

ENCYCLOPEDIA

of

RF and MICROWAVE

ENGINEERING

VOLUME I



KAI CHANG, *Editor*

ENCYCLOPEDIA OF

RF AND MICROWAVE ENGINEERING

VOLUME 1

Kai Chang, Editor

The *Encyclopedia of RF and Microwave Engineering* is available online at
<http://www.mrw.interscience.wiley.com/erfme>

 **WILEY-INTERSCIENCE**

A John Wiley & Sons, Inc., Publication

ENCYCLOPEDIA OF

RF AND MICROWAVE ENGINEERING

VOLUME 2

Kai Chang, Editor

The *Encyclopedia of RF and Microwave Engineering* is available online at
<http://www.mrw.interscience.wiley.com/erfme>

 **WILEY-INTERSCIENCE**

A John Wiley & Sons, Inc., Publication

ENCYCLOPEDIA OF

RF AND MICROWAVE ENGINEERING

VOLUME 3

Kai Chang, Editor

The *Encyclopedia of RF and Microwave Engineering* is available online at
<http://www.mrw.interscience.wiley.com/erfme>

 **WILEY-INTERSCIENCE**

A John Wiley & Sons, Inc., Publication

ENCYCLOPEDIA OF

RF AND MICROWAVE ENGINEERING

VOLUME 4

Kai Chang, Editor

The *Encyclopedia of RF and Microwave Engineering* is available online at
<http://www.mrw.interscience.wiley.com/erfme>

 **WILEY-INTERSCIENCE**

A John Wiley & Sons, Inc., Publication

ENCYCLOPEDIA OF

RF AND MICROWAVE ENGINEERING

VOLUME 5

Kai Chang, Editor

The *Encyclopedia of RF and Microwave Engineering* is available online at
<http://www.mrw.interscience.wiley.com/erfme>

 **WILEY-INTERSCIENCE**

A John Wiley & Sons, Inc., Publication

ENCYCLOPEDIA OF

RF AND MICROWAVE ENGINEERING

VOLUME 6

Kai Chang, Editor

The *Encyclopedia of RF and Microwave Engineering* is available online at
<http://www.mrw.interscience.wiley.com/erfme>

 **WILEY-INTERSCIENCE**

A John Wiley & Sons, Inc., Publication

Copyright © 2005 by John Wiley & Sons, Inc. All rights reserved.

Published by John Wiley & Sons, Inc., Hoboken, New Jersey.

Published simultaneously in Canada.

No part of this publication may be reproduced, stored in a retrieval system, or transmitted in any form or by any means, electronic, mechanical, photocopying, recording, scanning, or otherwise, except as permitted under Section 107 or 108 of the 1976 United States Copyright Act, without either the prior written permission of the Publisher, or authorization through payment of the appropriate per-copy fee to the Copyright Clearance Center, Inc., 222 Rosewood Drive, Danvers, MA 01923, 978-750-8400, fax 978-646-8600, or on the web at www.copyright.com. Requests to the Publisher for permission should be addressed to the Permissions Department, John Wiley & Sons, Inc., 111 River Street, Hoboken, NJ 07030, (201) 748-6011, fax (201) 748-6008.

Limit of Liability/Disclaimer of Warranty: While the publisher and author have used their best efforts in preparing this book, they make no representations or warranties with respect to the accuracy or completeness of the contents of this book and specifically disclaim any implied warranties of merchantability or fitness for a particular purpose. No warranty may be created or extended by sales representatives or written sales materials. The advice and strategies contained herein may not be suitable for your situation. You should consult with a professional where appropriate. Neither the publisher nor author shall be liable for any loss of profit or any other commercial damages, including but not limited to special, incidental, consequential, or other damages.

For general information on our other products and services please contact our Customer Care Department within the U.S. at 877-762-2974, outside the U.S. at 317-572-3993 or fax 317-572-4002.

Wiley also publishes its books in a variety of electronic formats. Some content that appears in print, however, may not be available in electronic format.

Library of Congress Cataloging-in-Publication Data:

Wiley encyclopedia of RF and microwave engineering, 6 Volume Set / Kai Chang, editor-in-chief.

p. cm.

Includes bibliographical references and index.

ISBN 0-471-27053-9 (cloth)

1. Wireless communication systems—Encyclopedias. 2. Radio circuits—Encyclopedias. 3. Microwave circuits—Encyclopedias. I. Chang, Kai, 1948-

TK5103.2.W535 2005

621.382—dc22

2004024581

Printed in the United States of America

10 9 8 7 6 5 4 3 2 1

PREFACE

There has been rapid development in RF and microwave technologies during the past decade. RF and microwave wireless applications have been and continue to be among the hottest growth areas. Some of the expanding activities in these fields include wireless communications (mobile, cellular, and satellite), wireless sensors, local area networks, remote control and identification, global positioning systems (GPS), and intelligent highway and vehicle systems (IHVS). In view of these growing applications, it is timely to publish this *Encyclopedia of RF and Microwave Engineering*.

The Encyclopedia is intended to serve as a compendium of theory, design methods, applications, overview, and future trends of technologies. Each article is a self-contained unit and is written for both non-specialists and specialists. Some overlap among articles is allowed for easy study. It is hoped that this Encyclopedia will provide useful information for technicians, students, professors, engineers, managers, and researchers in today's rapidly changing high-frequency technologies.

The Encyclopedia consists of six volumes. The articles include an overview of each subject, followed by in-depth descriptions of important theory, technology developments, and applications. Each article includes a list of references for further study. Some articles are adapted from the *Encyclopedia of Electrical and Electronics Engineering*. Most of these articles have been revised and updated. Among the major topics are the following:

- Electromagnetics
- Numerical Methods
- Wave Propagation
- Transmission Lines
- Transmission Line Discontinuities
- RF Circuits
- RF Components and Devices
- RF Technology
- RF Integrated Circuits
- RF CMOS Technology
- RF Antennas

- RF Transmitters
- RF Receivers
- RF Systems
- Microwave Passive Components and Devices
- Microwave Active Components and Devices
- Microwave Semiconductor Devices and Processing
- Microwave Hybrid and Monolithic Integrated Circuits
- Microwave Antennas
- Microwave Transmitters
- Microwave Receivers
- Microwave Superconductors
- Microwave Systems
- Millimeter-wave and Submillimeter-wave Technologies
- RF and Microwave Measurements
- RF and Microwave Propagation
- RF and Microwave Photonics
- CAD Techniques and Modeling
- Modulation and Demodulation Techniques
- Packaging and Interconnects
- Frequency Synthesizers
- Signal and Baseband Processing
- Solid-state Devices
- Semiconductor Materials
- High Power Tubes
- Noise
- Low Power Electronics
- Radar Systems
- Communication Systems
- Navigation Systems
- Radio Technologies
- Remote Sensing
- Broadcasting

The Editor would like to thank Cassie Craig of Wiley for managing this project, and George Telecki of Wiley for his constant encouragement and support. The Editor would also like to thank all of the members of the Editorial Board for their suggestions and advice.

Kai Chang
College Station, Texas

CONTRIBUTORS

- VALENTINE A. AALO**, *Florida Atlantic University, Boca Raton, Florida*, Digital Radio
- MUHAMMAD TAHER ABUELMA'ATTI**, *King Fahd University of Petroleum and Minerals, Dhahran, Saudi Arabia*, Intermodulation Measurement
- SABURO ADACHI**, *Tohoku Institute of Technology, Sendai, Japan*, Conical Antennas
- ARLON T. ADAMS**, *Syracuse University, Syracuse, New York*, Helical Antennas
- ILESANMI ADESIDA**, *University of Illinois at Urbana-Champaign*, Gallium Nitride for Electronics
- R. S. ADVE**, *Research Associates for Defense Conversion Inc.*, Stripline Components
- M. AGETHEN**, *Innovative Processing AG (IPAG), Duisburg, Germany*, Noise, High-Frequency
- VOLKAN AKAN**, *Hacettepe University, Beytepe, Ankara, Turkey*, Conformal Mapping Techniques
- IGOR ALEXEFF**, *The University of Tennessee, Knoxville, Tennessee*, Directive Antennas
- M. ALI**, *University of South Carolina, Columbia*, Miniaturized Packaged (Embedded) Antennas for Portable Wireless Devices
- F. ALIMENTI**, *University of Perugia, Perugia, Italy*, Waveguide Discontinuities
- JEREMY E. ALLNUTT**, *Virginia Tech/Northern Virginia Center, Falls Church, Virginia*, Refraction and Attenuation in Troposphere
- PLINIO R. G. ALVES**, *University of Brasilia, Brasilia, DF, Brazil*, Antenna Accessories
- W. A. ANDERSON**, *State University of New York at Buffalo*, Thin Film Resistors
- ILTCHO ANGELOV**, *Chalmers University of Technology*, Frequency Converters and Mixers
- JAUME ANGUERA**, *Fractus S.A., Barcelona, Spain*, Fractal Shaped Antennas: A Review
- RODOLFO ARANEO**, *University of Rome "La Sapienza," Rome, Italy*, Electromagnetic Shielding
- ANA GARCÍA ARMADA**, *Universidad Carlos III de Madrid, Madrid, Spain*, Wireless Communications Systems
- F. ARNDT**, *University of Bremen, Germany*, Hybrid CAD Techniques: Mode-Matching Methods
- S. ASHOK**, *The Pennsylvania State University, University Park, Pennsylvania*, Schottky Barriers
- KAZUHIKO ATSUKI**, *University of Electro-Communications*, Microstrip Lines
- OSAMA O. AWADELKHARIM**, *The Pennsylvania State University, University Park, Pennsylvania*, Smart Materials
- AYDIN AYKAN**, *Tutzing, Germany*, Calibration of Circular Loop Antenna
- EZEKIEL BAHAR**, *University of Nebraska-Lincoln, Lincoln, Nebraska*, Radar Remote Sensing of Irregular Stratified Media with Multiple-Scale Features
- INDER J. BAHL**, *M/A-COM, Inc., Roanoke, Virginia*, Monolithic Microwave Integrated Circuits (MMICs)
- D. BAILLARGEAT**, *IRCOM, Limoges, France*, Dielectric Resonator Filters
- JAMES R. BAKER-JARVIS**, *U.S. Department of Commerce Boulder Laboratories, Boulder, Colorado*, Electromagnetic Ferrite Tile Absorber
- CONSTANTINE A. BALANIS**, *Arizona State University, Tempe, Arizona*, Antenna Parameters; Circular Waveguides
- PETER BALLING, ASC**, *Antenna Systems Consultant, ApS, Taastrup, Denmark*, Multibeam Antennas
- RAJEEV BANSAL**, *University of Connecticut, Storrs, Connecticut*, Submarine Antennas
- JAMES BAO-YEN TSUL**, *Wright-Patterson Air Force Base, Ohio*, Microwave Receivers
- BRUNO BARELAUD**, *University of Limoges, Limoges Cedex, France*, Active Filters: Tools and Techniques for Active-Filter Design
- R. M. BARRIO-GARRIDO**, *Universidad Carlos III de Madrid*, Stripline Components
- R. BARTNIKAS**, *IREQ/Institut de Recherche d'Hydro-Quebec*, Dielectric Measurement
- B. BAYARD**, *Jean Monnet University, St. Etienne, France*, Ferrite Isolators
- GERARD BEAUDIN**, *Observatoire de Paris-Meudon*, Millimeter-Wave Measurement
- BENJAMIN BEKER**, *University of South Carolina, Columbia, South Carolina*, Boundary Value Problems
- GERALD BENDIXEN**, *Rockwell Collins, Inc.*, Radio Navigation
- O. BENDOV**, *Dielectric Communications*, Television and FM Broadcasting Antennas
- MATTHEW BENNETT**, *Army Research Laboratory*, Radar Equipment
- JENNIFER T. BERNHARD**, *University of Illinois at Urbana-Champaign, Urbana, Illinois*, Reconfigurable Antennas
- R. M. BERTENBURG**, *Innovative Processing AG (IPAG), Duisburg, Germany*, Noise, High-Frequency
- PRAKASH BHARTIA**, *Natel Engineering Co., Inc., Chatsworth, California*, Hybrids and Couplers; Strip Transmission Lines
- ASOKE K. BHATTACHARYYA**, *Lincoln University*, Linear Antennas
- MAREK E. BIALKOWSKI**, *University of Queensland (Australia) and National University of Singapore*, Power Combiners and Dividers
- JENS BIEGERT**, *University of New Mexico, Albuquerque, New Mexico*, Pulse Compression
- MARIO BIEY**, *Politecnico di Torino*, Frequency-Domain Circuit Analysis
- S. BILA**, *IRCOM, Limoges, France*, Dielectric Resonator Filters
- LAURENT BILLONNET**, *University of Limoges, Limoges, Cedex, France*, Active Filters: Overview of Active-Filter Structures; Active Filters: Tools and Techniques for Active-Filter Design
- TREVOR S. BIRD**, *CSIRO, Sydney, Australia*, Antenna Feeds
- GEORGE L. BLEHER**, *Individual Consultants*, Radiation Monitoring
- PETER HARING BOLIVAR**, *Institut fuer Halbleitertechnik II, Aachen University, Germany*, Terahertz Science, Engineering and Systems—from Space to Earth Applications
- DONALD M. BOLLE**, *Polytechnic University*, Microwave Integrated Circuits
- CARMEN BORJA**, *Fractus S.A., Barcelona, Spain*, Fractal Shaped Antennas: A Review
- RENATO G. BOSISIO**, *École Polytechnique, Montreal, Quebec, Canada*, Quadrature Phase Shift Keying (QPSK); Six-Port Networks

- MATTHYS M. BOTHA**, *University of Illinois at Urbana–Champaign, Urbana, Illinois*, Finite Element Analysis
- MAURIZIO BOZZI**, *University of Pavia, Pavia, Italy*, Periodic Structures
- G. R. BRANNER**, *University of California, Davis*, Microwave and Radio Frequency Multipliers
- W. BROCKERHOFF**, *Innovative Processing AG (IPAG), Duisburg, Germany*, Noise, High-Frequency
- JOSEPH A. BRUDER**, *Air Force Research Laboratory, Radar Tracking*
- D. BUDIMIR**, *University of Westminster, London, United Kingdom*, Waveguide Components
- ROBERT J. BURKHOLDER**, *The Ohio State University, Columbus, Ohio*, Iterative Methods
- NATHAN A. BUSHYAGER**, *Georgia Institute of Technology, Atlanta, Georgia*, Electromagnetics, Time-Domain
- QUNSHENG CAO**, *University of Minnesota, Minneapolis, Minnesota*, Multiresolution Technique
- C.N. CAPSALIS**, *National Technical University of Athens, Athens, Greece*, Antenna Reverberation Chamber
- ANTÔNIO CARLOS**, *Federal University of Rio de Janeiro, Rio de Janeiro, Brazil*, Chebyshev Filters
- PAULO H. P. CARVALHO**, *University of Brasilia, Brasilia, DF, Brazil*, Antenna Accessories
- YVES CASSIVI**, *Ecole Polytechnique, Montreal, Quebec, Canada*, Impedance Transformers and Matching Networks
- MANUEL SIERRA CASTAÑER**, *Universidad Politecnica de Madrid, Madrid, Spain*, Monopulse Tracking Systems
- ROBERT H. CAVERLY**, *Villanova University, Villanova, Pennsylvania*, Microwave Switches
- HAKI CEBI**, *University of Colorado at Boulder*, Microwave Circuits
- SALVATORE CELOZZI**, *University of Rome “La Sapienza,” Rome, Italy*, Electromagnetic Shielding
- THOMAS P. CENCICH**, *University of Colorado at Boulder*, Frequency-Independent Antennas; Spiral Antennas
- R. CHAIR**, *The University of Mississippi, Oxford, Mississippi*, Microstrip Antennas, Broadband
- ANDREW K. CHAN**, *Texas A & M University*, Radar Signal Detection
- CHI HOU CHAN**, *City University of Hong Kong, Kowloon, Hong Kong*, Parallel Algorithms and Computing for Large-Scale Electromagnetic Simulation; Rough-Surface Scattering; Numerical Simulations and Applications in Microwave Remote Sensing
- KA FAI CHAN**, *City University of Hong Kong, Kowloon, Hong Kong SAR, China*, Parallel Algorithms and Computing for Large-Scale Electromagnetic Simulation
- HENG-CHIA CHANG**, *RF System, Blue 7 Communications, Inc., Fremont, California*, Phase Noise and Measurements
- HONG-YEH CHANG**, *National Taiwan University, Taipei, Taiwan*, Monolithic Millimeter-Wave Integrated Circuits
- KAI CHANG**, *Texas A&M University, College Station, Texas*, Gratings and Grating Antennas; Microwave Power Transmission; Rectifying Antennas (Rectennas); Ring Resonators and Circuits; Slotline Components
- KOOKRIN CHAR**, *Conductus, Inc.*, HTS Film Growth
- FU-CHIARNG CHEN**, *University of Illinois at Urbana–Champaign, Urbana, Illinois*, Radar Antennas
- GUANRONG CHEN**, *City University of Hong Kong, Kowloon, Hong Kong, China*, Stability of Nonlinear Systems
- Ji CHEN**, *University of Houston, Houston, Texas*, Transmission Lines and Parameters
- R. S. CHEN**, *Nanjing University of Science and Technology, Nanjing, P.R. China*, Ferrite Circulators
- RICHARD L. CHEN**, *University of Houston, Houston, Texas*, Transmission Lines and Parameters
- S. Y. CHEN**, *University of Illinois at Urbana–Champaign, Urbana, Illinois*, Electromagnetic Subsurface Remote Sensing
- VICTOR C. CHEN**, *U.S. Naval Research Laboratory, Washington, DC*, Radar Imaging
- YINCHAO CHEN**, *University of South Carolina, Columbia, South Carolina*, Enhancements of the Finite-Difference Time-Domain Method; Multiresolution Technique
- YUPENG CHEN**, *University of Central Florida, Orlando, Florida*, BiCMOS Devices and RF Integrated Circuits
- DAVID B. CHESTER**, *Intersil Corporation*, Pulse-Shaping Circuits
- KAR-MING CHEUNG**, *California Institute of Technology*, Radio-telemetry
- WENG C. CHEW**, *University of Illinois at Urbana–Champaign, Urbana, Illinois*, Electromagnetic Subsurface Remote Sensing; Green's Function Methods; High-Frequency Transmission Lines; Radar Antennas
- CHOONSIK CHO**, *University of Colorado at Boulder*, Microwave Circuits
- CHIU H. CHOI**, *University of North Florida, Jacksonville, Florida*, Bandstop Filters; Lowpass Filters
- JONGHOON CHOI**, *University of Michigan, Ann Arbor, Michigan*, Microwave Oscillators
- M. CHONGCHEAWCHAMNAN**, *Mahanakorn University of Technology, Bangkok, Thailand*, Radiofrequency Integrated Circuits
- DURGA P. CHOUDHURY**, *Northeastern University*, Superconducting Microwave Technology
- P. K. CHOUDHURY**, *Multimedia University, Selangor, Malaysia*, Electromagnetic Materials
- CHRISTOS G. CHRISTODOULOU**, *University of New Mexico, Albuquerque*, Antenna Radiation Patterns; Antennas
- CHRISTOS CHRISTOPOULOS**, *University of Nottingham, Nottingham, United Kingdom*, The Transmission-Line Matrix (TLM) Method
- MICHAEL T. CHRYSOMALLIS**, *Democritus University of Thrace, Xanthi, Greece*, Antenna Radiation Patterns
- CHUNG BOON-KUAN CHUNG**, *Multimedia University, Cyberjaya, Malaysia*, Antenna Anechoic Chambers
- SHYH-JUNG CHUNG**, *National Chiao-Tung University, Hsinchu, Taiwan, Republic of China*, Van Atta Array Reflector
- SERGIO A. CLAVIJO**, *Arizona State University, Tempe, Arizona*, Artificial Magnetic Conductor
- GEORGE COKKINIDES**, *University of South Carolina, Columbia, South Carolina*, Boundary Value Problems
- PAOLO COLANTONIO**, *Università degli Studi di Roma Tor Vergata, Rome, Italy*, Microwave Power Amplifiers
- GERALD W. COLLINS**, *GW Collins Consulting*, Transmitters for Analog Television
- F. M. COLLINS**, *Ohmcraft, Inc.*, Thin Film Resistors
- DOMINIQUE CROS**, *Université de Limoges*, Millimeter-Wave Measurement
- PAUL CROZAT**, *Université Paris–Sud*, Millimeter-Wave Measurement
- TIE JUN CUI**, *University of Illinois at Urbana–Champaign*, Radar Antennas
- ROGER DALKE**, *Institute for Telecommunication Sciences*, Radio Noise
- GILLES DAMBRINE**, *Institut d'Electronique et Microelectronique du Nord (IEMN)*, Millimeter-Wave Measurement
- DAVID J. DANIELS**, *ERA Technology, Surrey, United Kingdom*, Ground Penetrating Radar

- E. DANIELSSON**, *Royal Institute of Technology, Kista-Stockholm, Sweden*, SiC Device Technologies
- AFSHIN S. DARYOUSH**, *Drexel University, Philadelphia, Pennsylvania*, Microwave Photonics: Technological Evolutions and Its Applications
- NIROD K. DAS**, *Polytechnic University*, Microwave Integrated Circuits
- D. K. DAS-GUPTA**, *University of Wales, Bangor, Wales*, Dielectric Permittivity and Loss
- KENNETH DAVIES**, *National Oceanic and Atmospheric Administration*, Sky Wave Propagation at Medium and High Frequencies
- W. ALAN DAVIS**, *The University of Texas at Arlington*, Schottky Barrier Diodes and Their Applications
- WILLIAM A. DAVIS**, *Virginia Tech Antenna Group, Blacksburg, Virginia*, Antenna Theory
- W. R. DEAL**, *Northrop Grumman Space Technology, Redondo Beach, California*, Dielectric Resonator Oscillators
- FRANCO DE FLAVIIS**, *University of California at Los Angeles*, Phase Shifters
- MICHAEL P. DELISIO**, *University of Hawaii at Manoa*, Quasi-optical Circuits
- PETER DE MAAGT**, *European Space Research and Technology Centre (ESTEC), The Netherlands*, Terahertz Science, Engineering and Systems—from Space to Earth Applications
- GREGORY M. DEMYASHEV**, *Swinburne University of Technology, Melbourne, Australia*, Microwave Resonance Plasma Source
- MAKARAND DEO**, *Carleton University, Ottawa, Canada*, Neural Networks for Microwave Circuits
- M. DE QUEIROZ**, *Federal University of Rio de Janeiro, Rio de Janeiro, Brazil*, Chebyshev Filters
- DOMINIC DESLANDES**, *Ecole Polytechnique, Montreal, Quebec, Canada*, Impedance Transformers and Matching Networks
- DANIËL DE ZUTTER**, *Ghent University, Ghent, Belgium*, Skin Effect
- RODOLFO E. DIAZ**, *Arizona State University, Tempe, Arizona*, Artificial Magnetic Conductor
- JEAN-CLAUDE DIELS**, *University of New Mexico, Albuquerque, New Mexico*, Pulse Compression
- KUNG-HAU DING**, *Air Force Research Laboratory, Hanscom AFB, Massachusetts*, Computational Electromagnetic Scattering Models for Microwave Remote Sensing
- PAUL E. DODD**, *Sandia National Laboratories, Albuquerque, New Mexico*, Radiation Effects
- M. DOMEIJ**, *Royal Institute of Technology, Kista-Stockholm, Sweden*, SiC Device Technologies
- ALAN N. DUCKWORTH**, *Naval Research Laboratory*, Electronic Warfare
- VERNON E. DUNN**, *Space Systems/Loral*, Microwave Isolators
- J. F. DUQUE-CARRILLO**, *University of Extremadura*, Preamplifiers
- R. B. DYBDAL**, *The Aerospace Corporation*, Satellite Antennas
- TERRY C. EDWARDS**, *Engalco, Bridlington, East Yorkshire, United Kingdom*, Microstrip Circuits
- HERIBERT EISELE**, *University of Leeds, Leeds, United Kingdom*, Gunn or Transferred-Electron Devices and Circuits
- ABDELNASSER A. ELDEK**, *Center of Applied Electromagnetic Systems Research (CAESR) The University of Mississippi University, Mississippi*, Wideband Slot and Printed Antennas
- KIM ANDREW ELLIOT**, High-Frequency Broadcasting
- ATEF Z. ELSHERBENI**, *Center of Applied Electromagnetic Systems Research (CAESR) The University of Mississippi University, Mississippi*, Wideband Slot and Printed Antennas
- KIE B. EOM**, *The George Washington University, Washington, DC*, Radar Target Recognition
- HALIT EREN**, *Curtin University of Technology, Bentley, Australia*, Altimeters
- DANILO ERRICOLO**, *University of Illinois, Chicago*, Geometric Optics
- KARU P. ESSELLE**, *Macquarie University, Sydney, New South Wales, Australia*, Dielectric Resonators
- JOSEPH B. EVANS**, *University of Kansas, Lawrence, Kansas*, Local-Area Networks (LANs)
- MAREK T. FABER**, *Warsaw University of Technology, Warsaw, Poland*, Microwave Parametric Amplifiers
- ROBERT L. FAGALY**, *Tristan Technologies*, SQUIDS
- LU FAN**, *Texas A&M University*, Slotline Components
- J. A. BRANDÃO FARIA**, *Instituto Superior Técnico, Lisbon, Portugal*, Multiconductor Transmission Lines
- ALY E. FATHY**, *University of Tennessee, Knoxville*, PIN Diodes
- ORLA FEELY**, *University College Dublin, Dublin, Ireland*, Transient Circuit Analysis
- ZHIPING FENG**, *University of Colorado at Boulder*, Microwave Circuits; Packaging RF Devices and Modules
- EVA S. FERRE-PIKAL**, *University of Wyoming, Laramie, Wyoming*, Frequency Standards, Characterization
- ANDREA FERREIRO**, *Politecnico di Torino, Torino, Italy*, Microwave Measurements
- L. B. FERTIG**, *Georgia Institute of Technology*, Frequency Modulation
- DEJAN S. FILIPOVIC**, *University of Colorado, Boulder, Colorado*, Frequency-Independent Antennas; Spiral Antennas
- MATTHEW FOLKERT**, *du Treil, Lundin, & Rackley, Sarasota, Florida*, Antennas for Medium-Frequency Broadcasting
- KENNETH R. FOSTER**, *University of Pennsylvania, Philadelphia, Pennsylvania*, Biological Effects of Radiofrequency Energy as Related to Health and Safety
- DOUGLAS R. FREY**, *Lehigh University*, Gyrotors
- FABRIZIO FREZZA**, *“La Sapienza” University of Rome, Italy*, Leaky-Wave Antennas
- LEE-LUENG FU**, *California Institute of Technology*, Spaceborne Radar
- DAVID W. FUGATE**, *Electric Research and Management, Inc.*, Magnetic Shielding
- KYOHEI FUJIMOTO**, *University of Tsukuba, Fujisawa, Japan*, Antennas for Mobile Communications; Integrated Antenna Systems; Small Antennas
- ADRIAN K. FUNG**, *University of Texas at Arlington, Arlington, Texas*, Microwave Scattering Models for Earth Terrain
- CYNTHIA M. FURSE**, *University of Utah, Salt Lake City, Utah*, Dipole Antennas and Arrays; Monopole Antennas
- VINCENT F. FUSCO**, *Queen’s University of Belfast, Belfast, Northern Ireland*, Dielectric Resonator Oscillators
- ALESSANDRO GALLI**, *“La Sapienza” University of Rome, Italy*, Leaky-Wave Antennas
- YEOW BENG GAN**, *National University of Singapore, Singapore*, Electromagnetic Inverse Problems
- OM P. GANDHI**, *University of Utah, Salt Lake City*, Dipole Antennas and Arrays; Monopole Antennas
- MANUEL GARCIA**, *Lawrence Livermore National Laboratory, Livermore, California*, Integro-Differential Equations
- FRED GARDIOL**, *Swiss Federal Institute of Technology, Lausanne, Switzerland*, Measurement of Near Fields Using a Modulated Scatterer
- P. GARDNER**, *The University of Birmingham, Edgbaston, Birmingham, United Kingdom*, Feedforward Amplifiers

- R. GARG**, *Indian Institute of Technology Kharagpur, Kharagpur, India*, Coaxial Line Discontinuities
- G. G. GENTILI**, *Milan Polytechnic, Milan, Italy*, Orthomode Transducers
- RAMEZ L. GERGES**, *IEEE-ITSC Standards Committee, Goleta, California*, ITS Radio Service Standards & Wireless Access in Vehicular Environments (ITS-WAVE) at 5.9 GHz
- DAVID GESBERT**, *Stanford University*, Antenna Arrays for Mobile Communications
- RICHARD G. GEYER**, *U.S. Department of Commerce, Boulder Laboratories, Boulder, Colorado*, Electromagnetic Ferrite Tile Absorber
- FRANCO GIANNINI**, *Università degli Studi di Roma Tor Vergata, Rome, Italy*, Microwave Power Amplifiers
- DONALD P. GIEGLER**, *Individual Consultants*, Radiation Monitoring
- IAN A. GLOVER**, *University of Bradford, Bradford, West Yorkshire, United Kingdom*, Radiometry
- JOHN P. GODWIN**, *DirecTV*, Direct Satellite Television Broadcasting
- BAR-GIORA GOLDBERG**, *Sciteq Electronics, Inc.*, Frequency Synthesizers
- GARY W. GOO**, *The Aerospace Corporation*, Military Communication
- JAIDEVA C. GOSWAMI**, *Schlumberger Technology Corporation, Sugar Land, Texas*, Application of Wavelets to Electromagnetic Problems
- G. K. GOTHARD**, *Auburn University, Auburn, Alabama*, Integral Equations: Application to Open-Region Problems
- VICTOR L. GRANATSTEIN**, *University of Maryland, College Park, Maryland*, Microwave Tubes
- RICHARD R. GREENE**, *Technology for Communications International, Fremont, California*, Antennas for High-Frequency Broadcasting
- JERRY MICHAEL GRIMM**, *JMG Consulting, Irving, Texas*, Elliptic Filters
- AMADEU GRIOL**, *Universidad Politécnica de Valencia, Valencia, Spain*, Photonic Band Gap (PBG)
- ANDREAS GRONEFELD**, *Ruhr-Universität Bochum*, Standing Wave Meters and Network Analyzers
- ADNAN GÖRÜR**, *Niğde University, Niğde, Turkey*, Filter Theory
- MARCO GUGLIELMI**, *European Space Research and Technology Centre, Noordwijk, The Netherlands*, Multimode Equivalent Network Representations
- P. GULLON**, *IRCOM, Limoges, France*, Dielectric Resonator Filters
- K. C. GUPTA**, *University of Colorado at Boulder*, Microwave Circuits; Packaging RF Devices and Modules
- MRIDULA GUPTA**, *University of Delhi South Campus, New Delhi, India*, MOSFET Modeling
- R. S. GUPTA**, *University of Delhi South Campus, New Delhi, India*, MOSFET Modeling
- GERMÁN GUTIERREZ**, *Centellax, Inc., Carlsbad, California*, Variable-Frequency Oscillators
- SUSAN C. HAGNESS**, *University of Wisconsin-Madison, Madison, Wisconsin*, Finite-Difference Time-Domain Analysis
- PETER S. HALL**, *The University of Birmingham, Edgbaston, Birmingham, UK*, Microstrip Antenna Arrays
- RONALD E. HAM**, *Consultant*, Microwave Detectors
- PETER H. HANDEL**, *University of Missouri St. Louis*, Noise, Low-Frequency
- KEN-YA HASHIMOTO**, *Chiba University, Chiba, Japan*, Surface Acoustic Wave Filters
- HITOSHI HAYASHI**, *Nippon Telegraph and Telephone Corporation, Yokosuka, Kanagawa, Japan*, Radiofrequency Identification (RFID) Systems
- I.I. HERETAKIS**, *National Technical University of Athens, Athens, Greece*, Antenna Reverberation Chamber
- K. HESS**, *University of Illinois*, High-Field Effects
- DAVID A. HILL**, *National Institute of Standards and Technology*, Radiowave Propagation Ground Effects
- KURT HILTY**, *Swiss Federal Office of Metrology, Bern-Wabern, Switzerland*, Attenuation Measurement
- JACKIE E. HIPPI**, *Southwest Research Institute, San Antonio, Texas*, Radio Direction Finding
- TAN-HSIUNG HO**, *National Chiao-Tung University, Hsinchu, Taiwan, Republic of China*, Van Atta Array Reflector
- ALI KÖKSAL HOCAOĞLU**, *Information Technologies Research Institute, Gebze, Kocaeli, Turkey*, Buried-Object Detection
- WOLFGANG J.R. HOEFER**, *University of Victoria, Victoria, BC, Canada*, Electromagnetic Modeling; Fines
- CHRISTOPHER L. HOLLOWAY**, *U.S. Department of Commerce Boulder Laboratories, Boulder, Colorado*, Electromagnetic Ferrite Tile Absorber
- ERIC L. HOLZMAN**, *Northrop Grumman Corporation, Baltimore, Maryland*, Microstrip Transitions; Waveguide Oscillators
- WEI HONG**, *Southeast University, Nanjing, China*, Feedback Oscillators
- WILLIAM E. HORD**, *Microwave Applications Group, Santa Maria, CA*, Ferrite Phase Shifters
- HOTON HOW**, *Hotech, Inc., Belmont, Massachusetts*, Magnetic Microwave Devices; Microstrip Antennas
- DAVID A. HOWE**, *National Institute of Standards and Technology (NIST), Boulder, Colorado*, Frequency Stability
- LUNG-HWA HSIEH**, *Texas A&M University, College Station, Texas*, Ring Resonators and Circuits
- JOHN HUANG**, *Jet Propulsion Laboratory, Pasadena, California*, Reflectarray Antenna
- ROBERT D. HUNSUCKER**, *RP Consultants, Klamath Falls, Oregon*, Electromagnetic Waves in Ionosphere
- BERNARD HUYART**, *Ecole Nationale Supérieure des Télécommunications (ENST)*, Millimeter-Wave Measurement
- MOHAMED IBNKAHLA**, *Queen's University, Kingston, Ontario, Canada*, Analytical and Adaptive Modeling of Nonlinear High-Power Amplifiers; MIMO Systems for Wireless Communications
- T. KORYU ISHII**, *Marquette University, Milwaukee, Wisconsin*, Distributed Amplifiers
- YUKIO ITO**, *The Pennsylvania State University*, Piezoelectricity
- TATSUO ITOH**, *UCLA*, Slotlines
- R. LAWRENCE IVES**, *Calabazas Creek Research, Inc., Saratoga, California*, Gyrotrons
- DAVID R. JACKSON**, *University of Houston, Houston, Texas*, Leaky Modes and High-Frequency Effects in Microwave Integrated Circuits
- RAMAKRISHNA JANASWAMY**, *University of Massachusetts, Amherst, Massachusetts*, Signal Fading in Radiocommunications
- BERNARD JARRY**, *University of Limoges, Limoges, Cedex, France*, Active Filters: Overview of Active-Filter Structures; Active Filters: Tools and Techniques for Active-Filter Design
- DAVID C. JENN**, *Naval Postgraduate School*, Radar Cross Section
- A. R. JHA**, *JHA Technical Consulting Services, Cerritos, CA*, Cryogenic Electronics
- JIAN-MING JIN**, *University of Illinois at Urbana-Champaign, Urbana, Illinois*, Finite Element Analysis; Green's Function Methods
- J. RALPH JOHLER**, *Johler Associates*, Sky Wave Propagation at Low Frequencies

- ROBERT T. JOHNSON**, *U.S. Department of Commerce, Boulder Laboratories, Boulder, Colorado*, Electromagnetic Ferrite Tile Absorber
- RICHARD L. JOHNSON**, *Southwest Research Institute, San Antonio, Texas*, Radio Direction Finding
- WILLIAM T. JOINES**, *Duke University*, Guided Electromagnetic Waves
- EDWARD V. JULL**, *University of British Columbia, Vancouver, British Columbia, Canada*, Horn Antennas
- DARKO KAJFEZ**, *University of Mississippi, University, Mississippi*, *Q* Factor
- MOTOHISA KANDA**, *National Institute of Standards and Technology*, Electromagnetic Field Measurement
- NORIAKI KANEDA**, *Lucent Technologies, Holmdel, New Jersey*, The Yagi-Uda Antenna
- WENG LOCK KANG**, *The University of Tennessee, Knoxville, Tennessee*, Directive Antennas
- U. KARACAOGLU**, *INTEL Corp., ICG Wireless Networking Group-WPD, San Diego, California*, Radio-frequency Integrated Circuits
- NEMAI CHANDRA KARMAKAR**, *Monash University, Clayton, Victoria Australia*, Adaptive Array Antennas; Coaxial Lines and Waveguides; Electromagnetic-Bandgap-Assisted Bandpass Filters
- ROGER KAUL**, *U.S. Army Research Laboratory*, Microwave Limiters
- W. NEILL KEFAUVER**, *Lockheed Martin*, Antenna Compact Range; Antenna Testing and Measurements
- YUNJIN KIM**, *California Institute of Technology, Pasadena, California*, Radar Remote Sensing
- KATSUJI KIMURA**, *NEC Corporation*, Mixer Circuits
- CLIFFORD A. KING**, *Lucent Technologies*, Negative Resistance
- AHMED A. KISHK**, *University of Mississippi, University, Mississippi*, Method of Moments
- FRANCIS J. KLEMM**, *Naval Research Laboratory*, Electronic Warfare
- R. D. KOILPILLAI**, *Ericsson, Inc.*, Radiowave Propagation in Multipath Channels
- ERIK L. KOLLBERG**, *Chalmers University of Technology*, Frequency Converters and Mixers
- GÉZA KOLUMBÁN**, *Budapest University of Technology and Economics, Hungary*, Phase-Locked Loops
- SHOZO KOMAKI**, *Osaka University, Osaka, Japan*, Radio-on-Fiber (RoF) Systems
- MYUNG JIN KONG**, *University of South Carolina, Columbia, South Carolina*, Boundary Value Problems
- S.-M. KOO**, *Royal Institute of Technology, Kista-Stockholm, Sweden*, SiC Device Technologies
- V. KOMAROV**, *Washington State University*, Permittivity and Measurement
- N.K. KOVELIOTIS**, *National Technical University of Athens, Athens, Greece*, Antenna Reverberation Chamber
- PIOTR KOWALCZYK**, *Gdansk University of Technology, Gdansk, Poland*, Helmholtz Equations
- DENNIS KOZAKOFF**, *DeVry University, Alpharetta, Georgia*, Aperture Antennas
- CLIFFORD M. KROWNE**, *Microwave Technology Branch, Washington, DC*, Left-Handed Materials for Microwave Devices and Circuits
- A. KUMAR**, *High Speed Networking Laboratory, Detroit, Michigan*, Personal Area Networking with Bluetooth
- B.P. KUMAR**, *Sacramento State University*, Microwave and Radio Frequency Multipliers
- RONALD KWOK**, *California Institute of Technology*, Spaceborne Radar
- AKHLESH LAKHTAKIA**, *Pennsylvania State University, University Park, Pennsylvania*, Anisotropy and Bianisotropy; Chirality
- KING WAI LAM**, *City University of Hong Kong, Kowloon, Hong Kong SAR, China*, Parallel Algorithms and Computing for Large-Scale Electromagnetic Simulation
- PAOLO LAMPARIELLO**, *"La Sapienza" University of Rome, Italy*, Leaky-Wave Antennas
- JOY LASKAR**, *Georgia Institute of Technology, Atlanta*, RF/Wireless Packaging
- GIANLUCA LAZZI**, *North Carolina State University*, Dipole Antennas and Arrays; Monopole Antennas
- W. MARSHALL LEACH JR.**, *Georgia Institute of Technology, Atlanta, Georgia*, Radio-frequency Circuit Noise
- CHUNG-YI LEE**, *Qualcomm, Inc.*, Slotlines
- JAY K. LEE**, *Syracuse University, Syracuse, New York*, Helical Antennas
- JIN-FA LEE**, *The Ohio State University, Columbus, Ohio*, Iterative Methods
- JONG-WOOK LEE**, *Kyung Hee University, Korea*, Gallium Nitride for Electronics
- K. F. LEE**, *University of Mississippi, Oxford*, Dual- and Multi-frequency Microstrip Antennas; Microstrip Antennas, Broadband
- RICHARD Q. LEE**, *NASA Glenn Research Center, Cleveland, Ohio*, Notch Antennas
- SUNGJAE LEE**, *Purdue University, West Lafayette, Indiana*, Low-Noise Amplifiers: Device Noise Characterization and Design
- WILLIAM C.Y. LEE**, *AirTouch Communication*, Cellular Radio
- Y. C. LEE**, *University of Colorado, Chong-IL Park, Kyocera America, Inc.*, Packaging RF Devices and Modules
- LAWRENCE M. LEEMIS**, *The College of William & Mary, Williamsburg, Virginia*, Monte Carlo Simulation in Reliability
- PATT LEGGATT**, History of Wireless Communication
- K. W. LEUNG**, *City University of Hong Kong, Kowloon, Hong Kong SAR*, Dielectric Resonator Antennas
- CURT A. LEVIS**, *Ohio State University, Columbus, Ohio*, Friis Free-Space Transmission Formula; Radiowave Propagation Concepts
- RALPH LEVY**, *R. Levy Associates, La Jolla, California*, Waveguide Directional Couplers; Waveguide Junctions
- LE-WEI LI**, *National University of Singapore, Kent Ridge, Singapore*, Complex Media
- QIN LI**, *University of Washington, Seattle, Washington*, Computational Electromagnetic Scattering Models for Microwave Remote Sensing; Rough-Surface Scattering: Numerical Simulations and Applications in Microwave Remote Sensing
- ZHONG XIN LI**, *City University of Hong Kong*, Rough-Surface Scattering: Numerical Simulations and Applications in Microwave Remote Sensing
- ERNESTO LIMITI**, *Università degli Studi di Roma Tor Vergata, Rome, Italy*, Microwave Power Amplifiers
- KUN-YOU LIN**, *National Taiwan University, Taipei, Taiwan*, Monolithic Millimeter-Wave Integrated Circuits
- BERNABÉ LINARES-BARRANCO**, *National Microelectronics Center (CNM)*, Harmonic Oscillators, Circuits
- CLINTON L. LINGREN**, *Individual Consultants*, Radiation Monitoring
- LIANGHONG LIU**, *Virginia Commonwealth University, Richmond, Virginia*, Modulation-Doped FETs
- QING HUO LIU**, *Duke University, Durham, North Carolina*, Fast Fourier Transforms and Nufft

- REN-CHIEH LIU**, *National Taiwan University, Taipei, Taiwan*, Monolithic Millimeter-Wave Integrated Circuits
- JOHN LODGE**, *Communications Research Centre, Ottawa, Ontario*, Mobile Satellite Communications
- ALBERTO ASENSIO LOPEZ**, *Universidad Politecnica de Madrid, Madrid, Spain*, Monopulse Tracking Systems
- JAVIER RAMOS LÓPEZ**, *Universidad Carlos III de Madrid, Madrid, Spain*, Wireless Communications Systems
- WALT LOWERY**, *Symetrix, Inc.*, Radio Broadcast Studio Equipment
- L. LUCCI**, *University of Florence, Florence, Italy*, Corrugated Horn Antennas
- ERNST LUEDER**, *University of Stuttgart*, Filter Synthesis
- PAOLO LUGLI**, *University Rome*, Monte Carlo Analysis
- ANDRE LUITEN**, *University of Western Australia, Nedlands, Australia*, Q-Factor Measurement
- K. M. LUK**, *City University of Hong Kong, Kowloon, Hong Kong*, Dual- and Multifrequency Microstrip Antennas; Microstrip Antennas, Broadband
- JOHANN-FRIEDRICH LUY**, *Munich Technical University and DaimlerChrysler Research, Germany*, Digital Microwave Receivers; GeSi Alloys and Devices
- E. M. MA**, *Cypress Semiconductor Inc. (Minnesota)*, Thin Film Resistors
- ZHEWANG MA**, *University of Electro-Communications*, Microstrip Lines
- TOM G. MACKAY**, *University of Edinburgh, Edinburgh, United Kingdom*, Anisotropy and Bianisotropy
- KOICHI MAEZAWA**, *Nagoya University, Nagoya, Japan*, Resonant Tunneling Diodes
- ROBERT J. MAILLOUX**, *AFRL/SNH, Hanscom Air Force Base, Massachusetts*, Antenna Scanning Arrays
- IVAN A. MAIO**, *Politecnico di Torino*, Frequency-Domain Circuit Analysis
- C. L. MAK**, *City University of Hong Kong, Kowloon, Hong Kong*, Microstrip Antennas, Broadband
- J. A. G. MALHERBE**, *University of Pretoria, Pretoria, South Africa*, Lens Antennas
- DONALD C. MALOCHA**, *University of Central Florida*, Surface Acoustic Wave Applications
- GIULIANO MANARA**, *University of Pisa, Pisa, Italy*, Generalized Scattering Matrix Technique
- G. F. MANES**, *University of Florence, Italy*, Gallium Arsenide Technology and Applications
- CHRIS MANN**, *Rutherford Appleton Laboratory, UK*, Terahertz Science, Engineering and Systems—from Space to Earth Applications
- RAAFAT R. MANSOUR**, *University of Waterloo, Waterloo, Ontario, Canada*, High-Temperature Superconductors; Multiplexers
- RICARDO MARQUÉS**, *University of Seville, Seville, Spain*, Ferrite Loaded Waveguides
- JAVIER MARTÍ**, *Universidad Politécnica de Valencia, Valencia, Spain*, Photonic Band Gap (PGB)
- ALEJANDRO MARTÍNEZ**, *Universidad Politécnica de Valencia, Valencia, Spain*, Photonic Band Gap (PGB)
- K. T. MATHEW**, *Cochin University of Science and Technology, Cochin, India*, Perturbation Theory
- WOLFGANG MATHIS**, *University of Hannover, Germany*, Oscillator Design
- VLADIMIR MATIJASEVIC**, *Conductus, Inc.*, HTS Film Growth
- ARVYDAS MATULIONIS**, *Semiconductor Physics Institute*, Noise, Hot Carrier Effects
- J. H. MCCLELLAN**, *Georgia Institute of Technology*, Frequency Modulation
- JAMES W. MCCLYMONDS**, *Raytheon Systems Company*, Impatt Diodes and Circuits
- DAVID J. MCLAUGHLIN**, *University of Massachusetts, Amherst, Massachusetts*, Radar Polarimetry
- KENNETH K. MEI**, *City University of Hong Kong and Zhejiang University, Hangzhou, China*, Maxwellian Circuits; MEI Method
- LEONARDO R. A. X. MENEZES**, *University of Brasilia, Brasilia, DF, Brazil*, Antenna Accessories
- JAVIER GISMERO MENOYO**, *Universidad Politecnica de Madrid, Madrid, Spain*, Monopulse Tracking Systems
- WOLFGANG S. MENZEL**, *University of Ulm, Ulm, Germany*, Fineline Components
- FRANCISCO MESA**, *University of Seville, Seville, Spain*, Leaky Modes and High-Frequency Effects in Microwave Integrated Circuits
- KRZYSZTOF ARKADIUSZ MICHALSKI**, *Texas A&M University, College Station, Texas*, Coulomb Gauge in Electromagnetics; Electromagnetic Field Computation in Planar Multilayers
- ALAN MICKELSON**, *University of Colorado, Boulder, Colorado*, Active Antennas
- KONSTANTINOS MISIAKOS**, *NCSR "Demokritos," Athens, Greece*, Diodes
- RAJ MITTRA**, *Pennsylvania State University, University Park, Pennsylvania*, Enhancements of the Finite-Difference Time-Domain Method; Generalized Scattering Matrix Technique; Multiresolution Technique
- RYAN Y. MIYAMOTO**, *University of Hawaii at Manoa, Honolulu, Hawaii*, Retrodirective Systems
- ANANDA SANAGAVARAPU MOHAN**, *University of Technology, Sydney, New South Wales, Australia*, Dielectric Resonators
- ANURAG MOHAN**, *University of Delaware, Newark, Delaware*, Galerkin Method (Rayleigh-Ritz Method)
- MOHAMMAD NURUNNABI MOLLAH**, *Khulna University of Engineering and Technology, Khulna, Bangladesh*, Electromagnetic-Bandgap-Assisted Bandpass Filters
- MAURO MONGIARDO**, *University of Perugia, Perugia, Italy*, Transverse Resonance Technique
- AGOSTINO MONORCHIO**, *University of Pisa, Pisa, Italy*, Generalized Scattering Matrix Technique
- FERNANDO J. S. MOREIRA**, *Federal University of Minas Gerais, Belo Horizonte, Brazil*, Electromagnetic Wave Propagation
- CHIP MORGAN**, *CMBE, Inc.*, Low-Power Broadcasting
- D. P. MORGAN**, *Impulse Consulting, Northampton, United Kingdom*, Surface Acoustic Wave Devices
- ANTONIO MORINI**, *Università di Ancona, Ancona, Italy*, Directional Couplers
- HADIS MORKOÇ**, *Virginia Commonwealth University, Richmond, Virginia*, Modulation-Doped FETs
- STANLEY A. MOROZ**, *Naval Research Laboratory*, Electronic Warfare
- AMIR MORTAZAWI**, *University of Michigan, Ann Arbor, Michigan*, Microwave Oscillators
- MICHAL MROZOWSKI**, *Gdansk University of Technology, Gdansk, Poland*, Helmholtz Equations
- TH. MUELLER**, *DaimlerChrysler Research, Ulm, Germany*, Digital Microwave Receivers
- BRIAN MULKEEN**, *University College Dublin, Dublin, Ireland*, Transient Circuit Analysis
- BLAINE T. MURAKAMI**, *University of Hawaii at Manoa, Honolulu, Hawaii*, Retrodirective Systems
- RANDALL L. MUSSELMAN**, *USAF Academy, Colorado Springs, Colorado*, Electromagnetic Wave Scattering
- BRENT A. MYERS**, *Intersil Corporation*, Pulse-Shaping Circuits

- VIJAY NAIR**, *Intel Corporation, Hillsboro, Oregon*, Low-Noise Amplifiers
- KRISHNA NAISHADHAM**, *Massachusetts Institute of Technology, Lexington, Massachusetts*, Parameter Estimation from Electromagnetic Simulations Using Signal Models
- HISAMATSU NAKANO**, *Hosei University, Koganei, Tokyo, Japan*, Slot Antennas
- MYSORE NARAYANAN**, *Miami University, Oxford, Ohio*, Wideband Amplifiers
- RAFAEL NAVAS-GONZÁLEZ**, *Institute of Microelectronics of Seville, Seville, Spain*, Voltage-to-Frequency Converters
- JEAN-MICHEL NEBUS**, *Universite de Limoges*, Millimeter-Wave Measurement
- R. NESTI**, *National Institute for Astrophysics, Florence, Italy*, Corrugated Horn Antennas; Orthomode Transducers
- ROBERT D. NEVELS**, *Texas A&M University, College Station, Texas*, Coulomb Gauge in Electromagnetics, The
- H. K. NG**, *City University of Hong Kong, Kowloon, Hong Kong* SAR, Dielectric Resonator Antennas
- KWOK K. NG**, *Lucent Technologies*, Negative Resistance
- LAM NGUYEN**, *Army Research Laboratory*, Radar Equipment
- TIEN M. NGUYEN**, *The Aerospace Corporation*, Military Communication
- KENNETH V. NOREN**, *University of Idaho, Moscow, Idaho*, Elliptic Filters
- ROBERT NOWLIN**, *Arizona State University East, Mesa, Arizona*, Attenuators
- MICHAEL W. NURNBERGER**, *Navy Research Laboratory, Washington, University of Colorado, Boulder, Colorado*, Frequency-independent Antennas
- AARON T. OHTA**, *University of Hawaii at Manoa, Honolulu, Hawaii*, Retrodirective Systems
- ERIK ÖJEFORS**, *Uppsala University, Uppsala, Sweden*, Monolithic Antennas
- FRANK OLYSLAGER**, *Ghent University, Ghent, Belgium*, Skin Effect
- BAN-LEONG OOI**, *National University of Singapore, Singapore*, Printed Inductors
- GEOFFREY C. ORSAK**, *Southern Methodist University*, Noise and Interference Modeling
- JOHN M. OSEPCCHUK**, *Concord, Massachusetts*, Magnetrons; Microwave Heating
- M. ÖSTLING**, *Royal Institute of Technology, Kista-Stockholm, Sweden*, SiC Device Technologies
- CANER OZDEMIR**, *Mersin University, Mersin, Turkey*, Synthetic Aperture Radar
- HASAN PADAMSEE**, *Cornell University*, Superconducting Cavity Resonators
- SHANTANU KUMAR PADHI**, *Monash University, Australia*, Coaxial Lines and Waveguides
- R. K. PANDEY**, *The University of Alabama, Tuscaloosa, Alabama*, Ferroelectric Materials
- CONSTANTINOS PAPADIAS**, *Lucent Technologies*, Antenna Arrays for Mobile Communications
- ROBERT K. PARKER**, *Naval Research Laboratory, Washington, D.C.*, Microwave Tubes
- D. P. PATEL**, *Naval Research Laboratory*, Microwave Ferroelectric Devices
- CLAYTON R. PAUL**, *Mercer University, Macon, Georgia*, Coupled Transmission Lines; Electromagnetic Compatibility
- AROGYASWAMI PAULRAJ**, *Stanford University*, Antenna Arrays for Mobile Communications
- S. J. PEARTON**, *University of Florida, Gainesville, Florida*, Passivation
- JOSÉ CARLOS PEDRO**, *University of Aveiro, Portugal*, Intermodulation
- G. PELOSI**, *University of Florence, Italy*, Corrugated Horn Antennas; Orthomode Transducers
- ODILON M. C. PEREIRA-FILHO**, *Federal University of Minas Gerais, Belo Horizonte, Brazil*, Electromagnetic Wave Propagation
- MANUEL SIERRA PEREZ**, *Universidad Politecnica de Madrid, Madrid, Spain*, Monopulse Tracking Systems
- EDWARD PETERSON**, *Arizona State University East, Mesa, Arizona*, Attenuators
- STEPHANE PINEL**, *Georgia Institute of Technology, Atlanta*, RF/Wireless Packaging
- UMBERTO PISANI**, *Politecnico di Torino, Torino, Italy*, Microwave Measurements
- GREESHMA PISHARODY**, *University of Delaware, Newark, Delaware*, Galerkin Method (Rayleigh–Ritz Method)
- J. M. POND**, *Naval Research Laboratory*, Microwave Ferroelectric Devices
- PROTAP PRAMANICK**, *K & L Microwave, Inc., Salisbury, Maryland*, Hybrids and Couplers; Strip Transmission Lines
- JAYASIMHA PRASAD**, *Maxim, San Jose, California*, Heterojunction Bipolar Transistor
- CARLES PUENTE**, *Fractus S.A., Barcelona, Spain*, Fractal Shaped Antennas: A Review
- ANYONG QING**, *National University of Singapore, Singapore*, Electromagnetic Inverse Problems
- RONALD RACKLEY**, *du Treil, Lundin, & Rackley, Sarasota, Florida*, Antennas for Medium-Frequency Broadcasting
- MARK RADER**, *The University of Tennessee, Knoxville, Tennessee*, Directive Antennas
- KALADHAR RADHAKRISHNAN**, *Intel Corporation, Chandler, Arizona*, High-Frequency Transmission Lines
- M. RAHMAN**, Hankel Transforms
- JAIME RAMIREZ-ANGULO**, *New Mexico State University, Las Cruces, New Mexico*, Bandpass Filters
- R. KEITH RANEY**, *Johns Hopkins University, Laurel, Maryland*, Radar Altimetry
- N. RANGANATHAN**, *University of South Florida*, Integrated Circuits
- J. B. L. RAO**, *Naval Research Laboratory*, Microwave Ferroelectric Devices
- S. M. RAO**, *Auburn University, Auburn, Alabama*, Integral Equations: Application to Open-Region Problems
- JAMES C. RAUTIO**, *Sonnet Software, Inc., Phoenix, New York*, Applied Numerical Electromagnetic Analysis for Planar High-Frequency Circuits
- LEONHARD M. REINDL**, *Albert Ludwigs Universitat, Freiburg, Germany*, Surface Acoustic Wave Delay Lines
- MARC RESSLER**, *Army Research Laboratory*, Radar Equipment
- R. REUTER**, *Innovative Processing AG (IPAG), Duisburg, Germany*, Noise, High-Frequency
- PATRICK REYNAERT**, *KULeuven ESAT-MICAS, Leuven, Belgium*, Mixed-Signal CMOS RF Integrated Circuits
- DAVID F. RIVERA**, *Naval Undersea Warfare Center, Newport, Rhode Island*, Submarine Antennas
- I.D. ROBERTSON**, *University of Leeds, Leeds, United Kingdom*, Radiofrequency Integrated Circuits
- CHRISTOPHER T. RODENBECK**, *Texas A&M University, College Station, Texas*, Gratings, Grating Antennas
- ARMANDO A. RODRIGUEZ**, *Arizona State University, Tempe, Arizona*, Missile Guidance
- ÁNGEL RODRÍGUEZ-VÁZQUEZ**, *University of Seville, Spain*, Harmonic Oscillators, Circuits; Voltage-to-Frequency Converters

- ULRICH L. ROHDE**, *Synergy Microwave Corporation, Paterson, New Jersey*, Phase-Locked Oscillators and Frequency Synthesizers
- ARYE ROSEN**, *Drexel University, Philadelphia, Pennsylvania*, PIN Diodes
- TULLIO ROZZI**, *Università di Ancona, Ancona, Italy*, Directional Couplers
- THOMAS E. RUDEN**, *Newton Highlands, Massachusetts*, Magnetrans
- CLEMENS C.W. RUPPEL**, *Albert Ludwigs Universität, Freiburg, Germany*, Surface Acoustic Wave Delay Lines
- ANDREW RUSEK**, *Oakland University, Rochester, Michigan*, Reflectometers, Time-Domain
- PETER RUSSEK**, *Munich Technical University, Germany*, GeSi Alloys and Devices; Oscillator Design
- ANDERS RYDBERG**, *Uppsala University, Uppsala, Sweden*, Monolithic Antennas
- VICTOR RYZHII**, *University of Aizu, Heterostructures Devices*
- MAGDALENA SALAZAR-PALMA**, *Madrid Polytechnic University, Spain*, Direction of Arrival Estimation and Adaptive Processing Using a Conformal Phased Array; Stripline Components
- PABLO SANCHIS**, *Universidad Politécnica de Valencia, Valencia, Spain*, Photonic Band Gap (PGB)
- CARLES SANS**, *Agrotech Biotecnologia Aplicada SA, Spain*, Microwave Superconductor Devices
- TAPAN K. SARKAR**, *Syracuse University, Syracuse, New York*, Direction of Arrival Estimation and Adaptive Processing Using a Conformal Phased Array; Stripline Components
- RONAN SAULEAU**, *University of Rennes, Rennes, France*, Fabry-Perot Resonators
- B. SAUVIAC**, *Jean Monnet University, St. Etienne, France*, Ferrite Isolators
- MANOJ SAXENA**, *University of Delhi, New Delhi, India*, MOSFET Modeling
- ROLF SCHAUMANN**, *Portland State University, Portland, Oregon*, Circuit Tuning
- BURKHARD SCHIEK**, *Ruhr-Universität Bochum*, Standing Wave Meters and Network Analyzers
- DOMINIQUE M. M.-P. SCHREURS**, *K.U.Leuven, Leuven-Heverlee, Belgium*, Microwave Solid-State Devices
- THOMAS F. SCHUBERT JR.**, *University of San Diego, San Diego, California*, Feedback Amplifiers
- HERMANN SCHUMACHER**, *University of Ulm, Ulm, Germany*, Silicon-Germanium (Si-Ge)
- LEONARD M. SCHWAB**, *Germaine Development Corp., Smith Chart*
- JAMES R. SCHWANK**, *Sandia National Laboratories, Albuquerque, New Mexico*, Radiation Effects
- S. SELLERI**, *University of Florence, Italy*, Corrugated Horn Antennas; Orthomode Transducers
- DIPAK L. SENGUPTA**, *University of Detroit Mercy, Detroit, Michigan*, Conformal Antennas
- FRANCISCO J. GONZÁLEZ SERRANO**, *Universidad Carlos III de Madrid, Madrid, Spain*, Wireless Communications Systems
- FRED W. SEXTON**, *Sandia National Laboratories, Albuquerque, New Mexico*, Radiation Effects
- L. SHAFAL**, *University of Manitoba, Winnipeg, Manitoba, Canada*, Dielectric Loaded Antennas
- MARTY R. SHANEYFELT**, *Sandia National Laboratories, Albuquerque, New Mexico*, Radiation Effects
- ARVIND K. SHARMA**, *TRW, Redondo Beach, California*, Cavity Resonators
- WILLIAM M. SHERRILL**, *Southwest Research Institute, San Antonio, Texas*, Radio Direction Finding
- GRANT S. SHIROMA**, *University of Hawaii at Manoa, Honolulu, Hawaii*, Retrodirective Systems
- WAYNE A. SHIROMA**, *University of Hawaii at Manoa, Honolulu*, Quasioptical Circuits; Retrodirective Systems
- Y.H. SHUM**, *City University of Hong Kong, Kowloon, Hong Kong*, Dual- and Multifrequency Microstrip Antennas
- MOSHE SIDI**, *Technion—Israel Institute of Technology*, Multiple-Access Schemes
- FRANKLIN C. SILVA**, *University of Brasilia, Brasilia, DF, Brazil*, Antenna Accessories
- RAINEE N. SIMONS**, *NASA Glenn Research Center, Cleveland, Ohio*, Coplanar Stripline Transitions; Coplanar Waveguide Components
- GORDON G. SINCLAIR**, *Technology for Communications International, Fremont, California*, Antennas for High-Frequency Broadcasting
- O. N. SINGH**, *Banaras Hindu University, Varanasi, India*, Electromagnetic Materials
- KAZIMIERZ SIWIAK**, *TimeDerivative, Inc., Coral Springs, Florida*, Loop Antennas; Ultra-Wideband Radio
- MARK A. SLETTEN**, *Naval Research Laboratory, Washington, DC*, Radar Polarimetry
- PETER M. SMITH**, *McMaster University, Hamilton, Canada*, Acoustic Microwave Devices
- CHARLES E. SMITH**, *Center of Applied Electromagnetic Systems Research (CAESR) The University of Mississippi University, Mississippi*, Wideband Slot and Printed Antennas
- CHRISTOPHER M. SNOWDEN**, *Filtronic Compound Semiconductors and University of Leeds, Shipley, West Yorkshire, United Kingdom*, III-V Semiconductors
- RICHARD V. SNYDER**, *RS Microwave, Butler, New Jersey*, Frequency-Division Multiplexers
- JORDI SOLER**, *Fractus S.A., Barcelona, Spain*, Fractal Shaped Antennas: A Review
- SAMEER SONKUSALE**, *Tufts University, Medford, Massachusetts*, A/D and D/A Conversion Architectures and Techniques
- ROBERTO SORRENTINO**, *University of Perugia, Perugia, Italy*, Transverse Resonance Technique; Waveguide Discontinuities
- ANTHONY E. SPEZIO**, *Naval Research Laboratory*, Electronic Warfare
- S. SRIDHAR**, *Northeastern University*, Superconducting Microwave Technology
- DANIELA STAICULESCU**, *Georgia Institute of Technology, Atlanta*, RF/Wireless Packaging
- MANFRED STECHER**, *Rhode & Schwarz GmbH & Co.KG*, Magnetic Field Measurement
- MICHEL STEYAERT**, *KULeuven ESAT-MICAS, Leuven, Belgium*, Mixed-Signal CMOS RF Integrated Circuits
- BERND H. STRASSNER II**, *Sandia National Laboratories, Albuquerque, New Mexico*, Microwave Power Transmission; Rectifying Antennas (Rectennas)
- WARREN L. STUTZMAN**, *Virginia Tech Antenna Group, Blacksburg, Virginia*, Antenna Theory
- BINGZHI SU**, *University of Colorado, Chong-IL Park, Kyocera America, Inc.*, Packaging RF Devices and Modules
- ALMUDENA SUÁREZ**, *University of Cantabria, Santander, Cantabria, Spain*, Nonlinear Circuit Analysis; Nonlinear Circuit Design
- YOUNG-HO SUH**, *Mimix Broadband Inc., Houston, Texas*, Coplanar Stripline (CPS) Components
- SAMIA A. SULIMAN**, *The Pennsylvania State University, University Park, Pennsylvania*, Smart Materials
- AHMED IYANDA SULYMAN**, *Queen's University, Kingston, Ontario, Canada*, MIMO Systems for Wireless Communications

- CHEN SUN**, *Nanyang Technological University, Singapore*, Adaptive Array Antennas
- RAJI SUNDARARAJN**, *Arizona State University East, Mesa, Arizona*, Attenuators
- JAMES A. SVOBODA**, *Clarkson University, Potsdam, New York*, Circuit Stability
- ALLEN TAFLOVE**, *Northwestern University, Evanston, Illinois*, Finite-Difference Time-Domain Analysis
- R. S. TAHIM**, *RST Scientific Research, Inc., New York*, Microwave Mixers
- PAUL J. TALLERICO**, *Los Alamos National Laboratory*, Klystron
- JAMES M. TALLEY**, *Naval Research Laboratory*, Electronic Warfare
- MICHAEL A. TAMAMOTO**, *University of Hawaii at Manoa, Honolulu, Hawaii*, Retrodirective Systems
- J. TANG**, *Washington State University*, Permittivity and Measurement
- SERIOJA O. TATU**, *École Polytechnique, Montreal, Quebec, Canada*, Quadrature Phase Shift Keying (QPSK)
- ALEXANDER L. TAUBE**, *Swinburne University of Technology, Melbourne, Australia*, Microwave Resonance Plasma Source
- F. J. TEGUDE**, *Innovative Processing AG (IPAG), Duisburg, Germany*, Noise, High-Frequency
- FERNANDO L. TEIXEIRA**, *The Ohio State University, Columbus, Ohio*, Electromagnetic Wave Propagation; High-Frequency Transmission Lines
- MANOS M. TENTZERIS**, *Georgia Institute of Technology, Atlanta, Georgia*, Application of Wavelets to Electromagnetic Problems; Electromagnetics, Time-Domain; RF/Wireless Packaging
- VALERIA TEPPATI**, *Politecnico di Torino, Torino, Italy*, Microwave Measurements
- MARCO A. B. TERADA**, *New Mexico State University, Las Cruces, New Mexico*, Reflector Antennas
- D. G. THOMAS JR.**, *University of California, Davis*, Microwave and Radio Frequency Multipliers
- TUAN TON**, *Army Research Laboratory*, Radar Equipment
- GUIDO TORELLI**, *University of Pavia*, Preamplifiers
- ALESSANDRO TOSCANO**, *“Roma Tre” University, Rome, Italy*, Method of Lines
- P. T. TRAKADAS**, *National Technical University of Athens, Athens, Greece*, Antenna Reverberation Chamber
- WALTER J. TRYBULA**, *SEMATECH, Austin, Texas*, Surface Mount Technology
- FENG-CHI E. TSAI**, *University of Queensland, Queensland, Australia*, Power Combiners and Dividers
- LEUNG TSANG**, *University of Washington, Seattle*, Computational Electromagnetic Scattering Models for Microwave Remote Sensing; Rough-Surface Scattering: Numerical Simulations and Applications in Microwave Remote Sensing
- GEORGE A. TSIHRINTZIS**, *University of Piraeus, Piraeus, Greece*, Radar Applications
- HAIPING TSOU**, *California Institute of Technology*, Radiotelemetry
- KATSUTOSHI TSUKAMOTO**, *Osaka University, Osaka, Japan*, Radio-on-Fiber (RoF) Systems
- AHMET SERDAR TÜRK**, *Information Technologies Research Institute, Gebze, Kocaeli, Turkey*, Buried-Object Detection
- KENJI UCHINO**, *The Pennsylvania State University*, Piezoelectricity
- PYOTR YA. UFIMSTEV**, *University of California at Irvine, California*, Backscatter
- SHAMBHU J. UPADHYAYA**, *State University of New York at Buffalo*, Noise Generators
- RUEDIGER VAHLDIECK**, *Institut für Feldtheorie und Höchstfrequenztechnik and Swiss Federal Institute of Technology, Zurich, Switzerland*, Electromagnetic Modeling; Finlines
- ANDRÉ VANDER VORST**, *Université Catholique de Louvain, Louvain-la-Neuve, Belgium*, Waveguides
- ROBERT B. VAN DOVER**, *Bell Labs, Lucent Technologies*, Magnetic Materials
- JAKOB J. VAN ZYL**, *California Institute of Technology, Pasadena, California*, Radar Remote Sensing
- RODNEY G. VAUGHAN**, *Simon Fraser University, Burnaby, British Columbia, Canada*, Mobile Radio Channels
- LUCIO VEGNI**, *“Roma Tre” University, Rome, Italy*, Method of Lines
- RAJU D. VENKATARAMANA**, *University of South Florida*, Integrated Circuits
- S. VERDEYME**, *IRCOM, Limoges, France*, Dielectric Resonator Filters
- GUY VERNET**, *Université Paris – Sud*, Millimeter-Wave Measurement
- FERNANDO VIDAL-VERDÚ**, *University of Málaga, Málaga, Spain*, Voltage-to-Frequency Converters
- D. VINCENT**, *Jean Monnet University, St. Etienne, France*, Ferrite Isolators
- OSAMU WADA**, *Kobe University, Japan*, Indium Phosphide (InP)
- P. F. WAHID**, *University of Central Florida, Orlando, Florida*, Antennas
- H. R. WALKER**, *Pegasus Data Systems, Inc., Edison, New Jersey*, Intermediate-Frequency Amplifiers
- FRED L. WALLS**, *Total Frequency, Boulder, Colorado*, Frequency Standards, Characterization
- CHARLES C. WANG**, *The Aerospace Corporation*, Military Communication
- CHI WANG**, *Orbital Sciences Corporation, Dulles, Virginia*, Combline Filters
- D. X. WANG**, *City University of Hong Kong, Kowloon, Hong Kong, P.R. China*, Ferrite Circulators
- HUEI WANG**, *National Taiwan University, Taipei, Taiwan*, Monolithic Millimeter-Wave Integrated Circuits
- LIHONG V. WANG**, *Texas A&M University, College Station, Texas*, Medical Imaging with Microwave: Thermoacoustic Tomography
- MINSHENG WANG**, *Texas Instruments Incorporated*, Radar Signal Detection
- S. WANG**, *Washington State University*, Permittivity and Measurement
- ZEYI WANG**, *Tsinghua University, Beijing, China*, Capacitance Extraction
- ANDREW WEBB**, *University of Illinois at Urbana-Champaign, Urbana*, Magnetic Resonance Imaging
- KEVIN J. WEBB**, *Purdue University, West Lafayette, Indiana*, Low-Noise Amplifiers: Device Noise Characterization and Design
- RALF WEBER**, *Ericsson Eurolab Deutschland GmbH*, Mobile Communication
- DANIEL S. WEILE**, *University of Delaware, Newark, Delaware*, Galerkin Method (Rayleigh–Ritz Method)
- ANDREW R. WEILY**, *Macquarie University, Sydney, New South Wales, Australia*, Dielectric Resonators
- ROBERT WEIRATHER**, *Harris Corporation, Quincy, Illinois*, Transmitters for Digital Television
- DANIEL WEIS**, *Individual Consultants*, Radiation Monitoring
- JOSEPH F. WHITE**, *JFW Technology, Inc.*, Microwave Phase Shifters
- RAYMOND A. WILDMAN**, *University of Delaware, Newark, Delaware*, Galerkin Method (Rayleigh–Ritz Method)

- RONALD WILENSKY**, *Technology for Communications International, Fremont, California*, Antennas for High-Frequency Broadcasting
- JOHN E.C. WILLIAMS**, *Massachusetts Institute of Technology, Cambridge, Massachusetts*, Superconducting Electromagnets
- H. WONG**, *City University of Hong Kong, Kowloon, Hong Kong*, Microstrip Antennas, Broadband
- KIN-LU WONG**, *National Sun Yat-Sen University, Kaohsiung, Taiwan*, Microstrip Antennas, Compact
- KE WU**, *Ecole Polytechnique, Montreal, Quebec, Canada*, Impedance Transformers and Matching Networks; Six-Port Networks; Slow Wave Structures
- KE-LI WU**, *The Chinese University of Hong Kong, Shatin, NT, Hong Kong*, Low Temperature Co-Fired Ceramic (LTCC) Technology in RF and Microwave Engineering
- TE-KAO WU**, *Northrop-Grumman, Redondo Beach, California*, Frequency Selective Surfaces
- THOMAS X. WU**, *University of Central Florida, Orlando, Florida*, BiCMOS Devices and RF Integrated Circuits
- ZHIPENG WU**, *UMIST, Manchester, United Kingdom*, Electromagnetic Surface Waves
- TADEUSZ WYSOCKI**, *Curtin University of Technology, Mobile Communication*
- MING YAO XIA**, *Peking University, Beijing, China*, Rough-Surface Scattering: Numerical Simulations and Applications in Microwave Remote Sensing
- FUQIN XIONG**, *Cleveland State University, Cleveland, Ohio*, Amplitude Shift Keying
- XINYU XU**, *Canada*, Six-Port Networks
- DAO-XIAN XU**, *National University of Singapore, Singapore*, Printed Inductors
- JIANJUN XU**, *Carleton University, Ottawa, Canada*, Neural Networks for Microwave Circuits
- YUAN XU**, *Texas A&M University, College Station, Texas*, Medical Imaging with Microwave: Thermoacoustic Tomography
- MASATSUNE YAMAGUCHI**, *Chiba University, Chiba, Japan*, Surface Acoustic Wave Filters
- EIKICHI YAMASHITA**, *University of Electro-Communications, Microstrip Lines*
- XIAOMIN YANG**, *University of Central Florida, Orlando, Florida*, BiCMOS Devices and RF Integrated Circuits
- ERDEM YAZGAN**, *Hacettepe University, Beytepe, Ankara, Turkey*, Conformal Mapping Techniques
- WEI YE**, *National University of Singapore*, Radar Signal Processing
- TAT SOON YEO**, *National University of Singapore*, Radar Signal Processing
- WEN-YAN YIN**, *National University of Singapore, Kent Ridge, Singapore*, Complex Media
- FRANK S. YOUNG**, *Electric Power Research Institute*, Magnetic Shielding
- SIMON H. YUEH**, *California Institute of Technology*, Spaceborne Radar
- WENHUA YU**, *Pennsylvania State University, University Park, Pennsylvania*, Enhancements of the Finite-Difference Time-Domain Method
- WENJIAN YU**, *Tsinghua University, Beijing, China*, Capacitance Extraction
- TAE-YEOL YUN**, *Hanyang University, Seoul, Korea*, Piezoelectric Transducer Controlled Circuits
- E. K. N. YUNG**, *City University of Hong Kong, Kowloon, Hong Kong, P.R. China*, Ferrite Circulators
- S. ZEADALLY**, *High Speed Networking Laboratory, Detroit, Michigan*, Personal Area Networking with Bluetooth
- HANS-JÜRGEN ZEPERNICK**, *Cooperative Research Center for Broadband Telecommunications and Networking, Mobile Communication*
- C.-M. ZETTERLING**, *Royal Institute of Technology, Kista-Stockholm, Sweden*, SiC Device Technologies
- QI-JUN ZHANG**, *Carleton University, Ottawa, Canada*, Neural Networks for Microwave Circuits
- WENGE ZHANG**, *University of Colorado, Chong-IL Park, Kyocera America, Inc.*, Packaging RF Devices and Modules
- JIANYI ZHOU**, *Southeast University, Nanjing, China*, Feedback Oscillators
- LIN ZHOU**, *Duke University, North Carolina*, Rough-Surface Scattering: Numerical Simulations and Applications in Microwave Remote Sensing
- LEI ZHU**, *Nanyang Technological University, Singapore*, Coplanar Waveguide (CPW) Transmission Lines; Microwave Filters
- HERBERT ZIRATH**, *Chalmers University of Technology*, Frequency Converters and Mixers
- TAKIS ZOURNTOIS**, *Texas A&M University, College Station, Texas*, A/D and D/A Conversion Architectures and Techniques
- ZORAN ZVONAR**, *Analog Devices, Wilmington, Massachusetts*, Radio System Performance

Contents

<i>Preface</i>	v
<i>Contributors</i>	vii
A/D and D/A Conversion Architectures and Techniques to Attenuators	1
A/D and D/A Conversion Architectures and Techniques	1
Acoustic Microwave Devices	24
Active Antennas	34
Active Filters: Overview of Active-filter Structures	56
Active Filters: Tools and Techniques for Active-filter Design	70
Adaptive Array Antennas	88
Altimeters	103
Amplitude Shift Keying	117
Analytical and Adaptive Modeling of Nonlinear High-power Amplifiers	127
Anisotropy and Bianisotropy	137
Antenna Accessories	147
Antenna Anechoic Chambers	158
Antenna Arrays for Mobile Communications	164
Antenna Compact Range	177
Antenna Feeds	185
Antenna Parameters	217
Antenna Radiation Patterns	225
Antenna Reverberation Chamber	239
Antenna Scanning Arrays	251
Antenna Testing and Measurements	262
Antenna Theory	269
Antennas	284
Antennas for High-frequency Broadcasting	295
Antennas for Medium-frequency Broadcasting	301
Antennas for Mobile Communications	319
Aperture Antennas	365
Application of Wavelets to Electromagnetic Problems	377

Applied Numerical Electromagnetic Analysis for Planar High-frequency Circuits	397
Artificial Magnetic Conductor	413
Attenuation Measurement	434
Attenuators	452
Backscatter to Buried Object Detection	481
Backscatter	481
Bandpass Filters	494
Bandstop Filters	498
BiCMOS Devices and RF Integrated Circuits	499
Biological Effects of Radiofrequency Energy as Related to Health and Safety	511
Boundary-value Problems	523
Buried Object Detection	540
Calibration of a Circular Loop Antenna to Cryogenic Electronics	560
Calibration of a Circular Loop Antenna	560
Capacitance Extraction	565
Cavity Resonators	576
Cellular Radio	592
Chebyshev Filters	600
Chirality	610
Circuit Stability	622
Circuit Tuning	632
Circular Waveguides	643
Coaxial Line Discontinuities	653
Coaxial Lines and Waveguides	658
Compline Filters	674
Complex Media	694
Computational Electromagnetic Scattering Models for Microwave Remote Sensing	718
Conformal Antennas	750
Conformal Mapping Techniques	760
Conical Antennas	775
Coplanar Stripline (CPS) Components	780
Coplanar Stripline Transitions	810
Coplanar Waveguide Components	816
Coplanar Waveguide (CPW) Transmission Lines	821
Corrugated Horn Antennas	833
Coulomb Gauge in Electromagnetics, the	849
Coupled Transmission Lines	863
Cryogenic Electronics	882

Dielectric Loaded Antennas to Dual- and Multi-frequency Microstrip Antennas	893
Dielectric Loaded Antennas	893
Dielectric Measurement	916
Dielectric Permittivity and Loss	938
Dielectric Resonator Antennas	960
Dielectric Resonator Filters	974
Dielectric Resonator Oscillators	985
Dielectric Resonators	999
Digital Microwave Receivers	1014
Digital Radio	1021
Diodes	1033
Dipole Antennas and Arrays	1046
Direct Satellite Television Broadcasting	1052
Direction of Arrival Estimation and Adaptive Processing Using a Conformal Phased Array	1065
Directional Couplers	1076
Directive Antennas	1085
Distributed Amplifiers	1086
Dual- and Multi-frequency Microstrip Antennas	1098
Electromagnetic-bandgap-assisted Bandpass Filters to Enhancements of the Finite Difference Time Domain Method	1117
Electromagnetic-bandgap-assisted Bandpass Filters	1117
Electromagnetic Compatibility	1136
Electromagnetic Ferrite Tile Absorber	1151
Electromagnetic Field Computation in Planar Multilayers	1163
Electromagnetic Field Measurement	1190
Electromagnetic Inverse Problems	1200
Electromagnetic Materials	1216
Electromagnetic Modeling	1232
Electromagnetic Shielding	1248
Electromagnetic Subsurface Remote Sensing	1256
Electromagnetic Surface Waves	1270
Electromagnetic Wave Propagation	1280
Electromagnetic Wave Scattering	1295
Electromagnetic Waves in Ionosphere	1303
Electromagnetics, Time-domain	1318
Electronic Warfare	1333
Elliptic Filters	1353
Enhancements of the Finite Difference Time Domain Method	1361

Fabry-Perot Resonators to Friis Free-space Transmission Formula	1381
Fabry-Perot Resonators	1381
Fast Fourier Transforms and NUFFT	1401
Feedback Amplifiers	1418
Feedback Oscillators	1432
Feedforward Amplifiers	1439
Ferrite Circulators	1448
Ferrite Isolators	1473
Ferrite-loaded Waveguides	1486
Ferrite Phase Shifters	1497
Ferroelectric Materials	1504
Filter Synthesis	1521
Filter Theory	1548
Finite-difference Time-domain Analysis	1567
Finite Element Analysis	1589
Finline Components	1601
Finlines	1609
Fractal-shaped Antennas: a Review	1620
Frequency Converters and Mixers	1635
Frequency-division Multiplexers	1649
Frequency-domain Circuit Analysis	1659
Frequency-independent Antennas	1674
Frequency Modulation	1691
Frequency Selective Surfaces	1700
Frequency Stability	1706
Frequency Standards, Characterization	1720
Frequency Synthesizers	1729
Friis Free-space Transmission Formula	1733
Galerkin Method (Rayleigh-Ritz Method) to Gyrotrons	1735
Galerkin Method (Rayleigh-Ritz Method)	1735
Gallium Arsenide Technology and Applications	1749
Gallium Nitride for Electronics	1758
Generalized Scattering Matrix Technique	1767
Geometrical Optics	1777
Ge-Si Alloys and Devices	1796
Gratings, Grating Antennas	1806
Green's Function Methods	1817
Ground Penetrating Radar	1833

Guided Electromagnetic Waves	1846
Gunn or Transferred-electron Devices and Circuits	1857
Gyrators	1874
Gyrotrons	1883
Hankel Transforms to Hybrids and Couplers	1893
Hankel Transforms	1893
Harmonic Oscillators, Circuits	1915
Helical Antennas	1925
Helmholtz Equations	1936
Heterojunction Bipolar Transistor	1946
Heterostructures Devices	1963
High-field Effects	1970
High-frequency Broadcasting	1981
High-frequency Transmission Lines	1989
High-temperature Superconductors	2005
History of Wireless Communication	2015
Horn Antennas	2021
HTS Film Growth	2032
Hybrid CAD Techniques	2040
Hybrids and Couplers	2054
IMPATT Diodes and Circuits to ITS Radio Service Standards and Wireless Access in Vehicular Environments (ITS-WAVE) at 5.9 GHz	2067
IMPATT Diodes and Circuits	2067
Impedance Transformers and Matching Networks	2079
Indium Phosphide (InP)	2092
Integral Equations	2103
Integrated Antenna Systems	2113
Integrated Circuits	2147
Integro-differential Equations	2166
Intermediate-frequency Amplifiers	2175
Intermodulation	2189
Intermodulation Measurement	2215
Iterative Methods	2231
ITS Radio Service Standards and Wireless Access in Vehicular Environments (ITS-WAVE) at 5.9 GHz	2241
Klystron	2257
Klystron	2257

Leaky Modes and High-frequency Effects in Microwave Integrated Circuits to Low-temperature Cofired Ceramic (LTCC) Technology in RF and Microwave Engineering	2268
Leaky Modes and High-frequency Effects in Microwave Integrated Circuits	2268
Leaky-wave Antennas	2294
Left-handed Materials for Microwave Devices and Circuits	2303
Lens Antennas	2320
Linear Antennas	2336
Local-area Networks (LANs)	2352
Loop Antennas	2359
Low Noise Amplifiers	2368
Low Noise Amplifiers: Device Noise Characterization and Design	2379
Low-pass Filters	2383
Low-power Broadcasting	2385
Low-temperature Cofired Ceramic (LTCC) Technology in RF and Microwave Engineering	2393
Magnetic Field Measurement to Multiresolution Technique	2400
Magnetic Field Measurement	2400
Magnetic Materials	2412
Magnetic Microwave Devices	2425
Magnetic Resonance Imaging	2462
Magnetic Shielding	2473
Magnetrons	2482
Maxwellian Circuits	2514
Measurement of Near Fields Using a Modulated Scatterer	2522
Medical Imaging with Microwave: Thermoacoustic Tomography	2530
MEI Method	2540
Method of Lines	2548
Method of Moments	2554
Microstrip Antenna Arrays	2568
Microstrip Antennas	2580
Microstrip Antennas, Broadband	2602
Microstrip Antennas, Compact	2626
Microstrip Circuits	2637
Microstrip Lines	2647
Microstrip Transitions	2654
Microwave and Radio Frequency Multipliers	2663
Microwave Circuits	2704
Microwave Detectors	2736
Microwave Filters	2751

Microwave Heating	2763
Microwave Integrated Circuits	2773
Microwave Isolators	2786
Microwave Limiters	2792
Microwave Measurements	2802
Microwave Mixers	2812
Microwave Oscillators	2818
Microwave Parametric Amplifiers	2827
Microwave Phase Shifters	2836
Microwave Photonics: Technological Evolution and Its Applications	2851
Microwave Power Amplifiers	2871
Microwave Power Transmission	2906
Microwave Receivers	2919
Microwave Resonance Plasma Source	2934
Microwave Scattering Models for Earth Terrain	2948
Microwave Solid-state Devices	2968
Microwave Superconductor Devices	2980
Microwave Switches	2991
Microwave Tubes	2999
Military Communication	3007
Millimeter-wave Integrated Circuits	3021
Millimeter-wave Measurement	3046
MIMO Systems for Wireless Communications	3059
Miniaturized Packaged (Embedded) Antennas for Portable Wireless Devices	3068
Missile Guidance	3082
Mixed-signal CMOS RF Integrated Circuits	3095
Mixer Circuits	3102
Mobile Communication	3121
Mobile Radio Channels	3132
Mobile Satellite Communications	3150
Mode-matching Methods	3162
Modulation-doped FETs	3176
Monolithic Antennas	3203
Monolithic Microwave Integrated Circuits (MMICs)	3213
Monopole Antennas	3238
Monopulse Tracking Systems	3244
Monte Carlo Analysis	3255
Monte Carlo Simulation in Reliability	3269
Mosfet Modeling	3278

Multibeam Antennas	3317
Multiconductor Transmission Lines	3335
Multimode Equivalent Network Representations	3342
Multiple Access Schemes	3351
Multiplexers	3362
Multiresolution Technique	3369
Negative Resistance to Notch Antennas	3385
Negative Resistance	3385
Neural Networks for Microwave Circuits	3390
Noise and Interference Modeling	3397
Noise Generators	3408
Noise, High-frequency	3417
Noise, Hot Carrier Effects	3439
Noise, Low-frequency	3458
Nonlinear Circuit Analysis	3482
Nonlinear Circuit Design	3502
Notch Antennas	3534
Orthomode Transducers to Oscillator Design	3547
Orthomode Transducers	3547
Oscillator Design	3563
Packaging RF Devices and Modules to Pulse-shaping Circuits	3590
Packaging RF Devices and Modules	3590
Parallel Algorithms and Computing for Large-scale Electromagnetic Simulation	3614
Parameter Estimation from Electromagnetic Simulations Using Signal Models	3646
Passivation	3669
Periodic Structures	3675
Permittivity and Measurements	3693
Personal Area Networking with Bluetooth	3711
Perturbation Theory	3725
Phase Locked Loops	3735
Phase Locked Oscillators and Frequency Synthesizers	3767
Phase Noise and Measurements	3802
Phase Shifters	3810
Photonic Band Gap (PGB)	3823
Piezoelectric Transducer Controlled Circuits	3838
Piezoelectricity	3846
Pin Diodes	3858

Power Combiners and Dividers	3869
Preamplifiers	3891
Printed Inductors	3905
Pulse Compression	3915
Pulse-shaping Circuits	3925
Q-factor to Quasi-optical Circuits	3937
Q-factor	3937
Q-factor Measurements	3948
Quadrature Phase Shift Keying (QPSK)	3964
Quasi-optical Circuits	3977
Radar Altimetry to Rough-surface Scattering: Numerical Simulations and Applications in Microwave Remote Sensing	3989
Radar Altimetry	3989
Radar Antennas	4005
Radar Applications	4018
Radar Cross-section	4030
Radar Equipment	4055
Radar Imaging	4069
Radar Polarimetry	4080
Radar Remote Sensing	4096
Radar Remote Sensing of Irregular Stratified Layers	4122
Radar Signal Detection	4128
Radar Signal Processing	4148
Radar Target Recognition	4165
Radar Tracking	4173
Radiation Effects	4186
Radiation Monitoring	4217
Radio Broadcast Studio Equipment	4227
Radio Direction Finding	4249
Radio-frequency Identification Systems (RFID)	4263
Radio-frequency Integrated Circuits	4269
Radio Navigation	4292
Radio Noise	4297
Radio on Fiber Systems (RoF Systems)	4310
Radio Reception	4324
Radiometry	4342
Radiotelemetry	4350
Radiowave Propagation Concepts	4365

Radiowave Propagation Ground Effects	4371
Radiowave Propagation in Multipath Channels	4389
Reconfigurable Antennas	4405
Rectifying Antennas (Rectennas)	4418
Reflectarray Antenna	4428
Reflectometers, Time-domain	4436
Reflector Antennas (Parabolic Antennas, Dish Antennas)	4450
Refraction and Attenuation in Troposphere	4475
Resonant Tunneling Diodes	4484
Retrodirective Systems	4493
RF Circuit Noise	4507
RF/Wireless Packaging	4516
Ring Resonators and Circuits	4537
Rough-surface Scattering: Numerical Simulations and Applications in Microwave Remote Sensing	4549
Satellite Antennas to Synthetic Aperture Radar	4585
Satellite Antennas	4585
Schottky Barrier Diodes and Their Applications	4595
Schottky Barriers	4607
SiC Device Technologies	4613
Signal Fading in Radiocommunications	4619
Silicon-Germanium	4626
Six-port Networks	4641
Skin Effect	4669
Sky Wave Propagation at Low Frequencies	4675
Sky Wave Propagation at Medium and High Frequencies	4686
Slot Antennas	4696
Slotline Components	4717
Slotlines	4736
Slow Wave Structures	4744
Small Antennas	4761
Smart Materials	4799
Smith Chart	4814
Spaceborne Radar	4823
Spatial and Quasi-optical Power Combining	4837
Spice	4844
Spiral Antennas	4853
Squids	4869
Stability of Nonlinear Systems	4881

Standing Wave Meters and Network Analyzers	4896
Strip Transmission Lines	4918
Stripline Components	4931
Submarine Antennas	4937
Superconducting Cavity Resonators	4951
Superconducting Electromagnets	4965
Superconducting Filters and Passive Components	4974
Superconducting Microwave Technology	4990
Surface Acoustic Wave Applications	5002
Surface Acoustic Wave Delay Lines	5012
Surface Acoustic Wave Devices	5029
Surface Acoustic Wave Filters	5046
Surface Mount Technology	5058
Synthetic Aperture Radar	5067
Target Tracking to Tunnel Devices	5081
Target Tracking	5081
Telemedicine	5097
Telemetry	5106
Television and FM Broadcasting Antennas	5124
Television Antennas	5132
Television Broadcast Transmission Standards	5143
Terahertz Science, Engineering and Systems – from Space to Earth Applications	5175
Thermal Analysis and Design of Electronic Systems	5194
Thin Film Resistors	5213
Thin Films	5226
III-V Semiconductors	5237
Transceivers	5254
Transient Analysis	5268
Transmission Line Matrix (TLM) Method	5286
Transmission Line Theory	5297
Transmission Lines and Parameters	5310
Transmitters for Analog Television	5318
Transmitters for Digital Television	5327
Transmitters for FM Broadcasting	5337
Transverse Resonance Techniques	5357
Traveling Wave Antennas	5363
Traveling Wave Tubes	5373
Tunnel Devices	5380

UHF Receivers to Uniform Geometrical Theory of Diffraction	5391
UHF Receivers	5391
Ultra-wideband Radio	5402
Ultra-wideband Wireless Systems	5411
Underground Propagation	5423
Uniform Geometrical Theory of Diffraction	5433
Van Atta Array Reflector to Volterra Modeling in Analog, RF and Microwave Engineering	5456
Van Atta Array Reflector	5456
Variable-frequency Oscillators	5468
Very High Frequency Range	5477
Voltage-to-frequency Converters	5489
Volterra Modeling in Analog, RF and Microwave Engineering	5507
Waveguide Antennas to Wireless Communications Systems	5515
Waveguide Antennas	5515
Waveguide Components	5527
Waveguide Directional Couplers	5536
Waveguide Discontinuities	5543
Waveguide Junctions	5554
Waveguide Oscillators	5559
Waveguides	5569
Wavelength Meter	5587
Wavelet Transforms	5602
Wavelets	5623
Wideband Amplifiers	5630
Wideband Slot and Printed Antennas	5638
Wireless Communications Systems	5656
Yagi-Uda Antenna	5680
Yagi-Uda Antenna	5680
Index	5691

A/D AND D/A CONVERSION ARCHITECTURES AND TECHNIQUES

SAMEER SONKUSALE
 Tufts University
 Medford, Massachusetts
 TAKIS ZOURNTOS
 Texas A&M University
 College Station, Texas

1. INTRODUCTION

Data conversion is a broad area of activity that involves both theory and implementation. Our goal in this article is to provide a focused treatment of key fundamentals and an in-depth study of the latest approaches available for data converter design in communication systems. The coverage provided here should allow the reader to plan the design of a data converter integrated circuit or begin an independent investigation of the field.

Since the early 1990s, the transceiver core shown in Fig. 1 has provided a technological backdrop for the analog integrated circuit (IC) engineer. All popular communication devices, including mobile phones, wired modems, and network interface cards, are based on some variant of this system. Although simple in form, the core embodies a wide range of expertise, and usually requires a team of engineers to develop.

This article is concerned with the data conversion subsystem that interfaces the front-end and back-end portions of the transceiver core. A data converter translates signals between analog and digital representations.¹ Our emphasis is on data converters for mobile communication systems in which cost and power savings are a priority. Therefore, although much of our discussion is of a general nature, our presentation is geared toward CMOS integrated circuit implementation and applications with low to moderate bandwidths (e.g., communications with WCDMA, IEEE 802.11a/b, or Bluetooth protocols). The emerging trend in communications of higher data rates and greater mobility necessitates the use of economical IC technologies such as deep-submicrometer CMOS that facilitate full system integration.

The design of data converters can be challenging, particularly if a concurrence of speed, accuracy, and power efficiency are required [1]. Quite often, as one attempts to improve accuracy, the area and power dissipation of a data converter design increase substantially. The tradeoff between speed and converter accuracy is most evident with oversampled converters, in which the suppression of

quantization noise is closely related to the sampling rate. Broadband networking protocols such as WCDMA and IEEE 802.11b can require between 80 and 100 dB of dynamic range and signal bandwidths in the multi-megahertz range. Until 1997, such performance had not been achieved using standard CMOS fabrication [2–4].

The current state of the art (as of the end of 2003) for CMOS Nyquist-rate D/A technology provides 10-bit dynamic range at signal bandwidths up to 500 MHz [5], while CMOS Nyquist-rate A/D converters are achieving between 8 and 10 bits of dynamic range with signal bandwidths from 40 to 100 MHz [6–9]. Higher dynamic ranges (around 14 bits) at moderate speeds (up to 10 MHz) have been reported for CMOS architectures employing pipeline techniques. In Section 4, we provide a detailed discussion of the latest flash and pipeline techniques for the design of higher-speed converters.

Oversampled converters exhibit greater tolerance to component nonidealities than do their Nyquist-rate counterparts, so that 15-bit dynamic range can be readily achieved. Using feedback, the effective resolution of a coarse quantizer can be substantially increased (at the expense of reduced conversion speed). However, because of the higher sampling rates required (and limitations imposed by stability requirements on the degree of quantization noise shaping), the signal bandwidths of CMOS oversampled converter ICs are typically on the order of 1 MHz. Section 7 provides an introduction to oversampling techniques and an overview of proven architectures that achieve high resolution for narrowband applications.

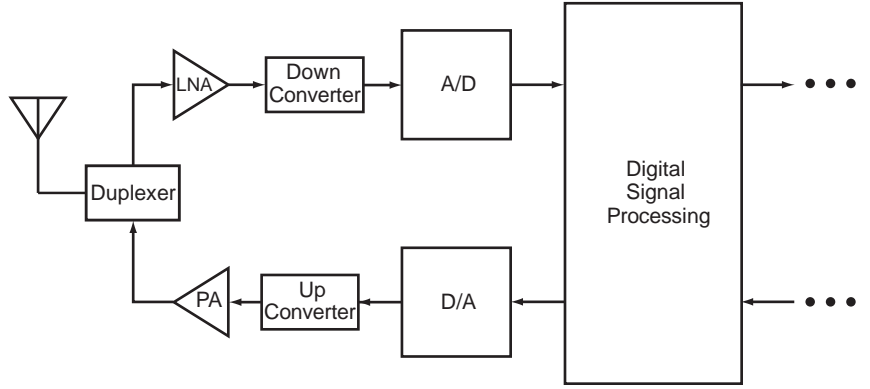
1.1. Overview of Data Conversion

Data converters are categorized as either *Nyquist-rate* or *oversampled* architectures. The former class of converter includes architectures that are typically open-loop and that operate at sampling rates that (usually) do not exceed 10 times the Nyquist rate. The Nyquist-rate D/A converter is the basis of many architectures and is formed by a series of passive or active elements, switches, and an output buffer, as shown in Fig. 2 (in binary-weighted form). Oversampled converters are feedback systems that operate with relatively high clock rates, up to 100 times the Nyquist rate or more. The kernel of the oversampled converter is the delta-sigma modulator, described in Section 7, which embeds a quantizer and filter within a feedback loop. The flash or parallel converter, described in Section 4, is perhaps the most straightforward type of Nyquist-rate A/D. A thermometer-coded binary number is generated through approximately 2^N parallel comparisons; conversion to conventional binary code (in addition to error correction) is performed by digital logic. The main advantage of this approach is speed. In Section 4, we present methods to “contain” the high complexity of the flash architecture by invoking pipeline techniques.

Nonidealities, particularly element-size mismatch, can reduce the dynamic range of data converters. Without mismatch compensation techniques (described below), the dynamic range of the converter is limited by the

¹We define *analog signals* as those with amplitudes that vary over a continuum, for example, signals such as voltage fluctuations induced by electromagnetic or acoustic waves impinging on transducers. Note that analog signals may be either discrete (i.e., sampled) or continuous in time. Digital signals are discrete in both amplitude and time. A system in which both analog and digital signals are used is called a *mixed-signal* system.

Figure 1. A generic wireless transceiver core for digital communication. The RF front end includes a low-noise amplifier (LNA) for the receiver and a power amplifier (PA) for the transmitter. The data conversion subsystem consists of an analog-to-digital (A/D) converter and a digital-to-analog (D/A) converter.



capabilities of the manufacturing technology, to—in the case of standard CMOS fabrication—approximately 10–12 bits. To see this, note that a D/A converter with N bits of accuracy, by definition, must satisfy

$$\text{Maximum error due to nonidealities} \leq \frac{V_{\text{LSB}}}{V_{\text{ref}}} = \frac{1}{2^N} \quad (1)$$

where the error associated with the converter must be less than the smallest possible change in the output voltage of the converter, defined as V_{LSB} (normalized by the reference voltage). If the D/A has a component mismatch error, which we assume to be the dominant source of error, of 0.1% (the minimum matching precision in standard CMOS [10]), we may write

$$\begin{aligned} 0.001 &\leq 2^{-N} \\ \Rightarrow \log_2(0.001) &\leq -N \log_2(2) \\ \Rightarrow N &\leq -\log_2(0.001) \approx 10. \end{aligned}$$

Therefore, the converter accuracy is limited to approximately 10 bits or 60 dB.

2. DATA CONVERTER FUNDAMENTALS

Data conversion can be viewed as a two-stage process of sampling followed by amplitude quantization, as shown in

Fig. 3. In many instances, the sampling operation is implicit in the functioning of the converter. However, it is often helpful to consider sampling as distinct from amplitude quantization, since certain performance degradations can be traced to sampling nonidealities.

In the case of D/A conversion, the sampling operation is simply a resampling and filtering of the digital input signal, which can be realized with digital circuits or software. In the A/D case, sampling is performed by an analog sample-and-hold (sometimes referred to as a “track-and-hold”) circuit, as shown in Fig. 4. The design of a suitable sample-and-hold can be challenging. Operating at the sampling rate of the converter, the sample-and-hold circuit must transition from “track” to “hold” mode with a minimum of error and provide an accurate measurement of the analog input with a minimum of signal feedthrough. The reader interested in a more in-depth discussion of sample-and-hold circuits is referred to the book by Johns and Martin [11, Chap. 8]; the remainder of our discussion will focus on the process of amplitude quantization.

The signal band of the data converter is the range of frequencies of width f_b from a minimum frequency (often DC) to a specified maximum frequency. For simplicity we assume throughout this article that the signal band begins at DC, where signals are restricted to the frequency range $[0, f_b]$. Sampling rates for bandlimited analog signals must exceed the Nyquist rate, denoted by $2f_b$, as shown in Fig. 5.

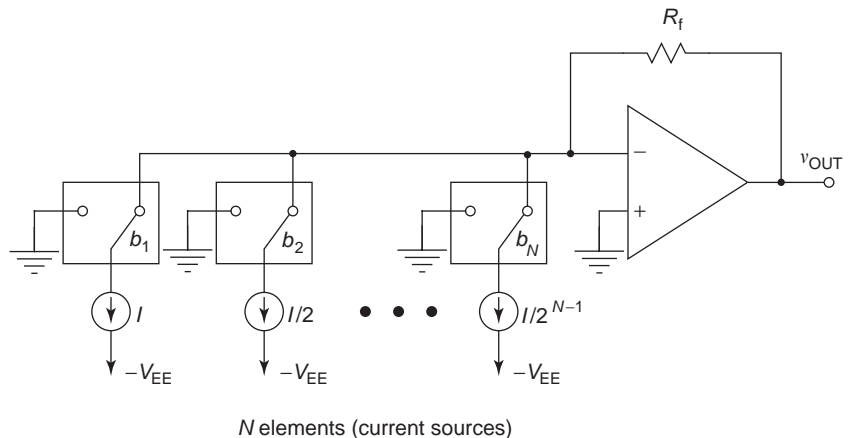


Figure 2. A binary-weighted N -bit Nyquist-rate D/A. Switching elements control current flow through the buffer based on bit values. The analog output voltage is expressed as $v_{\text{out}} = V_{\text{ref}} \sum_{i=1}^N 2^{-i} b_i$, where $V_{\text{ref}} = 2IR_f$.

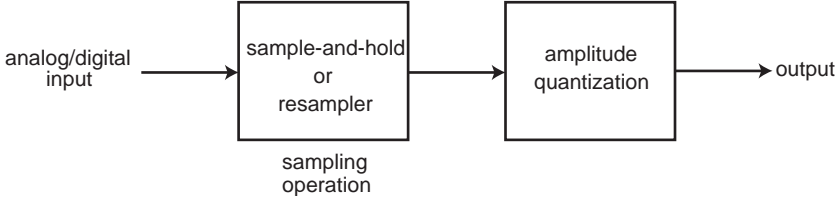


Figure 3. A conceptual view of the data conversion process.

For D/A converters, amplitude quantization can be expressed as a scaling of a digital input by an analog reference quantity. Formally, the amplitude quantization of an N -bit D/A converter (shown in general form in Fig. 6) is expressed as

$$v_{\text{out}} = V_{\text{ref}} \sum_{i=1}^N 2^{-i} b_i \quad (2)$$

where b_i are the bits of the input word, $\{b_1, b_2, \dots, b_N\}$, which may be in either signed or unsigned digital form; b_1 denotes the most significant bit (MSB); and b_N , the least significant bit (LSB). We assume that V_{ref} and v_{out} represent voltages, although other physical quantities (such as current) may be used. In the case of a thermometer code representation, $\{b_1, b_2, \dots, b_{2^N-1}\}$, of the digital input, we have

$$v_{\text{out}} = \frac{V_{\text{ref}}}{2^N} \sum_{i=1}^{2^N-1} b_i \quad (3)$$

We may provide a similar description for a generalized N -bit A/D converter, shown in Fig. 7. The relationship between analog input v_{in} and output bits is expressed as

$$v_{\text{in}} = V_{\text{ref}} \sum_{i=1}^N 2^{-i} b_i + v_Q \quad (4)$$

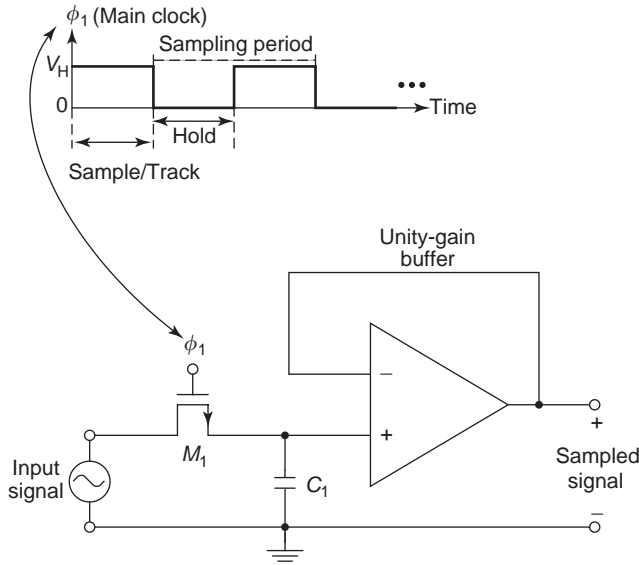


Figure 4. A conceptual sample-and-hold circuit. The sampling rate is set by the frequency of the main clock. During the sample phase, the switch M_1 is on and the capacitor voltage tracks the input signal voltage. During the hold phase, the switch opens and the voltage across C_1 can be read through a unity-gain buffer.

for binary-weighted encoding, or

$$v_{\text{in}} = \frac{V_{\text{ref}}}{2^N} \sum_{i=1}^{2^N-1} b_i + v_Q \quad (5)$$

for thermometer code converters. The variable v_Q denotes the quantization error, which we describe in detail below. These equations help us define the “staircase” characteristic that is often seen in A/D converter descriptions (please see Fig. 8). In addition to these equations, the ideal A/D has specific *transition* values for the analog input; Thus the transition points should occur $\frac{1}{2} V_{\text{LSB}}$ away from the midpoints of the staircase characteristic, as shown in Fig. 8. Assuming that v_{in} is within the designated limits of the converter, given by

$$-\frac{V_{\text{ref}}}{2^{N+1}} \leq v_{\text{in}} \leq \frac{2^{N+1} - 1}{2^{N+1}} V_{\text{ref}} \quad (6)$$

[note that the upperbound on v_{in} can be expressed as $V_{\text{ref}} - (V_{\text{LSB}}/2)$], the quantization error should satisfy

$$-\frac{V_{\text{ref}}}{2^{N+1}} \leq v_Q \leq \frac{V_{\text{ref}}}{2^{N+1}} \quad (7)$$

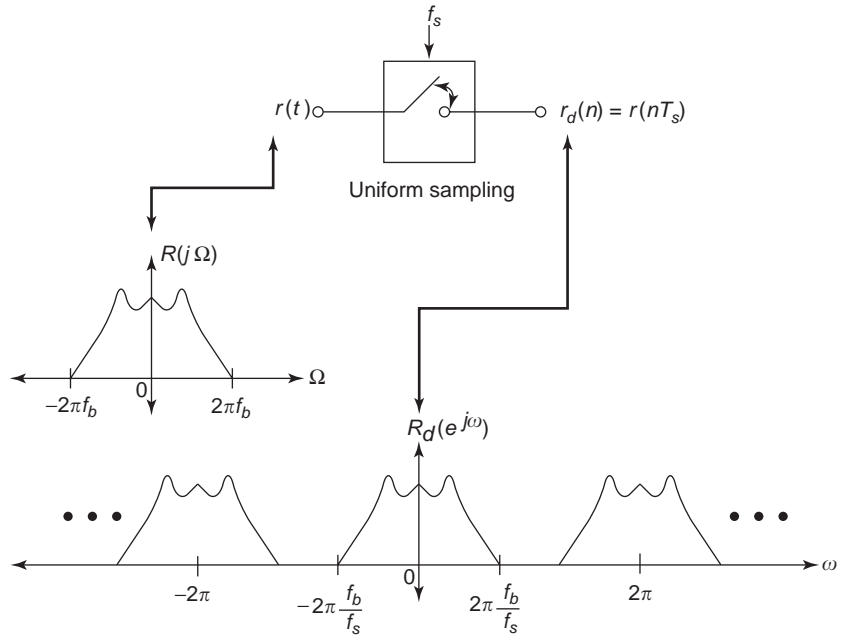
For dynamic measurements of converter performance, quantization error is often modeled as a uniformly distributed (zero-mean) uncorrelated random variable. Based on (7), the variance (i.e., power) of the quantization error is $V_{\text{LSB}}^2/12$. We can now derive the relationship between signal-to-quantization-noise ratio (SQNR) and N , the number of bits associated with an A/D converter. We assume that v_{in} is a sinusoidal input (commonly used for testing purposes) with amplitude that varies between 0 and V_{ref} [approximately within the bounds indicated by (6)]. We obtain the peak SQNR in units of dB as follows:

$$\begin{aligned} \text{SQNR} &= 10 \log_{10} \left(\frac{\text{power of sinusoidal input}}{\text{power of quantization error}} \right) \\ &= 10 \log_{10} \left(\frac{V_{\text{ref}}^2}{\frac{8}{V_{\text{LSB}}^2} \cdot \frac{1}{12}} \right) \\ &= 10 \log_{10} \left(\left(\frac{3}{2} \right) 2^{2N} \right) \\ &\approx 6.02N + 1.76 \end{aligned}$$

Thus we find that the resolution or peak SQNR of an N -bit converter is approximately $6N$ dB; therefore, we often say that 1 bit is equivalent to 6 dB.

The *signal-to-noise-and-distortion ratio* (SNDR) of a data converter is defined as the ratio of the signal power to the signal-band noise and distortion power measured at

Figure 5. An illustration of Shannon’s sampling theorem. The bandlimited analog input signal r is sampled uniformly in time at a sampling rate f_s [note that the sampling interval is given by $T_s = (1/f_s)$]. In the figure, the quantity Ω refers to frequency f in radians per second (i.e., $\Omega = 2\pi f$); the quantity ω is normalized frequency [i.e., $\omega = 2\pi(f/f_s)$] in radians per second. The sampled spectrum $R_d(e^{j\omega})$ consists of copies of the original spectrum $R(j\Omega)$ centered at integer multiples of the sampling frequency. To avoid aliasing (i.e., overlap and superposition of the copies), it is sufficient for f_s to exceed $2f_b$. Note that a generalized sampling theorem exists for bandpass signals that can reduce sampling rate requirements in many applications [12].



the output of the converter. *Noise* includes quantization error, modeled as a random process, and uncorrelated noise arising from circuit components. *Distortion* refers to signals that correlate with the input signal that are often harmonically related to frequency components of the input. The *signal-to-noise ratio* (SNR) is similar to the SNDR, but distortion frequency components are ignored in the calculation.

The DR of a data converter, obtained as illustrated in Fig. 9, is the ratio of the power level of the largest allowable input signal to the power level of the input signal corresponding to an SNDR of unity. The “largest allowable input signal” is the input signal that yields a specified drop in SNDR (sometimes 3 dB [13]) beyond the maximum SNDR. Dynamic range, SNDR, and SNR/SQNR are often expressed in units of bits (where, as mentioned above, 1 bit is equivalent to 6 dB). The *effective number of bits* (ENoB) is usually obtained by dividing the DR (in dB) by 6 dB/bit

and provides a measure of the true accuracy of the converter. For example, a 16-bit converter with a dynamic range of 72 dB is accurate to only 12 bits, and, therefore, has an ENOB of 12.

2.1. Nonidealities

Practical data converters typically fall short of ideal performance (specified, e.g., in terms of SNDR or DR). As mentioned, performance flaws can often be traced to mismatches between constituent elements. For example, in the binary-weighted D/A of Fig. 2, each current source must be exactly one-half the size of the next-larger current source in order to achieve an ideal characteristic. Any error in sizing results in a corresponding deviation of the converter characteristic from ideal. The precision with which these elements can be sized depends on the manufacturing technology.

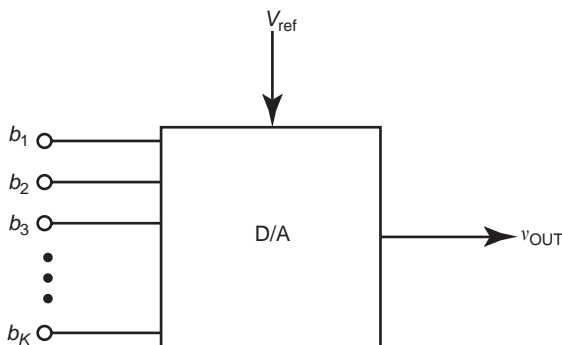


Figure 6. A generalized D/A converter. The binary input word $\{b_1, b_2, \dots, b_K\}$ describes a conventional (signed or unsigned) code ($K=N$) or a thermometer code ($K=2^N - 1$).

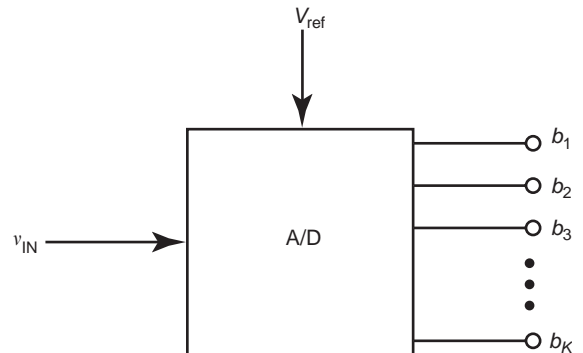


Figure 7. A generalized A/D converter. The analog input signal v_{in} is “within a least significant bit” of the binary output word, $\{b_1, b_2, \dots, b_K\}$. For conventional (signed or unsigned) codes, $K=N$, and for thermometer codes, $K=2^N - 1$.

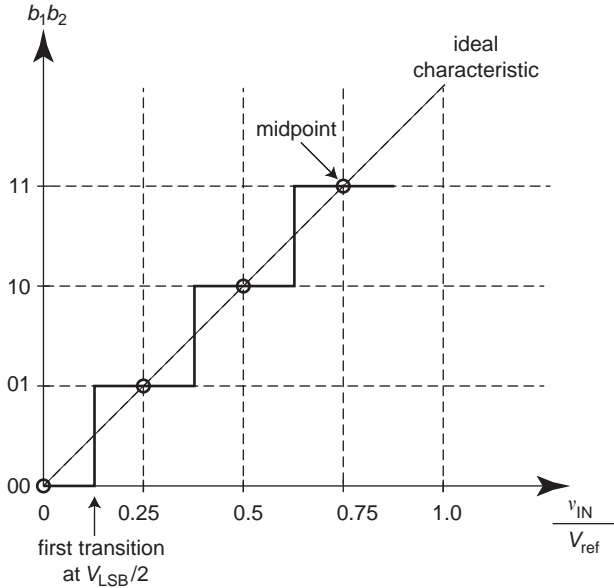


Figure 8. Ideal A/D staircase characteristic (shown here for a 2-bit converter), shown for positive values of v_{in} only. The midpoints of each output are indicated; transitions occur at analog input amplitudes $V_{LSB}/2$ away from the midpoints.

In Fig. 10, we superimpose the ideal and actual (D/A) characteristics to illustrate the various nonidealities that can be observed. For D/A converters, *offset error* is measured as the output corresponding to a zero input (i.e., the input defined by setting all bits to zero), often normalized

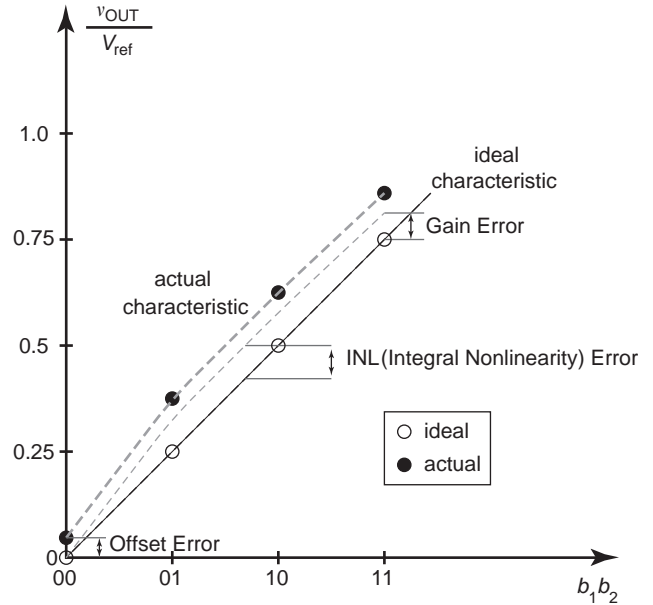


Figure 10. Plot of a 2-bit D/A converter characteristic. Deviations of the actual characteristic from ideal behavior are characterized using a variety of static metrics including offset, gain, and integral nonlinearity errors. Note that the offset error is typically removed before gain and nonlinearity errors are measured.

by V_{LSB} . To find the offset error for A/Ds, we measure the deviation of the lowest transition voltage of the input away from $V_{LSB}/2$. The notion of *gain error* is the endpoint difference between two straight lines (with offset error removed), as illustrated in Fig. 10; one line is defined by the ideal characteristic (for either A/D or D/A converters), and the second line has a slope computed using the extremes of zero and “full-scale” inputs.

Nonlinearity is characterized as either *differential* or *integral*, and is computed after offset error is removed. For D/A converters, differential nonlinearity (often abbreviated as DNL) is given by the difference between the largest step (between two adjacent binary input codes) and V_{LSB} ; integral nonlinearity (often abbreviated as INL) is the largest deviation of the actual characteristic from a straight line drawn between the endpoints of the characteristic [1]. Differential and integral non-linearities are calculated in much the same way for A/D converters. Differential nonlinearity is the difference between the largest increase in the analog input needed to generate a transition between consecutive digital output codes and V_{LSB} . Integral nonlinearity is largest difference between the actual A/D characteristic and the straight line formed by joining the endpoints of the actual characteristic.

SNDR vs. Input Signal Magnitude for a Hypothetical Data Converter

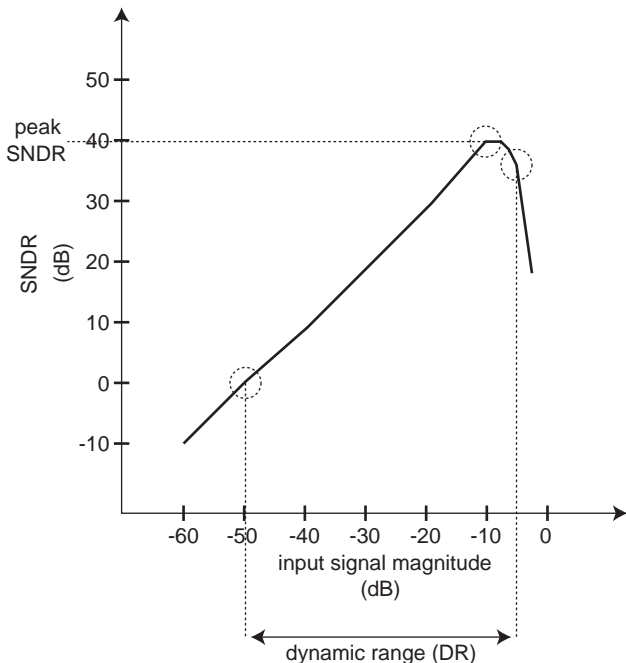


Figure 9. Illustration of SNDR variation with input signal magnitude for a hypothetical data converter. The peak SNDR and DR are indicated on the plot.

3. OVERVIEW OF D/A CONVERTER ARCHITECTURES

The digital-to-analog (D/A) converter is one of the basic building blocks of most analog/digital interface systems. For example, in audio-CD players and music synthesizers, D/A converters with accuracy as high as 16–24 bits are desired for speeds in the range of few kilohertz.

Telecommunication applications like radio transmitters require D/A converters (DACs) operating at hundreds of MHz for resolutions in the range of 10–15 bits.

There are several architectures for D/A converters depending on the speed, resolution, complexity, and area requirement [14]. In this section, we will focus on one particular type of D/A converter commonly known as a *current steering array*, which offers high-speed D/A conversion using current as a *unit* element for analog computation of digital input. Other formats such as switched-capacitor architectures or resistor ladder architectures are also used for D/A conversion. In switched-capacitor D/A converters, charge across unit capacitors is used as the *unit* for analog computation instead of current. Such architectures are popular in the design of a coarse D/A converters, also called *multiplying D/A converters* (MDACs) in pipelined A/D converters. Such architectures are introduced in another section on pipelined converters. A resistor ladder architecture uses voltage drop across the *unit* resistors as a basic *unit* for analog computation. More information about resistor ladder DACs and switched capacitor DACs can be found in the literature [1,11,14].

For most applications, the main performance measure for a D/A converter is its spurious-free dynamic range (SFDR). The SFDR measures the ability of the D/A converter to suppress the spurious harmonic tones generated as a result of circuit and system nonidealities. In case of current-steering D/A converters, the SFDR is limited by the matching of the unit current sources. Higher dynamic range is usually achieved through the use of dynamic element matching techniques discussed in brief toward the end of this section. There are three types of current steering D/A converters: binary-coded current steering DACs, thermometer-coded current steering DACs, and segmented current steering DACs. A conceptual binary-coded current steering DACs is shown in Fig. 2.

The binary DACs are not popular for high-resolution applications. This is because of the nonmonotonicity introduced due to current mismatch and momentary glitches during code transitions. Nonmonotonicity occurs because the amount of mismatch introduced by switching in of a new set of current sources for one LSB increase in

the input is greater than one LSB with an opposite sign. This causes the output to be nonmonotonic for increasing input. Glitches are another source of dynamic errors and are usually dominant during the worst-case code transition when input changes from 011...1 to 100...0. Because of finite delay in the ON time of the switches and mismatch therein, the MSB switch may turn on before (MSB goes from 0 to 1) the LSB switches (LSBs go from 1 to 0), causing a momentary output of all 1s. This glitch is equal to half the full scale and lasts as long as the delay mismatch between the MSB and the LSB switches. Such glitches are unacceptable for high-performance D/A converters since they affect the SFDR of the D/A converter.

The thermometer-coded D/A converter does not have the limitations described above. In a thermometer code D/A converter, all the current sources are of unit value, and are controlled by a monotonic thermometer code. A binary to thermometer digital logic is used to generate a thermometer code. Since an LSB increase in the digital input corresponds to a simple addition of another unit current source to the output, the monotonicity is guaranteed. Moreover, the glitch is completely eliminated as just one current source is switched on or off for one LSB change in the input. However, the main problem in a thermometer-decoded D/A converter is the complexity in the layout that is needed in generating a thermometer code for high-resolution binary input. Moreover the number of unit current sources to be individually controlled by the thermometer code increases exponentially. In most implementations, a combination of binary-coded D/A converters and a thermometer-coded D/A converter is used. An example for a $(M+K)$ -bit D/A converter is shown in the Fig. 11. Such converters are called segmented current steering DACs. A careful RAM-like physical layout usually achieves compact implementation of the thermometer-coded array. A segmented array offers a compromise between the complexity of layout for a thermometer-coded array and the amount of manageable glitch area from a binary-coded array.

In all the current steering D/A converters, the mismatch in the current sources introduces a systematic error wherein, for the same input, the error introduced is

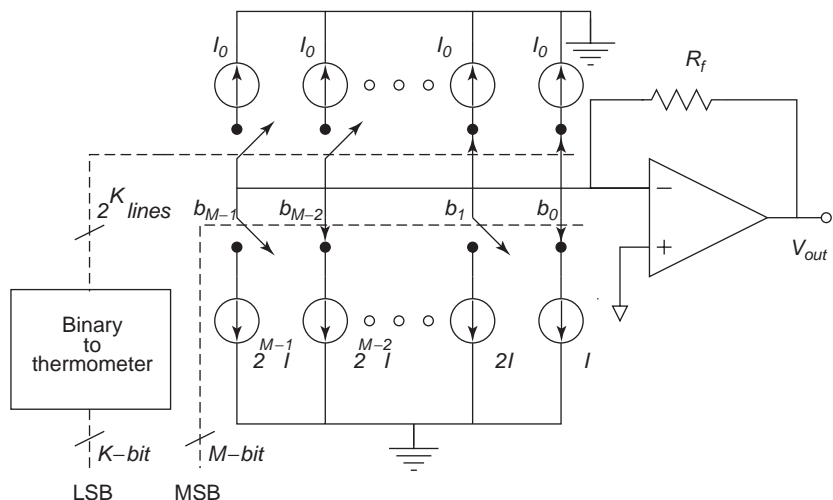


Figure 11. A popular segmented current steering D/A converter for $(N=M+K)$ -bit resolution. I is the unit current source, and currents are thermometer coded for the K most significant bits. The remaining M bits are implemented through a binary-weighted current steering D/A converter. The value of the unit current source in the binary-coded array is $I = 2^K I_0$, where I_0 is the unit current source for a thermometer array.

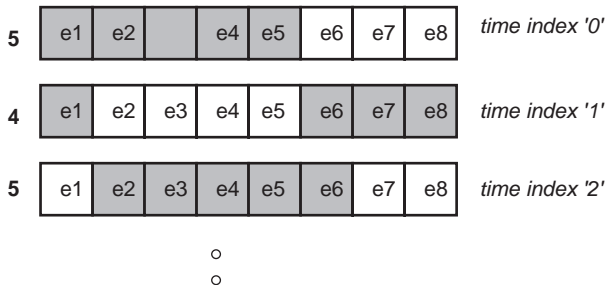


Figure 12. Data-weighted averaging illustrated for a 3-bit converter having eight unit current sources. The shaded squares correspond to the current sources chosen to generate the analog current-domain output. At time index 0, an input of 5 generates an output with a total mismatch error of $e_1 + e_2 + e_3 + e_4 + e_5$. At time index 1, the next four current sources (modulus 8) are chosen to generate an output with total mismatch error of $e_6 + e_7 + e_8 + e_1$. The next occurrence of 5 generates an output with total error of $e_2 + e_3 + e_4 + e_5 + e_6$, which is different from the previous occurrence of 5. A simple rotation scheme like this provides dynamic element matching through first-order shaping of the mismatch induced noise.

always the same because the same current sources are used in generating the output. Such systematic error introduces pattern noise in the form of spurious tones that appear as harmonics of the input signal frequency. Since harmonics are most undesirable in telecommunications and audio applications, techniques are needed to alleviate this problem. A dynamic element matching (DEM) techniques provide one such solution. Various DEM algorithms have been proposed in the literature offering different flavors, but their end goal is the same [14–17]. The main purpose of the DEM algorithm is to provide either random scrambling or permutation of the current sources such that the amount of error introduced by the D/A converter is not the same for the same input applied at two different time instants. This removes the systematic nature of the error signal and thus alleviate the problem of harmonics. However, depending on the schemes used, the harmonics either move at higher frequency or cause an increase in the noise floor (which can be tolerated in audio and telecommunication applications). A data-weighted averaging (DWA) technique proposed by Redman-White [14] is shown in Fig. 12. The technique provides first-order shaping of mismatch induced noise. However this technique still carries harmonics at higher frequency. Many variants of this technique have been suggested in the literature to avoid such tones [14,17].

4. OVERVIEW OF HIGH-SPEED A/D CONVERTER ARCHITECTURES

This section reviews the existing data converter architectures suitable for high-speed applications, with more emphasis on the analog-to-digital (A/D) converter design. A brief overview of digital-to-analog (D/A) converters is also provided for completeness. The architectures for the A/D converter discussed below are “flash,” “two-step,”

“interpolation,” “folding,” and “multistage” A/D converters. All the architectures discussed in this section pertain to single-channel ADC implementation. Time interleaved ADC perform parallel A/D conversion with a number of single-channel ADCs connected in parallel, offering high speed for a given resolution. However this is achieved at the cost of higher power consumption and increased area. Design issues related to time-interleaved A/D converters is discussed in detail in the literature [18], and is not discussed here. For communication applications, a behavioral survey and analysis of the A/D converters can also be found [19].

4.1. Flash Converters

Flash A/D converters are potentially the fastest ADCs and relatively easy to design compared to other architectures. Figure 13 shows the block diagram of a simple flash ADC. For an N -bit resolution, flash ADC consists of a resistor ladder that subdivides the main reference voltage into 2^N equally spaced voltage levels, and the $2^N - 1$ comparators to compare the input signal against these voltage levels. The output of a flash ADC is a thermometer code that is then passed on to the encoder to generate the binary output. Comparators usually consists of a moderate-gain preamplifiers followed by a regenerative-type latch to achieve high speeds. A sample comparator circuit is shown in Fig. 14. Transistors M_1 and M_2 along with the diode connected load form the input preamplifier. The preamplifier amplifies the difference between the input V_{in} and the

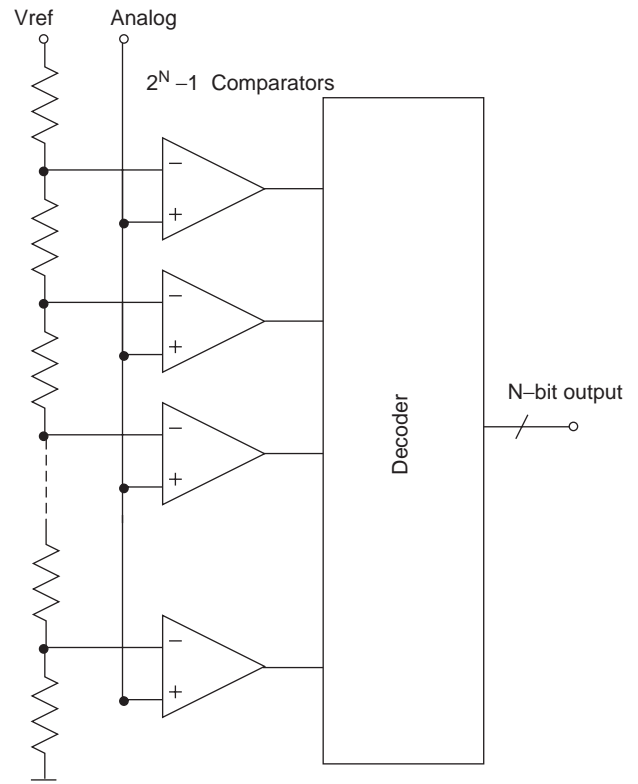


Figure 13. Conceptual flash A/D converter for an N -bit resolution.

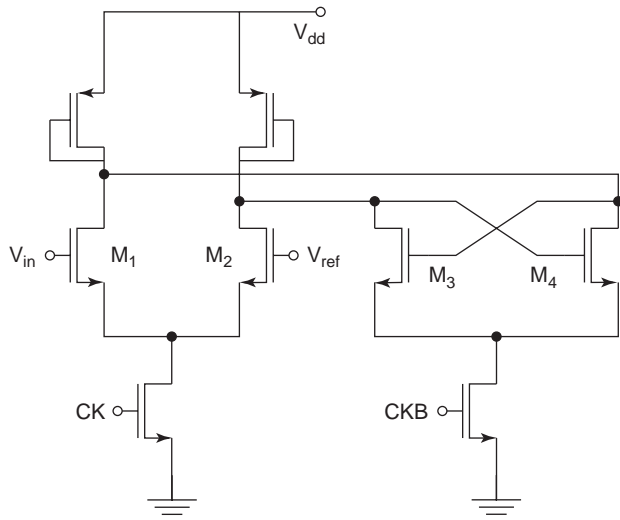


Figure 14. A simple comparator schematic: M_1 – M_2 form the input differential pair for preamplification. Transistors M_3 – M_4 form a positive-feedback latch for regeneration. CKB is opposite in phase to CK .

reference V_{ref} during clock phase CLK . This amplified difference is regenerated by the positive-feedback latch formed by transistors M_3 and M_4 , during clock phase $CLKB$. More comparator architectures can be found in the literature [1,11,18,20]. Flash ADC essentially performs distributed, parallel processing of the input signal, with no potential need for an explicit front-end sample-and-hold amplifier (SHA), resulting in the highest speeds among the data converter architectures. However, the number of components (e.g., resistors and comparators) increase exponentially with the overall resolution N of the converter. Also, higher resolutions are difficult to achieve from flash ADC because of various static and dynamic nonlinearities.

The main source of static nonlinearity in flash ADC appears from the offsets in the comparators and the resistor mismatch in the reference ladder. Input device transistors having large area is therefore needed to reduce the amount of offset, at the cost of increased nonlinear input capacitance. Large input capacitance at the input of the flash ADC also increases the load on the buffer driving the ADC, increasing its power consumption. Apart from large die-size and increased power consumption, flash ADCs also suffer from various issues such as metastability, kickback noise, slew-dependent sampling point, and clock jitter [1]. Metastability arises when the input to the flash A/D converter is very close to one of the comparator thresholds, which results in long settling times to regenerate the outputs to logic levels. This causes indeterminate latch outputs that are decoded incorrectly to give erroneous digital outputs. Metastability can be removed through gray coding as an intermediate step between the thermometer and binary codes [1]. Sparkles are also a source of static nonlinearity that arise directly from resistor mismatch and comparator offsets. Sparkles are caused when the comparator gives an *out-of-sequence* zero instead of a one due to these offsets. It is also caused by mismatch in

the sampling instants of the preamplifiers in the comparator array. Such sparkles can also be caused by slew-dependent sampling points. This occurs for rapidly varying input signals due to finite time between the tracking and the latching phase for certain implementations of the comparator. The rapidly varying input signal at the preamplifier input can cause the comparator to change its decision erroneously during the finite time between the latch phase and track phase. Such sparkles are removed through *bubble correction* in the thermometer to binary encoder. However, *bubble correction* can detect and correct for only a limited number of occurrences of sparkles. Gray-coding provides a soft degradation in performance for increasing number sparkles in the thermometer code and is therefore used in most flash A/D converter implementations. The slew-dependent sampling point and clock jitter can be minimized through the use of a dedicated sample and hold in front of the flash ADC at the expense of more power and area.

Two-step converter architectures trade speed for lower power consumption, small real estate, and lower input capacitance. Alternate architectures such as interpolation and folding maintain the one-step distributed nature of flash A/D conversion, and reduce the power consumption and real estate requirement of the pure flash ADC by reducing the number of preamplifiers and the latches needed in the implementation. Interpolation and averaging have also been shown to improve the differential nonlinearity performance (DNL) of the ADC [1,18].

4.2. Two-Step Converters

Figure 15 shows a two-step ADC architecture that has relatively small die size and low power consumption compared to flash ADCs. In a two-step ADC, the coarse flash A/D converter produces the most significant bit (MSB) decisions and the fine-flash ADC produces the least significant bit (LSB) decisions. The coarse D/A converter generates the coarse analog estimate of the input that has been resolved by the coarse A/D converter. This estimate is then subtracted from the input to generate the residue to be processed by the fine-flash ADC. The residue of the first stage is same as the quantization noise of the first stage, which indicates the portion of the input that is not resolved by the coarse A/D converter. The digital output of the coarse and fine ADC can be added appropriately to give the final ADC output.

Comparing the number of comparators needed in the two-step architecture versus the flash architecture, we can see that significant area savings can be achieved. An 8-bit flash ADC will require 256 comparators, whereas a two-step ADC, with a 4-bit MSB stage and a 4-bit LSB stage, will need only 32 comparators, which is a significant savings in the area. However, the speed of the two-step converter is less than that of a pure flash A/D converter, due to additional delays introduced by the D/A converter and the subtractor. The throughput of the two-step can be made comparable to the flash A/D converter, by adding a sample and hold between the two stages for pipelining. Pipelining can be extended to more than two stages and is covered in detail in a section on multi-stage converters.

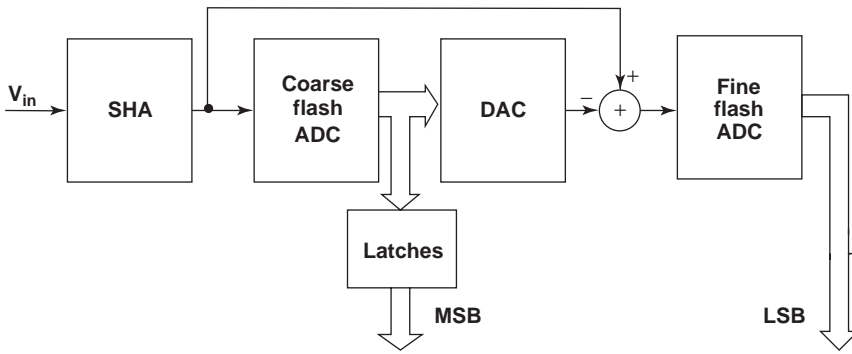


Figure 15. Conceptual schematic of a two-step A/D converter.

A main problem with the two step converter shown in Fig. 15 is that the residue generated for the fine-flash ADC is much smaller in magnitude, requiring that the coarse D/A converter and the subtracter be accurate to the overall resolution of the converter. To solve this problem, the residue output can be first passed through an inter-stage gain amplifier with a value of 2^M , where M is the resolution of the MSB stage, so as to make the signal swings same for both the coarse and fine ADCs. This also relaxes the offset requirement for the comparator of the fine-flash ADC. As in pipelined converter, if digital error correction is used, the accuracy requirements of the coarse A/D converter is greatly relaxed too. Some implementations of the two-step architecture can be found in the literature [21–23].

4.3. Interpolation-Based Flash Architectures

To reduce the input capacitance, power dissipation, and large area required from flash A/D converters, interpolation

can be used. The main idea behind interpolation is to use the linear region of the adjacent preamplifiers to generate additional thresholds for comparison, and hence reduce the number of preamplifiers needed for a given resolution [1,11,18,20].

In flash converters, the linearity of the preamplifier in the comparator is a nonissue, since only the sign of the amplifier outputs is needed for making a decision. However, in case of interpolating flash A/D converters, the linearity of the preamplifiers is needed at least over a small range of the input signal. The overall one-step nature of the flash conversion is still maintained in the interpolating flash A/D converters. Figure 16 shows the basic architecture for interpolation in flash A/D converters for a case of interpolation by 2. For this example, an additional output is generated as an average of the two adjacent preamplifier outputs using a resistor or capacitive dividers as shown in the figure. Since, the additional output resembles a preamplifier output for the threshold at the midpoint of the adjacent comparator thresholds, the number

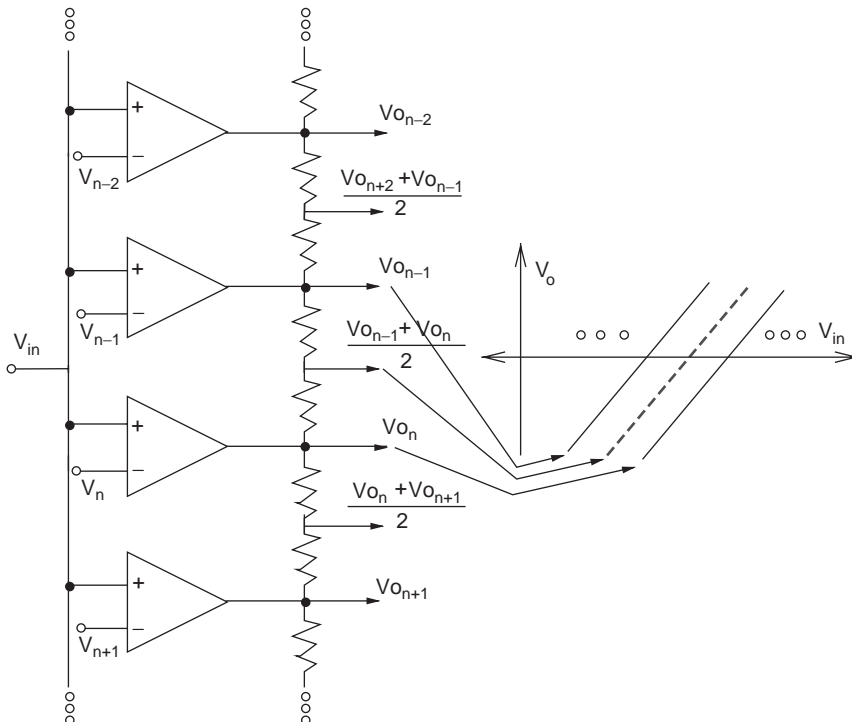


Figure 16. Conceptual schematic of an interpolating A/D converter using resistors. The interpolation is by 2. The dotted line indicates the interpolated waveform generated from the adjacent preamplifier outputs. The outputs V_o feed the latch to regenerate to logic levels (latch not shown).

of preamplifiers has been reduced by 2 for this flash A/D converter for the given resolution. Thus a reduction in the number of preamplifiers is achieved for a given resolution by interpolation. But the overall number of latches required is still the same as in a pure flash A/D converter. To further reduce component count and power consumption, interpolation is generally used alongside *folding* to enable further area and power savings [24]. Folding will be discussed in detail in the next section. Interpolation can also be pipelined to offset the lower speed and bandwidth attributed to resistive loads, to increase throughput [25].

Interpolation indicates that effective resolution of the flash A/D converter can be increased by interpolating between the outputs of the adjacent preamplifiers. An interesting property of the interpolation is that it improves the differential nonlinearity of the original flash converter. This is evident in Fig. 16, which shows that the effective interpolated reference threshold (level) generated lies between the thresholds of the adjacent preamplifiers, which guarantees that the differential nonlinearity for the interpolated threshold is bounded and is less than that of its pure flash counterpart. The reduction in DNL increases with the factor of interpolation. Since the accuracy of the interpolation depends on the linearity of the preamplifiers, a wider range between the preamplifiers would be required for a higher interpolation factor. Any nonlinearity when interpolating between preamplifiers not in the linear region, can cause deviation of the interpolated threshold from its ideal value or even a deadband around the interpolated threshold. The main problems of interpolation are the added time constants introduced by the interpolation resistors and capacitances from the following latches, sacrificing speed of conversion. The reduction in bandwidth scales approximately with the square of the interpolation factor, thereby making interpolation not feasible for factor exceeding 4. A conceptual schematic of a folding ADC is illustrated in Fig. 17.

4.4. Folding A/D Converters

In folding A/D converter (shown in Fig. 17), the speed trade-off of the two-step converter is mitigated by generating

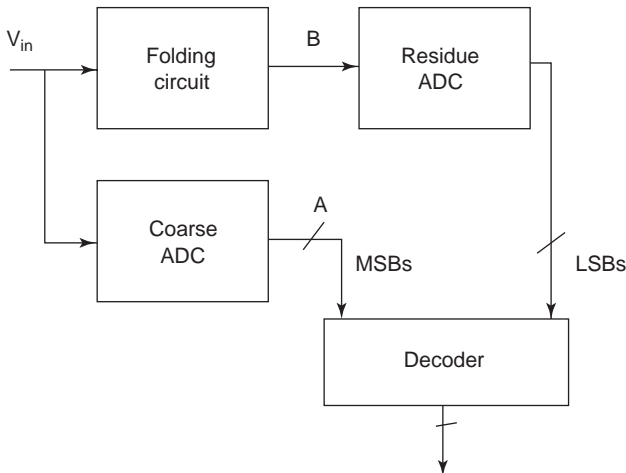


Figure 17. Conceptual schematic of a folding A/D converter.

the residue for the fine flash ADC of Fig. 15 in parallel using a separate analog preprocessor and is generated independent of the coarse MSB flash stage [1,11,26]. This eliminates the need for the D/A converter and a subtractor, resulting in power savings and reduced delay. The analog pre-processor uses a technique called “folding” to generate the residue independent of the MSB decisions. A simple voltage mode differential folding circuit for a folding factor of 4 is shown in Fig. 18. A folding factor is defined as the number of times the output changes sign (or direction) as the input V_{in} varies over its input range. The input-output characteristic of the folding circuit is also shown in Fig. 18. The ideal expected folder waveform is shown by the triangular dotted line. This is related to the sawtoothlike residue output of the first stage in the two-step ADC through simple reversal of signs and level shift operations. Hence, the folder output waveform can be used by the fine-flash stage instead of the sawtoothlike ideal residue output to generate LSBs. The operation of the circuit in Fig. 18 is given below. When the input is below V_{r1} , transistors $M_1, M_3, M_5,$ and M_7 are off and $M_2, M_4, M_6,$ and M_8 are on. A total of $2I_b$ flows through R_1 and $3I_b$ flows through R_2 , pulling down voltage at node $OUT -$ by $I_b R$ below the voltage at node $OUT +$. When input is equal to V_{r1} , equal currents $I_b/2$ flow through transistors M_1 and M_2 . However, transistors $M_3, M_5,$ and M_7 are still off and $M_4, M_6,$ and M_8 are still on. This, in essence, steers current $I_b/2$ from resistor R_2 to R_1 , causing equal currents of $2.5I_b$ to flow through both resistors and voltages at the node $OUT +$ and $OUT -$ are equal. As input is increased from V_{r1} , but maintained less V_{r2} , M_1 turns on and M_2 turns off. A total of $3I_b$ current now flows through R_1 and $2I_b$ flows through R_2 . This causes node $OUT +$ to be $I_b R$ lower than the node $OUT -$. As input approaches V_{r2} , M_3 begins to turn on and M_4 begins to turn off, causing the current to steer from R_1 to R_2 , and the output at node $OUT +$ and $OUT -$ changes direction. The circuit behaves in a similar manner as V_{in} is increased further. The number of times the output slope changes sign is equivalent to the number of times, the excess current steers between R_1 and R_2 . This number is also equal to the folding factor of the ADC.

It is to be noted for best performance, the folding circuit should have exactly one differential pair switch for any given input voltage, which mandates that the reference levels should be spaced far apart. However, this will cause saturation of the outputs for inputs closer to the midpoint of the two reference levels and none of the differential pairs would switch, resulting in deadband and inaccurate folder output around this input region. The main advantage of folding is that it maintains the one-step operation of flash, and does not need a subtractor and interstage D/A converter as in two-step converter, potentially achieving high speeds. Even though the sample-and-hold amplifier is not ideally needed for the folding A/D converter, it is used nevertheless to avoid input dependent errors resulting from clock skew and jitter. In spite of speed improvements, folding suffers from a few drawbacks. One of them is the increased frequency specifications for the design of the folding circuit. If a ramp input varying from 0 to full scale is applied to the folder with folding factor n , the output of the folder will change from V_{min} to V_{max} , n times.

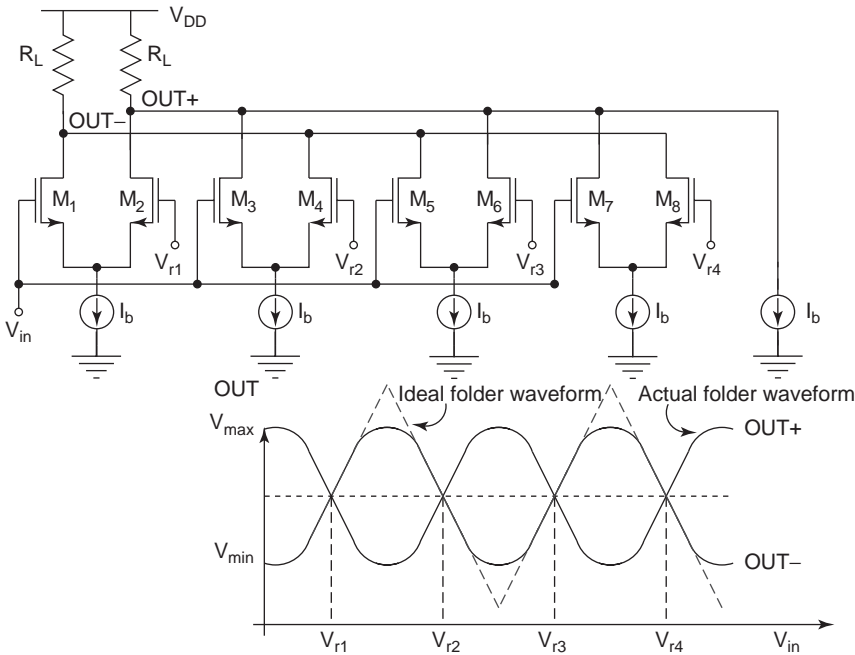


Figure 18. Differential folding circuit that has a folding factor of 4. The folder output feeds the latches that regenerate its output to logic levels. In case of folding and interpolating ADC, the outputs of the folder may be averaged by a resistor network.

This effect results in frequency multiplication by n . Hence the bandwidth and slewing requirements for the folder is n times the maximum allowable input frequency. Therefore, folding with a high folding factor is not effective at high operating frequencies. Another drawback of the folding is substantial nonlinearity in the folder waveform. Comparing the ideal dotted waveform and the actual waveform in Fig. 18, it can be seen that the output of the folder is grossly inaccurate toward the peaks V_{\max} and V_{\min} . The effect is similar to residue errors in a two-step converter or a pipelined converter which cause integral nonlinearity or differential nonlinearity. To alleviate this problem, double folding can be used, where the folding waveform is replicated with an additional shift of half the distance between the two reference levels. This ensures that in the region where one of the folders exhibit nonlinearity due to rounding effect, the other folder exhibits high linearity. Then depending on the input level an appropriate folder can be chosen.

The other main drawback of the folding architecture is the need for synchronization in absence of sample-and-holds between the MSB output and the output of the fine stage following the folder. Furthermore, any offset in the MSB stage may result in gross overall error with the magnitude as high as half of the full scale. Folding is usually used along with interpolation to further alleviate the linearity requirement of the folder and for obvious area savings due to reduced number of preamplifiers [1,24]. When interpolation is used between folder outputs for additional comparison thresholds, the nonlinearity of the folder output waveform does not directly affect the overall linearity and resolution of the converter, since the A/D converter extracts all its information from the location of the comparison thresholds (or zero crossings) and not from the amplitude of the folding waveform. However, this does not imply that the folder waveform can be nonlinear, since the accuracy of the comparison thresholds generated after

interpolation depends on the linearity of the individual folder waveforms over a large input range. The folding operation can also be pipelined to increase throughput and relax design requirements on the individual folders [6,27].

4.5. Multistage Converters

A multistage converter is a natural extension of the two-step converter discussed in Section 4.2, where more than two stages are used for digitization [1,11,18,28,29]. The second stage in the two-step ADC will also now consist of a sub-D/A converter and subtractor to generate a residue output that can be further digitized by the following stages that may appear identical to the first two stages. Use of an interstage gain amplifier relaxes the resolution requirement of the D/A converter and subtractor and also enables the use of the same flash ADC for all its stages. The bandwidth and the gain of the amplifier used in the MDAC is limited by the op-amp (operational amplifier) settling time, which depends on the speed and resolution specifications of the overall ADC. For an A/D converter without calibration, the finite op-amp gain needed is usually of the order of 2^{M+1} , where M is the number of remaining bits resolved by the following stages in the ADC. The overall speed of the multistage ADC reduces the conversion rate by the number of stages in the ADC, for the same reasons as in a two-step converter. This also puts stringent requirement on the timing skew for the subtractors for each stage. To alleviate this problem, a sample-and-hold amplifier is added at every stage to hold the amplified residue before passing on to the next stage [1,30]. This also increases the overall throughput of the system; the speed is limited by the delay of only one stage. Such an ADC is also called “pipelined” ADC because of the inherent concurrency of the operations. The pipelined converter is discussed in greater detail in the following section.

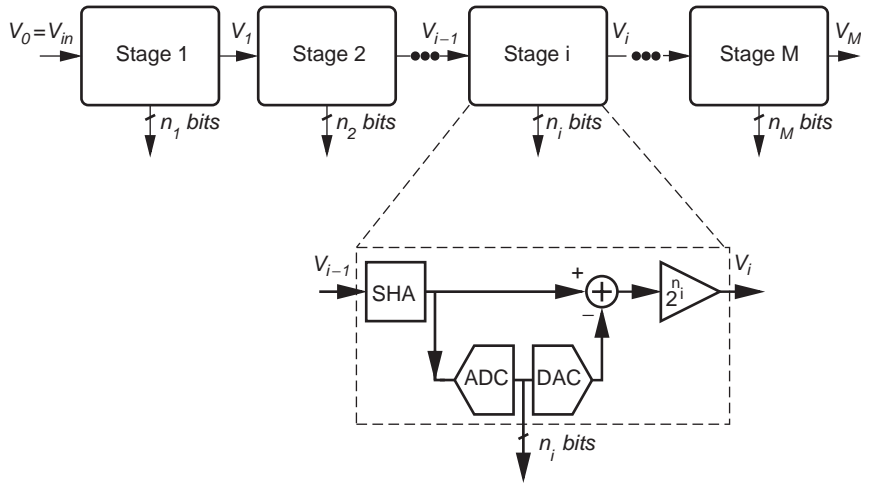


Figure 19. A generic block diagram of a pipelined ADC.

4.6. Pipelined Analog-to-Digital Converters

Pipelined A/D converters (ADCs) are multistage converters that use interstage sample-and-hold amplifiers to enable pipelining and concurrent processing of the input signal [1,18,31–33]. The residue output of one stage is kept on hold and the pipeline stage is not tied up for the fine LSB decisions to be carried out by the following stages. On the contrary, it can sample the next input data for conversion, while the previously held residue signal in the subsequent stage is digitized to make the LSB decisions. Thus pipelined A/D converters behave in concurrent manner and the overall data rate becomes independent of the number of stages. The overall speed is limited only by the speed of one pipeline stage, and therefore a pipelined converter can achieve close to the speeds achieved by flash ADC. Also, the complexity of the pipelined converter ideally scales linearly with the resolution desired, compared to flash which is exponentially related to the desired resolution. This is really beneficial for ADCs with resolutions greater than 8 bits at higher speeds.

5. BASIC PRINCIPLES OF PIPELINED A/D CONVERSION

A simplified block diagram of a multibit per stage pipelined ADC is shown in the Fig. 19. Each stage i resolves its input (or in other words, quantizes its input) into n_i bits of digital output using a coarse ADC (typically a flash-type converter) and then uses a coarse DAC, a subtractor, and an interstage gain amplifier of gain 2^{n_i} to amplify the unresolved input which we had defined as the residue. The operation of D/A conversion, subtraction, and amplification is designated as a MDAC (multiplying D/A conversion) operation. In switched-capacitor implementation, each stage has two nonoverlapping phases of operation: The sampling phase and the MDAC phase. During sampling phase, the residue output of the previous stage (or input if the stage in the first stage in the pipeline) is sampled and held later for subtraction. During this phase, a coarse decision is also made. During the MDAC phase, the MDAC operation is carried out. This is the time when the sampler of the following stage will be

active. The waveform for consecutive pipeline stages is shown in Fig. 20.

When stage 1 is sampling input sample for time index n , stage 2 is performing MDAC operation over the residue output of stage 1 corresponding to sample $n - 1$, and stage 3 is sampling this residue output corresponding to sample $n - 1$, and so on. A pipelined converter therefore exhibits a concurrent nature of processing of input, enabling high-speed operation. As mentioned earlier, the complexity of the pipeline, measured in the number of stages, scales linearly with the desired resolution and therefore pipelined A/D converters show substantial power and area savings for high-resolution applications at high speed.

In the pipeline architecture, as in all multistage ADC, the most significant bits are resolved by the stages earlier in the pipeline and the least significant bits are resolved later in the pipeline. A simple example for a pipeline would be a 1-bit per stage architecture ($n_i = 1$). Each stage of such a pipeline will consist of a simple 1-bit comparator as a coarse ADC, a multiply-by-2 DAC (MDAC) that performs coarse D/A conversion, subtraction, and interstage amplification by 2. A conventional switched-capacitor implementation of a one-bit pipeline stage is shown in Fig. 21. A single ended circuit is shown for simplicity. V_{ref} is the value of the reference voltage, where the complete resolvable input range is $\{-V_{ref}, +V_{ref}\}$ [18,34,35].

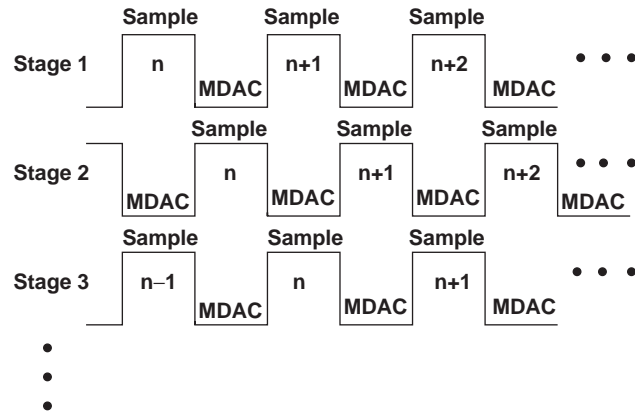


Figure 20. Timing diagram of a pipelined ADC.

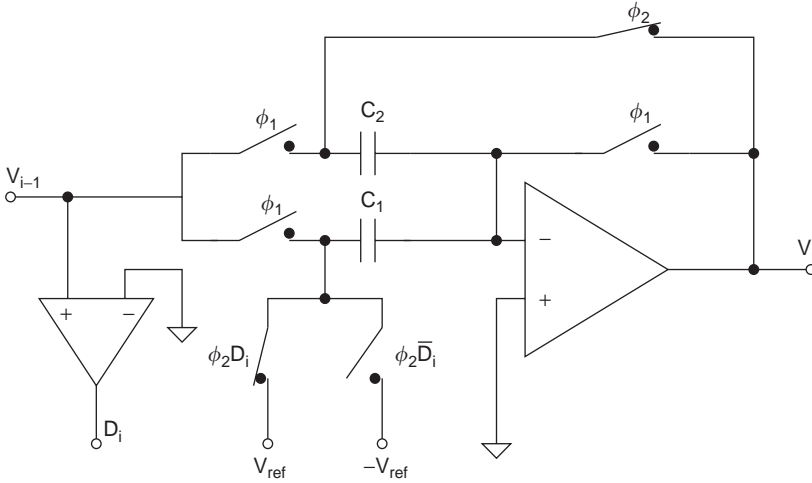


Figure 21. Switched-capacitor (SC) 1-bit pipeline stage (ϕ_1 -sampling phase, ϕ_2 -multiply-by-2/subtract phase).

Each stage consists of two nominally equal capacitors C_1 and C_2 , an operational amplifier (op-amp), and a comparator. During the sampling phase ϕ_1 , the comparator produces a digital output D_i by comparing its input V_{i-1} with comparator threshold V_{th}

$$D_i = \begin{cases} 1 & \text{if } V_{i-1} \geq V_{th} \\ -1 & \text{if } V_{i-1} < V_{th} \end{cases} \quad (8)$$

where $V_{th}(=0)$ is the threshold voltage of the comparator. The bipolar representation $\{-1, +1\}$ for the digital bit D_i is chosen instead of $\{0,1\}$ to facilitate analysis of the pipelined ADC for differential inputs. During the multiply-by-2/subtract (ϕ_2) phase, known as the MDAC phase, the circuit generates a residue voltage output V_i given by

$$V_i = K \left[\left(1 + \frac{C_1}{C_2} \right) V_{i-1} - \frac{C_1}{C_2} D_i V_{ref} \right] \quad (9)$$

$$K = \frac{A_0}{1 + \frac{C_1}{C_2} + A_0}$$

where the parameter K is an op-amp gain error coefficient (ideally unity) and A_0 is the finite op-amp gain. V_{i-1} is the residue output of the previous stage (for the first stage, the input is $V_0 = V_{in}$). The output residue voltage of the stage i is then passed to the next stage $i+1$, and the same operation continues. Ideally, we expect the residue output voltage to be

$$V_i = 2V_{i-1} - D_i V_{ref} \quad (10)$$

The ideal residue output of a one-bit pipeline stage is shown in Fig. 22, assuming $\{-V_{ref}, +V_{ref}\}$ as the resolvable input range. We see that as input is increased from $-V_{ref}$ to $+V_{ref}$, the output spans the full scale twice, once for the output $D_i = -1$ and for the output $D_i = +1$.

For a multibit per stage pipeline, consider a simple conceptual switched-capacitor implementation in Fig. 23, which indicates a n_i bit per stage output realization. When no error correction is used (see following section), a n_i bit per stage pipeline stage consists of a total of n_i capacitors $C_1, C_2, \dots, C_{2n_i}$. During the sampling phase the sub-ADC

compares the input with a set of reference voltages possibly a reference ladder to generate the raw bit decisions. At this time the input is also sampled across the 2^{n_i} capacitors. During the MDAC phase, one of the capacitors is connected across the operational amplifier, and the thermometer code corresponding to the raw bit decisions made is applied to the remaining capacitors. This produces an amplified residue output of this stage that will be processed by subsequent sections. The ideal expression for the residue output is given by

$$V_i = 2^{n_i} V_{i-1} - \sum_{k=1}^{k=n_i} 2^{(n_i-k)} D_{Sn_{i-1}+k} V_{ref} \quad (11)$$

The digital output of stage i is $\{D_i : i = Sn_{i-1} + 1, Sn_{i-1} + 2 \dots Sn_i\}$, where $D_{Sn_{i-1}+1}$ is the stage i MSB and D_{Sn_i} is the stage i LSB. Here the variable Sn_i indicates an index to conveniently tag the digital output of the stage i

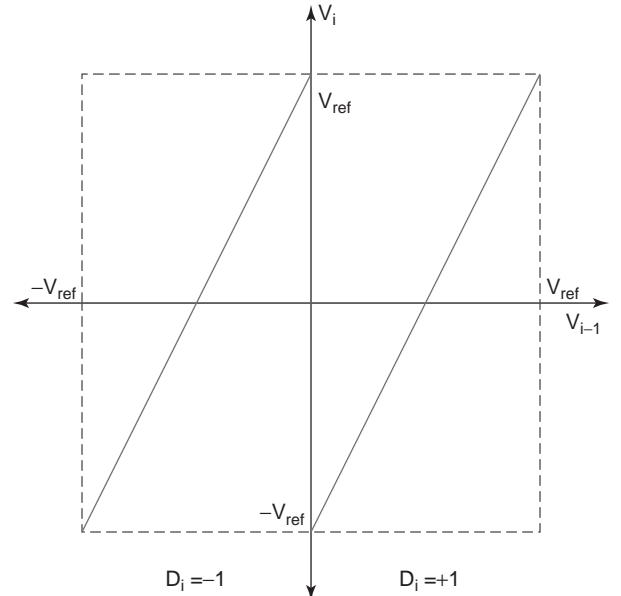


Figure 22. Ideal residue output of a 1-bit pipeline stage.

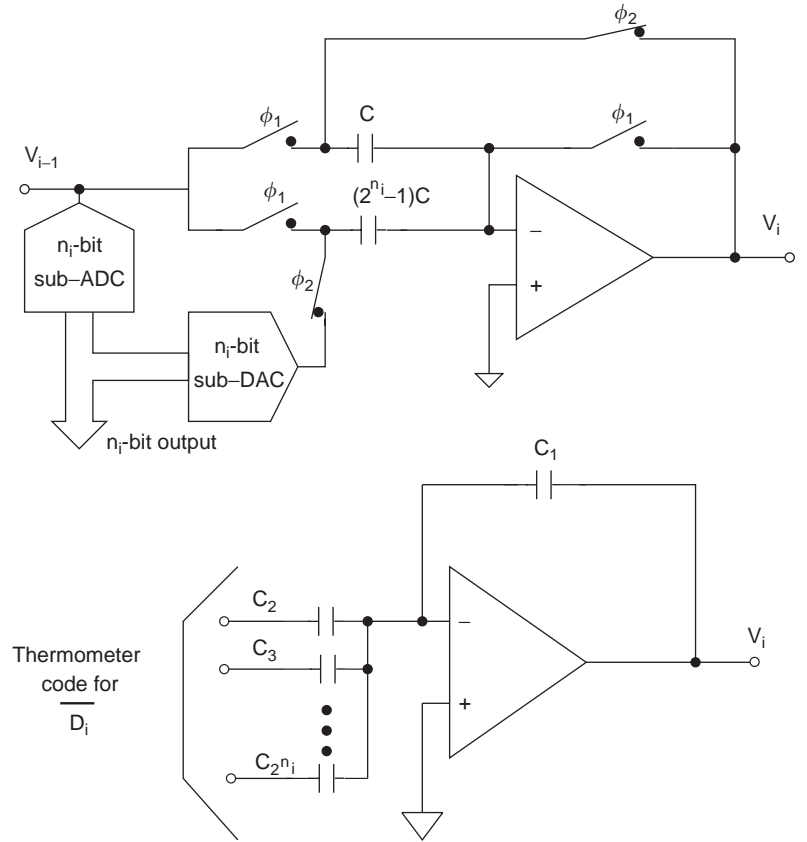


Figure 23. Example of a switched-capacitor (SC) implementation of a multibit pipeline stage.

and is given by

$$S n_i = \sum_{k=1}^{k=n_i} n_k \tag{12}$$

$$S n_0 = 0$$

The ideal residue output for a multibit pipeline stage looks similar to the one-bit case and is shown for a 2-bit pipeline stage in Fig. 24. The bipolar digital outputs for each region are also highlighted in the figure. The main points to note from the residue output plots for an ideal pipeline stage, is that the output spans the complete range of $\{-V_{ref}, +V_{ref}\}$, so that each stage input has the same dynamic range. This guarantees linearity for the complete pipelined converter. As is evident from the Eqs. (9) and (10) for a singlebit pipeline, the accuracy of a pipeline stage and hence of the overall converter depends on the accuracy of the residue output generated by the pipeline stage. We see that gain errors are introduced in the overall transfer characteristic because of the term K attributed to the finite amplifier gain and the term C_1/C_2 , which deviates from the ideal value of 1 because of poor capacitor matching. The same case is also valid for any multibit pipeline stage. For comparator offsets, the output of the pipeline stage will exceed the allowable input range of the following stage. This results in the *missing decision levels* in the overall ADC transfer characteristic. This is undesirable, since the information about the input is completely lost and cannot be recovered further. Other sources of errors due to capacitor ratio mismatch and finite amplifier gain

error result in *missing codes* in the overall transfer characteristics if the overall gain is less than nominal. Although this is undesirable, it is preferred over the case with missing decision levels, since the information about the input is not lost and can be recovered through calibration. Finally, it can also be seen that any nonlinearity in the operational amplifier will affect the linear output curve of the residue and contribute to the overall

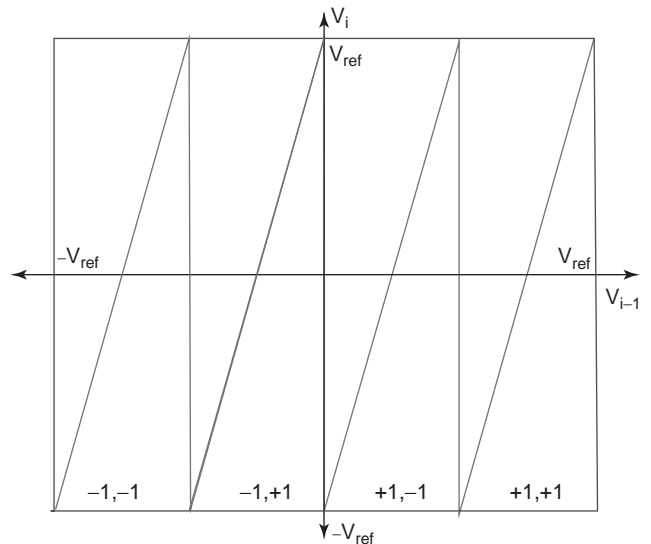


Figure 24. Ideal residue output of a 2-bit pipeline stage.

INL of the ADC. These nonidealities along with errors due to finite amplifier settling and charge injection errors usually limit the overall resolution of the ADC to 8–10 bits without calibration in today's CMOS processes. Charge injection errors can be minimized using bottom-plate sampling techniques [11], and the effect due to comparator offsets can be mitigated through the use of error correction or redundancy [31]. This concept is discussed in the next section.

6. DIGITAL ERROR CORRECTION THROUGH REDUNDANCY

Nonlinearity due to comparator offsets can be mitigated through the use of redundancy [18,31]. For example, with one-bit error correction in a n_i bit per stage pipeline, the interstage gain is chosen as $2^{(n_i-1)}$ instead of 2^{n_i} allowing redundancy so that inputs closer to comparator thresholds that would possibly result in swings beyond the allowable input range can now be resolved by the following pipeline stages.

Consider the modified switched capacitor implementation that incorporates one-bit redundancy (Fig. 25). The stage now consists of two comparators with thresholds on either side of $V_{th} = 0$, one at $V_{ref}/4$ and the other at $-V_{ref}/4$. Also, three different D/A converter outputs are used during the MDAC phase. The main idea behind redundancy is to let prevent the overrange of the residue output when the input is between the two thresholds. This prevents any missing decision levels and improved DNL performance. The expression for the residue output of this 1.5-bit pipeline stage is

$$V_i = 2V_{i-1} - D_i V_{ref} \quad (13)$$

where D_i is just a conceptual term that can have one of three values $\{-1, 0, 1\}$ instead of the previous bipolar representation $\{-1, 1\}$.

Table 1 suggests the relationship between D_i and D_{i1} and D_{i2} . The residue output of a 1.5-bit pipeline stage is shown in Fig. 26. The transfer characteristic of a 1.5-bit pipeline stage suggests that comparator offsets of up-to

Table 1. Relationship between D_i , D_{i1} , and D_{i2}

D_i	D_{i1}	D_{i2}
-1	-1	-1
0	+1	-1
+1	+1	+1

$|V_{ref}/4|$ can be tolerated without the residue exceeding the following stages resolvable input range.

The digital outputs of individual pipeline stages are now combined by overlapping the adjacent bits as shown in the Fig. 27. A unipolar representation is used for this illustration where the digital output is 00 when input is less than $-V_{ref}/4$, and 01 when the input is between $-V_{ref}/4$ and $+V_{ref}/4$ and 11 when input is greater than $+V_{ref}/4$.

However, to correct for errors due to capacitor ratio mismatch and finite amplifier gain, calibration schemes (also called error correction schemes in the literature) have to be used. Redundancy will not suffice enough to guarantee a good linearity from the converter, since the shape of the curve still depends on the capacitor ratio mismatch and the finite amplifier gain. Calibration has become an essential building block in today's pipelined data converters designed in deep-sub-micrometer CMOS due to poor technology parameters for realization of analog components such as capacitors, amplifiers, and reference circuits. Without calibration, the resolution of the data converters is limited to 8–10 bits for speeds under 100 MHz in CMOS.

6.1. Linearity Improvement Techniques

Data converters designed in digital CMOS technology for low-cost implementations and to facilitate higher integration do not offer high resolution because of poor component matching, low amplifier gains attributed to lowering supply voltages, charge injection errors, and offset errors. For example, in case of a current steering D/A converter, it is necessary that all the unit current sources be matched to each other. Otherwise, the D/A converter will exhibit nonuniform output transitions, giving rise to static

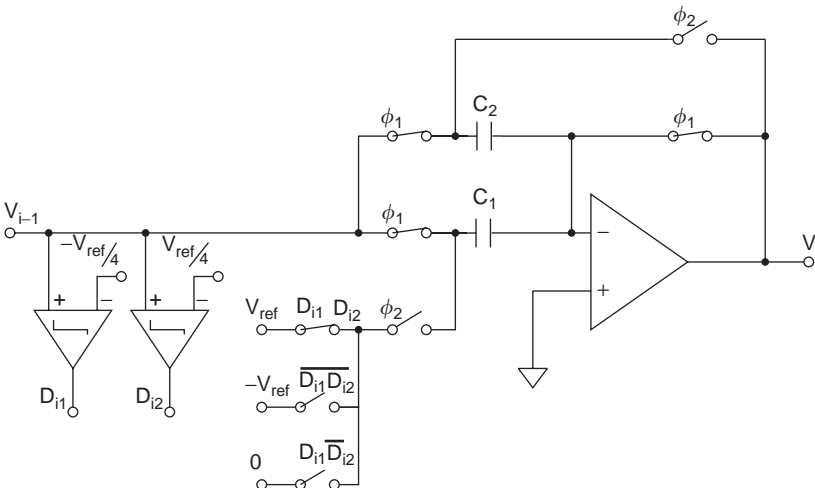


Figure 25. A 1.5-bit pipeline stage that exhibits one-bit redundancy.

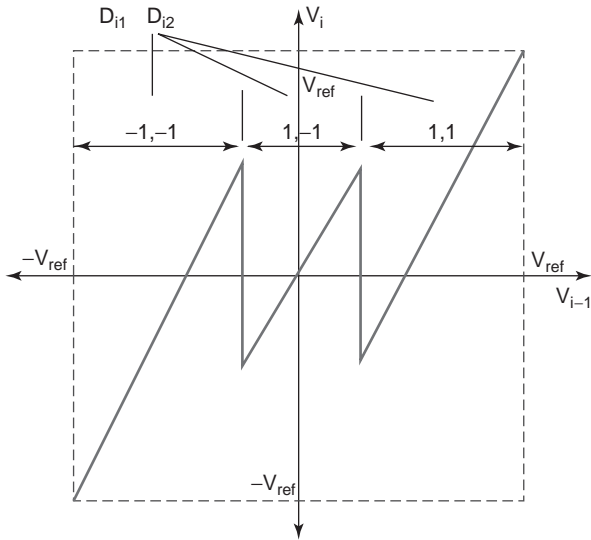


Figure 26. A 1.5-bit pipeline stage that exhibits one-bit redundancy.

nonlinearities that are measured as differential nonlinearity (DNL) and integral nonlinearity (INL) errors. These errors result in poor spectral performance measured by the spurious-free dynamic range (SFDR). When such nonideal D/A converters are used in oversampling A/D converters, the mismatch error adds directly at the input and in most implementations, and is not noise-shaped, resulting in spurious tones in baseband. The nonideal D/A converter used in multibit per stage pipelined A/D converter architectures also gives rise to spurious tones and therefore degrades the dynamic range of the overall A/D converter. Similar issues due to mismatch, offsets, charge injections, and finite amplifier gain errors arise in all architectures for data converters. Therefore, precision techniques need to be developed at both circuit and system levels to improve the resolution performance of the A/D converters.

Dithering and dynamic element matching are two popular techniques that have been widely used to improve the accuracy and the linearity of the converter. *Dithering* involves addition of a pseudorandom dither signal at the input that is either subtracted digitally from the output (a subtractive dither scheme) or not subtracted from the output (an additive dither scheme). The overall result in

both cases is an average linearization of the overall converter transfer characteristic, especially around sharp discontinuities [36]. The linearity improvement depends on the magnitude of the dither and that of the discontinuity. A subtractive dither scheme enables high linearity improvement, compared to the additive dither scheme. However, both cases suffer from reduced input dynamic range. *Dynamic element matching* (DEM) techniques, on other hand, perform permutation of the unit elements to convert the systematic error into an error spectrum that is either shaped out of the band of interest or contributes only to increased noise floor. Any spurious tones due to systematic error is removed through DEM schemes. Various DEM schemes have been proposed in the literature depending on the application [2,11,18,36–39].

Self-calibration is another way to push the resolution performance of the data converters. Many self-calibration schemes have been proposed in the literature for pipelined and multistage ADC [34,35,40–47]. Some of these schemes are implemented in analog domain (e.g., capacitor error-averaging [48], capacitor trimming [46]), and some of them are implemented in digital domain [40–42]. Capacitor error averaging involves mitigating the effect of the capacitor mismatch through averaging of the pipeline output over all permutations of the capacitors. This yields better overall accuracy at the cost of lower speed and increased complexity. Self-trimming of the elements that exhibit mismatch also improve the overall accuracy, but the techniques are usually expensive and can be calibrated only once.

Digital self-calibration schemes have proved to be more robust compared to analog self-calibration schemes [35,40,42] because of their ease of implementation in today’s CMOS technology and lower cost. Most of the digital schemes employ techniques to correct for errors by measuring code error transitions in the ADC transfer characteristics. This is achieved by providing appropriate input stimuli [41,42] to the ADC during the calibration phase. The scheme proposed in Ref. 34 performs calibration of both capacitor ratio mismatch and finite amplifier gain in the analog domain for a pipelined A/D converter. It performs continuous calibration by using an extra pipeline stage that is constantly being calibrated in the background while the ADC is in use. Once the extra stage is calibrated, it replaces an active pipeline stage that will be taken out for calibration. Such techniques involving redundant computation show promise for future calibration schemes in emerging CMOS technologies. A few promising digital calibration schemes based on adaptive signal processing techniques have been proposed to correct for errors introduced by finite amplifier gain and capacitor ratio mismatch in a pipeline stage [7,35,44]. One of these schemes needs a separate calibration signal to be added to the input for background calibration, through an adaptive technique for measurement of the gain error introduced for the calibration signal. This technique, proposed in Refs. 35 and 44, adaptively corrects for the residue errors in the pipeline with the use of a slow high-resolution ADC (typically a $\Sigma - \Delta$ ADC) for calibration. This is achieved at the cost of slight increase in hardware and power consumption.

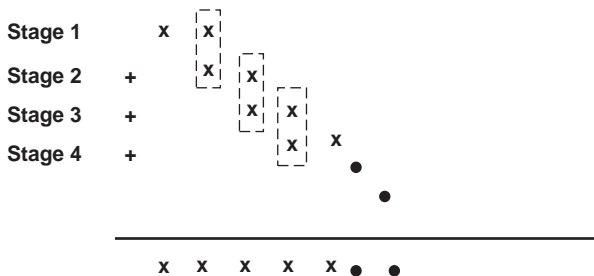


Figure 27. A 1.5-bit pipeline stage that exhibits one-bit redundancy.

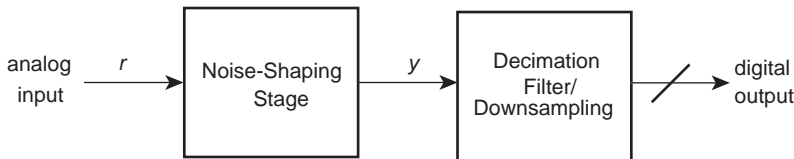


Figure 28. An oversampled analog-to-digital converter. The noise-shaping stage operates at the oversampled clock rate, producing the digital output y that is decimated (filtered and downsampled) to a lower clock rate.

7. OVERSAMPLED CONVERSION

Like Nyquist-rate converters, oversampled converters assume the general form of Fig. 3² in which amplitude quantization is also referred to as *noise shaping*. In this section, we cover the basic topologies and methods for achieving noise shaping of analog and digital signals.

An oversampled A/D takes the form shown Fig. 28. Here, the noise-shaping stage is implemented using mainly analog circuitry. Configured as a D/A, the oversampled converter appears as shown in Fig. 29. The noise-shaping stage is completely digital in this system, and therefore any deviation from ideal performance can usually be attributed to imperfections in the Nyquist-rate D/A [17].

All oversampled converters in popular use are derived from the delta-sigma (or sigma-delta) modulator (Fig. 30). It is no wonder, then, that the terms “oversampled” and “delta-sigma” have become interchangeable. A readable and general overview of discrete-time delta-sigma modulation can be found in Ref. 49. Although oversampled converters are often based on a single delta-sigma modulator, it is also possible to interconnect multiple delta-sigma modulators to form a *cascaded* design [2,17]. Well-known variants of the cascaded form include the MASH and Leslie-Singh architectures [50,51]. It is possible to achieve greater SNR performance at lower oversampling ratios with cascading; a more detailed discussion of this approach is provided below.

We note that for oversampled A/D conversion, the delta-sigma modulator is implemented in mixed-signal form, as depicted in Fig. 31. The quantizer block is comprised of a simple Nyquist-rate A/D (generating the output y) and a complementary Nyquist-rate D/A (providing a suitable feedback signal) in cascade. Often, the D/A block is implemented as a thermometer-coded current steering design with dynamic element matching. The use of element matching techniques is necessary to avoid SNR degradation from nonlinearities in the D/A characteristic. For oversampled D/A conversion, the delta-sigma modulator is implemented in purely digital form. Thus the modulator loop itself can be expected to perform ideally. However, the problem of mismatch is now relegated to the cascaded Nyquist-rate D/A, which must be sufficiently linear to allow the oversampled converter to achieve maximum resolution.

Oversampled converters can be developed using a wide range of architectures and technologies. A survey of state-of-the-art oversampled high-speed analog-to-digital converters is provided in Table 2. The results are sorted by

²The exception is the case of continuous-time delta-sigma modulation (in which H is realized with continuous-time analog circuitry) in which the sampling operation and amplitude discretization occur simultaneously.

signal bandwidth in descending order. With the exception of the technique employed by Paul et al. [52], each design employs a conventional delta-sigma modulator architecture. We see that CMOS oversampled A/Ds now process megahertz-range bandwidths, attaining resolutions of up to 15 bits. Specifically, SNDRs greater than 80 dB are achieved using the basic formula of discrete-time loop filtering and multibit quantization in a cascade (MASH) configuration.

7.1. Design of the Delta-Sigma Modulator

In delta-sigma D/A conversion, the noise shaping stage is implemented digitally, and the system is described in discrete time. In A/D conversion, the delta-sigma modulator is a mixed-signal system, and either continuous-time or discrete-time design descriptions for the loop filter are used.³ We shall present much of our discussion in a manner that is applicable to either discrete- or continuous-time by employing operator notation; for instance, the symbol H denotes a linear filter that may be considered to be either $H(z)$ or $H(s)$, depending on the context.

The design of the delta-sigma modulator typically proceeds in the frequency domain. Using the pseudolinear model of Fig. 32, the operation of the delta-sigma modulator can be described mathematically as follows:

$$y = G_s r + G_n e_Q \quad (14)$$

where G_s and G_n denote the signal and noise transfer functions, respectively. Both transfer functions are shown conceptually in Fig. 33, where it is seen that, within the designated signal band of the modulator, the magnitude of G_s is roughly unity, while the magnitude of G_n approximates 0 (and describes the noise shaping characteristic of the loop).

The design of the delta-sigma modulator begins with the selection of an appropriate noise transfer function. The loop filter H is in general a two-input system as shown in Fig. 30. Using the expressions for loop filter output

$$\sigma = H_1 r + H_2 y \quad (15)$$

(where H_1 and H_2 describe the responses of H to its first and second inputs, respectively) and overall output according to the pseudolinear model

$$y = e_Q + \sigma \quad (16)$$

³Note, however, that although the modulator loop filter may be described in continuous time, the delta-sigma modulator is itself a sampled-data system. Therefore, the overall system must be converted to discrete time as described in Ref. 56 to obtain a correct description of modulator operation.

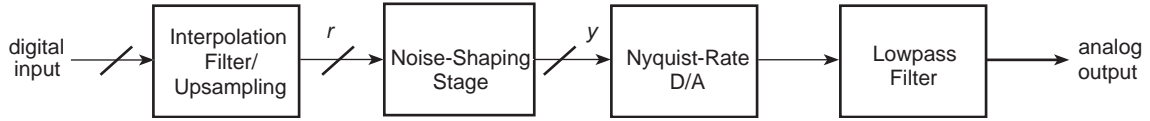


Figure 29. An oversampled digital-to-analog converter. The digital input signal is first upsampled to the oversampled data rate before being encoded by the purely digital noise-shaping stage.

we obtain the closed-loop expression for y as follows:

$$y = H_1(1 - H_2)^{-1}r + (1 - H_2)^{-1}e_Q \quad (17)$$

Therefore, the signal and noise transfer functions are given by $G_s = H_1(1 - H_2)^{-1}$ and $G_n = (1 - H_2)^{-1}$. Special attention is paid to the selection of G_n since the level of noise attenuation dictates overall performance and modulator stability [57]. A G_n that exhibits an aggressive profile can drive the system into instability. As a rule of thumb, the peak gain of G_n should be less than 1.5 for single-bit quantization to reduce the likelihood of instability. If finer quantization is employed, the noise transfer function can be more aggressive. Although a sufficient condition exists to ensure stability in the multibit case [58], it is thought to be too conservative, and most designers rely on simulation to assess modulator robustness. Nevertheless, it is important that simulation not be misconstrued as proof of stability, and the designer should anticipate the onset of instability, however infrequent.

A design recipe for achieving any desired SQNR (signal-to-quantization-noise ratio) has been provided [57]. A toolbox developed by Schreier [59] based on Matlab provides an outstanding array of scripts to assist the designer from noise transfer function design to full block-level realization, and is highly recommended. Using this toolbox, we generated the plots of Figs. 34 and 35. These graphs indicate the performance achievable with single- and multibit designs, respectively, in terms of peak SQNR versus (normalized) signal bandwidth. Various orders are shown and optimum noise transfer function zero placement has been used.

The realization of the loop filter H can proceed in several ways; a popular continuous-time structure is shown in Fig. 36. In the continuous-time case where there is significant parametric uncertainty (brought on by mismatch between active and passive circuit elements), loop filter sensitivity is an important issue, particularly for higher-order designs. Filter tuning may be necessary to mitigate

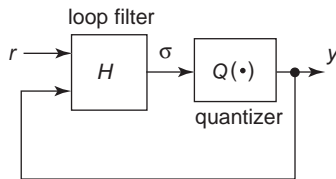


Figure 30. The basic delta-sigma modulator. The output y is a noise-shaped version of the input r . The *quantizer* element is a clocked device, and the *loop filter* is a linear time-invariant (LTI) system. The clock rate of the system is often many times higher than the specified signal bandwidth. For D/A conversion, the modulator is implemented entirely in digital form; for A/D converters, the modulator is a mixed-signal loop.

the effects of sensitivity [60]. The main advantage of using more sensitive realizations is that some savings in hardware complexity can be achieved. A thorough treatment of discrete-time loop filter realizations is provided in the documentation accompanying the toolbox by Schreier [59].

Cascaded architectures use multiple delta-sigma modulators to achieve greater attenuation of quantization noise without the need to increase oversampling ratio. Figure 37 shows the general form of a cascaded noise-shaper. The main challenge in the design of oversampled A/Ds is that the transfer functions $G_i(z)$ must match quantities that are realized with analog hardware (as shown below). For oversampled D/As, mismatch is not an issue since all blocks (including the modulators) are realized digitally and perfect matching is possible. The analysis in the case of a cascade of modulators proceeds as follows. The outputs of the first, second, and third modulators can be written as:

$$y_1 = H_{11}(1 - H_{12})^{-1}r + (1 - H_{12})^{-1}e_{Q1} \quad (18)$$

$$y_2 = H_{21}(1 - H_{22})^{-1}e_{Q1} + (1 - H_{22})^{-1}e_{Q2} \quad (19)$$

and

$$y_3 = H_{31}(1 - H_{32})^{-1}e_{Q2} + (1 - H_{32})^{-1}e_{Q3} \quad (20)$$

where H_{ij} denotes the j th loop filter transfer function associated with modulator $i \in \{1,2,3\}, j \in \{1,2\}$. The overall noise-shaped output can be written as

$$y = y_1 - G_1y_2 - G_2y_3 \quad (21)$$

$$\begin{aligned} &= H_{11}(1 - H_{12})^{-1}r + [(1 - H_{12})^{-1} - G_1H_{21}(1 - H_{22})^{-1}]e_{Q1} \\ &\quad - [G_1(1 - H_{22})^{-1} + G_2H_{31}(1 - H_{32})^{-1}]e_{Q2} \\ &\quad - G_2(1 - H_{32})^{-1}e_{Q3} \end{aligned} \quad (22)$$

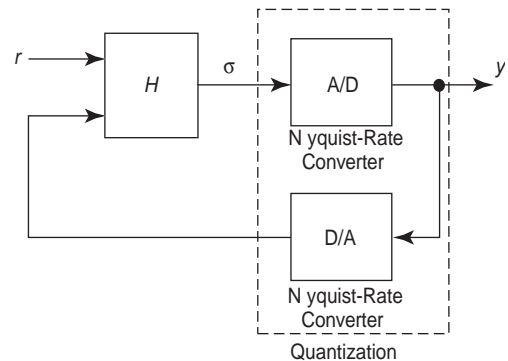


Figure 31. A mixed-signal delta-sigma modulator used in oversampled A/D conversion.

Table 2. Reported High-Speed Oversampled Architectures for A/D Conversion^a

Peak SNDR (dB)	Signal BW, OSR	Technology	Architecture, Quantization Supply, Power Consumption	Ref.
43	990 MHz, 9	InAlAs/InGaAs, bipolar	CT ^b 2nd-order lowpass, single-bit, 8 V, 1.5 W	[53]
55	50 MHz, 32	InP, bipolar	CT 2nd-order lowpass, single-bit, ± 5 V, 1 W	[54]
71	9 MHz, 1	1.2- μ m-Si CCD-CMOS	Oversampled pipelined lowpass, multibit, 5/4/3.3 V, 324 mW	[52]
87	2 MHz, 16	0.5- μ m-Si CMOS	SC ^c cascaded (2-2-1) lowpass, multibit, 2.5 V, 150 mW	[2]
90	1.25 MHz, 8	0.5- μ m-Si CMOS	SC cascaded (2-1-1) lowpass, multibit, 5 V, 270 mW	[3]
89	1.25 MHz, 8	0.6- μ m-Si CMOS	SC cascaded pipeline lowpass, multibit, 5/3 V, 550 mW	[4]
82	1.1 MHz, 24	0.5- μ m-Si CMOS	SC cascaded (2-1-1) lowpass, single-bit, 3.3 V, 200 mW	[51]
76	1 MHz, 2000	AlInAs/GaInAs, bipolar	CT 4th-order bandpass, single-bit, ± 5 V, 3.2 W	[55]
77	0.5 MHz, 32	0.35- μ m-SoI BCMOS	SC 2nd-order lowpass, multibit, 2.7 V, 12 mW	[38]

^aThe results indicate the typical performance possible with conventional delta-sigma modulation techniques.

^bContinuous time.

^cSwitched-capacitor.

from which we see that if the matching conditions

$$G_1 = (1 - H_{12})^{-1}[H_{21}^{-1}(1 - H_{22})] \quad (23)$$

and

$$G_2 = -G_1(1 - H_{32})^{-1}[H_{31}^{-1}(1 - H_{32})] \quad (24)$$

are met, then y becomes

$$y = H_{11}(1 - H_{12})^{-1}r - G_2(1 - H_{32})^{-1}e_{Q3} \quad (25)$$

where e_{Q3} is a residual error that is, in general, strongly attenuated relative to the original single-stage quantization error, e_{Q1} .

Note that the conditions (23) and (24) can imply that the digitally realized transfer functions G_1 and G_2 match responses of filters made from analog components. Thus, in the case of cascaded oversampled A/Ds, careful analog circuit design or the use of adaptive filtering may be necessary to ensure that (23) and (24) approximately hold. In spite of this potential shortcoming, cascaded architectures have achieved the highest performance levels in practice (as shown in the literature). Another distinct advantage of using cascaded noise shaping is that stability may be guaranteed if delta-sigma modulators of order ≤ 2 are employed throughout the design.

7.2. Architectural Choices

We may consider various options in the design of delta-sigma modulators, including the choice of quantizer

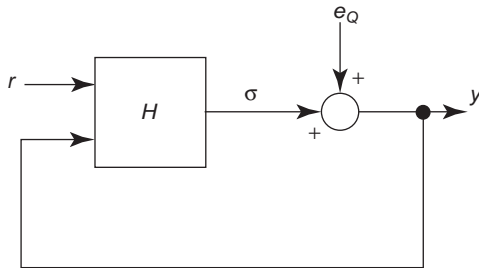


Figure 32. The pseudolinearized model of the delta-sigma modulator. By using a uniformly distributed random variable e_Q , it is possible to approximate the behavior of the actual delta-sigma modulator.

size, higher-order loop filtering, and continuous-time techniques.

7.2.1. Single-Bit or Multibit Quantization? In general, the in-band noise power for multibit mixed-signal delta-sigma modulators is dominated by component nonidealities, and not by quantization noise. The mismatch amongst elements comprising the quantizer D/A is a dominant noise source (even if mitigated by the use of dynamic element matching). Therefore, multibit modulators are used for higher-speed applications in which lower oversampling ratios mean that the ideal SQNR (signal-to-quantization-noise ratio) of the architecture is moderate (generally less than 90 dB). On the other hand, with the perfect linearity of a single-bit quantizer, single-bit delta-sigma modulators can come much closer to ideal SQNR performance at high oversampling ratios. Thus they are used for narrowband applications (particularly digital audio) in which high resolution is a priority.

Both single-bit and multibit delta-sigma modulators are susceptible to spurious tones, albeit for different reasons. In the single-bit case, dithering as described by

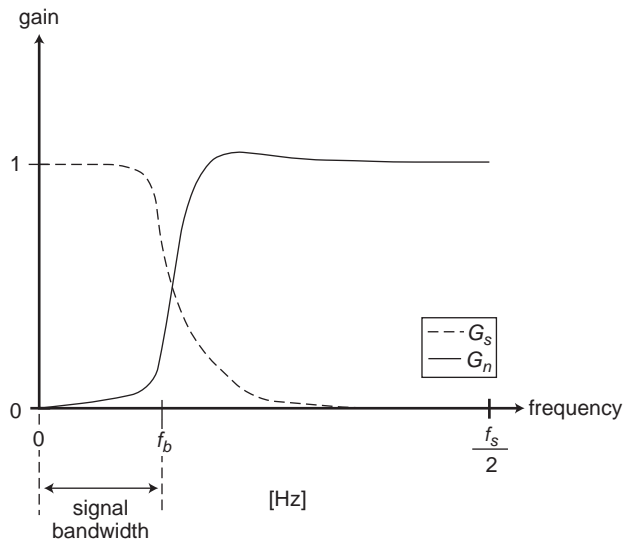


Figure 33. Depictions of modulator noise transfer function (G_n) and signal transfer function (G_s).

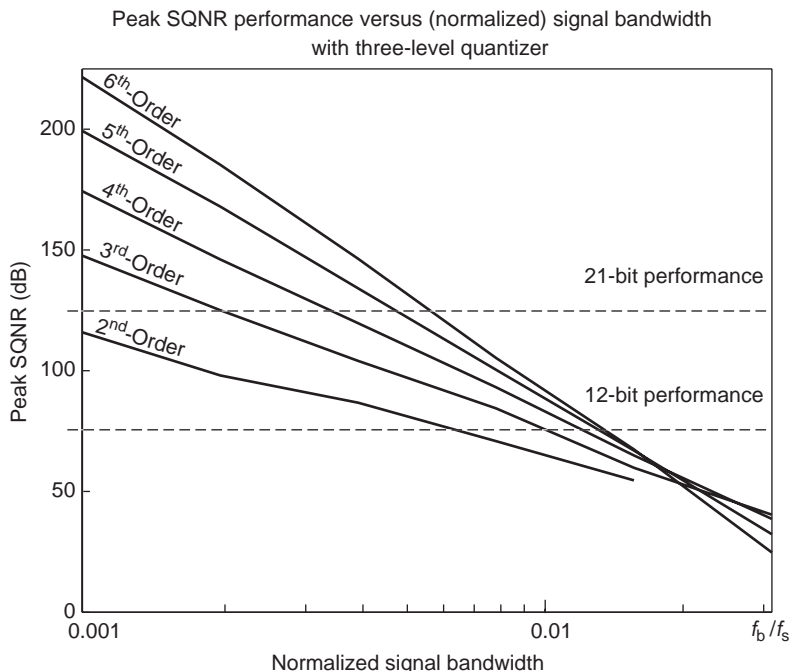


Figure 34. Resolution of single-bit delta-sigma modulators of various orders versus sample-rate-normalized signal bandwidth. The noise-transfer function out-of-band gain is set to 1.5 for all designs.

Norsworthy [61] can be applied to diffuse tones with only a slight impact on dynamic range. Multibit modulators can exploit various techniques for randomizing the selection of D/A elements. This helps to minimize tones generated by any periodicities in the dynamic element matching strategy.

In the case of oversampled D/A conversion, the delta-sigma modulator is implemented digitally; therefore, there are no linearity issues associated with a multibit quantizer. However, a single-bit architecture can be advantageous because the digital circuitry is simplified.

Multiplication of a multibit filter coefficient by a single-bit quantity is trivial. An additional complication with multibit delta-sigma D/A converters is that the noise-shaping loop is typically followed by a Nyquist-rate D/A. Therefore, because the Nyquist-rate D/A appears “open loop” in cascade with a digital delta-sigma modulator, it must be highly linear.

7.2.2. Higher-Order/Coarser Quantizer or Lower-Order/Finer Quantizer? A current trend in broadband CMOS delta-sigma A/D converters is the use of low (typically less

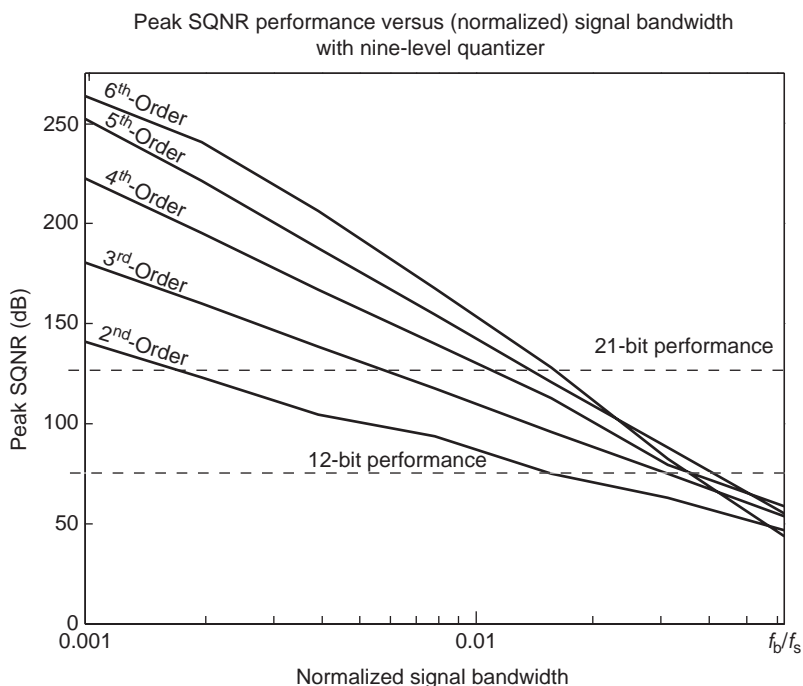


Figure 35. Resolution of 3-bit delta-sigma modulators of various orders versus sample-rate-normalized signal bandwidth. The noise transfer function out-of-band gain is set to 6.0 for all designs.

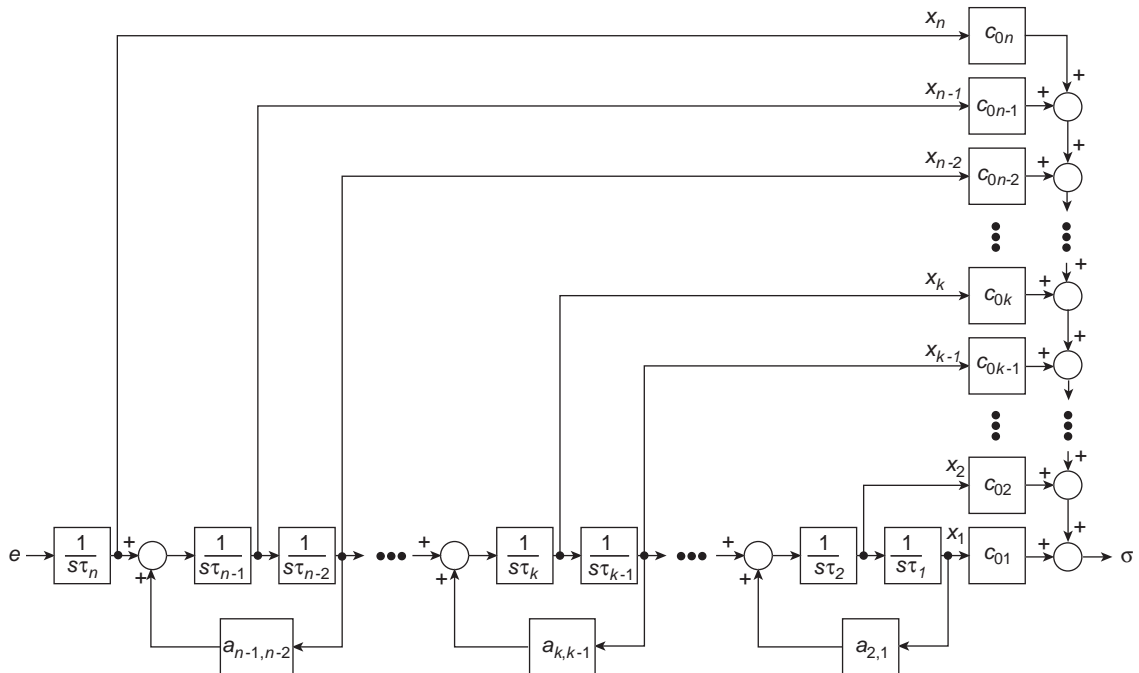


Figure 36. A common loop filter realization for continuous-time delta-sigma modulators (odd order case). If n is even, the leftmost integrator is omitted.

than fourth) order loop filters with finer quantization (up to 5 bits). Such a combination often makes sense because stability is more manageable at lower orders, and greater signal bandwidths can be used because of the SNR “boost” provided by a larger quantizer. A given peak SQNR specification may be achieved either by using a loop filter with sufficiently high order (given a quantizer of fixed size), or by employing a quantizer with sufficiently many bits (given a fixed order for H). The choice is dictated by such considerations as power consumption, chip area, or the designer’s own expertise. While higher-order loop filters may result in more analog power consumption, the use of a coarse quantizer helps to conserve digital power consumption at higher sampling rates. Area usage can increase exponentially with the number of quantizer bits; in spite of this, a number of designers have managed to produce compact multibit designs.

7.2.3. Continuous-Time or Discrete-Time H ? The use of continuous-time loop filtering provides two primary advantages: (1) the maximum clock rate (and hence the oversampling ratio) of the system can be much higher than with discrete-time loop filtering and (2) a sample-and-hold circuit preceding the noise shaping stage of the converter is unnecessary. With discrete-time designs based on switched-capacitor technology, the unity-gain bandwidths of the integrator opamps are required to be between 3 and 5 times the sampling rate of the system [11]. This can place a restrictive upper bound on the maximum rate with which the modulator can be clocked. In contrast, the maximum sampling rate of continuous-time modulators is determined by

considerations of excess loop delay (for which compensation is possible) and quantizer metastability [62,63], which are, in general, less severe constraints on the maximum sampling frequency. The sampling operation of a continuous-time modulator occurs at the quantization stage, therefore, a sample-and-hold circuit preceding the modulator is not needed. However, because the signaling scheme of the modulator is in continuous time, any quantizer sampling imperfections (sampling jitter or quantizer metastability), can severely degrade SNR performance. Quantizer metastability is usually the more significant noise source, and strategies exist to counter it (at the expense of greater loop delay).

8. CONCLUSION

This article provides an overview of modern A/D and D/A converter design for integrated circuits. Nyquist-rate and oversampled techniques are covered with an emphasis on fundamental concepts and key strategies for high-performance design.

Nyquist-rate architectures are most suitable for higher bandwidth applications with modest resolution requirements. Flash, folding, and pipelined techniques for converter design offer varying tradeoffs between hardware complexity and conversion speed. Oversampled converters based on delta-sigma modulation are appropriate for narrowband wide-dynamic-range applications. System requirements dictate the selection of noise shaping architecture, modulator loop filter realization, and quantizer characteristics.

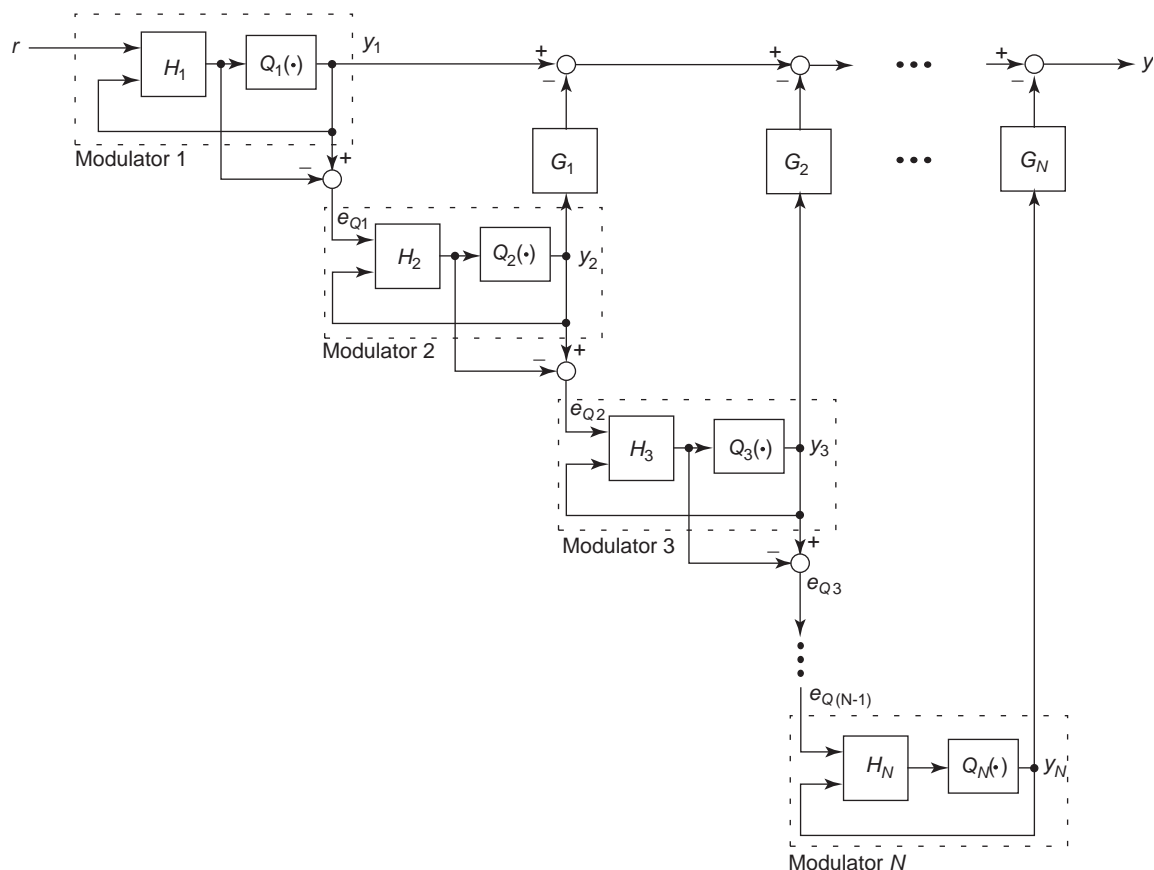


Figure 37. The general form of a cascaded noise-shaping architecture. The delta-sigma modulators are either digital or mixed-signal blocks (depending on the application), and the filter G_i are digital filters.

BIBLIOGRAPHY

1. B. Razavi, *Principles of Data Conversion System Design*, IEEE Press, 1995.
2. K. Vleugels, S. Rabii, and B. A. Wooley, A 2.5-V sigma-delta modulator for broadband communications applications, *IEEE J. Solid-State Circ.* **36**:1887–1899 (2001).
3. I. Fujimori, L. Longo, A. Hairapetian, K. Seiyama, S. Kovic, J. Cao, and S.-L. Chan, A 90-dB SFDR 2.5-MHz output-rate ADC using cascaded multibit delta-sigma modulation at $8 \times$ oversampling ratio, *IEEE J. Solid-State Circ.* **35**: 1820–1828 (2000).
4. T. L. Brooks, D. H. Robertson, D. F. Kelly, A. Del Muro, and S. W. Harston, A cascaded sigma-delta pipeline A/D converter with 1.25 MHz signal bandwidth and 89 dB SNR, *IEEE J. Solid-State Circ.* **32**:1896–1906 (1997).
5. A. van den Bosch, M. A. F. Borremans, M. S. J. Steyaert, and W. Sansen, A 10-bit 1-G Sample/s Nyquist current-steering CMOS D/A converter, *IEEE J. Solid-State Circ.* **36**:315–324 (2001).
6. M.-J. Choe, B.-S. Song, and K. Bacrania, An 8-b 100-M Sample/s CMOS pipelined folding ADC, *IEEE J. Solid-State Circ.* **36**:184–194 (2001).
7. J. Ming and S. H. Lewis, An 8-bit 80-M Sample/s pipelined analog-to-digital converter with background calibration, *IEEE J. Solid-State Circ.* **36**:1489–1497 (2001).
8. R. C. Taft and M. R. Tursi, A 100-MS/s 8-b CMOS subranging ADC with sustained parametric performance from 3.8 V down to 2.2 V, *IEEE J. Solid-State Circ.* **36**:331–338 (2001).
9. L. Sumanen, M. Waltari, and K. A. I. Halonen, A 10-bit 200-MS/s CMOS parallel pipeline A/D converter, *IEEE J. Solid-State Circ.* **36**:1048–1055 (2001).
10. A. Hastings, *The Art of Analog Layout*, Prentice-Hall, 2001.
11. D. A. Johns and K. Martin, *Analog Integrated Circuit Design*, Wiley, 1997.
12. A. Oppenheim and R. Schaffer, *Discrete-Time Signal Processing*, Prentice-Hall, 1989.
13. K. Vleugels, *Broadband Oversampling Analog-to-Digital Conversion for Digital Communications*, Ph.D. dissertation, Stanford Univ., 2002.
14. R. van de Plassche, *CMOS Integrated Analog-to-Digital and Digital-to-Analog Converters*, Kluwer Academic Publishers, 2003.
15. L. Carley, A noise-shaping coder topology for 15+ bit converters, *IEEE J. Solid-State Circ.* **24**:267–273 (April 1989).
16. R. Schreier and B. Zhang, Noise-shaped multi-bit D/A converter employing unit elements, *IEE Electron. Lett.* **31**: 1712–1713 (Sept. 1995).
17. G. C. Temes, S. Shu, and R. Schreier, Architectures for $\Delta\Sigma$ DACs, in S. Norsworthy, R. Schreier, and G. Temes, eds., *Delta-Sigma Converters: Theory, Design and Simulation*, IEEE Press, 1997, pp. 309–332.

18. M. Gustavvson, J. J. Wikner, and N. N. Tan, *CMOS Data Converters for Communications*, Kluwer Academic Publishers, 2000.
19. R. H. Walden, Analog-to-digital converter survey and analysis, *IEEE J. Select. Areas Commun.* **17**:539–550 (April 1999).
20. M. Choi and A. Abidi, A 6-b 1.3-Gsample/s A/D converter in 0.35- μm CMOS, *IEEE J. Solid-State Circ.* **36**:1847–1858 (Dec. 2001).
21. B.-S. Song, S.-H. Lee, and M. F. Tompsett, A 10-b 15-MHz CMOS recycling two-step A/D converter, *IEEE J. Solid-State Circ.* **25**:1328–1338 (1990).
22. H. Van Der Ploeg and R. Remmers, A 3.3 V 10 b 25 M sample/s two-step ADC in 0.35 μm CMOS, *Proc. 1999 IEEE Int. Solid State Circuits Conf.*, Feb. 1999, pp. 318–319.
23. W. Colleran and A. Abidi, A 10-b, 75-MHz two-stage pipelined bipolar A/D converter, *IEEE J. Solid-State Circ.* **28**:1187–1199 (Dec. 1993).
24. R. van de Grift, I. Rutten, and M. van der Veen, An 8-bit video ADC incorporating folding and interpolation techniques, *IEEE J. Solid-State Circ.* **22**:944–953 (Dec. 1987).
25. K. Kusumoto, A. Matsuzawa, and K. Murata, A 10-b, 20-MHz 30-mW pipelined interpolating CMOS ADC, *IEEE J. Solid-State Circ.* **28**:1200–1206 (Dec. 1993).
26. J. van Valburg and R. van de Plassche, An 8-b 650-MHz folding ADC, *IEEE J. Solid-State Circ.* **27**:1662–1666 (Dec. 1992).
27. M.-J. Choe, B. Song, and K. Barcania, A 13 b 40 M Sample/s CMOS pipelined folding ADC with background offset trimming, *Proc. 2000 IEEE Int. Solid State Circuits Conf.*, Feb. 2000, pp. 36–37.
28. C. Moreland, M. Elliott, F. Murden, J. Young, M. Hensley, and R. Stop, A 14 b 100 M sample/s 3-stage A/D converter, *Proc. 2000 IEEE Int. Solid State Circuits Conf.*, Feb. 2000, pp. 34–35.
29. H. Pan and M. E. A. Segami, A 3.3 V, 12 b, 50 M Sample/s A/D converter in 0.6 μm CMOS with over 80 dB SFDR, *Proc. 2000 IEEE Int. Solid State Circuits Conf.*, Feb. 2000, pp. 40–41.
30. T. Shimizu, M. Hotta, K. Maio, and S. Ueda, A 10-bit 20-MHz two-step parallel A/D converter with internal s/h, *IEEE J. Solid-State Circ.* **24**:13–20 (Feb. 1989).
31. S. H. Lewis, H. S. Fetterman, G. F. Gross, Jr., R. Ramachandran, and T. R. Viswanathan, A 10-b 20-M sample/s analog-to-digital converter, *IEEE J. Solid State Circ.* **27**(3):351–358 (March 1992).
32. Y.-I. Park, S. Karthikeyan, F. Tsay, and E. Bartolome, A 10 b 100 M sample/s CMOS pipelined ADC with 1.8 v power supply, *Proc. 2001 IEEE Int. Solid State Circuits Conf.*, Feb. 2001, pp. 130–131.
33. D. Kelly, W. Yang, I. Mehr, M. Sayuk, and L. Singer, A 3 V 14b 75 MSPS CMOS ADC with 85 dB SFDR at nyquist, *Proc. 2001 IEEE Int. Solid State Circuits Conf.*, Feb. 2001, pp. 134–135.
34. J. Ingino and B. Wooley, A continuously calibrated 12-b, 10-MS/s, 3.3-V A/D converter, *IEEE J. Solid State Circ.*, **33**(12):1920–1931 (Dec. 1998).
35. S. Sonkusale, J. Van der Spiegel, and K. Nagaraj, True background calibration technique for pipelined ADC, *IEE Electron. Lett.* **36**(9):786–788 (April 2000).
36. R. Jewett, K. Poulton, K. C. Hsieh, and J. Doernberg, A 12 b 128 M Sample/s ADC with 0.05 lsb dnl, *Proc. 1997 IEEE Int. Solid State Circuits Conf.*, Feb. 1997, pp. 138–139.
37. P. Yu, S. S. Joharapurkar, A. Chugh, B. A. R., X. Du, S.-U. Kwak, Y. Papantonopoulos, and T. Kuyel, A 14 b 40 M Sample/s pipelined ADC with dfca, *Proc. 2001 IEEE Int. Solid State Circuits Conf.*, Feb. 2001, pp. 136–137.
38. J. Grilo, I. Galton, K. Wang, and R. G. Montemayor, A 12-mW ADC delta-sigma modulator with 80 dB of dynamic range integrated in a single-chip bluetooth transceiver, *IEEE J. Solid-State Circ.* **37**:271–278 (2002).
39. A. Shabra and H.-S. Lee, Oversampled pipeline A/D converters with mismatch shaping, *IEEE J. Solid-State Circ.* **37**:566–578 (2002).
40. H. S. Lee, A 12-b 600 ks/s digitally self-calibrated pipelined algorithmic ADC, *IEEE J. Solid State Circ.* **29**(4):509–515 (April 1994).
41. A. N. Karanicolas, S.-H. Lee, and K. L. Barcania, A 15-b 1-M sample/s digitally self-calibrated pipeline ADC, *IEEE J. Solid State Circ.* **28**(12):1207–1215 (Dec. 1993).
42. U.-K. Moon and S. B. S., Background digital calibration techniques for pipelined ADC's, *IEEE Trans. Circ. Syst. II: Analog Digital Signal Process.* **44**(2):102–109 (Feb. 1997).
43. S.-U. Kwak, B. S. Song, and K. Barcania, A 15-b 5-M sample/s low-spurious CMOS ADC, *IEEE J. Solid State Circ.* **32**(12):1866–1875 (Dec. 1997).
44. S. Sonkusale, J. Van der Spiegel, and K. Nagaraj, Background digital error correction technique for pipelined analog-digital converters, *Proc. 2001 IEEE Int. Symp. Circuits and Systems*, May 2001, pp. 408–411.
45. S. H. Lee and B. S. Song, Digital-domain calibration of multistep analog-to-digital converters, *IEEE J. Solid State Circ.* **27**(12):1679–1688 (Dec. 1992).
46. Y. M. Lin, B. Kim, and P. Gray, A 13-b 2.5-MHz self-calibrated pipelined A/D converter in 3- μm CMOS, *IEEE J. Solid State Circ.* **26**:628–636 (April 1991).
47. H. S. Lee, D. A. Hodges, and P. R. Gray, A self-calibrating 15 bit CMOS A/D converter, *IEEE J. Solid State Circ.* **19**(6):813–819 (Dec. 1984).
48. B. S. Song, M. F. Tompsett, and K. R. Lakshmikumar, A 12-bit 1-M sample/s capacitor error-averaging pipelined A/D converter, *IEEE J. Solid State Circ.* **23**(6):1324–1333 (Dec. 1988).
49. P. Aziz, H. Sorensen, and J. Van der Spiegel, Overview of sigma-delta converters, *IEEE Signal Process. Mag.*, **27**:66–84 (Jan. 1996).
50. M. Rebeschini, The design of cascaded $\Delta\Sigma$ ADCs, in S. Norsworthy, R. Schreier, and G. Temes, eds., *Delta-Sigma Data Converters: Theory, Design and Simulation*, IEEE Press, 1997, pp. 193–218.
51. Y. Geerts, A. M. Marques, M. S. J. Steyaert, and W. Sansen, A 3.3-V, 15-bit, delta-sigma ADC with a signal bandwidth of 1.1 MHz for ADSL applications, *IEEE J. Solid-State Circ.* **34**:927–936 (1999).
52. S. A. Paul, H.-S. Lee, J. Goodrich, T. F. Alailima, and D. D. Santiago, A Nyquist-rate pipelined oversampling A/D converter, *IEEE J. Solid-State Circ.* **34**:1777–1787 (1999).
53. S. Jaganathan, S. Krishnan, D. Mensa, T. Mathew, Y. Betser, Y. Wei, D. Scott, R. Urteaga, and M. Rodwell, An 18-GHz continuous-time $\Sigma\text{-}\Delta$ analog-digital converter implemented in InP-transferred substrate HBT technology, *IEEE J. Solid-State Circ.* **36**:1343–1350 (2001).
54. J. F. Jensen, G. Raghavan, A. E. Cosand, and R. H. Walden, A 3.2-GHz second-order delta-sigma modulator implemented in InP HBT technology, *IEEE J. Solid-State Circ.* **30**:1119–1127 (1995).
55. G. Raghavan, J. F. Jensen, J. Laskowski, M. Kardos, M. G. Case, M. Sokolich, and S. Thomas, Architecture, design, and test of continuous-time tunable intermediate-frequency bandpass delta-sigma modulators, *IEEE J. Solid-State Circ.* **36**:5–13 (2001).

56. R. Schreier and B. Zhang, Delta-sigma data converters employing continuous-time circuitry, *IEEE Trans. Circ. Syst. I: Fund. Theory Appl.* **43**:324–332 (1996).
57. R. Adams and R. Schreier, Stability theory for $\Delta\Sigma$ modulators, in S. Norsworthy, R. Schreier, and G. Temes, eds., *Delta-Sigma Data Converters: Theory, Design and Simulation*, IEEE Press, 1997, pp. 141–164.
58. C. Wolff, J. G. Kenney, and L. R. Carley, CAD for the analysis and design of $\Delta\Sigma$ converters, in S. Norsworthy, R. Schreier, and G. Temes, eds., *Delta-Sigma Data Converters: Theory, Design and Simulation*, IEEE Press, 1997, pp. 447–467.
59. R. Schreier, The delta-sigma toolbox (version 2.0), Jan. 2000, URL <http://www.mathworks.com> (search author's last name "Schreier" in Matlab Central file exchange).
60. T. Zourntos, *Compensation of Delta-Sigma Modulators: Stabilization, Signal Restoration and Integrated Circuits*, Ph.D. dissertation, Univ. Toronto, 2003.
61. S. R. Norsworthy, Quantization errors and dithering in $\Delta\Sigma$ modulators, in S. Norsworthy, R. Schreier, and G. Temes, eds., *Delta-Sigma Data Converters: Theory, Design and Simulation*, IEEE Press, 1997, pp. 75–140.
62. J. A. Cherry and W. M. Snelgrove, Clock jitter and quantizer metastability in continuous-time delta-sigma modulators, *IEEE Trans. Circ. Syst. II: Analog Digital Signal Process.* **46**:661–676 (1999).
63. J. A. Cherry and W. M. Snelgrove, Excess loop delay in continuous-time delta-sigma modulators, *IEEE Trans. Circ. Syst. II: Analog Digital Signal Process.* **46**:376–389 (1999).

ACOUSTIC MICROWAVE DEVICES

PETER M. SMITH
 McMaster University
 Hamilton, Canada

1. INTRODUCTION

Since the first experiments on piezoelectricity by the Curie brothers in 1880, many devices have employed mechanical waves to process electrical signals. While their frequency of operation is usually well beyond the audible range, these waves are referred to as *acoustic waves* because of their mechanical nature. From an electrical standpoint, their principal benefits stem from the relatively low velocities of acoustic waves, which are in the order of 10^5 times lower than the velocity of electromagnetic waves. This leads to very small devices that can be made to meet very stringent specifications.

In virtually all radiofrequency (RF) and microwave applications, the acoustic waves are generated and detected in crystals through piezoelectricity, which couples electric fields to mechanical deformations. There are two broad types of devices:

- *Bulk acoustic wave* (BAW) resonators employ surface electrodes to generate mechanical waves that travel through the interior ("bulk") of the crystal. They have proved to be compact and reliable, and have become ubiquitous in high-precision oscillators having a

fundamental frequency of up to 20 MHz. Their resonant frequency depends on the exterior dimensions of the crystal. At high frequencies, standalone bulk crystal resonators become too thin and fragile for most applications.

- *Surface acoustic wave* (SAW) devices employ transducers to generate waves that propagate along the surface of a crystal [1]. They overcome the frequency limitations of the bulk acoustic wave resonators because the frequency of operation becomes independent of the crystal thickness. They also make the acoustic waves accessible along their entire propagation path, thus permitting sampling of the waves at arbitrary points.

2. BAW DEVICE STRUCTURES

At microwave frequencies, the most practical structure for employing bulk acoustic waves is known as the *thin-film bulk acoustic wave* (FBAW) resonator. It consists of a thin-film piezoelectric layer grown between two metal electrodes. The film is normally in the order of $1\ \mu\text{m}$ thick, and the structure is often built on an airbridge in order to isolate it mechanically from the substrate. This is illustrated in Fig. 1.

In general, the FBAW offers less flexibility than does its SAW counterpart. Its main advantage is the ability to integrate multiple FBAWs with electronic circuitry, where they can be used as high- Q circuit elements in filters having passband frequencies of up to ~ 10 GHz.

3. SAW DEVICE STRUCTURES

3.1. SAW Delay Line

A SAW delay line, illustrated in Fig. 2, is the simplest device of its type. It consists of two thin-film metallic transducers placed on the surface of a piezoelectric substrate. Common substrates are listed in Table 1. The transducers are usually created using a single-step photolithographic process and are made of a light metal such as aluminum to minimize the effect of their mass on the substrate. The

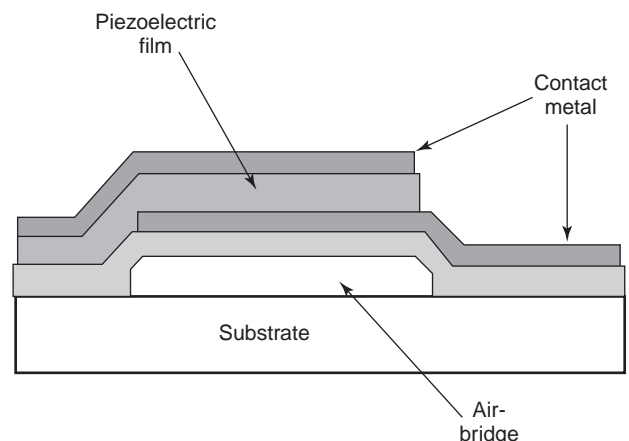


Figure 1. FBAW resonator structure.

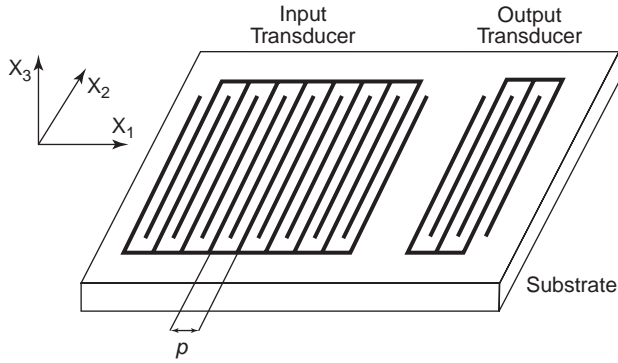


Figure 2. SAW delay line.

photolithographic resolution in the fabrication process limits the frequency of operation of SAW delay lines, where an achievable linewidth of $0.5\ \mu\text{m}$ limits the frequency of operation to $\sim 2\ \text{GHz}$.

The principal benefit of employing SAW devices as delay lines is the large group delays that are possible. For example, a device having a distance (center to center) between transducers of $0.5\ \text{cm}$ would produce a delay in the order of $1.5\ \mu\text{s}$. In addition, because the wave velocity is frequency-independent, this delay would apply to all frequency components that the device supports.

The structure of the transducers varies, but the most common type by far is the *interdigital transducer* (IDT), which consists of an array of parallel strips (“fingers”) of alternating polarity. When a RF signal is applied to the input IDT, the electric fields between the metal strips induce mechanical deformations that propagate as waves in the crystal. These waves in turn generate an electric potential between the strips in the output IDT, which produces a current in the load.

The frequency response of the device can be estimated by recognizing that a modulated pulse can approximate the impulse response of each IDT. The frequency response for a device having two identical transducers is thus

$$|H(f)| \approx A \left| \frac{\sin \left[\frac{N\pi(f - f_0)}{f_0} \right]}{\frac{N\pi(f - f_0)}{f_0}} \right|^2 \quad (1)$$

where A is a constant and N is the number of finger pairs in each transducer. f_0 is the device’s center frequency given by

$$f_0 = \frac{v}{p} \quad (2)$$

Here, v is the acoustic wave phase velocity in the transducer region and p is the finger periodicity, shown in Fig. 2.

The insertion loss of a SAW delay line is often high. Since both IDTs are bidirectional three-port (one electrical, two acoustic) devices, each IDT will contribute an inherent 3 dB loss (6 dB in total) when the two electrical ports are matched to the source and load, respectively. This matched condition unfortunately also results in the maximum level of acoustic wave regeneration by each IDT, and leads to severe multipath interference known as *triple-transit interference* (TTI). Consequently, most SAW delay lines are intentionally mismatched at the electrical ports so that acoustic regeneration is reduced. An insertion loss of between 20 and 30 dB is common.

The frequency response of SAW delay lines usually exhibits several other distortions attributed to second-order effects. The dominant effects are direct electromagnetic coupling (“feedthrough”) between input to output transducers, reflections from finger edges, acoustic beam diffraction, and bulk wave interference.

3.2. SAW Transversal Filter

The SAW transversal filter is a generalization of the delay line in which the relative efficiency of individual IDT fingers is varied so that the frequency response of the transducer can be tailored. The control is commonly achieved either by *apodization*, which consists of varying the individual finger lengths, or by *withdrawal weighting*, which involves selectively removing fingers. These techniques are illustrated in the device shown in Fig. 3.

In a first-order design process, each finger in an IDT is represented by a delta function whose magnitude is proportional to the length. The impulse response of the IDT is then a sequence of weighted delta functions separated by $\tau = p/2v$ seconds. This representation corresponds directly to the one commonly used for the design of finite-impulse-response (FIR) digital filters, for which there are extensive design tools. One of the most common of these tools is the Remez exchange algorithm, for which computer programs are readily available [2], but other optimization algorithms can also be used. Once the equivalent digital FIR filter has been designed, the SAW filter is obtained by making the finger lengths proportional to the tap weights of the digital filter. If the transducer has an impulse response that is symmetric, then its frequency response will exhibit a linear phase. This property is important in communications applications.

Care must be exercised when designing a SAW filter having two apodized transducers. Since in this case the acoustic beam generated by the first apodized transducer will not be uniform across acoustic aperture, the signal detected by each finger in the second transducer will seldom be proportional to its length. Because of the

Table 1. Common Substrates Used in Surface Acoustic Wave Devices

Substrate	Cut	Velocity v (m/s)	k^2 (%)	Temperature Coefficient (ppm/K)
Quartz	ST-X	3158	0.116	0
Lithium niobate	Y-Z	3488	4.82	+ 94
Lithium niobate	128° -X	3992	5.44	+ 75
Lithium tantalate	Y-Z	3230	0.66	+ 35

Source: Morgan [17].

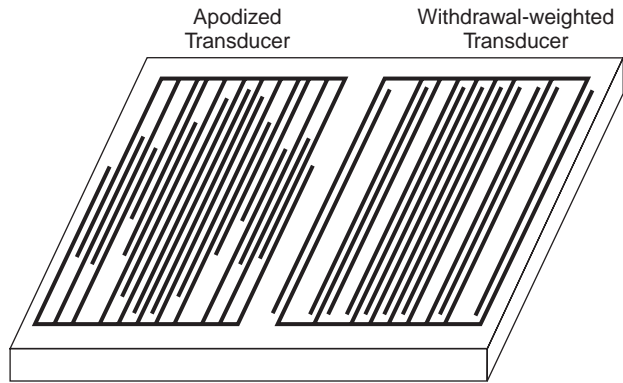


Figure 3. SAW device employing an apodized transducer and a withdrawal-weighted transducer.

difficulties that this behavior introduces in the design process, the second transducer is rarely apodized. In this case, withdrawal weighting is an attractive option.

3.3. Dispersive SAW delay line

Both the SAW delay line and transversal filter are usually designed to have a linear phase response. There are situations, however, where a nonlinear phase response is desirable. For example, a frequency-modulated (“chirp”) impulse response is often used to improve the range and resolution of radar systems.

A dispersive SAW delay line can be made by varying the finger positions of a delay line. Alternatively, grooves of varying periodicity can be etched into the substrate, as shown in Fig. 4, to create a *reflective array compressor* (RAC) [3]. The various frequency components in the acoustic beam will be reflected efficiently in the region where the grooves have a periodicity equal to half the acoustic wavelength. The frequency components will thus travel different distances and will reach the output transducer with differing delays. The phase response of the filter is obtained by integrating the radial frequency with respect to time, so a nonconstant delay can produce a desired nonlinear phase response.

3.4. Single-Mode SAW Resonator

An array of metal strips or grooves on the surface of the substrate can reflect SAW energy. If we place such arrays on the far sides of a one- or two-transducer device as shown in Fig. 5, we can create an acoustic resonant cavity. Resonance will occur, and the acoustic energy will be trapped in the cavity when the acoustic wave has a

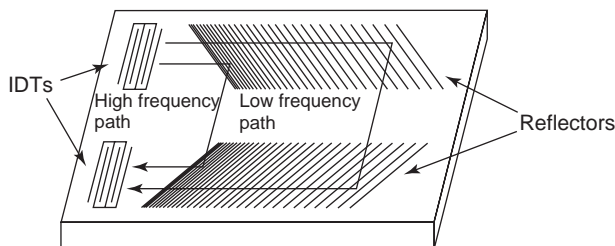


Figure 4. Reflective array compressor (RAC).

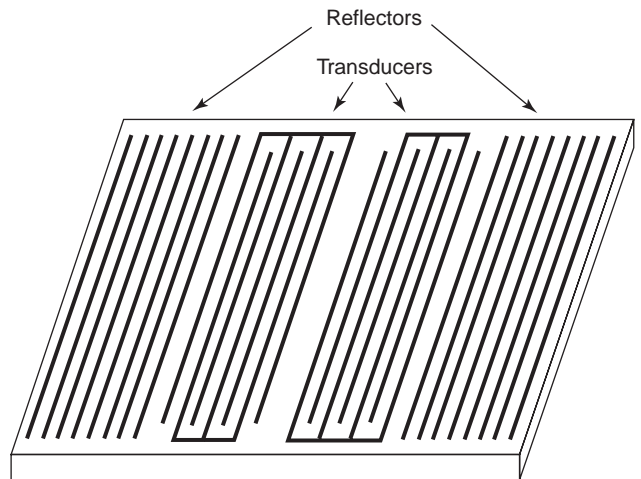


Figure 5. SAW resonator.

wavelength that is approximately equal to an even multiple of the reflector strip periodicity.

When properly designed, a SAW resonator can achieve a quality factor, measured as the inverse of the fractional bandwidth, equal to about 10,000. In addition, the SAW resonator usually has a low insertion loss because the acoustic energy is trapped in the cavity. An insertion loss of less than 2 dB is easily achievable.

3.5. Multimode SAW Resonator

If we allow the acoustic energy in two identical resonant cavities to couple, the resonant frequency of the combined structure will split into two resonant frequencies. This property is often used to produce resonators that exhibit a higher fractional bandwidth than do single-cavity resonators, while still maintaining their low insertion loss.

The resonators can be longitudinally coupled, in which case two acoustic cavities are placed in line and the reflector array that they share is shortened to allow the acoustic energy to “leak” into the adjacent cavity. This approach allows the designer to precisely control the coupling between the cavities. Alternatively, the cavity length can be increased sufficiently to permit two or more modes to exist within the single cavity. However, at frequencies not reflected by the reflector arrays, the SAW waves will be able to freely propagate between transducers in these inline structures. This leads to poor out-of-band rejection.

The resonators may also be transversely coupled. In this case the acoustic cavities are placed in parallel, with a very narrow gap (usually a grounded metal strip) between them. Acoustic energy is coupled between the cavities through the evanescent “tail ends” of the transverse energy distribution of each cavity. This approach gives limited control over the coupling between cavities, but leads to excellent out-of-band rejection, in the order of 60 dB.

3.6. Low-Loss Structures

The previous paragraphs have described many “first generation” SAW devices, which can be divided into high-loss filters with outstanding frequency response

characteristics, and low-loss narrowband resonant devices with responses over which the designer has limited control. A “second generation” type of device has emerged that can provide both low loss and control over the shape of the frequency response.

Designing transducers that launch acoustic energy primarily at one port can reduce the insertion loss. This is done by introducing wave reflections within each IDT that add in phase with waves propagating in the desired direction, but that add out of phase with waves propagating in the opposite direction. Since the standard IDT is symmetric, it cannot generate unsymmetric output unless the substrate is unsymmetrical. We must employ instead transducers that have multiple electrodes, often of varying width, per period. Several examples of structures, known as *single-phase unidirectional transducers* (SPUDTs), are given in Ref. 4. These devices require higher photolithographic resolution, and their fabrication presents difficulties at frequencies above 1 GHz.

A second approach to reducing the insertion loss is to employ multiple bidirectional transducers that are alternately connected to the input and output ports. Since each input transducer (unless located at the ends) has a receiving transducer at both acoustic ports, and since each output transducer (unless located at the ends) has a transmitting transducer at each port, very little acoustic energy is lost. These devices, known as *interdigitated interdigital transducers* (IIDTs), are not subject to the same fabrication limitations at high frequencies as the devices described in the previous paragraph, but they often exhibit severe ripples in the frequency response.

3.7. SAW Ladder Networks

One-port SAW resonators have been increasingly used as circuit elements in ladder networks [5]. These filters, known as *impedance element filters*, offer low insertion loss and high power-handling capability. They are therefore often used in the output stage of wireless transceivers.

The basic configuration for an impedance element filter is given in Fig. 6, which also shows the typical frequency response of the circuit elements. The resonant frequencies of the shunt and series elements are offset so that the antiresonant frequency of the shunt elements matches the resonant frequency of the series elements. The result is a filter with a wider bandwidth than achievable with individual resonators, with sharp transition bands and good close-in stopband suppression.

4. SUBSTRATES

4.1. SAW Substrates

At low frequencies, most BAW devices employ a cylindrical quartz crystal that is polished on the two faces, on which are placed metal electrodes. Since the fundamental resonant frequency is inversely proportional to the distance between the two faces, the crystal becomes extremely thin at high frequencies, and impractical at microwave frequencies.

In the case of the FBAW, the thin-film piezoelectric substrate must be easily deposited and processed. The

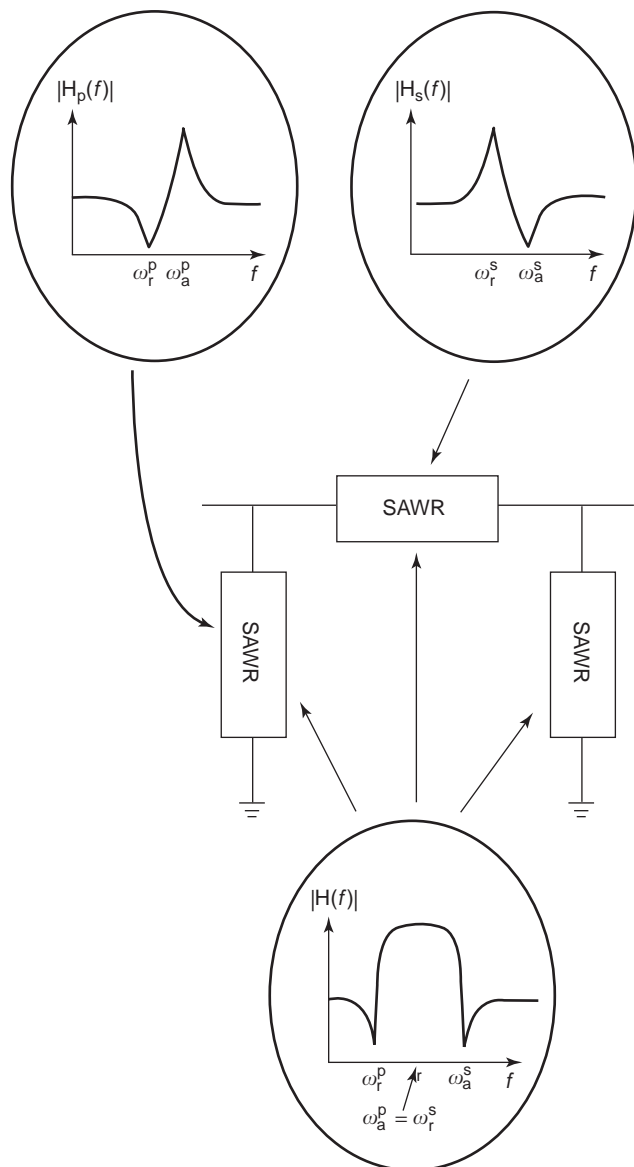


Figure 6. Configuration of impedance element filter employing SAW resonators.

most commonly used materials are aluminum nitride (AlN) and zinc oxide (ZnO).

4.2. SAW Substrates

There are currently many substrates in use for SAW devices. The most common are lithium niobate (LiNbO_3), quartz (SiO_2), and lithium tantalate (LiTaO_3), which are cut at various angles to the crystalline axes. Table 1 summarizes the most important properties of some of the more common crystal cuts.

The phase velocity v of the wave, combined with the photolithographic resolution of device fabrication process, determine the maximum sampling frequency of the transducers. Clearly, since IDT electrodes must be at most half a wavelength apart, a high velocity is desirable at microwave frequencies.

The coupling coefficient k^2 provides an indication of the electromechanical coupling efficiency. It is computed by evaluating the fractional velocity difference between waves propagating under metallized and free surfaces. Filters built on substrates with a higher k^2 can achieve lower insertion loss and wider bandwidths.

The temperature coefficient determines the effect of temperature changes on the acoustic phase velocity. This parameter is particularly important in oscillator applications where the cost of controlling the substrate temperature is excessive.

In general, LiNbO₃ crystals are used for wideband devices such as transversal filters, where the device may be placed in a temperature-controlled environment, or where small passband shifts due to temperature variations are of minor concern.

Quartz is usually preferred for narrowband applications, such as for resonators to be used in oscillators, where minor frequency shifts due to temperature variations are of major concern. The ST-X cut of quartz, with its zero first-order temperature coefficient at room temperature, is ideal for this type of application.

LiTaO₃ is often selected as a compromise between the two other substrates. Its temperature coefficient is lower than that of LiNbO₃, but its coupling coefficient is higher than for quartz.

There has been considerable interest in the use of multilayer substrates. A substrate that shows great promise is diamond because of its hardness, which leads to a high acoustic velocity. Since it is not piezoelectric, the diamond substrate must be layered with a piezoelectric thin film such as zinc oxide (ZnO). Nakahata reported that a silicon substrate coated with diamond and ZnO films can support a SAW having a velocity of 10,500 m/s and an electromechanical coupling coefficient k^2 of 1.5% [6]. Commercial diamond-based SAW devices operating well above 2 GHz are now available.

5. APPLICATIONS

5.1. Nyquist Filter

Consider a communication system designed to transmit digital bits (assume that each bit is transmitted as a delta function for now) every T seconds. The frequency response of the transmitted information must be restricted to the available channel bandwidth, which makes the impulse response of the channel infinite in length. Unless special steps are taken, successive bits will produce intersymbol interference (ISI). The solution is usually to employ a Nyquist filter in the transmitter.

To minimize this interference, it is important that the channel's impulse response be zero at all sampling instances $t = T_0 + nT$, $n \neq 0$, where T_0 is the delay through the channel. A channel with an ideal rectangular frequency response and a bandwidth of $1/2T$ Hz would have a sinc impulse response

$$\text{sinc}\left(\frac{t}{T}\right) = \frac{\sin(\pi t/T)}{\pi t/T} \quad (3)$$

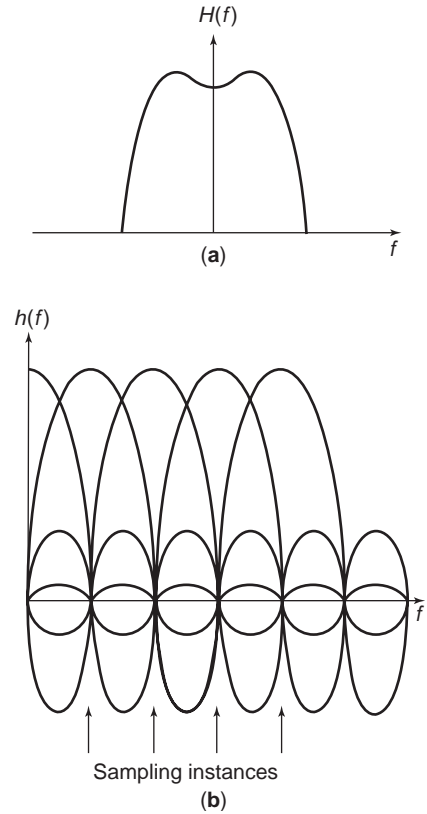


Figure 7. (a) Raised-cosine Nyquist filter frequency response; (b) impulse response of Nyquist filter.

which has the desired property. Other functions, such as the *raised-cosine function* [7], have the same property and are easier to realize. Any deviation from these precise frequency responses by the channel filter will quickly degrade the performance of the system.

The frequency response of the channel filter must be modified to account for the frequency response of the transmitted bit, which in practice cannot be a true delta function. If we assume a rectangular bit (with its sinc-shaped frequency response), a corresponding $1/\text{sinc}$ response must be superimposed on the frequency response of the channel filter. The resulting frequency response and its time-domain properties are illustrated in Fig. 7.

Because of their performance, reproducibility, and their ability to operate at intermediate frequencies (so that a single filter can operate on the combined in-phase and quadrature signals instead of requiring a baseband filter for each of these signals), SAW filters are often used in these applications [8].

5.2. Satellite Subchannelizers

Satellites usually have several transponders, and these are often leased to users. For example, the standard bandwidth of a C-band (6/4-GHz) satellite channel is 40 MHz, of which 36 MHz is usable because of the required guard bands between channels. In a conventional system, the user must lease the entire channel, regardless of whether the bandwidth is needed. The high cost of leasing the entire channel can be a major deterrent.

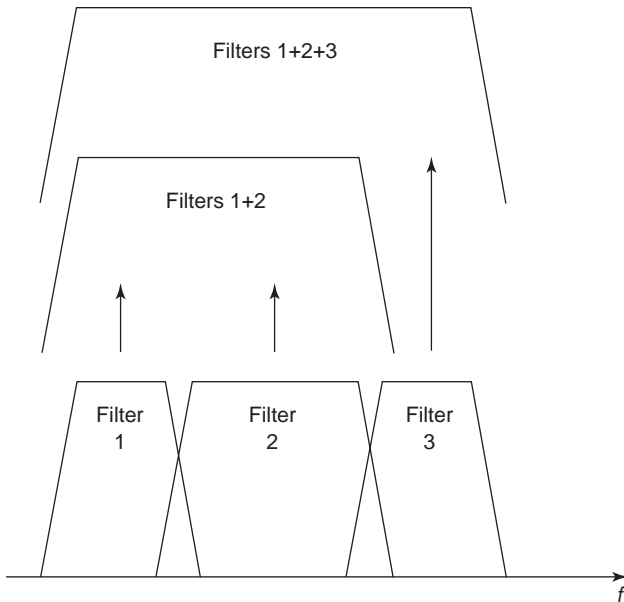


Figure 8. Filters in a SAW filter-bank seamlessly combine to dynamically vary channel bandwidth.

The high selectivity of SAW filters makes it possible to divide the satellite channel into three or more subchannels, possibly of varying bandwidth. Furthermore, if the magnitude and phase of these filters are carefully controlled, it is possible to combine two or more of these subchannels to form a contiguous channel of higher bandwidth, up to the full bandwidth of the transponder. Such a system is illustrated in Fig. 8. The Inmarsat-3 satellite uses this type of system to service its mobile users [9].

5.3. Wireless Handsets

Wireless communications systems require inexpensive, rugged, and compact components that consume very little power. Low-loss SAW devices excel in all four attributes, and have been widely adopted by all major manufacturers [10]. Cellular telephones are currently the largest market for SAW devices, at over 1 billion units per year.

SAW longitudinally coupled resonator filters are often used in the front end to remove out-of-band signal interference. A waveguide-coupled resonator filter is then used to select the desired channel. Figure 9 illustrates the possible uses of SAW components in a wireless handset.

5.4. SAW Oscillators

Stable oscillators require a narrowband device in their feedback path whose passband frequency can be precisely established. The frequency response of the device should also present a low insertion loss and be highly stable. Finally, for volume applications, the response must be easily reproducible.

SAW resonators meet all of these requirements, and are lightweight and rugged. When compared to other technologies, they can be manufactured at a low cost. For these

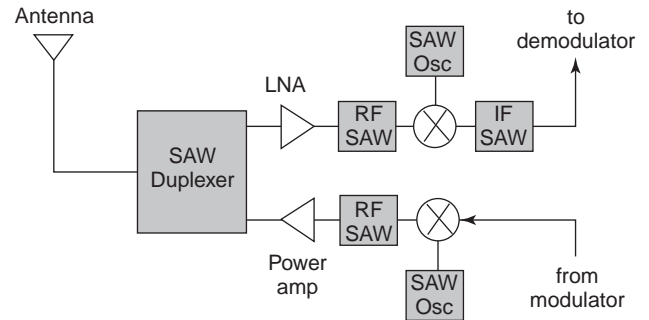


Figure 9. Block diagram of a wireless transceiver. Shaded blocks routinely use SAW devices.

reasons, SAW oscillators are widely used whenever signals in the range from 50 MHz to 2 GHz are required.

Oscillator stability is usually categorized as either short- or long-term. *Short-term stability* refers to output frequency variations lasting less than 1 s and caused by random thermal vibrations and the discrete nature of electric charge. *Long-term stability* encompasses effects due to temperature variations and component aging.

Short-term stability can be improved by selecting a high- Q feedback filter, an amplifier with low flicker noise and noise factor, and a clean power supply. In the case of SAW oscillators, it is also important to isolate the SAW device from mechanical vibrations, since the piezoelectric substrate can convert the vibrations to electrical signals. Short-term stability is usually measured in terms of single-sideband phase noise, which describes the oscillator output power density, normalized to the power of the carrier, at specific offset frequencies. A 500-MHz SAW oscillator, for example, is typically able to achieve phase noise levels of -130 dBc/Hz at 1 kHz offset from the carrier (dBc refers to decibels with respect to the carrier). The phase noise then typically drops to about -175 dBc/Hz at 100 kHz offset, and levels off [11].

Long-term stability can be improved by placing the oscillator in a temperature-controlled environment. Placing the SAW device in a package with thermal characteristics that are similar to those of the substrate also helps reduce mechanical stresses. Because component aging occurs predominantly early in its life, it is also important to “burn in” all oscillator components by subjecting them to high signal levels and high temperatures for an extended period of time. SAW oscillator long-term stability is usually measured in parts per million (ppm), and a good design can achieve 1 ppm per year at a fixed temperature or about 20 ppm over a temperature variation of 50 K.

5.5. SAW Chirp Fourier Transformer

The SAW chirp Fourier transformer is an analog circuit that is able to perform a finite-bandwidth windowed Fourier transform. The circuit is based on a simple algebraic manipulation of the formula for the Fourier transform $S(\omega)$ of a time signal $s(t)$:

$$S(\omega) = \int_{-\infty}^{\infty} s(t)e^{-j\omega t} dt \quad (4)$$

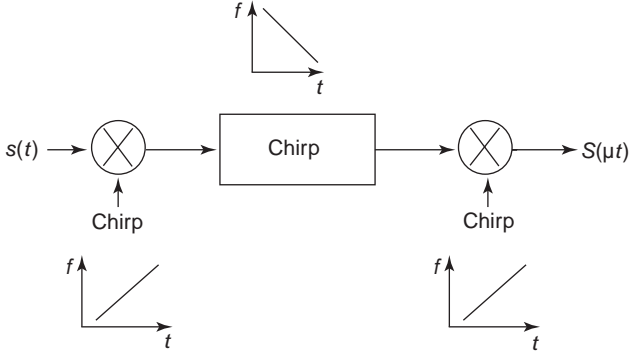


Figure 10. A multiply-convolve-multiply SAW Fourier transformer.

Substituting $-2\omega t = (t - \omega)^2 - t^2 - \omega^2$ and $\omega = \mu t$, we obtain

$$S(\omega) = S(\mu t) = e^{-j(\mu/2)t^2} \int_{-\infty}^{\infty} (s(\tau) e^{-j(\mu/2)\tau^2}) e^{j(\mu/2)(t-\tau)^2} d\tau \quad (5)$$

This expression can clearly be represented by the circuit shown in Fig. 10, which involves a multiplication by a linear frequency-modulated (FM) signal, followed by a convolution with another FM signal having a frequency variation opposite that of the first. The output of the convolver is then multiplied by a third FM signal having the same frequency variation as that of the first signal. A similar transformation can show that the dual circuit, consisting of a convolve–multiply–convolve system, produces the same result.

In a practical system, the convolutions can be performed by feeding the signal into a SAW chirp filter having a linear group delay. The multiplying signals can be provided by impulsing SAW chirp filters, but are usually generated digitally because this approach makes it easier to compensate for imperfections in the convolving SAW chirp filters.

While the SAW chirp Fourier transformer has not been widely used in commercial applications, studies have shown that it could be very competitive in some communications satellite applications [12].

6. ACOUSTIC WAVE PROPAGATION

A solution to the acoustic wave propagation in a piezoelectric substrate requires that both Maxwell's and Newton's equations be solved simultaneously in a nonisotropic medium. These two sets of equations are linked through the piezoelectric relationships. The equations that rule the behavior are

$$\nabla \times \mathbf{E} = -\frac{\partial \mathbf{B}}{\partial t} = -\boldsymbol{\mu} \frac{\partial \mathbf{H}}{\partial t} \quad (6)$$

$$\nabla \times \mathbf{H} = \frac{\partial \mathbf{D}}{\partial t} = \frac{\partial}{\partial t} (\boldsymbol{\epsilon}^T \mathbf{E} + \mathbf{d} \mathbf{T}) \quad (7)$$

$$\nabla_s \mathbf{v} = \frac{\partial \mathbf{S}}{\partial t} = \frac{\partial}{\partial t} (\mathbf{d}' E + \mathbf{s}^E \mathbf{T}) \quad (8)$$

$$\nabla \cdot \mathbf{T} = \boldsymbol{\rho} \frac{\partial \mathbf{v}}{\partial t} \quad (9)$$

where

- \mathbf{B} = magnetic flux density vector
- \mathbf{d} = (3×6) piezoelectric strain coefficient matrix
- \mathbf{D} = electric flux density vector
- \mathbf{E} = electric field vector
- $\boldsymbol{\epsilon}^T$ = (3×3) electric permittivity matrix
- \mathbf{H} = magnetic field vector
- $\boldsymbol{\mu}$ = (3×3) magnetic permeability matrix
- \mathbf{s}^E = (6×6) compliance coefficient matrix
- \mathbf{S} = strain vector
- \mathbf{T} = stress vector
- $\boldsymbol{\rho}$ = diagonal (3×3) material density matrix
- \mathbf{v} = particle velocity vector = $\partial \mathbf{u} / \partial t$
- \mathbf{u} = particle displacement vector

Here, $\nabla \times$ represents the curl and the prime refers to the transpose of a matrix. Assuming the standard abbreviated subscript notation described in Ref. 13, we have

$$\nabla \cdot = \begin{bmatrix} \frac{\partial}{\partial x} & 0 & 0 & 0 & \frac{\partial}{\partial z} & \frac{\partial}{\partial y} \\ 0 & \frac{\partial}{\partial y} & 0 & \frac{\partial}{\partial z} & 0 & \frac{\partial}{\partial x} \\ 0 & 0 & \frac{\partial}{\partial z} & \frac{\partial}{\partial y} & \frac{\partial}{\partial x} & 0 \end{bmatrix} = (\nabla_s)' \quad (10)$$

$$\nabla \times = \begin{bmatrix} 0 & -\frac{\partial}{\partial z} & \frac{\partial}{\partial y} \\ \frac{\partial}{\partial z} & 0 & -\frac{\partial}{\partial x} \\ -\frac{\partial}{\partial y} & \frac{\partial}{\partial x} & 0 \end{bmatrix} \quad (11)$$

The wave solutions obtained by solving these equations, subject to boundary conditions, can be classified by their propagation properties. The most common types are bulk waves, Rayleigh waves, Bluestein–Gulyaev waves, and leaky waves.

6.1. Bulk Waves

Bulk acoustic waves are waves that propagate in the interior of the substrate, so that they are subject to the substrate boundary conditions only when they strike the boundaries. A bulk wave will in general have a particle motion that is composed of a superposition of three fundamental modes. These are known as the *fast longitudinal wave*, whose particle motion is in the same direction as the wave, and two *slower transverse waves*, whose particle motions are perpendicular to the wave. The latter are usually termed *fast-shear* and *slow-shear* waves, owing to their different phase velocities (in some crystal directions, these two waves could have the same velocity). Since these components travel independently, their relative magnitudes and phases will be determined by the launching conditions. In a piezoelectric substrate, each of these wave components will have a phase velocity that depends on its propagation direction.

6.2. Rayleigh Waves

Rayleigh waves satisfy the Maxwell and Newton equations in a piezoelectric half-space. Their motion is retrograde elliptical in the sagittal plane (defined by axes x_1, x_3 in Fig. 2), and their velocity is lower than that of all other waves. This slow velocity leads to very low propagation loss because the acoustic power is confined to within about 1 wavelength of the surface and does not leak into the substrate.

6.3. Bluestein–Gulyaev Waves

Bluestein–Gulyaev waves, also called *surface transverse waves* (STWs), contain particle motion only in the x_2 direction and can be generated with the traditional IDT structure. In general, the energy will propagate at a non-zero angle to the surface, which makes the wave lossy. However, if the surface is subjected to a periodic stress, the STW can be guided parallel to the surface so that it behaves very much like a surface wave; it is then called a *surface-skimming bulk wave* (SSBW). IDTs or reflector arrays built with a heavier or thicker metal film are usually used to guide the wave.

For particular substrate cuts, STW or SSBW can be the dominant acoustic modes. They have a higher velocity than do Rayleigh waves, so they are sometimes used instead of their Rayleigh counterparts in high-frequency devices.

6.4. Leaky Waves

For some substrates, it is possible to satisfy the surface boundary conditions with waves that travel at a velocity that is higher than that of the slow shear wave. Such waves are referred to as “leaky waves” because they are not confined to the surface and their acoustic energy leaks into the substrate. However, in some cases their electromechanical coupling coefficient is higher than that for Rayleigh waves and their propagation loss is small enough to make them practical. In addition, many of these substrates offer very small temperature coefficients. For these reasons, leaky waves are being increasingly used, particularly at high frequencies.

7. DEVICE MODELS

7.1. Introduction

Attempts to accurately model surface wave devices have met with varying success. The electromechanical interactions that are central to their operation require that both Maxwell’s and Newton’s equations be solved for the given boundary conditions. Until recently (as of 2003), the computational requirements to fully model even the simplest devices have been excessive. As a result, varying levels of simplification have been adopted in order to generate useful design tools. Effects that have not been predictable with these simplified models have been classified as “second-order effects,” with several techniques used to minimize their effect on the desired behavior of the device [14].

7.2. Impulse Response Model

The impulse response model was first derived by Hartmann et al. [15] as an alternative to more complicated

equivalent circuit approaches. It provides more information on a SAW device’s performance than does the delta function model described by Eq. (1) because it includes information on electrical impedances and can cater to transducers with nonuniform electrode spacing.

The process of modeling a SAW device with the impulse response model involves three steps:

1. Each electrode is replaced with a half-cycle of a sine wave whose magnitude is proportional to the length of the electrode.
2. If electrode spacing is not uniform, then the magnitude of each i th half-cycle is further scaled by $f_i^{3/2}$, where f_i is the instantaneous frequency at that point in the transducer.
3. The frequency response is obtained by taking the Fourier transform of the resulting impulse response. This technique is illustrated in Fig. 11.

The input impedance of a transducer can be computed from the impulse response model through energy conservation arguments. The equivalent circuit consists of a radiation conductance, representing acoustic energy generation, in parallel with a radiation susceptance, corresponding to energy absorption and regeneration in the transducer, and with a static capacitance. The radiation conductance of an IDT with uniformly spaced electrodes is found to be

$$G_a(f) = 8k^2 C_s f_0 N^2 \left| \frac{\sin \left[\frac{N\pi(f - f_0)}{f_0} \right]}{\frac{N\pi(f - f_0)}{f_0}} \right|^2 \quad (12)$$

while the radiation susceptance is the Hilbert transform of $G_a(f)$ and is given by

$$B_a(f) = 8k^2 C_s f_0 N^2 \frac{\sin \left[\frac{2N\pi(f - f_0)}{f_0} \right] - \frac{2N\pi(f - f_0)}{f_0}}{2 \left[\frac{N\pi(f - f_0)}{f_0} \right]^2} \quad (13)$$

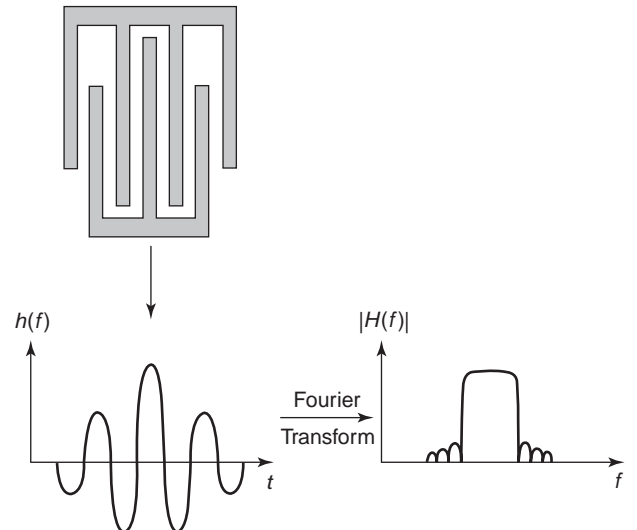


Figure 11. Impulse response model of a transducer.

The static capacitance for the transducer is

$$C_t = NC_s \quad (14)$$

In Eqs. (12) through (14), k^2 is the electromechanical coupling constant, C_s is the capacitance per finger pair, and N is the number of finger pairs in the transducer. The equivalent circuit values for transducers with nonuniformly spaced electrodes can be found in Ref. 15.

7.3. Coupling-of-Modes Model

The *coupling-of-modes* (COM) model is a phenomenological description of the behavior of propagating waves that are subjected to a periodic disturbance in their propagation medium. The technique is ideally suited to the computation of the behavior of SAW structures that contain a large number of equally spaced transducer fingers or reflector strips. The COM approach is very numerically efficient, but is only accurate over fractional bandwidths of about 10%. It also must be slightly modified to model devices that employ leaky waves.

Consider two sinusoidal waves having complex amplitudes $w^+(x)$ and $w^-(x)$ propagating in a transducer region in the $+x_1$ and $-x_1$ directions shown in Fig. 2, respectively. Because of reflections and acoustic generation at the electrodes, these waves will be coupled to each other so that

$$\begin{aligned} \frac{\partial w^+(x)}{\partial x} &= -j\delta w^+(x) + j\kappa w^-(x) + j\alpha V \\ \frac{\partial w^-(x)}{\partial x} &= j\delta w^-(x) - j\kappa^* w^+(x) - j\alpha^* V \\ \frac{\partial I(x)}{\partial x} &= -2j\alpha^* w^+(x) - 2j\alpha w^-(x) + j\omega C_0 V \end{aligned} \quad (15)$$

where κ is the distributed reflection coefficient, α is the distributed transduction coefficient, V is the applied voltage, ω is the radian frequency, C_0 is the static capacitance per unit length of the transducer, and δ is a measure of frequency deviation from the Bragg frequency given by

$$\delta = \beta - \frac{\pi}{a} \quad (16)$$

where β is the propagation constant and a is the electrode separation. The terms containing V and the equation for the incremental current $I(x)$ can be disregarded when dealing with reflector arrays.

If we write Eq. (15) in matrix form, we obtain

$$\begin{aligned} \frac{\partial \mathbf{w}(x)}{\partial x} &= \mathbf{C}\mathbf{w}(x) + \mathbf{f}V \\ \frac{\partial I(x)}{\partial x} &= \mathbf{N}\mathbf{w}(x) + j\omega C_0 V \end{aligned} \quad (17)$$

where

$$\mathbf{w}(x) = \begin{bmatrix} w^+(x) \\ w^-(x) \end{bmatrix}, \quad \mathbf{C} = \begin{bmatrix} -j\delta & j\kappa \\ -j\kappa^* & j\delta \end{bmatrix}, \quad \mathbf{f} = \begin{bmatrix} j\alpha \\ -j\alpha^* \end{bmatrix}$$

and $\mathbf{N} = [-2j\alpha^* \quad -2j\alpha]$, the general solution for the waves is

$$\mathbf{w}(x) = \mathbf{V}_e \mathbf{E}(x) \mathbf{V}_e^{-1} \mathbf{w}(0) + (\mathbf{V}_e \mathbf{E}(x) \mathbf{V}_e^{-1} - \mathbf{I}) \mathbf{C}^{-1} \mathbf{f} V \quad (18)$$

where \mathbf{V}_e is the 2×2 matrix containing the eigenvectors of \mathbf{C} in its columns, \mathbf{I} is the 2×2 unit matrix, and

$$\mathbf{E}(x) = \begin{bmatrix} e^{\lambda_1 x} & 0 \\ 0 & e^{\lambda_2 x} \end{bmatrix} \quad (19)$$

for which λ_1 and λ_2 are the eigenvalues of \mathbf{C} [16]. In the case of transducers, the solution requires an expression for the current, which is obtained by integrating the incremental current over the length of the transducer. For a transducer of length L_T , we get

$$\begin{aligned} I &= \mathbf{N} \mathbf{V}_e \Lambda^{-1} (\mathbf{E}(L_T) - \mathbf{I}) \mathbf{V}_e^{-1} \mathbf{w}(0) + \{ \mathbf{N} [\mathbf{V}_e \Lambda^{-1} (\mathbf{E}(L_T) - \mathbf{I}) \mathbf{V}_e^{-1} \\ &\quad + L_T \mathbf{I}] \mathbf{C}^{-1} \mathbf{f} + j\omega C_t \} V \end{aligned} \quad (20)$$

where $C_t = xC_0$ is the total static capacitance of the transducer and

$$\Lambda = \begin{bmatrix} \lambda_1 & 0 \\ 0 & \lambda_2 \end{bmatrix} \quad (21)$$

The admittance parameters for the device can be computed as

$$y_{ij} = \left. \frac{I_i}{V_j} \right|_{V_k=0, k \neq j} \quad (22)$$

where the subscripts identify the transducers in the device. Scattering parameters are then obtained from the admittance parameters by using standard transformations.

7.4. Green's Function Model

The Green's function models for SAW devices were first developed in the 1970s, with many simplifications applied to make the numerical computations tractable with the resources available at that time. The most common assumption at that time was that the substrate interface was stress-free [17]. The technique has attracted considerable attention more recently because of its ability to model essentially all aspects of a SAW device's performance and to take into account all acoustic propagation modes.

A Green's function describes the behavior of a structure due to a point source. This source can be an electrical charge on the surface of the substrate, or a mechanical stress due to, for example, the mass of a surface electrode. In the k domain (corresponding to the Fourier transform of these terms), these relationships can be summarized as

$$\begin{bmatrix} \bar{u}_1(k_1) \\ \bar{u}_2(k_1) \\ \bar{u}_3(k_1) \\ \bar{\phi}(k_1) \end{bmatrix} = \begin{bmatrix} \bar{G}_{11}(k_1) & \bar{G}_{12}(k_1) & \bar{G}_{13}(k_1) & \bar{G}_{14}(k_1) \\ \bar{G}_{21}(k_1) & \bar{G}_{22}(k_1) & \bar{G}_{23}(k_1) & \bar{G}_{24}(k_1) \\ \bar{G}_{31}(k_1) & \bar{G}_{32}(k_1) & \bar{G}_{33}(k_1) & \bar{G}_{34}(k_1) \\ \bar{G}_{41}(k_1) & \bar{G}_{42}(k_1) & \bar{G}_{43}(k_1) & \bar{G}_{44}(k_1) \end{bmatrix} \quad (23)$$

$$\times \begin{bmatrix} \bar{T}_5(k_1) \\ \bar{T}_4(k_1) \\ \bar{T}_3(k_1) \\ \bar{D}_3(k_1) \end{bmatrix}$$

where the overbar indicates a Fourier transform. G_{ij} are Green's functions, ϕ is the electric potential, and u_i, T_i, D_3 are elements of the displacement, stress, and electric flux density vectors, respectively.

A convenient method to evaluate all the Green's functions was proposed by Peach [18]. For an assumed x_1 component of the acoustic wavenumber given by k_1 , the possible x_3 components can be evaluated by solving Eqs. (6)–(9). The solution can be written as an eighth-order eigenvalue problem, where the k_3 terms are the eigenvalues, and the eigenvectors are the partial waves that make up the solution. The boundary conditions determine the relative contributions of these partial waves. The $\tilde{G}_{ij}(k_1)$ terms are then readily obtained.

The singular terms in the $\tilde{G}_{ij}(k_1)$ functions must be quantified so that the spatial domain Green's functions $G_{ij}(x_1, \omega)$ can be obtained. This step is often the most time consuming, but it is necessary because these singular points determine the long-range effect of the sources. The spatial domain Green's functions are then convolved over all sources and the overall device behavior is obtained.

Recently, a periodic Green's function methodology was introduced that is well suited to the analysis of long periodic structures [19]. This approach limits the analysis to that of a single period, which greatly reduces the computation requirements.

7.5. Finite-Difference Time-Domain Model

The finite-difference time-domain (FDTD) method was first introduced by Yee for the simulation of electromagnetic wave propagation [20]. It involves the discretization of the wave equations in both time and space, which then leads to a numerical solution of the wave propagation problem. The technique's main benefits are that it permits the description of wave propagation in nonuniform and nonlinear media, and it can easily include a wide range of boundary conditions. The technique is particularly well suited to broadband analyses, because the spectral response can be computed from the structure's time response to a narrow Gaussian impulse excitation.

There has been some early work on the extension of the method to the propagation of ultrasonic waves through piezoelectric media [21]. Stability considerations require that a quasistatic approximation be imposed on Eqs. (6)–(9), so that they can be reduced to

$$\nabla_s \mathbf{v} = \hat{\mathbf{s}}^E \frac{\partial \mathbf{T}}{\partial t} \quad (24)$$

$$\nabla \cdot \mathbf{T} = \rho \frac{\partial \mathbf{v}}{\partial t} \quad (25)$$

where the stiffened compliance matrix is defined as

$$\hat{\mathbf{s}}^E = \mathbf{s}^E - \mathbf{d}'(\boldsymbol{\epsilon}^T)^{-1} \mathbf{d} = (\hat{\boldsymbol{\epsilon}}^E)^{-1} \quad (26)$$

In the saggital plane, the resulting time-stepping equations become

$$-\mathbf{V}_{i+(1/2),j+(1/2)}^{n+(1/2)} = \mathbf{V}_{i+(1/2),j+(1/2)}^{n-(1/2)} + \frac{\Delta t}{2\rho\Delta x} \hat{\mathbf{T}}_{i+(1/2),j+(1/2)}^n \quad (27)$$

$$\mathbf{T}_{i,j}^{n+1} = \mathbf{T}_{i,j}^n + \frac{\Delta t}{2\Delta x} \hat{\boldsymbol{\epsilon}}^E \hat{\mathbf{v}}_{i,j}^{n+(1/2)} \quad (28)$$

where the superscripts refer to the time instant and the subscripts indicate the gridpoint index. In Eqs. (27) and (28), we have

$$\hat{\mathbf{T}}_{i+(1/2),j+(1/2)}^n = \begin{bmatrix} T_1|_{i+1,j+1}^n - T_1|_{i,j+1}^n + T_1|_{i+1,j}^n - T_1|_{i,j}^n \\ + \cdots + T_5|_{i+1,j+1}^n - T_5|_{i+1,j}^n + T_5|_{i,j+1}^n - T_5|_{i,j}^n \\ T_6|_{i+1,j+1}^n - T_6|_{i,j+1}^n + T_6|_{i+1,j}^n - T_6|_{i,j}^n \\ + \cdots + T_4|_{i+1,j+1}^n - T_4|_{i+1,j}^n + T_4|_{i,j+1}^n - T_4|_{i,j}^n \\ T_5|_{i+1,j+1}^n - T_5|_{i,j+1}^n + T_5|_{i+1,j}^n - T_5|_{i,j}^n \\ + \cdots + T_3|_{i+1,j+1}^n - T_3|_{i+1,j}^n + T_3|_{i,j+1}^n - T_3|_{i,j}^n \end{bmatrix} \quad (29)$$

$$\hat{\mathbf{v}}_{i,j}^{n+(1/2)} = \begin{bmatrix} v_1|_{i+(1/2),j+(1/2)}^{n+(1/2)} - v_1|_{i-(1/2),j+(1/2)}^{n+(1/2)} + v_1|_{i+(1/2),j-(1/2)}^{n+(1/2)} - v_1|_{i-(1/2),j-(1/2)}^{n+(1/2)} \\ 0 \\ v_3|_{i+(1/2),j+(1/2)}^{n+(1/2)} - v_3|_{i+(1/2),j-(1/2)}^{n+(1/2)} + v_3|_{i-(1/2),j+(1/2)}^{n+(1/2)} - v_3|_{i-(1/2),j-(1/2)}^{n+(1/2)} \\ v_2|_{i+(1/2),j+(1/2)}^{n+(1/2)} - v_2|_{i+(1/2),j-(1/2)}^{n+(1/2)} + v_2|_{i-(1/2),j+(1/2)}^{n+(1/2)} - v_2|_{i-(1/2),j-(1/2)}^{n+(1/2)} \\ v_3|_{i+(1/2),j+(1/2)}^{n+(1/2)} - v_3|_{i-(1/2),j+(1/2)}^{n+(1/2)} + v_3|_{i+(1/2),j-(1/2)}^{n+(1/2)} - v_3|_{i-(1/2),j-(1/2)}^{n+(1/2)} \\ + \cdots + v_1|_{i+(1/2),j+(1/2)}^{n+(1/2)} - v_1|_{i+(1/2),j-(1/2)}^{n+(1/2)} + v_1|_{i-(1/2),j+(1/2)}^{n+(1/2)} - v_1|_{i-(1/2),j-(1/2)}^{n+(1/2)} \\ v_2|_{i+(1/2),j+(1/2)}^{n+(1/2)} - v_2|_{i-(1/2),j+(1/2)}^{n+(1/2)} + v_2|_{i+(1/2),j-(1/2)}^{n+(1/2)} - v_2|_{i-(1/2),j-(1/2)}^{n+(1/2)} \end{bmatrix} \quad (30)$$

Further development of the FDTD method for piezoelectric substrates is expected in the future.

7.6. Diffraction and Beamsteering

Surface acoustic waves are generated by sources of finite aperture and are therefore subject to diffraction effects. As is done in optics, the effects are classified as near-field (Fresnel) effects and far-field (Fraunhofer) effects. In SAW devices, the Fraunhofer region is of most interest.

Many of the techniques developed for optics can be applied to SAW, with the small modification that the velocity, and therefore the wavenumber, of the waves depend on the direction of propagation. The wave velocity in a specified direction is computed by solving the stiffened Christoffel equation, as outlined in Ref. 13.

A commonly used method of computing the effect of diffraction is known as the *angular spectrum of waves* (ASoW) technique. If we ignore any wave dependence in the x_3 direction, the amplitude of the surface wave ψ at a point (x, y) on the surface of the substrates can be written [22]

$$\psi(x, y) = \int_{-\infty}^{\infty} \Psi(k_y) e^{-j(k_x x + k_y y)} dk_y \quad (31)$$

where $\Psi(k_y)$ is the Fourier transform of the wave amplitude at a reference point $x = 0$, while k_x and k_y are x_1 and x_2 components of the wavenumber for a wave propagating at an angle ϕ to the x_1 axis shown in Fig. 2. The signal detected at the receiving transducer is calculated by integrating $\psi(x, y)$ over all receiving electrodes.

Because of the anisotropy of SAW substrates, the acoustic wavefront does not always propagate in the direction that is normal to the electrodes. This effect, known as *beamsteering*, must be considered when positioning the receiving transducer.

BIBLIOGRAPHY

1. R. M. White and F. W. Voltmer, Direct piezoelectric coupling to surface elastic waves, *Appl. Phys. Lett.* **7**(12):314–316 (1965).
2. J. H. McClellan, T. W. Parks, and L. R. Rabiner, A computer program for designing optimum FIR linear phase digital filters, *IEEE Trans. Audio Electroacoust.* **21**(6):506–526 (1973).
3. R. C. Williamson and H. I. Smith, The use of surface elastic wave reflection gratings in large time-bandwidth pulse compression filters, *IEEE Trans. Microwave Theory Tech.* **MTT-21**(4):195–205 (1973).
4. M. Solal, P. Dufilie, and P. Ventura, Innovative SPUDT based structures for mobile radio applications, *1994 IEEE Ultrason. Symp. Proc.*, Cannes, France, 1994, pp. 17–22.
5. M. Hikita, N. Shibagaki, T. Akagi, and K. Sakiyama, Design methodology and synthesis techniques for ladder-type SAW resonator coupled filters, *1993 IEEE Ultrason. Symp. Proc.*, Baltimore, MD, 1993, pp. 15–24.
6. H. Nakahata, K. Higaki, S. Fujii, A. Hachigo, K. Kitabayashi, K. Tanabe, Y. Seki, and S. Shikata, SAW devices on diamond, *1995 IEEE Ultrason. Symp. Proc.*, Seattle, WA, 1995, pp. 361–370.
7. H. Stark and F. B. Tuteur, *Modern Electrical Communications*, Prentice-Hall, Englewood Cliffs, NJ, 1979.

8. J. C. B. Saw, T. P. Cameron, and M. S. Suthers, Impact of SAW technology on the system performance of high capacity digital microwave radio, *1993 IEEE Ultrason. Symp. Proc.*, Baltimore, MD, 1993, pp. 59–65.
9. R. C. Peach, F. Z. Bi, and B. van Osch, The application of surface acoustic wave filters to communications satellite design, *Proc. AIAA 15th Int. Commun. Satellite System Conf.*, San Diego, CA, 1994.
10. J. Machui, J. Bauregger, G. Riha, and I. Schropp, SAW devices in cellular and wireless phones, *1995 IEEE Ultrason. Symp. Proc.*, Seattle, WA, 1995, pp. 121–130.
11. G. K. Montress, T. E. Parker, and D. Andres, Review of SAW oscillator performance, *1994 IEEE Ultrason. Symp. Proc.*, Cannes, France, 1993, pp. 43–54.
12. P. M. Bakken and A. Rønnekleiv, SAW-based chirp Fourier transform and its application to analogue on-board signal processing, *Int. J. Satellite Commun.* **7**(4):283–293 (1989).
13. B. A. Auld, *Acoustic Fields and Waves in Solids*, 2nd ed., Vol. 1, Kruger, Malabar, FL, 1990.
14. C. K. Campbell, *Surface Acoustic Wave Devices*, Academic Press, Boston, 1998.
15. C. S. Hartmann, D. T. Bell, Jr., and R. C. Rosenfeld, Impulse response model design of acoustic surface-wave filters, *IEEE Trans. Microwave Theory Tech.* **MTT-21**(4):162–175 (1973).
16. Y. Xu and P. M. Smith, A theoretical and experimental study of coupled SAW resonator filters, *IEEE Trans. Ultrason. Ferroelectr. Freq. Control* **UFFC-42**(4):717–725 (1995).
17. D. P. Morgan, *Surface-Wave Devices for Signal Processing*, Elsevier, Amsterdam, 1991.
18. R. C. Peach, A general Green function analysis for SAW devices, *1995 IEEE Ultrason. Symp. Proc.*, Seattle, WA, 1995, pp. 221–226.
19. V. P. Plessky and T. Thorvaldsson, Periodic Green's functions analysis of SAW and leaky SAW propagation in a periodic system of electrodes on a piezoelectric crystal, *IEEE Trans. Ultrason. Ferroelectr. Freq. Control* **UFFC-42**(2):280–293 (1995).
20. K. S. Yee, Numerical solution of initial boundary value problems involving Maxwell's equations in isotropic media, *IEEE Trans. Anten. Propag.* **AP-14**:302–307 (1966).
21. P. M. Smith and W. Ren, Finite-difference time-domain techniques for SAW device analysis, *2002 IEEE Ultrason. Symp. Proc.*, Munich, Germany, 2002, pp. 313–316.
22. T. L. Szabo and A. J. Slobodnik, Jr., The effect of diffraction on the design of acoustic surface wave devices, *IEEE Trans. Sonics Ultrason.* **SU-20**(3):240–251 (1973).

ACTIVE ANTENNAS

ALAN MICKELSON
University of Colorado
Boulder, Colorado

1. INTRODUCTION TO ACTIVE ANTENNAS

A good place to start a discussion of active antennas might well be to define what we mean by an *active antenna* as is

done in two review articles on active integrated antennas [2,3]. An antenna is a structure that converts electromagnetic energy propagating in free space into voltage and current¹ in an electrical circuit and vice versa. In a transceiver system, the antenna is used to both receive and transmit free-space waves. At minimum, a transceiver then must consist of a signal source that serves to drive the antenna as well as a receiver circuit that reads out the signal from the antenna. Until relatively recently, practically all antenna systems operating in the microwave frequency regime (operation frequencies greater than 1 billion cycles per second, or 1 GHz) went to great lengths to isolate the antenna from the circuits—that is, to find ways to make system operation independent of the antenna's electrical characteristics. In contradistinction, an active antenna is one in which the antenna actually serves as a circuit element of either the driver or readout circuit. To really understand why this is different from conventional antenna driving or readout will require us to take a bit of a historical trip through the last century or so.

Actually, the first antenna of all time was an active one. Heinrich Hertz back in 1884 [4] was the first person to demonstrate that one could generate radiowaves and that they would propagate from a transmitter to a receiver at the speed of light. The apparatus used is schematically depicted in Fig. 1. The idea of the transmitter is that, by discharging an induction coil (a wire looped about a magnetic core such that the composite device can store significant amounts of magnetic energy) into a sparkgap, one can generate a current in the 5-mm-diameter wire. The voltage in the sparkgap induces a current in the wire, which in turn induces a voltage in the wires, and this voltage in turn induces current such that the voltage and current propagate along the two pieces of the wire to either side of the sparkgap as waves, appearing much like a one-dimensional slice through a water wave propagating away from the point where a pebble has struck the water's surface (the sparkgap). A wave will propagate rectilinearly until it encounters an obstruction, at which point it can suffer reflection and transmission from the barrier that the obstruction presents. There will then be reflections off the metal spheres on the ends of the wire. The spark will generate a broad spectrum of frequencies—that is, different lengths of waves. The reflections off the two ends, though, will tend to cancel each other except at certain special frequencies. The effect at these wrong frequencies is much like the effect of throwing a handful of pebbles into the pond and noting that, in between the points where the pebble struck, the waves are much less

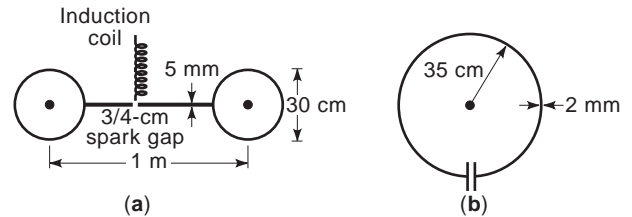


Figure 1. Hertz apparatus for (a) transmitting and (b) receiving radiowaves, where the transmitting antenna serves to choose a specific frequency of the sparkgap voltage to transmit to the receiving antenna, which also serves to pick out this special frequency from the free-space waveform and turn this electromagnetic disturbance into a voltage across the receiver antenna gap.

distinct than they are far from where the handful struck the surface. The special frequencies are ones that just fit into the region between the spheres. The current needs to be zero at the two ends in order to fit, whereas the voltage needs to be maximum at the ends. The current and voltage waves at the right frequency may appear as depicted in Fig. 2. The Hertz transmitter is the archetypical active antenna. The source is the sparkgap, which is actually placed in the antenna. The antenna then acts as a filter to pick the right frequency out of a large number of frequencies that could be launched from the sparkgap. The receiver is picked to be of a length to also select this primary frequency.

Hertz-style sparkgap transmitters, after further development and popularization by Marconi, were the primary ones in use for some 50 years after Hertz until they were banned for by the Federal Communications Commission (FCC). Indeed, sparkgap transmitters do exhibit some rather severe drawbacks. The main problem is that the simple resonant dipole antenna (i.e., a straight-wave antenna with a gap used to feed in current) is a pretty lousy frequency filter; that is, if one increases the frequency by 50%, there is 75% as much power transmitted at this frequency as at the first resonance, which is called the *fundamental*. There is a second resonance at twice the frequency of the first resonance and others at each integer multiple of the fundamental. Therefore, with increasing frequency the transmitted power decreases a little and then flattens out around the second resonance, decreases a little, flattens out at the third resonance, and so on, as is illustrated in Fig. 3. If the spark discharge is really broadband (i.e., if it really generates a large number of frequencies

¹A recurring theme in this article will be that voltage and current can be independently measured only at low frequency. Active antennas are useful in the frequency regime where we cannot really operationally have independent voltage and current, but only a combination of the two that forms a wave. It would really be better to define an antenna as a structure that converts waves propagating in free space to waves propagating in a guiding structure and vice versa. Such wording is a bit overpowering and requires a bit too much qualification for the second sentence of an introduction.

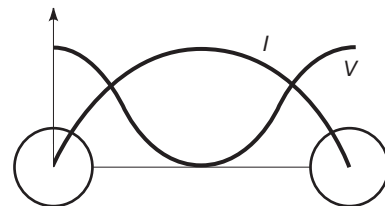


Figure 2. Current and voltage waveforms for the lowest-order (least number of zeros) waveform for the Hertz transmitter of Fig. 1a. The current must go to zero at the points where the wire ends, whereas the potential will be highest there.

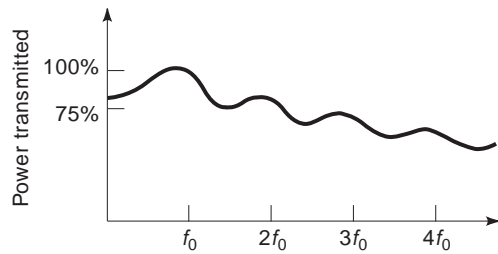


Figure 3. A sketch of what the transmission as a function of frequency might look like for the Hertzian dipole antenna of Figs. 1 and 2.

where the highest frequency may be many times the lowest), then what is transmitted by the antenna will also be broadband, albeit with somewhat higher transmission at the fundamental frequency and its harmonics than in between. In the very early days of radio, this was somewhat acceptable, although I would imagine that any information that one tried to impress on such a broadband carrier would be rather severely degraded on reception. However, the demise of the sparkgap transmitter was really instigated by the early success of radio, which caused the available frequency bands to begin to fill up rapidly. This band filling was a motivation for the formation of the FCC in 1934, which was then charged with allocation of frequency bands. That as allocation was necessary was in and of itself a justification for a (1934) ban on sparkgap transmitters, which were needlessly wasting bandwidth.

In a later experiment, Hertz noticed that the waves he was generating would tend to have a component that hugged the ground and could therefore travel over the horizon and, in fact, across the Atlantic Ocean, skimming along the surface of the water. Other researchers noticed that the effect became more pronounced at wavelengths longer than the roughly 2 m wavelength that Hertz originally used. (For the relation between frequency and wavelength for some important frequency bands, see Table 1.) In order for wave transmission to be useful, however, the transmitted signal needs to carry information. To impress information on the wave is said to be *modulating* the carrier. One can modulate either the heights (amplitudes) of the wave or the frequency of the wavetrain. The discovery of a technique to *amplitude-modulate* the waves coming off an antenna (in 1906) then led to the inception of AM radio in bands with wavelengths greater than 300 m, which corresponds to roughly 1 MHz. AM radio became commercial in 1920. By the 1930s, other researchers noted that waves with frequencies around 10 MHz, corresponding to a wavelength around 30 m, could be quite efficiently propagated over the horizon by bouncing the wave off the ionosphere. This led to the radio bands known as *shortwave*. In 1939, a researcher realized a technique to modulate the frequency of the wave. This realization led in the 1950s to FM radio, which was allocated the band around 100 MHz with a corresponding wavelength around 3 m. However, the FM technique was used first during World War II as a radar modulation technique. Radars today, as will be

Table 1. A Listing of the Allocated Microwave and Millimeter-Wave Bands as Defined by the Frequency and Wavelength Range within Each Band

Band Designation	Frequency (GHz)	Wavelength
L	1–2	15–30 cm
S	2–4	7.5–15 cm
C	4–8	3.75–7.5 cm
X	8–12	2.5–3.75 cm
Ku	12–18	1.67–2.5 cm
K	18–26	1.15–1.67 cm
Ka	26–40	0.75–1.15 cm
Q	33–50	6–9 mm
U	40–60	5–7.5 mm
V	50–75	4–6 mm
E	60–80	3.75–5 mm
W	75–110	2.7–4 mm
D	110–170	1.8–2.7 mm
G	140–220	1.4–2.1 mm
Y	220–325	0.9–1.4 mm

brought up in a subsequent paragraph, are at frequencies above roughly 1 GHz or wavelengths below 30 cm.

There is a fundamental difference between circuits that operate at frequencies whose corresponding wavelengths are less than the maximum circuit dimension and those circuits that are large compared to the carrier wavelength. The effect is closely related to the concept of impedance. As was mentioned above, in the wire antenna, the voltage and current feed each other and thereby travel on the antenna as waves. The same effect takes place in a circuit. At any point along the path (line) in a circuit, one defines the ratio of voltage at one frequency to the current at the same frequency as the impedance at that frequency. If the impedance tends to preserve the phase relation (where the wave peaks lie, relatively), then we would say that the impedance is *resistive*. If the impedance tends to drive the voltage peaks forward with respect to the current peaks, we say that the impedance is *capacitive*; in the converse case we say that the impedance is *inductive*. In a small circuit, one generally tries to carefully craft passive components—resistors, capacitors, and inductors—such that they exhibit large local impedance; that is, large impedance within their physical dimension. The lines (wires) between them have little or no effect on the electromagnetic disturbance passing through the circuit, then, as the impedances in the wires are small and reasonably constant with length. When the circuit is large (compared to the highest frequency into which any signal handled by the circuit can be decomposed), the lines themselves become circuit elements, and they themselves must be carefully crafted in order to exhibit the proper impedances. To illustrate, consider the parallel-plate capacitor of Fig. 4. The capacitance is maximized by maximizing the permittivity ϵ (a material parameter that denotes the ratio of electrical displacement to applied electric field) and area A while minimizing the plate spacing d . However, that the capacitance depends on the plate spacing d is the important point here. Consider the circuit of Fig. 5. The only ground in the figure is the one on the battery, but the wires connecting the circuit elements together in essence form

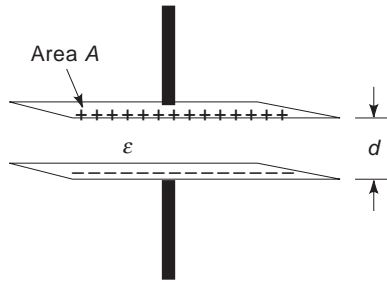


Figure 4. Schematic depiction of a parallel-plate capacitor in which the flow of a current will tend to change the upper plate, causing a voltage difference between upper and lower plates. The *capacitance* is defined as the ratio of the amount of change of the upper plate to the magnitude of the voltage this change induces between the plates.

at each point a capacitor, with a point on the wire that is carrying charge as the upper plate and the ground as the lower. This capacitance value changes as a function of position along the wire. For a small enough circuit (relative to the wavelength of the highest frequency carried by the circuit), the effect is not too important, as the wire-ground pair is not optimized for capacitance value and the position-varying effect is small. For a large circuit, the effect is disastrous, as we'll consider below.

Consider the circuit of Fig. 6. The idea is to discuss what happens when impedances aren't carefully controlled. Let's first say that the circuit is short (compared to wavelength). If the load resistor R_L is not matched to (i.e., isn't equal to) the resistance of the source R_S , some amount of reflection will occur at R_L , propagate back to R_S , be reflected with a minus sign times the reflection at R_L , propagate back to R_L , and so on. The reflections add up perfectly out of phase (i.e., simply subtract from one another) at the source and load, and the amount of power supplied to the load is less than optimal. In this limit of a small-circuit case, it is as if the load will not allow the source to supply as much power as it is capable of. Let's now say that the line is "nice" but long compared to a wavelength. Then the same argument applies to the reflections, but in this case the source doesn't know that the load is there until several wave periods have passed (several maxima and minima of the waveform have left the source), so the source supplies all the power it can. The power, though, is not allowed to be fully absorbed by the load, and some amount of the power will rattle around the line until it is radiated or absorbed. As we mentioned above, in a long enough circuit the wire itself becomes a distributed element—that is, one with an impedance of its own. If the distance to the nearest ground is not kept fixed

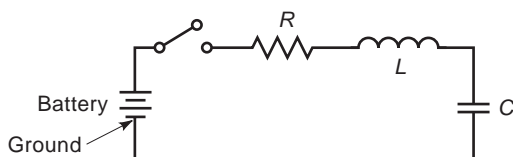


Figure 5. A circuit with lumped elements connected by wire segments.

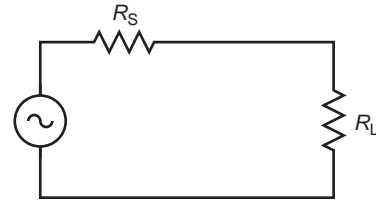


Figure 6. A circuit in which one is trying to supply power from a source with internal resistance R_S to a load with resistance R_L . The power transfer is maximized only when R_S and R_L are equal, in which case half the power supplied by the source is supplied to the load, the other half being dissipated in the source and causing it to heat.

along the line, this impedance becomes dependent on the position. In this case, we would have distributed reflections all along the line and the circuit would probably not work at all. This spatially variable impedance line is flexible, though, as illustrated by the drawing of a coaxial cable in Fig. 7. The idea is that, if the line brings along its own ground plane in the form of a grounded outer conductor, the impedance of the line can be kept constant with distance. The problem becomes the connection of the line to the source and load. A byproduct of this problem is a measurement reality. That reality is that a sufficiently high frequency one can no longer accurately sample voltage or current individually. Voltage sampling requires a measurement circuit that exhibits a high resistive impedance parallel to the impedance, which separates the sampling points of this composite voltage probe, whereas a current probe requires a small parallel impedance. Such probes are not impedance matched and disrupt the normal operation of the circuit under test. High-frequency circuit probes must use carefully impedance-matched termination, and thereby can only sample the power of waves propagating on the circuit's lines.

Before going on to discuss the "conventional" solution versus the "new" active-antenna solution, perhaps we should summarize a bit. In AM, shortwave, and FM applications, the wavelengths are greater than meters. If one considers typical receivers, the whole circuit will generally

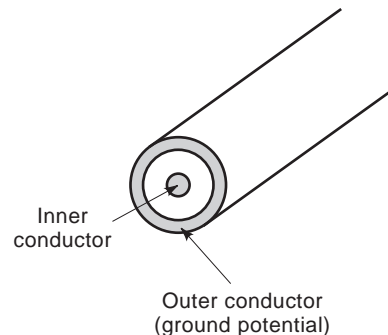


Figure 7. A coaxial cable in which signals are carried on an inner conductor and in which the grounded outer conductor serves to carry the ground plane along with the signal in order to give a constant impedance along the line.

be small compared to the carrier wavelength. This is also to say that in all of these cases, the antennas will be active in the sense that the antenna presents an impedance to the circuit. One needs pieces of line comparable to a wavelength to really match or isolate a component. However, from here on we won't be interested in the low-frequency case but rather in the well-above-1-GHz case. During World War II, radar was the application that drove the frequencies above 1 GHz (wavelength less than 30 cm). In a radar, one sends out a pulse and, from the return scattered wave, tries to infer as much as possible about the target. Target resolution is proportional to wavelength. There has been a constant drive to shorten wavelength. Therefore, as is indicated by Table 1, one notes that bands have been allocated out to 100s of GHz. Presently, however, there are a plethora of nonmilitary drivers for pushing to higher frequencies. These relate to compactness and lower power dissipation. But as we'll see, the conventional solution, which was developed for radars, is really not conducive to compactness nor to the pressures of cost minimization of the commercial market.

A typical conventional transmitter may appear as that schematically depicted in Fig. 8. A main concept here is that the transmission lines and matching networks are being used to isolate the oscillator from the amplifier and the amplifier from the antenna, in contrast to the situation in an active antenna. There were a number of reasons why the conventional solution took on the form that it did. Among them was the urgency of World War II. Radar was developed rapidly in both Great Britain and the United States in the 1930s and 1940s. Rapid development required numerous researchers working in parallel. When operating frequencies exceeded 1 GHz (corresponding to 30 cm wavelengths), matching networks, whose main requirement is that they must consist of lines of lengths comparable to a wavelength, became convenient to construct (in terms of size) for ground-based radar. In this case, then, the oscillators could be optimized independently of the amplifiers, which in turn could be optimized independently of the antennas and the receiver elements. The impedances of the individual pieces didn't matter, as the matching networks could be used to effectively transform the effective impedances looking into an element into something completely different for purposes of matching pieces of the network to each other. There are costs associated with such a solution, though, such as total system size as well as the tolerances that components must satisfy. However, once the technique was in place, the industry standardized on the conventional solution and perfected it to the point where it was

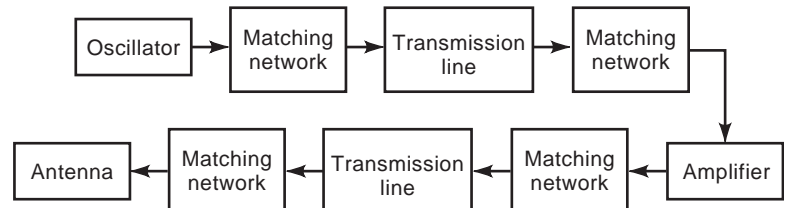


Figure 8. Schematic of a conventional RF microwave transmitter in which each individual element of the transmitter is matched to each other element.

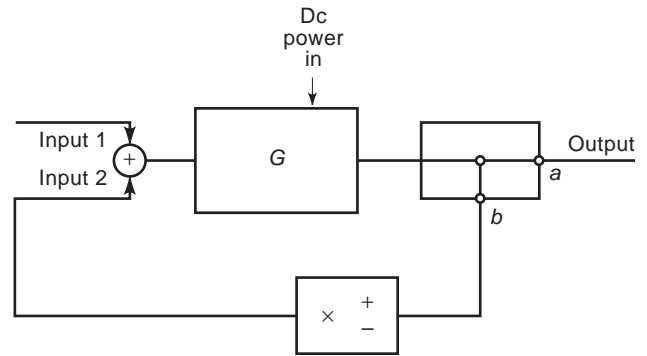


Figure 9. Schematic depiction of a feedback system that can operate as an oscillator when G is greater than 1, the feedback is positive, and there is a delay in feeding back the output to the input.

hard to challenge. The reemergence of the active solution really owes itself to two independent technologies, the emergence of high-frequency solid-state devices and the development of planar circuit and planar antenna technology.

A single frequency of electromagnetic energy must be generated in an *oscillator*—that is, a circuit that converts DC electrical power to AC electromagnetic power at the proper frequency. The basic operation of an oscillator can be described with respect to Fig. 9. What is shown here schematically is an amplifier in which a portion b (< 1) of the output is fed back to the input with either a plus or a minus sign. When the feedback is off ($b = 0$), then the signal out will be just G times the input. When the feedback is negative, the output will be less than G times the input. However, in the negative feedback mode, the stability to noise increases since fluctuations will be damped; that is, if the output fluctuates up, this lowers the effective input, whereas if the output fluctuates down, the output is driven up. The opposite is true in the positive-feedback case. In the positive-feedback case, if there were no fluctuation, any input would cause the output to increase until all the DC power in as well as all of the input signal would show up at the output. (This is all of the power that can show up at the output. This behavior is typical of unstable operation.) This would not be such an interesting case. However, there are always fluctuations of the input, and the positive feedback will cause these to grow. If there is a delay from output to input, then fluctuations with a period corresponding to this delay will be favored, as a rise in the input would show up as a rise in the output one period later, and rapidly all the DC power in would be converted to power out at this magic frequency. A real

circuit would operate a bit more interestingly than our ideal one. In a real circuit, as the fluctuations build up, the gain would be affected and some elements would absorb power, but the oscillations still would take place, although perhaps with a different frequency and amplitude from what one would have predicted from nondynamic measurements.

The transistor was first demonstrated in 1947, with publication in 1948 [5], with the diode not far behind [6]. Although the field-effect transistor (FET) was proposed in 1952 [7], it was not until the mid-1960s that the technology had come far enough that it could be demonstrated [8]. The high-electron-mobility transistor (HEMT) is a modification of the FET which allows for higher-frequency (and lower-noise) operation than the FET. The heterojunction bipolar transistor (HBT) is a more complex three-dimensional structured yet still integrated circuit (IC)-compatible semiconductor device that is now replacing the FET/HEMT in certain high-frequency applications. Two-terminal transferred electron devices (TEDs) were used before the FET for microwave applications and are still in use but tend to have a much lower wallplug efficiency, especially as the amplifying device of an oscillator. Radar systems, however, were already in use in the late 1930s. Essentially all of the microwave sources in radars up until the 1970s operated on principles that required that the source have physical dimensions larger than a wavelength, and perhaps many wavelengths. This fact almost required the use of conventional solution. Transistors, though, can have active areas with dimensions of micrometers; even packaged hybrid devices can have complete packages of dimensions smaller than a millimeter. The transistor can, therefore, act as an amplifier with dimensions much smaller than a wavelength and does not, therefore, need to be placed in a conventional solution design.

The last piece of our story of the new active-antenna era involves the development of printed-circuit technology, along with slot and patch antennas. The two most common planar “open waveguide” designs are microstrip line and coplanar waveguide (CPW). Depictions of these waveguide lines are given in Fig. 10. The idea behind the microstrip line is to propagate electromagnetic energy along the line by confining the electric field between the upper signal line and a lower ground plane. As the upper line carries current, a magnetic field encircles the upper line. As power flow takes place in a direction perpendicular to the electric and magnetic fields, the power flow is beneath the signal line in the dielectric. As we discussed before, on a low-frequency wire, the voltage and current waveforms couple to generate a wave. The coupling of the electric and magnetic fields in the microstrip is analogous to the coupling of voltage and current on the Hertz antenna wire, except that the microstrip line can be electrically long in the sense that the distance from the signal line to the ground plane is kept constant so that the impedance can be kept constant, as with the earlier-discussed coaxial cable. Lines that carry along their ground planes are generally referred to as *transmission lines*. Components (i.e., capacitors and inductors) can be built into the line by doing such things as changing the width or cutting gaps

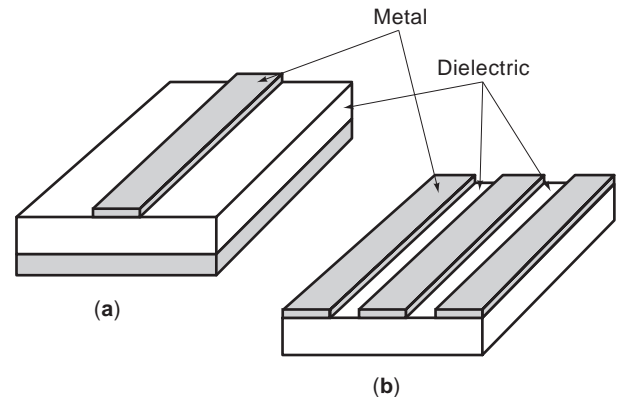


Figure 10. Views of (a) a microstrip and (b) a coplanar waveguide line. In the microstrip, the ground plane is the lower electrode, whereas in the coplanar waveguide the ground plane is placed on the surface of the dielectric substrate.

into the upper line or putting slits in the ground plane. In this sense, we can still describe transmission-line circuits by conventional circuit theory if we use a special circuit model for the line itself. The CPW line is quite similar to the microstrip line except that there the ground planes are on top of the dielectric slab. Either of these line types is reasonably easy to fabricate, as one needs only to buy a metal-coated dielectric plate and then pattern the needed shapes by photographically defining the patterns using a technique known as *photolithography*, a process common to all present-day circuit fabrication. These planar structures are quite compatible with transistor technology, as is indicated by the simple transistor oscillator circuit depicted in Fig. 11. The gap in the line on the drain side is there in order to provide the proper feedback for oscillation. In this case, the total oscillator linear dimension can be less than a wavelength.

In order to have an active antenna, one needs to have a radiating element—that is, a passive-antenna element in the active antenna. Certain antenna technologies are compatible with microstrip and CPW technologies, and these antenna types are illustrated in Fig. 12. The idea behind either of these antenna types is that the patch or slit is designed to have one of its dimensions in the plane match the operating wavelength such that the structure resonates (such as we had discussed in conjunction with the Hertz dipole antenna). In the case of fundamental mode operation of the patch antenna, the resonating direction is

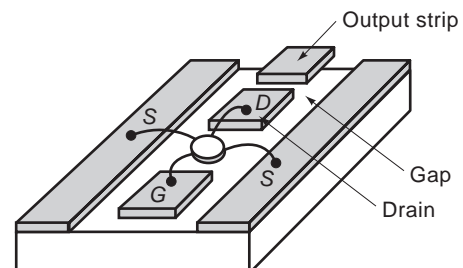


Figure 11. A simple transistor oscillator implemented in CPW technology.

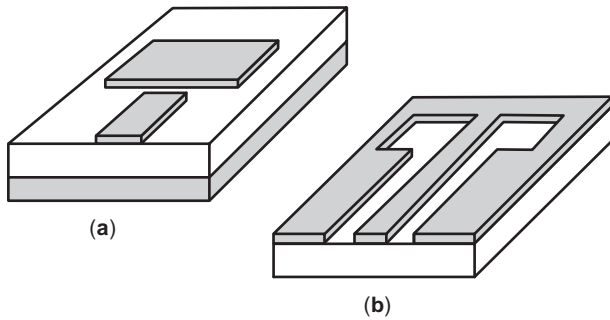


Figure 12. A depiction of (a) a patch antenna in a microstrip line and (b) a slot antenna in a CPW line.

the direction of the patch that lies along the direction of the feedline and extends from the end of the feedline to the end of the patch. The other dimension must be chosen such that it does not resonate, which requires that its dimension not correspond too closely to a resonance along that direction. A possible choice is to make this dimension smaller than the other so that its length is too short to resonate. However, square patches are also possible as the feedline will favor the resonance along the feed direction. Now, in a microstrip configuration, the electric field points primarily from the upper conductor to the ground plane. For the patch antenna, this configuration is illustrated in Fig. 13. The downward-pointing electric field component along the edges of the patch that are directed along the same direction as the input feedline (resonating direction) will then have a field pattern as sketched in Fig. 13a, and this downward component of the electric field along the edges perpendicular to the feedline direction (where it has been assumed that there is no resonance along this direction) will have a field pattern as sketched in Fig. 13b, with

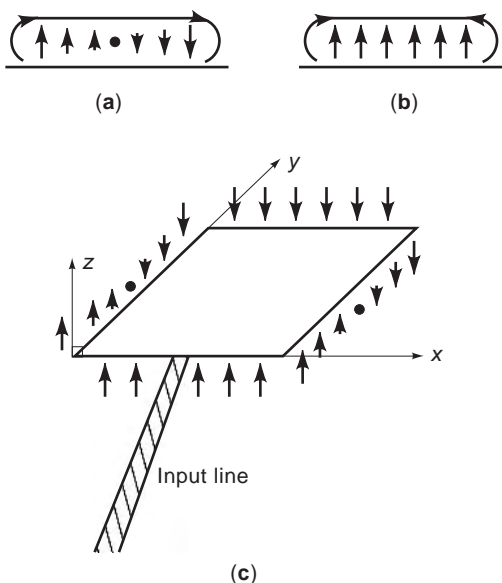


Figure 13. Illustration of the electric field directions along (a) the nonradiating edge and (b) the radiating edge, and (c) a schematic depiction of the edge fields around the patch.

a composite sketch given in Fig. 13c. The important part of the sketches, however, is really the so-called fringing fields in Fig. 13a—that is, the fields that point neither up nor down but rather point across. Along the input *radiating edge*, that is, the edge that is perpendicular and connects to the input line, electric field lines point along the direction of the feedline extending from some distance out in the dielectric to the edge. Along the other *radiating edge*, the other edge that is perpendicular to the input feedline but at the other side of the patch, there is a field pointing out (i.e., in phase with the electric field of the input radiating edge) from the edge into the dielectric. These two stripes of field, in phase and a resonating distance apart, then combine together to create an upwardly radiating wave field. The non radiating edges, those that are along the direction of the input feedlines, do not give rise to fringe field contributions as well, but these fringe field contributions are out of phase with each other and thereby cancel and do not contribute to the radiation from the patch. The operation of a slot antenna can be explained by a similar argument if one notes that the radiating edges must be those edges that lie along the direction of the feedline that is the downward-pointing magnetic field (the dominant component of the magnetic field that rings the currents) that takes the part of the electric field in the slot antenna’s operation.

We have now introduced all the pieces necessary to describe the new resurgence in active-antenna research. A possible active-antenna design could appear as in Fig. 14 [9], where the transistor is actually mounted right into the patch antenna element, and therefore the design can be quite compact; that is, the source plus oscillator plus antenna can all be fit into less than a wavelength area. The design of Fig. 14, which comes from R. Compton’s group at Cornell, will be discussed further in the next section.

There are a number of advantages to the use of active antenna ideas. One is that an active antenna can be made compact. Compactness in itself is advantageous,

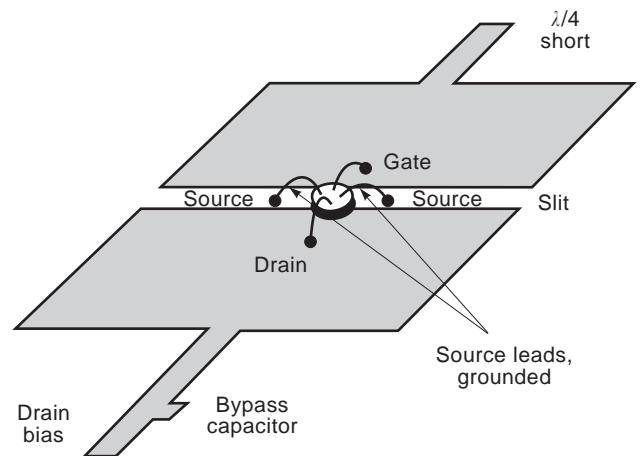


Figure 14. Depiction of the upper surface metallization of a microstrip active patch antenna discussed in Ref. 7. The short circuit on the gate together with the slit between gate and drain provides the proper feedback delay to cause oscillation.

as throughout the history of microelectronics, miniaturization has led to lowered costs. There are really two more advantages, though, that relate to compactness. One is that the power-handling capabilities of a device go down with increasing frequency. We would therefore like to find ways to combine the power from several devices. One can try to add together outputs from various oscillators in the circuit before feeding them to the elements, but this goes back to the conventional solution. A more advantageous design is to make an array of antennas, with proper spacing relative to the wavelength and antenna sizes, and add the power of the “locked” oscillators in the array quasioptically in free space.² The locking requires that the oscillators “talk” to each other such that the phases of all the array elements stay in a given relation. As will be discussed in more detail in the next section, however, an important problem at present in the active-antenna field relates to keeping elements locked yet still being able to modulate the output as well as steer the beam in order to be able to electronically determine on output direction. These issues will be discussed in Section 2 and in more detail in Section 3.

2. SOME QUANTITATIVE DISCUSSION OF ASPECTS OF ACTIVE ANTENNAS

Antennas are structures that convert free-space radiation to guided radiation and vice versa. In order to carry out this operation efficiently, antennas must have some dimension that is significant compared to a wavelength. Antenna design then must require a full treatment of the electromagnetic field, including its geometric structure to sub-wavelength accuracy and its polarization. Such analysis requires the full apparatus of Maxwell’s field equations. An early motivation for the use of the active-antenna concept was that of using the field generating devices in proximity to the antenna such that the physical length of an electromagnetically small antenna could be augmented by the characteristics of the generating mechanism. Presently, attention has turned to higher frequencies, but the active-antenna concept that an antenna and a circuit be coupled such that the circuit can be used to alter the antennas characteristics is the same. An interesting point is that although the operating frequency of active antennas is usually high, that is, higher than the frequency regime at which integrated electronic circuits operate, the driving circuit tends to be small in total extent relative to the operating wavelength and therefore circuit theory concepts still apply to active-antenna design although these circuit theory concepts must be judiciously combined with electromagnetic theory. The usual formulation couples a high-frequency form of transmission-line theory with circuit theory as applied to microwave/millimeter-wave

²An amplifier is an oscillator biased above threshold, but without feedback. An array of active antennas carefully designed to have no internal feedback can be used to amplify weak signals. This is an alternative to having the array itself generate the initial signal, and the design if such amplifiers is also a part of the field of quasioptical power combining. This topic is reviewed in Ref. 10.

circuits. We will presently work from Maxwell’s theory to high-frequency transmission-line theory as it applies to guidance and radiation. We will introduce the somewhat specialized circuit formulation, which includes transmission lines and planar antennas that is usually applied to the high-frequency integrated active-antenna problem.

Maxwell’s equations are the basic defining equations for all electromagnetic phenomena, and they are expressible in MKSA units as [11]

$$\begin{aligned}\nabla \times \mathbf{E} &= -\frac{\partial \mathbf{B}}{\partial t} \\ \nabla \times \mathbf{H} &= \mathbf{J} + \frac{\partial \mathbf{D}}{\partial t} \\ \nabla \cdot \mathbf{D} &= \rho \\ \nabla \cdot \mathbf{B} &= 0\end{aligned}$$

where \mathbf{E} is the electric field vector, \mathbf{B} is the magnetic induction vector, \mathbf{H} is the magnetic field vector, \mathbf{D} is the electric displacement vector, \mathbf{J} is the current density vector, and ρ is the volume density of charge. Each of these field quantities is a function of three spatial coordinates, which define a coordinate vector \mathbf{r} , and of the time t . The del operator ∇ and its associated operations of the curl $\nabla \times$ and the divergence $\nabla \cdot$ operate on these spatial coordinates. An additional important quantity is \mathbf{S} , the Poynting vector, defined by

$$\mathbf{S} = \mathbf{E} \times \mathbf{H}$$

If one is to take the divergence of \mathbf{S} , one finds

$$\nabla \cdot \mathbf{S} = \nabla \cdot (\mathbf{E} \times \mathbf{H})$$

where, if one assumes a free-space region

$$\mathbf{D} = \epsilon_0 \mathbf{E}$$

$$\mathbf{B} = \mu_0 \mathbf{H}$$

where free-space implies current-free

$$\mathbf{J} = 0$$

and charge-free

$$\rho = 0$$

where ϵ_0 is the permittivity of free space and μ_0 is the permeability of free space, one can use vector identities and Maxwell’s equations to obtain

$$\nabla \cdot \mathbf{S} = -\frac{\epsilon_0}{2} \frac{\partial}{\partial t} (\mathbf{E} \cdot \mathbf{E}) - \frac{\mu_0}{2} \frac{\partial}{\partial t} (\mathbf{H} \cdot \mathbf{H})$$

Integrating this equation throughout a volume V and using Gauss’ theorem

$$\int \nabla \cdot \mathbf{S} dV = \int \mathbf{S} \cdot d\mathbf{A}$$

where $d\mathbf{A}$ is the unit normal pointing out of the surface of the volume V , one finds that

$$\int \mathbf{S} \cdot d\mathbf{A} = -\frac{\partial}{\partial t} W_e - \frac{\partial}{\partial t} W_m$$

where W_e is the electric energy density

$$W_e = \frac{\epsilon_0}{2} \int \mathbf{E} \cdot \mathbf{E} dV$$

and W_m is the magnetic energy density

$$W_m = \frac{\mu_0}{2} \int \mathbf{H} \cdot \mathbf{H} dV$$

The interpretation of these equations is that the amount of \mathbf{S} flowing out of V is the amount of change of the energy within V . One therefore associates energy flow with $\mathbf{S} = \mathbf{E} \times \mathbf{H}$. This is important in describing energy flow in wires as well as transmission lines and waveguides of all types. As was first described by Heavyside [12], the energy flow in a wire occurs not inside the wire but around it; that is, as the wire is highly conductive, there is essentially no field inside it except at the surface where the outer layer of oscillating charges have no outer shell to cancel their effect. There is therefore a radial electric field emanating from the surface of the wire that combines with an azimuthal magnetic field that rings the current flow to yield an $\mathbf{E} \times \mathbf{H}$ surrounding the wire and pointing down its axis. Likewise, for a structure to radiate electromagnetic power upward from its surface requires that crossed components of \mathbf{E} and \mathbf{H} exist on an upward-pointing surface of the conductor.

Now, we would like to apply Poynting's theorem to the study of circuits that may contain antennas. A circuit, in general, will contain conductors that guide charges and currents, and these conductors will be surrounded by materials that are permeated by electromagnetic fields generated by the charges and currents in the conductors. It was Pocklington in 1897 [13] who made the formal structure of the fields around a wire a bit more explicit and, in the effort, also formed the basis for the approximation on which most of circuit and transmission-line theory rests, the quasistatic approximation. The result of his study of monochromatic (single-frequency) fields on wires could be summarized as follows. If one considers a small enough region around the axis of a wire conductor, one could construct an xyz Cartesian coordinate system where the axis of the wire is the z axis. As the fields close to the wire are stronger than those farther away, one can show that close enough to the wire all of the field quantities $\mathbf{f}(x, y, z, t)$ vary as

$$\mathbf{f}(x, y, z, t) = \Re\{\mathbf{f}(x, y)p(z, t)\}$$

where the propagation function $p(z, t)$ will generally take the form

$$p(z, t) = a_f e^{i\beta z - i\omega t} + a_b e^{-i\beta z - i\omega t}$$

where the a_f and a_b are complex constants, β a propagation constant and ω the angular frequency of the assumed field's source. That is, the above states that the fields consist of forward- and backward-propagating waves multiplied by a transverse field configuration. If one assumes

that the velocity of propagation of the above-defined wave is $v = (\mu\epsilon)^{-1/2}$, where the speed of light the speed of light $c = (\mu_0\epsilon_0)^{-1/2}$ is generally reduced by materials that have μ and ϵ different from their free-space values, then one can write that

$$\beta = \frac{\omega}{v}$$

The result that $\mathbf{f}(x, y)$ is independent of z , when substituted into Maxwell's equations, results in the relations in which

$$\nabla_t \times \mathbf{E}_t = \rho$$

$$\nabla_t \times \mathbf{H}_t = \mathbf{J}_z$$

where

$$\nabla_t = \hat{e}_x \frac{\partial}{\partial x} + \hat{e}_y \frac{\partial}{\partial y}$$

is just the transverse, and therefore two-dimensional, gradient operator and the \mathbf{f}_t are the transverse field quantities. These equations are just the electro- and magneto-static equations for the transverse fields, whereas the propagation equation above shows that these static transverse field configurations can be just propagated forward [if the wire is perfectly terminated such that the a_b of the $p(z, t)$ equation is zero but the a_f , the forward-going coefficient is nonzero] as if they corresponded to a propagating plane-wave field configuration. If the magnetic field is caused by the current in the wire, it rings the wire, whereas if the electric field is static, it must appear to emanate from charges in the wire and point outward at right angles to the magnetic field. The Poynting vector \mathbf{S} then points along the direction of propagation, that is, along the wire. If the wire is somehow terminated, for example in an open or short circuit termination, then the dominant electric field may be along the direction of the wire's axis [this is the case where the a_b may be close to or equal to the a_f in the $p(z, t)$ equation], and the Poynting vector \mathbf{S} may have a significant component at right angles to the propagation direction. In fact, in an antenna structure, one open-terminates a wire at a length (half-wavelength) from a feed-point such that the electric field is strongly and homogeneously pointing along the axis of the wire during each half of the wave period. As the current guided along the wire and also changes direction each half-period, the Poynting vector can be maintained in an upwardly pointing direction throughout the wave period. It is reasonably straightforward to generalize this thin wire theory to more general conductor shapes and non-Cartesian geometries, but always with the result that the conductors can be laid out in such manner that they can be used to control the electromagnetic energy flow through controlling the forward and backward excitation coefficients of transverse field configurations that closely resemble static field structures.

If we wish to guide electromagnetic energy along conductors and radiate energy by changing the guiding structure in a controlled manner, then one must design the guiding and radiating structures such that the quasistatic picture comes close to being the actual one. An approximate theory that is based on Pocklington's quasistatic

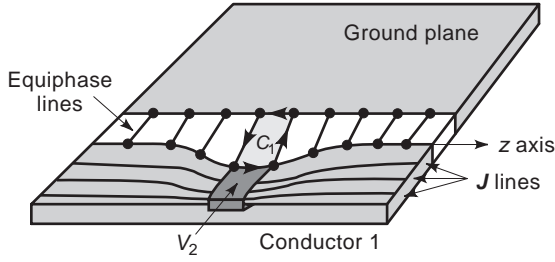


Figure 15. A sketch of a two-conductor transmission line where some equipotentials and some current lines are drawn in, as well as a volume V_1 with outward-pointing normal $d\mathbf{A}_1$. There is also an outward-pointing normal $d\mathbf{A}_2$ associated with the area bounded by contour C_2 .

approximation is one called *transmission-line theory*. To derive this theory, first consider the two-wire transmission line of Fig. 15. If we are to have something that we can actually call a transmission line, then we would hope that we can find equiphase fronts of the electromagnetic disturbance propagating in the gap crossing the gap conductor and that we can find lines along which the current flows on the current-carrying conductor. Otherwise, if the equiphases closed on themselves and/or we had eddies in the current, it would be hard to think of the structure as any form of guiding structure. Let's say we form an area in the gap with two walls of the four-sided contour C_1 surrounding this area following equiphases an infinitesimal distance dz from each other. We could then write

$$\int \nabla \times \mathbf{E} \cdot d\mathbf{A}_1 = - \int \frac{\partial \mathbf{B}}{\partial t} \cdot d\mathbf{A}_1$$

where $d\mathbf{A}_1$ corresponds to an upward-pointing normal from the enclosed area. One generally defines the integral as

$$\int \mathbf{B} \cdot d\mathbf{A}_1 = \phi$$

where ϕ is the magnetic flux. We further often define the flux as the inductance of the structure times the current by

$$\phi = Li$$

The integral with the curl in it can be rewritten by Stokes' theorem as

$$\int \nabla \times \mathbf{E} \cdot d\mathbf{A}_1 = \oint_{C_1} \mathbf{E} \cdot d\boldsymbol{\ell}$$

where C_1 is the contour enclosing the area. If we define

$$v = \int \mathbf{E} \cdot d\boldsymbol{\ell}$$

on the two equiphase lines of the contour C_1 , where v is an AC voltage (this is the main approximation shown above, as it is only strictly true for truly static fields), then, noting that v doesn't change along two of the boundaries of the contour (because they are the infinitesimal walls on constant voltage plates) and making the other two connecting lines infinitesimal, we note that the relation between the

curl of \mathbf{E} and the magnetic field reduces to

$$v(z+dz) - v(z) = \frac{\partial}{\partial t}(Li)$$

where it has been tacitly assumed that geometric deviations from rectilinear are small enough that one can approximately use Cartesian coordinates, which could be rewritten in the form

$$\frac{\partial v}{\partial z} = \ell \frac{\partial i}{\partial t} \quad (1)$$

where ℓ is an inductance per unit length, which may vary with longitudinal coordinate z if the line has longitudinal variation of geometry. A similar manipulation can be done with the second and third of Maxwell's equations. Taking

$$\nabla \cdot (\nabla \times \mathbf{H}) = \nabla \cdot \mathbf{J} + \frac{\partial}{\partial t} \nabla \cdot \mathbf{D}$$

and noting that the divergence of a curl is zero, substituting for $\nabla \cdot \mathbf{D}$ we find

$$\nabla \cdot \mathbf{J} + \frac{\partial \rho}{\partial t} = 0$$

which is the equation of charge conservation. Integrating this equation over a volume V_2 that encloses the current-carrying conductor whose walls lie perpendicular to the current lines gives

$$\int \nabla \cdot \mathbf{J} dV_2 = - \frac{\partial}{\partial t} \int \rho dV_2$$

where the total change Q , given by

$$Q = \int \rho dV_2$$

is also sometimes defined in terms of capacitance C and voltage v by

$$Q = Cv$$

Noting that

$$\int \nabla \cdot \mathbf{J} dV_2 = \int \mathbf{J} \cdot d\mathbf{A}_2$$

where $d\mathbf{A}_2$ is the outward-pointing normal to the boundary of the volume V_2 and where one usually defines

$$i = \int \mathbf{J} \cdot d\mathbf{A}_2$$

and letting the volume V have infinitesimal thickness, one finds that

$$\int \mathbf{J} \cdot d\mathbf{A}_2 = i(z+dz) - i(z)$$

Putting this together with the equations above, we find

$$\frac{\partial i}{\partial z} = c \frac{\partial v}{\partial t} \quad (2)$$

where c is the capacitance per length of the structure, where longitudinal variations in line geometry will lead to a longitudinal variation of c . The system of partial differential equations for the voltage and current have a circuit representation, as schematically depicted in Fig. 16a. One can verify this by writing Kirchoff's laws for the nodes

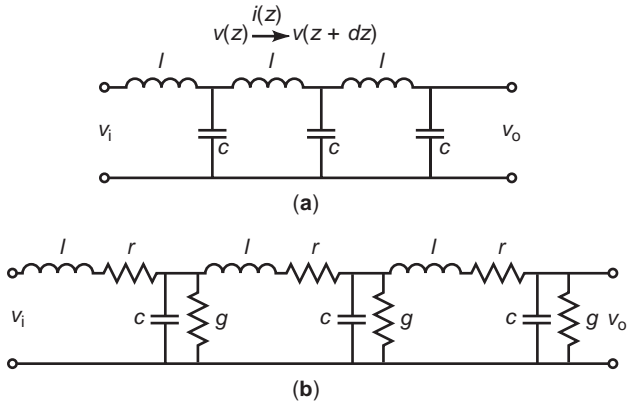


Figure 16. A circuit equivalent for (a) a lossless and (b) a lossy transmission line. The actual stages should be infinitesimally long, and the l s and c s can vary with distance down the line. In reality, one can find closed-form solutions for the waves in nominally constant l and c segments and put them together with boundary conditions.

with $v(z + dz)$ and $v(z)$ using the relations

$$v = \ell \frac{\partial i}{\partial t}$$

and

$$i = c \frac{\partial v}{\partial t}$$

Fig. 16b illustrates the circuit equivalent for a lossy (and therefore dispersive) transmission line, where the r represents the resistance encountered by the current in the metallization and where the g represents any conductance of the substrate material that might allow leakage to ground. A major point of the diagram is that the structure need not be uniform in order to have a transmission-line representation, although one may find that irregularities in the structure will lead to longitudinally varying inductances and capacitances.

Clearly, the solution to the circuit equations will have a wave nature that will exhibit propagation characteristics, which we discussed previously. In a region with constant ℓ and c , one can take a z derivative of Eq. (1) and a t derivative of Eq. (2) and substitute to obtain

$$\frac{\partial^2 v}{\partial z^2} - \ell c \frac{\partial^2 v}{\partial t^2} = 0$$

which is a wave equation with solutions

$$v(z, t) = v_f \cos(\omega t - \beta z + \phi_f) + v_b \cos(\omega t + \beta z + \phi_b) \quad (3)$$

where v_f is the amplitude of a forward-going voltage wave, v_b is the amplitude of a backward-going voltage wave, and

$$\frac{\omega}{\beta} = \sqrt{\ell c}$$

Similarly, taking a t derivative of Eq. (1) and a z derivative of Eq. (2) and substituting gives

$$\frac{\partial^2 i}{\partial z^2} - \ell c \frac{\partial^2 i}{\partial t^2} = 0$$

which will have a solution analogous to the one in Eq. (3), but with

$$v_f = \sqrt{\frac{\ell}{c}} i_f$$

$$v_b = \sqrt{\frac{\ell}{c}} i_b$$

which indicates that we can make the identification that the line phase velocity v_p is given by

$$v_p \triangleq \frac{\omega}{\beta} = \sqrt{\ell c}$$

and the line impedance Z_0 is given by

$$Z_0 = \sqrt{\frac{\ell}{c}}$$

Often, we assume that we can write (the sinusoidal steady-state representation)

$$v(z, t) = \text{Re}[v(z)e^{j\omega t}]$$

$$i(z, t) = \text{Re}[i(z)e^{j\omega t}]$$

such that we can write that

$$\frac{\partial v}{\partial z} = -j\omega \ell i$$

$$\frac{\partial i}{\partial z} = -j\omega c v$$

with solutions

$$v(z) = v_f e^{-j\beta z} + v_b e^{j\beta z}$$

$$i(z) = i_f e^{-j\beta z} + i_b e^{j\beta z}$$

Let's say now that we terminate the line with a lumped impedance Z_ℓ at location ℓ . At the coordinate ℓ , then, the relations

$$Z_\ell i(\ell) = v_f e^{-j\beta \ell} + v_b e^{j\beta \ell}$$

$$Z_0 i(\ell) = v_f e^{-j\beta \ell} - v_b e^{j\beta \ell}$$

hold, and from them we can find

$$v_f = \frac{1}{2}(Z_\ell + Z_0)i(\ell)e^{j\beta \ell}$$

$$v_b = \frac{1}{2}(Z_\ell - Z_0)i(\ell)e^{-j\beta \ell}$$

which gives

$$v(z) = \frac{i(\ell)}{2} [(Z_\ell + Z_0)e^{j\beta(\ell-z)} + (Z_\ell - Z_0)e^{-j\beta(\ell-z)}]$$

$$i(z) = \frac{i(\ell)}{2Z_0} [(Z_\ell + Z_0)e^{j\beta(\ell-z)} - (Z_\ell - Z_0)e^{-j\beta(\ell-z)}]$$

allowing us to write

$$Z(z - \ell) = \frac{v(z - \ell)}{i(z - \ell)} = Z_0 \frac{Z_\ell + jZ_0 \tan \beta(z - \ell)}{Z_0 + jZ_\ell \tan \beta(z - \ell)} \quad (4)$$

This equation allows us to, in essence, move the load from the plane ℓ to any other plane. This transformation can be

used to eliminate line segments and thereby use circuits on them directly. However, note that line lengths in which the line is at least comparable to a wavelength are necessary in order to significantly alter the impedance. At the plane $z = \ell$, then, we can further note that the ratio of the reflected voltage coefficient v_b and the forward-going v_f , which is the voltage reflection coefficient, is given by

$$\mathcal{R} = \frac{Z_\ell - Z_0}{Z_\ell + Z_0}$$

This is the reflection we discussed in the last section, which causes the difference between large and small circuit dimension.

One could question the utility of discussing Poynting vectors and transmission lines when the discussion was on active antennas. The answer really is that any antenna system, at whatever frequency or of whatever design, is a system for directing power from one place to another. To direct power from one place to another requires constantly keeping the Poynting vector pointed in the right direction. As we can surmise from the transmission-line derivation, line irregularities may cause the Poynting vector to wobble (with attendant reflections down the line due to attendant variations in the ℓ and c), but the picture must stay close to “correct” for power to get from one end of the system to another. For this reason, active antennas, even at very high (100s of GHz) frequencies can still be discussed in terms of transmission lines, impedances, and circuit equivalents, although greater care must be used in applying these concepts at increasingly higher frequencies.

The next piece of an active antenna that needs to be discussed is the active element. Without too much loss of generality, we will take our device to be a field-effect transistor (FET). A field-effect transistor (FET) is a device first described by Schockley in 1952 [7], but the MESFET (metal semiconductor FET) was not realized until 1965 [8] when gallium arsenide (GaAs) fabrication techniques became more workable. It should be pointed out that the silicon MOSFET (metal oxide semiconductor FET) is the workhorse device of digital electronics and therefore the most common of all electronic devices presently in existence by a very large margin. The GaAs MESFET was an important structure in the development of discrete microwave components and was used in early development of monolithic microwave circuitry (MMIC). High-electron-mobility transistors (HEMTs) and heterostructure bipolar transistors (HBTs) in such material systems as InP now are replacing GaAs MESFETs as both discrete and integrated components. In the present, though, the FET (and for some characteristics, the GaAs MESFET) will be used as a prototype device as its characteristics are reasonably archetypical of solid-state microwave devices. A top view of an FET might appear as in Fig. 17. As is shown clearly in the figure, an FET is a three-terminal device with gate, drain, and source regions. A cross section of the active region (where the gate is very narrow) might appear as in Fig. 18. The basic idea is that the highly doped n region causes current to flow through the ohmic contacts from drain to source (i.e., electrons flow from source to drain), but the current is controlled in magnitude by the electric field generated by the reverse bias voltage applied to the

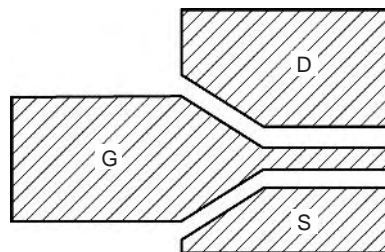


Figure 17. Schematic depiction of a top view of the metallized surface of an FET, where G denoted gate, D drain, and S source.

gate electrode. The situation is described a bit more in Fig. 19, where bias voltages are defined and a typical I–V curve for DC operation is given. Typically the bias would be supplied by a circuit such as that of Fig. 20. In what follows, we will simply assume that the biases are properly applied and isolated and consider the AC operation. An AC circuit model is given in Fig. 21. If one uses the proper number of circuit values, these models can be quite accurate, but the values do vary from device to device, even when the devices were fabricated at the same time and even on the same substrate. Usually, the datasheet with a device will, instead of specifying the circuit parameters, specify the device S parameters, which are defined as in Fig. 22 and can be measured in a straightforward manner by a network analyzer. The S parameters are defined by the equation

$$\begin{pmatrix} V_1^- \\ V_2^- \end{pmatrix} = \begin{pmatrix} S_{11} & S_{12} \\ S_{21} & S_{22} \end{pmatrix} \begin{pmatrix} V_1^+ \\ V_2^+ \end{pmatrix}. \quad (5)$$

An important parameter is the transfer function of the transistor circuit, which can be defined as the ratio of the v_o to the v_i as defined in Fig. 21. To simplify further analysis, we will ignore the package parasitics R_g and R_d with respect to other circuit parameters, and thereby we will carry out further analysis on the circuit depicted in Fig. 23. The circuit can be solved by writing a simultaneous system of equations for the two nodal voltages v_i and v_o . These sinusoidal steady-state equations become

$$j\omega C_{gd}(v_o - v_i) + g_m v_i + j\omega C_{ds} v_o + \frac{v_o}{R_{ds}} + \frac{v_o}{Z_L} = 0$$

The system can be rewritten in the form

$$v_o \left[j\omega (C_{gd} + C_{ds}) + \frac{1}{R_{ds}} + \frac{1}{Z_L} \right] = v_i [-g_m + j\omega C_{gd}]$$

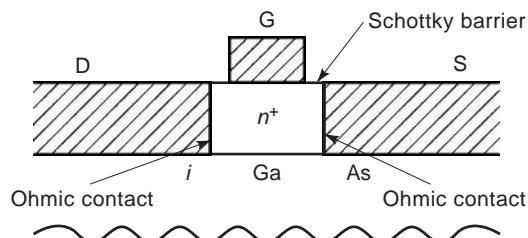


Figure 18. Schematic depiction of the cross section of the active region of a GaAs FET, Specific designs can vary significantly in the field-effect family.

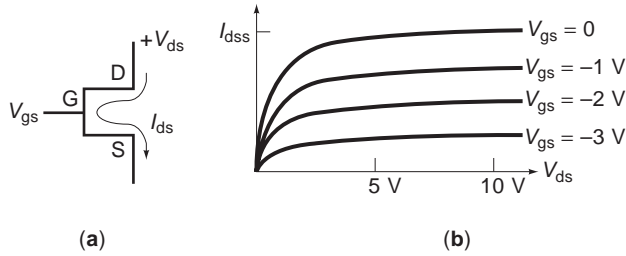


Figure 19. (a) Circuit element diagram with voltages and currents labeled for (b), where a typical I - V curve is depicted.

which gives us our transfer function T in the form

$$T = \frac{v_o}{v_i} = \frac{-g_m + j\omega C_{gd}}{j\omega(C_{gd} + C_{gs}) + \frac{1}{R_{ds}} + \frac{1}{Z_L}}$$

Often we are interested in open-circuit parameter—that is, the circuit transfer function when Z_L is large compared to other parameters. We often call this parameter G the *open-circuit gain*. We could write this open-circuit gain in the form

$$G = \left. \frac{v_o}{v_i} \right|_{oc} = \frac{-g_m R_{ds} + j\omega C_{gd} R_{ds}}{j\omega(C_{gd} + C_{gs})R_{ds} + 1}$$

It is useful to look at approximate forms. It is generally true that

$$C_{gd} \ll C_{ds}, C_{gs}$$

but for usual operating frequencies it is also generally true that

$$\frac{1}{\omega C_{ds}} \ll R_{ds}$$

Using both of the equations in our equations for T and G , we find

$$T = \frac{-g_m R_{ds}}{1 + \frac{R}{Z_L}}$$

$$G = -g_m R_{ds}$$

Clearly, one sees that the loaded gain will be less than the unloaded gain, as we would expect. Making only the first of our two approximations above, we can write these

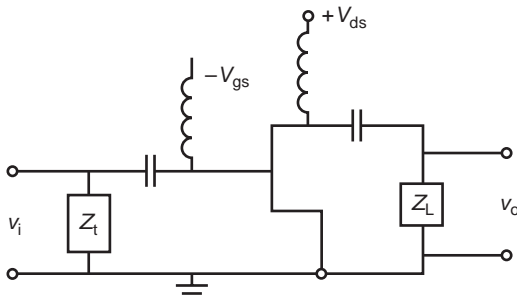


Figure 20. Typical FET circuit including the bias voltages v_{gs} and v_{ds} as well as the AC voltages v_i and v_o , where the conductors represent AC blocks and the capacitors DC blocks.

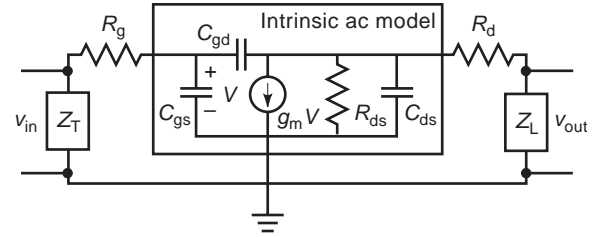


Figure 21. Intrinsic model for a common-source FET with external load and termination impedances and including gate and drain resistive parasitics, where Z_T is the gate termination impedance, R_g is the gate (metallization) resistance, C_{gs} is the gate-to-source capacitance, C_{gd} is the gate-to-drain capacitance, g_m is the channel transconductance, R_{ds} is the channel (drain-to-source) resistance, C_{ds} is the channel capacitance, R_d is the drain (metallization) resistance, and Z_L is the load impedance.

equations as

$$T = \frac{-g_m R_{ds}}{1 + j\omega\tau_{ds} + \frac{R_{ds}}{Z_L}}$$

$$G = \frac{-g_m R_{ds}}{1 + j\omega\tau_{ds}}$$

where the τ_{ds} is a time constant given by

$$\tau_{ds} = \frac{1}{C_{ds} R_{ds}}$$

We see that, in this limit, the high-frequency gain is damped. Also, an interesting observation could be that, at some frequency ω , an inductive load could be used to cancel the damping and obtain a purely real transfer function at that frequency. This effect is the one that allows us to use the transistor in an oscillator.

Let us now consider an oscillator circuit. The basic idea behind the oscillator circuit is illustrated in the one-port diagram of Fig. 24. The transistor's gain, together with feedback to the input loop through the capacitor C_{gd} , can give the transistor an effective negative input impedance that can lead to oscillation if the real and imaginary parts of the total impedance (i.e., Z_T in parallel with the Z_i of the transistor plus load) cancel. The idea is much like that illustrated in Fig. 25 of a feedback network. One sees that the output of the feedback network can be expressed as

$$v_o = G(j\omega)[v_i - H(j\omega)v_o]$$

or, by rearranging terms, one finds that

$$\frac{v_o}{v_i} = \frac{G(j\omega)}{1 + G(j\omega)H(j\omega)}$$

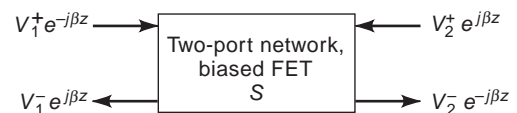


Figure 22. Schematic depiction of an FET as a two-port device that defines the quantities used in the S matrix of Eq. (5).

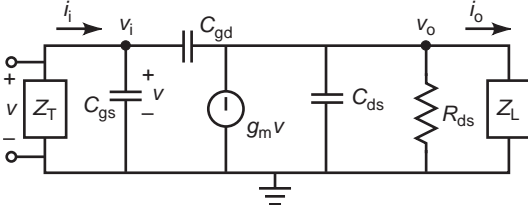


Figure 23. Simplified transistor circuit used for analyzing rather general amplifier and oscillator circuits, where the circuit parameter definitions are as in Fig. 22.

which clearly will exhibit oscillation—that is, have an output voltage without an applied input voltage—when

$$H(j\omega) = -\frac{1}{G(j\omega)}$$

What we need to do to see if we can achieve oscillation is to investigate the input impedance of our transistor and load seen as a one-port network. Clearly we can write the input current of Fig. 23 as

$$i_i = j\omega C_{gs}v_i + j\omega C_{gd}(v_i - v_o)$$

and then using the full expression for T to express v_o as a function of v_i , one finds

$$Z_i = \frac{i_i}{v_i} = j\omega C_{gs} + j\omega C_{gd} \left(1 + \frac{g_m - j\omega C_{gd}}{j\omega(C_{gd} + C_{ds}) + \frac{1}{R_{ds}} + \frac{1}{Z_L}} \right)$$

which can be somewhat simplified to yield

$$Z_i = j\omega C_{gs} + j\omega C_{gd} \left[\frac{g_m R_{ds} + 1 + j\omega\tau_{ds} + \frac{R_{ds}}{Z_L}}{1 + j\omega\tau_{ds} + \frac{R_d}{Z_L}} \right]$$

We can again invoke a limit in which $\omega\tau_{ds} \ll 1$ and then write

$$Z_i = j\omega C_{gs} + j\omega C_{gd} \left[\frac{Z_L(1 + g_m R_{ds} + R_{ds})}{R_{ds} + Z_L} \right]$$

Perhaps the most interesting thing about this expression is that one notes that if

$$Z_L = j\omega L$$

and

$$g_m R_{ds} \gg 1$$

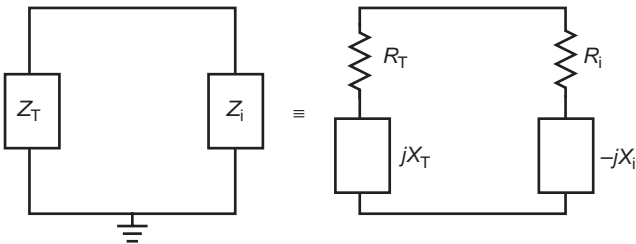


Figure 24. Diagram depicting the transistor and its load as a one-port device that, when matched to its termination so that there is no real or imaginary part to the total circuit impedance, will allow for oscillations.

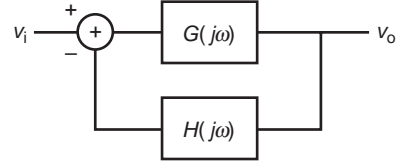


Figure 25. Depiction of a simple feedback network.

then clearly

$$R_i < 0$$

Whether X_i can be made to match any termination is another question that we will take up in the next paragraph.

As was mentioned earlier, generally the datasheet one obtains with an FET has plots of the frequency dependence of the S parameters rather than values for the equivalent-circuit parameters. Oscillator analysis is, therefore, usually carried out using a model of the circuit such as that depicted in Fig. 26, where the transistor is represented by its measured S matrix. The condition for oscillation in such a system can be expressed in either of the forms

$$\Gamma_i \Gamma_T = 1$$

or

$$\Gamma_o \Gamma_L = 1$$

where the Γ s are as defined in the caption of Fig. 26. If both Z_T and Z_L were passive loads—that is, loads consisting of resistance, inductance, and capacitance, then we would have that

$$\begin{aligned} |\Gamma_T| &< 1 \\ |\Gamma_L| &< 1 \end{aligned}$$

and the conditions for unconditional stability (nonoscillation at any frequency) would be that

$$\begin{aligned} |\Gamma_i| &< 1 \\ |\Gamma_o| &< 1 \end{aligned}$$

Clearly, we can express Γ_i and Γ_o as series of reflections such that

$$\begin{aligned} \Gamma_i &= S_{11} + S_{12}\Gamma_L S_{21} + S_{12}\Gamma_L S_{22}\Gamma_L S_{21} \\ &\quad + S_{12}\Gamma_L S_{22}\Gamma_L S_{22}\Gamma_L S_{21} + \dots \\ \Gamma_o &= S_{22} + S_{21}\Gamma_T S_{12} + S_{21}\Gamma_T S_{11}\Gamma_T S_{12} \\ &\quad + S_{21}\Gamma_T S_{11}\Gamma_T S_{11}\Gamma_T S_{12} + \dots \end{aligned}$$

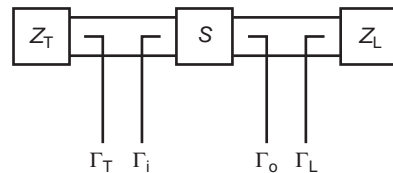


Figure 26. Schematic depiction of an oscillator circuit in which the transistor is represented by its S matrix and calculation is done in terms of reflection coefficients Γ_T looking into the gate termination, Γ_i looking into the gate source port of the transistor, Γ_o looking into its drain source port, and Γ_L looking into the load impedance.

Using the fact that

$$\sum_{n=0}^{\infty} x^n = \frac{1}{1-x}$$

we can reexpress the Γ s as

$$\Gamma_i = S_{11} + \frac{S_{12}S_{21}\gamma_L}{1 - S_{22}\Gamma_L}$$

$$\Gamma_o = S_{22} + \frac{S_{12}S_{21}\Gamma_T}{1 - S_{22}\Gamma_T}$$

If we define the determinant of the \mathbf{S} matrix to be Δ and be given by

$$\Delta = S_{11}S_{22} - S_{12}S_{21}$$

and a transistor κ parameter by

$$\kappa = \frac{1 - |S_{11}|^2 - |S_{22}|^2 + |\Delta|^2}{2|S_{12}S_{21}|}$$

then some tedious algebra leads to the result that stability requires

$$\kappa > 1$$

$$\Delta < 1$$

At frequencies where these condition are not satisfied, oscillation can occur if the load and termination impedances, Z_L and Z_T , respectively, are chosen properly. Oscillator design is discussed in various texts [11,14–16]. Generally, though, oscillator design involves finding instability points and not predicting the dynamics once oscillation is achieved. The next paragraph will discuss these dynamics.

If a transistor circuit is designed to be unstable, then as soon as the DC bias is raised to a level whereby the circuit achieves the set of unstable values, the circuit's output within the range of unstable frequencies rises rapidly and dramatically. The values that we took in the equivalent AC circuit, though, were small-signal parameters. As the circuit output increases, the signal will eventually no longer be small. The major thing that changes in this limit is that the input resistance to the transistor saturates, such that [17,18]

$$R_i = -R_{i\phi} + mv^2$$

where the plus sign on the nonlinearity is necessary, for if it were negative the transistor would burn up or else burn up the power supply. Generally, the m has to be determined empirically, as nonlinear circuit models have parameters that vary significantly from device to device. For definiteness, let's assume that the Z_T is resistive and the Z_L is purely inductive. At the oscillation frequency, the internal capacitance of the transistor then should cancel the load inductance, but to consider dynamics we need to put in both the C and L , as dynamics take place in the time domain. The dynamic circuit to consider is then as depicted in Fig. 27. The loop equation for this circuit in the time domain would be

$$L \frac{\partial i}{\partial t} + (R_i + R_T)i + \frac{1}{C} \int idt = 0$$

Recalling the equivalent circuit of Fig. 23 and recalling that

$$C_{gs} \gg C_{gd}$$

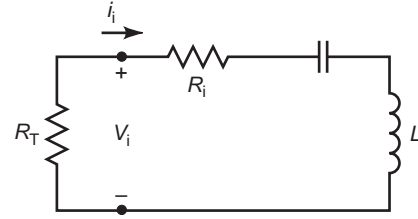


Figure 27. Circuit used to determine the dynamical behavior of a transistor oscillator.

we see that, approximately at any rate, we should have the relation between v_i and i_i that

$$i = C_{gs} \frac{\partial v}{\partial t}$$

Using this $i - v$ relation in the preceding, we find that

$$\frac{\partial^2 v}{\partial t^2} - \frac{R_i - R_T}{L} \left(1 - \frac{mv^2}{R_i - R_T}\right) \frac{\partial v}{\partial t} + \frac{v}{LC} = 0$$

which we could rewrite in terms of other parameters as

$$\frac{\partial^2 v}{\partial t^2} - \varepsilon(1 - \gamma^2 v^2) \frac{\partial v}{\partial t} + \omega_0^2 v = 0$$

which is the form of Van der Pol's equation (see, e.g., Refs. 17 and 18), which is an equation that describes the behavior of essentially any oscillator.

Now that we have discussed planar guiding structures and at least one example of a dynamical element that we can insert into a planar circuit, the time has arrived to discuss the planar antenna structures. Perhaps the best way to gain understanding of the operation of a patch antenna is by considering a cavity resonator model of one. A good review of microstrip antennas is given in Carver and Mink [19] and is reprinted in Ref. 20. Let's consider a patch antenna and coordinate system as is illustrated in Fig. 28. The basic idea behind the cavity model is to consider the region between the patch and ground plane as a resonator. If the resonator were a perfect one, an idealized set of boundary conditions would be satisfied that would allow no exchange of energy between the resonator and its surroundings. In actual operation, it is the inaccuracy of the idealized boundary conditions that gives rise to the transduction mechanism whereby an antenna can convert

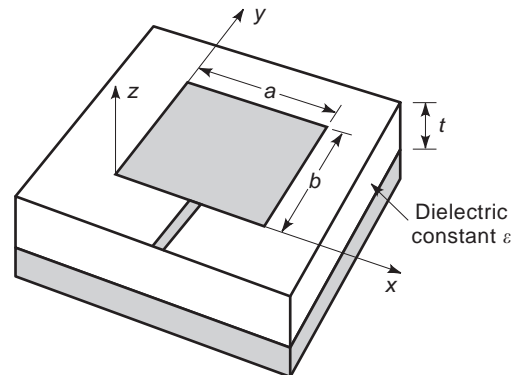


Figure 28. A patch antenna and Cartesian coordinate system.

guided waves to radiated waves and vice versa. We will assume the idealized conditions that there is only a z -directed electric field underneath the patch and that this field achieves maxima on the edges (open-circuit boundary condition). The magnetic field will be assumed to have both H_x and H_y components (only an H_x component in what we call the fundamental mode), and tangential components of these on the edges will be zero. (This boundary condition is the one consistent with the open circuit condition on the electric field and is exact as the thickness of the layer approaches zero, as there can be no component of current normal to the edge at the edge, and it would be the normal component of the current that generates the transverse \mathbf{H} field.) The electric field satisfying the open circuit condition can be seen to be given by the modes

$$e_{mn} = \frac{\lambda_{mn}}{\sqrt{\epsilon a b t}} \cos k_n x \cos k_m y$$

where

$$k_n = \frac{n\pi}{a}$$

$$k_m = \frac{m\pi}{b}$$

$$\lambda_{mn} = \begin{cases} 1, & m = 0 \text{ and } n = 0 \\ \sqrt{2}, & m = 0 \text{ or } n = 0 \\ 2, & m \neq 0 \text{ and } n \neq 0. \end{cases}$$

The \mathbf{H} field corresponding to the \mathbf{E} field then will consist of modes

$$\mathbf{h}_{mn} = \frac{1}{j\omega\mu} \frac{\lambda_{mn}}{\epsilon a b t} [\hat{e}_x k_m \cos k_n x \sin k_m y - \hat{e}_y k_n \sin k_n x \cos k_m y]$$

Now what we will call the fundamental mode is the one with $m = 1$ and $n = 0$. We can excite such a mode by choosing the dimension b to be resonant, that is, to correspond to a half of a wavelength in the structure. The dimension transverse to this must then be chosen to be nonresonant. This can be achieved by, for example, making this dimension less than a half-wavelength, but this is not the only way by any means. Now the basic transduction operation of the antenna must be due to the fact that the boundary conditions are not quite exact and the antenna can accept energy from the feedline and radiate it into free space. Let us consider this transduction operation in the antenna's fundamental mode. One might recall from the earlier argument that accompanied Fig. 13 that the z -directed field gives rise to a fringe field at the edges $y = 0$ and $y = b$ such that there are strips of y -directed electric field at the substrate surface for $y \leq 0$ and $y \geq b$. Because the boundary conditions are not quite correct on \mathbf{H} , there will also be strips of x -directed magnetic fields in these regions. As the Poynting vector is given by $\mathbf{E} \times \mathbf{H}$, we note that these strips will give rise to a z -directed Poynting vector at each of these edges. As these edges are a half-wavelength apart and the fields are in phase and Poynting-vector-like directed, these radiating edges will give rise to an upward-radiated field. Similar arguments could be applied to the

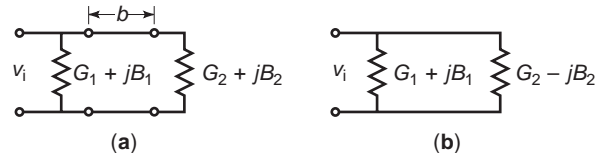


Figure 29. (a) A transmission-line model for a patch antenna, and (b) its circuitual equivalent as resonance.

edges at $x = 0$ and $x = a$. However, the x -directed field at $x \leq 0$ has a change of sign at the middle of the edge and is pointwise oppositely directed from the x -directed electric field at $x \geq a$. These fields, therefore, only give rise to very weak radiation, as there is significant cancellation. Analysis of the slot antenna requires that we first interchange the role of the \mathbf{E} and \mathbf{H} fields and realize that the radiating edges in the case of the slot are the edges that are along the direction of the feedline structure. Thus, in the CPW structure, the dominant electric fields are in the gaps between the conductors while the dominant magnetic field in the gaps points into the substrate. The end of the center conductor splits the downward-pointing magnetic field into two phases, one to the right of the center conductor and one to the left, defining the radiating edges of the structure in terms of the null of the z -directed magnetic field.

The picture of the patch antenna as two radiating strips allows us to represent it with a transmission line as well as a circuit model. The original idea is due to Munson [21]. The transmission line model is depicted in Fig. 29. The idea is that one feeds onto an edge with an admittance (inverse impedance) of $G_1 + jB_1$ and then propagates to a second edge with admittance $G_2 + jB_2$. When the circuit is resonant, then the length of transmission line will simply complex conjugate the given load [see Eq. (4)], leading to the circuit representation of Fig. 29b. The slot admittance used by Munson [21] was just that derived for radiation from a slit in a waveguide [22] as

$$G_1 + jB_1 = \frac{\pi a}{\lambda_0 Z_0} [1 - j0.636 \ln k_0 t]$$

where Z_0 is the impedance of free space of $377\Omega(\sqrt{\pi_0/\epsilon_0})$, λ_0 is the free-space wavelength, and k_0 is the free-space propagation vector, and where a and t are defined as per Fig. 28. When the edges are identical (as for a rectangular patch), one can write

$$G_2 + jB_2 = G_1 + jB_1$$

to obtain the input impedance in the form

$$Z_i = \frac{1}{Y_i} = \frac{1}{2G_1}$$

We have now considered all of the pieces, and therefore it is time to consider a couple of actual active-antenna designs. Figure 30 depicts one of the early designs from Kai Chang's group at Texas A&M [23]. Essentially, the patch here is being used precisely as the feedback element of an amplifier circuit (as was described in combination with Fig. 9). A more compact design is that of Fig. 14 [9]. There, the transistor is actually mounted directly into the patch antenna. The slit between the gate and drain yields a

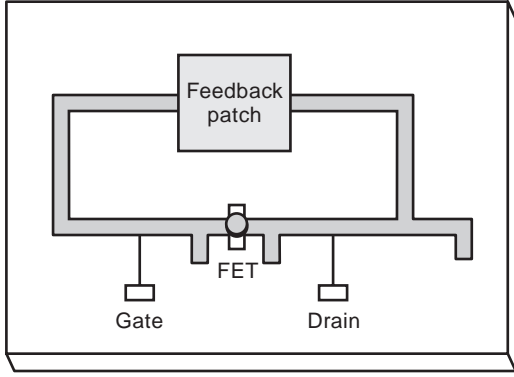


Figure 30. A design of a microstrip active radiating element.

capacitive feedback element such that the effective AC circuit equivalent of this antenna might well appear as depicted in Fig. 31. The capacitor/inductor pair attached to the gate lead form what is often referred to as a *tank circuit*, which (if the load were purely real) defines a natural frequency through the relation

$$\omega = \sqrt{\frac{1}{LC}}$$

As was discussed at some length in Section 1, a major argument for the use of active antennas is that they are sufficiently compact that they can be arrayed together. Arraying is an important method for free-space power combining, which is necessary due to the fact that, as frequency increases, the power-handling capability of active devices decreases. However, element size also decreases with increasing frequency such that use of multiple coherently combined elements can allow one to fix total array size and power more or less independently of frequency even though the number of active elements to combine increases. In the next paragraph, we'll consider some of the basics of arrays. The interested reader might also want to consult a relatively recent review article [10].

Consider a linear array such as is depicted in Fig. 32. Now let's say that the elements are nominally identical apart from phases that are set by the array operator at each of the elements. The complex electric field far from the n th element due to only the n th element would then be given by

$$\mathbf{E}_n = \mathbf{E}_e e^{i\phi_n}$$

where the \mathbf{E}_e is the electric field of a single element. To find out what is radiated in the direction θ due to the

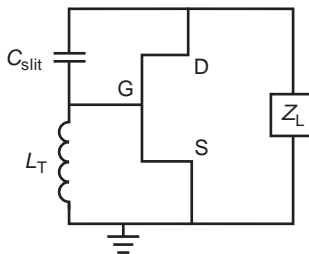


Figure 31. AC circuit equivalent of the active antenna of Fig. 14.

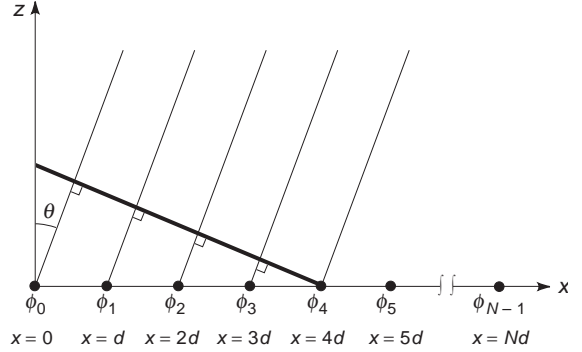


Figure 32. Depiction of a linear array of N identical radiating elements.

whole array, we need to sum the fields from all of the radiators, giving each radiator the proper phase delay. Each element will get a progressive phase shift $kd \sin\theta$ due to its position (see Fig. 32), where k is the free-space propagation factor, given by

$$k = \frac{2\pi}{\lambda}$$

where λ is the free-space wavelength. With this, we can write for the total field radiated into the direction θ due to all n elements

$$\mathbf{E}_t(\theta) = \mathbf{E}_e \sum_{n=0}^{N-1} e^{-inkd \sin \theta} e^{i\phi_n}$$

The sum is generally referred to as the *array factor*. The intensity, then, in the θ direction is

$$I_t(\theta) = I_e \left| \sum_{n=0}^{N-1} e^{-inkd \sin \theta} e^{i\phi_n} \right|^2$$

One notes immediately that, if one sets the phases ϕ_n to

$$\phi_n = nkd \sin \theta$$

then the intensity in the θ direction is N^2 times the intensity due to a single element. This is the effect of coherent addition. One gets a power increase of N plus a directivity increase of N . To illustrate, let's consider the broadside case where we take all the ϕ_n to be zero. In this case, we can write the array factor in the form

$$\left| \sum_{n=0}^{N-1} e^{-ind \sin \theta} \right|^2 = \left| \frac{1 - e^{-iNkd \sin \theta}}{1 - e^{-ikd \sin \theta}} \right|^2$$

which in turn can be written as

$$AF = \frac{\sin^2 \left(N \frac{kd}{2} \sin \theta \right)}{\sin^2 \left(\frac{kd}{2} \sin \theta \right)} \quad (6)$$

which is plotted in Fig. 33. Several interesting things can be noted from the expression and plots. One thing to note is that, for kd less than π , there is only one central lobe in the pattern. Another thing to note is that the pattern becomes increasingly directed with increasing N . This is just the directivity effect. If the array had a power-combining

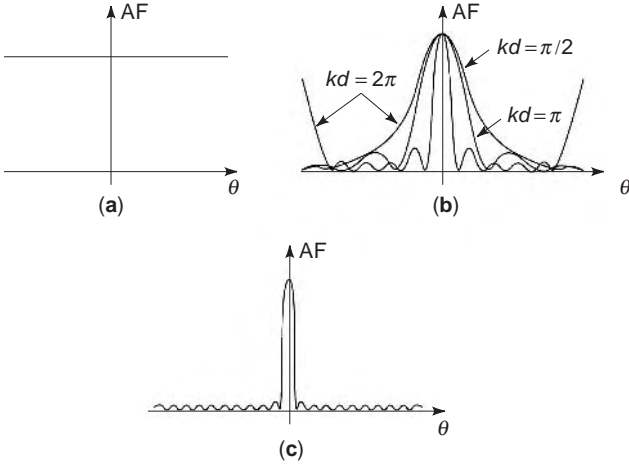


Figure 33. Plots of the array factor of Eq. (6), where (a) $N=1$, (b) $N=5$ and $kd = \pi/2, \pi$, and 2π , and (c) $N=10$ and $kd = \pi$.

efficiency of 100% (which we have built into our equations by ignoring actual couplings, etc.), then the total power radiated could only be N times that of a single element. However, it is radiated into a lobe that is only $1/N$ times as wide as that of a single element.

If we are to realize array gain, however, we need to be certain that the array elements are identical in frequency and have fixed phase relations in time. This can only take place if the elements are locked together. The idea of locking is probably best understood in relation to the Van der Pol equation [24–26], with an injected term, such that

$$\frac{\partial^2 v}{\partial t^2} - \frac{R_{i\phi} - R_T}{L} \left(1 - \frac{mv^2}{R_{i\phi} - R_T} \right) \frac{\partial v}{\partial t} + \omega_0^2 v = A \cos \omega_i t$$

where $R_{i\phi}$ is the input resistance of the transistor circuit as seen looking into the gate–source port and R_T is the external termination resistor placed between the gate and the common source. In the absence of the locking term, one can see that oscillation will take place with a primary frequency (and some harmonics) at angular frequency ω_0 with amplitude $\sqrt{R_{i0} - R_T/m}$ such that

$$v(t) \approx \sqrt{\frac{R_{i0} - R_T}{m}} \cos(\omega_0 t)$$

Without being too quantitative, one can say that, if ω_i is close enough to ω_0 and A is large enough, the oscillation will lock to ω_i in frequency and phase. If ω_i is not quite close enough and A not quite big enough (how big A needs to be is a function of how close ω_i is), then the oscillation frequency ω_0 will be shifted such that

$$v(t) = A_0 \cos((\omega_0 + \Delta\omega)t + \phi)$$

where $\Delta\omega$ and ϕ are functions of ω_i and A . These ideas are discussed in a number of places, including Refs. 1,17,18, and 24–26. In order for our array to operate in a coherent mode, the elements must be truly locked. This locking can occur through mutual coupling or through the injection of an external signal to each of the elements.

Ideally, we would like to be able to steer the locked beam. A number of techniques for doing this are presently

under investigation. A reasonably recent review article covering such techniques is [27]. Much of the thinking stems from the work of Stephan and coworkers [28–31]. One of the ideas brought out in these works was that, if the array were mutually locked and one were to try to inject one of the elements with a given phase, all the elements would lock to that phase. However, if one were to inject two elements at the locked frequency but with different phases, then the other elements would have to adjust themselves to these phases. In particular, if one had a locked linear array and one were to inject the two end elements with phases differing by ϕ , then the other elements would equally share the phase shift such that there would be a linear phase taper of magnitude ϕ uniformly distributed along the array. A different technique was developed by York [32,33] based on work he began when working with Compton [34,35]. In this technique, instead of injecting the end elements with the locked frequency and different phase, one injects the array with frequencies that are detuned from the desired center frequency. If the amplitudes of these injected frequencies are set to values that are not strong enough to lock the elements to these injected frequencies, then the elements would retain their “free-running” frequencies, but would obtain phase shifts from the injected signal as the oscillation within the element attempts to satisfy the contradictory operation instructions that are being fed to the element. If the elements of the array were locked because of mutual feedback, trying to inject either end of the array with “detuned” frequencies would then tend to give the elements a linear taper—that is, one in which the phase varies linearly with distance down the array—with much the same result as the technique of Stephan [28–31]. This will just linearly steer the mainlobe of the array off broadside and to a new direction. Such linear scanning is certainly what is needed for many commercial applications such as tracking or transmitting with minimum power to a given location. Another technique that again uses the locking-type ideas is the technique of changing the biases on each of the array’s active devices [36–38]. Changing the bias of a transistor will alter the free-running frequency at which the active antenna wants to oscillate. For an element locked to another frequency, then, changing the bias will just change the phase. In this way one can individually set the phase on each element. There are problems with this approach (as with all the others to present, which is why this area is still one of active research). One is that addressing each bias line represents a great increase in the complexity that we were trying to minimize by using an active antenna solution. The other is that the maximum phase shift obtainable with this technique is $\pm\pi$ from one end of the array to the other, a limitation that is shared by the phase shifts at the ends technique. In many phased array applications, of which electronic warfare is a typical one, one wants to have “true time delay,” which means that one would like to have as much as a π phase shift between adjacent elements. Essentially none of the techniques addressed to present can seem able to satisfy this requirement. Yet true time delay could open up a set new set of applications that could further drive work in this area. Work, however, continues. But already the

discussion has impinged on the topic of the next section, that of future application areas, and, therefore, now is a propitious time to begin this third section.

3. APPLICATIONS OF AND PROSPECTS FOR ACTIVE ANTENNAS

As was discussed earlier, active antennas were the first antennas of Hertz [4] although perhaps the greatest driver of more recent advances in this area has been power combining at high frequencies [10]. The power-combining area is becoming a subarea of high-power microwave/millimeter-wave devices by itself. However, there are numerous motivations other than simple power combining to pursue the study of active antennas. In this section, the aim is to run through a whole potpourri of past, present, and future applications. The applications to be touched on in this section are by no means exhaustive, but hopefully are representative.

Perhaps the earliest application of the active-antenna concept (following that of Hertz) was aimed at solving the small-antenna problem. As we recall, an antenna can be modeled (roughly) by a series RLC network with the R representing the radiation resistance. The input impedance of such a combination is given by

$$Z_i = \frac{1 - \frac{\omega^2}{\omega_0^2} + j\omega RC}{j\omega C}$$

and so we see that, when the operation frequency ω is well below the resonant frequency

$$\omega_0 = \frac{1}{\sqrt{LC}}$$

and the inverse of the RC time constant

$$\tau = RC$$

then the antenna appears as a capacitor and radiates quite inefficiently. The problem of reception is similar. Apparently, already in 1928 Westinghouse had a mobile antenna receiver that used a pentode as an inductive loading element in order to boost the amount of low-frequency radiation that could be converted to circuit current. In 1974, two works discussed transistor-based solutions to the short aerial problem [39,40]. In Ref. 40, the load circuit appeared as in Fig. 34. The idea was to generate an inductive load whose impedance varied with frequency, unlike a regular inductor, but so as to increase antenna bandwidth. The circuit's operation is not intuitively obvious. It is possible that most AM, shortwave, and FM receivers employ some short antenna solution regardless of whether the actual circuit designers are aware that they are employing active antenna techniques.

More recent efforts aimed at miniaturization have been concentrated on efficient amplification by single active-antenna elements rather than solving the small-antenna problem. For example, handheld wireless communication requires not only compact antenna elements but also compact and efficient amplification at the element. High-efficiency F class amplifiers were already under study in

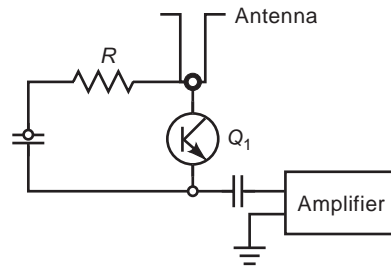


Figure 34. A circuit taken from Ref. 37 in which a transistor circuit is used to load a short antenna. Analysis shows that, in the frequency regime of interest, the loading circuit appears, when looking toward the antenna from the amplifier terminals, to cancel the strongly capacitive load of the short antenna.

1993 [41] followed by studies of lower-frequency class E amplifiers [42]. Efforts at fabricating integrated active-antenna elements employing high efficiency amplifiers have used resonant (if modified) patch elements, and have therefore in order to remain compact have carried out demonstrations at higher frequencies (S and C bands) where the resonant patches are more compact because of the smaller wavelengths, as is evidenced by work at Tatsuuo Itoh's group at UCLA in [43,44]. Kalialakis et al. attempted to make the active antenna not only efficient but also duplex and thereby a candidate for a transceiver [45].

Another set of applications where active devices are used as loading elements is in the >100 -GHz regime. Developments in this regime are reviewed in Refs. 1 and 46. To date, most work at frequencies greater than 100 GHz has involved radioastronomical receivers. A problem at such frequencies is a lack of components, including circuit elements so basic as waveguides. Microstrip guides already start having extramode problems at Ku band. Coplanar waveguides can go higher, although to present, rectangular metallic waveguides are the preferred guiding structures past about 60 GHz. In W band (normally narrowband, about 94 GHz—see Table 1), there are components, as around 94 GHz there is an atmospheric window of low propagation loss. However, waveguide tolerances, which must be a small percentage of the wavelength, are already severe in W band, where the wavelength is roughly 3 mm. Higher frequencies pretty much have to be handled in free space or, as one says, quasioptically. Receivers must therefore by nature be downconverting in this >100 GHz regime. Indeed, these types of solutions are the ones being demonstrated by the group at Michigan [46], where receivers will contain multipliers and downconverting mixers right in the antenna elements in order that CPW can be used to carry the downconverted signals to the processing electronics. Millimeter-wave/terahertz radioastronomy seems to be a prime niche for quasioptical active-antenna solutions.

The first applications of active antennas where solid-state components were used as gain elements were for power boosting [47–52]. By 1960, solid-state technology had come far enough that antennas integrated with diodes and transistors could be demonstrated. These early demonstrations of *antennafiers* [48] could be considered as the precursors of the high-efficiency integrated antennas we

mentioned in an earlier paragraph, but judging from the reference lists of these more recent works [43,44], there doesn't seem to be much of causal relationship. In fact, this early integrated active-antenna technology was to remain a laboratory curiosity per se until the 1980s, when further improvements in microwave devices were to render the technology more practical. The motivation at that point in time was primarily large gain. Large power gain, however, really requires combining the outputs of multiple solid-state devices. Power combining (see reviews in Refs. 10, 53, and 54), though, can be hard to achieve. There is a theorem that grew out of the early days of radiometry and radiative transfer (in the 1800s) known variously as the *brightness theorem*, the *Lagrange invariant*, or later the (later) *second law of thermodynamics*. (See, for example, Ref. 55 for some discussion of the Lagrange invariant.) The theorem essentially states that one cannot increase the brightness of a source by passive means. This theorem practically means that if one tries to combine two nominally identical but non-phase-locked sources by taking their outputs, and attempting to launch those two outputs into the same direction in space such that the two beams occupy the same spatial location in space, the resulting power density per steradian can be no greater than that of either of the nominally identical sources. Other power that was intended to go into this desired direction will have gone in some other direction. This seems to preclude any form of power combining. There is a proviso here, though. At the time the brightness theorem was first formulated, there were no coherent radiation sources. If one takes the output of a coherent radiation source, splits it in two, and adds it back together in phase, then the brightness, which was halved, can be restored. If two sources are phase locked, they are essentially one source. Therefore, locked sources can be coherently added if they are properly phased. A major portion of the power-combining field is therefore associated with techniques to lock individual radiating elements together into coherent sources and/or to amplify the output of weak sources in arrays of devices that lock to the source and to each other. It turns out that a powerful method with which to carry out such power combining employs the techniques that are generally referred to as *free-space power combining*.

A number of groups are working on developing compact elements for free-space power combining. Examples of free-space power-combining schemes have already appeared in Fig. 14 [9] and 30 [22]. In designs where the elements are spatially packed tightly enough, proximity can lead to strong enough nearest-neighbor coupling so that an array will lock to a common frequency and phase. Closeness of elements is also desirable in that arrays with less than $\lambda/2$ spacing will have no sidelobes sapping power from the central array beam. In designs that don't self-lock, one must either inject a locking signal on bias lines or spatially from a horn to try to lock to all elements simultaneously. A method for carrying out power combining in a self-locking array is to use the so-called *grid oscillator* solution [56,57]. The actual structure of a grid appears as in Fig. 35. The operating principle of the grid is actually quite a bit different from that of the arrays of weakly coupled individual elements. Note that there is no ground

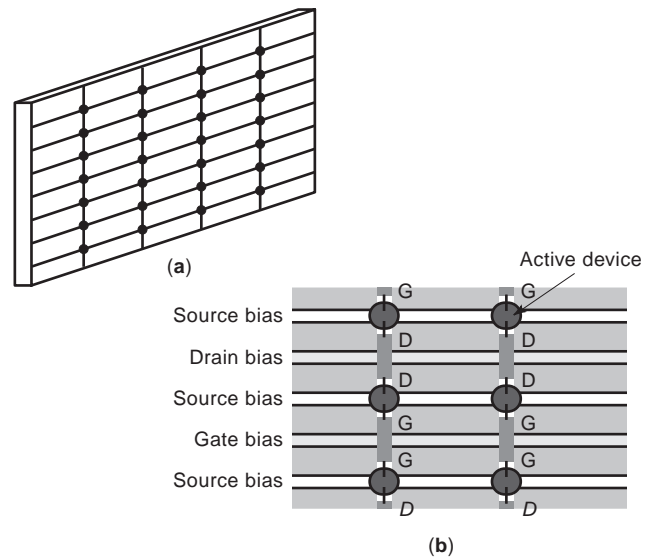


Figure 35. Schematic depiction of (a) the active surface of a grid oscillator and (b) a breakout of an internal region of the grid showing the active device placement relative to the bias lines.

plane at all on the back, and there is no ground plane either, per se, on the front side. Direct optical measurements of the potentials on the various lines of the grid [58], however, show that the source bias lines act somewhat as AC grounds. In this sense, either a drain bias line, together with the two closest source biases, or a gate bias line together with the two horizontally adjacent bias lines appears somewhat like CPW. The CPW lines, however, are periodically loaded ones with periodic active elements alternated with structures that appear like slot antennas. The radiating edges of the slots are, for the drain bias lines, the vertical AC connection lines between drain and drain or, for the gate bias CPW, the horizontal AC gate-to-gate convection lines. Indeed, the grid is known to lock strongly along the rows and more weakly between columns. As adjacent-row elements are sharing a patch radiator, this should be expected behavior. In a major sense, this strong locking behavior of the grid is both an advantage and a disadvantage. It is advantageous that the grid is compact (element spacing can be $\leq \lambda/6$) and further that it is easy to get the rows to lock to each other. However, the compactness is also a disadvantage in that it is quite hard to get any more functionality on the grid. Much effort has been given in this area to generate functionality by stacking various grid-based active surfaces such as amplifying surfaces, varactor surfaces for frequency shifting and modulation, or doubling surfaces. A problem with stacking is, of course, diffraction as well as alignment. Alignment tolerance adds to complexity. Diffraction tends to ease alignment tolerance, but in an inelegant manner. A 100-transistor array with $\lambda/6$ spacing will have an extent of roughly 1.5λ per side. As the diffraction angle is something like the wavelength divided by the array diameter, the diffraction angle for such an array is a major portion of a radian. One can say that grids are quasioptical, but in optics one seldom uses apertures too much smaller than a millimeter, for which the diffraction angle

would be roughly a thousandth of a radian. As far as pure combining efficiency goes, grids are probably the optimal solution. However, more functionality may well be hard to obtain with this solution. But then, as was previously mentioned, free-space power combining is itself becoming a subarea of high-power microwave/millimeter-wave sources as is evidenced by a review article [10].

Another application area of active antennas is that of proximity detection [59]. The idea is that an oscillator in an antenna element can be very sensitive to its nearby (within several wavelengths) environment. As was discussed previously, variation in distances to ground planes change impedances. The proximity of any metal object will, to some extent, cause the oscillator to be aware of another ground plane in parallel with the one in the circuit. This will change the impedance that the oscillator sees and thereby steer the oscillator frequency. The active antenna of Ref. 59 operated as a self-oscillating mixer; that is, the active element used the antenna as a load, whereas the antenna also used a diode mixer between itself and a low-frequency external circuit. The antenna acted both as a transmitting and receiving antenna. If there were something moving near the antenna, the signal reflected off the object and rereceived might well be at a different frequency than the shifting oscillator frequency. These two frequencies would then beat in the mixer, be downconverted, and show up as a low-frequency beat note in the external circuit. If such a composite device were to be used in a controlled environment, one could calibrate the output to determine what is occurring. Although Navarro and Chang [1, p. 130] mention such applications as automatic door openers and burglar alarms, I personally don't know how far the technology has gone into such commercial application. The original paper [59], though, seemed to have a different application in mind, as the term *Doppler sensor* appeared in the title. If one were to carefully control the immediate environment of the self-oscillating mixer, then reflections off more distant objects received by the antenna would beat with the stable frequency of the oscillator. The resulting beat note of the signals would then be the Doppler shift of the outgoing signal on reflection off the surface of the moving object, and from it one could determine the normal component of the object's velocity. It is my understanding that some low-cost radars operate on such a principle. As with other applications, though, the active-antenna principle, if due only to size constraints, becomes even more appealing at millimeter-wave frequencies, and at such frequencies power constraints favor use of arrays.

An older field that seems to be going through an active-antenna renaissance is that of retroreflection. A retro-reflector is a device that, when illuminated from any arbitrary direction, will return a signal directly back to the source. Clearly, retroreflectors are useful for return calibration as well as for various tracking purposes. An archetypical passive retroreflector would be a corner cube. Another idea for a passive reflector is a Van Atta array [60]. Such an array uses wires to interconnect the array elements such that the phase progression of the incident signal is conjugated and thereby returned in the direction of the source. As was pointed out by Friis in the 1930s,

though, phase conjugation is carried out in any mixer in which the local oscillator frequency exceeds the signal frequency [61]. This principle was already being exploited in 1963 for implementing retroreflection [62]. This work didn't seem to catch on, perhaps due to technology. A review in 1994 [63] and designs for such arrays were demonstrated and presented at the 1995 International Microwave Symposium [64,65]. For a more recent demonstration, a group of UCLA researchers borrows from the term *phase conjugation* from the optics literature in order to describe their work [66]. Work in this area of retrodirective arrays continues [67].

Although much has been done in the area of active antennas in general and active integrated antennas in particular, much remains to be done, and the area remains an active one at this point in time. Although the field of active antennas began with the field of radiofrequency, it still seems to be a field in its infancy and one that should continue to grow and change with advances in technology.

BIBLIOGRAPHY

1. J. A. Navarro and K. Chang, *Integrated Active Antenna and Spatial Power Combining*, Wiley, New York, 1995.
2. K. Chang, R. A. York, P. S. Hall, and T. Itoh, Active integrated antennas, *IEEE Trans. Microwave Theory Tech.* **50**:937–944 (March 2002).
3. Y. Qian and T. Itoh, Progress in active integrated antennas and their applications. *IEEE Trans. Microwave Theory Tech.* **46**:1891–1900 (Nov. 1998).
4. H. Hertz, *Electric Waves*, Macmillan, 1983.
5. J. Bardeen and W. Brittain, The transistor: A semiconductor triode, *Phys. Rev.* **74**:435 (1948).
6. W. Shockley, The theory of p-n junctions in semiconductors and p-n junction transistors, *Bell Syst. Tech. J.* **28**:435 (1949).
7. W. Shockley, A unipolar field-effect transistor, *Proc. IEEE* **40**:1365–1376 (1952).
8. C. A. Mead, Schottky-barrier gate field-effect transistor, *Proc. IEEE* **54**:307–308 (1966).
9. R. A. York, R. D. Martinez, and R. C. Compton, Active patch antenna element for array applications, *Electron. Lett.* **26**:494–495 (March 1990).
10. M. P. DeLisio and R. A. York, Quasi-optical and spatial power combining, *IEEE Trans. Microwave Theory Tech.* **50**:929–936 (March 2002).
11. K. Chang, *Microwave Solid-State Circuits and Applications*, Wiley, New York, 1994.
12. See, for example, Chap. 3 of B. J. Hunt, *The Maxwellians*, Cornell Univ. Press, Cornell, NY, 1991.
13. H. C. Pocklington, Electrical oscillations in wires, *Proc. Cambridge Phil. Soc.* 324–333 (1897).
14. D. M. Pozar, *Microwave Engineering*, Addison-Wesley, Reading, MA, 1990.
15. P. E. Gray and C. L. Searle, *Electronic Principles, Physics, Models and Circuits*, Wiley, New York, 1967.
16. R. E. Collin, *Foundations for Microwave Engineering*, 2nd ed., MacGraw-Hill, New York, 1992.
17. K. Y. Chen, P. D. Biernacki, A. Lahrichi, and A. R. Mickelson, Analysis of an experimental technique for determining Van der Pol parameters of a transistor oscillator. *IEEE Trans. Microwave Theory Tech.* **MTT-46**:914–922 (1998).

18. B. Van der Pol, Forced oscillations in a circuit with a non-linear resistance, *Phil. Mag.* **3**:65–80 (Jan. 1927).
19. K. R. Carver and J. W. Mink, Microstrip antenna technology, *IEEE Trans. Anten. Propag.* **AP-29**:2–24 (Jan. 1981).
20. D. M. Pozar and D. H. Schaubert, eds., *Microstrip Antennas*, IEEE Press, Piscataway, NJ, 1995.
21. R. E. Munson, Conformal microstrip antennas and microstrip phased arrays. *IEEE Trans. Anten. Propag.* **AP-22**:74–78 (1974).
22. R. F. Harrington, *Time Harmonic Electromagnetic fields*, McGraw-Hill, New York, 1961 (the equation in question is on p. 276).
23. K. Chang, K. A. Hammer, and G. K. Gopalakrishnan, Active radiating element using FETsource integrated with microstrip patch antenna, *Electro. Lett.* **24**:1347–1348 (Oct. 1988).
24. R. Adler, A study of locking phenomena in oscillators, *Proc. IRE* **34**:351–357 (June 1946).
25. R. Adler, A study of locking phenomena in oscillators, *Proc. IEEE* **61**:1380–1385 (Oct. 1973).
26. K. Kurokawa, Injection locking of microwave solid-state oscillators, *Proc. IEEE* **61**:1386–1410 (Oct. 1973).
27. R. A. York and T. Itoh, Injection and phase-locking techniques for beam control, *IEEE Trans. Microwave Theory Tech.* **46**:1920–1929 (Nov. 1998).
28. K. D. Stephan, Inter injection locked oscillators for power combining and phased arrays, *IEEE Trans. Microwave Theory Tech.* **34**:1017–1025. (Oct. 1986).
29. K. D. Stephan and W. A. Morgan, Analysis of inter-injection-locked oscillators for integrated phased arrays, *IEEE Trans. Anten. Propag.* **35**:771–781 (July 1987).
30. K. D. Stephan and S. L. Young, Mode stability of radiation-coupled inter-injection-locked oscillators for integrated phased arrays. *IEEE Trans. Microwave Theory Tech.* **36**:921–924 (May 1988).
31. W. A. Morgan and K. D. Stephan, An X-band experimental model of a millimeter-wave inter-injection-locked phased array system, *IEEE Trans. Anten. Propag.* **36**:1641–1645 (Nov. 1988).
32. R. A. York, Nonlinear analysis of phase relationships in quasi-optical oscillator arrays, *IEEE Trans. Microwave Theory Tech.* **41**:1799–1809 (Oct. 1993).
33. P. Liao and R. A. York, A new phase-shifterless beam scanning technique using arrays of coupled oscillators, *IEEE Trans. Microwave Theory Tech.* **41**:1810–1815 (Oct. 1993).
34. R. A. York and R. C. Compton, Quasi-optical power combining using mutual synchronized oscillator arrays, *IEEE Trans. Microwave Theory Tech.* **39**:1000–1009 (June 1991).
35. R. A. York and R. C. Compton, Coupled-oscillator arrays for millimeter-wave power-combining and mode-locking, *IEEE MTT-S Int. Microwave Symp. Digest*, June 1992, pp. 429–432.
36. P. S. Hall and P. M. Haskins, Microstrip active patch array with beam scanning, *Electron. Lett.* **28**:2056–2057 (Oct. 1992).
37. P. S. Hall, I. L. Morrow, P. M. Haskins, and J. S. Cahale, Phase control in injection-locked microstrip active antennas, *IEEE MTT-S Int. Microwave Symp. Digest*, 1994, pp. 1227–1230.
38. A. Zarrang, P. S. Hall, and M. Cryan, Active antenna phase control using subharmonic locking, *Electron. Lett.* **31**:842–843 (1995).
39. T. S. M. Maclean and P. A. Ransdale, Short active aerials for transmission, *Int. J. Electron.*, **36**:261–269 (Feb. 1974).
40. P. K. Rangole and S. S. Midha, Short antenna with active inductance, *Electron. Lett.*, **10**:462–463 (Oct. 1974).
41. C. Duvanaud, S. Dietsche, G. Paraut, and J. Obregon, High-efficiency class F GaAsFETamplifiers operating with very low bias voltages for use in mobile telephones at 1.75 GHz, *IEEE Microwave Guided Wave Lett.*, **3**:268–270 (Aug. 1993).
42. T. B. Mader and Z. B. Popović, The transmission-line-high-efficiency class-E amplifier, *IEEE Microwave Guided Wave Lett.*, **5**:290–292 (Sept. 1995).
43. V. Radišić, Y. Qian, and T. Itoh, Novel architectures for high-efficiency amplifiers for wireless application, *IEEE Trans. Microwave Theory Tech.* **46**:1901–1909 (Nov. 1998).
44. W. R. Deal, V. Radišić, Y. Qian, and T. Itoh, Integrated-antenna push-pull power amplifier, *IEEE Trans. Microwave Theory Tech.*, **47**:1418–1425 (Aug. 1999).
45. C. Kallialakis, M. J. Cryan, P. S. Hal, and P. Gardner, Analysis and design of integrated active circulator antennas, *IEEE Trans. Microwave Theory Tech.* **48**:1017–1023 (June 2000).
46. G. M. Rebeiz, Millimeter-wave and terahertz integrated circuit antennas, *Proc. IEEE* **80**:1748–1770 (Nov. 1996).
47. A. D. Frost, Parametric amplifier antennas, *Proc. IRE* **48**:1163–1164 (June 1960).
48. J. R. Copeland and W. J. Robertson, Antenna-verters and antennafiers, *Electronics* 68–71 (Oct. 1961).
49. M. E. Pedinoff, The negative conductance slot amplifier, *IRE Trans. Microwave Theory Tech.* **9**:557–566 (Nov. 1961).
50. W. J. Robertson, J. R. Copeland, and R. G. Verstraete, Antennafier arrays, *IEEE Trans. Anten. Propag.* **2**:227–233 (March 1964).
51. K. Fujimoto, Active antennas: Tunnel-diode-loaded dipole, *Proc. IEEE* **53**:174 (Feb. 1964).
52. H. H. Meinke, Tunnel diodes integrated with microwave antenna systems, *Radio Electron. Eng.* **31**:76–80 (Feb. 1966).
53. K. J. Russell, Microwave power combining techniques, *IEEE Trans. Microwave Theory Tech.* **27**:472–478 (May 1979).
54. K. Chang and C. Sun, Millimeter-wave-power-combining techniques, *IEEE Trans. Microwave Theory Tech.* **31**:91–107 (1983).
55. M. Born and E. Wolf, *The Principles of Optics*, 5th ed., Pergamon Press, New York, 1975.
56. Z. B. Popovic, M. Kim, and D. B. Rutledge, Grid oscillators, *Int. J. Infrared Millimeter Waves* **9**:647–654 (July 1988).
57. Z. B. Popovic, R. M. Weikle, M. Kim, and D. B. Rutledge, A 100-MES FETplanar grid oscillator, *IEEE Trans. Microwave Theory Tech.* **39**:193–200 (Feb. 1991).
58. K. Y. Chen, P. D. Biernacki, S. Bucheit, and A. R. Mickelson, Noninvasive experimental determination of charge and current distributions on an active surface, *IEEE Trans. Microwave Theory Tech.* **44**:1000–1009 (1996).
59. B. M. Armstrong, R. Brown, F. Rix, and J. A. C. Stewart, Use of microstrip impedance-measurement technique in the design of BARITT piplex Doppler sensor, *IEEE Trans. Microwave Theory Tech.* **28**:1437–1442 (Dec. 1980).
60. E. D. Sharp and M. A. Diab, Van Atta reflector array, *IRE Trans. Anten. Propag.* **8**:436–438 (July 1960).
61. H. T. Friis and C. Feldman, A multiple-unit steerable antenna for short-wave reception, *Bell Sys. Tech. J.* **16**:337–419 (1937).
62. C. Y. Pon, Retrodirective array using the heterodyne technique, *IEEE Trans. Anten. Propag.* **12**:176–180 (1964).
63. B. S. Hewitt, The evolution of radar technology into commercial systems, *IEEE MTT-S Int. Microwave Symp. Digest*, 1994, pp. 1271–1274.
64. C. W. Poblantz and T. Itoh, A conformal retrodirective array for radar applications using a heterodyne phase scattering

element, *IEEE MTT-S Int. Microwave Symp. Digest*, 1995, pp. 905–908.

65. Y. Chang, D. C. Scott, and H. R. Fetterman, Microwave phase conjugation using antenna coupled nonlinear optically pumped surface, *IEEE MTT-S Int. Microwave Symp. Digest*, 1995, pp. 1303–1306.
66. Y. Chang, H. R. Fetterman, I. L. Newberg, and S. K. Panaretos, Microwave phase conjugation using antenna arrays, *IEEE Trans. Microwave Theory Tech.*, **46**:1910–1919 (Nov. 1998).
67. S. L. Karode and V. F. Fusco, Self-tracking duplex communication link using planar retrodirective antennas, *IEEE Trans. Anten. Propag.* **47**:993–1000 (June 1999).

ACTIVE FILTERS: OVERVIEW OF ACTIVE-FILTER STRUCTURES

LAURENT BILLONNET
BERNARD JARRY
IRCOM University of Limoges
Limoges, Cedex, France

1. INTRODUCTION

Telecommunication services and products fueled by Internet, mobile, and space markets, have grown spectacularly since the early 1990s with no signs of slowing down. The use of microwave, millimeter-wave, and more generally high-frequency circuits, for today's applications, concerns at the same level detection systems (radars, intrusion sensors, etc.), the medical domain, and also various communication systems (e.g., telephone, PCS, data transfer, Internet by satellite, military applications, WLAN, Bluetooth). Such systems employ different RF functions or subsystems. Basic blocks can be divided into two categories. The first category concerns passive blocks or functions such as multiplexers, delays, couplers, isolators and connection sections (e.g., transmission lines). The second category focuses instead on active blocks, that is, blocks that use basic active components (transistors) or more complex subsystems. Basic subsystems to consider in this case are amplifiers, mixers, oscillators, and filters. Amplifiers are generally used to extract the information signal from noise in a front-end receiver or to increase the signal level in a transmitter chain. Mixers are used to upconvert or downconvert (modulate or demodulate) the working frequency of a signal to enable its transmission through a particular media (e.g., for hertzian transmission) or in a particular dedicated frequency band (e.g., in a given channel between a base station and a satellite or as a relay between two satellites). Oscillators are frequency sources most often used in association with mixers. The frequencies generated drive the up- or downconversion during a modulation/demodulation process. Finally, another essential block in a communication system is a filter. What is a filter [1]? A filter performs an electrical function used for a frequency selection process. This process can consist in

preserving a frequency band. We then speak either of low-pass, bandpass, or highpass filters. These filters are used to process a signal that must be transmitted to another part of a chain. The process can also consist in rejecting frequency bands. We speak in this case of bandstop filters. These filters are used to eliminate the effect or influence of a parasitic signal next to the frequency of a working signal. Note that lowpass or highpass filters may be considered, depending on their use (selection or rejection) as rejecting filters.

With the need of compact size and light weight for new satellite and PCS applications, the translation from classical waveguide-type technologies to planar integrated processes has become unavoidable. If passive filters solutions are first considered, reducing insertion losses and, as a result, increasing battery life and noise performance, the use of high- Q volumic resonators is needed. The latter cannot be reached by use of conventional planar MIC or MMIC technologies where unloaded Q factor does not exceed 200–300 and rapidly decreases with increasing frequency. The solution cannot then be found on the basis of conventional frequency selective passive circuits. One well-known limitation is the ratio between insertion loss and bandwidth. Their product is a constant for a given realization of passive filtering structure.

One promising way that naturally comes to mind to overcome these drawbacks, and specifically losses compensation, is the integration of passive filters with active components or devices. As we show it in this article, on the basis of this idea, different configurations of microwave active filters (MAFs) have been developed, and new types are under intensive search and study nowadays.

The key features of MAFs are:

- Gain control without distortion of the frequency response
- Frequency tuning capability (in Hz)
- Frequency agility for fast-tuned filters (in Hz/s)
- Capability of modifying specified poles to improve response selectivity
- Possibility of implementing automatic frequency control techniques
- Easy use of MIC/MMIC and integrated technologies
- Small filter dimensions and weight

However, in comparison to purely passive structures, implementation of active devices is accompanied with undesirable factors to take into account, such as:

- Noise figure increase
- Critical power-handling behavior
- Dynamic range reduction
- Electrical stability
- Stability of active parts under variations of external mechanical, climatic, optical, or electromagnetic conditions

In the design of microwave active filters, first task of researchers has then been to deal with imperfect active devices and lossy passive components [2]. The situation was

similar to that encountered before the advent of high-performance op-amps (operational amplifiers) in the 1950s and 1960s, when audiofrequency active RC filter designs were attempted. By adapting some of the active solutions used at lower frequency, investigators have then devised a number of interesting circuits. In this section, we first talk about the different families of filters. We evaluate different ways of classifying MAFs and show that two main categories can be finally considered. For the first category, we describe, from a general point of view, various compensation techniques and detail more specifically filters based on the use of gyrators and negative-impedance converters (NICs). At this step, we emphasize different problems that must be faced by RF and microwave designers in comparison to low-frequency classical designs. The second category is based on filters resulting from the application of methods and concepts used primarily at low frequency. As an example, this section sums up the different ways of considering and implementing recursive and transversal (R&T) filters for the microwave purpose.

2. MAF CLASSIFICATION

Most MAFs can be classified into several levels of a consideration depending on their basic topology structure, type of passive and active elements used, resonator configurations, guiding structures, application domain, working frequency band, and other factors. Major problem for MAF classification resides in the fact that there is still no systematic method to predict which active solution is the best to fit given specific functional requirements.

From our point of view, active filter structures at microwaves can be divided into two main categories:

- Active filters resulting from the improvement of classical microwave passive structures (category 1)
- Active filters resulting from the application, in the microwave domain, of methods and concepts primarily used at low frequency (category 2)

In fact, active-filter categories can, using the same approach, be defined by considering how the active components or functions improve the basic passive structures:

- If the active parts are used as correction blocks (e.g., for loss compensation), then the corresponding active filter belongs more to the first category;
- If the improvement is done through the benefit of a typical active property (except compensation, e.g., through nonreciprocity, unilaterality, or gain), then the second category is indicated.

Depending on the way the active parts contribute to the response improvement, the resulting filter can belong to one or the other category. As an example, consider the simple case of a classical LC filter for which the response improvement is realized through the use of an “active inductance”:

- If the active inductance consists in a classical passive inductance in which losses are compensated with a

NIC (a negative resistance), the global filter rather belongs to the first category.

- On the other hand, if the active inductance results from the capacitive load of a gyrator (which specific role, as we will see later, is to invert an impedance), then the global filter is of the second category.

Most realizations to date use the compensation principle and then belong to category 1 [3–6]. However, as it will be shown further, original approaches now tends to design circuits of category 2.

3. COMPENSATION TECHNIQUES

Referring to filter category 1, we show here various approaches to compensate (from a general point of view) the response of filter structures. Considering circuits using either distributed elements (in microstrip or coplanar technology) or lumped elements (using, e.g., monolithic integrated processes), compensation can be done in three basic ways.

3.1. Amplifiers for Loss Compensation

A first solution is used for resonator-based planar or volumic structures. It consists in compensating for the passive losses of one or more resonator thanks to the feedback of an amplifier. In terms of the compensation, the two-port amplifier is equivalent to a one-port negative resistance, as will be shown below. Following this principle, an example of a three-pole filter realized on a duroid substrate is given in Fig. 1 [7]. In this case, only the central resonator losses are directly compensated by the amplifier of adequate phase and gain values. These values are calculated to maintain the electrical stability (see Active filters: tools and techniques for active-filter design, Section 2). Input and output coupling values have been chosen to perform a 400 MHz bandwidth at 12 GHz. Figure 2 shows the improvement provided by the amplifier. Measurements of the filter in Fig. 3 show a perfect loss compensation within the passband. Poor input matching is due to a nonperfect matching of the amplifier. The same approach has been applied to volumic structures [8] for a third-order dielectric resonator (DR) filter for which the central resonator is compensated by an active loop [9].

3.2. Active Matching Approach

This active matching technique has already been successfully used and described at lower frequencies for broad-

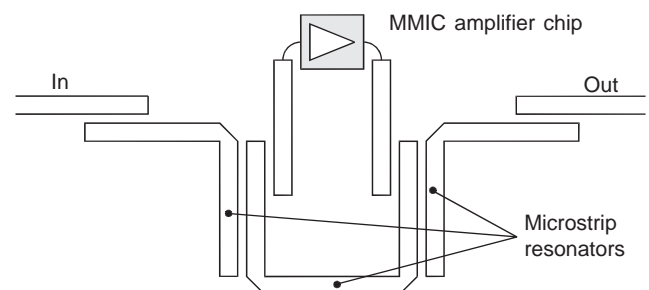


Figure 1. Topology of a third-order planar active filter.

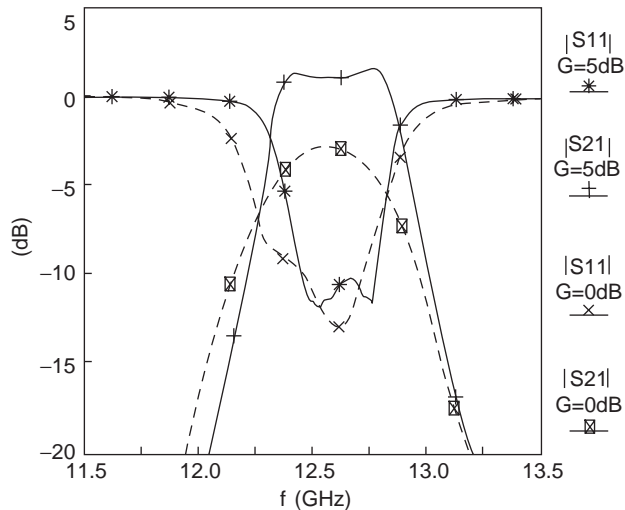


Figure 2. Simulated passive and compensated third-order planar filter responses.

band matching [10,11]. As an example, the filter consists here of a cascade association of three sections (Fig. 4) [12]. First and last sections act respectively as input and output matching networks. PHEMT active devices in common-gate and common-drain configurations have been used instead of passive elements to achieve wideband matching simultaneously as gain performances. The bandpass filter response is obtained by the intermediate section composed of a passive lumped-element network that sets the filter center frequency. The main goals of the common-gate and common-drain stages are to improve selectivity, compensate for the passive network losses, and match the filter to $50\ \Omega$ external impedances.

At high frequencies, the common-gate configuration is unilateral, whereas the common-drain configuration becomes nonunilateral, thus being capable of achieving both

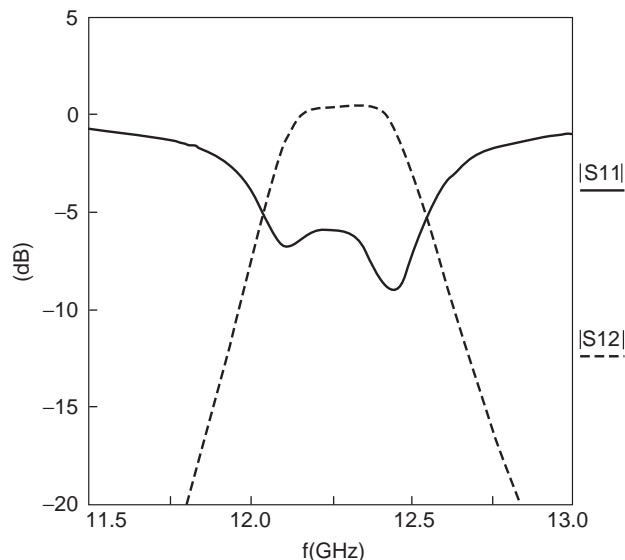


Figure 3. Measured third-order planar filter response.

input and output matchings to $50\ \Omega$ impedances. It can be shown [13] that the voltage transfer function of the passive section realizes a bandpass filter response. Replacing the common-gate and common-drain transistors in Fig. 4 by their equivalent models, it can be demonstrated that S_{21} is proportional to the voltage transfer function, thus realizing a bandpass filter response. Figure 5 shows the layout of the monolithic microwave integrated circuit (MMIC) using ED02Ah GaAs process from OMMIC [14]. Dimensions of the chip are $1.5 \times 1\ \text{mm}^2$. Total DC power consumption is 80 mW. Figure 6 shows a comparison between computer-simulated and measured results. The active filter operates at 31.825 GHz with 0.5 dB gain and 1.5 GHz with $-3\ \text{dB}$ bandwidth. Active matching approach appears to be suitable to achieve broadband performance with $|S_{ii}| < -12\ \text{dB}$. At the central frequency, the noise factor of the filter is equal to the minimum noise factor of 4 dB. The $-1\ \text{dB}$ compression point occurs for an input power of $+3\ \text{dBm}$. Noise performance and power-handling capabilities are discussed in the article on active-filter design tools and techniques, cited above (in Section 3.1).

3.3. Filtering/Matching Approach with Gain

The method is derived from classical lumped matching technique but it differs in the fact that a preliminary matching step is performed on the active part. This alternative method combines amplification and filtering functions based on the use of an active element with cascaded passive lumped filtering sections also contributing to the matching of the active part. A circuit example using this approach is presented in Fig. 7 [12]. The basic methodology first consists in simply doing a preliminary matching of a single transistor at the central frequency thanks to two inductances at the input and output. Wideband matching and filtering principles are then simultaneously realized by lumped passive filtering sections placed either before or after the preliminary matched active device while maintaining gain in the passband.

In comparison to a classical method, the preliminary matching using only two components achieves a significant reduction in the number of elements of the matching sections that can then be achieved much more simply. The chip size is only $1.5 \times 1\ \text{mm}$. Total DC power consumption is 20 mW. Figure 8 shows a comparison between computer-simulated and measured results. This filter operates at 14.12 GHz. The gain is near 0 dB, and the $-3\ \text{dB}$ bandwidth is 1.77 GHz. Good performances are obtained, especially for the input matching ($|S_{11}| = -17.26\ \text{dB}$). Simulated noise factor is equal to 2.7 dB at the center frequency.

3.4. Gytrators and NICs

The last compensation approach consists in using gyrators or NICs. Gytrators (impedance inverters) and NICs are functions initially used at low frequency. Their role is to build a given impedance through an intermediate load impedance. Thus, the impedance at a gyrator input is inversely proportional to the load impedance of the gyrator. In the NIC case, the input impedance is proportional to the negative of the load impedance of the NIC.

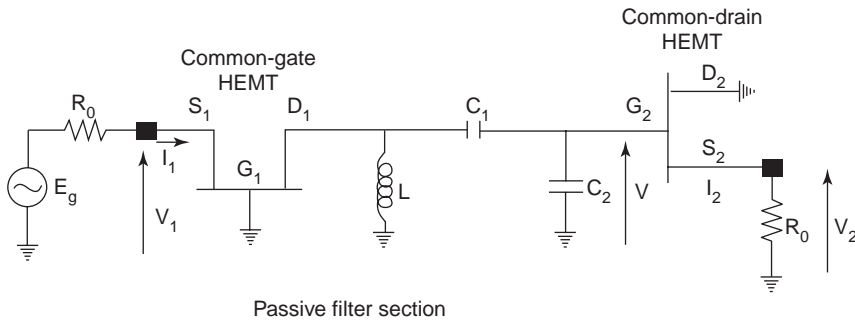


Figure 4. Actively matched passive lumped filter.

In most cases, NICs are dedicated to the compensation of losses and of resistive parts. However, overcompensation has already been used for oscillator design [15,16]. Gytrators are more classically used for high-value reactance design (in particular, for inductances) and for ideal inductances [17,18].

3.4.1. Design Problems at Microwaves. A large number of gyrators and NICs topologies have been investigated. Most of them come from the low frequency domain, where transistors and op amps can be considered as ideal transconductances and amplifiers with infinite gain, respectively.

At microwaves, gyrators and NICs topologies can be divided into two categories. As an example, we consider the NIC case here:

- In Fig. 9, high-gain transistors are considered as high-value transconductances. Input impedance of the global circuit then depends only on the three load impedances Z_1 , Z_2 , Z_3 , and is given by:

$$Z_{in} = -\frac{Z_1 Z_2}{Z_3}$$

- For the second category, transistors are modeled as finite-value transconductances. In Fig. 10, input impedance depends not only on a load impedance Z but

also on the two transconductances g_1 and g_2 , and is given by:

$$Z_{in} = -\frac{1}{g_1 g_2 Z}$$

However, whatever category is considered, investigator has to face some problems inherent to the microwave domain:

- Transconductances values cannot be infinite.
- Transistors cannot be modeled as simply as at low frequency, even in the linear regime.
- Passive components are not ideal and present losses or unwanted distributed effects.
- Interconnecting elements (in general transmission-line sections) lead to nonnegligible effects on the whole circuit response.

Considering the example of Fig. 10 at microwaves, when loaded with a pure resistance R , the circuit can provide a complex input impedance, even with a positive real part. Therefore, even if the idea of a simple transposition of low-frequency concepts to microwaves is promising, more complex compensation means must be considered.

3.4.2. Design Methodologies. In many cases, for negative-resistance circuits, designers just try to fit the negative real part of the desired impedance and accommodate as best as possible with the parasitic or unwanted imag-

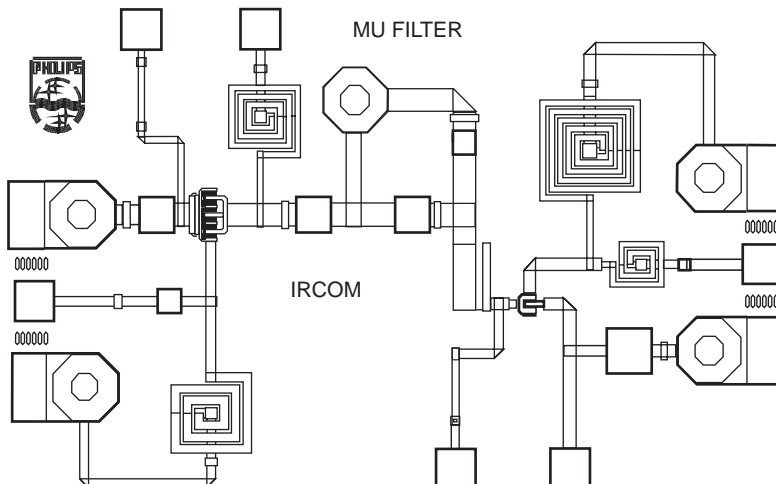


Figure 5. Layout of the actively matched passive lumped filter.

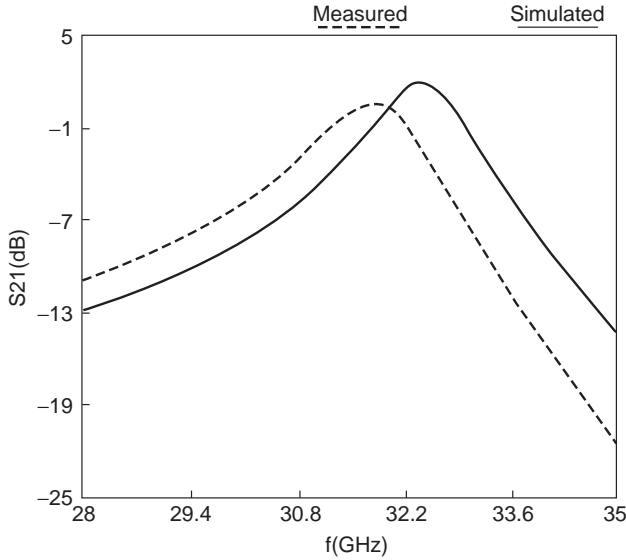


Figure 6. Comparison between simulated and measured S_{21} parameter of the actively matched passive lumped filter.

inary part when associating it to the rest of the filter [19,20]. This is the same for active inductances when designers try to fit only the imaginary part without sufficiently factoring in the parasitic real part, thus leading to poor- Q -factor inductances. Most part of the time, this tendency is only due to the lack of a systematic procedure. Some researchers have derived interesting methodologies to overcome these problems. Among all the attempts, one of the most interesting and simplest has been done by Sussman-Fort [21].

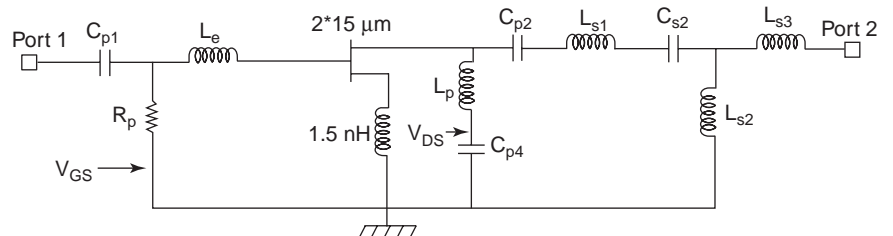
To explain the method, we come back to the topology of Fig. 10. Consider now the two-port NIC represented by its chain matrix (classically four parameters: A , B , C , and D) and loaded with an impedance Z . The input impedance is given by:

$$Z_{in} = \frac{AZ + B}{CZ + D} \quad (1)$$

Considering that a pure load resistance R at port 2 does not lead to $-R$ at the input at microwaves, the question we now consider is whether the corresponding Z_{in} can still be made to be a negative resistance by choosing a special load impedance Z . To answer this, we set $Z_{in} = -R$ in (1) and solve for the required Z as follows:

$$Z = -\frac{DR + B}{CR + A} = -Z' \quad (2)$$

Figure 7. Schematic of the preliminary matched filter structure.



Referring to (2), Z may be interpreted as the negative of the impedance Z' looking into port 2 when port 1 (the input) is terminated with the negative of the desired input impedance (here R is the negative of $-R$).

The design approach then simply consists in terminating the input of the circuit with the negative of the desired impedance, and to synthesize the negative of the impedance seen at port 2 under this condition. In our example, we then first load the input with R , look at the resulting impedance Z' at port 2, and try to synthesize $-Z'$, that is, Z .

A restriction must, however, be emphasized in the fact that the real part of Z must be positive to lead to a passive network to synthesize at port 2. If not, the procedure turns to a nonsense approach since a negative resistance will still have to be synthesized at port 2.

Note that this general procedure can also be applied for the design of ideal inductance. In that case, the procedure leads to synthesize the negative of the impedance seen at port 2 when the input is loaded by a negative inductance. The procedure applies for NICs as well as for gyrators. In any case, the impedance needed at port 2 can be synthesized using any adequate CAD software based, for example, on the real frequency technique.

To further facilitate the design, additional preliminaries can be applied before using this technique:

- In the case of infinite transconductance NICs or gyrators, each transistor can be replaced by a cascade association of two or more transistors to emulate as close as possible an infinite transconductance value [22].
- In the case of a finite-value transconductance NIC or gyrator, each transistor can be substituted with two transistors in a cascade configuration [21]. The desired effect here is to reduce the parasitics of the transistors.

However, in both cases, the synthesis steps cannot be skipped and are not sufficient to get close enough to the ideal case. Moreover, the cascade approach increases power consumption and degrades the power-handling capabilities (and in particular the compression point).

Another interesting design approach [23] can be associated with the Sussman-Fort basic approach for the complex load impedance synthesis. It relies on an original assisted visual representation of the design process.

Until now, there have been two main approaches to synthesize broadband matching and compensation networks for microwave active circuits. The first approach is based on the analytic theory by Fano [24] and Youla [25]; the second is the use of the already mentioned real frequency

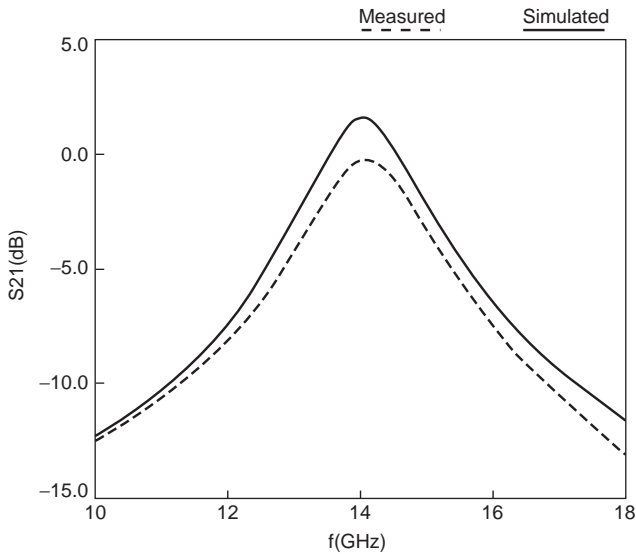


Figure 8. Simulated and measured S_{21} parameter of the preliminary matched filter.

technique (RFTs) by Carlin and Yarman [26]. Unfortunately, these approaches involve several limitations:

- It is difficult to apply them directly for the design of complex active circuits (i.e., circuits with several matching/compensation networks).
- With the synthesis techniques above, network configurations and elements result from fully formalized, complicated numerical procedures. Therefore, the designer has only very limited possibilities to control these configurations and elements.
- If distributed-element matching networks have to be designed, both the analytical procedures and RFTs lead to networks made from commensurate transmission lines. However, in practice, it may be

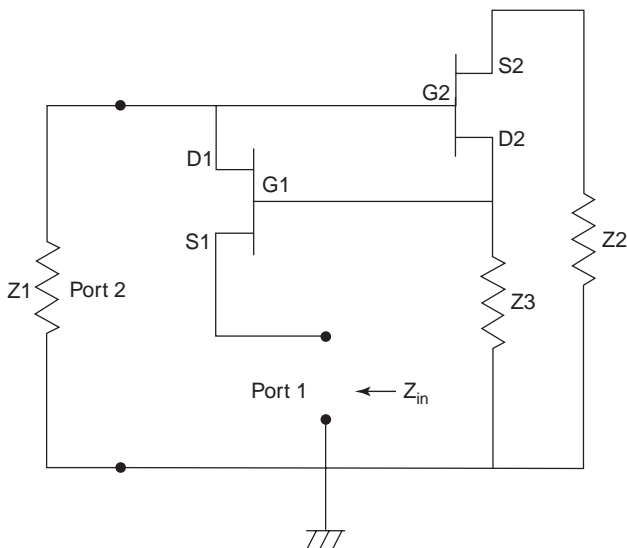


Figure 9. Example of a high-transconductance NIC topology.

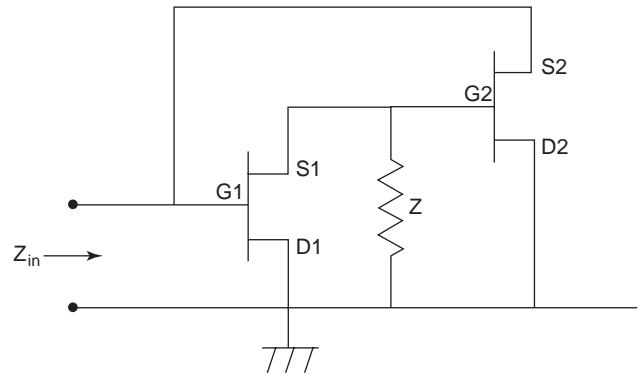


Figure 10. Example of a finite-value transconductance NIC topology.

preferable to employ networks consisting of noncommensurate lines, or mixed lumped/distributed-element networks.

To overcome these limitations, a new decomposition synthesis approach has been introduced for designing linear and nonlinear active circuits with passive matching/compensation networks. This method supposes that the design of active circuit is accomplished in two steps:

- Determination of acceptable regions of the matching/compensation networks immittances at sample frequencies over a frequency band of interest, according to a set of circuit specification ranges (noise, gain, matching levels)
- Synthesis of matching/compensation networks based on the acceptable immittance regions.

This technique allows the user to select a suitable network configuration and to directly control all the network elements for successful fabrication. Lumped, distributed noncommensurate line and mixed (lumped/distributed) networks of moderate complexity can then be designed. The approach is implemented in the software tool LOCUS, offering simple and fast means to produce solutions

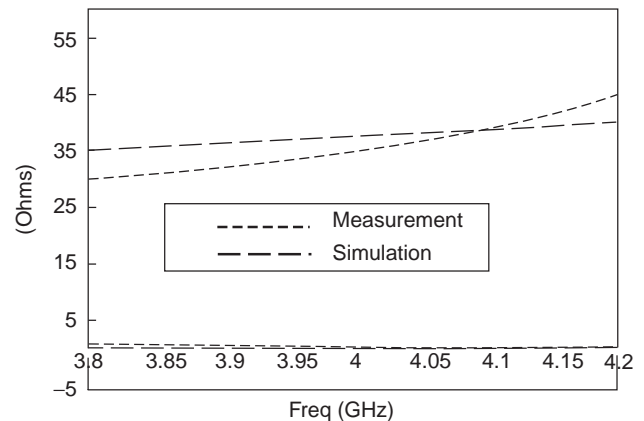


Figure 11. Simulated and measured imaginary part of the 1.5 nH active inductance.

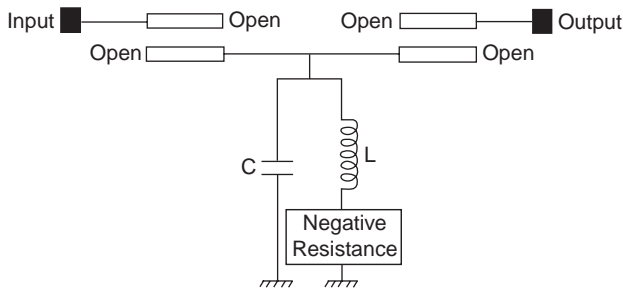


Figure 12. Basic LC shunt bandpass filter topology.

without the need for complicated circuit theory and mathematics. Other approaches have been developed by Yarman [27].

3.4.3. Circuit Examples. We give here three application examples of the compensation principle. The first example concerns the design of an ideal inductor in the 3.8–4.2 GHz band for a high- Q filter at 4 GHz [28]. Here, a spiral MMIC inductor is cascaded with a negative-impedance converter to obtain a high- Q inductor. Topology used is of infinite transconductance NIC type. The circuit has been drawn with the elements of the HB200 UMS (United Monolithic Semiconductors) process [29]. The size of the MMIC chip is 2.2×1.8 mm. Figure 11 shows simulated and measured results. The imaginary part is close to the expected value and losses are perfectly compensated.

The active inductance can then be used to design selective band-pass filters. Basic topology is presented in Fig. 12 [28]. Coupled lines are used at the input and output of the circuit to decouple the LC resonator and control the filter selectivity. Response of the filter achieves a Q factor of 1000 with a perfect loss compensation at the center frequency. A photograph of the filter is given in Fig. 13. Note the input and output coupling elements and the capacitance in parallel with the compensated spiral inductor.

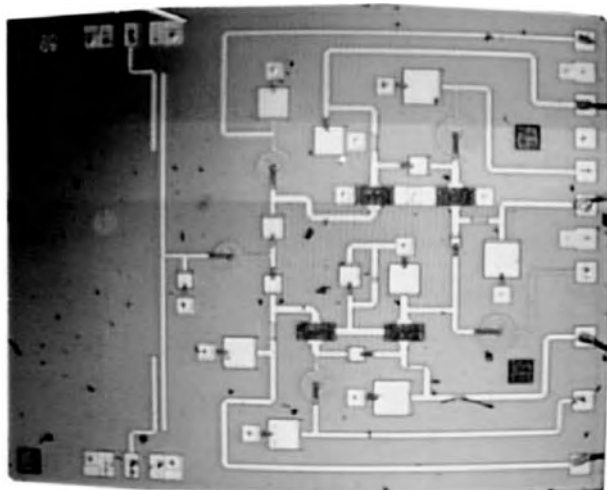


Figure 13. Photograph of the actively compensated LC shunt bandpass filter.

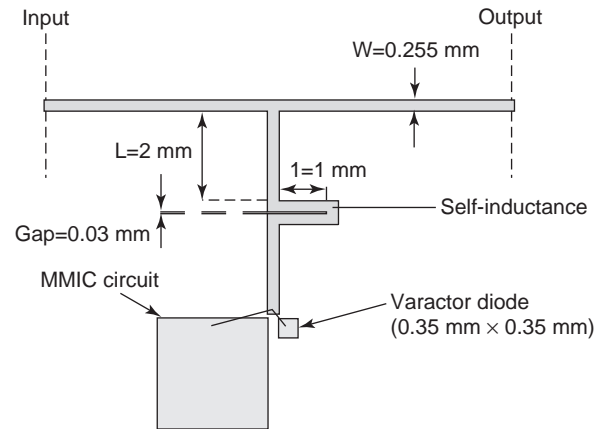


Figure 14. Layout of the tunable compensated bandstop filter.

The second example focuses on an active tunable bandstop filter using lumped elements [28]. We use here pseudolumped inductors built and synthesized in microstrip technology. Center frequency is optimized at 2 GHz. This filter can be tuned in frequency by using a varactor diode. Losses of the microstrip inductors and of the varactor diode are compensated by the negative-resistance circuit of Fig. 10. In a first step, characteristics of lumped inductors are studied according to the different geometric dimensions to determine an electrical equivalent schematic. This study is realized thanks to classical EM-CAD software packages. We use here an alumina substrate ($\epsilon_r = 9.8$; $h_s = 635 \mu\text{m}$). For this filter, the inductor chosen is realized with a single meander of length 1 mm, gap $30 \mu\text{m}$, and strip width $255 \mu\text{m}$. Layout of the filter including the MMIC chip is shown in Fig. 14. Measurements are shown in Fig. 15. Note that this bandstop filter is tunable in frequency over a wide band (nearly one octave). Tunability is also one interesting capability of active filters. It gives the property of being reconfigurable in frequency. Other examples of response tunability will be given and commented in the next sections. In this case, the tuning range varies from 1.3 to 2.6 GHz (66% of center frequency). The losses are well compensated as intended.

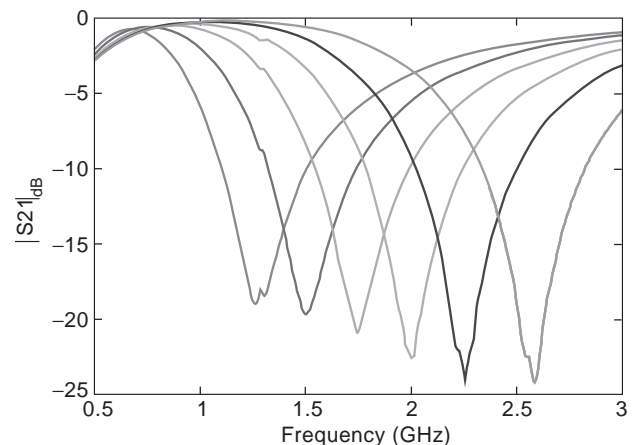


Figure 15. Measured tuned response of the compensated bandstop filter.

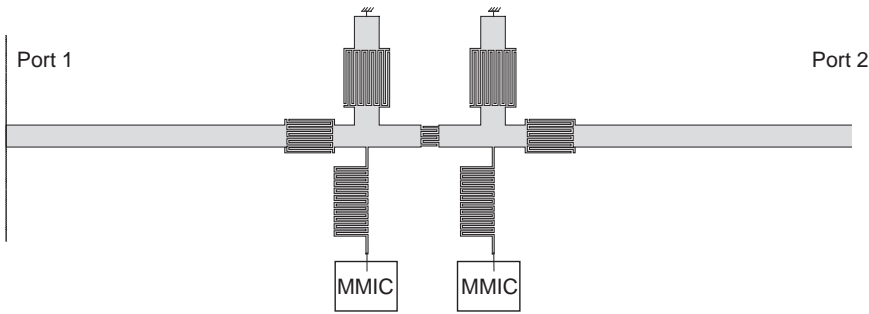


Figure 16. Layout of the two-pole active bandpass filter.

In the third example, we use the same type of NIC chip to compensate for the losses of a two-pole microstrip bandpass filter [30]. Interdigital capacitors and meander inductors are used to obtain a center frequency at 1.6 GHz. Compensation is made at one end of the inductors as shown in Fig. 16. Figure 17 shows the simulated response of the filter using the measured results of the MMIC chip. This figure also illustrates the response that would be obtained at the same frequency (due to the imaginary part of the MMIC impedance) without the negative real part of the MMICs. As can be seen, the difference of level obtained at the center frequency is more than 16 dB.

4. LOW-FREQUENCY CONCEPTS AT MICROWAVE APPLICATION TO RECURSIVE FILTER DESIGN

This section focuses on filters of category 2: active filters resulting from the application, in the microwave domain, of methods of filtering and concepts firstly used at low frequency.

4.1. Theoretical Background

Active filters have, for many years, focused at low frequency on operational amplifier approaches because of the abilities of such components to compensate for the

intrinsic losses of passive components, and for the overall amplification also provided. Although the physical constraints are strongly different, these advantages carry over to microwave frequencies, thus showing an increasing interest in adapting low-frequency techniques for use in microwave systems. One of these techniques includes the design of recursive and transversal filters. Application of such concepts to filtering structures clearly must employ MMIC technology [31].

Recursive and transversal filters are governed by the following time-domain (3) and frequency-domain (4) equations, where $x(t)$ [$y(t)$] is the input [output] of the system:

$$y(t) = \sum_{k=0}^N a_k x(t - k\tau) - \sum_{p=1}^P b_p y(t - p\tau) \quad (3)$$

$$H(f) = \frac{Y(f)}{X(f)} = \frac{\sum_{k=0}^N a_k e^{-2j\pi f k \tau}}{1 + \sum_{p=1}^P b_p e^{-2j\pi f p \tau}} \quad (4)$$

Implementation of the corresponding (N:P)-order filter requires multiple constant delay increments τ , amplitude weighting elements $\{a_k\}$ and $\{b_p\}$, and a mean of combining the elementary delayed signal components.

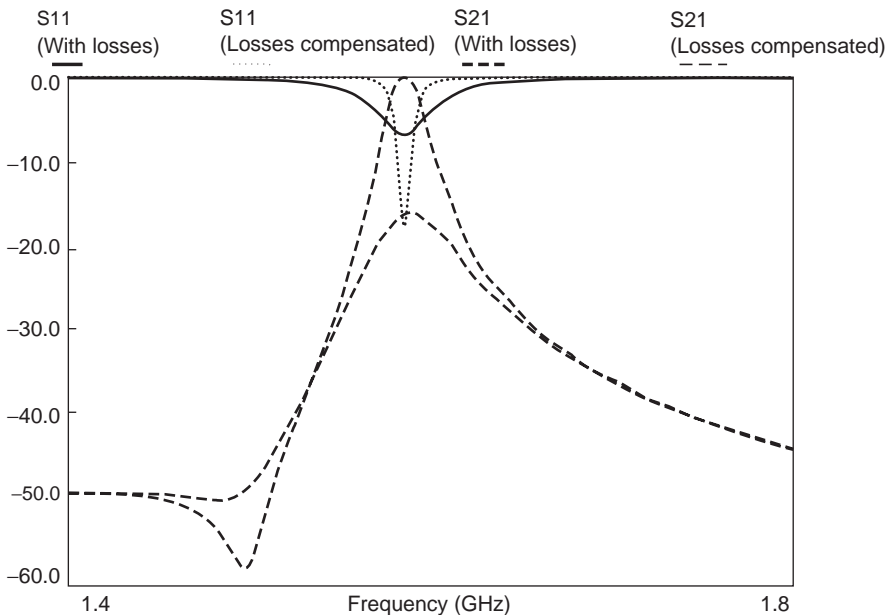


Figure 17. Influence of the negative real part of the MMIC on loss compensation of the two-pole bandpass filter.

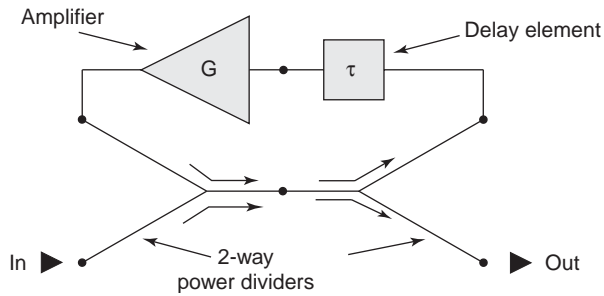


Figure 18. Topology of the first-order microwave recursive filter.

4.2. Power Matching Approach

Several approaches have been investigated to implement recursive responses. A first approach [31,32] consists in identifying a transversal filter with a distributed amplifier to get a ladder-type structure. However, this technique impose respectively a lowpass filter and a highpass filter before and after each transistor of the structure, to simultaneously realize the necessary delay time τ , and contribute to the response selectivity.

Another simple solution consists in considering combiners at microwaves, as power dividers/combiners [33]. This approach enables filter branches to be easily associated and then to be designed separately, each of them matched to the same impedance (in general, $50\ \Omega$), naturally leading to the identification of the weighting parameters as microwave amplifiers [34–36].

Following these principles for MMIC design purpose, we consider here a first-order recursive filter, shown in Fig. 18 [37]. Power dividers/combiners are built in MMIC technology with lumped-element cells in order to minimize the size of the final device. Each power divider/

combiner requires five lumped components. Delay time τ is built with a lowpass T cell. A one-stage pseudoresistive amplifier, including two RL series circuits for the matching of a single FET, is chosen here [38], thus again reducing the dimensions of the resulting circuit. For electrical stability reasons that we discuss in the article on active-filter design tools and techniques (cited above, in Section 3.1), the amplifier gain is adjusted to obtain the ratio $|S_{21}|_{\max}/|S_{21}|_{\min} = 10$ (20 dB) in the 7.5–12.5 GHz range. Figure 19 shows the layout of the filter, following OMMIC MMIC process design rules [14]. The circuit is implemented on an $100\text{-}\mu\text{m}$ -thick GaAs substrate. Dimensions of the chip are 2.0×1.5 mm. Perfect agreement between simulated and measured results is shown in Fig. 20.

4.3. Voltage Matching Approach

Considering that voltage matching and input/output signals combination can be more easily obtained over wider frequency bands than power matching, an alternative technique consists in synthesizing the filter responses owing to the use of voltage-matched devices [13]. At a last step, the whole circuit is matched to $50\ \Omega$ external impedances using FETs as described in Section 3.2. The classical recursive flow graph can be identified to the idealized series–shunt feedback model where an ideal adder is used to loop a unilateral forward active path $\mu(j\omega)$ with a passive path $\beta(j\omega)$. Under these assumptions, the overall transfer function can be identified as the transfer function of a first-order recursive filter if $\mu(j\omega) = 1$ and $\beta(j\omega) = -b_1 e^{-j\omega\tau}$.

The design procedure begins by first determining the circuit that realizes the voltage summation function at the input of the feedback. Then, the passive feedback device must provide the necessary delay time imposed by the

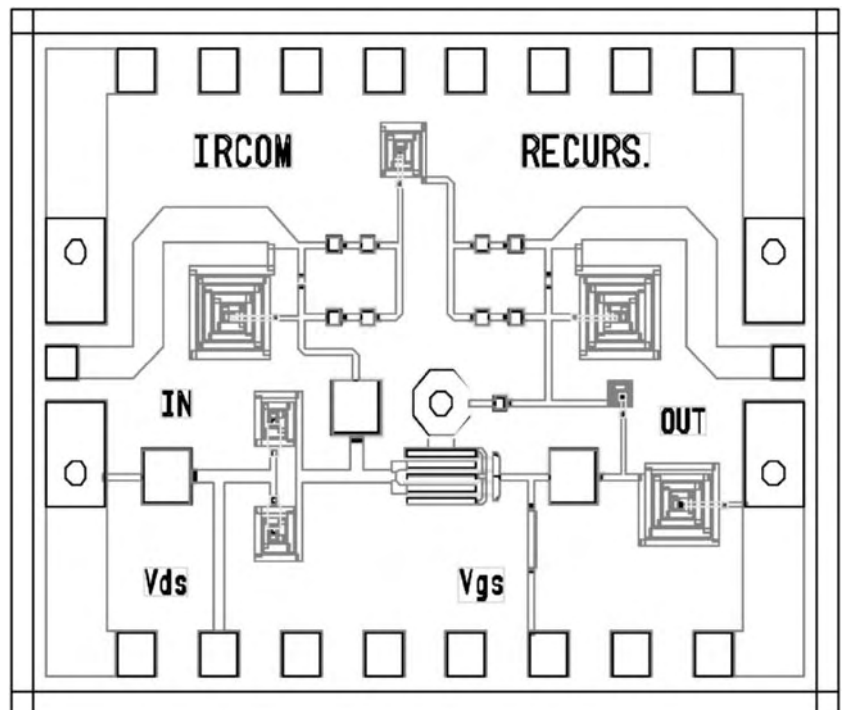


Figure 19. Layout of the first-order microwave recursive filter.

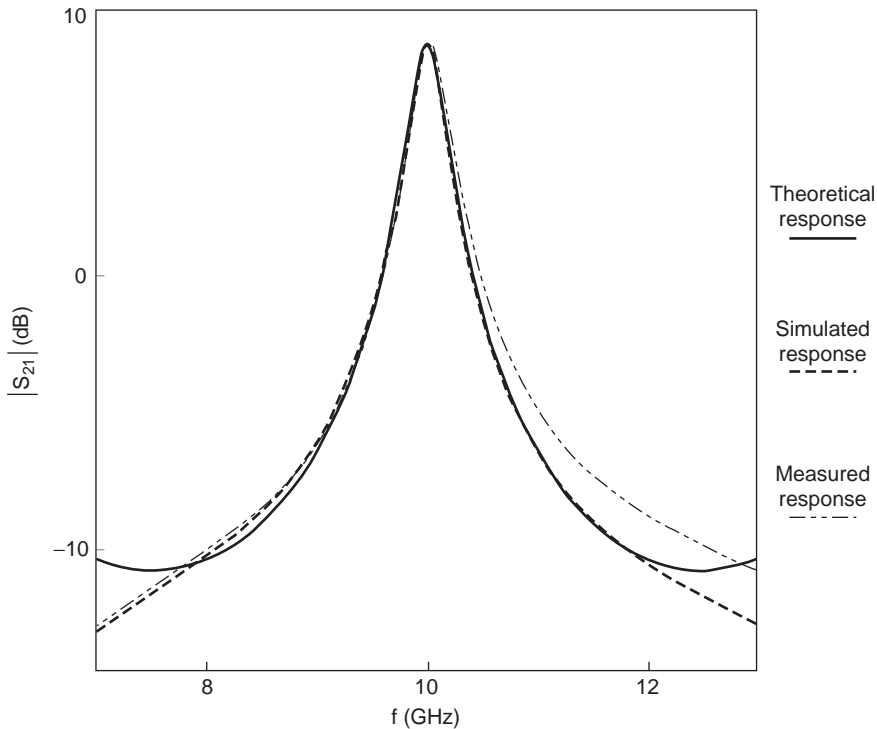


Figure 20. Theoretical, simulated, and measured response of the first-order recursive filter.

recursive process. Finally, a unilateral microwave active device must be employed in the forward branch in order to allow the feedback scheme to operate as intended. By verifying adequate relations between the impedances of the different blocks within the structure [13], the filter voltage gain appears to be of the recursive type:

$$G_V = K \left(\frac{\mu}{1 - \mu e^{-j\omega\tau}} \right)$$

Finally, for integration in microwave systems, two impedance transformers are required to match the filter to $50\ \Omega$ external impedances: a common-gate MESFET at the input and a common-drain MESFET at the output (Fig. 21), which must simultaneously provide a voltage matching of the loop and a power matching of the complete structure. Moreover, an attracting outstanding feature is the capability of the common-gate stage T_1 to produce power gain, making it a significant factor in the composi-

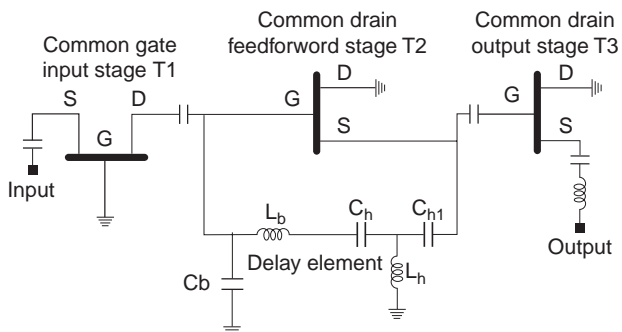


Figure 21. Electrical schematic of the voltage-matched first-order recursive filter.

tion of the overall noise figure of the filter. The loop gain can be controlled by the bias voltage of the common drain amplifier T_2 placed within the feedforward branch of the loop. A conventional lumped highpass cell and a lowpass cell are used to provide the necessary delay time τ for the desired filter center frequency. The filter has been fabricated using a $0.2\text{-}\mu\text{m}$ -gate-length PHEMT foundry process (ED02Ah from OMMIC [14]), and implemented on a $100\text{-}\mu\text{m}$ -thick GaAs substrate. Dimensions of the corresponding MMIC chip are $1 \times 1.5\ \text{mm}^2$. Total DC power consumption of the filter is $30\ \text{mW}$. Figure 22 shows a comparison between measured and simulated responses of the filter.

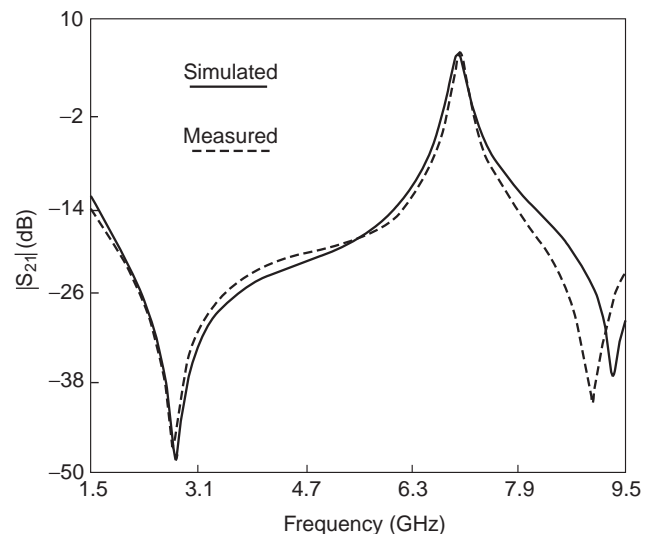


Figure 22. Simulated and measured voltage-matched first-order recursive filter response.

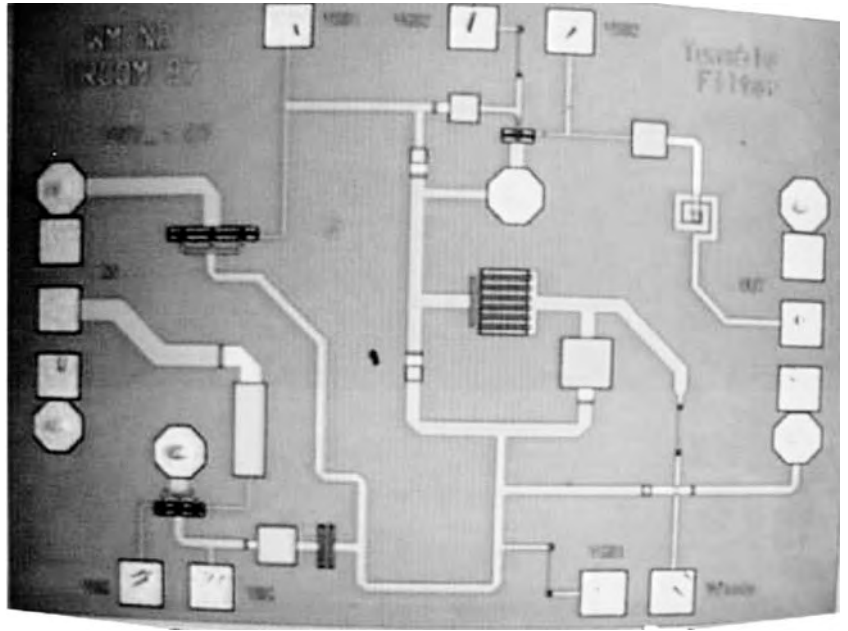


Figure 23. Photograph of the MMIC varactor-tuned first-order recursive filter.

The circuit is operating at 7 GHz with 5.1 dB gain at the center frequency and 140 MHz at 3 dB bandwidth. The out-of-band rejection is better than 20 dB, with 2 GHz from passband edges. The measured -1 dB compression point occurs for an input power of -15 dBm, and the simulated noise figure is 5.5 dB at the center frequency.

4.4. Frequency Tunable Recursive Filters

Recursive and transversal filters can simply provide tunable responses because of arbitrary analog phase shifter structures. As an example, we present the expression of a recursive transfer function shifted over a frequency band noted Δf :

$$\begin{aligned}
 H(f - \Delta f) &= \frac{\sum_{k=0}^N a_k e^{-2j\pi(f-\Delta f)k\tau}}{1 + \sum_{p=1}^P b_p e^{-2j\pi(f-\Delta f)p\tau}} \\
 &= \frac{\sum_{k=0}^N a_k e^{-2j\pi f k \tau} e^{jk\phi}}{1 + \sum_{p=1}^P b_p e^{-2j\pi f p \tau} e^{jp\phi}}
 \end{aligned}
 \tag{5}$$

with $\phi = 2\pi\Delta f\tau = 2\pi\Delta f/f_0$. This expression clearly shows that recursive responses can be tuned by the introduction of a variable phase shift in each branch of the filter. Consequently, many “recursivelike” filter structures can take advantage of this concept to be turned into tunable versions.

For most applications, 10% of tuning range is not sufficient and emphasizes the need for a real phase shifter function. A phase shifter structure for “recursivelike” filter purpose is proposed in Ref. 39. Maximum phase shift measured is 55° . Gain is near 7.5 dB in the 3–5 GHz frequency band. Noise factor of the phase shifter is 4.5 dB at 4 GHz.

Another tunable filter example is based on the design concepts outlined in Section 4.3. A tunable filter is realized by introducing a phase shift into the feedback loop of a voltage-matched recursive structure [13]. Filter tuning at the desired center frequency is accomplished through variation of the equivalent capacitor of a varactor diode that replaces a capacitance of the initial delay-time section. Correct adjustment of the bias point of the transistor T_2 (see Fig. 21) ensures a constant gain level over the frequency tuning range when the series diode resistance varies with the bias voltage.

A photograph of the filter is shown in Fig. 23. Dimensions of the MMIC chip are 2×1.5 mm². The measured transmission parameter of the filter is shown in Fig. 24. A frequency shift from 7.03 to 9.5 GHz (30% of relative

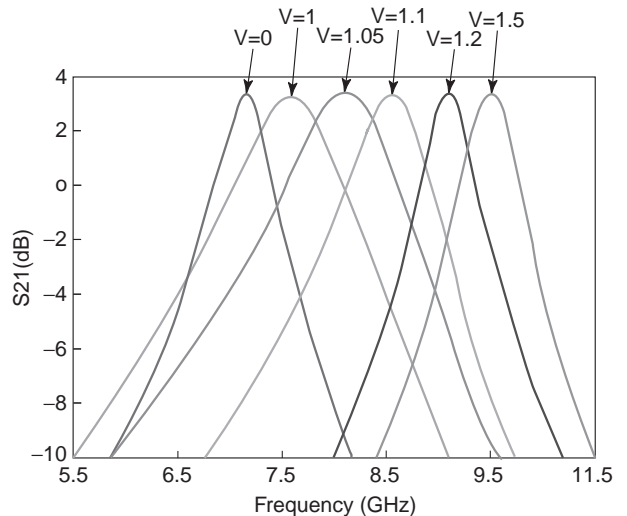


Figure 24. Measured S_{21} parameter of the tunable first-order recursive filter.

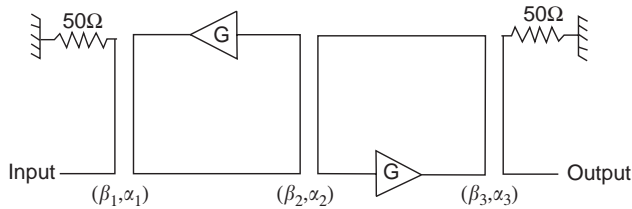


Figure 25. Second-order ring resonator active recursive filter.

tuning band) is achieved with a constant gain level of 3.5 dB across the tuning band. Moreover, the filter exhibits a good $50\ \Omega$ matching over the 2.5-GHz tuning band ($S_{ii} < -10\ \text{dB}$; $i = 1, 2$). The expected noise figure is 5 dB at center frequencies. The measured $-1\ \text{dB}$ compression point occurs for an input power of $-10\ \text{dBm}$. Maximum total DC power consumption is 46 mW.

4.5. High-Order Recursive Filters

For high-order filter design, a first alternative approach consists in coupling microstrip planar ring resonators, each resonator realizing a pole of the recursive transfer function.

The general transfer function of these ring resonator filters, where K and $\{K_n\}$ are functions of the coupling values and the amplifier gains can be expressed as:

$$S_{21}(f) = \frac{Ke^{-j\pi(f/f_0)}}{1 + \sum_{n=1}^N K_n e^{-2n\pi(f/f_0)}}$$

We give here an example of a second-order filter implemented in coplanar technology [40]. Many studies have shown that, in most cases, coplanar waveguides can be a good alternative to microstrip lines because of greater ease and flexibility in the design [41,42]. Because all conductors are located on the same plane, the ground connections for the active chips through via holes or ground report are eliminated, thus leading in more ease for connecting the active parts (here the amplifiers/phase shifters) and in more compact designs. Another advantage

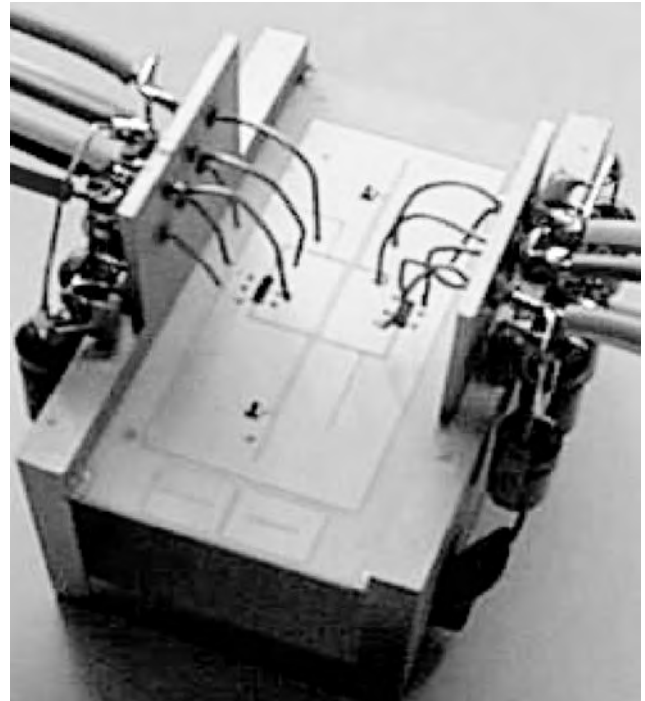


Figure 27. Photograph of the two-pole ring resonator recursive filter on its test fixture.

of coplanar technology is that each element characteristic can be adjusted and improved through additional geometric parameters. According to this degree of freedom, high-directivity couplers can then be easily achieved by minimizing the difference between the phase velocities of the two normal modes [43].

In our example, we consider three pairs of parallel coupled lines with up to two amplifiers within each passive ring resonator to achieve a second-order structure. The considered topology is shown in Fig. 25. With a methodology discussed in the article on active-filter design tools and techniques alluded to above, the noise performance of such structures can be analytically optimized. We use here the same amplifier/phase shifter as in Section 4.4. The

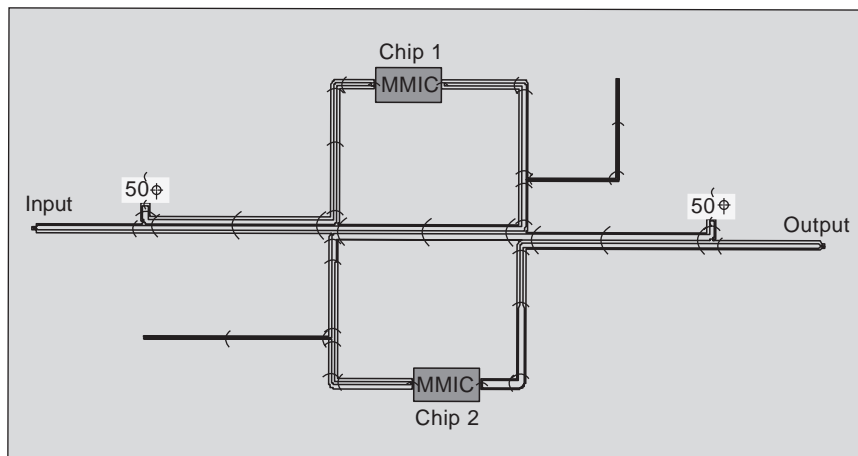


Figure 26. Two-pole ring resonator recursive filter layout in coplanar technology.

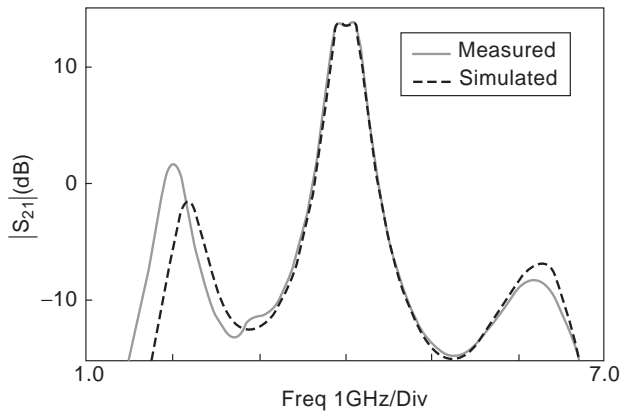


Figure 28. Comparison between simulation and measurements of the two-pole active ring resonator filter.

objective is to achieve a bandwidth $\Delta f = 120$ MHz with a ripple $\delta = 0.2$ dB within the passband. With $|G| = 2.2$, $F_A = 4.5$ at 4 GHz, the center frequency, we obtain $|S_{21}| = 13.7$ dB, $|S_{ii}| < -12$ dB. The noise figure is estimated to 6.5 dB. Figure 26 shows the layout of the active filter implemented on a 635- μm -thick alumina substrate ($\epsilon_r = 9.6$). Dimensions of the filter are 38×18 mm. A photograph of the circuit on its test fixture is given in Fig. 27.

Figure 28 shows a perfect agreement between simulated and experimental results. The gain of the filter is equal to 13.6 dB at 4 GHz. At center frequency, S_{11} and S_{22} are less than -10 dB. Power consumption is about 24 mW.

A second alternative for high-order filter design resides on the fact that classical “ladder type” high-order recursive filter design can become greatly complex considering the n -way dividers/combiners and the stability analysis of such multifeedback structures.

In the proposed approach [44], classical recursive filter concepts are extended by decomposing the response as a set of unitary terms. Each of these corresponds to a first-order function characterized by its own weighting coefficients $\{a_i, b_i\}$ and delay-time parameters τ_i . The obvious advantage of this approach is a more flexible way to

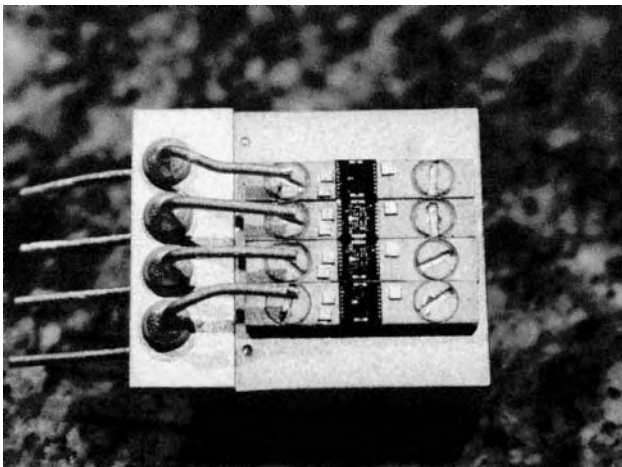


Figure 29. Test fixture of the four-cell filter configuration.

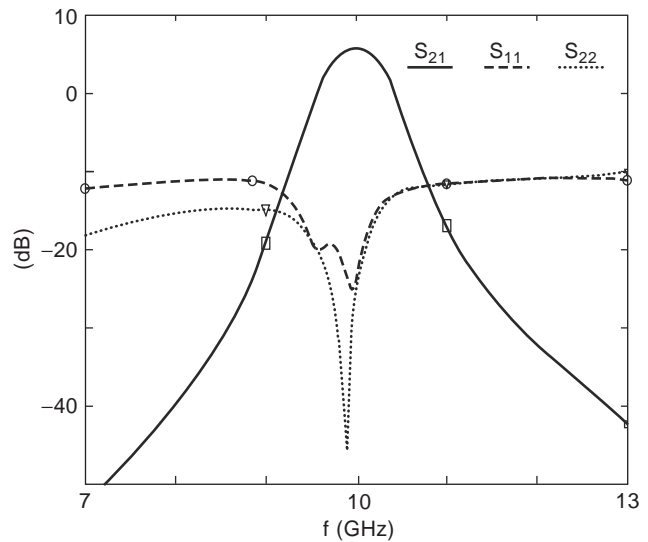


Figure 30. Measured S_{21} parameter of the four-cell filter with pairs of pole at 9.7 and 10.3 GHz.

individually control each pole frequency, selectivity, and also stability, thus simultaneously maintaining the global filter stability when cascading n unitary cells for a n th-order response. This also enables a tuning of the bandwidth and of the center frequency, whereas the classical approach does not give such flexibility. At least by cascading several elements of the same type, this approach also takes great advantage of MMIC technology reproducibility.

A physical implementation is shown in Fig. 29. Four 2×2 mm first-order tunable version of the chip of Fig. 19 are cascaded. Various response shapes can be obtained in terms of gain and bandwidth by adjusting center frequencies of the individual poles. Figure 30 shows excellent results obtained in the 4-chip configuration when two poles are located at 9.7 GHz and two at 10.3 GHz. Gain at center frequency is near 6 dB for a 670 MHz bandwidth. Good matching of the structure and -40 dB out-of-band rejection can also be noted in this case.

BIBLIOGRAPHY

1. R. V. Snyder, All the world is a filter, *IEEE MTT-S NewsL.* 5–10 (Fall 1990).
2. S. E. Sussman-Fort, Design concepts for microwave GaAs FET active filters, *IEEE Trans. Microwave Theory Tech.* **MTT-37**(9): 1418–1424 (1989).
3. H. Trabelsi and C. Cruchon, A varactor-tuned active microwave bandpass filter, *IEEE Microwave Guided Wave Lett.* **2**(6): 231–232 (1992).
4. S. R. Chandler, I. C. Hunter, and J. G. Gardiner, Active varactor tunable bandpass filter, *IEEE Microwave Guided Wave Lett.* **3**(3): 70–71 (1993).
5. U. Karacaoglu, I. D. Robertson, and M. Guglielmi, Microstrip bandpass filters using MMIC negative resistance circuits for loss compensation, *IMS'94, IEEE MTT-S Int. Microwave Symp. Digest*, 1994, pp. 613–616.

6. B. Hopf, I. Wolff, and M. Guglielmi, Coplanar MMIC active bandpass filters using negative resistance circuits, *IMS'94, IEEE MTT-S Int. Microwave Symp. Digest*, 1994, pp. 1183–1185.
7. A. Brucher, C. Cenac, M. Delmond, F. Delpino, B. Madrangeas, Ph. Meunier, V. Madrangeas, L. Billonnet, and B. Jarry, Several methodologies for active filter design at microwaves, *Int. J. RF Microwave Comput. Aided Eng.* **7**(3): 250–267 (1997).
8. F. Delpino, V. Madrangeas, L. Billonnet, B. Jarry, and P. Guillon, Dual mode dielectric resonator microwave active filters, *Microwave Opt. Technol. Lett.* **7**: 330–332 (1994).
9. B. Madrangeas, B. Jarry, P. Guillon, J. Larroque, B. Theron, and D. Parise, Three-pole DR microwave bandpass active filter, *IEE Proc. H.* **139**(2): 205–207 (1992).
10. K. B. Niclas, Active matching with comun gate MESFET, *IEEE Trans. Microwave Theory Tech.* **MTT-33**(6): 492–499 (1996).
11. R. S. Pengelly, J. R. Suffolk, J. R. Cockrill, and J. A. Turner, A comparison between actively and passively matched S-band GaAs monolithic FET amplifiers, *IEEE MTT-S Int. Microwave Symp. Digest*, 1981, pp. 367–369.
12. J. Tissier, W. Mouzannar, L. Billonnet, B. Jarry, and P. Guillon, Novel alternative design methods based upon combined amplification, matching and filtering approaches in MMIC technology, *IMS'2000, IEEE MTT-S Int. Microwave Symp. Digest*, 2000, Vol. 1, pp. 409–412.
13. W. Mouzannar, L. Billonnet, B. Jarry, and P. Guillon, A new design concept for wideband frequency-tunable and high-order MMIC microwave active recursive filters, *Microwave Opt. Technol. Lett.* **24**(6): 380–385 (2000).
14. ED02Ah monolithic process, *OMMIC, ED02Ah Design Manual*, GaAs Foundry and ASIC Design Center, <http://www.ommic.fr> (2000).
15. V. M. T. Lam and P. C. L. Yip, Microwave oscillator phase noise reduction using negative resistance compensation, *Electron. Lett.* **29**(4): 379–380 (1993).
16. A. V. Grebennikov, Stability of negative resistance oscillator circuits, *Int. J. Electric. Eng. Ed.* **36**: 242–254 (1999).
17. S. El Khoury, The design of active floating positive and negative inductors in MMIC technology, *IEEE Microwave Guided Wave Lett.* **5**(10): 321–323 (1995).
18. G. F. Zhang and J. L. Gautier, Broad-band, lossless monolithic microwave active floating inductor, *IEEE Microwave Guided Wave Lett.* **3**(4): 98–100 (1993).
19. U. Karacaoglu and I. D. Robertson, A MMIC active bandpass filter with FET negative resistance elements, *Microwave J.*, **7**: 76–79 (1996).
20. A. Brucher et al., Negative resistance monolithic circuits for microwave planar active filter losses compensation, *Proc. EuMC'95, 25th European Microwave Conf.* 1995.
21. S. E. Sussman-Fort, An NIC-based negative resistance circuit for microwave active filters, *Int. J. Microwave Millimeter Wave Comput. Aided Eng.* **4**(2): 130–139 (1994).
22. S. E. Sussman-Fort and L. Billonnet, Microwave, biquadratic, active-RC filter development, *Int. J. RF Microwave Comput. Aided Eng.* **2**(8): 102–115 (1998).
23. L. I. Babak, and M. V. Cherkashin, Interactive “visual” design of matching and compensation networks for microwave active circuits, *IMS'2001, IEEE MTT-S Int. Microwave Symp. Digest*, 2001.
24. R. M. Fano, Theoretical limitations on the broadband matching of arbitrary impedances, *J. Franklin Inst.*, **249**(1): 57–83, (Jan. 1950), **249**(2): 39–154 (Feb. 1950).
25. D. C. Youla, A new theory of broadband matching, *IEEE Trans. Circuit Theory*, **CT-11**(1): 30–50, (Mar. 1964).
26. B. S. Yarman and H. J. Carlin, A Simplified “Real Frequency” technique applied to broad-band multistage microwave amplifiers, *IEEE Trans. on Microwave Theory Techniques*, **MTT-30**(12): 2216–2222 (Dec. 1982).
27. A. Aksen and B. S. Yarman, A computer aided design technique for hybrid and monolithic microwave amplifiers employing distributed equalizers with lumped discontinuities, *IMS'2001, IEEE MTT-S Int. Microwave Symp. Digest*, 2001.
28. F. Biron, J. Ph. Plaze, L. Billonnet, D. Cros, B. Jarry, and P. Guillon, Design procedure for loss compensation of planar microwave filters using negative resistances for tunable bandstop and bandpass applications, *Proc. GAAS'2000, 8th European Gallium Arsenide and Related III-V Compounds Applications Symp.*, 2000, pp. 443–447.
29. HB200 monolithic process, UMS United Monolithic Semiconductors, www.ums-gaas.com.
30. J. Ph. Plaze, L. Billonnet, B. Jarry, and P. Guillon, A 2-pole bandpass filter assisted by a MMIC impedance for losses compensation and frequency control, *Proc. EuMC'2001, 31th European Microwave Conf.*, 2001.
31. C. Rauscher, Microwave active filters based on transversal and recursive principles, *IEEE Trans. Microwave Theory Tech.* **MTT-33**(12): 1350–1360 (1985).
32. M. J. Schindler, and Y. Tajima, A novel MMIC active filter with lumped and transversal elements, *IEEE Trans. Microwave Theory Tech.* **MTT-37**(12): 2148–2153 (1989).
33. L. Billonnet, B. Jarry, and P. Guillon, Theoretical and experimental analysis of microwave tunable recursive filters using power dividers, *IMS'93, IEEE MTT-S Int. Microwave Symp. Digest*, 1993, Vol. 1, pp. 185–188.
34. L. Billonnet et al., Design concepts for microwave recursive and transversal filters using Lange couplers, *IMS'92, IEEE MTT-S Int. Microwave Symp. Digest*, 1992, Vol. 2, pp. 925–928.
35. M. Danestig, H. Johansson, A. Ouacha, and S. Rudner, Low-noise active recursive MMIC filters, *IMS'97, IEEE MTT-S Int. Microwave Symp. Digest*, 1997.
36. R. Malmqvist, M. Danestig, S. Rudner, and C. Svensson, Analysis of intermodulation and noise performance for recursive active microwave integrated filters, *Proc. EuMC'99, 29th European Microwave Conf.*, 1999, pp. 60–63.
37. M. Delmond, L. Billonnet, B. Jarry, and P. Guillon, Microwave tunable active filter design in MMIC technology using recursive concepts, *IMS'95, IEEE MMWMC-S Microwave and Millimeter-Wave Monolithic Circuits Symp. Digest*, 1995, pp. 105–108.
38. P. K. Ikäläinen, An RLC matching network and applications in 1–20 GHz monolithic amplifier, *IEEE MTT-S Int. Microwave Symp. Digest*, 1990, pp. 503–506.
39. A. Cenac, L. Nénert, L. Billonnet, B. Jarry, and P. Guillon, MMIC broadband analog phase shifter and gain circuit for frequency-tunable microwave planar multipole active filter categories, *Microwave Opt. Technol. Lett.* **25**(5): 311–318 (2000).
40. L. Nénert, L. Billonnet, B. Jarry, P. Guillon, C. Quendo, E. Rius, and G. Tanné, Compact high-order planar ring-resonator filters optimized in noise in coplanar technology,

- IMS'2001, IEEE MTT-S Int. Microwave Symp. Digest*, 2001, Vol. 3, pp. 1441–1444.
41. M. Houdart, Coplanar lines: application to broadband microwave integrated circuits, *Proc. EuMC'76, 6th European Microwave Conf.*, 1976, pp. 49–53.
 42. L. Nenert, A. Cenac, L. Billonnet, B. Jarry, P. Guillon, C. Quendo, E. Rius, and G. Tanne, Use of coplanar technology advantages for tunable active planar looped filter structures optimised in noise, *Proc. EuMC'2000, 30th European Microwave Conf.*, 2000.
 43. E. Rius, T. Le Gouguec, K. Hettak, J. Ph. Coupez, and S. Toutain, Broadband high directivity 3 dB coupler using coplanar waveguide technology, *IMS'95, IEEE MTT-S Int. Microwave Symp. Digest*, 1995, pp. 671–674.
 44. M. Delmond, L. Billonnet, B. Jarry, and P. Guillon, High-order monolithic active recursive filter based upon multicellular approach, *IMS'96, IEEE MTT-S Int. Microwave Symp. Digest*, 1996, Vol. 2, pp. 623–626.

ACTIVE FILTERS: TOOLS AND TECHNIQUES FOR ACTIVE-FILTER DESIGN

LAURENT BILLONNET
 BERNARD JARRY
 BRUNO BARELAUD
 University of Limoges
 Limoges Cedex, France

1. INTRODUCTION

Whatever the application is, all communications systems—whether cellular, PCS, cable or satellite—require, in increasing quantity, a range of microwave filters with near-ideal characteristics to maximize communication capacity and signal processing efficiency and thus lower system costs. To satisfy these demands, engineers try to come up with design innovations and improved manufacturing processes of new filtering devices to reduce the cost of high-frequency communications. Since the early 1990s, engineers have also been increasingly interested in using active techniques for their compatibility with planar integrated monolithic technologies. Since the first microwave circuit was designed using a GaAs-based process, more and more attempts have been done nowadays to switch to silicon-based processes because of the resulting compact size and low-cost aspects.

We follow and gradually illustrate this tendency in this article. We first discuss the use of CAD tools for microwave and RF filter design, focusing particularly on optimization tools. We emphasize that, without any strong microwave design background and experience, this kind of tool unavoidably leads to nonreproducible and nonsystematic solutions. We then show the necessary implementation of analytical procedures to set and verify some essential characteristics of low-noise active devices, with examples of electrical stability criteria and noise performance calculation, prediction, and optimization. These two

examples are illustrated through many integrated filter designs and measurements.

Section 3 deals with the description of tools and techniques for filter improvements. We first begin with an extended consideration of compensation techniques based not only on loss compensation but also on response selectivity and circuit dimensions. The technique is illustrated with the design of a one-pole interdigital filter and a two-pole coplanar filter in which response and size have been improved using this approach. We then generalize this principle to the “active-impedance profile” (AIP) technique and present an example application to multistandard and pseudomultipole filters.

In Section 4, novel approaches and new technologies for new microwave and RF communications needs are detailed. We first discuss the new application constraints driven by new communication standards. We then discuss GaAs processes to silicon-based technologies, emphasizing the differences between the two technologies in terms of processes themselves, and in terms of CAD tools, component implementation, compactness, relative size, and cost with two basic circuit examples. Migration to silicon-based processes also involves novel implementation approaches among which differential circuits. This last approach is illustrated with experimental results.

2. ANALYTICAL TOOLS AND PROCEDURES FOR ACTIVE FILTER DESIGN

2.1. Numerical CAD Optimization Tools

Since 1980, scientific production on microwave filters has grown extensively. This extension finds its sources from a technical perspective in:

- A permanent growth in device complexity
- A constant objective of reduction in size and weight
- The use of new materials and new technologies (superconductor materials, MEMs, planar monolithic technologies, etc.)

However, any experimented engineer knows that this growth of production is fueled mostly by novel modern computing systems and by the extraordinarily growing computation capabilities.

Without this computation power, many application would still be only perspectives:

- The development of precise electromagnetic simulation methods for planar (2D or 2.5D) or volumic (3D) circuits, such as the finite-element method, method of lines, or modal analysis
- The development of numerical synthesis methods taking into account a larger number of parameters such as losses or process limitations
- Global analysis methods simultaneously coupling in a single step various sorts of analysis that are sometimes very different

IMS'2001, IEEE MTT-S Int. Microwave Symp. Digest, 2001, Vol. 3, pp. 1441–1444.

41. M. Houdart, Coplanar lines: application to broadband microwave integrated circuits, *Proc. EuMC'76, 6th European Microwave Conf.*, 1976, pp. 49–53.
42. L. Nenert, A. Cenac, L. Billonnet, B. Jarry, P. Guillon, C. Quendo, E. Rius, and G. Tanne, Use of coplanar technology advantages for tunable active planar looped filter structures optimised in noise, *Proc. EuMC'2000, 30th European Microwave Conf.*, 2000.
43. E. Rius, T. Le Gouguec, K. Hettak, J. Ph. Coupez, and S. Toutain, Broadband high directivity 3 dB coupler using coplanar waveguide technology, *IMS'95, IEEE MTT-S Int. Microwave Symp. Digest*, 1995, pp. 671–674.
44. M. Delmond, L. Billonnet, B. Jarry, and P. Guillon, High-order monolithic active recursive filter based upon multicellular approach, *IMS'96, IEEE MTT-S Int. Microwave Symp. Digest*, 1996, Vol. 2, pp. 623–626.

ACTIVE FILTERS: TOOLS AND TECHNIQUES FOR ACTIVE-FILTER DESIGN

LAURENT BILLONNET
BERNARD JARRY
BRUNO BARELAUD
University of Limoges
Limoges Cedex, France

1. INTRODUCTION

Whatever the application is, all communications systems—whether cellular, PCS, cable or satellite—require, in increasing quantity, a range of microwave filters with near-ideal characteristics to maximize communication capacity and signal processing efficiency and thus lower system costs. To satisfy these demands, engineers try to come up with design innovations and improved manufacturing processes of new filtering devices to reduce the cost of high-frequency communications. Since the early 1990s, engineers have also been increasingly interested in using active techniques for their compatibility with planar integrated monolithic technologies. Since the first microwave circuit was designed using a GaAs-based process, more and more attempts have been done nowadays to switch to silicon-based processes because of the resulting compact size and low-cost aspects.

We follow and gradually illustrate this tendency in this article. We first discuss the use of CAD tools for microwave and RF filter design, focusing particularly on optimization tools. We emphasize that, without any strong microwave design background and experience, this kind of tool unavoidably leads to nonreproducible and nonsystematic solutions. We then show the necessary implementation of analytical procedures to set and verify some essential characteristics of low-noise active devices, with examples of electrical stability criteria and noise performance calculation, prediction, and optimization. These two

examples are illustrated through many integrated filter designs and measurements.

Section 3 deals with the description of tools and techniques for filter improvements. We first begin with an extended consideration of compensation techniques based not only on loss compensation but also on response selectivity and circuit dimensions. The technique is illustrated with the design of a one-pole interdigital filter and a two-pole coplanar filter in which response and size have been improved using this approach. We then generalize this principle to the “active-impedance profile” (AIP) technique and present an example application to multistandard and pseudomultipole filters.

In Section 4, novel approaches and new technologies for new microwave and RF communications needs are detailed. We first discuss the new application constraints driven by new communication standards. We then discuss GaAs processes to silicon-based technologies, emphasizing the differences between the two technologies in terms of processes themselves, and in terms of CAD tools, component implementation, compactness, relative size, and cost with two basic circuit examples. Migration to silicon-based processes also involves novel implementation approaches among which differential circuits. This last approach is illustrated with experimental results.

2. ANALYTICAL TOOLS AND PROCEDURES FOR ACTIVE FILTER DESIGN

2.1. Numerical CAD Optimization Tools

Since 1980, scientific production on microwave filters has grown extensively. This extension finds its sources from a technical perspective in:

- A permanent growth in device complexity
- A constant objective of reduction in size and weight
- The use of new materials and new technologies (superconductor materials, MEMs, planar monolithic technologies, etc.)

However, any experimented engineer knows that this growth of production is fueled mostly by novel modern computing systems and by the extraordinarily growing computation capabilities.

Without this computation power, many application would still be only perspectives:

- The development of precise electromagnetic simulation methods for planar (2D or 2.5D) or volumic (3D) circuits, such as the finite-element method, method of lines, or modal analysis
- The development of numerical synthesis methods taking into account a larger number of parameters such as losses or process limitations
- Global analysis methods simultaneously coupling in a single step various sorts of analysis that are sometimes very different

From the beginning of their careers today's engineers can use numbers of synthesis, analysis, and statistical tools, and more importantly of optimization tools that can strongly help the design. For the beginner, the danger is in believing that this complete set of tools can lead, with security, to synthesis and analysis of any microwave function without either a strong knowledge or preliminary analytical studies. In particular, the riskiest tool is, without any doubt, the optimizer, which is still for some designer a "miracle" (or panacea) tool that always leads to the "best" solution.

In fact, any optimiser must be used with great care and attention:

- In practice, it should be used only at the last step of a design, after the synthesis procedure, to fine-tune the different parameters of the problem. If not, it does not mean any reproducibility in the approach and is based only on a hazardous random starting point. It does not enable any understanding or feedback of the results obtained.
- It never leads in a systematic way to "the" best solution, but usually only to a mathematically local set of parameters.
- Depending on the number of optimization constraints and the nature of each separate constraint (response level, noise, compression point, etc.), the major difficulty is the weight of the different constraints from one to the other. The optimizer then does not permit one to systematically analyze the influence of a given parameter (geometric or electrical) on the whole set of circuit characteristics.

Using such tools without any theoretical background, without experience, or without any preliminary analytical study, even simplified, does not reveal an efficient, fast, and operational investigator. The primary objective must be the implementation of rigorous analytical procedures to investigate any problem that can be encountered at each design step of an active device.

2.2. Examples of Analytical Tools and Procedures at Microwaves

We describe here two examples of analytical procedures that can facilitate understanding of the influence of a parameter on a given filter characteristic. These two examples focus on low-noise circuits in the linear regime.

2.2.1. Analysis and Optimization of Noise Performance.

For any applications using circuits with active elements, the problem of noise performance is a critical point that must be studied. In this subsection, the purpose is not to describe well-known methods or formalisms classically applied at the component level (e.g., how to determine the optimal loads of a transistor to be at the minimum noise power); rather this discussion is dedicated to determining

- The contribution of an active function in terms of system components, to the noise of a more complex structure (e.g., an amplifier within a recursive filter, or a negative resistance within a resonator-based filter)
- The optimal location of an active function within a global structure [1]
- An analytical optimization method of the noise characteristics of a global structure in which is integrated an active function, while maintaining given filtering characteristics

The discussion here is intended to help the designer better predict the influence of active parts or components by analytical means.

Several methodologies have been studied to evaluate or model noise performances, depending on the type of electrical parameters that are considered. Here, we choose to use a noise-wave formalism described by Wedge and Rutledge [2]. This formalism takes advantage of the S -parameter description. However, other formalisms using currents or voltages instead of power waves also exist, based on the same principles.

Analytical derivation of noise performance using the noise-wave formalism is done by gradually reconnecting parts of a global device for which S parameters and the noise matrix are known. An interesting way to illustrate the approach is to evaluate the noise factor of microwave active recursive filters. Other structures are studied in Ref. 3. As shown in Fig. 1, the noise-wave formalism consists in modeling the noise of a two-port device with internal noise-wave generators c_1 and c_2 .

Their contribution to the output scattering waves b_1 and b_2 can be expressed in the following manner, where S is the scattering matrix of the two-port Q :

$$\begin{pmatrix} b_1 \\ b_2 \end{pmatrix} = \begin{pmatrix} S_{11} & S_{12} \\ S_{21} & S_{22} \end{pmatrix}_Q \begin{pmatrix} a_1 \\ a_2 \end{pmatrix} + \begin{pmatrix} c_1 \\ c_2 \end{pmatrix} \quad (1)$$

Regarding the first-order recursive topology of the article ACTIVE FILTERS: OVERVIEW OF ACTIVE-FILTER STRUCTURES, Section 4.2, the circuit consists in two power dividers/combiners, one delay element, and one amplifier. Depending on where the amplifier is placed within the structure (in the feedback or in the direct branch), two topologies can be derived (Fig. 2). In the passband case, the problem is then to find, for each topology, the gain value G , noise factor value F_A , and the two coupling values

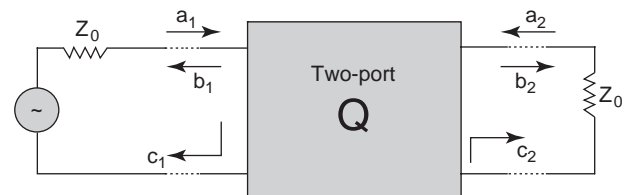


Figure 1. Two-port circuit described by noise waves and scattering parameters.

- A systematic approach for the analytical derivation of noise performances

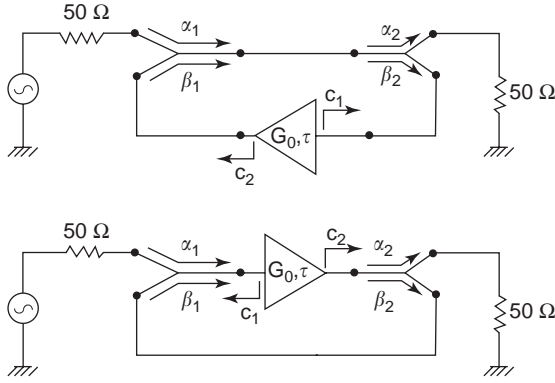


Figure 2. First-order recursive filter topologies: amplifier placed (a) in the feedback branch and (b) in the direct branch.

at the input and output of the filter, to obtain a given response shape with a minimum noise factor at center frequency. To calculate the minimum noise factors of the two topologies, we first consider the R and V selectivity parameters that set the filtering performances. These parameters must not be modified during the improvement process of the noise factor and set the frequency shape of the response. f_0 is the center frequency.

$$R = \frac{|S_{21}|_{\max}}{|S_{21}|_{\min}} = \frac{|S_{21}(f_0)|}{|S_{21}(f_0/2)|}, \quad V = \frac{R-1}{R+1} \quad (2)$$

The two corresponding filters are considered as equivalent when they are characterized by the same V parameter even if they do not achieve the same gain at the center frequency f_0 . The transfer functions of the two topologies can then be expressed as follows with the selectivity parameter $V = \beta_1\beta_2G_0$, $G = G_0 e^{-2j\pi f\tau}$, where G_0 is a positive real gain and the delay time τ is introduced:

$$H_i(f) = \frac{K_i}{1 - V e^{-2j\pi f\tau}} \quad (3)$$

For topology 1 (Fig. 2a), the transfer function and the noise factor at f_0 , the center frequency, are analytically derived through the reconnecting method, as functions of β_1 , G_0 , and F_A (the noise factor of the amplifier that can also be derived from the same noise-wave formalism):

$$H_1(f) = \frac{\alpha_1\alpha_2}{1 - G\beta_1\beta_2}; \quad F_1 = 1 + \left(\frac{\beta_1}{\alpha_1}\right)^2 (F_A - 1)G_0^2 + \left(\frac{\beta_2 - \beta_1G_0}{\alpha_1\alpha_2}\right)^2 \quad (4)$$

F_1 can also be expressed as a function of β_1 , G_0 , F_A and more importantly of V to maintain the filter response shape. For a given amplifier, β_1 appears as a degree of freedom that can be used to optimize the noise factor. It can even be shown that for the optimal value of $\beta_1 = \beta_{1\text{opt}}$, $F_1 < F_A$ when $G_0 \rightarrow \infty$.

Using the same methodology for topology 2, the transfer function $H_2(f)$ and the corresponding noise factor F_2

are given by:

$$H_2(f) = \frac{G\alpha_1\alpha_2}{1 - G\beta_1\beta_2}; \quad F_2 = 1 + \frac{(F_A - 1)}{\alpha_1^2} + \left(\frac{\beta_2 - \beta_1G_0}{\alpha_1\alpha_2G_0}\right)^2 \quad (5)$$

The expression of $\beta_{1\text{opt}}$ is the same as for topology 1 but leads to $F_2 > F_A$ at f_0 . The analytical procedure enables us to find that topology 1 is better than topology 2 in terms of the noise factor, which could not have been derived by using a classical CAD optimizer. Simulations show on one hand the noise factors increase when the selectivity increases, and on the other hand when the gain is increased (for the same F_A of the amplifier), the noise factor of the filter decreases as expected.

To experimentally validate our approach, we have designed a first-order recursive filter from topology 1 in MMIC technology. This filter, the layout of which is given in Fig. 3, has the same filtering performance as that described in Section 4.2 (Fig. 20) of the article over-viewing active-filter structures [cited above, immediately following Eq. (1)]. Couplings (through the use of Lange couplers [4,5]) and gain values are chosen to obtain the lowest noise factor according to the analysis presented. Measured noise figure is equal to 2.1 dB, in contrast to the initial 11.7 dB.

2.2.2. Analytical Tools for Electrical Stability Analysis and Optimization. Several stability criteria are used at microwaves to evaluate the electrical stability of a circuit. Most techniques used are based on the Rollett factor K [6,7] defined through two-port S parameters. However, these factors are not quantitative, and additional parameters must be calculated to get more information. Plots of μ factor [8] or stability circles can then be calculated to give the reader an idea of the stability margin and the location, respectively, of the load impedances that can lead to instability.

In terms of design, these criteria present many disadvantages:

- In most cases, filters are designed to be terminated (directly or in cascade with other modules) with 50 Ω impedances. In case of conditional stability, the

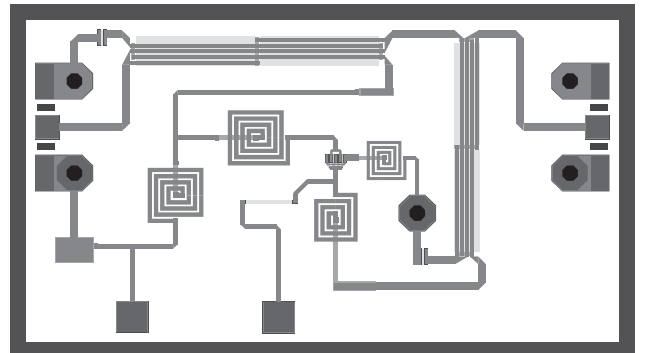


Figure 3. Layout of the low-noise first-order active recursive filter.

Rollett factor does not predict the impedances for which the instability is observed. It is then necessary to plot the stability circles, thus clearly complicating the engineer's work.

- Another important point directly concerns the validity of classical parameters. Indeed, interpretation of classical parameters (including stability circles) leads to a valid evaluation of stability only when the circuit is intrinsically stable, independently of the terminations. The designer must then, in a first step, be sure of the intrinsic stability of the device.
- Finally, for more complex circuits, classical stability parameters cannot analytically predict the influence of a component or a circuit characteristic, and therefore lead to efficient modification of the adequate parameter in case of instability.

Many researchers have attempted to solve the problem with methods derived from Bode's theory [9] among which Ohtomo [10] and Platzker [11]. We describe this last approach here. The normalized determinant function (NDF) approach is an extension of Bode's theory for circuits with more than two ports and multiple feedbacks. Without discussing the details, analysis of a mathematical complex function leads to a plot in an image complex plane. The function considered here is defined as the ratio of the determinant of the nodal description matrix of the circuit when all the sources are in ON state, to the determinant of the same matrix when all the sources are in OFF state. Interpretation of the resulting plot in the image plane results from Cauchy's theorem. If the plot encircles the origin of the image plane in the clockwise direction, then the circuit is unstable. There are as many instabilities as encirclements. Frequencies of instabilities can be extracted by searching the roots of the NDF.

The originality of the method resides in the return ratio (RR) principle [12], which allows analysis with a classical CAD package. With this method, each transistor is modeled as a voltage-controlled current source. All these sources, one by one, are driven by an external voltage instead of their initial internal voltage. The corresponding

RR is then defined as the ratio of the initial internal voltage to the external one. At each step of the calculation, all sources for which the RR has been calculated are turned off. Finally, expression of the NDF is derived from the n RRs (for a n -source or a n -transistor circuit).

Note that this approach, when numerically used through a CAD package, does not allow any interpretation of any parameter on the circuit stability. However, in this case, classical optimization is still possible.

With a strict calculation approach, analytical expression of the NDF can be obtained, thus allowing the evaluation of each parameter influence not only on the stability itself but also on the frequency where instabilities occur. To illustrate this point, we consider the first-order filter discussed in Section 4.2 (Fig. 19) of the article cited above [following Eq. (1)], where Lange couplers are used for division/summation of the signals within the structure [13]. We first model the ideal amplifier of the structure with an equivalent voltage-controlled current source terminated with two $50\ \Omega$ impedances. In Fig. 4, the ideal amplifier has been replaced by its equivalent dependent source. Because of the unilaterality property of this source, we now obtain a new open-loop two-port device loaded by a generator of internal impedance $50\ \Omega$ at the input, and with a $50\ \Omega$ impedance at the output. Initial input and output ports are also assumed to be terminated with a $50\ \Omega$ impedance. The current source is controlled by an external voltage V_{ext} .

The NDF is then derived through the RR calculation. It shows that the zeros location in the complex plane for $\text{NDF}(f)$ (i.e., the location of instabilities) is equivalent to the zeros location of the denominator of the transfer function of the filter $H(f)$. In other words, zeros of the NDF are equivalent to the poles of the response.

Using the same principles, we now consider a second-order recursive filter, for which the two amplifiers G_1 and G_2 are substituted with dependent current sources. Calculation of the NDF is obtained in two steps corresponding to the calculation of the two RRs:

$$\text{NDF}(f) = (1 + \text{RR}_1(f)) \cdot (1 + \text{RR}_2(f))$$

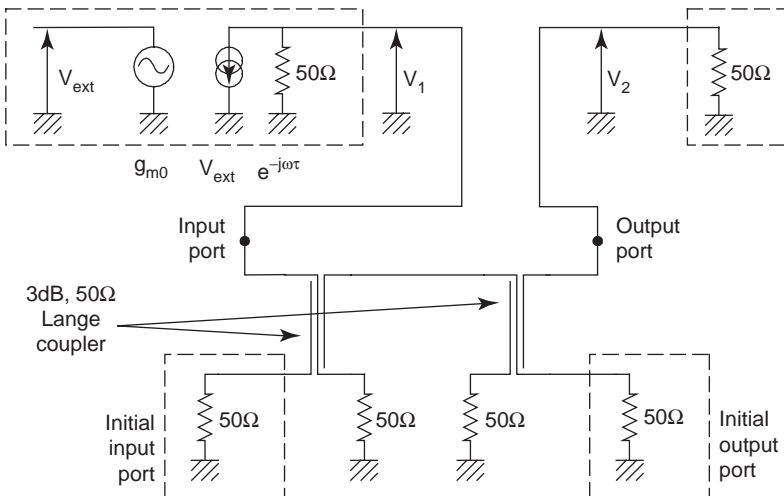


Figure 4. New “open loop” equivalent circuit of a first-order recursive filter.

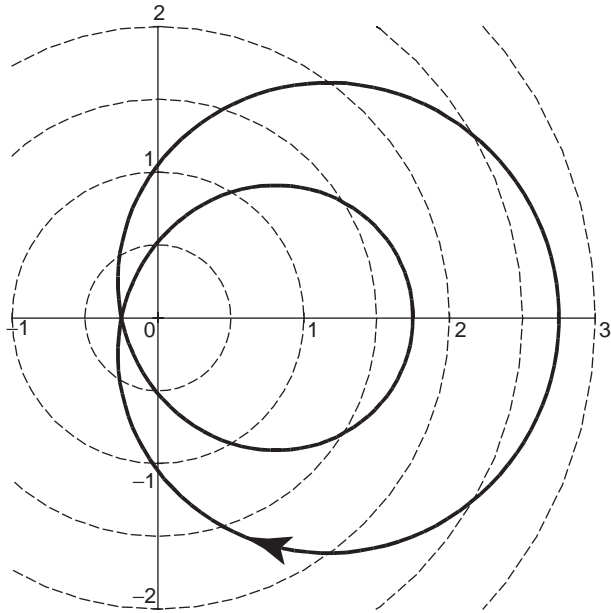


Figure 5. Unstable case of a second-order recursive filter: NDF plot for $G_1 = -5$ and $G_2 = -2$.

Here again, the NDF is the same as the denominator of the transfer function of the filter, thus validating the NDF calculation process. Figure 5 shows how instability can be predicted when the NDF encircles the origin for $G_1 = -5$ and $G_2 = -2$. In the same manner, Fig. 6 illustrates the stable state of the circuit, when the NDF does not encircle the origin for $G_1 = -4$ and $G_2 = -2$.

3. EXAMPLES OF PERFORMANCE IMPROVEMENT

For most engineers and researchers, the use of active components or functions is limited to loss compensation of passive structures. Nevertheless, active parts can play various roles in a global system. By identifying two main filter families in the active-filter structure overview article cited above, we have underlined a filter category for which active functions play an essential role. Gain, unilaterality or phase shift are directly implicated in the response and do not operate only for a simple loss compensation.

In fact, it is reasonable to imagine that active modules associated to passive filters could enable

- A significant reduction in size of the circuits
- An improvement of the response selectivity, even the control or the reconfigurability of the working band (passband or stopband)
- An automatic control process of frequency and level of the response elicited by external parasitics (e.g., temperature drift)
- Novel topologies for original filter structures
- Improved variable components [14]

In this section, we illustrate the possible improvements of filter responses and size due to such techniques for the

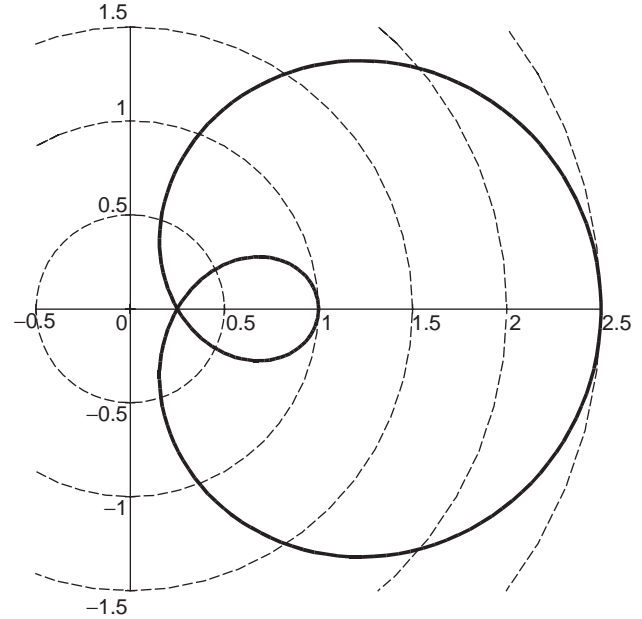


Figure 6. Stable case of a second-order recursive filter: NDF plot for $G_1 = -3$ and $G_2 = -3$.

two filter categories identified in the active-filter structure overview article cited above. We also describe automatic frequency control techniques and show an experimental validation.

3.1. Loss Compensation and Size Reduction

Miniaturized high-selectivity microwave bandpass filters are highly desirable for the next generation of satellite and mobile communications systems. Traditional interdigital and combline filters [15] based on TEM mode coupling are well suited for the design of narrowband passive filters. Unfortunately, the design of such filters with classical technologies (e.g., microstrip technology) leads to very high insertion losses in the operating band, especially when high selectivity is required. Indeed, due to low unloaded Q factors, it is not possible to obtain narrowband bandpass filters achieving 0 dB insertion losses with only passive elements, except with superconducting techniques.

An original technique is presented here, using classical passive interdigital filters in association with a MMIC active component circuit. Two filters, one of the first order and one of the second order, are discussed in reference to microstrip and coplanar technologies, respectively [16].

3.1.1. First-Order Microstrip Filter. A very classical first-order filter is studied using a standard design procedure [16]. The initial passive structure is designed to fit the following characteristics: 3.46 GHz for the center frequency and 91 MHz for the 3 dB bandwidth (2.63%). Measured insertion losses of the passive filter are about 7 dB at the center frequency. In a second step, the passive filter is geometrically modified in order to insert the MMIC circuit, while keeping the same center frequency. By taking into account the value of the imaginary part of the active

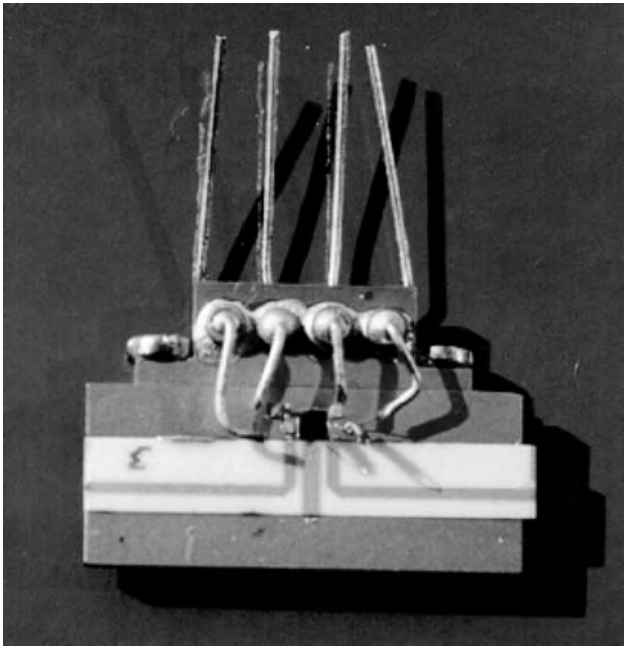


Figure 7. Photograph of the active one-pole microstrip filter.

component, the length of the resonator can be approximately divided by 2. A photograph of the active microstrip filter is shown in Fig. 7. Comparison of passive parts of the two versions are compared in Fig. 8. Measurements in Fig. 9 show a 3.27 GHz central frequency at a 85 MHz 3 dB bandwidth (2.6%). The insertion losses have been compensated at 0 dB.

3.1.2. Second-Order Coplanar Bandpass Filter. Many studies have shown that coplanar wave-guides can be considered as a good alternative to microstrip lines for many applications [17]. It is well known that low-level coupling coefficients are needed when designing narrowband bandpass filters. In the case of interdigital filters, a separating ground plane can be placed between the two coupled strips in order to obtain low-level couplings. With this approach, it is possible to efficiently control low coupling coefficients by adjusting the dimension of this ground plane. This method allows one to design compact low-coupled sections [18]. Another advantage of the coplanar technology is the flexibility in the design of the passive circuits. Indeed, a large number of geometric parameters can be chosen to design any transmission line with a given impedance. Electrical characteristics can then be improved by properly defining the ratio of the strip length to the slot length.

By taking into account all these advantages, a second-order filter is designed in coplanar technology. In this case, two MMIC components are placed at the open end of each resonator. A layout and a photograph of the coplanar active filter are respectively shown in Figs. 10 and 11. Measurements have been made over a wide frequency range in order to verify the bandstop responses (Fig. 12). No spurious resonances appear up to 9.5 GHz. Measurements also show a 1.98 GHz center frequency and a 75 MHz 3 dB

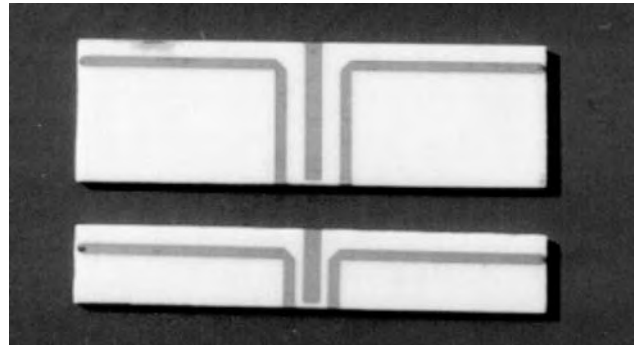


Figure 8. Comparison of the initial and optimized passive parts of the one-pole filter.

bandwidth (3.8%). In comparison to the purely passive case, the imaginary part of the MMIC chip has increased the response selectivity; 0 dB insertion losses have also been measured. In order to compare the reduction in size provided by the imaginary part of the active component, the same filter without the active components has been simulated. The center frequency of the filter is shifted to 2.6 GHz, resulting in a size reduction of about 0.8. Insertion losses are -7 dB in this case.

3.2. Active-Impedance Profile

In the previous subsection, interdigital structures were presented and improved in microstrip and coplanar technologies. However, these structures are not adequate when frequency switching or tuning is needed. Generally, the response of a passive filter is optimal at a given frequency. Tunability of the center frequency then implies a variation of one of the filter component parameters (such as electrical lengths) that can damage one or more electrical characteristics of the filters (matching, losses, bandwidth, etc.). In particular, for all planar filters using a varactor-based tuning or a switching process, any decrease of the center frequency is associated with a proportional reduction in bandwidth [19,20].

Nevertheless, beyond loss compensation and circuit size reduction, results presented above indicate a significant

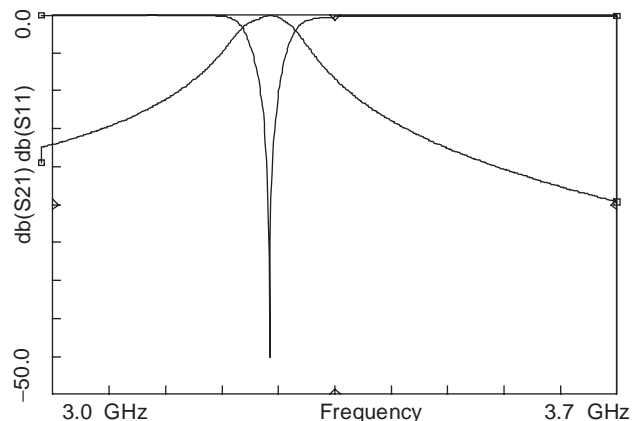


Figure 9. Experimental results of the active one-pole microstrip filter.

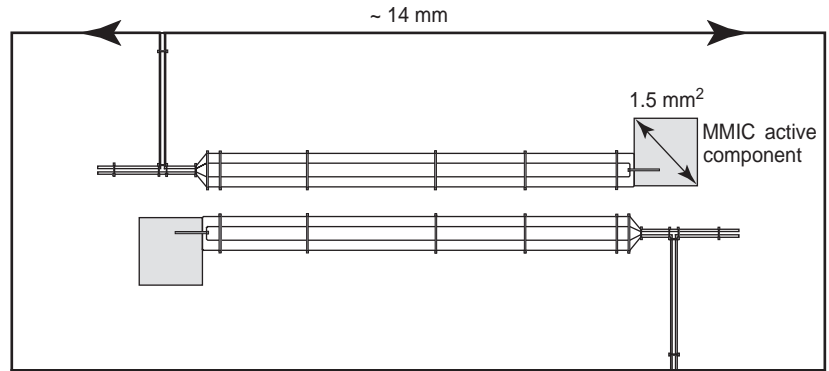


Figure 10. Layout of the compensated coplanar two-pole filter.

increase of the response selectivity in comparison to the corresponding passive filters. It should then be possible, using the same approach, to control simultaneously the bandwidth and the center frequency owing to the imaginary parts presented by compensation circuits.

In particular, it can easily be verified by simulations that these imaginary parts contribute to the improvement of the response in two ways:

- The value of the imaginary part at the input of the compensation circuit sets or corrects the center frequency of the filter. At a given frequency, this value is equivalent to a resonator length added to or withdrawn from a passive resonator.
- For this filter topology, the slope of the imaginary part around the chosen center frequency directly commands the response selectivity.

We now show two examples to illustrate how these simple impedance considerations, called active-impedance-profile (AIP), can be interpreted and applied for the design of multistandard and pseudomultipole filters.

3.2.1. Application of AIP to Multistandard Filters for Mobile Communications. The objective here is to build electrically tunable filters for multistandard mobile communication applications. To do this, frequency tuning must be achieved while maintaining a correct and constant level within the passband. Losses due to the passive

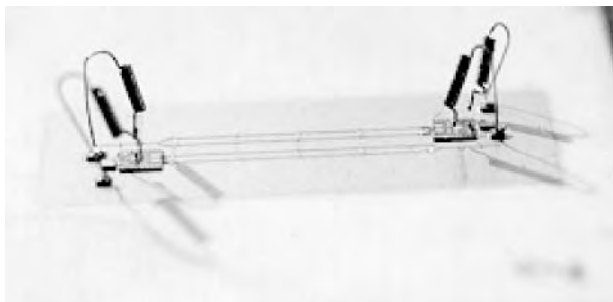


Figure 11. Photograph of the compensated coplanar two-pole filter.

parts of the circuit, but also those introduced by the tuning elements, must be compensated and controlled.

Generally, the response of a passive filter is optimal at a given frequency. To control the effects of one of the tuning parameters on filter performance, the filter structure has to be selected in reference to the target application. In our case, several tests on various elementary resonator-based structures have shown that interdigital filter structures exhibit an acceptable tolerance concerning the center frequency variation [21]. For example, a 10% increase of the resonator electrical length (by means of an additional capacitor at the end of the resonator or by the physical modification of the resonator length) achieves a 10% decrease of f_0 with a limited effect (less than 3%) on the bandwidth.

We apply our technique to the design of a second-order interdigital bandpass filter in coplanar technology. The filter topology is the same as in Fig. 10. The center frequency is electronically tuned in relation to the biasing voltages supplied to the varactor diodes located on the resonators. Each NIC-based AIP circuit is placed onto the ground plane (near the open end of each resonator) and is connected in series (using a bounding wire) with a varactor diode at the open end of the resonator. The filter is intended here to cover three telecommunications standards at

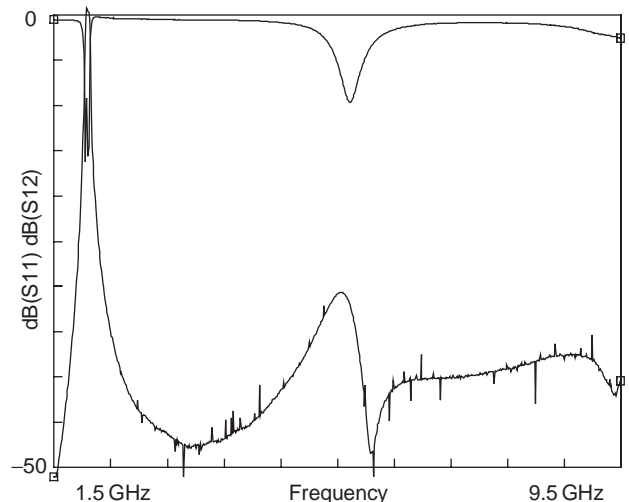


Figure 12. Experimental results of the compensated coplanar two-pole filter over a wide frequency range.

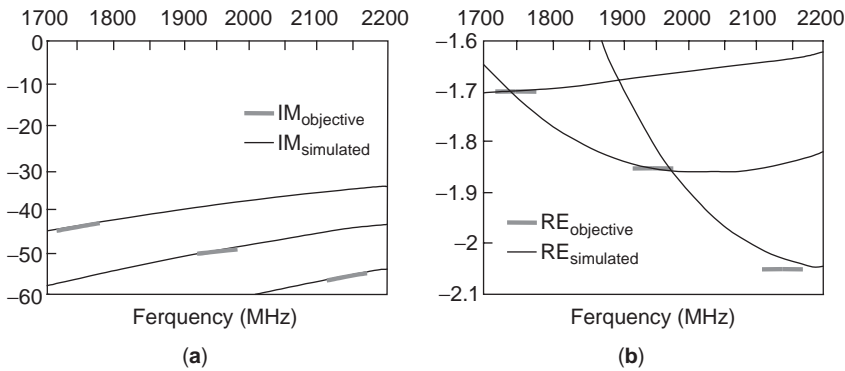


Figure 13. Objective and simulated AIP+diode impedance: (a) imaginary part; (b) real part.

- 1748 MHz (DCS1800 transmission band)
- 1950 MHz (UMTS transmission band)
- 2140 MHz (UMTS reception band)

For all standards, the objective bandwidth is set to 60 MHz relative to the UMTS standard. The design process is then done in four steps:

1. The designer sets the circuit dimensions referring to the desired center frequencies for the different communication standards and to the desired circuit size reduction.
2. This step focuses on the search, for each standard (three in this example), of the impedance characteristics in terms of real and imaginary parts to produce through the AIP associated with the varactor diode.
3. Considering that the switching between the standards is made through the varactor diode, one varactor bias voltage must be chosen in a third step for each standard. These choices can be set by the designer, but in a more general approach, an optimization process can help in finding the most adequate biasing points.
4. This last step consists in finding the real and imaginary part profiles over a frequency band covering all the standards. This impedance profile is obtained by deembedding the varactor diode impedance from the one obtained in step 3 around each standard center frequency.

Figure 13 shows the imaginary and real parts of the set AIP/varactor diode obtained at step 3 with classical packaged abrupt junction varactor diodes and for the three chosen bias voltages. A good agreement is obtained for each bias point between the objective correction impedance around each standard center frequency and the impedance performed.

Figure 14 shows the excellent results obtained for the global filter. A constant bandwidth of 60 MHz is obtained for each standard with a perfect loss compensation within the passbands.

3.2.2. Application of AIP to Pseudomultipole Filter. We now present the design of a pseudomultipole filter, based

on a one-pole passive filter topology. We apply the AIP technique to enlarge the bandwidth of the response. We start from the passive one-pole topology of Fig. 15. Transmission response initially presents a poor selectivity and a nonnegligible loss level at the center frequency (about 5 dB).

The idea is now to use the impedance profile principle to enlarge the response bandwidth. The objective is to search for the imaginary part to add to the passive filter, by means of the AIP, to reproduce the one-pole resonance not only at the initial central frequency but also at different frequency points in the objective passband. Figure 16 presents the imaginary parts of the AIP respectively necessary for a simple loss compensation (no effect of the imaginary part) and for a pseudomultipole effect. With this imaginary part profile, the resonance condition is reproduced for each frequency of the objective bandwidth. The result is a pseudomultipole filter based on a one-pole topology. The real part of the AIP allows for loss compensation, while the corresponding imaginary part increases the bandwidth with a flat gain, and with good rejection levels. The bandwidth of the filter is then 240 MHz for the same center frequency. Filter response is presented in Fig. 17 and validates the approach.

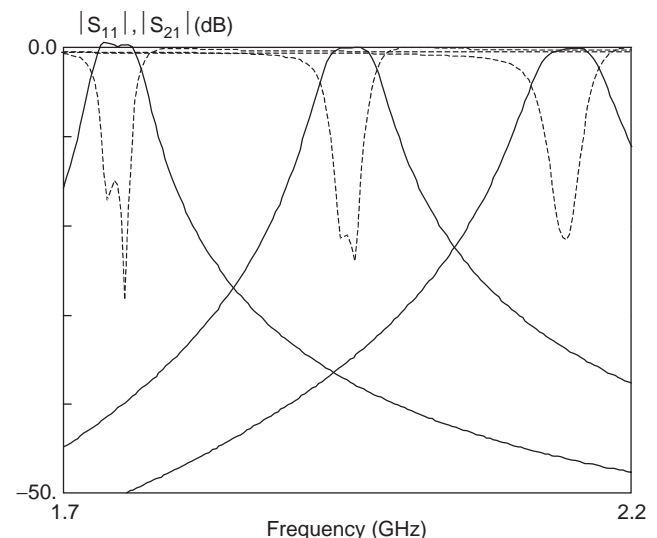


Figure 14. Simulated results of the 3-standard active filter.

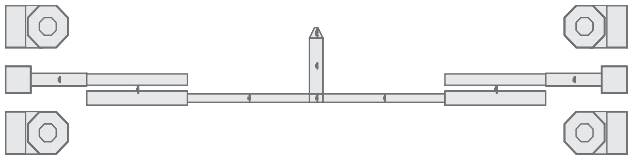


Figure 15. Distributed one-pole filter topology.

3.3. Automatic Frequency Control Techniques

This section deals with the application of phase-locked and magnitude-locked loops to achieve the automatic frequency control of microwave active filters. Indeed, analog filters are characteristically vulnerable to fabrication tolerances and temperature drifts and must be stabilized and controlled. Automatic frequency control (AFC) using the popular master–slave approach is the most feasible solution to control these characteristics [22]. This problem has been solved for a microwave filter [23–25] by using a typical phase-locked loop (PLL) based on a voltage-controlled oscillator (VCO) matched to the slave filter.

In contrast to the VCO-PLL, we propose here automatic frequency control based on the use of a voltage-controlled filter (VCF) PLL. We also propose an AFC based on the use of a VCF-based magnitude locked loop (MLL). These two techniques are attractive because they simplify the frequency control circuitry. They are applied to control the center frequency of a microwave bandpass VCF, implemented in planar hybrid technology on a duroid substrate and tunable over the 3.8–4.9 GHz range.

We first present a theoretical analysis establishing the control technique principles using a VCF and a MLL or a PLL. A transient-time analysis validates these results at low frequencies. We present measured results for a microwave tunable bandpass filter.

3.3.1. Theoretical Analysis. Figures 18 and 19 present an automatic tuning schemes using VCFs based on a MLL

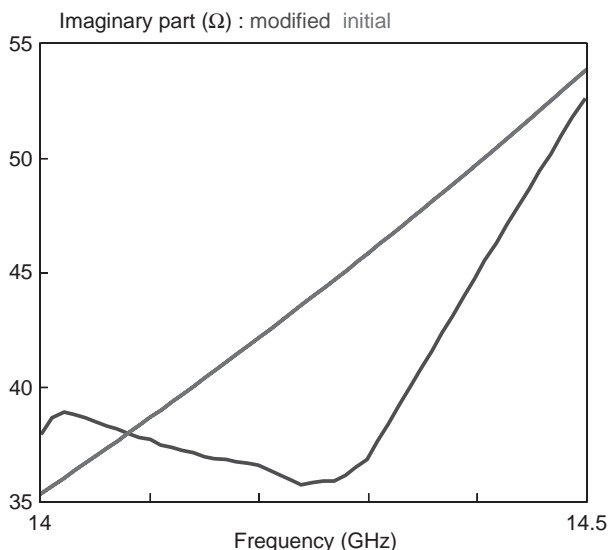


Figure 16. Loss compensation and pseudomultipole (AIP) profile imaginary parts for the distributed one-pole filter.

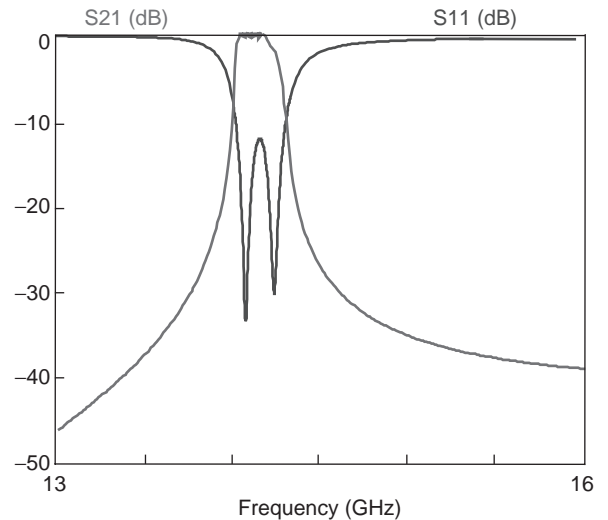


Figure 17. Global pseudomultipole AIP-based filter response.

and a PLL, respectively. Theoretical principles of the two techniques are pointed out by considering the particular case of an ideal second-order biquadratic band-pass VCF.

The voltage-controlled center frequency expression is given by $\omega_0(t) = \omega_0(t=0) + KV_c(t)$, where K is the VCF conversion factor (in radians per second per volt) and V_c the control voltage (volts). In the MLL-based AFC circuit scheme of Fig. 18, the amplitude of the reference signal is compared to VCF signal. The magnitude error is amplified and returned to control the filter center frequency ω_0 . The loop is magnitude-locked when the term $\Delta\omega = \omega_r - \omega_0$ is minimized ($\Delta\omega \rightarrow 0$) with ω_r , the reference signal frequency.

In the PLL-based AFC circuit of Fig. 19, the master filter is phase-locked to the reference signal. The phase of the reference signal is compared to the phase of the signal after the biquad filter by a phase comparator. The phase error is filtered out by the lowpass filter, then amplified and fed back to adjust the center frequency ω_0 of the filter. The loop is locked when the difference between the phase of the bandpass filter output signal and the phase of the reference signal is minimized, resulting in $\omega_0 \approx \omega_r$.

The differential equations that govern the control system based on a MLL or a PLL are given by Quintanel et al. [26]. The control response can be characterized for different tracking signal shapes by numerically solving the equations. Results given in Figs. 20 and 21 are obtained by considering $f_r(t)$ as frequency steps. Others results show that the system based on a MLL or a PLL is able to accurately track different time-variable reference frequencies, like ramps or steps. It is also shown that for the same parameter values, the PLL method is more accurate than the MLL technique. In Figs. 20 and 21, the control system based on a MLL is not able to track the reference signal for negative variations. The control system locks on a nonvalid solution. A method to solve this problem consists in taking a smaller $f_0(t=0)$ value to be sure to start with a positive variation and avoid a negative one.

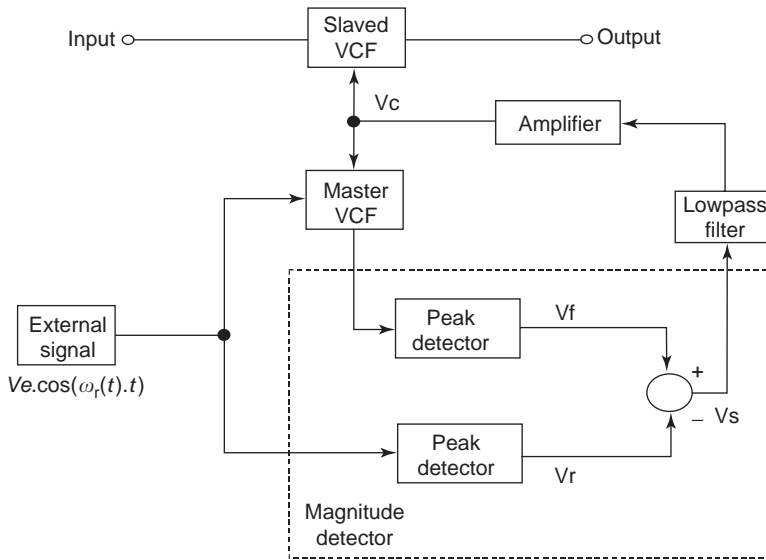


Figure 18. Automatic tuning scheme using a VCF based on a MLL.

3.3.2. AFC Systems Applied at Microwave Frequencies. In this section, we present an application of the AFC methods discussed above to a tunable microwave filter. Figure 22 presents the final functional scheme using the MLL or the PLL techniques. The VCF is a microwave bandpass planar filter based on a distributed half-wave hybrid resonant structure. The tunable element is a varactor diode used as a voltage-controlled capacitor (VCC). It is placed at the middle of the resonator to electronically tune the filter center frequency. The filter is implemented on a duroid substrate with a thickness of 0.5 mm and a dielectric constant of 2.43. It is tunable over the 3.8–4.9 GHz range. The VCC is a MACOM beam-lead constant-gamma GaAs varactor (MA46580).

To split the power reference signal between the reference and the filtered channels, we use a two-way Wilkinson power divider. The Wilkinson divider is fabricated on a duroid substrate and matched to $50\ \Omega$ at all ports. It exhibits a good isolation between output ports over the

3–5 GHz range. Phase detection is realized by using a microwave double-balanced mixer. Magnitude detection is achieved with zero-bias Schottky diodes. All RF elements are implemented on a duroid substrate. A DC amplifier is used to amplify the error signal of the loop.

Measurements are performed for different external reference frequencies and for each control technique. Table 1 summarizes the tracking performances of the two control techniques. The results demonstrate that the AFC based on a PLL or a MLL is possible and feasible in the microwave frequency domain. The PLL method offers a precision error varying from 0% to 0.19% over the 4.0–4.6 GHz range. Finally, the MLL method has a precision of 0.5–3.6% over the same frequency range. The control technique based on a PLL offers a better precision than does the MLL method because the losses of the microwave filter at the center frequency are not constant over the tuning frequency range. Nevertheless, the MLL technique is attractive for microwave applications

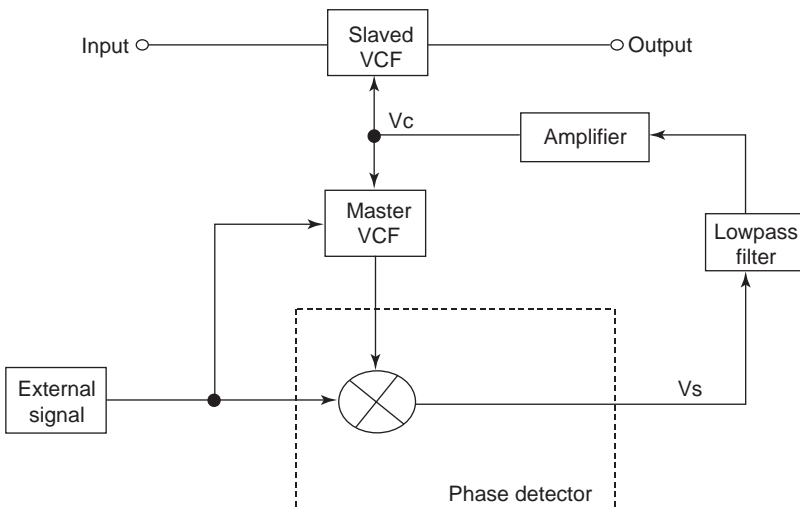


Figure 19. Automatic tuning scheme using a VCF based on a PLL.

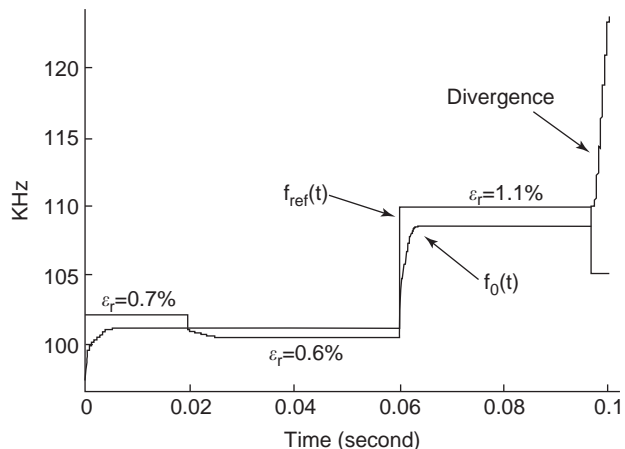


Figure 20. System response to frequency steps with a MLL control system.

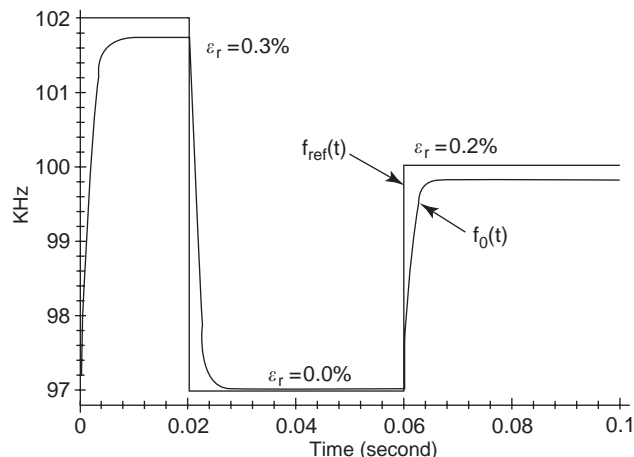


Figure 21. System response to frequency steps with a PLL control system.

because it avoids the critical phase sensitivity of the PLL method.

4. NEW APPROACHES AND NEW TECHNOLOGIES

The preceding paragraphs have shown that microwave and RF filter design is a complex art because it involves a nonnegligible number of steps, each step needing a wide spectrum of competences. In addition to a strong theoretical background, this diversity supposes the definition of a rigorous and efficient work methodology. However, even when all these tools are well known and effectively used, designers must keep in mind that, around all these skills and competences, new technologies and new needs that can modify their own approaches arise daily.

In this section, we give a brief review of new needs and new technologies in which planar active filters can be involved.

4.1. New needs and constraints

Migration of microwave systems for public market applications, in particular for mobile communications, has led to new unavoidable constraints:

- For mass production, cost considerations are essential. In practice, it is necessary to minimize the design time, and to make the design processes more reliable. Inherently, this is based on reliable low-cost integrated technologies.
- From the communication standards point of view, frequency bands allocated to different services are increasingly narrow, while the demand is always increasing. So the objective is to use at best these frequency bands in order, on one hand, to avoid interferences between services, and on the other hand, to augment the systems capabilities.

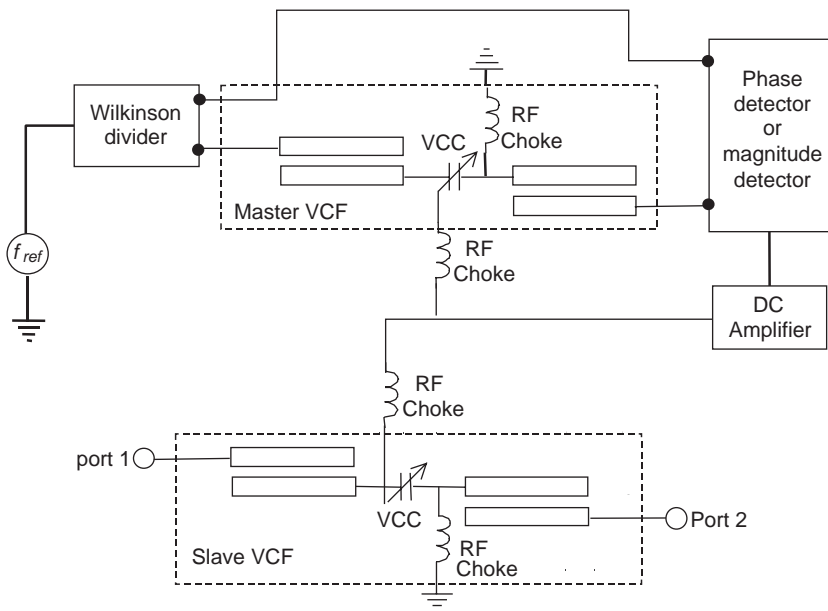


Figure 22. Microwave filter slaved to control system based on a PLL or a MLL.

Table 1. Tracking Performance of the Control Systems

F_{ref} (GHz)	4	4.1	4.2	4.3	4.4	4.5	4.6
f_0 (GHz) PLL method	4.005	4.092	4.197	4.302	4.398	4.503	4.600
f_0 (GHz) MLL method	4.005	4.092	4.171	4.250	4.363	4.495	4.635
ε_r % PLL method	0.12	0.19	0.007	0.004	0.004	0.006	0
ε_r % MLL method	0.12	0.19	0.6	1.1	0.8	0.1	0.7

- Device miniaturization is an essential constraint, synonymous with commercial success, especially for mobile handsets. From a technical perspective, this miniaturization involves a capability of integrating pre- or postprocessing digital circuits with analog microwave functions. At this step, mixed analog–digital technologies and methods are required.
- Finally, in terms of daily use, acceptable power autonomy of mobile handsets involves the use of low-current and low-consumption processes and circuits.

In any recent telecommunication system, filters take in a large number an important place in front-end transmitters/receivers; For example

- A duplexer located after an antenna is classically composed of two filters separating the transmission/reception frequency bands.
- In the reception channel, a filter can be found before the input low-noise amplifier (LNA) to improve its high-level signal performances, and simultaneously eliminate parasitic frequencies coming at the input of the front-end receiver.
- In the same channel, two other filters can be found, one after the LNA before the first downconversion mixer, and another one at intermediate frequency before the baseband downconversion.
- In the transmission channel, a filter can be found after each element of the chain, to eliminate or reduce noise and other possible distortions, linear or nonlinear.

With these considerations, and with the wide diversity of mobile telecommunication standards, it has rapidly become necessary to design multimode/multistandard portable terminals that could allow users to roam on a global scale. For this reason, frequency-tunable active filters have found an increasing interest. Indeed, tunable filter capabilities obviously lead to

- Elimination of redundant functions such as standard switches or analog/digital converters (ADCs)
- Considerable reduction in size of the global system
- Lower system complexity, and associated constraints

Because of their interesting gain capability, tunable active filters can replace very advantageously the LNAs and their associated filters. This approach can then permit (1) Elimination of one or more amplifiers in the transmission/reception chain and (2) Distribution of different constraints of noise, power-handling behavior, and response performance imposed on the other functions, thus relaxing

these specific constraints and providing more ease in the design of each functional block.

In this way, the use of tunable active filters is very attractive. However, to apply this principle with success, it is necessary to adapt the design tools, even to create new ones, but more importantly to adapt the original design method to new technologies.

4.2. New Integrated Technologies for Microwave Design: Silicon versus Gallium Arsenide

Even though some technologies have existed basically unchanged for decades, they can be seen in a totally novel aspect when used at frequencies for which they were not originally implemented. In this way, silicon-based technologies (Si and SiGe technologies) can be considered as novel for microwave active-filter applications.

Silicon-based technologies have been widely used at low frequencies for both digital and analog applications [27]. Because of the great advances of silicon and silicon–germanium technologies since the mid-1990s, silicon-based ICs have found an increasing importance for RF and microwave applications. Since 1998 only, some articles on the international scientific production have reported some interesting elements concerning the transposition of circuits classically implemented on GaAs to silicon-based processes [28,29]. Table 2 presents some general comparison elements between GaAs and SiGe capabilities.

The term *SiGe BiCMOS HBT* refers to heterojunction bipolar transistor, for which the base is doped with germanium. With this technology, chips work much faster while ensuring the reliability and the stability of such a process. These chips can be designed for wireless applications, increasing the performance of these products while decreasing their size and power consumption. Besides, the BiCMOS HBT SiGe technology takes advantage of the integration capability of CMOS process, which leads to greater compactness.

There are two different ideas on the issue of using SiGe technology. On one hand, Si and SiGe technologies are found to be very advantageous, because of their capability to achieve more compact and cost-effective circuits. On the other hand, the degree of maturity of Si/SiGe technologies is still not comparable to that of GaAs technologies. According to some designers, Si technology does not enable

Table 2. Comparison Elements of GaAs versus SiGe

Substrate type	Transistors	f_t (GHz)	F_{min} (dB)	Cost (\$/mm ²)
GaAs	PHEMT	>70	0.9 at 12 GHz	1000
SiGe	HBT-CMOS	>40	0.7 at 2 GHz	700
	BiCMOS	>50		

integration of a complete microwave system. It may then be necessary to use mixed technologies, which tends to be more expensive than a complete development on GaAs.

Moreover, in spite of obvious advantages of cost-effectiveness and compactness, SiGe technology involves some nonnegligible constraints, one of the most important of which is still the lack of a proper library model in conventional microwave and high-frequency circuit simulators. To become more familiar with Si and SiGe technologies, and before confronting the realization of circuits, designers will often have to test several processes through their design kits to have in mind the problems that have to be faced:

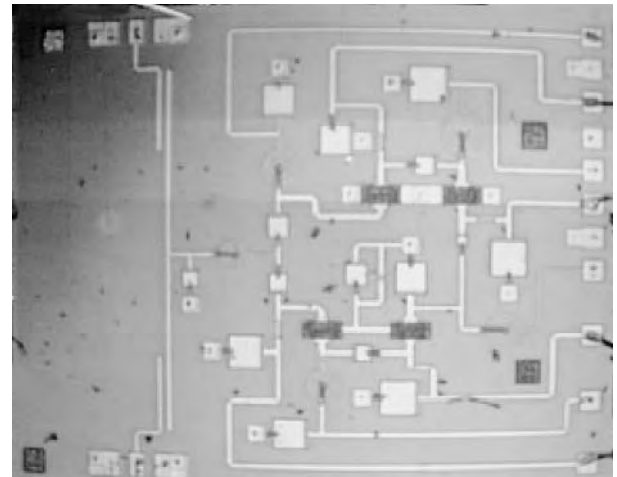
1. The first major problem is encountered at the level of the CAD tools. Because of the classical use of silicon technology for digital and analog applications at low frequencies, most component libraries were developed primarily for CAD software using the same approach. Of course, the design philosophy of these circuits is very far from that used for microwave analog circuits.
2. The second problem arises from the fact that some component models are sometimes not available in simulator libraries or not parameterized, thus making any optimization a difficult task. As a result, some components such as inductors are not available because they are not classically used at low frequencies. They have to be designed using specific tools. In some processes, this is also the case for varactor diodes.
3. From the design perspective, this third problem arises from the specific conductivity of the doped silicon (SiGe) substrate and its poor isolation (some tenths of an $\Omega \cdot \text{cm}$ compared to $10^5 \Omega \cdot \text{cm}$ for pure silicon). This leads to considerable increase in the number of parasitic capacitors in a circuit. For example, in the case of the MOSFET, it is necessary to take into account not only the parasitic capacitors C_{gs} and C_{gd} but also capacitors C_{db} , C_{bs} , and C_{gb} (parasitic capacitors between the substrate and respectively the drain, the source, and the gate). These capacitances are nonnegligible regarding the other capacitances of the circuits.

Note that these problems are now partially solved; some SiGe foundries now supply models for classical CAD packages, with microwave design facilities such as constant gain, stability, and noise circles.

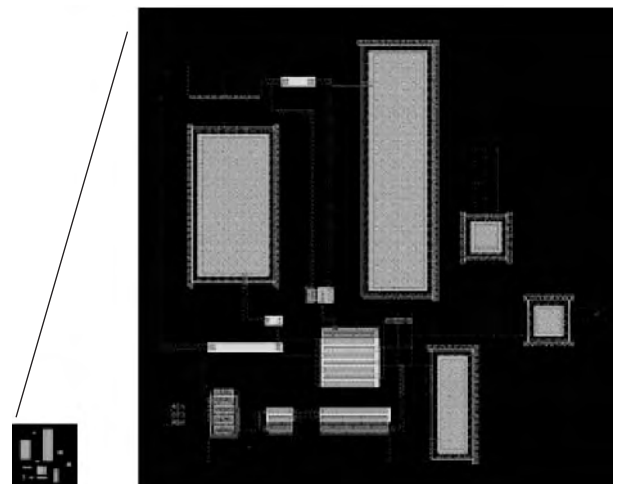
Design rules of Si-based technology are also very different from those used with GaAs processes, even for the design of simple circuits. For technological reasons, the ground plane of a circuit on silicon is located on the top of the substrate. It is then not possible to strictly consider microstrip lines. However, some reports have shown the feasibility of transmission lines in polymers, such as benzocyclobutene (BCB), allowing performances close to those obtained with GaAs [28]. Particular attention should be also paid to the leakage currents due to the specific conductivity of the substrate. To solve this problem, many manufacturers use guard rings. These guard rings are buried layers, surrounding partially or totally the component to be protected by acting as a p-n junction biased in inverse. All these protection processes clearly allow a more

compact implementation in comparison to GaAs, leading to very different design rules and component placement than those applied for conventional microwave GaAs technology. This mainly explains the differences in size that can be observed for the same function from one technology to the other. To illustrate these differences in terms of component implementation, size, consumption, and cost, we now give two comparative design examples and the corresponding layouts.

Example 1. In a first-order filter based on a parallel LC resonator, ports are decoupled by low-value capacitances. [The GaAs version is discussed in Section 3.4.3 (see also Fig. 12) of the active-filter structure overview article cited above; see also Ref. 30 of this present article.] In the same way, a SiGe version has been realized [30] using the BYR process from AMS [31]. This filter is designed to work in the UMTS reception band (2110–2170 MHz). Transistors are BiCMOS HBTs and PMOS. Losses are perfectly compensated within the passband. Figures 23a and 23b



(a)



(b)

Figure 23. Layouts of the active LC filter in (a) GaAs and (b) SiGe (+ zoom) technologies.

compare the two circuit layouts. The high-compactness of the SiGe version can be easily noted. The reduction in surface is done with a ratio of 150 corresponding to a reduction of cost of 170. With other circuits found in the literature, the mean reduction ratio in surface and in cost can be estimated respectively at 50 and 55. With the technologies used, the power consumption ratio is ~ 21 (48 mW for SiGe version against 1040 mW for the GaAs version).

Example 2. In this example, two different NIC topologies have voluntarily been chosen to try to emphasize one or the other technology. The GaAs version uses the ED02Ah process from OMMIC [32] with HEMT transistors. The circuit works in the 1.9–2.3 GHz range and belongs to the infinite transconductance NIC category (see active-filter structure overview article cited above). The SiGe version has been realized with the AT46000 from ATMEL [33]. It is based on a classical differential topology using BiCMOS transistors. This circuit works in the 0.1–3 GHz range. Figures 24a and 24b compare the two circuit layouts. The reduction in size here is ~ 55 , corresponding to a cost ratio

of 65. Power consumption is divided by 4 (18 mW for the SiGe version vs. 73 mW for the GaAs version). Simulation results of these two NICs inserted within a filter give a clear advantage to the SiGe version.

4.3. Realisation Examples

Example 1 focuses on a topology proposed in Refs. 34 and 35. It consists of a grounded active inductor using a low-cost 0.8- μm BiCMOS HBT technology [30]. This inductor topology is based on the use of two HBTs in a feedback configuration. Note that in this case there is no need for an integrated inductor (Fig. 25).

The quality factor Q_1 is biased by a voltage-controlled current source built with bipolar transistors. V_{tune} allows tuning of the associated real part while maintaining the inductance value. Using this approach, a quality factor of some thousands can be performed for an inductance value of 9.20 nH.

By associating a capacitor in parallel with the active inductance, a bandpass response can also be obtained. The active LC resonator is decoupled by two small value capacitors. Figures 26 and 27 respectively present the layout of

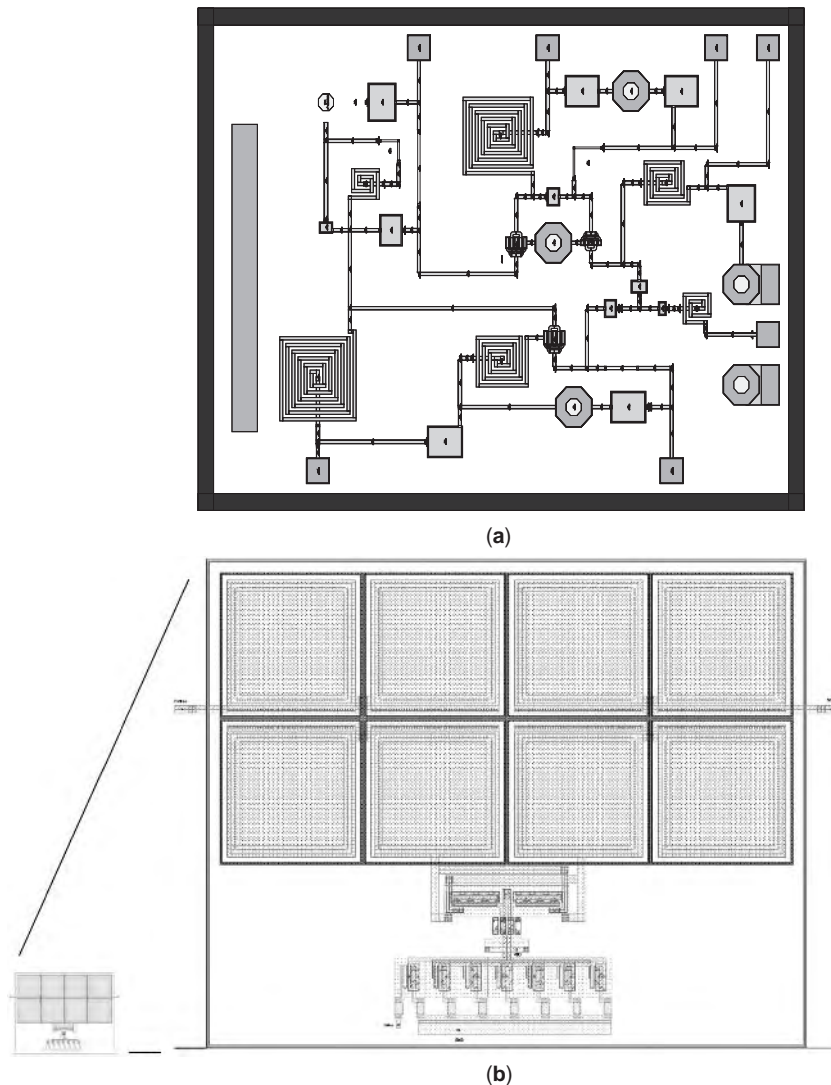


Figure 24. Layouts of the two negative-resistance chips in (a) GaAs and (b) SiGe (+ zoom) technologies.

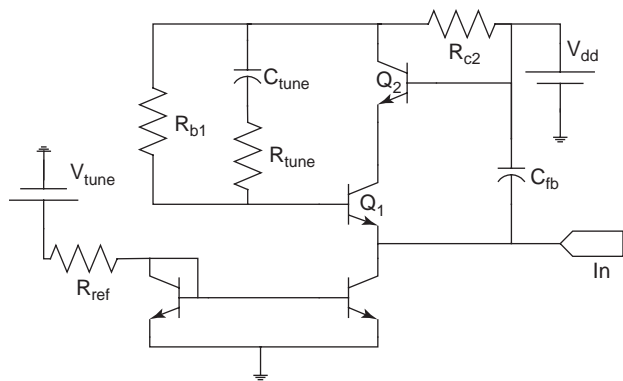


Figure 25. Schematic of the active inductor.

the filter and the simulated response. Dimensions of this circuit are $150 \times 170 \mu\text{m}$. Total consumption is about 15 mW. Losses are totally compensated at 1.86 GHz, with a quality factor of ~ 150 .

4.4. Differential Circuits

For many years, differential structures have been limited to low-frequency applications. Differential structures have the following advantages compared to single-ended topologies:

- They are insensitive to noise and interference coupled through supply lines and substrate.

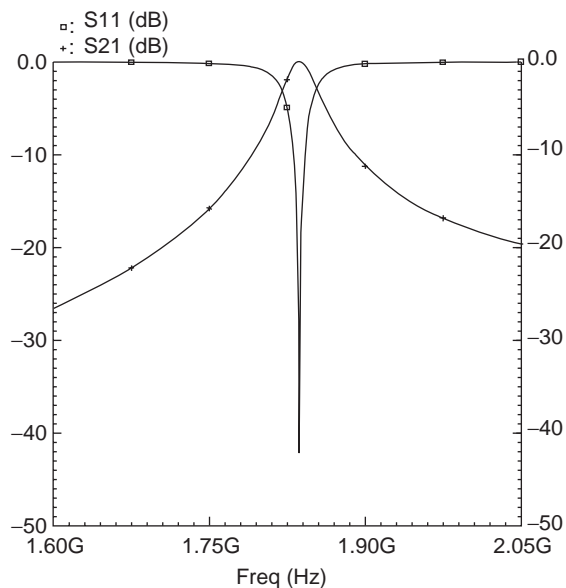


Figure 27. Layout-based simulated results of the integrated active LC filter.

- Many linearization methods used for transconductance stages can also be used for low-noise amplifiers and filters using this approach.
- They have smaller even-order distortion.

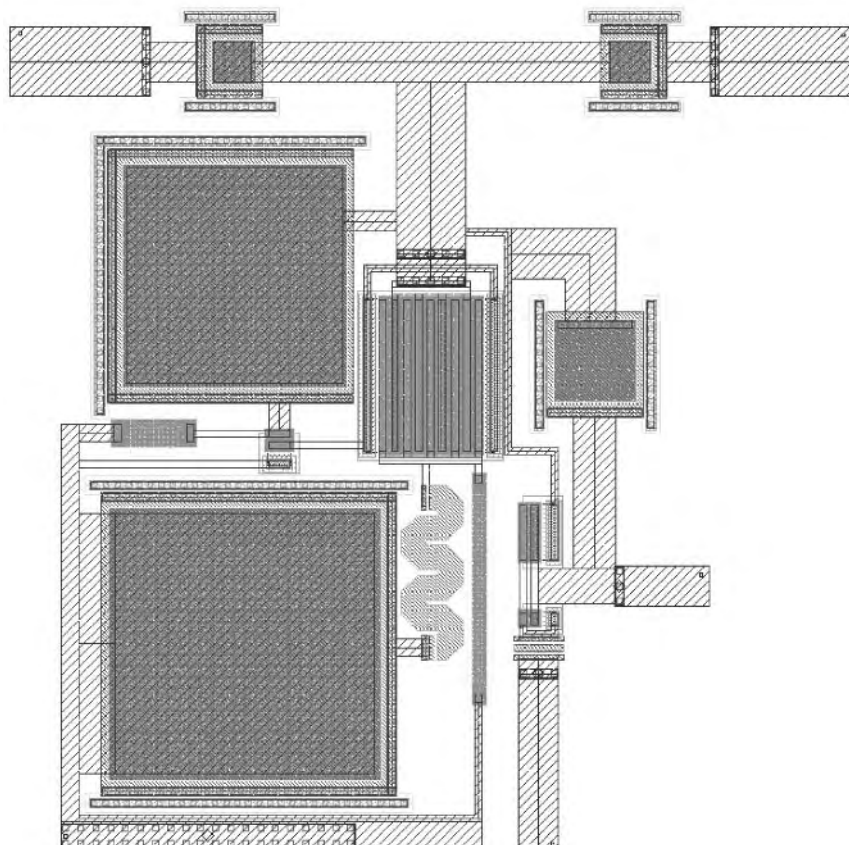


Figure 26. Layout of the integrated active LC filter in BiCMOS HBT technology.

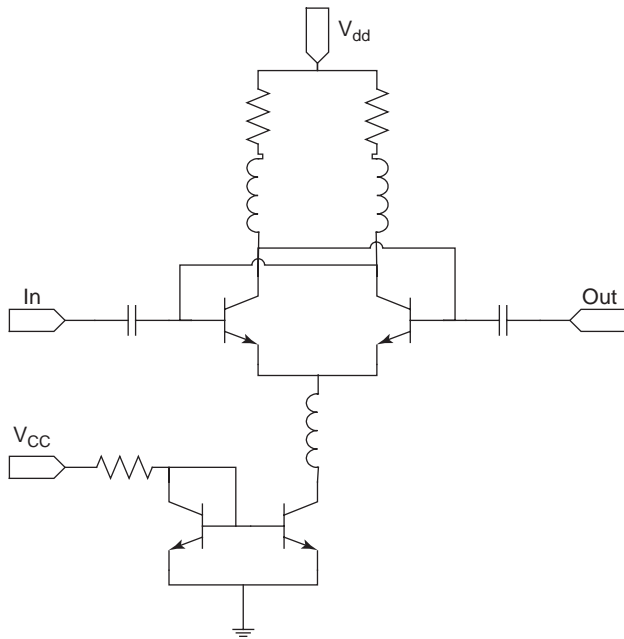


Figure 28. Schematic of the differential negative resistance.

Example 1 (above) focuses on a differential LC active filter in which losses are compensated with a differential negative resistance [36]. We begin with a brief description of the negative-resistance topology. The circuit uses a BiCMOS SiGe HBT technology. Such topologies generally present a real part of the impedance not strongly frequency-dependent and are recommended for wideband applications. A schematic and the layout of the circuit are presented in Figs. 28 and 29, respectively. Three integrated inductors are used to bias and stabilize HBTs. A current source sets the emitter current. Symmetric performances are obtained between the two ports. The imaginary part can be considered as a negative capacitance. Circuit dimensions are $690 \times 800 \mu\text{m}$. The negative resistance performed is about -10Ω at 1.8 GHz. The imaginary part is equivalent to a -2.4 pF negative capacitance. Power consumption is about 46 mW.

A differential LC filter circuit is now presented. The previous differential negative resistance is used to compensate for insertion losses introduced by the inductors of the resonator. Two transconductances are also used to tune the center frequency and the gain of the filter. A schematic of this circuit is presented in Fig. 30. A band-pass response is obtained with a quality factor of ~ 125 at 2 GHz. The S parameters are presented in Fig. 31. The noise figure is $\sim 4.5 \text{ dB}$ at 2 GHz.

Finally, we show a 2-GHz single-ended first-order recursive filter integrated using the QuBIC4 silicon MMIC

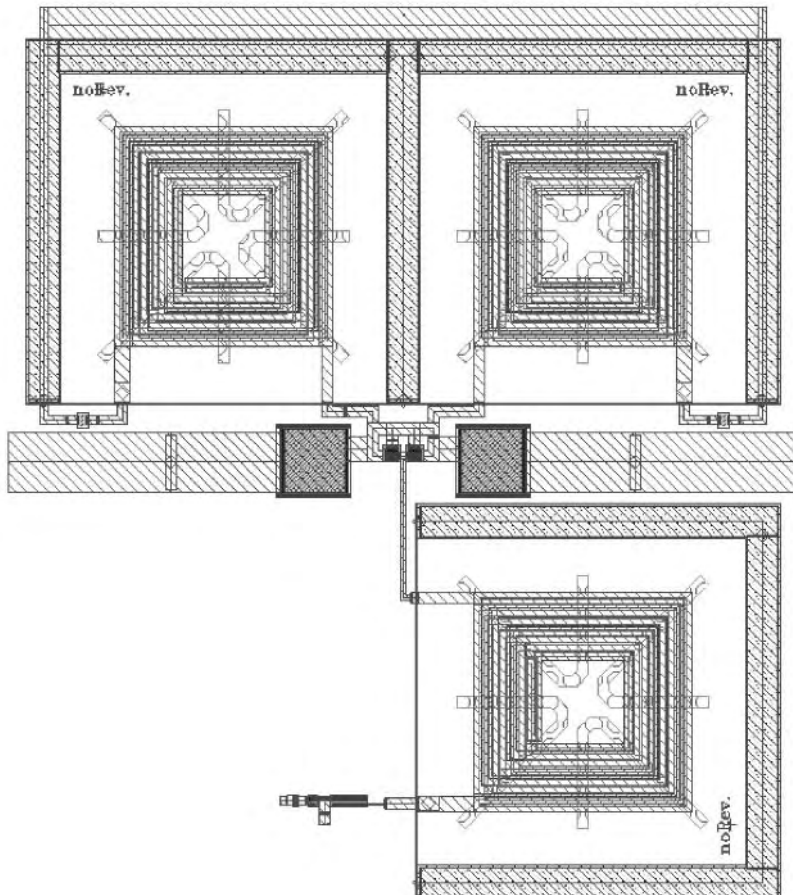


Figure 29. Layout of the differential negative resistance.

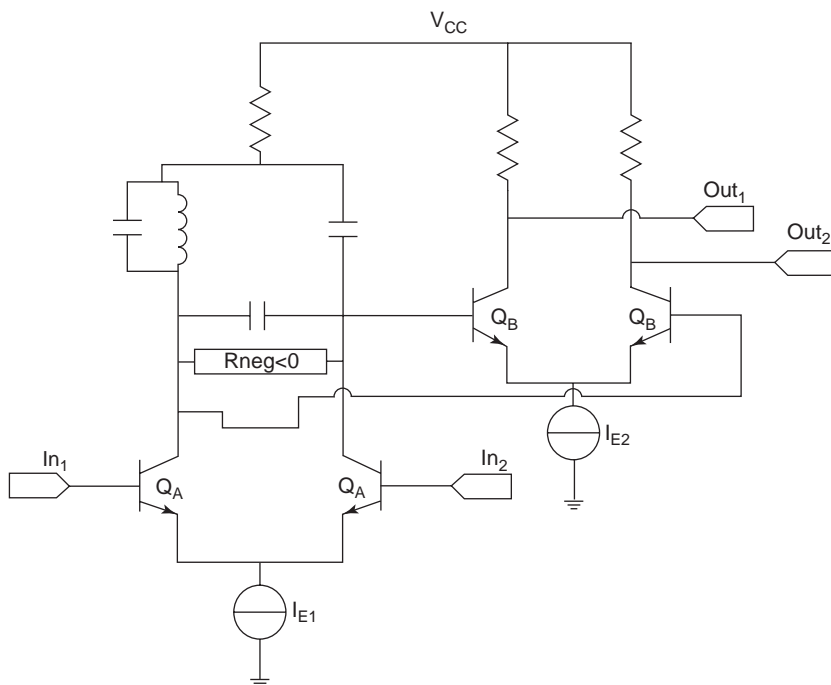


Figure 30. Schematic of the differential filter.

process from Philips [37]. The differential property is used here for an original recombination of input and delayed feedback signals within a first-order recursive structure. Figure 32 presents the basic principle of the circuit. With A_d , the differential-mode voltage gain of the amplifier structure, the voltage gain of the filter can be expressed as a first-order recursive filter response:

$$G_v(f) = \frac{V_{out}(f)}{V_{in}(f)} = \frac{-\frac{A_d}{2}}{1 + \frac{A_d}{2} e^{-j2\pi f\tau}}$$

The circuit layout is shown in Fig. 33. Dimensions of the chip are 1.12×1 mm. Measurements presented in Fig. 34 are in good agreement with simulations. Input/output matching is less than -12 dB within the passband. The filter exhibits a 260 MHz 3 dB bandwidth at 1.94 GHz, with a gain close to 10 dB for a power consumption of 32 mW. Input/output matchings are lower than -12 dB for 1 GHz around the center frequency. Isolation, which is not

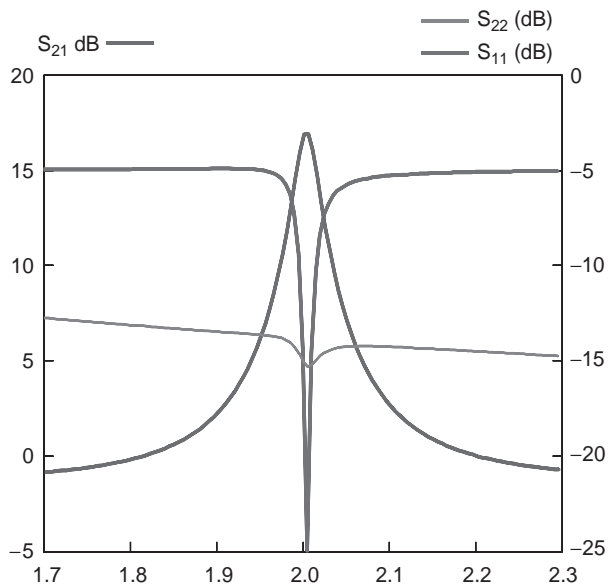


Figure 31. S parameters of the differential filter.

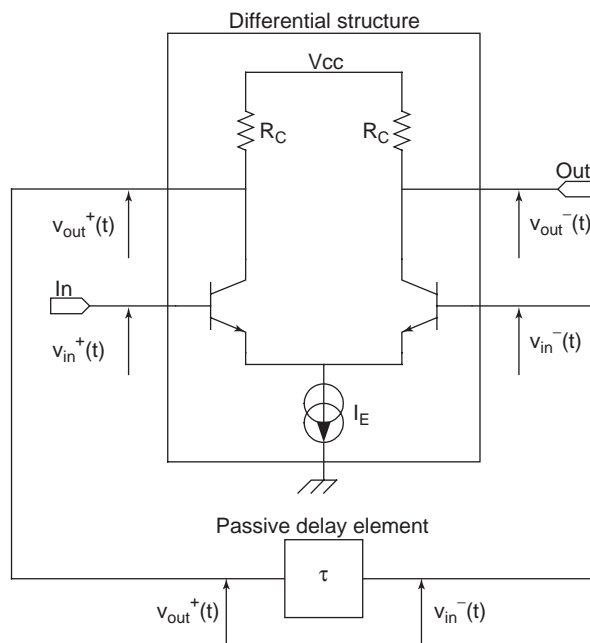


Figure 32. Schematic of a differential-based recursive filter.

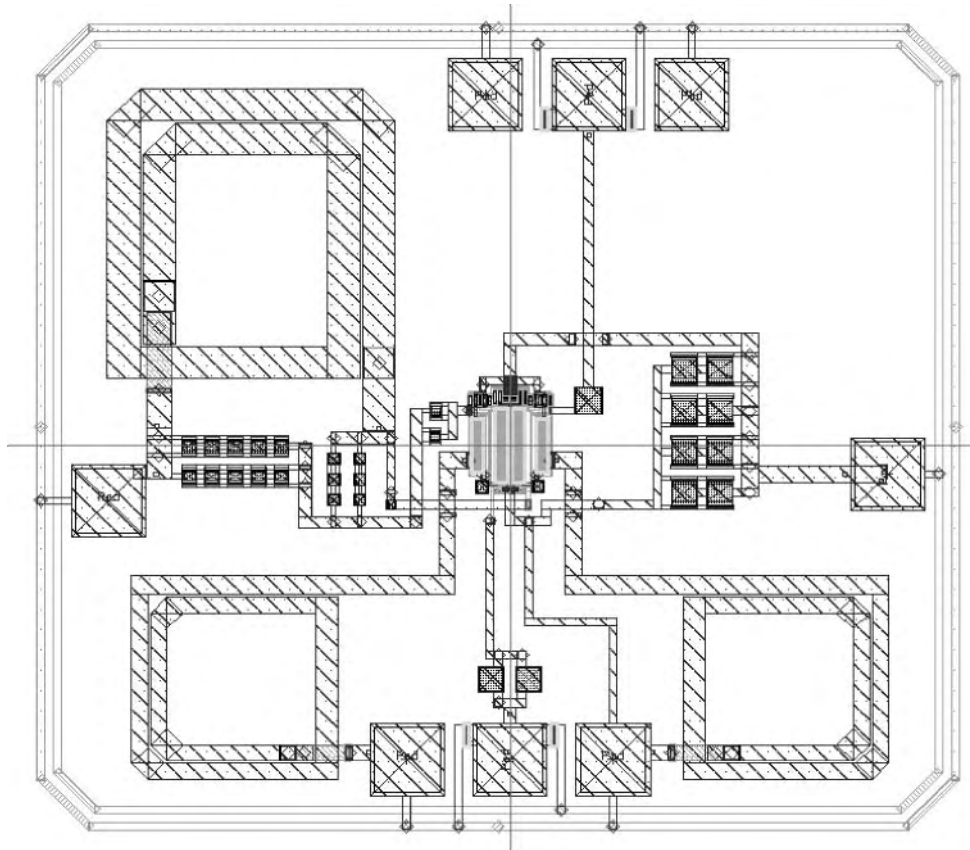


Figure 33. Differential-based recursive filter layout.

presented here, is greater than 30 dB in the 0.5–3.5 GHz range. The noise figure is equal to 4.6 dB at the center frequency. The -1 dB compression point is obtained for an output power of -11.7 dBm.

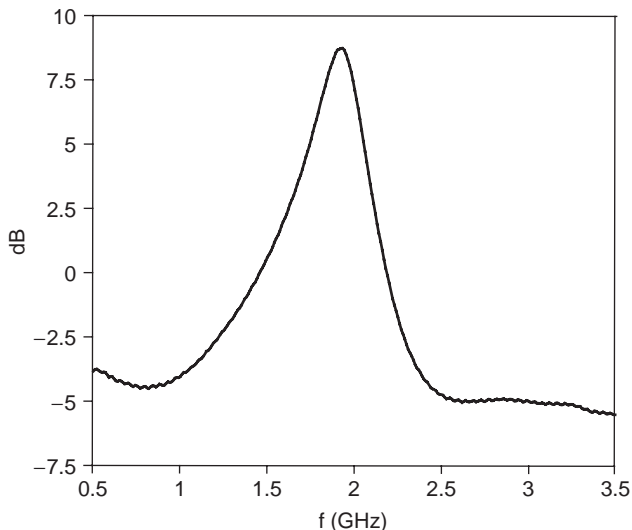


Figure 34. Measured gain of the differential-based recursive filter.

BIBLIOGRAPHY

1. P. Gardner and D. K. Paul, Optimum noise measure configurations for transistor negative resistance amplifiers, *IEEE Trans. Microwave Theory Tech.* **MTT-45**(5):580–586 (1997).
2. S. Wedge and D. Rutledge, Wave techniques for noise modeling and measurement, *IEEE Trans. Microwave Theory Tech.* **MTT-40**:2004–2012 (1992).
3. H. Ezzedine, L. Billonnet, B. Jarry, and P. Guillon, Optimization of noise performance for various topologies of planar microwave active filters using noise wave techniques, *IEEE Trans. Microwave Theory Tech.* **MTT-46**(12):2484–2492 (1998).
4. J. Lange, Interdigitated stripline quadrature hybrid, *IEEE Trans. Microwave Theory Tech.* **MTT-17**:1150–1151 (1969).
5. R. M. Osmani, Synthesis of Lange couplers, *IEEE Trans. Microwave Theory Tech.* **MTT-29**(2):168–170 (1981).
6. J. Rollett, Stability and power-gain invariants of linear two-ports, *IRE Trans. Circ. Theory* **9**(1):29–32 (1962).
7. R. P. Meys, Review and discussion of stability criteria for linear 2-ports, *IEEE Trans. Circ. Syst.* **37**(11):1450–1452 (1990).
8. M. L. Edwards, A new criterion for linear 2-port stability using a single geometrically derived parameter, *IEEE Trans. Microwave Theory Tech.* **MTT-40**(12):2303–2311 (1992).
9. H. W. Bode, *Network Analysis and Feedback Amplifier Design*, Van Nostrand, New York, 1945.
10. M. Ohtomo, Stability analysis and numerical simulations of multidevice amplifiers, *IEEE Trans. Microwave Theory Tech.* **MTT-41**(6/7):983–990 (1993).

11. A. Platzker, W. Struble, and K. T. Kketzler, Instabilities diagnosis and the role of K in microwave circuits, *IMS'93, IEEE MTT-S Int. Microwave Symp. Digest*, 1993, pp. 1185–1187.
12. A. Platzker and W. Struble, A rigorous yet simple method for determining stability of linear N-port networks, *Proc. GaAs IC Symp.* 1993, pp. 251–254.
13. M. Delmond, L. Billonnet, B. Jarry, and P. Guillon, Microwave tunable active filter design in MMIC technology using recursive concepts, *IMS'95, IEEE MMWMC-S Microwave and Millimeter-Wave Monolithic Circuits Symp. Digest*, 1995, pp. 105–108.
14. S. Kolev, B. Delacressonnière, and J.-L. Gautier, Using a negative capacitance to increase the tuning range of a varactor diode in MMIC technology, *IEEE Trans. Microwave Theory Tech.* **MTT-49**(12):2425–2430 (2001).
15. G. Matthaei, L. Young, and E. M. T. Jones, *Microwave Filters, Impedance-Matching Networks, and Coupling Structures*, Artech House, 1964.
16. F. Biron, L. Billonnet, B. Jarry, P. Guillon, G. Tanné, E. Rius, F. Mahé, and S. Toutain, Microstrip and coplanar bandpass filters using MMIC negative resistance circuits for insertion losses compensation and size reduction, *Proc. EuMC'99, 29th European Microwave Conf.* 1999, Vol. 1, pp. 72–75.
17. M. Houdart, Coplanar lines: Application to broadband microwave integrated, *Proc. EuMC'76, 6th European Microwave Conf.* 1976, pp. 49–53.
18. E. Rius, T. Le Gougec, K. Hettak, J. Ph. Coupeze, and S. Toutain, Broadband high directivity 3dB coupler using coplanar waveguide technology, *IMS'95, IEEE MTT-S Int. Microwave Symp. Digest*, 1995, pp. 671–674.
19. Y. H. Shu, J. A. Navarro, and K. Chang, Electronically switchable and tunable coplanar waveguide-slotline band-pass filters, *IEEE Trans. Microwave Theory Tech.* **MTT-39**(3): 548–554 (1991).
20. J. A. Navarro, and K. Chang, Varactor-tunable uniplanar ring resonators, *IEEE Trans. Microwave Theory Tech.* **MTT-41**(5):760–766 (1993).
21. G. Tanné, E. Rius, F. Mahé, S. Toutain, F. Biron, L. Billonnet, B. Jarry, and P. Guillon, Improvements in losses and size of frequency tunable coplanar filter structures using MMIC negative resistance chips for multistandard mobile communication systems, *IMS'2000, IEEE MTT-S Int. Microwave Symp. Digest*, 2000, Vol. 2, pp. 1165–1168.
22. Y. P. Tsvividis and J. O. Voorman, *Integrated Continuous-Time Filters*, IEEE Press, New York, 1993.
23. P. Katzin, B. Bedart, and Y. Ayasli, Narrow-band MMIC filter with automatic tuning and Q-factor control, *IEEE MTT-S Int. Microwave Symp. Digest*, 1993, pp. 403–406.
24. V. Aparin and P. Katzin, Active GaAsMMIC bandpass filters with automatic frequency tuning and insertion loss control, *IEEE J. Solid-State Circ.* **30**(10):1068–1073 (1995).
25. H. Serhan, B. Jarry, and P. Guillon, Automatic frequency control techniques for microwave active filters, *IMS'97, IEEE MTT-S Int. Microwave Symp. Digest*, 1997.
26. S. Quintanel, H. Serhan, B. Jarry, L. Billonnet, and P. Guillon, Theoretical and experimental analysis of automatic frequency control techniques for microwave active filters, *Microwave Opt. Technol. Lett.* **27**(1):23–27 (2000).
27. P. R. Gray and R. G. Meyer, *Analysis and Design of Analog Integrated Circuits*, Wiley, 1977.
28. J. D. Cressler, A new contender for Si-based RF and microwave circuit applications (invited paper), *IEEE Trans. Microwave Theory Tech.* **MTT-46**(5):572–589 (1998).
29. D. Li and Y. Tsvividis, Active LC filters on silicon, *IEE Proc. Circ. Devices Syst.* **147**(1) (2000).
30. H. Bazzi, F. Biron, S. Bosse, L. Delage, B. Barelaud, L. Billonnet, and B. Jarry, Microwave planar active filters in GaAs and SiGe technologies, *IMS'2002, IEEE MTT-S Int. Microwave Symp. Digest*, 2002.
31. BYR monolithic process, AMS, www.advanced-monolithic.com/index.html.
32. ED02Ah monolithic process, OMMIC, *ED02Ah Design Manual*, GaAs Foundry and ASIC Design Center, <http://www.ommic.fr> (2000).
33. AT46000 monolithic process, ATMEL, www.eu.atmel.com.
34. K. W. Kobayashi and A. K. Oki, A novel heterojunction bipolar transistor VCO using an active tunable inductance, *IEEE Microwave Guided Wave Lett.* **4**(7):235–237 (1994).
35. J. Caldinhas Vaz, L. Delage, and J. Costa Freire, GHz SiBiCMOS active inductors, *ConfTele 2001*, Figueira da Foz, Portugal, 2001.
36. H. Bazzi, S. Bosse, L. Delage, B. Barelaud, L. Billonnet, and B. Jarry, Using HBT BiCMOS differential structures at microwaves in SiGe technologies, *Proc. GAAS'2002, 10th European Gallium Arsenide and Related III-V Compounds Applications Symp.*, 2002.
37. QuBIC4 monolithic process, PHILIPS, www-eu3.semiconductors.philips.com/index.html.

ADAPTIVE ARRAY ANTENNAS

CHEN SUN
Nanyang Technological
University
Singapore
NEMAI C. KARMAKAR
Monash University
Victoria, Australia

1. INTRODUCTION

Demands for better-quality and new value-added services of existing wireless communication infrastructures have risen beyond all expectations. It is estimated that half a billion handsets will be put into the context of the third-generation system (UMTS, IMT 2000), which will provide an up to 2 MB (megabytes of) bandwidth for each user [1]. The challenging demand is to increase the spectrum efficiency and the system capacity of the current wireless networks. These demands have brought technological challenges to service providers. Because of the ability of suppressing interference and combating against fading and providing new services, adaptive array antennas or “smart” antennas have become one of the key technologies to realize third-generation (3G) and even fourth-generation (4G) wireless communications. We start with an overview of the evolution of wireless communication systems, calling for new technologies to support its new applications and improved qualities. Adaptive array antennas or smart antennas turn out to be solutions in the process of the evolution. We will present various applications of smart antenna technologies in wireless communications.

After that, different architectures of adaptive array antennas are presented with illustrations followed by descriptions of some algorithms. Finally, we compare the adaptive array antennas architectures and their suitability to different applications.

2. DEMANDS FOR ADAPTIVE ARRAY ANTENNAS

In 1899, Guglielmo Marconi transmitted signals across the English Channel, between Wimereux and Dover. In 1901, the first transatlantic wireless transmission was demonstrated [2]. Intrigued by that, scientists and engineers had been investigating new wireless communications methods and services. The era of wireless communications had just begun.

The wireless communication industry has experienced phenomenal technological advancement manifested in various application scenarios, including wireless remote control, codeless telephony, paging, wireless networks, terrestrial cellular telephone systems, and satellite communications [3]. Among them, the cellular telephone systems have been developing from the first-generation systems that were deployed firstly by Nippon Telephone and Telegraph (NTT). Through the 2G systems [i.e., Global System for Mobile Communications (GSM) and Digital Cellular System 1800 (DCS 1800) in Europe, Personal Communication System 1900 (PCS 1900), interim standard 95 (IS-95) and IS-136 in North America and Personal Digital Cellular (PDC) in Japan], the wireless system is evolving to the 3G system [i.e., wideband code-division multiple access (WCDMA) and CDMA 2000], and will approach the 4G system in the near future [3–5].

The 3G system is a universal, multifunctional, globally compatible digital mobile radio system. It allows users to communicate anyone, anywhere, at anytime. The system integrates paging, cordless, cellular, wireless network, and satellite communication systems into a single mobile terminal. The user can use the 3G terminal for conventional voice phonecall, broadband access to the Internet, high-speed package data services, and position tracking [3–12].

The main features of 3G and beyond communications systems are

- *High-Data-Rate Communications.* The minimum requirements of the user data rates in different environments are 144 kbps (kilobits per second) for vehicular applications, 384 kbps for pedestrian, 2 Mbps for indoor office, and 9.6 kbps for satellite communications. These goals require a significantly increased frequency efficiency that is measured by the bps/Hz.
- *New Services.* New services include intelligent transportation, position location (PL) services, and ad hoc networks. These location-aware services require new techniques to provide position information.
- *More Subscribers.* The wireless communications will be so ubiquitous that more subscribers or users are accommodated. This feature demands a dramatic increase in the mobile radio system capacity measured by the number of users within a given frequency spectrum.

During the migration from the 2G system to the 3G system, great efforts have been directed toward the development of the modulation, coding, and protocols on the 2G systems, such as code-division multiple access (CDMA) with IS-95, time-division multiple access (TDMA) with IS-136, and GSM. These techniques have been exhausted to the limit because of the large number of subscribers within the limited channel capacity. Antennas have gained much interest among researchers. The smart antenna system, in the form of adaptive arrays, can mitigate three major impairments caused by wireless channels: *fading*, *delay spread*, and *cochannel interference*. It can also bring many benefits to the existing wireless communication system, such as the enhancement of coverage for portable mobile applications, improved signal-to-interference ratio (SIR) and an increased channel capacity [13,14], lower transmitted power, and higher transmission data rate. Employing adaptive array antennas into current wireless communication infrastructures also brings value-added services, such as general packet radio service (GPRS), users' PL, and the intelligent transportation system [13,15].

3. CURRENT APPLICATIONS OF ADAPTIVE ARRAY ANTENNAS

Along with the evolving development of smart antenna technologies, the applications of adaptive array antennas have extended from the early forms such as diversity and sectoring to the recent employment such as space-division multiple access (SDMA) and multiple-input multiple-output (MIMO) communications. In this section, we give a brief introduction on some applications of adaptive array antennas in the wireless communications.

3.1. Diversity Scheme

The earliest application of adaptive array antennas is diversity. The scheme has found many applications over the years. It has been in wide use in a variety of present-day microwave systems [16–20]. The aims of this scheme are to extract information from several independent signal paths, to combine the multiple signals, and to reduce the effect of excessively high signal fade [21]. Because the probability of two independent signals having a deep fade at the same time is rare, combining them reduces the effect of the fades.

There are many mechanisms to provide diversity. They are space diversity (with spaced array elements), frequency diversity [multicarrier CDMA, orthogonal frequency division multiplexing (OFDM)], angle of arrival (AOA) or angular diversity (impinging waves with different directions), polarization diversity (transmitting signals with different polarized waves), time diversity (signal repetition), and multipath diversity (rake receiver technique) [16]. Among them, space diversity is the easiest one to implement. However, space diversity needs an array antenna with sufficient interelement spacing. Therefore, considering space limitation in a mobile phone, the polarization diversity provides a compact installation [22–26].

Geographically there are two kinds of diversity schemes: the macroscopic diversity scheme and the microscopic

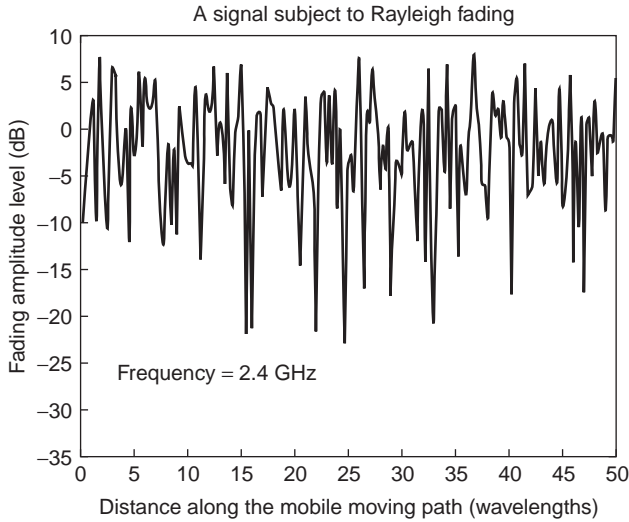


Figure 1. Rayleigh fading envelope.

diversity scheme. A *macroscopic diversity scheme* is used to combat against random shadowing effects where the signal power may drop to a point lower than the value predicted by a long-distance path loss model. The undulation of terrain contours determines the duration of the envelope variations during a long-term fading. The diversity scheme is employed by selecting signals from two separated base stations. On the other hand, in the *microscope cells*, clusters surround mobile users. Time dispersion caused by multipath propagation delays and the random frequency modulation due to varying Doppler shifts on different multiple signals result in fluctuations of the signal power at both base stations (BSs) and mobile terminals. This is commonly known as *Rayleigh fading* (see Fig. 1) [21]. Figure 2 shows the envelope correlation of two signal samples at distance/spacing ζ , where λ is wavelength of the carrier signal. The model assumes that the direction of arrivals (DoAs) of multipath signals are

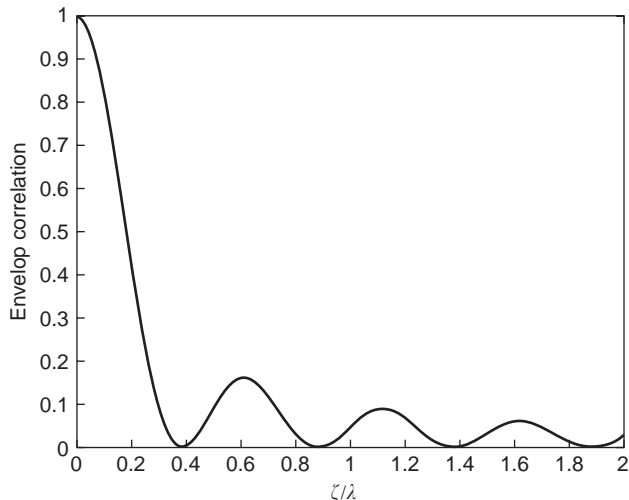


Figure 2. Envelope correlation spacing in a two-dimensional (2D) Clarke scenario.

uniformly distributed over 360° . Spacing of 0.13λ achieves a correlation lower than 0.7. For practical implementations of a microscopic diversity scheme, array antennas with interelement spacing of 0.38λ for a mobile station (MS) or tens of wavelength for a BS can provide independent signals at separate elements [17]. Ericsson has proved the improvement of the uplink performance employing both space and polarization diversities [27,28]. The international team of Ericsson has built a testbed to study the performance of the smart antenna receiver for digital advanced mobile phone service (AMPS). The uplink receiver uses space and polarization diversities. The interelement spacing is 15λ . The system provides a 3.5 dB gain in signal-to-noise ratio (SNR).

3.2. Sectoring

The ultimate goal of implementing a wireless cellular system is to achieve high capacity while satisfying quality-of-service (QoS) expectations. Cell splitting is a simple way to reduce cochannel interference (CCI). Currently most existing cellular and personal communication service (PCS) systems [3] make use of the sectoring technique in addition to the spatial diversity scheme. Each cell is divided into radial sectors with widebeam directional antennas installed at the BS [3,4,18,29]. Typically, those cells are divided into three sectors, which are 120° wide or six sectors that are 60° wide. Let us consider a cellular system with the cluster size of 7. The 120° cell sectoring reduces the number of the first-tier CCIs from 6 to 2 and brings a 6.8 dB SIR gain [1]. In addition to CCI suppression, another attractive benefit of sectoring is that frequency resources can be reused more frequently; thereby each cell can accommodate a larger traffic density without adding extra base stations.

Higher-order sectorization can be employed via beamforming or employing directional panel antennas to increase the frequency reuse and thus further improve the system capacity [29]. Sectoring via adaptive beamforming even allows more flexible allocation of transmit power at the BS [29]. However, handover will be initiated more frequently. Therefore, the system complexity is also increased.

3.3. Interference Suppression with Adaptive Beamforming

Adaptive antennas date back to 1959. The original work was attributed to L. C. Van Atta's work, *Electromagnetic Reflection* [U.S. Patent 29,080,002 (1959)]. Since then, adaptive beamforming techniques have been employed to remove unwanted noise and jamming from the output, mainly in military applications [4]. With the thriving commercial wireless communication industry and the advancing microprocessor technologies, the adaptive beamforming techniques have found their applications in commercial wireless communications. With powerful DSP hardware at the baseband, algorithms could control antenna beam patterns adaptively to the real signal environment, forming beams toward the desired signals while forming nulls to cochannel interferers. Thus, the system performance is optimized in terms of link quality and system capacity.

Field trials of both multibeam antennas and adaptive arrays have demonstrated performance improvements. Promising results substantiate the potential benefits of the adaptive beamforming technologies [30–37]. Meta-wave has extensively studied the range increase of multibeam antennas. Employing a 24-beam 15° beamwidth system, switching combining from two strongest directional beams achieves a 5 dB gain in a typical cellular environment [30]. An increased interference tolerance of 9 dB in the IS-136 system with a four-element adaptive antenna is demonstrated by Ericsson [31–33,37]. Lucent/AT&T has demonstrated the operation with an equal-power interferer next to the desired mobile terminal several miles from the base station in an IS-136 system with a four-element adaptive antenna [33]. Field trials have also been done for Digital European Cordless Telecommunications (DECT) system under the European TSUNAMI project [34]. Commercial products include a four-beam smart antenna incorporated into a GSM base station product by Nortel, and adaptive array processing using two base-station antennas incorporated into an IS-136 base station product by Ericsson [33–36].

However, the extensive implementation of adaptive antennas has been a problem. Because of system complexity, the fabrication cost, and the operational expenditure, adaptive antennas are limited to base stations or military applications. Researchers are endeavoring to make low-profile and low-power-consumption antennas for mobile terminals. Parasitic array antennas have become an active research topic. The antennas normally has one active element connected to the radiofrequency (RF) port, and beam pattern adaptation is achieved by switching among parasitic elements or by adjusting the loaded reactance at the passive elements. Being a less complicated structure, it offers an economical way to design low power consumption adaptive array antennas.

3.4. Space-Division Multiple Access

Filtering in the space domain separates spectrally and temporally overlapping signals from multiple MSs. Thus, the spatial dimension can be exploited as a hybrid multiple-access technique complementing existing multiple access schemes such as frequency-division multiple access (FDMA), TDMA, and CDMA. This approach is usually referred to as *space-division multiple access* (SDMA). The realization of this filtering technique is accomplished by using a smart antenna, which is capable of modifying its time, frequency, and spatial response by means of the amplitude and phase weighting and the internal feedback control (see Fig. 3). The SDMA scheme enables multiple users within the same radio cell to be accommodated on the same frequency or timeslot. Thus, it will increase the system capacity significantly [13,38–43]. The concept of the SDMA scheme is demonstrated by the TSUNAMI project. A uniform linear array consists of eight elements with a beamforming card developed by ERA Technology [44] used at the BS. The multiple signal classification (MUSIC) algorithm is used to find the direction of the MS. The Kalman filter is used to track the MS [34].

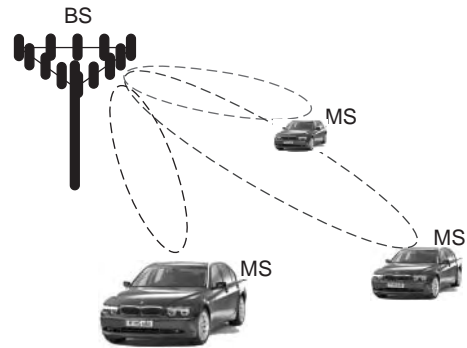


Figure 3. Space-division multiplexing (SDM) using spot beams at BS.

In addition to applications at terrestrial cellular systems, the SDMA scheme has been employed in satellite communications where each spot beam services a geographic area [39]. For an L-band mobile satellite communication system, to increase the frequency reuse in the spatial domain, multiple-beam satellite antennas are used for coverage of Canada and the United States. In comparison with a single-beam antenna, frequency reuse is increased by a factor of 4/3 using a four-beam antenna and 12/3 using a 12-beam antenna [39]. In Japan, a six-beam satellite antenna is used for 22-GHz band satellite broadcasting [45].

4. INCOMING APPLICATIONS OF ADAPTIVE ARRAY ANTENNAS

In addition to the aforementioned applications, new applications will be incorporated into future wireless communications standards of the 3G and 4G systems. Extensive investigations have been carried out to bring these new applications into reality.

4.1. Ad Hoc Networks

An ad hoc network is a dynamic wireless network established by peer-to-peer communications among mobile nodes (e.g., laptops, PDAs) without the help of any infrastructure such as a wire/wireless backbone [9,46–50]. The concept is shown in Fig. 4, in which each mobile terminal directs its beam toward the neighboring node to form a mesh where each node is a potential router. Changing together a sequence of neighboring nodes dynamically changes the routing of an information packet from an information source to a destination. Researchers are investigating media access control (MAC) protocols of ad hoc networks. Adaptive array antennas are a critical part, as many MAC protocol designs include the antenna beam pattern control [47,48]. With a properly oriented beam (toward the desired node), each node can resolve signals from neighboring nodes. The idea is the same as for an SDMA system. The DoA information from the antenna is used in routing selection. Another important issue of the ad hoc network is power consumption. Because mobile terminals for an ad hoc network have a limited battery life (around 3–4 h for a laptop), adaptive array

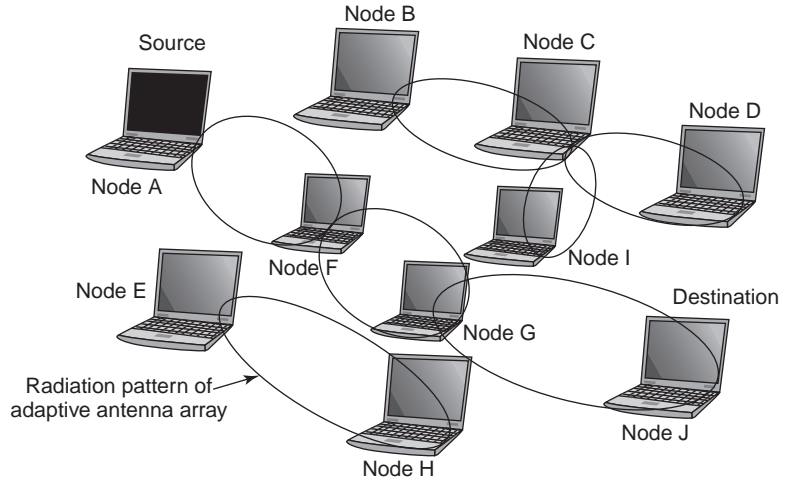


Figure 4. Ad hoc network with directional antenna at each mobile terminal.

antennas for this application are also required to have easy beam pattern control and consume as little power as possible.

4.2. Position-Location-Based Services

Safety is the primary motivation for PL services. In the United States, the Federal Communications Commission has mandated PL services within 125m accuracy on wireless emergency calls [13,18,51]. Using adaptive antennas, direction finding systems provide a mobile user’s position information. This location information aids emergency rescue, law enforcement, and other emergency calls. With the position location information, other promising applications such as accident reporting, navigational services, automated billing, fraud detection, roadside assistance, and cargo tracking are also becoming reality [15].

Currently, there are many existing PL systems, including the Global Positioning System (GPS), Global Navigation Satellite System (GLONASS), signpost navigation, and cellular geolocation [13]. Among them, cellular geolocation is the most attractive. It only needs to implement the smart antenna system, which has DoA estimation ability, into the existing wireless communication systems. The realization is based mainly on three mechanisms [51]: beacon location methods, DoA estimation techniques, and time-difference-of-arrival (TDoA) techniques. The concept of geolocation technique is shown in Fig. 5. The BSs located near the MSs estimate the DoA of the impinging wave from the terminal. From the DoA estimate, a line of bearing (LoB) from the base station to the mobile transmitter can be drawn. Multiple LoBs, drawn from different BS locations, intersect at the estimated location of the mobile terminal.

4.3. High-Data-Rate Transmission over MIMO Systems

The goal of the 3G communications systems is to provide high-data-rate transmission [5–8,11,52]. The goal urges a significant increase of channel capacity or, say, spectrum efficiency. MIMO systems have shed light in the tunnel to higher-data-rate transmissions. In commercial and

economical aspects the MIMO system is the most promising candidate as it offers such a significant capacity upgrade that high-data-rate transmission can be achieved [52–59].

Multipath fading has long been viewed as impairment to the wireless communications link. Techniques such as diversity combining, equalization, and adaptive beamforming have been investigated to reduce the fading. A different view is that exploiting multipath fading realizes higher-data-rate transmission. In a multipath-rich environment, antenna arrays that provide uncorrelated signal outputs are installed at both transmitters and receivers to build MIMO wireless communication channels [60–65]. The multipath phenomenon achieves an information-theoretic channel capacity that increases with the number of array antenna elements. In Fig. 6, Tx and Rx are the numbers of transmit antennas and receive antennas. We observe that the capacity grows significantly when Tx and Rx increase.

Transmission STC through MIMO systems takes advantage of spatial and temporal diversities to increase the data rate over fading channels [53]. Field tests and experimental results substantiate the capacity gain achieved by MIMO systems [66,67]. Lucent Technologies has achieved

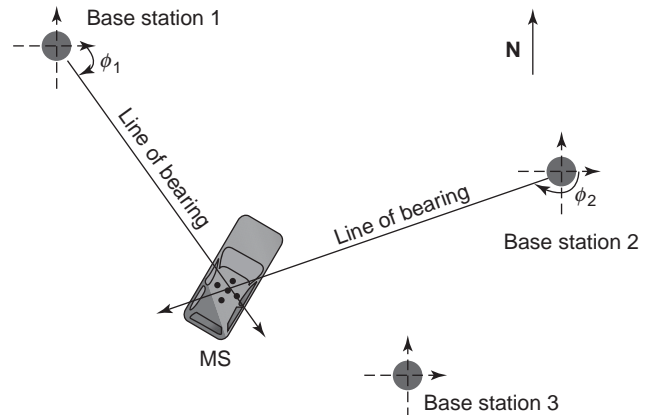


Figure 5. Concept of cellular geolocation.

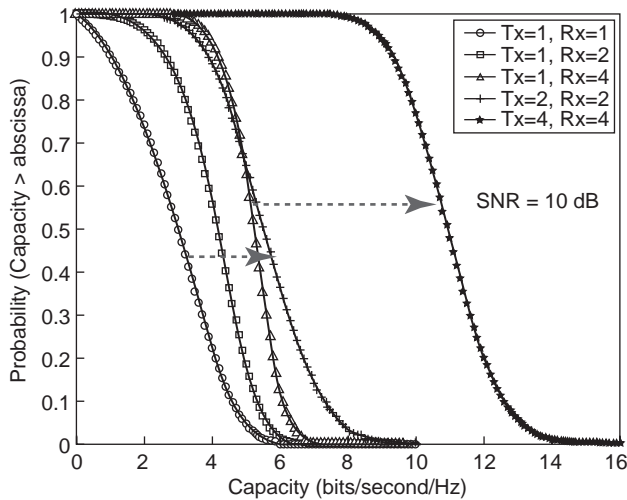


Figure 6. MIMO information-theoretic channel capacities with different numbers of transmit antenna and receive antennas.

a transmission data rate of 40 bps/Hz at a 30 dB SNR indoor flat fading environment using 8 transmit and 12 receive antennas vertical Bell Labs layered spacetime (V-BLAST) architecture [68,69].

5. ARCHITECTURES AND IMPLEMENTATIONS OF ADAPTIVE ARRAY ANTENNAS

In the previous section, we presented the applications of smart antenna technologies. Various applications require different functions from adaptive array antennas. For example, SDMA requires fine beamforming ability. PL services demand for DoA estimation, and MIMO systems require decorrelation among signal samples. In this section, we examine various realizations and implementation issues of adaptive array antennas. Figure 7 shows the tree structure of various smart antenna implementation architectures.

5.1. Switched-Beam Antennas

A switched-beam antenna system consists of several highly directive, fixed, predefined beams [13,14,18,63,70–72]. In practice, multiple beams can be formed by a beamforming

network, which consists of an involved feeding system and multiple input ports. The feeding network that provides adequate excitation to the array elements can steer the beam pattern to the desired direction. It can be implemented at either RF stage or intermediate-frequency (IF) stage. The functional block diagram of a switched-beam antenna is shown in Fig. 8. An example of the beam-forming network is the Butler matrix [14,18,71,73], which consists of power splitters and phase shifters. It has been used extensively over the years in radar, electronic warfare (electronic support measures), and satellite systems. Figure 9 depicts a 4 × 4 Butler matrix. Figure 10 illustrates the produced beam patterns with the 4 × 4 Butler matrix.

The receiver chooses from the one of the several beams to give the best performance. The decision making stage can be implemented at the IF stage, based on the criterion of the maximum received power using a received signal strength indicator (RSSI) or at the baseband digital stage by examining the lowest signal bit error rate (BER). In Ref. 74, an 8 × 8 Butler matrix is used to generate eight Woodward Lawson beams. Microstrip patch antennas are chosen as the array elements. Mutual coupling between elements is reduced to a level of less than – 15 dB by using H-shaped slot feeding technique. Measurement results show that 13 dBi directivity gain is achieved for the eight beams covering a 114° angular range. A beam selector chooses either one of the eight fixed beams or two neighboring beams by examining the output signal BER.

In a sense, a switched beam is an extension of the conventional sector beam antenna in that it divides a sector into several microsectors [63]. Therefore, the switched-beam antenna system is the easiest solution to upgrade the existing system, which employs 120° sector antennas and dual diversity per sector. However, switched-beam antennas also have drawbacks. They do not exploit multipath. In addition, the signal power from the mobile terminal drops greatly when the mobile terminal moves into the margin of a beam or the area between two beams. Furthermore, owing to the inability to distinguish a desired user from interferers, switched-beam antennas are not effective in combating against CCI. If a strong interfering signal is at the center of a selected beam and the desired user is away from the center of that beam, the interfering signal can be enhanced far more than the desired signal. One solution of the aforementioned problems has

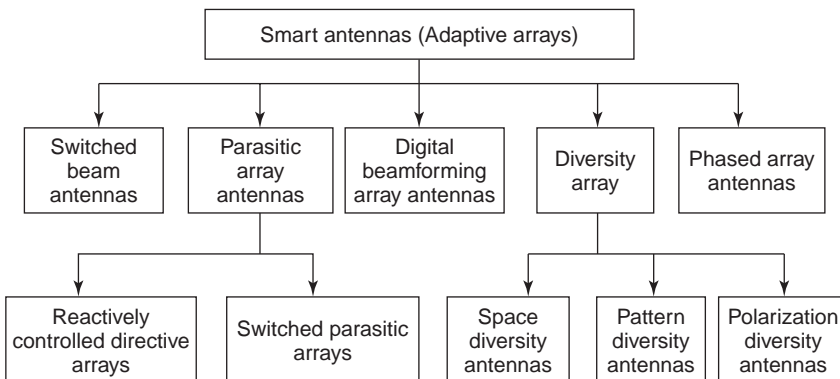


Figure 7. Various architectures of adaptive array antennas.

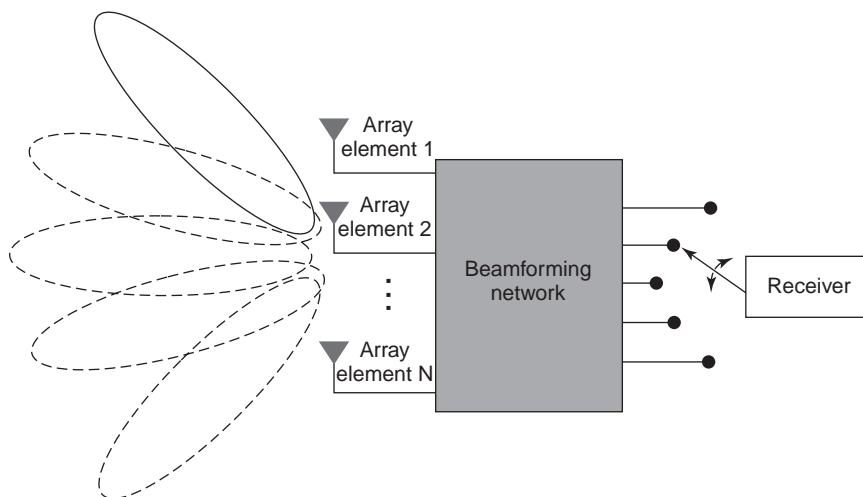


Figure 8. Functional block diagram of switched-beam antennas.

been presented in Refs. 75–77, where phase shifters are added to the switching system. The structure achieves a smoother transition from one beam to another.

5.2. Phased-Array Antennas

Research and development (R&D) of phased-array antennas for radar systems has been ongoing in the United States since 1950s [78]. Since then, phased-array antennas have been extensively utilized in radar, military scenarios, and satellite communications. Now the antennas are used more for space-based communications applications because of their advantages in scanning, reconfigurability, weight, and power. In satellite communications, adaptive array antennas function as input–output ports of the link at both satellite and ground segments. In Japan, phased-array antennas were first applied when Japanese Defense developed a passive array antenna consisting of element antennas equipped with phase shifters and power divider/combiners in the 1960s [78]. The Communication Research laboratory (CRL) and National Space Development Agency of Japan (NASDA) developed an onboard Ka-band (20/30-GHz) scanning spot beam active phased array

antenna for the experimental high data rate (gigabit) communication satellite [79]. Both the transmit and receive antennas use a meanderline polarizer and 64 pyramidal horn element antennas, and realize circularly polarized scanning spot beams. Each antenna is connected with four independent 4-bit digital phase shifters to achieve four independent beams, respectively. In Australia a 12-element land mobile terminal phased-array antenna is designed for continuous tracking of the Mobilesat satellite while the terminal is moving [80]. The role of a phased-array antenna for mobile terminal in satellite communication scenario is to enable transmission and reception of microwave signals and to track the satellite while the vehicle is moving. As shown in Fig. 11, the terminal is equipped with phased-array antenna as the mobile antenna, an antenna electronic unit (AEU), a transceiving unit, and a satellite tracking unit. The functional block diagram of the mobile antenna is depicted in Fig. 12. The beamforming network consists of power dividers, couplers, switches, phase shifters, biasing networks, and

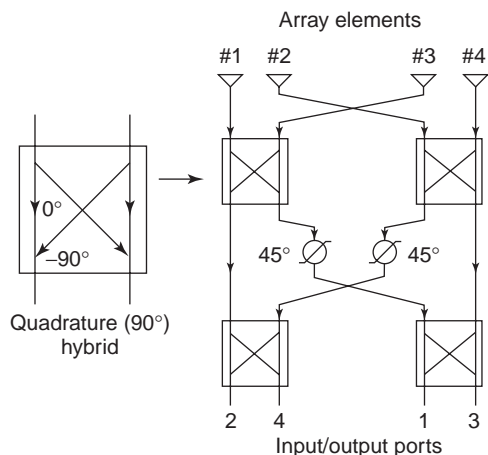


Figure 9. A four-port Butler matrix for fixed beamforming [71].

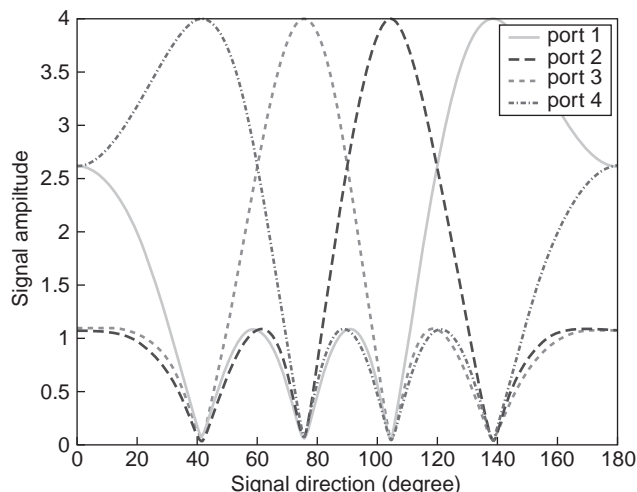


Figure 10. A set of four beams produced using a 4 × 4 Butler matrix. (This figure is available in full color at <http://www.mrw.interscience.wiley.com/erfme>.)

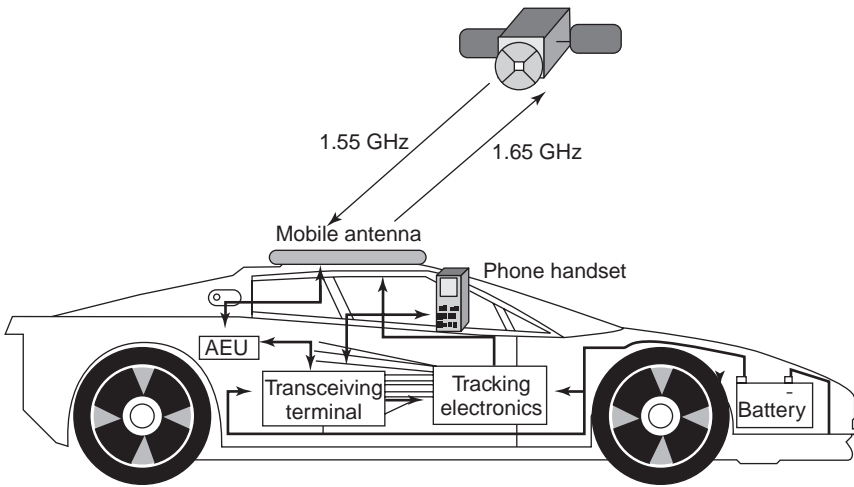


Figure 11. Functional block diagram of a mobile satellite communication terminal and a phased-array antenna mounted on a car.

circularly polarized (CP) patch antennas as array elements. The system conforms with the Australian mobile satellite specifications:

- *Polarization.* right-hand circular
- *Frequency.* 1646.5–1660.5 MHz for transmission; 1545.0–1559.0 MHz for reception
- *Coverage.* full 360° in azimuth and 28–66° in elevation
- *Gain.* 10–12 dBi desirable with a minimum of 7 dBi

In the design presented in Ref. 80, single-feed stacked patch elements presented in Ref. 75 (see Fig. 13) are selected as the best candidates for constructing the planar phased array. The detailed view of the developed multilayer phased-array antenna is shown in Fig. 14. The multilayer design includes stacked CP patch antenna arrays and two foam layers to achieve an increased antenna beamwidth, a slotted ground layer for coupling, and an antenna beamforming network layer as shown in Fig. 15. The beamforming network layer consists of a 12-way feed power division/combination network as required for 12 patch antenna elements arranged in two rings of 8 and 4 elements. Twelve 3-bit digital phase shifters (including a 180° switched-line phase shifter and 45° and 90° loaded line phase shifters), located at the outputs of the 12-way divider, are coupled to individual antenna elements via aperture coupling.

Phased-array antennas contain a multitude of radiating elements, typically arranged in a rectangular or triangular tessellation. Beam pattern steering of phased-array antennas is achieved by implementing phase shift of signals from array elements [18,63,70,75,80–82]. Dynamic phased arrays make use of the DoA information from a desired user and steer a beam maximum toward that user, thus improving the capabilities of a switched-beam antenna [63]. Tracking is needed to continuously steer the beam toward the desired user. However, the disadvantage of the phased-array antenna is the relatively high cost as expensive PIN diodes are used in phase shifters required by beamforming networks [75].

5.3. Digital Beamforming Array Antennas

The technological progress of DSP has introduced the concept of beamforming in the digital stage [14,18,37,39,63,70,82–84]. In comparison with switched-beam antennas and phased-array antennas, smoother pattern direction tuning and higher-resolution direction finding can be achieved with high-speed DSP and high-resolution ADC. The functional block diagram of a DBF array antenna is shown in Fig. 16. Each downconversion channel has a low-noise amplifier, a frequency converter, and an ADC. Signals received by individual antenna elements are downconverted to the baseband, digitized, and then fed into a DSP chip where algorithms are carried out. A fine steering is achievable by employing high-resolution sampling and

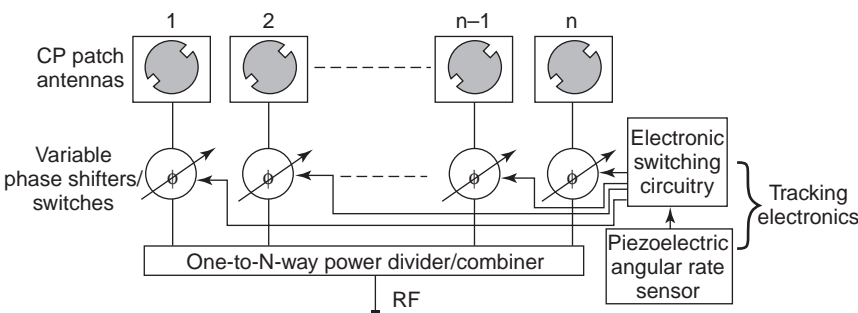


Figure 12. Functional block diagram of a phased-array antenna at land mobiles for satellite communications.

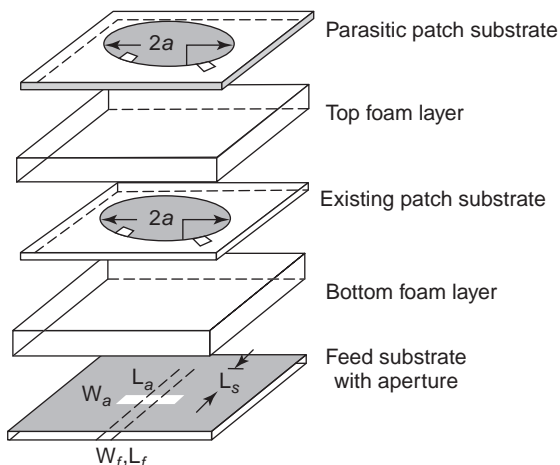


Figure 13. Stacked patch with perturbation segments [75].

quantization in an A/D conversion process. Many beamforming and DoA estimation algorithms have been studied [3,4,8,37,39,63,85–89]. Simulations and tests show that they are fruitful in improving the system capacity and enhancing system performance [37,39,87].

However, high-resolution A/D conversion dissipates a substantial amount of DC power. Furthermore, since a DBF antenna needs the same number of A/D converters as does the number of antenna elements, the fabrication cost increases with the number of antenna elements. In addition, because A/D conversion cannot be carried out directly in the RF stage, same amount of power are also consumed at the frequency converters [14,82,90]. For these reasons, the use of DBF antennas has been restricted to military applications, satellite communications, or at the base station for terrestrial wireless communications.

5.4. Parasitic Array Antennas

To circumvent the disadvantages of the aforementioned systems, adaptive beamforming based on parasitic antennas has been explored [82,90–107]. In a parasitic array antenna, the active element, which is excited by the transmitted or

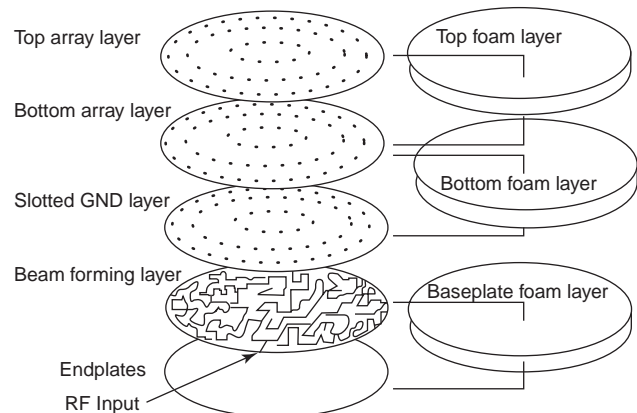


Figure 14. Detailed view of the developed multilayer phased-array antenna.

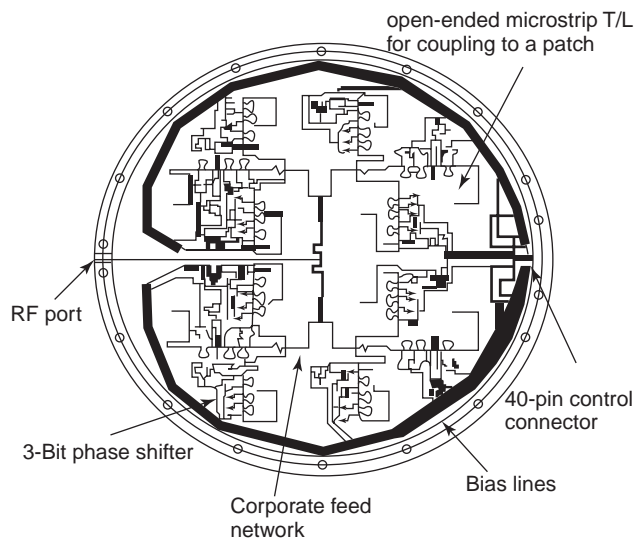


Figure 15. Detailed view of the beamforming layer.

the received signal sources, is surrounded by a number of parasitic elements, which are not connected to the signal source. In the presence of neighboring elements, the performance of each element depends not only on that element’s current but also the currents of neighboring elements. For resonant elements with no current excitation of their own, a substantial current could be induced by radiation from another source [108]. The far-field radiation pattern is formed by superposition of the radiation of all antenna array elements [109]. Thus, by changing the radiation of each element, it is possible to direct the antenna beam toward desired directions.

The use of parasitic elements for controlling antenna beam patterns goes back to the work of Yagi and Uda during the 1930s [108]. This antenna array has been patented in various forms for numerous applications. Various electronically steered Yagi–Uda arrays have been designed. A reflector formed by short-circuited elements is arranged behind the active element. Figure 17 illustrates the formation of Yagi-Uda array with the switched parasitic elements. By controlling the states (ON or OFF) of the PIN diode switches of the parasitic elements, different sets of short-circuited monopoles function as directors and reflectors around the active central monopole. Therefore, directive beams are steered toward the desired directions [91–93,96,97,100,102,103]. Instead of using one active element at a fixed position, multiple active elements give more choices of producing multiple beams [97,98,101,107]. Similar to those wire antenna elements switched by diodes, it is also possible to use switches to control the radiation pattern of parasitic patch elements and thereby change the beam direction of a parasitic patch array antenna [99]. The aforementioned antennas are categorized as “switched parasitic antennas” [105]. Using switched parasitic antennas, beam directions can be selected only among predefined directions. Analogous to switched-beam antennas, this limits performance.

Another category of parasitic array antennas is the “reactively controlled directive array antenna,” which

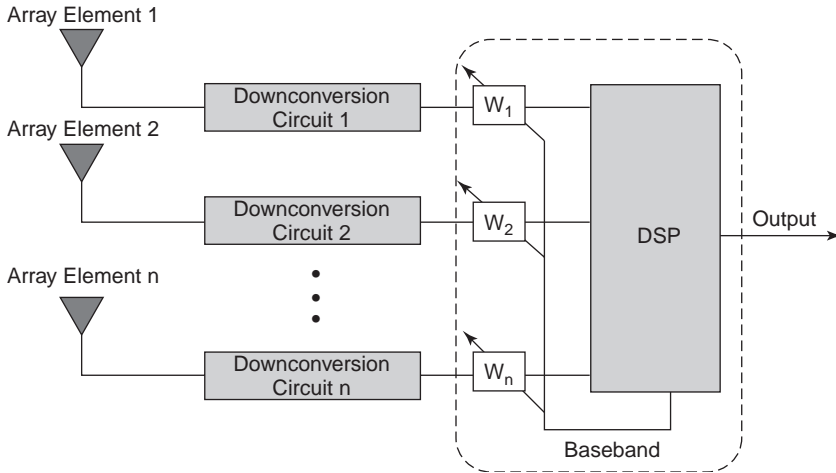


Figure 16. Functional block diagram of DBF array antennas.

dates back to Harrington’s work in 1978 [94]. The parasitic array is formed with one active and several surrounding monopoles on the ground plane. The functional block diagram is shown in Fig. 18. Changing the reactance of the parasitic elements alters the radiation of each element. Therefore, by adjusting the reactance loaded on the parasitic elements, directive beam patterns can be formed. With this configuration, it is possible to achieve a smoother beam pattern tuning. In Ref. 95, the array elements are realized microstrip patches. The loads on the parasitic elements are carried out by terminating a transmission line by a variable-reflection phase shifter. Adaptive beamforming is realized by the steepest-gradient optimization method. More recently, extensive investigations on adaptive beamforming and DoA estimation using this type of structure are carried out. A seven-element antenna called the *electronically steerable parasitic array radiator* (ESPAR) [90,104,110–112] has been developed.

Figure 19 shows the configuration of a seven-element ESPAR antenna. One active central element (monopole) is surrounded by six parasitic elements uniformly placed on a circular grid of radius R on a circular grounded baseplate. The length of each monopole L and the radius R of the circular grid are one-quarter wavelength ($\lambda/4$) of the transmitting RF signal at 2.484 GHz. According to Harrington [94], wide spacing among elements (e.g., $\lambda/2$) leads to reduced gain and significant backlobes. Moreover, further reduction of interelement spacing to $\lambda/8$ leads to a

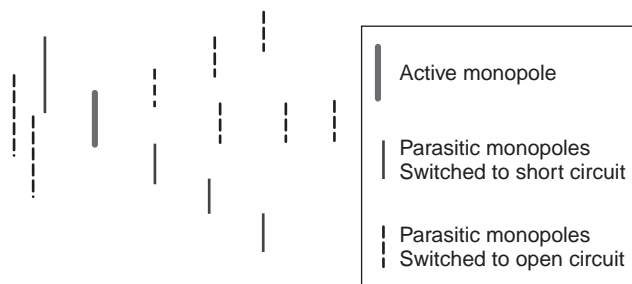


Figure 17. Structure of a switched parasitic array antenna.

supergain array. Therefore, a realistic design for spacing $= \lambda/4$ is chosen. The baseplate transforms monopoles with their images to dipoles with a length of $2L$. The central monopole is connected to a RF receiver, and each parasitic monopole is loaded with a tunable varactor that is realized with a reversely biased diode.

The working principle of ESPAR antennas is different from that for DBF array antennas. The antenna generates a directional beam based on tuning load reactances (x_1, x_2, \dots, x_6) on the parasitic monopoles. Signals received or transmitted from the central RF port excite the parasitic monopoles with substantial induced mutual currents on them. Let us first assume that the antenna is working in transmitting mode, where vectors \mathbf{i} and \mathbf{v} represent the currents and the voltages on the monopoles, respectively:

$$\mathbf{i} = [i_0 \ i_1 \ i_2 \ i_3 \ i_4 \ i_5 \ i_6]^T \quad (1)$$

$$\mathbf{v} = [v_0 \ v_1 \ v_2 \ v_3 \ v_4 \ v_5 \ v_6]^T \quad (2)$$

The superscript “T” represents the transpose; i_0 and v_0 represent the current and the voltage on the active central

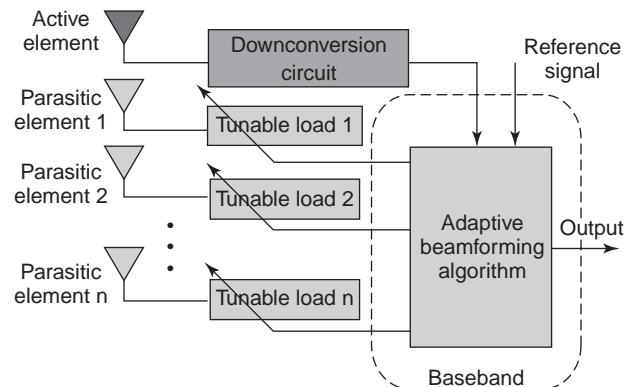


Figure 18. Functional block diagram of reactively controlled directive array antennas.

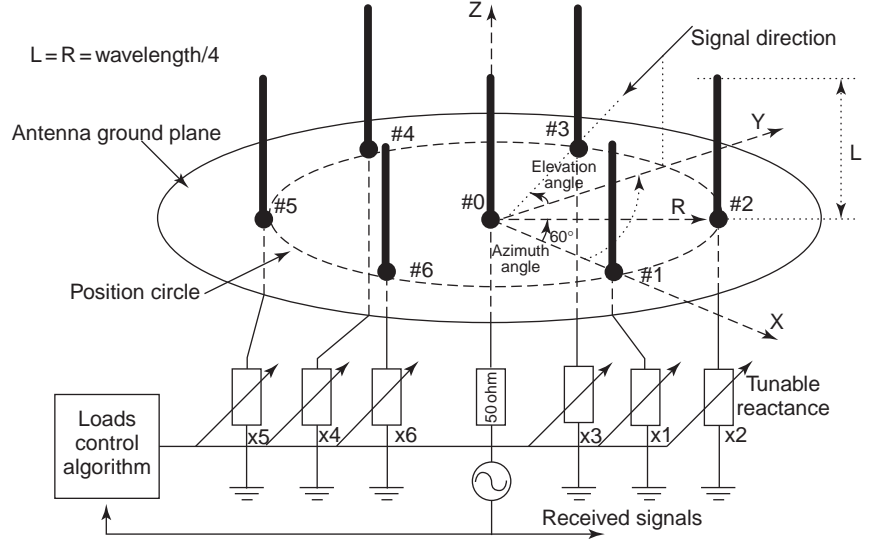


Figure 19. Configuration of a seven-element ESPAR antenna. The length of each monopole L and the radius R of the circular grid are one-quarter wavelength $\lambda/4$ of the transmitting RF signal at 2.484 GHz.

element (0), respectively. Mutual admittances are represented by the matrix \mathbf{Y}_C with each entity y_{ij} denoting the mutual admittance between the i th element and the j th element. The induced currents are represented with mutual admittances:

$$\mathbf{i} = \mathbf{Y}_C \mathbf{v} = \begin{bmatrix} y_{00} & y_{01} & y_{02} & y_{03} & y_{04} & y_{05} & y_{06} \\ y_{10} & y_{11} & y_{12} & y_{13} & y_{14} & y_{15} & y_{16} \\ y_{20} & y_{21} & y_{22} & y_{23} & y_{24} & y_{25} & y_{26} \\ y_{30} & y_{31} & y_{32} & y_{33} & y_{34} & y_{35} & y_{36} \\ y_{40} & y_{41} & y_{42} & y_{43} & y_{44} & y_{45} & y_{46} \\ y_{50} & y_{51} & y_{52} & y_{53} & y_{54} & y_{55} & y_{56} \\ y_{60} & y_{61} & y_{62} & y_{63} & y_{64} & y_{65} & y_{66} \end{bmatrix} \begin{bmatrix} v_0 \\ v_1 \\ v_2 \\ v_3 \\ v_4 \\ v_5 \\ v_6 \end{bmatrix}. \quad (3)$$

These values can be obtained using a numerical electromagnetic code (NEC) simulator [113]. The voltages on the active central monopole and the m th parasitic monopole are represented by v_0 and v_m , respectively. Let z_0 be the characteristic impedance at the RF port and v_s represent the transmitted voltage signal source with the amplitude and the phase from the driving RF port at the central element. Following the analysis in [90], we obtain

$$\mathbf{i} = v_s (\mathbf{Y}_C^{-1} + \mathbf{X}_L)^{-1} \mathbf{u}_1 \quad (4)$$

where $\mathbf{X}_L = \text{diag}[z_0, jx_1, \dots, jx_6]$ and $\mathbf{u}_1 = [1 \ 0 \ 0 \ 0 \ 0 \ 0 \ 0]^T$. The far-field radiation pattern is the superposition of all monopoles' radiation patterns [108]. Therefore, the far-field current signal in the azimuthal direction ϕ with its amplitude and the phase is represented as

$$y_{\text{far}}(\phi) = \mathbf{i}^T \mathbf{p} \mathbf{h} \alpha(\phi) = [(\mathbf{Y}_C^{-1} + \mathbf{X}_L)^{-1} \mathbf{u}_1]^T \mathbf{p} \mathbf{h} \alpha(\phi) v_s \quad (5)$$

where $\alpha(\phi)$ is the 7×1 dimensional steering vector corresponding to azimuth angle ϕ . It is expressed as

follows:

$$\alpha(\phi) = \begin{bmatrix} 1 & e^{j(\pi/2) \cos(\phi)} & e^{j(\pi/2) \cos(\phi - (\pi/3))} & e^{j(\pi/2) \cos(\phi - (2\pi/3))} \\ e^{j(\pi/2) \cos(\phi - \pi)} & e^{j(\pi/2) \cos(\phi - (4\pi/3))} & e^{j(\pi/2) \cos(\phi - (5\pi/3))} \end{bmatrix}^T \quad (6)$$

In (5), we denote $(\mathbf{Y}_C^{-1} + \mathbf{X}_L)^{-1} \mathbf{u}_1$ as \mathbf{w}_E and term it the “equivalent-weight vector” because of its resemblance to a (7×1) -dimensional beamforming weight vector in the array processing literature [90]. According to the reciprocity theory for radiation patterns [108], if the antenna is working in the receiving mode, the voltage signal, say, $y(t)$ at the RF port is expressed as

$$y(t) = \mathbf{w}_E^T \alpha(\phi) s(t) \quad (7)$$

where $s(t)$ represents the far-field impinging current waves with the amplitude and the phase in the azimuthal direction ϕ . It is clear that \mathbf{w}_E is dependent on the reactance values of the reactances at those parasitic elements; therefore a beamsteering pattern is achieved by properly adjusting reactance values. For the designed ESPAR antenna, the adjustable load reactances at the parasitic elements are realized with reversely biased diodes as shown in Fig. 20. The implementation achieves a frequency-dependent reactance value ranging from $-45.8j\Omega$ to $-3.6j\Omega$.

Since the load reactances and switches are realized by the diodes, there is only a small leakage current. Therefore, the power consumption of the parasitic array antennas is very small. Furthermore, the system normally has only one RF port and one subsequent downconversion circuit. In terms of power consumption and fabrication cost, it is obvious that parasitic array antennas are suitable for mass implementations of adaptive array antennas, especially for battery-powered portable mobile terminals.

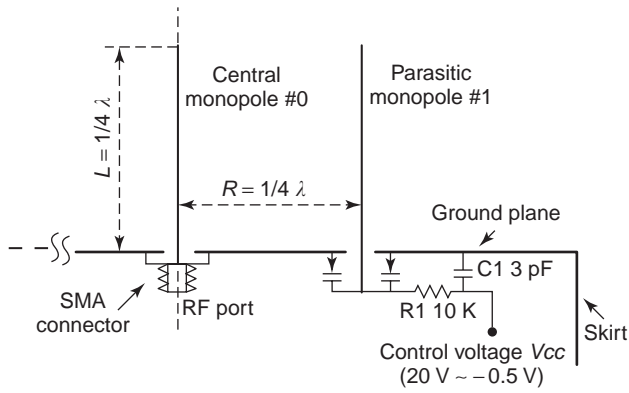


Figure 20. Vertical cross-sectional view of ESPAR antenna and a reactance circuit of one of the six parasitic elements. The length of each monopole is one-quarter wavelength ($\lambda/4$) of the transmitting RF signal at the frequency of 2.484 GHz [90].

5.5. Diversity Antennas

Diversity antennas combat against multipath fading and improve channel quality for a given radio spectrum in comparison with that from a single-port antenna [13,20,35,105,114]. Because the correlation among signals from the multiple ports of array antennas undermines diversity combining performance [16,20], the challenge of diversity antenna design is how to achieve signal decorrelation. This is particularly difficult in handphones where antenna elements are mounted within small spacing, for a given incident wave distribution scenario.

Colburn et al. [115] have presented three candidate dual-diversity antenna configurations: two side-mounted

planar-inverted F antennas (PIFAs), a back-mounted PIFA with a top-mounted helix, and a top-mounted PIFA with a flip monopole. Experimental results show sufficient signal decorrelation of these configurations. The diversity gain obtained with polarization diversity has been demonstrated with dual-polarized diversity obtained by an aperture-coupled patch antenna or by two slanted dipoles over an infinite ground plane [24]. Vaughan [102] presented diversity antennas using various parasitic array antenna structures. In one of the designs, three directional patterns are formed with three subsets of a parasitic array as shown in Fig. 17. By selecting one of the patterns pointing in different directions, angular diversity advantage is achieved. In another design, 16 parasitic monopoles are placed uniformly in the circle of radius 0.25 wavelength, and an active monopole is located at the center of the circle. The directional beam pattern with 90° half-power beamwidth (HPBW) is rotated, 360/16° each step, by shifting switch setting of parasitic elements. For adjacent beam patterns with 22.5° angular spacing, the envelope correlation of complex beam patterns is 0.91. For patterns with larger angular separation, say, 45°, the envelope correlation of 0.7 is achieved. The Virginia Tech Antenna Group has evaluated the envelope correlation, power imbalance, and diversity gain with space diversity, polarization diversity, and pattern diversity at handheld terminals [116]. The spatial diversity is achieved with two parallel half-wavelength dipoles with inter-element spacing variable from 0.1 to 0.5 wavelength. The dual-polarization diversity antenna is constructed with a dipole and a printed wheel antenna separated vertically by 0.3 wavelength. As for the pattern diversity, it is achieved with two dipoles, with 0.25 wavelength interelement

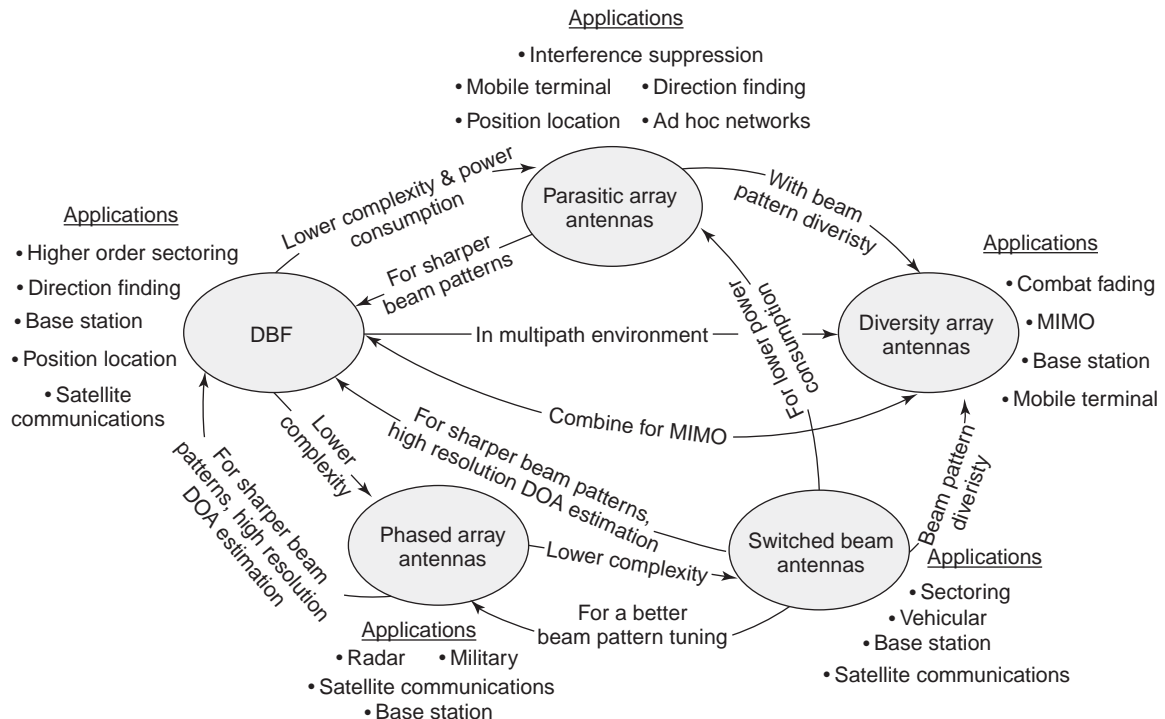


Figure 21. Relation of various adaptive array antenna structures and their applications.

Table 1. Comparison of Various Adaptive Array Antennas and Related References

Adaptive Array Architecture	Implementation stage	Decision–Control Stage	Applications	Refs.
Switched-beam antenna	RF/IF	Baseband/IF	Cellular base station, satellite communications	13, 14, 18, 63, 70–77
Phased-array antenna	RF	Baseband	Military, radar, satellite communications	18, 63, 70, 78–82
Digital beamforming (DBF)	Baseband DSP	Baseband	Cellular base station, satellite communications, radar, high-resolution direction finding	3, 4, 8, 14, 18, 37, 39, 63, 70, 82–89
Parasitic array	RF	Baseband	Power consumption limited mobile terminal, direction finding	82, 90–108, 110–112
Diversity array	Providing uncorrelated signals at RF stage	Baseband/IF	Mobile terminals, combating multipath fading, MIMO communications	20, 24, 105, 115, 116

spacing, connected to a quadrature (90°) hybrid (see Fig. 9). The structure provides two orthogonal beams at the two ports. Measured results in various multipath environments have clearly justified the feasibility of diversity at handheld terminals.

6. CONCLUSIONS

The wireless communications system is evolving with a fast pace. Better-quality wireless communications, new services and applications will become available with the technological advances. With different structures, adaptive array antennas play important roles in the evolution of wireless communications systems. Figure 21 and Table 1 generalize the tradeoff between the performance and complexities of various forms of adaptive array antennas, implementation stages and some of their applications. For applications where cost and power consumption are the main limiting factors, parasitic array antennas and switched-beam antennas are suitable. DBF array antennas and phased-array antennas dominate in the applications such as satellite communications and BS applications, where high performance is desired. In addition to combating fading, diversity antennas can also be employed to realize high-speed MIMO wireless transmissions.

BIBLIOGRAPHY

- G. L. Stuber, *Principle of Mobile Communication*, 2nd ed., Kluwer Academic Publishers, 2001.
- A. Paulraj, R. Nabar, and D. Gore, *Introduction to Space-Time Wireless Communications*, Cambridge Univ. Press, 2003.
- T. S. Rappaport, *Wireless Communications: Principles and Practice*, 2nd ed., Prentice-Hall PTR, Upper Saddle River, NJ, 2002.
- J. S. Blogh and L. Hanzo, *Third-Generation Systems and Intelligent Wireless Networking: Smart Antennas and Adaptive Modulation*, IEEE Press, 2002.
- S. Y. Hui and K. H. Yeung, Challenges in the migration to 4G mobile systems, *IEEE Commun. Mag.* **41**(12):54–59 (Dec. 2003).
- L. M. Correia and R. Prasad, An overview of wireless broadband communications, *IEEE Commun. Mag.* **35**(1):28–33 (Jan. 1997).
- P. Chaudhury, W. Mohr, and S. Onoe, The 3GPP proposal for IMT-2000, *IEEE Commun. Mag.* **37**(12):72–81 (Dec. 1999).
- P. H. Lehne and M. Pettersen, An overview of smart antenna technology for mobile communications systems, *IEEE Commun. Surve.* **2**(4):2–13 (fourth quarter, 1999).
- M. Frodigh, S. Parkvall, C. Roobol, P. Johansson, and P. Larsson, Future-generation wireless networks, *IEEE Pers. Commun. Mag.* **8**(5):10–17 (Oct. 2001).
- J. H. Park, Wireless internet access for mobile subscribers based on the GPRS/UMTS network, *IEEE Commun. Mag.* **40**(4):38–49 (April 2002).
- T. S. Rappaport, A. Annamalai, R. M. Buehrer, and W. H. Tranter, Wireless communications: Past event and a future perspective, *IEEE Commun. Mag.* **40**(5):148–161 (May 2002).
- J. D. Vriendt, P. Lainé, C. Lerouge, and X. F. Xu, Mobile network evolution: A revolution on the move, *IEEE Commun. Mag.* **40**(4):104–111 (April 2002).
- G. V. Tsoulos, Smart antennas for mobile communication systems: benefits and challenges, *Electron. Commun. Eng. J.* **11**(2):84–94 (April 1999).
- A. U. Bhohe and P. L. Perini, An overview of smart antenna technology for wireless communication, *Proc. IEEE Aerospace Conf.* March 2001, Vol. 2, pp. 875–883.
- T. S. Rappaport, J. H. Reed, and B. D. Woerner, Position location using wireless communications on highways of the future, *IEEE Commun. Mag.* **34**(10):33–41 (Oct. 1996).
- M. Schwartz, W. R. Bennett, and S. Stein, *Communication Systems and Techniques*, McGraw-Hill, 1966.
- W. C. Jakes, *Microwave Mobile Communications*, Wiley, 1974.
- J. C. Liberti and T. S. Rappaport, *Smart Antennas for Wireless Communications: IS-95 and Third Generation CDMA Applications*, Prentice-Hall PTR, Upper Saddle River, NJ, 1999.
- D. G. Brennan, Linear diversity combining techniques, *IEEE Proc.* **91**(2):331–356 (Feb. 2003).
- R. Vaughan and J. B. Andersen, *Channels, Propagation and Antennas for Mobile Communications*, IEEE UK, 2003.
- W. C. Y. Lee, *Mobile Communications Engineering, Theory and Applications*, 2nd ed., McGraw-Hill, New York, 1997.

22. M. R. Andrew, P. P. Mitra, and R. de Carvalho, Tripling the capacity of wireless communications using electromagnetic polarization, *Nature* **409**:316–318 (Jan. 2001).
23. T. Svantesson, A physical MIMO radio channel model for multi-element multi-polarized antenna systems, *Proc. IEEE 54th Vehicular Technology Conf.*, Oct. 2001, pp. 1083–1087.
24. B. Lindmark and M. Nilsson, On the available diversity gain from different dual-polarized antennas, *IEEE J. Select. Areas Commun.* **19**(2):1193–1204 (Feb. 2001).
25. R. U. Nabar, H. Bolcskei, V. Erceg, D. Gesbert, and A. J. Paulraj, Performance of multiantenna signaling techniques in the presence of polarization diversity, *IEEE Trans. Signal Process.* **50**(10):2553–2562 (Oct. 2002).
26. C. Sun and N. C. Karmakar, Environment-oriented beamforming for space-time block coded multiuser MIMO communications, *Proc. IEEE Antennas and Propagation Society Int. Symp.*, June 2004, Vol. 2, pp. 1744–1747.
27. B. Hagerman, T. Ostman, K. J. Molnar, and G. E. Bottomley, Field test performance results for D-AMPS in PCS bands with array processing, *Proc. IEEE 47th Vehicular Technology Conf.*, Kyoto, Japan, May 1997, Vol. 3, pp. 1582–1586.
28. K. Molnar, Space-time processing in an evolution of IS-136 system, *Proc. 5th Stanford Smart Antennas Mobile Wireless Communications Workshop*, 1998.
29. K. I. Pedersen, P. E. Mogensen, and J. Ramiro-Moreno, Application and performance of downlink beamforming technique in UMTS, *IEEE Commun. Mag.* **41**(10):134–143 (Oct. 2003).
30. Y. Li, M. Feuerstein, P. Perini, and D. Reudink, Gain improvement of a cellular base station multibeam antenna, *Proc. IEEE 46th Vehicular Technology Conf.*, May 1996, Vol. 3, pp. 1680–1684.
31. S. Anderson, U. Forssen, J. Karlsson, T. Witzschel, P. Fischer, and A. Krug, Ericsson/Mannesmann GSM field-trials with adaptive antennas, *Proc. IEEE 47th Vehicular Technology Conf.*, May 1997, Vol. 3, pp. 1587–1591.
32. S. Anderson, U. Forssen, J. Karlsson, T. Witzschel, P. Fischer, and A. Krug, Ericsson/Mannesmann GSM field-trials with adaptive antennas, *Proc. IEEE Colloquium on Advanced TMP Techniques and Applications*, Oct. 1996, Vol. 1996/234, pp. 6/1–6/6.
33. J. H. Winters and G. D. Golden, Adaptive antenna applique field test, *Proc. 4th Workshop on Smart Antennas in Wireless Mobile Communications*, 1997.
34. G. V. Tsoulos, M. Beach, and J. McGeehan, Wireless personal communications for the 21st century: European technological advances in adaptive antennas, *IEEE Commun. Mag.* **35**(9):102–109 (1997).
35. J. H. Winters, Smart antennas for wireless systems, *IEEE Personal Commun. Mag.* **5**(1):23–27 (Feb. 1998).
36. Ericsson Press Releases, Ericsson and Mannesman rollout the world's first GSM adaptive antenna base stations, (online), <http://www.ericsson.com/press/archive/2000Q2/20000417-0026.html>.
37. A. O. Boukalov and S. G. Häggman, System aspects of smart-antenna technology in cellular wireless communications—an overview, *IEEE Trans. Microwave Theory Tech.* **48**(6):919–929 (June 2000).
38. M. Marcus and S. Das, The potential use of adaptive antennas to increase land mobile frequency reuse, *Proc. IEEE Int. Conf. Radio Spectrum Conversation Techniques*, Birmingham, UK, Sept. 1983, pp. 113–117.
39. J. Litva, *Digital Beamforming in Wireless Communications*, Artech House, Norwood, MA, 1996.
40. T. Ohgane, Y. Ogawa, and K. Itoh, A study on a channel allocation scheme with an adaptive array in SDMA, *Proc. IEEE 47th Vehicular Technology Conf.*, May 1997, Vol. 2, pp. 725–729.
41. G. V. Tsoulos, J. McGeehan, and M. Beach, Space division multiple access (SDMA) field trials. Part 1: Tracking and BER performance, *IEEE Proc. Radar Sonar Nav.* **145**(1):73–78 (Feb. 1998).
42. C. Sun and N. C. Karmakar, Null-forming SDMA scheme based on channel responses correlation coefficient, *Proc. IEEE Antennas and Propagation Society Int. Symp.*, June 2003, Vol. 1, pp. 85–88.
43. C. Sun and N. C. Karmakar, Duplicate channel allocation of null-forming based SDMA in the presence of antenna array mutual coupling, *Proc. IEEE 4th Int. Conf. Information, Communication and Signal Processing*, Singapore, Dec. 2003, Vol. 2, pp. 1096–1100.
44. DBF1108 Digital Beamforming Device 0361.82.01.92, ERA Technology Ltd., Leatherhead, Surrey, UK.
45. S. Makino and N. Miyahara, Satellite onboard reflector antennas, *IEICE Trans. Commun.* **E86-B**(3):944–953 (March 2003).
46. C. K. Toh, *Wireless ATM and Ad-Hoc Networks*, Kluwer Academic Publishers, 1997.
47. A. Nasipuri, S. Ye, J. You, and R. E. Hiromoto, A MAC protocol for mobile ad hoc networks using directional antennas, *Proc. IEEE Wireless Communications and Networking Conf.*, Sept. 2000, Vol. 3, pp. 1214–1219.
48. Y. Ko, V. Shankarkumar, and N. H. Vaidya, Medium access control protocols using directional antennas in ad hoc networks, *Proc. 19th Annual Joint Conf. IEEE Computer and Communications Societies*, March 2000, Vol. 1, pp. 13–21.
49. C. K. Toh, *Ad Hoc Mobile Wireless Networks: Protocols and Systems*, Prentice-Hall, Upper Saddle River, NJ, 2001.
50. R. Ramanathan and J. Redi, A brief overview of ad hoc networks: Challenges and directions, *IEEE Commun. Mag.* **40**(5):20–22 (May 2002).
51. K. J. Krizman, T. E. Biedka, and T. S. Rappaport, Wireless position location: fundamentals, implementation strategies, and sources of error, *Proc. IEEE 47th Vehicular Technology Conf.*, May 1997, Vol. 2, pp. 919–923.
52. A. J. Paulraj, D. A. Gore, R. U. Nabar, and H. Bolcskei, An overview of MIMO communications—a key to gigabit wireless, *Proc. IEEE* **92**(2):198–218 (Feb. 2004).
53. A. F. Naguib, N. Seshadri, and A. R. Calderbank, Increasing data rate over wireless channels, *IEEE Signal Process. Mag.* **17**(3):76–92 (May 2000).
54. R. T. Derryberry, S. D. Gray, D. M. Ionescu, G. Mandyam, and B. Raghothaman, Transmit diversity in 3G CDMA systems, *IEEE Commun. Mag.* **40**(4):68–75 (April 2002).
55. R. D. Murch and K. B. Letaief, Antenna systems for broadband wireless access, *IEEE Trans. Inform. Theory* **40**(4):76–83 (April 2002).
56. D. Gesbert, L. Haumont, H. Bolcskei, R. Krishnamoorthy, and A. J. Paulraj, Technologies and performance for non-line-of-sight broadband wireless access networks, *IEEE Commun. Mag.* **40**(4):86–95 (April 2002).
57. D. Avidor, D. Furman, J. Ling, and C. Papadias, On the financial impact of capacity-enhancing technologies to wireless operators, *IEEE Wireless Commun. Mag.* **10**(4):62–65 (Aug. 2003).
58. S. D. Blostein and H. Leib, Multiple antenna systems: Their role and impact in future wireless access, *IEEE Commun. Mag.* **41**(7):94–101 (2003).

59. S. N. Diggavi, N. Al-Dhahir, A. Stamoulis, and A. R. Calderbank, Great expectations: The value of spatial diversity in wireless networks, *IEEE Proc.* **92**(2):219–270 (Feb. 2004).
60. J. Salz, Digital transmission over cross-coupled linear channels, *AT&T Tech. J.* **64**(6):1147–1159 (1985).
61. G. J. Foschini and M. J. Gans, On limits of wireless communications in fading environment when using multiple antennas, *Wireless Pers. Commun.* **6**(3):311–335 (March 1998).
62. E. Telatar, Capacity of multi-antenna Gaussian channels, *Eur. Trans. Telecommun.* **10**(6):589–595 (Nov. 1999).
63. R. Janaswamy, *Radiowave Propagation and Smart Antennas for Wireless Communications*, Kluwer, Amsterdam, 2001.
64. M. A. Khalighi, K. Raof, and G. Jourdain, Capacity of wireless communication systems employing antenna arrays, a tutorial study, *Wireless Pers. Commun.* **23**(3):321–352 (Dec. 2002).
65. D. Gesbert, M. Shafi, D. Shiu, P. J. Smith, and A. Naguib, From theory to practice: An overview of MIMO space-time coded wireless systems, *IEEE J. Select. Areas Commun.* **21**(3):281–302 (April 2003).
66. G. J. Foschini, Layered space-time architecture for wireless communication in a fading environment when using multi-element antennas, *Bell Labs Tech. J.* **2**(1):41–59 (1996).
67. G. J. Foschini, G. D. Golden, R. A. Valenzuela, and P. W. Wolniansky, Simplified processing for high spectral efficiency wireless communication employing multi-element arrays, *IEEE J. Select. Areas Commun.* **17**(11):1841–1852 (Nov. 1999).
68. P. W. Wolniansky, G. J. Foschini, G. D. Golden, and R. A. Valenzuela, V-BLAST: An architecture for realizing very high data rates over the rich-scattering wireless channel, *Proc. URSI Int. Symp. Signals, Systems, and Electronics*, 1998, pp. 295–300.
69. G. D. Golden, C. J. Foschini, R. A. Valenzuela, and P. W. Wolniansky, Detection algorithm and initial laboratory results using V-BLAST space-time communication architecture, *Electron. Lett.* **35**(1):14–16 (Jan. 1999).
70. L. C. Godara, Applications of antenna arrays to mobile communications, part I: Performance improvement, feasibility, and system considerations, *IEEE Proc.* **85**(7):1029–1030 (1997).
71. B. Pattan, *Robust Modulation Methods & Smart Antennas in Wireless Communications*, Prentice-Hall PTR, Upper Saddle River, NJ, 2000.
72. S. Bello Fiore, C. A. Balanis, J. Foutz, and A. S. Spanias, Smart-antenna systems for mobile communication networks. Part 1. Overview and antenna design, *IEEE Anten. Propag. Mag.* **44**(3):145–154 (2002).
73. J. P. Shelton and K. S. Kelleher, Multiple beams from linear arrays, *IEEE Trans. Anten. Propag.* **9**(2):154–161 (March 1961).
74. H. Novak, *Switched Beam Adaptive Antenna System*, Ph.D. dissertation, Technische Univ. Wien, Vienna, Austria, Nov. 1999.
75. N. C. Karmakar, *Antennas for Mobile Satellite Communications*, Ph.D. dissertation, Univ. Queensland, Australia, Aug. 1998.
76. N. C. Karmakar and M. E. Bialkowaski, A compact switched-beam array antenna for mobile satellite communications, *Microwave Optical Technol. Lett.* **21**(3):186–191 (May 1999).
77. N. C. Karmakar and M. E. Bialkowaski, A beam-forming network for a circular switched-beam phased array antenna, *IEEE Microwave Wireless Compon. Lett.* **11**(1):186–191 (Jan. 2001).
78. Y. Konishi, Phased array antennas, *IEICE Trans. Commun.* **E86-B**(3):954–867 (March 2003).
79. S. Takatsu, H. Aruga, T. Sakura, H. Nakaguro, A. Akaishi, N. Kadowaki, and T. Araki, Development results of Ka-band multibeam active phased array antenna for Gigabit Satellite, *Proc. Int. Symp. Antennas and Propagation*, Fukuka, Aug. 2003, Vol. 1, pp. 177–180.
80. M. E. Bialkowski and N. C. Karmakar, A two-ring circular phased array antenna for mobile satellite communications, *IEEE Trans. Anten. Propag.* **41**(3):14–23 (June 1999).
81. R. A. Hansen, *Phased Array Antennas*, Wiley, 1998.
82. T. Ohira, Adaptive array antenna beamforming architectures as viewed by a microwave circuit designer, *Proc. IEEE Asia-Pacific Microwave Conf.* Sydney, Australia, Dec. 2000, pp. 828–833.
83. Y. Ogawa and T. Ohgane, Advances in adaptive antenna technologies in Japan, *IEICE Trans. Commun.* **E84-B**(7):1704–1712 (2001).
84. R. A. Soni, R. M. Buehrer, and R. D. Benning, Intelligent antenna system for cdma2000, *IEEE Signal Process. Mag.* **19**(4):54–67 (2002).
85. B. Widrow, P. E. Mantey, L. J. Griffiths, and B. B. Goode, Adaptive antenna systems, *IEEE Trans. Anten. Propag.* **55**(12):2143–2159 (Dec. 1967).
86. B. D. V. Veen and K. M. Buckley, Beamforming: A versatile approach to spatial filtering, *IEEE ASSP Mag.* **5**(2):4–24 (April 1988).
87. L. C. Godara, Application of antenna arrays to mobile communications, part II: Beam-forming and direction-of-arrival considerations, *IEEE Proc.* **85**(8):1195–1245 (Aug. 1997).
88. S. Anderson, B. Hagerman, H. Dam, U. Forssen, J. Karlsson, F. Kronstedt, S. Mazur, and K. J. Molnar, Adaptive antennas for GSM and TMP systems, *IEEE Pers. Commun. Mag.* **6**(3):74–86 (1999).
89. S. Bellofiore, J. Foutz, C. A. Balanis, and A. S. Spanias, Smart-antenna systems for mobile communication networks. Part 2. Beamforming and network throughput, *IEEE Anten. Propag. Mag.* **44**(4):106–114 (Aug. 2002).
90. C. Sun, A. Hirata, T. Ohira, and N. C. Karmakar, Fast beamforming of electronically steerable parasitic array radiator antennas: Theory and experiment, *IEEE Trans. Anten. Propag.* **52**(7):1819–1832 (2004).
91. L. Himmel, S. H. Dodington, and E. G. Parker, *Electronically Controlled Antenna System*, U.S. Patent 3,560,978 (Feb. 2, 1978).
92. S. H. Black and R. B. Formeister, *Direction Finding System*, U.S. Patent 3,725,938 (April 3, 1973).
93. M. Gueguen, *Electronically Step-by-Step Rotated Directive Radiation Beam Antenna*, U.S. Patent 3,856,799 (Nov. 5, 1974).
94. R. F. Harrington, Reactively controlled directive arrays, *IEEE Trans. Anten. Propag.* **AP-26**(3):390–395 (May 1978).
95. R. Dinger, Reactively steered adaptive array using microstrip patch elements at 4 GHz, *IEEE Trans. Anten. Propag.* **32**(8):848–856 (Aug. 1984).
96. R. Milne, A small adaptive array antenna for mobile communications, *Proc. Antennas and Propagation Society Int. Symp.*, June 1985, Vol. 23, pp. 797–800.
97. D. V. Thiel, S. O’Keefe, and J. W. Lu, Electronic beam steering in wire and patch antenna systems using switched

- parasitic elements, *Proc. IEEE Antennas and Propagation Society Int. Symp.*, 1996, Vol. 1, pp. 21–26.
98. A. Sibille, C. Roblin, and G. Poncelet, Circular switched monopole arrays for beam steering wireless communications, *IEEE Electron. Lett.* **33**(7):551–552 (March 1997).
 99. S. L. Preston, D. V. Thiel, J. W. Lu, S. G. O’Keefe, and T. S. Bird, Electronic beam steering using switched parasitic patch elements, *Electron. Lett.* **33**(1):7–8 (Jan. 1997).
 100. S. L. Preston, D. V. Thiel, T. A. Smith, S. G. O’Keefe, and J. W. Lu, Base-station tracking in mobile communications using a switched parasitic antenna array, *IEEE Trans. Anten. Propag.* **46**(6):841–844 (1998).
 101. S. L. Preston, D. V. Thiel, and J. W. Lu, A multibeam antenna using switched parasitic and switched active elements for space-division multiple access applications, *IEICE Trans. Electron.* **E82-C**(7):1202–1210 (1999).
 102. R. Vaughan, Switched parasitic elements for antenna diversity, *IEEE Trans. Anten. Propag.* **47**(2):399–405 (Feb. 1999).
 103. T. Svantesson and M. Wennstrom, High-resolution direction finding using a switched parasitic antenna, *Proc. IEEE 11th Signal Processing Workshop*, Aug. 2001, pp. 508–511.
 104. T. Ohira and K. Gyoda, Electronically steerable passive array radiator antennas for low-cost analog adaptive beamforming, *Proc. IEEE Conf. Phased Array Systems and Technology*, May 2000, pp. 101–104.
 105. D. Thiel and S. Smith, *Switched Parasitic Antennas for Cellular Communications*, Artech House, Norwood, MA, 2001.
 106. C. Sun and N. C. Karmakar, A DOA estimation technique based on a single-port smart antenna for position location services, *Proc. Asia-Pacific Microwave Conf.*, Kyoto, Japan, Nov. 2002, Vol. 1, pp. 196–199.
 107. P. K. Varlamos and C. N. Capsalis, Direction-of-arrival estimation (DoA) using switched parasitic planar arrays and the method of genetic algorithms, *Wireless Pers. Commun.* **28**(1):59–75 (Jan. 2004).
 108. C. A. Balanis, *Antenna Theory: Analysis and Design*, 2nd ed., Wiley, 1997.
 109. S. Leonov and A. Leonov, *Handbook of Computer Simulation in Radio Engineering, Communications, and Radar*, Artech House, Norwood, MA, 2001.
 110. T. Ohira and K. Gyoda, Hand-held microwave direction-of-arrival finder based on varactor-tuned analog aerial beamforming, *Proc. IEEE Asia-Pacific Microwave Conf.*, Taipei, Taiwan, ROC, Dec. 2001, pp. 585–588.
 111. C. Sun, A. Hirata, T. Ohira, and N. C. Karmakar, Experimental study of a fast beamforming algorithm for ESPAR antennas, *Proc. European Conf. Wireless Technologies*, Munich, Oct. 2003, pp. 241–244.
 112. C. Sun, A. Hirata, T. Ohira, H. Yamada, and N. C. Karmakar, A novel antenna array calibration with a linear space error correction, *Proc. European Conf. Wireless Technologies*, Munich, Oct. 2003, pp. 301–304.
 113. (Online), <http://www.qsl.net/wb6tpu/swindex.html>.
 114. R. Jana and S. Dey, 3G wireless capacity optimization for widely spaced antenna arrays, *IEEE Pers. Commun. Mag.* **7**(6):32–35 (Dec. 2000).
 115. J. S. Colburn, Y. Rahmat-Samii, M. A. Jensen, and G. J. Pottie, Evaluation of personal communications dual-antenna handset diversity performance, *IEEE Trans. Vehic. Technol.* **47**(3):737–746 (Aug. 1998).
 116. C. B. Dietrich, Jr., K. Dietze, J. R. Nealy, and W. L. Stutzman, Spatial, polarization, and pattern diversity for wireless handheld terminals, *IEEE Trans. Anten. Propag.* **49**(9):1271–1281 (2001).

ALTIMETERS

HALIT EREN
Curtin University of Technology
Bentley, Australia

1. INTRODUCTION

Altitude, for the purposes of this article, is the elevation of an object above a given level. (In astronomy, navigation, and surveying, altitude means the angular height of a celestial body above the plane of the horizon.) *Altimeters* are instruments that measure altitude. Altimeters represent an advanced technology, finding diverse commercial and military applications ranging from air transport to space exploration. Many companies (Table 1) offer a wide range of altimeters and altimeter-related products.

There are three main types of altimeter:

1. The pressure altimeter, which uses changes in the atmospheric pressure to infer altitudes.
2. The radio detection and ranging (or *radar*) altimeter, which measures the time required for a continuous wave (CW) or pulse of radio energy to travel from an object in the atmosphere to the ground and back.
3. The optical altimeter, based on laser optics, operating mainly on pulsed energy transmission, as in the case of laser radar (LIDAR).

Altimeters are usually associated with aircraft, but they are also used in applications such as geodesy and surveying, navigation weapon guidance systems, parachute jumping, and mountaineering. The accuracy and the sophistication of the sensors and the associated electronics and computing power of altimeters depend on the measurement requirements. For example, in remote sensing applications, the selection of the sensors depends on the platform of the operation, as illustrated in Fig. 1.

Altimeters can be divided into two categories:

1. Instruments that measure the altitude of an object above a fixed Earth reference level (e.g., sea level).
2. Instruments that measure the distance between an object and some earth reference.

Instruments in the first category are of the barometric types that use the static air pressure at some altitude to infer height above a reference level. The second category is much broader and is based on the use of electromagnetic waves to determine altitudes. Some devices in this category are radar altimeters, laser altimeters, and the Global Positioning System (GPS).

2. BAROMETRIC ALTIMETERS

Barometric altimeters are based on the measurement of pressure, which varies depending on the atmospheric layers. Atmosphere of the Earth may be divided into several layers: troposphere (0–16 km from sea level),

Table 1. List of Manufacturers and Suppliers

Aeronautical Instrument & Radio Co. 234 Garibaldi Avenue Lodi, NJ 07644 Tel: 973-473-0034 Fax: 973-473-8748	Garmin International, Inc. 1200-T E, 151st St. Olathe, KS 66062 Tel: 913-397-8200 Fax: 913-397-8282	Pathfinder Instruments 2075 Corte Del Nogal, Suite X Carlsbad, CA 92009 Tel: 800-284-9698 Fax: 760-438-3953
Aerospace Industries, Inc. 333 N, Broadway, Suite 3011-T Jericho, NY 11753 Tel: 888-200-2681 Fax: 516-932-3307	GEC-Marconi Hazeltine Corp. 164-T Totowa Road, P.O. Box 975 Wayne, NJ 07474-0975 Tel: 973-633-6000 Fax: 973-633-6431	PLX, Inc. 40-T W, Jefryn Blvd. Deer Park, NY 11729 Tel: 800-586-4190 Fax: 516-586-4196
A. I. R., Inc. 8401 Baseline Road Boulder, CO 80303 Tel: 303-499-1701 Fax: 303-499-1767	Honeywell Inc. P.O. Box 524 Minneapolis, MN 55440 Tel: 612-951-1000 Fax: 612-951-2294	Rockwell, Collins Commercial Avionic 400-T Collins Road N.E. Cedar Rapids, IA 52498 Tel: 319-295-4085 Fax: 319-295-4777
Allen Osborne Associates, Inc. 756-T Lakefield Rd., Bldg, J Westlake Village, CA 91361 Tel: 805-495-8420 Fax: 805-373-6067	Jewell Electrical Instruments 124 Joliette Street Manchester, NH 03102 Tel: 603-669-6400 Fax: 603-669-5962	Shelby Jones Co., Inc. 8800 West Chester Pike Upper Darby, PA 19082 2619 Tel: 800-377-6060 Fax: 610-449-7010
AlliedSignal Inc. 101 Columbia Rd., Customer Operations Morristown, NJ 07962 Tel: 800-707-4555 Fax: 602-365-3348	Landis & Staefa, Inc. 1000 Deerfield Pkwy Buffalo Grove, IL 60089 Tel: 847-215-1050 Fax: 847-215-9026	Scientific Sales, Inc. P.O. Box 6725-T Lawrenceville, NJ 08648 Tel: 800-788-5666 Fax: 609-844-0466
American Paulin System 1455-T Rocky Knolls Road Cottonwood, AZ 86326 Tel: 520-634-0980	Laser Technology, Inc. 7070 S. Tucson Way, Dept. T Englewood, CO 80112 Tel: 800-873-8916 Fax: 303-649-9710	Terra Tech, Inc. P.O. Box 5547 Eugene, OR 97405 0547 Tel: 541-345-0597
Atmospheric Instruments Research Inc. 8401 Baseline Rd., Dept. T Boulder, CO 80303 Tel: 303-499-1701, Ext. 300 Fax: 303-499-1767	Leica, Herbrugg CH; 9435 Herbrugg Switzerland Tel: 41 (71) 70 33 84 Fax: 41 (71) 70 39 99	UMA, Inc. 260 Main St. Dayton, VA 22821 Tel: 703-879-2040 Fax: 703-879-2738
Azimuth Corp. 13-T Park Drive Westford, MA 01886 3511 Tel: 978-692-8500 Fax: 978-629-8510	Magellan Corp. 960 Overland Court San Dimas, CA 91773 Tel: 909-394-5000 Fax: 909-394-7050	Watrous & Co., Inc. Griffing Street, P.O. Box 996 Cutchogue, NY 11935 0996 Tel: 516-734-5504 Fax: 516-734-7931
COSCO, Inc. 95 N, Lincoln St. Denver, CO 80203 Tel: 800-372-6726 Fax: 303-777-3331	Optech Inc. 100 Wildcat Road North York, ON M3J3H4 Canada Tel: 416-661-5904 Fax: 416-661-4168	

stratosphere (16–50 km), mesosphere (50–80 km), thermosphere (80–640 km), and exosphere (outer space). To determine the altitude of an object, the atmospheric pressure is compared with a reference pressure by a mechanism such as shown in Fig. 2. Over the years, many different mechanisms have been developed for barometric

altitude measurements. However, they all rely on the use of a relation between air pressure and altitude.

In most modern barometric altimeters, integrated circuit (IC) pressure transducers are used, as shown in Fig. 3. A wide variety of pressure transducers are available with different specifications that are suitable

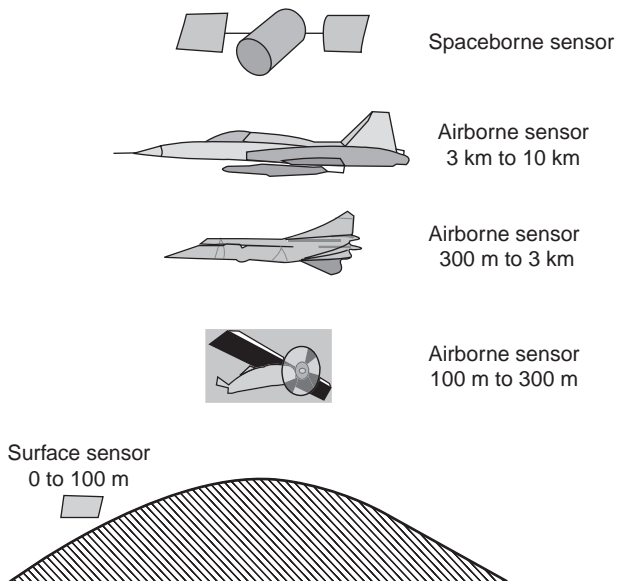


Figure 1. Use of altimeters at various altitudes. Altimeters are designed to operate accurately at certain ranges. Developed in recent (as of 2003) years, the altimeters carried by the geostationary satellites offer very high accuracy.

for a large range of barometric altimeter applications. The performance of pressure transducers depends on the characteristics of the atmospheric pressure.

2.1. Principles of Operation and the Effect of Atmospheric Pressure

Certain assumptions are made to allow the altitude–pressure relationship to be simplified so that the altitude above sea level at any point in Earth’s atmosphere can be related to air pressure by a single-valued function. The assumptions are often referred to as a *standard atmosphere* and are primarily concerned with the atmospheric conditions at sea level, chemical composition of the atmosphere, and atmospheric temperature distribution. These assumptions are based on a mixture of observations, measurements, and theories that are internationally accepted.

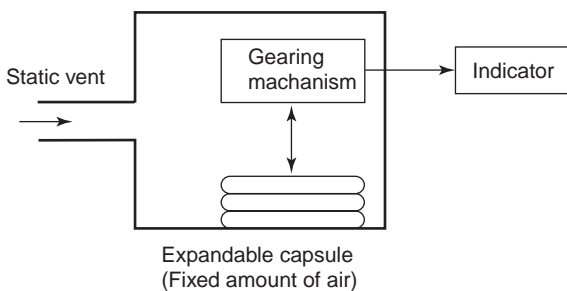


Figure 2. A typical barometric altimeter. In this type a constant volume of air is trapped in the bellows. Depending on the air pressure in the chamber, the bellows changes its volume. The change in volume is scaled by a gearing mechanism connected to an analog indicator.

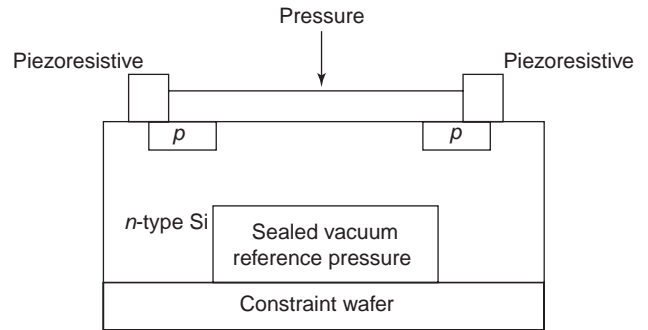


Figure 3. A barometric altimeter based on piezoresistive integrated circuit. The characteristics of silicon allow construction of a thin diaphragm that can be deflected by an applied pressure, thus resulting in changes in resistance of the piezoresistive elements located on the diaphragm. The signal-processing and voltage regulation circuits are also integrated in the IC chip.

The concept of the standard atmosphere has a threefold purpose: (1) it sets a reference for testing, design, and performance comparisons between instruments and the body carrying the altimeter, such as an aircraft, a balloon, or a parachute jumper; (2) it allows the derivation of the pressure–altitude relationship to be simplified both mathematically and physically within the altimeter; and (3) finally, if all objects with altitude-measuring devices are set to the same reference, the vertical separation between these objects when they are in common airspace can be reliably inferred and safety can be increased. The International Standard Atmosphere (ISA) assumptions are summarized as follows:

1. The temperature at sea level T_0 and the pressure at sea level P_{s0} are assumed to be constant at $T_0 = 288.15$ K and $P_{s0} = 101,325$ Pa (1013.25 mbar, 29.92 in.Hg).
2. The temperature decreases linearly with increasing height until a height known as the *tropopause* is reached, above which the temperature remains constant until the *stratopause* height is reached. The region below the tropopause is known as the *troposphere*. The law relating temperature T to altitude H to the tropopause height is given by

$$T = T_0 - LH \tag{1}$$

where L is the temperature decrease rate and is defined to be -6.5×10^{-3} K/m. At and above the tropopause (11,000 m), T remains constant at $T = T_T = 216.65$ K (-56.5°C).

3. The stratopause is defined to occur at 20,000 m. The region between the tropopause and the stratopause is known as the *stratosphere*.
4. At heights above the stratopause the temperature starts to increase linearly with height; this region is known as the *chemosphere* (top of the stratosphere, all of the mesosphere, and lower part of the thermosphere). The temperature increase rate is defined to be 1.0×10^{-3} K/m. The chemosphere is defined to have a height limit of 32,004 m. The temperature in

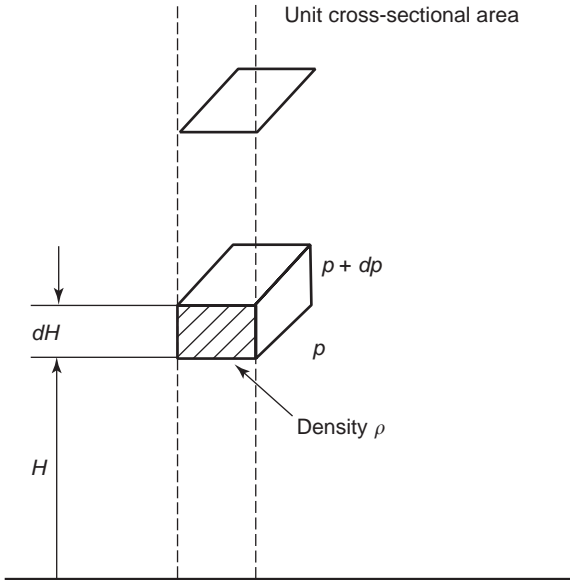


Figure 4. Change in the atmospheric pressure due to air density. These changes in the air pressure can be related to altitude by using the gas laws.

the chemosphere is given by

$$T = T_T + L(H - H_S) \tag{2}$$

where H_S is the height of the stratopause.

Using these assumptions, the altitude–static pressure relationship can now be derived by considering Fig. 4. A small change in pressure dp of air with density ρ , due to a small change in height dH , can be found by equating the forces acting in the vertical plane on an elemental volume of air, so that

$$-dp = \rho g dH \tag{3}$$

where g is the gravitational acceleration. From the ideal gas law

$$p = \rho R_a T \tag{4}$$

where T is the air temperature (in Kelvins) and R_a is the gas constant for a unit mass of dry air.

Combining Eqs. (1) and (2) through the variable ρ results in the following equation:

$$\frac{-dp}{p} = \frac{g}{R_a T} dH \tag{5}$$

The value of g , the gravitational acceleration, is known to decrease with increasing distance from the center of Earth. The equation governing this is

$$g = \frac{R^2}{(R + H)^2} g_0 \tag{6}$$

where R is the radius of Earth and g_0 is the gravitational acceleration at Earth’s surface, where its value is approximately equal to 9.807 m/s^2 . This degradation of g ,

however, can be assumed to be insignificant in the evaluation of the pressure altitude. This additional assumption further simplifies the derivation.

The assumptions stated imply that the relation between the pressure altitude and the static pressure must be derived separately in three regions, namely the troposphere, the stratosphere, and the chemosphere. First, considering the troposphere, by substitution of Eq. (1) into Eq. (5), and integrating both sides to eliminate the dp and dH , we obtain

$$-\int_{P_{s0}}^{P_s} \frac{1}{p} dp = \frac{g_0}{R_a} \int_0^H \frac{1}{T_0 - LH} dH \tag{7a}$$

where P_{s0} is the pressure at height $H = 0$ and P_s is the pressure at height H . Using the integration rule $(1/u)du = \ln|u| + c$ and the equality $\ln A - \ln B = \ln(A/B)$, we have

$$\ln \frac{P_s}{P_{s0}} = \frac{g_0}{R_a L} \ln \frac{T_0 - LH}{T_0} \tag{7b}$$

Solving for P_s gives

$$P_s = P_{s0} \left(1 - \frac{L}{T_0} H\right)^{g_0/LR_a} \tag{8}$$

Similarly, for the two other regions of concern, their appropriate temperature equations, $T = T_T$ and Eq. (2) can be substituted into Eq. (5) and integrated.

Considering the constants implied in the ISA and additionally noting that $R_a = 287.053 \text{ J/(K} \cdot \text{kg)}$, the following equations are found to relate the static pressure to the pressure altitude H_p

1. Troposphere (– 914.4 to 11,000 m):

$$P_s = 1013.25(1 - 2.25577 \times 10^{-5} H_p)^{5.255879} \text{ mbar} \tag{9}$$

2. Stratosphere (11,000 m to 20,000 m):

$$P_s = 226.32e^{0.0001576885(H_p - 11,000)} \text{ mbar} \tag{10}$$

3. Chemosphere (20,000–32,004 m):

$$P_s = 54.7482[1 + 4.61574 \times 10^{-6}(H_p - 20,000)]^{-34.163215} \text{ mbar} \tag{11}$$

It can be seen that these relationships are nonlinear. The nonlinearity can be observed graphically by plotting altitude on the horizontal axis against pressure as shown in Fig. 5.

2.2. Construction, Errors, and Use of Barometric Altimeters

A barometric altimeter must be able to display altitude linearly; therefore, a linearization, such as the gain adjustment, is necessary. The linearization is usually done by a calibratable mechanism to allow for variations in aneroid chambers. This mechanism introduces a gain that counters the nonlinear effects of pressure versus height, by means of nonlinear compression/expansion of the aneroid chamber. Gearing is also introduced, so that one

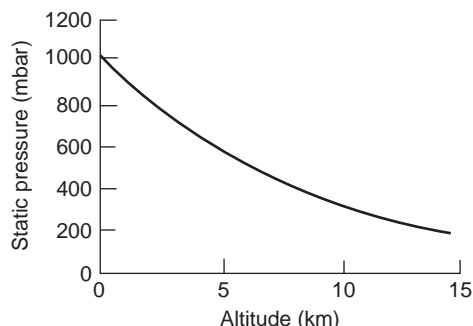


Figure 5. Static pressure versus pressure altitude. The pressure changes in a nonlinear manner. Linearization techniques must be employed to measure and display altitudes by barometric methods.

revolution of the altimeter pointer is equivalent to a 330 m height displacement.

The linearizing part of the mechanism of an aneroid barometric altimeter is usually located at the center of the altimeter body. The temperature compensation is realized via a bimetallic strip, which alters its curvature as temperature increases. These features are necessary to compensate for the changes in the modulus of elasticity of the material that the aneroid chamber is made from. For example, if the sea-level temperature of an aneroid chamber were to decrease, its elasticity would increase. Since the chamber has a vacuum, it is in natural shape when fully expanded (i.e., at very low atmospheric pressure). If the chamber material becomes more elastic, it tries to resume its original shape. This results in the display of a height greater than the actual height. Since the atmospheric pressure decreases as the chamber is moved away from sea level, the extra height effect of the elasticity of the chamber increases as the altitude increases.

The static pressure port is placed on the backplate of the altimeter for use in a small aircraft. In modern aircraft this port is connected to a line that is in turn connected to either a pitot tube or a static vent. The pitot tube is often seen as a small probe-like object pointed forward and located at the front of the aircraft to measure the airspeed. In altitude measurements, it fulfills the function of supplying a static pressure that is independent of the velocity of the aircraft.

It is important to note that pitot tubes can introduce errors into altitude measurements. The tubes are mechanically designed to introduce minimum errors and also are positioned on the aircraft so that the attitude does not affect the airflow onto the tube. A badly designed or positioned pitot tube can cause shockwaves to occur at high air velocities and also cause extra air to be forced into the static measurement holes, thus increasing the pressure.

In an effort to attempt to alleviate some of the problems caused by pitot tubes, the use of static vents has become common in modern aviation. They are designed to be mounted flush on the fuselage of an aircraft. In particular, these vents find extensive use in military applications where the removal of the probe-like pitot tube has improved stealth capabilities.

One problem common to all types of static-pressure-driven instruments is ice formation and water buildup inside the tubes or vents. To prevent ice formation, these tubes and vents contain heating elements. Where there is ice, there can be water. Variations in pressure and temperature can cause water to condense in tubes and ports. In the interests of instrument functionality and minimization of errors, there must be provisions to check static lines for water and remove it.

A typical modern barometric altimeter is approximately 35×30 mm and has a liquid crystal display (LCD). It can also function as a barometer and can be set for the minimum and maximum altitudes, the absolute altitude, the speed of ascent and descent, the reduced and absolute air pressures, the weather forecast, and time and altitude alarms. Typically, the range of measurement of the barometric altimeter is -700 to $10,000$ m, and it updates information once every second. It has a pressure range from 600 to 1100 mbar with $\pm 0.5\%$ accuracy and 0.1 mbar resolution. The altitude resolution is about 0.1 m. Altimeters with high precision find applications in geosciences, surveying, aviation, meteorology, recreation, and the laboratory.

2.3. Further Comments on Application of Barometric Altimeters in Aircraft

Barometric altimeters find extensive use in most modern aircraft as backup instruments. These altimeters are composed mechanically of sector gears, pinion, backlash springs, crankshafts, aneroid capsules, and pointers on a dial. A series of pointers on a graduated dial may be used to indicate altitude in hundreds, thousands, or tens of thousands of feet or meters. The barometric dial records the air pressure in millibars. Because atmospheric pressure is measured relative to sea level, the pressure altimeter must be manually adjusted in order to compensate for variations in pressure caused by weather changes.

In aircraft, the barometric altimeters can be set to show either altitude above sea level or altitude above an airfield once the height of the airfield above the sea level is known. If the pilot wishes to adjust the altimeter to display the height above sea level, the corrected sea-level pressure needs to be entered. When the corrected sea-level pressure is compared with the pressure at the airfield, the height of the airfield from sea level can be found. The sea-level pressure at that particular time must be known, however, because it may differ from the ISA assumption, indicating that the height of the airfield is higher or lower than what it actually is. Airfields continuously broadcast updated information on the pressure so that the pilot may correct the altimeter. The correct setting is called QNH, the adjusted sea-level pressure.

On the other hand, a pilot may wish to set the altimeter so that it displays the altitude above a particular airfield. To do this the pressure height of the airfield needs to be entered into the altimeter. Such pressures are denoted QFE and are given relative to the sea-level pressure. For example, an airfield 304.8 m above sea level, on a day when the sea-level pressure is as per ISA (1013.25 mbar), has a QFE of 977.4 mbar. This value is calculated from

Eq. (9). In summary, the barometric pressure knob is used to correct any variation in the sea-level pressure from the ISA assumed value of 1013.25 mbar.

Recalling the ISA assumptions, the temperature variations and airspeed effects are ignored. However, these effects can be taken into account by the application of computers and suitable analog-to-digital converters (ADCs) to the real-time signals generated by the instruments. The computers use complex models to take into account many variables affecting the altitude measurements. This means that the computer-driven altitude display can be corrected in real time, so that the pilot has a very accurate altitude reading at all times.

Altimeters are prone to the following errors: (1) instrument errors due to manufacture, installation, maintenance, and so on; (2) instrument lag; and (3) position error due to placement of vents and blockage of the static vents by ice. In response, the availability of computers has prompted the development of advanced pressure-measuring devices, such as the vibrating pressure sensor and the solid-state capsule pressure sensor.

As illustrated in Fig. 6, vibrating sensors work on the principles of detecting change in the natural resonant frequency of a vibrating system within a cylinder as the air pressure changes. This means that the electrical output of this sensor, when amplified, will be a frequency that changes proportionally with the pressure it is exposed to. Modern ADCs can detect very small differences in output frequency due to density variations as well as the large frequency variations due to pressure changes. This type of setup, which is enclosed, is very rugged and is in wide use today in commercial aircraft.

The second type of sensor, the capsule type, typically uses a vacuum chamber. The difference between these and the older aneroid chambers is in the materials from which the diaphragm is constructed. Typical materials are silicon, quartz, or ceramic compounds. These newer diaphragm materials are chemically engineered to have perfect mechanical properties in that they are very linear, do not suffer from hysteresis, and have a very stable modulus of elasticity.

The capsule-type transducers rely on two main methods. The first method involves the impregnation of the

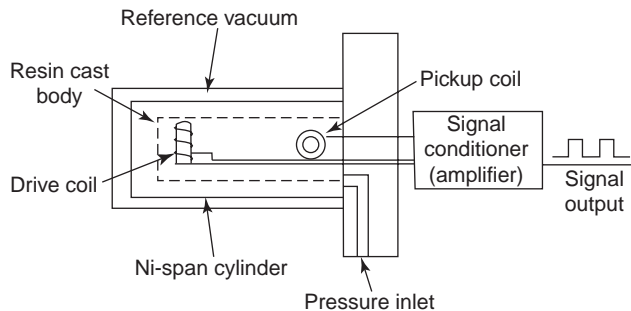


Figure 6. Vibrating sensor barometric altimeter. The natural frequency of the vibrating element depends on the air pressure inside a cylinder chamber. The signal of natural vibration is picked up and processed to obtain the pressure, and hence the altitude of the mechanism above sea level.

diaphragm with a Wheatstone bridge, thus allowing an excitation to be applied and a pressure-dependent voltage to appear at the output. This voltage varies with the change in resistance of the impregnated resistors as the diaphragm flexes due to pressure, similarly to a resistive strain gauge. The second method is to form an area of metallization on the bottom side of the diaphragm and the bottom of the vacuum chamber. This creates a capacitor, and these sensors are highly sensitive to small variations in its capacitance. However, temperature variations and accelerations can severely affect both these types of sensors. Thus the temperature is measured near the device and fed into the ADC for correction. For the acceleration effect, ensuring that the device is mounted so that its axis of movement is orthogonal to the acceleration is sufficient compensation. It should be noted that these devices are designed to be minimally sensitive to gravitational effects.

It can be concluded that barometric altimeters are likely to continue to be used extensively in the near future to measure altitudes of up to 15,000 m. Radar altimeters are expected to expand their role of providing accurate landing references, and low-altitude radar altimeters will continue to be used mainly for special-purpose military operations.

3. RADAR (RADIO) ALTIMETRY

Radar and laser altimeters, also termed *active ranging sensors*, are based on the transmission of electromagnetic or optical energy directed at an object and the detection of the reflected energy from the object. The reflected energy is suitably processed to reveal information about the altitude as well as other parameters such as the atmospheric conditions, including pollution. Radar altimeters can provide height information at high altitudes, where barometric systems are not effective. They can also provide high-quality images, as illustrated in Fig. 7.

Aviation radar altimeters, which have been in use for many years, measure height above the ground or sea. They transmit either continuous waves (CW) or pulsed waves and normally operate in the 4.2–4.4-GHz band to provide inputs to, for example, automatic landing systems or autostabilization systems for aircraft and helicopters. The basic operating principles of radio and radar altimeters are similar. The only difference is that the term *radio altimeter* often refers to continuously modulated waves, whereas the term *radar altimeter* refers to pulsed waves, mainly used in aircraft, spacecraft, and satellites.

3.1. Radar Altimeters Used in Satellites

The radar altimeter is a single-frequency radar system that broadcasts a pulsed tone directly downward, as illustrated in Fig. 8. It has highly sensitive devices for signal detection and processing. A satellite altimeter is a nadir-pointing active microwave sensor designed to measure characteristics of the surface of Earth. The time it takes for the reflected signal to be received directly is translated into the height above the terrain.

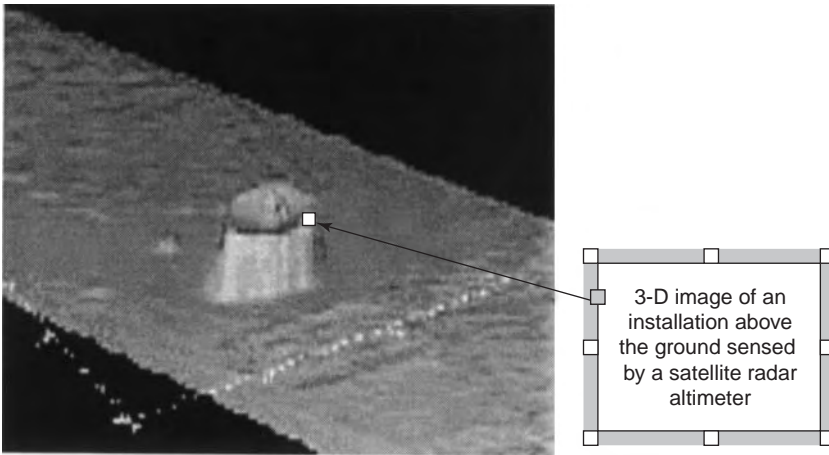


Figure 7. A typical example of remote sensing. Active remote sensors transmit electromagnetic energy and pick up the return signals. By appropriate data processing three-dimensional images can be constructed.

If a pulse is transmitted toward a target surface at an accurately measured time t_1 , it reflects back to the source after a time t_2 . The time difference $t_d = t_1 - t_2$ is equal to the round-trip distance to the reflecting surface divided by the propagation speed c :

$$t_d = \frac{2h}{c} \text{ or } h = \frac{ct_d}{2} \tag{12}$$

The accuracy of the measured distance h can be expressed by

$$\Delta h = \Delta c \frac{t_d}{2} + c \frac{\Delta t_d}{2} \tag{13}$$

Here, the time difference accuracy Δt_d depends mainly on the sharpness of the pulse, which is equal to

$$\Delta t = \frac{1}{B} \tag{14}$$

where B is the signal bandwidth.

If the speed of the pulse is taken to be constant, the range resolution can be found from

$$\Delta h = \frac{c}{2B} \tag{15}$$

Higher accuracy is achieved by detailed analysis of the received signal; this is achieved by averaging a large number

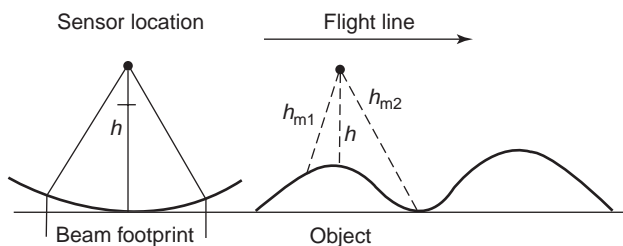


Figure 8. Geometry of a pulse-limited radar altimeter. The pulse intersects the nearest point on the ground, and the illuminated disk spreads rapidly. This gives a maximum size for the footprint. The geometry of the beam-limited altimeter is similar.

of echoes. Range errors can arise from pulse dispersion due to backscattering from the rough surface and to the propagation characteristics of the atmosphere. Consequently, the returned pulse is distorted and fading occurs, as illustrated in Fig. 9. The distortion in the waveform of the echo signal makes the altimeter signal less than perfect.

There are different types of radar altimeters, such as beam-limited altimeters, pulse-limited altimeters, synthetic aperture radar altimeters, imaging altimeters, and scanning altimeters. The operation principles of the altimeters are similar, but they vary in size of footprint, direction of the beam, and purpose of usage. The details in the differences of these altimeters are not given in this article, but interested readers can find further information in the references (e.g., Elachi [1]).

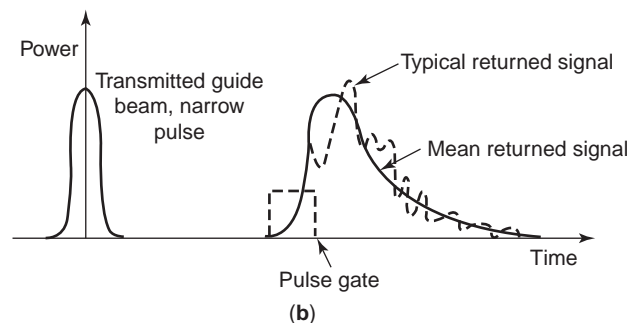
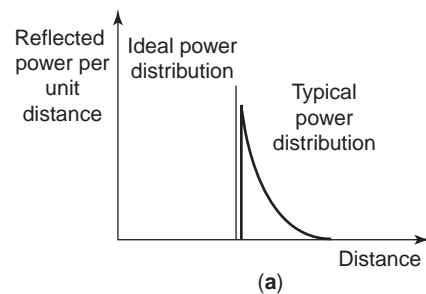


Figure 9. Waveforms of returned pulses: (a) ideal power distribution and typical power distribution of the returned signal—the distortion is due to imperfect mirroring of the signal back to the sensor; (b) pulse shape of wide-beam, narrow-pulse altimeter.

In most modern radar altimeters, high measurement accuracy is required. This necessitates good information on the effect of the ionosphere and atmosphere as well as sound understanding of the errors introduced by the sensor dynamics and signal-processing electronics. The signal-processing electronics comprises many components such as oscillators, modulators, mixers, power amplifiers, filters, demodulators, digitizers, compressors, and computers. All these devices have to be of good quality and highly accurate. Judicious selection of all the discrete components and circuits is necessary for good conformity and matching.

The first satellite altimeter was tested in 1973, as parts of several Skylab missions conducted by the United States. At that time, a typical resolution was 1–2 m; modern altimeters are capable of resolutions down to 2 cm (TOPEX/Poseidon). As an example, the discussion here focuses on one of the latest satellite altimeters, for the NASA TOPEX/Poseidon satellite used in oceanic applications.

The TOPEX/Poseidon mission, a joint mission between NASA and the Centre Nationale d'Etudes Spatiales (CNES), the French space agency, was designed to make high-precision measurements of the ocean surface possible. The application areas of this system are mainly for weather reports and predictions, in geodesy and geophysics. The TOPEX altimeter was the first dual-frequency satellite altimeter operating in space to perform these important measurements. The TOPEX used several methods for determining distance, such as the round-trip time discussed previously, and the shape of the reflected pulse. In particular, the shape of the reflected pulse provided a wealth of information on wave height in the ocean and the sea-surface windspeeds.

The TOPEX altimeter uses a 13.6-GHz signal as its primary pulse, and a secondary frequency of 5.3 GHz. The use of two frequencies is helpful in removing the adverse effects of variations in the propagation speed of the pulse due to variations in the atmospheric conditions of Earth.

NASA has built a self-calibration mechanism into the TOPEX altimeter. While over land, twice a day, the altimeter spends 5 min calibrating itself. The TOPEX is known to be extremely reliable and robust because of this self-calibration capability and its ability to compensate for ionospheric effects.

To obtain a high degree of precision, the satellite that carries TOPEX needs to know its exact position relative to points on Earth. The GPS helps the satellite determine its position with a precision of about 2 cm. A laser Doppler system and a ground station are also used to verify this reading. Another satellite system with importance for altitude measurements has been the Geosat follow-on meteorological-oceanographic (GFO METOC) satellite. It is owned by the U.S. Navy and is used for determining thermal fronts, eddies, ice edge locations, surface windspeeds, and wave heights.

The GFO and the GPS systems mentioned above are also used for position and altitude determinations, but their design is more elaborate than is needed for the accuracy of TOPEX. In these systems, an onboard water vapor detector is used to help correct ionospheric interference. Essentially,

the GFO was a test to determine whether a low-cost, light-weight, and compact satellite could be used to provide the U.S. Navy and its associated agencies with real-time ocean data. But the expectations for the GFO to replace TOPEX in a cost-effective manner have failed so far.

Spaceborne altimeters are primarily pulse-limited, and therefore they cannot deliver the required accuracy of surface height measurements over icy land. This is because the spreading and slope of the reflected pulse cause severe errors. In addition, during land height measurements, sudden changes in the slopes of the topography often result in a loss of tracking. Although techniques have been developed to improve the spatial resolution of radar altimeters for accurate elevation estimates over the terrain, most of them result in a significant increase in cost and complexity compared with a conventional altimeter.

In a typical noise-modulated radar altimeter, the principle of operation is based on the dependence of the cross-correlation function of the random modulation (Gaussian noise) on the finite correlator bandwidth, smoothing methods, extraneous noise disturbance, component characteristics, and changes in altitude during measurements.

3.2. Radio Altimeters

Like radar altimetry, radio altimetry is based on the use of electromagnetic (EM) waves to determine the distance between a reference point and an object that reflects the waves. Radio altimeters are used mostly in aircraft. Unlike radar altimetry, radio altimetry is based on continuous EM waves. Generally, it uses a frequency-modulated (FM) carrier, whose frequency is varied at a constant rate. The carrier reaches the surface below and reflects back to the transmitter with a delay. The reflection appears as a time-shifted version of the transmitted signal; thus the phase shift can be utilized. This time difference equates to a frequency difference, which can easily be detected using a superheterodyne receiver. Figure 10 illustrates the time difference in the transmitted and received signals. A typical radio altimeter operates at about 4.3 GHz. A low-frequency (100-Hz) triangular waveform modulates the carrier over a range of about ± 50 MHz.

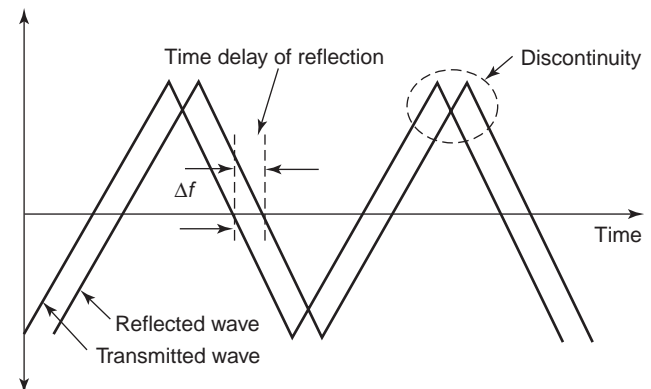


Figure 10. The transmitted and received waveforms of a radio altimeter. The time difference between the transmitted waveform and the reflected wave from the target is an indication of the distance between the two objects.

All radio and radar altimeters have three basic components: one or two antennas, a transmitter receiver, and an indicator. The type of antenna varies, depending on where it is fixed on the aircraft (on a flat or skewed area under the fuselage). Antennas are designed specifically for each system, so changing the unit also involves changing the antenna. The transmitter–receiver is the core of the device. The indicator consists of an electronic digital display or a common analog display.

As mentioned before, frequency differences can be measured using a superheterodyne receiver. In the signal-processing section, the received signal is multiplied with the transmitted signal on an instantaneous basis. In this way, according to the superheterodyne principle, a sum and a difference frequency are created. A lowpass filter is used to remove the component containing the sum of the frequencies, leaving only the difference, as required for further processing. The difference frequency can then be applied to a signal processor for digital display, or perhaps to a frequency-to-voltage converter allowing the altitude to be displayed in analog form. This technique allows the display of instantaneous altitudes as well as changes in altitude.

It is important to note that in the determination of altitudes by radar altimeters the speed of an EM wave in air is assumed to be constant: 3×10^8 m/s. Although this assumption may be valid in some situations, the presence of water vapor in the atmosphere can affect the speed and introduce serious errors in the measurements. Apart from this common shortcoming of radio altimeters, specific altimeters have their own. For example, a conventional FM counter radio altimeter has the following shortcomings: (1) the step error can be severe, (2) an upper measurable limit is introduced by the spurious beat, and (3) there is a tendency to overcount because of unwanted far-distance propagation. The step errors can be reduced by the *modulation synchronous phase-switching method*, using switching-type phase shifters placed at the transmitting (or receiving) antenna feeders. This results in an increase in the phase at every period of the frequency modulation. The upper limits and overcounting errors can be eliminated by the *frequency offset method*. In this method, the time-varying phase shifts are made at higher rates than the modulation repetitions.

Used in an aircraft, the radio altimeter measures its distance above the ground rather than above sea level. A cathode-ray tube indicates the time that a pulse of radio energy takes to travel from the aircraft to the ground and back to the aircraft. The altitude is equal to one-half the time multiplied by the speed of the pulse. Radio altimeters are used especially in automatic navigation and instrument landing systems (ILSs). They are also used in remote sensing applications for military intelligence gathering, mapping, and surveying.

4. LASER ALTIMETERS

Laser altimeters are essentially a form of laser range finding devices, and are used widely for accurate distance measurements. The operation principles are similar to

those of radar altimeters in depending on the time difference between the transmitted and received signals. Thus, the distance is measured by timing a light pulse traveling from a laser light emitter and back to a detector located in the vicinity of the transmitter.

Laser rangefinders are commonly used in land surveying. Airborne laser measurements can be used to directly measure topography, stream channel cross sections, gully cross sections, soil surface roughness, vegetation canopy heights, and vegetation cover and distributions. These laser measurements can be used for the estimation of forest biomass and volume, aerodynamic roughness, and leaf area indices. Airborne laser altimeters provide quick and accurate measurements for evaluating changes in land surface features and can be an additional and useful tool for remote sensing of watershed properties and water resource management.

In laser altimeter applications, three measurement techniques are used: (1) the interferometric method, which is extensively used in short-distance measurements, up to 100 m in free air; (2) amplitude-modulated laser beam telemetry, suitable for distances of 100 m–50 km; and (3) the pulsed laser radar method, for altitudes over 10 km. All these methods are based on the measurement of the propagation time of the laser pulse over the distance under investigation. Therefore, the evaluation of the true geometric distance depends on corrections for factors such as the air refractivity, the beam angles, and the signal processing techniques. On the basis of these principles, various types of laser altimeters are available commercially, depending on the application requirements and the range of the altitudes. In extra-long-range applications, optical radar altimeters, which are based on sending infrared pulses of about 5 ns duration, are found to be accurate.

4.1. Amplitude-Modulated Laser Beam Altimeters

Although interferometric methods for distance measurements are extensively used for short-distance applications, they are clearly not suitable for long-range distance measurements. For those a common method involves amplitude modulation of the laser beam. In this method the modulated beam is projected toward the target and the light returned from the target is collected by a telescope to be sent to a detector, as illustrated in Fig. 11. The phase of the amplitude modulation of the returning light is compared with that of the emitted light. The differences in the phases occur because of the time required for the light to travel to the target and back to the telescope. To describe the operations, an equation can be written in terms of intensities of transmitted beam $I(t)$ and the received beam $I(t - \tau)$

$$I(t) = \alpha I(t - \tau) \quad (16)$$

where τ is the transit time, or propagation time delay, of the lightbeam, and α is the attenuation coefficient, which takes into account propagation efficiency and losses during transmission. The transit time for the sinusoidal modulation, the geometric distances, and the refractive index

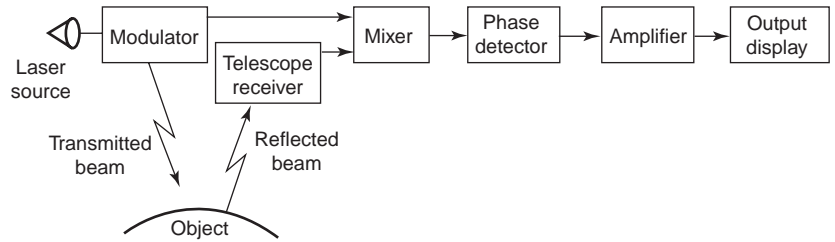


Figure 11. A laser-beam-modulated altimeter. The phase difference between the transmitted and returned signals is measured. The phase comparison technique allows the evaluation of altitudes at high precision from distances of several hundred kilometers.

of the spectral distribution of the lightbeam can be used to find the relationship between the phase shift Φ and the total pathlength L

$$\Phi = \frac{2\pi n_g L}{\lambda_v} \quad (17)$$

where n_g is the group index of refraction of air and the λ_v is the wavelength in vacuum.

4.2. Pulsed Laser Radar

Another approach to laser-based altitude measurement is to make use of the round-trip transit time for a very short pulse, as illustrated in Fig. 9b. Often the acronym LIDAR (light detection and ranging) is used, as an optical counterpart of “radar.” Using lasers to measure altitude results in good accuracy and spatial resolution, but in doing so the advantage of all-weather capability of a microwave altimeter is lost. Such measurements can only be carried out in favorable atmospheric conditions.

Pulsed laser radars commonly use Q -switched laser switches with high peak power. The accuracy of the time measurement depends on the characteristics of the propagation medium and on the resolving capabilities of the photodetector and the timing system. In topographical applications, the statistical characteristics of the received signals for the short-pulse laser altimeters can be directly related to the statistics of the surface profile. In the signal analysis the effects of laser speckle, shot noise, and the surface profile of the ground target need to be considered carefully.

In pulsed radar applications, the altitude to be measured can be found from the expression

$$E_R = \frac{E_0 A_R \eta A_T t^2}{\Omega_0 L^2 \Omega_T} \quad (18)$$

where E_0 is the transmitted pulse energy, A_T and A_R are the areas of the target and the received system, Ω_0 and Ω_T are the solid angles over which the emitted and reflected energy are spread, t is the atmospheric transmission time, η is the diffusion or reflection coefficient, and E_R is the received energy. This equation indicates that the energy follows an inverse-square law. If the intensity of the returned signal is high, Eq. (18) can be used for altitude measurements. If it is low, various probability methods (e.g., the Poisson distribution) are used to estimate the number of photoelectrons.

Solid-state lasers can deliver pulses with time duration of typically 20 ns and peak power up to 1000 MW. Semi-

conductor laser diodes provide high-efficiency pumping of solid-state lasers with the promise of long-lived, reliable operation. In the next generation of laser altimeters, 100-W quasi-CW laser diode bars are likely to find applications. Even with the use of power laser equipment to generate the transmitted signals, the pulse intensity of the returned signals is very weak. To overcome this problem, highly sensitive photodiodes and photomultipliers are used for detection.

In this article, two different systems are discussed in order to explain the scope and the potential of practical laser altimeters: the shuttle laser altimeter (SLA) and the raster scanning airborne laser (RASCAL). The first type, the SLA, is in its second generation of development. Constructed by NASA, this altimeter is used to determine the shape of land surfaces and vegetation canopies. At present, the accuracy of the SLA-2 is within ≈ 1.5 m (vertically) for each 100-m-diameter footprint. The signal-processing component of the system is able to recognize the differences between the reflection from the soil surface and the reflections from other objects; hence the information can be separated and relief plots can be computed.

The mission objective was to compile a database of laser echo returns for every possible surface condition on Earth. The SLA-2 is constructed as an engineering experiment, and NASA is planning the introduction of a third-generation altimeter, the SLA-3. This instrument is planned to have an ultrahigh repetition rate, a smaller footprint than SLA-2, and the ability to penetrate vegetation canopies so that it can provide a contour of the surface under the canopy.

Operation of the SLA-2 is very complex, but it can be broken down into the following three major components: the laser transmitter (a Q -switched, diode-pumped Nd:YAG device, by McDonnell-Douglas), the 38-cm-diameter telescope antenna, and the altimeter receiver connected to a waveform digitizer. A variable-gain amplifier is used to accommodate a greater range of return amplitudes of the returned signals, thus increasing the accuracy and the altitude range. The actual laser return-pulse detection is performed via a silicon avalanche photodiode detector, which in turn is connected directly to the waveform digitizer.

The second altimeter is the RASCAL, also from NASA. The operational principle of the RASCAL is similar to that of the SLA, but the device is configured specifically to operate in aircraft. The RASCAL sensor was developed in 1995 at the Goddard Space Flight Center for airborne mapping of surface topography. The RASCAL is a

second-generation laser altimeter with application to both Earth (airborne) and other planetary surface (space-based) topography determinations. It differs from earlier nadir-profiling laser altimeters by an increase in pulse repetition rate by two orders of magnitude and provision for a near-contiguous scan pattern. It was first operated in a NASA airborne remote sensing program station in California in September 1995, where its high spatial resolution (better than 2 m) in three-dimensional images of topography was demonstrated.

The complicated part of RASCAL is the need for accurate positioning of the laser relative to the aircraft and Earth. Through the use of the aircraft's GPS and inertial navigation system, the NASA team has, in its words, "brute-forced" the solution to this problem and gained a reliable model for exact positioning information. The accuracy of this system has been described as "not as good as [it] should be," and there are plans to build a laser capable of 1 ns pulse width at 10 kHz to help correct this. The return-pulse energy-sampling system is not at its optimum yet, either. By the use of the RASCAL, so far, postprocessed data have been used to re-create many footprints with diameters of 1 m, spaced approximately every 1.5 m in both directions in a pattern 100 m wide. An average accuracy of better than 20 cm with a precision of ± 5 cm is achievable.

A plot obtained from the RASCAL system data is shown Fig. 7. It showed up in postprocessing, when the analyzing team apparently did not realize that they had flown over a satellite tracking station. Although the desired accuracy is lacking, this typical plot shows the potential of the system.

Besides terrestrial applications, laser altimeters, LIDARs, and other ranging systems have been important parts of space missions to the Earth's moon, asteroids, and Mars; and more are planned and contemplated in the future exploration of the solar system. In 1997 the *Mars Global Surveyor* (MGS) entered into orbit around Mars. One of the four scientific instruments on the MGS is the Mars orbiter laser altimeter (MOLA), which has started to map the topography of the planet with unprecedented accuracy. In 1999 the *Near Earth Asteroid Rendezvous* (NEAR) spacecraft, which carries the NEAR laser rangefinder (NLR), arrived at the asteroid Eros. The NLR was to study the shape and the dynamics of the body of Eros for a period of a year. The MOLA and the NLR, along with the Clementine laser altimeter that went to the moon in 1992, represent a new class of active remote sensing instruments for investigations of science in the solar system.

5. GLOBAL POSITIONING SYSTEM (GPS)

The GPS was begun 1978 and completed in 1994 with 21 active and 3 spare satellites. The GPS allows users to determine their exact position, velocity, and time at any time of day, in any weather conditions, free of charge. In discussions of the GPS, it is convenient to break the system into three blocks or segments: the space segment, the user segment, and the control segment.

5.1. The Space Segment

The GPS satellites orbit Earth at an approximate altitude of 20,000 km, and have an orbit period of 12 sidereal hours. The orbits have been arranged so that a user can have a direct line of sight to at least four satellites at all times at any place on Earth.

Each satellite transmits a unique code, which is based on a pseudorandom sequence allocated before launching. Having received this code, the users can employ autocorrelation techniques to recover these sequences. Given an accurate time reference and the propagation time from the satellite to the receiver, the distance can be determined. If the distances from each satellite in sight and the locations of satellites are known, the relative position and thus the coordinates of the receiver can be calculated easily. For precise calculations, the clock references of the GPS satellites must be known exactly. The clocks on the satellites are known to be stable within 0.003 s per 1000 years.

The satellites transmit signals at 1575.42 and 1227.60 MHz; these two transmissions are known as the L1 and L2 signals. The L1 signal is described as being made up of a *precision* code (P) and a *coarse acquisition* code (C/A). The L2 contains only the P code, which when encrypted is called the "Y code."

5.2. The User Segment

Users of the GPS often have handheld GPS receivers. A receiver determines a pseudorange to work out the time that the signal takes to reach to the receiver. Performing this operation for more satellites in sight, the receiver can work out where the user is either on the face of or above Earth.

The P and C/A codes are sometimes referred as the *precise positioning service* (PPS) and the *standard positioning service* (SPS), respectively. As these names would suggest, the PPS is more accurate than the SPS; this is due to a smaller bit period in the P code. The PPS has been withheld from public use, but is earmarked to be released for civilian use in the near future. A third frequency, which will give better accuracy, is planned to be released for the public. However, the Russian Global Navigation Satellite System (GLONASS) uses a single frequency, thus giving better accuracy for civilian use.

5.3. The Control Segment

The control segment consists of operators of the GPS network at a number of stations on Earth. The requirement of this segment is to maintain the GPS time, monitor and control the satellite orbit positions, and predict variations for compensation of any detected inaccuracies. The network has a master control station situated in Colorado Springs in the United States, and five additional monitoring stations. The positions of these stations are known precisely, and they are used to check and calibrate the GPS. The stations are distributed roughly along the equator and are geographically suitable for general system maintenance. At the moment, the number of stations is said not to be sufficient; however, more stations are being

planned to allow the determination of precise orbital paths of the satellites.

5.4. Theory of Operation

The theory of operation of the GPS is too complicated for detailed treatment in this article. Here, a brief explanation will be given to provide a basic understanding of GPS-based altimeters, particularly concerning accuracy and errors.

The GPS makes use of the time of arrival; that is, the satellites send out signals that contain some information such as the exact time of signal transmission and satellite locations. Once received, the information in the signal can be processed to calculate the time taken for the signal to arrive from the satellite at the receiver. By repeating this operation with the information from at least four satellites, the latitude, longitude, and height of the user can be determined in reference to the satellites and thus, in turn, in reference to fixed points on Earth.

Each satellite transmits a binary phase shift-keyed sequence that is spread spectrally, by its pseudorandom code; this allows all of the satellites to transmit on the same L1 and L2 carriers. They all use the same bandwidths at 2.0463 MHz for the C/A codes and 20.98 MHz for the P codes. This is called *code-division multiple access* (CDMA), and it relies on the properties of pseudorandom codes to work.

Pseudorandom codes have the property of strong autocorrelation. This means that when a pseudorandom code is overlaid on itself and correlated, the result will be slightly negative for all positions except an identical overlaying, in which the result becomes positive. A delay time is added to the internally generated pseudorandom code, to provide a positive, strong correlation with the received signal.

If the internal clock of the GPS receiver were exactly synchronized with the satellite's clock, the measured time delay would be representative of the actual physical distance between the satellite and the receiver. It is very unlikely, however, that the satellite and receiver clocks will be synchronized exactly. As a result, some differences in time, called *clock bias*, arise. The GPS receivers must determine the magnitude of the clock bias by taking delay times of the other satellites into consideration. This means that the measured delay times are the combination (physical distance)/(speed of light) + (clock bias) as explained above.

It is convenient to define a *pseudorange*, which is the delay time multiplied by the speed of light. This is a pseudodistance from the receiver to the satellite, with clock bias factored in. The actual process that the receiver executes can be summarized as follows:

1. The receiver tracks four or more satellites and determines the delay time from each satellite.
2. The receiver calculates all the pseudoranges (i.e., multiplies the times by c).
3. The receiver then corrects the pseudorange results for errors such as the satellite clock difference, the clock bias, the ionospheric effects, and time.

The information sent by satellites, for the computation, is in the form of 50-bps (bits per second) frames superimposed on the C/A and P codes, called the *NAV messages*. It takes about 12.5 min to download 25 of the 1500-bit frames to the receiver. The precise position of the satellite, the clock time, and other relevant information is included in the NAV message. Because of the time required to download the message, the NAV message is defined to be valid for 4 h.

4. When all of the pseudoranges have been corrected, the receiver performs a simultaneous solution of four equations with four unknowns. The four unknown quantities are the Cartesian coordinates x, y, z and the time.

Now that the receiver has solved the equations, the latitude, longitude, and altitude of the user can be calculated and displayed. The accuracy of these results depends on statistical analysis, and thus on the percentage of time of availability of satellites.

The GPS has a number of errors that need to be considered in altitude determinations. Some of these are the receiver clock error, the multipath error, and the ionospheric and tropospheric propagation errors.

As mentioned, the U.S. Department of Defense (DoD) is planning to allow civilian users to use the PPS system instead of the SPS. This will give substantial improvement in accuracy of the position and altitude determinations, as shown in Table 2. In this table, the formal specified accuracies are shown in bold. The percentages 50%, 63%, and 95% are the probable fractions of time for the receiver to be located within the given distances of an exact position calculated statistically. For example, the measured vertical height of the receiver in the SPS system is within 140 m of the central value 95% of the time. This can be compared with 28 m for the PPS system. The distance error of 140 m is clearly too large to be useful in aircraft applications, at low altitudes, but may be acceptable at high altitudes.

A method of improving this accuracy is called *differential GPS* (DGPS), and it can help provide an SPS user with subcentimeter accuracy in many cases. The DGPS uses a ground station that is geodetically fixed (with exact latitude and longitude), and it continuously tracks all visible satellites. Given the precise location and altitude of the DGPS station, and that the satellites transmit their

Table 2. Accuracy in GPS Systems

	Accuracy					
	50% of Time		63% of Time		95% of Time	
	PPS	SPS	PPS	SPS	PPS	SPS
Position (m)						
Horizontal	8	40	10.5	50	21	100
Vertical	9	47	14	70	28	140
Spherical	16	76	18	86	36	172
Velocity (x, y, z) (m/s)	0.07	—	0.1	—	0.2	—
Time (ns)	68	115	100	170	100	340

positions in the NAV message, the DGPS can apply corrections based on the measured delay times. By transmitting corrected information about the visible satellite positions to a GPS receiver via a radio channel, the computation at the receiver can be improved.

The GPS is a powerful tool for accurate determination of altitudes if one has access to a PPS system, and an altitude accuracy better than 100 m can be achieved even with the SPS system. Handheld GPS receivers are now commonly available for a few hundred dollars in consumer retail outlets.

6. REMOTE SENSING

Remote sensing is the science of detecting, measuring, and analyzing an object on the ground from a distance. It comprises mainly measurements of electromagnetic radiation from the ground, in the form of energy reflected by active sensors or emitted by passive sensors in various spectral ranges picked up by aircraft or satellites. Also, remote sensing may encompass aerial photography and similar methods whose results are generally displayed in the form of photographlike images. In aircraft applications, images from different flight paths can be combined to allow an interpreter to perceive features in three dimensions, and identify specific types of rock, soil, vegetation, and other entities, where they have distinctive reflectance values in different spectral regions of the electromagnetic radiation.

Remote sensing systems are made from distinct components as shown in Fig. 12: (1) an active or a passive remote sensor that employs detecting mechanisms to sense or scan the object, (2) a device for recording and imaging of the information received, and (3) the analysis and display system that makes the information useful. In some cases, analysis and display systems are combined and operate concurrently with the sensing system to process and display the data instantaneously. In other cases, the data are recorded and analyzed later. The displays are usually in the form of aerial photographs or television pictures.

An important feature of remote sensing is the identification of signatures, which is used to sense the desired objects against a complex background or surroundings. For example, it may be necessary to identify a particular mineral, crop blight, or type of air or water pollution. Signature, as applied to imagery, usually refers to visual characteristics that identify the subject and separate it from other similar objects.

Image formation is another important aspect of remote sensing. In this regard, there are two categories of

systems: (1) imaging sensor systems, which can be subdivided into framing systems (e.g., aerial photographic cameras, vidicons) and scanning systems, (e.g., radar), and (2) nonimaging sensor systems, also known as spectral data systems (e.g., spectroradiometers, radar scatterometers).

Remote sensors may be surface-based and stationary or mobile, or airborne in aircraft, helicopters, or balloons; or carried aboard spacecraft, such as satellites, a space shuttle, or a space station. These bases are known as the *sensor platforms*. The resolution, or detail, with which a remote sensor can monitor a subject generally depends on the distance from the sensor platform to the object. Generally, remote sensors that employ the shortest wavelengths provide the best resolution. For example, microwave sensors, which operate at wavelengths longer than those of thermal infrared sensors, can be expected to have poorer resolution. However, the longer wavelengths have the best penetrating power. Microwaves, for example, can penetrate through clouds, whereas visible light and infrared light do not. Therefore, microwave radar systems are often used to sense subjects that are not visible to optical wavelength laser radar systems. Also, microwave systems can be used to penetrate vegetation for geologic mapping, to monitor snow depths, to indicate soil moisture, and so on.

Remote sensing finds many applications, such as in military equipment; air transport; deep-space research; geography; environmental monitoring such as oceanography, hydrology, meteorology, and pollution control; monitoring snow depth and ice cover, flood control, hydroelectric generation, and water transport management; agriculture and forestry; and lightning and fire sensing. The geographic and geologic applications include land-use and terrain mapping, geological mapping, and detection of mineral deposits. Oceanographic applications encompass monitoring of waves, currents, temperatures, salinity, turbidity, and other parameters and phenomena related to oceans and seas.

The technology of remote sensors varies from system to system. For example, in a typical infrared remote sensing system, the thermal infrared energy is detected by an optical-mechanical scanner. The detector is cooled by a liquid nitrogen or liquid helium jacket that encloses it, and a rotating mirror directs radiation coming from various directions onto the sensor. Infrared radiation permits mapping surface temperatures to a precision of less than a degree and thus shows the effects of phenomena that produce temperature variations, such as groundwater movements.

In another system, Landsat images are commonly used. They are produced with data obtained from a multispectral scanner carried aboard certain U.S. Landsat satellites orbiting Earth at an altitude of about 900 km. Images covering an area of over 185 km² are available for virtually every part of Earth's surface. Scanner measurements are made in four spectral bands: green and red in the visible portion of the spectrum, and two infrared bands. The data are usually displayed by arbitrarily assigning different colors to the bands and then superimposing these to make representative images.

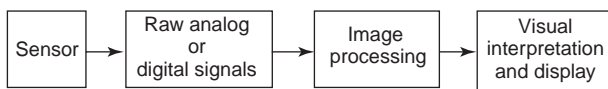


Figure 12. Components of remote sensing for image processing. The sensed signals are stored and processed either online or offline.

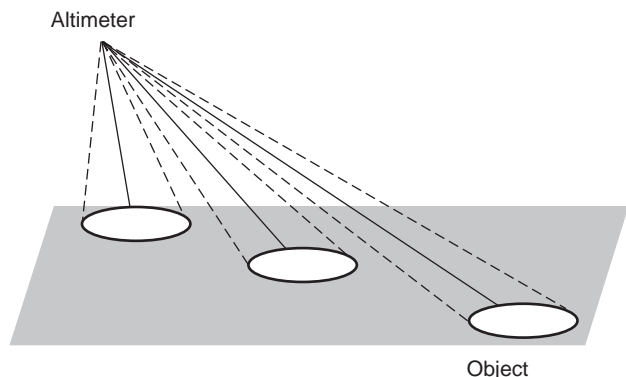


Figure 13. The geometry of a scanning beam altimeter. The scanning is realized either electronically or mechanically. Processing of the returned signals from each scan gives accurate three-dimensional images.

Topographic mapping of the earth, moon, and planets can be accomplished with high resolution and accuracy using satellite laser altimeters. These systems employ nanosecond laser pulses and microradian beam divergences to achieve submeter vertical range resolution from orbital altitudes of several hundred kilometers.

Conventional altimeters provide a topographic surface profile. In most cases the surface topography is required over an area. This can be achieved by multiple orbit traces displaced across the track by successive revolutions of an element making a large number of accurately positioned orbital passes. Often a multibeam or scanning beam altimeter is used to provide three-dimensional images. The corresponding geometry is illustrated in Fig. 13. The accurate performance of the altimeter depends on the effects of the target surface characteristics, spacecraft pointing jitter, and waveform digitizer characteristics. The ranging accuracy is critically dependent on the pointing accuracy and stability of the altimeter, especially over high-relief terrain where surface slopes are large. At typical orbital altitudes of several hundred kilometers, single-shot accuracy of a few centimeters can be achieved when the pointing jitter is on the order of 10μ rad or less.

7. SURFACE HEIGHT MEASUREMENT AND HEIGHT ACCURACY

Surface height measurement is an important concept associated with altimeter technology. In general, height measurement has many applications, ranging from the microscopic scale of measuring step heights in wafers in integrated circuits and height measurements of machined metal surfaces, to the very large scales of ice formation on Earth's surface and wave heights in the oceans. Consequently, the instrumentation suitable for these measurements ranges from microscopes and interferometers to GPS and satellite radar.

In large-scale applications, many methods are used to determine heights on land: (1) spirit leveling (most accurate but slow), (2) measuring vertical angles and distances

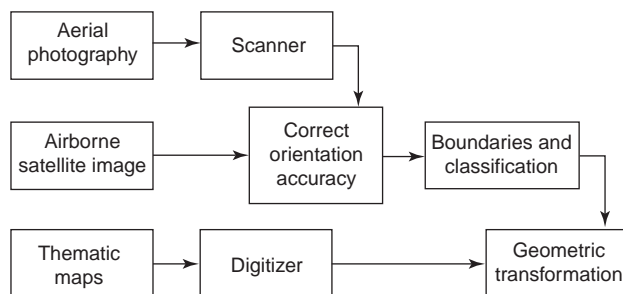


Figure 14. Use of different methods in remote sensing. Several methods are combined electronically to give extremely accurate mapping. In this particular case aerial photography, airborne satellite images, and digitized thematic maps are combined.

(accurate and faster), (3) measuring differences in atmospheric pressure, (4) using photographic techniques such as aerial surveying, and (5) using radar and satellite systems. The last two techniques are accurate but require expensive and sophisticated equipment, as discussed earlier. Often, more than one technique is employed to obtain accurate geographic information, as illustrated in Fig. 14.

In spirit leveling, a horizontal telescope fitted with crosshairs, rotating around a vertical axis on a tripod, is used to adjust a bubble, which is exactly centered. The reading on a graduated vertical staff is observed through the telescope. If such staffs are placed on successive ground points, and the telescope is truly leveled, the difference between the readings at the crosshairs will equal that between the heights of the points. By moving the level and the staffs alternately along a path or road and repeating this procedure, differences in height can be measured accurately over long horizontal distances. In some stringent surveys, the error may be kept to less than a centimeter over a distance of 100 km.

For faster work in hilly areas, where lower accuracy is usually acceptable, trigonometric height determination is employed, using a theodolite to measure vertical angles and measuring or calculating the distances by triangulation. To increase precision, the observations are made simultaneously in both directions so that aerial refraction is eliminated.

The third method of height determination depends on measurements of atmospheric pressure differences with a sensitive aneroid barometer, which can respond to pressure differences small enough to correspond to 0.3–0.6 m in height. To obtain reliable results, it is necessary to use a reference barometer, as the air pressure changes constantly. An alternative to the barometer for the pressure measurements is the use of an apparatus for measuring the boiling point of a liquid, since the boiling temperature depends on the atmospheric pressure.

A relatively new method of surface height measurement is the use of satellite and radar systems. The analysis of the signals received simultaneously from several satellites gives heights as accurately as positions. Heights determined in this way are useful in previously unmapped areas as a check on results obtained by faster relative

methods, but they are not accurate enough for mapping developed areas or for engineering projects. For example, absolute and relative height measurements with the differential GPS systems are accurate to about 30 m, whereas in photogrammetric surveys subcentimeter accuracy can be achieved over a wide area, typically 5 km^2 .

Another application of the satellite systems is in the oceans, to measure the sea level, since the surface of the sea acts as a reflector for radar waves. The accuracy of the measurements depends on how precisely the satellite orbit is known, and on the reduction of dynamic effects on the sea surface such as semidiurnal and diurnal tides.

A typical application of altimeters is in aircraft to determine their height above the surface. Radar systems are often used for geometric height estimation of civil and military aircraft. A typical system consists of a standard altimeter backed up with secondary surveillance radar (SSR) operating on mode S coupled to an omnidirectional antenna fixed under the airplane. The geometric height is derived by various methods, such as the trilateration method, and the systematic errors are compensated for by deriving the profile of the effect on height measurements of the bias in range measurements. Various curve-fitting techniques are used, which estimate both the geometric height and any nonzero systematic errors.

High single-point precision and high point density can be obtained by airborne laser altimetry, using GPS positioning and inertial navigation system (INS) attitude determination. However, these methods are subject to various error sources, which include (1) internal laser sensor errors; (2) GPS and INS errors; (3) atmospheric effects; (4) terrain roughness, reflectivity, and slope; (5) presence, height, and type of vegetation; and (6) integration and synchronization of laser, GPS, and INS. When well calibrated, laser altimeters can give subcentimeter accuracy. However, the accuracy may be very sensitive to terrain type, terrain coverage, and filters used to remove undesired objects, such as buildings and trees. In particular, pointing accuracy, which depends on the pointing jitter of the scanning mirror and INS attitude determination, is a main error source, especially over high-relief terrain.

BIBLIOGRAPHY

1. C. Elachi, *Spaceborne Radar Sensing Applications and Techniques*, Institute of Electrical and Electronics Engineers, New York, 1988.

FURTHER READING

- N. Ackroyd and R. Lorimer, *A GPS Users' Guide*, Lloyd's of London Press, New York, 1994.
- H. J. Buiten and J. P. G. W. Clevers, *Land Observation by Remote Sensing: Theory and Applications*, Gordon & Breach Science, Yverdon, Switzerland, 1993.
- B. Clarke, *GPS Aviation Applications*, McGraw-Hill, New York, 1996.
- R. P. G. Collinson, *Introduction to Avionics*, Chapman & Hall, London, 1996.
- N. E. Fancey, I. D. Gardiner, and R. A. Vaughan, *The Determination of Geophysical Parameters from Space*, Institute of Physics, Philadelphia, 1996.
- A. Helfrick, *Practical Aircraft Electronic Systems*, Prentice-Hall, Englewood Cliffs, NJ, 1995.
- E. H. J. Pallett and S. Coyle, *Automatic Flight Control Systems*, Blackwell Scientific, Oxford, 1993.
- RASCAL laser altimeter instrument home page (online), available at <http://denali.gsfc.nasa.gov/research/laser/rascal/index.html>.
- J. F. Ready, *Industrial Applications of Lasers*, 2nd ed., Academic Press, San Diego, 1997.
- P. A. Roocke, *Intelligent Barometric Altimeter*, thesis, School of Electrical and Computer Engineering, Curtin Univ. Technology, Perth, Western Australia, 1990.
- R. Rummel and F. Sanso, *Satellite Altimetry in Geodesy and Oceanography*, Springer-Verlag, Berlin, 1993.
- G. Seeber, *Satellite Geodesy*, de Gruyter, Berlin, 1993.
- G. Siouris, *Aerospace Avionics Systems*, Academic Press, San Diego, 1993.
- SLA (Shuttle Laser Altimeter) home page (online), available at <http://ssppgse.gsfc.nasa.gov/hh/tas/experiments/sla.html>.
- TOPEX altimeter home page (online), available at http://podaac.jpl.nasa.gov:2031/SENSOR_DOCS/topex_alt.html.

AMPLITUDE SHIFT KEYING

FUQIN XIONG
Cleveland State University
Cleveland, Ohio

1. INTRODUCTION

In some digital communication systems, such as satellite communication and cellular telephone systems, digital message data, such as binary 0 and 1, must be impressed on a high-frequency carrier signal before being transmitted. The carrier is usually a voltage signal such as a cosine function of time t

$$s(t) = A \cos(2\pi f_c t + \theta)$$

where A is the amplitude, f_c is the carrier frequency, and θ is the initial phase. Each of these three parameters or a combination of some of them can be used to carrier the message data. The process of impressing a message on to a carrier by associating one or more parameters of the carrier with the message is called modulation, and the process of extracting the message from the modulated signal is called demodulation.

The most important properties of a modulation scheme are the bandwidth efficiency, bit error probability, and system complexity.

The *bandwidth efficiency* is defined as number of bits per unit bandwidth (1 Hz) that a modulation scheme communicates, and it is determined by the power spectral

density (PSD) of a digitally modulated signal. Even though the carrier signal of a digitally modulated signal is a deterministic signal, the data bits that modulate the carrier are typically random. Therefore the digitally modulated signal is typically a random signal. For random signals, their spectral property is described by PSD [1, App. A], unlike that for deterministic signals where spectrum can be found using Fourier series or Fourier transform, depending on whether the signal is periodical or aperiodic, respectively.

Bit error probability is also commonly referred as *bit error rate* (BER), although the latter is only an approximation of the former. It is largely determined by the signal energy to noise energy ratio or simply signal-to-noise ratio (SNR), as well as signaling format. One modulation scheme may need less SNR than the other for the same BER, then we say the former is more power efficient than the latter.

System complexity refers to mainly complexities of the modulator, demodulator, and synchronization subsystems, which are also determined by signalling format.

The three basic digital modulations are the amplitude shift keying (ASK), frequency shift keying (FSK), and phase shift keying (PSK). As these terms suggest, while keeping all other parameters of the carrier unchanged, ASK uses the data to vary the amplitude, FSK uses the data to change the frequency, and PSK uses the data to control the phase of the carrier, respectively. Binary forms of all three of them are the simplest ones, where the modulating digital message are binary. If the messages are M -ary, where M is an integer, then the modulations are MASK, MFSK, or MPSK.

Both ASK and FSK are the simplest to implement, but ASK is more bandwidth-efficient; that is, for the same system bandwidth ASK can transmit more data. ASK and PSK have the same bandwidth efficiency, but PSK is more power-efficient, that is, for the same SNR (signal-to-noise ratio), the PSK has a lower bit error rate. However, PSK is more difficult to implement than ASK. Even though PSK has gained more popularity, ASK and FSK are still used in many communication systems because of their implementation simplicity.

This article is about ASK. We will first introduce the simplest ASK, the On-Off keying (OOK), in Section 2. After that we will describe a general form M -ary ASK (MASK) in Section 3, where a general form of the power spectral density expression is given and optimum detection and its error probability expression is derived. In Section 4, bipolar symmetric MASK and its PSD, BER, modulator, and demodulator are presented. Section 5 discusses unipolar MASK and its PSD, BER, modulator and demodulator. MASK and MPSK are compared in Section 6. Finally, in Section 7, two advanced forms of modulations related to ASK, the QAM, and ASK-OFDM are briefly discussed.

2. ON-OFF KEYING

The simplest ASK scheme is the binary unipolar ASK also known as *on-off keying* (OOK), where binary data 1 and 0

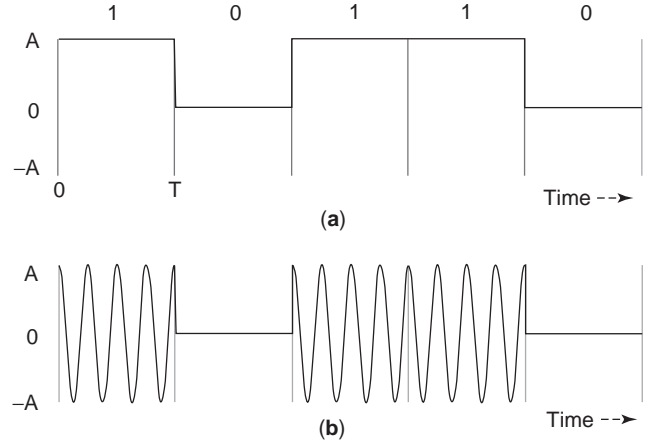


Figure 1. OOK waveforms: (a) data waveform; (b) modulated OOK signal waveform.

are represented by the presence and the absence of a carrier burst, respectively. The OOK signal set is

$$\begin{aligned} s_1(t) &= A \cos 2\pi f_c t \text{ for } a = 1, \quad 0 \leq t \leq T \\ s_2(t) &= 0 \text{ for } a = 0, \quad 0 \leq t \leq T \end{aligned} \quad (1)$$

where a is the binary data. Figure 1 illustrates an OOK signal, where (b) is the baseband data waveform corresponding to the data sequence (10110). The baseband waveform voltage is either A volts or 0, depending on whether the data bit is 1 or 0. When the data bit is 1, there is a burst of carrier signal of A volts in (b), otherwise there is not.

In the following we examine the properties of OOK in terms of its spectrum and bit error probability. We will give expressions without derivations. We defer the derivations to the section on noncoherent unipolar M -ary ASK, of which OOK is only one special case.

2.1. Power Spectral Density and Bandwidth

It is well known that for a bandpass random signal $s(t)$, the PSD is completely determined by the PSD of its complex envelope or equivalent baseband signal [1–3]

$$\Psi_s(f) = \frac{1}{2} [\Psi_{\tilde{s}}(f - f_c) + \Psi_{\tilde{s}}(-f - f_c)] \quad (2)$$

where $\Psi_{\tilde{s}}(f)$ is the PSD of the complex envelope. Thus it suffices to have $\Psi_{\tilde{s}}(f)$ instead of $\Psi_s(f)$.

Assuming that the random data bits are uncorrelated and equally likely, the baseband PSD expression of OOK is given by [1, p. 422]

$$\Psi_{\tilde{s}}(f) = \frac{A^2 T}{4} \left(\frac{\sin \pi f T}{\pi f T} \right)^2 + \frac{A^2}{4} \delta(f) \quad (3)$$

where $\delta(f)$ is the Dirac delta function, which is a discrete spectral line at zero frequency, reflecting the DC component

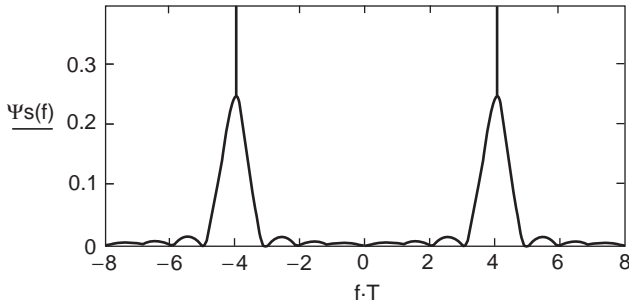


Figure 2. PSD of OOK and unipolar MASK with a rectangular pulse, from Eqs. (3) and (2), with $A = \sqrt{2}$ and $T = 1$.

of the baseband signal. The rest is a continuous part of the PSD, representing the variation in the data sequence.

Figure 2 shows the PSD of OOK. In the figure we set $A = \sqrt{2}$ and $T = 1$ for unity average symbol pulse energy and $f_c = 4/T$. In fact, the shape of the PSD in this figure is for any unipolar M -ary ASK with rectangular pulse. From the figure we can see that the main spectral components are within the null-to-null bandwidth, which is $2/T$. That is, the null-to-null bandwidth is twice the symbol rate.

2.2. Modulator and Demodulator

The modulator of OOK is very simple (Fig. 3a). The binary data sequence is used as a control signal that connects the output with the oscillator through the switch when the bit is 1 and disconnects the switch when the bit is 0. The demodulator can be in two different forms: the coherent (Fig. 3b) and the noncoherent (Fig. 3c). The coherent demodulator requires a carrier recovery circuit that synchronizes in frequency and phase the local oscillator in the receiver with the received signal

$$r(t) = s(t) + n(t)$$

where $n(t)$ is the additive white Gaussian noise (AWGN) whose two-sided power spectral density is $N_0/2$. The

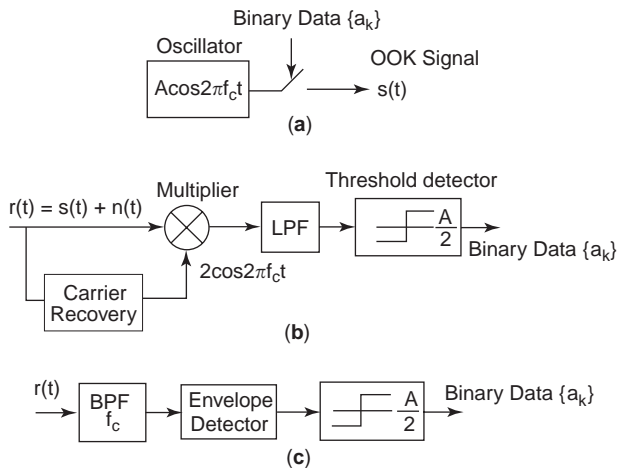


Figure 3. OOK modem: (a) modulator; (b) coherent demodulator; (c) noncoherent demodulator.

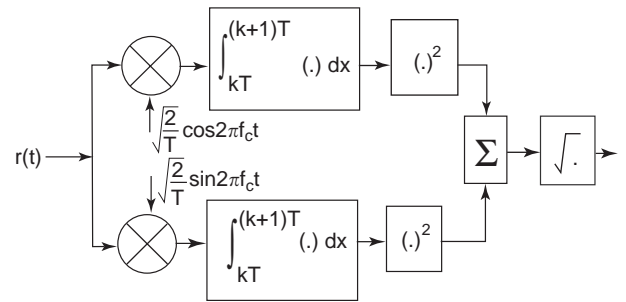


Figure 4. Quadrature envelope detector.

received signal is first multiplied with the recovered carrier $2 \cos 2\pi f_c t$, and the product then passes a lowpass filter (LPF). The LPF rejects the double-frequency part of the product and high-frequency noise. The result is $A + n$, where n is the residual noise. This signal is sent to the threshold detector, whose threshold is set at $A/2$. If the signal is above $A/2$ threshold, the output is set to 1; otherwise the output is set to 0. In the noncoherent demodulator, the first stage is a bandpass filter (BPF) with a center frequency of f_c and adequate bandwidth. This BPF has the function of selecting the desired signal and rejecting the noise. The filtered signal then passes an envelope detector, which extracts the envelope of the modulated carrier, namely, the noise-corrupted baseband pulses. Finally, the noise-corrupted baseband pulses pass the threshold detector to produce the binary data sequence.

The envelope detector can be implemented in the form of a quadrature detector as shown in Fig. 4. It can also be approximately implemented in other forms. For example, the well-known AM demodulator consisting of a diode followed by a resistor and a capacitor in parallel is an envelope detector.

2.3. Bit Error Probability

Bit error probability expressions for OOK are given below without proof. Later we can see that these expressions can be derived as special cases from M -ary cases.

The bit error probability for coherent demodulation of OOK is

$$P_b = Q\left(\sqrt{\frac{E_b}{N_0}}\right) \quad (4)$$

where E_b is the average bit energy and

$$Q(x) = \int_x^\infty \frac{1}{\sqrt{2\pi}} e^{-\frac{u^2}{2}} du \quad (5)$$

is the Q function. The bit error probability for noncoherent demodulation of OOK is [5].

$$P_b = \frac{1}{2} \exp\left(-\frac{E_b}{2N_0}\right) + \frac{1}{2} Q\left(\sqrt{\frac{E_b}{N_0}}\right) \quad (6)$$

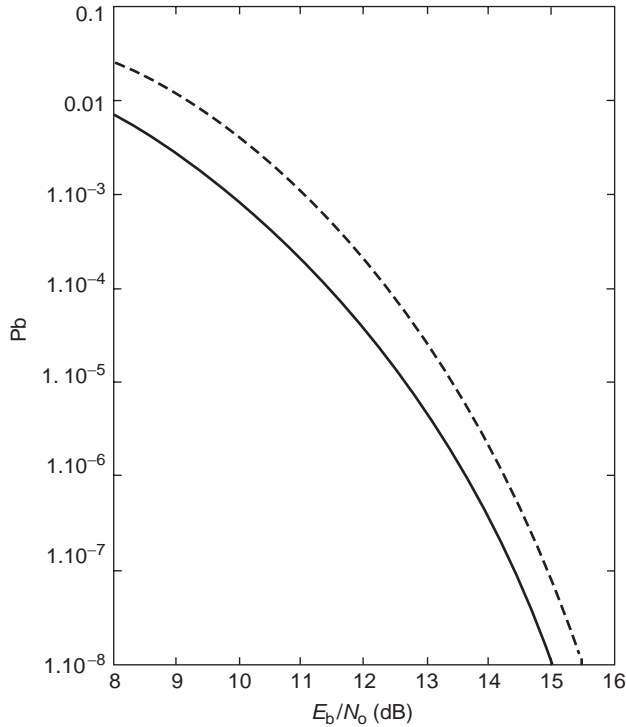


Figure 5. OOK bit error probabilities: solid line—coherent demodulation; dotted line—noncoherent demodulation.

Figure 5 shows the BERs of coherent and noncoherent OOK; the former demodulator has a better BER. The noncoherent is relatively easier to implement since it does not require the carrier synchronization. The noncoherent demodulator is more robust against channel impairments such as fading and also is suitable for systems where synchronization is difficult such as a frequency-hopping multiple-access system.

3. M -ARY ASK (MASK)

OOK is simple but not bandwidth-efficient. To improve bandwidth efficiency, we need to go from binary to M -ary, where M is usually a power of 2.

In M -ary ASK (MASK), data bits are grouped into n -tuples, where $n = \log_2 M$. Each n -tuple is mapped into an amplitude A_i . Thus a symbol in MASK is a burst of carrier signal with an amplitude determined by the n -tuple and it represents n bits instead of only one bit as in OOK. As we will see later (Sections 4.1 and 5.1), the bandwidth of the MASK signal's PSD is determined by the symbol duration. By keeping the symbol duration the same, an MASK system and an OOK system will need the same bandwidth, but the bit rate of the MASK system will be n times that of the OOK system.

In the basic symbol period $[0, T]$, an MASK signal with a pulseshape $p(t)$ can be expressed as

$$s_i(t) = A_i p(t) \cos 2\pi f_c t, \quad 0 \leq t \leq T \quad (7)$$

for $i = 1, 2, \dots, M$. The distribution of amplitudes varies. The most common choices are the symmetric uniform spacing bipolar distribution and uniform spacing unipolar distribution. The amplitudes of the symmetric uniform spacing bipolar distribution is given by

$$A_i = (2i - 1 - M)A, \quad i = 1, 2, \dots, M \quad (8)$$

where $A > 0$. The amplitude spacing is $2A$. For example, if $M = 4$, then $A_i \in (-3A, -A, A, 3A)$. The amplitude distribution of the uniform spacing unipolar distribution is given by

$$A_i = (i - 1)A, \quad i = 1, 2, \dots, M \quad (9)$$

The amplitude spacing is A . If $M = 4$, then $A_i \in (0, A, 2A, 3A)$. OOK is just a special case of the unipolar MASK when $M = 2$.

A bipolar MASK can be demodulated only coherently since noncoherent demodulation cannot distinguish the sign of the signal. A unipolar MASK can be demodulated noncoherently as well as coherently. However, it is generally used in a system where coherent demodulation is difficult; thus noncoherent demodulation is preferred. If coherent demodulation is feasible, the symmetric uniform spacing bipolar MASK is preferred over the uniform spacing unipolar MASK since the former has better BER performance. In the following two sections, we will discuss coherent symmetric uniform spacing bipolar MASK and noncoherent uniform spacing unipolar MASK. But first, we examine the power spectral densities of both.

3.1. Power Spectral Density

Consider a sequence of MASK symbols in the form of

$$s(t) = \sum_{k=-\infty}^{\infty} A_k p(t - kT \cos 2\pi f_c t), \quad -\infty < t < \infty \quad (10)$$

where A_k are the amplitudes controlled by the data n -tuples. Assuming that the data are uncorrelated, the PSD of the complex envelope of the bandpass MASK signal is [1, (A.18)]

$$\Psi_s(f) = \frac{\sigma_A^2 |P(f)|^2}{T} + \left(\frac{m_A}{T}\right)^2 \sum_{k=-\infty}^{\infty} \left|P\left(\frac{k}{T}\right)\right|^2 \delta\left(f - \frac{k}{T}\right) \quad (11)$$

where $P(f)$ is the Fourier transform of $p(t)$, σ_A^2 is the variance of A_k , and m_A is the mean value of A_k .

Now let us assume that $p(t)$ is rectangular with unit amplitude; then

$$|P(f)| = \left| T \frac{\sin \pi f T}{\pi f T} \right| \quad (12)$$

and

$$P \frac{k}{T} = T \frac{\sin \pi k}{\pi k} = \begin{cases} T, & k = 0 \\ 0, & k \neq 0 \end{cases}$$

then the PSD of the complex envelope of the bandpass MASK signal is

$$\Psi_s(f) = \sigma_A^2 T \left(\frac{\sin \pi f T}{\pi f T} \right)^2 + (m_A)^2 \delta(f) \quad (13)$$

3.2. Optimum Detection and Error Probability

It is well known from detection theory that for a noise-corrupted signal, the optimum detection starts by correlating the signal with a set of orthonormal basis functions from which the signal is constructed [4, Chap. 2] [1, App. B]. The outputs of the correlators are called sufficient statistics. Then, based on the probability distributions of the sufficient statistics and the detection criterion (usually minimum error probability), the detection rule is established.

To derive the optimum demodulator of the MASK, we first assume that the pulse shaping function is the unit amplitude rectangular pulse; then we can rewrite (7) in terms of an orthonormal basis function $\phi(t)$

$$s_i(t) = A_i \cos 2\pi f_c t = s_i \phi(t), \quad 0 \leq t \leq T \quad (14)$$

Note that there is only one basis function

$$\phi(t) = \sqrt{\frac{2}{T}} \cos 2\pi f_c t \quad (15)$$

and its energy is normalized, that is, $\int_0^T \phi^2(t) dt = 1$ and s_i is the projection of $s(t)$ onto the orthonormal basis function, given by

$$s_i = \int_0^T s_i(t) \phi(t) dt = A_i \sqrt{\frac{T}{2}} \quad (16)$$

Assuming that the received signal is

$$r(t) = s_i(t) + n(t)$$

then the sufficient statistic is the correlator output

$$r = \int_0^T r(t) \phi(t) dt \quad (17)$$

and the detector compares r to s_i and chooses the closest (minimum distance decision rule) [1].

The error probability of the coherent detection for an MASK with equal amplitude spacings can be derived as follows. Assuming an AWGN channel with two-sided noise PSD of $N_0/2$, we obtain

$$r = \int_0^T r(t) \phi(t) dt = \int_0^T [s_i(t) + n(t)] \phi(t) dt = s_i + n$$

where n is Gaussian with zero mean and a variance of $N_0/2$ [1, App. B]. Thus r is Gaussian with mean s_i and variance $N_0/2$.

$$f(r/s_i) = \frac{1}{\sqrt{\pi N_0}} \exp \left[-\frac{(r - s_i)^2}{N_0} \right] \quad (18)$$

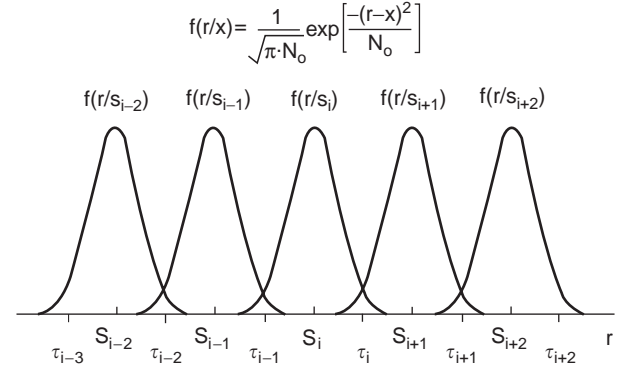


Figure 6. Thresholds and decision regions for MASK. (From Xiong [1], copyright © 2000 Artech House.)

Now we assume that signals s_i are equally spaced. Figure 6 shows the probability distribution densities of r conditioned on equally spaced s_i , where τ_i are thresholds. This figure can help us derive the error probability.

Assuming that, s_i is transmitted, a symbol error occurs when the noise n exceeds in magnitude one-half the distance between two adjacent levels. This probability is the same for each s_i except for the two outside levels, where an error can occur in one direction only. Assuming all amplitude levels are equally likely, the average symbol error probability is

$$P_s = \frac{M-1}{M} \Pr \left(|r - s_i| > \frac{\Delta}{2} \right)$$

where Δ is the distance between adjacent signal levels, and also is the distance between adjacent thresholds. Thus

$$\begin{aligned} P_s &= \frac{M-1}{M} \Pr \left(|r - s_i| > \frac{\Delta}{2} \right) \\ &= \frac{M-1}{M} \frac{2}{\sqrt{\pi N_0}} \int_{\Delta/2}^{\infty} e^{-x^2/N_0} dx \\ &= \frac{M-1}{M} \frac{2}{\sqrt{2\pi}} \int_{\Delta/\sqrt{2N_0}}^{\infty} e^{-x^2/2} dx \end{aligned}$$

That is

$$P_s = \frac{2(M-1)}{M} Q \left(\sqrt{\frac{\Delta^2}{2N_0}} \right) \quad (19)$$

Note that this expression is applicable to any uniformly spaced MASK, whether it is bipolar or unipolar, symmetric or asymmetric.

Now if the MASK signal's pulse shaping function is an arbitrary energy function rather than rectangular, we can write (7) as

$$s_i(t) = A_i p(t) \cos 2\pi f_c t = s_i \phi(t), \quad 0 \leq t \leq T \quad (20)$$

where

$$\begin{aligned} \phi(t) &= \sqrt{2/E_p} p(t) \cos 2\pi f_c t \\ s_i &= A_i \sqrt{E_p}/2 \end{aligned} \tag{21}$$

where E_p is the energy of pulseshaping signal $p(t)$ in $[0, T]$. Note that $\int_0^T \phi^2(t) dt \cong 1$ for $f_c \gg 1/T$. Thus for most practical cases where $f_c \gg 1/T$, the optimum demodulator for the rectangular pulse case is still applicable for other pulseshapes and the symbol error probability expression (19) is still valid.

4. BIPOLAR SYMMETRIC M-ARY ASK

As mentioned in the previous section, a bipolar MASK can be demodulated only coherently and is preferred over the unipolar MASK since the former has better BER performance. In this section, we will examine coherent symmetric uniform-spacing bipolar MASK in terms of its PSD, system structure, and BER.

4.1. Power Spectral Density and Bandwidth

The PSD of the complex envelope of the symmetric bipolar MASK (not necessarily uniformly spaced) is obtained by setting $m_A = 0$ in (11):

$$\Psi_s(f) = \frac{\sigma_A^2 |P(f)|^2}{T} \tag{22}$$

The above shows that the PSD of symmetric bipolar MASK is determined by the PSD of the pulseshaping function $p(t)$. If the pulse is rectangular, then, from (13), we have

$$\Psi_s(f) = \sigma_A^2 T \left(\frac{\sin \pi f T}{\pi f T} \right)^2 \tag{23}$$

The passband PSD can be obtained by substituting the baseband PSD expressions into (2). Figure 7 shows the passband PSD of the bipolar MASK with rectangular pulse (where we set $\sigma_A^2 T = \frac{1}{2}$). The null-to-null bandwidth is $2/T$. Note that unlike the PSD for OOK there is no discrete spectral line at the carrier frequency.

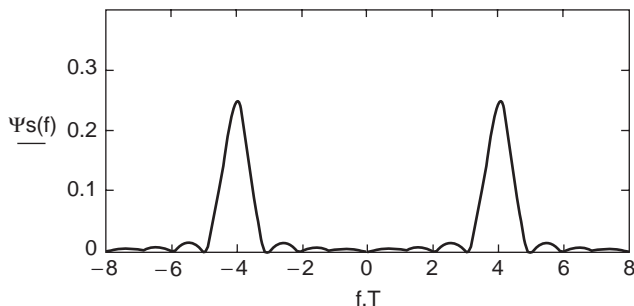


Figure 7. PSD of bipolar MASK with rectangular pulse, and $\sigma_A^2 T = \frac{1}{2}$.

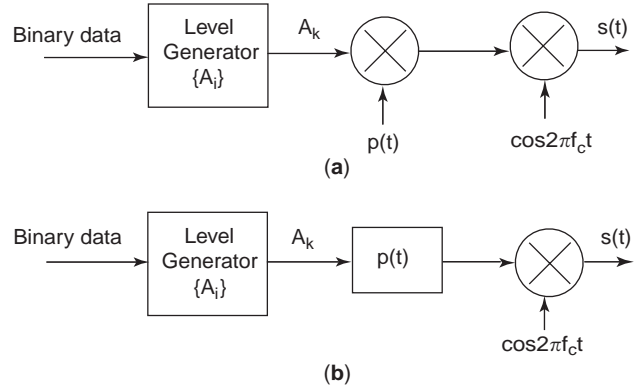


Figure 8. MASK modulator. (From Xiong [1], copyright © 2000 Artech House.)

4.2. Modulator and Demodulator

The modulator is shown in Fig. 8. Figure 8a is a direct implementation of (7). The level generator takes $n = \log_2 M$ bits from the binary datastream and maps them into an amplitude level $A_k \in \{A_i\}$, where the subscript k indicates the k th symbol interval. The mapping is preferably gray-coding so that the n -tuples representing the adjacent amplitudes differ by only one bit. The functions of the remaining blocks are self-explanatory. The equivalent implementation is shown in Fig. 8b. It is more practical for hardware implementation. The $p(t)$ multiplier is replaced with a filter with an impulse response $p(t)$. In order to generate a pulse $A_i p(t)$, the input to the filter must be an impulse $A_i \delta(t)$. In practice, this can be realized by a very narrow pulse with amplitude A_i .

The optimum receiver implementing the minimum distance rule is shown in Fig. 9, where the last block is a threshold detector. Figure 9a is a direct implementation of (17) and the minimum distance rule. In Fig. 9b, the correlation with $p(t)$ is replaced by a matched filter and a sampler [1, p. 419]. Figure 9b is more practical for hardware implementation.

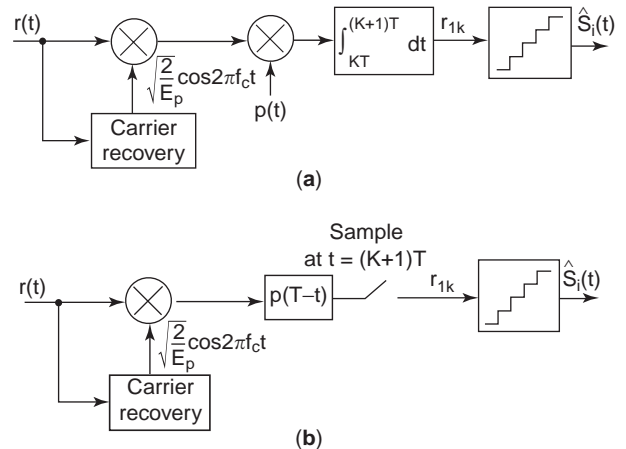


Figure 9. Optimum coherent demodulators for MASK. (From Xiong [1], copyright © 2000 Artech House.)

The threshold detector has $M-1$ thresholds, each placed in the middle of two signal points (refer to Fig. 7). The correlator computes the r , and the threshold detector is actually computing the distance of r to the amplitudes s_i , $i=1, 2, \dots, M$ and chooses the smallest. Note that the reference signal can be any scaled version of $\phi(t)$ as long as the thresholds are scaled accordingly.

The recovery of coherent carrier and the symbol timing clock are assumed in the coherent demodulator. A description of techniques of carrier and timing recovery is beyond the scope of this article, but it can be found in common communication books.

4.3. Error Probability

The error probability of bipolar symmetric uniformly spaced MASK is obtained from (19), but we need to figure out what Δ is. For bipolar symmetric uniformly spaced MASK, the amplitudes A_i are given in (8). In terms of signal projection s_i , from (21) we can write

$$\begin{aligned} s_i &= A_i \sqrt{E_p/2} = (2i-1-M)A \sqrt{E_p/2} \\ &= (2i-1-M)A_0, \quad i=1, 2, \dots, M \end{aligned} \quad (24)$$

where $A_0 = A \sqrt{E_p/2}$. Then

$$\Delta = |s_i - s_{i-1}| = 2A_0$$

Thus from (19) we have

$$P_s = \frac{2(M-1)}{M} Q \left(\sqrt{\frac{2A_0^2}{N_0}} \right) \quad (25)$$

The symbol error probability can be expressed in terms of the average energy of the signals. The average symbol energy of the signals is

$$\begin{aligned} E_s &= \frac{1}{M} \sum_{i=1}^M E_i = \frac{1}{M} \sum_{i=1}^M s_i^2 \\ &= \frac{1}{M} \sum_{i=1}^M (2i-1-M)^2 A_0^2 = \frac{1}{M} \frac{M(M^2-1)A_0^2}{3} \\ &= \frac{1}{3} (M^2-1)A_0^2 \end{aligned} \quad (26)$$

As a result, (25) becomes

$$P_s = \frac{2(M-1)}{M} Q \left(\sqrt{\frac{6E_s}{(M^2-1)N_0}} \right) \quad (27)$$

Since the average energy per bit is $E_b = E_s / \log_2 M$, (27) can be written as

$$P_s = \frac{2(M-1)}{M} Q \left(\sqrt{\frac{6(\log_2 M)E_b}{(M^2-1)N_0}} \right) \quad (28)$$

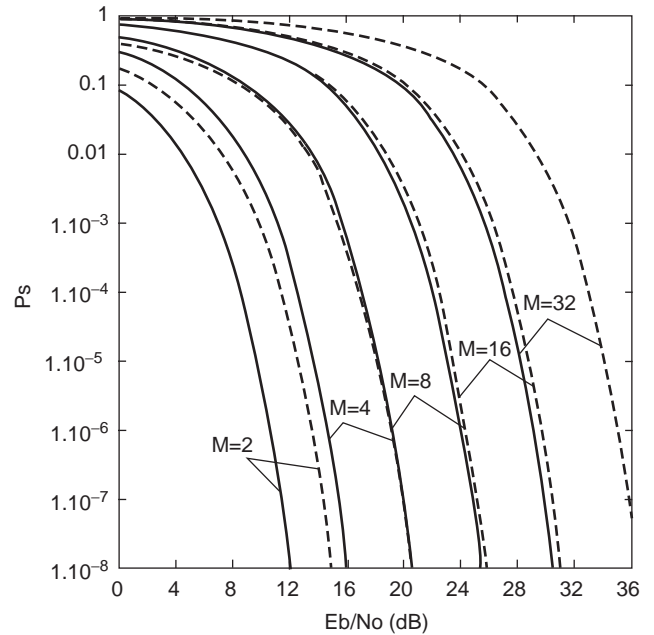


Figure 10. Symbol error probability of coherent bipolar symmetric uniformly spaced MASK (solid line) and coherent unipolar uniformly spaced MASK (dotted line).

Figure 10 shows the curves of the symbol error probability of the bipolar symmetric uniformly spaced MASK versus E_b/N_0 . We emphasize that (27) to (28) depend on only average energy of the signal symbols, not the function form of $p(t)$. In general, bit error probability is not simply related to symbol error probability. However, for Gray coded¹ n -tuple-to-amplitude mapping, the adjacent symbols differ by only one bit. At high signal-to-noise ratios, the most likely errors are the adjacent symbols, so in this case

$$P_b \approx \frac{P_s}{\log_2 M} \quad (29)$$

5. UNIPOLAR M -ARY ASK

As pointed out in Section 2, a unipolar MASK can be demodulated noncoherently as well as coherently. Even though coherent unipolar MASK is not a usual choice since the symmetric bipolar MASK is better in terms of BER, for the sake of completeness and also because of the ease in doing this, we will present the error probability expression. Then we will focus on the noncoherent unipolar MASK. But first we examine its power spectral density.

¹The bits-to-amplitude mapping could be arbitrary as long as the mapping is one-to-one. However, a method called Gray coding is usually used. Gray coding assigns n -tuples with only one-bit difference to two adjacent amplitudes. When an M -ary symbol error occurs, it is most likely that the signal is detected as one of the signals with the adjacent amplitudes; thus only one of the n bits is in error. Gray coding keeps the bit error rate at the minimum for a given symbol error rate.

5.1. Power Spectral Density and Bandwidth

In general, the PSD of unipolar MASK is given by (11). For uniformly spaced amplitudes and rectangular symbol pulse, the PSD of the complex envelope is given in (13). The passband PSD shape is shown in Fig. 2.

For the amplitudes given in (9), the mean value of the amplitudes is

$$m_A = \frac{1}{M} (0 + A + \dots + (M-1)A) = \frac{(M-1)A}{2}$$

and then

$$\Psi_s(f) = \sigma_A^2 T \left(\frac{\sin \pi f T}{\pi f T} \right)^2 + \frac{(M-1)^2 A^2}{4} \delta(f) \quad (30)$$

5.2. Modulator and Demodulator

The structure of modulator for unipolar MASK is almost the same as that for bipolar MASK as shown in Fig. 8. The difference is only in the settings of the level generator due to the signal's unipolarity. The signal levels are now only positive and equally spaced.

The structure of coherent demodulator for unipolar MASK is almost the same as that for bipolar MASK as shown in Fig. 9. The difference is only in the settings of the threshold detector due to the signal's unipolarity. The thresholds now are only positive and equally spaced.

The structure of noncoherent demodulator for unipolar MASK is almost the same as that for OOK as shown in Fig. 3. The difference is in the threshold detector, which must now have multiple equally-spaced thresholds.

5.3. Coherent Demodulation and Error Probability

The symbol error probability is again given by (19), but we need to figure out what Δ is. For unipolar uniformly spaced MASK, the amplitudes are given in (9). In terms of signal projection s_i , from (21) we can write

$$s_i = A_i \sqrt{E_p/2} = (i-1)A \sqrt{E_p/2} \quad (31)$$

$$= (i-1)A_0, \quad i = 1, 2, \dots, M$$

where $A_0 = A \sqrt{E_p/2}$. Then

$$\Delta = |s_i - s_{i-1}| = A_0$$

Thus from (19) we have

$$P_s = \frac{2(M-1)}{M} Q \left(\sqrt{\frac{A_0^2}{2N_0}} \right) \quad (32)$$

The average symbol energy of the signals is

$$\begin{aligned} E_s &= \frac{1}{M} \sum_{i=1}^M E_i = \frac{1}{M} \sum_{i=1}^M s_i^2 \\ &= \frac{1}{M} \sum_{i=1}^M (i-1)^2 A_0^2 = \frac{1}{M} \sum_{j=0}^{M-1} j^2 A_0^2 \\ &= \frac{1}{6} (2M^2 - 3M + 1) A_0^2 \end{aligned}$$

Table 1. Comparison between Bipolar and Unipolar Uniformly Spaced MASK

M	2	4	8	16	32	64	∞
$R(M)$	2	2.8	3.333	3.647	3.818	3.908	4
$10 \log R(M)$ (dB)	3.01	4.472	5.229	5.619	5.819	5.919	6.02

As a result, (32) becomes

$$P_s = \frac{2(M-1)}{M} Q \left(\sqrt{\frac{3E_s}{(2M^2 - 3M + 1)N_0}} \right) \quad (33)$$

In terms of average energy per bit, (33) can be written as

$$P_s = \frac{2(M-1)}{M} Q \left(\sqrt{\frac{3(\log_2 M)E_b}{(2M^2 - 3M + 1)N_0}} \right) \quad (34)$$

This expression is plotted in Fig. 10 (dotted line). The P_b at high SNRs can be estimated by (29). When $M=2$, the unipolar MASK is OOK, $P_s = P_b$. Substituting $M=2$ into (34), we obtain the exact expression in (4).

Comparing (28) and (34) reveals that the ratio of the expression in the square root sign of (28) over that of (34) is

$$R(M) = \frac{2(2M^2 - 3M + 1)}{M^2 - 1}$$

Table 1 shows some values of $R(M)$. It shows that the bipolar uniformly spaced MASK is superior to the unipolar uniformly spaced MASK. The asymptotic ratio is 4 or 6 dB. This confirms the statement we said earlier that coherent unipolar MASK is not a usual choice since the symmetric bipolar MASK is better in terms of BER.

5.4. Noncoherent Demodulation and Error Probability

When carrier synchronization is difficult or beyond simple system complexity, noncoherent unipolar MASK can be used. The noncoherent demodulator is the same as that for OOK in Fig. 3c except that the threshold detector must have multiple thresholds. The thresholds and symbol error probability for noncoherent demodulation of the unipolar uniformly spaced MASK in AWGN channel has been derived [6]. We summarize the derivation here and present the results.

Recall that the unipolar uniformly spaced MASK signal set is $(0, A, 2A, \dots, (M-1)A)$. When the amplitude $A_0 = 0$ is transmitted, the output of the envelope detector (Fig. 4), denoted as η , has Rayleigh distribution (the first probability density function (pdf) in Fig. 11). An error will occur if the envelope η has a value greater than the threshold γ . The probability of error for this case will be

$$p(e|A_0) = \int_{\gamma}^{\infty} \frac{\eta}{\sigma^2} \exp\left(-\frac{\eta^2}{2\sigma^2}\right) d\eta$$

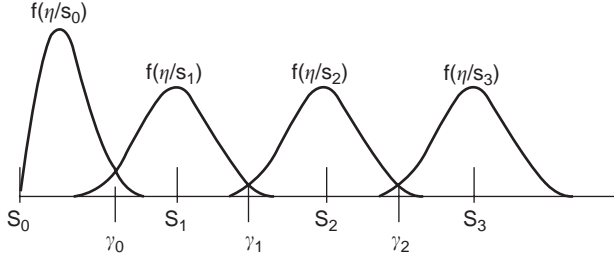


Figure 11. Threshold and decision regions for unipolar noncoherent MASK ($M=4$).

where $\sigma^2 = N_0/2$ is the variance² of the AWGN [1,7]. At high signal-to-noise ratio, the optimum threshold (γ_0) can be closely approximated by $\sqrt{E_{\min}}/2$ [8], where $E_{\min} = A^2 T/2$ is the energy of the symbol with the minimum non-zero amplitude. Therefore

$$p(e|A_0) = \exp\left(-\frac{E_{\min}}{4N_0}\right)$$

The other case that should be considered separately is the case when the symbol A_{M-1} is transmitted (see the last pdf in Fig. 11). In this case, the probability density function of the envelope η is Rician and is centered at $(M-1)\sqrt{E_{\min}}$. An error will occur if the value of the envelope η has a value less than the threshold. At high signal-to-noise ratio, the Rician distribution is closely approximated by a Gaussian distribution [8]. Using the Gaussian approximation, the probability of error for this case will be

$$p(e|A_{M-1}) \approx \int_{-\infty}^{\gamma_{M-2}} \frac{1}{\sigma\sqrt{2\pi}} \exp\left[-\frac{(\eta - (M-1)\sqrt{E_{\min}})^2}{2\sigma^2}\right] d\eta$$

Since we have used the Gaussian approximation, the threshold will be taken as the intersection of the adjacent probability density functions $p(\eta|A_{M-1})$ and $p(\eta|A_{M-2})$, that is, $\gamma_{M-2} = (M-1.5)\sqrt{E_{\min}}$, then

$$p(e|A_{M-1}) \approx Q\left(\sqrt{\frac{E_{\min}}{2N_0}}\right)$$

All other transmitted symbols have the same Rician distribution with different means. Because of the equal spacing of these signals and their thresholds, they have equal probability of error. Regardless of what symbol was transmitted, we can assume that the Rician pdf is centered at the zero point and an error will occur if η exceeds the upper or lower threshold, that is, if $\eta > \sqrt{E_{\min}}/2$ or $\eta < -\sqrt{E_{\min}}/2$. Since the Gaussian approximation has symmetric pdf around its mean, the average probability

²The envelope detector must be a quadrature receiver with orthonormal reference carriers.

of error can be expressed as

$$\begin{aligned} p(e|A_i) &\approx 2 \int_{\gamma_i}^{\infty} \frac{1}{\sigma\sqrt{2\pi}} \exp\left(-\frac{\eta^2}{2\sigma^2}\right) d\eta \\ &= 2Q\left(\sqrt{\frac{E_{\min}}{2N_0}}\right), \quad i=1, \dots, M-2 \end{aligned}$$

Multiplying the three conditional probabilities by $(1/M)$, $(1/M)$ and $[(M-2)/M]$, respectively, and adding them will give

$$P_s = \frac{1}{M} \left[\exp\left(-\frac{E_{\min}}{4N_0}\right) + (2M-3)Q\left(\sqrt{\frac{E_{\min}}{2N_0}}\right) \right]$$

The average symbol energy E_s is related to the minimum symbol energy by

$$\begin{aligned} E_s &= \frac{1}{M} \sum_{i=1}^M E_i = \frac{1}{M} \sum_{i=1}^M (i-1)^2 \left(A^2 \frac{T}{2}\right) = \frac{1}{M} \sum_{j=0}^{M-1} j^2 \left(A^2 \frac{T}{2}\right) \\ &= \frac{1}{6} (2M^2 - 3M + 1) \left(A^2 \frac{T}{2}\right) = \frac{1}{6} (2M^2 - 3M + 1) E_{\min} \end{aligned}$$

or

$$E_{\min} = \frac{6E_s}{2M^2 - 3M + 1} = 2B_M E_s$$

where

$$B_M = \frac{3}{2M^2 - 3M + 1} \quad (35)$$

This equation can be written in terms of E_s/N_0 using the following equation

$$P_s = \frac{1}{M} \left[\exp\left(-\frac{E_s}{2N_0} B_M\right) + (2M-3)Q\left(\sqrt{\frac{E_s}{N_0} B_M}\right) \right] \quad (36)$$

or in terms of E_b/N_0

$$\begin{aligned} P_s &= \frac{1}{M} \left[\exp\left(-\frac{1}{2} (\log_2 M) B_M \frac{E_b}{N_0}\right) \right. \\ &\quad \left. + (2M-3)Q\left(\sqrt{(\log_2 M) B_M \frac{E_b}{N_0}}\right) \right] \end{aligned} \quad (37)$$

where E_b is the average energy per bit. When $M=2$, the above reduces to the P_b expression for OOK (6). Figure 12 shows the symbol error probability given above for noncoherent demodulation (dotted lines), together with those for coherent demodulation. From the figure we can see that the noncoherent demodulation incurs a small performance degradation. When M is high, the degradation is negligible.

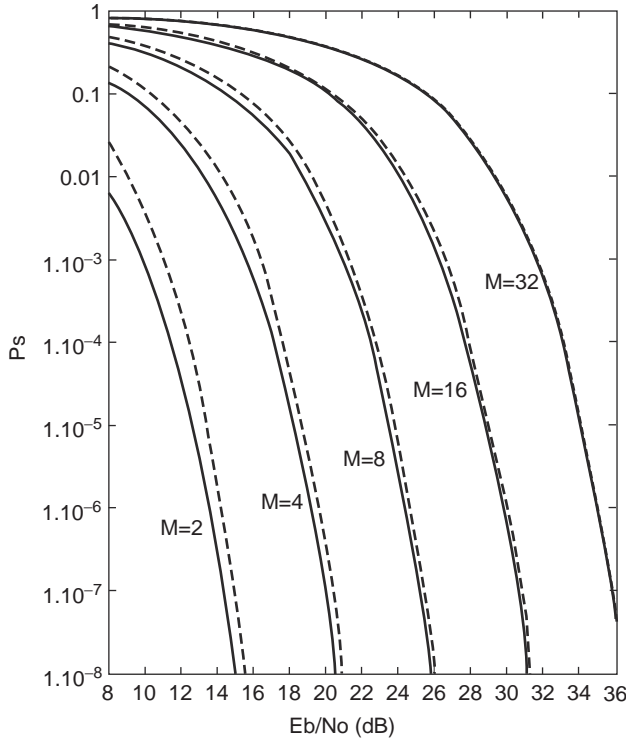


Figure 12. Symbol error probability of unipolar uniformly spaced MASK: solid line—coherently demodulated; dotted line—noncoherently demodulated.

6. COMPARISON WITH MPSK

For the same symbol rate and the pulshape, MPSK and MASK have the same PSD and hence the same bandwidth. Thus it makes sense to compare their BER performances.

In comparison to MPSK, starting from $M = 4$, the error probability of bipolar MASK is inferior to that of the MPSK. The P_s of the MPSK is given by [1, (4.24)]

$$P_s \approx 2Q\left(\sqrt{\frac{2E_s}{N_0}} \sin \frac{\pi}{M}\right) \tag{38}$$

Comparing (38) and (27), the ratio (MASK over MPSK) of the arguments inside the square root sign of the Q function is

$$R_M = \frac{3}{(M^2 - 1) \sin^2 \frac{\pi}{M}} \tag{39}$$

and is tabulated in Table 2. If $M \geq 32$ the degradation is constantly 5.17 dB. This is easily seen from (39). For

Table 2. Power Penalty of MASK over MPSK

M	2	4	8	16	32	64	128
$R(M)$	1	0.4	0.325	0.309	0.305	0.304	0.304
$10 \log R(M)$ (dB)	0	-3.98	-4.88	-5.10	-5.16	-5.17	-5.17

large M , $\sin \pi/M \cong \pi/M$, and $R_M \cong 3/\pi^2 \cong 0.304$. Another fact is that in both bipolar MASK and MPSK, for the same error probability, the power increase is 6 dB for doubling M for large M . This means in terms of increasing bandwidth efficiency with increased M , both schemes pay the same penalty in BER performance. However, MASK still has a fixed 5.17 dB disadvantage against MPSK. This shows MASK is inferior to MPSK in terms of error probability. However, we will see that going to two-dimensional MASK, namely, QAM, improves error rate performance significantly. As a result, QAM is superior to MPSK when $M > 4$. We will briefly discuss QAM in the next section.

7. ADVANCED MODULATIONS RELATED TO ASK

Two important modulations arise from ASK. One is the quadrature amplitude modulation or QAM. Another is the ASK-OFDM (orthogonal frequency division multiplexing).

QAM is constructed by adding two MASK signals together as below [$p(t)$ is pulshape]

$$s_i(t) = A_{i1}p(t) \cos 2\pi f_c t - A_{i2}p(t) \sin 2\pi f_c t$$

As can be seen, the second carrier is a sine function that is orthogonal to the first carrier. The first component is the in-phase or I component, and the second component is the quadrature or Q component. The system complexity of QAM doubles that of MASK since it requires I and Q branches in its modulator and demodulator. However, the BER performance of QAM is much better than MASK. In fact, the BER performance of an M -ary QAM is exactly the same as that of a \sqrt{M} -ary MASK whose bandwidth efficiency is only half that of QAM [13]. Also the BER performance of an M -ary QAM is even better than that of MPSK when $M > 4$. For example, for the same BER, the MPSK needs 1.65, 4.20, and 7.02 dB more SNR for $M = 8, 16,$ and 32 , respectively [1].

Orthogonal frequency-division multiplexing is a bandwidth-efficient multiple-carrier modulation scheme, especially good for frequency-selective fading channels, where data are separated into N datastreams. Each of them modulates a subcarrier. Then these N modulated signals are summed to form the final signal, which in turn modulates a higher-frequency carrier for transmission. The common modulations used in OFDM are QAM or MPSK [9]. Noncoherent OOK or MASK were also proposed to be used in frequency-hopping multiple-access system since carrier synchronization is difficult in such system [11,12]. An OFDM scheme that uses QAM or MPSK or noncoherent MASK (including OOK) requires that the N subcarriers be separated in frequency by $1/T$ for them to be orthogonal to each other so that they can be separated in the demodulator. These types of OFDM can be conveniently implemented by the pair of inverse fast Fourier transform (IFFT) for modulation and FFT for demodulation [10]. MASK-OFDM has been proposed [13], where coherent MASK is used for modulation that requires a frequency separation of only $1/2 T$ and can be conveniently implemented by the pair of fast cosine transform (FCT)

and inverse FCT (IFCT) for modulation and demodulation, respectively. Since the BER performance of MASK is inferior to that of QAM, the order of the MASK has to be reduced to \sqrt{M} to match the BER performance of QAM. By doing so, the bandwidth advantage of MASK-OFDM is lost. However, the system complexity of MASK-OFDM is reduced in comparison to that of QAM-OFDM.

BIBLIOGRAPHY

1. F. Xiong, *Digital Modulation Techniques*, Artech House, Boston/London, 2000.
2. J. G. Proakis, *Digital Communications*, 2nd Ed., New York: McGraw-Hill, 1989.
3. S. Haykin, *Digital Communications*, Wiley, New York, 1988.
4. H. L. Van Trees, *Detection, Estimation, and Modulation Theory, Part I*, Wiley, New York, 1968.
5. F. G. Stremmer, *Introduction to Communication Systems*, 3rd Ed., Addison-Wesley, 1990.
6. A. J. Al-Dweik and F. Xiong, Frequency-hopped multiple-access communication with noncoherent OFDM-MASK in AWGN channels, *Int. Conf. Military Communications (MIL-COM) 2001*, McLean, VA, Oct. 28–31 2001.
7. A. D. Whalen, *Detection of Signals in Noise*, Academic Press, 1971.
8. R. E. Ziemer and W. H. Tranter, *Principles of Communications*, Houghton-Mifflin, 1985.
9. A. R. S. Bahai and B. R. Saltzberg, *Multi-Carrier Digital Communications, Theory and Applications of OFDM*, Kluwer/Plenum, 1999.
10. S. B. Weinstein and P. M. Ebert, Data transmission by frequency division multiplexing using the discrete Fourier transform, *IEEE Trans. Commun.* **19**(5): 628–634 (Oct. 1971).
11. S. H. Kim and S. W. Kim, Frequency-hopped multiple-access communication with multicarrier on-off keying in Rayleigh fading channels, *IEEE Trans. Commun.* **48**(10): 1692–1701 (Oct. 2000).
12. A. Al-Dweik and F. Xiong, FHMA communication with noncoherent OFDM-ASK in AWGN channels, *IEEE Trans. Commun.* **51**(1): 33–36 (Jan. 2003).
13. F. Xiong, M-ary amplitude shift keying OFDM system, *IEEE Trans. Commun.* **51**(10): 1638–1642 (Oct. 2003).

ANALYTICAL AND ADAPTIVE MODELING OF NONLINEAR HIGH-POWER AMPLIFIERS

MOHAMED IBNKAHLA
Queen's University
Kingston, Ontario, Canada

1. INTRODUCTION

Communication channels are equipped with high-power amplifiers (HPA), which are used to amplify the transmit-

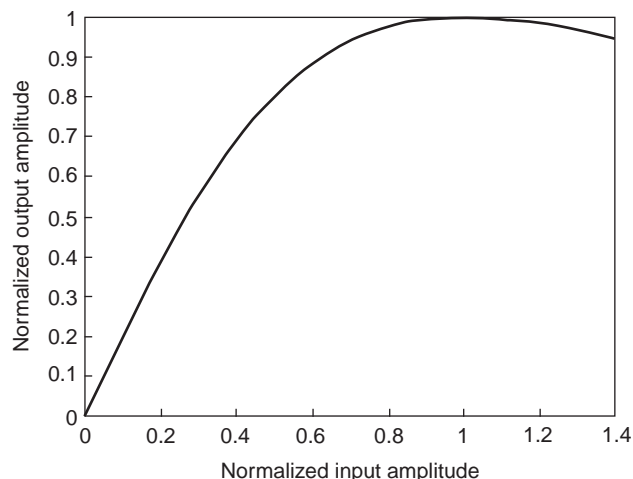


Figure 1. Example of amplitude conversion of a TWT amplifier.

ted signal in order to reach an acceptable signal-to-noise ratio (SNR). In general, these amplifiers have nonlinear characteristics. For example, traveling-wave-tube (TWT) amplifiers (see examples of amplitude and phase conversions in TWT amplifiers in Figs. 1 and 2, respectively) and solid-state power (SSP) amplifiers are widely used in satellite communications for their excellent power efficiency [15]. However, these amplifiers cause nonlinear distortions to the transmitted signals, due to their nonlinear behavior.

For low input levels, the output power of a nonlinear HPA is essentially a linear function of the input power. As the input drive increases, the output power increases nonlinearly until the point of maximum power output is reached. Beyond this point (referred to as “saturation”), any additional increase in the input power level does not result in an additional increase in output power (see, e.g., Fig. 1). The operating point of the TWT is usually given in terms of input or output backoff from saturation. Generally, an amplifier will be most efficient when it operates at or near saturation.

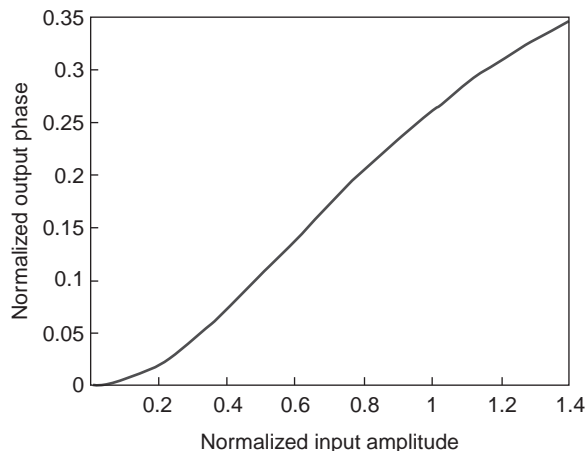


Figure 2. Example of phase conversion of a TWT amplifier.

The closer an amplifier is driven to saturation, the greater the amount of distortion it produces. Distortion may also be produced in the phase, which may change nonlinearly with the input power level.

HPA modeling serves a variety of purposes. For example, if the required measured physical data are unavailable, an analytical model is desirable. This model can be used in order to run computer simulations that measure a variety of signal and channel configurations without imposing instrumentation limitations. The analytical expressions derived by the model can be used in order to conduct performance analysis of the communication channel, to study the efficiency of the design through computer simulations, or to optimize the channel resources over various amplifier and channel conditions. Moreover, analytical models can be used in order to design and optimize the different parts of the transmitter and the receiver, such as modulation scheme and predistortion technique at the transmitter; and demodulation scheme, detection device, and equalization algorithm at the receiver. This article presents a survey of nonlinear amplifier models, including memoryless amplifiers and amplifiers with memory. There is a special focus on adaptive neural network (NN) approaches.

2. NONLINEAR MEMORYLESS HIGH-POWER AMPLIFIERS

2.1. Signal Representation

TWT amplifiers exhibit two nonlinear conversions: amplitude-to-amplitude (AM/AM) and amplitude-to-phase (AM/PM) conversions. Two equivalent frequency-independent representations have been proposed for these nonlinearities: amplitude-phase (A-P) representation and in-phase – quadrature (I-Q) representation [24].

Let the TWT input wave be expressed as

$$x(t) = r(t) \cos(\omega_0 t + \phi_0) \quad (1)$$

where ω_0 is the carrier frequency and $r(t)$ and ϕ_0 are the input signal amplitude and phase, respectively.

For the A-P representation, the output signal is expressed as

$$y(t) = A(r(t)) \cos(\omega_0 t + \phi(r(t)) + \phi_0) \quad (2)$$

where $A(r)$ and $\phi(r)$ are the AM/AM and AM/PM conversions, respectively.

For the I-Q representation, the output signal is represented by its in-phase and quadrature components

$$p(t) = P(r(t)) \cos(\omega_0 t + \phi_0) \quad (3)$$

$$q(t) = -Q(r(t)) \sin(\omega_0 t + \phi_0) \quad (4)$$

where $P(r)$ and $Q(r)$ are the in-phase and quadrature conversions, respectively. These can be shown from the

AM/AM and AM/PM conversions to be:

$$P(r) = A(r) \cos(\phi(r)) \quad (5)$$

$$Q(r) = A(r) \sin(\phi(r)) \quad (6)$$

2.2. Nonlinear Distortion Effect on Digitally Modulated Signals

When the input signal is digitally modulated, the HPA nonlinearity rotates the signal constellation. This causes an alteration in the decision region. Figure 3 displays the effect of nonlinearity on the constellation of a 16-quadrature amplitude modulation (16-QAM) signal. The decision regions are used by the receiver to decode the received symbols. If a received symbol falls in the decision region of a certain constellation point, then the receiver decides that the transmitted symbol is that particular constellation point.

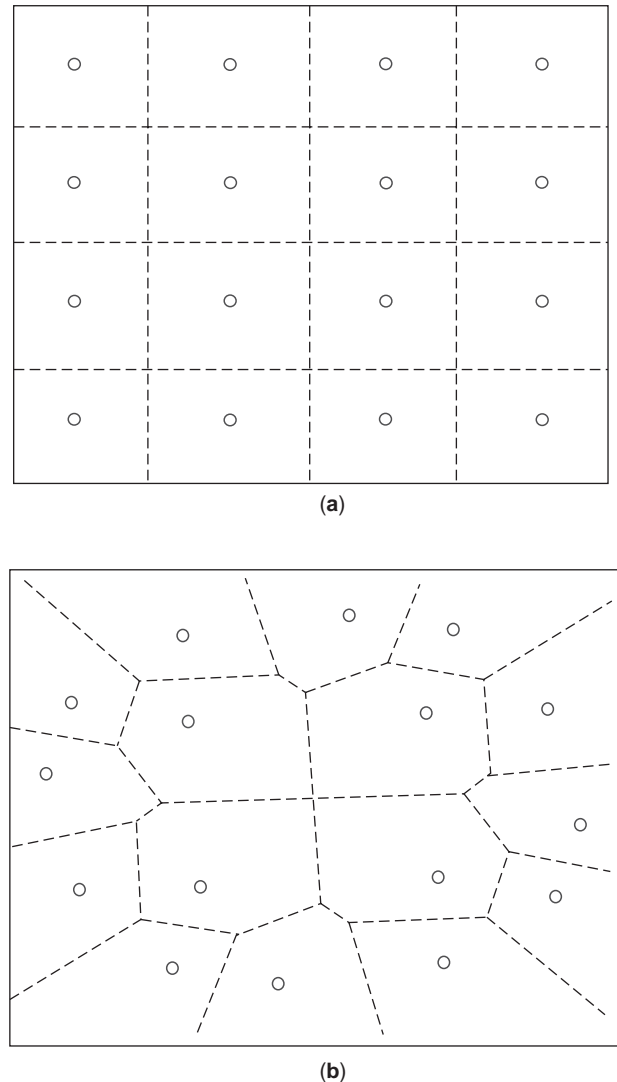


Figure 3. TWT input (a) and output (b) constellations with amplifier working close to saturation.

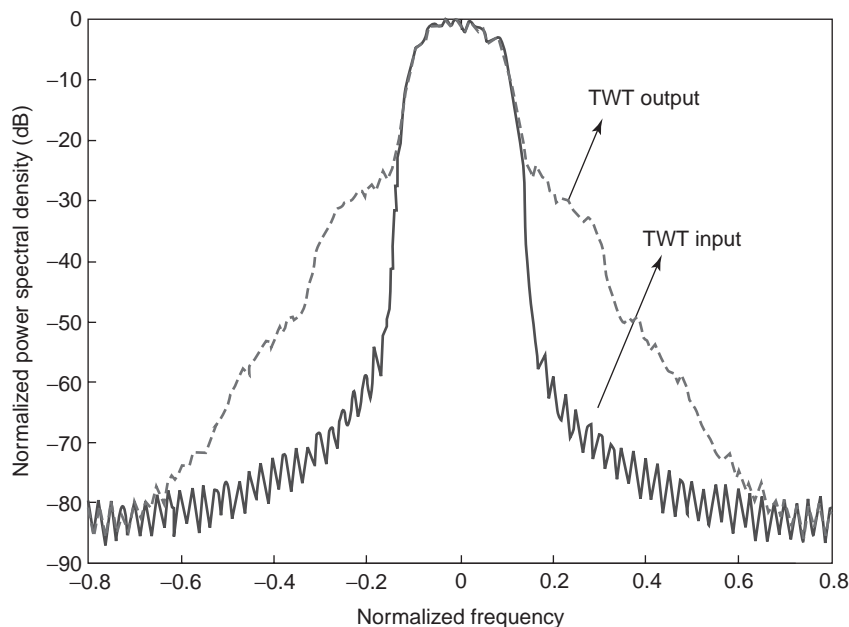


Figure 4. Example of spectral regrowth generated by a TWT amplifier.

When the decision regions are distorted, the receiver can no longer use the ideal decision regions of the transmitted constellation in order to decode the received signal. The receiver must know the constellation at the output of the amplifier, which is difficult since the characteristics and the operating point of the amplifier may change. Moreover, as can be seen in Fig. 3b, some symbols become closer to each other in the distorted constellation, leading to an increase in the symbol error rate (SER).

2.3. Intermodulation Distortions and Spectral Regrowth

Another major consequence of amplifier nonlinearities is the generation of intermodulation distortion (IMD) products [17]. IMD products are located at frequencies above and below those of the input carriers, and at frequency intervals equal to separations between input carriers. IMD products cannot be easily eliminated through filtering, as they are located close to the desired input signal bandwidth. IMD products not only corrupt the amplified signal itself but also cause adjacent-channel interference due to spectral regrowth (Fig. 4), which is more serious because it acts as interference to the adjacent channels. This interference is tightly controlled by the communications standards being used, and must be reduced to the allowable limit. Thus, this phenomenon has a direct impact on the system capacity and performance.

Distortion is most often evaluated in terms of the ratio of the carrier to the third-order IMD products (i.e., IMD terms closest to the carrier). IMD terms can also be non-symmetric. This imbalance is due to the presence of both amplitude- and phase-induced IMD products [17].

Interference produced in the adjacent channel is characterized by the adjacent-channel power ratio (ACPR), which is the power in the main channel divided by the power in the lower plus upper adjacent channels [25].

HPA amplifier design depends on tradeoffs between three main performance indicators: output power, efficiency, and sideband regrowth. However, a certain amount of power amplifier nonlinearity has to be accepted in order to guarantee satisfactory amplifier efficiency.

Moreover, these amplifiers not only are nonlinear, but also can possess memory. If the reciprocal of the bandwidth of the input signal is much larger than the memory of the amplifier (as is the case for most amplifiers driven with narrowband signals), then the amplifier can be modeled as memoryless for that particular input signal. This means that the output is a function of the input at the present time only.

An accurate and verified simulation model for an HPA is required to reliably study the effects of the nonlinearity on the system level, and to give an insight into the problem of finding an appropriate tradeoff between power amplifier efficiency and system capacity. Therefore, an optimal operating point is imperative in order to maximize the output power and minimize the degradation due to distortions.

2.4. Amplifier Backoff

Backoff (BO) defines how far the HPA is operating from the saturation point. The *input saturation power* is defined as the maximum power that can be provided by the amplifier with the highest efficiency. Beyond saturation, the amplifier has no more gain in power. There are two ways of defining backoff: (1) relative to the input [input backoff (IBO)] and (2) relative to the output [output backoff (OBO)]. IBO is the ratio of the saturation power to the desired drive (input) power. OBO is the ratio of the saturation power to the actual output power. Increasing the IBO or OBO reduces nonlinear distortions, but also leads to less output power.

3. ANALYTICAL MODELS

Considerable work has been done in the literature for developing analytical expressions of TWT characteristics. The analytical models have been categorized based on the form of the mathematical representation to elucidate the general characteristics of the models falling in each category.

3.1. Power Series

The power series representation is one of the most commonly used methods to represent nonlinear devices because it identifies the contribution of different power terms. Since the AM/AM conversion, $A(r)$, is an odd function of r , and the AM/PM conversion, $\phi(r)$, is an even function, the following expansion is generally assumed

$$A(r) = \sum_{m=0}^{\infty} a_m r^{2m+1} \quad (7)$$

$$\phi(r) = \sum_{m=0}^{\infty} p_m r^{2m} \quad (8)$$

where parameters $\{a_m\}$ and $\{p_m\}$ have to be determined (e.g., through an optimization procedure).

The power series or Taylor expression must be used with some caution because the series may not converge for all values and sometimes converges slowly. The series requires a large number of terms and heavy computation. The power series model can closely approximate the amplifier curve for a limited range. A common drawback with this model is the explosion of the predicted variable magnitude. This occurs when large values are assigned to some predictions. This type of behavior necessitates the censoring of the predicted variable value. Hence, it is difficult to test strong nonlinearities in simulation when there is a very large envelope variation in the input signal.

The classic work using this model was performed by Chapman and Millard [4]. They accounted for the effect of the AM/PM conversion, which was represented by a single constant coefficient k determined through a measured technique:

$$\phi(r) = kr^2 \quad (9)$$

This relation does not hold over the complete operating region of the TWT amplifier.

Medhurst and Roberts [21] proposed a representation of the AM/AM characteristic by using the sum of the linear and cubic terms and used a two-tone test for verification:

$$y(t) = a_1 x(t) + a_3 x^3(t) \quad (10)$$

3.2. Softlimiter Approach

The input/output relationship can simply be modeled as an ideal softlimiter that has two distinct regions: the perfect linear region and the saturation region. However, the linear region of a practical TWT amplifier is not as perfectly linear as that of the soft limiter. Moreover, this representation does not give a completely realistic model

of the TWT. The limitation of this model is that it requires the envelope amplitude function $A(r)$ not to fall off beyond saturation.

3.3. Exponential Expression

Berman and Mahle [2] gave a three-parameter analytical expression of the AM/PM conversion, which gives reasonably good agreement over the whole range, especially for small input power and above saturation

$$\phi(r) = k_1(1 - \exp(-k_2 r^2)) + k_3 r^2 \quad (11)$$

where k_1 , k_2 , k_3 are the TWT constants obtained from a measured transfer characteristic by a cut-and-dry method or by an optimization routine. The slope for zero input power is given by $2k_1 k_2$. Moreover, for a large input signal power, $\phi(r)$ approaches $k_3 r^2$.

Thomas et al. [27] proposed a four-parameter formula for $A(r)$. The amplitude nonlinearity was analytically modeled by fitting the single-carrier input/output power data with a portion of cosine centered around saturation. This leads to the following function representation

$$A(r) = \begin{cases} 10^{\alpha[\cos(\log_{10}(r/r_s)/\beta)-1]}, & r > r_s \\ r, & r < r_s \end{cases} \quad (12)$$

where r_s is the input saturation power and α and β are constants chosen to fit the data that can be calculated through optimization routines.

3.4. Error Function

The error function closely follows the AM-AM characteristics of a typical TWT amplifier. However, this approach can result in higher error for different amplifiers which may not follow the typical characteristic closely. Pawula [22] presented the input-output relationship of nonlinearity by an error function characteristic using

$$A(r) = \alpha \sqrt{\frac{\pi}{2}} \operatorname{erf}\left(\frac{r}{\beta}\right) \quad (13)$$

where α is the gain parameter and β is the limiter parameter.

3.5. Bessel Functions

The Bessel function was also considered for analytical modeling because of its analytical and numerical convenience as it simplifies the calculation of the output spectrum. However, it requires a large number of terms to fit the measured data.

Kaye et al. [18] came up with the quadrature model and used a sum of Bessel functions of the first kind of order 1. In order to compute the power spectra of the outputs of the nonlinearities in the I-Q representation, they suggested to represent them by a convergent series of functions that are, on one hand, simple to determine from the measured data and, on the other hand, convenient for the power spectrum calculations. This model is

expressed as

$$P(r)[\text{or } Q(r)] = \sqrt{2} \sum_{m=1}^L b_m J_1 \left(\frac{\sqrt{2}r(2m-1)\pi}{R} \right), \quad (14)$$

$$r \leq \frac{R}{2\sqrt{2}}$$

where $J_1(\cdot)$ is the Bessel function of the first kind of order 1.

Simbo and Potano [26] used a complex Bessel function expansion to simultaneously account for the AM/AM and AM/PM conversion of the TWT. Group delay and amplitude variation preceding the input of the nonlinear device was modeled using a Fourier series expression. However, the function has a high computational complexity for the calculation of the coefficients:

$$A(r)e^{j\phi(r)} = \sum_{m=1}^L b_k J_1(\alpha m r) \quad (15)$$

where $\{b_m\}$ are complex coefficients, and α is a constant that scales the input level.

For the I-Q representation, Hetrakul and Taylor [9] proposed two-parameter formulas using a modified Bessel function of the first kind

$$P(r) = C_1 r e^{-C_2 r^2} J_0(C_2 r^2) \quad (16)$$

$$Q(r) = S_1 r e^{-S_2 r^2} J_1(S_2 r^2) \quad (17)$$

where, $J_k(\cdot)$ is the modified Bessel function of the first kind of order k . The coefficients C_1 , C_2 , S_1 , S_2 are computed from a conventional optimization subroutine, so as to yield the least-squares fit to the actual measured data. The Bessel function approximation needs four coefficients to give a good fit to the TWT nonlinearity, up to and beyond saturation. Note that for large input power values, the formulas approach certain constants.

3.6. Rational Functions: Saleh's Model

A very comprehensive work was published by Saleh [24] for both A-P and I-Q representations. The model presented by Saleh is widely used in the literature. It is a frequency-independent model and can be made frequency-dependent by adding filters that reflect the frequency selectivity:

A-P Representation. The AM/AM and AM/PM curves are modeled as

$$A(r) = \frac{\alpha_a r}{1 + \beta_a r^2} \quad (18)$$

$$\phi(r) = \frac{\alpha_p r^2}{1 + \beta_p r^2} \quad (19)$$

Note that for a large value of r , $A(r)$ is proportional to $1/r$ and $\phi(r)$ approaches a constant.

I-Q Representation. The in-phase and quadrature curves are modeled as follows:

$$P(r) = \frac{\alpha_P r}{1 + \beta_P r^2} \quad (20)$$

$$Q(r) = \frac{\alpha_Q r^3}{(1 + \beta_Q r^2)^2} \quad (21)$$

Note that for a large value of r , both $P(r)$ and $Q(r)$ are proportional to $\frac{1}{r}$.

Saleh used a minimum mean-square-error (MMSE) procedure for fitting the formulas to the experimental data. With only two parameters, this is the most widely used model for TWT amplifiers in the literature. Note that, for high input power signals, $A(r)$ and $\phi(r)$ approach $\alpha_a/\beta_a r$ and α_p/β_p , respectively. Therefore, this model is suited for amplifiers that have these specific asymptotic behaviors.

4. NEURAL NETWORKS FOR MODELING MEMORYLESS TWT AMPLIFIERS

This section employs multilayer neural networks [8] to model TWT amplifiers. The main advantage of NN models over classical models is that they offer better MSE approximation performance than do classical TWT models [12]. NNs are adaptive, which makes them appropriate for online modeling. Classical models are based on offline optimization procedures that do not allow online modeling. Moreover, NNs can model a variety of nonlinear amplifiers using the same parametrized structure (e.g., a structure with five neurons). Only the NN weight values change from one TWT model to another. On the contrary, most classical models have been designed for specific families of TWT amplifiers (e.g., TWTs having a given asymptotic behavior). Therefore, they may not always be appropriate for emerging generations of TWT and SSP amplifiers.

4.1. NN Structure and Learning Algorithms:

Figure 5 shows the modeling scheme of a TWT characteristic using a two-layer neural network (NN) [10]. The NN has a scalar input, M neurons in the first layer, and a scalar output. A set of input-output data (collected from the physical TWT measurements, or from the transmission channel input-output signals) is presented to the NN. The network output at time n is expressed as

$$s(n) = \sum_{k=1}^M c_k f(w_k x(n) + b_k) \quad (22)$$

where $x(n)$ is the input sample at time n and f is the activation function (which is taken in this article as the hyperbolic tangent function); $\{w_k\}$, $\{b_k\}$, and $\{c_k\}$, $k = 1, \dots, M$, are the NN weights. We denote the vector containing the network weights by θ : $\theta = [w_1, \dots, w_M, b_1, \dots, b_M, c_1, \dots, c_M]^T$ where $(\cdot)^T$ denotes the transpose.

To perform the modeling task, the NN weights are updated using a learning algorithm that minimizes the squared error between the TWT output and the NN outputs

$$J(n) = \frac{1}{2} \|e(n)\|^2 \quad (23)$$

where

$$e(n) = y(n) + N_0(n) - s(n) \quad (24)$$

where $y(n)$ is the TWT output and $N_0(n)$ is a zero-mean white Gaussian noise with variance σ^2 .

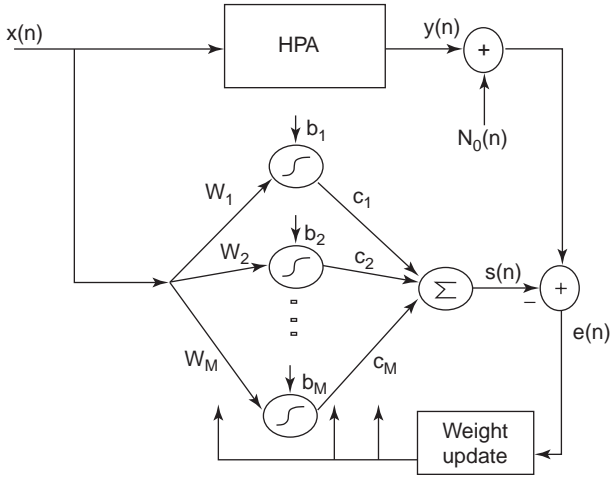


Figure 5. NN adaptive modeling of a nonlinear TWT amplifier.

In the following, we present two approaches to update the NN weights: the classical backpropagation (BP) algorithm and natural gradient (NG) algorithm.

The BP algorithm follows the ordinary gradient descent to update the weight vector θ :

$$\theta(n+1) = \theta(n) - \mu \nabla_{\theta}(J(n)) \quad (25)$$

where μ is a small positive constant, and ∇_{θ} is the ordinary gradient with respect to θ :

$$\nabla_{\theta}(J(n)) = -e(n) \cdot \nabla_{\theta} s(n) \quad (26)$$

$$= -e(n) \cdot \begin{pmatrix} x(n)c_1 f'(w_1 x(n) + b_1) \\ \vdots \\ x(n)c_M f'(w_M x(n) + b_M) \\ f(w_1 x(n) + b_1) \\ \vdots \\ f(w_M x(n) + b_M) \\ c_1 f'(w_1 x(n) + b_1) \\ \vdots \\ c_M f'(w_M x(n) + b_M) \end{pmatrix}$$

The NG algorithm follows the steepest-descent direction of the loss function, which is given by [1]

$$-\tilde{\nabla}_{\theta} J(n) = -G^{-1} \nabla_{\theta} J(n) \quad (27)$$

where G^{-1} is the inverse of the Fisher information matrix (FIM):

$$G = [g_{ij}(\theta)] = \left[E \left(\frac{\partial J(n)}{\partial \theta_i} \frac{\partial J(n)}{\partial \theta_j} \right) \right] \quad (28)$$

Therefore, the NG algorithm adjusts the NN weights as follows:

$$\theta(n+1) = \theta(n) - \mu G^{-1} \nabla_{\theta}(J(n)) \quad (29)$$

The calculation of the expectations in the FIM requires knowledge of the probability distribution functions (pdf values) of x and s , which are not always available. Moreover, the calculation of the inverse of the FIM is computationally very costly. A modified Kalman filter technique has been proposed [1] for an online estimation of the FIM inverse

$$\hat{G}^{-1}(n+1) = (1 + \varepsilon_n) \hat{G}^{-1}(n) - \varepsilon_n \hat{G}^{-1}(n) \nabla_{\theta} s(n) (\nabla_{\theta} s(n))^t \hat{G}^{-1}(n) \quad (30)$$

where $\nabla_{\theta} s(n)$ is the ordinary gradient of s [see Eq. (26)], and ε_n is a positive updating rate. The choice of ε_n depends on how fast/stable the algorithm is desired to be. For example, if $\varepsilon_n = c_e/n$ (where c_e is a small positive constant), then Kalman filtering is equivalent to an online calculation of the arithmetic mean. However, when ε_n is a constant, the convergence is faster but the algorithm may be less stable.

In order to reach a good tradeoff between convergence speed and stability, we will use a search-and-converge method in which ε_n is defined by

$$\varepsilon_n = \frac{\varepsilon_0 + \frac{c_e n}{\tau}}{1 + \frac{c_e n}{\tau \varepsilon_0} + \frac{n^2}{\tau}} \quad (31)$$

where τ is a positive time constant, and ε_0 is a small positive constant. Here, small n corresponds to a “search” phase (where ε_n is close to ε_0), and large n corresponds to a “converge” phase (ε_n is equivalent to c_e/n).

Simulation Example 1. Here, a neural network composed of $M = 5$ neurons is used to model the AM/AM characteristic of a TWT amplifier. The NG and the BP algorithms are compared. The simulations show that the value of $\mu = 0.005$ represents a good tradeoff (for each algorithm) between convergence speed and stability. Figure 6a shows the learning curve for each algorithm. It can be seen that the NG descent has a much faster convergence. The resulting MSE approximation performances are 9×10^{-6} and 3.0×10^{-5} for the NG and BP algorithms, respectively. Figure 6b illustrates the resulting AM/AM models and the original TWT input–output data that have been used for learning. Note that, for this amplifier, classical models such as Saleh [24] and Thomas [27] expressions give 1.4×10^{-4} and 2.0×10^{-4} as MSE errors, respectively. Therefore, the NG approach outperforms both the classical models and the BP algorithm. For asymptotic behavior, NN models approach a constant (due to the shape of the neuron activation function), which is desirable in TWT modeling as it ensures stability for high input power fluctuations. The desired asymptotic constant can be included as an additional constraint value during the learning process. Finally, the odd and even BP algorithms can be employed (if needed by the user to ensure strict even

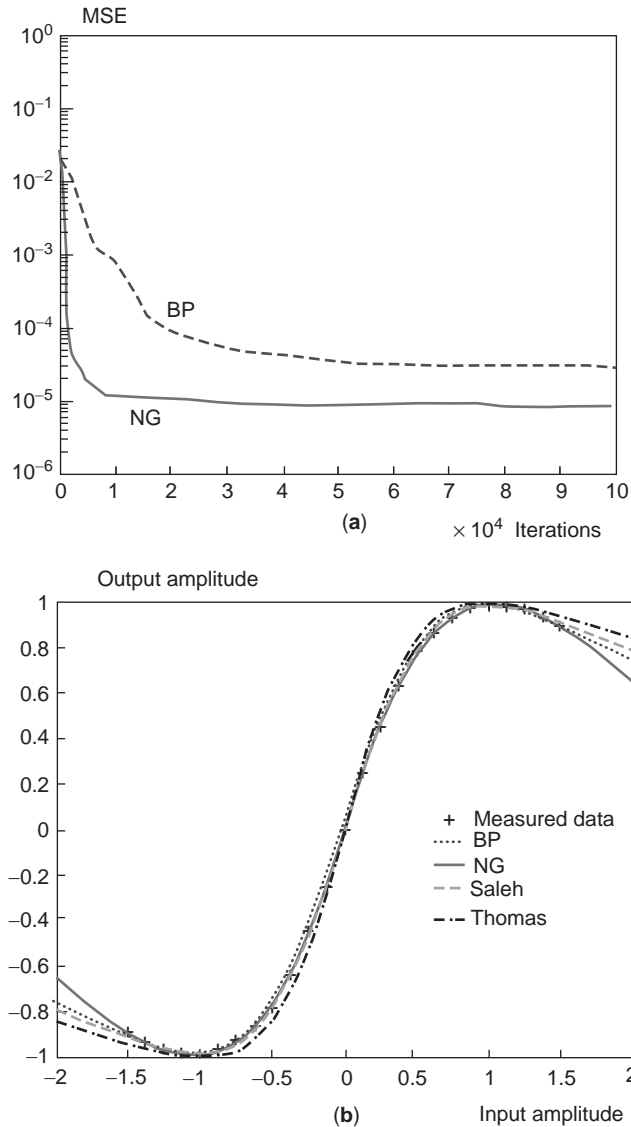


Figure 6. Modeling the AM/AM conversion of Intelsat IV TWT amplifier: (a) learning curves of the BP and NG algorithms; (b) comparison between the different models. (This figure is available in full color at <http://www.mrw.interscience.wiley.com/erfme>.)

or odd characteristics) [10]. See Table 1 for additional computer simulation results.

5. MODELING AND IDENTIFICATION OF NONLINEAR AMPLIFIERS WITH MEMORY

As discussed above, some nonlinear amplifiers may contain a memory that cannot be neglected. Moreover, the

transmission channel may also be considered as a nonlinear system with memory. This is because the uplink and downlink channels may introduce some memory because of thermal and electrical effects, multi-path propagation, or other filtering processes in the channel [15]. Several approaches, including those discussed below, have been proposed in the literature to model nonlinear amplifiers with memory.

5.1. Volterra Model

In the Volterra model, the input–output relationship is expressed as follows

$$\begin{aligned}
 y(t) = & h_0 + \int_{-\infty}^{+\infty} h_1(\tau_1)x(t - \tau_1)d\tau_1 \\
 & + \int_{-\infty}^{+\infty} \int_{-\infty}^{+\infty} h_2(\tau_1, \tau_2)x(t - \tau_1) \\
 & \times x(t - \tau_2)d\tau_1d\tau_2 \\
 & + \int_{-\infty}^{+\infty} \int_{-\infty}^{+\infty} \int_{-\infty}^{+\infty} h_3(\tau_1, \tau_2, \tau_3)x(t - \tau_1) \\
 & \times x(t - \tau_2)x(t - \tau_3)d\tau_1d\tau_2d\tau_3 + \dots
 \end{aligned} \tag{32}$$

where the Volterra kernels $\{h_1(\tau_1), h_2(\tau_1, \tau_2), h_3(\tau_1, \tau_2, \tau_3), \dots\}$ have to be obtained through an optimization or adaptive procedure.

Volterra series can approximate nonlinear amplifier characteristics [3,16,28,30] and predistortion devices [3,6,16] relatively well. The major drawback of this model is its complexity, which increases immensely with the length of the memory and the order of the nonlinearity.

5.2. Wiener Model (Filter–Memoryless Nonlinearity or Two-Box Model)

In this model, the amplifier is modeled by a linear filter followed by a memoryless nonlinearity (Fig. 7). This model is very simple and can provide a good approximation of the memory and the nonlinearity. The characterization of the filter and nonlinearity can be made through adaptive or optimization procedures [11,24].

5.3. Wiener–Hammerstein Model (Three-Box Model)

The amplifier is modeled by a linear filter followed by a memoryless nonlinearity followed by a linear filter (Fig. 8). This model has been shown to accurately predict intermodulation products and yield excellent characterization of several TWT and SSP amplifier behaviors. The different boxes can be determined through measurement and data processing [5], or they can be determined

Table 1. MSE Performance of Different Models for Approximation of I-Q and A-P TWT Characteristics

Characteristic	BP NN	NG NN	Saleh [24]	Hetrakul–Taylor [9]	Thomas et al. [27]	Berman and Mahle [2]
In-phase	6.1×10^{-3}	2.6×10^{-4}	3.20×10^{-3}	3.30×10^{-3}	—	—
Quadrature	6.2×10^{-3}	2.7×10^{-4}	5.20×10^{-4}	1.60×10^{-3}	—	—
AM/AM	3.0×10^{-5}	9.0×10^{-6}	1.40×10^{-4}	—	2.00×10^{-4}	—
AM/PM	8.1×10^{-5}	3.2×10^{-6}	1.38×10^{-4}	—	—	8.00×10^{-4}

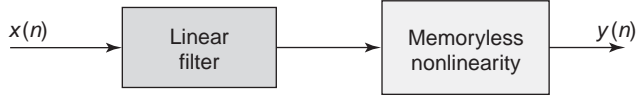


Figure 7. Wiener model.

adaptively (e.g., using neural networks and adaptive filtering) [11]. In this model, a physical interpretation of the different parts of the model can be easily made. This leads to an easy design and optimization of communication system (predistortion, equalization, IMD calculation, etc.).

5.4. Parallel Wiener Model

This model is composed of several parallel Wiener blocks that are summed together to yield the output. These models are more complicated than the two-box and the three-box models, but may yield better accuracy if the nonlinearity is complicated [19].

5.5. Memory Polynomial

The memory polynomial model (see Fig. 9) is composed of a cascade of polynomials separated by unit delays. The output can be expressed in discrete time as

$$y(n) = \sum_{k=0}^L F_k(x(n-k)) \tag{33}$$

where $F_k(x)$ is the k^{th} polynomial.

An extension of this model has been proposed in Ref. 20, allowing the unit delays to be sparse delay taps. This allows longer-time-constant memory effects to be modeled in parallel with short-time-constant effects using fewer parameters. The different parameters in this model can be characterized using an adaptive sliding-window approach.

The following section details the Wiener modeling approach using neural networks and adaptive filtering.

6. WIENER MODELING USING ADAPTIVE FILTERING AND NEURAL NETWORKS

The nonlinear channel to be modeled in this section is a nonlinear Wiener system composed of a linear filter $H(z) = \sum_{k=0}^{N_h-1} h_k z^{-k}$ followed by a zero-memory amplitude nonlinearity $g(\cdot)$ (Fig. 10). The phase nonlinearity is not considered in this section, but it can easily be included in the scheme with small changes to the algorithm [11,13,14].

The nonlinear system output signal is corrupted by a zero-mean additive white Gaussian noise (AWGN) $N_0(n)$. It can be expressed at time n as

$$d(n) = y(n) + N_0(n)$$

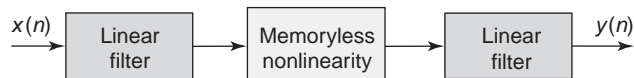


Figure 8. Wiener-Hammerstein model (three-box model).

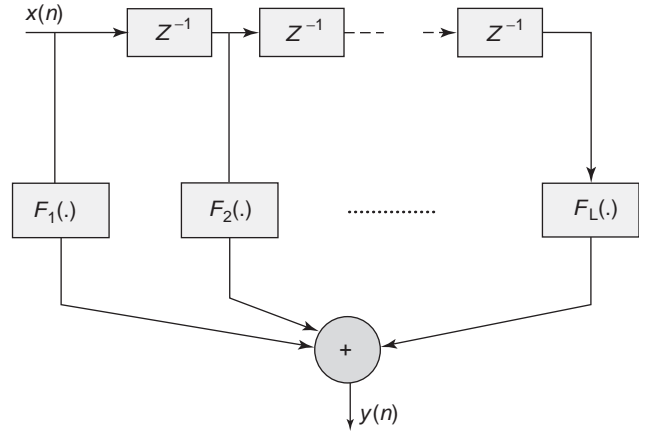


Figure 9. Memory polynomial model.

where

$$y(n) = g\left(\sum_{k=0}^{N_h-1} h_k x(n-k)\right) \tag{34}$$

The NN model (Fig. 10) is composed of an adaptive filter, $Q(z) = \sum_{k=0}^{N_q-1} q_k z^{-k}$, followed by a two-layer (zero-memory) adaptive neural network. The two-layer NN is composed of a scalar (real-valued) input, M neurons in the input layer, and a scalar output.

The adaptive structure has two goals:

1. Identify the linear filter H by the adaptive filter Q .
2. Model the nonlinearity $g(\cdot)$ by the zero-memory nonlinear NN.

The learning is performed by using the input-output signals only (i.e., we consider the unknown nonlinear system as a blackbox).

The NN output at time n is expressed as

$$\begin{aligned} s(n) &= \sum_{k=1}^M c_k f\left(w_k \sum_{i=0}^{N_q-1} q_i x(n-i) + b_k\right) \\ &= \sum_{k=1}^M c_k f(w_k Q^t X(n) + b_k) \end{aligned} \tag{35}$$

where $\{w_k\}$, $\{b_k\}$, and $\{c_k\}$ (where $k=1, \dots, M$) are the NN weights, $Q = [q_0 \ q_1 \ \dots \ q_{N_q-1}]^T$, and $X(n) = [x(n) \ x(n-1) \ \dots \ x(n-N_Q+1)]^T$.

The network and filter parameters are updated in order to minimize the loss function J_n (or squared error) between the system output and the NN output

$$J(n) = \frac{1}{2} \|e(n)\|^2 \tag{36}$$

where

$$e(n) = d(n) - s(n) \tag{37}$$

We denote the system parameter vector to be updated by $\theta = [w_1 w_2 \dots w_M b_1 b_2 \dots b_M c_1 c_2 \dots c_M q_0 q_1 \dots q_{N_q-1}]^T$. The BP and NG approaches that can be used to update the system are

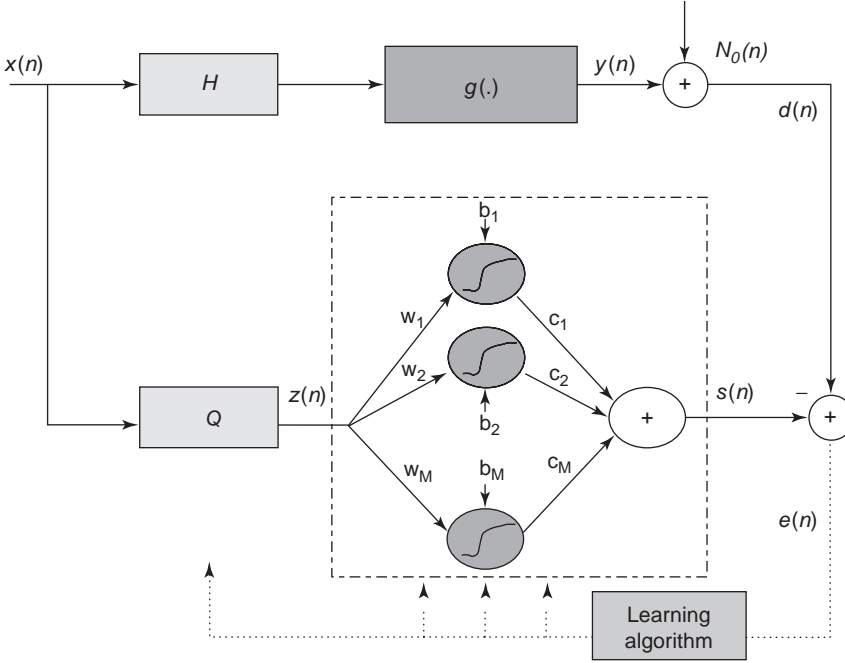


Figure 10. Neural network modeling and identification structure.

BP Algorithm. The BP algorithm updates the weights according to the ordinary gradient descent

$$\theta(n+1) = \theta(n) - \mu \nabla_{\theta} J(n) \quad (38)$$

where μ is a small positive constant, and ∇_{θ} represents the ordinary gradient with respect to vector θ , which is expressed as

$$\nabla_{\theta} J(n) = -e(n) \nabla_{\theta} s(n) \quad (39)$$

where

$$\nabla_{\theta} s(n) = \begin{pmatrix} c_1 \mathbf{Q}^t \mathbf{X}(n) f'(w_1 \mathbf{Q}^t \mathbf{X}(n) + b_1) \\ \vdots \\ c_M \mathbf{Q}^t \mathbf{X}(n) f'(w_M \mathbf{Q}^t \mathbf{X}(n) + b_M) \\ c_1 f'(w_1 \mathbf{Q}^t \mathbf{X}(n) + b_1) \\ \vdots \\ c_M f'(w_M \mathbf{Q}^t \mathbf{X}(n) + b_M) \\ f(w_1 \mathbf{Q}^t \mathbf{X}(n) + b_1) \\ \vdots \\ f(w_M \mathbf{Q}^t \mathbf{X}(n) + b_M) \\ x(n) \sum_{k=1}^M c_k w_k f'(w_k \mathbf{Q}^t \mathbf{X}(n) + b_k) \\ \vdots \\ x(n - N_Q + 1) \sum_{k=1}^M c_k w_k f'(w_k \mathbf{Q}^t \mathbf{X}(n) + b_k) \end{pmatrix} \quad (40)$$

where f' denotes the first derivative of f .

The NG Algorithm. The NN weights are updated according to the NG descent

$$\theta(n+1) = \theta(n) - \mu \tilde{\nabla}_{\theta} J(n) \quad (41)$$

where $\tilde{\nabla}_{\theta}$ represents the NG

$$-\tilde{\nabla}_{\theta} J(n) = -\Gamma^{-1} \nabla_{\theta} J(n)$$

where Γ^{-1} is the FIM inverse:

$$\Gamma = [\gamma_{i,j}] = \left[E \left(\frac{\partial J(n)}{\partial \theta_i} \frac{\partial J(n)}{\partial \theta_j} \right) \right] \quad (42)$$

Here again, the FIM can be approximated online using a modified Kalman technique

$$\hat{\Gamma}^{-1}(n+1) = (1 + \varepsilon_n) \hat{\Gamma}^{-1}(n) - \varepsilon_n \hat{\Gamma}^{-1}(n) \times \nabla_{\theta} s(n) (\nabla_{\theta} s(n))^t \hat{\Gamma}^{-1}(n) \quad (43)$$

where $\nabla_{\theta} s(n)$ is the (ordinary) gradient of $s(n)$ [see Eq. (40)].

Simulation Example 2. For the unknown structure to be identified, the following amplitude nonlinearity is taken:

$$g(x) = \frac{\alpha x}{1 + \beta x^2}, \quad \alpha = 2, \quad \beta = 1$$

The input signal has been taken as a white Gaussian sequence with variance 1 and filter H is taken as $H = [1.49 \ 1.36 \ 1.07 \ 0.67 \ 0.27 \ -0.057 \ -0.263 \ -0.325 \ -0.263 \ -0.125]^T$. The noise variance is $\sigma = 0.002$ and the learning rate is fixed to $\mu = 0.007$.

Filter Q is composed of 10 weights that have been initialized with 0 values. The NN is composed of $M = 5$ neurons. Figure 11 displays the learning curves of the BP and NG algorithms. The NG algorithm is faster and yields a lower MSE than does the BP algorithm (the MSE after

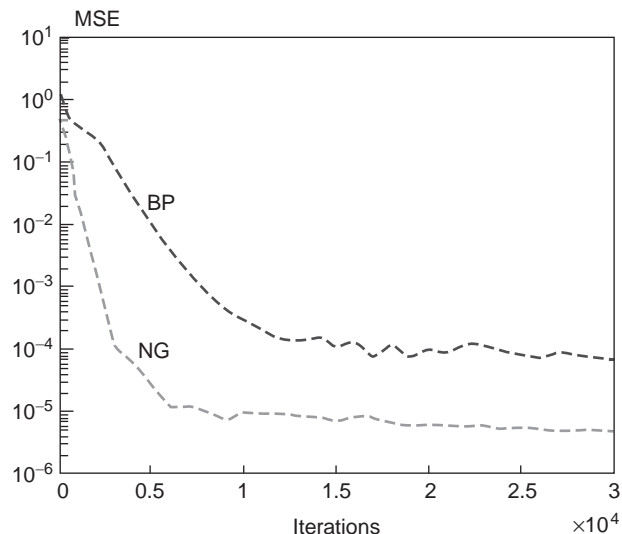


Figure 11. MSE learning curve for identification of the filter nonlinearity model. (This figure is available in full color at <http://www.mrw.interscience.wiley.com/erfme>.)

convergence equals 5×10^{-5} for the NG and 5.5×10^{-4} for the BP.

Figure 12 shows the frequency responses of the exact filter and the models obtained through the BP and NG algorithms, respectively. The frequency responses of the models are scaled versions of the exact filter frequency response. The amplitude conversion model obtained by the memoryless NN compensates for the scaling factor introduced by the adaptive filter. Figure 13 shows the AM/AM curves obtained through the NG and BP algorithms, respectively, which fit very well with the exact nonlinearity.

One major advantage of this NN adaptive approach is that it allows one to identify (or extract) the memoryless nonlinearity and estimate the memory of the amplifier, even in the case where the amplifier is not physically composed of separated blocks (i.e., a linear filter followed by a memoryless nonlinearity).

In Ref. 11, an adaptive structure composed of an adaptive filter, followed by a memoryless NN followed by an adaptive filter, has been used to characterize an SSP amplifier using physical measured data. The adaptive structure was able to extract the amplifier memoryless nonlinearity and characterize its frequency response. See also Refs. 7, 23, and 29 for other NN and adaptive

Figure 12. Filter frequency response: true filter and model. (This figure is available in full color at <http://www.mrw.interscience.wiley.com/erfme>.)

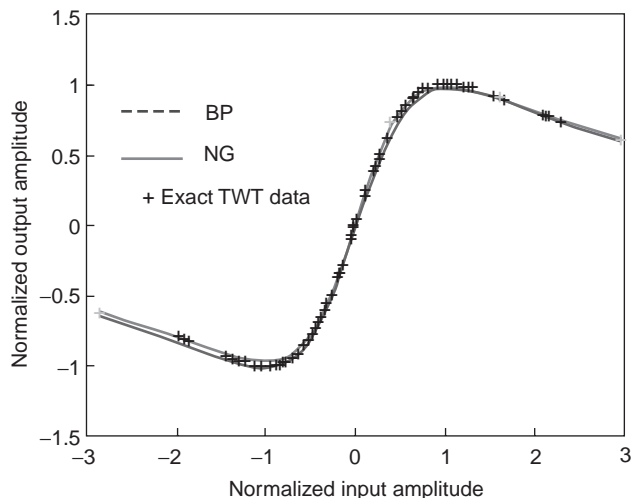
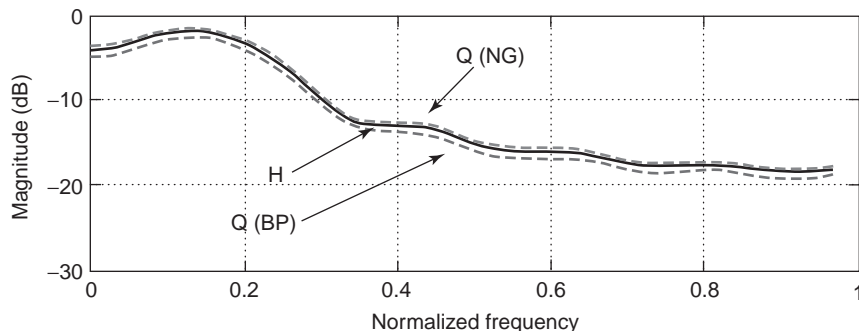


Figure 13. Identification of the memoryless nonlinearity. (This figure is available in full color at <http://www.mrw.interscience.wiley.com/erfme>.)

approaches used to efficiently model, identify, simulate, and characterize nonlinear microwave circuits with memory.

Acknowledgments

This work has been supported in part by the Natural Sciences and Engineering Research Council of Canada (NSERC), the Ontario Premier’s Research Excellence Award (PREA), and Communications Information Technology Ontario (CITO).

BIBLIOGRAPHY

1. S. I. Amari, H. Park, and K. Fukumizu, Adaptive method for realizing natural gradient learning for multi-layer perceptrons, *Neural Comput.* **12**:1399–1409 (2000).
2. A. L. Berman and C. E. Mahle, Nonlinear phase shift in traveling-wave tubes as applied to multiple access communications satellites, *IEEE Trans. Commun. Technol.* **COM-18**(1): 37–48 (Feb. 1970).
3. E. Biglieri, S. Barberis, and M. Catena, Analysis and compensation of nonlinearities in digital transmission systems, *IEEE J. Select. Areas Commun.* **6**:42–50 (Jan. 1988).
4. R. C. Chapman and J. B. Millard, Intelligible crosstalk between frequency modulated carriers through AM-PM conversion, *IEEE Trans. Commun. Syst.* **CS-12**:160–166 (June 1964).

5. C. J. Clark, C. P. Silva, A. A. Moulthrop, and M. S. Muha, Power-amplifier characterization using a two-tone measurement technique, *IEEE Trans. Microwave Theory Techn.* **50**(6):1590–1602 (June 2002).
6. A. D'Andrea, V. Lottici, and R. Reggiannini, RF power amplifier linearization through amplitude and phase predistortion, *IEEE Trans. Commun.* **44**(11), (Nov. 1996).
7. X. Ding, V. K. Devabhaktuni, B. Chattaraj, M. C. E. Yagoub, M. Deo, J. Xu, and Q. J. Zhang, Neural-network approaches to electromagnetic-based modeling of passive components and their applications to high-frequency and high-speed nonlinear circuit optimization, *IEEE Trans. Microwave Theory Techn.* **52**(1):436–449 (Jan. 2004).
8. S. Haykin, *Neural Networks: A Comprehensive Foundation*, IEEE Press, 1997.
9. P. Hetrakul and D. P. Taylor, The effects of nonlinearity on binary CPSK signal transmission, *IEEE Trans. Commun.* **COM-24**:546–553 (May 1976).
10. M. Ibnkahla, J. Sombrin, F. Castanié, and N. J. Bershad, Neural networks for modeling non linear memoryless channels, *IEEE Trans. Commun.* **45**(7):768–771 (July 1997).
11. M. Ibnkahla, N. J. Bershad, J. Sombrin, and F. Castanié, Neural network modeling and identification of non linear channels with memory: Algorithms, applications and analytic models, *IEEE Trans. Signal Process.* **46**(5), (May 1998).
12. M. Ibnkahla, Applications of neural networks to digital communications—a survey, *EURASIP J. Appl. Signal Process.* **80**:1185–11215 (2000).
13. M. Ibnkahla, Nonlinear system identification using neural networks trained with natural gradient descent, *EURASIP J. Appl. Signal Process.* 1229–1237 (Dec. 2003).
14. M. Ibnkahla, J. Yuan, and R. Boutros, Neural networks for transmission over nonlinear channels, in M. Ibnkahla, ed., *Signal Processing for Mobile Communications Handbook*, CRC Press, 2004, Chap. 19.
15. M. Ibnkahla, Q. Rahman, A. Sulyman, H. Al-Asady, J. Yuan, and A. Safwat, High speed satellite mobile communications: Technologies and challenges, *Proc. IEEE* (special issue on gigabit wireless communications: technologies and challenges) 312–339 (Feb. 2004).
16. G. Karam and H. Sari, A data predistortion technique with memory for QAM radio systems, *IEEE Trans. Commun.* **39**(2):336–344 (Feb. 1991).
17. A. Katz, TWT linearization, *Microwave J.* 78–89 (April 1996).
18. A. R. Kaye, D. A. George, and M. J. Eric, Analysis and compensation of bandpass nonlinearities for communications, *IEEE Trans. Commun.* 965–972 (Oct. 1972).
19. H. Ku, M. D. McKinley, and J. S. Kenney, Quantifying memory effects in RF power amplifiers, *IEEE Trans. Microwave Theory Techn.* **50**(12):2843–2849 (Dec. 2002).
20. H. Ku and J. S. Kenney, Behavioral modeling of power amplifiers considering IMD and spectral regrowth asymmetries, *Proc. IMS 2003*, Philadelphia, PA, 2003.
21. R. G. Medhurst and J. H. Roberts, Distortion of SSB transmission due to AM-PM conversion, *IEEE Trans. Commun. Syst.* **CS-12**:166–176 (June 1964).
22. R. Pawula, The effects of quadratic AM-PM conversion in frequency-division multiplexed multiple-access communication satellite systems, *IEEE Trans. Commun.* **28**(10):1785–1793 (Oct. 1980).
23. D. Root, J. Wood, and N. Tuffillaro, New techniques for nonlinear behavioral modeling of microwave/RF ICs from simulation to nonlinear microwave measurements, *Proc. DAC 2003*, June 2003, pp. 85–90.
24. A. Saleh, Frequency-independent and frequency-dependent nonlinear models of TWT amplifiers, *IEEE Trans. Commun.* **29**(11) (1981).
25. J. F. Sevic and J. Staudinger, Simulation of power amplifier adjacent-channel power ratio for digital wireless communication systems, *Proc. IEEE 47th Vehicular Technology Conf. VTC'97*, Phoenix, AZ, May 4–7, 1997, pp. 681–685.
26. O. Simbo and B. A. Potano, A general theory for intelligible crosstalk between frequency-division multiplexed angle-modulated carriers, *IEEE Trans. Commun.* **COM-24**(9) (Sept. 1976).
27. M. Thomas, M. Weidner, and S. Durrani, Digital amplitude-phase keying with M-ary alphabets, *IEEE Trans. Commun.* **22**:168–180 (1974).
28. J. Vuolevi, *Analysis Measurement and Cancellation of the Bandwidth and Amplitude Dependence of Internodulation Distortion in RF Power Amplifiers*, Ph.D. dissertation, Univ. Oulou, Finland, 2001.
29. J. Xu, M. Yagoub, R. Ding, and Q. Zhang, Neural based dynamic modeling of nonlinear microwave circuits, *Proc. IEEE MTTTS 2002*, June 2003, pp. 1101–1104.
30. G. T. Zhou, Analysis of spectral regrowth of weakly nonlinear power amplifiers, *IEEE Commun. Lett.* **4**(11):357–359 (Nov. 2000).

ANISOTROPY AND BIANISOTROPY

TOM G. MACKAY
University of Edinburgh
Edinburgh, United Kingdom
AKHLESH LAKHTAKIA
Pennsylvania State University
University Park, Pennsylvania

1. LINEAR ANISOTROPY AND BIANISOTROPY

Free space or vacuum is isotropic. Its electromagnetic response characteristics are contained in the frequency-domain constitutive relations

$$\left. \begin{aligned} \underline{D}(\underline{r}, \omega) &= \varepsilon_0 \underline{E}(\underline{r}, \omega) \\ \underline{H}(\underline{r}, \omega) &= \mu_0^{-1} \underline{B}(\underline{r}, \omega) \end{aligned} \right\} \quad (1)$$

wherein \underline{r} is the position vector and ω is the angular frequency. The induction field phasors $\underline{D}(\underline{r}, \omega)$ and $\underline{H}(\underline{r}, \omega)$ are scalar multiples of the primitive field phasors $\underline{E}(\underline{r}, \omega)$ and $\underline{B}(\underline{r}, \omega)$, respectively. The constants of proportionality—the permittivity $\varepsilon_0 = 8.854 \times 10^{-12}$ F/m and the permeability $\mu_0 = 4\pi \times 10^{-7}$ H/m of free space—are fundamental to the structure of modern electromagnetic theory [1].

The dielectric media that students are introduced to in their first electromagnetism course are also isotropic, with

$$\left. \begin{aligned} \underline{D}(\underline{r}, \omega) &= \varepsilon(\omega) \underline{E}(\underline{r}, \omega) \\ \underline{H}(\underline{r}, \omega) &= \mu_0^{-1} \underline{B}(\underline{r}, \omega) \end{aligned} \right\} \quad (2)$$

as the constitutive relations. The permittivity scalar ε must be complex-valued and frequency-dependent due to causality. Isotropic magnetic media are described by the constitutive relations

$$\left. \begin{aligned} \underline{D}(\underline{r}, \omega) &= \varepsilon_0 \underline{E}(\underline{r}, \omega) \\ \underline{H}(\underline{r}, \omega) &= \mu^{-1}(\omega) \underline{B}(\underline{r}, \omega) \end{aligned} \right\} \quad (3)$$

wherein the permeability scalar μ is frequency-dependent and complex-valued. Electromagnetically, the most complex of all isotropic media are the isotropic chiral media [2] whose constitutive relations

$$\left. \begin{aligned} \underline{D}(\underline{r}, \omega) &= \varepsilon(\omega) \underline{E}(\underline{r}, \omega) + \chi(\omega) \underline{B}(\underline{r}, \omega) \\ \underline{H}(\underline{r}, \omega) &= \mu^{-1}(\omega) \underline{B}(\underline{r}, \omega) + \chi(\omega) \underline{E}(\underline{r}, \omega) \end{aligned} \right\} \quad (4)$$

employ three complex-valued scalars: ε , μ , and χ .

The induction and the primitive field phasors are aligned in all linear isotropic media, because the constants of proportionality in Eqs. (1)–(4) are scalars. In contrast, the macroscopic properties of anisotropy and bianisotropy denote the directionality of the primitive field phasors relative to the induction field phasors. Specifically, a medium is termed *dielectrically anisotropic* if $\underline{D}(\underline{r}, \omega)$ is not aligned with $\underline{E}(\underline{r}, \omega)$, and *magnetically anisotropic* if $\underline{H}(\underline{r}, \omega)$ is not aligned with $\underline{B}(\underline{r}, \omega)$. In a linear dielectric-magnetic medium, the field phasors are related in the frequency-domain constitutive relations¹

$$\left. \begin{aligned} \underline{D}(\underline{r}, \omega) &= \underline{\varepsilon}(\omega) \cdot \underline{E}(\underline{r}, \omega) \\ \underline{B}(\underline{r}, \omega) &= \underline{\mu}(\omega) \cdot \underline{H}(\underline{r}, \omega) \end{aligned} \right\} \quad (5)$$

by the 3×3 dyadics (i.e., second-rank Cartesian tensors) of permittivity $\underline{\varepsilon}$ and permeability $\underline{\mu}$. Any $n \times n$ dyadic can be interpreted as a $n \times n$ matrix throughout this article [3, Chapter 1].

Many examples of anisotropic dielectric media arise in the context of crystal optics [4,5]. The uniaxial and orthorhombic biaxial crystals, which may be characterized by the permittivity dyadics

$$\underline{\varepsilon}_{\text{uni}}(\omega) = \varepsilon_{11}(\omega) \underline{\hat{x}\hat{x}} + \underline{\hat{y}\hat{y}} + \varepsilon_{33}(\omega) \underline{\hat{z}\hat{z}} \quad (6)$$

and

$$\underline{\varepsilon}_{\text{ortho}}(\omega) = \varepsilon_{11}(\omega) \underline{\hat{x}\hat{x}} + \varepsilon_{22}(\omega) \underline{\hat{y}\hat{y}} + \varepsilon_{33}(\omega) \underline{\hat{z}\hat{z}} \quad (7)$$

respectively, are widely studied; here and hereafter, the Cartesian unit vectors are denoted by $\underline{\hat{x}}$, $\underline{\hat{y}}$, and $\underline{\hat{z}}$. Nematic and smectic liquid crystals are also described by Eqs. (6) and (7), respectively [6,7]. Permeability dyadics with forms analogous to (6) and (7) may be employed to describe diamagnetic and paramagnetic crystals [5]. An important noncrystalline example of anisotropic dielectric behavior is provided by an electron plasma in thermal motion, biased by a static magnetic field [3, Chapter 7]. The corresponding permittivity dyadic has the gyrotropic form

$$\underline{\varepsilon}_{\text{gyro}}(\omega) = \varepsilon_{11}(\omega) (\underline{\hat{x}\hat{x}} + \underline{\hat{y}\hat{y}}) + \varepsilon_{33}(\omega) \underline{\hat{z}\hat{z}} + \varepsilon_{12}(\omega) (\underline{\hat{x}\hat{y}} - \underline{\hat{y}\hat{x}}) \quad (8)$$

¹It is convenient for the solution of boundary-value problems in engineering practice to interchange the roles of $\underline{B}(\underline{r}, \omega)$ and $\underline{H}(\underline{r}, \omega)$ in frequency-domain constitutive relations.

when the biasing magnetostatic field is oriented parallel to $\underline{\hat{z}}$. Magnetically biased ferrites may be characterized in terms of a permeability dyadic analogous to the $\underline{\varepsilon}_{\text{gyro}}$ of (8) [3, Chapter 7].

The generalization from anisotropy to bianisotropy is achieved through the introduction of the magnetoelectric dyadics $\underline{\zeta}(\omega)$ and $\underline{\xi}(\omega)$; thereby, the bianisotropic constitutive relations emerge as [8,9]

$$\left. \begin{aligned} \underline{D}(\underline{r}, \omega) &= \underline{\varepsilon}(\omega) \cdot \underline{E}(\underline{r}, \omega) + \underline{\zeta}(\omega) \cdot \underline{H}(\underline{r}, \omega) \\ \underline{B}(\underline{r}, \omega) &= \underline{\zeta}(\omega) \cdot \underline{E}(\underline{r}, \omega) + \underline{\mu}(\omega) \cdot \underline{H}(\underline{r}, \omega) \end{aligned} \right\} \quad (9)$$

If a particular medium is nonhomogeneous, its constitutive dyadics are functions of the position vector \underline{r} ; thus, the nonhomogeneous counterparts of (9) are as follows:

$$\left. \begin{aligned} \underline{D}(\underline{r}, \omega) &= \underline{\varepsilon}(\underline{r}, \omega) \cdot \underline{E}(\underline{r}, \omega) + \underline{\zeta}(\underline{r}, \omega) \cdot \underline{H}(\underline{r}, \omega) \\ \underline{B}(\underline{r}, \omega) &= \underline{\zeta}(\underline{r}, \omega) \cdot \underline{E}(\underline{r}, \omega) + \underline{\mu}(\underline{r}, \omega) \cdot \underline{H}(\underline{r}, \omega) \end{aligned} \right\} \quad (10)$$

In the remainder of this article, unless stated otherwise, homogeneity is assumed.

The most commonplace example of bianisotropy arises when a linear isotropic dielectric and/or magnetic medium rigidly attached to a constantly moving reference frame is considered from a stationary reference frame. From the perspective of a stationary observer, the moving medium is bianisotropic [3,10]. Thus, if an isotropic dielectric-magnetic medium with permittivity ε and permeability μ is traveling with uniform velocity \underline{v} , then the constitutive dyadics of the moving medium from the perspective of a stationary observer are

$$\left. \begin{aligned} \underline{\varepsilon}_{\text{mov}} &= \varepsilon [\alpha \underline{I} + (1 - \alpha) \underline{\hat{v}\hat{v}}] \\ \underline{\zeta}_{\text{mov}} &= \beta \underline{\hat{v}} \times \underline{I} \\ \underline{\zeta}_{\text{mov}} &= -\beta \underline{\hat{v}} \times \underline{I} \\ \underline{\mu}_{\text{mov}} &= \mu [\alpha \underline{I} + (1 - \alpha) \underline{\hat{v}\hat{v}}] \end{aligned} \right\} \quad (11)$$

where $\underline{I} = \underline{\hat{x}\hat{x}} + \underline{\hat{y}\hat{y}} + \underline{\hat{z}\hat{z}}$ denotes the 3×3 identity dyadic and

$$\alpha = \frac{1 - \varepsilon_0 \mu_0 |\underline{v}|^2}{1 - \varepsilon \mu |\underline{v}|^2}, \quad \beta = \frac{|\underline{v}| (\varepsilon \mu - \varepsilon_0 \mu_0)}{1 - \varepsilon \mu |\underline{v}|^2}, \quad \underline{\hat{v}} = \frac{1}{|\underline{v}|} \underline{v} \quad (12)$$

More exotic examples of bianisotropy arise from direct generalizations of the anisotropic forms (6)–(8). For example, (7) leads to the conceptualization of the orthorhombic biaxial bianisotropic form [11,12]

$$\underline{\gamma}_{\text{ortho}} = \gamma_{11} \underline{\hat{x}\hat{x}} + \gamma_{22} \underline{\hat{y}\hat{y}} + \gamma_{33} \underline{\hat{z}\hat{z}}, \quad (\gamma = \varepsilon, \xi, \zeta, \mu) \quad (13)$$

Media described by the gyrotropic form (8), when mixed with isotropic chiral media [2] and homogenized, give rise to the class of bianisotropic media known as *Faraday chiral media* (FCM) [13,14]. These are described by the constitutive dyadics

$$\underline{\gamma}_{\text{FCM}} = \gamma_{11} (\underline{\hat{x}\hat{x}} + \underline{\hat{y}\hat{y}}) + \gamma_{33} \underline{\hat{z}\hat{z}} + \gamma_{12} (\underline{\hat{x}\hat{y}} - \underline{\hat{y}\hat{x}}), \quad (14)$$

$$(\gamma = \varepsilon, \xi, \zeta, \mu)$$

with $\underline{\xi}_{\text{FCM}} = -\underline{\zeta}_{\text{FCM}}$.

Artificial bianisotropic media have been fabricated since at least the 1890s, when Bose [15] reported experimental results on the passage of microwaves through an ensemble of jute spirals. But the fabrication of artificial bianisotropic media intensified only about a century later, following renewal of interest in chirality [2]. Electrically small wire structures with twists have to be represented by both electric and magnetic dipoles, insofar as scattering is concerned [16]. Hence, ensembles of twisted wires—which can be fabricated in many ways [17,18]—are effectively bianisotropic continua at sufficiently low frequencies.

In the most general linear scenario, each of the four constitutive dyadics $\underline{\underline{\varepsilon}}$, $\underline{\underline{\zeta}}$, $\underline{\underline{\xi}}$, and $\underline{\underline{\mu}}$ contains nine complex-valued scalars; in matrix notation, we obtain

$$\underline{\underline{\gamma}} = \begin{pmatrix} \gamma_{11} & \gamma_{12} & \gamma_{13} \\ \gamma_{21} & \gamma_{22} & \gamma_{23} \\ \gamma_{31} & \gamma_{32} & \gamma_{33} \end{pmatrix}, \quad (\gamma = \varepsilon, \zeta, \xi, \mu) \quad (15)$$

However, for consistency with the special theory of relativity, all linear media must satisfy the Post constraint [19,20]

$$\text{Trace} \left[(\underline{\underline{\mu}})^{-1} \cdot (\underline{\underline{\zeta}} + \underline{\underline{\xi}}) \right] = 0 \quad (16)$$

Hence, a maximum of 35 independent, complex-valued, frequency-dependent parameters are needed to characterize a bianisotropic medium. The number of parameters may be further reduced by imposing conditions such as Lorentz reciprocity [21]

$$\underline{\underline{\varepsilon}} = \underline{\underline{\varepsilon}}^T, \quad \underline{\underline{\zeta}} = -\underline{\underline{\zeta}}^T, \quad \underline{\underline{\mu}} = \underline{\underline{\mu}}^T \quad (17)$$

where the superscript ^T denotes the *transpose*. Also, if the effects of dissipation are neglected, then the approximation [3, Section 2.5]

$$\underline{\underline{\varepsilon}} = \underline{\underline{\varepsilon}}^+, \quad \underline{\underline{\zeta}} = \underline{\underline{\zeta}}^+, \quad \underline{\underline{\mu}} = \underline{\underline{\mu}}^+ \quad (18)$$

may be implemented, with the superscript ⁺ indicating the *conjugate transpose*.

2. POINT GROUPS FOR LINEAR CONSTITUTIVE DYADICS

The specific form of the constitutive dyadics of a medium reflects the spacetime symmetry of the underlying medium physics. In particular, it is the *point group symmetry* of the anisotropic or bianisotropic medium that determines the form of Eq. (15) [22]. Each point group consists of all those space, time and spacetime transformations that bring the medium into self-coincidence. The number of different point groups is 122. These are conventionally divided into the three classes [23,24]: G_1 and G_2 containing 32 point groups each, and G_3 containing 58 point groups. Class G_1 describes those media which are invariant under the time-reversal operation. Lorentz-reciprocal media (17), including anisotropic diamagnetic and paramagnetic media, belong to G_1 . The 32 point groups of G_1 give rise to the seven classical crystallographic systems—

triclinic, monoclinic, orthorhombic, tetragonal, trigonal, hexagonal and cubic [5]—whose point groups and associated constitutive dyadic forms are listed in Table 1. (The 230 *space groups* corresponding to the 32 point groups of G_1 —which specify the symmetry elements of the underlying Bravais lattice—may be found in standard sources such as Ref. 25. The class G_2 does not contain the time reversal operation, whereas point groups of G_3 contain the time-reversal operation in combination with rotation–reflection operations. The classes G_2 and G_3 describe magnetic media (ferromagnetics, antiferromagnetics and ferrimagnetics [23]) and the most general bianisotropic media [26]. The 90 point groups belonging to G_2 and G_3 , together with their corresponding constitutive dyadic forms, are cataloged elsewhere [22,24].

3. PLANE-WAVE PROPAGATION

In the frequency domain, the source-free Maxwell curl postulates are given as [3]

$$\left. \begin{aligned} \nabla \times \underline{\underline{H}}(\underline{\underline{r}}, \omega) + i\omega \underline{\underline{D}}(\underline{\underline{r}}, \omega) &= \underline{\underline{0}} \\ \nabla \times \underline{\underline{E}}(\underline{\underline{r}}, \omega) - i\omega \underline{\underline{B}}(\underline{\underline{r}}, \omega) &= \underline{\underline{0}} \end{aligned} \right\} \quad (19)$$

wherein an $\exp(-i\omega t)$ time dependency has been assumed for the field phasors. The combination of (19) with the bianisotropic constitutive relations (9) yields a self-consistent system of differential equations that may be conveniently expressed in six-vector/dyadic notation as

$$[\underline{\underline{L}}(\nabla) + i\omega \underline{\underline{K}}(\omega)] \cdot \underline{\underline{F}}(\underline{\underline{r}}, \omega) = \underline{\underline{0}} \quad (20)$$

The linear differential operator $\underline{\underline{L}}(\nabla)$ and 6×6 constitutive dyadic $\underline{\underline{K}}(\omega)$ have the representations

$$\underline{\underline{L}}(\nabla) = \begin{bmatrix} \underline{\underline{0}} & \nabla \times \underline{\underline{I}} \\ -\nabla \times \underline{\underline{I}} & \underline{\underline{0}} \end{bmatrix}, \quad \underline{\underline{K}}(\omega) = \begin{bmatrix} \underline{\underline{\varepsilon}}(\omega) & \underline{\underline{\zeta}}(\omega) \\ \underline{\underline{\xi}}(\omega) & \underline{\underline{\mu}}(\omega) \end{bmatrix} \quad (21)$$

and the 6-vector electromagnetic field phasor $\underline{\underline{F}}(\underline{\underline{r}}, \omega)$ is defined as

$$\underline{\underline{F}}(\underline{\underline{r}}, \omega) = \begin{bmatrix} \underline{\underline{E}}(\underline{\underline{r}}, \omega) \\ \underline{\underline{H}}(\underline{\underline{r}}, \omega) \end{bmatrix} \quad (22)$$

Eigenanalysis of the system

$$[\underline{\underline{L}}(i\mathbf{k}) + i\omega \underline{\underline{K}}(\omega)] \cdot \underline{\underline{F}}_0 = \underline{\underline{0}} \quad (23)$$

is very fruitful for the development of plane-wave solutions

$$\underline{\underline{F}}(\underline{\underline{r}}, \omega) = \underline{\underline{F}}_0 \exp(i\mathbf{k} \cdot \underline{\underline{r}}) \quad (24)$$

of (20), where \mathbf{k} is the wavevector. In general, the associated dispersion relation

$$\det[\underline{\underline{L}}(i\mathbf{k}) + i\omega \underline{\underline{K}}(\omega)] = 0 \quad (25)$$

provides a polynomial of degree four in the components of \mathbf{k} . While the derivation of the roots \mathbf{k} of (25) and the

Table 1. The 32 Point Groups of G_1 in the International Notation^a

Medium Type	Crystal System	Point Group	Constitutive Dyadic Form	Number of real-valued scalars
Isotropic	Cubic	23 $m\bar{3}$ 432	$\begin{pmatrix} c_1 & 0 & 0 \\ 0 & c_1 & 0 \\ 0 & 0 & c_1 \end{pmatrix}$	2
		$\bar{4}3m$ $m\bar{3}m$		
Uniaxial	Tetragonal	4 $\bar{4}$ 4/m 422	$\begin{pmatrix} c_1 & 0 & 0 \\ 0 & c_1 & 0 \\ 0 & 0 & c_3 \end{pmatrix}$	4
		4/m \bar{m} $\bar{4}2m$ 4/m $\bar{m}m$		
	Hexagonal	6 $\bar{6}$ 6/m 622	$\begin{pmatrix} c_1 & 0 & 0 \\ 0 & c_1 & 0 \\ 0 & 0 & c_3 \end{pmatrix}$	4
	Trigonal	3 $\bar{3}$ 32	$\begin{pmatrix} c_1 & 0 & 0 \\ 0 & c_1 & 0 \\ 0 & 0 & c_3 \end{pmatrix}$	4
		3 m $\bar{3}m$		
Biaxial	Orthorhombic	222 $mm2$ mmm	$\begin{pmatrix} c_1 & 0 & 0 \\ 0 & c_2 & 0 \\ 0 & 0 & c_3 \end{pmatrix}$	6
	Monoclinic	2 m 2/m	$\begin{pmatrix} c_1 & 0 & r_1 \\ 0 & c_2 & 0 \\ r_1 & 0 & c_3 \end{pmatrix}$	7
	Triclinic	1 $\bar{1}$	$\begin{pmatrix} c_1 & r_1 & r_2 \\ r_1 & c_2 & r_3 \\ r_2 & r_3 & c_3 \end{pmatrix}$	9

^aThe conventional constitutive dyadic forms are also listed [5]; therein, c_n denotes a complex-valued constitutive parameter whereas r_n denotes a real-valued constitutive parameter. Source: Ref. 23.

associated eigenvectors \mathbf{F}_0 is mathematically straightforward, it is a task best undertaken with the aid of a symbolic manipulation package because the process involves unwieldy expressions.

Propagation in a direction parallel to the unit vector $\hat{\mathbf{a}}$ requires determination of the wavenumber k , which is the magnitude of the wavevector $\underline{\mathbf{k}} = k\hat{\mathbf{a}}$. In general, two distinct complex-valued solutions—say, k_1 and k_2 —emerge for every $\hat{\mathbf{a}}$. This phenomenon is known as *birefringence*, and every anisotropic/bianisotropic medium is generally birefringent. The difference between the real parts of k_1 and k_2 gives rise to optical rotation, which is the change in the tilt angle of the vibration ellipse of a plane wave on either reflection from or transmission through a birefringent layer. This phenomenon is commonly exploited in the construction of optical waveplates, polarizers, and prisms [4, Chapter 14], as well as microwave gyrators, isolators, and circulators [27, Section 6.8]. The operations of many liquid crystal devices are also based on birefringence [28]. The difference between the imaginary parts of k_1 and k_2 , called *dichroism*, is a measure of differential absorption of two orthogonally polarized plane waves incident on a birefringent layer.

If a wavenumber is independent of $\hat{\mathbf{a}}$, the corresponding solution $\mathbf{F}_0 \exp(ik\hat{\mathbf{a}} \cdot \mathbf{r})$ represents an *ordinary* plane wave;

otherwise, the solution represents an *extraordinary* plane wave. The amplitude vectors $\underline{\mathbf{E}}_0$ and $\underline{\mathbf{H}}_0$ of an ordinary plane wave are always normal to the direction of propagation, but those of an extraordinary plane wave may not be. The amplitude vectors $\underline{\mathbf{D}}_0$ and $\underline{\mathbf{B}}_0$ of both ordinary and extraordinary plane waves are normal to $\hat{\mathbf{a}}$. The time-averaged Poynting vector of an ordinary plane wave is aligned with the direction of propagation, but that of an extraordinary plane wave is generally not. Incidental unirefringence (i.e., $k_2 = k_1$) may arise for a specific $\hat{\mathbf{a}}$ —for instance, when $\hat{\mathbf{a}} = \hat{\mathbf{z}}$ in a uniaxial dielectric medium with permittivity specified by (6). Pathological unirefringence (i.e., $k_2 = k_1$ for all $\hat{\mathbf{a}}$) can also arise, for example, in a uniaxial dielectric–magnetic medium whose permittivity dyadic is a scalar multiple of its permeability dyadic [29]. Anomalous unirefringence is also possible for a specific $\hat{\mathbf{a}}$, when, in addition to $k_2 = k_1$, the amplitude vector $\mathbf{F}_{0_2} = ik_1 \mathbf{r} \cdot \hat{\mathbf{a}} \mathbf{F}_{0_1}$ turns out to be a function of \mathbf{r} whereas \mathbf{F}_{0_1} is spatially uniform [30]; the coalescence of the two plane waves—which exhibits a linear dependence on propagation distance—is known as a *Voigt wave* [31].

Many accounts of plane-wave propagation in complex media are available in the scientific literature. For comprehensive descriptions of plane-wave solutions in

anisotropic media, Ref. 3 is recommended. Propagation in bianisotropic media is an active area of research, using standard eigenanalysis [32], and results are also available for nonhomogeneous examples such as cholesteric liquid crystals [6,7] and helicoidal bianisotropic media [2,33]. The exquisitely beautiful palette of electromagnetic consequences of anisotropy and bianisotropy becomes evident in crystal optics [34,35].

4. DYADIC GREEN FUNCTIONS IN SPECTRAL FORM

In the presence of a six-vector electromagnetic source term $\underline{\mathbf{S}}(\underline{\mathbf{r}}, \omega)$, the Maxwell curl postulates (20) become

$$[\underline{\mathbf{L}}(\nabla) + i\omega\underline{\mathbf{K}}(\omega)] \cdot \underline{\mathbf{F}}(\underline{\mathbf{r}}, \omega) = \underline{\mathbf{S}}(\underline{\mathbf{r}}, \omega) \quad (26)$$

The linearity of (26) implies that its solution may be expressed in terms of a dyadic Green function $\underline{\mathbf{G}}(\underline{\mathbf{r}} - \underline{\mathbf{r}}', \omega)$ as

$$\underline{\mathbf{F}}(\underline{\mathbf{r}}, \omega) = \underline{\mathbf{F}}_h(\underline{\mathbf{r}}, \omega) + \int_{V'} \underline{\mathbf{G}}(\underline{\mathbf{r}} - \underline{\mathbf{r}}', \omega) \cdot \underline{\mathbf{S}}(\underline{\mathbf{r}}', \omega) d^3\underline{\mathbf{r}}' \quad (27)$$

where field and source points are represented by $\underline{\mathbf{r}}$ and $\underline{\mathbf{r}}'$, respectively, with all source points confined to the region V' . The field $\underline{\mathbf{F}}_h(\underline{\mathbf{r}}, \omega)$ represents the solution to the source-free version of (26); thus, $\underline{\mathbf{F}}_h(\underline{\mathbf{r}}, \omega)$ is the complementary function. The dyadic Green function itself arises as the solution to the differential equation

$$[\underline{\mathbf{L}}(\nabla) + i\omega\underline{\mathbf{K}}(\omega)] \cdot \underline{\mathbf{G}}(\underline{\mathbf{r}} - \underline{\mathbf{r}}', \omega) = \delta(\underline{\mathbf{r}} - \underline{\mathbf{r}}') \underline{\mathbf{I}} \quad (28)$$

in which the role of the source term is taken by the product of the Dirac delta function $\delta(\underline{\mathbf{r}} - \underline{\mathbf{r}}')$ and the 6×6 identity dyadic $\underline{\mathbf{I}}$. As the present context is that of unbounded space completely filled by a homogeneous medium, $\underline{\mathbf{G}}(\underline{\mathbf{r}} - \underline{\mathbf{r}}', \omega)$ is also required to satisfy the Sommerfeld radiation condition [36].

The method of Green functions is a powerful tool in the analysis of electromagnetic fields. However, the explicit delineation of the dyadic Green function for anisotropic and bianisotropic media continues to provide a

the Fourier transform of (28) yields

$$\underline{\tilde{\mathbf{G}}}(\underline{\mathbf{q}}, \omega) = \frac{1}{i\omega} \frac{\text{adj}[\underline{\tilde{\mathbf{A}}}(\underline{\mathbf{q}}, \omega)]}{\det[\underline{\tilde{\mathbf{A}}}(\underline{\mathbf{q}}, \omega)]} \quad (30)$$

where

$$\underline{\tilde{\mathbf{A}}}(\underline{\mathbf{q}}, \omega) = \begin{bmatrix} \underline{\mathbf{0}} & \frac{1}{\omega}(\underline{\mathbf{q}} \times \underline{\mathbf{I}}) \\ -\frac{1}{\omega}(\underline{\mathbf{q}} \times \underline{\mathbf{I}}) & \underline{\mathbf{0}} \end{bmatrix} + \underline{\mathbf{K}}(\omega) \quad (31)$$

While the analytic properties of the inverse Fourier transform

$$\underline{\mathbf{G}}(\underline{\mathbf{R}}, \omega) = \left(\frac{1}{2\pi}\right)^3 \frac{1}{i\omega} \int_q \frac{\text{adj}[\underline{\tilde{\mathbf{A}}}(\underline{\mathbf{q}}, \omega)]}{\det[\underline{\tilde{\mathbf{A}}}(\underline{\mathbf{q}}, \omega)]} \exp(i\underline{\mathbf{q}} \cdot \underline{\mathbf{R}}) d^3\underline{\mathbf{q}} \quad (32)$$

for anisotropic media are known [40], numerical techniques are needed to explicitly evaluate (32).

5. DYADIC GREEN FUNCTIONS IN CLOSED FORM

Closed-form representations of dyadic Green functions are available for all isotropic media [2]. In contrast, those representations have been found for only a limited set of anisotropic and bianisotropic media [37,39].

For a uniaxial dielectric-magnetic medium characterized by the constitutive dyadics

$$\left. \begin{aligned} \underline{\varepsilon}_{\text{uni}} &= \varepsilon_{11} \left(\hat{\mathbf{x}}\hat{\mathbf{x}} + \hat{\mathbf{y}}\hat{\mathbf{y}} \right) + \varepsilon_{33} \hat{\mathbf{z}}\hat{\mathbf{z}} \\ \underline{\mu}_{\text{uni}} &= \mu_{11} \left(\hat{\mathbf{x}}\hat{\mathbf{x}} + \hat{\mathbf{y}}\hat{\mathbf{y}} \right) + \mu_{33} \hat{\mathbf{z}}\hat{\mathbf{z}} \end{aligned} \right\} \quad (33)$$

the 3×3 dyadic components of the 6×6 dyadic Green function

$$\underline{\mathbf{G}}_{\text{uni}}(\underline{\mathbf{r}} - \underline{\mathbf{r}}', \omega) = \begin{bmatrix} \underline{\mathbf{G}}_{\text{uni}}^{ee}(\underline{\mathbf{r}} - \underline{\mathbf{r}}', \omega) & \underline{\mathbf{G}}_{\text{uni}}^{em}(\underline{\mathbf{r}} - \underline{\mathbf{r}}', \omega) \\ \underline{\mathbf{G}}_{\text{uni}}^{me}(\underline{\mathbf{r}} - \underline{\mathbf{r}}', \omega) & \underline{\mathbf{G}}_{\text{uni}}^{mm}(\underline{\mathbf{r}} - \underline{\mathbf{r}}', \omega) \end{bmatrix} \quad (34)$$

are given as [41]

$$\left. \begin{aligned} \underline{\mathbf{G}}_{\text{uni}}^{ee}(\underline{\mathbf{r}} - \underline{\mathbf{r}}', \omega) &= -i\omega\mu_{11} \left[\left(\varepsilon_{33}\varepsilon_{\text{uni}}^{-1} + \frac{\nabla\nabla}{\omega^2\varepsilon_{11}\mu_{11}} \right) \underline{\mathbf{g}}_e(\underline{\mathbf{r}} - \underline{\mathbf{r}}', \omega) - \underline{\mathbf{T}}(\underline{\mathbf{r}} - \underline{\mathbf{r}}', \omega) \right] \\ \underline{\mathbf{G}}_{\text{uni}}^{em}(\underline{\mathbf{r}} - \underline{\mathbf{r}}', \omega) &= -\varepsilon_{11}\varepsilon_{\text{uni}}^{-1} \cdot (\nabla \times \underline{\mathbf{I}}) \cdot \left[\mu_{33}\underline{\mathbf{g}}_\mu(\underline{\mathbf{r}} - \underline{\mathbf{r}}', \omega)\underline{\mu}_{\text{uni}}^{-1} + \underline{\mathbf{T}}(\underline{\mathbf{r}} - \underline{\mathbf{r}}', \omega) \right] \\ \underline{\mathbf{G}}_{\text{uni}}^{me}(\underline{\mathbf{r}} - \underline{\mathbf{r}}', \omega) &= -\mu_{11}\underline{\mu}_{\text{uni}}^{-1} \cdot (\nabla \times \underline{\mathbf{I}}) \cdot \left[-\varepsilon_{33}\underline{\mathbf{g}}_e(\underline{\mathbf{r}} - \underline{\mathbf{r}}', \omega)\varepsilon_{\text{uni}}^{-1} + \underline{\mathbf{T}}(\underline{\mathbf{r}} - \underline{\mathbf{r}}', \omega) \right] \\ \underline{\mathbf{G}}_{\text{uni}}^{mm}(\underline{\mathbf{r}} - \underline{\mathbf{r}}', \omega) &= -i\omega\varepsilon_{11} \left[\left(\mu_{33}\underline{\mu}_{\text{uni}}^{-1} + \frac{\nabla\nabla}{\omega^2\varepsilon_{11}\mu_{11}} \right) \underline{\mathbf{g}}_\mu(\underline{\mathbf{r}} - \underline{\mathbf{r}}', \omega) + \underline{\mathbf{T}}(\underline{\mathbf{r}} - \underline{\mathbf{r}}', \omega) \right] \end{aligned} \right\} \quad (35)$$

formidable challenge to theoreticians [37–39]. A spectral representation may be provided as the spatial Fourier transform [8]

$$\underline{\tilde{\mathbf{G}}}(\underline{\mathbf{q}}, \omega) = \int_{\underline{\mathbf{R}}} \underline{\mathbf{G}}(\underline{\mathbf{R}}, \omega) \exp(-i\underline{\mathbf{q}} \cdot \underline{\mathbf{R}}) d^3\underline{\mathbf{R}} \quad (29)$$

with $\underline{\mathbf{R}} = \underline{\mathbf{r}} - \underline{\mathbf{r}}'$. For the homogeneous bianisotropic medium characterized by the 6×6 constitutive dyadic $\underline{\mathbf{K}}(\omega)$,

The scalar Green functions $\underline{\mathbf{g}}_e(\underline{\mathbf{r}} - \underline{\mathbf{r}}', \omega)$ and $\underline{\mathbf{g}}_\mu(\underline{\mathbf{r}} - \underline{\mathbf{r}}', \omega)$ in (35) are defined by

$$\underline{\mathbf{g}}_\gamma(\underline{\mathbf{R}}, \omega) = \frac{\exp\left(-i\omega^2\varepsilon_{11}\mu_{11}\sqrt{\gamma_{33}\underline{\mathbf{R}} \cdot \underline{\gamma}_{\text{uni}}^{-1} \cdot \underline{\mathbf{R}}}\right)}{4\pi\sqrt{\gamma_{33}\underline{\mathbf{R}} \cdot \underline{\gamma}_{\text{uni}}^{-1} \cdot \underline{\mathbf{R}}}}, \quad (36)$$

($\gamma = \varepsilon, \mu$)

while the dyadic $\underline{T}(\underline{r} - \underline{r}', \omega)$ is specified as

$$\begin{aligned} \underline{T}(\underline{R}, \omega) &= \left(\frac{\varepsilon_{33}}{\varepsilon_{11}} \underline{g}_\varepsilon - \frac{\mu_{33}}{\mu_{11}} \underline{g}_\mu \right) \frac{(\underline{R} \times \hat{\underline{z}})(\underline{R} \times \hat{\underline{z}})}{(\underline{R} \times \hat{\underline{z}})^2} \\ &+ \left[\underline{I} - \hat{\underline{z}}\hat{\underline{z}} - \frac{2(\underline{R} \times \hat{\underline{z}})(\underline{R} \times \hat{\underline{z}})}{(\underline{R} \times \hat{\underline{z}})^2} \right] \\ &\times \frac{g_\varepsilon \sqrt{\varepsilon_{33} \underline{R} \cdot \underline{\varepsilon}_{\text{uni}}^{-1} \cdot \underline{R}} - g_\mu \sqrt{\mu_{33} \underline{R} \cdot \underline{\mu}_{\text{uni}}^{-1} \cdot \underline{R}}}{i\omega \sqrt{\varepsilon_{11} \mu_{11}} (\underline{R} \times \hat{\underline{z}})^2} \end{aligned} \quad (37)$$

Although analytical progress has been reported towards closed-form dyadic Green functions for general uniaxial bianisotropic media described by the constitutive dyadics

$$\underline{\gamma}_{\text{uni}} = \gamma_{11} \underline{I} + (\gamma_{33} - \gamma_{11}) \hat{\underline{z}}\hat{\underline{z}}, \quad (\gamma = \varepsilon, \zeta, \zeta, \mu) \quad (38)$$

the case remains unsolved [39,42].

Closed-form representations of dyadic Green functions are available for the bianisotropic example provided by a uniformly moving isotropic dielectric–magnetic medium. In the case where $|\underline{v}|$ in (11) is smaller than the phase velocity of a wave in the stationary medium, the 3×3 dyadic Green functions (34) of the moving medium are [3,37]

$$\left. \begin{aligned} \underline{G}_{\text{mov}}^{ee}(\underline{r} - \underline{r}', \omega) &= -i\omega\mu\sqrt{\alpha^3} \left(\underline{I} + \frac{\underline{\varepsilon}_{\text{mov}} \cdot \nabla \nabla}{\mu(\omega\varepsilon\alpha)^2} \right) \frac{\exp(-i\omega\varepsilon\alpha\sqrt{\underline{\mu}\underline{R} \cdot \underline{\varepsilon}_{\text{mov}}^{-1} \cdot \underline{R}})}{4\pi\sqrt{\varepsilon\underline{R} \cdot \underline{\varepsilon}_{\text{mov}}^{-1} \cdot \underline{R}}} \\ \underline{G}_{\text{mov}}^{em}(\underline{r} - \underline{r}', \omega) &= \frac{1}{i\omega} \underline{\varepsilon}_{\text{mov}}^{-1} \cdot [\nabla \times \underline{I} - i\omega(\hat{\underline{v}} \times \underline{I})] \cdot \underline{G}_{\text{mov}}^{mm}(\underline{r} - \underline{r}', \omega) \\ \underline{G}_{\text{mov}}^{me}(\underline{r} - \underline{r}', \omega) &= -\frac{1}{i\omega} \underline{\mu}_{\text{mov}}^{-1} \cdot [\nabla \times \underline{I} - i\omega(\hat{\underline{v}} \times \underline{I})] \cdot \underline{G}_{\text{mov}}^{ee}(\underline{r} - \underline{r}', \omega) \\ \underline{G}_{\text{mov}}^{mm}(\underline{r} - \underline{r}', \omega) &= -i\omega\varepsilon\sqrt{\alpha^3} \left(\underline{I} + \frac{\underline{\mu}_{\text{mov}} \cdot \nabla \nabla}{\varepsilon(\omega\mu\alpha)^2} \right) \frac{\exp(-i\omega\mu\alpha\sqrt{\varepsilon\underline{R} \cdot \underline{\mu}_{\text{mov}}^{-1} \cdot \underline{R}})}{4\pi\sqrt{\underline{\mu}\underline{R} \cdot \underline{\mu}_{\text{mov}}^{-1} \cdot \underline{R}}} \end{aligned} \right\} \quad (39)$$

Dyadic scalarization and factorization techniques are commonly implemented in establishing solutions to (28). In outline, the procedure is as follows. Formally

$$\underline{G}(\underline{r} - \underline{r}', \omega) = [\underline{L}(\nabla) + i\omega\underline{K}(\omega)]^\dagger \underline{W}(\underline{r} - \underline{r}', \omega) \quad (40)$$

where the adjoint operation indicated by superscript \dagger is defined implicitly via

$$[\underline{L}(\nabla) + i\omega\underline{K}(\omega)]^\dagger \cdot [\underline{L}(\nabla) + i\omega\underline{K}(\omega)] = \mathcal{H}(\nabla, \underline{r}, \omega) \underline{I} \quad (41)$$

The scalar Green function $W(\underline{r} - \underline{r}', \omega)$ in (40) is specified by the action of the scalar fourth-order operator $\mathcal{H}(\nabla, \underline{r}, \omega)$ in (41) as

$$\mathcal{H}(\nabla, \underline{r}, \omega) W(\underline{r} - \underline{r}', \omega) = \delta(\underline{r} - \underline{r}') \quad (42)$$

The construction of the adjoint operator $[\underline{L}(\nabla) + i\omega\underline{K}(\omega)]^\dagger$ for anisotropic and bianisotropic media involves straightforward, albeit lengthy, matrix–algebraic operations.

However, solutions to the fourth-order partial differential equation represented by (42) are generally elusive.

The general unavailability of the dyadic Green functions in closed form has meant that a cornerstone of electromagnetic scattering theory—the Huygens principle—has been formulated exactly only for the simplest of anisotropic media [43,44]. Field representations in non-Cartesian coordinate systems are generally unavailable; and the very few counterexamples [45,46] are exceedingly awkward to handle and restricted in scope.

6. DEPOLARIZATION DYADICS

Although closed-form representations of dyadic Green functions are relatively scarce, often in electromagnetic analyses it is sufficient to construct approximative solutions of restricted validity. An important example occurs in the homogenization of particulate composite materials [47,48], wherein the scattering response of an electrically small particle embedded within a homogeneous ambient medium is required. Relative to Eqs. (26) and (27), the particle represents an equivalent source $\underline{S}(\underline{r}, \omega)$; and the field $\underline{F}(\underline{r}, \omega)$ is sought for $\underline{r} \in V$ (i.e., in the source region). Provided the particle is sufficiently small compared with the electromagnetic wavelengths, the Rayleigh

approximation

$$\underline{F}(\underline{r}, \omega) \approx \underline{F}_h(\underline{r}, \omega) + \underline{D}(\underline{r}, \omega) \cdot \underline{S}(\underline{r}, \omega) \quad (43)$$

may be implemented, where

$$\underline{D}(\underline{r}, \omega) = \int_V \underline{G}(\underline{r} - \underline{r}', \omega) d^3 \underline{r}' \quad (44)$$

is the 6×6 *depolarization dyadic* of a region of the same shape, orientation, and size as the particle [48]. In the limiting case of a vanishingly small particle, the depolarization dyadic is nonzero because of the singularity of the Green function at the origin.

Consider an ellipsoidal particle with surface parameterized as

$$\underline{r}_e(\theta, \phi) = \eta \underline{U} \cdot \hat{\underline{r}}(\theta, \phi) \quad (45)$$

where $\hat{\underline{r}}(\theta, \phi)$ is the radial unit vector specified by the spherical polar coordinates θ and ϕ . The shape dyadic \underline{U} is a real-valued 3×3 dyadic with positive eigenvalues [49]; the normalized lengths of the ellipsoid semi-axes are specified by the eigenvalues of \underline{U} . In the limit $\eta \rightarrow 0$, the 6×6

depolarization dyadic for the ellipsoidal particle embedded within a homogeneous bianisotropic medium (with 3×3 constitutive dyadics $\underline{\underline{\epsilon}}_{\text{amb}}, \underline{\underline{\xi}}_{\text{amb}}, \underline{\underline{\zeta}}_{\text{amb}}$, and $\underline{\underline{\mu}}_{\text{amb}}$) is given as [50]

$$\underline{\underline{\mathbf{D}}}^{U/\text{amb}} = \begin{bmatrix} \underline{\underline{D}}_{ee}^{U/\text{amb}} & \underline{\underline{D}}_{em}^{U/\text{amb}} \\ \underline{\underline{D}}_{me}^{U/\text{amb}} & \underline{\underline{D}}_{mm}^{U/\text{amb}} \end{bmatrix} \quad (46)$$

where

$$\underline{\underline{D}}_{\lambda\lambda'}^{U/\text{amb}} = \underline{\underline{U}}^{-1} \cdot \underline{\underline{\tilde{D}}}_{\lambda\lambda'}^{U/\text{amb}} \cdot \underline{\underline{U}}^{-1}, \quad (\lambda, \lambda' = e, m) \quad (47)$$

$$\begin{aligned} & \underline{\underline{\tilde{D}}}_{\lambda\lambda'}^{U/\text{amb}} \\ &= \frac{1}{4\pi i \omega} \int_{\phi=0}^{2\pi} \int_{\theta=0}^{\pi} \frac{(\hat{\mathbf{q}} \cdot \underline{\underline{\tau}}_{\lambda\lambda'} \cdot \hat{\mathbf{q}}) \hat{\mathbf{q}} \hat{\mathbf{q}} \sin \theta d\theta d\phi}{(\hat{\mathbf{q}} \cdot \underline{\underline{\epsilon}}_{\text{amb}} \cdot \hat{\mathbf{q}})(\hat{\mathbf{q}} \cdot \underline{\underline{\mu}}_{\text{amb}} \cdot \hat{\mathbf{q}}) - (\hat{\mathbf{q}} \cdot \underline{\underline{\xi}}_{\text{amb}} \cdot \hat{\mathbf{q}})(\hat{\mathbf{q}} \cdot \underline{\underline{\zeta}}_{\text{amb}} \cdot \hat{\mathbf{q}})} \end{aligned} \quad (48)$$

$$\underline{\underline{\tau}}_{ee} = \underline{\underline{\mu}}_{\text{amb}}, \quad \underline{\underline{\tau}}_{em} = -\underline{\underline{\xi}}_{\text{amb}}, \quad \underline{\underline{\tau}}_{me} = -\underline{\underline{\zeta}}_{\text{amb}}, \quad \underline{\underline{\tau}}_{mm} = \underline{\underline{\epsilon}}_{\text{amb}} \quad (49)$$

$$\underline{\underline{\tilde{\gamma}}}_{\text{amb}} = \underline{\underline{U}}^{-1} \cdot \underline{\underline{\gamma}}_{\text{amb}} \cdot \underline{\underline{U}}^{-1}, \quad (\gamma = \epsilon, \xi, \zeta, \mu) \quad (50)$$

and

$$\hat{\mathbf{q}} = \hat{\mathbf{x}} \sin \theta \cos \phi + \hat{\mathbf{y}} \sin \theta \sin \phi + \hat{\mathbf{z}} \cos \theta \quad (51)$$

Thus, (48) provides the components of the integrated singularity of the dyadic Green function.

Explicit evaluations of the surface integrals in (48) are available for several classes of anisotropic media. For a spherical particle (i.e., $\underline{\underline{U}} = \underline{\underline{I}}$) immersed in the orthorhombic biaxial dielectric medium described by (7), the 3×3 depolarization dyadics are [51]

$$\left. \begin{aligned} \underline{\underline{D}}_{ee}^{I/\text{ortho}} &= \frac{1}{i\omega\epsilon_0} (D_x \hat{\mathbf{x}}\hat{\mathbf{x}} + D_y \hat{\mathbf{y}}\hat{\mathbf{y}} + D_z \hat{\mathbf{z}}\hat{\mathbf{z}}) \\ \underline{\underline{D}}_{em}^{I/\text{ortho}} &= \underline{\underline{D}}_{me}^{I/\text{ortho}} = \underline{\underline{0}} \\ \underline{\underline{D}}_{mm}^{I/\text{ortho}} &= \frac{1}{3i\omega\mu_0} \underline{\underline{I}} \end{aligned} \right\} \quad (52)$$

with

$$\left. \begin{aligned} D_x &= \frac{\sqrt{\epsilon_{22}}}{(\epsilon_{22} - \epsilon_{11})\sqrt{\epsilon_{33} - \epsilon_{11}}} [F(v_1, v_2) - E(v_1, v_2)] \\ D_y &= \frac{1}{\epsilon_{22} - \epsilon_{11}} \left\{ \frac{\epsilon_{11} - \epsilon_{22}}{\epsilon_{33} - \epsilon_{22}} - \sqrt{\frac{\epsilon_{33} - \epsilon_{11}}{\epsilon_{22}}} \right. \\ & \left. \left[\frac{\epsilon_{11}}{\epsilon_{33} - \epsilon_{11}} F(v_1, v_2) - \frac{\epsilon_{22}}{\epsilon_{33} - \epsilon_{22}} E(v_1, v_2) \right] \right\} \\ D_z &= \frac{1}{\epsilon_{33} - \epsilon_{22}} \left[1 - \sqrt{\frac{\epsilon_{22}}{\epsilon_{22} - \epsilon_{11}}} E(v_1, v_2) \right] \end{aligned} \right\} \quad (53)$$

where $F(v_1, v_2)$ and $E(v_1, v_2)$ are elliptic integrals of the first and second kinds [52], respectively, and their arguments are

$$v_1 = \tan^{-1} \sqrt{\frac{\epsilon_{33} - \epsilon_{11}}{\epsilon_{11}}}, \quad v_2 = \sqrt{\frac{\epsilon_{33}(\epsilon_{22} - \epsilon_{11})}{\epsilon_{22}(\epsilon_{33} - \epsilon_{11})}} \quad (54)$$

The form of the depolarization dyadics (52) also arises for an ellipsoidal particle embedded in an isotropic dielectric

medium [51,53]. The depolarization dyadics for uniaxial dielectric media follow from (52) as special cases (e.g., $\epsilon_{11} = \epsilon_{22}$) [54]. Furthermore, the depolarization dyadics for gyrotropic dielectric media (8) are precisely the same as those for uniaxial dielectric media, since the surface integrals in (48) are insensitive to skew-symmetric dyadic components [50]. In addition to the representation (52) for spherical/ellipsoidal particles, depolarization dyadics associated with certain infinitely long cylindrical particles in biaxial anisotropic media have also been derived [55,56]. Closed-form representations of depolarization dyadics are not available for the general bianisotropic medium (15), but are established for certain ellipsoidal particles embedded in uniaxial bianisotropic media [50].

7. HOMOGENIZATION

Consider the electromagnetic response of an assembly of particulate media. Provided that the component particles are small compared with the electromagnetic wavelengths, the assembly may be viewed as an effectively homogeneous composite medium (HCM) [47,48]. By the process of homogenization, complex anisotropic and bianisotropic media may be conceptualized—and fabricated—even when the component media themselves are relatively simple. A variety of formalisms have been developed for the purpose of estimating the constitutive properties of HCMs. Three widely used homogenization formalisms—namely, those of Maxwell Garnett, Bruggeman and the strong property fluctuation theory (SPFT)—are outlined in this section. The HCM considered is that arising from two particulate component media, labeled as a and b , which are characterized by the 6×6 constitutive dyadics $\underline{\underline{\mathbf{K}}}_a$ and $\underline{\underline{\mathbf{K}}}_b$, respectively, at the angular frequency ω of interest. The volume fractions of the media a and b are denoted by f_a and $f_b = 1 - f_a$, respectively.

The Maxwell Garnett homogenization formalism is perhaps the simplest and most often utilized formalism. If medium a is present as identically oriented, ellipsoidal particles described by the shape dyadic $\underline{\underline{U}}^a$, then the Maxwell Garnett estimate of the HCM constitutive dyadic is [57]

$$\underline{\underline{\mathbf{K}}}_{\text{MG}} = \underline{\underline{\mathbf{K}}}_b + f_a \underline{\underline{\alpha}}^{a/b} \cdot \left(\underline{\underline{I}} - i\omega f_a \underline{\underline{D}}^{I/b} \cdot \underline{\underline{\alpha}}^{a/b} \right)^{-1} \quad (55)$$

The 6×6 depolarization dyadic $\underline{\underline{D}}^{I/b}$ is that associated with a sphere embedded in medium b , while the dyadic $\underline{\underline{\alpha}}^{a/b}$ is the generalized polarizability density dyadic

$$\underline{\underline{\alpha}}^{a/b} = (\underline{\underline{\mathbf{K}}}_a - \underline{\underline{\mathbf{K}}}_b) \cdot \left[\underline{\underline{I}} + i\omega \underline{\underline{D}}^{U^a/b} \cdot (\underline{\underline{\mathbf{K}}}_a - \underline{\underline{\mathbf{K}}}_b) \right]^{-1} \quad (56)$$

of a particle of medium a embedded in medium b . The estimate (55) is valid for $f_a < 0.3$ only. However, this limitation has been overcome in recent (as of 2004) incremental and differential refinements to the Maxwell Garnett formalism [58]. If $\underline{\underline{D}}^{I/b}$ is replaced by $\underline{\underline{D}}^{U^a/b}$ in (55), then the HCM constitutive dyadic estimate of the Bragg-Pippard formalism [59] results.

The Bruggeman formalism rests on the assertion that the net polarizability density is zero throughout the HCM.

A characteristic feature is that the component media a and b are treated symmetrically. Thus, the Bruggeman homogenization formalism has the advantage over the Maxwell Garnett formalism of being applicable for all volume fractions $f_a \in (0,1)$ [47]. For component media a and b distributed as ellipsoids with shape dyadics $\underline{\underline{U}}^a$ and $\underline{\underline{U}}^b$, respectively, the Bruggeman estimate of the HCM constitutive dyadic $\underline{\underline{K}}_{\text{Br}}$ is obtained by solving the equation [57]

$$f_a \underline{\underline{\alpha}}^{a/\text{Br}} + f_b \underline{\underline{\alpha}}^{b/\text{Br}} = \underline{\underline{0}} \quad (57)$$

with $\underline{\underline{\alpha}}^{a/\text{Br}}$ and $\underline{\underline{\alpha}}^{b/\text{Br}}$ defined and interpreted similarly to $\underline{\underline{\alpha}}^{a/b}$. Half a century after its intuitive initial enunciation [60], Eq. (57) was found to arise naturally within the SPFT [61,62]. For isotropic dielectric–magnetic media, the HCM permittivity and permeability may be extracted simply from (57) as roots of quadratic polynomials. But for anisotropic and bianisotropic media, (57) represents a nonlinear relation in terms of the HCM constitutive parameters embodied in $\underline{\underline{K}}_{\text{Br}}$. Iterative solutions to the nonlinear forms of (57) are straightforwardly computed by applying the Jacobi method [63], for example.

The SPFT provides an approach to homogenization based on the iterative refinement of the Bruggeman estimate $\underline{\underline{K}}_{\text{Br}}$. Unlike the Maxwell Garnett and Bruggeman formalisms, the SPFT accommodates a comprehensive description of the distributional statistics of the component media [61]. Thereby, coherent scattering losses may be accounted for. Successive SPFT iterates recruit successively higher-order spatial correlation functions. Suppose that the particulate geometries of both component media a and b are characterized by the ellipsoidal shape dyadic $\underline{\underline{U}}$. Then the n th-order SPFT estimate of the HCM constitutive dyadic is obtained as [62]

$$\underline{\underline{K}}_{\text{Dy}}^{[n]} = \underline{\underline{K}}_{\text{Br}} - \frac{1}{i\omega} \left(\underline{\underline{I}} + \underline{\underline{\Sigma}}^{[n]} \cdot \underline{\underline{D}}^{U/\text{Br}} \right)^{-1} \cdot \underline{\underline{\Sigma}}^{[n]} \quad (58)$$

wherein the subscript Dy on $\underline{\underline{K}}_{\text{Dy}}^{[n]}$ derives from the central equation in the SPFT, namely, the Dyson equation [61]. The mass operator term $\underline{\underline{\Sigma}}^{[n]}$ —which is an infinite series—is defined in terms of the dyadic Green function $\underline{\underline{G}}_{\text{Br}}(\underline{\underline{R}}, \omega)$ associated with $\underline{\underline{K}}_{\text{Br}}$, together with the normalized polarizability density dyadic $\underline{\underline{\chi}}_l = -i\omega \underline{\underline{\alpha}}^{l/\text{Br}}$ ($l = a, b$). In the derivation of (58), the long-wavelength approximation is invoked. For $n = 0$ and $n = 1$, the SPFT estimates of the HCM constitutive dyadic are degenerate with those of the Bruggeman formalism:

$$\underline{\underline{K}}_{\text{Dy}}^{[0]} = \underline{\underline{K}}_{\text{Dy}}^{[1]} = \underline{\underline{K}}_{\text{Br}} \quad (59)$$

At the level of the so-called bilocal approximation (i.e., $n = 2$), the mass operator is given by

$$\underline{\underline{\Sigma}}^{[2]} = \left(\underline{\underline{\chi}}_a - \underline{\underline{\chi}}_b \right) \cdot \left[\mathcal{P} \int \Gamma(\underline{\underline{R}}) \underline{\underline{G}}_{\text{Br}}(\underline{\underline{R}}) d^3 \underline{\underline{R}} \right] \cdot \left(\underline{\underline{\chi}}_a - \underline{\underline{\chi}}_b \right) \quad (60)$$

and $\underline{\underline{K}}_{\text{Dy}}^{[2]}$ is thus delivered by (58). In (60), \mathcal{P} denotes principal value integration and $\Gamma(\underline{\underline{R}})$ is a two-point covariance function. Evaluations of the mass operator (60) for physically motivated choices of $\Gamma(\underline{\underline{R}})$ have revealed that $\underline{\underline{K}}_{\text{Dy}}^{[2]}$ is largely insensitive to the precise form of the

covariance function [64]. Finite integral representations of $\underline{\underline{K}}_{\text{Dy}}^{[2]}$ are available for both anisotropic [64,65] and bianisotropic [62] composites. In addition, the SPFT iterative procedure converges at the level $n = 2$, at least for weakly anisotropic composites [66].

The constitutive dyadic forms that result from homogenization processes have been extensively investigated [63]. HCMs with biaxial symmetry have come under particular scrutiny [67]. A biaxial HCM arises when the component media present two distinct distinguished axes. These distinguished axes can have either a geometric origin (e.g., component media present as spheroids) or an electromagnetic origin (e.g., component media characterized by uniaxial constitutive dyadics). Furthermore, orthorhombic biaxial HCM structures generally develop, provided that the distinguished axes of the component media are mutually perpendicular; for nonperpendicular distinguished axes, the more general monoclinic or triclinic biaxial HCM form arises.

8. NONLINEAR ANISOTROPY

A general description of bianisotropic nonlinearity (and, therefore, also anisotropic nonlinearity) proceeds as follows: The nonlinear constitutive relations are expressed in six-vector/dyadic notation as [68]

$$\underline{\underline{C}}(\underline{\underline{r}}, \omega) = \underline{\underline{K}}_0 \cdot \underline{\underline{F}}(\underline{\underline{r}}, \omega) + \underline{\underline{Q}}(\underline{\underline{r}}, \omega) \quad (61)$$

where $\underline{\underline{K}}_0$ is the 6×6 constitutive dyadic of free space, and the six-vector

$$\underline{\underline{C}}(\underline{\underline{r}}, \omega) = \begin{bmatrix} D(\underline{\underline{r}}, \omega) \\ B(\underline{\underline{r}}, \omega) \end{bmatrix}. \quad (62)$$

The six-vector $\underline{\underline{Q}}(\underline{\underline{r}}, \omega)$ is the sum of linear and nonlinear parts

$$\underline{\underline{Q}}(\underline{\underline{r}}, \omega) = \underline{\underline{Q}}^{\text{lin}}(\underline{\underline{r}}, \omega) + \underline{\underline{Q}}^{\text{nl}}(\underline{\underline{r}}, \omega) \quad (63)$$

The linear part

$$\underline{\underline{Q}}^{\text{lin}}(\underline{\underline{r}}, \omega) = \left(\underline{\underline{K}}^{\text{lin}}(\omega) - \underline{\underline{K}}_0 \right) \cdot \underline{\underline{F}}(\underline{\underline{r}}, \omega) \quad (64)$$

involves $\underline{\underline{K}}^{\text{lin}}$ as the 6×6 constitutive dyadic to characterize the linear response of the nonlinear medium. The exclusively nonlinear response of the medium, under the simultaneous stimulation by an ensemble of $M > 1$ fields $\underline{\underline{F}}(\underline{\underline{r}}, \omega_m)$, ($m = 1, 2, \dots, M$), is characterized by the six-vector $\underline{\underline{Q}}^{\text{nl}}(\underline{\underline{r}}, \omega)$. At the frequency $\omega = \omega_{\text{nl}}$, the j th element of $\underline{\underline{Q}}^{\text{nl}}(\underline{\underline{r}}, \omega_{\text{NL}})$ is given by

$$\begin{aligned} & \mathcal{Q}_j^{\text{nl}}(\underline{\underline{r}}, \omega_{\text{nl}}) \\ &= \sum_{j_1=1}^6 \sum_{j_2=1}^6 \cdots \sum_{j_m=1}^6 \cdots \sum_{j_M=1}^6 \\ & \times \left\{ \chi_{jj_1 j_2 \dots j_m \dots j_M}^{\text{nl}}(\omega_{\text{nl}}; \mathcal{W}) \prod_{n=1}^M [F_{j_n}(\underline{\underline{r}}, \omega_n)] \right\} \end{aligned} \quad (65)$$

for $j \in [1, 6]$, where $\mathcal{W} = \{\omega_1, \omega_2, \dots, \omega_M\}$ and not all members of \mathcal{W} have to be distinct. The angular frequency ω_{nl} is the

sum

$$\omega_{\text{nl}} = \sum_{m=1}^M a_m \omega_m, \quad a_m = \pm 1 \quad (66)$$

If $a_n = -1$, then $F_{j_n}(r, \omega)$ in (65) should be replaced by its complex conjugate. The nonlinear susceptibility tensor

$$\chi_{j_1 j_2 \dots j_M}^{\text{nl}}(\omega_{\text{nl}}; \mathcal{W}) \quad (67)$$

delineates the nonlinear constitutive properties. A vast range of nonlinear electromagnetic phenomena may be described in terms of (65) [69,70].

The homogenization of nonlinear anisotropic composites has been carried out with various homogenization formalisms [71,72], including the Maxwell Garnett [68,73] and Bruggeman [73,74] formalisms, and the SPFT [75]. For example, the anisotropic dielectric HCM with permittivity dyadic given by the sum of linear and nonlinear contributions

$$\underline{\underline{\epsilon}}(\omega) = \underline{\underline{\epsilon}}^{\text{lin}}(\omega) + \underline{\underline{\chi}}^{\text{nl}}(\omega) |\underline{\underline{E}}(\omega)|^2 \quad (68)$$

is found to arise from isotropic nonlinear component media distributed as ellipsoidal particles [74,75]. Furthermore, the degree of nonlinearity exhibited by the HCM described by (68) can exceed the degree of nonlinearity present in the component phases. This nonlinearity enhancement—which is itself an anisotropic phenomenon—has significant potential for technological applications [76].

BIBLIOGRAPHY

1. E. J. Post, Separating field and constitutive equations in electromagnetic theory, in W. S. Weiglhofer and A. Lakhtakia, eds., *Introduction to Complex Mediums for Optics and Electromagnetics*, SPIE Press, Bellingham, WA, pp. 2003, pp. 3–26.
2. A. Lakhtakia, Chirality, in K. Chang, ed., *Encyclopedia of RF and Microwave Engineering*, Wiley, Hoboken, NJ, 2005.
3. H. C. Chen, *Theory of Electromagnetic Waves*, TechBooks, Fairfax, VA, 1993.
4. M. Born and E. Wolf, *Principles of Optics*, 6th ed., Pergamon Press, Oxford, UK, 1980.
5. J. F. Nye, *Physical Properties of Crystals*, Clarendon Press, Oxford, UK, 1985.
6. S. Chandrasekhar, *Liquid Crystals*, 2nd ed., Cambridge Univ. Press, Cambridge, UK, 1992.
7. P. G. de Gennes and J. A. Prost, *The Physics of Liquid Crystals*, 2nd ed., Clarendon Press, Oxford, UK, 1993.
8. J. A. Kong, Theorems of bianisotropic media, *Proc. IEEE* **60**:1036–1046 (1972).
9. W. S. Weiglhofer, Constitutive characterization of simple and complex mediums, in W.S. Weiglhofer and A. Lakhtakia, eds., *Introduction to Complex Mediums for Optics and Electromagnetics*, SPIE Press, Bellingham, WA, 2003, pp. 27–61.
10. C. T. Tai, *Dyadic Green Functions in Electromagnetic Theory*, 2nd ed., IEEE Press, Piscataway, NJ, 1994.
11. W. S. Weiglhofer and A. Lakhtakia, On electromagnetic waves in biaxial bianisotropic media, *Electromagnetics* **19**:351–362 (1999).
12. T. G. Mackay and W. S. Weiglhofer, Homogenization of biaxial composite materials: bianisotropic properties, *J. Opt. A: Pure Appl. Opt.* **3**:45–52 (2001).
13. N. Engheta, D. L. Jaggard, and M. W. Kowarz, Electromagnetic waves in Faraday chiral media, *IEEE Trans. Anten. Propag.* **40**:367–374 (1992).
14. W. S. Weiglhofer and A. Lakhtakia, The correct constitutive relations of chiroplasmas and chiroferrites, *Microwave Opt. Technol. Lett.* **17**:405–408 (1998).
15. J. C. Bose, On the rotation of polarisation of electric waves by a twisted structure, *Proc. Roy. Soc. Lond. A* **63**:146–152 (1898).
16. A. Lakhtakia, ed., *Selected Papers on Natural Optical Activity*, SPIE Optical Engineering Press, Bellingham, WA, 1990.
17. I. P. Theron and J. H. Cloete, The optical activity of an artificial non-magnetic uniaxial chiral crystal at microwave frequencies, *J. Electromagn. Waves Appl.* **10**:539–561 (1996).
18. K. W. Whites and C. Y. Chung, Composite uniaxial bianisotropic chiral materials characterization: Comparison of predicted and measured scattering, *J. Electromagn. Waves Appl.* **11**:371–394 (1997).
19. E. J. Post, *Formal Structure of Electromagnetics*, Dover, New York, 1997.
20. A. Lakhtakia and W. S. Weiglhofer, Constraint on linear, spatiotemporally nonlocal, spatiotemporally nonhomogeneous constitutive relations, *Int. J. Infrared Millim. Waves* **17**:1867–1878 (1996).
21. C. M. Krowne, Electromagnetic theorems for complex anisotropic media, *IEEE Trans. Anten. Propag.* **32**:1224–1230 (1984).
22. V. Dmitriev, Some general electromagnetic properties of linear homogeneous bianisotropic media following from space and time-reversal symmetry of the second-rank and antisymmetric third-rank constitutive tensors, *Eur. Phys. J. Appl. Phys.* **12**:3–16 (2000).
23. A. S. Nowick, *Crystal Properties via Group Theory*, Cambridge Univ. Press, Cambridge, UK, 1995.
24. V. Dmitriev, Tables of the second rank constitutive tensors for linear homogeneous media described by the point magnetic groups of symmetry, *Prog. Electromagn. Res.* **28**:43–95 (2000).
25. T. Hahn, ed., *International Tables for Crystallography*. Vol. A: *Space-Group Symmetry*, 5th ed., Kluwer Academic Publishers, Dordrecht, The Netherlands, 2002.
26. D. B. Litvin, Point group symmetries, in W. S. Weiglhofer and A. Lakhtakia, ed., *Introduction to Complex Mediums for Optics and Electromagnetics*, SPIE Press, Bellingham, WA, 2003, pp. 79–102.
27. R. E. Collin, *Foundations for Microwave Engineering*, McGraw-Hill, New York, 1966.
28. S. D. Jacobs, ed., *Selected Papers on Liquid Crystals for Optics*, SPIE Optical Engineering Press, Bellingham, WA, 1992.
29. A. Lakhtakia, V. K. Varadan, and V. V. Varadan, Plane waves and canonical sources in a gyroelectromagnetic uniaxial medium, *Int. J. Electron.* **71**:853–861 (1991).
30. A. Lakhtakia, Anomalous axial propagation in helicoidal bianisotropic media, *Opt. Commun.* **157**:193–201 (1998).
31. W. Voigt, On the behaviour of pleochroitic crystals along directions in the neighbourhood of an optic axis, *Phil. Mag.* **4**:90–97 (1902).
32. A. Lakhtakia, Frequency-dependent continuum electromagnetic properties of a gas of scattering centers, *Adv. Chem. Phys.* **85**(2):311–359 (1993).
33. A. Lakhtakia and W. S. Weiglhofer, Further results on light propagation in helicoidal bianisotropic mediums: oblique propagation, *Proc. Roy. Soc. Lond. A* **453**:93–105 (1997); erratum 454:3275 (1998).
34. P. J. Collings, *Liquid Crystals*, Princeton Univ. Press, Princeton, NJ, 1990.

35. C. D. Gribble and A. J. Hall, *Optical Mineralogy: Principles and Practice*, University College London Press, London, UK, 1992.
36. L. B. Felsen and N. Marcuvitz, *Radiation and Scattering of Waves*, IEEE Press, Piscataway, NJ, 1994.
37. W. S. Weiglhofer, Analytic methods and free-space dyadic Green's functions, *Radio Sci.* **28**:847–857 (1993).
38. W. S. Weiglhofer, Frequency-dependent dyadic Green functions for bianisotropic media, in T. W. Barrett and D. M. Grimes, eds., *Advanced Electromagnetism: Foundations, Theory and Applications*, World Scientific, Singapore, pp. 376–389, 1995.
39. F. Olyslager and I. V. Lindell, Electromagnetics and exotic media: A quest for the holy grail, *IEEE Anten. Propag. Mag.* **44**(2):48–58 (2002).
40. P. G. Cottis and G. D. Kondylis, Properties of the dyadic Green's function for an unbounded anisotropic medium, *IEEE Trans. Anten. Propag.* **43**:154–161 (1995).
41. W. S. Weiglhofer, Dyadic Green's functions for general uniaxial media, *IEE Proc. Part H* **137**:5–10 (1990).
42. W. S. Weiglhofer and I. V. Lindell, Analytic solution for the dyadic Green function of a nonreciprocal uniaxial bianisotropic medium, *Arch. Elektron. Übertrag.* **48**:116–119 (1994).
43. N. R. Ogg, A Huygen's principle for anisotropic media, *J. Phys. A: Math. Gen.* **4**:382–388 (1971).
44. A. Lakhtakia, V. K. Varadan and V. V. Varadan, A note on Huygens's principle for uniaxial dielectric media, *J. Wave-Mat. Interact.* **4**:339–343 (1989).
45. X. B. Wu and K. Yasumoto, Cylindrical vector-wave-function representations of fields biaxial Ω -medium, *J. Electromagn. Waves Appl.* **11**:1407–1423 (1997).
46. J. C. Monzon, Three-dimensional field expansion in the most general rotationally symmetric anisotropic material: Application to scattering by a sphere, *IEEE Trans. Anten. Propag.* **37**:728–735 (1989).
47. A. Lakhtakia, ed., *Selected Papers on Linear Optical Composite Material*, SPIE Optical Engineering Press, Bellingham, WA, 1996.
48. A. Lakhtakia, On direct and indirect scattering approaches for homogenization of particulate composites, *Microwave Opt. Technol. Lett.* **25**:53–56 (2000).
49. A. Lakhtakia, Orthogonal symmetries of polarizability dyadics of bianisotropic ellipsoids, *Microwave Opt. Technol. Lett.* **27**:175–177 (2000).
50. B. Michel and W. S. Weiglhofer, Pointwise singularity of dyadic Green function in a general bianisotropic medium, *Arch. Elektron. Übertrag.* **51**:219–223 (1997); erratum **52**:310 (1998).
51. W. S. Weiglhofer, Electromagnetic depolarization dyadics and elliptic integrals, *J. Phys. A: Math. Gen.* **31**:7191–7196 (1998).
52. I. S. Gradshteyn and I. M. Ryzhik, *Table of Integrals, Series, and Products*, Academic Press, London, 1980.
53. H. Fricke, The Maxwell–Wagner dispersion in a suspension of ellipsoids, *J. Phys. Chem.* **57**:934–937 (1953).
54. B. Michel, A Fourier space approach to the pointwise singularity of an anisotropic dielectric medium, *Int. J. Appl. Electromagn. Mech.* **8**:219–227 (1997).
55. P. G. Cottis, C. N. Vazoura, and C. Spyrou, Green's function for an unbounded biaxial medium in cylindrical coordinates, *IEEE Trans. Anten. Propag.* **47**:195–199 (1999).
56. W. S. Weiglhofer and T. G. Mackay, Needles and pillboxes in anisotropic mediums, *IEEE Trans. Anten. Propag.* **50**:85–86 (2002).
57. W. S. Weiglhofer, A. Lakhtakia, and B. Michel, Maxwell Garnett and Bruggeman formalisms for a particulate composite with bianisotropic host medium, *Microwave Opt. Technol. Lett.* **15**:263–266 (1997); erratum **22**:221 (1999).
58. B. Michel, A. Lakhtakia, W. S. Weiglhofer, and T. G. Mackay, Incremental and differential Maxwell Garnett formalisms for bianisotropic composites, *Compos. Sci. Technol.* **61**:13–18 (2001).
59. J. A. Sherwin and A. Lakhtakia, Bragg–Pippard formalism for bianisotropic particulate composites, *Microwave Opt. Technol. Lett.* **33**:40–44 (2002).
60. D. A. G. Bruggeman, Berechnung verschiedener physikalischer Konstanten von heterogenen Substanzen, I. Dielektrizitätskonstanten und Leitfähigkeiten der Mischkörper aus isotropen Substanzen, *Ann. Phys. Lpz.* **24**:636–679 (1935).
61. L. Tsang and J. A. Kong, Scattering of electromagnetic waves from random media with strong permittivity fluctuations, *Radio Sci.* **16**:303–320 (1981).
62. T. G. Mackay, A. Lakhtakia, and W. S. Weiglhofer, Strong-property-fluctuation theory for homogenization of bianisotropic composites: Formulation, *Phys. Rev. E* **62**:6052–6064 (2000); erratum **63**:049901 (2001).
63. B. Michel, Recent developments in the homogenization of linear bianisotropic composite materials, in O. N. Singh and A. Lakhtakia, eds., *Electromagnetic Fields in Unconventional Materials and Structures*, Wiley, New York, 2000, pp. 39–82.
64. T. G. Mackay, A. Lakhtakia, and W. S. Weiglhofer, Homogenisation of similarly oriented, metallic, ellipsoidal inclusions using the bilocal-approximated strong-property-fluctuation theory, *Opt. Commun.* **197**:89–95 (2001).
65. N. P. Zhuck, Strong-fluctuation theory for a mean electromagnetic field in a statistically homogeneous random medium with arbitrary anisotropy of electrical and statistical properties, *Phys. Rev. B* **50**:15636–15645 (1994).
66. T. G. Mackay, A. Lakhtakia, and W. S. Weiglhofer, Third-order implementation and convergence of the strong-property-fluctuation theory in electromagnetic homogenization, *Phys. Rev. E* **64**:066616 (2001).
67. T. G. Mackay and W. S. Weiglhofer, A review of homogenization studies for biaxial bianisotropic materials, in S. Zouhdi, A. Sihvola, and M. Arsalane, eds., *Advances in Electromagnetics of Complex Media and Metamaterials*, Kluwer, Dordrecht, The Netherlands, 2003, pp. 211–228.
68. A. Lakhtakia and W. S. Weiglhofer, Maxwell Garnett formalism for weakly nonlinear, bianisotropic, dilute, particulate composite media, *Int. J. Electron.* **87**:1401–1408 (2000).
69. R. W. Boyd, *Nonlinear Optics*, Academic Press, London, 1992.
70. T. Kobayashi, Introduction to nonlinear optical materials, *Nonlin. Opt.* **1**:91–117 (1991).
71. J. P. Huang, J. T. K. Wan, C. K. Lo, and K. W. Yu, Nonlinear ac response of anisotropic composites, *Phys. Rev. E* **64**:061505 (2001).
72. A. V. Goncharenko, V. V. Popelnukh, and E. F. Venger, Effect of weak nonsphericity on linear and nonlinear optical properties of small particle composites, *J. Phys. D: Appl. Phys.* **35**:1833–1838 (2002).
73. O. Levy and D. Stroud, Maxwell Garnett theory for mixtures of anisotropic inclusions: application to conducting polymers, *Phys. Rev. B* **56**:8035–8046 (1997).
74. M. N. Lakhtakia and A. Lakhtakia, Anisotropic composite materials with intensity-dependent permittivity tensor: The Bruggeman approach, *Electromagnetics* **21**:129–138 (2001).
75. T. G. Mackay, Geometrically derived anisotropy in cubically nonlinear dielectric composites, *J. Phys. D: Appl. Phys.* **36**:583–591 (2003).
76. R. W. Boyd, R. J. Gehr, G. L. Fischer, and J. E. Sipe, Nonlinear optical properties of nanocomposite materials, *Pure Appl. Opt.* **5**:505–512 (1996).

ANTENNA ACCESSORIES

PLINIO R. G. ALVES
 LEONARDO R. A. X. MENEZES
 PAULO H. P. CARVALHO
 FRANKLIN C. SILVA
 University of Brasilia
 Brasilia, DF, Brazil

1. ATTENUATORS

Attenuators are circuits designed to introduce a well-known loss between input and output ports [1]. The power ratio, expressed in decibels, between input and output represents the loss in these circuits. The main use of attenuators is in measurement of the standing-wave ratio (SWR) in antennas and of the transmission coefficient. In the case of the SWR measurement [2], a variable-loss attenuator is used between the generator and the slotline. One adjusts the attenuation value to maintain equal outputs in the stationary wave detector at the maximum and minimum points. SWR in decibels is, then, equal to the difference between the readings of the attenuator.

The external circuits connected to the input and output ports of the attenuator should present purely resistive impedances. These will always be matched to the input and output impedances of the component. Therefore, the resistors always constitute the attenuator circuit. In general, these resistive circuits use the T and Π circuit topologies. Figure 1 shows the T topology, where R_1 , R_2 , and R_3 form the circuit. The external circuitry presents purely resistive impedances (Z_i , Z_o) at the input and output of the attenuator. Figure 2 shows the configuration of the section Π . If the input and output impedances are the same ($Z_i = Z_o$), the circuits T and Π become symmetric, that is, $R_1 = R_2$.

1.1. Attenuator Design

The designer has two concerns in the project of an attenuator: (1) attenuation in decibels and (2) input and output impedances. The attenuation is

$$ATT = 10 \log_{10} N \tag{1}$$

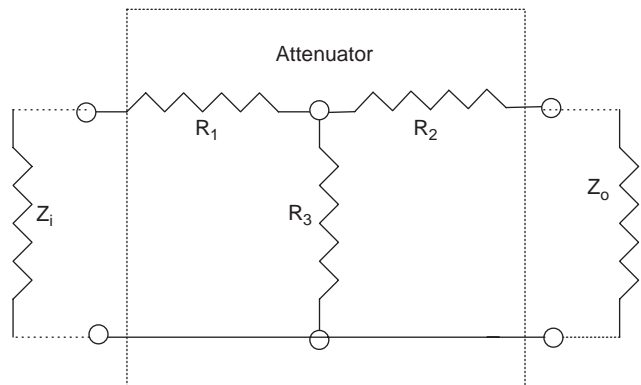


Figure 1. Resistors configuration for the T attenuator; Z_i and Z_o are the input and output resistive impedances presented to the attenuator by external circuits.

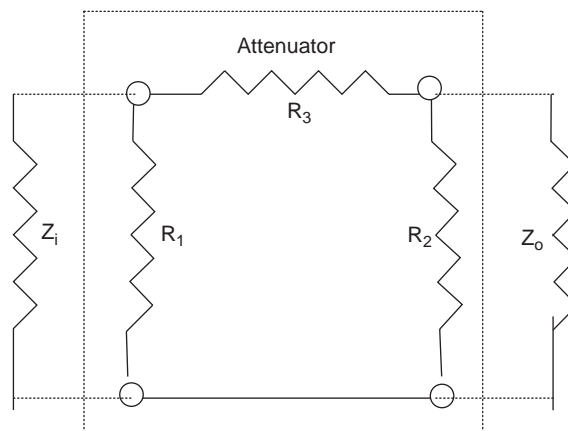


Figure 2. Resistors configuration for the Π attenuator; Z_i and Z_o are input and output resistive impedances presented to the attenuator by external circuits.

where ATT it is attenuation (in dB) and N is the ratio between the power absorbed by the circuit (from the generator) and the power delivered to the load.

The design starts from the desired input and output impedances, and from the value of obtained in Eq. (1). Equations (2)–(4) give the resistance that composes the T circuit:

$$R_3 = \frac{2(NZ_i Z_o)^{1/2}}{N - 1} \tag{2}$$

$$R_1 = Z_i \frac{N + 1}{N - 1} - R_3 \tag{3}$$

$$R_2 = Z_o \frac{N + 1}{N - 1} - R_3 \tag{4}$$

Equations (5)–(7) give the resistance for type Π circuits:

$$R_3 = \frac{1}{2(N - 1)} \left(\frac{Z_i Z_o}{N} \right)^{1/2} \tag{5}$$

$$\frac{1}{R_1} = \frac{1}{Z_i} \frac{N + 1}{N - 1} - \frac{1}{R_3} \tag{6}$$

$$\frac{1}{R_2} = \frac{1}{Z_o} \frac{N + 1}{N - 1} - \frac{1}{R_3} \tag{7}$$

Equations (2)–(7) are also valid for symmetric circuits (it is sufficient that $Z_i = Z_o$).

The T and Π attenuators are applied to unbalanced systems such as coaxial cable. Bifilar lines feed many antennas that are intrinsically balanced, such as the dipole antennas. In this case, the T and Π circuits change into the balanced version and are designated as H and O sections, respectively. Figure 3 shows the H-circuit resistor configuration and Fig. 4, the O-circuit configuration. In relation to the T and Π circuits, the resistors R_3 and R_1 , R_2 are distributed in the inferior branch. All project equations shown above are valid for this case. However, it is necessary to take the half of the values of the respective

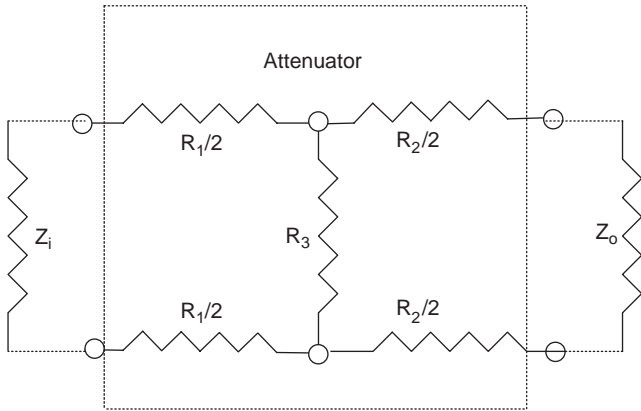


Figure 3. Balanced attenuator of H type. The R_1 and R_2 resistors from the T circuit are distributed in the inferior arms.

resistors and distribute them in the superior and inferior branches of their circuits.

1.2. Attenuators in Waveguides

Waveguides usually feed high-frequency antennas. In this case, the attenuators are built starting from a very thin tapered geometry resistive card. Figure 5 displays the construction of the waveguide attenuator and shows, how the attenuator device introduces this card in a section of slotted guide. The double-arrow shown in the upper part of the midsection of the figure illustrates the card displacement. The adjustment of the penetration depth in the slot allows one to control the dissipation of power and the desired attenuation. The slot should be made in the middle of the broad wall, as this is the area where it propagates the maximum power inside the guide and therefore where introduction of the resistive card allows the greatest dynamic control of attenuation. The attenua-

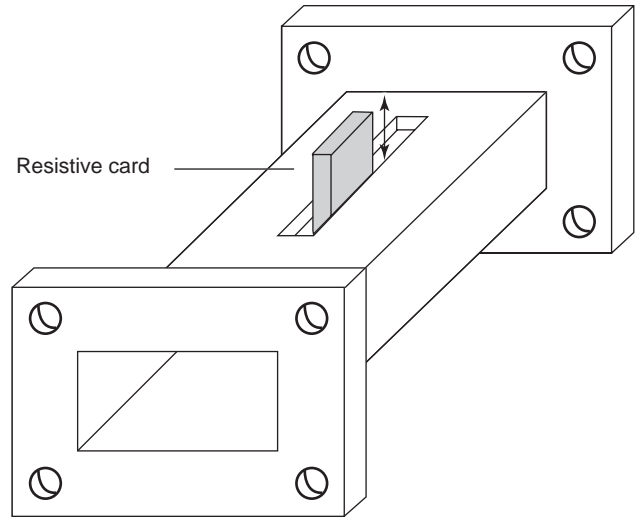


Figure 5. Waveguide attenuator.

tion variation with the depth of insertion of the card is nonlinear for this attenuator type. Figure 5, illustrates that SWR in the input and output ports of the attenuator can be improved if the extremities of the card are tapered.

2. BALUNS

Although knowledge of the impedance values between two terminals, is important, it is not enough to connect this impedance correctly to a transmission line, because of the existence of couplings between the terminals and ground.

The equivalent circuit of Fig. 6 represents these couplings to ground. Two special cases are considered in detail [3]:

1. When $Z_2 = Z_3$ in magnitude and phase. In this case, the impedance AB is balanced. Therefore, the voltages between A to ground and B to ground have the same magnitude and opposite phase.
2. When either Z_2 or Z_3 is zero. In this case, one side is at ground potential and the impedance is unbalanced. An example of a balanced line is a parallel wire line (twin lead). The unbalanced lines are generally coaxial. Other types of line can exist,

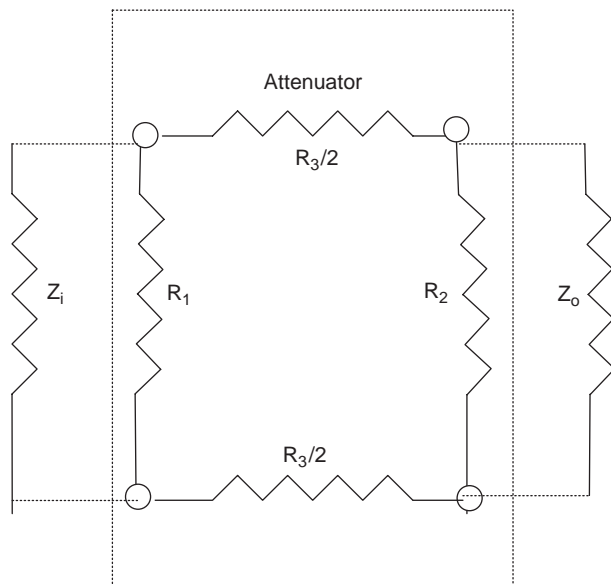


Figure 4. Balanced attenuator of O type. The R_3 resistor from the Π circuit is distributed in the inferior arm.

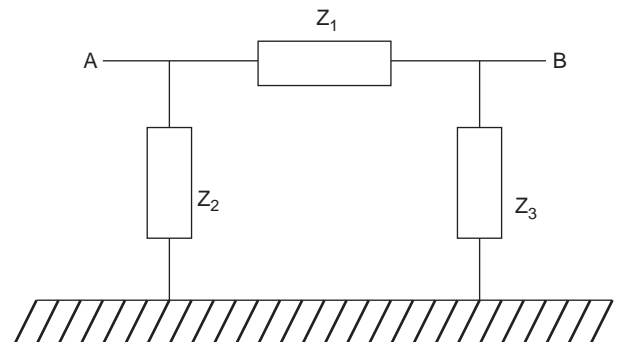


Figure 6. Equivalent circuit of impedance AB .

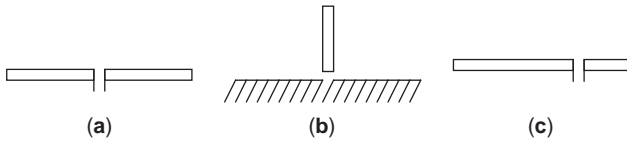


Figure 7. (a) Dipole antenna with symmetric feeding; (b) monopole antenna fed in the base; (c) dipole antenna with asymmetric feeding.

where the conductors present different couplings to the ground. An unusual example of this case is the twin lead with conductors of different thicknesses.

Since conductors have different potentials with respect to ground, the capacitance of the each conductor to the ground is also different. Therefore, the current in both conductors can vary.

The antennas are generally designed for balanced or unbalanced input impedances. This simplifies connection of the lines to the antenna. Connection to a symmetric antenna requires a balanced line, while an antenna where one of the feeding points is at ground potential requires an unbalanced input.

A simple example of a balanced antenna is the dipole antenna shown in Fig. 7a. Figure 7b illustrates a monopole, which is an unbalanced antenna. Figure 7c shows a dipole antenna with the feeding point between the center and the end (this is a procedure used to achieve different input impedance values); this antenna has a current imbalance, which prevents it from being fed satisfactorily by either a balanced or unbalanced line.

It is usually necessary to feed a balanced antenna with a coaxial cable and (although less frequent) an unbalanced antenna, with a balanced line. Such connections require special components to ensure satisfactory operation of the system [4]. These devices are balanced-to-unbalanced converters, also known as *baluns*, which ensure that the voltages and/or currents in the two lines are similar in magnitude.

If a coax cable is connected directly in a balanced antenna, currents will be induced in the external part of the external mesh of the cable. This will cause radiation of electromagnetic fields in unwanted directions. These currents cause an imbalance in the current distribution of the antenna. This affects the radiation diagram by altering the mainlobe (sometimes drastically) and the gain of the antenna. In the reception case, interference signals can be induced in the external part of the coaxial and coupled inside of the cable feeding the receiver.

The difficulties associated with the connection between an unbalanced and a balanced system can be understood considering the coax line below a ground plane. Figure 8

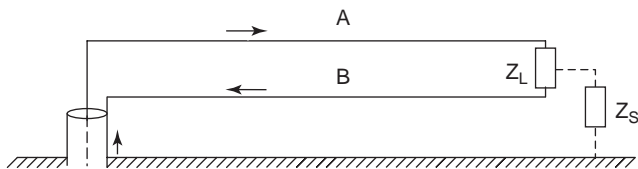


Figure 8. Unbalanced line connected to a balanced line.

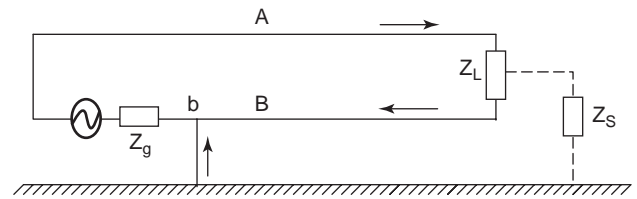


Figure 9. Idealized generator of the circuit shown in Fig. 3.

illustrates the connection between the system and the parallel wire line. In this figure, Z_L is the load impedance and Z_S is the impedance associated with the support structures. The resulting currents in this system are equivalent to the ones created by the ideal generator shown in Fig. 9.

The currents in lines A and B are not necessarily the same. The total current leaving point *b* in Fig. 9 flows into the line. However, the total current in *b* comes from line B and the connection with ground. The main purpose of baluns is to ensure that the currents in lines A and B (Fig. 8) are similar.

Figure 10 illustrates a device capable of introducing symmetry in the line with respect to ground. The symmetry is essential in all kinds of baluns or balanced systems. Figure 11 shows the equivalent representation of this kind of balun.

In this case $I_A = I_B$. Even so, if the length *FC* (Fig. 10) is small, the coax cable is almost short-circuited and very little power is delivered to the load. In order to achieve satisfactory operation, the length *FC* should be of the order of a quarter-wavelength ($\lambda/4$). Because of this restriction, the type of balun shown in Fig. 10 is inherently narrowband.

A possible solution to increase the bandwidth is to wind the coaxial under a coil form of length *FC*. This introduces a high impedance to the system. However, there are design limitations. One of them is in the lower frequency range. In this case, the impedance of the winding is lower in comparison to load (seen at the input of the twin-lead line). The upper limit is at the resonance point of the space between the windings. A technique used to increase the inductive effect is to wind the cable in ferrite cores, providing a high impedance level on a wider frequency band. Careful designs of structures of this type allow their operation in frequency bands ratios up to 10:1 [5].

The most commonly used baluns are those based on $\lambda/4$ short-circuited line sections. Such an arrangement is shown in Fig. 12. In this way, high impedance is obtained

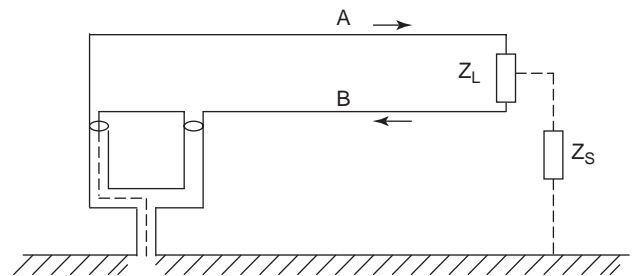


Figure 10. Connection by means of a balun.

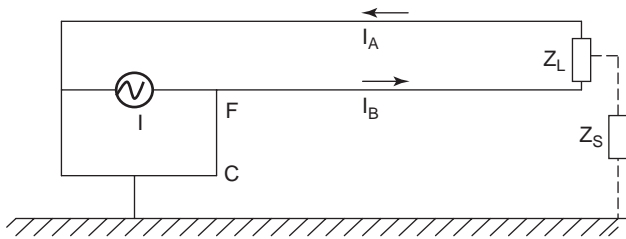


Figure 11. Equivalent circuit of the circuit shown in Fig. 5.

from point *B* toward the external side of the outer mesh of the coaxial line. This prevents the current from flowing into the outer side of the external mesh of the cable.

In practice, the characteristic impedance of the transmission line is usually real, whereas that of the antenna element is complex. It is frequently desirable to operate the balun at a length other than a quarter-wavelength, in order to take advantage of the shunt reactance presented by the balun to the load, for impedance-matching purposes.

Among many coupling matching networks that can be used to connect the transmission line to the antenna, we can introduce a quarter-wavelength transformer (see Fig. 24). If the impedance of the antenna is real, the transformer is attached directly to the load. However, if the antenna impedance is complex, the transformer is placed at a distance *l* away from the antenna. The distance *l* is chosen so that the impedance toward the load, at *l*, is real.

If the transformer is a two-wire line section, and the line is a coaxial cable, obviously the coaxial line cannot be connected directly to the two-wire line. In this case, a balun may be used to connect the transformer to the coaxial line.

3. RADIO FREQUENCY CHOKES

A radiofrequency (RF) choke coil is an inductance designed to offer a high impedance to alternating currents over the frequency range for which the coils are to be used. This result is obtained by increasing the inductance of the coil and decreasing the distributed capacitance. The result is that the inductance is in parallel resonance with the distributed capacitance somewhere in the desired operating frequency range.

A typical RF choke coil consists of one or more universal wound coils mounted on an insulating rod; it can

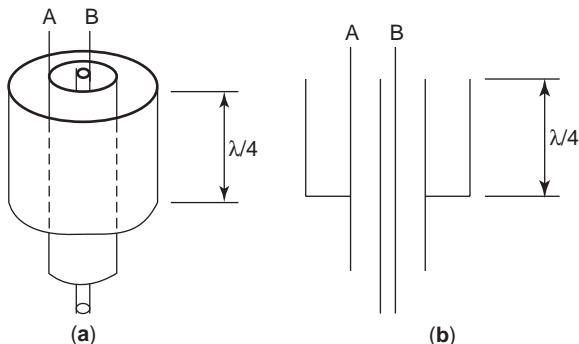


Figure 12. (a) Balun bazooka; (b) cross section of the balun.

also be made by a series of ferrite beads wrapped in deep narrow slots in a slotted bobbin. A long single-layer solenoid is sometimes used.

Proper use of slug-type magnetic cores improves the performance of RF chokes. These cores increase the inductance, and hence the impedance of the coil, without materially affecting the distributed capacitance.

One particular use of chokes is to minimize common-mode (CM) currents on wires and cables. The inductance is usually of the order of 5 mH. This value is achieved using high-permeability ferrites. In these cases, saturation of the choke is not an issue.

The choke behaves as a common-mode filter. The most common type of ferrite used for electromagnetic compatibility is composed of NiZn. Below 10 MHz, the ferrite behaves as an inductance. Above this value it can be seen as a frequency-dependent resistor with peak loss at about 100 MHz.

Several types of cable use ferrite chokes to prevent CM currents. The main advantage of this approach is that the choke does not filter differential-mode (DM) currents, so it will prevent (up to 100 MHz, at least) some of the electromagnetic interference effects of common-mode (CM) currents.

4. COAXIAL CABLE

Coaxial cable is used in antenna engineering to connect the transmitter to the antenna, particularly at high frequencies. This is largely because of convenient construction and practically perfect shielding between fields both inside and outside the line. The range of impedances that may be obtained most conveniently by coaxial lines is 30–100 Ω. However, since the cable is an unbalanced structure, its connection to a dipole needs a balun transformer. Figure 13 shows its configuration with the dimensions of interest; *d* is the internal conductor diameter, and *b* is the outer conductor diameter. Its characteristic impedance is given by

$$Z_0 = \frac{60}{\sqrt{\epsilon_r}} \ln \frac{b}{d} \tag{8}$$

where ϵ_r is the relative permittivity of the medium.

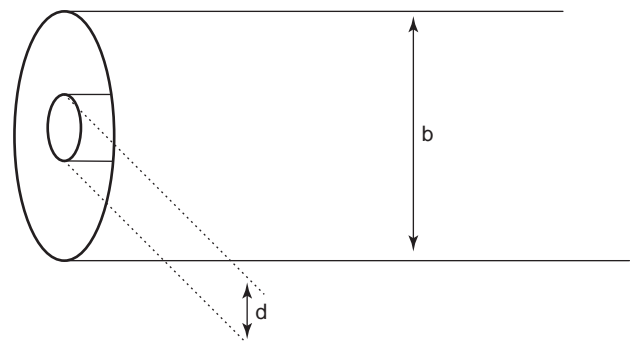


Figure 13. Geometry of a coaxial cable. A dielectric of relative permittivity ϵ_r fills the space between the inner and the outer conductors.

The attenuation α_c of a coaxial line due to ohmic losses in the conductor is

$$\alpha_c = \frac{4.343R_s}{Z_0\pi} \left(\frac{1}{b} + \frac{1}{d} \right) \text{ (dB/m)} \quad (9)$$

where

$$R_s = \sqrt{\frac{\pi f \mu}{\sigma}} \Omega$$

where f is measured in hertz; μ , in H/m (henries per meter); and σ is the conductivity in S/m (siemens per meter).

The attenuation α_d of the coaxial line due to losses in the dielectric is

$$\alpha_d = \frac{27.3\sigma Z_0}{\ln(b/d)} \text{ (dB/m)} \quad (10)$$

Breakdown will occur in an air-filled coaxial line at atmospheric pressure when the maximum electric field E_m reaches a value of approximately 2.9×10^6 V/m. The average power P that can be transmitted on matched coaxial lines under these conditions is

$$P = \left(\frac{E_m^2}{480} \right) b^2 \frac{\ln(b/d)}{(b/d)^2} \text{ W} \quad (11)$$

The first high-order TE (transverse electric) mode that will propagate in a coaxial cable experiences cutoff when the average circumference is about equal to wavelength, so

$$\lambda_c \approx \frac{\pi}{2(b+d)} \quad (12)$$

5. INSULATORS

A material is said to be an “insulator” if this is its most dominant characteristic. This does not mean that other electric effects, such as conductivity or magnetism, are not present; they are just less significant. From a macroscopic point of view, the constitutive relationship of the material, specifically in the case of the insulating ones (dielectrics), is given by

$$\mathbf{D} = \epsilon \mathbf{E} \quad (13)$$

where \mathbf{E} is the electric field intensity vector and \mathbf{D} is the electric flux density vector.

From the microscopic perspective, it is better to use the relationship introduced by Lorentz [6], where two terms contribute to the vector density of electric flow: the *vector electric field* by the vacuum permittivity and the *vector polarization* \mathbf{P} . Mathematically, this is

$$\mathbf{D} = \epsilon_0 \mathbf{E} + \mathbf{P} \quad (14)$$

$$\epsilon_0 = 8.856 \times 10^{-12} \text{ F/m}$$

Contributions of the material to the behavior of vector \mathbf{P} are different for solids, liquids, and gases. These contributions are too complicated to be summarized here (for more details, see Ref. (6)). However, for linear materials, \mathbf{P} is directly proportional to \mathbf{E} ; therefore

$$\mathbf{P} = \epsilon_0 \chi_e \mathbf{E} \quad (15)$$

where χ_e is the electric susceptibility to the medium.

Substituting Eq. (15) in Eq. (14), one returns to Eq. (13), since

$$\epsilon = \epsilon_0(1 + \chi_e) \quad (16)$$

Therefore there is no difference between this perspective and that of the constitutive relationship.

In the term that defines the loss of energy in Poynting’s theorem, the vector current density (which considers the conduction current) is in phase with the intensity of the vector electric field. In the general characterization of the dielectrics presenting losses, the complex permittivity is introduced:

$$\epsilon = \epsilon' - j\epsilon'' \quad (17)$$

This is introduced in Maxwell’s equations as the current $j\omega(\epsilon' - j\epsilon'')\mathbf{E}$, where the second term is in phase with the electric field. Both ϵ' and ϵ'' are, in general, functions of frequency. Table 1 lists values of ϵ'/ϵ_0 and ϵ''/ϵ' for some representative materials used in antenna engineering as well as the breakdown fields for some materials.

Table 1. Characteristics of Insulating Materials

Material Composition	ϵ'/ϵ_0 at 10^8 Hz	ϵ''/ϵ' at 10^8 Hz	Breakdown Field (V/m) at 25°C
Ceramics			
Aluminum oxide (alumina)	8.8	0.00030	—
Porcelain (dry process)	5.04	0.0078	—
Plastics			
Polyethylene	2.26	0.00020	47.2×10^6
Polytetrafluorethylene (Teflon)	2.1	<0.00020	39.4×10^6
Adhesives			
Epoxy resin (Araldite CN-501)	3.35	0.034	15.9×10^6
Glass			
Fused quartz	3.78	0.00020	16.1×10^6

Source: Data taken from Ref. 1.

6. LIGHTNING ARRESTERS

Lightning is an atmospheric phenomenon of harmful consequences. It is caused by the accumulation of electric charges in a cloud, and the consequent discharge on the terrestrial surface. This effect occurs mainly on structures that offer conditions favorable to discharge. The best protection against atmospheric discharges is the enclosure of a site with a grounded conductive structure. Even so, such protection, although not expensive, becomes impracticable.

The antennas must be immune (impervious) to atmospheric discharges, and must maintain integrity as the lightning current flows to the ground. Protection against the direct and induced effects of lightning must be designed in to avoid damage to operators, equipment, and construction. For antennas, several techniques can be used, such as

- Protective conductors on radome [7] (so as to avoid degradation of antenna performance)
- Grounded towers (positioning the antennas below the tower summit as much as possible)
- Lightning arresters [mainly in high-frequency (HF) operation, where the antennas are relatively large structures]

Common types of lightning arresters are varistors, gas discharge devices, and semiconductors. No type is suitable for all applications, and each one may be combined with another into a hybrid device. A simple lightning arrester can be assembled by maintaining a gap between the structure to be protected and the ground. These gaps are adjusted to the minimum width to prevent arcing when the transmitter is in operation.

7. PHASE SHIFTERS

A *phase shifter* is a two-port component that provides a fixed or variable change in phase of the traveling wave. The shift occurs with respect to a “reference” (the line without the component) and a “test” (the line and the component) lengths; therefore it is always understood as the phase difference between the two cases. The shift may be fixed or variable. The variable phase shift uses mechanical or electronic techniques to change the phase dynamically. The main applications of these devices are test, measurement systems, modulation devices, and phased-array antennas. The use of phase shifters in antenna systems provides controllable steering of the main beam of the radiation pattern without moving the antenna. There are several ways to implement these components for communication systems. The type of phase shifter used in this process depends on the kind of antenna being used, including its cost and power requirements.

7.1. Fixed and Variable Phase Shifters

The shifters can provide fixed or variable phase shifts. The fixed phase shifters are usually extra transmission-line

sections of certain length to shift the phase with respect to the reference line. The variable shifters use mechanical or electronic means to achieve a dynamical range of phase difference. In the case of antenna systems, the main use of variable phase shifters is beamsteering, while fixed shifters are more frequently used for beamforming (pattern synthesis).

The mechanically tuned phase shifter usually consists of variable short circuits used with hybrids or, in the case of waveguide components, a dielectric slab with variable position in the guide. Step motors move the slab across the guide (from its center toward outer walls), therefore accomplishing maximum or minimum phase shift.

Another method for obtaining the desired mechanically tuned phase shift is to combine variable short circuits and hybrid circuits. The movement of the short circuit along a transmission line results in the phase shift, therefore making it appear shorter or longer.

There are two classes of electronically tuned phase shifters depending on component cost, weight, and power-handling capability: ferrite and switching circuit shifters. The *ferrite shifter* uses slabs of this magnetic material inside waveguides. Since the electrical properties of ferrite vary with the applied bias magnetic field, this process can yield the desired phase shift. Ferrite phase shifters are essentially low-cost, bulky, high-power-handling-capability devices. The switching circuit shifters are essentially low-power pin (positive–intermediate–negative) diodes or FETs used as switching (ON–OFF states) elements. Depending on the applied bias current in these devices, these devices will work either as short or open circuits. The phase shift is the result of an extra section of transmission line added to the switching element. Therefore, depending on the bias current, the wave traveling along the transmission line will have an additional traveling path. Since these devices are binary switches, only discrete phase shifts are possible. The construction of a continuously variable shifter demands the use of several of these switching elements. The design of variable phase shifters depends on the expression of the variable shift in respect to a specific position or applied bias magnetic field or current. In all cases, the procedures depend on the topology of the device and its mathematical models.

7.2. Ferrite Phase Shifters

Ferrite phase shifters are common in power applications in waveguide technology. The ferrite phase shifter is a result of the combination of two properties of this medium: (1) dependence of the velocity of the propagating waves on the direction of propagation of the wave relative to the ferrite slab and (2) application of a bias magnetic field. Ferrite is an anisotropic medium; therefore, the propagation constant (and the velocity of propagation) is an important factor in the ferrite phase shifters, which are commonly used in power applications in waveguide technology. The anisotropic properties of ferrites are also critical factors if a magnetic field is applied. This is a macroscopic result of the microscopic interaction between the fields and the atomic nuclei.

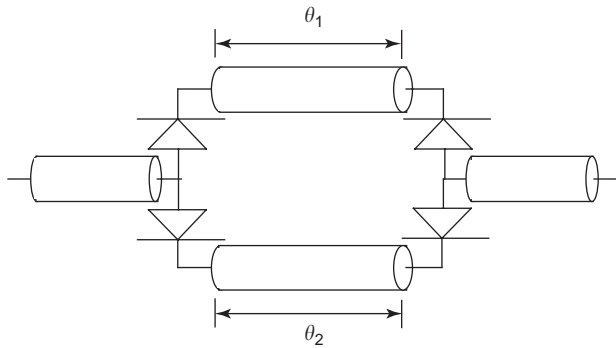


Figure 14. PIN switching circuit phase shifter representation. Application of the bias current results in change in electrical length of the line. The resulting shift is the difference in the electrical angle between direct polarization and reverse polarization.

The phase shift in these devices is the difference between the forward and backward traveling waves. This is a nonreciprocal phase shift, which is dependent on an applied external magnetic field. Accurate design of these devices is not straightforward because of the complexity of the mathematical models of ferrites. A detailed procedure is shown by Pozar [8] and Bornemann [9].

7.3. Switching Circuit Phase Shifters

The switching circuit phase shifter uses solid-state technology (pin diodes). In these applications, pin diodes behave as ON-OFF elements. The switching circuit shifters are common to several manufacturing technologies such as microstrip, coplanar guides and lines, slotlines, waveguides, and finlines. The diodes act as binary switches along the line (Fig. 14). With the bias applied, the diode will behave as a short circuit for the incoming wave. Therefore, the phase transmitted signal has two possible states, determined by which diode is polarized. A variable phase shift results from the mounting of several diodes on the line. The returning wave enters a hybrid circuit and then the antenna.

8. PLANAR TECHNOLOGY

Planar transmission lines are the basic transmission media for microwave integrated circuits (MICs) when the hybrid or monolithic technology is used. Figure 15 shows the cross section of the three basic planar transmission lines: stripline, microstrip, and slotline. Several other configurations are possible, such as listed by Bhat and Koul [10]. All are variations of the three main types. Each one offers certain advantages, depending on the circuit type and its application. Some of these configurations are the suspended stripline, the suspended microstrip, the inverted microstrip, the coplanar guide, and the coplanar stripline. Planar designs using special substrates have been applied at frequencies up to 10.0 GHz.

A designer can perform several microwave circuits and electric functions with planar transmission lines. Therefore, this constitutes a very important technology for the

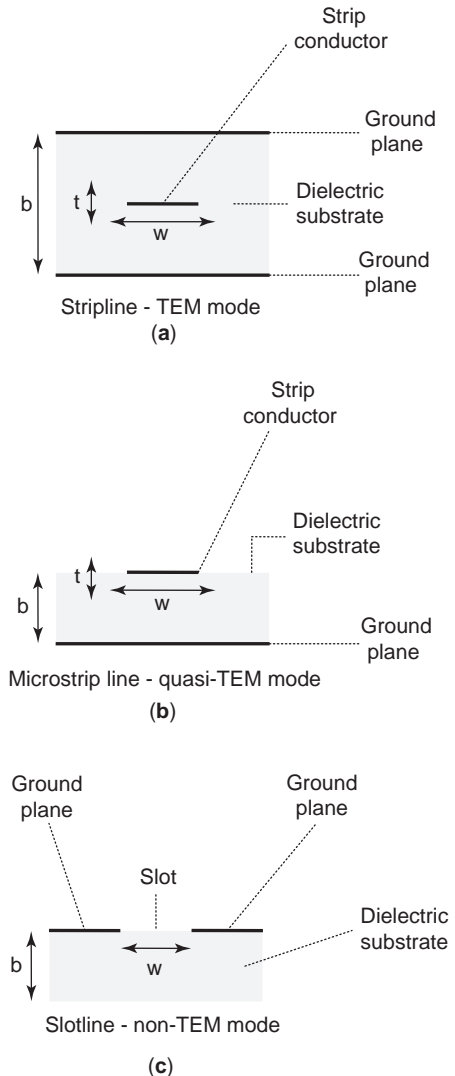


Figure 15. Basic planar transmission lines: (a) stripline, TEM (transverse electric mode); (b) microstrip line, quasi-TEM mode; (c) slotline, non-TEM mode.

development of antenna accessories in the microwave range. These components, called *distributed circuits*, are generally of the order of a wavelength or more (in the propagation medium). Thus, in the lower microwave range these circuits can have large dimensions. In this case, one uses lumped components.

However, several lumped components can be obtained starting from planar technology. These components are called *microwave integrated circuits* (MICs). Figure 16 illustrates lumped and distributed circuits in planar technology.

The most important project parameters for planar transmission lines are

- Effective dielectric constant
- Characteristic impedance
- Dispersion
- Losses
- Working frequency limitations

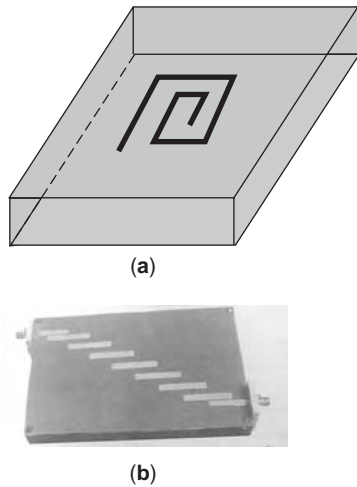


Figure 16. Lumped and distributed MICs: (a) spiral inductor (lumped element); (b) bandpass interdigital filter (distributed MIC). (Courtesy of the Department of Electrical Engineering, University of Brasilia.)

Antenna accessories that can be manufactured for planar technology include directional couplers, hybrid rings, power dividers, and impedance matchers [11,12]. These components are generally used in antenna feeds, for impedance matching between the antenna and transmission system, and for antenna measurement.

The effect of the electromagnetic coupling between two parallel transmission lines (sufficiently near to each other) constitutes the design framework of several microwave devices (especially for antennas). An example is the directional coupler, which has wide application in circuits and telecommunication systems. It performs several electrical functions, such as the separation and combination of signal power (received or delivered from/to antennas). It also allows the sampling of power and separation of incident and reflected waves of a system. This separation is used for power control or performance measurements.

Couplers are either conductively or electromagnetically coupled transmission line circuits with three, four, or more ports. In general, a directional coupler is a four-port device, with two of its ports mutually decoupled, with respect to the other two. Figure 17 shows the block diagram of a directional coupler. From the theoretical point of view, if port 1 receives a microwave signal, this power will be delivered to ports 2 and 3, but no power will appear in port 4. Port 4 is decoupled from port 1. On the other hand, if port 2 receives the microwave signal, then this signal will be divided between ports 1 and 4, and port 3 will be decoupled, in relation to port 2.

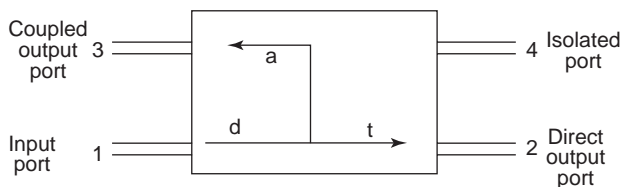


Figure 17. Block diagram of a directional coupler.

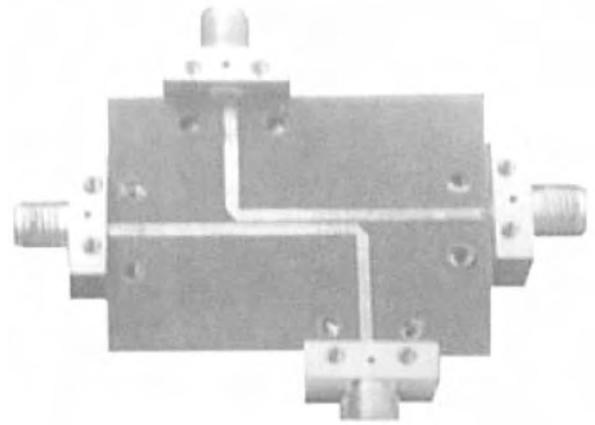


Figure 18. Directional couplers in $\lambda/4$ parallel lines, in the microstrip technology. (Courtesy of the Department of Electrical Engineering, University of Brasilia.)

In the special case where the power is equally divided between ports 2 and 3, the coupler is called a “hybrid” or 3-dB directional coupler. If the phase difference is 90° between ports 2 and 3, the coupler is termed to “ 90° hybrid” or “quadrature hybrid”. Another hybrid design provides 180° between the output ports.

Different topologies of directional couplers exist [11,12]. Figure 18 shows a directional coupler in the topology of parallel lines of $\lambda/4$ length. As in any directional coupler, a fraction of the incident power in the primary branch is coupled to the secondary branch. In fact, when a microwave signal is incident in port 1, port 2 receives part of its power. In this topology, another part of the power will be coupled to port 3. This coupling occurs through the gap, and practically no power will be coupled to port 4, which is terminated by the load. The load has the same value of the characteristic impedance of the coupler lines. In parallel line couplers, the smaller is the gap between branches of the coupler, the greater is the coupling. The spacing between conductors can compromise high coupling designs.

The main parameters of a directional coupler are the coupling, directivity, isolation, and transmission factors. The *coupling factor* is defined by the relationship between the power in the coupled (port 3) and input (port 1) ports; this factor is a measurement of the coupling. The *transmission factor* is defined by the relationship between the power in ports 2 and 1. The *directivity* is the relationship between the power in the isolated (port 4) and coupled (port 3) ports; this measures the undesirable coupling. The *isolation* is the relationship between powers in the isolated (port 4) and input (port 1) ports.

Figure 19a shows a coupler in branchline topology [11,12]. In this directional coupler, a larger coupling factor can be obtained. It also allows keeping DC (direct-current) continuity between the ports, which is an interesting feature for phase shifter design (as shown in Fig. 19b). It allows high power levels. The branchline coupler uses branching transmission lines to couple 3–9 dB. The length of all branches of this coupler is $\lambda/4$. However, the widths, and consequently the impedances, of these branches are

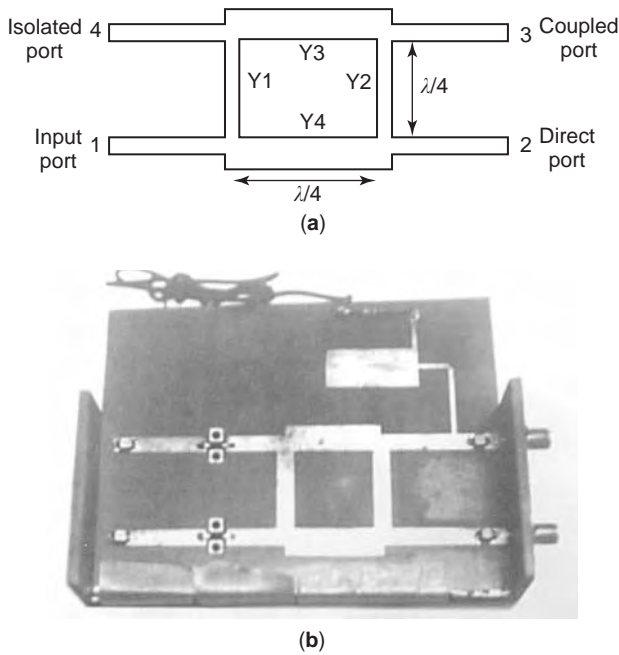


Figure 19. (a) Branchline coupler structure; (b) branchline coupler in a phase shifter circuit. (Courtesy of the Department of Electrical Engineering, University of Brasilia.)

different: Y_1, Y_2, Y_3, Y_4 . The operating principle of this coupler can be presented in the following way. When the input port (port 1) receives a signal, the energy will be divided and will propagate in clockwise and counterclockwise sense through the branches. The power in each output (ports 2–4) will depend on the phase relationships between the propagating signals. In a 3-dB coupler, the power is divided equally between the coupled (port 2) and matched (port 3) ports. Port 4 is the isolated one.

A special version of branch line coupler is the hybrid ring (Fig. 20). The ring has a 1.5λ circumference and all sections of equal impedance. It can be assembled using several technologies such as coaxial lines, stripline, microstrip lines, or even waveguides. The operating principle is the same as that of the branchline coupler. The signal injected in the input port is divided into two opposite-

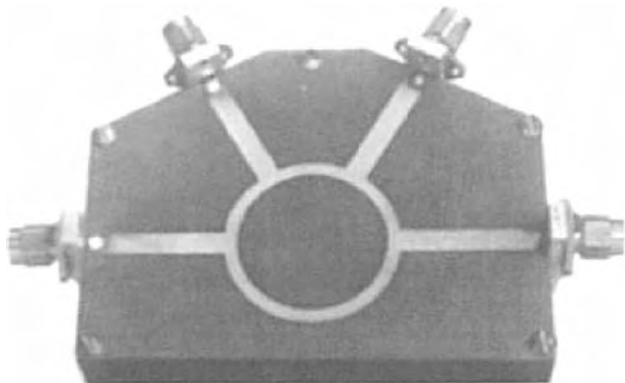


Figure 20. Hybrid ring. (Courtesy of the Department of Electrical Engineering, University of Brasilia.)

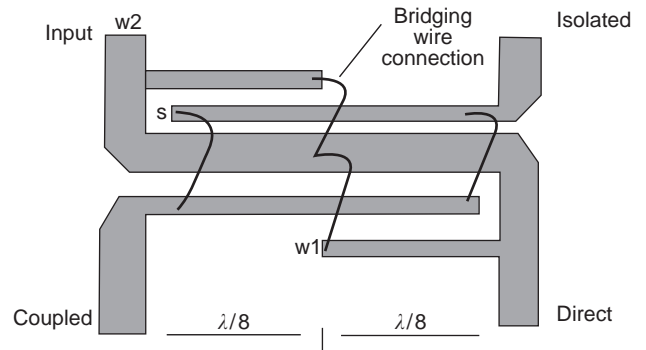


Figure 21. Lange coupler.

direction propagating waves. In the coupled output port, the two signals arrive in phase and reinforce each other, providing an output signal. In the direct output port, the signal that propagates counterclockwise travels a length of 1.25λ and the signal propagating clockwise travels 0.25λ . The two signals arrive at this port in phase, providing an output signal at this port. For the same reason, there is an isolated port that has no output signal. The output signals in the direct and coupled ports are 180° out of phase.

Another topology of directional coupler is the Lange coupler (Fig. 21). The Lange coupler is well adapted to microstrip technology [13]. It is an interdigital structure with superior performance in comparison to the parallel line coupler. Its bandwidth can be greater than one octave. The Lange coupler, which is compatible with tandem topology (Fig. 22), makes it possible to obtain power coupling near 3 dB, with a combination of two inferior-order couplers, if their design dimensions are feasible.

Power dividers are used in antenna feeds and performance measurements. Directional couplers and hybrid rings can be used as power dividers. The branchline coupler output signals are in phase quadrature (90° out of phase). The hybrid rings output signals that are in opposite phases. However, in several microwave applications, such as parallel feeds for phased-array antennas, the input has to be divided into an arbitrary number of signals with equal power and in phase. A symmetric power divider of n branches provides the successive division of the input signal into n signals with the same power and phase at all frequencies. This power divider can also be used as a signal combiner by inverting the input and the output ports.

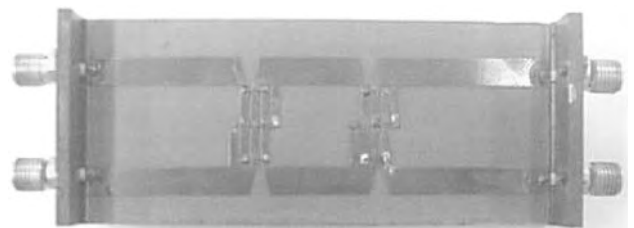


Figure 22. Lange Coupler in tandem topology. (Courtesy of the Department of Electrical Engineering, University of Brasilia.)

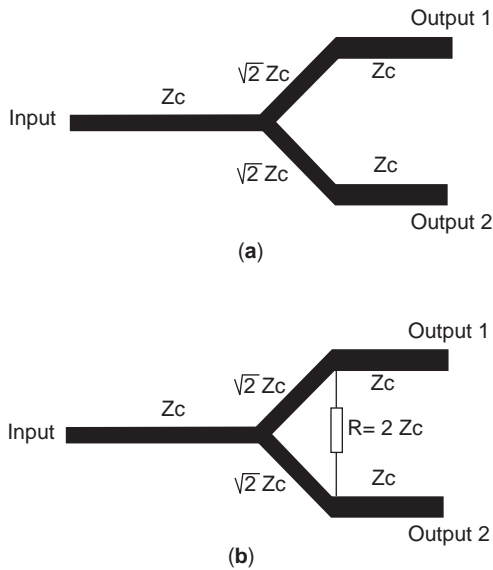


Figure 23. Unmatched and matched two-way power dividers.

There are several kinds power dividers and combiners. One of them is the two-branch power divider, shown in Fig. 23. It is also possible to obtain output signals in phase, but with different power levels.

Impedance-matching circuits are another type of antenna accessory. They are also manufactured in planar technology [2]. These circuits are commonly used in antenna feeds, avoiding power losses caused by mismatch. In most cases, the load will have an impedance different from that of the transmission line. This is the case in telecommunication systems, where the output impedance of the generator is usually different from the input impedance of the antenna. The problem is how to reduce or eliminate the resulting reflections and high voltage standing-wave ratios (VSWRs).

One method is to cascade transmission-line sections (planar structures) or lumped components with different impedances between the mismatched transmission line and its terminations (the system output and the antenna input). The antenna input impedance is then transformed. This new impedance value seen at the output point (the end of the transmission line) can be matched to the system for maximum power transfer.

Different topologies and technologies are used in impedance-matching circuits. Examples involve the use of stub association and quarter-wave transformers. Figure 24a shows a schematic of a quarter-wave impedance transformer. The impedance Z_1 can be matched to a transmission line of characteristic impedance Z_s with a section of transmission line that is a quarter-wave long based on the wavelength in the transmission line. This characteristic impedance of the matching section is shown as $Z_t = \sqrt{Z_s Z_1}$. The microstrip feed on Fig. 24b is planar, allowing the patch and the feed to be printed on a single metallization layer. The impedance of the edge-fed patch can be transformed by using a quarter-wave matching section of a microstrip transmission line, as shown in Figs. 24a and 24c. Another kind of quarter-wave

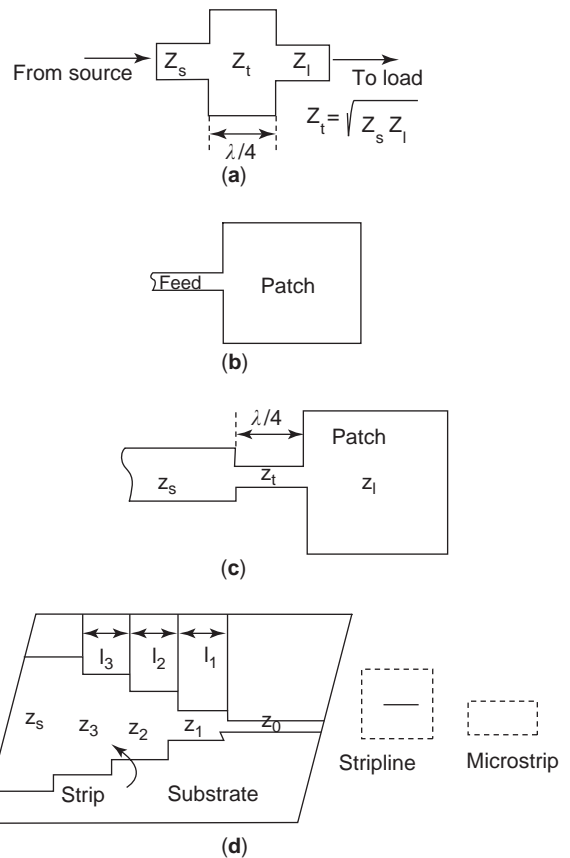


Figure 24. (a) Quarter-wave impedance transformer. (b) Top view of patch antenna. (c) Microstrip edge feed with quarter-wave transformer. (d) Multisection quarter-wave transformer.

transformer is the multisection quarter-wave transformer, as shown in Fig. 24d. This kind of transformer is commonly used in wideband systems.

9. TWIN-LEAD LINE

The bifilar (twin-lead) line is a two-wire parallel conductor line that carries the power from the generator to the antenna. Each wire carries equal and opposite currents (180° out of phase). However, since the wires are spaced by a certain distance, their radiated fields do not cancel out completely. If the two wires were located in the same place in space, there would be no radiated field. However, since this is not possible, there will be a certain amount of radiation loss. Keeping the distance between the parallel wires small (typically of the order of 1% of the wavelength of the radiowave) can reduce this loss. The spacing between conductors is a constraint of the physical limitations of the line construction. Parallel conductor lines, open-wire lines, two-wire lines, two-wire cable, and two-wire ribbon cable are also bifilar lines.

9.1. Types of Bifilar Lines

The bifilar line is usually supported a fixed distance apart. Usually insulating rods, called “spacers,” or molded

plastics such as polystyrene provide the support. The spacers have to be placed at small length intervals to prevent the wires from moving apart from each other. These lines are air-insulated, since air is the medium between them. The spacers have little effect on the impedance behavior of the line. However, flexible dielectric separation (molded) lines have several advantages over air-insulated types. In this type, a plastic coating similar to a ribbon surrounds the conductors. These lines maintain uniform spacing between conductors. They are also less bulky, weigh less, and are easier to install. One common example of the flexible dielectric bifilar line is the television receiving cable (called "ribbon cable" or two-wire cable).

9.2. Uses of Bifilar Lines

In television reception applications, polyethylene molded ribbon bifilar lines are available with spaces of 2.54 mm (1 in.) and 1.27 mm ($\frac{1}{2}$ inch) with conductor sizes of AWG (American Wire Gauge) 18 (diameter of 2.053 mm). These lines have characteristic impedances of 450 and 300 Ω , respectively. The attenuation is quite low for these receiving applications (typically under 0.03 dB/m for applications under 20 m). There is also the 75- Ω bifilar line, which has AWG 12 conductors (diameter of 1.024 mm) with close spacing between them (see Ref. 14 for a detailed description). The spacing keeps most of the fields confined to the solid dielectric instead of the surrounding air.

The bifilar line is also used in amateur radio applications and LF to VHF (low- to very-high frequency) antennas, although for higher-frequency applications, the coaxial line tends to be used more frequently because of its superior characteristics. The lines are simple to assemble. However, the designer should avoid sharp bends. These bends tend to change the characteristic impedance of the lines, which cause reflections at each bend and power mismatch.

9.3. Design Equations of Bifilar Lines

The analysis of bifilar transmission lines uses Maxwell equations subjected to the appropriate boundary conditions. The main parameters of the bifilar transmission line are

- Characteristic impedance

$$Z_0 = \frac{\eta}{\pi} \cosh^{-1} \left(\frac{d}{2r} \right) = \frac{120}{\sqrt{\epsilon_r}} \cosh^{-1} \left(\frac{d}{2r} \right) \quad (18)$$

where r is the radius of the conductors, d is the spacing between them, and ϵ_r is the relative dielectric of the surrounding medium (Fig. 25).

- Attenuation

$$A \text{ (dB/m)} = 8.686 \left(\frac{1}{\pi r} \sqrt{\frac{\omega \mu}{\sigma}} \left[\frac{d/2r}{\sqrt{(d/2r)^2 - 1}} \right] + \frac{\pi}{\lambda} \left(\frac{\epsilon''}{\epsilon'} \right) \right) \quad (19)$$

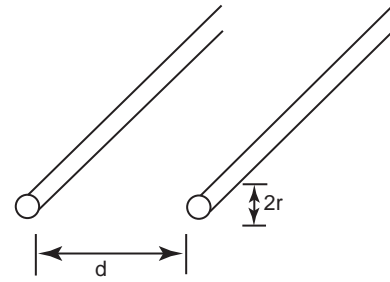


Figure 25. Geometry of the bifilar line. In the molded plastic casing, the dielectric surrounding the lines has the shape of a ribbon. Since most of the field is inside the ribbon, the line is less susceptible to external influences.

where μ is the permeability of the surrounding medium, ω is the operating frequency, σ is the loss in the conductors, and ϵ''/ϵ' is relative loss of the dielectric constant.

- Propagation constant

$$\beta = \frac{\omega}{c} \quad (20)$$

where c is the speed of light in a medium that surrounds the conductors. In the case of the ribbon transmission line, ϵ_r is 2.56 with $(\epsilon''/\epsilon') = 0.7$. If the wire is made of copper, then σ is 58 MS/m. In this case, since most of the field is inside the dielectric, the relative dielectric constant ϵ_r is approximately 2.56.

BIBLIOGRAPHY

1. *Reference Data for Radio Engineers*, 6th ed., Howard (a subsidiary of International Telephone and Telegraph Corp.), Indianapolis, 1981.
2. R. E. Collin, *Foundations for Microwave Engineering*, 2nd ed., McGraw-Hill, New York, 1992.
3. A. W. Rudge, K. Milne, A. D. Olver, and P. Knight, *The Handbook of Antenna Design*, Vols. 1, 2, Peter Peregrinus, Stevenage, UK, 1986.
4. H. Jasik, *Antenna Engineering Handbook*, McGraw-Hill, New York, 1961.
5. W. L. Weeks, *Antenna Engineering*, McGraw-Hill, New York, 1968.
6. S. Ramo, J. R. Whinnery, and T. Van Duzer, *Fields and Waves in Communication Electronics*, 3rd ed., Wiley, New York, 1994, pp. 678–682.
7. R. H. Golde, *Lightning*, Vols. 1, 2, Academic Press, New York, 1981.
8. D. M. Pozar, *Microwave Engineering*, Addison-Wesley, Reading, MA, 1990.
9. J. Uher, J. Bornemann, and U. Rosenberg, *Waveguide Components for Antenna Feed Systems, Theory and CAD*, Artech House, Norwood, MA, 1993.
10. B. Bhat and S. Koul, *Stripline-like Transmission Lines Microwave Integrated Circuits*. Wiley, New York, 1989.
11. E. A. Wolff and R. Kaul, *Microwave Engineering and Systems Applications*, Wiley, New York, 1988.
12. L. A. Trinogga, G. Kaizhou, and I. C. Hunter, *Practical Microstrip Circuit Design*, Ellis Horwood, 1991.

13. J. Lange, Interdigitated stripline quadrature hybrid, *IEEE Trans. Microwave Theory Tech.* **MTT-17**: 1150–1151 (Dec. 1969).
14. G. Hall, ed., *The ARRL Antenna Book*, 15th ed., The American Radio League, Newington, CT, 1988, pp. 24.15–24.25.

ANTENNA ANECHOIC CHAMBERS

BOON-KUAN CHUNG
Multimedia University
Cyberjaya, Malaysia

1. INTRODUCTION

Electromagnetic wave measurements involving very low signal levels are commonly performed in laboratory facilities that provide high isolation from external electromagnetic environment. Shielded enclosures with isolation performance in excess of 100 dB prevent extraneous energy from masking measurements of the intended signals. However, an electromagnetic wave generally propagates in all directions, and waves reflected by the walls, ceiling, and floor of the shielded enclosure will give rise to a complex wavefront at the test region where the test antenna is to be placed. As it is desirable to provide an environment for electromagnetic energy to propagate between the transmitter and the receiver in a simple and well-defined manner, waves propagating toward the walls, ceiling, and floor of the enclosure must be absorbed using a suitable absorbing material. The shielded enclosure with the entire inner surfaces covered with wave absorber to create a nonreflecting environment equivalent to free space is known as the *anechoic chamber*. With no echo, the anechoic chamber provides a “quiet” environment for electromagnetic wave measurements.

Anechoic chambers were initially utilized as a means to improve the accuracy of indoor radiofrequency (RF) measurements during World War II in response to the increasing need to test RF devices, antennas, and radar signature in a controlled environment, with all-weather capability and minimum electromagnetic interference. Throughout the years, many chambers have been designed with the capabilities to perform a wide variety of measurements, including antenna gain, directivity, radiation pattern, phase, polarization, impedance, radar cross section (RCS), radiation hazards, and electromagnetic compatibility (EMC) testing. Others have been designed for specific types of measurement.

Anechoic chambers are conventionally utilized in the microwave region (above 1000 MHz). In the 1990s, an increasing number of low-frequency (30–1000-MHz) electromagnetic anechoic and semianechoic test chambers were manufactured in response to the rapid growth in electronic and telecommunication industries. Products must meet both emission and immunity requirements of EMC regulations before they can be marketed. A full anechoic chamber is commonly used to determine the immunity of

products to an impinging electromagnetic field. As for the emission limit, interference emissions from electronic products are referenced to measurements performed on an ideal open-area test site (OATS) having a perfectly conducting infinite ground-plane. A semi-anechoic chamber in which the conductive floor is not covered with wave absorbing material can be used as the alternative test site for this measurement. International standards are being developed to qualify full anechoic chamber for use in both immunity and emission EMC measurements.

2. SHAPES OF ANECHOIC CHAMBER

The most common geometric shapes for anechoic chamber design are those of rectangular shape, due to the simplicity of constructing the chamber structure and ease of lining the absorbers. One deficiency of this simple geometry, however, is that the absorbers on the sidewalls, ceiling, and floor scatter a considerable amount of waves that are approaching at large angle of incidence with respect to the normal direction of the absorbers (as illustrated in Fig. 1). These wide-angle reflections are especially crucial at lower frequencies, where the absorbers are less effective in absorbing incident waves. As a result, the reflected waves add with the direct path signal at the test region and form an interference field (with sharp peaks and nulls), giving rise to errors in various wave propagation measurements.

In the 1960s, the tapered-shape chamber was invented to overcome the limitation of rectangular chambers at low frequencies (below 1 GHz) [1]. The diverging geometry of the tapered chamber (see Fig. 2) greatly reduces the wide-angle reflection problem. As a result, less expensive absorbers can be used at the tapered section. Additional cost saving is attained because a smaller surface area in the chamber and thus fewer wave absorbers are required. The tapered chamber has been designed, tested, and used at frequencies as low as 30 MHz. However, these improvements are not achieved without tradeoff. For example, only a single-source antenna can be placed at the taper apex, which limits the measurements involving multiple sources, moving sources, and bistatic radar cross section. The path loss is different from that of free space, making the chamber unsuitable for measurements involving

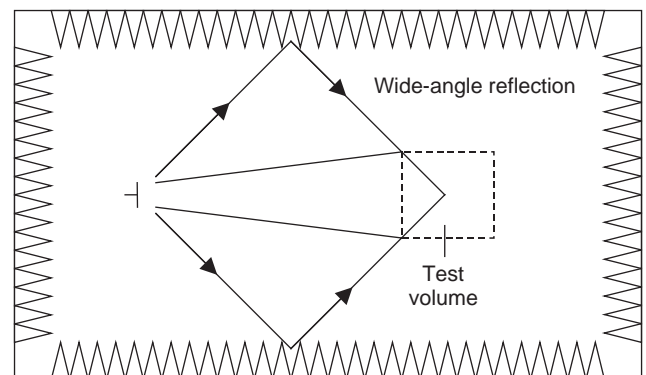


Figure 1. Plan view of a simple rectangular anechoic chamber.

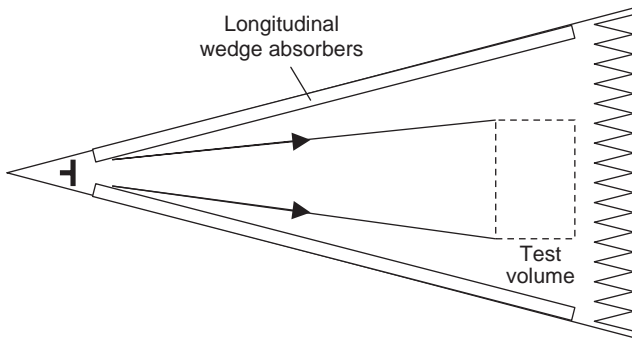


Figure 2. Diverging geometry of a tapered chamber.

absolute field strength. At higher frequencies, the rectangular chamber is preferred since the antenna can be configured in a highly directional radiation pattern and the level of wide-angle reflection can be controlled. In addition, absorbers with good absorbing properties at these frequencies can easily be manufactured at low cost.

A quasitapered chamber has been designed and evaluated from 100 MHz to 93 GHz [2]. It consists of a small rectangular room, connected to a tapered section, and then followed by a larger rectangular room where the test region is located. This design incorporates the performance advantages of a fully tapered chamber at low frequencies and provides some flexibility of a rectangular chamber at high frequencies.

Microwave antenna and RCS measurements usually require that the target under test be illuminated by a uniform plane wave. This is achieved only in the far-field region and often dictates a very large distance. To reduce the room area required, the compact-range anechoic chamber uses large offset parabolic reflector to produce an approximate plane wave at a much shorter range. The parabolic reflector is illuminated by a broadband horn antenna feed placed at the focal point of the reflector (as shown in Fig. 3). The diverging spherical wavefront is converted into a plane wave with very flat phase front and small amplitude taper over the test zone, making the compact range equivalent to a much larger conventional antenna test range. The offset focal point eliminates scattering and shadowing from the feed and feed support. However, limited cross-polarization isolation can be achieved.

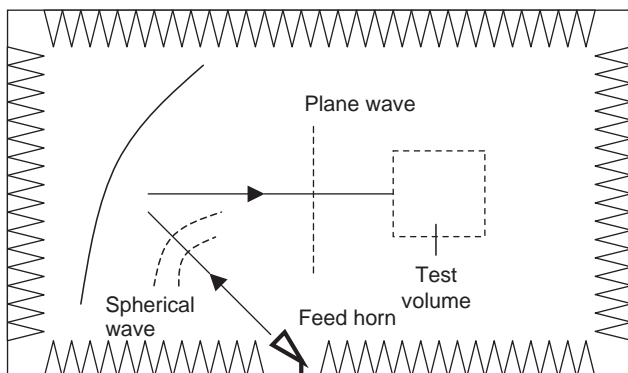


Figure 3. Compact range anechoic chamber configuration.

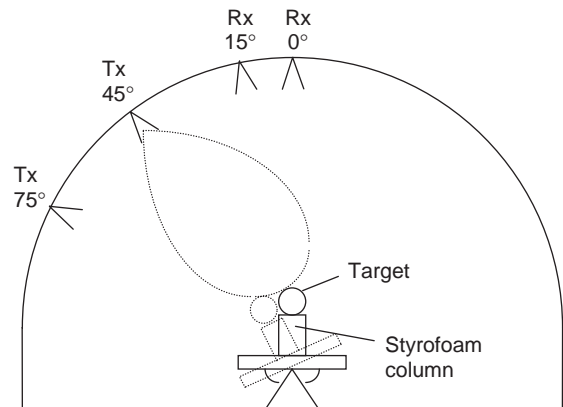


Figure 4. Dome-shaped anechoic chamber for monostatic and bistatic RCS measurements.

A few dome-shaped chambers have been designed and built [3,4] to facilitate a variety of monostatic as well as bistatic RCS measurements at a constant range. A number of antennas are mounted on the dome surface (see Fig. 4) inside the chamber as receivers to detect the electromagnetic waves scattered from radar targets placed at the center of the spherical space.

Anechoic chambers that are built specifically for EMC tests are usually not suitable for microwave RCS and antenna measurements. Similarly a microwave anechoic chamber is seldom suitable for EMC tests, due to differences in the measurement techniques and test-site validation criteria. Nevertheless, a major limitation has been the availability of ultrawideband wave absorber that can provide adequate reflectivity performance covering the frequency bands of EMC test requirements and microwave frequencies.

3. ELECTROMAGNETIC WAVE ABSORBERS

Much research has focused on developing absorbers with superior absorbing properties such as low normal incidence reflection, low forwardscatter and backscatter at wide-angle incidence, lower usable frequency, wide bandwidth, and reduced absorber thickness in the course of improving the “quietness” of anechoic chambers, cost-efficiency, and required room size. The idea of using material that provides wave impedance near that of free space at the front surface gradually tapers to that of a lossy medium at the back surface has dominated this area of development. One implementation of such idea is to shape the absorbing material into a wedge or pyramid shape (see Fig. 5) in contrast to a flat front surface.

An extremely broadband absorber can be made with pyramidal shaped urethane foam impregnated with carbon black. The height of the pyramid must be greater than quarter wavelength to function efficiently. A 60-cm-thick pyramidal foam absorber may offer a reflectivity level below -40 dB over the frequency range 1–40 GHz at normal incidence. Optimum performance of the electrically thick foam absorber is obtained by adjusting the percentage carbon loading of the foam material. For frequencies as low as 30 MHz, 2.5-m-thick absorbers were used for con-

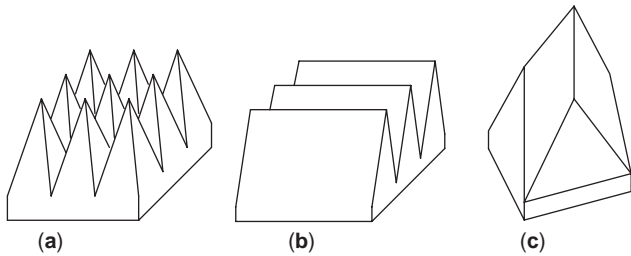


Figure 5. Pyramid (a), wedge (b), and twisted pyramid (c).

struction of anechoic chambers during the 1970s. The bulky size gives rise to high cost of material, difficulty of installation, and large room space requirement, thus limiting its use at the lower frequency range of the spectrum.

The wedge-shaped absorber gives better absorbing characteristics compared to the pyramidal-shaped absorber for wave directions nearly parallel to the ridge of the wedge. It can be used at the tapered section of chamber with diverging geometry.

The twisted pyramid structure has been used in the fabrication of thick absorbers because of its improved mechanical strength. The pyramid is “twisted” by 45° with respect to the base as shown in Fig. 5. The droop with age will be less for the twisted pyramid tips compared to the standard pyramid tips. However, its reflectivity performance is generally not as good as the standard pyramid.

Microscopic particles of metal can be dispersed in a nonconducting matrix to adjust the effective conductivity of the material. The resistive material can be coated onto a hollow pyramid-shaped substrate with a height of quarter-wavelength to realize a wideband absorber. A large absorber has been constructed with adequate mechanical strength and light weight for construction of EMC test chamber.

Wide band absorption can also be achieved by increasing the material loss tangent with respect to depth from a flat outer surface. A variation of this approach is to use multiple layers of carbon-impregnated foam. The layers have an increasing loss tangent from the front layer toward the bottom layer, hence achieve an electrical taper that yield a material with good reflectivity level over a wide frequency range.

To achieve low reflectivity using taper length less than a quarter-wavelength, a different carbon loading for the foam pyramids must be used. If the carbon loading is too high, the impedance taper will be too abrupt, causing the incident wave to be reflected from the region near the pyramid tips instead of penetrating into the absorber medium. On the other hand, if the carbon loading is too low, the incident wave that penetrates the absorber medium will not be sufficiently absorbed. With a carbon loading that gives optimum reflectivity of -20 dB for the 200–1000 MHz range, the performance of the pyramids may not be adequate at higher frequencies where the required reflectivity is below -40 dB for the typical applications in designing antenna and radar cross-section measurement chamber.

Ferrite tile is a new generation of low-frequency wideband absorber that has been widely used in many EMC

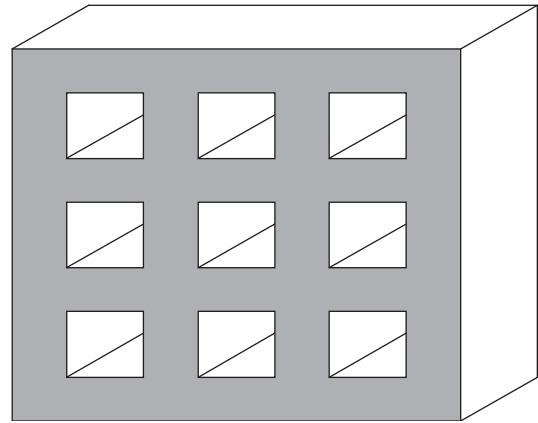


Figure 6. Geometry of a ferrite grid.

test chambers. The ferrite tile (NiZn) with a thickness of 6.3 mm may offer a reflectivity level below -15 dB over the frequency range of 30–600 MHz, but the reflectivity deteriorates rapidly as the frequency increases [5]. The ferrite grid (see Fig. 6) is a variant of ferrite tile. Because of the square air section, the ferrite material can be considered as having an equivalent permittivity and an equivalent permeability. The filling factor or fraction of space occupied by ferrite can be selected in order to place a reflectivity null at a desired frequency. Ferrite grid with a thickness of 19 mm can be used to cover the frequency range of 30–1000 MHz. An exponentially tapered ferrite grid is also investigated in an effort to widen the bandwidth to 2400 MHz.

A method to improve the reflectivity of ferrite tiles and grids is by simply adding a dielectric layer between the ferrite and the metal wall of the screened room [5]. The dielectric layer can be commercial plywood with dielectric constant of ~ 2.0 . However, the thickness of the dielectric must be properly chosen in order to give an optimum performance over a wider bandwidth. A multi-layer approach with different types of ferrite and/or magnetic composite materials separated by air space is under investigation.

Electrically thin urethane foam pyramids that are optimized to operate at 200–1000 MHz have been combined with ferrite tiles that are effective at 30–600 MHz. This hybrid absorber provides the required performance to cover the frequency range of 30–1000 MHz. The carbon loading of the pyramids must not be too high; otherwise the low-frequency performance of the ferrite tiles will be degraded.

The weight of ferrite and hybrid absorbers (> 30 kg/m²) are generally heavier than foam absorbers. The strength of the room must be strong enough to support the weight of the absorbers. A special room structure will be necessary in constructing the large anechoic chamber. On the other hand, the use of 2.5-m-thick pyramid absorbers requires a screened room size larger than $20 \times 10 \times 9$ m height in order to construct a 10-m-range anechoic chamber. The required cost and space are substantial. Hence, there is much interest in trying to reduce the required investment while still maintaining adequate performance.

Small and medium-size foam absorbers are conventionally glued onto the chamber wall using rubber-based contact adhesive. Pyramids longer than 1 m are usually supplied with metal baseplate to be installed onto a rail-and-clip mounting system on the chamber wall in order to ensure installation reliability. Ferrite tiles can be installed using glue. However, because of weight and sharp edges of the tile, overhead net must be installed as safety measure to prevent fallen tile from injuring the personnel who enter the room. A more secure method is to install a plywood panel onto the wall and then fasten the ferrite tile through a centre hole onto the plywood panel using self-tapping screws. The gap between adjacent tiles can then be precisely controlled to give better reflectivity performance, in contrast to using adhesive in which some glue may be trapped between the tiles. The plywood panel also acts as the dielectric backing to improve the performance of the ferrite tile.

In addition to electrical and mechanical specifications of the absorber, the fire retardant property of the absorber must also be considered in order to comply with building safety codes. Lifespan and maintenance needs of the absorber may also be an aspect to consider in the absorber selection criteria.

4. SIZE OF ANECHOIC CHAMBER

Wave measurements are usually performed at far field so that uniform field distribution can be obtained. The measurement facility must be sufficiently large to accommodate the source and the receiver at a separation defined by the Rayleigh range criterion. For an antenna aperture D of 1 m diameter, the separation distance must be greater than $2D^2/\lambda$, which is 67 m at 10 GHz and 6.7 m at 1 GHz. At lower frequencies, the separation must be longer than $\lambda_{\max}/2\pi$ (where λ_{\max} is the maximum wavelength to be measured) so that the coupling between the transmitter and receiver antennas is radiative rather than reactive.

Absorber reflectivity is a function of the wave impedance. The wave impedance near a dipole-type source is higher than intrinsic wave impedance of free space, while the wave impedance near a current loop source is lower than the intrinsic wave impedance. For RF absorber to work efficiently, the distance between the radiation source and the absorber must be greater than $\lambda_{\max}/2\pi$. In general, the thickness of a pyramidal foam absorber must be greater than $\lambda_{\max}/4$ to be effective. However, in order to provide absorber reflectivity better than -40 dB, the height of pyramid shall be several wavelengths. For antenna aperture of 1 m diameter operating at 1 GHz, the size of the screened room may have to be larger than $8 \times 2 \times 10$ GHz, the Rayleigh range criterion can be met for antenna aperture smaller than 0.3 m diameter. For larger antenna, near-field measurement techniques may be used.

5. SCREENED ROOM

The ideal environment for taking RF wave measurements should be free from electromagnetic energy not directly associated with the measurements. The isolation require-

ment is necessary to prevent extraneous energy from masking measurements of electromagnetic field of interest and to protect nearby systems from interference caused by the energy generated by radiation source used in the measurement setup.

RF-shielded enclosures are widely used for various types of RF measurements in the increasingly crowded electromagnetic environment. A volume of space completely enclosed by metal plates will be shielded against electromagnetic radiation. However, ventilation holes and access doors to the screened room, as well as cables penetrating the shielding walls for signal-power interconnection purposes, will cause leakage of electromagnetic waves. Different construction methods will give rise to varying degrees of imperfection that determine the shielding effectiveness. The required shielding design is a function of the purpose of the shield, type of equipment involved, the measurement distance, and the sensitivity of the information being processed.

The geometry of the anechoic chamber must not be too complex so that the screened room can easily be constructed, the shielding effectiveness can be under controlled, and the RF absorbers can properly be lined on the chamber walls, ceiling and floor.

The screened room is commonly fabricated from sheet copper, aluminum, or steel. The most common material is 24-gauge galvanized/zinc-plated steel sheet laminated to wooden board. Sheetmetal offers more than 120 dB shielding effectiveness. However, the total shielding effectiveness of screened room is usually limited by the presence of holes and/or seams, high-impedance discontinuities, and wires/cables passing through holes in the shield. In all practical cases, shielding effectiveness in excess of 120 dB can rarely be achieved [6]. Doors, vents, filters, and piping must be carefully designed and constructed to maintain the shielding integrity. On the other hand, standing waves due to resonance effects may cause certain areas within a screened enclosure to exhibit poorer performance.

A smaller screened enclosure is commonly constructed as a modular clampup structure using prefabricated wooden panels laminated with sheetmetal. The panels are tied together to form the six-sided freestanding room by a framework made of plated steel. A metal-to-metal seal between the panels is provided by the clamping unit, which consists of two metal straps brought together by a number of screws. The shielding performance is dependent on the degree of electrical continuity between the panels and the absence of cracks or breaks between the panels. Installation workmanship is critical. Cleanliness is required around the edges of the panels. Painting of the shielding panels is not recommended because the paint may capillarize under the clamping straps, thus negating the shielding properties of the system. A few problems of the modular construction are the floor panels tend to become loose under varying loads and constant stresses caused by people moving about the room. Expensive maintenance and recertification are required. Water will cause contamination and corrosion of the clamped seams and degrade the shielding effectiveness. The wooden core will swell with moisture and damage the shielding integrity. Hence, modular screened enclosure is not suitable for climate that

has continuous high humidity unless marine-grade plywood is used.

When the required room size exceeds 20 m^2 , welded construction must be considered. A large modular system may not be cost-effective because of the required steel support structure to carry the weight of the screened room ceiling panels. Welded enclosure is structurally reliable and provides long-term high-performance shielding. Low-carbon steel is commonly used because of its relatively low materials cost. However, it has the tendency to rust when exposed to moisture. The corrosion can be protected with paints containing a large amount of zinc. Galvanized steel is not suitable because it produces toxic gas in the welding process.

Architectural shielding system is a method where metal foil or sheet metal is built into the walls, floor, and ceiling of existing or new construction. It is used for application requiring moderate shielding performance. Soldering and shielding tapes are used to join together the metal shields to form a continuous barrier.

A standing wave will be reinforced by reflections between the opposing walls, and between the ceiling and the floor, causing cavity resonance to be established in the screened room. The absorber must provide sufficient damping of Q factors of the resonant modes. Hence, an RF absorber must be applied over the entire inner surfaces of the enclosure to create an anechoic environment. The strength of the shielding structure must be strong enough to support the weight of the RF absorber.

The appearance, physical layout, lighting, HVAC properties, and environmental requirements will depend on the operational purpose of the anechoic chamber. Air conditioning and controlled humidity are generally required to ensure the lifespan of RF absorber in an anechoic chamber.

6. PERFORMANCE CRITERIA

The performance of the antenna anechoic chamber is defined by the uniformity of the illuminating field over a given region known as the “quiet zone”, the region in which

the test antenna is to be placed. The illuminating field across the quiet zone may have small amplitude ripple due to interference of the direct signal with reflections from various mounting structures, cables, turntable, obstacles on or near the range surface, and irregularities in the range surface. The “quietness” of the zone is then defined as the average ratio of reflected energy to that of the direct signal. However, there is no standardized figure of merit for an anechoic chamber. The “free-space voltage standing-wave ratio” field probe technique is recommended by IEEE Standard 149-1979 to evaluate the quietness level. An antenna with stated directivity is used as the probe. The probe carriage is oriented perpendicular to the axis of the chamber to enable the probe to move continuously along a transverse line. The interference pattern of the field is recorded along with the linear motion of the probe. A typical result is shown in Fig. 7. Measurements are made for horizontal and vertical transverse directions with both horizontal and vertical polarizations. A standard-gain horn antenna is generally used as the probe. The directivity of the probe antenna will affect the results obtained.

The radiation pattern of antenna is conventionally measured at far-field distance between the transmitter and the receiver antennas. In an anechoic chamber, the size of the quiet zone is dictated by the Rayleigh range criterion to ensure that the phase variation of the direct wave from the center to the edge of the quiet zone is less than 22.5° (equivalent to $\lambda/16$). Larger phase variation may cause the measured antenna pattern to depart appreciably from the true far-field pattern. For a fixed range distance $R = 10 \text{ m}$, the width of the quiet zone decreases with frequency from 1.22 m at 1 GHz to 0.39 m at 10 GHz.

There must be minimum amplitude variation of the field within the quiet zone. If the antenna under test (AUT) is configured as the receiver antenna, the effect of wide-angle reflection (from the walls, ceiling, and floor of the anechoic chamber) may be reduced by the use of directional transmitting antenna. Hence, the acceptable tolerance for the level of reflected wave below the direct wave amplitude depends on the radiation pattern of the

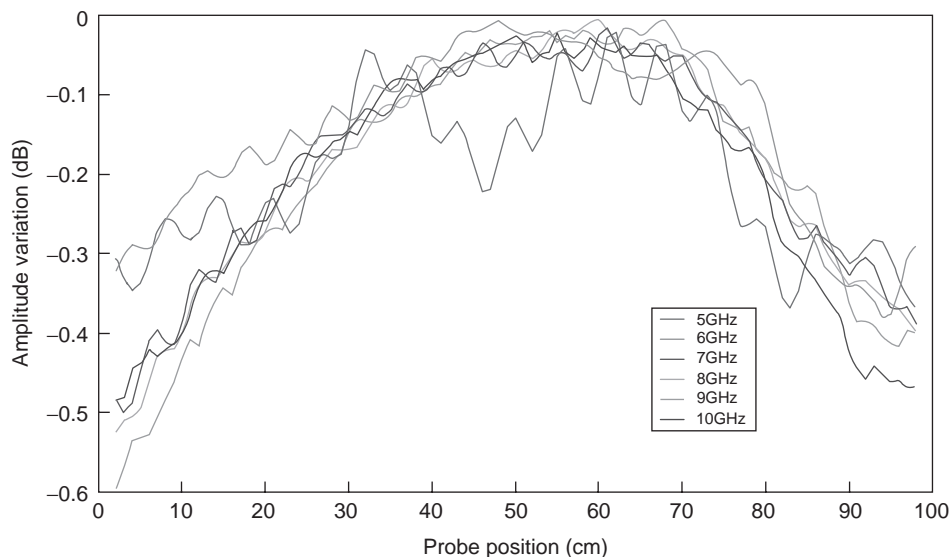


Figure 7. Amplitude variations within the quiet zone. (This figure is available in full color at <http://www.mrw.interscience.wiley.com/erfme>.)

AUT and the source antenna. The directivity of the source antenna must not be too high, to ensure that the amplitude taper from the center to the edge of the quiet zone will not adversely affect the measurement accuracy. For antenna polarization measurement, cross-polarization isolation of the source antenna and the anechoic chamber must be better than that for the AUT.

The performance criteria employed to evaluate an anechoic chamber depend on the type of measurements to be made in the chamber. For RCS measurements, the performance criterion of the chamber is its apparent radar cross section measured in the absence of the scatterer. This is, in effect, the total system sensitivity of the measurement system. It determines the smallest RCS that can be reliably measured. The accuracy, however, is not specified because it does not depend on just a few parameters but on a complex combination of a number of factors. These include the calibration technique, data processing algorithm, signal-to-noise ratio, as well as the nature of the target in terms of the scattering mechanism involved in the wave-target interaction such as edge diffraction, creeping wave, traveling wave, and coupling between constituents in a dense medium.

For EMC-radiated emission measurements, the site validation requirements are defined in international standard CISPR 16 (and ANSI C63.4 in the United States; EN50147-2 in the Europe). The measurement site shall be validated with a method involving a series of normalized site attenuation (NSA) measurements for 30–1000 MHz frequencies. The *site attenuation* is defined as the ratio of the voltage input to a matched and balanced lossless tuned dipole radiator, to that at the output of a similarly matched balanced lossless tuned dipole receiver antenna. The NSA measurements are carried out for the given transmitter-receiver separation and heights above a flat conductive surface for both horizontal and vertical polarizations. The measured NSA data shall be compared to that calculated for an ideal site.

7. ABSORBER AND CHAMBER MODELING

The calculations of the interference field in an anechoic chamber are often inaccurate because of the lack of a proper model to characterize the scattering behavior of absorbers when they are lined up on the chamber walls. With the transmitter located at one end of the chamber and the receiver located at the other end, the reflected waves in magnitude and phase must be known in order to calculate the total field due to the sum of the direct wave and the reflected waves. Absorber manufacturers usually specify only the reflectivity at normal incidence due to the limitation of the large waveguide or large coaxial line used to carry out the measurement. In fact, the reflectivity at oblique incidence may deteriorate rapidly with increasing incident angle. An engineering model that describes the behaviors of the absorber as a function of incident angle, frequency, and polarization, in magnitude and phase, is required for calculation of the sum of waves propagating directly toward the receiver and those reflected from the chamber walls and ceilings.

Theoretical models for pyramidal and wedge absorbers have been developed to calculate absorber reflectivity using the known complex permittivity and permeability, as well as the conductivity, of the bulk material [7]. However, multiple samples extracted from several places of a real absorber may show large differences in the bulk parameters. The calculated absorber reflectivity based on the bulk parameters may not be accurate. Furthermore, the final use of the absorber is not as a small isolated absorber element. The great variation of bulk parameters as well as gaps in lining the absorber material over the area illuminated by a plane wave may result in large error of the actual reflection coefficient compared to the calculated value. The mounting methods used in the absorber installation (thickness of adhesive, mounting bracket, etc.) may also contribute to additional errors. In some situations, the RF absorber is illuminated at near field by a spherical wave rather than a plane wave. Therefore, the assumption of plane wave illumination in the calculation will be invalid.

On the other hand, wave energy incident on the absorber will be scattered in virtually all directions in much the same way as on a rough surface. A geometric optic modeling method that traces the rays of electromagnetic waves propagating from the transmitter to the receiver assumes specular reflection at the walls, ceiling, and floor. The calculated field quantities may not compare well with the measurement data. The only reliable method to give a good prediction of the performance is to perform a complete 3D solution of Maxwell's equations over the entire interior of the chamber. This method is very laborious in terms of specifying the exact dimensions of the chamber structure and fixtures and absorber material properties, and it involves extremely long computation time. In all practical cases, it is very difficult to characterize the chamber fixtures (antenna mast, turntable, lighting, CCTV camera, "honeycomb" waveguide vents, penetration panels, etc.) and imperfection in lining the absorbers for an exact computer simulation. Hence, the use of ray-tracing method together with a suitable model for the absorber-lined surfaces will suffice for prediction of the chamber performance as a first approximation prior to the chamber construction.

An anechoic chamber usually represents a substantial investment both financially and in building space. Hence, there is much interest in trying to reduce the required investment while still maintaining adequate performance. With a suitable computer simulation tool, together with a reasonable absorber model, the anechoic chamber geometry may be optimized to achieve the cost-effectiveness target.

BIBLIOGRAPHY

1. H. E. King et al., Characteristics of a tapered anechoic chamber, *IEEE Trans. Anten. Propag.* **AP-15**:488–490 (May 1967).
2. R. B. Dydal, VHF to EHF performance of a 90-ft quasi-tapered anechoic chamber, *IEEE Trans. Anten. Propag.* 579–581 (July 1973).
3. A. K. Fung, Remote sensing at the University of Texas at Arlington, *IEEE Geosci. Remote Sens. Soc. Newsl.* 23–27 (Sept. 1994).

4. B. K. Chung, H. T. Chuah, and J. W. Bredow, A microwave anechoic chamber for radar cross-section measurement, *IEEE Anten. Propag. Mag.* **39**(3):21–26 (June 1997).
5. C. L. Holloway et al., Comparison of electromagnetic absorber used in anechoic and semi-anechoic chambers for emission and immunity testing of digital devices, *IEEE Trans. Electromagn. Compat.* **39**(1):33–47 (Feb. 1997).
6. L. H. Hemming, *Architectural Electromagnetic Shielding Handbook: A Designer and Specification Guide*, IEEE Press, 1992.
7. E. F. Kuester and C. L. Holloway, Improved low-frequency performance of pyramidal-cone absorbers for application in semi-anechoic chambers, *Proc. IEEE Int. Symp. Electromagnetic Compatibility*, 1989, pp. 394–398.

FURTHER READING

- W. H. Emerson, Electromagnetic wave absorbers and anechoic chambers through the years, *IEEE Trans. Anten. Propag.* 484–490 (July 1973).
- D. J. Edwards and R. F. Burbidge, An experimental investigation into the performance of asymmetric screened rooms for electromagnetic measurements, *Proc. IEEE Int. Conf. Electromagnetic Compatibility*, 1990, pp. 114–118.
- B. T. DeWitt and W. D. Burnside, Electromagnetic scattering by pyramidal and wedge absorbers, *IEEE Trans. Anten. Propag.* 971–984, (July 1988).
- R. B. Schulz, V. C. Plantz, and D. R. Brush, Shielding theory and practice, *IEEE Trans. Electromagn. Compat.* **30**(3):187–201 (1988).
- L. H. Hemming, *Architectural Electromagnetic Shielding Handbook: A Designer and Specification Guide*, IEEE Press, 1992.
- E. F. Buckley, Outline of evaluation procedures for microwave anechoic chambers, *Microwave J.* **6**(8) (Aug. 1963).
- R. Janaswamy, Oblique scattering from lossy periodic surfaces with application to anechoic chamber absorbers, *IEEE Trans. Anten. Propag.* **40**:162–169 (1992).
- S. R. Mishra and T. J. F. Pavlasek, Design of absorber-lined chambers for emc measurements using a geometrical optics approach, *IEEE Trans. Electromagn. Compat.* **26**:111–119 (1984).

ANTENNA ARRAYS FOR MOBILE COMMUNICATIONS

AROGYASWAMI PAULRAJ
 DAVID GESBERT
 Stanford University
 Stanford, California
 CONSTANTINOS PAPADIAS
 Lucent Technologies
 New Jersey

Wireless cellular networks are growing rapidly around the world, and this trend is likely to continue for several years. The progress in radio technology enables new and improved services. Current wireless services include transmission of voice, fax, and low-speed data. More bandwidth-consuming interactive multimedia services such as

video-on-demand and Internet access will be supported in the future. Wireless networks must provide these services in a wide range of environments, spanning dense urban, suburban, and rural areas. Varying mobility needs must also be addressed. Wireless local loop networks serve fixed subscribers. Microcellular networks serve pedestrians and other slow-moving users, and macrocellular networks serve high-speed vehicle-borne users. Several competing standards have been developed for terrestrial networks. AMPS (advanced mobile phone system) is an example of a first-generation frequency-division multiple-access analog cellular system. Second-generation standards include GSM (global system for mobile) and IS-136, using time-division multiple access (TDMA); and IS-95, using code-division multiple access (CDMA). IMT-2000 is proposed to be the third-generation standard and will use mostly a wideband CDMA technology.

Increased services and lower costs have resulted in an increased airtime usage and number of subscribers. Since the radio (spectral) resources are limited, system capacity is a primary challenge for current wireless network designers. Other major challenges include (1) an unfriendly transmission medium, with multipath transmission, noise, interference, and time variations; (2) the limited battery life of the user's handheld terminal; and (3) efficient radio resource management to offer high quality of service.

Current wireless modems use signal processing in the time dimension alone through advanced coding, modulation, and equalization techniques. The primary goal of smart antennas in wireless communications is to integrate and exploit efficiently the extra dimension offered by multiple antennas at the transceiver in order to enhance the overall performance of the network. Smart antenna systems use modems that combine the signals of multi-element antennas in both space and time. Smart antennas can be used for both receive and transmit, both at the base station and at the user terminal. The use of smart antennas at the base alone is more typical, since practical constraints usually limit the use of multiple antennas at the terminal. See Fig. 1 for an illustration.

Spacetime processing offers various advantages. The first is array gain; multiple antennas capture more signal energy, which can be combined to improve the signal-to-noise ratio (SNR). Next, spatial diversity obtained from multiple antennas can be used to combat channel fading. Finally, spacetime processing can help mitigate intersymbol interference (ISI) and cochannel interference (CCI). These leverages can be traded for improvements in

- Coverage: square miles per base station
- Quality: bit error rate (BER); outage probability
- Capacity: erlangs per hertz per base station
- Data rates: bits per second per hertz per base station

1. EARLY FORMS OF SPATIAL PROCESSING

1.1. Adaptive Antennas

The use of adaptive antennas dates back to the 1950s with their applications to radar and antijam problems. The

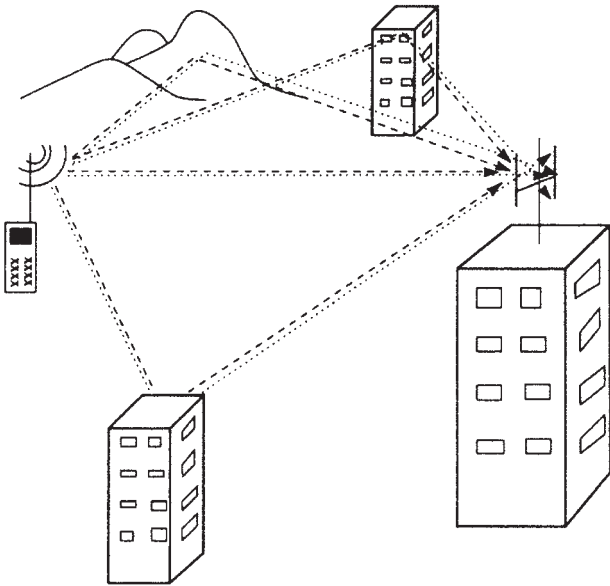


Figure 1. The user signal experiences multipath propagation and impinges on a two-element array on a building rooftop.

primary goal of adaptive antennas is the automatic generation of beams (beamforming) that track a desired signal and possibly reject (or *null*) interfering sources through linear combining of the signals captured by the different antennas. An early contribution in the field of beamforming was made in 1956 by Altman and Sichak, who proposed a combining device based on a phase-locked loop. This work was later refined in order to incorporate the adjustment of antenna signals in both phase and gain, allowing improved performance of the receiver in the presence of strong jammers. Howells proposed the sidelobe canceler for adaptive nulling. Optimal combining schemes were also introduced in order to minimize different criteria at the beamformer output. These include the minimum mean-squared error (MMSE) criterion, as in the LMS algorithm proposed by Widrow; the signal-to-interference-and-noise ratio (SINR) criterion proposed by Applebaum, and the minimum-variance beamformer distortionless response (MVDR) beamformer proposed by Capon. Further advances in the field were made by Frost, Griffiths, and Jim among several others. A list of references in beamforming can be found in Refs. 1 and 13.

Besides beamforming, another application of antenna arrays is direction-of-arrival (DoA) estimation for source or target localization purposes. The leading DoA estimation methods are the MUSIC and ESPRIT algorithms [2]. In many of the beamforming techniques (e.g., in Capon's method), estimation of the source direction is an essential step. DoA estimation is still an area of active research.

Antenna arrays for beamforming and source localization are, of course, of great interest in military applications. However, their use in civilian cellular communication networks is now gaining increasing attention. By enabling the transmission and reception of signal energy from selected directions, beamformers play an important role in improving the performance of both the base-to-mobile (forward) and mobile-to-base (reverse) links.

1.2. Antenna Diversity

Antenna diversity can alleviate the effects of channel fading, and is used extensively in wireless networks. The basic idea of space diversity is as follows. If several replicas of the same information-carrying signal are received over multiple branches with comparable strengths and exhibit independent fading, then there is a high probability that at least one branch will not be in a fade at any given instant of time. When a receiver is equipped with two or more antennas that are sufficiently separated (typically several wavelengths), they offer useful diversity branches. Diversity branches tend to fade independently; therefore, a proper selection or combining of the branches increases link reliability. Without diversity, protection against deep channel fades requires higher transmit power to ensure the link margins. Therefore, diversity at the base can be traded for reduced power consumption and longer battery life at the user terminal. Also, lower transmit power decreases the amount of cochannel user interference and increases the system capacity.

Independent fading across antennas is achievable when radiowaves impinge on the antenna array with sufficient angle spread. Paths coming from different arriving directions will add differently (constructive or destructive manner) at each antenna. This requires the presence of significant scatterers in the propagation medium, such as in urban or hilly terrain.

Diversity also helps to combat large-scale fading effects caused by shadowing from large obstacles (e.g., buildings or terrain features). However, antennas located in the same base station experience the same shadowing. Instead, antennas from different base stations can be combined to offer a protection against such fading (*macro diversity*).

Antenna diversity can be complemented by other forms of diversity. Polarization, time, frequency, and path diversity are some examples. These are particularly useful when physical constraints prevent the use of multiple antennas (e.g., at the handheld terminal). See Ref. 3 for more details.

Combining the different diversity branches is an important issue. The main options used in current systems are briefly described below. In all cases, independent branch fading and equal mean branch powers are assumed. However, in nonideal situations, branch correlation and unequal powers will result in a loss of diversity gain. A correlation coefficient as high as 0.7 between instantaneous branch envelope levels is considered acceptable.

1.2.1. Selection Diversity. Selection diversity is one of the simplest forms of diversity combining. Given several branches with varying carrier-to-noise ratios (C/N), selection diversity consists in choosing the branch having the highest instantaneous C/N . The performance improvement from selection diversity is evaluated as follows: Let us suppose that M branches experience independent fading but have the same mean C/N , denoted by Γ . Let us now denote by Γ_s the mean C/N of the selected branch. Then it

can be shown that [4]

$$\Gamma_s = \Gamma \sum_{j=1}^M \frac{1}{j}$$

For instance, selection over two branches increases the mean C/N by a factor of 1.5. More importantly, the statistics of the instantaneous C/N is improved. Note that selection diversity requires a receiver behind each antenna.

Switching diversity is a variant of selection diversity. In this method, a selected branch is held until it falls below a threshold T , at which point the receiver switches to another branch, regardless of its level. The threshold can be fixed or adaptive. This strategy performs almost as well as the selection method described above, and it reduces the system cost, since only one receiver is required.

1.2.2. Maximum-Ratio Combining. Maximum-ratio combining (MRC) is an optimal combining approach to combat fading. The signals from M branches are first cophased to mutual coherence and then summed after weighting. The weights are chosen to be proportional to the signal level to maximize the combined C/N . It can be shown that the gain from MRC in mean C/N is directly proportional to the number of branches:

$$\Gamma_s = M\Gamma$$

1.2.3. Equal-Gain Combining. Although optimal, MRC is expensive to implement. Also, MRC requires accurate tracking of the complex fading, which is difficult to achieve in practice. A simpler alternative is given by equal-gain combining, which consists in summing the cophased signals using unit weights. The performance of equal-gain combining is found to be very close to that of MRC. The SNR of the combined signals using equal gain is only 1 dB below the SNR provided by MRC [4].

2. EMERGING APPLICATION OF SPACETIME PROCESSING

While the use of beamforming and space diversity proves useful in radiocommunication applications, an inherent limitation of these techniques lies in the fact that they exploit signal combining in the space dimension only. Directional beamforming, in particular, heavily relies on the exploitation of the spatial signatures of the incoming signals but does not consider their temporal structure. The techniques that combine the signals in both time and space can bring new advantages, and their importance in the area of mobile communications is now recognized [5].

The main reason for using spacetime processing is that it can exploit the rich temporal structure of digital communication signals. In addition, multipath propagation environments introduce signal delay spread, making techniques that exploit the complete spacetime structure more natural.

The typical structure of a spacetime processing device consists of a bank of linear filters, each located behind a branch, followed by a summing network. The received

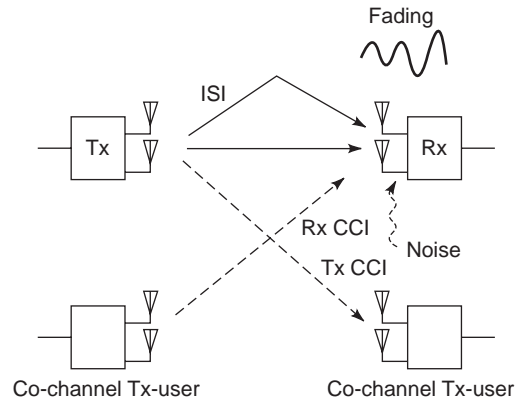


Figure 2. Smart antennas help mitigate the effects of cellular radio propagation.

spacetime signals can also be processed using nonlinear schemes, for example, maximum-likelihood sequence detection. The spacetime receivers can be optimized to maximize array and diversity gains, and to minimize

1. Intersymbol interference (ISI), induced by the delay spread in the propagation channel. ISI can be suppressed by selecting a spacetime filter that equalizes the channel or by using a maximum-likelihood sequence detector.
2. Cochannel (user) interference (CCI), coming from neighboring cells operating at the same frequency. CCI is suppressed by using a spacetime filter that is orthogonal to the interference's channel. The key point is that CCI that cannot be rejected by space-only filtering may be handled more effectively using spacetime filtering.

Smart antennas can also be used at the transmitter to maximize array gain and/or diversity and to mitigate ISI and CCI. In the transmit case, however, the efficiency of spacetime processing schemes is usually limited by the lack of accurate channel information.

The major effects induced by radio propagation in a cellular environment, are pictured in Fig. 2. The advantages offered by spacetime processing for receive and transmit are summarized in Table 1.

In the following sections, we describe channel models and algorithms used in spacetime processing. Both simple and advanced solutions are presented, and tradeoffs

Table 1. Advantages of Spacetime Processing

For transmit (Tx)	Reduces Tx CCI Maximizes Tx diversity Reduces ISI Increases Tx EIRP
For receive (Rx)	Reduces Rx CCI Maximizes Rx diversity Eliminates ISI Increases C/N

highlighted. Finally, we describe current applications of smart antennas.

3. CHANNEL MODELS

Channel models capture radio propagation effects and are useful for simulation studies and performance prediction. Channel models also help in motivating appropriate signal-processing algorithms. The effects of radio propagation on the transmitted signal can be broadly categorized into two main classes: fading and spreading.

Fading refers to the propagation losses experienced by the radio signal (on both the forward and reverse links). One type of fading, called *selective fading*, causes the received signal level to vary around the average level in some regions of space, frequency, or time. *Channel spreading* refers to the spreading of the information-carrying signal energy in space, and on the time or frequency axis. Selective fading and spreading are complementary phenomena.

3.1. Channel Fading

3.1.1. Mean Path Loss. The mean path loss describes the attenuation of a radio signal in free-space propagation, due to isotropic power spreading, and is given by the well-known inverse square law:

$$P_r = P_t \left(\frac{\lambda}{4\pi d} \right)^2 G_t G_r$$

where P_r and P_t are the received and transmitted powers, λ is the radio wavelength, d is the range, and G_t , G_r are the gains of the transmit and receive one-element antennas, respectively. In cellular environments, the main path is often accompanied by a surface-reflected path that may interfere destructively with the primary path. Specific models have been developed that consider this effect. The path loss model becomes [4]

$$P_r = P_t \left(\frac{h_t h_r}{d^2} \right)^2 G_t G_r$$

where h_t, h_r are the effective heights of the transmit and receive antennas, respectively. Note that this particular path loss model follows an inverse fourth-power law. In fact, depending on the environment, the path loss exponent may vary from 2.5 to 5.

3.1.2. Slow Fading. Slow fading is caused by long-term shadowing effects of buildings or natural features in the terrain. It can also be described as the local mean of a fast fading signal (see below). The statistical distribution of the local mean has been studied experimentally and shown to be influenced by the antenna height, the operating frequency, and the type of environment. It is therefore difficult to predict. However, it has been observed that when all the abovementioned parameters are fixed, then the received signal fluctuation approaches a normal distribution when plotted on a logarithmic scale (i.e., in decibels) [4].

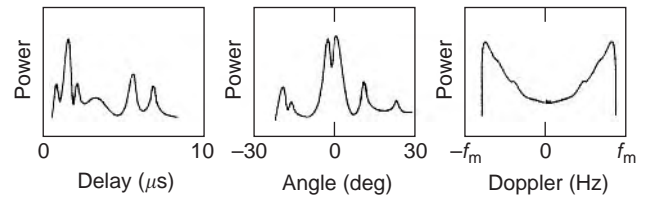


Figure 3. The radio channel induces spreading in several dimensions. These spreads strongly affect the design of the space-time receiver.

Such a distribution is called lognormal. A typical value for the standard deviation of shadowing distribution is 8 dB.

3.1.3. Fast Fading. The multipath propagation of the radio signal causes path signals to add up with random phases, constructively or destructively, at the receiver. These phases are determined by the pathlength and the carrier frequency, and can vary extremely rapidly along with the receiver location. This gives rise to *fast fading*: large, rapid fluctuations of the received signal level in space. If we assume that a large number of scattered wavefronts with random amplitudes and angles of arrival arrive at the receiver with phases uniformly distributed in $(0, 2\pi)$, then the in-phase and quadrature phase components of the vertical electrical field E_z can be shown to be Gaussian processes [4]. In turn, the envelope of the signal can be well approximated by a Rayleigh process. If there is a direct path present, then it will no longer be a Rayleigh distribution but becomes a Rician distributed instead.

3.2. Channel Spreading

Propagation to or from a mobile user, in a multipath channel, causes the received signal energy to spread in the frequency, time, and space dimensions (see Fig. 3, and also Table 2 for typical values). The characteristics of the spreading [that is to say, the particular dimension(s) in which the signal is spread] affects the design of the receiver.

3.2.1. Doppler Spread. When the mobile user is in motion, the radio signal at the receiver experiences a shift in the frequency domain (called the *Doppler shift*), the amplitude of which depends on the path direction of arrival. In the presence of surrounding scatterers with multiple directions, a pure tone is *spread* over a finite spectral bandwidth. In this case, the Doppler power spectrum is defined as the Fourier transform of the time autocorrelation of the

Table 2. Typical Delay, Angle, and Doppler Spreads in Cellular Radio Systems

Environment	Delay Spread (μs)	Angle Spread (deg)	Doppler Spread (Hz)
Flat rural (macro)	0.5	1	190
Urban (macro)	5	20	120
Hilly (macro)	20	30	190
Microcell (mall)	0.3	120	10
Picocell (indoors)	0.1	360	5

received signal, and the Doppler spread is the support of the Doppler power spectrum. Assuming scatterers uniformly distributed in angle, the Doppler power spectrum is given by the so-called classical spectrum:

$$S(f) = \frac{3\sigma^2}{2\pi f_m} \left[1 - \left(\frac{f - f_c}{f_m} \right)^2 \right]^{-1/2},$$

$$f_c - f_m < f < f_c + f_m$$

where $f_m = v/\lambda$ is the maximum Doppler shift, v is the mobile velocity, f_c is the carrier frequency, and σ^2 is the signal variance. When there is a dominant source of energy coming from a particular direction (as in line-of-sight situations), the expression for the spectrum needs to be corrected according to the Doppler shift of the dominant path f_D

$$S(f) + B\delta(f - f_D)$$

where B denotes the ratio of direct to scattered path energy.

The Doppler spread causes the channel characteristics to change rapidly in time, giving rise to the so-called *time selectivity*. The coherence time, during which the fading channel can be considered as constant, is inversely proportional to the Doppler spread. A typical value of the Doppler spread in a macrocell environment is about 200 Hz at 30 m/s (65 mi/h) in the 1900-MHz band. A large Doppler spread makes good channel tracking an essential feature of the receiver design.

3.2.2. Delay Spread. Multipath propagation is often characterized by several versions of the transmitted signal arriving at the receiver with different attenuation factors and delays. The spreading in the time domain is called *delay spread* and is responsible for the selectivity of the channel in the frequency domain (different spectral components of the signal carry different powers). The coherence bandwidth, which is the maximum range of frequencies over which the channel response can be viewed as constant, is inversely proportional to the delay spread. Significant delay spread may cause strong intersymbol interference, which makes necessary the use of a channel equalizer.

3.2.3. Angle Spread. *Angle spread at the receiver* refers to the spread of directions of arrival of the incoming paths. Likewise, *angle spread at the transmitter* refers to the spread of departure angles of the paths. As mentioned earlier, a large angle spread will cause the paths to add up in a random manner at the receiver as the location of the receive antenna varies; hence it will be a source of *space-selective fading*. The range of space for which the fading remains constant is called the coherence distance and is inversely related to the angle spread. As a result, two antennas spaced by more than the coherence distance tend to experience uncorrelated fading. When the angle spread is large, which is usually the case in dense urban environments, a significant gain can be obtained from space

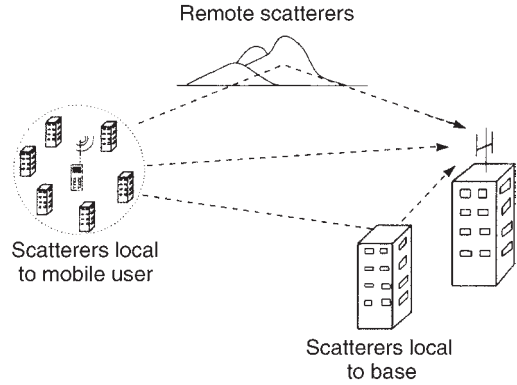


Figure 4. Each type of scatterer introduces specific channel spreading characteristics.

diversity. Note that this usually conflicts with the possibility of using directional beamforming, which typically requires well-defined and dominant signal directions, that is, a low angle spread.

3.3. Multipath Propagation

3.3.1. Macrocells. A macrocell is characterized by a large cell radius (up to a few tens of kilometers) and a base station located above the rooftops. In macrocell environments, the signal energy received at the base station comes from three main scattering sources: scatterers local to the mobile, remote dominant scatterers, and scatterers local to the base (see Fig. 4 for an illustration). The following description refers to the reverse link but applies to the forward link as well.

The scatterers local to the mobile user are those located a few tens of meters from the handheld terminal. When the terminal is in motion, these scatterers give rise to a Doppler spread, which causes time-selective fading. Because of the small scattering radius, the paths that emerge from the vicinity of the mobile user and reach the base station show a small delay spread and a small angle spread.

Of the paths emerging from the local-to-mobile scatterers, some reach remote dominant scatterers, such as hills or high-rise buildings, before eventually traveling to the base station. These paths will typically reach the base with medium to large angle and delay spreads (depending, of course, on the number and locations of these remote scatterers).

Once these multiple wavefronts reach the vicinity of the base station, they usually are further scattered by local structures such as buildings or other structures that are close to the base. These scatterers local to the base can cause large angle spread; therefore they can cause severe space-selective fading.

3.3.2. Microcells. Microcells are characterized by highly dense built-up areas, and by the user’s terminal and base being relatively close (a few hundred meters). The base antenna has a low elevation and is typically below the rooftops, causing significant scattering in the vicinity of the base. Microcell situations make the propagation

difficult to analyze, and the macrocell model described earlier no longer can be expected to hold. Very high angle spreads along with small delay spreads are likely to occur in this situation. The Doppler spread can be as high as in macrocells, although the mobility of the user is expected to be limited, due to the presence of mobile scatterers.

3.4. Parametric Channel Model

A complete and accurate understanding of propagation effects in the radio channel requires a detailed description of the physical environment. The *specular model*, to be presented below, provides only a simplified description of the physical reality. However, it is useful, as it describes the main channel effects and provides the means for a simple and efficient mathematical treatment. In this model, the multiple elementary paths are grouped according to a (typically small) number L of main path clusters, each of which contains paths that have roughly the same mean angle and delay. Since the paths in these clusters originate from different scatterers, the clusters typically have near-independent fading. Based on this model, the continuous-time channel response from a single transmit antenna to the i th antenna of the receiver can be written as

$$f_i(t) = \sum_{l=1}^L \alpha_i(\theta_l) \alpha_l^R(t) \delta(t - \tau_l) \quad (1)$$

where $\alpha_l^R(t)$, θ_l , and τ_l are respectively the fading (including mean path loss and slow and fast fading), the angle, and the delay of the l th receive path cluster. Note that this model also includes the response of the i th antenna to a path from direction θ_l , denoted by $\alpha_i(\theta_l)$. In the following we make use of the specular model to describe the structure of the signals in space and time. Note that in the situation where the path cluster assumption is not acceptable, other channel models, called *diffuse* channel models, are more appropriate [6].

4. DATA MODELS

This section focuses on developing signal models for spacetime processing algorithms. The transmitted information signal is assumed to be linearly modulated. In the case of a nonlinear modulation scheme, such as the Gaussian minimum shift keying (GMSK) used in the GSM system, linear approximations are assumed to hold. The baseband equivalent of the transmitted signal can be written [7]

$$u(t) = \sum_k g(t - kT) s(k) + n(t) \quad (2)$$

where $s(k)$ is the symbol stream, with rate $1/T$, $g(t)$ is the pulse shaping filter, and $n(t)$ is an additive thermal noise. Four configurations for the received signal (two for the reverse link and two for the forward link) are described below. These are also depicted in Fig. 5. In each case, one assumes $M > 1$ antennas at the base station and a single antenna at the mobile user.

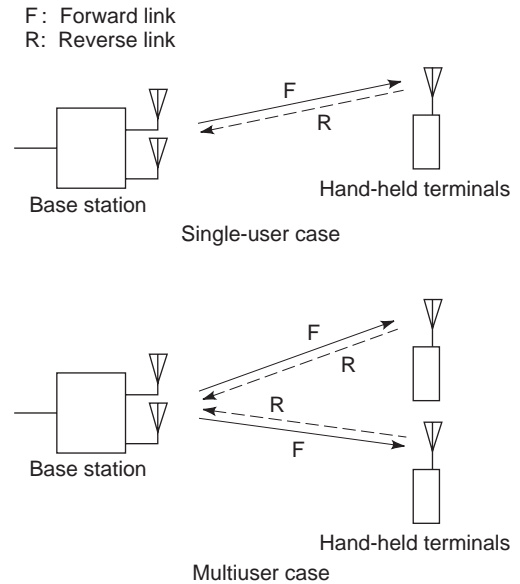


Figure 5. Several configurations are possible for antenna arrays, in transmit (T) and in receive (R).

4.1. Reverse Link

We consider the signal received at the base station. Since the receiver is equipped with M antennas, the received signal can be written as a vector $\mathbf{x}(t)$ with M entries.

4.1.1. Single-User Case. Let us assume a single user transmitting towards the base (no CCI). Using the specular channel model in Eq. (1), the received signal can be written as follows:

$$\mathbf{x}(t) = \sum_{l=1}^L \mathbf{a}(\theta_l) \alpha_l^R(t) u(t - \tau_l) + \mathbf{n}(t) \quad (3)$$

where $\mathbf{a}(\theta_l) = (a_1(\theta_l), \dots, a_M(\theta_l))^T$ is the vector array response to a path of direction θ_l , and where T refers to the transposition operator.

4.1.2. Multiuser Case. We now have Q users transmitting toward the base. The received signal is the following sum of contributions from the Q users, each of them carries a different set of fading, delays, and angles:

$$\mathbf{x}(t) = \sum_{q=1}^Q \sum_{l=1}^{L_q} \mathbf{a}(\theta_{lq}) \alpha_{lq}^R(t) u_q(t - \tau_{lq}) + \mathbf{n}(t) \quad (4)$$

where the subscript q refers to the user index.

4.2. Forward Link

4.2.1. Single-User Case. In this case, the base station uses a transmitter equipped with M antennas to send an information signal to a unique user. Therefore, spacetime processing must be performed *before* the signal is launched into the channel. As will be emphasized later,

this is a challenging situation, as the transmitter typically lacks reliable information on the channel.

For the sake of simplicity, we will assume here that a space-only beamforming weight vector \mathbf{w} is used, as the extension to spacetime beamforming is straightforward. The baseband signal received at the mobile station is scalar and is given by

$$x(t) = \sum_{l=1}^L \mathbf{w}^H \mathbf{a}(\theta_l) \alpha_l^F(t) u(t - \tau_l) + n(t) \quad (5)$$

where $\alpha_l^F(t)$ is the fading coefficient of the l th transmit path in the forward link. Superscript H denotes the transpose conjugation operator. Note that path angles and delays remain theoretically unchanged in the forward and reverse links. This is in contrast with the fading coefficients, which depend on the carrier frequency. Frequency-division duplex (FDD) systems use different carriers for the forward and reverse links, which result in $\alpha_l^F(t)$ and $\alpha_l^R(t)$ being nearly uncorrelated. In contrast, time-division duplex (TDD) systems will experience almost identical forward and reverse fading coefficients in the forward and reverse links. Assuming, however, that the transmitter knows the forward fading and delay parameters, transmit beamforming can offer array gain, ISI suppression, and CCI suppression.

4.2.2. Multiuser Case. In the multiuser case, the base station wishes to communicate with Q users, simultaneously and in the same frequency band. This can be done by superposing, on each of the transmit antennas, the signals given by Q beamformers $\mathbf{w}_1, \dots, \mathbf{w}_Q$. At the m th user, the received signal waveform contains the signal sent to that user, plus an interference from signals intended for all other users. This gives

$$x_m(t) = \sum_{q=1}^Q \sum_{l=1}^{L_q} \mathbf{w}_q^H \mathbf{a}(\theta_{lm}) \alpha_{lm}^F(t) u_q(t - \tau_{lm}) + n_m(t) \quad (6)$$

Note that each information signal $u_q(t)$ couples into the L_m paths of the m th user through the corresponding weight vector \mathbf{w}_q , for all q .

4.3. A Nonparametric Model

The data models above build on the parametric channel model developed earlier. However, there is also interest in considering the end-to-end channel impulse response of the system to a transmitted symbol rather than the physical path parameters. The channel impulse response includes the pulseshaping filter response, the propagation phenomena, and the antenna response as well. One advantage of looking at the impulse response is that the effects of ISI and CCI can be described in a better and more compact way. A second advantage is that the nonparametric channel relies only on the channel linearity assumption.

We look at the reverse-link and single-user case only. Since a single scalar signal is transmitted and received over several branches, this corresponds to a single-input multiple-output (SIMO) system, depicted in Fig. 6. The model below is also easily extended to multiuser channels. Let $\mathbf{h}(t)$ denote the $M \times 1$ global channel impulse response.

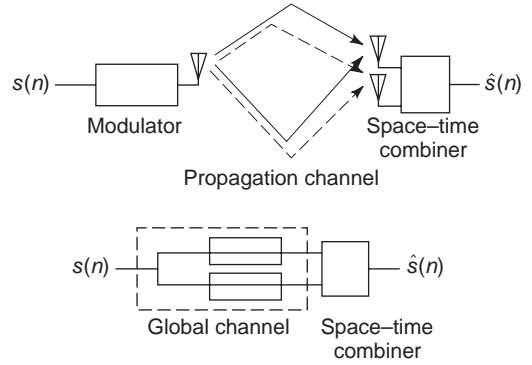


Figure 6. The source signal $s(n)$ can be seen as driving a single-input multiple-output filter with M outputs, where M is the number of receive antennas.

The received vector signal is given by the result of a (noisy) convolution operation:

$$\mathbf{x}(t) = \sum_k \mathbf{h}(t - kT) s(k) + \mathbf{n}(t) \quad (7)$$

From Eqs. (2) and (3), the channel response may also be expressed in terms of the specular model parameters through

$$\mathbf{h}(t) = \sum_{l=1}^L \mathbf{a}(\theta_l) \alpha_l^R(t) g(t - \tau_l) \quad (8)$$

4.3.1. Signal Sampling. Consider sampling the received signal at the baud (symbol) rate, that is, at $t_k = t_0 + kT$, where t_0 is an arbitrary phase. Let N be the maximum length of the channel response in symbol periods. Assuming that the channel is invariant for some finite period of time [i.e., $\alpha_l^R(t) = \alpha_l^R(t_0 + jT - \tau_l)$], the received vector sample at time t_k can be written as

$$\mathbf{x}(k) = \mathbf{H} \mathbf{s}(k) + \mathbf{n}(k) \quad (9)$$

where \mathbf{H} is the sampled channel matrix, with size $M \times N$, whose (i, j) term is given by

$$[\mathbf{H}]_{ij} = \sum_{l=1}^L a_i(\theta_l) \alpha_l^R g(t_0 + jT - \tau_l)$$

and where $\mathbf{s}(k)$ is the vector of N ISI symbols at the time of the measurement:

$$\mathbf{s}(k) = (s(k), s(k-1), \dots, s(k-N+1))^T$$

To allow for the presence of CCI, Eq. (9) can be generalized to

$$\mathbf{x}(k) = \sum_{q=1}^Q \mathbf{H}_q \mathbf{s}_q(k) + \mathbf{n}(k) \quad (10)$$

where Q denotes the number of users and q the user index. Most digital modems use sampling of the signal at a rate higher than the symbol rate (typically up to 4 times). Oversampling only increases the number of scalar observations per transmitted symbol, which can be regarded

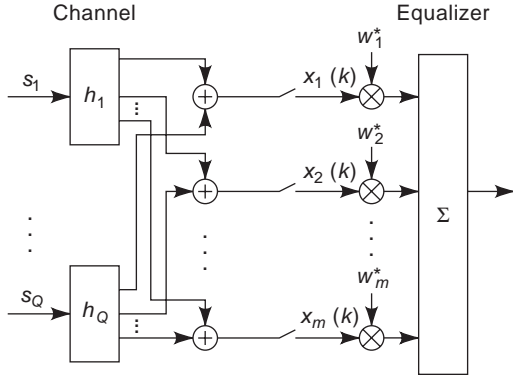


Figure 7. Structure of the spatial beamformer. The spacetime beamformer is a direct generalization that combines in time the outputs of several spatial beamformers.

mathematically as increasing the number of channel components, in a way similar to increasing the number of antennas. Hence the model above also holds true when sampling at $T/2$, $T/3$, and so on. However, although mathematically equivalent, spatial oversampling and temporal oversampling lead to different signal properties.

4.4. Structure of the Linear Spacetime Beamformer

Space combining is now considered at the receive antenna array. Let \mathbf{w} be an $M \times 1$ space-only weight vector (a single complex weight is assigned to each antenna). The output of the combiner, denoted by $y(k)$ is as follows:

$$y(k) = \mathbf{w}^H \mathbf{x}(k)$$

The resulting beamforming operation is depicted in Fig. 7. The generalization to spacetime combining is straightforward. Let the combiner have m time taps. Each tap, denoted by $\mathbf{w}(i)$, $i = 0, \dots, m-1$, is an $M \times 1$ space weight vector defined as above. The output of the spacetime beamformer is now written as

$$y(k) = \sum_{i=0}^{m-1} \mathbf{w}(i)^H \mathbf{x}(k-i) \quad (11)$$

which can be reformulated as

$$y(k) = \mathbf{W}^H \mathbf{X}(k) \quad (12)$$

where $\mathbf{W} = (\mathbf{w}(0)^H, \dots, \mathbf{w}(m-1)^H)^H$ and $\mathbf{X}(k)$ is the data vector compactly defined as $\mathbf{X}(k) = (\mathbf{x}(k)^H, \dots, \mathbf{x}(k-m+1)^H)^H$.

4.5. ISI and CCI Suppression

The formulation above gives insight into the algebraic structure of the spacetime received data vector. It also allows us to identify the conditions under which the suppression of ISI and/or CCI is possible. Recalling the signal model in Eq. (9), the spacetime vector $\mathbf{X}(k)$ can be in turn written as

$$\mathbf{X}(k) = \mathcal{H} \mathbf{S}(k) + \mathbf{N}(k) \quad (13)$$

where $\mathbf{S}(k) = (s(k), s(k-1), \dots, s(k-m+N+2))^T$ and where

$$\mathcal{H} = \begin{pmatrix} \mathbf{H} & 0 & \dots & 0 \\ 0 & \mathbf{H} & \ddots & \vdots \\ \vdots & \ddots & \ddots & 0 \\ 0 & \dots & 0 & \mathbf{H} \end{pmatrix} \quad (14)$$

is an $mM \times (m+N-1)$ -channel matrix. The block Toeplitz structure in \mathcal{H} stems from the linear time-invariant convolution operation with the symbol sequence.

Let us temporarily assume a noise-free scenario. Then the output of a linear spacetime combiner can be described by the following equation:

$$y(k) = \mathbf{W}^H \mathcal{H} \mathbf{S}(k) \quad (15)$$

In the presence of Q users transmitting towards the base station, the output of the spacetime receiver is generalized to

$$y(k) = \sum_{q=1}^Q \mathbf{W}^H \mathcal{H}_q \mathbf{S}_q(k) \quad (16)$$

4.5.1. ISI Suppression. The purpose of equalization is to compensate for the effects of ISI induced by the user's channel in the absence of CCI. Tutorial information on equalization can be found in Refs. 7 and 8. In general, a linear filter \mathbf{W}_q is an equalizer for the channel of the q th user if the convolution product between \mathbf{W}_q and the channel responses yields a Dirac function, that is, if \mathbf{W}_q satisfies the following so-called zero-forcing condition:

$$\mathbf{W}_q^H \mathcal{H}_q = (0, \dots, 0, 1, 0, \dots, 0) \quad (17)$$

Here, the location of the 1 element represents the delay of the combined channel–equalizer impulse response. Note that from an algebraic point of view, the channel matrix \mathcal{H}_q should have more rows than columns for such solutions to exist: $mM \geq m+N-1$. Therefore, it is essential to have enough degrees of freedom (number of taps in the filter) to allow for ISI suppression. Note that zero-forcing solutions can be obtained using temporal oversampling at the receive antenna only, since oversampling by a factor of M provides us theoretically with M baud rate branches. However, having multiple antennas at the receiver plays an important role in improving the conditioning of the matrix \mathcal{H} , which in turn will improve the robustness of the resulting equalizer in the presence of noise. It can be shown that the condition number of the matrix \mathcal{H}_q is related to some measure of the correlation between the entries of $\mathbf{h}(t)$. Hence, a significant antenna spacing is required to provide the receiver with sufficiently decorrelated branches.

4.5.2. CCI Suppression. The purpose of CCI suppression in a multiple-access network is to isolate the contribution of one desired user by rejecting that of others. One way to achieve this goal is to enforce *orthogonality*

between the response of the spacetime beamformer and the response of the channel of the users to be rejected. In other words, in order to isolate the signal of user q using \mathbf{W}_q , the following conditions must be satisfied (possibly approximately):

$$\mathbf{W}_q^H \mathcal{H}_f = 0 \quad \text{for all } f \neq q \in [1, \dots, Q] \quad (18)$$

If we assume that all the channels have the same maximum order N , Eq. (18) provides as many as $(Q-1)(m+N-1)$ scalar equations. The number of unknowns is again given by mM (the size of \mathbf{W}_q). Hence a receiver equipped with multiple antennas is able to provide the number of degrees of freedom necessary for signal separation. This requires $mM \geq (Q-1)(m+N-1)$. At the same time, it is desirable that the receiver capture a significant amount of energy from the desired user; hence an extra condition on \mathbf{W}_q should be $\mathbf{W}_q^H \mathcal{H}_q \neq 0$. From an algebraic perspective, this last condition requires that \mathcal{H}_q and $\{\mathcal{H}_f\}_{f \neq q}$ should not have the same column subspaces. The required subspace misalignment between the desired user and the interferers in spacetime processing is a generalization of the condition that signal and interference should not have the same direction, needed for interference nulling using beamforming.

4.5.3. Joint ISI and CCI Suppression. The complete recovery of the signal transmitted by one desired user in the presence of ISI and CCI requires both channel equalization and separation. A spacetime beamformer is an exact solution to this problem if it satisfies both Eq. (17) and Eq. (18), which can be further written as

$$\begin{aligned} \mathbf{W}_q^H (\mathcal{H}_1, \dots, \mathcal{H}_{q-1}, \mathcal{H}_q, \mathcal{H}_{q+1}, \dots, \mathcal{H}_Q) \\ = (0, \dots, 0, 1, 0, \dots, 0) \end{aligned} \quad (19)$$

where the location of the 1 element designates both the index of the user of reference and the reconstruction delay. The existence of solutions to this problem requires the multiuser channel matrix $\mathcal{H}_* \stackrel{\text{def}}{=} (\mathcal{H}_1, \dots, \mathcal{H}_Q)$ to have more rows than columns: $mM \leq Q(m+N-1)$. Here again, smart antennas play a critical role in offering a sufficient number of degrees of freedom. If, in addition, the global channel matrix \mathcal{H}_* has full column rank, then we are able to recover any particular user using spacetime beamforming. In practice, though, the performance of an ISI-CCI reduction scheme is limited by the SNR and the condition number \mathcal{H}_* .

5. SPACETIME ALGORITHMS FOR THE REVERSE LINK

5.1. General Principles of Receive Spacetime Processing

Space processing offers several important opportunities to enhance the performance of the radiolink. First, smart antennas offer more resistance to channel fast fading through maximization of *space diversity*. Then, space combining increases the received SNR through array gain, and allows for the suppression of interference when the user of reference and the cochannel users have different DoAs.

Time processing addresses two important goals. First, it exploits the gain offered by path diversity in delay-spread channels. As the channel time taps generally carry independent fading, the receiver can resolve channel taps and combine them to maximize the signal level. Second, time processing can combat the effects of ISI through equalization. Linear zero-forcing equalizers address the ISI problem but do not fully exploit path diversity. Hence, for these equalizers, ISI suppression and diversity maximization may be conflicting goals. This is not the case, however, for maximum-likelihood sequence detectors.

Spacetime processing allows us to exploit the advantage of both the time and space dimensions. Spacetime (linear) filters allow us to maximize space and path diversity. Also, spacetime filters can be used for better ISI and CCI reduction. However, as mentioned above, these goals may still conflict. In contrast, spacetime maximum-likelihood sequence detectors (see below) can handle harmoniously both diversity maximization and interference minimization.

5.2. Channel Estimation

Channel estimation forms an essential part of most wireless digital modems. Channel estimation in the reverse link extracts the information that is necessary for a proper design of the receiver, including linear (spacetime beamformer) and nonlinear (decision feedback or maximum-likelihood detection) receivers. For this task, most existing systems rely on the periodic transmission of training sequences, which are known to both the transmitter and receiver and are used to identify the channel characteristics. The estimation of \mathcal{H} is usually performed using the nonparametric FIR model in Eq. (9), in a least-squares manner or by correlating the observed signals against decorrelated training sequences (as in GSM). A different strategy consists in addressing the estimation of the physical parameters (path angle and delays) of the channel using the model developed in Eq. (8). This strategy proves useful when the number of significant paths is much smaller than the number of channel coefficients.

Channel tracking is also an important issue, necessary whenever the propagation characteristics vary (significantly) within the user slot. Several approaches can be used to update the channel estimate. The *decision-directed method* uses symbol decisions as training symbols to update the channel response estimate. Joint data-channel techniques constitute another alternative, in which symbol estimates and channel information are recursively updated according to the minimization of a likelihood metric: $\|\mathbf{X} - \mathcal{H}\mathbf{S}\|^2$.

5.3. Signal Estimation

5.3.1. Maximum-Likelihood Sequence Detection (Single User). Maximum-likelihood sequence detection (MLSD) is a popular nonlinear detection scheme that, given the received signal, seeks the sequence of symbols of one particular user that is most likely to have been transmitted. Assuming temporally and spatially white Gaussian noise,

maximizing the likelihood reduces to finding the vector \mathbf{S} of symbols in a given alphabet that minimizes the following metric:

$$\min_{\mathbf{S}} \|\mathbf{X} - \mathcal{H}\mathbf{S}\|^2 \quad (20)$$

where the channel matrix \mathcal{H} has been previously estimated. Here, $\|\cdot\|$ denotes the conventional euclidean norm. Since \mathbf{X} contains measurements in time and space, the criterion above can be considered as a direct extension of the conventional ML sequence detector, which is implemented recursively using the well-known Viterbi algorithm [7].

MLSD offers the lowest BER in a Gaussian noise environment, but is no longer optimal in the presence of co-channel users. In the presence of CCI, a solution to the MLSD problem consists in incorporating in the likelihood metric the information on the statistics of the interferers. This, however, assumes that the interferers do not undergo significant delay spread. In general, though, the optimal solution is given by a multiuser MLSD detection scheme (see below).

5.3.2. Maximum-Likelihood Sequence Detection (Multi-user). The multiuser MLSD scheme has been proposed for symbol detection in CCI-dominated channels. The idea consists in treating CCI as other desired users and detecting all signals simultaneously. This time, the Q symbol sequences $\mathbf{S}_1, \mathbf{S}_2, \dots, \mathbf{S}_Q$ are found as the solutions to the following problem

$$\min_{\{\mathbf{S}_q\}} \left\| \mathbf{X} - \sum_{q=1}^Q \mathcal{H}_q \mathbf{S}_q \right\|^2 \quad (21)$$

where again all symbols should belong to the modulation alphabet. The resolution of this problem can be carried out theoretically by a multiuser Viterbi algorithm. However, the complexity of such a scheme grows exponentially with the number of users and the channel length, which limits its applicability. Also, the channels of all the users are assumed to be accurately known. In current systems, such information is very difficult to obtain. In addition, the complexity of the multiuser MLSD detector falls beyond current implementation limits. Suboptimal solutions are therefore necessary. One possible strategy, known as *onion peeling*, consists in first decoding the user having the largest power and then subtracting it out from the received data. The procedure is repeated on the residual signal, until all users are decoded. Linear receivers, described below, constitute another form of suboptimal but simple approach to signal detection. Minimum mean square error detection is described below.

5.3.3. Minimum Mean-Squared Error Detection. The spacetime minimum mean-squared error (STMMSE) beamformer is a spacetime linear filter whose weights are chosen to minimize the error between the transmitted symbols of a user of reference and the output of the beamformer defined as $y(k) = \mathbf{W}_q^H \mathbf{X}(k)$. Consider a situation with Q users. Let q be the index of the user of reference.

\mathbf{W}_q is found by

$$\min_{\mathbf{W}_q} E|y(k) - s_q(k-d)|^2 \quad (22)$$

where d is the chosen reconstruction delay. E here denotes the expectation operator. The solution to this problem follows from the classical normal equations:

$$\mathbf{W}_q = E[\mathbf{X}(k)\mathbf{X}(k)^H]^{-1} E[\mathbf{X}(k)s_q(k-d)^*] \quad (23)$$

The solution to this equation can be tracked in various manners, for instance, using pilot symbols. Also, it can be shown that the intercorrelation term in the right-hand side of Eq. (23) corresponds to the vector of channel coefficients of the decoded user, when the symbols are uncorrelated. Hence Eq. (23) can also be solved using a channel estimate.

STMMSE combines the strengths of time-only and space-only combining, hence is able to suppress both ISI and CCI. In the noise-free case, when the number of branches is large enough, \mathbf{W}_q is found to be a solution of Eq. (19). In the presence of additive noise, the MMSE solution provides a useful tradeoff between the so-called zero-forcing solution of Eq. (19) and the maximum-SNR solution. Finally the computational load of the MMSE is well below that of the MLSD. However, MLSD outperforms the MMSE solution when ISI is the dominant source of interference.

5.3.4. Combined MMSE-MLSD. The purpose of the combined MMSE-MLSD spacetime receiver is to be able to deal with both ISI and CCI using a reasonable amount of computation. The idea is to use a STMMSE in a first stage to combat CCI. This leaves us with a signal that is dominated by ISI. After channel estimation, a single-user MLSD algorithm is applied to detect the symbols of the user of interest. Note that the channel seen by the MLSD receiver corresponds to the convolution of the original SIMO channel with the equalizer response.

5.3.5. Spacetime Decision Feedback Equalization. The *decision feedback equalizer* is a nonlinear structure that consists of a spacetime linear feedforward filter (FFF) followed by a nonlinear feedback filter. The FFF is used for precursor ISI and CCI suppression. The nonlinear part contains a decision device that produces symbol estimates. An approximation of the postcursor ISI is formed using these estimates and is subtracted from the FFF output to produce new symbol estimates. This technique avoids the noise enhancement problem of the pure linear receiver and has a much lower computational cost than MLSD techniques.

5.4. Blind Spacetime Processing Methods

The goal of blind spacetime processing methods is to recover the signal transmitted by one or more users, given only the observation of the channel output and minimal information on the symbol statistics and/or the channel structure. Basic available information may include the type of modulation alphabet used by the system. Also, the fact that

channel is quasi-invariant in time (during a given data-frame) is an essential assumption. Blind methods do not, by definition, resort to the transmission of training sequences. This advantage can be directly traded for an increased information bit rate. It also helps to cope with the situations where the length of the training sequence is not sufficient to acquire an accurate channel estimate. Tutorial information on blind estimation can be found in Ref. 9.

Blind methods in digital communications have been the subject of active research since the late 1970s. It was only recently recognized, however, that blind techniques can benefit from utilization of the spatial dimension. The main reason is that oversampling the signal in space using multiple antennas, together with the exploitation of the signal channel structure, allows for efficient channel and beamformer estimation techniques.

5.4.1. Blind Channel Estimation. A significant amount of research work has been focused lately on identifying blindly the impulse response of the transmission channel. The resulting techniques can be broadly categorized into three main classes: higher-order statistics (HOS) methods, second-order statistics (SOS) methods, and maximum-likelihood (ML) methods.

HOS methods look at third- and fourth-order moments of the received data and exploit simple relationships between those moments and the channel coefficients (assuming the knowledge of the input moments) in order to identify the channel. In contrast, the SOS of the output of a scalar (single input–single output) channel do not convey sufficient information for channel estimation, since the second-order moments are phase-blind.

In SIMO systems, SOS does provide the necessary phase information. Hence, one important advantage of multiantenna systems lies in the fact that they can be identified using second-order moments of the observations only. From an algebraic point of view, the use of antenna arrays creates a low-rank model for the vector signal given by the channel output. Specifically, the channel matrix \mathcal{H} in Eq. (14) can be made tall and full-column-rank under mild assumption on the channels. The low-rank property allows one to identify the column span of \mathcal{H} from the observed data. Along with the Toeplitz structure of \mathcal{H} , this information can be exploited to identify the channel.

5.4.2. Direct Estimation. Direct methods bypass the channel estimation stage and concentrate on the estimation of the spacetime filter. The use of antenna arrays (or oversampling in time or space in general) offers important advantages in this context, too. The most important one is perhaps the fact that, as was shown in Eq. (17), the SIMO system can be inverted exactly using a spacetime filter with finite time taps, in contrast with the single-output case.

HOS methods for direct receiver estimation are typically designed to optimize a nonlinear cost function of the receiver output. Possible cost functions include Busgang cost functions [Sato, decision-directed, and constant modulus (CM) algorithms] and kurtosis-based cost functions. The most popular criterion is perhaps the CM criterion, in which the coefficients of the beamformer \mathbf{W} are updated

according to the minimization (through gradient-descent algorithms) of

$$J(\mathbf{W}) = E[|y(k)|^2 - 1]^2$$

where $y(k)$ is the beamformer output.

SOS techniques (sometimes also referred to as “algebraic techniques”) look at the problem of factorizing, at least implicitly, the received data matrix \mathbf{X} into the product of a block-Toeplitz channel matrix \mathcal{H} and a Hankel symbol matrix \mathbf{S}

$$\mathbf{X} \approx \mathcal{H} \mathbf{S} \quad (24)$$

A possible strategy is as follows. Because \mathcal{H} is a tall matrix, the row span of \mathbf{S} coincides with the row span of \mathbf{X} . Along with the Hankel structure of \mathbf{S} , the row span of \mathbf{S} can be exploited to uniquely identify \mathbf{S} .

6. MULTIUSER RECEIVER

The extension of blind estimation methods to a multiuser scenario poses important theoretical and practical challenges. These challenges include an increased number of unknown parameters, more ambiguities caused by the problem of user mixing, and a higher complexity. Furthermore, situations where the users are not fully synchronized may result in an abruptly time-varying environment that makes the tracking of the channel or receiver coefficients difficult.

As in the nonblind context, multiuser reception can be regarded as a two-stage signal equalization plus separation. Blind equalization of multiuser signals can be addressed using extensions of the aforementioned single-user techniques (HOS, CM, SOS, or subspace techniques). Blind separation of the multiuser signals needs new approaches, since subspace methods alone are not sufficient to solve the separation problem. In CDMA systems, the use of different user spreading codes makes this possible. In TDMA systems, a possible approach to signal separation consists in exploiting side information such as the finite-alphabet property of the modulated signals. The factorization Eq. (24) can then be carried out using alternate projections (see Ref. 10 for a survey). Other schemes include adjusting a spacetime filter in order to restore the CM property of the signals.

6.1. Spacetime Processing for Direct-Sequence Code-Division Multiple Access

Direct-sequence CDMA (DSCDMA) systems are expected to gain a significant share of the cellular market. In CDMA, the symbol stream is spread by a *unique* spreading code before transmission. The codes are designed to be orthogonal or quasi-orthogonal to each other, making it possible for the users to be separated at the receiver. See Ref. 11 for details. As in TDMA, the use of smart antennas in CDMA systems improves the network performance.

We first introduce the DSCDMA model; then we briefly describe spacetime CDMA signal processing.

6.1.1. Signal Model. Assume $M > 1$ antennas. The received signal is a vector with M components and can be

written as

$$\mathbf{x}(t) = \sum_{q=1}^Q \sum_{k=-\infty}^{\infty} s_q(k) \mathbf{p}_q(t - kT) + \mathbf{n}(t)$$

where $s_q(k)$ is the information bitstream for user q and $\mathbf{p}_q(t)$ is the composite channel for user q that embeds both the physical channel $\mathbf{h}_q(t)$ (defined as in the TDMA case) and the spreading code $c_q(p)$ of length P :

$$\mathbf{p}_q(t) = \sum_{p=0}^{P-1} c_q(p) \mathbf{h}_q\left(t - \frac{pT}{P}\right)$$

6.1.2. Spacetime Receiver Design. A popular single-user CDMA receiver is the rake combiner. The rake receiver exploits the (quasi)orthogonal codes to resolve and coherently combine the paths. It uses one correlator for each path and then combines the outputs to maximize the SNR. The weights of the combiner are selected using diversity combining principles. The rake receiver is a matched filter to the spreading code plus multipath channel.

The spacetime rake is an extension of the above. It consists of a beamformer for each path followed by a rake combiner (see Fig. 8). The beamformer reduces the CCI at the rake input and thus improves the system capacity.

7. SPACETIME ALGORITHMS FOR THE FORWARD LINK

7.1. General Principles of Transmit Spacetime Processing

In transmit spacetime processing, the signal to be transmitted is combined in time and space before it is radiated by the antennas to encounter the channel. The goal of this operation is to enhance the signal received by the desired user, while minimizing the energy sent toward cochannel users. Spacetime processing makes use of the spatial and temporal signature of the users to differentiate them. It may also be used to pre-equalize the channel, that is, to reduce ISI in the received signal. Multiple antennas can also be used to offer transmit diversity against channel fading.

7.2. Channel Estimation

The major challenge in transmit spacetime processing is the estimation of the forward link channel. Further, for

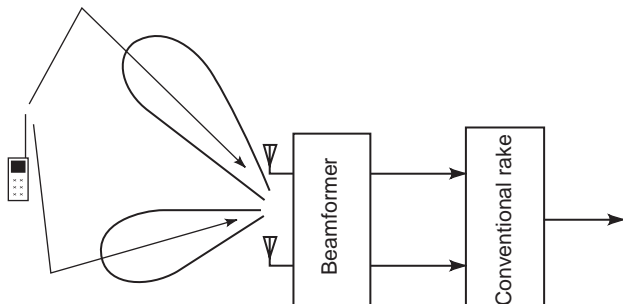


Figure 8. The spacetime rake receiver for CDMA uses a beamformer to spatially separate the signals, followed by a conventional rake.

CCI suppression, we need to estimate the channels of all cochannel users.

7.2.1. Time-Division Duplex Systems. TDD systems use the same frequency for the forward link and the reverse link. Given the reciprocity principle, the forward and reverse link channels should be identical. However, transmit and receive take place in different time slots; hence the channels may differ, depending on the ping-pong period (time duration between receive and transmit phases) and the coherence time of the channel.

7.2.2. Frequency-Division Duplex Systems. In frequency-division duplex (FDD) systems, reverse and forward links operate on different frequencies. In a multipath environment, this can cause the reverse and forward link channels to differ significantly.

Essentially, in a specular channel, the forward and reverse DoAs and times of arrival (ToAs) are the same, but not the path complex amplitudes. A typical strategy consists in identifying the DoAs of the dominant incoming path, then using spatial beamforming in transmit in order to focus energy in these directions while reducing the radiated power in other directions. Adaptive nulls may also be formed in the directions of interfering users. However, this requires the DoAs for the cochannel users to be known.

A direct approach for transmit channel estimation is based on feedback. This approach involves the user estimating the channel from the downlink signal and sending this information back to the transmitter. In the sequel, we assume that the forward channel information is available at the transmitter.

7.2.3. Single-User Minimum Mean-Squared Error. The goal of spacetime processing in transmit is to maximize the signal level received by the desired user from the base station, while minimizing the ISI and CCI to other users. The spacetime beamformer \mathbf{W} is chosen so as to minimize the following MMSE expression

$$\begin{aligned} & \min_{\mathbf{W}} \left(E \|\mathbf{W}^H \mathcal{H}_q^F \mathbf{S}_q(k) - s_q(k-d)\|_2^2 \right. \\ & \left. + \alpha \sum_{k=1, k \neq q}^Q \mathbf{W}^H \mathcal{H}_k^F \mathcal{H}_k^{FH} \mathbf{W} \right) \end{aligned} \quad (25)$$

where α is a parameter that balances the ISI reduction at the reference mobile and the CCI reduction at other mobiles. d is the chosen reconstruction delay. \mathcal{H}_q^F is the block Toeplitz matrix [defined as in Eq. (14)] containing the coefficients of the forward link channel for the desired user. $\mathcal{H}_k^F, k \neq q$, denotes the forward channel matrix for the other users.

7.3. Multiuser Minimum Mean-Squared Error

Assume that Q cochannel users, operating within a given cell, communicate with the same base station. The multiuser MMSE problem involves adjusting Q spacetime beamformers so as to maximize the signal level and minimize the ISI and CCI at each mobile. Note that CCI that

originates from other cells is ignored here. The base communicates with user q through a beamformer \mathbf{W}_q . All beamformers \mathbf{W}_q , $q = 1, \dots, Q$, are jointly estimated by the optimization of the following cost function:

$$\min_{\mathbf{W}_q, q=1, \dots, Q} \sum_{q=1}^Q \left(E \|\mathbf{W}_q^H \mathcal{H}_q^F \mathbf{S}_q(k) - s_q(k-d)\|_2^2 \right. \\ \left. + \alpha \sum_{k=1, k \neq q}^Q \mathbf{W}_k^H \mathcal{H}_q^F \mathcal{H}_q^{FH} \mathbf{W}_k \right) \quad (26)$$

It turns out that the problem above decouples into Q independent quadratic problems, each having the form shown in Eq. (25). The multiuser MMSE problem can therefore be solved without difficulty.

7.4. Spacetime Coding

When the forward channel is unknown or only partially known (in FDD systems), transmit diversity cannot be implemented directly as in TDD systems, even if we have multiple transmit antennas that exhibit low fade correlation. There is an emerging class of techniques that offer transmit diversity in FDD systems by using spacetime channel coding. The diversity gain can then be translated into significant improvements in data rates or BER performance.

The basic approach in spacetime coding is to split the encoded data into multiple datastreams, each of which is modulated and simultaneously transmitted from a different antenna. Different choices of data-to-antenna mapping can be used. All antennas can use the same modulation and carrier frequency. Alternatively, different modulation (symbol waveforms) or symbol delays can be used. Other approaches include use of different carriers (multicarrier techniques) or spreading codes. The received signal is a superposition of the multiple transmitted signals. Channel decoding can be used to recover the data sequence. Since the encoded data arrive over uncorrelated faded branches, diversity gain can be realized.

8. APPLICATIONS OF SPACETIME PROCESSING

We now briefly review existing and emerging applications of spacetime processing that are currently deployed in base stations of cellular networks.

8.1. Switched-Beam Systems

Switched-beam systems (SBSs) are nonadaptive beamforming systems that involve the use of four to eight antennas per sector at the base station. Here the system is presented for receive beamforming, but a similar concept can be used for transmit. The cell usually consists of three sectors that cover a 120° angle each. In each sector, the outputs of the antennas are combined to form a number of beams with predesigned patterns. These fixed beams are obtained through the use of a Butler matrix. In most current cellular standards (including analog FDMA and digital FDMA-TDMA), a sector and a channel-timeslot pair

are assigned to one user only. In order to enhance the communication with this user, the base station examines, through an electronic *sniffer*, the best beam output and switches to it. In some systems, two beams may be picked up and their outputs forwarded to a selection diversity device. Since the base also receives signals from mobile users in surrounding cells, the sniffer should be able to detect the desired signal in the presence of interferers. To minimize the probability of incorrect beam selection, the beam output is validated by a color code that identifies the user. In digital systems, beam selection is performed at baseband, after channel equalization and synchronization.

SBSs provide array gain, which can be traded for an extended cell coverage. The gain brought by SBS is given by $10 \log m$, where m is the number of antennas. SBSs also help combat CCI. However, since the beams have a fixed width, interference suppression can occur only when the desired signal and the interferer fall into different beams. As a result, the performance of such a system is highly dependent on propagation environments and cell loading conditions. The SBS also experiences several losses, such as cusping losses (since there is a 2–3 dB cusp between beams), beam selection loss, mismatch loss in the presence of nonplanar wave fronts, and loss of path diversity.

8.2. Reuse within Cell

Since cellular communication systems are (increasingly) interference-limited, the gain in CCI reduction brought by the use of smart antennas can be traded for an increase in the number of users supported by the network for a given quality of service. In current TDMA standards, this capacity improvement can be obtained through the use of a smaller frequency reuse factor. Hence, the available frequency band is reused more often, and consequently a larger number of carriers are available in each cell.

Assuming a more drastic modification of the system design, the network will support several users in a given frequency channel in the same cell. This is called “reuse within cell” (RWC). RWC assumes these users have sufficiently different spacetime signatures so that the receiver can achieve sufficient signal separation. When the users become too closely aligned in their signatures, spacetime processing can no longer achieve signal recovery, and the users should be handed off to different frequencies or timeslots. As another limitation of RWC, the spacetime signatures (channel coefficients) of each user needs to be acquired with good accuracy. This can be a difficult task when the powers of the different users are not well balanced. Also, the propagation environment plays a major role in determining the complexity of the channel structure. Finally, angle spread, delay spread, and Doppler spread strongly affect the quality of channel estimation. As an additional difficulty, the channel estimation required in forward link spacetime processing is made difficult in FDD systems.

9. SUMMARY

Smart antennas constitute a promising but still emerging technology. Spacetime processing algorithms provide

powerful tools to enhance the overall performance of wireless cellular networks. Improvements, typically by a factor of 2 in cell coverage or capacity, are shown to be possible according to results from field deployments using simple beamforming. Greater improvements can be obtained from some of the more advanced spacetime processing solutions described in this article. The successful integration of spacetime processing techniques will, however, also require a substantial evolution of the current air interfaces. Also, the design of spacetime algorithms must also be application- and environment-specific.

BIBLIOGRAPHY

1. R. A. Monzingo and T. W. Miller, *Introduction to Adaptive Arrays*, Wiley, New York, 1980.
2. D. Johnson and D. Dudgeon, *Array Signal Processing*, Prentice-Hall, Englewood Cliffs, NJ, 1993.
3. J. D. Gibson, ed., *The Mobile Communications Handbook*, CRC Press, Boca Raton, FL, 1993.
4. W. C. Jakes, *Microwave Mobile Communications*, Wiley, New York, 1974.
5. *Proc. 4th Workshop on Smart Antennas in Wireless Mobile Communications*, Center for Telecommunications and Information Systems Laboratory, Stanford Univ., Stanford, CA, 1997.
6. R. S. Kennedy, *Fading Dispersive Communication Channels*, Wiley, New York, 1969.
7. J. G. Proakis, *Digital Communications*, McGraw-Hill, New York, 1989.
8. S. U. H. Qureshi, Adaptive equalization, *Proc. IEEE*, **53**:1349–1387 (1985).
9. S. Haykin, ed., *Blind Deconvolution*, Prentice-Hall, Englewood Cliffs, NJ, 1994.
10. Special issue on blind identification and estimation, *Proc. IEEE*, to be published 1998.
11. M. K. Simon et al., *Spread Spectrum Communications Handbook*, McGraw-Hill, New York, 1994.
12. A. Paulraj and C. B. Papadias, Space-time processing for wireless communications, *IEEE Signal Process. Mag.* **14**(6):49–83 (Nov. 1997).
13. S. U. Pillai, *Array Signal Processing*, Springer-Verlag, New York, 1989.

ANTENNA COMPACT RANGE

W. NEILL KEFAUVER
Lockheed Martin
Denver, Colorado

1. INTRODUCTION

Bringing large antenna measurements indoors has been a very necessary technology since antennas measurement began, and the antenna compact range is one solution.

The father of the compact range is R. C. Johnson, who patented (U.S. 3,302,205) the concept of compact ranges for the measurement in 1967 based on his research at the Air Force's Rome Laboratories [1]. His research centered on testing for radar cross section (RCS), but he also used the technique to evaluate high-gain antennas as well. Compact ranges were further improved in the following decades to solve two major problems in the world of microwave testing: security and environmental control. Generically, the measurements in a specific range are made on an "article," a term used throughout this text. An article can be an antenna, a model including one or more antennas for interactions, or just a model in the case of RCS measurements.

Direct characterization of electrically large articles requires immense outdoor facilities that have high maintenance costs and limited operational time due to weather conditions. The primary types of large articles needing extensive evaluation during the design-and-build stage are antennas for space and structures designed to have low RCS. Neither of these items should be moved outside until it is ready for use. Space antennas are very lightweight and fragile in conventional environments and are often integrated into sophisticated electronics that are very sensitive to contamination and electromagnetic interference. While these antennas can handle the rigors of outer space, the outdoor measurement method simply introduces too high a risk, and case of very high frequencies, has unacceptable propagation variations. The security issues with RCS measurement, along with the cost of building a full-scale operational test article with each design change, would never have allowed outdoor testing as the primary research tool. RCS is mentioned here only because compact ranges for measuring antennas probably would never have been developed without the need to measure the radar cross section.

By 1980 there a fully validated technique with superior accuracy had been developed to measure antennas that eliminated all the problems found in outdoor ranges and in compact ranges: near-field measurements. The primary reason for growth of compact ranges in the 1980s was the absolutely essential need for the compact range in the RCS community, and the gradual acceptance of near-field measurement technology as the compact range could provide direct measurements instantaneously. In this article we will discuss the capabilities that compact ranges provide for the user attempting to perform evaluations of antennas and satellite systems.

2. BASIC PHYSICS

An antenna compact range is designed to do one thing very well, namely, to deliver a collimated wave of microwave fields to a test article. The collimated wave will simulate the far field that the article will see in its final application. The basics of the process are also straightforward, taking a point source antenna with a fairly broad beamwidth and placing it at the focus of an offset reflector, which, due to the surface—usually a section of a paraboloid—will cause all the rays projecting from the focus to cross the plane of the test article simultaneously (see Fig. 1).

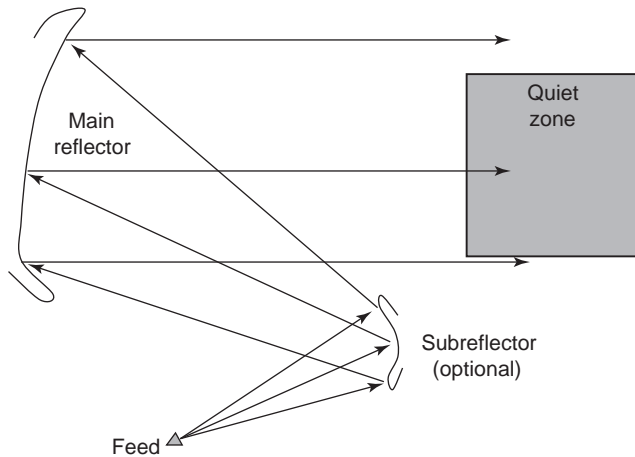


Figure 1. Basic antenna compact range schematic.

In a conventional far-field range this collimation is caused by sheer distance; the standard engineering term for minimum far field distance is $2D^2/\lambda$. This relationship of the diameter enclosing the article to wavelength will result in a phase curvature of 22.5° on an article of diameter D centered in the range between the outside edge and center of the article. Ideally, both the edge and the center on the same plane will see a phase difference of zero. This property arises because a plane wave has no phase curvature, only direction. The obvious advantage of a compact range is that testing at higher frequencies does not require a longer range—a conventional far-field requirement becomes inverse linearly with wavelength. If one wishes to build and test a 4-m aperture at 3 GHz, one would need a 320 m (1050 ft) range; at 36 GHz this distance would increase to 3.84 km (2.4 mi). In contrast, the compact range size for the same measurement is fixed or even slightly smaller because of reduction in edge diffraction for electrically large reflectors. More importantly, this requirement is the minimum to ensure reasonable prediction of pattern, which for many challenging telecommunication requirements utilizing frequency reuse and multiple beams, the standard distance requirement will not yield the high accuracy needed to ensure successful system operation.

2.1. Advantages

Antenna compact ranges have a huge size advantage over conventional outdoor ranges and are impervious to weather conditions. They also have an important advantage over near-field ranges. Compact ranges are significantly larger physically for the same testing requirements—typically 3 times the largest expected test article versus $1\frac{1}{2}$ times for a near-field range. However, the compact range performs a direct measurement that needs little additional processing for comparison of performance requirements, and the near-field range will require extensive data processing. The operator who is trained to take measurements in a far field will see results in an antenna compact range that look very similar to those that would have been obtained from measurements in a conventional range. The tricky

issues arise in separating the range interaction with the measurement. Seemingly endless papers on the design of a compact range to minimize the range interactions have been written [2–6]. For satellite system measurements, the antenna compact range does truly shine because the direct measurement of special system requirements as well as conventional antenna pattern characterization can be performed.

The special system measurements are discussed below and can often have millions of dollars associated with values of less than a decibel. Effective isotropic radiated power (EIRP) is a direct measurement of the satellite's capacity to deliver the required power to the coverage of the antenna pattern. Although each component in the system may have been evaluated to high accuracy in its benchtest, the integrated spacecraft test providing integrated system results is where the engineer can finally know whether the unit will perform as designed. G/T is the reciprocal measurement of spacecraft performance—whether the receiver will deliver the designed sensitivity. The primary concern to be evaluated in the antenna compact range for this measurement is that the noise measurement be accurate; if the noise temperature of the room is not true blackbody-ambient, the final number may be meaningless. Errors can arise from several noise sources, including fluorescent lights and computers. However, for both these measurements, because the full gain of the antenna system is in the link, high accuracies can be obtained with very few measurements.

2.2. Disadvantages

Compact ranges are expensive relative to indoor far-field ranges of similar physical size because the reflector will probably double the cost. This author would say that this is not a disadvantage of the antenna compact range, for several reasons:

1. A compact range should be considered only when the tests to be performed are sufficiently extensive to generate a capital investment and the requirements will not be satisfied by alternative methods. The cost of an equivalent outdoor far-field range of several miles is similar for the infrastructure, but the property maintenance cost will continually increase. The cost for a near-field scanner will be lower, but the throughput can be much lower, depending on the test requirements, and iterative troubleshooting of system problems will typically take much longer because of staff training.
2. Although the compact range can do a wonderful job of testing small articles and low-cost antennas, the engineering requirements will never direct the designer to build such a range. This would be equivalent to using an electron scanning microscope to examine a thumbprint. Yes, the system can do the task, but why would you buy one?
3. Once one has established that the antennas you are testing are too complicated and the requirements too tight to be done using a conventional far-field method, then the antenna compact range is justified.

Having made the decision to build the antenna compact range will solve many of your future problems and has minimal maintenance costs as the most expensive piece of equipment—the reflector—never moves and is far away from any operation activities. One item that is difficult to estimate is the impact of the need to rotate a spacecraft or even an antenna in the gravity field found on Earth. For spacecraft antennas designed for zero gravity, the Earth's gravity field can cause significant deflections that will dynamically change as the article rotates. For some designs the cost would be astronomical—particularly unfurlable (deployable) antennas that cannot support their weight to eliminate this deflection. Some structures, because of the surface tolerances required for proper performance, may not be stable enough even for rigid reflectors to test in an antenna compact range. Additionally, some accommodation must be made in the positioning system to offset any imbalance the test article may put on the positioning structure. This problem does not occur in planar near-field scanners, making them very popular for these special testing issues where only minimal movement of the test article is allowed.

3. APPLICATIONS

The primary applications of compact ranges are to evaluate the microwave performance parameters of full or scaled models of antennas, spacecrafts, and airplanes. The compact range does a very good job of simulating the microwave operational environment to facilitate the measurement of the radar cross section, antenna patterns, and spacecraft radiation parameters.

3.1. Radar Cross Section

The compact range became very popular in the 1970s as an efficient method to measure radar cross section—the microwave signal reflected from an object illuminated by a radar pulse (primarily in the direction of the radar). The compact range brought this testing inside and allowed small-scale models to be tested without weatherization. In addition, the designer now had physical security to develop new designs in order to lower the cross section if desired. As these techniques continued to improve, the ease of performing antenna measurements in the same facilities using the same equipment popularized the use of compact ranges for measuring antennas as well. Ultimately the needs for antenna measurements to be more accurate caused changes in the reflector designs, resulting in some very specialized reflector designs for difficult antenna measurements. Two obvious differences between antenna measurements and RCS measurements are that the antenna (1) receives a signal having only a single path loss (targets have a two path loss) and (2) may cause a very high degree of reflection in the range while working perfectly (very few targets have high-level reflections). Difference 1 would mean that the range should require much less power to perform an accurate measurement; differ-

ence 2 would require the user to check data routinely for range interaction. The primary method is to perform a “range walk.” Range walks are achieved by measurement of many frequencies to reconstruct the time response of the range over several times its physical length or using the hardware gating to remove responses not due to the antenna in the collimated wave.

3.2. Antenna Measurements

The major difference in measuring RCS and antenna patterns from the test setup is that the receiver detector is moved from the feed to the antenna under test. Because of the need to pass signals from the antenna to the receiver, a second model tower may also be required so that a coaxial cable can be run back through the range (RCS towers are usually microwave-“transparent”—cables are not). Additionally, particularly if an entire spacecraft is tested, the tower must have sufficient strength to support a large load. The quiet zone must have much higher performance than a RCS measurement because often the antennas will have shaped patterns with low sidelobes. Erroneously low sidelobes can be measured on an antenna in a range due to taper of the quiet-zone amplitude since the amplitude taper of the antenna aperture is how sidelobes are reduced. The compact range can also cause increased sidelobes due to range interactions. To evaluate these two scenarios, the range operator has three available methods: field probing of the quiet zone using a less directive source, measuring the antenna oriented differently in the quiet zone, or performing a “range walk” where the time-domain response of the range is imaged using a frequency chirp (the Fast Fourier transform (FFT) of the frequency chirp will produce the time-domain response). “Range walk” can also be implemented directly in the time domain at a fixed frequency using hardware gating to determine where in the range the pulses are being generated by reflections delaying the signal.

3.2.1. Compensation From Field Probing. The best approach to minimize risk of pattern measurement error from quiet-zone anomalies is to gather an extensive set of field probe data during certification of the range as a required baseline for operation of the range. If this set of data is not established as an initial requirement, it will be very difficult to convince any user of the need for the data since the contributions will often be hidden below the measurement envelope. Ideally these data will be complex phasor measurements of the field over the entire plane with sufficient density to facilitate a reasonable prediction of the fields on the test article. Ultimately these data can be applied to the antenna pattern to show the level of purity of the quiet zone relative to the antenna pattern.

The method employed for this compensation is to use quiet-zone data as near-field data. If the envelope of the two-dimensional FFT of the field probe exceeds the expected envelope of the antenna pattern, the measurement will be flawed. The transform of the field probe gives the wavenumber distribution of the quiet-zone fields; the wavenumber converts to angular information using the

direct relationships $k_x/k_0 = \cos \phi \sin \theta$, $k_y/k_0 = \sin \phi \sin \theta$, and $k_z/k_0 = \cos \theta$. The contribution of compact range errors to the first sidelobe measurement is more subtle. Because a perfect plane-wave circular aperture will transform to a -17 -dB sidelobe, the envelope test is not sufficient. What needs to be evaluated is the convolution response of the two patterns. A first-order approach is to apply the measured amplitude and phase-taper to the predicted antenna aperture and bound the contribution. Alternately, the pattern from integrating the quiet-zone measurements directly should be the ideal constant aperture mentioned above with a -17 -dB first sidelobe. The discrepancy of the first sidelobe from theoretical can be used to predict the threshold of the first sidelobe measurement error. If the sidelobe is off by 1 dB, then the quiet-zone error is -37 dB for the first sidelobe due to amplitude taper. The quiet zone integrated in this case should be the size of the antenna aperture being tested, not the nominal size of the range quiet zone. This type of error evaluation obviously requires very detailed and accurate knowledge of the quiet zone and will also require gathering at least two planes of data to fully encompass the test article.

3.2.2. Compensation for Polarization. The other measurement best performed immediately prior to measuring the test article is an evaluation of the range polarization symmetry using a purely polarized source. Since compact ranges are of an inherently asymmetric geometry, there should be no expectation of the vertical and horizontal polarization would be identical. If a circularly polarized source antenna is used in the compact range, the issue becomes even more complicated: (1) the beam off the reflector will be squinted by the geometry, (2) the cross-polarized horn will be squinted in the opposite direction, and (3) the normalization factor between the two measurements must be determined, which may be complicated by drift for the time it takes to reconfigure the feed. An alternative method is to measure the complete polarization matrix to allow use of lower polarization purity with post-processing of the measured data. This technique allows for accurate measurement of wideband antennas using simple source; if a dual-polarized source horn is used, then the pattern can be collected and compensated by a simple inversion of the 2×2 polarization matrix (P^{-1}) and the measured two-element vector E_{aut}^m .

$$E_{\text{aut}} = P^{-1} * E_{\text{aut}}^m$$

The polarization matrix is typically measured by using a linearly polarized gain standard that must have the same response in both orientations and is expected to be an almost pure polarization device. If the gain standard is clocked 90° in the chamber, the resulting responses should be identical. The measured response then can be normalized by inverting the matrix, so that the antenna can be rotated to any polarization orientation in the chamber and the same maximum field response will be measured using the P -matrix compensation if the orthogonal polarizations define an ellipse.

Obviously, even this compensation method will not eliminate the polarization errors, but it is good for establishing a lower bound for the range accuracy. If measurement of the range as described is performed, gathering at least the diagonal points, then the limit on measuring the axial ratio of an antenna or equivalently the cross-polarization of a linear antenna can be established. If the test article is significantly larger than the gain standard, this bound still applies, but the error will probably be greater because data for an increasing quiet-zone area are being gathered. The quiet-zone data mentioned above help in determining how significant the additional contributions are off axis. The compensation method described above is still valid on axis for validating measurement accuracy because fundamentally the fields of an antenna are independent of its rotation around the z axis of the range. Using the field probe data and the technique described by Rose et al. [9], additional improvement of the measurements can be achieved.

3.3. System Integration

In system integration, a compact range often is more useful than other types of ranges. The test article can effectively be flown through its operational environment with all the systems integrated, and direct evaluation of performance parameters can be evaluated instantaneously. The instantaneous evaluation can sometimes significantly reduce total test duration and, if the accuracy is acceptable, greatly reduce the amount of postprocessing analysis required to certify performance of a system. One measurement requirement in which this capability is advantageous is in measuring active arrays. One can program the array to track the positioner on a peak or a null and get a continuous response, whereas a near-field range would have to do this measurement by interpolation and require full collections instead of single-point checks.

4. REFLECTOR TYPES

Design of reflectors have become more sophisticated over the years as modeling tools have improved, but the basic principle is unchanged—how to get the maximum performance in a quiet zone for a sufficiently large reflector. This section addresses the solutions; the more complicated the design, the more specialized the application—as is the case for most test tools, the more the performance is optimized for one attribute, the less capable the design will be for general use. A range optimized for testing low cross-polarization will have problems measuring low frequency, a range optimized for measuring radar cross section will not perform antenna measurements nearly as well, and a range optimized for testing satellite systems will not facilitate testing of antenna components or radar cross section.

4.1. Prime Focus

Prime focus reflectors as shown in Fig. 2 are the most common compact range reflectors and can be ordered from several vendors with small variations in design. The major

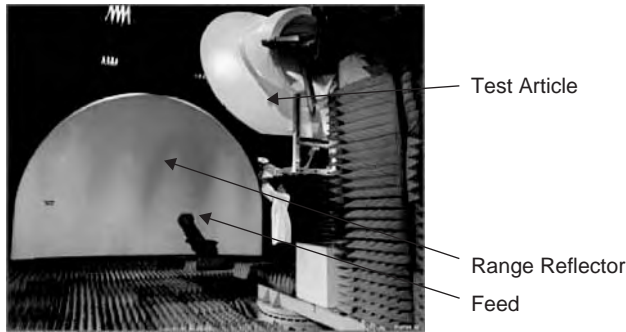


Figure 2. Example of a prime focus reflector. (Courtesy of Lockheed Martin, Sunnyvale, CA operations.)

problem with a prime focus reflector is the cross-polarization created by the reflection of the feed pattern off the reflector. Many antenna requirements in the telecommunications industry require quiet-zone cross-polarization (XPOL) to be limited to less than -40 dB to accurately measure the ability of the test antenna to perform polarization reuse. *Polarization reuse* is where the antenna can receive and separate two signals whose only distinguishing characteristic is polarization. The minimal XPOL level needed to maintain acceptable bit error rates is typically 30 dB. For a prime focus reflector the geometry will generate XPOL for even a pure linearly polarized feed, due to the polarization rotation from reflecting off the doubly curved surface. While the cross-polarization is symmetric across the reflector's axis of symmetry and will tend to cancel out for applications where the test article is similarly aligned [3], for a complex multibeam spacecraft antenna this situation is seldom the case. Cross-polarization of the quiet zone can be decreased by increasing the focal length of the reflector—unfortunately the directivity of the feed horn will also have to increase until eventually the designers will find that they need a second reflector to collimate the feed sufficiently to obtain the needed focal length of the main reflector. This limit in the prime focus design is the starting point for a dual-reflector design. Once a second reflector is introduced into the system, the two reflectors can be designed with intentional cross-polarization cancellation [7].

4.2. Dual Reflector

The photo in Fig. 3 shows a typical dual-reflector compact range (although extremely large, 20 m in diameter). In the foreground is the pylon where the antenna or RCS target can be mounted, at the bottom of the photo is the back of the subreflector, and in front of the subreflector is an array of feeds to cover various frequency bands. The center of the photo is the large rolled edge main reflector constructed from many panels.

The first obvious reason for a dual-reflector system is the reduction in overall range size to meet a requirement within a minimal physical footprint [8]. While the cross-polarization of a range can be reduced by increasing the focal length, the feed will ultimately end up on the other side of the test article—an unacceptable geometry,

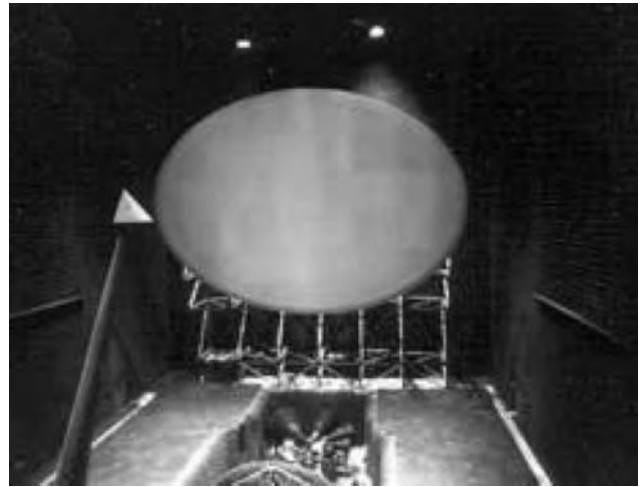


Figure 3. Example of a dual-reflector system. (Courtesy of Composite Optics Incorporated.)

resulting in increasing the size of the chamber, resulting in higher costs to maintain the facility. The alternative is to introduce a subreflector, which would move the feed back toward the main reflector, and if several additional design constraints are imposed, the primary sources of compact range cross-polarization will also be reduced dramatically. The subreflector can be Cassegrain or Gregorian; ranges have been created using both geometries. The initial advantage of the Gregorian configuration is that the subreflector is beyond the focal point of the main reflector and can be designed to be further out of the quiet zone. Classical examples of this design are the DASA (now the European Aeronautic Defense and Space Company) compact ranges built for several companies, such as Loral, SPAR Canada, Astrium, and RCA. In the DASA range the geometry is set horizontally rather than vertically, allowing the overall range height to be only slightly greater than that of the main reflector. In most compact ranges the subreflector and feed are located below the main reflector, resulting in a much taller facility for the same-size reflector.

4.3. Other Reflector Types

Other types of systems have been developed for specialized measurement applications, including multiple subreflector systems and modified single-cylindrical-reflector designs; these alternate designs arise from various needs. MI-Technologies produces a cylindrical reflector because it maximizes the quiet-zone area with minimal installation and manufacturing difficulty, while XPOL contamination is reduced by postprocessing [9]. The original compact range design by Scientific Atlanta combined a parabolic cylinder with a rolled edge parabolic dish, these can be found at all facilities in the United States. Ultimately, the end user has to determine whether the design needs to be customized for the article testing requirements or whether a general-purpose system is sufficient. With the advent of modern processing capabilities, many sources of measurement errors can be removed in the processing without

designing them out of the original range. With compact ranges in particular, this problem always arises because a range that did a splendid job of testing one article may be inadequate for the next article because of changes in size, frequency, pattern type, and other variables that cannot be anticipated in the original design. The problem is simple, the compact range is ultimately an antenna, and if the antenna you are testing is optimized for performance to specific requirements, quite often the compact range is not. That said, the compact range will give you very acceptable results on a broad range of designs without any additional data analysis; this feature alone can drastically reduce the time from prototype to final design. The final design can then be carefully evaluated at an alternative range to verify that the range does not affect the measured performance requirements.

4.4. Edge Treatments

The edge treatments for compact ranges are used to ease the boundary conditions of conventional reflector designs; for the purposes of packaging and weight, the conventional reflector designer may not have to worry about sharp edge transitions that represent less than 0.01% of the total aperture power. In a compact range these discontinuities are deliberately reduced with edge treatments because they can cause elevated sidelobes. The three common solutions in order of preference in common use are serrated, blended, and absorber [2,4]. Serrated is the most popular because of the ease of implementation; a technician can easily stamp out a series of triangles to place about the reflector edge in a day with a brief description of the desired sizes. The blended edge treatment is difficult because you are trying to force a doubly curved surface to be continuous as you change it from concave to convex without causing significant discontinuities through at least two derivatives. Performing this operation accurately requires elaborate sheetmetal forming capabilities with only marginal improvements over serrations in many test applications—if the compact range aperture is always going to be larger than 10 wavelengths, the extra work cannot be justified. The absorber treatment requires consistent control of the reflectivity of the dielectric materials that you are using and may result in failure if the materials used are not tightly controlled. Realistically, most absorber manufacturers have problems in maintaining precise controls on the material's dielectric properties. Also, lossy materials do not have effectively frequency-independent behavior as does metal, which render the designs even less stable. In addition, absorber materials are often fragile, which means that the range may require frequent repair with materials that may not be equivalent to the originals.

5. ERROR SOURCES

Error sources in the compact range arise from several areas. There is an emerging method utilizing the generic ANSI Z-540/ISO25 standard that is gaining acceptance for quantification of these areas for RCS. One can safely assume that if the range is acceptable for RCS using this

methodology, it will also be able to test antennas of similar size to a normal accuracy. The major issue in determining the accuracy of the compact range relative to other measurement methods is the need to know the limits of the reflector's collimation ability. The basic tool for evaluating this quantity is the field probe (which is also used in far field range certification). The field probe simply introduces a low-gain antenna, although still having a good front:back ratio, in the "quiet" zone where the test article is to be placed after range evaluation. For a conventional far-field range, the ripples in the "quiet" zone are typically due to wall reflections for indoor ranges or ground reflections for outdoor ranges. In a compact range these ripples will typically be caused by the reflector edge diffraction; the radiation from the feedpoint and the subreflector, if used, will also cause ripples. Ripples from the feed and subreflector can usually be time-gated with modern instrumentation. However, the reflector diffraction cannot be gated and usually serves as the lower limit frequency for a particular reflector.

5.1. Reflector Surface

The limit for the ultimate high frequency of a reflector is typically the precision of the reflector surface. Present-day manufacturers will certify surface tolerances to 0.1 mm (0.004 in.) RMS (root mean squared) or less for reflectors up to 10 m (30 feet)—this surface corresponds to a loss of 0.1 dB at 36 GHz. The more important issue is how these errors will manifest themselves in the pattern of a high-performance antenna. The RMS valuation is supposed to be coupled to a Gaussian distribution of surface errors. If the reflector is built from multiple panels (all large reflectors are due to transportation and manufacturing issues), the quiet zone may have a significant systematic error due to the alignment of the panels. The misalignment will cause errors in the pointing of the antenna and feed orientation. The techniques of photogrammetry and automated triangulation by theodolites are used to minimize this contribution to range errors. Likewise, a correlated machining error could cause a false sidelobe in the antenna pattern; even a properly built reflector will produce sidelobes due to the edge transitions. In most instances these sidelobes can be pinpointed by using a secondary test position in the compact range. Range induced sidelobes will move as a result of change in the chamber orientation, whereas the true antenna pattern should be independent of the chamber orientation. Many of the processing techniques developed for RCS analysis and near-field measurements have applications in isolating quiet-zone errors in the antenna measurements, and with a proper understanding of the source can sometimes allow the measurements to be accurately compensated.

5.2. Feed Pattern

The feed pattern will significantly affect the measurement of several antenna parameters: polarization, gain, and sidelobe envelope. The feed controls the taper of the quiet-zone fields, and the designer has to choose between range ripple due to edge illumination and edge taper due to feed directivity. This problem is equivalent to Gibb's

phenomenon in communication theory. The dangerous part of this problem is that it can deceptively make an antenna look better than it really is by reducing the edge illumination of the test article. Additionally, because it is a first-order effect, it can be isolated only by large lateral displacement. Typically, if the error is significant, the article cannot be moved a large amount laterally because it will then be outside the defined quiet zone. Location of the feed can also be problematic, as most feeds are corrugated waveguide horns used to minimize cross-polarization and will not maintain a stable phase center over the full frequency band of operation. All these effects are easily isolated by field probing, but depending on the test article, the pattern may be much more severely affected than obvious from first glance at the quiet-zone data. The issue is that the observed range response is the convolution of the quiet zone with the antenna's pattern. For a low-gain antenna, this problem is negligible because the quiet zone is almost a Dirac function relative to the pattern variation of the test article. The range collimates virtually all the power in one direction, yielding a spatial impulse response, and the test article has an insufficient beamwidth to be affected by the angular width of the spatial impulse versus that of a Dirac function. Once the test article approaches the size of the range, the correlated function will no longer be swamped by the beamwidth of the test article and the pattern will begin to show errors due to the process of integrating the compact range fields by the large-aperture antenna. The obvious result is that the higher the performance the antenna, the higher the quality of the compact range that is needed to measure it. This problem is to determine what the various multiple reflector compact ranges were designed to solve. For example, by changing from a point source to an additional source aperture, the polarization and taper of the quiet zone could be improved. The trade off when this solution is implemented is that the subreflector size now becomes the fundamental limit to the lowest usable frequency for the compact range.

5.3. Multipath

Most compact range multipath arises from three sources: chamber wall reflections, direct-feed radiation, and reflector diffraction. Chamber wall reflections are minimized by anechoic material. Since the reflector collimates the signal, the sidewalls are treated uniformly, unlike the case for a rectangular range, where the sidewall absorber is thicker in the area of specular reflection. The backwall is treated just like a conventional range, where the thickness of the absorber is about a wavelength at the lowest test frequency. The direct-feed radiation can typically be time-gated by either hardware or software because of the significant lead in arrival time. The diffraction of the reflector is usually the limiter on range operation because the arrival time is almost simultaneous with the plane wave from the reflector, and it contaminates the quiet-zone polarization and causes amplitude and phase ripple; hence the emphasis area of modeling the diffraction and synthesizing of reflector designs to reduce this effect.

5.4. Test Article Interaction

One of the most important measurement issues to verify when using an antenna compact range for measurements is the interaction with the test article. When calibrating a range with a gain standard, the article is often not in the facility or is oriented away from the direction in which it will be characterized. In a conventional far field the interaction level will be minimal as a result of the path loss associated with secondary bounces. In a compact range, however, the path loss is minimal so that a highly directive test article can reflect a significant signal level into the feed system, leading to a very rapidly varying standing wave in the chamber due to the error signal traversing the range 3 times to once for the calibrated signal. The behavior is similar to the interaction between the feed and the subreflector commonly addressed by a scattering cone or similar device to eliminate the standing wave. Several solutions can be taken to avoid this problem, such as absorber baffles about the feed, gating by software or hardware, and repeating measurements at multiple locations in the chamber. The most troubling issue with this error is that it appears only when the test article is being measured and is highly sensitive to the orientation of the article. If the test article has flat surfaces, such as those of a phased array or a spacecraft, or if the article is a large reflector, the issue must be evaluated. Typically, the expected level of the contaminant can be found through the classical "range walk" as the interaction impulse is beyond the length of the facility.

6. SPECIALIZED TESTING REQUIREMENTS

Particular test articles require specific facility equipment; in particular, antenna compact ranges are often pulsed systems employed to minimize the chamber multipath. The receivers used with antenna compact ranges must usually be frequency-agile to facilitate rapid data acquisition and also enhance or replace the hardware pulsing capability. Depending on the type of data results desired, extensive processing of the data may sometimes need to be performed, and depending on the type of system and engineering needs, the facility may require a high degree of shielding.

6.1. Pulsed Systems

Pulsed systems arise from the radar world, where the operator, when operating a monostatic radar, transmits a pulse and then switches to the receiver front end to observe reflections downrange from objects. The antenna compact range can be operated the same way and quickly eliminates signals significantly delayed in time in the range such as the backlobe of the feed or diffraction from the subreflector, as these signals will arrive significantly ahead of the main reflector's collimated wave. In a typical compact range this delay will be many nanoseconds whereas the risetime of the antenna under test will be almost instantaneous. There are two obvious drawbacks to a pulsed system: (1) the lower the duty cycle, the lower the system dynamic range; and (2) for large test articles, it is

possible to have a pulse smaller than the risetime on the article because of the limited bandwidth. Overall, although pulsing is an excellent tool to help minimize range errors in measurements, especially if the range is already configured to perform RCS measurements as well, there are other ways to accomplish the same result without these tradeoffs.

6.2. Frequency-Agile Receivers

With the advent of the Agilent 8510/8530, MI-Technologies 1797 and similar receivers using frequency-agile sources, the user now has the capability to take a virtually unlimited number of frequencies at each position as the unit is rotated in the range with virtually no additional time overhead for testing. The advantage to these receivers is that the dynamic range limitation of a pulsed system is eliminated and instead, the data can be carefully evaluated postacquisition for range/antenna-generated time-domain pulses. The major problem with these systems is the tendency to accumulate large blocks of data that can be processed only by extensive computational tools. As the computers continue to improve, this problem has been increasingly eliminated—for instance, in 1985, when this type of processing was required, one often would need a dedicated mainframe, whereas in 2003 the same processing activity using general application software was reduced from hours to minutes, and the asset cost is now negligible. The advantage of this type of system is that one can achieve high-quality and high-quantity measurements using a PC, an HPIB (Hewlett-Packard interface bus) card, a network analyzer, and a commercial positioner system in an existing range. The increased capabilities have had two impacts on antenna measurements—engineers routinely asking for more data and less investment in new infrastructure other than compact ranges and near-field ranges. The outdoor direct measurement has been abandoned because of cost and the limited quality of the measurement and this work has moved indoors.

6.3. Extensive Postprocessing

Antenna compact ranges are fundamentally limited in their polarization symmetry, which has led to postprocessing techniques of varying degrees of sophistication. Since the reflector is offset by design and therefore asymmetric relative to the feed, regardless of the F/D ratio, there will be some residual imbalance in the quiet zone, whether it lies in the cross-polarization or the amplitude taper as the unit or feed polarization is rotated. With sufficient knowledge of the quiet zone, these errors can be corrected to the first order in much the same way as the imperfections of the network analyzer testset are calibrated out.

The simplest level of calibration is to take the quasi-static approach to the quiet zone and assume that measurement at a given point represents the response of the quiet zone. The operator can create a 2×2 matrix of points to establish whether the measured response was using a pure polarization source such as a standard-gain horn, with matrix components of HH , HV , VH , and VV

responses, where H is horizontal and V is vertical orientations of the polarization standard. Even if one were not to compensate the data, this measurement should be taken to establish error bounds. If the matrix is inverted, then the bias can be removed from the data. Obviously, this technique can be expanded to include higher-order terms in the quiet zone with additional measurements increasing the accuracy of the compensation method. The standard-gain horn can also be replaced with a more symmetric probe to increase the accuracy of matrix measurements. Ultimately, the limit to this approach is similar to the near-field probe compensation—you can consistently measure the quiet zone to only a finite accuracy, and the higher the order of compensation, the less stable.

6.4. Shielding

Shielding of the range can be particularly important if the testing is done using spacecraft receivers, which are very sensitive and may even be damaged by ground-based signals. Typically there risk is greater involved in getting stray signals in the measurement that complicate the analysis of data. Shielding is accomplished using the standard techniques from the electromagnetic compatibility community of placing the test article in a Faraday cage (welded steel enclosure) to isolate it from external sources and then additionally lining the range with absorber material to reduce reflections. Using this technique, the stray signal levels can be reduced by 100 dB, although quite often the test instrumentation will also need to be removed from the cage to achieve these levels.

7. CONCLUSIONS

The antenna compact range is a very useful tool in the science of evaluating antenna performance. Careful development of this technology has virtually eliminated the need for outdoor testing and lowered the cost and risk of testing fragile spacecraft antennas. The capabilities of range reflectors rapidly matured in the late 1980s to facilitate very clean direct measurements of antennas with minimal effort in compensating the range errors. The chief technology competitor to the antenna compact range is the near-field scanner, which requires much more data processing as well as a much more detailed working knowledge of antenna theory since the measured data do not correspond directly to the needed far-field pattern. The antenna compact range is a very cost-effective tool to evaluate antennas with modest performance requirements. For antennas with extremely low cross-polarization and sidelobe performance requirements, the technology becomes limited since the test antenna may outperform the range.

BIBLIOGRAPHY

1. R. C. Johnson, *Antenna Range for Providing a Plane Wave for Antenna Measurements*, U.S. Patent 3, 302, 205 (Jan. 31, 1967).

2. S. Brumley, Low frequency operation, design and limitations of compact range reflector, paper presented at 16th Annual Antenna Measurement Techniques Association, Oct. 3, 1994.
3. D. W. Hess, Cross-polarized pattern measurements on point source compact ranges, paper presented at 16th Annual Antenna Measurement Techniques Association, Oct. 3, 1994.
4. T.-H. Lee, Performance trade-off between serrated edge and blended edge compact range reflectors, *IEEE Trans. Anten. Propag.* **44**(1) (Jan. 1996).
5. D. A. Leatherwood and E. B. Joy, Range-field plane wave model determined from spherical probing data, paper presented at 19th Annual Antenna Measurement Techniques Association, Nov. 17, 1997.
6. J. R. Newhouse et al., Helendale measurement facility uncertainty analysis, paper presented at 23rd Annual Antenna Measurement Techniques Association, Oct. 21, 2001.
7. R. A. Shore, A simple derivation of the basic design equation for offset dual reflector antennas with rotational symmetry and zero cross polarization, *IEEE Trans. Anten. Propag.* **AP-33**(1):114–116 (Jan. 1985).
8. C. W. I. Pistorius et al., Dual chamber Gregorian subreflector system, *IEEE Trans. Anten. Propag.* **37**(3):305–313 (March 1987).
9. C. Rose et al., High accuracy cross-polarization measurements using a single reflector compact range, available online at *MI-Technologies.com*.

ANTENNA FEEDS

TREVOR S. BIRD
CSIRO
Sydney, Australia

1. INTRODUCTION

1.1. Definition and General Description

According to the *Macquarie Dictionary*, a “Feed” is a “Feeding mechanism.” The term “antenna feeds” describes many types of antennas in common use. Feeds are a means of supplying energy to (or receiving energy from) a “secondary antenna,” such as a reflector, lens, or beam waveguide, via a transmission line or waveguide. Hence, an antenna feed is often referred to as a “primary feed.” Everyday applications of antennas with feeds include satellite communications, radar, radio telescopes, deep-space probes, and terrestrial microwave and millimeter-wave radiolinks. Some examples are shown in Figs. 1 and 2. Depending on the application, secondary antennas can be designed to produce beams that are highly directional to minimize the effects of interference and noise or shaped to cover a specific region or angular segment. For example, shaped beams allow reuse of the frequency spectrum in another region as in the case of satellite coverage on the Earth’s surface. In other applications, such as broadcasting, secondary antennas and feeds can be used to produce beams tailored to suit the demographics around the



(a)



(b)



(c)

Figure 1. Some applications of feed antennas: (a) 64-m radio telescope at Parkes, Australia; (b) three 4.5-m offset-fed reflector multibeam Earth stations at SES-ASTRA, Luxembourg, give over 110° coverage of the geostationary satellite arc; (c) 0.9-m spherical Luneburg lens; (d) shaped-beam satellite antenna; (e) omnidirectional reflector antenna.

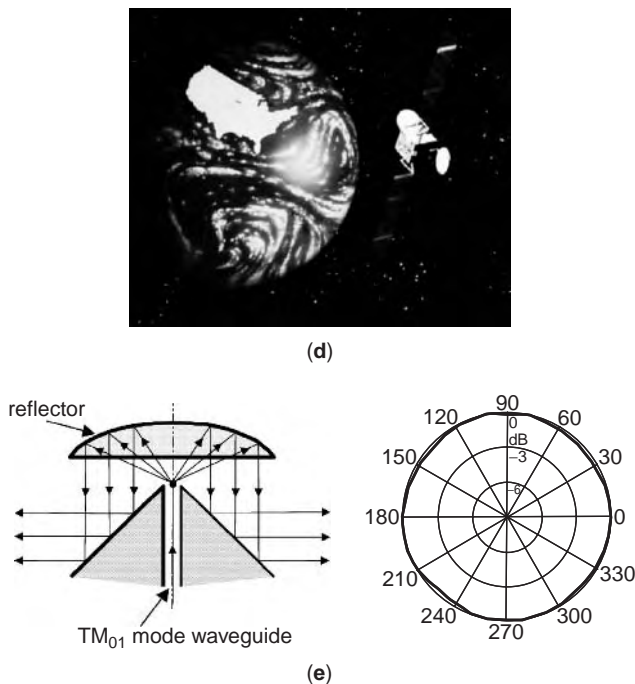


Figure 1. (Continued).

transmitter. The secondary antenna can be used to illuminate another device such as in a beam waveguide system for a reflector or a particle accelerator.

Feed antennas come in many different shapes and sizes, ranging from simple dipoles and waveguides to horns and printed antennas such as microstrip patches, arrays, and traveling-wave antennas. The choice of feed in any given situation is often a complex decision and depends on the type of application and secondary antenna. Factors to be considered when selecting a feed antenna include the frequency of operation, bandwidth, polarization requirements, impedance properties, the transmission line connecting to the feed, and mechanical aspects such as the size, volume and weight, available materials, and cost.

Secondary antennas are typically capable of extremely wide bandwidth performance and are, in practice, severely restricted by the bandwidth limitations of the feed antenna and its associated network, the feed system. There have been significant advances in improving the performance of feed systems, especially in regard to wideband and multiband operation.

The most common type of secondary antenna is the parabolic reflector (Fig. 2a). This has a point focus and, when illuminated by a feed emitting a spherical wave, it produces a narrow pencil beam. Other secondary antennas are cylindrical or spherical reflectors (Fig. 2b), which require a line-source feed to produce a pencil beam, lenses (Figs. 1c and 2c), and reflectarrays (Fig. 2d). Reflectarrays combine the techniques of reflectors and printed circuit antennas. A standard reflectarray consists of an array of microstrip patches or dipoles printed on a thin dielectric substrate. The elements of the printed array are suitably phased to convert a spherical wave from a conventional

feed into a plane wave. The advantage is that the antenna is planar, has low volume, and is potentially lightweight. Phasing of the printed array is achieved with patches that have different size, different length delay lines, or varying angles of rotation.

In some applications, the aim is to shape the secondary radiation pattern and the role of the antenna feed is simply to give the correct illumination. For example, an array feed or a corrugated horn can be used to illuminate a shaped reflector system for a satellite system that will produce a shaped secondary pattern to cover selected Earth coverage regions (see Fig. 1d). Another application is a mobile base station antenna that requires an omnidirectional pattern. A suitable feed antenna and a shaped reflector are able to produce a 360° coverage as shown in Fig. 1e. Secondary antennas with elliptical beamshapes can be used to maximize the radiated field intensity within an angular region that has different beamwidths in two orthogonal planes. Such antennas are used in radar, Earth stations, and satellite applications to provide an elliptical footprint on Earth.

1.2. Historical Perspective

The first feed antennas date back to the pioneering work of Heinrich Hertz during his demonstration of the consequences of James Clerk Maxwell's equations, which were published a decade earlier. In 1888, Hertz employed a half-wavelength dipole in front of a cylindrical parabolic reflector to demonstrate the opticslike properties of electromagnetic waves at about 60 cm [1]. Other feeds and antennas now used as basic feeds were discovered prior to 1900 by Lodge (circular waveguide), Bose (dielectric rod and pyramidal horn), and Rayleigh [2]. From the early 1900s to the 1930s, little work on feeds appears to have occurred, mainly because of the outstanding success of long-range low-frequency communications where directly radiating antennas were the natural choice.

The rising interest in microwave techniques in the 1930s resulted in major developments in antenna feeds. The then new applications using ultrahigh frequencies and microwaves, such as radar and point-to-point communications, required many new antennas, and reflectors, in particular, became extremely important because of their versatility, effectiveness, and practicability. In short, feeds became an area of significant interest and research. The MIT Radiation Laboratory series of books published in the late 1940s, and especially the volume edited by Silver [3], did much to establish the basis of reflector and feed antenna design. It is significant that Silver's book was the primary reference for a generation of feed designers and is still a great source of information. With radar, and the deployment of terrestrial microwave systems for communications, reflectors came into common use. These used simple waveguides or horns, rear-radiating feeds [4] or arrays such as the Yagi-Uda or logperiodic arrays [5]. The creation of new applications in the 1950s, such as radio astronomy and satellite communications, added new dimensions to feed design with requirements for low noise and low cross-polarization. These demands resulted in new feed antennas, including the dual-mode Potter horn

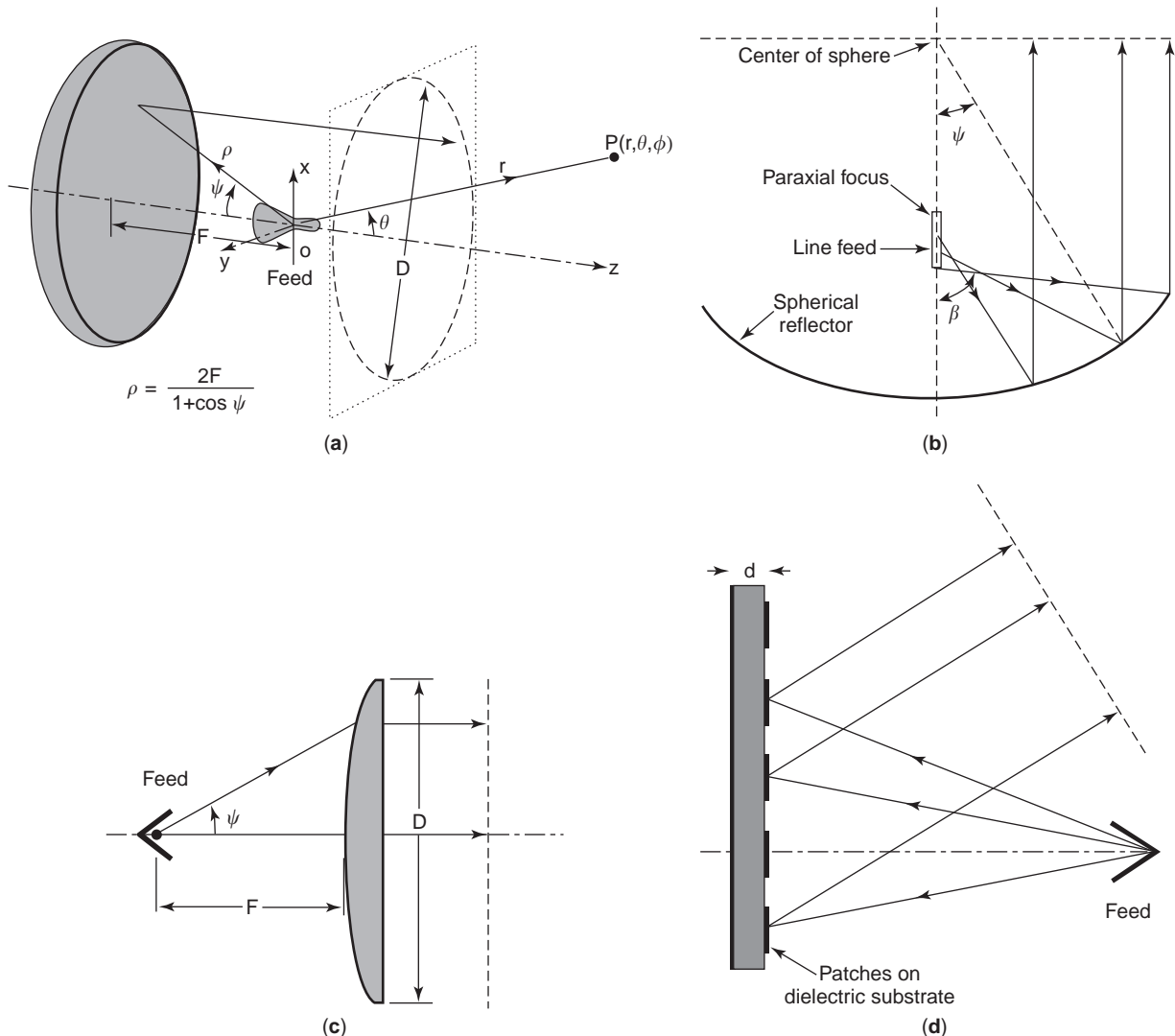


Figure 2. Examples of secondary antennas: (a) parabolic reflector; (b) spherical reflector; (c) two-dimensional lens; (d) reflectarray.

[6], the corrugated horn (see Thomas [7] for an historical summary of this important feed), multimode horns [8], stepped horns, and dielectric-lined feeds. Many of the most influential papers on horns written prior to 1976 have been collected by Love [9], and a more recent survey is given by Olver et al. [10]. Array feeds were investigated first in the early 1960s [11] and over the next two decades were adopted in radar and satellite communications for producing scanned and shaped beams with reflectors. In the 1980s and early 1990s, compact corrugated horns covering octave bandwidths were developed, while easy to manufacture, high-performance feeds, such as axially corrugated horns, were widely adopted. Major advances in electromagnetic modeling have allowed the development of horns whose performance can be tailored by computer optimization. In more recent years, improvements in the theoretical understanding of printed antennas has resulted in microstrip and printed slot or Vivaldi arrays being used as feeds.

1.3. Design of Feeds

A feed antenna should be designed to suit the secondary antenna to obtain the best overall performance. This is usually expressed in terms of the signal level, whether received or transmitted, immunity to noise or interference, and frequency of operation. There are essentially two ways of designing the overall antenna. The first way, called the *transmit mode of operation*, specifies the combined radiation pattern of the feed and the secondary antenna that meets the system requirements when both are transmitting signals. Figure 2a depicts a parabolic¹ reflector operating in the transmit mode. The electromagnetic field radiated by the feed is called the *primary field* and the radiation pattern, the *primary pattern*. The

¹This refers to a paraboloid or part of a paraboloidal surface as for an offset-fed parabolic reflector.

illuminated antenna is the secondary antenna and the associated radiated field is the secondary field.

In the second approach, called the *receive mode of operation*, the antenna feed is designed to match the fields produced in the secondary antenna due to a specific illumination; for example, plane-wave illumination is used for a directive beam. In most common situations the two approaches are equivalent (due to the principle of reciprocity [5]) and are often used interchangeably. If the fields are matched in the focal region of a reflector or lens, this is called focal plane matching. Optimum antenna gain and minimum cross-polarization are achieved simultaneously if the feed aperture field (represented by the complex vector \mathbf{E}_a) is conjugate matched to the focal field of the reflector or lens (\mathbf{E}_f). This is expressed approximately by

$$\mathbf{E}_{\text{acp}} \approx \mathbf{E}_{\text{fcp}}^*, \quad \mathbf{E}_{\text{axp}} \approx -\mathbf{E}_{\text{fxp}}^* \quad (1)$$

where the subscripts cp and xp denote the copolar and cross-polar components of the fields and the asterisk indicates the complex conjugate. This approach is applicable to single feeds or arrays in the focal region.

The design of the feed antenna's primary or aperture field depends on the geometry of the secondary antenna. For example, the geometry of a symmetric parabolic reflector is defined simply by its diameter D and its focal length F (see Fig. 2a). However, in the symmetric case there is usually some blockage by the feed and the supporting struts close to where the energy is strongest. The offset parabolic reflector geometry is slightly more complex, but the advantage is the ability to design the antenna to avoid blockage by the feed or to move this blockage toward a region on the aperture where the field is weak. For a given F/D ratio, the half-subtended angle at the feed is given by

$$\theta_c = \arctan\left(\frac{8F/D}{16(F/D)^2 - 1}\right) \quad (2)$$

In typical reflectors, F/D has a value from 0.6 to 0.3, which corresponds to half-subtended angles from $\sim 45^\circ$ to 80° . Particular applications require specific feed illuminations and the choice of illumination for the secondary antenna is a compromise between gain, sidelobes, beamwidth, and spillover, which are determined by the characteristics of the primary feed antenna. We return to this compromise at the end of the next section.

1.4. Characteristics of Primary Feed Antennas

It is usual to describe the performance of an antenna in terms of its far-field radiation characteristics and its terminal impedance or reflection coefficient into a specified transmission line. Some important terms used to describe feed antennas are

1. Radiation pattern
2. Gain
3. Phase center

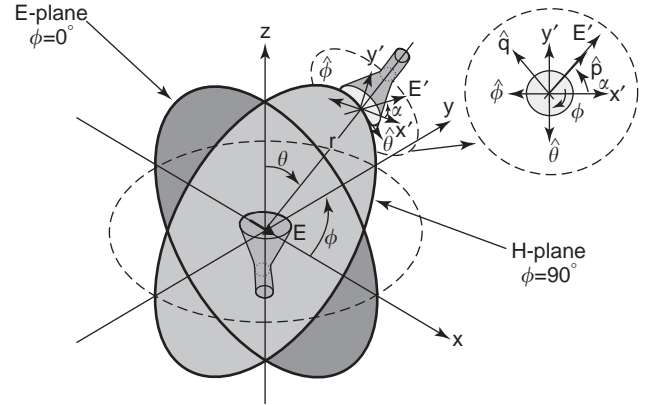


Figure 3. Geometry for radiated fields from feeds.

4. Polarization
5. Input match
6. Bandwidth
7. Spillover
8. Edge illumination and edge taper

These terms are defined below.

1.4.1. Radiation pattern. In the far field of an antenna, the amplitude of the electromagnetic fields radiated is proportional to $1/r$, where r is the distance from the antenna (see Fig. 3). Plots of the magnitude of the radiated power at a constant distance r are called *radiation power patterns*. The power pattern P in a given direction (θ, ϕ) is

$$P(\theta, \phi) = 4\pi r^2 P_r(r, \theta, \phi) \quad (3)$$

where P is the power density per unit solid angle, P_r is the power density (in W/m^2), and r, θ, ϕ are the spherical polar coordinates (see Fig. 3). The power density is the radial component of the Poynting vector given by

$$P_r(r, \theta, \phi) = \frac{1}{2\eta} |\mathbf{E}|^2 \quad (4)$$

where \mathbf{E} is the electric field intensity (V/m) transverse to the direction of wave propagation. The quantity $\eta = \sqrt{\mu_0/\epsilon_0}$ is the wave impedance in free space (μ_0 and ϵ_0 are the permeability and permittivity of free space) and is approximately $120\pi\Omega$.

The power pattern of a feed usually consists of a maximum beam in the main direction and a series of subsidiary maxima called *sidelobes*. These are numbered consecutively from the mainbeam. Usually, the power pattern (3) is normalized to the maximum value and graphs are constructed of this function as contours or intensity plots in two dimensions, or in one-dimensional pattern cuts. The magnitude of the pattern is usually expressed in decibels (dB). The most common type of pattern cut for feeds is a plot of P at a constant angle ϕ , the so-called azimuth cut.

The half-power beamwidth (HPBW) is the angle subtended at the half-power or -3 dB points of the

normalized power pattern. The beamwidth between first nulls (BWFN) and the -12 dB power beamwidth are also used.

1.4.2. Gain. The power gain of an antenna in a given direction (θ, ϕ) is defined as the ratio of the power intercepted by a large sphere enclosing the antenna when that same power density at (θ, ϕ) is radiated in all directions (i.e., isotropically) and the total power input to the antenna.² The power density at (θ, ϕ) is given by (4). If this power were radiated isotropically, the power that would be radiated on a large sphere of radius r would be given by (3). Therefore, if P_{in} is the power incident on the antenna, the power gain function G is

$$G(\theta, \phi) = \frac{P(\theta, \phi)}{P_{\text{in}}} \quad (5)$$

The maximum value of (5) is the maximum power gain and is often used to describe the performance of an antenna. Usually when the term *gain* is used, maximum power gain is being referred to.

Directivity is similar to gain except that the reference power is in the radiated field. Thus the directivity function D is defined as

$$D(\theta, \phi) = \frac{P(\theta, \phi)}{P_{\text{T}}} \quad (6)$$

where P_{T} is the total radiated power and is obtained by integrating the power density P_{r} over a surface enclosing the antenna. For aperture antennas, it is common to integrate the power density over the aperture, rather than the far-field sphere, as this is easier to do. A special case of (6) is where the antenna is excited by sources with uniform amplitude and phase distribution (or illumination) over its aperture area A . The maximum directivity in this case is $D_0 = 4\pi A/\lambda^2$.

The aperture efficiency η_{a} is the ratio of the maximum directivity D_{max} given by (6), and the directivity of a uniformly illuminated aperture

$$\eta_{\text{a}} = \frac{D_{\text{max}}}{D_0} \quad (7)$$

Most practical feeds have aperture efficiencies in excess of 60%, and in excess of 90% can be achieved over limited bandwidths.

Gain and directivity are related through the antenna efficiency, which is the ratio of gain and directivity or equivalently the ratio of total radiated power and the power incident at the antenna input. Antenna efficiency (η_{ae}) is equal to the product of the mismatch efficiency (η_{m}), conversion efficiency (η_{c}), and the aperture efficiency η_{a} . In a lossless, matched feed, the antenna efficiency equals the aperture efficiency.

²This compares with the IEEE definition (Std. 145–1993 §2.165) for gain, which uses the power *accepted* by the antenna. The present definition is more convenient for feeds and differs from the IEEE definition by the factor $1/(1 - |\Gamma_{\text{in}}|^2)$ for single mode excitation where Γ_{in} is the input reflection coefficient.

1.4.3. Phase Center. The phase center is the apparent origin of the spherical wave radiating from an antenna. Because phase varies significantly over the full sphere, this center is not unique for all applications because it depends on the solid angle over which the radiated field is incident on the secondary antenna. The phase center is obtained experimentally by rotating the antenna about its axis and determining the position on the axis where the measured phase function variation is minimized over the desired angle for illuminating the secondary antenna. This can be time-consuming as the phase center is usually different for each pattern cut. An alternative approach is to calculate the phase center from measured or numerically obtained data. One approach is to average the phase center from locations d_n of N pattern cuts. Thus, the phase center d_{pc} is given by

$$d_{\text{pc}} = \frac{1}{N} \sum_{n=1}^N d_n \quad (8)$$

The phase center in the n th azimuth plane is given by [12]

$$kd_n = \frac{(A_0 B_1 - A_1 B_0)}{(A_0 A_2 - A_1^2)} \quad (9)$$

where $k = 2\pi/\lambda$, $A_0 = \sum_{i=1}^M \theta_i$, where M is the number of data points of the phase function $\Phi(\theta_i, \phi_n)$, θ_i is the i th angle of the n th pattern cut ϕ_n , $A_1 = \sum_{i=1}^M \cos \theta_i$, $A_2 = \sum_{i=1}^M \cos^2 \theta_i$, $B_0 = \sum_{i=1}^M \Phi(\theta_i, \phi_n)$, and $B_1 = \sum_{i=1}^M \Phi(\theta_i, \phi_n) \cos \theta_i$. The simplest case of (8) corresponds to a single cut ($N=1$). A better estimate is to average the phase centers of the two principal plane patterns ($N=2$). With circularly symmetric feeds, an average of the two principal planes plus the intercardinal plane (45° and 135°) phase centers ($N=4$) is usually sufficiently accurate for most purposes.

1.4.4. Polarization. Although the fields radiated by feed antennas are usually complicated, they can be resolved into two components on any chosen surface, such as the far-field sphere (see Fig. 3) or on the secondary antenna. Without loss of generality, we will consider here only the former. The two components are the desired polarization or the copolarized component (denoted by the vector $\hat{\mathbf{p}}$) and the usually undesired cross-polarized component (given by $\hat{\mathbf{q}}$). Further, there are two main types of polarization, linear and circular. There is no unique way of defining the components of these polarizations. For feeds, the common method is to define co- and cross-polarization in the manner in which they are measured in practice. In the case of predominantly linearly polarized feeds, the copolar component is obtained as for conventional far-field measurement, by aligning the test antenna on boresight with the polarization of the distant source antenna. Maintaining this alignment, the test antenna is then rotated about the phase center. The signal received at the test antenna is the copolar pattern. If the polarization of the distant antenna is now rotated through $\pm 90^\circ$ and the radiation pattern remeasured, the received signal is the cross-polar pattern of the test antenna. If the test antenna is rotated in the plane of the principal electric field com-

ponent, the pattern cut is called the *E-plane* (see Fig. 3). The orthogonal plane is called the *H-plane cut*. For feed antennas it is common also to measure the pattern in the 45° and 135° planes. The co- and cross-polarized field components are obtained from the spherical field components by means of

$$\begin{bmatrix} E_p \\ E_q \end{bmatrix} = \begin{bmatrix} \cos(\phi - \alpha) & -\sin(\phi - \alpha) \\ -\sin(\phi - \alpha) & -\cos(\phi - \alpha) \end{bmatrix} \cdot \begin{bmatrix} E_\theta \\ E_\phi \end{bmatrix} \quad (10)$$

where E_θ and E_ϕ are the spherical components in the θ and ϕ directions, ϕ is the azimuth angle, and α is the polarization angle referenced to the x axis of the coordinate system (Fig. 3).

Cross-polarization becomes important in antenna design when two orthogonal polarizations are used to transmit two separate channels. Frequency reuse by dual polarization effectively doubles the available system bandwidth. The antenna, and the feed in particular, is the means by which isolation is maintained between the channels. Signals may be sent or received in either linearly polarized vertical and horizontal components or circularly polarized where the signals rotate in space and time in a right- or left-hand sense.

1.4.5. Input Match. This is the input reflection coefficient of the feed antenna when it is excited at its input. Usually this is measured with the feed alone; however, care must be taken to ensure that reflection from the secondary antenna does not significantly affect the match. If this occurs, a matching vertex plate can be added to the reflector or lens to reduce the reflection.

1.4.6. Bandwidth. The bandwidth of the feed antenna is the continuous frequency range over which the feed performance is acceptable. The parameter measured is often the input reflection coefficient, and the acceptable level depends on the application. In satellite ground stations and radio astronomy, a commonly used maximum level is -17.7 dB (VSWR = 1.3). The percentage bandwidth is used to compare the performance of different feeds. This is calculated from the minimum and maximum frequencies, f_{\min} and f_{\max} over which the parameter meets the criterion, thus

$$\% \text{ bandwidth} = 200 \frac{(f_{\max} - f_{\min})}{(f_{\max} + f_{\min})}$$

1.4.7. Spillover. In transmit mode, the energy from a feed antenna that is not incident on the secondary antenna is called *spillover*. In receive mode, received spillover is an important contributor to the overall antenna noise temperature. Considerable effort goes into minimizing the amount of spillover in systems requiring low antenna noise temperatures such as radio astronomy and deep-space probes. Spillover efficiency η_{spill} is the ratio of the power intercepted by the secondary antenna to the total power radiated by the feed.

1.4.8. Edge Illumination and Edge Taper. *Edge illumination* is the ratio of the field strength radiated by the feed in

the direction of the edge of the secondary antenna and its level at the center of the secondary antenna, where field strength is measured on a sphere of radius equal to the distance to the center of the secondary antenna. *Edge taper* is a related quantity, and gives the ratio of the feed field strength at the center of the secondary antenna relative to the level at the edge. The difference between edge illumination and edge taper (apart from the sign) is the free-space loss between the sphere and the edge. In a symmetric reflector antenna, the edge is the reflector rim and the intersection point is the vertex. For a paraboloid with focal length F and diameter D

$$\begin{aligned} \text{Edge taper (dB)} &= 20 \log_{10} \left(1 + \frac{1}{4(F/D)^2} \right) \\ &- \text{edge illumination (dB)} \end{aligned} \quad (11)$$

The choice of primary feed illumination for a secondary antenna (e.g., reflector F/D) is often a compromise between spillover efficiency (η_{spill}) and the secondary antenna aperture efficiency (η_{sae}). As the feed beamwidth is increased, the edge taper decreases and η_{sae} increases. At the same time, the spillover loss increases (η_{spill} decreases), causing the overall antenna efficiency to decrease. Consequently, there is an optimum edge taper that maximizes the overall antenna efficiency and, therefore, gain for a given secondary antenna. A -12 dB edge illumination is recommended for a paraboloid as a compromise between gain, sidelobes, and spillover (noise). With this edge illumination, a paraboloid with $F/D = 0.4$ has an edge taper of 14.9 dB. Further increase in edge taper results in lower sidelobes and wider beamwidth in the secondary pattern. A similar argument applies for a lens, except that a lower edge taper can be used in receive-only applications because the feed spillover radiation contributes to the sidelobes close to the mainbeam rather than the rear lobes of the antenna.

1.5. Types of Feed Antennas

Antenna feeds can be grouped into four basic categories as shown in Table 1. The class of aperture antennas is the most extensive and has the property that the area normal to the direction of propagation of the radiation from the antenna determines the gain and beamwidth. Linear antennas are distinguished by their physical appearance and how the dominant currents are supported on line elements. Traveling-wave antennas derive essentially from fields or currents that propagate along the antenna and radiate in the endfire direction with gain that is approximately proportional to the length of the antenna. Most

Table 1. Types of Antenna Feeds

Aperture	Linear	Traveling-Wave	Compound
Waveguides	Dipole	Dielectric rod	Arrays
Horns	Yagi-Uda	Profiled slot	Beam waveguide
Microstrip patch	Logperiodic	Vivaldi	Splash plate
Slots	Zigzag	Linefeeds	Dichroic reflector
Rear-radiating			
Short backfire			

linear arrays belong to this category also. Compound feeds are made up of several antenna types including aperture or traveling antennas with reflectors, lenses, or grids. In the following sections, different feed types will be described according to this classification.

2. APERTURE FEED ANTENNAS

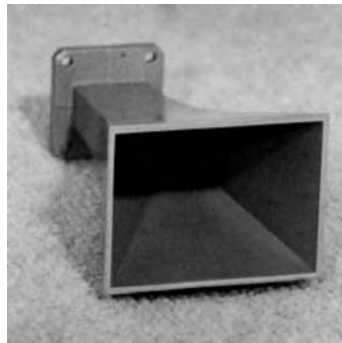
Aperture antennas radiate from a surface that serves as the interface between the circuit attached to the transmitter or receiver and the radiation field. Actual or equivalent electric and magnetic currents flow on this surface, and the radiated fields and impedance properties can be derived from these currents. The equivalence principle says there is no unique surface but, for horns,

the aperture is commonly taken as the opening and the external walls. For slot antennas, the aperture is usually the opening and the surrounding metallic surface, while for rectangular microstrip antennas the aperture is sometimes taken as a pair of rectangular “slots” formed between the edges of the patch and the ground plane. Examples of some aperture antennas are shown in Fig. 4.

Some of the simplest and most commonly used aperture feeds are based on smooth metallic waveguides and their extension by flaring into horns. The main types of waveguide and horn feed have rectangular or circular cross sections. In feed applications, the radiation in the forward direction is the fundamental concern and, to a reasonable approximation, these functions are given by the radiation of the first waveguide mode.



(a)



(b)



(c)



(d)



(e)



(f)

Figure 4. Examples of aperture antennas: (a) waveguide feeds—left to right, rectangular, circular, and coaxial; (b) pyramidal horn; (c) circular waveguide with choke ring; (d) corrugated horn; (e) cup feed; (f) profiled superelliptical corrugated horn.

A commonly used model for radiation from aperture feeds is the E -field model. It is so called because the field is derived from the electric fields in the aperture and corresponds physically to an aperture opening out into an infinite ground plane. The model is useful for predicting the field in the forward direction and, of course, it predicts zero fields behind the conductor. The fields radiated by simple waveguide and horn feeds are a spherical wave of the form

$$\mathbf{E} = jk \frac{\exp(-jkr)}{2\pi r} (\hat{\theta} F(\theta, \phi) \cos \phi - \hat{\phi} \cos \theta G(\theta, \phi) \sin \phi); \quad |\theta| \leq 90^\circ \quad (12a)$$

$$\mathbf{H} = \frac{1}{\eta} \hat{\mathbf{r}} \times \mathbf{E} \quad (12b)$$

where $k = 2\pi/\lambda$, λ is the free-space wavelength, and the functions $F(\theta, \phi)$ and $G(\theta, \phi)$ depend on the aperture geometry. The radial field components are small in the far field and are neglected in (12), although they are important when the secondary antenna is in the near field of the feed. Assuming that the waveguide aperture is in a ground plane or the waveguide wall is thick, F and G are approximately given by the E -field model and are listed in Table 2 for rectangular, circular, coaxial, and corrugated waveguides. Other waveguide cross sections, such as the elliptic and polygonal shapes, have the same form as (12), although the functions are not expressible in terms of simple functions and must be computed by other methods. The effect of a finite-size ground plane or flange can be included in the E -field model simply by the method of geometrical or physical theory of diffraction

[5,13]. The main effect on the mainbeam of the finite ground plane is to change the multipliers (known as *Huygens factors*) in (12), respectively 1 and $\cos \theta$ of the $\hat{\theta}$ and $\hat{\phi}$ vector components.

When $F(\theta, \phi)$ and $H(\theta, \phi) = \cos \theta G(\theta, \phi)$ are independent of ϕ , the radiation pattern is axisymmetric; furthermore, if F and H are identical, the cross-polarized field is zero. Ideal corrugated horns have these properties if the “balanced hybrid condition” is satisfied. For smooth-wall circular horns, F and H are generally different, although the phase of these functions may be almost the same. Equation (12) shows that, for feeds with axisymmetric patterns, the peak cross-polarization is in the intercardinal planes and equals $|F(\theta) - H(\theta)|/2$; thus the cross-polarization depends on the difference between the E - and H -plane pattern functions. The copolar pattern in the intercardinal planes is $|F(\theta) + H(\theta)|/2$, that is, the average of the E - and H -plane pattern functions.

2.1. Feeds with Circular and Related Cross Section

Circular aperture antennas find wide application as feeds because of their geometric symmetry, low cross-polarization, and ease of manufacture. Examples of this type of feed are illustrated in Fig. 5.

A circular waveguide (Fig. 5a) is an efficient feed for moderately deep reflectors or lenses where the half-cone angle is around 60° . It has an almost equal E - and H -plane pattern (pattern symmetry) for pipe diameters in the range of 0.7–1.2 wavelengths depending on the size of the flange at the aperture. Higher efficiencies may be obtained by the addition of parasitic rings as shown in Fig. 5b. A coaxial waveguide (Fig. 5c) operating in

Table 2. Simple Waveguide Feeds

Type of Feed	$F(\theta, \phi)$	$G(\theta, \phi)$	Notes
Aperture			
TE ₀₁ -mode rectangular waveguide	$\frac{2ab}{\pi} S\left(U \frac{b}{2}\right) C\left(V \frac{a}{2}\right)$	$F(\theta, \phi)$	a and b are the width and height of the waveguide
TE ₁₁ -mode circular waveguide	$2\pi a J_1(k_c a) \frac{J_1(wa)}{k_c wa}$	$2\pi a J_1(k_c a) \frac{k_c J_1'(wa)}{k_c^2 - w^2}$	a is the waveguide radius; $k_c a = 1.8412$
TE ₁₁ -mode coaxial waveguide	$\frac{2\pi a [Z_1(k_c a, k_c b) J_1(wa) - Z_1(k_c b, k_c b) J_1(wb)]}{k_c wa}$	$\frac{2\pi a k_c [Z_1(k_c a, k_c b) J_1'(wa) - \frac{b}{a} Z_1(k_c b, k_c b) J_1'(wb)]}{k_c^2 - w^2}$	a and b are outer and inner conductor radii; $k_c a \approx 2/(1 + (b/a))$ and is the first root of $J_1'(k_c a) Y_1'(k_c b) - J_1'(k_c b) Y_1'(k_c a) = 0$
HE ₁₁ -mode corrugated waveguide	$2\pi a J_1(k_\rho a) \frac{k_\rho J_0(wa)}{k_\rho^2 - w^2}$	$F(\theta, \phi)$	a is the waveguide radius; $k_\rho a = 2.4048$

Key: $U = w \cos \phi$, $V = w \sin \phi$, $w = k \sin \theta$, J_p is a Bessel function of order p , and J_p' is its first derivative; Y_1 is a Bessel function of second kind and Y_1' is its first derivative:

$$S(x) = \frac{\sin x}{x}, \quad C(x) = \frac{\cos x}{1 - \left(\frac{2x}{\pi}\right)^2}, \quad Z_1(x, y) = J_1(x) - \frac{J_1'(y)}{Y_1'(y)} Y_1(x)$$

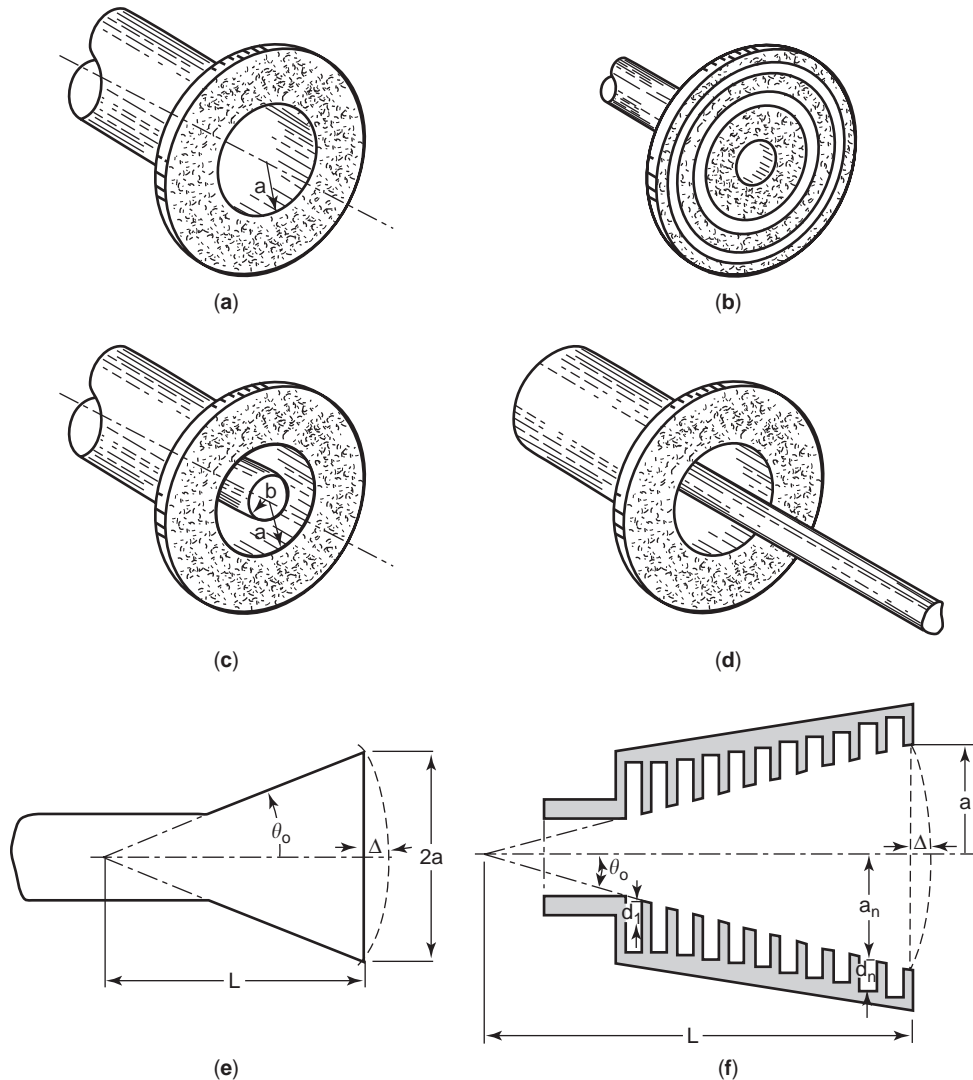


Figure 5. Circular waveguides and horn antennas: (a) circular waveguide; (b) circular waveguide with parasitic rings; (c) coaxial waveguide; (d) rear-radiating coaxial waveguide; (e) conical horn; (f) corrugated horn. (Parts (b)–(d) from Bird [14], courtesy of IEEE.)

predominantly the TE_{11} mode has potentially greater flexibility of available radiation patterns because of the extra degree of freedom given by the internal conductor. Figure 5d shows a self-supporting radiating coaxial waveguide (sometimes called a “tomato can”) feed for a reflector. Here the inner conductor extends all the way to the vertex of the reflector, allowing the feed to be driven from a transmission line or waveguide inside this conductor.

Flaring the circular or coaxial waveguide produces a conical horn (Fig. 5e) that has a more directive radiation pattern. The quality of the pattern depends on many factors, including the size of the output aperture, the internal structure of the flare, and the means of exciting the flared section. As an example, a horn with transverse internal corrugations (Fig. 5f), the so-called corrugated horn, is very commonly used in satellite communications and radio astronomy because of its low cross-polarization. When the depth of the corrugations is about a quarter-

wavelength, almost pure polarized radiation patterns result. Several other types of feeds with circular or elliptical cross section are discussed in the following sections.

2.1.1. Circular and Coaxial Waveguide. Smooth-wall circular or coaxial waveguide and horns are most frequently excited in the first waveguide mode, the TE_{11} mode (see Fig. 6a). The transverse field components of this mode in circular waveguide are

$$\mathbf{E}_t = A_0 \left[\hat{\rho} \frac{J_1(k_c \rho)}{k_c \rho} \cos \phi - \hat{\phi} J_1(k_c \rho) \sin \phi \right] e^{-j\beta z} \quad (13a)$$

and

$$\mathbf{H}_t = Y_W \hat{z} \times \mathbf{E}_t, \quad (13b)$$

where $k_c = 1.8412/a$ is the cutoff wavenumber, a is the waveguide radius, $Y_W = \beta/k\eta$ and $\beta = \sqrt{k^2 - k_c^2}$, J_1 is the

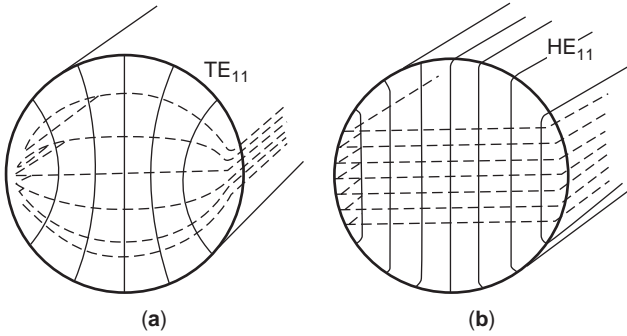


Figure 6. Electric and magnetic fields in (a) smooth-wall circular waveguide and (b) corrugated waveguide (— electric; - - - magnetic).

Bessel function of first order, A_0 is a constant, and (ρ, ϕ, z) are the cylindrical polar coordinates.

When the TE_{11} mode is incident on the open end as in Fig. 6a, an external field is produced and the TE_{1n} and TM_{1n} ($n = 1, 2, \dots$) modes are excited in order to satisfy the boundary conditions. These modes radiate and also propagate back into the waveguide; the dominant component is due to the reflected TE_{11} mode. This coupling to other modes is often ignored as a first approximation, but it should be included for accurate design. To first order, the aperture fields [$z = 0$ in (13)] expressed in terms of rectangular components are

$$\mathbf{E}_a = \hat{x} \frac{A_0}{2} [J_0(k_c \rho) + J_2(k_c \rho) \cos 2\phi] + \hat{y} \frac{A_0}{2} J_2(k_c \rho) \sin 2\phi \tag{14a}$$

$$\mathbf{H}_a = Y_w \hat{z} \times \mathbf{E}_a \tag{14b}$$

These equations show that the TE_{11} mode has both x - and y -field components and, therefore, so does the radiated fields. The principal aperture field polarization is maximum on axis and the cross-polarized component is maximum in the intercardinal (45° and 135°) planes. When a center conductor of radius b is introduced into circular waveguide, as in Fig. 5c, the basic properties of a TE_{11} -mode excited coaxial waveguide are similar, but there are significant differences as shown in Figs. 7–9. The fields radiated by circular and coaxial waveguide are given in Table 2. The -12 dB semiangle of the principal radiation patterns for circular ($b = 0$) and coaxial waveguides ($b > 0$) is shown in Fig. 7, and the maximum cross-polar level is given in Fig. 8. The E - and H -plane patterns of circular waveguide are approximately the same when $ka \sim 3.4$ ($a \sim 0.55\lambda$), and this results in a cross-polar minimum for the same ka value (Fig. 8). Coaxial waveguide also has a cross-polar minimum, (as shown in Fig. 8), which depends on the inner–outer conductor ratio (b/a).

The reflection coefficient S_{11} of the TE_{11} mode in circular waveguide due to the aperture mismatch is

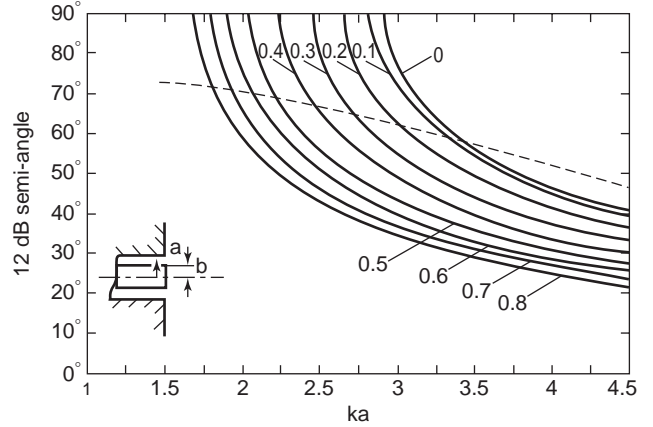


Figure 7. The 12 dB semiangle of far-field radiation pattern of a coaxial waveguide, (— E plane; - - - H plane; parameter is b/a). (From Bird [14], courtesy of IEEE.)

approximately

$$S_{11} = \left(\frac{1 - y_{11}}{1 + y_{11}} \right) \tag{15}$$

where the admittance of the TE_{11} mode in circular waveguide is given by

$$y_{11} = 9.617 \frac{k}{\beta} \int_0^\infty \left(\frac{w\sqrt{1-w^2}}{(ka)^2} \frac{J_1^2(kaw)}{(w^2 - (1.84118/ka)^2)^2} + 0.087 \frac{J_1^2(kaw)}{w\sqrt{1-w^2}} \right) dw \tag{16}$$

As shown in Fig. 9, Eq. (15) has a minimum when $ka \sim 3.4$ ($a \sim 0.55\lambda$), which is coincident with the condition for minimum cross-polarization. Providing $a > \lambda$, the TE_{11} mode reflection coefficient is < -30 dB. Coaxial waveguide has a large mismatch, as Fig. 9 shows, when the inner–outer conductor diameter ratio exceeds ~ 0.3 . By means of a pair of capacitive and inductive coaxial irises, it

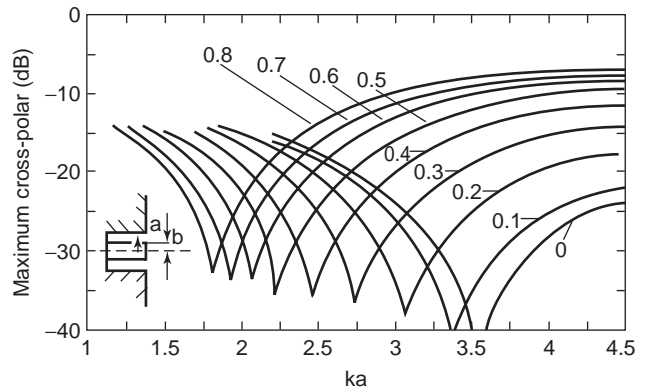


Figure 8. Maximum cross-polar level relative to peak copolar level within a 75° semiangle versus normalized frequency ka (parameter is b/a). (From Bird [14], courtesy of IEEE.)

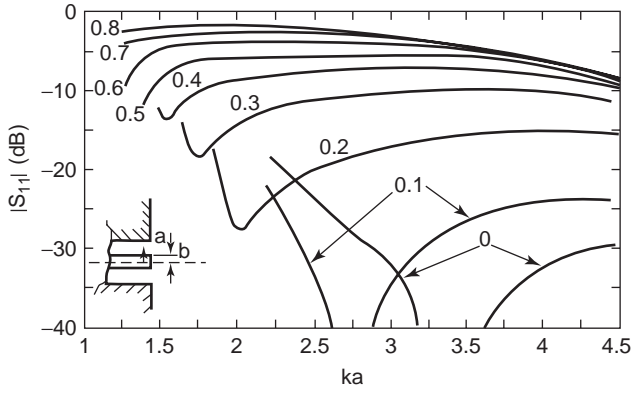


Figure 9. Reflection coefficient at the aperture of coaxial waveguide (parameter is b/a). (From Bird et al. [15], courtesy of IEEE.)

is possible to match coaxial feeds with inner-outer conductor ratios of ≤ 0.6 over $>17\%$ bandwidth. This is achieved by stepping down to an inner-to-outer conductor diameter of 0.3 and matching into this guide using the technique described by Bird et al. [15].

The maximum gain predicted by the E -field model for circular waveguide is

$$G_{\max} = 0.209(ka)^2 \frac{k}{\beta} \left(1 + \frac{\beta}{k}\right)^2 \left(\frac{|1 + S_{11}|^2}{1 - |S_{11}|^2}\right) \quad (17)$$

where the mode is above cutoff. For frequencies well above cutoff ($\beta \approx k$), $G_{\max} \approx 0.837 (ka)^2$ and the maximum aperture efficiency is 83.7%.

Circular horns are desirable for dual-polarized applications because of their geometric symmetry. However, this does not ensure low cross-polarization and thereby high polarization isolation. We have seen that the TE_{11} mode of circular waveguide has a radial directed electric field at the wall and, therefore, cross-polarized fields arise to satisfy the boundary conditions. Cross-polarization is transferred from the aperture to the radiation field, but this can be reduced in some situations by exciting other modes.

Cross-polar patterns of rationally symmetric feeds have a characteristic null on axis. If the symmetry is broken and other modes excited, it is possible to have cross-polarization on axis. Equality of the E - and H -plane patterns may be difficult or impossible to achieve in practice over any reasonable bandwidth. In feed applications, reasonably low cross-polarization can be achieved in the secondary pattern by selecting the geometry so that the E - and H -plane patterns cross over at around the -10 to -14 dB level. Choke rings either inside the horn or at the aperture (Fig. 5b) are useful for tailoring the radiation pattern of small horns to minimize cross-polarization over a moderate bandwidth [16]. Figure 7 shows that up to a certain ka value, the E -plane beamwidth is wider than the H -plane beamwidth. By placing a 0.2 – 0.26λ deep choke ring concentric with the aperture, the E -plane beamwidth can be reduced to almost the same as the H -plane beamwidth.

2.1.2. Conical Horn. If a circular aperture is flared into a conical horn as shown in Fig. 5e, the field at the aperture has a spherical wavefront. In simple terms, when the TE_{11} mode reaches the flare, it expands outward in order to satisfy the wall conditions and forms a spherical wave that propagates to the aperture. Therefore, the distance between a planar and a spherical wavefront is approximately given by [5]

$$\delta \approx \frac{1}{2} \frac{\rho'^2}{L} \quad (18)$$

where ρ' is the radial distance from the axis to the field point on the aperture and L is the distance from the horn apex to the aperture. The result is that (14) is modified by the application of the phase factor $\exp(-jk\delta)$ and the radiated fields are now given approximately by the functions

$$\begin{aligned} F(\theta, \phi) &= L_0(\theta) - L_2(\theta) \quad \text{and} \\ G(\theta, \phi) &= L_0(\theta) + L_2(\theta) \end{aligned} \quad (19)$$

where

$$\begin{aligned} L_m(\theta) &= 2\pi \int_0^a J_m(k_c \rho') J_m(k \sin \theta \rho') \\ &\quad \times \exp(-jk\rho'^2/2L) \rho' d\rho' \end{aligned} \quad (20)$$

Equation (19) gives reasonable results providing the semicone angle $\theta_0 = \arctan(a/L)$ is less than $\sim 30^\circ$.

The radiation pattern of the conical horn is strongly dependent on the flare angle. In Fig. 10 the E - and H -plane patterns are plotted as a function $\Delta = (a/\lambda)\tan(\theta_0/2)$, which is the distance in wavelengths between the spherical wavefront and the aperture (see Fig. 5e). As the angle is increased, the patterns broaden and lose distinctive sidelobes. The phase center in these two principal planes has been calculated from (8) over the angular range defined by the -12 dB semiangles. The results given in Fig. 11 show when Δ is small, the phase center is near the aperture. However, as Δ increases, the phase centers in the two planes move toward the apex at a different rate. When $\Delta > 0.8$, the phase center is almost at the apex.

The radiation performance of the conical horn can be improved by changing the surface of the horn, with corrugations, for example, or by introducing discontinuities to excite high-order modes, particularly the TM_{11} mode. The Potter horn discussed in Section 2.1.6 uses steps placed near the throat to produce such improvements.

2.1.3. Corrugated Horns. The corrugated horn is widely used as a feed antenna for reflector antennas and lenses because it can radiate fields with a high degree of axial symmetry. Smooth-wall circular waveguides and horns have, in general, different E - and H -plane patterns because the electric and magnetic field components in the pipe satisfy different types of boundary conditions on the walls (see Fig. 6). In simple terms, the tangential electric field of the TE_{11} mode experiences a short circuit at the wall while the tangential magnetic field experiences an open circuit.

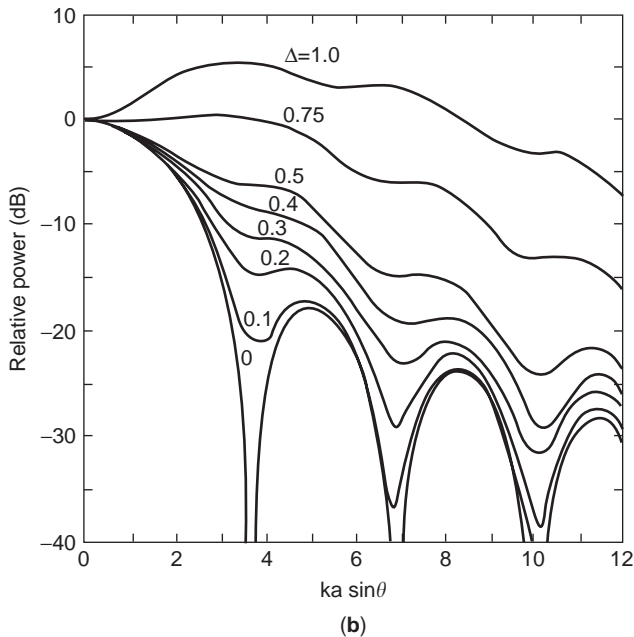
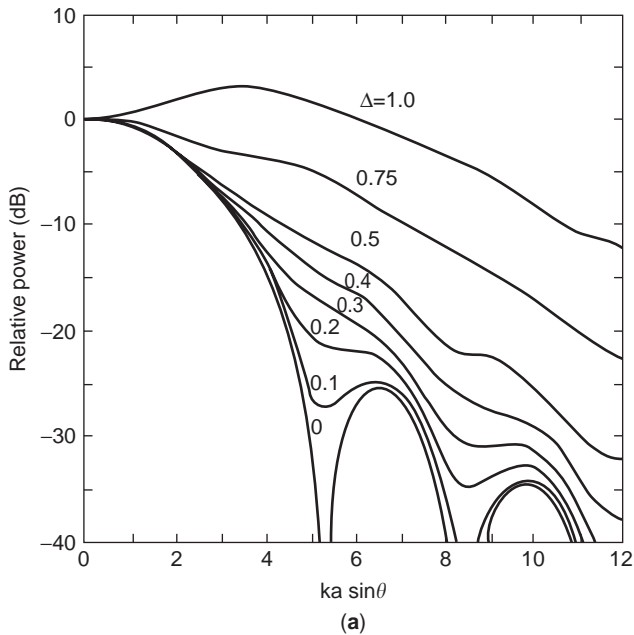


Figure 10. Normalized radiation patterns of conical horn where $\Delta = (a/\lambda) \tan(\theta_0/2)$ is the parameter: (a) *E* plane; (b) *H* plane.

The end result is that the field lines in the waveguide are curved. By modifying the wall surface conditions, such as corrugating the surface, covering it with dielectric or inserting strips, the wall impedance experienced by the mode can be altered and the field lines made almost unidirectional, which results in low cross-polarization.

The corrugated surface was one of the first used to create alternative wall impedances and has proved most successful in circular waveguide and horns. When there are many corrugations per waveguide (typically greater than about five per wavelength) and the corrugation depth is approximately $\lambda/4$ (where λ is the free-space wavelength), the radial transmission line formed by the

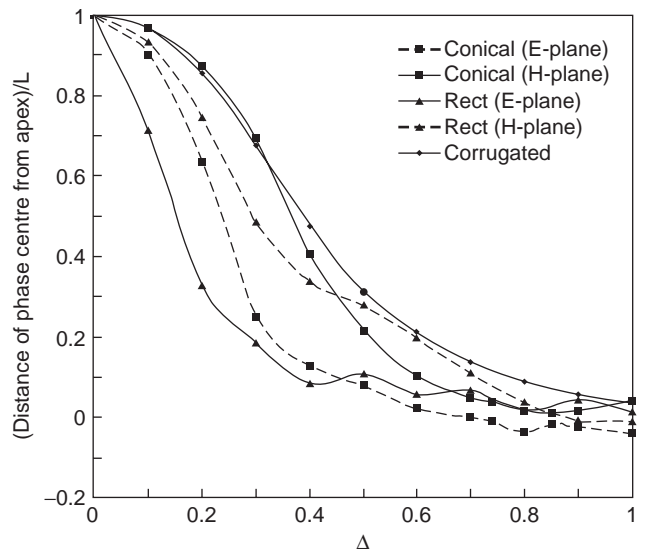


Figure 11. Phase center location for the principal planes of conical, corrugated, and rectangular horns.

slots transforms the short circuit for the electric field into an open circuit while having only a second-order effect on the transverse magnetic field. This creates a nonzero axial electric field at the corrugated surface, allowing a zero circumferential component. Consequently, the modes in the corrugated waveguide or horn are no longer TE or TM to the longitudinal (propagation) direction and, because both axial field components are generally nonzero, they are called “hybrid modes.” The principal mode used for feed horns is the HE_{11} mode, shown in Fig. 6b. An axisymmetric radiation pattern is produced if the HE_{11} mode operates at the “balanced hybrid condition,” which is achieved when the corrugations are approximately $\lambda/4$ deep. Under this condition, the horn has low cross-polarization, pattern symmetry, and low sidelobes, which are almost ideal for many applications and gives rise to the popularity of these hybrid-mode feed horns [17,18].

At the balanced hybrid condition, the aperture electric field of the HE_{11} mode is approximately

$$\mathbf{E}_a = \hat{x}A_0J_0(k_\rho\rho) \tag{21}$$

and the magnetic field is as given by (14b); J_0 is the zero-order Bessel function, A_0 is a constant, and $k_\rho a = 2.4048$. The far zone field radiated by the HE_{11} mode is provided in Table 2. The maximum gain of the corrugated waveguide under these conditions is $G_{\max} \approx 0.692(ka)^2$ and the maximum aperture efficiency of 69.2%.

The conical corrugated horn may be modeled by the same method described above for smooth-wall conical horn. The radiated fields are given approximately by (12), where

$$F(\theta, \phi) = L_0(\theta) = G(\theta, \phi) \tag{22}$$

where $L_0(\theta)$ is as given by (20), wherein $m = 0$ and k_c is replaced by k_ρ .

The radiation pattern of a corrugated horn operating in the balanced HE_{11} mode is given by the set of universal

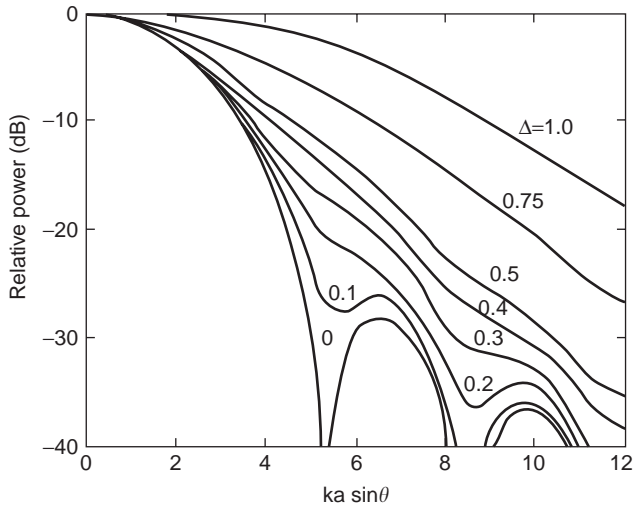


Figure 12. Normalized radiation pattern of corrugated horn with balanced hybrid mode, where Δ is the parameter.

curves shown in Fig. 12 plotted as a function of $\Delta = (a/\lambda) \tan(\theta_0/2)$. When $\Delta > 0.4$, the shape of the horn's pattern changes very little with Δ , indicating that the pattern and gain become virtually independent of aperture size. This is called “gain-saturated” and means that the horn is suitable for wideband operation. For $\Delta < 0.4$, the horn is said to be narrowband.

By virtue of the high pattern symmetry, the phase center for the corrugated conical horn is the same in all planes. Figure 11 gives the phase center location as a function of Δ based on the pattern over the -12 dB beamwidth.

The reflection coefficient of the HE_{11} balanced hybrid mode at the aperture is relatively low in most practical cases. If required, it can be calculated from (14) and the self-admittance

$$y_{11} = \frac{5.783k}{(ka)^2 \beta} \int_0^\infty \frac{w(2-w^2)}{\sqrt{1-w^2}} \frac{J_0^2(kaw)}{(w^2 - (2.4048/ka)^2)^2} dw \quad (23)$$

This equation predicts that when $a > 1.1\lambda$, the HE_{11} -mode reflection from the aperture is < -30 dB.

The corrugated horn equations given in Table 2 and Eq. (22) are useful only for narrowband feed design near the balanced hybrid condition. In a typical conical corrugated horn, there are 5–10 slots per wavelength, the slot width-to-pitch ratio (w/p) is > 0.75 , and the slot depth is approximately [19]

$$d_n \approx \frac{\lambda}{4} \exp\left(\frac{2}{5ka_n}\right) \quad (24)$$

where a_n is the radius of the corrugated surface at the n th slot (see Fig. 5f). Wideband feed design requires more accurate design methods and to achieve optimal performance, the input throat region, the flare from the input, and the profile to the aperture must be considered. The corrugated horn is limited to a continuous bandwidth performance of about 2:1. Thomas et al. [20] discuss

matching of corrugated horns and wideband design in detail.

The standard design of a corrugated horn starts from the smooth-wall input circular waveguide with a section of about a wavelength long where the depth of the corrugations are gradually decreased from a half-wavelength to a quarter-wavelength deep as the horn is widened. Following this input transition, a linear taper can be used for the horn profile, although some other profiles, such as “hour-glass” (sine-squared), have been found more effective. To achieve the widest bandwidth operation, the first four or five slots of the input section may need to terminate in a short-circuited coaxial waveguide—known as “ring-loaded slots.” These slots present a capacitive reactance over a bandwidth considerably wider than that of the conventional constant-width slot. The design of ring-loaded slots is described by James and Thomas [19]. The final part of the design is tapering the profile from the initial transition to the final output diameter. Corrugated horns with a profiled corrugated internal surface [21] produce a more compact design while maintaining high performance. A number of different profiles have been attempted in order to achieve low sidelobes and cross-polarization. The hyperbolic [10], or the identical Gaussian [22], profile has been found very effective overall for designing compact horns. Thus, if a_i is the radius of the input section, a_o is the output or aperture radius, and L is the length of the profile section, the horn profile as a function of axial distance (z) is given by

$$a(z) = a_i \sqrt{1 + \left(\frac{z}{L}\right)^2 \left(\left(\frac{a_o}{a_i}\right)^2 - 1\right)} \quad (25)$$

2.1.4. Horns with Axial Corrugations. Horns with internal axial corrugations (or internal short-circuited ring slots) are widely used as feeds for direct broadcast by satellite applications. As well as having good performance, they are relatively inexpensive to manufacture, especially by die casting. There are several different types of axially corrugated horn. One particular configuration is the choked aperture feed shown in Fig. 13a. It has choke rings in the aperture plane and also internal ring slots [23]. Although a simple prime-focus feed, it has an excellent performance over nearly an octave bandwidth.

Through the selection of a number of internal axial corrugations, a combination of TE_{11} , TM_{11} , and TE_{12} modes are produced in the aperture. These modes are maintained by a compensating action of the TE_{11} mode in the coaxial corrugations, which vary in length from about 0.37λ at the throat to about 0.25λ at the aperture. At least two corrugations are needed to achieve reasonable performance, but little is gained from using more than four corrugations.

2.1.5. Scrimp Horn. Originally devised by Wolf [24], the scrimp horn (Fig. 13b) is a compact and lightweight feed element for satellite antenna feed arrays. The scrimp horn has high aperture efficiency (typically $> 80\%$), operating bandwidth of about 20%, low cross-polarization, and better sidelobes than do most similar sized horns. The scrimp horn has three main sections: a conical horn input section,

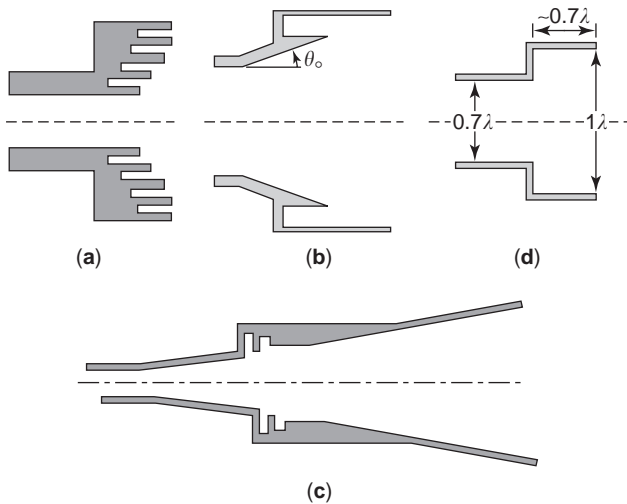


Figure 13. Circular horn feeds: (a) circular horn with axial corrugations; (b) scrimp horn; (c) Potter horn; (d) stepped horn.

a short-circuited coaxial waveguide section, and a cylindrical output waveguide section that terminates in the aperture. A TE_{11} mode in a circular waveguide of between 0.75λ and 0.95λ is input to the conical horn section, and this generates a standing wave in the coaxial waveguide section, which is dominated by a TE_{11} mode. The semian- gular of the flare (θ_0 in Fig. 13b) of the conical horn is typically $15\text{--}25^\circ$, and the length of the coaxial waveguide is about 0.25λ . This input TE_{11} mode in the conical horn oscillates in odd phase to the TE_{11} mode in the output section and to ensure continuity of the fields, additional higher-order modes, mainly TM_{11} and TE_{12} , are generated. These modes are superimposed with the fundamental TE_{11} mode to produce a field distribution in the aperture that is low in cross-polarized components. The aperture diameter can be from about $\sim 1.2\lambda$ to $\sim 1.8\lambda$ depending on the required edge taper.

2.1.6. Multimode and Stepped Circular Horns. The basic idea of multimode and stepped horns is to excite modes in addition to the fundamental mode in such a way as to improve the aperture efficiency, shape the radiation pattern or reduce cross-polarization. An early feed antenna that was designed for low cross-polarization characteristics is the dual-mode horn (Fig. 13c) described by Potter [6]. In this horn, a combination of TE_{11} and TM_{11} modes that are approximately in the ratio 1:0.3 in the aperture modes are excited in a smooth-wall horn. The modes are brought into the correct phase relationship over the length of the horn. This concept has been extended by several workers, including Takabayashi et al. [25], where a double-band dual-mode conical horn design is described. The band separation is not given and, as is typical with this type of design, the individual bandwidths are quite narrow ($\sim <5\%$).

Another approach [26] uses a thin dielectric ring in the flare of the horn, producing a rotationally symmetric beam and low sidelobe levels over a bandwidth greater than 25%.



Figure 14. The 13-element multibeam feed system for the Parkes (Australia) radio telescope.

Instead of inserting discontinuities inside the horn to generate higher-order modes, the horn profile can also be stepped. A horn of this type, which is useful for closely packed arrays, is the one-wavelength diameter dual-mode stepped horn in Fig. 13d [27]. This feed is excited by a traveling TE_{11} mode and an evanescent TM_{11} , which is produced at the step, is brought into phase over a $\sim 0.7\lambda$ uniform section to the aperture.

An example of multisteped circular horns are the elements of the multibeam array feed for the Parkes radio telescope [28], which has been in operation since early 1997 (the horns and receiver cryogenics are shown in Fig. 14). Bandwidths of about 20% can be achieved with these types of horns.

Aperture efficiencies in excess of 90% can be obtained with circular horns by exciting the right combination of modes using steps. For example, Bhattacharyya and Goyette [29] achieved both high aperture efficiency and low cross-polarization by exciting only TE-type modes in appropriate amplitudes and suppressing undesired TM modes.

Excitation of two or more hybrid modes in corrugated horns can also be used to improve aperture efficiency over a narrow band. For example, Thomas [30] showed that if the HE_{11} and HE_{12} hybrid modes were excited, the feed gave an increased efficiency of 12% over a single-mode design. Thomas and Bathkar [31] were able to achieve very low sidelobes with a multimode corrugated horn.

2.1.7. Profiled and Optimized Circular Horns. The profile of smooth-wall or corrugated horns can be optimized to achieve a desired performance. This is done either by using known information on the effect of conventional pro-

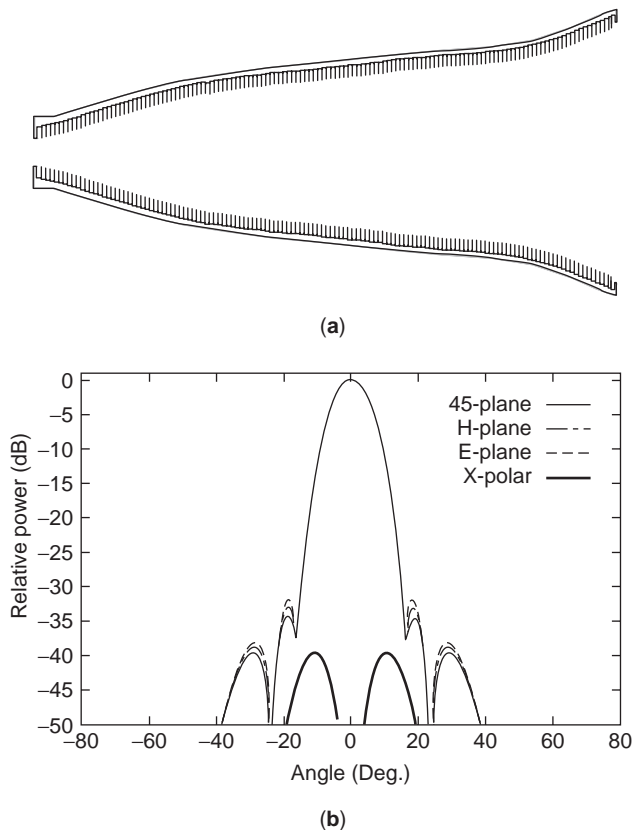


Figure 15. Profiled corrugated horn: (a) geometry; (b) radiation pattern at 11.7 GHz [33].

files, by combining some of these profiles [22,32], or through direct optimization [33]. The former approach is illustrated by the use of Gaussian/hyperbolic profiles (25), which produce a beam with low cross-polarization over very wide bandwidths. Direct optimization is achieved using the profile and/or slot depths of each corrugation as parameters. An alternative approach that is more efficient is to fix the slot width-to-pitch ratio and optimize the profile by defining splines. An example of a horn designed by this method for a Ku-band transmit/receive feed application is shown in Fig. 15 [33]. Through these means, excellent performance can be realized with very compact structures.

2.1.8. Dual- and Multiband Feeds. Some applications require feeds that operate in two or more frequency bands simultaneously. Two basic ways to achieve this are to multiband the feed or to use dichroic reflectors (see Section 5.4). A common dual-band feed is a coaxial horn structure where the high-frequency band is diverted into an inner (usually) circular horn and the low-frequency band is handled by an outer coaxial waveguide. The two bands often share a tapered section that leads to the aperture. The match of the outer coaxial horn is strongly affected by the diameter of the inner pipe, and, to keep this at an acceptable level, this waveguide is sometimes loaded with dielectric or has an aperture choke ring. To improve the match and the pattern, the dielectric loading some-

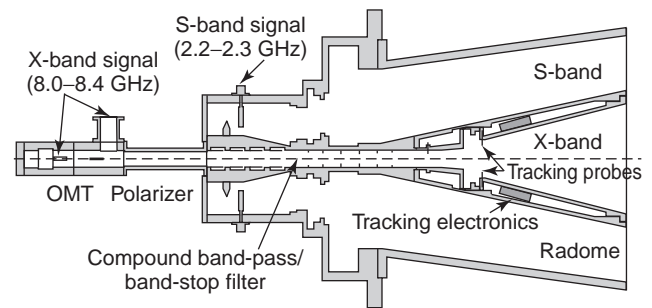


Figure 16. Dual-band coaxial horn for S- and X-band operation [34].

times protrudes into the common horn. The concentric coaxial feed concept can be extended to three or more bands with increasing difficulty for matching and inputting signals.

Multiple-step Potter-type horn designs can be used for coaxial structures, as demonstrated by James et al. [34] in providing a simultaneous dual-band/dual circularly polarized feed for a Cassegrain reflector antenna. Figure 16 shows a cross-sectional view of the complete feed design to provide S/X-band operation and satellite tracking. The inner section is a Potter horn for X-band (including provision of tracking) operation, and the outer S-band system has a coaxial waveguide geometry. In both horns, multiple steps are used in the throat region of the horn to provide a symmetrical low cross-polarization radiation pattern over the $\sim 5\%$ bandwidth of each band. The input to the dual-polarized coaxial horn is through four orthogonal probes (two excited in anti-phase to couple the TE_{11} -mode) and the X-band horn is input through a compound band-pass/band-stop filter in circular waveguide where both irises and ring-loaded slots were utilized in the design to achieve the required performance. Another example of a coaxial feed is the compact dual-band feed of Henderson and Richards [35] suitable for small front-fed parabolic reflectors. This feed is integrated with a diplexer and septum polarizer to provide dual-circular polarization in both bands.

An alternative approach to multiband horn design is shown in Fig. 17 [36]. This dual-depth corrugated horn (see inset to Fig. 17) operates in three relatively narrow frequency bands to provide transmit and receive in X-band and receive-only in Ka-band. The X-band receive signal is obtained from a junction of four waveguides that are arranged radially at 90° . A similar junction is used to inject the transmit signal at X-band. Ka-band is extracted from the rear of the corrugated horn. Another example is given by Green and Smith [37] for a dual-band corrugated horn design where operation is required in Ku/Ka-bands separated by a ratio of 1.5:1.

2.1.9. Elliptical Horns. Horns with elliptical cross section are used to feed reflectors or lenses that are noncircularly symmetric, particularly when low cross-polarization or circular polarization is required. The field in the aperture of an elliptical horn is tapered in the two

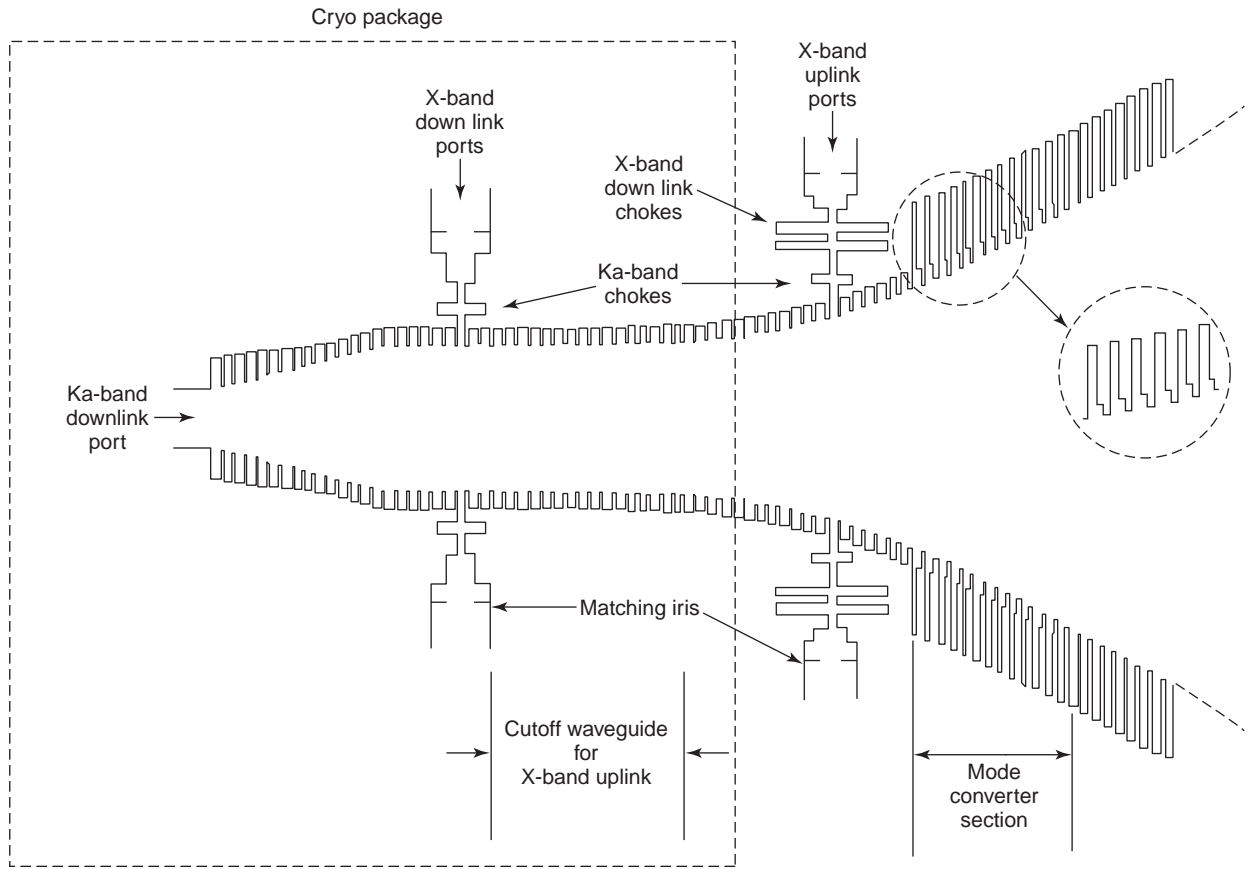


Figure 17. A triband X/X/Ka horn. (From Chen et al. [36], courtesy of IEEE.)

principal planes, resulting in lower sidelobes in the E plane than for a rectangular horn. The dominant modes of the air-filled horn are the TE_{c11} (even) and TE_{s11} (odd) modes, corresponding to the electric field maximum aligned with the minor and the major axes, respectively.

In an elliptical waveguide or horn (Fig. 18), the fields are expressed in terms of Mathieu functions, which are readily calculated via a computer but that, unlike circular geometries, preclude closed-form expressions for the F and G functions in (12). For an elliptical aperture radiating in the TE_{c11} mode, the fields are obtained from

$$F(\theta, \phi) = N_x + N_y \tan \phi \text{ and } G(\theta, \phi) = N_x - N_y \cot \phi \quad (26)$$

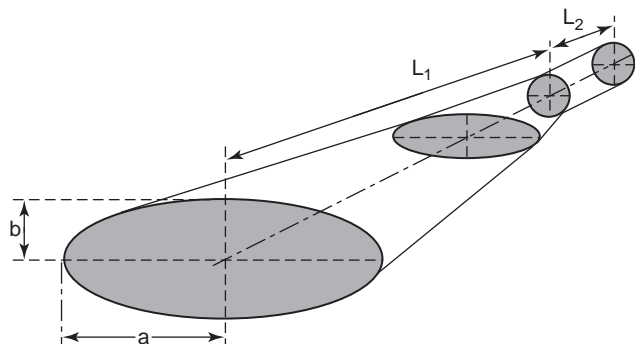


Figure 18. Geometry of elliptical horn.

where

$$N_x = \int_0^{\xi_0} \int_0^{2\pi} [Ce_1(\xi)ce'_1(\eta) \sinh \xi \cos \eta + Ce'_1(\xi)ce_1(\eta) \cosh \xi \sin \eta] \times \exp(jkae \sin \theta(\cosh \xi \cos \eta \cos \phi + \sinh \xi \sin \eta \sin \phi)) d\eta d\xi \quad (27a)$$

$$N_y = \int_0^{\xi_0} \int_0^{2\pi} [Ce_1(\xi)ce'_1(\eta) \cosh \xi \sin \eta - Ce'_1(\xi)ce_1(\eta) \sinh \xi \cos \eta] \times \exp(jkae \sin \theta(\cosh \xi \cos \eta \cos \phi + \sinh \xi \sin \eta \sin \phi)) d\eta d\xi \quad (27b)$$

where a is the length of the semi-major axis, $ce_1(\eta, q)$ and $Ce_1(\xi, q)$ are the ordinary and modified even Mathieu functions of order 1 respectively, a prime on the Mathieu functions denotes the first derivative, q is the first zero of $Ce'_1(\xi, q) = 0$ and is implied in (27), e is the eccentricity of the aperture, and $\cosh \xi_0 = 1/e$. The aperture mismatch for the TE_{c11} mode is < -30 dB for $a > \lambda$ providing $e < 0.9$.

The patterns in the two principal planes are generally different, although for some geometries it can be shown that the beam can be highly symmetric for some eccentricities. For example, a horn of length 5.09λ that is fed

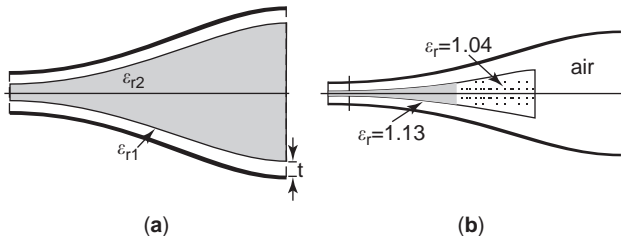


Figure 19. Dielectric-lined horns: (a) cone-loaded; (b) profiled ultrawideband.

from an elliptical waveguide with semi-major axis 0.42λ and eccentricity 0.422, gives good beam symmetry for an aperture with semi-major axis 2.65λ when $e \approx 0.67$ [38].

Elliptical corrugated horns have been designed and used in some applications [39,40], although the bandwidth is somewhat limited ($\sim 10\%$), probably because of the excitation of high-order modes.

2.1.10. Dielectric-Loaded Horns. Horns that are partially loaded with a central dielectric cone or core are capable of very wideband operation (Fig. 19). Between the core of permittivity ϵ_{r2} and the metal wall is a material of thickness t with a permittivity ϵ_{r1} close to 1. An estimate of the optimum gap thickness for circular, dielectric-lined horns, which is valid for large apertures, is [41]

$$t \approx \frac{\lambda}{4\pi\sqrt{\epsilon_{r2} - \epsilon_{r1}}} \ln \left(\frac{\sqrt{\epsilon_{r2} + \epsilon_{r1}}}{\sqrt{\epsilon_{r2} - \epsilon_{r1}}} \right) \quad (28)$$

However, the horn performance is not sensitive to the gap thickness. Dielectric-lined horns support a hybrid mode similar to a corrugated horn [42], but which is not band-limited by the slot depth of the corrugations. The potential of the dielectric-loaded horn has been made possible by the advent of accurate design software and also high-quality low-loss dielectric materials. For example, Clark and James [43] showed that a partially filled circular dielectric-loaded horn (Fig. 19b) could have high performance with respect to return loss, cross-polarization, pattern symmetry, and phase center stability over a bandwidth ratio of $> 30:1$. However, as frequency increases, the main frequency dependency is in the general reduction in beamwidth.

Many different types of dielectric-loaded horns have been developed. Some use a solid dielectric with permittivity of ~ 2.5 , and others use foam materials with permittivity close to 1. The wider bandwidth horns use a dielectric permittivity of between 1.1 and 1.2 for the inner core and also a thin airgap.

Other types of dielectric-lined horns have been shown to give excellent performance [44]. An estimate for gap thickness is given by (28), but is often profiled to suit the horn profile. In a rectangular dielectric-lined horn, if the airgap is small, the field in the horn appears approximately uniform in the principal direction, compared with an air-filled guide that has a cosine dependence. The result is a radiation pattern in both principal planes with a sinc-function dependence. The elliptical dielectric-lined horn has lower sidelobes compared to the rectangular horn for the same beamwidth, indicating that the latter has a slightly lower efficiency when used as a feed.

A practical difficulty with the dielectric-loaded horn is obtaining suitable dielectric materials with a permittivity of ~ 1.2 with an acceptable low loss (loss tangent $< 5 \times 10^{-4}$). One approach is to simulate the required dielectric by forming alternate layers of low-loss materials such as PTFE and low-loss, low-density, expanded polystyrene foam in a sandwich construction. With several layers of foam and PTFE per wavelength, and adjusting the relative thickness of the two materials or cutting holes in the material, a simulated material of the required permittivity with low loss can be achieved [45].

2.2. Rectangular Feeds

Rectangular horns that operate predominantly in the fundamental TE_{10} mode³ radiate fields where the E - and H -plane patterns are significantly different. Equation (12) and Table 2 give the radiated field. The quantity a is the aperture width in the H plane, and b is the height in the E plane. The different patterns can be advantageous in some array feed applications or where the secondary structure is not axisymmetric, as in a pillbox reflector. The reason for this difference is seen through the TE_{10} -mode aperture fields. The E plane of this mode's field is almost uniform, while in the H plane the field is cosine-tapered. The radiation by single-mode rectangular and pyramidal horns is detailed in many texts on antennas and is not repeated here [5,10]. In addition, a design procedure for so-called standard-gain horns is provided in these references. We note, however, that although the standard-gain horn design maximizes gain for given aperture dimensions, this is usually not a good design strategy for feed antennas because the pattern shape is often unsuitable, and high sidelobes occur in the E plane, causing significant spillover loss.

The radiation pattern of a rectangular horn radiating in the TE_{10} mode is given by the set of universal curves shown in Fig. 20 as a function of $\Delta = (w/\lambda) \tan(\theta_0/2)$, where $w = b$ in the E plane and $w = a$ in the H plane. An open-ended rectangular waveguide or small flare-angle horn is an effective feed antenna if the aperture dimensions are suitably chosen. For a symmetric reflector or lens, the aperture dimensions are usually chosen to equalize the E - and H -plane patterns across the mainbeam, although the cross-polar level in the intercardinal planes remains high. The rectangular horn dimensions for maximum gain with a given reflector F/D has been determined by Truman and Balanis [46]. The dimensions are shown in Fig. 21 for various horn slant lengths (where infinity corresponds to uniform waveguide).

The phase center in the two principal planes of a flared rectangular horn is given in Fig. 11, which was obtained from the patterns over the angular range defined by the -12 dB semiangles in the E and H planes. In this figure, L is the distance from the apex to the aperture in each plane. Similar to the conical horn, the phase centers are significantly different in the two planes, except when the aperture size is large and they are close to the horn apex.

³The TE_{10} and TE_{01} modes are fundamental modes of rectangular waveguide with the electric field aligned in the y and x directions, respectively. The latter is obtained from the former by rotating the waveguide clockwise by 90° .

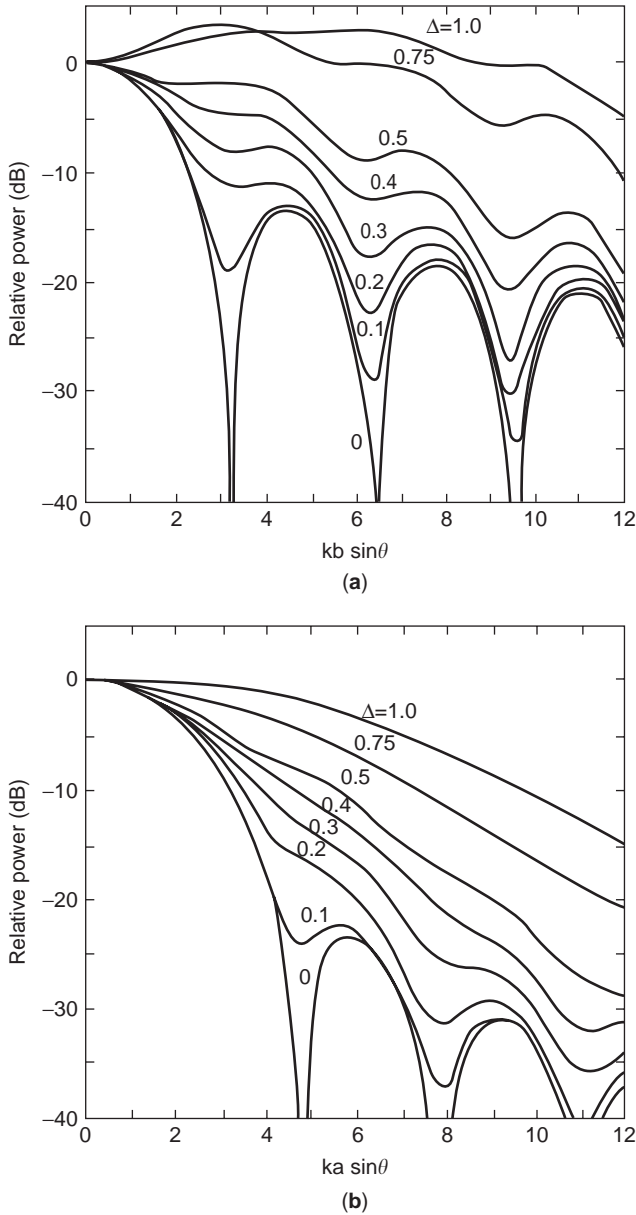


Figure 20. Normalized pattern of rectangular horn: (a) E plane; (b) H plane.

The reflection coefficient of the TE_{10} mode at the aperture is given by (15) and the mode self-admittance

$$\begin{aligned}
 y_{11} = & \frac{2jk^2}{\pi ab\beta} \left(\int_0^{z_0} d\alpha \int_0^{a \sec \alpha} dx + \int_{z_0}^{\pi/2} d\alpha \int_0^{b \csc \alpha} dx \right) \\
 & \times \exp(-jkx)(b - x \sin \alpha) \\
 & \times \left(\frac{1}{k_c} \left(1 + \left(\frac{k_c}{k} \right)^2 \right) \sin(k_c x \cos \alpha) \right. \\
 & \left. + \left(1 - \left(\frac{k_c}{k} \right)^2 \right) (a - x \cos \alpha) \cos(k_c x \cos \alpha) \right)
 \end{aligned} \quad (29)$$

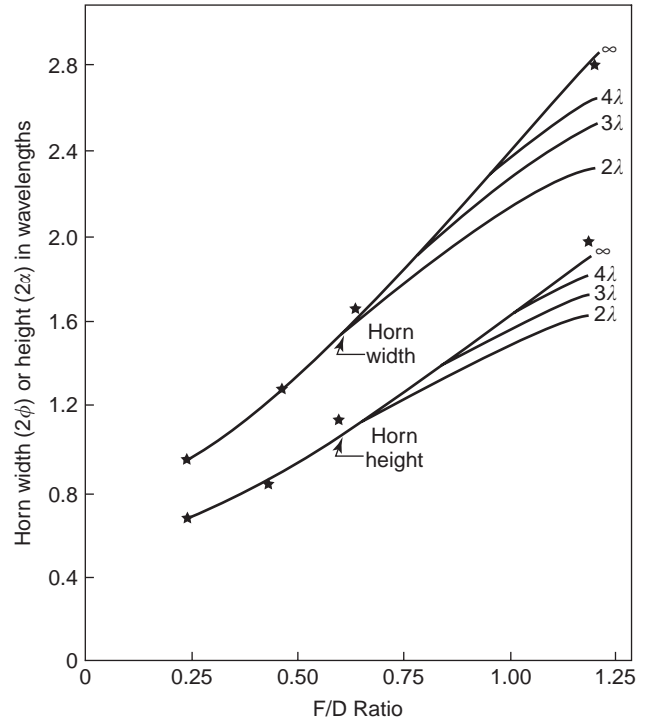


Figure 21. Optimum horn dimensions versus reflector F/D ratio for various rectangular horn lengths. (From Truman and Balanis [46], courtesy of IEEE.)

where $k_c = \pi/a$ and $\alpha_0 = a \tan(b/a)$. The aperture mismatch is -30 dB for $a > 2\lambda$ and $a < b < 2a$. When the height (b) is small compared with the width (a), as with some sectoral horns, the aperture mismatch can be significant (~ -20 dB).

2.2.1. Multimode Feeds. A way to improve the pattern of rectangular horns is to excite one or more additional modes to the TE_{10} mode to make the patterns in the two planes more identical or to reduce sidelobes. Beamshaping in rectangular horns can be achieved in the same way as with circular horns. As described by Cohn [8], changes of flare angle introduced along the length of the horn can be used to excite the required mixture of high-order modes, which must be brought into correct phase at the aperture. In particular, flare-angle changes can generate the TE_{12}/TM_{12} mode pair, and relative to the TE_{10} mode, the amplitude of the TE_{12}/TM_{12} modes is

$$A_{TE_{12}-TM_{12}} \approx \frac{2}{3} j \frac{(\theta_1 - \theta_2)s}{\lambda} \quad (30)$$

provided the flare angle change $|\theta_1 - \theta_2|$ is small ($< 25^\circ$), where s is the width of waveguide at the transition. Since the mixture of the TE_{12}/TM_{12} modes leads the phase of the TE_{10} -mode by 90° , this phase must be removed with a length of waveguide that gives 270° phase shift. Despite this complication, especially in designing the several flares to avoid breaking the condition described above, good pattern symmetry can be achieved over moderate bandwidths ($\sim 30\%$).

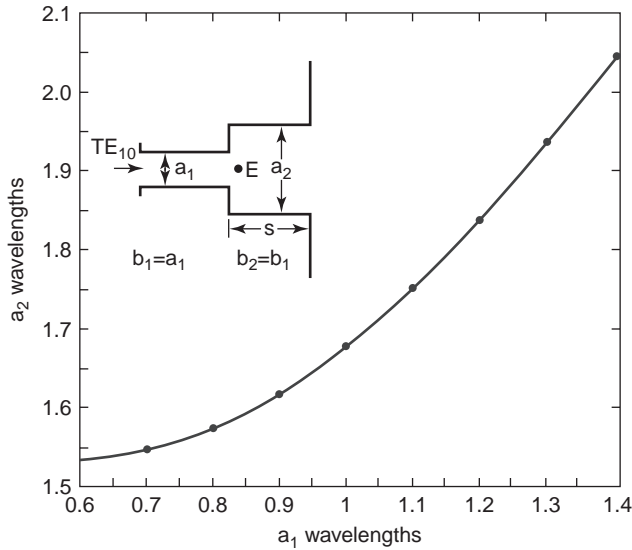


Figure 22. Width a_2 in the H plane required to produce a TE_{30} mode with amplitude $\frac{1}{3}$ of the TE_{10} mode in the aperture of a dual-mode rectangular horn, which is excited from a square waveguide with side length a_1 .

Rectangular horns are often used as feed elements in arrays to produce shaped beams from secondary reflectors for satellite communications. In such cases, the efficient illumination of the reflector is crucial, and this can be achieved with multimode horns. Multimode rectangular horns employ TE_{m0} ($m = 1, 3, 5, \dots$) modes with approximate amplitude of $1/m$ to improve the aperture field uniformity. This results in higher aperture efficiencies than horns with the fundamental mode alone, typically $>90\%$. The aperture dimension in the H plane of these horns needs to be at least $m\lambda/2$ for efficient excitation and for these modes to propagate. However, significant improvement in performance is achieved by exciting the TE_{30} mode in addition to the fundamental TE_{10} mode [3]. The TE_{30} mode is produced with an H -plane step, and Fig. 22 shows the dimension of the step in a square waveguide needed to produce a TE_{30} mode with an amplitude one-third that of the TE_{10} mode in the output waveguide [47]. This step excites the TE_{30} mode approximately 180° out of phase with the transmitted TE_{10} mode, and a length of waveguide s is required to equalize the mode phases at the aperture.

2.2.2. Diagonal Horn. Another type of dual-mode horn is the diagonal horn due to Love [48, 49]. Two spatially orthogonal modes TE_{10} and TE_{01} are excited with equal amplitude and phase in a square waveguide. This waveguide is then flared into the required aperture dimensions. The principal electric field of the diagonal horn is along one of the diagonals. While principal plane patterns are the same, in the intercardinal plane the copolar pattern is different and the cross-polarization is unacceptably high for most dual-polarized applications. The horn has optimal performance when the aperture size is relatively large

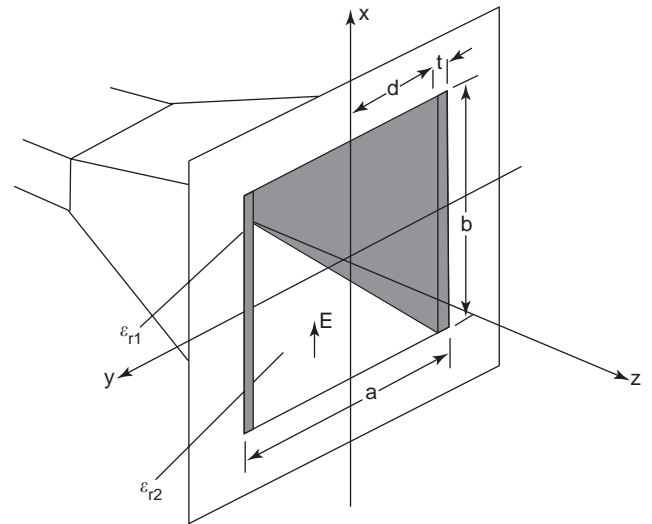


Figure 23. Dielectric-lined rectangular horn.

and, therefore, is suitable mainly for long-focal-length or dual-reflector applications.

2.2.3. Dielectric-Loaded Rectangular Horns. Another form of dielectric-loaded rectangular horn has a dielectric lining the wall parallel to the E plane. Dielectric loading of feed arrays of rectangular waveguides and pyramidal horns provides an extra degree of freedom in the design of shaped beams for satellite antennas. It improves the illumination efficiency of the array and can be applied to both small- and large-aperture horns. Usually the dielectric is placed on the walls that are parallel to the principal electric field, as in Fig. 23. The aperture field is almost uniform in the H plane if the dielectric thickness t is chosen to be approximately [50]

$$t \approx \frac{\lambda}{4\sqrt{\epsilon_{r1} - \epsilon_{r2}}} \quad (31)$$

where λ is the free-space wavelength and ϵ_{r1} and ϵ_{r2} are the dielectric constants in regions shown in Fig. 23. At the center frequency when t is given by (31), the radiation pattern of the dielectric-loaded horn is obtained from (12), where $F = G$ and F is given by

$$F(\theta, \phi) = 2bdS \left(U \frac{b}{2} \right) \left[S(Vd) + \frac{2t \cos\left(\frac{V\alpha}{2}\right) + \frac{2t}{\pi} V \sin(Vd)}{1 - \left(\frac{2t}{\pi} V\right)^2} \right] \quad (32)$$

where S , U , and V are defined in Table 2 while a , b , and d are defined in Fig. 23. The factor in the square brackets determines the H -plane pattern and the first term predominates if t/d is small. Consequently, for thin dielectric layers, the E - and H -plane radiation patterns have almost the same shape.

Another property of dielectric-loaded horns is that their gain can be greater than the corresponding unloaded

horn. For a uniform waveguide satisfying (31), with $\epsilon_{r2} = 1$ the relative aperture efficiency is

$$\frac{\eta_{\text{load}}}{\eta_{\text{unload}}} = \frac{\pi^2 d^2}{2a(a-t)} \left(1 + \frac{2t}{\pi d}\right)^2 \sqrt{1 - \left(\frac{\lambda}{2a}\right)^2} \quad (33)$$

where the subscripts “load” and “unload” refer to loaded and unloaded waveguide cases. Equation (33) shows, that for most commonly available dielectrics, an increase occurs only if $a > \lambda$. With dielectric loading, the H -plane beamwidth is usually less than in the unloaded case. This is important in array feed applications for satellites because the reflector edge is often overilluminated and, therefore, dielectric loading should help improve antenna efficiency. However, ohmic loss in the dielectric decreases the gain, but the thinner the dielectric layer, the lower the loss.

2.3. Rear-Radiating Feeds

In prime-focus-fed symmetric reflectors, blockage by the feed and feed support struts causes reduced gain and increased sidelobe levels. The loss of performance due to strut blockage can be eliminated by employing a self-supporting or axial feed antenna. Mechanical support is provided in this case by the transmission line, which extends from the reflector vertex to the feed. Such feeds have a long history, and many different types have been reported. Some examples are shown in Fig. 24.

All rear-radiating feeds depend for their operation on the efficient transition from the feeder line in the axial conductor to the radiator. Usually, it is this feature that limits the usable bandwidth to only a few percent of the operating frequency. For example, the match from the resonant dipole disk feed [3] shown in Fig. 24a is narrowband, and this is even worse for the feed in Fig. 24b, which incorporates a resonant ring to improve the radiation pattern [51]. In the Cutler feed [4] (Fig. 24c), two radiating slots are excited by a cavity driven from the waveguide transmission line. A tuning screw in the cavity improves the match, although the design remains essentially narrowband. The cup feed (an example is shown in Fig. 24d [52]) is distinguished by its axial symmetry, and a number of designs have been tried in order to achieve an effective transition from the circular waveguide to the cup region. An example of a cup feed design is a circular waveguide version of the Cutler feed using an annular slot; another design [53] uses coaxial waveguide sections at the end of the cup to improve the match. Both of these designs are relatively narrowband (approximately 5%). However, Schwerdtfeger [54] was able to achieve up to 20% bandwidth by exciting dipoles within the cup with a thin TEM transmission line.

The cup feed developed by Poulton and Bird [52] shown in Fig 24d uses a simple transition from circular waveguide to excite the cup. This produces a bandwidth of about 20%, and its symmetry allows dual polarization to be used. The waveguide to cup transition is most effective when the inner–outer conductor radius ratio (b/a) is ~ 0.5 . Radiation from the cup is due predominantly to the TE_{11} coaxial waveguide mode in the cup. This radiates in the

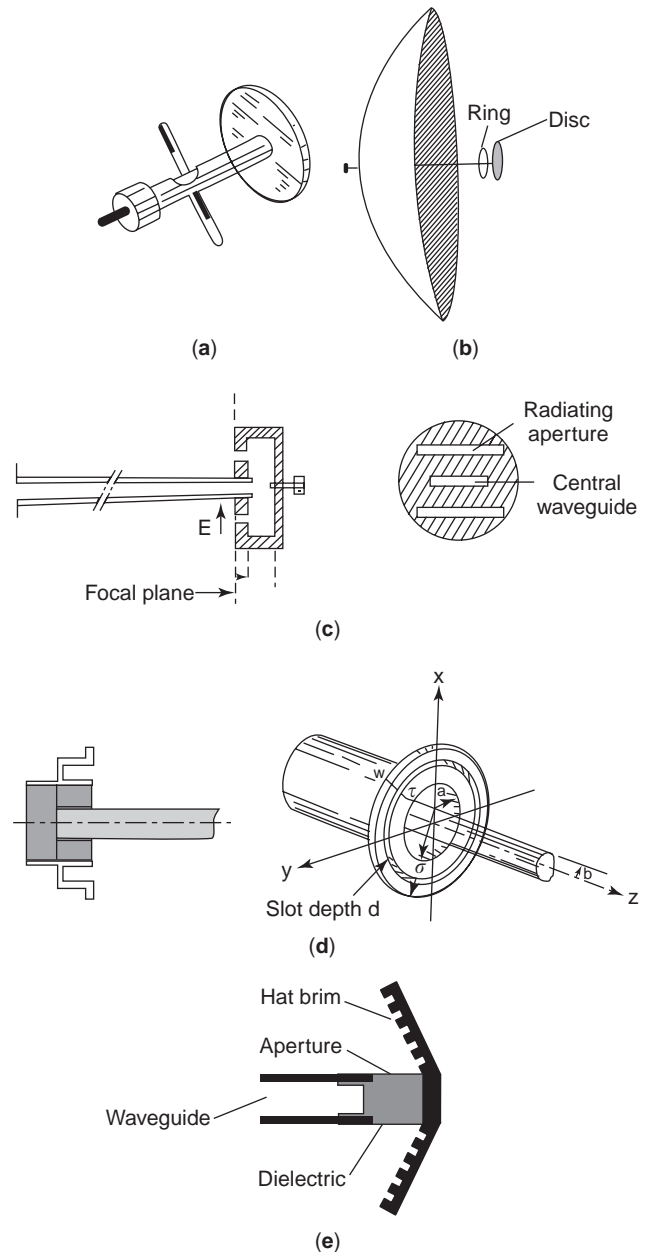


Figure 24. Rear-radiating feed antennas: (a) dipole and disk fed by transmission line (after Silver [3]); (b) the same as (a) with ring; (c) rectangular waveguide with radiating slots (after Cutler [4]); (d) cup feed (Poulton and Bird [52], Bird [55], courtesy of IEEE); (e) hat feed (after Kildal and Yang [57]).

presence of the supporting central conductor, which has a significant effect when the central conductor diameter is even moderately large. To keep cross-polar levels below -20 dB, the central conductor radius should be kept relatively small, typically $b/a < 0.3$ and $ka > 2.5$. A cup feed excited with an air-filled circular waveguide has a relatively poor performance with poor pattern symmetry and, as a result, has high levels of cross-polarization. Significantly improved performance is obtained by dielectric-loading the central conductor and this also provides mechanical support for the cup. The main disadvantage

of dielectric loading is matching into the feeder waveguide. Further improvement in the pattern is possible by adjusting the size of the flange surrounding the aperture and by inclusion of a concentric ring slot. The ring slot flange considerably improves the radiation performance over a narrow band (typically 5–10%) [55].

The “hat” feed of Kildal [56] and Kildal and Yang [57] shown in Fig. 24e uses a circular waveguide transmission line, a circumferential slot, and a corrugated reflecting brim. An iris-matching network is used in the waveguide to give a good match over a $\sim 15\%$ bandwidth. The feed is excited by a propagating TE_{11} mode in the waveguide, and this excites radial waveguide modes in the dielectric aperture. The $\lambda/4$ -deep corrugations ensure that the radiation pattern is symmetric with little spillover radiation. The beamwidth is relatively broad for a flat brim, but this can be reduced by angling the brim as shown in Fig. 24e.

2.4. Microstrip Feeds

Microstrip patch antennas are a possible alternative to horns in feed applications or as a feeder for a horn. The advantages of microstrip as a feed are its ease of integration with the system electronics, compact size, reduced weight, and lower volume compared with a horn. Multi-layer patch antennas can provide a return loss of 10 dB or better over a $\geq 50\%$ bandwidth. Microstrip feed antennas are used singly or in arrays and can be incorporated in a cavity or a horn to improve the radiation performance for feed applications where low noise temperature is required [58,59].

Microstrip antennas are suitably shaped printed circuits that are designed to radiate at discontinuities [60,61]. The most common types are rectangular and circular patches. Two simple models are used to describe these antennas. These are the cavity and transmission-line models. In the cavity model, the antenna, which is excited by a probe or a slot in the ground plane, sets up resonances in the cavity formed between the patch and the ground plane. The antenna radiates through currents set up around the edge of the patch. To take a circular patch, for example, the radius of the patch a is determined by the desired mode and its resonance frequency. The TM_{11} mode has suitable characteristics for feed antennas, and its resonance occurs at the first root of $J_1(k\sqrt{\epsilon_r}a) = 0$, where J_1 is the first-order Bessel function and ϵ_r is the dielectric constant of the substrate, which gives $a \approx 0.61\lambda/\sqrt{\epsilon_r}$. In the transmission-line model of a rectangular microstrip patch antenna, the radiation appears to occur at two rectangular apertures on either side of the patch, and these apertures are connected by a parallel-plate transmission line, which is the length ℓ of the patch. Now assume a patch of width w lies in the y - z plane on a substrate of thickness h . The radiated fields are given by (12), where F is approximately

$$F(\theta, \phi) = whS\left(\frac{kw}{2} \sin \theta \sin \phi\right) \cos\left(\frac{k\sqrt{\epsilon_r}\ell}{2} \cos \theta\right) \quad (34)$$

where the function $S(x)$ is defined in Table 2 and $G(\theta, \phi) = F(\theta, \phi)$. The first factor in (34) is due to the radiation

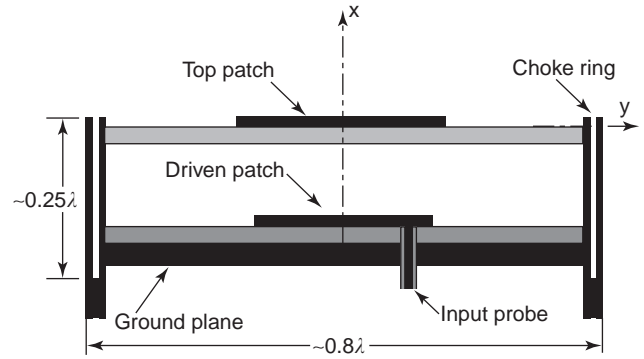


Figure 25. Two-layer circular microstrip antenna in a cavity with a choke ring.

pattern of the $w \times h$ apertures at the ends of the patch, while the second factor is a consequence of the pathlength between these apertures. In this geometry, the E plane is the $\phi = 0$ plane and the H plane corresponds to $\theta = 90^\circ$. Further discussion of the design of microstrip antennas is beyond the scope of this review; for further information, the reader should consult specialized texts [60,61].

The patterns given by (12) and (34) are asymmetric and produce high cross-polarization. By designing the ground-plane size (typically a diameter of $\sim 0.8\lambda$) and incorporating a choke at the edge of the ground plane, the pattern symmetry, and hence cross-polar performance, can be considerably improved over a ~ 5 – 10% bandwidth. The chokes also assist to reduce the spillover energy and rear lobes, which is important in low-noise applications. An example of a two-layer microstrip patch feed is shown in Fig. 25 [58,59].

2.5. Short-Backfire Antenna

A useful narrowband feed is the short-backfire antenna, particularly in low-frequency applications when compactness and light weight are important [62]. It has a relatively directive pattern, low sidelobes, and low rear lobes. The short-backfire antenna consists of two parallel-plate reflectors, spaced about $\lambda/2$ apart, and a driven element, a $\sim \lambda/2$ dipole shown in Fig. 26, placed about midway between the reflectors. In this arrangement the backfire antenna is basically a modified endfire array. One of the

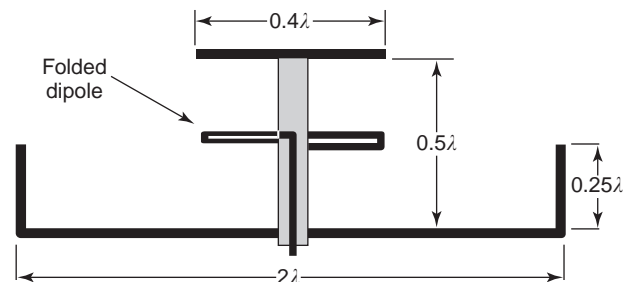


Figure 26. Geometry of a circular short backfire antenna fed by a folded dipole.

reflectors is small, and the energy concentrated between the reflectors radiates through this reflector. The larger rear reflector has a skirt of about $\lambda/4$ to reduce the side-lobes. Due to the resonant structure, the antenna has only about a 3% bandwidth. Rectangular waveguide versions of this antenna have also been proved useful.

3. LINEAR ANTENNA FEEDS

Historically, one of the earliest feeds for a reflector was a half-wave dipole, which was fed from a transmission line via a balun. The dipole is backed by a circular disk set about $\lambda/4$ away to produce a unidirectional radiation pattern (see Fig. 24a) [3, Chap. 8]. The disk diameter is $0.5-1\lambda$, depending on the required edge taper. Alternative to the circular disk, one or more parasitic elements can achieve a similar effect. This type of feed is relatively narrowband.

The extension of the parasitic array is the Yagi-Uda array and the logperiodic antennas (Fig. 27) [5,49,63,64]. These are often used as feeds, especially at low frequencies for practical considerations, such as low weight, and also because the latter can operate over relatively wide bandwidths. Other practical advantages are that they are low-profile, which minimizes blockage, and have relatively simple input requirements. A major disadvantage in wide-

band applications is the defocusing caused by axial phase center movement with frequency. The optimum feed design for maximum antenna gain changes with the angle subtended by the secondary antenna (e.g., F/D for a paraboloid). In narrowband applications, the Yagi-Uda or log-periodic array is placed at the focal point of the secondary antenna and defocusing loss is negligible.

The Yagi-Uda array consists of a center-driven dipole element with a number of parasitic elements arranged in the same plane. These parasitic elements increase the gain of the antenna over that of a single dipole. A longer parasitic element is a reflector and is opposite the main radiation direction. The shorter elements lying in the direction of the main radiation are called *directors*. Varying the length and spacing of the elements relative to the driven element optimizes the radiation pattern. The input match is sensitive to the first reflector element, and usually only one or possibly two reflectors are needed to control the rear radiation and hence the pattern front-to-back ratio. The typical dimensions of a Yagi-Uda feed for a reflector with $F/D = 0.4$ are given in Fig. 27a. The classical Yagi-Uda array has a limited bandwidth of $\sim 2\%$ and the directivity increases approximately with the number of directors.

The bandwidth of a linear antenna may be increased significantly by means of a logperiodic geometry that feeds all elements in the array instead of a single dipole (Fig. 27b). The logperiodic antenna consists of dipole elements arranged in a plane that have a constant ratio (τ) between the element's distance from the apex (x_n) and the dipole lengths (l_n). Successive dipole elements are excited by reversing the phase. The pattern depends on the apex angle (α) and element spacing (d_n) (Fig. 27b), usually expressed in terms of the parameter $\sigma = d_n/(2l_n)$. Higher gains occur with large τ and σ and small α . For broadband designs, logperiodic antennas with large α are favored, as the phase center is closer to the apex and suffers less from defocusing loss. Details of the optimum design of log periodic feeds are given by Imbriale [65].

The tapered zigzag antenna (Fig. 27c) has properties similar to those of the classical linear logperiodic array and can be more convenient to fabricate. It has found use as a wideband feed for a reflector with F/D ratios from ~ 0.4 to 0.5 . To ensure that correct scaling is achieved, the wire is replaced with a plane metal sheet that tapers along the antenna. As well as the parameter τ , the design of the logperiodic zigzag antenna depends on the two angles α and β shown in Fig. 27c as described by Lo and Lee [64, Chap. 9]. Of importance in feed design is that the E - and H -plane half-power beamwidths are similar when $\gamma = 2\alpha$.

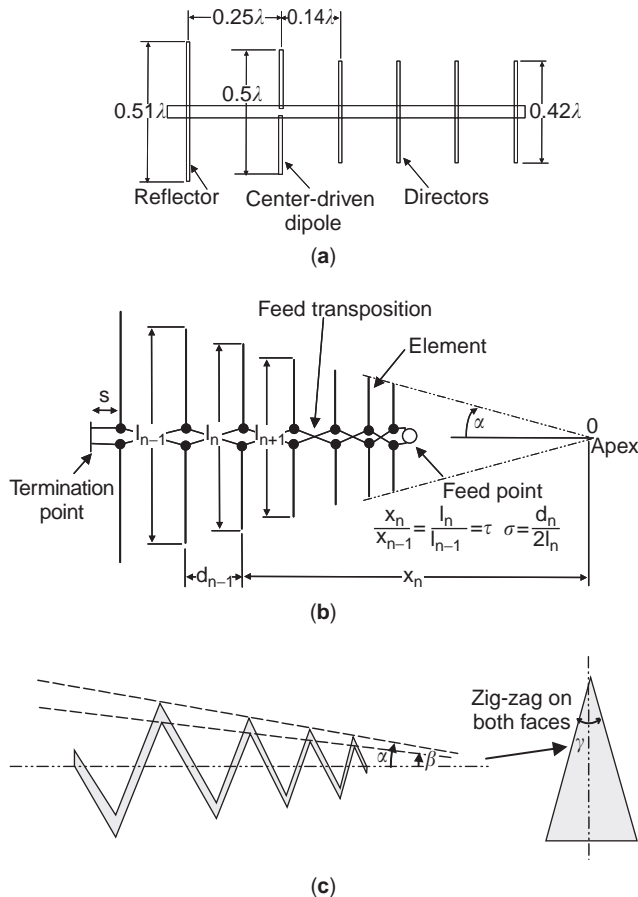


Figure 27. Linear feed antennas: (a) Yagi-Uda; (b) logperiodic; (c) zigzag.

4. TRAVELING-WAVE FEEDS

Traveling-wave antennas of the surface-wave type support a wave propagating along the antenna structure with a phase velocity $v < c$, producing an endfire beam. The distinctive feature of this type of antenna is that their directivity is proportional to their length. With traveling-wave antennas, the maximum directivity is achieved by meeting the Hansen-Woodyard condition [5], which requires that the phase difference between the surface wave and

the free-space wave be 180° at the termination of the antenna. Under this condition, the gain is $10 \log(10L/\lambda)$ dB and the beamwidth is $55\sqrt{\lambda/L}$ degrees, where L is the length.

Other excitation conditions give lower gain and side-lobe levels that are often more suitable for antenna feeds.

4.1. Dielectric Rod

The dielectric rod antenna is usually excited by an open-ended waveguide and has the property of a single lobe along the axis of the antenna. The wave traveling along the rod consists of hybrid modes whose fields exist inside and outside the dielectric. The radiation from a waveguide-fed dielectric rod has three main contributions: radiation from the waveguide-rod interface, radiation along the rod, and radiation at the end of the rod. To improve the match and prevent the occurrence of standing waves, the rod is often tapered either along its length or near its end. The choice of rod material is usually a compromise between size, directivity, and bandwidth. Both circular and rectangular dielectric-rod antennas are used [66,67]. Rods can be used in arrays and for ease of integration with electronics printed launchers have proved effective over a modest bandwidth (Fig. 28a) [68].

4.2. Traveling-Wave Slot

This type of antenna consists of a tapered slotline cut in a thin layer of metal, which is usually supported by a thin dielectric substrate on one side (Fig. 28b) [69,70]. The slotline is narrowed at one end to efficiently couple to the

feeding network and is tapered outward at the other end to improve radiation effectiveness. A traveling wave excited by the feed network propagates in the slot and radiates in an endfire direction at the tapered end. The energy in the traveling wave is tightly bound to the slotline when the separation distance is small compared to the free-space wavelength. An electric field is created across the slot, which produces a linearly polarized beam in the plane of the antenna (E plane). As the slotline width increases, radiation occurs most efficiently when the slotline width is about a half-wavelength. Tapered slot antennas have been found to have very wide bandwidths and the ability to generate a symmetric beam pattern despite their planar geometry.

The Vivaldi antenna (Fig. 28b) is one of a class of slot traveling-wave antennas and is characterized by an exponential curve for the taper in the slotline [71]. The antenna belongs to the class of aperiodic continuously scaled antenna structures, giving it the property of a theoretically infinite bandwidth. The Vivaldi antenna can produce a symmetric endfire beam (in both the E and H planes) with moderately high gain and low sidelobes. Figure 28b shows the basic geometry of the Vivaldi antenna and how the exponential taper is defined. Vivaldi antennas lend themselves well to being integrated with different types of circuits because of their planar construction. The radiating portion of the antenna is well separated and isolated from the nonradiating portion, allowing circuits to be integrated onto the dielectric at the nontapered end of the slot. It is common for the tapered slot to continue into a slotline circuit, which can then be fed by a microstrip/stripline to slotline transition or a finline. There are many variations of the Vivaldi antenna, including antipodal [72] and balanced configurations [73], which have, respectively, advantages of better feeding and lower cross-polarization than does the conventional Vivaldi. Arrays of Vivaldi antennas are used also as feeds for reflectors and lenses (Fig. 29).

4.3. Line-Source Feeds

Some secondary antennas, unlike the parabolic reflector, do not have a unique focus. Examples of such antennas are

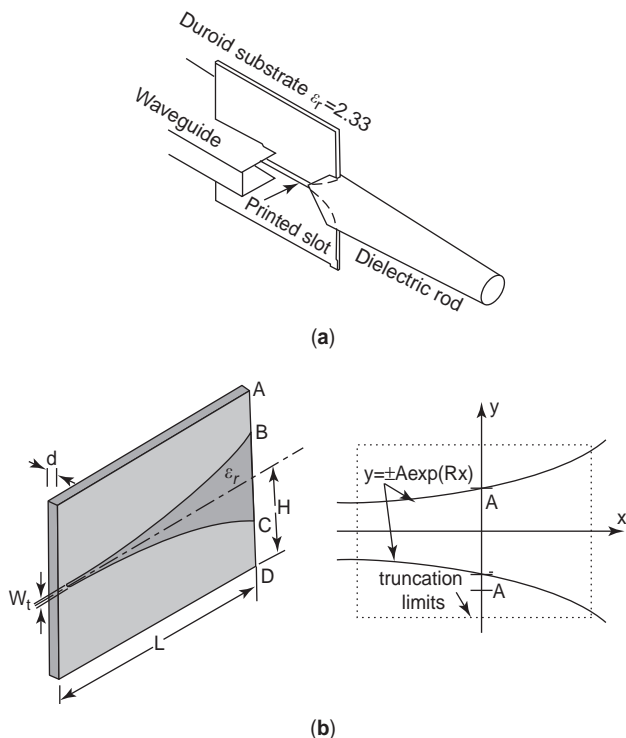


Figure 28. Traveling-wave feed antennas: (a) dielectric rod (From Qassim and McEwan [68], courtesy of IEE); (b) Vivaldi antenna.

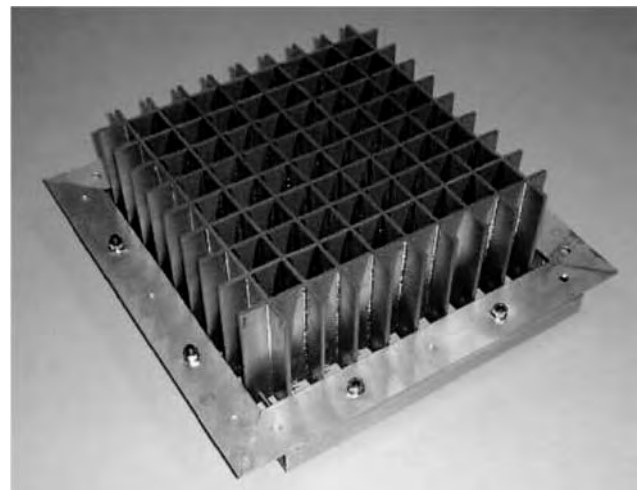


Figure 29. Dense-packed array of Vivaldi antenna elements for a focal plane array (courtesy of ASTRON).

spherical and cylindrical reflectors. In a spherical reflector (Fig. 2b), only the axial ray has a unique point focus on the axis and the remainder suffer from spherical aberration. There are several ways to correct for spherical aberration; one approach is to use a phased linefeed, which adds the incident radiation in correct phase at a single point. Rumsey [74] has detailed the condition for exciting a spherical reflector for maximum gain. This is a conjugate field match condition (1) where the feed produces a tangential electric field at the surface of a mathematical cylinder that just encloses it, equal to the conjugate of the field that would be produced by the reflector currents if the reflector were illuminated by a plane wave.

Linefeeds can be divided into two main types: those that use waveguides and those that use cables for phasing. A waveguide can support phase velocities higher than the velocity of light, and this gives the required aberration correction. Examples include channel waveguide, dielectric rod antennas, a combination of the previous two antennas as described by Love [75], and a slotted waveguide. In the latter, varying the slot length while maintaining a fixed slot width and constant slot spacing throughout controls the rate of radiation. Using the TE_{10} mode in a waveguide of rectangular cross section enables the phase velocity to be controlled by varying the cutoff wavelength, which depends on the wide dimension of the waveguide. The second approach is to use a linear array of radiating elements such as dipoles, microstrip patches, or Vivaldi elements, and achieve the correct phasing by adjusting the transmission-line lengths between the elements. The main limitation is that aberration correction can be maintained only over a very narrow bandwidth with conventional transmission lines. When the frequency is varied, phase errors arise and the gain of the antenna is reduced. This problem may be overcome by means of a correcting subreflector and a point feed in which the spherical aberration is corrected by introducing a correcting pathlength in air.

An example of a circularly polarized linefeed was a feed developed for the 300-m-diameter spherical reflector antenna at Arecibo [76,77]. This feed used slotted circular cylinders (Fig. 30a) with circumferential fins between each slot that acted as radial waveguides to provide the correct phasing between the two orthogonal fields within the fins. The slots and fins provided also a radiation pattern with the correct azimuthal dependence. To improve the illumination, a few of the upper feed elements of the azimuthally-directed slot fields were closed off to compensate for the finite length, and the spacing between the upper elements was reduced to lower spillover.

Another feed for spherical reflectors is the sectoral hoghorn shown in Fig. 30b [78]. This consists of a primary feed and a section of subreflector surface enclosed between parallel plates spaced $< \lambda/2$ apart. The aperture of the hoghorn is placed parallel to the incident rays in the receiving case. Energy from the spherical reflector is incident on the aperture of the hoghorn, and an appropriate pathlength is included in the parallel-plate region to produce in-phase addition of the incident energy at the primary feed.

A parabolic cylinder reflector antenna, which is a cylindrical reflector with a parabolic cross section, has a

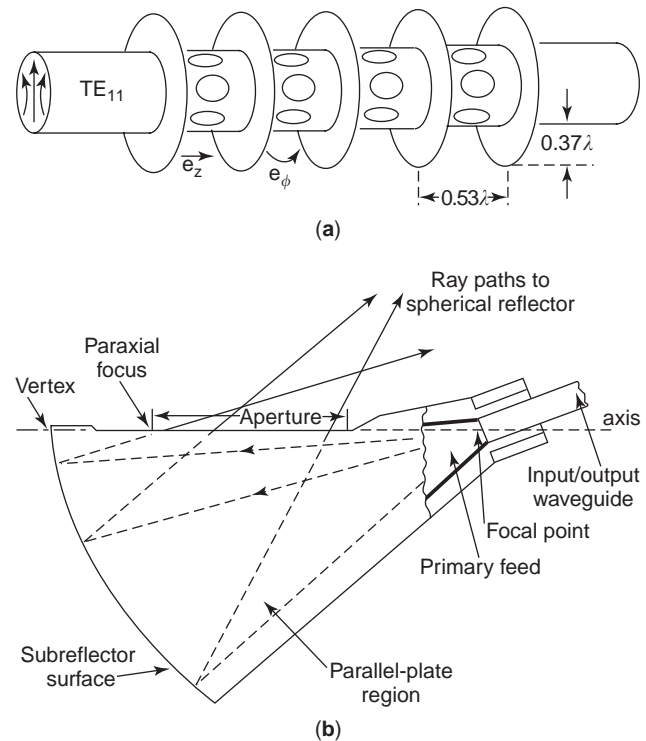


Figure 30. Line-source feeds: (a) slotted cylinder (From Love and Gustincic [76], courtesy of IEEE); (b) sectoral hoghorn (From Pratt and Shearman [78], courtesy of IEE).

linefeed along the focal line of the reflector. An example of a feed for this antenna is a linear array of crossed dipoles. The dipoles are located parallel and normal to the focal line, specifically, longitudinal and transverse polarizations. The two polarizations are fed separately through two completely branched transmission-line systems, exciting each dipole with identical amplitude and phase. The beam may be steered by adjusting the phasing of the elements. Another suitable feed for a parabolic cylinder is a pillbox horn [3]. These are usually single-polarization, although two polarizations can be obtained by stacking two orthogonally-polarized horns.

5. COMPOUND FEED ANTENNAS

Feeds for secondary antennas are sometimes made from a combination of the other types of feeds, reflectors, or resonant structures. The most common types of compound feeds are the array, beam waveguide, splash-plate (feed), and dichroic reflector.

5.1. Array Feeds

Single antenna feeds can be combined in arrays to create properties that are unattainable with more elementary antennas. Arrays of feeds are used for a variety of applications, including the creation of shaped beams, multiple pencil beams, beam scanning over a limited region of space, or correction of deficiencies in the reflector system arising from surface errors or misalignments. Single feeds or clusters are used to excite multiple beams. Overlapping

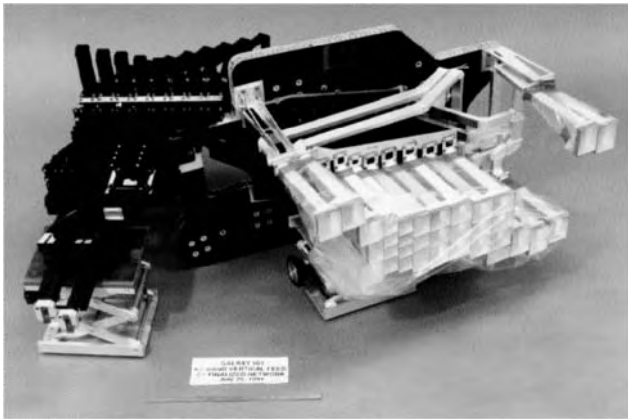


Figure 31. Array feed and beamforming network for the Galaxy IV satellite. (Courtesy of Hughes Aircraft Co.).

clusters can produce beams closer together than can arrays of single feeds. In pencil-beam applications where the array essentially compensates for the field distortion through the reflector, a natural design technique is conjugate-field matching (1). In this approach, the network connected to the array input excites the feeds so that the field in the aperture is the complex conjugate of the fields in the focal region that would be produced by a beam from the required direction. If there is more than one beam, then the array excitation is the conjugate of the superposition of focal fields of these beams.

The most common elements of feed arrays are waveguide horns, typically circular or rectangular cross section (see Figs. 14 and 31). The circular geometry is convenient for hexagonal array arrangements, while rectangular elements have advantages for producing shaped beams from satellites. Other types of array elements used for array feeds are tapered slot, dielectric rod, and microstrip patches.

Array feeds can also be phased to allow beam scanning over a limited angular range. If the spacing between elements is s , the maximum angular range the beam can be scanned before grating lobes appear is given by $\sin\theta_{\max} = \lambda/(2s)$. In typical practical arrays, $s \sim \lambda$ because of the physical size of the elements, and therefore the scan range of the feed is less than 30° . Grating lobes are not deleterious in some feed applications, except for lost power, provided these lobes do not illuminate the secondary antenna or a noisy source. The Vivaldi element allows greater close packing and therefore greater scan capability. Coaxial waveguides can also be used in arrays to achieve closer packing than with circular horns in applications requiring moderate bandwidths ($<20\%$) [79].

Another concern is the design of the individual elements in the array. For example, Amitay and Gans [80] showed that blindspots could exist as a result of forced aperture resonances in arrays of tapered rectangular horn elements with oversized (overmoded) apertures. The dominant contributor to these blindspots is the resonance of the equivalent transverse magnetic waveguide mode (TM_{12}). By appropriate design of the taper, these resonances can be avoided.

Another important effect to include in feed array design is the mutual coupling between the elements. Mutual

coupling affects both the input match and the radiated fields, particularly cross-polarization. Mutual coupling in finite arrays has been studied in detail for many different horn types, including rectangular [47,81], circular [82], and coaxial [83] apertures and also tapered-slot arrays [84]. The effect can be represented by a scattering matrix that is combined with the scattering matrices of the different elements constituting the array. The results obtained from a multimode analysis of mutual coupling are very accurate, and computer programs based on mode-matching methods have been widely used in satellite antenna and radio telescope feed array design [47,79]. In large arrays, prediction of the element patterns and array performance can be obtained using the Floquet periodic boundary conditions in combination with finite-element or finite-difference time-domain numerical methods (see Section 7).

5.2. Beam Waveguide

A beam waveguide feed uses a sequence of focusing elements to translate a beam pattern from a conventional feed horn to the secondary antenna. An example is shown in Fig. 32 for the NASA Deep Space Network [85]. The focusing elements may be reflectors or lenses, and sometimes polarizing grids are used to combine or separate two beams with orthogonal polarizations. The design technique commonly used is based on Gaussian beam propagation [86,87]. In this approach, the field radiated by the feed horn, usually a transversely corrugated horn, is represented by a sum of Gaussian beam modes. These modes have the characteristic that the amplitude has a Gaussian function variation with distance from the axis of propagation. The distance from the axis to the point where the Gaussian beam has decayed to $1/e$ of its value is called the beam waist (w), and this is a function of distance (z) along

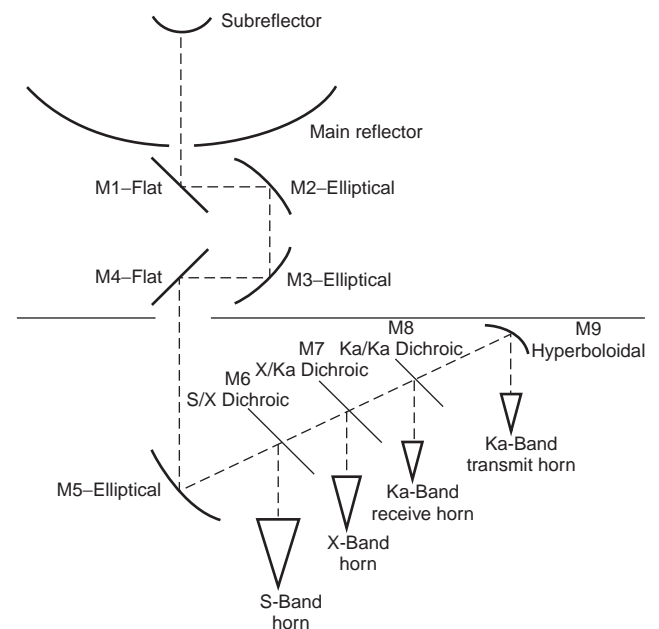


Figure 32. Geometry of beam waveguide system for the NASA Deep Space Network antenna DSS-25. (From Imbriale [85], courtesy of Wiley.)

the beam. Thus

$$w = w_0 \sqrt{1 + \left(\frac{\lambda z}{\pi w_0^2}\right)^2} \quad (35)$$

where w_0 is the minimum beam waist radius, which occurs where the radius of curvature of the wavefront is infinite, corresponding to a plane wave. The path through the sequence of reflectors, lenses, and grids can be represented step by step as a series of spreading transverse Gaussian beams. Each transformation from input to output beam through the focusing element can be represented by a 2×2 *ABCD* matrix, and the complete system can be found by concatenating these matrices. The *ABCD* matrices of different focusing elements is described by Kitsuregawa [86] and also Goldsmith [87], who also give many more details than there is space to record here. Ultimately, the method leads to output Gaussian beams that can be summed to give the field emanating from the beam waveguide. Kitsuregawa [86] provides a design procedure from feed horn to output reflector and design equations. If the focusing elements are moderate in size (say, >10 wavelengths, the minimum size for a beam waveguide element, but <50 wavelengths), it is prudent to calculate the effect of diffraction through the system using a more rigorous analysis method than Gaussian beams before completing the system design.

5.3. Splash-Plate Feeds

A splash-plate feed is a version of a self-supporting feed (Fig. 33). An open-ended waveguide irradiates a small reflector, the “splash-plate,” that is usually located a short distance s away. The splash plate then illuminates the

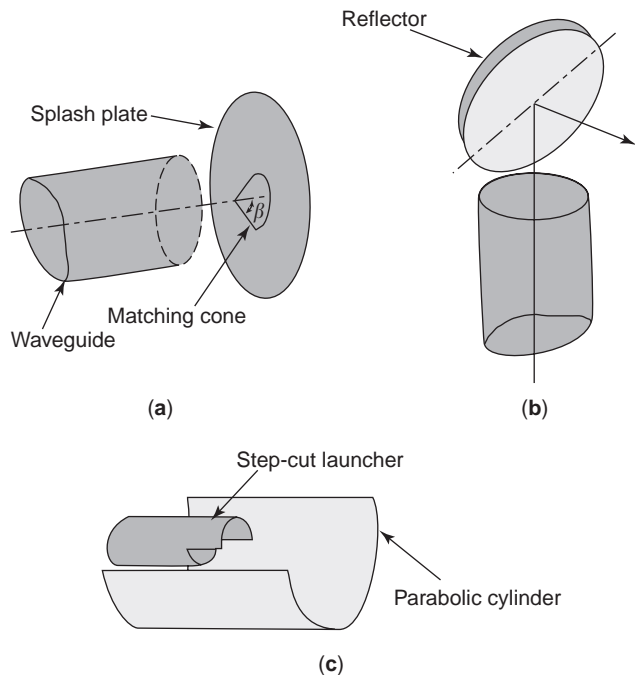


Figure 33. Splash-plate feeds: (a) vertex plate with matching cone; (b) periscope; (c) step-cut Vlasov mode converter.

secondary antenna, commonly a parabolic reflector. From image theory, the radiation pattern is approximately equal to that of the waveguide situated a distance s behind the plate and directed at the reflector, plus the edge diffraction field due to the rim of the splash plate [88]. Struts or a dielectric insert in the waveguide are often used to support the plate, which is usually about a wavelength in diameter and fitted with a cone or knob at the center to minimize the reflections back in the feed. The reflection coefficient in the waveguide is approximately given by [12]

$$\Gamma \approx \Gamma_{wg} + \frac{G_{wg}\lambda}{8\pi s} \left[\frac{R_1 R_2}{(R_1 + s)(R_2 + s)} \right]^{1/2} e^{-j(2ks + \theta_{wg})} \quad (36)$$

where Γ_{wg} is the reflection coefficient of the waveguide alone, s is the distance from the waveguide phase center to the splash plate, R_1 and R_2 respectively are the principal radii of curvature at the center of the splash plate, G_{wg} is the maximum gain of the waveguide, and θ_{wg} is a phase constant that depends on the reference plane in the waveguide; $\theta_{wg} = 0$ at the waveguide aperture.

The periscope feed in Fig. 33b is used to convert the beamshape to provide a more appropriate edge illumination for a secondary antenna. A third type of splash plate, the Vlasov mode converter shown in Fig. 33c, converts zero-azimuth index modes from high-power microwave and millimeter-wave sources into TE_{11} or HE_{11} modes for use in plasma heating and conventional antenna systems.

5.4. Dichroic Reflector

In the usual arrangement, a dichroic reflector (or frequency-selective surface) consists of an array of resonant slots or patches on a surface that is illuminated by signals in two frequency bands (see Fig. 34). The resonant elements are designed to reflect the fields of one feed in one frequency band and to transmit the fields of the second feed in the second band. In this way, a dual-band feed can be designed for a secondary reflector. The resonant patch approach uses a grid of crossed dipoles, resonant rings, concentric loops, or dumbbell-shaped patches printed on a dielectric surface that has the profile of the desired sub-reflector for the primary reflector [87]. These patches resonate at the frequency of the feed at the secondary focus of the surface, usually the higher of the two bands. The second feed is placed in the prime focus of the primary

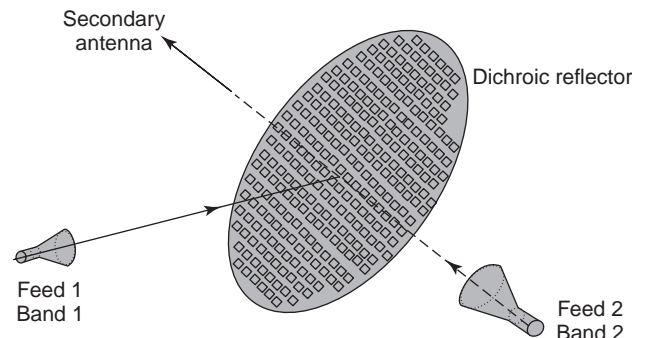


Figure 34. Dichroic reflector.

reflector, and at low frequencies the grid of patches and the dielectric is almost transparent. The complementary approach to resonant patches is to use a metallic reflector with resonant slots or perforations. Here the reflector reflects the signals at frequencies below the cutoff frequency of the slots and is transparent above this cutoff frequency. More frequency bands can be accommodated using more than one dichroic reflector as shown in Fig. 32.

6. FEED SYSTEMS

Following the feed antenna is usually a circuit consisting of waveguide, printed circuits, finline, or coaxial cables, and the design of these is a separate topic in itself. However, an overview of feed antennas would be incomplete without some mention of the circuit following the feed, which is commonly called the *feed system*. There are several major types of feed systems, depending on the application. Three types of feed system will be briefly mentioned, namely, diplexers, beamforming networks, and comparator networks for monopulse tracking.

6.1. Diplexing

After the feed antenna, the orthomode transducer (OMT) and (for circular polarization) a polarizer are basic components of the feed system. Uher et al. [89] detail design techniques for waveguide components used in feed systems. To date, the maximum continuous bandwidth achieved by both polarizers and OMTs is about 50%, and this limits the feed system configurations possible when considering multiband operation over wide frequency ranges. The means of diplexing several frequency bands can considerably complicate the feed system design. One of the “simpler” diplexing techniques is to use a series of dichroic plates to deflect selectively a given band to an appropriate feed system (Fig. 32). This type of diplexing can be designed using Gaussian beam optics analysis [87].

For dual-frequency operation, a number of feed system configurations are possible. If the individual bandwidths are small (typically less than 10%) and the overall bandwidth ratio to cover the two bands is less than $\sim 40\%$, then diplexing can take place at the OMT ports before the signals are combined through the OMT into a common waveguide and through the polarizer. In that case we need consider only a single polarized signal in the diplexer and associated filters. These are usually built in rectangular waveguide to maintain polarization purity. A feed system for reception of dual linear and circularized polarized signals is shown in Fig. 35.

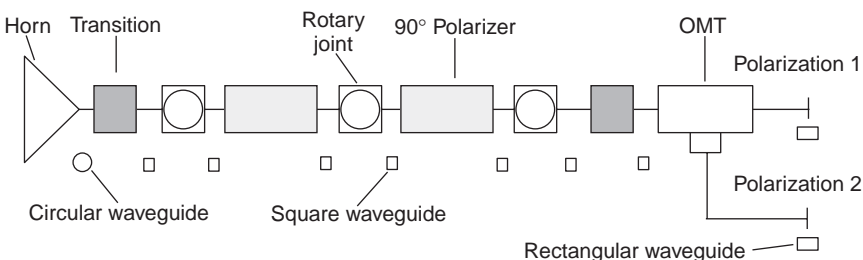


Figure 35. Schematic of a feed system for a dual linear/circular receive-only antenna.

For larger bandwidth requirements, it has been necessary to develop more sophisticated feed configuration schemes. An example of a dual-band, dual-polarized feed system for both circular and linear polarization is shown in Fig. 36 and has a very wideband dielectric-loaded horn. The lower-frequency band has a bandwidth of 24%, while the upper band has a bandwidth of 19%, with an interband separation ratio of $\sim 3.7:1$ [90]. The bands of this feed system are separated in a coaxial orthomode-junction diplexer where the center core of the coaxial waveguide is a loaded circular waveguide, which uses a low-loss dielectric with a permittivity of 2.4. This coaxial junction is matched to the horn with a dielectric of 1.15 permittivity by a dielguide section. The horn, dielguide section through to the coaxial junction, and beyond the highband rejection filter in the coaxial waveguide were completely analyzed by mode-matching methods, which was essential to obtain a workable design.

6.2. Beamforming Networks

A beamforming network (BFN) is required for an array feed to produce either a fixed illumination, as for the case of a shaped beam for a satellite, or variable illumination, if the feed is phased for radar systems. In satellite applications, the standard approach for producing contoured beams is with a parabolic reflector and an array feed of which the amplitude and phase at the input of each feed is supplied by a BFN, which must be low loss, low volume and light weight [91]. Typically, for Ku⁺ and Ka⁺ band these networks are realized in waveguide technology and for C band and lower frequencies, in TEM line. The BFN may need to be reconfigured into a number of fixed beams for different satellite orbital locations. The main components are power dividers, often 1-to-2-way, 1-to-4-way, or 1-to-8-way, fixed or variable, lengths of waveguide for phasing, variable phase shifters, and microwave switches. To achieve the best performance, the power divider couplers need to be accurately known and made. Accurate computer-aided design (CAD) software is used for this purpose and, with software based on methods such as mode matching, BFNs can be designed and built for flight without any trimming. An example of a beamforming network for a reflector providing a beam covering continental United States, Puerto Rico, Alaska, and Hawaii is shown in Fig. 37 [92]. The array itself is shown in Fig. 31. When the beam is scanned, rather than fixed, variable phase shifters are usually required. There are several ways of doing this, including uniform amplitude illumination over the array with variable phasing to steer the beam and use of Butler matrices with intervening phase shifters to

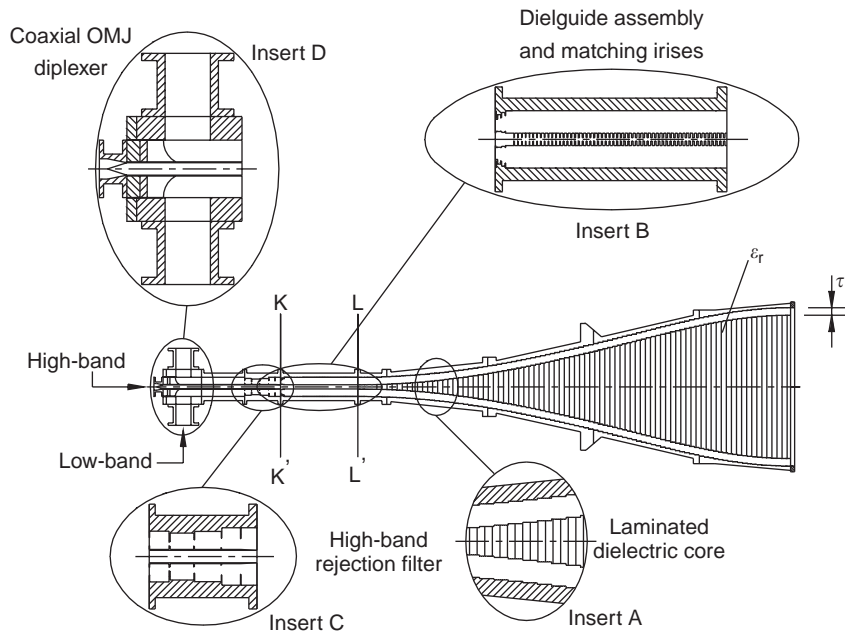


Figure 36. Dielectric cone-loaded feed system for dual-band applications. (From James et al. [90], courtesy of IEEE.)

produce multiple simultaneous beams. More details are given by Lo and Lee [64] and Mailloux [93].

6.3. Monopulse Feeds

A monopulse feed for a reflector or lens allows searching and tracking in radar and communications. The aim of such a feed is to produce sum, azimuth difference, and elevation difference signals from which tracking information can be obtained [94]. Among the available designs that use a secondary antenna there are three main types:

1. The first type uses four or five feeds arranged orthogonally in the focal plane of the secondary antenna. One arrangement uses four multimode rectangular feed horns and a suitable feed network to balance the efficiency of the sum and difference beams. A practical implementation of this design is given by Lee and Chu [95] (see Fig. 38a). These multimode horn designs suffer from different phase centers and different beamwidths between the sum and difference beams, which results in poor

efficiency for the sum beam and high spillover for the difference beam.

2. The second method uses a single circular waveguide input to a corrugated horn from a beamforming network, which produces appropriate modes to give the three tracking signals. In one implementation of this, due to Watson et al. [96], the beamforming network produces a combination of TM_{01} and TE_{21} modes.

3. The third method employs a single multimode horn and four input waveguides that control the modes excited in the horn by means of a comparator network (see Figs. 38b and 39). As shown in Fig. 40, a corrugated horn can be used in this case where the HE_{11} mode provides the sum beam while combinations of orthogonal HE_{21} modes with H_{01} and E_{02} modes of corrugated waveguide provide azimuth and elevation difference beams [97,98]. The challenge in this type of monopulse feed design is balancing the diameter of the horn at the junction, which gives the correct mode excitation, with the size of the input waveguides and also phasing the modes at the aperture.

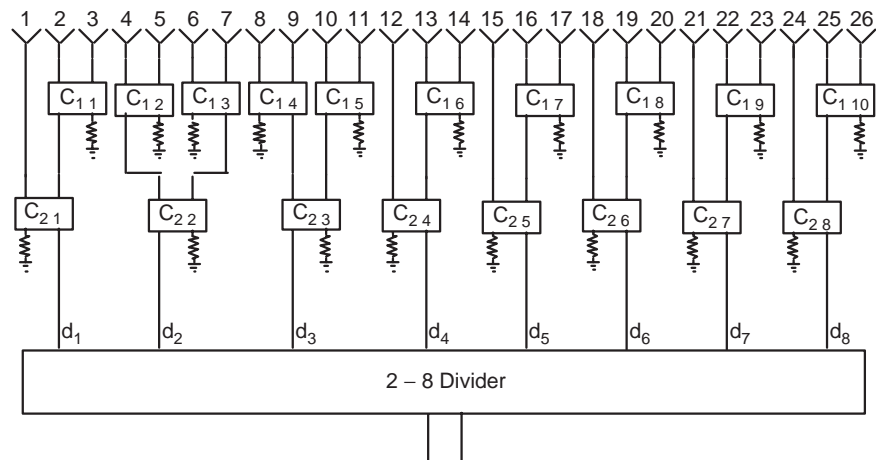


Figure 37. Beamforming network layout for the vertical transmit beam, where C_{mn} is the coupling value. (From Bird and Sroka [92].)

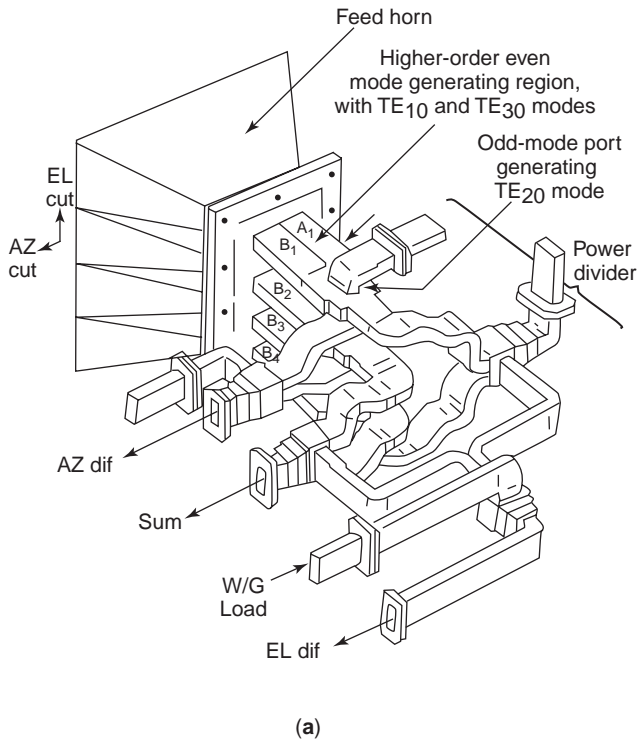


Figure 38. Monopulse tracking feeds: (a) multifeed array (From Lee and Chu [95], courtesy of IEEE); (b) multimode monopulse feed.

Rectangular waveguide can be used, but square waveguide allows better performance. While greater beam efficiency is obtained for all beams at the center frequency, the bandwidth for best performance is typically narrow (~2%) and the match is often poor for the difference beam (reflection coefficient ~ -10 dB).

7. DESIGN METHODS

A feature of modern antenna feed design is the extent to which accurate computer software is now used. Electromagnetic software is used to analyze both the antenna and

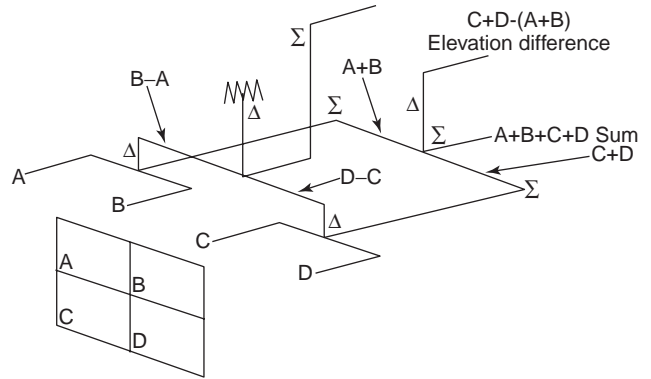
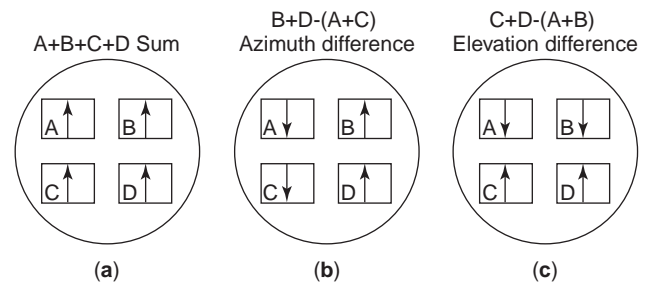


Figure 39. Schematic of a monopulse comparator (Σ and Δ respectively indicate sum and difference ports of four-port magic-T junctions). (After Zhang et al. [98], courtesy of Wiley.)

the feed system. While many analysis methods are available, the main software packages are based on five principal analysis methods: the finite-difference time-domain (FDTD), the finite-element method (FEM), mode matching (MM), method of moments (MoM), and the transmission-line matrix (TLM) method [99]. In the past, the most widely used were MoM and the MM technique because radiation is easily and accurately incorporated. However, with improvements in artificial boundary conditions, the accuracy of the more general finite methods such as FDTD and FEM is approaching that of the traditional methods. Hybrid methods are also used, and these can give additional flexibility. Methods used to design components



Signal	Aperture distribution	Modes
Sum		
Azimuth difference		
Elevation difference		

Figure 40. Mode excitations used to create (a) sum, (b) azimuth difference, and (c) elevation difference patterns; (d) desired aperture field distribution in horn and associated modes. (After Zhang et al. [98], courtesy of Wiley.)

relevant to antenna feeds are reviewed in articles by Steer et al. [100] and Arndt et al. [101].

The most accurate method currently available for aperture-type feeds employs a combination of MM and MoM. The former is used to analyze the internal structure and MoM, the outer structure. To analyze a device by the mode-matching method, the scattering matrix solution of the transverse modal coefficients is required at each discrete boundary surface that describes the geometry of the structure. By cascading these matrices, we can completely characterize the device [10,101]. This technique has been used with great success in analyzing numerous waveguide horns, arrays, and components. While a common elemental or building-block solution required to analyze complex structures in circular waveguide components is the junction between two circular waveguides, other scattering matrix solutions are available for junctions between coaxial waveguides, partially filled circular waveguides, rectangular waveguides, elliptical waveguides, and ridged waveguides as well as junctions between rectangular and circular waveguides. In all cases, however, the basic procedure remains the same. Radiation from the outer structure is expressed as a summation of elementary radiating current sources, called a *Green function integral equation*. The currents are approximated by many simple functions, called *shape functions*, such as triangular functions for line currents [99] and the “rooftop tiles” of Rao et al. [102] for surface currents. The mode matching and integral equations are solved together to give the mode amplitudes in the aperture and the external currents. Once these are known, the radiated field is found by summing the contributions from all modes and sources. It is important to include all high-order terms in the radiation calculation, especially when the feed and reflector are within the Fresnel (near-field) zone, as ignoring these terms can lead to significant errors in predicting cross-polarization and phase center. This particular approach can predict the performance of horn antennas very accurately down to the -60 dB level of the radiation pattern.

Proprietary electromagnetics software, such as Ansoft’s HFSS [103] and CST Microwave Studio [104], is now achieving impressive results that more specialized software achieved in the past. As an example, Fig. 41 shows the three-dimensional drawing of a quad-band feed system that has been analysed with Microwave Studio. The results for the input reflection coefficient for all bands show excellent agreement with accurate mode-matching software and measurement.

Another aspect of design is optimization of performance and, until only relatively recently, computer speed limited the degree this was possible. Now, for example, horns are regularly designed by MM to suit particular performance criteria by optimizing the profile [33]. Optimizers are also employed in many electromagnetics software packages to adjust the geometry to peak the performance [100].

8. FUTURE OUTLOOK

The developments in antenna feeds go in parallel with new applications and improvements in software, materials, devices, and manufacturing methods. The inexorable

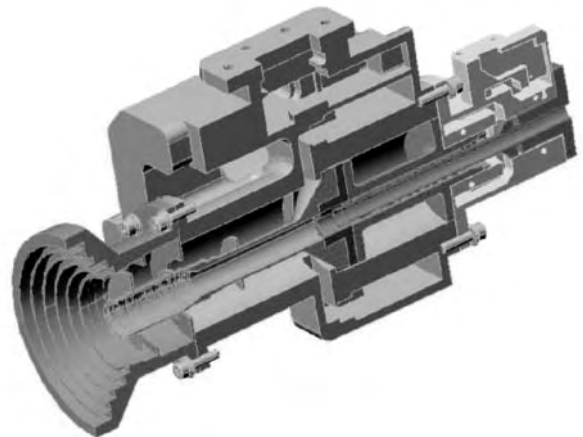


Figure 41. Cutaway drawing of a quad-band feed system analyzed completely with computer software. (© CSIRO.)

push for higher levels of integration in future systems should see active devices, both receivers and transmitters, fully integrated with the feed antenna. At the moment, lower bandwidth capability and higher initial cost of these units is limiting wider use of integrated feeds. The ability to manufacture a feed antenna has, in the past, limited some of the antennas that are used. With further improvements in software, materials, and computer-aided manufacture, some of these limitations should reduce. Of the feed antennas themselves, we expect to see more multi-band and wideband feeds, which will allow system designers to provide greater flexibility and functionality. Some examples of these wideband feeds that will be more widely used are dielectric-lined horns and arrays of traveling-wave slots. The means of extracting the different frequency bands or wideband signals from these antennas remains a challenging problem.

Antenna feeds are by definition used in conjunction with other antennas forming a system. In the past, these antennas were designed separately, and the effect of the interactions between them was ignored as insignificant or calculated approximately. Effects such as scattering from reflectors, feeds, struts, or the supporting structure itself can be important contributors to cross-channel interference in communication systems. It is expected that future computers and software will allow the design and optimization of complete antenna systems as a matter of course. Encouraging steps have been made in this direction in recent years. While these developments depend heavily on improvements in computers, software, and display technology, the search continues for the most accurate and fastest electromagnetics methods for analysis and optimization of antenna feeds.

BIBLIOGRAPHY

1. J. H. Bryant, *Heinrich Hertz—the Beginning of Microwaves*, IEEE Inc., New York, 1988.
2. J. F. Ramsay, Microwave antenna and waveguide techniques before 1900, *Proc. IRE* **46**:405–415 (1958).
3. S. Silver, *Microwave Antenna Theory and Design*, McGraw-Hill, New York, 1949.

4. C. C. Cutler, *Directional Microwave Antenna*, U.S. Patent 2,442,184 (1947).
5. C. A. Balanis, *Antenna Theory: Analysis and Design*, Harper & Row, New York, 1982.
6. P. D. Potter, A new horn antenna with suppressed sidelobes and equal beamwidths, *Microwave J.* **6**:71–78 (June 1963).
7. B. MacA. Thomas, A review of the early developments of circular-aperture hybrid-mode corrugated horns, *IEEE Trans. Anten. Propag.* **AP-34**:930–935 (1986).
8. S. B. Cohn, Flare-angle changes in a horn as a means of pattern control, *Microwave J.* **13**:41–46 (Oct. 1970).
9. A. W. Love, ed., *Electromagnetic Horn Antennas*, IEEE Press, New York, 1976.
10. A. D. Olver, P. J. B. Clarricoats, A. A. Kishk, and L. Shafai, *Microwave Horns and Feeds*, Peter Peregrinus, London, 1994.
11. P. C. Loux and R. W. Martin, Efficient aberration correction with a transverse focal plane array technique, *IRE Int. Convention Record* **12**:125–131 (1964).
12. W. V. T. Rusch and P. D. Potter, *Analysis of Reflector Antennas*, Academic Press, New York, 1970.
13. S. G. Hay, F. R. Cooray, and T. S. Bird, Accurate modelling of edge diffraction in arrays of circular and rectangular horns, *Journées Internationales de Nice sur les Antennes (JINA)* 645–648 (1996).
14. T. S. Bird, TE₁₁ mode excitation of flanged circular coaxial waveguides with an extended center conductor, *IEEE Trans. Anten. Propag.* **AP-35**:1358–1366 (1987).
15. T. S. Bird, G. L. James, and S. J. Skinner, Input mismatch of TE₁₁ mode coaxial waveguide feeds, *IEEE Trans. Anten. Propag.* **AP-34**:1030–1033 (1986).
16. G. L. James, Cross-polarization performance of flanged cylindrical and conical waveguides, *Proc. IREE (Australia)*, **40**:180–184 (1979).
17. B. MacA. Thomas, Design of corrugated conical horns, *IEEE Trans. Anten. Propag.* **AP-26**:367–372 (1978).
18. P. J. B. Clarricoats and A. D. Olver, *Corrugated Horns and Microwave Antennas*, Peter Peregrinus, London, 1984.
19. G. L. James and B. MacA. Thomas, TE₁₁ to HE₁₁ cylindrical waveguide mode converters using ring-loaded slots, *IEEE Trans. Microwave Theory Tech.* **MTT-30**:278–285 (1982).
20. B. MacA. Thomas, G. L. James, and K. J. Greene, Design of wide-band corrugated conical horns for Cassegrain antennas, *IEEE Trans. Anten. Propag.* **AP-34**:750–757 (1986).
21. G. L. James, Design of wide-band compact corrugated horns, *IEEE Trans. Anten. Propag.* **AP-32**:1134–1138 (1984).
22. C. del Rio, R. Gonzalo, and M. Sorolla, High purity Gaussian beam excitation by optimal horn antenna, *Proc. Int. Symp. Antennas and Propagation (ISAP)*, 1996, pp. 1133–1136.
23. Z. Ying, A. A. Kishk, and P.-S. Kildal, Broadband compact horn feed for prime-focus reflectors, *Electron. Lett.* **31**:1114–1115 (1995).
24. H. Wolf, The Scrimphorn, a new compact multimode horn for array application, *Proc. JINA* 446–449, 1988.
25. M. Takabayashi, H. Deguchi, S. Makino, and T. Katagi, A design method of double bands dual mode conical horn antenna by using generalized transmission equation, *Proc. ISAP*, 1996, Vol. 2, pp. 922–925.
26. T. Satoh, Dielectric-loaded horn antenna, *IEEE Trans. Anten. Propag.* **AP-20**:199–201 (1972).
27. K. Raghavan, D. N. Paul, and P. S. Bains, *Low Cross-Polarization Radiator of Circularly Polarized Radiation*, U.S. Patent 4, 972, 199 (1990).
28. L. Staveley-Smith, W. E. Wilson, T. S. Bird, M. J. Disney, R. D. Ekers, K. C. Freeman, R. F. Haynes, M. W. Sinclair, R. A. Vaile, R. L. Webster, and A. E. Wright, The Parkes 21 cm multibeam receiver, *Publ. Astron. Soc. Austral.* **14**(3):243–248 (1996).
29. A. Bhattacharyya and G. Goyette, Step horn antenna with high aperture efficiency and low cross-polarization, *Electron. Lett.* **38**:1495–1496 (2002).
30. B. MacA. Thomas, Prime-focus one- and two-hybrid-mode feeds, *Electron. Lett.* **6**:460–461 (1970).
31. R. F. Thomas and D. A. Bathkar, *A Dual Hybrid Mode Feed Horn for DSN Antenna Performance Enhancement*, JPL DSN Progress Report 42-22, 1974, pp. 101–108.
32. G. G. Gentili, E. Martini, R. Nesti, and G. Pelosi, Performance analysis of dual profile corrugated circular waveguide horns for radioastronomy applications, *IEE Proc. Microwave Anten. Propag.* **148**:119–122 (2001).
33. C. Granet and T. S. Bird, Optimization of corrugated horn radiation patterns via a spline-profile, *ANTEM*, Montreal, Canada, July 27–29, 2002, pp. 307–310.
34. G. L. James, P. R. Clark, G. R. Graves, and T. S. Bird, The S/X-band feed for the Tasmanian Earth Resources Satellite Station (TERSS), *J. Electric. Electron. Eng. Austral.* **15**:307–314 (1995).
35. R. I. Henderson and P. J. Richards, Compact circularly-polarised coaxial feed, *IEE Int. Conf. Antennas and Propagation (ICAP)*, 1995, pp. 327–330.
36. J. C. Chen, P. H. Stanton, and H. F. Reilly, X/X/Ka-band horn design, *Proc. IEEE Antennas and Propagation Society Int. Symp.*, 1996, Vol. 3, pp. 2022–2025.
37. D. Green and D. Smith, Wide flare-angle horn antenna with means for radiating low levels of crosspolarization in two widely separated frequency bands, *Proc. IEEE Antennas and Propagation Society Int. Symp.*, 1996, Vol. 3, pp. 2026–2029.
38. S. Amari and J. Bornemann, A study of the symmetry of field patterns of elliptic horns fed by elliptic apertures, *Proc. IEEE Antennas and Propagation Society Int. Symp.*, 1996, Vol. 3, pp. 1992–1995.
39. M. E. J. Jeuken and L. F. G. Thurlings, The corrugated elliptical horn antenna, *Proc. IEEE Antennas and Propagation Society Int. Symp.*, 1975, pp. 9–12.
40. R. F. E. Guy and R. W. Ashton, Cross-polar performance of an elliptical corrugated horn antenna, *Electron. Lett.* **15**:400–402 (1979).
41. E. Lier, A dielectric hybrid mode antenna feed: A simple alternative to the corrugated horn, *IEEE Trans. Anten. Propag.* **AP-34**:21–29 (1986).
42. G. L. James, Propagation and radiation from partly filled elliptical waveguide, *IEE Proc.* **136**(Part H):195–201 (1989).
43. P. R. Clark and G. L. James, Ultra-wideband hybrid-mode feeds, *Electron. Lett.* **31**:1968–1969 (1995).
44. E. Lier, Y. Rahmat-Samii, and S. R. Rengarajan, Application of rectangular and elliptical dielectric core feed horns to elliptical reflector antennas, *IEEE Trans. Anten. Propag.* **AP-39**:1592–1597 (1991).
45. P. R. Clark and G. L. James, Analysis of hybrid-mode feed horns with simulated dielectric material, *Proc. IEEE Antennas and Propagation Society Int. Symp.*, 1994, Vol. 2, pp. 772–775.
46. W. M. Truman and C. A. Balanis, Optimum design of horn feeds for reflector antennas, *IEEE Trans. Anten. Propag.* **AP-22**:585–586 (1974).

47. T. S. Bird, Mode matching analysis of arrays of stepped rectangular horns and application to satellite design, *Proc. IEEE Int. Conf. Antennas and Propagation (ICAP)*, 1991, pp. 849–852.
48. A. W. Love, The diagonal horn antenna, *Microwave J.* **5**:117–122 (March 1962).
49. R. C. Johnson and H. Jasik, eds., *Antenna Engineering Handbook*, McGraw-Hill, New York, 1984.
50. G. N. Tsandoulas and W. D. Fitzgerald, Aperture efficiency enhancement in dielectrically loaded horns, *IEEE Trans. Anten. Propag.* **AP-20**:69–74 (1972).
51. P.-S. Kildal, A small dipole fed resonant reflector antenna with high efficiency, low cross-polarization and low side-lobes, *IEEE Trans. Anten. Propag.* **AP-33**:1386–1391 (1985).
52. G. T. Poulton and T. S. Bird, Improved rear-radiating cup feeds, *Proc. IEEE Antennas and Propagation Society Int. Symp.*, 1986, Vol. 1, pp. 79–82.
53. D. W. Griffin, *Improvements in or Relating to Radiating Waveguide Feeders for Radio-frequency Electromagnetic Waves*, UK Patent 825, 532 (1959).
54. R. Schwerdtfeger, A coaxial dual mode feed system, *Proc. IEEE Antennas and Propagation Society Int. Symp.*, 1979, pp. 286–289.
55. T. S. Bird, A ring-slot flange for rear-radiating cup feeds, *Proc. IEEE Antennas and Propagation Society Int. Symp.*, 1987, Vol. II, pp. 672–675.
56. P.-S. Kildal, The hat feed: A dual-mode rear radiating waveguide antenna having low cross-polarization, *IEEE Trans. Anten. Propag.* **AP-35**:1010–1016 (1987).
57. P.-S. Kildal and J. Yang, FDTD optimization of the bandwidth of the hat feed for mm-wave reflector antennas, *Proc. IEEE Antennas and Propagation Society Int. Symp.*, 1997, Vol. 3, pp. 1638–1641.
58. A. A. Kishk and L. Shafai, Optimization of microstrip feed geometry for prime focus reflector antennas, *IEEE Trans. Anten. Propag.* **AP-37**:445–451 (1989).
59. A. K. Singh and G. Kumar, EMCP microstrip antennas as feed for satellite receiver, *Proc. IEEE Antennas and Propagation Society Int. Symp.*, 1996, Vol. 2, pp. 1274–1277.
60. J. R. James and P. S. Hall, *Handbook of Microstrip Antennas*, Peter Peregrinus, London, 1989.
61. R. A. Sainati, *CAD of Microstrip Antennas for Wireless Applications*, Artech House, Boston, 1996.
62. A. Kumar and H. D. Hristov, *Microwave Cavity Antennas*, Artech House, Norwood MA, 1989.
63. A. W. Rudge, K. Milne, A. D. Olver, and P. Knight, eds., *The Handbook of Antenna Design*, Vols. 1 and 2, Peter Peregrinus, London, 1986.
64. Y. T. Lo and S. W. Lee, *Antenna Handbook*, Van Nostrand-Reinhold, New York, 1988.
65. W. A. Imbriale, Applications of the method of moments to thin-wire elements and arrays, in R. Mittra, ed., *Numerical and Asymptotic Techniques in Electromagnetics*, Springer-Verlag, New York, 1975.
66. D. G. Kiely, *Dielectric Aerials*, Methuen, London, 1953.
67. C. Salema, C. Fernandes, and R. K. Jha, *Solid Dielectric Horn Antennas*, Artech House, Boston, 1998.
68. K. A. S. Qassim and N. J. McEwan, Focal plane dielectric rod arrays with printed launchers, *IEE Int. Conf. Antennas and Propagation (ICAP)*, 1993, Vol. 2, pp. 792–795.
69. L. R. Lewis, M. Fasset, and J. Hunt, A broadband stripline array element, *Proc. IEEE Antennas and Propagation Society Int. Symp.*, 1974, pp. 335–337.
70. D. H. Schaubert, E. L. Kollberg, T. L. Korzeniowski, T. Thungren, J. F. Johansson, and K. Yngvesson, Endfire tapered slot antennas on dielectric substrates, *IEEE Trans. Anten. Propag.* **AP-33**:1392–1400 (1985).
71. P. J. Gibson, The Vivaldi aerial, *Proc. 9th European Microwave Conf.*, Brighton, UK, 1979, pp. 101–105.
72. E. Gazit, Improved design of Vivaldi antenna, *IEE Proc.* **135**:89–92 (1988).
73. J. D. S. Langley, P. S. Hall, and P. Newham, Novel ultrawide-bandwidth Vivaldi antenna with low crosspolarisation, *Electron. Lett.* **29**:2004–2005 (1993).
74. V. H. Rumsey, On the design and performance of feeds for correcting spherical aberration, *IEEE Trans. Anten. Propag.* **AP-18**:343–351 (1970).
75. A. W. Love, Spherical reflecting antennas with corrected line sources, *IRE Trans. Anten. Propag.* **AP-10**:529–537 (1962).
76. A. W. Love and J. J. Gustincic, Line source feed for a spherical reflector, *IEEE Trans. Anten. Propag.* **AP-16**:132–134 (1968).
77. A. W. Love, Scale model development of a high efficiency dual polarized line feed for the Arecibo spherical reflector, *IEEE Trans. Anten. Propag.* **AP-21**:628–639 (1973).
78. T. Pratt and E. D. R. Shearman, Sectoral hoghorn: A new form of line feed for spherical reflector aerials, *Electron. Lett.* **5**:1–2 (1969).
79. T. S. Bird, Coaxial feed array for a short focal-length reflector, *Proc. IEEE Antennas and Propagation Society Int. Symp.*, 1997, Vol. 3, pp. 1618–1621.
80. N. Amitay and M. J. Gans, Design of rectangular horn arrays with oversized aperture elements, *IEEE Trans. Anten. Propag.* **AP-29**:871–884 (1981).
81. T. S. Bird, Analysis of mutual coupling in finite arrays of different-sized rectangular waveguides, *IEEE Trans. Antennas Propag.* **AP-38**:166–172 (1990).
82. M. C. Bailey and C. W. Bostian, Mutual coupling in a finite array of circular apertures, *IEEE Trans. Anten. Propag.* **AP-22**:178–184 (1974).
83. T. S. Bird, Mutual coupling in arrays of coaxial waveguides and horns, *IEEE Trans. Anten. Propag.* **AP-52**:821–829 (2004).
84. D. H. Schaubert, J. A. Aas, M. E. Cooley, and N. E. Buris, Moment method analysis of infinite stripline-fed tapered slot antenna arrays with a ground plane, *IEEE Trans. Anten. Propag.* **AP-42**:1161–1166 (1994).
85. W. A. Imbriale, *Large Antennas of the Deep Space Network*, Wiley-Interscience, Hoboken, NJ, 2003.
86. T. Kitsuregawa, *Advanced Technology in Satellite Communication Antennas*, Artech House, Boston, 1990.
87. P. F. Goldsmith, *Quasioptical Systems—Gaussian Beam Quasioptical Propagation and Applications*, IEEE Press, Piscataway, NJ, 1998.
88. G. L. James, *Geometrical Theory of Diffraction for Electromagnetic Waves*, 3rd ed., Peter Peregrinus, London, 1986.
89. J. Uher, J. Bornemann, and U. Rosenberg, *Waveguide Components for Antenna Feed Systems: Theory and CAD*, Artech House, Boston, 1993.
90. G. L. James, P. R. Clark, and K. J. Greene, Diplexing feed assemblies for application to dual-reflector antennas, *IEEE Trans. Anten. Propag.* **AP-51**:1024–1029 (2003).
91. F. Alessandri, M. Mongiardo, and R. Sorrentino, Computer-aided design of beam forming networks for modern satellite antennas, *IEEE Trans. Microwave Theory Tech.* **MTT-40**:1117–1127 (1992).

92. T. S. Bird and C. Sroka, Design of the Ku-band antennas for the Galaxy HS601C satellites, *J. Electric. Electron. Eng. Austral.* **12**:267–273 (1992).
93. R. J. Mailloux, *Phased Array Antenna Handbook*, Artech House, Boston, 1993.
94. S. M. Sherman, *Monopulse Principles and Techniques*, Artech House, Dedham, MA, 1984.
95. K. M. Lee and R. S. Chu, Design and analysis of a multimode feed horn for a monopulse feed, *IEEE Trans. Anten. Propag.* **AP-36**:171–181 (1988).
96. B. K. Watson, N. D. Dang, and S. Ghosh, A mode extraction network for RF sensing in satellite reflector antennas, *Proc. IEE Int. Conf. Antennas and Propagation (ICAP)*, 1981, pp. 323–327.
97. P. J. B. Clarricoats and R. D. Elliot, Multimode corrugated waveguide feed for monopulse radar, *Proc. IEE* **128** (Part H):102–110 (1981).
98. H. Z. Zhang, C. Granet, and M. A. Sprey, A compact Ku-band monopulse horn, *Microwave Opt. Technol. Lett.* **34**:9–13 (2002).
99. W. X. Zhang, *Engineering Electromagnetism: Functional Methods*, Ellis Horwood, New York, 1991.
100. M. B. Steer, J. W. Bandler, and C. M. Snowden, Computer-aided design of RF and microwave circuits and systems, *IEEE Trans. Microwave Theory Tech.* **MTT-50**:996–1005 (2002).
101. F. Arndt, J. Brandt, V. Catina, J. Ritter, I Rullhusen, J. Dauelsberg, U. Hilgefort, and W. Wessel, Fast CAD and optimization of waveguide components and aperture antennas by hybrid MM/FE/MoM/FD methods—state-of-the-art and recent advances, *IEEE Trans. Microwave Theory Tech.* **MTT-52**:292–305 (2004).
102. S. M. Rao, D. R. Wiltron, and A. W. Glisson, Electromagnetic scattering by surfaces of arbitrary shape, *IEEE Trans. Anten. Propag.* **AP-30**:409–418 (1982).
103. www.ansoft.com/.
104. www.cst.de/Content/Products/MWS/Overview.aspx.

ANTENNA PARAMETERS

CONSTANTINE A. BALANIS
Arizona State University
Tempe, Arizona

1. INTRODUCTION

An antenna is a communication system component that is designed to radiate or receive electromagnetic waves. In other words, the antenna is the electromagnetic transducer that is used to convert, in the receiving mode, free-space waves to guided waves, and in the transmitting mode, guided waves to free-space waves, as shown in Fig. 1. The Thevenin equivalent of the antenna in the transmission-line mode is shown in Fig. 2. In a modern RF–microwave system, the antenna must also act as a directional device to optimize or accentuate the transmitted or received energy in some directions while suppressing it in the others. The antenna serves to an RF and microwave system the same purpose that eyes and eyeglasses serve for a human.

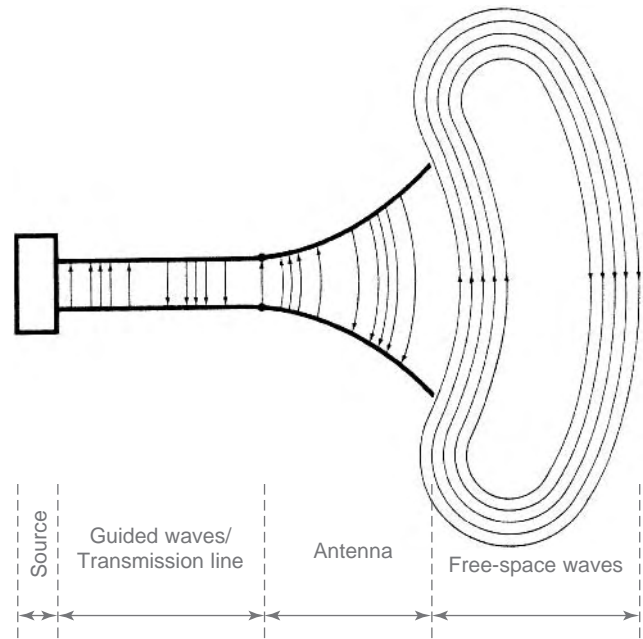


Figure 1. Antenna as a transitional device.

The history of antennas dates back to James Clerk Maxwell, who unified the theories of electricity and magnetism, and eloquently represented their relations through a set of profound equations best known as *Maxwell's equations*. His work was first published in 1873. He also showed that light was electromagnetic, and that both light and electromagnetic waves travel by wave disturbances of the same speed. In 1886, Professor Heinrich Rudolph Hertz demonstrated the first wireless electromagnetic system. In his laboratory, he was able to produce at a wavelength of 4 m a spark in the gap of a transmitting $\lambda/2$ dipole, which was then detected as a spark in the gap of a nearby loop. It was not until 1901 that Guglielmo Marconi was able to send signals over long distances. He performed, in 1901, the first transatlantic transmission from Poldhu in Cornwall, England, to St. John's in Newfoundland [1].

From Marconi's inception through the 1940s, antenna technology was centered primarily on wire-related radiating elements and frequencies up to about UHF. It was not until World War II that modern antenna technology was launched and new elements (waveguide apertures, horns, reflectors, etc.) were introduced, especially for RF and

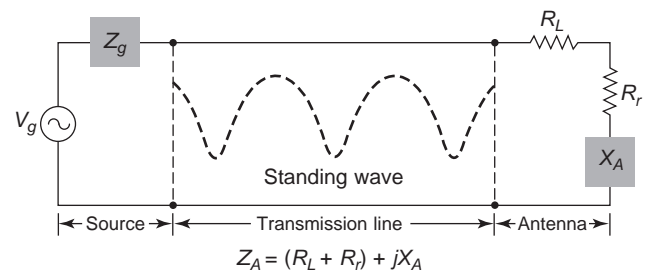


Figure 2. Thevenin equivalent in transmission mode.

microwave frequencies. A contributing factor to this new era was the invention of microwave sources (such as the klystron and magnetron) with frequencies of 1 GHz and above.

While a new era in antennas was launched, during World War II, the advances made in computer architecture and wireless communications technology during the 1960s–1990s have had a major impact on the advances of modern antenna technology, and they are expected to have an even greater influence on antenna engineering in this new millennium. Beginning primarily in the early 1960s, advanced numerical and computational methods were introduced that allowed previously intractable complex antenna system configurations to be analyzed and designed very accurately. Antenna design plays a critical role in overall system design since the success of a system relies strongly on the performance of the antenna. Detailed analysis, design, and measurements of antennas can be found in Ref. 2. A tutorial on antennas is described in Ref. 3.

2. ANTENNA ELEMENTS

Prior to World War II most antenna elements were of the wire type (long wires, dipoles, helices, rhombuses, fans, etc.), and they were used either as single elements or in arrays. During and after World War II, many other radiators, some of which may have been known for some time and others of which were relatively new, were put into service. This created a need for better understanding and optimization of their radiation characteristics. Many of these antennas were of the aperture type (such as open-ended waveguides, slots, horns, reflectors, lenses), and they have been used for communication, radar, remote sensing, and deep-space applications on both airborne and Earth-based platforms. Many of these operate at RF and microwave frequencies.

Prior to the 1950s, antennas with broadband pattern and impedance characteristics had bandwidths not much greater than about 2:1. In the 1950s, a breakthrough in antenna evolution was created that extended the maximum bandwidth to as great as 40:1 or more. Because the geometries of these antennas are specified by angles instead of linear dimensions, they have ideally an infinite bandwidth. Therefore, they are referred to as *frequency-independent* [2]. These antennas are used primarily in the 10–10,000 MHz region in many applications, including TV, point-to-point communications, and feeds for reflectors and lenses.

It was not until almost 20 years later that a fundamental new radiating element, which has received a lot of attention and many applications since its inception, was introduced. This occurred in the early 1970s when the *microstrip* or *patch* antenna was reported [2]. This element is simple, lightweight, inexpensive, low-profile, and conformal to the surface. Microstrip antennas and arrays can be flush-mounted to metallic and other existing surfaces. Operational disadvantages of microstrip antennas include low efficiency, narrow bandwidth, and low power-handling capabilities. Major advances in millimeter-wave antennas have been made in recent years, including integrated antennas where

active and passive circuits are combined with radiating elements in one compact unit (monolithic form).

The unparalleled advances in telecommunications have brought a dramatically increased interest and activity in antenna design. This has resulted in many new elements and design concepts [4], including increased interest in adaptive arrays and “smart” antennas [5–7]. A short description on the analysis and modeling of antennas can also be found in Ref. 8.

3. FUNDAMENTAL PARAMETERS AND FIGURES-OF-MERIT

To describe the performance of an antenna, definitions of various parameters are necessary. Some of the parameters are interrelated, and not all of them need to be specified for complete description of the antenna performance. Parameter definitions will be given in this article. Many of the definitions in quotation marks are from the *IEEE Standard Definitions of Terms for Antennas* (IEEE Standard 145-1983) [9]. This is a revision of the IEEE Standard 145-1973. Many of these definitions relating to parameters and figures-of-merit (including directivity, gain, input impedance, effective area, polarization, etc.) that characterize the performance of the antenna system can also be found in the literature [2,3,8].

The space surrounding an antenna is usually subdivided into three regions: the reactive near-field region, the radiating near-field (Fresnel) region, and the far-field (Fraunhofer) region, as shown in Fig. 3. These regions are so designated to identify the field structure in each. Although no abrupt changes in the field configurations are noted as the boundaries are crossed, there are distinct differences among them. The boundaries separating these regions are not unique, although various criteria have been established and are commonly used to identify the regions [2]. The following definitions in quotation marks are from Ref. 9.

The *reactive near-field region* is defined as “that region of the field immediately surrounding the antenna wherein the reactive field predominates.” For most antennas, the outer boundary of this region is commonly taken to exist at a distance $R < 0.62\sqrt{D^3/\lambda}$ from the antenna, where λ is the wavelength and D is the largest dimension of the antenna.

The *radiating near-field (Fresnel) region* is defined as “that region of the field of an antenna between the reactive near-field region and the far-field region wherein radiation fields predominate and wherein the angular field distribution is dependent upon the distance from the antenna.” The radial distance R over which this region exists is $0.62\sqrt{D^3/\lambda} \leq R < 2D^2/\lambda$ (provided D is large compared to the wavelength). This criterion is based on the maximum phase error of $\pi/8$ radians (22.5°). In this region the field pattern is, in general, a function of the radial distance and the radial field component may be appreciable.

The *far-field (Fraunhofer) region* is defined as “that region of the field of an antenna where the angular field distribution is essentially independent of the distance from the antenna.” In this region, the real part of the power density is dominant. The radial distance defining the far-field region is $R \geq 2D^2/\lambda$ (provided D is large compared to

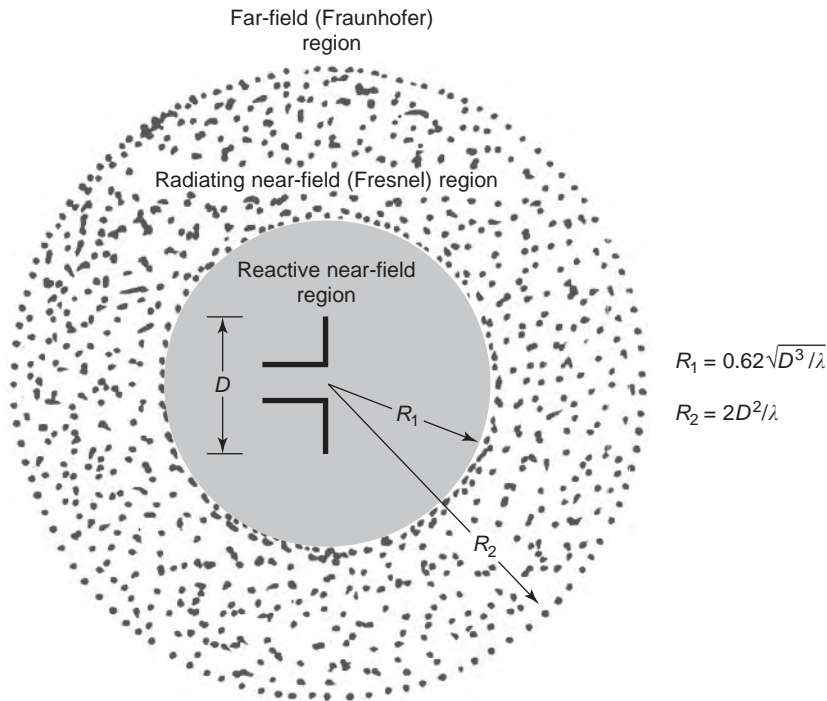


Figure 3. Field regions surrounding an antenna.

the wavelength). The outer boundary is ideally at infinity. The criterion is also based on the maximum phase error of $\pi/8$ radians (22.5°). In this region, the field components are essentially transverse to the radial direction, and the angular distribution is independent of the radial distance.

An *antenna pattern* is defined as a graphical representation, usually in the far-field region, of one of the antenna's parameters. For a complete description, the parameters of interest are usually plotted as a function of the spherical angles θ , ϕ . Parameters of interest include amplitude, phase, polarization, and directivity. An amplitude pattern usually consists of a number of lobes, as shown in Fig. 4, where the first quadrant has been deleted to visualize the directional part of the pattern.

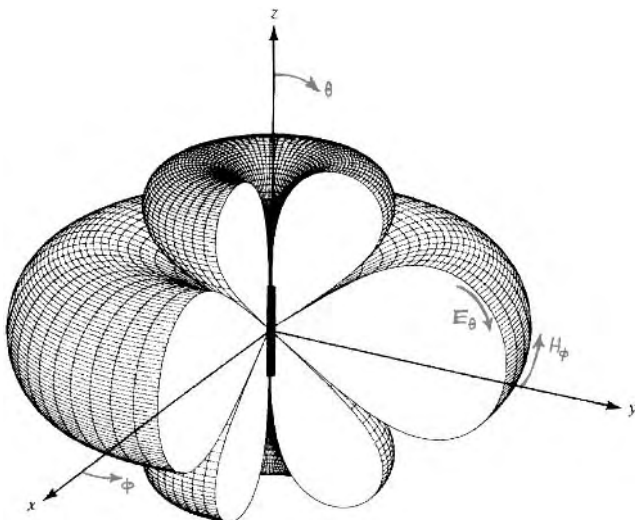


Figure 4. Three-dimensional pattern of $l = 1.25\lambda$ dipole.

A *main- (major) lobe* is defined as “the radiation lobe containing the direction of maximum radiation. In certain antennas, such as multi-lobed or split-beam antennas, there may exist more than one major lobe.”

A *sidelobe* is defined as “a radiation lobe in any direction other than that of the major lobe.” The amplitude level of a sidelobe relative to the mainlobe (usually expressed in decibels) is referred to as *sidelobe level*.

The antennas, based on their amplitude radiation pattern, can be classified into three categories: isotropic, directional, and omnidirectional. An *isotropic* antenna/radiator is defined as “a hypothetical lossless antenna having equal radiation in all directions.” Although it is ideal and not physically realizable, it is often taken as a reference for expressing the directive properties of actual antennas. A *directional* antenna is one “having the property of radiating or receiving electromagnetic waves more effectively in some directions than in others. This term is usually applied to an antenna whose maximum directivity is significantly greater than that of a half-wavelength dipole.” A special case of a directional radiator is the *omnidirectional* antenna, which is defined as one “having an essentially nondirectional pattern in a given plane and a directional pattern in any orthogonal plane.” An example of an omnidirectional pattern is shown in Fig. 4 that is the pattern of a symmetric linear dipole of length $l = 1.25\lambda$. That pattern is nondirectional in the azimuth plane [$f(\phi)$, $\theta = 90^\circ$] and directional in the elevation plane [$g(\theta)$, $\phi = \text{constant}$].

For a linearly polarized antenna, performance is often described in terms of the principal *E*-plane and *H*-plane amplitude patterns. The *E plane* is defined as “the plane containing the electric-field vector and the direction of maximum radiation,” while the *H plane* is “the plane containing the magnetic-field vector and the direction of maximum radiation.” Although it is very difficult to illustrate

the principal planes without considering a specific example, it is the usual practice to orient most antennas so that at least one of the principal plane patterns coincides with one of the geometric principal planes. Figure 4 illustrates the omnidirectional pattern of a linear dipole of length $l = 1.25\lambda$. For this example, any elevation plane pattern ($\phi = \text{constant}$, $0^\circ \leq \theta \leq 180^\circ$) represents the principal E plane while the azimuth x - y plane pattern ($\theta = 90^\circ$, $0^\circ \leq \phi \leq 360^\circ$) is the principal H plane. The E -plane pattern follows the vector of the electric field while the H -plane follows the vector of the magnetic field. For this example, because of the symmetry of the dipole antenna and its omnidirectional amplitude pattern, we have an infinite number of principal E -plane patterns and only one principal H plane. For most other directional antennas, there is usually only one principal E plane and only one principal H plane.

An antenna is often represented by an equivalent circuit with antenna impedance Z_A , as shown in Fig. 2. The antenna impedance Z_A consists of the *radiation resistance* R_r , the *loss resistance* R_L , and an imaginary part X_A [$Z_A = R_A + jX_A = (R_r + R_L) + jX_A$]. The radiation resistance is the resistance that accounts for antenna radiation or scattering. The loss resistance is the element that accounts for the conductive and dielectric losses of the antenna. Expressions for R_r and R_L for dipoles and small circular loops can be found, respectively, in Chapters 4 and 5 of Ref. 2.

Input impedance is defined as “the impedance presented by an antenna at its terminals.” It is expressed at the terminals as the ratio of the voltage to current or the ratio of the appropriate components of the electric to magnetic fields, and it is usually complex. When the antenna impedance Z_A is referred to the input terminals of the antenna, it reduces to the input impedance.

Radiation efficiency is defined as “the ratio of the total power radiated by an antenna to the net power accepted by an antenna from the connected transmitter.” Using the equivalent circuit representation of an antenna of Fig. 2, the radiation efficiency of the antenna can be expressed as

$$e_r = \frac{R_r}{R_r + R_L} \quad (1)$$

Power density S is defined as the power density (W/m²) of the fields radiated by the antenna. In general, the power density is complex. In the reactive near field, the imaginary component is dominant. In the far field, the real part is dominant. In equation form, the power density \mathbf{S} is expressed as

$$\mathbf{S} = \frac{1}{2} \mathbf{E} \times \mathbf{H}^* = \mathbf{S}_r + j\mathbf{S}_i \quad (2)$$

where \mathbf{E} and \mathbf{H} are the fields radiated by the antenna (* indicates complex conjugate). The real part of (2) is usually referred to as *radiation density*.

Radiation intensity U is defined as “the power radiated from an antenna per unit solid angle (steradian).” The radiation intensity is usually defined in the far field and is related to the real part of the power density by

$$U = r^2 S_r \quad (3)$$

where r is the spherical radial distance.

Beamwidth is defined as the angular separation between two directions in which the radiation intensity is identical, with no other intermediate points of the same value. When the intensity is one-half of the maximum, it is referred to as *half-power beamwidth*.

An *isotropic radiator* is defined as “a hypothetical, lossless antenna having equal radiation intensity in all directions.” Although such an antenna is an idealization, it is often used as a convenient reference to express the directive properties of actual antennas. The radiation density S_{r0} of an isotropic radiator and corresponding intensity U_0 are defined, respectively, as

$$S_{r0} = \frac{P_r}{4\pi r^2} \quad (4a)$$

$$U_0 = \frac{P_r}{4\pi} \quad (4b)$$

where P_r represents the power radiated by the antenna.

Directivity is one of the most important figures-of-merit that describes the performance of an antenna. It is defined as “the ratio of the radiation intensity in a given direction from the antenna to the radiation intensity averaged over all direction.” Using Eq. (4b), it can be written as

$$D = \frac{U(\theta, \phi)}{U_0} = \frac{4\pi U(\theta, \phi)}{P_r} \quad (5)$$

where $U(\theta, \phi)$ is the radiation intensity in the direction θ, ϕ and P_r is the radiated power. For antennas radiating both electric field components (E_θ and E_ϕ), partial directivities D_θ and D_ϕ associated, respectively, with E_θ and E_ϕ (and their corresponding radiation intensities U_θ and U_ϕ), can be defined as [2]

$$D_\theta = \frac{4\pi U_\theta}{(P_{\text{rad}})_\theta + (P_{\text{rad}})_\phi} \quad (6a)$$

$$D_\phi = \frac{4\pi U_\phi}{(P_{\text{rad}})_\theta + (P_{\text{rad}})_\phi} \quad (6b)$$

where the total directivity D is then the sum of the two, or

$$D = D_\theta + D_\phi \quad (6c)$$

If the direction of observation is not specified, directivity in general implies the direction of maximum radiation intensity (maximum directivity) expressed as

$$D_0 = \frac{U_m(\theta, \phi)}{U_0} = \frac{4\pi U_m(\theta, \phi)}{P_r} \quad (7)$$

The directivity is an indicator of the relative directional properties of the antenna. As defined by Eqs. (5)–(7), the directional properties of the antenna in question are compared to those of an isotropic radiator. Figure 5 displays the three-dimensional directivity pattern of a $\lambda/2$ dipole and an isotropic source. In each angular direction, only the greater directivity between the two radiators is shown. As can be seen, the directivity of the $\lambda/2$ dipole is

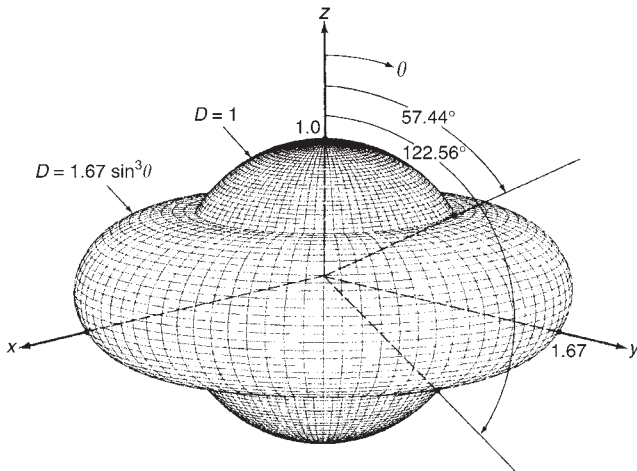


Figure 5. Three-dimensional directivity pattern of $\lambda/2$ dipole.

greater than that of an isotropic source for angles of $57.44^\circ < \theta < 122.56^\circ$ with a maximum value of 1.67 (or 2.23 dB) at $\theta = 90^\circ$. In the other angular region ($0^\circ \leq \theta < 57.44^\circ$ and $180^\circ \geq \theta > 122.56^\circ$), the directivity of the isotropic source ($D = 1$ or 0 dB) is greater than that of the $\lambda/2$ dipole. This allows us to relate the directivity of the element in question to that of an isotropic radiator by simply adding (if expressed in decibels) the relative directivities of one element to another. This procedure is analogous to that used to determine the overall gain of cascaded amplifiers.

Gain is probably the most important figure-of-merit of an antenna. It is defined as “the ratio of the radiation intensity in a given direction, to the radiation intensity that would be obtained if the power accepted by the antenna were radiated isotropically.” Antenna gain is expressed as

$$G = \frac{4\pi U(\theta, \phi)}{P_a} \quad (8)$$

where P_a is the accepted (input) power of the antenna. If the direction is not specified, it implies the direction of maximum radiation (maximum gain). In simplest terms, the main difference between the definitions of directivity and gain is that the directivity is based on the radiated power (assuming that all input power is radiated) while the gain is based on the accepted (input) power. Since all of the accepted (input) power is not radiated (because of losses), the two are related by

$$P_r = e_{cd} P_a \quad (9)$$

where e_{cd} is the radiation efficiency of the antenna as defined by (1). By using (5), (8) and (9), the gain can be expressed as

$$G = e_{cd} \frac{4\pi U(\theta, \phi)}{P_r} = e_{cd} D \quad (10)$$

For a lossless antenna, its gain is equal to its directivity. As with the directivity, there can be partial gains G_θ and

G_ϕ , analogous to (6a)–(6b), related to the electric field components E_θ and E_ϕ (and their corresponding intensities U_θ and U_ϕ).

For each antenna, whether it is a linear or aperture antenna, there is a parameter referred to it as *vector effective length* \mathbf{l}_e (in some places it is referred to as *vector effective height* \mathbf{h}_e), which is used to determine the voltage induced on the open-circuit terminals of the antenna when a wave impinges on it, as shown in Fig. 6. The vector effective length \mathbf{l}_e for an antenna is usually a complex vector quantity represented by

$$\mathbf{l}_e(\theta, \phi) = \hat{\mathbf{a}}_\theta \ell_\theta(\theta, \phi) + \hat{\mathbf{a}}_\phi \ell_\phi(\theta, \phi) \quad (11)$$

The vector effective length is a far-field quantity, and it is related to the far-field \mathbf{E}_a radiated by the antenna, with equivalent current I_{in} in its terminals, by [2]

$$\mathbf{E}_a = \hat{\mathbf{a}}_\theta E_\theta + \hat{\mathbf{a}}_\phi E_\phi = -j\eta \frac{k I_{in}}{4\pi r} \mathbf{l}_e e^{-jkr} \quad (11a)$$

The effective length represents the antenna in its transmitting and receiving modes, and it is particularly useful in relating the open-circuit voltage V_{oc} of receiving antennas, as shown in Fig. 6. This relation can be expressed as

$$V_{oc} = \mathbf{E}^i \cdot \mathbf{l}_e \quad (12)$$

where V_{oc} is the open-circuit voltage at antenna terminals, \mathbf{E}^i is the incident electric field, and \mathbf{l}_e is vector effective length.

Polarization of a radiated wave is defined as “the figure traced as a function of time by the extremity of the vector (electric or magnetic field) at a fixed location in space, and the sense in which it is traced, as observed along the direction of propagation.” Based on the definition of

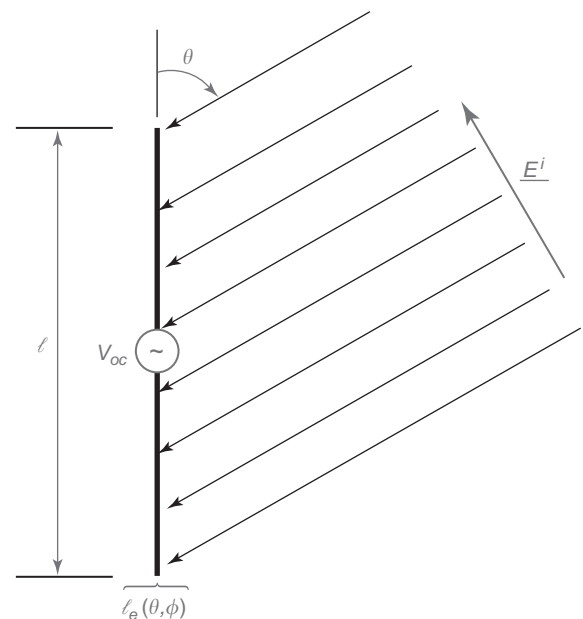


Figure 6. Geometry for vector effective height.

the polarization of a radiated wave, we can now state that the *antenna polarization* in a given direction is determined by the polarization of the fields radiated by the antenna. In general, the polarization of an antenna is classified as *linear*, *circular*, or *elliptical*. Although linear and circular polarizations are special cases of elliptical, in practice they are usually treated separately. Circular and elliptical polarizations also are classified according to the rotation of the transmitted field vectors; the rotation can be either *clockwise (right-hand)* or *counterclockwise (left-hand)* as viewed in the direction of propagation. For more details about polarization of electromagnetic fields and that of antennas, the reader is referred to Refs. 2 and 10.

Polarization efficiency (polarization mismatch or polarization loss factor) is defined as “the ratio of the power received by an antenna from a given plane wave of arbitrary polarization to the power that would be received by the same antenna from a plane wave of the same power flux density and direction of propagation, whose state of polarization has been adjusted for a maximum received power” and is represented by

$$p_e = \frac{|\mathbf{l}_e \cdot \mathbf{E}^i|^2}{|\mathbf{l}_e|^2 |\mathbf{E}^i|^2} \quad (13a)$$

where \mathbf{l}_e is the vector effective length of Eq. (11). The polarization mismatch between the antenna and the incident wave can also be represented by a polarization loss factor (PLF) [2], represented here also by p_f , which is defined by referring to Fig. 7 as

$$p_f = \text{PLF} = |\hat{\rho}_w \cdot \hat{\rho}_a|^2 = |\cos(\psi_p)|^2 \quad (13b)$$

In (13a) $\hat{\rho}_w$ and $\hat{\rho}_a$ are unit vectors representing, respectively, the polarizations of the incident wave and of the

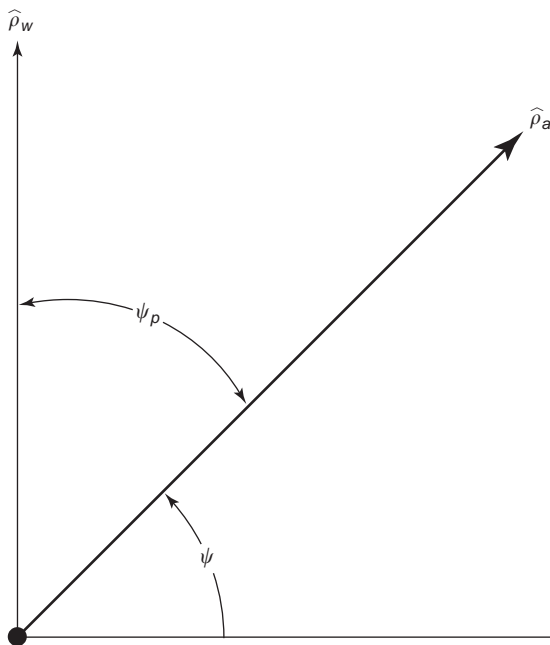


Figure 7. Polarization vector for antenna and impinging wave.

antenna [2]. The polarization efficiency of (13a) or the polarization loss factor of (13b), which represent the same polarization mismatch, is an important factor that must be included in the power budget of communications systems but is sometimes neglected.

When an incident wave impinges on an antenna, as shown in Fig. 8, the amount of power received by the antenna and transferred to the load/receiver can be determined using what is referred to as the *effective area*, which is an *equivalent area* representing the antenna, whether it is a wire, aperture, reflector, or other components. In a given direction, the *effective area* is defined as “the ratio of the available power at the terminals of a receiving antenna to the power flux density of a plane wave incident on the antenna from that direction, *the wave being polarization matched to the antenna*. If the direction is not specified, the direction of maximum radiation intensity is implied.” The maximum effective area is related to the antenna gain by [2]

$$A_{em} = p_{e,f} e_r \frac{\lambda^2}{4\pi} G_0 \quad (14)$$

where $p_{e,f}$ represents either the polarization efficiency p_e of (13) or polarization loss factor p_f of (13b), G_0 is the maximum gain of the antenna, and e_r is the impedance-matching efficiency between the transmission line and the antenna defined as

$$e_r = (1 - |\Gamma_{in}|^2) \quad (15)$$

where Γ_{in} is the reflection coefficient at the input terminals of the antenna. When multiplied by the power density of the incident wave that impinges on the antenna, the maximum effective area determines the maximum power that is delivered to a matched load connected to the antenna (assuming no other losses, such as transmission-line losses between the antenna and the load/receiver).

Aperture efficiency, usually expressed in percent, is defined as the ratio of antenna’s maximum effective area to its physical area, which can also be expressed on the ratio of the maximum directivity of the aperture to the standard directivity, or

$$\varepsilon_{ap} = \frac{A_{em}}{A_p} = \frac{D_0}{D_s} \quad (16)$$

where A_p is the physical area of the antenna and D_s is standard directivity of antenna ($4\pi A_p/\lambda$ when $A_p \gg \lambda^2$ and with radiation confined to a half-space).

For a rectangular aperture mounted on an infinite ground plane and with a triangular aperture distribution, its aperture efficiency is 75%. However, for an aperture with a sinusoidal aperture distribution, its aperture efficiency is 81% [2]. Again, we see that the aperture distribution, which satisfies the wave equation and the boundary conditions of the structure, determines its aperture efficiency. If an aperture could support an ideal uniform field distribution, which is seldom physically realizable, its aperture efficiency would be 100%.

Every object with a physical temperature above zero ($0 \text{ K} = -273^\circ\text{C}$) radiates energy. The amount of energy ra-

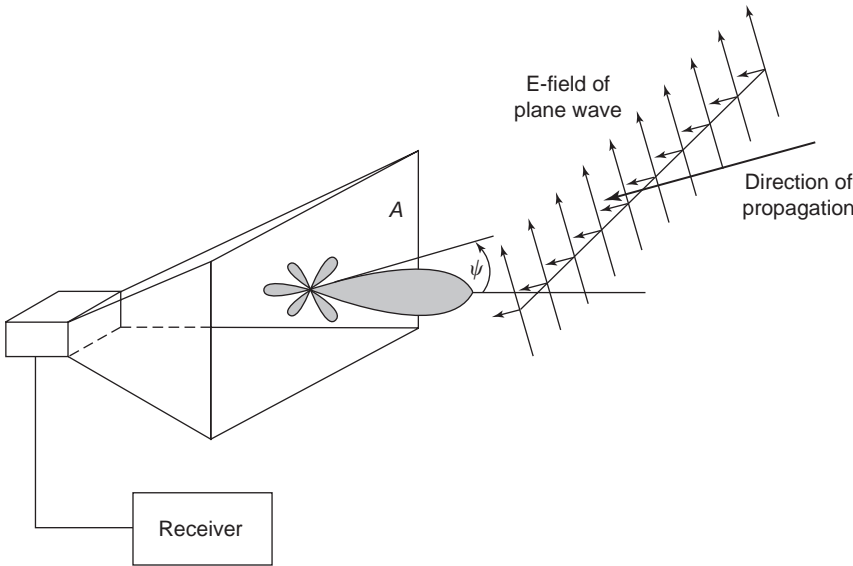


Figure 8. Geometry for defining effective area.

diated is usually represented by an equivalent temperature T_B , better known as *brightness temperature*, and it is defined as

$$T_B(\theta, \phi) = \varepsilon(\theta, \phi)T_m = [1 - |\Gamma(\theta, \phi)|^2]T_m \quad (17)$$

where T_B is brightness temperature (K), ε is emissivity (dimensionless), T_M is molecular (physical) temperature (K), and $\Gamma(\theta, \phi)$ is the reflection coefficient of the surface for the polarization of the wave.

The brightness temperature emitted by the different energy sources is intercepted by antennas, as shown in Fig. 9, and it appears at their terminals as an antenna temperature T_A [2]. The temperature appearing at the terminals of an antenna is that given by (17), and it is

weighted by the gain pattern $G(\theta)$ of the antenna. In equation form, this is expressed as

$$T_A = \frac{\int_0^{2\pi} \int_0^\pi T_B(\theta, \phi)G(\theta, \phi) \sin \theta d\theta d\phi}{\int_0^{2\pi} \int_0^\pi G(\theta, \phi) \sin \theta d\theta d\phi} \quad (17a)$$

where T_A is antenna temperature [effective noise temperature of antenna radiation resistance (K)] and $G(\theta, \phi)$ is gain (power) pattern of the antenna.

Assuming no losses or other contributions between the antenna and the receiver, the noise power transferred to the receiver is given by [2]

$$P_r = kT_A\Delta f \quad (18)$$

where

- P_r = antenna noise power (W)
- k = Boltzmann's constant (1.38×10^{-23} J/K)
- T_A = antenna temperature (K)
- Δf = bandwidth (Hz).

To account for other noise contributions to the receiver, such as those from the transmission line, the reader is referred to Ref. 2.

Specific amplitude radiation pattern requirements usually cannot be achieved by a single antenna element, because single elements usually have relatively wide radiation patterns and low directivities. To design antennas with very large directivities, it is usually necessary to increase the electrical size of the antenna. This can be accomplished by enlarging the electrical dimensions of the chosen single element. However, mechanical problems are usually associated with very large elements.

An alternative way to achieve large directivities and control the amplitude pattern, without increasing the size

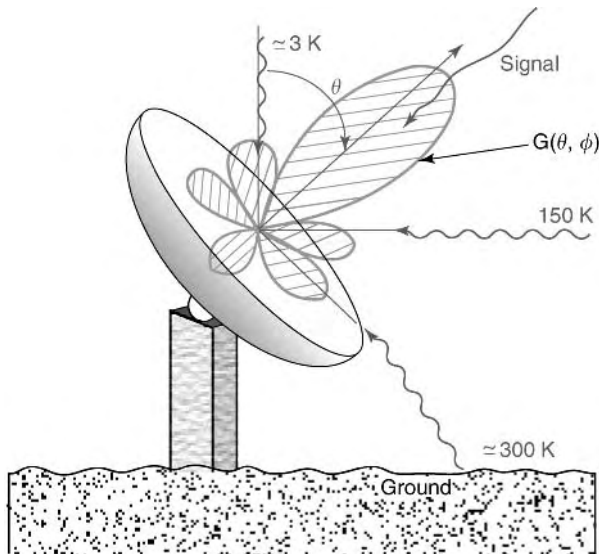


Figure 9. Geometry for antenna and brightness temperatures.

of the individual elements, is to use multiple single elements to form an *array*. An *array* is really a sampled version of a very large single element. In an array, the mechanical problems of large single elements are traded for the electrical problems associated with the feed networks of arrays. However, with today's solid-state technology, very efficient and low-cost feed networks can be designed.

Arrays are the most versatile antenna systems. They find wide applications not only in many spaceborne systems but in many Earth-bound missions as well. In most cases, the elements of an array are identical; this is not necessary, but it is often more convenient, simpler and more practical. In general, the radiation characteristics of an array depend on many factors, including

1. The geometric configuration of the overall array (linear, circular, rectangular, spherical, etc.)
2. The relative displacement between the elements
3. The excitation amplitude of the individual elements
4. The excitation phase of the individual elements
5. The relative pattern of the individual elements

Therefore the designer has many controls or degrees of freedom that can exercise in order to make the antenna very versatile and meet the specifications of the design.

With arrays, it is practical to not only *synthesize* almost any desired amplitude radiation pattern, but the mainlobe can be scanned, resulting in a *scanning* array, by controlling the relative phase excitation between the elements. This is most convenient for applications where the antenna system is not readily accessible, especially for spaceborne missions. The beamwidth of the mainlobe along with the sidelobe level can be controlled by the relative amplitude excitation (distribution) between the elements of the array. In fact, there is a tradeoff between the beamwidth and the sidelobe level based on the amplitude distribution of the elements [2]. The spacing between the elements can be used to control many characteristics of an array, including the pattern, beamwidth, bandwidth, input impedance, and sidelobe level.

There are a plethora of array designs. Two classic array configurations include the Yagi-Uda and log-periodic arrays [2]. The Yagi-Uda is a popular antenna used by amateur radio enthusiasts and for TV. The log-periodic array, because of its large and attractive bandwidth, is probably the most widely used home TV antenna. Arrays of waveguides, horns, reflectors and microstrips are also very popular [11]. Microstrip arrays will play a key role in the realization of unique designs of adaptive and smart antennas for wireless communications.

Designs of uniform distribution arrays include the broadside, endfire, and scanning arrays. Classic non-uniform distribution arrays include the binomial, Dolph-Tschebyscheff, Woodward-Lawson, Fourier transform, and Taylor (Tschebyscheff error and line source) [2]. There are many other array designs, too numerous to name here. However there are two prominent types of arrays that are outstanding candidates for wireless communications: adaptive arrays and smart antennas [5-7].

In *adaptive antenna arrays* [12,13], the amplitude and phase distribution between the elements are adaptively chosen to improve signal reception or transmission in certain directions and reduce noise and interference in all other directions. Adaptive signal processing algorithms are often used in conjunction with the array architecture to obtain an optimum set of weights that maximizes *signal-to-noise ratio* (SNR) and minimizes *mean-square error* (MSE). In this context, such adaptive arrays are commonly referred to as "smart antennas" [5-7]. In *code-division multiple-access* (CDMA) applications, such as cellular and mobile communications, smart antennas at the base station can form a mainbeam toward the subscriber and low-level sidelobes or ideally nulls toward interfering signals. Through adaptive beamforming, smart antennas can penetrate through buildings and cover areas that are otherwise unattainable by a single-element antenna at the base station. In addition, smart antennas can more effectively alleviate problems due to multipath, fading, and time dispersion. This results in an improved system performance compared to an isotropic antenna. Also, dynamic beamforming in smart antennas enhances antenna gain in the direction of the subscriber, thus extending signal coverage. Coverage enhancement can reduce manufacturing cost in cellular and mobile communications by requiring a smaller number of base stations within a given area.

4. CONCLUSIONS

Antenna engineering has enjoyed a very successful period since the 1940s. Responsible for its success have been the introduction and technological advances of some new elements of radiation, such as aperture antennas, horns, reflectors, frequency-independent antennas, and microstrip/patch antennas. Excitement has been created by the advancement of numerical methods that have been instrumental in analyzing many previously intractable problems. Another major factor in the success of antenna technology has been the advances in the computer architecture and wireless communications. Today antenna engineering is considered a truly fine engineering science.

Although a certain level of maturity has been attained, there are many challenging opportunities and problems to be solved. Unique and innovative adaptive and smart antenna designs for wireless communication are creating new enthusiasm and interest in the exploding wireless communication technology. Phased-array architecture integrating monolithic MIC technology is still a challenging problem. Integration of new materials into antenna technology offers many advantages, and numerical methods will play key roles in their incorporation and system performance. Computational efficiency in numerical methods will allow modeling, design, and optimization of antennas on complex platforms without the need of supercomputing capabilities. Innovating antenna designs to perform complex and demanding system functions always remain a challenge. New basic elements are always welcomed and offer refreshing opportunities.

BIBLIOGRAPHY

1. J. D. Kraus, *Antennas since Hertz and Marconi*, *IEEE Trans. Anten. Propag.* **AP-33**:131–137 (Feb. 1985).
2. C. A. Balanis, *Antenna Theory: Analysis and Design*, Wiley, New York, 1997.
3. C. A. Balanis, Antenna theory: A review, *Proc. IEEE* **80**:7–23 (Jan. 1992).
4. Special issue on wireless communications, *IEEE Trans. Anten. Propag.* **AP-46** (June 1998).
5. J. C. Liberti, Jr., and T. S. Rappaport, *Smart Antennas for Wireless Communications: IS-95 and Third Generation CDMA Applications*, Prentice-Hall PTR, Englewood Cliffs, NJ, 1999.
6. T. S. Rappaport, ed., *Smart Antennas: Adaptive Arrays, Algorithms, & Wireless Position Location*, IEEE, 1998.
7. S. Bellofiore, J. Foutz, R. Govindarajula, I. Bahceci, C. A. Balanis, A. S. Spanias, J. M. Capone, and T. M. Duman, Smart antenna system, analysis integration, and performance for mobile ad-hoc networks (MANETs), *IEEE Trans. Anten. Propag.* (special issue on wireless communications) **50**(5):571–581 (May 2002).
8. C. A. Balanis and A. C. Polycarpou, Antennas, in *Encyclopedia of Telecommunications*, Wiley, Hoboken, NJ, 2003, pp. 179–188.
9. IEEE Standard Definitions of Terms for Antennas, IEEE Standard 145-1983, *IEEE Trans. Anten. Propag.* **AP-31**(Part II of two parts):5–29 (Nov. 1983).
10. C. A. Balanis, *Advanced Engineering Electromagnetics*, Wiley, New York, 1989.
11. Special issue on phased arrays, *IEEE Trans. Anten. Propag.* **47**(3) (March 1999).
12. Special issue on adaptive antennas, *IEEE Trans. Anten. Propag.* **AP-24** (Sept. 1976).
13. Special issue on adaptive processing antenna systems, *IEEE Trans. Anten. Propag.* **AP-34** (Sept. 1986).

ANTENNA RADIATION PATTERNS

MICHAEL T. CHRYSOMALLIS
Democritus University of
Thrace
Xanthi, Greece
CHRISTOS G.
CHRISTODOULOU
The University of New Mexico
Albuquerque, New Mexico

1. ANTENNAS AND FUNDAMENTAL PARAMETERS

An antenna is used to either transmit or receive electromagnetic waves. It serves as a transducer converting guided waves into free-space waves in the transmitting mode or vice versa in the receiving mode. Antennas or aeri- als can take many forms according to the radiation mechanism involved and can be divided in different categories. Some common types are wire antennas, aperture antennas, reflector antennas, lens antennas, traveling-wave antennas, frequency-independent antennas, horn antennas,

and printed and conformal antennas, [1, pp. 563–572]. When applications require radiation characteristics that cannot be met by a single radiating element, multiple elements are employed. Various configurations are utilized by suitably spacing the elements in one or two dimensions. These configurations, known as *array antennas*, can produce the desired radiation characteristics by appropriately feeding each individual element with different amplitudes and phases that allows a mechanism for increasing the electric size of the antenna. Furthermore, antenna arrays combined with signal processing lead to smart antennas (switched-beam or adaptive antennas) that offer more degrees of freedom in the wireless system design [2]. Moreover, active antenna elements or arrays incorporate solid-state components producing effective integrated antenna transmitters or receivers with many applications [1, pp. 190–209; 2].

Regardless of the antenna considered, certain fundamental figures of merit describe the performance of an antenna. The response of an antenna as a function of direction is given by the antenna pattern. This pattern commonly consists of a number of lobes, where the largest one is called the *mainlobe* and the others are referred to as *sidelobes*, *minorlobes*, or *backlobes*. If the pattern is measured sufficiently far from the antenna so there is no change in the pattern with distance, the pattern is the so called '*far-field pattern*'. Measurements at shorter distances yield '*near-field patterns*', which are a function of both angle and distance. The pattern may be expressed in terms of the field intensity, called *field pattern*, or in terms of the Poynting vector or radiation intensity, which are known as *power patterns*. If the pattern is symmetric, a simple pattern is sufficient to completely specify the variation of the radiation with the angle. Otherwise, a three-dimensional diagram or a contour map is required to show the pattern in its entirety. However, in practice, two patterns perpendicular to each other and perpendicular to the mainlobe axis may suffice. These are called the '*principal-plane*' patterns, the *E* plane and the *H* plane, containing the *E* and *H* field vectors, respectively. Having established the radiation patterns of an antenna, some important parameters can now be considered such as radiated power, radiation efficiency, directivity, gain, and antenna polarization. All of them are considered in detail in this article.

Here, scalar quantities are presented in italics, while vector quantities are in boldface, for example, electric field ***E*** (vector) of $E(=|\mathbf{E}|)$ (scalar). Unit vectors are boldface with a circumflex over the letter; $\hat{\mathbf{x}}$, $\hat{\mathbf{y}}$, $\hat{\mathbf{z}}$, and $\hat{\mathbf{r}}$ are the unit vectors in *x*, *y*, *z*, and *r* directions, respectively. A dot over the symbol means that the quantity is harmonically time-varying or a phasor. For example, taking the electric field, $\dot{\mathbf{E}}$ represents a space vector and time phasor, but \dot{E}_x is a scalar phasor. The relations between them are $\dot{\mathbf{E}} = \hat{\mathbf{x}}\dot{E}_x$ where $\dot{E}_x = E_1 e^{j\omega t}$.

The first section of this article introduces several antenna patterns, giving the necessary definitions and presenting the common types. The field regions of an antenna are also pointed out. The most common reference antennas are the ideal isotropic radiator and the very short dipole. Their fields are used to show the calculation

BIBLIOGRAPHY

1. J. D. Kraus, *Antennas since Hertz and Marconi*, *IEEE Trans. Anten. Propag.* **AP-33**:131–137 (Feb. 1985).
2. C. A. Balanis, *Antenna Theory: Analysis and Design*, Wiley, New York, 1997.
3. C. A. Balanis, Antenna theory: A review, *Proc. IEEE* **80**:7–23 (Jan. 1992).
4. Special issue on wireless communications, *IEEE Trans. Anten. Propag.* **AP-46** (June 1998).
5. J. C. Liberti, Jr., and T. S. Rappaport, *Smart Antennas for Wireless Communications: IS-95 and Third Generation CDMA Applications*, Prentice-Hall PTR, Englewood Cliffs, NJ, 1999.
6. T. S. Rappaport, ed., *Smart Antennas: Adaptive Arrays, Algorithms, & Wireless Position Location*, IEEE, 1998.
7. S. Bellofiore, J. Foutz, R. Govindarajula, I. Bahceci, C. A. Balanis, A. S. Spanias, J. M. Capone, and T. M. Duman, Smart antenna system, analysis integration, and performance for mobile ad-hoc networks (MANETs), *IEEE Trans. Anten. Propag.* (special issue on wireless communications) **50**(5):571–581 (May 2002).
8. C. A. Balanis and A. C. Polycarpou, Antennas, in *Encyclopedia of Telecommunications*, Wiley, Hoboken, NJ, 2003, pp. 179–188.
9. IEEE Standard Definitions of Terms for Antennas, IEEE Standard 145-1983, *IEEE Trans. Anten. Propag.* **AP-31**(Part II of two parts):5–29 (Nov. 1983).
10. C. A. Balanis, *Advanced Engineering Electromagnetics*, Wiley, New York, 1989.
11. Special issue on phased arrays, *IEEE Trans. Anten. Propag.* **47**(3) (March 1999).
12. Special issue on adaptive antennas, *IEEE Trans. Anten. Propag.* **AP-24** (Sept. 1976).
13. Special issue on adaptive processing antenna systems, *IEEE Trans. Anten. Propag.* **AP-34** (Sept. 1986).

ANTENNA RADIATION PATTERNS

MICHAEL T. CHRYSOMALLIS
Democritus University of
Thrace
Xanthi, Greece
CHRISTOS G.
CHRISTODOULOU
The University of New Mexico
Albuquerque, New Mexico

1. ANTENNAS AND FUNDAMENTAL PARAMETERS

An antenna is used to either transmit or receive electromagnetic waves. It serves as a transducer converting guided waves into free-space waves in the transmitting mode or vice versa in the receiving mode. Antennas or aerials can take many forms according to the radiation mechanism involved and can be divided in different categories. Some common types are wire antennas, aperture antennas, reflector antennas, lens antennas, traveling-wave antennas, frequency-independent antennas, horn antennas,

and printed and conformal antennas, [1, pp. 563–572]. When applications require radiation characteristics that cannot be met by a single radiating element, multiple elements are employed. Various configurations are utilized by suitably spacing the elements in one or two dimensions. These configurations, known as *array antennas*, can produce the desired radiation characteristics by appropriately feeding each individual element with different amplitudes and phases that allows a mechanism for increasing the electric size of the antenna. Furthermore, antenna arrays combined with signal processing lead to smart antennas (switched-beam or adaptive antennas) that offer more degrees of freedom in the wireless system design [2]. Moreover, active antenna elements or arrays incorporate solid-state components producing effective integrated antenna transmitters or receivers with many applications [1, pp. 190–209; 2].

Regardless of the antenna considered, certain fundamental figures of merit describe the performance of an antenna. The response of an antenna as a function of direction is given by the antenna pattern. This pattern commonly consists of a number of lobes, where the largest one is called the *mainlobe* and the others are referred to as *sidelobes*, *minorlobes*, or *backlobes*. If the pattern is measured sufficiently far from the antenna so there is no change in the pattern with distance, the pattern is the so called '*far-field pattern*'. Measurements at shorter distances yield '*near-field patterns*', which are a function of both angle and distance. The pattern may be expressed in terms of the field intensity, called *field pattern*, or in terms of the Poynting vector or radiation intensity, which are known as *power patterns*. If the pattern is symmetric, a simple pattern is sufficient to completely specify the variation of the radiation with the angle. Otherwise, a three-dimensional diagram or a contour map is required to show the pattern in its entirety. However, in practice, two patterns perpendicular to each other and perpendicular to the mainlobe axis may suffice. These are called the '*principal-plane*' patterns, the *E* plane and the *H* plane, containing the *E* and *H* field vectors, respectively. Having established the radiation patterns of an antenna, some important parameters can now be considered such as radiated power, radiation efficiency, directivity, gain, and antenna polarization. All of them are considered in detail in this article.

Here, scalar quantities are presented in italics, while vector quantities are in boldface, for example, electric field \mathbf{E} (vector) of $E (= |\mathbf{E}|)$ (scalar). Unit vectors are boldface with a circumflex over the letter; $\hat{\mathbf{x}}$, $\hat{\mathbf{y}}$, $\hat{\mathbf{z}}$, and $\hat{\mathbf{r}}$ are the unit vectors in *x*, *y*, *z*, and *r* directions, respectively. A dot over the symbol means that the quantity is harmonically time-varying or a phasor. For example, taking the electric field, $\dot{\mathbf{E}}$ represents a space vector and time phasor, but \dot{E}_x is a scalar phasor. The relations between them are $\dot{\mathbf{E}} = \hat{\mathbf{x}}\dot{E}_x$ where $\dot{E}_x = E_1 e^{j\omega t}$.

The first section of this article introduces several antenna patterns, giving the necessary definitions and presenting the common types. The field regions of an antenna are also pointed out. The most common reference antennas are the ideal isotropic radiator and the very short dipole. Their fields are used to show the calculation

and meaning of the different parameters of antennas covered in this article. The second section begins with a treatment of the Poynting vector and radiation power density, starting from the general case of an electromagnetic wave and extending the definitions to a radiating antenna. After this, radiation performance measures such that the beam solid angle, directivity, and gain of an antenna are defined. In the third section the concepts of wave and antenna polarization are discussed. Finally, in the fourth section, a general case of antenna pattern calculation is considered, and numerical solutions are suggested for radiation patterns that are not available in simple closed-form expressions.

2. RADIATION FROM ANTENNAS

2.1. Radiation Patterns

The radiation pattern of an antenna is, generally, its most basic requirement since it determines the spatial distribution of the radiated energy. This is usually the first property of an antenna that is specified, once the operating frequency has been stated. An *antenna radiation pattern* or *antenna pattern* is defined as a graphical representation of the radiation properties of the antenna as a function of space coordinates. Since antennas are commonly used as parts of wireless telecommunication systems, the radiation pattern is determined in the far-field region where no change in pattern with distance occurs. Using a spherical coordinate system, shown in Fig. 1, where the antenna is at the origin, the radiation properties of the antenna depend only on the angles ϕ and θ along a path or surface of constant radius. A trace of the radiated or received power at a constant radius is called a *power pattern*, while the spatial variation of the electric or magnetic field along a constant radius is called an *amplitude field pattern*. In practice, the necessary information from the complete three-dimensional pattern of an antenna can be received by taking a few two-dimensional patterns, according to the complexity of radiation pattern of the specific antenna. Usually, for most applications, a number of plots of the pattern as a function of θ for some particular values of ϕ , plus a few plots as a function of ϕ for some particular values of θ , give the needed information.

Antennas usually behave as reciprocal devices. This is very important since it permits the characterization of the antenna as either a transmitting or receiving antenna. For example, radiation patterns are often measured with the test antenna operating in the receive mode. If the antenna is reciprocal, the measured pattern is identical when the antenna is in either a transmit or a receive mode. If non-reciprocal materials, such as ferrites and active devices, are not present in an antenna, its transmitting and receiving properties are identical.

The radiation fields from a transmitting antenna vary inversely with distance, while the variation with observation angles (ϕ , θ) depends on the antenna type. A very simple but basic configuration antenna is the ideal or very short dipole antenna. Since any linear or curved wire antenna may be regarded, as being composed of a number of short dipoles connected in series, the knowledge of this antenna is

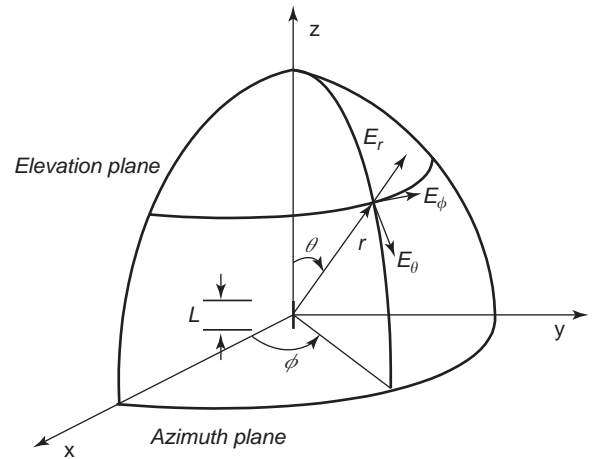


Figure 1. Spherical coordinate system for antenna analysis purposes. A very short dipole is shown with its no-zero field component directions.

useful. So, we will use the fields radiated from an ideal antenna to define and understand the radiation pattern properties. An ideal dipole positioned symmetrically, at the origin of the coordinate system and oriented along the z axis, is shown in Fig. 1. The pattern of electromagnetic fields, with wavelength λ , around a very short wire antenna of length $L \ll \lambda$, carrying a uniform current $I_0 e^{j\omega t}$, is described by functions of distance, frequency, and angle. Table 1 summarizes the expressions for the fields from a very short dipole antenna as [3,4] $E_\phi = H_r = H_\theta = 0$ for $r \gg \lambda$ and $L \ll \lambda$. The variables shown in these relations are as follows: I_0 = amplitude (peak value in time) of current (A), assumed to be constant along the dipole; L = length of dipole (m); $\omega = 2\pi f$ = radian frequency, where f is the frequency in Hz; t = time (s); $\beta = 2\pi/\lambda$ = phase constant (rad/m); θ = azimuthal angle (dimensionless); c = velocity of light $\approx 3 \times 10^8$ m/s; λ = wavelength (m); j = complex operator = $\sqrt{-1}$; r = distance from center of dipole to observation point (m); and ϵ_0 = permittivity of free space = 8.85 pF/m.

It is to be noted that E_θ and H_ϕ are in time phase in the far field. Thus, electric and magnetic fields in the far field of the spherical wave from the dipole are related in the same manner as in a plane traveling wave. Both are also proportional to $\sin \theta$; that is, both are maximum when $\theta = 90^\circ$ and minimum when $\theta = 0^\circ$ (in the direction of the dipole axis). This variation of E_θ or H_ϕ with angle can be presented by a *field pattern* (shown in Fig. 2), where the length r of the radius vector is proportional to the value of the far field (E_θ or H_ϕ) in that direction from the dipole. The pattern in Fig. 2a is the three-dimensional far-field pattern for the ideal dipole, while the patterns in Figs. 2b and 2c are two-dimensional and represent cross sections of the three-dimensional pattern, showing the dependence of the fields with respect to angles θ and ϕ .

All far-field components of a very short dipole are functions of I_0 , the dipole current; L/λ , the dipole length in terms of wavelengths; $1/r$, the distance factor; $j e^{j(\omega t - \beta r)}$, the phase factor; and $\sin \theta$, the pattern factor that gives the variation of the field with angle. In general, the expression for the field of any antenna will involve these factors.

Table 1. Fields of an Ideal or Very Short Dipole

Component	General Expression for All regions	Far Field Only
E_r	$\frac{I_0 L e^{j(\omega t - \beta r)} \cos \theta}{j\omega\epsilon_0 4\pi r} \left(\frac{2j\beta}{r} + \frac{2}{r^2} \right)$	0
E_θ	$-\frac{I_0 L e^{j(\omega t - \beta r)} \sin \theta}{j\omega\epsilon_0 4\pi r} \left(\beta^2 - \frac{j\beta}{r} - \frac{1}{r^2} \right)$	$\frac{j(L/\lambda) I_0 e^{j(\omega t - \beta r)} \sin \theta}{2\epsilon_0 c r}$
H_ϕ	$\frac{I_0 L e^{j(\omega t - \beta r)} \sin \theta}{4\pi r} \left(j\beta + \frac{1}{r} \right)$	$\frac{j(L/\lambda) I_0 e^{j(\omega t - \beta r)} \sin \theta}{2r}$

For longer antennas with complicated current distribution, the field components generally are functions of the terms defined above, which are grouped and designated as the *element factor* and the *space factor*. The element factor includes everything except the current distribution along the source, which is the space factor of the antenna. If, for example, we consider the case of a finite dipole antenna, we can produce the field expressions by dividing the antenna into a number of very short dipoles and summing all the contributions. The element factor is equal to the field of the very short dipole located at a reference point, while the space factor is a function of the current distribution along the source, the latter usually described by an integral. The total field of the antenna is taken by the product of the element and space factors. This procedure is known as *pattern multiplication*.

A similar procedure is used in array antennas, which are used when it is necessary to design antennas with directive characteristics. The increased electrical size of an array antenna due to the use of more than one radiating

elements gives better directivity and special radiation patterns. The total field of an array is determined by the product of *the field of a single element* and *the array factor* of the array antenna. If we use isotropic radiating elements, the pattern of the array is simply the pattern of the array factor. The array factor is a function of the geometry of the array and the excitation phase. Thus, changing the number of elements, their geometric arrangement, their relative magnitudes, their relative phases, and their spacing, we take different patterns. Figure 3 shows some cases of characteristic patterns of an array antenna with two isotropic point sources as radiating elements, by using different values of the above mentioned quantities, which produce different array factors.

2.2. Common Types of Radiation Patterns

An *isotropic source* or *radiator* is an ideal antenna that radiates uniformly in all directions in space. Although no practical source has this property, the concept of the iso-

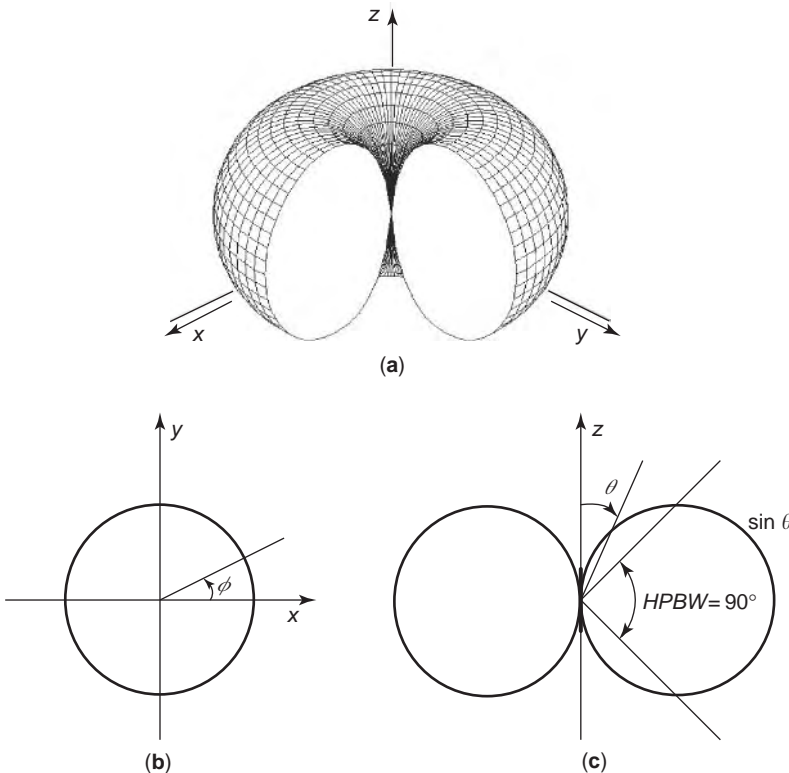


Figure 2. Radiation field pattern of far field from an ideal or very short dipole: (a) three-dimensional pattern plot; (b) E -plane radiation pattern polar plot; (c) H -plane radiation pattern polar plot.

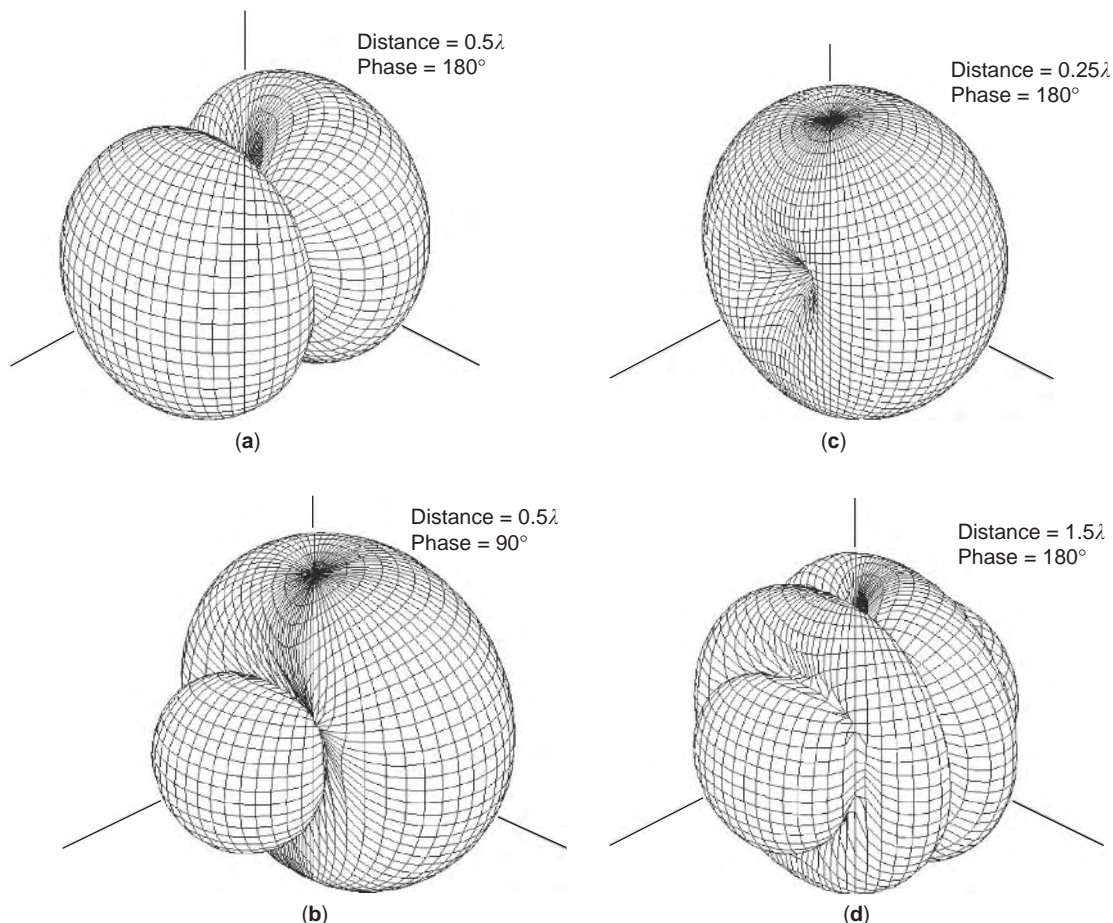


Figure 3. Three-dimensional graphs of power radiation patterns for an array of two isotropic elements of the same amplitude and (a) opposite phase, spaced 0.5λ apart; (b) phase quadrature, spaced 0.5λ apart; (c) opposite phase, spaced 0.25λ apart; and (d) opposite phase, spaced 1.5λ , apart.

tropic radiator is very useful and is often used as a reference for expressing the directive properties of actual antennas. It is worth recalling that the power flux density S at a distance r from an isotropic radiator is $P_t/4\pi r^2$, where P_t is the transmitted power, since all the transmitted power is evenly distributed on the surface of a spherical wavefront with radius r . The electric field intensity is calculated as $\sqrt{30P_t}/r$ (using the relation from electric circuits, power = E^2/η , where η = the characteristic impedance of free space = $377\ \Omega$).

On the contrary, a *directional* antenna is one that radiates or receives electromagnetic waves more effectively in some directions than in others. An example of an antenna with a directional radiation pattern is that of an ideal or very short dipole, shown in Fig. 2. It is seen that this pattern, which resembles a doughnut with no hole, is nondirectional in the azimuth plane, which is the xy plane characterized by the set of relations [$f(\phi)$, $\theta = \pi/2$], and directional in the elevation plane, which is any orthogonal plane containing the z axis characterized by [$g(\theta)$, $\phi = \text{constant}$]. This type of directional pattern is designated as an *omnidirectional pattern* and is defined as one having an essentially nondirectional pattern in a given plane, which for this case is the azimuth plane and a directional

pattern in any orthogonal plane, in this case the elevation plane. The omnidirectional pattern—also known as broadcast-type—is used for many broadcast or communications services where all directions are to be covered equally well. The horizontal-plane pattern is generally circular, while the vertical-plane pattern may have some directivity in order to increase the gain.

Other forms of directional patterns are pencil-beam, fan-beam, and shaped-beam patterns. The *pencil-beam pattern* is a highly directional pattern that is used to obtain maximum gain and when the radiation pattern is to be concentrated in as narrow an angular sector as possible. The beamwidths in the two principal planes are essentially equal. The *fan-beam pattern* is similar to the pencil-beam pattern except that the beam cross section is elliptical in shape rather than circular. The beamwidth in one plane may be considerably broader than the beamwidth in the other plane. As with the pencil-beam pattern, the fan-beam pattern generally implies a rather substantial amount of gain. The *shaped-beam pattern* is used when the pattern in one of the principal planes must preferably have a specified type of coverage. A typical example is the cosecant type of pattern, which is used to provide a constant radar return over a range of angles in the

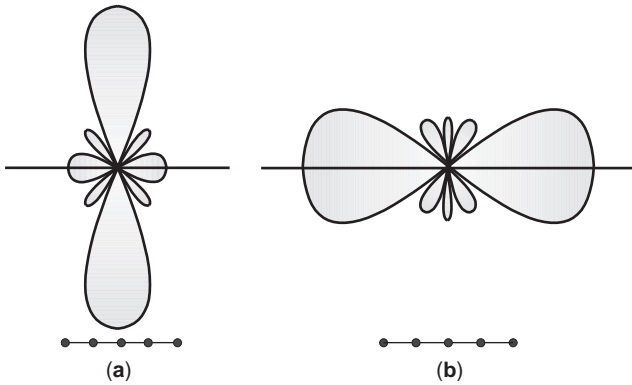


Figure 4. Polar plots of a linear uniform amplitude array of five isotropic sources with 0.5λ spacing between the sources: (a) broadside radiation pattern (0° phase shift between successive elements); (b) endfire radiation pattern (180° phase shift).

vertical plane. The pattern in the other principal plane is usually a pencil-beam pattern but may sometimes be a circular pattern as in certain types of beacon antennas. In addition to these pattern types, there are a number of pattern shapes used for direction finding and other purposes that do not fall under the categories already mentioned. These patterns include the well-known figure-of-eight pattern, the cardioid pattern, split-beam patterns, and multilobed patterns whose lobes are of substantially equal amplitude. For those patterns, which have particularly unusual characteristics, it is generally necessary to specify the pattern by an actual plot of its shape or by the mathematical relationship that describes its shape.

Antennas are often referred to by the type of pattern they produce. Two terms that usually characterize array antennas, are broadside and endfire. A *broadside antenna* is one for which the mainbeam maximum is in a direction normal to the plane containing the antenna. An *endfire antenna* is one for which the mainbeam is in the plane containing the antenna. For example, the short dipole antenna is a broadside antenna. Figure 4 shows the two cases of broadside and endfire radiation patterns, which are produced from a linear uniform array of isotropic sources of 0.5 wavelength spacing, between adjacent elements. The type of radiation pattern is controlled by the choice of phase shift angle between the elements. Zero phase shift produces a broadside pattern and 180° phase shift leads to an endfire pattern, while intermediate values produce radiation patterns with the mainlobes between these two cases.

2.3. Characteristics of Simple Patterns

For a linearly polarized antenna, as a very short dipole antenna, performance is often described in terms of two patterns (Figs. 2b and 2c). Any plane containing the z -axis has the same radiation pattern since there is no variation in the fields with angle ϕ (Fig. 2b). A pattern taken in one of these planes is called an *E-plane pattern* because it is parallel to the electric field vector \mathbf{E} and passes through the antenna in the direction of the beam maximum. A

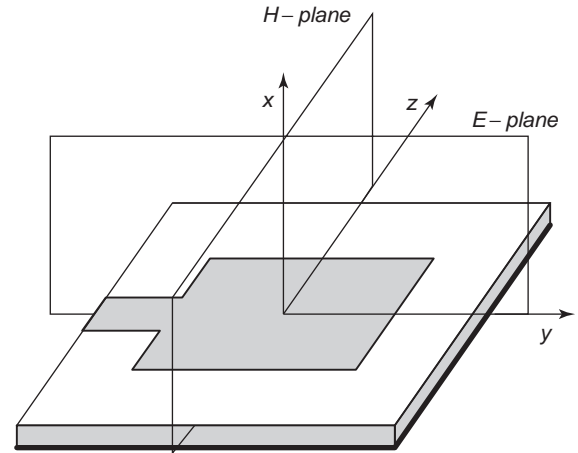


Figure 5. The principal plane patterns of a microstrip antenna: (a) the xy plane or *E*-plane (azimuth plane, $\theta = \pi/2$) and (b) the xz plane or *H* plane (elevation plane, $\phi = 0$).

pattern taken in a plane orthogonal to an *E* plane and cutting through the short dipole antenna, the xy plane in this case, is called an *H-plane pattern* because it contains the magnetic field H and also passes through the antenna in the direction of the beam maximum (Fig. 2c). The *E*- and *H*-plane patterns, in general, are referred to as the *principal-plane patterns*. The pattern plots in Figs. 2b and 2c are called *polar patterns* or *polar diagrams*. For most types of antennas it is a usual practice to orient them so that at least one of the principal-plane patterns coincides with one of the geometric principal planes. This is illustrated in Fig. 5, where the principal planes of a microstrip antenna are plotted. The xy plane (azimuthal plane, $\theta = \pi/2$) is the principal *E* plane, and the xz plane (elevation plane, $\phi = 0$) is the principal *H* plane.

A typical antenna power pattern is shown in Fig. 6. In Fig. 6a depicts a polar plot in linear scale; Fig. 6b shows the same pattern in rectangular coordinates in decibels. As can be seen, the radiation pattern of the antenna consists of various parts, which are known as *lobes*. The *mainlobe* (or *mainbeam* or *major lobe*) is defined as the lobe containing the direction of maximum radiation. In Fig. 6a the mainlobe is pointing in the $\theta = 0$ direction. In some antennas there may exist more than one major lobe. A *minor lobe* is any lobe except the mainlobe. Minor lobes are composed of sidelobes and backlobes. The term *sidelobe* is sometimes reserved for those minor lobes near the mainlobe but is most often taken to be synonymous with minor lobe. A *backlobe* is a radiation lobe in, approximately, the opposite direction to the mainlobe. Minor lobes usually represent radiation in undesired directions, and they should be minimized. Sidelobes are normally the largest of the minor lobes. The level of side or minor lobes is usually expressed as a ratio of the power density in the lobe in question to that of the mainlobe. This ratio is often termed the *sidelobe ratio* or *sidelobe level*, and desired values depend on the antenna application.

For antennas with simple shape patterns, the half-power beamwidth and sidelobe level in the two principal planes specify the important characteristics of the

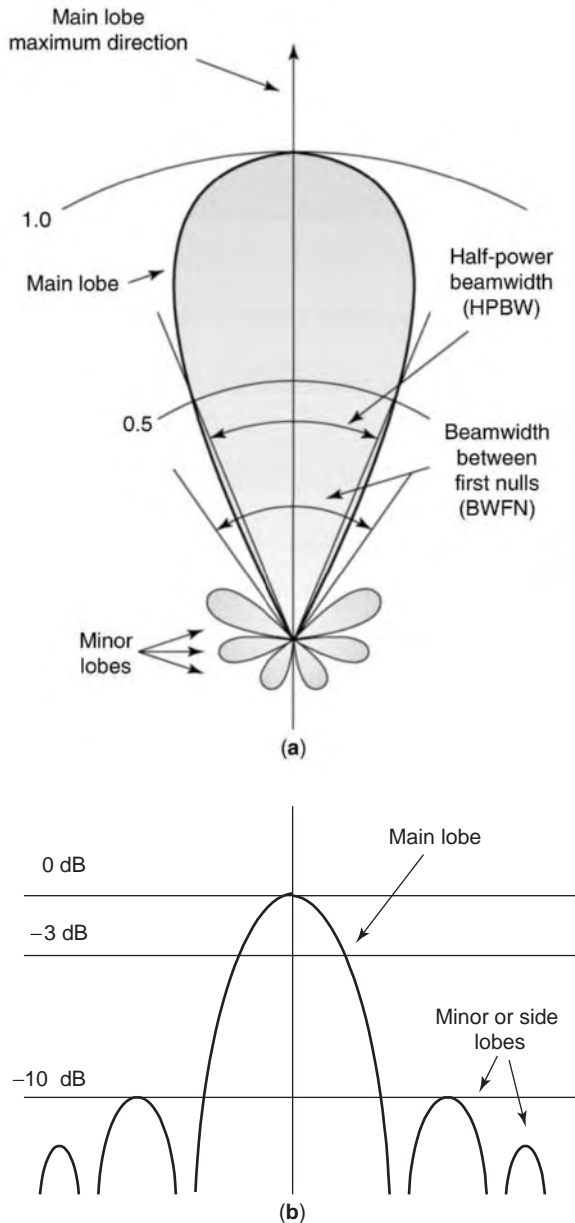


Figure 6. Antenna power patterns: (a) a typical polar plot in linear scale; (b) a plot in rectangular coordinates in decibel (logarithmic) scale. The associated lobes and beamwidths are also shown.

patterns. The *half-power beamwidth* (HPBW) is defined in a plane containing the major maximum beam, as the angular width within which the radiation intensity is one-half the maximum value of the beam. The *beamwidth between first nulls* (BWFN) or beamwidths 10 or 20 dB below the pattern maximum are also sometimes used. Both of them are shown in Fig. 6. However, the term *beamwidth* by itself is usually reserved to describe the 3-dB beamwidth. The beamwidth of the antenna is a very important figure of merit in the overall design of an antenna application. As the beamwidth of the radiation pattern increases, the sidelobe level decreases, and vice versa. So there is a tradeoff between sidelobe ratio and beamwidth of a pattern.

The beamwidth of the antenna is also used to describe the resolution capabilities of the antenna to distinguish between two adjacent radiating sources or radar targets. The most common resolution criterion states that the resolution capability of an antenna to distinguish between two sources is equal to half the first null beamwidth, which is generally used to approximate the half-power beamwidth. This means that two sources separated by angular distances equal to or greater than the HPBW of an antenna, with a uniform distribution, can be resolved. If the separation is smaller, then the antenna will tend to smooth the angular separation distance.

2.4. Field Regions of an Antenna

For convenience, the space surrounding a transmitting antenna is divided into several regions, although, obviously, the boundaries of the regions cannot be sharply defined. The names given to the various regions denote some pertinent prominent property of each region.

In free space there are mainly two regions surrounding a transmitting antenna: the *near-field region* and the *far-field region*. The near-field region can be subdivided into two regions, the *reactive near field* and the *radiating near field*.

The first and innermost region, which is immediately adjacent to the antenna, is called the *reactive or induction near-field region*. Of all the regions, it is the smallest in coverage and derives its name from the reactive field, which lies close to every current-carrying conductor. In this region the reactive field, which decreases with either the square or the cube of the distance, dominates over all radiated fields, the components of which decrease with the first power of distance. For most antennas, the outer boundary of this region is taken to extend to a distance $r < 0.62\sqrt{D^3/\lambda}$ from the antenna as long as $D \gg \lambda$, where D is the largest dimension of the antenna and λ is the wavelength [3]. For the case of an ideal or very short dipole, for which $D = \Delta z \ll \lambda$, this distance is approximately one-sixth of a wavelength ($\lambda/2\pi$). At this distance from the very short dipole the reactive and radiation field components are individually equal in magnitude.

Between the reactive near-field and far-field regions lies the *radiating near-field region*, where the radiation fields dominate but the angular field distribution still depends on the distance from the antenna. For an antenna focused at infinity, which means that the rays at a long distance from the transmitting antenna are parallel, the radiating near-field region is sometimes referred to as the *Fresnel region*, a term taken from the fields of optics. The boundaries of this region are taken to be between the end of the reactive near-field region, $0.62\sqrt{D^3/\lambda}$, and the starting distance of the far-field region, $r < 2D^2/\lambda$ [3].

The outer boundary of the near-field region lies where the reactive field intensity becomes negligible with respect to the radiation field intensity. This occurs at distances of either a few wavelengths or a few times the major dimension of the antenna, whichever is larger. The *far-field or radiation region* begins at the outer boundary of the near-field region and extends outward indefinitely into free

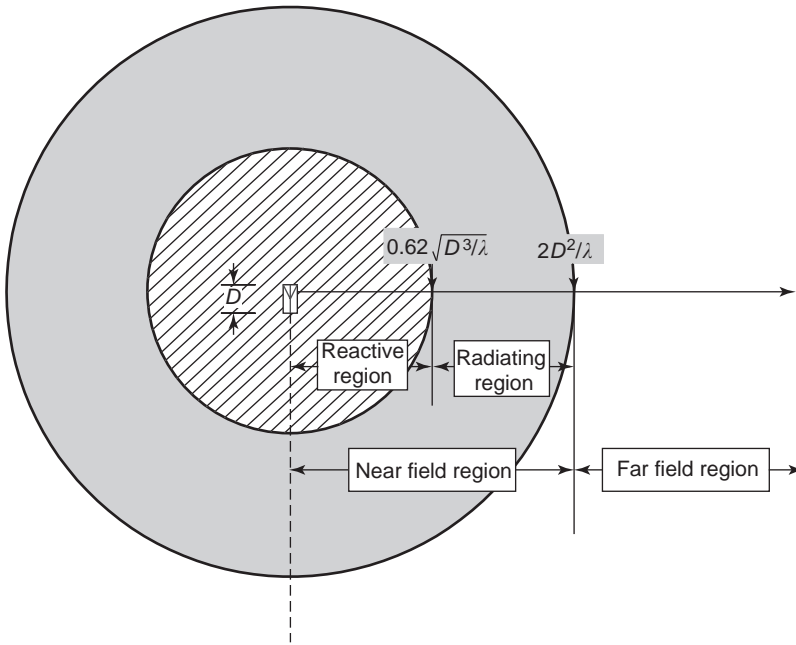


Figure 7. Field regions of an antenna and some commonly used boundaries.

space. In this region the angular field distribution of the field of the antenna is essentially independent of the distance from the antenna. For example, for the case of a very short dipole, the $\sin\theta$ pattern dependence is valid anywhere in this region. The far-field region is commonly taken to exist at distances $r > 2D^2/\lambda$ from the antenna, and for an antenna focused at infinity it is sometimes referred to as the *Fraunhofer region*. All three regions surrounding an antenna and their boundaries are illustrated in Fig. 7.

3. ANTENNA PERFORMANCE MEASURES

3.1. Poynting Vector and Radiation Power Density

In an electromagnetic wave, electric and magnetic energies are stored in equal amounts in the electric and magnetic fields, which together constitute the wave. The power flow is found by making use of the Poynting vector \mathbf{S} , defined as

$$\mathbf{S} = \mathbf{E} \times \mathbf{H} \quad (1)$$

where \mathbf{E} (V/m) and \mathbf{H} (A/m) are the field vectors. Since the Poynting vector represents a surface power density (W/m^2), the integral of its normal component over a closed surface always gives the total power through the surface

$$\oint_A \mathbf{S} \cdot d\mathbf{A} = P \quad (2)$$

where P is the total power (W) flowing out of closed surface A and $d\mathbf{A} = \hat{\mathbf{n}}dA$, where $\hat{\mathbf{n}}$ is the unit vector normal to the surface. The Poynting vector \mathbf{S} and the power P in the relations above are instantaneous values.

Normally, it is the time-averaged Poynting vector \mathbf{S}_{av} , which represents the average power density, that is of

practical interest, and is given by

$$\mathbf{S}_{\text{av}} = \frac{1}{2} \text{Re}(\dot{\mathbf{E}} \times \dot{\mathbf{H}}^*) \quad (\text{W/m}^2) \quad (3)$$

where the term Re stands for the real part of the complex number and the asterisk $*$ denotes the complex conjugate. Note that $\dot{\mathbf{E}}$ and $\dot{\mathbf{H}}$ in Eq. (3) are respectively the expressions for the electric and magnetic fields written as complex numbers to include the change with time. Thus, for a plane wave traveling in the positive z direction with electric and magnetic field components in x and y directions, respectively, the electric field is $\mathbf{E} = \hat{\mathbf{x}}E_x e^{j\omega t}$, while in Eq. (1) it is $\mathbf{E} = \hat{\mathbf{x}}E_{x0}$. The $\frac{1}{2}$ factor appears because the fields represent peak values and should be omitted for RMS (root-mean-square) values.

The average power P_{av} flowing outward through a closed surface can now be obtained by integrating Eq. (3):

$$P_{\text{av}} = \oint_A \text{Re} \dot{\mathbf{S}} \cdot d\mathbf{A} = \frac{1}{2} \oint_A \text{Re}(\dot{\mathbf{E}} \times \dot{\mathbf{H}}^*) \cdot d\mathbf{A} = P_{\text{rad}} \quad (\text{W}) \quad (4)$$

Consider the case where the electromagnetic wave is radiated by an antenna. If the closed surface is taken around the antenna within the far-field region, then this integration results in the average power radiated by the antenna. This is called *radiation power* P_{rad} , while Eq. (3) represents the *radiation power density* S_{av} of the antenna. The imaginary part of Eq. (3) represents the reactive power density stored in the near field of an antenna. Since the electromagnetic fields of an antenna in its far-field region are predominately real, Eq. (3) suffices for our purposes.

The average power density radiated by the antenna as a function of direction, taken on a large sphere of constant radius in the far-field region, results in the *power pattern*

of the antenna. As an example, for an isotropic radiator, the total radiation power is given by

$$P_{\text{rad}} = \iint_A \mathbf{S}_i \cdot d\mathbf{A} = \int_0^{2\pi} \int_0^\pi [\hat{\mathbf{r}}\mathbf{S}_i(r)] \cdot [\hat{\mathbf{r}}r^2 \sin\theta \, d\theta \, d\phi] \quad (5)$$

$$= 4\pi r^2 S_i$$

where, because of symmetry, the Poynting vector $\mathbf{S}_i = \hat{\mathbf{r}}S_i(r)$ is taken independent of the spherical coordinate angles θ and ϕ , having only a radial component.

From Eq. (5) the power density can be found:

$$\mathbf{S}_i = \hat{\mathbf{r}}S_i = \hat{\mathbf{r}} \left(\frac{P_{\text{rad}}}{4\pi r^2} \right) \quad (\text{W/m}^2) \quad (6)$$

This result can also be reached if we assume that the radiated power expands radially in all directions with the same velocity and is evenly distributed on the surface of a spherical wavefront of radius r .

As we will see later, an electromagnetic wave may have an electric field consisting of two orthogonal linear components of different amplitudes, E_{x0} and E_{y0} , respectively, and a phase angle between them δ . Thus, the total electric field vector, called an *elliptically polarized vector*, becomes

$$\dot{\mathbf{E}} = \hat{\mathbf{x}}\dot{E}_x + \hat{\mathbf{y}}\dot{E}_y = \hat{\mathbf{x}}E_{x0}e^{j(\omega t - \beta z)} + \hat{\mathbf{y}}E_{y0}e^{j(\omega t - \beta z + \delta)} \quad (7)$$

which at $z = 0$ becomes

$$\dot{\mathbf{E}} = \hat{\mathbf{x}}\dot{E}_x + \hat{\mathbf{y}}\dot{E}_y = \hat{\mathbf{x}}E_{x0}e^{j\omega t} + \hat{\mathbf{y}}E_{y0}e^{j(\omega t + \delta)} \quad (8)$$

So $\dot{\mathbf{E}}$ is a complex vector (phasor vector) that is resolvable into two components $\hat{\mathbf{x}}\dot{E}_x$ and $\hat{\mathbf{y}}\dot{E}_y$. The total $\dot{\mathbf{H}}$ field vector associated with $\dot{\mathbf{E}}$ at $z = 0$ is then

$$\dot{\mathbf{H}} = \hat{\mathbf{y}}\dot{H}_y - \hat{\mathbf{x}}\dot{H}_x = \hat{\mathbf{y}}H_{y0}e^{j(\omega t - \zeta)} - \hat{\mathbf{x}}H_{x0}e^{j(\omega t + \delta - \zeta)} \quad (9)$$

where ζ is the phase lag of \dot{H}_y with respect to \dot{E}_x . From Eq. (9) the complex conjugate magnetic field can be found changing only the sign of exponents.

Now the average Poynting vector can be calculated using the fields defined above:

$$\begin{aligned} \mathbf{S}_{\text{av}} &= \frac{1}{2} \text{Re}[(\hat{\mathbf{x}} \times \hat{\mathbf{y}})\dot{E}_x\dot{H}_y^* - (\hat{\mathbf{y}} \times \hat{\mathbf{x}})\dot{E}_y\dot{H}_x^*] \\ &= \frac{1}{2} \hat{\mathbf{z}} \text{Re}(\dot{E}_x\dot{H}_y^* + \dot{E}_y\dot{H}_x^*) \\ &= \frac{1}{2} \hat{\mathbf{z}} \text{Re}(E_{x0}H_{y0} + E_{y0}H_{x0}) \cos \zeta \end{aligned} \quad (10)$$

It should be noted that \mathbf{S}_{av} is independent of δ , the phase angle between the electric field components.

In a lossless medium, $\zeta = 0$, because electric and magnetic fields are in time phase and $E_{x0}/H_{x0} = E_{y0}/H_{y0} = \eta$, where η , is the intrinsic impedance of the medium that is real. If $\mathbf{E} = \sqrt{E_{x0}^2 + E_{y0}^2}$ and $\mathbf{H} = \sqrt{H_{x0}^2 + H_{y0}^2}$ are the amplitudes of the total \mathbf{E} and \mathbf{H} fields, respectively, then

$$\begin{aligned} \mathbf{S}_{\text{av}} &= \frac{1}{2} \hat{\mathbf{z}} \frac{E_{x0}^2 + E_{y0}^2}{\eta} = \frac{1}{2} \hat{\mathbf{z}} \frac{E^2}{\eta} \\ &= \frac{1}{2} \hat{\mathbf{z}} (H_{x0}^2 + H_{y0}^2) \eta = \frac{1}{2} \hat{\mathbf{z}} H^2 \eta \end{aligned} \quad (11)$$

These expressions are the most general form of radiation power density of an elliptically polarized wave or of an elliptically polarized antenna, respectively, and hold for all cases, including the linear and circular polarization cases, which will introduce later on.

3.2. Radiation Intensity

Radiation intensity is a far-field parameter, in terms of which any antenna radiation power pattern can be determined. Thus, the antenna power pattern, as a function of angle, can be expressed in terms of its radiation intensity as [3]:

$$\begin{aligned} U(\theta, \phi) &= S_{\text{av}} r^2 \\ &= \frac{r^2}{2\eta} |\mathbf{E}(r, \theta, \phi)|^2 \\ &= \frac{r^2}{2\eta} [|\mathbf{E}_\theta(r, \theta, \phi)|^2 + |\mathbf{E}_\phi(r, \theta, \phi)|^2] \\ &\approx \frac{1}{2\eta} [|\mathbf{E}_\theta(\theta, \phi)|^2 + |\mathbf{E}_\phi(\theta, \phi)|^2] \end{aligned} \quad (12)$$

where

$$\begin{aligned} U(\theta, \phi) &= \text{radiation intensity (W/unit solid angle)} \\ S_{\text{av}} &= \text{radiation density or radial component of Poynting vector (W/m}^2\text{)} \\ \mathbf{E}(r, \theta, \phi) &= \text{total transverse electric field (V/m)} \\ \mathbf{H}(r, \theta, \phi) &= \text{total transverse magnetic field (A/m)} \\ r &= \text{distance from antenna to point of measurement (m)} \\ \eta &= \text{intrinsic impedance of medium (\Omega per square)} \end{aligned}$$

In Eq. (12) the electric and magnetic field are expressed in terms of spherical coordinates.

What makes radiation intensity important is that it is independent of distance. This is because in the far field the Poynting vector is entirely radial, which means that the fields are entirely transverse and E and H vary as $1/r$.

Since the radiation intensity is a function of angle, it can also be defined as the power radiated from an antenna per unit solid angle. The measure of a solid angle is the steradian. One *steradian* is described as the solid angle with its vertex at the center of a sphere that has radius r , which is subtended by a spherical surface area equivalent to that of a square of size r^2 . But the area of a sphere of radius r is given by $A = 4\pi r^2$, so in a closed sphere there are $4\pi r^2/r^2 = 4\pi$ sr. For a sphere of radius r , an infinitesimal area dA on its surface can be written as

$$dA = r^2 \sin\theta \, d\theta \, d\phi \quad (\text{m}^2) \quad (13)$$

and therefore the element of solid angle $d\Omega$ of a sphere is given by

$$d\Omega = \frac{dA}{r^2} = \sin\theta \, d\theta \, d\phi \quad (\text{sr}) \quad (14)$$

Thus, the total power can be obtained by integrating the radiation intensity, as given by Eq. (12), over the entire

solid angle of 4π , as

$$P_{\text{rad}} = \oint_{\Omega} U(\theta, \phi) d\Omega = \int_0^{2\pi} \int_0^{\pi} U(\theta, \phi) \sin \theta d\theta d\phi \quad (15)$$

As an example, for the isotropic radiator ideal antenna, the radiation intensity $U(\theta, \phi)$ will be independent of the angles θ and ϕ and the total radiated power will be

$$\begin{aligned} P_{\text{rad}} &= \oint_{\Omega} U_i d\Omega = U_i \int_0^{2\pi} \int_0^{\pi} \sin \theta d\theta d\phi \\ &= U_i \oint_{\Omega} d\Omega = 4\pi U_i \end{aligned} \quad (16)$$

or $U_i = P_{\text{rad}}/4\pi$, which is the power density of Eq. (6) multiplied by r^2 .

Dividing $U(\theta, \phi)$ by its maximum value $U_{\text{max}}(\theta, \phi)$, we obtain the *normalized antenna power pattern*:

$$U_n(\theta, \phi) = \frac{U(\theta, \phi)}{U_{\text{max}}(\theta, \phi)} \quad (\text{dimensionless}) \quad (17)$$

A term associated with the normalized power pattern is the beam solid angle. The *beam solid angle* Ω_A is defined as the angle through which all the power from a radiating antenna would flow if the power per unit solid angle were constant over this angle and equal to its maximum value (Fig. 8). This means that, for typical patterns, the solid beam angle is approximately equal to the half-power beam width (HPBW):

$$\Omega_A = \int_0^{2\pi} \int_0^{\pi} U_n(\theta, \phi) \sin \theta d\theta d\phi = \oint_{4\pi} U_n(\theta, \phi) d\Omega \quad (\text{sr}) \quad (18)$$

If the integration is done over the mainlobe, the *mainlobe solid angle*, Ω_M , is defined, and the difference of $\Omega_A - \Omega_M$

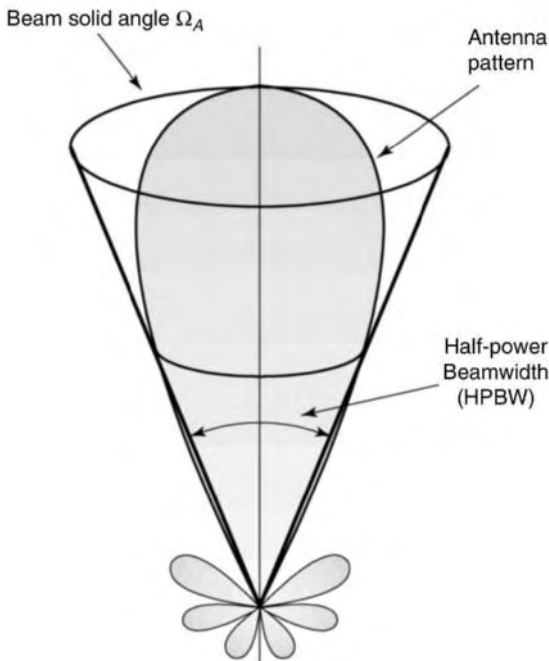


Figure 8. Power pattern and beam solid angle of an antenna.

gives the *minor-lobe solid angle*. These definitions hold for patterns with clearly defined lobes. The *beam efficiency* (BE) of an antenna is defined as the ratio of Ω_M/Ω_A and is a measure of the amount of power in the major lobe compared to the total power. A high beam efficiency means that most of the power is concentrated in the major lobe and that minor lobes are minimized.

3.3. Directivity and Gain

A very important antenna parameter that indicates how well an antenna concentrates power into a limited solid angle is its *directivity* D . The *directivity* of an antenna is defined as the ratio of the maximum radiation intensity to the radiation intensity averaged over all directions. The average radiation intensity is calculated by dividing the total power radiated by 4π sr. Hence

$$\begin{aligned} D &= \frac{U_{\text{max}}(\theta, \phi)}{U_{\text{av}}} = \frac{U_{\text{max}}(\theta, \phi)}{U_i} = \frac{U_{\text{max}}(\theta, \phi)}{P_{\text{rad}}/4\pi} \\ &= \frac{4\pi U_{\text{max}}(\theta, \phi)}{P_{\text{rad}}} \quad (\text{dimensionless}) \end{aligned} \quad (19)$$

since from Eq. (16), $P_{\text{rad}}/4\pi = U_i$. So, alternatively, the directivity of an antenna can be defined as the ratio of its radiation intensity in a given direction, which usually is taken to be the direction of maximum radiation intensity, divided by the radiation intensity of an isotropic source with the same total radiation intensity. Equation (19) can also be written

$$\begin{aligned} D &= \frac{U_{\text{max}}(\theta, \phi)}{P_{\text{rad}}/4\pi} \\ &= \frac{4\pi U_{\text{max}}(\theta, \phi)}{\oint_{4\pi} U(\theta, \phi) d\Omega} \\ &= \frac{4\pi}{\oint_{4\pi} U(\theta, \phi)/U_{\text{max}}(\theta, \phi) d\Omega} \\ &= \frac{4\pi}{\oint_{4\pi} U_n(\theta, \phi) d\Omega} \\ &= \frac{4\pi}{\Omega_A} \end{aligned} \quad (20)$$

Thus, the directivity of an antenna is equal to the solid angle of a sphere, which is 4π sr, divided by the antenna beam solid angle Ω_A . We can say that by this relation the value of directivity is derived from the antenna pattern. It is obvious from this relation that the smaller the beam solid angle, the larger the directivity, or stated in a different way, an antenna that concentrates its power in a narrow mainlobe has a great value of directivity.

Obviously, the directivity of an isotropic antenna is unity. By definition, an isotropic source radiates equally in all directions. If we use Eq. (20), then $\Omega_A = 4\pi$ since $U_n(\theta, \phi) = 1$. This is the smallest directivity value that one can attain. However, if we consider the directivity in a specified direction, for example, $D(\theta, \phi)$ its value can be smaller than unity. As an example, let us calculate the

directivity of the very short dipole antenna. We can calculate its normalized radiated power using the electric or the magnetic field components, given in Table 1. Using the electric field E_θ for far-field region, from Eq. (12), we have

$$U_n(\theta, \phi) = \frac{U(\theta, \phi)}{U_{\max}(\theta, \phi)} = \frac{E_\theta^2(\theta, \phi)}{[E_\theta^2(\theta, \phi)]_{\max}} = \sin^2 \theta \quad (21)$$

and

$$D = \frac{4\pi}{\oint \int_{4\pi} U_n(\theta, \phi) d\Omega} = \frac{4\pi}{\int_0^{2\pi} \int_0^\pi \sin^3 \theta d\theta d\phi} = \frac{3}{2} = 1.5 \quad (22)$$

Alternatively, we can work using power densities instead of power intensities. The power flowing in a particular direction can be calculated using Eq. (3) and using the electric and magnetic far-field components given in Table 1:

$$S_{\text{av}} = \frac{\eta}{2} \left(\frac{I_0 L \beta}{4\pi r} \right)^2 \sin^2 \theta \quad (\text{W/m}^2) \quad (23)$$

By integrating over all angles the total power flowing outward is given by

$$P_T = \frac{\eta}{12\pi} (I_0 L \beta)^2 \quad (\text{W}) \quad (24)$$

The directivity of a very short dipole antenna can be found from the ratio of the maximum power density to the average power density. For the very short dipole antenna, the maximum power density is in the $\theta = 90^\circ$ direction (Fig. 2) and the average power density is found by averaging the total power P_T from Eq. (24) over a sphere of surface area $4\pi r^2$:

$$D = \frac{S_{\text{av}}}{P_T/4\pi r^2} = \frac{(\eta/2)(I_0 L \beta/4\pi r)^2}{(\eta/12\pi)(I_0 L \beta)^2/4\pi r^2} = \frac{3}{2} \quad (25)$$

Thus, the directivity of a very short dipole is 1.5, which means that the maximum radiation intensity is 1.5 times the power of the isotropic radiator. This is often expressed in decibels, such that

$$D = 10 \log_{10}(d) \text{ dB} = 10 \log_{10}(1.5) = 1.76 \text{ dB} \quad (26)$$

Here, we use small (lowercase) letters to indicate absolute value and capital (uppercase) letters for the logarithmic value of the directivity, which is a common symbolism in the field of antennas and propagation.

In some cases it is convenient to use simpler expressions for directivity estimation instead of the exact ones. For antennas characterized by a radiation pattern consisting of one narrow mainlobe and negligible minor lobes, the beam solid angle can be approximated by the product of the half-power beamwidths in two perpendicular planes, and the directivity can be given by the expression

$$D = \frac{4\pi}{\Omega_A} \approx \frac{4\pi}{\Theta_{1r} \Theta_{2r}} = \frac{41,253}{\Theta_{1d} \Theta_{2d}} \quad (27)$$

where Θ_{1r} , Θ_{2r} and Θ_{1d} , Θ_{2d} are the half-power beamwidths in two perpendicular planes in radians and degrees, respectively.

The gain of an antenna is another basic property in the total characterization of an antenna. Gain is closely associated with directivity, which is dependent on the radiation patterns of an antenna. The *gain* is commonly defined as the ratio of the maximum radiation intensity in a given direction to the maximum radiation intensity produced in the same direction from a reference antenna *with the same power input*. Any convenient type of antenna may be taken as a reference antenna. Often the type of the reference antenna is dictated by the application area, but the most commonly used one is the isotropic radiator, the hypothetical lossless antenna with uniform radiation intensity in all directions. So

$$G = \frac{U_{\max}(\theta, \phi)}{U_i} = \frac{U_{\max}(\theta, \phi)}{P_{\text{in}}/4\pi} \quad (\text{dimensionless}) \quad (28)$$

where the radiation intensity of the reference antenna of isotropic radiator is equal to the power in the input P_{in} of the antenna divided by 4π .

Real antennas are not lossless, which means that if they accept an input power P_{in} , the radiated power P_{rad} generally will be less than P_{in} . The *antenna efficiency* k is defined as the ratio of these two powers

$$k = \frac{P_{\text{rad}}}{P_{\text{in}}} = \frac{R_r}{R_r + R_{\text{loss}}} \quad (\text{dimensionless}) \quad (29)$$

where R_r is the *radiation resistance* of the antenna. R_r is defined as an equivalent resistance in which the same current flowing at the antenna terminals will produce power equal to that produced by the antenna. R_{loss} is the *loss resistance* that comes from any heat loss due to the finite conductivity of the materials used to construct the antenna or due to losses associated by the dielectric structure of the antenna. So, for a real antenna with losses, its radiation intensity at a given direction $U(\theta, \phi)$ will be

$$U(\theta, \phi) = k U_0(\theta, \phi) \quad (30)$$

where $U_0(\theta, \phi)$ is the radiation intensity of the same antenna with no losses.

Substituting Eq. (30) into (28) yields the definition of gain in terms of the antenna directivity:

$$G = \frac{U_{\max}(\theta, \phi)}{U_i} = \frac{k U_{\max}(\theta, \phi)}{U_i} = k D \quad (31)$$

Thus, the gain of an antenna over a lossless isotropic radiator equals its directivity if the antenna efficiency is $k = 1$ and is less than the directivity if $k < 1$.

The values of gain may lie between zero and infinity, while for directivity the values range between unity and infinity. However, while directivity can be computed from either theoretical considerations or from measured radiation patterns, the gain of an antenna is almost always

determined by a direct comparison of measurement against a reference, usually the standard gain antenna.

Gain is also expressed in decibels

$$G = 10 \log_{10}(g) \text{ dB} \quad (32)$$

where, as in Eq. (26), small and capital letters denote absolute and logarithmic values, respectively. The reference antenna used is sometimes declared as subscript; for example, dBi means decibels over isotropic.

4. POLARIZATION

4.1. Wave and Antenna Polarization

Polarization refers to the physical orientation of the radiated waves in space. It is known that the direction of oscillation of an electric field is always perpendicular to the direction of propagation. An electromagnetic wave whose electric field oscillation occurs only within a plane containing the direction of propagation is called *linearly polarized* or *plane-polarized*. This is because the locus of oscillation of the electric field vector within a plane perpendicular to the direction of propagation forms a straight line. On the other hand, when the locus of the tip of an electric field vector forms an ellipse or a circle, the electromagnetic wave is called an *elliptically polarized* or *circularly polarized wave*.

The decision to label polarization orientation according to the electric intensity is not as arbitrary as it seems; as a result, the direction of polarization is the same as the direction of the antenna. Thus, vertical antennas radiate vertically polarized waves and, similarly, horizontal antennas radiate waves whose polarization is horizontal. For some time there has been a tendency to transfer the label to the antenna itself. Thus people often refer to antennas as “vertically” or “horizontally polarized”, whereas it is actually only their radiations that are so polarized.

It is a characteristic of antennas that the radiation they emit is polarized. These *polarized waves* are deterministic, which means that the field quantities are definite functions of time and position. On the other hand, other forms of radiation, for example, light emitted by *incoherent* sources such as the sun or light globes, have a random arrangement of field vectors and is said to be *randomly polarized* or *unpolarized*. In this case the field quantities are completely random and the components of the electric field are uncorrelated. In many situations the waves may be partially polarized. In fact, this case can be seen as the most general situation of wave polarization; a wave is *partially polarized* when it may be considered to consist of two parts, one completely polarized and the other completely unpolarized. Since we are interested mainly in waves radiated from antennas, we consider only polarized waves.

4.2. Linear, Circular, and Elliptical Polarization

Consider a plane wave traveling in the positive z direction, with the electric field at all times in the x direction as shown in Fig. 9a. This wave is said to be *linearly polarized* (in the x direction) and its electric field as a function of

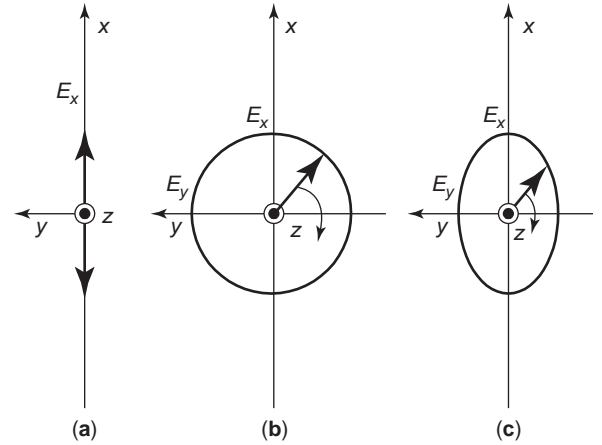


Figure 9. Polarization of a wave: (a) linear; (b) circular; (c) elliptical.

time and position can be described by

$$E_x = E_{x0} \sin(\omega t - \beta z) \quad (33)$$

In general, the electric field of a wave traveling in the z direction may have both an x and a y component, as shown in Figs. 9b and 9c. If the two components E_x and E_y are of equal amplitude, the total electric field at a fixed value of z rotates as a function of time with the tip of the vector forming a circular trace and the wave is said to be *circularly polarized* (Fig. 9b).

Generally, the wave consists of two electric field components, E_x and E_y , of different amplitude ratios and relative phases. Obviously, there are magnetic fields (not shown in the Fig. 9, to avoid confusion) with amplitudes proportional to and in phase with E_x and E_y , but orthogonal to the corresponding electric field vectors. In this general situation, at a fixed value of z the resultant electric vector rotates as a function of time, where the tip of the vector describes an ellipse, called the *polarization ellipse*, and the wave is said to be *elliptically polarized* (Fig. 9c). The polarization ellipse may have any orientation that is determined by its tilt angle, as suggested in Fig. 10, and the ratio of the major to minor axes of the polarization ellipse is called the *axial ratio* (AR). Since the two cases of linear and circular polarization can be seen as two particular cases of elliptical polarization, we will analyze the latter one. Thus, for a wave traveling in the positive z direction, the electric field components in the x and y directions are

$$E_x = E_{x0} \sin(\omega t - \beta z) \quad (34)$$

$$E_y = E_{y0} \sin(\omega t - \beta z + \delta) \quad (35)$$

where E_{x0} and E_{y0} are the amplitudes in x and y directions, respectively, and δ is the time-phase angle between them. The total instantaneous vector field \mathbf{E} is

$$\mathbf{E} = \hat{\mathbf{x}}E_{x0} \sin(\omega t - \beta z) + \hat{\mathbf{y}}E_{y0} \sin(\omega t - \beta z + \delta) \quad (36)$$

At $z = 0$, $E_x = E_{x0} \sin \omega t$ and $E_y = E_{y0} \sin(\omega t + \delta)$. The expansion of E_y gives

$$E_y = E_{y0}(\sin \omega t \cos \delta + \cos \omega t \sin \delta) \quad (37)$$

Using the relation for E_x , we take $\sin \omega t = E_x/E_1$ and $\cos \omega t = \sqrt{1 - (E_x/E_1)^2}$, while the introduction of these terms in Eq. (37) eliminates ωt , giving the following relation, after rearranging:

$$\frac{E_x^2}{E_1^2} - \frac{2E_x E_y \cos \delta}{E_1 E_2} + \frac{E_y^2}{E_2^2} = \sin^2 \delta \tag{38}$$

If we represent this with

$$a = \frac{1}{E_1^2 \sin^2 \delta} \quad b = \frac{2 \cos \delta}{E_1 E_2 \sin^2 \delta} \quad c = \frac{1}{E_2^2 \sin^2 \delta}$$

Eq. (38) takes the form

$$aE_x^2 - bE_x E_y + cE_y^2 = 1 \tag{39}$$

which is the equation of an ellipse, the polarization ellipse, shown in Fig. 10. The line segment OA is the semi-major axis, and the line segment OB is the semi-minor axis. The tilt angle of the ellipse is τ . The axial ratio is

$$AR = \frac{OA}{OB} \quad (1 \leq AR \leq \infty) \tag{40}$$

From this general case, the cases of linear and circular polarization can be found. Thus, if there is only E_x ($E_{y0} = 0$), the wave is linearly polarized in the x direction and if there is only E_y ($E_{x0} = 0$), the wave is linearly polarized in the y direction. When both E_x and E_y exist, for linear polarization they must be in phase or inverse to each other. In general, the necessary condition for linear polarization is that the time-phase difference between the two components must be a multiple of π . If $\delta = 0, \pi, 2\pi, \dots$ and $E_{x0} = E_{y0}$, the wave is linearly polarized but in a plane at an angle of $\pm \pi/4$ with respect to the x axis ($\tau = \pm \pi/4$). If the relation of amplitudes of E_{x0} and E_{y0} is different, then the tilt angle will be related to E_{y0}/E_{x0} ratio value.

If $E_{x0} = E_{y0}$ and $\delta = \pm \pi/2$, the wave is circularly polarized. Generally, circular polarization can be achieved only

when the magnitudes of the two components are the same and the time-phase angle between them is an odd multiple of $\pi/2$.

Consider the case that $\delta = \pi/2$. Taking $z = 0$, from Eqs. (34)–(36) at $t = 0$, it is $\mathbf{E} = \hat{\mathbf{y}}E_{y0}$, while one-quarter cycle later, at $\omega t = \pi/2$, it becomes $\mathbf{E} = \hat{\mathbf{x}}E_{x0}$. Thus, at a fixed position ($z = 0$) the electric field vector rotates as a function of time tracing a circle. The sense of rotation, also referred to as the *sense of polarization*, can be defined by the sense of rotation of the wave as it is observed toward or along the direction of propagation. Thus the above mentioned wave rotates clockwise if it is observed toward the direction of travel (viewing the wave approaching) or counterclockwise observing the wave from the direction of its source (viewing the wave moving away). Thus, unless the wave direction is specified, there is a possibility of ambiguity. The most generally accepted notation is that of the IEEE, by which the sense of rotation is always determined observing the field rotation as the wave is viewed as it travels away from the observer. If the rotation is clockwise, the wave is *right-handed or clockwise circularly polarized* (RH or CW). If the rotation is counterclockwise, the wave is *left-handed or counterclockwise circularly polarized* (LH or CCW). Yet, an alternate way to define the polarization is with the aid of helical-beam antennas. A right-handed helical-beam antenna radiates (or receives) right-handed regardless of the position from which it is viewed while a left-handed one at the opposite direction.

Although linear and circular polarizations can be seen as special cases of elliptical, usually, in practice, elliptical polarization refers to other than linear or circular. A wave is characterized as elliptically polarized if the tip of its electric vector forms an ellipse. For a wave to be elliptically polarized, its electric field must have two orthogonal linearly polarized components, E_{x0} and E_{y0} , but different magnitudes. If the two components are not of the same magnitude, the time-phase angle between them must not be 0 or multiples of π , while in the case of equal magnitude, the angle must not be an odd multiple of $\pi/2$. Thus, a wave that is not linearly or circularly polarized is elliptically polarized. The sense of its rotation is determined according to the same rule as for the circular polarization. So, a wave is *right-handed or clockwise elliptically polarized* (RH or CW) if the rotation of its electric field is clockwise and it is *left-handed or counterclockwise elliptically polarized* (LH or CCW) if the electric field vector rotates counterclockwise. In addition to the sense of rotation, elliptically polarized waves are characterized by their axial ratio AR and their tilt angle τ . The tilt angle is used to identify the spatial orientation of the ellipse and can be measured counterclockwise or clockwise from the reference direction (Fig. 10). If the electric field of an elliptically polarized wave has two components of different magnitude with a time-phase angle between them that is an odd multiple of $\pi/2$, the polarization ellipse will not be tilted. Its position will be aligned with the principal axes of the field components, so that the major axis of the ellipse will be aligned with the axis of the larger field component and the minor axis, with the smaller one.

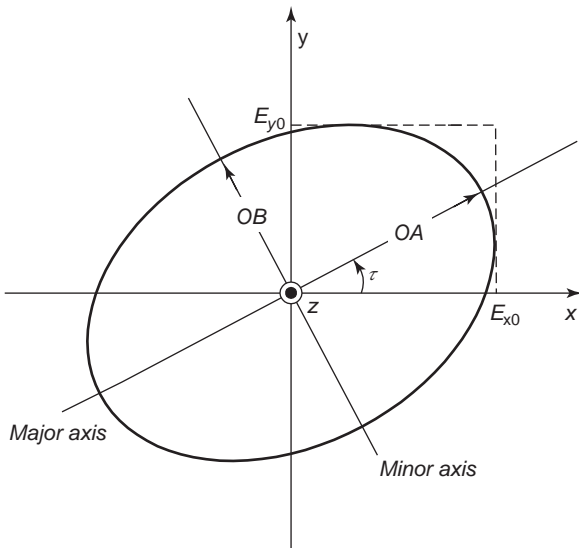


Figure 10. Polarization ellipse at $z = 0$ of an elliptically polarized electromagnetic wave.

4.3. The Poincaré Sphere and Antenna Polarization Characteristics

The polarization of a wave can be represented and visualized with the aid of a Poincaré sphere. The polarization state is described by a point on this sphere where the longitude and latitude of the point are related to parameters of the polarization ellipse. Each point represents a unique polarization state. On the Poincaré sphere the north pole represents left circular polarization while the south pole, right circular polarization, and the points along the equator linear polarization of different tilt angles. All other points on the sphere represent elliptical polarization states. One octant of the Poincaré sphere with polarization states is shown in Fig. 11a, while the full range of polarization states is shown in Fig. 11b, which presents a rectangular projection of the Poincaré sphere.

The polarization state described by a point on the Poincaré sphere can be expressed in terms of

1. The longitude and latitude of the point, which are related to the parameters of the polarization ellipse

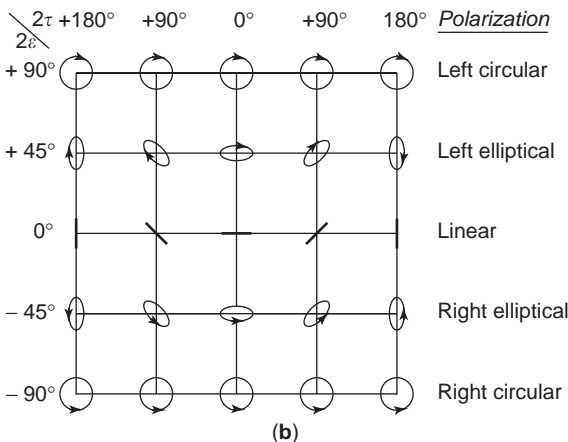
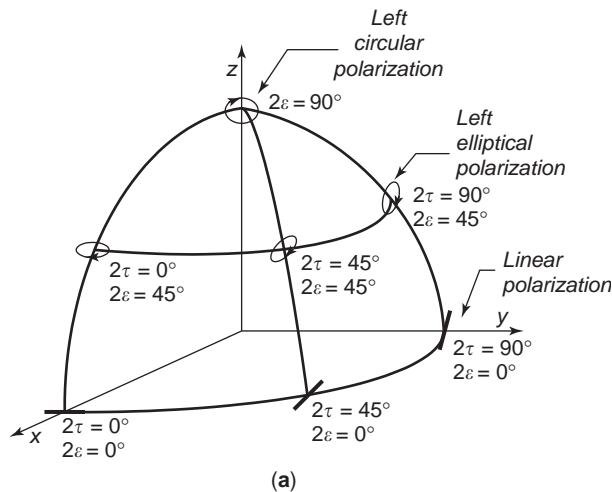


Figure 11. Polarization states of an electromagnetic wave with the aid of Poincaré sphere: (a) one octant of Poincaré sphere with polarization states; (b) the full range of polarization states in rectangular projection.

by the relations

$$L(\text{longitude}) = 2\tau \text{ and } l(\text{latitude}) = 2\varepsilon$$

where τ = tilt angle with values between $0 \leq \tau \leq \pi$ and $\varepsilon = \cot^{-1}(\mp AR)$ with values between $-\pi/4 \leq \varepsilon \leq +\pi/4$. The axial ratio (AR) is negative and positive for right- and left-handed forms of polarization, respectively.

2. The angle subtended by the great circle drawn from a reference point on the equator and the angle between the great circle and the equator:

$$\begin{aligned} \text{Great-circle angle} &= 2\gamma \text{ and equator} \\ &\text{-- great-circle angle} = \delta \end{aligned}$$

with $\gamma = \tan^{-1}(E_{y0}/E_{x0})$ with $0 \leq \gamma \leq \pi/2$ and δ = time-phase difference between the components of electric field ($-\pi \leq \delta \leq +\pi$).

All these quantities, τ , ε , γ and δ , are interrelated by trigonometric formulas [5], and the knowing of (τ, ε) can determine the (γ, δ) and vice versa. As a result, the polarization state can be described by either of the two these sets of angles. The geometric relation between these angles is shown in Fig. 12.

The polarization state of an antenna is defined as the polarization state of the wave radiated by the antenna when it is transmitting. It is characterized by the axial ratio AR, the sense of rotation and the tilt angle, which identifies the spatial orientation of the ellipse. However, care is needed in the characterization of the polarization of a receiving antenna. If the receiving antenna has a polarization that is different from that of the incident wave, a polarization mismatch occurs. In this case the amount of power extracted by the receiving antenna from the incident wave will be lower than the expected value because of the polarization loss. A figure of merit that can be used as a measure of polarization mismatch is the *polarization loss factor* (PLF), defined as the cosine raised by a power of 2 relative to the angle between the polarization states of the antenna in its transmitting mode and the incoming

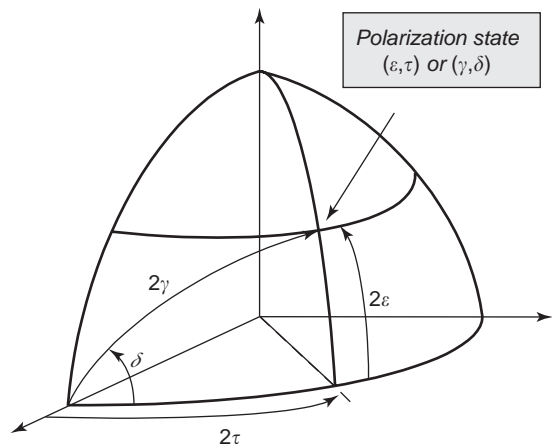


Figure 12. One octant of Poincaré sphere showing the relations of angles τ , ε , γ , and δ that can be used to describe a polarization state.

wave. Alternatively, another quantity that can be used to describe the relation between the polarization characteristics of an antenna and an incoming wave is the *polarization efficiency*, also known as *loss factor* or *polarization mismatch*. It is defined as the ratio of the power received by an antenna from a given plane wave of arbitrary polarization to the power that would be received by the same antenna from a plane wave of the same power flux density and direction of propagation, whose state of polarization has been adjusted for a maximum received power.

In general, an antenna is designed for a specific polarization. This is the desired polarization and is called *copolariation* or *normal polarization*, while the undesired polarization, usually taken in the direction orthogonal to the desired one, is known as *cross-polarization* or *opposite polarization*. The latter can be due to a change of polarization characteristics, known as *polarization rotation*, during the propagation of waves. In general, an actual antenna does not completely discriminate against a cross-polarized wave because of engineering and structural restrictions. The directivity pattern obtained over the entire direction on a representative plane for cross-polarization with respect to the maximum directivity for the normal polarization, called *antenna cross-polarization discrimination*, is an important factor in determining the antenna performance.

The *polarization pattern* gives the polarization characteristics of an antenna and is the spatial distribution of the polarization of its electric field vector radiated by the antenna taken over its radiation sphere. The description of the polarizations is done by specifying reference lines, which are used to measure the tilt angles of polarization ellipses or the directions of polarization for the case of linear polarizations.

5. EVALUATION OF ANTENNA PATTERN AND DIRECTIVITY (GENERAL CASE)

5.1. Derivation of Electromagnetic Fields

As already pointed out, the radiation pattern of an antenna is generally its most basic property and it is usually the first requirement to be specified. Of course, the patterns of an antenna can be measured in the transmitting or receiving mode, selecting in most cases the receiving mode if the antenna is reciprocal. But to find the radiation patterns analytically, we have to evaluate the fields radiated from the antenna. In radiation problems, the case where the sources are known and the fields radiated from these sources are required is characterized as an analysis problem. It is a very common practice during the analysis process to introduce auxiliary functions that will aid in the solution of the problem. These functions are known as *vector potentials*, and for radiation problems the most widely used ones are the *magnetic vector potential* \mathbf{A} and the *electric vector potential* \mathbf{F} . Although it is possible to calculate the electromagnetic fields \mathbf{E} and \mathbf{H} directly from the source current densities, it is simpler to first calculate the electric current \mathbf{J} and magnetic current \mathbf{M} and then evaluate the electromagnetic fields. The vector potential \mathbf{A} is used for the evaluation of the electromagnetic field generated by a known harmonic electric current density \mathbf{J} .

The vector potential \mathbf{F} can give the fields generated by a harmonic magnetic current that, although physically unrealizable, has specific applications in some cases as in volume or surface equivalence theorems. Here, we restrict ourselves to the use of the magnetic vector potential \mathbf{A} , which is the potential that gives the fields for the most common wire antennas.

Using the appropriate equations from electromagnetic theory, the vector potential \mathbf{A} can be found as [3]

$$\mathbf{A} = \frac{\mu_0}{4\pi} \iiint \mathbf{J} \frac{e^{-j\beta r}}{r} dv \quad (41)$$

where $k^2 = \omega^2 \mu_0 \epsilon_0$, μ_0 and ϵ_0 are the magnetic permeability and electric permittivity of the air, respectively; ω is the radian frequency; and r is the distance from any point in the source to the observation point. The fields can then be given by

$$\mathbf{E} = -\nabla V - j\omega \mathbf{A} \quad (42a)$$

and

$$\mathbf{H} = \frac{1}{\mu_0} \nabla \times \mathbf{A} \quad (42b)$$

In Eq. (42a) the scalar function V represents an arbitrary electric scalar potential that is a function of position. The fields radiated by antennas with finite dimensions are spherical waves and in the far-field region, the electric and magnetic field components are orthogonal to each other and form a TEM (transverse electric mode) wave. Thus in the far-field region, Eqs. (42) simplify to

$$\mathbf{E} \approx -j\omega \mathbf{A} \Rightarrow \begin{cases} E_r \approx 0 \\ E_\theta \approx -j\omega A_\theta \\ E_\phi \approx -j\omega A_\phi \end{cases} \quad (43a)$$

and

$$\mathbf{H} \approx \frac{1}{\eta} \hat{\mathbf{r}} \times \mathbf{E} \Rightarrow \begin{cases} H_r \approx 0 \\ H_\theta \approx -\frac{E_\phi}{\eta} \\ H_\phi \approx +\frac{E_\theta}{\eta} \end{cases} \quad (43b)$$

So, the problem becomes that of evaluating the function \mathbf{A} from the specified electric current density on the antenna, first, and then, using Eqs. (43), the \mathbf{E} and \mathbf{H} fields are evaluated and the radiation pattern is extracted. For example, for the case of a very short dipole, the magnetic vector potential \mathbf{A} is given by

$$\mathbf{A} = \hat{\mathbf{z}} \frac{\mu_0 I_0}{4\pi r} e^{-jkr} \int_{-L/2}^{L/2} dz = \hat{\mathbf{z}} \frac{\mu_0 I_0 L}{4\pi r} e^{-jkr} \quad (44)$$

Using Eq. (44), the fields shown in Table 1 can be evaluated.

5.2. Numerical Calculation of Directivity

Usually, the directivity of a practical antenna is easier to evaluate from its radiation pattern using numerical methods. This is especially true when radiation patterns are so complex that closed-form mathematical expressions are

not available. Even if these expressions exist, because of their complex form, the integration necessary to find the radiated power is very difficult to perform. A numerical method of integration, like the Simpson or trapezoid rule can greatly simplify the evaluation of radiated power and give the directivity, helping in this way to provide a method of general application that necessitates only the function or a matrix with the values of the radiated field. However, in many cases the evaluation of the integral that gives the radiated power, using a series approximation, proves to be enough to give the correct value of directivity.

Consider the case where the radiation intensity of a given antenna can be written as

$$U(\theta, \phi) = Af(\theta)g(\phi) \tag{45}$$

which means that it is separable into two functions, where each is a function of one variable only and A is a constant. Then P_{rad} from Eq. (15) will be

$$P_{\text{rad}} = A \int_0^{2\pi} \left(\int_0^\pi f(\theta)g(\phi) \sin \theta d\theta \right) d\phi \tag{46}$$

If we take N uniform divisions over the π interval of variable θ and M uniform divisions over the 2π interval of variable ϕ , we can calculate the two integrals by a series approximation, respectively, as

$$\int_0^\pi f(\theta) \sin \theta d\theta = \sum_{i=1}^N [f(\theta_i) \sin \theta_i] \Delta\theta_i \tag{47a}$$

and

$$\int_0^{2\pi} g(\phi) d\phi = \sum_{j=1}^M g(\phi_j) \Delta\phi_j \tag{47b}$$

Introducing Eq. (47) in Eq. (46), we obtain

$$P_{\text{rad}} = A \left(\frac{\pi}{N} \right) \left(\frac{2\pi}{M} \right) \sum_{j=1}^M \left\{ g(\phi_j) \left[\sum_{i=1}^N f(\theta_i) \sin \theta_i \right] \right\} \tag{48}$$

A computer program can easily evaluate this equation. The directivity is then given by Eq. (19), which is repeated here:

$$D = \frac{4\pi U_{\text{max}}(\theta, \phi)}{P_{\text{rad}}}$$

In the case where θ and ϕ variations are not separable, P_{rad} can also be calculated by a computer program by a slightly different expression

$$P_{\text{rad}} = B \left(\frac{\pi}{N} \right) \left(\frac{2\pi}{M} \right) \sum_{j=1}^M \left\{ \sum_{i=1}^N F(\theta_i, \phi_j) \sin \theta_i \right\} \tag{49}$$

where we consider that in this case $U(\theta, \phi) = BF(\theta, \phi)$.

For more information on radiation patterns, in general, and radiation patterns of specific antennas the reader is encouraged to check Refs. 2–13.

BIBLIOGRAPHY

1. J. G. Webster, ed., *Wiley Encyclopedia of Electrical and Electronics Engineering*, Vol. 1, Wiley, New York, 1999.
2. S. Drabowitch, A. Papiernik, H. Griffiths, J. Encinas, and B. L. Smith, *Modern Antennas*, Chapman & Hall, London, 1998.
3. C. A. Balanis, *Antenna Theory, Analysis and Design*, Wiley, New York, 1997.
4. J. D. Kraus, *Antennas*, McGraw-Hill, New York, 1988.
5. J. D. Kraus and R. Marhefka, *Antennas*, McGraw-Hill, New York, 2001.
6. J. D. Kraus and K. R. Carver, *Electromagnetics*, McGraw-Hill, New York, 1973.
7. W. L. Stutzman and G. A. Thiele, *Antenna Theory and Design*, Wiley, New York, 1981.
8. W. L. Weeks, *Antenna Engineering*, McGraw-Hill, New York, 1968.
9. S. A. Schelkunoff and H. T. Friis, *Antenna Theory and Practice*, Wiley, New York, 1952.
10. E. Jordan and K. Balmain, *Electromagnetic Waves and Radiating Systems*, Prentice-Hall, New York, 1968.
11. T. A. Milligan, *Modern Antenna Design*, McGraw-Hill, New York, 1985.
12. R. C. Johnson (and H. Jasik, editor of first edition), *Antenna Engineering Handbook*, McGraw-Hill, New York, 1993.
13. Y. T. Lo and S. W. Lee, eds., *Antenna Handbook: Theory, Applications and Design*, Van Nostrand Reinhold, New York, 1988.

ANTENNA REVERBERATION CHAMBER

N.K. KOUVELIOTIS
 P.T. TRAKADAS
 I.I. HERETAKIS
 C.N. CAPSALIS
 National Technical University of
 Athens
 Athens, Greece

1. INTRODUCTION

During the last few years there has been increasingly widespread study of the electromagnetic interference of equipment to either one of its component sections or to another apparatus operating in the close vicinity. This has been caused by the continuous development of electronic and electric systems that use the electromagnetic spectrum for information transfer purposes [1]. For this reason, there is a growing interest among scientific communities globally in the development of methods and structures that can determine and identify the electromagnetic interference phenomena. The scientific field that covers the principles of electromagnetic interference and deals with the harmonic coexistence of complex electric and electronic systems is electromagnetic compatibility (EMC). According to Williams [1], EMC is defined as the ability of a device, system, or equipment component to

satisfactorily operate in its electromagnetic environment without introducing unwanted electromagnetic disturbances in any apparatus that functions in that environment.

In order to ensure that the fundamental principles of EMC are followed, several tests have to be carried out. A piece of equipment, according to its classification, has to undergo tests related to conducted emission and conducted immunity, as well as radiated emission and radiated immunity. For every equipment unit, the corresponding EMC standards present the appropriate tests together with the proposed methods and structures. A very crucial parameter for determination of conformity of the equipment examined, within the limits and restrictions outlined in the appropriate EMC standard, is the test site that will host the measurements performed according to the standard.

The test sites that are often used and proposed by the majority of the standards are the open-area test site (OATS), the anechoic chamber, the screened room, and more recently the reverberation chamber. An OATS consists of a perfectly conducting ground plane placed on an ellipsoidal area that is free of reflecting obstacles and electromagnetic noise from the surrounding environment. It is used mostly for radiated emissions tests. The anechoic chamber is a closed structure with walls coated with a radiosorbent material in order to absorb the unwanted reflections of the propagating waves. Moreover, it provides a high-quality shielding of the test structure, ensuring that environmental electromagnetic noise is absent or under a very low level. The screened room is a test site often used for immunity tests, due to the low cost and easy constructed structure.

A form of screened room used for emission and immunity tests is the *reverberation chamber* [2], which consists of a highly conductive enclosure that provides high shielding for the electrical and electronic equipment being tested therein. The main feature that distinguishes it from the other closed cavities is the presence of one or more stirrers, which modify the internal distribution of the electromagnetic field, providing the desired electromagnetic environment for the EMC tests being carried out. It is also referred to as a mode-stirred chamber.

Reverberation chambers were first introduced for measuring the shielding effectiveness of cables, connectors, and enclosures according to specified military standards. The International Electrotechnical Commission (IEC) has established a standard (IEC 61000-4-21 [2]) that regards the test methods and procedures for using reverberation chambers for radiated immunity, radiated emissions, and shielding effectiveness measurements. It also describes the methods that have to be adopted for the proper calibration of a reverberation chamber.

The reverberation chamber (see structure shown in Fig. 1) consists of a highly conductive electrically large cavity whose smallest dimension is very large compared to the wavelength at the lowest usable frequency (LUF). The LUF [2,3] is a crucial parameter for determining the proper operation of a reverberation chamber and will be analytically discussed later in this article. As mentioned previously, the main feature of a mode-stirred chamber

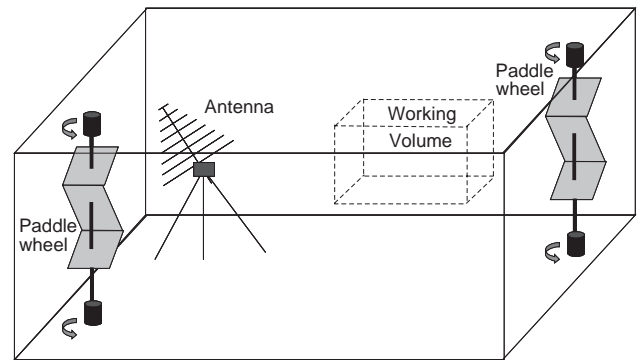


Figure 1. Structure of reverberation chamber.

is the presence of a stirrer, which forms the appropriate field conditions, which will be described later. It usually appears in the shape of a paddle wheel, although several alternative methods of stirring have been proposed in the more recent literature and discussed later in this article. The choice of the kind of the stirrer as well as the position inside the chamber where it is fixed to operate are basic parameters for determining the stirrer effectiveness, as will be shown later.

The main function of a stirrer (or *tuner*, as it is also referred to) is to significantly vary the field boundary conditions in the chamber through its movement or rotation. When the stirrer has moved to a sufficient number of positions, the number of modes propagating in the closed cavity has been significantly increased (usually over 60 modes) and the field variations that are caused by its movement provide a set of fields that cover all the directions and polarizations. The cavity is then multimoded, and this is interpreted by the relative stability of the field magnitude and direction between all the chamber points within uncertainty limits. The electromagnetic environment that derives from this situation is statistically uniform and statistically isotropic when it is considered as the average value for a sufficient number of stirrer positions. However, in some cases (usually in immunity tests) the maximum value is computed for the corresponding number of stirrer positions. Thus, as will be discussed later, the choice of the number of stirrer positions during the EMC test or the calibration of the chamber forms a very critical parameter for the evaluation of the results and the proper operation of the chamber itself.

There are two basic procedures for stirrer rotation: (1) mode stirring and (2) mode tuning [4,5]. In procedure 1, the stirrer moves continuously during the test and the average field is computed or measured; in procedure 2, the stirrer (or tuner) moves at distinct positions with a predefined angle of separation to allow the field to become stable and a maximum measurement or computation is performed.

The reverberation chamber study requires the use of statistical theory to predict the field conditions inside the chamber, as the field is stochastic in nature in contrast to the anechoic chamber, where the field is deterministic. This property of the mode-stirred chamber enhances the ability of performing repeatable EMC tests, due to the

uniformity and the isotropic conditions over the working volume where the equipment under test (EUT) is positioned. This feature allows tests to be performed with a high degree of reliability without requiring the rotation of the EUT or the interchange of the antennas' polarization between horizontal and vertical as demanded when an anechoic chamber is used. Consequently, tests are performed in a quick and easy manner and are repeatable, which is usually problematic because of the long duration of the tests and the accuracy and credibility requirements of the results.

Construction of a reverberation chamber is a low-cost and easily performed procedure because of the simple and low-demand structure, as is readily seen in Fig. 1. This advantage allows for mobility in manufacture of the chamber, which can be moved and set up wherever the EUT is intended to operate (in situ measurement); thus the EUT does not have to be transferred to the laboratory for testing, which is usually inconvenient for large objects. Furthermore, the multipath propagation environment that is accomplished in a mode-stirred chamber represents the actual conditions under which the EUT is designed to routinely operate. This is a very important property, as according to EMC principles, the EUT should be tested as close as possible to its real-life operating environment [6].

The ability of a reverberating enclosure to store a high amount of energy is another significant feature. The field strengths that are generated are usually very high, corresponding to a large value for the chamber's quality factor (Q) compared to proposed EMC test sites. The Q [2] of an enclosure is another critical parameter for determining the acceptable performance of a mode-stirred chamber, and the methods of calculation and measurement of which are described analytically later in this article.

However, the use of the reverberation chamber is not a panacea for EMC tests. The statistical nature of the electromagnetic environment inside the chamber proper may have some drawbacks as it may be difficult to predict the field at a certain point. Moreover, the LUF proposes some restrictions with regard to the use of the chamber at relatively low frequencies. It then relies on the cavity dimensions, the stirrer effectiveness, and the quality factor to determine whether the chamber can be used at the desired low level of the frequency range. Additionally, when the EUT fails the test, no information is provided regarding the direction and polarization of the field due to the isotropic and randomly polarized electromagnetic environment [7].

The performance of a reverberation chamber has been tested both theoretically and experimentally as reported in the more recent literature. The theoretical approach [8–13] is based almost entirely on the use of an appropriate numerical electromagnetic method, which can compute the fields within the enclosure with high reliability and derive results for the statistics or the main reverberation chamber characteristics. The strong benefit of this chamber's realization is the ability to easily evaluate different conditions related to alternating the chamber's dimensions or shape, the stirrer shape or size, wall materials, and other parameters. Thus, an optimization of the

chamber's operation can be carried out by performing different tests with relatively tolerable time limits. The experimental procedure is based on the assessment of measurement results acquired from a manufactured mode-stirred chamber or from a screened room properly transformed to serve as a reverberating enclosure.

The use of reverberation chambers for testing various types of antennas and especially electrically small antennas used in terminal mobile or generally wireless devices is a reliable alternative compared to the widespread anechoic chamber structure. The usual small size of these antennas, combined with the relatively high-frequency spectrum in which they are designed to operate, enhances the adoption of a mode-stirred chamber for measuring the characteristics of such antennas as few restrictions based on dimensions or LUF are imposed. Moreover, the multipath environment in which these types of antennas are designed to operate is best described with the use of a reverberation chamber [14].

Many studies presented in the more recent literature suggest ways for measuring the radiation efficiency of antennas in a mode-stirred chamber [15–18]. By locating a transmitting antenna and an antenna to be tested in this kind of chamber for different chamber configurations (due to the alternating environment that the stirrers produce), the received power of the tested antenna is a stochastic variable. The radiation efficiency of the tested antenna can be assessed by computing the average value of the received power over all the different stirrer positions and comparing it with the average received power of a reference antenna with a predetermined radiation efficiency. However, the results seem to be strongly dependent on the orientation and polarization of the antenna tested, and an uncertainty of 2–3 dB is produced. This can be reduced by replacing the transmission antenna with either a helical circularly polarized antenna or three orthogonally polarized fixed antennas. In addition to the radiation efficiency, the input impedance of antennas operating near lossy materials that simulate the human tissue properties can be determined with the use of reverberation chambers [19]. These conditions are assumed to be very close to the free-space environment.

After approximately 20 years since reverberation chambers were first introduced, only now is their use in EMC tests, according to the present standards, becoming appreciable. This acceptance is predicted to become more intense in the near future as emission standards will demand that tests be carried out at frequencies greater than 1 GHz and as the tests at high frequencies of EUTs with electrically large dimensions turn out to be complicated. Reverberation chambers have also proved to be very reliable for bioelectromagnetic testing, due to their advantage of providing a uniform environment conducive to a parallel implementation in which multiple tests can be performed, resulting in an increased number of statistical samples and therefore in a more precise set of results [20].

In the following sections, we outline the basic characteristics of a mode-stirred chamber. The field uniformity, the statistical properties, the LUF, the quality factor, the alternative ways of chamber's stirring, and the numerical

methods used to simulate the reverberation performance will be presented on the basis of information acquired from the available literature.

2. FIELD UNIFORMITY

As also mentioned before, field uniformity is a basic feature of a reverberation chamber. It can be interpreted as the ability of the electromagnetic field inside the chamber to be statistically isotropic, statistically homogeneous, and randomly polarized. The term *isotropic* represents the equal statistics of the electromagnetic environment in any given direction. The homogeneous property implies that all spatial locations at a sufficient distance from any metal surfaces inside the chamber are statistically equivalent. The random phase between all waves reflects the random polarization.

After a reverberation chamber is constructed or is modified to a high degree, a calibration procedure has to be carried out to ensure that the chamber meets the requirements of adequate chamber performance. Therefore, the fields should be tested to verify that the same magnitude for all polarizations throughout the chamber is achieved, within certain limits of uncertainty. This procedure is also used to determine the LUF of the chamber, which will delineate the frequency operating range of the enclosure.

The setup for the calibration procedure is depicted in Fig. 1. The calibration is performed over a volume, including the testbench and the EUT inside the chamber, which is called the “test” or “working” volume [2]. The working volume is thought to be placed at a distance of $\lambda/4$ m at the lowest frequency of operation from any antenna, tuner, or other reflecting object. For example, for a chamber having a LUF of 100 MHz, this distance is calculated to be 0.75 m. Measurement of the field uniformity should be done in the absence of the EUT or any other support equipment and it is carried out at the eight corner points of the working volume and for the three individual axes (x, y, z) at each location. Thus, the use of isotropic probes is suggested to allow access to each axis and collecting the maximum data of the electric field at each location that will be worked out for the field uniformity assessment. The fields inside the chamber are excited with the use of an antenna that points to one of the chamber’s corners to avoid direct illumination of the working volume, which can result in degradation of the proper operation of the reverberation chamber. For that reason, a logperiodic antenna is used because of its high directivity patterns. However, as was reported in the more recent literature [21,22], the direct path between the generating antenna and the EUT, apart from not disturbing the desired electromagnetic environment inside the chamber, effectively describes the real conditions of EUT operation. A reference antenna is also employed for recording electric field measurements, which are used for the determination of certain factors of the chamber’s behavior (i.e., chamber calibration factor and chamber loading factor [2]).

The data recording is repeated while the stirrer is rotating either continuously (mode stirring) or at distinct

positions (mode tuning). For the mode-stirring technique, the use of as many samples as possible, provided these samples are independent [2], contributes to enhanced chamber operation. Moreover, the considerably shorter test time achieved compared to the mode-tuning technique is another significant advantage. However, the response of the field sensors and the EUT to the rapidly changing field is usually problematic and should be significantly considered each time this stirring method is enforced. The procedure for chamber calibration is similar to that adopted for the mode-tuning technique.

For the case of mode tuning, the number of tuner positions (i.e., number of samples) is a critical parameter for field uniformity assessment. The number of tuner steps capable of providing the required field uniformity is shown to be dependent on the frequency of operation according to the IEC specification. This approval is derived from the fact that for every chamber there is a frequency at which the overmoded condition no longer exists and the reverberation characteristics vanish. Compensation can be obtained by increasing the number of tuner steps in order to restore the optimum chamber performance. Table 1 depicts the recommended [2] number of samples (or tuner steps) required for the chamber calibration at each frequency examined and at each point of the working volume. The choice of more or fewer tuner positions (but not less than 12) will probably improve the field uniformity.

After obtaining the required data for the electric field using the procedure mentioned earlier, the field uniformity should be determined by enforcing an appropriate method. In one method presented in the literature, the acquired data are reduced by discarding 25% of the values that have the maximum variation among the eight points (i.e., $i = 1, \dots, 8$) and then requiring the variation of the remaining data to be usually within 6 dB. However, the excluded data are eliminated without regard to any “weight,” thus resulting in unknown uncertainties. For this reason the method proposed by the IEC standard [2] is widely accepted and employed in the literature.

The IEC specification utilizes the standard deviation method, which computes the standard deviation of the data among the eight points for the three polarizations and that, according to the frequency tested, should be beyond a proposed upper limit. The limits for each frequency range are depicted in Table 2 [2].

To calculate the standard deviation, the maximum value of the magnitude of the electric field over the number of the discrete tuner steps, determined according to Table 1, at each of the eight points and for each polarization is recorded and then normalized to the square root of the average input power over one tuner rotation:

$$E_{x,y,z}^i = \frac{E_{\max,x,y,z}^i}{\sqrt{P_{\text{in}}}} \quad (1)$$

where $E_{x,y,z}^i$ is the normalized value of the magnitude of the electric field for each of the three polarizations x, y, z and at each of the eight points ($i = 1, \dots, 8$), $E_{\max,x,y,z}^i$ represents the maximum, over the number of tuner steps,

Table 1. Number of Samples Required for Chamber Calibration

Frequency ^a	Number of samples
f_1-3f_1	50
$3f_1-6f_1$	18
$6f_1-10f_1$	12
$>10f_1$	12

^a(f_1 : lowest examined frequency)

recorded value at each point ($i=1,\dots,8$) and for each polarization, and P_{in} is the input power over one tuner rotation.

The average value of the normalized maximum of the electric field for each polarization obtained by Eq. (1) over the eight locations of the working volume is computed in the next step. For the x axis this is symbolized by $\langle E_x \rangle_8$ and calculated by the following equation:

$$\langle E_x \rangle_8 = \frac{\sum_{i=1}^8 E_x^i}{8} \quad (2)$$

where E_x^i is the normalized maximum magnitude of the x component of the electric field, derived by Eq. (1), at each of the eight points of the working volume.

For the y and z polarizations the equations are derived in a straightforward manner. Moreover, the average $\langle E \rangle_{24}$ of the normalized maximum values over all of the eight locations and the three polarizations is regarded as well:

$$\langle E \rangle_{24} = \frac{\sum E_{x,y,z}^i}{24} \quad (3)$$

which is interpreted as the sum of the 24 rectangular electric field maximum values divided by the number of the computed or measured values at all points and for all polarizations. The IEC specification allows the total number of values (i.e., 24) to be replaced by nine measurements or computed results if the frequency of examination is above $10f_1$, where, according to Table 1, f_1 is the lower frequency of the range in which the chamber is tested for its operation.

The standard deviation σ for each field component and for the total dataset, which will finally determine the field uniformity conditions in the reverberation chamber, is computed from the following equation:

$$\sigma = \alpha^* \sqrt{\frac{\sum (E_{x,y,z}^i - \langle E_{x,y,z} \rangle)^2}{N - 1}} \quad (4)$$

where N is the number of values in the sample examined (i.e., 8 or 24 or 9), $\langle E_{x,y,z} \rangle$ represents the average value over the eight points of the normalized maximum magnitude $E_{x,y,z}^i$ of the x, y, z component or over the total set of 24 or 9 measurements, respectively, and α is a constant equal to 1.06 for $N \leq 20$ or equal to 1 for $N > 20$. To express the standard deviation in decibels, the following equation is utilized:

$$\sigma(\text{dB}) = 20^* \log \left(\frac{\sigma + \langle E_{x,y,z} \rangle}{\langle E_{x,y,z} \rangle} \right) \quad (5)$$

Table 2. Standard Deviation Limits for Field Uniformity Determination

Frequency	Standard Deviation Limit (dB)
80–100 MHz	4
100–400 MHz	4 dB at 100 MHz with linear decrease to 3 dB at 400 MHz
> 400 MHz	3

The field uniformity criterion is thought to be satisfied if the standard deviations for each of the three polarizations and for the total dataset is under the limits specified in Table 2.

If the chamber meets the field uniformity criterion, it is regarded as calibrated in the frequency range tested, and the lowest frequency of this range is generally assumed to be its LUF. Then, the number of tuner steps required to obtain the uniformity may be reduced in order to gain valuable test time when an EUT will be introduced for testing.

The problems arise when the field uniformity criterion is not satisfied and therefore the chamber is not calibrated. The literature, as well as in the IEC specification [2], describes methods for improving the achieved field uniformity or obtaining the uniformity conditions when a chamber fails the calibration test. As mentioned in the IEC standard, increasing the number of tuner steps (or samples) by 10% or 50% could result in field uniformity.

A reduction of the size of the working volume (which should not be smaller than the size of the EUT that is intended to be tested) is another method proposed to achieve the required uniformity but only if the fail margin is relatively small. Additionally, by increasing the number of tuners or altering the size of tuners or their positions inside the chamber (e.g., by placing them on the ceiling instead of one wall [10]), the field uniformity may improve or be achieved if the criterion described above is not satisfied. As also stated in the recent literature [9], the uniformity when two stirrers in the form of the paddle wheel rotate at different speeds is improved, compared to the case in which one stirrer or two stirrers with equal speeds are utilized. This is interpreted by the observation that the alteration of boundary conditions increases with time and the modes inside the chamber are multiplied and consequently an overmoded condition is obtained. The use of a sufficient paddle ratio [10] (i.e., ratio of paddle sizes) seems to provide an increase in the effectiveness of the tuner, which subsequently improves the field conditions. Also, as illustrated by Harima [9], with a stirrer having a width greater than 3λ and positioned at a distance of over 1λ from the wall surface, the field uniformity is improved and the uncertainty of the prediction in measurements is minimized.

The properties of the chamber tested influence to a high degree the uniformity obtained. For the case of a large chamber, the field is found to be uniform at relatively low frequencies because of the overmoded condition that is observed in a chamber with large dimensions compared to the excitation wavelength. A proposed dimension of a

reverberation chamber found in the literature [8] is greater than 10λ , where λ is the excitation wavelength. The walls of a mode-stirred chamber are theoretically assumed to be perfect electric conductors, but in practical cases, the value of the reflection coefficient is less than unity. As also shown by Harima [9], as the reflection coefficient on the chamber's walls approaches unity with the appropriate choice of the constructed material, the uniformity improves. Some studies [e.g., 5] propose the use of absorbing materials (e.g., ferrite tiles) inside the chamber for improving the field uniformity, especially at low frequencies. The aim for this modification of the reverberating enclosure has been the reduction of the Q of the enclosure, which contributes in a broader resonance bandwidth that increases the field uniformity. This situation, however, results in the reduction of the available energy inside the chamber, requiring higher input power in order to compensate for the power loss. On the contrary, the use of acoustic diffusors [13] leads to better field homogeneity, due to the shifting of modes that is observed in frequency ranges where no or only a few modes are present. These structures are alternatively placed vertically or horizontally to eliminate the influence of the incident field.

An important issue that should be addressed each time a calibration of a reverberation chamber is performed is the loading effect [2,23]. After calibration is completed, the EUT should be placed inside the chamber so that the EMC test can be conducted. The introduction of the EUT in the enclosure will inevitably "load" the chamber, that is, absorb a significant amount of the energy available, which will no longer be used for generating the desired field conditions in the cavity. As a result, the input power should be increased, as mentioned previously.

No test should be carried out in a calibrated mode-stirred chamber without encountering the loading effects. For this reason, the average power received by a reference antenna injected in the chamber with the EUT in place should be recorded for a number of tuner steps equal to those used during the calibration. The eight measurements obtained from the calibration are compared to the data from this single measurement, and the chamber is not considered as loaded if the average value of the power received by the reference antenna, when the EUT is present, does not exceed the uniformity of the average field magnitude recorded during the calibration procedure. In a different case, a factor defined as the *chamber loading factor* (CLF) is introduced to compute the appropriate level of the input power capable of providing the desired amount of stored energy. The CLF is derived by calculating the ratio between (1) the measurement acquired when the EUT is placed in the chamber and (2) the mean value obtained during calibration. The chamber loading limit should also be determined by testing the field uniformity at conditions where tough loading is present.

3. STATISTICAL CHARACTERIZATION OF THE FIELD

A basic feature of a reverberating enclosure is the nature of the generated electromagnetic environment, which is purely stochastic in contrast to the alternate EMC sites

where the field is found to be deterministic. Therefore, research on the statistical properties of the field conditions inside a mode-stirred chamber turns out to be a very challenging task. In the more recent literature, the statistical behavior of a reverberation chamber has gained significant attention and an adequate number of mathematical models have been derived for the characterization of such a behavior. The received power of the antenna placed inside the chamber, which is directly related to the electric field squared, is statistically characterized with the use of theoretical prediction models. Other magnitudes that are statistically described in the literature are the maximum received power (i.e., maximum electric field squared), the rectangular component of the electric field, and the maximum value(s) of the rectangular component of the electric field. Because of the statistical nature of the electromagnetic environment in a reverberation chamber, the test conditions at the EUT can be established or monitored.

When the reverberation properties are assumed to be perfect (i.e., in an ideal mode-stirred chamber), then the spatial mean value of the field for a fixed boundary condition and the corresponding average of the field at a fixed location for variable boundary conditions (called the "ensemble average") are equivalent. The variable boundary conditions are accomplished by either rotating the stirrer or altering the configuration of the objects required for performing the EMC test in the chamber. Figure 2 demonstrates the probability density function (pdf) of the field at a location in a reverberation chamber with perfect conditions normalized by the ensemble average or the spatial mean value. It can be readily seen that as the number of the samples (i.e., different boundary conditions) is increased, the average magnitude of the field in the chamber at any location (or the "expected" value) converges to the spatial mean value. The uncertainty of this mean value is expressed by the width of the curve shown in Fig. 2, and as it can be easily derived, it shows a remarkable improvement as the number of samples grows [2].

Apart from the average value of the chamber field, the maximum magnitude, which is widely used for radiated immunity testing, also seems to be influenced by the number of the alternate boundary conditions. In Fig. 3, the pdf of the normalized by the mean value maximum magnitude of the electric field at a given location in the chamber is demonstrated. It can be noted that with the increase of the number of tuner steps (or boundary conditions), the distribution converges to a single value and the uncertainty improves as a result of the narrower width of the curve. This property, combined with the isotropic and homogeneous nature of the field in the chamber, and with the fact that the electromagnetic environment is characterized by its mean value, is used for the determination of the maximum value of all components at all locations in the working volume of the chamber by measuring or computing the mean of a specific component at a specific location. This assumption is, of course, used within some uncertainty but it is a very vigorous prediction.

When a large number of modes are present in a reverberation chamber (i.e., when the chamber is overmoded), the energy in a given mode is thought to be a random

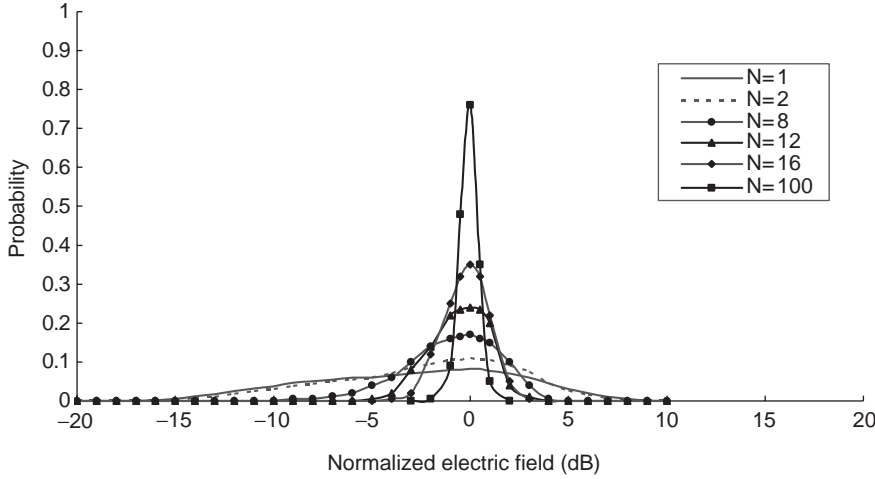


Figure 2. Probability density function of the normalized value of the electric field at a fixed location with different number (N) of tuner steps.

variable depending on the position of the tuner [24]. The field at a given point is the sum of the contributions of the propagating modes in the chamber and is characterized by six parameters (in-phase and quadrature component in each direction). According to the central-limit theorem, each component should be normally distributed, as it is thought to be the sum of a large number of modes' amplitudes that are random variables. Also, all six components are independent and identically distributed when the distance of the point of examination and a reflecting object is large enough and, likewise, have zero means if the antenna in the chamber does not directly illuminate the location examined. That's the reason why the antenna in Fig. 1 points to the wall or to a corner opposite the EUT. According to these features, the magnitude of the total field at a location inside the mode-stirred chamber, follows the X distribution with 6 degrees of freedom, and has the following pdf [24,25]

$$f(|E_t|) = \frac{|E_t|^5}{8\sigma_t^6} \exp\left(-\frac{|E_t|^2}{2\sigma_t^2}\right) \quad (6)$$

where $|E_t|$ is the magnitude of the total field and σ_t^2 is the variance. The magnitude of any of the three electric field components (e.g., the E_x component) is again X -distributed but with only 2 degrees of freedom or in other words follows the Rayleigh distribution [24,25]

$$f(|E_x|) = \frac{|E_x|}{\sigma_x^2} \exp\left(-\frac{|E_x|^2}{2\sigma_x^2}\right) \quad (7)$$

where $|E_x|$ is the magnitude of the E_x component and σ_x^2 is the variance. The received power P_r of the antenna is proportional to the electric field squared and as a result is exponentially distributed [24,25]

$$f(P_r) = \frac{1}{2\sigma_r^2} \exp\left(-\frac{P_r}{2\sigma_r^2}\right) \quad (8)$$

where σ_r^2 is the variance.

The abovementioned statistical distributions apply for the case where the antenna, used to inject the appropriate amount of power in the chamber, does not directly

illuminate the EUT. But according to EMC requirements, the test should be done under conditions as close as possible to those under which the EUT is intended to operate. Most EUTs are designed to function in urban environments, where a direct path between the electromagnetic wave source and the EUT exists. Therefore, a model for predicting the electric field strength involving both deterministic and stochastic components has to be adopted. According to mobile communication environments, when a direct path is present, the multipath propagation phenomena are best described by the Rice distribution [21,22,26,27]

$$p_r(r) = \frac{r}{\sigma_{\text{Rice}}^2} \exp\left[-\frac{r^2 + r_s^2}{2\sigma_{\text{Rice}}^2}\right] I_0\left(\frac{rr_s}{\sigma_{\text{Rice}}^2}\right) \quad (9)$$

where r is a random variable, r_s a dominant component, σ_{Rice}^2 denotes the variance, and $I_0(\cdot)$ represents the Bessel function of the first kind and zero order. The Rician distribution is often described in terms of a parameter K defined as

$$K = 10 \log \frac{r_s^2}{2\sigma_{\text{Rice}}^2} \text{ dB} \quad (10)$$

which can be interpreted as the ratio of the dominant wave power over the power of the multipath components.

As shown in other studies [21,22], the fundamental properties of the reverberation chamber are satisfied to a high degree despite of the presence of the direct component, which is usually referred to as the "unstirred" component, due to its uninfluenced nature with regard to alteration in the chamber boundary conditions. The proposed Rice distribution [22] for the case of an unstirred component is well satisfied with the factor K lying between 1.2 and 1.5 for the majority of the frequencies examined. The uniformity tests for all the frequency ranges revealed a generated electromagnetic environment compliant with the requirements of the IEC standard [2], cited in the previous section.

The previously mentioned distributions apply to the field amplitude. The phase of the electric field component is another significant parameter to study. When the

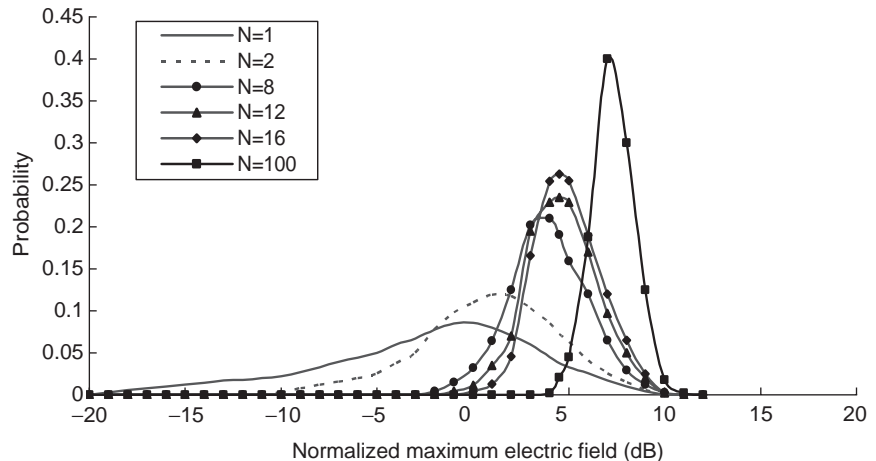


Figure 3. Probability density function of the normalized maximum field magnitude at a fixed location with different number (N) of tuner steps.

antenna in the chamber does not directly illuminate the EUT, the magnitude of a rectangular component is Rayleigh distributed and the phase φ is uniformly distributed [28]. Therefore, it can be predicted by the following pdf:

$$f(\varphi) = \frac{1}{2\pi}, \quad -\pi < \varphi \leq \pi \quad (11)$$

The case of the presence of the unstirred component, where the electromagnetic field is partially stirred, is considered by assuming two real independent Gaussian fields, that have nonzero mean values but the same variance σ_g^2 . Consequently, the resulting field is the complex superposition of real and imaginary Gaussian fields with different means, leading to the Rice distribution for the field magnitude [Eq. (9)] and the phase distributed according to the following pdf [28]

$$f(\varphi) = \frac{1}{2\pi} \exp\left(-\frac{|E_u|^2}{2\sigma_g^2}\right) [1 + b\sqrt{\pi}e^{b^2}(1 + \operatorname{erf}(b))] \quad (12)$$

where $b = (1/\sigma_g\sqrt{2})(E_r \cos \varphi + E_i \sin \varphi)$, E_r, E_i are the means of the real and imaginary Gaussian fields, respectively, and E_u stands for the unstirred component.

There are many ways to test the behavior of a reverberation chamber and verify that it is calibrated and ready to be employed for performing EMC tests. An apparent procedure for determining the quality of the generated electromagnetic field conditions inside the chamber is to calculate the field uniformity or the statistical distribution of the field and require satisfaction of the proposed limits or distributions, respectively. Some additional ways which more or less give an indication of the proper chamber operation have been suggested in the literature.

The most widely known and commonly utilized test, apart from the field uniformity and statistical verification, is the stirring ratio test (or range test). This test determines the ability of the paddle to significantly vary the chamber boundary conditions and, consequently, the field strength at a given point. Ladbury and Goldsmith [29] defined a *stirring ratio* as the ratio of the maximum value

of the field divided by the minimum value at a fixed point. A value of 20 dB or greater proved adequate to generate the desired electromagnetic environment and revealed a significant improvement with an increase in the number of samples or tuner steps.

Similar to the stirring ratio test, the maximum : average ratio of the field strength or the received power is another indicative magnitude for determining the chamber's operation. Typical measurements [29] have shown a range of 6–8 dB to be adequate, and this improved again with the increase in the number of samples. This range is predicted by the nature of the chi-square (χ^2) distribution and appears to be important for immunity tests where the maximum values are most commonly used.

4. LOWEST USABLE FREQUENCY

The frequency above which the chamber operates according to the fundamental properties described in Sections 2 and 3 is assumed to be the lowest usable frequency. The LUF is generally determined by the effectiveness of the stirrer and the quality factor of the chamber. Its scope is about 3–5 times the first chamber resonance. In the IEC 61000-4-21 standard [2], it is assumed to be the lowest frequency above which the field uniformity requirements are achieved.

With another approach [3], the LUF is considered to be the frequency at which the chamber, due to the variable environment that is created by the movement of the tuners, hosts an electromagnetic environment with 60 modes. For a rectangular enclosure the LUF can be determined by the following equation [2]

$$N = \frac{8\pi}{3}abd \frac{f^3}{c^3} - (a+b+d) \frac{f}{c} + \frac{1}{2} \quad (13)$$

where N is number of modes, f is the frequency of propagation, c is the wave speed of propagation, and a, b, d are the dimensions of the rectangular enclosure. Equation (13), however, is a theoretical approach for determination of LUF, and an experimental verification should be per-

formed each time a chamber calibration is done. As derived by Eq. (13), the LUF depends primarily on the chamber's dimensions as they define the modal structure as a function of frequency. A commonly accepted guideline sets the LUF border at the frequency where the minimum tuner dimension is $\lambda/2$. However, the use of larger tuners, apart from improving the field uniformity, may result in lower LUF.

The dependence of the LUF on the chamber's dimensions, quality factor, and stirrer effectiveness can be conversely used, as for a given value of the LUF the minimum chamber requirements with regard to the later characteristics, can be specified. Arnaut [30] gives a theoretical expression for determination of LUF, depending on the chamber mode density and the number of available cavity modes. The use of wave diffractors shows that an increase or a decrease on the average mode density depends on their shape or position in the chamber. Additionally, as depicted by Petirsch and Schwab [13], the use of diffusors seems to increase the density of resonances at lower frequencies, which results in reduction of the minimum operating frequency of the reverberation chamber.

5. QUALITY FACTOR

An important parameter for determination of satisfactory reverberation chamber performance is the quality factor (often referred to as Q). As mentioned previously, the ability of a mode-stirred chamber to store high-intensity fields is a very important feature that distinguishes this kind of chamber from the other types of screened rooms. This ability is expressed through the quality factor, which is defined as the ratio of the energy stored in the chamber to the losses that occur in the enclosure and is depicted in the following equation [31]

$$Q = \frac{\omega U}{W_L} \quad (14)$$

where $\omega = 2\pi f$ is the angular frequency of operation, U is the energy stored in the chamber, and W_L stands for the losses.

One dominant factor of losses in a reverberation chamber is related to losses in the walls. These losses depend on the material that is used for the construction of the chamber and apparently are on low level when a highly conductive material is employed, such as copper and aluminum sheets or galvanized steel. On the contrary, copper and aluminum screen and flame spray give a low value for the quality factor of the chamber [2]. Apart from the walls' losses, some other types of losses that result in decrease in the Q value are the number of absorbing objects in the chamber, which "load" the chamber as shown before for the case of the EUT, the leakage through apertures and losses due to the dissipated power in the loads of receiving antennas. However, when a comparison is needed between different chambers with regard to the quality factor obtained, only wall losses are taken into account [31].

An expression for the determination of the chamber Q is given in the IEC 61000-4-21 standard [2]

$$Q = \frac{16\pi^2 V}{n_{Tx} n_{Rx} \lambda^3} \left\langle \frac{P_{avrec}}{P_{input}} \right\rangle \quad (15)$$

where V is the chamber volume (m^3), λ is the wavelength (m), $\langle P_{avrec}/P_{input} \rangle$ stands for the ratio of the average received power to the input power for one complete tuner rotation, and n_{Tx} , n_{Rx} are the efficiency factors of the transmit and receive antennas, respectively. These latter factors are set to 0.75 in the case of logperiodic antennas or 0.9 for horn antennas, if manufacturer's data are not available.

In the literature, a theoretical expression for the quality factor of a rectangular reverberation chamber has been derived [32]. For a chamber with dimensions a , b , c , this expression is

$$Q = \frac{3}{2} \frac{V}{S\delta_w} \frac{1}{1 + \frac{3\pi}{8k} \left(\frac{1}{a} + \frac{1}{b} + \frac{1}{c} \right)} \quad (16)$$

where V is the volume of the chamber, S is the sum of the areas of the chamber's walls, k stands for the wavenumber in free space, and δ_w is the wall skin depth, which is expressed by [33]

$$\delta_w = \frac{1}{\sqrt{\pi f \mu \sigma}} \quad (17)$$

where f is the frequency of propagation and μ, σ are the wall's permeability and conductivity, respectively.

In order to produce Eq. (16), the field inside the chamber was expressed through a series of cavity modes and then the average was taken over the ensemble of all these modes. It was additionally assumed that an equal amount of energy was in each mode, which is typical for random fields. Dunn [32] adopted a method, based on local plane waves, for the derivation of the Q of the chamber, which had the advantage of being applicable to nonseparable geometries (e.g., to a chamber with curved walls). The assumptions made were the random nature of the field well away from the walls and the large dimension of the chamber compared to the wavelength. The final expression that was derived identically agrees with (16) except for its adaptability to other than rectangular chamber geometries.

As can be observed in Eq. (16), minimization of the sum of the areas of the chamber's walls can result in an increase of the quality factor. Consequently, a spherical chamber stores larger amounts of energy compared to a rectangular, circular, or cubical chamber but will result in poorer spatial field uniformity due to the focus of the field at the chamber's center. Therefore, the arbitrary shape of the reverberation chamber is a very challenging topic to deal with, and similar to Dunn [32], Hill [34] has investigated this topic by introducing a reflection coefficient method for the determination of the quality factor. The expression derived is applicable to general wall materials and is transformed to the approach presented in Ref. 32, with utilization of highly conducting walls with small skin depth. In the following section, an expression for the qual-

ity factor of a mode-stirred chamber with vibrating walls is presented, based on an analysis performed using cavity theory.

6. ALTERNATIVE MEANS OF MODE STIRRING

Up to this point, the traditional reverberation chamber (i.e., rectangular chamber with rotating metallic paddle wheels) was assumed, and its features and properties have been presented. However, during the last few years the EMC community has also studied alternative ways of stirring the propagating modes inside a mode-stirred chamber, instead of using the traditional method. One motive for this study has been the complex structure of a chamber operating with paddle wheels, thus limiting its flexibility and mobility for in situ measurements. Additionally, the attempt to improve the performance of a mode-stirred chamber, especially at low frequencies, has also motivated this particular issue.

Since the objective for the constitution of an overmoded electromagnetic environment is the alteration of the chamber boundary conditions, this can be achieved by performing an alternative modification in some of the chamber characteristics. One apparent means of varying the chamber boundary conditions is to modify the chamber dimensions. This can be achieved by either moving one or more walls of the chamber, resulting in a moving-wall mode-stirred chamber [22], or by providing a chamber with flexible conductive walls that vibrate during the EMC test, thus introducing the vibrating reverberation chamber [26,35,36]. In the study presented in Ref. 22, the moving-wall mode-stirred chamber depicted in Fig. 4 was examined.

Assuming that the EUT is directly illuminated by a source antenna, the fields inside the chamber were analyzed with the use of a ray-tracing method [37], which was extended to best describe the direct-path status. The field was found to be homogeneous over a range of frequencies higher than 450 MHz and also Rice distributed at a specified point (due to the presence of the direct-path signal). Consequently, a LUF of ~ 450 MHz was predicted for that specific chamber. The length of the chamber was varied in a random manner, while extended simulation results showed that field homogeneity did not depend significantly on the range of variation.

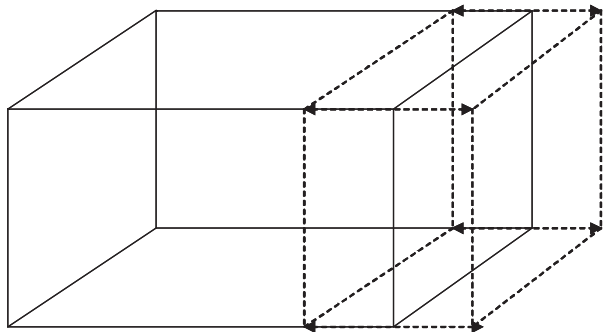


Figure 4. The moving-wall mode-stirred chamber.

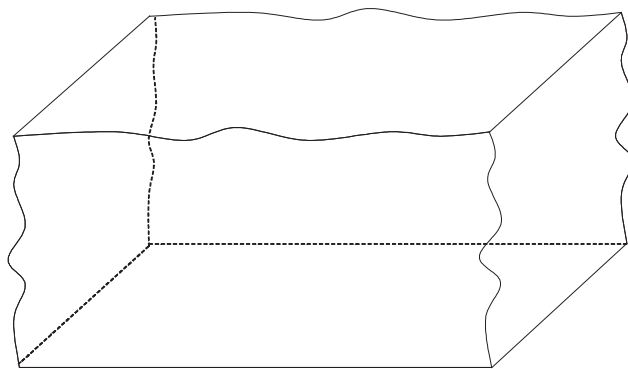


Figure 5. The vibrating reverberation chamber.

Another type of chamber with variable dimensions is the vibrating reverberation chamber shown in Fig. 5. The vibrating reverberation chamber consists of flexible walls made of highly conductive material to isolate the external electromagnetic environment. By vibrating the walls of the chamber, the number of the propagating modes is increased, resulting in a uniform environment. Because of the greater resonance frequency shift [36], the operating frequency range is increased and includes the lower frequencies. Another advantage of this chamber is its flexible structure, which enables it to be used for in situ measurements and does not occupy much laboratory space (or occupies no space if it is small enough to be folded).

A theoretical examination of the field conditions inside a vibrating reverberation chamber is presented in Refs. 26 and 35, where the finite-difference time-domain (FDTD) method [38] is applied. This numerical method is commonly used for the computation of the electromagnetic fields in a specified space in the time domain and provides the value of the electric or magnetic field at any given point inside the examination volume. Thus, it is a very good selection criterion for derivation of the magnitude of the electric field in a mode-stirred chamber, as is shown in the literature [26,35].

With the use of a continuous-wave [35] or pulsed [26] excitation in a vibrating reverberation chamber with a dipole antenna, the field uniformity was examined according to the rules defined in the IEC 61000-4-21 standard [2]. The vibrating surfaces were modeled according to the procedure described in Ref. 39, and the walls were assumed to be highly conductive. When a continuous wave excitation was employed, the field values were recorded after the field has reached the steady state situation. On the other hand, when a pulsed excitation was applied to the dipole antenna, the field values were computed by applying a discrete Fourier transform to derive the desired values over a wide frequency range.

The results from these two studies [26,35] reveal that the required field uniformity is obtained for all the frequencies within the frequency ranges examined (300 MHz–1 GHz for a chamber of dimensions $1 \times 1 \times 1$ m and 100 MHz–1.9 GHz for a larger chamber with dimensions $2 \times 2 \times 2$ m). In the same bands, the field was found to satisfy the Rice distribution, which was introduced by the direct-path signal. Additionally, the number of sam-

ples required for the field uniformity to be below the specified level [2] seems to be less than that proposed by the IEC specification, while the uniformity is improved as the frequency increases. From these observations it is concluded that the vibrating reverberation chamber provides a lowest LUF and requires fewer samples for obtaining the acceptable uniformity level compared to the traditional rectangular mode-stirred chamber.

Another theoretical study [31] on vibrating reverberation chambers demonstrates the ability of this chamber to store higher amounts of energy, resulting in a higher quality factor compared to the traditional mode-stirred chamber. The quality factor was computed through the relationship depicted in Eq. (14) for a chamber with highly conducting vibrating walls of the structure shown in Fig. 5. The FDTD method adopted for the theoretical simulation and a dipole antenna was again used for the field excitation. The stored energy was computed through the triple integral of the square of the electric field magnitude over the entire chamber volume. The chamber losses were focused only on the walls (as mentioned before when comparing different reverberating chambers, only walls losses are regarded) and were calculated by applying a double integral at the square magnitude of the magnetic field at each surface, which represents the forego currents. The quality factor for the rectangular reverberation chamber was computed by applying Eqs. (16) and (17) for the case of aluminum walls. The result derived proved the ability of the vibrating reverberation chamber to provide a higher quality factor compared to the traditional reverberation chamber, especially at high frequencies, with values ranging from 47 to 65 dB, whereas the rectangular chamber yielded a quality factor range of 45–50 dB for the same frequency band (300 MHz–2 GHz).

Apart from the theoretical approaches with regard to the usefulness of the vibrating reverberation chamber, some interesting experimental studies have appeared in the more recent literature. In Ref. 40, a screened room with walls made of conductive cloth was transformed in a vibrating mode-stirred chamber with the use of a fan placed outside the enclosure but close to the walls. The electromagnetic environment inside the chamber was found uniform for frequencies higher than ~ 450 MHz, and the field was found to be Rice distributed as a monopole antenna directly illuminated the examined area of the chamber. Leferink et al. [36] investigated a vibrating reverberation chamber with walls made of flexible conducting material and hanging in strings for several parameters: resonance frequency variation, voltage standing-wave ratio, stirring ratio, probability density function, and cumulative density function. The results derived showed adequate operation performance of the chamber, especially at low frequencies, where a high stirring ratio was observed.

Apart from the two alternative ways for mode stirring described earlier in this article, some others have been suggested in the literature. More specifically, frequency stirring [41], shows that field uniformity can be obtained by altering the bandwidth of the frequency modulation of the source, where a smaller bandwidth is required at high frequencies and vice versa, leading to a reduced effective-

ness of this technique at this late range. The intrinsic reverberation chamber [42], which uses nonparallel walls, where the ceiling is not parallel to the floor and at most two walls are placed perpendicular and fixed field diffusers, is another more recently proposed alternate structure of reverberation chamber. The use of a set of wires [43] or corrugated walls [44] inside the reverberating enclosure reveals that the field uniformity and the general operational conditions of a mode-stirred chamber are improved to a significant degree. One study [16] proved that for the case of radiation efficiency measurement of terminal antennas, the rotation of the EUT (i.e., the antenna) results in an improved accuracy for this measurement; and this stirring method is referred to as “platform stirring.”

7. CONCLUSION

An EMC test site, the reverberation chamber, was studied in this article. By describing its main features, the advantages that arise with the use of such a structure were outlined. Although not widespread, the reverberation chamber has been adopted at a standard level for EMC tests and is commonly used for antenna measurements, due to its compact size and uniform electromagnetic environment. In conjunction with the different ways of altering the mode distribution, measurements are performed with reliable accuracy and repeatability. Thus, when used for measurements not requiring a large test site or a very low operating frequency range (e.g., for mobile or wireless antenna measurements), the mode-stirred chamber is the best solution for performing the appropriate tests for each case. Research on reverberation chambers is being conducted continuously, with intense interest throughout the scientific community, because of the different operating conditions and structures that it provides. As expected, its characteristics will continue to be investigated and optimized in the near future, by fully utilizing the accoutrements provided by the current technology.

BIBLIOGRAPHY

1. T. Williams, *EMC for Product Designers — Meeting the European EMC Directive*, 2nd ed., Newnes, 1996.
2. Standard IEC 61000-4-21, *Electromagnetic Compatibility (EMC) — Part 4: Testing and Measurement Techniques, Sec. 21: Reverberation Chambers*, 2001.
3. M. O. Hatfield, E. A. Godfrey, and G. J. Freyer, Investigations to extend the lower frequency limit of reverberation chambers, *Proc. IEEE Int. Symp. Electromagnetic Compatibility*, 1998, pp. 20–23.
4. M. Petirsch, W. Kurner, I. Sottriffer, and A. Schwab, Comparing different measurement approaches in a mode-stirred chamber, *Proc. IEEE Int. Symp. Electromagnetic Compatibility*, 1999, pp. 929–933.
5. D. Svetanoff, J. Weibler, R. Cooney, M. Squire, S. Zielinski, M. Hatfield, and M. Slocum, Development of high performance tuners for mode-stirring and mode-tuning applications, *Proc. IEEE Int. Symp. Electromagnetic Compatibility*, 1999, pp. 29–34.

6. C. Christopoulos, *Principles and Techniques of Electromagnetic Compatibility*, CRC Press, 1995.
7. K. GoldSmith, Reverberation chambers — what are they? *IEEE EMC Society Newsl.* (1999).
8. L. Bai, L. Wang, B. Wang, and J. Song, Reverberation chamber modeling using FDTD, *Proc. IEEE Int. Symp. Electromagnetic Compatibility*, 1999, pp. 7–11.
9. K. Harima, FDTD analysis of electromagnetic fields in a reverberation chamber, *IEICE Trans. Commun.* **E81-B-10**:1946–1950 (1998).
10. L. Bai, L. Wang, B. Wang, and J. Song, Effects of paddle configurations on the uniformity of the reverberation chamber, *Proc. IEEE Int. Symp. Electromagnetic Compatibility*, 1999, pp. 12–16.
11. C. F. Bunting, K. J. Moeller, C. J. Reddy, and S. A. Scarce, A two dimensional finite-element analysis of reverberation chambers, *IEEE Trans. Electromagn. Compat.* **41**:280–289 (1999).
12. T. H. Lehman, G. J. Freyer, M. O. Hatfield, J. M. Ladbury, and G. H. Koepke, Verification of fields applied to an EUT in a reverberation chamber using numerical modeling, *Proc. IEEE Int. Symp. Electromagnetic Compatibility*, 1998, pp. 28–33.
13. M. Petirsch, and A. J. Schwab, Investigation of the field uniformity of a mode-stirred chamber using diffusors based on acoustic theory, *IEEE Trans. Electromagn. Compat.* **41**:446–451 (1999).
14. K. Rosengren and P. S. Kildal, Study of distributions of modes and plane waves in reverberation chambers for the characterization of antennas in a multipath environment, *Microwave Opt. Technol. Lett.* **30**:386–391 (2001).
15. P. Hallbjorner, Reflective antenna efficiency measurements in reverberation chambers, *Microwave Opt. Technol. Lett.* **30**:332–335 (2001).
16. K. Rosengren, P. S. Kildal, C. Carlsson, and J. Carlsson, Characterization of antennas for mobile and wireless terminals in reverberation chambers: improved accuracy by platform stirring, *Microwave Opt. Technol. Lett.* **30**:391–397 (2001).
17. P. S. Kildal and C. Carlsson, Detection of a polarization imbalance in reverberation chambers and how to remove it by polarization stirring when measuring antenna efficiencies, *Microwave Opt. Technol. Lett.* **34**:145–149 (2002).
18. P. Hallbjorner, A model for the number of independent samples in reverberation chambers, *Microwave Opt. Technol. Lett.* **33**:25–28 (2002).
19. P. S. Kildal, C. Carlsson, and J. Yang, Measurement of free-space impedances of small antennas in reverberation chambers, *Microwave Opt. Technol. Lett.* **32**:112–115 (2002).
20. P. Corona, J. Ladbury, and G. Latmiral, Reverberation chamber research—then and now: A review of early work and comparison with current understanding, *IEEE Trans. Electromagn. Compat.* **44**:87–94 (2002).
21. P. Corona, G. Ferrara, and M. Migliaccio, Reverberating chamber electromagnetic field in presence of an unstirred component, *IEEE Trans. Electromagn. Compat.* **42**:111–115 (2000).
22. N. K. Kouveliotis, P. T. Trakadas, and C. N. Capsalis, Theoretical investigation of the field conditions in a vibrating reverberation chamber with an unstirred component, *IEEE Trans. Electromagn. Compat.* **45**:77–81 (2003).
23. M. O. Hatfield, A calibration procedure for reverberation chambers, *Proc. IEEE Int. Symp. Electromagnetic Compatibility*, 2000, pp. 621–626.
24. J. G. Kostas and B. Boverie, Statistical model for a mode-stirred chamber, *IEEE Trans. Electromagn. Compat.* **33**:366–370 (1991).
25. D. A. Hill, Plane wave integral representation for fields in reverberation chambers, *IEEE Trans. Electromagn. Compat.* **40**:209–217 (1998).
26. N. K. Kouveliotis, P. T. Trakadas, and C. N. Capsalis, FDTD modeling of a vibrating intrinsic reverberation chamber, *Prog. In Electromagn. Res.* **39**:47–59 (2003).
27. P. Hallbjorner, Reverberation chamber with variable received signal amplitude distribution, *Microwave Opt. Technol. Lett.* **35**:376–377 (2002).
28. M. Migliaccio, On the phase statistics of the electromagnetic field in reverberating chambers, *IEEE Trans. Electromagn. Compat.* **43**:694–695 (2001).
29. J. M. Ladbury and K. Goldsmith, Reverberation chamber verification procedures, or, how to check if your chamber ain't broke and suggestions on how to fix it if it is, *Proc. IEEE Int. Symp. Electromagnetic Compatibility*, 2000, pp. 17–22.
30. L. R. Arnaut, Operation of electromagnetic reverberation chambers with wave diffractors at relatively low frequencies, *IEEE Trans. Electromagn. Compat.* **43**:637–653 (2001).
31. N. K. Kouveliotis, P. T. Trakadas, and C. N. Capsalis, FDTD calculation of quality factor of vibrating intrinsic reverberation chamber, *Electron. Lett.* **38**:861–862 (2002).
32. J. M. Dunn, Local, high-frequency analysis of the fields in a mode-stirred chamber, *IEEE Trans. Electromagn. Compat.* **32**:53–58 (1990).
33. S. Ramo, J. R. Whinnery, and T. Van Duzer, *Fields and Waves in Communication Electronics*, Wiley, New York, 1965.
34. D. A. Hill, A reflection coefficient derivation for the Q of a reverberation chamber, *IEEE Trans. Electromagn. Compat.* **38**:591–592 (1996).
35. N. K. Kouveliotis, P. T. Trakadas, and C. N. Capsalis, Examination of field uniformity in vibrating intrinsic reverberation chamber using the FDTD method, *Electron. Lett.* **38**:109–110 (2002).
36. F. B. J. Leferink, J. C. Boudenot, and W. Etten, Experimental results obtained in the vibrating intrinsic reverberation chamber, *Proc. IEEE Int. Symp. Electromagnetic Compatibility*, 2000, pp. 639–644.
37. L. Cappetta, M. Feo, V. Fiumara, V. Pierro, and I. M. Pinto, Electromagnetic chaos in mode-stirred reverberation enclosures, *IEEE Trans. Electromagn. Compat.* **40**:185–192 (1998).
38. A. Taflove, *Computational Electrodynamics: The Finite Difference Time Domain Method*, Artech House, Norwood, MA, 1995.
39. N. K. Kouveliotis, P. T. Trakadas, A. I. Stefanogiannis, and C. N. Capsalis, Field prediction describing scattering by a one dimensional smooth random rough surface, *Electromagnetics* **22**:27–35 (2002).
40. N. K. Kouveliotis, P. T. Trakadas, I. I. Hairidakis, and C. N. Capsalis, Experimental investigation of the field conditions in a vibrating intrinsic reverberation chamber *Microwave Opt. Technol. Lett.* **40**:35–38 (2004).
41. D. A. Hill, Electronic mode stirring for reverberation chambers, *IEEE Trans. Electromagn. Compat.* **36**:294–299 (1994).
42. F. B. J. Leferink, High field strength in a large volume: The intrinsic reverberation chamber, *Proc. IEEE Int. Symp. Electromagnetic Compatibility*, 1998, pp. 24–27.
43. J. Perini and L. S. Cohen, An alternative way to stir the fields in a mode-stirred chamber, *Proc. IEEE Int. Symp. Electromagnetic Compatibility*, 2000, pp. 633–637.

44. E. A. Godfrey, Effects of corrugated walls on the field uniformity of reverberation chambers at low frequencies, *Proc. IEEE Int. Symp. Electromagnetic Compatibility*, 1999, pp. 23–28.

ANTENNA SCANNING ARRAYS

ROBERT J. MAILLOUX
AFRL/SNH
Hanscom Air Force Base,
Massachusetts

1. INTRODUCTION

There is a growing need for electronically scanned antenna arrays for both commercial and military applications. In the past the technology was driven by the need for military radars to find and track a multitude of fast-moving targets, and that led to the technology of large ground-based scanning arrays with narrow beamwidths, high gain, and thousands of control elements. More recent military trends have included the development of lightweight airborne arrays that now include solid-state transmit/receive (TR) modules at every element. The signal processing aspect of array systems has been exploited for the purpose of suppressing external noise in both commercial and military systems, and for providing simultaneous multiple functions or communication links. Research studies for wireless base station technology now include angle diversity, polarization diversity, and adaptive optimization algorithms in addition to the traditional space diversity. There is no limit to the demand for additional functions that would be useful if array technology could eventually lead to the idealized but cost-effective blackbox with huge bandwidth or multiple frequency bands and multiple beams. Unfortunately there is a limit to the rate of advances in the technology, but it is clear that these new applications will drive scanning array development for many years. This article describes some of the traditional and new features that can be incorporated into scanning arrays to meet these challenging new requirements.

The most fundamental requirement of a scanning array is to provide more gain and a narrower beamwidth than possible with a single-antenna element, and to move that beam to various observation angles. Array gain and beamwidth for broadside radiation are basically the same as for any equal-size aperture antenna, except for dissipative losses. The gain, as defined below, includes dissipative losses, but not mismatch losses, which are accounted separately. The maximum array gain when the array is scanned to some angle θ , is given as

$$G = \frac{4\pi A}{\lambda^2} \epsilon_a \epsilon_t \cos \theta \tag{1}$$

where A is the antenna area, λ is the wavelength, ϵ_a is the aperture efficiency that normalizes the directivity to that of a uniformly illuminated aperture ($\epsilon_a = 1$ for uniform), ϵ_t

accounts for loss in the feed network and antenna, and $\cos \theta$ is the array projector factor.

For a linear array of length L , the 3dB beamwidth (in radius) is given as

$$\theta_3 = \frac{B(0.886) \cos \theta}{(L/\lambda)} \tag{2}$$

where B is the beam broadening factor. It is unity for uniform illumination across the array and larger for array illuminations that produce lower sidelobes. For a rectangular arm, with sides L_1 and L_2 , the beamwidths θ_3 and θ_3 are written as above with L_1 and L_2 substituted for L and using the appropriate broadening factors in each plane.

Figure 1a illustrates how scanning is implemented in an array that scans in one dimension. Each antenna element is fed by an RF signal that is time-delayed by the sequence Δ , 2Δ , and so on across the array, where $\Delta = d_x \sin \theta_0/c$, and c is the velocity of light. This sequence of

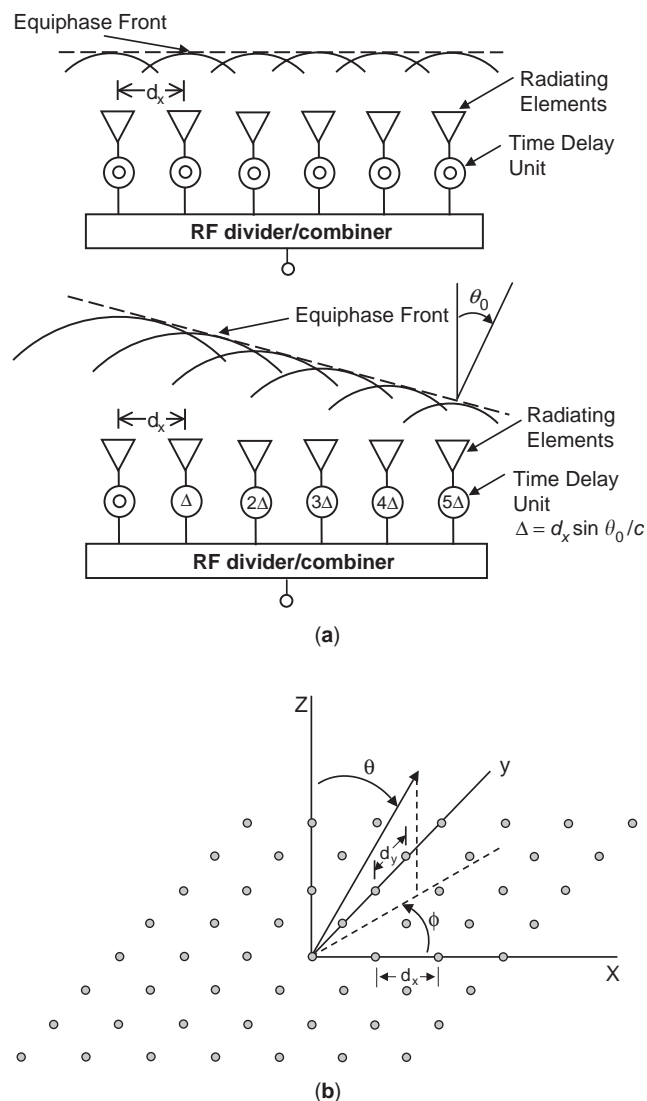


Figure 1. (a) Radiation from a linear antenna array; (b) two-dimensional scanning array.

time delays causes the radiation from the various antenna elements to add and form a coherent phase front (shown dashed) at some chosen angle θ_0 . The array beamwidth and gain are dependent on array size in ways that are described in the following section.

2. ARRAY SCANNING AND ITS CONSTRAINTS

Figures 1a and 1b show the array element grid locations and spatial angles. In the plane $\phi = 0$, the far-field pattern of a linear array of N elements located in a plane at $x_n = nd_x$ is written

$$E(\theta, \phi) = \sum_{n=1}^N a_n f_n(\theta, \phi) e^{jkn d_x u} \tag{3}$$

where $u = \sin \theta$ and $k = 2\pi/\lambda$ and $f_n(\theta, \phi)$ is the far-field element pattern of the n th element in the array environment. In general, the element patterns $f_n(\theta, \phi)$ are different for each array element even though all the elements are the same. These differences occur because each element pattern includes the scattered radiation from all other elements, from the array edges, and any scattering from the mounting structure. For most simple elements, like dipoles and slots, the currents or fields on the antennas differ by only a constant, and one can adjust the feed weights to compensate for these interaction effects.

For the purpose of illustration, we assume that all the element patterns $f_n(\theta, \phi)$ are the same [and given by $f(\theta, \phi)$]. The expression (3) becomes

$$E(\theta, \phi) = f(\theta, \phi) \sum_{n=1}^N a_n e^{jkn d_x u} \tag{4}$$

When this separation can be made, the pattern is expressed as the product of an element pattern $f(\theta, \phi)$ and an array factor (the indicated summation).

The coefficients a_n are chosen to move the array’s peak radiation to some desired angle θ_0 and to produce a specified sidelobe level. In principle, one would choose to steer the beam using time-delay devices, using the coefficients defined as

$$a_n = |a_n| e^{-jkn d_x u_0} \tag{5}$$

for $k = 2\pi/\lambda$ and $u_0 = \sin \theta_0$. In this expression the wave-number k is the same as that used in Eq. (3), and it varies linearly with frequency. The expression (3) thus has the frequency-dependent form of a signal that has passed through a length $n d_x u_0$ of coaxial line, and so is time-delayed by $n\Delta = n d_x u_0/c$. With this excitation the far-field radiation will always peak at u_0 for all frequencies, and the array bandwidth is limited only by device operation. This is immediately evident since inserting (5) into (4) leads to an expression with the exponent equal to zero at $u = u_0$. This state is highly desirable, but time-delay devices are costly and lossy and can constitute a major architectural issue in the design of array systems. This is one of the constraints that will be discussed later.

2.1. Array “Squint”

In lieu of using time delays at every element, it is more common to use phase shifters to control arrays. In this case, to move a principal maximum to some θ_0 at a single frequency ($\lambda = \lambda_0, k = k_0$), the required phased element excitations are given by

$$a_n = |a_n| e^{-jk_0 n d_x u_0} \tag{6}$$

Substituting Eq. (6) into Eq. (4) results in

$$E(\theta, \phi) = f(\theta, \phi) \sum_{n=1}^N a_n e^{j2\pi((u/\lambda) - (u_0/\lambda_0))n d_x} \tag{7}$$

The pattern has a maximum value at $u = u_0(\theta_0, \phi_0)$ when $\lambda = \lambda_0$. However, for a signal at some other frequency, since phase shifters produce a phase change that is nearly independent of frequency, Eq. (7) shows a peak at the angle θ whose sine is

$$\sin \theta = \left(\frac{\lambda}{\lambda_0} \right) \sin \theta_0 \tag{8}$$

This beam angle moves, or squints, as a function of frequency as indicated in Fig. 2, with the beam peak farthest from broadside at the lowest frequency and nearest to broadside for the highest frequency. This is called *array squint*.

This squint angle change can be interpreted in terms of a fractional bandwidth by assuming an array beamwidth of Δu and assuming that the beam is placed exactly at the angle θ_0 at center frequency f_0 . Then defining the upper and lower usable frequencies to be those at which the gain is reduced to half of the angle θ_0 results in the fractional bandwidth

$$\frac{\Delta f}{f_0} = \frac{\Delta u}{\sin \theta_0} \sim \frac{1}{(L/\lambda) \sin \theta_0} \tag{9}$$

where L is the array length. Arrays with narrow beamwidths Δu thus have less bandwidth and inverse proportionally less bandwidth as the scan angle is increased. Since the beamwidth is inversely proportional to array length, larger arrays suffer more severe squint loss than do smaller arrays for a given instantaneous bandwidth.

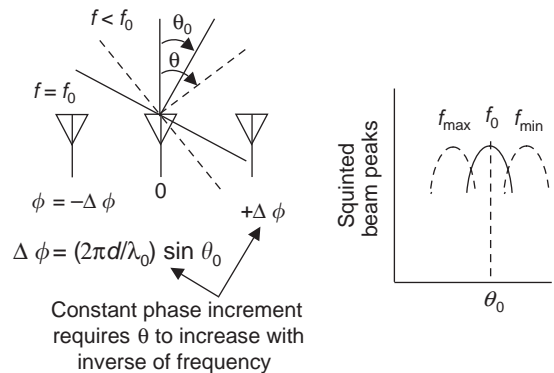


Figure 2. Frequency-sensitive beam “squint” for phase steered array.

Bandwidth requirements that result in the need to introduce time delays at every element become a major constraint in array design.

2.2. Grating Lobes

A second constraint restricts array element spacing and is a result of the array periodicity. The periodicity imposes constraints on element spacing in order to avoid the formation of unwanted radiation peaks, called *grating lobes*.

The grating lobe phenomenon is apparent from an inspection of Eq. (10). Consider the one-dimensional array with elements at the locations nd_x and operating at the frequency λ scanned by phase shifters. The pattern given by Eq. (7) becomes

$$E(\theta, \phi) = f(\theta, \phi) \sum_{n=1}^N |a_n| e^{jknd_x(\sin \theta - \sin \theta_0)} \quad (10)$$

The summation has its maximum when the exponent is zero for all n . This occurs at the peak of the mainbeam of the array, but the summation is also maximum when the exponent is set equal to any multiple p times $j2\pi n$. At these peaks, or grating lobes, the array factor is as large as it is at the mainbeam location $\theta = \theta_0$. These grating lobe angles are given by the angles θ_p for which

$$\sin \theta_p = \sin \theta_0 + \frac{p\lambda}{d_x} \quad p = \pm 1, \pm 2, \dots \quad (11)$$

for

$$\sin |\theta_p| \leq 1$$

Grating lobes can be avoided by restricting the element normalized spacing d_x/λ and the scan angle θ_0 . Using Eq. (11) and imposing the criteria that $\sin |\theta_p| \leq 1$ gives the spacing that excludes all grating lobes

$$\frac{d_x}{\lambda_0} < \frac{1}{1 + \sin \theta_0} \quad (12)$$

This condition means that the spacing must be less than $\lambda/2$ for scanning to endfire ($\theta_0 = 90^\circ$) and accordingly somewhat greater for lesser scan angles. Spacings greater than one wavelength always produce grating lobes.

The two-dimensional rectangular lattice array of Fig. 1 also has sets of grating lobes. These arise from the evident periodicities in the array factor. The pattern of this array is (at frequency f_0)

$$E(\theta, \phi) = f(\theta, \phi) \sum_{n=1}^N \sum_{m=1}^M |a_{nm}| e^{jk[(u-u_0)nd_x + (v-v_0)md_y]} \quad (13)$$

where $u = \sin \theta \cos \phi$ and $v = \sin \theta \sin \phi$. This pattern has grating lobes at

$$u_p = u_0 + \frac{p\lambda}{d_x} \quad (14)$$

$$v_q = v_0 + \frac{q\lambda}{d_y}$$

subject to the condition that these lobes fall within the unit circle

$$u_p^2 + v_q^2 < 1 \quad (15)$$

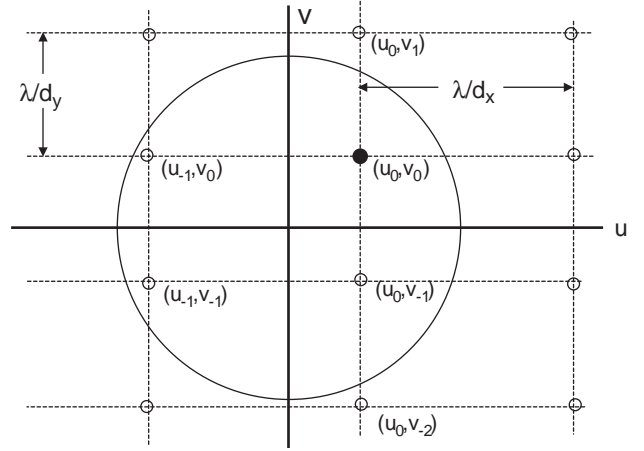


Figure 3. Grating lobe locations for two-dimensional rectangular grid array.

A sketch of the location of these lobes is given in Fig. 3, which indicates the primary beam at (u_0, v_0) and others at various (u_p, v_q) locations. The spacing d_x is chosen to illustrate a case such that for $u_0 = 0$ there are no other u_p lobes ($u_p \neq 0$) within the allowed circle, but with the scan angle (and direction cosine) u_0 were increased, as shown, the lobe at the left with u_{-1}, v_0 enters the circle and therefore radiates. In the other plane the spacing d_y/λ_0 is chosen larger and even with $v_0 = 0$ there already is a lobe (u_0, v_{-1}) that radiates. The specific criterion for excluding these lobes is given by Eq. (15), but for wide scan angles in both planes, this amounts to keeping the spacings very close to one-half wavelength.

2.3. Array Elements and Mutual Coupling

Scanned arrays can use a wide variety of basic elements, provided that they can fit within the allowed interelement spacing of Eq. (12). This poses no problem at the lower frequencies, but above 3 GHz or so it becomes a major constraint, since elements, phase control, and often TR modules may need to fit in a spacing on the order of a half-wavelength on a side. Figure 4 shows several of the basic elements used for array antennas. These are ordered relative to bandwidth, even though bandwidth is only one among many criteria for selection. The microstrip patch antenna of Fig. 4a as described by Herd [1] is one variation of this printed circuit antenna that is inexpensive to fabricate with computer controlled fabrication processes. The traditional microstrip patch (not shown) is driven by an inline microstrip transmission line on the dielectric substrate over ground. That technology is very narrowband, but the proximity-coupled patch in this figure uses a smaller patch or open-ended line on a substrate beneath the surface patch. The resulting double-tuning broadens the operating bandwidth to 10–15%. The dielectric loaded waveguide element of Fig. 4b is more expensive to fabricate and feed, although large two-dimensional grids of waveguides are efficiently fabricated and used for high-power radar arrays. Typically the bandwidth of waveguides in arrays is less than 40%. Figure 4c shows

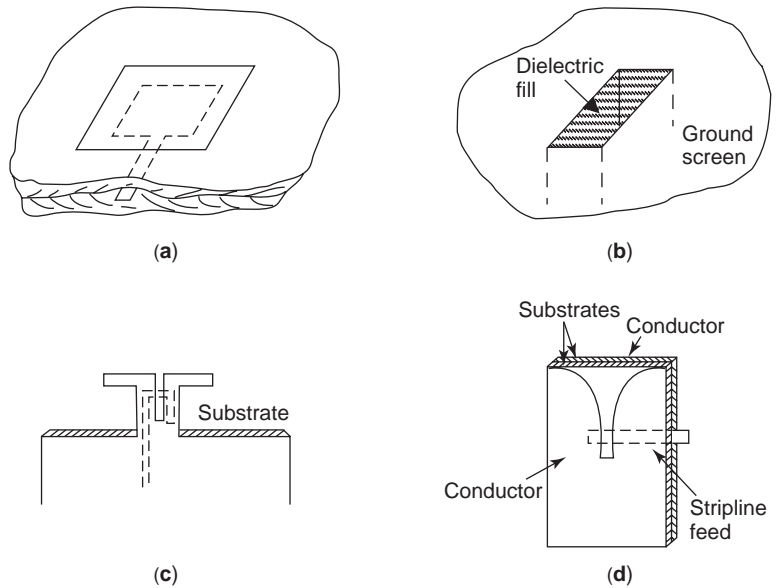


Figure 4. Elements for scanning arrays: (a) proximity-coupled microstrip patch (ground screen beneath lower substrate); (b) dielectric-loaded waveguide; (c) dipole/balun radiating element; (d) stripline-fed flared-notch element.

one version of a horizontal dipole element fed by a balun. This particular feed combination [2] operates over about 40% bandwidth, but some dipole arrays operate over bandwidths in excess of 2:1. The flared-notch element of Fig. 4d is the widest-band element used to date in arrays [3]. The element can be designed and balun fed to achieve up to 10:1 bandwidth in a scanning environment when spaced approximately a half-wavelength apart at the highest frequency.

Restricting element spacings to about a half-wavelength improves the scanning characteristics of the array in addition to eliminating grating lobes. Scan behavior is dictated by electromagnetic coupling between the various array elements, and this coupling, called *mutual coupling* or *mutual impedance*, must be accounted for in the array design. This subject is treated in many journal publications, for example the paper by Wu [4] and texts by Balanis [5] and others, and won't be described further here except to note that it causes the element impedance to vary with each scan and so makes array matching difficult. In addition, it can cause a phenomenon called *array blindness* as described by Farrell and Kuhn [6] that can reduce the array radiation to zero within the normal scan range. This disastrous result appears as an effective open or short circuit at the array input ports, with all signal reflected back from the elements. To avoid building an array that is "blind" at some angles, designers now typically perform the full electromagnetic analysis of the array (or an infinite array with the same elements and spacings) before construction, or they perform measurements in an electromagnetic simulator or a small test array.

Whatever the element and array grid, the occurrence of blindness is usually reduced by decreasing the spacing beyond that given in Eqs. (12) and (15). For normally well-behaved elements that do not have a dielectric substrate at the array face (like waveguides or dipoles), Knittel et al. [7] have shown that making the dimensions smaller than required by 10% or so will avoid blindness. Arrays with

dielectric covers or with antennas printed on dielectric substrates may have additional blindness due to surface waves that propagate along the dielectric.

2.4. Array Pattern Synthesis

A number of very useful pattern synthesis procedures have been developed over the years. These fall roughly into two categories: methods for synthesizing "shaped" patterns that follow some prescribed shape like a conical sector to fill a given area or a cosecant-squared pattern for ground radar, and methods for providing a very narrow beam in one or two orthogonal planes. These latter are often called "pencil beam" synthesis procedures. It is not generally necessary to solve the full electromagnetic coupling problem when performing the synthesis studies, for one can synthesize on the basis of antenna currents or slot aperture fields, and then later use the computed mutual impedances to obtain the array excitation parameters. In addition, it is seldom necessary to synthesize scanned patterns since, for a periodic array, scanning just translates the pattern in u - v coordinates.

The basis for most aperture syntheses is the Fourier transform relationship between aperture field and far field for a continuous aperture. Arrays periodic in one or two dimensions have far-field patterns describable by discrete Fourier transform pairs. In one dimension the array factor at wavelength λ is written

$$F(u) = \sum_{n=-(N-1)/2}^{(N-1)/2} a_n e^{jkn d_x u} \quad (16)$$

where the sum is taken symmetrically about the array center. The coefficients a_n are the array element excitation and are given from orthogonality as

$$a_n = \frac{d_x}{\lambda} \int_{-\lambda/2d_x}^{+\lambda/2d_x} F(u) e^{-jkn d_x u} du \quad (17)$$

In this expression the integral is taken over the periodic distance in u space, namely, halfway to the two nearest grating lobes for a broadside beam. Used in this way, the technique gives the best mean-square approximation to the desired pattern. This feature is lost if spacings are less than a half-wavelength, although the technique is still useful. This Fourier transform synthesis is especially useful for shaped beam patterns, but it also serves as basis for many pencil-beam procedures as well.

A second technique that has found extensive application to shaped beam pattern synthesis is the Woodward synthesis method [8]. This approach uses an orthogonal set of pencil beams to synthesize the desired pattern. The technique has important practical utility because the constituent orthogonal beams are naturally formed by a Butler [9] matrix or other multiple-beam system.

Other techniques for periodic array synthesis are based on the polynomial structure of the far-field patterns. These include the method of Schelkunov [10] and the Dolph–Chebyshev method [11]. Among the most successful and used methods are the pencil-beam synthesis technique of Taylor [12] and the associated monopulse synthesis technique of Bayliss [13] (see Fig. 5). These techniques are derived as improvements to the equal-ripple method of Dolph–Chebyshev, and result in more realizable aperture distributions, improved gain, and other advantages. Figures 5a–b show the array factors for 50-element arrays with -40 dB Taylor and Bayliss distribution with $\bar{n} = 8$. Note that the first sidelobe in both cases is very close to -40 dB with respect to the pattern maximum. In general, the discretizing of continuous distributions introduces errors in the synthesized pattern, and these are more significant for small arrays or for arrays that are forced to have very low sidelobes. Usually discretizing the continuous distribution is not a problem, but when it is, a number of iterative techniques are used to converge to the original desired pattern. Space here precludes giving a detailed description of these procedures, but they are described in detail in a number of references. Notable among these is the work of Elliott [14].

Finally, in addition to these classic synthesis procedures, there have been many iterative numerical solutions to the synthesis problem. These have, in general, been shown to be efficient and useful. One such procedure has utility for both shaped and pencil beams. This procedure, described by Bucci et al. [15], is called the “method of alternating projection” or the “intersection” method, and produces a synthesis that is a best fit, or projection subject to some specified norm, to a desired pattern function, usually the region between an upper and lower “mask.” Space precludes including the details of this procedure, but Fig. 6 shows the upper (dashed) and lower (dotted) masks and the synthesized pattern. The mechanics of the process is to choose an initial guess at the currents (or the far-field pattern itself), compute the radiated power pattern using Eq. (16), “project” this to the nearest point on or between the upper or lower masks, and then use Eq. (17) to compute the exciting currents a_n , truncating the series at $n = N$. This new set of currents is subjected to the same procedure, and the process is repeated until the pattern is converged. The procedure is dependent on making a real-

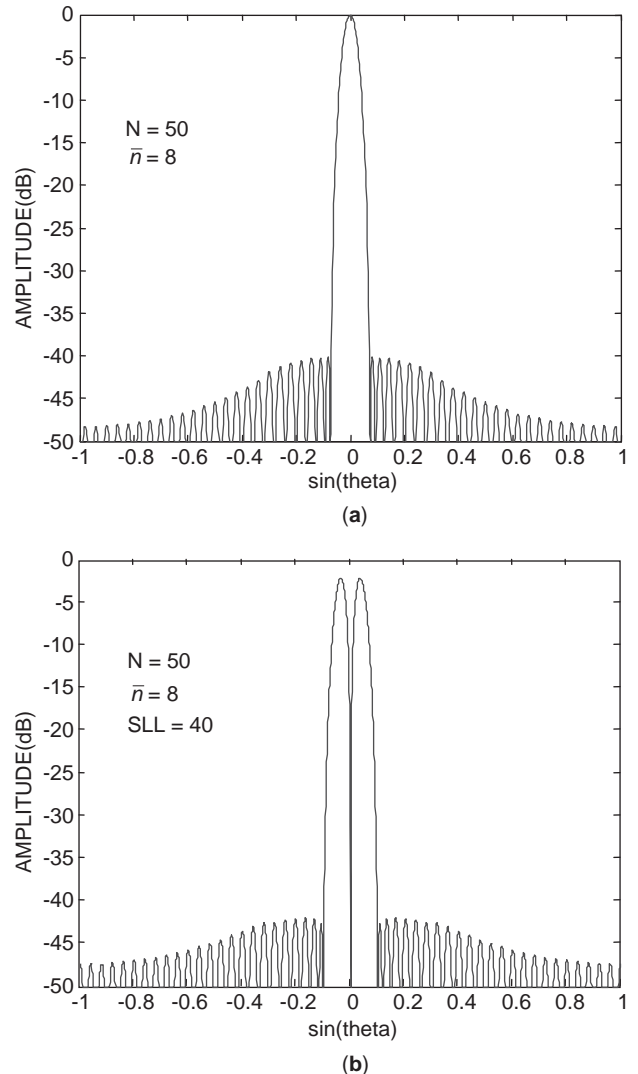


Figure 5. Pattern synthesis by discretized continuous distributions (50-element array examples): (a) Taylor pattern for -40 -dB sidelobes using $\bar{n} = 8$; (b) Bayliss difference pattern for -40 -dB sidelobes using $\bar{n} = 8$.

istic initial guess, and on choosing a mask set that bounds a realizable solution, but has been found very convenient for many situations.

2.5. Array Error Effects

The ability to actually produce the synthesized patterns with a real array depends on the errors in the amplitude and phase of the currents or fields at the array aperture. Fundamental limits on phase shifter or amplitude control tolerance, the discretization of the desired phase, and amplitude in the aperture can lead either to random or correlated errors across the array. The average array sidelobe level (SL), far from the beam peak, and due to random error in amplitude and phase errors is given below in a form normalized to the beam peak

$$SL_{d10} = 10 \log_{10} \sigma^2 \quad (18)$$

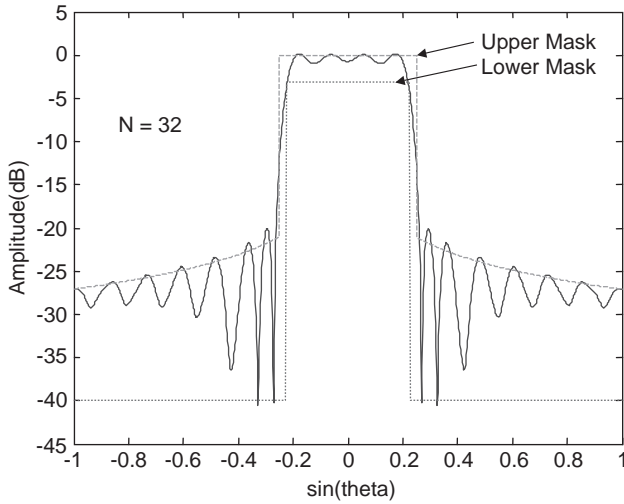


Figure 6. Antenna pattern synthesis using the method of alternating projections (32-element array).

where the variance $\sigma^2 = (\bar{\Phi}^2 + \bar{\delta}^2)/N\epsilon_a$ and $\bar{\Phi}^2$ and $\bar{\delta}^2$ are the amplitude ratio variance and phase variance, N is the number of array elements, and ϵ_a is aperture efficiency.

2.6. Adaptive Arrays for Radar and Communication

Military systems have used adaptive antenna principles for jammer and other interference suppression for many years. In most early military systems these took the form of sidelobe cancelers, with one or several low-gain auxiliary antennas used to form nulls in the sidelobe regions of the composite pattern formed by the primary antenna and the cancelers. Fully adaptive arrays, wherein all elements of the array are controlled according to the adaptive algorithms, provide far more control than do sidelobe cancelers, but are far more costly and complex. One method, used when the direction of arrival of some desired signal is known, is due to Howells and Applebaum [16]. In terms of the total signal received by all ports of the array and weighted by the feed network, the array output is

$$E = \sum w_n e_n \quad (19)$$

or in vector form

$$E = \mathbf{W}^T \mathbf{e}, \quad (20)$$

where the signals and weights are shown as column vectors. The signal to noise ratio is given as

$$S/N = \frac{\mathbf{W}^\dagger \mathbf{M}_s \mathbf{W}}{\mathbf{W}^\dagger \mathbf{M} \mathbf{W}} \quad (21)$$

where \dagger denotes the conjugate transpose (Hermetian transpose).

The matrices \mathbf{M}_s and \mathbf{M} are the covariance matrices of the signal and noise. The noise covariance matrix is

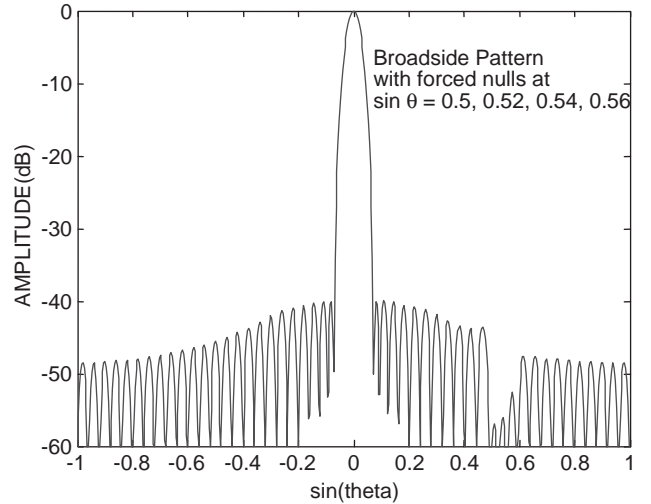


Figure 7. Pattern adapted to suppress interference at $\sin \theta = 0.50, 0.52, 0.54, \text{ and } 0.56$.

written as the outer product

$$\mathbf{M} = \overline{\mathbf{e}^* \mathbf{e}^T} = \begin{bmatrix} \overline{e_1^* e_1} & - & - & \overline{e_1^* e_N} \\ - & - & - & - \\ - & - & - & - \\ \overline{e_N^* e_1} & - & - & \overline{e_N^* e_N} \end{bmatrix} \quad (22)$$

where the included terms are only the noise sources, with no desired signal present. The \mathbf{M}_s has the same form, but includes only the desired signal. Subject to these conditions, the optimum weight vector \mathbf{W} is given as

$$\mathbf{W} = \mathbf{M}^{-1} \mathbf{W}_0 \quad (23)$$

where \mathbf{W}_0 is the quiescent steering vector, which is usually known for most radar applications. Communication networks can use this algorithm using known or measured direction of arrival data.

Figure 7 shows the pattern of an array with the same -40 dB steering vector as Fig. 5a, but subject to strong interfering sources at $\sin \theta = 0.5, 0.52, 0.54, 0.56$. The resulting pattern isn't significantly distorted from that of Fig. 5a, but it does have nulls moved to the required angles. More serious pattern distortion would occur if the elimination of many more interfering signals were needed or if the interfering signals occupied a part of the main-beam.

3. ARRAY APPLICATIONS, CONTROL, AND ARCHITECTURE

3.1. Applications

The preceding sections of this article have outlined a number of the constituents that make up phased-array technology, as well as a number of constraints that dictate element spacing, bandwidth, achievable sidelobe levels,

and other properties. Present and future applications place new demands on this ubiquitous technology, but actually place separate groups of demands that result in quite different array architectures, and using very different modes of control.

Wireless mobile communication alone includes a huge number of varied requirements, from various satellite links to aircraft and ground-based users to base station needs and even to new projections for array needs in individual handheld cellphones. Many of these requirements are detailed in the review papers by Godora [17] and Dietrich et al. [18] and the book edited by Tsoulos [19].

Arrays will reduce the problem of limited channel bandwidth, multipath fading, and insufficient range by providing higher directivity with tailored beamshapes and the suppression of cochannel interference. The various wireless requirements span frequency ranges from UHF (Ultrahigh Frequency) to EHF (Extrahigh Frequency) and define array sizes from a few to many hundreds of elements. Of these requirements, the satellite systems often require large antenna systems at both ends of the communication link, with highly complex scanning or multibeam systems on the satellites and usually single-beam arrays with tens to hundreds of elements at airborne or Earth stations. Bands of frequencies up to approximately 44 GHz are used by civilian and military systems. Military airborne satellite terminals might have arrays with hundreds of elements.

Most existing wireless base station systems use fixed-beam arrays with a single element in azimuth, but enough elements in the vertical plane to provide narrow elevation beamwidths ($<10^\circ$). The typical three-sided cluster arrangement of Fig. 8 has three groups of three arrays each to cover three contiguous 120° sectors. Of the three-column arrays that face any particular sector, one transmits while the other two receive independent channels and provide time diversity to eliminate multipath fading. Some systems offer orthogonal polarizations to provide polarization diversity. Systems with small arrays are also being developed to provide angle diversity with scanning or fixed multiple beams. Either function can result in increased range and elimination of interference from competing signals [17].

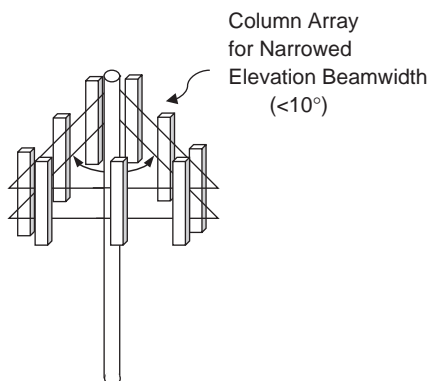


Figure 8. Typical wireless cellular telephone base station arrays using four-column arrays for each 120° sector.

More recent experiments conducted with handheld and vehicle mounted arrays have shown significantly reduced fading and multipath interference rejection, so it seems that soon even handheld cellphones may have small arrays of a few elements.

Applications to military and civilian radar occupy the high-end array technology needs, with airborne multi-function arrays requiring hundreds to a few thousands of elements, while ground- and space-based arrays with tens to hundreds of thousands of elements have been investigated.

3.2. Array Control Modalities

Analog, optical, and digital technologies have been applied to the control of array antennas. The application of one or another of these technologies depends on system requirements and the constraints described earlier. This choice is also a function of time, since microwave analog technology is well established and still advancing rapidly through the use of circuit and solid-state device integration, while optical and digital technologies are far less mature but offer significant advantageous features for certain applications.

The most basic control circuits for each of these modalities are shown in Fig. 9. Analog control, shown in its simplest form in Fig. 9a, might consist of a circulator or TR switch to separate transmit and receive channels at the array level, followed by a corporate power divider network that weights the element level signals to provide for low sidelobe array illumination. This network could include simultaneous or switched sum-and-difference beam formation. Phase shifters or time-delay devices scan the beam in one or two dimensions. This basic network suffers from losses in the circulator, the power divider, and the phase or time control devices, and at microwave frequencies these could add to half the power. For this reason it is becoming more common to use solid-state TR modules at some subarray level or at each element as shown in Fig. 9b. Here separate feeds are used for transmit and receive that often have very different sidelobe requirements, and each port is routed to a TR module where it passes through a power amplifier on transmit or a low-noise amplifier on receive. The solid-state module usually includes a circulator for separating the two channels. Two fundamental constraints come into play: (1) time-delay devices are required if the instantaneous system bandwidth exceeds that of Eq. (9), and (2) spacing must be on the order of a half-wavelength at the highest frequency. However, these analog devices are basically switched lines, and must be on the order of the array aperture length, so at the higher frequencies it is difficult to fit the lines and control switches in the interelement area. These two constraints lead to the use of a subarray architecture for wideband arrays, discussed in a later section.

Figure 9c shows a basic optical network for array control. In this simplified circuit an optical signal is amplitude-modulated by an RF signal, the optical power divided into a channel for each antenna element, and then time-delayed by a switched-fiber time-delay unit. After detec-

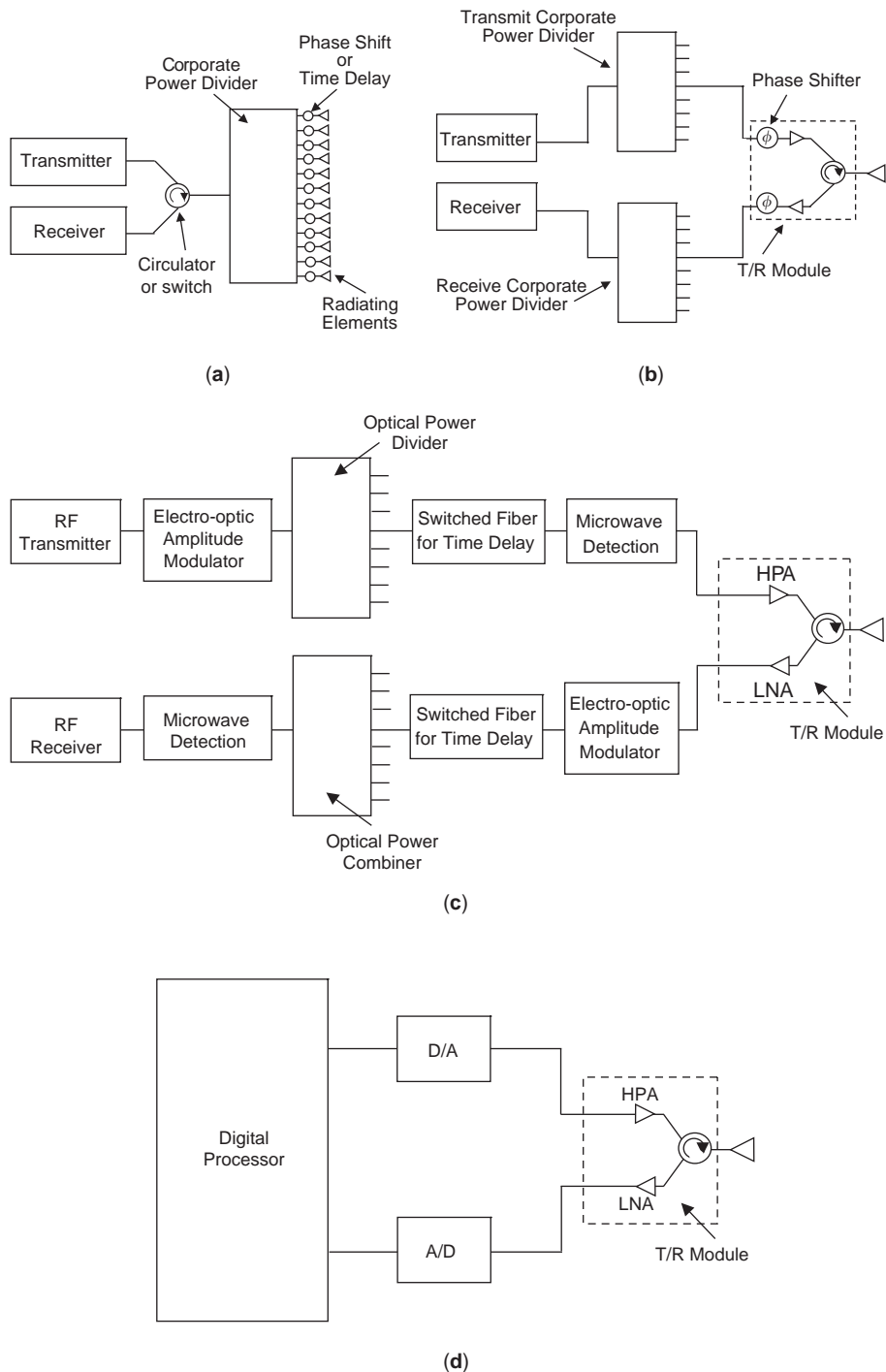


Figure 9. Array control modalities: (a) analog control using passive components; (b) analog control using active components; (c) optical control; (d) digital control.

tion the RF signal is amplified and radiated. The received signal is handled in a similar manner. This RF/optical path is very inefficient and may require amplification elsewhere in the network. The technology can provide accurate time delay with little dispersion, as required for large arrays with wide bandwidth.

Actual networks that are configured for photonic array control are often far more complex than the simple one shown in the figure, and may use independent optical

sources for each control port, as done by Lee et al. [20]. Still further in the future, photonic systems may use multiple interconnect networks for forming independent multiple beams with MEMS (micro-electromechanical system) mirror switches as described by Morris [21].

The primary obstacles to widespread use of photonic array control are network losses and device size constraints. Without amplification in the transmit and receive channels, modulation, detection, and power divider

losses can exceed 10dB, and this, coupled with the size constraints, may mean that for many years photonic time-delay control will be useful primarily at the subarray level.

Figure 9d shows a rudimentary digital beamforming network. This technology will eventually provide the ultimate degree of antenna control, and will present the signal processing computer with digital signals that are preprocessed to give optimal antenna performance. The digital beamforming network will obtain sidelobes as low as achievable from a given calibration network, provide multiple simultaneous beams or receive with arbitrary weightings on each beam, provide time-delay and wide-band operation using subbanding techniques, provide for array failure detection and correction, and “idealize” the antenna system itself by providing entirely separate control for each channel path through the array or subarray. Finally, it will allow fully adaptive control using virtually any algorithm without network changes.

This digital control is well within the state-of-the-art now, but currently not practical for large arrays. Limiting factors are A/D and D/A (or synthesizer) bandwidth, computer speed and storage requirements, power requirements, and size. The loss in the digitizing process also mandates use of solid-state modules at the array elements and the A/D sampling is usually done after downconversion to a suitable intermediate frequency. Considering all these factors leads to some very real and practical applications for relatively small arrays (or for some large but narrowband military arrays), and for many more applications for digital beamforming at the subarray level.

3.3. Control Architectures

3.3.1. Space-Fed Lens and Reflector Antennas. Figure 10a shows a space-fed lens array, which, in its simplest form, is just an alternate to the constrained “corporate feed” implied in Figs. 1a and 1b. This configuration shows an array face, fed by a single antenna that illuminates the back face of the aperture. The lens is active in that there is phase control at every element in the lens. The main advantage of this configuration is that it reduces the cost and weight of the system by eliminating the corporate feed. It is therefore applicable to lower-cost ground-based arrays as well as to very large space-based radar systems. Not shown are active reflect arrays that are configured like the lens geometry, but with shorted (short-circuited) lines that use phase shifters to vary the effective line lengths. This is a wide-angle scanning technology similar to that in the space-fed lens. In addition there is a class of space-fed structures including passive reflectors that can be scanned over limited angular regions. All of these space-fed scanning systems have instantaneous bandwidths limited by the use of phase control (or passive reflector) at the objective aperture.

3.3.2. Multiple-Beam Arrays. One last category of scanner is the multiple-beam array shown schematically in Fig. 10b, where each input port excites and independent beam in space. These can be produced with a digital beamformer, but in addition there are a variety of antenna

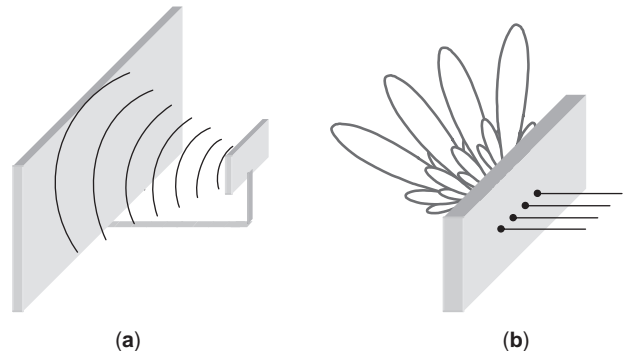
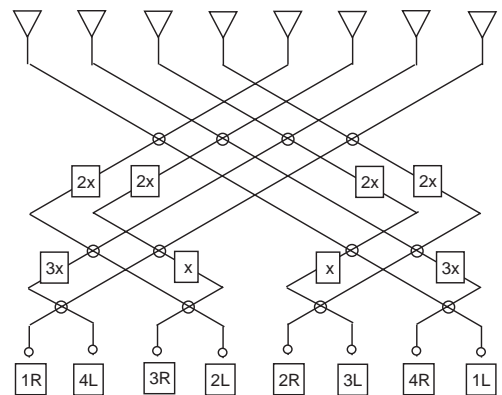


Figure 10. Phase shift and passive lens arrays: (a) space-fed array; (b) multiple-beam array.

hardware concepts that produce multiple beams, including Butler matrices [9,22] (Fig. 11), which involve a circuit implementation of the fast Fourier transform (FFT) and radiate orthogonal sets of beams with uniform aperture illumination. Lens and reflector systems have the advantage of being wideband scanners, since their beam locations do not vary with frequency. A particularly convenient implementation is the Rotman lens [23] of Fig. 12, a variant of the earlier Gent bootlace lens [24] that has the special feature of forming three points of perfect focus for one plane of scan. The Rotman lens can provide good wide-angle scanning out to angles exceeding 45°. Multiple-beam lenses and reflectors have been chosen for satellite communication systems, and in that application serve to either produce switched individual beams or use clusters of beams to cover particular areas on Earth. Figure 12 shows a sketch of a Rotman lens, illustrating the



$x = \pi/8$ radians phase shift
 ⊗ Hybrid coupler convention: Straight through arms have no phase shift, while coupled arms have 90° phase shift

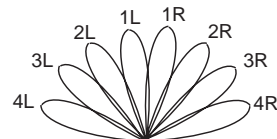


Figure 11. Eight-element, eight-beam Butler matrix and radiated beams.

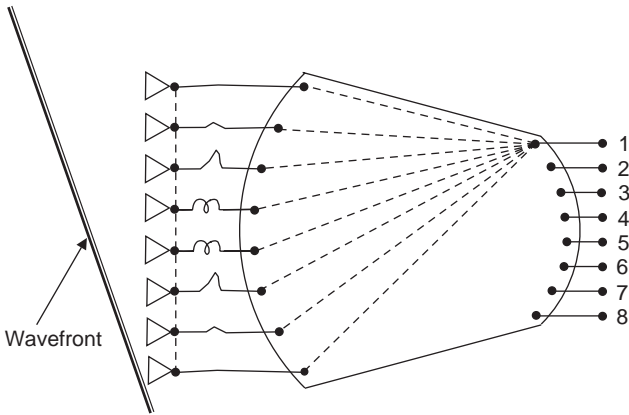


Figure 12. Rotman lens showing ray tracings and radiated wavefront.

several ray paths through the lens, and the associated radiating wavefront.

3.3.3. Control for Wideband and Fractional Bandwidth “Wideband” Arrays. The phenomenon called “squint” [see Fig. 2 and Eqs. (8), (9)] dictates the need for including time-delay steering for very wideband arrays and for very large arrays with even modest “fractional” bandwidth. These two categories of wideband arrays are distinctly different, and require completely different architectures. Figures 13 and 14 outline several approaches to providing time delay for the various relevant conditions. Figure 13 shows two possible architectures for very wideband (octave or multioctave) or multiple-band control. The sketch at left (Fig. 13a) shows one TR module and one time delay unit per element, and provides exact time delay and the ultimate bandwidth subject to antenna element

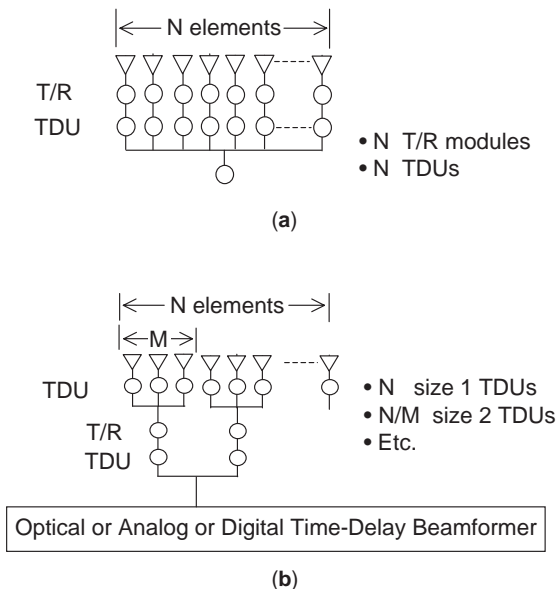


Figure 13. Array architectures for multioctave bandwidth or multiple-band antennas: (a) array with time-delay units; (b) array with cascaded time-delay units.

design (which can now be up to 10:1 in some cases). The TR amplification at the elements is necessary because time-delay units are lossy (depending on their length and technology). Recalling that an array 100 wavelengths long needs nearly 100 wavelengths of excess line switched in series with the outermost elements for scan to 60°, it becomes clear that significant loss can be expected. In addition to loss, there is little room behind each element to include the time-delay units and amplification, so this most basic of architectures is impractical for most applications except for relatively small, very wideband arrays.

Figure 13b shows a more practical configuration for providing element-level time-delay, and, like the sketch in Fig. 13a, provides the exact time delay at every element. This configuration provides small increments of time delay at each element, perhaps up to two or three wavelengths, then after grouping these elements into subarrays and amplifying, provides longer delays at successive levels of subarraying. Very long delays can then be pro-

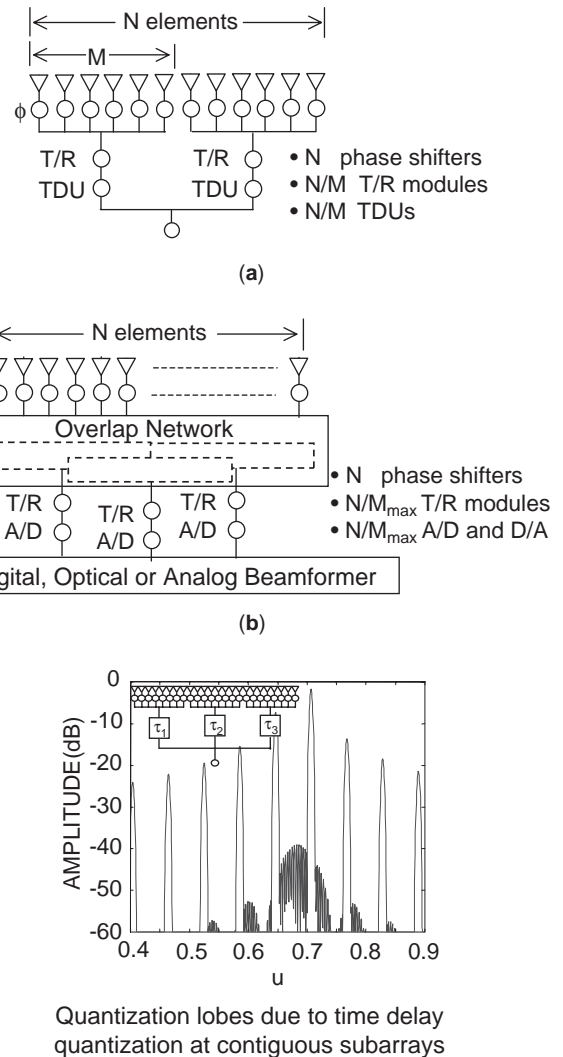


Figure 14. Architectures for large “wideband” arrays with fractional bandwidth: (a) phased arrays with time-delayed contiguous subarrays; (b) phased array with time-delayed overlapped subarrays.

vided by a beamformer using optical, analog, or digital time delay. In this case the optical and analog time delay is provided by a switched line configuration, and so retains the wideband features of the basic apertures. Digital beamformers don't presently support octave or multioctave bandwidth at microwave frequencies, but can provide accurate time delay over narrower bandwidths at a multitude of frequencies through subbanding and filtering. In these cases, the digital beamformer can provide multiband beams that point in the same direction using the network of cascaded time-delay units.

Figure 13a addressed truly wideband signal control, but very large arrays require time delay when the instantaneous bandwidth may be only a few percent, but still exceeding that of Eq. (9). Certainly the configuration of Fig. 13b will readily satisfy this condition, too, but several other options are available when the bandwidth is modest. Architectural solutions for such fractional bandwidth, but "wideband" arrays are shown in Fig. 14. The obvious solution, shown in Fig. 14a, consists of using phase shifters at the element level, and after amplification, inserting time delays at the subarray level. This solution is simple, is easy to build, and provides room for including analog, optical, or digital time delay at the subarray level, but can produce significant quantization lobes as shown in the insert. The configuration in Fig. 14b is highly schematic, but intended to indicate that by producing special, shaped subarray patterns, one can use the subarray patterns as an angular filter to remove the quantization lobes. These special networks, called *overlapped subarray* or *transform feeds*, have been developed as space-fed or constrained microwave networks, and, as detailed by Mailloux [25], do provide good pattern control at the expense of increased complexity. Digital control seems particularly appropriate for these overlapped feed networks because of the added degree of flexibility it provides.

4. CONCLUSION

This article has briefly described a variety of technologies and concepts that are fundamental to antenna scanning arrays. This technology has grown out of the military investments for radar, but now has an increasing role in commercial as well as military systems. One goal of the article has been to explain how the physical constraints of the interelement spacing and array squint necessary lead to different system architectures depending on the desired application. A second goal has been to briefly address present and new applications in light of the changing availability of analog, optical, and digital control technology. It seems reasonable to expect that this growing list of new array applications will continue to require an expanding collection of control modalities, components, and architectures for the foreseeable future.

BIBLIOGRAPHY

1. J. Herd, Full wave analysis of proximity coupled rectangular microstrip antenna arrays, *Electromagnetics* (Jan. 1992).
2. B. Edward and D. Rees, A broadband printed dipole with integrated balun, *Microwave J.* **30**:339–344 (May 1987).
3. N. Schuneman, J. Irion, and R. Hodges, Decade bandwidth tapered notch antenna array element, *Proc. 2001 Antenna Applications Symp.*, Monticello, IL, Sept. 19–21, 2001, pp. 280–294.
4. C. P. Wu, Analysis of finite parallel plate waveguide arrays, *IEEE Trans. Anten. Propag.* **AP-18**(3):328–334 (1970).
5. C. A. Balanis, *Antenna Theory: Analysis and Design*, Wiley, New York, 1997, Chap. 8.
6. G. F. Farrell, Jr. and D. H. Kuhn, Mutual coupling effects in infinite planar arrays of rectangular waveguide horns, *IEEE Trans. Anten. Propag.* **AP-16**:405–414 (1968).
7. G. H. Knittel, A. Hessel, and A. A. Oliner, Element pattern nulls in phased arrays and their relation to guided waves, *Proc. IEEE*, **56**:1822–1836 (1968).
8. P. M. Woodward, A method of calculating the field over a plane aperture required to produce a given polar diagram, *Proc. IEE* (Lond.) **93**(Part 3A):1554–1555 (1947).
9. J. Butler and R. Loe, Beamforming matrix simplifies design of electronically scanned antennas, *Electron. Design* **9**:170–173 (April 12, 1961).
10. S. A. Schelkunov, A mathematical theory of linear array, *Bell Syst. Tech. J.* **22**:80–107 (1943).
11. C. L. Dolph, A current distribution for broadside arrays which optimizes the relationship between beamwidth and sidelobe level, *Proc. IRE* **34**:335–345 (June 1946).
12. T. T. Taylor, Design of line source antennas for narrow beamwidth and low sidelobes, *IEEE Trans. Anten. Propag.* **AP-3**:16–18 (Jan. 1955).
13. E. T. Bayliss, Design of monopulse antenna difference patterns with low sidelobes, *Bell Syst. Tech. J.* **47**:623–640 (1968).
14. R. S. Elliott, On discretizing continuous aperture distributions, *IEEE Trans. Anten. Propag.* **AP-25**:617–621 (Sept. 1977).
15. O. M. Bucci, G. Delia, and G. Romito, A generalized projection technique for the synthesis of conformal arrays, *Proc. IEEE AP-S Int. Symp.* 1995, pp. 1986–1989.
16. S. P. Applebaum, Adaptive arrays, *IEEE Trans. Anten. Propag.* **AP-24**:585–598 (Sept. 1976).
17. L. C. Godora, Application of antenna arrays to mobile communications. Part II: Beamforming and direction-of-arrival considerations, *IEEE Proc.* **83**(8):1195–1245 (Aug. 1997).
18. C. B. Dietrich, Jr., W. L. Stutzman, B. Kim, and K. Dietze, Smart antennas in wireless communications: Base-station diversity and handset beamforming, *IEEE Anten. Propag. Mag.* **42**(5):145–151 (Oct. 2000).
19. G. V. Tsoulos, ed., *Adaptive Antennas for Wireless Communication*, IEEE Press, 2001.
20. J. J. Lee, R. Y. Loo, S. Livingston, V. I. Jones, J. B. Lewis, H. -W. Yen, G. L. Tagonau, and M. Wechsberg, Photonic wideband array antennas, *IEEE Trans. Anten. Propag.* **AP-43**(9):966–982 (Sept. 1995).
21. A. Morris III, In search of transparent networks, *IEEE Spectrum* **38**(10):47–51 (Oct. 2001).
22. J. L. Butler, Digital, matrix, and intermediate frequency scanning, in R. C. Hansen, ed., *Microwave Scanning Antennas*, Peninsula Publishing, Los Altos, CA, 1985, Chap. 3.
23. W. Rotman and R. F. Turner, Wide angle microwave lens for line source applications, *IEEE Trans. Anten. Propag.* **AP-11**:623–632 (1963).

24. H. Gent, The bootlace aerial, *Roy. Radar Estab. J.* 47–57 (Oct. 1957).
25. R. J. Mailloux, *Phased Array Antenna Handbook*, Artech House, Norwood, MA, 1994, Chap. 8.

ANTENNA TESTING AND MEASUREMENTS

W. NEILL KEFAUVER
 LOCKHEED MARTIN
 Denver, Colorado

Antenna testing uses many creative technological solutions to get what is an easily stated and critical function of a wireless communication, radar, or remote sensing system. The criterion is simply what level of power will my antenna deliver to or receive from a remote location defined by the antenna's usage. This remote location is almost always in the "far field" of the antenna, the far field of an antenna is the distance beyond which the pattern of antenna can be accurately approximated as $F(\theta, \phi) e^{-jkr}/r$. The engineering criterion for this distance is $2D^2/\lambda$, where λ is the wavelength of the signal and D is the antenna aperture's largest dimension in the same units as the wavelength; this relationship corresponds to a phase error of 22.5° across the antenna aperture relative to ideal. This article discusses the techniques used to evaluate antennas and the decades of effort to get the answer without having to put up with all the risks and delays of trying to obtain the information after the system is in the field.

1. HISTORY

In the early days of antenna measurements the technology was based on simple approximation of the operational environment, where measurements were performed outdoors at a sufficient distance to assume that the pattern was not changing with distance. One would build a tower outside to minimize antenna interactions with the ground, mount the antenna, and point it toward a transmitter a great distance away on the basis of the $2D^2/\lambda$ criterion. Using conventional motor control mechanisms already developed for telescopes and artillery among other applications, the user could obtain a reasonable response with the microwave detector—sometimes a crystal detector for just power, but over time the mixer became the sensor of choice as it has better dynamic range, can give phase information, and allows one to further filter the signal after converting the transmit signal to an intermediate-frequency signal. The data were recorded by synchronizing the motors of the range controller to a turntable and plotting using a pen and translation motor keyed to the amplitude of the received signal.

With the advent of widespread computing in the 1970s, the ranges began to automate, alleviating the menial task of manually reading data off charts and inputting them into the analysis computer. One of the first algorithms

implemented in the computer was calculation of circularly polarized data from linear measurements, eliminating the need for the rotating linear measurement to determine axial ratio of the antenna where the source antenna was spun continuously while scanning the remaining axes. The calculation of polarization using this method led to investigation of other information that could be derived from having digital data of the complex fields. Test articles no longer needed to be precisely aligned in the range; only knowledge of the location was necessary. Data processing could be used to correct misalignment, calibrate against gain standards, compensate for range polarization impurity, and software time-gate the data to reduce multipath. With all this improved capability to measure data, the increase in the technical knowledge, particularly mathematical, was dramatic. The arrival of compact range and near-field testing in the same decade represented an outgrowth of the metrology breakthroughs in automated testing spearheaded by several universities (particularly Ohio State) and the National Institute of Standards and Technologies (NIST). Since then the equipment has increased in complexity and capability to support the increasingly stringent antenna operational requirements.

2. APPLICATIONS

The vast majority of antennas are used in communications; however, there are more specialized antennas used for remote sensing and power transfer.

2.1. Communications

Beginning with Marconi, we have been using antennas to communicate at a distance, and the applications of these antennas have become more sophisticated over the decades. Today the most complex antennas are built for spacecraft to exacting requirements to optimize the distribution of power and reception of signals from geosynchronous orbit. These antennas will often have hundreds of beams working simultaneously to transfer received signals to transmit back to the final destination through a sophisticated communication subsystem. These antennas will often transmit two different signals simultaneously on the same frequency using polarization orthogonality to optimize the bandwidth utilization. In addition, the beams will be shaped to match specified coverage areas on Earth so that power is not wasted outside the coverage area. At the other end of the scale of complexity is the venerable monopole found on your radio, pager, or cellular phone and most portable communication devices; the only requirement expected of the monopole is to transfer some small percentage of the power to and from space into the communication device. In between these two antennas there are a host of applications requiring varying complexity, base-station antennas with single or multiple beams for cellular phones, television and radio transmit antennas for more efficient horizon coverage, reflectors for deep-space probes, whip antennas for cars, blade antennas for planes, and GPS patches for location finding.

2.2. Remote Sensing

An antenna used for remote sensing is either trying to measure a physical phenomenon, such as temperature or a radiated signal. Radar and astronomy antennas are specific examples of this application, where the information is not embedded in the signal but arises from the properties of the detected signal. Antennas used in radiometer work (a type of astronomy) need to have high-beam efficiency because the signal is very similar to the entire surrounding environment. Antennas used for signal detection need to have sensitivity over the desired coverage area and frequency, but are typically of a much broader band than are communication antennas because the signal source may change over time intentionally.

2.3. Radar

Radar is the one application where a device learns useful information while trying to talk to itself; the antennas employed for radar applications are typically highly directional in order to maximize power in a desired location. In specialized applications the pointing can be done using sophisticated microwave electronics almost instantaneously such as the AEGIS or AWACS system. More generally the radar is either pointed or swept through an area using rotation mechanisms, or for the radar gun, the antenna is manually pointed by the operator.

2.4. Astronomy

Most ground-based antennas used in astronomy have to be measured after installation because the individual antenna is too large to fit into a conventional measurement facility; range testing of these antennas is normally limited to the feed assembly and final performance is predicted using detailed modeling. Space-based astronomy usually has antennas that are thoroughly tested on the ground but require additional calibration as they settle into orbital operation. Antennas used in astronomy are some of the most efficient power conversion systems built because they have to resolve a signal of millikelvins from the background radiation of the universe. Also, because of the high sensitivity with which they are designed, the final assembly will need calibration to achieve optimal performance.

3. ANTENNA PATTERN MEASUREMENT REQUIREMENTS

Requirements for radiation performance of antennas can easily be divided into three areas by physical properties—frequency, solid angle, and polarization. Within each of these properties, depending on the application, there will be a large list of more specific requirements. Section 4 details many of these terms; the important item to remember is that all radiation behavior of the antenna is based on these three fundamental properties.

4. TERMINOLOGY

Antenna technology, like all technical specialties, has its own language, and I will now review some of the common

parameters when specifying an antenna's performance against system requirements using nonrigorous terminology. All of these terms have a pure mathematical relationship that can be developed rigorously and that can be found in any of the reference materials [1–6]. Antenna measurements require development of the method to convert raw response to an accurate, widely accepted version of these parameters. One reliable source of standard definitions for antennas is the IEEE [7]. These parameters are as follows:

Isotropic—a theoretical antenna that radiates a pure polarization uniformly in all directions¹

Gain—the improvement in the signal strength over an isotropic radiator

Directivity—the ratio of the signal received in the direction of interest relative to a standard radiating source, usually isotropic, less frequently a dipole

Beam width—usually half-power, the angular width in a plane containing the beam peak between the crossover points on either side of the peak

Cross-polarization—amount of power in the field polarization that is orthogonal to the one you are using

Polarization—relationship between the two orthogonal components of a traveling wave normal to the direction of propagation

Mainbeam—solid angle between the beam peak and the sign reversal of the detected signal (the signal usually goes through zero)

Sidelobes—pattern structure outside the main beam, usually desired to be minimal

Efficiency—amount of power delivered to the antenna that is radiated

Beam efficiency—amount of power radiated that is in the mainbeam

Axial ratio—ratio of the minimum to maximum linear response of measured signal at a specific angle

VSWR/return loss—amount of power reflected by antenna into the desired impedance

Mechanical boresight—orientation of the test article relative to coordinate system, usually defined as the z axis

Electrical boresight—location of the pattern peak relative to the mechanical boresight specified through test article physical geometry

Link margin—amount of power available relative to the required power to close the communication link between two antennas

Geometry—typically either θ/ϕ or azimuth/elevation coordinate system

G/T—gain of the antenna above the system noise temperature; defines sensitivity to received signals

¹Such a device is not even remotely achievable physically but is the most commonly used reference for all performance parameters.

EIRP—effective isotropic radiated power or power density at a defined distance, measured complete efficiency of the transmitter

Bandwidth—frequency range over which the antenna meets design requirements

Because of the brevity of this section, I will only try to introduce the function of each of these particular parameters for evaluating an antenna. The physical entity most easily understood is also one of the hardest to measure to the desired accuracy is gain. Gain is so significant because all other system performance parameters are limited by this entity. It is difficult to measure with high accuracy because there are so many possible ways to get significant error. For instance, the antenna must be aligned with a known gain standard to high accuracy (less than 0.5°), and it must not be significantly affected by the test environment. If the antenna picks up a stray emission 30 dB below the test signal, the error will be 0.27 dB or $\pm 6\%$. Because of the strong interaction of the antenna with its environment, it is very difficult to go below this level. Measurements at frequencies below 1 GHz are typically not directive and sensitive to multipath, and measurements above 1 GHz have stability problems due to the thermal drift moving the response significantly from the time when a standard was measured to when the antenna data were completed.

5. METHODS

The methods of evaluating antenna performance have diversified as the computational capabilities have increased. An antenna generates a three-dimensional radiation field, which for the purposes of most antenna applications can be described using an angular coordinate system; the dependence on distance is inversely proportional to distance, with no higher-order terms in the far field of the antenna. Unfortunately, reducing the field description problem to two spatial dimensions still leaves a great deal of complexity, especially if frequency is still a variable as well. Conventionally, a range has to be designed to rotate an antenna on two orthogonal axes to create a surface about the antenna (a sphere). Usually the antenna is rotated because it is easier than building an arch to allow the antenna to remain stationary. If this method is used, then a complete set of radiation data can be collected utilizing either three rotational axes or two axes and a dual-polarized source antenna with a switch.

5.1. Far-Field Range

Far-field ranges are either indoor or outdoor—indoor ranges became common after the development of commercially inexpensive anechoic materials to reduce multipath of the signal inside the room in the 1950s. Outdoor ranges were the first method developed as the need to characterize antennas became prevalent during World War II and are still used to this day for specific applications at low frequencies and involving extremely large test articles. Multipath problems in outdoor ranges usually

arise from one source—the reflection from the ground approximately halfway between the source antenna and the test article. The ground reflection is typically controlled through geometry by using ground bounce coherently at low frequencies (below 1 GHz). Otherwise the ground bounce is reduced by radiation fences or building sites on opposite sides of canyons or adjacent hills to reduce the power reflected into the test article by most of the ground outside the mainbeam of the source antenna.

5.1.1. Outdoor. The outdoor range often employs a secondary reference antenna in close proximity to the test article. This second antenna is used to deal with the outdoor range phenomenon of scintillation and to minimize cable runs. Outdoor ranges tend to be expensive to maintain because of property costs and frequent weather-related outages. The outdoor range does have the advantage of testing the article in an environment similar to production usage in some cases such as cellular base stations. If an outdoor range is retrofitted with a modern frequency-agile receiver, the user can take advantage of the same techniques pioneered in RCS (radar cross section) measurements, where you can apply either a software or hardware time gate to reduce multipath in the measured signal. The concept is simple—if the bounce from the ground is delayed by 10 ns, for example, then all signals are filtered out outside of approximately ± 5 ns from arrival in the direct path. The limitation to this technique is the bandwidth of the antenna and the separation of the arrival time—the longer the range and the shorter the towers, the less able the operator is to eliminate the ground bounce.

Figure 1 shows a typical range walk depicted the contribution of different signals to the response of the antenna separated in range and shows how time gating can be applied to eliminate some of the extraneous signal paths. The data were generated by using postprocessing of a stepped-frequency measurement. Making simple changes to the range configuration can isolate several of the additional pulses shown in the figure. If a cable length is introduced in between the source antenna and the

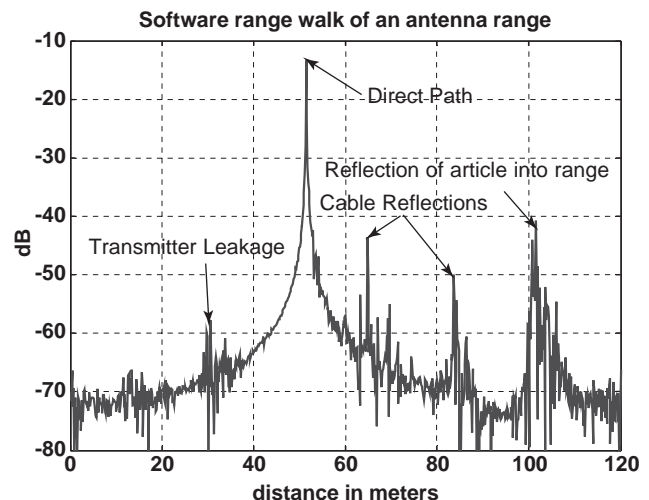


Figure 1. Antenna range “range walk.”

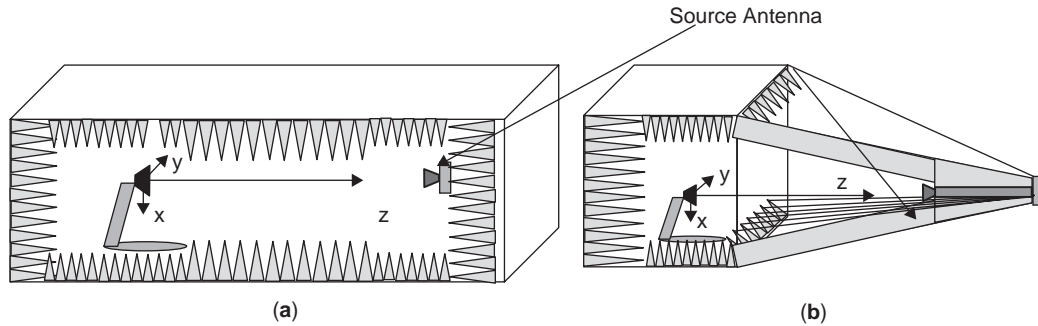


Figure 2. Chamber geometries: (a) rectangular; (b) tapered.

transmitter, the pulses associated with the cable should move out twice as far as the direct-path signal in the cable within the same time. The reflection of the test article should change as it is rotated relative to the antenna. Replacing the source antenna with a load can isolate the transmitter leakage. These diagnostic techniques are typical in any range setup and are key in ensuring that the antenna measurements are as good as can be done with the equipment. More importantly, these techniques have universal application and show the importance of a range walk in evaluating the performance of the range.

5.1.2. Indoor. Indoor ranges come in several types—rectangular (Fig. 2a), tapered (Fig. 2b), and dual-tapered are the most common. The rectangular chamber ideally has two square faces with long rectangles forming the walls, ceiling, and floor. The center of each face is treated with thick anechoic material to minimize specular reflections. This type of chamber typically provides a very clean quiet zone but is limited to higher frequencies due to the reflectivity of the sidewalls. The tapered chamber is specifically optimized for low-frequency measurements. The tapered chamber is intentionally flared from a point near the source's physical location to a large square aperture at volume where the antenna under test (AUT) is located. The chamber then terminates in a backwall of an extra-deep absorber to eliminate further chamber reflections. This chamber is more costly to build than a rectangular one and is plagued by a frequency-sensitive source point to mount the source antenna for optimal performance. The dual-tapered chamber basically bolts two large metal horns together and applies thick anechoic to the AUT end while attempting to reduce the bounce off the throat for a conventional tapered chamber. Full reciprocity does not apply straightforwardly to either the tapered or dual-tapered range because the source antenna is not in “free” space; therefore the anechoic material is used to optimize the delivery of fields to the region in which the AUT is located and the source that is selected has to be compatible with the chamber geometry. The operator does not care which antenna transmits and which receives but is extremely concerned as to how the antenna interacts with the chamber throat. This behavior makes three antenna calibrations impossible in a taper chamber. For a rectangular chamber, spatial reciprocity does apply since typically antennas can be physically interchanged with

the same response resulting, so multipath can be evaluated with ambivalence to it arising from the AUT or the source. The theoretical reciprocity of the antenna to transmit or receive is not what is important in measurements. Since the traditional method of calibrating an antenna for gain is by substituting a standard, the reciprocity of physical location is important since we are replacing an antenna with a known standard and neglecting the coupling to the chamber. This step usually predominates over all other error sources in the measurement because the accuracy of knowledge of the gain standard in the AUT environment is often poorly known or assumed to be much better than it really is. The uncertainty comes from the two devices that have significantly different patterns and are sensitive to multipath from different directions. In narrow ranges the gain standard may often interact with the source, causing significant errors, particularly if there are large flat surfaces. Often the test article itself will have large collimated reflections due to testing it in the environment in which it will be used. These terms can usually be isolated by time-domain (range walk) methods and can be surprisingly large. The important criterion is the tradeoff of facility size for article testing, namely, if you test in a small facility, the risk of the test article having a large RCS that interferes with the direct antenna measurement increases; as R increases, the contribution from the RCS decreases much faster than does the total loss on the link. The chamber can and will introduce additional errors depending on the type of antenna and measurement being performed. Possible errors include specular scattering off the flat surfaces of the absorber, reflections from the positioners, and even radiation from some lighting systems (particularly for antenna temperature measurements).

5.1.3. Pattern Synthesis. A specialized case for antenna measurements are techniques specifically modified to synthesize plane waves using means other than distance. The obvious reason for developing these other techniques was to eliminate the need for facilities many times the size of the antenna under test. However, if the cross section of the chamber is only slightly larger than the antenna, the far-field criterion causes the length of the range to increase in direct proportion to frequency. This type of range, although the cost would increase linearly, would degrade quickly once the range length increases to more

than twice the range width. This ratio applies when the angle of incidence on the wall is 60° off normal.

Unfortunately, as the chamber becomes longer, the specular wall reflections are at a lower angle, causing increased multipath as the reflectivity of the absorber decreases with angle. Absorber reflectivity decreases off normal incidence because the medium has been intentionally thinned geometrically to match to free space over several wavelengths using pyramids or wedges. As the field becomes parallel to the top of the absorber, the faces of geometric structures become visible and the transition from free space to carbon-loaded dielectric is instantaneous instead of spread over wavelengths.

Three well-known types of ranges are applied to eliminate the need for a long range: compact, near-field, and extrapolation. The following sections will briefly cover each type.

5.2. Compact Range

Although this concept is covered extensively in another article, briefly, the basic concept is that a point source of a conventional range is converted into an approximate plane wave using a reflector system. This concept was explored in the 1960s and perfected in the 1980s as modeling tools became more effective. Primary limitations to this measurement technique are the purity of the plane wave, which is limited by the reflector size and surface accuracy in addition to conventional multipath. Since the plane wave is synthesized instantaneously, this solution is desirable for applications in which speed is more important than accuracy. In particular, for situations where the amount of data required is minimal, such as peak gain, beamwidth, and cross-polarization, this type of range will allow the user to turn around hardware more quickly than using near-field scanning methods since only the data needed for the direct measurement of requirements are gathered. In the case of RCS measurements, the sheer volume of positional data required by near-field measurements necessitate that any realistic measurements be done using either a compact or far-field range.

5.3. Near-Field Range

Near-field measurements were developed in the 1970s to improve the accuracy of measurement methods. With near-field measurements, the far-field criterion ($2D^2/\lambda$) was eliminated and the concern over the purity of the plane wave was eliminated as well using powerful mathematical function space transforms. The ultimate limitation in far-field measurements has always been knowledge of the real distance between two antennas asymptotically to the far field. When one wishes to determine the coordinate system of the test antenna, all the uncertainties in the gain standard, the source, and the test antenna must be minimized to push measurement uncertainties under 0.5 dB. An example of this concern is that if one measures an antenna in a 100 m range, the knowledge of the relative position of the two antennas to the source must be less than 50 cm to get the positional error of the gain measurement under 0.05 dB. The quiet-zone variance over that 50 cm will need to be less than 0.05 dB to achieve an overall accuracy of <0.1 dB. In near-field ranges the first term is not rele-

vant and the second term is minimized by probe compensation. For many users this level of accuracy is beyond their needs and requires excellent mathematical skills, which has slowed the proliferation of this technology. One advantage of near-field measurement is that data can accurately be calculated for any position in space outside the measurement surface and fairly accurately calculated all the way into the test antenna. The limitations of near-field measurements are threefold: volume of data, processing of data, and knowledge of the probe pattern that has been convolved into the near-field measurement data.

5.3.1. Planar. Planar near-field measurements were the first geometry attempted because of the simplicity of the associated mathematics, which can be distilled to the following pair of simple equations, although it took a decade of research to become confident with the results:

$$\begin{aligned} \mathbf{P}(\mathbf{k})\mathbf{A}(\mathbf{k}) &= \iint [\mathbf{P}(x, y, 0) \otimes \mathbf{E}(x, y, 0)] \\ &\quad \times e^{-j\vec{k} \cdot \vec{r}(x, y, 0)} dx dy \\ \mathbf{E}(\mathbf{r}) &= \iint \mathbf{A}(\mathbf{k}) \frac{e^{j\vec{k} \cdot \vec{r}}}{r} \sin \theta d\theta d\phi \end{aligned} \quad (1)$$

When the probe being used to measure the fields over the planar surface is nonisotropic (*reality*), then the near-field measured value is the convolution of the probe pattern ($\mathbf{P}(x, y, 0)$) with the test antenna pattern which then must be divided out using known probe pattern characteristics by wavenumber ($\mathbf{P}(\mathbf{k})$) before the second equation. Obviously, to find the test antenna fields, the probe fields must be quantified. Often the isotropic approximation is used when the test antenna is highly directive and pointed perpendicular to the scan plane. Along the way to making this measurement method viable, many approximations had to be evaluated to quantify their contribution to a real measurement. First, the surface of a planar scanner is not closed except at infinity; this error term is called *truncation*. Moreover, the measured voltage is at discrete locations—the maximum sample spacing is limited by the Nyquist criterion to a half-wavelength without significant loss of information. The Nyquist criterion is normally applied in signal processing where the maximum frequency is harder to define sometimes, for antenna measurements the maximum frequency has to be the transmit frequency of the antenna, and sampling at twice the transmit frequency corresponds to sampling every half-wavelength. There are additional new error terms quantified by Newell and Yaghjian [8] in their papers on error analysis of this method. Note that for the far-field pattern case the second integral degenerates to an identity because wavenumber and direction are equivalent and the distance dependence is eliminated. Orthogonality with the Green function ensures that $\mathbf{A}(\mathbf{k}) = \mathbf{A}(\theta, \phi)$ with $\mathbf{A}(r) = 0$ since radial fields do not propagate.

5.3.2. Spherical. Because many antennas have important pattern characteristics extending into the back hemisphere and the method of near-field measurements had worked so well in the planar geometry, the mathematical

extraction techniques were extended to spherical data collection methods. The mathematics is far more complicated computationally by the need for spherical Bessel functions and Legendre polynomials to perform the spatial function decomposition; planar function expansions required only trigonometric functions that are conveniently self-inverting through the FFT (fast Fourier transform). The spherical function coefficient calculations require the use of full two-dimensional integrations to determine the best fit of coefficients to the antenna pattern. The positional sensitivity of the function expansion also increases dramatically as the near fields are measured over spheres closer to the size of the antenna. The implementation commercially usually involves building a facility that is identical to a far-field range except for having higher-grade rotary stages for accurate location of the test article. Several ranges have been built that move the probe instead of the test antenna to minimize the dynamic loading of the test antenna as its center of mass moved about the support tower. In this special case the positional uncertainty of the sphere surface can be reduced relative to the coordinate system, allowing for much more accurate measurements on antennas that have significant deflection under gravity.

5.3.3. Cylindrical. Cylindrical near-field measurement capabilities are easily added to either of the ranges described above by adding an extra axis of position control. Cylindrical measurements are optimized for fan beam antennas such as cellphone base stations and some more sophisticated radar applications such as the cosecant squared beams. The mathematical function set is more easily dealt with because we are back to using trigonometric functions for evaluating the function coefficients—with processing times for a similar-sized collection process such as planar data by taking advantage of the FFT. Typically the antenna will be rotated while a linear scan mechanism takes the second axis of data. The following equation expresses the mathematical flow of the processing:

$$\begin{aligned}
 & \mathbf{P}_A(k_z, n)\mathbf{A}(k_z, n) \\
 &= \oint \int [\mathbf{P}(0, \theta, z) \otimes \mathbf{E}(r_0, \theta, z)] e^{-j \vec{k} \bullet (z \sin n\theta)} \\
 & \mathbf{P}_B(k_z, n)\mathbf{B}(k_z, n) \\
 &= \oint \int [\mathbf{P}(0, \theta, z) \otimes \mathbf{E}(r_0, \theta, z)] e^{-j \vec{k} \bullet (z \cos n\theta)} \quad (2) \\
 \mathbf{E}(\mathbf{r}) &= \int \sum_n \left(\mathbf{A}(k_z, n) \times \frac{H_n^1(r)}{H_n^1(r_0)} \right. \\
 & \left. + \mathbf{B}(k_z, n) \times \frac{H_n^2(r)}{H_n^2(r_0)} \right) \frac{e^{jk_z \bullet \vec{r}}}{r}
 \end{aligned}$$

Note that the values in the final fields require both a summation and degenerate integral for far-field evaluation. Similar to the planar case, as r becomes large, the k and r vectors provide a significant product only when coincident, due to the function space orthogonality for a particular angle in θ . The other obvious introduction is a normalization factor for Bessel function H to resolve the

r dependence of the function. The magnitude of trigonometric functions does not vary with distance and thus does not have to be normalized to the integration surface. The cosine and sine functions are mathematically similar to the $+$ and $-$ of the conventional k -space expansions; the only difference is that the function has to be mapped to a finite number of functions in θ . Further reading on each of the geometries is available; for instance, the work by Yaghjian [8] is excellent in detailing the nuances of the measurement method.

5.4. Extrapolation Range

An extrapolation range measurement is used to very precisely determine the gain of an antenna at one orientation angle. The method measures the fields in the direction desired over an extended range from the near field to at least a reasonable far-field distance. Obviously this method is limited to antennas where this set of data can be taken with reasonably small structure—antennas typically have gains from 0 to 30 dB and frequencies above 500 MHz. The set of data from the antenna is then fitted to a polynomial, and the coefficient equivalent to the conventional power drop of distance squared is used to calculate the gain of the antenna. This method has the advantage that multipath is measured and then filtered directly by the processing. The obvious disadvantage of this method is that it requires a priori knowledge of the beam peak location if that is the direction in which accurate knowledge of gain is required. In conventional applications to general gain standards, this information is not considered to be in question, but for a generalized case this knowledge would have to be obtained by one of the other methods mentioned above.

6. OTHER REQUIREMENTS AND MEASUREMENT CRITERIA

6.1. Health Checks

All the methods described above require extensive checking during operation to obtain reasonable accuracies—margins for accurate gain measurements are small since the residual error terms, even in the best facilities, can quickly approach the system requirements. Additionally, only rarely is the measurement repeated let alone checked in an alternate facility, so the performance of the range must be carefully monitored. The result is that any range delivering data on high-performance antennas has an extensive health check capability—items regularly evaluated are the repeatability of the working standards in the range, the long-term stability of the range measurement system, the range alignment, the range multipath, range polarization purity, and system crosstalk.

6.2. Standards

Standards are needed for traceability of measurements to the engineering definitions we covered above. The most ubiquitous standard is the pyramidal horn; these antennas are widely accepted as working standards because direct gain calibration of each arbitrary antenna would require three antennas in the same frequency band and

the pyramidal horn is sufficiently accurate without direct evaluation to allow measurements to be calibrated by substitution with reasonable accuracy. Also, the gain of the horn is accurately predicted to less than 0.25 dB, often by computation, due to its excellent match and directivity. Other antennas are often used as standards of comparison but tend to be less robust in a working laboratory environment and are also difficult to model with the same confidence of accuracy. Of less concern because their error contributions are usually smaller by an order of magnitude are standards of distance, angle, frequency, and linearity. However, to accurately evaluate antenna performance parameters, these other items need to be quantified and documented. With the advent of automated network analyzers, lasers, and synthesizers, these terms should always be less than 0.1 dB.

6.3. Calibration

Range calibration is typically done by introducing one of the standards mentioned above in place of the antenna under test and comparing the measured response. In cases where the response would greatly differ between the two antennas, the one with the high power level is attenuated using a device of known loss and low mismatch, and a commercial microwave attenuator will often suffice. In some of the more complex facilities calibration will also evaluate polarization and will be required on multiple ports because of the antenna complexity. The accuracy of the calibration always is a cost driver in any measurement activity, and therefore tradeoffs must be made between accuracy and speed.

6.4. Gain by Comparison

Gain by comparison is used in all except the most exacting requirements because of the simplicity described in the standards section. Additionally, although the standard agreed to by industry for antenna gain excludes the device mismatch, it is usually embedded in the data and addressed by the device mismatch requirement for microwave measurements. Why I raise this piece of specific information is to emphasize that measured data do not typically correspond to a specific definition for a parameter—harmless approximations are frequently made, and since they do not change the uncertainty of most measurements, they are seldom mentioned in the final data. One obvious exception to this generally relaxed measurement approach is the calibration of a gain standard. When a customer requires the antenna measurement knowledge more accurately than the theoretical prediction of the gain standard, other measurement methods are applied. The best known of these is the three-antenna calibration.

6.5. Three-Antenna Measurements

In theory, three-antenna measurements only require the operator to introduce an alternate antenna at both ends of the chamber sequentially and take an additional measurement. In practice, this measurement is complicated by the source interaction with the chamber and is thus

limited to rectangular chambers. The other readily available solution is to have two nearly identical source antennas allowing one to use the second antenna as the source and also as the test antenna. The equation system is fairly simple if device mismatch is neglected:

$$\begin{aligned} P_{r1} &= P_t \frac{G_1 G_2}{4\pi r^2} \\ P_{r2} &= P_t \frac{G_3 G_2}{4\pi r^2} \\ P_{r3} &= P_t \frac{G_1 G_3}{4\pi r^2} \end{aligned} \quad (3)$$

The term P is treated as a vector of received voltage at the receive reference plane and is a vector because of the unknown polarization of the antennas tested, thus requiring two orthogonal orientations to measure the overall polarization. If this effect is neglected (which is usually possible when determining gain standards), then the antenna can be aligned for optimal delivered power and the only requirement is inversion of the set of equations, resulting in the following scalar result:

$$\begin{aligned} G_1 &= \frac{P_{r1} P_{r3} 4\pi r^2}{P_{r2} P_t} \\ G_2 &= \frac{P_{r1} P_{r2} 4\pi r^2}{P_{r3} P_t} \\ G_3 &= \frac{P_{r2} P_{r3} 4\pi r^2}{P_{r1} P_t} \end{aligned} \quad (4)$$

The result still requires knowledge of the total power transmitted, which is, of course, impacted by mismatch losses, as well as knowledge of the distance between the two antennas. When this result is combined with the extrapolation measurement mentioned above, the distance dependence of the calculation can be eliminated with the polynomial fit. The method also works best for antennas of matched polarization because of the ability to neglect the additional measurements, reducing test drift and detailed understanding of the interaction between gain and polarization. The importance of the result in Eq. (4) is that no calibrated components are required in the measurement, eliminating the need for traceability to an externally calibrated standard.

7. CONCLUSIONS

Antennas are a major component of any wireless application, including telephony, the Internet, and even many remote control systems as well as important science tools such as remote Earth sensing and radio astronomy. Since the build to tolerance of antenna patterns is always unknown through direct physical probing of the device or visual inspection, a different technology was required. As a result, a myriad of solutions have been used to gather information on the radiation characteristics of antennas. The solution can be as simple as a point-to-point connection of two antennas in the far field and as complicated as a multiport spherical near field with many options in between. The most important item in any measurement

solution is that precision (repeatability) of the measurement is significantly better than the measurement accuracy. As a result, good antenna ranges can provide reasonable error estimates for an arbitrary antenna measurement based on knowledge of the range without requiring significant modifications for the particular antenna pattern. The range design selection can then be based on the electrical/physical size of the test article, the weight of the article, the amount of data required, and the frequency to be tested. No particular range design is the best solution to all problems, but understanding how all the types work is key to making a good selection.

BIBLIOGRAPHY

1. J. Kraus and R. Marhefka, *Antennas*, McGraw-Hill, New York, 2001.
2. T. Milligan, *Modern Antenna Design*, McGraw-Hill, New York, 1985.
3. C. A. Balanis, *Antenna Theory, Analysis and Design*, Wiley, New York, 1996.
4. D. Slater, *Near-Field Antenna Measurements*, Artech House, Boston, 1991.
5. J. E. Hansen, *Spherical Near-Field Measurements*, Peter Peregrinus, London, 1988.
6. W. Stutzman and G. Thiele, *Antenna Theory and Design*, Wiley, New York, 1997.
7. *IEEE Standard Definitions of Terms for Antennas*, IEEE, 1993.
8. A. Yaghjian, *Plane-Wave Theory of Time-Domain Fields: Near-Field Scanning Applications*, Wiley-IEEE Computer Society Press, May 27, 1999.

ANTENNA THEORY

WILLIAM A. DAVIS
 WARREN L. STUTZMAN
 Virginia Tech Antenna Group
 Blacksburg, Virginia

1. INTRODUCTION

This article introduces the foundation concepts of antennas. Radiation of antennas provide the emphasis of the presentation. Methods of describing antennas include critical characteristics such as impedance, gain, beamwidth, and bandwidth. These parameters provide the primary information needed for full analysis of a communication system. To address a basic question raised by communication system designers, the fundamental limits of antennas are also presented to relate antenna size and bandwidth. The presentation is closed with a brief overview of the transient analysis of antennas as is appropriate for ultra wideband systems.

2. FUNDAMENTALS

2.1. Maxwell's Equations

Antenna properties are analyzed according to the basic laws of physics. These laws have been collected into a set of equations commonly referred to as *Maxwell's equations*. (The presentation in this section follows the textbook by Stutzman and Thiele [1] where a more detailed treat may be found.) In most antenna applications, we analyze sinusoidally varying sources in a linear environment. For such time-harmonic fields with a radian frequency of ω , the phasor form of Maxwell's equations as

$$\nabla \times \mathbf{E} = -j\omega \mathbf{B} - \mathbf{M} \quad (1)$$

$$\nabla \times \mathbf{H} = j\omega \mathbf{D} + \mathbf{J} \quad (2)$$

$$\nabla \cdot \mathbf{D} = \rho \quad (3)$$

$$\nabla \cdot \mathbf{B} = m \quad (4)$$

The quantities, \mathbf{E} , \mathbf{H} , \mathbf{D} , and \mathbf{B} , describe the physical terms of electric and magnetic field intensities and the electric and magnetic field densities, respectively. The cross and dot are the curl and divergence differential operators respectively. A supplementary equation that can be deduced from the second and third equations is

$$\nabla \cdot \mathbf{J} = -j\omega \rho \quad (5)$$

and is denoted the continuity equation to explicitly describe the electric current density \mathbf{J} in terms of the movement of volumetric electric charge, ρ . A similar relationship holds for the magnetic current density \mathbf{M} and volumetric magnetic charge m . These latter two quantities have not been identified as actual physical quantities to date, but are found to be extremely useful in analysis. In fact, the concept of magnetic current is identical to the concept of ideal voltage sources in electrical networks.

Maxwell's equations define relationships between the field quantities, but do not explicitly provide information about the media in which the fields exist. The material is usually characterized by three terms: permittivity ϵ , permeability μ , and conductivity σ . Sometimes the material conductivity is given in inverse form as the resistivity $\rho = 1/\sigma$. These terms relate the field density and intensity terms as well as the portion of the current due to conduction. Thus, we have $\mathbf{D} = \epsilon \mathbf{E}$, $\mathbf{B} = \mu \mathbf{H}$, and $\mathbf{J} = \sigma \mathbf{E}$ to give

$$\nabla \times \mathbf{E} = -j\omega \mu \mathbf{H} - \mathbf{M}_i \quad (6)$$

$$\nabla \times \mathbf{H} = (\sigma + j\omega \epsilon) \mathbf{E} + \mathbf{J}_i \quad (7)$$

$$\left(\epsilon - \frac{\sigma}{j\omega} \right) \nabla \cdot \mathbf{E} = \rho_i \quad (8)$$

$$\mu \nabla \cdot \mathbf{H} = m_i \quad (9)$$

and

$$\nabla \cdot \mathbf{J}_i = -j\omega \rho_i \quad (10)$$

where the i subscript denotes the impressed sources in the system, equivalent to the independent sources of circuit

theory. We find the medium description in the above equations limited in two ways: (1) the medium is described by scalar quantities, implying isotropic medium, and (2) the material parameters have been extracted from the derivatives, implying a constant, homogeneous medium. These simplifications are valid for antenna problems. It should be noted that Eqs. (8) and (9) can be obtained from Eqs. (7) and (6), respectively, with the appropriate continuity relations, such as Eq. (10).

If multiple frequencies are present, the solution to the equations can be found for each frequency separately and the results combined to form the total solution. A linearity restriction is used to ensure that the analysis would be properly performed for a single frequency. For nonlinear media and some complex problems, it is advantageous to solve the equivalent time-domain equations and obtain the frequency-domain fields through a Fourier (or Laplace) transform process. Computationally, the Fourier transform is usually obtained using a fast Fourier transform (FFT).

2.2. Wave Equations

In the far field of antennas, the solution of Maxwell's equations are solutions to the wave equation in source-free regions. The wave equation can be obtained by eliminating either \mathbf{E} or \mathbf{H} from Eqs. (6)–(9) with no impressed sources as

$$(k^2 + \nabla^2) \begin{Bmatrix} \mathbf{E} \\ \mathbf{H} \end{Bmatrix} = 0 \quad (11)$$

where $k = \omega \sqrt{\mu(\epsilon - \sigma/j\omega)}$. The quantity k is referred to as the *propagation constant* or *wavenumber* and can be written in terms of the phase and amplitude constants as $(\beta - j\alpha)$. In most antenna problems of interest, it is common to use β instead of k since the media is generally lossless. We will retain k for generality.

The solutions to Eq. (11) can be written in terms of either traveling or standing waves; traveling waves are more common for antenna applications. The traveling-wave solution to the electric field has a plane-wave solution form of

$$\mathbf{E}(\mathbf{r}) = \mathbf{E}_+ e^{-j\mathbf{k}\cdot\mathbf{r}} + \mathbf{E}_- e^{j\mathbf{k}\cdot\mathbf{r}} \quad (12)$$

The corresponding magnetic field is given by

$$\mathbf{H}(\mathbf{r}) = \frac{1}{\eta} \mathbf{k} \times [\mathbf{E}_+ e^{-j\mathbf{k}\cdot\mathbf{r}} - \mathbf{E}_- e^{j\mathbf{k}\cdot\mathbf{r}}], \quad \eta = \sqrt{\frac{\mu}{\left(\epsilon - \frac{\sigma}{j\omega}\right)}} \quad (13)$$

The form of Eq. (13) is called a *generalized plane wave* propagating along $\pm \mathbf{k}$ with the restriction that $\mathbf{k}\cdot\mathbf{E} = 0$, since the divergence is zero. The direct solution of the general differential forms of Maxwell's equations can be obtained analytically in special cases and numerically in most other cases. Numerical procedures typically use finite differences (FD), the finite difference-time domain (FDTD) method, or finite-element (FE) techniques [2]. The alternative is to transform the equations into integral forms for solution, where the solution structure is written

in integral form and the integral equation are used to solve for the field quantities.

2.3. Auxiliary Functions

Auxiliary functions are used to extend the solution of the wave equation beyond the simple traveling plane-wave form. If the magnetic sources are zero, then we can expand the magnetic flux density in terms of the curl of an auxiliary function, the magnetic vector potential \mathbf{A} [3], or

$$\mathbf{H} = \frac{1}{\mu} \nabla \times \mathbf{A} \quad (14)$$

The corresponding electric field intensity in simple media (using the Lorentz gauge for the potential) is given by

$$\mathbf{E} = \frac{1}{j\omega\mu\epsilon} [k^2 \mathbf{A} + \nabla \nabla \cdot \mathbf{A}] \quad (15)$$

This use of a gauge condition completes the specification of the degrees of freedom for \mathbf{A} . The magnetic-vector potential must satisfy the Helmholtz equation given by

$$(k^2 + \nabla^2) \mathbf{A} = -\mu \mathbf{J} \quad (16)$$

having a solution in free space (no boundary) of

$$\mathbf{A}(\mathbf{r}) = \mu \int_V \mathbf{J}(\mathbf{r}') \frac{e^{-jk|\mathbf{r}-\mathbf{r}'|}}{4\pi|\mathbf{r}-\mathbf{r}'|} dv \quad (17)$$

for the geometry of Fig. 1. This general form can be specialized to the far-field case for an antenna located near the origin by expanding $R = |\mathbf{r}-\mathbf{r}'|$ in a binomial series as

$$\begin{aligned} R = |\mathbf{r}-\mathbf{r}'| &= \sqrt{r^2 - 2\mathbf{r}\cdot\mathbf{r}' + r'^2} \\ &= r - \frac{\mathbf{r}\cdot\mathbf{r}'}{r} + \frac{r'^2}{2r} - \frac{(\mathbf{r}\cdot\mathbf{r}')^2}{2r^3} + \dots \end{aligned} \quad (18)$$

for r' sufficiently small. Only the first term in this expansion, r , needs to be retained for use in the denominator of Eq. (17). However, more accuracy is needed for R in the exponential to account for phase changes; so the second term of the expansion is also used in the exponential:

$$R \approx r - \hat{\mathbf{r}}\cdot\mathbf{r}' \quad (19)$$

The complete far-field approximation becomes

$$\mathbf{A}(\mathbf{r}) \approx \mu \frac{e^{-jkr}}{4\pi r} \int_V \mathbf{J}(\mathbf{r}') e^{j\mathbf{k}\cdot\mathbf{r}'} dv \quad (20)$$

which is the familiar Fourier transform representation.

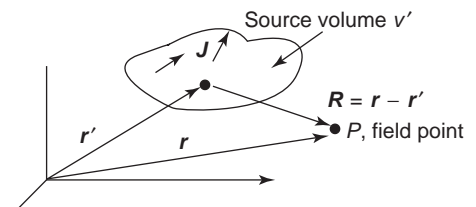


Figure 1. Coordinates and geometry for solving radiation problems.

In the far field where Eq. (20) is applicable, we may approximate the corresponding electric and magnetic fields as

$$\mathbf{E} \approx -j\omega[\mathbf{A} - \hat{\mathbf{r}}(\hat{\mathbf{r}} \cdot \mathbf{A})] \quad (21)$$

and

$$\mathbf{H} \approx \frac{k}{j\mu} [\hat{\mathbf{r}} \times \mathbf{A}] \quad (22)$$

The second term in Eq. (21) simply removes the radial portion \mathbf{A} from the electric field.

The definition of the minimum far-field distance from the source is where errors resulting in the parallel-ray approximation to the radiation become insignificant. The distance where the far field begins r_{ff} is taken to be that value of r for which the pathlength deviation due to neglecting the third term of Eq. (18) is a 16th of a wavelength. This corresponds to a phase error (by neglecting the third term) of $2\pi/\lambda \times \lambda/16 = \pi/8$ rad = 22.5° . If D is the maximum dimension of the source, r_{ff} is found to be

$$\frac{(D/2)^2}{2r_{\text{ff}}} = \frac{\lambda}{16} \quad (23)$$

Solving for r_{ff} gives

$$r_{\text{ff}} = \frac{2D^2}{\lambda} \quad (24)$$

The far-field region is $r \geq r_{\text{ff}}$ and r_{ff} is called the *far-field distance*, or *Rayleigh distance*. The far-field conditions are summarized as follows:

$$r \gg \frac{2D^2}{\lambda} \quad (25a)$$

$$r \gg D \quad (25b)$$

$$r \gg \lambda \quad (25c)$$

The condition $r \gg D$ is needed in association with the approximation $R \approx r$ the denominator of Eq. (17) for use in the magnitude dependence. The condition $r \gg \lambda$ follows from $kr = (2\pi r/\lambda) \gg 1$ which was used to reduce Eq. (15) to Eq. (21), neglecting terms that are inversely proportional to powers of kr greater than unity. Usually the far field is taken to begin at a distance given by Eq. (24), where D is the maximum dimension of the antenna. This is usually a sufficient condition for antennas operating in the UHF region and above. At lower frequencies, where the antenna can be small compared to the wavelength, the far-field distance may have to be greater than $2D^2/\lambda$ as well as D and λ in order that all conditions in Eq. (25) are satisfied.

The far-field region is historically called the *Fraunhofer region*, where rays at large distances from the transmitting antenna are parallel. In the far-field region the radiation pattern is independent of distance. For example, the $\sin \theta$ pattern of an ideal dipole is valid anywhere in its far field. The zone interior to this distance from the center of the antenna, called the *near field*, is divided into two subregions. The reactive near-field region is closest to the antenna and is that region for which the reactive field dominates over the radiative fields. This region extends to a distance $0.62\sqrt{D^3/\lambda}$ from the antenna, as long as $D \gg \lambda$. For an ideal dipole, for which $D = \Delta z \ll \lambda$, this distance is

$\lambda/2\pi$. Between the reactive near-field and far-field regions is the radiating near-field regions in which the radiation fields dominate and where the angular field distribution depends on the distance from the antenna. For an antenna focused at infinity, this region is sometimes referred to as the Fresnel region. We can summarize the field region distances for cases where $D \gg \lambda$ as follows [1]:

<u>Region</u>	<u>Distance from antenna (r)</u>	
Reactive near field	0 to $0.62\sqrt{D^3/\lambda}$	(26a)
Radiating near field	$0.62\sqrt{D^3/\lambda}$ to $2D^2/\lambda$	(26b)
Far field	$2D^2/\lambda$ to ∞	(26c)

2.4. Duality

Duality provides an extremely useful way to complete the development of the solution form as well as equating some forms of antennas. To complete the previous set of equations for the magnetic current and charge, we simply note that we can change the variable definitions to obtain an identical form of equations. Specifically, we replace

$$\mathbf{E} \rightarrow \mathbf{H} \quad (27a)$$

$$\mathbf{H} \rightarrow -\mathbf{E} \quad (27b)$$

$$\mathbf{J} \rightarrow \mathbf{M} \quad (27c)$$

$$\mathbf{A} \rightarrow \mathbf{F} \quad (27d)$$

$$\mu \rightarrow \varepsilon, \varepsilon \rightarrow \mu \quad (27e)$$

and

$$k \rightarrow k, \eta \rightarrow \frac{1}{\eta} \quad (27f)$$

The quantity \mathbf{F} is the electric vector potential for \mathbf{M} , analogous to the magnetic vector potential for \mathbf{J} . The solution forms for \mathbf{J} and \mathbf{M} can be combined for the total solution as

$$\mathbf{E} = \frac{1}{j\omega\mu\varepsilon} [k^2\mathbf{A} + \nabla\nabla \cdot \mathbf{A}] - \varepsilon\nabla \times \mathbf{F} \quad (28a)$$

and

$$\mathbf{H} = \frac{1}{j\omega\mu\varepsilon} [k^2\mathbf{F} + \nabla\nabla \cdot \mathbf{F}] + \mu\nabla \times \mathbf{A} \quad (28b)$$

The alternate use of duality is to equate similar dual problems numerically. A classic problem is the relationship between the input impedance of a slot dipole and strip dipole. The two structures are complements within the plane and have input impedances that satisfy

$$Z_{\text{slot}}Z_{\text{strip}} = \frac{\eta^2}{4} = \frac{\mu}{4\varepsilon} \quad (29)$$

This relationship incorporates several equivalencies, but most importantly the electric and magnetic quantities are scaled appropriately by η to preserve the proper units in the dual relationship. For a $72\text{-}\Omega$ strip dipole, we find the complementary slot dipole has an input

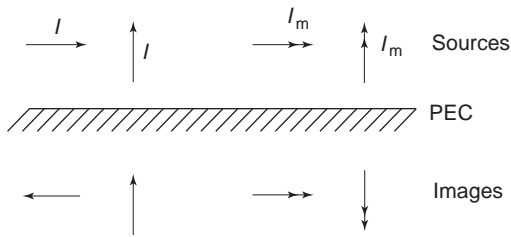


Figure 2. Images of electric (I) and magnetic (I_m) elemental currents over a perfect electric ground plane.

impedance of $Z_{\text{slot}} = 493.5 \Omega$. Self-complementary planar antennas such as spirals have an input impedance of 188.5Ω .

2.5. Images

Many antennas are constructed above a large metallic structure referred to as a *ground plane*. As long as the structure is greater than a half-wavelength in radius, the finite plane can be modeled as an infinite structure for all but radiation behind the plane. The advantage of the infinite structure that is a perfect electric conductor (PEC) is that the planar sheet can be replaced by the images of the antenna elements in the plane. For the PEC, the images are constructed to provide a zero, tangential electric field at the plane. Figure 2 shows the equivalent current structure for the original and the image problems.

It is common to feed antennas at the ground plane through a coaxial cable. If the ground is a good conductor, planar, and very large in extent, it approximates a perfect, infinite, ground plane. Then the equivalent voltage for the imaged problem is twice that of the source above the ground plane. The vertical electric current in Fig. 2 fed at the ground plane is called a monopole; it together with its image form a dipole and

$$Z_{\text{monopole}} = \frac{1}{2} Z_{\text{dipole}} \quad (30)$$

Since the corresponding field is radiated into only a half-space, the directivity of the antenna defined as the peak power density in the far field compared to the average power density over a sphere is double for the ground-plane-fed antenna as

$$D_{\text{monopole}} = 2 D_{\text{dipole}} \quad (31)$$

3. ANTENNA CHARACTERISTICS

There are a number of characteristics used to describe an antenna as a device. Characteristics such as impedance and gain are common to any electrical device. On the other hand, a property such as radiation pattern is unique to the antenna. In this section we discuss patterns and impedance. Gain is discussed in the following section. We begin with a discussion of reciprocity.

3.1. Reciprocity

Reciprocity plays an important role in antenna theory and can be used to great advantage in calculations and mea-

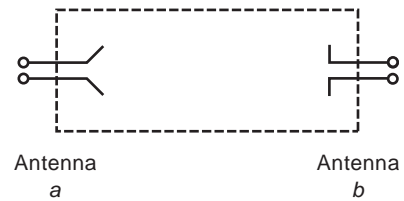


Figure 3. Two-port device representation for coupling between antennas.

surements. Fortunately, antennas usually behave as reciprocal devices. This permits characterization of the antenna as either a transmitting or receiving antenna. For example, radiation patterns are often measured with the test antenna operating in the receive mode. If the antenna is reciprocal, the measured pattern is identical when the antenna is in either a transmit or a receive mode. In fact, the following general statement applies: If nonreciprocal materials are not present in an antenna, its transmitting and receiving properties are identical. A case where reciprocity may not hold is when a ferrite material or active devices are included as a part of the antenna.

Reciprocity is also helpful when examining the terminal behavior of antennas. Consider two antennas, a and b shown in Fig. 3. Although connected through the intervening medium and not by a direct connection path, we can view this as a two-port network. For an antenna system, a property of reciprocity is the equality of the mutual impedances:

$$Z_{ab} = Z_{ba} \text{ for reciprocal antennas} \quad (32)$$

If one antenna is rotated around the other, the output voltage as a function of rotation angle becomes the radiation pattern. Since the coupling mechanism is via mutual impedances Z_{ab} and Z_{ba} , they must correspond to the radiation patterns. For example, if antenna b is rotated in the plane of Fig. 3, the pattern in that plane is proportional to the output of a receiver connected to antenna b due to a source of constant power attached to antenna a . For reciprocal antennas, Eq. (32) implies the transmitting and receiving patterns for the rotated antenna are the same.

Reciprocity can be stated in integral form by cross-multiplying Maxwell's equations by the opposite field for two separate problems, integrating and combining, and taking the resultant enclosing surface to infinity to obtain [4]

$$\int_V [(\mathbf{J}_a \cdot \mathbf{E}_b - \mathbf{M}_a \cdot \mathbf{H}_b)] dv = \int_V [(\mathbf{J}_b \cdot \mathbf{E}_a - \mathbf{M}_b \cdot \mathbf{H}_a)] dv \quad (33)$$

This form will be used in the next section to develop a formula for antenna impedance.

3.2. Antenna Impedance

Reciprocity can be used to obtain the basic formula for the input impedance of an antenna. If we define the two systems (a and b) for Eq. (33) as (a) the antenna current distribution in the presence of the antenna structure and (b) the same antenna current in free space ($\mathbf{J}_a = \mathbf{J}_b = \mathbf{J}$),

then we can apply Eq. (33) to obtain

$$\int_V (\mathbf{J} \cdot \mathbf{E}_b) dv = \int_V (\mathbf{J} \cdot \mathbf{E}_a) dv = -IV_a \quad (34)$$

Since $V_a = IZ$,

$$Z = -\frac{1}{I^2} \int_V (\mathbf{J} \cdot \mathbf{E}_b) dv \quad (35)$$

Thus, if the current distribution on the antenna is known, or can be estimated, then (35) simply provides a means for computing the antenna impedance Z by integrating the near field radiated by the antenna current in free space times the current distribution itself. A common approach to this computation results in the induced EMF method [5] for determining the input impedance to an antenna. The radiation resistance can be estimated using conservation of energy.

3.3. Radiation Patterns

The radiation pattern of an antenna is the angular variation of the radiation level around the antenna. This is perhaps the most important characteristic of an antenna. In this section we present definitions associated with patterns and develop the general procedures for calculating radiation patterns.

3.3.1. Radiation Pattern Basics. A radiation pattern (or, antenna pattern) is a graphical representation of the radiation (far-field) properties of an antenna. The radiation fields from a transmitting antenna vary inversely with distance (e.g., $1/r$). The variation with observation angles (θ, ϕ), however, depends on the antenna.

Radiation patterns in general can be calculated in a manner similar to that used for the ideal dipole if the current distribution on the antenna is known. This calculation is performed by first finding the vector potential using Eq. (20). As a simple example consider a filament of current along the z axis and located near the origin. Many antennas can be modeled by this line source; straight-wire antennas are good examples. In this case the vector potential has only a z component and the vector potential integral is one-dimensional:

$$A_z = \mu \frac{e^{-j\beta r}}{4\pi r} \int_z I(z') e^{j\beta z' \hat{\mathbf{z}} \cdot \hat{\mathbf{r}}} dz' \quad (36)$$

where β has been used for typical radiation media. Because of the symmetry of the source, we expect that the radiation fields will not vary with ϕ . This lack of variation is because as the observer moves around the source, such that ρ and z are constant, the appearance of the source remains the same; thus, its radiation fields are also unchanged. Therefore, for simplicity we will confine the observation point to a fixed ϕ in the xy plane ($\phi = 90^\circ$) as shown in Fig. 5. Then from Fig. 5 we see that

$$\rho^2 = x^2 + y^2 \quad (37)$$

$$z = \rho \cos \theta \quad (38)$$

$$y = \rho \sin \theta \quad (39)$$

Applying the general geometry of Fig. 1 to this case, $\mathbf{r} = y\hat{\mathbf{y}} + z\hat{\mathbf{z}}$ and $\mathbf{r}' = z'\hat{\mathbf{z}}$ lead to $\mathbf{R} = \mathbf{r} - \mathbf{r}' = y\hat{\mathbf{y}} + (z - z')\hat{\mathbf{z}}$ and

$$R = \sqrt{y^2 + (z - z')^2} = \sqrt{y^2 + z^2 - 2zz' + (z')^2} \approx r - z' \cos \theta \quad (40)$$

in the far field. This expression for R is used in the radiation integral of Eq. (36) to different degrees of approximation. In the denominator (which affects only the amplitude) we let

$$R \approx r \quad (41)$$

We can do this because in the far field r is very large compared to the antenna size, so $r \gg z' \geq z' \cos \theta$. In the phase term, we must be more accurate when computing the distance from points along the line source to the observation point and use both terms in Eq. (40). Using this far-field approximation in Eq. (36) yields

$$A_z = \mu \int I(z') \frac{e^{-j\beta(r-z' \cos \theta)}}{4\pi r} dz' = \mu \frac{e^{-j\beta r}}{4\pi r} \int I(z') e^{j\beta z' \cos \theta} dz' \quad (42)$$

where the integral is over the extent of the line source.

The electric field is found from Eq. (21), which is

$$\mathbf{E} \approx -j\omega [\mathbf{A} - \hat{\mathbf{r}}(\hat{\mathbf{r}} \cdot \mathbf{A})] = -j\omega A_\theta \hat{\boldsymbol{\Theta}} = j\omega \sin \theta A_z \hat{\boldsymbol{\Theta}} \quad (43)$$

Note that this result yields the components of \mathbf{A} that are perpendicular to $\hat{\mathbf{r}}$. This form is an important general result for z -directed sources that is not restricted to line sources.

The radiation fields from a z -directed line source (any z -directed current source in general) are E_θ and H_ϕ , and are found from Eqs. (21) and (22). The only remaining problem is to calculate A_z , which is given by Eq. (20) in general and by Eq. (42) for z -directed line sources. Calculation of A_z is the focus of linear antenna analysis. We will return to this topic after pausing to further examine the characteristics of the far-field region.

The ratio of the radiation field components as given by Eqs. (21) and (22) yields

$$E_\theta = \frac{\omega\mu}{\beta} H_\phi = \eta H_\phi \quad (44)$$

where $\eta = \sqrt{\mu/\epsilon}$ is the intrinsic impedance of the medium, 377Ω in a vacuum. An interesting conclusion can be made at this point. The radiation fields are perpendicular to each other and to the direction of propagation $\hat{\mathbf{r}}$, and their magnitudes are related in general by η .

These are the familiar properties of a plane wave. They also hold for the general form of a transverse electromagnetic (TEM) wave, which has both the electric and magnetic fields transverse to the direction of propagation. Radiation from a finite antenna is a special case of a TEM wave, called a *spherical wave*, which propagates radially outward from the antenna and the radiation fields have no radial components. Spherical-wave behavior is also characterized by the $e^{-j\beta r}/4\pi r$ factor in the field expressions; see Eq. (42). The $e^{-j\beta r}$ phase factor indicates a traveling wave propagating radially outward from the

origin and the $1/r$ magnitude dependence leads to constant power flow just as with the infinitesimal dipole. In fact, the radiation fields of all antennas of finite extent display this dependence with distance from the antenna.

Radiation patterns can be understood by examining the ideal dipole. The fields radiated from an ideal dipole are shown in Fig. 4a over the surface of a sphere of radius r that is in the far field. The length and orientation of the field vectors follow from Eq. (43); they are shown for an instant of time for which the fields are peak. The angular variation of E_θ and H_ϕ over the sphere is $\sin \theta$. An electric field probe antenna moved over the sphere surface and oriented parallel to E_θ will have an output proportional to $\sin \theta$ (see Fig. 4b). Any plane containing the z axis has the same radiation pattern since there is no ϕ variation in the fields. A pattern taken in one of these planes is called an *E-plane pattern* because it contains the electric vector. A pattern taken in a plane perpendicular to an *E-plane* and cutting through the test antenna (the xy plane in the dipole case) is called an *H-plane pattern* because it contains the

magnetic field H_ϕ . The *E-* and *H-plane* patterns, in general, are referred to as *principal plane patterns*. The *E-* and *H-plane* patterns for the ideal dipole are shown in Figs. 4b and 4c. These are polar plots in which the distance from the origin to the curve is proportional to the field intensity; they are often called polar patterns or polar diagrams.

The complete pattern for the ideal dipole is shown in isometric view with a slice removed in Fig. 4d. This solid polar radiation pattern resembles a doughnut with no hole. It is referred to as an *omnidirectional pattern* since it is uniform in the xy plane. Omnidirectional antennas are very popular in ground-based applications with the omnidirectional plane horizontal. When encountering new antennas, one should attempt to visualize the complete pattern in three dimensions.

Another way to view radiation field behavior is to note that spherical waves appear to an observer in the far field to be a plane wave. This “local plane-wave behavior” occurs because the radius of curvature of the spherical wave is so large that the phase front is nearly planar over

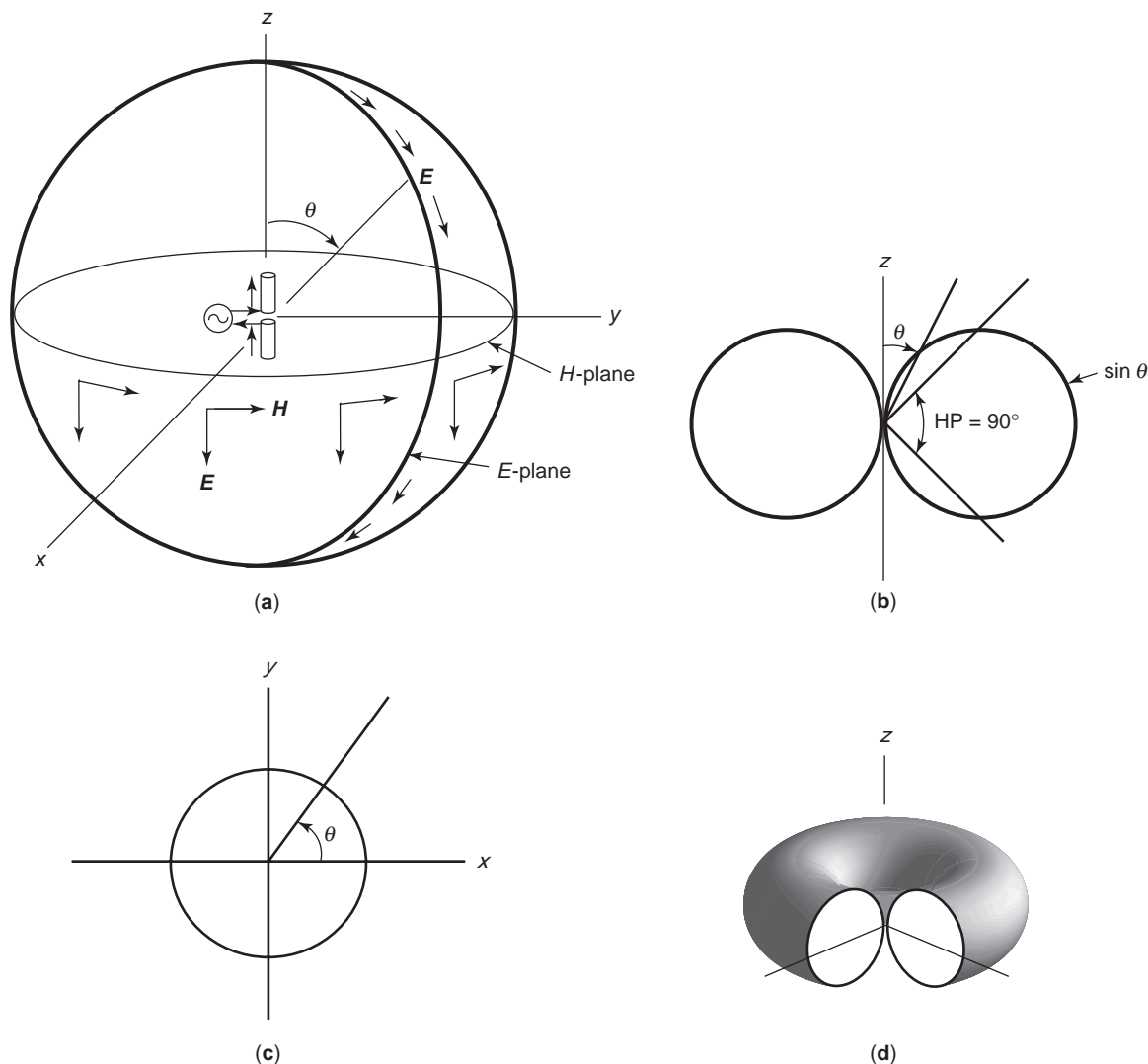


Figure 4. Radiation from an ideal dipole: (a) field components; (b) *E*-plane radiation pattern polar plot; (c) *H*-plane radiation pattern polar plot; (d) three-dimensional pattern plot. From [1]

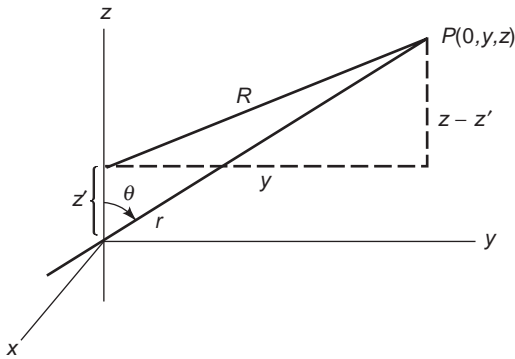


Figure 5. Geometry used for field calculations of a line source along the z axis.

a local region. If parallel lines (or rays) are drawn from each point in current distribution as shown in Fig. 6, the distance R to the far field is geometrically related to r by Eq. (19), which was derived by neglecting high-order terms in the expression for R in Eq. (18). The parallel-ray assumption is exact only when the observation point is at infinity, but it is a good approximation in the far field. Radiation calculations often start by assuming parallel rays and then determining R for the phase by geometrical techniques. From the general source shown in Fig. 6, we see that

$$R = r - r' \cos \alpha \quad (45)$$

Using the definition of dot product, we again have Eq. (19):

$$R = r - \hat{\mathbf{r}} \cdot \mathbf{r}' \quad (46)$$

This form is the same general approximation to R for the phase factor in the radiation integral for the general case previously developed. Notice that if $\mathbf{r}' = z' \hat{\mathbf{z}}$, as for line sources along the z axis, (46) reduces to (40).

3.3.2. Steps in the Evaluation of Radiation Fields. The derivation for the fields radiated by a line source can be generalized for application to any antenna. The analysis of

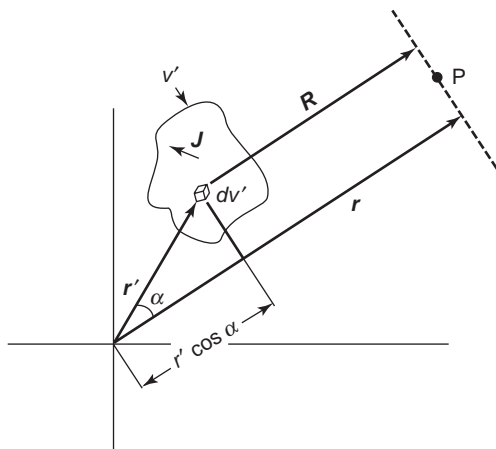


Figure 6. Parallel-ray approximation for far-field calculations of radiation from a general source.

the line source, and its generalizations, can be reduced to the following three-step procedure:

1. Find \mathbf{A} . Select a coordinate system most compatible with the geometry of the antenna, using the notation of Fig. 1. In general, use Eq. (17) with r in the magnitude factor and the parallel-ray approximation of Eq. (46) for determining phase differences over the antenna. These yield

$$\mathbf{A} = \mu \frac{e^{-j\beta r}}{4\pi r} \int_V \mathbf{J} e^{j\beta \hat{\mathbf{r}} \cdot \mathbf{r}'} dv' \quad (47)$$

For z -directed line sources on the z axis

$$\mathbf{A} = \hat{\mathbf{z}} \mu \frac{e^{-j\beta r}}{4\pi r} \int_z I(z') e^{j\beta z' \cos \theta} dz' \quad (48)$$

which is Eq. (42).

2. Find \mathbf{E} . In general, use the component of

$$\mathbf{E} = -j\omega \mathbf{A}_t \quad (49)$$

(where the “ t ” subscript denotes transverse to $\hat{\mathbf{r}}$). This result is expressed formally as

$$\mathbf{E} = -j\omega \mathbf{A} + j\omega (\hat{\mathbf{r}} \cdot \mathbf{A}) \hat{\mathbf{r}} = -j\omega (A_\theta \hat{\Theta} + A_\phi \hat{\Phi}) \quad (50)$$

which arises from the component of \mathbf{A} tangent to the far-field sphere. For z -directed sources, this form becomes

$$\mathbf{E} = j\omega A_z \sin \theta \hat{\Theta} \quad (51)$$

which is Eq. (43).

3. Find \mathbf{H} . In general, use the plane-wave relation

$$\mathbf{H} = \frac{1}{\eta} \hat{\mathbf{r}} \times \mathbf{E} \quad (52)$$

This equation expresses the fact that in the far field the directions of \mathbf{E} and \mathbf{H} are perpendicular to each other and to the direction of propagation, and also that their magnitudes are related by η . For z -directed sources

$$H_\phi = \frac{E_\theta}{\eta} \quad (53)$$

which is Eq. (44).

The most difficult step is the first, evaluating the radiation integral. This topic will be discussed many times throughout this encyclopedia, but to immediately develop an appreciation for the process, we will present an example. This uniform line source example will also serve to provide a specific setting for introducing general radiation pattern concepts and definitions.

3.3.3. Example: The Uniform Line Source. The uniform line source is a line source for which the current is constant along its extent. If we use a z -directed uniform line source centered on the origin and along the z axis, the current is

$$I(z') = \begin{cases} I_0 & x' = 0, y' = 0, |z'| \leq \frac{L}{2} \\ 0 & \text{elsewhere} \end{cases} \quad (54)$$

where L is the length of the line source (see Fig. 5). We first find A_z from Eq. (48) as follows:

$$A_z = \mu \frac{e^{-j\beta r}}{4\pi r} \int_{-L/2}^{L/2} I_0 e^{j\beta z' \cos \theta} dz' \tag{55}$$

$$= \mu \frac{e^{-j\beta r}}{4\pi r} I_0 L \frac{\sin [(\beta L/2) \cos \theta]}{(\beta L/2) \cos \theta}$$

The electric field from (51) is then

$$\mathbf{E} = j\omega A_z \sin \theta \hat{\Theta} = j\omega \mu I_0 L \frac{e^{-j\beta r}}{4\pi r} \sin \theta \frac{\sin [(\beta L/2) \cos \theta]}{(\beta L/2) \cos \theta} \hat{\Theta} \tag{56}$$

The magnetic field is simply found from this result using $H_\phi = \mathbf{E}_\theta / \eta$.

3.3.4. Radiation Pattern Definitions. Since the radiation pattern is the variation over a sphere centered on the antenna, r is constant and we have only θ and ϕ variations of the field. It is convenient to normalize the field expression such that its maximum value is unity. This is accomplished as follows for a z -directed source that has only a θ component of \mathbf{E}

$$F(\theta, \phi) = \frac{E_\theta}{E_\theta(\max)} \tag{57}$$

where $F(\theta, \phi)$ is the normalized field pattern and $E_\theta(\max)$ is the maximum value of the magnitude of E_θ over a sphere of radius r .

In general, E_θ can be complex-valued and, therefore, so can $F(\theta, \phi)$. In this case the phase is usually set to zero at the same point that the magnitude is normalized to unity. This is appropriate since we are interested only in relative phase behavior. This variation is, of course, independent of r .

As an example, an element of current on the z axis has a normalized field pattern of

$$F(\theta) = \frac{(I\Delta z/4\pi)j\omega\mu(e^{-j\beta r}/r)\sin\theta}{(I\Delta z/4\pi)j\omega\mu(e^{-j\beta r}/r)} = \sin\theta \tag{58}$$

and there is no ϕ variation.

The normalized field pattern for the uniform line source is from Eq. (56)

$$F(\theta) = \sin\theta \frac{\sin [(\beta L/2) \cos \theta]}{(\beta L/2) \cos \theta} \tag{59}$$

and again there is no ϕ variation. The second factor of this expression is the function $\sin(u)/u$, and we will encounter it frequently. It has a maximum value of unity at $u=0$; this corresponds to $\theta=90^\circ$, where $u=(\beta L/2)\cos\theta$. Substituting $\theta=90^\circ$ in Eq. (59) gives unity, and we see that $F(\theta)$ is properly normalized.

In general, a normalized field pattern can be written as the product

$$F(\theta, \phi) = g(\theta, \phi) f(\theta, \phi) \tag{60}$$

where $g(\theta, \phi)$ is the element factor and $f(\theta, \phi)$ is the pattern factor. The pattern factor comes from the integral over the current and is due only to the distribution of current in space. The element factor is the pattern of an infinitesimal

current element in the current distribution as in Eq. (58). For example, for a z -directed current element the total pattern is given by the element factor

$$F(\theta) = g(\theta) = \sin\theta \tag{61}$$

Actually this factor originates from Eq. (43) and can be interpreted as the projection of the current element in the θ direction. In other words, at $\theta=90^\circ$ we see the maximum length of the current, whereas at $\theta=0^\circ$ or 180° we see the end view of an infinitesimal current that yields no radiation. The $\sin\theta$ factor expresses the fraction of the size of the current as seen from the observation angle θ . On the other hand, the pattern factor $f(\theta, \phi)$ represents the integrated effect of radiation contributions from the current distribution, which can be treated as being made up of many current elements. The pattern value in a specific direction is then found by summing the parallel rays from each current element to the far field with the magnitude and phase of each included. The radiation integral of Eq. (47) sums the far-field contributions from the current elements and, when normalized, yields the pattern factor.

Antenna analysis is usually easier to understand by considering the antenna to be transmitting as we have here. However, most antennas are reciprocal and thus their radiation properties are identical when used for reception, as discussed in Section 3.1.

For the z -directed uniform line-source pattern (59), we identify the factors as

$$g(\theta) = \sin\theta \tag{62}$$

and

$$f(\theta) = \frac{\sin [(\beta L/2) \cos \theta]}{(\beta L/2) \cos \theta} \tag{63}$$

For long line sources ($L \gg \lambda$) the pattern factor of Eq. (63) is much sharper than the element factor $\sin\theta$, and the total pattern is approximately that of Eq. (63), that is, $F(\theta) \approx f(\theta)$. Hence, in many cases we need work only with $f(\theta)$, which is obtained from Eq. (48). If we allow the beam as in Fig. 7 to be scanned, the element factor

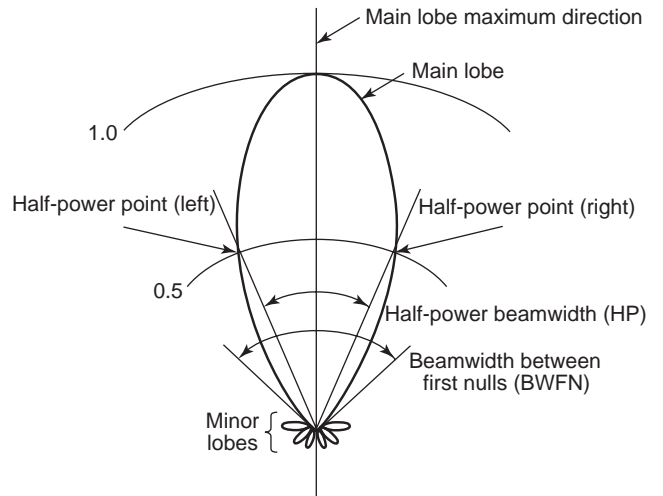


Figure 7. A typical power pattern polar plot. From [1].

becomes important as the pattern maximum approaches the z axis.

This concept of element and pattern factors can also be extended to arrays. If we consider an array to be made of a collection of identical elements with input currents of I_n , we can write the vector potential as

$$\begin{aligned} \mathbf{A} &= \mu \frac{e^{-j\beta r}}{4\pi r} \int_V \mathbf{J} e^{j\beta \hat{\mathbf{r}} \cdot \mathbf{r}'} dv' \\ &= \sum_n I_n \mu \frac{e^{-j\beta r}}{4\pi r} \int_V \mathbf{J}_0(\mathbf{r}' - \mathbf{r}_n) e^{j\beta \hat{\mathbf{r}} \cdot \mathbf{r}'} dv' \\ &= \sum_n I_n e^{j\beta \hat{\mathbf{r}} \cdot \mathbf{r}_n} \left[\mu \frac{e^{-j\beta r}}{4\pi r} \int_V \mathbf{J}_0(\mathbf{r}') e^{j\beta \hat{\mathbf{r}} \cdot \mathbf{r}'} dv' \right] \\ &= \mathbf{A}_0(\mathbf{r}) \sum_n I_n e^{j\beta \hat{\mathbf{r}} \cdot \mathbf{r}_n} = \mathbf{A}_0(\mathbf{r}) AF \end{aligned} \quad (64)$$

Expanding this result to the electric field and then to pattern, we have

$$\mathbf{F}(\theta, \phi) = g_a(\theta, \phi) f(\theta, \phi) \quad (65)$$

where g_a represents the *element pattern* of the basic array element and f represents AF which is called the *array factor*. The array factor includes the phasing effects between the elements. For a large array, the array factor dominates the far-field pattern of the array.

Frequently the directional properties of the radiation from an antenna are described by another form of radiation pattern, the power pattern. The power pattern gives angular dependence of the power density and is found from the θ, ϕ variation of the r component of the Poynting vector [1]. For z -directed sources $H_\phi = E_\theta/\eta$ so the r component of the Poynting vector is $\frac{1}{2} E_\theta H_\phi = |E_\theta|^2/(2\eta)$ and the normalized power pattern is simply the square of its field pattern magnitude $P(\theta) = |F(\theta)|^2$. The general normalized power pattern is

$$P(\theta, \phi) = |F(\theta, \phi)|^2 \quad (66)$$

The normalized power pattern for a z -directed current element is

$$P(\theta, \phi) = \sin^2 \theta \quad (67)$$

and for a z -directed uniform line source is

$$P(\theta) = \left\{ \sin \theta \frac{\sin[(\beta L/2) \cos \theta]}{(\beta L/2) \cos \theta} \right\}^2 \quad (68)$$

Frequently patterns are plotted in decibels. It is important to recognize that the field (magnitude) pattern and power pattern are the same in decibels. This follows directly from the definitions. For the field intensity in decibels

$$|F(\theta, \phi)|_{\text{dB}} = 20 \log |F(\theta, \phi)| \quad (69)$$

and for power in decibels

$$\begin{aligned} P(\theta, \phi)_{\text{dB}} &= 10 \log P(\theta, \phi) = 10 \log |F(\theta, \phi)|^2 \\ &= 20 \log |F(\theta, \phi)| \end{aligned} \quad (70)$$

and we see that

$$P(\theta, \phi)_{\text{dB}} = |F(\theta, \phi)|_{\text{dB}} \quad (71)$$

3.3.5. Radiation Pattern Parameters. A typical antenna power pattern is shown in Fig. 7 as a polar plot in linear units (rather than decibels). It consists of several lobes. The *main lobe* (or *main beam* or *major lobe*) is the lobe containing the direction of maximum radiation. The direction of the main lobe is often referred to as the *boresight direction*. There is also usually a series of lobes smaller than the main lobe. Any lobe other than the main lobe is called a *minor lobe*. Minor lobes are composed of side lobes and back lobes. Back lobes are directly opposite the main lobe, or sometimes they are taken to be the lobes in the half-space opposite the main lobe. The term *side lobe* is sometimes reserved for those minor lobes near the main lobe, but is most often taken to be synonymous with *minor lobe*; we will use the latter convention.

The radiation from an antenna is represented mathematically through the radiation pattern function $F(\theta, \phi)$ for the field and $P(\theta, \phi)$ for power. This angular distribution of radiation is visualized through various graphical representations of the pattern, which we discuss in this section. Graphical representations also are used to introduce definitions of pattern parameters that are commonly used to quantify radiation pattern characteristics.

A three-dimensional plot as in Fig. 4d gives a good overall impression of the entire radiation pattern, but cannot convey accurate quantitative information. Cuts through this pattern in various planes are the most popular pattern plots. They usually include the E - and H -plane patterns; see Figs. 4b and 4c. Pattern cuts are often given various fixed ϕ values, leaving the pattern a function of θ alone; we will assume that is the case here. Typically the sidelobes are alternately positive- and negative-valued. In fact, a pattern in its most general form may be complex-valued. Then we use the magnitude of the field pattern $|F(\theta)|$ or the power pattern $P(\theta)$.

A measure of how well the power is concentrated into the mainlobe is the (relative) sidelobe level, which is the ratio of the pattern value of a sidelobe peak to the pattern value of the mainlobe. The largest sidelobe level for the whole pattern is the maximum (relative) sidelobe level, frequently abbreviated as SLL. In decibels it is given by

$$\text{SLL} = 20 \log \left| \frac{F(\text{SLL})}{F(\text{max})} \right| \quad (72)$$

where $|F(\text{max})|$ is the maximum value of the pattern magnitude and $|F(\text{SLL})|$ is the pattern value of the maximum of the highest sidelobe magnitude. For a normalized pattern, $F(\text{max}) = 1$.

The width of the main beam is quantified through the half-power beamwidth (HPBW), which is the angular separation of the points where the mainbeam of the power pattern equals one-half the maximum value

$$\text{HPBW} = |\theta_{\text{HPleft}} - \theta_{\text{HPright}}| \quad (73)$$

where $\theta_{\text{HPBW, left}}$ and $\theta_{\text{HPBW, right}}$ are points to the "left" and "right" of the main beam maximum for which the

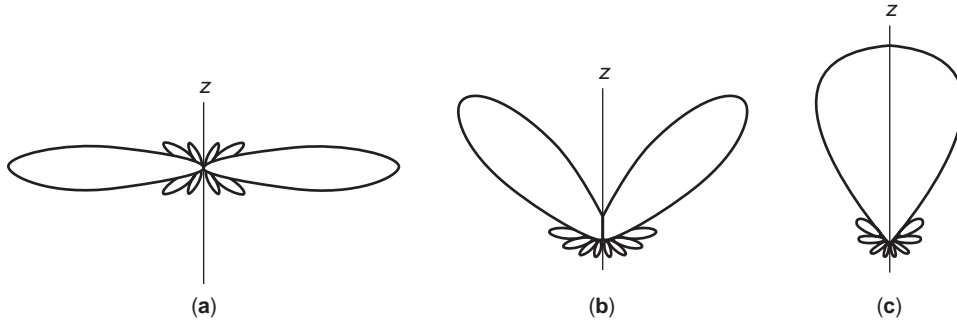


Figure 8. Polar plots of uniform line source patterns: (a) broadside; (b) intermediate; (c) endfire.

normalized power pattern has a value of one-half (see Fig. 8). On the field pattern $|F(\theta)|$ these points correspond to the value $1/\sqrt{2}$. For example, the $\sin \theta$ pattern of an ideal dipole has a value of $1/\sqrt{2}$ for θ values of $\theta_{\text{HPBW, left}} = 135^\circ$ and $\theta_{\text{HPBW, right}} = 45^\circ$. Then $\text{HPBW} = |135^\circ - 45^\circ| = 90^\circ$. This is shown in Fig. 4b. Note that the definition of HPBW is the magnitude of the difference of the half-power points and the assignment of left and right can be interchanged without changing HPBW. In three dimensions the radiation pattern major lobe becomes a solid object and the half-power contour is a continuous curve. If this curve is essentially elliptical, the pattern cuts that contain the major and minor axes of the ellipse determine what the Institute of Electrical and Electronic Engineers (IEEE) defines as the principal half-power beamwidths.

Antennas are often referred to by the type of pattern they produce. An isotropic antenna, which is hypothetical, radiates equally in all directions, giving a constant radiation pattern. An omnidirectional antenna produces a pattern that is constant in one plane; the ideal dipole of Fig. 4 is an example. The pattern shape resembles a doughnut. We often refer to antennas as being broadside or endfire. A broadside antenna is one for which the mainbeam maximum is in a direction normal to the plane containing the antenna. An endfire antenna is one for which the mainbeam is in the plane containing the antenna. For a linear current on the z axis, the broadside direction is $\theta = 90^\circ$ and the endfire directions are 0° and 180° . For example, an ideal dipole is a broadside antenna. For z -directed line sources several patterns are possible. Figure 8 illustrates a few $|f(\theta)|$ patterns. The entire pattern (in three dimensions) is imagined by rotating the pattern about the z axis. The full pattern can then be generated from the E -plane patterns shown. The broadside pattern of Fig. 8a is called the *fan beam*. The full three-dimensional endfire pattern for Fig. 8c has a single lobe in the endfire direction. This single lobe is referred to as a *pencil beam*. Note that the $\sin \theta$ element factor, which must multiply these patterns to obtain the total pattern, will have a significant effect on the endfire pattern.

4. ANTENNA PERFORMANCE MEASURES

Antennas are devices that are used in systems for communications or sensing. There are many parameters used to quantify the performance of the antenna as a device, which in turn impacts on system performance. In this

section we consider the most important of these parameters when they are employed in their primary application area of communication links, such as the simple communication link shown in Fig. 9. We first discuss the basic properties of a receiving antenna. The receiving antenna with impedance Z_A and terminated in load impedance Z_L is modeled as shown in Fig. 10. The total power incident on the receiving antenna is found by summing up the incident power density over the area of the receive antenna, called *effective aperture*. How an antenna converts this incident power into available power at its terminals depends on the type of antenna used, its pointing direction, and polarization. In this section we discuss the basic relationships for power calculations and illustrate their use in communication links.

4.1. Directivity and Gain

For system calculations it is usually easier to work with directivity rather than its equivalent, maximum effective aperture. The maximum effective aperture of an antenna is related to the effective length of the antenna. Using reciprocity, it can be shown that the effective length is given by

$$\mathbf{h}(\theta, \phi) = \left[\frac{\mathbf{E}(\theta, \phi)}{j\omega\mu I_{\text{in}} \frac{e^{-jkr}}{4\pi r}} \right]^* = \left[\frac{1}{I_{\text{in}}} \int_V \mathbf{J} e^{j\beta\hat{\mathbf{r}} \cdot \mathbf{r}'} dv' \right]^* \quad (74)$$

with the corresponding open-circuit voltage given as

$$V_{\text{oc}} = \mathbf{h}^*(\theta, \phi) \cdot \mathbf{E}^i(\theta, \phi) \quad (75)$$

The power available from the antenna is realized when the antenna is terminated in a conjugately matched impedance of $Z_L = R_r - jX_A$ assuming $R_{\text{ohmic}} = 0$. The maximum available power is then

$$P_{\text{Am}} = \frac{1}{8} \frac{|V_{\text{oc}}|^2}{R_{\text{rad}}} = \frac{1}{8} \frac{|\mathbf{h}^*(\theta, \phi) \cdot \mathbf{E}^i(\theta, \phi)|^2}{R_{\text{rad}}} = \frac{1}{8} \frac{|\mathbf{h}|^2 |\mathbf{E}^i|^2}{R_{\text{rad}}} p \quad (76)$$

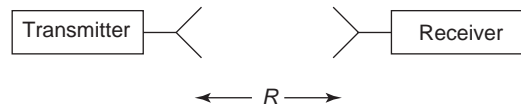


Figure 9. A communication link.

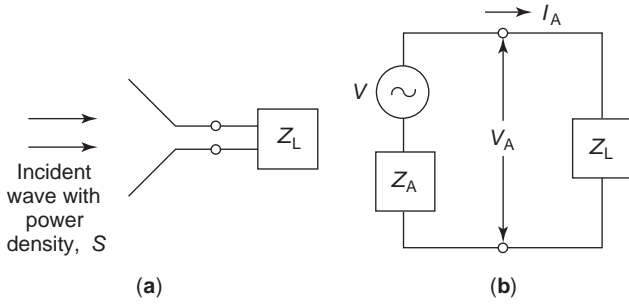


Figure 10. Equivalent circuit for a receiving antenna: (a) receive antenna connected to a receiver with load impedance Z_L ; (b) equivalent circuit.

where p is the polarization factor

$$p(\theta, \phi) = \frac{|\hat{h}^* \cdot \bar{\mathbf{E}}_{\text{inc}}|^2}{|\hat{h}^*|^2 |\bar{\mathbf{E}}_{\text{inc}}|^2} \quad (77)$$

The quantity represents the fractional power received compared to the total possible received power under perfect polarization match conditions. It is also called polarization efficiency and varies from 0 to 1.

The available power can also be calculated by examining the incident wave. The power density, Poynting vector magnitude, in the incoming wave is

$$S = \frac{1}{2} |\mathbf{E} \times \mathbf{H}^*| = \frac{1}{2} \frac{|\mathbf{E}^i|^2}{\eta} \quad (78)$$

with $\eta \approx 120\pi$ in a vacuum. The available power is found using the maximum effective aperture A_{em} , which is the collecting area of the antenna. The receiving antenna collects power from the incident wave in proportion to its maximum effective aperture

$$P_{\text{Am}} = S A_{\text{em}} p \quad (79)$$

and using Eq. (74) for the effective length, we have

$$A_{\text{em}} = \frac{\eta |\mathbf{h}_{\text{max}}|^2}{4R_{\text{rad}}} = \frac{\eta |\mathbf{E}_{\text{max}}|^2}{4R_{\text{rad}} |\omega \mu I_{\text{in}} \frac{e^{-jkr}}{4\pi r}|^2} = \frac{\eta^2 S_{\text{max}}}{(\omega \mu)^2 \frac{P_{\text{rad}}}{\pi} \frac{1}{4\pi r^2}} = \frac{\lambda^2}{4\pi} D \quad (80)$$

where the radiated power is given in terms of the input current and radiation resistance. The factor D in Eq. (80) is directivity defined as the ratio of the maximum radiated power density to the total radiated power defines the antenna directivity as

$$D = \frac{S_{\text{max}}}{P_{\text{rad}}/4\pi r^2} = \frac{\text{maximum power density}}{\text{average power density}} \quad (81)$$

For a short dipole, the effective length and radiation resistance R_r are respectively equal to $\Delta z \left[\frac{2\pi}{3} \eta \left(\frac{\Delta z}{\lambda} \right)^2 \right]$, giving and effective aperture of [1]

$$A_{\text{em}}(\text{short dipole}) = \frac{3}{2} \frac{\lambda^2}{4\pi}, \quad \text{where } D = \frac{3}{2} \quad (82)$$

The maximum effective aperture of an ideal dipole is independent of its length Δz (as long as $\Delta z \ll \lambda$). However, it is important to note that R_{rad} is proportional to $(\Delta z/\lambda)^2$ so

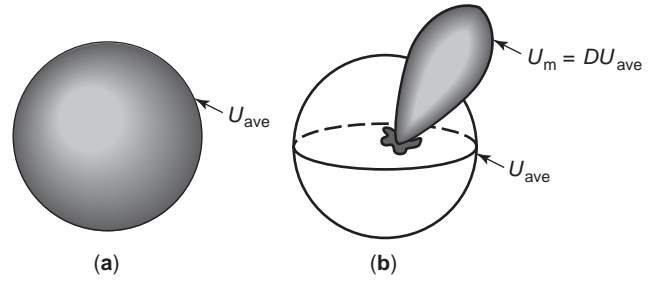


Figure 11. Illustration of directivity: (a) radiation intensity distributed isotropically; (b) radiation intensity from an actual antenna.

that even though A_{em} remains constant as the dipole is shortened, its radiation resistance decreases rapidly and it is more difficult to realize this maximum effective aperture because of the required conjugate impedance match of the receiver to the antenna.

Directivity is defined more directly through an inverse dependence on beam solid angle as

$$D = \frac{4\pi}{\Omega_A} \quad (83)$$

where

$$\Omega_A = \iint |F(\theta, \phi)|^2 d\Omega \quad (84)$$

This directivity definition has a simple interpretation. Directivity is a measure of how much greater the power density at a fixed distance is in a given direction than if all power were radiated isotropically. This view is illustrated in Fig. 11. For an isotropic antenna, as in Fig. 11a, the beam solid angle is 4π , and thus Eq. (83) gives a directivity of unity.

The directivity of the ideal dipole can be written in the following manner:

$$D = \frac{3}{2} = \frac{4\pi}{\lambda^2} \frac{3}{8\pi} \lambda^2 \quad (\text{ideal dipole}) \quad (85)$$

Grouping factors this way permits identification of A_{em} from Eq. (80). Thus

$$D = \frac{4\pi}{\lambda^2} A_{\text{em}} \quad (86)$$

This relationship is true for any antenna. For an isotropic antenna the directivity by definition is unity, so from Eq. (86) with $D = 1$, or

$$A_{\text{em}} = \frac{\lambda^2}{4\pi} \quad (\text{isotropic antenna}) \quad (87)$$

Comparing this to $D = 4\pi/\Omega_A$, we see that

$$\lambda^2 = A_{\text{em}} \Omega_A \quad (88)$$

which is also a general relationship. We can extract some interesting concepts from this relation. For a fixed wavelength, A_{em} and Ω_A are inversely proportional; that is, as the maximum effective aperture increases (as a result of increasing its physical size), the beam solid angle decreases, which means that power is more concentrated in angular space (i.e., directivity goes up).

For a fixed maximum effective aperture (i.e., antenna size), as wavelength decreases (frequency increases), the beam solid angle also decreases, leading to increased directivity.

In practice, antennas are not completely lossless. Earlier we saw that power available at the terminals of a transmitting antenna was not all transformed into radiated power. The power received by a receiving antenna is reduced to the fraction e_r (radiation efficiency) from what it would be if the antenna were lossless. This is represented by defining effective aperture

$$A_e = e_r A_{em} \quad (89)$$

and the available power with antenna losses included, analogous to Eq. (79), is

$$P_A = S A_e \quad (90)$$

This simple equation is very intuitive and indicates that a receiving antenna acts to convert incident power (flux) density in W/m^2 to power delivered to the load in watts. Losses associated with mismatch between the polarization of the incident wave and receiving antenna as well as impedance mismatch between the antenna and load are not included in A_e . These losses are not inherent to the antenna, but depend on how it is used in the system. The concept of gain is introduced to account for losses on an antenna, that is, $G = e_r D$. We can form a gain expression from the directivity expression by multiplying both sides of Eq. (86) by e_r and using Eq. (89):

$$G = e_r D = \frac{4\pi}{\lambda^2} e_r A_{em} = \frac{4\pi}{\lambda^2} A_e \quad (91)$$

For electrically large antennas effective aperture is equal to or less than the physical aperture area of the antenna A_p , which is expressed using aperture efficiency ϵ_{ap} :

$$A_e = \epsilon_{ap} A_p \quad (92)$$

It is important to note that although we developed the general relationships of Eqs. (76), (80), and (92) for receiving antennas, they apply to transmitting antennas as well. The relationships are essential for communication system computations, which we consider next.

4.2. Antennas in Systems

Antennas are used in a variety of applications. The primary application that most people think of is communications. The other major application is sensing, including radar (navigational, surveillance, and ground-penetrating) and radiometry. There is a new interest in transient, broadband application — called “ultrawideband” because of the large bandwidth. This section will consider these systems aspects of antennas.

4.3. Communication Links

We are now ready to completely describe the power transfer in the communication link of Fig. 9. If the transmitting antenna were isotropic, it would have power

density at distance R of

$$S = \frac{U_{av}}{R^2} = \frac{P_t}{4\pi R^2} \quad (93)$$

where P_t is the time-average input power (P_{in}) accepted by the transmitting antenna. The quantity U_{av} denotes the time-average radiation intensity given in the units of power per solid angle (see Fig. 11). For a transmitting antenna that is not isotropic but has gain G_t and is pointed for maximum power density in the direction of the receiver, we have for the power density incident on the receiving antenna:

$$S = \frac{G_t U_{av}}{R^2} = \frac{G_t P_t}{4\pi R^2} \quad (94)$$

Using this in Eq. (90) gives the available received power as

$$P_r = S A_{er} = \frac{G_t P_t A_{er}}{4\pi R^2} \quad (95)$$

where A_{er} is the effective aperture of the receiving antenna and we assume it to be pointed and polarized for maximum response. Now from Eq. (91) $A_{er} = G_r \lambda / 4\pi$, so Eq. (95) becomes

$$P_r = P_t \frac{G_t G_r \lambda^2}{(4\pi R)^2} \quad (96)$$

which gives the available power in terms of the transmitted power, antenna gains, and wavelength. Or, we could use $G_t = 4\pi A_{et} / \lambda^2$ in Eq. (91), giving

$$P_r = P_t \frac{A_{et} A_{er}}{R^2 \lambda^2} \quad (97)$$

which is called the *Friis transmission formula* [1].

The power transmission formula Eq. (96) is very useful for calculating signal power levels in communication links. It assumes that the transmitting and receiving antennas are matched in impedance to their connecting transmission lines, have identical polarization, and are aligned for polarization match. It also assumes the antennas are pointed toward each other for maximum gain. If any of the abovementioned conditions are not met, it is a simple matter to correct for the loss introduced by polarization mismatch, impedance mismatch, or antenna misalignment.

The antenna misalignment effect is easily included by using the power gain value in the appropriate direction. The effect and evaluation of polarization and impedance mismatch are additional considerations. Figure 10 shows the network model for a receiving antenna with input antenna impedance Z_A and an attached load impedance Z_L , which can be a transmission line connected to a distant receiver. The power delivered to the terminating impedance is

$$P_D = pq P_r \quad (98)$$

where

P_D = power delivered from antenna

P_r = power available from receiving antenna

p = polarization efficiency (or polarization mismatch factor), $0 \leq p \leq 1$

q = impedance mismatch factor, $0 \leq q \leq 1$
 A_e = effective aperture (area)

An overall efficiency, or total efficiency ϵ_{total} , can be defined that includes the effects of polarization and impedance mismatch:

$$\epsilon_{\text{total}} = pq \epsilon_{\text{ap}} \quad (99)$$

Then $P_D = \epsilon_{\text{total}} P_r$. It is convenient to express Eq. (98) in decibel form

$$P_D(\text{dBm}) = 10 \log p + 10 \log q + P_r(\text{dBm}) \quad (100)$$

where the unit dBm is power in decibels above a milliwatt; for example, 30 dBm is 1 W. Both powers could also be expressed in units of decibels above a watt, dBW. The power transmission formula Eq. (96) can also be expressed in dB form as

$$\begin{aligned}
 P_r(\text{dBm}) &= P_t(\text{dBm}) + G_t(\text{dB}) + G_r(\text{dB}) \\
 &\quad - 20 \log R(\text{km}) - 20 \log f(\text{MHz}) - 32.44
 \end{aligned} \quad (101)$$

where $G_t(\text{dB})$ and $G_r(\text{dB})$ are the transmit and receive antenna gains in decibels, R (km) is the distance between the transmitter and receiver in kilometers, and f (MHz) is the frequency in megahertz.

4.4. Effective Isotropically Radiated Power (EIRP)

A frequently used concept in communication systems is that of effective (or equivalent) isotropically radiated power, EIRP. It is formally defined as the power gain of a transmitting antenna in a given direction multiplied by the net power accepted by the antenna from the connected transmitter. Sometimes it is denoted as ERP, but this term, effective radiated power, is usually reserved for EIRP with antenna gain relative to that of a half-wave dipole instead of gain relative to an isotropic antenna.

As an example of EIRP, suppose an observer is located in the direction of maximum radiation from a transmitting antenna with input power P_t . Then the EIRP can be expressed as

$$\text{EIRP} = P_t G_t \quad (102)$$

For a radiation intensity U_m , as illustrated in Fig. 11b, and $G_t = 4\pi U_m / P_t$, we obtain

$$\text{EIRP} = P_t \frac{4\pi U_m}{P_t} = 4\pi U_m \quad (103)$$

The same radiation intensity could be obtained from a lossless isotropic antenna (with power gain $G_i = 1$) if it had an input power P_{in} equal to $P_t G_t$. In other words, to obtain the same radiation intensity produced by the directional antenna in its pattern maximum direction, an isotropic antenna would have to have an input power G_t times greater. Effective isotropically radiated power is a frequently used parameter. For example, FM radio stations often mention their effective radiated power when they sign off at night.

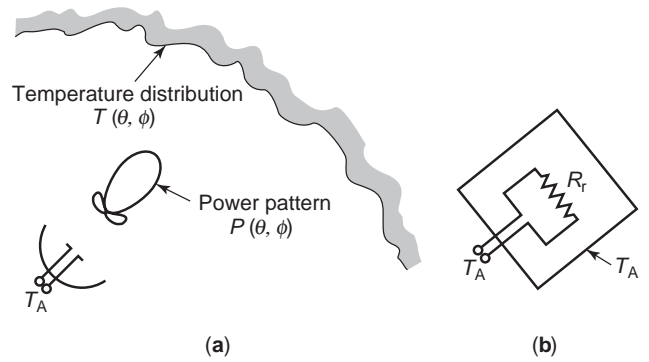


Figure 12. Antenna temperature: (a) an antenna receiving noise from directions (θ, ϕ) producing antenna temperature T_A ; (b) equivalent model.

4.5. Noise and Antenna Temperature

Receiving systems are vulnerable to noise and a major contribution is the receiving antenna, which collects noise from its surrounding environment. In most situations a receiving antenna is surrounded by a complex environment as shown in Fig. 12a. Any object (except a perfect reflector) that is above absolute zero temperature will radiate electromagnetic waves. An antenna picks up this radiation through its antenna pattern and produces noise power at its output. The equivalent terminal behavior is modeled in Fig. 12b by considering the radiation resistance of the antenna to be a noisy resistor at a temperature T_A such that the same output noise power from the antenna in the actual environment is produced. The antenna temperature T_A is not the actual physical temperature of the antenna, but is an equivalent temperature that produces the same noise power, P_{NA} , as the antenna operating in its surroundings. This equivalence is established by assuming the model of Fig. 12b, the noise power available from the noise resistor in bandwidth Δf at temperature T_A is

$$P_{\text{NA}} = k T_A \Delta f \quad (104)$$

where

P_{NA} = available power due to antenna noise (W)
 k = Boltzmann's constant = 1.38×10^{-23} J/K
 T_A = antenna temperature (K)
 Δf = receiver bandwidth (Hz).

Such noise is often referred to as *Nyquist* or *Johnson noise* for system calculations. The system noise power P_N is calculated using the total system noise temperature T_{sys} in place of T_A in Eq. (104) with $T_{\text{sys}} = T_A + T_r$ where T_r is the receiver noise temperature.

Antenna noise is important in several system applications including communications and radiometry. Communication systems are evaluated through "carrier-to-noise ratio," which is determined from the signal power and the system noise power as

$$\text{CNR} = \frac{P_D}{P_N} \quad (105)$$

where $P_N = kT_{\text{sys}}\Delta f$ denoting the system noise power. This noise power $kT_{\text{sys}}\Delta f$ equals the sum of P_{NA} and noise power generated in the receiver connected to the antenna.

Noise power is found by first evaluating antenna temperature. As seen in Fig. 12a, T_A is found from the collection of noise through the scene temperature distribution $T(\theta, \phi)$ weighted by the response function of the antenna, the normalized power pattern $P(\theta, \phi)$. This is expressed mathematically by integrating over the temperature distribution:

$$T_A = \frac{1}{\Omega_A} \int_0^\pi \int_0^{2\pi} T(\theta, \phi) P(\theta, \phi) d\Omega \quad (106)$$

If the scene is of constant temperature T_0 over all angles, T_0 comes out of the integral and then

$$T_A = \frac{T_0}{\Omega_A} \int_0^\pi \int_0^{2\pi} P(\theta, \phi) d\Omega = \frac{T_0}{\Omega_A} \Omega_A = T_0 \quad (107)$$

using Eq. (84) for Ω_k . The antenna is completely surrounded by noise of temperature T_0 and its output antenna temperature equals T_0 independent of the antenna pattern shape.

In general, antenna noise power P_{NA} is found from Eq. (104) using T_A from Eq. (106) once the temperature distribution $T(\theta, \phi)$ is determined. Of course, this depends on the scene, but in general $T(\theta, \phi)$ consists of two components: sky noise and ground noise. Ground noise temperature in most situations is well approximated for soils by the value of 290 K, but is much less for surfaces that are highly reflective as a result of reflection of low temperature sky noise. Also, smooth surfaces have high reflection for near grazing incidence angles.

Unlike ground noise, sky noise is a strong function of frequency. Sky noise is made up of atmospheric, cosmic, and manmade noise. Atmospheric noise increases with decreasing frequency below 1 GHz and is due primarily to lightning, which propagates over large distances via ionospheric reflection below several MHz. Atmospheric noise increases with frequency above 10 GHz due to water vapor and hydrometeor absorption; these depend on time, season, and location. It also increases with decreasing elevation angle. Atmospheric gases have strong, broad spectral lines, such as water vapor and oxygen lines at 22 and 60 GHz, respectively.

Cosmic noise originates from discrete sources such as the sun, moon, and “radio stars” as well as our (Milky Way) galaxy, which has strong emissions for directions toward the galactic center. Galactic noise increases with decreasing frequency below 1 GHz. Manmade noise is produced by power lines, electric motors, and other equipment and usually can be ignored except in urban areas at low frequencies. Sky noise is very low for frequencies between 1 and 10 GHz, and can be as low as a few K for high elevation angles.

Of course, the antenna pattern strongly influences antenna temperature; see Eq. (106). The ground noise temperature contribution to antenna noise can be very low for high-gain antennas having low sidelobes in the direction of Earth. Broadbeam antennas, on the other hand, pick up a significant amount of ground noise as well as sky noise. Losses on the antenna structure also contribute to antenna

noise. A figure of merit used with satellite Earth terminals is G/T_{sys} , which is the antenna gain divided by system noise temperature usually expressed in dB/K. It is desired to have high values of G to increase signal and to have low values of T_{sys} to decrease noise, giving high values of G/T_{sys} .

4.5.1. Example: Direct Broadcast Satellite Reception. Reception of high-quality television channels at home in the 1990s, with an inexpensive, small terminal, is the result of three decades of technology development, including new antenna designs. DirecTV (trademark of Hughes Network Systems) transmits from 12.2 to 12.7 GHz with 120 W of power and an EIRP of about 55 dBW in each 24 MHz transponder that handles several compressed digital video channels. The receiving system uses a 0.46-m (18-in.)-diameter offset fed reflector antenna. In this example we perform the system calculations using the following link parameter values:

$$f = 12.45 \text{ GHz (midband)}$$

$$P_t(\text{dBW}) = 20.8 \text{ dBW (120 W)}$$

$$G_t(\text{dB}) = \text{EIRP (dBW)} - P_t(\text{dBW}) = 55 - 20.8 = 34.2 \text{ dB}$$

$$R = 38,000 \text{ km (typical slant pathlength)}$$

$$G_r = \frac{4\pi}{\lambda^2} e_{\text{ap}} A_p = \frac{4\pi}{(0.024)^2} 0.7 \left(\pi \frac{0.46}{4} \right)^2 = 2538$$

$$= 34 \text{ dB (70\% aperture efficiency)}$$

The received power of a polarized matched system from Eq. (101) is

$$P_D(\text{dBm}) = 20.8 + 34.2 + 34 - 20 \log(38,000)$$

$$- 20 \log(12,450) - 32.44 = -113.9 \text{ dBm} \quad (108)$$

This is 2×10^{-12} W! Without the high gains of the antennas (68 dB combined), this signal would be hopelessly lost in noise.

The receiver uses a 67 K noise temperature low-noise block downconverter. This is the dominant receiver contribution, and when combined with antenna temperature leads to a system noise temperature of $T_{\text{sys}} = 125$ K. The noise power in the effective signal bandwidth $\Delta f = 20$ MHz is

$$P_N = kT_{\text{sys}} \Delta f$$

$$= 1.38 \times 10^{-23} \cdot 125 \cdot 20 \times 10^6 = 3.45 \times 10^{-14} \quad (109)$$

$$= -134.6 \text{ dBW}$$

Thus the carrier-to-noise ratio from Eqs. (105) and (108) is

$$\text{CNR}(\text{dB}) = P_D(\text{dBW}) - P_N(\text{dBW})$$

$$= -116.9 - (-134.6) = 17.7 \text{ dB} \quad (110)$$

4.6. Antenna Bandwidth

Bandwidth is a measure of the range of operating frequencies over which antenna performance is acceptable.

Bandwidth is computed in one of two ways, percentage bandwidth or ratio bandwidth. Let f_U and f_L be the upper and lower frequencies of operation for which satisfactory performance is obtained. The center (or sometimes the design frequency) is denoted as f_C . Then bandwidth as a percent of the center frequency B_p is

$$B_p = \frac{f_U - f_L}{f_C} \times 100 \quad (111)$$

Bandwidth is also defined as a ratio B_r by

$$B_r = \frac{f_U}{f_L} \quad (112)$$

The bandwidth of narrowband antennas is usually expressed as a percent, whereas wideband antennas are described with B_r . Resonant antennas have small bandwidths. For example, the half-wave dipoles have bandwidths of up to 16%, (f_U and f_L determined by the voltage standing-wave ratio $\text{VSWR}=2.0$). On the other hand, antennas that have traveling waves on them rather than standing waves (as in resonant antennas) have larger bandwidths.

5. FUNDAMENTAL LIMITS OF ANTENNAS

Antenna designers are often asked to make an antenna smaller without sacrificing performance from the system. To be able to address this design possibility with communications system designers, the fundamental limits of antennas have been developed. The basic work, by Wheeler [6] and Chu [7], resulted in an approximate expression for the minimum radiation Q , or quality factor, of a small antenna. Extensions and corrections have been presented by Harrington [8], Collin and Rothschild [9], Fante [10], and McLean [11]. Further work by the authors improved the lower bound estimate on the fundamental limit by evaluating the total stored energy that is available for energy dissipation in a cycle. For small antennas, all the approaches provide the same result. The total stored energy approach allows an extension to larger structures, providing a higher bound for larger antenna structures as well as correcting the inconsistent results for circular polarized antennas.

The bound for the radiation Q is given by [7]

$$Q = \frac{1 + 2(ka)^2}{(ka)^3 [1 + (ka)^2]} \quad (113)$$

where the Q or quality factor of the antenna provides a measure of the center frequency compared to bandwidth. This Q is based on the bandwidth of the input impedance to the antenna and does not account for the source impedance, commonly called the “unloaded” Q . To give a common measure for experimental data, we translate the commonly used VSWR measure of 2 relative to the resistance at the center of the band to an equivalent 3-dB quality factor. For a given VSWR and bandwidth, Q may be determined as [12]

$$Q = \frac{\text{VSWR} - 1}{\text{BW}_{\text{VSWR}} \sqrt{\text{VSWR}}} \quad (114)$$

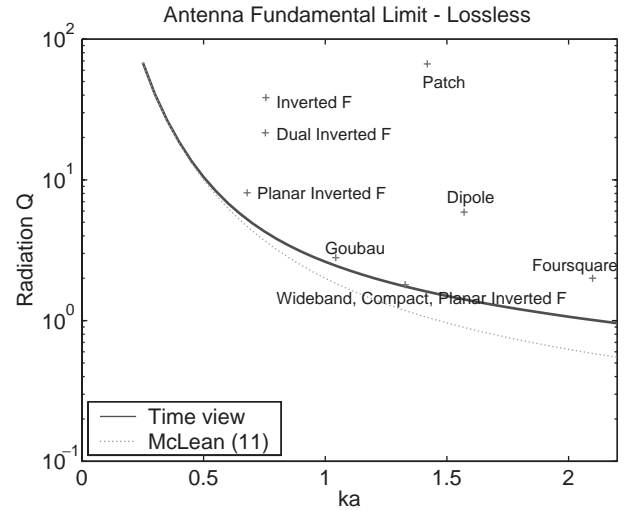


Figure 13. Sample antennas and their fundamental limits from experiment/computation.

It is customary to calculate VSWR based on a perfect matched impedance, so that $\text{VSWR}=1$ at the center frequency where the reactance of the antenna at midband is tuned out. This leaves the antenna resistance at midband as the characteristic impedance. For a $\text{VSWR}=2$, Eq. (114) reduces to

$$Q = \frac{1}{\sqrt{2} \text{BW}_{\text{VSWR}=2}} \quad (115)$$

Also, from Eq. (114) we see that a $\text{VSWR}=2.62$ gives bandwidth is equivalent to a 3dB bandwidth of the unloaded input impedance.

The relationship between Q and antenna size given by Eq. (113) is plotted in Fig. 13 as the solid line. Also shown are data for several typical antennas for communication applications. In order to provide a consistent application of fundamental limits, we evaluate the Q as the inverse of the fractional bandwidth with respect to the 3dB impedance limits as used in Eq. (111). All the antennas evaluated do indeed fall above the fundamental limit definition. To go below the limit, it is generally required that loss must be added to the antenna, producing an inefficient antenna.

6. TRANSIENT ANTENNA CONCEPTS

Current technology is demanding extremely wideband antennas for ultrawideband (UWB) applications. UWB antennas typically require a minimum of a 25% bandwidth and are best evaluated using time-domain approaches. We present some of the concepts to give the reader a start toward understanding UWB antenna systems.

A fundamental view of the antenna first comes from the Friis transmission forms of Eqs. (96) and (97). If an antenna system has constant gain with frequency, the received signal is inversely proportional to frequency squared. Conversely, if the system has constant effective aperture, the received signal is proportional to frequency squared. A more direct view is to modify the effective length definition in Eq. (74) for frequency domain applica-

tions to the transient domain:

$$\mathbf{h}(\theta, \phi; t) = \frac{1}{I_{\text{in}}} \int_V \mathbf{J} \left(\mathbf{r}'; t + \frac{\hat{\mathbf{r}} \cdot \mathbf{r}'}{c} \right) dv' \quad (116)$$

and

$$V_{\text{oc}}(t) = \mathbf{h}(\theta, \phi; t) \odot \mathbf{E}^i(\theta, \phi; t) \quad (117)$$

where the “ \odot ” denotes a vector dot product with time convolution. Transient fields radiated from an antenna are obtained from the field forms previously developed as

$$\mathbf{A}(\mathbf{r}; t) \approx \mu \frac{1}{4\pi r} \int_V \mathbf{J} \left(\mathbf{r}'; t - \frac{r}{c} + \frac{\hat{\mathbf{r}} \cdot \mathbf{r}'}{c} \right) dv \quad (118)$$

with the corresponding electric and magnetic fields given as

$$\mathbf{E} \approx -\frac{\partial}{\partial t} [\mathbf{A} - \hat{\mathbf{r}}(\hat{\mathbf{r}} \cdot \mathbf{A})] \quad (119)$$

and

$$\mathbf{H} \approx -\frac{1}{\eta} [\hat{\mathbf{r}} \times \mathbf{E}] \quad (120)$$

The two important aspects of this transient representation are the computation of the effective length, which is also fundamental to the radiated field. In addition to this effective length of the antenna, the field also contains a time derivative. For an impulse-type system, it is desired that the effective length be a transient impulse. For such impulse antennas, the reception is given by the time derivative of the transmitter waveform.

The input reflection properties of the antenna are indicative of the efficiency of the antenna and should not be considered as the primary aspect needed for transient radiation. Several broadband antennas such as the Archimedian spiral and the log-periodic dipole provide excellent reflection properties over the bandwidth. However, these antennas have poor UWB transmission properties, leading to a chirp response due to phase dispersion of the structures. Excellent results are obtained with the TEM horn, disk-cone, and Vivaldi antennas, but these antenna are too large for many applications. These antennas provide a smooth transition of the transmit waveform to space, with minimal reflection over the band of interest.

The pattern properties of a transient antenna are typically represented by a transient waveform in selected directions rather than a continuous plot in for a single frequency. All of these transient properties are transformations from the basic concepts presented in the frequency domain, but with concepts of convolution and pulse response becoming dominant players. Further discussion of transient properties of antennas is beyond the scope of this article, but may be inferred from the development presented in the frequency domain.

7. SUMMARY

This article has provided the foundation concepts of antennas. The emphasis has focused on the radiation properties of antennas and the methods of characterizing antennas. Critical components include impedance, gain, beamwidth, and bandwidth as are needed for communication systems.

A system designer must incorporate these parameters into a full analysis of the communication system.

BIBLIOGRAPHY

1. W. L. Stutzman and G. A. Thiele, *Antenna Theory and Design*, 2nd ed., Wiley, New York, 1998.
2. A. F. Peterson, S. L. Ray, and R. Mittra, *Computational Methods for Electromagnetics*, IEEE Press, New York, 1998.
3. C. A. Balanis, *Advanced Engineering Electromagnetics*, Wiley, New York, 1989, p. 256.
4. R. F. Harrington, *Time-Harmonic Electromagnetic Fields*, McGraw-Hill, New York, 1961, p. 117.
5. E. C. Jordan and K. G. Balmain, *Electromagnetic Waves and Radiating Systems*, 2nd ed., Prentice-Hall, New York, 1968, p. 555.
6. H. A. Wheeler, Fundamental limitations of small antennas, *Proc. IEEE* **69**:1479–1484, Dec. 1947.
7. L. J. Chu, Physical limitations on omni-directional antennas, *J. Appl. Phys.* **19**:1163–1175, Dec. 1948.
8. R. F. Harrington, Effect of antenna size on gain, bandwidth, and efficiency, *J. Res. Nat. Bur. Stand.* **64-D**:1–12, Jan./Feb. 1960.
9. R. E. Collin and S. Rothschild, Evaluation of antenna Q, *IEEE Trans. Anten. Propag.* **AP-12**:23–27, Jan. 1964.
10. R. L. Fante, Quality factor of general ideal antennas, *IEEE Trans. Anten. Propag.* **AP-17**:151–155, Mar. 1969.
11. J. S. McLean, A reexamination of the fundamental limits on the radiation Q of electrically small antennas, *IEEE Trans. Anten. Propag.* **44**:672–675, May 1996.
12. K. R. Carver and J. W. Mink, Microstrip antenna technology, *IEEE Trans. Anten. Propag.* **AP-29**:2–24, Jan. 1981.

ANTENNAS

C. G. CHRISTODOULOU
University of New Mexico
Albuquerque, New Mexico

P. F. WAHID
University of Central Florida
Orlando, Florida

1. HISTORY OF ANTENNAS

Since Marconi's first experiments with transmitting electromagnetic waves in 1901, antennas have found several important applications over the entire radiofrequency range, and numerous designs of antennas now exist. Antennas are an integral part of our everyday lives and are used for a multitude of purposes, such as cell phones, wireless laptop computers, TV, and radio. An antenna is used to either transmit or receive electromagnetic waves, and it serves as a transducer converting guided waves into free-space waves in the transmitting mode or vice versa, in the receiving mode. All antennas operate on the same basic principles of electromagnetic theory formulated by James Clark Maxwell. Maxwell put forth his unified theory of electricity and magnetism in 1873 [1] in his famous

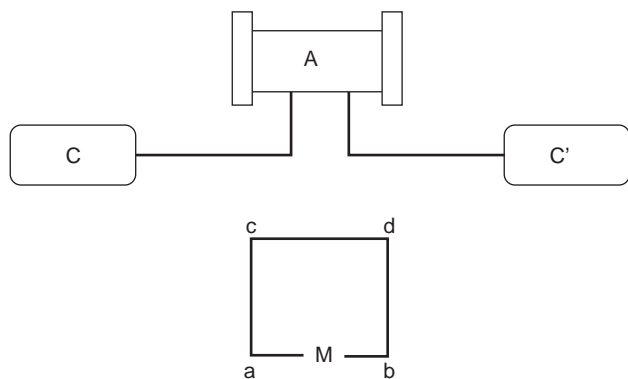


Figure 1. Heinrich Hertz' radio system.

book *A Treatise on Electricity and Magnetism*. His theory was met with much skepticism and it wasn't until 1886 that Heinrich Hertz [2], considered the father of radio, was able to validate this theory with his experiments. The first radio system, at a wavelength of 4 m, consisted of a $\lambda/2$ dipole (transmitting antenna) and a resonant loop (receiving antenna) as shown in Fig. 1 [3]. By turning on the induction coil, sparks were induced across gap A, which were detected across gap B of the receiving antenna.

Almost a decade later, Guglielmo Marconi, in 1901, was able to receive signals across the Atlantic in St. Johns, Newfoundland, sent from a station he had built in Poldhu, Cornwall, England. Marconi's transmitting antenna was a fan antenna with 50 vertical wires supported by two 6-m guyed wooden poles. The receiving antenna was a 200-m wire pulled up with a kite [3]. For many years since Marconi's experiment, antennas operated at low frequencies, up to the UHF region and were primarily wire-type antennas. The need for radar during World War II launched antenna design into a new era and opened up the entire RF spectrum for their use. Since the 1950s many antennas types such as reflector, aperture, and horn antennas came into use, most of them operating in the microwave region. Their use ranged from communications to astronomy to various deep-space applications. These antennas have been discussed in a plethora of books, some of these have been included in the Bibliography [4–23].

A good explanation of how an antenna can act as a radiator or a receiver is given in Refs. 20 and 23. To understand how an antenna radiates, consider a pulse of electric charge moving along a straight conductor. A static electric charge or a charge moving with a uniform velocity does not radiate. However, when charges are accelerated along the conductor and decelerated on reflection from its end, radiated fields are produced along the wire and at each end [20,21]. The *IEEE Standard Definitions of Terms for Antennas* [24] and Balanis [25] provide good sources of definitions and explanations of the fundamental parameters associated with antennas.

2. TYPES OF ANTENNAS

Modern antennas or antenna systems require careful design and a thorough understanding of the radiation

mechanism involved. Selection of the type of antenna to be used is determined by electrical and mechanical constraints and operating costs. The electrical parameters of the antenna include the frequency of operation, gain, polarization, radiation pattern, and impedance. The mechanical parameters of importance include the size, weight, reliability, and manufacturing process. In addition, the environment under which the antenna is to be used also must be considered, including the effects of temperature, rain, wind vibrations, and the platform that the antenna is mounted. Antennas are shielded from the environment through the use of radomes whose presence is taken into account while designing the antenna.

Antennas can be classified broadly into the following categories: wire antennas, reflector antennas, lens antennas, traveling-wave antennas, frequency-independent antennas, horn antennas, and conformal antennas. In addition, antennas are very often used in array configurations, such as in phased-array or adaptive array antennas, to improve the characteristics of an individual antenna element.

2.1. Wire Antennas

Wire antennas were among the first type of antennas used and are the most familiar type to the average person. These antennas can be linear or in the form of closed loops. The thin linear dipole antenna is used extensively, and the half-wavelength dipole antenna has a radiation resistance of $73\ \Omega$, very close to the $75\text{-}\Omega$ characteristic impedance of feedlines such as the coaxial cable. It has an omnidirectional pattern as shown in Fig. 2, with a half-power beamwidth of 78° . Detailed discussions on dipole antennas of different lengths and their various applications can be found in Ref. 25.

Loop antennas can have several different shapes, such as circular, square, or rectangular. Electrically small loops are those whose overall wire extent is less than one-tenth of a wavelength. Electrically large loops have circumferences that are of the order of a wavelength. An electrically small circular or square loop antenna can be treated as an infinitesimal magnetic dipole with its axis perpendicular to the plane of the loop. Various configurations of polygonal loop antennas have been investigated [26,27], including the ferrite loop, where a ferrite core is placed in the loop antenna to increase its efficiency. Loop antennas are inefficient with high ohmic losses and are often used as receivers and as probes for field measurements. The radiation pattern of a small loop antenna has a null perpendicular to the plane of the loop and a maximum along the plane of the loop. An electrically large antenna has a maximum radiation perpendicular to the plane of the loop and is regarded as the equivalent to the half-wavelength dipole.

Dipole and loop antennas find applications in the low-medium-frequency ranges. They have wide beamwidths, and their behavior is greatly affected by nearby obstacles or structures. These antennas are often placed over a ground plane. The spacing above the ground plane determines the effect of the ground plane has on the radiation pattern and the increase in directivity [21].

Thick dipole antennas are used to improve the narrow bandwidth of thin dipole antennas. Examples of these are

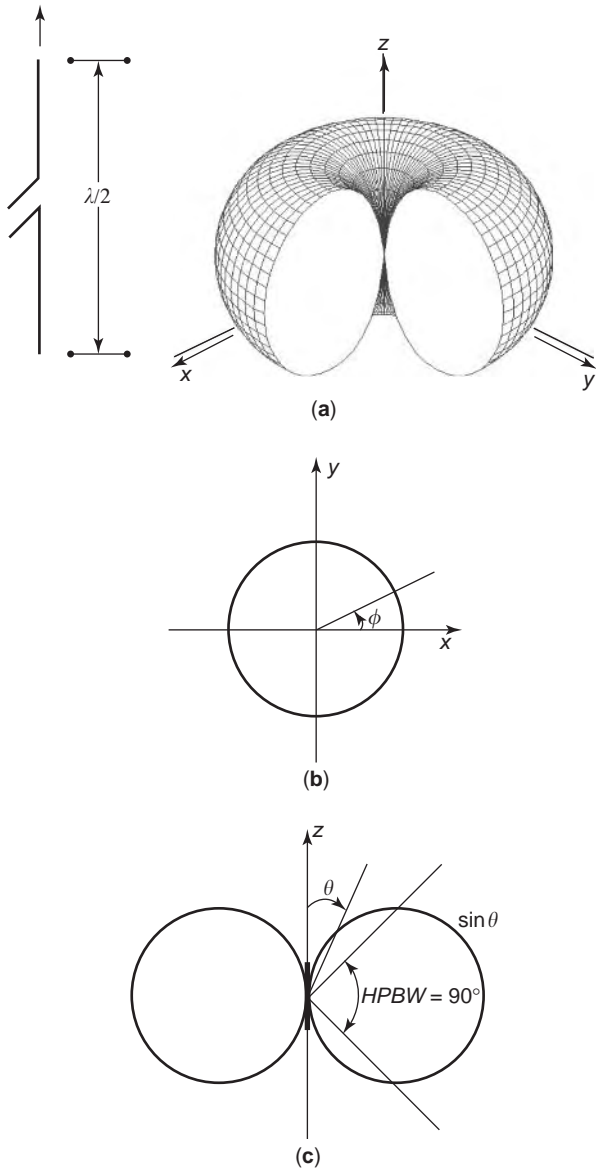


Figure 2. A half-wavelength dipole and its radiation pattern.

the cylindrical dipole, the folded dipole, and the biconical antennas. The use of a sleeve around the input region and the arms of the dipole also results in broader bandwidths.

2.2. Reflector Antennas

Since World War II, when reflector antennas gained prominence for their use with radar systems, these antennas have played an important role in the field of communications. Love [28] has published a collection of papers on reflector antennas. Reflector antennas have a variety of geometrical shapes and require careful design and a full characterization of the feed system (the system that illuminated the reflector surface with electromagnetic fields). Silver [5] presents the technique for analysis based on aperture theory and physical optics. Other methods such as the geometric theory of diffraction (GTD) and fast Fourier transform (FFT) along with various optimization tech-

niques [29] are now used for a more accurate design of these antennas.

The plane reflector is the simplest type of a reflector and can be used to control the overall system radiation characteristics [21]. The corner reflector has been investigated by Kraus [30], and the 90° corner reflector is found to be the most effective. The feeds for corner reflectors are generally dipole antennas placed parallel to the vertex. These antennas can be analyzed in a rather straightforward manner using the method of images. Among curved reflectors, the paraboloid is the most commonly used. The paraboloid reflector shown in Fig. 3 is formed by rotating a parabolic reflector about its axis. The reflector transforms a spherical wave radiated from a feed at its focus into a plane wave.

To avoid blockage caused by the feed placed at the focal point in a front-fed system, the feed is often offset from the axis [31]. The Cassegrain reflector is a dual-reflector system using a paraboloid as the primary and a hyperboloid as the secondary reflector with a feed along the axis of the paraboloid.

The Gregorian dual-reflector antenna uses an ellipse as the subreflector. The aperture efficiency in a Cassegrain antenna can be improved by modifying the reflector surfaces [28]. Most paraboloidal reflectors use horn antennas (conical or pyramidal) for their feeds. With a paraboloidal reflector, beam scanning by feed displacement is limited. A spherical reflector provides greater scanning but requires more elaborate feed design since it fails to focus an incident plane to a point. Spherical reflectors can suffer from a loss in aperture and increased minor lobes due to blockage by the feed.

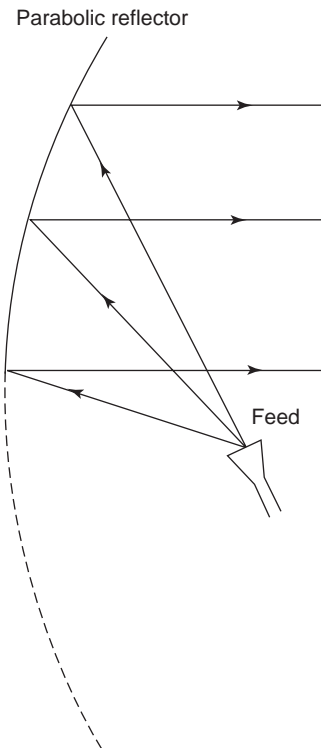


Figure 3. A parabolic reflector antenna with its feed.

2.3. Lens Antennas

At larger wavelengths, reflectors become impractical because of the necessity for large feed structures and tolerance requirements. At low frequencies, the lens antenna is prohibitively heavy. Both lens antennas and parabolic reflectors use free space as a feed network to excite a large aperture. The feed of a lens remains out of the aperture and thus eliminates aperture blockage and high sidelobe levels. Dielectric lens antennas are similar to optical lenses, and the aperture of the antenna is equal to the projection of the rim shape. Lenses are divided into two categories: single-surface and dual-surface. In the *single-surface lens* one surface is an equiphase surface of the incident or emergent wave and the waves pass through normal to the surface without refraction.

In a *dual-surface lens*, refraction occurs at both lens surfaces. Single-surface lenses convert either cylindrical or spherical waves to plane waves. Cylindrical waves require a line source and a cylindrical lens surface, and spherical waves require a point source. The far field is determined by diffraction from the aperture. Dual-surface lenses allow more control of the pattern characteristics. Both surfaces are used for focusing, and the second surface can be used to control the amplitude distribution in the aperture plane. These simple lenses are many wavelengths thick if their focal length and aperture are large compared to a wavelength. The surface of the lens can be zoned by removing multiples of wavelengths from the thickness. The zoning can be done in either the refracting or nonrefracting surface as shown in Fig. 4. The zoned

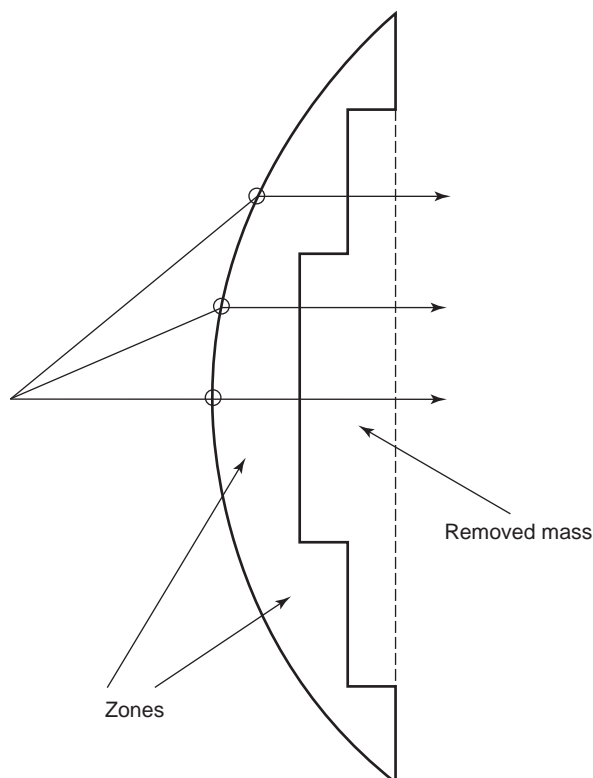


Figure 4. Zoned lenses.

lens is frequency-sensitive and can give rise to shadowing losses at the transition regions [5].

Artificial dielectric lenses in which particles such as metal spheres, strips, disks, or rods are introduced in the dielectric have been investigated by Kock [32]. The size of the particles has to be small compared to the wavelength. Metal plate lenses using spaced conducting plates are used at microwave frequencies. Since the index of refraction of a metal plate medium depends on the ratio of the wavelength to the spacing between the plates, these lenses are frequency-sensitive. The Luneberg lens is a spherically symmetric lens with an index of refraction that varies as a function of the radius. A plane wave incident on this lens will be brought to a focus on the opposite side. These lens antennas can be made using a series of concentric spherical shells, each with a constant dielectric.

2.4. Traveling-Wave Antennas

Traveling-wave antennas [33] are distinguished from other antennas by the presence of a traveling wave along the structure and by the propagation of power in a single direction. Linear wire antennas are the dominant type of traveling-wave antennas. Linear wave antennas with standing-wave patterns of current distributions are referred to as *standing-wave* or *resonant antennas*, where the amplitude of the current distribution is uniform along the source but the phase changes linearly with distance. There are in general two types of traveling-wave antennas: (1) the *surface-wave antenna*, which is a slow-wave structure, where the phase velocity of the wave is smaller than the velocity of light in free space and the radiation occurs from discontinuities in the structure; and (2) a *leaky-wave antenna*, which is a fast-wave structure, where the phase velocity of the wave is greater than the velocity of light in free space. The structure radiates all its power with the fields decaying in the direction of wave travel.

A long-wire antenna, many wavelengths in length, is an example of a traveling-wave antenna. The "beverage" antenna is a thin wire placed horizontally above a ground plane. The antenna has poor efficiency but can have good directivity and is used as a receiving antenna in the low-mid-frequency range. The V antenna is formed by using two beverage antennas separated by an angle and fed from a balanced line. By adjusting the angle, the directivity can be increased and the sidelobes can be made smaller. Terminating the legs of the V antenna in their characteristic impedances makes the wires nonresonant and greatly reduces backradiation. The rhombic antenna consists of two V antennas. The second V antenna brings the two sides together, and a single terminating resistor can be used to connect the balanced lines. An inverted V over a ground plane is another configuration for a rhombic antenna.

The pattern characteristics can be controlled by varying the angle between the elements, the lengths of the elements, and the height above ground. The helical antenna [21] is a high-gain broadband endfire antenna. It consists of a conducting wire wound in a helix. It has found applications as feeds for parabolic reflectors and for various space communications systems. A popular and practical antenna is the Yagi-Uda antenna [34,35], shown

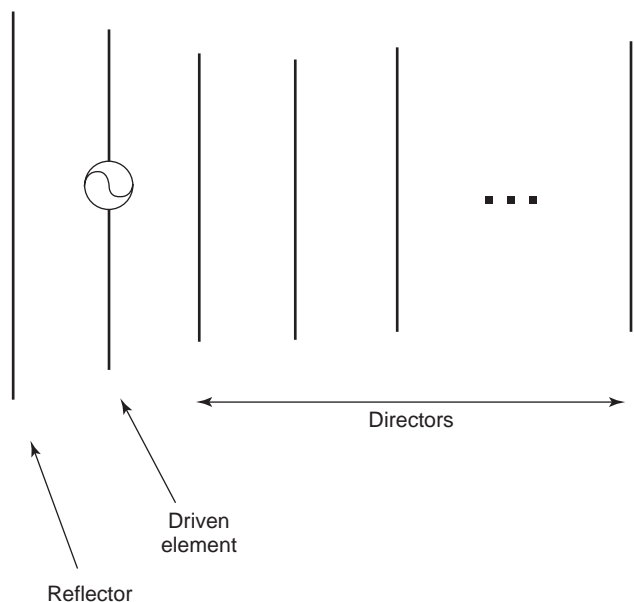


Figure 5. A Yagi-Uda antenna.

in Fig. 5. It uses an arrangement of parasitic elements around the feed element to act as reflectors and directors to produce an endfire beam. The elements are linear dipoles with a folded dipole used as the feed. The mutual coupling between the standing-wave current elements in the antenna is used to produce a traveling-wave unidirectional pattern.

2.5. Frequency-Independent Antennas

Frequency-independent antennas or self-scaling antennas were introduced in the early 1950s, extending antenna bandwidths by greater than 40% [36]. Ideally, an antenna will be frequency-independent if its shape is specified only in terms of angles. These antennas have to be truncated for practical use, and the current should attenuate along the structure to a negligible value at the termination. Examples of these antennas are the eight-element log-periodic circular configuration shown in Fig. 6.

2.6. Horn Antennas

The electromagnetic horn antenna is characterized by attractive qualities such as a unidirectional pattern, high gain, and purity of polarization. Horn antennas are used as feeds for reflector and lens antennas and as a laboratory standard for other antennas. A good collection of papers on horn antennas can be found in Ref. 37. Horns can be of a rectangular or circular shape as shown in Fig. 7.

Rectangular horns derived from a rectangular waveguide can be pyramidal or sectoral E -plane and H -plane horns. The E -plane sectoral horn has a flare in the direction of the E -field of the dominant TE_{10} mode in the rectangular waveguide, and the H -plane sectoral horn has a flare in the direction of the H -field. The pyramidal horn has a flare in both directions. The radiation pattern of the horn antenna can be determined from a knowledge of the aperture dimensions and the aperture field distribution. The flare angle of the horn and its dimensions affect the

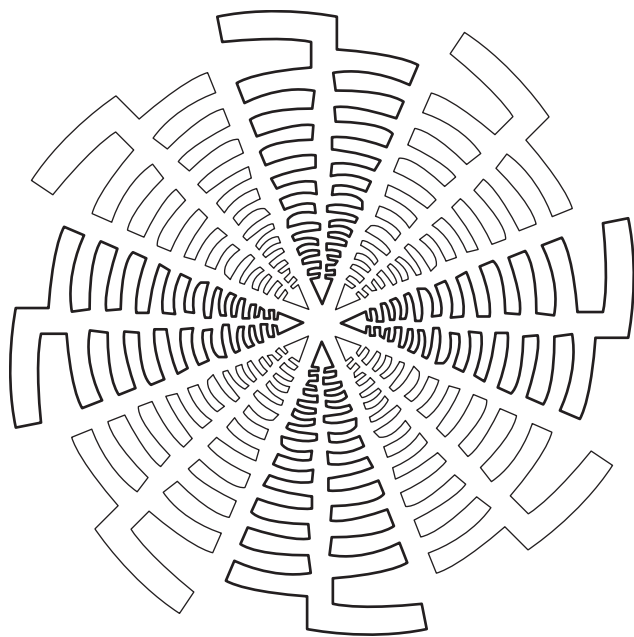


Figure 6. An eight-element log-periodic circular antenna.

radiation pattern and its directivity. Circular horns derived from circular waveguides can be either conical, biconical, or exponentially tapered.

The need for feed systems that provide low cross-polarization and edge diffraction and more symmetric patterns led to the design of the corrugated horn [38]. These horns have corrugations or grooves along the walls that present equal boundary conditions to the electric and magnetic fields when the grooves are $\lambda/4$ to $\lambda/2$ deep. The conical corrugated horn, referred to as the *scalar horn*, has a larger bandwidth than do the small-flare-angle corrugated horns.

2.7. Conformal Antennas

Microstrip antennas have become a very important class of antennas since they received attention in the early 1970s. These antennas are lightweight, easy to manufacture using printed-circuit techniques, and compatible with MMICs (monolithic microwave integrated circuits). An additional attractive property of these antennas is that they are low-profile and can be mounted on surfaces; that is, they can be made to “conform” to a surface and hence are referred to as *conformal antennas*. The microstrip antenna consists of a conducting “patch” or radiating element that may be square, rectangular, circular, triangular, or of another shape, etched on a grounded dielectric substrate as shown in Fig. 8.

These antennas are an excellent choice for use on aircraft and spacecraft. Microstrip antennas have been investigated extensively over the past twenty years and the two volumes published by James and Hall [39] provide an excellent description of various microstrip antennas, including their design and usage. Microstrip antennas are fed either using a coaxial probe, a microstrip line, or proximity coupling or through aperture coupling. A major disadvantage of these antennas is that they are poor radiators and have a very narrow frequency bandwidth.

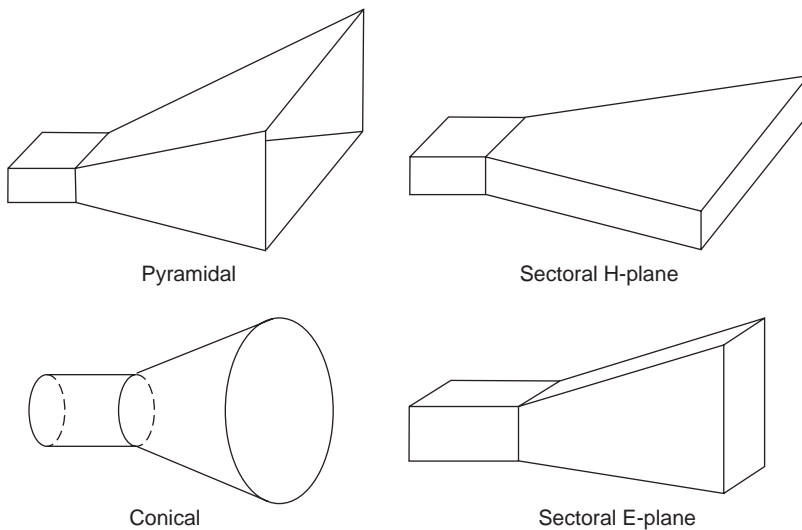


Figure 7. Examples of horn antennas.

They are often used in an array environment to achieve the desired radiation characteristics. Larger frequency bandwidths are obtained by using stacked microstrip antennas.

2.8. Antenna Arrays

Antenna arrays are formed by suitably spacing radiating elements in a one- or two-dimensional lattice. By suitably feeding these elements with relative amplitudes and phas-

es, these arrays produce desired directive radiation characteristics. The arrays allow a means of increasing the electric size of the antenna without increasing the dimensions of the individual elements. Most arrays consist of identical elements such as dipoles, helices, large reflectors, or microstrip elements. The array has to be designed such that the radiated fields from the individual elements add constructively in the desired directions and destructively in the other directions. Arrays are generally classified as *endfire* arrays that produce a beam directed along the axis of the array, or *broadside* arrays producing a beam directed in a direction normal to the array. The beam direction can be controlled or “steered” using a phased-array antenna in which the phase of the individual elements is varied. Frequency-scanning arrays are an example where beam scanning is done by changing the frequency. Adaptive array antennas produce beams in predetermined directions. By suitably processing the received signals, the antenna can steer its beam toward the direction of the desired signal and simultaneously produce a null in the direction of an undesired signal.

2.9. Reconfigurable Antennas

With the advent of RF microelectromechanical system (MEMS) switches, a new class of antennas has emerged that are capable to radiate more than one pattern, at different frequencies and with multiband characteristics [40–42]. A MEMS-switched reconfigurable antenna can be dynamically reconfigured within a few microseconds to serve different applications at different frequency bands, which are necessary in radar and modern telecommunication systems. RF MEMS switches are used to connect antennas together to create different configurations (linear, planar, circular arrays, etc.), which results in a reduction of architectural complexity, and hence cost, of any communication devices while simultaneously enhancing performance. Figure 9 depicts a fractal antenna with only its diagonal elements activated through RF MEMS switches. By activating six diagonal elements, the antenna works as a rotated array consisting of triangular elements.

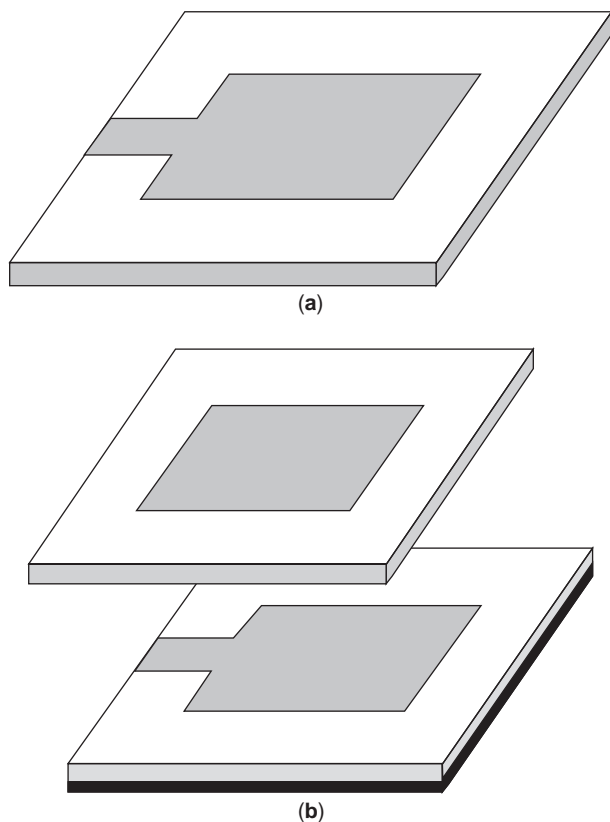


Figure 8. (a) A microstrip antenna and (b) a stacked microstrip antenna.

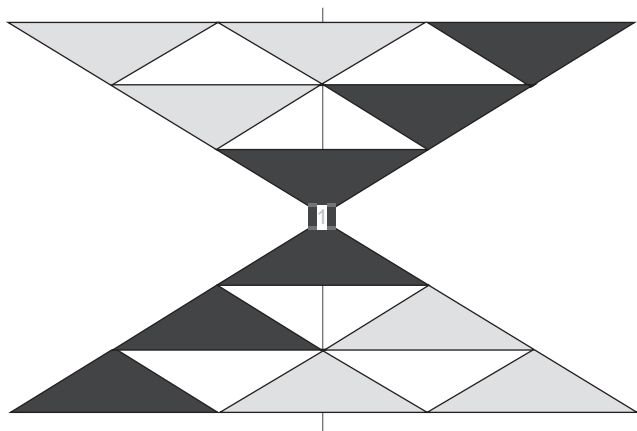


Figure 9. A fractal antenna with six activated elements.

3. APPLICATIONS AND IMPACT ON SYSTEMS

Antennas enjoy a very large range of applications, in both the military and commercial sectors. The most well known applications of antennas to the average person are those associated with radio, TV, and communication systems. Today, antennas find extensive use in biomedicine, radar, remote sensing, astronomy, navigation, RF identification, controlling space vehicles, collision avoidance, air traffic control, GPS, pagers, wireless telephone, and wireless local-area networks (LANs). These applications cover a very wide range of frequencies as shown in Table 1 [2,3,43]:

3.1. Antennas in Communication Systems

Antennas are one of the most critical components in a communication system since they are responsible for the proper transmission and reception of electromagnetic waves. The antenna is the first part of the system that will receive or transmit a signal. A good design can relax some of the complex system requirements involved in a

communication link and increase the overall system performance.

The choice of an antenna for a specific application (cellular, satellite-based, ground-based, etc.) depends on the platform to be used (car, ship, building, spacecraft, etc.), the environment (sea, space, land), the frequency of operation, and the nature of the application (video, audio data, etc.). Communication systems can be grouped in several different categories.

3.1.1. Direct (Line-of-Sight) Links. This is transmission link established between two highly directional antennas. The link can be between two land-based antennas (radio relays); between a tower and a mobile antenna (cellular communication), between a land-based antenna and a satellite antenna (Earth–space communication), or between two satellite antennas (intraspace communication). Usually these links operate at frequencies between 1 and 25 GHz. A typical distance between two points in a high capacity, digital microwave radio relay system is about 30 mi.

3.1.2. Satellites and Wireless Communications. Antennas on orbiting satellites are used to provide communications between various locations around Earth. In general, most telecommunication satellites are placed in a geostationary orbit (GEO), about 22,235 mi above Earth as shown in Fig. 10. There are also some satellites at lower-Earth orbits (LEOs) that are used for wireless communications. Modern satellites have several receiving and transmitting antennas that can offer services such as video, audio, data transmission, and telephone communication in areas that are not hardwired. Moreover, direct TV is now possible through the use of a small 18-in. reflector antenna, with 30 million users in the United States today [44,45].

Satellite antennas for telecommunications are used either to form a large area-of-coverage beam for broadcasting or spot beams (with a small area of coverage) for point-to-point communications. Also, multibeam antennas

Table 1. Frequency Bands and General Usage

Band Designation	Frequency Range	Usage
Very low frequency (VLF)	3–30 kHz	Long-distance telegraphy, navigation; antennas are physically large but electrically small; propagation is accomplished using Earth’s surface and the ionosphere; vertically polarized waves
Low frequency (LF)	30–300 kHz	Aeronautical navigation services; long-distance communications; radio broadcasting; vertical polarization
Medium frequency (MF)	300–3000 kHz	Regional broadcasting and communication links; AM radio.
High frequency (HF)	3–30 MHz	Communications, broadcasting, surveillance, CB (Citizens’ band) radio (26.965–27.225 MHz); ionospheric propagation; vertical and horizontal propagation
Very high frequency (VHF)	30–300 MHz	Surveillance, TV broadcasting (54–72 MHz), (76–88 MHz), and (174–216 MHz), FM radio (88–108 MHz); wind profilers
Ultrahigh frequency (UHF)	300–1000 MHz	Cellular communications, surveillance TV (470–890 MHz).
L	1–2 GHz	Long-range surveillance, remote sensing
S	2–4 GHz	Weather, traffic control, tracking, hyperthermia
C	4–8 GHz	Weather detection, long-range tracking
X	8–12 GHz	Satellite communications, missile guidance, mapping
Ku	12–18 GHz	Satellite communications, altimetry, high-resolution mapping
K	18–27 GHz	Very-high-resolution mapping
Ka	27–40 GHz	Airport surveillance
Submillimeter waves	—	In experimental stage

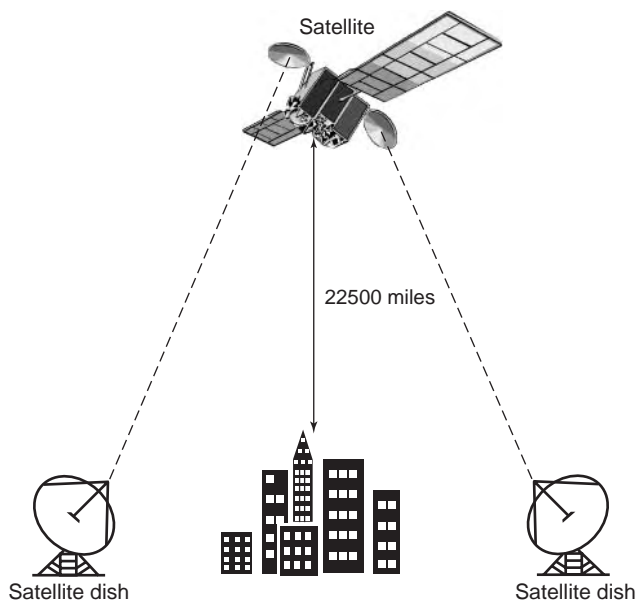


Figure 10. A satellite communication system.

are used to link mobile and fixed users that cannot be linked economically via radio or land-based relays [46–49].

The impact of antennas on satellite technology continues to grow. For example, very-small-aperture terminal (VSATs) dishes at Ku band, which can transmit any combination of voice, data, and video using satellite network-

ing, have become valuable tools for several small and large companies. Most satellites operate at the L, S, or Ku band, but increasing demand for mobile telephony and high-speed interactive data exchange is pushing the antenna and satellite technology into higher operational frequencies [50]. Future satellites will be equipped with antennas at both the Ku and the Ka bands. This will lead to greater bandwidth availability. For example, the ETS-VI (Engineering Test Satellite) [a Japanese satellite comparable to NASA’s TDRS (tracking and data relay satellite)], carries five antennas: an S-band phased array, a 0.4-m reflector for 43/38 GHz, for uplinks and downlinks, an 0.8-m reflector for 26/33 GHz, a 3.5-m reflector for 20 GHz, and a 2.5-m reflector for 30 and 6/4 GHz. Figure 11 shows a few typical antennas used on satellites and spacecrafts. It is expected that millions of households, worldwide, will have access to dual Ku/Ka band dishes later in this (twenty-first) century.

3.1.3. Personal/Mobile Communication Systems. The vehicular antennas used with mobile satellite communications constitute the weak link of the system. If the antenna has high gain, then tracking of the satellite becomes necessary. If the vehicle antenna has low gain, the capacity of the communication system link is diminished. Moreover, handheld telephone units require ingenious design because of the lack of “real estate” on the portable device.

There is more emphasis now on enhancing antenna technologies for wireless communications, especially in cellular communications, which will enhance the link

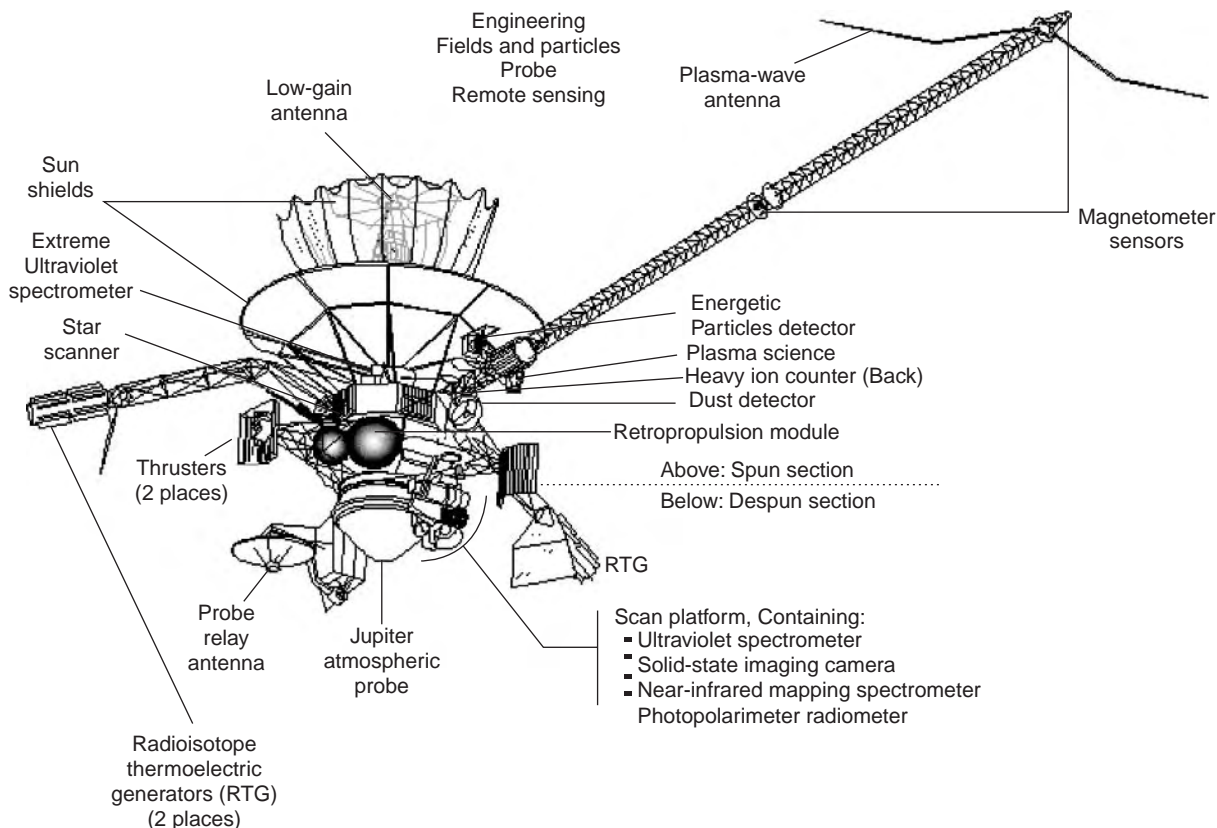


Figure 11. Line drawing of the Galileo spacecraft showing several of the antennas used on board. [Courtesy NASA, JPL (Jet Propulsion Laboratory).]

performance and reduce the undesirable visual impact of antenna towers. Techniques that utilize “smart” antennas, fixed multiple beams, and neural networks are now being utilized to increase the capacity of mobile communication systems, whether it is land-based or satellite-based [51]. It is anticipated that later in this century the “wire” will no longer dictate where we must go to use the telephone, fax, send or receive electronic mail (e-mail), or run a computer. This will lead to the design of more compact and more sophisticated antennas.

3.2. Antennas for Biomedical Applications

In many biological applications the antenna operates under very different conditions than do the more traditional free-space, far-field counterparts. Near fields and mutual interaction with the body dominate. Also, the antenna radiates in a lossy environment rather than free space. Several antennas, from microstrip antenna to phased arrays, operating at various frequencies, have been developed to couple electromagnetic energy in or out of the body. Most medical applications can be classified into two groups [52]: (1) therapeutic and (2) informational. Examples of therapeutic applications are hyperthermia for cancer therapy, enhancement of bone and wound healing, nerve stimulation, neural prosthesis, microwave angioplasty, treatment of prostatic hyperplasia, and cardiac ablation. Examples of informational applications are tumor detection using microwave radiometry, imaging using microwave tomography, measurement of lung (pulmonary) water content, and dosimetry.

Therapeutic applications are further classified as invasive and noninvasive. Both applications require different types of antennas and different restrictions on their design. In the noninvasive applications (not penetrating the body), antennas are used to generate an electromagnetic field to heat some tissue. Antennas such as helical coils, ring capacitors, dielectrically loaded waveguides, and microstrip radiators are attractive because of their compactness. Phased arrays are also used to provide focusing and increase the depth of penetration. The designer has to choose the right frequency, size of the antenna, and the spot size that the beam has to cover in the body. The depth of penetration, since the medium of propagation is lossy, is determined by the total power applied or available to the antenna. Invasive applications require some kind of implantation in the tissue. Many single antennas and phased or nonphased arrays have been used extensively for treating certain tumors. A coaxial cable with an extended center conductor is a typical implanted antenna. This type of antenna has also been used in arteries to soften arterial plaque and enlarge the lumen of narrowed arteries.

Antennas have also been used to stimulate certain nerves in the human body. As the technology advances in the areas of materials and in the design of more compact antennas, more antenna applications will be found in the areas of biology and medicine.

3.3. Radio Astronomy Applications

Another field where antennas have made a significant impact is astronomy. A *radio telescope* is an antenna

system that astronomers use to detect RF radiation emitted from extraterrestrial sources. Since radio wavelengths are much longer than those in the visible region, radio telescopes make use of very large antennas to obtain the resolution of optical telescopes. Today, the most powerful radio telescope is located in the plains of San Augustin, near Socorro, New Mexico. It is made of an array of 27 parabolic antennas, each about 25 m in diameter. Its collecting area is equivalent to a 130-m antenna. This antenna is used by over 500 astronomers to study the solar system, the Milky Way Galaxy, and extraterrestrial systems. Arecibo, Puerto Rico is the site of the world's largest single-antenna radio telescope. It uses a 300-m spherical reflector consisting of perforated aluminum panels. These panels are used to focus the received radiowaves on movable antennas placed about 168 m above the reflector surface. The movable antennas allow the astronomer to track a celestial object in various directions in the sky.

Antennas have also been used in constructing a different type of a radio telescope, called a *radio interferometer*. It consists of two or more separate antennas that are capable of receiving radiowaves simultaneously but are connected to one receiver. The radiowaves reach the spaced antennas at different times. The idea is to use information from the two antennas (interference) to measure the distance or angular position of an object with a very high degree of accuracy.

3.4. Radar Applications

Modern airplanes, both civilian and military, have several antennas on board used for altimetry, speed measurement, collision avoidance, communications, weather detection, navigation, and a variety of other functions [43,53–55]. Each function requires a certain type of antenna. It is the antenna that makes the operation of a radar system feasible. Figure 12 shows a block diagram of a basic radar system.

Scientists in 1930 observed that electromagnetic waves emitted by a radio source were reflected back by aircrafts (echoes). These echoes could be detected by electronic equipment. In 1937, the first radar system, used in Britain for direction finding of enemy guns, operated at 20–30 MHz. Since then, several technological developments have emerged in the area of radar antennas. The desire to operate at various frequencies lead to the development of several very versatile and sophisticated antennas. Radar antennas can be ground-based, mobile, satellite-based, or placed on any aircraft or spacecraft. The space shuttle orbiter, for example, has 23 antennas. Among these, four C-band antennas are used for altimetry, two to receive and two to transmit. There are also six L-band antennas and three C-band antennas used for navigation purposes.

Today, radar antennas are used for coastal surveillance, air traffic control, weather prediction, surface detection (ground-penetrating radar), mine detection, tracking, air defense, speed detection (traffic radar), burglar alarms, missile guidance, mapping of Earth's surface, reconnaissance, and other applications.

In general, radar antennas are designed as part of a very complex system that includes high-power klystrons,

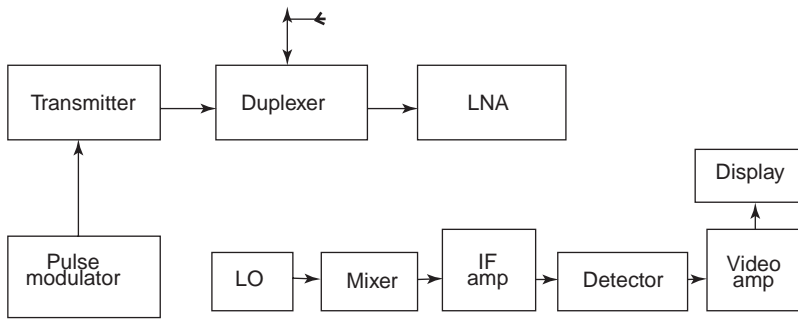


Figure 12. A basic radar system (IF = intermediate frequency; LNA = low-noise amplifier; LO = local oscillator).

traveling-wave tubes, solid-state devices, integrated circuits, computers, signal processing, and a myriad of mechanical parts. The requirements of the radar antennas vary depending on the application (continuous-wave, pulsed radar, Doppler, etc.) and the platform of operation. For example, the 23 antennas on the space shuttle orbiter must have a useful life of 100,000 operational hours over a 10-year period or about 100 orbital missions. The antennas also have to withstand a lot of pressure and a direct lightning strike. The antenna designer will have to meet all of these constraints along with the standard antenna problems such as polarization, scan rates, and frequency agility.

3.5. Impact of Antennas in Remote Sensing

Remote sensing is a radar application in which antennas such as horns, reflectors, phased arrays, and synthetic apertures are used to monitor conditions on Earth from an airplane or a satellite to infer the physical properties of the planetary atmosphere and surface or to photograph or map images of objects.

There are two types of remote sensing—active and passive (radiometry)—and both are in wide use. In the *active* case, a signal is transmitted and the reflected energy, intercepted by radar as shown in Fig. 13, is used to determine several characteristics of the illuminated object such as temperature or shape. In the *passive* case, the antenna detects energy radiated by thermal radiation from the objects on Earth. Radiometers are used to measure the ther-

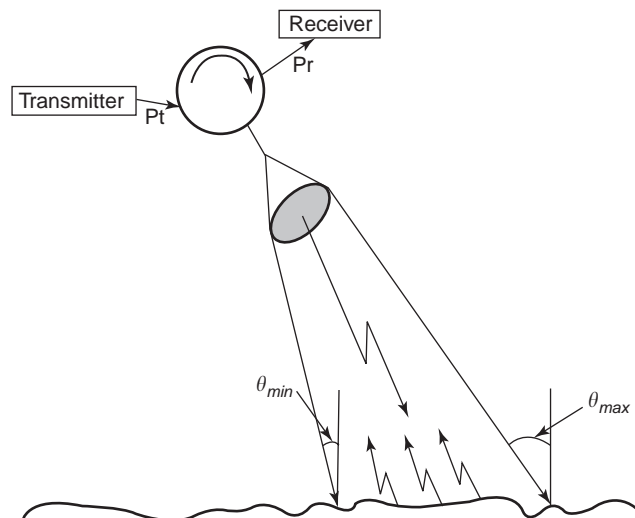


Figure 13. Active remote sensing (scatterometer).

mal radiation of the ground surface and/or atmospheric conditions [13,56,57].

Most antennas associated with radiometers are downward-looking, where radiation patterns possess small, close-in sidelobes. Radiometer antennas require a very careful design to achieve high beam efficiency, low antenna losses, low sidelobes, and good polarization properties. The ohmic loss in the antenna is perhaps the most critical parameter since it can modify the apparent temperature observed by the radiometer system.

The degree of resolution of a remote-sensing map depends on the ability of the antenna system to separate closely spaced objects in range and azimuth. To increase the azimuth resolution, a technique called *synthetic aperture* is employed. Basically, as an aircraft flies over a target, the antenna transmits pulses assuming the value of a single radiating element in a long array. Each time a pulse is transmitted, the antenna, in response to the aircraft's motion, is further along the flight path. By storing and adding up the returned signals from many pulses, the single antenna element acts as the equivalent of a very large antenna, hundreds of feet long. Using this approach, an antenna system can produce maps approaching the quality of good aerial photographs. This synthetic aperture antenna becomes a "radio camera" that can yield excellent remote imagery. Figure 14 shows an image of the air (thick with dust and smoke) over the Mediterranean Sea.

Today, antennas are used in remote-sensing applications for both the military and civilian sectors. For example, in the 1960s the United States used remote-sensing imaging from satellites and aircraft to track missiles activities over Cuba. In 1970s, remote sensing provided NASA with needed maps of the lunar surface before the *Apollo* landing. Also, in July 1972, NASA launched the first Earth Resource Technology Satellite (ERTS-1). This satellite provided data about crops, minerals, soils, urban growth, and other Earth features. This program still continues its original success using the new series of satellites "the Landsats." In 1985, British scientists noted the "ozone depletion" over the Antarctica. In 1986, U.S. and French satellites sensed the Chernobyl nuclear reactor explosion that occurred in the Ukraine. Landsat images from 1975 to 1986 proved to be very instrumental in determining the deforestation of Earth, especially in Brazil. In 1992, hurricane "Andrew," the most costly natural disaster in the history of the United States, with winds of 160 miles per hour, was detected on time by very-high-resolution radar on satellites. Because of the ability to detect the hurricane from a distance, on time, through sophisticated antennas and imagery, the casualties

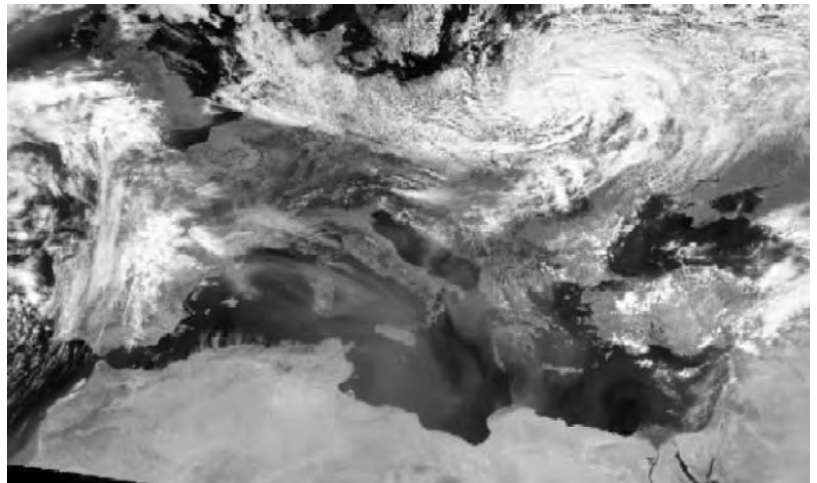


Figure 14. The air over the Mediterranean Sea (thick with smoke and dust). This sea image shows most of the Algerian coastline to be on fire. (Courtesy NASA Goddard Center.)

from this hurricane were low. In 1993, during the flooding of the Mississippi River, antenna images were used to assist in emergency, planning, and locating threatened areas. Finally, NASA, using antennas, managed to receive signals from Mars and have the entire world observe the “pathfinder” maneuver itself through the Rocky Martian terrain.

BIBLIOGRAPHY

1. J. C. Maxwell, *A treatise on Electricity and Magnetism*, Oxford Univ. Press, London, 1873, 1904.
2. H. R. Hertz, *Electric Waves*, Macmillan, London, 1893; Dover, New York, 1962.
3. J. D. Kraus, Antennas since Hertz and Marconi, *IEEE Trans. Anten. Propag.* **AP-33**:131–137 (Feb. 1985).
4. J. Aharoni, *Antennae*, Oxford Univ. Press, London, 1946.
5. S. Silver, *Microwave Antenna Theory and Design*, MIT Radiation Lab. Series, Vol. 12. McGraw-Hill, New York, 1949.
6. S. A. Schelkunoff and H. T. Friis, *Antenna Theory and Practice*, Wiley, New York, 1952.
7. S. A. Schelkunoff, *Advanced Antenna Theory*, Wiley, New York, 1952.
8. E. A. Laport, *Radio Antenna Engineering*, McGraw-Hill, New York, 1952.
9. R. E. Collin and F. J. Zucker, eds., *Antenna Theory*, Parts 1 and 2, McGraw-Hill, New York, 1969.
10. R. S. Elliot, *Antenna Theory and Design*, Prentice-Hall, New York, 1981.
11. W. L. Stutzman and G. A. Thiele, *Antenna Theory and Design*, Wiley, New York, 1981.
12. A. W. Rudge, K. Milne, A. D. Olver, and P. Knight, eds., *The Handbook of Antenna Design*, Vols. 1 and 2, Peter Peregrinus, London, 1982.
13. R. C. Johnson and H. Jasik, *Antenna Engineering Handbook*, McGraw-Hill, New York, 1961, 1984.
14. K. F. Lee, *Principles of Antenna Theory*, Wiley, New York, 1984.
15. W. L. Weeks, *Antenna Engineering*, McGraw-Hill, New York, 1984.
16. R. E. Collin, *Antennas and Radiowave Propagation*, McGraw-Hill, New York, 1985.
17. J. R. Wait, *Introduction to Antennas and Propagation*, IEE, Hithin Herts, UK, 1986.
18. L. V. Blake, *Antennas*, Wiley, New York, 1966; Artech House, Norwood, MA, 1987.
19. E. Wolff, *Antenna Analysis*, Wiley, New York, 1966; Artech House, Norwood, MA, 1988.
20. Y. T. Lo and S. W. Lee, eds., *Antenna Handbook: Theory Applications and Design*, Van Nostrand Reinhold, New York, 1988.
21. J. D. Kraus, *Antennas*, McGraw-Hill, New York, 1950, 1988.
22. F. R. Connor, *Antennas*, Edward Arnold, London, 1989.
23. C. A. Balanis, *Antenna Theory: Analysis and Design*, Wiley, New York, 1982, 1996.
24. *IEEE Standard Definitions of Terms for Antennas*, IEEE Standard, 145-1993; reprinted in *IEEE Trans. Anten. Propag.* **AP-27**(6):3–29 (1993).
25. C. A. Balanis, Antenna theory: A review, *Proc. IEEE* 80(1): 7–23 (Jan. 1992).
26. T. A. Mulligan, *Modern Antenna Design*, McGraw-Hill, New York, 1985.
27. T. Tsukiji and S. Tou, On polygonal loop antennas, *IEEE Trans. Anten. Propag.* **AP-28**(4):571–575 (July 1980).
28. A. E. Love, ed., *Reflector Antennas*, IEEE Press, New York, 1978.
29. P. J. Wood, *Reflector Analysis and Design*, Peter Peregrinus, London, 1980.
30. J. D. Kraus, The corner reflector antenna, *Proc. IRE* **28**:513–519 (Nov. 1940).
31. A. W. Rudge, Off-set parabolic reflector antennas: A review, *Proc. IEEE* **66**(12):1592–1618 (Dec. 1978).
32. W. E. Kock, Metal lens antennas, *Proc. IRE* **34**:828–836 (Nov. 1946).
33. C. H. Walter, *Traveling Wave Antennas*, McGraw-Hill, New York, 1965.
34. S. Uda, Wireless beam of short electric waves, *J. IEE (Jpn.)* 1209–1219 (Nov. 1927).
35. H. Yagi, Beam transmission of ultra short waves, *Proc. IEE* **26**:715–741 (June 1928).
36. V. H. Rumsey, *Frequency Independent Antennas*, Academic Press, New York, 1966.
37. A. W. Love, ed., *Electromagnetic Horn Antennas*, IEEE Press, New York, 1976.

38. P. J. B. Clarricoats and A. D. Olver, *Corrugated Horns for Microwave Antennas*, Peter Peregrinus, London, 1984.
39. J. R. James and P. S. Hall, *Handbook of Microstrip Antennas*, Vols. 1, 2, Peter Peregrinus, London, 1989.
40. J. L. Eaves and E. K. Reedy, (eds.), *Principles of Modern Radar*, Van Nostrand Reinhold, New York, 1987.
41. J. Griffiths, *Radio Wave Propagation and Antennas*, Prentice-Hall Int., London, 1987, Chapters 8, 9.
42. F. J. Ricci, *Personal Communications Systems Applications*, Englewood Cliffs, NJ, Prentice-Hall, 1997.
43. T. T. Ha, *Digital Satellite Communications*, Macmillan, New York, 1986.
44. M. Rubelj, P. F. Wahid, C. G. Christodoulou, A microstrip array for direct broadcast satellite receivers, *Microwave Opt. Technol. Lett.* **15**(2):68–72 (June 1997).
45. W. L. Pritchard and J. A. Sciulli, *Satellite Communications Systems Engineering*, Prentice-Hall, Englewood Cliffs, NJ, 1986.
46. L. H. Van Tress, ed., *Satellite Communication Systems*, IEEE Press, New York, 1979.
47. S. D. Dorfman, *Satellite Communications in the 21st Century*, Strategies Summit, Telecom '95 (IUT), Geneva, Switzerland, Oct. 10, 1995.
48. A. H. El Zooghby, C. G. Christodoulou, and M. Georgiopoulos, Performance of radial basis functions for direction of arrival estimation with antenna arrays, *IEEE Trans. Anten. Propag.* (Nov. 1997).
49. C. H. Durney, Antennas and other electromagnetic applicators in biology and medicine, *Proc. IEEE*, **80**(1) (Jan. 1992).
50. M. I. Skolnik, *Introduction to Radar Systems*, 2nd ed., McGraw-Hill, New York, 1980.
51. D. K. Barton, *Radar Systems Analysis*, Artech House, Dedham, MA, 1976.
52. G. W. Stimson, *Introduction to Airborne Radar*, Hughes Aircraft Company, Radar Systems Group, El Segundo, CA, 1983.
53. C. T. Swift, Passive microwave remote sensing of the ocean—a review, *Bound. Layer Meteorol.* **18**:25–54 (1980).
54. R. H. Dicke, The measurement of thermal radiation at microwave frequencies, *Rev. Sci. Instrument.* **17**:268–275 (1946).
55. J. K. Smith, MEMS and advanced radar, Tutorial Session on MEMS for Antenna Applications, *1999 Antenna Applications Symp.*, Allerton Park, Monticello, IL, Sept. 15–17, 1999.
56. E. R. Brown, RF-MEMS switches for reconfigurable integrated circuits, *IEEE Trans. Microwave Theory Technol.* **46**(11):1868–1880 (Nov. 1998).
57. N. S. Barker and G. M. Rebeiz, Distributed MEMS true-time delay phase shifters and wide-band switches, *IEEE Trans. Microwave Theory Technol.* **46**(11):1881–1890 (Nov. 1998)

FURTHER READING

- J. R. Reid, An Overview of micro-electro-mechanical systems (MEMS), Tutorial Session on MEMS for Antenna Applications, *1999 Antenna Applications Symp.*, Allerton Park, Monticello, IL, Sept. 15–17, 1999.
- W. H. Weedon, W. J. Payne, G. M. Rebeiz, J. S. Herd and M. Champion, MEMS-switched reconfigurable multi-band antenna: design and modeling, *Proc. 1999 Antenna Applications Symp.*, Allerton Park, Monticello, IL, Sept. 15–17, 1999.
- W. J. Payne and W. H. Weedon, Stripline feed networks for reconfigurable patch antennas, *Proc. 2000 Antenna Applications Symp.*, Allerton Park, Monticello, IL, Sept. 2000.

ANTENNAS FOR HIGH-FREQUENCY BROADCASTING

RONALD WILENSKY
 GORDON G. SINCLAIR
 RICHARD R. GREENE
 Technology for Communications
 International
 Fremont, California

1. INTRODUCTION

High-frequency (HF) broadcasting uses discrete bands within the frequency range from 2 to 30 MHz (Table 1). These bands are based on international agreements that also permit broadcasting at other frequencies on a non-interference basis. HF, also known as *shortwave*, is very effective for transmitting voice and program material over distances of thousands of kilometers. While HF broadcasting's role is changing as the world becomes more interconnected by satellites and cable, it is still used extensively for broadcasting across national borders by governmental and private organizations. The implementation of digital HF broadcasting will improve the quality of the received signals and is likely to increase the popularity of HF broadcasts.

2. GENERAL CHARACTERISTICS

The path between an HF transmitter and a receiver may be either along Earth's surface, by means of ground waves, or via the ionosphere, by means of sky waves. Ground waves are reliable but at HF frequencies are limited to a few kilometers over land. HF broadcasting uses sky waves exclusively. Sky waves are radiowaves that radiate away from Earth's surface at some "takeoff angle" (TOA) above the horizon. Sky waves may pass through the ionosphere, or they may be absorbed or refracted back to Earth's surface. The refraction mode is the propagation mode of interest to shortwave broadcasters. The electrical characteristics of the ionosphere change with time of day and hours of daylight (season), and electrical activity of the sun (sunspot number). In addition, the ionosphere's ability to propagate and refract HF radiowaves varies significantly with frequency; therefore, broadcasters must carefully select frequencies that will produce the best propagation paths at any given time.

HF signals propagate by refraction from the E and F layers of the ionosphere, regions of charged particles located approximately 100–400 km above Earth's surface. HF broadcasts must use optimum frequencies in order to obtain useful signal strength at the receiver. Optimum frequencies, normally referred to as FOTs (frequency of optimum transmission) vary widely during a 24-h period. A typical day's ionospheric activity begins with the buildup of a D layer, a layer that forms only on the sunlit side of Earth. The D layer strongly absorbs low HF frequencies, so daytime frequencies must always be high enough to get through it. At night the D layer disappears and FOTs drop. Late at night even the E and F layers may

Table 1. HF Broadcast Bands

Band (MHz)	Frequencies (MHz)	Comments
2	2.300–2.495	
3	3.200–3.400	
4	3.950–4.000	ITU regions 1 and 3 only
5	4.750–5.060	5.0 MHz excluded for time signals
6	5.900–6.200	
7	7.100–7.350	7.1–7.3 MHz excluded in ITU region 2
9	9.400–9.900	
11	11.600–12.100	
13	13.570–13.870	
15	15.100–15.800	
17	17.480–17.900	
19	18.900–19.020	
21	21.450–21.850	
26	25.670–26.100	

diminish significantly, especially at times of low solar activity or long winter nights, when FOTs may drop to the bottom of the band. The subject of propagation of radiowaves via the ionosphere is vast; additional references may be found in this encyclopedia and in the Further Reading list at the end of this article. Because the FOT can vary widely over the course of a single day, HF broadcasting antennas should be capable of transmitting over as many of the allocated bands as possible.

Coverage area is a function of the antenna's takeoff angle and beamwidth. Local coverage requires high TOAs, on the order of 90° , while long-range coverage requires that the signal takeoff at a low angle. The coverage area where the signal is first refracted back to Earth is known as the *first-hop footprint*. The angle of arrival will normally be the same as the takeoff angle. The "hopping" process may continue as many as 2 or 3 more times, ionospheric conditions permitting. Multihop signals are usually terminated if they reach longitudes of dawn or dusk. The limit of good-quality HF service is generally taken to be 6000 km; this distance represents the approximate end of the second-hop coverage area.

HF broadcasting typically uses transmitter carrier powers of 50–500 kW, with a few systems using 1000 kW. Currently, HF transmissions use double-sideband (DSB) amplitude modulation to allow signals to be received and demodulated by simple and inexpensive receivers. More recent plans calling for the conversion of HF broadcasting to single sideband have been shelved in favor of conversion to digital broadcasting using a worldwide standard that was promulgated in 2003. Digital test transmissions commenced in 2003 with encouraging initial results, and some broadcasters predict widespread implementation of digital broadcasting by 2010.

A DSB AM signal with carrier power P and modulation index m , where $0 < m \leq 1$, has an average power of $(1 + m^2/2)P$ and peak envelope power of $(1 + m)^2P$. For 100% modulation ($m = 1$), average and peak power levels are thus $1.5P$ and $4P$, respectively. An antenna excited by a fully modulated 500-kW transmitter must therefore be designed to withstand the currents of a 750-kW source and the voltages and fields of a 2000-kW source.

3. GENERAL ANTENNA CHARACTERISTICS

HF broadcasting antennas must have radiation patterns that match the requirements for a particular target service area. The antenna's gain, horizontal beamwidth, and vertical angle of radiation [takeoff angle (TOA)] must be chosen carefully in order to provide a strong signal in the audience area. This requires taking into account the ionospheric propagation characteristics, distance to the audience area, and geometric shape of the audience area. Antenna selection is aided by computerized propagation prediction programs such as VOACAP and IONCAP, which calculate TOAs, FOTs, gain, and signal strengths.

Despite the variability of the ionosphere as a refracting medium, some general rules apply to the selection of HF broadcasting antennas. HF broadcasting antennas generally operate in the 6–21 MHz frequency bands. Antennas that serve distant audiences have low TOAs, narrow horizontal beams, and high gain of 15–30 dBi (dBi is the antenna gain in decibels above an isotropic radiator). Antennas that serve nearby audiences have higher TOAs, broader or even omnidirectional beams, and lower gains in the range 9–14 dBi. These antennas are often designed to operate down to 2.3 or 3.2 MHz, frequencies that are required for propagation over short distances, particularly at night and when sunspot activity is low.

HF broadcasting antennas are almost without exception horizontally polarized. Although vertically polarized HF antennas have many desirable characteristics, such as low TOA and broad azimuthal patterns, their gain is reduced by several decibels if the ground in front of the antenna is not highly conductive. The gain of horizontally polarized antennas is much less dependent on ground conductivity. At low TOAs poor ground conductivity reduces the gain of a horizontally polarized antenna by only a few tenths of a decibel. The ground losses associated with vertically polarized antennas may be partially overcome by siting the antenna very close to seawater, which has excellent electrical conductivity, or by installation of an artificially enhanced ground made from a large mesh of copper wires. In most situations, such solutions are neither desirable nor possible; consequently, horizontal polarization remains the primary choice for HF broadcasting antennas.

HF broadcasting antennas fall into two main classes: log-periodics and dipole arrays. Log-periodics are wide-band, generally not steerable, and limited to 250 kW of carrier power. Dipole arrays are limited in bandwidth, but can handle more power and are capable of being steered, or "slewed" electrically by up to $\pm 30^\circ$. This allows broadcasters to serve different target areas with the same antenna. An alternative approach to steering the beam rotates the entire antenna; rotatable antennas are rarely used, however, owing to the cost and complexity of the steering mechanisms and the associated structures.

4. LOG-PERIODIC ANTENNAS

Log-periodic antennas (LPAs) are a class of frequency-independent antennas first developed in the 1960s. In the HF band LPAs have been used mainly for communications, but

since the 1970s have been increasingly used for broadcasting. Unlike a single-dipole array, whose operation is limited to a one-octave (2–1) frequency range, an LPA can operate over nearly a 4-octave (16–1) frequency range, covering all of the international broadcast bands from 5.9 through 21 MHz.

LPAs constitute a series of half-wave dipoles spaced along a transmission line where all electrical lengths (lengths of both the dipoles and intervening transmission lines) follow a geometric progression. The ratio of successive smaller lengths is a constant, commonly called the *scaling constant* and represented by the Greek letter τ . By convention, the progression starts with the longest element so that τ is less than 1 and typically in the range 0.8–0.92. LPAs are fed at their high-frequency end, where the radiators are smallest. Current flows up the internal antenna feedline until it reaches a group of radiators, called the *active region*, which are approximately one-half wavelength wide at the excitation frequency. The active region radiates in the direction of the smaller radiators. LPAs typically have balanced input impedances of 100–400 Ω and maximum VSWR of 1.8–1 or less.

A highly desirable feature of LPAs is the ability to tailor their radiation patterns to satisfy different broadcasting requirements. The designer can control the way the radiation pattern varies with frequency by making the pattern dependent on frequency. This is not true for dipole arrays, whose patterns vary with frequency in a way that cannot be controlled.

The radiation pattern of an LPA is determined by the number and arrangement of the curtains. In some LPAs the TOA is designed to decrease as frequency increases. This helps reach audiences at varying distances, since long paths generally propagate best using higher frequencies, while at the same time requiring low TOAs. In other cases the TOA is kept constant, which is very useful for broadcasting to a fixed geographic area. The horizontal beamwidth of an LPA can also be controlled by the designer, although in most situations a fixed beamwidth is most useful.

The physical size of an LPA depends on the antenna's frequency range (principally its low-frequency limit) and radiation pattern characteristics. While the relationships among these characteristics are complex, the following relationships generally apply:

1. The largest radiators of an LPA are approximately one-half wavelength long at the lowest operating frequency. Thus, the lower an antenna's frequency limit, the larger the physical size.
2. The TOA of any horizontally polarized antenna is given by the formula

$$\text{TOA} = \sin^{-1} \frac{\lambda}{4h} \quad (1)$$

where λ is the wavelength at the operating frequency and h is the height above ground of the radiating element with the highest current. Thus, for a low TOA, an antenna's height will be large compared to its wavelength; conversely, high TOAs require lower heights.

3. The horizontal beamwidth of an antenna varies inversely with its horizontal radiating aperture

(the physical width of the active region relative to the wavelength at the operating frequency). Narrow beamwidths require larger apertures and physical size than do broad beamwidths.

LPAs have been designed to operate at transmit powers of 500 kW with 100% amplitude modulation; however, these antennas are large and expensive. Power levels exceeding 250 kW are better handled by dipole arrays. The most cost-effective power range for high-power LPAs is 50–250 kW, with 100-kW versions the most common.

Antenna radiators must have a large electrical diameter to prevent corona discharge at high power levels, since the electric field perpendicular to the surface of a conductor is inversely proportional to the electrical diameter of the conductor. Although radiators can be made from large-diameter tubes or pipes, the resulting structures are expensive and mechanically unreliable. A more reliable and less expensive means of increasing electrical diameter is to form two small-diameter (8–12 mm) wire cables into a triangular tooth (Fig. 1). Radiators with large electrical diameters have lower Q and broader bandwidth than do thin radiators. In an LPA, lower Q results in a greater the number of radiators in the active region, which decreases the power in each radiator. The larger active region also provides a small increase in antenna gain.

4.1. Examples of Log-Periodic Antennas

4.1.1. Short-Range LPAs. To cover short distances, an HF antenna must direct energy at high angles with peak radiation at vertical incidence (i.e., TOA = 90°). According to Eq. (1), the active region at each frequency must be approximately 0.25 wavelength at the operating frequency. Figure 1 illustrates a two-curtain LPA that provides a vertically incident pattern giving primary coverage from 0 to 1500 km. Short-range antennas have low-frequency operating limits in either the 2.3- or 3.2-MHz bands. The upper frequency limit is usually set at 18 MHz to cover areas in the 1000–1500 km range.

The short-range LPA has a maximum gain of 9 dBi at vertical incidence and produces a nearly circular horizon-

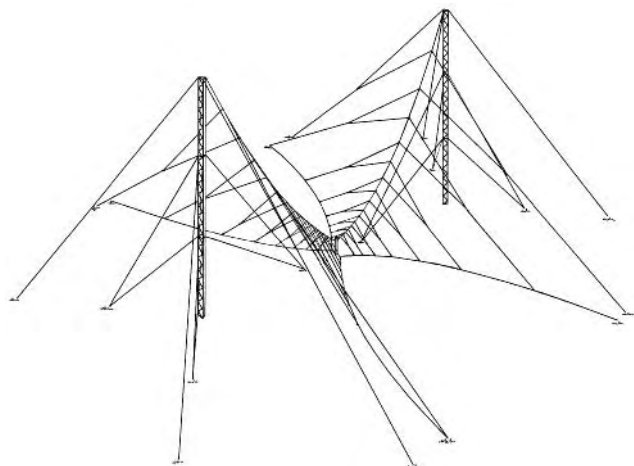


Figure 1. Two-curtain short-range omnidirectional log-periodic antenna.

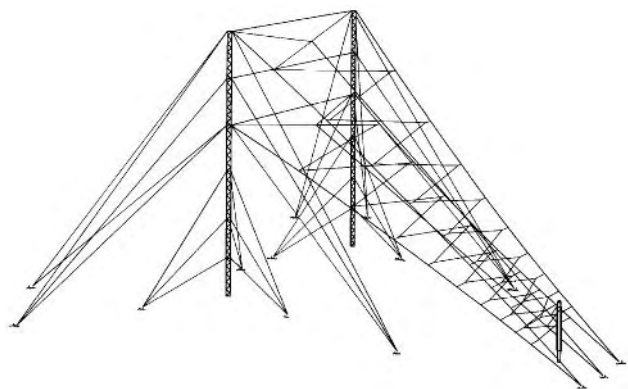


Figure 2. Two-curtain medium-range directional log-periodic antenna.

tal pattern. The elevation pattern has its -3 -dB points at approximately 50° above the horizon. The antenna obtains its high-angle coverage by firing energy downward into the ground, which in turn reflects it upward. A ground screen minimizes losses in the imperfectly conducting Earth. The short-range LPA is the only horizontally polarized antenna for which a ground screen provides meaningful gain enhancement.

4.1.2. Medium-Range LPAs. A two-curtain LPA suitable for broadcasting over distances of 700–2000 km is illustrated in Fig. 2. While similar to the LPA shown in Fig. 1, this antenna fires obliquely into the ground, rather than vertically, producing a lower TOA and narrower elevation pattern than the short-range LPA. Antennas of this type have TOAs in the range of 20 – 45° , with gains of 14 and 10 dBi respectively, and horizontal patterns having -3 -dB beamwidths of 68 – 90° .

4.1.3. Long-Range LPAs. A four-curtain LPA (Fig. 3) provides vertical and horizontal patterns that are narrower than those of the two-curtain LPA. This antenna provides gain of up to 18 dBi and low TOA in the range of 12 – 20° . The -3 -dB horizontal beamwidth is 38° . This pattern provides excellent coverage for broadcasts beyond 1500 km.

5. DIPOLE ARRAYS

Dipole arrays are rectangular or square arrays of half-wave dipoles mounted in front of a reflecting screen (Fig. 4). Dipole arrays have high power handling capacity and provide a wide variety of different radiation patterns

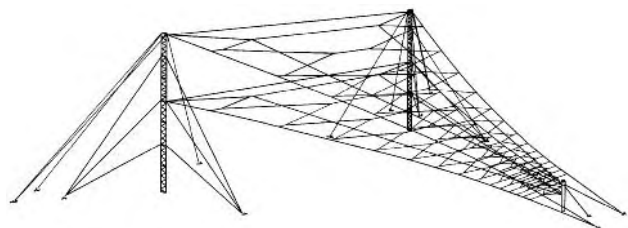


Figure 3. Four-curtain long-range directional log-periodic antenna.

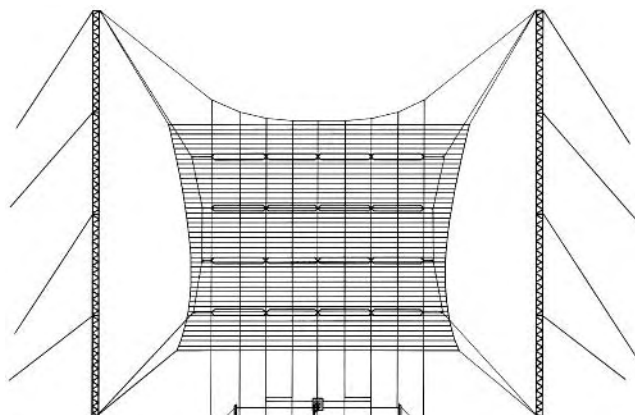


Figure 4. 4×4 dipole array with reflecting screen.

to serve different broadcasting requirements. Beams of dipole arrays can be steered in both the vertical and horizontal planes without moving the entire antenna.

Dipole arrays containing four or more dipoles have low VSWR over a 1-octave frequency range. Arrays with fewer than four dipoles generally have narrower impedance bandwidths. Unlike an LPA, one dipole array cannot cover the entire shortwave frequency range, which is 4 octaves wide. However, two dipole arrays, one operating in the 6/7/9/11-MHz bands and the other in the 13/15/17/19/21/26-MHz bands, can cover the frequencies used in international broadcasting. The dimensions of a dipole array are determined by its design frequency f_0 , which is approximately equivalent to the arithmetic mean of the lowest and highest operating frequencies. The design wavelength, λ_0 (meters) is $300/f_0$ (MHz). Horizontal and vertical centers of the dipoles are spaced at $0.5\lambda_0$ wavelengths.

The dipoles in the array are interconnected by a set of balanced transmission lines. The transmission lines terminate at a single feedpoint having a balanced impedance of 200 – 330Ω . The input VSWR of a dipole array is generally 1.5 – 1 or less in its operating bands.

The most commonly used dipole arrays are described by the standard nomenclature AHRS $m/n/h$; “H” indicates that the antenna is horizontally polarized; “R” that it has an aperiodic (i.e., nonresonant) reflecting screen, and “S” (if present) that the antenna beam can be slewed horizontally or vertically. m and n are integers that indicate, respectively, the number of vertical columns and the number of dipoles in each column; h is the height of the lowest dipole above ground in wavelengths at the antenna design frequency. The m , n , and h parameters determine the antenna’s radiation patterns. Most common values are $m = 2$ or 4 , $n = 2, 4$, or 6 , and $h = 0.5$ – 1.0 . The radiation patterns for various dipole arrays (Table 2) demonstrate the wide variety of radiation patterns which dipole arrays can provide.

The number of vertical columns m determines the horizontal aperture of the antenna. For $m > 1$, the -3 dB horizontal beamwidth (HBW) at frequency f is approximately $100^\circ(f_0/mf)$. At $f = 1.34f_0$, the upper frequency limit of a 1-octave bandwidth, the minimum HBW is 75° divided by m .

The number of dipoles in each column (n) and height of the lowest dipole (h) determine the TOA and elevation

Table 2. Radiation Patterns of Typical Dipole Arrays over 2–1 Bandwidth

Array Type	TOA	– 3 dB HBW	– 3 dB VBW	Gain (dBi)
AHRS 2/2/0.5	13–25°	40–70°	13–25°	18–15
AHRS 4/2/0.5	13–25°	20–35°	13–25°	21–18
AHRS 2/4/0.5	7–14°	40–70°	7–14°	21–18
AHRS 4/3/0.5	8–16°	20–35°	8–16°	23–18
AHRS 4/4/0.5	7–14°	20–35°	7–14°	24–19
AHRS 4/4/1.0	5–10°	20–35°	5–10°	24–19
AHRS 4/6/0.5	4–8°	30–35°	4–8°	25–20

Note: The first value in the range is the highest frequency; the second value is the lowest frequency.

pattern beamwidth. In typical dipole arrays $h \leq 1.0$ and $n \leq 6$ (larger values would result in very tall and expensive antennas). The effective height of radiation is the average height above ground of all the excited dipoles. The effective height can be used in Eq. (1) to calculate the TOA.

Modern dipole arrays use reflecting screens to suppress radiation behind the antenna and increase forward gain by nearly 3 dB. A typical screen consists of horizontal wires with a vertical separation of $0.04\text{--}0.06\lambda_0$. The screen is placed approximately $0.25\lambda_0$ behind and parallel to the plane of the dipoles. It extends approximately $0.125\text{--}0.25\lambda_0$ beyond the edges of this plane. Screens for 2-, 4-, and 6-high arrays have 25–35 wires, 50–75 wires, and 75–100 wires. These parameters produce a backlobe which is 12–15 dB below the gain of the mainbeam. The backlobe may be reduced further by adding more screen wires. Halving the vertical spacing by doubling the number of wires reduces the backlobe by 6 dB, although there is a tradeoff—screens with more wires impose greater loads on the support towers.

6. SLEWING DIPOLE ARRAYS

Phase delays can be inserted via RF switches in the internal feedlines of a dipole array to slew, or steer, the pattern in the horizontal plane. Horizontal slews of up to $\pm 30^\circ$ relative to boresight are accomplished by switching in delay lines that introduce a progressive phase delay from column to column. Phase delays greater than 30° should not be used since the result would be high VSWR and excessive sidelobe levels. For maximum horizontal coverage with minimum complexity and cost, slewing systems should provide angular steps equal to approximately 50–75% of the HBW. Thus, a five-position slewing system providing 10–15° steps is suitable for a 4-wide array, which has a minimum HBW of 19°.

Vertical slew may be accomplished by switching off one or more pairs of dipoles in each column. For example, 6-high arrays commonly have three vertical slew positions. The lowest TOA is obtained with all six dipoles excited. Medium/high-angle slews are obtained by exciting only the bottom four and bottom two dipoles, respectively.

Slewing of a dipole array can cause resonances near the lower frequency limit. Resonances always produce voltages much higher than normal, and may also cause excessive VSWR. Resonances are caused by circulating currents that flow between the interconnected dipoles. At a circulating current resonance, some dipoles have nega-

tive input resistance and thus act as a power source rather than a power sink. Circulating current resonances are 50–250 kHz wide, comparable to the width of a broadcast band. In 4- and 6-high arrays, multiple resonances can occur, preventing operation in one or more bands. Resonant frequencies are determined by the pathlength between the dipoles and can be changed by altering this length. The prediction and measurement of circulating current resonances is an important part of both the design and construction of dipole arrays.

7. TRANSMISSION LINES, SWITCHING SYSTEMS, AND BALUNS

A broadcast station's transmitters are connected to its antennas via a feed system that includes balanced and/or coaxial transmission lines. All but the simplest feed systems also include switching, usually provided by a matrix of switches, which select the antennas that are to be connected to the transmitters. Feed systems generally include balanced-to-unbalanced (balun) transformers to match the balanced impedance of most high-power HF antennas to the unbalanced impedance of modern transmitters.

8. RIGID COAXIAL LINE

RF output is typically taken from the transmitter by means of a rigid coaxial transmission line. Coax sizes range from $6\frac{1}{8}$ -in. EIA standard for 100 kW to 9-in. standard (nominal, not standardized) for 500 kW. Characteristic impedance is usually 50 or 75 Ω . Coax lines outside the transmitter building require constant pressurization with 3–10 psi (lb/in.²) of dry air to prevent condensation of moisture. Lines within the building do not require pressurization.

9. SWITCH MATRIX

The typical switch matrix comprises a number of rows and columns of motorized single-pole, double-throw switches. Typically, transmitters feed the rows of switches; in turn, the columns of switches feed the antennas. The matrix configuration allows any transmitter–antenna combination while prohibiting the connection of two transmitters to a single antenna, or two antennas to a single transmitter. A typical switch matrix comprising 5 rows and 6 columns is shown in Fig. 5.

Switch matrices can be either balanced or unbalanced. Balanced matrices have impedance levels of 300–330 Ω .

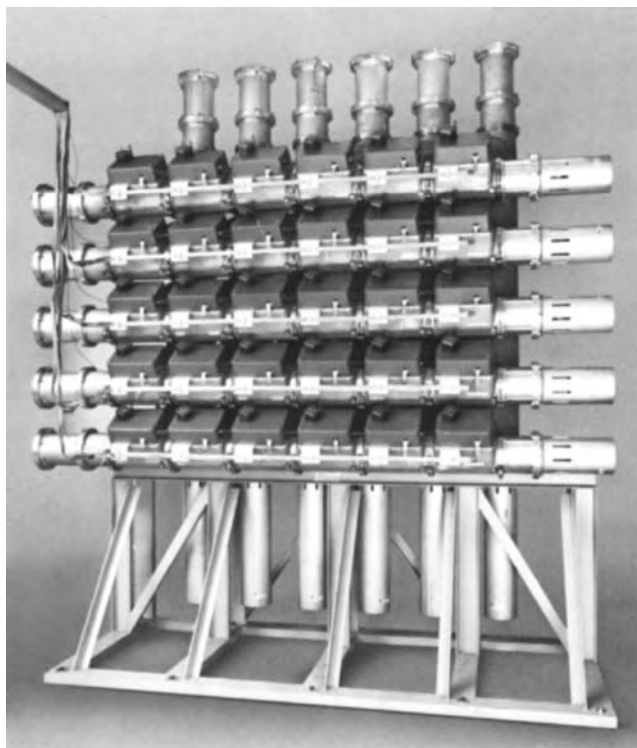


Figure 5. Coaxial switch matrix, 5 rows \times 6 columns.

Unbalanced matrices are either 50 or 75 Ω . Balanced matrix switches are generally shielded to minimize RF radiation in the vicinity of the switch. Coaxial matrix switches are inherently shielded by nature of their construction. Coaxial switch matrices generally preferred in new installations because they are smaller in size and have greater RF isolation between the switches.

10. BALUNS

The input of a balun matches the impedance of the coaxial portion of the system, usually 50 or 75 Ω ; the output matches the balanced impedance of the antenna, usually 300 Ω . Some transmitters are equipped with baluns that use a network of motorized adjustable components that are set to different values for each transmitter operating frequency. Another type of balun is a completely passive device designed to operate over a wide range of frequencies without tuning. A broadband balun consists of a coaxial section that converts the RF power to a balanced mode, and a tapered balanced transmission line that transforms the impedance to 300 Ω . A typical broadband balun is 33 m long and operates at 5.9–26 MHz.

11. BALANCED TRANSMISSION LINE

A balanced, or “open wire,” transmission line is commonly used to feed high-power RF to antennas. This line usually consists of two pairs of copper, aluminum, aluminum-clad steel, or copper-clad steel wire cables held at a fixed distance by means of high-voltage insulators. The line is

held under tension 3–6 m above ground by poles spaced at 15–25-m intervals. Open wire transmission line costs less than rigid coax and is much easier to repair.

12. FEED SYSTEM CONFIGURATIONS

HF broadcasting stations generally use one of three types of feed systems: (1) all balanced, (2) all unbalanced, or (3) combined balanced–unbalanced. The balanced system is used when the transmitter includes its own balun and therefore provides a balanced output. The RF switches and transmission lines will be balanced and have an impedance level that matches that of the antennas. In the unbalanced system, all feeders from the transmitter to the RF switches and from the switches to the antenna are coaxial lines. Each antenna has a broadband balun whose frequency range matches that of the antenna. In the combined unbalanced/balanced system, coaxial feeders are used between the transmitters and switch matrix and from the switch matrix to an area outside but near the transmitter building in which broadband baluns are placed. Balanced open wire transmission lines interconnect the baluns to the antennas.

The balanced system is used primarily at small stations that contain a small number of transmitters and antennas. It is the least expensive of the three systems. In stations containing a large number of transmitters, a balanced switch matrix will occupy a large amount of space and is therefore not desirable. The unbalanced system is the most expensive and is preferred when there are environmental concerns that necessitate maximum shielding of the transmission-line system. The combined unbalanced/balanced system is the one most commonly used at modern stations because it provides a good trade-off between cost, size, and performance.

FURTHER READING

- G. Braun, *Planning and Engineering of Shortwave Links*, Hayden, London, 1982.
- R. E. Collin and Z. A. Zucker, *Antenna Theory*, Vols. 1 and 2, McGraw-Hill, New York, 1969.
- K. Davies, *Ionospheric Radio*, Peter Peregrinus, London, 1990.
- J. M. Goodman, *HF Communication Science and Technology*, Van Nostrand, New York, 1992.
- G. Jacobs and T. J. Cohen, *The Shortwave Propagation Handbook*, Cowan, Port Washington, NY, 1979.
- R. C. Johnson, ed., *Antenna Engineering Handbook*, 3rd ed., McGraw-Hill, New York, 1993.
- J. A. Kuecken, *Antennas and Transmission Lines*, Howard Sams, Indianapolis, 1969.
- Y. T. Lo and S. W. Lee, *Antenna Engineering Handbook*, Van Nostrand, New York, 1988.
- W. L. Stutzman and G. A. Thiele, *Antenna Theory and Design*, Wiley, New York, 1981.
- W. Wharton, S. Metcalfe, and G. Platts, *Broadcasting Transmission Engineering Practice*, Butterworth-Heinemann, London, 1992.
- J. Wood, *History of International Broadcasting*, Peter Peregrinus, London, 1992.

ANTENNAS FOR MEDIUM-FREQUENCY BROADCASTING

RONALD RACKLEY
MATTHEW FOLKERT
du Treil, Lundin, & Rackley
Sarasota, Florida

The beginnings of medium-frequency broadcast antennas (530–1700 kHz) can be traced to the early 1920s. The first antennas constructed were made of a pair of steel or wooden masts supporting an antenna structure consisting of a vertical wire or wire cage, sometimes accompanied by a horizontal section consisting of a wire or flat surface or cage of wires. The antennas with the horizontal members were referred to as T- or L-type antennas. Figure 1 illustrates the physical characteristics of the early medium-frequency antennas. Most of these antennas did not exceed a physical height of 50–70 electrical degrees. In 1924, Ballantine [1] showed that longer antennas would result in a substantial gain in the horizontal plane radiation. Heights were then increased to as much as 135 electrical degrees with the first commercial antennas being constructed in the early 1930s.

During the 1930s the present type of medium-frequency broadcast antenna, a self-supporting or guyed tower in which a base-insulated tower is utilized as the radiating element with an accompanying ground system, was developed. The classic paper by Chamberlain and Lodge [2] spearheaded this development and offered many advantages over the earlier antennas. The radiation efficiency of a nondirectional radiator was often more than double when this new type of design was put into service and the cost of such a structure decreased significantly as the number of required towers was cut in half. It was also found necessary to use breakup insulators to reduce guywire current. Figure 2 shows a single-tower radiator of this type. As the number of medium-frequency broadcast stations increased during the 1930s, it was necessary to develop directional antenna systems to minimize interference between stations. A directional antenna consists of multiple towers used in a phased-array configuration and excited with various amplitude and phase relationships to form a pattern in the desired shape. The single excited tower radiating element made the directional antenna concept an economically feasible possibility. The first directional antenna system designed by Dr. Raymond M. Wilmotte, was constructed by WSUN in St. Petersburg, Florida and

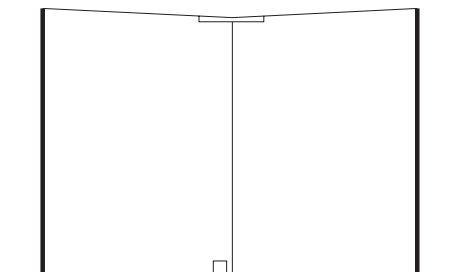


Figure 1. Early AM antenna utilizing two vertical masts supporting the radiating structure.

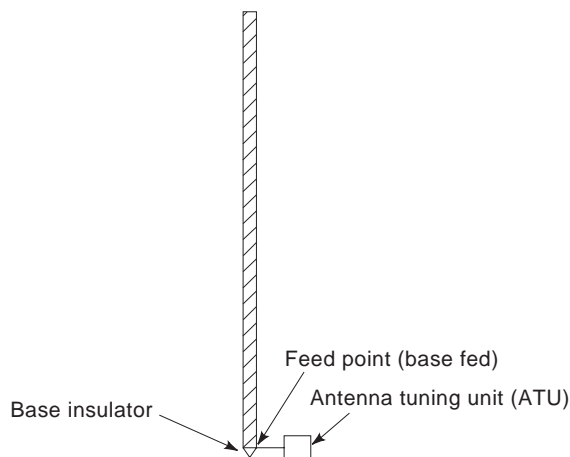


Figure 2. Present antenna configuration using the tower as the radiating element. Structure can be self-supporting or supported with guywires.

employed two towers to produce a radiation pattern null toward cochannel station WTMJ in Milwaukee, Wisconsin to resolve a nighttime interference controversy.

The 1940s brought further development to the design of medium-frequency broadcast antennas. Top-loading, sectionalizing, and improved ground systems were introduced to improve antenna efficiency as well as to control vertical radiating characteristics. The number of towers used in directional arrays was increased to as many as nine elements as the power dividing and phasing systems were improved.

Since the 1940s, there has not been significant development in the area of the antenna element itself as self-supporting and guyed radiating towers continue to be used much as they were at that time. In the 1960s, three 12-tower arrays were constructed at WJBK in Detroit, Michigan, CFGM in Toronto, Canada, and KLIF in Dallas, Texas. These were the largest arrays of driven elements ever constructed for medium-frequency broadcast use. New developments since then have principally involved auxiliary equipment used to test and monitor the antenna system and the means by which the antenna is theoretically analyzed. Digital antenna monitors are used today to accurately monitor the relative current magnitudes and phase relationships of the towers in a directional array while portable solid-state field strength meters are used to measure radiation patterns. Advances have also been made with improved RF current meters, sampling transformers, and impedance measuring equipment. The design of medium-frequency broadcast antennas for optimized performance has also seen tremendous advances with the introduction of numerical solutions to electromagnetic problems and nodal modeling of feeder systems made economically possible with personal computers vastly simplifying both design and implementation.

1. GENERAL ANTENNA CHARACTERISTICS

The medium-frequency range is generally defined from 300 to 3000 kHz. The portion of the band allocated to AM

broadcasting is from 530 to 1700 kHz in North America. The channels for the individual broadcast stations are spaced 10 kHz apart. In contrast, within the medium-frequency broadcast band in other regions of the world, the stations are spaced 9 kHz apart.

1.1. Electrical

The typical antenna used for medium-frequency broadcasting is electrically equivalent to one or more base-excited monopoles over a finite perfectly conducting ground plane. In directional antenna systems, where more than one element is employed, the amplitude and phase of the current to each monopole are varied in relationship to one another to determine the pattern size and shape. The height of each monopole can vary in height from as little as 45 to as much as 225 electrical degrees. This translates to a range of physical heights of 25–200 m within the medium-frequency band. In a few rare instances taller towers are employed; they are center-fed and known as *Franklin Antennas*.

1.2. Mechanical

A self-supported or guyed steel tower is usually used as the radiating element. The tower can be triangular or square in cross section and can have a face width ranging from a fraction of a meter to several meters. A ground system consisting of copper wires typically extends radially from the base of each tower a length of 90 electrical degrees from the tower base. Normal practice is to use 120 wires equally spaced (every 3 degrees) and equal in length except where they would overlap between adjacent towers for the ground system. Overlapping of wires is avoided by shortening them and bonding them to a transverse conductor (usually a copper strap).

1.3. Propagation

The electromagnetic field propagates from a medium-frequency antenna system in two modes. The first mode travels along the surface of the ground and is referred to as *ground-wave propagation*. The second mode radiates directly into space and refracts from the ionosphere before reaching the target area and is referred to as *sky-wave propagation*. Effective sky-wave propagation is severely attenuated during daytime hours and is significant only at night. Ground-wave propagation is dependent on the characteristics of the terrain over which the signal propagates. Propagation models for ground-wave and sky-wave signals, as they affect spectrum management and individual station authorization, are prescribed by the government agency having jurisdiction within the country where a station is located. The agency with jurisdiction over stations operation within the United States is the Federal Communications Commission (FCC), while many foreign countries use propagation standards published by the ITU/CCIR.

2. STATION CLASSIFICATIONS

The FCC of the United States regulates all medium-wave radio broadcasting in the United States. The FCC has

classified all medium-frequency radio stations into categories defining their coverage areas and power levels [3]. An *unlimited* time station can broadcast at all times during the daytime and nighttime, whereas a *limited* time station (usually daytime) can only broadcast at certain specified times. A *primary* service area is defined as the area within close proximity to the station and where ground-wave propagation provides a high-quality signal. A *secondary* service area is more distant from the station and usually depends on sky-wave propagation during nighttime hours.

Under the international agreements governing medium-wave broadcasting in the Western Hemisphere (ITU Region III), there are three classes of frequency allotments. By bilateral agreements among the North American countries, certain channels or frequencies are reserved for use by stations providing various classes of service.

2.1. Clear Channel

A *clear channel* classification is assigned to stations covering wide service areas and is subdivided into three classes:

1. *Class A*. Unlimited stations assigned to primary and secondary service area. Power levels range between 10 and 50 kW.
2. *Class B*. Unlimited service assigned to primary service areas only. Power levels range between 0.25 and 50 kW.
3. *Class D*. Limited service daytime or unlimited service with no nighttime service or nighttime power less than 0.25 kW. Power levels range between 0.25 and 50 kW.

2.2. Regional Channel

A *regional channel* classification is assigned to stations serving a principal center of population and the surrounding rural areas and is subdivided into two classes:

1. *Class B*. Unlimited service assigned to a primary service area. Power levels range between 0.25 and 50 kW.
2. *Class D*. Limited service daytime or unlimited service with no nighttime service or nighttime power less than 0.25 kW. Power levels range between 0.25 and 50 kW.

2.3. Local Channel

A *local channel* classification is assigned to stations serving a community and the surrounding suburban and rural areas and consists of one class:

1. *Class C*. Unlimited service assigned to a primary service area. Power level range between 0.25 and 1 kW.

3. ALLOCATION STUDIES

Before a medium-frequency station can be licensed, an analysis is required to determine compliance with rules governing acceptable interference levels between stations. In the United States, the analysis is based on propagation models and conductivity maps as defined in the Code of Federal Regulations [3].

3.1. Propagation Models

Field strength algorithms exist that can be used to predict the coverage of a particular antenna system. The *equivalent-distance ground-wave model* is a prediction method used for daytime ground-wave field strength calculations when signals propagate over one or more conductivity regions. The *1992 FCC Skywave Model* (47 CFR 73.183) is a prediction method used for most nighttime field strength calculations within the United States. The *Region 2 Annex II Figure 4 Skywave Model* is a predication method used for nighttime sky-wave field strength calculations between the United States and Central and South America, and the Caribbean Islands. Also, the *US–Canada Bilateral Agreement, Annex II Figure 4A Skywave Model* is a predication method used for nighttime sky-wave field strength calculations between the United States and Canada. Propagation models and techniques for determining allowable interference differ substantially from one part of the world to another. Propagation models for other regions of the world are specified in regional agreements administered by the International Telecommunications Union (ITU) in Geneva, Switzerland.

3.2. Ground Conductivity Maps

The calculation of ground-wave field strength levels depend on predicted ground conductivity and dielectric constant values for the area of interest. It is an acceptable simplification for most engineering analysis to define ground conductivity with a fixed dielectric constant. Predicted conductivities are usually presented in the form of a map or computer model delineating boundaries between regions of different conductivities. The M3 map is included in the FCC rules and shows predicted ground conductivity for the continental United States. The region 2 map covers a larger area and shows predicted ground conductivity for much of the Western Hemisphere. The M3 map is used for calculations between stations within the United States while the region 2 map is used between stations in the United States and stations in Canada, Central America, and the Caribbean. Other countries utilize conductivity maps developed for their own regions.

3.3. Field Strength Contours

When analyzing the coverage from a given antenna system, it is useful to calculate field strength contours at various levels to determine if the station is providing adequate coverage to the target area and if interference exists between stations on cochannel or adjacent channel frequencies. A field strength level of 50–25 mV/m is considered necessary to provide premium service to heavily

Frequency separation (kHz)	Contour of proposed station (classes B, C and D) (mV/m)	Contour of any other station (mV/m)
0	0.005	0.100 (Class A)
	0.025	0.500 (Other classes)
	0.500	0.025 (All classes)
10	0.250	0.500 (All classes)
	0.500	0.250 (All classes)
20	5.0	5.0 (All classes)
30	25.0	25.0 (All classes)

Figure 3. Daytime protection limits as specified by the Federal Communications Commission. Protection limits are instituted to reduce cochannel and adjacent-channel interference.

built-up urban and industrialized areas, whereas a field strength of 5 mV/m is often considered to be satisfactory for the less heavily built-up surrounding areas. A field strength of 2.0 mV/m provides service to residential areas and 0.5 mV/m is the minimum signal level for service to rural areas in nontropical regions of the world.

3.4. Daytime Allocation Study

A daytime allocation study involves the calculation of ground-wave field strength contours to determine if interference exists between stations on cochannel or adjacent channel frequencies. The required protections as specified by the FCC are given in Fig. 3. The most stringent protection is afforded to cochannel stations with decreasing protection levels to the first, second, and third adjacent channels chosen to eliminate *splatter* between the signals of nearby stations.

3.5. Nighttime Allocation Study

A nighttime allocation study involves the calculation of nighttime skywave field strength levels to determine if interference exists between stations on cochannel or adjacent frequency channels. In contrast to the daytime study in which field strength contours are determined, the nighttime study involves point-to-point calculations. In the United States, the method for determining protection between stations requires calculating the received interfering field strengths from all cochannel and first-adjacent-channel stations. The square root of the sum of the squares (RSS) is calculated using all the interfering signals in descending order and determines the overall interference level. The levels of interference which are defined by the FCC are the 50% and 25% RSS levels. The 50% RSS level includes only the stations that contribute a signal level of at least 50% to the running RSS total, whereas the 25% RSS level includes all stations that contribute a signal level of at least 25% to the running RSS total. When a station is newly licensed or undergoes a major change (increase in power or modified pattern), it cannot increase interference to existing stations above the 25% RSS level. If a station presently causes interference at a level between 25 and 50% of another station, its interference contribution cannot be increased at all, and, if it presently caused interference above the 50% level, its

interfering signal must be decreased at the affected station by at least 10% under the present FCC rules. The service area of a station during nighttime hours is considered to be the area that is defined by the 50% RSS boundary.

4. ANTENNA DESIGN

Antenna design involves the selection of physical and electrical parameters that meet all design requirements as determined by the allocation studies while simultaneously providing a satisfactory level of interference-free coverage to the proposed coverage area, including the “community of license,” from the selected transmitter site.

4.1. Mechanical

4.1.1. Radiating Elements. Two types of radiating elements are typically used in medium-frequency broadcast antenna system today: self-supporting or guyed towers. A self-supporting tower consists of a free-standing tapered steel structure. A guyed tower is usually of uniform cross section and is supported by insulated steel guy cables or nonconductive cables attached at multiple levels. Either type of tower can be top-loaded (with a horizontal steel circular cap or a portion of the guy wires connected directly to the tower to achieve greater electrical height with a physically shorter structure) or sectionalized (when the tower is broken into sections and a series inductance is inserted between them to reduce the reactance of the upper sections). In some cases, where towers on the order of a wavelength tall are employed, they are center fed. Such center-fed towers are known as *Franklin antennas*.

4.1.2. Feedpoint. The feedpoint is the location at which the radiating element is fed power from the transmission line. A series feed system feeds the power across a tower’s base insulator, whereas a tower may be shunt-fed either with a slant wire attached part way up its structure or with a wire skirt at its base. A major advantage of grounded tower radiators with skirt wires is the elimination of isolation components for lighting circuits. This is especially true for very high-power operation of stations outside the United States. A Franklin antenna may be fed across either an insulator or gap in a wire skirt at approximately one half of its height. Some type of balun (usually a quarter-wave line section) must be employed to isolate the circuit across the ground level insulator of a Franklin antenna.

4.1.3. Ground System. The ground system is a conductive screen or grid of wires imbedded in the ground around the base of each radiating element to allow ground currents to return directly to its base. A typical ground system consists of 120 buried copper wires, equally spaced, extending radially outward from each radiating element base to a minimum distance of 90 electrical degrees. An exposed copper mesh may also be used around the base when high voltages are expected.

When multiple elements are used to form an array, the ground radial wires from adjacent towers will often over-

lap. When this occurs, a copper transverse strap or cable is employed for bonding the radials together so that they do not extend into the area where they would overlap.

4.1.4. Lighting System. A system of beacons or continuously illuminated lights mounted on each tower at various heights is often required for towers above a certain height. Series excited towers must have some means of coupling the ac power to the lighting circuit on the towers while the wiring may proceed directly from ground level up a shunt-fed grounded tower. Lighting chokes, which provide a high impedance at the RF frequency while conducting ac current are often used for connecting the lighting circuits on towers across their base insulators. Another method employed uses a *ring* transformer that is constructed so that the primary and secondary have sufficient spacing between them to withstand typical base voltages while adding only a slight amount of capacitance across the base as far as the RF energy is concerned.

4.1.5. Lightning Protection. Because of the relatively tall and conductive nature of a medium-frequency antenna system, they are very susceptible to lightning strikes. Additionally, high transient voltages can be induced at their bases due to distant lightning strikes and they are subject to high static buildup under certain environmental conditions. Therefore it is necessary to include a system to protect the radiating elements and associated tuning components from being damaged by lightning strikes. A tower protection system usually consists of a pointed vertical rod or rods at its top, extending above the tower lighting beacon if one is employed, a conductive circuit such as an RF choke across the tower base to provide a low impedance path to ground (for series-excited towers) and a set of arc gaps directly across its feedpoint.

4.2. Electrical

Electrical parameters are chosen such that size and shape of an antenna pattern meet the radiation limits identified in the allocation studies. Antenna patterns fall into two broad categories: directional and nondirectional. Where a power level to provide satisfactory coverage can be had without any interference to other stations, a new facility may employ a nondirectional antenna consisting of only one radiating element. Otherwise, a multielement array (directional antenna) must be employed to meet the protection requirements. The parameters used to design a directional antenna pattern include the field ratios and phase relationships between elements, the number of elements, the height of each element, and the physical orientation of each element. These are the factors that determine the size and shape of the pattern such that the amount of energy radiated is controlled in any given direction.

4.2.1. Electrical Parameters. The following example (Table 1) shows how the electrical design parameters are typically specified for a four element array. Note that

Table 1. Electrical Design Parameters in a Four-Element Array

Tower No.	Field Ratio	Phase (degrees)	Spacing (degrees)	Bearing (degrees)	Height (degrees)
1	1.000	0.0	0.0	0.0	90.0
2	1.000	+90.0	90.0	0.0	90.0
3	1.000	+180.0	180.0	0.0	90.0
4	1.000	+270.0	270.0	0.0	90.0

tower 1 is used as reference with phase, spacing, and bearing set to zero.

The field ratio gives the relative magnitude of the radiated field from each element. The spacing and bearing of each element is given with respect to the reference element. The relative electrical phase relationships between the elements are also specified. The bearing of each element (physical orientation) is given in true degrees azimuth. The spacing and height of each element are given in electrical degrees. A plan of the preceding example is shown in Fig. 4, while the horizontal pattern is shown in Fig. 5.

4.2.2. Pattern Shape. The shape of a radiation pattern is controlled by varying the electrical parameters and the geometry of the individual radiating elements (usually towers). The most elementary directional antenna radiation patterns are developed using two-tower arrays of elements. More towers are added as necessary to meet more complicated radiation pattern requirements.

4.2.2.1. Theoretical Pattern. A theoretical radiation pattern can be calculated using the following formulation, which represents the inverse distance field at 1 km for a given azimuth and elevation angle

$$E(\phi, \theta)_{th} = \left| K \sum_{i=1}^n F_i f_i(\theta) / S_i \cos \theta \cos(\phi_i - \phi) + \phi_i \right| \quad (1)$$

where

K = multiplying constant that determines basic pattern size

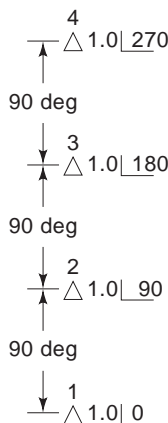


Figure 4. Orientation of antenna array for a given set of field parameters. The current magnitude and phase is given relative to tower 1.

- n = number of elements in directional array
- i = i th element in array
- F_i = field ratio of i th element in array at $\theta = 0$
- θ = vertical elevation angle measured from horizontal plane
- $f_i(\theta)$ = vertical plane radiation characteristic of i th element in array
- S_i = electrical spacing of i th element from reference point
- ϕ_i = orientation (with respect to true north) of i th element in array
- ϕ = azimuth (with respect to true north)
- ϕ_i = electrical phase angle of current in i th element in array

Figure 6 shows the reference coordinate system.

4.2.3. K Factor. The multiplying constant K can be obtained by numerically integrating the effective field intensity as calculated at each vertical angle in half space. Calculation at 5° or 10° intervals is satisfactory for results that are acceptable from an engineering standpoint

$$K = \frac{E_s \sqrt{P}}{e_h} \quad (2)$$

where E_s is the horizontal radiation from a standard isotropic radiator in half-space at 1 km distance and 1 kW power level, P is the antenna input power, and e_h is the

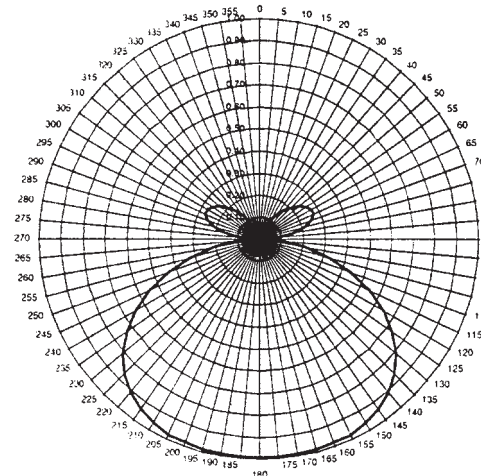


Figure 5. Horizontal pattern of field parameters given in Fig. 4. Use of multiple towers produces pattern directivity.

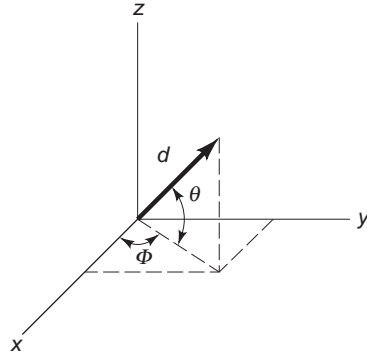


Figure 6. Definition of reference coordinate system. $\theta = 0$ in the x - y plane.

root-mean-square effective field strength in half space

$$e_h = \left\{ \frac{\pi\Delta}{180} \left[\frac{e_a^2(0)}{2} + \sum_{m=1}^N e_a^2(m\Delta) \cos(m\Delta) \right] \right\}^{1/2} \quad (3)$$

where Δ is the interval between vertical elevation angles, $N = (90/\Delta) - 1$ (number of intervals minus one), and $e_a(m\Delta)$ is the RMS field strength at angle $m\Delta$.

$$e_a(m\Delta) = \left\{ \sum_{i=1}^n \sum_{j=1}^n F_i f_i(m\Delta) F_j f_j(m\Delta) \cos \psi_{ij} J_0[S_{ij} \cos(m\Delta)] \right\}^{1/2} \quad (4)$$

where

- $j = j$ th element
- $f_i(m\Delta)$ = vertical radiation characteristic of i th element
- F_j = field ratio of j th element
- $f_j(m\Delta)$ = vertical radiation characteristic of j th element
- ψ_{ij} = difference in phase angles of currents in i th and j th elements
- S_{ij} = spacing between i th and j th elements
- $J_0(x)$ = Bessel function of first kind and zero order

4.2.3.1. Vertical Plane Radiation Characteristic. The vertical plane radiation characteristics show the relative field being radiated at a given vertical angle (θ), with respect to the horizontal plane. The general form is

$$f(\theta) = \frac{E(\theta)}{E(0)} \quad (5)$$

where $E(\theta)$ is the radiation from an element at angle θ and $E(0)$ is the radiation from an element in the horizontal plane.

Assuming sinusoidal current distribution for a typical element that is not top-loaded or sectionalized, the vertical

radiation is

$$f(\theta) = \frac{\cos(G \sin \theta) - \cos G}{(1 - \cos G) \cos \theta} \quad (6)$$

where G is the electrical height of the element. For a top-loaded element, the vertical radiation is

$$f(\theta) = \frac{\cos B \cos(A \sin \theta) - \sin \theta \sin B \sin(A \sin \theta) - \cos(A + B)}{\cos \theta [\cos B - \cos(A + B)]} \quad (7)$$

where A is the physical height of the element in electrical degrees, B is the difference between the apparent electrical height and the actual physical height in electrical degrees, and G is the apparent electrical height, $A + B$.

For a sectionalized element the vertical radiation is

$$f(\theta) = \frac{\sin J[\cos B \cos(A \sin \theta) - \cos G] + \sin B[\cos D \cos(C \sin \theta) - \sin \theta \sin D \sin(C \sin \theta)] - \cos J \cos(A \sin \theta)}{\cos \theta [\sin J(\cos B - \cos G) + \sin B(\cos D - \cos J)]} \quad (8)$$

where A is the physical height of the lower section of the element in electrical degrees, B is the difference between the apparent electrical height of the lower section of the element and the physical height of the lower section of the element, C is the physical height of the entire element in electrical degrees, D is the difference between the apparent height of the element and the physical height of the entire element (D will be zero if the sectionalized tower is not top loaded), and

$$G = A + B$$

$$H = C + D$$

$$J = H - A$$

4.2.3.2. Standard Pattern. The FCC has also defined a standard pattern that is an envelope around the theoretical pattern and is intended to provide a tolerance within which the actual operating pattern can be maintained. All designs must be based on the standard pattern and are calculated as follows:

$$E_{std} = 1.05 \sqrt{E^2 + Qg^2(\theta)} \quad (9)$$

where

- $Q = 10\sqrt{P}$ or $0.025E_{rss}$ (whichever is greater)
- P = power (kW)
- $E_{rss} = E_1 \sqrt{\sum_i^n F_i^2}$
- E_1 = reference field
- F_i = field ratio of the i th element
- $g(\theta) = f_s(\theta)$, if the shortest element is shorter than $\lambda/2 = \sqrt{f_s^2(\theta) + 0.0625/1.030776}$, otherwise
- $f_s(\theta)$ = vertical radiation characteristic of the shortest element

4.2.3.3. Pattern Augmentation. The FCC rules include a provision to augment the standard pattern to take into account actual operating conditions when radiation is greater than the standard pattern in certain directions. Radiation is augmented over a specified azimuthal span and is calculated as follows:

$$E_{\text{aug}}(\theta) = \sqrt{E_{\text{std}}^2(\theta) + A \left[g(\theta) \cos\left(\frac{180D_a}{S}\right) \right]^2} \quad (10)$$

where

E_{std} = standard radiation pattern

$A = E_{\text{aug}}^2(\theta) - E_{\text{std}}^2(\theta)$ at central azimuth of augmentation

S = azimuthal span of augmentation centered on central azimuth of augmentation

D_a = absolute difference between azimuth of calculation and central azimuth of augmentation; note that D_a cannot exceed $S/2$ for augmentation within a particular span

4.2.4. Pattern Size. The size of an antenna pattern is the magnitude of the radiation and is determined by the term K as introduced in the previous section. The term K is evaluated by calculating the total power radiated from the antenna. The total power radiating from any antenna structure can be determined by integrating the power flowing outward from a closed surface completely enclosing the antenna. The Poynting vector expresses the rate of power flow in watts/meter² at a given point in space and is expressed as

$$P = \mathbf{E} \times \mathbf{H} \quad (11)$$

where P is the power flow (W/m²), \mathbf{E} is the electric field intensity vector (V/m), and \mathbf{H} is the magnetic field intensity vector (A/m).

In the far field, the two field vectors \mathbf{E} and \mathbf{H} are orthogonal and related in free space by the permeability and permittivity of air and is expressed as

$$H = \sqrt{\varepsilon_0/\mu_0} E \quad (12)$$

where $\mu_0 = 4\pi \times 10^{-7}$ permeability (H/m), $\varepsilon_0 = 1/\mu_0 c^2$ permittivity (f/m), and $c = 299.776 \times 10^6$ velocity of light (m/s).

The intrinsic impedance of free space is defined as

$$Z_c = \mathbf{E}/\mathbf{H} = \sqrt{\varepsilon_0/\mu_0} = 376.71 \Omega \quad (13)$$

The total amount of power flowing in free space from a given source is

$$p = E^2/Z_c \quad (14)$$

The total power radiated is calculated by integrating over a closed surface enclosing the source and can be

expressed as

$$P = \int p dS = (1/Z_c) \int E^2 dS \quad (15)$$

where P is the total power radiated (watts), Z_c is the intrinsic impedance (ohms), E is the total field at the closed surface (V/m), and dS is the incremental area on the closed surface (m²).

If a sphere is chosen as the closed surface then the integration becomes

$$dS = d \cos \theta d\theta d\phi \quad (16)$$

Substituting Eq. (16) into Eq. (15) yields the total power radiating from a given source:

$$P = (1/Z_c) \int_0^{2\pi} \int_{-\pi/2}^{+\pi/2} E^2 d^2 \cos \theta d\theta d\phi \quad (17)$$

4.2.4.1. Isotropic Antenna in Free Space. If the radiating source is isotropic, the power radiates equally in all directions and Eq. (17) becomes

$$P = (1/Z_c) E_0^2 d^2 \int_0^{2\pi} \int_{-\pi/2}^{+\pi/2} \cos \theta d\theta d\phi \quad (18)$$

$$P = 4\pi(1/Z_c) E_0^2 d^2 \quad (19)$$

Solving Eq. (19) for E_0 , the root-mean-square (RMS) field intensity of an isotropic radiator is

$$E_0 = \sqrt{\frac{PZ_c}{4\pi d^2}} \quad (20)$$

For 1 kW of power at a distance of 1 km, Eq. (20) yields

$$E_0 = 173.14 \text{ mV/m}$$

4.2.4.2. Isotropic Antenna in Half-Space. On placing the isotropic radiator in a half-space over a perfectly conducting plane, the limits of integration change and Eq. (18) becomes

$$P = (1/Z_c) E_0^2 d^2 \int_0^{2\pi} \int_0^{+\pi/2} \cos \theta d\theta d\phi \quad (21)$$

Solving Eq. (21) for E_0 , the maximum RMS field intensity of an isotropic radiator half-space is

$$E_0 = \sqrt{\frac{PZ_c}{2\pi d^2}} \quad (22)$$

For 1 kW of power at a distance of 1 km, Eq. (19) yields

$$E_0 = 244.86 \text{ mV/m}$$

4.2.4.3. Current Element in Free Space. If we replace the isotropic radiating source with an infinitesimally small

vertical current element, the field intensity term is

$$E = E_0 \cos \theta \tag{23}$$

and Eq. (17) becomes

$$P = (1/Z_c) \int_0^{2\pi} \int_{-\pi/2}^{+\pi/2} (E_0 d \cos \theta)^2 d\theta d\phi \tag{24}$$

Solving Eq. (24) for E_0 , the maximum RMS field intensity at $\theta = 0$ is

$$E_0 = \sqrt{\frac{3PZ_c}{8\pi d^2}} \tag{25}$$

For 1 kW of power at a distance of 1 km, Eq. (25) yields

$$E_0 = 212.05 \text{ mV/m}$$

4.2.4.4. Current Element in Half-Space. On placing the current element just above a perfectly conducting plane, the limits of integration change and Eq. (24) becomes

$$P = (1/Z_c) \int_0^{2\pi} \int_0^{+\pi/2} (E_0 d \cos \theta)^2 d\theta d\phi \tag{26}$$

Solving Eq. (26) for E_0 , the maximum RMS field intensity at $\theta = 0$ is

$$E_0 = \sqrt{\frac{3PZ_c}{4\pi d^2}} \tag{27}$$

For 1 kW of power at a distance of 1 km, Eq. (27) yields

$$E_0 = 299.89 \text{ mV/m}$$

4.2.4.5. Center-Fed Conductor in Free Space. Now replace the radiating source with a center-fed conductor in free space of length $2G$ having a sinusoidal current distribution, the field intensity term is

$$E = E_0 \left[\frac{\cos(G \sin \theta) - \cos G}{(1 - \cos G) \cos \theta} \right] \tag{28}$$

and Eq. (14) becomes

$$P = (1/Z_c) \int_0^{2\pi} \int_{-\pi/2}^{+\pi/2} \left\{ E_0 \left[\frac{\cos(G \sin \theta) - \cos G}{(1 - \cos G) \cos \theta} \right] \right\}^2 \times d^2 \cos \theta d\theta d\phi \tag{29}$$

Equation (29) has been solved by Ramo and Whinnery [15], the maximum RMS field intensity of a center-fed

conductor in free space

$$E_0 = \frac{\left[\frac{\cos(G \sin \theta) - \cos G}{\cos \theta} \right] \sqrt{\frac{PZ_c}{2\pi d^2}}}{\{\gamma + \ln(2G) - \text{Ci}(2G) + 0.5[\text{Si}(4G) - 2 \sin(2G)] \sin(2G)\} + 0.5[\gamma + \ln G - 2\text{Ci}(2G) + \text{Ci}(4G)] \cos(2G)}^{1/2} \tag{30}$$

where γ is Euler's constant = 0.57721566, Ci is the cosine integral function, Si is the sine integral function, and $2G$ is the length of the conductor.

For 1 kW of power at a distance of 1 km and defining the angle of radiation as well as the electrical length of the radiating element.

$$\theta = 0^\circ \quad \text{and} \quad G = 90^\circ$$

Equation (30) yields a maximum field intensity of

$$E_0 = 221.78 \text{ mV/m}$$

4.2.4.6. Vertical Conductor in Half-Space. The final step in this process is to determine the maximum field intensity of a vertical conductor in half-space (a monopole over perfecting conducting ground plane of infinite extent). Again, the limits of integration change such that Eq. (29) becomes

$$P = (1/Z_c) \int_0^{2\pi} \int_0^{+\pi/2} \left\{ E_0 \left[\frac{\cos(G \sin \theta) - \cos G}{(1 - \cos G) \cos \theta} \right] \right\}^2 \times d^2 \cos \theta d\theta d\phi \tag{31}$$

It follows from the previous analysis that solving for Eq. (31) yields

$$E_0 = \frac{\left(\frac{\cos(G \sin \theta) - \cos G}{\cos \theta} \right) \sqrt{\frac{PZ_c}{2\pi d^2}}}{\{\gamma + \ln(2G) - \text{Ci}(2G) + 0.5[\text{Si}(4G) - 2 \sin(2G)] \sin(2G)\} + 0.5[\gamma + \ln G - 2\text{Ci}(2G) + \text{Ci}(4G)] \cos(2G)}^{1/2} \tag{32}$$

For 1 kW of power at a distance of 1 km, and

$$\theta = 0^\circ \quad \text{and} \quad G = 90^\circ$$

Equation (32) yields a maximum field intensity of

$$E_0 = 313.66 \text{ mV/m}$$

4.2.5. Pattern Synthesis. The antenna designer is required to fit a pattern within a given set of radiation limits as defined by the allocation studies. As this defines the general shape and size of the pattern, a set of field parameters must be chosen with regard to the number, height, and physical orientation of the towers. Useful

techniques have been developed to synthesize the design of antenna patterns. The general expression given in Eq. (1) for calculating the pattern shape is simplified for a two-element array, which is used as the basic building block for pattern synthesis.

Using element 1 as the reference, the field ratio F_2 can be defined as

$$F_2 = E_1/E_2 \quad (33)$$

The difference in phase angle, α_2 , has two components:

$$\alpha_2 = S \cos \phi \cos \theta + \Psi_2 \quad (34)$$

The first term of Eq. (34) relates to the space phase difference, and the second term relates to the time phase difference between E_1 and E_2 .

If the towers are of equal height, it can be shown that the total field is

$$E = E_1 f(\theta) \sqrt{2F_2} \left[\frac{1 + F_2^2}{2F_2} + \cos(S \cos \phi \cos \theta + \Psi_2) \right]^{1/2} \quad (35)$$

where

$$f(\theta) = f_1(\theta) = f_2(\theta)$$

If $F_2 = 1$ and $f(0) = 1$, Eq. (35) further reduces to

$$E = 2E_1 \cos\left(\frac{S}{2} \cos \phi + \frac{\Psi_2}{2}\right) \quad (36)$$

It follows from Eq. (36) that nulls occur in the pattern when

$$S \cos \phi + \Psi_2 = \pm 180^\circ \quad (37)$$

Any number of horizontal plane patterns from Eq. (36) can be generated by varying spacing and phase relationships of one element to the other. These patterns are then used as basic building blocks when computing patterns for multielement arrays. The most common technique for computing these patterns is known as *pattern pair multiplication*.

4.2.5.1. Pattern Pair Multiplication. Multielement arrays can be designed by multiplying the pattern of individual elements with the pattern of an array of vertical radiators having the same locations, relative amplitudes, and phases as the individual elements. As an example, take the two array patterns as shown in Figs. 7 and 8. Using Eq. (36), the array patterns can be expressed as follows

$$E_a = 2E_{1a} \cos\left(\frac{\pi}{4} \cos \phi + \frac{\pi}{4}\right) \quad (38)$$

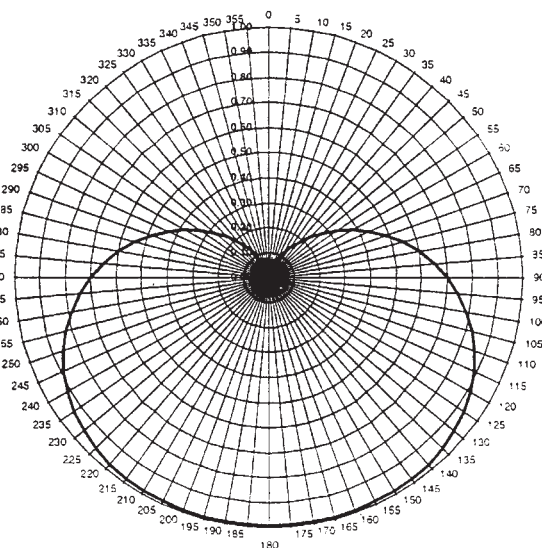


Figure 7. Horizontal pattern of a two-element array ($S = 90^\circ$ and $\Psi_2 = 90^\circ$). Pattern is broad with no radiation at 0° .

when $S = \pi/2$ and $\Psi_2 = \pi/2$

$$E_b = 2E_{1b} \cos\left(\frac{\pi}{2} \cos \phi + \frac{\pi}{2}\right) \quad (39)$$

when $S = \pi$ and $\Psi_2 = \pi$.

The resulting equation for the combined pattern is simply the product of individual arrays

$$E_a = 2E_{1a} \cos\left(\frac{\pi}{4} \cos \phi + \frac{\pi}{4}\right) 2E_{1b} \cos\left(\frac{\pi}{2} \cos \phi + \frac{\pi}{2}\right) \quad (40)$$

and Fig. 5 shows the combined pattern.

4.2.5.2. Array Simplification. The four-tower array as illustrated in the previous section can be simplified if equal spacing is maintained between the towers, which is frequently the case for medium-frequency inline arrays used in broadcasting. Using Eqs. (38) and (39) the following field relationships can be defined as

$$F_a = 1.0/\underline{+90}$$

$$F_b = 1.0/\underline{+180}$$

The four-tower array can be reduced to a three-tower array using the following relations:

$$\text{Tower 3} = F_a \times F_b = 1.00/\underline{+270}$$

$$\text{Tower 2} = F_a \times F_b = 1.41/\underline{+135}$$

$$\text{Tower 1} = \text{reference} = 1.00/\underline{+0}$$

The horizontal pattern for this set of parameters is shown in Fig. 9. Comparing Fig. 5 with Fig. 9 reveals little

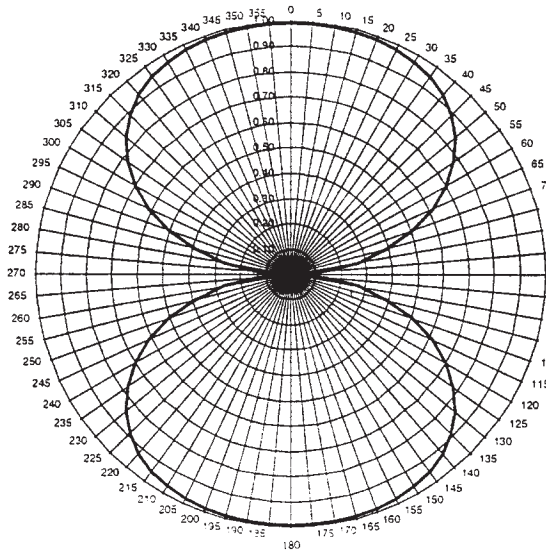


Figure 8. Horizontal pattern of a two-element array ($S = 180^\circ$ and $\Psi_2 = 180^\circ$). Pattern is symmetric with equal radiation at 0° and 180° .

difference in pattern shape with the economical advantage of saving the cost of one tower.

4.2.6. Antenna Impedance. The base impedance defines the relationship of the voltage to the current in both magnitude and phase at the base of each radiating element. This is a complex quantity and is typically given in the following form:

$$Z_b = R_b + jX_b \tag{41}$$

where R_b is the base resistance (ohms) and X_b is the base reactance (Ω).

The base resistance R_b has two components

$$R_b = R_r + R_1 \tag{42}$$

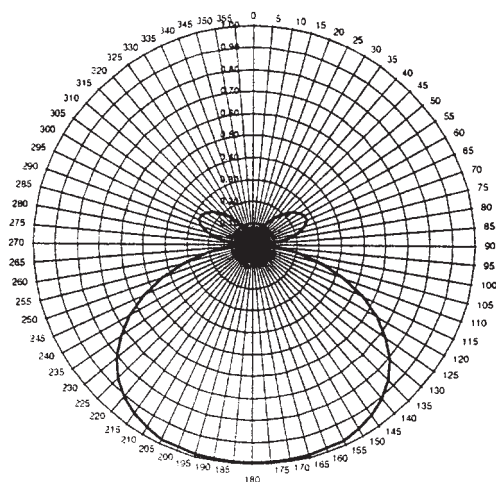


Figure 9. Horizontal pattern of a three-element array. Combined pattern produces greater directivity with no radiation at 0° .

where R_r is the radiation resistance (Ω) and R_1 is the loss resistance (Ω).

The radiation resistance determines the total power radiated from the antenna while the loss resistance takes into account all dissipative losses associated with the antenna and the ground system. It is the ratio of these two quantities that determines the efficiency of an antenna system. As the height of the radiating element decreases below 90 electrical degrees, the loss resistance becomes an appreciable percentage of the radiation resistance, thus decreasing the overall efficiency of the antenna system.

It is important to take into account all series and shunt reactance found between the base of the antenna and the point at which the matching networks are connected to the antenna. Knowing an accurate impedance at this point of the antenna is very important when designing the feeder system for a multielement antenna system.

It follows then that the power radiated from a given antenna element is given as

$$P_r = I_b^2 R_r \tag{43}$$

where I_b is the base current (A).

4.2.6.1. Self-Impedance Using Traditional Methods. The traditional method of determining the self-impedance (the impedance of a single radiating element apart from the influence of other radiating elements in close proximity) of a vertical radiating element uses the theory of nonuniform transmission lines as introduced by Schelkunoff [4]. This method assumes a single radiator of uniform cross section over an infinite perfectly conducting ground plane. The first order approximation is given as

$$Z_b = Z_0 \left[\frac{A \sin G + j(B - C) \sin G - j(2Z_0 - D) \cos G}{(2Z_0 + D) \sin G + (B + C) \cos G - j(A \cos G)} \right] \tag{44}$$

where

- $Z_b = R_b + jX_b$ base self-impedance (Ω)
- $Z_0 = 60[\ln(2G/a) - 1]$ average characteristic impedance (Ω)
- $G =$ antenna height (degrees)
- $a =$ antenna height (degrees)
- $A = 60[\gamma + \ln(2G) - \text{Ci}(2G)] + 30[\gamma + \ln G - 2\text{Ci}(2G) + \text{Ci}(4G)] \cos(2G) + 30[\text{Si}(4G) - 2\text{Si}(2G)] \sin(2G)$
- $B = 60\text{Si}(2G) + 30[\text{Ci}(4G) - \ln G - \gamma] \sin(2G) - 30\text{Si}(4G) \cos(2G)$
- $C = 60[\text{Si}(2G) - \sin(2G)]$
- $D = 60[\ln(2G) - \text{Ci}(2G) + \gamma - 1 + \cos(2G)]$
- $\gamma = 0.5772$ Euler's constant
- $\text{Ci} =$ cosine integral function
- $\text{Si} =$ sine integral function

4.2.6.2. Impedance of the Elements in Directional Array Using Traditional Methods. The impedance for an individual element of a directional array is not only dependent on its own current but also the current induced in it due to

mutual coupling from other elements in the array. The relationship between the voltages and currents of the individual elements are given in terms of mutual impedance. The matrix of equations for a three-element array will be

$$V_1 = I_1 Z_{11} + I_2 Z_{21} + I_3 Z_{31}$$

$$V_2 = I_1 Z_{12} + I_2 Z_{22} + I_3 Z_{32}$$

$$V_3 = I_1 Z_{13} + I_2 Z_{23} + I_3 Z_{33}$$

where V_1 and I_1 are the base voltage and current for element 1, Z_{11} is the self-impedance of element 1, and Z_{21} is the mutual impedance between element 1 and element 2.

The values for mutual impedance as a function of element separation and height have been solved by Brown [5] and Cox [6]. The equations are

$$Z_{21} = R_{21} + jX_{21} \quad (45)$$

where

$$\begin{aligned} R_{21} = & \frac{15}{\sin \beta l_1 \sin \beta l_2} \{ \cos \beta \Delta [\text{Ci}(u_1) - \text{Ci}(u_0) + \text{Ci}(v_1) - \text{Ci}(v_0)] \\ & + 2\text{Ci}(y_0) - \text{Ci}(y_1) - \text{Ci}(s_1)] \\ & + \sin \beta \Delta [\text{Si}(u_1) - \text{Si}(u_0) + \text{Si}(v_0) - \text{Si}(v_1) \\ & - \text{Si}(y_1) + \text{Si}(s_1)] \\ & + \cos \beta L [\text{Ci}(w_1) - \text{Ci}(v_0) + \text{Ci}(x_1) - \text{Ci}(u_0) + 2\text{Ci}(y_0) \\ & - \text{Ci}(y_1) - \text{Ci}(s_1)] \\ & + \sin \beta L [\text{Si}(w_1) - \text{Si}(v_0) + \text{Si}(u_0) - \text{Si}(x_1) \\ & - \text{Si}(y_1) + \text{Si}(s_1)] \} \end{aligned} \quad (46)$$

$$\begin{aligned} X_{21} = & \frac{15}{\sin \beta l_1 \sin \beta l_2} \{ \cos \beta \Delta [\text{Si}(u_0) - \text{Si}(u_1) + \text{Si}(v_0) - \text{Si}(v_1) \\ & + \text{Si}(y_1) - 2\text{Si}(y_0) + \text{Si}(s_1)] \\ & + \sin \beta \Delta [\text{Ci}(u_1) - \text{Ci}(u_0) + \text{Ci}(v_0) - \text{Ci}(v_1) \\ & - \text{Ci}(y_1) + \text{Ci}(s_1)] \\ & + \cos \beta L [\text{Si}(v_0) - \text{Si}(x_1) + \text{Si}(u_0) - \text{Si}(x_1) \\ & - 2\text{Si}(y_0) + \text{Si}(y_1) + \text{Si}(s_1)] \\ & + \sin \beta L [\text{Ci}(w_1) - \text{Ci}(v_0) + \text{Ci}(u_0) - \text{Ci}(x_1) \\ & - \text{Ci}(y_1) + \text{Ci}(s_1)] \} \end{aligned} \quad (47)$$

where l_1 and l_2 are the heights of elements 1 and 2, respectively, d is the distance between elements, and

$$L = l_1 + l_2$$

$$\Delta = l_2 - l_1$$

$$w_0 = \beta \left[\sqrt{d^2 + l_1^2} + l_1 \right] = v_0$$

$$w_1 = \beta \left[\sqrt{d^2 + L^2} + L \right]$$

$$v_1 = \beta \left[\sqrt{d^2 + \Delta^2} - \Delta \right]$$

$$x_0 = \beta \left[\sqrt{d^2 + l_1^2} - l_1 \right] = u_0$$

$$x_1 = \beta \left[\sqrt{d^2 + L^2} - L \right]$$

$$u_1 = \beta \left[\sqrt{d^2 + \Delta^2} + \Delta \right]$$

$$y_0 = \beta d = s_0$$

$$y_1 = \beta \left[\sqrt{d^2 + l_2^2} + l_2 \right]$$

$$s_1 = \beta \left[\sqrt{d^2 + l_2^2} - l_2 \right]$$

Once the mutual impedances are known, the preceding matrix of equations is solved for the ratio of the voltage to the current in each element that defines the impedance of that element.

Operating impedances may be calculated with fair accuracy using the traditional method of calculating self- and mutual impedances as presented herein for tower heights up to approximately 120 electrical degrees. For taller towers, it has been standard practice to design matching units very conservatively and with components to provide a wide adjustment range. As presented in the next section, modern moment method analysis gives excellent results for all tower heights with properly chosen assumptions.

4.2.6.3. Impedance Determination Using Moment Methods. Moment method antenna modeling has proved to be a very useful tool in overcoming the limitations of traditional antenna theory. The moment method technique divides each radiator into a large number of individual segments for which corresponding current values can be calculated. In order for this technique to be useful in the design of a medium-frequency antenna system, it is necessary to relate the fields as produced by the antennas system to the drive point conditions of the antenna (voltage, current, and impedance).

A convenient method for specifying a medium-frequency directional antenna system uses field parameters that easily allow the designer to determine the radiation characteristics of any given antenna configuration. The field parameters for each tower in a directional antenna array are the ratios of the magnitudes and phases, relative to an arbitrary reference, of the electric field component of the radiation that results from integrating the current

over the length of that particular tower or element of the directional antenna. Because field parameters are the standard method of specifying directional antennas, most notably with the FCC, it is necessary to relate these parameters to the driving point conditions (base voltage and current) in order to utilize modern moment method techniques to design these antennas. Once the driving point conditions are determined, the antenna feed system can be designed to provide the necessary power division and phase relationship between the elements in the array.

The means of exciting the antenna model with numerical electromagnetics code (NEC) [18] and MININEC [19] involves voltage sources. A problem involving a monopole over perfectly conducting ground plane excited with $1 + j0$ volts at the base would yield the current distribution on the monopole and the fields, both electric and magnetic, produced by the monopole.

4.2.7. Field Parameters versus Voltage Drives [21]. The field parameters are calculated by ratioing the electric fields as produced by each element in the directional array to an arbitrary reference. The electric field produced by a finite current element over a perfectly conducting ground plane is proportional to the current in the wire and can be expressed as follows

$$\vec{E} \propto \int_0^l \vec{I} dz \tag{48}$$

where \vec{I} is the current distribution of the current element, dz is the incremental distance along the current element, and l is the length of the current element.

A close approximation for the solution of Eq. (48) is found using moment method techniques by summing the current moments of each element. The mathematical representation is

$$\vec{E} \propto \sum_{i=0}^n \vec{I}_i l_i \tag{49}$$

where \vec{I}_i is the current in the i th segment and l_i is the length of the i th segment.

Four terminal network theory can now be used to relate the field parameters to the driving voltages for each tower in a directional array. Using a two-tower array as an example, the following set of equations is formulated

$$\begin{aligned} \vec{E}_1 &= \vec{T}_{11}\vec{V}_1 + \vec{T}_{12}\vec{V}_2 \\ \vec{E}_2 &= \vec{T}_{21}\vec{V}_1 + \vec{T}_{22}\vec{V}_2 \end{aligned}$$

where \vec{E}_1 is the field radiated from tower 1, \vec{V}_1 is the voltage drive of tower 1, \vec{T}_{11} is the current moment summation of tower 1, and \vec{T}_{12} is the current moment summation of tower 2 (as induced by the current in tower 1).

As can be seen from the above equations, to determine the T elements of the matrix, it is necessary to calculate the current summations by individually exciting each tower in the array. For example, to determine the elements, T_{11} and T_{21} it is necessary to excite tower 1 with voltage V_1 while grounding tower 2. The current moment summations are calculated for each tower. The same procedure is

used to determine the elements, T_{21} and T_{22} , by exciting tower 2 with voltage V_2 while grounding tower 1. Using matrix algebra, the drive point voltages can be determined from the field parameters by inverting the T matrix and multiplying by the field parameters

$$[\vec{V}] = [\vec{F}][\vec{T}]^{-1} \tag{50}$$

where $[\vec{F}]$ is the set of field parameters as determined from the calculated electric fields and $[\vec{T}]^{-1}$ is the inverted current summation matrix.

The drive voltages for a given set of field parameters can now be determined. With these drive voltages the drive point currents and impedances are calculated, which determines the power division and phase relationships of the directional array elements.

It is possible to adjust an antenna system using moment method modeling with little, if any, experimentation, if the conditions at the site approach the ideal in terms of flat terrain and an absence of nearby reradiating structures. Even where conditions are not ideal, moment method modeling is a very useful tool in relating current drives to field parameters and reducing the amount of trial-and-error work necessary to achieve the required radiation pattern.

5. DIRECTIONAL ANTENNA FEEDER SYSTEMS

Once the base impedances of the individual elements in the antenna system have been calculated, it is possible to design the feeder system to provide the required current amplitude and phase for each tower in the array. Figure 10 shows a block diagram of the basic components that comprise a directional antenna feeder system.

Computer modeling techniques have been developed to analyze the feeder systems making it possible to obtain exact theoretical solutions for bandwidth analysis. The advance of computational capabilities has allowed the

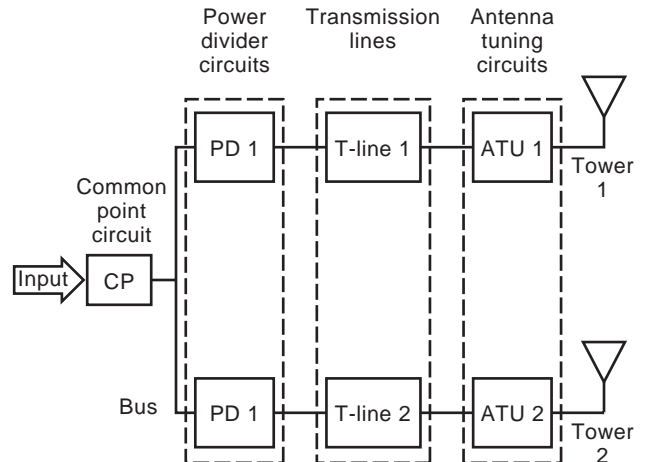


Figure 10. Basic components of a two-tower directional antenna feeder system. Additional towers can be added to the bus using similar networks.

development of new approaches for the design of power dividing, phasing, and matching networks. The two areas of concern when designing the feeder system are the impedance and the pattern bandwidth which directly impact the quality of the audio within the entire coverage area.

5.1. Nodal Analysis

The technique of nodal analysis is well known in the field of electrical engineering. This technique works very well when predicting the bandwidth performance of directional antenna phasing and coupling equipment, since admittance values can be given for each component and the tower bases can be modeled as nodes with self- and mutual admittance values determined using moment method analysis. An exact solution for carrier and side-band currents and impedances can be found for every branch in a system. This solves the problem with simpler techniques that assume a set of base current parameters to determine operating impedances, which, when presented to the system of networks, yield a different set of base current parameters and render the starting assumptions invalid.

5.2. Power Dividing Circuits

Prior to the 1970s, two traditional circuits were used for the purpose of dividing the power between the towers of a directional antenna system in virtually all cases. The circuits are shown on Fig. 11. The first circuit is a *series* or *tank* type of power divider which goes back to the earliest days of radio and the *parallel* or *Ohm's law* design, which became popular during the 1950s.

Both circuits of Fig. 11 function primarily as power dividers, with separate networks necessary for phase adjustments. Both can introduce high system Q, thus possibly restricting bandwidth. The series circuit circulates all of the power fed into the system through a parallel tuned antiresonant circuit, and the parallel circuit can result in relatively high circulating current due to the low resistance presented when several tower feeds are tied together across a common bus. The high Q of such circuits could

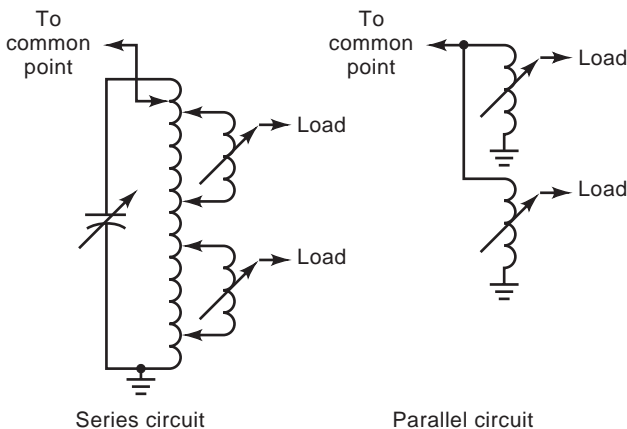


Figure 11. Traditional power divider circuits principally used in early medium-wave antenna designs.

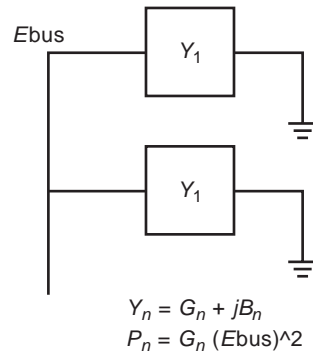


Figure 12. General power divider principle. The bus voltage is determined by the parallel combination of admittances produced by each tower and the input power.

serve to counteract bandwidth problems inherent in an array design. This would require careful system modeling to be effective and was not practical when such systems were built.

The general principle for all power divider circuits is illustrated in Fig. 12. If the common feed for all power dividing circuits is considered to be a voltage bus, the power delivered to each tower is determined by the conductance value presented to the bus by that tower's power dividing circuit. The voltage for the desired bus impedance can be determined and then the circuits necessary to present the required conductances, when terminated in the transmission lines, can be designed.

It is usually desirable to design for a bus impedance of 50 Ω when 50-Ω transmission lines are used, unless another factor suggests otherwise. Such an alternative situation would arise where one tower in a system needs much higher power than any of the others and could be fed directly off the bus without adjustment capability and satisfy the requirements for optimum overall phase shift. For example, a 25-Ω bus would feed half of its power directly to a 50-Ω transmission line.

5.2.1. Modern Power Divider Circuits. Any network that can adjust the conductance presented across the bus for a tower feed can be used as a power divider circuit. It is not necessary to have the same type of power divider network for every tower in an array. From the standpoint of adjustability and bandwidth, it is often desirable to have different types of intermixed networks in a given system.

Figures 13a–13f show several power divider circuits. Each one shown is capable of serving for control of both power and phase, making separate phase adjustment networks unnecessary. If properly applied, the circuits of Fig. 13 can generally lead to lower power dividing and phasing network Q than attainable with either power divider from Fig. 11. Most of the circuits of Fig. 13 do not offer separate controls for both power and phase. This is not a great disadvantage, because the circuits that do only offer totally independent control when connected to load impedances that remain constant. This is not the case for any power divider that is feeding elements in an array

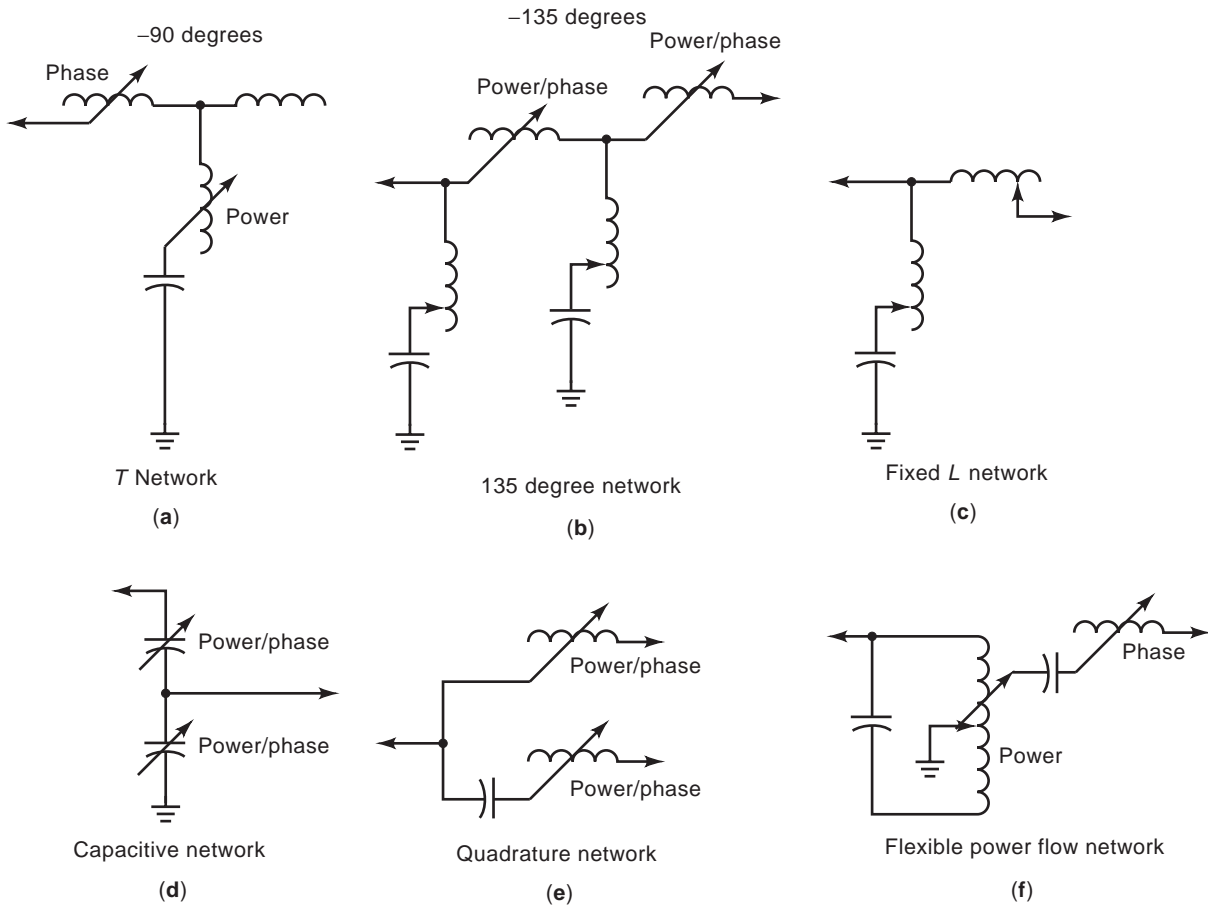


Figure 13. Modern power divider circuits. The selection of a particular circuit is dependent on overall system and load characteristics.

because effects of mutual coupling between the elements make each tower’s impedance change as the current flowing in the other towers change.

The low *Q* circuits of Fig. 13 are popular modern alternatives to the traditional power dividers of Fig. 11. For some directional arrays with highly volatile power division, however, the traditional power dividers, with their higher *Q*, may be desirable if easy adjustability is important. Proper system modeling could be used to minimize the high-*Q* effects or actually use them to improve overall system bandwidth.

Figures 14–17 show how the basic power divider circuits of Fig. 13 can be applied in phasing system design. Figure 14 offers good control and a 50-Ω bus, but can be simplified to Fig. 15 if the proper value is chosen for the power divider coil of the lowest power tower so that the capacitor necessary to antiresonate it is of the same reactance magnitude as the top tower’s fixed *L* network shunt coil. This would be possible in a case where the lowest power tower would not change power flow direction. In the process, the power divider *Q* is lowered by the elimination of a parallel antiresonant circuit across the bus.

Figure 16 shows how, if the phase shift requirements allow it, the high-power tower feed can be connected directly to the bus, eliminating the three components of the

L network. The circuit of Fig. 17 is identical to the circuit of Fig. 16, except that the bus has been divided with the series *L*–*C* slope network. In the case shown, the high-power towers need to have the phase shift of their feed tailored to track the lower-power tower in order to preserve pattern bandwidth. This is the purpose of the *L*–*C* slope network as shown.

As can be seen from the circuit of Fig. 17, high-*Q* circuits can be inserted at appropriate locations in phasing equipment to effectuate broadbanding. Such processes require modeling of total system performance, such as with nodal analysis, in order to be effective. In many cases, it may be necessary to improve pattern bandwidth with high-*Q* circuits added after the common bus, with an additional network to improve impedance bandwidth included in the common point matching circuit.

5.3. Phasing and Matching Circuits

The conventional *T* network is the basic building block for antenna matching and phase shifting functions. Figure 18 shows the circuit for this network type. If the series input and output branches exhibit overall inductive reactance with the shunt branch having overall capacitive reactance,

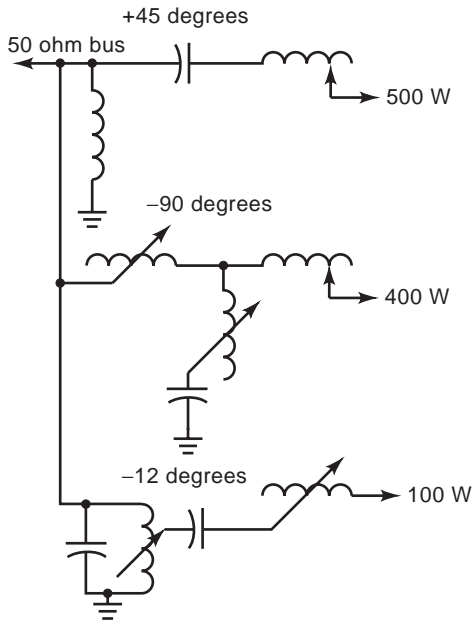


Figure 14. Mixed use of power divider circuits. Power division and system phase shifts determine the best combination of power divider circuits.

the network will produce negative phase shift and is said to be lagging. Conversely, if the series branches are capacitive and the shunt branch is inductive, the network will produce a positive phase shift and is said to be leading. The values chosen for each component determine the impedance transformation, the phase shift as well as the bandwidth performance.

Referring to Fig. 18, the following equations can be used to determine the impedance transformation and

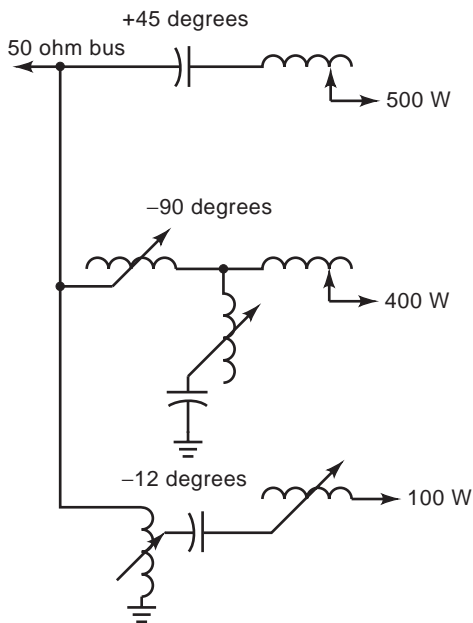


Figure 15. Simplification by elimination of parallel components as compared to Fig. 14.

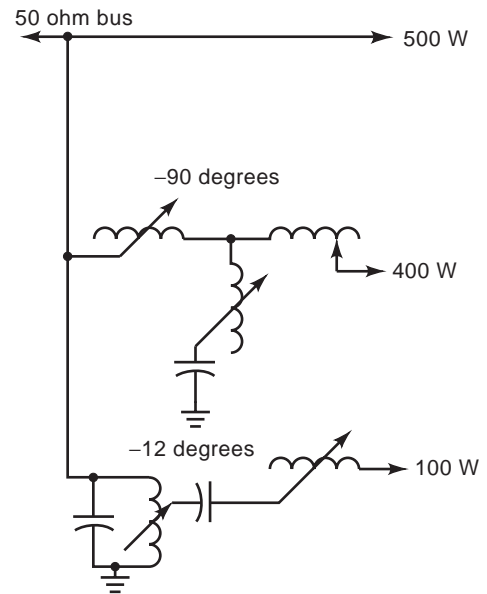


Figure 16. Direct feed to highest power tower. Another simplification which reduces the number of components.

phase shift of a *T* network

$$X_1 = \frac{\sqrt{R_i R_o}}{\sin \beta} - \frac{R_i}{\tan \beta} \tag{51}$$

$$X_2 = \frac{\sqrt{R_i R_o}}{\sin \beta} - \frac{R_o}{\tan \beta} \tag{52}$$

$$X_3 = -\frac{\sqrt{R_i R_o}}{\sin \beta} \tag{53}$$

where R_i is the input resistance (ohms), R_o is the output resistance (Ω), and β is the phase angle.

Although conventional thinking would suggest that optimum bandwidth performance results with the phase

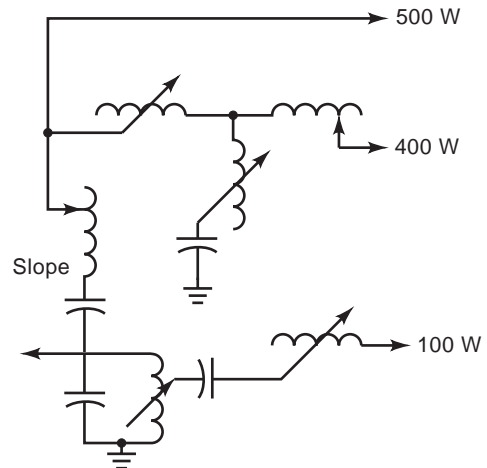


Figure 17. Split bus with pattern bandwidth improvement. Improved pattern bandwidth is most noticeable in the minima regions of radiation.

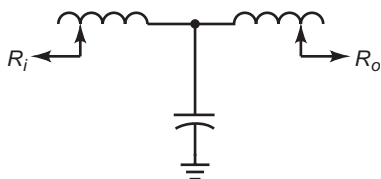


Figure 18. *T* network: basic circuit for impedance matching and phase shift. Circuit shown is for a phase lagging network.

shift of a *T* network adjusted to 90°, the family of curves on Fig. 19 indicate otherwise. There is an optimum *T* network phase shift for each transformation ratio and these values are generally lower than 90°.

Figure 19 also shows that the VSWR bandwidth worsens as the transformation ratio increases. The negative impact of transforming an impedance to one that is very much higher (or lower) can be lessened by cascading networks together. Figure 20 shows how two networks can be cascaded to achieve a gradual stepup of resistance that requires that only one additional shunt branch be added alongside the normal *T* network configuration. Figure 21 shows the bandwidth performance of such a circuit designed with two cascaded networks. For the cost of an additional network branch, there is an approximate three to one improvement in sideband VSWR.

6. PROCUREMENT AND INSTALLATION

Once authorization has been received to construct a new or modify an existing medium-wave antenna system, it is necessary to prepare a request for quotation to procure the necessary equipment. The document necessary to receive a competitive quotation includes a detailed description of the required equipment usually in the form of a specification as well as a detailed statement of work that outlines all additional labor required outside of the manufacturing of the equipment. This usually includes any labor associ-

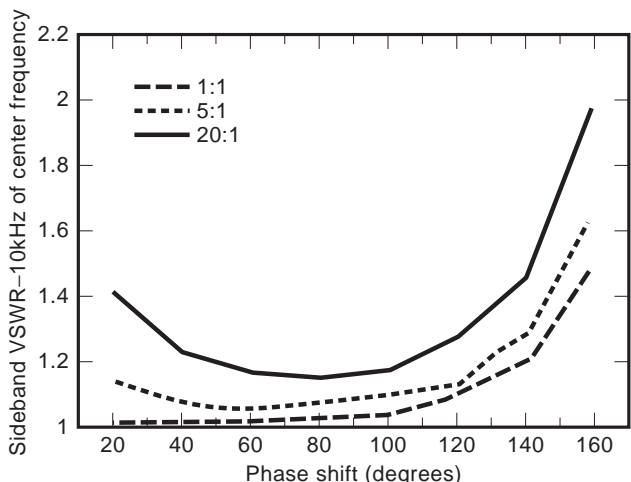


Figure 19. *T* network sideband VSWR versus phase shift for various transformation ratios. Smaller transformation ratios produce better sideband VSWR.

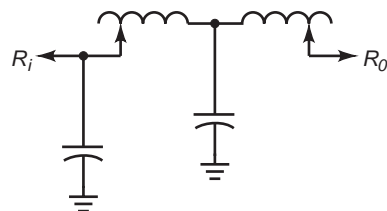


Figure 20. Cascaded *T* and *L* networks for optimizing phase shift and transformation ratio. Such a configuration results in better impedance bandwidth with fewer components.

ated with installation and adjustments in the field. It is also important to specify the terms of a warranty if it is not already expressed in an off-the-shelf product. A line item must also be included for shipping.

It is recommended to request quotations from a number of reputable manufacturers to encourage a competitive bid. The evaluation of the bids should not only consider the price but also the quality of the product being proposed as well as how long it will take to deliver the product. It may be necessary to visit the prospective proposers’ plants to ascertain their interest and commitment in providing you a quality product in a timely manner. Recommendations from others in the field of broadcasting are also invaluable when making a decision between quotations.

When overseeing the installation of a medium-wave antenna system there are a number of areas to which one should pay special attention. For each tower, the connections of the ground system must be made and checked very carefully, since they will ultimately be below ground level and not visible. For directional antennas, the spacings and orientations of the elements must be carefully determined with reference to true north with a careful survey using celestial reference data.

The governing authorities of the country in which the new or modified medium-frequency antenna system is being constructed will usually require the system to be tested to confirm compliance with the radiation characteristics as outlined in the construction permit. Once the system has been adjusted to theoretical parameters,

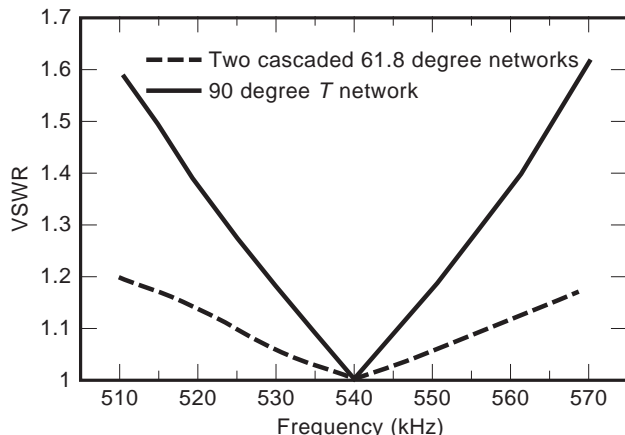


Figure 21. VSWR introduced by network for transformation ratio of 20:1. Cascaded networks produce significant improvement with sideband VSWR for high transformation ratios.

a number of measurements are necessary to confirm compliance.

7. ANTENNA ADJUSTMENT

After the equipment has been installed and properly connected, the branches of the individual networks must be set to their design values. This involves using an impedance bridge and a frequency generator or a network analyzer to set the required reactance value at the operating frequency. Care must be taken when making these measurements to take into account all stray reactances that are inherent in an antenna system with long conductors between components (series inductive reactance) with close proximity to a grounded surface (shunt capacitive reactance). High-power systems, where physical dimensions are large, have very large stray impedances.

The electrical lengths of the sampling transmission lines must be measured to determine the values to which the antenna monitor will be adjusted. This is a critical step in the adjustment of the antenna system as errors interjected at this juncture will make it very difficult if not impossible to bring the antenna system into adjustment. A procedure has been developed for making such a measurement using an impedance bridge and a frequency generator by measuring the adjacent resonant frequencies of the line when it is in a short-circuited condition. The equation for calculating the length based on the two measurements is

$$\Psi_L = \frac{180}{(f_H/f_L) - 1} \quad (54)$$

where Ψ_L is the line length at lower frequency (degrees), f_H is the higher frequency (kHz), and f_L is the lower frequency (kHz).

Once the network branches have been set to their theoretical levels, low power can be applied to the system and the common point impedance adjusted to match the system to the transmitter. The phasor is then adjusted to bring the antenna monitor to the theoretical values as previously calculated. During this process it is oftentimes found that the adjustment of the ratio or phase to one tower will have an affect on the ratios and phases of other towers. The amount of interdependence between towers is determined by how closely the towers are coupled as well the component layout design within the phasor and ATU cabinets. While making these adjustments, the common point impedance must continually be readjusted to insure a proper load to the transmitter.

When the antenna monitor has been adjusted to theoretical parameters, a field strength meter is used to measure the radiated field levels at critical radials. The critical radials are usually located at the places where the pattern shape has inflections, that is, the pattern minima and minor lobe maxima. In the United States, the FCC requires that a number of measurements be made on each radial, ratioed to nondirectional reference measurements, averaged, and then multiplied by the measured unattenuated nondirectional measured field to determine the predicted

level of radiation in a given direction. The inherent accuracy of a field intensity meter is largely dependent on the local environment in which a measurement is taken. Powerlines and other reradiating structures necessitate that a number of measurements be taken to achieve reasonable results. The FCC requires at least twenty measurements be made on each radial between the distances of 2 and 20 m. A number of close-in measurements, less than 2 miles, are also required for the nondirectional analysis.

At this point, there may be a one or more radials at which the measured radiation exceeds the maximum level specified in the construction permit. It may be necessary to adjust the antenna parameters away from their initial values to bring the pattern into compliance. A common approach used to bring a radiation pattern into compliance involves placing a number of field intensity monitors at locations on the critical radials and adjusting parameters until the pattern is in. While one person adjusts the parameters, the monitors at locations on the critical radials report variations in signal strength after each adjustment. Once the pattern appears to come into adjustment based on individual measurements at each point, the entire radial must be remeasured to confirm the adjustment. If the pattern is still out of adjustment, the procedure must be repeated. This method requires that the points monitored all represent their associated radials, a condition that often is not obtained, particularly with directional antenna patterns with deep radiation nulls. This method is generally a useful technique for patterns with minima that are not extremely deep, and where conductivity near the antenna is uniform and few reradiation sources affect the measurements.

7.1. Complex-Plane Mapping

Complex-plane mapping is an alternate approach that has been developed to adjust an antenna pattern. This technique is based on the knowledge that the field found at any point as produced by the antenna system is a vector quantity, having both magnitude and phase. In theory, the resultant vector field at any point in the far field can be calculated by adding the individual vectors as contributed from each radiating element in the array. It is theoretically straightforward to determine the change in the resultant vector at a point of interest when one or more of the ratios or phases of the radiating element is varied. In the real world, however, it is often impossible to accurately correlate the field strength measurements taken with a field intensity meter that measures only the magnitude of a signal with a theoretically determined resultant due to reradiation and variations in the ground characteristics.

The problem of how to determine the magnitude and phase of the resultant vector for each radial of interest is solved by making a series of trial measurements. First, a reference measurement is made by taking a sample of field strength readings at each radial of interest. These measurements are ratioed with the nondirectional measurements and for each critical measurement radial. Next, only one of the parameters of antenna is changed. Usually, the tower having the least interaction with the others in the array is chosen so that the adjustment is simplified.

The magnitude is changed by an appropriate amount with all other parameters remaining the same and the field strength measurements are taken at the same points. Again the readings are ratioed with the nondirectional measurements and averaged. Finally, the magnitude of the tower that has changed is returned to the original value and the phase of that tower is changed by an appropriate amount. The measurements are retaken and analyzed as before. The results of all three trials (A, B, and C) are plotted on polar paper as circles with radii corresponding to the calculated averages for each measurement radial. The theoretical vectors for each radiating element are also plotted. Knowing that the field of the radiating element was changed in both magnitude (trial B) and phase (trial C), the delta (difference) vectors can be plotted. The magnitudes and phases of the delta vector gives the necessary information to determine the positions of the resultant vectors for the various radials for the beginning (trial A) operating parameters.

Once the actual resultant vectors have been determined for each radial of interest, one is able to predict the impact of parameter variations to the individual radials themselves. In extremely difficult cases of signal scatter along measurement radials corresponding to deep radiation pattern nulls, it may be necessary to apply the complex plane mapping technique to individual measurement points rather than to entire radials in order to avoid analysis ambiguity. The pattern is brought into adjustment by making changes that will simultaneously change the field strengths at each radial in accordance with the previously calculated limits. Once the required adjustment has been determined and made, measurements are taken at all radials to access compliance. If compliance is confirmed, a full set of measurements is made to be filed with the proof of performance to be submitted to the proper governing authorities.

8. DETUNING TO CONTROL RERADIATION

Sometimes there are objects, usually other radio antenna towers or high-tension power lines, capable of scattering sufficient radiofrequency (RF) energy to distort a medium-wave radio station's antenna radiation pattern located near its transmitter site. Most such objects can be made transparent to the medium-wave RF energy if properly treated.

A tower located near a transmitter site may be detuned by installing the necessary apparatus to control its current distribution to minimize reradiation. For a short tower (shorter than a quarter-wavelength), it is often sufficient to insulate its base or produce an impedance pole at its base with an arrangement of skirt wires and a detuning network.

For a taller tower or any critically located shorter tower, a null in tower current at a height somewhat above its base may be necessary for proper detuning. The correct treatment to produce the detuned condition and the corresponding current distribution for verification are best determined using the moment method directional antenna

analysis procedures (with the field of the tower to be detuned set to zero) described herein.

Control over the tower current may be achieved by either placing a reactance across its base or tuning the open end of a wire skirt mounted on it. In general, it will be necessary to place the null in tower current at approximately one-third of its height for towers up to approximately a half-wavelength tall. For structures taller than a half-wavelength, it may be necessary to produce more than one current distribution null. Two or more wire skirts may be required for this purpose.

Sampling loops may be mounted at the appropriate height or heights on a tower to verify the placement of current nulls corresponding to the detuned condition. They may be connected to detectors near the tower's base to facilitate observation during adjustment efforts and to verify continued detuning. For such sampling loops to be useful, they must not be mounted within a wire skirt span.

It is often sufficient to eliminate objectionable reradiation from a high tension power line by insulating the ground conductor running along the tops of adjacent support towers, thus breaking up the loops of current flowing in them. To maintain the integrity of the power line's protection system, insulators with arc gaps to conduct transient energy from the ground conductor to the support towers may be employed. When ground wire insulation is not sufficient to reduce high-tension powerline reradiation to an acceptable level, individual towers may be detuned utilizing wire skirts and detuning networks to control their current distribution.

9. MULTIPLE-FREQUENCY DIPLEXING

It is possible for a medium-wave antenna to radiate more than one frequency. Filters are employed to keep RF energy at each frequency out of a transmitter at the other frequency where a spurious signal might be generated.

For a nondirectional antenna, a series network providing an impedance zero at the desired frequency and an impedance pole at the undesired frequency and a shunt network providing an impedance pole at the desired frequency and an impedance zero at the undesired frequency to ground are normally placed at the feedpoint. For diplexed directional antennas, it is typical to have series filters at the tower bases but shunt filters only across the system input terminals (the common point).

BIBLIOGRAPHY

1. S. Ballantine, On the optimum transmitting wavelength for a vertical antenna over perfect earth, *Proc. IRE* **12**: 833-839 (1924).
2. A. B. Chamberlain and W. B. Lodge, The broadcast antenna, *Proc. IRE* **24**:11-35 (1936).
3. *Code of Federal Regulations*, 47 Parts 73.1-73.190.
4. S. A. Schelkunoff, Theory of antennas of arbitrary size and shape, *Proc. IRE* **29**:493-521 (1941).
5. G. H. Brown, Directional antennas, *Proc. IRE* **25**:81-145 (1937).

6. C. R. Cox, Mutual impedance between vertical antennas of unequal heights, *Proc. IRE* **35**:1367–1370 (1947).
7. G. J. Burke and A. J. Poggio, *Numerical Electromagnetics Code (NEC)—method of moments*. NOSC Technical Document 116, Vol. 2, Jan. 1981.
8. J. W. Rockway et al., *The MININEC System: Microcomputer Analysis of Wire Antennas*, Artech House, Norwood, MA, 1988.
9. R. D. Rackley, Modern methods in mediumwave directional antenna feeder system design, *Proc. NAB Broadcast Eng. Conf.*, 1991, pp. 43–54.
10. C. E. Smith, *Theory and Design of Directional Antennas*, Smith Electronics, Cleveland, 1949.
11. J. D. Kraus, *Antennas*, 2nd ed., McGraw-Hill, New York, 1988.
12. E. A. Laport, *Radio Antenna Engineering*, McGraw-Hill, New York, 1952.
13. C. T. Tai, Dipoles and monopoles, in R. C. Johnson and H. Jasik, eds., *Antenna Engineering Handbook*, 2nd ed., McGraw-Hill, New York, 1984.
14. H. T. Head, J. A. Lundin, Medium-frequency broadcast antennas, in R. C. Johnson and H. Jasik, eds., *Antenna Engineering Handbook*, 2nd ed., McGraw-Hill, New York, 1984.
15. S. Ramo and J. Whinnery, *Fields and Waves in Modern Radio*, Wiley, New York, 1944.
16. H. P. Williams, *Antenna Theory and Design*, Vol. 2, Sir Isaac Pitman, London, 1950.
17. J. Layton, *Directional Broadcast Antennas: A Guide to Adjustment, Measurement, & Testing*, TAB Books, Blue Ridge Summit, PA, 1974.
18. J. E. Cunningham, *The Complete Broadcast Antenna Handbook—Design, Installation, Operation & Maintenance*, TAB Books, Blue Ridge Summit, PA, 1977.
19. G. Bingeman, Optimizing impedance and pattern bandwidths of a phased array, *BM/E* 84–94 (1980).
20. G. Bingeman, Broadband your antenna with an external network, *BM/E* 262–272 (1984).
21. J. B. Hatfield, Relative currents and fields in an am directional array, *IEEE Trans. Broadcast* **35**:176–184 (1989).

ANTENNAS FOR MOBILE COMMUNICATIONS

KYOHEI FUJIMOTO
University of Tsukuba
Fujisawa, Japan

1. GENERAL

Antennas used for mobile communications are not necessarily specialized types of antenna; ordinary antenna types can be used. However, there are several distinctions in performance between mobile and fixed communications with respect to design methodology for antennas in mobile communications:

1. Parameters for antenna design are variations of field strength, which decays in proportion to the distance

between the fixed station and the mobile terminals, as mobile terminals move.

2. The field strength at a receiving point varies irregularly, depending on the environmental conditions, mainly due to the multipath propagation, which causes multipath fading. This variation usually takes a statistically Rayleigh distribution or Nakagami-Rice distribution.

3. Environmental conditions are also varied as mobile terminals move and affect mobile system performance, sometimes significantly. A typical example is the proximity effect caused by materials near an antenna element, which vary the antenna performance. The operator who holds a portable mobile terminal can significantly perturb antenna performance, which could be hazardous to humans. The human interface remains one of the most important issues in operating mobile terminals. The proximity effect is a problem that virtually cannot be avoided in mobile terminals; in particular, as equipment becomes smaller, the influence of nearby materials may not be easily reduced; it must be allowed for in the antenna design. Also, the equipment onto which an antenna element is mounted may itself act as a radiator, so the antenna element and the body of the equipment must be treated together as an antenna system.

4. Antennas for mobile terminals should also be designed to be robust against mechanical and physical environmental conditions. In the field, antennas should be mechanically tolerable against the operator's rough handling and also shock, vibration, and other disturbances that might rupture the antenna elements. It should also be durable against the variation of outdoor physical conditions such as temperature and humidity.

5. Requirements for system performance, concerning both mechanical and electrical conditions, should be satisfied. Small size, light weight, low cost, and yet realization of highest performance obtainable are desired. Antenna performance should meet the system specifications. In zoned systems, radiation patterns have to match the zoned patterns to avoid interference, and performance is also subject to variations in field strength according to movement of the mobile terminals and environmental conditions in the propagation path. Antennas should have sufficiently high gain to satisfy requirements for the link budget, and should function properly for rejection of interference and mitigation of multipath fading.

Frequency reuse capabilities, the type of information, modulation, and personalization of mobile terminals are some of the many factors that are of concern to antenna designers. Table 1 summarizes the influence of system requirements on antenna design [1].

Design of antennas for mobile communications thus must focus on propagation, the system, the environment, and the antenna. The antenna should be considered as an integral part of the overall system as depicted in Fig. 1. Mobile antenna design is no longer confined to small, lightweight, low-profile, or flush-mounted, omnidirectional radiators on a well-defined flat ground plane; rather, it involves the creation of a sophisticated electromagnetic

Table 1. Requirements for Mobile Antenna Design (from [1] with permission from Wiley)

Requirement	Implication
Antenna as a system	Not as an isolated receive/transmit terminal
Designed to accommodate propagation effects	Some degree of polarization or pattern diversity control embodied, leading to “smart” adaptive antenna arrays
Compatible with environmental conditions	Pattern characteristics to match stone requirements and allow for nearby obstacles
Integration of antenna with vehicle or platform	To include hand and body effects and possible hazard considerations
Latest manufacturing technology	Exploitation of new composite materials and integrated electronic technology
User-friendly and reliable performance	Minimum of moving parts and switches; high reliability of mechanical design
EMC constraints	Reduction of spurious radiation and coupling
Multimedia applications	Increased bandwidth requirements

configuration that plays a significant role in signal processing during operation in a generally ill-defined time-varying environment. It should be emphasized again that antennas employed for mobile communications should be designed while factoring in all the parameters that concern propagation, system requirements, and environmental conditions.

2. BRIEF HISTORICAL REVIEW

Variation of related parameters and evolution of antenna systems with time are shown in Table 2 in

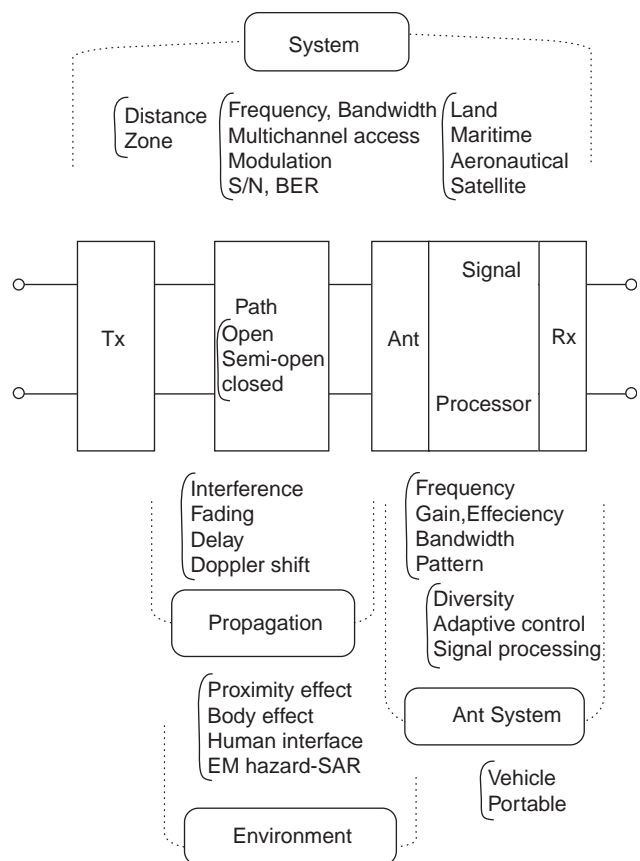


Figure 1. Antenna systems as an integral part of a mobile communication system. (From [1] with permission from Wiley.)

terms of frequency bands, systems, antenna, and propagation.

The first mobile communication was initiated in 1885 with wireless telegraph between trains and stations, which was developed by Thomas Edison [2]. Trolley wires were used as the antenna, which coupled electrostatically with a metal sheet installed on the ceiling of the train, and thereby the telegraph signal was received. Edison also experimented with communication on a vehicle in 1901 [3] using a thick cylindrical antenna placed on the roof of the vehicle. The practical mobile communication services started with wireless telegraph on ships in 1889 developed by Guglielmo Marconi using long vertical wire antennas in various forms such as T, inverted L, and umbrella shapes. It is interesting to note that portable equipment appeared in 1910 [4].

World Wars I and II both introduced the need for advanced antenna systems and promoted evolution of novel design and technology [5]. Wire antennas were firmly established in the 1920s, while present-day microwave antenna design and technology was commonplace in the 1950s. In the 1960s a new antenna era emerged, triggered by the revolutionary progress in semiconductors and integrated circuits, attributed initially to the Cold War defense industry but subsequently carried forward into the commercial sector. Quite simply, the demand instigated designers to create compact, lightweight, low-cost, easy-to-manufacture radiating structures, compatible with the newly conceived integrated electronic packages. The most notable one has been the creation of printed antenna technology, which lends itself to multifunction antenna devices [6]. Some of the salient factors that have increasingly influenced antenna design in this era and continue to do so today are noted in Table 3, which clearly emphasizes that communications, particularly mobile communication systems, are the most significant drivers of antenna technology at present.

Mobile communication systems have made rapid progress since mobile phone systems were introduced in 1979. The early analog systems, called the *first-generation* (1G) systems, conveyed mostly voice, but demonstrated benefit of communication on the move. This then became a good impetus for advances in mobile systems, which dealt with both voice and data in digital form. The digital systems were referred to as *second-generation* (2G) systems, and subsequently advanced to the *third*

Table 2. Developments in Mobile Communication Antenna Technology (from [1] with permission from Wiley.)

	1900–	1950–	1970–	1990–	2000–
Frequency System	Telegraph/telephone for train, ship, aircraft, police cars, portable receiving and transmitting	150 MHz < Voice system for business, navigation, taxis, tone pagers	800 MHz < Mobile phones	1.9 GHz < Satcom, voice, and data channel for aircraft, personal phones, microzones, TV-type images, wireless local-area network	2 GHz < Wireless-IP
Antenna	Monopole/dipole, whip, top-loaded monopole, inverted L, loop	Blades, coil loaded ferrite, helical	Corner reflector, leaky coaxial cable, diversity configurations, body-integrated planar inverted F, bifilar helix, microstrip antenna and arrays, parallel-plate, printed antennas	Adaptive signal processing, meanderline, normal mode helix, ceramic chip antennas	Intelligent software algorithms, wideband, multi-band antennas

generation (3G), which has demonstrated transmission of image, both still and moving. Table 4 outlines the evolution of mobile systems with time. Some typical widely used systems worldwide are also shown. The second-generation systems had shown advantages of digital systems over analog systems with respect to increasing the available capacity and services provided. More significantly, the digital system has enabled the achievement of global standardization of mobile communications. The typical European digital system, GSM (Global Systems for Mobile Communications), which initiated the operation of digital mobile system in the world, has paved the way for the third-generation systems, in which CDMA (code-division multiple-access) technology has been applied with increased capacity and services, including access to the Internet.

Now the systems referred to as the IMT-2000 (International Mobile Telecommunication Systems)/UMTS (Universal Mobile Telecommunication Services) have made even further progress toward fourth-generation systems, which can deploy extended services with higher-quality and higher-capacity transmission.

Antenna technology has progressed with the advancement of these mobile systems. The macrozone systems have been changed to smaller zones such as microzone and even picozones. Propagation problems have been modified according to changes in zone size, and antenna design has followed suit. Mobile phone systems initiated with automobile telephone systems have now evolved into handheld phone systems, and today the number of handheld phone users has far surpassed that of automobile phone users. There have been notable changes in antenna design for mobile phones since the early 1990s. Monopole was the main antenna for mobile phones; however, planar antennas, typically a planar inverted-F antenna (PIFA), have prevailed in most mobile phones and in some systems, particularly GSM systems, and variations of PIFA have been used as built-in antennas. Presently, use of a built-in antenna has become a worldwide trend in mobile phones. Further advancement is expected to include antenna systems such as adaptive arrays, antennas capable of adaptive performance control of environmental conditions, and antennas with more sophisticated functions, yet with smaller and more compact structure.

Table 3. Salient Factors Influencing Antenna Design (from [1] with permission from Wiley)

Factor	Trends
Spectral congestion and utilization	Wider bandwidth operation, improved performance, interference rejection, use of millimeter and submillimeter antennas
Explosive growth in mobile/personal communication systems	New compact user-friendly higher-performing antennas for cellular terrestrial operation of handsets and vehicles
Escalating information and processing speeds	Wide-bandwidth “smart” antennas with pattern agility and fast scan acquisition, antennas for microwaves
Growth in satellite communications	Higher-performance spaceborne antennas offering multifunction operation and reduced payloads, small high-performance handset antennas
Link with IN and ATM networks	Small high-performance antennas for mobile terminals
Traffic information and control	Specifically designed antennas for systems
New materials	Redesign of existing, and creation of new, robust antenna structures to simplify manufacture and operation
Impact of computer modeling and computer-controlled measurement	Strengthens design methods to create higher-performing equipment, compatible antennas at lower cost
Public awareness of electromagnetic radiation	Preference for lower transmitted powers, environmentally friendly antennas, and antenna platforms

Table 4. Evolution of Mobile Communication Systems (from [1] with permission from Wiley)

		Year	
1980–	1990–	2000–	2010–
1G (analog)	2G (digital)	3G (CDMA)	4G
Voice AMPS,	Voice and data IS-54, GSM, PDC PHS DECT	Multimedia UMTS, IMT- 2000, Wireless ATM	Wireless LAN
TACS, JTACS		Mobile SAT- COM	Ubiquitous NW
NTT, NMT	Cdma-one	Mobile + IP NW Cdma – 2000	Mobile–optical NW ITS

3. TRENDS

Mobile systems are now being advanced toward fourth-generation systems, beyond IMT-2000/UMTS, which offer various new services with higher data rate, video transmission capability, and other advanced facilities. Main regional standards bodies have decided the preferred technology for IMT-2000, for example

- UWC-1336, a TDMA-based proposal from the United States
- WCDMA, a joint proposal from Japan and Europe
- cdma-2000, advanced from cdma-one, adopted in the United States and Japan

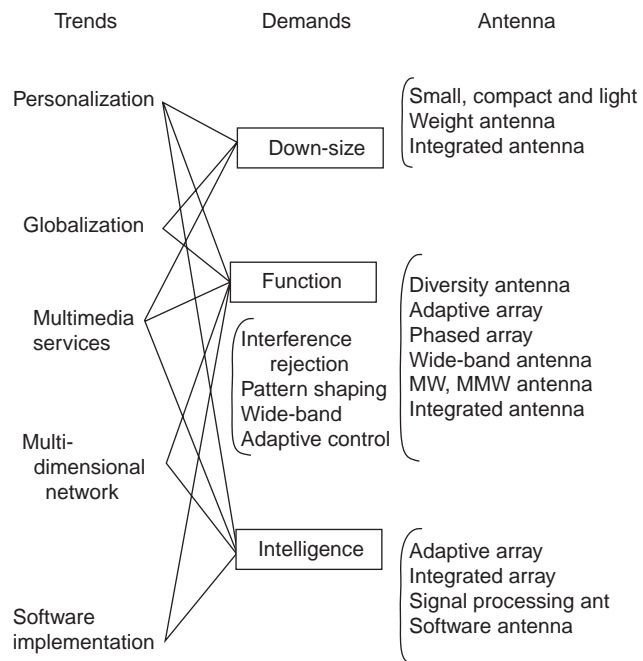


Figure 2. Typical trend of mobile communication and antennas. (From [1] with permission from Wiley.)

The WCDMA (wideband CDMA) system features high-quality and variable multirate services, multimedia transmission, and international roaming. Antenna systems with intelligent functions realized by adaptive signal processing and software implementation are expected to appear in future advanced systems. The typical trends in modern mobile communications are listed in Fig. 2 [1] and discussed in the following paragraphs.

3.1. Personalization

Personalization has been accelerated by downsizing hardwares in both mobile and base stations. Increase in information content, including games, movies, and music, which attracted many users, also accelerated the development of personalization features for mobile phone users. Mobile phones are presently no longer “telephones,” but information terminals, which deal with computer data, moving images, message exchange, and so forth. In other aspects, the downsizing of mobile terminals has also provided impetus for the personalization of mobile systems because the smaller handsets are more convenient to carry and easier to operate. One of the main problems encountered is the realization of smaller antennas for downsized handsets without degrading system performance. Downsizing of base stations (BSs) has also required antennas to be small in size and light in weight as a consequence of the increased number of base stations to serve an increased number of subscribers and the need for more efficient use of each channel.

Zone size has decreased; hence BS antennas are provided with less space for installation. Lightweight antennas are required for mounting on the wall of a building, and microstrip antenna (MSA) arrays are a typical example of downsized and lightweight antennas.

3.2. Globalization

Globalization has been realized by using satellite on the orbits of LEO or MEO (low- or medium-Earth orbit) as well as GEO (geostationary or geosynchronous orbit). Globalization is realized by not only satellite systems but also by wired network systems such as IP (Internet Protocol) cored network and wireless systems that enable mobile terminals to roam worldwide. One objective of IMT-2000 is the establishment of worldwide multimedia services.

3.3. Multimedia Services

Mobile systems are now capable of transmitting video images, both still and moving, as well as voice and data. Since the transmission rate has gradually increased from the order of kilo- to megabits per second (kbps to Mbps), various services, including TV-phone, movies, and large-scale packet data transmission, have become available. FOMA (the third-generation system in Japan), for instance, which employs WCDMA, can presently carry data of 384 kbps; however, it will be 2 Mbps in near future

and eventually 10 Mbps, by which various multimedia services will be provided. Antenna should have enough wideband to meet the requirements for multimedia transmissions.

3.4. Multidimensional Networks

Mobile communication systems are now being integrated into multidimensional networks that embrace multiinformational media, multitransmission media, and multilayered networks. Information media consist of both voice and nonvoice systems, including digital voice, sound, still and moving images, and computer data. Transmission media consist of both wire and wireless lines, including IP networks, radio, and optical links. Land, maritime, aeronautical, and satellite systems will be integrated into complex multilayered networks, thus allowing seamless communications worldwide regardless of time and space. The demand for more intelligent antennas that are integrated with signal processing, adaptive control, and software will continue unabated.

3.5. Software Implementation

Implementation of software to antenna systems will be increased in order to enhance the performance of antennas, including intelligent performance. An example is a mobile terminal that installs software, in which one system can be switched to another system, when a user desires to use a different system. For example, a user who is operating GSM may switch to operating PDC when entering a PDC [Personal Digital Cellular (Japan)] zone.

4. TYPICAL ANTENNA ELEMENTS

Various antenna elements have been used for mobile communications. There are no specific type of antenna elements, but the design differs when it is applied to practical mobile systems. In particular, specific design considerations are taken for antennas used in mobile terminals, as was mentioned in the previous section.

Typical antenna elements are shown in Fig. 3. Linear elements are (see Fig. 3) (a) dipole, (b) monopole, (c) loop, (d) inverted-L antenna, (e) inverted-F antenna, (f) normal-mode helical antenna (NMHA), and (g) meanderline antenna. Typical planar elements are (h) microstrip antenna (MSA), (i) planar inverted-F antenna (PIFA), (j) parallel-plate antenna, and (k) slot. Typical bulk-structured antennas are (l) small chip antennas, in which an antenna element such as small normal-mode helix, inverted L, or inverted F is encapsulated by ceramic material with high permeability. In the ceramic chip antenna, an inverted-F, meanderline, or other pattern may be printed on the surface of the ceramic substrate.

5. ANTENNAS FOR BASE STATIONS

Figure 4 shows important items to consider in designing a base-station antenna. Although “antenna design” in the narrow sense means electrical design, in reality it includes a wider area, and it is important to derive the antenna

hardware specifications from system requirements. In order to determine the hardware specifications, it is necessary to perform an evaluation that compares electrical and mechanical characteristics with a tradeoff between performance and cost, as shown in Fig. 5. Performance and cost considerations are sometimes the first step, while determination of the electrical and mechanical design is the second step [1].

In designing the practical antenna, it is important to assess how the antenna hardware will be installed after manufacturing. Installation fees may exceed the cost of the antennas themselves. It is important to consider not only the reduction of construction cost, but also the creation of an antenna design that facilitates installation.

5.1. Propagation Problems

Propagation problems differ depending on the environmental conditions. Propagation in mobile communication occurs within a diffraction region and is not free-space propagation. Propagation path loss in free space is simple and is proportional to the square of the distance, whereas in mobile communications it depends on various factors, such as the propagation environment, antenna height, and frequency.

Mobile propagation environments are very complex, but are roughly categorized into four basic types [7]:

- *Open Area.* There are few obstacles, such as high trees or buildings, in the propagation path. Roughly speaking, free spaces measuring about 300–400 m in length lie between the base and mobile stations.
- *Suburban Area.* There are some obstacles around the mobile stations, but they are not dense. Roughly speaking, this may be an area of trees and low-height houses.
- *Urban Area.* There are many buildings or other high structures. Roughly speaking, this is an area with high, adjacent buildings, or a densely mixed area of buildings and high trees.
- *Closed Area.* Propagation is confined to limited areas such as building, tunnels, subway stations, and underground streets.

5.2. Propagation Path Loss Characteristics

Although there are many aspects of mobile propagation, path loss characteristics are most closely related to the antenna design. Path loss in a mobile propagation environment exceeds that in free space because of the existence of various obstacles. Figure 6 shows measured field strength versus distance from the antenna with respect to base-station antenna height. These measurements were recorded at a frequency of 453 MHz with vertical polarization and a mobile station height of 3 m [7].

5.3. Base-Station Antenna Techniques

5.3.1. Requirements for Base Station Antenna Systems. The earliest mobile phone systems were installed in automobiles and other moving vehicles; then the

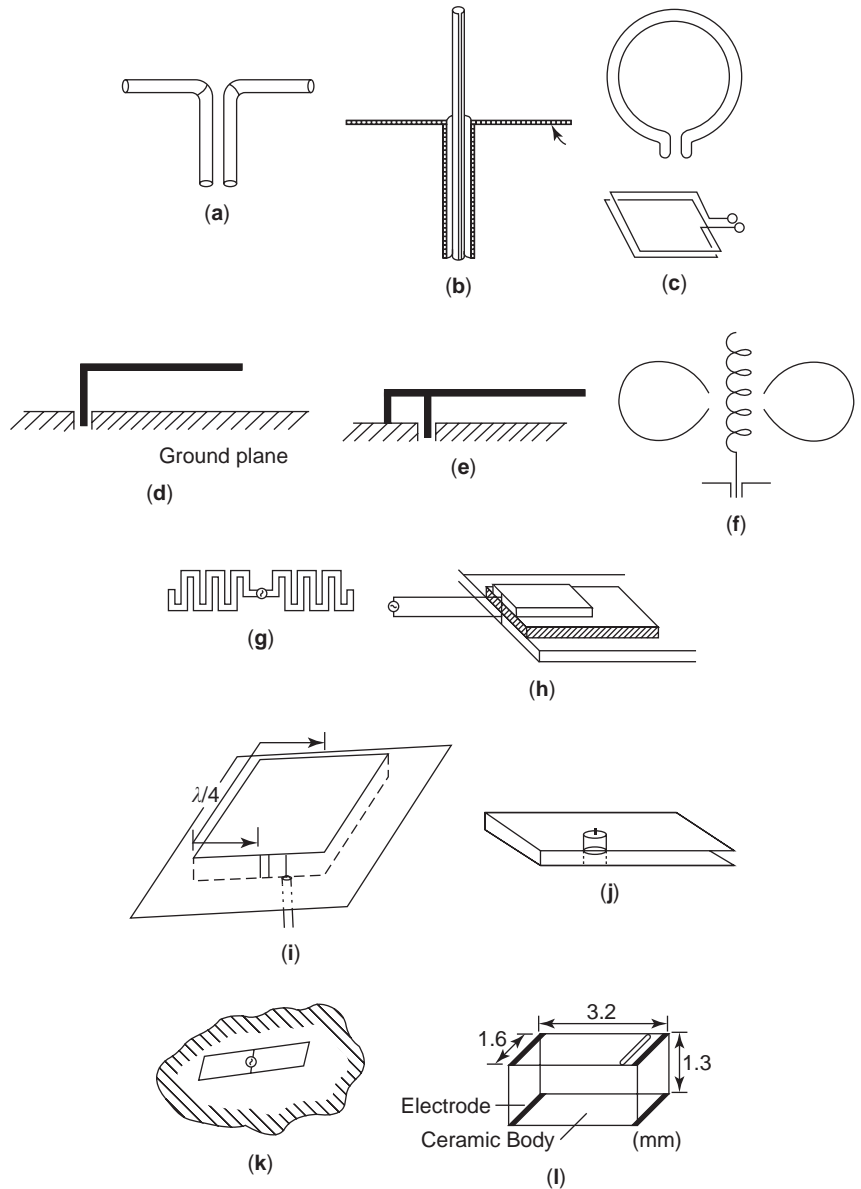


Figure 3. Typical antenna elements: (a) dipole; (b) monopole; (c) loop; (d) inverted L; (e) inverted F; (f) normal-mode helical antenna; (g) meanderline antenna; (h) microstrip antenna; (i) planar inverted F; (j) parallel plate; (k) slot; (l) chip antenna.

development of portable telephone systems subsequently followed. Mobile phone systems adopt a cellular structure, and antennas are designed to meet the requirements for the systems that operate within that structure. The necessary antenna technology is illustrated in Fig. 7. In order for the base station to communicate with the mobile stations located in the service area, base-station antennas must radiate uniformly inside the area. Moreover, antenna gain should be as high as possible. Since the pattern of the service area is specified, antenna gain cannot be increased by narrowing the beamwidth in the horizontal plane. Therefore, the antenna beam is usually narrowed in the vertical plane to increase gain; a vertical array of linear antennas is used for this purpose. Antennas with a gain from 7 to 15 dBi are normally used for base-station antennas in cellular systems.

Since a base station communicates with many mobile stations simultaneously, multiple channels must be

handled. This requires wide-frequency characteristics and a function for branching and/or combining the channels. Hence, base stations in the cellular system use one antenna for both transmitting and receiving. The required bandwidth of the antenna, for example, in the 800-MHz band Japanese PDC system, is more than 7% for the specified voltage standing-wave ratio (VSWR) of < 1.5. Furthermore, antennas are designed for sharing by several systems (e.g., analog and digital systems), for which a wider frequency bandwidth is required. Thus the PDC antenna in the 800-MHz band requires a frequency coverage of 810–960 MHz, with a 17% relative bandwidth.

Due to the rapid growth of mobile phone subscribers, effective use of communication channels has been encouraged worldwide. The cellular system has been introduced to increase the channel capacity by adopting the frequency reuse concept, and base-station antennas are designed to

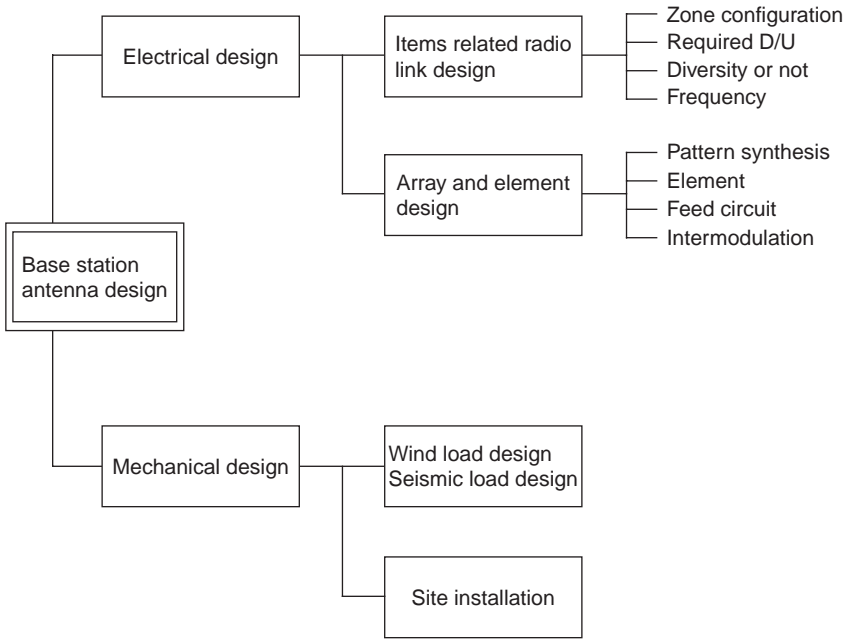


Figure 4. Important items in designing base-station antenna. (From [1] with permission from Wiley.)

match the frequency reuse concept. Tilted mainbeam and shaped patterns are two major design concepts.

Another important issue that warrants specific consideration in mobile communications is mitigation of multipath fading. One way to overcome this problem is to apply diversity antenna systems. Diversity systems have been studied since the 1960s, and thus far their effectiveness has been confirmed both experimentally and theoretically. Reception diversity first applied to commercial systems was for the “advanced mobile phone system” (AMPS) in the United States in 1982. It was also employed in the large-capacity mobile systems in Japan.

Various antenna technologies for base stations other than diversity systems have been developed to enhance the system performance. Adaptive array is one of them and has been studied extensively in the United States, Europe, and Japan. Major issues in the process of adaptive array development are communication frame format for beamforming, beamforming algorithms, array calibration, and simplification of hardware. The world’s first application of the adaptive array was to the PHS (personal handy-phone system) base-station antennas in Japan in

1998. PHS system is a likely system for application of the adaptive array, because PHS employs a TDD (time-division duplex) system and allows slow movement of mobile terminals, so that estimation of the propagation channel property for downlink can also be used for uplink, resulting in rendering application of adaptive array feasible.

A field test using the adaptive array in IMT-2000 has been performed and the usefulness of the adaptive array was confirmed; however, practical allocation has not yet been completed.

5.3.2. Type of Antenna. Base-station antenna configurations depend on the size and shape of the service area, the number of cells, and the number of channels. For the limited service areas within a restricted angle in the horizontal plane, a corner reflector antenna is often used. When the service area is wide, as in a macrozone system, a linear array antenna, which has high directivity in the vertical plane, is used.

In the early stage of cellular system development, the base-station antenna was designed mainly to achieve higher gain, and array antennas excited uniformly were

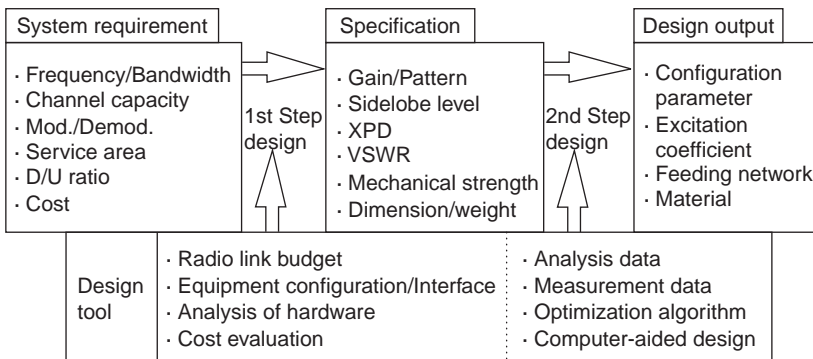


Figure 5. Design steps of base-station antenna. (From [1] with permission from Wiley.)

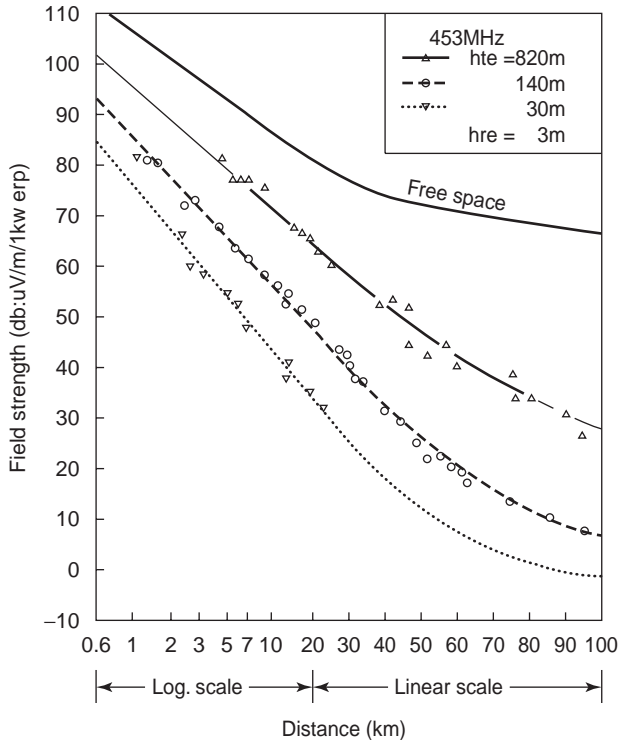


Figure 6. Measured field strength with respect to distance from a base station ($f = 450$ MHz, urban area). (From [1] and [7] with permission from Wiley and IEICE, respectively.)

often used. However, the design concept of the base-station antenna has shifted from attaining not only high gain but also a greater ratio of desired-to-undesired (D/U) signal strength, as cells have been divided into smaller sub-cells in order to increase the effectiveness of frequency reuse. Mainbeam tilting, either mechanically or electrically, has been adopted throughout the world and cochannel interference was reduced by about 10 dB, as can be observed in Fig. 8. Beam tilting was recognized to be essential for enhancing frequency reuse, and suppression of sidelobes adjacent to the mainbeam, achieved by synthe-

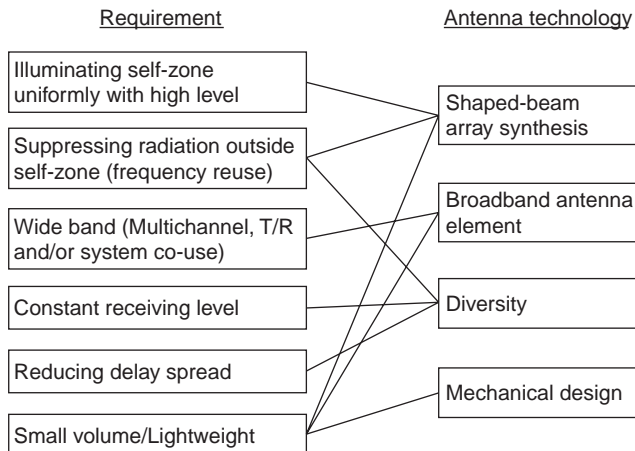


Figure 7. System requirements and necessary antenna technology. (From [1] with permission from Wiley.)

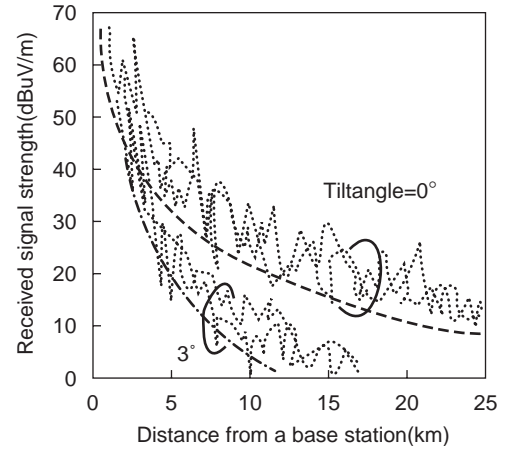


Figure 8. Interference reduction by means of beam tilting. (From [1] and [7] with permission from Wiley and IEICE, respectively.)

sizing array antenna patterns appropriately, was also effective in decreasing the distance between cells. Figure 9 depicts the effectiveness of reducing the sidelobe.

As for diversity antennas, space diversity, in which two antennas are used with separation of 5–10 wavelengths, has been commonly used. Other diversity schemes such as the pattern diversity [8] and polarization diversity [8] have also been applied to base-station antennas in commercial systems.

Polarization diversity has gained new understanding, as improved performance compared with that using space diversity has been recognized in urban areas, particularly in dense metropolitan areas such as central Tokyo [9]. This is attributed to increase in cross-polarization components in mobile phone propagation with increase in mobile phone users. When a mobile phone is held at talk position, the unit is slanted and produces both vertical and horizontal polarization components. Consequently, polarization diversity performs better than does space diversity. Polarization diversity was employed in the cdma-one system, and presently in the IMT-2000 systems.

Figure 10 categorizes the types of base station antennas with respect to functions and antenna characteristics.

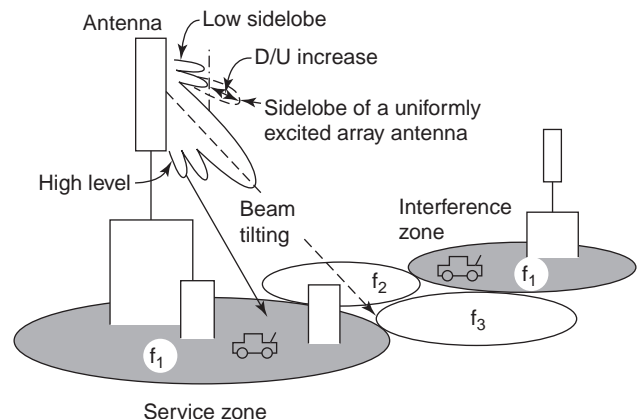


Figure 9. Sidelobe reduction for frequency reuse. (From [1] and [8] with permission from Wiley and IEICE, respectively.)

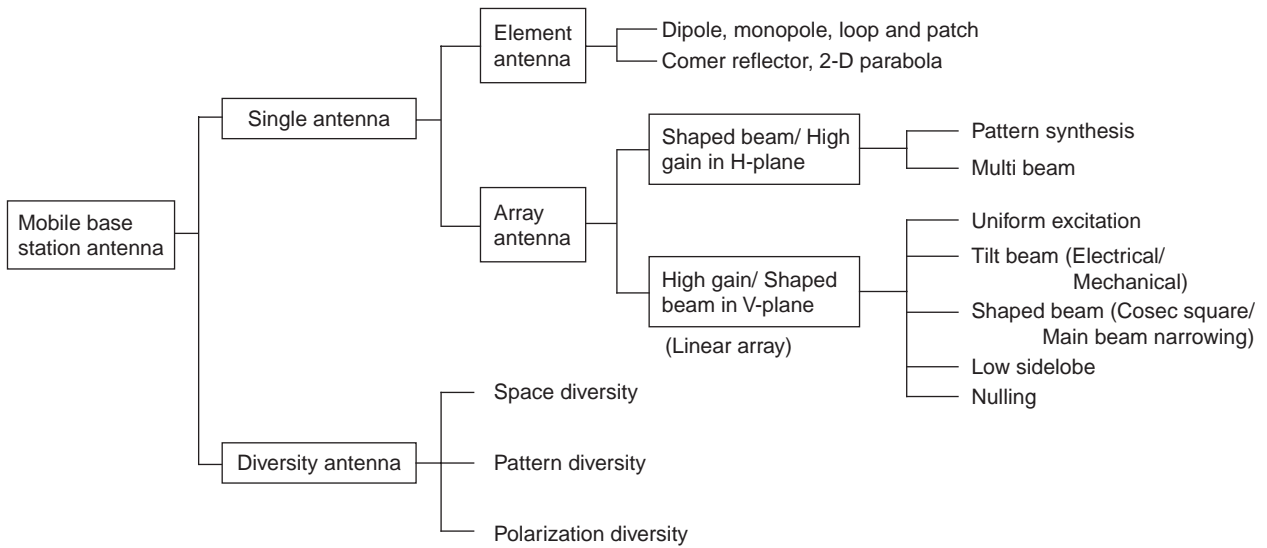


Figure 10. Types of base-station antennas categorized by function and characteristics. (From [1] with permission from Wiley.)

5.3.3. Design of Shaped-Beam Antennas. A base station antenna in a cellular system is required to radiate energy at as low a level as possible toward the cell where the same frequency is used; conversely, it must illuminate the service area at as high a level as possible. There are two types of shaped-beam antennas: (1) a sector beam in the horizontal plane and (2) a cosecant beam in the vertical plane.

5.3.3.1. Frequency Reuse Distance. From the cellular system shown in Fig. 11 [10], the following formula can be derived

$$N = \frac{1}{3} \left(\frac{D}{R} \right)^2, \tag{1}$$

where N is the number of cells, R is the radius of a cell, and D is the distance between the centers of adjacent cells [11]. The worst value of the carrier-to-interference ratio (CIR), expressed in decibels, appears at the edge of the cell and is given by

$$\text{CIR} = -\alpha \cdot 10 \log \frac{R}{D - R} \tag{2}$$

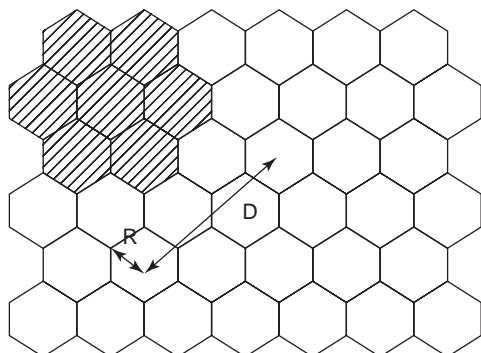


Figure 11. Cellular system. (From [1] and [10] with permission from Wiley and IEICE, respectively.)

where α is the attenuation constant of the path loss characteristic curve. In (2), $(C/I)_{\text{ANT}}$, the antenna pattern difference between the desired wave direction (θ_d, ψ_d) and the interference wave direction (θ_i, ψ_i) , expressed in decibels, is not included.

Therefore, the total CIR of antenna pattern $P(\theta, \psi)$, expressed in decibels, is obtained by

$$\text{CIR} = -\alpha \cdot 10 \log \frac{R}{D - R} + (C/I)_{\text{ANT}} \tag{3}$$

$$(C/I)_{\text{ANT}} = \frac{P(\theta_d, \psi_d)}{P(\theta_i, \psi_i)} \tag{4}$$

Figure 12 shows the relation between D/R and CIR when $(C/I)_{\text{ANT}}$ is varied and $\alpha = 3$ [10]. From this figure, the significance of $(C/I)_{\text{ANT}}$ can be understood.

Figure 13 shows the typical radiation pattern of a base station antenna in the vertical plane and radiation levels

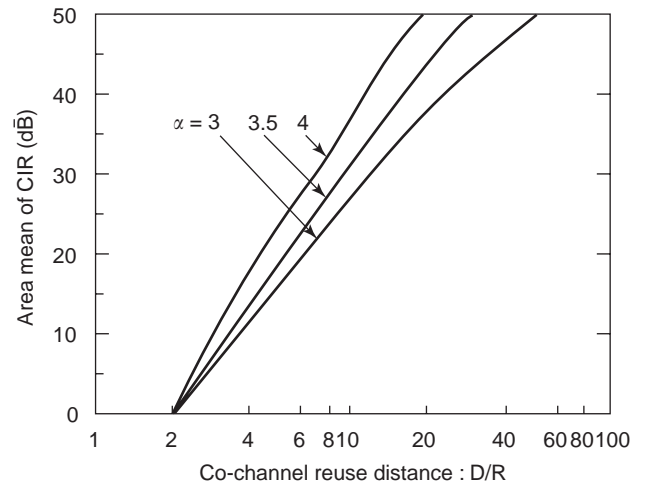


Figure 12. Relation between D/R and CIR. (From [1] and [10] with permission from Wiley and IEICE, respectively.)

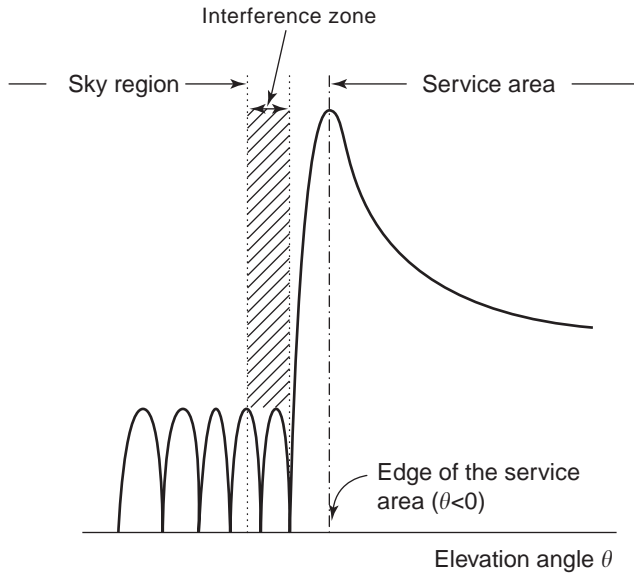


Figure 13. Typical radiation pattern of base station in the vertical (y) plane. (From [1] and [10] with permission from Wiley and IEICE, respectively.)

at the edge of the cell and toward the interference direction. If the two directions are sufficiently separated compared to 50% of the main beamwidth of the antenna, interference points exist in the sidelobe region of the radiation pattern, and the sidelobe level must be decreased to increase $(C/I)_{ANT}$.

If the interference direction approaches the desired direction (N becomes small), interference lines may exist in the mainbeam as well as the desired direction. To increase $(C/I)_{ANT}$ in this case, it is necessary to increase the length of the antenna or to narrow the main beamwidth with beam shaping techniques without increasing the length of the antenna.

When sector beams with the angle of θ_S are used in place of omnidirectional (circular) beams, the interference distance $(D-R)$ in Eq. (2) lengthens to $(D^2 + R^2 - 2DR \cos \theta_S)^{1/2}$,

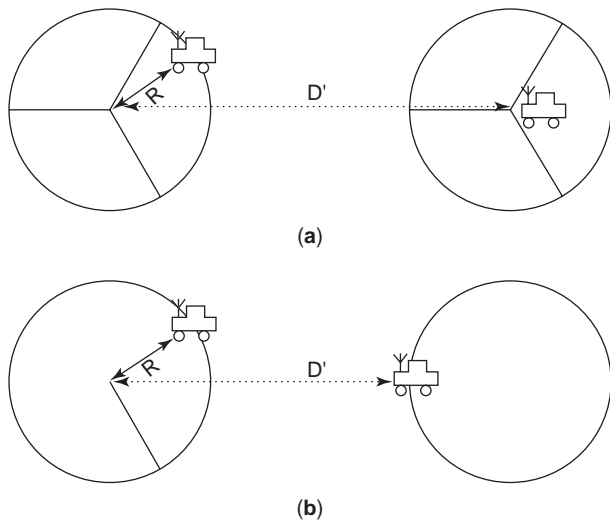


Figure 14. Interference distance of (a) sector beam and (b) omnidirectional beams. (From [1] with permission from Wiley.)

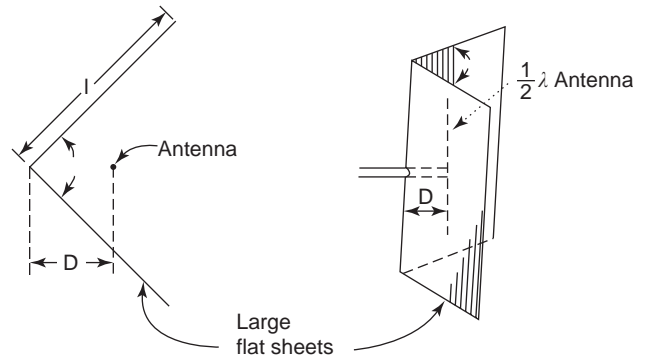


Figure 15. Fundamental configuration of a corner reflector antenna. (From [1] with permission from Wiley.)

as shown in Fig. 14. These are more advantageous in frequency reuse than omnidirectional beams.

5.3.3.2. Sector Beams. A sector beam should effectively cover the service area of a hemisphere or a sector. In addition, the frequency reuse distance with a sector zone arrangement is shorter than that with a circular zone arrangement. Typical antennas having a sector beam are an antenna with a corner reflector, and a two-dimensional parabolic reflector fed by two primary radiators [12].

The corner reflector antenna has an advantage that the beamwidth can be adjusted by controlling the aperture angle of the reflector. Figure 15 shows the fundamental configuration of the corner reflector antenna. The antenna element may be a vertically arrayed antenna. With the vertically arrayed antenna, the corner reflector can achieve high directivity by narrowing the mainbeam in the vertical plane and can radiate a shaped radiation beam by controlling the excitation coefficient.

Figure 16 shows the relationship between the aperture angle of the corner reflector and a half-power beamwidth in the horizontal plane, as well as the relationship between the aperture angle and the directivity when the primary radiator is a half-wavelength dipole. Sector beams with 60–180° beamwidth can be obtained by

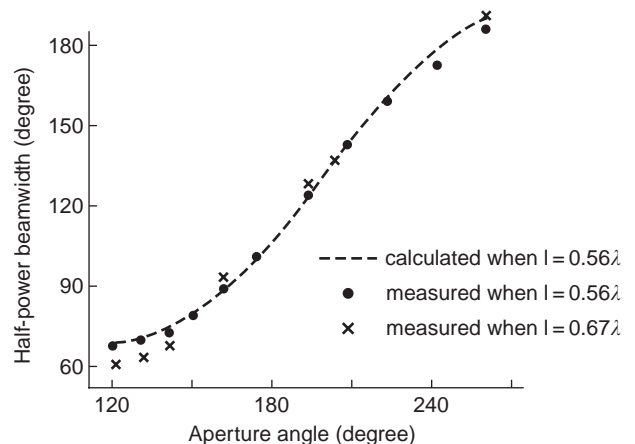


Figure 16. Aperture angle versus half-power beamwidth in a corner reflector antenna. (From [1] and [13] with permission from Wiley and IEICE, respectively.)

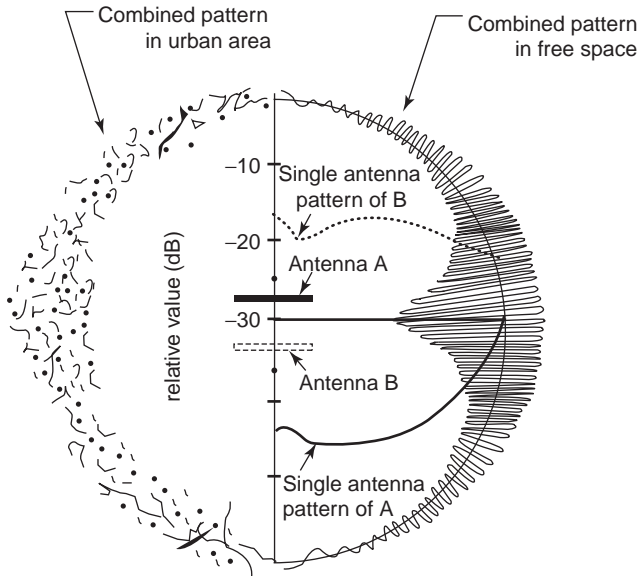


Figure 17. Omnidirectional pattern by combining two 180° sector beam antennas. (From [1] and [8] with permission from Wiley and IEICE, respectively.)

setting the aperture angle from 60° to 270° [13]. The results shown in Fig. 16 are somewhat different from those presented by Kraus [14], in which an infinite corner width is assumed. When the aperture angle is 180°, corresponding to a flat plate, the beamwidth becomes approximately 120°. To obtain a sector beam with a beamwidth more than 120°, a corner reflector with an aperture angle of more than 180° is needed.

If two sector beam antennas of 180° beamwidth are combined with moderate spacing (approximately $> 6\lambda$), an omnidirectional pattern is realized, as shown in Fig. 17. In this case, large ripples appear in the direction of $\pm 90^\circ$ due to the interference of the two patterns. However, measurements confirm that these ripples disappear in a multipath environment as shown in Fig. 17.

A design method of a corner reflector beam antenna having a dual frequency has been reported [15]. To realize a dual-frequency corner reflector antenna, it is necessary to prepare a dual-frequency primary radiator. This is possible with a dipole with a closely spaced parasitic element

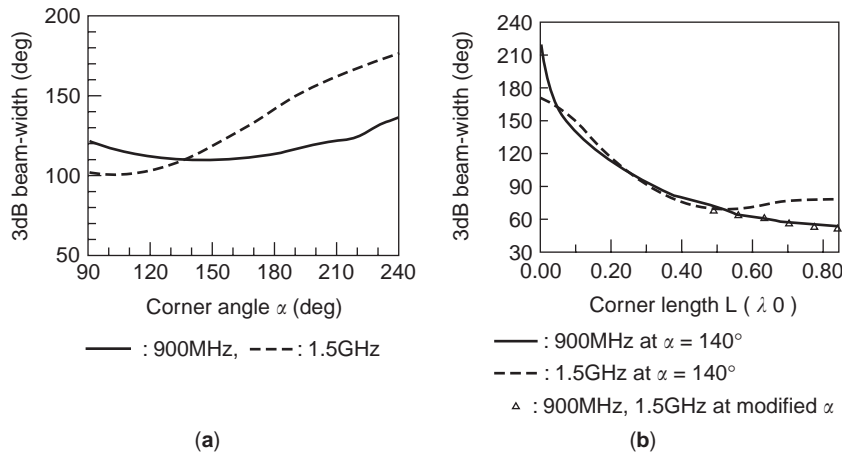


Figure 19. Typical design curves for corner reflector antenna of 900 MHz and 1.5 GHz. (From [1] and [15] with permission from Wiley and IEICE, respectively.)

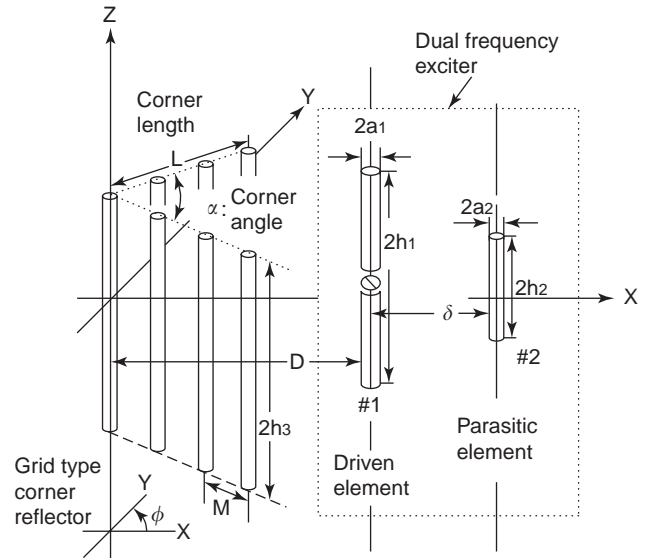


Figure 18. Geometry of a dual-frequency corner reflector antenna. (From [1] and [15] with permission from Wiley and IEICE, respectively.)

as shown in Fig. 18. This antenna has the advantage of being very compact. By using the primary radiator shown in Fig. 18, sector beams of equal beamwidth for frequencies f_1 and f_2 can be obtained by selecting the aperture angle α , distance d between reflector and primary radiator, and the width of the corner l . Typical design curves are shown in Fig. 19 for frequency bands of 900 and 1500 MHz.

5.3.3.3. Shaped Beams in the Vertical Plane. When a limited horizontal area is to be illuminated with equal received signal level from an antenna fixed at a certain height, as shown in Fig. 20, it is known that an antenna with a cosecant squared shaped-beam pattern in the vertical plane is used. If the path loss is larger than that in free space ($\propto r^2$) as in the case of mobile communication systems, the p th power order of a cosecant shaped-beam power pattern is necessary to achieve equal received signal levels at all points in the area. However, in cellular systems, the significance of the shaped beam is recognized

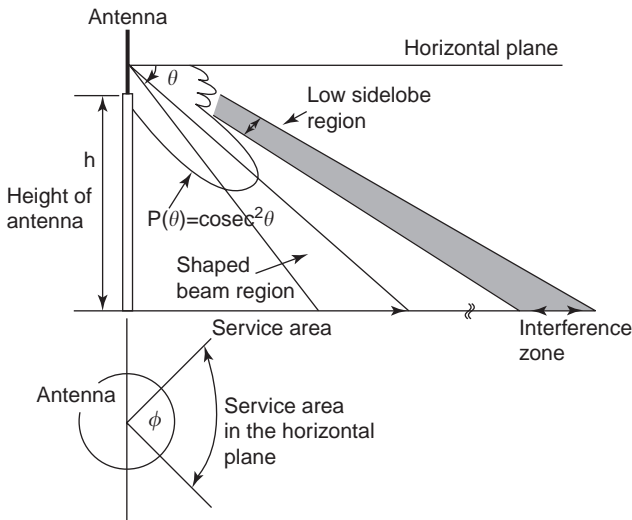


Figure 20. Shaped beam for illuminating service area uniformly and low sidelobes for interference reduction. (From [1] with permission from Wiley.)

in suppression of the radiation toward the cell, where the same frequency is reused, rather than in illumination of the self-zone uniformly, as illustrated in Fig. 21. If frequencies are reused, and the cells are closely spaced, a part of the mainbeam will illuminate the reuse cell. Therefore, it may be effective to tilt the mainbeam down to suppress the interference, even if the received signal level within the self-zone weakens. By reducing the main beamwidth while maintaining the length of the antenna, it is possible to increase $(C/I)_{ANT}$.

5.3.3.4. Beam Tilt. The principal idea of the beam tilt-down technique is to tilt the main beam in order to suppress the level toward the reuse cell and to increase $(C/I)_{ANT}$. In this case the carrier level also decreases in the zone edge. However, the interference level decreases more than the carrier level, so the total $(C/I)_{ANT}$ increases. This is an advantage from the viewpoint of

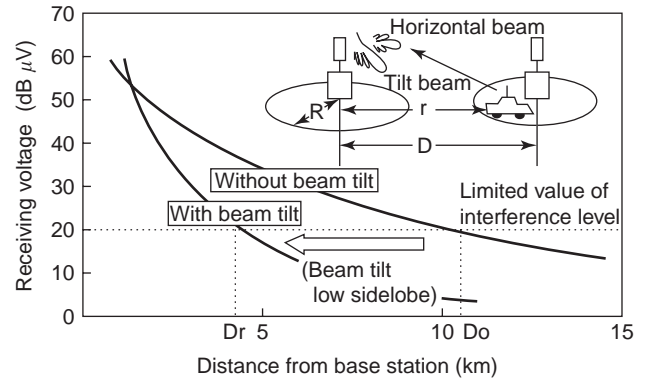


Figure 22. Beam tilting effect showing interference reduction with and without beam tilting. (From [1] with permission from Wiley.)

system design, and this technique is used in most cellular systems in the world. Figure 22 compares antennas with and without beam tilt, verifying the effectiveness of the beam tilt technique [16]. It can be easily understood from this figure that the distance from the base station inside which the interference level exceeds the threshold level of the system can be significantly reduced. In Japan, beam tilt is attained electrically by adjusting the excitation coefficient of the array, while in Europe it is achieved mainly mechanically.

5.3.3.5. Shaped Beam with a Locally Suppressed Sidelobe Level. For reducing the interference, sidelobe levels in some limited angles are suppressed. A pattern synthesized with locally suppressed sidelobe levels was first studied in the field of radar [17]. However, since sidelobe suppression is performed in the direction close to the mainbeam, and sidelobe level is closely related to the main beamwidth, it must be carried out very carefully. As shown in Fig. 23, a mainbeam 30% narrower than that of a uniformly excited array was obtained by suppressing only several sidelobes near the mainbeam and setting the other sidelobes at a comparatively high level [18]. An antenna with this radiation pattern can increase the

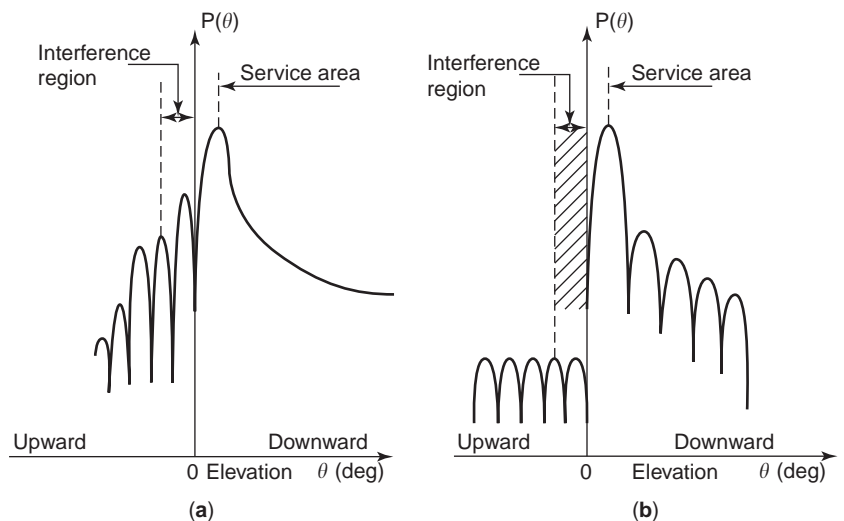


Figure 21. Synthesized patterns (a) with smooth cosecant beam having high sidelobe level and (b) constant rippled pattern having low sidelobe level. (From [1] with permission from Wiley.)

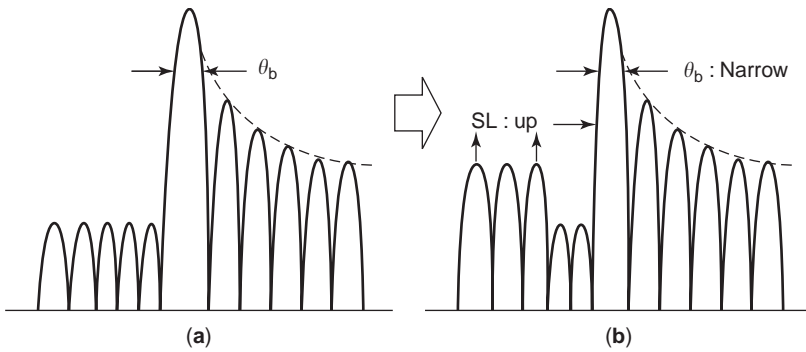


Figure 23. Narrow mainbeam designed by suppressing (a) sidelobe uniformly and (b) several restricted sidelobes. (From [1] with permission from Wiley.)

level at the zone edge by approximately 1.5 dB if the interference level is kept constant. This is a great advantage in system design.

5.4. Diversity Antenna Systems

5.4.1. Effect of Reception Diversity. The effect of reception diversity of the base station was first reported in 1965 [19]. It was shown that fading reduction could be achieved by placing two antennas approximately 10 wavelengths apart in the horizontal (*x*) plane. Figure 24 shows the cumulative probability of received level using either one isolated antenna or two antennas with a correlation coefficient ρ_e of 0, 0.5, and 0.8, respectively [20]. From this observation, it can be understood that the received level at a probability of 1% with the diversity antenna exceeds that with a single antenna by 8 dB.

Although two or more ports are necessary to carry out reception diversity, this method significantly reduces fading.

As a result, the transmitter power of the mobile station is reduced, and the quality of the transmission is enhanced. This is a great advantage from the total-system perspective. Reception diversity in the base station has been in commercial use in AMPS since 1982 in the United States and in NTT's large-capacity system since 1985 in Japan.

5.4.2. Configuration of Base-Station Diversity Antennas.

Many versions of base-station antennas are in use for commercial mobile systems in the United States, the United Kingdom, and Japan [10]. Sector beam antennas with a 3 dB beamwidth of 60° and 120° are used.

There are three types of diversity antenna schemes: space diversity, pattern diversity, and polarization diversity. In these three systems, space diversity is most commonly used.

Figure 25 depicts the pattern diversity antenna for an omnizone. Two antennas are arrayed as shown in Fig. 17 at 90° to each other [8]. Whereas 180° sector beam antennas for synthesizing an omnidirectional pattern are placed apart in space, the centers of the two omnidirectional antennas coincide with the center of the platform, and the spacing between the two antennas is regarded as zero.

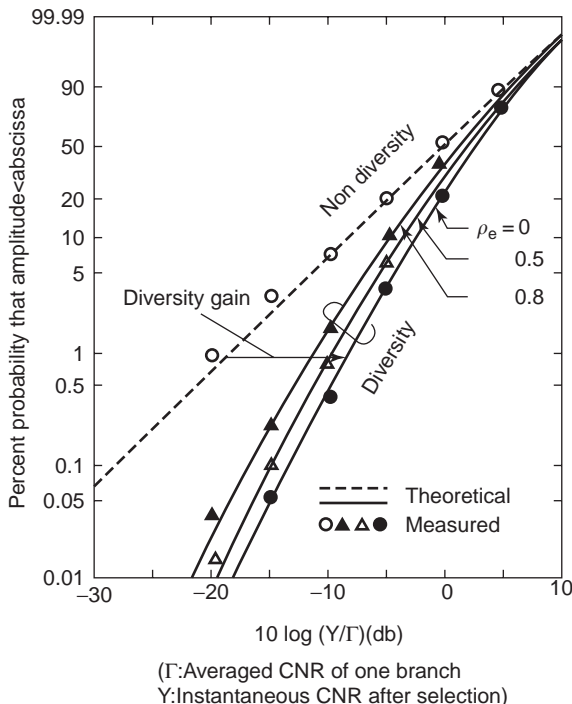


Figure 24. Diversity effect versus correlation coefficient ρ_e . (From [1] and [20] with permission from Wiley and IEICE, respectively.)

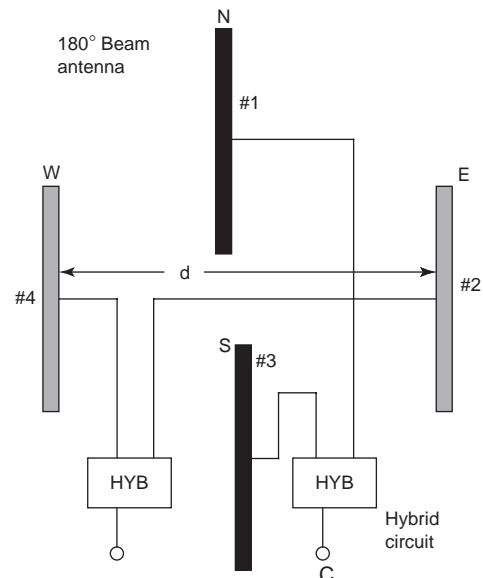


Figure 25. A 180° sector beam antenna configuration. (From [1] with permission from Wiley.)

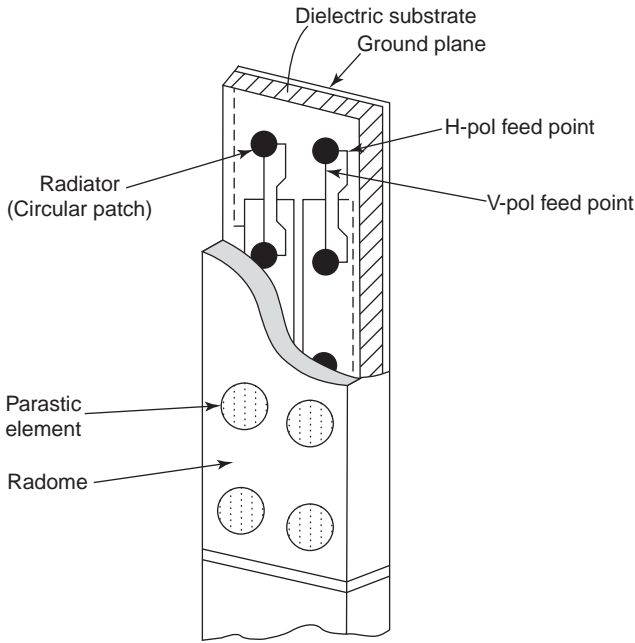


Figure 26. Configuration of a polarization diversity antenna configuration (60° sector beam). (From [1] with permission from Wiley.)

Therefore, the difference of the received power for each antenna is considered to produce the difference in the radiation pattern. When the space of two 180° sector beam antennas shown in Fig. 25 is six wavelengths, the correlation coefficient between two antennas is observed by the experiment to be less than 0.2 in urban areas. Figure 26 presents an example of a polarization diversity antenna developed by NTT [21]. It appears as a single antenna and has the advantage of small volume. The antenna element is a circular microstrip antenna with two feeding ports for diversity reception, which are orthogonal to each other. The correlation coefficient is as low as 0.2 in urban areas.

5.4.3. Design of the Base-Station Diversity Antenna. When the received power level at the receiving terminals of the antennas takes a Rayleigh distribution, the

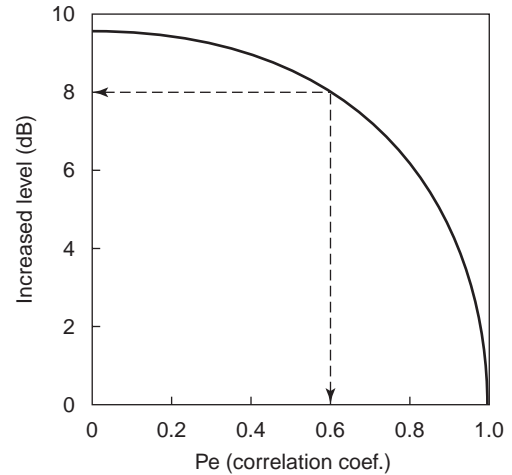


Figure 27. Increased CNR level versus correlation coefficient. (From [1] with permission from Wiley.)

relationship between the correlation coefficient of the diversity terminals and carrier-to-noise (CNR) level at the cumulative probability of 1% is as shown in Fig. 27. From this figure, it can be understood that the ideal improvement of CNR is 9.5 dB (when the correlation coefficient is 0), and that the improvement of CNR remains at 8 dB even if the correlation coefficient rises to 0.6. It is usual, therefore, to design the diversity antenna using such antenna spacing or antenna radiation patterns in order to achieve a correlation coefficient of <0.6.

5.5. Practical Base-Station Antennas [22]

In Japan, mobile telephone services began in 1979. After the liberalization of mobile communication services in 1988 and terminal markets in 1994, the number of subscribers of mobile phones increased rapidly. The personal digital communication system PDC began service in 1994. Four operators provided digital cellular services using frequency bands of 900 MHz and 1.5 GHz. In 2001, the third-generation system IMT-200 using 2GHz began service. The frequency bands used for mobile communications in Japan are shown in Fig. 28.

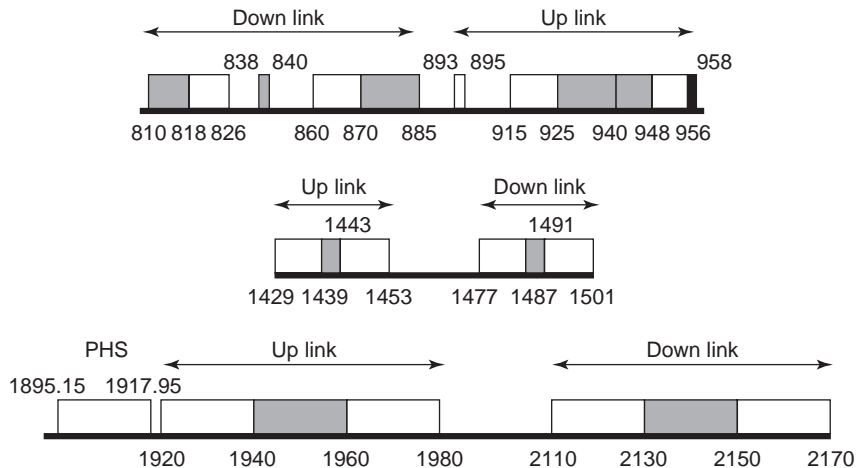


Figure 28. Frequency allocation for the Japanese cellular systems. (From [23] with permission from IEICE.)

Base-station antennas are designed to operate in dual and triple bands, employ the electronic dual-beam beam tilting technique, and use diversity systems, not only the space diversity scheme but also polarization and pattern diversity schemes. The small cell, with a radius of < 1 km, has been used in the high-density areas such as metropolitan Tokyo. A large number of base station antennas were installed on civil buildings. Rigorous requirements such as conservation of installation space, light weight, and low wind load are also allowed for in the design.

PHS (personal handy-phone system) services began in 1995. The cell size was designed to be very small, with a radius of 100–500 m. Base-station antennas are installed on various structures such as telephone pole, building walls, and telephone booth rooftops. Low-cost and very-lightweight antennas have been used for base stations. PHS was the first system in the world to apply practical adaptive antennas. In addition, PHS has been employed to operate a WLL (wireless local loop) system, where 12 base-station antennas are used to compose an adaptive array based on the DBF (digital beamforming) technique, in which a multibeam is attained. The mainbeam and adaptive antenna performance contribute to increase the system capacity.

5.5.1. Base-Station Antennas for Cellular Systems. Typical cell parameters of second-generation mobile communication systems in Japan are shown in Table 5 [22]. Frequency reuse by means of four-cell repetition gives nearly the maximum frequency spectrum utilization within most mobile systems. To achieve this repetition pattern, interference reduction is essential. The antenna beam is tilted downward and sidelobes directing cells, where the same frequency is used, are suppressed. The three-sector cell configuration is also effective for achieving the four-cell repetition pattern, as it reduces the number of cells that might experience interference. For two-branch reception diversity, two antennas are employed. One of these antennas is shared as a transmitter antenna. As for the sector cell configuration, the six-sector format has been used in order to increase the system capacity.

Antenna specifications are shown in Table 6. The antenna gain in the 900-MHz band is 17 dBi for 120° beamwidth in the horizontal plane. Determination of antenna gain in the 1500-MHz band is based on the gain in the 900-MHz band by considering the loss increase in high-frequency bands. The bandwidth of the 900-MHz digital

Table 6. Specifications of Base Station Antenna

Item	Specifications
Antenna height	5.4 m
Antenna gain	17 dBi (810–956 MHz) 17.5 dBi (1429–1503 MHz)
Sidelobe level below the horizontal direction	Less than –20 dB
Electrical beam tilt	Type 1: 0–5° Type 2: 3–11°
Beamwidth in a horizontal plane	120°

system is 146 MHz, which is 17% in relative bandwidth. The relative bandwidth of the 1500-MHz band is 6%. The sidelobe levels are required to be less than –20 dB. By means of electrical beam tilting, the antenna can be designed flexibly to match a variety of cell radii and building heights. For building height H , beam tilt angle α is determined by the relation $\tan \alpha = H/R$, where R is the cell radius.

Figure 29 shows a typical base-station antenna installation [23].

5.5.2. Dual-Frequency Antenna. The outside view of a dual-frequency antenna is shown in Fig. 30. This antenna is composed of three cylindrical blocks. Beside the antenna, a beam tilt box is attended. The box has two terminals of 900- and 1500-MHz bands. The antenna is connected to the beam tilt box with six coaxial cables whose lengths are 5 m, respectively. The antenna and coaxial cables are used at the dual-frequency bands. The configuration of the antenna feed network is shown in Fig. 31. All antenna components such as radiators, transmission lines, and power dividers are mounted on the same dielectric substrate. The beam tilt panel (contained in the beam tilt box) is separated from the antenna body and placed on the antenna base. All components shown in Fig. 31 are

Table 5. Parameters and Specifications of Base Station (from [1] with permission from Wiley)

System Parameters	Specifications	
Frequency bands	Uplink	Downlink
800-MHz analog	915–940	860–885
800-MHz digital	940–956	810–826
1500-MHz digital	1429–1441	1477–1489
	1453–1465	1501–1513
Cell radius	0.5–3 km	
Frequency reuse	Four-cell repeat pattern	
Sector configuration	Three-sector cell	
Diversity scheme	Two-branch switching	

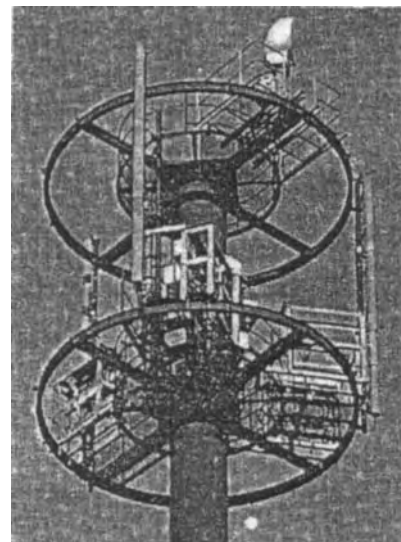


Figure 29. Installation of dual-frequency base-station antennas. (From [23] with permission from IEICE.)

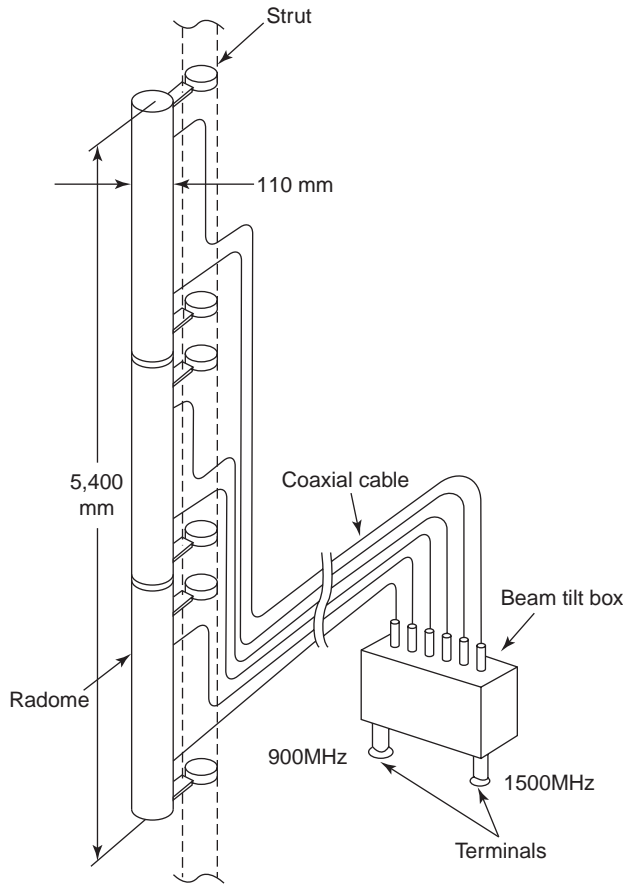


Figure 30. Exterior view of a base-station antenna. (From [1] with permission from Wiley.)

commonly used in dual-frequency bands. Array elements are excited through the feed network composed of transmission lines and power dividers. Each element of the feed network has wide frequency band characteristics. Array elements are designed for dual-frequency operation. An element number of 26 is selected to achieve the required antenna gain. Because grating lobe suppression at higher frequencies is important in determining radiator spacing, the array element spacing of one wavelength in the 1500-MHz band was chosen. At 900 MHz, the array element spacing becomes 0.6λ . The desired excitation coefficients (amplitude and phase) of array elements are achieved by designing the feed network. Excitation amplitudes are determined by setting power ratios at power dividers. Excitation phases are determined by setting the length of transmission lines. Here, because the line length is frequency-dependent, changes in excitation phases occur in dual-frequency operation. Accordingly, low-sidelobe characteristics will be degraded in dual-frequency operation.

The electrical beam tilt is achieved by imparting a specific phase difference to subarrays (composed of M array elements) [24]. This phase difference is achieved at a beam tilt panel. The wavefront of the subarrays is tilted by θ_{t0} as shown by solid lines. The beam tilt angle is set to θ_{tt} as shown by the broken line. Change in electrical beam tilt is achieved by replacing the beam tilt panel. When θ_{tt} does not equal to θ_{t0} , abrupt phase jumps between the edges of

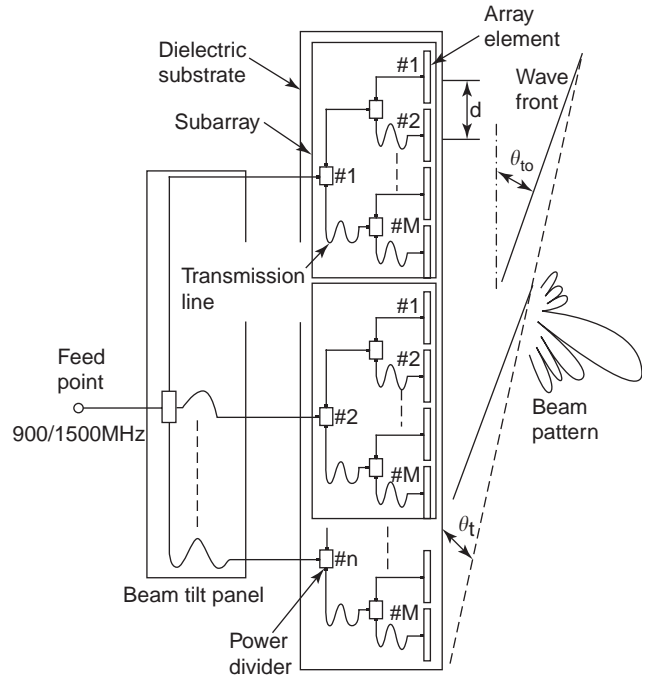


Figure 31. Feed network of a base-station antenna. (From [1] with permission from Wiley.)

subarrays occur. This phase jump produces many grating lobes in the low-sidelobe area. Here, the number of subarray element M is the key factor in determining the grating lobe positions. In this case, six subarrays, with element numbers 5, 4, 4, 4, 4, and 5, are employed (viz., M numbers are 4 and 5).

A practical base-station antenna is shown in Fig. 32. As dual-band array elements, the dual radiator configuration is employed. Printed dipole configurations are used as the 900- and 1500-MHz elements. The 1500-MHz element is placed in front of the 900-MHz element. Stubs are inserted between array elements in order to suppress mutual coupling due to small element spacing of 0.6λ . A reflector is placed behind these radiators to achieve a 120° beam in the horizontal plane. The radome diameter is 110 mm.

A cross-sectional view of the antenna is shown in Fig. 33. The main feature of this configuration is the sidewalls attached to both sides of the reflector. Adding sidewalls is effective to achieve 120° beamwidth using a small reflector size. Figure 34 shows the design chart for selecting radiator position. By using this chart, radiator position of 0.05 m is found for the 800-MHz band (810–960 MHz), and 0.07 m for the 1500-MHz band (1429–1501 MHz). Measured radiation patterns are shown in Figs. 35a (800-MHz band), and 35b (1500-MHz). The bandwidths of the 800- and 1500-MHz bands, respectively, are 17% and 5%. Measured antenna gains for the type 2 antenna are shown in Fig. 36. At a tilt angle of 6° , an antenna gain of 17.1 dBi is achieved in the 900-MHz band. Here, losses of the tilt panel of 1.2 dB and that of coaxial cables (5 min length) of 0.9 dB are included. At 1465 MHz, antenna gain is 17.7 dBi, loss of a tilt panel is 1.8 dB, and that of a coaxial cable is 1.0 dB.

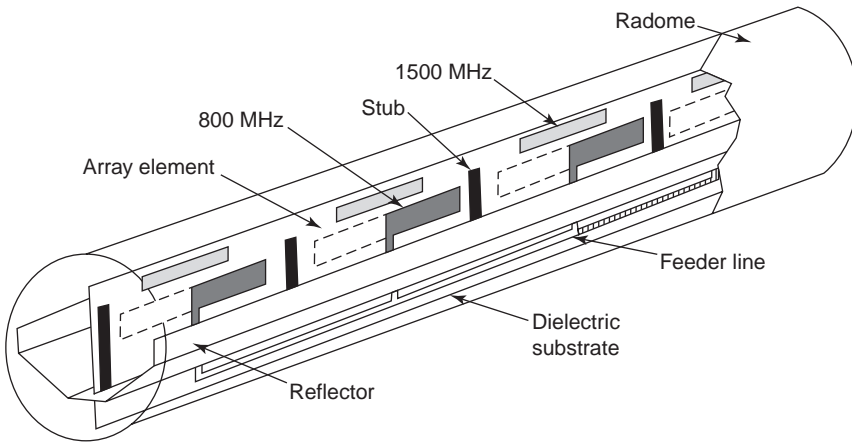


Figure 32. Inside view of a base-station antenna. (From [1] with permission from Wiley.)

5.5.3. Triple-Band Antenna. The IMT-2000 system uses a 2-GHz band, and additional antennas to dual-band antennas or exchange of dual-band antennas have been required. Since there have been little space to install new antennas, multiband antennas have been developed: two types of dual-band antennas, which operate at 900 MHz/2GHz and 1.5 GHz/2GHz, and one triple-band antenna, covering 0.9, 1.5, and 2 GHz bands. In IMT-200 systems, new sector beam antennas having 60° beamwidth are required in addition to 90° and 120° sector beam antennas. By adding a parasitic element to dual-band antennas, triple-band antennas have been attained. Two horizontal parasitic elements are used for increasing the bandwidth at 900-MHz bands. Figure 37 illustrates antenna configuration [25]. Current flows shown by arrows on the elements in Fig. 38 indicate operation of three frequencies each [26]. Radiation patterns for each frequency are shown in Fig. 39 [26].

5.5.4. Dual-Beam Antenna. In cellular systems, six-sector cells are employed to increase the system capacity. Thus 18 antennas maximum are needed when the diversity system is applied; reduction of the number of antennas is desired to ease facilitate antenna installation on the tower.

Figure 40 shows a 60° dual-beam antenna [27]. Two radiators are combined by a 90° hybrid circuit. By excitation of ports A and B, respectively, beams of A and B are generated. By setting separation D of the radiator at 0.5λ , the beamwidth of each beam becomes 60°, centering at $\theta_T = 30^\circ$ directions. Two sidewalls are attached in order to

refine beam shapes. Antenna configuration is shown in Fig. 41. Two vertical array antennas are arranged side by side. Subarrays are combined with a hybrid circuit. By connecting each port of the hybrid circuits to a beam tilt panel, electrical beam tilt is achieved. Radiation pattern of this antenna is shown in Fig. 42. The main parameter in designing the low-sidelobe characteristic is length T of a sidewall. This result shows the effectiveness of the sidewall. By increasing the height, sidelobes near 70° can be reduced effectively. Measured and designed characteristics are shown in Fig. 43. A parasitic element is placed in front of the radiator to achieve excellent 60° beamwidth and low-sidelobe characteristics [28].

The dual-beam antenna is introduced into a six-sector system as shown in Fig. 44. Two dual-beam antennas are combined to achieve four-beam system as shown in Fig. 44a. Then, three 4-beam-antennas are mounted on an antenna tower. The diversity system is employed in all sectors. As a result, the six-sector system is achieved by employing six dual-beam antennas. This is very simple

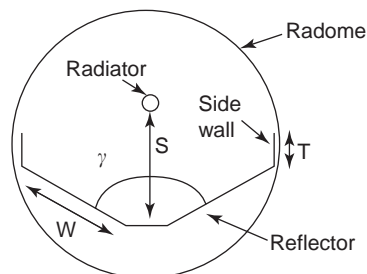


Figure 33. Cross-sectional view of a corner reflector antenna. (From [1] with permission from Wiley.)

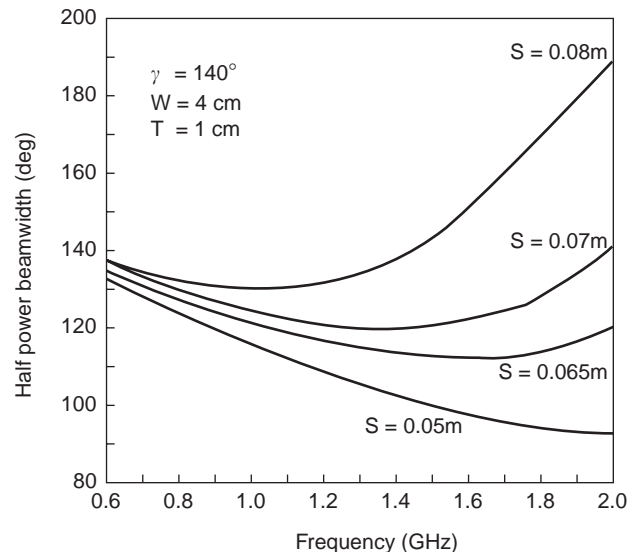
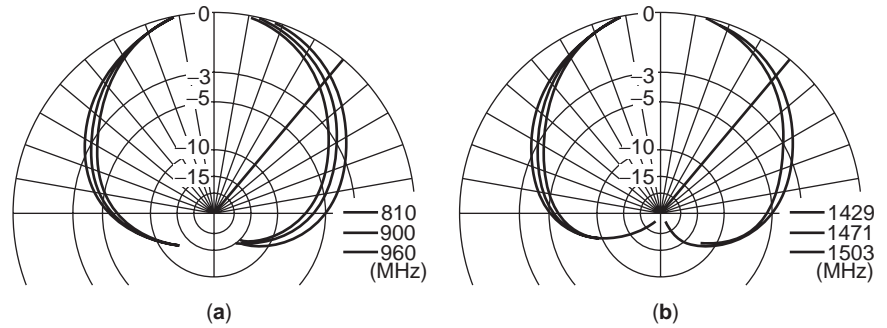


Figure 34. Design chart of corner reflector antenna; half-power beamwidth versus frequency with respect to location of radiator. (From [1] with permission from Wiley.)

Figure 35. Radiation patterns in the horizontal plane: (a) 800-MHz band; (b) 1500-MHz band. (From [1] with permission from Wiley.)



compared with the conventional antenna, which requires 12 antennas.

5.6. Diversity Antenna

5.6.1. Space Diversity. Shared use of an antenna element for reception and transmission is a mandatory necessity for reducing the number of antennas. The approach to accommodate two-sector elements inside a cylindrical radome is being applied to most base-station antennas in order to reduce the apparent number of antennas for multisector cell sites. An example of this scheme is illustrated in Fig. 45, which is a top view of a three-sector antenna system consisting of three poles that contain two radiating elements each.

Pole 1 contains two vertical arrays, $A_{1,1}$ and $A_{3,2}$, facing two azimuth angles of 0° for sector 1, and 240° for sector 3, respectively. Array $A_{1,1}$ is to receive the signal $Rx_{1,1}$ to be combined with $Rx_{1,2}$ received by array $A_{1,2}$, in pole 2 for diversity of sector 1. $A_{1,1}$ is commonly used for transmitting the signal Tx_1 for sector 1. Tx_2 is the signal transmitted by array $A_{2,1}$, which is shared for receiving the signal $Rx_{2,1}$ from the 120° direction. $Rx_{2,2}$ is received by array $A_{2,2}$ in pole 3 and combined with $Rx_{2,1}$ for diversity of sector 2. Transmission and diversity reception of sector 3 will be made in the same manner. This configuration needs three antenna poles separated by 10 wavelengths each for the three-sector space diversity system.

5.6.2. Polarization Diversity. Polarization diversity, on the other hand, does not require two spatially separated antennas. Multiple dipole elements with orthogonal polar-

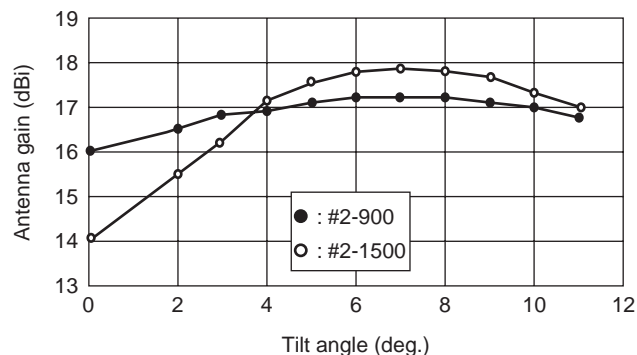


Figure 36. Gain versus beam tilt angle. (From [1] with permission from Wiley.)

ization can be alternately mounted on one piece of dielectric substrate in a vertical radome. Elements for the orthogonal polarization may be of vertical/horizontal or $+45^\circ/-45^\circ$ cross-dipoles depending on the particular design.

Polarization diversity is a well-known diversity technique; however, it has not been used in cellular phone systems. This was because it was not necessarily useful in the propagation environment, where mobile terminals were found mostly in automobiles and vertical polarization components predominated, as the mobile station employed were a vertical trunk-lid element.

However, as the number of handheld phone subscribers has increased, propagation conditions have changed. Horizontal polarization components sometimes exceed vertical polarization components, as users hold their phones in a tilted position, typically 60° from zenith at talk position. The polarization diversity is then recognized effective in the field where both vertical and horizontal polarization components exist.

Figure 46 shows a top view of a polarization diversity antenna having compact structure, which should be compared with Fig. 45. This is an antenna consisting of a single piece of vertical pole containing three-sector transmitting and receiving arrays with diversity capability

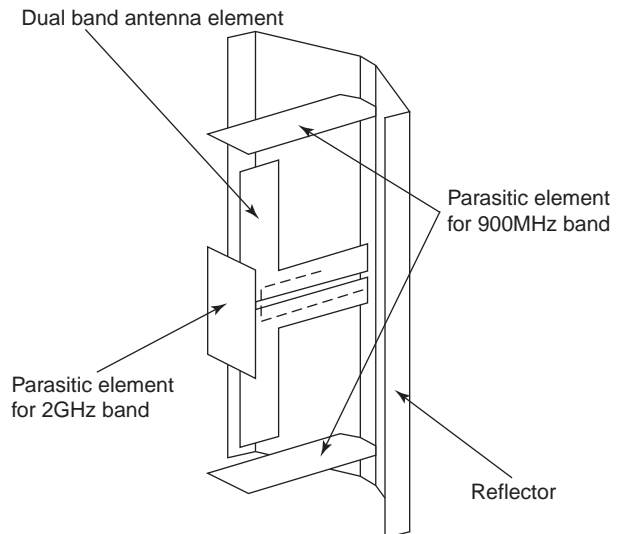


Figure 37. Configuration of a triple-band antenna. (From [25] with permission from IEICE.)

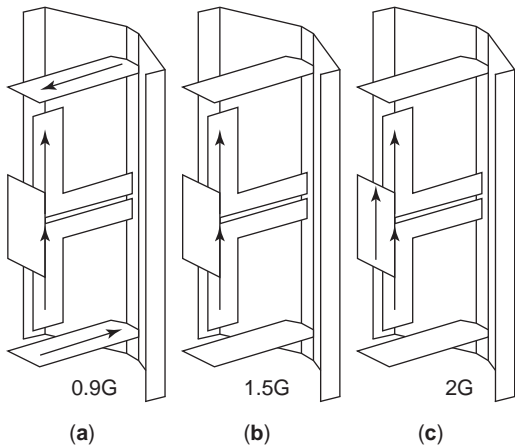


Figure 38. Current flow on the dipole element: (a) 900-MHz band; (b) 1.5-GHz band; (c) 2-GHz band. (From [26] with permission from IEICE.)

inside. Three vertical arrays, A_1 , A_2 , and A_3 , are bound together in the shape of a triangular pillar and are accommodated in a cylindrical radome. Array A_1 , for example, contains a set of vertical and horizontal dipoles stacked alternately on a dielectric substrate to receive vertically polarized signal $Rx-V_1$ and horizontally polarized signal $Rx-H_1$ for sector 1. Either vertical or horizontal dipole elements of array A_1 , or both, can be shared for transmission of the signal Tx_1 . The other two arrays, A_2 and A_3 , have configurations identical to that of A_1 . A number of tests [29–32] have confirmed the effectiveness of polarization diversity.

Figure 47a shows the cumulative distribution of the received level at a base station using space diversity, while the handheld phone transmitted signals from a line-of-sight location in the base-station coverage area. The two solid lines on the left hand show the received levels at the two separate vertical ports, and the dotted line shows the cumulative distribution of selection-combine diversity. Figure 47b shows a line-of-sight location with polarization diversity reception. The two solid lines show the distribution of output levels of vertical and horizontal ports, and the dotted line again shows that of selection-combined diversity. As can be seen, the polarization diversity gain is 12.0 dB at the 1% level of cumulative distribution whereas that of space diversity is 6.2 dB, suggesting the effectiveness of polarization diversity. Similar results were ob-

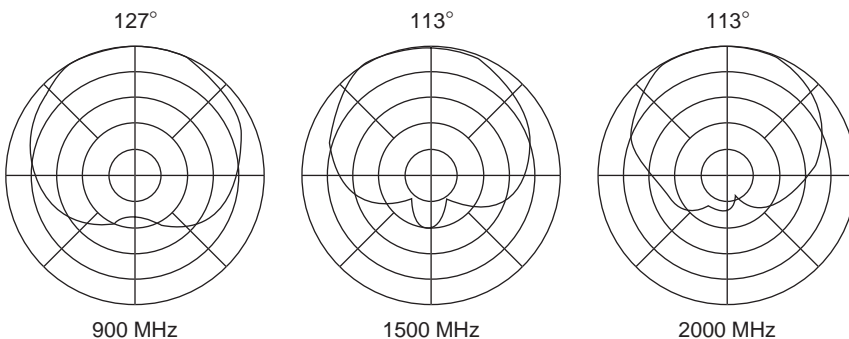


Figure 39. Radiation patterns at three frequencies. (From [26] with permission from IEICE.)

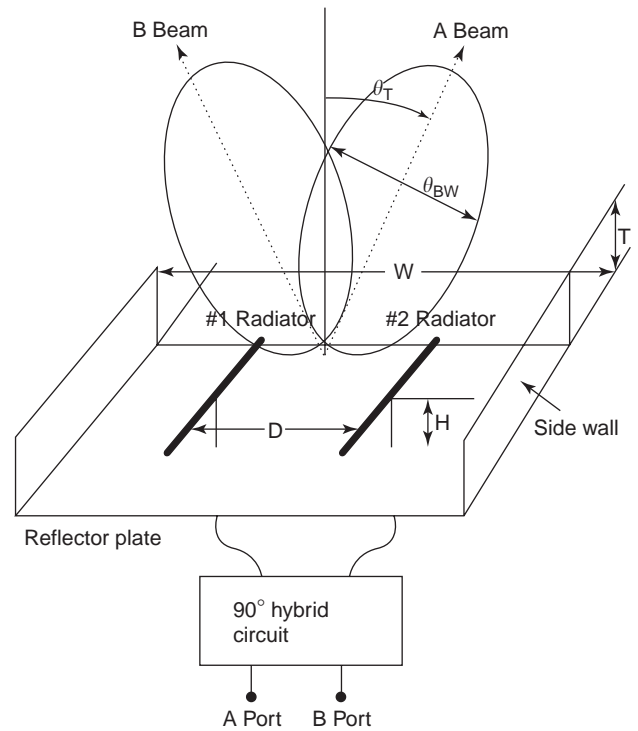


Figure 40. A 60° dual-beam antenna configuration. (From [1] with permission from Wiley.)

tained for the case where the mobile transmitted signals from the out-of-sight area (see results shown in Figs. 47c and 47d). Although the effect is not as significant as that in the line-of-sight case, diversity gain still is greater for polarization diversity (PD) than space diversity (SD).

Polarization diversity antennas feature reduction in size and weight to cope with stringent environmental requirements. Presently, polarization diversity antennas have been employed in all cdma-one base stations and some PDC base stations of KDDI of Japan [33,34]. This has resulted in easy cell site selection and reduction of construction cost because of the simple structure of the antenna in addition to superior performance.

Figure 48 shows the inner structure of this type of antenna and radome housing. Arrays for three sectors are accommodated in the shape of triangular tube in a cylindrical radome of 23 cm diameter. In this example, three subarrays are stacked to achieve high gain. Downtilting is

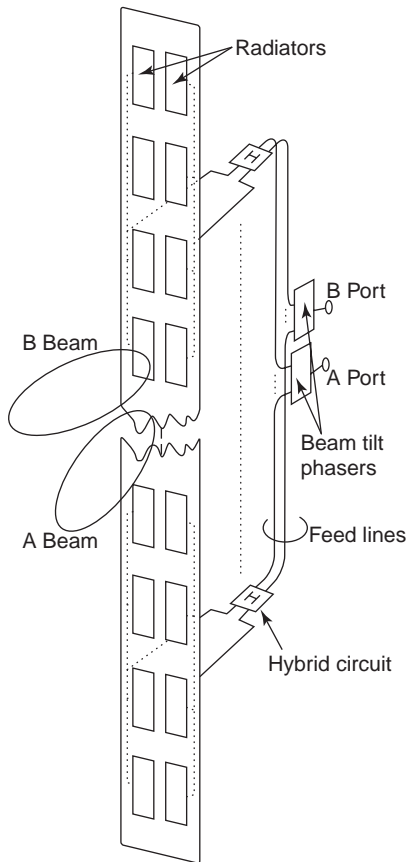


Figure 41. Configuration of dual-beam antenna. (From [1] with permission from Wiley.)

performed by changing the phase angles of top and bottom subarrays in opposite sense relative to the central subarray. The tilting is given independently to each transmit/receive and vertical/horizontal polarization combination. Each subarray consists of three vertically polarized dipoles and horizontally polarized dipoles stacked alternately [35].

Figure 49 shows a simplified structure of the dipoles consisting of the vertical array in vertical polarization [36]. A pair of dipoles is arrayed to reduce the beamwidth

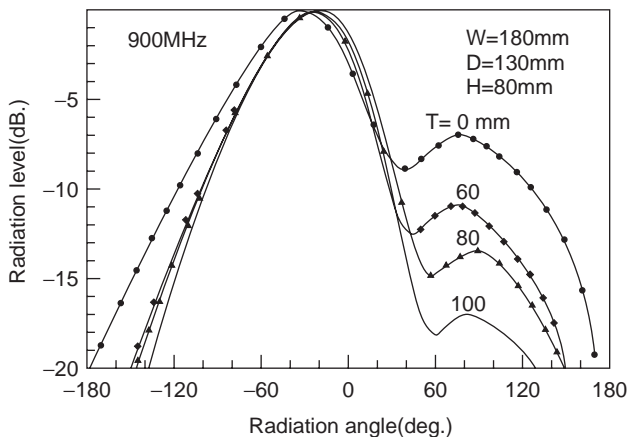


Figure 42. Radiation pattern with reduced sidelobes by means of sidewalls. (From [1] with permission from Wiley.)

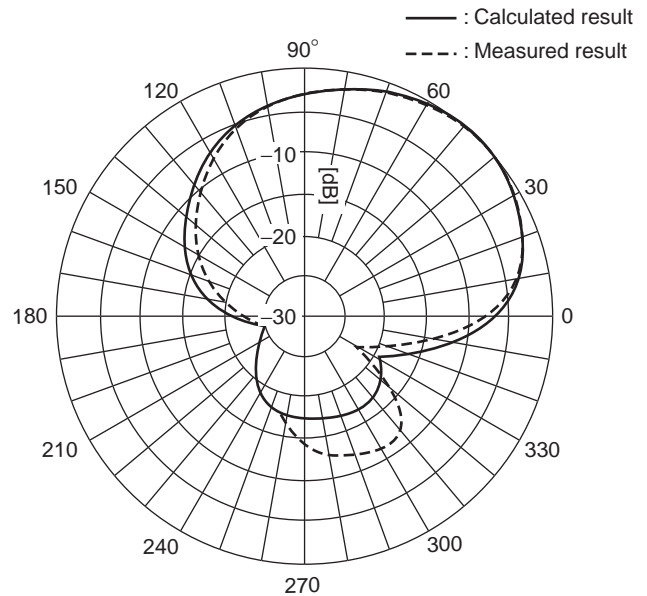


Figure 43. Measured and calculated radiation patterns: $D = 0.32\lambda$, $W = 0.684\lambda$, and $H = 0.14\lambda$. (From [1] with permission from Wiley.)

in the H plane to match that of the E plane. Similar dipoles are used for the horizontal polarization arrays. The protruded portion of the parasitic element is effective in widening the frequency range in which the beamwidth in the magnetic plane is kept constant. Table 7 lists the specifications of newly developed antennas.

One major potential feature of this antenna is the capability of transmission diversity using different polarizations. Radiation patterns in the horizontal plane of this antenna for vertical and horizontal polarizations are shown in Fig. 50. Great care has been taken to keep the beamwidth in both polarizations for transmit and receive bands almost identical. Cross-polarization characteristics are quite important for such antennas. Figure 51 shows those of the polarization diversity antenna.

5.7. Antennas for Micro/Picocellular Systems [37]

Cellular phone services have been extended to include inside tunnels, subway stations, inside large buildings, underground shopping malls, and other highly populated areas. In order to provide services for these areas, the relay station is installed between the outside base station and the areas to be covered. The relay station has a booster, which receives a downlink signal from the outside station, amplifies it, and reradiates it. As for the uplink signal, the operation is reversed in the same way. A flat antenna is used for the booster. For example, for tunnel systems, a planar, notched structure, two-element half-wave dipole antenna is used. The antenna configuration is shown in Fig. 52. The antenna is installed on the wall of the tunnel at a very low height. The radiation pattern is Figure 8 in both E and H planes, with a null at the direction normal to the antenna element.

In the tunnel system, an optical fiber cable is used from the outside station to the relay station.

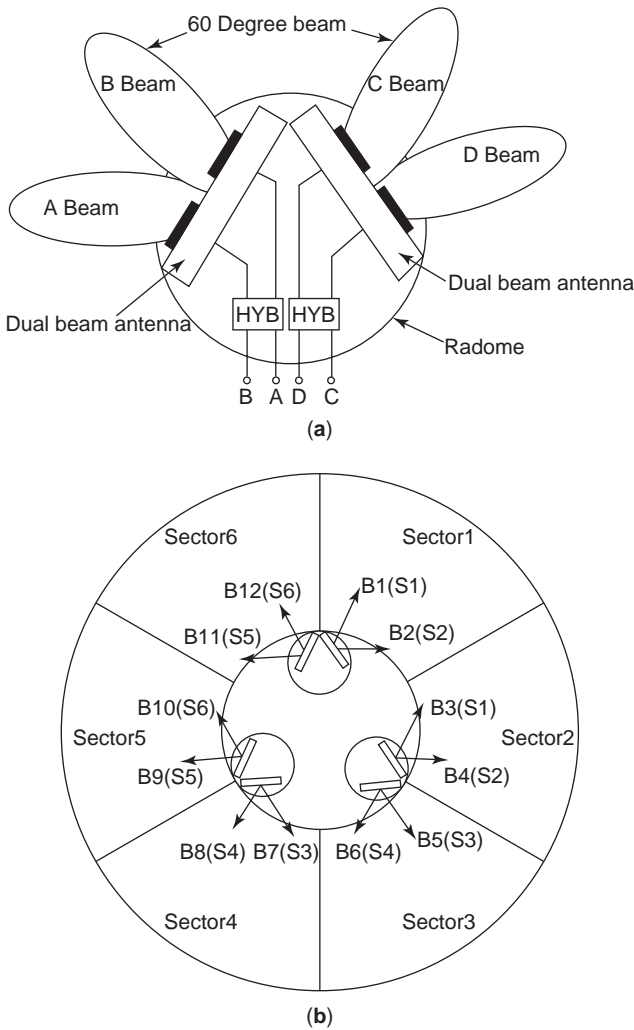


Figure 44. Installation of dual-beam antenna for a six-sector cell: (a) four-beam configuration with dual-beam antenna by four antenna elements; (b) diversity layout for six-sector cell. (From [1] with permission from Wiley.)

5.8. Antennas for PHS (Personal Handy-Phone System)

5.8.1. Collinear Array and Diversity Antennas. In the PHS system, the TDD (time-division duplex) transmission scheme is employed. This system provides service at the 1900-MHz band. A block diagram of the transmission systems with transmission diversity is shown in Fig. 53 [38]. The base station (BS) has two antennas and receivers. The portable station (PS) has only one antenna and receiver. In a TDD system, a single carrier frequency is used to provide two-way communication (upward channel; PS to BS, and downward channel; BS to PS). The BS is able to predict the received signal strength at the PS because of the reciprocity between upward and downward channels. The BS receives upward link signal from the PS using the reception diversity method, and measures the received signal strength during the receiving period. In addition, it predicts which antenna gives the highest received signal strength at the PS. Then, the selected antenna is used for transmission. The signal frame consists of four channels, in which CH1 is the control channel, and CH2 to CH4 are

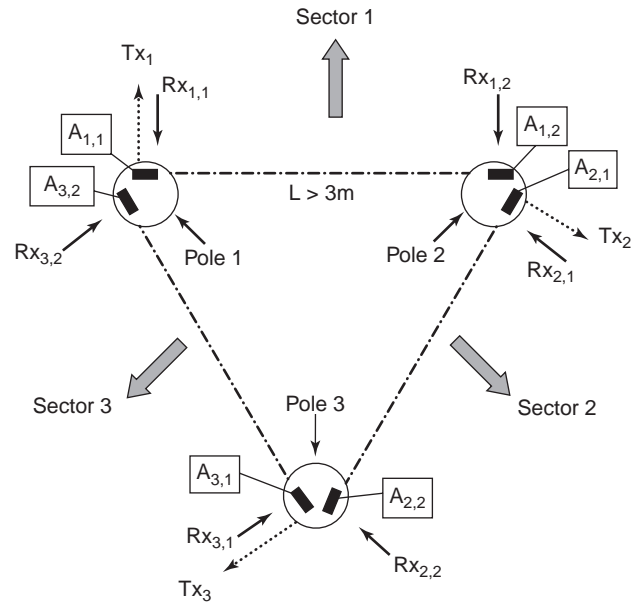


Figure 45. Three-sector space diversity system scheme. (From [1] with permission from Wiley.)

user channels. At CH2, transmission and reception is repeated in every 2.5 ms. In this short time interval, propagation conditions are supposedly stable. Thus, the same propagation condition in an upward channel is supposed to exist in a downward channel.

Diversity antenna setups are shown in Fig. 54. The antenna installed orthogonal to a road has superior diversity gain. For antenna separation (s) larger than 50 cm, sufficient diversity gains are achieved.

A typical omnidirectional collinear antenna configuration is shown in Fig. 55 [39]. The inner microstrip patch antennas are excited. The cylindrical parasitic elements are used as omnidirectional radiators. The element separation is 0.7 λ . Five radiation elements are employed for the upper and lower antennas, respectively. Antennas are covered with a radome whose diameter is 17 mm. Antenna beam-width in the vertical plane is 16°; antenna gain is 7.5 dBi.

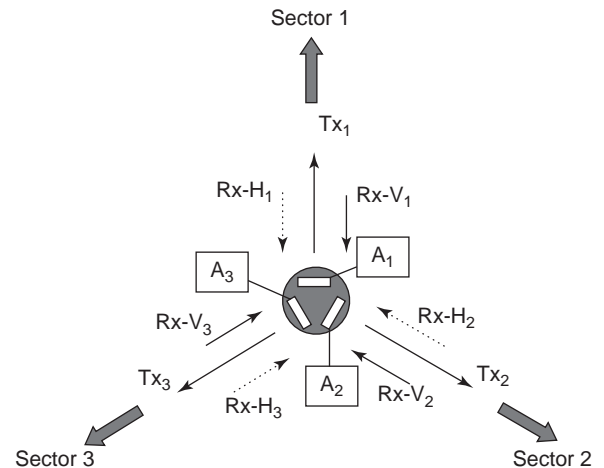


Figure 46. Three-sector polarization diversity system scheme. (From [1] with permission from Wiley.)

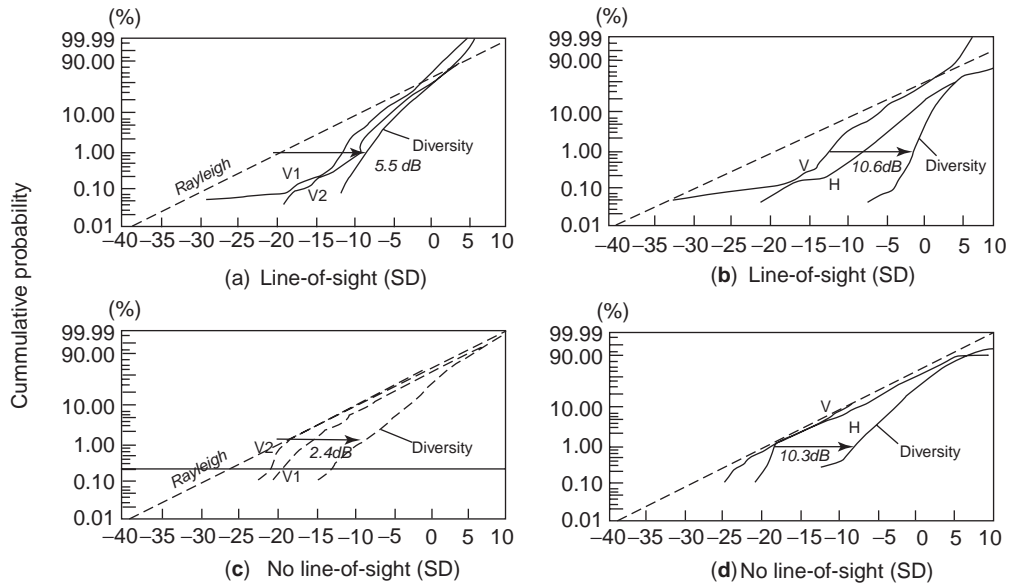


Figure 47. Cumulative distribution of received level at a base station: (a, b) for mobile phones in line of sight; (c, d) for mobile phones out of line of sight. (From [1] with permission from Wiley.)

5.9. Adaptive Array Antenna [40]

Among the endeavors to reduce the interference and improve the spectrum efficiency, as transmitting data and the number of users are increasing, the adaptive array antenna has been one of the most significant areas of study for antenna engineers. The first testbed for base stations in mobile communications in Japan was developed by the CRL (Communication Research Laboratories) in 1989. The four-element square array with an element spacing of 0.444λ was used and 256-kbps GMSK signals sent by a mobile station were received by the base station. Reduction of intersymbol interference (ISI) and about

20 dB improvement in E_b/N_0 performance with BER of 10^{-2} were obtained in the practical field test [41]. Since then, research activities concerned with the adaptive array antenna increased dramatically after 1995, aiming at application to PHS and IMT-2000.

The adaptive array system was first introduced in 1998. The block diagram of an adaptive base station antenna applied to PHS is shown in Fig. 56 [42]. Four antennas are used for transmission and reception. Adequate weight is determined in the CPU module for the output signal of each antenna to achieve the best BER value by using the constant-modulus algorithm (CMA) concept. An

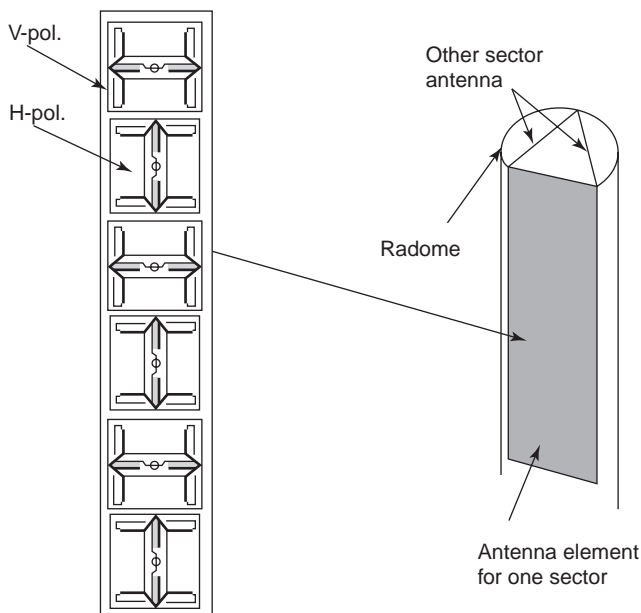


Figure 48. Radome housing of polarization diversity antenna. (From [23] with permission from IEICE.)

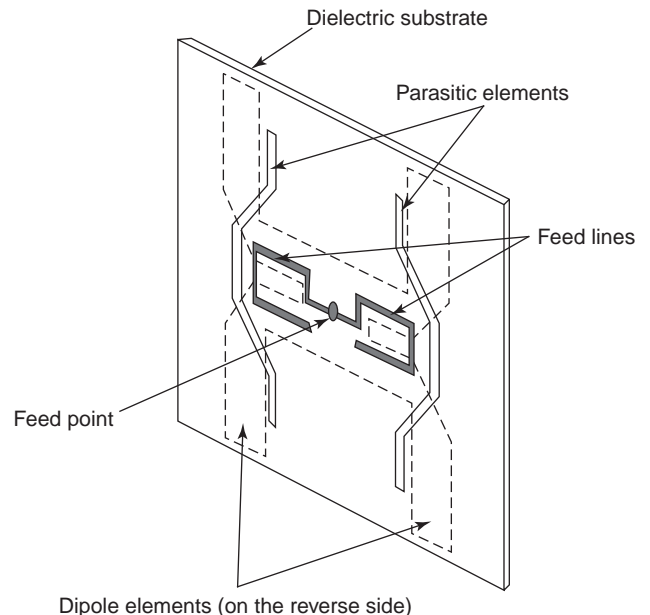


Figure 49. Scheme of dipoles consisting of vertical array. (From [1] with permission from Wiley.)

Table 7. Specifications of Polarization Diversity Antenna (from [1] with permission from Wiley)

a. Electrical Specifications			
Type	AN-951-1	AN-951-3	
Antenna element	Array of two printed dipoles		
Frequency range	818–958 MHz		
Gain	16 dBi	12 dBi	
VSWR	1.5		
– 3 dB beamwidth (vertical plane)	~ 18°	~ 5.5°	
– 3 dB beamwidth (horizontal plane)	~ 70°		
Cross-polarization ratio	> 30 dB		
Isolation between V–H ports	> 40 dB		
Isolation between sector beams	> 40 dB		
b. Mechanical Specifications			
Type	AN-951-1	AN-951-3	
Radome height	~ 3200 mm	~ 1200 mm	
Radome diameter	239 mm		
Rated wind velocity	60 m/s (survival)		
Connector	BFX-20D		
Weight (with electrical tilt box)	~ 124 kg	~ 94 kg	

antenna radiation pattern maximum is achieved in the desired signal direction, and pattern nulls are achieved in the undesired signal directions. An example of a practical base-station adaptive antenna is shown in Fig. 57. Each antenna has gain of 10 dBi. Antenna spacing is 5 wavelengths. A radio unit is installed at the foot of the antenna.

A study to determine antenna spacing has been conducted [43]. The antenna setup is shown in Fig. 58. In this case, four $\frac{1}{2}\lambda$ dipole antennas are used for the base-station antenna. Here the antenna spacing is denoted as d . The measured results of SINR (signal-to-interference noise ratio) for various antenna spacing are shown in Fig. 59. Here, Φ_d and Φ_i , respectively, denote the direction of desired signal and interference. In every interference angle, SINR increases for wide antenna spacing. SINR saturates

near the antenna spacing of 5 wavelengths. Hence, antenna spacing of a base station is determined to be 5 wavelengths.

Variations in the antenna radiation pattern in the case of interference suppression are shown in Fig. 60 [44]. A deep pattern null is achieved in the direction of interference. Adaptive antenna performance of interference suppression is ensured.

A field test was conducted with a conventional space diversity antenna whose transmission power was 500 mW and an adaptive antenna whose total transmission power was 125 mW [45]. Nearly the same communication quality in the same cell size was confirmed. As a result, a 6 dB increase in antenna gain was obtained. Received power was also compared with that of a conventional diversity antenna. The average received power of the adaptive antenna was 3 dB higher than that of the conventional diversity antenna.

5.10. Adaptive Array Antenna for Wireless Local Loop (WLL) [46]

An adaptive array antenna system (AAAS) applied to the WLL system is called super-*PHS-WLL*, because the PHS standards are applied to the WLL, and wideband radios and spatial channel processing are employed to enhance system performance. By means of adaptive beamforming, the channel capacity is increased, the number of multipath signals is reduced, the coverage is expanded, and the flexible configuration of the coverage for each base station to match the local propagation environment is made feasible.

The system concept is briefly illustrated in Fig. 61 with an example of a system configuration composed of a BS (base station), single- and four-line SUs (subscriber units), and connection to the local exchange. The operating frequency of the system is the same as that of the PHS (1880–1930 MHz), and the TDMA-SDMA system for channel access and the duplex system TDD (time-division duplex) are employed.

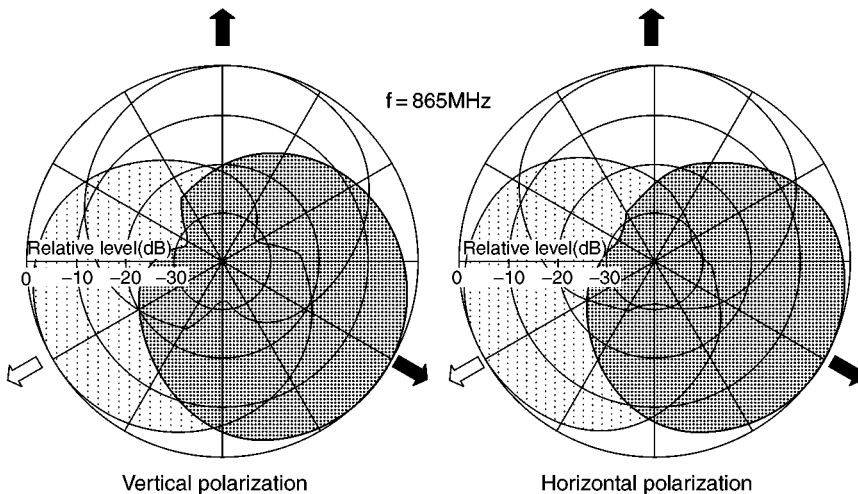


Figure 50. Horizontal plane patterns of three-sector antenna in vertical and horizontal polarizations. (From [1] with permission from Wiley.)

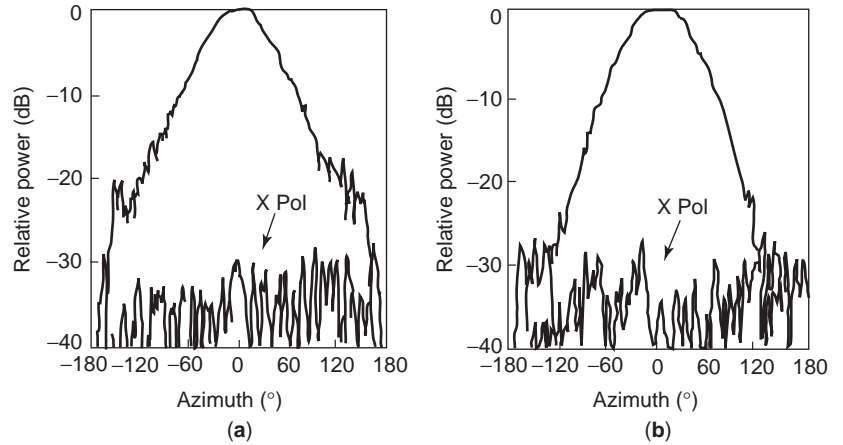


Figure 51. Cross-polarization characteristics of polarization diversity antenna. (From [1] with permission from Wiley.)

The AAAS, which produces multibeam by DBF (digital beamforming) technology, performs the function of SDMA. The beams automatically direct to a plural number of SUs, wherever they are located. The received signal at the BS in the multipath environment is processed adaptively to enhance the processing gain, thereby improving the quality of the link. It also contributes to rejection of interference by directing a null against it and enhancing the reuse of the same frequency, thereby increasing the number of channels.

The system performance that can dynamically adapt to the changeable propagation environment is achieved by DBF technology. The DBF software processes in real time the phase and the time differences among the incoming signals in the multipath environment so that the signal transmission can be directed to each desired SU. By this means a stable and robust link can be established.

Other factors that enhance channel capacity are the multiple-frequency operation using a plural number of wideband radios in addition to the AAAS and use of the PHS standard TDD, which has four timeslots in one da-

taframe that can be used for both transmitting and receiving four channels at the same time in one frequency.

A base station of the super-PHS-WLL system, which has been operated, consists of 12 antennas and 12 radios, and uses 16 radiofrequencies for 16-multiplex operation. By combining the spatial channel processing with the AAAS, a spatial channel efficiency of ~ 2.5 is achieved. Consequently, the voice channel capacity achieved is ≤ 155 ; that is, 4 (timeslot) \times 16 (frequency) \times 2.5 (spatial channel efficiency) $- 5$ (control channel). It can serve 2730 subscribers as the total traffic capacity, and is capable of covering up to ~ 15 km.

6. ANTENNAS FOR SMALL MOBILE TERMINALS

6.1. Technical Subjects Pertaining to Design of Small Mobile Terminal Antennas

In designing antennas for handsets, the first considerations are generally that the antennas should have

- Small size
- Light weight
- Compact structure
- Low profile, or flush mounting
- Robustness
- Flexibility
- Low cost

plus additional requirements for specific applications. Parameters pertaining to communication system, propagation problems, and environmental conditions, are summarized in Fig. 1. In fact, all of these parameters should generally be considered in the handset antenna design. When systems require particular specifications, the antenna should be designed specifically to satisfy the requirements, depending on the systems. Propagation problems have now been diversified to include complicated environments such as indoor malls, subway stations, and bridge underpasses. Also, problems now include

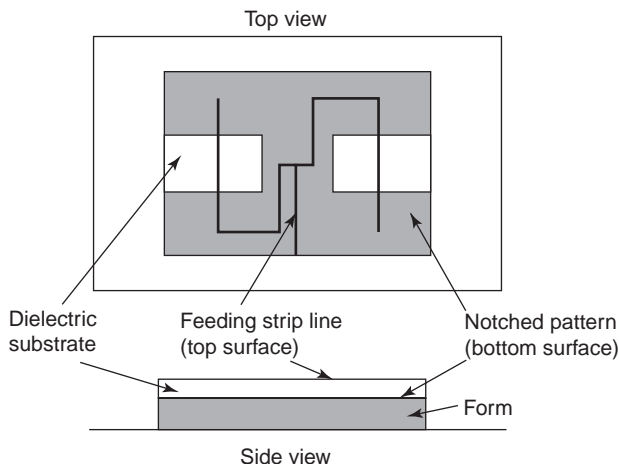


Figure 52. Planar notched structure two-element half-wave dipole antenna. (From [23] with permission from IEICE.)

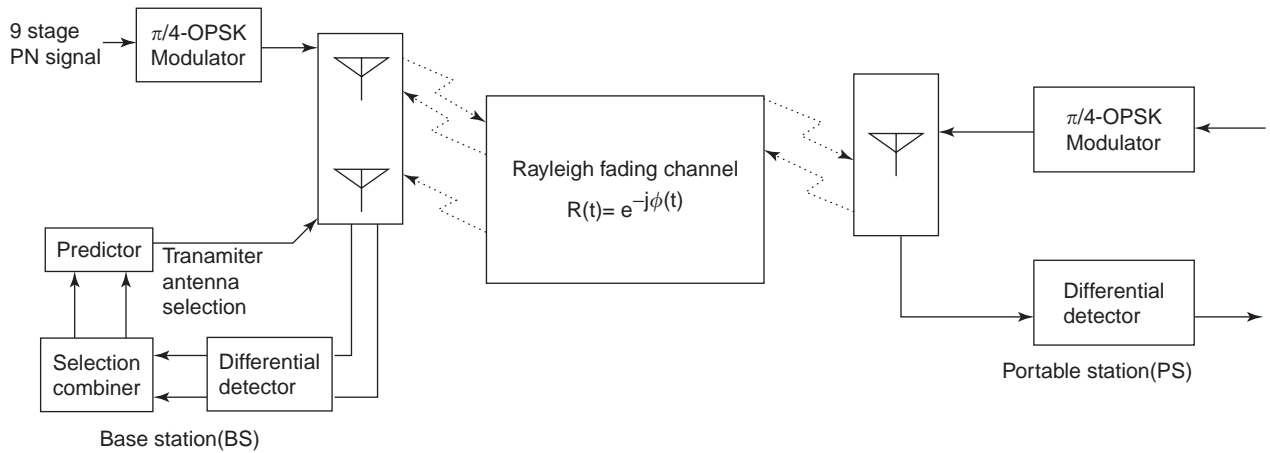


Figure 53. Block diagram of linear predictive transmitting diversity antenna system. (From [1] with permission from Wiley.)

higher-frequency regions such as microwaves and millimeter waves.

6.2. Design Concept of Antenna Systems for Small Mobile Terminals [47]

Figure 1 presents essential parameters necessary for designing antenna systems for mobile communications. Antenna design, as was mentioned previously, relates to system requirements, propagation problems, and environmental conditions. When designing an antenna, whether for a fixed station or a mobile station, designers should factor in these parameters.

In the 1950s and 1960s, antennas used for mobile terminals were mostly simple monopoles of about a quarter-wavelength. A monopole was usually mounted on top of the equipment case, as shown in Fig. 62. Figure 63a illustrates a model of this type of antenna. Since the case was

made of metal in those days, it was simply considered as a group plane (GPL), as shown in Fig. 63b. By taking the image of the antenna element into account, the model was treated as a half-wave dipole, as shown in Fig. 63c. Thus no particular attention was paid to designing this sort of antenna at that time, and just a quarter-wavelength element was used. When an antenna for small portable equipment was designed, the concept was expanded to consider the body of the equipment as a part of antenna, since it was noted that the antenna image could hardly be considered while current flow on the equipment body should have been accounted for. The model shown in Fig. 63 equivalently illustrates an antenna system that is composed of a monopole and the (metal) case. This model can be treated equivalently by an asymmetric dipole as shown in Fig. 64 and is further decomposed into two parts: a short, thick dipole and a long, thin dipole as shown in Fig. 65. Decomposed two parts are equivalently expressed

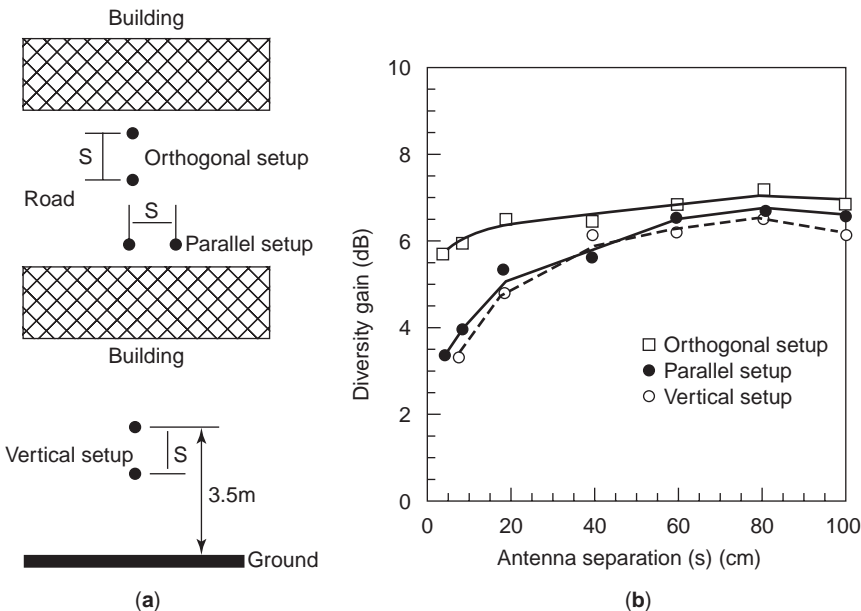


Figure 54. Diversity antenna: (a) antenna installation; (b) diversity gain. (From [1] with permission from Wiley.)

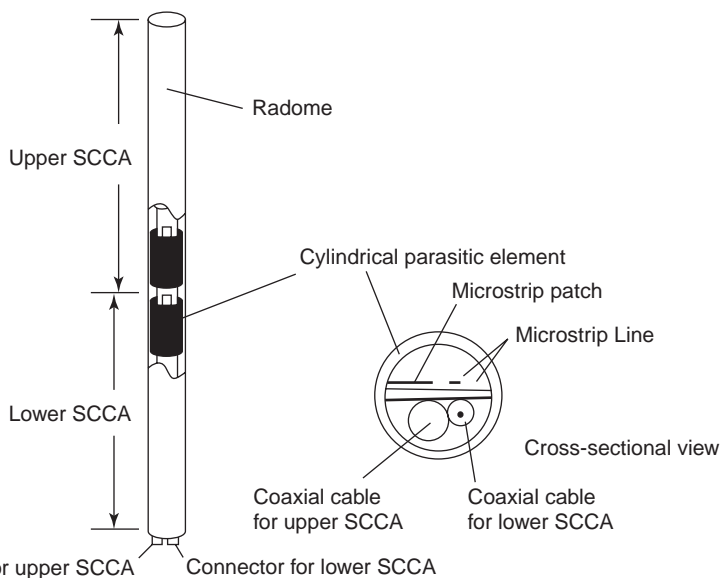


Figure 55. Configuration of typical omnidirectional collinear antenna. (From [23] with permission from IEICE.)

by two dipoles: one thin and long dipole and another one thick and short dipole. The antenna system shown in Fig. 64 is then treated as a parallel combination of these two dipoles. This was the first treatment that illustrated the concept in which the case was considered to be a part of the radiator [48]. However, this concept was not recognized until a detailed analysis of the antenna system was introduced, and the contribution of the case to the radia-

tion was clarified [49]. Through the analysis, the current distributions on the case as well as on the antenna element were shown for various dimensions of antenna element and the case. It was clarified that currents on the case, excited by the antenna element, may contribute to producing fields that have horizontal as well as vertical polarization, although this depends on the dimensions of the case. The more interesting result was that almost no

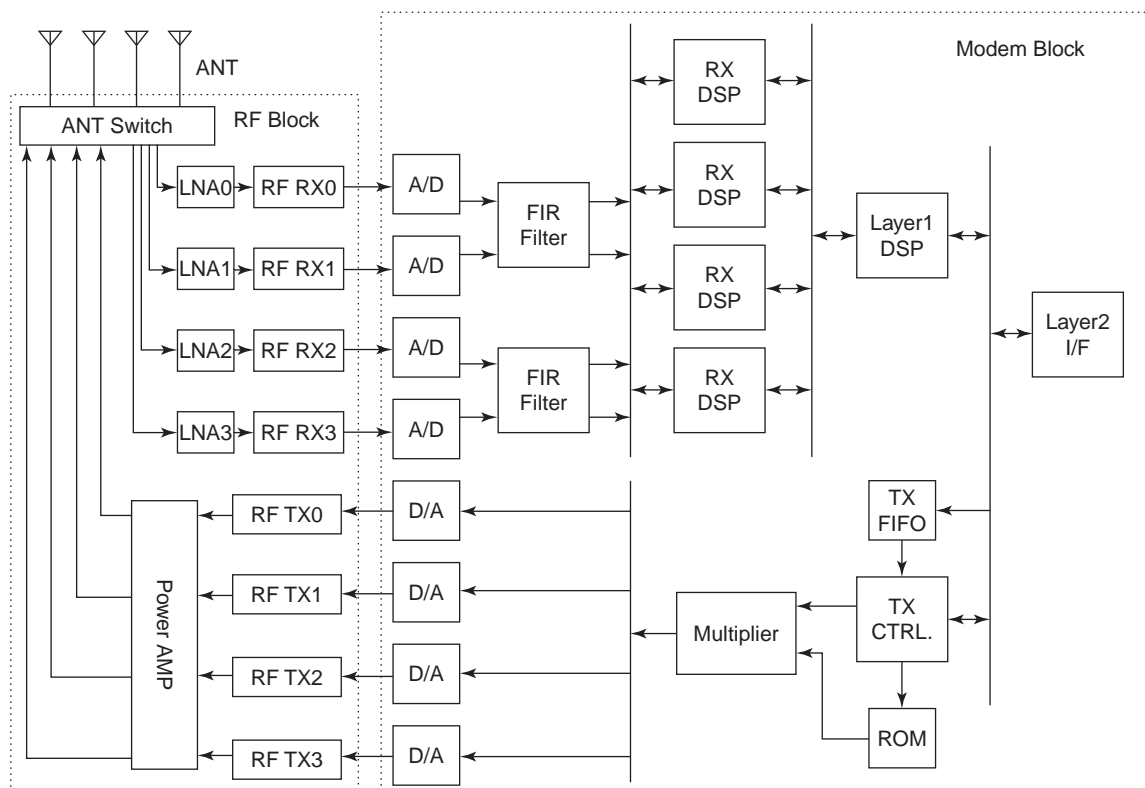


Figure 56. Block diagram of adaptive antenna system for a base station. (From [1] with permission from Wiley.)



Figure 57. An example of practical base-station adaptive antenna. (From [1] with permission from Wiley.)

current flow on the case was observed in the system where a half-wavelength element was used. This was advantageous in reducing the influence of the user's hand on antenna performance, because the variation of impedance or frequency due to the handheld effect can be decreased as a result of a reduction in the current on the case. In practice, however, a half-wavelength element that is fed between the element and the case cannot be used, because the feedpoint impedance becomes very high. Instead, a monopole with length of $\frac{3}{8}\lambda$ or $\frac{5}{8}\lambda$ has been employed in practice for PDC handsets or other mobile terminals, since it has the appropriate input impedance for matching to the load and yet the current flow on the case is very small. It is very interesting to note that the analysis presented in Ref. 49 provided the essential design concept for developing antennas for PDC handsets and other small mobile terminals presently used.

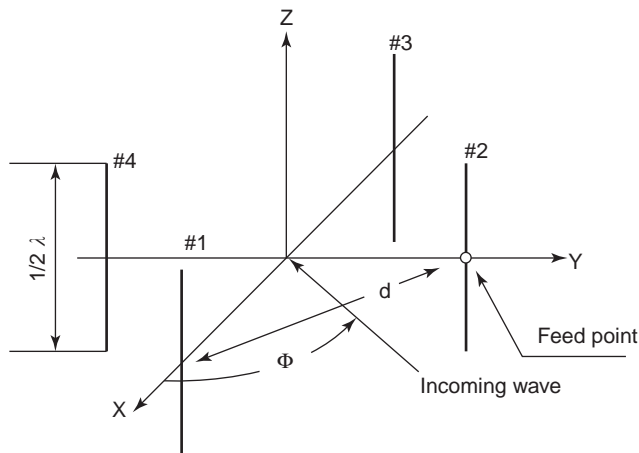


Figure 58. Base-station antenna setup for determining spacing. (From [1] with permission from Wiley.)

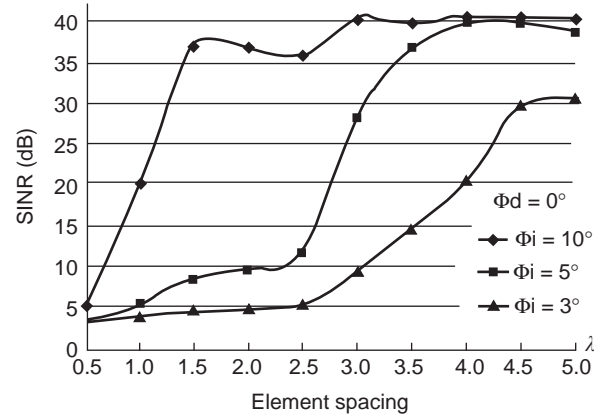


Figure 59. SINR characteristics with respect to antenna spacing d . (From [1] with permission from Wiley.)

From the 1980s to present, downsizing of mobile terminals has made remarkable progress and, accordingly, antenna size, except for monopole elements, has accordingly decreased. The downsizing was advantageous for users; however, it posed a serious problem for antenna designers, as the antenna design should be such that antenna performance should remain unchanged, even though the antenna size becomes more compact. Fortunately, this problem has not been widely experienced, as antenna performance was not as significantly degraded as was expected. There was the assistance of the conducting materials existing in the equipment, which contributed to radiation as part of the radiator. The typical conducting material in the equipment is a rectangular shielding plate or box, where RF and other circuits are included. Usually a built-in antenna element is placed on this plate or box, and it acts as a ground plane (GPL). As a GPL performs as a part of radiator, when a small antenna element is placed on it and induces current on it, the antenna size is equivalently increased, and hence antenna performance is enhanced. Antenna gain and bandwidth may be increased, although this depends on the size of GPL and the type of antenna. A typical example of GPL performance can be observed in PDC handsets, where a PIFA is used as a built-in antenna. A bandwidth of $\leq 17\%$ can be achieved, although that of a PIFA in free space is ordinarily only

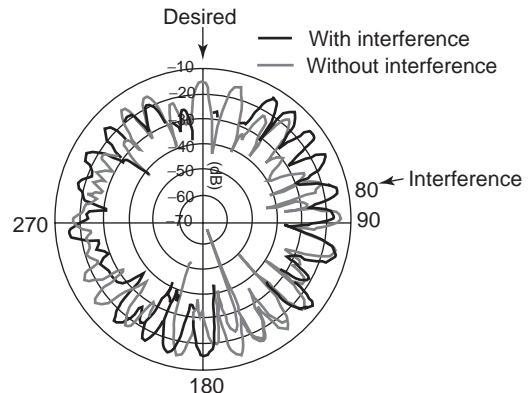


Figure 60. Radiation patterns with and without interference. (From [1] with permission from Wiley.)

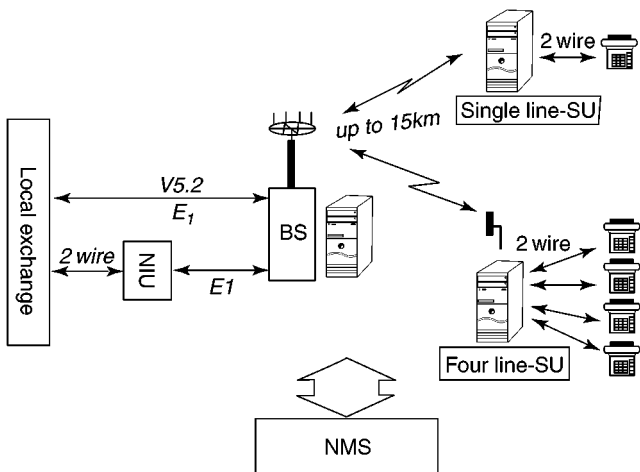


Figure 61. System concept of PHS WLL. (From [41] with permission from IEEE.)

1–2%. A gain increase of several decibels is also observed. It is interesting to note that the GPL had been used as part of the radiator without any conscious effort; that is, it was not intentionally applied in the design of small handset antennas.

Effective use of a GPL can be seen in another case, where the radiation mode is increased with the help of current on the GPL. Modal increase in is one of the most significant concepts for developing a small antenna. By introducing multimode into a small antenna system, enhanced antenna performance may be expected, so that a practically useful small antenna may be realized. This concept was applied to a pager antenna system, where a small rectangular loop antenna was used [50], and a dipole mode was produced in addition to the loop mode. Figure 66 shows the antenna model, where a coaxial cable is

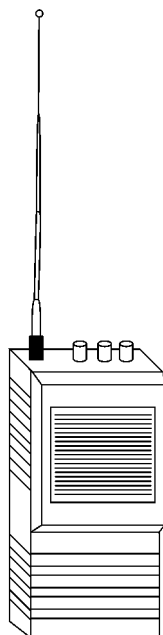


Figure 62. Monopole antenna placed on the top of small portable equipment. (From [47] with permission from IEEE.)

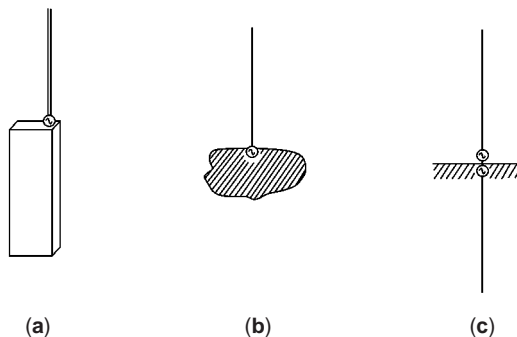


Figure 63. Model of portable equipment with a monopole: (a) equivalent expression; (b) monopole on the ground plane; (c) equivalent dipole. (From [47] with permission from IEEE.)

directly connected to the loop input terminal without using a balun. The direct connection of a balanced system (the loop terminal) to an unbalanced line (a coaxial cable) is not common; however, the connection was intentionally done in order to produce the dipole mode in the antenna system. By this means, unbalanced currents are produced on the terminals and then flow into both the ground parts (GPL) of the printed-circuit board (PCB) and the surface of the loop element. These unbalanced currents lead to produce a dipole mode (Fig. 67a) in addition to the loop mode (Fig. 67b). Then, the radiation pattern, which is actually the receiving pattern, is almost omnidirectional as a result of the combined patterns of the loop and the dipole, with a 90° phase difference. In addition, combination of both the dipole and the loop modes produces receiving patterns that allow the pager to have appreciable sensitivity in various situations, for example, with the pager unit laid down, or placed so as to stand erect on a desk. This concept—the use of a dual mode, similar to the loop and dipole—is very useful for creating small antennas. The dual mode may be a combination of electric and magnetic modes, or inductive and capacitive modes, and so on. It can be applied in designing antennas for any other small antenna terminals.

There are both advantages and disadvantages in utilizing current on the GPL inside mobile terminals. The advantage is the enhancement of antenna performance.

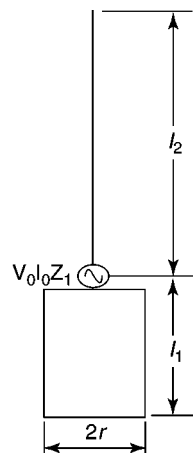


Figure 64. An asymmetric dipole consisting of a monopole and portable equipment. (From [47] with permission from IEEE.)

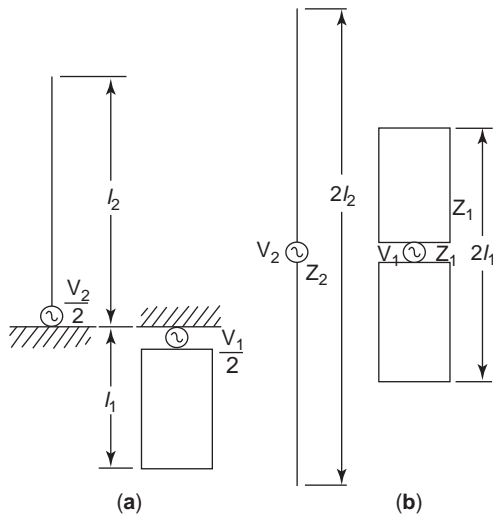


Figure 65. Equivalent models of antenna shown in Fig. 64: (a) equivalent expression with a thin, long monopole and a thick, short monopole, standing on the ground plane and (b) their equivalent expression with dipoles, taking out the ground plane. (From [47] with permission from IEEE.)

On the contrary, the disadvantage is the possible degradation of antenna performance due to the effect of adjacent materials, including the human body. In fact, more than 6 dB gain degradation has been observed in the talk position of mobile phones, mainly due to the effect of a user's hand. A hand holding a handset varies the currents on the GPL, and thus the impedance and frequency, so that antenna gain and efficiency deteriorate. The human head, when the handset is at talk position, also varies antenna performance in the same way as does the hand. Antenna gain is also decreased by the influence of the hand and the head, which both absorb radiation power.

With the increase in current distribution on the GPL inside the handsets, the radiation toward the human head may increase, and so would the SAR (specific absorption rate). To reduce the undesired radiation toward the human head and thus the SAR value in the head, the appropriate selection of antenna type, the method of feeding it, and the place and method of mounting the antenna element on the equipment should all be seriously considered. Thus, fur-

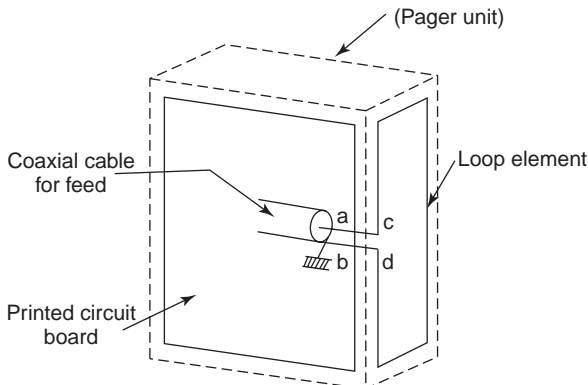


Figure 66. Schematic expression of a pager antenna system. (From [47] with permission from IEEE.)

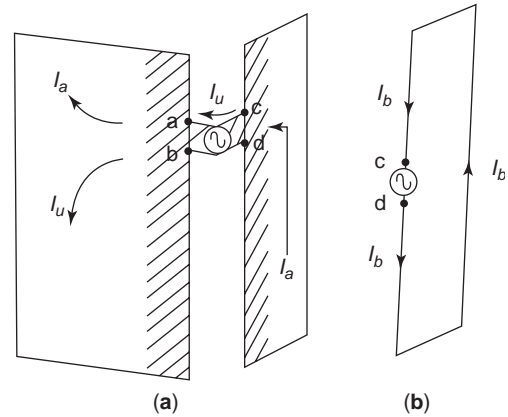


Figure 67. Equivalent expression of a pager antenna system; (a) dipole mode; (b) loop mode. (From [47] with permission from IEEE.)

ther consideration in designing the handheld phone antenna is needed in order to improve the SAR problem and antenna performance at the same time.

Use of an internal antenna, replacing a monopole, which has long been used in mobile terminals, is a trend in today's mobile terminals. Possible antenna characteristics desired for the latest mobile terminals are to have

1. A magnetic current as a radiating source
2. Balance
3. Two modes (e.g., two polarization components)

For item 1 the objective is to create a built-in antenna by making an antenna small and of low profile, or flush-mounted. A magnetic current source, such as a loop or slot, is effectively used by being placed on the GPL such that the source current is parallel to the GPL. With this structure, the EM field produced in front of the GPL is doubled by the additional field due to the image of the source current. As a result, antenna gain is doubled, compared with an antenna system in free space, yet the antenna is small and of low profile. By adequate balancing (item 2), the currents on the GPL, generated by the antenna element, can be reduced, so that the human body effect can be mitigated. In practice, a loop, a normal-mode helical dipole, a meanderline dipole, and any other type of antenna having a balanced structure, so that no unbalanced current flow is generated on the GPL, can be used for this purpose. As for item 3, it has been shown that an antenna having two modes such as a dipole and a loop can contribute to enhance antenna performance so that antenna size is minimized. In other aspects, an antenna having two polarizations components, such as vertical and horizontal polarizations, can, to some extent, reduce multipath fading [51]. An L-shaped loop [52] can be used as one of the candidates for this purpose.

Now, by combining any one or all of items 1, 2, and 3 with the conventional design concept, an advanced antenna system can be developed. Item 3 indicates that the GPL is not purposely utilized for enhancing antenna performance, but rather is separate from the antenna system. This is then an advanced concept that should be applied

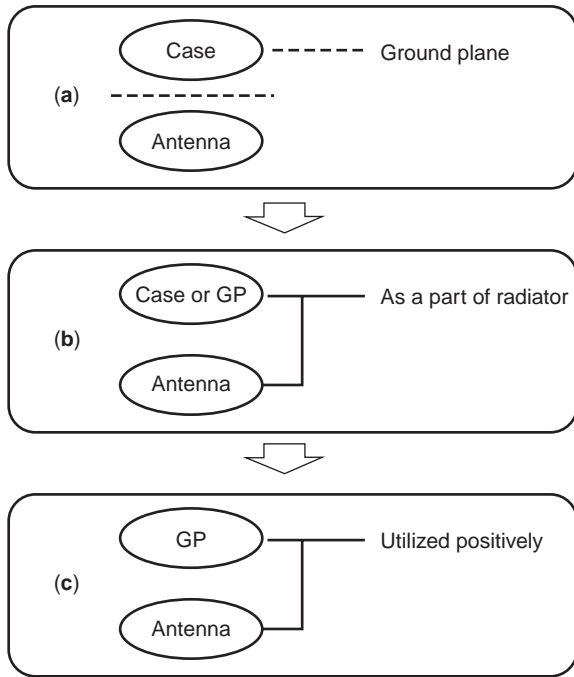


Figure 68. Three stages in development of antenna design concept. (From [47] with permission from IEEE.)

for designing an antenna, which should be developed further.

The design concept explained above is depicted in Fig. 68, where the steps are as follows:

- First stage*—use of a quarter-wavelength monopole and its image
- Second stage*—combined design of a monopole and the equipment case (metal) as a radiator
- Third stage*—utilization of GPL to enhance performance of a built-in small antenna
- Fourth stage*—separation of GPL from the antenna system

The next stage will be design of antenna with a concept in which the device, function, or software is integrated into an antenna system so that sophisticated functions such as adaptive control and signal processing can be achieved. Applying the concept of an integrated antenna system (IAS) is a promising way to realize such antennas. Unification of a device into an antenna structure will bring a new antenna having enhanced performance, or improved characteristics. Integration of functions or software into the antenna structure may also create a new antenna system that performs with intelligence. Figure 69 illustrates this concept.

6.3. Typical Antenna Elements Used for Mobile Terminals

Typical antenna elements used for small mobile terminals include MP (monopole), NMHA (normal-mode helical antenna), PIFA (planar inverted-F antenna), ceramic chip, meanderline, and MSA (microstrip antenna). A majority of PDC mobile terminals employ an MP element and a

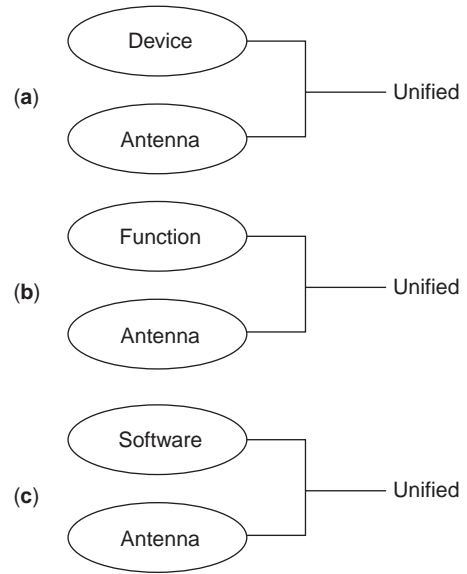


Figure 69. Advanced concept of antenna design. (From [47] with permission from IEEE.)

built-in PIFA as a pair element of diversity antenna (Fig. 70). An NMHA element placed on the top of an MP element was formerly used as an extension of the MP element in order to reduce the length of the MP; however, the design concept has been modified to employ an NMHA element as the replacement of the MP, when the MP element is retracted into the handset unit. An NMHA element has been used as the main antenna of PHS mobile terminals, since the operating frequency is 1.5 GHz, so that the antenna length can be short enough to be directly mounted on the unit body.

6.3.1. Monopole. Monopole is the most simple, thin, lightweight, low-cost, and hence useful as an antenna element for small mobile terminals. Hence it has long been

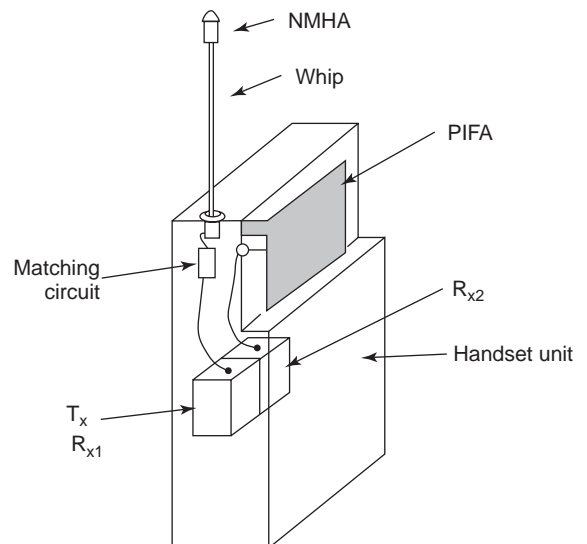


Figure 70. Antenna systems in PDC. (From [1] with permission from Wiley.)

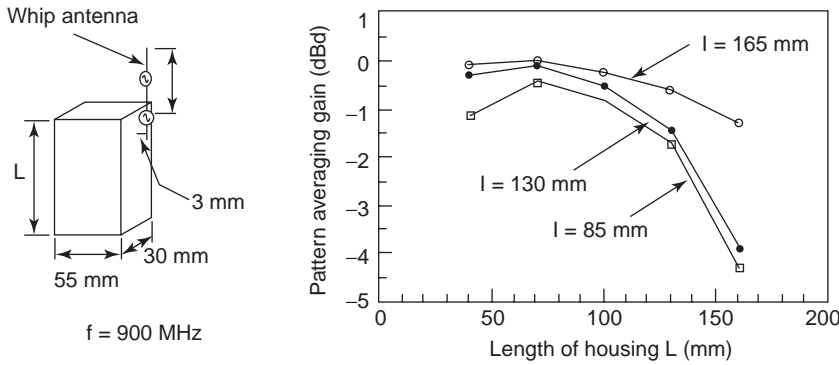


Figure 71. Gain of a monopole with respect to the length of housing. (From [1] with permission from Wiley.)

used as typical antenna element for small mobile terminals.

Antenna performance depends on not only antenna element but also the dimensions of the ground plane, on which the antenna element is mounted. Figure 71 illustrates MP gain with respect to the length of housing when mounted on a rectangular conducting box [53]. The dimensions of the box are shown in the figure. Current distributions on the antenna element and the surface of the box are shown in Fig. 72, for (a) a case where a $\frac{1}{4}\lambda$ MP is used (a) and a case where a $\frac{1}{2}\lambda$ dipole is fed at its bottom (b) [54]. Amplitude of the current distributions is shown by hatched lines. The current distributions are obtained by using a wire grid model, in which the method of moments is applied. When the element length S is $\frac{3}{8}\lambda$ or $\frac{5}{8}\lambda$, current flows are observed to be relatively small as shown in Fig. 73, and yet input impedance characteristics are adequate to match the load impedance as shown in Fig. 74 [55].

6.3.2. Normal-Mode Helical Antenna (NMHA). In order to keep the antenna small, a traveling-wave structure is utilized, and NMHA is a typical example of this design. NMHA is a helical antenna that radiates in the direction normal to the helical axis, and the radiation patterns are essentially the same as that of a short dipole (Fig. 75). The dimensions of the helix are usually much smaller than the operating wavelength; the length of an individual turn is a small fraction of a wavelength λ , and the axial length is also much less than $\frac{1}{4}\lambda$. With this structure, a NMHA is

equivalently expressed by an array of small loops and short monopoles (Fig. 76) [56]. Inductive impedance is increased by the array of loops and compensates the capacitive impedance of short monopoles. As a consequence, the helical structure can be arranged to have self-resonance property, although the antenna length (in the axial direction) is considerably shorter than that of a conventional resonant-monopole or dipole antenna. In this way the antenna efficiency can be improved and extension of the antenna length may lead to increased bandwidth. The NMHA has been used in modern mobile phones worldwide.

The antenna model shown in Fig. 77 is considered [57]. The impedance characteristics of an antenna with dimensions of helical diameter $D_h = 0.018\lambda$, pitch $P = 0.006\lambda$, and wire diameter $2a = 0.0002\lambda$ are shown in Fig. 78, where the number of turns M_T used as a parameter. Figure 79 shows the radiation efficiency with respect to the pitch P . Figure 80 illustrates the relationships between D_h and P . Figure 80a shows the parameter used for the number of turns M_T , while Fig. 80b shows the radiation resistance R at resonance.

6.3.3. Meanderline Antenna. The meanderline antenna also has the traveling-wave structure, which enables reduction of the antenna length. It has a periodical array structure of alternative square patterns as shown in Fig. 81. With this pattern, the extended wire can be made much longer than the initial antenna (dipole)

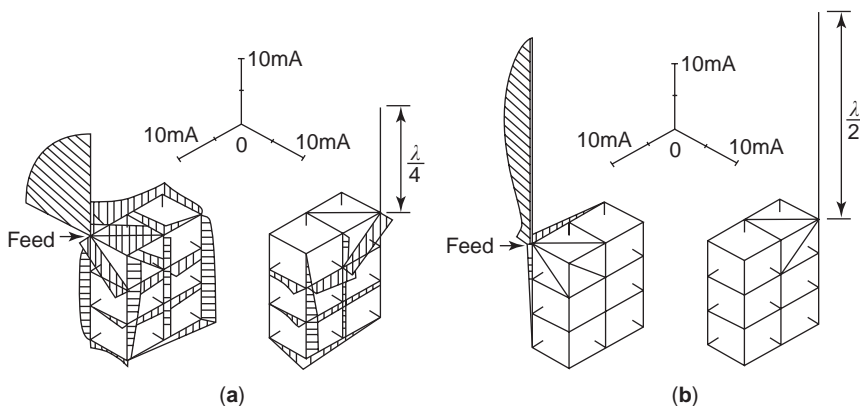


Figure 72. Current distributions on the antenna element and the surface of the rectangular conducting box: (a) a bottom-fed $\frac{1}{4}\lambda$ MP; (b) a bottom-fed $\frac{1}{2}\lambda$ dipole. (From [49] with permission from IEICE.)

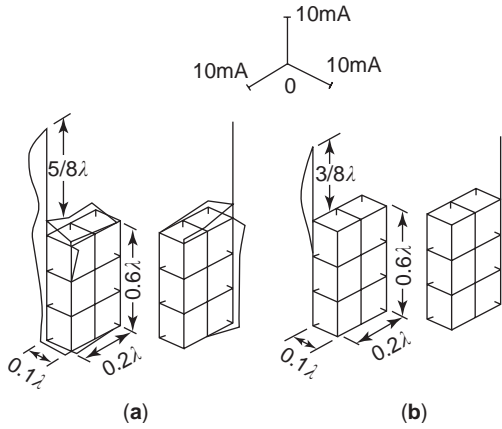


Figure 73. Current flows on the antenna element and rectangular conducting box when the antenna length is $\frac{3}{8}\lambda$ and $\frac{5}{8}\lambda$. (From [49] with permission from IEICE.)

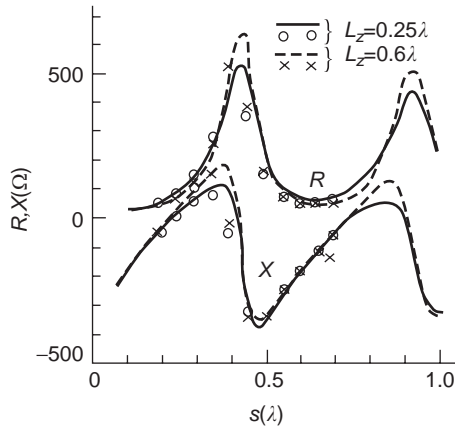


Figure 74. Impedance characteristics with respect to length of box. (From [49] with permission from IEICE.)

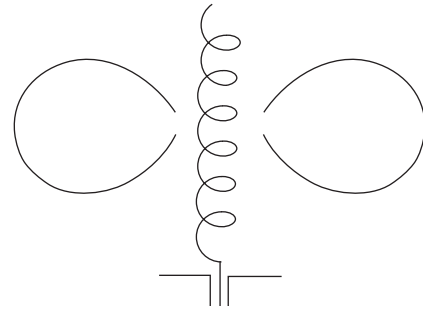


Figure 75. Normal-mode helical antenna (NMHA) and its equivalent expression.



Figure 76. Equivalent expression of NMHA.

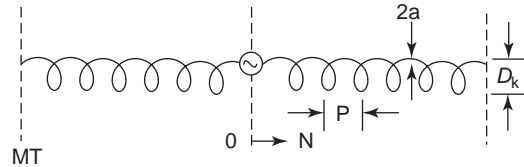


Figure 77. Model of NMHA. (From [50] with permission from Research Studies Press.)

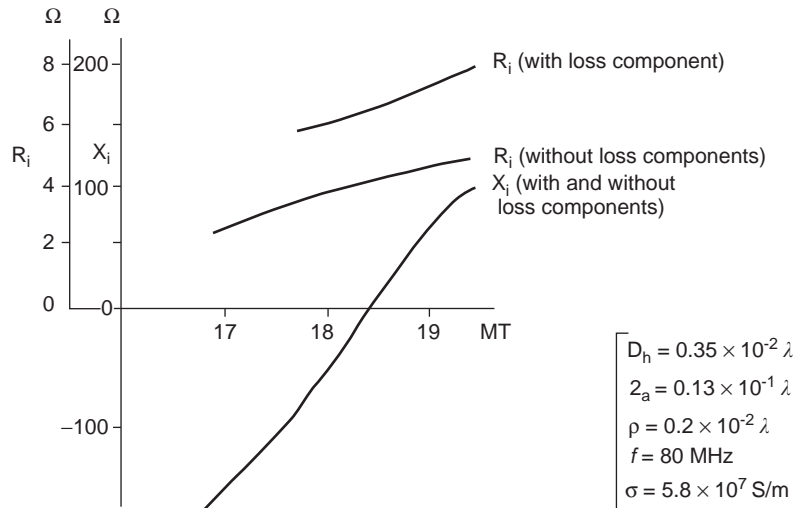


Figure 78. Impedance characteristics of a NMHA. (From [50] with permission from Research Studies Press.)

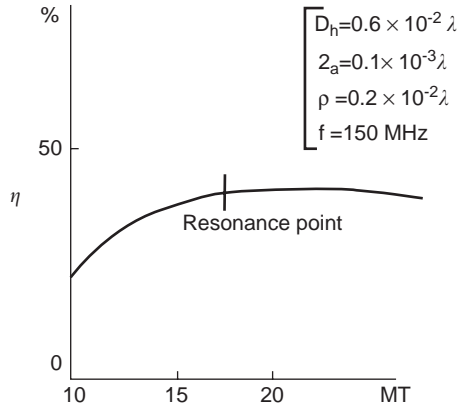


Figure 79. Radiation efficiency ρ versus number of turns MT . (From [50] with permission from Research Studies Press.)

length, so that the self-resonance can be attained. The resonance frequency is then lower and radiation resistance is higher than that of a dipole of the same length. This in turn implies that the antenna is effectively made small.

In this section a meanderline dipole antenna, such as that shown in Fig. 81, where dimensional parameters are given, is considered [58]. Figure 82 shows the equivalent expression of the antenna, which consists of a series connection of short-circuited two-wire transmission lines (a) and a monopole (b). Using this model, design parameters can be found. At first, a relationship between the resonance frequency f_0 and the wire diameter b /pitch p is obtained as shown in Fig. 83. Here the planar line of width b is replaced equivalently by a wire of diameter d . When the resonance frequency f_0 is given, the number of turns N can be determined with prior knowledge of the wire radius b and the antenna width w using Fig. 84. As the antenna length becomes shorter, the radiation resistance R_{rad} decreases. The ratio of R_{rad} of a meanderline antenna to that of a half-wave dipole is shown in Fig. 85 as a function of the antenna size reduction ratio R_e in comparison with a half-wave dipole. Figure 86 shows radiation efficiency η and number of turns N with respect to the length l of the antenna.

When a meanderline monopole antenna is placed on a finite ground plane ($59 \times 25.4 \text{ mm}^2$) as shown in Fig. 87 [59], variation of the input impedance with respect to the antenna length L_{ax} is as shown in Fig. 88. When the antenna length $L_{\text{a,x}}$ is 73 mm and the number of segments is

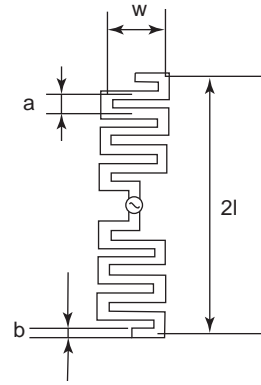


Figure 81. Meanderline antenna. (From [58] with permission from IEICE.)

48, resonance occurs at two frequencies, 0.95 and 2.39 GHz (two-band operation), and the resonance impedance is about 25Ω at these two frequencies. Figure 89 shows the first resonance frequency f_0 versus antenna length L_{ax} . The empirical equation is derived as

$$f_0 = 22.69 L_{\text{ax}}^{-0.7392} \quad (5)$$

when $e_1 = e_2 = 3 \text{ mm}$, the substrate thickness t_s and width W_s are 3.17 mm and 11 mm, respectively, and the size of the ground plane is $59 \times 29.4 \text{ mm}^2$.

6.3.4. Inverted-F Antenna (IFA). The IFA shown in Fig. 90 can be treated in the same way as the antenna shown in Fig. 91a with its image. The IFA shown in Fig. 91a is equivalently decomposed into two parts: an ILA with its image (b) and two 2-wire short-circuited-transmission lines (c). The two-wire transmission lines compensate capacitive impedance of the ILA and at the same time step up the input impedance so that matching to the 50- Ω load is made feasible. The input impedance of IFA is expressed by

$$Z_{\text{in}} = 4Z_a \cap 2Z_b \quad (6)$$

where Z_a denotes the input impedance of the antenna shown in Fig. 91b, Z_b is the impedance of the short-circuited two-wire transmission line with length h and width S , and \cap expresses the parallel combination of impedances.

The input impedance of an IFA can be adjusted by selecting S and h , appropriately. An example is shown in Fig. 92 [60].

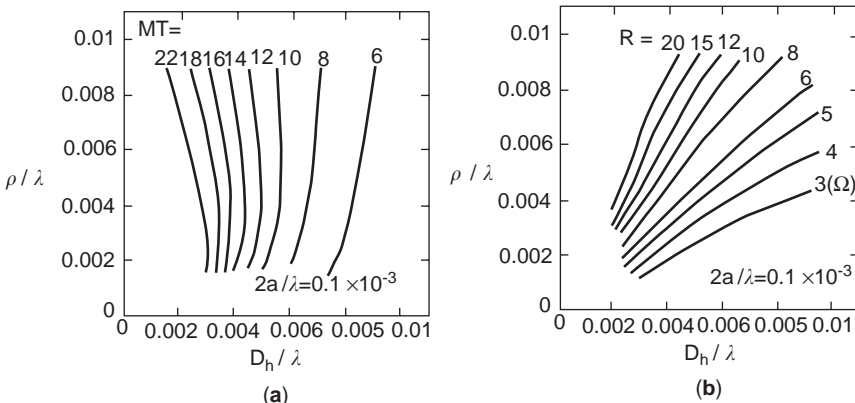


Figure 80. D_h versus P : (a) with parameter of number of turns MT and (b) with parameter of radiation resistance R at resonance. (From [50] with permission from Research Studies Press.)

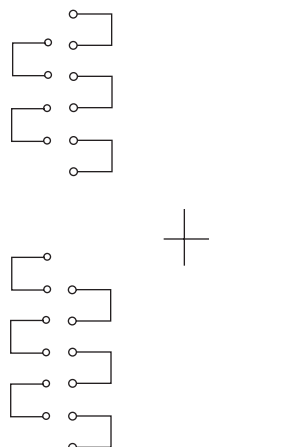


Figure 82. Equivalent expression of a meanderline antenna. (From [58] with permission from IEICE.)

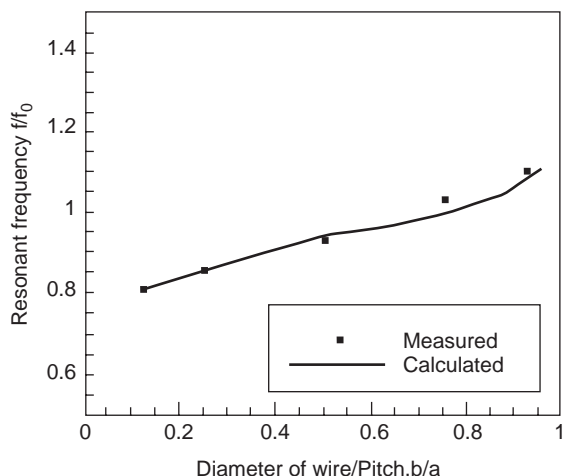


Figure 83. Resonance frequency versus wire diameter/pitch: b/p . (From [58] with permission from IEICE.)

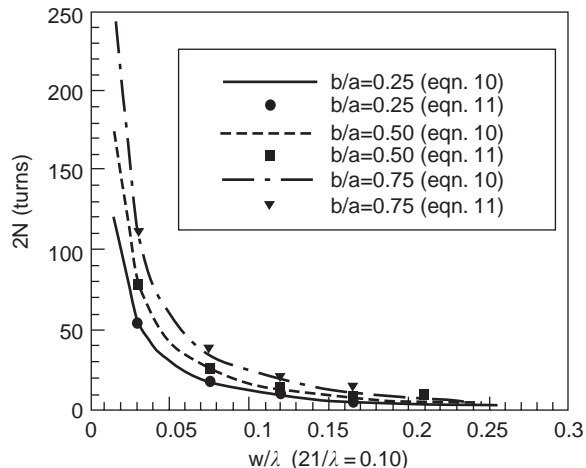


Figure 84. Number of turns N versus antenna width; parameter is the wire radius. (From [58] with permission from IEICE.)

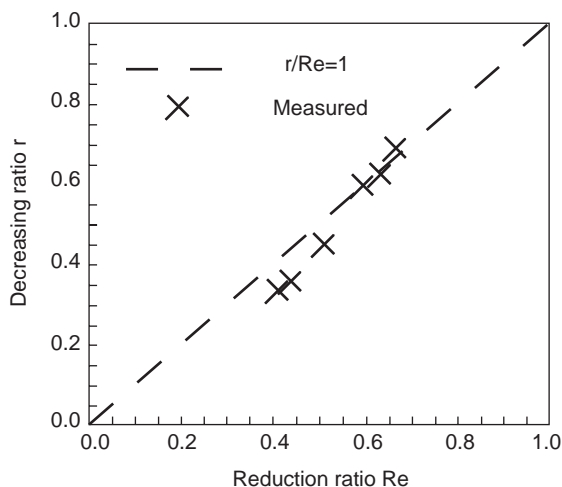


Figure 85. Ratio r of radiation resistance R_{rad} of an antenna to that of a half-wave dipole versus antenna size reduction ratio R_e in comparison with a half-wave dipole. (From [58] with permission from IEICE.)

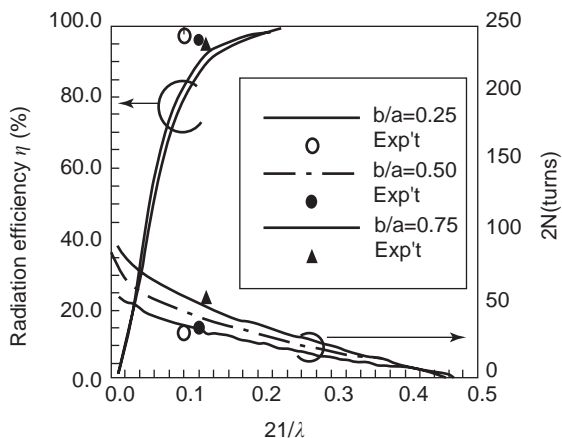


Figure 86. Radiation efficiency η and number of turns N with respect to the length l of the antenna. (From [58] with permission from IEICE.)

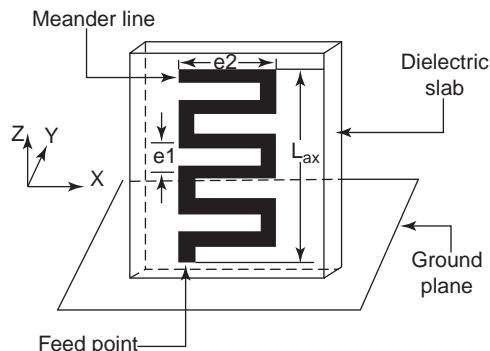


Figure 87. Meanderline antenna placed on finite-size ground plane. (From [59] with permission from CRC.)

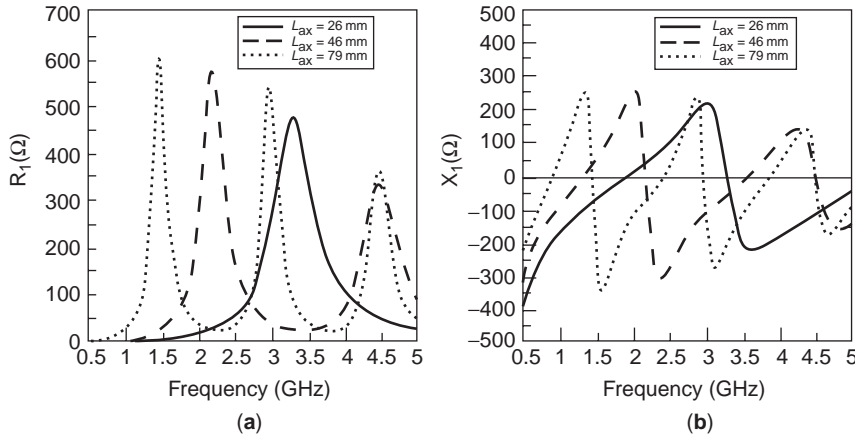


Figure 88. Variation of input impedance of a meanderline antenna versus antenna length. (From [59] with permission from CRC.)

6.3.5. Planar Inverted-F Antenna (PIFA). The planar inverted-F antenna is apparently a modification of the IFA with replacement of the IFA’s linear horizontal element with a planar element. However, the PIFA differs from the IFA in its radiation principle. The PIFA’s source of radiation is the magnetic current on the peripheral aperture of the planar element, whereas that of IFA is the electric currents on the linear F-shaped vertical and horizontal elements. In addition, the peripheral aperture of the PIFA measures about a half-wavelength, whereas that of the IFA is about a quarter-wavelength.

Study of the PIFA structure has initially started with a half-wave slot placed on the side of a rectangular conducting body as shown in Fig. 93a. The slot is fed at a point near a short-circuited end in order to attain adequate impedance to match the load impedance. The idea was born in the process of development of handset antennas. The basic concept was to develop a small, low-profile antenna suitable for handset units. In order to ensure a low-profile or flush-mount structure, use of a magnetic current as a

source of radiation was considered. The slot antenna satisfies this requirement. Meanwhile, the microstrip antenna (MSA) had been known as a useful planar antenna, having a small and low-profile structure. Then an attempt was made to place that slot antenna on a ground plane to form a planar structure such as an MSA (Fig. 93b), and the performance was confirmed to be satisfactory for handset use. Finally, the antenna configuration was formulated to achieve the structure illustrated in Fig. 93c, in which the short-circuited part is reduced to decrease the antenna size. In a PIFA, the peripheral aperture of a half-wavelength contributes to radiation, whereas in MSA a patch end aperture of about a quarter-wavelength contributes to radiation.

In fact, an attempt was initially made to increase the bandwidth of a linear IFA by replacing the linear horizontal element with a planar element; however, this was not successful, as the bandwidth increase obtained was only 1–2%, unless otherwise increasing the height.

An example of the input impedance ($R + jX$) of a similar antenna model is shown in Fig. 94a [61]. The equivalent circuit of this antenna model is shown in Fig. 94b. It is interesting to note that in the equivalent circuit there is a reactance jX_a . The bandwidth enhancement of an antenna system, composed of a PIFA element placed on the handset unit, may attribute to this reactance. This reactance has constant impedance over a bandwidth much wider than that of the antenna system.

There are many variations of the PIFA element in practice. In fact, some PIFA elements can hardly be identified as PIFA components because the modified antenna structure differs entirely from the original structure.

6.3.6. Ceramic Chip Antenna. The ceramic chip antenna is a small ceramic bulk antenna in appearance, but is

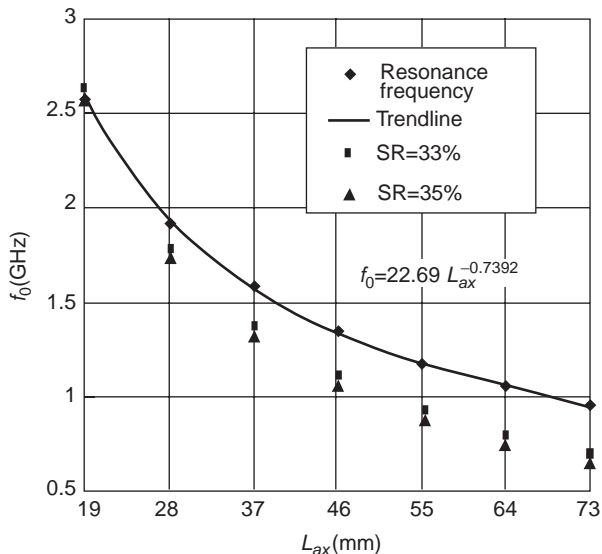


Figure 89. The first resonance frequency of a meanderline antenna versus antenna length. (From [59] with permission from CRC.)

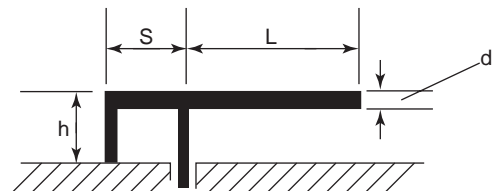


Figure 90. Inverted-F antenna.

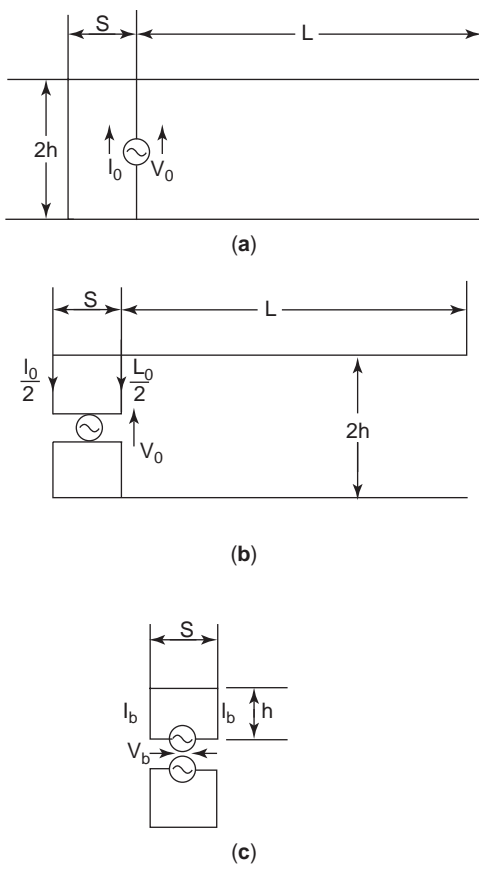


Figure 91. Equivalent expressions: (a) antenna model with its image element; (b) an IFA with its image; (c) two 2-wire transmission lines.

composed of an antenna element encapsulated by the ceramic material of high relative permeability. The antenna element is printed on the ceramic substrate and encapsulated by the ceramic material, which usually has a high

relative permeability of ≥ 20 . As a typical element, the meanderline, inverted-F, normal-mode helix, or other planar pattern is used. Use of plate ceramic, on which the antenna element is printed, is typical; however, there is another type—a small but bulky substrate that is structured with multi-layered very thin ceramic sheet, in which the antenna element is encapsulated. The antenna elements printed on the top and bottom surfaces of the ceramic substrate are connected by via wires.

One of the smallest ceramic chip antennas is 1.6 mm wide, 3.2 mm long, and 1.3 mm high as depicted in Fig. 95. This may be the world's smallest antenna at present; Fig. 96 illustrates an exploded view of the antenna structure. The thin ceramic substrate is composed of multilayered thin ceramic sheets. The antenna element used is a normal-mode helix, which is formed in the substrate by connecting printed patterns on the top- and bottom-layer via wires. This antenna has been used for small mobile terminals, in which the antenna is placed on a corner of the ground plane (GPL) as shown in Fig. 97. Usually a small part of the ground plane beneath the antenna element is taken out in order to avoid excessive loss due to the GPL. However, the antenna needs the help of the GPL; in other words, this antenna actually excites the GPL so that the small antenna and the GPL work as a combined antenna system. Thus the antenna performance depends on the size of the GPL, and how and where the antenna element is placed on the GPL.

Some examples of practical applications of small ceramic chip antenna are shown in Fig. 98, in which antenna mounting, operating frequency, antenna performance such as gain, bandwidth, and radiation patterns are illustrated.

In this type of antenna the resonant frequency can be controlled by the antennas flexible structure, and reasonably high gain and wide bandwidth may be realized, in addition to very small size and very light weight. Typically, this antenna has a gain of -5 to $+10$ dBi and a bandwidth of ~ 100 MHz in 5-GHz regions.

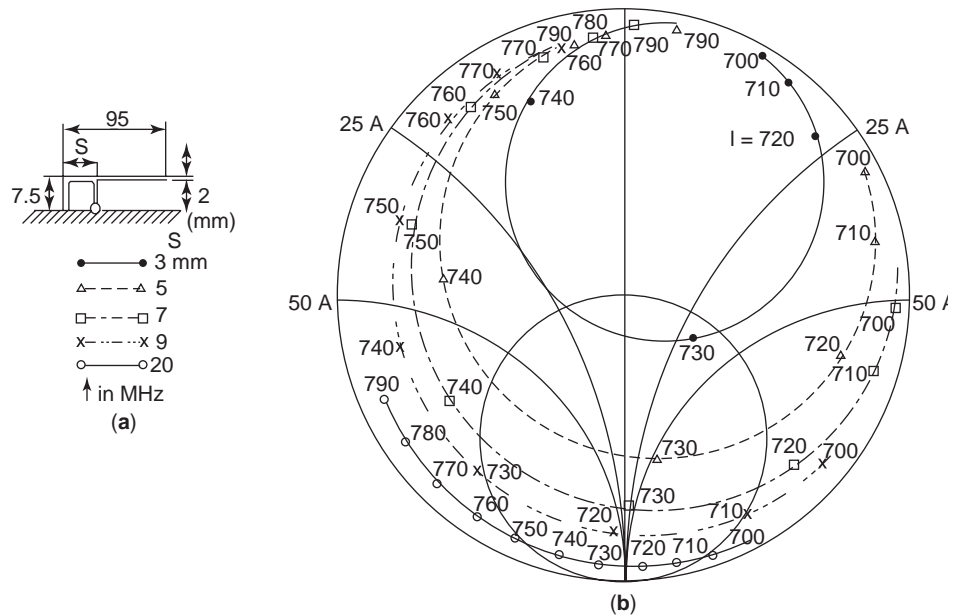


Figure 92. Input impedance of an IFA. (From [60] with permission from Research Studies Press.)

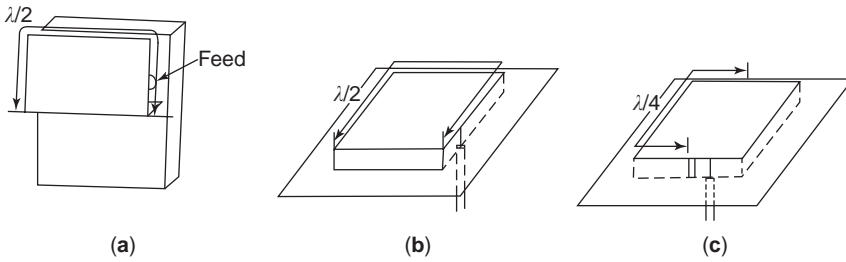


Figure 93. A PIFA evolved from a $\frac{1}{2}\lambda$ slot antenna on a rectangular conducting box.

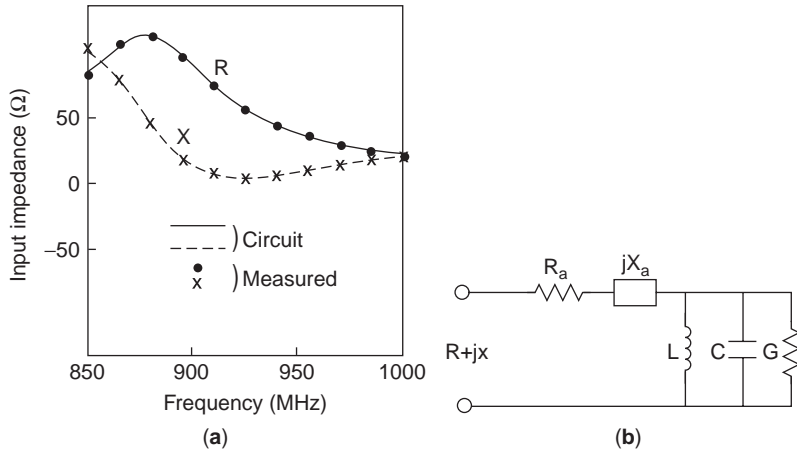


Figure 94. Input impedance of a PIFA on the ground plane: (a) impedance characteristics; (b) equivalent circuit. (From [1] and [61] with permission from Wiley and IEICE, respectively.)

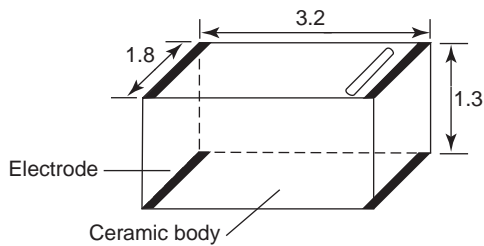


Figure 95. A small ceramic chip antenna. (Courtesy of Murata Mfg. Co., Japan.)

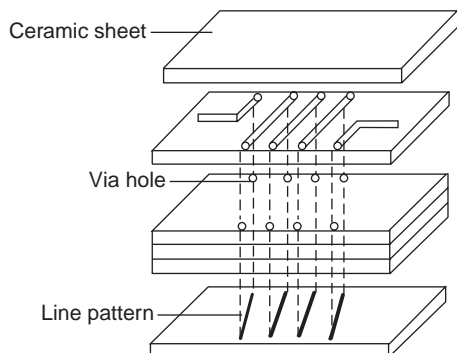


Figure 96. Exploded view of a small ceramic antenna. (Courtesy of Murata Mfg. Co., Japan.)

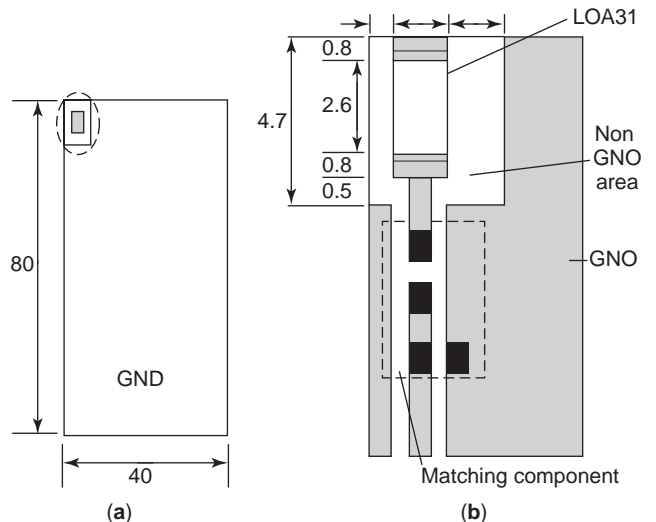


Figure 97. A ceramic antenna mounted on a ground plane: (a) mounted on a corner of the ground plane; (b) detail of the mounting. (Courtesy of Murata Mfg. Co., Japan.)

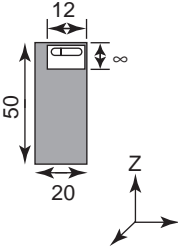
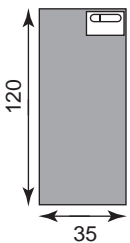
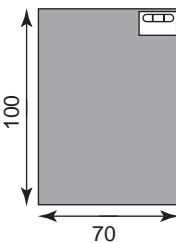
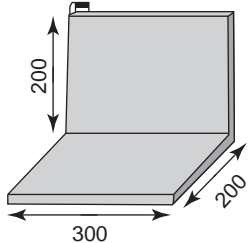
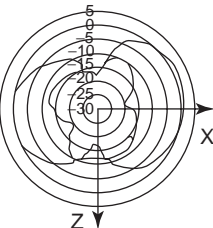
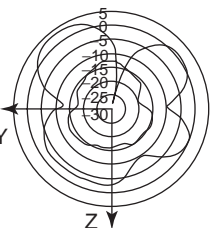
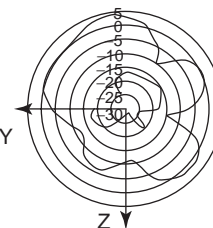
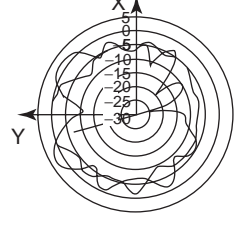
Application	Module	Cellular phone	PDA	Laptop PC
Mock-up board (non GND area 8x12) (unit:mm)				
10 (MHz)	2450	2450	2450	2450
B.W. (MHz)	450	160	210	140
Peak gain (dBi)	+2.0 (ZX plane)	+3.7 (YZ plane)	+2.7 (YZ plane)	+3.3 (XY plane)
Typical Directivities				

Figure 98. Practical applications of small ceramic antenna. (Courtesy of Murata Mfg. Co., Japan.)

6.4. Antennas for Small Mobile Terminals

6.4.1. Handset Antennas. The handset antenna used for the PDC system is an example that employs a monopole (MP), a normal-mode helical antenna (NMHA), and a planar inverted-F antenna (PIFA), as shown in Fig. 99 [62].

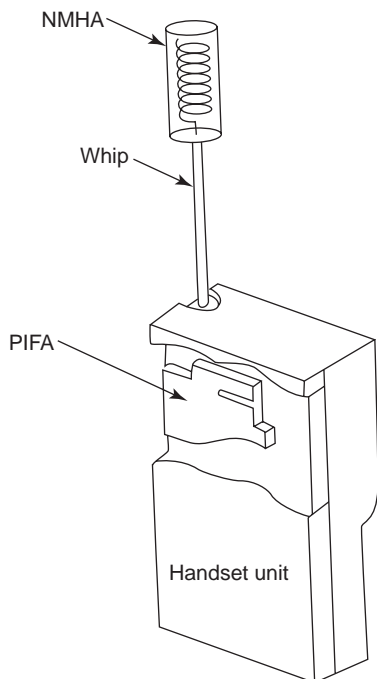


Figure 99. Antennas for a PDC handset. (From [63] with permission from IEICE.)

The NMHA element is placed on top of the MP. The MP element and the NMHA element are separated electrically. In the transmitting/receiving mode, the MP element is extracted outside the handset case and fed at the bottom. The NMHA is not active in this situation; only the MP element is operational. In the receiving mode, as the MP element is retracted inside the handset case and its bottom is disconnected from the feed terminals, only the NMHA acts as an antenna. In Fig. 99a, the MP element

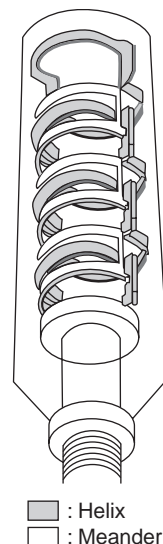


Figure 100. A meanderline helix used for small mobile terminals. (From [63] with permission from IEICE.)

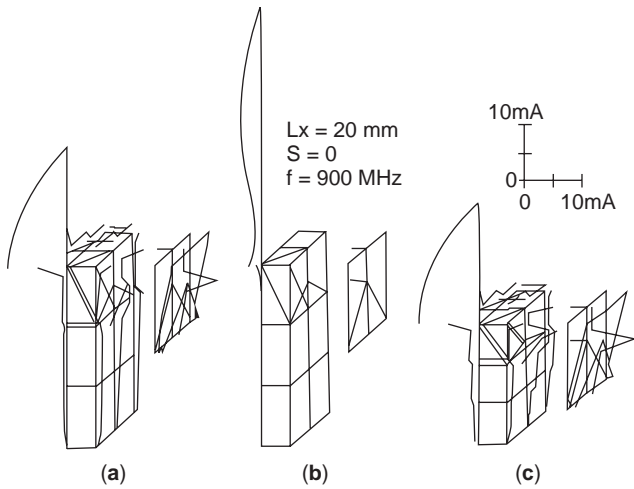


Figure 101. Current distributions on an antenna element and the unit: (a) $L_W \frac{1}{4}\lambda$ and L_Z 125 mm; (b) $L_W 0.54\lambda$ and L_Z 125 mm; (c) $L_W \frac{1}{4}\lambda$ and L_Z 83 mm. (From [1] and [64] with permission from Wiley and IEICE, respectively.)

is extracted from the unit and in Fig. 99b, it is retracted inside the unit.

The typical length of the MP element is either $\frac{3}{8}\lambda$ or $\frac{5}{8}\lambda$, because with these lengths, relatively small current flows on the handset unit and yet a better input impedance to match the load impedance is achieved than with $\frac{1}{2}\lambda$ and other lengths (Fig. 74) [55].

The typical length (extended) of the NMHA is about $\frac{1}{4}\lambda$. Lengths other than $\frac{1}{4}\lambda$ may be used if, for instance, a particular input impedance is specified. The gain of this type of antenna is generally about -0.5 dBd peak and about -9 dBd average in the horizontal plane, when the length is about $\frac{1}{4}\lambda$; however, this varies depending on the length of the handset unit.

A meanderline helix, shown in Fig. 100, has been used in some mobile terminals instead of NMHA [63].

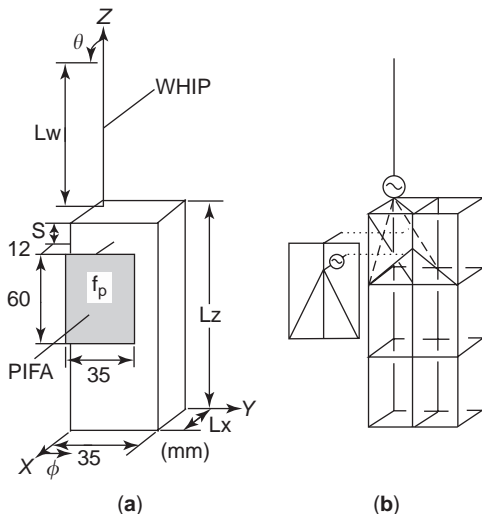


Figure 102. Antenna model used for the analysis: (a) dimensions and (b) wire grid model. (From [1] and [58] with permission from Wiley and IEICE, respectively.)

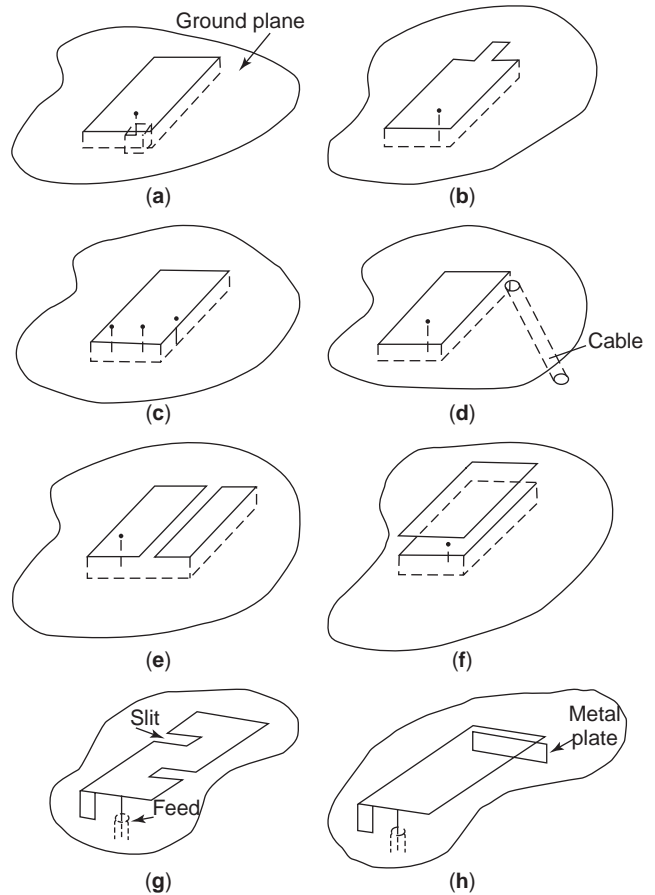


Figure 103. Configurations of planar element to achieve wide bandwidth or multiband operation. (From [1] and [55] with permission from Wiley and Denshi Sohgo Publishing Co., Japan, respectively.)

A PIFA element, a built-in antenna, is placed on the ground plane, which is actually a shielding plate for the RF circuits in the handset unit. The PIFA is employed as a pair of the diversity elements with the MP element. The PIFA is an antenna of rather narrow bandwidth, representing 1–2% in the relative bandwidth in free space. However, when it is mounted on a finite ground plane, the bandwidth usually increases. In practice, the bandwidth of an antenna system, which uses a built-in PIFA element in a handset unit, can be designed to have bandwidth wider than that of the whole-spectrum bandwidth of the PDC system. This is attributed to the handset unit,

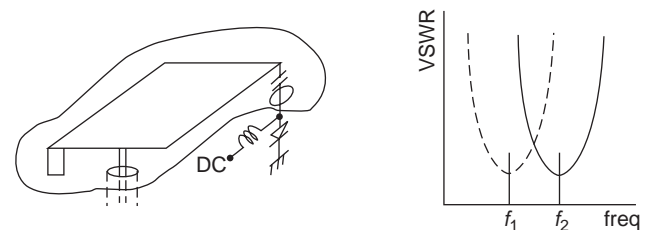


Figure 104. Switching circuit for dual-frequency resonance. (From [1] and [55] with permission from Wiley and Denshi Sohgo Publishing Co., Japan, respectively.)

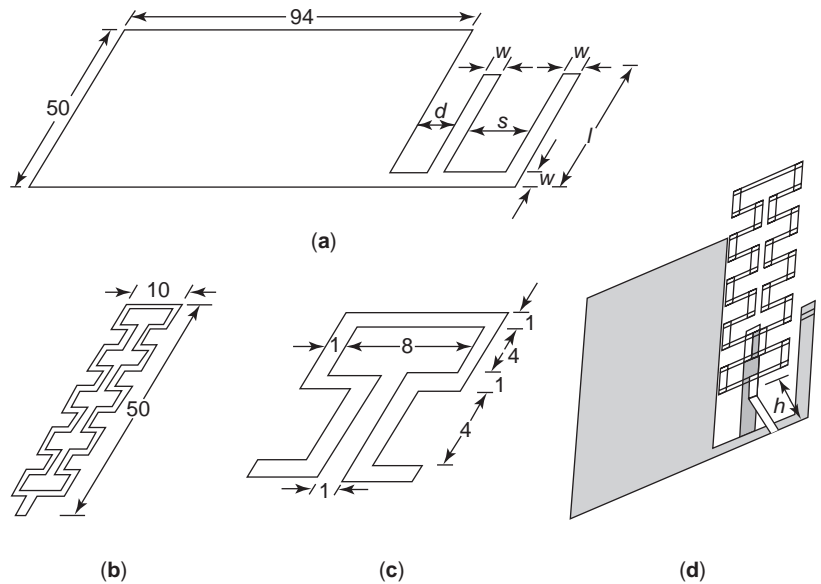


Figure 105. Antenna and printed circuit board (PCB): (a) PCB and parasitic metal strips (layer 1); (b) antenna geometry (layer 2); (c) detail of antenna geometry; (d) antenna height h from PCB. (From [67] with permission from IEEE.)

which acts as a part of the radiator, due to the current flow excited by the PIFA element.

Consequently, the impedance of the antenna system, which consists of an antenna element and the handset unit, is varied by the effect of the handset unit. Figure 101 illustrates an example of the current distributions on an antenna model [64] composed of an MP element, a PIFA element, and the handset unit. Figure 102 shows the antenna model used for the analysis and the dimensions. In the analysis the handset unit is simulated by a rectangular conducting box and modeled with wire grids, and the frequency is 900 MHz [64]. Figure 101 shows the current distributions for cases where (a) the length L_W of the MP = 83 mm ($\lambda/4$) and the length L_Z of the handset unit = 125 mm, (b) $L_W = 180$ mm (0.54λ) and $L_Z = 125$ mm, and (c)

$L_W = 83$ mm ($\lambda/4$) and $L_Z = 83$ mm. The PIFA, measuring 60×35 mm and placed at a distance 12 mm away apart from the handset unit surface, is assumed to be the same in all cases. Amplitudes of the current distributions are illustrated on each wire of the wire grid. The method of moment is applied to obtain these distributions. It has been shown that with an MP element of $\lambda/4$, much current flow on the handset unit is observed, while with that of 0.54λ (nearly a half-wavelength) almost no current flow is observed. This is a very important factor in designing handset antennas.

One of the more recent trends in mobile communications is for multimode handsets, which can operate for such frequency bands as 800 MHz (AMPS), 900 MHz (GSM, PDC), 1.5 GHz (PDC, GPS), 1.9 and 2 GHz (GSM, IMT-2000), 2.4 GHz (Bluetooth), and 5 GHz (WLAN, ITS). Thus, multifrequency antennas are desired. In the PDC system, for example, two bands are used; the lower bands are 810–828 MHz and 940–958 MHz, respectively, for receiving and transmitting, and the higher bands are 1477–1501 MHz and 1429–1453 MHz, respectively, for receiving and transmitting. In IMT-2000, 2-GHz bands are used. In order to design antennas that can operate at multifrequency bands, various techniques are used. The simplest technique is to increase the antenna length so that the resonance occurs at multiple-frequency bands. There are several methods for increasing antenna length; such as using a traveling-wave structure, loading impedance for multiple resonance, and arranging a matching circuit for multifrequency operation. For planar elements, some methods are shown in Fig. 103 [65], where part (a) shows a matching circuit, part (b) uses a small additional piece, part (c) uses additional pins, part (d) uses a cable as a reactance, part (e) shows the addition of a parallel parasitic element, part (f) shows the addition of a stacked element, part (g) uses slits on the planar element, and part (h) shows the addition of a loading element. When the bandwidth required is too wide to be covered by a matching

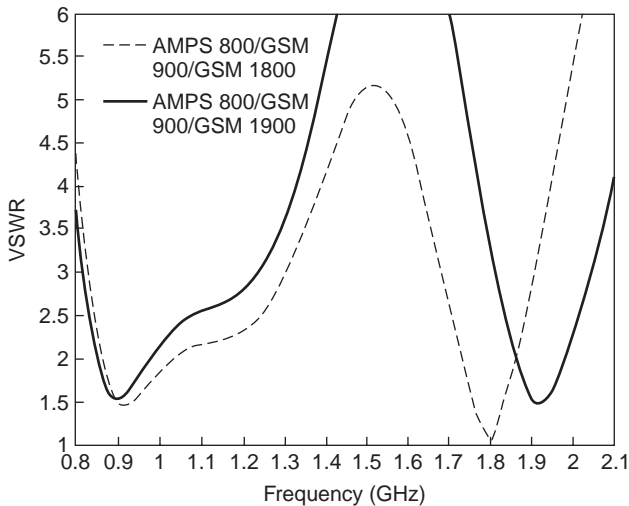


Figure 106. VSWR versus frequency: solid line— $l = 26.5$ mm, $h = 6$ mm; dotted line— $l = 29.5$ mm, $h = 5$ mm. Other fixed parameters are shown in Fig. 105. (From [67] with permission from IEEE.)

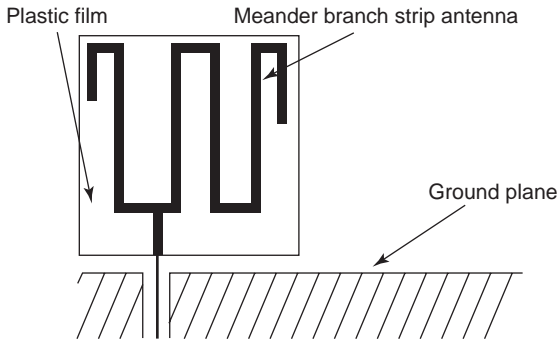


Figure 107. Configuration of a meanderline branch antenna (after [68]).

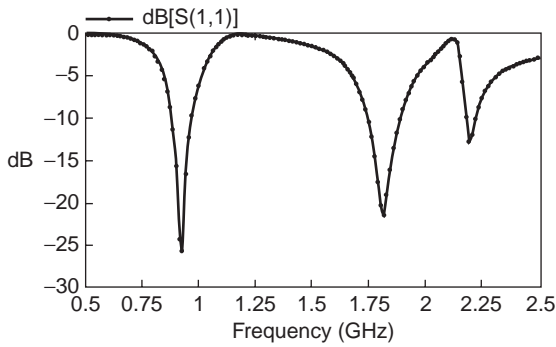


Figure 108. Calculated return loss characteristics of a branch antenna (after [68]).

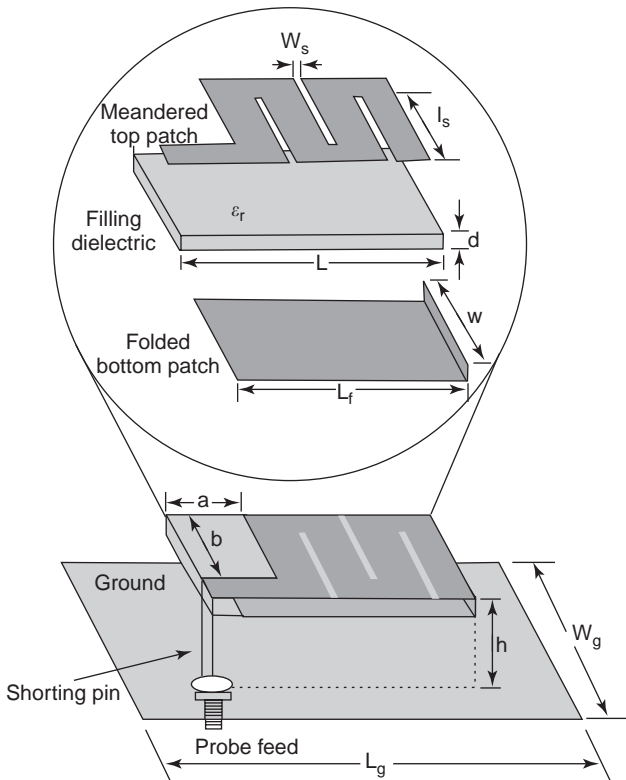


Figure 109. PIFA using planar meanderline. (From [69] with permission from IEEE.)

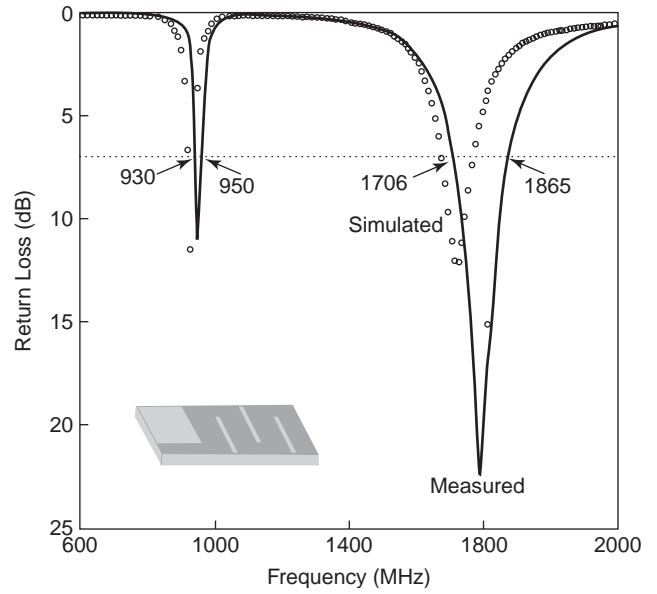


Figure 110. Measured and simulated return loss of an antenna: $l_s=7.5$ mm, $b=7$ mm $W_s=0.5$ mm. (From [69] with permission from IEEE.)

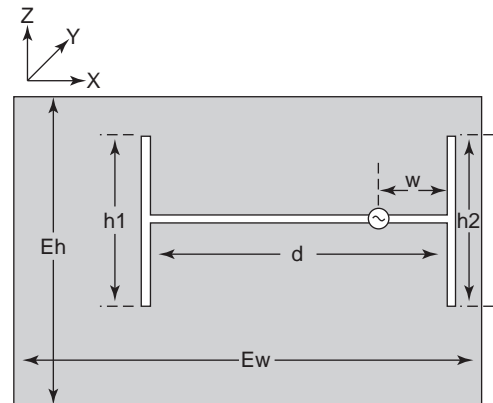


Figure 111. Basic structure of an H-type slot antenna ($E_w=70$ mm, $E_h=50$ mm). (From [70] with permission from IEICE.)

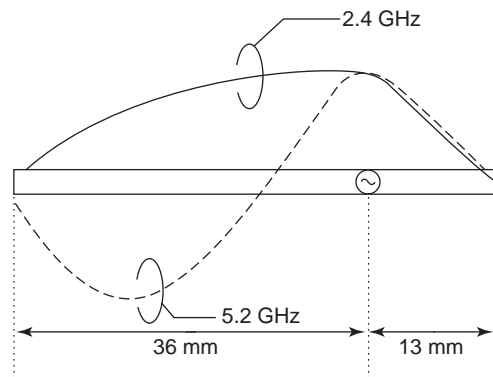


Figure 112. Magnetic current distribution on the straight slot by asymmetric feed. (From [70] with permission from IEICE.)

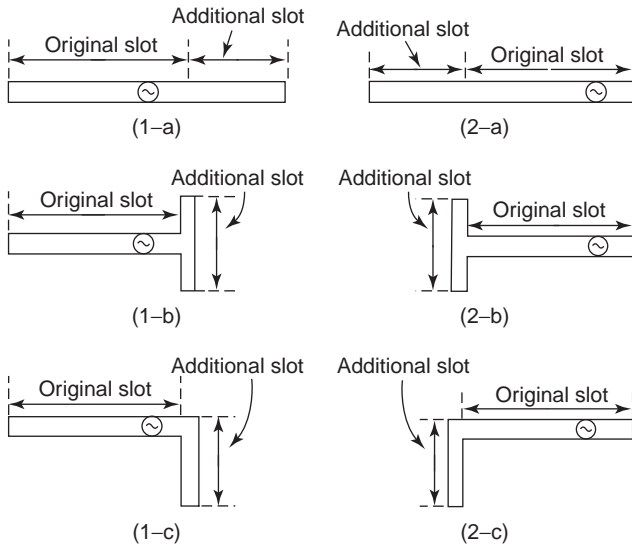


Figure 113. Additional slot structure: (1) addition at the right end; (2) addition at the left end, where (a) shows straight slot, (b) T-shaped slot, and (c) L-shaped slot. (From [70] with permission from IEICE.)

circuit, a switching circuit is used. An example of such a switching circuit is given in Fig. 104 [66], showing (a) a varactor circuit and (b) VSWRs for two frequencies. A MEMS (microelectronic switching) device can be used for this purpose.

Figure 105 shows an example of a triple-band antenna that uses a driven meanderline element and two coupled parasitic elements. The antenna operates effectively in the AMPS 800 (824–894 MHz), GSM 900 (880–960 MHz), and GSM 1900 (1850–1990 GHz) systems with a VSWR of <math><2.5</math>. The VSWR characteristics are shown in Fig. 106 [67].

Figure 107 shows another example of a multiband antenna composed of two branch elements fed by a short element [68]. The arms have different lengths; one arm is a quarter-wavelength at the lower-frequency region (e.g., GSM 900), while the other has a quarter-wavelength at the higher-frequency region (e.g., DCS 1800 and PCS 190). To shorten the wavelength, the arms can be structured in meanderline, spi-

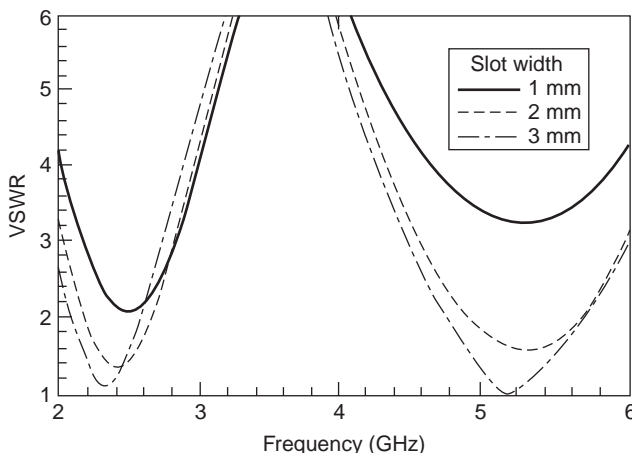


Figure 114. VSWR characteristics of an H-type slot antenna. (From [70] with permission from IEICE.)

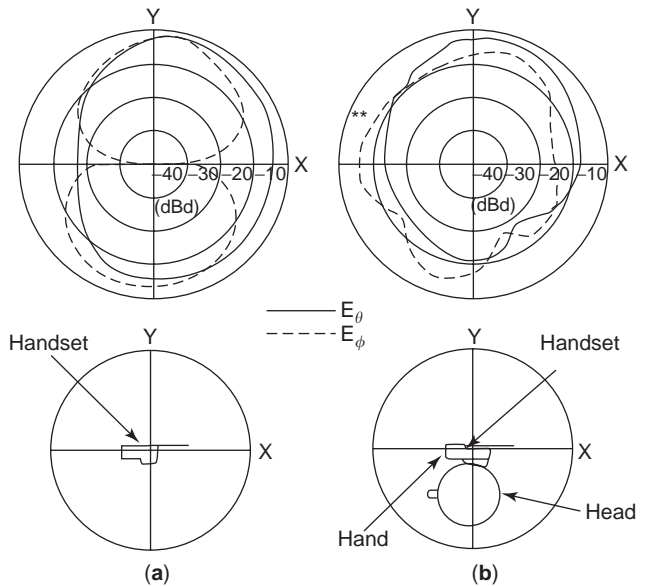


Figure 115. Radiation pattern of a handset antenna system: (a) in free space; (b) at talk position. (From [1] and [71] with permission from Wiley and IEICE, respectively.)

ral line, or other shapes. Figure 108 depicts the calculated return loss, which shows a dual-band operation.

Figure 109 illustrates a dual-band antenna modified from a PIFA by employing planar meanderline as the radiating element and folded to reduce the antenna size [69]. Return loss characteristics are illustrated in Fig. 110. Two-band operation at 900 and 1800 MHz is achieved with a small volume of $24 \times 10 \times 7.2 \text{ mm}^3$.

Figure 111 illustrates the basic structure of an H-shaped slot antenna that operates at two frequency bands: 2.4 and 5.2 GHz [70]. The basic principle of this antenna originates from an asymmetrically excited slot, on which two magnetic current flows that contribute to radiation in two bands are produced as shown in Fig. 112. By decomposing these two currents, a slot consisting of additional slots at the both right and left ends (Fig. 113), can be constituted and an H-shape antenna is created. VSWR characteristics are shown in Fig. 114. This antenna is designed for application to the Bluetooth (2.4 GHz) and the Wireless LAN systems (5.2 GHz).

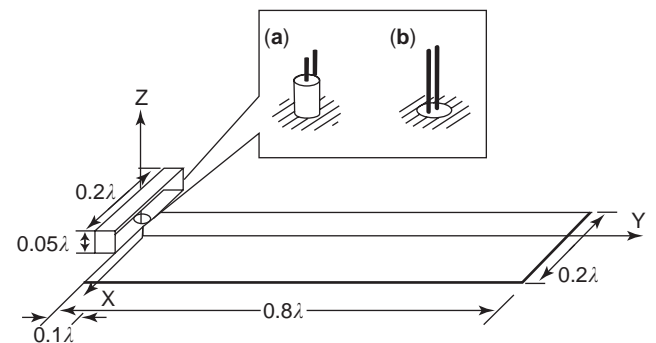


Figure 116. Loop antenna system: (a) unbalanced feed; (b) balanced feed. (From [1] and [71] with permission from Wiley and IEICE, respectively.)

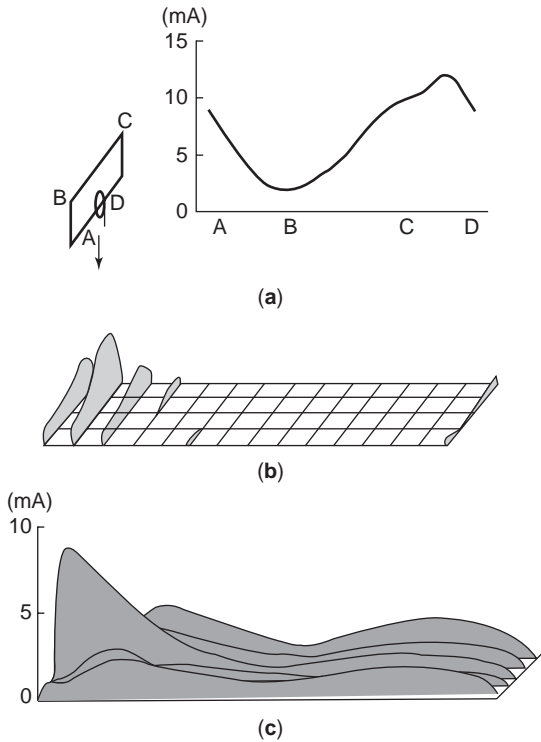


Figure 117. Current distribution in an unbalanced antenna system: (a) on loop element; (b) on ground plane (y axis); (c) on ground plane (x axis). (From [1] and [71] with permission from Wiley and IEICE, respectively.)

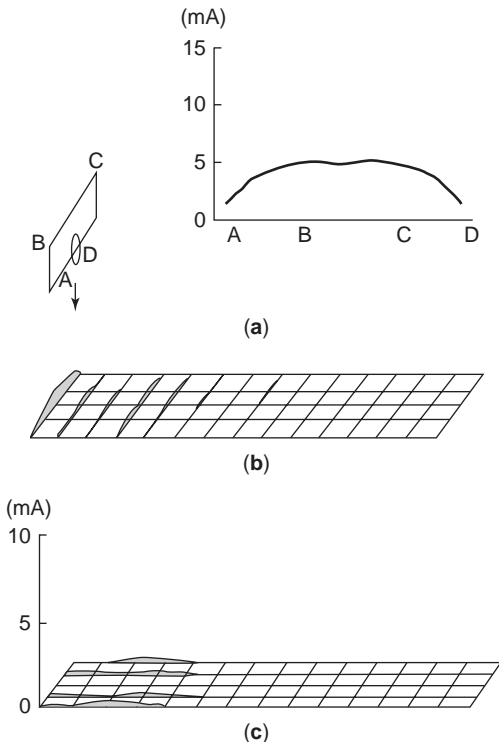


Figure 118. Current distribution in a balanced antenna system (similar to configuration in Fig. 117). (From [1] and [71] with permission from Wiley and IEICE, respectively.)

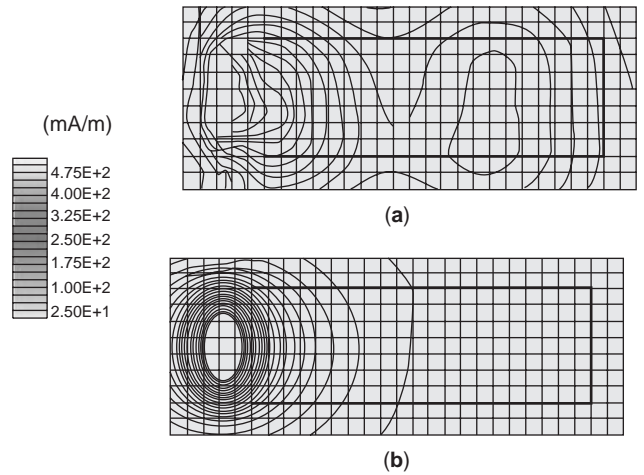


Figure 119. Measured current distributions of loop antenna system: (a) unbalanced system; (b) balanced system. (From [1] and [71] with permission from Wiley and IEICE, respectively.)

Antenna performance of a handset usually degrades at the talk position, due mainly to the effect of the human body such as the operator’s hand and head. The major reason for the degradation is the variation in the current flow on the handset unit. A typical example of distorted radiation patterns caused by the body effect is shown in Fig. 115, with the handset placed in free space and (b) at talk position.

Because the currents on the handset unit are produced by the excitation of the built-in PIFA, its variation is caused mainly by the body effects, the degradation of antenna performance may be avoided by decreasing such current flow. The reduction of such current flow can be realized by means of an antenna system that has balanced terminals and is fed with a balanced line [70]. An example that uses a loop antenna placed on a ground plane and fed with a two-wire line is shown in Fig. 116; Fig. 116a shows the feed with unbalanced line and Fig. 116b, with a balanced line. Figure 117 shows current distributions in an unbalanced structure: (a) on the antenna element, (b) on the ground plane (the y axis), and (c) on the ground plane (the x axis). Figure 118 shows similar current distributions in a balanced structure for comparison with the unbalanced structure. Figure 119 illustrates magnetic field distributions on the surface of the antenna system that correspond to current distributions. Figure 119a shows the distributions in the unbalanced structure and Fig. 119b, in the balanced structure.

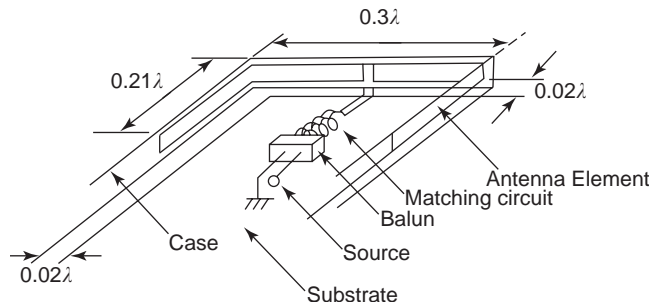


Figure 120. Configuration of one-wavelength (1λ) U-shaped dipole antenna (after [72]).

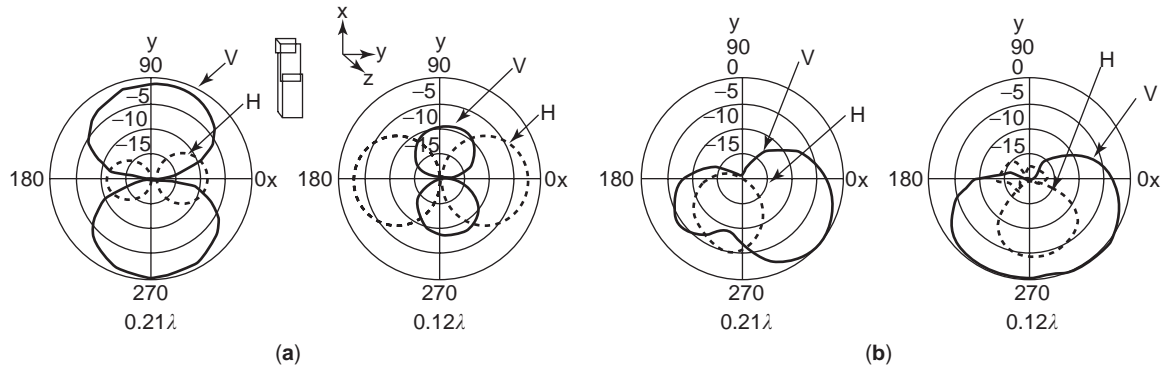


Figure 121. Radiation patterns: (a) in free space; (b) at talk position (after [72]).

It can be seen in Fig. 119 that a significant reduction in current flow can be realized using the balanced antenna structure. The antenna element is not necessarily a loop for this purpose, but any other element such as NMHA or meanderline, can be used, whenever the input terminals are balanced and fed with a balanced line. One should be careful if an antenna system has very asymmetric structure, even when the terminals have balanced structure and are fed with a balanced line. With the asymmetric structure, there may be some difficulty in achieving a truly electrically balanced structure, and thus some unbalanced currents flow at the terminals.

Practical application of a balanced-type antenna is seen in a latest handset. Figure 120 depicts a model of a U-shaped dipole and its dimensions [71]. The antenna has a balanced mode and is fed with a balanced line through a balun. The radiation performance of the antenna is shown in Fig. 121, where radiation patterns in free space and at talk position are shown. The antenna is located on top of the handset as shown in Fig. 122.

6.4.2. Diversity Antenna. It is very common to use two antenna elements in the diversity system. There has been an exception in a type of PDC handset, where a single antenna element is devised to perform diversity function

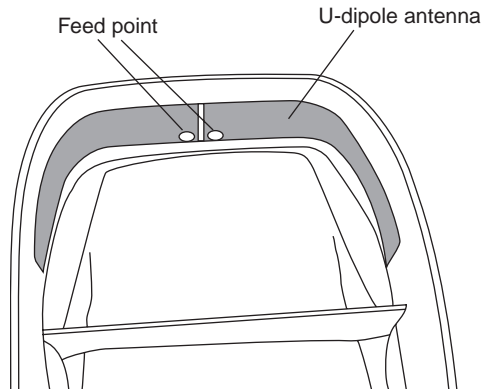


Figure 122. U-shaped antenna mounted on top of handset (after [72]).

[72]. An antenna is applied to a clam-shell type handset (Fig. 123), which consists of two parts, one of which flips to open and the other, to close the unit. Each of these two parts has circuitry on it, and some radiation currents flow on the ground plane of both parts. Thus they can be used as a radiator component as well as the antenna element. In order to achieve diversity function, the two parts are electrically separated, and two impedance components Z_1 and Z_2 are located between the two parts. This configuration is simplified in Fig. 124, where part (a) illustrates location of impedances and (b) expresses switching of impedances Z_1 and Z_2 for the diversity performance. Since the radiation pattern can be varied by changing the value of impedance, for instance, from Z_1 to Z_2 , pattern diversity can be achieved. Changing the impedance value contributes to variation in phase of the current flowing on the ground plane so that additional lower correlation coefficients can be obtained.

6.4.3. Antennas for PHS Terminals. The PHS (personal handy-phone system) has been used in Japan as an extension of the indoor use of cordless phones to outdoor applications. The communication areas are limited to small



Figure 123. Handset to which a single-antenna-element diversity system is applied.

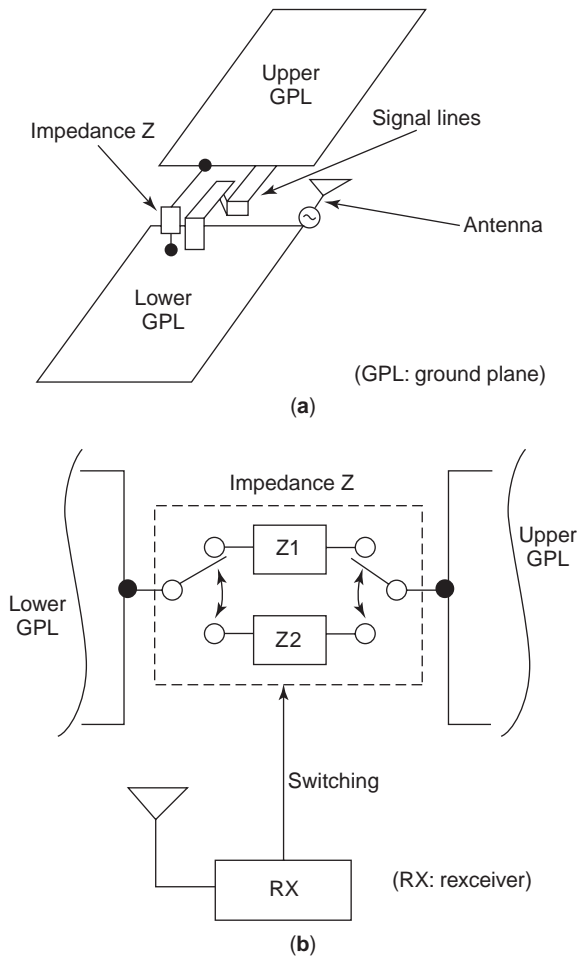


Figure 124. Diversity system using a single antenna element: (a) schematic expression; (b) circuitry to function diversity. (From [73] with permission from IEICE.)

zones, such as several hundred meters in diameter. The transmitter power of the mobile terminals is kept as low as 10 mW. The frequency band is 1895–1918 MHz. It should

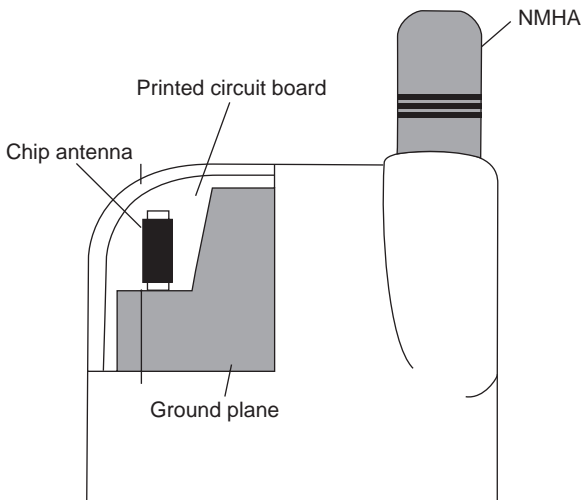


Figure 125. A chip antenna mounted at a corner of ground plane in a PHS unit. (Courtesy of Murata Mfg. Co., Japan.)

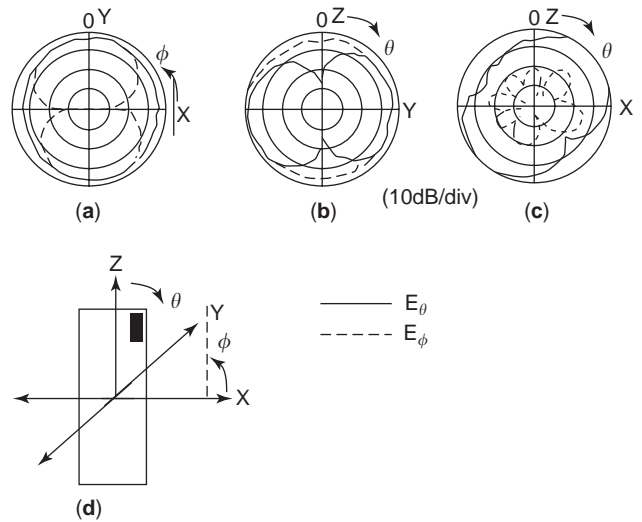


Figure 126. Radiation patterns: (a) x - y plane; (b) y - z plane; (c) x - z plane; (d) geometry. (Courtesy of Murata Mfg. Co., Japan.)

be noted that a faster data transmission can be handled by the PHS than by the PDC.

PHS mobile terminals use a single-antenna element, which is typically an MP, an NMHA, or a small chip antenna. Because the operating frequency is higher and the bandwidth is narrower than those in the PDC system, a smaller antenna element can be used. Then antenna design is easier than that in the PDC systems. The MP element has a structure similar to that in the PDC, but the length of the PDC is shorter than that of the PHS. An example of the inside view of a PHS is shown in Fig. 125, where mountings of both a chip antenna and an NMHA are shown. Figure 126 shows the radiation patterns. The gain is evaluated to be about -2 to -4 dBd at maximum and -4 to -7 dBd on average, depending on the plane measured.

BIBLIOGRAPHY

1. K. Fujimoto and J. R. James, eds., *Mobile Antenna Systems Handbook*, 2nd ed., Artech House, 2001.
2. E. Hawks, *Pioneers of Wireless*, Methuen, 1927.
3. S. Isobe, *From Chappe's Semaphore Telegraph to Satellite Communications*, KDD Data Center, 1968, p. 133 (in Japanese).
4. *Ibid.*, p. 134.
5. Historical papers on development in antennas and propagation, 1912 to 1962 *Proc. IRE* (50th anniversary issue) 692–717 (1962).
6. J. R. James and G. Andrasic, Multifunction printed antennas, in H. F. Lee and W. Chen, eds., *Microstrip and Printed Antennas*, Wiley, 1997, Chap. 6, pp. 273–324.
7. Y. O. Okumura and A. Akeyama, in Y. Okumura and M. Shinji, eds., *Radio Wave Propagation in Mobile Communications*, IEICE Press, 1986, pp. 24–59 (in Japanese).
8. N. Nakajima, H. Mishima, and Y. Yamada, Mobile communications antennas, in Y. Okumura and M. Shinji, eds., *Basic*

- Technology of Mobile Communications*, IEICE Press, 1985 (in Japanese).
9. M. Nakano, T. Satoh, and H. Arai, *Up-link Polarization Diversity Measurement of Hand-Held Terminal at 900MHz*, Technical Report AP95-13, IEICE, 1995, pp. 13–19 (in Japanese).
 10. Y. Yamada, Y. Ebine, and K. Tsunekawa, Base and mobile station antenna for land mobile radio systems, *Trans. IEICE*, **E74(6)**:1547–1555 (1991).
 11. M. Sakamoto, System configuration and control, in Y. Okumura and M. Shinji, eds., *Basic Technology of Mobile Communications*, IEICE Press, 1986, pp. 188–217.
 12. H. Mishima, Y. Ebine, and K. Watanabe, Base station antenna and multiplexer systems for land mobile telephone system, *Electric Commun. Lab. Tech. J.* **26(7)**:2011–2036 (1977).
 13. Y. Yamada, T. Nara, S. Kameo, Y. Chitani, and H. Abe, A *Variable Beamwidth Corner Reflector Antenna*, IEICE Natl. Convention Record 694, 1986.
 14. J. D. Kraus, *Antennas*, 2nd ed., McGraw-Hill, 2002, pp. 352–362.
 15. T. Suzuki and K. Kagoshima, Corner reflector antenna with the same beamwidth in two frequency bands, *Trans. IEICE* **J75-B-II(12)**:950–956 (1992).
 16. T. Nara, Y. Ebine, and N. Nakajima, *Beam Tilting Effect of Base Station Antenna*, IEICE Natl. Convention Record S5-15, 1985.
 17. R. S. Elliott, *Antenna Theory and Design*, Prentice-Hall, 1981, Chap. 5.
 18. M. Kijima and Y. Yamada, *Beam Narrowing Method for Radiation Pattern with Suppressing Some Sidelobes*, IEICE Tech. Report on Antennas and Propagation AP91-125, 1992.
 19. R. H. Clark, Statistical theory of mobile radio reception, *Bell System Tech. J.* **47(6)**:957–1000 (1968).
 20. Y. Yamada, K. Kagoshima, and K. Tsunekawa, Diversity antenna for base and mobile station in land mobile communication systems, *Trans. IEICE*. **E74(10)**:3202–3209 (1991).
 21. T. Nara, Y. Ebine, and Y. Yamada, *A Study of Vertical Space Diversity for Land Mobile Radio*, IEICE Natl. Convention Record 2362, 1986.
 22. M. Kijima, Y. Ebine, and Y. Yamada, Development of a dual-frequency base station antenna for cellular mobile radio, *IEICE Trans. Commun.* **E82-B(4)** (1999).
 23. H. Arai and K. Cho, Cellular and PHS base station antenna systems, *IEICE Trans. Commun.* **E-86-B(3)**: 980–992 (2003).
 24. Y. Yamada and M. Kijima, Low sidelobe and tilted beam base station antenna for smaller cell systems, *Proc. IEEE APS Int. Symp.*, 1989, pp. 138–141.
 25. Y. Ebine, *Design of Base Station Antennas for Next Generation Cellular Mobile Radios (IMT-2000)*, Tech. Report IEICE P-2000 (in Japanese).
 26. M. Karikomi, *Effect of Parasitic Elements for 0.9/1.5/2GHz Corner-Reflector Antenna with 120° Beamwidth*, IEICE Communications Society Convention Record B-I-80, 2002.
 27. Y. Yamada and M. Kijima, A slender two beam base station antenna for mobile radio, *Proc. IEEE APS Int. Symp.* 1994, pp. 352–355.
 28. Y. Ebine and M. Ito, Design of a dual beam antenna used for base station of cellular mobile radios, *IEICE Trans. Commun.* **J79-B-II(11)**: 909–915 (1996).
 29. H. Arai and M. Nakano, Up-link polarization diversity and antenna gain measurement of hand held terminal at 900 MHz, paper presented at *Int. Symp. on Multi-Dimensional Mobile Communications*, Nov. 1994.
 30. M. Nakano, T. Satoh, and H. Arai, *Up-link Polarization Diversity Measurement of Hand-Held Terminal at 900MHz*, Tech. Report IEICE AP95-13, May 1995, pp. 13–19 (in Japanese).
 31. M. Nakano, T. Satoh, and H. Arai, Up-link polarization diversity and antenna gain measurement of hand-held terminal, *IEEE AP-S Int. Symp. Digest*, 1995, pp. 1940–1943.
 32. M. Nakano, T. Satoh, and H. Arai, *Up-link Polarization Diversity and Antenna Gain Measurement of Hand-held Terminal*, IEICE Natl. Convention Record B-11, 1995 (in Japanese).
 33. M. Nakano, S. Aizawa, T. Satoh, T. Matsuoka, and H. Arai, Up-link polarization diversity measurement for cellular communication systems using hand-held terminal, *Proc. IEEE Antenna and Propagation Society Int. Symp.*, 66.8, July 1997, pp. 1360–1363.
 34. M. Nakano, S. Aizawa, T. Satoh, T. Matsuoka, and H. Arai, *Up-link Polarization Diversity for Cellular Communication System*, Technical Report IEICE A-P98-15, 1998, pp. 13–20 (in Japanese).
 35. M. Nakano, S. Aizawa, T. Satoh, T. Matsuoka, and H. Arai, *Small-Sized Polarization Diversity Antenna for Cellular Base Stations*, Natl. Society Convention Record IEICE B-1-42, 1997 (in Japanese).
 36. M. Nakano and T. Satoh, *Polarization Diversity for Base Stations on cdmaOne Cellular System*, Natl. Society Convention Record IEICE B-1-14, 1998 (in Japanese).
 37. Ref. 23, p. 984.
 38. Y. Kondo and K. Suwa, Linear predictive transmission diversity for TDMA/TDD personal communication systems, *IEICE Trans. Commun.* **E79-B(10)**:1586–1591 (1996).
 39. K. Cho et al., Bidirectional collinear antenna with arc parasitic plates, *Proc. IEEE AP-S Int. Symp.*, 1995, pp. 1414–1417.
 40. Ref. 23, pp. 989–990.
 41. T. Ohgane, Y. Kamio, N. Matsuzawa, T. Shinnmura, M. Mizuno, and H. Sasaoka, BER performance of CMA adaptive array for high speed GMSK mobile communications—a description of measurement in central Tokyo, *IEEE Trans. Vehic. Technol.* **42(4)**:484–490 (1993).
 42. T. Yokota et al., *The Development of PHS Base Station with Adaptive Array Antenna*, Natl. Society Convention Record IEICE B-5-74, 1998 (in Japanese).
 43. H. Yuan et al., *A Study of the Interelement Spacing on Adaptive Array Antenna for PHS Base Station*, Natl. Society Convention Record IEICE B-5-75, 1998 (in Japanese).
 44. J. Uchibori et al., *The Radiatio Characteristics of Adaptive Array Antenna for PHS Base Station*, Natl. Society Convention Record IEICE B-5-76, 1998 (in Japanese).
 45. Y. Fujitsuka et al., *A Field Test for the PHS Base Station with Adaptive Array Antenna*, Natl. Society Convention Record IEICE, B-5-77, 1998 (in Japanese).
 46. S. Kimura, Kyocera Super PHS-WLL technology, paper presented at Technical Seminars, 6th Vietnam Intl Exhibition on Communication, Computer & Office System and 4th Vietnam Int. Exhibition on Broadcasting Technology, Dec. 1997.
 47. H. Morishita, Y. Kim, and K. Fujimoto, Design concept of antennas for small mobile terminals and the future perspectives, *IEEE Anten. Propag. Mag.* **44(5)**:30–42 (2002).
 48. K. Fujimoto, A loaded antenna system applied to VHF portable communication equipment, *IEEE Trans. Vehic. Technol.* **VT-17(1)**: 5–12 (1968).

49. K. Hirasawa and K. Fujimoto, Characteristics of wire antennas on a rectangular conducting body, *Trans. IEICE* **J65-B(9)**:1133–1139 (1982) (in Japanese).
50. K. Fujimoto, A. Henderson, K. Hirasawa, and J. R. James, *Small Antennas*, Research Studies Press, Chap. 4, 1987, pp. 89–110.
51. H. Kuboyama, K. Hirasawa, and K. Fujimoto, UHF-bent-slot antenna system for portable equipment—II; receiving performance in urban areas, *IEEE Trans. Vehic. Technol.* **VT-36**:129–134 (1987).
52. H. Morishita, H. Furuuchi, and K. Fujimoto, Balance-fed L-type loop antenna system for handset, *Proc. 1999 Vehicular Technology Society Int. Conf.*, 1999, Vol. 3, pp. 1346–1350.
53. Ref. 1, pp. 333–334.
54. Ref. 50, p. 287.
55. K. Fujimoto, Y. Yamada, and K. Tsunekawa, *Antenna Systems for Mobile Communications*, 2nd ed., Denshi Sohgo Publishing, Japan, 1999, p. 55 (in Japanese).
56. J. D. Kraus, *Antennas* 2nd ed., McGraw-Hill, 2002, pp. 293–294.
57. Ref. 47, pp. 59–76.
58. T. Endo, Y. Sunahara, S. Satoh, and T. Katagi, Resonant frequency and radiation efficiency of meander line antenna, *Trans. IEICE* **J80 B-II(12)**:1044–1049 (1997) (in Japanese).
59. L. C. Godara, ed., in Handheld antennas, *Handbook of Antennas in Wireless Communications*, CRC Press, Boca Raton, FL; 2002, Chap. 12, pp. 12-8–12-10.
60. Ref. 47, pp. 120–121.
61. K. Satoh, K. Matsumoto, K. Fujimoto, and K. Hirasawa, Characteristics of a planar inverted-F antenna on a rectangular conducting body, *Trans. IEICE* **J71-B(11)**:1237–1243 (1988) (in Japanese).
62. Ref. 1, pp. 440–441.
63. K. Ogawa, High performance technologies for portable radio antennas; toward the harmony of antenna, propagation, human body and systems, *J. IEICE* **84(11)**:775–781 (2001).
64. K. Ogawa and T. Uwano, Analysis of a diversity antenna comprising a whip antenna and a planar inverted-F antenna for portable telephones, *Trans. IEICE* **J79-B(12)**:1008 (1996) (in Japanese).
65. Ref. 1, p. 445; Ref. 55, p. 125.
66. Ref. 1, p. 447.
67. M. Ali, G. J. Hates, H. S. Hwang, and R. A. Sadler, Design of multiband internal antenna for third generation mobile phone handsets, *IEEE Trans. Anten. Propag.* **51(7)**:1452–1461 (2003).
68. Z. Ying, Design of a branch multi-band antenna and efficiency enhancement, paper presented at Nordic Antenna Symp. 2000, Lund, Sweden, 2000.
69. H. T. Chen, K. L. Wong, and T. W. Chiou, PIFA with a meandered and folded patch for the dual-band mobile phone application, *IEEE Trans. Anten. Propag.* **51(9)**:2468–2471 (2003).
70. A. Itakura, Y. Okano, and M. Abe, A study on double resonance H-type slot antenna, *Trans. IEICE* **J86-B(12)**:2533–2542 (2003).
71. H. Morishita and K. Fujimoto, A balance-fed loop antenna system for handsets, *Trans. IEICE* **E82-A(7)**:1138–1143 (1999).
72. K. Egawa, T. Oga, and H. Haruki, A development of built-in antenna for W-CDMA visual terminals, *2002 Int. Symp. on Anten. and Propag.* YRP, Japan, pp. 235–238.
73. T. Fukasawa, K. Kopydama, S. Makino, *Diversity Antenna for Portable Telephone with Two Boxes*, Tech. Report IEICE AP2002-78, 2002, pp. 87–90.

APERTURE ANTENNAS

DENNIS KOZAKOFF
Devry University
Alpharetta, Georgia

1. INTRODUCTION

Aperture antennas are most commonly used at microwave and the millimeter-wave frequencies. There are a large number of antenna types for which the radiated electromagnetic fields can be considered to emanate from a physical aperture. Antennas that fall into this category include reflector antennas, lenses, and horn antennas. The geometry of the aperture may be square, rectangular, circular, elliptical, or virtually any other shape. The term “aperture antenna” usually has more to do with the method used to analyze the antenna than the actual form of the antenna. For instance, array antennas viewed as a continuous field function bounded by a conducting screen can be considered to be an aperture antenna. This would encompass so-called planar (flat-plate) waveguide and microstrip arrays.

Aperture antennas are very popular for aerospace applications because they can be flush-mounted onto the spacecraft or aircraft surface. Their aperture opening can be covered with an electromagnetic (dielectric) window material that is transparent to the RF energy to protect the antenna from the environmental conditions [1]. This is known as a *radome*, and it is implemented so as not to disturb the aerodynamic profile of the vehicle, which is of special importance to high-speed aircraft or missiles.

In order to evaluate the distant (far-field) radiation patterns, it is necessary to know the surface currents that flow on the radiating surfaces of the antenna aperture. In many instances, these current distributions may not be known exactly and only approximate or experimental measurements can provide estimates. A technique based on the equivalence principle allows one to make reasonable approximations to the electromagnetic fields on, or in the vicinity of, the physical antenna aperture structure, which can then be used to compute far field antenna radiation patterns.

Field equivalence, first introduced by Schelkunoff [2], is a principle by which the actual sources on an antenna aperture are replaced by equivalent sources on an external closed surface that is physically outside the antenna aperture. The fictitious sources are said to be *equivalent* within a region because they produce the same fields within that region. Another key concept is Huygens’ principle [3], which states that the equivalent source at each point on the external surface is a source of a spherical wave. The secondary wavefront can be constructed as the envelope of these secondary spherical waves [4].

Using these principles, the electrical and/or magnetic fields in the equivalent aperture region can be determined with these straightforward, but approximate, methods. The fields elsewhere are assumed to be zero. In most applications, the closed surface is selected so that most of it coincides with the conducting parts of the physical antenna aperture structure. This is preferred because the

49. K. Hirasawa and K. Fujimoto, Characteristics of wire antennas on a rectangular conducting body, *Trans. IEICE* **J65-B(9)**:1133–1139 (1982) (in Japanese).
50. K. Fujimoto, A. Henderson, K. Hirasawa, and J. R. James, *Small Antennas*, Research Studies Press, Chap. 4, 1987, pp. 89–110.
51. H. Kuboyama, K. Hirasawa, and K. Fujimoto, UHF-bent-slot antenna system for portable equipment—II; receiving performance in urban areas, *IEEE Trans. Vehic. Technol.* **VT-36**:129–134 (1987).
52. H. Morishita, H. Furuuchi, and K. Fujimoto, Balance-fed L-type loop antenna system for handset, *Proc. 1999 Vehicular Technology Society Int. Conf.*, 1999, Vol. 3, pp. 1346–1350.
53. Ref. 1, pp. 333–334.
54. Ref. 50, p. 287.
55. K. Fujimoto, Y. Yamada, and K. Tsunekawa, *Antenna Systems for Mobile Communications*, 2nd ed., Denshi Sohgo Publishing, Japan, 1999, p. 55 (in Japanese).
56. J. D. Kraus, *Antennas* 2nd ed., McGraw-Hill, 2002, pp. 293–294.
57. Ref. 47, pp. 59–76.
58. T. Endo, Y. Sunahara, S. Satoh, and T. Katagi, Resonant frequency and radiation efficiency of meander line antenna, *Trans. IEICE* **J80 B-II(12)**:1044–1049 (1997) (in Japanese).
59. L. C. Godara, ed., in Handheld antennas, *Handbook of Antennas in Wireless Communications*, CRC Press, Boca Raton, FL; 2002, Chap. 12, pp. 12-8–12-10.
60. Ref. 47, pp. 120–121.
61. K. Satoh, K. Matsumoto, K. Fujimoto, and K. Hirasawa, Characteristics of a planar inverted-F antenna on a rectangular conducting body, *Trans. IEICE* **J71-B(11)**:1237–1243 (1988) (in Japanese).
62. Ref. 1, pp. 440–441.
63. K. Ogawa, High performance technologies for portable radio antennas; toward the harmony of antenna, propagation, human body and systems, *J. IEICE* **84(11)**:775–781 (2001).
64. K. Ogawa and T. Uwano, Analysis of a diversity antenna comprising a whip antenna and a planar inverted-F antenna for portable telephones, *Trans. IEICE* **J79-B(12)**:1008 (1996) (in Japanese).
65. Ref. 1, p. 445; Ref. 55, p. 125.
66. Ref. 1, p. 447.
67. M. Ali, G. J. Hates, H. S. Hwang, and R. A. Sadler, Design of multiband internal antenna for third generation mobile phone handsets, *IEEE Trans. Anten. Propag.* **51(7)**:1452–1461 (2003).
68. Z. Ying, Design of a branch multi-band antenna and efficiency enhancement, paper presented at Nordic Antenna Symp. 2000, Lund, Sweden, 2000.
69. H. T. Chen, K. L. Wong, and T. W. Chiou, PIFA with a meandered and folded patch for the dual-band mobile phone application, *IEEE Trans. Anten. Propag.* **51(9)**:2468–2471 (2003).
70. A. Itakura, Y. Okano, and M. Abe, A study on double resonance H-type slot antenna, *Trans. IEICE* **J86-B(12)**:2533–2542 (2003).
71. H. Morishita and K. Fujimoto, A balance-fed loop antenna system for handsets, *Trans. IEICE* **E82-A(7)**:1138–1143 (1999).
72. K. Egawa, T. Oga, and H. Haruki, A development of built-in antenna for W-CDMA visual terminals, *2002 Int. Symp. on Anten. and Propag.* YRP, Japan, pp. 235–238.
73. T. Fukasawa, K. Kopydama, S. Makino, *Diversity Antenna for Portable Telephone with Two Boxes*, Tech. Report IEICE AP2002-78, 2002, pp. 87–90.

APERTURE ANTENNAS

DENNIS KOZAKOFF
Devry University
Alpharetta, Georgia

1. INTRODUCTION

Aperture antennas are most commonly used at microwave and the millimeter-wave frequencies. There are a large number of antenna types for which the radiated electromagnetic fields can be considered to emanate from a physical aperture. Antennas that fall into this category include reflector antennas, lenses, and horn antennas. The geometry of the aperture may be square, rectangular, circular, elliptical, or virtually any other shape. The term “aperture antenna” usually has more to do with the method used to analyze the antenna than the actual form of the antenna. For instance, array antennas viewed as a continuous field function bounded by a conducting screen can be considered to be an aperture antenna. This would encompass so-called planar (flat-plate) waveguide and microstrip arrays.

Aperture antennas are very popular for aerospace applications because they can be flush-mounted onto the spacecraft or aircraft surface. Their aperture opening can be covered with an electromagnetic (dielectric) window material that is transparent to the RF energy to protect the antenna from the environmental conditions [1]. This is known as a *radome*, and it is implemented so as not to disturb the aerodynamic profile of the vehicle, which is of special importance to high-speed aircraft or missiles.

In order to evaluate the distant (far-field) radiation patterns, it is necessary to know the surface currents that flow on the radiating surfaces of the antenna aperture. In many instances, these current distributions may not be known exactly and only approximate or experimental measurements can provide estimates. A technique based on the equivalence principle allows one to make reasonable approximations to the electromagnetic fields on, or in the vicinity of, the physical antenna aperture structure, which can then be used to compute far field antenna radiation patterns.

Field equivalence, first introduced by Schelkunoff [2], is a principle by which the actual sources on an antenna aperture are replaced by equivalent sources on an external closed surface that is physically outside the antenna aperture. The fictitious sources are said to be *equivalent* within a region because they produce the same fields within that region. Another key concept is Huygens’ principle [3], which states that the equivalent source at each point on the external surface is a source of a spherical wave. The secondary wavefront can be constructed as the envelope of these secondary spherical waves [4].

Using these principles, the electrical and/or magnetic fields in the equivalent aperture region can be determined with these straightforward, but approximate, methods. The fields elsewhere are assumed to be zero. In most applications, the closed surface is selected so that most of it coincides with the conducting parts of the physical antenna aperture structure. This is preferred because the

disappearance of the tangential electrical components over the conducting parts of the surface reduces the physical limits of integration. The formula to compute the fields radiated by the equivalent sources is exact, but it requires integration over the closed surface. The degree of accuracy depends on the knowledge of the tangential components of the electromagnetic fields over the closed surface.

Aperture techniques are especially useful for parabolic reflector antennas, where the aperture plane can be defined immediately in front of the reflector. Parabolic reflectors are usually electrically large. More surprisingly, aperture techniques can also be successfully applied to small-aperture waveguide horn antennas. However, for very small horn antennas with an aperture dimension of less than approximately one wavelength, the assumption of zero fields outside the aperture fails unless the horn is completely surrounded by a planar conducting flange [5]. In this section, the mathematical formulas will be developed to analyze the radiation characteristics of aperture antennas. Emphasis will be given to the rectangular and circular configurations because they are the most commonly used geometries. Because of mathematical complexities, the results will be restricted to the far-field region.

One of the most useful concepts is the far-field radiation pattern that can be obtained as a Fourier transform of the field distribution over the equivalent aperture, and vice versa. Fourier transform theory is extremely important to the analysis and synthesis of aperture antennas. Obtaining analytical solutions for many simple aperture distributions in order to design aperture antennas is useful. More complex aperture distributions, which do not lend themselves to analytical solutions, can be solved numerically. The increased capabilities of the personal computer (PC) have resulted in its acceptance as a conventional tool for the antenna designers. The Fourier transform integral is generally well behaved and does not present any fundamental computational problems.

Considering the use of the Fourier transform, first consider rectangular apertures in which one aperture dimension is large in wavelengths and the other is small in terms of wavelengths. This type of aperture is approximated as a line source and is treated with a one-dimensional Fourier transform [6]. For many kinds of rectangular aperture antennas such as horns, the aperture distributions in the two principal-plane dimensions are independent. These types of distributions are said to be separable. The total radiation pattern is the product of the pattern functions obtained from the one-dimensional Fourier transforms, which corresponds to the two principal-plane distributions.

If the rectangular aperture distribution cannot be separated, the directivity pattern is found in a similar manner to the line-source distribution, except that the aperture field is integrated over two dimensions rather than one dimension [7]. This double Fourier transform can also be applied to circular apertures.

For all aperture distributions, the following observations are made [8]:

1. A uniform amplitude distribution yields the maximum directivity (where nonuniform edge-enhanced

distributions for supergain are considered impractical), but at high sidelobe levels.

2. Tapering the amplitude at the center, from a maximum to a smaller value at the edges, will reduce the sidelobe levels compared with the uniform illumination, but it results in a larger (mainlobe) beamwidth and less directivity.
3. An inverse-taper distribution (amplitude depression at the center) results in a smaller (mainlobe) beamwidth but increases the sidelobe level and reduces the directivity when compared with the uniform illuminated case.
4. Depending on the aperture size in wavelengths and the phase errors, there is a frequency (or wavelength) for which the gain peaks, falling to smaller values as the frequency is either raised or lowered.

Finally, we consider aperture efficiencies. The *aperture efficiency* is defined as the ratio of the effective aperture area to the physical aperture area. The *beam efficiency* is defined as the ratio of the power in the mainlobe to the total radiated power. The maximum aperture efficiency occurs for a uniform aperture distribution, but maximum beam efficiency occurs for a highly tapered distribution. The aperture phase errors are the primary limitation of the efficiency of an antenna.

2. HUYGENS' PRINCIPLE

The principle proposed by Christian Huygens (1629–1695) is of fundamental importance to the development of wave theory [3]. Huygens' principle states that "Each point on a primary wavefront serves as the source of spherical secondary wavelets that advance with a speed and frequency equal to those of the primary wave. The primary wavefront at some time later is the envelope of all these wavelets" [9]. This is illustrated in Fig. 1 for spherical and

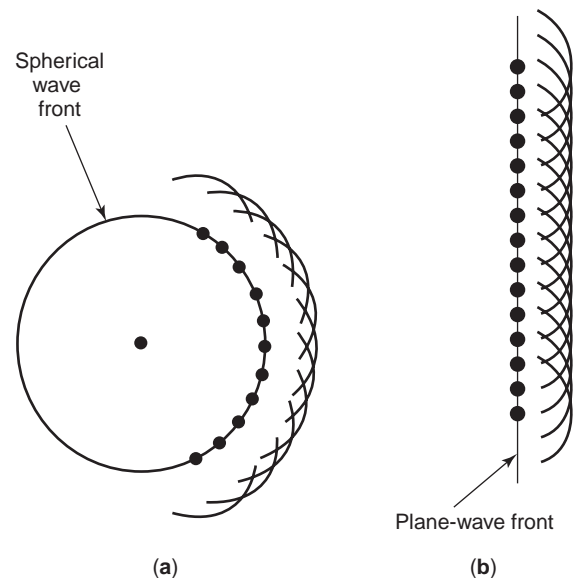


Figure 1. Spherical (a) planar and (b) wavefronts constructed with Huygens secondary waves.

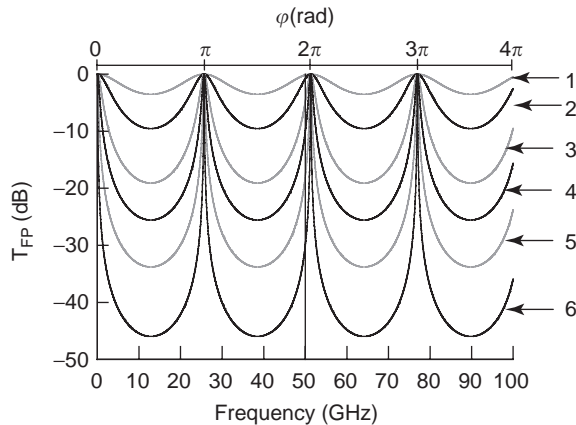


Figure 2. Diffraction of waves through a slit based on the Huygens principle.

plane waves modeled as a construction of Huygens' secondary waves. Actually, the intensities of the secondary spherical wavelets are not uniform in all directions but vary continuously from a maximum in the direction of wave propagation to a minimum of zero in the backward direction. As a result, there is no backward-propagating wavefront. The Huygens source approximation is based on the assumption that the magnetic and electric fields are related as a plane wave in the aperture region.

The situation shown in Fig. 2, shows an infinite electromagnetic plane wave incident on an infinite flat sheet that is opaque to the waves. This sheet has an opening that is very small in terms of wavelengths. Accordingly, the outgoing wave corresponds to a spherical wavefront propagating from a point source. That is, when an incoming wave comes against a barrier with a small opening, all except one of the effective Huygens point sources are blocked, and the energy coming through the opening behaves as a single point source. In addition, the outgoing wave emerges in all directions, instead of just passing straight through the slit.

On the other hand, consider an infinite plane electromagnetic wave incident on an infinite opaque sheet shown in Fig. 3 that has a larger opening of dimension a . The

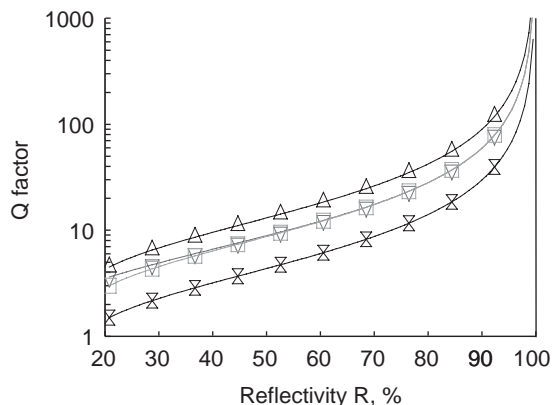


Figure 3. Plane wave incident on an opaque sheet with a slot of width a .

field everywhere to the right of the sheet is the result of the section of the wave that passes through this opening. If a is large in terms of wavelengths, the field distribution across the slot is assumed, as a first approximation, to be uniform. The total electromagnetic field at any point to the right of the opening is obtained by integrating the contributions from an array of Huygens sources distributed over the length a . We calculate the electric field at point P on a reference plane located at a distance R_0 from this opening by evaluating the integration of these Huygens sources [10]:

$$E = \int E_0 \frac{e^{-jkr}}{r} dy \quad (1)$$

For points near to the array, the integral does not simplify but can be reduced to the form of Fresnel integrals.

The actual evaluation of this integral is best achieved on a PC computer, which reduces the integral to a summation of N Huygens sources

$$E = \sum_{i=1}^N \frac{e^{-jkr_i}}{r_i} \quad (2)$$

where r_i is the distance from the i th source to point P . The field variation near the slot opening that is obtained in this way is commonly called a *Fresnel diffraction pattern* [4].

For example, let us consider the case in which the slot length a is 5 cm and the wavelength is 1.5 cm (corresponding to 20 GHz.) We can use Eq. (2) to compute the field along a straight line parallel to the slot. The field variation for $R_0 = 2.5$ cm shown in Fig. 4. For this case, R_0 is well within the near field (the so-called Fresnel region.) As we continue to increase R_0 , the shape of the field variation along this line continues to vary with increasing R_0 until we reach the far-field or Fraunhofer region (see the trends in Figs. 4b–4d). Once we have entered the Fraunhofer region, the pattern becomes invariant to range R_0 . For the distance to be in the far field, the following relationship must be met

$$R_0 \geq \frac{2a^2}{\lambda} \quad (3)$$

where a is the width of the slot and λ is the wavelength. Thus, the larger the aperture or the shorter the wavelength, the greater will be the distance at which the pattern must be measured if we wish to avoid the effects of Fresnel diffraction.

Huygens' principle is not without limitations as it neglects the vector nature of the electromagnetic field space. It also neglects the effect of the currents that flow at the slot edges. However, if the aperture is sufficiently large and we consider only directions roughly normal to the aperture, the scalar theory of Huygens' principle gives very satisfactory results.

Geometric optics (GO) techniques are commonly applied in reflector antennas to establish the fields in the reflector aperture plane. This procedure, referred to as

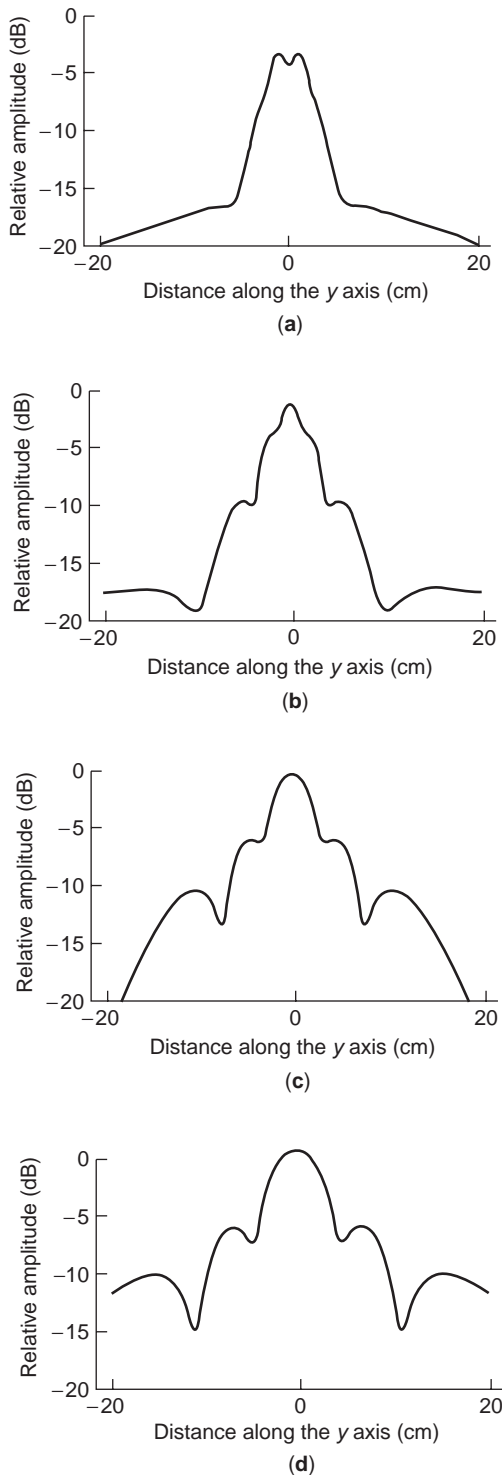


Figure 4. Electromagnetic field versus distance along the Y axis, with $R_0 = 2.5$ (a), 5(b), 15(c), and 20(d) cm.

the *aperture field method*, is employed as an alternative to the so-called induced-current method, which is based on an approximation for the electric current distribution on the reflector surface. The fields in the aperture plane can be thought of as an ensemble of Huygens sources. The radiation pattern can be computed via a numerical summation of these sources.

3. EQUIVALENCE PRINCIPLE

The ability to determine electromagnetic waves radiated fields via field equivalence principles is a useful concept, and the development can be traced by to Schelkunoff [2]. The equivalence principle often makes an exact solution easier to obtain or suggests approximate methods that are of value in simplifying antenna problems. Field equivalence principles are treated at length in the literature, and we will not consider the many variants here. The book by Collin and Zucker [11] is a useful source of reference. The basic concept is illustrated in Fig. 5, where the electromagnetic source region is enclosed by a surface S that is referred to as a *Huygens surface*.

In essence, Huygens' principle and the equivalence theorem shows how to replace actual sources by a set of equivalent sources spread over the surface S [12]. The equivalence principle is developed by considering a radiating source, electrically represented by current densities J_1 and M_1 . Assume that the source radiates fields E_1 and H_1 everywhere. We would like to develop a method that will yield the fields outside the closed surface. To accomplish this, a closed surface S is shown by the dashed lines that enclose the current densities J_1 and M_1 . The volume inside S is denoted by V . The primary task is to replace the original problem (Fig. 5a) by an equivalent one that will yield the same fields E_1 and H_1 (Fig. 5b). The formulation of the problem can be greatly facilitated if the closed surface is judiciously chosen so that the fields over most of—if not the entire—surface are known a priori.

The original sources J_1 and M_1 are removed, and we assume that there exists a field E, H inside V . For this field to exist within V , it must satisfy the boundary conditions on the tangential electric and magnetic field components on surface S . Thus on the imaginary surface S , there must exist equivalent sources [13]:

$$J_s = nx(H_1 - H) \tag{4}$$

$$M_s = -nx(E_1 - E) \tag{5}$$

These equivalent sources radiate into an unbounded space. The current densities are said to be equivalent

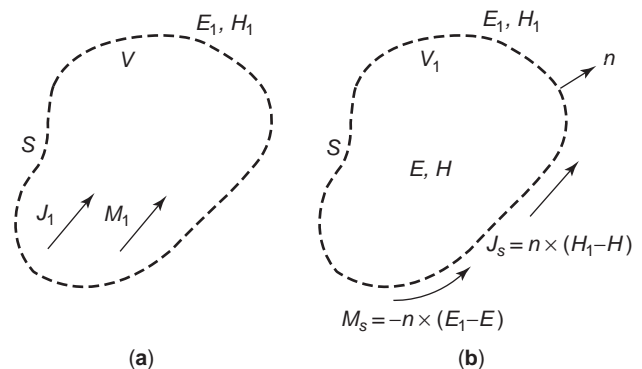


Figure 5. Equivalence principle with a closed Huygens surface S enclosing sources: (a) original problem; (b) equivalent problem.

only outside region V , because they produce the original field (E_1, H_1) . A field E or H , different from the original, may result within V .

The sources for electromagnetic fields are always electrical currents. However, the electrical current distribution is usually unknown. In certain structures, it may be a complicated function, particularly for slots, horns, reflectors, and lenses. With these types of radiators, the theoretical work is seldom based on the primary current distributions. Rather, the results are obtained with the aid of what is known as *aperture theory* [14]. This theory is based on the fact that an electromagnetic field in a source-free, closed region is completely determined by the values of tangential E or tangential H fields on the surface of the closed region. For exterior regions, the boundary condition at infinity may be employed to close the region. This is exemplified by the following case.

Without changing the E and H fields external to S , the electromagnetic source region can be replaced by a zero-field region with approximate distributions of electric and magnetic currents (J_s and M_s) on the Huygens surface. This example is overly restrictive and we could specify any field within S with a suitable adjustment. However, the zero-internal-field approach is particularly useful when the tangential electric fields over a surface enclosing the antenna are known or can be approximated. In this case, the surface currents can be obtained directly from the tangential fields, and the external field can be determined.

Assuming zero internal fields, we can consider the electromagnetic sources inside S to be removed, and the radiated fields outside S are then determined from the electric-magnetic surface current distributions alone. This offers significant advantages when the closed surface is defined as a *two-hemisphere region*, with all sources contained on only one side of the plane. If either the electric or magnetic field arising from these sources can be determined over the planar Huygens surface S , then the radiated fields on the far side of the plane can be calculated. The introduction of an infinite conducting sheet just inside of the Huygens surface here will not complicate the calculations of the radiated fields in the other half-space [15]. This infinite plane model is useful for antennas the radiation of which is directed into the right hemisphere (Fig. 6), and has found wide application in dealing with aperture antennas. For instance, if the antenna is a rectangular horn, it is assumed that the horn transitions into an infinite flange. All tangential fields outside the rectangular boundary along the infinite Huygens surface are taken to be zero.

When the limitations of the half-space model are acceptable, it offers the important advantage that either the electrical or magnetic currents need to be specified. However, knowledge of both is not required. It must be emphasized that any of the methods described before will produce exact results over the Huygens surface. In the analysis of electromagnetic problems, often it is easier to form equivalent problems that will yield the same solution only within a region of interest.

The steps that must be used to form an equivalent problem and solve an aperture antenna problem are as follows:

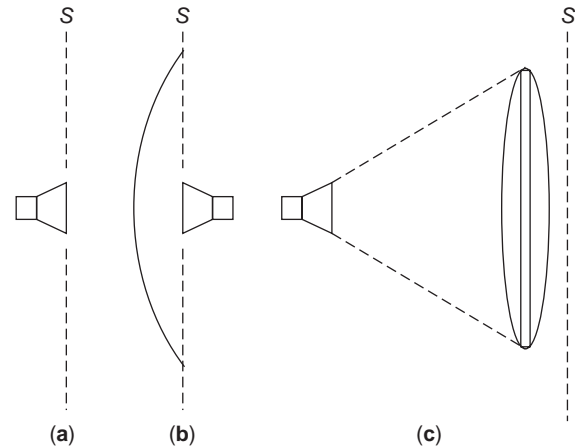


Figure 6. Some apertures yielding the same electromagnetic fields to the right side of the Huygens surface S : (a) horn; (b) parabola; (c) lens.

1. Select an imaginary surface that encloses the actual sources (the aperture). The surface must be judiciously chosen so that the tangential components of the electric field and/or the magnetic field are known, exactly or approximately, over its entire span. Ideally, this surface flat plane extending to infinity.
2. Over the imaginary surface S , form equivalent current densities J_s and M_s , assuming that the E and H fields within S are not zero.
3. Finally, solve the equivalent-aperture problem.

4. RECTANGULAR APERTURES

There are many kinds of antennas for which the radiated electromagnetic fields emanate from a physical aperture. This general class of antennas provides a very convenient basis for analysis that permits a number of well-established mathematical techniques to be applied and results in expressions for the distant radiation fields.

Horn and parabolic reflectors can be analyzed as aperture antennas. Incident fields are replaced by equivalent electric and magnetic currents. With use of vector potentials, the far fields are found as a superposition of each source. Generally, one can assume that the incident field is a propagating free-space wave, the electric and magnetic fields of which are proportional to each other. This will give the Huygens source approximation and allow us to use integrals of the electric field in the aperture plane. Each point in the aperture is considered as a source of radiation.

The first step involved in the analysis of aperture antennas is to calculate the electromagnetic fields over the aperture due to the sources on the rearward side of the infinite plane and to use these field distributions as the basis for the prediction of the distance fields on the forward half-space. The electromagnetic fields in the aperture plane cannot be determined exactly, but approximation distributions can be found by many different methods, which are dependent on the antenna. One can

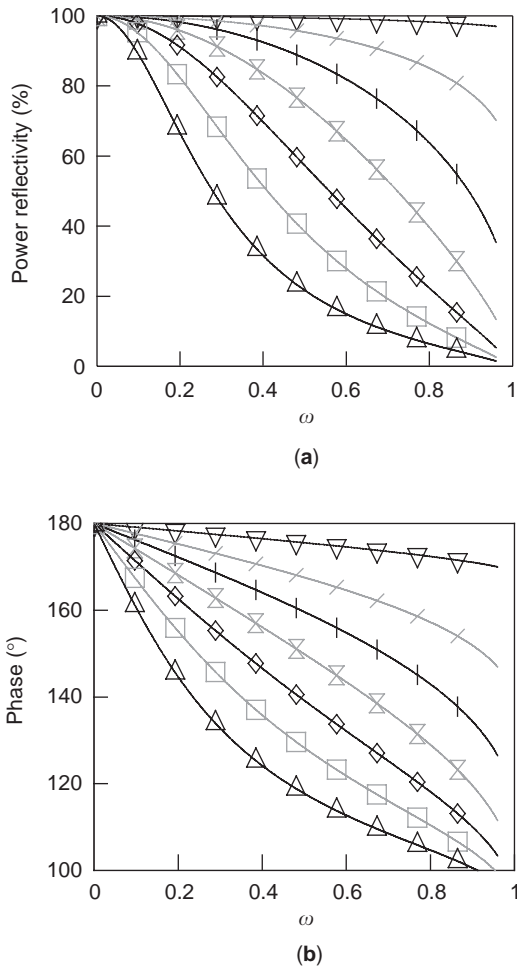


Figure 7. Coordinate system used to analyze a linear aperture of length L_w .

find the far-field radiation pattern for various distributions by, for instance, a Fourier transform relation.

Consider a line source of length L_w using the coordinate system illustrated in Fig. 7. Assume that the source is positioned in a ground plane of infinite extent. This model is simple and yet the analysis gives results that demonstrate the main features of the one-dimensional aperture. The line-source distribution does show a practical realization, namely, in a long one-dimensional geometry that has sufficient elements to enable it to be approximated by a continuous distribution. The applicable transform is [7,16]

$$E(\theta) = \int_{-\infty}^{\infty} E(x)e^{jkx \sin \theta} dx \tag{6}$$

and the inverse transform is

$$E(x) = \int_{-\infty}^{\infty} E(\sin \theta)e^{-jkx \sin \theta} d(\sin \theta) \tag{7}$$

where $k = 2\pi/\lambda$. For real values of θ , $-1 \leq \sin \theta \leq 1$, the distribution represents radiated power, while outside this region it represents reactive or stored power [17]. The field distribution $E(\sin \theta)$, or an angular spectrum, refers to a

distribution of plane waves. The angular spectrum finite aperture is the same as in the far-field pattern, $E(\theta)$. Now for a finite aperture, the Fourier integral representation [Eq. (6)] may be rewritten as [8] follows:

$$E(\theta) = \int_{-L_w/2}^{L_w/2} E(x)e^{jk \sin \theta} dx \tag{8}$$

For example, consider a so-called uniform distribution in which the amplitude is constant over the aperture region $-L_w/2 \leq x \leq L_w/2$:

$$E(x) = \frac{1}{L_w} \tag{9}$$

$E(x) = 0$ outside this region. The radiation pattern can be found by incorporating this into Eq. (8):

$$E(\theta) = \frac{1}{L_w} \int_{-L_w/2}^{L_w/2} e^{j2\pi x/\lambda \sin \theta} dx \tag{10}$$

We complete this straightforward integration and get the final result:

$$E(\theta) = \frac{\sin \frac{\pi L_w \sin \theta}{\lambda}}{\frac{\pi L_w \sin \theta}{\lambda}} \tag{11}$$

This $\sin(x)/x$ distribution is very important in antenna theory and is the basis for many practical antenna designs. It results in the narrowest radiation pattern beamwidth of any other distribution, but on the other hand has the highest first sidelobe level of -13.2 dB.

Another popular continuous aperture distribution is the cosine raised to a power n distribution. For all $-L_w/2 \leq x \leq L_w/2$, let

$$E(x) = \cos^n \frac{\pi x}{L_w} \tag{12}$$

and $E(x) = 0$ for all x outside this region. This popular distribution is illustrated in Fig. 8 for $n = 1, 2, 3$. To make a relative comparison of the two types of line-source

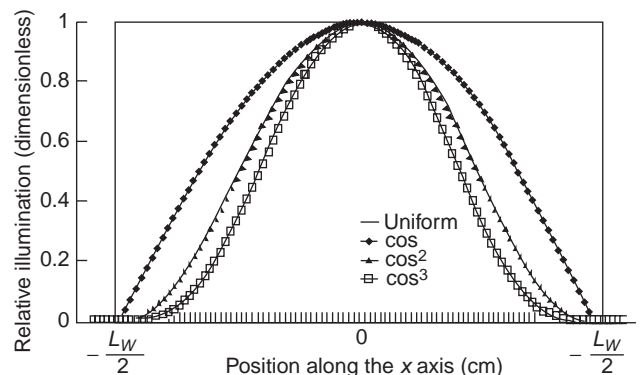


Figure 8. Some popular aperture distributions.

distribution discussed, we must first normalize the distributions to ensure that the total radiated power is the same relative to the uniform case. To do this, we multiply the radiation pattern expressions by the normalization constant:

$$C_p = \frac{1}{\int_{-L_w/2}^{L_w/2} E^2(x) dx} \quad (13)$$

To demonstrate, we computed the antenna radiation pattern for a one-meter-long line-source distribution for uniform, cosine, and cosine² distributions. For an assumed wavelength of 3 cm, the resulting antenna radiation patterns are shown in Fig. 9. These data indicate that the more heavily tapered the illumination, the greater the decrease in sidelobe levels, but this occurs for a penalty in reduced mainlobe directivity.

Many distributions actually obtained in practice can be approximated by one of the simpler forms or by a combi-

nation of simple forms. For example, a common linear aperture distribution is the cosine on a pedestal p :

$$E(x) = p + (1 - p) \cos \frac{\pi x}{L_w} \quad (14)$$

where $0 \leq p \leq 1$. This is a combination of a uniform plus a cosine-type distribution. The so-called triangular distribution is of interest

$$E(x) = 1 + \frac{x}{L_w/2} \quad (15)$$

for $-L_w/2 \leq x \leq 0$, and

$$E(x) = 1 - \frac{x}{L_w/2} \quad (16)$$

for $0 \leq x \leq L_w/2$.

In practice, the rectangular aperture is a common microwave antenna shape. Because of its configuration, the rectangular coordinate system shown in Fig. 10 is the

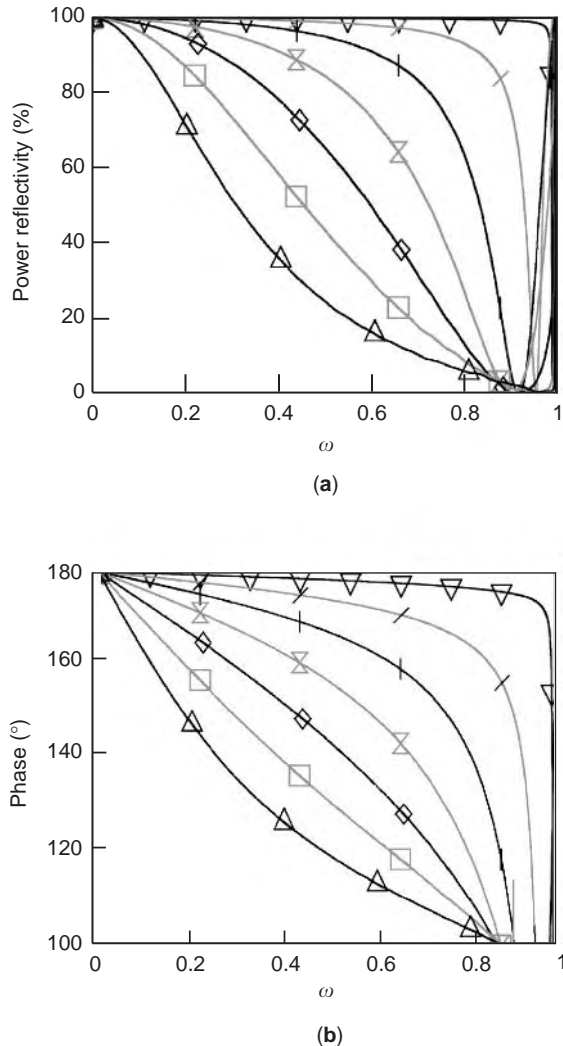


Figure 9. Radiation patterns of line sources for three different aperture distributions ($L_w = 1$ m, $\lambda = 3$ cm).

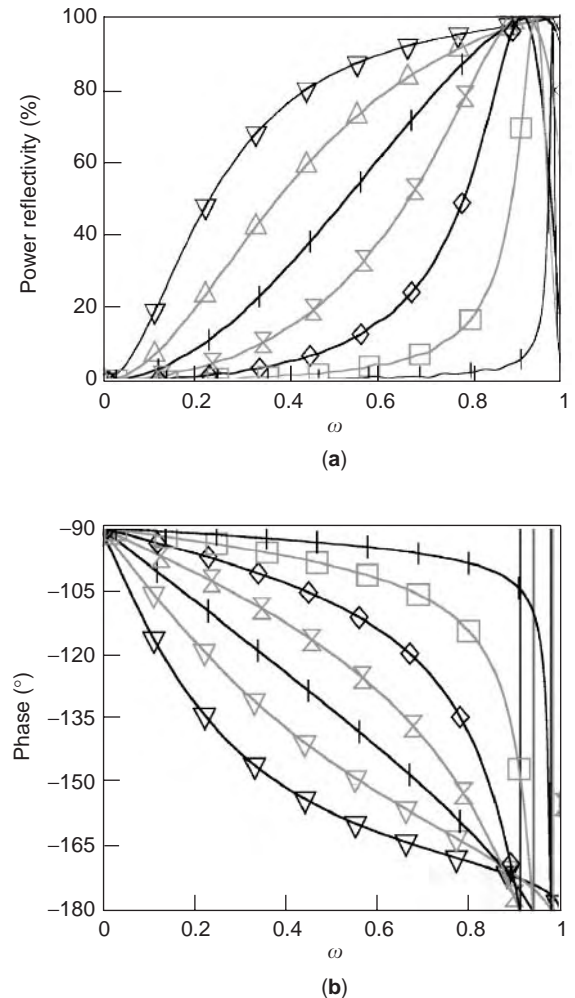


Figure 10. Coordinate system used to analyze rectangular aperture of dimensions $A_w B_w$.

most convenient system in which to express the electromagnetic fields at the aperture. Here, the aperture lies in the x - y plane and has a defined tangential aperture distribution $E(x,y)$. In keeping with the equivalence principle, we shall assume that the x - y plane is a closed surface that extends from $-\infty$ to $+\infty$ in the x - y plane. Outside the rectangular aperture boundaries we shall assume that the field distribution is zero for all points on the infinite surface. The task is then to find the fields radiated by the aperture; specifically, the pattern mainlobe beamwidths, the first sidelobe levels, and the directivity. Also shown in the figure is the superposition of a standard spherical coordinate system that will allow us to define a radiation pattern in terms of the two angle coordinates θ, ϕ .

Assuming a rectangular aperture of dimension A_w in the x plane and B_w in the y plane, the radiation pattern may then be obtained from the integral [18]

$$E(\theta, \phi) = \int_{-B_w/2}^{B_w/2} \int_{-A_w/2}^{A_w/2} E(x,y) e^{j(k_x x + k_y y)} dx dy \quad (17)$$

in which the directional wavenumbers are given by

$$k_x = k \sin \theta \cos \phi$$

$$k_y = k \sin \theta \sin \phi$$

These are also known as the x and y components of the propagation vector k [19].

For many types of antennas such as the rectangular horn antenna, the x and y functions are separable and may be expressed in the following form:

$$E(x,y) = E(x)E(y) \quad (18)$$

For these distributions, the pattern in the principal x - z plane can be determined from the line-source distribution $E(x)$ while the pattern in the y - z plane can be determined from the line-source distribution $E(y)$. We can illustrate this by assuming that both $E(x)$ and $E(y)$ are uniform distributions in which $E(x) = 1/A_w$ and $E(y) = 1/B_w$. We enter these into the Fourier transform relationship of Eq. (17) to get the following result:

$$E(\theta, \phi) = \frac{\sin \frac{k_x A_w}{2}}{\frac{k_x A_w}{2}} \frac{\sin \frac{k_y B_w}{2}}{\frac{k_y B_w}{2}} \quad (19)$$

From this pattern, we conclude that the principal plane radiation patterns of separable rectangular distributions correspond to the respective line-source distributions.

Next, we have applied this to an aperture size of $A_w = 75$ cm in the x dimension and $B_w = 125$ cm in the y dimension, an operating wavelength of 3 cm, and for simple cosine distributions in each plane. The results are plotted in Fig. 11, where it should be pointed out that $\phi = 0^\circ$ corresponds to the principal-plane radiation pattern in the x - z plane, $\phi = 90^\circ$ is the principal-plane pattern in the y - z plane, and $\phi = 45^\circ$ corresponds to the principal-plane

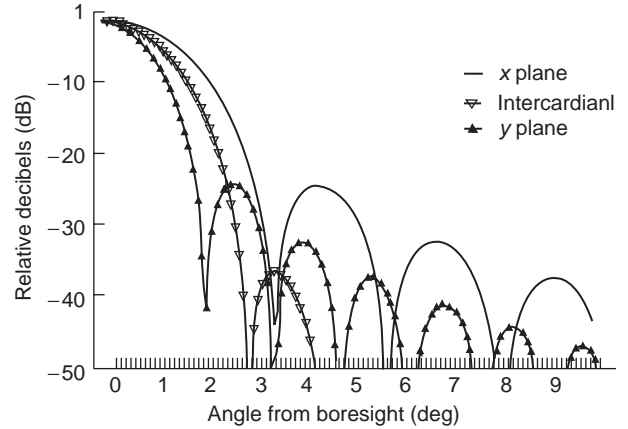


Figure 11. Radiation patterns for a rectangular aperture ($A_w = 75$ cm, $B_w = 125$ cm, $\lambda = 3$ cm).

pattern in the intercardinal plane. For nonseparable distributions, the integration of Eq. (17) is best carried out on a PC computer using numerical methods.

To generalize, we have applied a computer code to compute the secondary radiation patterns produced by uniform cosine raised to power n , cosine on a pedestal p , and triangular rectangular aperture distributions. The results shown in Table 1 compare the gain, mainlobe beamwidth, and the first sidelobe levels for each. All gain levels are compared with the uniform illumination case, and total radiated power is assumed in each case.

A uniform line-source or rectangular aperture distribution produces the highest directivity. However, the first sidelobe is only about -13.2 dB down. The results also show that the first sidelobe levels for a cosine illuminated aperture are -23 dB down but at a penalty of -0.91 dB in reduction of directivity compared to the uniform illuminated case. Other distributions have even lower first sidelobe levels but even greater reduction in directivity compared to the uniform illuminated case. Thus, aperture distributions used in practice must be a tradeoff or compromise between the desired directivity (or gain) and first sidelobe level.

5. CIRCULAR APERTURES

Circular aperture shape antennas form the largest single class of aperture antennas. For instance, the circular parabolic reflector is used extensively in satcom (satellite communications), terrestrial telecommunications, and radar applications.

The coordinate system used to analyze the radiation from a circular aperture of diameter D_w is the spherical coordinate system shown in Fig. 12, where the aperture lies in the x - y plane and radiation can be described in terms of the spherical coordinate components θ and ϕ . The radiation pattern from a circular aperture can be calculated by applying Huygens' principle in much the same way as we did for rectangular apertures. The simplest form of a circular aperture distribution is one in which the field does not vary with ϕ , that is, one that is rotationally

Table 1. Radiation Pattern Characteristics Produced by Various Linear Aperture Distributions

Distribution	Comments	Normalized Half-Power Beamwidth (deg) HPbw/K	Normalized Null-to-Null Beamwidth (deg) NULLbw*/K	Sidelobe Level (dB): SLL dB	Normalized Sidelobe Angle (deg) SLpos/K	Gain Relative to Uniform G_0 dB	Power Gain Factor Relative to Uniform G_0 power	Voltage Gain Factor Relative to Uniform G_0 volts
Uniform		50.67	114.67	-13.26	82.00	0.00	1.000	1.000
Cosine raised to power n	$n = 1$	68.67	172.00	-23.00	108.33	-0.91	0.810	0.900
	$n = 2$	82.67	229.33	-31.46	135.50	-1.76	0.666	0.816
	$n = 3$	95.33	286.67	-39.29	163.00	-2.40	0.576	0.759
	$n = 4$	106.00	344.00	-46.74	191.00	-2.89	0.514	0.717
	$n = 5$	116.67	402.00	-53.93	219.00	-3.30	0.468	0.684
Cosine on a pedestal p	$p = 0.0$	68.67	172.00	-23.01	108.33	-0.91	0.810	0.900
	$p = 0.1$	64.67	162.00	-23.00	98.00	-0.68	0.855	0.925
	$p = 0.2$	62.00	152.67	-21.66	97.00	-0.50	0.892	0.944
	$p = 0.3$	59.33	144.67	-20.29	93.67	-0.35	0.923	0.961
	$p = 0.4$	58.00	138.00	-18.92	90.67	-0.24	0.947	0.973
	$p = 0.5$	56.00	132.67	-17.65	88.33	-0.15	0.966	0.983
	$p = 0.6$	54.67	127.67	-16.53	86.67	-0.09	0.979	0.989
	$p = 0.7$	54.00	123.33	-15.55	85.00	-0.05	0.989	0.995
	$p = 0.8$	52.67	120.00	-14.69	83.83	-0.02	0.995	0.998
	$p = 0.9$	52.00	117.33	-13.93	82.67	-0.00	0.998	0.999
$p = 1.0$	50.67	114.67	-13.26	82.00	0.00	1.000	1.000	
Triangular		73.34	114.59	-26.52	164.00	-1.25	0.749	0.865

symmetric. This is not always true in practice; however, we will assume that to be the case here in order to demonstrate the methodology of analyzing circular apertures.

As was the case with rectangular apertures, a Fourier transform relationship exists between the antenna distribution and the far-field radiation pattern. For a circular symmetric aperture distribution, the radiation pattern can be written in normalized form [6]

$$E(u) = \frac{1}{\pi^3} \int_0^{2\pi} \int_0^\pi E(p) e^{jpu \cos(\phi - \phi')} p dp d\phi' \quad (20)$$

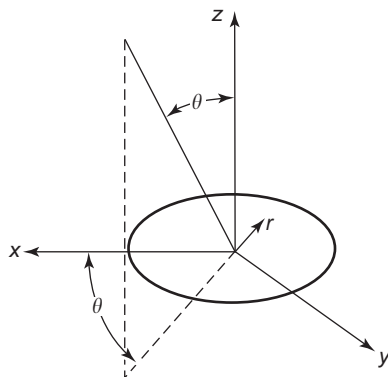


Figure 12. Coordinate system used to analyze a circular aperture of diameter D_w .

where

$$u = \frac{D_w \sin \theta}{\lambda}$$

and the normalized radius is

$$p = \frac{2\pi r}{D_w}$$

For a uniformly illuminated circular aperture, the normalized radiation pattern is expressed in terms of a first-order Bessel function

$$E(u) = \frac{2J_1(\pi u)}{\pi u} \quad (21)$$

which, in turn, can be expressed as

$$E(\theta) = \frac{2J_1 \frac{\pi D_w \sin \theta}{\lambda}}{\frac{\pi D_w \sin \theta}{\lambda}} \quad (22)$$

The uniformly illuminated circular aperture radiation pattern has a first sidelobe level of -17.6 dB compared with -13.2 dB for the uniformly illuminated rectangular aperture or line source. Other types of circular aperture distributions include the cosine raised to a power n

$$E(r) = \cos^n \frac{\pi r}{D_w} \quad (23)$$

where $0 \leq r \leq D_w/2$.

Table 2. Radiation Pattern Characteristics Produced by Various Circular Aperture Distributions

Distribution	Comments	Normalized Half-Power Beamwidth (deg) HPbw/K	Normalized Null-to-Null Beamwidth (deg) NULLbw*/K	Sidelobe Level (dB): SLL dB	Normalized Sidelobe Angle (deg) SLpos/K	Gain Relative to Uniform (dB) G_0 dB	Power Gain Factor Relative to Uniform G_0 power	Voltage Gain Factor Relative to Uniform G_0 volts
Uniform		59.33	140.00	-17.66	93.67	0.00	1.000	1.000
Cosine raised to power n	$n = 1$	74.67	194.67	-26.07	119.33	-1.42	0.721	0.849
	$n = 2$	88.00	250.00	-33.90	145.50	-2.89	0.514	0.717
	$n = 3$	99.33	306.67	-41.34	173.00	-4.04	0.394	0.628
	$n = 4$	110.00	362.67	-48.51	200.30	-4.96	0.319	0.564
	$n = 5$	120.00	420.00	-55.50	228.17	-5.73	0.267	0.517
Cosine on a pedestal p	$p = 0.0$	74.67	194.67	-26.07	119.33	-1.42	1.000	1.000
	$p = 0.1$	70.67	183.33	-25.61	112.67	-0.98	0.799	0.894
	$p = 0.2$	68.67	174.00	-24.44	107.83	-0.66	0.859	0.927
	$p = 0.3$	66.00	166.00	-23.12	104.17	-0.43	0.905	0.951
	$p = 0.4$	64.67	159.60	-21.91	101.33	-0.27	0.9388	0.9689
	$p = 0.5$	63.33	154.67	-20.85	99.47	-0.17	0.963	0.981
	$p = 0.6$	62.00	150.67	-19.95	97.83	-0.09	0.9789	0.9894
	$p = 0.7$	61.33	147.33	-19.18	96.47	-0.05	0.9895	0.9947
	$p = 0.8$	60.67	144.00	-18.52	95.27	-0.02	0.9958	0.9979
	$p = 0.9$	60.00	142.00	-17.96	94.57	-0.00	0.9991	0.9995
$p = 1.0$	59.33	140.00	-17.66	93.67	0.00	1.000	1.000	
Parabolic raised to power n	$n = 0$	59.33	140	-17.66	93.67	0.00	1.00	1.00
	$n = 1$	72.67	187.33	-24.64	116.33	-1.244	0.701	0.866
	$n = 2$	84.67	232.67	-30.61	138.67	-2.547	0.556	0.746
	$n = 3$	94.67	277.2	-35.96	160.17	-3.585	0.438	0.662
	$n = 4$	104.00	320.33	-40.91	181.33	-4.432	0.36	0.6

The so-called cosine on a pedestal p distribution is defined here as

$$E(r) = p + (1 - p) \cos \frac{\pi r}{D_w} \quad (24)$$

and the parabolic raised to a power n distribution is [15]

$$E(r) = \left[1 - \left(\frac{r}{D_w/2} \right)^2 \right]^n \quad (25)$$

To analyze the various circular aperture distributions, we can utilize a PC computer using numerical methods to perform the aperture integration of Eq. (20). To demonstrate the behavior of various distributions discussed, a computer code was applied to compute the secondary pattern characteristic produced by a uniform cosine raised to a power n , cosine on a pedestal p , and parabolic raised to power n distributions. The results shown in Table 2 compare the gain, beamwidth, and the first sidelobe levels of each. All gain levels are compared with the uniform illumination case.

6. BEAM EFFICIENCY

This discussion considers the effect of the aperture field distribution on the beam and aperture efficiencies. For many applications, the fraction of the total radiated energy that is in the main (null-to-null) antenna beam is important. This quantity, called the *beam efficiency* [20], can be used to judge the ability of the antenna to discriminate between signals received through its mainlobe and those through the minor lobes.

Before we delve into this subject, it is helpful to review some fundamentals. The mainbeam consists of the solid angle

$$\Omega_m = \theta_{hp} \phi_{hp} \quad (26)$$

where θ_{hp} and ϕ_{hp} are the half-power beamwidths of the mainlobes in the two principal planes, with minor lobes neglected. The total-beam solid angle Ω_a consists of the mainbeam solid angle plus the minor-lobe solid angle. Furthermore, the ratio of the mainbeam solid angle to the total-beam solid angle defines a property called the *beam efficiency* η_b :

$$\eta_b = \frac{\Omega_m}{\Omega_a} \quad (27)$$

In terms of the radiated intensity $E(\theta, \varphi)$ of a pencil beam with boresight at $(\theta = 0, \varphi = 0)$, the beam efficiency can be defined by [13]

$$\eta_b = \frac{\int_{-\theta_n/2}^{\theta_n/2} \int_{-\phi_n/2}^{\phi_n/2} E(\theta, \phi) E(\theta, \phi)^* \sin \theta d\phi d\theta}{\int_0^\pi \int_0^{2\pi} E(\theta, \phi) E(\theta, \phi)^* \sin \theta d\phi d\theta} \quad (28)$$

where θ_n and ϕ_n are the null-to-null beamwidths in the two principal planes. Also, $E(\theta, \varphi)^*$ denotes the conjugate of $E(\theta, \varphi)$.

The directivity of the aperture antenna can be expressed as

$$D = \frac{4\pi}{\Omega_a} = \frac{4\pi A_p}{\lambda^2} \quad (29)$$

where A_p is the physical area of the aperture. The *aperture efficiency* is defined as the ratio of the effective aperture area A_e to the physical aperture area, or

$$\eta_a = \frac{A_e}{A_p} \quad (30)$$

so that the ratio of the aperture and beam efficiencies is [8]

$$\frac{\eta_a}{\eta_m} = \frac{A_e \Omega_a}{A_p \Omega_m} \quad (31)$$

where Ω_m is the mainbeam solid angle and Ω_a is the total-beam solid angle, both of which are measured in steradians (sr). It is important to recognize, then, that the beam efficiency and aperture efficiency are related to each other.

In general, the aperture and beam efficiencies must be multiplied by a gain degradation factor due to phase errors within the aperture given by [21]

$$\eta_{pe} = e^{-(2\pi\delta/\lambda)^2} \quad (32)$$

where δ is the RMS phase error over the aperture. It is assumed that the correlation intervals of the deviations are greater than the wavelength. The controlling effect of tapers on the beam and aperture efficiencies tends to decrease them as the phase error increases. The efficiencies are also reduced by the presence of other phase errors.

The curves in Fig. 13 show that the beam efficiency tends to increase with an increase in taper but the aperture efficiency decreases. Maximum aperture efficiency occurs for a uniform aperture distribution, but maximum beam efficiency occurs for a highly tapered distribution. In most cases a taper is used that is intermediate between the two extremes.

7. APERTURE SYNTHESIS

To demonstrate the principles in aperture synthesis, consider a one-dimensional line source of length L_w . Earlier, in Eqs. (6) and (7), a Fourier transform pair was defined

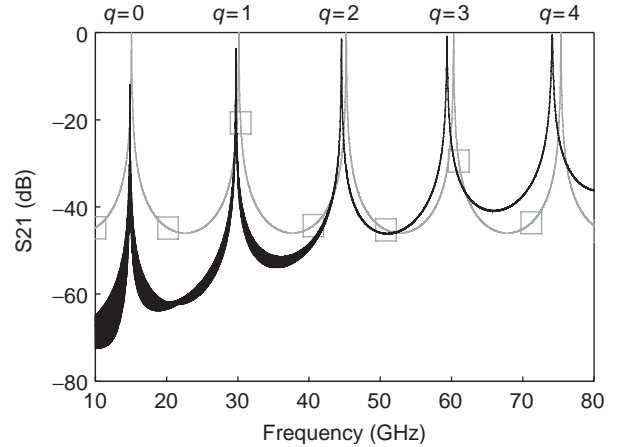


Figure 13. Form of beam and aperture efficiencies for an aperture as a function of taper.

relating the aperture distribution of a line source with the far-field radiation pattern. In the synthesis process, we wish to determine an aperture distribution that will result in a desired radiation that is not necessarily a symmetric beam; for instance, let us determine the well-known $\text{csc}^2\theta$ (cosecant² θ)-shaped beam used in a ground-mapping radar. In order to do this, we first express the illumination function as a sum of N uniform distributions that have relative weights c_m and a relative linear aperture phase function ϕ_m . This may be expressed mathematically as follows:

$$E(x) = \sum_{m=1}^N c_m e^{j\phi_m x} \quad (33)$$

The Fourier transform of this aperture distribution gives us an expression for the far-field radiation pattern:

$$E(\theta) = \int_{-L_w/2}^{L_w/2} \sum_{m=1}^N c_m e^{j(k \sin \theta + \phi_m)x} dx \quad (34)$$

which may be expressed in the form

$$E(\theta) = \sum_{m=1}^N c_m \frac{\sin\left((k \sin \theta + \phi_m) \frac{L_w}{2}\right)}{(k \sin \theta + \phi_m) \frac{L_w}{2}} \quad (35)$$

Thus, each coefficient c_m is responsible for a $(\sin x)/x$ type of beam, and there are N different beams. The coefficients may be obtained manually by estimating the number of independent beams and their relative magnitudes and positions in angle space needed to approximate the desired radiation pattern. The results may be extended by the reader to a two-dimensional aperture.

The preceding equations form the basis for Woodward's aperture synthesis technique [6,28], which quantifies the aperture illumination required to produce a given beam shape that is desired. Another antenna synthesis method

called the virtual array synthesis method was more recently published by Vaskelainen [22]. In this method, the geometry of the virtual array is chosen so that there will be a suitable synthesis method for that geometry, and the synthesis of the virtual array can be done accurately. The excitation values for the virtual array are transformed into the excitation values of the actual array geometry. Matrix operations are simple and large arrays can easily be synthesized. Further information on antenna pattern synthesis techniques is given in Refs. 23–27.

8. MODERN FULL-WAVE METHODS [29]

Some aperture antennas can be addressed with analysis approaches known as *full-wave methods*. The application of such methods has rapidly expanded with the explosion of high-power PC computers.

Analysis methods are called “full-wave” when they start with the fundamental equations of electromagnetics and discretize them such that they can be reduced to linear matrix equations suitable for solving by a computer. The advantage is that there are no approximations in principle, only the size of the discrete interval, which is usually between 10 and 20 intervals per wavelength. There are three primary full-wave methods used in electromagnetics: the finite-element method (FEM) [30–33], the method of moments (MoM) [34–36], and the finite-difference time-domain (FDTD) method [37,38]. The MoM discretizes Maxwell’s wave equations in their integral form, the finite-difference method (FDM) discretizes the equations in the differential form, and the FEM method discretizes the equations after casting them in a variational form. All three techniques have been applied to aperture antenna analysis [39–41].

The MoM method finds natural application to antennas because it is based on surfaces and currents, whereas the other two methods are based on volumes and fields. This means that for MoM, only the antenna aperture surface structure must be discretized and solved, whereas for FEM and FDTD, all volumes of interest must be discretized. For antenna radiation, the far field would require an inordinate amount of space were it not for the recent development of absorbing boundary conditions. These boundary conditions approximate the radiation conditions of infinite distance in the space very near the radiating structure.

The MoM works by solving for currents on all surfaces in the presence of a source current or field. The radiated field is then obtained by integration of these currents in much the same way as it was obtained in the physical optics (PO) approaches. Thus, the MoM can be applied to any aperture antenna that the PO technique can be applied to, unless the problem is too large for the available computer resources. Ensemble [42] is a commercially available software package that is a 2.5D (two and one-half-dimensional) MoM program used primarily for patch antennas or antennas that can be modeled as layers of dielectrics and conductors. If the top layer is a conductor with radiating holes, the holes are aperture antennas, which this program is designed to analyze.

There is another full-wave commercial software package that is widely used for aperture antenna problems: the high-frequency structure simulator (HFSS) [43]. This is a 3D FEM software package with extensive modeling and automatic meshing capability. It is best for horn antennas or other kinds of antennas formed by apertures in various nonlayered structures. The latest version uses the “perfectly matched layer” type of absorbing boundary conditions.

In practice, full-wave methods cannot be directly applied to high-gain aperture antennas such as reflectors or lenses without difficulties because these structures are usually many wavelengths in size, requiring a large amount of computational resources. Often, however, if there is symmetry in the problem that can be exploited, the number of unknowns for which to solve can be greatly reduced. For instance, a high-gain reflector antenna that has circular symmetry allows for body-of-revolution (BoR) symmetry [44,45] simplifications in the modeling. Similarly, a large lens requires a computer program with dielectric capability [46] in addition to BoR symmetry modeling.

BIBLIOGRAPHY

1. D. J. Kozakoff, *Analysis of Radome Enclosed Antennas*, Artech House, Norwood, MA, 1997.
2. S. A. Schelkunoff, Some equivalence theorems of electromagnetics and their application to radiation problems, *Bell Syst. Tech. J.*, **15**:92–112 (1936).
3. C. Huygens, *Traite de La Lumiere*, Leyden, 1690 (transl. into English by S. P. Thompson, Chicago, IL, Univ. Chicago Press, 1912).
4. J. D. Kraus and D. Fleisch, *Electromagnetics*, 5th ed., McGraw-Hill, New York, 1998.
5. C. A. Balanis, *Antenna Theory Analysis and Design*, Harper & Row, New York, 1982.
6. A. D. Oliver, Basic properties of antennas, in A. W. Rudge et al., eds., *The Handbook of Antenna Design*, IEE Electromagnetic Wave Series, Peter Peregrinus, Stevanage, UK, 1986, Chapter 1.
7. H. Jasik, Fundamentals of antennas, in R. C. Johnson, ed., *Antenna Engineering Handbook*, 3rd ed., McGraw-Hill, New York, 1993.
8. J. D. Kraus, *Antennas*, 2nd ed., McGraw-Hill, New York, 1988.
9. A. Sommerfeld, Theorie der Beugung, in P. Frank and R. von Mises, eds., *Die Differential und Integralgleichungen der Mechanik und Physik*, Vieweg, Braunschweig, Germany, 1935.
10. J. D. Kraus, *Radio Astronomy*, 2nd ed., Cygnus-Quasar Publishers, New York, 1956.
11. R. E. Collin and Z. J. Zucker, *Antenna Theory*, McGraw-Hill, New York, 1969.
12. W. L. Weeks, *Antenna Engineering*, McGraw-Hill, New York, 1968.
13. T. A. Milligan, *Modern Antenna Design*, McGraw-Hill, New York, 1985.
14. A. W. Rudge et al., *The Handbook of Antenna Design*, Peter Peregrinus, Stevanage, UK, 1986.
15. S. Silver, *Microwave Antenna Theory and Design*, McGraw-Hill, New York, 1949.

16. H. G. Booker and P. C. Clemmow, The concept of an angular spectrum of plane waves and its relation to that of polar diagram and aperture distribution, *Proc. IEEE* **97**:11–17 (1950).
17. D. R. Rhodes, The optimum line source for the best mean square approximation to a given radiation pattern, *IEEE Trans. Anten. Propag.* **AP-11**:440–446 (1963).
18. R. S. Elliot, *Antenna Theory and Design*, Prentice-Hall, Englewood Cliffs, NJ, 1987.
19. I. S. Sokolnikoff and R. M. Redhefer, *Mathematics of Physics and Modern Engineering*, McGraw-Hill, New York, 1958.
20. R. C. Hansen, Linear arrays, in A. W. Rudge et al., eds., *The Handbook of Antenna Design*, Peter Peregrinus, Stevanage, UK, 1986.
21. R. T. Nash, Beam efficiency limitations for large antennas, *IEEE Trans. Anten. Propag.* **AP-12**:918–923 (1964).
22. L. I. Vaskelainen, Virtual array synthesis method for planar array antennas, *IEEE Trans. Anten. Propag.* **46**:922–928 (1998).
23. R. J. Mailoux, *Phased Array Antenna Handbook*, Artech House, Norwood, MA, 1994.
24. E. Botha and D. A. McNamara, A contoured beam synthesis technique for planar antenna arrays with quadrantal and centro-symmetry, *IEEE Trans. Anten. Propag.* **41**:1222–1231 (1993).
25. B. P. Ng, M. H. Er, and C. Kot, A flexible array synthesis method using quadratic programming, *IEEE Trans. Anten. Propag.* **41**:1541–1550 (1993).
26. H. J. Orchard, R. S. Elliot, and G. J. Stern, Optimizing the synthesis of shaped beam antenna patterns, *IEEE Proc.* **132**(1):63–68 (1985).
27. R. F. E. Guy, General radiation pattern synthesis technique for array antennas of arbitrary configuration and element type, *Proc. IEEE* **135**(4):241–248 (1988).
28. P. M. Woodward, A method of calculating the field over a plane aperture required to produce a given polar diagram, *IEEE J.* **93**:1554–1558 (1947).
29. V. Tripp, *Full Wave Methods for Analysis of Aperture Antennas*, USDigiComm Corp., Stone Mountain, GA, 2003.
30. J. L. Volakis, A. Chatterjee, and L. C. Kempel, *Finite Element Methods for Electromagnetics*, IEEE Press, New York and Oxford Univ. Press, London, 1998.
31. P. P. Sylvester, G. Pelosi, ed., *Finite Elements for Wave Electromagnetics: Methods and Techniques*, IEEE Press, New York, 1994.
32. P. P. Sylvester and R. L. Ferrari, *Finite Elements for Electrical Engineers*, Cambridge Univ. Press, New York, 1992.
33. J. Jin, *The Finite Element Method in Electromagnetics*, Wiley-Interscience, New York, 1993.
34. R. F. Harrington, *Field Computation by Moment Methods*, Macmillan, New York, 1968.
35. E. K. Miller, L. Medgyesi-Mitschang, and E. H. Newman, eds., *Computational Electromagnetics, Frequency Domain Method of Moments*, IEEE Press, New York, 1992.
36. R. C. Hansen, ed., *Moment Methods in Antennas and Scattering*, Artech House, Norwood, MA, 1990.
37. A. Taflov, *Computational Electromagnetics: The Finite Difference Time Domain Method*, Artech House, Norwood, MA, 1995.
38. K. S. Kunz and R. J. Luebbers, *The Finite Difference Time Domain Method for Electromagnetics*, CRC Press, Cleveland, OH, 1993.
39. D. Chun, R. N. Simons, and L. P. B. Kotehi, Modeling and characterization of cavity backed circular aperture antenna with suspended stripline probe feed, *IEEE Antennas Propagation Soc. Int. Symp. 2000 Digest*, Salt Lake City, UT, 2000.
40. J. Y. Lee, T. S. Horng, and N. G. Alexopoulos, Analysis of cavity backed aperture antennas with a dielectric overlay, *IEEE Trans. Anten. Propag.* **42**(11):1556–1562 (Nov. 1994).
41. D. Sullivan and J. L. Young, Far-field time-domain calculation from aperture radiators using the FDTD method, *IEEE Trans. Anten. Propag.* **49**(3), 464–469 (March 2001).
42. Ensemble Software, version 6.1, Ansoft Corp., Four Station Square, Suite 200, Pittsburgh, PA 15219, Tel: 412-261-3200.
43. Ansoft Corp., Four Station Square, Suite 200, Pittsburgh, PA 15219, Tel: 412-261-3200.
44. Z. Altman and R. Mittra, Combining an extrapolation technique with the method of moments for solving large scattering problems involving bodies of revolution, *IEEE Trans. Anten. Propag.* **44**(4), 548–553 (April 1996).
45. A. D. Greenwood and J. M. Jin, Finite element analysis of complex axisymmetric radiating structures, *IEEE Trans. Anten. Propag.* **47**(8), 1260 (Aug. 1999).
46. J. M. Putnam and L. N. Medgyesi-Mitschang, Combined field integral equation for inhomogeneous two- and three-dimensional bodies: The junction problem, *IEEE Trans. Anten. Propag.* **39**(5), 667–672 (May 1991).

FURTHER READING

- C. A. Balanis, *Antenna Theory Analysis and Design*, Harper & Row, New York, 1982.
- E. T. Bayliss, Design of monopulse difference patterns with low sidelobes, *Bell Syst. Tech. J.* **47**, 623–650 (1968).
- R. N. Bracewell, Tolerance theory of large antennas, *IRE Trans. Anten. Propag.* **AP-9**, 49–58 (1961).
- W. N. Christiansen and J. A. Hogbom, *Radiotelescopes*, Cambridge Univ. Press, Cambridge, UK, 1985.

APPLICATION OF WAVELETS TO ELECTROMAGNETIC PROBLEMS

JAIDEVA C. GOSWAMI
Schlumberger Technology
Corporation
Sugar Land, Texas
MANOS M. TENTZERIS
Georgia Institute of Technology
Atlanta, Georgia

1. INTRODUCTION

Since the early nineteenth century, Fourier analysis has played an important role in almost all branches of science and engineering and in some areas of social science as well. In this method a function is transformed from one domain to another where many characteristics of the function are revealed. One usually refers to this transform

domain as the *spectral, frequency, or wavenumber* domain, while the original domain is referred to as *time or spatial domain*. In many applications, combined time–frequency analysis of a signal provides useful information about the physical phenomena; information that could not be extracted by either the time-domain or the frequency-domain analyses. For instance, in applications to identification and classification of targets based on the analysis of radar echo, time-domain scattering center analysis [1,2] provides information about the local features of the scatterer since these features appear as short timepulses. Frequency-domain analysis of radar echo using the singularity expansion method [3,4] provides information about the global features of the target. The combined time–frequency analysis can provide additional information, such as the dispersive nature of the target [5,6] and the dispersive nature of propagation in a transmission line [7].

Another area of interest to the electromagnetics community concerns solving boundary value problems arising from scattering and propagation of electromagnetic waves. Two of the main properties of wavelets vis-à-vis boundary value problems are their hierarchical nature and the vanishing moments properties. Because of their hierarchical (multiresolution) nature, wavelets at different resolutions (scales) are interrelated, a property that makes them suitable candidates for multigrid-type methods for solving partial-differential equations. On the other hand, the vanishing-moment property, causing wavelets, when integrated against a function of certain order, to render the integral zero, is attractive in sparsifying a dense matrix generated by an integral equation.

In applications to discrete datasets, wavelets may be considered as basis functions generated by dilations and translations of a single function. Analogous to Fourier analysis, there are wavelet series (WS) and integral wavelet transforms (IWTs). In wavelet analysis, WS and IWT are intimately related. The IWT of a finite-energy function on the real line evaluated at certain points in the timescale domain gives the coefficients for its wavelet series representation. No such relation exists between Fourier series and Fourier transform, which are applied to different classes of functions; the former is applied to finite-energy periodic functions, whereas the latter is applied to functions that have finite energy over the real line. Furthermore, Fourier analysis is global in the sense that each frequency (time) component of the function is influenced by all the time (frequency) components of the function. On the other hand, wavelet analysis is a local analysis. This local nature of wavelet analysis makes it suitable for time–frequency analysis of signals.

Wavelet techniques enable us to divide a complicated function into several simpler ones and study them separately. This property, along with fast wavelet algorithms that are comparable in efficiency to fast Fourier transform algorithms, makes these techniques very attractive in analysis and synthesis problems.

In this article we discuss some wavelet applications to electromagnetic problems. The organization of this article

is as follows. In the next section we give an overview of wavelet theory. Sections 3 to 6 deal with solution of integral equations arising from electromagnetic scattering and transmission-line problems. Differential equations, especially the multiresolution time-domain method, are considered in Section 7. Readers may refer to the literature [5–7] for time-frequency analysis of electromagnetic data.

2. WAVELET PRELIMINARIES

In this section we briefly describe the basics of wavelet theory to facilitate subsequent discussion on its application. More details on the topic may be found in the literature [8–16].

2.1. Multiresolution Analysis

As pointed out before, multiresolution analysis (MRA) plays an important role in the application of wavelets to boundary value problems. In order to achieve MRA we must have a finite-energy function (square integrable on the real line) $\phi(x) \in L^2(\mathbb{R})$, called a *scaling function*, that generates a nested sequence of subspaces

$$\{0\} \leftarrow \cdots \subset V_{-1} \subset V_0 \subset V_1 \subset \cdots \rightarrow L^2 \tag{1}$$

and satisfies the dilation (refinement) equation, namely

$$\phi(x) = \sum_k p_k \phi(2x - k) \tag{2}$$

with $\{p_k\}$ belonging to the set of square summable biinfinite sequences. The number 2 in (2) signifies “octave levels.” In fact, this number could be any rational number, but we will discuss only octave levels or scales. From (2) we see that the function $\phi(x)$ is obtained as a linear combination of a scaled and translated version of itself, and hence the term *scaling function*.

The subspaces V_j are generated by $\phi_{j,k}(x) := 2^{j/2} \phi(2^j x - k)$; $j, k \in \mathbb{Z}$, where $\mathbb{Z} := \{\dots, -1, 0, 1, \dots\}$. For each scale j , since $V_j \subset V_{j+1}$, there exists a complementary subspace W_j of V_j in V_{j+1} . This subspace W_j , called “wavelet subspace,” is generated by $\psi_{j,k}(x) := 2^{j/2} \psi(2^j x - k)$, where $\psi \in L^2$ is called the “wavelet.” From the discussion above, these results follow easily:

$$\begin{cases} V_{j_1} \cup W_{j_1} = V_{j_2} & j_2 = j_1 + 1 \\ V_{j_1} \cap V_{j_2} = V_{j_2} & j_1 > j_2 \\ W_{j_1} \cap W_{j_2} = \{0\} & j_1 \neq j_2 \\ V_{j_1} \cap W_{j_2} = \{0\} & j_1 \leq j_2 \end{cases} \tag{3}$$

The scaling function ϕ exhibits lowpass filter characteristics in the sense that $\hat{\phi}(0) = 1$, where a hat over the function denotes its Fourier transform. On the other hand, the wavelet function ψ exhibits bandpass filter characteristic in the sense that $\hat{\psi}(0) = 0$. Later in the article, we will see some examples of wavelets and scaling functions.

2.2. Properties of Wavelets

Some of the important properties that we will discuss in this article are given below:

- *Vanishing moment*—a wavelet is said to have a vanishing moment of order m if

$$\int_{-\infty}^{\infty} x^p \psi(x) dx = 0; \quad p = 0, \dots, m-1 \quad (4)$$

All wavelets must satisfy this condition for $p=0$.

- *Orthonormality*—the wavelets $\{\psi_{j,k}\}$ form an orthonormal basis if

$$\langle \psi_{j,k}, \psi_{l,m} \rangle = \delta_{j,l} \delta_{k,m}; \quad \text{for all } j, k, l, m \in \mathbb{Z} \quad (5)$$

where $\delta_{p,q}$ is the Krönercker delta defined in the usual way as

$$\delta_{p,q} = \begin{cases} 1 & p=q \\ 0 & \text{otherwise} \end{cases} \quad (6)$$

The inner product $\langle f_1, f_2 \rangle$ of two square integrable functions f_1 and f_2 is defined as

$$\langle f_1, f_2 \rangle := \int_{-\infty}^{\infty} f_1(x) f_2^*(x) dx$$

with $f_2^*(x)$, representing the complex conjugation of f_2 .

- *Semiorthogonality*—The wavelets $\{\psi_{j,k}\}$ form a semiorthogonal basis if

$$\langle \psi_{j,k}, \psi_{l,m} \rangle = 0; \quad j \neq l; \quad \text{for all } j, k, l, m \in \mathbb{Z} \quad (7)$$

2.3. Wavelet Transform Algorithm

Given a function $f(x) \in L^2$, the decomposition into various scales begins by mapping the function into a sufficiently high-resolution subspace V_M :

$$L^2 \ni f(x) \mapsto f_M = \sum_k a_{M,k} \phi(2^M x - k) \in V_M \quad (8)$$

Now since

$$\begin{aligned} V_M &= W_{M-1} + V_{M-1} \\ &= W_{M-1} + W_{M-2} + V_{M-2} \\ &= \sum_{n=1}^N W_{M-n} + V_{M-N}, \end{aligned} \quad (9)$$

we can write

$$f_M(x) = \sum_{n=1}^N g_{M-n}(x) + f_{M-N}(x) \quad (10)$$

where $f_{M-N}(x)$ is the coarsest approximation of $f_M(x)$ and

$$f_j(x) = \sum_k a_{j,k} \phi(2^j x - k) \in V_j \quad (11)$$

$$g_j(x) = \sum_k w_{j,k} \psi(2^j x - k) \in W_j \quad (12)$$

If the scaling functions and wavelets are orthonormal, it is easy to obtain the coefficients $\{a_{j,k}\}$ and $\{w_{j,k}\}$. However for the semiorthogonal case, we need a dual scaling function ($\tilde{\phi}$) and dual wavelet ($\tilde{\psi}$). Dual wavelets satisfy the ‘‘biorthogonality condition’’:

$$\langle \psi_{j,k}, \tilde{\psi}_{l,m} \rangle = \delta_{j,l} \cdot \delta_{k,m}, \quad j, k, l, m \in \mathbb{Z} \quad (13)$$

For the semiorthogonal case, both ψ and $\tilde{\psi}$ belong to the same space W_j for an appropriate j ; likewise ϕ and $\tilde{\phi}$ belong to V_j . One difficulty with semiorthogonal wavelets is that their duals do not have compact support. We can achieve compact support for both $\tilde{\phi}$ and $\tilde{\psi}$ if we forgo the orthogonality requirement that $V_j \perp W_j$. In such a case we get ‘‘biorthogonal wavelets’’ [17] and two MRAs, $\{V_j\}$ and $\{\tilde{V}_j\}$. In this article we will discuss application of orthonormal and semiorthogonal wavelets only.

3. INTEGRAL EQUATIONS

Integral equations appear frequently in practice, particularly the first-kind integral equations [18] in inverse problems. These equations can be represented as

$$L_K f = \int_a^b f(x') K(x, x') dx' = g(x) \quad (14)$$

where $f(x)$ is an unknown function, $K(x, x')$ is the known kernel that might be the system impulse response or Green’s function, and $g(x)$ is the known response function.

3.1. Electromagnetic Scattering

Consider the problem of electromagnetic scattering by an infinitely long metallic cylinder, as shown in Fig. 1. For such a problem, electric surface current J_{sz} is related to the incident electric field via an integral equation

$$j\omega\mu_0 \int_C J_{sz}(l') G(l, l') dl' = E_z^i(l) \quad (15)$$

where

$$G(l, l') = \frac{1}{4j} H_0^{(2)}(k_0 |\rho(l) - \rho(l')|) \quad (16)$$

with the wavenumber $k_0 = 2\pi/\lambda_0$. The electric field E_z^i is the z component of the incident electric field and $H_0^{(2)}$ is the second-kind Hankel function of order 0, and λ_0 is the wavelength in free space. Here, the contour of integration has been parameterized with respect to the chord length.

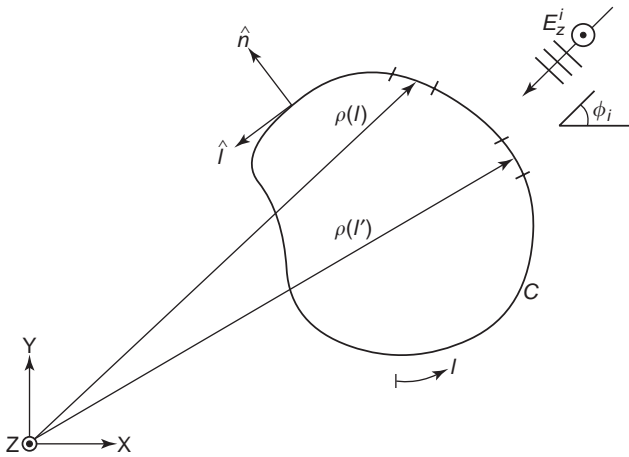


Figure 1. Cross section of an infinitely long metallic cylinder illuminated by a TM plane wave.

The field component E_z^i can be expressed as

$$E_z^i(l) = E_0 \exp[jk_0(x(l) \cos \phi_i + y(l) \sin \phi_i)] \quad (17)$$

where ϕ_i is the angle of incidence.

Scattering from a thin perfectly conducting strip, as shown in Fig. 2a, gives rise to an equation similar to (15). For this case, we have

$$\int_{-h}^h J_{sy}(z') G(z, z') dz' = E_y^i(z) \quad (18)$$

where $G(z, z')$ is as given by (16).

As a final example of the scattering problem, consider scattering from a thin wire as shown in Fig. 2b. Here the current on the wire and the incident field are related to each other as

$$\int_{-l}^l I(z') K_w(z, z') dz' = -E^i(z) \quad (19)$$

where the kernel K_w is given by

$$K_w(z, z') = \frac{1}{4\pi j \omega \epsilon_0} \frac{\exp(-jk_0 R)}{R^5} \times [(1 + jk_0 R) \times (2R^2 - 3a^2) + k_0^2 a^2 R^2] \quad (20)$$

$$E^i(z) = E_0 \sin \theta \exp(jk_0 z \cos \theta) \quad (21)$$

This kernel is obtained by interchanging integration and differentiation in the integrodifferential form of Pocklington's equation and using the reduced kernel distance $R = [a^2 + (z - z')^2]^{1/2}$, where a is the radius of the wire [19].

All the equations described thus far have the form of a first-kind integral equation, namely

$$\int_a^b f(x') K(x, x') dx' = g(x) \quad (22)$$

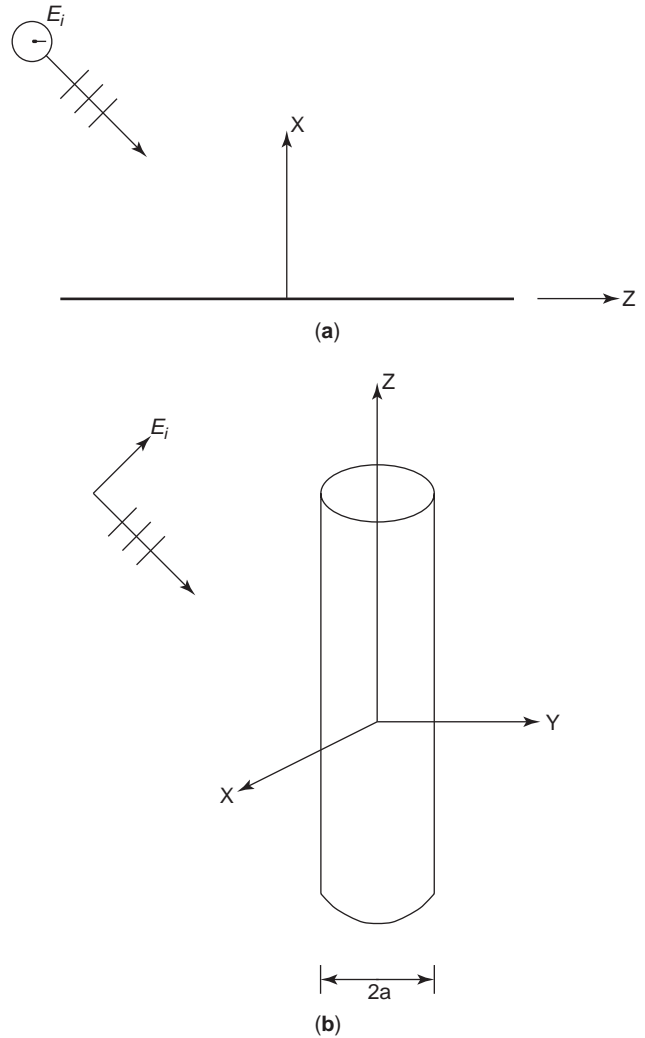


Figure 2. (a) A thin half-wavelength-long metallic strip illuminated by a TM wave; (b) a thin wire of length $l/2$ and thickness $l/1000$ illuminated by a plane wave.

where f is the unknown function and the kernel K and the functions g are known. Here the objective is to reconstruct the function f from a set of known data (possibly measured) g . The kernel K may be regarded as the impulse response function of the system.

Although we discuss the solution technique for first-kind integral equations only, the method can be extended to second-kind equations [20,21] and higher-dimensional integral equations [22].

3.2. Transmission-Line Discontinuity

As an example of electromagnetic propagation in a transmission line, consider the problem of characterizing one discontinuity of a coplanar waveguide, shown in Fig. 3. The problem can be formulated by separating the configuration of Fig. 3a into two parts with the help of the equivalence principle [23], according to which the slot regions can be replaced by equivalent surface magnetic

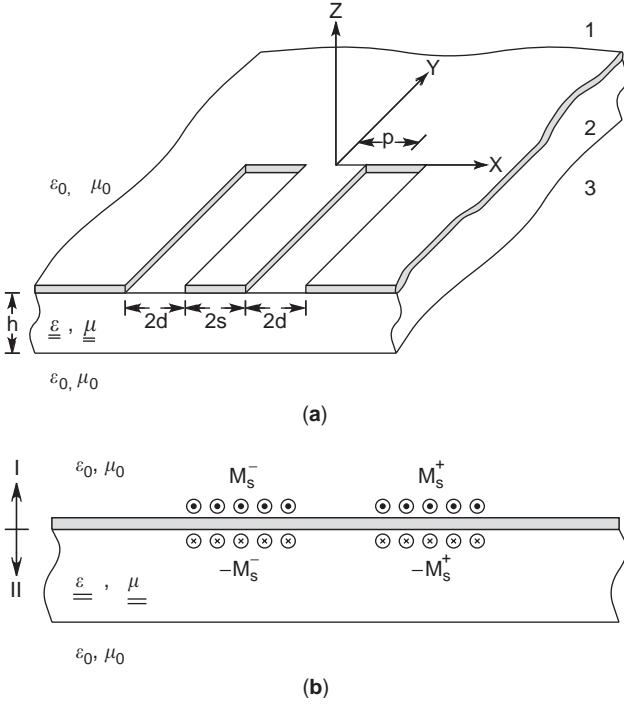


Figure 3. (a) Short-circuited coplanar waveguide with uniaxial substrate; (b) equivalent problem.

current, namely

$$\mathbf{M}_s(\mathbf{r}) = \mathbf{E}(\mathbf{r}) \times \hat{\mathbf{z}}; \quad \mathbf{r} \in \mathcal{D} := \mathcal{D}^+ \cup \mathcal{D}^- \quad (23)$$

where $\mathcal{D}^+ := \{x, y, z \mid x \in (s, s + 2d), y \in (-\infty, 0], z = 0\}$, and $\mathcal{D}^- := \{x, y, z \mid x \in (-s, -s - 2d), y \in (-\infty, 0], z = 0\}$. Then we can write the magnetic field integral equation by enforcing the boundary condition

$$\hat{\mathbf{z}} \times \mathbf{H}(\mathbf{r}) = 0; \quad \mathbf{r} \in \mathcal{D} \quad (24)$$

with $\mathbf{H}(\mathbf{r}) = \mathbf{H}_1(\mathbf{r}) - \mathbf{H}_2(\mathbf{r})$. The magnetic field is given by

$$\begin{aligned} \mathbf{H}(\mathbf{r}) &= \int_{\mathcal{D}^+} \underline{\mathbf{G}}^{HM}(\mathbf{r}, \mathbf{r}') \cdot \mathbf{M}_s^+(\mathbf{r}') d\mathbf{r}' \\ &+ \int_{\mathcal{D}^-} \underline{\mathbf{G}}^{HM}(\mathbf{r}, \mathbf{r}') \cdot \mathbf{M}_s^-(\mathbf{r}') d\mathbf{r}' \end{aligned} \quad (25)$$

$$\underline{\mathbf{G}}^{HM}(\mathbf{r}, \mathbf{r}') = \underline{\mathbf{G}}^{HM,I}(\mathbf{r}, \mathbf{r}') + \underline{\mathbf{G}}^{HM,II}(\mathbf{r}, \mathbf{r}') \quad (26)$$

where the superscripts I and II denote two half-spaces (see Fig. 3b). Details on solving discontinuity problem using wavelets in spectral domain may be found in Ref. 22.

4. MATRIX EQUATION GENERATION

In this section, we will attempt to solve integral equations discussed in the last section. The first step in solving any integral or differential equation is to convert these into a matrix equation to be solved for the unknown coefficients.

The goal is to transform Eq. (14) into a matrix equation

$$\mathbf{Z}i = v \quad (27)$$

where \mathbf{Z} is a two-dimensional matrix, sometimes referred to as the *impedance matrix*, i is the column vector of unknown coefficients to represent f , and v is another column vector related to g . Computation time depends largely on the way we obtain and solve (27). In the following section we describe conventional and wavelet basis functions that are used to represent the unknown function.

4.1. Conventional Basis Functions

The unknown function $f(x)$ can be written as

$$f(x) = \sum_n i_n b_n(x) \quad (28)$$

where $\{b_n\}$ form a complete set of basis functions. These bases may be “global” (entire-domain), extending the entire length $[a, b]$ or be “local” (subdomain), covering only a small segment of the interval, or a combination of both. Some of the commonly used subdomain basis functions are shown in Fig. 4.

For an exact representation of $f(x)$, we may need an infinite number of terms in the series presented above. However, in practice, a finite number of terms suffice for a given acceptable error. Substituting the series representation of $f(x)$ into the original equation (14), we get

$$\sum_{n=1}^N i_n L_K b_n \approx g \quad (29)$$

For the present discussion we will assume N to be large enough that this representation is exact. Now by taking the inner product of (29) with a set of *weighting functions* or *testing functions* $\{t_m; m = 1, \dots, M\}$, we get a set of linear equations

$$\sum_{n=1}^N i_n \langle t_m, L_K b_n \rangle = \langle t_m, g \rangle; \quad m = 1, \dots, M \quad (30)$$

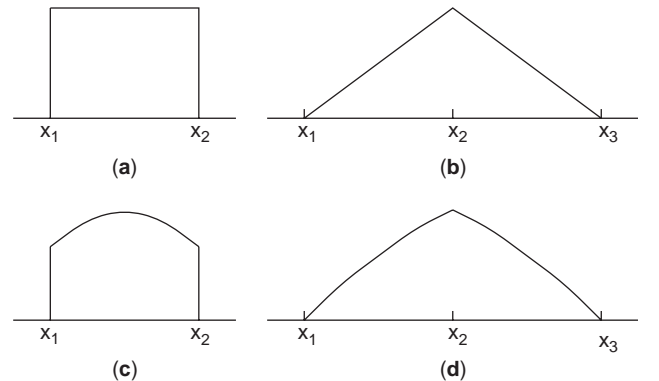


Figure 4. Typical subdomain basis functions: (a) piecewise constant, (b) piecewise linear, (c) piecewise cosine, and (d) piecewise sine functions.

which can be written in the matrix form as

$$[Z_{mn}][i_n] = [v_m] \tag{31}$$

where

$$Z_{mn} = \langle t_m, L_K b_n \rangle; \quad m = 1, \dots, M; \quad n = 1, \dots, N$$

$$v_m = \langle t_m, g \rangle; \quad m = 1, \dots, M$$

The solution of the matrix equation gives the coefficients $\{i_n\}$ and thereby the solution of the integral equations. Two main choices of the testing functions are (1) $t_m(x) = \delta(x - x_m)$, where x_m is a discretization point in the domain; and (2) $t_m(x) = b_m(x)$. In the former case the method is called *point matching*, whereas the latter method is known as the *Galerkin method*. The method so described and those to be discussed in the following sections are generally referred to as “method of moments” (MoM) [24]. We will call MoM with conventional bases as “conventional MoM” and the method with wavelet bases, “wavelet MoM.” Observe that the operator L_K in the preceding paragraphs could be any linear operator—differential as well as integral.

4.2. Wavelet Bases

Conventional bases (local or global), when applied directly to the integral equations, generally lead to a dense (fully populated) matrix Z . As a result, the inversion and the final solution of such a system of linear equations are very time-consuming. In later sections it will be clear why conventional bases give a dense matrix while wavelet bases produce sparse matrices. Observe that conventional MoM is a single-level approximation of the unknown function in the sense that the domain of the function (e.g., $[a, b]$), is discretized only once, even if we use nonuniform discretization of the domain. Wavelet MoM as we will discuss, on the other hand, is inherently multi-level in nature.

Beylkin et al. [25] first proposed the use of wavelets in sparsifying an integral equation. Alpert et al. [20] used “waveletlike” basis functions to solve second-kind integral equations. In electrical engineering, wavelets have been used to solve integral equations arising from electromagnetic scattering and transmission-line problems [22,26–40]. In what follows we briefly describe four different ways in which wavelets have been used in solving integral equations.

4.2.1. Use of Fast Wavelet Algorithm. In this method, the impedance matrix Z is obtained via the conventional method of moments using basis functions such as triangular functions, and then wavelets are used to transform this matrix into a sparse matrix [26,27]. Consider a matrix W formed by wavelets. This matrix consists of the decomposition and reconstruction sequences and their translates. We have not discussed these sequences here, but

readers may find these sequences in any standard book on wavelets [e.g., 8–16].

Transformation of cite original MoM impedance matrix into the new wavelet basis is obtained as

$$WZW^T \cdot (W^T)^{-1}i = Wv \tag{32}$$

which can be written as

$$Z_w \cdot i_w = v_w \tag{33}$$

where W^T represents the transpose of the matrix W . The new set of wavelet-transformed linear equations are

$$Z_w = WZW^T \tag{34}$$

$$i_w = (W^T)^{-1}i \tag{35}$$

$$v_w = Wv \tag{36}$$

The solution vector i is then given by

$$i = W^T(WZW^T)^{-1}Wv \tag{37}$$

For orthonormal wavelets $W^T = W^{-1}$ and the transformation (32) is “unitary similar.” It has been shown [26,27] that the impedance matrix Z_w is sparse, which reduces the inversion time significantly. Discrete wavelet transform (DWT) algorithms can be used to obtain Z_w . Readers may find the details of discrete wavelet transform (octave scale transform) in any standard book on wavelets. In some applications it may be necessary to compute the wavelet transform at nonoctave scales. Readers are referred to the literature [7,41,42] for details on such algorithms.

4.2.2. Direct Application of Wavelets. In another method of applying wavelets to integral equations, wavelets are directly applied; that is, first the unknown function is represented as a superposition of wavelets at several levels (scales) along with the scaling function at the lowest level, prior to using Galerkin’s method described before.

In terms of wavelets and scaling functions we can write the unknown function f in (14) as

$$f(x) = \sum_{j=j_0}^{j_n} \sum_{k=K_1}^{K(j)} w_{j,k} \psi_{j,k}(x) + \sum_{k=K_1}^{K(j_0)} a_{j_0,k} \phi_{j_0,k}(x) \tag{38}$$

where we have used the multiscale property (10).

It should be pointed out here that the wavelets $\{\psi_{j,k}\}$ by themselves form a complete set; therefore, the unknown function could be expanded entirely in terms of the wavelets. However, to retain only a finite number of terms in the expansion, the scaling function part of (38) must be included. In other words, $\{\psi_{j,k}\}$, because of their bandpass

filter characteristics, extract successively lower and lower frequency components of the unknown function with decreasing values of the scale parameter j , while $\phi_{j_0,k}$, because of its lowpass filter characteristics, retains the lowest frequency components or the coarsest approximation of the original function.

In Eq. (38), the choice of j_0 is restricted by the order of the wavelet, while the choice of j_u is governed by the physics of the problem. In applications involving electromagnetic scattering, as a “rule of thumb” the highest scale, j_u , should be chosen such that $1/2^{j_u+1}$ does not exceed $0.1\lambda_0$, where λ_0 is the operative wavelength.

When (38) is substituted in (14), and the resultant equation is tested with the same set of expansion functions, we get a set of linear equations

$$\begin{bmatrix} [Z_{\phi,\phi}] & [Z_{\phi,\psi}] \\ [Z_{\psi,\phi}] & [Z_{\psi,\psi}] \end{bmatrix} \begin{bmatrix} [a_{j_0,k}]_k \\ [w_{j,n}]_{j,n} \end{bmatrix} = \begin{bmatrix} \langle v, \phi_{j_0,k'} \rangle_{k'} \\ \langle v, \psi_{j',k'} \rangle_{j',k'} \end{bmatrix} \quad (39)$$

where the ψ term of the expansion function and the ϕ term of the testing function give rise to the $[Z_{\phi,\psi}]$ portion of the matrix Z . A similar interpretation holds for $[Z_{\phi,\phi}]$, $[Z_{\psi,\phi}]$, and $[Z_{\psi,\psi}]$.

By carefully observing the nature of the submatrices, we can explain the “denseness” of the conventional MoM and the “sparseness” of the wavelet MoM. Unlike wavelets, the scaling functions discussed in this article do not possess the vanishing moments properties. Consequently, for two pulse or triangular functions ϕ_1 and ϕ_2 (usual bases for the conventional MoM and suitable candidates for the scaling functions), even though $\langle \phi_1, \phi_2 \rangle = 0$ for nonoverlapping support, $\langle \phi_1, L_K \phi_2 \rangle$ is not very small since $L_k \phi_2$ is not small. On the other hand, as is clear from the vanishing-moment property (4) of a wavelet of order m , the integral vanishes if the function against which the wavelet is being integrated behaves as a polynomial of a certain order “locally.” Away from the singular points the kernel has a polynomial behavior locally. Consequently, integrals such as $(L_K \psi_{j,n})$ and the inner products involving wavelets are very small for nonoverlapping support.

Because of its “total positivity” property [11, pp. 207–209], the scaling function has a “smoothing” or “variation diminishing” effect on a function against which it is integrated. The smoothing effect can be understood as follows. If we convolve two pulse functions, both of which are discontinuous but totally positive, the resultant function is a linear B -spline (triangular function) that is continuous. Likewise, if we convolve two linear B -splines, we get a cubic B -spline that is twice continuously differentiable. Analogous to these, the function $L_K \phi_{j_0,k}$ is smoother than the kernel K itself. Furthermore, because of the MRA properties that give

$$\langle \phi_{j,k}, \psi_{j',l} \rangle = 0, \quad j \leq j' \quad (40)$$

the integrals $\langle \phi_{j_0,k'}, (L_K \psi_{j,n}) \rangle$ and $\langle \psi_{j',n'}, (L_K \phi_{j_0,k}) \rangle$ are quite small.

The $[Z_{\phi,\phi}]$ portion of the matrix, although diagonally dominant, usually does not have entries that are very

small compared to the diagonal entries. In conventional MoM case, all the elements of the matrix are of the form $\langle \phi_{j,k'}, (L_K \phi_{j,k}) \rangle$. Consequently, we cannot, threshold such a matrix in order to sparsify it. In wavelet MoM case, the entries of $[Z_{\phi,\phi}]$ occupy a very small portion (5×5 for linear and 11×11 for cubic spline cases) of the matrix, while the rest contain entries whose magnitudes are very small compared to the largest, entry; hence a significant number of entries can be set to zero without affecting the solution appreciably.

4.2.3. Wavelets in Spectral Domain. In the previous section, we have used wavelets in the space domain. The local support and vanishing-moment properties of wavelet bases were used to obtain a sparse matrix representation of an integral equation. In some applications, particularly in spectral-domain methods in electromagnetics, wavelets in the spectral domain may be quite useful. Whenever we have a problem in which the unknown function is expanded in terms of the basis function in the space (time) domain while the numerical computation takes place in the spectral (frequency) domain, we should look at the space–spectral window product in order to determine the efficiency of using a particular basis function. According to the “uncertainty principle,” the space–spectral window product of a square integrable function cannot be less than 0.5; the lowest value is possible only for functions of Gaussian class. Because of the nearly optimal space–spectral window product of the cubic spline and the corresponding semiorthogonal wavelet, the improper integrals appearing in many spectral-domain formulations of integral equations can be evaluated efficiently. This is due to the fact that higher-order wavelets generally have faster decay in the spectral domain. The spectral-domain wavelets have been used to solve the transmission-line discontinuity problem [22].

4.2.4. Wavelet Packets. The discrete wavelet packet (DWP) similarity transformation has been used to obtain a higher degree of sparsification of the matrix than is achievable using the standard wavelets [38]. It has also been shown that the DWP method gives faster matrix-vector multiplication than do some of the fast multipole methods.

In the standard wavelet decomposition process, first we map the given function to a sufficiently high-resolution subspace (V_M) and obtain the approximation coefficients $\{a_{M,k}\}$ (see Section 2). The approximation coefficients $\{a_{M-1,k}\}$ and wavelet coefficients $\{w_{M-1,k}\}$ are computed from $\{a_{M,k}\}$. This process continues; that is, the coefficients for the next-lower level $M-2$ are obtained from $\{a_{M-1,k}\}$, and so on. Observe that in this scheme, only approximation coefficients $\{a_{j,k}\}$ are processed at any scale j ; the wavelet coefficients are merely the outputs and remain untouched. In a wavelet packet, the wavelet coefficients are also processed, which, heuristically, should result in a higher degree of sparsity since in this scheme, the frequency bands are further divided compared with the standard decomposition scheme.

4.3. Intervallic Wavelets

Wavelets on the real line have been used to solve integral equations arising from electromagnetic scattering and waveguiding problems. The difficulty with using wavelets on the entire real line is that the boundary conditions need to be enforced explicitly. Some of the scaling functions and wavelets must be placed outside the domain of integration. Furthermore, because of truncation at the boundary, the vanishing-moment property is not satisfied near the boundary. Also, in signal processing uses of these wavelets lead to undesirable jumps near the boundaries. We can avoid this difficulty by periodizing the scaling function as [10, Sect. 9.3]

$$\phi_{j,k}^p := \sum_l \phi_{j,k}(x+l) \tag{41}$$

where the superscript “p” implies periodic case. Periodic wavelets are obtained in a similar way. It is easy to show that if $\hat{\phi}(2\pi k) = \delta_{k,0}$, which is generally true for the scaling functions, then $\sum_k \phi(x-k) \equiv 1$. If we apply the last relation, which is also known as the “partition of unity” to (41), we can show that $\{\phi_{0,0}^p\} \cup \{\psi_{j,k}^p; j \in \mathbb{Z}^+ := \{0, 1, 2, \dots\}, k = 0, \dots, 2^j - 1\}$ generates $L^2([0,1])$.

Periodic wavelets have been used in other studies [35–37]. However, as mentioned elsewhere [10, Sect. 10.7], unless the function that is being approximated by the periodized scaling functions and wavelets has the same values at the boundaries, we still have “edge” problems at the boundaries. To circumvent these difficulties, wavelets, constructed especially for a bounded interval, have been introduced in [40]. Details on intervallic wavelets may be found in the literature [40,43–45]. Most of the time, we are interested in knowing the formulas for these wavelets rather than delving into the mathematical rigor of their construction. These formulas may be found in the literature [16,40].

Wavelets on a bounded interval satisfy all the properties of regular wavelets that are defined on entire real line; the only difference is that in the former case, there are a few special wavelets near the boundaries. Wavelets and scaling functions whose support lies completely inside the interval have properties that are exactly same as those of regular wavelets. As an example consider semiorthogonal wavelets of order m . For this case the scaling functions (B -splines of order m) have support $[0, m]$, whereas the corresponding wavelet extends the interval $[0, 2m - 1]$. If we normalize the domain of the unknown function from $[a, b]$ to $[0, 1]$ then there will be 2^j segments at any scale j (discretization step = 2^{-j}). Consequently, in order to have at least one complete inner wavelet, the following condition must be satisfied:

$$2^j \geq 2m - 1 \tag{42}$$

For j satisfying this condition, there are $m - 1$ boundary scaling functions and wavelets at 0 and 1, and $2^j - m + 1$ inner scaling functions and $2^j - 2m + 2$ inner wavelets. Figure 5 shows all the scaling functions and wavelets for $m = 2$ at the scale $j = 2$. All the scaling functions for $m = 4$

and $j = 3$ are shown in Fig. 6a, while Fig. 6b gives only the corresponding boundary wavelets near $x = 0$ and one inner wavelet. The rest of the inner wavelets can be obtained by simply translating the first one whereas the boundary wavelets near $x = 1$ are the mirror images of ones near $x = 0$.

5. NUMERICAL RESULTS

In this section we present some numerical examples for applications of wavelets to time–frequency analysis and integral equations. The purpose of these results is to give readers an idea of how wavelets can be applied. These examples can certainly be solved by other methods more efficiently, but they help understand wavelet approach in a simpler way.

Because of page limitations, we present only one example from electromagnetic scattering problems, the one for a cylindrical geometry. Numerical results for strip and wire problems can be found in Ref. 31. Results for spectral-domain applications of wavelets to transmission-line discontinuity problems may be found in Ref. 22. For more applications of wavelets to electromagnetic problems, readers may refer to Ref. 39.

The matrix equation (39) is solved for a circular cylindrical surface [40]. The surface current distribution is computed using linear and cubic spline wavelets. The wavelet MoM results are compared with the conventional MoM results. To obtain the conventional MoM results, we have used triangular functions for both expanding the unknown current distribution and testing the resultant equation. The conventional MoM results have been verified with a series solution [23]. The results of the conventional MoM and the wavelet MoM agree very well.

We want to show how “thresholding” affects the final solution. By “thresholding,” we mean setting those elements of the matrix to zero that are smaller (in magnitude) than some positive number δ ($0 \leq \delta < 1$), called the threshold parameter, times the largest element of the matrix.

Let z_{\max} and z_{\min} be the largest and the smallest elements of the matrix in (39). For a fixed value of the threshold parameter δ , define percent relative error (ϵ_δ) as [40]

$$\epsilon_\delta := \frac{\|f_0 - f_\delta\|_2}{\|f_0\|_2} \times 100 \tag{43}$$

and percent sparsity (S_δ) as

$$S_\delta := \frac{N_0 - N_\delta}{N_0} \times 100 \tag{44}$$

where f_δ represents the solution obtained from (39) when the elements whose magnitudes are smaller than δz_{\max} have been set to zero. Similarly, N_δ is the total number of elements left after thresholding. Clearly, $f_0(x) = f(x)$ and $N_0 = N^2$, where N is the number of unknowns.

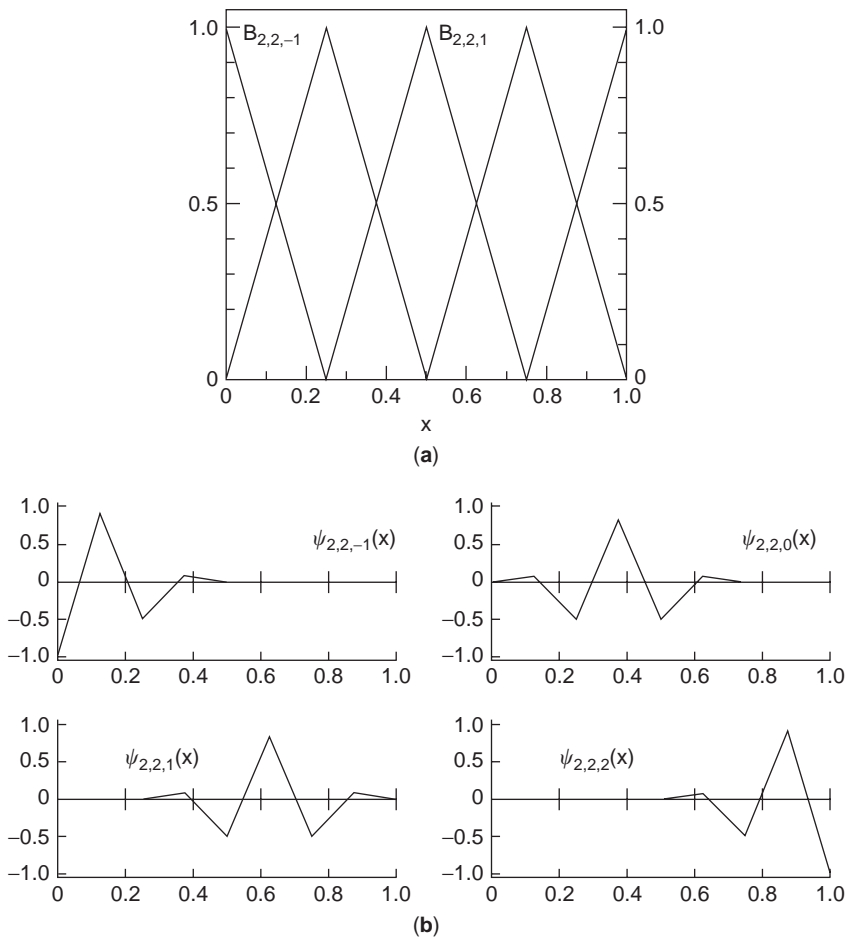


Figure 5. (a) Linear spline ($m=2$) scaling functions on $[0,1]$; (b) linear spline wavelets on $[0,1]$. The subscripts indicate the order of spline (m), scale (j), and the position (k), respectively [40].

Table 1 gives an idea of the relative magnitudes of the largest and the smallest elements in the matrix for conventional and wavelet MoM. As is expected, because of their higher vanishing moment property, cubic spline wavelets give the higher ratio, z_{\max}/z_{\min} .

The matrix elements with $\delta=0.0002$ for the linear spline case are shown in Fig. 7. Figures 8 and 9 give an idea of the pointwise error in the solution for linear and cubic spline cases for different values of threshold parameter.

It is worth pointing out here that regardless of the size of the matrix, only 5×5 in the case of the linear spline and 11×11 in the case of the cubic splines remain unaffected by thresholding; a significant number of the remaining elements can be set to zero without causing much error in the solution.

6. SEMIORTHOGONAL VERSUS ORTHOGONAL WAVELETS

Both semiorthogonal and orthogonal wavelets have been used for solving integral equations. A comparative study of their advantages and disadvantages has been reported [31]. The orthonormal wavelet transformation, because of its unitary similar property, preserves the condition

number (κ) of the original impedance matrix Z ; semiorthogonal wavelets do not. Consequently, the transformed matrix equation may require more iterations to converge to the desired solution. Some preliminary results comparing the condition number of matrices for different cases are given in Table 2 (where ON = orthonormal and SO = semiorthogonal).

In applying wavelets directly to solve integral equations, one of the most attractive features of semiorthogonal wavelets is that closed-form expressions are available for such wavelets [16,40]. Few of the continuous ON wavelets can be written in closed form.

One thing to be kept in mind is that, unlike signal processing applications where one usually deals with a discretized signal and decomposition and reconstruction sequences, here in the boundary value problem we often have to compute the wavelet and scaling function values at any given point. For a strip/thin-wire case, a comparison of the computation time and sparsity is summarized in Tables 3 and 4 [31].

Semiorthogonal wavelets are symmetric and hence have generalized linear phase [11, pp. 160–174], an important factor in function reconstruction. It is well known [10, Sect. 8.1] that symmetric or antisymmetric, real-valued, continuous, and compactly supported ON scaling functions and wavelets do not exist. Finally, in using

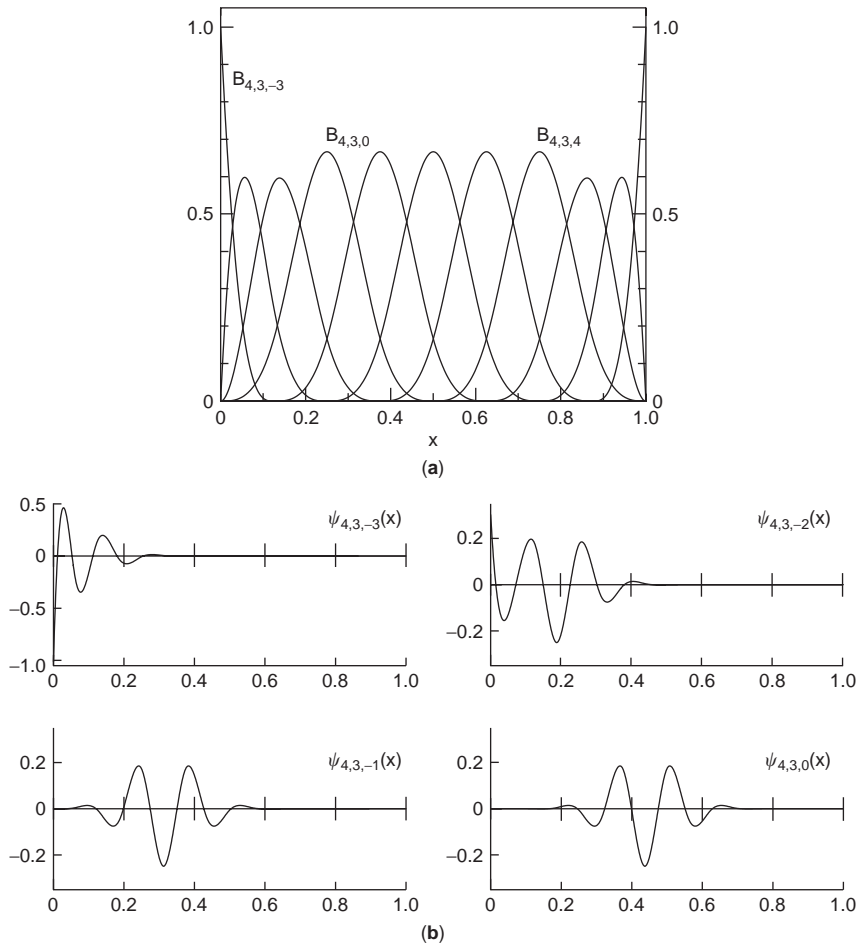


Figure 6. (a) Cubic spline ($m = 4$) scaling functions on $[0,1]$; (b) cubic spline wavelets on $[0,1]$. The subscripts indicate the order of spline (m), scale (j), and the position (k), respectively [40].

wavelets to solve spectral domain problems, as discussed before, we need to look at the time–frequency window product of the basis. Semiorthogonal wavelets approach the optimal value of the time–frequency product, which is 0.5, very fast. For instance, this value for the cubic spline wavelet is 0.505. It has been shown [46] that this product approaches to ∞ with the increase in smoothness of ON wavelets.

7. DIFFERENTIAL EQUATIONS

An ordinary differential equation (ODE) can be represented as

$$Lf(x) = g(x); \quad x \in [0, 1] \tag{45}$$

Table 1. Relative Magnitudes of Largest and Smallest Elements of Matrix for Conventional and Wavelet MoM ($\alpha = 0.1\lambda_0$)

	Conventional MoM	Wavelet MoM ($m = 2$)	Wavelet MoM ($m = 4$)
Z_{\max}	5.377	0.750	0.216
Z_{\min}	1.682	7.684×10^{-8}	8.585×10^{-13}
Ratio	3.400	9.761×10^6	2.516×10^{11}

Source: Ref. 40.

with

$$L = \sum_{j=0}^m a_j(x) \frac{d^j}{dx^j} \tag{46}$$

and some appropriate boundary conditions. If the coefficients $\{a_j\}$ are independent of x , then the solution can be obtained via a Fourier method. However, in the ODE case, with nonconstant coefficients, and in PDEs, we generally use finite-element or finite-difference-type methods.

7.1. Multigrid Method

In the traditional finite-element method (FEM), local bases are used to represent the unknown function and the solution is obtained by Galerkin’s method, similar to the approach described in previous sections. For the differential operator, we get sparse and banded stiffness matrices that are generally solved using iterative techniques, such as the Jacobi method.

One disadvantage of conventional FEM is that the condition number (κ) of the stiffness matrix grows as $O(h^{-2})$, where h is the discretization step. As a result, the convergence of the iterative technique becomes slow and the solution becomes sensitive to small perturbations in the matrix elements. If we study how the error

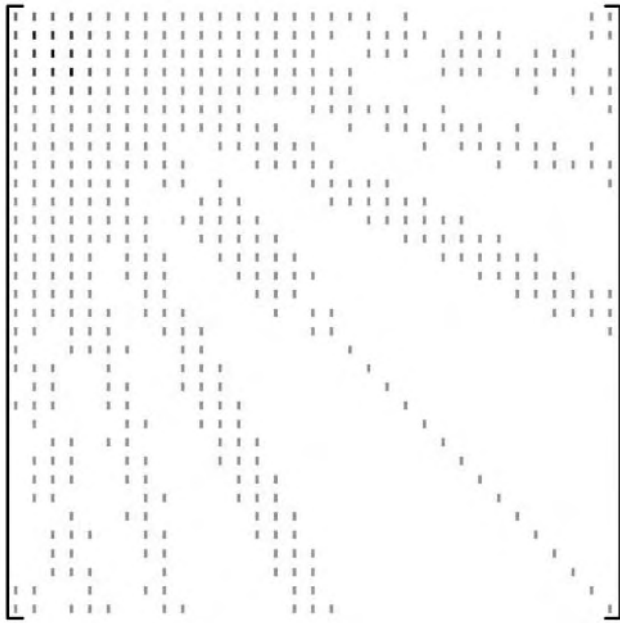


Figure 7. A typical grayscale plot of the matrix elements obtained using linear wavelet MoM. The darker color represents larger magnitude. (This figure is available in full color at <http://www.mrw.interscience.wiley.com/erfme>.)

decreases with iteration in iterative techniques, such as the Jacobi method, we find that the error decreases rapidly for the first few iterations. After that, the rate at which the error decreases slows down [47, pp. 18–21]. Such methods are also called “high-frequency methods” since these iterative procedures have a “smoothing” effect on the high-frequency portion of the error. Once this portion is eliminated, convergence becomes quite slow. After the first few iterations, if we could rediscritize the domain with coarser grids and thereby go to lower

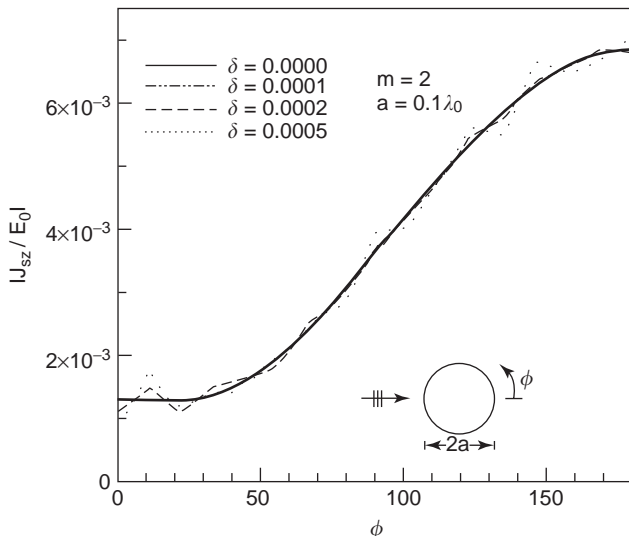


Figure 8. The magnitude of surface current distribution computed using linear ($m = 2$) spline wavelet MoM for different values of the threshold parameter δ [40].

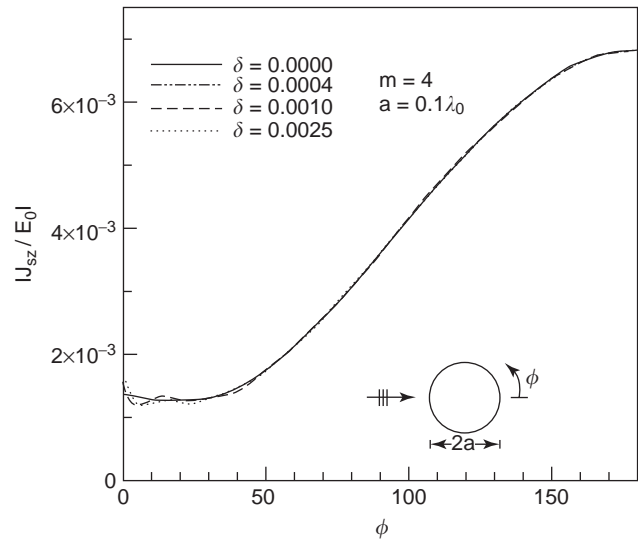


Figure 9. The magnitude of surface current distribution computed using cubic ($m = 4$) spline wavelet MoM for different values of the threshold parameter δ [40].

frequency, the convergence rate would be accelerated. This leads us to a multigrid-type method.

Multigrid or hierarchical methods have been proposed to overcome the difficulties associated with the conventional method [47–63]. In this technique one performs a few iterations of the smoothing method (Jacobi type), and then the intermediate solution and the operator are projected to a coarse grid. The problem is then solved at the coarse grid, and by interpolation one goes back to the finer grids. By going back and forth between finer and coarser grids, the convergence can be accelerated. It has been shown for elliptic PDEs, that for wavelet-based multilevel methods, the condition number is independent of discretization step [i.e., $\kappa = O(1)$] [58]. The multigrid method is too involved to discuss in this article. Readers are encouraged to look at the references provided at the end of this article.

Multiresolution aspects of wavelets have also been applied in evolution equations [62,63]. In evolution problems, the space and time discretizations are interrelated to gain a stable numerical scheme. The timestep must be determined from the smallest space discretization. This makes the computation quite complex. A spacetime adaptive method has been introduced [63] where wavelets have been used to adjust the spacetime discretization steps locally.

7.2. Multiresolution Time-Domain (MRTD) Method

The explosive growth in wireless communications (3G Cellular Systems, 802.11 WLANs) has spawned a great deal of research in electronic packaging for high-performance devices. Silicon-embedded components, ultracompact efficient antenna technology, and micromachining technology are critical to meet the cost and performance requirements for a higher level of multifunction integration in the development of wireless transceivers, since they can

Table 2. Effect of Wavelet Transform Using Semiorthogonal and Orthonormal Wavelets on Condition Number of Impedance Matrix^a

Basis and Transform	Number of Unknowns	Octave Level	δ	S_δ	ϵ_δ	Condition Number κ	
						Before Threshold	After Threshold
Pulse and none	64	NA ^b	NA ^b	0.0	2.6×10^{-5}	14.7	—
Pulse and SO	64	1	7.2×10^{-2}	46.8	0.70	16.7	16.4
Pulse and ON	64	1	7.5×10^{-3}	59.7	0.87	14.7	14.5

^aThe original impedance matrix is generated using pulse basis functions.

^bData not available.

considerably reduce the MMIC real estate and the amount of needed discrete elements. In addition, advances in device processing are enabling the creation of increasingly compact microwave circuits. These circuits incorporate a high degree of functionality through the combination of many microwave components in close proximity. These advanced devices often utilize geometries with high aspect ratios, small feature size, and moving parts. These characteristics, which are necessary to the operation of these devices, often lead to difficulties in predicting performance. The simulation of these complex devices requires the use of extremely small elements or cells, which can tax many simulation tools beyond their limits. This has led to the use of a combination of methods, such as full-wave simulation and microwave circuit simulation, or, if higher accuracy is required, the use of a parallel full-wave simulator on specialized hardware. For the modeling of all of these wireless elements, time-domain full-wave techniques demonstrate numerous advantages since they are robust and easy to program, and they can use wideband excitations that allow for one simulation to cover the entire frequency band of interest and can be easily parallelized on relatively inexpensive hardware, making it possible to simulate large structures.

The FDTD [67,70] method is one of the most mature and versatile time-domain numerical techniques and has been used for a wide variety of structures. The use of variable gridding along with effective parallelization approaches allows fine details of large structures to be modeled. Curves and diagonal elements can be modeled using stair stepping. In addition, a wide variety of FDTD enhancements make possible the modeling of small gaps, multielectric/membrane configurations and resonating passives. Macroscopic results, such as *S* parameters and impedances, can be determined by probing and comparing voltages and currents at different points in the structure. The multiresolution time-domain technique (MRTD)

Table 3. Comparison of CPU Time (in seconds) per Matrix Element for Spline, Semiorthogonal, and Orthonormal Basis Function [31]

	Wire	Plate
Spline	0.12	0.25×10^{-3}
SO wavelet	0.49	0.19
ON wavelet	4.79	4.19

Source: Ref. 31.

[62,65] is an adaptive generalization of the FDTD technique that is based on the principles of multiresolution analysis and makes use of wavelets to alleviate the computational burdens of FDTD for complex or large structures, such as multilayer packages or MEMS, where the position of the boundaries is time changing and the membrane thickness is much smaller than any other detail in the transverse direction. The MRTD technique allows the cell resolution to vary with both time and position. The wavelets can be used to represent higher levels of detail along with higher-frequency content. As fields propagate through the structure, the resolution can be varied to allow for the rapidly changing fields.

The multiresolution time-domain (MRTD) technique uses a wavelet discretization of Maxwell's equations to provide a time- and space-adaptive electromagnetic modeling scheme. The advantage of this method is that it can use much larger cells than similar methods [64], such as finite-difference time-domain (FDTD). The number of basis functions used in each cell can be varied as a function of space and time [71]. In this way, grids of complex structures can use high-resolution cells in areas of large field variation and lower-resolution cells elsewhere. The multiresolution time-domain technique draws its name from the application of multiresolution principles to Maxwell's equations. In the application of the method, the electric and magnetic fields are expanded into a scaling and wavelet functions and then inserted into Maxwell's equations. The method of moments is then applied to these equations. This leads to a time marching scheme much like the finite-difference time-domain technique. The advantage of this technique over other methods is that wavelets can be added or subtracted during to the simulation at any point in the grid. In this way the grid can react to both complex geometry and rapid changes in the field as it propagates through the grid. The choice of wavelet basis functions determines the characteristics of the MRTD scheme. The Battle-Lemarie [72,73], the Daubechies [10], and other wavelet basis (e.g., biorthogonal wavelets [17,68,74]) have been successfully applied and demonstrated significant savings in memory and execution time requirements by one and two orders of magnitude, respectively [75–79] with respect to the FDTD technique. The stability and dispersion performance of entire-domain (e.g., Battle-Lemarie) MRTD schemes has been investigated for different stencil sizes and for zero-resolution wavelets [80]. Analytical expressions for the maximum stable timestep have been derived. Larger

Table 4. Comparison of Percentage Sparsity (S_δ) and Percentage Relative Error (ϵ_δ) for Semiorthogonal and Orthonormal Wavelet Impedance Matrices as a Function of Threshold Parameter (δ)

Scatterer/Octave Levels	Number of Unknowns		Threshold δ	Sparsity S_δ		Relative Error ϵ_δ	
	SO	ON		SO	ON	SO	ON
Wire/ $j=4$	29	33	1×10^{-6}	34.5	24.4	3.4×10^{-3}	4.3×10^{-3}
			5×10^{-6}	48.1	34.3	3.9	1.3×10^{-3}
			1×10^{-5}	51.1	36.5	16.5	5.5×10^{-2}
Plate/ $j=2, 3, 4$	33	33	1×10^{-4}	51.6	28.1	1×10^{-4}	0.7
			5×10^{-4}	69.7	45.9	4.7	5.2
			1×10^{-3}	82.4	50.9	5.8	10.0

Source: Ref. 31.

stencils decrease the numerical phase error, making it significantly lower than FDTD for low and medium discretizations. Stencil sizes greater than 10 offer a smaller phase error than does FDTD even for discretizations close to 50 cells per wavelength. The enhancement of wavelets further improves the dispersion performance for discretizations close to the Nyquist limit (23 cells per wavelength) making it comparable to that of much denser grids (10–15 cells per wavelength), although it decreases the value of the maximum timestep guaranteeing the stability of the scheme. The finite-domain Haar basis functions (Fig. 10) provide a convenient tool for the transition from FDTD to MRTD due to their compact support, and to their similarity with the FDTD pulse basis, thus providing an effective demonstration tool for this section. In order to create an efficient scheme, Wavelet systems are usually chosen to create sparse discretizations of the modeled equations. The multiresolution time-domain (MRTD) [62] technique makes possible the application of wavelet decomposition principles to the space discretization of Maxwell's equa-

tions. The practical outcome of this application is a time-space-adaptive grid. This grid is very useful because the resolution can be customized to match a given structure using a minimum number of grid points. Through careful application of thresholding [64], this effect can be enhanced by allowing the resolution to be changed based on the requirements of representing the waveform as a function of time. The use of wavelets, however, is not without a price and the application of localized effects becomes difficult.

The quantities that are found directly in MRTD are the values of the wavelet/scaling coefficients; the field values must be reconstructed by summing all coefficients that overlap at any given point. Because all wavelet coefficients cover multiple grid locations, the application of effects at individual points in the grid is challenging. Changing the values of wavelet coefficients to alter the field values at one point effects the values at many other points. Careless coefficient modification can lead to nonphysical field values and unstable algorithms.

The Haar wavelet family is in many ways one of the simplest; however, it has many properties that make its application to practical structures favorable [64]. Most importantly, it is finite-domain and when reconstructed leads to finite areas of constant field value (equivalent gridpoints [66]). Using this property, it is possible to apply pointwise effects in the MRTD grid when an arbitrary level of Haar wavelets is used.

This section discusses the fundamentals of the MRTD derivation and techniques that can be used for the intracell modeling of PECs and dielectric interfaces with Haar MRTD to apply PEC effects at individual equivalent gridpoints. These techniques use wavelet reconstruction/decomposition to apply pointwise effects in the MRTD grid and makes possible the use of the MRTD timespace-adaptive grid for complex structures. Using this method, large, sparse cells can be used in homogeneous areas surrounding high-resolution structures while high-resolution grids can be used to represent fine features. Various examples from large-scale MEMS, packaging, antenna and interconnecting structures demonstrate the potentials of MRTD technique for system-level analysis, design, and optimization.

7.2.1. Fundamentals of MRTD. To clearly present the MRTD method, a brief derivation of 2D Haar MRTD is presented, as well as a partial listing of the properties of

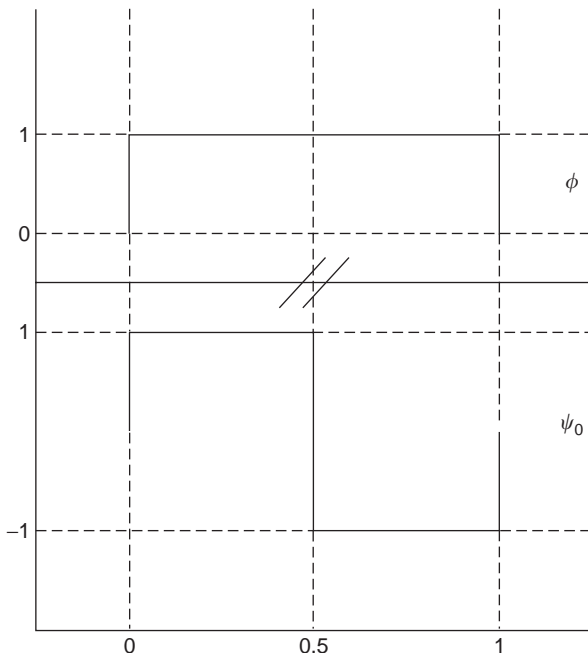


Figure 10. Haar scaling function ϕ and wavelet ψ_0 .

Haar wavelet expansions. The extension to 3D and other basis functions is straightforward.

7.2.1.1. Haar Basis Functions. Haar basis functions are based on pulses in space. The Haar scaling function ϕ , as well as the Haar mother wavelet ψ_0 , are presented in Fig. 10. The scaling function is simply a pulse function over a given domain. The wavelet function is based on the scaling function, and consists of two pulses, each of half the domain of the scaling function and of the opposite magnitude. The inner product of either function with itself is 1, while the inner product of the two functions is 0 [65].

The Haar wavelets of higher resolution levels are based on the mother wavelet. For each level of resolution the number of wavelets is doubled while the domain of each is halved. The magnitude of each function is modified so that the inner product of each wavelet function with itself is one. The inner product of any wavelet coefficient with any other wavelet coefficient, at any resolution level, or with the scaling function, is 0 [65]. Figure 11 presents the wavelet coefficients for wavelet resolution levels 1 and 2. We assume that the maximum used wavelet resolution is r_{\max} .

The reconstruction of the wavelets yields some interesting properties. When the coefficients of the expansion are summed to determine field values, the function appears as a pulsetrain. The pulses have the domain of half of the highest resolution wavelet. Furthermore, these

pulses overlap the constant valued sections of the highest-resolution wavelets. A linear combination of the wavelet and scaling functions has as many degrees of freedom as the number of coefficients used. There are $2^{r_{\max} + 1}$ functions used per level, and any finite real value can be represented at the center of each half of the r_{\max} level wavelets.

The effect of the variable grid when it is used to represent electromagnetic fields can be easily seen. If the field value can be approximated as constant across the half-domain of the highest-resolution wavelet, there is no need for increasing resolution. If the field has more rapid variation, each increase in resolution doubles the effective resolution of the cell. High-resolution cells can be used to represent rapid field variation (such as impressed currents and discontinuity effects) while low-resolution cells can be used elsewhere.

7.2.1.2. Haar MRTD Derivation. The equations

$$\frac{dE_x}{dt} = \frac{1}{\epsilon} \frac{dH_z}{dy} \tag{47}$$

$$\frac{dE_y}{dt} = -\frac{1}{\epsilon} \frac{dH_z}{dx} \tag{48}$$

$$\frac{dH_z}{dt} = \frac{1}{\mu} \left[\frac{dE_x}{dy} - \frac{dE_y}{dx} \right] \tag{49}$$

represent the 2D TE_z mode of Maxwell's equations for source-free, lossless, isotropic media. These functions will be used to demonstrate the expansion of Maxwell's equations in this article as a compromise between completeness and space requirements. The expansion of the E_x field in (47) in terms of Haar scaling and wavelet functions is

$$\begin{aligned} E_x(x,y) = & \sum_{n,i,j} h_n(t) \left[{}_n E_{i,j}^{x,\phi\phi} \phi_i(x)\phi_j(y) \right. \\ & + \sum_{r=0}^{r_{\max}} \sum_{p=0}^{2^r-1} {}_n E_{i,j,r,p}^{x,\psi\psi} \psi_{i,p}^r(x)\phi_j(y) \\ & + \sum_{r=0}^{r_{\max}} \sum_{p=0}^{2^r-1} {}_n E_{i,j,r,p}^{x,\phi\psi} \phi_i(x)\psi_{j,p}^r(y) \\ & \left. + \sum_{r=0}^{r_{\max}} \sum_{p=0}^{2^r-1} \sum_{s=0}^{r_{\max}} \sum_{q=0}^{2^s-1} {}_n E_{i,j,r,p}^{x,\psi\psi} \psi_{i,p}^r(x)\psi_{j,q}^s(y) \right] \end{aligned} \tag{50}$$

where ${}_n E_{i,j}^{x,\phi\phi}$ is the coefficient corresponding to scaling function in x and y that represents the electric field in the i, j cell at timestep n . $\psi_{j,p}^r$ denotes a wavelet of resolution r at the p position $[(p - 0.5)/2^r]$ of the j cell. Other coefficients have similar definition. The time dependence is assumed to be constant for each timestep using the pulse $h_n(t)$, although efforts have been published where wavelets have been used in the time domain as well [77].

In a 2D expansion wavelets and scaling functions are used in both the x and y directions. The terms in (50) represent the products of the basis functions in both

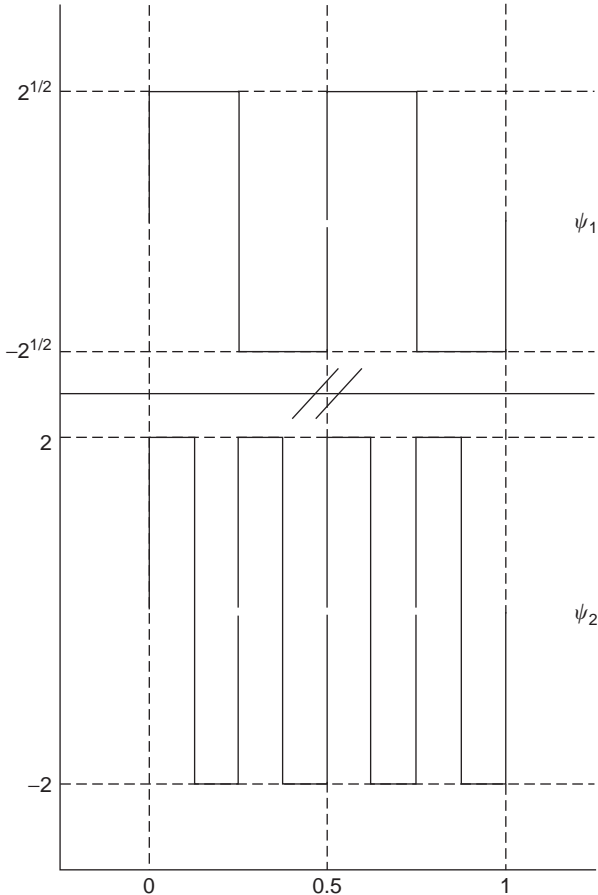


Figure 11. Haar wavelets at resolutions 1 and 2.

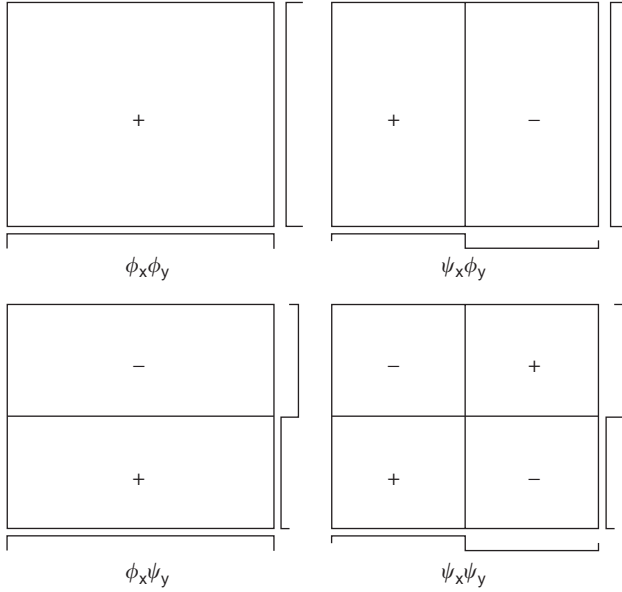


Figure 12. 2D Haar coefficients for $r_{\max} = 0$.

directions. For each of these products, one coefficient results. The four groups of coefficients represent the scaling x /scaling y , wavelet x /scaling y , scaling x /wavelet y , and wavelet x /wavelet y coefficients. There are $2^{2(r_{\max} + 1)}$ wavelets for a maximum resolution r_{\max} . For a maximum resolution level $r_{\max} = 0$, the four coefficients in 2D [one for each product term in (50)] are presented in Fig. 12.

When the E and H -field expansions are inserted into (47)–(49), the method of moments can be applied to determine update equations for each of the wavelet/scaling coefficients [65]. It has been shown [65,66] that the offset between the E and H fields in this expansion yields the best dispersion properties and locates the equivalent gridpoints in the same pattern as in the FDTD Yee cell [67]. In the 2D case, as in the 1D case presented above, the equivalent gridpoints are at the center of the constant valued sections of the highest-resolution wavelets. In Fig. 12 these are the locations of the + and – in the $\psi_x \psi_y$ function.

The update equations for this case are

$$\begin{aligned} n\mathbf{E}_{i,j}^x &= n-1\mathbf{E}_{i,j}^x + \frac{\Delta t}{\epsilon\Delta y} (\mathbf{U}_{E_{x1} n-1} \mathbf{H}_{i,j}^z \\ &+ \mathbf{U}_{E_{x2} n-1} \mathbf{H}_{i,j-1}^z) \end{aligned} \quad (51)$$

$$\begin{aligned} n\mathbf{E}_{i,j}^y &= n-1\mathbf{E}_{i,j}^y + \frac{\Delta t}{\epsilon\Delta x} (\mathbf{U}_{E_{y1} n-1} \mathbf{H}_{i,j}^z \\ &+ \mathbf{U}_{E_{y2} n-1} \mathbf{H}_{i-1,j}^z) \end{aligned} \quad (52)$$

$$\begin{aligned} n\mathbf{H}_{i,j}^z &= n-1\mathbf{H}_{i,j}^z + \frac{\Delta t}{\mu} \left[\frac{1}{\Delta y} (\mathbf{U}_{H_{E_{x1} n-1}} \mathbf{E}_{i,j}^x \right. \\ &+ \mathbf{U}_{H_{E_{x2} n-1}} \mathbf{E}_{i,j+1}^x) - \frac{1}{\Delta x} (\mathbf{U}_{H_{E_{y1} n-1}} \mathbf{E}_{i,j}^y \\ &\left. + \mathbf{U}_{H_{E_{y2} n-1}} \mathbf{E}_{i+1,j}^y) \right] \end{aligned} \quad (53)$$

These equations are written in a matrix form similar to that used in Ref. 65, where, for example, each $n\mathbf{E}_{i,j}^x$ is the vector of the scaling and wavelet coefficients that represent the electric field in the i, j cell at timestep n . The \mathbf{U} matrices are the results of the inner products from the method of moments. Equations (51)–(53) form an explicit set of equations that can be used in a time marching scheme similar to the FDTD method [67]. The resolution can be varied on a cell-by-cell basis, and can also be changed as a function of time [64]. The timestep for this method

$$\Delta t = \frac{1}{c \sqrt{\left(\frac{2^{r_{\max}} + 1}{\Delta x}\right)^2 + \left(\frac{2^{r_{\max}} + 1}{\Delta y}\right)^2}} \quad (54)$$

is the same as FDTD for a cell spacing equal to the equivalent gridpoint spacing [64,65].

7.2.2. Subcell Modeling in MRTD. The method presented in the previous section allows a timespace-variable grid to be used to model Maxwell equations. While not presented, it is possible to continuously vary the dielectric constant continuously through a cell [68,79]. Using this method, arbitrary structures consisting of only dielectrics can be modeled efficiently. However, the addition of PEC structures adds difficulties. A novel technique has been introduced that allows for the intracell modeling of multiple PEC's [81] using MRTD grids, a development that would eliminate one of the major roadblocks in the minimization of memory requirements using this type of adaptive simulator.

The PEC boundary condition requires that electric fields tangential to PECs be set to zero. In (51)–(53) update equations are presented that allow the determination of wavelet/scaling coefficients at a future timestep based on the wavelet/scaling coefficients of the surrounding fields at previous timesteps. If the PEC structure is the size of an MRTD cell, all the scaling/wavelet coefficients can be zeroed to apply the boundary condition. If the PEC structure is smaller than the cell, however, the scaling/wavelet coefficients must be modified such that the field values at non-PEC locations are unchanged while the field values at PEC locations are zeroed.

One way to determine the seating/wavelet coefficients that zero selected fields while leaving other fields unchanged is to use the reconstruction matrix. For example, the $n\mathbf{E}_{i,j}^x$ matrices in (51)–(53) can be transformed into field values by multiplying with a matrix that represents the summation of the fields at the appropriate equivalent gridpoints. In this case

$$\mathbf{E}_R = \mathbf{R}\mathbf{E}_W \quad (55)$$

where \mathbf{E}_R is the reconstructed fields, \mathbf{E}_W is the wavelet coefficients, and \mathbf{R} is the reconstruction matrix. It was previously noted that there are as many independent points that can be reconstructed in \mathbf{E}_R as there are coefficients in \mathbf{E}_W . Thus, \mathbf{R} is square. For the case of

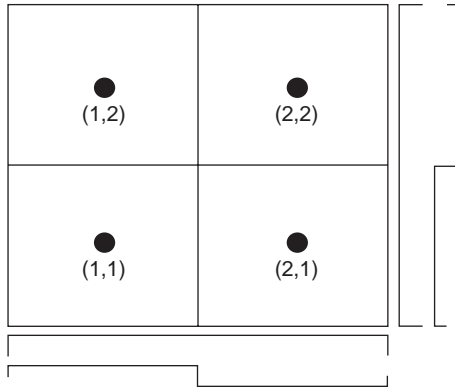


Figure 13. Coordinates for reconstructed fields.

$r_{\max} = 0$, and (55) can be expanded as

$$\begin{bmatrix} \mathbf{E}_{1,1} \\ \mathbf{E}_{1,2} \\ \mathbf{E}_{2,1} \\ \mathbf{E}_{2,1} \end{bmatrix} = \begin{bmatrix} 1 & 1 & 1 & 1 \\ 1 & 1 & -1 & -1 \\ 1 & -1 & 1 & -1 \\ 1 & -1 & -1 & 1 \end{bmatrix} \begin{bmatrix} {}_n\mathbf{E}_{i,j}^{x,\phi\phi} \\ {}_n\mathbf{E}_{i,j}^{x,\psi\phi} \\ {}_n\mathbf{E}_{i,j}^{x,\phi\psi} \\ {}_n\mathbf{E}_{i,j}^{x,\psi\psi} \end{bmatrix} \quad (56)$$

if the coordinates for the reconstructed fields are given as in Fig. 13.

Just as \mathbf{R} can be used to reconstruct the field coefficients from their scaling/wavelet values, \mathbf{R}^{-1} can be used to decompose the field values to scaling/wavelet coefficients. Thus, the application of a PEC boundary condition to an individual equivalent gridpoint can be accomplished by reconstructing the fields, zeroing the fields tangential to PECs, and then decomposing back to scaling/wavelet coefficients. However, a more efficient method results when the reconstruction/decomposition matrices are applied directly to the MRTD update equations.

By using the reconstruction/decomposition matrices directly on (51)–(53) a pointwise update equation results. For example, multiplying (51) by \mathbf{R} , using $\mathbf{H}_{i,j}^z = \mathbf{R}^{-1}\mathbf{R}\mathbf{H}_{i,j}^z$, and defining $\mathbf{U} = \mathbf{R}\mathbf{U}\mathbf{R}^{-1}$ yield

$$\begin{aligned} \mathbf{R}_n\mathbf{E}_{i,j}^x &= \mathbf{R}_{n-1}\mathbf{E}_{i,j}^x + \frac{\Delta t}{\epsilon\Delta y} (\mathbf{U}'_{E_{x1}}\mathbf{R}_{n-1}\mathbf{H}_{i,j}^z \\ &+ \mathbf{U}'_{E_{x2}}\mathbf{R}_{n-1}\mathbf{H}_{i,j-1}^z) \end{aligned} \quad (57)$$

which gives an update on the electric field points in terms of the magnetic field points.

Using this equation, it is possible to zero the field points that are tangential to PECs by multiplying with a matrix \mathbf{I}_p , which is the identity matrix with zeros in the rows corresponding to PEC locations. As (57) is an update equation, and the initial values of all fields are 0, multiplying the electric field vectors in (57) with \mathbf{I}_p is redundant.

The new update equation with PEC locations zeroed is

$$\begin{aligned} \mathbf{R}_n\mathbf{E}_{i,j}^x &= \mathbf{R}_{n-1}\mathbf{E}_{i,j}^x + \frac{\Delta t}{\epsilon\Delta y} (\mathbf{I}_p\mathbf{U}'_{E_{x1}}\mathbf{R}_{n-1}\mathbf{H}_{i,j}^z \\ &+ \mathbf{I}_p\mathbf{U}'_{E_{x2}}\mathbf{R}_{n-1}\mathbf{H}_{i,j-1}^z) \end{aligned} \quad (58)$$

By multiplying (58) with \mathbf{R}^{-1} and defining $\mathbf{U}^p = \mathbf{R}^{-1}\mathbf{I}_p\mathbf{U}\mathbf{R}$, the PEC MRTD update equation is

$$\begin{aligned} {}_n\mathbf{E}_{i,j}^x &= {}_{n-1}\mathbf{E}_{i,j}^x + \frac{\Delta t}{\epsilon\Delta y} (\mathbf{U}_{E_{x1}}^p {}_{n-1}\mathbf{H}_{i,j}^z \\ &+ \mathbf{U}_{E_{x2}}^p {}_{n-1}\mathbf{H}_{i,j-1}^z) \end{aligned} \quad (59)$$

This equation is the same as (51) except for the use of the \mathbf{U}_p matrices. Thus, it is possible to implement subcell PEC modeling in MRTD while changing only the inner product matrices. This method adds no increase in computational overhead, and simply requires the additional memory to store the \mathbf{U} matrices.

7.2.3. Examples. To test the method, a PEC screen in a 2D parallel-plate waveguide was simulated. An expanded view of the grid surrounding the screen is presented in Fig. 14. The areas where the PEC is applied are shaded. A maximum wavelet resolution of 2 was used. In this simulation, the voltage at the output of the screen was probed. When compared to the results of an FDTD simulation of the same structure (Fig. 15), the maximum difference in magnitude is shown on the order of 10–12% of the peak field value. This is within the numerical accuracy of Matlab [69], which was used for the simulations, showing that the techniques are identical.

7.2.3.1. CPW–Microstrip Transition. The CPW–microstrip transition simulated is shown in Fig. 16. The loss of this transition can be optimized over a wide frequency range with the use of FDTD and design curves for various packaging specifications can be derived. The plot in Fig. 17 shows S_{21} of this transition for a variety of lengths of the

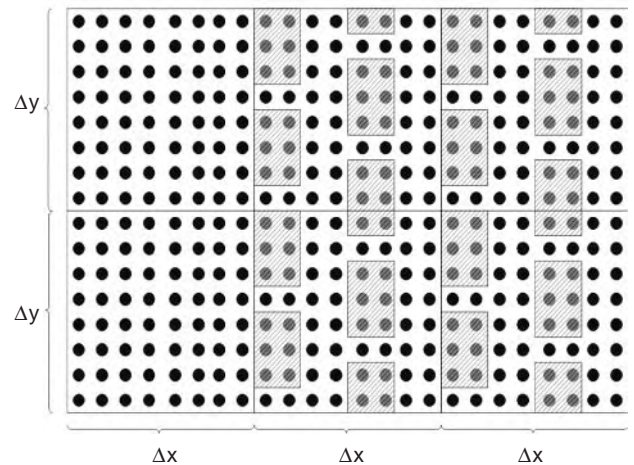


Figure 14. Grid used to represent PEC screen.

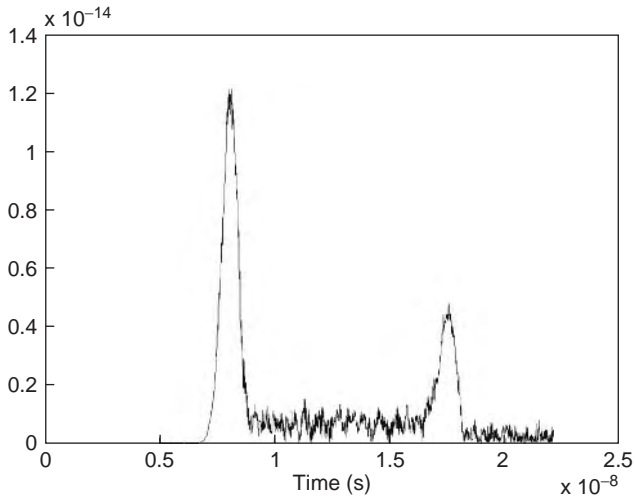


Figure 15. Difference between FDTD and MRTD results.

central straight section from 10 to 20 GHz. This data was obtained using time-domain voltage probes at the input (V_1) and output (V_2) of the transition, converting them to frequency domain through the use of a discrete Fourier transform and identifying the reflected voltage through the use of a reference input voltage (V_{ref}) derived by the simulation of a through CPW line [64]. In addition, the use of the full-wave FDTD, which provides the values of all electromagnetic components throughout the geometry, offers a more intuitive visualization of the circuit. For example, in the transition the electric fields have to change smoothly from a coplanar waveguide mode to a microstrip mode, in order to minimize the local reflections. Thus, in the design process it is desirable to identify where this transition takes place and optimize the tapering. Figure 16 is a plot of total electric field for a transverse cross section of the transition. It can be seen that at the position of this cross section, the field is mostly in a CPW mode, although a microstrip mode has started developing below and at the edges of the signal line there. The relative amplitudes of the E field could provide an intuitive design rule for the spacing between the CPW ground and signal line, so as not to suppress the microstrip mode.

7.2.3.2. Microstrip-Line Coupling. Embedded transmission lines are commonly used in multilayer packages, where

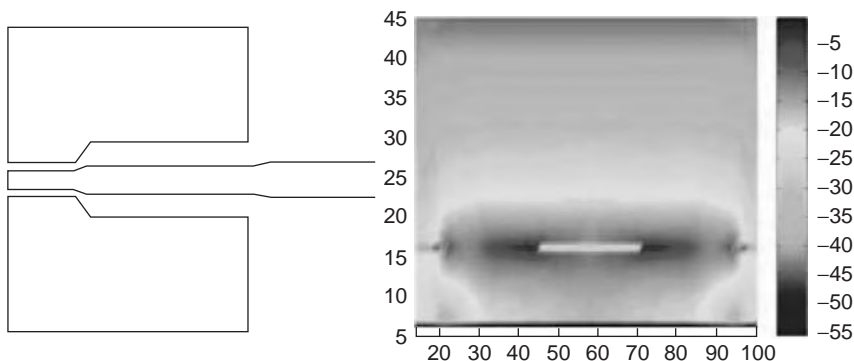


Figure 16. CPW–microstrip transition; E -field distribution.

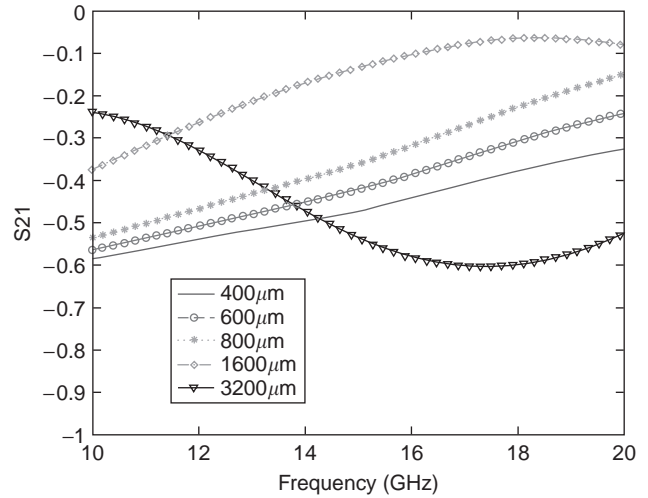


Figure 17. S_{21} for various central linewidths. (This figure is available in full color at <http://www.mrw.interscience.wiley.com/erfme>.)

the use of noncontinuous grounds could lead to increased crosstalk effects. In this article, the FDTD technique is used for the estimation of the coupling of the finite-ground microstrip lines of Fig. 18 [66]. The results for different line spacing and for a ground connecting via (optimized design) presented in Fig. 19 have been obtained by combining two simulations, an even/odd-mode excitation. In addition, to reduce the unwanted crosstalk, the electric and the magnetic field distributions have been calculated and plotted along a transverse cross section. It is apparent that most of the coupling is through the magnetic field lines, leading to the design conclusion that attempts to reduce the coupling should focus on magnetic shielding.

7.2.3.3. MEMS Capacitive Switch. One example of a MEMS structure that benefits from simulation in MRTD [67] is the MEMS capacitive switch shown in Fig. 20. The gap between the plates in the switch is $\frac{1}{175}$ th of the substrate thickness. The simulation of this device in FDTD is tedious and slow because of the large number of cells that must be used in order to accurately represent the very small gap and substrate.

In MRTD, the number of cells can be reduced by using the built-in adaptive gridding capability of the method. In addition, further efficiencies can be obtained in large

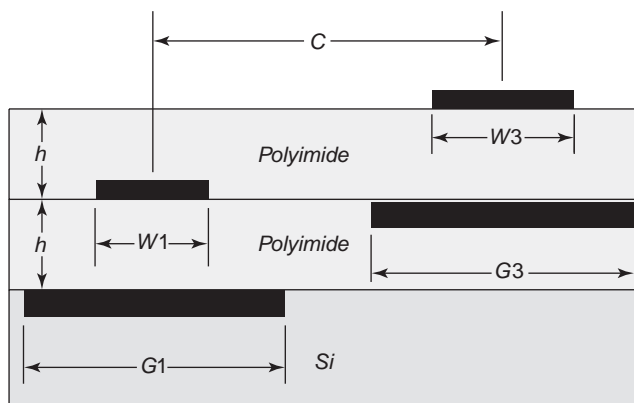


Figure 18. Embedded finite-ground microstrip lines.

simulations featuring this structure by allowing fewer cells to be used when the electric field variation near the cell is low.

7.2.3.4. LTCC Antenna Development. A via-fed stacked cavity-backed patch antenna has been designed (based on a 10-layer LTCC process) for IEEE 802.11a 5.8 GHz band [68] as shown in Fig. 21. The heights of the lower and upper patches (400 mils, 400 mils) are respectively 8 mils (2 LTCC GL550 layers) and 32 mils.

The input impedance and radiation characteristics of the stacked-patch antenna are shown in Figs. 22 and 23 respectively. The 10-dB return loss bandwidth of the antenna is about 4.

7.2.4. Concluding Remarks. The multiresolution time domain (MRTD) is a wavelet-based extension of FDTD. It demonstrates a very high efficiency in the calculation of the scattering parameters as well as its the estimation of the packaging effects and of the parasitic crosstalk between neighboring geometries. In addition, its inherent capability of global electromagnetic field calculation as well as MRTD’s multi-PEC cell allows for the identifica-

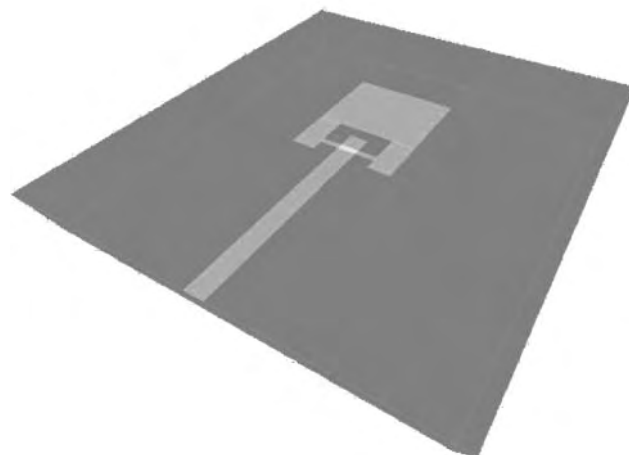


Figure 20. MEMS switch feeding capacitive stub.

tion of “hotspots” of high field concentration and for the derivation of physically driven solutions for improvement of the overall system-on-package efficiency. The time/space-adaptive grid of MRTD allows it to be used to model finely detailed structures. Areas of the grid containing small features can use increased resolution, while homogenous areas can use low resolution. It is important to note that this technique can be used to model structures with continuous dielectric variations, and thus composite cells, that is, those with multiple PEC and dielectric regions per cell, can be modeled. Furthermore, the pointwise expansion of MRTD equations can be used in the future to model other subcell components, such as lumped elements and equivalent circuits.

Acknowledgment

J. C. Goswami wishes to thank Profs. Charles K. Chui, Anrew K. Chan, Robert Novels, and Raj Mittra, with whom he worked on some of the topics discussed in this article.

M. Tenzeris wishes to acknowledge the support of the Georgia Electronic Design Center, the Georgia Tech NSF

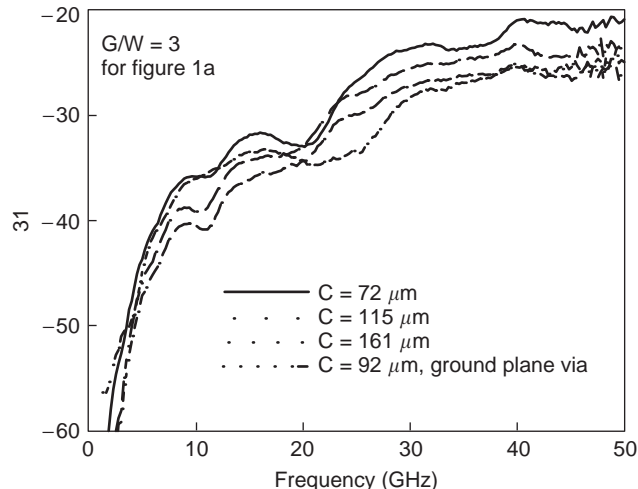


Figure 19. S_{31} for different line separations.

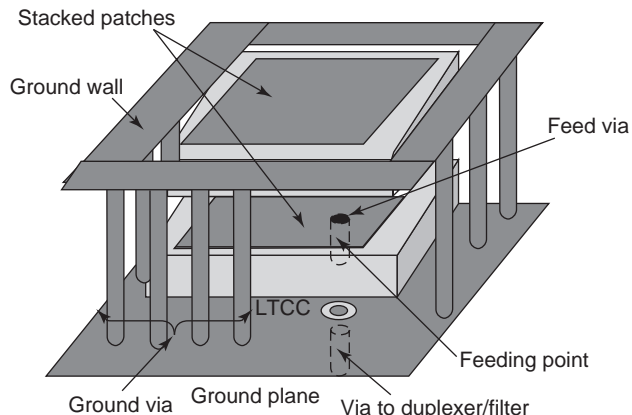


Figure 21. Double-patch cavity-backed antenna for 5.725–5.825-GHz applications.

Packaging Research Center, and NSF CAREER Award 9964761. He would also like to acknowledge the assistance and the contributions of his graduate students, Nathan Bushyager and Edan Dalton.

BIBLIOGRAPHY

1. M. P. Hurst and R. Mittra, Scattering center studies via Prony's method, *IEEE Trans. Anten. Propag.* **35**:986–988 (Aug. 1987).
2. R. Carriere and R. L. Moses, High resolution radar target modeling using a modified Prony estimator, *IEEE Trans. Anten. Propag.* **40**:13–18 (Jan. 1992).
3. C. E. Baum, The singularity expansion method, in L. B. Felsen, ed., *Transient Electromagnetic Fields*, Springer-Verlag, New York, 1976, pp. 130–176.
4. M. A. Morgan, Singularity expansion representations of fields and currents in transient scattering, *IEEE Trans. Anten. Propag.* **32**:466–473 (May 1984).
5. H. Kim and H. Ling, Wavelet analysis of radar echo from finite-size target, *IEEE Trans. Anten. Propag.* **41**:200–207 (Feb. 1993).
6. A. Moghaddar and E. K. Walton, Time-frequency distribution analysis of scattering from waveguide cavities, *IEEE Trans. Anten. Propag.* **41**:677–680 (May 1993).
7. J. C. Goswami, A. K. Chan, and C. K. Chui, An application of fast integral wavelet transform to waveguide mode identification, *IEEE Trans. Microwave Theory Tech.* **43**:655–663 (1995).
8. Y. Meyer, *Wavelets: Algorithms and Applications*, SIAM, Philadelphia, 1993.
9. S. Mallat, A theory of multiresolution signal decomposition: The wavelet representation, *IEEE Trans. Pattern Anal. Machine Intell.* **11**:674–693 (1989).
10. I. Daubechies, *Ten Lectures on Wavelets*, CBMS-NSF Series in Applied Math. Vol. 61, SIAM, Philadelphia, 1992.
11. C. K. Chui, *An Introduction to Wavelets*, Academic Press, Boston, 1992.
12. C. K. Chui, *Wavelets: A Mathematical Tool for Signal Analysis*, SIAM, Philadelphia, 1997.
13. G. Strang and T. Nguyen, *Wavelets and Filter Banks*, Wellesley-Cambridge Press, Wellesley, MA, 1996.
14. M. Vetterli and J. Kovačević, *Wavelets and Subband Coding*, Prentice-Hall, Englewood Cliffs, NJ, 1995.
15. A. N. Akansu and R. A. Haddad, *Multiresolution Signal Decomposition*, Academic Press, San Diego, 1992.
16. J. C. Goswami and A. K. Chan, *Fundamentals of Wavelets: Theory, Algorithms, and Applications*, Wiley, New York, Feb. 1999.
17. A. Cohen, I. Daubechies, and J. C. Feauveau, Biorthonormal bases of compactly supported wavelets, *Commun. Pure Appl. Math.* **45**:485–500 (1992).
18. G. M. Wing, *A Primer on Integral Equations of the First Kind*, SIAM, Philadelphia, 1991.
19. J. H. Richmond, Digital solutions of the rigorous equations for scattering problems, *Proc. IEEE* **53**:796–804 (Aug. 1965).
20. B. K. Alpert, G. Beylkin, R. Coifman, and V. Rokhlin, Wavelet-like bases for the fast solution of second-kind integral equations, *SIAM J. Sci. Comput.* **14**:159–184 (1993).
21. J. Mandel, On multi-level iterative methods for integral equations of the second kind and related problems, *Num. Math.* **46**:147–157 (1985).
22. J. C. Goswami, An application of wavelet bases in the spectral domain analysis of transmission line discontinuities, *Int. J. Num. Model.* **11**:41–54 (1998).
23. R. F. Harrington, *Time-Harmonic Electromagnetic Fields*, McGraw-Hill, New York, 1961.
24. R. F. Harrington, *Field Computation by Moment Methods*, IEEE Press, New York, 1992.
25. G. Beylkin, R. Coifman, and V. Rokhlin, Fast wavelet transform and numerical algorithms I, *Commun. Pure Appl. Math.* **44**:141–183 (1991).
26. R. L. Wagner, P. Otto, and W. C. Chew, Fast waveguide mode computation using wavelet-like basis functions, *IEEE Microwave Guided Wave Lett.* **3**:208–210 (1993).
27. H. Kim and H. Ling, On the application of fast wavelet transform to the integral-equation of electromagnetic scattering problems, *Microwave Opt. Technol. Lett.* **6**:168–173 (March 1993).
28. B. Z. Steinberg and Y. Leviatan, On the use of wavelet expansions in method of moments, *IEEE Trans. Anten. Propag.* **41**:610–619 (1993).
29. K. Sabetfakhri and L. P. B. Katehi, Analysis of integrated millimeter-wave and submillimeter-wave waveguides using orthonormal wavelet expansions, *IEEE Trans. Microwave Theory Tech.* **42**:2412–2422 (1994).
30. B. Z. Steinberg, A multiresolution theory of scattering and diffraction, *Wave Motion* **19**:213–232 (1994).
31. R. D. Nevels, J. C. Goswami, and H. Tehrani, Semi-orthogonal versus orthogonal wavelet basis sets for solving integral equations, *IEEE Trans. Anten. Propag.* **45**:1332–1339 (1997).
32. Z. Xiang and Y. Lu, An effective wavelet matrix transform approach for efficient solutions of electromagnetic integral equations, *IEEE Trans. Anten. Propag.* **45**:1332–1339 (1997).
33. Z. Baharav and Y. Leviatan, Impedance matrix compression (IMC) using iteratively selected wavelet basis, *IEEE Trans. Anten. Propag.* **46**:226–233 (1997).
34. R. D. Nevels and R. E. Miller, A comparison of moment impedance matrices obtained by direct and transform matrix methods using wavelet basis functions, *Proc. IEEE Trans. AP-S Int. Symp.*, 1997.
35. B. Z. Steinberg and Y. Leviatan, Periodic wavelet expansions for analysis of scattering from metallic cylinders, *Proc. IEEE Antennas and Propagation Society Symp.* June 1994, pp. 20–23.
36. G. W. Pan and X. Zhu, The application of fast adaptive wavelet expansion methods in the computation of parameter matrices of multiple lossy transmission lines, *Proc. IEEE Antennas Propagation Society Symp.* June 1994, pp. 29–32.
37. G. Wang, G. W. Pan, and B. K. Gilbert, A hybrid wavelet expansion and boundary element analysis for multi-conductor transmission lines in multilayered dielectric media, *IEEE Trans. Microwave Theory Tech.* **43**:664–675 (March 1995).
38. W. L. Golik, Wavelet packets for fast solution of electromagnetic integral equations, *IEEE Trans. Anten. Propag.* **46**:618–624 (1998).
39. *Int. J. Num. Model. Electron. Networks Devices Fields* (special issue on wavelets in electromagnetics) **11** (1998).
40. J. C. Goswami, A. K. Chan, and C. K. Chui, On solving first-kind integral equations using wavelets on a bounded interval, *IEEE Trans. Anten. Propag.* **43**:614–622 (1995).
41. C. K. Chui, J. C. Goswami, and A. K. Chan, Fast integral wavelet transform on a dense set of time-scale domain, *Num. Math.* **70**:283–302 (1995).

42. J. C. Goswami, A. K. Chan, and C. K. Chui, On a spline-based fast integral wavelet transform algorithm, in H. L. Bertoni, L. Carin, L. B. Felsen, and S. U. Pillai, eds., *Ultra-Wideband Short Pulse Electromagnetics 2*, Plenum Press, New York, 1995, pp. 455–463.
43. E. Quak and N. Weyrich, Decomposition and reconstruction algorithms for spline wavelets on a bounded interval, *Appl. Comput. Harm. Anal.* **1**:217–231 (June 1994).
44. A. Cohen, I. Daubechies, and P. Vial, Wavelets on the interval and fast wavelet transform, *Appl. Comput. Harm. Anal.* **1**:54–81 (Dec. 1993).
45. P. Auscher, Wavelets with boundary conditions on the interval, in C. K. Chui, ed., *Wavelets: A Tutorial in Theory and Applications*, Academic Press, Boston, 1992, pp. 217–236.
46. C. K. Chui and J. Z. Wang, High-order orthonormal scaling functions and wavelets give poor time-frequency localization, *Fourier Anal. Appl.* 415–426 (1996).
47. W. Hackbusch, *Multigrid Methods and Applications*, Springer-Verlag, New York, 1985.
48. A. Brandt, Multi-level adaptive solutions to boundary value problems, *Math. Comput.* **31**:330–390 (1977).
49. W. L. Briggs, *A Multigrid Tutorial*, SIAM, Philadelphia, 1987.
50. S. Dahlke and I. Weinreich, Wavelet-Galerkin methods: An adapted biorthogonal wavelet basis, *Constr. Approx.* **9**:237–262 (1993).
51. W. Dahmen, A. J. Kurdila, and P. Oswald, eds., *Multiscale Wavelet Methods for Partial Differential Equations*, Academic Press, San Diego, 1997.
52. H. Yserentant, On the multi-level splitting of finite element spaces, *Num. Math.* **49**:379–412 (1986).
53. J. Liandrat and Ph. Tchamitchian, *Resolution of the 1D Regularized Burgers Equation Using a Spatial Wavelet Approximation*, NASA Report, ICASE 90-83, Dec. 1990.
54. R. Glowinski, W. M. Lawton, M. Ravachol, and E. Tenenbaum, Wavelet solution of linear and nonlinear elliptic, parabolic, and hyperbolic problems in one space dimension, in R. Glowinski and A. Lichniewsky, eds., *Computing Methods in Applied Sciences and Engineering*, SIAM, Philadelphia, 1990, pp. 55–120.
55. P. Oswald, On a hierarchical basis multilevel method with nonconforming P1 elements, *Num. Math.* **62**:189–212 (1992).
56. W. Dahmen and A. Kunoth, Multilevel preconditioning, *Num. Math.* **63**:315–344 (1992).
57. P. W. Hemker and H. Schippers, Multiple grid methods for the solution of Fredholm integral equations of the second kind, *Math. Comput.* **36** (Jan. 1981).
58. S. Jaffard, Wavelet methods for fast resolution of elliptic problems, *SIAM J. Num. Anal.* **29**:965–986 (1992).
59. S. Jaffard and Ph. Laurençot, Orthonormal wavelets, analysis of operators, and applications to numerical analysis, in C. K. Chui, ed., *Wavelets: A Tutorial in Theory and Applications*, Academic Press, Boston, 1992, pp. 543–601.
60. J. Xu and W. Shann, Galerkin-wavelet methods for two-point boundary value problems, *Num. Math.* **63**:123–144 (1992).
61. C. Guerrini and M. Piraccini, Parallel wavelet-Galerkin methods using adapted wavelet packet bases, in C. K. Chui and L. L. Schumaker, eds., *Wavelets and Multilevel Approximation*, World Scientific, 1995, pp. 133–142.
62. M. Krumpholz and L. P. B. Katehi, MRTD: new time-domain schemes based on multiresolution analysis, *IEEE Trans. Microwave Theory Tech.* **44**:555–571 (1996).
63. E. Bacry, S. Mallat, and G. Papanicolaou, A wavelet based space-time adaptive numerical method for partial differential equations, *Math. Model. Num. Anal.* **26**:793–834 (1992).
64. E. M. Tentzeris, A. Cangellaris, L. P. B. Katehi, and J. Harvey, Multiresolution time-domain (MRTD) adaptive schemes using arbitrary resolutions of wavelets, *IEEE Trans. Microwave Theory Tech.* **50**:501–516 (Feb. 2002).
65. T. Dogaru and L. Carin, Application of Haar-wavelet-based multiresolution time-domain schemes to electromagnetic scattering problems, *IEEE Trans. Anten. Propag.* **50**:774–784 (June 2002).
66. C. Sarris and L. P. B. Katehi, Fundamental gridding-related dispersion effects in multiresolution time-domain schemes, *IEEE Trans. Microwave Theory Tech.* **49**:2248–2257 (Dec. 2001).
67. K. S. Yee, Numerical solution of initial boundary value problems involving Maxwell's equations in isotropic media, *IEEE Trans. Anten. Propag.* **14**:302–307 (March 1966).
68. T. Dogaru and L. Carin, Scattering analysis by the multi-resolution time-domain method using compactly supported wavelet systems, *IEEE Trans. Microwave Theory Tech.* **50**:1752–1760 (July 2002).
69. Matlab, The MathWorks, 3 Apple Hill Drive, Natick, MA 01760-2098.
70. A. Taflove, *Computational Electrodynamics*, Artech House, Norwood, MA, 1995.
71. E. Tentzeris, R. Robertson, A. Cangellaris, and L. P. B. Katehi, Space and time-adaptive gridding using MRTD, *Proc. IEEE MTT-S Int. Microwave Symp. Digest*, 1997, pp. 337–340.
72. G. Battle, A block spin construction of ondelettes. Part I: Lemarie functions, *Commun. Math. Phys.* **110**:601–615 (1987).
73. P. G. Lemarie, Ondelettes a localization exponentielles, *J. Math. Pure Appl.* **67**:227–236 (1998).
74. M. Fujii and W. J. R. Hoefer, Application of Biorthogonal interpolating wavelets to the Galerkin Scheme of time-dependent Maxwell's equations, *IEEE Microwave Wireless Compon. Lett.* **11**:22–24 (Jan. 2001).
75. E. Tentzeris, M. Krumpholz, and L. P. B. Katehi, Application of MRTD to printed transmission lines, *Proc. Microwave Theory and Techniques Symp. (MTT-S)*, 1996, pp. 573–576.
76. E. Tentzeris, R. Robertson, M. Krumpholz, and L. P. B. Katehi, Application of the PML absorber to the MRTD schemes, *IEEE Trans. Anten. Propag.* **47**:1709–1715 (Nov. 1999).
77. E. Tentzeris, J. Harvey, and L. P. B. Katehi, Time adaptive time-domain techniques or the design of microwave circuits, *IEEE Microwave Guided Wave Lett.*, **9**:96–98 (1999).
78. K. Goverdhanam, E. Tentzeris, M. Krumpholz, and L. P. B. Katehi, An FDTD multi-grid based on multiresolution analysis, *Proc. Antennas and Propagation Society Symp. (AP-S)*, 1996, pp. 352–355.
79. R. L. Robertson, M. Tentzeris, and L. P. B. Katehi, Modeling of dielectric-loaded cavities using MRTD, *Int. J. Num. Model. (special issue on wavelets in electromagnetics)* **11**:55–68 (1998).
80. M. Tentzeris, R. Robertson, J. Harvey, and L. P. B. Katehi, Stability and dispersion analysis of Battle-Lemarie based MRTD schemes, *IEEE Trans. Microwave Theory Tech.* **47**:1004–1013 (July 1999).
81. N. Bushyager and M. Tentzeris, Composite cell MRTD method for the efficient simulation of complex microwave structures, *Proc. 2003 IEEE European Microwave Symp.* Munich, Germany, Oct. 2003, Vol. 1, pp. 77–80.

APPLIED NUMERICAL ELECTROMAGNETIC ANALYSIS FOR PLANAR HIGH-FREQUENCY CIRCUITS

JAMES C. RAUTIO
Sonnnet Software, Inc.
Phoenix, New York

1. INTRODUCTION

Both commercial and military wireless applications push limits for size and performance. In the 1970s troops had to make educated guesses about the battlefield situation. Today, frontline troops can have a real-time display showing where every one is, even including the enemy. Cell-phones of the 1980s were the size of a book. Today, they have greater coverage and are so small that they get lost in a pocket. Technology drives these advances. A critical part of this technology is electromagnetic (EM) analysis.

Wireless technology achieves these dramatic advances by shifting functionality from printed circuit boards (PCB) and discrete components (e.g., inductors, capacitors, resistors, transistors) to monolithic integrated circuits. These radiofrequency integrated circuits (RFICs) can be on silicon (Si) or gallium arsenide (GaAs). Another choice, midway between RFIC and PCB, is low-temperature cofired ceramic (LTCC). For example, if you were to open your cellphone, you would see a tiny piece of ceramic connected to the antenna. That little piece of ceramic is an LTCC circuit that replaces a PCB and numerous discrete elements formerly occupying a volume almost as large as your entire modern cellphone.

Other portions of your cellphone might include Si RFICs. Formerly restricted to digital/computer applications, silicon integrated circuits can now be used to shrink entire PCB assemblies down to the size of a few grains of sand. For example, silicon RFICs are widely used for radiofrequency identification (RFID) tags. Costing pennies and the size of a credit card, RFID tags use an embedded Si RFIC to transmit information whenever they receive an appropriate radio signal. You might use this when you buy gasoline or pay a toll. Demanding military applications, where high frequency and high power are important, can make use of the superior, but more expensive, GaAs.

Figure 1 shows a photomicrograph of a GaAs MMIC (monolithic microwave integrated circuit) wafer. During the design phase it is common to place multiple designs on a single GaAs wafer. The circuit in the center is a two-stage 1.2–3.2-GHz 1-W GaAs amplifier with 20 dB small-signal gain. It was fabricated on a 75- μm -thick wafer and is 2.98 mm on each side. Electromagnetic analysis is absolutely critical in achieving success on first fabrication for circuits like this.

In all of these applications, it is important to squeeze every gram of performance out of the selected technology, and to do that with the smallest possible size and the shortest possible design and fabrication time.

The high-frequency design process widely used prior to the 1990s began with an approximate design, then the

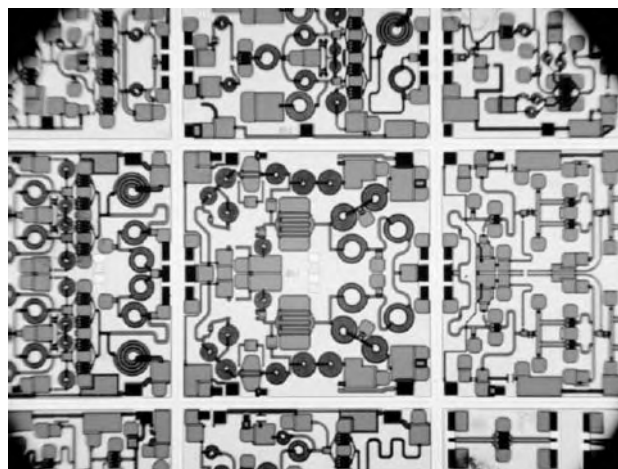


Figure 1. During the design phase, multiple circuits are usually placed on a single GaAs wafer. Here, in the center of this photomicrograph, is a two-stage 1.2–3.2-GHz 1-W GaAs MMIC amplifier with 20 dB small-signal gain. (Image courtesy of M/A-COM, Inc., A Tyco Electronics Company.)

circuit was built. The technology to complete a design with one fabrication simply did not exist. Thus, after building the circuit using these early design approaches, measurements would invariably show that its performance did not meet requirements. For example, an amplifier might not have enough gain, or a filter might be set for the wrong frequency. This was fully expected.

After the initial failure, the designer would review exactly how the circuit failed to meet expectations and then incrementally tune the circuit (a process called “tweaking”), or possibly redesign and refabricate the circuit with the hope that it would perform better the second time around. This redesign–refabricate cycle might be exercised half a dozen times before the desired performance was achieved.

Then, in the 1980s, high-frequency designers started making RF circuits on silicon and gallium arsenide. Now, instead of a few days for fabrication, GaAs RFICs required 3–6 months for fabrication and the cost for fabrication was around \$50,000 each time. Tweaking a circuit was no longer possible. Five or six redesign–refabricate iterations were too expensive and took far too long. This is where the technology of numerical electromagnetics found its first widespread application.

2. APPLICATION EXAMPLE

Prior to the advent of RFICs, components like inductors were literally a simple coil of wire. The approximate inductance was calculated using simple formulas. Then with the inductor in the circuit, it could be tweaked, if desired, to the exact inductance by bending the wire or tuning a small ferrite slug.

Figure 2 shows a spiral inductor on silicon. The venerable coil of wire has been flattened into a spiral so that it can be placed on the flat surface of a silicon IC. This results in several non-inductor-like characteristics. First, recall that the magnetic field in the old coil of wire is just

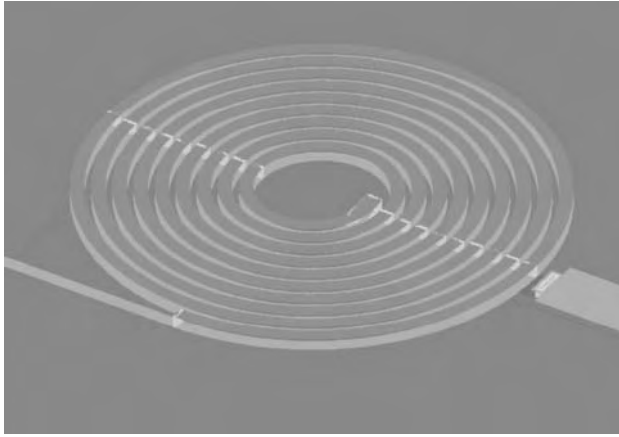


Figure 2. An 8.25-turn spiral inductor on silicon has thick conductors that must be modeled with two sheets of conductor to accurately include the skin effect and current crowding on inductance and loss.

like that of the classical bar magnet, with all the magnetic field going through the center of the coil and then loosely spreading around the outside and finding its way back to the other end.

In a spiral inductor, some of the returning magnetic field pushes back through in between the spiral turns. The magnetic field that penetrates the plane of the spiral pushes and pulls the current in the spiral turns, the result is called “current crowding.” This increases the already high resistive loss of the tiny conductors in the inductor. In addition, while the spiral inductor is on top of the silicon substrate, there may be a conducting ground plane on the bottom side of the silicon. There is extra capacitance to this ground plane that can be significant. Making things more difficult, the semiconducting silicon substrate itself allows current to flow, further modifying this extra capacitance and increasing loss.

Note that this inductor is actually modeled as two thin sheets very close to each other. This is because the thickness of the metal is about the same as the gap between the spiral turns. In this case, both sheets are needed for the highest accuracy at high frequency because the current actually flows close to the surface of the metal (“skin effect”). Since there are two sheets of skin effect current in the actual inductor (one flowing on top of the thick metal, the other on the bottom), two sheets of current are used to model the inductor. So, while it initially looks like just one inductor, we actually have two very tightly coupled inductors, one directly on top of the other, and that is the way it is analyzed. This simple inductor is not so simple.

The Z axis is magnified for the inductor of Fig. 2, the metal thickness is $2.8\ \mu\text{m}$, and the gap between lines is $3.2\ \mu\text{m}$. No vias connecting the edges of the sheets, and no additional sheets are used as they are not needed. Testing to see if edge vias or additional sheets are needed is easily done by simply adding them, reanalyzing, and comparing the results. Typically we find that this simple two-sheet model is sufficient when the gap is on the order of the thickness, as we have here.

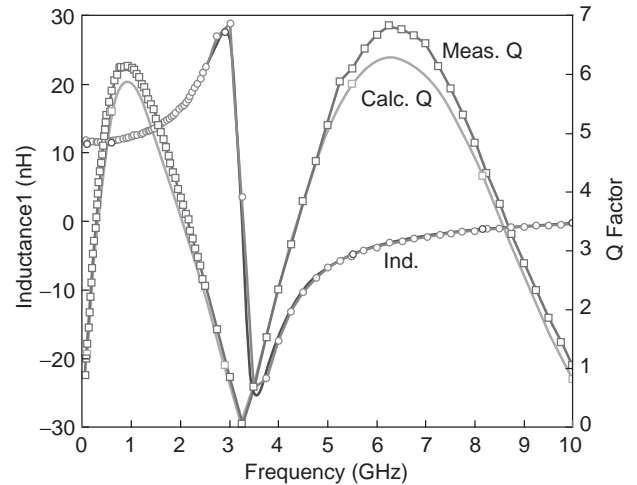


Figure 3. Measured (thin lines) versus calculated (thick lines) inductance and Q for the spiral inductor of Fig. 2.

Measured versus calculated data for this inductor are shown in Fig. 3. The quality factor (Q) is related to resistive loss; higher Q indicates lower loss. These results are typical of the kind of agreement usually seen with EM analysis. With this kind of capability, the high-frequency designer can now modify the design on the computer to achieve exactly the desired response, and then build the circuit once. Once a rare event, achieving complete success on the first fabrication for even the most complicated circuits is now common.

Figure 4 shows the current distribution on the inductor. First notice that there is high current on the edges. This edge concentration of current is characteristic of planar circuits and causes increased loss. Inclusion of this high edge current requires use of a very small subsection size. If a large subsection size is used, the high edge current cannot be included in the analysis and the loss is underestimated.

Note also that the high edge current is present on only one edge of some of the interior turns of the inductor. This

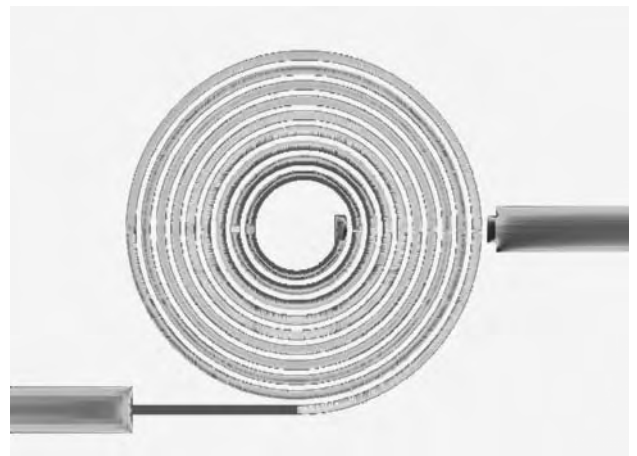


Figure 4. High current on the edges of planar conductors significantly increases loss. The effect of current crowding causes current to switch from side to side, further increasing loss. Current on the bottom side of the thick metal is shown.

is the current crowding referred to above, where the inductor magnetic field penetrating the plane of the inductor pushes and pulls the current on the spiral turns to one edge or the other. This additionally increases loss and if not included in the analysis, results in an optimistic estimate of loss. Current distribution visualization is an important diagnostic tool.

This spiral analysis uses a new type of meshing, “conformal meshing,” which allows accurate and fast analysis. This spiral was analyzed in 5 min 9 s per frequency on a 3-GHz Pentium. Conformal meshing is discussed in detail below.

3. CIRCUIT THEORY ANALYSIS OF RFICS

Prior to the 1980s, most RF design was based on approximate circuit theory. The performance of any electrical circuit can be described in terms of voltage [measured in volts (V)] and current [amperes (A)] at a specified frequency [hertz (Hz)]. For example, a wall outlet might be described as providing 115 V at up to 15 A at 60 Hz.

This is true for RF circuits, only the frequency is much higher. For example, the radio signal going to the antenna of your cellphone might be 1 V at 20 mA at 900 MHz. This is a different voltage, different current, and different frequency, but basically the same idea.

The interplay between voltage and current (assuming a single fixed frequency) are mathematically described in terms of Ohm’s law, Kirchhoff’s current law, and Kirchhoff’s voltage law. We won’t detail these laws here, other than to point out that they are easily implemented in a computer. This was done just as soon as computers started to become widely available in the 1970s.

With the combination of computers and circuit theory, RF designers could quickly analyze their proposed designs consisting of inductors, capacitors, resistors, and transistors. This worked well, up to a point. At higher frequencies, the inductor was no longer just an inductor. Capacitance and resistance become important as well. In addition, there might be unwanted coupling between two different inductors. All this was not too much of a problem, because the designers could build their circuit, then tweak the design with a soldering iron, screwdriver, and pliers to achieve the desired performance.

Then, in the 1980s, circuits started getting smaller. Si and GaAs RFICs generated substantial interest. In the 1990s LTCC (with a dozen or more layers in one tiny ceramic block) saw development. As things became smaller and packed more closely together, tweaking a circuit simply was not possible. Effects that circuit theory did not include, such as stray coupling, became important. When a design did not work the first time, it was a complete refabrication. Designers could not wait years for the completion of multiple redesign–refabricate iterations.

4. ELECTROMAGNETIC ANALYSIS

In the 1980s, with the introduction of the IBM PC, serious computer power became available on the desktop at reasonable cost. Although initially starting with a clock

rate under 4 MHz, the PC became steadily faster achieving multi-GHz clock rates with the turn of the century. It was the advent of fast inexpensive desktop computing that allowed the next step in RFIC design to take place.

Clearly, something more precise than circuit theory with its volts and amperes was required. This turned out to be electromagnetics, which describes circuits in terms of electric field and magnetic field. We are all familiar with the static (i.e., unchanging) electric field surrounding the head of a longhaired youngster touching a Van de Graph generator. We are also familiar with the static magnetic field surrounding a bar magnet.

The interplay between electric field and magnetic field is governed by Maxwell’s equations. For a description of Maxwell’s equations appropriate for the college-bound high school senior, see Ref. 1. Maxwell’s equations deal with more than just static electric and magnetic fields. They completely describe how changing (i.e., dynamic) electric and magnetic fields behave. For a quick explanation, Maxwell’s equations state that a changing electric field generates a magnetic field. It also works in reverse; a changing magnetic field generates an electric field.

Remember that cellphone transmitting a signal at 900 MHz? Its signal, which consists of changing electric and magnetic fields interwoven together and each completely dependent on the other for their existence, changes direction and then back again 900 million times a second. How they do this and what happens as a result is completely covered by Maxwell’s equations.

The mathematical details are discussed later in this article; and while the top-level concepts are relatively simple, the detailed math is complicated. To appreciate the complexity, note that both the electric and magnetic fields are vector fields. In other words, any computer analysis must determine both the direction and magnitude for both electric and magnetic fields everywhere in the circuit being analyzed. This is not a trivial problem.

Additionally, if the analysis is for a specific frequency (i.e., a frequency-domain analysis), the phase of each field at each point in the circuit must be determined. In an alternative approach, the EM analysis generates signals at all frequencies simultaneously. This is EM analysis in the time domain, and now the magnitudes and directions of both fields must be determined as a function of time everywhere in the circuit.

4.1. Volume Meshing EM Analysis

There is tremendous complexity within Maxwell’s equations. This means that there is also a huge diversity in methods of solution. Four general approaches have seen wide application in high-frequency design. All the approaches rely on meshing the high-frequency circuit into many small subsections. Maxwell’s equations are then applied to find the electric and magnetic fields for each subsection in the entire mesh.

The most general class of techniques relies on meshing the entire volume of the problem. The approach called “finite elements” meshes the entire volume into small tetrahedral cells. A technique known as finite-difference time domain (FDTD), or a related technique known as

finite integration technique (FIT), meshes the entire volume into tiny rectangular cells. For both techniques, when a more accurate solution is required; simply use more and smaller cells or tetrahedra.

Of course, a finer mesh means the analysis time increases. As with all EM analyses, analysis time can easily exceed tens of hours. The analysis time is strongly related to the number of cells or subsections. Thus, there is a practical upper limit on the complexity of the circuit that can be analyzed using electromagnetics. Where this upper limit occurs depends on the specific EM analysis used and the type of circuit being analyzed.

The different EM analysis techniques all have their relative advantages and disadvantages. This is important to understand as using an EM analysis on an inappropriate type of problem can result in analysis times 10–1000 times longer, if indeed the problem can be done at all.

Volume meshers are ideal for 3D arbitrary structures that can have any shape and structure whatsoever. A classic example is a cellphone held close to a human head (Fig. 5).

A disadvantage of meshing a problem using tetrahedra is that linear current flow is not well represented. This is easily seen by viewing a finite-element current distribution. The current distribution can lack the smoothness that is characteristic of a true current distribution. In addition, the high current that is naturally present at any sharp metal edges can be indistinct, if present at all.

Fortunately, the response of a circuit is not strongly dependent on the exact current distribution. Thus, useful data can easily result even if the current distribution is not exactly calculated. However, an extremely high accuracy solution might be elusive.

The finite-element method works in the frequency domain. In other words, the analysis assumes that there is a signal at only one specific frequency at any one time. In order to obtain data at 100 frequencies, 100 analyses must be performed. There are interpolation approaches that can provide a spectrally rich dataset after completing a full analysis at fewer frequencies as discussed below.

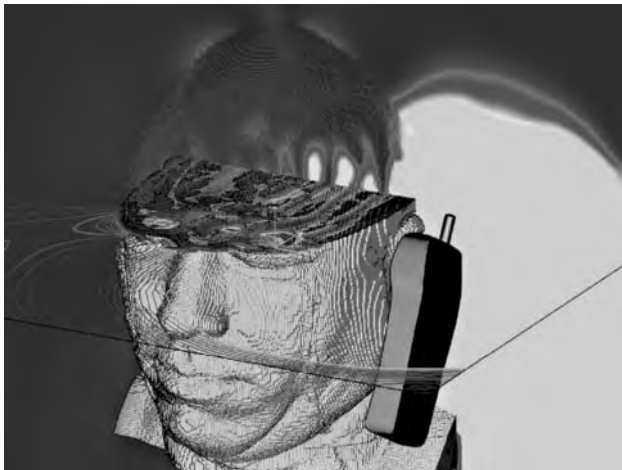


Figure 5. Volume meshing tools excel for 3D arbitrary geometries. Problems of critical importance can be solved easily.

FDTD and FIT are time-domain approaches that assume that all frequencies are present in the circuit at the same time. This is done by exciting the circuit with an impulse (actually a narrow Gaussian pulse, to avoid numerical problems). The impulse contains energy at all frequencies, and the circuit response is analyzed as a function of time. After the time impulse response is calculated, it is transformed to the frequency domain. In this way, a spectrally rich dataset is generated at all frequencies present in the original impulse input without need for interpolation.

The advantage of a time-domain analysis is that the circuit response at all frequencies is determined in a single analysis. The disadvantage is that the analysis can handle an impulse input on only one port (i.e., input or output terminal/connector) at a time. Thus, in order to completely characterize a circuit with, say, 15 ports, 15 complete time-domain analyses are required. The finite-element approach also suffers from this same problem.

While both finite-element and the time-domain analyses can, and are, used for planar circuit analysis, they are usually much slower than tools specifically designed for planar analysis. Thus, volume meshing tools should typically be used for planar circuits only when a specialized planar tool is not available, or if there is an important nonplanar aspect to the circuit. In addition, the volume meshing tools can be used to double-check the results of a planar tool, assuming that the circuit is not too complicated.

4.2. Surface Meshing EM Analysis

Silicon and GaAs RFICs, and LTCC circuits are all planar circuits. In general, use of a volume meshing tool to analyze these, and other planar circuits, is inappropriate. Both faster analysis times and higher accuracy are realized by using EM tools made specifically for planar circuits. Such tools take advantage of the fact that these kinds of circuits are mostly planar (with short vias connecting circuit on different layers) and embedded in layered dielectric. In addition, each layer of dielectric must be uniform within itself, with the possible exception of very small volumes (e.g., a small hole in a layer of dielectric). These specializations allow these tools to subsection only the surface of the metal in the circuit. This is far more efficient and accurate than subsectioning the entire volume of a planar circuit.

There are two basic kinds of surface meshing planar EM tools: (1) those intended for unshielded circuit analysis and (2) those used for shielded circuit analysis (i.e., a circuit contained in a conducting box). In both cases, the circuit metal (and only the circuit metal) is meshed into a set of small subsections. As with the volume meshers, smaller subsections mean higher accuracy, but at the cost of increased analysis time. And also as with the volume meshers, at some point the number of subsections increases the analysis time to tens of hours, setting an upper limit to the level of circuit complexity that can be analyzed. Exactly where this upper level is can vary widely depending on the type of circuit and specific tool

being used. No single tool is superior for all planar circuits.

Both types of surface meshing approaches first calculate the coupling between every possible pair of subsections, namely, put current on one subsection and calculate the voltage induced in another subsection. If there are 100 subsections, then the calculated pairwise coupling is stored in a 100×100 matrix. The analysis then inverts the 100×100 matrix to yield the current distribution and total circuit response. Since this is a frequency-domain analysis, this process must be repeated at each frequency of interest. The principal difference between unshielded and shielded analysis is the means by which they calculate the coupling between subsections. Unshielded EM analysis calculates the subsection-to-subsection coupling by means of numerical integration. For shielded analysis, the coupling is calculated by using the fast Fourier transform (FFT). Each approach has advantages and disadvantages.

The advantage of the unshielded/numerical integration approach is that the subsections can be of any shape, size, or orientation (e.g., triangle or rectangle, or even polygon). This is because the numerical integration takes place over the area of the subsection. Since numerical integration is easily performed over any desired area, any desired size subsection can be used. The disadvantage of the unshielded analysis is that the numerical integration introduces numerical integration error. Special care must be taken to avoid numerical integration error in the vicinity of poles, which result from surface waves present in unbounded media. Depending on the specific circuit, design requirements, mesh, and frequency of analysis, the numerical integration error may or may not be important. Fortunately, this is typically of concern only when high accuracy is required.

Shielded analyses use a 2D FFT (fast Fourier transform) to calculate the coupling. Recall that in digital signal processing, a time signal must first be uniformly time-sampled prior to using the FFT. The same is true with FFT-based EM analysis, except that the planar surface of the circuit substrate is first uniformly space-sampled in two dimensions. This means that the shielded/FFT based analysis starts with a fine uniform underlying FFT mesh. The FFT mesh can easily be 1024×1024 cells, so the individual cell size can be about the same size as a pixel on a computer screen. Nevertheless, the principal disadvantage of shielded/FFT analysis is that, like a picture on a computer screen, the circuit outline is first pixilated so that its edges follow the fine FFT mesh.

The FFT also brings the shielded analysis its principal advantage. Because there is no numerical integration, there is no numerical integration error. The coupling between each pair of subsections is calculated to full numerical precision. Thus, the accuracy and dynamic range of shielded/FFT EM analysis is the highest that can be obtained. The accuracy of shielded EM analysis is quantitatively explored below.

Generally, if high accuracy or the effect of a shielding box might be important, a shielded/FFT analysis should be used. If accuracy is not of the highest importance or the effect of shielding sidewalls cannot be allowed, then an

unshielded analysis can be used. There are additional considerations in selecting the appropriate analysis technique for a given problem, too numerous to discuss here. Ideally, a high-frequency planar circuit designer will have access to both shielded and unshielded tools and will be able to use each as appropriate. The tradeoff between the two is very much like the tradeoff between analog cell-phones (unshielded/numerical integration) and digital cellphones (shielded/FFT). Many of the same issues arise.

5. COMPANION MODELING

The usual EM-based high-frequency design flow is

1. Design the circuit using circuit theory, optimize to meet all requirements.
2. Lay out the circuit.
3. Analyze the circuit using EM.
4. If the circuit meets requirements, build the circuit.
5. Otherwise, change (i.e., “tweak”) the layout in hopes of improving performance.
6. Return to step 3 and see if the changes worked.

This design process can be performed manually, or with the use of automated optimization algorithms. Automated optimization algorithms that drive an EM analysis should be used only if the design already yields nearly the desired response due to the typically long time required for high-accuracy EM analysis. This design flow represents a huge advance over that of the 1980s, when a fabrication rather than EM analysis, was used in step 3. This greatly increased the time and expense to design completion.

A modification of the abovementioned approach, called “companion modeling” [2], can substantially further reduce the time and expense. This process adds structure to the tweaking step, step 5, in the design flow:

- 5a. Determine a mapping between the critical parameters of the circuit theory model and the layout. For example, associate the length of a transmission line in the circuit theory model with a specific dimension in the layout. This process is called “space mapping” [3].
- 5b. Optimize the circuit theory model to match the EM analysis results.
- 5c. Note the changes in the critical parameters of the circuit theory model. Reverse those changes in the layout. For example, if the optimized circuit theory transmission line became $10\mu\text{m}$ shorter, then lengthen that transmission line (in the layout) by $10\mu\text{m}$.

Step 5b is counterintuitive. The circuit theory result meets all requirements. The initial EM analysis does not. So the high-frequency designer instinctively wants to optimize the layout (using EM analysis) to match the circuit theory. The problem is that any EM-based optimization is very slow. Unless the result is close, this will be a long and possibly never-ending process. Instead, step 5b optimizes the desired circuit theory result to match the not-so-good

EM result. Now the optimization loop uses the much faster circuit theory. With proper selection of critical parameters, an answer is obtained quickly. Then proceeding to step 5c, if a decrease of $10\ \mu\text{m}$ in a transmission-line length changes the good circuit theory response so as to match the not-so-good EM result, we reason that an increase of $10\ \mu\text{m}$ should make the not-so-good EM result nearly match the desired circuit theory response. Just reverse the changes, and the layout can be quickly tweaked into the desired response. The entire loop usually needs to be performed only 2 or 3 times before it is exited at step 4.

Although companion modeling (a special case of a general technique known as *space mapping*) is not presently widely known, the power of this approach means that it is likely to become, in some form, the primary design flow approach for EM-based high-frequency design.

6. DIVIDE-AND-CONQUER ANALYSIS STRATEGY

No matter what approach is used to solve a problem, for some problem size, the time required becomes too large to obtain a solution in a reasonable length of time. This can happen easily when using EM analysis tools. Analysis times of days or even weeks can be easily seen. Problems that are too large for computer memory or take too long to analyze still need a solution of some kind.

Divide-and-conquer strategies are useful in many of these situations. Figure 6 shows a typical parallel-coupled line bandpass filter. While this filter is still easily analyzed as one complete filter, it serves to illustrate the divide-and-conquer strategy.

This filter is divided into eight subcircuits. Now, rather than analyzing the entire filter at once, each of the eight subcircuits is analyzed separately. Because the EM analysis time is typically proportional to the number of subsections cubed, performing eight small analyses is much faster than performing one large analysis.

After the eight subcircuits are analyzed, they are all connected together by circuit theory nodal analysis and the S parameters of the two-port filter result. In modern EM analysis software, this entire process is automatic once the user has specified the circuit subdivisions. A disadvantage of this approach is that coupling between the different sections is not included. Such coupling occurs

only between line segments that are not perpendicular to the dividing line. Thus, one should not specify any horizontal circuit dividing lines for this particular circuit as such lines are parallel to the filter's coupled lines. The coupling between resonators is critical to the filter performance and must be included. Thus, all dividing lines in this filter are perpendicular to the coupled lines of the filter.

With the circuit divided as shown, coupling between nonadjacent resonators is not included. If such coupling is important, as is the case with elliptic function filters, then this approach should not be used in a manner that causes such coupling to be eliminated from the analysis.

Extremely precise de-embedding of tightly coupled ports is required for success of this approach, as described in Section 11. If there is any port discontinuity left in any of the subcircuit ports, that remaining port discontinuity is inserted in the center of the resonators of the complete circuit. This disrupts the filter response.

Manual modification of the automatically generated netlist (which is used by circuit theory to connect all eight subcircuits together) allows an even faster analysis. Note that subcircuit S_8 is identical to subcircuit S_1 (with a rotation). Thus, switching subcircuit S_8 references to subcircuit S_1 with appropriate attention to node numbering can eliminate all references in the netlist to subcircuit S_8 .

By noting other symmetries, only four of the eight subcircuits need to be analyzed electromagnetically. This modification further cuts the analysis time by half. Measured, and calculated results are shown in Fig. 7.

7. ERROR EVALUATION

Accuracy is the primary reason in using EM analysis. If accuracy is not an issue, then the high-frequency designer should use circuit theory, which is much faster. Accuracy directly impacts whether success on first fabrication is achieved. Because of the critical importance of success on first fabrication, the issue of accuracy cannot be left to chance. All handwaving, subjective, nonquantitative claims of "high accuracy" should be ignored if such statements are made in the absence of hard quantitative data.

Because EM analysis always has some degree of error, success on first fabrication cannot be guaranteed. In a complicated circuit, there are many sources of error. Often

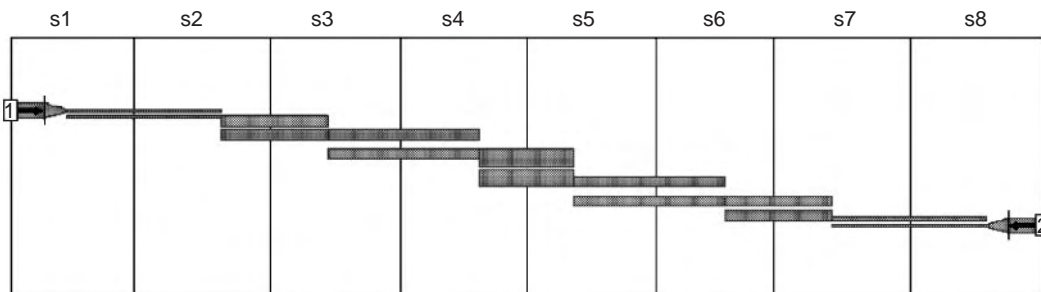


Figure 6. A parallel-coupled line bandpass filter is divided into eight smaller sections for much more rapid analysis.

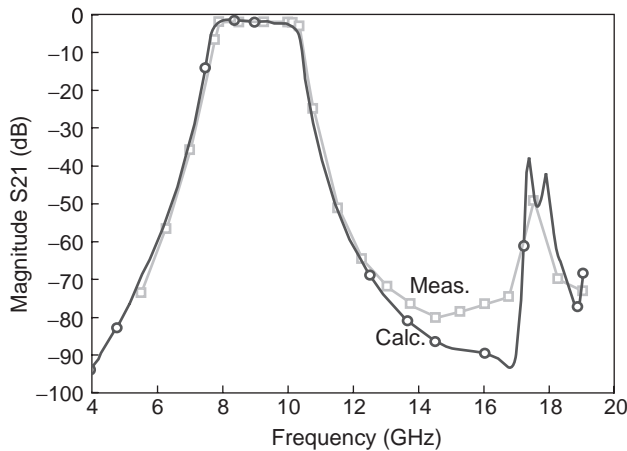


Figure 7. Measured versus calculated data show visually identical results nearly everywhere validating the divide-and-conquer approach for this filter.

these errors average out, so there is no problem. However, sometimes the errors add together in the same direction, sometimes by chance, and sometimes causally. When the errors add together, the result is a design failure. There is always a risk of failure. The successful high-frequency designer works aggressively to minimize that risk. In that way, rather than getting, say, 5 out of 10 designs to succeed on first fabrication, the knowledgeable designer sees 9 out of 10 designs succeed. The competitive advantage is substantial.

An attitude sometimes seen among high-frequency designers is that several percent error is not a problem. This can be true, depending on the circuit and on the requirements. Several percent error in the transmission-line characteristic impedance for a branchline coupler is not likely to be a problem. Several percent error in the velocity of propagation for a 5% bandwidth filter will require at least one additional fabrication. The informed designer will know when to, and when not to strive to realize absolute minimum analysis error.

A widely held, and usually untested, belief is that as long as the subsection size is small with respect to the wavelength, then EM analysis error is small. This is incorrect. In fact, subsection size must be small with respect to how rapidly (as a function of position) the current distribution changes. Thus, as described below, subsection width must be small with respect to linewidth in addition to being small with respect to wavelength. Specific quantitative knowledge of EM analysis error is critical to the design engineer's success.

The most common approach to accuracy validation involves the widespread "good agreement between measured and calculated" (GABMAC) plot, examples of which are shown in Figs. 3 and 7. While certainly important as a final reality check, the GABMAC plot is of little value for quantitative determination of analysis error as differences can be additionally due to measurement and fabrication error. Determining the magnitude of the analysis error by itself in such tests is nearly impossible.

Each of the following tests are easily performed on any EM analysis. Intended to supplement, not replace, the

usual GABMAC test, these tests use simple circuits that are easily analyzed on any EM tool and allow precise quantitative evaluation of analysis error.

7.1. The Stripline Standard

Exact theoretical solutions are known for a small set of planar problems. Such problems allow the precise evaluation of analysis error. Any and all differences between calculated data and the exact answer is analysis error.

Stripline is one such problem that has an exact solution and has been used to precisely evaluate the error of EM analysis [4]. For example, as applied to a shielded planar EM analysis, the following empirically determined upper bounds are found for analysis error

$$e_{z0} \leq \frac{16}{N_W} \quad (1)$$

$$e_V \leq 2 \left(\frac{16}{N_L} \right)^2 \quad (2)$$

where

e_{z0} = percent error in characteristic impedance

e_V = percent error in velocity of propagation

N_W = number of cells across width of line

N_L = number of cells per wavelength along length of line

These upper bounds are met nearly in equality for most of their range.

Figure 8 shows a performance plot where analysis error is plotted versus analysis time on a 3-GHz Pentium. For each data point, N_W is doubled. N_L is held constant at 1024 cells per wavelength. N_W is taken up to 1024, and although larger values can be evaluated, a larger value of N_L would be required in order to continue to see convergence. Even as it is, the error convergence starts to slow down for large N_W . It is important to note that the convergence to the exact correct answer is smooth, the error decreasing by about half each time N_W is doubled.

When the convergence is smooth, Richardson extrapolation [5,6] can be used to arrive at a nearly exact answer

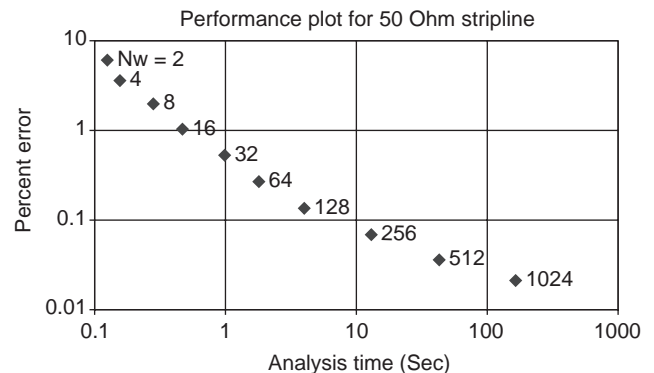


Figure 8. A performance plot shows the precise analysis error versus analysis time for an exactly known zero-thickness lossless stripline. Note the logarithmic scale on both axes.

based on two lower accuracy results. For this dataset, Richardson extrapolation converges to 0.002% error, one order of magnitude better. Note that this performance plot can be viewed as a lower bound (i.e., best possible speed/accuracy performance) for a given EM analysis. Most practical circuits are more complicated. If one were able to generate a performance plot for a more complicated circuit, the analysis time would be longer, moving the performance curve to the right. In addition, there would be more sources of error, thus moving the performance curve up. Thus the stripline standard performance plot represents a kind of starting line for the race to analyze a circuit both as quickly and as accurately as possible.

For metal-insulator-metal (MIM) capacitors [7], common on RFICs, the following upper bounds are also nearly met in equality over most of their range:

$$e \cong \frac{5.12}{1/N_A + 1/N_B} \quad (3)$$

where

e = percent capacitance error
 N_A = number of cells among capacitor length
 N_B = number of cells across capacitor length

These equations may be used to evaluate and simply subtract the error from a single EM analysis of an MIM capacitor. In fact, the analysis error of the MIM capacitor is so well behaved that an EM analysis can be used to directly determine the amount of capacitance due to fringing field, usually a very small amount.

7.2. The Zero-Length Coupled Line

Another approach is to use a coupled pair of microstrip lines. There is no exact solution for such a structure; however, there is a degenerate case that is of interest for error evaluation: the zero-length coupled line.

No EM analysis can analyze a zero-length coupled line directly. Rather, they must analyze a finite length of line and then de-embed to zero length. The exact answer is simply that all reflection coefficients and all coupled transmission coefficients must be zero, or $-\infty$ dB. Because all EM analyses have error, something other than $-\infty$ dB results. This result is the noise floor of the analysis.

Figure 9 shows that the noise floor for a shielded planar analysis is around -130 dB. Generally analysis results should not be trusted down to any more than 20 dB above the noise floor. The noise floor for this specific EM analysis has been found to range between -100 and -180 dB, depending on the circuit and mesh size used.

7.3. The Thick Stripline Benchmark

Another benchmark is thick stripline [8]. The characteristic impedance is known for the selected geometry (Fig. 10) to better than $\pm 0.0006\%$. This upper bound on the error is estimated by using the thick stripline equations for the line of Fig. 10, except that the thickness set to zero. That answer is then compared with the known exact

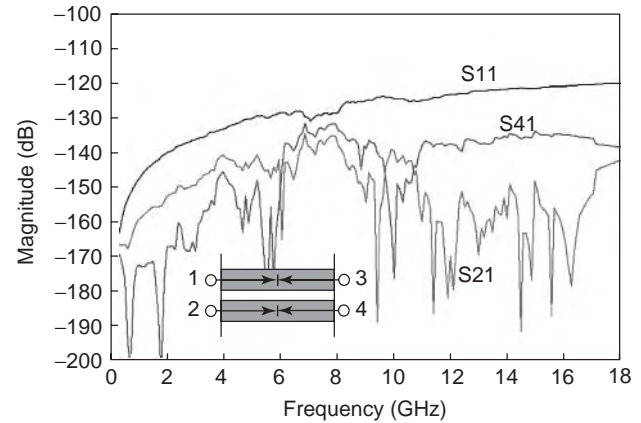


Figure 9. The exact value of S_{11} , S_{21} , and S_{41} of a zero-length coupled line should be $-\infty$ dB. The calculated values, plotted here, show that the analysis numerical noise floor is below -120 dB.

solution for zero-thickness stripline. It is at zero thickness that the thick stripline equations have maximum error; thus the difference at zero thickness is an upper bound on the thick stripline equation error when using nonzero thickness. In addition, when the zero-thickness result is compared to the result with thickness, as in Fig. 10, it is found that the characteristic impedance changes by 25% between the two cases.

Thus, we have a structure whose correct answer is known very precisely and that is also strongly dependent on the parameter of interest: thickness. This is ideal for a benchmark. Thickness is modeled in a planar analysis with multiple sheets [9]. As the number of sheets increase, and as N_W increases, the result should converge to the exact answer, as seen in Fig. 11. Note once more that the smooth convergence, with the error decreasing by about half each time, allows a Richardson extrapolation [5,6] to provide a nearly exact answer.

The error convergence has been shown to be good for this specific shielded EM analysis; a similar convergence test can be performed to quantify the expected error due to thickness for an actual design situation. In practice, it has been found that multisheet models for thickness are needed when either the width of the line, or the gap

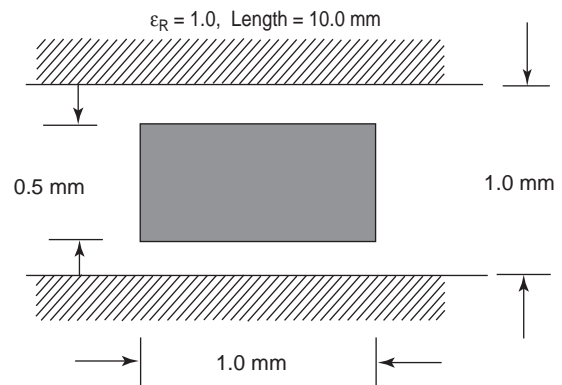


Figure 10. An extremely thick stripline is used to test the multisheet model for accuracy.

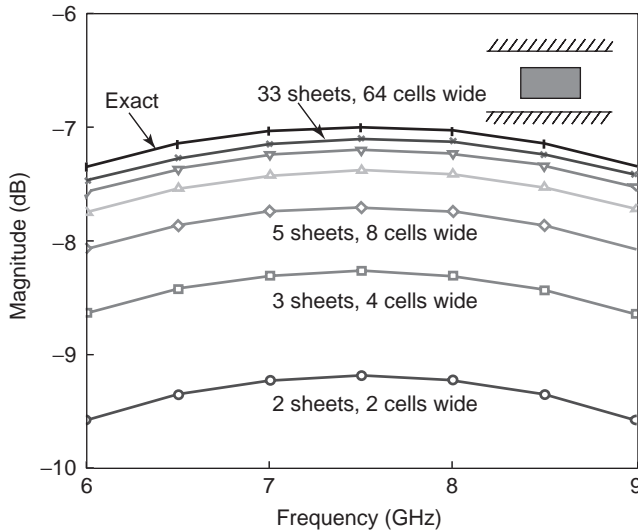


Figure 11. As the number of zero-thickness sheets used to represent this very thick stripline increases, S_{11} converges to the exact answer.

between lines, is on the order of or less than the thickness of the lines. In some RFIC situations, this can be common.

Extreme cases of thickness are becoming common as decreasing loss becomes important in RFIC design. For example, a $6\ \mu\text{m}$ metal thickness combined with a $2\ \mu\text{m}$ gap between lines would require perhaps half a dozen sheets for accurate analysis at high frequency. In this case, it is possible to simulate coupling between such closely spaced thick lines by using the two-sheet model and modifying the permittivity and permeability of nearby dielectric to compensate for the coupling that is otherwise underestimated by the two-sheet model.

8. ELECTROMAGNETIC INTERPOLATION

When using a frequency-domain analysis, which includes all the planar approaches described above, a complete analysis must be performed at each frequency. If data at 100 frequencies are required, then 100 complete analyses must be performed.

In order to reduce the number of analyses required, interpolation can be used. Substantial work in this area has been accomplished since the mid-1990s, with spectacular results. A recent (at time of writing) publication in this area, including an extensive bibliography, is Ref. 10. Here, we briefly describe only a simple approach to give an idea of what can be done.

8.1. Linear Interpolation

In high school, we are introduced to linear interpolation, where we are given two data points: (x_0, y_0) and (x_1, y_1) . We then calculate the coefficients a and b of the equation

$$y = ax + b \quad (4)$$

that passes through the two points. We can then perform an interpolation by using this equation to calculate y for

all desired values of x . While simple algebra is all that is required, the solution of this problem can also be cast in the form of a 2×2 matrix. The solution for a and b is obtained by inverting the matrix. For EM analysis, x is the frequency and y is the calculated data (usually S , Y , or Z parameters), which is complex (real and imaginary, or magnitude and angle).

8.2. Cubic Spline Interpolation

At the next level, we have the cubic spline. The process is identical to that above, except that it uses an equation that is a bit more complicated:

$$y = a_3x^3 + a_2x^2 + a_1x + a_0 \quad (5)$$

Now there are four unknown a coefficients; thus we require four data points and we invert a 4×4 matrix to solve for the four coefficients. Once that task is done, we may evaluate the equation for any and all values of x (frequency) that we desire and realize many data points after having only calculated data at four frequencies.

8.3. Padé Rational Polynomial Interpolation

The cubic spline has problems for interpolating high-frequency data. For example, if impedance or admittance is being interpolated, y might need to go to infinity (i.e., a pole). At a given frequency (x), and with finite coefficients, the result of a cubic spline cannot go to infinity. This suggests that we use a ratio of two polynomials, for example

$$y = \frac{a_3x^3 + a_2x^2 + a_1x + a_0}{b_2x^2 + b_1x + 1} \quad (6)$$

where, we have four unknown coefficients in the numerator (providing for three “zeros” in the resulting function and setting the amplitude of y at $x = 0$) and two unknown coefficients in the denominator (providing for two poles in the resulting function). With a total of six unknowns, we now require six data points. In a manner similar to that seen for the cubic spline, with six data points, we can write six linear equations (by multiplying both sides by the denominator polynomial), resulting in a 6×6 matrix. Solution of the matrix yields the six unknown coefficients.

The total number of terms both numerator and denominator must be less than or equal to the total number of data points taken. However, their distribution between numerator and denominator is arbitrary. More recent research has been directed toward finding a distribution that is optimum in some way for a given set of data.

This ratio of two polynomials is known as a *Padé rational polynomial*. By noting the similarity to the Laplace transform of a lumped circuit, we note that, given a sufficient number of terms, the Padé rational polynomial can exactly represent an arbitrary lumped circuit. However, it cannot exactly represent a distributed circuit. Thus, for high-frequency circuits, the Padé rational polynomial is generally bandlimited.

8.4. Applied Interpolation Issues

As typically applied to EM analysis, at least two analyses are initially performed. This yields two data points. Then several interpolations are formed, either with different numbers of data points, or with a different distribution of coefficients between numerator and denominator. The differences between these different interpolations (all based on the same data) are treated as an estimate of the interpolation error. While the true interpolation error can be as much as 20 dB greater than the estimate, the estimated error does tend to correctly show the frequency at which the true error is highest. The next data point is then taken at this highest error frequency. The iterative algorithm proceeds until the maximum estimated error is below a user-selected threshold.

Early application of the Padé rational polynomial to high-frequency EM analysis was limited in bandwidth, dynamic range, and occasional failure to converge. However, more recent results now provide a much more robust implementation. Basically, in addition to the actual high-frequency circuit data at each frequency, the interpolation can also make use of the tremendous amount of information contained within the method-of-moments (MoM) matrix used by the EM analysis, for example, frequency derivative information.

The advanced techniques can easily interpolate over a $1000 \times$ bandwidth (e.g., from 0.1 to 100 GHz) with analysis at 15–20 frequencies, or over a small bandwidth with analysis at only four or five frequencies, no matter how complex the response (see Fig. 12).

Even so, today's interpolation algorithms do still exhibit failure modes of which the informed designer should be aware. In one failure mode, the interpolation fails when an attempt is made to interpolate data that are below the analysis noise floor. The noise floor depends strongly on the specific EM technique, specific circuit, specific meshing, and specific frequency. Observed noise floors range from 40 to over 180 dB down for the different types of planar analyses. Special caution should be exercised

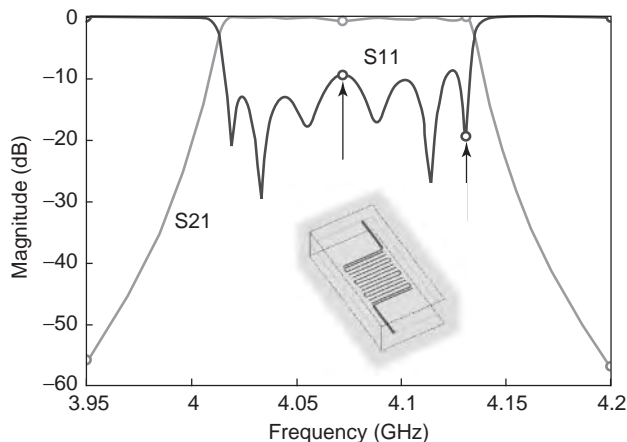


Figure 12. Only four frequencies were analyzed for this six-resonator filter: the start, stop, and the two arrowed frequencies. All the remaining data are interpolated. The interpolated data are visually identical to those from a full calculation.

whenever interpolation is invoked on data that approach to within 20 dB of the noise floor.

The second failure mode is seen in shielded analysis. Early algorithms could fail with only one box resonance. Modern algorithms are more robust, providing accurate data even with large numbers of box resonances; however, the number of data points required for convergence can be excessive. Thus, even though the resulting data are still accurate, analysis time can become excessive.

9. CONFORMAL MESHING

As described above, one advantage of the unshielded EM analysis is that the required numerical integration can be performed over any arbitrary subsection as desired. In practice, arbitrary size, shape, and orientation rectangles and triangles are used. More advanced techniques additionally include arbitrary polygons.

Shielded analyses use the FFT to calculate the coupling between subsections. While the FFT provides unsurpassed accuracy and dynamic range, it requires a fine underlying uniform FFT mesh. These tiny FFT mesh cells are joined together into larger rectangular subsections.

In order to increase speed, both shielded and unshielded analyses try to maximize use of large subsections. Large subsections substantially reduce the size of the matrix, thus speeding the analysis. However, large subsections also decrease analysis accuracy, especially when the subsections are so large that the natural high edge current is not allowed to form.

The arbitrary triangles of the unshielded analysis are a distinct advantage in analyzing arbitrary smoothly curving circuits. A few triangles can easily form a piecewise linear representation of a curving edge, especially when the error introduced by ignoring the high edge current is acceptable. However, when high edge current must be included, a large number of narrow rectangular subsections must be inserted on the conductor edges, rapidly increasing the subsection count and analysis time.

Merging the small FFT cells of the shielded analysis can be severely limited by curving geometries. Even the largest rectangular subsections must still be small, thus limiting the reduction in the number of subsections. As a small compensation, the high accuracy yielded by the small subsections is still seen. To alleviate this bottleneck, conformal meshing [11] was developed. The tiny FFT cells are still present, so the accuracy and dynamic range provided by the FFT remains uncompromised. However, instead of merging the cells into larger rectangular subsections, the cells are merged into large subsections that both cover the entire width of a transmission line and curve to follow arbitrary curving edges. In this way, a subsection count reduction of 100 times or more can be achieved. Since matrix solve time increases with the subsection count cubed, a $100 \times$ reduction in subsection count realizes a $1,000,000 \times$ faster analysis.

Normally large subsections that cover the entire width of a transmission line result in decreased accuracy because high edge current is not allowed. This is not the case with conformal mesh because the mesh automatically

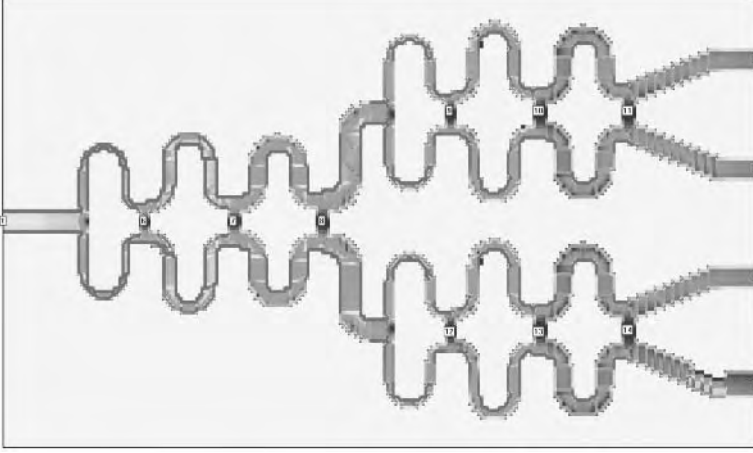


Figure 13. Conformal meshing allows analysis of this four-way power splitter including the critical high edge current in 19 s per frequency on a 3-GHz Pentium.

includes the high edge current in the conformal subsections. Thus we simultaneously achieve two seemingly contradictory goals: the fast analysis of a few large subsections and the accurate analysis of many small subsections.

Figures 2–4, presented and discussed above, show a circular 8.25-turn spiral inductor that was analyzed using conformal meshing. No other form of meshing and no other technique of analysis has yet been found to successfully analyze this inductor, including the effect of conductor thickness and high edge current. While one other approach was found to be able to complete an analysis, the result was overwhelmed with numerical noise due to the large problem size. Using conformal meshing, the inductor requires 5 min 9 s per frequency on a 3-GHz Pentium. Six frequencies were analyzed and interpolated to provide the plotted data.

Figure 13 shows a four-way power splitter analyzed using conformal meshing. Note that the high edge current is well represented, even though the analysis required only 19 s per frequency on a 3-GHz Pentium.

Conformal meshing marks a major advance in the size of problem for which numerical EM analysis can achieve fast and accurate results.

10. SHIELDED ELECTROMAGNETIC ANALYSIS THEORY

Because of the complexity of Maxwell's equations, there are innumerable methods of solution, each approach having advantages and disadvantages for a given type of problem. In this section, we describe one approach to the analysis of planar circuits in a shielded environment using the method of moments [12]. This particular solution is detailed in Refs. 13 and 14.

For the geometry of Fig. 14, we can treat the perfectly conducting sidewalls as a rectangular waveguide propagating in the z direction. The rectangular waveguide TE (transverse electric) and TM (transverse magnetic) modes in each dielectric region form a complete orthogonal basis for any source-free field. We sum all the TE and TM modes (over the composite summation index i) in each region so as to match tangential electric fields at the interface

between the two regions ($z = h$)

$$\mathbf{E}_t^{(1)} = \sum_i V_i \frac{\sin(k_{iz}^{(1)} z)}{\sin(k_{iz}^{(1)} h)} \mathbf{e}_i \quad (7)$$

$$\mathbf{H}_t^{(1)} = \sum_i V_i Y_i^{(1)} \frac{\cos(k_{iz}^{(1)} z)}{\sin(k_{iz}^{(1)} h)} \mathbf{h}_i \quad (8)$$

$$\mathbf{E}_t^{(0)} = \sum_i V_i \frac{\sin(k_{iz}^{(0)} (c - z))}{\sin(k_{iz}^{(0)} (c - h))} \mathbf{e}_i \quad (9)$$

$$\mathbf{H}_t^{(0)} = \sum_i V_i Y_i^{(0)} \frac{\cos(k_{iz}^{(0)} (c - z))}{\sin(k_{iz}^{(0)} (c - h))} \mathbf{h}_i \quad (10)$$

where

$$Y_{i,TE}^{(p)} = -jk_{iz}^{(p)} / \omega\mu_p$$

$$Y_{i,TM}^{(p)} = -j\omega\epsilon_p / k_{iz}^{(p)}$$

$$k_{i,z}^{(p)} = (k_p^2 - k_x^2 - k_y^2)^{1/2}$$

$$k_p = \omega(\mu_p\epsilon_p)^{1/2}$$

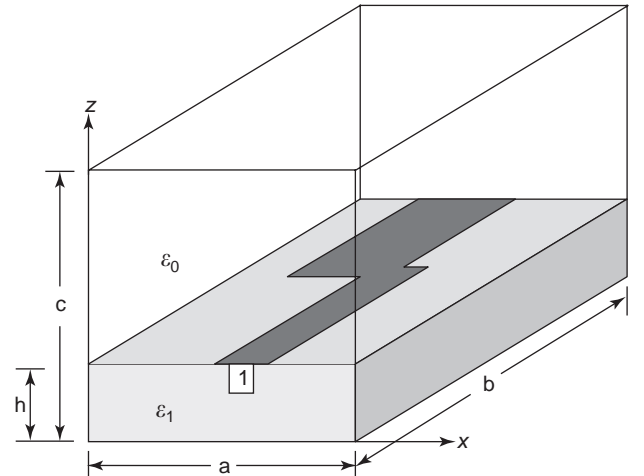


Figure 14. Shielded electromagnetic analysis views the conducting sidewalls of the shielding box as rectangular waveguide. The fields for each layer are written as a sum of waveguide modes.

$$\begin{aligned}
 k_x &= m\pi/a \\
 k_y &= n\pi/b \\
 \mathbf{e}_{i,\text{TE}} &= N_1 g_1 \mathbf{u}_x - N_2 g_2 \mathbf{u}_y \\
 \mathbf{e}_{i,\text{TM}} &= N_2 g_1 \mathbf{u}_x - N_1 g_2 \mathbf{u}_y \\
 \mathbf{h}_I &= \mathbf{u}_z \times \mathbf{e}_i \\
 g_1 &= \cos(k_x x) \sin(k_y y) \\
 g_2 &= \sin(k_x x) \cos(k_y y) \\
 N_1 &= (2/ab)^{1/2}, \quad m=0, \quad n \neq 0 \\
 N_1 &= 0, \quad m \neq 0, \quad n=0 \\
 N_1 &= 2(n/b)(ab/(n^2 a^2 + m^2 b^2))^{1/2}, \quad m \neq 0, \quad n \neq 0 \\
 N_2 &= 0, \quad m=0, \quad n \neq 0 \\
 N_2 &= (2/ab)^{1/2}, \quad m \neq 0, \quad n=0 \\
 N_2 &= 2(m/a)(ab/(n^2 a^2 + m^2 b^2))^{1/2}, \quad m \neq 0, \quad n \neq 0
 \end{aligned}$$

The modal admittances are those of the standing-wave modes, which differ from the more usual traveling-wave modes by the imaginary factor j . The amplitude of the i th mode (V_i) is determined as described below.

Note that the equations above, and this entire approach, maintain full validity for any degree of lossy or conductive substrates. The only change required is that the characteristic impedances and wavenumbers presented above become complex.

10.1. Calculating the Coupling between Subsections

The central problem is to determine the voltage on one subsection (the “field” subsection) caused by current on another subsection (the “source” subsection). It is this pairwise coupling that fills the moment matrix for every possible source–field pair of subsections.

In order to proceed, we must first assume a specific current distribution for the source subsection. We use the “rooftop” current distribution [15] (Fig. 15). In Fig. 15, the height indicates the current density over the rectangular area of the subsection. Several rooftops are overlapped to yield a piecewise linear approximation to the current in the direction of current flow (Fig. 16). Rooftops are placed side by side to yield a stepwise approximation to the actual current distribution in the direction transverse to current flow.

A given area must be subsectioned twice, once for x -directed current and a second time for y -directed current. Figure 17 shows how the x - and y -directed subsections overlap. Note that the centers of the x -directed and y -directed rooftops must be offset. This offset is required in order to allow current to flow from one rooftop to the next.

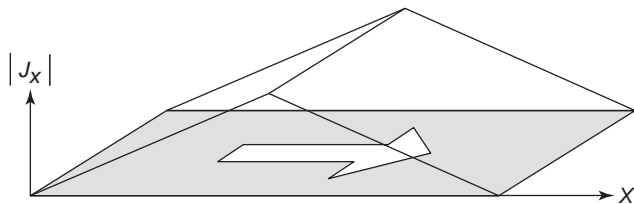


Figure 15. The vertical direction represents the current density on a rectangular subsection. Current is flowing in the x direction. This is called a “rooftop” basis function.

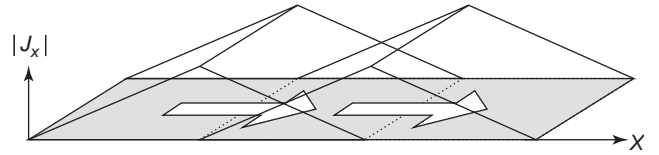


Figure 16. The total current from the sum of two overlapping rooftop basis functions yields a piecewise linear approximation to the current in the direction of the current flow.

We now evaluate the V_i so that the discontinuity in tangential H field at $z = h$ equals the rooftop current at the source subsection. With \mathbf{J}_s representing the rooftop current distribution centered on the source subsection at (x_0, y_0) , we have

$$V_i = -Z_i \iint \mathbf{J}_s(x, y, x_0, y_0) \cdot \mathbf{e}_i(x, y) dx dy \quad (11)$$

$$Z_i^{-1} = Y_i^{(0)} \text{ctn}[k_{iz}^{(0)}(c - h)] - Y_i^{(1)} \text{ctn}[k_{iz}^{(1)}h] \quad (12)$$

Note that Z_i is just the impedance of the topcover and ground plane transformed by the intervening rectangular waveguide to the surface of the substrate (at $z = h$) and connected in parallel. Extension of this technique to multiple layers requires only the modification of Z_i .

When the full forms of the vector fields \mathbf{J}_s and \mathbf{e}_i are inserted above, the expression for V_i becomes complicated; however, it is simply the sine and cosine integrals. Analytic evaluation of the integrals is tedious but straightforward. The V_i are then used in Eqs. (7)–(10) to determine the tangential electric fields everywhere due to the subsection current distribution \mathbf{J}_s .

Within the framework of the method of moments, the \mathbf{J}_s (one for each subsection) represent “basis” or “expansion” functions. The total current on a circuit is a sum of all the \mathbf{J}_s . To complete the method of moments, we must select “testing” functions. Here, we choose a Galerkin technique, in that the testing functions are the same as the basis functions.

Now, given a specific source subsection with current \mathbf{J}_s impressed on it, we calculate the voltage on a specific field subsection by multiplying the tangential electric field by a rooftop testing function centered on the field subsection and integrating over the area of the field subsection. This integration is of the same form as Eq. (11). It is once more a tedious but straightforward sine and cosine integration that is performed analytically.

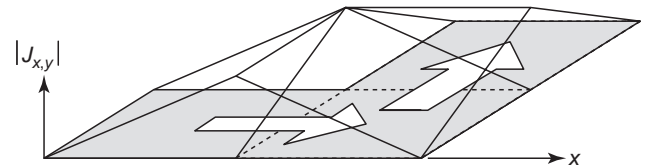


Figure 17. When a y -directed rooftop basis function overlaps half of an x -directed rooftop, current can flow around a corner. Note how the center of any x -directed rooftop must be offset from the center of any y -directed rooftop.

10.2. Solving the Moment Matrix

The process described above is repeated for every possible pair of source–field subsections. For N subsections, this fills an $N \times N$ impedance matrix, $\underline{\underline{Z}}$. The amplitude of the current density on each subsection is stored in the $N \times 1$ vector $\underline{\underline{J}}$ and the total voltage on each subsection is stored in the $N \times 1$ vector $\underline{\underline{V}}$. The resulting matrix equation is

$$\underline{\underline{V}} = \underline{\underline{Z}} \underline{\underline{J}} \quad (13)$$

Typically most of the numerical effort is in inverting the $\underline{\underline{Z}}$ matrix. This operation is of order N^3 . Values of N up to 30,000 can now be solved in about an hour on a 3-GHz Pentium. Prior to solving the matrix, we designate a few subsections as “port” subsections. Port subsections are subsections to which we plan to make outside circuit connections. After the matrix is solved, we have

$$\underline{\underline{J}} = \underline{\underline{Y}} \underline{\underline{V}} \quad (14)$$

In order to meet the boundary condition of zero voltage on a conductor, we set the voltage on all nonport subsections to zero. Once we do that, we see that we don’t even need to solve for most of the $\underline{\underline{Y}}$ matrix. If solving the matrix with LU (lower/upper) decomposition, we still must do the full decomposition. However, nearly the entire back solve step is no longer needed.

With the nonport subsection voltages set to zero, we only need the portions of the $\underline{\underline{Y}}$ matrix that deal exclusively with port subsections. If there are two port subsections, the result is a 2×2 matrix. After converting current density $\underline{\underline{J}}$ to current, and possibly changing signs (when circuit theory positively directed current is of direction opposite that of EM analysis positively directed current), this is actually the $\underline{\underline{Y}}$ matrix of the circuit and is the solution to the problem.

If the current distribution is required, additional back solve effort is applied, yielding a larger portion of the $\underline{\underline{Y}}$ matrix. For example, if there are N total subsections and two of these subsections represent ports, we need either a $2 \times N$ or a $N \times 2$ portion of the $\underline{\underline{Y}}$ matrix. Then we use Eq. (14) to calculate $\underline{\underline{J}}$ for any possible port excitations.

10.3. Application of the Fast Fourier Transform

The summation of Eqs. (7)–(10) over i is actually a two-dimensional summation over rectangular waveguide mode numbers m and n for all TE and TM rectangular waveguide modes. Performing this summation repeatedly is very slow. It is performed more efficiently by making a simple trigonometric modification.

Simplifying to one dimension for illustrative purposes, one form of the required summation for a source subsection located at x_0 and a field subsection located at x_1 is

$$S = \sum_{m=0}^M C_m \cos \frac{m\pi x_0}{M} \cos \frac{m\pi x_1}{M} \quad (15)$$

For the complete summation, the summation index m goes to infinity. However, if x_0 and x_1 are restricted to integers

in the range from 0 to M and we take advantage of the periodicity of the trigonometric functions, the entire summation may be performed over the indicated summation range by appropriate modification of the C_m .

This summation is starting to look like a Fourier cosine series, except for one problem. We have the product of two cosines, instead of one. This is easily remedied by rewriting the summation as the sum of two summations:

$$2S = \sum_{m=0}^M C_m \cos \frac{m\pi(x_0 + x_1)}{M} + \sum_{m=0}^M C_m \cos \frac{m\pi(x_0 - x_1)}{M} \quad (16)$$

Both summations are now a cosine series easily and rapidly summed by specialized FFT (fast Fourier transform) algorithms. In fact a single FFT cosine transform provides results for all possible values of $x_0 + x_1$ and $x_0 - x_1$ after taking into account the periodicity in M .

10.4. Improving Speed and Memory Requirements

For the actual two-dimensional summation (over all TE and TM waveguide mode numbers m and n), the 2D cosine transform is performed using a 2D FFT specialized for the cosine transform. Because the C_m depend on both the basis and testing functions, an additional 2D transform is required each time a different type of source or field subsection is used. For a single layer, typically three 2D FFTs are required, one each for x/x , y/y , and x/y coupling. Depending on the specific basis and testing functions, a sine transform may be required instead.

Multiple layers are accommodated by modification of Eq. (12). The modification is such that both extremely thin and extremely thick layers have no impact on accuracy or analysis time. This also changes the C_m in the summation above, so the FFTs must be repeated once more. This approach, when completely including all coupling between all layers, easily accommodates up to several hundred layers.

As mentioned above, all metal must be subsectioned twice, once for x -directed current, and a second time for y -directed current. Further, the center of all x -directed rooftops are offset with respect to the centers of the y -directed subsections. This offset is realized by restricting subsection center coordinates to either even or odd values. This means that the 2D FFTs need be performed for only half of the values of (x_0, y_0) and (x_1, y_1) . With further specialized modification, the size of the required FFTs is cut by half in both dimensions, resulting in a $4 \times$ speed increase.

Different basis and testing functions require only the modification of V_i in Eqs. (7)–(10). Other basis functions that have been implemented in shielded analysis include vias (for conducting current vertically through layers), and triangles [16]. Triangles are used to fill in the staircase that would otherwise exist when meshing with rectangular subsections. However, when comparing analysis results with and without the use of triangles, they are found to provide an advantage only when the transmission line is one or two rectangular subsections wide. If

there is symmetry along one centerline axis in the circuit, the FFTs need to include only half of the m or n modes, resulting in a further doubling of the FFT speed.

Unshielded analysis must also calculate coupling between subsections. In this case, it is worthwhile to store certain intermediate results that depend only on the dielectric geometry. In shielded analysis, the corresponding results are always calculated when needed. This is because the FFT-based calculation of these results is so fast that storing them for later use would actually slow down the analysis.

Matrix storage reduction is also possible. The most significant reduction is realized by noting that the \underline{Z} matrix is symmetric. It is relatively simple to organize LU decomposition so that storage is required for only half the matrix, cutting memory requirements by half.

Provided extremely low-frequency data are not required, all calculations can be performed in single precision, cutting storage requirements by half again. For both single and double precision, careful attention to avoiding loss of precision when dividing by the pivot element is critical. If there is potential loss of precision, then rows and columns must be pivoted. Rigorous testing for potential matrix solve problems requires running literally thousands of cases. Checking for success in only a few cases is certain to leave hidden problems.

Intel architecture computers utilize a specialized FPU (floating-point unit) that performs all calculations using 80 bits of precision. One way to minimize numerical precision problems is to leave the result of continuing calculations (e.g., dot products) and critical numbers (e.g., the pivot element) in the FPU, thus avoiding the precision loss caused by repeated truncation to single or double precision.

11. DE-EMBEDDING ELECTROMAGNETIC DATA

Whether derived from electromagnetic analysis or from measurement, high-frequency data must be properly “de-embedded” if accurate results are to be obtained. In the early days of high-frequency measurement, slotted-line techniques were used. With these approaches, a standing wave is measured on a length of transmission line (e.g., rectangular waveguide). Then, with knowledge of the transmission-line characteristic impedance, the standing-wave measurements can be converted into S -parameter data.

De-embedding approaches analogous to slotted-line measurements are in use today in planar EM analyses, primarily in unshielded environment analyses. While easily implemented, such slotted-line techniques are compromised by the necessity to independently determine the transmission line characteristic impedance. This is usually done by a separate 2D cross-sectional EM analysis. Two additional sources of error are thus introduced: (1) error inherent in the cross-sectional EM analysis and (2) error due to the determination of the characteristic impedance.

This second source of error is due to the fact that the characteristic impedance must be determined from linear

functionals of the cross-sectional fields. For example, voltage is determined by selecting a path from the line to ground and integrating the electric field over that path. While unique for lossless homogeneous media, results can range over 20% or more for typical inhomogeneous microstrip media, depending on which circuit parameters (power, current, or voltage) are calculated and which path integrals are taken. This uncertainty in the “correct” value of characteristic impedance translates directly into error in the final result.

11.1. Modern De-embedding Algorithms

For modern high-frequency measurements, a device under test (DUT) is placed in a test fixture. The test fixture is typically microstrip for connections to the DUT, and either coax or ground–signal–ground (GSG) probepads for connection to the measurement equipment. In order to characterize and remove the effect of the test fixture, a series of known standards are inserted at the location of the DUT and measured. Typical standards might include a short (circuit), open (circuit), load, and through. However, both slotted-line and many modern de-embedding approaches suffer from the fact that characteristic impedance must be independently determined. This is because these approaches cannot directly measure voltage at any point in the circuit.

In contrast, shielded EM analyses can determine both the voltage and current directly and unambiguously at ports. The shielded analyses use infinitesimal gap voltage sources at the edge of the substrate; a side view is shown in Fig. 18. Because the gap source is immediately adjacent to a perfect ground reference (the sidewall), the voltage is unique and precisely determined. With both port current and voltage known uniquely and unambiguously, the port input impedance is known as well.

11.2. De-embedding the Port Discontinuity

The problem with box sidewall ports is that the port input impedance also includes fringing fields excited by the port. The port fringing fields can be viewed as a port discontinuity including both series inductance and shunt capacitance. When loss is present, resistance and conductance may additionally be part of the port discontinuity. Now, the de-embedding problem becomes characterization of the port discontinuity.

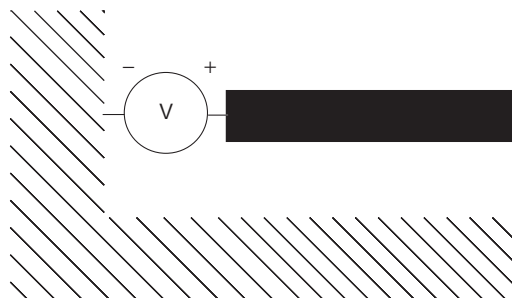


Figure 18. The shielded electromagnetic analysis uses an infinitesimal gap voltage source to excite the circuit, shown here from the side.

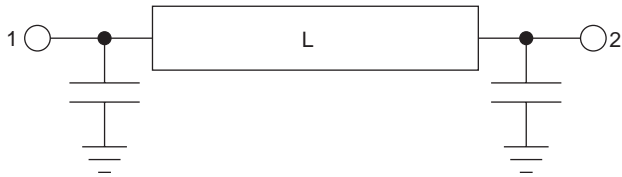


Figure 19. The L length through line shown schematically includes the port discontinuities, shown here as pure shunt capacitance. The $2L$ length through has the same port discontinuity and twice the length of the transmission line.

For the most straightforward de-embedding approach, the port discontinuity is specialized to pure shunt admittance. This is realized in the EM analysis by forcing uniform voltage along the length of the gap. This disallows transverse current at the port, effectively short-circuiting out any series port inductance. That this assumption is correct is tested as part of the de-embedding process, as described below.

The de-embedding procedure [17] first analyzes two standards, an L length through and a $2L$ length through. A schematic of the L length through including port discontinuities is shown in Fig. 19. Alternatively, only a single $2L$ length through with an internal port at L from each box wall port may be analyzed. The data for the L length through is then obtained by exciting the $2L$ length box wall ports in an odd mode to determine Y parameters of the L length through.

To characterize the port discontinuity, first convert the data for the L and $2L$ length throughs to $ABCD$ cascading parameters. Then invert the $ABCD$ parameters for the $2L$ length through and pre- and postmultiply the result by the $ABCD$ parameters for the L length through. This leaves only a cascade of the port discontinuity with itself; this is called the *double-port discontinuity*.

If the $2L$ line includes a third internal port, as mentioned above, then data for a single-port discontinuity can be uniquely determined [18]. However, if the port discontinuity is specialized to a pure shunt admittance, then the single-port discontinuity can be determined only on the basis of the L and $2L$ length $ABCD$ parameters.

If the port discontinuity is a pure shunt admittance, then $A=D=1.0$ and $B=0.0$. This leaves the C (of the $ABCD$ parameters) equal to the double-port discontinuity shunt admittance. The single-port discontinuity is determined by simply dividing C by 2.

If these conditions on A , B , and D are not met, then either the port discontinuity is not a pure shunt admittance, or another failure mode (discussed later) has occurred. If the more general technique described in Ref. 18 is used, then this self-consistency check is not possible and de-embedding failure will not be detected until it is realized that the analysis calculated incorrect results; however, a general port discontinuity can be characterized.

Once the port discontinuity has been characterized, the DUT data are de-embedded by inverting the single-port discontinuity $ABCD$ matrix and pre- and postmultiplying the DUT $ABCD$ data.

This de-embedding approach is valid for both lossless and lossy situations, including metal loss, dielectric loss, and—under the restrictions noted below—radiation loss.

11.3. Determination of Characteristic Impedance

This de-embedding approach has absolutely no need for knowledge of the characteristic impedance of the transmission lines, as it deals directly only with the terminal (port) voltages and currents. However, additional information can be obtained by de-embedding the $ABCD$ parameters (in the same way the DUT was de-embedded) of the L length through. Then, by noting the $ABCD$ parameters for an ideal TEM through line of length L

$$\begin{bmatrix} A & B \\ C & D \end{bmatrix} = \begin{bmatrix} \cos(\beta L) & jZ_0 \sin(\beta L) \\ j\frac{\sin(\beta L)}{Z_0} & \cos(\beta L) \end{bmatrix} \quad (17)$$

we can then determine [19] the “TEM equivalent” characteristic impedance Z_0 and wavenumber β of the L length line by equating (17) with the calculated $ABCD$ parameters of the L length through. We emphasize that this determination of the characteristic impedance is not required in any way for the actual de-embedding process itself.

Once the de-embedded $ABCD$ parameters of the L length through have been obtained, they can be used (by inverting them and then pre- or postmultiplying (as desired) the DUT $ABCD$ parameters) to shift the reference plane of the DUT data into the box. This is sometimes done to remove the port connecting transmission lines.

11.4. De-embedding Failure Mechanisms

This de-embedding approach fails if the through standards allow propagation of more than one transmission-line mode. This is easily detected in the double-port discontinuity data as A , B , and D are different from the values stated above. In addition, the L length line must be long enough that the port fringing fields on each end do not interact with each other. A length of at least one substrate thickness, and preferably two, is usually all that is required. If this condition is not met, then once more, A , B , and D are different from the above-stated values.

An additional failure mechanism is sometimes exhibited when radiation is allowed. Shielded analyses approximate radiation by making the topcover resistive, usually 377Ω per square. The box conducting sidewalls form a rectangular waveguide. The topcover must be positioned far enough above the DUT that it is not involved in fringing fields (i.e., near field) of the DUT. Placing the topcover above the DUT by about the size of the DUT is usually sufficient.

A radiation related de-embedding failure mode is seen when the sidewalls of the box containing the L length through form a cutoff rectangular waveguide but the sidewalls of the $2L$ length through form a propagating waveguide. Thus, the L length through does not see radiation loss, but the $2L$ length through does. The error introduced is typically small because the radiation loss for a simple through line is typically small. However, careful

inspection of the S parameters of an otherwise lossless passive structure can in this case actually show a small gain. If high-accuracy S parameters including radiation loss are important, then one should take care to make sure that the box containing the L length through is large enough to allow propagation up to the topcover. This failure mode is not detected by inspection of A , B , and D as in other failure modes.

A final failure mechanism occurs if one of the standards excites a box resonance. This resonance appears in the de-embedded data and also causes the values of A , B , and D for the port discontinuity to differ from the values stated above.

For typical high-frequency applications, the port discontinuity capacitance is a few tenths of a picofarad. Occasionally, such a port discontinuity is unimportant for a specific application and de-embedding can be skipped.

11.5. De-embedding Multiple Coupled Ports

In the case of multiple coupled ports, A , B , and D of the $ABCD$ matrices above all become, themselves, matrices. For example, if there are two ports on one side of the box, both of which are to be de-embedded, the L and $2L$ length throughs each become a pair of coupled lines and each element of the $ABCD$ matrix becomes a 2×2 matrix.

The approach is fully valid, no matter how many ports and no matter how tightly coupled they are. Analyses with several hundred ports, as tightly coupled as desired, are easily performed. The very high accuracy of this de-embedding technique for tightly coupled ports is critical in the success of divide-and-conquer analysis strategies, as described above.

12. CONCLUSION

The field of applied high-frequency numerical electromagnetics began in the 1990s and has reached an advanced state of development. Today, numerical electromagnetics is considered a necessary part of nearly any high-frequency design. The designer can now complete numerous design iterations in days, or even in hours, that previously would have taken weeks or months. Once the design is complete, success on first fabrication is now regularly enjoyed.

Future advancements in this field are likely to be outside the realm of Maxwell's equations. Specifically, interoperability with design frameworks, faster computers, and a maturation of the generally accepted RF design cycle are all likely to see activity in the near future. Numerical electromagnetics promises to play an important role in the future of both commercial and military high-frequency design.

BIBLIOGRAPHY

1. K. Breitfelder and M. Geselowitz, IEEE Virtual Museum, Microwave Featured Exhibit, Institute of Electrical and Electronics Engineers, April 2003 (online) <http://www.ieee-virtual-museum.org/> (Feb. 4, 2004).

2. J. Estes, R. Lucero, A. Pavio, and L. Zhao, Optimization of multi-layer circuits using companion models and space mapping, *MTT Int. Microwave Symp. Digest*, Workshop WFA, June, 2003.
3. J. W. Bandler, R. M. Biernacki, S. H. Chen, P. A. Grobelny, and R. H. Hemmers, Space mapping technique for electromagnetic optimization, *IEEE Trans. Microwave Theory Tech.* **42**:2536–2544 (Dec. 1994).
4. J. C. Rautio, An ultra-high precision benchmark for validation of planar electromagnetic analyses, *IEEE Trans. Microwave Theory Tech.* **42**(11):2046–2050 (Nov. 1994).
5. R. C. Booton, *Computational Methods for Electromagnetics and Microwaves*, Wiley, New York, 1992.
6. W. H. Press, B. P. Flannery, S. A. Teukolsky, and W. T. Vetterling, *Numerical Recipes*, Cambridge Univ. Press, Cambridge, UK, 1986.
7. E. H. Lenzing and J. C. Rautio, A model for discretization error in electromagnetic analysis of capacitors, *IEEE Trans. Microwave Theory Tech.* **46**(2):162–166 (Feb. 1998).
8. S. B. Cohn, Problems in strip transmission lines, *IRE Trans. MTT* **3**:119–126 (March 1955).
9. J. C. Rautio and V. Demir, Microstrip conductor loss models for electromagnetic analysis, *IEEE Trans. Microwave Theory Tech.* **51**(3):915–921 (March 2003).
10. M. Mattes and J. R. Mosig, A novel adaptive sampling algorithm based on the survival-of-the-fittest principle of genetic algorithms, *IEEE Trans. Microwave Theory Tech.* **52**(1):265–275 (Jan. 2004).
11. J. Rautio, A conformal mesh for efficient planar electromagnetic analysis, *IEEE Trans. Microwave Theory Tech.* **52**(1):257–264 (Jan. 2004).
12. R. F. Harrington, *Field Computation by Moment Methods*, Macmillan, New York, 1968; reprinted IEEE, 1993.
13. J. C. Rautio, *A Time-Harmonic Electromagnetic Analysis of Shielded Microstrip Circuits*, Ph.D. dissertation, Syracuse Univ., Syracuse, NY, 1986.
14. J. C. Rautio and R. F. Harrington, An electromagnetic time-harmonic analysis of shielded microstrip circuits, *IEEE Trans. Microwave Theory Tech.* **MTT-35**:726–730 (Aug. 1987).
15. A. W. Glisson and D. R. Wilton, Simple and efficient numerical methods for problems of electromagnetic radiation and scattering from surfaces, *IEEE Trans. Anten. Propag.* **AP-28**:593–603 (1980).
16. J. C. Rautio, Triangle cells in an electromagnetic analysis of arbitrary microstrip circuits, *MTT Int. Microwave Symp. Digest*, June 1990, pp. 701–704.
17. J. C. Rautio, A de-embedding algorithm for electromagnetics, *Int. J. Microwave Millimeter-Wave Comput.-Aided Eng.* **1**(3):282–287 (July 1991).
18. L. Zhu and K. Wu, Unified equivalent circuit model of planar discontinuities suitable for field theory-based CAD and optimization of M(H)MICs, *IEEE Trans. Microwave Theory Tech.*, **47**(9):1589–1602 (Sept. 1999).
19. J. C. Rautio, A new definition of characteristic impedance, *MTT Int. Symp. Digest*, June 1991, pp. 761–764.

FURTHER READING

D. G. Swanson, Jr. and W. J. R. Hoefer, *Microwave Circuit Modeling Using Electromagnetic Field Simulation*, Artech House, Norwood, MA, 2003.

- J. S. Hong and M. J. Lancaster, *Microstrip Filters for RF/Microwave Applications*, Wiley, New York, 2001.
- C. W. Sayre, *Complete Wireless Design*, McGraw-Hill Telecom, New York, 2001.
- I. D. Robertson, *MMIC Design*, IEEE, New York, 1995.

ARTIFICIAL MAGNETIC CONDUCTOR

RODOLFO E. DIAZ
 SERGIO A. CLAVIJO
 Arizona State University
 Tempe, Arizona

1. INTRODUCTION

An artificial magnetic conductor (AMC) [1,2] is a nearly lossless reactive surface, usually realized as a printed circuit board, that presents a reflection coefficient of the order of $+1$ to incident plane waves and simultaneously inhibits the propagation of surface waves across its surface over a prescribed band of frequencies (the so-called bandgap). Because of the in-phase reflection coefficient at the surface, the total tangential magnetic field is close to zero over its operational band, thus emulating the properties of a theoretical perfect magnetic conductor (PMC). However, whereas a true PMC would allow the grazing propagation of waves with vertical magnetic field over its surface while suppressing waves with vertical electric field, the AMC suppresses propagation of both types of waves. This combination of properties yields the following experimentally verified desirable features:

1. The radiation from a proximate, horizontal electric dipole (a wire antenna) is reflected in phase, augmenting the dipole's gain instead of canceling it, as would occur over a conventional conducting ground plane.
2. The input impedance of the dipole is increased.
3. The radiated power along the surface is dramatically reduced, leading to backlobe suppression and further increased broadside gain.

When properly designed, the AMC surface-wave bandgap will correspond to the same frequency band over which the AMC exhibits a high surface impedance, thus enabling realization of an efficient, electrically thin antenna structure. Because of features 1 and 2, the AMC is classified as a high-impedance surface. Because of feature 3, the AMC can also be classified as an artificially soft surface [3] since, for an arbitrary point source located at the center of the AMC, simultaneous cancellation of E_ϕ and H_ϕ over the surface corresponds to the suppression of radially propagating TE and TM surface waves. Because the suppression of surface waves occurs over a well-defined frequency range, the AMC is classified as an electromagnetic bandgap (EBG) structure. However, because this behavior

results from a texture with periodicity much smaller than the free-space wavelength and does not involve periodic structure resonances, the AMC is classified as a metamaterial or artificial magnetodielectric.

The latter definition is adopted here as the most appropriate. In Section 2 the artificial anisotropic magnetodielectric parameters of the AMC are derived from quasistatic analysis of its physical features. It is then shown that these parameters are sufficient to completely explain the features enumerated above. In particular it is demonstrated that the permittivity and permeability normal to the surface are the key parameters that control the surface-wave suppression properties of the AMC. The degree of control available to the engineer for designing an AMC, including its thickness, operational frequency, bandwidth of favorable reflection coefficient, and bandwidth of surface-wave suppression, is the subject of Section 3. Section 4 applies the results of Section 3 to develop a design approach for typical AMCs. Section 5 places the AMC in the context of earlier and later developments of other artificial magnetic conductors found in the literature. Finally, Section 6 highlights more recent successful applications of the AMC ranging from tunable antenna ground planes to applications as a suppressor of crosstalk between collocated antennas.

2. THE AMC AS A TWO-LAYER ARTIFICIAL UNIAXIAL ANISOTROPIC MAGNETODIELECTRIC

Figure 1 shows the original AMC embodiment, invented at UCLA in the late 1990s by Sievenpiper et al. [1,2]. It consists of an electrically thin, planar, periodic structure with vertical conductors (vias) that terminate on a periodic array of planar conductors [the frequency-selective surface (FSS)], above a conducting ground plane, that can be fabricated using low-cost printed circuit technologies.

The normal incidence reflection coefficient of this AMC surface can be derived immediately from its transmission-line representation. It turns out that for typical configurations the dielectric constant of the substrate is not a critical parameter because its thickness is so small that the electric field throughout its volume is nearly zero. The effect of the vias can likewise be ignored since for a normal incidence wave the electromagnetic fields are transverse to them and therefore are nearly invisible (or, stated another way, the transverse polarizability of thin metallic cylinders perpendicular to both E and H fields is negligible). Therefore, the groundplane is a short circuit in the transmission line of free space, above which, at a distance

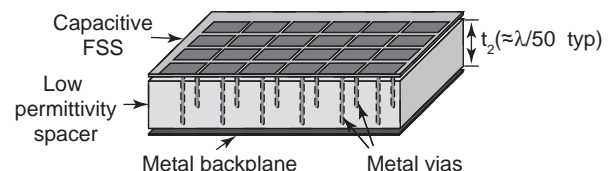
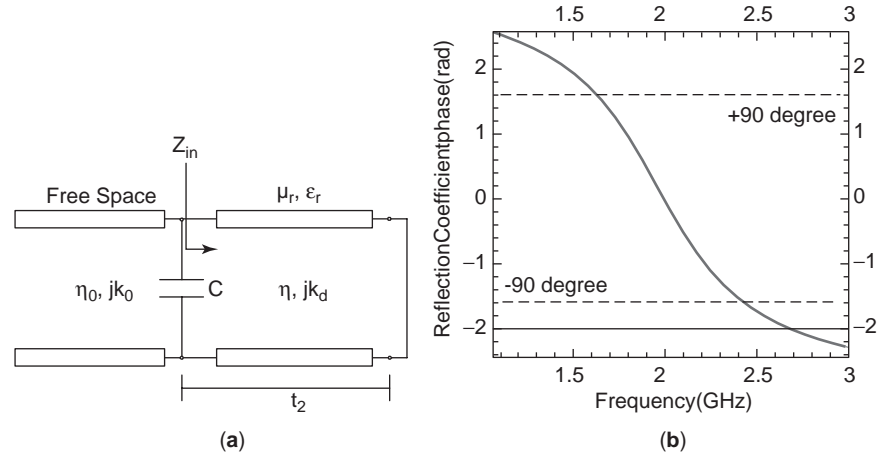


Figure 1. Sievenpiper high-impedance surface.

Figure 2. Transmission-line representation of the normal incidence reflection properties of the AMC (a) yields the typical reflection phase–frequency plot (b). In the example of (b) the center or resonance frequency is 2 GHz and the useful reflection coefficient band extends from 1.65 to 2.35 GHz.



t_2 , there is a large shunt capacitance. The value of the shunt capacitance is chosen to resonate the short circuit so that just above the capacitive sheet the short (circuit) is electrically a quarter-wavelength away at the design frequency. Clearly the phase angle of the reflection coefficient is 0° at this frequency and must vary from $+180^\circ$ at DC to -180° at the frequency where the short is electrically a half-wavelength away. The operational band of the AMC, from the standpoint of favorable reflection coefficient, is then defined as the frequency band bounded by the $+$ and -90° phase frequencies, since at those frequencies the radiation from the image of a horizontal electric dipole does not subtract from the source radiation. It is also the band of frequencies for which the wave impedance for plane wave incidence is greater than that of free space. Figure 2 illustrates these considerations.

The fractional bandwidth of a typical Sievenpiper AMC structure is defined by its normal incidence reflection properties using the transmission-line model. The impedance of the transmission line is the dielectric substrate's impedance for normally incident TEM waves η with its corresponding propagation constant $\beta = k_d$. The input impedance of the short(-circuit) transmission for normal incidence is

$$Z_{in} = j\eta \tan(k_d t_2) \quad (1a)$$

With the assumption of an electrically thin structure ($\tan(k_d t_2) = k_d t_2$), this impedance can be simplified as

$$Z_{in} = j\omega\mu_D\mu_0 t_2 = j\omega L \quad (1b)$$

Therefore, the transmission line can be replaced by its total series inductance L , which is then in series with the short circuit forming a tank LC circuit with the FSS capacitor, of resonant frequency $\omega_0 = (LC)^{-1/2}$. (It should be noted that the inductance involved here has nothing to do with the via rods; they are essentially transparent to a normally incident plane wave.)

The reflection coefficient of this simplified circuit tuned to resonate at a center frequency of ω_0 can be obtained

easily as a function of frequency:

$$\Gamma(\omega) = \frac{j\omega t_2 \mu_D \mu_0 - \eta_0 \left(1 - \left(\frac{\omega}{\omega_0}\right)^2\right)}{j\omega t_2 \mu_D \mu_0 + \eta_0 \left(1 - \left(\frac{\omega}{\omega_0}\right)^2\right)} \quad (2)$$

Defining f_{up} as the frequency at which the phase of the reflection coefficient of Eq. (2) crosses -90° , $\Gamma = -j_1$, and f_{low} the frequency at which it crosses $+90^\circ$, $\Gamma = j_1$, and substituting these two values of Γ into the equation, it is easy to show that for thin high-impedance surfaces, the bandwidth $BW = f_{up}/f_{low}$ is given by

$$\frac{BW - 1}{\sqrt{BW}} = \frac{\omega_{+90} - \omega_{-90}}{\omega_0} = 2\pi\mu_D \frac{t_2}{\lambda_0} \quad (3)$$

Thus, to support a 10% instantaneous bandwidth an AMC with purely dielectric, nonpermeable ($\mu_D = 1$) substrate need be only $\frac{1}{62}$ th of a wavelength thick. In applications requiring wide instantaneous bandwidth, for example, to accommodate an octave frequency range ($BW = 2$), the AMC thickness must be over a tenth of a free-space wavelength thick ($t_2 = 0.113 \lambda_0$). This thickness may be too large for some applications, and thus magnetically loaded AMCs ($\mu_D > 1$) have been designed. The limiting case of a Sievenpiper AMC is one whose thickness is a full $\lambda_0/4$, and whose FSS capacitance has gone to zero. The exact phase bandwidth for this thick case (maximum instantaneous bandwidth for an AMC) is 3–1 or 100% fractional bandwidth.

The transmission-line model of the reflection coefficient of the AMC just described illustrates the fact that the AMC derives its in-phase reflection coefficient property from a “quarter-wave ground plane” effect. This in itself is not a novel accomplishment since physically thin but electrically quarter-wave-thick ground-plane structures are trivial to construct using high-dielectric-constant materials. However, such structures are useless in practice for gain enhancement of antennas because the preferred mode of radiation of a horizontal dipole above a dielectrically clad ground plane is into the surface waves and not

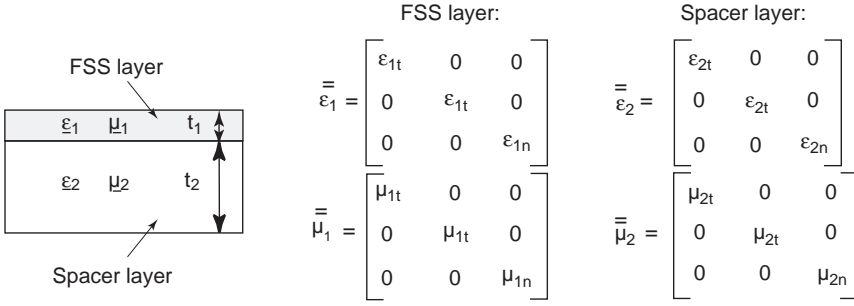


Figure 3. Effective medium model and parameters for AMC.

into free space. The key to the usefulness of the AMC is therefore that its surface-wave suppression properties occur in the same band in which the reflection coefficient is in phase. This can be accomplished only by exploiting its anisotropic degrees of freedom.

In the following analysis we assume that the periodicity of the unit cells in the AMC is very small compared to the wavelength so that it can be modeled in terms of effective medium theory, treating the quasielectrostatic and quasimagnetostatic features separately. We also assume a square lattice, with equal periods in both the x and y directions. Because of the form of the AMC structure, we choose to separate the effective medium into two distinct layers. The “spacer” layer or “rodded medium” layer consists of a regular array of conducting vias connected to the conducting backplane. This is covered by a capacitive “FSS” layer, which consists of a regular array of metal patches. Although the FSS layer can be infinitely thin in theory, we assign it a finite (and somewhat arbitrary) thickness in the effective medium representation. Because of the symmetry of the structure, both layers can be modeled with uniaxial permittivity and permeability tensors. Figure 3 shows the effective media model layers and associated permittivity and permeability tensors.

2.1. Effective Medium Model for the Substrate

In order to derive the values for the elements of these tensors, first consider a medium consisting of an array of infinite rods. When an electric field exists throughout the whole space (such as in the low-frequency limit of a wave traveling through this “forest” of rods), symmetry considerations allow us to concentrate on one unit cell of the array. In the quasielectrostatic limit, that cell has PEC plates at $z=0$ and $z=h$ (arbitrary) and PMC walls all around, as in Fig. 4.

As Fig. 4 suggests, the actual shape of the PMC boundary of the unit cell cannot possibly be a significant factor in the quasistatic effective medium behavior of this

array, and so we take it to be a cylindrical boundary of equal cross-sectional area. If the array is immersed in free space, the only polarization vector is that inside the rods, and thus the only excess current in this space comes from the rod current $\partial P/\partial t$. Assuming that the rods are metal, this is purely a conduction current. It creates a circulating magnetic field inside the unit cell that starts at the surface of the rod and vanishes on the surrounding PMC surface (since H tangential to a PMC must vanish). Integration of the magnetic energy inside the unit cell and setting it equal to $\frac{1}{2} I^2 L$ yields

$$L = \frac{\mu h}{4\pi} \left[\ln\left(\frac{1}{\alpha}\right) + \alpha - 1 \right]; \quad \alpha = \frac{\pi a^2}{d^2} \quad (4)$$

where α is the ratio of the rod’s cross-sectional area, to the cross-sectional area of the unit cell.

The circuit describing the unit cell is then the capacitance of the cell $\epsilon_0 \epsilon_D A/h$ in parallel with the inductance. The effective capacitance of that circuit is

$$C_{\text{eff}}(\omega) = \frac{1}{j\omega} Y = \frac{1}{j\omega} \left(j\omega \frac{\epsilon_D \epsilon_0 A}{h} + \frac{1}{j\omega L} \right) \quad (5)$$

$$= \frac{\epsilon_D \epsilon_0 A}{h} - \frac{1}{\omega^2 L}$$

The effective permittivity is then the effective capacitance of that circuit divided by the capacitance of the empty unit cell:

$$\epsilon_{\text{eff}}(\omega) = \epsilon_D - \frac{1}{\omega^2 \epsilon_0 \frac{\mu A}{4\pi} \left[\ln\left(\frac{1}{\alpha}\right) + \alpha - 1 \right]} \quad (6)$$

Thus, at low frequencies it is negative, and it crosses zero at the so-called plasma frequency, defined as the frequency at which the unit cell resonates.

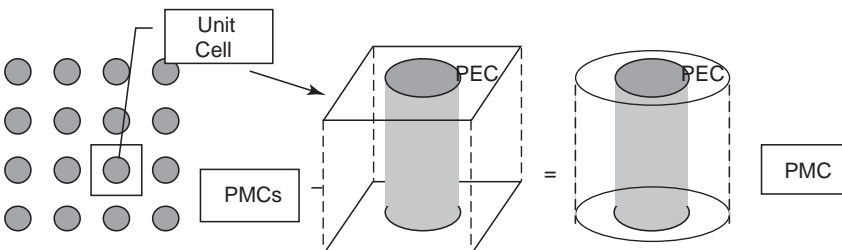


Figure 4. Equivalent unit cell for the rodded medium.

This medium was analyzed on the basis of its periodic structure properties by Brown [4], under the assumption of thin rods arrayed in a square lattice. His solution is obtained from solving the equation

$$\cos\left(\frac{2\pi l}{\lambda} n\right) = \cos\left(\frac{2\pi l}{\lambda}\right) + \frac{\lambda}{2l} \frac{\sin\left(\frac{2\pi l}{\lambda}\right)}{\ln\left(\frac{l}{2\pi\rho}\right) + F\left(\frac{d}{\lambda}\right)} \quad (7)$$

where l is the distance between rods, n is the effective refractive index referenced to the background in which the wavelength is measured, and the correction function F can be approximated by

$$F\left(\frac{d}{\lambda}\right) \approx 0.15 \left(\frac{d/\lambda}{0.5}\right)^2 \quad (8)$$

Setting $\epsilon_{\text{eff}}^{\text{Brown}}(\lambda) = n^2$, the results of Brown's model can be compared to the effective medium model. Figure 5 shows the comparison for rods of radius 0.18 mm, spaced 2.4 mm center to center in a Cartesian array. Note the close agreement. For rods that are not thin compared to the separation between them (breakdown of Brown's equation), the quasistatic analysis above continues to be self-consistent. However, for rod separations that are not a small fraction of the wavelength, Brown's equation correctly predicts the periodic structure scattering above the frequency where the effective permittivity crosses zero. The quasistatic model does not include this phenomenon. Therefore, in designing an AMC where the negative values of the normal permittivity are crucial, Eq. (6) and its derivation can be used. It has the advantage that it allows the designer to consider the effect of loading the vias with lumped elements such as series inductors, and evaluate the effect this would have on the effective med-

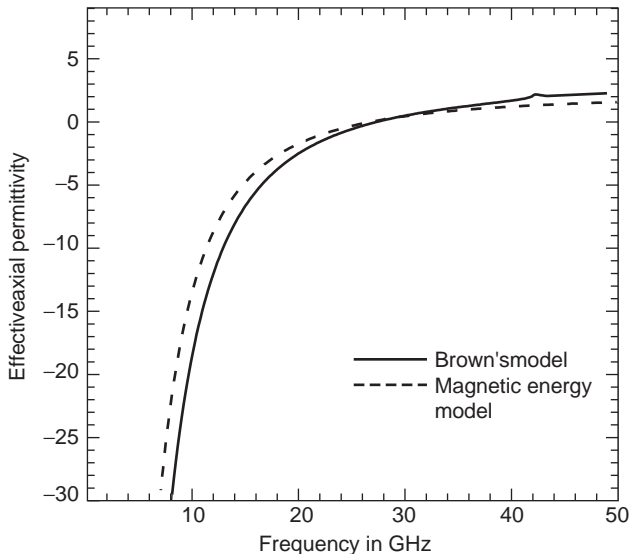


Figure 5. Comparison of the effective axial permittivity of the rodded medium in the quasistatic approximation (red dashed curve) and in the periodic solution of Brown (black curve).

ium properties of the AMC. However, for predicting the AMC performance at frequencies where the normal permittivity of the substrate becomes positive, it is mandatory to use Brown's equation.

The reader might wonder how a thin substrate consisting of this periodic array of vias can be modeled by the same equations that describe a medium of infinitely long rods. The answer lies in the terminating metal plates of the capacitive FSS layer. The current in the via rod continues onto the FSS metal plates and spreads radially out within the unit cell all the way to the end of the periodic cell. Thus the upper metal plates act as a ground plane mirroring the lower ground plane and thus creating, by virtue of the theory of images, effectively infinite rods. That this mechanism is crucial to the proper functioning of AMCs has been proved by electrically disconnecting the via rods from the FSS layer. In that case the AMC's TM surface suppression properties quickly vanish as the separation between the vias exceeds the height of the vias.

The transverse permittivity of the rodded medium is obtained by simply invoking the Clausius–Mosotti formula for a two-dimensional array of infinite metallic cylinders. The effective property is due to the transverse polarization of the rods and is simply given by

$$\epsilon_{xx2} = \epsilon_{yy2} = \epsilon_D \left(\frac{1 + \alpha}{1 - \alpha} \right) \quad (9)$$

The transverse permeability can be deduced from the following argument. A TEM wave traveling along the rods (z direction) must experience ϵ_{xx} and μ_{yy} (or ϵ_{yy} and μ_{xx}) and yet must have a phase velocity equal to that of the background dielectric:

$$v_{\text{phase}} = \frac{c}{(\epsilon_D \mu_D)^{1/2}} \quad (10)$$

It follows that for this rodded medium

$$\mu_{xx} = \mu_{yy} = \frac{\epsilon_D}{\epsilon_{xx}} \mu_D \quad (11)$$

Finally, the z -directed permeability of the rodded layer is deduced by recognizing that a PEC rod excludes the magnetic field from its interior, thus reducing the cell permeability and creating an effective unit cell that is diamagnetic:

$$\mu_{zz} = (1 - \alpha) \mu_D \quad (12)$$

2.2. Effective Medium Model for the FSS

Next we must consider the FSS layer. For the single-layered ‘‘Cohn square’’ structure that makes up the FSS layer of the original Sievenpiper embodiment of an AMC (Fig. 1), the effective permittivity in the x and y directions comes from the edge-to-edge capacitance induced whenever there is a planar component of the electric field. For both TM waves (magnetic field perpendicular to the plane

of incidence) and TE waves (electric field perpendicular to the plane of incidence), there is such a planar electric field, and so it is expected that both cases experience an effective transverse (x - y) permittivity. However, the only case where the magnetic field is affected by the (assumed extremely thin) metal squares of the FSS is when it has a component perpendicular to the plane (the TE case). The eddy currents induced on the squares repel the magnetic field and allow it to flow only through the gaps between the squares. Thus it is expected that the TE case will exhibit a normal permeability that is depressed below the value of free space. These effective constitutive properties can be derived rigorously from the classic case of the periodic strip surface as a shunt obstacle in the transmission line of free space.

First, for the following derivations we will need to define the TE and TM impedances and propagation constants for uniaxial anisotropic media where the x - and y -axis properties are equal and the z (normal to the plane) properties are different. These expressions are [5,6]

$$Z_n^{\text{TM}} = \frac{k_{zn}^{\text{TM}}}{\omega \epsilon_0 \epsilon_{xn}} \quad Z_n^{\text{TE}} = \frac{\omega \mu_0 \mu_{xn}}{k_{zn}^{\text{TE}}} \quad (13)$$

$$k_{zn}^{\text{TM}} = k_0 \sqrt{\mu_{yn} \epsilon_{xn} - \left(\frac{k_x}{k_0}\right)^2 \frac{\epsilon_{xn}}{\epsilon_{zn}}} \quad (14)$$

$$k_{zn}^{\text{TE}} = k_0 \sqrt{\mu_{xn} \epsilon_{yn} - \left(\frac{k_x}{k_0}\right)^2 \frac{\mu_{xn}}{\mu_{zn}}}$$

2.2.1. The TM Case. When a wave with its E field in the x - z plane and H field in the y direction is incident at an angle θ as shown in Fig. 6 on a Cohn square FSS in free space, its total tangential E field on the metal squares goes to zero. It follows that for narrow gaps between the squares, the total E field in the x direction in that plane also tends to zero in the gaps aligned with the x direction. To first order the only relevant field is the one concentrated in the gaps aligned with the y axis, implying that the behavior of the Cohn square FSS [7] must be the same as that from a plane of parallel infinite strips aligned with the y axis. The solution for this latter case is well known [8].

According to Ref. 8 considering the plane of the strips a shunt obstacle, the input admittance for arbitrary angles

of incidence is

$$Y_{\text{in}} = Y_0 \cdot \left[1 + j \cdot \frac{4d}{\lambda_0 \cos \theta} \cdot \ln \left(\csc \frac{\pi b'}{2d} \right) \right] \quad (15)$$

Realizing that k_{z0} is just $2\pi/\lambda_0 \cos \theta$, we have

$$Y_{\text{in}} = Y_0 \left[1 + j \frac{2d}{\pi} k_{z0} \ln \left(\csc \frac{\pi b'}{2d} \right) \right] \quad (16)$$

where Y_0 is the admittance of free space, d the periodic unit length, k_{z0} the propagation constant of the incident plane wave in the z direction corresponding to a free-space propagation constant $k_0 = \omega/c$, and b' the gap between the strips.

If, however, the FSS layer were modeled as a material layer of thickness t_1 with uniaxial anisotropic properties, the input admittance could also be obtained using the transmission-line equation where the load is the free space behind the FSS and the transmission line is the FSS layer

$$Y_{\text{in}} = Y_0 \frac{\cos k_{z1} t_1 + j \left(\frac{k_{z0}/\omega \epsilon_0}{k_{z1}/\omega \epsilon_0 \epsilon_x} \right) \sin k_{z1} t_1}{\cos k_{z1} t_1 + j \left(\frac{k_{z1}/\omega \epsilon_0 \epsilon_x}{k_{z0}/\omega \epsilon_0} \right) \sin k_{z1} t_1} \quad (17)$$

where k_{z1} is the z -directed propagation constant in the FSS equivalent material layer, given by

$$\left(\frac{k_{z1}}{k_0} \right)^2 = \mu_y \epsilon_x - \left(\frac{k_x}{k_0} \right)^2 \frac{\epsilon_x}{\epsilon_z} \quad (18)$$

where ϵ_x , ϵ_z and μ_y are the relevant constituent parameters of the material tensor for TM incidence and k_x is the propagation constant in the x direction of the waves in all the layers. Under the assumption that t_1 is small and that the permittivity of the FSS layer in the z direction and the permeability in the y direction are 1 (since the ideal FSS is infinitely thin), Eq. (17) reduces to

$$Y_{\text{in}} = Y_0 \frac{1 + j \frac{k_{z0}/\omega \epsilon_0}{k_{z1}/\omega \epsilon_0 \epsilon_x} k_{z1} t_1}{1 + j \frac{k_{z1}/\omega \epsilon_0 \epsilon_x}{k_{z0}/\omega \epsilon_0} k_{z1} t_1} = Y_0 \frac{1 + j \epsilon_x k_{z0} t_1}{1 + j \frac{(k_{z1})^2 t_1}{\epsilon_x k_{z0}}} \quad (19a)$$

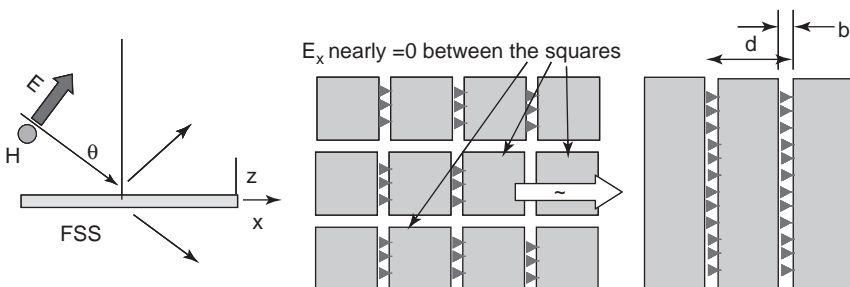


Figure 6. Incidence of a plane TM wave onto the Cohn square FSS can be approximated with the problem of the scattering from a strip array.

and since $kz_1^2 = k0^2 \epsilon_x (1 - (kx/k0)^2) = k0^2 \epsilon_x (kz_0/k0)^2$, it follows that $kz_1^2/kz_0 = kz_0 \epsilon_x$ and, again assuming $kz_0 t_1$ very small compared to 1, Eq. (19a) becomes

$$Y_{\text{in}} = Y_0 \frac{1 + j \epsilon_x k_{z0} t_1}{1 + j k_{z0} t_1} \approx Y_0 [1 + j \epsilon_x k_{z0} t_1] \quad (19b)$$

Comparing Eq. (19b) to Eq. (16), we conclude that the FSS layer has an effective x -directed relative permittivity equivalent to a pure shunt capacitance that is angle-independent, given by

$$\epsilon_x = \frac{2d}{\pi t_1} \ln \left(\csc \frac{\pi b'}{2d} \right) \quad (20a)$$

Since the FSS layer is not floating in space but supported by a dielectric substrate, the result of Eq. (20) is increased in practice by the average relative permittivity ϵ_{avg} of the dielectric materials surrounding the FSS and the final result for the transverse effective relative permittivity is

$$\epsilon_{xx} = \frac{2d}{\pi t_1} \ln \left(\csc \frac{\pi b'}{2d} \right) \epsilon_{\text{avg}} \quad (20b)$$

For thin gaps the logarithm term simplifies to $\ln(2d/\pi b')$. It should be noted that this result is simply the statement $\epsilon_1 = C_{\text{FSS}}/t_1$, where C_{FSS} is the capacitance in farads per square of the FSS sheet.

2.2.2. The TE Case. The TE case is analyzed following a parallel procedure. The z -directed propagation constant in the uniaxial medium for TE is given by

$$\left(\frac{k_{z1}}{k_0} \right)^2 = \epsilon_y \mu_x - \left(\frac{k_x}{k_0} \right)^2 \frac{\mu_x}{\mu_z} \quad (21)$$

Knowing that t_1 is small, the input impedance for the material layer model is given by Eq. (22), while the TE incidence result from Ref. 8 for the FSS as a shunt obstacle is still given by Eq. (16):

$$Y_{\text{in}} = Y_0 \frac{1 + j \frac{k_{z1}/\omega \mu_0 \mu_x}{k_{z0}/\omega \mu_0} k_{z1} t_1}{1 + j \frac{k_{z0}/\omega \mu_0}{k_{z1}/\omega \mu_0 \mu_x} k_{z1} t_1} \quad (22)$$

$$= Y_0 \frac{1 + j \left(\frac{k_{z1}}{k_{z0}} \right)^2 \frac{k_{z0} t_1}{\mu_x}}{1 + j k_{z0} \mu_x t_1}$$

But we know that μ_x is approximately 1 and that $k_z = k_0 \cos \theta$, so that

$$Y_{\text{in}} \approx Y_0 \left(1 + j \left(\frac{k_{z1}}{k_0} \right)^2 \frac{k_{z0} t_1}{\cos^2 \theta \mu_x} \right) \quad (23)$$

Finally, using Eq. (21), and $k_x = k_0 \sin \theta$, we have

$$Y_{\text{in}} = Y_0 \left[1 + j \frac{k_{z0} t_1}{\cos^2 \theta} \left(\epsilon_y - \sin^2 \theta \frac{1}{\mu_z} \right) \right] \quad (24)$$

In order for Eq. (24) to be equivalent to Eq. (16), the θ -dependent terms must vanish. This can happen only if ϵ_y is the inverse of μ_z :

$$\epsilon_{yy} = \frac{1}{\mu_{z \text{ strips}}} = \frac{2d}{\pi t_1} \ln \left(\csc \frac{\pi b'}{2d} \right) \quad (25)$$

This relation shows us that the normal permeability of the strip layer is the inverse of the transverse permittivity because to the extent that the structure concentrates the in-plane E field, to the same extent that it squeezes the normal H field. In other words if we were to consider a TEM wave guided along the strips of the strip medium, it would have to travel at the speed of light, yet its concentration of electric field is equivalent to an increased permittivity. Therefore the squeezing of the H field must be equivalent to a depressed (diamagnetic) permeability exactly the inverse of the increased permittivity. The depression of the normal permeability is therefore a geometric effect proportional to the ratio of gap area to blocking metal area. (Note that if we were to ignore the effective normal permeability of the FSS, we would be forced to model the FSS as an angle-dependent shunt capacitance.)

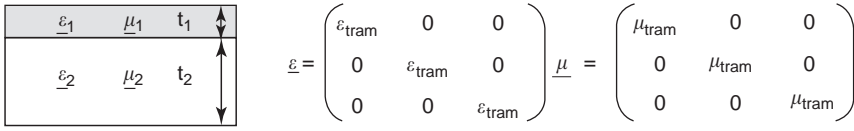
Therefore, since for the case of the Cohn square FSS the number of gaps per unit cell is double that found in the strip medium, we can write

$$\mu_{zz} = 2 \frac{\epsilon_{\text{avg}}}{\epsilon_{xx}} \quad (26)$$

where it is recognized that the squeezing of the magnetic field lines is a purely geometric effect and therefore any enhancement of the transverse permittivity due to the dielectric supporting the FSS must be ignored. Finally, as discussed during the derivation above, because the FSS is thin, ϵ_{zz} , μ_{xx} , and μ_{yy} are all simply equal to unity.

Thus, using an effective medium model, it is possible to derive closed-form expressions for a two-layer equivalent uniaxial magnetodielectric medium that should mimic all the properties of the AMC. This model is summarized in Fig. 7.

The method of derivation has been detailed above to allow the engineer to obtain equivalent representations for alternative designs. For instance, if a different capacitive FSS is used, it follows that the transverse permittivity of the FSS layer is simply $\epsilon_1 = C_{\text{FSS}}/t_1$. The normal permeability of the FSS, however, is not as easy to determine since it requires solving the quasimagnetostatic eddy current problem for determining the blockage of the magnetic field. As a rule of thumb, any FSS that obtains its capacitance from maximally blocking metal structures will obey Eq. (26). Maximally blocking structures are those where the closed metal paths cover the largest possible area with minimized perimeter. So, for instance,



$$\underline{\underline{\epsilon}} = \begin{pmatrix} \epsilon_{\text{tram}} & 0 & 0 \\ 0 & \epsilon_{\text{tram}} & 0 \\ 0 & 0 & \epsilon_{\text{tram}} \end{pmatrix} \quad \underline{\underline{\mu}} = \begin{pmatrix} \mu_{\text{tram}} & 0 & 0 \\ 0 & \mu_{\text{tram}} & 0 \\ 0 & 0 & \mu_{\text{tram}} \end{pmatrix}$$

$\epsilon_{1\text{tran}} = \frac{2d}{\pi t_1} \ln \left(\frac{d2}{\pi b'} \right) \epsilon_{\text{avg}}$ $\epsilon_{1\text{zz}} = 1$ $\mu_{1\text{tran}} = \mu_D$ $\mu_{1\text{zz}} = \frac{2\epsilon_{\text{avg}}}{\epsilon_{1\text{tran}}} \mu_D$ <p style="text-align: center;">FSS Layer</p>	$\epsilon_{2\text{tran}} = \epsilon_D \left(\frac{1 + \alpha}{1 - \alpha} \right)$ $\epsilon_{2\text{zz}} = \epsilon_D - \frac{1}{\omega^2 \epsilon_0 \frac{\mu A}{4\pi} \left[\ln \left(\frac{1}{\alpha} \right) + \alpha - 1 \right]}$ $\mu_{2\text{tran}} = \frac{\epsilon_D}{\epsilon_{2\text{tran}}} \mu_D \quad \mu_{2\text{zz}} = (1 - \alpha) \mu_D$ <p style="text-align: center;">Via array Substrate</p>
---	--

Figure 7. Summary of effective media parameters for the Sievenpiper AMC.

Cohn squares, hexagonal patches, or even closed square loops are maximally blocking. However, a gapped loop is the opposite of a maximally blocking structure since at low frequency the magnetic field can cross through the area inside the loop, owing to the interruption of eddy current by the gap. In such low-blockage cases the normal permeability can be estimated by rearranging the metal into parallel strips, calculating the capacitance of that “equivalent” strip medium and then using Eqs. (20) and (26).

Clearly, two FSS layers attaining the same capacitance, one using Cohn squares (which maximally block magnetic flux) and one using multilegged dipoles (with minimal blockage) will yield extremely different μ_{normal} values. The consequences of the choice of FSS topology is manifested in the surface-wave suppression properties of the AMC.

3. ELECTROMAGNETIC PROPERTIES IN TERMS OF THE EQUIVALENT EFFECTIVE MEDIA MODEL

The effective media model of the AMC is now used to calculate the surface-wave propagation properties of the structure. It is shown that the negative axial permittivity of the lower layer is the parameter responsible for the TM surface-wave properties and the creation of the lower band edge, while the highly diamagnetic normal permeability of the upper layer pushes the onset of TE surface waves above the resonant frequency of the AMC, thus creating the upper band edge.

The problem of solving the two-layer grounded slab is a boundary value problem, which can be solved completely using the wave equation subject to the appropriate boundary conditions. This solution is simplified by using the transverse resonance method (TRM), whereby the eigenvalue problem for a wave traveling in a preferred direction can be solved as a resonant transmission line in the transverse plane. The transverse resonance condition in the transverse plane is simply

$$Z_{\text{up}} + Z_{\text{down}} = 0 \quad (27)$$

where Z_{up} is the input impedance looking up and Z_{down} the input impedance looking down the transmission line, as seen in Fig. 8. The reference plane where the TRM is applied may be any convenient location along the equivalent transmission line (Fig. 8), and in this analysis it is chosen to be the outer surface of the AMC.

For a grounded two-layer slab as suggested in Fig. 8, the TR condition equality becomes

$$Z_0(Z_1 - Z_2 \tan(k_{z2}t_2) \tan(k_{z1}t_1)) + Z_1(jZ_2 \tan(k_{z2}t_2) + jZ_1 \tan(k_{z1}t_1)) = 0 \quad (28)$$

where Z_0 , Z_1 , and Z_2 are the corresponding wave impedances in layers 0 (air), 1, and 2 and the corresponding propagation constants k_{z1} and k_{z2} are as given in Eqs. (13) and (14). From this point on, the subscripts 0, 1, and 2 will refer to layers 0, 1, and 2, respectively, as shown in Fig. 8. As a rule, the fictitious thickness of the FSS is set to $t_1 = t_2/100$.

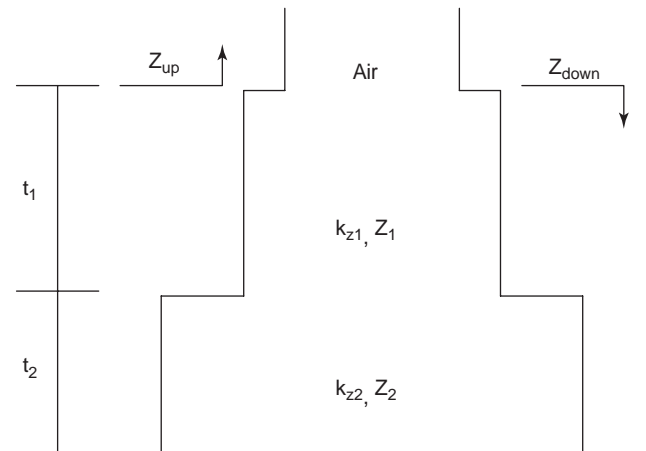
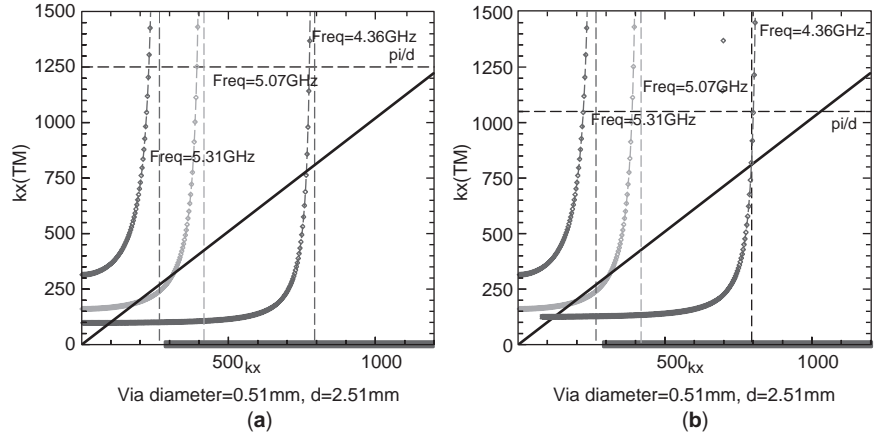


Figure 8. TRM applied to a two-layer grounded slab.

Figure 9. Graphical solution of the transverse resonance equation for TM waves showing the onset of the bandgap (lack of intersection) as frequency is increased: (a) via diameter = 0.51 mm, $d = 2.51$ mm; (b) via diameter = 0.51 mm, $d = 3.05$ mm. (This figure is available in full color at <http://www.mrw.interscience.wiley.com/erfme>.)



3.1. TM Surface Waves

Recognizing that the continuity of Maxwell's equations requires a common propagation constant in the x direction, namely k_x , for all the layers, and as we are seeking guided-wave solutions, we restrict the impedance of the air, layer 0, to that of an evanescent wave, defined as follows:

$$Z_0 = \frac{\alpha_z}{j\omega\epsilon_0} \quad (29)$$

Solving (28) for α_z , we have

$$\alpha_z = \frac{k_{z1}}{\epsilon_{x1}} \times \frac{\frac{k_{z2}}{k_0\epsilon_{x2}} \tan(k_{z2}t_2) \cos(k_{z1}t_1) + \frac{k_{z1}}{k_0\epsilon_{x1}} \sin(k_{z1}t_1)}{\frac{k_{z1}}{k_0\epsilon_{x1}} \cos(k_{z1}t_1) - \frac{k_{z2}}{k_0\epsilon_{x2}} \tan(k_{z2}t_2) \sin(k_{z1}t_1)} \quad (30)$$

However, since $k_x = \sqrt{k_0^2 - k_{z0}^2} = \sqrt{k_0^2 + \alpha_z^2}$, and since we are assuming that the propagation constant of air will be that of an evanescent wave, we obtain an equation of the following form:

$$k_x(\text{TM}) = \sqrt{k_0^2 + \alpha(k_{z1}(k_x), k_{z2}(k_x))^2} \quad (31)$$

This is a transcendental equation that cannot be inverted analytically. However, the solution can be illustrated graphically by inserting a real-valued $k_x > 0$, into the right-hand side of (31) and seeing where the curve $y = k_x(\text{TM})$ intersects the line $y = k_x$. The assumption of a solution of the form $e^{-\alpha_z z}$ in air implies that only those solutions with positive α_z correspond to guided waves. The absence of such a solution indicates the onset of the bandgap.

The TM case of the AMC is very similar to the Fakir bed of nails of King et al. [6]. The constitutive properties affecting the results are ϵ_z , ϵ_x , and μ_y . The relevant physical parameters according to the effective medium model are substrate permittivity, rod radius, and rod separation (size of the unit cell). Figure 9a shows a typical solution for a structure with the following characteristics: $t_2 = 1.57$ mm,

$\epsilon_D = 4.5$, via diameter = 0.51 mm, periodicity = 2.51 mm. Three frequencies were selected: 4.36, 5.07, and 5.31 GHz. It can be seen that at low frequencies there are always two intersections with the $y = k_x$ line and therefore two guided-wave solutions.

As frequency is increased, the $y = k_x(\text{TM})$ curve slides to the left, bringing the two solutions closer together until at the band edge the two coalesce into a single solution that then disappears (no intersection). In this example then the lower band edge where TM waves are suppressed occurs just above 5.07 GHz. Figure 9b shows the effect of changing the via separation. Changes in both radius and via separation provide a means for changing the inductance in the effective medium model, but the separation is the stronger control parameter. In Fig. 9b a 20% increase in the via separation moves the band edge to below 5.07 GHz.

It is clear that the appropriate choice of the physical dimensions determines the negative ϵ_{zz} of the via array substrate and therefore the position of the TM surface band edge that may or may not coincide with the $+90^\circ$ normal incidence reflection phase point of the AMC. The solution shown in Fig. 9 has the same characteristics as the King et al. Fakir structure. As those authors mention [6], in addition to the first two solutions, there are an infinite number of additional intersections, with an infinite number of tangential curves (higher-order modes). However, those intersections correspond to modes of extremely high reactance, which would exist only extremely close to the surface. Furthermore, they correspond in the example to values of k_x that exceed the periodic unit limit π/d ; therefore they are not relevant to the physical situation.

3.2. TE Surface Waves

Following the same procedure as for the TM case, the solution for α_z is as follows:

$$\alpha_z = -\frac{k}{\mu_{x1}} \times \frac{\frac{k_{z2}}{\omega\mu_0\mu_{x2}} \cot(k_{z2}t_2) \cos(k_{z1}t_1) + \frac{k_{z1}}{\omega\mu_0\mu_{x1}} \sin(k_{z1}t_1)}{\frac{k_{z1}}{\omega\mu_0\mu_{x1}} \cos(k_{z1}t_1) + \frac{k_{z2}}{\omega\mu_0\mu_{x2}} \cot(k_{z2}t_2) \sin(k_{z1}t_1)} \quad (32)$$

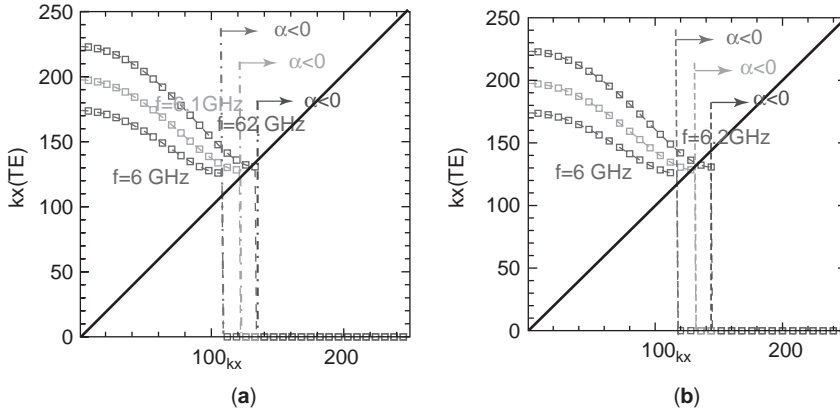


Figure 10. Graphical solution of the transverse resonance equation for TE waves showing the onset of guided surface waves as frequency is increased: (a) typical Cohn square FSS AMC; (b) after artificially raising μ_z by 20%. (This figure is available in full color at <http://www.mrw.interscience.wiley.com/erfme>.)

Again, setting $k_x = \sqrt{k_0^2 + \alpha_z^2}$, we have the following transcendental equation:

$$k_x(\text{TE}) = \sqrt{k_0^2 + \alpha(k_{z1}(k_x), k_{z2}(k_x))^2} \quad (33)$$

The solution to this transcendental equation can also be illustrated graphically.

For the TE case, the constitutive parameters involved in the solution of Eq. (33) are μ_z , μ_x , and ε_y . But since μ_x is assumed to be one, and since ε_y is higher than 1 and therefore promotes the guidance of surface waves, the only parameter that can lead to suppression of surface waves is μ_z . Figure 10a shows the dependence of this solution on frequency for an AMC with the following characteristics: $t_2 = 1.57$ mm, with a square-shape FSS element supplying a capacitance of 0.4 pF and printed on an $\varepsilon_D = 4.5$ dielectric substrate.

At low frequencies no intersection between the $y = k_x(\text{TE})$ curve and the $y = k_x$ line occurs because the total electrical thickness of the guiding structure is less than a quarter-wavelength. For this AMC the normal incidence reflection coefficient resonance occurs at 5.5 GHz. This means that the electrical thickness of the structure is $\lambda/4$ at that frequency, and if this were a conventional isotropic dielectric structure with high permittivity, TE surface waves would begin to propagate at that frequency. However, as Fig. 10 shows, the intersection does not occur until 6.2 GHz.

To prove that it is the depressed normal μ_z of the FSS that is responsible for this upward shift of the TE band edge, Fig. 10b shows the result for an FSS that blocks less of the magnetic field; μ_z has been raised by 20%. Now the band edge occurs at 6.1 GHz. The structure has the same characteristics as in the previous example: $t_2 = 1.57$ mm, $\varepsilon_D = 4.5$. The reduction in blockage would arise, for instance, by going from a Cohn squares FSS design to a design that uses overlapping dipoles.

In Fig. 10, on the same graphs the boundary at which α_z changes from positive to negative has been denoted. At those boundaries the curve representing the right-hand side of Eq. (33) is stopped, because after that point the solution is an improper mode. The mode goes from proper to improper near the point at which k_x is approximately equal to k_0 .

In summary, the surface-wave suppression properties, and therefore the bandwidth, of the Sievenpiper AMC are controlled by the negative value of the normal permittivity of the via array substrate and the depressed normal permeability of the FSS layer. The position of the band edges relative to the $\pm 90^\circ$ phase shift points of the reflection coefficient is in general arbitrary except for the fact that the TE band edge can occur only above the 0° phase frequency (the reflection coefficient resonance). The physical implementation of these structures and the degree to which the surface-wave suppression bandwidth can be designed is treated in the next section.

3.3. Reflection Coefficient

The reflection coefficient for a generalized two-layer anisotropic grounded slab can be found through the use of Eqs. (13) and (14) and an equivalent transmission-line representation of assumed infinitely wide slabs (Fig. 11).

The input impedance of the AMC is the short circuit rolled back through the two media of lengths t_1 and t_2 . Thus, after finding Z_{12} of Fig. 11, we will use that impedance as the load impedance for the line of length t_1 :

$$Z_{12}^{\text{TE, TM}} = jZ_2^{\text{TE, TM}} \tan(k_{z2}^{\text{TE, TM}} t_2) \quad (34)$$

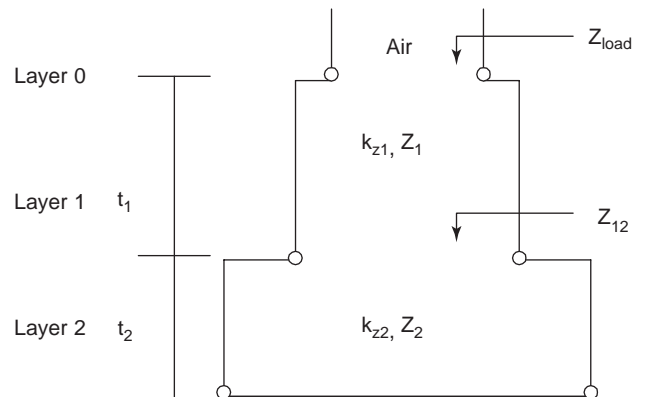


Figure 11. Equivalent transmission-line representation of a two-layer anisotropic grounded slab.

Table 1. Anisotropic Constitutive Parameters for a 10 mm Thick AMC Resonating at 2 GHz

Layer n	Anisotropic Constitutive Parameters			
	ϵ_{ntr}	ϵ_{nz}	μ_{ntr}	μ_{nz}
1	876.46	1	1	0.01
2	4.8	$\sim(-450)$	1	1

This yields the desired load impedance of the two-layer anisotropic medium:

$$Z_{load}^{TE, TM} = Z_1^{TE, TM} \times \frac{jZ_2^{TE, TM} \tan(k_{z2}^{TE, TM} t_2) + jZ_1^{TE, TM} \tan(k_{z1}^{TE, TM} t_1)}{Z_1^{TE, TM} - Z_2^{TE, TM} \tan(k_{z2}^{TE, TM} t_2) \tan(k_{z1}^{TE, TM} t_1)} \quad (35)$$

Now, using this result and the definition of the reflection coefficient, we can find the generalized reflection coefficient for a two-layer anisotropic grounded slab as a function of frequency and angle of incidence $\theta_i = a \sin(k_x/k_0)$.

Since the structure is grounded and assumed lossless, the magnitude of the reflection coefficient will be 1 for any frequency and angle of incidence. But clearly the phase of the reflected wave will change with frequency and angle since the electrical thickness of the layers will also change. The reflection coefficient was calculated for an AMC 10 mm thick with anisotropic constitutive parameters at the center of the band as shown in Table 1.

The corresponding reflection coefficient phase can be seen in Figs. 12a and 12b for TE and TM waves, respectively, for normal incidence, 45° angle of incidence, and angles almost grazing parallel to the surface.

Clearly, the curve shapes are similar, all exhibiting a change in the reflection coefficient phase from +90° to -90°, crossing the 0° phase point, which signals total in-phase reflection. The angle of incidence dependence of the FSS admittance in the TE case, that is, the presence of $\mu_z < 1$, is what causes the shift in the curves for that case (Fig. 12a). It has been pointed out [9] that a more stationary behavior would be obtained for the TE case if

$\mu_z < 0$ were involved in direct analogy to the negative ϵ_z involved in the TM case. The relevance of these curves to the performance of an antenna extremely close to the AMC is not necessarily obvious. Such a proximate antenna has its near field in contact with the AMC so that the interaction between the antenna and the AMC involves not only reflection of its radiated plane-wave spectrum but also coupling of the evanescent portion of that spectrum to the spectrum of leaky- and surface-wave modes supported by the AMC. In other words, a complete picture of the antenna-AMC interaction involves the complete k -space spectrum of the AMC surface’s complex impedance and reflection coefficient [10]. This is why both analyses have been presented above. However, it is true, on the basis of the reaction theorem [11], that for an observation point far from the (assumed infinite) surface of the AMC, the antenna pattern of a current source such as a horizontal dipole can be entirely determined from the surface’s TE and TM plane-wave reflection coefficients (the only electromagnetic property not so determined is the impedance and therefore the efficiency of the resulting radiator).

Thus consider the case of an end-fed quarter-wave horizontal dipole directly over a thick (33-mm) AMC with a low-dielectric-constant substrate ($\epsilon_D = 1.07$) designed with a resonant frequency of 1080 MHz (FSS capacitance of 0.54 pF) and 1-mm-diameter vias 34 mm apart. The lower (TM) band edge is at 770 MHz and the upper (TE) band edge at 1380 MHz (a 1.77-1 bandwidth). In the E plane of the monopole, the TM reflection coefficient dominates. Figure 13a shows the resulting antenna pattern for 0.699 GHz (just below the band edge), 1.075 GHz (center of the band), 1.376 GHz (above the center but still inside the band), and 1.526 GHz (just outside the band.) A +3 dB gain increase is seen at the center of the band when compared to the other in-band frequencies. Outside the band the gain is lower. In all cases we have a well-behaved nearly identical dipolelike pattern. In the H plane the TE reflection coefficient dominates. The calculated pattern at the same frequencies is shown in Fig. 13b. There we see a more significant change in pattern shape with frequency as expected from the shift in the reflection coefficient phase seen in Fig. 12a.

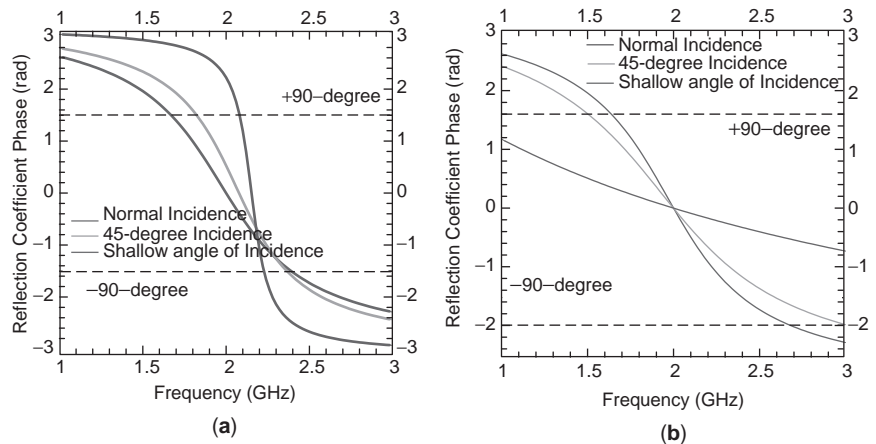


Figure 12. Reflection coefficient phase versus frequency as a function of angle of incidence for an AMC resonant at 2 GHz: (a) TE case; (b) TM case. (This figure is available in full color at <http://www.mrw.interscience.wiley.com/erfme>.)

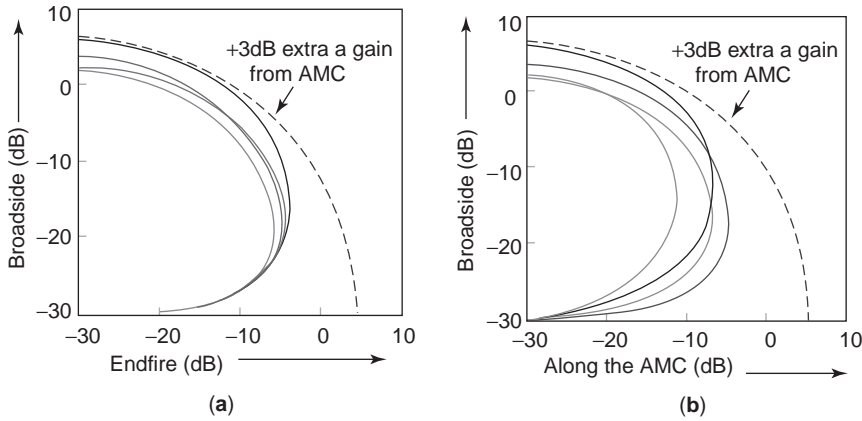


Figure 13. Antenna patterns on the principal planes of a horizontal quarter-wave monopole over an AMC with 0.7 GHz TM band edge and 1.53 GHz TE band edge (red curve = 0.699 GHz, black curve = 1.075 GHz, blue curve = 1.376 GHz inside the band, magenta curve = 1.526 GHz): (a) *E* plane; (b) *H* plane. (This figure is available in full color at <http://www.mrw.interscience.wiley.com/erfme>.)

The effective medium model allows us to calculate the reflection coefficient of the AMC outside its operational band. If we go well above the band, the TM solution admits of higher-order modes (the modes found by King et al. in Fakir’s bed of nails). Around 2 GHz the first of these modes intersects the $y = k_x$ line with a propagation constant just below k_0 ; in other words, the mode is leaky. This intersection manifests itself in the TM reflection coefficient calculation and leads to an antenna pattern with a sharp cusp, characteristic of leaky-wave antennas [12].

Figure 14a shows this result. The effective medium model allow us to not only predict that result but also devise a method for extinguishing the offending mode selectively. As is well known, higher-order modes are extremely sensitive to loss. Therefore adding a small amount of loss to the substrate ($\epsilon_D = 1.07 - j0.05$) essentially erases the leaky-wave contribution and preserves the dipolelike pattern outside the band as seen in Fig. 14b.

4. DESIGN PROCEDURE FOR AMCs

Although transverse resonance can be used directly to find the propagation characteristics of waves in the AMC, it is a graphical and tedious process. Automatic complex root-finding routines do not add to our physical insight. Unfortunately, the transcendental equations describing the propagating modes involve trigonometric functions that cannot be inverted. In this section equivalent-circuit ele-

ments and approximations regarding the electrical size of the material are used to simplify the equations and thus enable us to locate the guiding solutions of the effective medium model.

4.1. Approximation Method for TM Waves

By noting that the FSS layer is simply a capacitor that contributes the additional phase shift to create a quarter-wave grounded thin slab, the AMC can be modeled by a single uniaxial anisotropic layer over which there is an infinitesimally thin capacitive shunt element. In that case the transverse resonance equation [Eqs. (30) and (31)] become

$$k_{xTM} = \sqrt{\frac{\epsilon_0^2(k_{z2})^2}{(\epsilon_0\epsilon_{xx2} \cot(k_{z2}t_2) - Ck_{z2})^2} + k_0^2} \quad (36)$$

where C is the capacitance of the FSS and of course k_{z2} is a function of k_{xTM} per Eq. (14) (as a further approximation we note that, by definition, the AMC is an electrically thin structure; thus the product $k_{z2}t_2 < 1$ and the cotangent function can be approximated by $1/k_{z2}t_2$).

In the graphical solution illustrated in Fig. 9, we can see the close resemblance of the $y = k_{xTM}$ curves to secant functions. Thus the guiding properties arise when a secantlike curve just grazes the diagonal $y = k_x$ line.

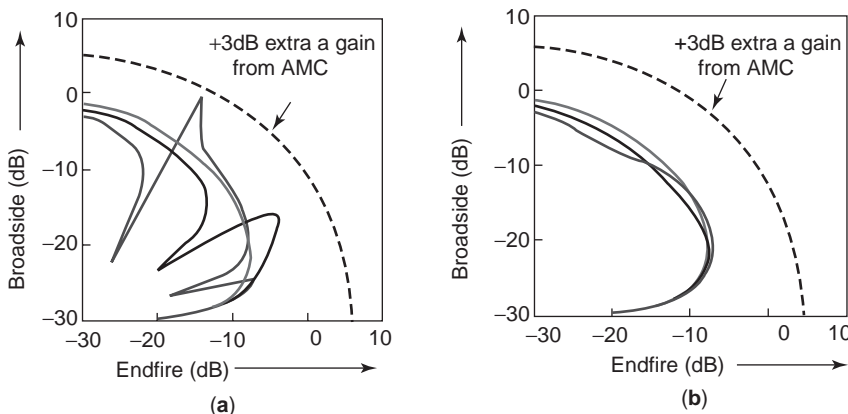


Figure 14. Antenna patterns on the *E* plane of the horizontal monopole of Fig. 13, above the AMC bandgap; the existence of a leaky wave near 2 GHz causes severe distortion of the pattern (a) that can be corrected by adding a small amount of loss to the substrate (b) (red curve = 1.83 GHz, black curve = 1.90 GHz, blue curve = 1.98 GHz). (This figure is available in full color at <http://www.mrw.interscience.wiley.com/erfme>.)

Thus the guiding properties of the AMC can be characterized by determining the following two parameters that fix the secant function:

- The value of k_x when the secant function approaches infinity,
- The value of y when k_x TM is zero.

The first value must correspond to the pole in k_x of Eq. (36). The pole occurs at

$$k_{x\text{TM}\infty} = k_0 \sqrt{\mu_{yy2} \epsilon_{zz2} \left(1 - \left(\frac{k_{0\text{res}}}{k_0} \right)^2 \right)} \quad (37)$$

where $k_{0\text{res}}$ is the free-space wavenumber at the resonant frequency.

The second value can be found simply by finding the y -axis intercept:

$$k_{x\text{TM}}|_{k_x=0} = k_0 \sqrt{1 + \left(\frac{k_0 \mu_{yy2} t_2 k_{0\text{res}}^2}{k_0^2 - k_{0\text{res}}^2} \right)^2} \quad (38)$$

Therefore, in order to find the curve for the lowest-order mode solution of TM waves, we will use the following secant function

$$y(k_x) = (k_{x\text{TM}}|_{k_x=0}) \sec\left(\frac{\pi}{2k_{x\text{TM}\infty}} k_x\right) \quad (39)$$

where $k_{x\text{TM}\infty}$ and $k_{x\text{TM}}|_{k_x=0}$ are as given in (37) and (38), respectively. Of course, once we have an analytic expression as in Eq. (39), the frequency at which an intersection no longer occurs can be directly determined by recognizing that the osculation point (the band edge) occurs at the point where the secant curve has slope equal to one. Therefore by taking the first derivative of Eq. (39), setting it equal to 1.0 and then finding the frequency at which that point exactly equals k_x reveals the band edge.

Figure 15 shows the close agreement between the exact transcendental equation from Eq. (31) and the analytic secant function from Eq. (39). The error in the prediction of the band edge, that is, the frequency at which the curve detaches the 45° line, is only ~2%.

4.2. Approximation Method for TE Waves

For the TE case we have already seen that the FSS cannot be regarded simply as a shunt capacitor, since the normal component of the permeability is not one. We then proceed by first rewriting the transcendental equation in the form

$$k_{x\text{TE}} = k_0 \sqrt{\frac{\left[\frac{k_{z1}}{k_0} \left(\frac{\mu_{xx1}}{k_{z1}} - \frac{\mu_{xx2}}{k_{z2}} \tan(k_{z1}t_1) \tan(k_{z2}t_2) \right) \right]^2}{\mu_{xx1} \left(\frac{\mu_{xx2}}{k_{z2}} \tan(k_{z2}t_2) + \frac{\mu_{xx1}}{k_{z1}} \tan(k_{z1}t_1) \right)}}} + 1 \quad (40)$$

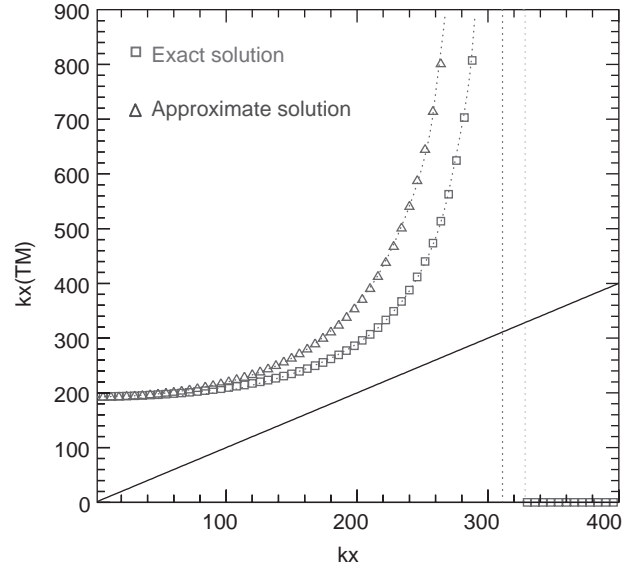


Figure 15. Comparison of the exact solution and the design equation (39) for a 1.57-mm AMC resonant at 5.5GHz with a substrate dielectric constant of 4.5, rod radius of 0.2mm, and via separation of 2.51 mm. (This figure is available in full color at <http://www.mrw.interscience.wiley.com/erfme>.)

Simplifying by assuming that $[\tan(k_{z2}t_2)]/k_{z2} = t_2$ (for the substrate layer) introduces a small error, which in the TM case was negligible, but in this case this small error is accentuated when multiplied by the small values from the $\tan(k_{z1}t_1)$ term. Therefore the ratio mentioned above needs to be fixed to a value to ensure that the solution stays close to the exact solution. Since guided waves first appear when k_x is near k_0 , we fix the ratio as follows:

$$c_2 = \frac{\tan\left(k_0 \sqrt{\epsilon_{y2} \mu_{x2} - \frac{\mu_{x2}}{\mu_{z2}} t_2}\right)}{k_0 \sqrt{\epsilon_{y2} \mu_{x2} - \frac{\mu_{x2}}{\mu_{z2}}}} \quad (41)$$

Now we can assume that the FSS layer has an infinitely thin thickness, and therefore, the tangent function involving $k_{z1}t_1$ can be simplified to its argument. Performing all these simplifications leads to the following version of Eq. (40):

$$\left(\frac{k_x}{k_0}\right)^2 = \frac{\left[1 - \mu_{xx2} c_2 t_1 (k_0)^2 \left(\epsilon_{yy1} - \left(\frac{k_x}{k_0}\right)^2 \frac{1}{\mu_{zz1}} \right) \right]^2}{(k_0)^2 (\mu_{xx2} c_2 + \mu_{xx1} t_1)^2} + 1 \quad (42)$$

Solving for k_x , we encounter a second-order polynomial in k_x squared of the form

$$\left(\frac{k_x}{k_0}\right)^4 \left(\frac{\beta}{\mu_{z1}}\right)^2 - \left(\frac{k_x}{k_0}\right)^2 \left(\chi - \frac{2\beta}{\mu_{z1}} + \frac{2\epsilon_{y1}\beta^2}{\mu_{z1}}\right) + \chi + 1 - 2\beta\epsilon_{y1} + \epsilon_{y1}^2\beta^2 = 0 \quad (43)$$

where $\beta = k_0^2 \mu_{y2} t_1 c_2$ and $\chi = (k_0 (\mu_{y2} c_2 + \mu_{y1} t_1))^2$.

The solution of this polynomial will yield four solutions for guided waves. However, only the real solutions with an attenuation constant $\alpha > 0$ are proper solutions. To complete our design equations, we have to find the point at which $\alpha = 0$, or in other words, where proper solutions begin to propagate. Hence, using Eq. (32) and using the same approximations that lead to Eq. (43), this point in k_x becomes

$$k_x = \sqrt{\mu_{z1} \left(k_0^2 \epsilon_{y1} - \frac{1}{\mu_{y2} t_1 c_2} \right)} \quad (44)$$

Figure 16 shows the exact solution and our new approximated design equation (43). The error in the prediction of the TE band edge is less than 0.5%.

4.3. Design of Surface-Wave Bandwidth

The design equations of Sections 4.1 and 4.2 allow us to more easily determine the surface-wave bandwidth of operation of an AMC. For the TM waves the objective is to find the osculation point between the secant function and the $y = k_x$ line. In order to find this point using Eq. (39), we first have to find the value of k_x for which the derivative of the secant function is one. As an intermediate step to this calculation we encounter a quadratic equation in sine functions that, after a change of variable of the form $U = \sin(x)$, can be solved as

$$U = \frac{-\pi(k_{xTM}|_{k_x=0})}{4k_{xTM\infty}} + \sqrt{\left(\frac{\pi k_{xTM}|_{k_x=0}}{4k_{xTM\infty}} \right)^2 + 1} \quad (45)$$

Then, the k_x point of interest is the inverse of this sine function multiplied by a constant,

$$k_{xTM} = \frac{2k_{xTM\infty}}{\pi} \arcsin(U) \quad (46)$$

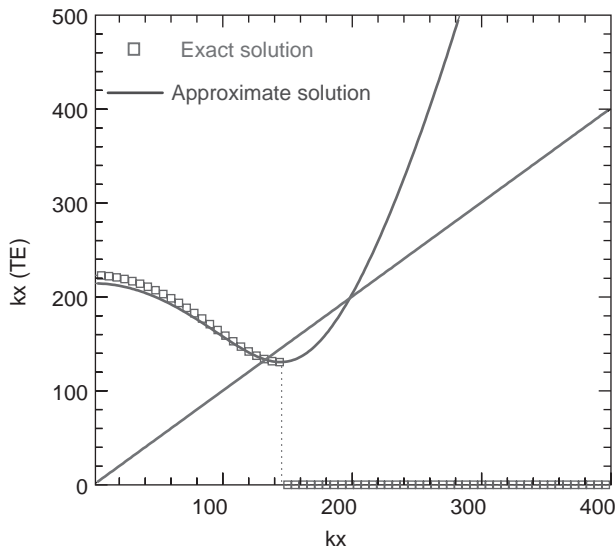


Figure 16. Comparison of the exact solution and the design equation (43) for a 1.57-mm AMC resonant at 5.5 GHz with a substrate dielectric constant of 4.5. (This figure is available in full color at <http://www.mrw.interscience.wiley.com/erfme>.)

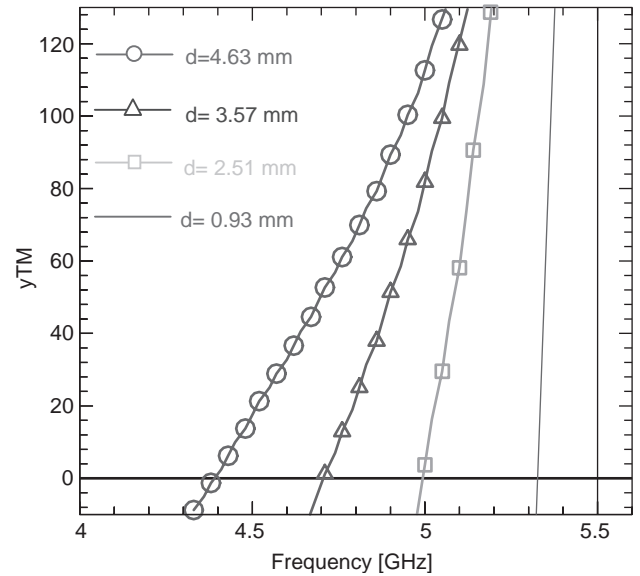


Figure 17. TM band edge for different via spacing d ; the TM band edge is identified as the zero-crossing values of the curves. (This figure is available in full color at <http://www.mrw.interscience.wiley.com/erfme>.)

This point indicates the value of k_x only where a 45° line is tangential to the curve. When this value is substituted into Eq. (39), then the ordinate of this point is found. Therefore, as this ordinate approaches k_{xTM} itself, we have the desired intersection. The resulting equation to find the intersection is still not invertible but its graphical solution allows us to find **all** the TM band edges associated with any range of input physical parameters of the AMC. For instance, Fig. 17 shows the difference $y_{TM} = K_{xTM} - y(K_{xTM})$ versus frequency for an AMC as the via periodic unit length is changed. For each periodic unit length the point where the curve crosses zero is the TM band edge.

For the TE band edge, four roots will be found from Eq. (43). These solutions are proper guided waves only if these are real and positive values, and only when they lie to the left of the k_x value (the $\alpha_z = 0$ boundary) given by Eq. (44). As an example, Fig. 18 shows the roots of Eq. (43) for the resonance frequency ($f_1 = 5.5$ GHz) and for a frequency 11% higher ($f_2 = 6.1$ GHz). For f_1 we have TE surface-wave suppression since the boundary at which $\alpha_1 = 0$ (corresponding to f_1) occurs at $k_x = 0$ and no real solutions exist. As frequency increases, the $\alpha_2 = 0$ (corresponding to f_2) boundary moves to the right and the complex solutions of Eq. (43) approach the real axis of the complex plane. The blue curve of Fig. 18 shows that we have two real solutions for frequency f_2 but that one of them is an improper solution (lying outside the $\alpha_2 > 0$ region) and the other is just inside the region. Hence, a TE surface wave is excited for frequency f_2 and the TE surface-wave suppression band edge is found.

4.4. Design Guidelines

In the design of the AMC the first step is to determine the thickness based on the desired bandwidth of operation [according to Eq. (3)]. Then the FSS capacitance required

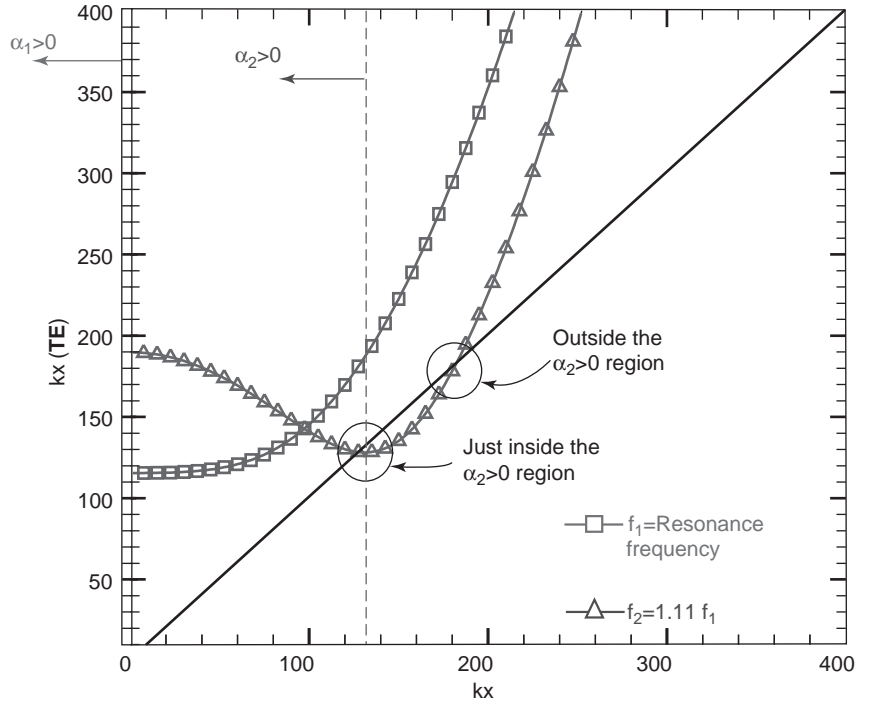


Figure 18. TE band edge determination procedure. The roots of equation (43) have to be real and positive and lie in the $\alpha > 0$ region. (This figure is available in full color at <http://www.mrw.interscience.wiley.com/erfme>.)

to obtain resonance at the desired thickness is given by

$$C = \frac{1}{\omega_{\text{res}} \eta_0 \sqrt{\frac{\mu_{\text{trans}2}}{\epsilon_{\text{trans}2}}}} \times \cot\left(\frac{\omega_{\text{res}}}{c_0} \sqrt{\mu_{\text{trans}2} \epsilon_{\text{trans}2}} \cdot t_2\right) \quad (47)$$

where ω_{res} is the angular frequency of resonance; η_0 is the intrinsic impedance of free space; $\mu_{\text{trans}2}$ and $\epsilon_{\text{trans}2}$ are the relative transverse permeability and permittivity, respectively, of layer 2 (the via array region); c_0 is the speed of light in free space; and t_2 is the thickness of the via array layer.

If the capacitance required is not too large, a Cohn squares array can be designed approximately using the equations for the strip grating [Eq. (20)]. This will give the engineer a reasonable estimate of the required periodic unit and gap dimensions. The exact design can then be fine-tuned using a full-wave electromagnetic solver. If the required capacitance is large, then equation 20 may give a periodic unit that is too large (too close to $\lambda/4$) or a gap width that is too small to manufacture accurately. Then a multilayer design is required for use of the parallel-plate capacitance obtained from overlapping metal plates. The following rules of thumb for typical AMCs may be used. Up to a capacitance of 1 pF/square, Cohn squares are appropriate; to obtain capacitances as high as 15 pF/square requires overlapping Cohn squares. The choice of FSS design is also driven by cost considerations, where a single-layer design has obvious advantages from minimization of manufacturing steps. To exceed the 1 pF/square limit in a single layer, interdigital capacitor (ICAP)

designs have been fabricated that offer FSS capacitance levels up to 5 pF/square [13].

Almost arbitrarily large values of capacitance are achievable simply by placing the two layers very close to each other, that is by using a very thin dielectric spacer with the metal pattern etched one side and registered appropriately above the first metal pattern on the top of the substrate. However, it must be realized that then the manufacturing tolerance on the thickness of the dielectric spacer becomes the critical parameter in controlling the resonant frequency of the AMC.

Figure 19 shows the most general case of two-overlapping arrays of Cohn squares. Such a design will have both the original edge-to-edge capacitance and a much stronger parallel-plate contribution of the form $C_p = \epsilon A/d$. The capacitance per square of the case in Fig. 19 is deduced by recognizing the equivalent circuit of Fig. 20.

The FSS capacitance would then be

$$C_{\text{eq}} = 2C_e + \frac{C_{p11}C_{p12}}{C_{p11} + C_{p12}} + \frac{C_{p21}C_{p22}}{C_{p21} + C_{p22}} \quad (48)$$

where C_e is the edge-to-edge capacitance (as in the strip medium).

As mentioned earlier, a Cohn square FSS is maximally blocking; therefore Eq. (26) correctly predicts the normal permeability, and the procedure using Eqs. (43) and (44) enables a direct prediction of the maximum attainable TE band edge that results automatically from this choice.

If a maximally blocking design is not required or if adding series inductance to the FSS is desirable (providing an additional measure of tuneability) [13], other shapes, such as overlapping Jerusalem crosses, can be used. Figure 21 shows the basic cross element, while

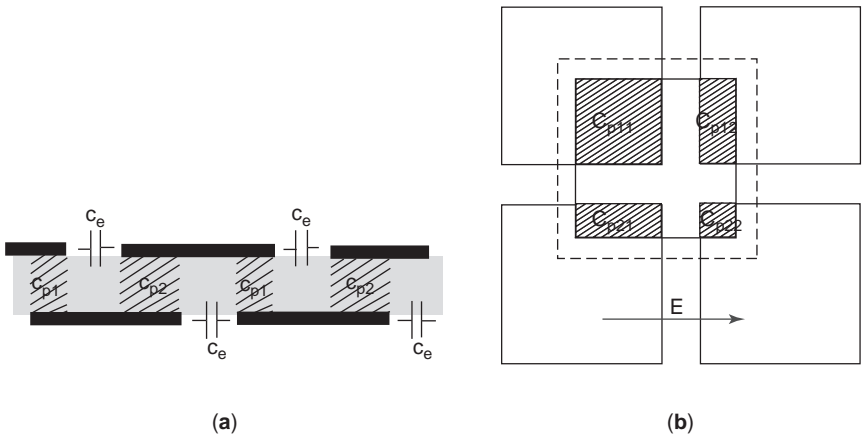


Figure 19. Side (a) and top (b) views of a two-layer FSS with Cohn squares.

Fig. 22 shows how the overlapping is accomplished in a two-layer design. In the Jerusalem cross case, the eddy currents cannot flow around the outer perimeter because of the breaks in the pattern; therefore only small eddy currents will be formed on the arms of the cross and in its center. With the chosen proportions the parallel-plate capacitance in the overlapping regions can be quite high, while making the arms thin enough to yield a significant amount of series inductance.

The design problem is to find the physical dimensions l_1 , l_2 , and l_3 of Fig. 21 in order to achieve the capacitance with a moderate-thickness spacer. The equivalent circuit with a moderate-thickness spacer. The equivalent circuit is the same as in Fig. 20, except that each C_{p11} , C_{p12} , C_{p21} , and C_{p22} is the result of two parallel-plate capacitors in parallel. Also since the crosses are set symmetrically in the center of the cell, then all the capacitances have the same value and the equivalent capacitor is $2C$, where C is the capacitance of one parallel-plate capacitor.

After designing the FSS to attain the needed capacitance and TE blockage, the next step is to ensure that the surface-wave suppression band coincides with or exceeds the $\pm 90^\circ$ phase reflection bandwidth. The via array in the substrate controls the lower band edge. Its primary design parameter is the via spacing or periodic unit cell. This is because most reasonable via diameters chosen will work

well provided the spacing between the vias is adjusted properly. Thus we can assume that selection of the via diameter will be based on manufacturing convenience. The purpose of the via array is to create a negative ϵ_{zz} such that the TM waves guided by the substrate are of the Fakir bed of nails type, and then to place the cutoff of these waves at the desired band edge frequency. These requirements place obvious constraints on the design. It should be noted that the periodicity of the via array must match the periodic unit of the FSS metal patches because it is the termination on a (relatively) large metal plate that allows the current in the short vias to appear almost uniform along the length of the via, and thus enable the finite substrate to behave as the rodged medium with infinitely long rods.

Since the permittivity is a strong function of frequency, the right value of inductance for the via array region must be chosen precisely with respect to the desired bandwidth. Clearly, if the value of the normal permittivity of the substrate becomes greater than one inside the desired

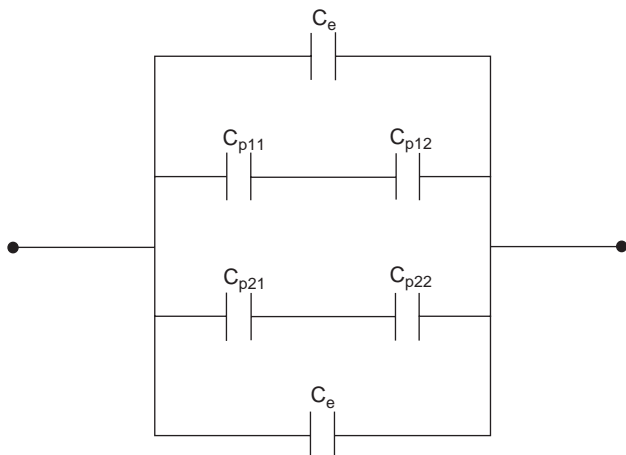


Figure 20. Equivalent circuit of a two-layer FSS with squares as its element shapes.

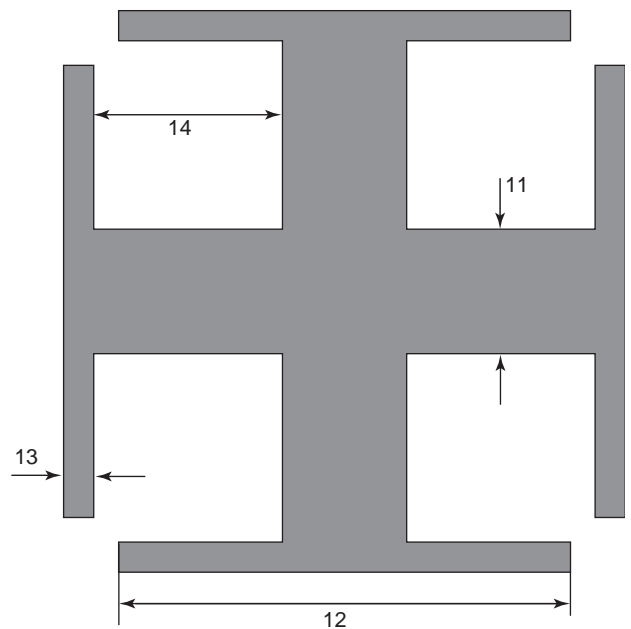


Figure 21. Jerusalem cross element.

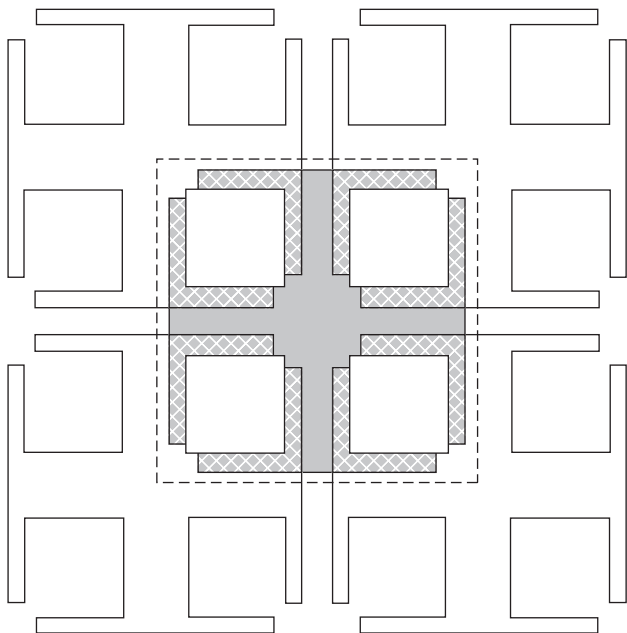


Figure 22. Two-layer Jerusalem cross FSS.

operating band, the substrate will be able to support conventional TM surface waves. Thus, the first general guideline to ensure surface-wave suppression is to maintain the normal permittivity at <1 within the bandwidth of interest. Given a choice of substrate dielectric constant, the normal permittivity is controlled over the band by controlling the zero-crossing frequency, that is, the frequency at which ϵ_{zz} changes from negative to positive values. Figure 23 illustrates the effect of the via spacing on this zero-crossing point for a substrate with a relative dielectric constant of 4.5.

The vertical lines define the extent of the desired bandwidth of operation (Γ_{BW}). In this figure the case in which the vias are one-ninth of a free-space wavelength

apart (at the reflection phase resonance) gives the most negative normal permittivity because its zero-crossing frequency is far above the high-impedance frequency band of operation. However it also gives the most rapidly varying value of ϵ_{zz} over the band, and this turns out to limit the surface-wave suppression bandwidth since the oscillation point will occur at a higher frequency for more negative values of permittivity. To maximize the TM bandwidth, we want the slowest possible varying normal permittivity that nevertheless does not cross 1 inside the band of operation. For this case a via spacing of the order of $\frac{1}{8}$ -wavelength ($\lambda/8$) would be the best. Clearly, in Fig. 23 the dielectric constant ϵ_D of the substrate plays an important role in determination of the bandwidth because it controls the asymptotic high-frequency limit of ϵ_{zz} and therefore the slope of the curve over the bandwidth of operation.

As a rule of thumb, to maximize the TM bandwidth, it is advisable to put the zero crossing of ϵ_{zz} as close as possible to the upper end of the band and to minimize the slope of the curve. This means that substrate dielectric constant is chosen as low as possible and the via spacing is chosen as large as possible within the constraint of not getting close enough to $\lambda/4$ in the dielectric where periodic effects start to alter the zero-crossing frequency. To maximize the TE bandwidth, we have to allow for the normal H field to be blocked as much as possible. FSS consisting of metal squares are maximally blocking, while FSS consisting of crossed dipoles would be minimally blocking. Although it is true that interdigitated capacitor designs enable the creation of high capacitance FSS with only one side of metal (no need for overlap), such metal arrangements are full of gaps and are not maximally blocking; therefore they typically result in a reduced TE surface wave bandgap.

Finally, the blocking performance of the FSS is indirectly affected by the thickness and composition of the via array substrate because to obtain zero-degree reflection

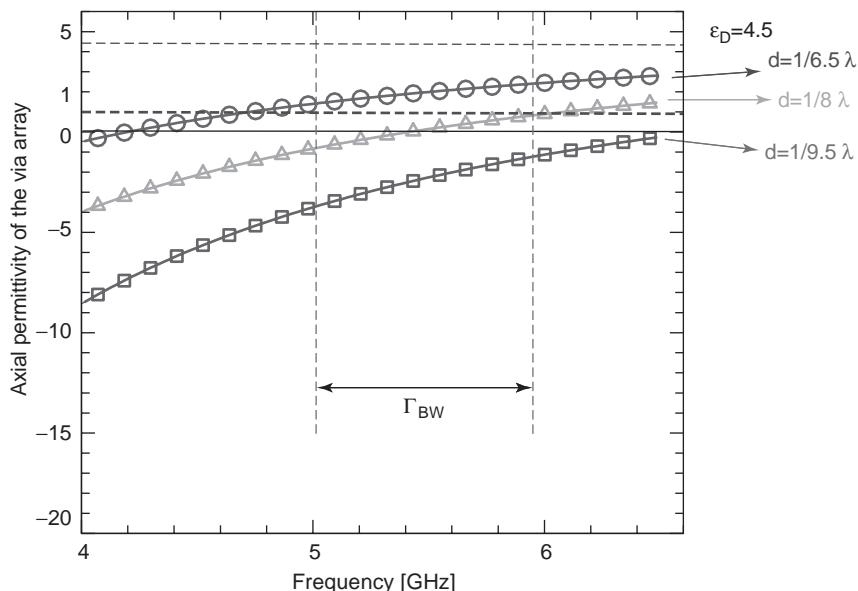


Figure 23. Zero crossing of ϵ_{zz2} as a function of via spacing. (This figure is available in full color at <http://www.mrw.interscience.wiley.com/erfme>.)

coefficient at the desired center frequency the total phase shift supplied by the FSS and the substrate must be equivalent to a quarter-wavelength. Therefore, if the substrate is made too thick, or has too high a dielectric constant, the FSS capacitance will be too small, and hence the FSS patches will be too small or the gaps will be too large to adequately block the normal magnetic field.

It should be emphasized that whenever FSS designs are used that utilize thin metal lines, slots, or gaps, that block the current flow on plates, or overlapping regions that require the current to “neck down” to deliver the charge to the parallel-plate capacitors, there is bound to be a significant amount of inductance in series with the capacitance. This inductance may manifest itself as an apparent frequency dependence on the capacitance that raises the capacitance with frequency and therefore reduces the bandwidth of the original design by detuning it. In the extreme case, the inductance can resonate the FSS capacitance and create multiple high-impedance bands, each with its own default value of TE band edge [14]. The use of such inductive FSS also requires additional care in selection of the periodic unit because the ratio of FSS capacitance to FSS inductance is affected by the absolute size of the unit cell. Whereas the capacitance of an overlapping FSS is proportional to the area of the cell, the inductance is clearly proportional to the length of the cell.

5. REVIEW OF MORE RECENT LITERATURE ON AMCs

The operational definition of an artificial magnetic conductor adopted in this article includes the AMC’s response to both free traveling plane waves (the in-phase reflection coefficient) and evanescent plane waves (near-field impedance increase and suppression of surface waves)—in other words, the effect of the AMC on the entire k -space spectrum of the radiator. Both conditions must be present for the AMC to constitute a gain-increasing ultrathin ground plane for low-profile antennas. On purpose we have avoided classifying the AMC as a photonic bandgap (PBG) or electromagnetic bandgap (EBG) structure because such structures typically operate as three-dimensional frequency-selective filters; that is, EBGs and PBGs usually operate in the frequency range where the periodicity of their inhomogeneities is comparable to a quarter of the wavelength in the dielectric [15]. In contrast, the Sievenpiper family of AMCs operates in the range of frequencies where the periodicity is a small fraction of the wavelength. For conventional communication requirements of bandwidths of the order of 10%, the periodic unit can be of the order of $\lambda/50$. Only when the bandwidth has to be pushed to 2–1 does it become necessary to increase the via separation close to the quarter-wave point.

These considerations are important when tracing the heritage and ongoing history of the AMC in the literature. For instance, the term *artificial magnetic conductor* has been applied in the literature to “quarter-wave ground-planes” rendered thin by the inclusion of FSS layers [16]. However, if the ground plane contains no vias to suppress TM surface waves, the only useful suppression will occur

when the filtering properties of the FSS come into play, that is, when the periodic unit of the FSS is comparable to $\lambda/4$. Such a structure should simply be classified as a frequency-selective surface. Similarly, just because a surface exhibits an in-phase reflection coefficient to plane waves does not mean that it will increase the gain of proximate horizontal antennas and qualify it as an AMC. For this reason, references in the literature that consider and measure only plane-wave reflection coefficients are not very useful to the designer of AMCs.

Because the Sievenpiper AMC is used as a surface below the antenna, its “bulk” EBG properties are seldom, if ever, used and appear to be irrelevant in practice. This fact is highlighted by the ease with which a horizontal monopole on the AMC is fed by penetrating the ground plane, thus exposing the center conductor of a coaxial cable (coax) line to an array of vias in its near field. The vias simply play the role of an extension of the coax transmission line’s (absent) outer conductor. Clearly, any wave that might be radiated by the exposed center conductor in the via array region is stymied by the large negative permittivity of that substrate.

There is one structure labeled as PBG in the literature that is very close in spirit to the AMC, and this is the uniplanar compact photonic bandgap (UCPBG) [17]. This structure uses no vias, but its textured ground plane contains both capacitive patches and inductive segments of line. Their combination creates a surface that can guide slow waves up to a resonant forbidden band. Many useful devices have been constructed using that structure ranging from slow-wave compact filters to “TEM” closed waveguides. Indubitably the UCPBG could be analyzed and designed in terms of effective medium theory in the same way as the AMC subject of this article.

The history of the AMC in its present form can be directly traced to Ref. 18, where it was shown that the reflection coefficient band of a tripole array FSS can be moved arbitrarily low in frequency by overlapping tripole layers so that the overlap parallel-plate capacitance tunes the surface. Only plane-wave transmission and reflection coefficients were measured. In Ref. 19 the tripole layers are revisited and it is pointed out that the 100% reflection bandgap disappears at shallow angles of incidence for TM waves because there are no vias connecting the multiple overlapping tripole layers. In Ref. 20 a diamond lattice of multiple overlapping crossed dipole FSS layers connected to each other with vias is studied. A plane-wave reflection coefficient bandgap is reported together with a bulk bandgap assessed by inserting collinear coax probes into the center of the material.

The first reported measurement of a surface-wave bandgap appears in Ref. 21. Overlapped tripole and crossed dipole FSS layers connected with vias were studied for TM surface-wave properties as well as for normal incidence reflection coefficient properties. TM surface waves were found to exist inside only a portion of the reflection bandgap. “Variation of the symmetry” was the approach used to attempt to modify the size and location of the bandgap.

After a symposium paper in 1998 [21], Sievenpiper’s Ph.D. dissertation [1] contains proof of both TE and TM

surface-wave bandgap properties, and subsequent papers, including those noted in Section 5 (above), have thoroughly examined the extent to which the AMC properties can be designed and even dynamically altered. Still, misuse of the AMC happens occasionally as in Ref. 22, where a patch antenna intended to operate at Ku band (13–15 GHz) is surrounded by a Sievenpiper AMC (the PBG of the title), and yet the chosen parameters for the via array region (via diameter 0.2 mm, spacing 2.44 mm, and substrate dielectric constant) can be shown to give a zero-crossing frequency well below the band of operation. In fact, calculation of the ϵ_z properties reveals a normal permittivity varying from 3.6 to 5.7 (positive!) over the range where experiments were performed. It is therefore not surprising that the author's results were unimpressive. For a correct application of the AMC to patch antennas, the reader is referred to Rahmat-Samii's paper [23], which also reports a circularly polarized curl antenna with good axial ratio in the bandgap. The patch antenna had a 3 dB gain enhancement accompanied by skirt suppression and 15 dB suppression of the backlobe. The AMC was also used for mutual coupling reduction (8 dB improvement) in a microstrip patch array.

A careful study of the backlobe suppression properties of the AMC is found in Ref. 24. The authors show that the AMC effect on antenna match (S_{11}) essentially follows the antenna's own trend in free space. Using the AMC as a reflector, very high front-to-back shielding in the near field and somewhat less in the far field are shown. They also investigated a double (back-to-back) AMC versus the regular AMC backed by its PEC ground plane and found that the former has similar backlobe suppression but incurs more dielectric loss. This is contrasted with a full-wave simulation of back-to-back PMC surfaces, which have much poorer backlobe suppression than does the AMC. This result emphasizes that the AMC is not a PMC because it also suppresses TE waves.

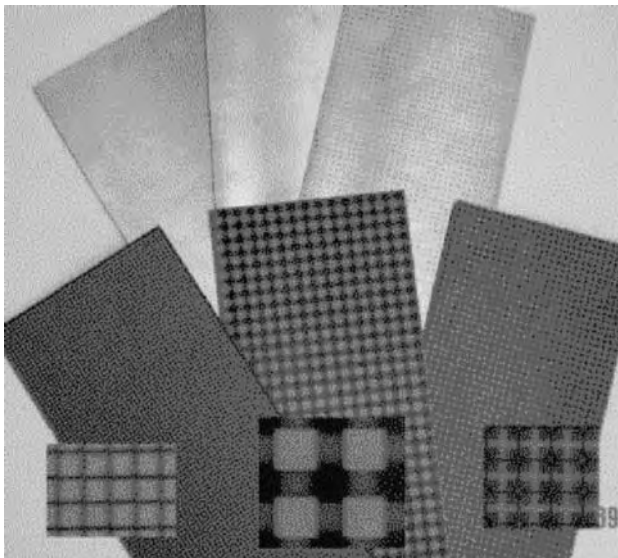


Figure 24. Fabricated AMC designs I, II, and III, from left to right. A zoomed image shows the design in more detail.

Table 2. Summary of the Most Relevant Parameters of the Three Different AMCs Designed

Parameters	Designs		
	I	II	III
$C_{\text{FSS}}(\text{pF})^a$	0.915	$0.915 + L_{\text{FSS}}$	$0.915 + L_{\text{FSS}}$
t_2 (mm)	1.5748	1.5748	1.5748
d (mm)	2.5146	8.3312	3.9624
ϵ_D	4.5	4.5	4.5
11 (mm) ^b	N/A	N/A	0.8382
12(mm) ^b	N/A	N/A	2.3114
13(mm) ^b	N/A	N/A	0.2286
14(mm) ^b	N/A	N/A	1.143
SW BW(GHz)	3.65–4.1	2.85–3.4	3.41–3.5

^a“+” means that the FSS inductance has to be taken into account.

^b“Jerusalem cross” dimensions shown in Fig.21.

6. MORE RECENT APPLICATIONS OF AMC

As an example of the versatility of the design procedure outlined above, we designed three different AMCs whose $\pm 90^\circ$ phase operating bands are not necessarily coincident with the surface-wave band. The fabricated designs are shown in Fig. 24.

The goal of the first design was to set the TM as well as the TE band edges close to the $\pm 90^\circ$ band; therefore the appropriate via separation and magnetic field blockage were calculated to yield the surface-wave bandwidth given in Table 2, while the normal incidence reflection bandwidth is 3.57–4.01 GHz. The goal of the second design was to set the TE band edge just above the -90° phase point by tailoring the magnetic blockage appropriately, while at the same time using the via spacing to move the TM band edge well below the $+90^\circ$ phase point. The normal reflection bandwidth is 3.23–3.33 GHz. The last design is meant only to block TM surface waves using the via array but to allow TE waves to propagate by using a low magnetic blockage (Jerusalem cross) FSS, shown in Fig. 21. Again, the following normal reflection bandwidth for this case is 3.33–3.64 GHz. Table 2 shows the most important dimensions of the AMCs fabricated as well as their predicted surface-wave band, defined by the TM and TE band edge.

Figure 25 shows the equivalent circuit for the FSS. Since in two of these cases the current flow through the FSS is considerably constricted by the geometry of the

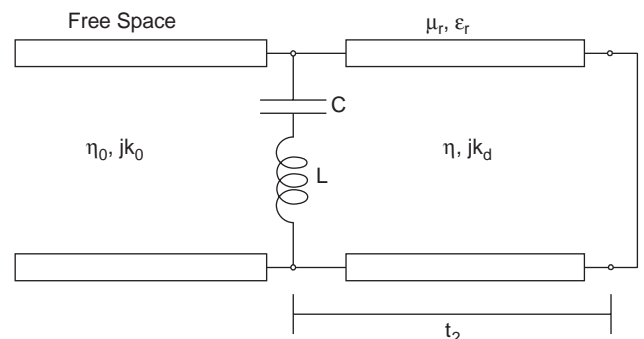


Figure 25. Equivalent circuit for the AMC when its FSS inductance is relevant.

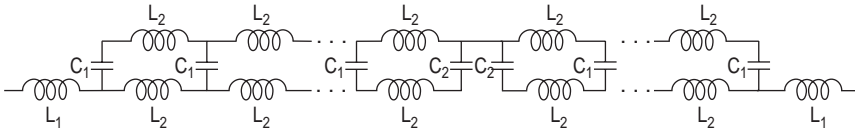


Figure 26. Equivalent distributed LC circuit for an FSS with two overlapping layers with Jerusalem crosses as its elements.

pattern, the series inductance of each design must also be taken into account. As a rule of thumb, Marcuvitz' [8, pp. 221–228] results for a strip inductive medium provide a reasonable closed-form estimate for this inductance (with the result that tightly packed Cohn squares have almost zero inductance). Thus, for design I a purely capacitive FSS is appropriate, since the inductance from the FSS is negligible ($L_{\text{FSS}} = 0.03 \text{ nH}$).

For design II we used large Cohn squares that have little overlap capacitance. In this case, the inductance, calculated from Marcuvitz' data [8, pp. 221–228], is not negligible anymore ($L_{\text{FSS}} \approx 0.87 \text{ nH}$) and has to be taken into account in the design. For design III, the FSS equivalent circuit is a distributed LC circuit, shown in Fig. 26, where the series inductances can be calculated using Marcuvitz' method [8, pp. 284–285], and the capacitors are small parallel-plate capacitors. The inductance from the FSS is manifested in the frequency-dependent effective capacitance deduced from the circuit from Fig. 26.

The phase of the reflection coefficient was measured experimentally on a basic Naval Research Laboratory (NRL) arch setup. Figure 27 shows a typical measurement test setup for determining the surface-wave properties of AMCs. A pair of broadband tapered notch antennas is used for linear polarization where TM waves are attained when the antennas are oriented in a vertical plane and TE waves when they are oriented in a horizontal plane. Therefore a through measurement, where the direct ray is blocked with absorbing material, only allows waves tightly attached to the surface to propagate to the receiving antenna. The results are usually referenced to waves over metal (making it notoriously difficult to measure the TE waves). The experimentally and theoretically measured phase of the normal reflection coefficient is shown in Fig. 28. We can observe that the inductance tends to shift the AMC resonance to lower frequencies, and to narrow the $\pm 90^\circ$ frequency band. An oddity of such a plane-wave measurement of the properties of an AMC is

that the magnitude of the reflection coefficient shows a sharp dip exactly at the resonant frequency. This is not entirely unexpected since at resonance any losses in the dielectrics inside a resonator should be magnified. It appears odd, because every measurement made of the gain and efficiency of antennas proximate to an AMC have shown at least a $+3 \text{ dB}$ gain increase at band center. We must remember, however, that the efficiency of an antenna is ultimately connected to its ability to couple energy from its near field into propagating free-space waves and that the mechanism of that coupling is not measured by the plane-wave reflection coefficient.

The TM measurements and the predicted TM band edges for the three designs are shown in Fig. 29. For the TE surface wave, the fields are zero over the metal; therefore, when the AMC can support TE wave propagation, we have the band edge. Figure 30 shows the TE surface-wave measurements and the theoretically predicted TE band edges.

A brief review of the latest applications in which AMCs are used include the following. McKinzie and Fahr [25] used the AMC as part of a low-profile polarization diversity compact antenna. Two orthogonal bent-wire monopoles were placed in close proximity ($\lambda_0/200$) to an AMC right on top of each other, where λ_0 is the free-space wavelength at the AMC's resonance. The monopoles are parallel to the surface, and their centers are coincident. The experiments, compared to a conventional two-port probe-fed patch antenna, show an improved return loss bandwidth, a 5–10 dB reduction in mutual coupling, and improved radiation efficiency.

In applications such as 802.11 and Bluetooth radios, two antennas located on the same platform must have low mutual coupling to minimize interference. Rogers et al. [26] used the AMC as a reactive edge treatment that reduces the mutual coupling of two antennas mounted on the top and side of a 16-mm-wide screen surrogate laptop computer. Two 2.4-GHz AMCs were also placed

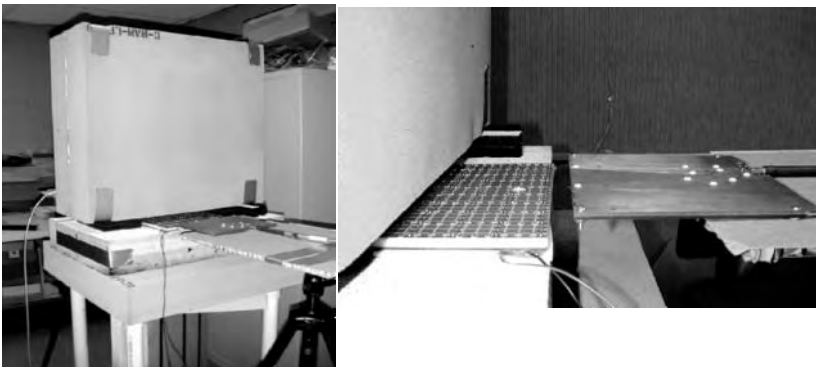


Figure 27. Surface-wave measurement test setup. (Photos courtesy of Titan Aerospace Electronics Corporation.)

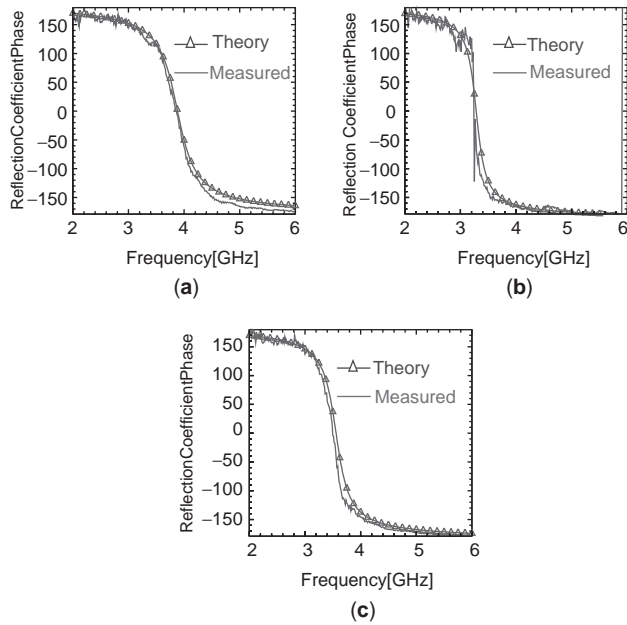


Figure 28. Theoretical and measured reflection coefficient phase of the three AMC design examples. a) Design I. b) Design II and c) Design III. (This figure is available in full color at <http://www.mrw.interscience.wiley.com/erfme>.)

between the antennas, on the top and side of the surrogate laptop, so that coupling between the two antennas is reduced. In the resulting experiments, the coupling

between the antennas (S_{21}), shows isolation of 45 dB, 20 dB above the case without edge treatment. The properties of the AMC used were calculated using the design equations in this article and agree with the authors' measurements, except for a slight increase in the band center, mentioned by the authors as due to the truncation of the AMC into a thin strip.

Bandwidth can be increased by magnetically loading the AMC, as seen in Eq. (3). This increase was demonstrated in Ref. 27. It is shown that the bandwidth increases by a factor of >4 . Thus, the AMC of dimensions $411 \times 411 \times 33$ mm operated between 240 and 400 MHz. The magnetic material used was barium cobalt hexaferrite with uniaxial permeability $\mu_{r,xy} = 30 - j1.0$ and $\mu_{r,z} = 1.0 - j0.03$ at approximately 200 MHz. It was engineered in such a way that the reflection bandwidth and surface-wave bandwidth align. In the final design the via array region was subdivided into two parts. In one of them the magnetic material was placed as far as possible from the FSS layer and the vias spaced 9 times closer together than in the rest of the via array region. No surface-wave measurements were available at those low frequencies because of the difficulty associated with the smallness of the AMC.

Sanchez and Paller [28] propose a new method for tuning the AMC. Essentially, it changes the parallel plate capacitance of the FSS by changing its geometry. The authors used concentric square loops for the upper FSS layer. The loops are segmented and can be completed by bridging the gaps using switches, as shown in Fig. 31, and

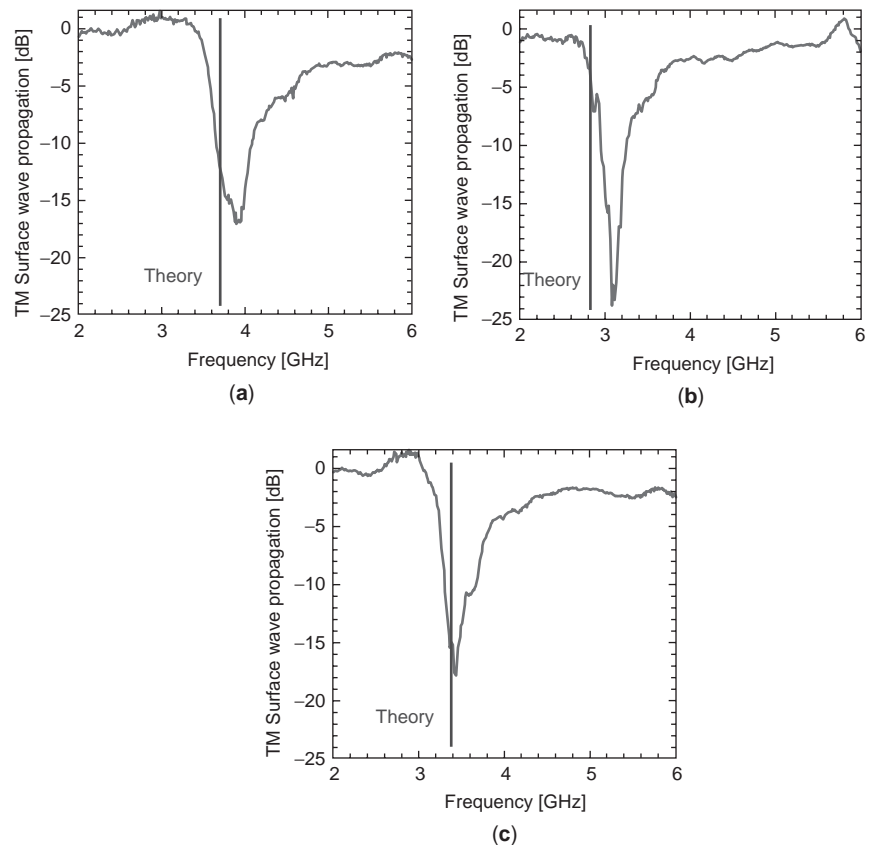


Figure 29. TM surface-wave propagation measurement and theoretically predicted TM band edges for designs I (a), II (b), and III (c). (This figure is available in full color at <http://www.mrw.interscience.wiley.com/erfme>.)

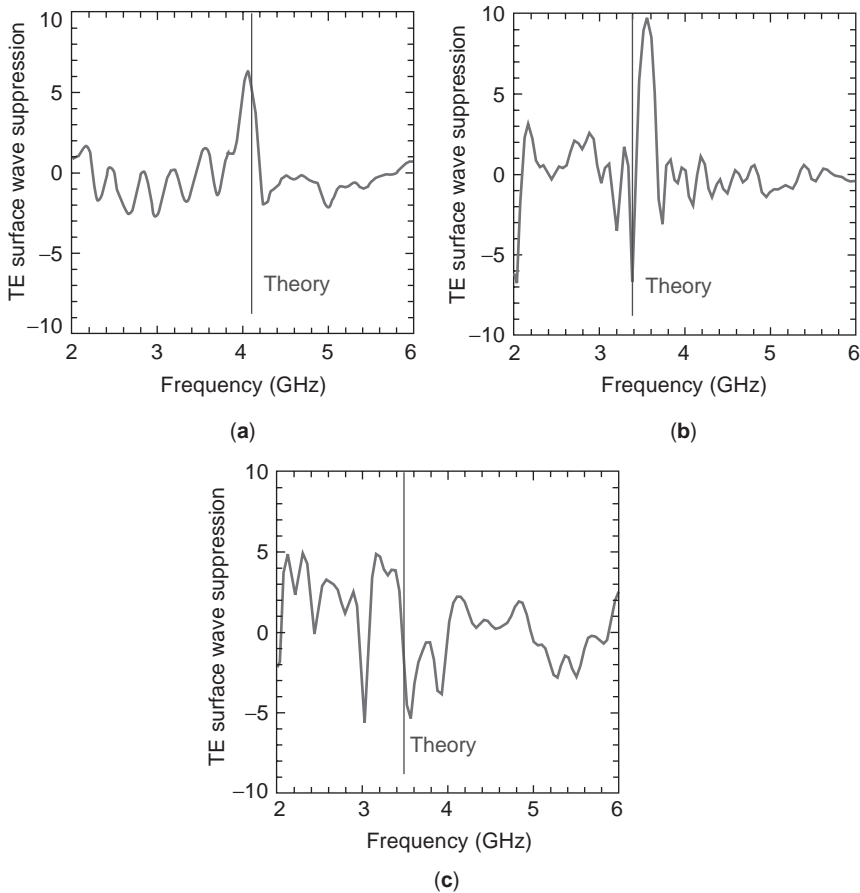


Figure 30. TE surface-wave propagation measurement and theoretically predicted TE band edges for designs I (a), II (b), and III (c). (This figure is available in full color at <http://www.mrw.interscience.wiley.com/erfme>.)

in this way the density of the overlapping patches can be changed by turning the switches on and off. There are 2^N tuning states for an N -loop FSS. It is shown that the

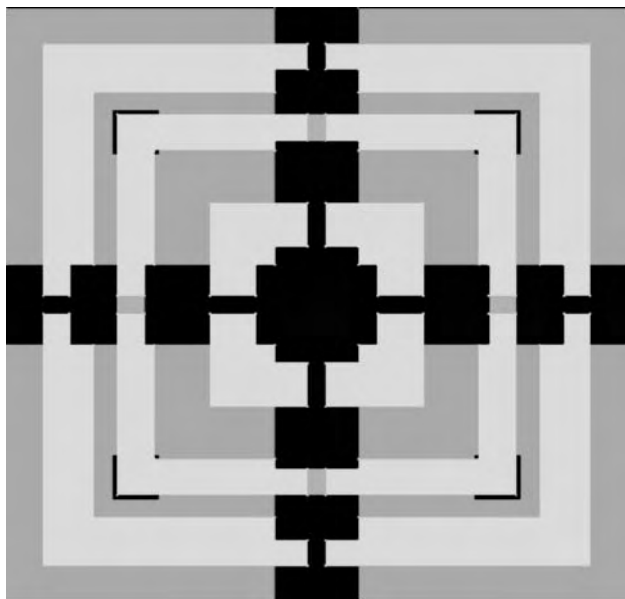


Figure 31. Eight-state concentric square loops shaping the top FSS unit cell. The lower FSS squares are also shown.

surface-wave band will follow the high-impedance band. By changing the capacitance of the FSS, the surface-wave suppression properties will also change accordingly.

Sievenpiper et al. [29] use the AMC as a beamsteering device. By changing the electrical properties of the impedance surface through varactors in the FSS layer, as a function of position, a reflecting surface with controllable phase angle of reflection is created. It is shown that the AMC can therefore be used as a reflecting device that can steer a microwave beam over a $\pm 40^\circ$ range in two dimensions.

Acknowledgments

The authors would like to thank Mr. John Turtle and Dr. Livio Pols of AFRL/SNHA, Hanscom AFB, Massachusetts for their excellent technical management of the Reconfigurable Apertures program (RECAP) under which most of this work was originally developed. Thanks are also given to Prof. James Aberle of ASU, Dr. Will McKinzie of McKintek LLC, Dr. Dave Auckland of Etenna Corporation, Mr. Victor Sanchez, and Dr. Eric Caswell of Titan Corporation for their valuable insight, technical collaboration, and management during the various phases of the program. Special thanks are due to the reviewer of this contribution, whose careful analysis and invaluable comments greatly enhanced our exposition of the subject.

BIBLIOGRAPHY

1. D. F. Sievenpiper, *High-Impedance Electromagnetic Surfaces*, Ph.D. dissertation, Univ. California, Los Angeles, Jan. 1999.
2. D. Sievenpiper, L. Zhang, R. Jimenez Broas, N. Alexopoulos, and E. Yablonovitch, High-impedance electromagnetic surfaces with a forbidden frequency band, *IEEE Trans. Microwave Theory Tech.* **47**(11):2059–2074 (Nov. 1999).
3. P. Kildal, Artificially soft and hard surfaces in electromagnetics, *IEEE Trans. Anten. Propag.* **38**(10):1537–1544 (Oct. 1990).
4. J. Brown, *Microwave Lenses*, Methuen, London, Wiley, New York, 1953, pp. 59–61.
5. R. J. King, Groundwave propagation over horizontally layered anisotropic media, *Appl. Phys.* **5**:187–196 (1974).
6. R. J. King, D. V. Thiel, and K. S. Park, The synthesis of surface reactances using an artificial dielectric, *IEEE Trans. Anten. Propag.* **AP-31**:471–476 (May 1983).
7. S. Cohn, Analysis of the metal-strip delay structure for microwave lenses, *J. Appl. Phys.* **20**:257–262 (March 1949).
8. N. Marcuvitz, *Waveguide Handbook*, Peter Peregrinus, London, 1993, pp. 218–221.
9. C. R. Simovski, P. de Maagt, S. A. Tretyakov, M. Paquay, and A. A. Sochava, Angular stabilisation of resonant frequency of artificial magnetic conductors for TE-incidence, *Electron. Lett.* **40**(2):92–93 (Jan. 22, 2004).
10. P. C. Clemmow, *The Plane Wave Spectrum Representation of Electromagnetic Fields*, Pergamon Press, London, 1966.
11. V. H. Rumsey, Reaction concept in electromagnetic theory, *Phys. Rev.* **94**(6):1483–1491 (1954).
12. H. Y. D. Yang, and J. Wang, Surface waves of printed antennas on planar artificial periodic dielectric structures, *IEEE Trans. Anten. Propag.* **49**(3):444–450 (2001).
13. S. Rogers, W. McKinzie, and G. Mendolia, AMC's comprised of interdigital capacitor FSS layers enable lower cost applications, *Proc. IEEE Int. Antennas and Propagation Symp.*, Columbus, OH, June 22–27, 2003, Vol. 2, pp. 411–414.
14. R. E. Diaz and W. E. McKinzie, *Multi-resonant High-Impedance Electromagnetic Surfaces*, U.S. Patent 6,512,494 B1 (Jan. 28, 2003).
15. D. Dawn and Y. Ohashi, A novel electromagnetic bandgap metal plate for parallel plate mode suppression in shielded structures, *IEEE Microwave Wireless Compon. Lett.* **12**(5):166–168 (May 2002).
16. A. Monorchio, G. Manara, and L. Lanuzza, Synthesis of artificial magnetic conductors by using multilayered frequency selective surfaces, *IEEE APLett.* **1**:196–199 (2002).
17. F. Yang, K. Ma, Y. Qian, and T. Itoh, A novel TEM waveguide using uniplanar compact photonic-bandgap (UC-PBG) structure, *IEEE Trans. Anten. Propag.* **47**:2092–2098 (Nov. 1999).
18. A. S. Barlevy, D. F. Sievenpiper, and Y. Rahmat-Samii, Photonic bandgap (PBG) structures of multiple metallic periodic screens: Efficient electromagnetic characterization, *Proc. IEEE Antennas and Propagation (AP) Society Int. Symp.* 1998, June 1998, Vol. 2, pp. 1216–1219.
19. A. S. Barlevy and Y. Rahmat-Samii, Characterization of electromagnetic band-gaps composed of multiple periodic tripods with interconnecting vias: Concept, analysis, and design, *IEEE Trans. Anten. Propag.* **49**(3):343–353 (March 2001).
20. D. F. Sievenpiper, E. Yablonovich, J. N. Winn, S. Fan, P. R. Villeneuve, and J. D. Joannopoulos, 3D metallo-dielectric photonic crystals with strong capacitive coupling between metallic islands, *Phys. Rev. Lett.* **80**(13):2829–2832 (March 30, 1998).
21. D. Sievenpiper and E. Yablonovich, Eliminating surface currents with metallodielectric photonic crystals, *IEEE MTT-S Int. Microwave Symp. Digest*, June 1998, Vol. 2, pp. 663–666.
22. F. Tavakkol-Hamedani, L. Shafai, and Gh. Z. Rafi, Comparison of PBG and perfect magnetic conductor surface effects on the performance of finite microstrip antennas, *Proc. IEEE AP Society Int. Symp.* 2002, June 2002, Vol. 3, pp. 748–751.
23. Y. Rahmat-Samii, The marvels of electromagnetic band gap (EBG) structures: Novel microwave and optical applications, *Proc. 2003 SBMO/IEEE MTT-S Int.*, Sept. 2003, Vol. 1, pp. 265–275.
24. D. Kim, M. Kim, H. Xin, and J. Hacker, 2 GHz electromagnetic crystal reflector antenna, *Electron. Lett.* **39**(15):1096–1098 (July 24, 2003).
25. W. E. McKinzie and R. R. Fahr, A low profile polarization diversity antenna built on an artificial magnetic conductor, *Proc. IEEE AP Society Int. Symp.*, June 2002, Vol. 1, pp. 762–765.
26. S. Rogers, J. Marsh, W. McKinzie, and G. Mendolia, AMC edge treatments enable high isolation between 802.11b and Bluetooth/spl trade/ antennas on laptop computers, *IEEE AP Society Int. Symp.*, June 2003, Vol. 2, pp. 38–41.
27. R. Diaz, Magnetic loading of artificial magnetic conductors for bandwidth enhancement, *Proc. IEEE AP Society Int. Symp.*, June 2003, Vol. 2, pp. 431–434.
28. V. Sanchez and E. Paller, A tunable artificial magnetic conductor using switched capacitance in a concentric overlapping geometry, *Proc. IEEE AP Society Int. Symp.*, June 2003, Vol. 2, pp. 439–442.
29. D. Sievenpiper, J. Schaffner, J. Song, R. Loo, and G. Tangonan, Two-dimensional beam steering using an electrically tunable impedance surface, *IEEE Trans. Anten. Propag.* **51**:2713–2722 (Oct. 2003).

ATTENUATION MEASUREMENT

KURT HILTY
Swiss Federal Office of
Metrology
Bern-Wabern, Switzerland

When a signal is sent along any transmission path, many different mechanisms degrade it. Because of finite conductivity, every cable shows a resistive loss. Furthermore, the dielectric loss and the skin effect may be significant at higher frequencies, and imperfect screening of cables leads to radiation losses which might be quite important at higher frequencies. Single-mode optical fibers have two main intrinsic loss mechanisms, scattering loss and absorption loss. Scattering loss is dominated by Rayleigh scattering, and below 1600 nm absorption losses are caused mainly by OH absorption. Fibers that are bent too tightly or cabled too poorly may have, in addition, bend losses because of nonguided modes. Connectors show losses because of nonideal contacts and imperfect impedance matching, which reflect part of the signal to the transmitter. Filters built in the transmission path have

BIBLIOGRAPHY

1. D. F. Sievenpiper, *High-Impedance Electromagnetic Surfaces*, Ph.D. dissertation, Univ. California, Los Angeles, Jan. 1999.
2. D. Sievenpiper, L. Zhang, R. Jimenez Broas, N. Alexopoulos, and E. Yablonovitch, High-impedance electromagnetic surfaces with a forbidden frequency band, *IEEE Trans. Microwave Theory Tech.* **47**(11):2059–2074 (Nov. 1999).
3. P. Kildal, Artificially soft and hard surfaces in electromagnetics, *IEEE Trans. Anten. Propag.* **38**(10):1537–1544 (Oct. 1990).
4. J. Brown, *Microwave Lenses*, Methuen, London, Wiley, New York, 1953, pp. 59–61.
5. R. J. King, Groundwave propagation over horizontally layered anisotropic media, *Appl. Phys.* **5**:187–196 (1974).
6. R. J. King, D. V. Thiel, and K. S. Park, The synthesis of surface reactances using an artificial dielectric, *IEEE Trans. Anten. Propag.* **AP-31**:471–476 (May 1983).
7. S. Cohn, Analysis of the metal-strip delay structure for microwave lenses, *J. Appl. Phys.* **20**:257–262 (March 1949).
8. N. Marcuvitz, *Waveguide Handbook*, Peter Peregrinus, London, 1993, pp. 218–221.
9. C. R. Simovski, P. de Maagt, S. A. Tretyakov, M. Paquay, and A. A. Sochava, Angular stabilisation of resonant frequency of artificial magnetic conductors for TE-incidence, *Electron. Lett.* **40**(2):92–93 (Jan. 22, 2004).
10. P. C. Clemmow, *The Plane Wave Spectrum Representation of Electromagnetic Fields*, Pergamon Press, London, 1966.
11. V. H. Rumsey, Reaction concept in electromagnetic theory, *Phys. Rev.* **94**(6):1483–1491 (1954).
12. H. Y. D. Yang, and J. Wang, Surface waves of printed antennas on planar artificial periodic dielectric structures, *IEEE Trans. Anten. Propag.* **49**(3):444–450 (2001).
13. S. Rogers, W. McKinzie, and G. Mendolia, AMC's comprised of interdigital capacitor FSS layers enable lower cost applications, *Proc. IEEE Int. Antennas and Propagation Symp.*, Columbus, OH, June 22–27, 2003, Vol. 2, pp. 411–414.
14. R. E. Diaz and W. E. McKinzie, *Multi-resonant High-Impedance Electromagnetic Surfaces*, U.S. Patent 6,512,494 B1 (Jan. 28, 2003).
15. D. Dawn and Y. Ohashi, A novel electromagnetic bandgap metal plate for parallel plate mode suppression in shielded structures, *IEEE Microwave Wireless Compon. Lett.* **12**(5):166–168 (May 2002).
16. A. Monorchio, G. Manara, and L. Lanuzza, Synthesis of artificial magnetic conductors by using multilayered frequency selective surfaces, *IEEE APLett.* **1**:196–199 (2002).
17. F. Yang, K. Ma, Y. Qian, and T. Itoh, A novel TEM waveguide using uniplanar compact photonic-bandgap (UC-PBG) structure, *IEEE Trans. Anten. Propag.* **47**:2092–2098 (Nov. 1999).
18. A. S. Barlevy, D. F. Sievenpiper, and Y. Rahmat-Samii, Photonic bandgap (PBG) structures of multiple metallic periodic screens: Efficient electromagnetic characterization, *Proc. IEEE Antennas and Propagation (AP) Society Int. Symp.* 1998, June 1998, Vol. 2, pp. 1216–1219.
19. A. S. Barlevy and Y. Rahmat-Samii, Characterization of electromagnetic band-gaps composed of multiple periodic tripods with interconnecting vias: Concept, analysis, and design, *IEEE Trans. Anten. Propag.* **49**(3):343–353 (March 2001).
20. D. F. Sievenpiper, E. Yablonovich, J. N. Winn, S. Fan, P. R. Villeneuve, and J. D. Joannopoulos, 3D metallo-dielectric photonic crystals with strong capacitive coupling between metallic islands, *Phys. Rev. Lett.* **80**(13):2829–2832 (March 30, 1998).
21. D. Sievenpiper and E. Yablonovich, Eliminating surface currents with metallodielectric photonic crystals, *IEEE MTT-S Int. Microwave Symp. Digest*, June 1998, Vol. 2, pp. 663–666.
22. F. Tavakkol-Hamedani, L. Shafai, and Gh. Z. Rafi, Comparison of PBG and perfect magnetic conductor surface effects on the performance of finite microstrip antennas, *Proc. IEEE AP Society Int. Symp.* 2002, June 2002, Vol. 3, pp. 748–751.
23. Y. Rahmat-Samii, The marvels of electromagnetic band gap (EBG) structures: Novel microwave and optical applications, *Proc. 2003 SBMO/IEEE MTT-S Int.*, Sept. 2003, Vol. 1, pp. 265–275.
24. D. Kim, M. Kim, H. Xin, and J. Hacker, 2 GHz electromagnetic crystal reflector antenna, *Electron. Lett.* **39**(15):1096–1098 (July 24, 2003).
25. W. E. McKinzie and R. R. Fahr, A low profile polarization diversity antenna built on an artificial magnetic conductor, *Proc. IEEE AP Society Int. Symp.*, June 2002, Vol. 1, pp. 762–765.
26. S. Rogers, J. Marsh, W. McKinzie, and G. Mendolia, AMC edge treatments enable high isolation between 802.11b and Bluetooth/spl trade/ antennas on laptop computers, *IEEE AP Society Int. Symp.*, June 2003, Vol. 2, pp. 38–41.
27. R. Diaz, Magnetic loading of artificial magnetic conductors for bandwidth enhancement, *Proc. IEEE AP Society Int. Symp.*, June 2003, Vol. 2, pp. 431–434.
28. V. Sanchez and E. Paller, A tunable artificial magnetic conductor using switched capacitance in a concentric overlapping geometry, *Proc. IEEE AP Society Int. Symp.*, June 2003, Vol. 2, pp. 439–442.
29. D. Sievenpiper, J. Schaffner, J. Song, R. Loo, and G. Tangonan, Two-dimensional beam steering using an electrically tunable impedance surface, *IEEE Trans. Anten. Propag.* **51**:2713–2722 (Oct. 2003).

ATTENUATION MEASUREMENT

KURT HILTY
Swiss Federal Office of
Metrology
Bern-Wabern, Switzerland

When a signal is sent along any transmission path, many different mechanisms degrade it. Because of finite conductivity, every cable shows a resistive loss. Furthermore, the dielectric loss and the skin effect may be significant at higher frequencies, and imperfect screening of cables leads to radiation losses which might be quite important at higher frequencies. Single-mode optical fibers have two main intrinsic loss mechanisms, scattering loss and absorption loss. Scattering loss is dominated by Rayleigh scattering, and below 1600 nm absorption losses are caused mainly by OH absorption. Fibers that are bent too tightly or cabled too poorly may have, in addition, bend losses because of nonguided modes. Connectors show losses because of nonideal contacts and imperfect impedance matching, which reflect part of the signal to the transmitter. Filters built in the transmission path have

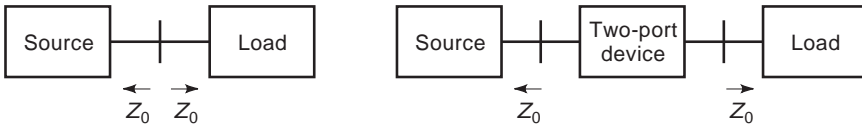


Figure 1. Attenuation measurement in a matched system.

losses in the passband caused by finite conductivity and probably dielectric losses. Wireless transmission paths, such as microwave links, satellite links, and broadcast or mobile communication, are affected by scattering caused by rain, clouds, and multiple reflections.

The two examples following clearly show how additional attenuation or losses influence a system:

In a radar system a total loss of 2 dB in the feeder system and the duplexer wastes 37% of the transmitter power. During the development of the different parts, the losses have to be measured very carefully to minimize the total loss.

Satellite systems quite often operate with cooled front ends at the receiver because the signals to be picked up are extremely weak. Therefore the front ends often operate with noise temperatures of 5 K. An additional loss of 0.1 dB from an uncooled waveguide would raise the noise temperature to 7 K.

These examples show how important it is to measure the losses of the different parts of a transmission system as accurately as possible to optimize system parameters.

Many different methods and a variety of systems for measuring attenuation have been developed. The most important techniques are described in the following sections.

1. ATTENUATION

1.1. Definition

In the field of loss measurement, the most important terms are attenuation, insertion loss, mismatch loss, and voltage loss [1,2]. These terms are discussed in the following sections.

1.1.1. Attenuation. According to Beatty [3], *attenuation* is defined as the decrease in power level at the load caused by inserting a device between a Z_0 source and load, where Z_0 is the characteristic impedance of the line. Figure 1 shows the basic idea of such an attenuation measurement.

Attenuation is mostly expressed by a logarithmic scale in decibels (dB) or in nepers. The attenuation of a two-port device is defined as follows [4]:

In decibels:

$$A = 10 \log \left[\frac{\text{power delivered to a matched load by a matched source}}{\text{power delivered to the same load when the two-port device is inserted}} \right] \quad (1)$$

In nepers:

$$A = \frac{1}{2} \ln \left[\frac{\text{power delivered to a matched load by a matched source}}{\text{power delivered to the same load when the two-port device is inserted}} \right] \quad (2)$$

Because $\log(x) = \ln(x)/\ln(10)$, the following relationship between decibels and nepers is valid:

Attenuation in decibels = $8.6858 \times$ attenuation in nepers.

Attenuation is a property only of a two-port device.

1.1.2. Insertion Loss. In practical applications neither the source nor the load have an impedance exactly equal to Z_0 , the characteristic impedance of a line. Therefore source and load have a reflection coefficient of r_s and r_L , respectively. Let P_1 be the power delivered from the source to the load and P_2 be the power absorbed by the same load when the two-port device is inserted (Fig. 2).

Then the loss is defined by

$$L_1 = 10 \log \frac{P_1}{P_2} \quad (3)$$

The insertion loss depends on the property of the device and the reflection coefficients of the source and the load.

1.1.3. Scattering Parameters. Two-port networks, especially at radiofrequencies, are very well characterized by scattering parameters.

A two-port device inserted between a source and a load is shown in Fig. 3.

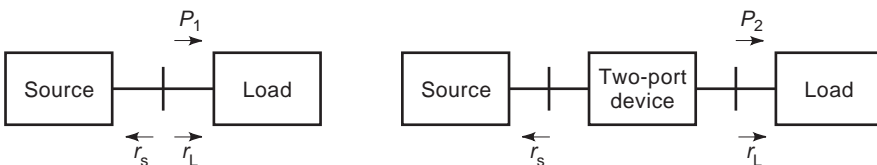


Figure 2. Insertion loss measurement in a nonmatched system.

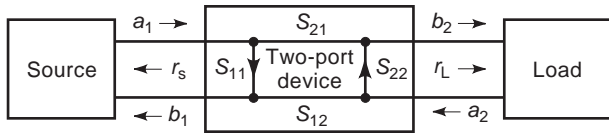


Figure 3. Scattering parameters for a two-port device inserted between source and load.

The complex wave amplitudes a_1 , a_2 , b_1 , and b_2 shown in Fig. 3 are related as follows:

$$b_1 = s_{11}a_1 + s_{12}a_2 \quad (4)$$

and

$$b_2 = s_{21}a_1 + s_{22}a_2 \quad (5)$$

Setting up the signal flow graph for the configuration in Fig. 3 and using the nontouching loop rules of Mason [5,6], the insertion loss is given by the following expression:

$$L_I = 20 \log \frac{|(1 - r_s s_{11})(1 - r_L s_{22}) - r_s r_L s_{12} s_{21}|}{|s_{21}| \cdot |1 - r_s r_L|} \quad (6)$$

For a matched system where $r_s = r_L = 0$, Eq. (6) delivers the attenuation

$$A = 20 \log \frac{1}{|s_{21}|} \quad (7)$$

Equations (6) and (7) clearly show that the insertion loss L_I depends on the property of the two-port device and the reflection coefficients of the source r_s and the load r_L . Otherwise the attenuation is the pure property of the two-port device.

1.1.4. Voltage Loss. Voltage loss is used only for applications in the DC-to-UHF part of the spectrum where voltage is well defined. According to Warner [4], it is defined as follows:

$$L_V = 20 \log \left[\frac{\text{voltage at the input of the two-port device}}{\text{voltage at the output of the two-port device}} \right] \quad (8)$$

and using the scattering parameters

$$L_V = 20 \log \frac{|(1 + s_{11})(1 - r_L s_{22}) + r_L s_{12} s_{21}|}{|s_{21}(1 - r_L)|} \quad (9)$$

Note that L_V is independent of the source reflection coefficient r_s .

When $s_{11} = 0$ and $r_L = 0$, the voltage loss is equal to the attenuation.

1.1.5. Mismatch Loss. At higher frequencies every real two-port device has an input and output reflection coefficient that differs from zero. Therefore, there is always a mismatch between the source and the two-port device and between the two-port device and the load (Fig. 4). This reflects part of the incoming and outgoing wave toward

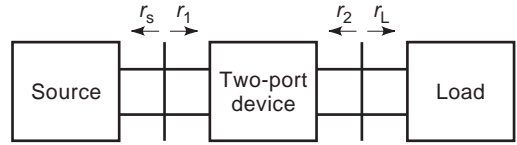


Figure 4. Mismatch loss of a two-port device between a source and a load.

the source and toward the two-port device, respectively, resulting in additional losses.

The mismatch loss between the source and the two-port device is expressed as:

$$L_{m1} = 10 \log \frac{\text{power absorbed at the input of the two-port device}}{\text{maximal available power from the source}} \quad (10)$$

According to Fig. 3 the mismatch loss is given by

$$L_{m1} = \frac{(1 - |r_s|^2)(1 - |r_1|^2)}{|1 - r_s r_1|^2} \quad (11)$$

Similarly, the mismatch loss between the two-port device and the load is given by

$$L_{m2} = 10 \log \frac{\text{power absorbed by the load}}{\text{maximal available power at the output of the two-port device}} \quad (12)$$

and with the parameters of Fig. 4

$$L_{m2} = 10 \log \frac{(1 - |r_2|^2)(1 - |r_L|^2)}{|1 - r_2 r_L|^2} \quad (13)$$

If several two-port devices are cascaded, the mismatch loss between them has to be calculated similarly and taken into account.

2. ATTENUATOR

Apart from the natural losses in devices and transmission paths, manufactured devices have well-defined losses. These devices, called *attenuators*, are used for measurement and for adjusting power levels to a defined value in transmission systems. Attenuators are probably the most important devices in measurement systems and therefore exist in a large number of different forms [7–9], such as symmetric, coaxial, waveguide, optical, fixed-value, and variable-loss. The important properties of attenuators are frequency range, attenuation accuracy, attenuation variation versus frequency, input and output impedance match (reflection coefficient), power handling capacity, and phase linearity.

2.1. Balanced-Line Attenuator

Balanced lines are used especially in telecommunications and lately in local-area networks and in-house

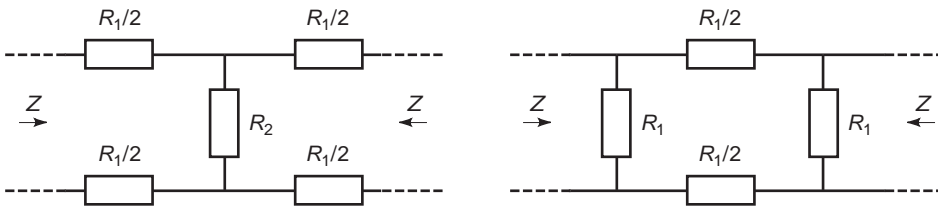


Figure 5. Basic symmetric double-T and double-Π attenuation circuits.

communications systems. Therefore, there is a demand for balanced-line attenuators. Chains of symmetric double-T or double-Π circuits, as shown in Fig. 5, are mostly used [10].

The reference handbooks [10] give formulas and tables to determine the circuit elements for a given line impedance and different element attenuations. The circuit has to be symmetric to the ground plane and well matched to the line impedance. Special techniques are given to optimize the circuit for small frequency dependence.

Variable-value attenuators are commercially available for different impedances (150 Ω, 120 Ω) in the frequency range from DC to several megahertz and have attenuation ranges from 0 to 132 dB.

2.2. Coaxial-Line Attenuator

2.2.1. Fixed-Value Coaxial Attenuator. Coaxial attenuators generally have multioctave bandwidth or frequently operate from DC to several gigahertz (GHz). Coaxial transmission lines are generally operated in the transverse electromagnetic (TEM) mode and therefore an obvious solution for attenuators is to use lumped elements that are small compared to the wavelength. There are four major constructions: T circuit, Π circuit, distributed lossy line, and distributed thin-film technology.

2.2.1.1. T-Circuit Attenuator. The T-attenuator circuit is shown in Fig. 6. The values of R_1 and R_2 are calculated from the following formulas, where K is the transmission coefficient [7,10]:

$$R_1 = Z_0 \frac{K - 1}{K + 1} \tag{14}$$

$$R_2 = \frac{2Z_0K}{K^2 - 1} \tag{15}$$

The attenuation in decibels is given by

$$A(\text{dB}) = 20 \log K \tag{16}$$

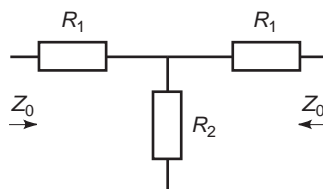


Figure 6. T-attenuator circuit.

Resistive rods for R_1 are often used, and disk resistors are used for R_2 , or film resistors are used for both R_1 and R_2 .

2.2.1.2. Π-Circuit Attenuator. Techniques similar to the T circuit are used for the Π circuit shown in Fig. 7, and the corresponding formulas are as follows [7,10]:

$$R_1 = Z_0 \frac{K + 1}{K - 1} \tag{17}$$

$$R_2 = Z_0 \frac{K^2 - 1}{2K} \tag{18}$$

At higher microwave frequencies the elements of the T and Π attenuators have dimensions comparable to the wavelength, and therefore the reactance of the elements becomes more important and thus degrades the performance of the attenuator.

2.2.1.3. Lossy-Line Attenuator. Distributed lossy-line attenuators, explained by Weber [11], have very favorable performance. As long as the attenuation is not very high, they have a flat attenuation response and an excellent impedance match. The center conductor of the transmission line is made mostly of lossy material using thin film deposited on a substrate with a circular cross section. The disadvantage of lossy-line attenuators is that they have a lower frequency limit depending on their physical length.

2.2.1.4. Thin-Film Attenuator. Distributed thin-film attenuators [12] use a resistive material deposited on a dielectric substrate for the series and shunt losses (Fig. 8).

Strip transmission lines and narrow ground electrodes on the longitudinal sides are added to the input and output terminals. The characteristic impedance and the attenuation are constant and given as follows [7]:

TART numbered equation (19)

$$Z_0 = \rho \sqrt{\frac{D - a}{4a}} \quad (\Omega) \tag{19}$$

$$\alpha = \sqrt{\frac{4}{a(D - a)}} \quad (\text{in nepers per unit length}) \tag{20}$$

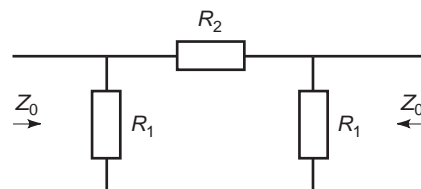


Figure 7. Π-attenuator circuit.

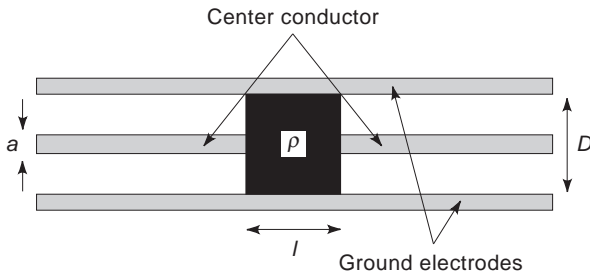


Figure 8. Distributed thin-film attenuator element.

Equation (20) shows that the attenuation is independent of the resistivity of the film as long as the film is homogenous. The attenuation depends only on the geometry and therefore is insensitive to temperature changes.

2.2.2. Variable-Value Coaxial Attenuator. There are two types of variable attenuators: continuous variable attenuators and step attenuators. Continuous variable attenuators have the advantage of being noninterruptive when changing attenuation. This feature is important for some measurements, for example, receiver sensitivity measurements. On the other hand, these attenuators may sometimes lack accuracy, settability, impedance match, high insertion loss and have limited bandwidth.

Step attenuators are very accurate and have the following qualities: good reproduceability, low insertion loss, excellent impedance match, and wide operating bandwidth. But most step attenuators are interruptive when changing the attenuation value.

2.2.2.1. Continuously Variable Attenuator

2.2.2.1.1. Piston Attenuator (Waveguide beyond Cutoff Attenuation). The piston attenuator is one of the oldest continuously variable microwave attenuators [13]. It is used especially as a precision attenuator or for handling high power levels. This type of attenuator uses a waveguide below its cutoff frequency. According to transmission-line theory, the amplitude of a wave launched into such a waveguide decays exponentially. So the attenuation is calculable. Most constructions use a circular cross section and a magnetic coupling that generates the lowest cutoff higher-order transverse electric mode (TE_{11}). Figure 9 shows the simplified construction of a piston attenuator. By sliding the two concentric cylinders into each other, the physical displacement of the coupling coil is changed and therefore also the attenuation. Special care must be taken to avoid unwanted higher order modes.

Attenuation as a function of wavelength is given per unit length as [10]

$$A = \frac{2\pi \cdot 20}{\lambda_c \cdot \ln 10} \sqrt{1 - \left(\frac{\lambda_c}{\lambda}\right)^2} \quad \text{in decibels per unit length} \quad (21)$$

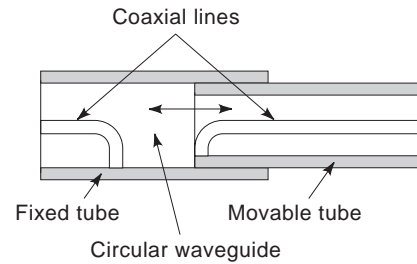


Figure 9. Principle of a piston attenuator.

where λ_c is the cutoff wavelength of the waveguide and λ is the free-space wavelength.

If the operating frequency is chosen to be much lower than the cutoff frequency, the term λ_c/λ is negligibly small for the operating frequency band, and a flat attenuation frequency response is achieved. The advantages of cutoff attenuators are that they are calculable and that high accuracy is achieved (0.001 dB/10 dB for 60 dB attenuation). For this reason, cutoff attenuators are often used as standard attenuators. Their main disadvantage is the high insertion loss (15 to 20 dB) because tight coupling has to be avoided so as not to stimulate higher modes.

2.2.2.1.2. Resistant Card, T-, or Π-Type Attenuator. Several constructions of variable attenuators using resistive cards or resistive films are on the market [9]. The variable card attenuator operates like a potentiometer. A resistive film is fixed on a substrate so that the resistance between the input and the output is varied with a movable coaxial wiper, and thus the amount of attenuation changes. This type of attenuator does not have good input and output impedance matches. More sophisticated constructions use T- or Π-type structures where the series and the shunt resistors are changed simultaneously. Therefore the input and output ports of these attenuators are quite well matched. The minimum insertion loss is on the order of 4 dB, and they operate up to several gigahertz.

2.2.2.1.3. Lossy-Line Attenuator. Lossy-line attenuators use a lossy center conductor partly covered with a thin sliding shield [7]. This effectively changes the length of the resistive conductor and thus the attenuation. Some constructions use microstrip lines with variable lossy walls [9]. This type of attenuator is limited in its maximal attenuation because of the length of the device.

2.2.2.1.4. Pin Attenuator. Pin attenuators change the loss in either a step or continuous mode. The series and shunt resistors are by *pin* diodes, electronic devices that change their conductivity. The diodes are controlled by a bias current. Various types of circuits are available, such as series, shunt, bridged T, and Π [9]. *Pin* attenuators are electronic circuits and therefore may produce harmonics. Below about 10 MHz, the *pin* diode exhibits some rectifying behavior. At much higher frequencies,

the *pin* diode behaves more like a variable resistor. Because of the matching circuits for input and output and the bias network, most devices operate in a limited frequency band. Attenuation from 2 to 80 dB is achieved.

2.2.2.1.5. Step Attenuator. Step attenuators always use a set of fixed attenuators that are switched into a line by different mechanisms. The steps are mostly 0.1, 1, and 10 dB. The 0.1-dB steps generally cover a range of 1.1 dB, the 1-dB steps a range of 11 dB, and the 10-dB steps cover a range up to 110 dB. The step attenuator has excellent repeatability, covers a wide frequency range (e.g., DC to 26.5 GHz), has a good impedance match, and mostly has a flat frequency response of the attenuation value.

In the turret-type coaxial attenuator a set of coaxial fixed attenuators is placed in a cylindrical arrangement. With a rotary motion the different elements (e.g., 0 dB, 10 dB, 20 dB, ...) are switched between the junctions of the transmission line.

Another type of step attenuator uses a variety of fixed attenuation elements. The different attenuation elements are cascaded by switches or bypassed. The switches may be activated manually or electrically.

2.3. Waveguide Attenuator

Waveguide attenuators work mostly in the entire usable waveguide bandwidth, which is not quite half an octave. To attenuate a wave propagated in a waveguide, either the electric or the magnetic field or even both are influenced. As an example, a resistive card inserted into the waveguide parallel to the *E* field attenuates it. Another technique uses lossy walls that influence the current in the waveguide wall. Most of these attenuators are not phase-invariant.

2.3.1. Fixed-Value Waveguide Attenuator. The waveguide flap attenuator (Fig. 10) and the side-vane attenuator (Fig. 11) [7] are very popular.

The flap attenuator is based on a resistive card inserted in the center of the waveguide parallel to the *E* field. The more the card dives into the waveguide, the more the *E* field is weakened, and therefore attenuation increases. A smooth card shape is chosen to minimize the reflection caused by the discontinuity.

The side-vane attenuator (Fig. 11) influences the *E* field similarly. The vane is always completely inside the waveguide, but it uses the fact that the *E* field varies along the broad side. For the most popular TE₁₀ mode, the *E* field is zero at the sidewall and has its maximum in the center of

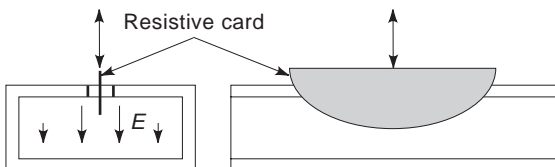


Figure 10. Principle of a waveguide flap attenuator.

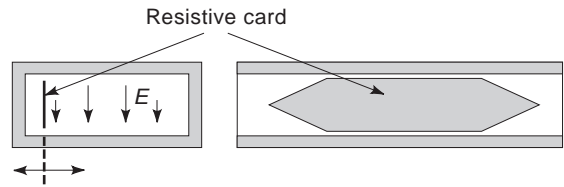


Figure 11. Principle of a side-vane attenuator.

the waveguide. Therefore the position of the resistive card defines the attenuation value. A smooth shape minimizes the reflection of the discontinuity.

Several constructions of lossy-wall attenuators exist. One version is shown in Fig. 12 [14].

Section 2 with equally spaced slots filled with a lossy material defines the attenuation. Sections 1 and 3 are configured to minimize the reflection due to the discontinuity in the wall. The lossy-wall attenuator withstands high power because the dissipated heat is transferred to any cooling system.

2.3.2. Variable-Value Waveguide Attenuator

2.3.2.1. Flap and Side-Vane Attenuator. By adding a mechanism that changes the position of the resistive card, the fixed-value-flap and side-vane attenuator are easily transformed into a variable-value attenuator. It is often used as a settable attenuator.

2.3.2.2. Rotary-Vane Attenuator. The rotary-vane attenuator was invented in the early 1950s by E. A. N. Whitebread (Elliot H. Brothers, London) and A. E. Bowen (Bell Telephone Laboratories). It was proposed and developed as a precision waveguide attenuator [15–19]. The rotary-vane attenuator consists of three sections of waveguide that have a resistive film spanned across the waveguide, as shown in Fig. 13. The middle section has a circular cross section and can be rotated with respect to the two fixed-end sections. Figure 13 illustrates the principle of a rotary-vane attenuator. For clarity, the transitions from a round to a rectangular waveguide at both ends are omitted.

The electric field is perpendicular to all resistive films whenever the films are aligned. In this case no current flows in the resistive film, and therefore no attenuation occurs. If the center part is rotated by an angle θ , the component $E_{\sin \theta}$ in θ produce a current flowing in the resistive film and are absorbed. Thus the resulting

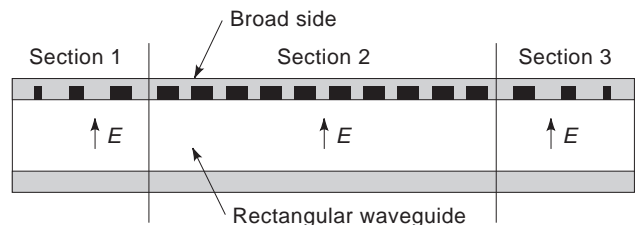


Figure 12. Lossy-wall attenuator.

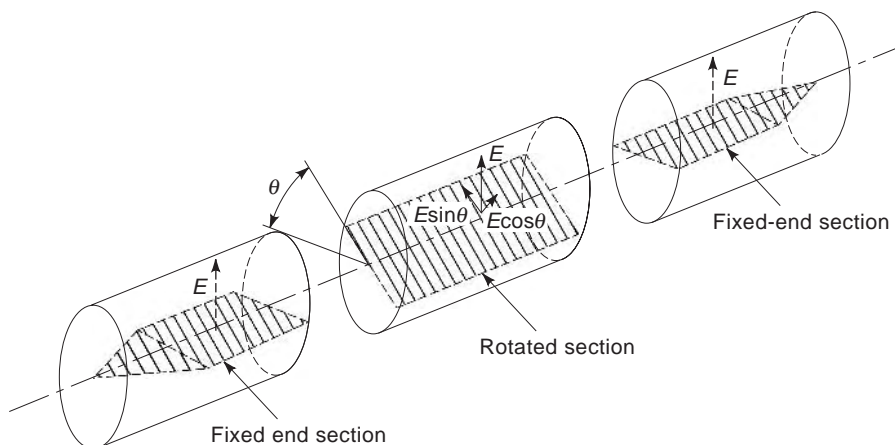


Figure 13. Principle of a rotary-vane attenuator.

attenuation is given by

$$A(\text{dB}) = -40 \log(\cos \theta) + A_0 \quad (22)$$

The rotary-vane attenuator has the following advantages:

- The attenuation is almost independent of the frequency.
- The phase shift is very small. The phase variations are smaller than 1° up to 40 dB attenuation.
- The input and output VSWRs are very low under all conditions.
- The attenuation is not sensitive to the resistive film as long as its attenuation is high enough.
- The attenuation is not sensitive to temperature changes.

Rotary-vane attenuators are commercially available for most of the known waveguide bands. They typically have an accuracy of 2% of the reading in decibels or 0.1 dB, whichever is greater.

2.4. Attenuator for Optical Fibers

Attenuators have to be adapted to an optical fiber system. Therefore different attenuators for single-mode or multi-mode applications are available and mostly operate within

one or two wavelength windows. Various attenuation techniques are used to reduce the transmitting light, such as lateral or axial displacement of the fibers or optical prisms, and inserting absorbing filters.

2.4.1. Fixed- or Adjustable-Value Attenuator. A pair of lenses is used in most fiberoptic attenuators to collimate the light of the input fiber and to refocus it to the output fiber. Any attenuation mechanism, such as absorbing filters or absorbing glass with variable thickness can be inserted into the optical beam path. Attention has to be given to the attenuation mechanism so that there is very little polarization-dependent loss. Fixed-value attenuators are commercially available for a range of 3–40 dB with an accuracy of 0.5–1 dB.

2.4.2. Variable-Value Attenuator. The reflection type variable attenuator often combines a series of 10 dB steps for the high values and a continuous variable attenuation of up to 10 or 15 dB. Figure 14 shows the basic configuration of an optical section [20].

A rod lens collimates the light of the fiber into a spatial beam that passes two neutral-density filters (ND filters). The second rod lens focuses the spatial beam into the output fiber. The ND filter must have high uniformity, little attenuation change with time, and flat spectral transmittance. This is achieved by vacuum-depositing Ni

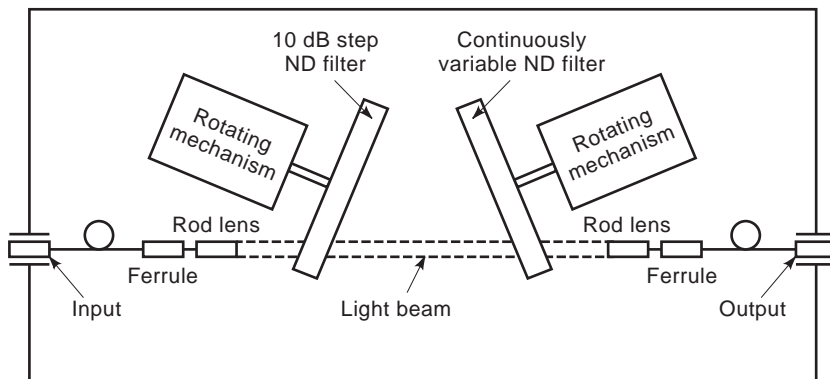


Figure 14. Basic configuration of an optical section.

and Cr alloys onto a glass substrate. The ND filters are the reflecting type. To avoid multiple reflections and to ensure that the light is not reflected into the input lead, the two filters are inclined at a small angle with respect to the optical axis.

Commercially available attenuators of this type have an insertion loss of about 3.5 dB, a range of up to 65 dB, and an accuracy of about ± 0.5 dB per 10 dB. They are available for wavelengths of 850, 1300, and 1550 nm.

2.5. Calculable Attenuation Standards

Many attenuators have been described in the previous sections, but only a few are suitable as attenuation standards. An attenuation standard is a device that can be traced to the SI units by an unbroken chain. The application of the described standards depend on the frequency band and the technique used in the measurement system.

2.5.1. Kelvin–Varley Divider. The Kelvin–Varley divider (KVD) was described for the first time by Varley in 1866 [21]. It is a resistive voltage divider and operates from DC up to several hundred kilohertz. Figure 15 shows an example of a four-decade Kelvin–Varley divider.

Each decade consists of 11 equal resistors except for the last decade, which has only 10. The decades are connected by switches that always span two resistors. The value of the resistors of each following decade is reduced by a factor of 5. The four-decade Kelvin–Varley divider allows varying the output-to-input voltage ratio from zero to one in steps of one part in 10^4 . The unloaded KVD has a constant input impedance that is independent of the switch setting, whereas the output resistance varies with the setting. The original type of KVD (Fig. 15) requires either very large or very small resistance values because each decade needs 5 times larger values. Due to

stray capacitance, the divider reacts similarly to an RC filter. For example, a 100 k Ω input impedance limits the 3 dB bandwidth to about 100 kHz. To avoid large resistance values, modified constructions with a resistor shunting the decades have been developed.

Two major errors determine the accuracy: deviations of the resistors from nominal values and the resistances of the switch contacts and leads. The first three or four decades are the most sensitive, and therefore these resistors often are adjustable. Several calibration techniques have been developed and are described in the literature [22,23].

Today commercially available Kelvin–Varley dividers have up to seven decades, have an absolute linearity of ± 1 part in 10^7 , and long term stability of ± 1 part in 10^6 per year.

2.5.2. Inductive-Voltage Divider. The inductive-voltage divider (IVD), also called a *ratio transformer*, is an exceptionally accurate variable attenuation standard. It consists of a number of very accurately tapped autotransformers. The autotransformers are connected together by high quality switches. The IVD operates from 10 Hz to about 100 kHz, and the greatest accuracy is achieved at about 1 kHz. In 1962 Hill and Miller [24] described a multidecade IVD with seven decades and a resolution of 1 part in 10^7 . Figure 16 shows the principle of a seven-decade IVD with a setting of 0.4324785. The output-to-input voltage ratio can be set from zero to one.

The tapped autotransformers are constructed by winding exactly equal lengths of copper wire on a high permeability toroidal core. A superalloy having an extremely high permeability ($> 100,000$) and low hysteresis loss is preferred as a core material. For an exact division of the tapped autotransformer, it is not necessary to have a 100% coupling between the ten inductors [4]. But the 10 self-inductances and the 45 mutual inductances have to be exactly equal.

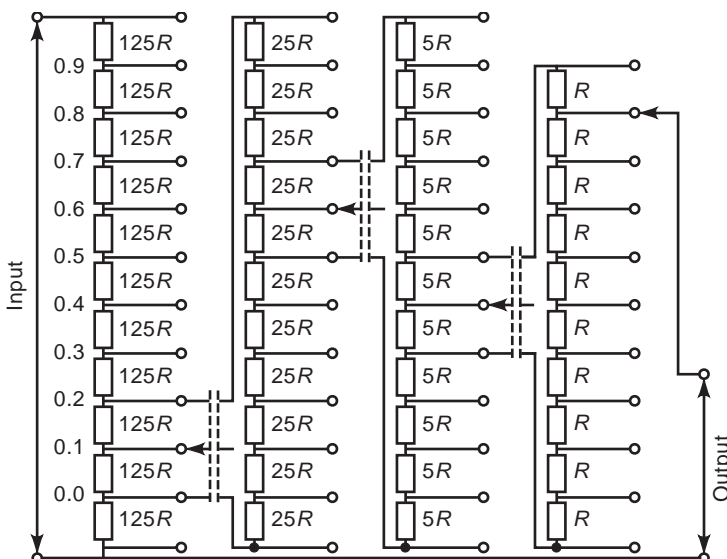


Figure 15. Principle of a four-decade Kelvin–Varley divider.

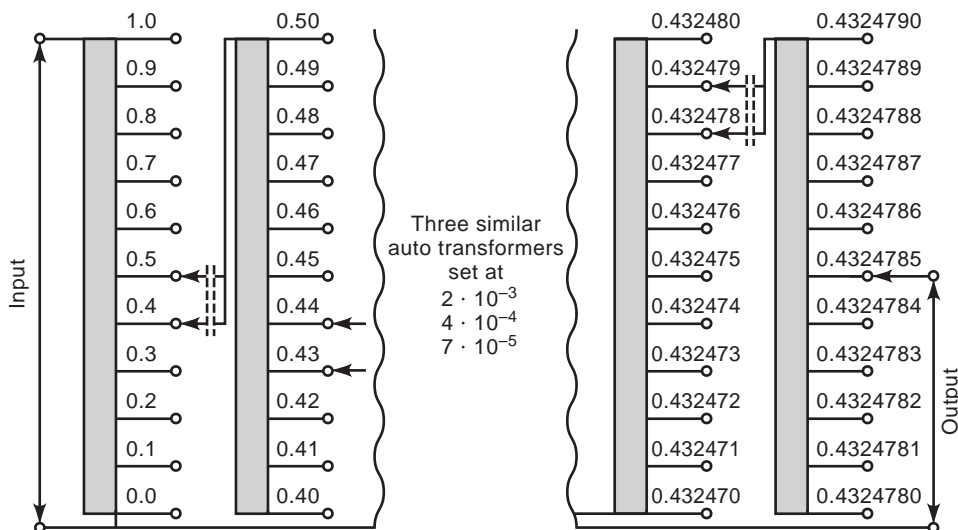


Figure 16. Principle of a seven-decade IVD.

The following error sources limit the accuracy of IVDs:

Inequality in the series resistances and the leakage inductances of the sections in each autotransformer

Inhomogenities in the magnetic cores

Distributed admittances between the windings

Internal loading caused by the later stages

Impedances of the connecting leads and switch contacts

Variations in the input voltage, frequency, and ambient temperature

With careful design, these errors can be minimized. Programmable binary IVDs with 30 bits, a resolution of 1 part in 10^9 , and a linearity of 0.1 ppm have been developed [25].

IVDs with eight decades and an accuracy of four parts in 10^8 are commercially available.

2.5.3. Intermediate-Frequency Piston Attenuator. The IF piston attenuator is based on the same principle as the attenuator previously described for RF, but it is designed to operate at a specific, fixed frequency, mostly 30 or 60 MHz. As Eq. (21) shows, attenuation depends on the cutoff wavelength λ_c , the free-space wavelength λ , and the displacement of the two coils. The waveguide dimensions, which can be determined, define the cutoff wavelength, and the displacement can be measured very precisely. Therefore the IF piston attenuator is used as a calculable standard. Figure 17 shows a simplified diagram of an IF piston attenuator.

The standard IF piston attenuator consists of a high-precision circular cylinder that has excellent conductivity, a fixed coil, and a movable coil mounted on a piston. The piston attenuator operates in the H_{11} (TE_{11}) mode that has the lowest attenuation. A well-designed metal strip filter

in front of the fixed coil attenuates the higher modes. To allow smooth movement and to avoid any scratches, the plunger carrying the moving coil is insulated. Equation (23) expresses the attenuation per unit length more precisely

$$A = \frac{s_{11}}{r} \sqrt{1 - \left(\frac{\lambda_c}{\lambda}\right)^2} \cdot \epsilon - \frac{\delta}{r} \tag{23}$$

in nepers per unit length, where $\lambda_c = 2\pi r/s_{11}$, λ_c is the cutoff wavelength, λ is the free-space wavelength, s_{11} the first zero of the Bessel function $J_1 = 1.8411838$, r the radius of the cylinder, and δ is the skin depth.

Highly accurate standard attenuators use a laser interferometer to accurately determine the displacement of the coil. Yell [26,27] and Bayer [28] developed extremely accurate IF piston attenuators with a dynamic range of 120 dB, a resolution of 0.0001 dB, and an accuracy of 0.0002 dB/10 dB over the linear range of 90 dB.

2.5.4. Rotary-Vane Attenuator. The principle of the rotary-vane attenuator is described in Section 2.3.2.2. Because the attenuation is given by the equation

$$A(\text{dB}) = -40 \log(\cos \theta) + A_0 \tag{24}$$

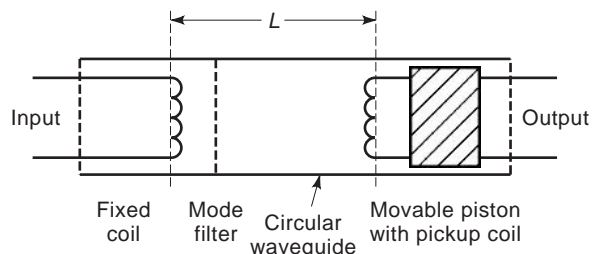


Figure 17. Simplified IF piston attenuator.

where A_0 is the insertion loss at a setting of $\theta=0$, the device can be used as a calculable primary standard.

The rotating angle θ of the center vane has to be determined very precisely, especially for higher attenuation values. As an example, a rotational angle accuracy of $\pm 0.001^\circ$ results in an attenuation accuracy of ± 0.01 dB at a setting of 60 dB. Especially precise optical readouts have been developed by national standards laboratories [29–31] to allow an angular resolution of $\pm 0.001^\circ$. Following are the main error sources for precision rotary-vane attenuators:

- Misalignment of the end vanes
- Insufficient attenuation of the central vane
- Incorrect readout of the rotational angle
- Eccentricity of the rotor
- Leakage of the rotating joints
- Internal reflections at the ends of the three vanes

Careful design of the attenuator results in an accuracy of ± 0.0015 dB up to 16 dB at 10 GHz.

2.5.5. Comparison of Attenuation Standards. The attenuation standards mentioned previously are used in various precision measurement systems, such as RF, IF, or LF substitution. The standards have very different accuracy depending on the attenuation setting. Figure 18 shows a comparison of different precision

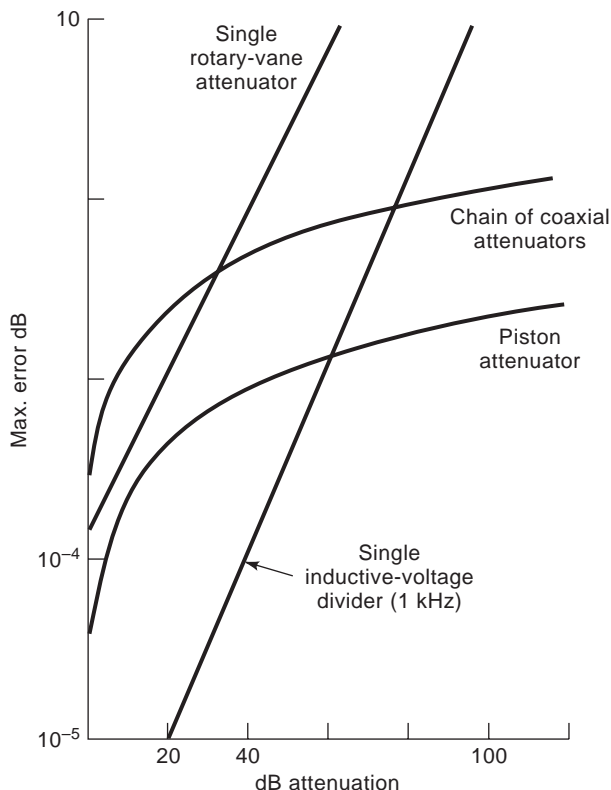


Figure 18. Comparison of attenuation standards.

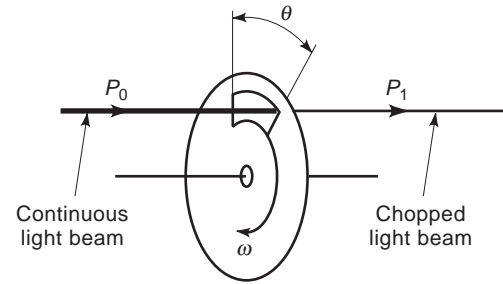


Figure 19. Principle of an optical chopping system.

attenuation standards used in national metrology laboratories [32].

2.5.6. Optical Attenuation Standards. Imamura [33] shows one solution of a calculable optical attenuation standard that is used to calibrate precision attenuators. The key element is a rotating disk with a well-defined opening. The device operates as an optical chopping system (Fig. 19).

As long as the response of the detector is slow compared to the rotational speed ω , the ratio of P_1 to P_0 defines the attenuation. In this case the attenuation depends only on the opening angle θ (in radians) and is given by the following equation:

$$A = -10 \cdot \log \frac{P_1}{P_0} = -10 \cdot \log \frac{\theta}{2\pi} \quad (25)$$

An opening angle of 36° defines an attenuation of 10 dB. Special care has to be paid to the diffraction of light at the edges of the disk openings and the stability of the light source and the sensor. The overall accuracy is estimated to be ± 0.008 dB for 10 dB attenuation.

3. MEASUREMENT OF ATTENUATION

Various kinds of measurement systems are used depending on the frequency range, the type of attenuator, the required accuracy, and the available standards. Most of the modern attenuation measurement systems are computer- or microprocessor-controlled. They use the same principle as the manual systems but operate much faster. If maximum accuracy is required, manually controlled measurement systems are often preferred.

3.1. Low-Frequency Measurement Systems

Low-frequency attenuation measurements are used mainly in communication systems where voice, video, and data have to be transmitted with as little distortion as possible. Dedicated test systems have been developed for testing and adjusting the communication systems working either with coaxial lines (50 or 75 Ω) or balanced lines (124, 150, or 600 Ω).

3.1.1. Direct Measurement. Operation of communication systems requires a great number of test systems for

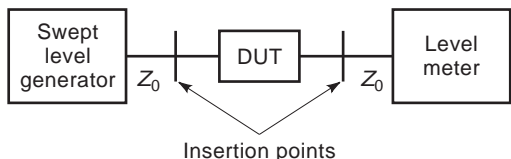


Figure 20. Principle of a direct measurement system.

which low-cost test systems that are easily handled were developed. The systems are based on current, voltage, or power measurement and operate in a frequency band from 200 Hz up to 30 MHz. The test system (Fig. 20) consists of a tuneable generator with a known constant output level and a wideband voltmeter or a high-sensitivity, selective superheterodyne receiver.

Many test systems can be switched to operate in either coaxial-line (50 or 75 Ω) or balanced-line (124, 150, or 600 Ω) configuration. In the balanced-line mode the test systems have a limited frequency range of 200 Hz to several MHz depending on the impedance selected. In the selective-level meter mode, bandwidths of 25 Hz–3.1 kHz are used, and the dynamic range achieved is on the order of 80 dB. The attenuation measurement accuracy in the frequency range indicated is about 1 dB.

3.1.2. Low-Frequency Substitution Method. The LF substitution method is based on a precisely calibrated low-frequency reference attenuator used in a parallel or a serial configuration (Fig. 21).

Because the attenuation of the device under test (DUT) is compared with that of the reference attenuator, neither the output level of the generator nor the absolute level indication of the receiver have to be known. The only requirements are that generator and receiver remain stable during measurements. The accuracy is determined mainly by the calibration of the reference attenuator.

3.2. Radiofrequency and Microwave Measurement Systems

In radiofrequency and microwave ranges many different measurement principles are known. They all have their own characteristics; one is meant to measure low values of attenuation, another to measure high values, a third to achieve highest accuracy. The most popular measurement principles are discussed in the following sections.

3.2.1. Power Ratio Method. The power ratio method [4,40] (Fig. 22) is very simple for measuring attenuation.

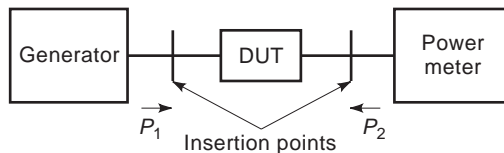


Figure 22. Principle of the power ratio method.

It is commonly used as long as maximum accuracy is not required.

The method is based on the linearity of the power meter or the receiver used. First the power P_1 of the generator is measured without the device under test (DUT) and then P_2 is measured with the DUT inserted. The attenuation of the DUT is calculated by the ratio of P_2 to P_1 :

$$A(\text{dB}) = 10 \log \frac{P_2}{P_1} \tag{26}$$

To measure attenuation, the insertion points have to be matched by either tuners or matching pads. The square-law characteristic of the power sensors and the noise limit the dynamic range to about 40 dB. If a tuned receiver is used instead of a power meter, the measurement range is extended to about 100 dB.

Several error sources influence the accuracy:

- The stability of the generator and the detector system
- The frequency stability of the generator
- The matching at the insertion points
- The square-law region of the detector system
- The crosstalk for high-attenuation measurement

Commercially available systems using a tuned receiver achieve a measurement uncertainty of 0.1 dB at 50 dB attenuation. These systems are easily automated by controlling the instruments with a computer.

In national standards laboratories very sophisticated systems have been developed resulting in an accuracy of 0.06 dB at 50 dB attenuation [34,35].

3.2.2. Voltage Ratio Method. The voltage ratio method makes use of high-resolution AC digital voltmeters (AC DVMs) available now. Because the AC DVMs work up to only several MHz, the RF signals have to be downconverted to low frequency. Figure 23 shows the principle of a

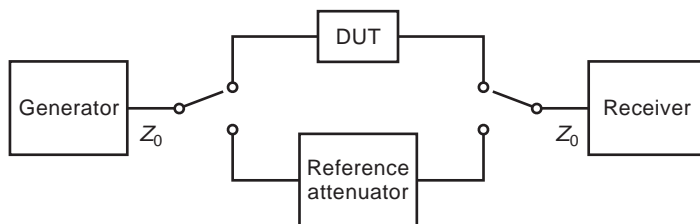


Figure 21. Principle of a LF substitution method.

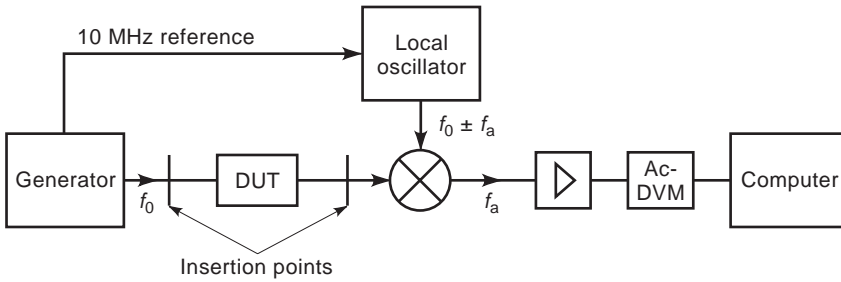


Figure 23. Principle of the voltage ratio method.

voltage ratio system working at an audiofrequency of 50 kHz.

If a synthesizer locked to the same reference frequency is used as a signal generator and local oscillator, a very stable audiofrequency f_a (e.g., 50 kHz) is generated. The audiofrequency signal is amplified and measured with an AC DVM. If U_1 is the voltage measured with the two insertion points clamped together and U_2 is the voltage with the DUT inserted, the attenuation is given by

$$A(\text{dB}) = 20 \log\left(\frac{U_2}{U_1}\right) + C \quad (27)$$

where C is the correction factor in decibels for the non-linearity of the amplifier and the DVM.

The dynamic range of the direct system is about 20–30 dB. More sophisticated systems achieve an uncertainty less than 0.001 dB for 20 dB attenuation. By adding a gauge block technique, for example, a calibrated step attenuator (10, 20, 30, 40, 50, 60, 70 dB) in series with the DUT in the RF path, the range is extended to 90 dB with excellent accuracy of 0.001 dB [32].

The error sources which limit the measurement uncertainty are

- The matching of the insertion points
- The generator output level stability
- The AF amplifier stability
- The AF amplifier and AC DVM linearity
- The mixer linearity
- The gauge block attenuator stability and reproducibility
- The crosstalk for high attenuation measurement

3.2.3. IF Substitution Method. The IF substitution method [4,40] (Fig. 24) gives good accuracy, operates over a large dynamic range, and is used up to very high frequencies. Most systems operate in a parallel substitution mode.

The signal passing through the DUT is mixed to an IF of 30 or 60 MHz. This signal is compared with the signal of the 30-MHz reference oscillator and the standard attenuator by a narrowband 30 MHz receiver (mostly with synchronous detection). In the first phase the insertion points are clamped together, and the standard attenuator is adjusted until there is no switching signal (i.e., 1 kHz)

detectable any longer. The reading A_1 of the standard attenuator is taken. In a second phase the DUT is inserted, the standard attenuator is adjusted so that the signal of the standard attenuator equals the signal of the mixer, and the reading A_2 is taken. The attenuation of the DUT is given by the difference A_2 minus A_1 between readings.

A piston attenuator, an inductive-voltage divider, or a high-precision resistive attenuator can be used as a standard attenuator.

In national standards laboratories very-high-precision piston attenuators with a resolution of 0.0001 dB over a 100 dB range have been used in a parallel substitution system. The accuracy achieved is better than 0.001 dB per 10-dB step [27,32,36].

Accuracy of about 0.002 dB and a dynamic range of 100 dB have been achieved by using a seven-decade 50-kHz inductive voltage divider in a parallel substitution system [37].

Weinert [38] proposed a parallel IF complex vector substitution system using a high precision IF attenuator. The system has a single-step dynamic range of 140 dB and a display resolution of 0.001 dB.

The following error sources limit the accuracy and the dynamic range:

- The matching at the insertion points
- The level stability of the signal source
- The mixer linearity
- The noise balance
- The level stability of the IF reference oscillator
- The standard attenuator resolution and stability
- The crosstalk for high attenuation measurement

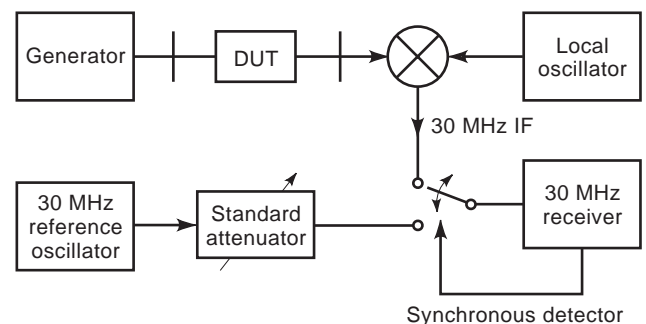


Figure 24. Principle of the IF substitution method.

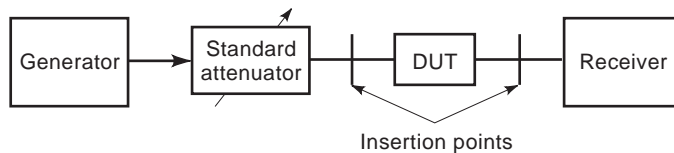


Figure 25. Principle of the series RF substitution method.

3.2.4. RF Substitution Method. In the RF-substitution method [4,40] (Fig. 25), the reference standard attenuator and the DUT operate at the same frequency. Because the attenuation of the reference standard is compared either in a series or in a parallel substitution system with the DUT, the results are independent of the receiver characteristics. A rotary-vane attenuator, a piston attenuator, or a chain of well-matched and precisely calibrated attenuators (e.g., step attenuator) is used as a reference standard.

In the first step the insertion points are clamped together, and the reference standard is adjusted to a value A_1 according to the estimated attenuation of the DUT. The receiver shows the reading U_1 . In the second step the DUT is inserted, and the reference standard is adjusted to get the same reading U_1 at the receiver A_2 . The attenuation of the DUT is calculated as the difference between the two decibel readings of the reference attenuator, A_1 minus A_2 .

3.2.5. Scalar Measurement. All attenuation measurement systems described in the previous sections provide scalar measurements. There are many commercial scalar network analyzers available (Fig. 26) [8,39]. These analyzers measure the input reflection and the attenuation of the device under test. Because mostly wideband detectors are used, the magnitude of only two quantities can be determined.

The signal of the sweep generator is divided by a power splitter into reference and measurement paths. The directional bridge or coupler measures the reflected wave of the DUT. The analyzer forms the ratio A/R , which is proportional to the input reflection coefficient of the DUT. Using a third detector, the attenuation is measured by calculating the ratio B/R . Most scalar network analyzers are microprocessor- or computer-controlled and offer simple correction methods. The calibration for reflection measurements is frequently done by

using open and short circuits, and a connect through normalization is used for the transmission path. Because these analyzers are broadband systems, they operate very fast and are easily expandable to highest frequencies. Commonly used scalar network analyzers operate from 10 MHz to 18 GHz or 26 GHz, and often their frequency range can be extended to 50 GHz in coaxial lines and to 110 GHz in waveguides. The dynamic range is limited to about 75 dB by the square-law characteristic of the detectors and noise. The measurement accuracy achieved is quite reasonable, for example, 0.6 dB measuring a 30-dB attenuator. The insertion points have to be well matched.

The following errors influence the measurement uncertainty:

- The harmonics of the sweep generator
- The matching of the insertion points
- The square-law characteristic of the detectors
- The sweep generator level stability

3.2.6. Vector Measurement. Vector measurements enable characterization of a two-port circuit completely. In addition to the magnitude, the phase of the scattering parameters is also determined. There are two major concepts for measuring the complex parameters of a two-port device: the vector network analyzer and the six-port technique.

Modern vector network analyzers [8,39,40] measure all four scattering parameters— s_{11} , s_{21} , s_{12} , and s_{22} —without the necessity of turning the DUT around. Therefore they are symmetrical (Fig. 27) and measure in both directions.

The basic concept looks similar to that of the scalar network analyzer. The signal of the generator is divided into reference and measurement paths. In forward measurements, the directional bridge A determines the reflected signal, bridge B determines the transmitted signal,

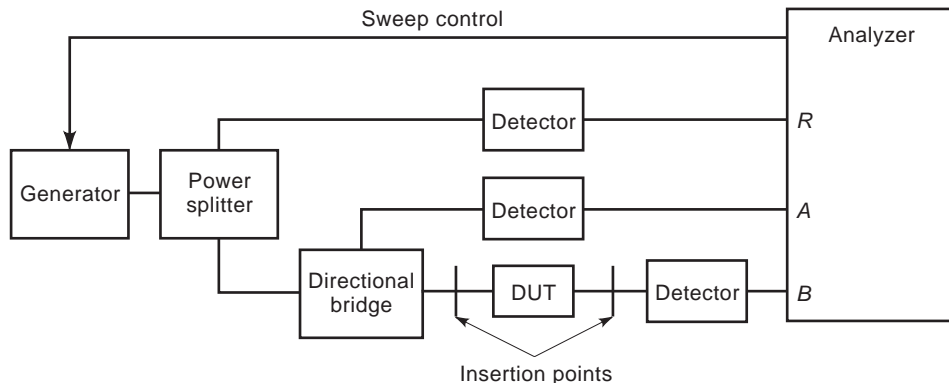


Figure 26. Principle of a scalar network analyzer.

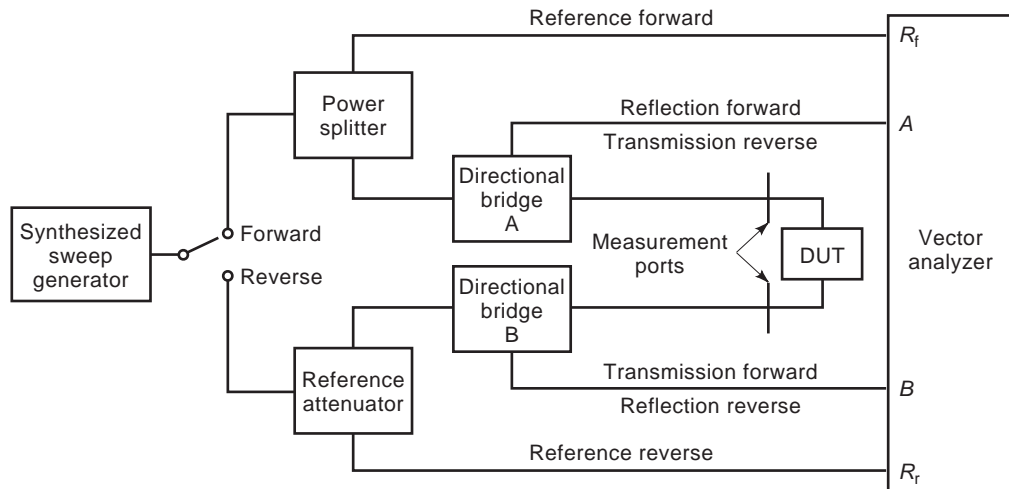


Figure 27. Principle of a vector network analyzer.

and vice versa for the reverse case. Instead of using diode detectors, the signals are downconverted to an intermediate frequency and analyzed in magnitude and phase. Synthesized sweep generators and synchronous detection are being used to obtain high accuracy for magnitude and phase measurements. Because the complex signals are measured, the main errors due to component imperfections may be corrected. Frequently a 12-term error model is applied to correct the source and load match, the bridge characteristics, the transmission leakage crosstalk, and downconverter characteristics. In the first phase well-known standards (e.g., open, short, line) are measured, and the 12 error parameters are determined. In the second phase the DUT is measured and the data corrected according to the calculated error terms. Several different techniques for measuring the error parameters are used, such as open–short–load, transmission–reflect line, and line–reflect line. Each technique uses different kinds of reference standards, such as short and open circuits, well-defined lines, and known loads.

Excellent performance is achieved by using the 12-term error correction technique. For example, at 20 GHz, load and source match better than -38 dB return loss, transmission tracking is better than 0.06 dB and crosstalk is less than -104 dB. As a result a 30 dB attenuator can be measured at 20 GHz with an uncertainty of 0.07 dB.

Vector network analyzers are commercially available in coaxial configurations in frequency bands from about 100 kHz to 50 GHz and in waveguides up to 110 GHz. Some specially dedicated systems operate in waveguides up to 1000 GHz.

The measuring uncertainty is defined mainly by the following parameters:

- Accuracy of the reference standards
- Stability of the generator and of the detection system
- Stability of the connection cables
- Repeatability of the connectors
- Accuracy of the built-in software to calculate the error parameters and DUT scattering parameters

The six-port technique is another method for measuring the complex scattering parameters of a device. The magnitude and the phase of the signal are calculated from four scalar power measurements made with detectors arranged as shown in Fig. 28 [8,40].

The four power sensors gather enough information to calculate the magnitude and phase of the reflection of the DUT and the power launched into it. The calibration of the six-port device is rather complicated because a set of quadratic equations has to be solved. The quadratic equations can be linearized and solved for both calibration and measurement [8,40].

The simplicity of the detection system is an advantage of the six-port device especially for wideband applications and very high operating frequencies. Compared to the vector network analyzer, the six-port device requires more calibration and more complicated mathematics.

Two six-port devices connected in the configuration shown in Fig. 29 are required to provide attenuation measurements.

The dividing circuit includes phase adjustments to obtain different ratios b_1/b_2 at the terminals of the DUT. Using state-of-the-art power sensors the dynamic range of a dual six-port device is as large as 60 dB.

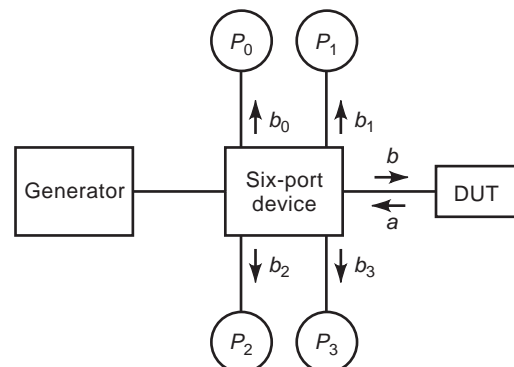


Figure 28. Principle of six-port technique for reflection measurement.

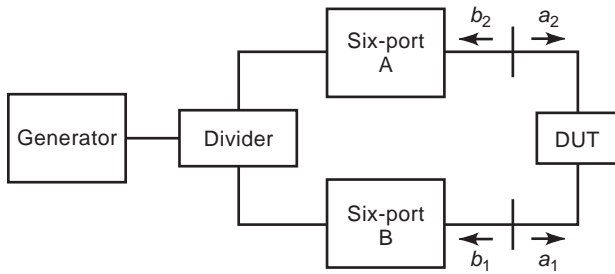


Figure 29. Principle of a dual six-port for s-parameter measurement.

To achieve maximum accuracy, through-connection, reflection line (TRL) calibration is frequently used. Because the six-port device determines the complex parameters during the calibration process, the test ports appear to be well matched. The measurement uncertainties are primarily limited by the calibration standards, mainly the reflection standard (short or open). Real-time operation is limited by the computing time and the response time of the power sensors.

3.3. Fiberoptics

Three main methods [41,42] are used for attenuation measurements: the insertion loss technique, the cutback technique, and the backscattering method. The first two methods perform two-point (end-to-end) measurements and the last performs a one-ended characterization. Some of the methods are standardized [43,44].

3.3.1. Insertion Loss Method. The insertion loss technique consists of a stable laser source and a stable, accurate, optical power meter. The power P_2 of the laser source is sent into the DUT (e.g., an optical fiber), and the power P_3 is measured at the far end. The attenuation is given by the ratio of the two power levels as

$$A(\text{dB}) = 10 \log \left(\frac{P_3}{P_2} \right) \tag{28}$$

To achieve more accurate measurements in the first phase, the power of the source is directly measured and is remeasured in the second phase with the DUT inserted. More sophisticated measuring systems use a configuration shown in Fig. 30.

A second power sensor measures the power level of the source instantaneously by a power divider. In this config-

uration the power stability of the source is less important because P_1 is always used as a reference. By using cooled detectors, a dynamic range of ≤ 90 dB is achieved.

The accuracy of the measurements are determined by the following factors:

- The power level and wavelength stability of the source
- The calibration and stability of the power sensors
- The reproducibility of the connectors
- The linearity of the detectors

The measurement uncertainties for the insertion loss technique are on the order of 0.9 dB including the connector reproducibility. Sophisticated systems reach over a limited dynamic range of 50 dB and uncertainty of 0.2 dB.

3.3.2. Cutback Method. The cutback method [41,45] (Fig. 31) is the most accurate technique, but it is destructive. This method was developed to measure the attenuation of fibers as a function of the wavelength. Using a light source combined with a monochromator, a fiber can be tested at any wavelength from 800 to 1600 nm with a spectral width of 3 nm. The light from the source is projected into the fiber by a lens.

The power $P_2(\lambda)$ is measured at the far end of the fiber (test length l_t) by using a cooled detector. Then the fiber is cut back to a short length of 2–3 m without changing the projecting conditions, and the power $P_1(\lambda)$ is recorded. If the power loss in the short length of fiber is assumed to be negligible, the attenuation is given by the following equation:

$$A(\lambda) = 10 \log \frac{P_2(\lambda)}{P_1(\lambda)} \tag{29}$$

Assuming a uniform fiber, the attenuation coefficient per unit length of the fiber is given by

$$\alpha(\lambda) = \frac{A(\lambda)}{(l_t - l_r)} \tag{30}$$

where l_t and l_r are given in kilometers. The achieved uncertainty for cable length of several kilometers is about 0.02 dB/km for multimode fibers and 0.004 dB/km for single mode.

3.3.3. Backscattering Method. The backscattering method is a one-ended measurement based on Rayleigh scattering in an optical fiber [41,46]. Figure 32 shows

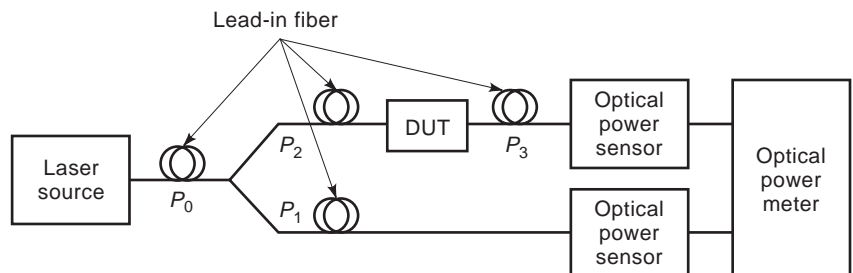


Figure 30. Principle of the insertion loss method.

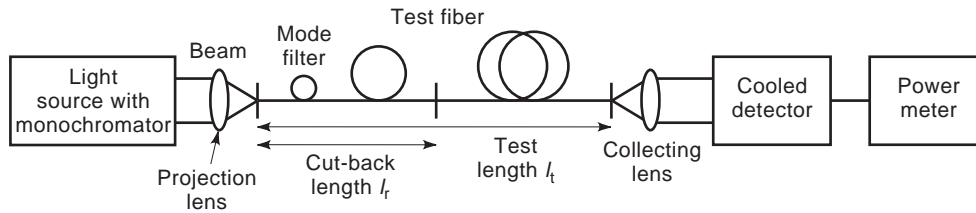


Figure 31. Principle of the cutback method.

the principle of an optical time-domain reflectometer (OTDR).

A laser pulse is projected into the fiber by a coupler, and the backscattered power is measured. The backscattered power is related to the attenuation loss of the fiber, and the measured time delay is related to the distance in the fiber. The attenuation is calculated by using two values of the backscattered power at different time delays (different locations along the fiber). The OTDR has the advantage of providing attenuation and reflection information along the fiber. A typical recording is shown in Fig. 33.

The length of the pulse is responsible for the deadzone, where no measurement is possible. A lead-in fiber allows masking of the deadzone. From the measured data details in the fiber path, such as connector loss or splice loss, irregularities of attenuation and defects can be analyzed.

Commercially available OTDRs have a dynamic range of about 35 dB and cover distances up to 65 km depending on the fiber loss. A well-calibrated OTDR can produce a measurement uncertainty of about 0.02 dB/km.

4. ERRORS AND UNCERTAINTIES IN ATTENUATION MEASUREMENTS

Whenever measurements are made, the results differ from the true or theoretically correct values. The differences are the result of errors in the measurement system, and it should be the aim to minimize these errors. In practice there are limits because no measurement instruments operate perfectly. A statement of measurement uncertainty reflects the quality of the measured results, and it has to be accompanied by a statement of confidence.

The International Committee for Weights and Measures (CIPM) [47] has published a guide for expressing uncertainty in measurements which has been adopted by the European Cooperation for Accreditation of Laboratories (EA) [48]. According to the guide, uncertainty is grouped in two categories: type A and type B:

Type A evaluation is the result of statistical analysis of a series of repeated observations and therefore includes random effects.

Type B evaluation is by definition other than type A, for example, judgment based on data of calibration certificates, experiences with instruments, and manufacturers' specifications.

4.1. Type A Evaluation of Uncertainty Components

Random effects result in errors that vary unpredictably. For an estimate of the standard deviation $s(q_k)$ of a series of n readings, q_k is obtained from

$$s(q_k) = \sqrt{\frac{1}{(n-1)} \sum_{k=1}^n (q_k - \bar{q})^2} \quad (31)$$

where \bar{q} is the mean of n measurements.

The random component of uncertainty is reduced by repeating the measurements. This yields the standard deviation of the mean $s(\bar{q})$

$$s(\bar{q}) = \frac{s(q_k)}{\sqrt{n}} \quad (32)$$

The standard uncertainty of the input estimate \bar{q} is the experimental standard deviation of the mean (for $n \geq 10$)

$$u(\bar{q}) = s(\bar{q}) \quad (33)$$

4.2. Type B Evaluation of Uncertainty Components

Systematic effects that remain constant during measurements but change if the measurement conditions are altered cannot be corrected and therefore contribute to uncertainty. Other contributions arise from errors that are not possible or impractical to correct for, such as from calibration certificates or manufacturers' specifications. Most of these contributions are adequately represented by a symmetrical distribution. In RF metrology three main distributions are of interest: normal, rectangular, and U-shaped.

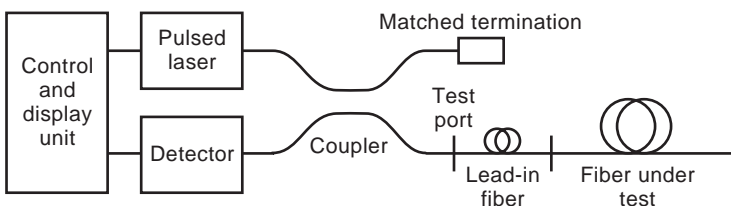


Figure 32. Principle of an optical time-domain reflectometer.

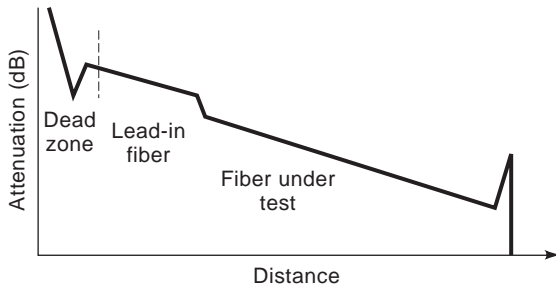


Figure 33. Typical backscattering signature of a fiber.

4.2.1. Normal Distribution. Uncertainties derived from multiple contributions are assumed to be normally distributed. Accredited calibration laboratories issue calibration certificates calculated for a normal distribution and a minimum level of confidence of 95% (approximate coverage factor $k = 2$). The standard uncertainty associated with the estimate x_i is given by

$$u(x_i) = \frac{\text{uncertainty}}{k} \tag{34}$$

4.2.2. Rectangular Distribution. This means that there is equal probability that the true value lies between limits. This is the case for most manufacturers' specifications that give a semi-range limit a_i :

$$u(x_i) = \frac{a_i}{\sqrt{3}} \tag{35}$$

4.2.3. U-Shaped Distribution. This distribution is applicable to mismatch uncertainty [49]. Because the phases of the reflection coefficients (of source, DUT, load) in scalar measurement are not known, the mismatch loss has to be taken into account as an uncertainty. The mismatch uncertainty is asymmetric to the measured result, and normally the larger of the two limits $M = 20 \log(1 - |\Gamma_G| |\Gamma_L|)$ is used. The standard uncertainty is calculated as

$$u(x_i) = \frac{M}{\sqrt{2}} \tag{36}$$

4.3. Combined Standard Uncertainty

The combined standard uncertainty for uncorrelated input quantities is calculated as the square root of the sum of the squares of the individual standard

uncertainties:

$$u_c(y) = \sqrt{\sum_{i=1}^m u_i^2(y)} \tag{37}$$

4.4. Expanded Uncertainty

The expanded uncertainty U defines an interval in which there is the true value with a specified confidence level. Normally accredited calibration laboratories are asked to use the coverage factor $k = 2$ (approximately 95% confidence level), giving

$$U = k \cdot u_c(y)$$

4.5. Uncertainty in Attenuation Measurement

Let us assume a simple attenuation measuring setup, shown in Fig. 34, consisting of a generator, two matching circuits, and a receiver. In the first phase, when the two insertion points are clamped together, the receiver measures $P_1(f)$ (often called a *normalization*). In the second phase the DUT is inserted, and the receiver reads the values $P_2(f)$.

Attenuation as a function of the frequency is calculated from the ratio of the two sets of readings:

$$A(f) = 10 \log \left[\frac{P_2(f)}{P_1(f)} \right] \tag{38}$$

The following errors contribute to the uncertainty of the measurement:

The statistical errors of n repeated measurements (type A) are given by the arithmetic experimental standard deviation:

$$s(A) = \sqrt{\frac{1}{(n-1)} \sum_{k=1}^n (A_k - \bar{A})^2} \tag{39}$$

(\bar{A} is the arithmetic mean of the measurements)

The standard uncertainty is calculated from

$$u_s(A) = s(\bar{A}) = \frac{s(A)}{\sqrt{n}} \tag{40}$$

The generator level stability a_G is taken from the manufacturer's specification and is assumed to be rectangularly distributed. The uncertainty is calculated

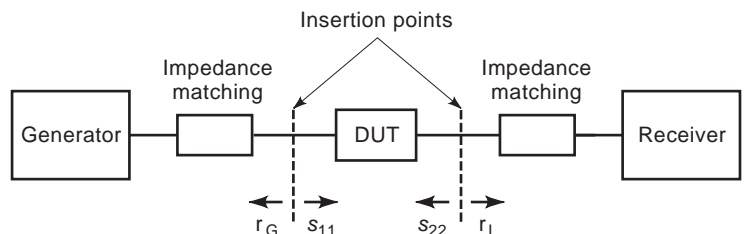


Figure 34. Example of an attenuation measurement system.

as follows:

$$u_G = \frac{a_G}{\sqrt{3}} \quad (41)$$

The receiver level linearity and stability a_R is taken from the manufacturer's specification. The uncertainty is calculated as

$$u_R = \frac{a_R}{\sqrt{3}} \quad (42)$$

The noise level of the receiver influences the measurement of high attenuation values. It is given in the manufacturer's specification and contributes to the uncertainty as

$$u_N = \frac{a_N}{\sqrt{3}} \quad (43)$$

The crosstalk of the measurement system a_I is determined by measurements and regarded as limits, and therefore contributes to the uncertainty as

$$u_I = \frac{a_I}{\sqrt{3}} \quad (44)$$

Two mismatch losses have to be taken into account, one during the normalization (often also called *calibration*) phase and the second while measuring the DUT.

4.5.1. Normalization Phase. The maximum mismatch loss [49] is calculated from the reflection coefficients of the source and the receiver as

$$M_C = 20 \log(1 - |r_G||r_L|) \quad (45)$$

As in scalar measurements, the phases of the reflection coefficients are unknown. The mismatch loss contributes to the measurement uncertainty and is normally assumed to be U-shaped-distributed:

$$u_C = \frac{M_C}{\sqrt{2}} \quad (46)$$

4.5.2. Measurement Phase. There are two mismatch losses [49] that have to be considered: one between the generator and the input of the DUT and the other between the output of the DUT and the receiver. In addition, for small attenuation values the interaction between the input and the output connections has to be considered. The maximum limits of the mismatch loss that have to be used for the uncertainty are given by

$$M_m = 20 \log \frac{|1 - |r_G s_{11}| - |r_L s_{22}| - |r_G r_L s_{11} s_{22}| - |r_G r_L s_{21} s_{12}|}{1 - |r_G r_L|} \quad (47)$$

The uncertainty is given by

$$u_m = \frac{M_m}{\sqrt{2}} \quad (48)$$

The total uncertainty is calculated either from linear values or from decibel values as long as they are small:

$$u_c(A) = \sqrt{u_s^2 + u_G^2 + u_R^2 + u_N^2 + u_I^2 + u_C^2 + u_m^2} \quad (49)$$

The expanded uncertainty is calculated using a coverage factor $k = 2$ (approximately 95% confidence level) as

$$U(A) = k \cdot u_c(A) = 2 \cdot u_c(A) \quad (50)$$

The uncertainty has to be calculated for all the measurement frequencies to find the maximum value of the uncertainty.

BIBLIOGRAPHY

1. D. M. Kerns and R. W. Beatty, *Basic Theory of Waveguide Junctions and Introductory Microwave Network Analysis*, Pergamon, New York, 1967.
2. R. W. Beatty, *Applications of Waveguide and Circuit Theory to the Development of Accurate Microwave Measurement Methods*, NBS Monograph 137, U.S. Government Printing Office, Washington, DC, 1973.
3. R. W. Beatty, Insertion loss concepts, *Proc. IEEE* **52**:663 (1964).
4. F. L. Warner, *Microwave Attenuation Measurement*, IEE Monograph Series 19, Peter Peregrinus, London, 1977.
5. S. J. Mason, Feedback theory-some properties of signal flow graphs, *Proc. IRE* **41**:1144-1156 (1953).
6. N. Kuhn, Simplified signal flow graph analysis, *Microw. J.* (11):59-66 (1963).
7. S. F. Adam, *Microwave Theory and Applications*, Prentice-Hall, Englewood Cliffs, NJ, 1969.
8. G. H. Bryant, *Principles of Microwave Measurements*, IEE Electrical Measurement Series 5, Peter Peregrinus, London, 1993.
9. T. S. Laverghetta, *Modern Microwave Measurements and Techniques*, Artech House, Norwood, MA, 1998.
10. *Reference Data for Engineers*, 7th ed., Sams, Indianapolis, IN, 1985.
11. E. Weber, Precision Metalized Glass Attenuators, *Technique of Microwave Measurements*, MIT Radiation Lab Series Vol. 11, McGraw-Hill, New York, pp. 751-774.
12. S. F. Adam, Precision thin-film coaxial attenuators, *Hewlett-Packard J.* 12-19 (June 1967).
13. C. G. Montgomery, *Technique of Microwave Measurements*, MIT Radiation Lab Series Vol. 11, McGraw-Hill, New York.
14. W. Bolinger, private communication.
15. H. L. Kundsén, Champs dans un guide rectangulaire à membrane conductrice, *L'Onde Electrique* (April 1953).
16. B. P. Hand, A precision waveguide attenuator which obeys a mathematical law, *Hewlett-Packard J.* **6**(5) (1955).
17. G. C. Southworth, *Principles and Applications of Waveguide Transmission*, Van Nostrand, Princeton, NJ, 1950, pp. 374-376.
18. B. P. Hand, Broadband rotary vane attenuator, *Electronics* **27**:184-185 (1954).
19. P. F. Mariner, An absolute microwave attenuator, *Proc. IEE* **109B**:415-419 (1962).

20. T. Imanura, MN 9002A Standard optical attenuator, *Anritsu Tech. Rev.* **14**:32-41 (1991).
21. C. F. Varley, On a new method of testing electronic resistance, *Math. Phys. Sect. Br. Assoc. Adv. Sci.* 14-15 (1866).
22. M. L. Morgan and J. C. Riley, Calibration of a Kelvin-Varley standard divider, *IRE Trans.* **I-9**(1):243-273 (1960).
23. A. F. Dunn, Calibration of a Kelvin-Varley voltage divider, *IEEE Trans. Instrum. Meas.* **IM-3**:129-139 (1964).
24. J. J. Hill and A. P. Miller, A seven-decade adjustable-ratio inductively coupled voltage divider with 0.1 part per million accuracy, *Proc. IEE* **109**:157-162 (1962).
25. S. Avramov et al., Automatic inductance voltage divider bridge for operation from 10 Hz to 100 kHz, *IEEE Trans. Instrum. Meas.* **42**:131-135 (1993).
26. R. Yell, NPL MK 3 WBCO attenuator, *IEEE Trans. Instrum. Meas.* **IM-27**:388-391 (1978).
27. R. Yell, Developments in waveguide below cutoff attenuators at NPL, *IEE Colloq. Digest* **49**:1/1-1/5 (1981).
28. H. Bayer, Consideration of a rectangular waveguide below cutoff piston attenuator as calculable broad-band attenuation standard between 1 MHz and 2.6 GHz, *IEEE Trans. Instrum. Meas.* **IM-29**:467-471 (1980).
29. F. L. Warner, D. O. Watton, and P. Herman, A very accurate X-band rotary vane attenuator with an absolute digital angular measurement system, *IEEE Trans. Instrum. Meas.* **IM-21**:446-450 (1972).
30. W. E. Little, W. Larson, and B. J. Kinder, Rotary vane attenuator with an optical readout, *J. Res. NBS* **75C**:1-5 (1971).
31. W. Larson, *The Rotary Vane Attenuator as an Interlaboratory Standard*, NBS Monograph 144, U.S. Government Printing Office, Washington DC, Nov. 1975.
32. H. Bayer, F. Warner, and R. Yell, Attenuation and ratio-national standards, *Proc. IEEE* **74**:46-59 (1986).
33. T. Imamura, MN9002 Standard optical attenuator, *Anritsu Tech. Rev.* **14**:32-41 (1991).
34. G. F. Engen and R. W. Beatty, Microwave attenuation measurements with accuracies from 0.0001 to 0.06 dB over a range of 0.01 to 50 dB, *J. Res. NBS* **64C**:139-145 (1960).
35. H. Bayer, An error analysis for the RF-attenuation measuring equipment of the PTB applying the power method, *Metrologia*, **11**:43-51 (1975).
36. D. L. Hollway and F. P. Kelly, A standard attenuator and the precise measurement of attenuation, *IEEE Trans. Instrum. Meas.* **IM-13**:33-44 (1964).
37. F. L. Warner, P. Herman, and P. Cumming, Recent improvements to the UK national microwave attenuation standards, *IEEE Trans. Instrum. Meas.* **IM-32**(1):33-37 (1983).
38. F. K. Weinert, High performance microwave ratio meter employs parallel if complex vector substitution, *Microwave J.* **24**:51-85 (1981).
39. Hewlett-Packard, *Understanding the Fundamental Principles of Vector Network Analysis*, HP Application Note 1287-1, 1997; *Exploring the Architectures of Network Analyzers*, HP Application Note 1287-2, 1997; *Applying Error Correction to Network Analyzer Measurement*, HP Application Note 1287-3, 1997.
40. G. F. Engen, *Microwave Circuit Theory and Foundations of Microwave Metrology*, IEE Electrical Measurement Series Vol. 9, Peter Peregrinus, London, 1992.
41. O. D. D. Soares, ed., Trends in optical fibre metrology, *Part VI: Optical Fibre Characterisation, Calibration Standards*, Fibre Characterization and Measurement, pp. 353-397; NATO ASI Series E, Applied Sciences, Kluwer, Dordrecht, 1995, Vol. 285.
42. C. Hentschel, *Fibre Optics Handbook*, Hewlett-Packard, HP 13100-5952-9654, Hewlett-Packard, Boblingen, Germany, 1989.
43. International Electrotechnical Commission, *Optical Fibres - Part 1: Generic Specification*, IEC 793-1 (11/92).
44. International Telecommunications Union, *Definition and Test Methods for the Relevant Parameters of Single Mode Fibres*, ITU-T G 650 (03/93).
45. T. Jones, *Attenuation and Cut-off Wavelength Measurement*, National Physical Laboratory, Optical Fibre Measurement Course, April 27-28, 1993.
46. D. J. Ives and B. Walker, *Optical Time Domain Reflectometry*, National Physical Laboratory, Optical Fibre Measurement Course, April 27-28, 1993.
47. International Organization for Standardization, *Guide to the Expression of Uncertainty in Measurement*, 1st ed., International Organization for Standardization, Geneva, 1993; corrected and reprinted 1995.
48. European Cooperation for Accreditation of Laboratories, *Expression of the Uncertainty of Measurement in Calibration*, EAL-R2, 1st ed., April 1997; *Examples*, EAL-R2-S1, 1st ed., Nov. 1997.
49. I. A. Harris and F. L. Warner, Re-examination of mismatch uncertainty when measuring microwave power and attenuation, *IEE Proc. H* **128**(1):35-41 (1981).

ATTENUATORS

RAJI SUNDARARAJN
EDWARD PETERSON
ROBERT NOWLIN
Arizona State University East
Mesa, Arizona

Attenuators are linear, passive, or active networks or devices that attenuate electrical or microwave signals, such as voltages or currents, in a system by a predetermined ratio. They may be in the form of transmission-line, stripline, or waveguide components. Attenuation is usually expressed as the ratio of input power (P_{in}) to output power (P_{out}), in decibels (dB), as

$$\text{Attenuation (A)} = 10 \log_{10} \frac{P_{in}}{P_{out}} = 20 \log \frac{E_{in}}{E_{out}} = 20 \log \frac{E_1}{E_2} \quad (1)$$

This is derived from the standard definition of attenuation in Nepers (Np), as

$$\text{Attenuation (A)} = \alpha \Delta x = - \ln \frac{|E_2|}{|E_1|} \quad (2)$$

where α is attenuation constant (Np/m) and Δx is the distance between the voltages of interest (E_1 and E_2).

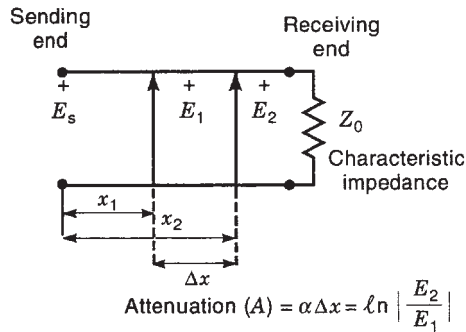


Figure 1. Concept and definition of attenuation.

Figure 1 illustrates this concept. The relation between N_p and dB is

$$1N_p = 8.686 \text{ dB} \tag{3}$$

Here the load and source are matched to the characteristic impedance. The decibels are converted to the attenuation ratio as follows: $P_{in}/P_{out} = \log_{10}^{-1} \text{ dB}/10$ or $V_{in}/V_{out} = \log_{10}^{-1} \text{ dB}/20$.

The most commonly used method in attenuators is to place resistors at the center of an electric field. Due to the electric field, there is current induced, resulting in ohmic loss.

1. APPLICATION

There are many instances when it is necessary to reduce the value, or level, of electrical or microwave signals (such as voltages and currents) by a fixed amount to allow the rest of the system to work properly. Attenuators are used for this purpose. For example, in turning down the volume on a radio, we make use of a variable attenuator to reduce the signal. Almost all electronic instruments use attenuators to allow for the measurement of a wide range of voltage and current values, such as voltmeters, oscilloscopes, and other electronic instruments. Thus, the various applications in which attenuators are used include the following:

- To reduce signal levels to prevent overloading
- To match source and load impedances to reduce their interaction
- To measure loss or gain of two-port devices
- To provide isolation between circuit components, or circuits or instruments so as to reduce interaction among them
- To extend the dynamic range of equipment and prevent burnout or overloading equipment

2. TYPES

There are various types of attenuators based on the nature of circuit elements used, type of configuration, and kind of adjustment. They are as follows:



Figure 2. Fixed coaxial attenuator. (Courtesy of Weinschel Associates.)

- Passive and active attenuators
- Absorptive and reflective attenuators
- Fixed and variable attenuators

A fixed attenuator is used when the attenuation is constant. Variable attenuators have varying attenuation, using varying resistances for instance. The variability can be in steps or continuous, obtained either manually or programmably. There are also electronically variable attenuators. They are reversible, except in special cases, such as a high-power attenuator. They are linear, resistive, or reactive, and are normally symmetric in impedance. They include waveguide, coaxial, and striplines, as well as calibrated and uncalibrated versions. Figures 2–4 show fixed, manual step, and continuously variable commercial attenuators, respectively.

Based on their usage, IEEE Std 474 classifies them as

Class I	Standard
Class II	Precision
Class III	General-purpose
Class IV	Utility

Typical commercial attenuators are listed below:

WA 1 (0–12.4 GHz), WA 2 (0–3 GHz), coaxial, fixed attenuators: 1–60 dB; 5 W av./1 kW peak

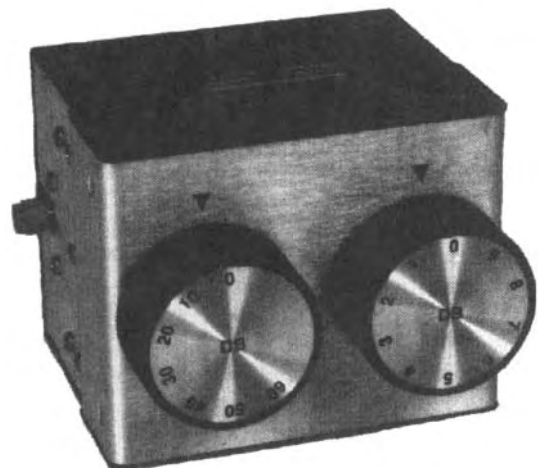
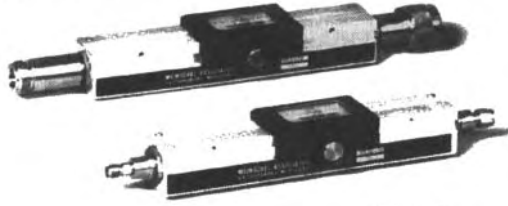


Figure 3. Manual step attenuator. (Courtesy of Weinschel Associates.)

953B - 10 - 34



953K - 3

Figure 4. Continuously variable attenuator. (Courtesy of Weinschel Associates.)

WA 115A manual step attenuators: 0–18 GHz, 0–9 dB, 1-dB steps

VA/02/100 continuously variable attenuators, resistive, 0–2 GHz, 5 W av./0.5 kW peak

HP 84904L programmable step attenuator, direct current (DC) to 40 GHz, 0–11 dB, 1-dB steps

HP 84906K programmable step attenuator, DC to 26.5 GHz, 0–90 dB, 10-dB steps

HP 84904L programmable step attenuator, DC to 40 GHz, 0–70 dB, 10-dB steps

HP 8495B manual step attenuator, DC to 18 GHz, 0–70 dB, 10-dB steps

HP 355F programmable step attenuator, DC to 1 GHz, 0–120 dB, 10-dB steps

HP 8493A coaxial fixed attenuator, DC to 12.4 GHz

Based on their utility, military attenuators are classified as:

Class I	For use as a primary standard
Class II	For use as a secondary standard, and in lab and precision test equipment
	A—with lumped constant or distributed shunt and series elements
	B—with lossy-line pads
Class III	For use in general field equipment
Class IV	For use in equipment where precision and stability are secondary considerations

Typical military specifications for fixed coaxial attenuators are as follows:

Mil-A-3933/1: attenuators, fixed, coaxial line, DC to 3 GHz, class IIA, low power

Mil-A-3933/2: attenuators, fixed, coaxial line, 1–4 GHz, class IIB, medium power

Mil-A-3933/10: attenuators, fixed, coaxial line, DC to 18 GHz, class III, medium power

Mil-A-3933/26: attenuators, fixed, coaxial line, 0.4–18 GHz, class IV low power

3. SPECIFICATIONS

To specify an attenuator, the purpose of the attenuator should be known. Attenuators are used to provide protec-

tion, reduce power, and extend the dynamic range of the test equipment. In choosing an attenuator, the frequency range of operation should be considered since the accuracy depends on the frequency. Attenuation involves placing resistive material to absorb the signal's electric field. This means, there will always be some reflection. So, attenuators must be designed to minimize reflection. This is quantified in terms of voltage standing-wave ratio (VSWR). Another factor to be considered is the insertion loss, which is the ratio of power levels with and without the component insertion. If it is a variable step attenuator, the step size is to be known. Thus, the parameters available in the specs are as follows:

dB rating

VSWR

Accuracy

Power rating

Stepsize (if variable)

Frequency band

Degree of stability (measured by the change in attenuation due to temperature, humidity, frequency, and power level variations)

Characteristic impedance of attenuator

Repeatability

Life

Degree of resolution (difference between actual attenuation and measured value)

The definitions of various parameters used in selecting attenuators are given below.

3.1. Electrical Parameters and Definitions (from MIL-HDBK-216)

Attenuation. A general transmission term used to indicate a decrease in signal magnitude. This decrease in power is commonly expressed in decibels (dB) as

$$\text{Attenuation (A)} = 10 \log_{10} \frac{P_{\text{in}}}{P_{\text{out}}}$$

Deviation of Attenuation from Normal. Difference in actual attenuation from the nominal value at 23°C and an input power of 10 mW at a specified reference frequency or frequency range. When used in a frequency range, it involves the frequency sensitivity.

Frequency Sensitivity. This is the peak-to-peak variation in the loss of the attenuator through the specified frequency range.

Frequency Range. Range of frequency over which the accuracy of attenuator is specified.

Insertion Loss. Amount of power loss due to the insertion of the attenuator in the transmission system. It is expressed as a ratio of the power delivered to that part of the system following the attenuator, before and after the insertion.

Characteristic Insertion Loss. This is the insertion loss in a transmission line or waveguide that is reflectionless in both directions from the inserted attenuator.

Power-Handling Capabilities. Maximum power that can be applied to the attenuator under specified conditions and durations without producing a permanent change in the performance characteristics that would be outside of specification limits.

Power Sensitivity. This is the temporary variation in attenuation (dB/W) under steady-state conditions when the input power is varied from 10 mW to maximum input power.

Stability of Attenuation. Capability of attenuator to retain its parameters when subjected to various environmental conditions.

Operating Temperature Range. Temperature range of the attenuator can be operated with maximum input power.

Temperature Sensitivity. Temperature variation in attenuation [dB/(dB × °C)] over the operating range.

Input VSWR. This is the level of reflected signal created at the attenuator input when the output is terminated with a load with the same characteristic impedance as the source.

Output VSWR. This is the level of reflected signal created at the attenuator output when the input is terminated with a load with the same characteristic impedance as the source.

4. PASSIVE ATTENUATORS

4.1. Resistance Networks for Attenuators

Typically T, pi, or L designs are used for attenuators. Figure 5 shows four commonly used symmetric (input and output resistors of equal value) configurations. The formulas for the resistance values in ohms for these pads when the characteristic resistance $R_0 = 1 \Omega$ are given

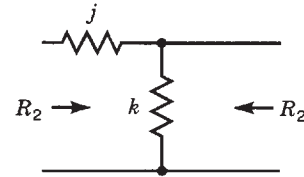


Figure 6. Unsymmetric matching L attenuator.

below. If R_0 is other than 1Ω , multiply each of the resistance values (a , b , c , $1/a$, $1/b$, and $1/c$) by R_0 , where

$$a = \frac{10^{\text{dB}/20} - 1}{10^{\text{dB}/20} + 1} \tag{4}$$

$$b = \frac{2 \times 10^{\text{dB}/20}}{10^{\text{dB}/10} - 1} \tag{5}$$

$$c = (10^{\text{dB}/20} - 1) \tag{6}$$

Simple wirewound resistors are used in audio applications. Nonreactive wirewound resistors, such as mica card, Aryton-Perry winding, woven resistors are used for high frequencies. For coaxial applications (over 26.5 GHz), thin-film resistors are used. For higher frequencies, distributive resistive films, such as nichrome alloy film, on a high-quality ceramic substrate, such as alumina or sapphire, is used. An unsymmetrical pad is shown in Fig. 6, and the formulas for this pad are

$$j = \frac{R_1 - kR_2}{k + R_2} \tag{7}$$

$$k = \left[\frac{R_1 R_2^2}{(R_1 - R_2)} \right]^{1/2} \text{ where } R_1 > R_2 \tag{8}$$

$$\text{Minimum loss (dB)} = 20 \log \left\{ \left[\frac{(R_1 - R_2)}{R_2} \right]^{1/2} + \left(\frac{R_1}{R_2} \right)^{1/2} \right\} \tag{9}$$

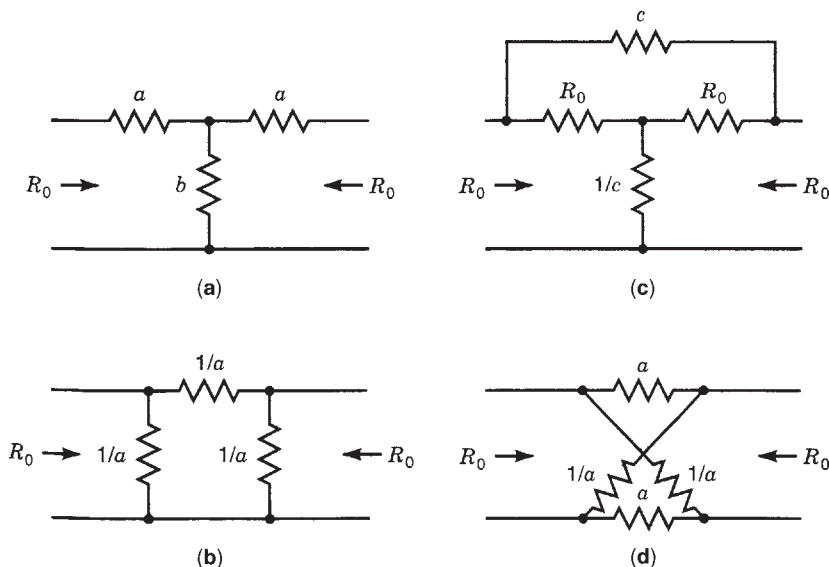


Figure 5. Symmetric pads with matched impedances: (a) T pad; (b) pi pad; (c) bridged T pad; (d) balanced pad.

Table 1. Resistance Values for Attenuator Pads When $R_0 = 1 \Omega^a$

dB ^b	T Pad		Pi Pad		Bridged T Pad		Balanced Pad	
	a	b	$1/b$	$1/a$	c	$1/c$	a	$1/a$
0.1	0.0057567	86.853	0.011514	173.71	0.011580	86.356	0.0057567	173.71
0.2	0.011513	43.424	0.023029	86.859	0.023294	42.930	0.011513	86.859
0.3	0.017268	28.947	0.034546	57.910	0.035143	28.455	0.017268	57.910
0.4	0.023022	21.707	0.046068	43.438	0.047128	21.219	0.023022	43.438
0.5	0.028775	17.362	0.057597	34.753	0.059254	16.877	0.028775	34.753
0.6	0.034525	14.465	0.069132	28.965	0.071519	13.982	0.034525	28.965
0.7	0.040274	12.395	0.080678	24.830	0.083927	11.915	0.040274	24.830
0.8	0.046019	10.842	0.092234	21.730	0.096478	10.365	0.046019	21.730
0.9	0.051762	9.6337	0.10380	19.319	0.10918	9.1596	0.051762	19.319
1.0	0.057501	8.6668	0.11538	17.391	0.12202	8.1954	0.057501	17.391
2.0	0.11462	4.3048	0.23230	8.7242	0.25893	3.8621	0.11462	8.7242
3.0	0.17100	2.8385	0.35230	5.8481	0.41254	2.4240	0.17100	5.8481
4.0	0.22627	2.0966	0.47697	4.4194	0.58489	1.7097	0.22627	4.4194
5.0	0.28013	1.6448	0.60797	3.5698	0.77828	1.2849	0.28013	3.5698
6.0	0.33228	1.3386	0.74704	3.0095	0.99526	1.0048	0.33228	3.0095
7.0	0.38248	1.1160	0.89604	2.6145	1.2387	0.80727	0.38248	2.6145
8.0	0.43051	0.94617	1.0569	2.3229	1.5119	0.66143	0.43051	2.3229
9.0	0.47622	0.81183	1.2318	2.0999	1.8184	0.54994	0.47622	2.0999
10.0	0.51949	70.273 ^c	1.4230	1.9250	2.1623	46.248 ^c	0.51949	1.9250
20.0	0.81818	20.202 ^c	4.9500	1.2222	9.0000	11.111 ^c	0.81818	1.2222
30.0	0.93869	6330.9 ^c	15.796	1.0653	30.623	3265.5 ^c	0.93869	1.0653
40.0	0.980198	2000.2 ^c	49.995	1.0202	99.000	1010.1 ^c	0.980198	1.0202
50.0	0.99370	632.46 ^c	158.11	1.0063	315.23	317.23 ^c	0.99370	1.0063
60.0	0.99800	200.00 ^c	500.00	1.0020	999.00	100.10 ^c	0.99800	1.0020
70.0	0.99937	63.246 ^c	1581.1	1.0006	3161.3	31.633 ^c	0.99937	1.0006
80.0	0.99980	20.000 ^c	5000.0	1.0002	9999.0	10.001 ^c	0.99980	1.0002
90.0	0.99994	6.3246 ^c	15.811	1.0001	31.622	3.1633 ^c	0.99994	1.0001
100.0	1.0000	2.0000 ^c	50.000	1.0000	99.999	1.0000 ^c	1.0000	1.0000

^aIf $R_0 \neq 1 \Omega$, multiply all values by R_0 . (From Ref. data for *Radio Engineers*, 1985.)

^bFor other decibel values, use formulas in text.

^cThese values have been multiplied by 10^3 .

Typical values for the pads in Fig. 5 are shown in Table 1, and those of Fig. 6 are shown in Table 2.

For a broadband match between impedances R_1 and R_2 , use the minimum-loss L pad (Fig. 6).

4.2. Power Dissipation within a T Pad

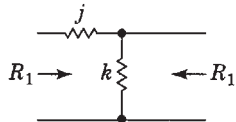
Table 3 lists values of power dissipation within a T pad. The values are for an input of 1 W; for other input powers, multiply the values by the input power.

5. INSERTION LOSS

An attenuator is used to introduce attenuation between a source and a load. Due to the introduction of the attenuator, there is change in the current. This loss is designated as insertion loss, which depends on the configuration.

Usually, the load and source impedances are matched. Figure 7 illustrates this concept. If I_{L0} is the load current without the attenuator pad and I_L is the current with the attenuator pad, then the ratio I_L/I_{L0} is called the *insertion loss*, one of the parameters of the attenuates. Figure 7a shows the source and load connected without an attenuator, and Fig. 7b shows the same system with an attenuator. (The quantities I_L , R_{in} , and R_{out} depend on the attenuator configuration.) The quantities insertion loss (I_L), input resistance (R_{in}), and output resistance (R_{out}) depend on the attenuator configuration. The value of each of the three resistors of the T (Fig. 8) and pi (Fig. 9) attenuators can be chosen independently of others. This enables the three-design criteria of input resistance, output resistance, and insertion loss to be met. In many situations, the only function of the pad is to provide matching between source and load; and although attenua-

Table 2. Resistance Values and Attenuation for L Pad^a



R_1/R_2	j	k	dB
20.0	19.49	1.026	18.92
16.0	15.49	1.033	17.92
12.0	11.49	1.044	16.63
10.0	9.486	1.054	15.79
8.0	7.484	1.069	14.77
6.0	5.478	1.095	13.42
5.0	4.472	1.118	12.54
4.0	3.469	1.155	11.44
3.0	2.449	1.225	9.96
2.4	1.833	1.310	8.73
2.0	1.414	1.414	7.66
1.6	0.9798	1.633	6.19
1.2	0.4898	2.449	3.77
1.0	0	∞	0

^aFor $R_2 = 1\Omega$ and $R_1 > R_2$. If $R_2 \neq 1\Omega$, multiply values by R_2 . For ratios not in the table, use the formulas in the text. (From Ref. data for *Radio Engineers*, 1985.)

Examples of use of table:

If $R_1 = 50\Omega$ and $R_2 = 25\Omega$, then $R_1/R_2 = 2.0$, and $j = k = 1.414 \times 25\Omega = 35.35\Omega$.

If $R_1/R_2 = 1.0$, minimum loss = 0 dB.

For $R_1/R_2 = 2.0$, the insertion loss with the use of j and k for matching is 7.66 dB above that for $R_1/R_2 = 0$.

tion will be introduced, this may not be a critical design parameter. This allows a simpler type of pad to be designed, requiring only two resistors; it is known as an “L pad.”

Figure 10 shows an L attenuator, which can be derived from either a T or a pi attenuator, simply by removing one of the resistors. As shown, different configurations are required depending on whether $R_S > R_L$ or $R_S < R_L$.

5.1. T Attenuator Insertion Loss

The T attenuator contains resistors R_1 , R_2 , and R_3 ; these form a T configuration, as shown in Fig. 6. Insertion loss is usually measured in dB, defined as $I_L(\text{dB}) = -20 \log I_L$ or $|20 \log I_L|$, the amount of attenuation required. The insertion loss I_L is given as

$$I_L(\text{dB}) = \frac{I_L}{I_{L0}} = \frac{R_3(R_S + R_L)}{(R_S + R_1 + R_3)(R_2 + R_3 + R_L) - R_3^2} \quad (10)$$

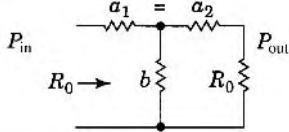
The input and the output of resistances of the attenuator are given by

$$R_{in} = R_1 + \frac{R_3(R_2 + R_L)}{R_2 + R_3 + R_L} \quad (11)$$

and

$$R_{out} = R_2 + \frac{R_3(R_1 + R_S)}{R_1 + R_3 + R_S} \quad (12)$$

Table 3. Power Dissipation in T Pad^a



dB	Watts, Input Series Resistor	Watts, Shunt Resistor	Watts, Output Series Resistor
0.1	0.00576	0.0112	0.005625
0.3	0.0173	0.0334	0.016113
0.5	0.0288	0.0543	0.025643
0.7	0.0403	0.0743	0.034279
0.9	0.0518	0.0933	0.0421
1.0	0.0575	0.1023	0.0456
1.2	0.0690	0.120	0.0523
1.4	0.0804	0.11368	0.0582
1.6	0.0918	0.1525	0.0635
1.8	0.103	0.1672	0.0679
2.0	0.114	0.1808	0.0718
2.2	0.126	0.1953	0.0758
2.4	0.137	0.2075	0.0787
2.6	0.149	0.2205	0.0818
2.8	0.160	0.232	0.0839
3.0	0.170998	0.242114	0.085698
3.2	0.182	0.2515	0.0870
3.4	0.193	0.2605	0.0882
3.6	0.204	0.2695	0.0890
3.8	0.215	0.2775	0.0897
4.0	0.226	0.285	0.0898
5	0.280	0.3145	0.0884
6	0.332	0.332	0.0833
7	0.382	0.341	0.0761
8	0.430	0.343	0.0681
9	0.476218	0.33794	0.0599527
10	0.519	0.328	0.0519
12	0.598	0.3005	0.0377
14	0.667	0.266	0.0266
16	0.726386	0.23036	0.0182460
18	0.776	0.1955	0.0123
20	0.818	0.1635	0.0100
30	0.938	0.0593	0.0010
40	0.980	0.0196	0.0001

^aFor 1 W-input and matched termination. If input $\neq 1\text{w}$, multiply values by P_{in} . (From Ref. data for *Radio Engineers*, 1985.)

In many cases, the attenuator also has to match the load and the source impedance. In this case, $R_1 = R_2 = R$ and $R_{in} = R_{out} = R_0$. Thus

$$R_0 = R + \frac{R_3(R + R_0)}{(R_3 + R + R_0)} \quad (13)$$

and the insertion loss is given by

$$I_L = \frac{R_3}{R_3 + R + R_0} \quad (14)$$

and

$$R = R_0 \frac{1 - I_L}{1 + I_L} \quad (15)$$

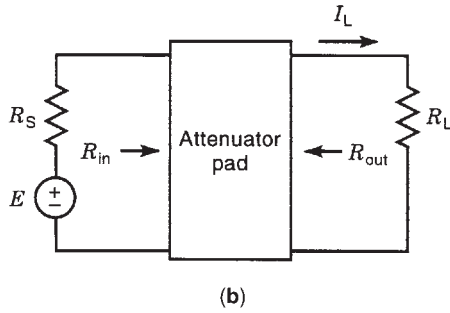
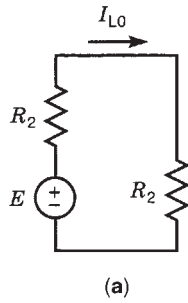
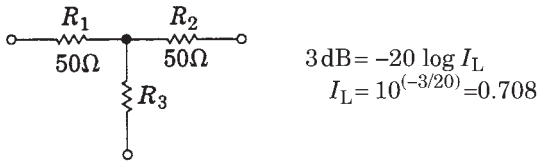


Figure 7. Definition of characteristic insertion loss: (a) original setup without attenuator; (b) original setup with attenuator between source and load.

and

$$R_3 = \frac{2R_0 I_L}{1 - (I_L)^2} \tag{16}$$

Example 1 (T Attenuator). A T-type attenuator is required to provide 3×0 dB insertion loss and to match 50Ω input and output. Find the resistor values,



using the following equations:

$$R = R_0 \frac{1 - I_L}{1 + I_L} = 50 \left(\frac{1 - 0.708}{1 + 0.708} \right) = 8.55 \Omega$$

$$R_3 = \frac{2R_0 I_L}{1 - (I_L)^2} = \frac{2 \times 50 \times 0.708}{1 - (0.708)^2} = 141.6 \Omega$$

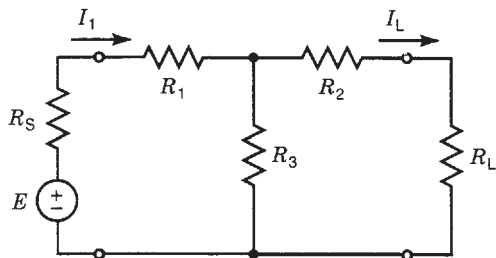


Figure 8. T attenuator configuration.

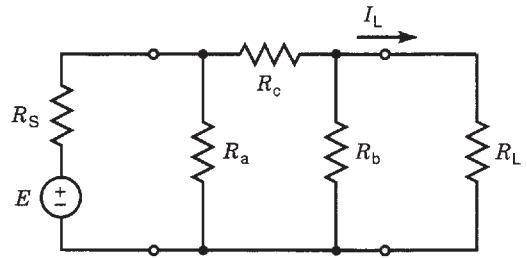


Figure 9. Pi attenuator configuration.

Check:

$$I_L = \frac{R_3}{R_3 + R + R_0} = \frac{141.6}{141.6 + 8.55 + 50} = 0.708$$

5.1.1. The Pi Attenuator Insertion Loss. Figure 9 shows a pi attenuator formed by resistors R_a , R_b , and R_c . The insertion loss and conductances G_{in} and G_{out} are given by

$$I_L = G_c \frac{G_S + G_L}{(G_S + G_a + G_c(G_b + G_c + G_L) - G_c^2)} \tag{17}$$

$$G_{in} = G_a + \frac{G_c(G_b + G_L)}{G_b + G_c + G_L} \tag{18}$$

$$G_{out} = G_b + \frac{G_c(G_a + G_S)}{G_a + G_c + G_S} \tag{19}$$

where $G = 1/R$; thus $G_L = 1/R_L$ and so on.

The same pi attenuator can be realized using a T attenuator with R_1 , R_2 , and R_3 values using the Y- Δ

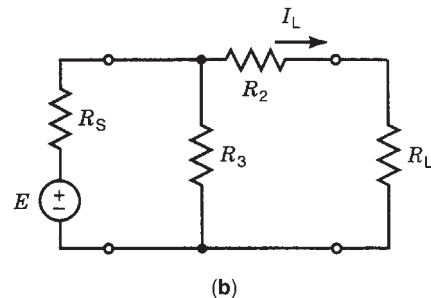
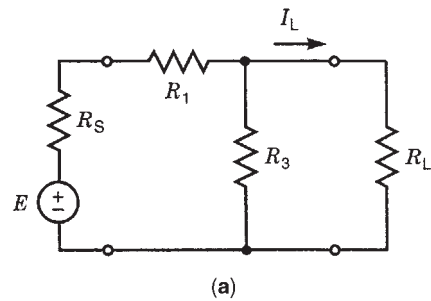


Figure 10. L attenuator configuration:(a) $R_S < R_1$; (b) $R_S > R_1$.

transformation:

$$R_a = \frac{R_1 R_2 + R_1 R_3 + R_2 R_3}{R_2} \quad (20)$$

$$R_b = R_a \frac{R_2}{R_1} \quad (21)$$

$$R_c = R_a \frac{R_2}{R_3} \quad (22)$$

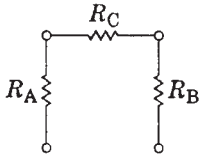
The selection between pi and T is based on the value of resistors that can be used in practice. With matching source and load impedances, the values of the pi attenuator are

$$R_a = R_b = R_0 \frac{1 + I_L}{1 - I_L} \quad (23)$$

and

$$R_c = R_0 \frac{1 - (I_L)^2}{2I_L} \quad (24)$$

Example 2 (Pi Attenuator). Repeat Example 1 using a pi attenuator



$$R_L \text{ (dB)} = 3 = -20 \log I_L$$

$$I_L = 10^{(-3/20)} = 0.708$$

using the following equations:

$$R_A = R_B = R_0 \frac{1 + I_L}{1 - I_L} = 50 \left(\frac{1 + 0.708}{1 - 0.708} \right) = 292.46 \Omega$$

$$R_C = R_0 \left(\frac{1 - (I_L)^2}{2I_L} \right) = 50 \left(\frac{1 - (0.708)^2}{2 \times 0.708} \right) = 17.61 \Omega$$

5.1.2. The L Attenuator Insertion Loss. An L attenuator can be derived from a T or pi attenuator by removing one resistor. As shown in Fig. 10, two configurations are obtained depending on $R_S > R_L$ or $R_S < R_L$. Simple circuit theory shows that for $R_S > R_L$, we have

$$R_S = R_{in} = R_1 + \frac{R_3 R_L}{R_3 + R_L} \quad (25)$$

and

$$R_L = R_{out} = \frac{R_3 (R_1 + R_S)}{R_3 + R_1 + R_S} \quad (26)$$

from which it can be shown that

$$R_1 = \sqrt{R_S (R_S - R_L)} \quad (27)$$

and

$$R_3 = \frac{R_S^2 - R_L^2}{R_1} \quad (28)$$

and when we put $R_2 = 0$, the insertion loss is calculated as

$$I_L = \frac{R_3 (R_S + R_L)}{(R_S + R_1 + R_3)(R_3 + R_L) - R_3^2} \quad (29)$$

Example 3. Design an L attenuator to match a 300-Ω source to a 50-Ω load and determine insertion loss. Here $R_S > R_L$ using the following equation:

$$R_1 = \sqrt{R_S (R_S - R_L)} = \sqrt{300(300 - 50)}$$

$$= \sqrt{300 \times 250} = 273.86 \Omega$$

Using the following equation:

$$R_3 = \frac{R_S^2 - R_L^2}{R_1} = \frac{300^2 - 273.86^2}{273.86} = 54.775 \Omega$$

$$R_L = \frac{R_3 (R_S + R_L)}{(R_S + R_1 + R_3)(R_3 + R_L) - R_3^2}$$

$$= \frac{54.775 (300 + 50)}{(300 + 273.86 + 54.775)(54.775 + 50) - (54.775)^2}$$

$$= 0.305$$

$$R_L \text{ (dB)} = -20 \log 0.305 = 10.3 \text{ dB}$$

For $R_S < R_L$, we have

$$R_{in} = \frac{R_3 (R_2 + R_L)}{R_2 + R_3 + R_L} \quad (30)$$

and

$$R_{out} = R_2 + \frac{R_3 R_S}{R_3 + R_S} \quad (31)$$

and

$$R_2 = \sqrt{R_L (R_L - R_S)} \quad (32)$$

and

$$R_3 = \frac{R_L^2 - R_S^2}{R_2} \quad (33)$$

The corresponding insertion loss is

$$I_L = \frac{R_3 (R_S + R_L)}{(R_S + R_3)(R_2 + R_3 - R_L) - R_3^2} \quad (34)$$

Example 4. Design an L attenuator to match 50-Ω source to 75-Ω load and determine the insertion loss $R_S < R_L$,

using the following equation:

$$R_2 = \sqrt{R_L(R_L - R_S)} = \sqrt{75(75 - 50)} = 43.3 \Omega$$

using the following equations:

$$R_3 = \frac{R_L^2 - R_2^2}{R_2} = \frac{75^2 - 43.3^2}{43.3} = 86.6 \Omega$$

$$R_L = \frac{R_3(R_S + R_L)}{(R_S + R_3)(R_2 + R_3 + R_L) - R_3^2}$$

$$= 0.0123 = 38.2 \text{ dB}$$

6. FIXED ATTENUATORS

Fixed attenuators, commonly known as “pads,” reduce the input signal power by a fixed amount, such as 3, 10, and 50 dB. For example, an input signal of 10 dBm (10 mW) passing through a 3-dB fixed attenuator will exit with a power of 10 dBm – 3 dB = 7 dBm (5 mW). Figure 2 shows a fixed coaxial commercial attenuator. A typical datasheet for a fixed coaxial attenuator is as follows (courtesy of Weinschel Associates):

Frequency	0–3 GHz
Attenuation	50 dB
Accuracy	±0.10 dB (DC) ±0.15 dB (0–2 GHz) ±0.13 dB (0–3 GHz)
VSWR	1.15 (0–1 GHz) 1.20 (1–3 GHz)
Input power	1 W av., 1 kW peak at –30°–70°C
Connectors	Type N; St. St.; m, f
Length	68 mm (2.7 in.)
Diameter	210 mm (0.83 in.)
Weight	100 g (3.6 oz)
Power sensitivity	<0.005 dB/dB × W; bidirectional in power
Temperature stability	<0.0004 dB/dB × °C

6.1. Applications

Fixed attenuators are used in numerous applications. In general, they can be classified into two distinct categories:

1. Reduction in signal level
2. Impedance matching of a source and a load

Those in the first category are used in the following situations:

- Operation of a detector in its square-law range for most efficient operations.
- Testing of devices in their small signal range.

- Reduction of a high-power signal to a level compatible with sensitive power measuring equipment, such as power sensors and thermistor mounts.

Those in the second category are used in the following situations:

- Reduction of signal variations as a function of frequency. The variations here are caused by a high VSWR. The attenuator provides a reduction in these variations and a better match.
- Reduction in frequency pulling (changing the source frequency by changing the load) of solid-state sources by high reflection loads.

6.2. Types

Based on construction, fixed attenuators are available in coaxial, waveguide, and stripline configurations. The various types are:

1. Waveguide vane
2. Rotary vane (fixed)
3. Directional coupler
4. T or pi
5. Lossy line
6. Distributed resistive film

6.2.1. Coaxial Fixed Attenuators. T or pi configurations are most commonly used both at low and high frequencies. At low frequencies, normal wirewound resistors are used. At high frequencies, thin-film resistors are used. Figures 11 and 12 show T and pi fixed attenuators. Thin-film resistors designed for microwave frequencies are used in place of carbon resistors. These resistors employ a nichrome alloy film on a high-quality ceramic substrate to ensure a firmly bonded film with low-temperature coefficients. This type of construction makes the resistors extremely stable at high frequencies. The skin effect of these resistors is excellent, used extensively in the microwave applications.

The T and pi configurations are obtained by placing the resistors in series on the center conductor and in shunt, contacting both the center and outer conductor. Thus, the T configuration can be fabricated with one shunt flanked by two series resistors and the pi configuration, with one series flanked by two shunt resistors. The series resistors in the T and pi configurations have less than 1 W capacity, thereby severely limiting the use at high-power applications, unless an elaborate heatsinking is provided. Power attenuators usually have huge sinks to handle high-power applications.

6.2.2. Resistive Card Attenuator. In a fixed dissipative, waveguide-type resistive card attenuator, the card is bonded in place (Fig. 13). It is tapered at both ends to maintain a low-input and low-output VSWR over the useful waveguide band. Maximum attenuation per length is obtained when the card is parallel to the *E* field

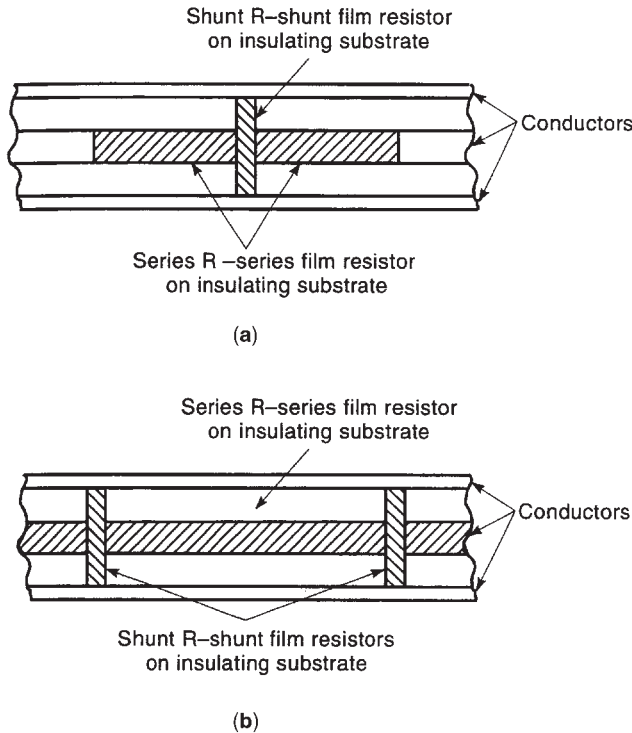


Figure 11. T/pi fixed attenuator configuration: (a) T section; (b) pi section.

and at the center, where the TE_{10} mode is maximum. The conductivity and the dimensions of the card are adjusted, by trial and error, to obtain the desired attenuation, which is a function of frequency. The attenuation increases with increase in frequency. In power applica-

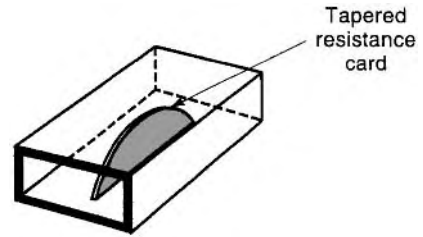


Figure 13. Fixed resistive card attenuator configuration.

tions, ceramic-type absorbing materials are used instead of a resistive card.

7. VARIABLE ATTENUATORS

A variable attenuator has a range, such as 0-20 dB or 0-100 dB. The variation can be continuous or in steps, obtained manually or programmably.

7.1. Step Attenuators

A series of fixed attenuators are mechanically arranged to offer discrete-step variation. The fixed attenuators are arranged in a rotatable drum or in a slab for switching between contacts. This arrangement provides discrete values of attenuation in each position and a high reliability factor. The step size can be 0.1, 1, or 10 dB. Stationary coaxial contacts provide the input and output of the device. These are used in applications requiring broadband flatness with low VSWR and satisfactory resettability over ranges from 0 to 120 dB. Their application range is DC to 18 GHz.

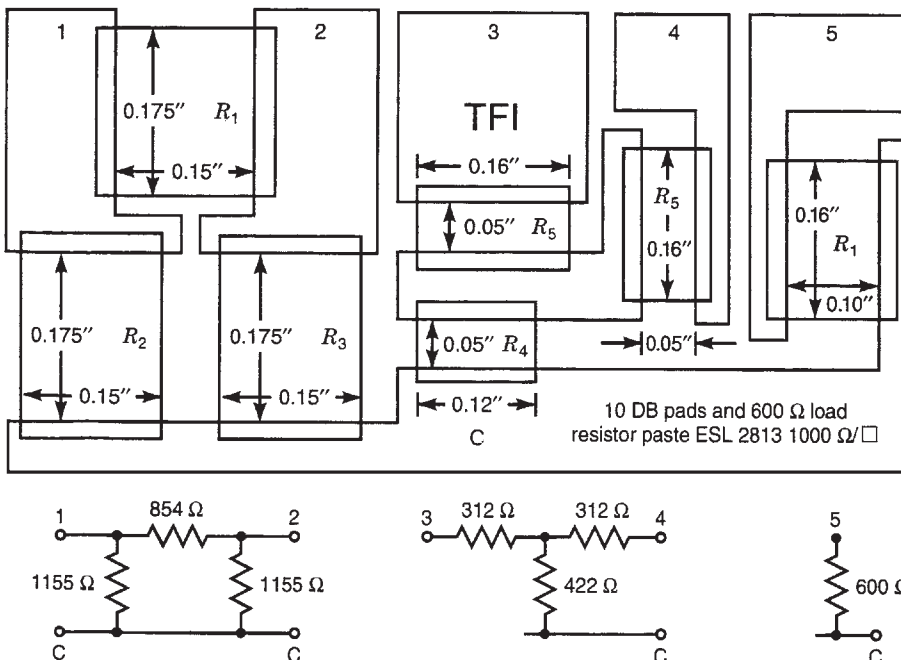


Figure 12. T/pi fixed-attenuator construction.

7.2. Manual Step Attenuators

Figure 3 shows a manual step attenuator. A typical datasheet looks as follows:

Frequency	0–4, 0–8, 0–12.4, 0–18 GHz
Attenuation	0–9, 0–60, 0–69
Stepsize	1, 10, 1 dB, respectively, for the range given above
VSWR	1.20, 1.25, 1.40, 1.50 for the frequency ranges given above 1.25, 1.30, 1.45, 1.60, for the frequency range given above
Connectors	N/SMA; St. St.
Height	83 mm (3.3 in.)
Depth	79 mm (3.1 in.) (excludes shaft and knob)
Width	65, 65, 118 mm (2.6, 2.6, 4.7 in.) for the three attenuation ranges given above

7.3. Continuously Variable Attenuators

Figure 4 shows a continuously variable attenuator. Typical specs are

Frequency	1–18 GHz, 1 W av./1 kW peak
Connectors	St. St., M, F; type N, SMA
Zero loss	Typically 0.5–1 dB
Attenuation	0–9, 0–60, 0–69 dB

The various types of continuously variable attenuators are

- Lossy wall
- Movable vane (Flap)
- Rotary vane
- Variable coupler
- Absorptive type
- Coaxial resistive film
- Variable T
- Waveguide below cutoff (piston)

7.4. Programmable and Solenoid Attenuators

7.4.1. Programmable. These are rapid switching attenuators with high accuracy and repeatability, useful for remote and computerized applications. Switching speeds can be as low as 30 ns. Two varieties of the programmable attenuators are the step-controlled and voltage-controlled types. The attenuation is varied by controlling the electrical signal applied to the attenuator. These signals can be in the form of either a biasing current or binary digit. The biasing can be pulses, square waves, or sine waves. A typical datasheet for coaxial programmable step attenuator is as follows:

Frequency	DC to 40 GHz
Attenuation	0–11 dB, in steps of 1 dB
Maximum VSWR	1.3–12.4 GHz 1.7–34 GHz 1.8–40 GHz

Insertion loss	0.8 dB + 0.04 GHz 0 dB setting
Repeatability	0.03 dB
Power rating average	1 W
Peak	50 W
Maximum pulse width	10 μ s
Life	5 million cycles per section minimum

7.4.2. Solenoid. A typical datasheet would be as follows:

Voltage	20–30 V
Speed	< 20 ms
Power	2.7 W
RF connectors	2.4 mm, F
Shipping weight	291 g (10.3 oz)

7.5. Lossy Wall Attenuator

Figure 14 shows lossy wall variable attenuator. It consists of a glass vane coated with a lossy material, such as aquadag or carbon. For maximum attenuation, the vane is placed in the center of the guide's wide dimension, where the electric field intensity is the maximum. A drive mechanism with a dial then shifts the vane away from the center so that the degree of attenuation is varied. This needs calibration by a precise attenuator. To match the attenuator to the waveguide, the vane can be tapered at each end; usually a taper of $\lambda g/2$ provides an adequate match. Thus, it is frequency sensitive and the glass dielectric introduces appreciable phase shift.

Attenuation may also be obtained by inserting a resistive element through a shutter. The plane of the element lies in the distribution of the electric field across the wide dimension of the waveguide and the result is a degree of attenuation, which increases with the depth of insertion. However, due to the discontinuity, there is reflection of energy.

7.6. Movable-Vane (Flap) Attenuator

Figure 15 shows a waveguide variable, dissipative attenuator. The card enters the waveguide through the slot in the broad wall, thereby intercepting and absorbing a portion of the TE_{10} wave. The card penetration, and hence the attenuation, is controlled by means of the hinge arrangement to obtain variable attenuation. The ratings are typically 30 dB and are widely used in microwave equipment. However, the attenuation is frequency sensitive and the phase of the output signal is a function of card penetration and hence attenuation. This may result in nulling when the attenuator is part of a bridge network. Since it is not simple to calculate the loss in dB, this type of attenuator has to be calibrated against a superior standard. To overcome these drawbacks, a rotary-vane attenuator is used.

7.7. Rotary-Vane Attenuator

The rotary-vane attenuator is a direct-reading precision attenuator that obeys a simple mathematical law, $A = -20 \log \cos^2 \theta = -40 \log \cos \theta$ dB. As such, it is frequency-independent, which is a very attractive criterion

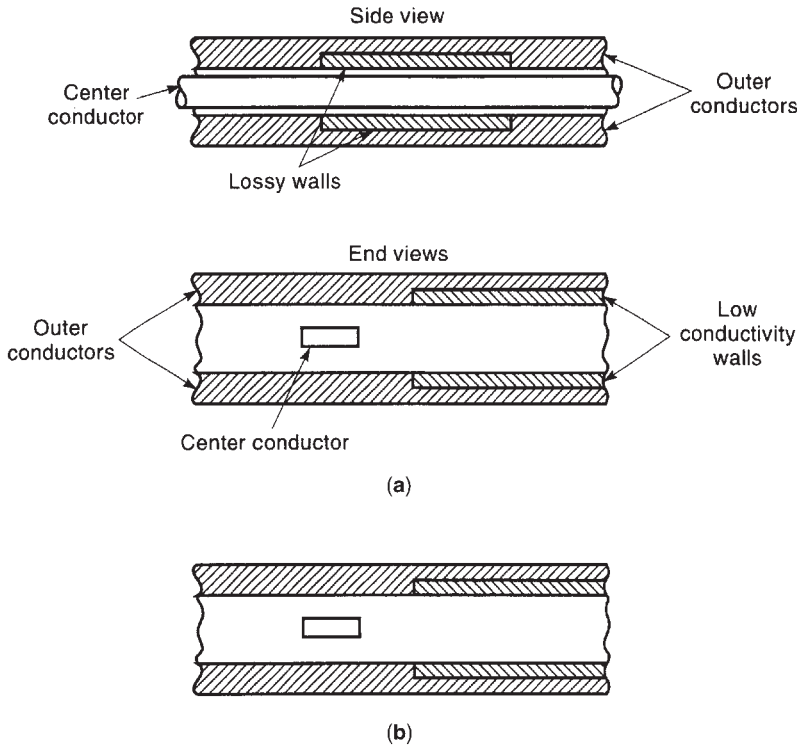


Figure 14. Lossy wall attenuator configuration: (a) minimum attenuator; (b) maximum attenuator.

for an attenuator. A functional diagram illustrates the operating principle of this attenuator. It consists of three sections of waveguide in tandem as shown (Fig. 16). A rectangular-to-circular waveguide transition containing a horizontal attenuator strip is connected to a rotatable circular waveguide containing an attenuator strip. This in turn is connected to a circular-to-rectangular waveguide transition containing a horizontal attenuator strip.

The incoming TE_{10} mode is transformed into the TE_{11} mode in the circular waveguide by the rectangular-to-circular waveguide transition with negligible reflections. The polarization of the TE_{11} mode is such that the e field is perpendicular to the thin resistive card in the transition section. As such, this resistive card has a negligible effect on the TE_{11} mode. Since the resistive card in the center can be rotated, its orientation relative to the electric field

of the incoming TE_{11} mode can be varied so that the amount by which this mode is attenuated is adjustable.

When all the strips are aligned, the electric field of the applied wave is normal to the strips and hence no current flows in the attenuation strips and therefore no attenuation occurs. In a position where the central attenuation strip is rotated by an angle θ , the electric field of the applied wave can be resolved into two orthogonally polarized modes; one perpendicular and one parallel to the resistive card. That portion which is parallel to the resistive slab will be absorbed, whereas the portion, which is polarized perpendicular to the slab, will be transmitted.

7.8. Variable Coupler Attenuator

These are basically directional couplers where the attenuation is varied by mechanically changing the coupling between two sections. This is accomplished by varying the spacing between coupled lines. These attenuators have a large range, high power handling capability, and retain calibration over a range of ambient conditions. They have a higher insertion loss at lower frequencies (Fig. 17).

7.9. Absorptive Attenuator

Figure 18 shows an absorptive variable attenuator. Attenuation is obtained by using a lossy dielectric material. The TEM electric field is concentrated in the vicinity of the center strip of the stripline. When the absorbing material is inserted in the high-field region, a portion of the TEM wave is intercepted and absorbed by the lossy dielectric. Thus, the attenuation increases. Since the characteristic impedance of the stripline changes with the dielectric

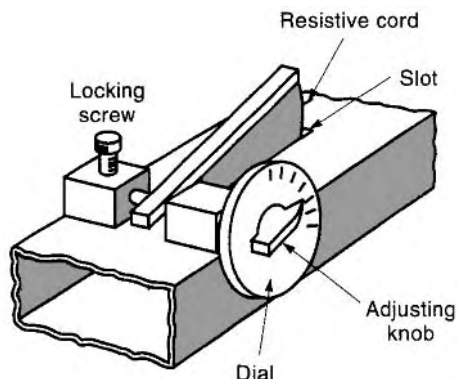


Figure 15. Movable-vane (flap) variable attenuator configuration.

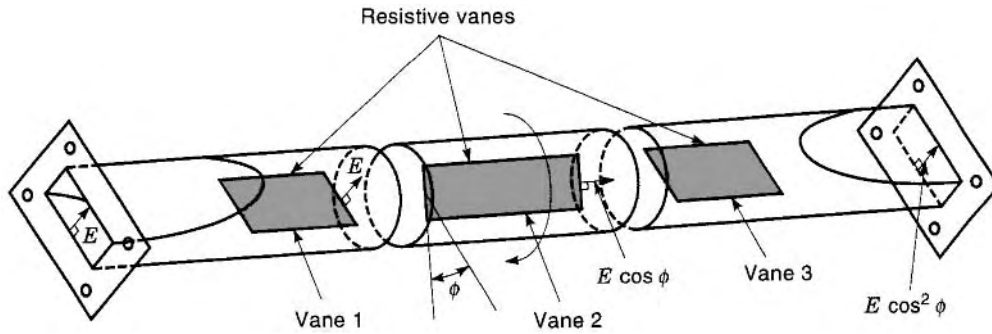


Figure 16. Rotary-vane attenuator configuration.

material insertion, the SWR tends to increase as the attenuation increases. To minimize this, the ends of the lossy material are tapered to provide a smooth impedance transformation into and out of the lossy section. SWR values of > 1.5 are possible over a limited frequency range. In general, the SWR deteriorates at low frequencies. The attenuation increases with increasing frequency for a fixed setting. This is another disadvantage, since this makes the calibration a cumbersome procedure. Compensation techniques are occasionally used to reduce this variation with frequency.

7.10. Coaxial Resistive Film Attenuator

Figure 19 shows a coaxial resistive film attenuator. In this configuration, if r is the RF resistance per unit length, by adjusting the length l , the series resistance $R = rl$ of the center conductor is changed; thus, the attenuation is variable. If I is the conduction current on the center conductor, the voltage drop is $V = RI = Ir l$. If E_i is the input voltage, then the output voltage is $E_o = E_i - r l I$ and the attenuation is

$$A = 20 \log \frac{E_i}{E_i - r l I} \text{ (dB)} \tag{35}$$

7.11. Variable T

The variable T attenuator is the same as the fixed attenuator except that the resistors are variable (Fig. 20). All three resistors are variable simultaneously to give good input/output VSWR.

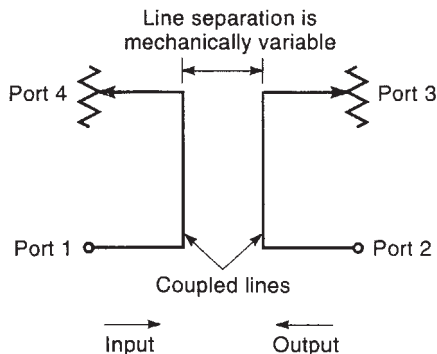


Figure 17. Variable coupler attenuator configuration.

7.12. Waveguide below Cutoff or Piston Attenuator

The simple principle of cutoff below frequency is used in the piston or the cutoff attenuator. The cylindrical waveguide used is operating at a frequency below cutoff. For high-power applications, a coaxial configuration is used. A simple waveguide cutoff attenuator is shown in Fig. 21. A metal tube, acting as a waveguide, has loops arranged at each end to couple from the coaxial lines into and out of the waveguide. One of the loops is mounted on a movable plunger or hollow piston so that the distance between the loops is variable. The input coupling loop converts the incoming TEM wave into the TE_{11} mode in the circular waveguide, while the output loop converts the attenuated TE_{11} mode back to TEM. The attenuator can be matched by adding Z_0 resistors. The attenuation is given as

$$A(\text{dB}) = 54.6 \frac{l}{\lambda_c} \sqrt{1 - \left(\frac{f}{f_c}\right)^2} \tag{36}$$

By choosing the diameter such that $\lambda_c \ll \lambda_o$, and hence $f/f_c \ll 1$, this equation reduces to

$$A(\text{dB}) = 54.6 \frac{l}{\lambda_c} \tag{37}$$

This was obtained from

$$\alpha = \frac{2\pi}{\lambda_{oc}} \text{ Np/m or } \alpha = \frac{54.6}{\lambda_{oc}} \text{ dB/m where } 1 \text{ Np} = 8.686 \text{ dB} \tag{38}$$

[If $\lambda_{oc} = 10 \text{ cm}$, and λ_o is much greater (10 times or more—in this case, 1 m or more), the attenuation

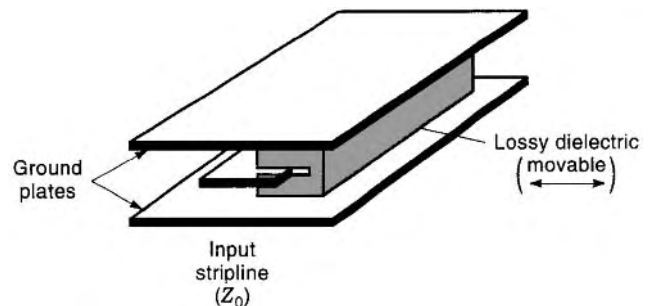


Figure 18. Absorptive-type variable attenuator configuration.

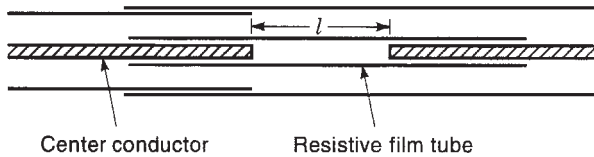


Figure 19. Coaxial resistive film attenuator configuration.

increases 5.45 dB per cm of outward movement of the plunger.]

The sliding cylindrical conductors allow length l to be varied, which varies the attenuation, since attenuation $A = \alpha l$, where α is the attenuation constant due to the cutoff effect, and l is the length of the circular guide. The cutoff wavelength is $\lambda_c = 1.706D$, where D is the diameter of the waveguide. Thus the attenuation is

$$A(\text{dB}) = 54.6 \frac{l}{\lambda_c} = 32 \frac{l}{D} \quad (39)$$

or

$$\Delta A(\text{dB}) = \frac{32}{D} \Delta l \quad (40)$$

The attenuation is independent of frequency; it depends only on the physical dimensions and hence can be accurately controlled by maintaining tight tolerances on the length and diameter of the circular guide. With ΔA linearly proportional to Δl , the cutoff attenuator is easily calibrated and hence particularly useful as a precision variable attenuator.

The cutoff attenuator is one of the most widely used precision variable attenuators in coaxial measurement equipment. This is a reflective-type attenuator, since the waveguide is essentially dissipationless. The signal is reflected rather than absorbed. For higher attenuation (> 10 dB), the SWR at both ports is very high (> 30). This can cause problems in certain applications.

This type of attenuator is very useful, but has the disadvantage of high insertion loss. Due to the nature of cutoff, the insertion loss is high, up to 15–20 dB. If this loss is overcome, piston attenuators are one of the most accurate attenuators available. Values of 0.001 dB/10 dB of attenuation over a 60 dB range are common. A good input/output match is obtained using inductive loops within the waveguides. Excellent matching is obtained over the entire range of attenuation due to inductive loop coupling. Figure 22 shows a commercially available standard variable piston attenuator and the various calibration curves. It contains an accurately dimensioned tube acting

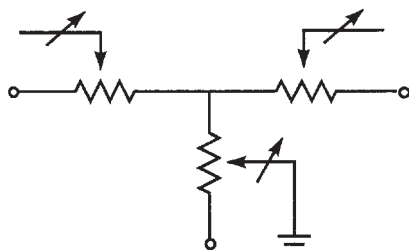


Figure 20. Variable T attenuator.

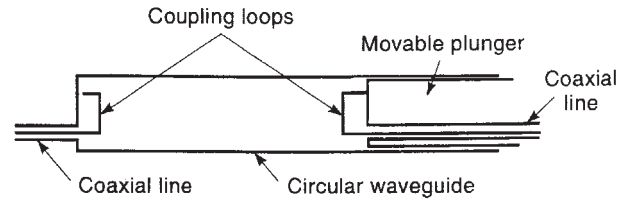


Figure 21. Coaxial variable cutoff attenuator configuration.

as a circular waveguide, below cutoff TE_{11} mode. Typical specifications are (courtesy of Weinschel Associates)

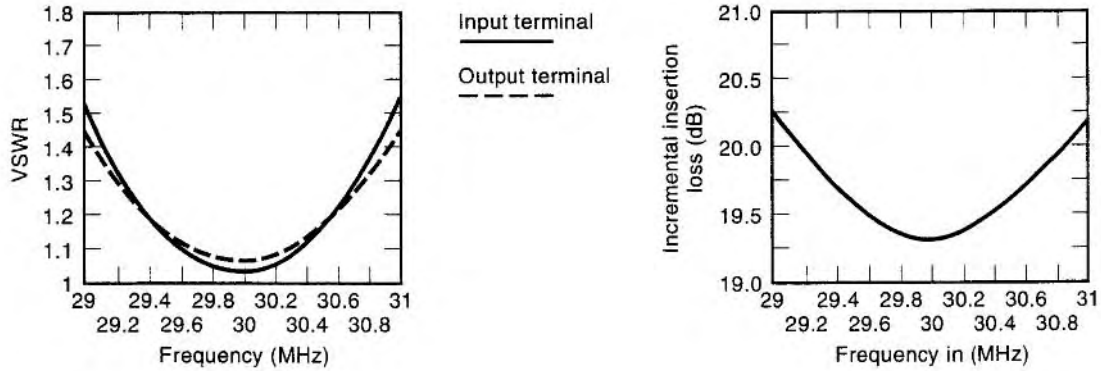
Frequency	30 MHz
Mode	TE_{11} cutoff
Range	0–120 dB
	12.5 dB zero insertion loss
VSWR	1.2 max in 50- Ω system
Connectors	Type N, panel-mounted
Accuracy	0.01 dB from 0 to 15 dB
	0.005 dB/10 dB from 15 to 100 dB
	0.01 dB/10 dB from 100 to 120 dB
Resolution	0.001 dB direct-reading digital indicator

7.12.1. Laser Piston Attenuator. Figure 23 shows a laser piston attenuator. The heart of this instrument is a precise stainless steel circular waveguide, operated in the TE_{11} cutoff mode. Laser light, traveling between two antennas in the center of the circular waveguide, measures directly the changes in actual separation of the two antennas along the same path as the TE_{11} mode propagates. The laser signal is converted to attenuation in dB and corrected for skin effect, the refractive index of air, and changes relative to temperature of the waveguide and pressure. The specifications are (courtesy of Weinschel Associates)

Operating frequency	Dual frequency 1.25 MHz + 0.05 MHz and 30.0 MHz + 0.1 MHz
Waveguide mode	TE_{11} , below cutoff
Incremental attenuation range	100 dB
Minimum insertion loss	10 dB nominal
Resolution	0.0001 dB for Δ dB, 0.002 dB for total loss
Attenuation readout	Front panel 7-digit LED or remotely via IEEE bus
Connectors	Type N jacks
VSWR (input and output)	1.2 max at 1.25 and 30 MHz in 50- Ω system
Accuracy	0.001 dB/10 dB + 0.0005 dB between 15 and 115 dB total loss
Weight	Net: 77 kg (170 lb); shipping: 145 kg (320 lb)
Accessories	Power supply, controller, calibration tape, two power cables, one 22-wire power cable, instruction/maintenance manual

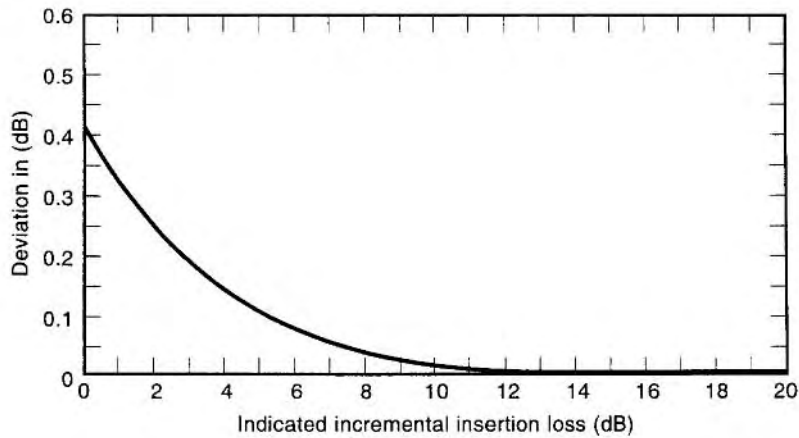


(a)



(b)

(c)



(d)

Figure 22. (a) Standard variable piston attenuator and (b–d) calibration curves. (b) Typical VSWR versus frequency of SPA-2 attenuator with frequency. (c) Typical variation of insertion loss of SPA-2 attenuator with frequency in a 50-Ω system. (d) Deviation versus indicated incremental insertion. Typical deviation from linearity for the model SPA-2 operating frequency is 30.0 MHz.

8. ACTIVE ATTENUATORS

8.1. pin Diode Attenuators

The normal diode junction consists of a p-type material brought together with an n-type material to form the familiar pn junction. The pin diode is distinguished from the normal pn junction type by an area called an *intrinsic region* sandwiched between the p⁺-doped and n⁺-doped

silicon layers. This intrinsic layer has almost no doping and thus has a very large resistance. When a variable DC control voltage forward-biases the pin diode, the DC bias or control current causes it to behave as almost a pure resistance at RF frequencies, with a resistance value that can be varied over a range from 1 Ω to 10 kΩ. As the bias current is increased, the diode resistance decreases. This relation makes the pin diode ideally suited as a variable



Figure 23. Laser piston attenuator. (Courtesy of Weinschel Associates.)

attenuator for leveling and amplitude modulating a RF signal.

These attenuators provide local oscillator, IF, and RF signal level control throughout communications, measurement, and control circuits. One example is the reduction in the output of a receive mixer in a code-division multiple-access (CDMA) base station prior to the IF amplifier. Also, to provide one step of transmit level control with little degradation of the noise figure (NF), it could be used in a CDMA handset transmit chain between the mixer (upconverter) and the bandpass filter (Fig. 24). Since the attenuator is purely passive, it produces no additive noise and the NF is essentially its insertion loss. Even in the attenuator mode, the effect on the noise figure would be minimal.

In personal communication service (PCS) systems, the base stations may be fed from multiple picocells that are physically separated from it by up to 100ft or more of coaxial cable. The signal levels coming into the base station will vary depending on the cable length and individual transponder power. It is desirable to keep the signals at uniform levels coming into the base station; to do so, it may be necessary to attenuate the stronger signals. An attenuator can be easily inserted for this purpose.

The upper end of a receiver's linear dynamic range is determined by the largest signal it can handle without being overdriven and producing unacceptable levels of distortion caused by device nonlinearities. Inserting an attenuator before a low-noise amplifier (LNA) in the presence of strong, in-band signals produces better reception by preventing them from overdriving the receiver's front end. This effectively shifts the dynamic range

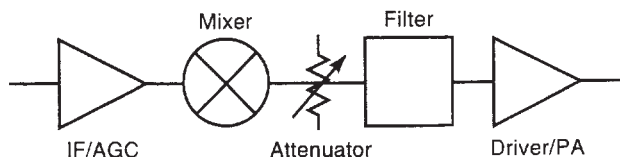


Figure 24. CDMA handset transmit application.

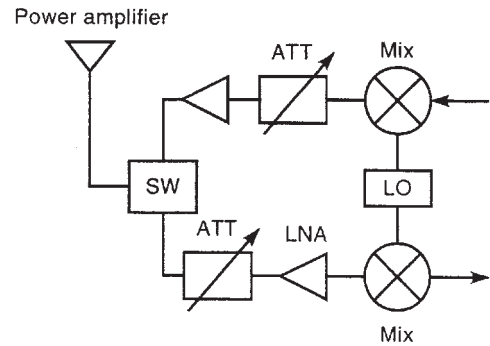


Figure 25. Functional block diagram of a digital cellular phone, using variable attenuators.

upward by the amount of attenuation. It must be remembered that when inserted into the system, the attenuator will also present a load and a source impedance to the previous and succeeding stages, respectively, hence the importance of the attenuator impedance match.

RF variable attenuators are used to control the transmitting and receiving signal power levels to prevent strong-weak adjacent signals from seriously degrading the bit error rate (BER) of digital mobile communication systems, such as TDMA or CDMA. Figure 25 shows the basic RF functional block diagram of a typical digital cellular phone system, where variable attenuators are required.

8.2. Characteristics of the pin Diode

The approximate high frequency equivalent circuit of a pin diode is shown in Fig. 26. Here, R_I is the effective resistance of the intrinsic (I) layer, given by

$$R_I = \frac{k}{I_{DC}^x} \tag{41}$$

where I_{DC} is the DC bias current in mA, and k and x are device-dependent empirical constants. Although shown as a variable, this resistance is constant with respect to the RF signal. The high-frequency resistance function is plotted in Fig. 27 for the Hewlett-Packard HPND-4165 diode. For a specific diode design, the exponent X is usually a constant. For the HPND-4165, X is typically 0.92. The constant k and therefore R_I , however, are highly dependent on the fabrication and process control and its value can vary by as much as 3:1 from diode to diode. For analog applications, such as a variable attenuator, where repeatable attenuation with bias current is desired, the variation of R_I must be controlled. The HPND-4165 is



Figure 26. pin diode high-frequency equivalent circuit.

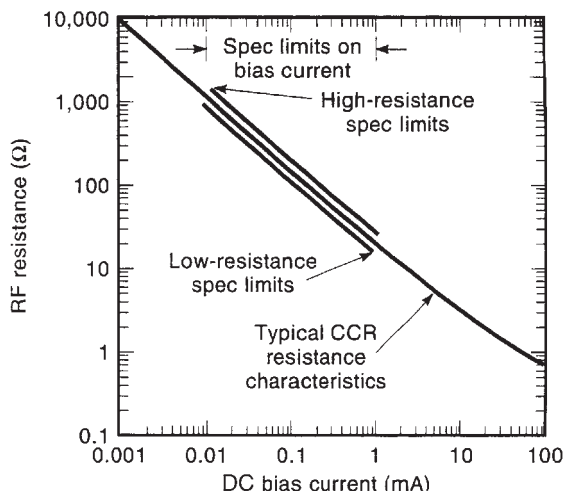


Figure 27. Typical RF resistance versus DC bias current for HPND-4165.

precisely controlled in manufacturing, and resistance values at specific bias points are specified and the slope of resistance versus bias matched with narrow limits. The specification limits of these parameters are shown in Table 4.

8.3. Applications

The pin diode is ideally suited to switch and attenuate RF signals. Since the pin diode is a RF variable resistor, the logical application is that of a variable attenuator. This attenuator may be either a step or a continuously variable type. Two of the simplest circuits are the series and shunt attenuators shown in Figs. 28 and 29.

Attenuation in the series pin circuit is decreased (more power appears at the output) as the RF resistance of the diode is reduced. This resistance is reduced by increasing the forward bias control current on the diode. The opposite occurs for the shunt configuration. The attenuation in the shunt circuit is decreased when the RF resistance of the diode increases because less power is absorbed in the diode and more appears at the output. If the control bias is switched rapidly between high and low (zero) values, then the circuit acts simply as a switch. When used as a switch, the attenuation that exists when the switch is ON is called

Table 4. HPND-4165 pin Diode Specifications

Parameter	HPND-4165	Test Conditions
High-resistance limit, R_H	1100–1660 Ω	10 μ A
Low-resistance limit R_L	16–24 Ω	1 mA
Maximum difference in resistance versus bias slope x	0.04	10 μ A and 1 mA

insertion loss. The attenuation provided when the switch is OFF is called *isolation*. If the diode is a pure resistance, the attenuation for the series and shunt circuit can be calculated as

$$A(\text{series}) = 20 \log \left(1 + \frac{R_I}{Z_0} \right) \tag{42}$$

$$A(\text{shunt}) = 20 \log \left(1 + \frac{Z_0}{2R_I} \right) \tag{43}$$

where $Z_0 = R_G = R_L =$ circuit, generator, and load resistance, respectively. In reviewing these equations, it is seen that the attenuation is not a function of frequency but only a ratio of circuit and diode resistances, which is a great advantage. As the bias on the diode is varied, the load resistance experienced by the source also varies. These circuits are generally referred to as reflective attenuators because they operate on the principle of reflection.

Many RF systems require that the impedance at both RF ports remain essentially constant at the design value Z_0 . Four such circuits and their pin diode counterparts are shown in Fig. 30. All four circuits operate on the principle of absorbing the undesired RF signal power in the pin diodes. In circuits (a), (b), and (c), the control current variation through each diode is arranged in such a way that the impedance at both RF ports remain essentially constant at the characteristic impedance (Z_0) of the system while the attenuation can be varied over a range of less than 1 dB to greater than 20 dB. In circuit (d), the input impedance is kept constant by using a distributed structure with a large number of diodes. The impedance variation of each diode is also shaped so that the diodes in the center of the structure vary more than those near the ports. The resulting tapered impedance

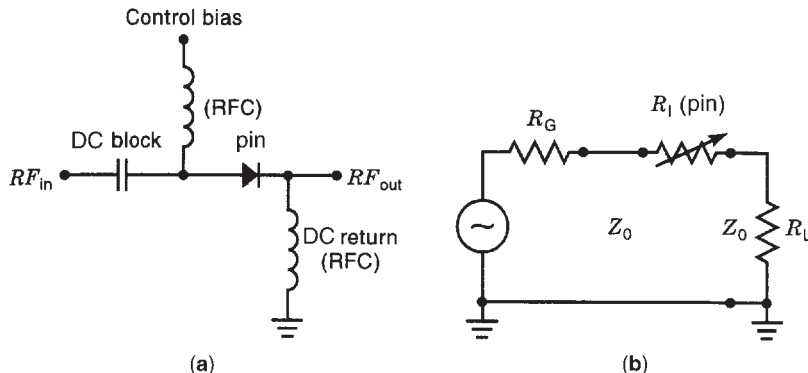


Figure 28. Series pin RF attenuator or switch: (a) complete circuit; (b) idealized RF equivalent circuit.

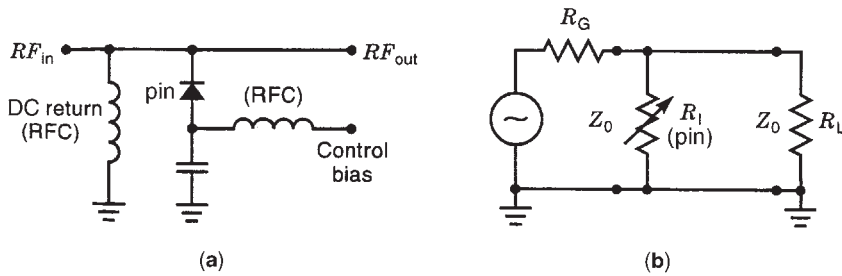


Figure 29. Shunt pin RF attenuator or switch: (a) complete circuit; (b) idealized RF equivalent circuit.

structure results in an essentially constant impedance at the ports, while the overall attenuation can be varied up to a range of 40–80 dB, depending on the length of the structure.

A pin diode pi attenuator such as that in Fig. 30a is often selected when designing a variable attenuator. The basic pi fixed attenuator is shown, along with its design equations, in Fig. 31. Shunt resistors R_1 and the series

resistor R_3 are set to achieve a desired value of attenuation, while simultaneously providing an input and output impedance that matches the characteristic impedance Z_0 of the system.

Three pin diodes can be used as shown in Fig. 32 to replace the fixed resistors of the pi circuit to create a variable attenuator. The attenuator provides good performance over the frequency range of 10 MHz to over

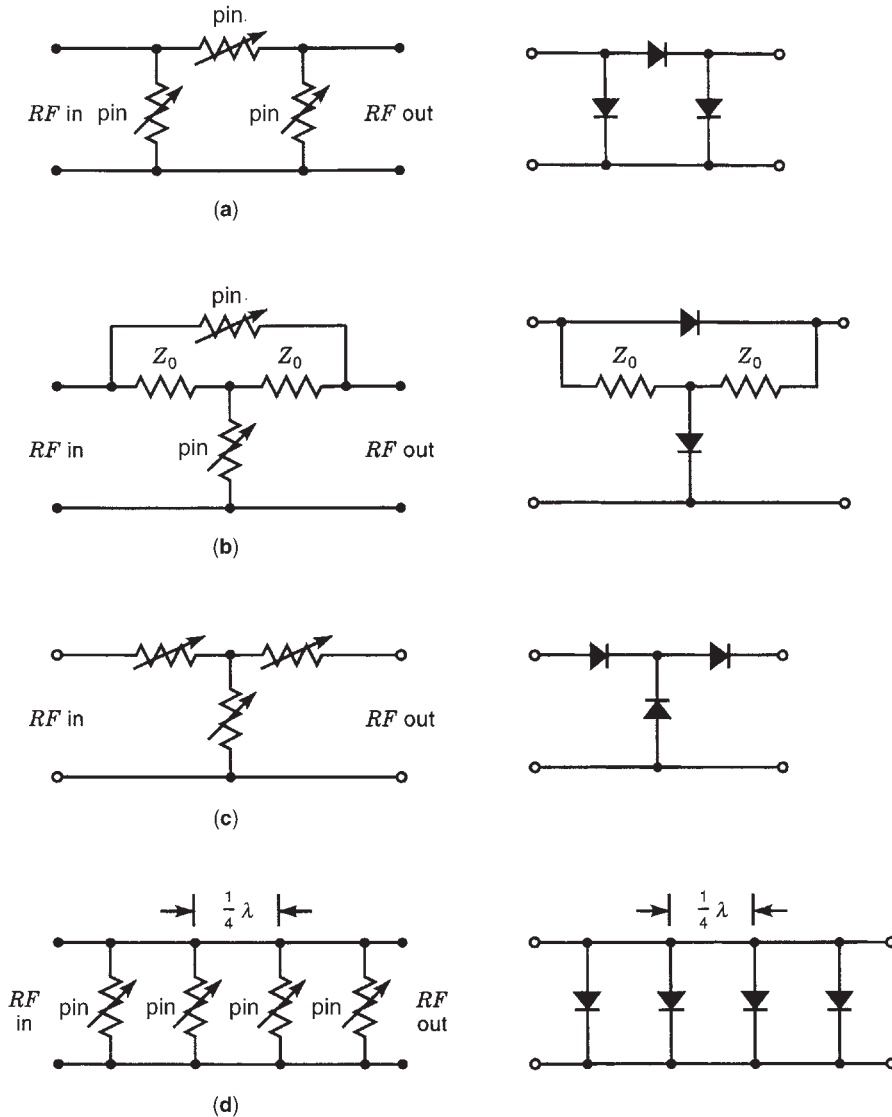


Figure 30. Constant impedance pin diode attenuators: (a) pi attenuator; (b) bridged T attenuator; (c) T attenuator; (d) resistive line attenuator.

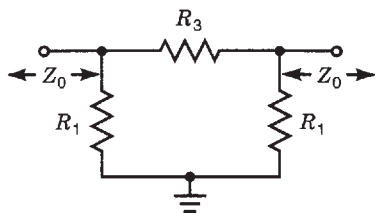


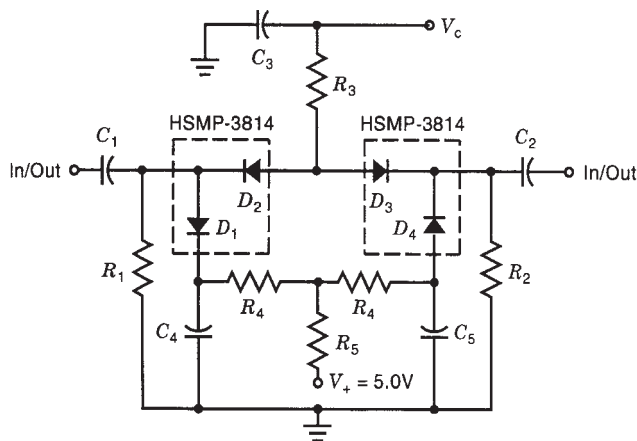
Figure 31. Fixed pi attenuator.

500 MHz. However, the use of three diodes as the three variable resistors in a pi attenuator results in a complex unsymmetric bias network. If resistor R_3 is replaced by two diodes, as shown in Fig. 33, the resulting attenuator is symmetric and the bias network is significantly simplified. V_+ is a fixed voltage, and V_c is the variable control voltage, which controls the attenuation of the network. The only drawback to using two series diodes in place of one is the slight increase in insertion loss. Resistors R_1 and R_2 serve as bias returns for series diodes D_2 and D_3 . Resistors R_3 and R_4 are chosen to match the specific characteristics of the pin diodes used. Properly selected, they will provide the correct split of bias current between series and shunt diodes required to maintain a good impedance match over the entire dynamic range of attenuation.

The pin diode variable attenuator is an excellent circuit used to set the power level of an RF signal from a voltage control; it is used widely in commercial applications, such as cellular phones, PCN (personal communication networks), wireless LANs (local-area networks), and portable radios.

8.4. GaAs NMESFET Attenuator

The GaAs *N*-semiconductor metal semiconductor field effect transistor (NMESFET) is used in microwave attenuator designs. The metal–semiconductor FET (MESFET) is a field-effect transistor that operates on the principle that the gate-to-source voltage controls the drain current. The MESFET is a device extension of a JFET, where the gate structure is a Schottky MN (metal–*N* semiconductor) junction.



Component	Value	Manufacturer and part number
R_1, R_2	560 Ω	Kyocera CR21-561JB1
R_3	330 Ω	Kyocera CR21-331JB1
R_4	1640 Ω	Kyocera CR21-162JB1
R_5	680 Ω	Kyocera CR21-6B1JB1
C_1-C_5	47,000 pF	Kyocera 08957473M2P03
D_1-D_4	-	Hewlett-Packard HSMP-3814

Figure 33. Wideband four-diode II attenuator.

In GaAs NMESFET attenuator designs, the devices are operated either in the linear region where the device is modeled as a voltage variable resistor or as an ON/OFF switch in conjunction with thin-film nichrome resistors to provide appropriate levels of attenuation. The channel resistance of the GaAs NMESFET is known to follow the classical theory for a FET in the linear region of operation. With the FET biased in the linear region, the resistance varies inversely to the gate voltage as shown below:

$$R_{ds} = R_{ds0} \left(\frac{1}{1 - (V_g/V_p)} \right) \tag{44}$$

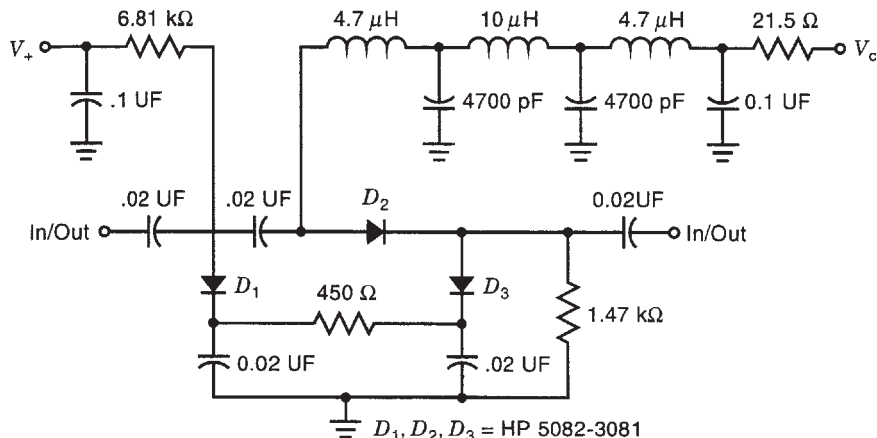


Figure 32. Three-diode pi attenuator.

$D_1, D_2, D_3 = \text{HP } 5082-3081$

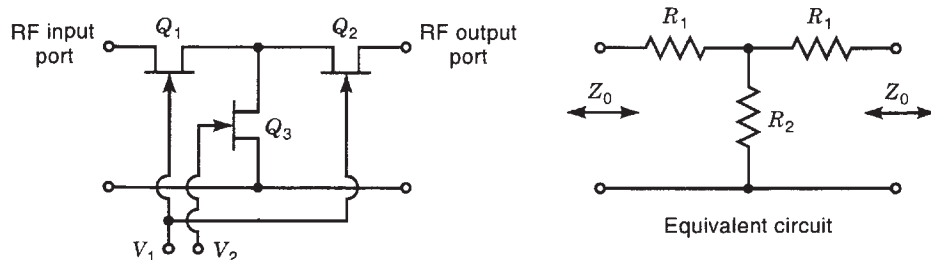


Figure 34. MESFET T attenuator.

where V_g = gate bias voltage (V), V_p = pinchoff voltage (V), and R_{ds0} = channel resistance (Ω) with $V_g = 0$ V.

As the gate voltage approaches the pinchoff voltage, the resistance becomes very high (relative to $50\ \Omega$). Conversely, as the gate voltage approaches zero, so does the channel resistance. For each attenuator configuration, two independent gate bias voltages are used; one to control the series MESFETs and one to control the shunt MESFETs. The T attenuator configuration is shown in Fig. 34, with one voltage controlling the series resistance arms, and another the shunt resistance arm. Table 5 gives the resistor values of the series and shunt resistances in a $Z_0 = 50\ \Omega$ system. The channel resistances of the MESFETs are matched as closely as possible for these resistances. A matched condition at the input and output port to Z_0 occurs when

$$Z_0^2 = R_1^2 + 2R_1R_2 \quad (45)$$

The resulting matched attenuation is

$$A = 20 \log \left(\frac{R_1 + R_2 + Z_0}{R_2} \right) \quad (46)$$

The pi attenuator configuration is shown in Fig. 35, with one voltage controlling the shunt resistance arms, and another the series resistance arm. Table 6 gives the values of the series and shunt resistances for different levels of attenuation in a $Z_0 = 50\ \Omega$ system. Shunt resistor R_1 and series resistor R_2 provide an input and output impedance that matches the characteristic impedance $Z_0 = 50\ \Omega$ of the system, while setting the desired level of attenuation. The

Table 5. T Attenuator Resistor Values for Different Levels of Attenuation

Attenuation (dB)	R_1 (Ω)	R_2 (Ω)
2	5.73	215.24
4	11.31	104.83
6	16.61	66.93
8	21.53	47.31
10	25.97	35.14
12	29.92	26.81
14	33.37	20.78
22	42.64	7.99

design equations are

$$R_1 = Z_0 \left[\frac{K + 1}{K - 1} \right] \quad (47)$$

$$R_2 = \frac{Z_0}{2} \left[K - \frac{1}{K} \right] \quad (48)$$

$$A(\text{dB}) = 20 \log K \quad (49)$$

where K is the input to output voltage ratio.

GaAs NMESFET digital attenuators allow a specific value of attenuation to be selected via a digital n bit programming word. In these designs, the NMESFET operates as an ON/OFF switch and is used in conjunction with nichrome thin-film resistors to provide the desired level of attenuation. Figure 36 shows the circuit configurations used for individual attenuator bits. The switched bridged T attenuator consists of the classical bridged T attenuator with a shunt and series FET. These two FETs are switched on or off to switch between the two states. The attenuation in dB is given by

$$A(\text{dB}) = 20 \log \left(\frac{Z_0 + R_2}{R_2} \right) \quad (50)$$

where $Z_0^2 = R_1R_2$.

The performance is determined by the FET characteristics in the on and off states and the realizability limit on required resistance values and their associated parasitics. The switched T or pi attenuators are similar in principle to the switched bridged T attenuator except for the circuit topology. These attenuators are normally used for high attenuation values. To obtain smaller values of attenuation, the thin-film resistors are replaced with appropriate channel resistances.

There are GaAs NMESFET digital RF attenuators on the market with excellent performance, in both step and continuously variable types. The variable or programmable class allows a specific value of attenuation to be selected from an overall range via an N -bit programming word. They are more flexible than step attenuators, as they allow any amount of attenuation to be set, but the cost is greater circuit complexity. Both types have a bypass state when no attenuation is selected, and the attenuation is just the insertion loss of the device. An example of each type is presented.

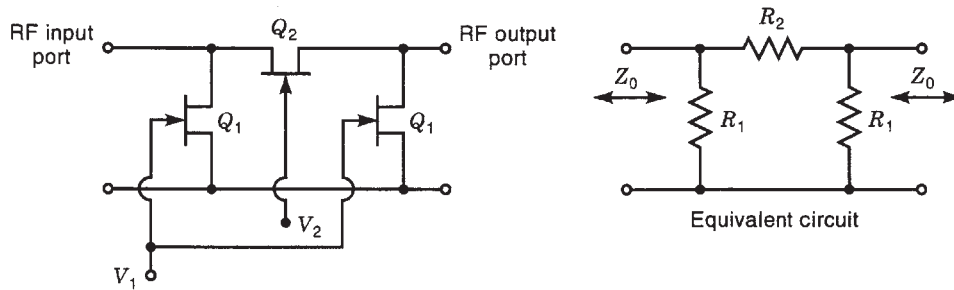


Figure 35. MESFET pi attenuator.

The RF Microdevices RF 2420 is a multistage monolithic variable or programmable attenuator that has as attenuation programmability over a 44 dB range in 2-dB steps. The attenuation is set by 5 bits of digital data. A functional block diagram of the RF 2420 is shown in Fig. 37. It consists of five cascaded, DC-coupled attenuator sections, each with its own logic translator. The logic translator converts the one-bit control signal, which uses logic levels approximating standard TTL logic, to the voltage levels required to switch the attenuator stage FETs. The RF input and output signal lines are biased at approximately V_{DD} , and therefore external DC blocking capacitors are required. An external V_{DD} bypass capacitor is also required.

A functional schematic of the RF portion of one attenuator section is shown in Fig. 38. A MESFET bridges the series resistor in a resistive pi attenuator, and two more MESFETs are connected as a double-pole single-throw (DPST) RF switch connecting the shunt branches of the pi attenuator to RF ground. In the bypass state, the bridge MESFET is in its high conductance state, and the DPST switch is open, so that the pi-attenuator is effectively removed from the circuit. When the attenuator bit is selected, the bridge MESFET is put into its low conductance state or cutoff state and the shunt FETs are put into their on state, so that the pi attenuator is connected into the RF series path. This attenuator has only moderate variation across a broad band of operation from 100 to 950 MHz, as illustrated in Fig. 39.

Furthermore, the attenuation varies smoothly and consistently with attenuator switch settings. Other features of the device are single 3–6-V supply operation, and

Table 6. Pi Attenuator Resistor Values for Different Levels of Attenuation

Attenuation (dB)	R_1 (Ω)	R_2 (Ω)
2	436	11.61
4	221	23.85
6	150.5	37.35
8	116.14	52.84
10	96.25	71.15
12	83.54	93.25
14	74.93	120.31
22	58.63	312.90

4 dB insertion loss, and the input and output have a low-VSWR 50- Ω match. All these features make the RF 2420 an excellent component for communications systems that require RF transmit power control by digital means. Typical applications are in dual mode IS-54/55 compatible cellular transceivers and TETRA systems. Figure 40 shows the complete schematic details of the RF 2420 being employed in a typical RF/IF switching attenuator application.

The RF Microdevice RF 2421 is a GaAs MESFET-switched step attenuator. It has a single-step digitally controlled attenuation of 10 dB. A functional block diagram of the device is shown in Fig. 41. The supply voltage range required is 2.7 V to 6 V DC. The input and output of the device have a low-voltage standing-wave ratio (VSWR) 50- Ω match, and the RF output can drive up to +16 dBm. It has 1.0 dB of insertion loss over the specified 500 MHz–3 GHz operating frequency range. The resistors are nickel chromium (nichrome) and provide excellent temperature stability. The RF ports are reversible, which means that the input signal can be applied to either port. The attenuation control pin has an internal pulldown resistor that causes the attenuator to be turned off when it is not connected. Figure 42 illustrates the RF 2421 being used to set the RF signal level in a communications system.

8.5. MOSFET Attenuators

Active voltage attenuators have many useful applications in analog integrated circuit design. Some of the applications are in the feedback loops of finite gain amplifiers and in the input stages of transconductance amplifiers. In discrete circuit design, the most popular way to design a finite-gain amplifier with precisely controlled gain, high linearity, and low output noise is to use operational amplifier and a voltage attenuator in the feedback loop. Here the voltage attenuator consists of two resistors connected in series as shown in the classical noninverting and inverting op amp gain configurations of Fig. 43. Resistor attenuators are not useful in integrated circuit design because of their large areas, low input impedance, large power dissipation, and parasitic capacitances, and precise resistance values cannot be realized.

Three MOS active voltage attenuator configurations useful for the realization of finite-gain amplifiers in mono-

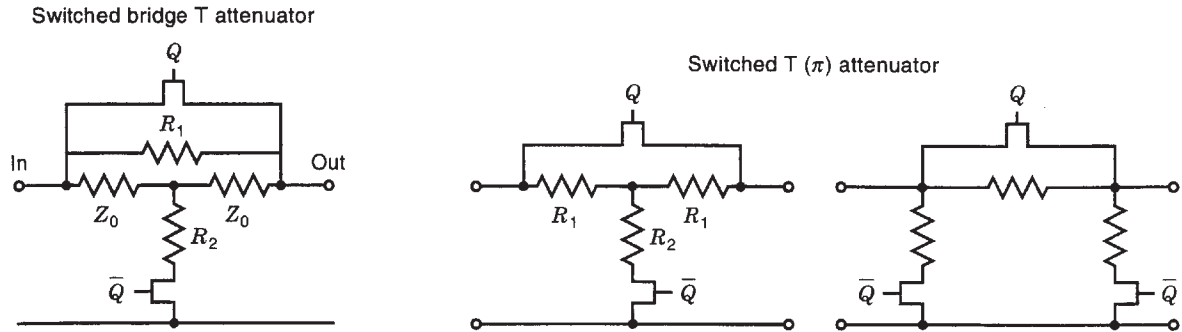


Figure 36. GaAs digital attenuator circuit configuration.

lithic circuits are presented. The attenuators are two single-input attenuators and a summing attenuator that has two inputs. These attenuators are simple in structure, consisting only of MOSFETs. Therefore, they are easy to fabricate in standard CMOS semiconductor processes. The attenuation factor is precisely controlled over a wide range of gains because it ideally depends only on the ratios of the dimensions of the MOSFETs.

Attenuator I, shown in Fig. 44, is an active linear voltage attenuator consisting of two n-channel MOSFETs fabricated in a common substrate. The capability to fabricate the MOSFETs in a common substrate has several advantages. First, both n-channel and p-channel attenuators can be monolithically fabricated in a standard CMOS process. Second, the required area of the attenuator is much smaller. As seen in Fig. 44, the substrate is common for both MOSFETs and is connected to the source of the bottom transistor M1. The circuit operates as a linear voltage attenuator when M1 is in the ohmic region and M2 is in the saturation region.

The operating conditions of the MOS attenuators in this section are derived as in the following equations,

where

V_{in}	Input voltage
V_{out}	Output voltage
V_{DD}	Drain supply voltage
V_B	Bias supply voltage 1
V_{BB}	Bias supply voltage 2
$V_{TON} = V_{TON1} = V_{TON2}$	Zero bias threshold voltage of M1 and M2
V_{T2}	Threshold voltage of M2 due to body bias effect
V_1	Input voltage 1
V_2	Input voltage 2
γ	Body effect parameter
ϕ	Barrier potential
I_D	Drain current
W	Width of channel
L	Length of channel
W_1, W_2	Width of channels 1,2
L_1, L_2	Length of channels 1,2
K'	Device constant, $\mu_n CoX$
μ_n	Mobility of electron
CoX	Gate oxide capacitance per unit area

The zero-bias threshold voltage of both MOSFETs is $V_{TON1} = V_{TON2} = V_{TON}$. The proper operating conditions will be met, provided

$$V_{TON} < V_{in} < V_{DD} + V_{T2} \tag{51}$$

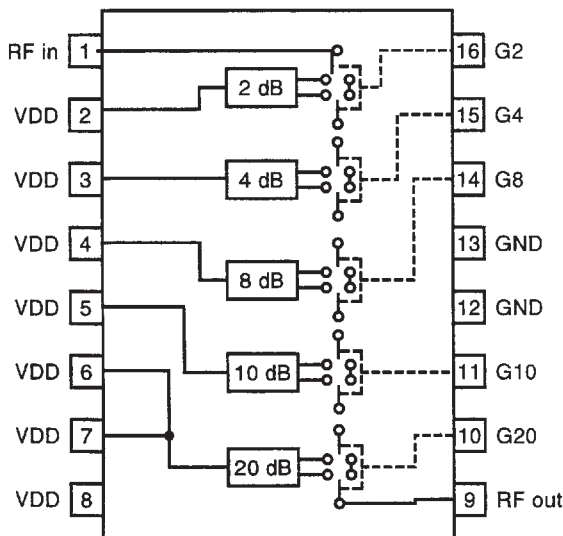


Figure 37. RF 2420 functional block diagram.

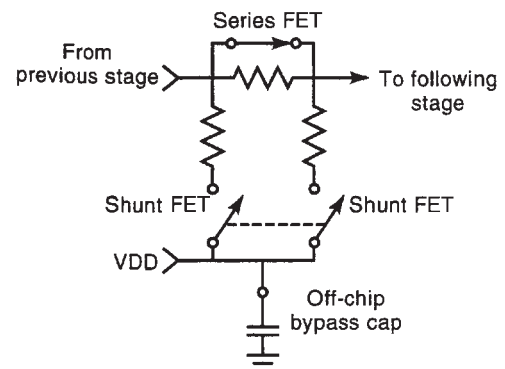


Figure 38. Functional schematic of RF 2420 (one attenuator section).

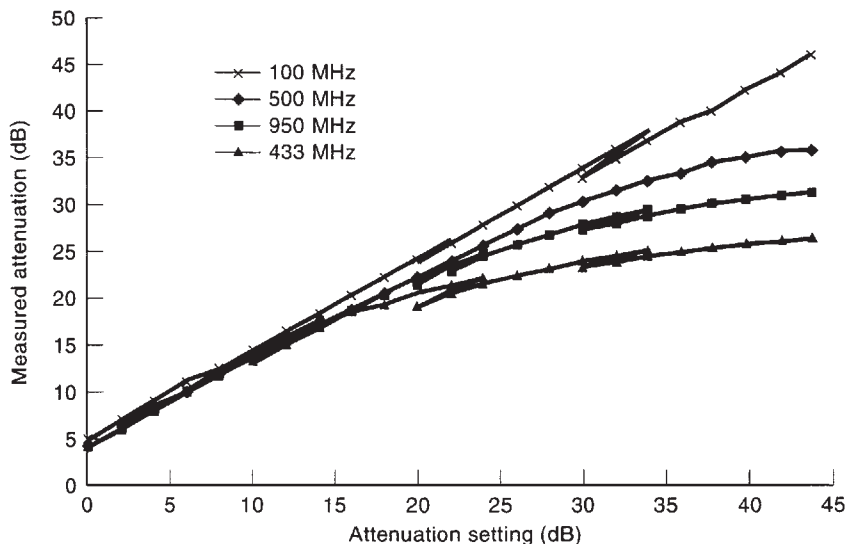


Figure 39. Attenuation and frequency response characteristics of RF 2420 5-bit digital RF attenuator.

where

$$V_{T2} = V_{TON} + \gamma(\sqrt{\phi + V_{out}} - \sqrt{\phi}) \quad (52)$$

Since M1 is operating in the ohmic region and M2 is in the saturation region, the drain current of each MOSFET is given by

$$I_{D1} = K' \frac{W_1}{L_1} \left(V_1 - V_{TON} - \frac{V_{out}}{2} \right) V_{out} \quad (53)$$

and

$$I_{D2} = K' \frac{W_2}{2L_2} (V_1 - V_{T2} - V_{out})^2 \quad (54)$$

Equating the two drain currents, the relationship between V_{in} and V_{out} is obtained as

$$2R \left(V_{in} - V_{TON} - \frac{V_{out}}{2} \right) V_{out} = \left\{ V_{in} - V_{TON} - V_{out} - \gamma(\sqrt{\phi + V_{out}} - \sqrt{\phi}) \right\}^2 \quad (55)$$

where

$$R = \frac{W_1/L_1}{W_2/L_2} \quad (56)$$

If each MOSFET in the attenuator is fabricated in a separate substrate and the substrate of each

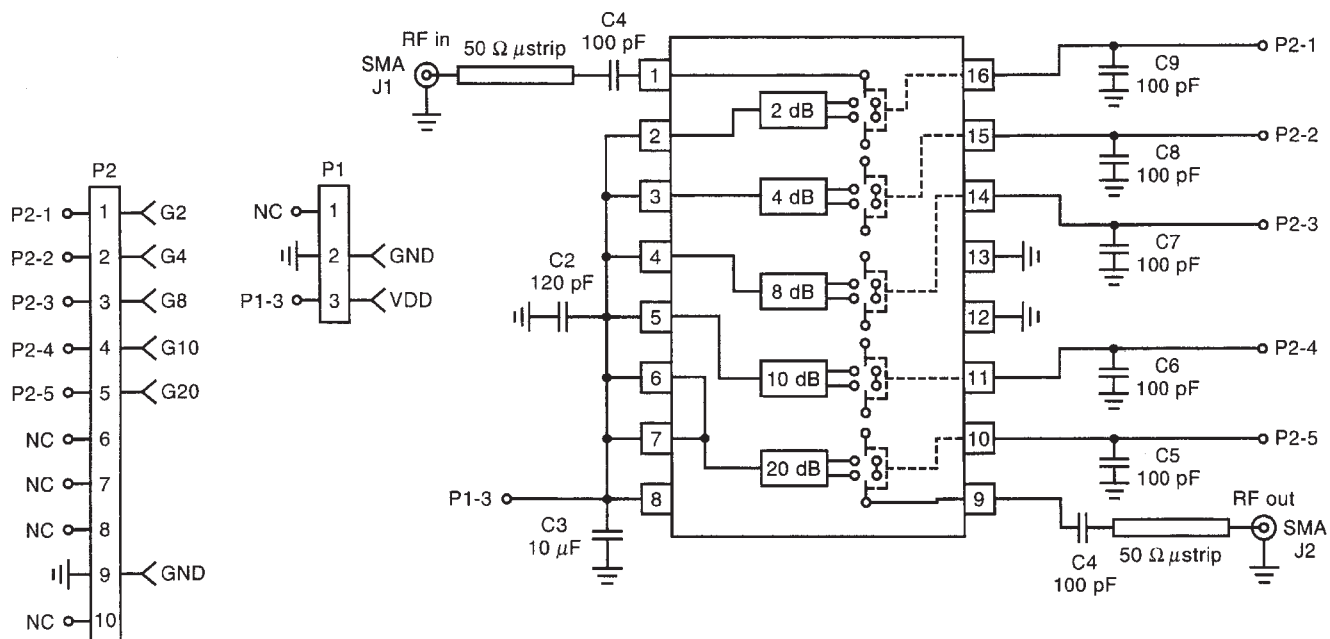


Figure 40. RF 2420 RF/IF switching attenuator schematic.

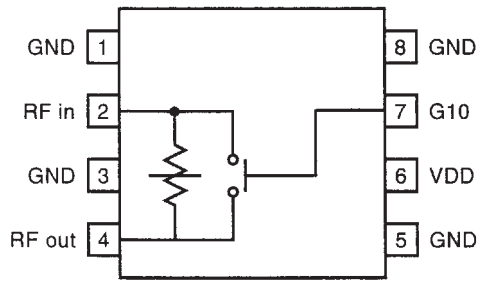


Figure 41. RF 2421 functional block diagram.

MOSFET is connected to its source ($\gamma = 0$), the DC transfer characteristic relating V_{in} and V_{out} becomes a linear equation:

$$V_{out} = \alpha(V_{in} - V_{TON}) \quad (57)$$

where α is the small-signal attenuation factor.

In this case, α is

$$\alpha = 1 - \sqrt{\frac{R}{R+1}} = 1 - \sqrt{\frac{W_1/L_1}{W_1/L_1 + W_2/L_2}} \quad (58)$$

Equation (57) is a special case of Eq. (55), when the bulk effect term due to γ is ignored. When the substrate is separate, the small-signal attenuation factor from Eq. (58) is precisely determined by width/length ratios. If the substrate is common, the relationship between the input and output is still very linear as given by Eq. (55) even though the equation appears to be a nonlinear quadratic.

Figure 45 shows the typical DC transfer characteristic of the attenuator consisting of M1 ($12 \times 10 \mu\text{m}^2$) and M2 ($3 \times 10 \mu\text{m}^2$) when the substrate is common ($\gamma \neq 0$) and $V_{DD} = 5\text{V}$. The DC transfer characteristic exhibits a high degree of linearity for the input range 2–5 V. The small-signal attenuation factor (α), which is the slope of the DC

transfer characteristic is 0.07824 at an input quiescent voltage of 3.5 V.

A finite-gain amplifier consisting of an ideal op amp and attenuator I in the feedback loop is shown in Fig. 44. Since the op amp is assumed ideal, we obtain

$$V_{in} = V_{out} = \alpha V'_{in} = \alpha V'_{out} \quad (59)$$

or

$$V'_{out} = \frac{1}{\alpha} V'_{in} \quad (60)$$

Thus, the DC transfer function of the amplifier is the inverse function of the DC transfer function of the attenuator in the feedback loop. Thus, the transfer function between the input V'_{in} and the V'_{out} of the amplifier is given by Eq. (55) when V_{out} is replaced by V'_{in} and V'_{in} by V'_{out} . The small-signal voltage gain

$$\left(A_V = \frac{V'_{out}}{V'_{in}} = \frac{1}{\alpha} \right)$$

is the reciprocal of the attenuator's attenuation factor in the feedback loop. Figure 46 illustrates the DC transfer characteristic of the finite-gain amplifier.

Two slightly different linear inverting voltage attenuator configurations consisting of two n-channel MOSFETs are shown in Fig. 47. These circuits operate as a linear inverting voltage attenuator when both transistors are in the saturation region. Assuming the zero-bias threshold of both of the MOSFETs is V_{TON} , the condition will be met, provided

$$V_{out} + V_{T2} < V_B < V_{DD} + V_{T2} \quad (61)$$

and

$$V_{TON} < V_{in} < V_{out} + V_{TON} \quad (62)$$

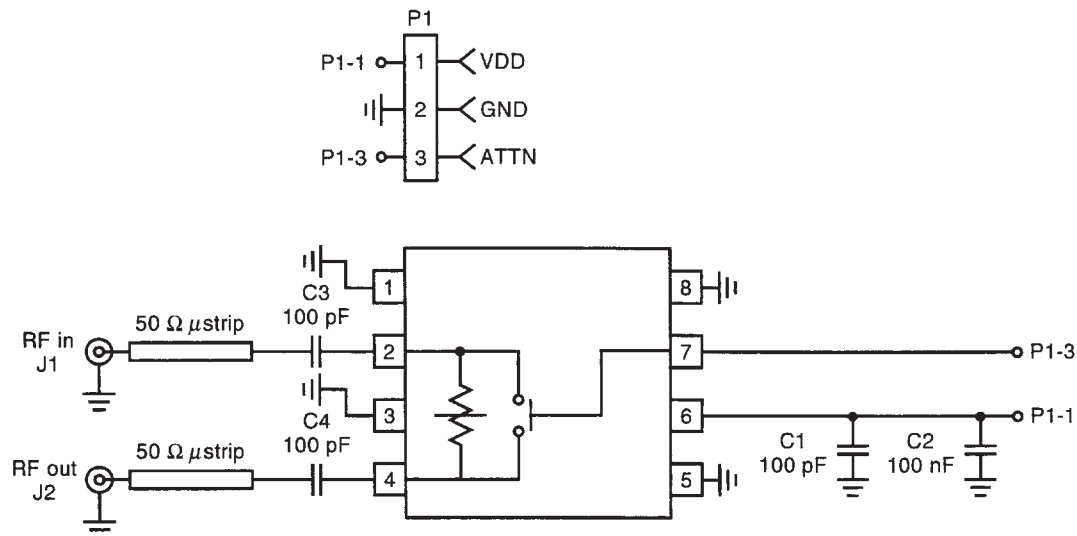


Figure 42. RF 2421 single-step 10-dB attenuator application.

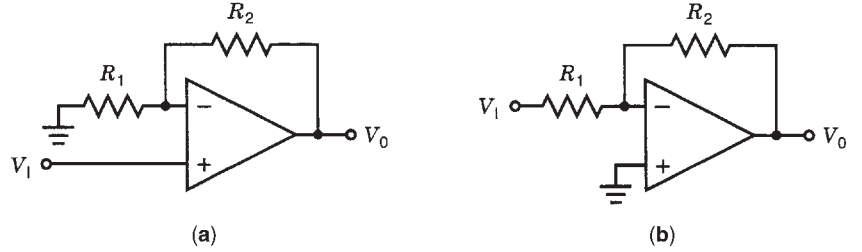


Figure 43. Op amp noninverting (a) and inverting (b) gain configuration.

Under this condition, the drain currents of the transistors are given by

$$I_{D1} = K' \frac{W_1}{2L_1} (V_{in} - V_{TON})^2 \tag{63}$$

$$I_{D2} = K' \frac{W_2}{2L_2} (V_B - V_{out} - V_{T2})^2 \tag{64}$$

where

$$V_{T2} = V_{TON} + \gamma(\sqrt{\phi + V_0} - \sqrt{\phi}) \tag{65}$$

Since the two drain currents are the same for the circuit, the DC transfer function relating V_{in} and V_{out} is found by equating Eqs. (63) and (64):

$$\begin{aligned} V_{out} + \gamma(\sqrt{\phi + V_{out}} - \sqrt{\phi}) \\ = -R_1 V_{in} + \{V_B + (R_1 - 1)V_{TON}\} \end{aligned} \tag{66}$$

where

$$R_1 = \sqrt{\frac{W_1/L_1}{W_2/L_2}} \tag{67}$$

If $\gamma = 0$ in Eq. (66), which corresponds to the case of circuit (b) in Fig. 47, where the substrate is separate, the DC transfer characteristic reduces to a linear equation:

$$V_{out} = \alpha V_I + \{V_B - (\alpha + 1)V_{TON}\} \tag{68}$$

In this case, the small-signal attenuator factor is

$$\alpha = -R_1 \tag{69}$$

which is precisely determined by the width/length ratios of the MOSFETs. From Eqs. (66) and (68), it is noted that the output DC operating voltage is controlled by V_B , independent of the attenuation factor.

The DC transfer characteristic between V_{in} and V_{out} calculated from Eq. (66) for the common substrate case, $R_1 = 0.1149$ and $V_B = 3.993$, and the DC transfer characteristics calculated from Eq. (68) for the separate substrate case, $R_1 = 0.1$ and $V_B = 3.449$ are shown in Fig. 50 for the range restricted by Eq. (62). The parameter values ($\gamma = 0.525 V^{1/2}$, $\phi = 0.6 V$, and $V_{TON1} = V_{TON2} = V_{TON} = 0.777 V$) were used in the calculation. The DC transfer function given by Eq. (66) for the common substrate case appears nonlinear, but the degradation from linearity due to practical values of γ is not significant. The small-signal attenuation factor α , the slope of transfer characteristic in Fig. 48, is -0.1 . The high degree of linearity supports the usefulness of both configurations in precision attenuator or finite-gain amplifier applications.

Figure 49 shows a finite-gain amplifier with attenuator II in the feedback loop of an op amp. Assuming that the op amp is ideal, we obtain

$$V'_{out} = \frac{1}{\alpha} V'_{in} \tag{70}$$

The transfer function of the amplifier is the inverse function of the transfer function of the attenuator in the feedback loop. The DC transfer function of the amplifier is given by Eq. (66) when V_{in} is replaced by V'_{out} and V_{out} is replaced by V'_{in} . If the substrate is separate, V_{in} replaces V'_{out} and V_{out} replaces V'_{in} in Eq. (68); then

$$V'_{out} = \frac{1}{\alpha} V'_I - \frac{1}{\alpha} \{V_B - (\alpha + 1)V_{TON}\} \tag{71}$$

where the small-signal attenuator factor $\alpha = -R_1$.

A summing attenuator is necessary to realize versatile multiple-input finite-gain amplifiers in integrated circuits. Figure 50 shows a two-input active linear inverting voltage summing attenuator that consists of two attenuators cascaded. For the summing attenuator, V_{BB} is used to control the output DC operating voltage, and input signals are designated as V_1 and V_2 .

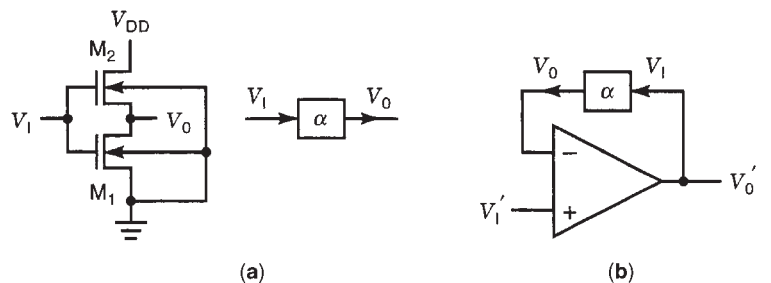


Figure 44. (a) Circuit and block diagram of attenuator I consisting of two n-channel MOSFETs, and (b) block diagram of amplifier consisting of an op amp and attenuator.

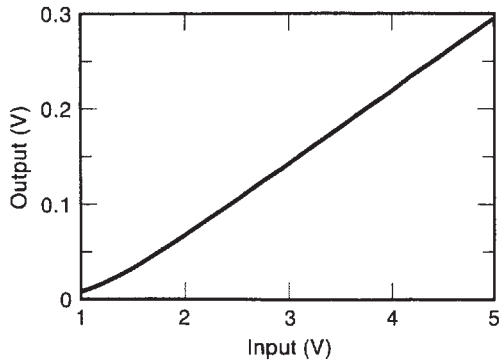


Figure 45. DC transfer characteristic of attenuator I ($\alpha = 0.07824$).

As for the inverting attenuator, the summing attenuator works when all the MOSFETs M1–M4 are operating in the saturation region. The DC transfer characteristics are found by equating the drain currents in the saturation region for each transistor. Assuming that the zero-bias threshold voltages for the four MOSFETs are matched at V_{TON} , the four transistors are in the saturation region, provided

$$2(V_{TON} + \gamma(\sqrt{\phi + V_{TON}} - \sqrt{\phi})) + V_{out} < V_{BB} < V_{DD} + V_{T4} \quad (72)$$

$$V_{TON} < V_1 < V_0 + V_{TON} \quad (73)$$

$$V_{TON} < V_2 < V_B + V_{TON} \quad (74)$$

By equating the drain currents of M3 and M4 given by

$$I_{D3} = K' \frac{W_4}{2L_3} (V_2 - V_{TON})^2 \quad (75)$$

and

$$I_{D4} = K' \frac{W_4}{2L_4} (V_{BB} - V_B - V_{T4})^2 \quad (76)$$

where

$$V_{T4} = V_{TON} + \gamma(\sqrt{\phi + V_0} - \sqrt{\phi}) \quad (77)$$

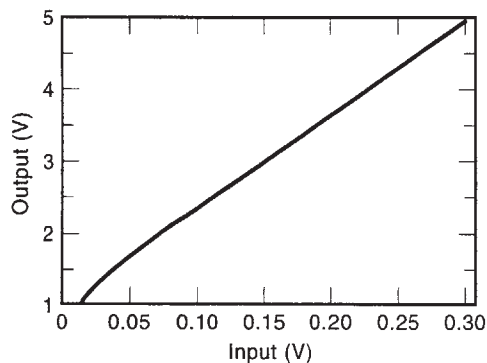


Figure 46. DC transfer characteristic of amplifier ($A_V = 1/\alpha = 12.78$).

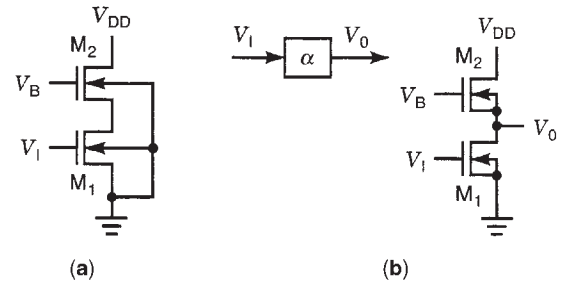


Figure 47. Circuit and block diagrams of linear inverting voltage attenuators consisting of two n-channel MOSFETs.

The DC transfer function between V_2 and V_B is obtained as

$$\begin{aligned} V_B + \gamma(\sqrt{\phi + V_B} - \sqrt{\phi}) \\ = -R_2 V_2 + \{V_{BB} + (R_2 - 1)V_{TON}\} \end{aligned} \quad (78)$$

where

$$R_2 = \sqrt{\frac{W_3 L_4}{L_3 W_4}} \quad (79)$$

Similarly, it can be shown that the DC transfer function between V_1 and V_0 is obtained as

$$\begin{aligned} V_0 + \gamma(\sqrt{\phi + V_0} - \sqrt{\phi}) \\ = -R_1 V_1 + \{V_B + (R_1 - 1)V_{TON}\} \end{aligned} \quad (80)$$

where

$$R_1 = \sqrt{\frac{W_1 L_2}{L_1 W_2}} \quad (81)$$

If $\gamma = 0$ in Eqs. (78) and (80), the equations become linear. This is realized if each transistor is fabricated in a separate substrate and the substrate of each transistor is connected to its source. In this case, the attenuation

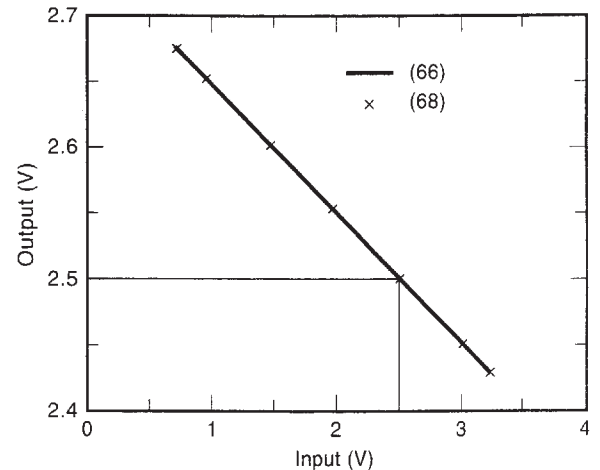


Figure 48. DC transfer characteristics of attenuator II linear inverting voltage attenuators.

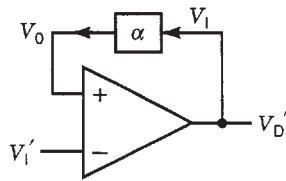


Figure 49. Amplifier consisting of op amp and attenuator II in the feedback loop.

factors are given by $\alpha_1 = -R_1$, and $\alpha_2 = -R_2$. Even when $\gamma \neq 0$, which is the case when the substrates are common, the transfer characteristics between V_1 and V_0 and between V_2 and V_0 are nearly linear as shown in Fig. 53 for practical values of γ . In the calculation of Fig. 51, $\gamma = 0.5255 \text{ V}^{1/2}$, $\phi = 0.6 \text{ V}$, and $V_{\text{TON}} = 0.777 \text{ V}$ were used, which are standard for a 2μ CMOS process and $R_1 = 0.1149$ and $R_2 = 0.1290$ were set such that the small-signal attenuation factors for V_1 and V_2 are both -0.1 . The operating points were set by $V_{\text{BB}} = 5.712 \text{ V}$ such that $V_{0\text{Q}} = 2.5 \text{ V}$ ($V_{\text{BQ}} = 3.993 \text{ V}$) when $V_{1\text{Q}} = V_{2\text{Q}} = 2.5 \text{ V}$.

Summing and subtracting amplifier configurations using the inverting attenuator and the inverting summing attenuator are shown in Fig. 52.

Circuit (a) in Fig. 52 functions as a summing amplifier and the circuit (b) functions as a subtracting amplifier, with controllable weights. Assuming ideal op amps and attenuators, we obtain

$$V_- = \alpha_1 V_1 + \alpha_2 V_2 + \{V_{\text{BB}} - (\alpha_1 + \alpha_2 + 2)V_{\text{TON}}\} \quad (82)$$

$$V_+ = \alpha V_0 + \{V_{\text{B}} - (\alpha + 1)V_{\text{TON}}\} \quad (83)$$

Equating V_- and V_+ , the output is given by

$$V_0 = \frac{\alpha_1}{\alpha} V_1 + \frac{\alpha_2}{\alpha} V_2 + \frac{1}{\alpha} \{V_{\text{BB}} - V_{\text{B}} - (\alpha_1 + \alpha_2 - \alpha + 1)V_{\text{TON}}\} \quad (84)$$

From Eq. (84), the circuit in Fig. 52a is a summing amplifier with a wide range of available gain from each

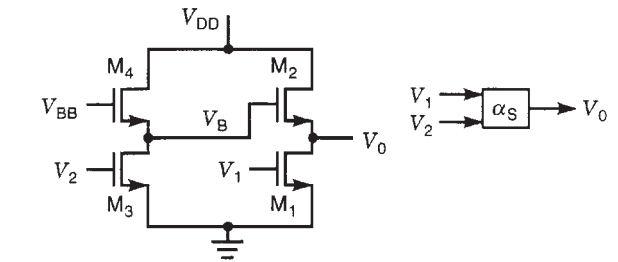
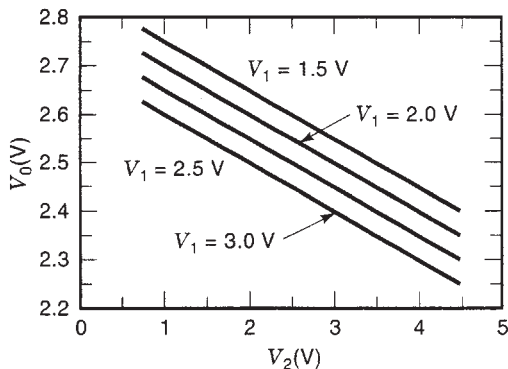


Figure 50. Circuit and block diagram of summing attenuator.

input. Similarly, for the circuit in Fig. 52b, we obtain

$$V_+ = \alpha_1 V_0 + \alpha_2 V_2 + \{V_{\text{BB}} - (\alpha_1 + \alpha_2 + 2)V_{\text{TON}}\} \quad (85)$$

$$V_- = \alpha V_1 + \{V_{\text{B}} - (\alpha + 1)V_{\text{TON}}\} \quad (86)$$

Equating V_+ and V_- , the output is given by

$$V_0 = \frac{\alpha}{\alpha_1} V_1 - \frac{\alpha_2}{\alpha_1} V_2 - \frac{1}{\alpha_1} \{V_{\text{BB}} - V_{\text{B}} - (\alpha_1 + \alpha_2 - \alpha + 1)V_{\text{TON}}\} \quad (87)$$

From Eq. (87), the circuit in Fig. 52b is a subtracting amplifier with a wide range of available gain for each input.

The active attenuator and the active summing attenuator have many desirable characteristics such as small size, nearly infinite impedance, low power dissipation, and precisely controllable attenuation ratio with excellent linearity. These attenuators and the finite-gain amplifiers obtained from these attenuators and op amps will find increased applications in analog integrated circuits.

8.6. Noise

Noise in a communication system can be classified in two broad categories, depending on its source. Noise generated by components within a communication system, such as resistive, extender, and solid-state active devices, comprise internal noise. The second category, external noise, results from sources outside a communication system, including atmospheric, manmade, and extraterrestrial sources.

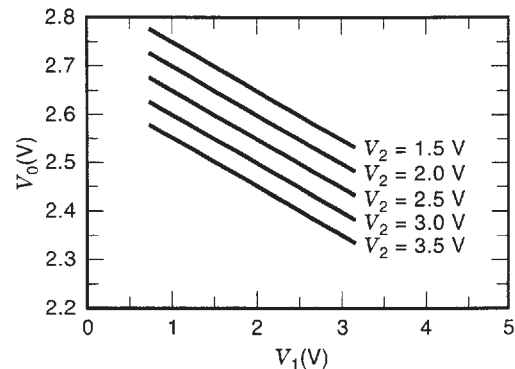


Figure 51. DC transfer characteristics of summing attenuator.

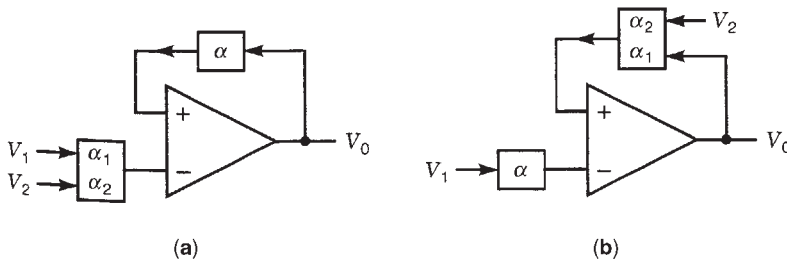


Figure 52. (a) Summing amplifier; (b) subtracting amplifier.

External noise results from the random motion of a charge carrier in electronic components. The three types are

1. Thermal noise: caused by random motion of free electrons in a conductor or semiconductor excited by thermal agitation
2. Shot noise: caused by random amount of discrete charge carriers in such devices as thermionic tubes or semiconductors in devices
3. Flicker noise: produced by semiconductors by a mechanism not well understood and is more severe the lower the frequency

Atmospheric noise results primarily from spurious radiowaves generated by the natural discharges within the atmosphere associated with thunderstorms. Manmade noise sources include high-voltage power-line discharge and computer-generated noise in electric motors.

Other noises include

- Generation–recombination noise: due to free carriers being generated and recombining in semiconductor material. They are random and can be treated as a shot noise process.
- Temperature fluctuation noise: the result of the fluctuating heat exchange between a small body, such as a transistor, and its environment due to the

fluctuations in the radiation and heat conduction processes.

9. RECENT TRENDS

Figure 53 shows a 4-dB step, 28-dB variable attenuator for a 1.9-GHz personal handy phone system transmitter fabricated using silicon bipolar technology with f_T of 15 GHz. The GaAs MESFET variable attenuator is configured with resistive pi attenuators and GaAs switches as shown. Step accuracy within 1.2 dB and total vector modulation error of less than 4% were realized for -15 dBm output. The attenuator consumes 21 mA with 2.7 V power supply and occupies 1.1×0.5 mm. This unit is being developed. This shows the technology trend.

Figure 54 shows the top view and cross section of a prototype optical microwave attenuator that can be

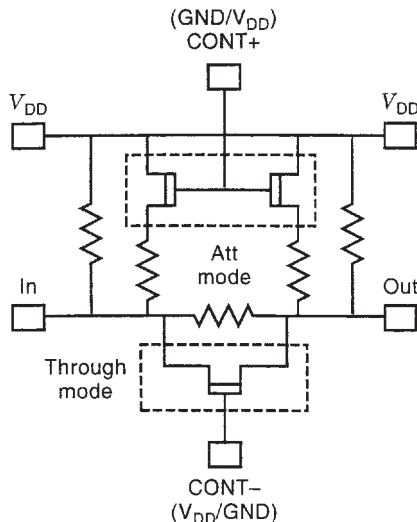


Figure 53. Variable attenuator using GaAs MESFET CONT+ / CONT- = VDD/GND in attenuation mode and CONT+ / CONT- = GND/VDD in through mode.

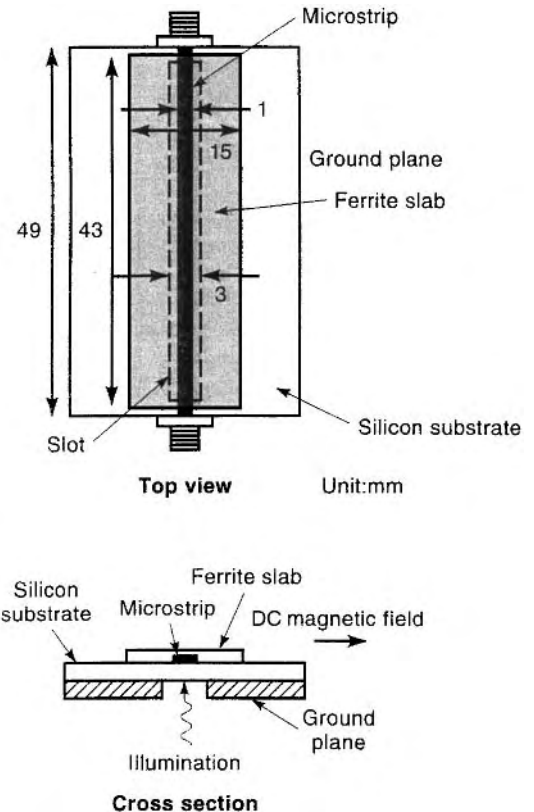


Figure 54. Microstrip–slotline attenuator on a silicon substrate with an override ferrite slab.

controlled by illuminating the silicon substrate. The maximum attenuation is 30 dB using laser diode illumination. It is a microstrip line whose substrate consists of silicon and ferrite slabs. The ferrite slab is overlaid on the microstrip. There is a slot on the ground plane under the strip. A white light from a xenon arc lamp with a parabolic mirror is focused by a lens to the silicon surface through the slot. The intensity of the light is not uniform along the slot direction. Due to the light, electron-hole pairs are induced and the permittivity and conductivity of the silicon are changed, which vary the phase and amplitude of the microwave. With 240 mW optical power illumination, an attenuation in the range of 17–26 dB was obtained in the frequency range from 8 to 12 GHz.

FURTHER READING

- F. G. Ananasso, A low phase shift step attenuator using PIN diode switches, *IEEE Trans. Microwave Theory Tech.* **MTT-28**(7) (July 1980).
- P. S. Bochert, *FET Attenuator, 0–1 GHz Applied Microwave and Wireless*, spring 1996.
- R. G. Brown et al., *Lines, Waves, and Antennas*, Ronald Press, New York, 1973.
- R. S. Elliot, *An Introduction to Guided Waves and Microwave Circuits*, Prentice-Hall, Englewood Cliffs, NJ, 1993.
- Engineering staff of the Microwave Division, *Microwave Theory and Measurements*, Hewlett-Packard Co., 1962.
- S. C. Harsany, *Principles of Microwave Technology*, Prentice-Hall, Englewood Cliffs, NJ, 1997.
- M. R. Haskard, *Thick Film Hybrids—Manufacture and Design*, Prentice-Hall, New York, 1988.
- Hewlett-Packard Application Note 1048, *A Low-Cost Surface Mount PIN Diode π Attenuator*, Hewlett Packard Co., 1996.
- Hewlett-Packard Application Note 922, *Applications of PIN Diodes*, Hewlett Packard Co., 1997.
- IEEE Std 474-1973, *Specifications and Test Methods for Fixed and Variable Attenuators, DC to 40 GHz*.
- T. Koryu Ishii, *Microwave Engineering*, Harcourt Brace Jovanovich, New York, 1989.
- J.-Y. Kim and R. L. Geiger, MOS active attenuators for analog ICS and their applications to finite gain amplifiers, *Proc. IEEE Int. Symp. Circuits and Systems*, 1994.
- J.-Y. Kim and R. L. Geiger, Performance Characterization of an active attenuator using two cascaded MOSFETS, *Proc. 36th Midwest Symp. Circuits and Systems*, 1993.
- J.-Y. Kim and R. L. Geiger, Characterization of linear MOS active attenuator and amplifier, *Electron. Lett.* **3**(7) (March 30, 1995).
- J.-Y. Kim and R. L. Geiger, An inverting MOS active attenuator for monolithic applications, *Proc. Midwest Electro-Technology Conf.* 1993.
- T. S. Laverghetta, *Practical Microwaves*, Prentice-Hall, Englewood Cliffs, NJ, 1996.
- R. LaVerne Libbey, *Video Attenuator Using a Multiplier and FET*, a publication of RCA, New Jersey, 1975.
- RF Microdevices, RF 2420 Programmable Attenuator Data Sheet, 1997.
- RF & Microwave Test Accessories Catalog, Hewlett-Packard, 1997/98.
- RF Microdevices Technical Application Note TA 0027, *Integrated, Single Step, 10 dB Attenuator for Power Control Applications*, 1997.
- RF Microdevices, RF 2421, *10 dB Switched Attenuator Data Sheet*, 1997.
- MIL-HDBK-216, military handbook, *R. F. Transmission Lines and Fittings*, Section 14, Attenuators, Nov. 1976.
- MIL-A-3933E, military specification, *Attenuators, Fixed, General Specification for 1985*.
- MIL-A-3933E, Suppl. 1, military specification, *Attenuators, Fixed, General Specification for 1985*.
- S. Otaka et al., A 1.9 GHz Si-bipolar variable attenuator for PHS transmitter, *IEEE J. Solid State Circuits* **32**(9):1424–1429 (Sept. 1997).
- Reference Data for Radio Engineers*, 1957, International Telephone and Telegraph Corp., New York.
- P. A. Rizzi, *Microwave Engineering—Passive Circuits*, Prentice-Hall, Englewood Cliffs, NJ, 1988.
- D. Roddy, *Microwave Technology*, Prentice-Hall, Englewood Cliffs, NJ, 1986.
- S. E. Sadow and C. H. Lee, Scattering parameter measurements on optoelectronic attenuator, *IEEE MIT-S Digest* (1994).
- H. W. Sams, *Reference Data for Radio Engineers*, 7th ed., 1985, Indianapolis, IN.
- G. E. Schafer and A. Y. Rumfelt, Mismatch errors in cascade-connected variable attenuators, *IRE Trans. Microwave Theory Tech.* (1959).
- H. Shimasaki, S. Matsuda, and M. Tsutsumi, Phase compensation in an optically controlled microwave attenuator, *IEEE MTT-S Digest* 1703–1706 (1997).
- V. A. Suprynovicz, *Electrical and Electronics Fundamentals—an Applied Survey of Electrical Engineering*, West Publishing, New York, 1987.
- V. F. Valey, *Modern Microwave Technology*, Prentice-Hall, Englewood Cliffs, NJ, 1987.
- A vector attenuator for feedforward amplifier and RF predistortion use, product features, *Microwave J.* (Oct. 1997).
- Weinschel Associates Catalogue, *Attenuators and Terminations*, 1998.
- R. E. Ziemer and W. H. Tranter, *Principles of Communications—Systems, Modulation, and Noise*, Wiley, New York, 1988.

BACKSCATTER

PYOTR YA. UFIMTSEV
 University of California at
 Irvine
 Irvine, California

The scattering of waves from an object is a diffraction process that transforms the incident wave into the waves propagating from the object in all possible directions. The *backscatter*, or *backscattering*, is the scattering of waves back toward the source of the incident wave. This process substantially depends on material properties of the scattering object, its shape, size, and spatial orientation relative to the incident wave, as well as on the frequency and polarization of the incident wave. One distinguishes three frequency regions with different physical properties of scattered waves. They are quasistatic, resonance, and quasioptical regions.

1. QUASISTATIC SCATTERING

In the quasistatic region (sometimes called the *Rayleigh region*), the wavelength λ of the incident wave is much greater than the maximum linear dimension l of the scattering object ($\lambda \gg l$). At a certain time t , the scattered field at small distances ($r \ll \lambda$) from the object is approximately the static field created by dipoles and multipoles induced by the incident wave in the scattering object at the same time t . Far from the object, the scattered field is an outgoing spherical wave. Its average power flux density (over one period of oscillations) relative to that of the incident wave, or radar cross section (RCS), is determined by the object's volume rather than the shape of the object, and it is proportional to λ^{-4} . Specifically, this dependence explains the blue color of the cloudless sky during the day. This color is due to the predominance of blue light scattered by small inhomogeneities of the air caused by fluctuations of its density. The violet light, which is shorter in wavelength, undergoes stronger relative scattering and as a result suffers higher attenuation while propagating through the atmosphere. Analytical expressions for quasistatic RCS of some scattering objects can be found in Refs. 1–3. For example, the axial RCS of perfectly conducting bodies of revolution is determined by the following approximation (p. 145 of Ref. 1)

$$\sigma \approx \frac{4}{\pi} k^4 V^2 \cdot \left(1 + \frac{e^{-\tau}}{\pi\tau}\right)^2 \quad (1)$$

where $k = 2\pi/\lambda$ is the wavenumber, V is the object's volume, and τ is the characteristic length-to-width ratio of the object. The quantity τ is found for each object's shape by the allowing the axial dimension of the object to

go to zero so as to obtain the correct result

$$\sigma = \frac{64}{9\pi} k^4 a^6 \quad (2)$$

for the circular disk with radius a . Table 8.2 in Ref. 2 (Vol. 2, pp. 558–561) contains explicit expressions for RCS found in this manner for a variety of bodies of revolution. The first term in this table (Eq. 8.1-87a on p. 558) contains a misprint. The letter b should be replaced by h .

In this frequency region, the scattered field can be expressed in terms of a convergent series in positive integer power of the wavenumber $k = 2\pi/\lambda$. The expansion coefficients are found from the solution of the recursive system of boundary value problems in potential theory (pp. 848–856 of Ref. 4). In practice it is possible to find only a few first coefficients. Direct numerical methods are efficient tools for the solution of quasistatic scattering problems [5–7].

2. RESONANCE SCATTERING

In the resonance frequency region, linear dimensions of scattering objects are comparable to the wavelength of the incident wave. Eigenoscillations excited by the incident wave in the scattering object can substantially influence the scattering properties. Frequencies of these oscillations are complex quantities. Their imaginary parts determine both the internal (thermal) losses inside the object and the external losses that are due to radiation into the surrounding medium. A major contribution to RCS is given by the radiation of those eigenoscillations, whose eigenfrequency real part and polarization are close to the incident wave frequency and polarization. If the quality factor of these oscillations is quite large, the amplitude and the intensity of the scattered wave sharply increase as the frequency of the incident wave approaches the real part of the frequency of eigenoscillations. This phenomenon is referred to as “resonance scattering.” It reveals itself, for example, in scatterings from thin metallic half-wavelength long wires and narrow strips (pp. 293–303 of Ref. 2). These scatterers are used, in particular, to create a chaff clutter for radars. Analytical and numerical data for scattering by thin wires are collected in Chap. 12 of Ref. 3. Recent analytical results for resistive wires are presented in Ref. 8.

The resonance scattering from wires can also be explained as being due to the constructive interference of multiple current waves arising from the wire ends. This process is investigated in detail in Refs. 9, 10, and 30. The total current generated by the incident plane wave in the perfectly conducting wire (Fig. 1) equals

$$J(z) = J_0(z) + \sum_{n=1}^{\infty} [J_n^+(z) + J_n^-(z)] \quad (3)$$

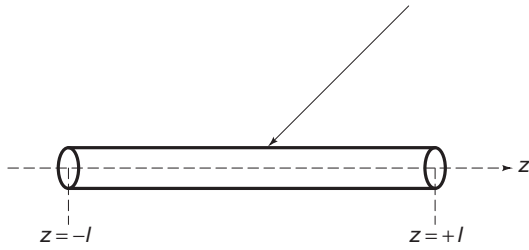


Figure 1. A thin wire excited by an incident wave. The radius of the wire is small compared with the wavelength. Such a wire can support traveling waves arising due to the multiple edge diffractions. A constructive interference of these waves results in the resonance behavior of the surface current and scattered field.

with the time dependence $\exp(-i\omega t)$ assumed and suppressed here and later. The term $J_0(z)$ is the current induced by the incident wave in the infinitely long wire ($-\infty \leq z \leq +\infty$). The terms $J_n^+(z)$ and $J_n^-(z)$ are multiple current waves. Waves $J_n^+(z)$ run in the positive z -direction from the left wire end $z = -l$ to the right end $z = +l$. Waves $J_n^-(z)$ run in the negative z direction from the right end $z = +l$ to the left end $z = -l$. The total length of the wire is $L = 2l$. When the wave $J_n^\pm(z)$ reaches the opposite end it undergoes diffraction and transforms into the wave $J_{n+1}^\mp(z)$. At the end points of the wire the total current and its components satisfy the conditions

$$J(\pm l) = 0, \quad J_1^+(-l) = -J_0(-l), \quad J_1^-(l) = -J_0(l) \quad (4)$$

$$J_{n+1}^+(-l) = -J_n^-(l), \quad J_{n+1}^-(l) = -J_n^+(l), \quad n = 1, 2, 3, \dots \quad (5)$$

In thin wires ($ka < 0.2$, a is the wire radius), the multiple current waves are described by the following approximate expressions

$$\begin{aligned} J_{2n}^+(z) &= -J_1^-(l) [\psi(kL) e^{ikL}]^{2n-2} \psi[k(l+z)] e^{ik(l+z)} \\ J_{2n+1}^+(z) &= J_1^+(l) [\psi(kL) e^{ikL}]^{2n-1} \psi[k(l+z)] e^{ik(l+z)} \\ J_{2n}^-(z) &= -J_1^+(l) [\psi(kL) e^{ikL}]^{2n-2} \psi[k(l-z)] e^{ik(l-z)} \\ J_{2n+1}^-(z) &= J_1^-(l) [\psi(kL) e^{ikL}]^{2n-1} \psi[k(l-z)] e^{ik(l-z)} \end{aligned} \quad (6)$$

with $n = 1, 2, 3, \dots$. Function $\psi(kz)$ is defined in Refs. 10 and 30 as

$$\psi(kz) = \frac{2 \ln \frac{i}{\gamma ka}}{\ln \frac{2ikz}{\gamma q} - E(2kz) e^{-2ikz}} \quad (7)$$

where

$$q = (ka)^2, \quad \gamma = 1.781 \dots, \quad \ln(i) = i\pi/2$$

and

$$E(x) = - \int_x^\infty \frac{e^{it}}{t} dt = \text{Ci}(x) + i\text{Si}(x) \quad (8)$$

Functions $\text{Ci}(x)$ and $\text{Si}(x)$ are the well-tabulated cosine and sine integrals, respectively. For small arguments ($x \ll 1$), function $E(x)$ reduces to $E(x) = \ln(\gamma x) - \ln(i) + O(x)$ and ensures the equality $\psi(0) = 1$. Equation (6) shows that all multiple edge waves starting with secondary waves ($n = 2, 3, 4, \dots$) are expressed approximately by the same function $\psi(x)$. As a result, the substitution of expressions (6) into Eq. (3) leads to the geometric series

$$\begin{aligned} \sum_{n=2}^{\infty} [J_n^+(z) + J_n^-(z)] &= f(k, z, l, a) \sum_{m=0}^{\infty} \{[\psi(kL) e^{ikL}]^2\}^m \\ &= \frac{f(k, z, l, a)}{D} \end{aligned} \quad (9)$$

which contains the resonance denominator $D(ka, kL) = 1 - [\psi(kL) e^{ikL}]^2$. The equation $D(ka, kL) = 0$ defines the complex resonant frequencies $\omega_{\text{res}} = ck_{\text{res}} = \omega'_{\text{res}} + i\omega''_{\text{res}}$, where c is the light velocity in vacuum. Due to the radiation loss, the quantity $\omega''_{\text{res}} = \text{Im}(\omega)$ is always negative ($\omega''_{\text{res}} < 0$). Therefore, for real frequencies ($\omega'' = 0$), the denominator $D(ka, kL)$ does not vanish. But it acquires minimum values when the frequency of the incident wave is close to the real part of the resonant, frequency ($\omega \approx \omega'_{\text{res}}$). This occurs when $kL \approx n\pi$ or $L \approx n\lambda/2$ with $n = 1, 2, 3, \dots$ and results in the current resonance. Under the normal incidence (the direction of the incident wave is

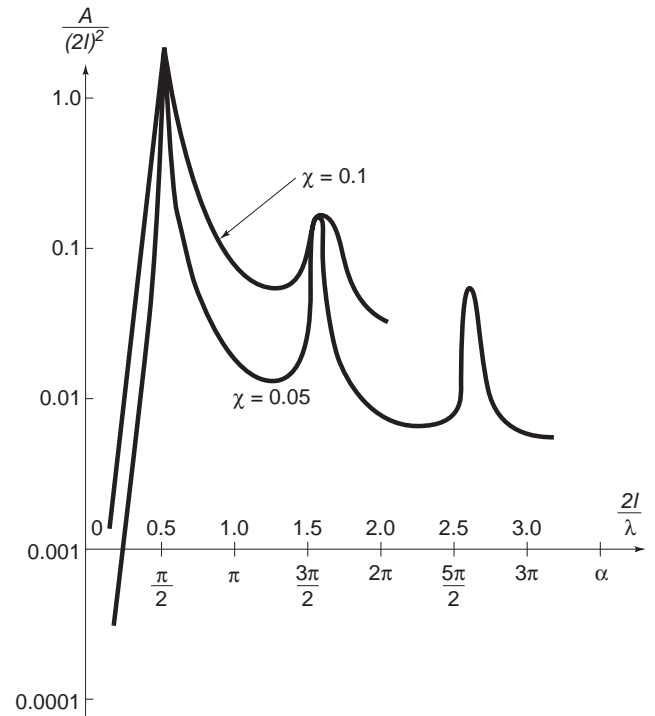


Figure 2. Integral cross section of thin wires (from Ref. 11). This quantity has the maximum (resonance) values for wires with the total length $L = 2l \approx (2n + 1)\lambda/2$, $n = 0, 1, 2, 3, \dots$. Along such wires from one end to another, each multiple edge wave acquires the phase shift of $(2n + 1)\pi$. Due to reflection at the end, it acquires an additional phase shift of π . As a result, this wave becomes equiphased with all other multiple edge waves. This leads to the resonance behavior for the current and scattered field.

perpendicular to the wire axis), only the odd resonances ($n=1,3,5,\dots$) are realized, due to the symmetry of the incident field [$E_z^{\text{inc}}(-z)=E_z^{\text{inc}}(z)$]. Figure 2, taken from a classic paper [11], illustrates the resonance behavior of scattering from thin wires. The incident wave direction is perpendicular to the wire axis. The quantity A in Fig. 2 is the total power of the field scattered in all directions. The maximum scattering occurs in the directions perpendicular to the wire and therefore in the backscattering direction as well. In Fig. 2, the quantity $\chi = 1/[2|\ln(ka)|]$ depends on the wire radius a , $2l=L$ is the wire length, and $a=kl$.

A similar interference of a specular reflection with surface diffracted rays (Fig. 3) explains the backscattering from perfectly conducting spheres and prolate spheroids at the upper end of the resonance region (p. 149 of Ref. 2 and pp. 822–848 of Ref. 4). However, an important difference exists between the resonances in scattering from wires and spheres. The resonance backscattering from wires is caused by the current resonance in the wires and it is accompanied by a simultaneous increase of the scattered field in other directions. This is a true resonance effect. The resonance scattering from spheres and spheroids is a simple equiphase interference in the single (backward) direction without the field increase in other directions. Additional data for the resonance backscattering can be found in Ref. 4 (pp. 822–848). As in the case of quasistatic scattering, direct numerical methods are also efficient for RCS calculations in the resonance frequency region [5–7].

3. QUASIOPTICAL SCATTERING

In the quasioptical frequency region, which is often referred to as the *high-frequency region*, linear dimensions of scatterers are much greater than the wavelength of the incident wave. For example, this occurs in the scattering of decimeter and centimeter radar waves by such objects as ships, airplanes, and missiles. In contrast to the quasistatic and resonance frequency regions, the scatterings by objects in the quasioptical region are determined mainly by the objects' local properties rather than by their whole volume.

Large dimensions and complex shapes of scattering objects allow the existence of various types of scattered fields. Some of them are illustrated in Fig. 4. Geometric

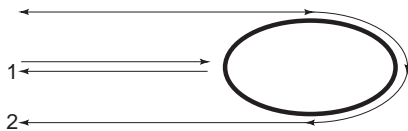


Figure 3. Backscattering from a body of revolution. The total scattered field consists of two components. One of them is a specular reflected ray (1); the other is a beam of diffracted rays (2) radiated by creeping waves traveling along the shadow side of the scattering body. The equiphase interference of these two components results in the resonance like increase of the scattered field.

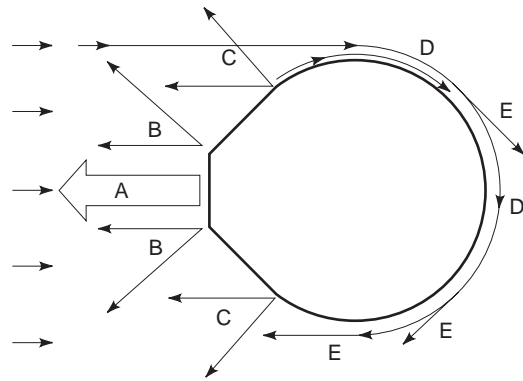


Figure 4. Backscattering from a convex opaque object. The main contributor to the scattered field is beam A reflected from the front planar facet of the object. Edge waves B are created at the edges. Edge waves C are created at the curvature discontinuities. At the shadow boundary, the incident wave excites creeping waves D , which propagate along the object's surface and radiate surface diffracted rays E . Additional creeping waves are excited at the curvature discontinuities.

optics rays and beams (A) reflected from the object provide the main contributions to backscattering. Diffraction of the incident wave at edges and at lines of curvature discontinuity or material discontinuity creates edge waves (B and C), which can be interpreted as diffracted rays. They represent the second-order contributions [12–15]. Diffracted waves arising from corners provide the third-order contributions [12–14]. At the shadow boundary on a smooth scattering surface, the incident wave excites creeping waves (D), which propagate along the shadow side of the object and radiate surface diffracted rays (E). Due to continuous radiation of these rays, the creeping waves attenuate exponentially and for this reason the contribution of surface diffracted rays (E) to backscattering is small [12,13]. However, for the objects with dimensions comparable to the wavelength, surface diffracted rays can give appreciable contributions, as it is mentioned already in the previous section (see also Fig. 3). Diffracted waves propagating along the scattering object can undergo multiple diffractions at geometric and material discontinuities and can transform into other types of waves. This process creates high-order contributions to backscattering [12–15]. A visual description of scattering from large objects, simple quantitative estimations of some contributions to backscattering, and relevant references are presented in Ref. 16.

High-frequency asymptotic methods are widely used to predict scatterings in this frequency region. They include geometric optics (GO) and its extension, geometric theory of diffraction (GTD); physical optics (PO) and its extension, physical theory of diffraction (PTD); and various modifications and extensions of GTD and PTD. These asymptotic techniques are discussed in ELECTROMAGNETIC WAVE SCATTERING and RADAR CROSS SECTIONS. The present article supplements these and concentrates mainly on the physical optics. This method is not so precise as GTD, PTD, and their extensions, but it allows useful estimations for the scattered fields in many practical problems that cannot be treated with other techniques.

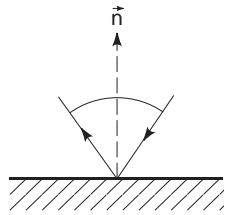


Figure 5. Reflection from a planar surface. The reflected ray lies in the plane that contains the incident ray and the unit normal vector \mathbf{n} to the reflecting surface.

Direct numerical methods, in their classical forms, are not efficient in the high-frequency region. Various combinations of these methods with the asymptotic techniques (so-called hybrid methods) represent a promising direction in the prediction of high-frequency scattering [17]. Additional information about numerical, hybrid, and asymptotic techniques used for the solution of scattering problems can be found in Ref. 6,13, and 18 and in the Further Reading list at the end of this article.

3.1. Geometric Optics Approximation

GO is used for approximate estimations of backscattering in many practical problems. The basic notion of GO involves the concept of rays. A ray is an infinitely narrow stream of the wave field moving with the light velocity along the lines perpendicular to the phase fronts. These lines are called *ray trajectories*. In free space they are straight lines. Electric and magnetic vectors of the ray field are perpendicular to each other and to the direction of propagation. GO reflected rays obey simple rules [19,20]: (1) the reflected ray lies in the incidence plane which contains the incident ray and the normal to the scattering surface at the reflection point (Fig. 5), (2) the angle of reflection equals the angle of incidence (Snell’s reflection law), and (3) the power inside an elementary hypothetical tube confined by neighboring rays is constant.

GO is a good approximation for the field reflected from large smooth scattering objects. It provides the leading term in the exact high-frequency asymptotic expansion of the reflected field. The reflection coefficient is found from

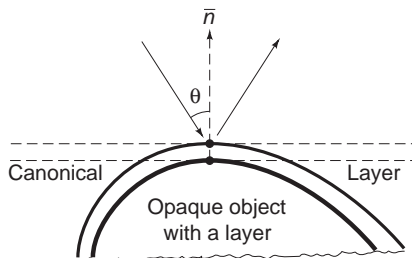


Figure 6. A scattered field at the reflection point on a coated scattering object is equal asymptotically (with $kR_{1,2} \rightarrow \infty$) to the field that would be reflected from a tangential layer with the same material properties. Due to losses, the contributions of rays and waves propagating along the object (inside the coating) become small and can be neglected.

the solution of an appropriate canonical problem. For opaque homogeneous objects, this is the Fresnel reflection coefficient, which determines the amplitude and phase of plane waves reflected from a planar boundary of a semi-infinite homogeneous medium [2, pp. 474–479]. For opaque objects coated with thin layers, the canonical problem is the reflection of plane waves from an infinite planar layer. This canonical layer is tangential to the scattering object (Fig. 6). It is homogeneous in the directions parallel to its surface and has the same material structure in depth as a real layer at the reflection point T . The canonical layer is placed on the planar boundary of a homogeneous medium with the same material properties as a real object at the tangency point. This implies that the field on a real coated object is determined exclusively by its local properties in the vicinity of the reflection point. Nonlocal contributions from various waves propagating along the object are not treated with this approach. Creeping and traveling waves [2, pp. 120 and 130] are examples of such waves.

According to this GO approach, the backscattering RCS of smooth coated objects equals

$$\sigma = |\mathbf{r}(0)|^2 \cdot \pi R_1 R_2 \text{ (m}^2\text{)} \tag{10}$$

where $r(0)$ is the reflection coefficient for the normal incidence ($\theta = 0$) and R_1, R_2 are principal radii of the curvature of the scattering surface at the reflection point T . In the case of isotropic objects and coatings, the reflection coefficient $r(0)$ does not depend on the incident wave polarization. Equation (10) is not valid for objects with planar faces when $R_1 = R_2 = \infty$. It also fails for objects that contain ruled elements (cylindrical, conical) with a rectilinear generatrix whose radius of curvature is infinite. In this case, the rays reflected by the object form the so-called reflected beams, which undergo the transverse diffusion while propagating from the object and for this reason lose their geometrical optics structure in the far zone.

3.2. Physical Optics Approximation

This method goes back to Macdonald [21] and is based on three concepts: GO, canonical planar layer, and equivalency principle.

The first step in the physical optics (PO) approximation is to use GO for the description of fields right on the scattering surface where GO approximation is still valid. The second step is to calculate the scattered field outside the object using the equivalency principle described in the following. Tangential components ($\mathbf{n} \times \mathbf{E}, \mathbf{n} \times \mathbf{H}$) of electric and magnetic vectors of the total field on the scattering surface (with the external unit normal \mathbf{n}) can be interpreted as equivalent magnetic and electric currents

$$\begin{aligned} \mathbf{j}_m &= -\mathbf{n} \times \mathbf{E} \text{ (V/m)} \\ \mathbf{j}_e &= \mathbf{n} \times \mathbf{H} \text{ (A/m)} \end{aligned} \tag{11}$$

In the PO approach, the equivalent currents are defined in the GO approximation. The total electromagnetic field on the scattering object is considered approximately as the

sum of the GO incident and reflected waves ($\mathbf{E}^{\text{GO}} = \mathbf{E}^{\text{inc}} + \mathbf{E}^{\text{ref}}$, $\mathbf{H}^{\text{GO}} = \mathbf{H}^{\text{inc}} + \mathbf{H}^{\text{ref}}$). Thus, the PO surface currents are defined as

$$\begin{aligned} \mathbf{j}_e^{\text{PO}} &= \mathbf{n} \times \mathbf{H}^{\text{GO}} \\ \mathbf{j}_m^{\text{PO}} &= -\mathbf{n} \times \mathbf{E}^{\text{GO}} \end{aligned} \quad (12)$$

This equation defines equivalent currents only on the illuminated side of the opaque scattering object. On the shadow side, these currents are assumed to be zero. In the particular case of perfectly conducting objects, the magnetic current does not exist ($\mathbf{j}_m^{\text{PO}} = \mathbf{0}$) due to the boundary condition $\mathbf{n} \times \mathbf{E} = \mathbf{0}$, and the electric current equals $\mathbf{j}_e^{\text{PO}} = 2\mathbf{n} \times \mathbf{H}^{\text{inc}}$ according to the GO approximation.

The scattered field is found by the integration of equivalent currents over the scattering surface S . Geometry of a sample scattering problem is shown in Fig. 7, where the quantity r is the distance between the integration (ρ, θ, ϕ) and observation (R, ϑ, φ) points. In the far zone ($R > k\rho_{\text{max}}^2$), the scattered field determined as

$$E_{\vartheta} = Z_0 H_{\phi} = ik(Z_0 A_{\vartheta}^e + A_{\vartheta}^m) \quad (13)$$

$$E_{\phi} = -Z_0 H_{\vartheta} = ik(Z_0 A_{\phi}^e - A_{\phi}^m)$$

$$\mathbf{A}^{e,m} = \frac{1}{4\pi R} \int_S \mathbf{j}_{e,m} e^{-ik\rho \cos \Omega} dS \quad (14)$$

$$\cos \Omega = \cos \vartheta \cos \theta + \sin \vartheta \sin \theta \cos(\varphi - \phi) \quad (15)$$

Here, $E_{\vartheta, \phi}$ is the electric field intensity (V/m), $H_{\vartheta, \phi}$ is the magnetic field intensity (A/m); \mathbf{A}^e is the electric potential vector (A), \mathbf{A}^m is the magnetic potential vector (V), and $Z_0 = \sqrt{\mu_0/\epsilon_0} \cong 377 \text{ } (\Omega)$ is the impedance of vacuum.

The PO approximation for the scattered field follows from Eqs. (13) and (14) when the PO approximation given by Eq. (12) is used for equivalent surface currents and the integration region is restricted to the illuminated part of the scattering surface. The line Γ shown in Fig. 7 is the boundary between the illuminated and shadow sides of the scattering surface S . The PO approach is usually

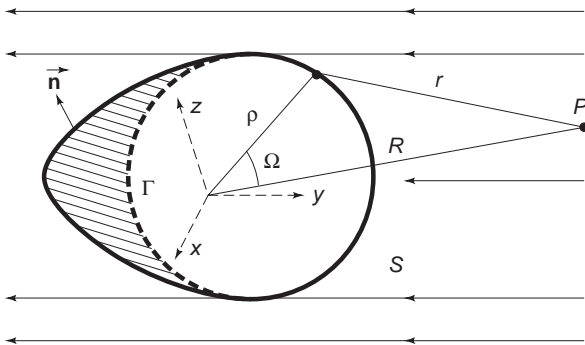


Figure 7. Schematics of a scattering problem: S is the surface of the scattering object; the dashed part of this surface (with the boundary Γ) is located in the shadow region which is hidden from the incident rays.

applied to large convex objects. However, it is also applicable to concave objects when the multiple GO reflections are taken into account.

3.2.1. Accuracy of PO. Approximate estimations for the PO scattered field [Eq. (13)] can be found by the application of asymptotic techniques to the integrals [Eq. (14)] with the PO currents [Eq. (12)]. The first term of the asymptotic expansion found in this way is correct for the fields scattered by smooth convex objects and planar plates in the specular directions predicted by GO. All higher-order terms in the PO asymptotic expansion are incorrect. Only two exceptions exist when PO provides the exact solution. The first is the scattering from the infinite perfectly conducting plane. The second is the scattering from the semiinfinite perfectly conducting paraboloid of revolution illuminated by the plane wave incident along the symmetry axis (22). In the latter case, the scattered field consists of only the GO reflected rays. Reference 22 also shows that PO provides the correct second term in the high-frequency asymptotic expansion for the specular backscattering from any convex perfectly conducting bodies of revolution when the incident wave propagates in the direction parallel to the symmetry axis.

The first term of the PO asymptotic expansion for the field scattered by smooth convex objects in specular directions represents the GO reflected rays [2, pp. 50–62]. Therefore, for such objects the PO value of RCS in specular directions is asymptotically (with $k \rightarrow \infty$) equivalent to the GO estimation. However, it is well known that GO is valid only away from the forward direction, i.e., from the shadow boundary of the incident rays. But PO is more general than GO and is applicable in the vicinity of this direction. All known results show that the first term of the PO asymptotic expansion for the field scattered in the forward direction is correct and leads to the following RCS for large opaque objects:

$$\sigma = 4\pi \frac{A^2}{\lambda^2} \text{ (m}^2\text{)} \quad (16)$$

Here, the quantity A is the area of the scattering object projection on the plane perpendicular to the direction of the incident wave propagation.

Reference 23 contains similar PO estimations for thin semitransparent plates. The field on the plate surface is defined by complex reflection and transmission coefficients which depend on the incidence angle (γ) and polarization of the incident wave. The incident wave with an arbitrary linear polarization can be decomposed into two independent waves with orthogonal polarizations. A decomposition is chosen such that either the electric or magnetic vector of the incident wave is parallel to the plate. In the first case, denote the reflection and transmission coefficients for the electric vector as $r_e(\gamma)$ and $t_e(\gamma)$, respectively. Similar coefficients, $r_h(\gamma)$ and $t_h(\gamma)$, for the magnetic vector describe the plate when the magnetic vector of the incident wave is parallel to the plate. Reference 2 (pp. 479–499) contains instructions for the calculation of these coefficients. Two directions of scattering are of

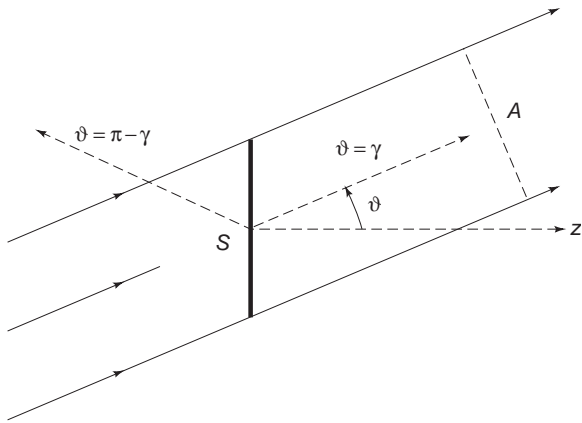


Figure 8. Directions of the forward ($\vartheta = \gamma$) and specular ($\vartheta = \pi - \gamma$) scattering from the plate S . The dashed line A denotes the projection of the plate S .

greatest interest. The first is the direction of specular reflection, $\vartheta = \pi - \gamma$, and the second is the forward direction, $\vartheta = \gamma$ (Fig. 8). According to (23), the PO approximations of RCS in the specular direction are given by

$$\sigma_e(\pi - \gamma) = 4\pi \frac{A^2}{\lambda^2} |r_e(\gamma)|^2 \tag{17}$$

$$\sigma_h(\pi - \gamma) = 4\pi \frac{A^2}{\lambda^2} |r_h(\gamma)|^2$$

and in the forward direction by

$$\sigma_e(\gamma) = 4\pi \frac{A^2}{\lambda^2} |1 - t_e(\gamma)|^2 \tag{18}$$

$$\sigma_h(\gamma) = 4\pi \frac{A^2}{\lambda^2} |1 - t_h(\gamma)|^2$$

where the quantity A is the same as in Eq. (16). This is the area of the plate projected on the plane perpendicular to the direction of the incident wave. Equations (17) and (18) are applicable for planar plates of an arbitrary shape under the condition $A \gg \lambda^2$. This means that the grazing angles ($\gamma \approx \pi/2$) cannot be treated with these equations.

Known results for perfectly conducting plates ($|r_{e,h}(\gamma)| = 1, |t_{e,h}(\gamma)| = 0$) show that PO estimations given in Eqs. (17) and (18) are correct. These equations also give the correct result, $\sigma_h(\pi/2) = 0$, for perfectly conducting plates under the grazing incidence. In this case, the incident wave does not undergo diffraction because its electric vector is perpendicular to the plate surface. PO describes satisfactorily the field scattered from large conducting plates not only in the specular and forward directions corresponding to mainlobes in the directivity pattern, but also in the directions of neighboring sidelobes. However, PO fails to predict a field level in minimums of the directivity pattern (Figs. 7–19 and 7–20 on p. 509 of Ref. 2) and does not satisfy the reciprocity principle.

The PO currents given by Eq. (12) are discontinuous on the shadow boundary of a scattering surface. The PO field

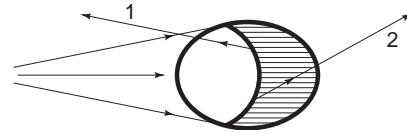


Figure 9. The PO current given by Eq. (12) is discontinuous at the shadow boundary of the scattering surface. This leads to spurious waves (1 and 2) in the case of a smooth scattering surface.

contains spurious waves from such a boundary in the case of smooth scattering surfaces (Fig. 9). A similar current discontinuity on scattering objects with edges results in edge waves. If the scattering edge is visible from the observation point, such an edge wave does exist. The PO edge waves coming from invisible edges are spurious shooting-through waves (Fig. 10). Such shooting-through waves do not occur in the backscattering direction. All PO spurious waves can be removed by neglecting the corresponding terms in the asymptotic expansion of the integral in Eq. (14). For real edge waves, even the first-order term of their PO asymptotic expansion is incorrect. This defect is remedied in PTD by the inclusion of the field radiated by the so-called nonuniform currents arising from the diffraction of the incident wave at edges [14,15,30].

One should emphasize a special role of PO in PTD. PO is a constitutive part of PTD. Therefore, the PO's first- and higher-order asymptotic terms are integral parts of the PTD asymptotic expansions for the total scattered field. For example, the terms with coefficients $(3d/16a)$ in the PTD equations (99) and (100) of (15) are exactly the PO's second-order terms in the asymptotic expansion of the field scattered by a perfectly conducting cylinder of finite length.

3.2.2. Polarization of the PO Scattered Field. In general cases, components E_ϑ and E_ϕ in Eq. (13) have different amplitudes and phases. This results in the elliptic polarization of the scattered field even in the case when the incident wave is linearly polarized. This means that the electric vector of the scattered field rotates with the angular frequency $\omega = k \cdot c$ and its endpoint traces an ellipse. The direction of rotation (clockwise or

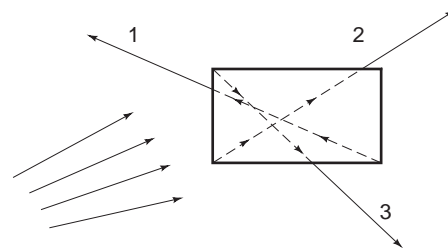


Figure 10. A scattered field is generated by the induced surface currents. Any approximations for these currents can result in the appearance of nonphysical components in the scattered field. In particular, the PO currents create spurious shooting-through edge waves (1, 2, and 3) passing through an opaque object.

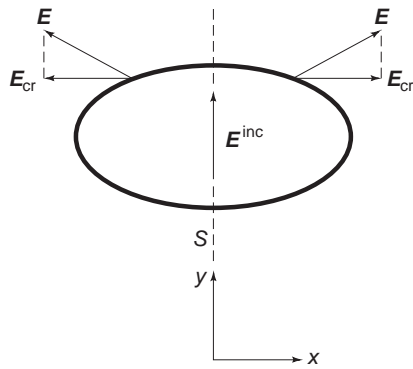


Figure 11. Backscattering without depolarization from a symmetric perfectly conducting surface S . The incident wave direction is parallel to the symmetry plane y - z . Vectors E_{cr} are the cross-polarized components of the reflected field. Due to the symmetry, they cancel each other.

counterclockwise) is determined by the phase shift between components E_β and E_ϕ . The lengths of the elliptical axes are determined by the amplitudes of these components. Due to diffraction, the scattered field can contain an electric field component perpendicular to the incident wave polarization. This phenomenon is known as *depolarization*, or *cross-polarization*.

The PO field scattered by arbitrary perfectly conducting objects in the backscattering direction does not contain the cross-polarized component [2, p. 56]. It is assumed only that no multiple GO reflections occur on the object's surface. This PO result is correct for scattering objects with certain symmetry. These are objects with a symmetry plane parallel to both the electric (or magnetic) vector of the incident wave and the direction of its propagation. Each element of such a scattering object may create the cross-polarized component. But because of the symmetry, the cross-polarized components from symmetric elements cancel each other in the backscattering direction (Fig. 11). A convex smooth body of revolution whose symmetry axis is parallel to the incident wave direction is a simple example of such an object. A symmetric plate, illuminated by the plane wave whose electric (or magnetic) vector and direction of propagation are parallel to the symmetry plane, is another example where the backscattered field does not contain a cross-polarized component (Fig. 12).

As stated previously, the first term of the PO high-frequency asymptotic expansion represents the GO reflected ray. This ray contains the cross-polarized component when the electric vector of the incident ray makes any angle different from 0° and 90° with the incidence plane at the reflection point. This is the case when PO correctly describes depolarization of the scattered field in the high-frequency asymptotic limit ($k \rightarrow \infty$). However, PO fails to predict all depolarization effects caused by the diffraction part of equivalent surface currents.

3.2.3. Bistatic RCS. Bistatic RCS determines the power flux density of electromagnetic waves scattered by the object in an arbitrary direction. The angle between the directions to the transmitter and receiver is called

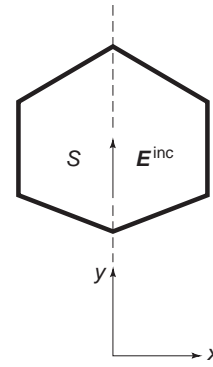


Figure 12. Backscattering without depolarization from a perfectly conducting plate S . The incident wave direction is parallel to the symmetry plane y - z . Cross-polarized components scattered by the left and right parts of the plate are symmetric and completely cancel each other.

the *bistatic angle*. Monostatic, or backscattering, RCS is a particular case of bistatic RCS when the bistatic angle equals zero. Some PO results for bistatic RCS have already been discussed. This section addresses the interrelationships between bistatic and monostatic RCS.

Using PO, one can prove the following statement:

For perfectly conducting bodies which are sufficiently smooth, in the limit of vanishing wavelength, the bistatic cross section is equal to the monostatic cross section at the bisector of the bistatic angle between the direction to the transmitter and receiver. [1, pp. 157–160; 2, p. 11]

There is a simple physical explanation for this result. As already stated, the first term of the PO asymptotic expansion for the field scattered by smooth objects exactly equals the GO expression for the reflected rays. The monostatic RCS caused by these rays is given by Eq. (10). In the case of perfectly conducting objects, this equation reduces to

$$\sigma = \pi R_1 R_2 \quad (19)$$

It should be noted that this equation is valid also for the bistatic RCS, which therefore *does not depend on the bistatic angle* $\beta = 2\vartheta$ (Figs. 5 and 6). This follows directly from Eqs. (5.32), (6.19), and (6.20), given by Fock [19, Chap. 8]:

$$\begin{aligned} \mathbf{E}(r) &= \frac{1}{2} \mathbf{E}(0) \sqrt{R_1 R_2} \frac{e^{iks}}{s} \\ \mathbf{H}(r) &= \frac{1}{2} \mathbf{H}(0) \sqrt{R_1 R_2} \frac{e^{iks}}{s} \end{aligned} \quad (20)$$

These expressions describe the field reflected by smooth convex objects at a far distance ($s \gg R_{1,2}$) from the reflection point for *any incidence angle* ($0 \leq \vartheta < \pi/2$). In the case of reflection from concave surfaces, the reflected field acquires the additional phase shift of $(-\pi/2)$ in passing through a focus of reflected rays. Vectors $\mathbf{E}(0)$ and $\mathbf{H}(0)$

denote the reflected field at the reflection point. Expressions (20) clearly show that the GO reflected field really does not depend on the incidence angle. As a result, the bistatic RCS does not depend on the bistatic angle and is the same as the monostatic RCS at the bisector direction that is perpendicular to the scattering surface at the reflection point. Thus, the cited equivalence between the bistatic and monostatic RCS is a pure GO effect and is fulfilled asymptotically (with $k \rightarrow \infty$) only in the ray region, away from the shadow boundary behind the scattering object. It is also clear that this equivalence is not valid when the scattered field contains multiple reflected rays arising from concave parts of the scattering surface. Reference 1 (pp. 160–183) presents additional results for bistatic RCS of some typical objects found using PO and other approximations.

In the case of coated smooth objects, Eq. (20) leads to the bistatic RCS

$$\sigma(\vartheta) = |r_{e,h}(\vartheta)|^2 \pi R_1 R_2 \tag{21}$$

where the reflection coefficients $r_{e,h}(\vartheta)$ depend on the polarization and direction of the incident wave. Therefore, the asymptotic equivalence between bistatic and monostatic RCS can be valid only for those bistatic angles where $|r_{e,h}(\vartheta)| = |r_{e,h}(0)|$.

This discussion relates to the situation where the bistatic scattered field is produced by a single scattering source (the reflection point). The field scattered by complex objects can have many sources (scattering centers) on the object’s surface. Figure 13 illustrates the bistatic scattering from the center located at the point (x_n, y_n, z_n) . The origin of Cartesian coordinates is somewhere inside the scattering object. The z axis is directed along the bisector of the bistatic angle β . In the far zone, the bistatic scattered field can be represented as the sum of partial contributions from all scattering centers [4, pp. 983–988]:

$$\mathbf{u}(\beta) = \frac{e^{ikR}}{R} \sum_n \mathbf{v}_n e^{-2ikz_n \cos(\beta/2)} \tag{22}$$

Here, \mathbf{u} is either the electric or magnetic vector of the total scattered field; R is the distance from the origin to the observation point. Vector \mathbf{v}_n determines the amplitude and

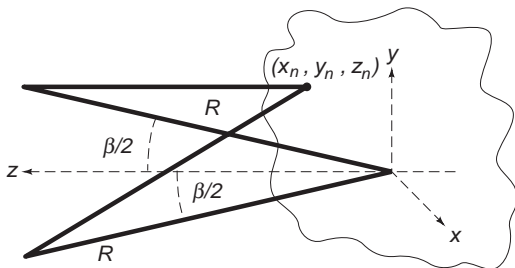


Figure 13. Geometry of the bistatic scattering problem. A solid winding line represents a scattering object with many scattering centers (x_n, y_n, z_n) . The scattering direction forms the angle β with the direction of the incident wave.

polarization of the wave generated by the n th scattering center. Suppose that vectors \mathbf{v}_n and the number of scattering centers are constant inside the $0 \leq \beta \leq \beta_{\max}$. Assume also that coordinates z_n of scattering centers do not depend on the bistatic angle β , while coordinates x_n and y_n can be functions of this angle. Under these conditions, the monostatic field scattered in the bisector direction equals

$$\mathbf{u}(0) = \frac{e^{ikR}}{R} \sum_n \mathbf{v}_n e^{-2ikz_n} \tag{23}$$

Comparisons of Eqs. (22) and (23) show that the bistatic RCS, $\sigma(\beta, k)$, at the frequency $\omega = c \cdot k$ will be equal to the monostatic RCS, $\sigma[0, k \cos(\beta/2)]$, at the frequency $\omega = c \cdot k \cdot \cos(\beta/2)$. This equality requires the additional assumption that each vector \mathbf{v}_n is constant in the frequency band $[c \cdot k \cos(\beta/2) \leq \omega \leq c \cdot k]$. The derivation, some applications, and restrictions of this equivalence relation are presented in Ref. 4 (pp. 983–988). In particular, this reference notes that this equivalence is not true for the bistatic scattering from spheres when the bistatic angle exceeds one degree and the sphere radius is less than 6λ . Before applying this equivalence in practice, we must first check carefully that all assumptions made in this scattering model are really fulfilled. One can expect that this approximate model can be reasonable only for small bistatic angles.

3.2.4. PTD as an Extension of PO. PTD is a natural extension of PO [14,15,24,30]. In PTD, the PO current given by Eq. (12) is considered as the uniform component (j^0) of the total surface current and is supplemented by the additional, nonuniform component (j^1). In contrast to the PO current that has the GO origin, the nonuniform current is caused by diffraction at smooth bendings, sharp edges, corners, and any other geometric discontinuity and material inhomogeneity on the scattering surfaces. Creeping and edge current waves are examples of such a current. The field generated by the nonuniform current represents the PTD contribution to the scattered field. Exact analytical expressions for nonuniform currents are not available. Therefore, one has to find their high-frequency approximations by the solution of appropriate canonical problems. In this manner, Fock developed special functions that describe the nonuniform current on smooth convex objects in the vicinity of the shadow boundary [19]. The Sommerfeld solution of the wedge canonical problem is used for the asymptotic description of the nonuniform current near perfectly conducting edges [14,15,24,30]. The concept of uniform and nonuniform currents plays a key role in PTD and those hybrid techniques that combine direct numerical methods with high-frequency asymptotic approximations [6,17,18]. Reference 15 shows that PTD properly defines the leading term in the high-frequency asymptotic expansions for primary and multiple edge waves. A close connection exists between PTD and GTD. The latter automatically follows from the PTD integrals when they are evaluated

by the stationary phase technique [15, pp. 136–138]. Some PTD results are presented in the next section.

4. BACKSCATTERING RCS OF SIMPLE SHAPES

This section contains examples of PO estimations for RCS of simple objects. Whenever possible, these estimations are accompanied by more precise PTD counterparts that include the contributions of primary edge waves generated by the nonuniform edge currents. Only objects with symmetry of revolution are considered. All given data are taken from Refs. 15, 16, and 30. Exact, numerical solutions of scattering problems for bodies of revolution can be found, for example, in Refs. 6, 18, and 25.

4.1. Semitransparent Disk

The geometry of this scattering problem is shown in Fig. 8. The backscattering direction is determined by the spherical coordinates $\vartheta = \pi - \gamma$, $\varphi = -\pi/2$. The disk radius is denoted by the letter a . The incident wave can have either E or H polarization. In the first case, the electric vector is perpendicular to the incidence plane and parallel to the disk face. The reflection and transmission coefficients, $r_e(\gamma)$, $t_e(\gamma)$, with respect to the electric vector. In the case of H polarization, the magnetic vector of the incident wave is perpendicular to the incident plane and parallel to the disk face. The reflection and transmission coefficients, $r_h(\gamma)$, $t_h(\gamma)$, determine the magnetic vector on the front ($z = -0$) and rear ($z = +0$) faces of the disk, respectively. According to Eq. (67) in (23), the backscattering RCS is given by

$$\begin{aligned}\sigma_e^{\text{PO}}(\gamma) &= |r_e(\gamma)|^2 \pi a^2 [J_1(2ka \sin \gamma)]^2 \cot^2 \gamma \\ \sigma_h^{\text{PO}}(\gamma) &= |r_h(\gamma)|^2 \pi a^2 [J_1(2ka \sin \gamma)]^2 \cot^2 \gamma\end{aligned}\quad (24)$$

where $J_1(x)$ is the Bessel function and the incidence angle is restricted by the values $0 \leq \gamma < \pi/2$. For perfectly conducting disks, one should put $r_e(\gamma) = -1$ and $r_h(\gamma) = +1$. Then, in the case of the normal incidence ($\gamma = 0$), Eq. (24) reduces to

$$\sigma_e^{\text{PO}} = \sigma_h^{\text{PO}} = \pi a^2 (ka)^2 \quad (25)$$

Figure 7-24 on p. 514 of Ref. 2 shows that this equation is in good agreement with the exact results when $ka \geq 5$. Note also that Eq. (18), with $A = \pi a^2 \cos \gamma$, determines the PO bistatic RCS of this disk for the forward direction ($\vartheta = \gamma$). PTD estimations for RCS of a perfectly conducting disk are presented in Chaps. 2 and 5 of Ref. 14. See also pp. 514–521 of Ref. 2. Some important corrections in the PTD expressions for bistatic scattering from a disk are given in Ref. 24. Contributions of multiple edge waves to forward scattering are presented in Ref. 15 (pp. 149–151).

4.2. Circular Cone

Geometric parameters of a perfectly conducting cone are shown in Fig. 14. The incident wave direction is parallel to the symmetry axis of the cone. The PO backscattering

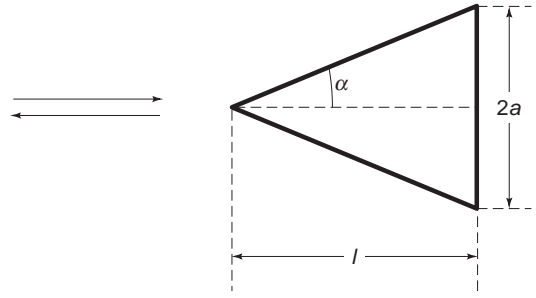


Figure 14. Backscattering from a truncated cone. The base diameter of the cone ($2a$) is large compared to the wavelength. The length of the cone (l) can be arbitrary. In the limiting case $l = 0$, the cone transforms into a disk.

RCS is given by Eqs. (17.06) and (17.09) in (4) [see also Eqs. (2.4.7) and Eq. (2.4.10) in Ref. 30]

$$\sigma^{\text{PO}} = \pi a^2 \cdot \left| \frac{1}{ka} \tan^2 \alpha \sin kl - \tan \alpha e^{ikl} \right|^2 \quad (26)$$

where the cone length equals $l = a \cot \alpha$. To clarify the physics in this equation, we rewrite it as

$$\sigma^{\text{PO}} = \pi a^2 \left| \frac{i}{2ka} \tan \alpha e^{-ikl} - \left(\tan \alpha + \frac{i}{2ka} \tan \alpha \right) e^{ikl} \right|^2 \quad (27)$$

The first term (with exponential e^{-ikl}) is related to the wave scattered by the cone tip. Comparison with the exact solution [3, Fig. 18.15, p. 691] shows that this PO approximation is quite satisfactory for all cone angles ($0 \leq \alpha \leq \pi/2$). The second term (with the exponential e^{ikl}) describes the edge wave contribution. This PO approximation is incorrect. PTD takes into account the additional contribution from the nonuniform (diffraction) currents located near the cone edge and provides a more accurate result, given by Eqs. (17.06) and (17.08) in Ref. 14 [see also Eqs. (2.4.7) and (2.4.9) in Ref. 30]

$$\sigma^{\text{PTD}} = \pi a^2 \cdot \left| \frac{1}{ka} \tan^2 \alpha \sin kl + \frac{\frac{2}{n} \sin \frac{\pi}{n}}{\cos \frac{\pi}{n} - \cos \frac{2\alpha}{n}} e^{ikl} \right|^2 \quad (28)$$

where $n = \frac{3}{2} + \alpha/\pi$. When the cone transforms into the disk ($\alpha \rightarrow \pi/2$, $l \rightarrow 0$) the previous expressions reduce to

$$\sigma^{\text{PO}} = \sigma^{\text{PTD}} = \pi a^2 (ka)^2 \quad (29)$$

which coincides with Eq. (25).

4.3. Paraboloid

The directrix of a paraboloid is given by the equation $r = 2pz$ where $p = a \tan \alpha$ (Fig. 15). The length of the paraboloid equals $l = a^2/(2p) = (a/2) \cot \alpha$. The angle α is formed by the symmetry axis z and the tangent to the directrix at the point $z = l$. The radius of the paraboloid base equals a . The incident wave propagates in the positive direction of the z axis. According to Eq. (18.02)

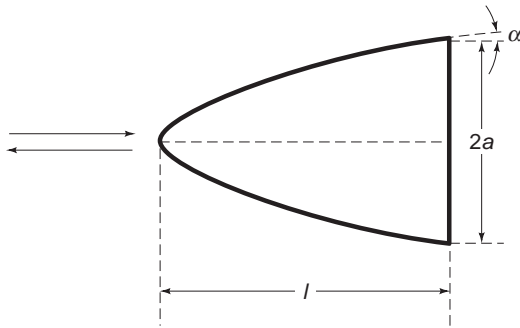


Figure 15. Backscattering from a truncated paraboloid. The base diameter of the paraboloid ($2a$) is large compared to the wavelength. The length of the paraboloid (l) can be arbitrary. In the limiting case $l = 0$, the paraboloid transforms into a disk.

in Ref. 14 (see also Sect. 2.5 in Ref. 30), the PO backscattering RCS of a perfectly conducting paraboloid equals

$$\sigma^{PO} = 4\pi a^2 \tan^2 \alpha \sin^2 kl \quad (30)$$

This equation can be written in another form as

$$\sigma^{PO} = \pi a^2 \tan^2 \alpha \cdot |e^{-ikl} - e^{ikl}|^2 \quad (31)$$

which is more convenient for the physical analysis. The term with the exponential e^{-ikl} gives the correct contribution of the specular reflection from the paraboloid tip. The term with the exponential e^{ikl} represents the edge wave contribution and is wrong. PTD includes the additional contribution from the nonuniform edge currents and provides the correct result, given by Eq. (18.04) in Ref. 14 [see also Eq. (2.5.4) in Ref. 30]

$$\sigma^{PTD} = \pi a^2 \left| \tan \alpha + \frac{\frac{2}{n} \sin \frac{\pi}{n}}{\cos \frac{\pi}{n} - \cos \frac{2\alpha}{n}} e^{2ikl} \right|^2 \quad (32)$$

where $n = \frac{3}{2} + \alpha/\pi$. When the paraboloid transforms into the disk ($\alpha \rightarrow \pi/2$ and $l \rightarrow 0$), these expressions reduce to Eq. (29).

4.4. Truncated Sphere

The geometry of this scattering problem is shown in Fig. 16. The angle α is formed by the tangent to the sphere generatrix and the symmetry axis. The sphere radius equals $\rho = a/\cos \alpha$, where a is the base radius. The length of the truncated sphere equals $l = \rho \cdot (1 - \sin \alpha)$. It is assumed that $l \leq \rho$. The PO backscattering RCS of a perfectly conducting sphere equals [14, Eq. (19.05); 30, Eq. (2.6.2)]

$$\sigma^{PO} = \pi a^2 \left| \frac{1}{\cos \alpha} - \frac{i}{2ka} - \left(\tan \alpha - \frac{i}{2ka} \right) e^{2ikl} \right|^2 \quad (33)$$

In this equation, the first two terms represent the specular reflection from the sphere, and both are correct. The third term (with the exponential e^{2ikl}) gives the contribution

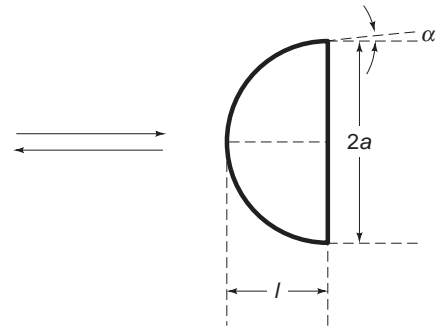


Figure 16. Backscattering from a truncated sphere. The base diameter of the sphere ($2a$) is large compared to the wavelength. The length of the sphere (l) can be arbitrary. In the limiting case $l = 0$, the sphere transforms into a disk.

from the edge and it is wrong. With $ka \gg 1$, Eq. (33) simplifies to

$$\sigma^{PO} = \pi a^2 \left| \frac{1}{\cos \alpha} - \tan \alpha e^{2ikl} \right|^2 \quad (34)$$

When $\alpha = 0$, the latter gives the RCS of a hemisphere, $\sigma = \pi a^2$. The PTD backscattering RCS is determined by Eq. (19.12) in Ref. 14 [Eq. (2.6.8) in Ref. 30]

$$\sigma^{PTD} = \pi a^2 \left| \frac{1}{\cos \alpha} + \frac{\frac{2}{n} \sin \frac{\pi}{n}}{\cos \frac{\pi}{n} - \cos \frac{2\alpha}{n}} e^{2ikl} \right|^2 \quad (35)$$

where $n = \frac{3}{2} + \alpha/\pi$. When the sphere transforms into the disk ($\alpha \rightarrow \pi/2, \rho \rightarrow \infty, l \rightarrow 0$), Eqs. (34) and (35) reduce exactly to Eq. (29).

4.5. Circular Cylinder with Flat Ends

The diameter and length of a perfectly conducting cylinder are assumed to be large as compared with the wavelength of the incident wave. PO and PTD estimations for backscattering RCS are developed in Chap. 3 of Ref. 14. They are also presented in Ref. 2 (pp. 308–312). PTD asymptotic expressions for bistatic RCS are given in Ref. 15 (pp. 152–154).

5. BACKSCATTERING FROM COMPLEX OBJECTS AND STEALTH PROBLEMS

Computer codes based on GTD, PTD, and on their hybridizations have been developed for prediction of high-frequency scattering from complex perfectly conducting objects. Relevant references can be found in Refs. 16 and 18 and in special issues of *Proc. IEEE* (1989), *IEEE Trans. Anten. Propag.* (1989), and *Annales des Telecommunications* (1995), which are mentioned in the Further Reading list. Note also the XPATCH code (based on the shooting-and-bouncing ray technique and PTD), which allows the calculation of backscattering from complex geometries. Information about this code is published in *IEEE Trans.*

Anten. Propag. Mag. **36**(1):65–69 (1994). Computer codes interfaced with graphical utilities of workstations can display three-dimensional chromatic views of scattering centers and magnitudes of their contributions to RCS. This is the end result of complicated computations. However, a part of this can be obtained without any computations. Nature can show us the location of all scattering centers if we bring a small metallized model of the scattering object into an anechoic optical chamber and illuminate the model by the light. Bright shining points (scattering centers) seen on a scattering object are exactly those from which the radar waves will be reflected toward the radar, if we look at the object from the light source direction. (The following text is taken from Ref. 16 and slightly modified.)

The locations of these points do not depend on the frequency of incident electromagnetic waves, and they are determined completely by the location of the light source (the radar), the observer, and the scattering object. These shining points obey the Fermat principle. This means that the path along the ray between the source, the reflection point, and the observer is extremal (minimal or maximal) in comparison with similar paths corresponding to neighboring points on the object's surface. A more detailed description of the Fermat principle is presented, for example, in Sect. 3.3.2 in Ref. 20.

Waves reflected from discrete shining points located on the smooth parts of the scattering object represent the usual geometric optics reflected rays. Waves reflected from discrete shining points located on edges, tips, and corners are diffracted rays. The farthest shining points on a smooth object—those located on the boundary between visible and invisible sides of the object—create surface diffracted rays.

As the orientation of the object is changed, the shining points move along the object. Some of them can merge with each other and create a brighter point. In this case our eyes (i.e., the radar) are located on a caustic that is the envelope of merged rays.

We can also observe bright shining lines and bright shining spots on the object, which contain an *infinite* number of continuously distributed shining points. Their important property is that the optical path through a shining point from the source to the observer is constant for all of these points. It is assumed here that the source and observer are far from the scattering object. All waves reflected from these points reach the observer with the same phase. From the mathematical point of view, each such point is a stationary point of the infinite order; the derivatives (of any higher order) of the wave phase along the shining line (or along the shining spots) are zero at these points.

Shining spots and lines located on smooth parts of the scattering surface generate powerful reflected beams (such as those radiated by reflector antennas) that represent the strongest contributors to RCS. Shining edge lines create edge-diffracted beams whose contributions can be comparable with those from ordinary reflected rays.

It is difficult to model in optics the electromagnetic properties of realistic scattering surfaces for the radar frequency band. But the optical modeling can be used to

identify the scattering centers and to control them by an appropriate shaping of the scattering surface. As it is well known, one of the basic ideas of the current stealth technology is to use an appropriate body shaping and to shift all reflected beams and rays away from the directions to the radar. See, for example, Refs. 2 and 16, and the radar cross-section handbooks mentioned in the reading list. Some interesting details about the development of stealth technology in the United States are presented in Refs. 26–28.

The second idea of stealth technology is traditional: to use radar absorbing materials (RAMs) and composite structures in order to reduce the intensity of reflected beams and rays. References 2, 16, and 29, and radar handbooks (mentioned in the reading list) describe fundamental concepts used in the design and application of RAMs. We present here some details taken from Ref. 16. In order to use RAMs efficiently, it is necessary to place an electric (magnetic) RAM in the region where the average electric (magnetic) field is maximal. Location of these regions in the vicinity of real objects depends on many factors, such as the radar frequency, geometry, size, and electrical properties of the object, as well as properties of materials intended for absorption. Identification of such regions and optimization of the RAM parameters to minimize RCS is a very complex problem. Its solution is attainable only in some simple cases. Most of these relate to absorbing layers on an infinite metallic plane. From the physical point of view such absorbing layers can be considered as open resonators that can support eigenoscillations. Frequencies of eigenoscillations are complex quantities. Their imaginary part is responsible for the loss inside the resonator and radiation from the resonator. It turns out that the minimal reflection from such resonators happens when the frequency of an incident wave is close to the real part of the resonator eigenfrequency.

Note that thin electric RAMs are not efficient when applied on metallic objects. This is due to the boundary condition; the tangential component of the electric field is very small on the metal surface. On the contrary, magnetic absorbing materials can be applied directly to the surface of a metallic object. This is an important advantage of magnetic materials over electric ones.

However, any RAMs (electric, magnetic, and hybrid) homogeneous in the direction parallel to the reflecting plate are not efficient for grazing incidence ($\theta \approx 90^\circ$, in Fig. 5). In this case, the reflection coefficient tends to unity independently of the incident wave polarization when $\theta \rightarrow 90^\circ$. This is a fundamental limitation of ordinary RAMs. They do not work against grazing incident waves. That is why ordinary RAMs do not reduce forward scattering. Actually, the RAM terminology is justified only for incidence angles that are not too far from $\theta = 0$ and when the reflection coefficient is small enough.

There is another reason why RAMs are not efficient against the forward scattering. Any large opaque scattering objects act like a lens focusing the scattered field in the forward direction. As shown in Refs. 15, 23, and 30, the forward scattering can be interpreted as the *shadow radiation* generated by the *black bodies* (perfectly absorbing objects whose reflection coefficient equal zero). In Ref. 23 (see also Refs. 15 and 30), it was established that the total

power of the shadow radiation in all directions equals *one-half* of the total power scattered by a *perfectly reflecting* body (of the same shape and size as the black body). This fundamental law means that the total power of the scattered field cannot be reduced with application of any radar absorbing coatings more than by a factor of 1/2.

Various geometric and material inhomogeneities on the scattering surface can partially transform the incident wave into surface waves propagating along absorbing layers. This may be used to further reduce the RCS. However, this idea has two essential defects: (1) any inhomogeneity creates an additional undesirable scattered field and (2) it is not a simple problem to design an absorbing layer that would allow the propagation of surface waves. To support surface waves with electric vector parallel to the incidence plane, the surface impedance must be inductive. But the surface impedance must be capacitive to support surface waves with the electric vector perpendicular to the incidence plane. This means that the surface impedance, and therefore the absorbing layer, must depend on the radar polarization with respect to the incidence plane. But this plane is different at different points of the scattering surface and different at the same point when the scattering object changes its orientation with respect to radar. It is very difficult and probably impossible to design such an absorber, especially against radars with circular polarization. However, for some chosen orientations of the object and for an appropriate polarization of the incident wave, this might not be a hopeless problem.

Development of efficient hybrid techniques and computer codes to predict RCS of large complex objects with realistic materials and research efforts to overcome the abovementioned physical limitations in RCS reduction represent challenging problems for future stealth technology. One can expect that future advanced computer codes will contain as necessary constitutive components the known high-frequency techniques (such as GTD, PTD, and the uniform theory of diffraction) extended for coated and composite objects. Diffraction coefficients used in these techniques can be determined by the numerical solution of appropriate canonical problems. Direct numerical methods should be used for calculation of scattering from those elements of the scattering object that cannot be treated by high-frequency methods. Diffraction interaction between the object's elements handled by high-frequency techniques and by direct numerical methods can be described by the surface integral equations.

BIBLIOGRAPHY

- J. W. Crispin Jr. and K. M. Siegel, eds., *Methods of Radar Cross-Section Analysis*, Academic Press, New York, 1968.
- G. T. Ruck, D. E. Barrick, W. D. Stuart, and C. K. Kirchbaum, *Radar Cross-Section Handbook*, Vols. 1 and 2, Plenum Press, New York, 1970.
- J. J. Bowman, T. B. A. Senior, and P. L. E. Uslenghi, eds., *Electromagnetic and Acoustic Scattering by Simple Shapes*, Hemisphere Publishing, New York, 1987.
- P. C. Fritch, ed., *Proc. IEEE* (Special issue on radar reflectivity) **53**(8) (Aug. 1965).
- M. N. O. Sadiku, *Numerical Techniques in Electromagnetics*, CRC Press, Boca Raton, FL, 1992.
- E. K. Miller, L. Medgyesi-Mitschang, and E. H. Newman, *Computational Electromagnetics*, IEEE Press, New York, 1991.
- P. P. Silvester and G. Pelosi, eds., *Finite Elements for Wave Electromagnetics*, IEEE Press, New York, 1994.
- P. Ya. Ufimtsev and A. P. Krasnozhen, Scattering from a straight thin wire resonator, *Electromagnetics* **12**(2):133–146 (1992).
- L. A. Vainshtein, Waves of current in a thin cylindrical conductor, II. The current in a passive oscillator, and the radiation of a transmitting antenna, *Sov. Phys., Tech. Phys.* **4**(6):617–626 (Dec. 1959).
- L. A. Vainshtein, Waves of current in a thin cylindrical conductor, III. Variational method and its application to the theory of ideal and impedance conductors, *Sov. Phys., Tech. Phys.* **6**(1):19–29 (July 1961).
- M. A. Leontovich and M. L. Levin, Towards a theory on the simulation of oscillations in dipole antennas, *Zh. Tech. Fiz.* **14**(9):481–506 (1944) (in Russian) (English transl. published in the following report: K. C. Chen, ed., SAND91-0720, UC-705, Sandia National Laboratories, Albuquerque, NM and Livermore, CA, Contract DE-AC04-76DP00789, Jan. 1992).
- J. B. Keller, Geometrical theory of diffraction, *J. Opt. Soc. Am.* **52**:116–130 (1962).
- R. C. Hansen, ed., *Geometrical Theory of Diffraction*, IEEE Press, New York, 1981.
- P. Ya. Ufimtsev, *Method of Edge Waves in the Physical Theory of Diffraction*, Soviet Radio Publishing House, Moscow, 1962, pp. 1–243, transl. U.S. Air Force, Foreign Technology Division, Wright-Patterson AFB, Ohio, 1971; Technical Report AD 733203, DTIC, Cameron Station, Alexandria, VA.
- P. Ya. Ufimtsev, Elementary edge waves and the physical theory of diffraction, *Electromagnetics* **11**(2):125–160 (1991).
- P. Ya. Ufimtsev, Comments on diffraction principles and limitations of RCS reduction techniques, *Proc. IEEE* **84**(12):1830–1851 (1996).
- D. P. Bouche, F. A. Molinet, and R. Mittra, Asymptotic and hybrid techniques for electromagnetic scattering, *Proc. IEEE* **81**:1658–1684 (1993).
- W. R. Stone, ed., *Radar Cross Sections of Complex Objects*, IEEE Press, New York, 1990.
- V. A. Fock, *Electromagnetic Diffraction and Propagation Problems*, Pergamon Press, London, 1965.
- M. Born and E. Wolf, *Principles of Optics*, Pergamon Press, New York, 1975.
- H. M. Macdonald, The effect produced by an obstacle on a train of electric waves, *Phil. Trans. Roy. Soc. Lond. Series A, Math. Phys. Sci.* **212**:299–337 (1912).
- C. E. Schensted, Electromagnetic and acoustic scattering by a semi-infinite body of revolution, *J. Appl. Phys.* **26**:306–308 (1955).
- P. Ya. Ufimtsev, Diffraction of electromagnetic waves at black-bodies and semi-transparent plates, *Radiophys. Quantum Electron.* **11**:527–538 (1968).
- P. Ya. Ufimtsev, Comments on “Comparison of three high frequency diffraction techniques,” *Proc. IEEE* **63**:1734–1737 (1975).
- R. D. Graglia et al., Electromagnetic scattering for oblique incidence on impedance bodies of revolution, *IEEE Trans. Anten. Propag.* **43**(1):11–26 (1995).

26. M. W. Browne, Two rival designers led the way to stealthy warplanes, *New York Times* (Science Times Section), May 14, 1991.
27. S. F. Browne, The secret ship, *Popular Sci.*, (Oct. 1993).
28. B. Rich and L. Janos, *Skunk Works*, Little, Brown, Boston–New York–London, 1994.
29. K. J. Vinoy and R. M. Jha, *Radar Absorbing Materials*, Kluwer Academic Publishers, Boston, 1996.
30. P. Ya. Ufimtsev, *Theory of Edge Diffraction in Electromagnetics*, Tech Science Press, Encino, CA, 2003.

FURTHER READING

This section contains short comments on some related references.

- P. C. Fritch, ed., *Radar Reflectivity*, special issue of *Proc. IEEE* **53**(8) (Aug. 1965). [The first attempt to sum up basic results in the field of RCS. Includes a comprehensive subject index, about 1500 titles (pp. 1025–1064).]
- J. W. Crispin Jr. and K. M. Siegel, eds., *Methods of Radar Cross Section Analysis*, Academic Press, New York, 1968. [Includes a short historical survey of high-frequency approximations. Contains results of such approximations for monostatic and bistatic RCS of simple objects. States a strategy of RCS calculations for complex objects. Some results are conveniently summarized in tables. Table 5 on p. 147 contains expressions for RCS in the Rayleigh region (for objects small in comparison with wavelength). High-frequency monostatic and bistatic RCS are given in Tables 7 and 8 on pp. 168, 169, 171.]
- G. T. Ruck, D. E. Barrick, W. D. Stuart, and C. K. Kirchbaum, *Radar Cross-Sections Handbook*, Plenum Press, New York, 1970. [This is a real encyclopedia of RCS, which includes most results obtained before 1970. It contains numerous theoretical and experimental results for both perfectly conducting and absorbing objects. The physical theory of diffraction (PTD) is mentioned here as the Sommerfeld–Macdonald technique. Equation (5.1-54), presented on p. 351, for the bistatic RCS of an ellipsoid is incorrect. In the particular case when an ellipsoid transforms into a sphere, this equation does not provide the bistatic RCS for the sphere, $\sigma = \pi a^2$. Instead it leads to the wrong quantity $\sigma = \pi a^2/(1 + \cos \beta)^2$, where β is the bistatic angle.]
- J. J. Bowman, T. B. A. Senior, and P. L. E. Uslenghi, eds., *Electromagnetic and Acoustic Scattering by Simple Shapes*, Hemisphere Publishing, New York, 1987. (Contains a comprehensive collection of theoretical results for RCS of simple objects which allow the exact solutions of diffraction problems. Both low-frequency and high-frequency approximations are presented as well.)
- M. Skolnik, ed., *Radar Handbook*, McGraw-Hill, New York, 1970. (Contains many results of measurements and calculations for RCS. Calculations were carried out mostly by the physical optics approach and GTD. Analytical expressions for RCS are not given.)
- W. R. Stone, ed., *Radar Cross Sections of Complex Objects*, special issue of *Proc. IEEE* **77**(5) (May 1989); W. R. Stone, ed., *Radar Cross Sections of Complex Objects*, special issue of *IEEE Trans. Anten. Propag.* **37**(5) (May 1989). [These two references contain many theoretical results concerning RCS for complex objects (perfectly conducting objects with complex shapes and simple objects with complex boundary conditions).]
- W. R. Stone, ed., *Radar Cross Sections of Complex Objects*, IEEE Press, New York, 1989. (This book consists of a collection of
- articles. It includes expanded versions of about half of the papers published in two previously mentioned special issues. It also contains papers written especially for this book and reprints of some earlier key papers.)
- J. M. Bernard, G. Pelosi, and P. Ya. Ufimtsev, eds., *Radar Cross Sections of Complex Objects*, special issue of French journal *Annales des Telecommunications* **50**(5–6) (May–June 1995) (published in English with abstracts translated into French). (Contains the asymptotic analysis of RCS for higher-order curved surfaces, physical theory of slope diffraction, PO and PTD analysis of trihedral corner reflectors, a selective review of some numerical methods for electromagnetic scattering, and some other results.)
- The following three books contain additional information on RCS. They include concise descriptions of basic exact and approximate techniques for prediction of RCS, they introduce methods of RCS enhancement and reduction, and they contain a large number of calculated and measured data for RCS of many typical simple and complex objects. The books complement each other, with emphasis on different aspects in the field of RCS.
- A. L. Maffett, *Topics for a Statistical Description of Radar Cross Section*, Wiley, New York, 1989. (This book treats the subject of RCS with special emphasis on statistical aspects and applications. It reflects broad interests of the author: from historical background and perspective through analytical and numerical methods of RCS calculation and RCS measurements to elements of detection theory, investigation of anisotropic layers, and the inverse problem for anisotropic materials with diagonal permittivity and permeability tensors.)
- A. K. Bhattacharyya and D. L. Sengupta, *Radar Cross Section Analysis and Control*, Artech House, Boston–London, 1991. [The book concentrates on deliberate changes of RCS (enhancement and reduction). It contains a useful table (p. 108) that represents in concise form the comparison of different methods available for RCS analysis, with discussion of their advantages, disadvantages, and possible applications. It also complements other books by inclusion of the Maluzhinets function, which plays a fundamental role in the theory of scattering by absorbing objects with sharp edges or with impedance discontinuities. The computer code for the calculation of this important function is provided in the appendix of the book.]
- E. F. Knott, J. F. Schaffer, and M. T. Tuley, *Radar Cross Section*, 2nd ed., Artech House, Boston–London, 1993. [This book presents updated material that covers most aspects of RCS: radar fundamentals, radar detection, RCS prediction, RCS reduction, radar absorbing materials, and RCS measurements. Chapter 14 can be especially useful for a brief review. It contains a table (p. 562) with RCS estimations, as well as the RCS data presentation formats and data reduction recipes.]
- P. Ya. Ufimtsev, Comments on diffraction principles and limitations of RCS reduction techniques, *Proc. IEEE* **84**:1830–1851 (1996). (RCS reduction techniques are discussed briefly from the physical point of view. Attention is concentrated on the physical structure of radar waves scattered from large objects. Possible passive and active techniques to control and reduce reflected beams, rays, and shadow radiation as well as potential limitations of these techniques are considered. In particular, it is emphasized that grazing reflected rays and shadow radiation cannot be eliminated by absorbing materials.)
- R. C. Hansen, ed., *Geometrical Theory of Diffraction*, IEEE Press, New York, 1981. (This book consists of a collection of articles. It

contains key papers on GTD, asymptotic solutions of some canonical problems, and applications-oriented papers.)

Many scattering objects contain nonmetallic materials, composites, and various layered structures. To simplify the solution of scattering problems for such objects, it is often practical to apply approximate boundary conditions. These conditions are enforced on the external surface of the object and contain important information about the internal structure of the scattering object. As a result, this approximation allows one to substantially reduce the spatial region under investigation. The two following books present the development and applications of this approximation technique.

- T. B. A. Senior and J. L. Volakis, *Approximate Boundary Conditions in Electromagnetics*, The Institution of Electrical Engineering, London, 1995.
- D. J. Hoppe and Y. Rahmat-Samii, *Impedance Boundary Condition in Electromagnetics*, Taylor & Francis, Washington, DC, 1995.
- P. Ya. Ufimtsev, *Theory of Edge Diffraction in Electromagnetics*, Tech Science Press, Encino, CA, 2003. [Among the fundamental results of this theory are the following: (1) The theory of black bodies that is important for understanding of physics of diffraction, especially of scattering at large bistatic angles. This theory also determines the diffraction limit for reduction of the total scattered power by application of radar absorbing coatings. (2) PTD estimations of RSC for bodies of revolution. (3) Extension of PTD for scattering objects with concave elements. (4) Analysis of diffraction problems (wedge, strips, dipoles) based on the parabolic equation method. (5) Investigation of multiple edge diffraction at a single strip and at an open resonator formed by two strips. Exact and asymptotic expressions are found for the current on the strip and for the far field that are valid for arbitrary directions of incidence and observation. These expressions allow the calculation of the current and the far field with arbitrary high precision].

BANDPASS FILTERS

JAIME RAMIREZ-ANGULO
New Mexico State University
Las Cruces, New Mexico

A bandpass filter is an electrical device that passes the spectral components of an electrical signal around a certain frequency f_0 with little or no attenuation, while it mostly rejects other spectral components (Fig. 1). Bandpass filters are common building blocks of many electronic systems. They find applications in diverse fields such as communications, audio, instrumentation, and biomedicine. To illustrate a typical application of a bandpass filter, consider the simultaneous transmission of n signals in one communications channel using frequency multiplexing techniques. The signals can share the same channel because their individual frequency spectra are shifted so that they occupy nonoverlapping regions (or bands) of the frequency spectrum. Frequency modulation is used to shift the baseband spectrum of each of the signals (centered originally at zero frequency or dc) to center frequencies $f_{01}, f_{02}, \dots, f_{0n}$ (Fig. 2). In order to avoid overlapping,

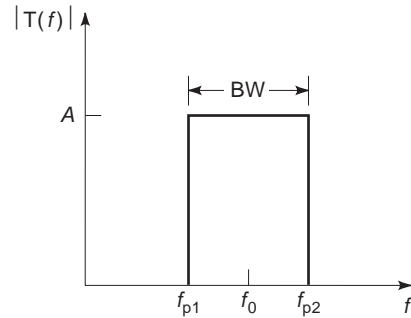


Figure 1. Frequency response of ideal bandpass filter.

the center frequencies must have a minimum separation of at least the bandwidth of the signals. Bandpass filters are used on the receiver side in order to select or “filter out” only one of the signals transmitted in the channel. A process called demodulation is used to shift the spectrum of the selected signal back to baseband (to a zero center frequency).

1. IDEAL BANDPASS FILTERS

Ideally, a bandpass filter is characterized by its center frequency f_0 and its bandwidth BW. The bandwidth is defined in terms of upper and lower passband edge frequencies f_{p1} and f_{p2} , respectively, and given by $BW = f_{p2} - f_{p1}$. Typically, f_{p1} and f_{p2} specify frequency points at which the gain decreases by a factor $\sqrt{2}$. The frequency response plot of Fig. 1 shows the gain A as a function of frequency f of an ideal bandpass filter. An important parameter of a bandpass filter is its selectivity factor S_F , which is expressed by $S_F = f_0/BW$. The selectivity is a measure of the filter’s ability to reject frequencies outside its passband. It is also a relative measure of the reciprocal bandwidth. Highly selective filters (also denoted narrowband filters) have a bandwidth that constitutes only a small fraction of f_0 . Narrowband filters with large selectivity factors (e.g., $S_F > 50$) are commonly required in communication systems. For ideal bandpass filters, the frequency range is divided into three regions: the passband region where the gain is approximately constant ($f_{p1} < f < f_{p2}$) and the lower and upper stopbands ($f < f_{p1}$ and $f > f_{p2}$, respectively), where the gain is ideally zero or the attenuation or reciprocal gain is infinite. The ideal bandpass filter has sharp transitions between the passband and the two stopbands.

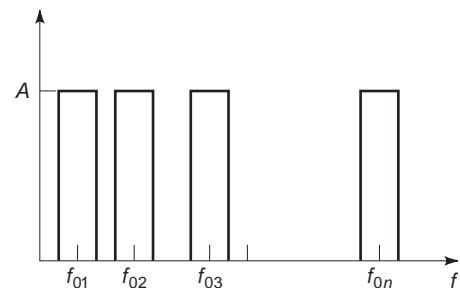


Figure 2. Spectrum of n signals in a communication channel.

2. PRACTICAL BANDPASS FILTERS

The typical frequency response of a practical passband filter is shown in Fig. 3. It has a relatively constant gain possibly with fluctuations (ripple) with maximum amplitude A_p within the passband. The passband edge frequencies f_{p1} and f_{p2} are defined, in this case, as the minimum and maximum frequencies with gain, $A - A_p$. The center frequency f_0 is commonly the center of geometry of the passband edge frequencies: $f_0 = \sqrt{f_{p1}f_{p2}}$. In a practical filter, there is a gradual transition between the passband and the upper and lower stopbands. Therefore, besides the passband and stopband there are also two transition bands. Two frequencies f_{s1} and f_{s2} , each denoted lower and upper stopband edge frequencies, respectively, define the stopbands in a practical bandpass filter. Stopband regions are characterized by a small gain with maximum value, $1/A_s$, where A_s is the stopband attenuation. Passband ripple A_p and stopband attenuation A_s are commonly specified in a logarithmic unit denoted decibel according to A_s (dB) = $20 \log A_s$. Practical bandpass filters can have monotonic decreasing gain or equal gain fluctuations (ripple) within both the passband and the stopband.

3. MATHEMATICAL CHARACTERIZATION OF A BANDPASS FILTER

The simplest bandpass filter is the second-order filter. It is characterized by the input-output relation or transfer function:

$$T(f) = \frac{jBwf}{f_0^2 + jBwf - f^2} \quad (1)$$

This transfer function is a complex function with magnitude and phase. The magnitude (frequency response) obtained from Eq. (1) has the form

$$|T(f)| = \frac{Bwf}{\sqrt{(f_0^2 - f^2)^2 + (Bwf)^2}} \quad (2)$$

The pole-zero plot (in the complex frequency plane also known as the *s plane*) of a second-order bandpass filter is shown in Fig. 4. It has a zero at the origin (shown as a circle) and two complex conjugate poles (shown as marks).

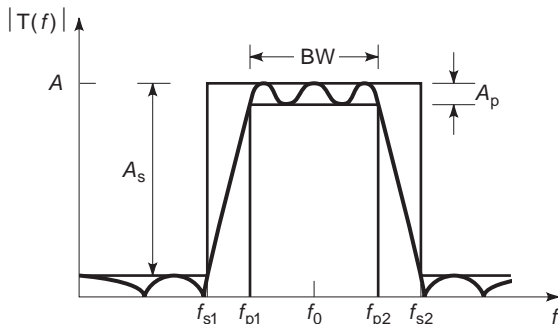


Figure 3. Practical bandpass filter.

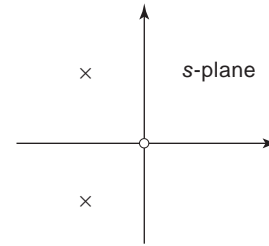


Figure 4. Pole-zero plot of second-order bandpass filter.

The selectivity is associated with the relative distance of the poles from the imaginary axis in the *s* plane. The distance from the origin to the poles corresponds to the center frequency in radians, $\omega_0 = 2\pi f_0$.

4. BANDPASS FILTER IMPLEMENTATIONS

Depending on the center frequency and selectivity, there exist several possible implementations of bandpass filters. In general, the higher the selectivity and the center frequency, the more complex the filter becomes. Two very important aspects are miniaturization and compatibility with very large scale integration (VLSI) systems technology. These have dictated the evolution of bandpass filters and of most other electronic circuits. *Compatibility* refers to the fact that the filter can be fabricated on a CMOS integrated circuit as a part of a VLSI system in CMOS technology. This technology allows for the fabrication of very complex analog and digital electronic systems with hundreds of thousands or even millions of transistors on a single integrated circuit. CMOS compatibility is crucial in order to reduce manufacturing costs and to increase system reliability. Automatic tuning and low power consumption are also important aspects for bandpass filters. Tuning consists in the process of adjusting the filter's response to compensate for unavoidable fabrication tolerances in the values of the filter elements. These tolerances cause the filter's response to deviate from the ideal (nominal) response. Low power is important for portable equipment like cellular phones and bioimplantable devices.

4.1. Passive Filters

For many years, most filters were exclusively implemented as *passive RLC* circuits using resistors, inductors, and capacitors [1]. Figure 5 shows an example of a resonant *RLC* circuit used as a bandpass filter. This filter is characterized by the transfer function of Eq. (1) with

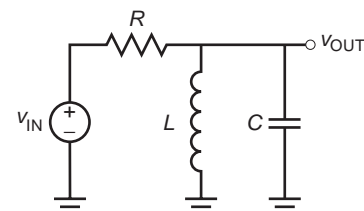


Figure 5. Second-order *RLC* bandpass filter.

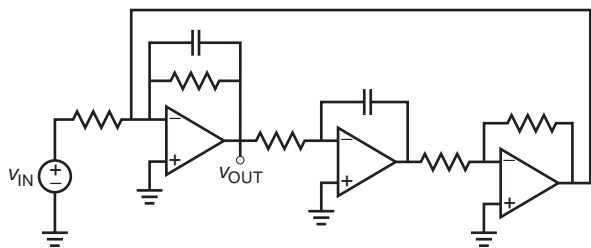


Figure 6. Second-order RC active filter.

$f_0' = 1/2\pi \cdot 1/\sqrt{LC}$ and $BW = 1/(CR)$. The transfer function of this circuit has the pole-zero plot shown in Fig. 4. Ceramic filters based on bulk electromechanical resonance phenomena in piezoelectric materials have been used in the radio frequency range specially for requirements of high selectivity and accurate center frequency. Inductors have several problems: (1) they have large physical dimensions and cannot be integrated unless their value is very small, (2) they are temperature-dependent, and (3) their value is subject to large manufacturing tolerances. They also have poor characteristics at low frequencies, and their value tends to change with time. RLC passive filters cannot be automatically tuned at the manufacturing stage. Additionally, RLC and ceramic filters are not compatible with CMOS VLSI technology.

4.2. RC Active Filters

In the 1960s, RC active filters using operational amplifiers, capacitors, and resistors led to the implementation of highly selective low-cost filters without inductors (Fig. 6). These filters are known as RC active filters [2]. They constituted the first step toward filter miniaturization. RC active filters were mass-produced in miniaturized form using thin-film and/or thick-film technology. These filters still required individual tuning. This was automatically done using computer-controlled laser beams that burn sections of resistor material to change the resistance and achieve the desired filter response. Within a short time, RC active filters replaced most inductor-based filters in the audio frequency range.

4.3. Monolithic Analog Filters

In the mid-1980s, RC active filters were replaced by fully integrated switched-capacitor filters [3]. These use only switches, operational amplifiers, and capacitors and can be fabricated in CMOS VLSI technology (see Fig. 7). Switched-capacitor filters require no tuning and can operate at center frequencies up to a few hundred kilohertz. Starting in the mid 1970s, surface acoustic wave (SAW) filters—another family of filters—were developed to implement filters for center frequencies spanning from 10 to several hundred megahertz. These filters are miniaturized filters that also require no tuning. They are based on the controlled propagation of electromechanical waves on the surface of a piezoelectric crystal with very small dimensions. SAW filters are not compatible with CMOS technology. But because of their excellent performance characteristics and low cost, they are currently

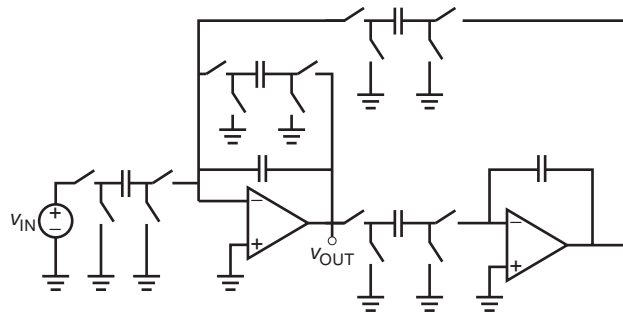


Figure 7. Second-order switched-capacitor filter.

being used to implement the intermediate frequency filter of most televisions.

More recently, electronically tunable elements in CMOS technology have allowed the integrated circuit implementation of active filters for center frequencies up to a few tens of megahertz. These filters are compatible with CMOS VLSI technology. Most of these implementations are based on electronically tunable elements called operational transconductance amplifiers (transconductors or OTAs) and include on-chip automatic tuning circuitry [4]. The tuning circuit continuously (or periodically) monitors the filter’s response and electronically adjusts the gain of the OTAs to tune the frequency response of the bandpass filter. This family of filters is known as OTA-C filters (see Fig. 8). They require no tuning and can be integrated as part of a VLSI system [5]. Figure 8a shows a conventional “voltage mode” filter, while Fig. 8b shows a “current mode” filter where input, output, and intermediate variables are represented by electrical currents rather than voltages as it is done in conventional “voltage mode” filters [6]. In analog signal processing systems, the range above 100 MHz is still based, to a large extent, on passive RLC filters. At these frequencies, high-quality, small-dimension inductors are available. A very recent trend for the implementation of high-frequency high-selectivity

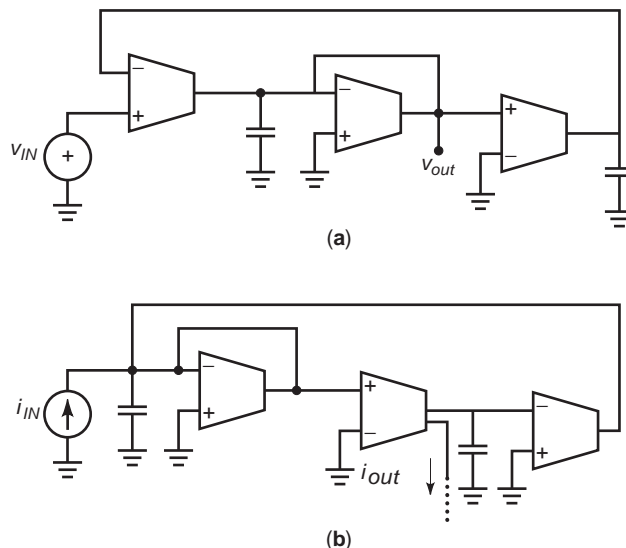


Figure 8. Second-order OTA-C bandpass filter: (a) voltage-mode implementation; (b) current-mode implementation.

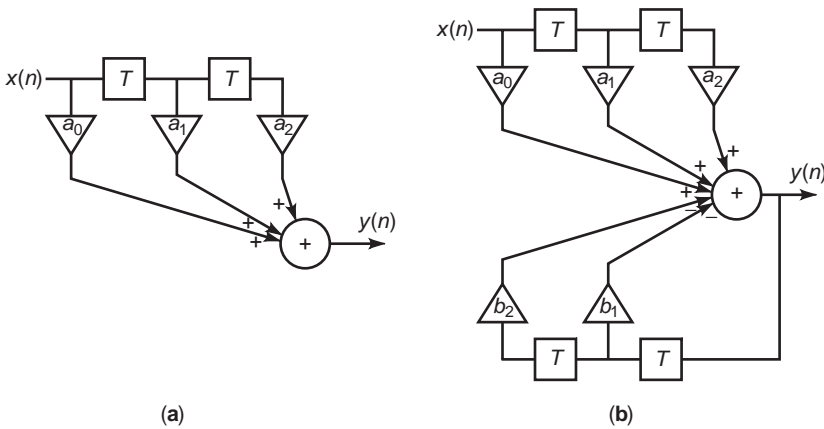


Figure 9. Second-order digital filters: (a) FIR filter; (b) IIR filters.

integrated analog filters is based on microelectromechanical (MEM) structures, which are based on electromechanical resonance. This approach has shown potential for the implementation of bandpass filters operating in the radio frequency range and with very high selectivity factors similar to those achievable with ceramic and SAW structures. These MEM-based filters, unlike the SAW filters, are CMOS VLSI-compatible.

4.4. Digital Filters

Currently, the availability of low-cost digital circuitry in VLSI systems has made it convenient to replace many traditional analog functions by digital ones and to process signals in the digital domain rather than in analog form. Successful implementation of digital filters for center frequencies up to a few megahertz, as standalone units or as part of a VLSI system has been achieved. Digital filters are fully integrated filters that are compatible with CMOS technology and require no tuning [7]. Their characteristics (f_0 , BW, or Q) can be easily reprogrammed for many different applications. A digital filter consists basically in various addition, multiplication, and delay operations applied to an ordered sequence of numbers that represent the digitized values of a signal. These digitized values are obtained by sampling the signal at regular time intervals ($t = T, 2T, 3T, \dots$) and transforming the sampled values into binary codes. In digital filters, present values $x(n) = x(nT)$ and past values $x(n-1) = x((n-1)T)$, $x(n-2) = x((n-2)T) \dots$ of both input and output signals are processed. The steps performed on these digitized values lead to an output sequence $y(n), y(n-1), y(n-2), \dots$, which can be transformed by means of a digital-to-analog converter into a filtered output signal $y(t)$. A digital filter is, therefore, an algorithm or sequence of mathematical steps that relates input and output sequences by means of multiplication, addition, and delay operations. A digital filter is mathematically characterized by a difference equation. There are two types of digital filters: finite impulse response (FIR) filters, where the current value of the output signal $y(n)$ depends only on the current and past values of the input signal; and infinite impulse response (IIR) filters, where the current value of the output signal depends also on past values of the output signal. For example, the difference equation of a second-order FIR

filter is expressed by

$$y(n) = a_0x(nT) + a_1x(n-1) + a_2x(n-2) \quad (3)$$

while the difference equation of a second-order IIR digital filter has the form

$$y(n) = a_0x(n) + a_1x(n-1) + a_2x(n-2) - b_1y(n-1) - b_2y(n-2) \quad (4)$$

where $a_0, a_1, a_2, b_1,$ and b_2 are multiplying coefficients; $x(n)$ and $y(n)$, stand for $x(t=nT)$ and $y(t=nT)$, are the current values of the input and output signals; and $x(n-1), x(n-2), y(n-1),$ and $y(n-2)$ correspond to the two previous values of the input and output signals, respectively. The values of the multiplying coefficients and the sampling frequency, $f_s = 1/T$, determine the selectivity and center frequency of the digital filter and can be easily reprogrammed. Figures 9a and 9b illustrate the block diagram of second-order FIR and IIR filters, respectively.

High-speed digital filters can be implemented using special-purpose VLSI hardware in the form of digital signal processors [6] or as relatively low-speed filters using software in general-purpose digital systems such as computers or microprocessors.

BIBLIOGRAPHY

1. A. B. Williams and F. J. Taylor, *Electronic Filter Design Handbook: LC Active and Digital Filters*, McGraw-Hill, New York, 1988.
2. M. K. Van Valkenburg, *Analog Filter Design*, Holt, Reinhart, Winston, Forth Worth, TX, 1982.
3. R. Schaumann, M. S. Ghauri, and K. R. Laker, *Design of Analog Filters: Passive, Active RC and Switched Capacitors*, Prentice-Hall, Englewood Cliffs, NJ, 1990.
4. J. Silva-Martinez, M. Steyaert, and W. Sansen, *High Performance CMOS Continuous-time Filters*, Kluwer Academic Publishers, Norwood, MA, 1995.
5. Y. P. Tsividis and J. O. Voorman, *Integrated Continuous Time Filters: Principles Design and Applications*, IEEE Press, Piscataway, NJ, 1992.

6. J. Ramirez-Angulo, K. Sanchez-Sinencio, and M. Robinson, Current mode continuous time filters: two design approaches, *IEEE Trans. Circ. Syst.* **39**:337–341 (1992).
7. R. Higgins, *Digital Signal Processing in VLSI*, Prentice-Hall, Englewood Cliffs, NJ, 1990.

BANDSTOP FILTERS

CHIU H. CHOI
 University of North Florida
 Jacksonville, Florida

A bandstop filter (also known as *band-reject*, *band-elimination*, or *notch filter*) suppresses a band of frequencies of a signal, leaving intact the low- and high-frequency bands. A bandstop filter specification can be expressed as shown in Fig. 1. In the stopband from f_3 Hz to f_4 Hz, the attenuation is at least A_s dB. In the passbands (below f_1 Hz and above f_2 Hz), the maximum attenuation is A_p dB. The bands from f_1 to f_3 and from f_4 to f_2 are called the *transition bands*. The filter requirement is said to be geometrically symmetric if $f_1 f_2 = f_3 f_4$.

An approach to designing a circuit (a bandstop filter) with a frequency response that satisfies the bandstop requirements shown in Fig. 1 is described below. It consists of two steps: the approximation of the requirements by a transfer function and the synthesis of the transfer function.

In the approximation part of the design process, it is desirable to find a transfer function with a frequency response that satisfies the bandstop requirements. To find that transfer function, first convert the bandstop requirements into the normalized lowpass requirements. For the case that the bandstop requirements are symmetric, the corresponding normalized lowpass requirements are shown in Fig. 2. The normalized passband frequency $F_p = 1$ and the passband attenuation is A_p dB. The normalized stopband frequency is

$$F_s = \frac{f_2 - f_1}{f_4 - f_3}$$

and the stopband attenuation is A_s dB.

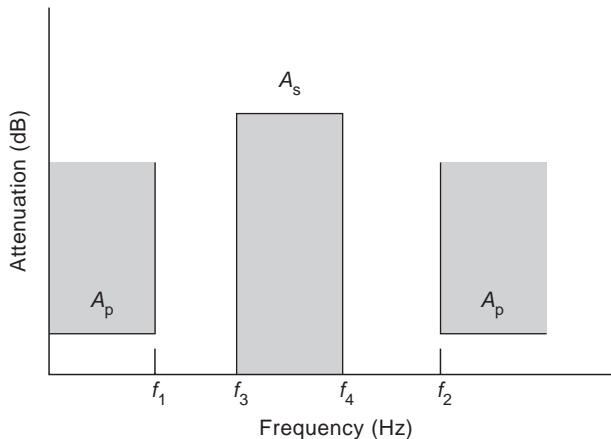


Figure 1. Bandstop filter specification.

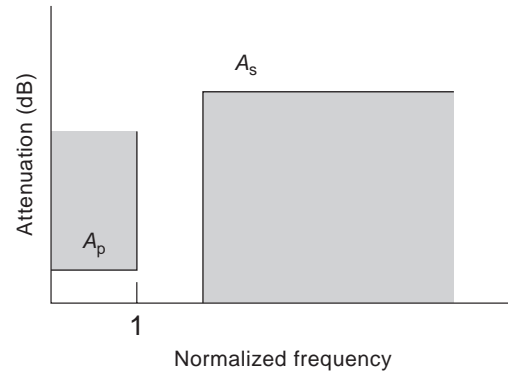


Figure 2. Normalized lowpass requirements.

With such lowpass requirements, we can obtain the corresponding lowpass transfer function $T_{LP}(s)$. (See LOWPASS FILTERS for more information about how to obtain the transfer function.) The bandstop filter transfer function $T_{BS}(s)$ is obtained by making the transformation

$$T_{BS}(s) = T_{LP}(s) \Big|_{s = \frac{B_s}{s^2 + (2\pi f_0)^2}}$$

where B is the bandwidth of the bandstop filter defined as

$$B = 2\pi(f_2 - f_1)$$

and f_0 is the center frequency of the bandstop requirement defined as

$$f_0 = \sqrt{f_1 f_2} = \sqrt{f_3 f_4}$$

To use this method when the requirement is not symmetric for the case where $f_1 f_2 > f_3 f_4$, we form a more stringent requirement by either decreasing f_2 or increasing f_4 , so that the symmetrical condition is met. The bandstop transfer function that satisfies the new requirements must also satisfy the original requirements. In case $f_1 f_2 < f_3 f_4$, we either increase f_1 or decrease f_3 and then apply the same procedure.

A simple example is provided to illustrate this concept. For the bandstop requirements $A_s = 25$ dB, $A_p = 3.01$ dB, $f_1 = 1$ kHz, $f_2 = 100$ kHz, $f_3 = 8$ kHz, and $f_4 = 12.5$ kHz; the corresponding normalized lowpass requirements are $A_s = 25$ dB, $A_p = 3.01$ dB, $F_p = 1$, and $F_s = 22$. Choosing a single-pole Butterworth approximation, the lowpass transfer function for the normalized lowpass requirements is

$$T_{LP}(s) = \frac{1}{s + 1}$$

which meets the stopband requirements easily. The bandstop transfer function is obtained by the transformation

$$T_{BS}(s) = \frac{1}{S + 1} \Big|_{S = \frac{2\pi(100 \times 10^3 - 1 \times 10^3)s}{s^2 + (2\pi 100 \times 10^3)(2\pi 1 \times 10^3)}}$$

which simplifies to

$$T_{BS}(s) = \frac{s^2 + 3.948 \times 10^9}{s^2 + 6.220 \times 10^5 s + 3.948 \times 10^9}$$

Note that the single-pole lowpass function has been transformed to a two-pole bandstop function. The above bandstop transfer function is in the so-called biquadratic form, which is an expression of the form

$$\frac{s^2 + a_1 + a_2}{s^2 + b_1 s + b_2} \quad (1)$$

There are a number of ways to synthesize and biquadratic function as an active network, such as the Friend biquad circuit [1,5], the Boctor circuit [2], and the summing four-amplifier biquad circuit [3,5]. The Friend or Boctor circuit uses one operational amplifier. The summing four-amplifier biquad circuit is much easier to tune. When $a_1 = 0$, the Bainter circuit can be used. The Bainter circuit [4] is shown in Fig. 3. For higher performance circuits, see Ref. 5 for the description of different bandstop circuit topologies.

The transfer function is

$$\frac{V_{out}(s)}{V_{in}(s)} = \frac{s^2 + \frac{R_{12}}{R_{11}R_{21}R_{31}C_1C_2}}{s^2 + \left(\frac{1}{R_{31}C_1} + \frac{1}{R_{32}C_1}\right)s + \frac{1}{R_{22}R_{31}C_1C_2}}$$

Comparing with Eq. (1), we obtain

$$a_1 = 0, \quad a_2 = \frac{R_{12}}{R_{11}R_{21}R_{31}C_1C_2}$$

$$b_1 = \frac{1}{R_{31}C_1} + \frac{1}{R_{32}C_1}, \quad b_2 = \frac{1}{R_{22}R_{31}C_1C_2}$$

Choose $C_1 = C_2 = 1$, $R_{12}/R_{11} = K$, $R_{31} = R_{32}$. Solving for the other values, we obtain

$$R_{21} = \frac{Kb_1}{2a_2}, \quad R_{22} = \frac{b_1}{2b_2}, \quad R_{31} = \frac{2}{b_1}$$

The impedance scaling method can be used to scale the values of R and C into the practical ranges. In general, a higher-order bandstop transfer function can be factorized

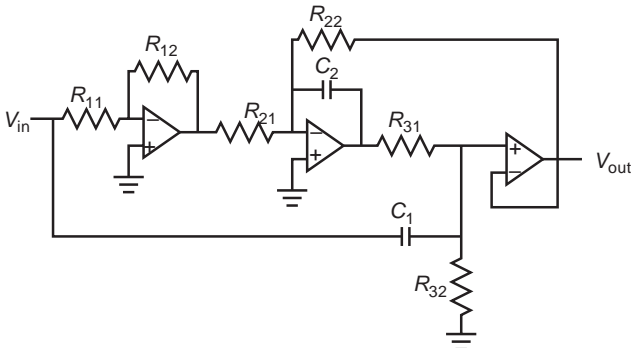


Figure 3. Bainter circuit.

into a product of biquadratic functions. Each biquadratic function can be synthesized by using the Bainter or other circuits. By cascading all the circuits together, the bandstop filter is realized.

BIBLIOGRAPHY

1. J. J. Friend et al., STAR, An active filter biquad section, *IEEE Trans. Circuits Syst.* **CAS-22**:115–121 (1975).
2. S. A. Boctor, Single amplifier functionally tunable low-pass notch filter, *IEEE Trans. Circ. Syst.* **CAS-22**:875–881 (1975).
3. G. Daryanani, *Principles of Active Network Synthesis and Design*, Wiley, New York, 1976.
4. J. R. Bainter, Active filter has stable notch and response can be regulated, *Electronics* 115–117 (Oct. 1975).
5. G. Moschytz and P. Horn, *Active Filter Design Handbook*, Wiley, New York, 1981.

BiCMOS DEVICES AND RF INTEGRATED CIRCUITS

YUPENG CHEN
XIAOMIN YANG
THOMAS X. WU
University of Central Florida
Orlando, Florida

1. INTRODUCTION

Since the late 1980s, the wireless communication market has expanded explosively mainly driven by increasing needs for high-performance, low-cost personal wireless communication equipments. Worldwide intensive research is being done in process technologies, circuit designs, system architectures, and communication standards to meet such demands. Technology advances in silicon germanium (SiGe) heterojunction bipolar transistors (HBTs) have created innovations in the semiconductor industry. The RF performance improvement of SiGe HBT by adding germanium to the base of the device will have a strong impact on modern radiofrequency integrated circuit (RFIC) design. Since IBM introduced the first commercial silicon germanium (SiGe) BiCMOS process in 1997, more and more SiGe products have emerged in the market, such as cellphones, wireless LAN, global positioning system (GPS) ICs, TV tuners, hard-disk-drive ICs, and optical carrier ICs. The estimated worldwide SiGe market growth is expected to exceed \$2.5 billion by the end of 2006 [1].

In this article, BiCMOS technology development focusing on the most recent achievements of SiGe BiCMOS technology is reviewed first. Several important figures of merit of SiGe device for RFIC designers such as f_T , f_{max} , BV_{CEO} (collector-emitter breakdown voltage with open base), and NF_{min} are discussed in detail. Next, from the RFIC designer's point of view, we begin with the stringent

system requirements of typical modern wireless communication standards. Commercial available technology options for RFIC are compared according to performance, power consumption, level of integration, and cost, with special emphasis on GaAs, RF CMOS, and SiGe BiCMOS. As a result, SiGe BiCMOS is an optimal device technology for implementing high-performance, low-power, and high-integration RFIC products. As important integration elements in the SiGe BiCMOS process, passive devices are also explored with respect to their impacts on RFIC design. This is expected to be followed by the design of key wireless system building blocks using SiGe BiCMOS technology. The most recently reported results of SiGe low-noise amplifiers (LNAs), power amplifiers (PAs), and integrated voltage-controlled oscillators (VCOs) are reviewed. Finally, future trends of RF integrated system adopting SiGe BiCMOS technology are discussed with respect to SiGe HBT technology (e.g., SiGe:C), integration level [e.g., RF SoC (RF system on chip)], and performance of on-chip passive devices (e.g., substrate transfer techniques).

2. BiCMOS DEVICES

It is well known that bipolar devices offer superior performance attributes for analog and RF circuits compared with plain CMOS [2]: more reliably modeled, less component variation, exhibiting better device-to-device matching, lower noise, increased bandwidth, easier matching to off-chip RF passive components, higher gain for a given layout size and power consumption level, and greater transconductance for a given current level. CMOS devices are also preferred because of their excellent switching performance with very high OFF-state resistance and lack of voltage drop when in the ON state. BiCMOS is a technology combining MOSFETs and bipolar devices into integrated circuits, which was proposed as early as 1969 [3]. Since then, BiCMOS technology has been applied to digital logic applications, which utilize the characteristics of high-speed bipolar and low-power CMOS on the same chip and RF and mixed-signal applications, which utilize bipolar RF and analog performance and CMOS digital integration capability. But as CMOS power supply voltage scaled down, the performance gap between bipolar and CMOS in digital logic began to narrow. Consequently, since the early 1990s there have been very few reports on developing BiCMOS for digital applications [4]. As

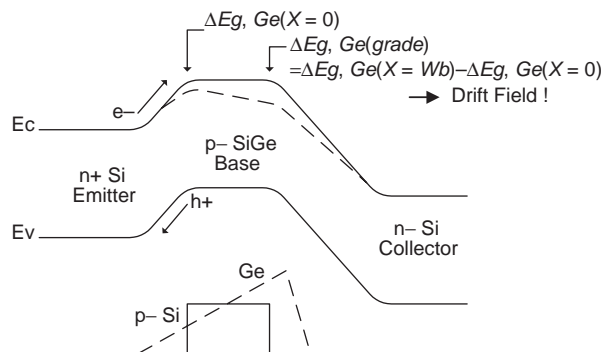


Figure 1. Engineered band diagram of SiGe HBT [6].

inspired by performance improvement of GaAs technology using heterojunction structure, germanium is introduced to the base of silicon BJT to form silicon germanium (SiGe) heterojunction bipolar transistors (HBTs) with enhanced RF performance. Since SiGe-based BiCMOS technology is currently a topic of great interest for research and wireless products development, our discussions will focus mainly on SiGe BiCMOS technology and its impact on RFIC design.

Table 1 demonstrates technology milestone for SiGe BiCMOS early development in IBM, a leader in SiGe BiCMOS technology. After that IBM introduced the first commercial silicon germanium (SiGe) BiCMOS process in 1997.

The essential operational differences between the SiGe HBT and the Si BJT are best illustrated by considering a schematic energy band diagram (Fig. 1). Two approaches are generally applied [7]. In the first approach, a graded germanium profile creates an electric field in the base region to accelerate the carriers that are diffusing from the emitter to the collector junction. In the second approach, the mobility of the minority carriers is increased in the base and the base resistance is reduced. Both approaches result in a higher f_T and lower base resistance.

A scanning electron microscopy (SEM) cross-sectional view of a 0.2- μm self-aligned selective epitaxial growth (SEG) SiGe HBT by ultrahigh vacuum/chemical vapor deposition (UHV/CVD) is shown in Fig. 2 [8], including an enlarged view of the active region, the key part of the SiGe HBT.

Device parameters such as f_T , f_{max} , NF_{min} , and BV_{CEO} are important figures of merit considered by RFIC designers for specific applications. f_T (short-circuit unity current

Table 1. SiGe BiCMOS Technology Early Development History from IBM Onward

Year	Key Technology
1982	UHV/CVD growth technique developed
1986	UHV/CVD epitaxial base silicon transistors fabricated
1987	SiGe based HBTs fabricated using MBE
1988	Graded-base SiGe polyemitter HBTs demonstrated, utilizing learning of double-polysilicon bipolar transistors
1993	Analog LSI circuit (1 gbps, 12 bits DAC) demonstrated, utilizing CMOS base processing
1993	SiGe HBTs with $f_T > 100$ GHz fabricated
1994	BiCMOS process in 200-mm CMOS fabricated, aligning processing with CMOS base
1996	RF technology with passive components, models, and design kit

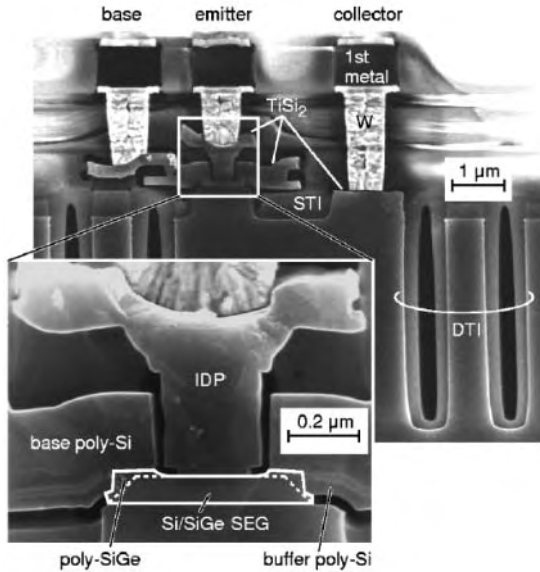


Figure 2. SEM cross-sectional view of a self-aligned SEG SiGe HBT [8].

gain frequency) and open emitter) to influence the dynamic range of device operation. The product of f_T and BV_{CEO} is referred to as the *Johnson limit* [12], which is an important figure of merit for high-frequency device. Many commercial foundries offer SiGe HBTs with several different BV_{CEO} values by using selective collector implantation optimized for both high-speed and wide-dynamic-range applications. We will discuss it later in SiGe RFIC power amplifier design.

Table 2 summarizes major SiGe HBT figures of merit that are important for RFIC applications. In addition, as with CMOS technologies, progressive vertical and lateral scaling of SiGe HBT results in better performance at lower power as indicated in Table 2.

Compared with III-V technologies, SiGe HBTs based on silicon substrate can inherently integrate with silicon CMOS, and standard silicon CMOS processes are by far one of the cheapest IC processing technologies available. Obviously, it is a cost-effective and processing-compatible way for SiGe BiCMOS processes to integrate the SiGe HBT into existing silicon CMOS core processes. That's exactly the method adopted by successful SiGe BiCMOS foundries. Historically, two different integration approaches have been used in SiGe BiCMOS processes [13]:

Table 2. IBM SiGe HBT Development across Four Generations

Parameter	0.5 μm	0.25 μm	0.18 μm	0.13 μm
Beta	100	100	200	400
V_A (V)	65	75	120	> 150
BV_{CEO} (V)	3.35	3.35	2.5	1.9
BV_{CBO} (V)	10.5	10.5	7.5	6
Peak f_T (GHz)	47	47	120	210
Peak f_{max} (GHz)	65	65	100	185
NF_{min} (dB)	0.8	0.8	0.4	< 0.3

Source: Refs. 13 and 14.

base-during-gate (BDG) integration and base-after-gate (BAG) integration. In the former approach, the HBTs are fabricated during the CMOS process (e.g., the IBM 0.5- μm SiGe BiCMOS process). In BAG, the HBTs are fabricated after the CMOS process to decouple the CMOS thermal cycle from the bipolar (e.g., IBM 0.25- and 0.18- μm SiGe BiCMOS) processes. The BAG approach is used in the most advanced SiGe BiCMOS technology such as 0.25 and 0.18 μm generations because it's difficult to fabricate HBT during a high thermal cycle of CMOS in these generations. f_{max} (maximum unity power gain frequency) are the parameters determining the frequency bandwidth of the device. f_T and f_{max} have been significantly improved over 200 GHz in the state-of-art SiGe BiCMOS 0.13- μm generation as shown in Fig. 3 [9].

In practical design, a good rule for high-quality RFIC design is $f_{design} < \frac{1}{10}f_T$. According to this rule, when f_T is over 200 GHz, SiGe HBT can be used for ultra-high-speed optical network applications that were previously the realm of III-V technologies.

The *noise figure* (NF), a standard metric of system noise performance, is defined as the degradation of signal-to-noise ratio (SNR) of an input signal as it passes through the system; NF is minimized when the device is presented with an optimized source reactance. A simplified formula for a SiGe HBT device is given as [6]

$$NF_{min} = 1 + \frac{1}{\beta} + \sqrt{2g_m r_b} \sqrt{\frac{1}{\beta} + \left(\frac{f}{f_T}\right)^2} \quad (1)$$

where β is the device current gain, g_m is the device transconductance, r_b is the base resistance, and f is the operation frequency. From this formula, the key to lower the noise figure is to reduce r_b and increase f_T [6]. Most recently reported SiGe transistors have $f_T > 350$ GHz [10] and $NF_{min} \leq 0.4$ dB at 10 GHz [11].

BV_{CEO} refers to the collector-emitter breakdown voltage with an open base. This parameter is quoted in device specifications of IC technology together with BV_{CBO} (collector-base breakdown voltage with an Passive elements such as inductors, capacitors, and resistors are also integrated into a typical SiGe BiCMOS process. Metallization and back-end processing in IC processes produce several metal layers utilized to build these passive components. A

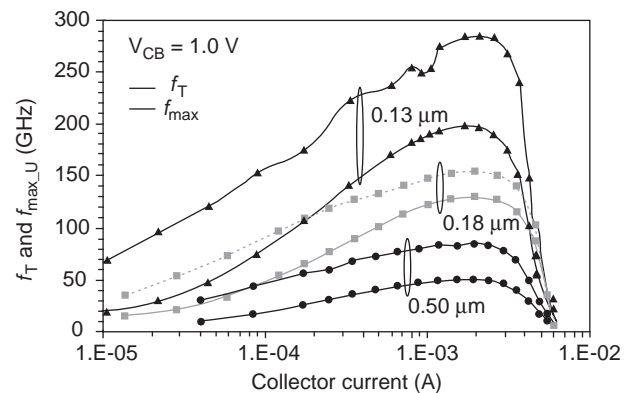


Figure 3. SiGe HBT f_T/f_{max} improvement across generations [9].

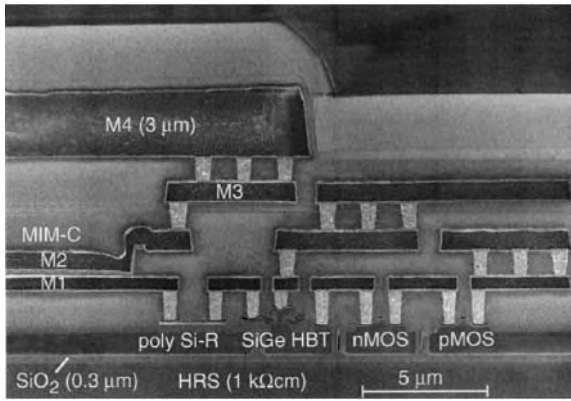


Figure 4. SEM cross section of a SiGe BiCMOS processes [8].

SEM cross-sectional view of a SiGe BiCMOS processes with the passives and metallization is shown in Fig. 4 [8]. High-quality-factor (Q) on-chip passive components are difficult to acquire in silicon substrate technology compared with III–V technology because of high silicon substrate loss. For example, it has been particularly challenging to achieve integrated inductors with Q values of 15–20 in the silicon process. Typical Q values for inductors in standard BiCMOS process can maximally reach about 10 (for inductances > 1 nH) [13]. In modern advanced SiGe BiCMOS processes, two types of methods are usually adopted to improve the performance of integrated inductors by decreasing metal series resistance and reducing substrate loss effects [14]: (1) additional thick top metal layer, copper metallization, deep-trench isolation, lightly doped substrate and (2) thick dielectric between inductor and substrate. Improved performance of passives in the IBM 0.18- μm SiGe BiCMOS process can be found in Table 3 [15]. We will discuss passive components for RFIC design using SiGe BiCMOS technology in Section 3.3.

Table 3. 0.18- μm SiGe BiCMOS Passive Device Performance from IBM Onward

Component		
Resistors	R_s (Ω/square) ^a	TCR ^b (ppm/ $^\circ\text{C}$)
Subcollector	8.1	1430
n^+ diffusion	72	1910
p^+ diffusion	105	1430
p^+ polysilicon	270	50
p polysilicon	1600	– 1178
TaN	142	– 750
Capacitors	C_p (fF/ μm^2)	V_{CC}^d (+5/– 5 ppm/V)
MIM ^c	1	< 45
MOS	2.6	– 7500/– 1500
Inductor	L (nH)	maximum Q at 5 GHz
Al-spiral inductor	$> = 0.7$	18
Varactor	tuning range	Q at 0.5 GHz
CB junction	1.64:1	90
MOS accumulation	3.1:1	300

Source: Ref. 15.

^aSheet resistance.

^bTemperature coefficient of resistance.

^cMetal–insulator–metal.

^dVoltage coefficient of capacitance.

3. BiCMOS RADIOFREQUENCY INTEGRATED CIRCUIT DESIGN

In the late 1980s, the first CMOS baseband analog and digital chips for the first-generation GSM (Group Special Mobile, now known as Global System Mobile) were fabricated in a 1.2- μm CMOS technology. Together with the progress of silicon bipolar technology (cutoff frequency f_T above 10 GHz) and worldwide spread use of mobile digital phones, a new and exciting area, radiofrequency integrated circuit (RFIC) technology, was created [7]. RF design moved from the PCB (printed circuit board) with discrete components to large-scale integration in silicon technology. Until recently, single-chip radio integration capabilities based on SiGe BiCMOS technology have been demonstrated [9]. A true single-chip radio supporting multiband, multistandard, and broadband communication may not just be a dream in the near future.

As stated above, RFIC is a relatively new area in contrast to other types of analog or microwave circuits. RFIC design has borrowed from both analog design techniques used at low frequencies and high-frequency design techniques used at microwave frequencies. However, RFIC design as a multidisciplinary area requires knowledge of many other areas besides integrated circuits, such as semiconductor device physics, wireless communication standards, signal and communication theory, microwave engineering, and system architectures.

From the circuit designer point of view, well-developed low-frequency analog circuit design and analysis techniques are fundamental knowledge references. Classical circuit building blocks can be used as prototypes or starting references for RFIC design. S parameters, shielding, impedance matching, and standing-wave ratios, which are important microwave system design concepts, are not totally but partially adopted in RFIC design. With the increasing of integration level of RFIC, new RFIC design has gradually acquired its own features [7]. The 50- Ω impedance matching culture has been stepped away. SPICE-like tools and system-level simulation packages including noise analysis have been adopted for highly integrated RFIC due to high-frequency substrate crosstalk and parasitic coupling.

3.1. Representative Wireless System Requirements

The rapidly growing commercial wireless personal and data communication market has been the strongest force driving the rapid development of RFIC technology. Since the early 1980s, the industry has undergone several generations of revolutionary changes. Figure 5 [16] schematically presents the scope of RFIC technologies in terms of the interplay among commercial wireless communication applications, available spectrum, and the kinds of elemental and compound semiconductors likely to be used.

From Fig. 5, we can find that modern RFIC designers are confronting with a wide range of system requirements with respect to different kinds of wireless applications. Table 4 compares some important specifications of several representative wireless communication standards.

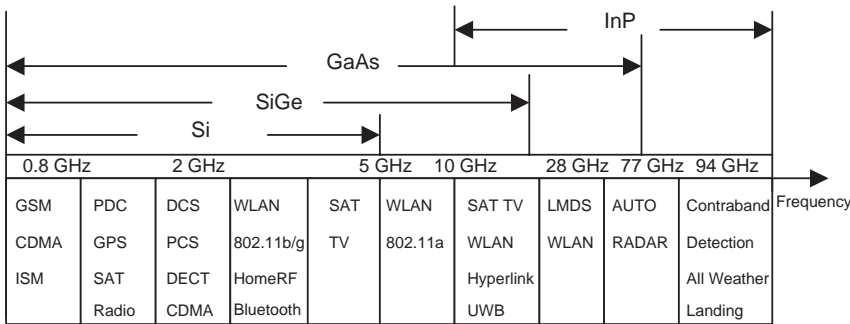


Figure 5. Commercial wireless communication applications [16].

It is clear that application-orientated system specifications vary in frequency, transmitter output power, receiver minimum sensitivity, and modulation schemes. In order to address such a broad application market, RFIC designers must satisfy constraints of not only performance but also flexibility and cost.

3.2. Technology Trends and Options for RFIC

Semiconductor technologies commercially available for RFIC design can be categorized as silicon and III–V compounds according to substrate type. Several semiconductor devices are based on these materials, including the silicon bipolar junction transistor (Si BJT), SiGe HBT, RF CMOS, GaAs metal semiconductor field-effect transistors (MESFETs), and GaAs and InP high-electron-mobility transistors (HEMTs). Each type of device has its own advantages or disadvantages as shown in Table 5.

Table 5 lists the key figures of merit normally considered by RFIC designers for various RF application standards. Obviously, no device technology does well in everything. Fortunately, different RF components require different device parameters. For example, the low-noise amplifier (LNA) needs devices with low-noise characteristics, the voltage-controlled oscillator (VCO) employs devices with low $1/f$ noise, and the power amplifier (PA) requires devices with high output power and high breakdown voltage. As a result, commercial wireless transceivers typically utilize a combination of different device technologies.

From the early 1980s, GaAs-based III–V compound technology has been the choice for RF and microwave applications because of their high level of performance for

GHz (gigahertz-range) frequency. Compared with silicon, they have higher electron mobility and saturation drift velocity, which means high device speed and a low noise figure. Because they are wide-bandgap materials, they also have high breakdown voltage, which is useful in high-power applications. The semiinsulating property of the III–V materials provides high device isolation and low dielectric loss for high-frequency integrated circuits. This property also decreases the loss of integrated passive components. The increased quality factor of passive elements can greatly improve the performance of the overall RF system. However, III–V technologies also suffer from inherent problems such as cost, integration level, and reliability issues. The III–V material wafer is normally smaller and more expensive than silicon. In addition, much effort should be taken to reduce leakage current and increase uniformity and yield. The overall high cost of III–V compounds is a tradeoff for their high performance.

Advances in silicon bipolar technology in the late 1980s, particularly in increasing the cutoff frequency, created an epoch in silicon RFIC. Some low-GHz RF front-end building blocks formerly implemented in GaAs technology have been replaced by silicon bipolar devices, while GaAs is still employed for low-noise amplifiers, power amplifiers, and RF switching, which belong to the high-frequency area near the antenna. But the vertical diffusion depth of base and the mobility of carriers in silicon set a limit of 30 GHz cutoff frequency for the bipolar transistor, which confines this bipolar component to the low-GHz front-end and analog mixed-signal area [7]. As discussed before, inspired by the heterobipolar approach in GaAs technologies, the SiGe HBT was introduced as an enhanced bipolar approach with superior RF performance.

Table 4. Comparison of Wireless Communication Standards

Standard	System	Frequency (MHz)	Data Rate (mbps)	Peak Transmit Power (dBm)	Minimum Sensitivity (dBm)	Modulation Scheme
DECT ^a	Coreless	1800	0.552	24	–83	GFSK
GSM	Cellular	900	0.014	33	–102	GMSK
CDMA	Cellular	900/1900	0.014	23	–104	BPSK/QPSK
WCDMA	Cellular	2000	2	27	–117	M-PSK
802.11b	Data	2400	11	20	–80	PSK-CCK
802.11a/802.11g	Data	5200	54	23	–82	OFDM
Bluetooth	Data	2400	0.723	0	–70	FSK
UWB	Data	3100~10600	>100	–	–	–

^aDigital Enhanced Cordless Telecommunications.

Table 5. Comparison of Various Semiconductor Device Technologies

Performance Metrics	SiGe HBT	Si BJT	Si CMOS	III-V MESFET	III-V HBT	III-V HEMT
Frequency response	+	0	0	+	++	++
1/f and phase noise	++	+	-	--	0	--
Broadband noise	+	0	0	+	+	++
Linearity	+	+	+	++	+	++
Output conductance	++	+	-	-	++	-
Transconductance/area	++	++	--	-	++	-
Power dissipation	++	+	-	-	+	0
CMOS integration	++	++	N/A	--	--	--
Output power density	+	0	-	++	+	++
Breakdown voltage	+	0	-	++	++	++
Passive performance	-	-	-	+	+	+
IC cost	0	0	+	-	-	--

Key: ++ excellent; + very good; 0 good; - fair; -- poor.

Source: Refs. 6 and 17.

Several practical RFIC design advantages for SiGe HBT are summarized as follows [18]:

- Low DC power consumption
- High breakdown voltage
- Improved noise performance with higher f_T and lower r_b
- Superior performance in 1/f noise characteristics over MOSFETs and MESFETs
- Higher early voltage V_A and βV_A
- Improved linearity over that in SiBJTs

With RF performance comparable to that of GaAs technology, LNA and PA, high-RF performance demanding blocks have been designed using SiGe technology rather than GaAs technology. We will investigate such a trend in detail later in this article. Besides the abovementioned high device performance, SiGe HBT can potentially be integrated with CMOS on the same silicon substrate (SiGe BiCMOS). This high integration ability creates the possibility of implementing a true single-chip RF system.

In the mid-1990s, at approximately the same time when SiGe HBT technology emerged, and driven by the tendency of increasingly shrinking microprocessor size, the scaling of CMOS resulted in marked improvement in RF performance at submicrometer feature size. Consequently, CMOS has become a viable option for RFIC design. Foundries also provide RF CMOS process optimized for RF applications [19]. But RF CMOS technology achieves the same performance level using novel circuit techniques, which may need higher power consumption or larger chip die size compared with SiGe BiCMOS.

The optimum technology option for RFIC in terms of performance, cost, and market is the first line for successful RFIC product developments. But for practical RFIC designers, this is always complicated by various application performance requirements (Table 4) regarding different building blocks, various device characteristics (Table 5), system cost, and market factors. For a whole RF system, a combination of technologies may achieve optimum system performance and cost compromise. In addition, this multidimensional decision function is strongly related with the development of device, circuit, and sys-

tem technology. The cost of SiGe BiCMOS technology will be gradually lowered with its wider applications. Combining performance, integration, and cost advantages together, SiGe BiCMOS should be one of the most promising technologies for RFIC design.

3.3. RFIC Passive Design in SiGe BiCMOS Technology

Passive components also play important roles in RFIC design. To reduce board-level components, passive devices should be integrated on chip as active devices. Integrated inductors, capacitors, varactors, and resistors have been developed based on the existing SiGe BiCMOS fabrication processes while avoiding any significant process alterations.

3.3.1. Inductor. RFIC designs require high-performance passive components, particularly the on-chip inductors. Integration of spiral inductors has numerous challenges. In particular, high Q (inductor quality factor), high self-resonance frequency, and low cost must be balanced in order to provide a competitive inductor. Circular and rectangular spirals are two popular shapes for on-chip inductors. The circular spiral is known to provide somewhat higher Q , while the rectangular version is more area-efficient [20]. For both of these inductor configurations, the bulk of the spirals are usually implemented in the topmost available metal, and connection to the center of the spiral is made with a crossunder of some lower level of metal.

Losses in inductors are due primarily to currents flowing in the inductors. Substrate and radiation losses also exist. The quality factor Q and the self-resonance frequency are the most common figures of merit. Q is used to describe loss performance of inductors. Many factors can influence the Q value, such as operating frequency, conductor metal conductivity, substrate resistivity, and geometric characteristics of inductor [21,22]. Q is frequency-dependent, increasing with the frequency up to a peak value, and drops at higher frequencies, owing to the fact that the reactance of input impedance dominated by the inductance at lower frequency rolls off at higher frequency because of the parasitic capacitances, which consist of the overlap capacitance between the spiral and underpass,

fringing capacitance between adjacent metal lines, and substrate capacitance between metal layer and grounded substrate.

In practical integrated inductor design, the geometric characteristics, such as linewidth, line spacing, number of turns, and inner diameter, should be carefully chosen to optimize the inductor Q at operating frequencies. The rise of Q is usually found with increasing linewidth, while there is no wide variation in inductance. This is because of the fact that the resistance of inductor decreases with increasing linewidth. The inner diameter also affects the inductor Q . The contribution of innermost turn to the total inductance is very small. The main effect of the innermost turn is on resistance. For this reason, hollow spirals are commonly used in RF applications to increase the Q factor. Increasing the number of turns of a given inductor always yields higher inductance. This increase in inductor design, as the increase of linewidth, spacing between the turns, or the inner diameter, may result in larger area. Usually, the larger the area, the higher the parasitic capacitance, and the lower the self-resonance frequency. Therefore, it is important to ensure that the self-resonance frequency is beyond the operating frequency range.

3.3.2. Capacitor. Besides inductors, capacitors with high Q at the operating frequency are also essential for the integration of RF circuits. The design goal is to achieve both a small series resistance for a high Q and a high capacitance/area ratio to minimize the area consumption. Three basic types of capacitors have been developed in SiGe technology: MOS (polysilicon gated capacitors on single-crystal silicon), PIP (polysilicon-insulator-polysilicon), and MIM (metal-insulator-metal)/MOM (metal-oxide-metal) capacitors. Each has its own place for use in different application spaces depending on capacitance desired and performance at the application frequency.

MOS capacitors are simply built from the gate oxide. These devices consist of silicided gate polysilicon, thin gate oxide, and FET well-doped silicon. They have the highest capacitance density among all the capacitors owing to the ultrathin oxide. But the Q value of these capacitors is relatively poor because of the high resistance of the doping. PIP capacitors are fabricated in double-polysilicon BiCMOS processes [23]. The capacitor structure is formed using p^+ -doped gate polysilicon as the bottom plate, a deposited oxide layer for the capacitor dielectric, and silicided extrinsic base polysilicon as the top electrode. The drawback of MOS and PIP capacitors is low quality factor (Q) due to high-resistance plates and capacitive losses at RF frequencies. This limits their use at RF. They are typically used for power supply bypass and decoupling. In contrast, MIM or MOM capacitors can be built using two interconnect layers with a very small series resistance for high Q . These capacitors are achieved by using a thin oxide film to form the capacitors in place of the thick intermetal dielectrics. MIM or MOM capacitors are preferred in narrowband applications, such as resonators, filters, and tank circuits, where high Q is needed [24].

3.3.3. Varactor. Voltage-variable capacitors (varactors) are required for tuning circuit designs, such as voltage-controlled oscillators (VCOs) for on-chip carrier frequency generation. The key figures of merit for varactors are (1) tunability (C_{\max}/C_{\min}), (2) C_V linearity for VCO gain variation, (3) quality factor Q , (4) tolerance, and (5) capacitance density. Two basic types of varactors are supported by SiGe BiCMOS technology: MOS varactors and junction varactors.

An accumulation-mode MOS varactor is achieved by connecting the drain and the source only, while adding the control voltage on the bulk [25]. The capacitance of this varactor is high in accumulation and decreases sharply as the device enters and goes further into depletion. This results in excellent tunability. However, it has the drawback of a narrow range across which the capacitance varies significantly from a low value to a high value. This in turn could limit the tuning range of the VCOs based on such varactors. Junction varactors are offered as an alternative to provide wider capacitance variation range and also more linearity. The collector-base (CB) junction varactor provides wider capacitance variation while maintaining a relatively high Q .

3.4. Wireless System Key Building Blocks

Figure 6 gives us a general view of RF heterodyne transceiver system. Some important building blocks that are necessary in all types of transceiver are listed in Table 6, with their main features and technology requirements. During practical RFIC design, several tradeoffs must be made under product performance and cost constraints. These tradeoffs have been summarized in the “RF design hexagon” as shown in Fig. 7 [26]. We will discuss some tradeoffs in the design of each building block.

3.4.1. Low-Noise Amplifiers (LNAs). The LNA is one of the key building blocks in the RF system. In the receiving chain closest to the antenna, the LNA receives a variety of signals coming from the antenna, and its function is to boost the signal without adding much noise. Since the LNA is at the first stage of receiving chain, its noise performance is the most critical for the entire receiver. Because of the wide amplitude range of the receiving signal, low noise and high linearity are both important figures of merit for LNA design [27]. The third-order input intercept point (IIP3) is the most common parameter used to measure circuit linearity by applying the two-tone test. The noise figure (NF) is often used to measure system noise performance. Application-dependent system specifications such as minimum detectable signal (MDS) or minimum sensitivity and spurious-free dynamic range (SFDR) can be determined from IIP3 and NF [26].

From the perspective of LNA designers, a seemingly simple structure with a few components means easy design, but the tradeoffs complicate the design. A matching network needs to be designed to satisfy both noise and power matching. The progressive decrease of supply voltage and maximum allowed power consumption with an almost constant dynamic range requirement of the system leads to great challenges in modern LNA design.

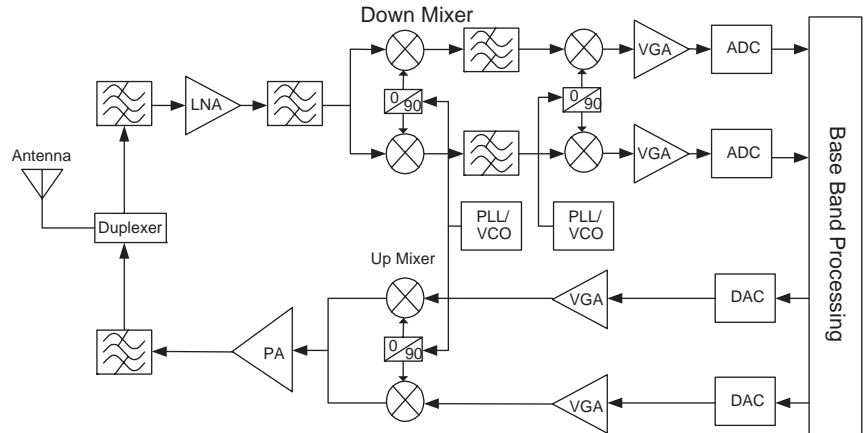


Figure 6. A general RF transceiver system.

Additionally, the LNA must provide enough gain to decrease the noise contributions from the following stages and consequently minimize the overall system noise. However, maximum gain is often limited by system linearity performance [28].

Noise figure (NF), DC power consumption (P_{DC}), power gain, and IIP3 are the most important design considerations for the LNA. They can be summarized into two figures of merit: $gain/(P_{DC} \cdot NF)$ and $IIP3/P_{DC}$. The results of comparing these two parameters for the best reported results in silicon and GaAs technology at 2 GHz [29] have indicated the potential advantage of SiGe technology for LNA, if DC power dissipation is a major consideration.

Table 7 summarizes the most recently reported results of RF LNA using SiGe BiCMOS technology, demonstrating a competitive noise figure and linearity compared with GaAs technology for various wireless applications.

3.4.2. Power Amplifier (PA). The power amplifier is the last building block in the transmitter chain of a transceiver system. Its function is to amplify the signal power to a level that is high enough for signal propagation through

an appropriate antenna into the air. It is one of the most challenging building blocks in a transceiver system.

The typical figures of merit of a practical power amplifier are efficiency, linearity, output power, ruggedness, and power gain. The most commonly used metric for efficiency is power-added efficiency (PAE), which indicates how power drawn from the supply is efficiently converted to RF power delivered to the load. The linearity of PA is usually specified as an adjacent-channel power ratio (ACPR) in dBc (decibels with respect to carrier), a measure of the spectral “spillover” due to amplifier nonlinearity into an adjacent frequency band by a digitally modulated waveform. Ruggedness is the ability to survive power mismatch conditions at the output using specific DC and RF drive conditions. Output power is defined by a wireless standard (see Table 4) and often exhibits a wide range of variation for mobile applications. Power gain is implicitly set by the maximum power generated by the preceding stage of the power amplifier together with output power requirements [37].

The linearity varies with different signal modulation schemes employed by different wireless standards (see

Table 6. Features and Requirements for Basic Wireless Building Blocks

Building Blocks	Main Features	Technology Requirements
LNA	Low-noise figure Gain per stage High linearity	Low NF_{min} , low HBT R_b High early voltage High f_T/f_{max}
Mixer	High linearity High port isolation Carrier leakage	High early voltage High f_T/f_{max} Isolation technologies (DT) Small mismatch
VCO	Low-phase noise	High-Q passives farther from carrier Low- $1/f$ -noise HBT closer to carrier Varactor tuning range (C/V)
Synthesizer	Tuning range (frequency/V) Low gain (K_v) variation Low-phase noise Low reference spurs Power consumption Chip area	Same as VCO Small FET asymmetry Small gate length for low supply operation Reduced area
PA	Power-added efficiency Gain per stage Robustness	Low loss matching and interconnect circuits (high-Q inductor, thick metal) Maximum available gain HBT High-breakdown-voltage HBT

Source: Ref. 15.

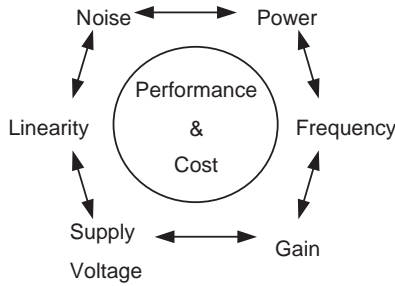


Figure 7. RFIC design hexagon [26].

Table 4). For wireless standards such as GSM, DECT, and Bluetooth employing constant envelope modulation schemes, nonlinear power amplifier (classes C, D, E, and F) can be used. For other wireless standards such as WLAN and WCDMA employing variable envelope modulation schemes, linear power amplifier (class AB) is typically used. Linearity can be a tradeoff with power-added efficiency in a practical power amplifier design, where nonlinear amplifiers often achieve higher efficiency than do linear ones [37].

In a practical RF power amplifier design several challenges are presented [29]. The PA must satisfy all the figures of merit discussed above under the constraint of cost for specific applications; the current trend toward decreased power supply (from 5 to 3 V and even lower) has also made it difficult to maintain the required output power and efficiency due to impedance matching limitations; power-added efficiency should not degrade significantly with a wide range of output power.

Key device figures of merit for RF power amplifiers are f_{\max} (bandwidth and high power gain), linearity, and breakdown voltage. Currently available technologies for RF commercial power amplifier are GaAs, SiGe, and CMOS. Because of the high linearity, efficiency, output power, and breakdown voltage, GaAs has been the dominant technology for the RF power amplifier since the early 1990s. However, GaAs amplifiers have the disadvantages of relatively high cost, low substrate thermal conductivity, and low integration ability with CMOS technology. More recent SiGe HBT technology with high f_{\max} , improved ruggedness, high linearity, and relatively high breakdown voltage has made SiGe a technology contender for RF power amplifier applications. As discussed before, SiGe devices can be engineered to have even higher breakdown voltage but with the compromise of lower f_{\max} . In portable wireless applications, a progressively reduced power supply makes breakdown voltage less critical, where SiGe can

be a good choice [29]. In addition, SiGe BiCMOS provides the ability to integrate the power amplifier with some related logic power amplified functions (implemented by CMOS). High-quality passive components offered by commercial SiGe BiCMOS processes enable the manufacture of fully integrated RF power amplifiers, including on-chip impedance matching and filtering.

The power amplifier is probably one of the last building blocks to be integrated into a single radio chip. By far, the only reported real single radio chip including PA is Bluetooth [38], which is a relatively low-RF performance demanding wireless standard.

More recently a significant amount of research effort has been taken to design RF power amplifiers using SiGe BiCMOS technology (see Table 8), which have demonstrated competitive power efficiency and linearity compared with GaAs technology for various wireless applications.

3.4.3. Integrated Voltage Controlled Oscillator (VCO).

The voltage-controlled oscillator (VCO) is a very important building block in the RF system and is often integrated into a phase-locked loop (PLL) or frequency synthesizer to serve as a frequency reference in a transceiver system [47]. For example, it is used as a local oscillator together with a mixer to downconvert the received RF signal to an IF signal. Typical figures of merit for VCO are frequency of oscillation, phase noise, frequency tuning range, output power, gain variation, and thermal stability. Phase noise is perhaps the most important characteristic of a VCO. Ideally, a VCO output signal is expected to have all signal power concentrated in one discrete frequency; however, all practical VCOs suffer from spectrum impurity. *Phase noise* is any noise that changes the frequency or phase of the oscillator signal and is usually specified in dBc/Hz, meaning noise power in a 1 Hz bandwidth with respect to carrier power.

A good equation for relative phase noise of a VCO can give us some insight into its function [48]:

$$\frac{1}{4Q^2} \left(\frac{\Delta\omega}{\omega_0} \right)^2 \frac{P_{\text{noise}}}{P_{\text{carrier}}} \quad (2)$$

Here, Q is the open loop quality factor, $\Delta\omega$ is the frequency offset, ω_0 is the center frequency, P_{noise} is the spectral density of each noise source, and P_{carrier} is the spectral density of the carrier. From this equation, there are several rules for decreasing the phase noise: (1) use high- Q passive components, (2) maximize the oscillation

Table 7. Some Recently Reported SiGe BiCMOS LNAs Compared with GaAs LNAs

Technology	Frequency (GHz)	Noise Figure (dB)	Gain (dB)	IIP3 (dBm)	Power Dissipation (mW)	Ref.
0.5 μm GaAs PHEMT	2.14	1.0	15.0	+7.3	25.5	30
0.5 μm SiGe BiCMOS	2.5	1.6	12.0	+8	20.625	31
0.5 μm SiGe BiCMOS	2.0	1.15	18.0	+15.8	N/A	32
0.5 μm SiGe BiCMOS	1.96	1.9	15.3	+7.6	13.5	33
0.2 μm SiGe BiCMOS	23	4.1	21.0	N/A	50	34
0.35 μm SiGe BiCMOS	5.2–6.6	2.3	17.0	–7	13	35
0.5 μm SiGe BiCMOS	0.88	1.4	15.7	+10.3	11.7	36

Table 8. Some Recently Reported SiGe BiCMOS PAs compared with GaAs PAs

Technology	Frequency (GHz)	Maximum output power (dBm)	Linearity (ACPR)	Maximum PAE (%)	Supply Voltage (V)	Linear Gain (dB)	Ref
GaAs HBT	1.95	24	– 42 dBc at 5 MHz – 55 dBc at 10 MHz	36	3.5	48	39
SiGe	1.88	30	– 46 dBc at 1.25 MHz	41	3.4	23	40
0.35 μmSiGe	5	31.5	N/A	24	N/A	20.6	41
SiGe	2.4	27.5	N/A	47	3.3	35	42
0.25 μmSiGe	1.95	24	– 30.7 dBc at 5 MHz – 41.3 dBc at 10 MHz	30	3.3	24	43
0.18 μmSiGe	2.2	10	N/A	25	1.3	13	44
SiGe	0.824 ~ 0.849	28.2	– 53.6 dBc at 885 kHz – 60.6 dBc at 1980 kHz	45	2.5	28	45
0.25 μmSiGe	5.3	25	N/A	24	2.4	26	46

swing, and (3) minimize the number of active and lossy passive devices in the oscillation path. Consequently, high- Q passive components such as inductors and varactors are critical limiting factors for the performance of VCO. Fully integrated VCO suffers from low-quality on-chip inductors and varactors. In addition to phase noise, frequency tuning range and VCO gain variation parameters also require high-quality passive components. Because of the lower $1/f$ noise of SiGe HBT compared with that of GaAs or Si CMOS, SiGe HBT is preferred for $1/f$ noise-sensitive circuits such as VCO. As discussed previously, more recent advances of SiGe BiCMOS passive device technology have greatly increased VCO performance. Table 9 summarizes the most recently reported VCO design using SiGe BiCMOS and GaAs technology.

4. FUTURE TRENDS

According to ITRS (International Technology Roadmap for Semiconductors) 2003 [16], the challenges for future RF transceivers using BiCMOS technology include the following: aggressive scaling of passive elements (capacitors and inductors); reducing the cost of BiCMOS technology while improving power and performance tradeoffs; improving signal isolation as more functions are integrated on a single chip; increasing difficulty with integrating bipolar devices in aggressively scaled CMOS nodes due to conflicting thermal budget requirements; improving the performance of active devices to levels that enable reconfiguration of the RF transceiver in a software-defined radio, a funda-

mental architectural simplification of the RF transceiver such as the direct synthesis and/or direct analog-to-digital conversion of the RF signal; enabling the scaling of bipolar power supply to reduce power consumption versus CMOS technology; and integrating new materials in a cost-effective manner to realize the high- Q inductors and high-density metal-insulator-metal (MIM) capacitors.

Future challenges can be summarized as follows: SiGe HBT device performance improvement, RFIC design technique development, and on-chip passive component performance and isolation enhancement.

4.1. SiGe HBT Device Performance Improvement

Carbon doping of SiGe HBTs (SiGe:C) is rapidly becoming the preferred approach for commercial SiGe technologies as a means to effectively suppress boron outdiffusion during fabrication [6], consequently facilitating management of the overall thermal budget and profile control. Continuous lateral and vertical scaling, novel device structure design, and improved fabrication techniques will further enhance SiGe HBT peak f_T and f_{max} . Improved device performance has led to optical and communication applications at frequencies greater than 20 GHz. The further increased performance of SiGe HBT also makes it possible to design a reconfiguring RF transceiver in a software-defined radio, which implements most of RF functions in the digital domain.

4.2. RFIC Design Technology Development

RF system-on-chip (RF SoC) usually means that RF analog/digital circuits are all integrated with memory blocks

Table 9. Some Recently Reported SiGe BiCMOS VCOs Compared with GaAs VCOs

Technology	Frequency (GHz)	Tuning Range (GHz)	Phase Noise	Power Supply (V)	Power Dissipation (mW)	Ref
GaAs HBT	5	0.290	– 118 dBc/Hz at 1 MHz	3.5	13.2	49
0.35 μmSiGe	4.7	0.509	– 107 dBc/Hz at 1 MHz	3	54	50
0.35 μmSiGe	11	0.5	– 85 dBc/Hz at 100 kHz	3.3	N/A	51
0.35 μmSiGe	47	7.05	– 104 dBc/Hz at 1 MHz	5.5	290	52
0.25 μmSiGe	2.3	N/A	– 102 dBc/Hz at 100 kHz	3	15.6	53
0.35 μmSiGe	20	0.600	– 85 dBc/Hz at 1 MHz	3.6	43.2	54
0.4 μmSiGe	28	4.1	– 84.2 dBc/Hz at 1 MHz	5	129	55
0.18 μmSiGe	6/9	0.3/0.45	– 106 dBc/Hz at 1 MHz/ – 104 dBc/Hz at 1 MHz	1.8	19.44	56

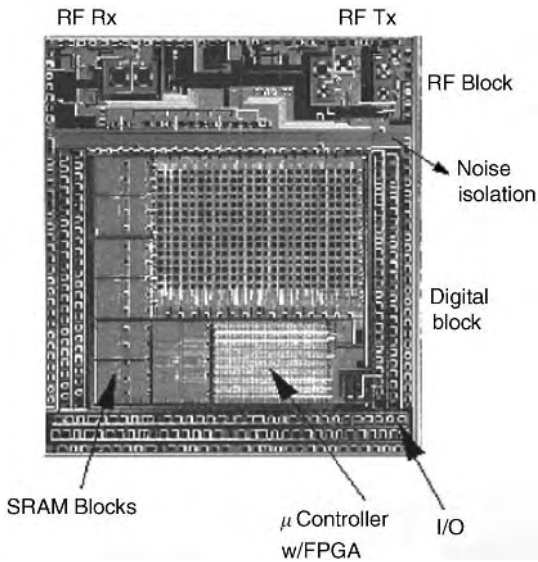


Figure 8. Highly integrated SoC solution using SiGe BiCMOS technology [9].

and microprocessors as a single-chip radio. High integration ability with superior RF performance has made SiGe BiCMOS a preferred choice for future RF SoC implementations [18]. IBM has demonstrated a highly integrated SoC design using 0.18- μm SiGe BiCMOS technology [9] (see Fig. 8). Multistandard and multiband wireless handsets employing RF SoC technique will not be a dream in the near future. Future developments of RFIC CAD techniques may change the RFIC design methodology to digital cell library-like designs (see Fig. 9) [57]. After picking up existing RF/analog cell libraries or IPs (intellectual properties) for different building blocks (e.g., LNA, PA, VCO) according to various applications (e.g., GSM, CDMA), future RF system designers can simply assemble them together to functionalize the whole system. Consequently, RFIC design will be an easy and quick instead of

tedious and complicated process. Available highly accurate RF/analog models that support scaling will enable RF SoC simulations, including all on-chip coupling parasitic effects.

4.3. On-Chip Passive Component Performance and Isolation Enhancement

The performance of active devices has been improved significantly, as discussed earlier. In contrast, relatively slow development of passive components will be the key bottleneck in the future RFIC designs. This is mostly the result of high RF loss of silicon substrate, which leads to not only low- Q passive devices but also large coupling through substrates. A lot of research has been done on substrate technologies for RF applications. A good review of modern substrate transfer techniques for RFIC, such as silicon-on-insulator (SoI), silicon-on-glass (SoG), and silicon-on-anything (SoA) is given in Ref. 58. Micromachining techniques have also been applied to RFIC to produce high-performance passive devices [59].

5. CONCLUSION

In this article, we have reviewed the advances of SiGe BiCMOS technologies. SiGe BiCMOS technology has exhibited many advantages over other existing RF semiconductor technologies, such as III-V compounds and RF CMOS, which will have a strong impact on future RFIC design. RFIC designs using SiGe BiCMOS technology are discussed in terms of passive components and some key RF building blocks. Future trends of RF integrated system adopting SiGe BiCMOS technology are also summarized.

Acknowledgements

The authors wish to thank George Remoundos from Agere Systems (Orlando, FL) and Brittin Kane from Insyte Inc. (St Petersburg, FL) for providing valuable materials on this topic.

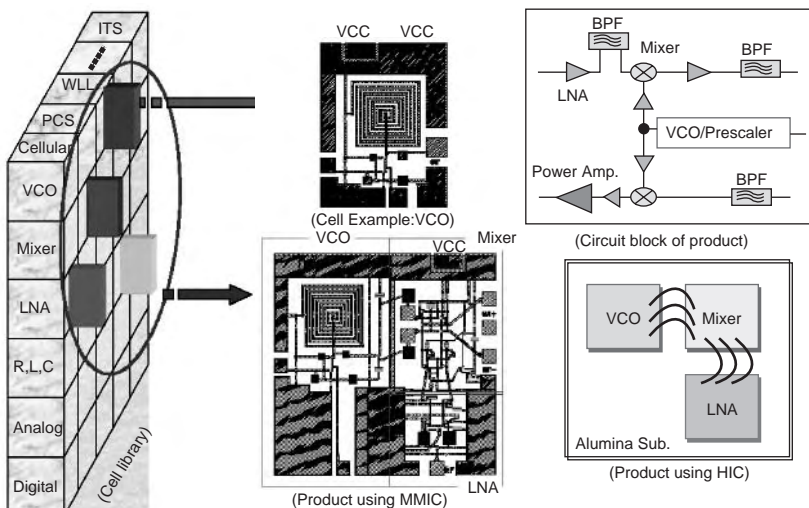


Figure 9. Cell library for quick RFIC design [57].

BIBLIOGRAPHY

1. *SiGe Advances in the Marketplace*, Pathfinder Research Inc., San Jose, CA, Sept. 2002.
2. D. A. Rich, M. S. Carroll, M. R. Frei, T. G. Ivanov, M. Mas-trapasqua, S. Moinian, A. S. Chen, C. A. King, E. Harris, J. De Blauwe, Vuong Hong-Ha, V. Archer, and K. Ng, BiCMOS technology for mixed-digital, analog, and RF applications, *IEEE Microwave Mag.* **3**(2):44–55 (June 2002).
3. H. C. Lin, J. C. Ho, R. R. Iyer, and K. Kwong, Complementary MOS-bipolar transistor structure, *IEEE Trans. Electron. Devices* **ED-16**(11):945–951 (Nov. 1969).
4. T. H. Ning, Why BiCMOS and SOI BiCMOS, *IBM J. Res. Devel.* **46**(2/3):181–186 (March/May 2002).
5. S. Subbanna, D. Ahlgren, D. Hatame, and B. Meyerson, How SiGe evolved into a manufacturable semiconductor production process, *Proc. IEEE Int. Solid-State Circuits Conf.*, 1999, pp. 66–67.
6. J. D. Cressler and G. Liu, *Silicon-Germanium Heterojunction Bipolar Transistors*, Artech House, Norwood, MA, 2003.
7. J. Sevenhans, The siliconradio decade, *IEEE Trans. Microwave Theory Tech.* **50**(1):235–244 (Jan. 2002).
8. K. Washio, SiGe HBT and BiCMOS technologies for optical transmission and wireless communication systems, *IEEE Trans. Electron. Devices* **50**(3):656–668 (March 2003).
9. A. J. Joseph, J. Dunn, G. Freeman, D. L. Hareme, D. Coolbaugh, R. Groves, K. J. Stein, R. Volant, S. Subbanna, V. S. Marangos, S. S. Onge, E. Eshun, P. Cooper, J. B. Johnson, Rieh Jae-Sung, B. Jagannathan, V. Ramachandran, D. Ahlgren, D. Wang, and X. Wang, Product applications and technology directions with SiGe BiCMOS, *IEEE J. Solid-State Circ.* **38**(9):1471–1478 (Sept. 2003).
10. J. S. Rieh, B. Jagannathan, H. Chen, K. T. Schonenberg, D. Angell, A. Chinthakindi, J. Florkey, F. Golan, D. Greenberg, S. J. Jeng, M. Khater, F. Pagette, C. Schnabel, P. Smith, A. Stricker, K. Vaed, R. Volant, R. D. Ahlgren, G. Freeman, K. Stein, and S. Subbanna, SiGe HBTs with cut-off frequency of 350 GHz, *Proc. Int. Electronic Devices Mtg.*, Dec. 2002, pp. 771–774.
11. D. Greenberg, B. Jagannathan, S. Sweeney, G. Freeman, and D. Ahlgren, Noise performance of a low base resistance 200 GHz SiGe Technology, *Proc. Int. Electronic Devices Mtg.*, Dec. 2002, pp. 787–790.
12. E. O. Johnson, Physical limitation on frequency and power parameters of transistors, *IEEE Int. Conv. Record* **27** (1965).
13. D. L. Hareme, D. C. Ahlgren, D. D. Coolbaugh, J. S. Dunn, G. G. Freeman, J. D. Gillis, R. A. Groves, G. N. Hendersen, R. A. Johnson, A. J. Joseph, S. Subbanna, A. M. Victor, K. M. Watson, C. S. Webster, and P. J. Zampardi, Current status and future trends of SiGe BiCMOS technology, *IEEE Trans. Electron. Devices* **58**(11):2575–2594 (Nov. 2001).
14. J. S. Dunn, D. C. Ahlgren, D. D. Coolbaugh, N. B. Feilchenfeld, G. Freeman, D. R. Greenberg, R. A. Groves, F. J. Guarin, Y. Hammad, A. J. Joseph, L. D. Lanzerotti, S. A. St. Onge, B. A. Orner, J. S. Rieh, K. J. Stein, S. H. Voldman, P. C. Wang, M. J. Zierak, S. Subbanna, D. L. Hareme, D. A. Herman, Jr., and B. S. Meyerson, Foundation of RF CMOS and SiGe BiCMOS technologies, *IBM J. Res. Devel.* **47**(2/3):101–138 (March/May 2003).
15. D. L. Hareme, A. Joseph, D. Coolbaugh, G. Freeman, K. Newton, S. M. Parker, R. Groves, M. Erturk, K. Stein, R. Volant, C. Dickey, J. Dunn, S. Subbanna, H. Zamat, V. S. Marangos, M. M. Doherty, O. Schreiber, T. Tanji, D. A. Herman, and B. S. Meyerson, The emerging role of SiGe BiCMOS technology in wired and wireless communications, *Proc. 4th Int. IEEE Inter. Caracas Conf. Devices, Circuit and System*, Aruba, April 2002, pp. D052-1–D052-17.
16. ITRS 2003 Roadmap (2003) (Online), <http://public.itrs.net>
17. K. Chang, I. Bahl, and V. Nair, *RF and Microwave Circuit and Component Design for Wireless Systems*, Wiley, New York, 2002.
18. D. Y. C. Lie, Xiaojun Yuan, L. E. Larson, Y. H. Wang, A. Senior, and J. Mecke, “RF-SoC”: Low-power single-chip radio design using Si/Ge BiCMOS technology, *Proc. 3rd Int. Conf. Microwave and Millimeter Wave Technology*, Aug. 2002, pp. 30–37.
19. IBM 180 nm technology brief (2003) (Online), <http://www.ibm.com>.
20. T. Lee, *The Design of CMOS Radio-Frequency Integrated Circuits*, Cambridge Univ. Press, Cambridge, UK, 1998.
21. I. Bahl, *Lumped Elements for RF and Microwave Circuits*, Artech House, Norwood, MA, 2003.
22. M. Park, S. Lee, C. S. Kim, H. K. Yu, and K. S. Nam, The detailed analysis of high Q CMOS-compatible microwave spiral inductors in silicon technology, *IEEE Trans. Electron. Devices* **45**(9):1953–1959 (Sept. 1998).
23. A. Pruijboom, D. Szmyd, R. Brock, R. Wall, N. Morris, Keng Fong, and F. Jovenin, QUBiC3: A 0.5 μm BiCMOS production technology with $f_T = 30$ GHz, $f_{max} = 60$ GHz and high-quality passive components for wireless telecommunication applications, *Proc. IEEE Bipolar/BiCMOS Circuits and Technology Meeting*, Sept. 1998, pp. 120–123.
24. J. N. Burghartz, M. Soyuer, K. A. Jenkins, M. Kies, M. Dolan, K. J. Stein, J. Malinowski, and D. L. Hareme, Integrated RF components in a SiGe bipolar technology, *IEEE J. Solid-State Circ.* **32**(9):1440–1445 (Sept. 1997).
25. P. Andreani and S. Mattisson, Brief papers on the use of MOS varactors in RFVCO's, *IEEE J. Solid-State Circ.* **35**(6):905–910 (2000).
26. B. Razavi, *RF Microelectronics*, Prentice-Hall, Upper Saddle River, NJ, 1998.
27. X. Yang, T. X. Wu, and J. McMacken, Design of LNA at 2.4 GHz using 0.25 μm CMOS technology, *Microwave Opt. Technol. Lett.* **36**(4):270–275 (2003).
28. J. Kucera, Low noise amplifier design, in J. M. Golio, and A. M. Shamsuddin, eds., *Commercial Wireless Circuits and Components Handbook*, CRC Press, Boca Raton, FL, 2003.
29. L. E. Larson, Integrated circuit technology options for RFICs—present status and future directions, *IEEE J. Solid-State Circ.* **33**(3):387–399 (March 1998).
30. S. Kumar, M. Vice, H. Morkner, and W. Lam, Enhancement mode GaAs PHEMT LNA with linearity control (IP3) and phased matched mitigated bypass switch and differential active mixer, *IEEE Microwave Symp. Digest*, June 2003, Vol. 3, pp. 1577–1580.
31. D. Wang, K. Krishnamurthi, S. Gibson, and J. Brunt, A 2.5 GHz low noise high linearity LNA/mixer IC in SiGe BiCMOS technology, *Proc. IEEE Radio Frequency Integrated Circuit Symp.*, May 2001, pp. 249–252.
32. Q. Liang, G. Niu, J. D. Cressler, S. Taylor, and D. L. Hareme, Geometry and bias current optimization for SiGe HBT cascode low-noise amplifiers, *Proc. IEEE Radio Frequency Integrated Circuit Symp.*, June 2002, pp. 407–410.
33. P. Shah, A 2 GHz low-distortion low-noise two-stage LNA employing low impedance bias terminations and optimum

- inter-stage match for linearity, *Proc. 26th European Solid-State Circuits Conf.*, Sept. 2000.
34. G. Schuppener, T. Harada, and Y. Li, A 23-GHz low-noise amplifier in SiGe heterojunction bipolar technology, *Proc. IEEE Radio Frequency Integrated Circuit Symp.*, May 2001, pp. 177–180.
 35. J. Sadowy, I. Telliez, J. Graffeuil, E. Tournier, L. Escotte, and R. Plana, Low noise, high linearity, wide bandwidth amplifier using a 0.35 μm SiGe BiCMOS for WLAN applications, *Proc. IEEE Radio Frequency Integrated Circuit Symp.*, June 2002, pp. 217–220.
 36. V. Aparin, E. Zeisel, and P. Gazzero, Highly linear SiGe BiCMOS LNA and mixer for cellular CDMA/AMPS applications, *Proc. IEEE Radio Frequency Integrated Circuit Symp.*, June 2002, pp. 129–132.
 37. A. Shirvani and B. A. Wooley, *Design and Control of RF Power Amplifiers*, Kluwer Academic Publishers, Boston, 2003.
 38. F. O. Eynde, J.-J. Schmit, V. Charlier, R. Alexandre, C. Sturman, K. Coffin, B. Mollekens, J. Craninckx, S. Terrijn, A. Monterastelli, S. Beerens, P. Goetschalckx, M. Ingels, D. Joos, S. Guncer, and A. Pontioglu, A fully-integrated single-chip SoC for Bluetooth, *Proc. IEEE Int. Solid-State Circuits Conf.*, Feb. 2001, pp. 196–197.
 39. V. T. S. Vintola, M. J. Matilainen, S. J. K. Kalajo, and E. A. Jarvinen, Variable-gain power amplifier for mobile WCDMA applications, *IEEE Trans. Microwave Theory Tech.* **49**(12):2464–2471 (Dec. 2001).
 40. X. Zhang, C. Saycocie, S. Munro, and G. Henderson, A SiGe HBT power amplifier with 40% PAE for PCS CDMA applications, *IEEE Microwave Symp. Digest*, June 2002, Vol. 2, pp. 857–860.
 41. N. Tanzi, J. Dykstra, and K. Hutchinson, A 1-watt doubly balanced 5 GHz flip-chip SiGe power amplifier, *Proc. IEEE Radio Frequency Integrated Circuit Symp.*, June 2003, pp. 141–144.
 42. A. Raghavan, D. Heo, M. Maeng, A. Sutono, K. Lim, and J. Laskar, A 2.4 GHz high efficiency SiGe HBT power amplifier with high-Q LTCC harmonic suppression filter, *IEEE Microwave Symp. Digest*, June 2002, Vol. 2, pp. 1019–1022.
 43. I. Rippke, J. Duster, and K. Kornegay, A fully integrated, single-chip handset power amplifier in SiGe BiCMOS for W-CDMA applications, *Proc. IEEE Radio Frequency Integrated Circuit Symp.*, June 2003, pp. 667–670.
 44. J. A. O'Sullivan, C. Delabie, K. G. McCarthy, A. Murphy, and P. J. Murphy, A fully integrated high efficiency SiGe HBT class F power amplifier at 2.2 GHz, *High Frequency Postgraduate Student Colloquium*, Sept. 2003, pp. 48–51.
 45. N. Srirattana, M. S. Qureshi, A. Aude, V. Krishnamurthy, D. Heo, P. E. Allen, and J. Laskar, SiGe HBT power amplifier for IS-95 CDMA using a novel process, voltage, and temperature insensitive biasing scheme, *Proc. Int. Symp. Circuits and Systems*, May 2003, Vol. 1, pp. 1-437–1-440.
 46. W. Bakalski, W. Simburger, R. Thuringer, A. Vasylyev, and A. L. Scholtz, A fully integrated 5.3 GHz, 2.4 V, 0.3 W SiGe-bipolar power amplifier with 50 spl Omega output, *Conf. European Solid-State Circuits*, Sept. 2003, pp. 561–564.
 47. X. Yang, T. X. Wu, and J. McMacken, A 5 GHz fast-switching CMOS frequency synthesizer, *Proc. 2002 IEEE Radio Frequency Integrated Circuit Symp.*, June 2002, pp. 479–482.
 48. B. Razavi, Challenges in the design of frequency synthesizers for wireless communications, *Proc. IEEE Custom Integrated Circuits Conf.*, May 1997, pp. 395–402.
 49. Y. Eo, K. Kim, B. Oh, Low noise 5 GHz differential VCO using InGaP/GaAs HBT technology, *IEEE Microwave Wireless Compon. Lett.* **13**:259–261 (July 2003).
 50. Y. G. Kim, H. S. Kim, J. H. Bac, J. H. Oh, and C. W. Kim, Fully integrated differential VCO with buffer amplifier using 0.35 μm SiGe BiCMOS for C-band wireless RF transceiver, *Proc. Radio and Wireless Conf.*, Aug. 2003, pp. 297–300.
 51. W. Wong, G. Cibiel, J.-G. Tartarin, E. Tournier, R. Plana, and O. Llopis, X band BiCMOS SiGe 0.35- μm voltage controlled oscillator in parallel and reflection topology and external phase noise improvement solution, *IEEE Radio Frequency Integrated Circuit Symp.*, June 2003, pp. 281–284.
 52. H. Li, H.-M. Rein, R. Kreienkamp, and W. Klein, 47 GHz VCO with low phase noise fabricated in a SiGe bipolar production technology, *IEEE Microwave Wireless Compon. Lett.* **12**(3):79–81 (March 2002).
 53. D. Wang and X. Wang, The performance comparison of CMOS vs bipolar VCO in SiGe BiCMOS technology, *IEEE Microwave Symp. Digest*, June 2003, Vol. 1, pp. A101–A104.
 54. K. Ettinger, A. Stelzer, C. G. Diskus, W. Thomann, J. Fenk, and R. Weigel, Single-chip 20-GHz VCO and frequency divider in SiGe technology, *IEEE Microwave Symp. Digest*, June 2002, Vol. 2, pp. 835–838.
 55. S. Hackl, J. Bock, G. Ritzberger, M. Wurzer, and A. L. Scholtz, A 28-GHz monolithic integrated quadrature oscillator in SiGe bipolar technology, *IEEE J. Solid-State Circ.* **38**(1):135–137 (Jan. 2003).
 56. H. Shin, Z. Xu, and M. F. Chang, A 1.8-V 6.9-GHz reconfigurable dual-band quadrature LC VCO in SiGe BiCMOS technology, *IEEE J. Solid-State Circ.* **38**(6):1028–1032 (June 2003).
 57. Flash communication market overview (online), <http://www.flash-comm.com>.
 58. R. Dekker, P. G. M. Baltus, and H. G. R. Maas, Substrate transfer for RF technologies, *IEEE Trans. Electron. Devices*, **50**(3):747–757 (March 2003).
 59. J. Y.-C. Chang, A. A. Abidi, and M. Gaitan, Large suspended inductors on silicon and their use in a 2 μm CMOS RF amplifier, *IEEE Electron. Device Lett.* **14**:246–248 (May 1993).

BIOLOGICAL EFFECTS OF RADIOFREQUENCY ENERGY AS RELATED TO HEALTH AND SAFETY

KENNETH R. FOSTER
University of Pennsylvania
Philadelphia, Pennsylvania

1. BIOLOGICAL EFFECTS OF RADIOFREQUENCY FIELDS—AN ONGOING CONTROVERSY

The biological effects of radiofrequency (RF) and microwave energy is a large and heterogeneous subject that spills over into biophysics, medicine, and engineering—and more recently, epidemiology, risk assessment, law, and public policy. The primary scientific literature on biological effects of RF fields contains several thousand papers, including many written in the 1960s or before.

This article examines biological effects of RF fields (3 kHz–300 GHz) with emphasis on potential hazards,

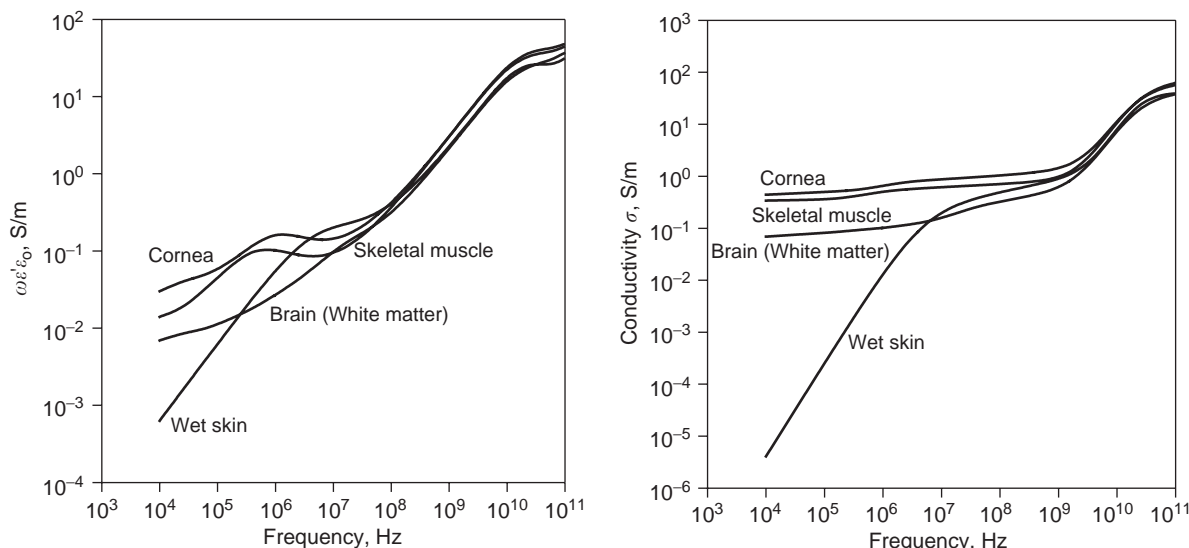


Figure 1. Dielectric properties of selected tissues: conductivity Φ and $\omega\epsilon'\epsilon_0$ (both in S/m) of selected tissues at 37°C. (Data from Ref. 2.)

specifically, effects that a person would perceive as adverse to health and safety. Its approach is tutorial rather than comprehensive, and its perspective follows that of major international exposure limits [established by IEEE and ICNIRP (International Committee on Non-Ionizing Radiation Protection)]. Its main emphasis will be on unequivocal effects that are potentially hazardous, which are principally thermal in nature. A concluding section will review major areas of controversy. Issues related to electromagnetic compatibility, for example, the interaction of RF fields with medical devices, are excluded from discussion. Additional sources are included in an annotated bibliography (see Further Reading section following the numbered references list).

2. EXPOSURE AND DOSE

In toxicology, *exposure* is the concentration or a potentially toxic agent in the external environment of a subject, and *dose* is the concentration of the substance in target tissues. For RF fields, the corresponding quantities are field levels external to the body, and those induced within body tissues by the exposure. The bioeffects literature refers to assessment of both quantities as “dosimetry.” Exposure is very different from risk, which is the probability of an adverse effect in an exposed individual and the severity of the effect.

The coupling between RF fields and the human body depends on the characteristics of the field (including frequency, polarization, and field strength) as well as the electrical characteristics of the biological target. Because of the wide range in these characteristics over the frequency range considered here, these coupling properties are quite diverse.

2.1. Bulk Electrical Properties of Tissue

The bulk electrical properties (dielectric properties) of tissue determine the propagation characteristics of

RF fields inside tissue; for a review, see Ref. 1. The bulk properties consist of the permittivity ϵ and conductivity σ . It is convenient to define the complex conductivity σ^* :

$$\sigma^* = \sigma + j\omega\epsilon\epsilon_0 \quad (1)$$

where ω is the frequency [in radians per second (rad/s)] and ϵ_0 is the permittivity of space (a constant). The real and imaginary parts of σ^* are shown in Fig. 1 for several representative soft tissues [2].

The dielectric properties of tissues exhibit dispersions (variations with frequency) due to the charging of cell membranes, dipolar losses in tissue water, and other effects. Charging of cellular membranes is chiefly responsible for the dispersion observed in tissue at megahertz (MHz) frequencies and below, while dipolar relaxation of tissue water is the dominant source of dispersion above ~ 1 GHz. Above ~ 100 MHz, tissue water content is the chief factor determining the dielectric properties of soft tissues.

2.2. Quantities Used to Characterize Exposure

Depending on the exposure scenario, different quantities are useful in characterizing exposure and dose. These include

1. For assessing external fields:
 - a. *External field strength* E_0 , measured in volts/meter (electric field) or amperes per meter (A/m) (magnetic field) (used principally at frequencies below 100 MHz¹ or in the near-field region of antennas).
 - b. *Incident power density* S , in W/m² (used principally at frequencies above 0.5 GHz or in the far fields of radiators).

¹All frequency ranges in this discussion are approximate.

2. For assessing internal fields:

- a. *Current density within the body* J_i (in A/m^2), used principally in the frequency range up to 10 MHz; a related measure is internal field strength E_i (V/m), which is related to the current density by Ohm's law

$$J_i = \sigma E_i \quad (2)$$

- b. *Total current passed into tissue* J , used chiefly to characterize contact currents, principally in the frequency range up to 100 MHz.
- c. *Internal electrical field strength* E_i , specifically, the electric field induced within body tissues, the *induced current density* J_i in A/m^2 .
- d. *Specific absorption rate* (SAR), defined as the power dissipation in watts per kilogram of tissue. In terms of the electric field E_i in the tissue

$$SAR = \frac{\sigma |E_i|^2}{\rho} \quad (3)$$

where ρ is the density (kg/m^3) of the tissue. The SAR can be expressed as a point value at a given instant in time, a value averaged over a specified time and distance, or a value averaged over the whole body of an animal (the whole-body SAR).

Under most circumstances, the SAR is the preferred dosimetric quantity for RF fields, particularly over the frequency range 100 kHz–10 GHz, and journal editors and referees typically insist that this information be included in papers submitted for publication. However, the SAR becomes less useful at frequencies above 10 GHz, where the energy is absorbed close to the tissue surface and the incident power density can be a more appropriate measure of exposure. The SAR is also less useful below 100 kHz, where little energy is absorbed by the tissue from the external field and contact currents become the dominant source of hazard.

Another parameter is specific-energy absorption (S.A.), the total absorbed energy in a pulse per kilogram of tissue, used principally for pulsed fields in the frequency range 300 MHz–10 GHz.

The SAR can be determined in a number of ways:

- By measuring the transient rate of temperature increase in the exposed object. A SAR of 1 W/kg produces a rate of temperature increase of $0.015^\circ C/min$ in high-water-content tissues. The rate of temperature increase can be measured using small temperature sensors, notably “nonperturbing” fiberoptic probes that are designed specifically for measurements in RF fields. Another approach is thermal imaging of the surface of the exposed object using an infrared camera, typically using phantom models to mimic animals. In either case, it is important to correct for effects of heat conduction in measurements of the rate of temperature increase.
- By modeling the exposure situation by computer, to determine the rate of absorption of the incident energy in the exposed object.

- By measuring the internal electric field in the exposed object with a small probe (taking care to avoid electrical artifacts).

Additional information may be necessary to characterize exposure, including the peak field strength or peak incident power density (for pulsed fields) or other description of the modulation characteristics of the field.

Inadequate dosimetry has been a longstanding problem in bioeffects studies. Many earlier studies reported only the incident field intensity, but did not determine the absorbed power in the exposed animals, and consequently the studies are difficult or impossible to interpret. Inadequate dosimetry is a particularly noticeable problem in numerous bioeffects studies in the Russian scientific literature, which frequently lacks even rudimentary information about the frequency and intensity of exposure.

A related problem has been the difficulty in distinguishing effects due to heating of the sample from those due to the fields themselves, that is, distinguishing thermal from nonthermal effects, due to the difficulty in adequately controlling temperature during an experiment. With careful experimental design, these problems are now solvable. However, adequate dosimetry and temperature control remain difficult and expensive to achieve. Typically, bioeffects studies, particularly those involving exposure of large animals and humans, require specially designed facilities and extensive engineering support including in some cases elaborate computational studies to determine exposure (Fig. 2).

3. COUPLING CONSIDERATIONS

The coupling between external fields and body tissues depends on the characteristics of exposure, which vary greatly in different exposure scenarios, as well on the geometry and electrical characteristics of the exposed subject.

There are numerous ways in which human subjects can be exposed to RF energy. The exposure scenarios can often be classified in one of three ways, which entail significant technical differences in determining exposure, described in the following text.

3.1. Contact Currents

In this exposure scenario, RF currents are passed into the body when a subject touches a conductive object in the presence of a field. Contact currents are a major potential occupational hazard in some occupational settings. For example, contact currents induced by touching broadcast transmission towers or secondary metallic structures (buildings, guywires, fencing, etc.) near the towers can induce hazardous contact currents.

The magnitude of the contact current is a function of source impedance and the impedance of the subject to ground, and is not simply related to the field strength in the vicinity of the subject. Contact currents can be measured by placing an ammeter between the source and the subject.



Figure 2. Eleanor R. Adair, noted bioeffects investigator [and immediate past chair of the ICES (formerly known as IEEE C95.1) standards committee] in microwave anechoic chamber used for RF bioeffects studies at Brooks Air Force Base, Texas.

3.2. Near-Field or Partial-Body Exposure

In localized regions near RF sources, very high RF fields can exist, possibly at acutely hazardous levels. Sources include medical equipment [such as magnetic resonance imaging (MRI) scanners], industrial equipment (e.g., induction heaters or microwave drying equipment), and radar and broadcast transmitters. Exposures to RF fields from such equipment typically occur in the near fields of RF sources, and to parts of the body. Partial-body exposure (albeit at thermally innocuous levels) is an everyday occurrence to a user of a mobile telephone or other portable transmitter.

Because of the complex electrical interaction between the transmitting antenna and the subject's body, exposure assessment in near-field exposures is a difficult matter. Exposure is typically determined using computer modeling or physical measurements on "phantom" models whose electrical properties approximate those of tissue at the pertinent frequency [3]. The measurements can include thermal measurement of SAR or direct measurement of the local field using small electrical probes inserted into the model. Figure 3 shows a commercial apparatus that employs a robot to move a small electric field probe about a "phantom" model of the head, which has become the most widely used method to measure SARs produced in the human head by mobile telephone handsets.



Figure 3. Commercial instrument used to measure SAR distribution produced by a mobile telephone in model of a human head. The robot arm moves an electric field probe inside a phantom model filled with a liquid whose electrical properties resemble those of a tissue. (From Ref. 3 with permission; available at <http://www.dasv4.com/welcome.html>.)

3.3. Far-Field Exposure

In a typical far-field exposure scenario, plane-wave energy is incident on large areas of the subject's body. This exposure scenario is important because of public concern about possible health hazards from broadcast transmitters, as well as in some occupational exposure settings, for example, for workers near radar transmitters.

Far-field exposure can be modeled by computer or measured experimentally, and, in comparison to with near-field exposures, is comparatively easy to accomplish. Consequently, a large literature exists on the subject (e.g., see Ref. 4). Initial studies, beginning in the 1960s, modeled the human body and experimental animals using homogeneous spheroids exposed to plane-wave irradiation. More recent studies have employed detailed anatomical models of the body with millimeter spatial resolution. A variety of thermal measurements have also been reported, most commonly for measurement of whole-body SAR [4].

As with other exposure scenarios, the coupling between an incident field and the body depends strongly on the frequency and other characteristics of the field. Figure 4 shows the whole-body average SAR in an isolated ellipsoid modeling an adult human, exposed to plane-wave irradiation of varying polarization. Below ~ 70 MHz, the SAR is proportional to the square of the frequency, and most of the energy is deposited near the body surface. This model exhibits a maximum near 70 MHz due to an electrical resonance, reflecting the antenna properties of the model. At higher frequencies, the whole-body SAR decreases (for a given incident power density) because the energy is deposited close to the surface. In addition, various parts of the body exhibit their own resonances; for example, the human head exhibits an antenna resonance at approximately 1 GHz. If the model is placed in contact with

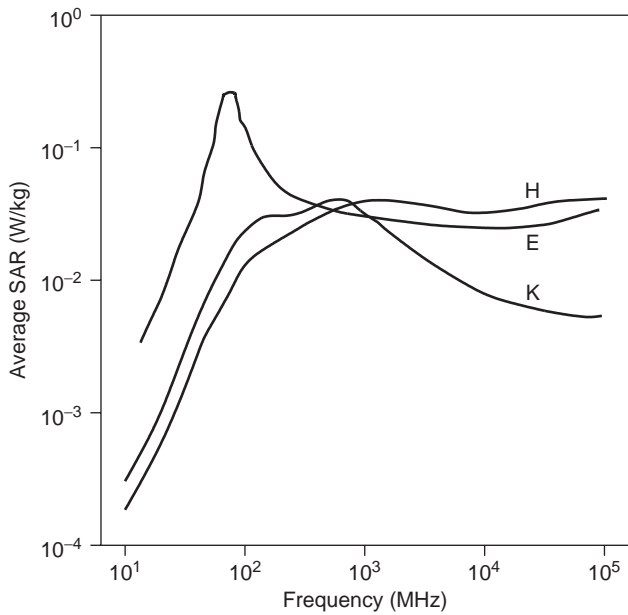


Figure 4. Whole-body average SAR in a prolate spheroidal model of man in a plane wave, as a function of frequency of the incident wave. The semi-major axis is 0.875 m, semi-minor axis 0.138 m, volume 0.07 m^3 . The SAR is given in W/kg, normalized to an incident power density of 10 W/m^2 (from Ref. 4). Three curves are shown, for E (electric field vertical), H (magnetic field vertical), and K (wave propagating from the top) polarizations.

ground, the induced currents (particularly those near the point of contact with ground) are increased as a result of image effects. Similar resonances occur in animals, but at higher frequencies reflecting the smaller body size, and with different SAR levels for a given incident exposure level (Fig. 5).

At sufficiently high frequencies, the wavelength of the incident energy is much smaller than the dimensions of the model and the exposure approaches the “quasi-optical” regime. In this case, the distribution of energy within the body is similar to that produced by a plane wave incident on an absorbing surface. For a plane wave incident on a plane surface of tissue, the SAR as a function of depth x into the tissue is given by

$$\text{SAR} = \frac{I_0 T}{\rho L} e^{-x/L} \quad (4)$$

where T is the fraction of energy transmitted in the tissue (the remaining part of the incident energy being reflected) and L is the energy penetration depth. In terms of the relative permittivity and conductivity of the tissue (ϵ' , σ), these quantities are

$$T = 1 - \frac{\sqrt{\epsilon^*} - 1}{\sqrt{\epsilon^*} + 1}^2 \quad (5)$$

$$L = \frac{-c}{2\omega \text{Im}(\sqrt{\epsilon^* \epsilon_0})}$$

where $\epsilon^* = \epsilon' - (j\sigma/2\pi f\epsilon_0)$ and c is the velocity of light. Energy penetration depths of microwaves

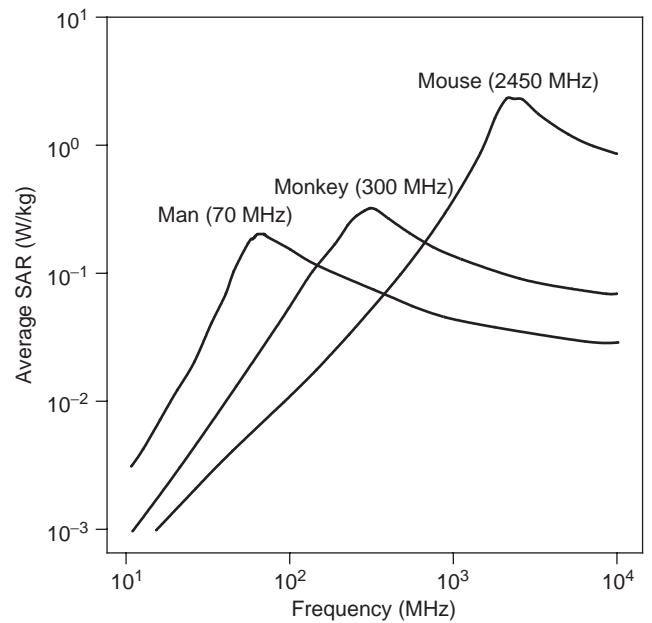


Figure 5. Whole-body absorption rates for spheroidal models of a human, a squirrel monkey, and a mouse, exposed to plane-wave irradiation at 10 W/m^2 in the E polarization. (From Ref. 4.)

into soft tissue such as muscle range from about 1 cm at 1 GHz to a few tenths of a millimeter at 100 GHz (Fig. 6).

4. INTERACTION MECHANISMS

The energy of photons of radiofrequency and microwave fields is several orders of magnitude (at least) below that needed to disrupt the weakest chemical bonds and create free radicals. Consequently, RF fields are nonionizing, in contrast to ionizing radiation such as X rays or ultraviolet light, which disrupt chemical bonds and create highly reactive free radicals.

Nevertheless, RF fields can interact with biological systems, most obviously by exerting forces on charges in tissue [5]. These forces act in the presence of random thermal agitation, which will overwhelm the effects of the fields if the forces are too small. The absorbed power in tissue will also generate heat and increase the local temperature, an obvious thermal mechanism for biological effects.

4.1. Thermal Mechanisms

Thermal mechanisms arise from the deposition of power in the biological system (as opposed to nonthermal effects, which result from direct interaction with the electric or magnetic fields).

4.1.1. Direct Effects of Temperature Increase. Biochemical reactions typically vary in rate by about $3\%/^\circ\text{C}$. However, some biological structures (e.g., thermal receptors in the human body or infrared receptors in some snake species) respond to very small changes in temperature, as little as a few hundredths of a degree or less. Thus, even modest temperature increases, particularly if they persist

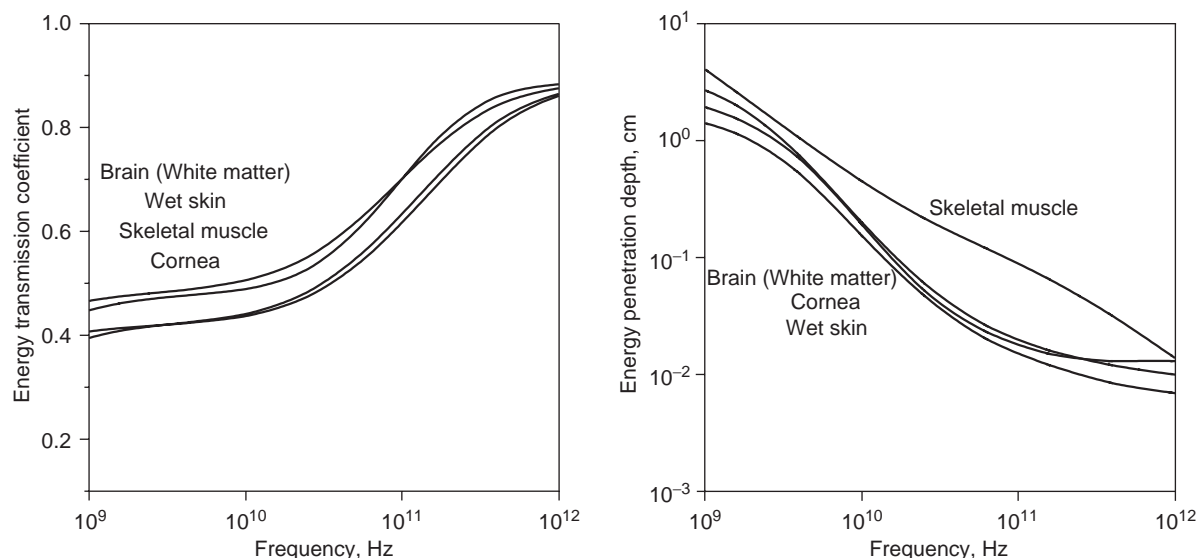


Figure 6. Energy penetration depths and transmission coefficients for several tissues.

over appreciable times, can elicit biological effects. Several classes of thermal effects can be identified.

4.1.2. Effects of Thermal Load on the Body. An additional heat load on the body due to exposure to RF energy can also elicit effects due to thermoregulatory responses. The natural rate of power generation in the human body (the basal metabolic rate) is about 1 watt per kilogram of body mass. Addition of heat by a RF field at levels comparable to or above this rate can produce significant physiological effects even in the absence of thermally damaging temperature increases anywhere in the body. These changes can be interpreted as normal thermoregulatory responses, and may explain, in part, various subtle physiological effects that have been reported in animals subjected to moderate levels of RF energy exposure. With typical values of the conductivity of tissue, field levels inside the body ranging from 100 V/m (3 kHz) to 30 V/m (1 GHz) will produce a SAR of 1 W/kg.

4.1.3. Effects of Local Temperature Increases. At SAR levels somewhat above 1 W/kg, depending on the duration of exposure, rate of cooling of the tissue by bloodflow, and other factors, local heating effects in tissue can become significant or even damaging. These include a variety of biological changes and, at sufficient heating levels, frank tissue damage.

4.1.4. Effects Due to Rate of Temperature Increase. Some thermal mechanisms depend on the rate of temperature increase (as opposed to the magnitude of increase). Pulsed microwave energy will generate acoustic transients in tissue by transient heating of tissue water with corresponding thermal expansion. These transients, under appropriate exposure conditions, can be perceived by human subjects as “clicks,” the so-called microwave auditory effect. This typically requires that the head of the subject be exposed to microsecond pulses of RF energy with a carrier frequency near 1 GHz, and peak field intensities

above 10,000 W/m². The pulses produce transient increases in tissue temperature of a few microdegrees, at a rate of about 1°C/s. This is sufficient to produce acoustic transients in the head in excess of 100 dB peak sound pressure [6]. The subject perceives these acoustic transients through normal hearing mechanisms.

Under more extreme exposure conditions, changes in membrane potentials and stimulation of cell membranes can occur, also related to the rates of temperature increase [7]. For example, mice exposed in the head to intense microwave pulses, leading to brain temperature increases of a few tenths of a degree within one second, exhibit a variety of involuntary body movements and other “stun” phenomena [8]. The extreme exposure levels needed to produce such effects are far above those encountered in realistic environments, and to achieve them generally requires that the animals be placed inside waveguides that are connected to high-powered military transmitters.

4.2. Nonthermal Mechanisms

Electric fields can exert forces on charges, and magnetic fields exert torques on magnetic dipoles in biological systems. This gives rise to several classes of “nonthermal” interaction mechanisms. (Whether the mechanisms result in observable biological effects under realistic exposure conditions is a different question, however.) Examples are described below.

4.2.1. Membrane Excitation. The dominant hazard mechanism for low-frequency currents is shock and other membrane excitation phenomena. Above a few kilohertz, the threshold current needed to excite membranes increases rapidly with frequency. With a few exceptions, over the entire frequency range considered in this article, the thresholds for producing biologically significant heating are lower than those for directly exciting cell

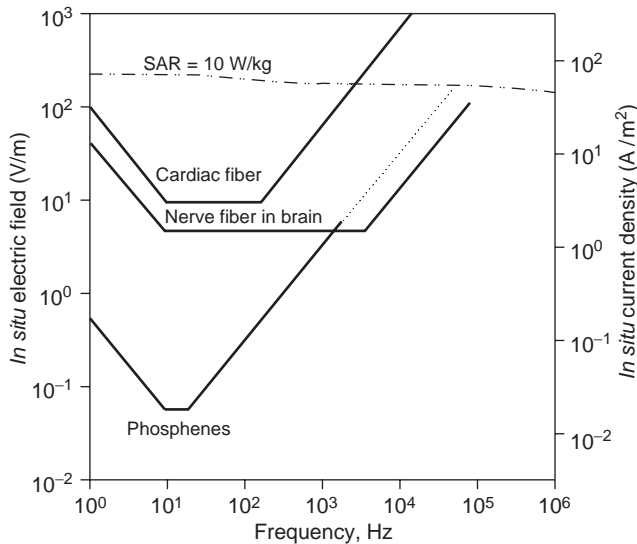


Figure 7. Estimated thresholds for different stimulatory effects (excitation of 10- μ m nerve fibers in the brain, excitation of cardiac fibers, production of phosphenes, together with current level for a SAR of 1 W/kg.

membranes (Fig. 7). Consequently, the dominant hazard mechanisms at RFs are thermal in nature.

4.2.2. Electroporation. Electric fields can create pores in cell membranes (electroporation) by inducing electrical breakdown. This requires membrane potentials of ~ 1 V, which in turn requires tissue field strengths that can exceed 10^4 – 10^5 V/m, which would be thermally damaging if sustained for more than brief periods. However, electroporation can be produced in the absence of thermal damage using brief pulses of RF fields, typically with carrier frequencies below 1 MHz. Electroporation is considered to be a factor in some kinds of electrical injury [9].

4.2.3. Field-Induced Forces. Electric fields exert forces on ions and torques on permanent dipoles, as well as forces and torques on induced dipoles (dielectrophoretic forces). Magnetic fields exert torques on magnetic dipoles. These forces are opposed by viscous drag from the surrounding medium, and occur in the face of random thermal agitation.

Dielectrophoretic forces on cells are well documented, and have important applications in biotechnology. However, biophysical considerations show that the forces to be expected on cells from RF fields at normal environmental levels are far too weak to overcome naturally occurring thermal agitation.

4.3. Other Proposed Mechanisms

Various scientists, including some prominent physicists, have suggested mechanisms for biological effects of weak RF fields. These include various quantum phenomena, nonlinear effects such as creation of solitons, and kinetic effects including disruption of “bound” water and excitation of molecular resonances (to name only a few proposed mechanisms). These theories remain speculative, and of-

ten are susceptible to criticism, for example, for failing to consider the effects of thermal agitation or viscous drag or other dissipative processes [10]. This remains a highly uneven and, in many places, highly contentious literature.

5. POTENTIAL ADVERSE EFFECTS OF RADIOFREQUENCY FIELDS IN HUMANS

This subject is wide and, particularly as it relates to possible chronic health effects in humans, very controversial. This article first considers the well-established hazards of RF energy, which underlie major exposure standards for electromagnetic fields. It then comments on possible effects of chronic exposure to RF and microwave fields on humans.

5.1. Thermal Death

Numerous studies have been conducted, beginning in the early 1960s, to determine lethal levels of exposures to RF and microwave energy for animals. The exposure level, in terms of incident power density, that will kill an animal varies considerably depending on species, frequency of the field, environmental conditions, pretreatment by drugs or other physiological manipulation, and other factors. In part this reflects the different absorption characteristics of different species for RF energy, and in part physiological differences among species, such as different capabilities for thermoregulation. Prior to death, animals typically exhibit circulatory failure and other signs of extreme heat stress, and the thresholds for lethality typically correlate with an increase in body temperature of several degrees above normal [11]. Clearly, similar effects would occur in a human, in the unlikely circumstance that he or she were exposed at comparable levels.

5.2. Perception and Pain

Thresholds for perception of contact currents have been measured for humans at several frequencies (Table 1). At frequencies below ~ 10 kHz, subjects report “mild tickling or pricking” sensations near the threshold for perception; at higher frequencies subjects report “faint warmth” [12], evidently reflecting two different mechanisms for perception (direct stimulation of membranes at low frequencies and cutaneous perception of warmth at higher frequencies).

The thresholds for perception of microwave energy have been measured by Blick et al. [13] over a wide range of microwave frequencies. These experiments used brief (10-s) exposures to microwave energy over an area of 0.024 m² on the backs of human volunteers (Table 2) [13]. The estimated increase in skin temperature at the threshold for perception is about 0.07°C over this entire frequency range [14]. The threshold for perception decreases with increasing frequency because of the shorter penetration depth into tissue and corresponding increase in SAR near the skin surface. Thresholds for pain under similar exposure conditions are approximately 100 times higher, and correspond to peak temperature increases of

Table 1. Ranges of Threshold Currents for Indirect Effects, Including Children, Women, and Men

Indirect Effect	Threshold Current (mA) at Frequency			
	50/60 Hz	1 kHz	100 kHz	1 MHz
Touch perception	0.2–0.4	0.4–0.8	25–40	25–40
Pain on finger contact	0.9–1.8	1.6–3.3	33–55	28–50
Painful shock/let-go threshold	8–16	12–24	112–224	Not determined
Severe shock/breathing difficulty	12–23	21–41	160–320	Not determined

Source: From Ref. 25.

several degrees Celsius at the surface of the skin [15]. These thresholds clearly reflect thermal phenomena.

5.3. Burns

Burns and other thermal damage are clear potential hazards of RF and microwave energy. Typically, human tissues can tolerate temperatures up to $\sim 43^\circ\text{C}$ for prolonged periods without damage; progressively higher temperatures will cause thermal damage in progressively shorter times [16].

While RF burns are an obvious potential hazard, few such injuries are reported. The exposures are very painful, causing the victim to withdraw from exposure before thermal injury occurs. Serious injuries generally require extreme exposure levels in which damage occurs quickly, or circumstances in which the victim is unable to voluntarily leave the area of exposure. There is a scattering of reports of burns produced by microwave ovens whose interlock mechanisms (which turn off the microwave power when the door is opened) have failed, and of burns to patients from medical treatments involving RF and microwave energy. There have been at least two reported cases of infants being placed deliberately in microwave ovens and suffering severe burns [17].

5.4. Other Adverse Thermal Effects

Many thermal effects have been demonstrated in animals, and analogous effects can be anticipated in humans as well. Deleterious effects include the following:

1. *Cataracts.* These are an established hazard of microwave energy, and have been reported occasionally in humans exposed to high intensity microwaves. Cataracts can be produced in animals at high exposure levels, generally $> 1000 \text{ W/m}^2$, where they are associated with temperature increases of several degrees in the eye. Such exposure levels are similar to those capable of producing skin burns. Occasional claims of cataract from low-level

microwave exposure have not been substantiated by animal studies and remain controversial [18].

2. *Adverse Reproductive Effects.* Development abnormalities have been convincingly demonstrated in animals exposed to microwave energy at near-lethal levels. These effects are associated with significant increases in body temperature, which is itself a well-established cause of birth defects [19,20]. Heating the testes to microwave energy to induce temporary sterility has been explored in China as a means of contraception. Some men have received more than 100 treatments, each raising the surface temperature of the scrotum to $40\text{--}42^\circ\text{C}$. No significant abnormalities were reported in a follow-up study in these men after cessation of treatment [21].

3. *Behavioral Disruption.* This has been observed in several species of animals exposed to microwaves at whole-body exposures of $4\text{--}6 \text{ W/kg}$, at several frequencies above 100 MHz [22]. In such studies, the animals are trained to carry out a task (e.g., pressing a lever to obtain food pellets) and exposed to microwave energy. At sufficient exposure levels, the animals stop performing the assigned task and begin a different behavior, typically one associated with thermoregulation (in rats, spreading saliva on the tail). The threshold SAR for behavioral disruption is approximately 4 W/kg in several species, and does not vary greatly with frequency (Table 3). The effect is reversible; that is, no lasting effects are observed in the animals after the exposure is terminated. Consequently it is not considered deleterious, although exposures that are sufficient to produce behavioral disruption are undoubtedly close to those that would be thermally injurious if sustained for sufficient lengths of time.

5.5. Mobile Phones and Health

The hazards discussed above are principally (if not exclusively) thermal in nature, and require high exposure levels. Much public and legal controversy has concerned the possibility of hazards from use of mobile telephones or

Table 2. Thresholds for Perception of Microwave Energy by Humans

Frequency (GHz)	Threshold for Perception (10 s Exposure, 0.024 m^2 Exposure Area) (W/m^2)	Approximate Energy Penetration Depth (m)	Approximate Temperature Increase at Skin Surface ($^\circ\text{C}$) at Threshold
2.45	630	0.01	0.06
7.5	195	0.003	0.05
10	196	0.002	0.07
35	88	4×10^{-4}	0.08
94	45	1×10^{-4}	0.05

Source: Adapted from Ref. 33.

Table 3. Thresholds for Behavioral Disruption in Different Animals

Species and Conditions	225 MHz	1.3 GHz (Pulsed)	2.45 GHz	5.8 GHz (Pulsed)
	(Continuous-Wave)		(Continuous-Wave)	
Norwegian rat power density SAR	—	10 mW/cm ² (2.5 W/kg)	128 mW/cm ² (5.0 W/kg)	20 mW/cm ² (4.9 W/kg)
Squirrel monkey power density SAR	—	—	45 mW/cm ² (4.5 W/kg)	40 mW/cm ² (7.2 W/kg)
Rhesus monkey power density SAR	8 mW/cm ² (3.2 W/kg)	57 mW/cm ² (4.5 W/kg)	67 mW/cm ² (4.7 W/kg)	140 mW/cm ² (8.4 W/kg)

Source: Adapted from Ref. 34.

living near cellphone base stations. The exposure levels encountered in these two situations are very different, but both are far below any threshold for a thermal hazard.

Certainly the most visible public issue has been the possibility that use of mobile telephones can cause brain cancer. Since the issue was first raised (by a nonscientist on a U.S. television show in 1992), several epidemiology studies have been completed, together with several long-term animal studies designed as cancer assays. The results so far have failed to identify a link between use of mobile telephones and cancer. A review of the literature published in 1999 found the evidence for a causal relationship between RF radiation from cellphones and cancer to be “weak to nonexistent” [23]. However, given the long time that it takes brain tumors to develop (years to decades between initiation and clinical diagnosis), the studies completed to date have only limited ability to address the question of possible long-term effects from use of mobile telephones.

A number of studies have been conducted to address health issues other than cancer. Many of them have reported effects of using mobile telephones on neurological function, response time, sleep, and other functions in human subjects. However, the effects have generally been insignificant, with no clear health significance. Reviews of the issue by a number of expert committees have generally concluded that no convincing evidence exists for a hazard from mobile phones or their base stations, but also that numerous open questions still remain.

6. TWO MAJOR WESTERN EXPOSURE LIMITS

Government and nongovernment agencies throughout the world have established guidelines for human exposure to electromagnetic fields. The rationale for two major Western limits [Institute of Electrical and Electronics Engineers (IEEE) standard C95.1-1999 [24] and the International Commission on Non-Ionizing Radiation Protection (ICNIRP) guideline [25]] is now considered (see also Table 4). The IEEE committee has recently been renamed International Committee on Electromagnetic Safety (ICES).

The standards are complex, and readers should refer to the original documents for authoritative statements of the limits. They have similar rationales but differ in many particulars. ICNIRP limits include “basic restrictions,” which are limits on absorbed power (or other measure of internal field) based directly on adverse health effects, and “reference levels,” which are limits on external field strength designed to ensure that the basic restrictions are not exceeded.

Each standard has two tiers: for “controlled” and “uncontrolled” environments (IEEE) or for occupational groups and the general public (ICNIRP). The “controlled” limits in IEEE C95.1 are intended for environments in which the exposed subjects are aware of the potential for exposure, and correspond roughly to occupational exposure guidelines in ICNIRP.

Table 4. Comparison of ICNIRP and IEEE Limits for Contact Current

A. ICNIRP Reference Levels for Time-Varying Contact Currents from Conductive Objects

Exposure Characteristics	Frequency Range	Maximum Contact Current (mA)
Occupational exposure	≤2.5 kHz	1.0
	2.5–100 kHz	0.4f ^a
	100 kHz–110 MHz	40
General public exposure	≤2.5 kHz	0.5
	2.5–100 kHz	0.2f ^a
	100 kHz–110 MHz	20

B. IEEE Induced and Contact Radiofrequency Currents^b

Frequency Range	Maximum Current (mA)		
	Through Both Feet	Through Each Foot	Contact
3–100 kHz	0.9f ^a	0.45f ^a	0.45f ^a
100 kHz–100 MHz	90	45	45

^aFrequency in kilohertz.

^bLimits for uncontrolled environments; limits for controlled environments are higher by a factor of ~2.

6.1. Limits to Whole-Body SAR

Both the IEEE and ICNIRP limits are designed to limit the whole-body average SAR to 0.4 W/kg (“controlled” or occupational) or 0.08 W/kg (“uncontrolled” or general public limits). The rationale, as described in ICNIRP is [25]

Established biological and health effects in the frequency range from 10 MHz to a few GHz are consistent with responses to a body temperature rise of more than 1°C. This level of temperature increase results from exposure of individuals under moderate environmental conditions to a whole-body SAR of approximately 4 W kg⁻¹ for about 30 minutes. A whole-body average SAR of 0.4 W kg⁻¹ has therefore been chosen as the restriction that provides adequate protection for occupational exposure. An additional safety factor of 5 is introduced for exposure of the public, giving an average whole-body SAR limit of 0.08 W kg⁻¹.

The IEEE and ICNIRP limits are compared for one exposure situation (general public for ICNIRP, uncontrolled environments for IEEE) in Fig. 8. The antenna resonance in the human at 70 MHz accounts for the lower limits near that frequency in both limits.

6.2. Limits to Partial-Body SAR

For the head and trunk, ICNIRP limits for partial body exposures are 2 W/kg (general public) and 10 W/kg (occupational), averaged over any 10 g mass of contiguous tissue. Limits elsewhere in the body are a factor of 2 higher. The corresponding limits in the present IEEE limit are 1.6 and 8 W/kg, averaged over 1 g of tissue (but is anticipated to change with a new edition of the limit to be released in 2003).

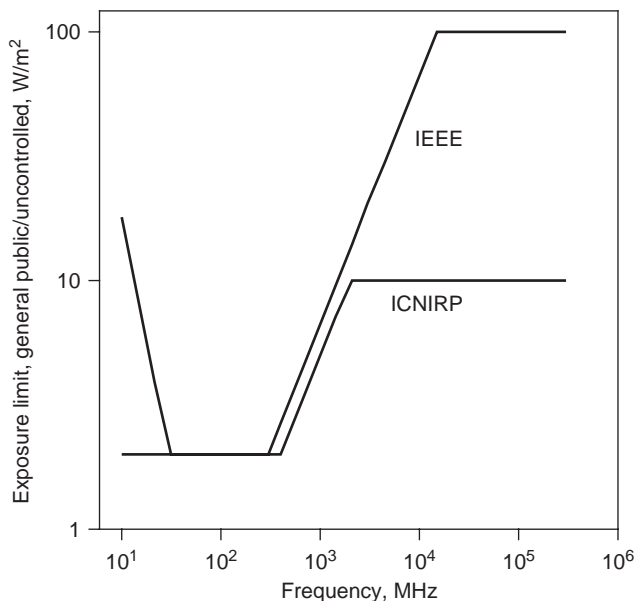


Figure 8. Comparison of ICNIRP and IEEE limits for general population/uncontrolled environments. Limits for occupational groups/controlled environments are generally 5 times higher than for the general public/uncontrolled environments.

6.3. Contact Currents

The limits in these two standards are compared in Fig. 8. The ICNIRP limits are somewhat more restrictive, but both sets of limits are clearly rather similar.

7. CONTROVERSIES AND UNRESOLVED ISSUES

The literature on biological effects and health hazards of RF energy is complex and frequently inconsistent and controversial even among scientists. Several areas of controversy are discussed below.

7.1. Many Reported Biological Effects of RF Energy

The scientific literature abounds with reports of biological effects of RF energy, including some at low exposure levels that the investigators considered “nonthermal.” The studies vary greatly in biological endpoint, exposure level, quality, and relevance to health and safety. Many of the studies are controversial, due to technical criticisms of the studies or the inability of other studies to confirm the initial findings [26].

Faced with an inconsistent and incomplete literature (the normal state of affairs in environmental health issues), health agencies typically employ a “weight of evidence” approach, using panels of experts to evaluate critically all relevant information. These panels normally give little weight to studies that are technically deficient or whose relevance to health is unclear. Health agencies typically point to the incompleteness of the scientific literature and the existence of open questions. For example, a 1999 review by the Royal Society of Canada concluded [27]

Scientific studies performed to date suggest that exposure to low intensity non-thermal RF fields do not impair the health of humans or animals. However, the existing scientific evidence is incomplete, and inadequate to rule out the possibility that these non-thermal biological effects could lead to adverse health effects. Moreover, without an understanding of how low energy RF fields cause these biological effects, it is difficult to establish safety limits for non-thermal exposures.

7.2. Reports of Adverse Health Effects of RF Energy at Low Exposure Levels

A major factor in the public controversy about the safety of RF energy is the existence of a scattering of reports in the medical literature of associations between adverse health outcomes and presumed exposure to RF energy. For example, there is one report of clusters of testicular cancer cases among police officers using radar guns [28]. One investigator has reported an increase in cancer mortality in Polish soldiers whose job classifications suggest exposure to RF radiation, compared to other soldiers used as controls [29]. A more recent epidemiology study by a French investigator reported an association between nonspecific health symptoms and residence near a mobile base station [30].

Perhaps even more perplexing, the medical literature of the former Soviet Union and its former Warsaw Pact

Table 5. Comparison of Five Different Exposure Limits for RF Energy at 2000 MHz^a.

Country	Limit for General Public Exposure to RF Fields (2000 MHz) for Extended Periods of Exposure (W/m ²) (Applies to Far-Field Exposure, Extended Duration)	Basis
ICNIRP (adopted in numerous countries worldwide)	10	Science-based
U.S. Federal Communications Commission Bulletin 65, <i>Evaluating Compliance with FCC Guidelines for Human Exposure to Radiofrequency Electromagnetic Fields</i> , Washington, DC, 1997.	10	Science-based
China: UDC 614.898.5 GB 9175-88	0.1	Science-based
Russia: <i>Sanitary Norms and Regulations 2.2.4/2.1.8.055-96</i>	0.1	Science-based
Switzerland: <i>Ordinance on Protection from Nonionising Radiation</i> (NISV) of Dec. 23, 1999	0.1	Precautionary
Typical maximum exposure from cellular base station mounted on 50-m tower (assuming a total effective radiated power of 2500 W in each sector, summed over all channels)	0.01	

^aThis 2000-MHz limit is similar to that used by many cellular telephones throughout the world. The limits are for long-term exposure to the general population.

allies contains numerous reports of adverse health effects in people exposed to RF energy. For example, Russian physicians have identified a “neurasthenic” syndrome among workers in radio equipment factories, which is characterized by diverse and nonspecific symptoms such as fatigue, anxiety, headache, and impotence [31]. The exposures to these subjects was undocumented, but almost certainly the levels of RF energy were far below Western exposure limits.

So far, these reports have carried little weight in Western assessments of possible health risks of RF energy, in part because of technical deficiencies in the studies and in part because of lack of independent confirming evidence. However, these reports would certainly tend to convince many nonscientists that health hazards do exist from low-level exposures to RF energy.

7.3. Large Variations in Exposure Limits to RF Energy throughout the World

The underlying philosophy in setting exposure limits to RF and microwave energy varies greatly in different countries, and there is a corresponding large variation in exposure limits. These limits can be classified as “science-based” (in that they were designed to avoid identified hazards, on the basis of detailed analysis of the relevant scientific literature) and “precautionary” (not designed to exclude particular hazards). The limits for general public exposure to 2000 MHz energy (similar to that emitted by many mobile telephone base stations) are compared in Table 5.

7.4. Science-Based Limits

One group of science-based limits consists of the IEEE and ICNIRP limits discussed above.

A very different group of science-based limits is in effect in Russia and most of its former Warsaw Pact allies. These limits are far lower (as much as 100 times, if the limits are expressed in terms of incident power density) than the

ICNIRP and the IEEE limits (as well as those of many other Western countries). The Russian standards clearly reflect a conviction that prolonged exposure to low-level RF fields causes health problems of many sorts. It has so far proved impossible to reconcile these two sets of limits, in part because of the brief nature of the Russian reports (many of which lack sufficient technical detail to permit expert evaluation) and in part because of technical limitations of the studies (which seldom provide information about exposure) [32]. This situation goes back for many years and is not likely to be resolved anytime soon.

7.5. Precautionary Limits

More recently, Italy, Switzerland, and a few other countries have adopted strict limits for RF exposure that are even below those of Russia. To a large extent, these limits reflect public fears about the safety of mobile telephone masts (whose exposure levels are invariably far below ICNIRP and other Western limits). These limits are not science-based, but are justified by the precautionary principle, and thus are designed to be highly restrictive due to uncertainty about the safety of RF energy at low exposure levels.

BIBLIOGRAPHY

1. K. R. Foster and H. P. Schwan, Dielectric properties of tissues—a review, in C. Polk and E. Postow, eds., *Handbook of Biological Effects of Electromagnetic Radiation*, 2nd ed., CRC press, Boca Raton, FL, 1995.
2. S. Gabriel, R. W. Lau, and C. Gabriel, The dielectric properties of biological tissues. 2. Measurements in the frequency range 10 Hz to 20 GHz, *Phys. Med. Biol.* **41**:2251–2269 (1996).
3. T. Schmid, O. Egger, and N. Kuster, Automated E-field scanning system for dosimetric assessments, *IEEE Trans. Microwave Theory Tech.* **44**:105–113 (1996).
4. C. H. Durney, H. Massoudi, and M. F. Iskander, *Radiofrequency Radiation Dosimetry Handbook*, 4th ed., Brooks Air

- Force Base, San Antonio, TX, Report USAFSAM-TR-85-73; available online at <http://www.brooks.af.mil/AFRL/HED/hedr/reports/handbook/home.html>.
5. H. P. Schwan and K. R. Foster, RF-field interactions with biological systems: Electrical properties and biophysical mechanisms, *Proc. IEEE* **68**:104–113 (1980).
 6. K. R. Foster and E. D. Finch, Microwave hearing: Evidence for thermoacoustic auditory stimulation by pulsed microwaves, *Science* **185**:256–258 (1974).
 7. F. S. Barnes, Cell membrane temperature rate sensitivity predicted from the Nernst equation, *Bioelectromagnetics* **5**:113–115 (1984).
 8. H. Wachtel, D. Brown, and H. Bassen, Critical durations of pulse microwave exposures that evoke body movements, *Proc. Bioelectromagnetics Soc. 12th Annual Meeting*, June 10–14, 1990, San Antonio, TX, p. 55.
 9. R. C. Lee, D. Zhang, and J. Hannig, Biophysical injury mechanisms in electrical shock trauma, *Ann. Rev. Biomed. Eng.* **2**:477–509 (2000).
 10. R. K. Adair, Biophysical limits on athermal effects of RF and microwave radiation, *Bioelectromagnetics* **24**:39–48 (2003).
 11. S. M. Michaelson and J. C. Lin, *Biological Effects and Health Implications of Radiofrequency Radiation*, Plenum Press, New York, 1987.
 12. I. Chatterjee, D. Wu, and O. P. Gandhi, Human body impedance and threshold currents for perception and pain for contact hazard analysis in the VLF-MF band, *IEEE Trans. Biomed. Eng.* **33**:486–494 (1986).
 13. D. W. Blick, E. R. Adair, W. D. Hurt, C. J. Sherry, T. J. Walters, and J. H. Merritt, Thresholds of microwave-evoked warmth sensations in human skin, *Bioelectromagnetics* **18**:403–409 (1997).
 14. P. J. Riu, K. R. Foster, D. W. Blick, and E. R. Adair, A thermal model for human thresholds of microwave-evoked warmth sensations, *Bioelectromagnetics* **18**:578–583 (1997).
 15. T. J. Walters, D. W. Blick, L. R. Johnson, E. R. Adair, and K. R. Foster, Heating and pain sensation produced in human skin by millimeter waves: Comparison to a simple thermal model, *Health Phys.* **78**:259–267 (2000).
 16. A. J. Welsh, Laser irradiation of tissue, in A. Schitzer and R. C. Eberhart, eds., *Heat Transfer in Medicine and Biology*, Vol. 2, Plenum Press, New York, 1985, p. 167.
 17. R. C. Alexander, J. A. Surrell, and S. D. Cohle, Microwave oven burns to children: An unusual manifestation of child abuse, *Pediatrics* **79**:255–260 (1987).
 18. S. F. Cleary, Microwave cataractogenesis, *Proc. IEEE* **68**:49–55 (1980).
 19. P. S. Nawrot, D. I. McRee, and R. E. Staples, Effects of 2.45 GHz microwave radiation on embryofetal development in mice, *Teratology* **24**:303–314 (1981).
 20. R. P. Jensh, Behavioral teratologic studies using microwave radiation: Is there an increased risk from exposure to cellular phones and microwave ovens? *Reprod. Toxicol.* **11**:601–611 (1997).
 21. Y. H. Liu, X. M. Li, R. P. Zou, and F. B. Li, Biopsies of human testes receiving multiple microwave irradiation—an histological and ultramicroscopical study, *J. Bioelectric.* **10**:213–230 (1991).
 22. J. A. D'Andrea, Microwave radiation absorption: Behavioral effects, *Health Phys.* **61**:29–40 (1991).
 23. J. E. Moulder, L. S. Erdreich, R. S. Malyapa, J. Merritt, W. F. Pickard, and Vijayalaxmi, Cell phones and cancer: What is the evidence for a connection? *Rad. Res.* **151**:513–531 (1999); available online at http://www.radres.org/rare_151_05_0513.pdf.
 24. IEEE Std C95.1-1991, 1999 ed., *IEEE Standard for Safety Levels with Respect to Human Exposure to Radiofrequency Electromagnetic Fields, 3 kHz to 300 GHz* (available from the Institute of Electrical and Electronics Engineers, Inc., Service Center, 445 Hoes Lane, Piscataway, NJ 08854-1331).
 25. International Commission on Non-Ionizing Radiation Protection, ICNIRP guidelines: Guidelines for limiting exposure to time-varying electric, magnetic, and electromagnetic fields (up to 300 GHz), *Health Phys.* **74**:494–522 (1998).
 26. K. R. Foster and W. F. Pickard, Microwaves: The risks of risk research, *Nature* **330**:531–532 (1987).
 27. Royal Society of Canada, *A Review of the Potential Health Risks of Radiofrequency Fields from Wireless Telecommunication Devices*, Ottawa, Canada, 1999, available online at www.rsc.ca/english/RFreport.html.
 28. R. L. Davis and F. K. Mostofi, Cluster of testicular cancer in police officers exposed to hand-held radar, *Am. J. Indust. Med.* **24**:231–233 (1993).
 29. S. Szmigielski, Cancer morbidity in subjects occupationally exposed to high frequency (radiofrequency and microwave) electromagnetic radiation, *Sci. Total Environ.* **180**:9–17 (1996).
 30. R. Santini, P. Santini, J. M. Danze, P. Le Ruz, and M. Seigne, Investigation on the health of people living near mobile telephone relay stations: Incidence according to distance and sex, *Pathol. Biol. (Paris)* **50**:369–373 (2002).
 31. N. J. Roberts and S. M. Michaelson, Epidemiological studies of human exposures to radiofrequency radiation. A critical review, *Int. Arch. Occup. Environ. Health.* **56**:169–178 (1985).
 32. M. H. Repacholi, Radiofrequency electromagnetic-field exposure standards, *IEEE Eng. Med. Biol.* **6**:18–21 (1987).
 33. P. J. Riu, K. R. Foster, D. W. Blick, and E. R. Adair, A thermal model for human thresholds of microwave-evoked warmth sensations. *Bioelectromagnetics* **18**:578–583 (1997).
 34. J. Osepchuk and R. C. Petersen, Safety standards for exposure to RF electromagnetic fields, *IEEE Microwave Mag.* 57–69 (June 2001).

FURTHER READING

A vast amount of material is available about health and safety issues related to RF energy, much available on the Internet. Below is a selection of sources for further reading.

BOOKS

- C. Polk and E. Postow, eds., *Handbook of Biological Effects of Electromagnetic Fields*, 2nd ed., CRC Press, Boca Raton, FL, 1996. (A collection of review chapters including biological effects of RF energy, dosimetry, and electrical properties of tissue.)
- S. M. Michaelson and J. C. Lin, *Biological Effects and Health Implications of Radiofrequency Radiation*, Plenum Press, New York, 1987 (a now-dated review, but with extensive discussion of earlier literature).
- O. P. Gandhi, ed., *Biological Effects and Medical Applications of Electromagnetic Energy*, Prentice-Hall, Englewood Cliffs, NJ, 1990. (Several excellent review articles on bioeffects, dosimetry, medical applications of RF energy.)

TUTORIALS AND REVIEWS

- M. H. Repacholi, Low-level exposure to radiofrequency fields: Health effects and research needs, *Bioelectromagnetics* **19**: 1–19 (1998). (Recent review of research questions related to biological effects of RF energy.)
- C.-K. Chou, H. Bassen, J. Osepchuk, Q. Balzano, R. Petersen, M. Meltz, R. Cleveland, J. C. Lin, and L. Heynick, Radiofrequency electromagnetic exposure: tutorial review on experimental dosimetry, *Bioelectromagnetics* **17**:195–208 (1996). (Excellent review of dosimetry.)
- K. A. Hossmann and D. M. Hermann, Effects of electromagnetic radiation of mobile phones on the central nervous system, *Bioelectromagnetics* **24**:49–62 (2003). (Review of possible neurologic effects of RF energy, with reference to mobile phones.)
- E. Litvak, K. R. Foster, and M. H. Repacholi, Health and safety implications of exposure to electromagnetic fields in the frequency range 300 Hz–10 MHz, *Bioelectromagnetics* **23**:68–82 (2002). (One of the few available reviews of biological effects of RF energy below 10 MHz.)
- J. D. Boice and J. K. McLaughlin, Epidemiological studies of cellular telephones and cancer risk—a review, Swedish Radiation Protection Authority, Stockholm, 2002; available online at http://www.ssi.se/ssi_rapporter/pdf/ssi_rapp_2002_16.pdf.

EXPERT REPORTS

- These reports of expert groups summarize the current status of knowledge about biological effects of RF energy, largely from the perspective of possible health risks of mobile phones and their base stations.
- Health Council of the Netherlands, *Mobile Telephones; an Evaluation of Health Effects*, Health Council of the Netherlands, The Hague, 2002, publication 2002; available online at <http://www.gr.nl/>.
- Independent Expert Group on Mobile Phones, *Mobile Phones and Health*, UK, May 2000; available online at <http://www.ie-gmp.org.uk/index.htm>.
- New Zealand Ministry for the Environment, *National Guidelines for Managing the Effects of Radiofrequency Transmitters*, Dec 2000; available online at <http://www.mfe.govt.nz/publications/rma/radio-freq-guidelines-dec00.pdf>.
- The Royal Society of Canada, *A Review of the Potential Health Risks of Radiofrequency Fields from Wireless Telecommunication Devices*, Ottawa, March 1999; available online at <http://www.rsc.ca/english/RFreport.html>.

INTERNET SITES

- Bioelectromagnetics Society, (the major professional society concerned with studies of possible health and safety issues related to RF energy); report available online at <http://bioelectromagnetics.org>.
- FAQ (frequently asked question) sheets related to electromagnetic fields and health by John Moulder at The Medical College of Wisconsin offers comprehensive and up-to-date reviews about mobile phones and health and other issues; available online at www.mcw.edu/gerc/cop/cell-phone-health-faq/toc.html.
- IEEE Committee on Man and Radiation (COMAR) prepares “technical information statements” on issues related to health and safety of electromagnetic fields; available online at <http://ewh.ieee.org/soc/embs/comar/>.

International Commission on Non-Ionizing Radiation Protection (ICNIRP) is an international agency that establishes exposure guidelines for electromagnetic fields; information available online at www.icnirp.de.

World Health Organization EMF Project offers an extensive array of information including “fact sheets” about health and safety issues related to RF energy, comparison of international exposure limits; available online at www.who.int/peh-emf/.

BOUNDARY-VALUE PROBLEMS

BENJAMIN BEKER
 GEORGE COKKINIDES
 MYUNG JIN KONG
 University of South Carolina
 Columbia, South Carolina

Many problems in electrical engineering require solution of integral or differential equations that describe physical phenomena. The choice as to whether integral or differential equations are used to formulate and solve specific problems depends on many factors, whose discussion is beyond the scope of this article. This article strictly concentrates on the use of the finite-difference method (FDM) in the numerical analysis of boundary value problems associated with primarily static and to some extent quasistatic electromagnetic (EM) fields. Although all examples presented herein deal with EM-related engineering applications, some numerical aspects of FDM are also covered. Since there is a wealth of literature in numerical and applied mathematics about the FDM, little will be said about the theoretical aspects of finite differencing. Such issues as the proof of existence or convergence of the numerical solution will not be covered, while the appropriate references will be provided to the interested reader. Instead, the coverage of FDM will deal with the details about implementation of numerical algorithms, compact storage schemes for large sparse matrices, the use of open boundary truncation, and efficient handling of inhomogeneous and anisotropic materials.

The emphasis will be placed on the applications of FDM to three-dimensional boundary value problems involving objects with arbitrary geometric shapes that are composed of complex dielectric materials. Examples of such problems include modeling of discrete passive electronic components, semiconductor devices and their packages, and crosstalk in multiconductor transmission lines. When the wavelength of operation is larger than the largest geometric dimensions of the object that is to be modeled, static or quasistatic formulation of the problem is appropriate. In electrostatics, for example, this implies that the differential equation governing the physics (voltage distribution) is of Laplace type for the source-free environment and of Poisson type in regions containing sources. The solution of such second-order partial-differential equations can be readily obtained using the FDM.

Although the application of FDM to homogeneous materials is simple, complexities arise as soon as inhomogeneity and anisotropy are introduced. The following discussion will provide essential details on how to overcome any potential difficulties in adapting FDM to boundary value problems involving such materials. The analytical presentation will be supplemented with abundant illustrations that demonstrate how to implement the theory in practice. Several examples will also be provided to show the complexity of problems that can be solved by using FDM.

1. BRIEF HISTORY OF FINITE DIFFERENCING IN ELECTROMAGNETICS

The utility of the numerical solution to partial-differential equations (or PDEs) utilizing finite-difference approximation to partial derivatives was recognized early [1]. Improvements to the initial iterative solution methods, discussed in Ref. 1, by using relaxation were subsequently introduced [2,3]. However, before digital computers became available, the applications of the FDM to the solution of practical boundary value problems was a tedious and often impractical task. This was especially true when a high level of accuracy was required.

With the advent of digital computers, numerical solution of PDEs became practical. They were soon applied to various problems in electrostatics and quasistatics such as in the analysis of microstrip transmission lines [4] among many others. The FDM found quick acceptance in the solution of boundary value problems within regions of finite extent, and efforts were initiated to extend their applicability to open region problems as well [5].

As a point of departure, it is interesting to note that some of the earliest attempts to obtain the solution to practical boundary value problems in electrostatics involved experimental methods. They included the electrolytic tank approach and resistance network analog technique [6], among others, to simulate the finite-difference approximations to PDEs.

Finally, it should be mentioned that in addition to the application of FDM to static and quasistatic problems, the FDM was also adapted for use in the solution of dynamic, full-wave EM problems in time and frequency domains. Most notably, the use of finite differencing was proposed for the solution to Maxwell's curl equations in the time domain [7]. Since then, a tremendous amount of work on the finite-difference time-domain (or FDTD) approach was carried out in diverse areas of electromagnetics. This includes antennas and radiation, scattering, microwave integrated circuits, and optics. The interested reader can consult the authoritative work in Ref. 8, as well as other articles on eigenvalue and related problems in this encyclopedia, for further details and additional references.

2. ENGINEERING BASICS OF FINITE DIFFERENCING

It is best to introduce the FDM for the solution of engineering problems, which deal with static and quasistatic electromagnetic fields, by way of example. Today, just

about every elementary text in electromagnetics—as well as newer, more numerically focused introductory EM textbooks—will have a discussion on FDM (e.g., pp. 241–246 of Ref. 9 and Sect. 4.4 of Ref. 10) and its use in electrostatics, magnetostatics, waveguides, and resonant cavities. Regardless, it will be beneficial to briefly go over the basics of electrostatics for the sake of completeness and to provide a starting point for generalizing FDM for practical use.

3. GOVERNING EQUATIONS OF ELECTROSTATICS

The analysis of electromagnetic phenomena has its roots in the experimental observations made by Michael Faraday. These observations were cast into mathematical form by James Clerk Maxwell in 1873 and verified experimentally by Heinrich Hertz 25 years later. When reduced to electrostatics, they state that the electric field at every point in space within a homogeneous medium obeys the following differential equations [9]

$$\nabla \times \vec{E} = 0 \quad (1)$$

$$\nabla \cdot \epsilon_0 \epsilon_r \vec{E} = \rho_v \quad (2)$$

where ρ_v is the volumetric charge density, ϵ_0 ($\approx 8.854 \times 10^{-12}$ F/m) is the permittivity of freespace, and ϵ_r is the relative dielectric constant. The use of the vector identity $\nabla \times \nabla \phi = 0$ in Eq. (1) allows for the electric field intensity, \vec{E} (V/m), to be expressed in terms of the scalar potential $\vec{E} = -\nabla \phi$. When this is substituted for the electric field in Eq. (2), a second-order PDE for the potential ϕ is obtained

$$\nabla \cdot (\epsilon_r \nabla \phi) = -\rho_v / \epsilon_0 \quad (3)$$

which is known as the *Poisson equation*. If the region of space, where the solution for the potential is sought, is source-free and the dielectric is homogeneous (i.e., ϵ_r is constant everywhere), Eq. (3) reduces to the Laplace equation $\nabla^2 \phi = 0$.

The solution to the Laplace equation can be obtained in several ways. Depending on the geometry of the problem, the solution can be found analytically or numerically using integral or differential equations. In either case, the goal is to determine the electric field in space due to the presence of charged conductors, given that the voltage on their surface is known. For example, if the boundaries of the charged conductors are simple shapes, such as a rectangular box, circular cylinder, or sphere, then the boundary conditions (constant voltage on the surface) can be easily enforced and the solution can be obtained analytically. On the other hand, when the charged object has an irregular shape, the Laplace equation cannot be solved analytically and numerical methods must be used instead.

The choice as to whether integral or differential equation formulation is used to determine the potential depends heavily on the geometry of the boundary value problem. For example, if the charged object is embedded within homogeneous medium of infinite extent, integral equations are the preferable choice. They embody the boundary conditions on the potential ϕ at infinity and

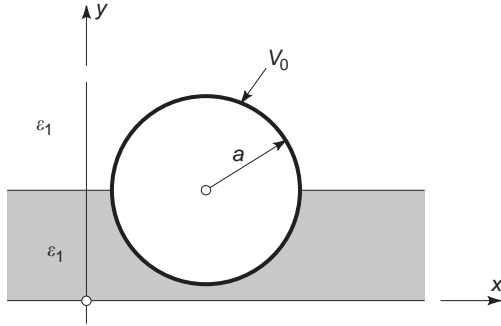


Figure 1. Charged circular cylinder embedded between two different dielectrics.

reduce the numerical effort to finding the charge density on the surface of the conductor (see Sect. 5.2 or 4.3 of Ref. 9 or 10 for further details).

On the other hand, when the boundary value problem includes inhomogeneous dielectrics (i.e., ϵ_r varying from point to point in space), the surface integral equation methods are no longer applicable (or are impractical). Instead, such problems can be formulated using volumetric PDE solvers such as the FDM.

It is important to note that similar considerations (to those stated above) also apply to the solution of the Poisson equation. In this case, in addition to the integration over the conductor boundaries, integration over the actual sources (charge density) must also be performed. The presence of the sources has the same effects on PDEs and FDM, as their effects must be taken into account at all points in space where they exist.

3.1. Direct Discretization of Governing Equation

To illustrate the utility and limitations of FDM and to introduce two different ways of deriving the numerical algorithm, consider the geometry shown in Fig. 1. Note that for the sake of clarity and simplicity, the initial discussion will be restricted to two dimensions.

The infinitely long, perfectly conducting circular cylinder in Fig. 1 is embedded between two dielectrics. To determine the potential everywhere in space, given that the voltage on the cylinder surface is V_0 , the FDM will be used. There are two approaches that might be taken to develop the FDM algorithm. One approach would be to solve Laplace (or Poisson) equations in each region of uniform dielectric

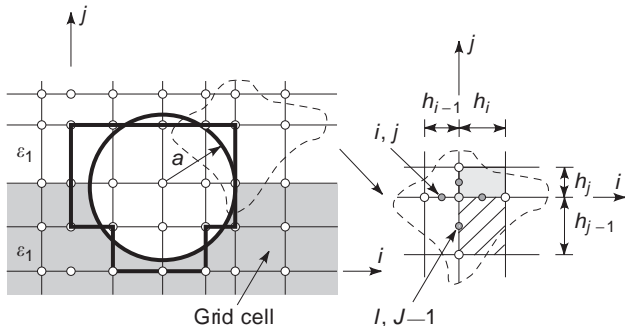


Figure 2. "Staircase" approximation to boundary of circular cylinder and notation for grid dimensions.

and enforce the boundary conditions at the interface between them. The other route would involve development of a general volumetric algorithm, which would be valid at every point in space, including the interface between the dielectrics. This would involve seeking the solution of a single, Laplace-type (or Poisson) differential equation:

$$\nabla \cdot (\epsilon_r(x, y) \nabla \phi) = \epsilon_r(x, y) \left(\frac{\partial^2 \phi}{\partial x^2} + \frac{\partial^2 \phi}{\partial y^2} \right) + \left(\frac{\partial \epsilon_r}{\partial x} \frac{\partial \phi}{\partial x} + \frac{\partial \epsilon_r}{\partial y} \frac{\partial \phi}{\partial y} \right) = \begin{cases} 0 \\ -\frac{\rho(x, y)}{\epsilon_0} \end{cases} \quad (4)$$

which is valid everywhere, except for the surface of the conductor.

The numerical approach to solving Eq. (4) starts with the approximation to partial derivatives using finite differences. This requires some form of discretization for the space (area or volume in two or three dimensions) where the potential is to be computed. The numerical solution of the PDE will lead to the values of the potential at a finite number of points within the discretized space. Figure 2 shows one possible discretization scheme for the cylinder in Fig. 1 and its surroundings. The points form a two-dimensional (2D) grid and need not be uniformly spaced. Note that the gridpoints, where the potential is to be computed, have to be defined all along the gridlines to allow for properly approximating the derivatives in Eq. (4). In other words, the gridlines cannot abruptly terminate or become discontinuous within the grid.

Using finite differences, the first-order derivative at any point in the grid can be approximated as follows

$$\begin{aligned} \left(\frac{\partial \phi}{\partial x} \right)_{i,j} &\approx \frac{(\phi_{I,J} - \phi_{I-1,j})}{(h_i + h_{i-1})/2} \\ &= \left[\left(\frac{\phi_{i+1,j} + \phi_{i,j}}{2} \right) - \left(\frac{\phi_{i,j} + \phi_{i-1,j}}{2} \right) \right] \frac{1}{(h_i + h_{i-1})/2} \\ &= \frac{\phi_{i+1,j} - \phi_{i-1,j}}{h_i + h_{i-1}} \end{aligned} \quad (5)$$

with the help of intermediate points I, J (darkened circles in Fig. 2). The approximation for the second derivatives can be obtained in a similar manner and is given by

$$\begin{aligned} \left[\frac{\partial}{\partial x} \left(\frac{\partial \phi}{\partial x} \right) \right]_{i,j} &\approx \frac{\left(\frac{\partial \phi}{\partial x} \right)_{I+1,j} - \left(\frac{\partial \phi}{\partial x} \right)_{I-1,j}}{(h_i + h_{i-1})/2} \\ &= \left[\left(\frac{\phi_{i+1,j} - \phi_{i,j}}{h_i} \right) - \left(\frac{\phi_{i,j} - \phi_{i-1,j}}{h_{i-1}} \right) \right] \\ &\quad \times \frac{1}{(h_i + h_{i-1})/2} \end{aligned} \quad (6)$$

Once all derivatives in Eq. (4) are replaced with their respective finite-difference approximations and all similar terms are grouped together, the discrete version of Eq. (4) takes on the following form:

$$\phi_{i,j} \approx \frac{1}{Y_{i,j}} (Y_{i+1}\phi_{i+1,j} + Y_{i-1}\phi_{i-1,j} + Y_{j+1}\phi_{i,j+1} + Y_{j-1}\phi_{i,j-1}) + \left\{ \begin{array}{c} 0 \\ \frac{(\rho_{i,j} + \rho_{i-1,j} + \rho_{i,j-1} + \rho_{i-1,j-1})}{\epsilon_0} \end{array} \right. \quad (7)$$

In this equation, the Y factors contain the material parameters and distances between various adjacent gridpoints. They are expressed below in a compact form:

$$Y_{i\pm 1} = \frac{2}{(h_i + h_{i-1})^2} \left\{ \begin{array}{l} (\epsilon_{i,j-1} + \epsilon_{i,j}) \left(\frac{3h_i + h_{i-1}}{h_i} \right) \\ (\epsilon_{i-1,j-1} + \epsilon_{i-1,j}) \left(\frac{h_{i-1} - h_i}{h_i} \right) \\ \left(\frac{h_i + 3h_{i-1}}{h_{i-1}} \right) \end{array} \right\} \quad (8)$$

$$Y_{j\pm 1} = \frac{2}{(h_j + h_{j-1})^2} \left\{ \begin{array}{l} (\epsilon_{i-1,j} + \epsilon_{i,j}) \left(\frac{3h_j + h_{j-1}}{h_j} \right) \\ (\epsilon_{i-1,j-1} + \epsilon_{i,j-1}) \left(\frac{h_{j-1} - h_j}{h_j} \right) \\ \left(\frac{h_j + 3h_{j-1}}{h_{j-1}} \right) \end{array} \right\} \quad (9)$$

$$Y_{i,j} = Y_{i+1,j} + Y_{i-1,j} + Y_{i,j+1} + Y_{i,j-1} \quad (10)$$

It is important to add that in deriving these equations, a particular convention for associating the medium parameters to individual grid cells was employed. Specifically, it was assumed that the medium parameter values of the entire grid cell were associated with (or assigned to) the lower left corner of that cell. For example, $\epsilon_{i,j}$ is assumed to be constant over the shaded grid cell area shown in Fig. 2, while $\epsilon_{i,j-1}$ is constant over the hatched area, which is directly below.

Observe what are the consequences of converting the continuous PDE given in Eq. (4) to its approximate discrete form stated in Eq. (7). First, the boundary value problem over the continuous space, shown in Fig. 1, was “mapped” onto a discrete grid (see Fig. 2). Clearly, if the number of gridpoints increases, then spacing between them will become smaller. This provides a better approximation to the actual continuous problem. In fact, in the

limit as the number of gridpoint reaches infinity, the discrete and continuous problems become identical.

In addition to illustrating the “mapping” of a continuous problem to its discrete analog, Fig. 2 also clearly demonstrates one of FDM’s undesirable artifacts. Note that objects with smooth surfaces are replaced with a “staircased” approximation. Obviously, this approximation can be improved by reducing the discretization grid spacing. However, this will increase the number of points where the potential has to be calculated, thus increasing the computational complexity of the problem. One way to overcome this is to use a nonuniform discretization, as depicted in Fig. 2. Specifically, finer discretization can be used in the region near the smooth surface of the cylinder to better approximate its shape, followed by gradually increasing the gridpoint spacing between the cylinder and grid truncation boundary.

At this point, it is also appropriate to add that other, more rigorous methods have been proposed for incorporating curved surfaces into the finite-difference type of algorithms. They are based on special-purpose differencing schemes, which are derived by recasting the same PDEs into their equivalent integral forms. They exploit the surface or contour integration and are used to replace the regular differencing algorithm on the curved surfaces or contours of smooth objects. This approach was already implemented for the solution of dynamic full-wave problems [11] and could be adapted to electrostatic boundary value problems as well.

Finally, Eq. (7) also shows that the potential at any point in space, which is source-free, is a weighted average of the potentials at the neighboring points only. This is typical of PDEs, because they represent physical phenomena only locally—that is, in the immediate vicinity of the point of interest. As will be shown later, one way to “propagate” the local information through the grid is to use an iterative scheme. In this scheme, the known potential, such as V_0 at the surface of the conducting cylinder in Fig. 1, is carried throughout the discretized space by stepping through all the points in the grid. The iterations are continued until the change in the potential within the grid is very small.

3.2. “Indirect” Discretization of Governing Equation

As shown in the previous section, appropriate finite-difference approximations were required for the first- and second-order derivatives in order to convert Eq. (4) to a discrete form. Intermediate points (I, J) were used midway between the regular grid nodes for obtaining average values of the potential, its first derivatives, and dielectric constants to facilitate the derivation of the final update equation for the potential. This can be avoided and an alternative, but equally valid finite-differencing scheme to that given in Eq. (7), which for the sake of brevity is restricted to the Laplace equation only, can be obtained. The first step is to simplify Eq. (4) by recasting it into an integrodifferential form. To achieve this, Eq. (4) should be integrated over a volume that completely encloses any one of the grid nodes. This will be referred to as the volume of the unit cell (V_U), which is bounded by

surface S_U (see Fig. 3). Stoke’s theorem is applied to replace the volume integration by a surface integral:

$$\int_{V_U} \nabla \cdot (\epsilon_r(x,y)\nabla\phi) dv = \oint_{S_U} (\epsilon_r(x,y)\nabla\phi) \cdot \hat{n} ds$$

$$= \oint_{S_U} \epsilon_r(x,y) \frac{\partial\phi}{\partial n} ds = 0 \tag{11}$$

where \hat{n} is the unit vector, normal to S_U and pointing out of it.

To illustrate this “indirect” discretization procedure in two dimensions, consider surface $S_{U,i,j}$ (i.e., just a contour) shown in Fig. 3, which completely encloses gridpoint i, j . The integral in Eq. (11) reduces to four terms, each corresponding to one of the faces of $S_{U,i,j}$. For example, the integral over the right edge (or face) of $S_{U,i,j}$ can be approximated as

$$\frac{\phi_{i+1,j} - \phi_{i,j}}{h_i} \left(\frac{h_{j-1}}{2} \epsilon_{i,j-1} + \frac{h_j}{2} \epsilon_{i,j} \right) \tag{12}$$

When the remaining integrals are evaluated and the like terms are grouped together, the final form of the “indirect” FDM algorithm is obtained. This algorithm is identical in form to that given earlier in Eq. (7). However, the weighting Y factors are different from those appearing in Eqs. (8) and (9). Their complete expressions are given by

$$Y_{\{i+1\}}^{\{i-1\}} = \left(h_{j-1} \epsilon_{\{i,j-1\}} + h_j \epsilon_{\{i,j\}} \right) \frac{1}{2h_{\{i-1\}}} \tag{13}$$

where $Y_{i,j}$ is the sum of all other Y s, the same as before [see Eq. (10)].

It should be added that this approach has been suggested several times in the literature—for example, in Refs. 12 and 13. Therein, Eq. (11) was specifically used to enforce the boundary conditions at the interface between different dielectrics only in order to “connect” FDM algorithms based on the Laplace equation for the homogeneous regions. However, there is no reason not to use Eq. (11) at every point in space, especially if the boundary

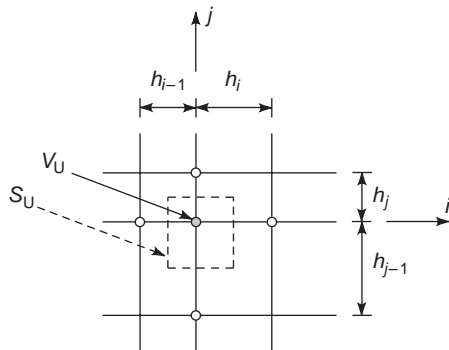


Figure 3. Closed surface completely enclosing a grid node.

value problem involves inhomogeneous media. This form of FDM scheme is completely analogous to that presented in the previous section. In fact, it is a little simpler to derive and involves fewer arithmetic operations.

3.3. Numerical Implementation in Two Dimensions

There are several important numerical issues that must be addressed prior to implementing FDM on the computer. Questions such as how to terminate the grid away from the region of interest and which form of the FDM algorithm to choose must be answered first. The following discussion provides some simple answers, postponing the more detailed treatment until later.

3.3.1. Simplistic Grid Boundary Truncation. Clearly, since even today’s computers do not have infinite resources, the computational volume (or space) must somehow be terminated (see Fig. 4). The simplest approach is to place the truncation boundary far away from the region of interest and to set the potential on it equal to zero. This approach is valid as long as the truncation boundary is placed far enough not to interact with the charged objects within, as for example the “staircased” cylinder shown in Fig. 4. The downside of this approach is that it leads to large computational volumes, thereby requiring unnecessarily high computer resources. This problem can be partly overcome by using a nonuniform grid, with progressively increasing spacing from the cylinder toward the truncation boundary. It should be added that there are other ways to simulate the open-boundary conditions, which is an advanced topic and will be discussed later.

3.3.2. Iteration-Based Algorithm. Several iteration methods can be applied to solve Eq. (7), each leading to different convergence rates (i.e., how quickly an acceptable solution is obtained). A complete discussion of this

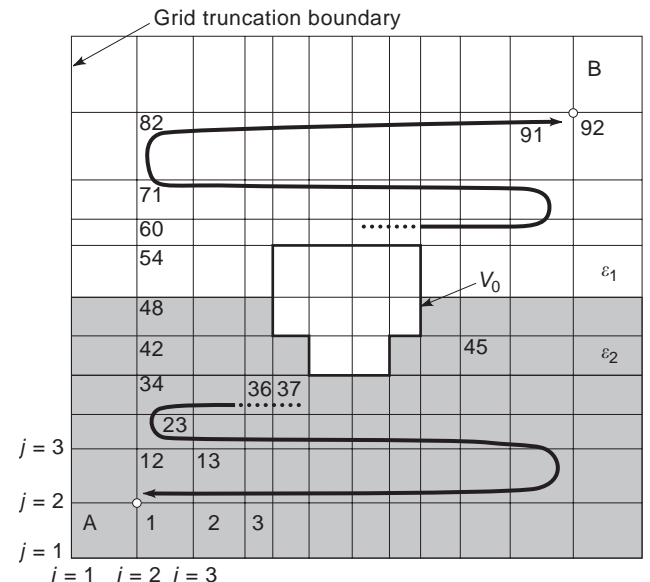


Figure 4. Complete discretized geometry and computational space for cylinder in Fig. 2.

topic, as well as of the accuracy of the numerical approximations in FDM, appears in Ref. 14 and will not be repeated here. The interested reader may also find Ref. 15 quite useful, because it covers such topics in more rigorous detail and includes a comprehensive discussion on the proof of the existence of the finite-differencing solution to PDEs. However, for the sake of brevity, this article deals with the most popular and widely used approach, which is called successive overrelaxation (SOR) (see, e.g., Ref. 14).

SOR is based on Eq. (7), which is rearranged as

$$\begin{aligned} \phi_{i,j}^{p+1} &\approx \phi_{i,j}^p + \frac{\Omega}{Y_{i,j}} (Y_{i+1}\phi_{i+1,j}^p + Y_{i-1}\phi_{i-1,j}^{p+1} + Y_{j+1}\phi_{i,j+1}^p \\ &\quad + Y_{j-1}\phi_{i,j-1}^{p+1} - Y_{i,j}\phi_{i,j}^p) \\ &= (1 - \Omega)\phi_{i,j}^p + \frac{\Omega}{Y_{i,j}} (Y_{i+1}\phi_{i+1,j}^p + Y_{i-1}\phi_{i-1,j}^{p+1} \\ &\quad + Y_{j+1}\phi_{i,j+1}^p + Y_{j-1}\phi_{i,j-1}^{p+1}) \end{aligned} \tag{14}$$

In this equation, superscripts p and $p + 1$ respectively denote the present and previous iteration steps and Ω is the so-called overrelaxation factor, whose value can vary from 1 to 2. Note that Ω accelerates the change in the potential from one iteration to the next at any point in the grid. It can be a constant throughout the entire relaxation (solution) process or be varying according to some heuristic scheme. For example, it was found that the overall rate of convergence is improved by setting Ω near 1.8 at the start of the iteration process and gradually reducing it to 1.2 with the numbers of iterations.

At this point, the only remaining task is to define the appropriate criteria for terminating the FDM algorithm. Although there are rigorous ways of selecting the termination criterion, the following approach, which seems to work quite well, is presented instead. As stated below, it is based on calculating the change in the potential between successive iterations at every point in the grid and comparing the maximum value to the (user-selectable) error criterion:

$$\text{ERR}_{\max} = \sum_{i=1}^{N_x} \sum_{j=1}^{N_y} \max(|\phi_{i,j}^{p+1} - \phi_{i,j}^p|) \tag{15}$$

Although it is simple, the redeeming feature of this approach is that the error is computed globally within the grid, rather than within a particular single grid node. The danger in monitoring the convergence of the algorithm at a single node may lead to premature termination or to an unnecessarily prolonged execution.

Now that an error on which the algorithm termination criterion is based has been defined, the iteration process can be initiated. Note that there are several ways to “march” through the grid. Specifically, the updating of the potential may be started from point A , as shown in Fig. 4, and end at point B , or vice versa. If the algorithm works in this manner, the solution will tend, to be artificially “biased” toward one region of the grid, and the potential is “more converged” in regions where the

iteration starts. The obvious way to avoid this is to change the direction of the “marching” process after every few iterations. As a result, the potential will be updated throughout the grid uniformly and will converge at the same rate. Note from Fig. 4 that the potential only needs to be computed at the internal points of the grid, since the potential at the outer boundary is (for now) assumed to be zero. Moreover, it should also be evident that the potential at the surface of the cylinder, as well as inside it, is known (V_0) and need not be updated during the iteration process.

3.3.3. Matrix-Based Algorithm. Implementation of the finite-difference algorithms is not restricted to relaxation techniques only. The solution of Eq. (4) for the electrostatic potential can also be obtained using matrix methods. To illustrate this, the FDM approximation to Eq. (4)—namely, Eq. (7)—will be rewritten as

$$\begin{aligned} (Y_{i+1}\phi_{i+1,j} + Y_{i-1}\phi_{i-1,j} + Y_{j+1}\phi_{i,j+1} + Y_{j-1}\phi_{i,j-1} \\ - Y_{i,j}\phi_{i,j}) \approx 0 \end{aligned} \tag{16}$$

This equation must be enforced at every internal point in the grid, except at the surface of and internal to the conductors, where the potential is known (V_0). For the particular example of the cylinder shown in Fig. 4, these points are numbered 1 through 92. This implies that there are 92 unknowns, which must be determined. To accomplish this, Eq. (16) must be enforced at 92 locations in the grid, leading to a system of 92 linear equations that must be solved simultaneously.

To demonstrate how the equations are set up, consider nodes 1, 36, and 37 in detail. At node 1 (where $i=j=2$), Eq. (16) reduces to

$$Y_3^i\phi_{12} + Y_3^j\phi_{2} - Y_{2,2}\phi_1 = 0 \tag{17}$$

where the fact that the potential at the outer boundary nodes $(i,j)=(1,2)$ and $(2,1)$ is zero was taken into account and superscripts i and j on Y were introduced as a reminder whether they correspond to $Y_{i\pm 1}$ or $Y_{j\pm 1}$. In addition, the potential at nodes $(i,j)=(2,2)$, $(3,2)$, and $(2,3)$ was also relabeled as ϕ_1 , ϕ_2 , and ϕ_{12} , respectively. Similarly, at nodes 36 ($i,j=4,5$) and 37 ($i,j=5,5$), Eq. (16) becomes

$$Y_5^i\phi_{37} + Y_3^i\phi_{35} + Y_6^j\phi_{44} + Y_4^j\phi_{25} - Y_{4,5}\phi_{36} = 0 \tag{18}$$

and

$$Y_4^i\phi_{36} + Y_4^j\phi_{26} - Y_{5,5}\phi_{37} = -Y_6^iV_0 - Y_6^jV_0 = V_{37} \tag{19}$$

where [in Eq. (19)] the known quantities (the potentials on the surface of the cylinder at nodes 5,6 and 6,5) were moved to the right-hand side.

Similar equations can be obtained at the remaining free grid nodes where the potential is to be determined. Once Eq. (16) has been enforced everywhere within the grid, the resulting set of equations can be combined into the following matrix form:

arrays can be used to find the index k (to identify ϕ_k) for grid coordinates (i, j) in the following manner:

1. Given i and j , compute $code = i \cdot N_y + j$.
2. Find the array index m , such that $code = CODE(m)$, using the bisection search algorithm.
3. Look up k using $k = INDEX(m)$, thereby identifying the appropriate ϕ_k , given i, j .

The criteria for selecting a particular sparsity coding scheme for the matrix $[Y]$ are (1) the minimization of storage requirements and (2) optimization of matrix operations—in particular, multiplication and LU factoring. One very efficient scheme is based on storing $[Y]$ using four one-dimensional arrays:

1. Real array $DIAG(i) =$ diagonal entry of row i
2. Real array $OFFD(i) =$ i th nonzero off-diagonal entry (scanned by rows)
3. Integer array $IROW(i) =$ index of first nonzero off-diagonal entry of row i
4. Integer array $ICOL(i) =$ column number of i th nonzero off-diagonal entry (scanned by rows)

Assuming a system of N equations, the arrays $DIAG$, $IROW$, $OFFD$, and $ICOL$ have N , $N+1$, $4N$, and $4N$ entries, respectively. Therefore, the total memory required to store a sparsity-coded matrix $[Y]$ is approximately 40N bytes (assuming 32-bit storage for both real and integer numbers). On the other hand, $4N^2$ bytes would be needed to store the full form of $[Y]$. For example, in a system with 1000 equations, the full storage mode requires 4 megabytes (MB), while the sparsity-coded matrix occupies only 40 kilobytes (KB) of computer memory.

Perhaps the most important feature of sparsity coding is the efficiency with which multiplication and other matrix operations can be performed. This is best illustrated by a sample FORTRAN code needed to multiply a matrix stored in this mode, by a vector $B(i)$:

```

DO I = 1, N
    C(I) = DIAG(I) * B(I)
    DO J = IROW(I), IROW(I+1) - 1
        C(I) = C(I) + OFFD(J) * B(ICOL(J))
    ENDDO
ENDDO

```

(23)

This double loop involves $5N$ multiplications and $4N$ additions, without the need of search and compare operations. To perform the same operation using the brute-force, full-storage approach would require N^2 multiplications and N^2 additions. Thus, for a system of 1000 unknowns, the sparsity-based method is at least 200 times faster than the full-storage approach in performing matrix multiplication.

To solve Eq. (20), $[Y]$ can be inverted and the inverse multiplied by $[V_0]$. However, for sparse systems, complete matrix inversion should be avoided. The reason is that, in

most cases, the inverse of a sparse matrix is full, for which the advantages of sparsity coding cannot be exploited. The solution of sparsity coded linear systems is typically obtained by using the LU decomposition, since usually the L and U factors are sparse. Note that the sparsity of the L and U factor matrices can be significantly affected by the ordering of the grid nodes (i.e., in which sequence $[\phi]$ was filled). Several very successful node ordering schemes that are associated with the analysis of electrical networks were reported for the solution of sparse matrix equations (see Ref. 16). Unfortunately, the grid node connectivity in typical FDM problems is such that the L and U factor matrices are considerably fuller than the original matrix $[Y]$, even if the nodes are optimally ordered. Therefore, direct solution techniques are not as attractive for use in FDM as they are for large network problems.

Unlike the direct solution methods, there are iterative techniques for solving matrix equations, which do not require LU factoring. One of them is the conjugate-gradient method [17–19].

This method uses a sequence of matrix/vector multiplications, which can be performed very efficiently using the sparsity coding scheme described above.

3.3.4. Convergence. Given the FDM equations in matrix form, either direct [16] or iterative methods [17–19] such as the conjugate-gradient method (CGM) can be readily applied. It is important to point out that CGM-type algorithms are considerably faster than direct solution, provided a good initial guess is used. One simple approach is to assume that the potential is zero everywhere, but on the surface of the conductor, and let this be an initial guess to start the CGM algorithm. For this initial guess, the convergence is very poor and the solution takes a long time. To improve the initial guess, several iterations of the SOR-based FDM algorithm can be performed to calculate the potential everywhere within the grid. It was found that for many practical problems, 10–15 iterations provide a very good initial guess for CGM.

From the performance point of view, the speed of CGM was most noticeable when compared to the SOR-based algorithm. In many problems, CGM was found to be an order of magnitude faster than SOR. In all fairness to SOR, its implementation, as described above, can be improved considerably by using the so-called multigrid/multilevel acceleration [20,21]. The idea behind this method is to perform the iterations over coarse and fine grids alternatively, where the coarse gridpoints also coincide with and are a part of the fine grid. This means that iterations are first performed over a coarse grid, then interpolated to the fine grid and iterated over the fine grid. More complex multigrid schemes involve several layers of grids with different levels of discretization, with the iterations being performed interchangeably on all grids.

Finally, it should be pointed out that theoretical aspects of convergence for algorithms discussed thus far are well documented and are outside the main scope of this article. The interested reader should consult Ref. 15, 18, or 19 for detailed mathematical treatment and assessment of convergence.

4. ADVANCED TOPICS

4.1. Open-Boundary Truncation

If the electrostatic boundary value problem consists of charged conductors in a region of infinite extent, then the simplest approach to truncate the computational (or FDM) boundary is with an equipotential wall of zero voltage. This has the advantage of being easy to implement, but leads to erroneous solution, especially if the truncation boundary is too close to the charged conductors. On the other hand, placing it too far from the region of interest may result in unacceptably large computational volume, which will require large computational resources.

Although some early attempts to overcome such difficulties [5] provided the initial groundwork, rigorous absorbing boundary truncation operators were more recently introduced [22–24] for dynamic problems, which can be modified for electrostatics. They are based on deriving mathematical operators that help simulate the behavior of the potential on a virtual boundary truncation surface, which is placed close to charged conductors (see Fig. 5). In essence, these operators provide the means for numerically approximating the proper behavior of the potential at infinity within a computational volume of finite extent.

Such absorbing boundary conditions (ABCs) are based on the fact that the potential due to any 3D charge distribution is inversely proportional to the distance measured from it. Consider an arbitrary collection of charged conductors shown in Fig. 5. Although it is located in free unbounded space, a fictitious surface will be placed around it, totally enclosing all conductors. If this surface is far away from the charged conductor system—namely, if \vec{r} is much greater than \vec{r}' —then the dominant radial variation of potential, ϕ , will be given by

$$\frac{1}{|\vec{r} - \vec{r}'|} \rightarrow \frac{1}{r} \quad (24)$$

If the fictitious boundary is moved closer toward the conductor assembly, then the potential will also include additional terms with higher inverse powers of r . These

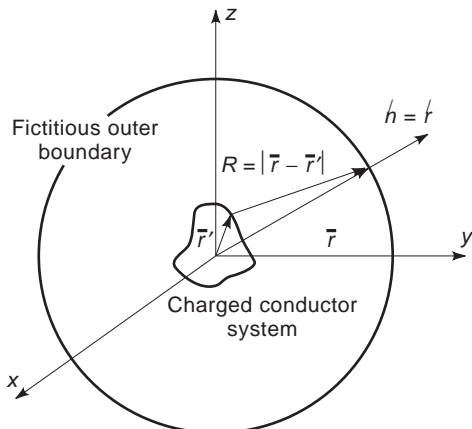


Figure 5. Virtual surface used for boundary truncation.

terms will contribute to the magnitude of the potential more significantly than those with lower inverse powers of r , as r becomes small.

The absorbing boundary conditions emphasize the effect of leading (dominant) radial terms on the magnitude of the potential evaluated on the fictitious (boundary truncation) surface. The ABCs provide the proper analytic means to annihilate the nonessential terms, instead of simply neglecting their contribution. Numerically, this can be achieved by using the so-called absorbing boundary truncation operators.

In general, absorbing boundary operators can be of any order. For example, as shown in Ref. 23, the first- and second-order operators in 3D have the following forms:

$$B_1 u = \frac{\partial u}{\partial r} + \frac{u}{r} = O\left(\frac{1}{r^3}\right) \rightarrow 0 \quad \text{as } r \rightarrow \infty \quad (25)$$

$$B_2 u = \left(\frac{\partial}{\partial r} + \frac{3}{r}\right) \left(\frac{\partial u}{\partial r} + \frac{u}{r}\right) = O\left(\frac{1}{r^5}\right) \rightarrow 0 \quad \text{as } r \rightarrow \infty \quad (26)$$

where u is the scalar electric potential function, ϕ , that satisfies the Laplace equation, and $r = |\vec{r}|$ is the radial distance measured from the coordinate origin (see Fig. 5). Since FDM is based on the iterative solution to the Laplace equation, small increases in the overall lattice (discretized 3D space whose planes are 2D grids) size do not slow the algorithm down significantly, nor do they require an excessive amount of additional computer memory. As a result, from a practical standpoint, the fictitious boundary truncation surface need not be placed too close to the region of interest, therefore not requiring the use of high-order ABC operators in order to simulate proper behavior of the potential at lattice boundaries accurately. Consequently, in practice, it is sufficient to use the first-order operator, B_1 , to model open boundaries. Previous numerical studies suggest that this choice is indeed adequate for many engineering problems [25].

To be useful for geometries that mostly conform to rectangular coordinates, the absorption operator B_1 , when expressed in Cartesian coordinates, takes on the following form

$$\frac{\partial u}{\partial x} \approx \mp \left(\frac{u}{x} + \frac{y}{x} \frac{\partial u}{\partial y} + \frac{z}{x} \frac{\partial u}{\partial z} \right) \quad (27)$$

$$\frac{\partial u}{\partial y} \approx \mp \left(\frac{u}{y} + \frac{x}{y} \frac{\partial u}{\partial x} + \frac{z}{y} \frac{\partial u}{\partial z} \right) \quad (28)$$

$$\frac{\partial u}{\partial z} \approx \mp \left(\frac{u}{z} + \frac{x}{z} \frac{\partial u}{\partial x} + \frac{y}{z} \frac{\partial u}{\partial y} \right) \quad (29)$$

where \mp signs correspond to the outward pointing unit normal vectors $\hat{n} = \pm(\hat{x}, \hat{y}, \hat{z})$ for operators in Eqs. (27), (28), and (29), respectively.

The finite-difference approximations to the preceding equations that have been employed in the open boundary

FDM algorithm are given by

$$u_{i+1,j,k} = u_{i-1,j,k} - \frac{(h_i + h_{i-1})}{(x_{i,j,k} - x_{\text{ref}})} \left[u_{i,j,k} + \frac{(y_{i,j,k} - y_{\text{ref}})(u_{i,j+1,k} - u_{i,j-1,k})}{(h_j + h_{j-1})} + \frac{(z_{i,j,k} - z_{\text{ref}})(u_{i,j,k+1} - u_{i,j,k-1})}{(h_k + h_{k-1})} \right] \quad (30)$$

$$u_{i,j+1,k} = u_{i,j-1,k} - \frac{(h_j + h_{j-1})}{(y_{i,j,k} - y_{\text{ref}})} \left[u_{i,j,k} + \frac{(x_{i,j,k} - x_{\text{ref}})(u_{i+1,j,k} - u_{i-1,j,k})}{(h_i + h_{i-1})} + \frac{(z_{i,j,k} - z_{\text{ref}})(u_{i,j,k+1} - u_{i,j,k-1})}{(h_k + h_{k-1})} \right] \quad (31)$$

$$u_{i,j,k+1} = u_{i,j,k-1} - \frac{(h_k + h_{k-1})}{(z_{i,j,k} - z_{\text{ref}})} \left[u_{i,j,k} + \frac{(x_{i,j,k} - x_{\text{ref}})(u_{i+1,j,k} - u_{i-1,j,k})}{(h_i + h_{i-1})} + \frac{(y_{i,j,k} - y_{\text{ref}})(u_{i,j+1,k} - u_{i,j-1,k})}{(h_j + h_{j-1})} \right] \quad (32)$$

where $(x, y, z)_{\text{ref}}$ are the x, y, z components of a vector pointing (referring) to the geometric center of the charged conductor assembly, with other quantities that appear in Eqs. (30)–(32) shown in Fig. 6. It is important to add that the $(x, y, z)_{i,j,k} - (x, y, z)_{\text{ref}}$ terms are the x, y, z components of a vector from the truncation boundary to the geometric center of the charged conductor system.

Notice that Fig. 6 graphically illustrates the FDM implementation of the open-boundary truncation on lat-

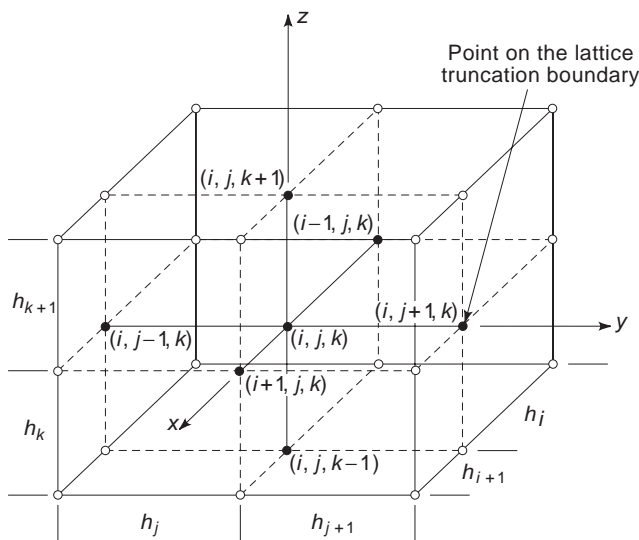


Figure 6. Detail of FDM lattice near the boundary truncation surface.

tice faces aligned along the xz plane. On this plane, the normal is in the y direction, for which Eq. (31) is the FDM equivalent of the first-order absorbing boundary operator in Cartesian coordinates. Similarly, Eqs. (32) and (30) are used to simulate the open boundary on xy and yz faces of the lattice, respectively.

When reduced to two dimensions, the absorption operator, B_1 , in Cartesian coordinates, takes on the form given below:

$$\frac{\partial u}{\partial x} \approx \mp \left(\frac{1}{x} + \frac{y}{x} \frac{\partial u}{\partial y} \right) \quad (33)$$

$$\frac{\partial u}{\partial y} \approx \mp \left(\frac{1}{y} + \frac{\partial u}{\partial x} \right) \quad (34)$$

The discrete versions of these equations can be written as

$$u_{i+1,j} = \mp \left\{ u_{i-1,j} - \frac{(h_i + h_{i-1})}{(x_{i,j} - x_{\text{ref}})} \left[u_{i,j} + \frac{(y_{i,j} - y_{\text{ref}})(u_{i,j+1} - u_{i,j-1})}{(h_j + h_{j-1})} \right] \right\} \quad (35a)$$

$$u_{i,j+1} = \mp \left\{ u_{i,j-1} - \frac{(h_j + h_{j-1})}{(y_{i,j} - y_{\text{ref}})} \left[u_{i,j} + \frac{(x_{i,j} - x_{\text{ref}})(u_{i+1,j} - u_{i-1,j})}{(h_i + h_{i-1})} \right] \right\} \quad (35b)$$

where, as before, \mp correspond to the outward pointing unit normal vectors $\hat{n} = \pm(\hat{x}, \hat{y})$ for operators in Eqs. (33) and (34) or (35a) and (35b), respectively. The points $x_{i,j}$ and $y_{i,j}$ denote those points in the grid that are located one cell away from the truncation boundary, while x_{ref} and y_{ref} correspond to the center of the cylinder in Figs. 2 and 4.

Finally, another approach to open-boundary truncation, which is worth mentioning, involves the regular finite-difference scheme supplemented by the use of electrostatic surface equivalence [26]. A virtual surface S_v is defined near the actual grid truncation boundary. The electrostatic potential due to charged objects, enclosed within S_v , is computed using the regular FDM algorithm. Subsequently, it is used to calculate the surface charge density and surface magnetic current, which are proportional to the normal and tangential components of the electric field on S_v .

Once the equivalent sources are known, the potential between the virtual surface and the grid truncation boundary can be readily calculated (for details, see Ref. 26). This procedure is repeated every iteration, and since the potential on the virtual surface is estimated correctly, it produces a physical value of the potential on the truncation boundary. As demonstrated in Ref. 26, this approach leads to very accurate results in boundary value problems with charged conductors embedded in open regions.

It is vastly superior to simply using the grounded conductor to terminate the computational space.

4.2. Inclusion of Dielectric Anisotropy

4.2.1. Network Analog Approach. Many materials such as printed-circuit board (PCB) and microwave circuit substrates, which are commonly used in electrical engineering, exhibit anisotropic behavior. The electrical properties of these materials vary with direction and have to be described by a tensor instead of a single scalar quantity. This section will examine how the anisotropy affects the FDM and how the algorithm must be changed to accommodate the solution of 3D problems containing such materials. The theoretical development presented below is a generalization of that available in Ref. 27 and is restricted to linear anisotropic dielectrics only.

In an attempt to provide a more intuitive interpretation to the abstract nature of the FDM algorithm, an equivalent-circuit model will be used for linear inhomogeneous, anisotropic regions. This approach is called *resistance network analog* [6]. It was initially proposed for approximating the solution of the Laplace equation in two dimensions experimentally, with a network of physical resistors whose values could be adjusted to correspond to the weighting factors [e.g., the Y s in Eq. (7)] that appear in the FDM algorithm. Since its introduction, the resistance network approach has been implemented numerically in the analysis of (1) homogeneous dielectrics in 3D (28) and (2) simple biaxial anisotropic materials (described by diagonal permittivity tensors) in 2D [29].

Since the resistance network analog gives a physical interpretation to FDM, the discretized versions of the Laplace equations for anisotropic media will be recast into this form. As the details of FDM were described earlier, only the key steps in developing the two-dimensional model are summarized below. Moreover, for the sake of brevity, the discussion of the three-dimensional case will be limited to the final equations and their pictorial interpretation.

The Laplace equation for boundary value problems involving inhomogeneous and anisotropic dielectrics in three dimensions is given by

$$\nabla \cdot (\epsilon_0 [\epsilon_r(x, y, z)] \cdot \nabla \phi(x, y, z)) = 0 \tag{36}$$

In this equation, $[\epsilon_r]$ stands for the relative dielectric tensor and is defined as

$$[\epsilon] = \begin{bmatrix} \epsilon_{xx} & \epsilon_{xy} & \epsilon_{xz} \\ \epsilon_{yx} & \epsilon_{yy} & \epsilon_{yz} \\ \epsilon_{zx} & \epsilon_{zy} & \epsilon_{zz} \end{bmatrix} \tag{37}$$

Since the material properties need not be homogeneous in the region of interest, the elements of $[\epsilon_r]$ are assumed to be functions of position. The dielectric is assumed to occupy only part of the modeling (computational) space, and its properties may vary from point to point. When Eq. (37) is substituted into Eq. (36) and rewritten in a

matrix form as

$$\begin{bmatrix} \frac{\partial}{\partial x} & \frac{\partial}{\partial y} & \frac{\partial}{\partial z} \end{bmatrix} \cdot \begin{bmatrix} \epsilon_{xx} \frac{\partial \phi}{\partial x} + \epsilon_{xy} \frac{\partial \phi}{\partial y} + \epsilon_{xz} \frac{\partial \phi}{\partial z} \\ \epsilon_{yx} \frac{\partial \phi}{\partial x} + \epsilon_{yy} \frac{\partial \phi}{\partial y} + \epsilon_{yz} \frac{\partial \phi}{\partial z} \\ \epsilon_{zx} \frac{\partial \phi}{\partial x} + \epsilon_{zy} \frac{\partial \phi}{\partial y} + \epsilon_{zz} \frac{\partial \phi}{\partial z} \end{bmatrix} = 0 \tag{38}$$

it provides the starting point for developing the corresponding FDM algorithm.

After eliminating the z -dependent terms and fully expanding the equation above by following the notation used throughout this article, the finite-difference approximation for the potential at every nodal point in a 2D grid is given by

$$\phi_{i,j}^{p+1} = (1 - \Omega) \phi_{i,j}^p + \frac{\Omega}{Y_{i,j}} \times \left\{ \begin{aligned} &(\phi_{i+1,j}^p Y_{i+1} + \phi_{i-1,j}^{p+1} Y_{i-1}) \\ &+ (\phi_{i,j+1}^p Y_{j+1} + \phi_{i,j-1}^{p+1} Y_{j-1}) \\ &+ (\phi_{i+1,j+1}^p Y_{i+1,j+1} + \phi_{i-1,j-1}^{p+1} Y_{i-1,j-1}) \\ &- (\phi_{i-1,j+1}^p Y_{i-1,j+1} + \phi_{i+1,j-1}^{p+1} Y_{i+1,j-1}) \end{aligned} \right\} \tag{39}$$

where

$$Y_{i\pm 1} = \left(\begin{array}{c} (\epsilon_{i,j-1}^{yy} + \epsilon_{i,j}^{yy}) \\ (\epsilon_{i-1,j-1}^{yy} + \epsilon_{i-1,j}^{yy}) \end{array} \right) \left(\frac{1}{h_i} + \frac{2}{h_i + h_{i-1}} \right) + \left(\frac{2}{h_i + h_{i-1}} \right) \left(\frac{2}{h_j + h_{j-1}} \right) [(\epsilon_{i,j}^{zy} + \epsilon_{i-1,j}^{zy}) - (\epsilon_{i-1,j-1}^{zy} + \epsilon_{i,j-1}^{zy})] \tag{40}$$

$$Y_{j\pm 1} = \left(\begin{array}{c} (\epsilon_{i-1,j}^{zz} + \epsilon_{i,j}^{zz}) \\ (\epsilon_{i-1,j-1}^{zz} + \epsilon_{i,j-1}^{zz}) \end{array} \right) \left(\frac{1}{h_j} + \frac{2}{h_j + h_{j-1}} \right) + \left(\frac{2}{h_i + h_{i-1}} \right) \left(\frac{2}{h_j + h_{j-1}} \right) [(\epsilon_{i,j-1}^{yz} + \epsilon_{i,j}^{yz}) - (\epsilon_{i-1,j-1}^{yz} + \epsilon_{i-1,j}^{yz})] \tag{41}$$

$$Y_{i\pm 1, j\pm 1} = Y_{i\pm 1, j} + Y_{i, j\pm 1} = \left(\frac{2}{h_i + h_{i-1}} \right) \left(\frac{2}{h_j + h_{j-1}} \right) [(\epsilon_{i,j}^{yz} + \epsilon_{i-1,j}^{yz} + \epsilon_{i,j-1}^{yz} + \epsilon_{i-1,j-1}^{yz}) + (\epsilon_{i-1,j}^{zy} + \epsilon_{i-1,j-1}^{zy} + \epsilon_{i,j-1}^{zy} + \epsilon_{i-1,j-1}^{zy})] \tag{42}$$

$$Y_{i,j} = Y_{i+1} + Y_{i-1} + Y_{j+1} + Y_{j-1} \tag{43}$$

Note that, unlike the treatment of isotropic dielectrics, the permittivity of each cell is now described by a tensor

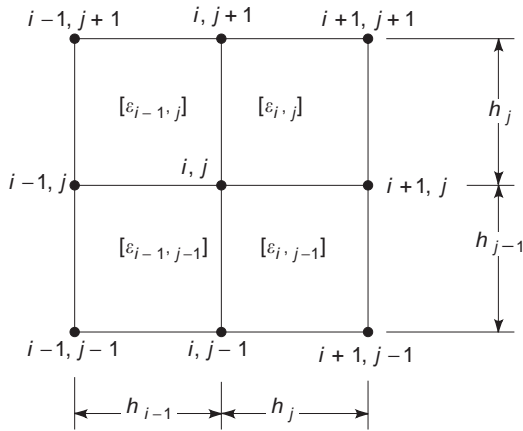


Figure 7. Detail with FDM cell for anisotropic medium in two dimensions.

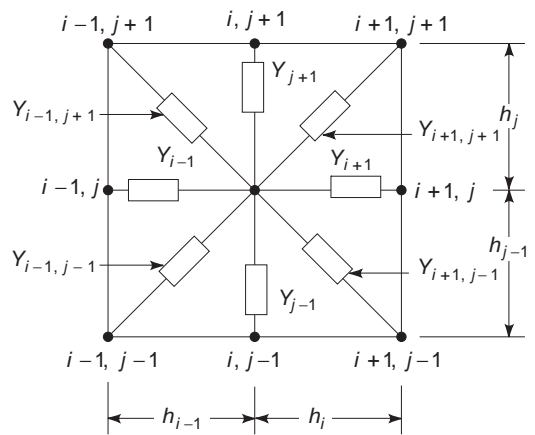


Figure 8. Network analog for 2D FDM algorithm at gridpoint i, j for arbitrary anisotropic medium.

(see Fig. 7). In addition, the presence of the anisotropy is responsible for added coupling between the voltage $\phi_{i,j}$ and voltages $\phi_{i\pm 1, j\pm 1}$ (actually all four combinations of the subscripts).

The symbols Y in Eq. (39) can be interpreted as admittances representing the “electrical link” between the gridpoint voltages. The resulting equivalent network for Eq. (39) can thus be represented pictorially as shown in Fig. 8.

Similarly, after fully expanding Eq. (36) in three dimensions, the following finite-difference approximation for the potential at every nodal point in a 3D lattice can be obtained:

$$\phi_{i,j,k}^{p+1} = (1 - \Omega)\phi_{i,j,k}^p + \frac{\Omega\phi_{\text{new}}}{Y_{i,j,k}} \quad (44)$$

where ϕ_{new} is defined as

$$\begin{aligned} \phi_{\text{new}} = & \phi_{i+1,j,k}^p(Y_{i+1} + Y_1^A) + \phi_{i-1,j,k}^{p-1}(Y_{i-1} - Y_1^A) \\ & + \phi_{i,j+1,k}^p(Y_{j+1} + Y_2^A) + \phi_{i,j-1,k}^{p-1}(Y_{j-1} - Y_2^A) \\ & + \phi_{i,j,k+1}^p(Y_{k+1} + Y_3^A) + \phi_{i,j,k-1}^{p-1}(Y_{k-1} - Y_3^A) \\ & + Y_4^A[(\phi_{i+1,j+1,k}^p - \phi_{i-1,j-1,k}^{p-1}) - (\phi_{i-1,j+1,k}^p + \phi_{i+1,j-1,k}^p)] \\ & + Y_5^A[(\phi_{i+1,j,k+1}^p + \phi_{i-1,j,k-1}^{p-1}) - (\phi_{i-1,j,k+1}^p + \phi_{i+1,j,k-1}^p)] \\ & + Y_6^A[(\phi_{i,j+1,k+1}^p + \phi_{i,j-1,k-1}^{p-1}) - (\phi_{i,j+1,k-1}^p + \phi_{i,j-1,k+1}^p)] \end{aligned} \quad (45)$$

and

$$Y_{i,j,k} = Y_{i+1} + Y_{i-1} + Y_{j+1} + Y_{j-1} + Y_{k+1} + Y_{k-1}$$

The Y terms appearing in Eqs. (44) and (45) are given by

$$\begin{aligned} Y_{i-1} = & \frac{2}{h_i + h_{i-1}} \left[T_{1,xx} \left(\frac{1}{h_{i-1}} - \frac{2}{h_i + h_{i-1}} \right) \right. \\ & \left. + T_{2,xx} \left(\frac{1}{h_{i-1}} - \frac{2}{h_i + h_{i-1}} \right) \right] \end{aligned} \quad (46)$$

$$\begin{aligned} Y_{i+1} = & \frac{2}{h_i + h_{i-1}} \left[T_{1,xx} \left(\frac{1}{h_i} + \frac{2}{h_i + h_{i-1}} \right) \right. \\ & \left. + T_{2,xx} \left(\frac{1}{h_i} + \frac{2}{h_i + h_{i-1}} \right) \right] \end{aligned} \quad (47)$$

$$\begin{aligned} Y_{j-1} = & \frac{2}{h_j + h_{j-1}} \left[T_{1,yy} \left(\frac{1}{h_{j-1}} - \frac{2}{h_j + h_{j-1}} \right) \right. \\ & \left. + T_{2,yy} \left(\frac{1}{h_{j-1}} + \frac{2}{h_j + h_{j-1}} \right) \right] \end{aligned} \quad (48)$$

$$\begin{aligned} Y_{j+1} = & \frac{2}{h_j + h_{j-1}} \left[T_{1,yy} \left(\frac{1}{h_j} + \frac{2}{h_j + h_{j-1}} \right) \right. \\ & \left. + T_{2,yy} \left(\frac{1}{h_j} - \frac{2}{h_j + h_{j-1}} \right) \right] \end{aligned} \quad (49)$$

$$\begin{aligned} Y_{k-1} = & \frac{2}{h_k + h_{k-1}} \left[T_{1,zz} \left(\frac{1}{h_{k-1}} - \frac{2}{h_k + h_{k-1}} \right) \right. \\ & \left. + T_{2,zz} \left(\frac{1}{h_{k-1}} + \frac{2}{h_k + h_{k-1}} \right) \right] \end{aligned} \quad (50)$$

$$\begin{aligned} Y_1^A = & \left(\frac{2}{h_j + h_{j-1}} \right) \left(\frac{2}{h_i + h_{i-1}} \right) (T_{1,yx} - T_{2,yx}) \\ & + \left(\frac{2}{h_k + h_{k-1}} \right) \left(\frac{2}{h_i + h_{i-1}} \right) (T_{1,zx} - T_{2,zx}) \end{aligned} \quad (51)$$

$$\begin{aligned} Y_2^A = & \left(\frac{2}{h_j + h_{j-1}} \right) \left(\frac{2}{h_i + h_{i-1}} \right) (T_{1,xy} - T_{2,xy}) \\ & + \left(\frac{2}{h_k + h_{k-1}} \right) \left(\frac{2}{h_j + h_{j-1}} \right) (T_{1,zy} - T_{2,zy}) \end{aligned} \quad (52)$$

$$\begin{aligned} Y_3^A = & \left(\frac{2}{h_k + h_{k-1}} \right) \left(\frac{2}{h_i + h_{i-1}} \right) (T_{1,xz} - T_{2,xz}) \\ & + \left(\frac{2}{h_k + h_{k-1}} \right) \left(\frac{2}{h_j + h_{j-1}} \right) (T_{1,yz} - T_{2,yz}) \end{aligned} \quad (53)$$

$$Y_4^A = 2 \left(\frac{2}{h_j + h_{j-1}} \right) \left(\frac{2}{h_i + h_{i-1}} \right) \times \left(\frac{T_{1,xy} + T_{2,xy}}{8} + \frac{T_{1,yx} + T_{2,yx}}{8} \right) \quad (54)$$

$$Y_5^A = 2 \left(\frac{2}{h_k + h_{k-1}} \right) \left(\frac{2}{h_i + h_{i-1}} \right) \times \left(\frac{T_{1,xz} + T_{2,xz}}{8} + \frac{T_{1,zx} + T_{2,zx}}{8} \right) \quad (55)$$

$$Y_6^A = 2 \left(\frac{2}{h_j + h_{j-1}} \right) \left(\frac{2}{h_k + h_{k-1}} \right) \times \left(\frac{T_{1,yz} + T_{2,yz}}{8} + \frac{T_{1,zy} + T_{2,zy}}{8} \right) \quad (56)$$

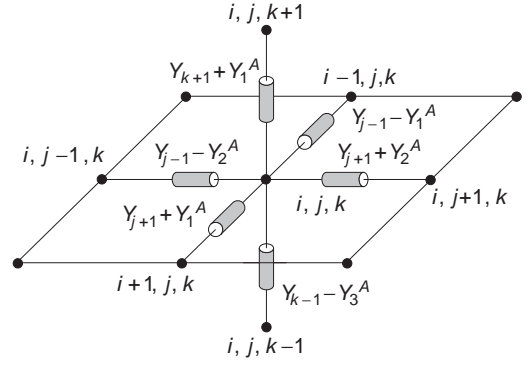


Figure 9. Network analog for 3D FDM algorithm at gridpoint i, j for anisotropic dielectric with diagonal permittivity tensor.

with the T terms having the following forms:

$$T_{1,xx} = \varepsilon_{i,j-1,k-1}^{xx} + \varepsilon_{i,j,k-1}^{xx} + \varepsilon_{i,j-1,k}^{xx} + \varepsilon_{i,j,k}^{xx} \quad (57a)$$

$$T_{2,xx} = \varepsilon_{i-1,j-1,k-1}^{xx} + \varepsilon_{i-1,j,k-1}^{xx} + \varepsilon_{i-1,j-1,k}^{xx} + \varepsilon_{i-1,j,k}^{xx} \quad (57b)$$

$$T_{1,yy} = \varepsilon_{i-1,j,k-1}^{yy} + \varepsilon_{i,j,k-1}^{yy} + \varepsilon_{i-1,j,k}^{yy} + \varepsilon_{i,j,k}^{yy} \quad (58a)$$

$$T_{2,yy} = \varepsilon_{i-1,j-1,k-1}^{yy} + \varepsilon_{i,j-1,k-1}^{yy} + \varepsilon_{i-1,j-1,k}^{yy} + \varepsilon_{i,j-1,k}^{yy} \quad (58b)$$

$$T_{1,zz} = \varepsilon_{i-1,j-1,k}^{zz} + \varepsilon_{i,j-1,k}^{zz} + \varepsilon_{i-1,j,k}^{zz} + \varepsilon_{i,j,k}^{zz} \quad (59a)$$

$$T_{2,zz} = \varepsilon_{i-1,j-1,k-1}^{zz} + \varepsilon_{i,j-1,k-1}^{zz} + \varepsilon_{i-1,j,k-1}^{zz} + \varepsilon_{i,j,k-1}^{zz} \quad (59b)$$

$$T_{1,xy} = \varepsilon_{i,j-1,k-1}^{xy} + \varepsilon_{i,j,k-1}^{xy} + \varepsilon_{i,j-1,k}^{xy} + \varepsilon_{i,j,k}^{xy} \quad (60a)$$

$$T_{2,xy} = \varepsilon_{i-1,j-1,k-1}^{xy} + \varepsilon_{i-1,j,k-1}^{xy} + \varepsilon_{i-1,j-1,k}^{xy} + \varepsilon_{i-1,j,k}^{xy} \quad (60b)$$

$$T_{1,xz} = \varepsilon_{i,j-1,k-1}^{xz} + \varepsilon_{i,j,k-1}^{xz} + \varepsilon_{i,j-1,k}^{xz} + \varepsilon_{i,j,k}^{xz} \quad (61a)$$

$$T_{2,xz} = \varepsilon_{i-1,j-1,k-1}^{xz} + \varepsilon_{i-1,j,k-1}^{xz} + \varepsilon_{i-1,j-1,k}^{xz} + \varepsilon_{i-1,j,k}^{xz} \quad (61b)$$

$$T_{1,yx} = \varepsilon_{i-1,j,k-1}^{yx} + \varepsilon_{i,j,k-1}^{yx} + \varepsilon_{i-1,j,k}^{yx} + \varepsilon_{i,j,k}^{yx} \quad (62a)$$

$$T_{2,yx} = \varepsilon_{i-1,j-1,k-1}^{yx} + \varepsilon_{i,j-1,k-1}^{yx} + \varepsilon_{i-1,j-1,k}^{yx} + \varepsilon_{i,j-1,k}^{yx} \quad (62b)$$

$$T_{1,yz} = \varepsilon_{i-1,j,k-1}^{yz} + \varepsilon_{i,j,k-1}^{yz} + \varepsilon_{i-1,j,k}^{yz} + \varepsilon_{i,j,k}^{yz} \quad (63a)$$

$$T_{2,yz} = \varepsilon_{i-1,j-1,k-1}^{yz} + \varepsilon_{i,j-1,k-1}^{yz} + \varepsilon_{i-1,j-1,k}^{yz} + \varepsilon_{i,j-1,k}^{yz} \quad (63b)$$

$$T_{1,zx} = \varepsilon_{i-1,j-1,k}^{zx} + \varepsilon_{i,j-1,k}^{zx} + \varepsilon_{i-1,j,k}^{zx} + \varepsilon_{i,j,k}^{zx} \quad (64a)$$

$$T_{2,zx} = \varepsilon_{i-1,j-1,k-1}^{zx} + \varepsilon_{i,j-1,k-1}^{zx} + \varepsilon_{i-1,j,k-1}^{zx} + \varepsilon_{i,j,k-1}^{zx} \quad (64b)$$

$$T_{1,zy} = \varepsilon_{i-1,j-1,k}^{zy} + \varepsilon_{i,j-1,k}^{zy} + \varepsilon_{i-1,j,k}^{zy} + \varepsilon_{i,j,k}^{zy} \quad (65a)$$

$$T_{2,zy} = \varepsilon_{i-1,j-1,k-1}^{zy} + \varepsilon_{i,j-1,k-1}^{zy} + \varepsilon_{i-1,j,k-1}^{zy} + \varepsilon_{i,j,k-1}^{zy} \quad (65b)$$

Note that Eq. (45) has a similar interpretation as its 2D counterpart Eq. (39). It can also be represented by an equivalent network, whose diagonal terms are shown in

Fig. 9. For clarity, the off-diagonal terms, which provide the connections of $\phi_{i,j,k}$ to the voltages at the remaining nodes in Eq. (45), are shown separately in Fig. 10.

4.2.2. Coordinate Transformation Approach. Coordinate transformations can be used to simplify the solution to electrostatic boundary value problems. Such transformations can reduce the complexity arising from complicated geometry or from the presence of anisotropic materials. In general, these methods utilize coordinate transformation to map complex geometries or material properties into simpler ones, through a specific relationship that links each point in the original and transformed problems, respectively.

One class of coordinate transformations, known as *conformal mapping*, is based on modifying the original complex geometry to one for which an analytic solution is available. This technique requires extensive mathematical expertise in order to identify an appropriate coordinate transformation function. Its applications are limited to a few specific geometrical shapes for which such functions exist. Furthermore, the applications are restricted to two-dimensional problems. Even though this technique can be very powerful, it is usually rather tedious and thus it is considered beyond the scope of this article. The interested reader can refer to Ref. 30, among others, for further details.

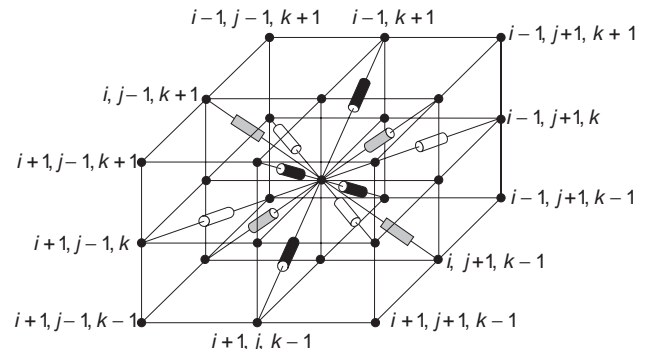


Figure 10. Network analog for 3D FDM algorithm at gridpoint i, j for arbitrary anisotropic dielectric.

The second class of coordinate transformations reduces the complexity of the FDM formulation in problems involving anisotropic materials. As described in the previous section, the discretization of the Laplace equation in anisotropic regions [Eq. (36)] is considerably more complicated than the corresponding procedure for isotropic media [Eq. (7)]. However, it can be shown that a sequence of rotation and scaling transformations can convert any symmetric permittivity tensor into an identity matrix (i.e., free space). As a result, the FDM solution of the Laplace equation in the transformed coordinate system is considerably simplified, since the anisotropic dielectric is eliminated.

To illustrate the concept, this technique will be demonstrated with two-dimensional examples. In 2D (no z dependence is assumed) the Laplace equation can be written as

$$\nabla \cdot ([\epsilon_r(x,y)]\nabla\phi) = 0 \tag{66}$$

where

$$[\epsilon_r] = \begin{bmatrix} \epsilon_{xx} & \epsilon_{xy} \\ \epsilon_{yx} & \epsilon_{yy} \end{bmatrix} \tag{67}$$

If the principal (crystal or major) axes of the dielectric are aligned with the coordinate system of the geometry, then the off-diagonal terms vanish. Otherwise, $[\epsilon_r]$ is a full symmetric matrix. In this case, any linear coordinate transformation of the form

$$\begin{bmatrix} x' \\ y' \end{bmatrix} = [A] \begin{bmatrix} x \\ y \end{bmatrix} \tag{68}$$

(where $[A]$ is a 2×2 nonsingular matrix of constant coefficients) also transforms the permittivity tensor as follows:

$$[\epsilon'] = [A]^{-1}[\epsilon_r][A] \tag{69}$$

Next, consider the structure shown in Fig. 11a. It consists of a perfect conductor (metal) embedded in an anisotropic dielectric, all enclosed within a rectangular conducting shell. The field within the rectangular shell must be determined given the potentials on all conductors. In this example, $[\epsilon_r]$ is assumed to be diagonal:

$$[\epsilon_r] = \begin{bmatrix} \epsilon_{xx} & 0 \\ 0 & \epsilon_{yy} \end{bmatrix} \tag{70}$$

By scaling the coordinates with

$$[A] = \begin{bmatrix} 1/\sqrt{\epsilon_{xx}} & 0 \\ 0 & 1/\sqrt{\epsilon_{yy}} \end{bmatrix} \tag{71}$$

the permittivity can be transformed into an identity matrix. The geometry of the structure is deformed as shown in Fig. 11b, with the corresponding rectangular

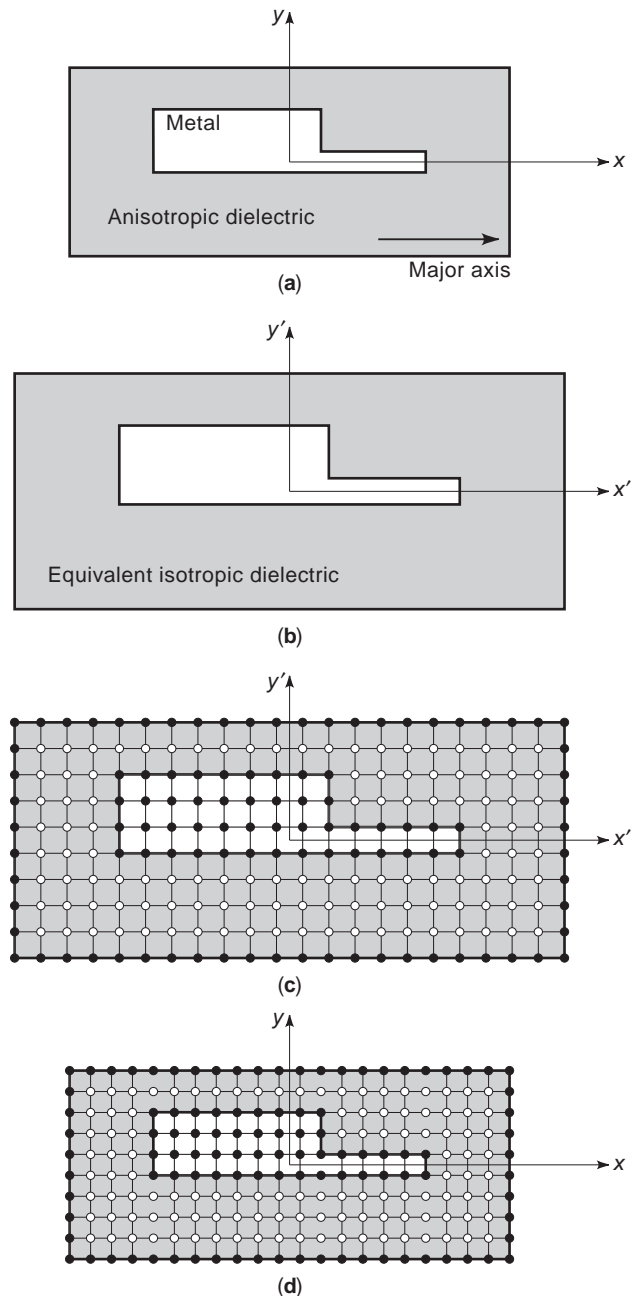


Figure 11. Graphical representation of coordinate transformation for homogeneous anisotropic dielectric with diagonal permittivity tensor.

discretization grid depicted in Fig. 11c. Note that the locations of the unknown potential variables are marked by white dots, while the conducting boundaries are represented by known potentials and their locations are denoted by black dots. The potential in the transformed boundary value problem can now be computed by applying the FDM algorithm, which is specialized for free space, since $[\epsilon_r]$ is an identity matrix.

Once the potential is computed everywhere, other quantities of interest, such as the E field and charge, can be calculated next. However, to correctly evaluate the

required space derivatives, transformation back to original coordinates is required, as illustrated in Fig. 11d. Note that in spite of the resulting simplifications, this method is limited to cases where the entire computational space is occupied by a single homogeneous anisotropic dielectric.

In general, when the principal (or major) axes of the permittivity are arbitrarily orientated with respect to the coordinate axes of the geometry, $[\epsilon_r]$ is a full symmetric matrix. In this case, $[\epsilon_r]$ can be diagonalized by an orthonormal coordinate transformation. Specifically, there exists a rotation matrix of the form

$$[A] = \begin{bmatrix} \cos \theta & -\sin \theta \\ \sin \theta & \cos \theta \end{bmatrix} \tag{72}$$

such that the product

$$[\epsilon'] = [A]^T [\epsilon_r] [A] \tag{73}$$

is a diagonal matrix. The angle θ is defined as the angle by which the coordinate system should be rotated to align it with the major axes of the dielectric.

Consider the structure shown in Fig. 12a, which is enclosed in a metallic shell. However, in this example the nonconducting region of interest includes both free space and an anisotropic dielectric. Furthermore, the major axis of $[\epsilon_r]$ is at 30° with respect to that of the structure. The effect of rotating the coordinates by $\theta = -30^\circ$ leads to a geometry shown in Fig. 12b. In the transformed coordinate system, the major axis of the permittivity is horizontal and $[\epsilon_r]$ is a diagonal matrix. Observe that this

transformation does not affect the dielectric properties of the free-space region (or of any other isotropic dielectrics, if present). However, the subsequent scaling operation for transforming the properties of the anisotropic region to free space is not useful. Such transformation also changes the properties of the original free-space region to those exhibiting anisotropic characteristics. Regardless of this limitation, the coordinate rotation alone considerably simplifies the FDM algorithm of Eq. (45) to

$$\begin{aligned} \phi_{\text{new}} = & \phi_{i+1,j,k}^p (Y_{i+1} + Y_1^A) + \phi_{i-1,j,k}^{p-1} (Y_{i-1} - Y_1^A) \\ & + \phi_{i,j+1,k}^p (Y_{j+1} + Y_2^A) + \phi_{i,j-1,k}^{p-1} (Y_{j-1} - Y_2^A) \end{aligned} \tag{74}$$

where all z -dependent (or k) terms have been removed.

Without the rotation, the permittivity is characterized by Eq. (67). Under such conditions, the corresponding FDM update equation includes four additional potential variables, as shown below:

$$\begin{aligned} \phi_{\text{new}} = & \phi_{i+1,j,k}^p (Y_{i+1} + Y_1^A) + \phi_{i-1,j,k}^{p-1} (Y_{i-1} - Y_1^A) \\ & + \phi_{i,j+1,k}^p (Y_{j+1} + Y_2^A) + \phi_{i,j-1,k}^{p-1} (Y_{j-1} - Y_2^A) \\ & + Y_4^A [(\phi_{i+1,j+1,k}^p - \phi_{i-1,j-1,k}^{p-1}) \\ & - (\phi_{i-1,j+1,k}^p + \phi_{i+1,j-1,k}^{p-1})] \end{aligned} \tag{75}$$

The simplification resulting from coordinate rotation in three dimensions is even more significant. In the general

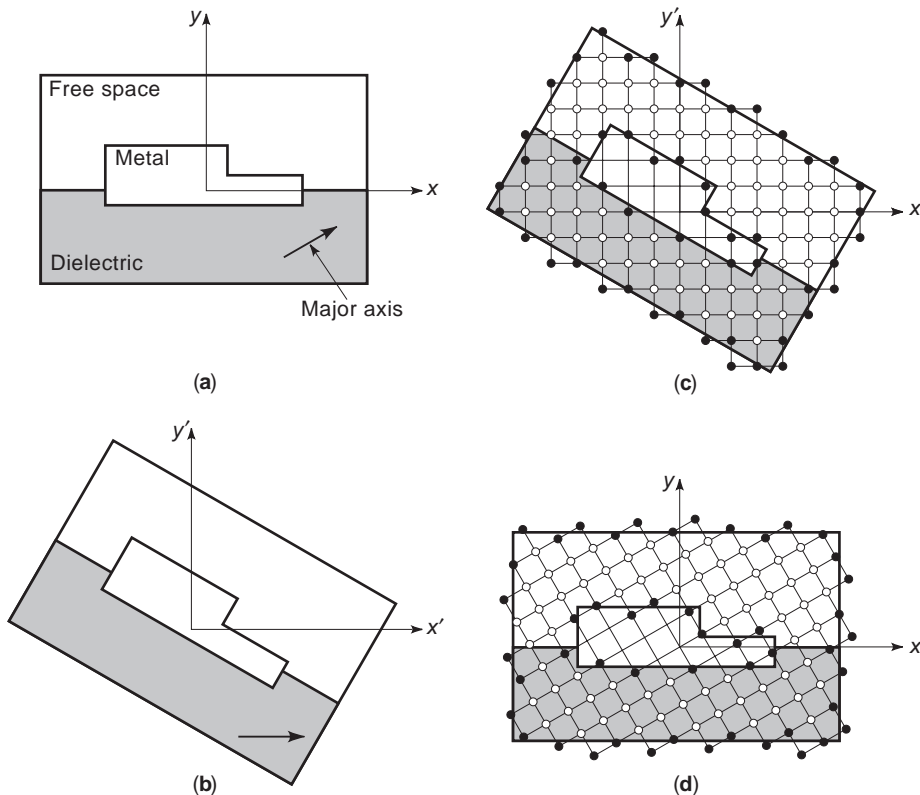


Figure 12. Graphical representation of coordinate transformation for inhomogeneous anisotropic dielectric with diagonal permittivity tensor.

case, the full FDM algorithm [Eq. (45)] contains 18 terms, while in the rotated coordinates the new equation has only 6.

Next, a rectangular discretization grid is constructed for the transformed geometry as shown in Fig. 12c, with the unknown potential represented by white dots and conducting boundaries denoted by black dots. As can be seen, the rotation complicates the assignment (or definition) of the boundary nodes. In general, a finer discretization may be required to approximate the metal boundaries more accurately.

Once the potential field is computed, the transformation back to the original coordinates is performed by applying the inverse rotation $[A]^T$, as illustrated in Fig. 11d. Note that in the original coordinate system, the grid is rotated and, as such, complicates the computation of electric field. In addition to the required coordinate mapping, this method is also limited to boundary value problems containing only one type of anisotropic dielectric, though any number of isotropic dielectric regions may be present.

The examples above illustrate that coordinate transformations are beneficial in solving a narrow class of electrostatic problems. Undoubtedly, considerable computational savings can be achieved in the calculation of the potential using FDM. However, the computational overhead associated with the pre- and postprocessing can be significant, since the geometry is usually complicated by such transformations.

5. SAMPLE NUMERICAL RESULTS

To illustrate the versatility of FDM in solving engineering problems that involve arbitrary geometries and inhomogeneous materials, consider the cross section of the microwave field-effect transistor (FET) shown in Fig. 13. Note that this device is composed of many different materials, each of different thickness and cross-sectional profile. The FET is drawn to scale, with the $1\ \mu\text{m}$ thickness of the

buffer layer serving as a reference. FDM can be used to calculate the potential and field distribution throughout the entire cross section of the FET. This information can be used by the designer to investigate such effect as material breakdown near the metallic electrodes. In addition, the computed field information can be used to determine the parasitic capacitance matrix of the structure, which can be used to improve the circuit model of this device and is very important in digital circuit design. Finally, it should be noted that the losses associated with the silicon can also be computed using FDM as shown in Eq. (25).

It should be added that in addition to displaying the potential distribution over the cross section of the FET, Fig. 13 also illustrates the implementation of open-boundary truncation operators. Since the device is located in an open boundary environment, it was necessary to artificially truncate the computation space (or 2D grid). Note that, as demonstrated in Ref. 25, only the first-order operator was sufficient to obtain accurate representation of the potential in the vicinity of the electrodes as well as near the boundary truncation surface.

A sample with three-dimensional geometry that can be easily analyzed with the FDM is shown in Fig. 14. The insulator in the multilayer ceramic capacitor is assumed to be anisotropic barium titanate dielectric, which is commonly used in such components. The permittivity tensor is diagonal and its elements are $\epsilon_{xx} = 1540$, $\epsilon_{yy} = 290$, and $\epsilon_{zz} = 1640$. To demonstrate the effect of anisotropy on this passive electrical component, its capacitance was calculated as a function of the misalignment angle between the crystal axes of the insulator and the geometry of the structure (see Fig. 15).

For the misalignment angle (or rotation of axes) in the yz plane, the capacitance of this structure was computed. The results of the computations are plotted in Fig. 16. Note that the capacitance varies considerably with the rotation angle. Such information is invaluable to a designer, since the goal of the design is to maximize the capacitance for the given dimensions of the structure.

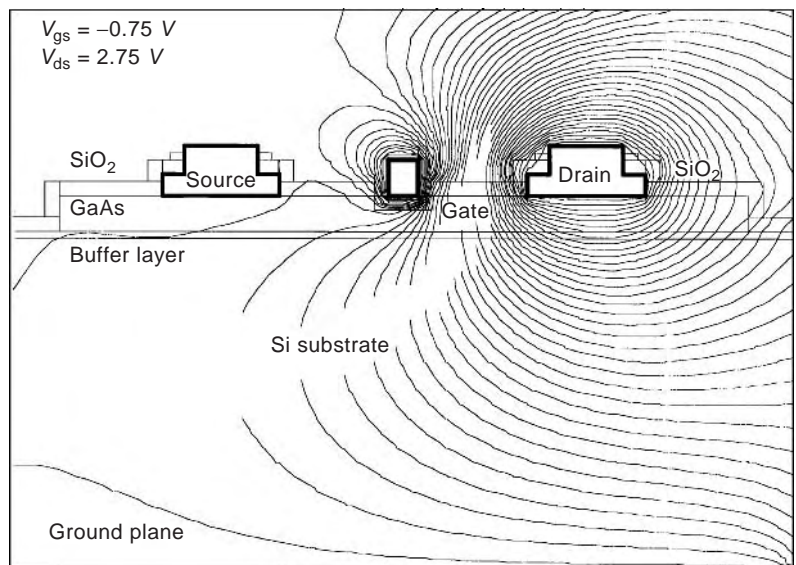


Figure 13. Equipotential map of DC-biased microwave FET. [From B. Beker and G. Cokkinides, Computer-aided quasi-static analysis of coplanar transmission lines for microwave integrated circuits using the finite difference method, *Int. J. MIMICAE* 4(1):111–119. Copyright © 1994, Wiley.]

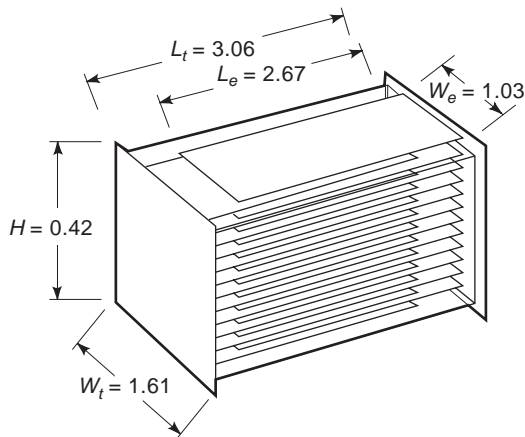


Figure 14. Geometry of a multilayer ceramic chip capacitor. All dimensions are in millimeters.

The preceding examples are intended to demonstrate the applicability of FDM to the solution of practical engineering boundary value problems. FDM has been used extensively in analysis of other practical problems. The interested reader can find additional examples where FDM was used in Refs. 31–37.

6. SUMMARY

Since the strengths and weaknesses of FDM were mentioned throughout this article, as were the details dealing with the derivation and numerical implementation of this method, they need not be repeated. However, the reader should realize that FDM is best suited for boundary value problems with complex geometries and arbitrary material composition. The complexity of the problem is the primary motivating factor for investing the effort into developing a general-purpose volumetric analysis tool.

Acknowledgments

The authors wish to express their sincere thanks to many members of the technical staff at AVX Corporation for initiating, supporting, and critiquing the development and implementation of many concepts presented in this arti-

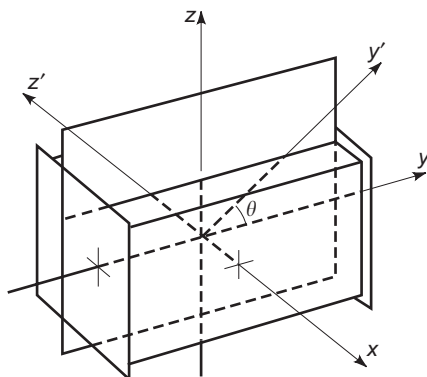


Figure 15. Definition of rotation angle for anisotropic insulator.

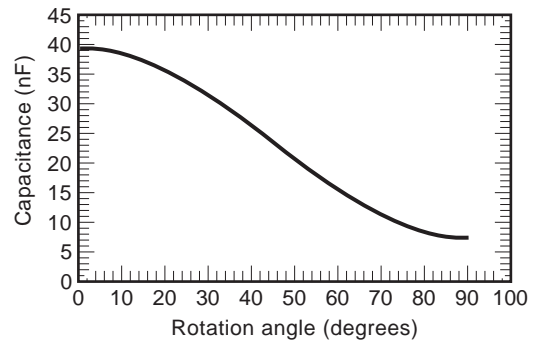


Figure 16. Capacitance of multilayer chip capacitor as a function of rotation angle of the insulator.

cle, as well as for suggesting practical uses of FDM. Many thanks also go to Dr. Deepak Jatkar for his help in extending FDM to general anisotropic materials.

BIBLIOGRAPHY

1. H. Liebmann, *Sitzungsber. Bayer. Akad. München* 385 (1918).
2. R. V. Southwell, *Relaxation Methods in Engineering Science*, Clarendon Press, Oxford, UK, 1940.
3. R. V. Southwell, *Relaxation Methods in Theoretical Physics*, Clarendon Press, Oxford, UK, 1946.
4. H. E. Green, The numerical solution of some important transmission line problems, *IEEE Trans. Microwave Theory Tech.* **17**(9):676–692 (1969).
5. F. Sandy and J. Sage, Use of finite difference approximation to partial differential equations for problems having boundaries at infinity, *IEEE Trans. Microwave Theory Tech.* **19**(5):484–486 (1975).
6. G. Liebmann, Solution to partial differential equations with resistance network analogue, *Br. J. Appl. Phys.* **1**(4):92–103 (1950).
7. K. S. Yee, Numerical solution of initial boundary value problems involving Maxwell's equations in isotropic media, *IEEE Trans. Anten. Propag.* **14**(3):302–307 (1966).
8. A. Taflove, *Computational Electrodynamics: The Finite-Difference Time-Domain Method*, Artech House, Boston, 1995.
9. N. N. Rao, *Elements of Engineering Electromagnetics*, 4th ed., Prentice-Hall, Englewood Cliffs, NJ, 1994.
10. S. R. H. Hoole and P. R. P. Hoole, *A Modern Short Course in Engineering Electromagnetics*, Oxford Univ. Press, New York, 1996.
11. T. G. Jurgens, A. Taflove, K. Umashankar, and T. G. Moore, Finite-difference time-domain modeling of curved surfaces, *IEEE Trans. Anten. Propag.* **40**(4):357–366 (1992).
12. M. Naghed and I. Wolf, Equivalent capacitances of coplanar waveguide discontinuities and interdigitated capacitors using three-dimensional finite difference method, *IEEE Trans. Microwave Theory Tech.* **38**(12):1808–1815 (1990).
13. M. F. Iskander, *Electromagnetic Fields & Waves*, Prentice-Hall, Englewood Cliffs, NJ, 1992, Sect. 4.8.
14. R. Haberman, *Elementary Applied Partial Differential Equations with Fourier Series and Boundary Value Problems*, Prentice-Hall, Englewood Cliffs, NJ, 1983, Chap. 13.
15. L. Lapidus and G. H. Pinder, *Numerical Solutions of Partial Differential Equations in Science and Engineering*, Wiley, New York, 1982.

16. W. F. Tinney and J. W. Walker, Direct solution of sparse network equations by optimally ordered triangular factorization, *IEEE Proc.* **55**(11) (1967).
17. W. T. Press, B. P. Flannery, S. A. Teukolsky, and W. T. Vetterling, *Numerical Recipes: The Art of Scientific Computing*, 2nd ed., Cambridge Univ. Press, Cambridge, UK, 1992, Section 2.7.
18. Y. Saad, *Iterative Methods for Sparse Linear Systems*, PWS Publishing, Boston, 1996.
19. G. H. Golub and C. F. Van Loan, *Matrix Computations*, 3rd ed., Johns Hopkins Univ. Press, Baltimore, 1996, Chap. 10.
20. R. E. Phillips and F. W. Schmidt, Multigrid techniques for the numerical solution of the diffusion equation, *Num. Heat Transfer* **7**:251–268 (1984).
21. J. H. Smith, K. M. Steer, T. F. Miller, and S. J. Fonash, Numerical modeling of two-dimensional device structures using Brandt's multilevel acceleration scheme: Application to Poisson's equation, *IEEE Trans. Comput. Aided Design Integrated Circ. Syst.* **10**(6):822–824 (1991).
22. A. Kherib, A. B. Kouki, and R. Mittra, Higher order asymptotic absorbing boundary conditions for the finite element modeling of two-dimensional transmission line structures, *IEEE Trans. Microwave Theory Tech.* **38**(10):1433–1438 (1990).
23. A. Kherib, A. B. Kouki, and R. Mittra, Asymptotic absorbing boundary conditions for the finite element analysis of three-dimensional transmission line discontinuities, *IEEE Trans. Microwave Theory Tech.* **38**(10):1427–1432 (1990).
24. R. K. Gordon and H. Fook, A finite difference approach that employs an asymptotic boundary condition on a rectangular outer boundary for modeling two-dimensional transmission line structures. *IEEE Trans. Microwave Theory Tech.* **41**(8):1280–1286 (1993).
25. B. Beker and G. Cokkinides, Computer-aided analysis of coplanar transmission lines for monolithic integrated circuits using the finite difference method, *Int. J. MIMICAE* **4**(1):111–119 (1994).
26. T. L. Simpson, Open-boundary relaxation, *Microwave Opt. Technol. Lett.* **5**(12):627–633 (1992).
27. D. Jatkar, *Numerical Analysis of Second Order Effects in SAW Filters*, Ph.D. dissertation, Univ. South Carolina, Columbia, SC, 1996, Chap. 3.
28. S. R. Hoole, *Computer-Aided Analysis and Design of Electromagnetic Devices*, Elsevier, New York, 1989.
29. V. K. Tripathi and R. J. Bucolo, A simple network analog approach for the quasi-static characteristics of general, lossy, anisotropic, layered structures, *IEEE Trans. Microwave Theory Tech.* **33**(12):1458–1464 (1985).
30. R. E. Collin, *Foundations for Microwave Engineering*, 2nd ed., McGraw-Hill, New York, 1992, App. III.
31. B. Beker, G. Cokkinides, and A. Templeton, Analysis of microwave capacitors and IC packages, *IEEE Trans. Microwave Theory Tech.* **42**(9):1759–1764 (1994).
32. D. Jatkar and B. Beker, FDM analysis of multilayer-multi-conductor structures with applications to PCBs, *IEEE Trans. Comput. Pack. Manuf. Technol.* **18**(3):532–536 (1995).
33. D. Jatkar and B. Beker, Effects of package parasitics on the performance of SAW filters, *IEEE Trans. Ultrason. Ferroelectric Freq. Control* **43**(6):1187–1194 (1996).
34. G. Cokkinides, B. Beker, and A. Templeton, Direct computation of capacitance in integrated passive components containing floating conductors. *IEEE Trans. Comput. Pack. Manuf. Technol.* **20**(2):123–128 (1997).
35. B. Beker, G. Cokkinides, and A. Agrawal, Electrical modeling of CBGA packages, *Proc. IEEE Electronics Computer Technology Conf.*, 1995, pp. 251–254.
36. G. Cokkinides, B. Beker, and A. Templeton, Cross-talk analysis using the floating conductor model, *Proc. ISHM-96, Int. Microelectronics Society Symp.*, 1996, pp. 511–516.
37. B. Beker and T. Hirsch, Numerical and experimental modeling of high speed cables and interconnects, *Proc. IEEE Electronics Computer Technology Conf.*, 1997, pp. 898–904.

BURIED OBJECT DETECTION

AHMET SERDAR TÜRK
 ALI KÖKSAL HOCAGLU
 Information Technologies
 Research Institute
 Gebze, Kocaeli, Turkey

1. INTRODUCTION

The subsurface detection and identification of buried geologic and synthetic (human-produced) structures is currently an important research area and a progressive technological concept on the global scale. The scope of the problem is very complex, and aspects of the topic depend on wide-area demands from the military to the commercial necessities. Some examples are the localization of the underground pipes, buried mines, and archeological or anthropological artifacts. The variety of unknown false and undesired targets under the ground complicates the object identification task. In addition, the medium involved is usually lossy and inhomogeneous. The size, geometry, constitution (dielectric, metallic, explosive, etc.), and depth of the target object and the characteristics of the medium (wet soil, sand, etc.) are the principal parameters for the detector designs. As yet, there is unfortunately still no single method or unique system that can detect all kinds of objects at arbitrary size, structure, depth, and soil. Therefore, a few numbers of the convenient sensor technologies are considered regarding to the specific situations. These sensors may have common, similar, or different capabilities for the detection of the desired targets.

This article is an introduction to buried-object detection and attempts to compile and present the available methods to readers who are potentially involved in physics, geophysics, civil engineering, archeology, or electrical engineering, regardless of their educational or academic background levels. On this scope, different sensor technologies and radar systems mainly based on the electromagnetic, acoustic, infrared, or chemical methods are examined with the cons and pros such as operating principles, strengths, limitations, and feasibilities. Furthermore, some convenient multisensor approaches for wide-range applications are discussed to attain the best detection performance level in each specific case.

2. SENSOR TYPES

The main sensors for buried-object detection are based on the electromagnetic, acoustic, seismic, and optical technologies. The electromagnetic sensors are divided into two groups: electromagnetic induction (EMI) and ground penetrating radar (GPR). The EMI or metal detector uses low-frequency electromagnetic fields to induce the eddy currents in metal components of buried objects. It is a very mature, popular, and relatively inexpensive sensor technology performed in a wide range of environments for conducting target detection. The main limitation of the EMI sensor is the possible metallic clutter of the medium, especially for the low-conductivity or small-metallic-content objects. The GPR is another widely used and established electromagnetic sensor type. The operating principle is the reflection and backscattering of the radiofrequency (RF) waves from buried metallic or dielectric objects. GPR detects all anomalies under the ground, even if nonmetal. The most important problems are the clutter due to the unwanted objects in soil and the buried targets that have constitutive parameters similar to those of soil. The acoustic and seismic sensors benefit from the sound or seismic wave reflection from the object principles. Although they are not completely established sensor technologies, such detector systems can have low false-alarm rates. Nevertheless, deep buried objects, rough surfaces, and vegetation/mineral-covered or frozen ground present the main difficulties in detection. Optical sensors use the infrared and hyper spectral band to distinguish the target from the temperature and light reflectance differences. If the heat absorbing capacity of the object is much more different from that of the soil, the sensor performance will be very satisfactory. The infrared detector can quickly scan wide areas from high altitudes. However, this is not a suitable sensor for deep-buried-object detection.

Beyond the main sensor technologies mentioned above, a few additional detector systems can be examined either for main sensor performance improvement or some specific applications such as explosive-materials detection. For instance, subsurface microwave tomography uses operating principles similar to those of GPR and achieves the high-resolution imaging of shallow buried objects, electrical impedance tomography determines the electrical conductivity distribution of the surface, and the X-ray sensor images the buried objects with X-ray radiation. Moreover, the systems based on electrochemical, piezo-

electric, nucleonic, and biological methods have proved useful just for the explosive vapor detection. Detailed discussions of all sensor types are presented in the following sections.

3. GROUND-PENETRATING RADAR

3.1. Overview

The terms *ground probing*, *subsurface detecting*, and *surface penetrating* refer to a wide range of electromagnetic methods designed for the detection and identification of buried artifacts or structures beneath the surface, generally termed *ground penetrating radar* (GPR). GPR uses the electromagnetic wave propagation and scattering principles to locate, quantitatively identify, and image the variations in electrical and magnetic properties under the ground. It may be performed from Earth's surface, from a land vehicle, or from an aircraft and has high-resolution in subsurface imaging equal to that of any geophysical method, approaching the centimeter range under the right conditions. Since GPR senses subsurface electrical inhomogeneities, the detection performance of the subsurface features such as depth, orientation, water density, size, and shape are related to the contrast in electrical and magnetic properties. The detection performance can be further improved by quantitative feature interpretation through modeling. The GPR technology is largely application-oriented. Implementation of its hardware and software determines the overall system performance characteristics. The detection range can vary from a few centimeters to tens meters. Metallic or dielectric structures can be detected. Identification of small objects even in the centimetric range is possible. Any metallic object and dielectric discontinuity can be detected by the GPR system in principle. The target may be a long, thin, cylindrical, or spherical object or a planar soil layer and can be classified according to its physical geometry and electrical constitution. All these performances strongly depend on the soil properties and the radar parameters, which are mainly operational frequency, transmitter power, system dynamic range, and electromagnetic wave polarization [1,4,7,13].

Two kinds of GPR systems—the impulse GPR and swept-frequency GPR—are employed in most current applications. The impulse GPR uses time-domain electromagnetic pulse radiation and scattering principles.

Table 1. Radar Cross Section Formulas of Basic Target Geometries

Object	Aspect Direction	RCS (dBsm)	Shape Parameters
Sphere	Omnidirectional	πR^2	Sphere radius R (m)
Cylinder	Broadside	$\frac{2\pi a d^2}{\lambda}$	Cylinder radius a (m) Cylinder length d (m)
Flat plate	Normal	$\frac{4\pi w^2 h^2}{\lambda^2}$	Plate width w (m) Plate length h (m)
Corner reflector, dihedral	Symmetry axis	$\frac{8\pi A^2}{\lambda^2}$	Reflector plate area A (m ²) Wavelength λ (m)
Corner reflector, rectangular trihedral	Symmetry axis	$\frac{4\pi L^4}{3\lambda^2}$	Sidelength L (m)

The shape of the impulse signal determines the frequency bandwidth. The object detection is done by means of the amplitude and time delay of the received pulse. In the case of the swept-frequency GPR, the operational band is clearly defined by the designer. The electromagnetic wave scattering problem is solved in the frequency domain. The target information is obtained from the amplitude and the phase of the received signal [1].

The GPR is not very different from conventional radar. The main differences are the short-range concept, near-field analysis, and lossy inhomogeneous propagation medium. The detection technique is usually based on the backscattered radiation signal from the underground object, but forward scattering can also be employed to yield target information in specific cases. Since this is a short-range radar, the clutter is the main problem for target detection and identification. The sources of the clutter are the antenna ringing, transmitter/receiver (T/R) coupling, the ground surface reflection, and unwanted (spurious) backscattering from other buried structures or soil inhomogeneities. The preventive measures such as proper antenna matching, shielding enclosure design, and adaptive methods for processing the signal should be taken to improve radar performance.

Selection of the center frequency, the bandwidth, and the power of the GPR system are the key factors in design. The electromagnetic wave reflection from the ground surface and the attenuation under the ground dramatically increase with the increasing frequency and the soil conductivity as given in Table 2. As a rule, material that has a high conductivity will have a large attenuation. Thus GPR object probing in sand, gravel, dry soil, and freshwater is much easier than in clay, wet, mineral soils, and salty water. Since the ground attenuation and reflection parameters indicate power loss and clutter, lower frequencies are used to detect deeply buried objects. Nevertheless, higher frequencies are needed for better resolution and detailed echo to determine small objects [4]. Thus, the ultrawideband (UWB) GPR is mostly preferred in order to benefit from both low and high frequencies. UWB antenna design is a significant area in terms of GPR performance. Transmitter and receiver antennas are designed to comply with the

existing hardware to radiate and couple the signal into the ground efficiently [3].

The object-oriented design procedure and critical parameters for GPR systems are discussed in Section 3.2. More specifically, suitable broadband antennas, appropriate continuous-wave (CW) or impulse signal generator design, low-noise RF receiver units, and signal processing techniques are discussed.

3.2. System Design Procedure

Ground penetrating radar has an enormously wide application area from underground structure exploration to small-object detection just beneath the surface. The operational principle consists in generation of impulse or radiofrequency (RF) power by the signal source, radiation of the electromagnetic wave by the transmitter antenna, characterization of the soil and air-Earth interface, reception of the backscattered electromagnetic wave from the target object by the receiver antenna, and finally, sensing, digitizing, and processing the received RF signal by the receiver (see Fig. 1). The critical parameters such as soil type and target properties strongly affect the detection performance. The main goal of the design is to provide application-oriented information and to illustrate the technical options available for the operator or designer. To operate the GPR successfully, the following requirements must be satisfied:

1. Sufficiently high power RF or impulse signal generator to attain the required penetration depth
2. Suitable antenna to couple the electromagnetic wave into the ground efficiently with sufficient bandwidth, high-gain, narrowbeam, and low-input reflection
3. Proper frequency bandwidth to obtain a sufficiently large scattered signal from the smallest buried object
4. Appropriate receiver hardware to achieve an adequate signal-to-noise (S/N) and signal to clutter ratios for the best target detection performance
5. Adaptive signal processing techniques to distinguish and classify the buried objects

Table 2. Propagation Losses at 100 MHz and 1 GHz in Different Soils

Material	Relative Dielectric Constant	Conductivity (mS/m)	Loss at 100 MHz (dB/m)	Loss at 1 GHz (dB/m)
Air	1	0	0	0
Asphalt, dry	2–4	1–10	2–15	20–150
Asphalt, wet	6–12	10–100	5–20	50–200
Clay	2–40	1–1000	5–300	50–3000
Concrete	4–20	1–100	1–25	10–250
Freshwater	81	0.1	0.1	1
Rock	4–10	0.1–1	0.01–1	0.1–10
Sand, dry	4–6	0.0001–1	0.01–2	0.1–20
Seawater	81	4	1000	10000
Snow	8–12	0.001–0.01	0.1–2	1–20
Sandy soil	4–30	0.1–10	0.1–5	1–50
Loamy soil	4–20	0.1–100	0.5–60	5–600
Clayey soil	4–15	0.1–1000	0.3–100	3–1000

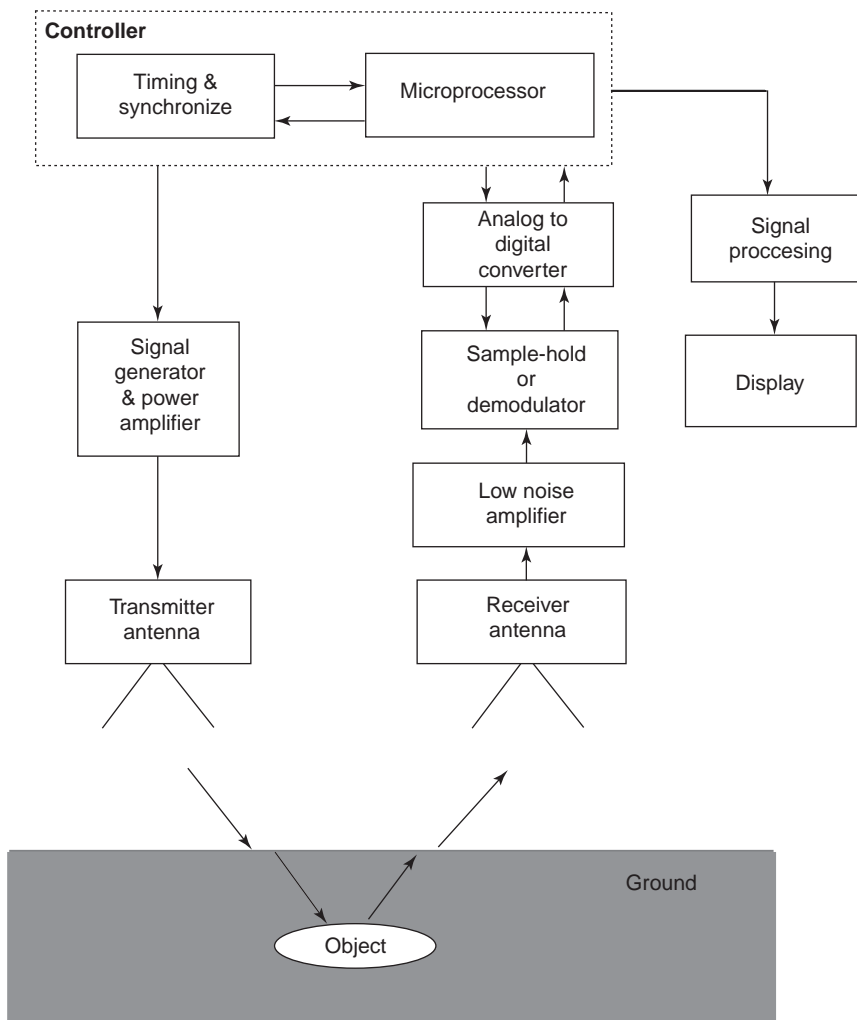


Figure 1. Block diagram of GPR operating system.

The electrical properties of the medium (soil) are important parameters in GPR design. The soil in concept is quasihomogeneous, and its electrical behavior may be defined by its constitutional parameters, namely, dielectric permittivity (ϵ), magnetic permeability (μ), and electrical conductivity (σ). Here, the relative dielectric and the magnetic constants (ϵ_r, μ_r) designate the effective wavelength, and the soil conductivity determines the propagation loss. The variability of both material parameters and local geologic conditions cause great difficulty in accurate prediction of propagation behavior. All of these parameters are generally the functions of frequency as well. For instance, RF propagation and ground surface reflectivity losses sharply increases after 3 GHz and in many cases, this fact physically limits the operational bandwidth. Nevertheless, when the buried objects decrease in size, the simulation results show that the radar cross section (RCS) values are insufficient before the resonance frequency region (see Fig. 3). As is well known, the RCS of a target object represents the object's electromagnetic wave backscattering level. Since the RCS depends on the electrical sizes (measurements with respect to wavelength) of the object and the effective wavelength is inversely proportional to the square root

of the soil dielectric constant, the GPR frequency can be shifted downward in high dielectric mediums (e.g., in wet soils). For example, the operating frequency must be at least 2 GHz to obtain sufficiently powerful backscattered signal from a 5-cm-diameter cylindrical target buried in dry soil. However, if this object were buried in wet soil, the frequency bandwidth about 1 GHz would be enough for the desired backscattering level. The range resolution in depth (ΔR_z) is another important performance parameter for GPR design. The thickness of the depth-range layers on the GPR screen is directly related to the range resolution (see Fig. 14). For impulse radars, the bandwidth (BW) expressed in (1) is inverse proportional to the downrange resolution

$$BW = \frac{c}{2 \cdot \Delta R_z \cdot \sqrt{\epsilon_r}} \quad (1)$$

where c is the free-space speed of light and ϵ_r is the relative permittivity of the soil. If it is presumed that $\epsilon_r = 9$ and $\Delta R_z = 2$ cm, the required bandwidth will be 2.5 GHz.

The radar equation given in (2) determines the detection range for a given target RCS in different parametric

cases, such as power, frequency, soil type, and antenna structure (see configuration in Fig. 2)

$$P_r = \frac{P_t G_t A_e RCS}{(4\pi R^2)^2 L} \quad (2)$$

$$L(\text{dB}) = L_a(\text{dB}) + L_{r1}(\text{dB}) + L_{s1}(\text{dB}) + L_{s2}(\text{dB}) + L_{r2}(\text{dB}) \quad (3)$$

where

- P_r = received power (W)
- P_t = transmitter power (W)
- G_t = transmitter antenna gain
- R = target detection range (m)
- A_e = receiver antenna effective area (m^2)
- RCS = radar cross-section of buried object (m^2)
- L = total propagation loss (except free space loss)
- L_a = transmitter and receiver antenna efficiency loss
- L_{r1} = surface reflectivity loss (air to ground)
- L_{r2} = surface reflectivity loss (ground to air)
- $L_{s1,2}$ = soil attenuation losses

The transmitter antenna gain (G_t) depends on the antenna type, geometry, and frequency. The gain at given frequency band is taken for stepped frequency GPR, while the peak gain (or the average gain) must be considered for an impulse GPR. Typical gains can be from minus a few decibels over isotropic to >10 dBi. The receiver effective area is expressed in terms of the antenna gain (4). The antenna efficiencies are generally related to the radiation losses due to the resistive loadings and impedance mismatching at the structures. Such losses are typically expressed in a few decibels:

$$A_e = \frac{G_r \lambda^2}{4\pi} \quad (4)$$

The RCS of the target depends on the object geometry and structure. However, the model formulas for canonical geometries given at Table 1 and the numerical simulation

plots for 5-cm-diameter cylindrical dielectric target shown in Fig. 3 are presented to express an author's opinion [18].

The reflectivity losses between air-ground and ground-air layers are subject to the problem of electromagnetic wave scattering from a dielectric surface. Too many parameters, such as antenna-ground surface and target-ground surface distances, dielectric constant of soil, antenna and target geometries, antenna radiation and target scattering waveshapes at surface, and tilt angles of antenna and object, are included in this formulation. In this case, some useful approximations are usually proposed for easy-to-calculate coherent estimations [1]. For example, the air-ground reflection loss is given by (5) presuming that the radiated wave on the surface is a uniformly distributed plane wave. Another generic method based on the transmission-line approach in Eq. (6) that uses the characteristic impedances of the air (Z_{air}) and the soil (Z_{soil}) is expressed as

$$L_{r1} = 20 \log_{10} \left(\frac{\sqrt{\epsilon_0} \cos \theta_1 - \sqrt{\epsilon_r} \cos \theta_2}{\sqrt{\epsilon_0} \cos \theta_1 + \sqrt{\epsilon_r} \cos \theta_2} \right) \quad (5)$$

(dB); (see Fig. 2)

$$L_{r1} = 20 \log_{10} \left(\frac{2Z_{\text{soil}}}{Z_{\text{soil}} + Z_{\text{air}}} \right) \quad (6)$$

(dB)

where

$$Z_{\text{air}} = 377 \Omega \quad \text{and} \quad Z_{\text{soil}} = \left(\sqrt{\frac{\mu_0 \mu_r}{\epsilon_0 \epsilon_r}} \right) \frac{\left(\cos \frac{\delta}{2} + j \sin \frac{\delta}{2} \right)}{(1 + \tan^2 \delta)^{1/4}} \quad (7)$$

Typical values for many soil materials, Z_{soil} is about 100Ω , hence $L_{r1} \approx 8$ – 10 dB and $L_{r2} \approx 5$ dB. Finally, soil attenuation losses are defined as

$$L_{s1,2} = 8.686 \cdot 2\pi f R \sqrt{\frac{\mu_0 \mu_r \epsilon_0 \epsilon_r}{2}} \left\{ \sqrt{(1 + \tan^2 \delta) - 1} \right\} \quad (8)$$

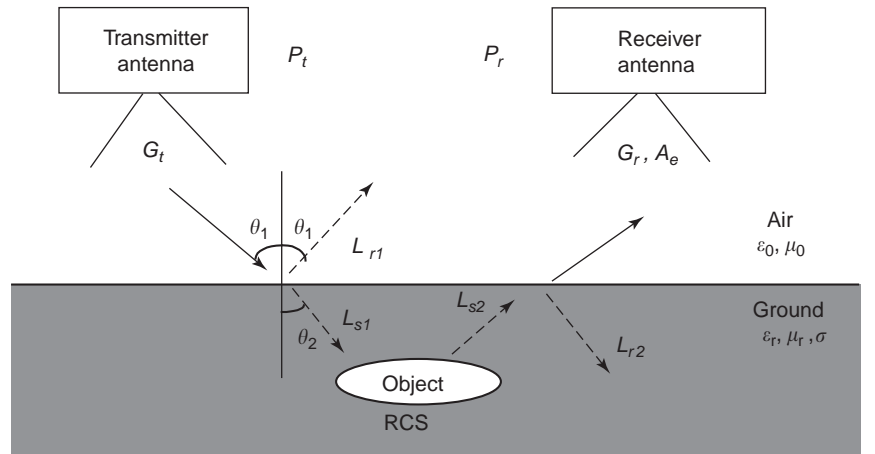


Figure 2. Propagation modeling of GPR system.

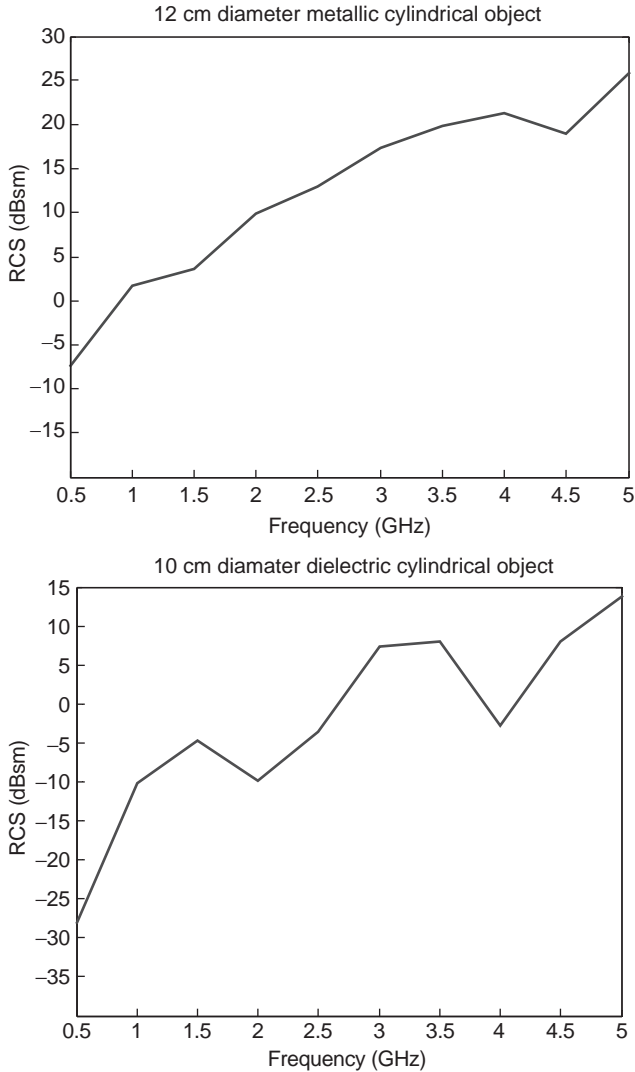


Figure 3. RCS behaviour of different cylindrical objects in air.

where δ is the soil propagation path loss in nepers per meter ($1 \text{ N} = 8.686 \text{ dB}$) in soil, f is the operating frequency, and R' is the pathlength in the soil. Table 2 exhibits the RF propagation losses in some soils at 100 MHz and 1 GHz.

As a general rule, the system noise threshold determines the minimum detectable signal (MDS) level. Detection of the target is possible if the received power backscattered from the object is sufficiently higher than both noise and clutter. The MDS can be calculated by (9) using the system frequency bandwidth (BW), the receiver noise figure (NF), and the required signal-to-noise ratio (SNR)

$$\text{MDS} = k \cdot T_0 \cdot \text{BW} \cdot \text{NF} \cdot \text{SNR} \quad (9)$$

where k is Boltzmann's constant and T_0 is room temperature in kelvins ($kT_0 \cong 4 \times 10^{-21} \text{ W/Hz}$). To obtain a received power, Pr , that exceeds this value, the MDS will not suffice for detection when clutter dominates the signal. The sources of the clutter are mostly the undesired cou-

pling signals from transmitter to receiver, the unwanted backscattering from other buried objects, and the reflection from the ground surface. For this reason, minimum SNR requirement of the system should be accurately estimated on the design to guarantee the physical radar detection range.

Design Example. Suppose that we want to detect a dielectric cylindrical object of 10 cm diameter that is buried up to $R = 100 \text{ cm}$. The system operating frequency is chosen 1 GHz. The soil is dry and loamy ($\epsilon_r = 4$). The transmitter antenna has 3 dBi gain, and the receiver antenna effective area is $A_e = 0.0012 \text{ m}^2$. Using (2)–(9), Table 2, and Fig. 3, we find that the two-way reflection losses are totally taken as 15 dB, the soil attenuation loss is 10 dB, the target has an RCS of -10 dBm^2 , and the overall power loss (dynamic range) is calculated as $\sim 94 \text{ dB}$. If we assume that the amplifier of the GPR receiver has a noise figure (NF) of 3 dB over 1 GHz bandwidth (BW), the MDS for the specified receiver characteristics yields $8 \times 10^{-10} \text{ W}$ or -91 dBW , considering a signal-to-noise ratio (SNR) of 20. Under the circumstances, the peak power of the transmitter must be at least 3 dBW or approximately 2 W. For a 50- Ω -impulse GPR system, this corresponds to 10 V peak voltage of the transmitter output.

3.3. Signal Sources and Modulation Methods

Many kinds of the modulation techniques can be employed for ground penetrating radar systems. The most frequently used GPR systems are the impulse radar that generates short pulses or impulses in the category of amplitude modulation (AM) and the swept or stepped-frequency radar that uses frequency modulation (FM) followed by a synthesized pulse.

Impulse GPR is commercially the most popular system preferred for a wide range of applications. The operational principle is based on the impulse signal generation at required peak power and frequency bandwidth. The signal sources generate monocycle or monopulse waveforms that can last for a few hundred picoseconds to a few nanoseconds. The impulse waveforms are generally Gaussian in shape and their frequency bandwidths start from a few hundred MHz up to a few GHz depending on the application (Fig. 6). The main difference between the monocycle and monopulse is in the frequency-domain behavior. The monopulse signal highly contains DC or low-frequency components. Nevertheless, the monopulse waveform has some physical advantages for time-domain radar signal transmission and radiation.

Frequency-modulated continuous-wave (FMCW) and stepped-frequency GPR systems are used when the targets of interest are shallow and an operational frequency of $\geq 1 \text{ GHz}$ has to be maintained. These systems are easier to design compared to the wideband impulse radars. Such swept- and stepped-frequency radars have the advantage of greater selection and control of the operational frequency bandwidth. This feature provides better radiation efficiency with high-power generators and high-gain antennas, lower noise level at narrower bands, and con-

sequently wider dynamic range in comparison to the impulse radar.

3.3.1. Impulse Generator Design. There are two major concerns in an impulse generator used in GPR applications: (1) the pulshape and plusewidth and (2) pulse amplitude. In many cases, both of these parameters are highly critical. The pulshape and plusewidth imply broadband characteristics, conducive to the detection of buried small objects. On the other hand, pulse amplitude implies system power related to the operational detection depth of the target in soil.

The shape of the pulse signal rigorously affects the operational frequency bandwidth of the GPR system. For example, a steplike pulse has a large amount of spectral energy at lower frequencies with the spectrum falling off as inverse frequency ($1/f$), while an impulselike pulse has a flat spectrum over the bandwidth. In every case, the high-frequency content of the pulse signal is limited by either the step risetime (T_s) or the impulse duration (T_d). For ideal impulse waveforms, the first null (f_0) in the spectrum occurs at $1/T_d$. The spectral power distribution of the impulse decreases rapidly beyond f_0 and typically follows an equation of the sinc function form. A monocycle signal can be analyzed as a pulse AM modulation of a RF sine-wave carrier. Thus, the spectrum of the monocycle impulse is shifted upward in the frequency domain with respect to the risetime and centered on the carrier frequency that corresponds to $1/T_d$. Generation of these various waveforms normally begins with a very fast-risetime-edge, steplike pulse. Then one takes the first derivative of the step risetime to obtain an impulse signal. To obtain a monocycle, the first derivative of an impulse or the second derivative of a step pulse is taken. In practice, this process can be implemented by adding a proper short-circuit-terminated transmission line to the impulse generator output. The UWB antenna and the wideband amplifier must be appropriately designed to avoid bandpass filtering, which can cause multicycling [4].

Various high-power switching transistors or FETs can be used to acquire the typical GPR pulses of a few hundred picoseconds to a few nanoseconds in duration. Avalanche transistors are often used to generate peak power levels from 50 W to several kilowatts. For the 3–10-GHz UWB band, selection of available devices is much smaller. Step recovery diodes (SRDs) can generate 50–200 ps edges with amplitudes of several volts [2].

The following is given as a monocycle impulse circuit design procedure especially for high-frequency and high-amplitude GPR applications:

- A fast risetime and high-amplitude square-wave generator
- Impulse generator with step recovery diodes
- Wideband impedance matching with resistors and high-speed Schottky diodes
- Impulse bandwidth improvement by short-circuit shunt stubs
- Wideband MMIC amplifier (if the signal power is insufficient)

The monocycle pulse generator shown in Fig. 4 is developed using transmission-line stubs realized by rigid cables, SRDs, and a Schottky diode, a MESFET and a monolithic microwave integrated circuit (MMIC) amplifier. At the input, a square-wave signal with a repetition frequency of 400 kHz is applied by a microprocessor. The risetime of the signal is shortened with a comparator circuit. The signal proceeds to the impulse generator, composed of SRDs in active mode [8]. Operating in active mode enable the designer to shape the impulse by adjusting the DC bias current drawing from the DC source. The MESFET is used particularly for the circuit isolation and wideband impedance matching. Finally, the first stub, which is at the gate of the MESFET, is used to generate a very short impulse. It is noted that, due to the MESFET buffer, the antenna cannot load back the circuit in an undesirable way. Figures 5 and 6 show the measured output monocycle pulse in time domain and in frequency domain, respectively. The measured waveform has less than 1.5 ns pulse duration in time domain, and its frequency domain bandwidth is approximately 2 GHz.

The design procedure of the avalanche-mode monocycle impulse generator is similar to that of the SRD circuit. The main difference is that an avalanche transistor is used instead of the short recovery diodes. The transistor is operated in avalanche breakdown mode used with switching by discharging the stored energy into the short transmission lines. These are output loads, which also include the transmitter antenna input impedance. The time-domain impulse signal output and its frequency-domain transformation of an avalanche-mode impulse generator are presented in Figs. 7 and 8.

3.3.2. FMCW and Stepped-Frequency Radar. The FMCW radar system transmits a sweeping RF carrier signal controlled by a voltage-controlled oscillator (VCO) over a selected frequency bandwidth. The operational frequency band can be selected by considering mainly the maximum depth and the minimum size of the buried object. The backscattered signal from the target object is mixed with a sample of the transmitted waveform and the results in a difference frequency, called the *intermediate frequency* (IF), is derived from an I/Q (in-phase/quadrature) mixer pair. The IF output contains the amplitude and phase data of the received signal. The phase information yields the range of the target since it is correlated with time delay. Only if there is a target on the scope will the IF signal be produced. If the variation in transmitter frequency is a linear function of time, then a target return will occur at a time T_r given by

$$T_r = \frac{2R}{u} \quad (10)$$

where R is the range in meters and u is the velocity of electromagnetic wave on the propagation path (air, ground, or both) in meters per second.

Since the FMCW radar essentially measures the phase of the IF signal, which is directly related to target range, it

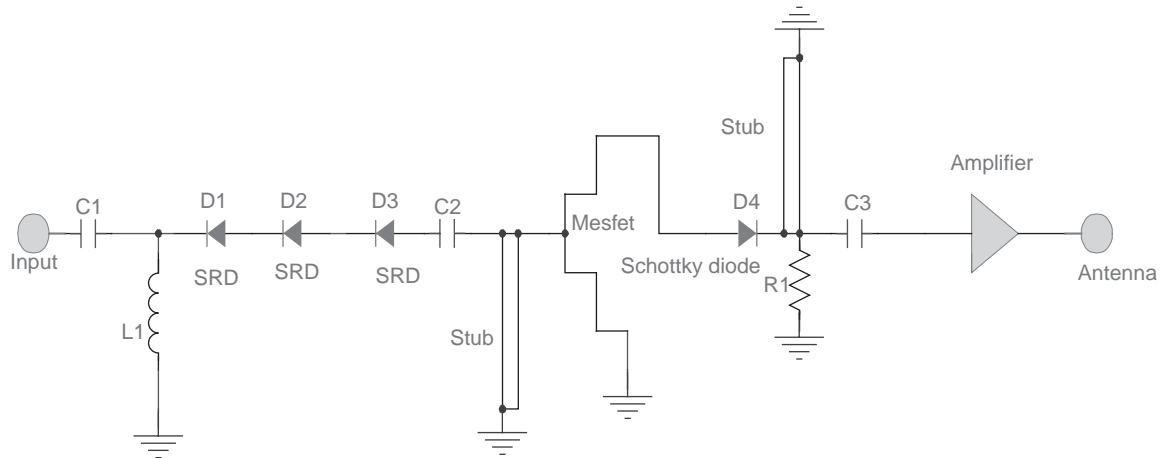


Figure 4. Schematic of the monocycle pulse generator.

requires a high degree of linearity of frequency sweep with time to avoid spectral widening of the IF, which indicates the system range resolution degradation. In practice, the sweeping nonlinearity levels should keep below 0.1% [1]. The amplifier and the antenna gain responses over the frequency band must also be linear for an appropriate system design. A time-domain equivalent to the impulse radar can be acquired by the inverse Fourier transformation.

Stepped-frequency radar is a continuous wave system that is sequentially repetitive at different frequencies as shown in Fig. 9. This kind of radar radiates a sequence of N number of carrier frequency steps and the amplitude and the phase of the received signal is stored. Downconversion to IF signal is similar in principle to that for FMCW radar. The complex Fourier transformation is applied to obtain the time-domain response of the reflected or backscattered target signal. The range resolution is defined as

$$\Delta R = \frac{u}{2N\Delta f} \quad (11)$$

where ΔR is the range resolution and Δf is the frequency increment of every step.

For both FMCW and stepped-frequency radar, it is evident that the thermal noise level is much lower than that of the receiver of the time-domain impulse radar. Nevertheless, the discrimination of the target backscattering signal from the ambiguous clutter at the receiver unit is a more difficult problem due to the futility of simple anti-aliasing filters. Therefore, some calibrating methods such as iterative range gating are usually employed for such systems.

3.4. GPR Antennas

The performance of GPR is highly dependent on the proper design of the transmitter and receiver (T/R) antenna pair. In practice, the transmitted GPR signal has broadband characteristics, which may vary from 10 MHz to 5 GHz for impulse system and from 1 to 8 GHz for stepped/swept-frequency systems. Therefore, wideband T/R antennas must be designed to reach the largest dynamic range, best focused illumination area, lowest T/R antenna coupling, reduced clutter, and uniformly shaped impulse

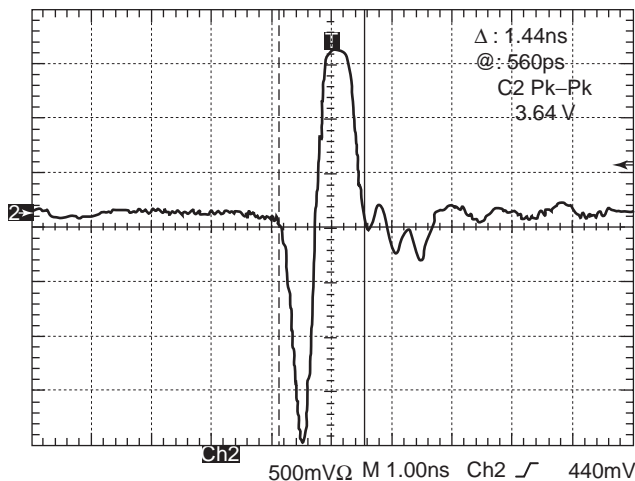


Figure 5. Measured output monocycle pulse in time domain.

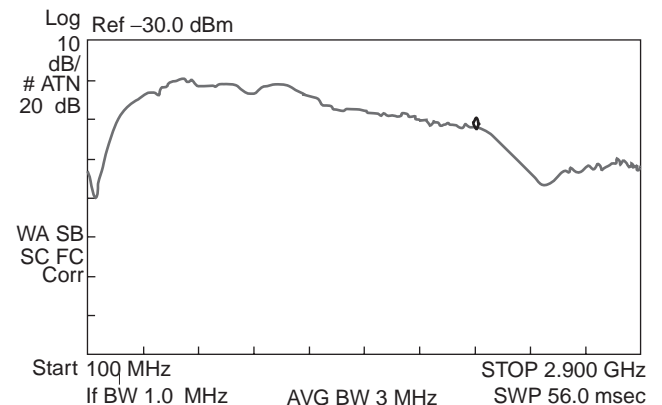


Figure 6. Frequency-domain transformation of the output monocycle pulse.

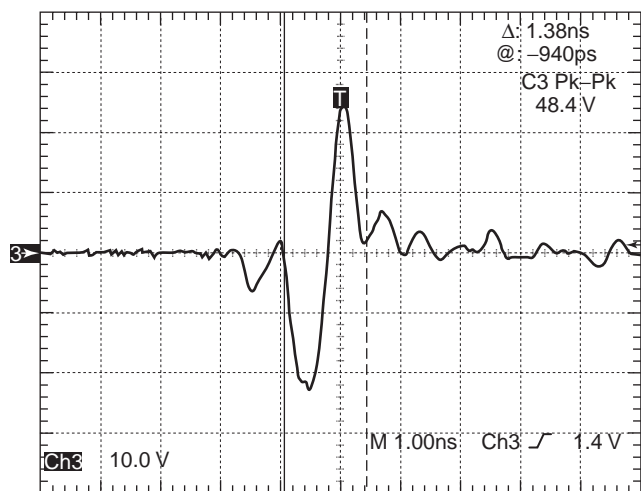


Figure 7. Time-domain signal output of the avalanche-mode impulse generator.

radiation [3]. These antennas should satisfy the following electrical characteristics over the operational frequency band such as high directivity gain, low input reflection level, suppressed side/backlobes, convenient polarization with respect to the target shape, high T/R shielding, and linear phase response (for impulse GPR). Moreover, some physical restrictions, such as lightweight requirements for movable handheld GPR, can also rigorously restrict the convenient antenna types. A useful reference to the general case of antennas in matter is given by King and Smith [9]. Further considerations in the selection of the suitable antenna types are subject to the types of targets and radar systems. On this scope, most popular ultrawideband (UWB) antenna models, such as dipole, bowtie, spiral, and TEM horn, are proposed for the impulse GPR system. For FMCW and stepped-frequency GPR, wideband-selective octave horns, dielectric filled open-ended waveguides, cavity-backed planar spirals, and pencil-beam dish antennas (only in certain specific cases) may be preferred because of their higher gain characteristics [1,6,11,12,18].

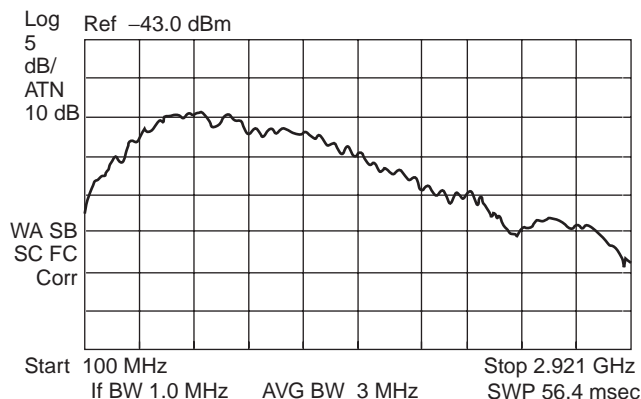


Figure 8. Frequency-domain behavior of the avalanche-mode impulse generator signal.

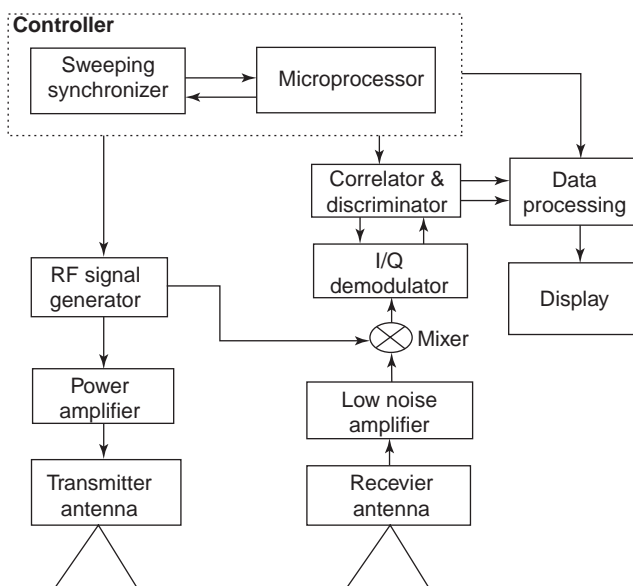


Figure 9. Block diagram of swept/stepped-frequency radar.

The simplest GPR antenna is an electrically small dipole element. It is a linearly polarized antenna that has far-field intensity proportional to its electrical length. Thus, the antenna gain and the radiation efficiency can be very small at lower frequencies. In order to avoid performance degradation, resonance dipoles such as half-wave are usually preferred for impulse GPR. Although the dipoles have a physical advantage especially for handheld GPR systems because of their small size, lightweight and easy-to-fabricate structures, and their frequency-dependent input impedance and radiation gain characteristics. Some dielectric and absorber loading techniques are usually employed to improve antenna frequency bandwidth [10]. The bowtie configuration is similar to the dipole wideband antenna frequently used for pulse radiation (Fig. 10c). The bowtie exhibit shows higher gain and wider band performance than does the simple dipole. For a circular object, the bowtie is a suitable antenna type since it produces linear polarization and has relatively good linear phase response over the wideband [3,10]. If the target is noncircular, with respect to electromagnetic wave scattering principles, circularly polarized planar antennas such as spirals may be preferred. The spiral is based on which Archimedian and logarithmic models, is theoretically a frequency-independent antenna (see Fig. 10). But in practice, both are bandlimited with respect to the feed radius for the upper frequency and the armlength for the lower frequency [3]. The frequency-domain responses of bowtie and spiral antennas are presented in Fig. 11.

When a wider band, lower-voltage standing-wave ratio (VSWR), higher gain, and narrower beamwidth are required, the TEM horn is one of the most promising antenna types for impulse GPR systems. Such a structure consists of a pair of triangular or circular slice-shaped conductors forming a V-dipole structure. It is characterized by L , d , α , and θ parameters, which correspond to the length of the antenna, the feedpoint gap, the conductor plate angle, and the elevation angle, respectively

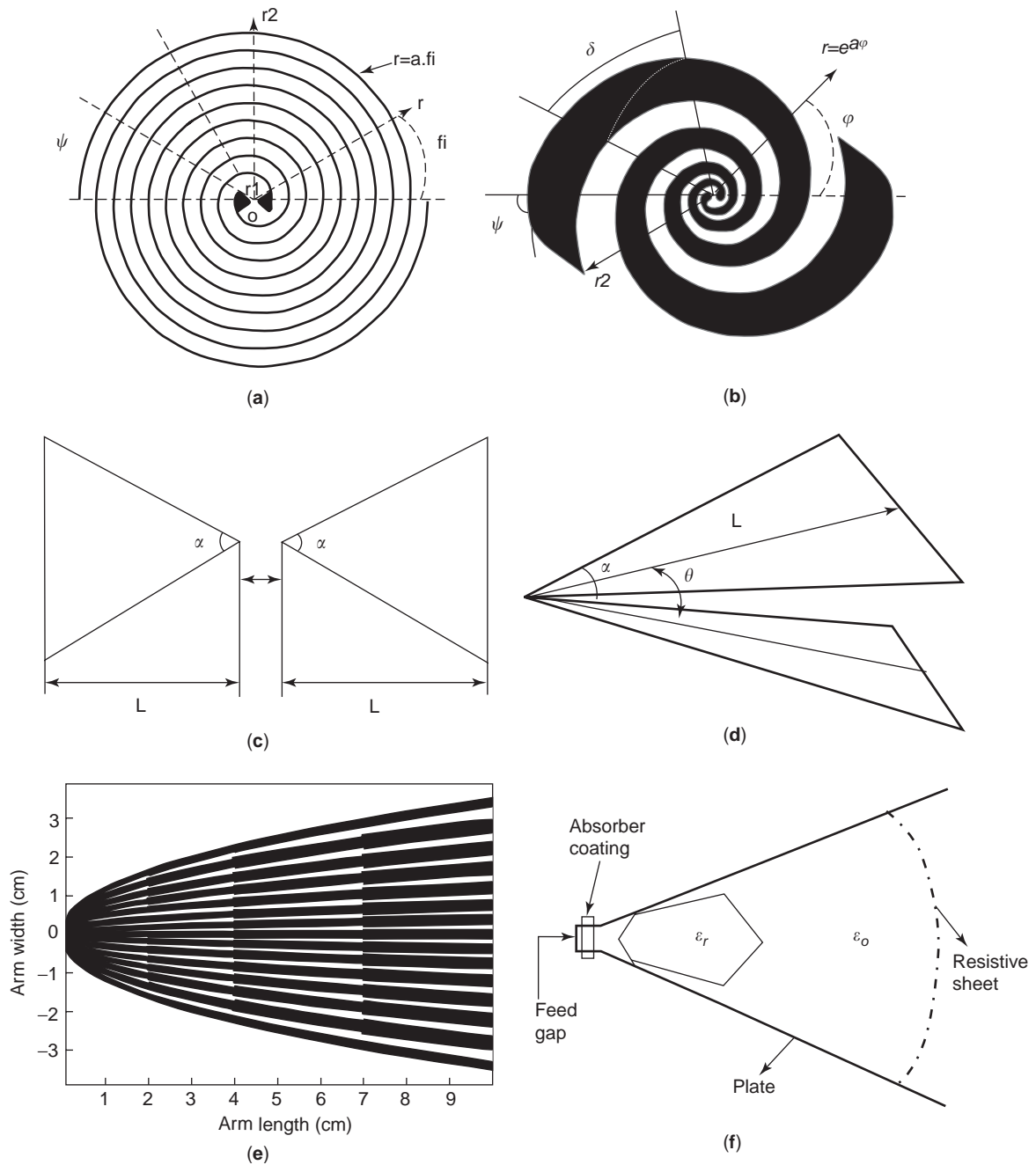


Figure 10. Wideband GPR antenna types: (a) Two-armed Archimedean spiral; (b) two-armed logarithmic spiral; (c) triangular plate bowtie; (d) triangular plate TEM horn; (e) grating model TEM horn arm (top view); (f) PDTEM horn geometry (side view).

(Fig. 10d). A TEM horn generally shows bandpass filter-like antenna gain behavior over a large bandwidth. In practice, its electrical dimensions strongly limit the lower operation frequency. Thus, dielectric-filling techniques are applied mostly to decrease the lower cutoff frequency due to certain physical restrictions in GPR applications [11]. In this case, the operational band of the antenna can be shifted downward in the frequency domain but the frequency bandwidth probably cannot be broadened. The partial-dielectric-loaded TEM (PDTEM) horn structure is proposed by Turk to achieve low VSWR (voltage stand-

ing-wave ratio) and high directivity gain with stable performance over the wideband [6]. The PDTEM structure is modeled as a microstrip line, and its geometry is designed to match the antenna output impedance to the feed source impedance (nominal, 50Ω) by decreasing the segment characteristic impedances along the antenna line. For this purpose, using multiangular dielectric profile loading and arranging the segment widths of the plate wings properly, one can implement an efficient geometric design for the TEM horn (see Fig. 10f). This approach is quite effective for higher frequencies where the electrical length

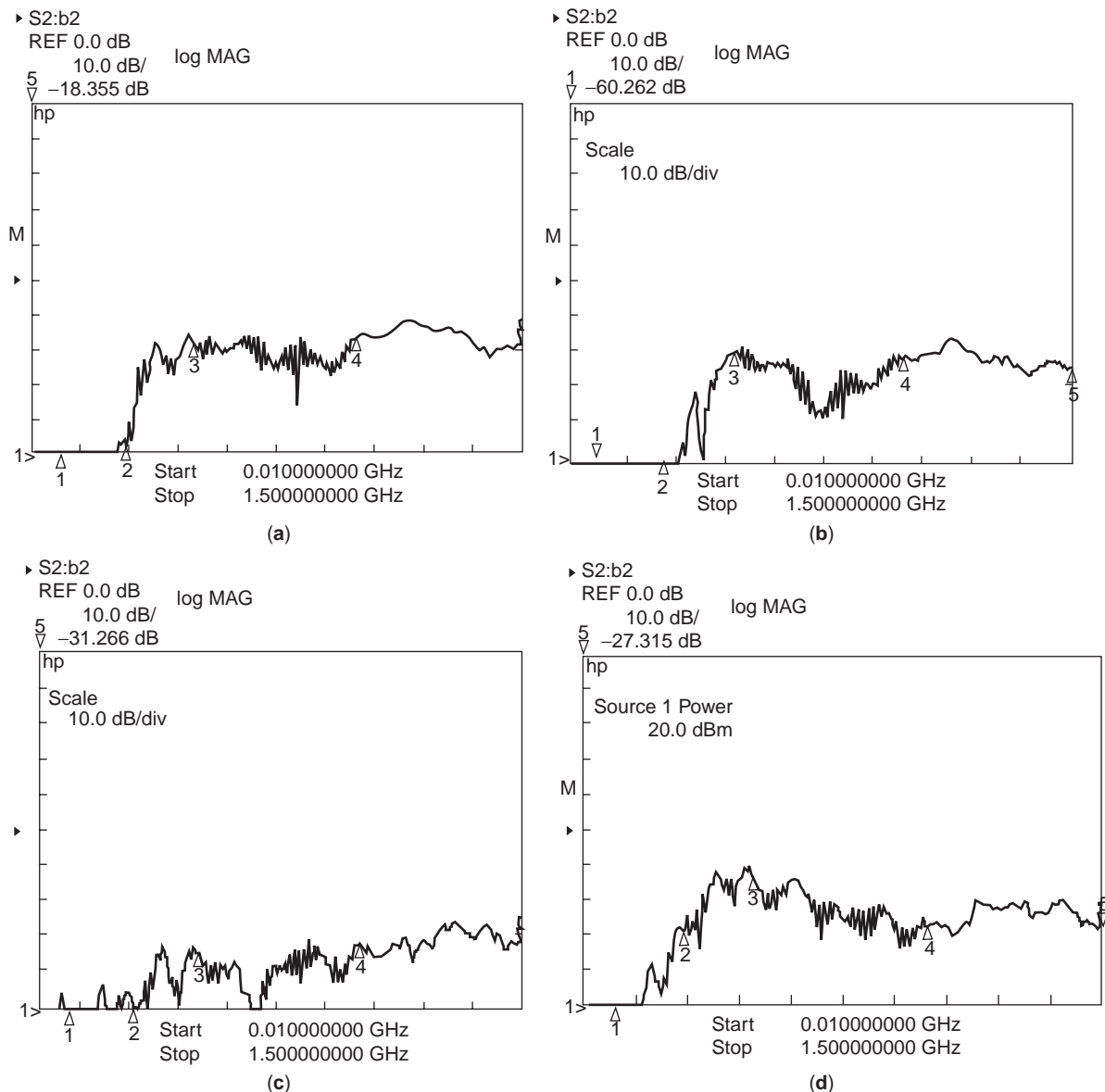


Figure 11. Measured frequency-domain S_{21} responses of the planar antennas for 60 cm dry soil: (a) logarithmic spiral ($r_1 = 0.5$ cm, $r_{2h} = 5.5$ cm, $r_{2v} = 7.3$ cm); (b) Archimedean spiral ($r_1 = 0.5$ cm, $r_2 = 8$ cm); (c) bowtie ($\alpha = 60^\circ$, $d = 0.5$ cm, $L = 7.3$ cm)—cross-polarization; (d) bowtie—copolarization.

of the antenna line is sufficiently long to transform output impedance. Nevertheless, the antenna output impedance strongly determines the matching performance rather than the characteristic impedance. An extensional resistive aperture loading is used to keep VSWR levels reasonable at lower frequencies. Finally, the feed gap is coated by a piece of low-conductivity absorber to improve the overall VSWR performance. The grating model arm structure is the metal-reduced version of the PDTEM horn antenna, which is recommended for multisensor (GPR combined with metal detector) systems (see Fig. 10e). Typical input reflection and antenna gain behaviors of TEM, PDTEM, and rigid horns are shown in Figs. 12 and 13.

Impedance matching is a critical step to improve the antenna gain and to reduce time-domain ringing effects.

Since most of the GPR impulse signals are generated by avalanche-mode transistors that produce impedance-dependent pulseshapes, the variability of the antenna impedance over the wide operational band must be stabilized by a matching circuit design. In addition, the antenna structure should be balanced to avoid structural imbalances using a wideband balun (balanced-to-unbalanced) transformer that has a sufficiently short risetime [3].

Standard-gain-horn, rigid-horn, dielectric-loaded waveguide, and dish antennas can also be considered for FMCW and stepped-frequency GPR systems. All of these models are high-gain and narrowbeam band-selective antennas that are used from L band to X band (from ~ 1 to ~ 10 GHz). The typical gain of the standard horn antenna is ~ 15 dBi over a 2–1 frequency bandwidth. To increase

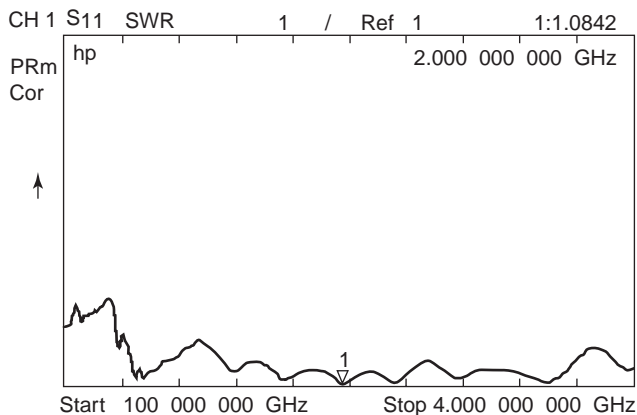


Figure 12. VSWR plot of PDTEM horn ($L=10$ cm, $\alpha=30^\circ$, $\theta=80^\circ$).

the antenna directivity gain with a narrower beamwidth, a model using proper dielectric loadings is available [12]. For multiband GPR operations, the rigid horn that yields ~ 10 dBi gain over 10–1 frequency bandwidth can be chosen (Fig. 13). When the highest gain and the narrowest beamwidth are highly necessary and the physical size of the antenna is not restricted (i.e., as in vehicle-mounted forward-looking systems), the dish antenna is an appropriate solution because of its high gain up to 30 dBi and pencil-beam characteristics. The electrical size of the dish aperture is directly related with the directivity gain and HPBW as follows [18]

$$G = 20 \log\left(\frac{D}{\lambda}\right) + 9.94 \text{ dBi} \quad (12)$$

$$\text{HPBW} = \frac{180\lambda}{\pi D} \text{ degrees} \quad (13)$$

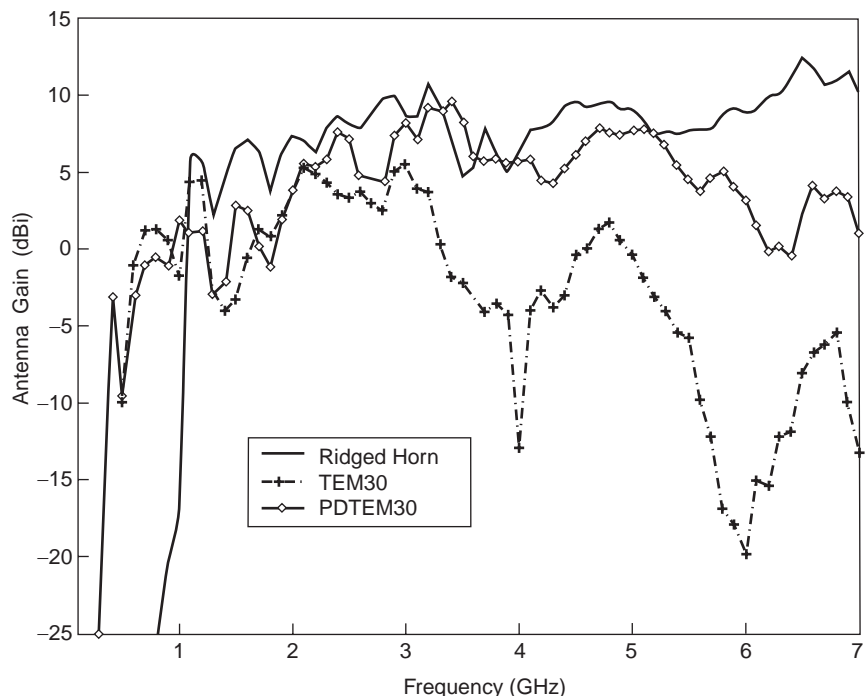


Figure 13. UWB antenna gain performances of GPR antennas.

where G is the antenna gain for 100% efficiency and D is the diameter of the circular dish.

3.5. Signal Processing Techniques

The development of advanced processing algorithms for GPR data is very important to achieve high performance for the detection and identification of objects. The signal processing methods are based on interpreting the backscattered signal parameters; these are the amplitude and the phase of the received signal for continuous or stepped-frequency GPR, and the time-domain shape of the received signal for impulse GPR. In both cases, the amplitude represents how much power is returned back from the target. The impulsive oscillations or the change in phase indicates the depth range of the target. For CW GPR, the phase difference between the transmitted and received signals indicates the depth of the target. The phase of the electromagnetic wave changes when propagating over the path proportional to its effective wavelength. Thus, every wavelength distance corresponds to 360° phase difference, but it is not easy to find the target range if the medium is inhomogeneous and cluttered. At this stage, advanced signal processing algorithms are needed to estimate the parameters adaptively from the raw data collected from inhomogeneous regions [1].

In the case of impulse radar, the received pulse signals are collected in the scanning direction. The *A*-scan and *B*-scan raw data series are obtained as shown in Fig. 14. *A*-scan data represent the received impulse signals for any scanning step. The *B*-scan plot is simply a two-dimensional (2D) representation of consecutive *A* scans in the scanning direction. Here, the x and y axes correspond to the scanning direction and the propagation time, respectively. Time also means the range, since the electromagnetic

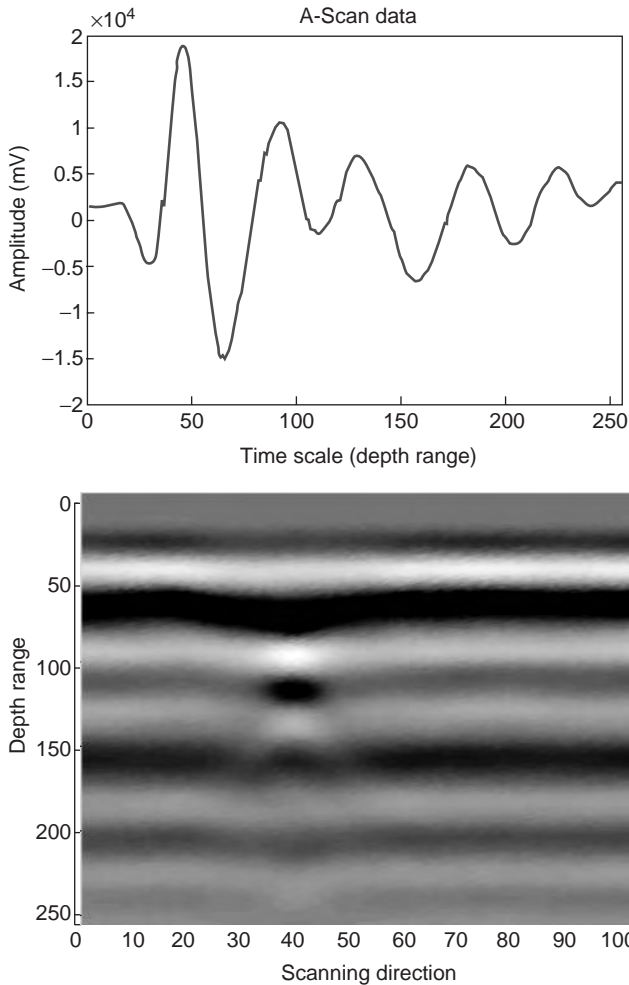


Figure 14. Measured A-scan and B-scan impulse GPR raw data.

wave has a velocity of

$$u = \frac{3 \times 10^8}{\sqrt{\epsilon_r \mu_r}} \text{ (m/s)} \tag{14}$$

where ϵ_r and μ_r respectively are the relative constitutional dielectric and magnetic coefficients of the propagation medium. Thus, if any anomaly occurs under the ground, the signal amplitude changes at the timescale to express the related depth range. When the soil structure is not well known, inhomogeneous and there are many unwanted buried objects, detection and discrimination of the target will be a difficult problem. Most of the GPR processing algorithms are based on background estimation, differentiated power density analysis, and subband processing of GPR data [1,5]. The main goal is to find the target emphasizing the anomalies under the ground. For background estimation and removal, an average A-scan dataset is calculated from multiple A-scan data that do not contain any signal from a target, and then this average is taken as a reference. The other A-scan data are calculated relatively. The magnitude of the GPR data after the background removal process is computed (see Fig. 15). Further processing can be done in several frequency

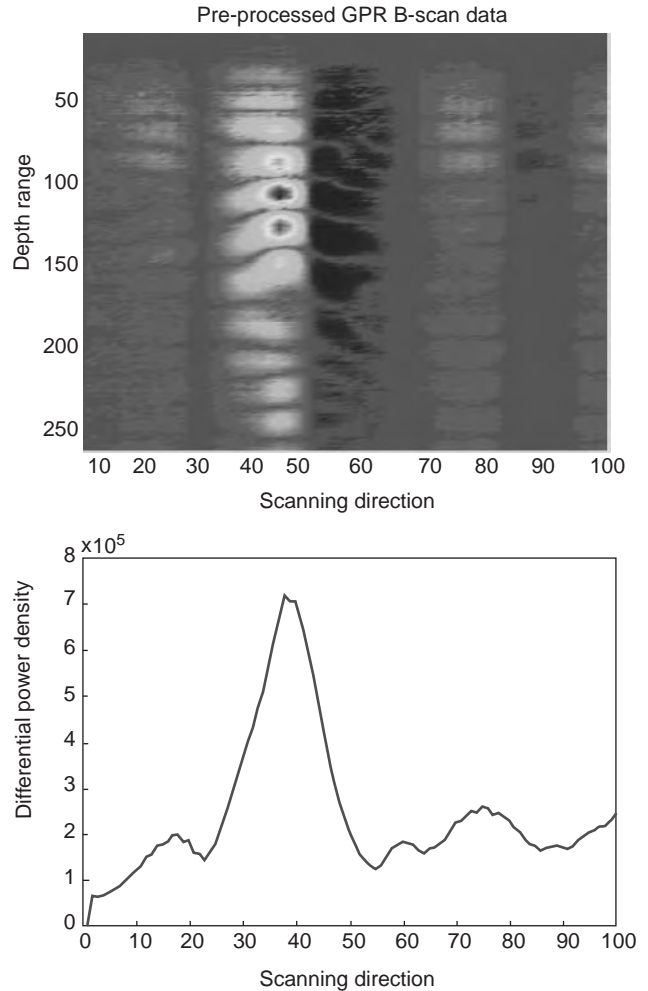


Figure 15. Processed A-scan and B-scan impulse GPR data.

bands separately. The advantage of subband processing is that it allows one to take into account the different target responses and clutter behaviors in different frequency regions. For example, the average RCS values of the probable target objects can be calculated for every subband, and some correlation algorithms can be estimated to discriminate and classify the detected objects.

4. ELECTROMAGNETIC INDUCTION (EMI) SENSOR

4.1. Overview

Electromagnetic induction (EMI), which is the basis for the metal detectors, is one of several sensor modalities widely deployed for subsurface buried-object detection and identification. The basic technology is very mature. The EMI sensors have been used for landmine detection in World War I, and EMI metal detectors were further developed during World War II. Afterward, usage of EMI sensors was also directed to detect conducting objects in other application areas such as mineral exploration, non-destructive body testing, archeological investigation, and security enforcement.

The operating principle of the EMI sensor is to transmit a time-varying primary electromagnetic field that induces currents in any metallic object that the primary field penetrates. When the primary field is abruptly turned off, eddy currents in the metallic object produce a secondary electromagnetic field that is measured by the receiver. The employed frequency range is generally limited to a few tens of kHz [13]. EMI sensors usually consist of a pair of transmitter and receiver coils (see Fig. 16). An electrical current flowing in the transmitter coil of the wire produces the primary field, and the electromagnetic waveform is often either a broadband pulse or a continuous wideband. The transmitted field induces a secondary current in the earth (ground) as well as in any buried conducting objects. This secondary current is usually detected by sensing the voltage induced in the same or another coil of wire, called the *receiver coil*. In the case of pulsed excitation, the transmit waveform is quenched quickly and the receiving coil measures the decaying secondary field that has been induced in the earth (ground) and subsurface objects. In the case of wideband excitation, the receiving coil is placed within the magnetic cavity so that it senses only the weak secondary field radiated by the earth and buried objects [14,16,17].

4.2. Operational Theory

The detection performance of the EMI sensor depends mainly on the system parameters, namely, the primary magnetic field level created by the transmitter coil, the target range, the eddy-current induction capability of the target object, and the receiver coil probe characteristics. Assuming that the fields are time-dependent and the coil position is stationary ($\partial S / \partial t = 0$), the electrical current/magnetic field and the magnetic field/electrical voltage transformation ratios of the transmitter and receiver coils are calculated by the related Maxwell equations given in (15) and (16):

$$\begin{aligned} \nabla \times \mathbf{E} &= -\mu \frac{\partial \mathbf{H}}{\partial t} \Rightarrow \oint_c \mathbf{E} d\mathbf{l} = -\mu \int_S \frac{\partial \mathbf{H}}{\partial t} d\mathbf{S} \\ &\Rightarrow V_{AB} = i2\pi f \mu N H S \cos \varphi \end{aligned} \quad (15)$$

$$\begin{aligned} \nabla \times \mathbf{H} &= \mathbf{J} + \varepsilon \frac{\partial \mathbf{E}}{\partial t} \Rightarrow \oint_c \mathbf{H} d\mathbf{l} = \int_S \mathbf{J} d\mathbf{S} + \varepsilon \int_S \frac{\partial \mathbf{E}}{\partial t} d\mathbf{S} \\ &\Rightarrow \oint_c \mathbf{H} d\mathbf{l} = I \end{aligned} \quad (16)$$

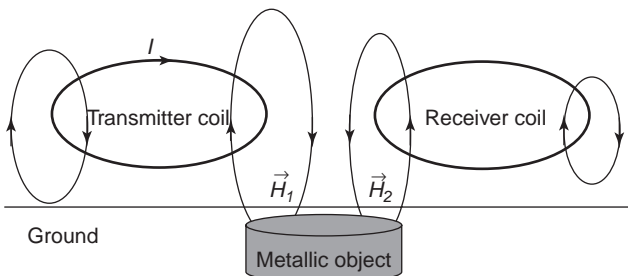


Figure 16. Electromagnetic induction system.

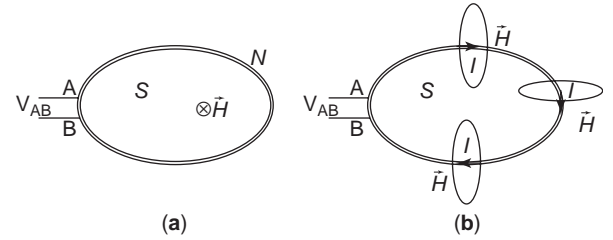


Figure 17. Schematic representations of operational theories of the receiver (a) and transmitter (b) coils.

where E is the electric field, H is the magnetic field, f is the frequency, N is the number of turns, S is the coil surface area of the coil, J is the current density, I is the coil current, φ is the angle between the magnetic field and the coil surface normal vectors, (ε, μ) is the dielectric permittivity and magnetic permeability of the coil material and V_{AB} is the induced voltage (see Fig. 17).

Equation (15) denotes that the coil probe sensitivity increases with the operation frequency, the number of coil turns, the magnetic permeability of the coil ferrite, and the effective area of the coil. The physical shapes of the coils are also important for the sensitivity in terms of the coil's effective area and the field pattern. The field amplitude is inverse proportional to the range. Since EMI sensors use very low frequencies, the ground surface reflectivity and the soil conductivity losses are very slight values. Nevertheless, the specific soil types that contain high conductive and magnetic molecules or particulars can cause some attenuation, and remarkable clutter levels can occur. The eddy currents set up in an object, and hence the induced field, depend on the size, shape, and composition of the object. Because of this, different objects generally have different EMI responses. The basic issues are then how much information about an object can be inferred from its EMI response, and whether that information can be used to distinguish between target and clutter. The objects that contain much more metallic elements will naturally produce more powerful eddy currents and secondary fields on the receiver coil, but the shape of the metallic part in the sense of the angular position with respect to the primary electromagnetic field vector will be an important parameter for detection sensitivity, as well.

4.3. System Performance

The system detection capability of buried metallic objects is generally a well-known parametric problem as mentioned above. It is possible to detect any small amount of metallic or metal-like object under the dynamic range limitations of the system. The range equation is not as complicated as that of a GPR. For instance, the soil attenuation and reflection loss parameters are not strong enough to affect system performance; even in most cases, the size of the metallic content of the object is the most effective system parameter. The experimental results presented in Ref. 14 show that the measured voltages (the receiver voltage, after eliminating from the transmitter–receiver coupling voltage) at the receiver

coil are 3000, 450, and 50 mV for the 15-mm-, 8-mm-, and 5-mm-diameter spherical aluminum objects, respectively. These figures decrease by half for the same size of iron objects.

The concept of EMI sensor capability involves not only detection of metal objects, but also discrimination of the targets of interest from clutter. The traditional detection technique is made based on the secondary field energy calculation method for the decision regarding the presence or absence of an object. In some physical applications, this approach can lead to excessively high false-alarm rates due to the presence of the other metal pieces or granules in soil. Several modifications of traditional EMI sensors are considered in order to facilitate the target discrimination and classification. Wideband sensor operation is one of the most promising methods. In this way, the frequency-dependent response of the induced field by a buried conducting object is used to distinguish the target from the clutter [15]. Another way is to use a simple phenomenological model that describes the measured time-domain waveform as a weighted sum of decaying exponentials to provide an accurate discrimination model for EMI sensors [17]. The measured EMI response can be modeled as a sum of decaying exponential signals whose characteristic decay rates are intrinsic to the interrogated target. Since the decay rates are not dependent on target/sensor orientation, decay rate estimation has been proposed as an effective and robust method for target identification by Ho et al. [17]. In general, the decay rates associated with metallic objects are slower than that of the earth (ground), so there is more energy in the received signal when a metallic object is present under the surface of the earth. This simple phenomenology allows very basic signal processing to be employed; for example, either an energy detector or the overall amplitude of the signal in a given time gate may be used when the goal is to detect any metallic subsurface object. Nevertheless, such processing can be the source of many false alarms in highly cluttered media.

5. ACOUSTIC AND SEISMIC SENSOR

5.1. Overview

Most technologies for the detection of shallow buried objects are electromagnetic methods. They measure the contrast in ferrous content, electrical conductivity, or dielectric constant between the object and the soil in which they are buried. Plastic objects have no or little such contrast because of their nonconductive constitutions. They have dielectric constants that are low, very close to the dielectric constant of dry soil. This makes them very difficult to detect by these technologies. Their acoustic compliance, on the other hand, makes them easier to detect by seismic and acoustic technologies. These methods search for buried objects by causing them to vibrate by introducing sound or seismic waves into the ground. As the materials with different properties vibrate differently, the pattern of ground motion leads to the detection and possibly the identification of the buried object.

Seismic sensors provide a means of sensing the mechanical properties of buried objects remotely. Seismic

technologies are commonly employed in exploration of oil. The equipment used in such applications is designed to find layered geology or use field techniques too expensive to apply. Geophones provide an inexpensive solution to record seismic data and thus sense buried objects. The main difficulty of this approach is to generate clean Rayleigh waves. Also, the geophones have to contact the ground to perform the measurements. This is not desirable for detecting objects containing explosives.

Seismic motion can also be generated by an airborne acoustic wave. A loudspeaker above the ground can be used for this purpose. A phenomenon called *acoustic-to-seismic coupling* occurs when an airborne acoustic wave is incident at the ground surface. This term refers to the coupling of acoustic energy into the ground as seismic motion. Acoustic-to-seismic coupling causes particles to vibrate on the soil surface. More recent techniques use a laser Doppler vibrometer (LDV) to measure and study the spatial pattern of particle velocity amplitude of the surface. A variety of sensors such as radars, microphones, and ultrasonic devices have also been tried to detect the vibrations and the backscattered sound.

There are three main approaches for buried-object detection using acoustics:

1. *The Linear Acoustic Technique.* This technique has proved to be an extremely accurate technology for locating buried landmines [19]. In this technique, loudspeakers insonify broadband acoustical noise over the soil and a laser Doppler velocimeter (LDV) equipped with X-Y scanning mirrors is used to detect increased soil vibration across a scan region.
2. *The Nonlinear Acoustic Technique.* This technique uses a single speaker to drive two tonal excitations to provide the airborne sound to produce A/S coupling [20]. An accelerometer is used to measure the surface acceleration.
3. *Excitation of Elastic Waves and Surface Displacement Measurement.* The main objective of this approach is to excite elastic waves in the soil and then measure the surface displacements [21]. It uses an electrodynamic shaker to excite elastic waves. As the waves propagate through a scan region, the surface displacements are measured using radar.

5.2. Linear Acoustic Techniques

Acoustic–seismic systems proposed by Sabatier et al. have shown great promise in detecting low metal mines [19,22]. In these systems, a loudspeaker above the ground surface insonifies the target region at the surface. Acoustic energy is coupled into the ground, producing vibrations. The velocity of the ground surface resulting from these vibrations is measured with a laser Doppler vibrometer (LDV) at several positions over a rectangular grid. The output of the system at a single spatial position is a collection of complex velocities at a set of frequencies, typically within the range from ~ 100 to 300 Hz for large objects and within 100–1000 Hz for small objects. The data collected over a

region form a three-dimensional (3D) complex image. This 3D image can be regarded as a stack of two-dimensional (2D) images, referred to as *spectral images*. These spectral images can be viewed as the displacement energy of the soil above the buried object at various frequencies. The analysis of these images leads to detection and identification of the buried object [23,24].

There are three different versions of the linear acoustic systems proposed by Sabatier et al:

1. The first version uses a stop-and-stare data collection scheme [19,22]. The LDV collects data staring at a single spatial position and then stares at a position close to the previous one. A region of interest is thus scanned by stopping and staring. The data are collected with some predefined spatial resolution, which obviously depends on the size of the object to be detected. As a rule, the spatial resolution is selected such that a minimum of three equally spaced positions is scanned along the major axis of the object to increase detection rate. The scantime of this type of data collection scheme may be too slow for some applications such as mine detection, where a faster scanning speed is always desirable.

2. A faster version of the linear acoustic system scans a region without stopping [25]. A laser beam continuously sweeps over an area by moving back and forth as shown in Fig. 18. The spatial resolution in downtrack can be adjusted by factoring in the size of the buried object. However, the cross-track resolution depends on the imaging techniques employed as well as the sweeping speed. Unlike the previous systems, spectral images are not readily available. Transforming the time-domain data into spectral images is a critical step in this second approach. The scanning speed of an area by the sweeping beam approach is faster than that of the stop-and-stare approach.

3. A much faster scanning speed is achieved using an array of LDVs placed on a moving platform [26]. Scanning of the area is performed by moving the platform. The LDVs on the platform are positioned such that they point to uniquely spaced positions in cross-track direction (see Fig. 19). When the platform is moved in the downtrack direction, each LDV scan the region along the path. Since this system uses more than one LDV, a normalization

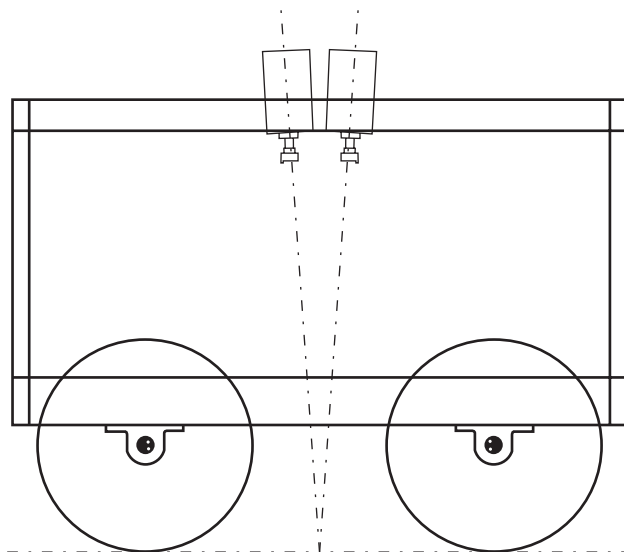


Figure 19. LDV array on a moving platform.

problem is likely to occur due to nonuniqueness of the LDVs.

5.3. Nonlinear Acoustic Techniques

Nonlinear acoustic technique proposed by Donskoy employs dual-frequency (f_1 and f_2) acoustic signal transmitted toward a buried object [20]. It relies on reception of a signal generated on the soil–buried object interface. This signal has frequencies different from the initially radiated signal. The dual-frequency sound causes an object to radiate a signal at the intermodulation frequencies ($f_1 \pm f_2$). Thus, the presence of the difference frequency in the radiated signal leads to detection of the object. Some solid object such as bricks, steel disks, tree roots, and rocks do not radiate this new signal with the difference frequency. This makes it easier to differentiate certain objects from debris.

Dynamic behavior of the buried object is strongly dependent on the stiffness of the soil and the buried object. The stiffness of solid objects such as rocks and shrapnel is usually much higher than that of the soil in which they are buried. Their burial of depth also affects their stiffness. The stiffness increases as the depth of the object increases. When the stiffness of the object is much higher than that of the soil, the nonlinear motion is not observable; rather, it is a linear motion. Therefore, the nonlinear acoustic technique is not sensitive to such solid objects and deeply buried objects. Donskoy explains this by modeling the buried object as a mass–spring system [20]. This model is discussed in Section 5.5.1.

5.4. Simultaneous Use of Elastic and Electromagnetic Waves

The detection system proposed by Scott et al. simultaneously uses elastic and electromagnetic waves [21]. Elastic surface waves are generated using an elastic wave transducer, which is an electrodynamic shaker in direct contact with the soil (see Fig. 20). The shaker is excited

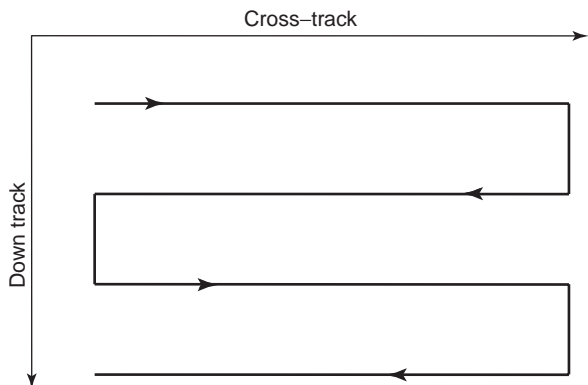


Figure 18. Sweeping scheme for laser measurement of the velocity of ground vibration.

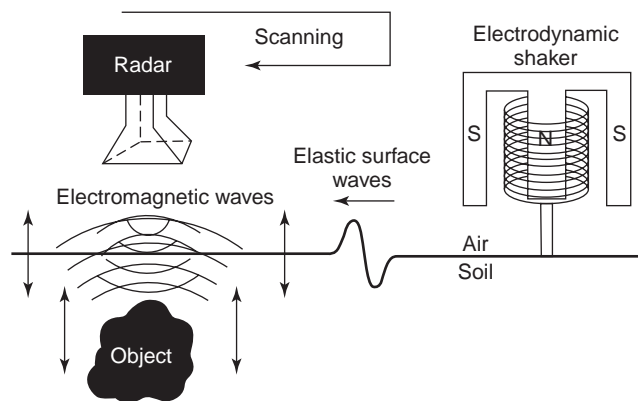


Figure 20. Use of elastic and electromagnetic waves for object detection.

with a differentiated Gaussian pulse with a center frequency of 400 Hz. The waves propagate through the scan region. A radar-based sensor is used to measure the surface displacements of the soil throughout the scan region. The displacements of the surface are measured as a function of time and position. The sensitivity of the radar is typically around 1 nm. As in the linear and nonlinear acoustic techniques, the technique relies on the flexible mechanical structure of the object to be detected. If the object is solid and inflexible, it will not exhibit resonant response. The surface displacements of the soil are then will not likely yield to the detection of the object. Flexible objects such as plastic pipes can be detected using this technology. The main advantage of this method is that it can be used even if the surface is covered with some vegetation. Electrical arc source and air acoustic source have also been investigated in place of the electrodynamic shaker.

5.5. Detection Algorithms

An important step in object detection by acoustic/seismic technology is to process the acquired data. The processing steps for detecting an object are dependent on the acquired data, sensor type, soil type, target type, and environmental conditions. For example, the acquired data can be in either time or frequency domain, and this may require applying different processing steps to prepare for further processing. Figure 21 shows a sensor output in the time domain. Each row represents the time-domain signals acquired by sweeping a region on the ground along the scan direction. The location of the buried object is shown by the dotted line in the same figure. A number of imaging techniques, such as short-time fast Fourier transform (FFT) and the Yule–Walker method, can be applied to obtain spectral images. In some cases, on the other hand, the sensor readily provides the spectral images as shown in Fig. 22. In the sample spectral images shown in the figure, the buried object is located at the lower left of the 8 × 12 grid with a spatial resolution of 2 cm. If multiple sensors are used to collect the signals at each row in Figs. 21 and 22, a processing step to equalize the channels may be necessary if the sensors are not unique. This step is

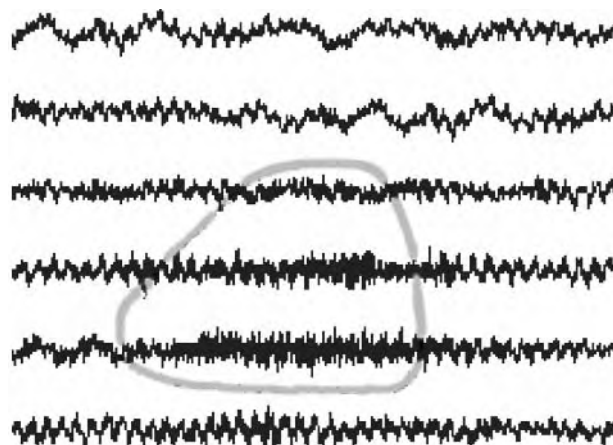


Figure 21. LDV measurements of an acoustic/seismic object detection system producing time-domain signals.

skipped if a single sensor is used to scan the same region by stopping and staring, as shown in Fig. 18. It is, therefore, necessary to design detection algorithms specific to the detection technique. Some examples of automated methods for detecting and discriminating buried objects from clutter objects are discussed below.

5.5.1. Model-Based Detection Techniques. Mathematical models are often used for detection and identification of objects. For buried objects, the depth and the physical properties of the objects and the soil are the common parameters of the models. Unfortunately, some of these parameters such as the depths of the objects are not known or sometimes their estimation is too time-consuming and impractical. These problems render the model useless even if a perfect model is available. Also, it is obvious that a general model for any type of buried object cannot

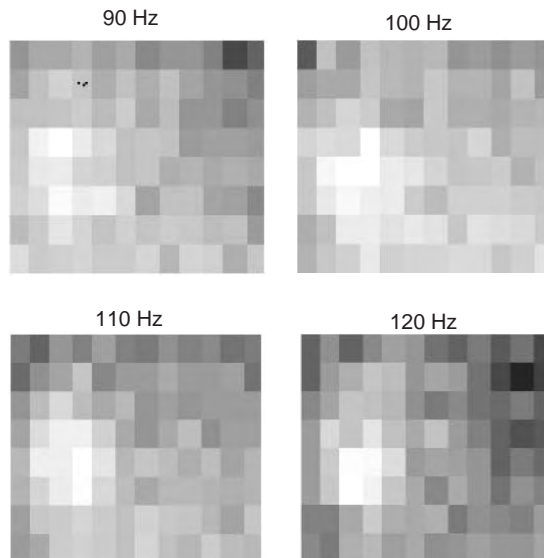


Figure 22. LDV measurements of an acoustic/seismic object detection system producing spectral images.

be given. Therefore, each model must be specific to each problem.

A mathematical model for a buried mine using coupled damped harmonic oscillators was developed by Donskoy to interpret acoustic measurements taken on the soil surface [20]. On the basis of this model, it can be shown that the transfer function of a buried mine is in the following form:

$$H(s) = \frac{V(s)}{F(s)} = K \frac{s^3 + n_1 s^2 + n_2 s}{s^4 + p_1 s^3 + p_2 s^2 + p_3 s + p_4} \quad (17)$$

where V is the velocity of the vibration on the surface of the ground and F is the driving acoustic force at a particular spatial location [27]. The coefficients are somewhat complicated functions of the model parameters. They are very difficult to estimate and are not given here. Assuming that $F(s)$ is nearly constant over all frequencies, the frequency spectrum of the velocity of the ground surface vibration is proportional to $|H(j\omega)|$ and it is what is actually measured by the LDV:

$$|V(j\omega)| \approx \left| \frac{(j\omega)^3 + n_1(j\omega)^2 + n_2(j\omega)}{(j\omega)^4 + p_1(j\omega)^3 + p_2(j\omega)^2 + p_3(j\omega) + p_4} \right| \quad (18)$$

A sample Bode diagram of the transfer function in (17) is shown in Fig. 23. This system has four poles and three transmission zeros. As the depth of the mine increases, the leftmost peak shifts to the left and the rightmost peak shifts to the right.

It can be easily verified that an autoregressive moving-average (ARMA) process with order (4,4) has the same form as shown in (17). This suggests that the acoustic measurements, namely, the velocity of the vibration of the ground surface, have frequency spectra that can be modeled by an ARMA process with order (4,4). This leads to pole analysis for detection of the buried objects [27].

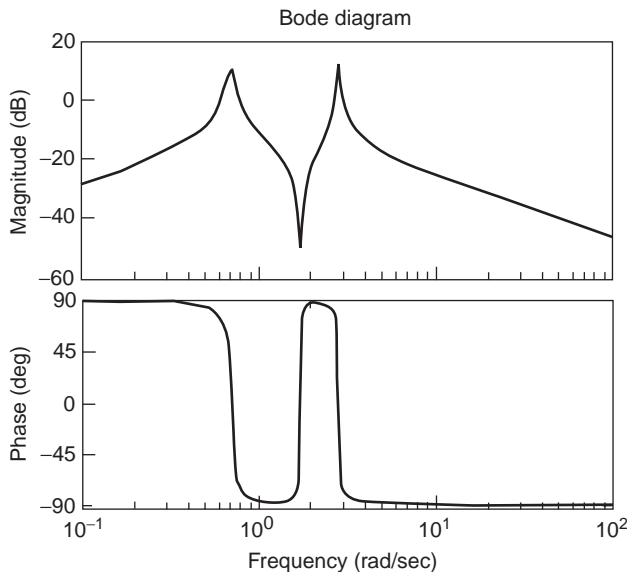


Figure 23. A sample Bode diagram of the transfer function in Eq. (17).

Observe that the change in the phase is dramatic at the same frequency of the leftmost peak of the magnitude plot in the Bode diagram in Fig. 23. Another approach uses this property to extract feature based on the phase information [28]. It significantly lowers false-alarm rates at given detection probabilities.

5.5.2. Shape-Based Detection. A common approach for object detection is to use shape information [23,24]. For buried objects, the spectral images usually provide good shape information. In Fig. 24, for example, the shape of the object shown in the spectral images at various bands is quite round. Thus, the *roundness* can be used as a feature.

Shape-based detection algorithms usually have a pre-processing step that may include background subtraction, normalization, and thresholding. Connected component analysis usually follows this step. Features such as eccentricity, minor-axis length, major-axis length, area, and compactness are found useful for discriminating different objects [23]. Hocaoglu et al. used independent component analysis to extract additional features to enhance the detection rate [24]. Similar features can also be applicable to the images representing the basis vectors of independent components.

6. OPTICAL DETECTORS

Detection of buried objects by optical sensing is regarded as one of the most promising techniques [29,30]. Its main advantage is that passive sensors are employed, which is very important especially in military applications. A common practice is to use several sensors (cameras) sensitive at different wavelengths. The spectrally reach reflection region (from 0.4 to 2.5 μm) is available for only daylight detection. The detection concepts using the midwave infrared (3–5 μm) and the longwave infrared (8–12 μm) are usually emphasized for a day/night system.

There are two main approaches for optical detection; the sensor can detect either (1) the thermal signature of the buried object itself or (2) a disturbance to the surface soil caused by the process of burying an object. The first approach uses the thermal contrast governed by the alternation of temperature over day and night and it is referred as the *thermal detection method*. As buried objects heat up at a rate different from that for soil, a thermal signature can be obtained to detect them. The latter is referred as the *nonthermal detection method*. The principal rationale behind the nonthermal detection method is that the spectral properties of the surface layer are different from those of the subsurface soil. The act of burying an object will bring some subsurface materials such as SiO_2 content of rocks and soils to the surface. Thus, the spectral properties of the soil above the buried object will be different from the spectral properties of the soil around the same region. The contrast between the spectral properties will lead to the detection of a freshly buried object exploiting the 8–9.4 μm Reststrahlen feature, which refers to absorption of energy as a function of silica content. The emissivity decreases more

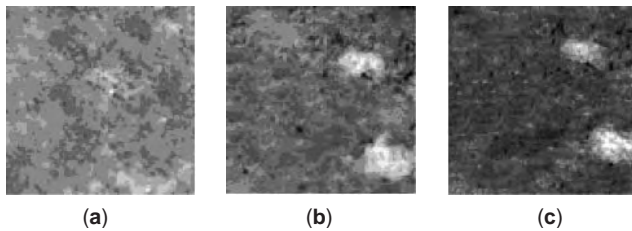


Figure 24. IR imagery taken at different times of day: (a) 8:00 A.M.; (b) 2:00 P.M.; (c) 3:00 P.M.

and also shifts as wavelengths become longer and as silica content increases.

Soil contains both large and small particles. In fact, many of the larger particles are usually coated with smaller particles. The smaller particles in the surface layer, on the other hand, tend to be cleared from the larger particles by wind and rain. This weathering process over time causes the clean large particle to dominate the surface layer, and thus changing the spectral property of the soil at the surface layer. When the soil is disturbed, the chemical composition of the surface will change. The weathering process over time will bring the surface to its original state. Therefore, this technique may not be suitable to detect objects that were buried a long time ago.

Both of these methods have extreme variability in performance. Their performances depend heavily on environmental conditions such as the humidity and the temperature. Figure 24 shows images of two buried objects in the thermal band, obtained by a thermal camera with an operating wavelength of 7.5–13 μm . The objects are 10 cm deep and they have circular shape with a diameter of 15 cm. The best contrast between the areas near the objects and the surrounding areas is obtained at the warmest time of the day. But, the objects lose heat more quickly at night. Thus, they show up as dark spots in the imagery, instead of the bright spots. Laser illumination or microwave radiation can be used to induce these differential temperature profiles.

7. OTHER SENSORS

In this section, the auxiliary sensor types generally used for the specific application areas or to improve detector performance, will briefly be presented with their operating principles, current capabilities, limitations, and further improvement potentials. Most of these sensor technologies, such as electrical impedance tomography, X-ray imaging, and explosive-material detectors, are still at the stage of prototyping or technical research [13].

Electrical impedance tomography (EIT) is a low-cost and basic measurement technique employed to obtain the conductivity distribution of the ground surface. The detection principle is based on the discrimination of the shallow buried objects that have electrical resistance different from that of soil. The ground surface is probed by many numbers of low-current electrodes to image the surface resistivity with a required resolution [31]. The detection capability of EIT is limited to the probing depth, which is usually less than 20 cm. It is also not convenient for quick-time wide-area scanning operations.

X-ray scattering is one of the highest-resolution buried-object detector technologies. The pencil beam of the X rays is emitted to the scanning area, and the backscattered rays are detected by the sensor [32]. The performance depends essentially on the X-ray absorbing characteristics of the target object. For instance, organic materials, soil layers, and explosives have less absorbing and more scattering characteristics than do metals. Solid objects are more easily distinguished than are clutters. Since higher X-ray energy sources are needed to penetrate deeper, these sensors are usually suitable for shallow buried targets.

Subsurface microwave tomography is actually a type of electromagnetic sensor. The operating principle and hardware units of the diffraction tomography system are similar to those of stepped-frequency GPR. However, such systems generally use higher frequencies up to millimeter bands and their detection process is based on solution of the inverse scattering problem. The sweeping microwave signal is radiated to the buried object, and the diffracted wave from the target is received. Wideband antennas, mostly dielectric-loaded horns, are employed for wave transmitting and receiving. Then, I/Q data signatures of the buried target are processed using some image reconstruction algorithms such as Born–Kirchhoff approximations. The diffraction tomography sensor can yield high-resolution subsurface mapping and target imaging [33]. Nevertheless, the detection depth is less than 10 cm, due to the strong soil attenuation at high frequencies, and they are not still convenient for real-time detection since the scanning time is usually very long.

In addition to these detector types, some biological, electrochemical, and piezoelectric sensor systems are employed for specific applications such as explosive-material detection, which may be very important especially for military applications (i.e., mine detection). Biological smell sensors can detect the vapors or the gases produced by the explosive components of objects. The electrochemical detector measures the changes in polymer electrical resistance of the explosive vapors. The piezoelectric sensor uses the resonant frequency shifting of various materials when exposed to the explosive vapors [13].

BIBLIOGRAPHY

1. D. J. Daniels, *Surface Penetrating Radar*, IEE Radar, Sonar, Navigation and Avionics Series 6, London, 1996.
2. Picosecond Pulse Labs Application Notes, www.picosecond.com.
3. A. S. Turk and B. Sen, Ultra-wide-band antenna designs for GPR impulse radar systems, *IEEE EMC Symp. Records*, May 2003.
4. D. S. A. Sahinkaya and A. S. Turk, UWB GPR for detection and identification of buried small objects, *SPIE Proc.* **5410**:174–184 (2004).
5. M. Sezgin, F. Kurugollu, I. Taşdelen, and S. Ozturk, Real time detection of buried objects by using GPR, *SPIE Proc.* **5415**:447–455 (2004).
6. A. S. Turk, Ultra wide band TEM horn design for ground penetrating impulse radar system, *Microwave Opt. Technol. Lett.* **41**(6):333–336 (June 2004).

7. L. C. Chan, D. L. Moffat, and L. Peters, A characterization of subsurface radar targets, *Proc. IEEE* **67**(7):991–1000 (July 1979).
8. J. S. Lee and C. Nguyen, Novel low-cost ultra-wideband, ultra-short-pulse transmitter with MESFET impulse-shaping circuitry for reduced distortion and improved pulse repetition rate, *IEEE Microwave Wireless Compon. Lett.* **11**(5) (May 2001).
9. R. W. P. King and G. S. Smith, *Antennas in Matter*, MIT Press, 1981.
10. K. L. Schlager, G. S. Smith, and J. G. Maloney, Optimization of bow-tie antenna for pulse radiation, *IEEE Trans. Anten. Propag.* **42**(7):975–982 (July 1994).
11. A. G. Yaravoy, A. D. Schukin, I. V. Kaploun, and L. P. Lightart, The dielectric wedge antenna, *IEEE Trans. Anten. Propag.* **50**(10):1460–1471 (Oct. 2002).
12. V. P. Chumachenko and A. S. Turk, Radiation characteristics of wide-angle H-plane sectoral horn loaded with dielectric of multiangular shape, *Int. J. Electron.* **88**(1):91–101 (Jan. 2001).
13. *Alternatives for Landmine Detection, RAND Science and Technology Policy*, RAND Corp., Santa Monica, CA, 2003.
14. S. Yamazaki, H. Nakane, and A. Tanaka, Basic analysis of a metal detector, *Proc. IEEE Instrumentation and Measurement Technology Conf.* Budapest, Hungary, May 21–23, 2001.
15. P. Gao, L. Collins, N. Geng, L. Carin, D. Keiswetter, and I. J. Won, Classification of landmine-like metal targets using wideband electromagnetic induction, *IEEE Trans. Geosci. Remote Sens.* **38**(3):1352–1361 (May 2000).
16. T. H. Bell, B. J. Barrow, and J. T. Miller, Subsurface discrimination using electromagnetic induction sensors, *IEEE Trans. Geosci. Remote Sens.* **39**(6):1286–1293 (June 2001).
17. K. C. Ho, L. M. Collins, L. G. Huettel, and P. D. Gader, Discrimination mode processing for EMI and GPR sensors for hand-held land mine detection, *IEEE Trans. Geosci. Remote Sens.* **42**(1):249–263 (Jan. 2004).
18. M. I. Skolnik, *Radar Handbook*, McGraw-Hill, New York, 1970.
19. J. M. Sabatier and N. Xiang, An investigation of a system that uses acoustic-to-seismic coupling to detect buried ant-tank mines, *IEEE Trans. Geosci. Remote Sens.* **39**:1146–1154 (2001).
20. D. M. Donskoy, Nonlinear vibro-acoustic technique for landmine detection, *SPIE Proc.* **3392**:211–217 (1998).
21. W. R. Scott, G. D. Larson, J. S. Martin, and P. H. Rogers, Seismic/electromagnetic system for landmine detection, *J. Acoust. Soc. Am.* **107**(5)(Part 2):28 (May 2000).
22. J. M. Sabatier and C. J. Hickey, Acoustic-to-seismic transfer function at the surface of a layered outdoor ground, *Proc. SPIE* **4038**:633–644 (2000).
23. A. K. Hocaoglu, P. Gader, J. Keller, and B. Nelson, Anti-personnel landmine detection and discrimination using acoustic data, *Subsurf. Sens. Technol. Appl.* **3**(2):75–93 (April 2002).
24. A. K. Hocaoglu and P. Gader, Continuous processing of acoustics data for landmine detection, *Proc. SPIE* **4742**:654–664 (Detection and remediation technologies for mines and mine like targets VII) (April 2002).
25. N. Xiang and J. M. Sabatier, Acoustic-to-seismic landmine detection using a continuously scanning laser Doppler vibrometer, *Proc. SPIE* **5089**:591–595 (Detection and remediation technologies for mines and minelike targets VIII) (April 2003).
26. R. D. Burgett, M. R. Bradley, M. Duncan, J. Melton, A. K. Lal, V. Aranchuk, C. F. Hess, J. M. Sabatier, and N. Xiang, Mobile mounted laser Doppler vibrometer array for acoustic landmine detection, *Proc. SPIE* **5089**:665–672 (Detection and remediation technologies for mines and minelike targets VIII) (April 2003).
27. A. K. Hocaoglu, P. D. Gader, and G. X. Ritter, Acoustic/Seismic imaging using spectral estimation for landmine detection, *Proc. Int. Conf. Requirements and Technologies for the Detection, Removal and Neutralization of Landmines and UXO*, Brussels, Belgium, 2004, Vol. 2, pp. 489–495.
28. T. Wang, J. Keller, P. D. Gader, and A. K. Hocaoglu, Phase signatures in acoustic-seismic landmine detection, *Radio Sci.* **39**(4):RS4S02 (2004).
29. J. Salisbury, L. Walter, N. Vergo, and D. D'Aria, *Infrared (2.1–2.5 mm) Spectra of Minerals*, Johns Hopkins Univ. Press, Baltimore, 1991.
30. S. Hong, T. W. Miller, H. Tobin, B. Borchers, J. M. Hendrickx, H. A. Lensen, P. B. Schwering, and B. A. Baertlein, Impact of soil water content on landmine detection using radar and thermal infrared sensors, *Proc. SPIE* **4394**:409–416 (Detection and remediation technologies for mines and minelike targets VI) (Oct. 2001).
31. A. Wexler, Electrical impedance imaging in two and three dimensions, *Clin. Phys. Physiol. Meas.* (Suppl. A): 29–33 (1988).
32. B. Towe and A. Jacobs, X-ray backscatter imaging, *IEEE Trans. Biomed. Eng.* **BME-28**:646–654 (1981).
33. A. A. Vertiy and S. P. Gavrilov, Modeling of microwave images of buried cylindrical objects, *Int. J. Infrared Millimeter Waves* **19**(9):1201–1220 (1998).

CALIBRATION OF A CIRCULAR LOOP ANTENNA *

AYDIN AYKAN
Tutzing, Germany

A time-varying magnetic field at a defined area S can be determined with a calibrated circular loop connected to the input of an appropriate measuring receiver (Fig. 5). There may be a passive or an active network between the loop and the output port. The measuring loop can also include a shielding over its circumference against any perturbation of strong and unwanted electric fields. The shielding must be interrupted at a point on the loop circumference.

Generally in the far field the streamlines of magnetic flux are uniform, but at near field, in the vicinity of the generator of a magnetic field, they depend on the source and its periphery. Figure 4 shows the streamlines of the electromagnetic vectors generated by the transmitting loop L1. In the near field, the spatial distribution of the magnetic flux $B = \mu_0 H$ over the measuring loop area is not known. Only the normal components of the magnetic flux, averaged over the closed-loop area, can induce a current through the loop conductor. The measuring loop must have a calibration (conversion) factor or set of factors that, at each frequency, expresses the relationship between the field strength impinging on the loop and indication of the measuring receiver. The calibration of a measuring loop requires the generation of a well-defined standard magnetic field on its effective receiving surface. Such a magnetic field is generated by a circular transmitting loop when a defined root-mean-square (RMS) current is passed through its conductor. The unit of the generated or measured magnetic field strength H_{av} is A/m (amperes per meter) and therefore is also an RMS value. The subscript "av" strictly indicates the average value of the spatial distribution, not the average over a period of T of a periodic function. This statement is important for near-field calibration and measuring purposes. For far-field measurements the result indicates the RMS value of the magnitude of the uniform field. The traceability of the calibration must be established for the calibration process, through linking the assigned value of any components to the International System of Units (SI). In the following we discuss the requirements for the near-zone calibration of a measuring loop.

1. CALCULATION OF STANDARD MAGNETIC FIELDS

To generate a standard magnetic field, a transmitting loop L1 is positioned coaxial and plane-parallel at a separation distance d from the loop L2 to be calibrated, as in Fig. 1. The analytical formula for the calculation of the average

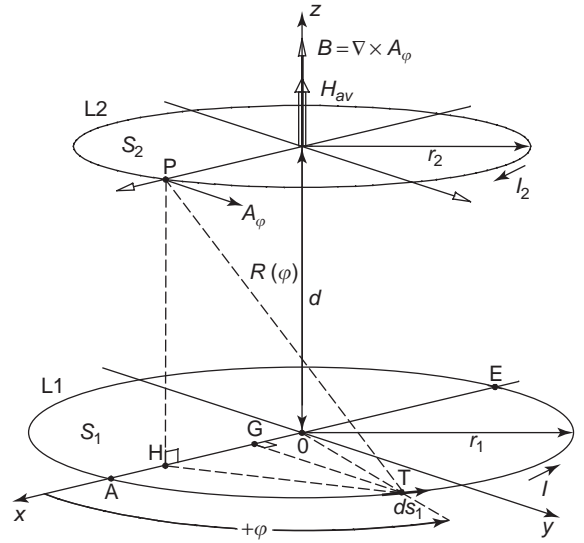


Figure 1. Configuration of two circular loops.

magnetic field strength H_{av} in A/m generated by a circular filamentary loop at an axial distance d including the retardation due to the finite propagation time was obtained earlier by Greene [1]. The average value of field strength H_{av} was derived from the retarded vector potential A_φ as a tangential component on the point P of the periphery of loop L2:

$$H_{av} = \frac{I r_1}{\pi r_2} \int_0^\pi \frac{e^{-j\beta R(\varphi)}}{R(\varphi)} \cos(\varphi) d\varphi \quad (1a)$$

$$R(\varphi) = \sqrt{d^2 + r_1^2 + r_2^2 - 2r_1 r_2 \cos(\varphi)} \quad (1b)$$

In these equations for thin circular loops, I is the transmitting loop RMS current in amperes, d is the distance between the planes of the two coaxial loop antennas in meters, r_1 and r_2 are filamentary loop radii of transmitting and receiving loops in meters, respectively, β is wavelength constant, $\beta = 2\pi/\lambda$, and λ is wavelength in meters.

Equations (1) give the exact results for the separation distances even from $d=0$. For $d=0$ the radii of the loops must be $r_1 \neq r_2$, otherwise the integral gives a singularity for $\varphi = \pi$, because for $r_1 = r_2$ the root in Eq. (1b) being zero.

The use of any approximate formula (Eq. 25 in Ref. 1 and Eqs. (2) in Ref. 2) is not suitable, because it imposes restrictions on the range applicability for the approximate equations. Using the expressions of maximum magnetic field H_{max} would also not be suitable for purposes of near-field calibration purpose (see Fig. 2 in Ref. 2).

Generally the Eqs. (1) can be determined by numerical integration. To this end we separate the real and imaginary parts of the integrand using Euler's formula

*This article is based on "Calibration of Circular Loop Antennas," by Aydin Aykan, which appeared in *IEEE Transactions on Instrumentation and Measurement*, Vol. 7, No. 2, © 1998 IEEE.

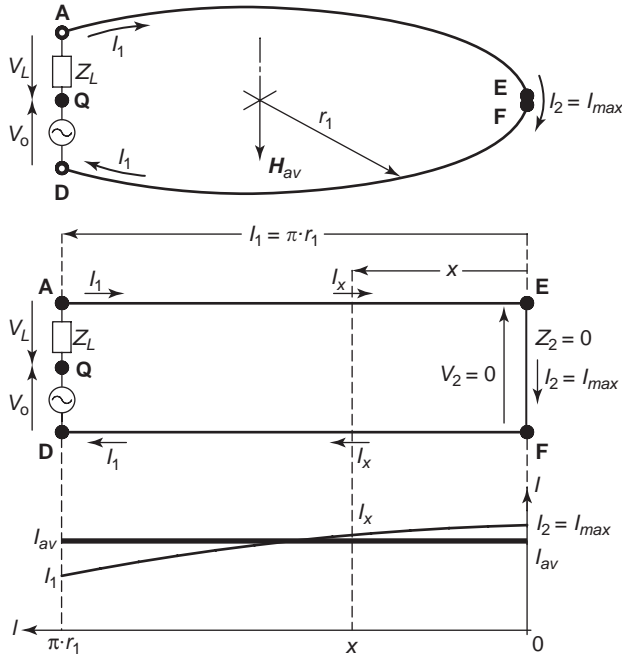


Figure 2. Current distribution on a circular loop.

$e^{-j\varphi} = \cos(\varphi) - j \sin(\varphi)$ and rewrite Eq. (1a) as

$$H_{av} = \frac{I r_1}{\pi r_2} (F - jG) \quad (2a)$$

where

$$F = \int_0^\pi \frac{\cos(\beta R(\varphi))}{R(\varphi)} \cos(\varphi) d\varphi \quad (2b)$$

$$G = \int_0^\pi \frac{\sin(\beta R(\varphi))}{R(\varphi)} \cos(\varphi) d\varphi \quad (2c)$$

and the magnitude of H_{av} is then obtained as

$$|H_{av}| = \frac{I r_1}{\pi r_2} \sqrt{F^2 + G^2} \quad (2d)$$

It is possible to evaluate the integrals in Eqs. (2) numerically with an appropriate mathematics software on a personal computer. Some mathematics software can directly calculate the complex integral of Eqs. (1). Hence, some of the following equations are written in complex form for convenience.

2. ELECTRICAL PROPERTIES OF CIRCULAR LOOPS

2.1. Current Distribution around a Loop

The current distribution around the transmitting loop is not constant in amplitude and in phase. A standing wave of current exists on the circumference of the loop. This current distribution along the loop circumference is discussed by Greene [1, pp. 323–324]. He has assumed the loop circumference $2\pi r_1$ to be electrically smaller than the

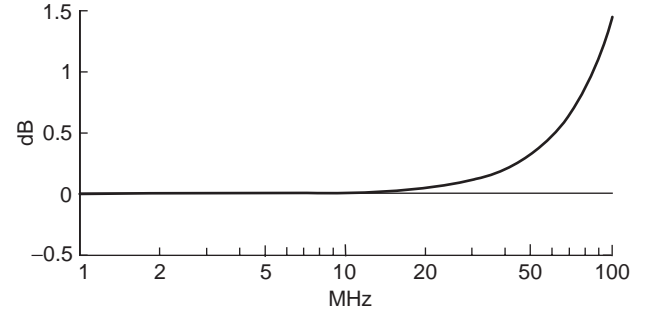


Figure 3. Deviation of I_{av}/I_1 for a loop radius 0.1 m as $20 \log(I_{av}/I)$ in decibels versus frequency.

wavelength λ and the loop current to be constant in phase around the loop and the loop proper to be sufficiently loss-free. The single-turn thin loop was considered as a circular balanced transmission line fed at points A and D and short-circuited at points E and F (Fig. 2).

In an actual calibration setup the loop current I_1 is specified at the terminals A and D. The average current was given as a function of input current I_1 of the loop [2]:

$$I_{av} = I_1 \frac{\tan(\beta \pi r_1)}{\beta \pi r_1} \quad (3)$$

The fraction of I_{av}/I_1 from Eq. (3) expressed in decibels gives the conditions for determining of the highest frequency f and the radius of the loop r_1 . The deviation of this fractions is plotted in Fig. 3.

The current I in Eq. (1a) must be substituted with I_{av} from Eq. (3). Since Eq. (3) is an approximate expression, it is recommended to keep the radius of the transmitting loop small enough for the highest frequency of calibration to minimize the errors. For the dimensioning of the radius of the receiving loop, these conditions are not very important, because the receiving loop is calibrated with an accurately defined standard magnetic field, but the resonance of the loop at higher frequencies must be taken into account.

2.2. Circular Loops with Finite Conductor Radii

A measuring loop can be constructed with one or more windings. The form of the loop is chosen as a circle because of the simplicity of the theoretical calculation and calibration. The loop conductor has a finite radius. At high frequencies the loop current flows on the conductor surface and shows the same proximity effect as two parallel, infinitely long cylindrical conductors. Figure 4 shows the cross section of two loops in intentionally exaggerated dimensions. The streamlines of the electric field are orthogonal to the conductor surface of the transmitting loop L1 and they intersect at points A and A'. The total conductor current is assumed to flow through a fictive thin filamentary loop with the radius $a_1 = \sqrt{r_1^2 - c_1^2}$, where $a_1 = \overline{OA} = \overline{QP} = \sqrt{\overline{OQ}^2 - \overline{QP}^2}$. The streamlines of the magnetic field are orthogonal to the streamlines of electric field. The receiving loop L2 with the finite conductor

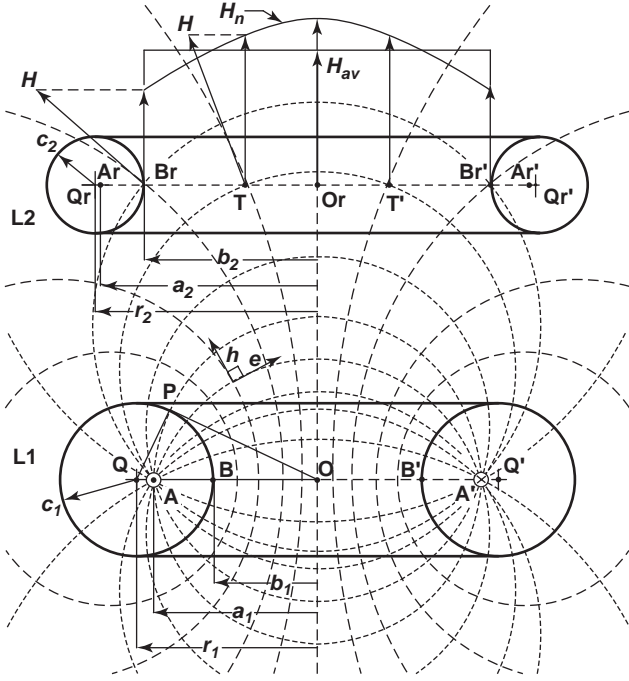


Figure 4. Filamentary loops of two loops with finite conductor radii and orthogonal streamlines of the electromagnetic vectors, produced from transmitting loop L1.

radius c_2 can encircle a part of magnetic field with its effective circular radius $b_2 = r_2 - c_2$.

The sum of the normal component of vectors H acting on the effective receive area $S_2 = \pi b_2^2$ induces a current in the conductor of the receiving loop L2. This current flows through the filamentary loop with the radius a_2 . The average magnetic field vector H_{av} is defined as the integral of vectors H_n over effective receiving area S_2 , divided by S_2 . The magnetic streamlines, which flow through the conductor and outside of loop L2, cannot induce a current through the conductor along the filamentary loop Ar, Ar' of L2. The equivalent filamentary loop radii a_1, a_2 and effective circular surface radii b_1, b_2 can be seen directly from Fig. 4.

The equivalent thin current filament radius a_1 of the transmitting loop L1:

$$a_1 = \sqrt{r_1^2 - c_1^2} \quad (4a)$$

The equivalent thin current filament radius a_2 of the receiving loop L2 is

$$a_2 = \sqrt{r_2^2 - c_2^2} \quad (4b)$$

The radius b_1 of the effective transmitting circular area of the transmitting loop L1 is

$$b_1 = r_1 - c_1 \quad (4c)$$

The radius b_2 of the effective receiving circular area of the receiving loop L2 is

$$b_2 = r_2 - c_2 \quad (4d)$$

2.3. Impedance of a Circular Loop

The impedance of a loop can be defined at chosen terminals Q, D as $Z = V/I_1$ (Fig. 2). Using Maxwell's equation with Faraday's law $\text{curl}(\mathbf{E}) = -j\omega\Phi_m$, we can write the line integrals of the electric intensity \mathbf{E} along the loop conductor through its cross section, along the path joining points D, Q and the load impedance Z_L between the terminals Q, A :

$$\int_{(AEFD)} \mathbf{E}_s ds + \int_{(DQ)} \mathbf{E}_s ds + \int_{(QA)} \mathbf{E}_s ds = -j\omega\Phi_m \quad (5a)$$

Here Φ_m is the magnetic flux. The impressed emf (electromotive force) V acting along the path joining points D and Q is equal and opposite to the second term of Eq. (5a):

$$V = - \int_{(DQ)} \mathbf{E}_s ds \quad (5b)$$

The impedance of the loop at the terminals D, Q can be written from Eqs. (5) dividing with I_1 as

$$Z = \frac{V}{I_1} = \frac{\int_{(AEFD)} \mathbf{E}_s ds}{I_1} + \frac{\int_{(QA)} \mathbf{E}_s ds}{I_1} + \frac{j\omega\Phi_m}{I_1} = Z_i + Z_L + Z_e \quad (6)$$

where Z_i indicates the internal impedance of the loop conductor. Because of the skin effect, the internal impedance at high frequencies is not resistive. For the calculation of the Z_i , we refer to Schelkunoff, [3, p. 263] and Ramo et al. [4, p. 185]. Z_L is a known load or a source impedance on Fig. 2. Z_e is the external impedance of the loop:

$$Z_e = j\omega \frac{\Phi_m}{I_1} = j\omega \frac{\mu_0 H_{av} S}{I_1} \quad (7a)$$

We can consider that the loop consists of two coaxial and coplanar filamentary loops (i.e., separation distance $d = 0$). The radii a_1 and b_1 are defined in Eqs. (4). The average current I_{av} flows through the filamentary loop with the radius a_1 and generates an average magnetic field strength H_{av} on the effective circular surface $S_1 = \pi b_1^2$ of the filamentary loop with the radius b_1 . From Eqs. (1) and (3) we can rewrite Eq. (7a), for the loop L1:

$$Z_e = j \frac{\tan(\beta\pi a_1)}{\beta\pi a_1} \mu_0 \omega a_1 b_1 \int_0^\pi \frac{e^{-j\beta R_0(\varphi)}}{R_0(\varphi)} \cos(\varphi) d\varphi \quad (7b)$$

$$R_0(\varphi) = \sqrt{a_1^2 + b_1^2 - 2a_1 b_1 \cos(\varphi)} \quad (7c)$$

The real and imaginary parts of Z_e are the radiation resistance and the external inductance of loops,

respectively:

$$\operatorname{Re}(Z_e) = \left| \frac{\tan(\beta\pi a_1)}{\beta\pi a_1} \right| \mu_0 \omega a_1 b_1 \int_0^\pi \frac{\sin(\beta R_0(\varphi))}{R_0(\varphi)} \cos(\varphi) d\varphi \quad (7d)$$

$$\operatorname{Im}(Z_e) = \frac{\tan(\beta\pi a_1)}{\beta\pi a_1} \mu_0 \omega a_1 b_1 \int_0^\pi \frac{\cos(\beta R_0(\varphi))}{R_0(\varphi)} \cos(\varphi) d\varphi \quad (7e)$$

From Eq. (7e) we obtain the external self-inductance:

$$L_e = \frac{\tan(\beta\pi a_1)}{\beta\pi a_1} \mu_0 a_1 b_1 \int_0^\pi \frac{\cos(\beta R_0(\varphi))}{R_0(\varphi)} \cos(\varphi) d\varphi \quad (7f)$$

Equations (7) include the effect of current distribution on the loop with finite conductor radii.

2.4. Mutual Impedance between Two Circular Loops

The mutual impedance Z_{12} between two loops is defined as

$$Z_{12} = \frac{V_2}{I_1} = \frac{Z_2 I_2}{I_1} \quad (8)$$

The impedance of Z_2 in Eq. (8) can be defined as in Eqs. (6):

$$Z_2 = \frac{V_2}{I_2} = Z_{2i} + Z_L + Z_{2e} \quad (9)$$

here Z_{2i} is the internal impedance, Z_L is the load impedance, and Z_{2e} is the external impedance of the second loop L2.

The current ratio I_2 to I_1 in Eq. (8) can be calculated from Eqs. (1), (3), and (4). The current I_1 of the transmit loop with separation distance d

$$I_1 = \frac{H_{av} \pi b_2}{\frac{\tan(\beta\pi a_1)}{\beta\pi a_1} a_1 \int_0^\pi \frac{e^{-j\beta R_d(\varphi)}}{R_d(\varphi)} \cos(\varphi) d\varphi} \quad (10a)$$

$$R_d(\varphi) = \sqrt{d^2 + a_1^2 + b_2^2 - 2a_1 b_2 \cos(\varphi)} \quad (10b)$$

and the current I_2 of the receive loop for the same H_{av} (here $d = 0$) is

$$I_2 = \frac{H_{av} \pi b_2}{\frac{\tan(\beta\pi a_2)}{\beta\pi a_2} a_2 \int_0^\pi \frac{e^{-j\beta R_0(\varphi)}}{R_0(\varphi)} \cos(\varphi) d\varphi} \quad (10c)$$

$$R_0(\varphi) = \sqrt{a_2^2 + b_2^2 - 2a_2 b_2 \cos(\varphi)} \quad (10d)$$

The general mutual impedance between two loops from Eqs. (8) and (9) is

$$Z_{12} = (Z_{2i} + Z_L + Z_{2e}) \frac{I_2}{I_1} = Z_{12i} + Z_{12L} + Z_{12e} \quad (11a)$$

here Z_{12i} is the mutual internal impedance, Z_{12L} denotes the mutual load impedance, and Z_{12e} is the external mutual impedance.

Arranging Eq. (7b) for Z_{2e} and the current ratio I_2/I_1 from Eqs. (10), we obtain the external mutual impedance:

$$Z_{12e} = j \frac{\tan(\beta\pi a_1)}{\beta\pi a_1} \mu_0 \omega a_1 b_2 \int_0^\pi \frac{e^{-j\beta R_d(\varphi)}}{R_d(\varphi)} \cos(\varphi) d\varphi \quad (11b)$$

The real part of Z_{12e} may be described as mutual radiation resistance between two loops.

The imaginary part of Z_{12e} divided by ω gives the mutual inductance

$$M_{12e} = \frac{\tan(\beta\pi a_1)}{\beta\pi a_1} \mu_0 a_1 b_2 \int_0^\pi \frac{\cos(\beta R_d(\varphi))}{R_d(\varphi)} \cos(\varphi) d\varphi \quad (11c)$$

Equations (11b) and (11c) include the effect of current distribution on the loop with finite conductor radii.

3. DETERMINATION OF THE ANTENNA FACTOR

The antenna factor K_H is defined as a proportionality constant with necessary conversion of units. K_H is the ratio of the average magnetic field strength H_{av} bounded by the loop to the measured output voltage V_L on the input impedance R_i of the measuring receiver.

$$K_H = \frac{H_{av}}{V_L} \text{ in } (\text{A/m}) \cdot \text{V}^{-1} \quad (12a)$$

Equation (12a) can also be expressed logarithmically:

$$k_H = 20 \log(K_H) \text{ in } \text{dB}(\text{A/m}) \cdot \text{V}^{-1} \quad (12b)$$

For evaluation of the antenna factor there are two methods. The first is by calculation of the loop impedances, and the second is with the well-defined standard magnetic field calibration.

3.1. Determination of the Antenna Factor by Computing from the Loop Impedances

If a measurement loop, (e.g., L2), has a simple geometric shape and a simple connection to a voltage measuring device with a known input impedance R_i , we can determine the antenna factor by calculation. In the case of the unloaded loop from Fig. 2, the open-circuit voltage is

$$V_0 = j\omega \mu_0 H_{av} S_2 \quad (13a)$$

For the case of the loaded loop the current is

$$I = \frac{V_0}{Z} = \frac{V_0}{R_L + Z_i + Z_e} \quad (13b)$$

The antenna factor from Eq. (12a) can be written with $V_L = Z_i I$ and Eqs. (13) and (1) as

$$K_H = \left| \frac{1}{j\omega \mu_0 S_2} \left(1 + \frac{Z_e}{R_L} + \frac{Z_i}{R_L} \right) \right| \text{ in } (\text{A/m}) \cdot \text{V}^{-1} \quad (14)$$

The effective loop area is $S_2 = \pi b_2^2$. The external loop impedance Z_e can be calculated with Eqs. (7). The internal

impedance Z_i is in general small in respect to external impedance Z_e , and can be neglected. For a more precise calculation of the internal impedance Z_i due to the skin effect, refer to Refs. 3 and 4.

3.2. Standard Magnetic Field Method

In the calibration setup in Fig. 5 we measure the voltages with standard laboratory measuring instrumentation with the 50Ω interface impedances. The device to be calibrated consists at least of a loop and a cable with an output connector. The measuring loop can also include a passive or active network between the terminals C, D and a coaxial shield on the circular loop conductor against unwanted electric fields, depending on its development and construction. The impedance Z_{CD} and the voltage V_{CD} at the terminals C, D is not accurately measurable. The behavior of the attenuation and/or the gain between the interfaces D, C and F cannot be accurately defined. Such a complex measuring loop must be calibrated with the standard magnetic field method through the calibration setup in Fig. 5. To prevent the deterioration of the magnetic field, produced by L1, we must place the attenuators sufficiently far from the transmitting loop using a twisted-pair balanced line. The attenuators (e.g., nominal 10 dB) must have the calibrated attenuations m for attenuator 1 and n for attenuator 2, and the calibrated interface resistances (nominal 50Ω). The shielding of the attenuators must be electrically connected at the points x . The ferrite pads on the twisted-pair line and on the coaxial cable attenuate the magnetic field scattering from the measuring transmission lines. The electrical length Le of the twisted transmission line must be taken into account and the equation (3) must be redefined for the average current I_{av} :

$$I_{av} = I_1 \frac{\tan(\beta(\pi a_1 + Le))}{\beta(\pi a_1 + Le)} \quad (15)$$

The usable highest frequency of the loop L1 decreases with the additional electrical length of the twisted-pair line. This consideration is used to define an appropriate length of the twisted-pair transmission line.

The antenna factor in Eqs. (12) can be fully defined for each frequency through the measurement of the transmitting loop current I_1 at the interface M' and voltage V_L at the interface F :

$$K_H = \frac{\left| \frac{I_1 \tan(\beta(\pi a_1 + Le))}{\pi a_1 + Le} \frac{a_1}{\pi b_2} \int_0^\pi \frac{e^{-j\beta R_d(\varphi)}}{R_d(\varphi)} \cos(\varphi) d\varphi \right|}{V_L} \quad (16a)$$

Here $r_1 = a_1, r_2 = b_2, Le$ is the electrical length of the twisted-pair transmission line and R_d defined with Eq. (10b). Attenuator 1 attenuates the current I_1 with the ratio m and hence the current through the interface M' becomes $m \cdot I_1$. The transmitting loop current is $I_1 = V_2/m \cdot R_2$. Consequently, the current flowing through the interface N' is $I_1/(n \cdot m)$. With the measuring receiver we can measure first the voltage V_2 at the interface M' to obtain the transmitting loop current I_1 , which produces the magnetic field H_{av} in the receiving loop L2. We then measure the voltage V_L at the interface F , which is produced by the same magnetic field H_{av} . With setting $\alpha = V_2/V_L$, we can write Eq. (16a) as

$$K_H = \left| \frac{\alpha \tan(\beta(\pi a_1 + Le))}{m} \frac{a_1}{R_2(\beta\pi a_1 + Le)} \frac{a_1}{\pi b_2} \int_0^\pi \frac{e^{-j\beta R_d(\varphi)}}{R_d(\varphi)} \cos(\varphi) d\varphi \right| \quad (16b)$$

Equation (16b) is expressed in SI units $[(A/m)V^{-1}]$ and can also be expressed logarithmically as

$$k_H = 20 \log(K_H) \text{ in dB}[(A/m) \cdot V^{-1}] \quad (16c)$$

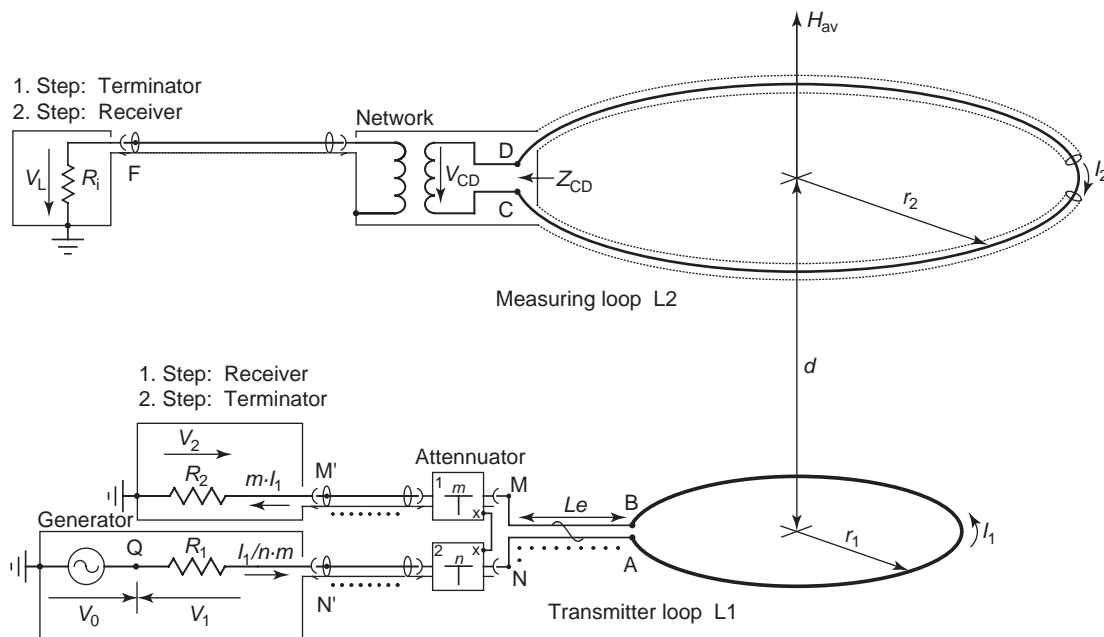


Figure 5. Calibration setup for circular loop antennas.

The ratio of the measured voltages is an attenuation and with an appropriate measuring setup the calibration is realized as an attenuation measurement. A network analyzer is generally used for this purpose instead of discrete measurements at each individual frequency with a signal generator and a measuring receiver. A network analyzer can normalize the frequency characteristic of the transmit loop current I_1 and gives a quick overview of the measured attenuation for the frequency band under consideration.

Equation (16b) reduces the calibration process of the loop to an accurate measurement of attenuation α for each frequency. The other terms of Eq. (16a) can be calculated depending on the geometric configuration of the calibration setup at the working frequency band of the measuring loop. The calibration uncertainties are also calculable with the given expressions. The uncertainty of the separation distance d between two loops must be taken into consideration as well. At a separation distance $d < a_1$, the change in the magnetic field is high (see Fig. 2 in Ref. 2).

For a calibration setup the separation distance d can be defined as small as possible. However, the effect of the mutual impedance must be taken into account in the calibration process, and a condition for definition of the separation distance d must be given (Fig. 5). If the second loop is open-circuited, that is, if the current $I_2 = 0$, the current I_1 is defined only from the impedances of the transmitting loop L1. In the case of a short-circuited second loop L2, I_2 is maximum and the value of I_1 will change depending on the supply circuit and loading of the transmitting loop. A current ratio q between these two cases can be defined as the condition of the separation distance d between the two loops.

It is assumed that the generator voltage V_0 is constant. The measuring loop L2 is terminated by Z_L . For $Z_L = 0$ and $V_{CD} = 0$, one obtains the current I_1 in the transmitting loop as

$$I_{1(Z_L=0)} = \frac{V_0}{R_1 + R_2 + Z_{AB} - \frac{Z_{12}^2}{Z_{CD}}} \quad (17a)$$

and for $Z_L = \infty$, that is, $I_2 = 0$

$$I_{1(Z_L=\infty)} = \frac{V_0}{R_1 + R_2 + Z_{AB}} \quad (17b)$$

The ratio of Eq. (17a) to Eq. (17b) is

$$q \equiv \left| \frac{I_{1(Z_L=0)}}{I_{1(Z_L=\infty)}} \right| = \left| \frac{R_1 + R_2 + Z_{AB}}{R_1 + R_2 + Z_{AB} \left(1 - \frac{Z_{12}^2}{Z_{AB}Z_{CD}} \right)} \right| \quad (18a)$$

here with the coupling factor $k = Z_{12}/\sqrt{Z_{AB}Z_{CD}}$ between two loops:

$$q = \left| \frac{R_1 + R_2 + Z_{AB}}{R_1 + R_2 + Z_{AB}(1 - k^2)} \right| \quad (18b)$$

where $R_1 = R_2 = 50 \Omega$ and Z_{AB} , Z_{CD} , and Z_{12} can be calculated from Eqs. (7) and (11). For greater accuracy one must try to keep the ratio q close to unity (e.g., $q = 1.001$).

The influence of the loading of the second loop on the transmitting loop can also be found experimentally. The change of voltage V_2 at R_2 in Fig. 5 must be considerably small (e.g., < 0.05 dB) when the measuring loop is short-circuited at the chosen separation distance d .

4. CONCLUSION

All equations in this article are written in their original exact form without approximations, which usually restrict their range of validity in applications regarding frequency range, distance, and other quantities. Also, no simplifications of the equations are made. All equations deliver the results directly in units of SI with an appropriate mathematical software on a personal computer. The electrical properties of the loops are calculable without approximation. The necessary conditions are given for the choice of dimensions of the measuring and transmitting circular loops and the separation distance d .

For calibration of circular loop antennas, the standard magnetic field method is recommended with the calibration setup in Fig. 5 and also for determination of the antenna factor K_H and k_H in Eqs. (16b) and (16c). The calibration process is based on the measurement of attenuation at each frequency on the same impedance level of 50Ω , using the standard laboratory equipment. The measurement can also be accelerated by using a network analyzer.

BIBLIOGRAPHY

1. F. M. Greene, The near-zone magnetic field of a small circular-loop antenna, *J. Res. Natl. Bur. Stand. Eng. Instrum.* **71C**(4): 319–326 (Oct.–Dec., 1967).
2. A. Aykan, Calibration of circular loop antennas, *IEEE Trans. Instrum. Meas.* **47**(2): 446–452 (April 1998).
3. S. A. Schelkunoff, *Electromagnetic Waves*, Van Nostrand, New York, 1943.
4. S. Ramo, J. R. Whinnery, and T. van Duser, *Fields and Waves in Communication Electronics*, 3rd ed., Wiley, New York, 1994.

CAPACITANCE EXTRACTION

WENJIAN YU
ZEYI WANG
Tsinghua University
Beijing, China

1. INTRODUCTION

Since the early 1950s, microwave circuits have evolved from discrete circuits to planar integrated circuits, then to multilayered and three-dimensional integrated circuits. With the increased circuit density, the multiconductor line in multilayered dielectric media has become the major form of the transmission line or interconnect. Multilayered routing reduces the area as well as the volume of the

circuit. However, as a result, electromagnetic coupling among conductors greatly influences circuit performance. In some microwave integrated circuits, this coupling effect is utilized to construct compact circuit components. But under most circumstances, it is regarded as a parasitic effect that must be modeled accurately for verification of the circuit's validity and performance.

In the related field of very-large-scale integration (VLSI) circuits, electromagnetic coupling among interconnects is also becoming increasingly important. With the introduction of deep-sub-micrometer (DSM) semiconductor technologies, the on-chip interconnect wire can no longer be considered equipotential jointing. The parasitic effects introduced by the wires display a scaling behavior that differs from that of active devices such as transistors, and these effects tend to gain importance as device dimensions are reduced and circuit speed is increased. In fact, they begin to dominate some of the relevant metrics of digital integrated circuits such as speed, energy consumption, and reliability. A typical recursive design flowchart of a state-of-the-art integrated circuit (IC) is shown in Fig. 1, where a postlayout step termed *parasitic extraction* precedes *gate-level simulation*. The task of parasitic extraction is to model the electromagnetic effects of the wire with parasitic components of capacitance, resistance, and inductance, so that a more accurate circuit simulation can be performed.

With the increase in working frequency and development of silicon technologies, the discrepancy between the microwave IC and the common VLSI circuit becomes marginal. Therefore, the electromagnetic modeling and accurate extraction of the interconnect parasitics have become a subject of advanced research in both fields to date. Among the three parasitic parameters, capacitance has attracted the most attention because it greatly influences time delay, power consumption, and the signal integrity and its calculation becomes complicated under DSM technologies.

In the following sections, the fundamental theory and contemporary methodology and algorithms of capacitance extraction will be discussed.

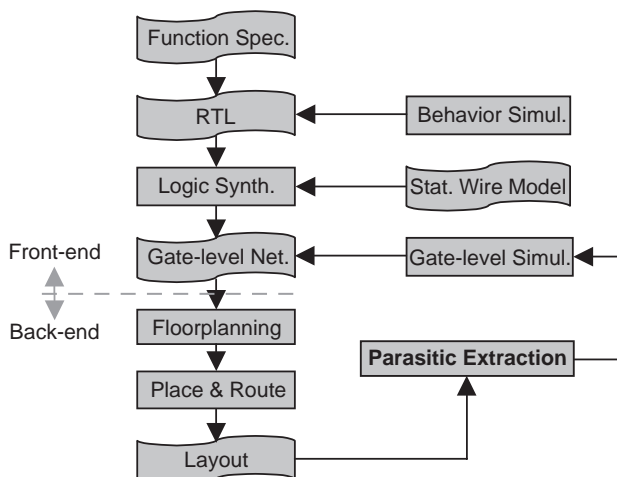


Figure 1. A typical flowchart of IC design.

2. PROBLEM FORMULATION

As is well known, the capacitor is a commonly used component in electric or electronic equipment. It is usually composed of two conductors insulated from each other. When charged, the two surfaces of the conductor facing each other carry equal and opposite charges Q and $-Q$, respectively (see Fig. 2). The electric potential difference between the two conductors $\phi_1 - \phi_2$ is called the *voltage* of the capacitor and is always denoted by V . Experiments and theoretical analyses show that, for a capacitor, Q is always proportional to V and thus the ratio Q/V is a constant determined by the structure of the capacitor. This ratio is called the *capacitance* of the capacitor and is denoted by C : $C = (Q/V)$.

In the International System of Units (SI), the unit of capacitance is the faraday (F). It expresses the capacitance of a capacitor that has one coulomb on one of its poles when the potential difference is 1 V. Other commonly used units of capacitance are μF (10^{-6} F), pF (10^{-12} F), and fF (10^{-15} F).

The capacitance of some simple capacitor can be calculated easily. For example, for the parallel-plate capacitor shown in Fig. 2, we have

$$C = \frac{\epsilon_0 \epsilon_r S}{d} \quad (1)$$

where ϵ_0 is the dielectric constant of free space and in SI, is expressed as

$$\epsilon_0 = \frac{1}{4\pi \times 9 \times 10^9} = 8.85 \times 10^{-12} \text{ C}^2/\text{N} \cdot \text{m}^2$$

where ϵ_r is the relative permittivity of the insulating material, S is the area of the plate, and d is the distance between two parallel plates.

Specific capacitors widely used in the design of microwave circuits include the interdigital capacitor and the metal-insulator-metal (MIM) capacitor. Figure 3 shows the physical layout of an interdigital capacitor with nine fingers, and Fig. 4 shows the cross-sectional view of an MIM capacitor with the GaAs process. The interdigital capacitor works with the electrostatic coupling between the intercrossed fingers, and has a very high Q value. So, it is widely used in the high-frequency microwave circuits.

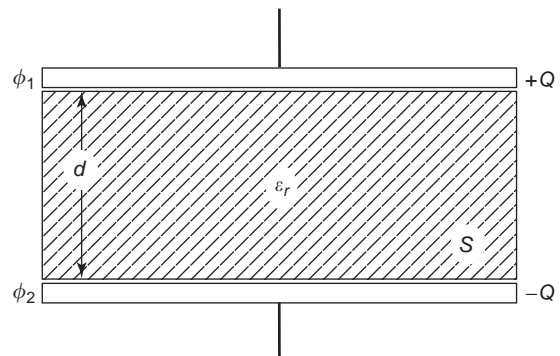


Figure 2. A parallel-plate capacitor.

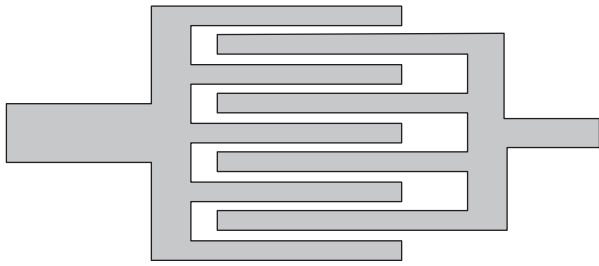


Figure 3. An interdigital capacitor.

The MIM capacitor has simple geometry and is easily fabricated, and its capacitance is controlled by the dimensions of the polar planes. Since the interdigital capacitor and the MIM capacitor are widely used, calculation of the parameters of their structures within given the working frequency and corresponding capacitor value becomes an important issue for both design and optimization. This can be regarded as the reverse procedure of capacitance extraction. For further discussion of this issue, please refer to the literature [39,40].

Actually, the capacitor has more generalized forms than that described above, which consists of two insulated conductors. The *capacitance* of a single conductor (conductor 1) is defined as if another conductor (conductor 2) were located at an infinite distance away to form a joint capacitor (conductors 1 + 2). For example, the capacitance of an isolated conductor sphere with radius of R can be calculated as $C = 4\pi\epsilon_0 R$.

Many conductor interconnect wires are involved in the microwave IC and the common VLSI circuit, and they are insulated by some dielectric such as oxide SiO_2 . The capacitance between any two wires reflects the electrostatic coupling effect between these wires, and calculating these capacitances with high accuracy is very important for analysis of the circuit's performance.

For an N -conductor system, such as the interconnect wires in an IC, an $N \times N$ capacitance matrix $[C_{ij}]_{N \times N}$ is defined by

$$Q_i = \sum_{j=1}^N C_{ij} U_j, \quad i = 1, 2, \dots, N, \quad (2)$$

where C_{ij} ($i \neq j$) is the coupling capacitance between conductors i and j , and C_{ii} is the self-capacitance or total capacitance of conductor i . Q_i is the induced charge on

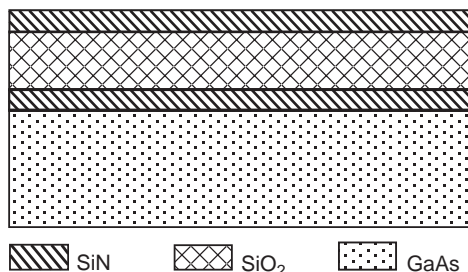


Figure 4. An MIM capacitor (cross-sectional view).

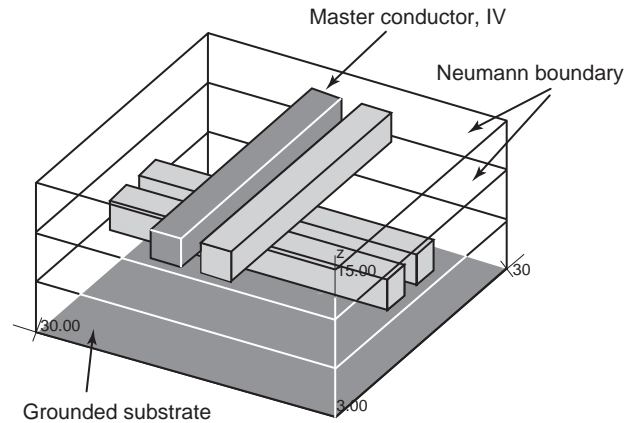


Figure 5. A structure involving 2×2 crossover interconnect wires.

conductor i , and U_j is the electric potential of conductor j (usually the known bias voltage).

Figure 5 shows a typical crossover wires in the VLSI system, where the coupling capacitances between any two conductors need to be calculated.

Accurate modeling of the wire capacitances in a state-of-the-art integrated circuit is not a trivial task. It is further complicated by the fact that the interconnect structure of contemporary integrated circuits is three-dimensional (see Fig. 5). The capacitance of such a wire is a function of its shape, environment, distance from the substrate, and distance to surrounding wires. Generally SiO_2 is the insulating material among interconnect wires in integrated circuits, although some materials with lower permittivity, and thus lower capacitance, are coming into use. The relative permittivity ϵ_r of several dielectrics commonly used in integrated circuits is presented in Table 1. It should also be pointed out that ϵ_r of air or vacuum is 1.

3. METHODOLOGY AND ALGORITHMS

With the advances in IC technology, the methodology of capacitance extraction has evolved from one-dimensional (1D), two-dimensional (2D), 2.5-dimensional (2.5D), to three-dimensional (3D) to meet the required accuracy. In this section, the 1D and 2D methods are briefly introduced. Then, the 2.5-D method and the mechanism of the modern commercial capacitance extraction tools that employ the 3D capacitance extractor are presented. Finally, we will discuss some details of algorithms of the 3D field solver for capacitance extraction.

3.1. 1D and 2D Methods

From the formula for calculation of parallel-plate capacitance [Eq. (1)], we can infer that the capacitance is proportional to the overlapping area between the conductors and inversely proportional to their separation distance. This is very important for capacitance extraction without a high degree of precision.

Table 1. Relative Permittivity of Several Commonly used Dielectric Materials

Dielectric Material	Silicon	Alumina (Package)	Silicon Nitride (Si ₃ N ₄)	Glassepoxy (PCB)	Silicon Dioxide	Polyimides (Organic)	Aerogels
Relative permittivity (ϵ_r)	11.7	9.5	7.5	5	3.9	3–4	~1.5

Figure 6 shows a typical microstrip structure, where there is only a single rectangular conductor over a ground plane. This structure is very different from the above parallel-plate model discussed because of the existence of the capacitance between the sidewalls of the wire and the substrate, called the *fringing capacitance*. To avoid the time-consuming numerical modeling of this geometry, an approximate 1D method can be used as a good engineering practice. The capacitance is assumed to be the sum of two components: (1) a parallel-plate capacitance determined by the vertical field between a wire of width w and the ground plane and (2) the fringing capacitance modeled by a cylindrical wire with radius equal to the conductor thickness H . So, this simple and practical 1D formula becomes

$$C = C_{\text{area}} + C_{\text{fringe}} = \frac{\epsilon \cdot w}{d} + \frac{2\pi\epsilon}{\log(d/H)}$$

where $w = W - H/2$ is a good approximation for the width of the parallel-plate capacitor (W is the width of the wire), d is the distance between the ground plane and the bottom of wire, and ϵ is the permittivity of the insulating material. With this formula, we obtain the approximate capacitance per unit length.

In another kind of 1D capacitance extraction, the area and perimeter parameters of interconnect geometries are first obtained. Then, a fine-tuned set of area and perimeter weights per routing layer can be used to calculate capacitance values as an inner product [1]:

$$C = (\text{area amount, perimeter amount}) \\ \cdot (\text{area weight, perimeter weight})$$

Such area and perimeter weights can be obtained by pre-characterization of an “average” environment of a wire. The area can be that from single layer or a combination of layer overlaps.

Usually, the 1D extraction method works well when the number of interconnect layers is restricted to only one or two. However, the current process technology often involves many more interconnect layers, and they are also of high density. So, several capacitance components of a wire embedded in the multilayered interconnect system may

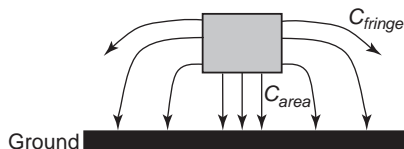


Figure 6. A conductor above a ground plane (cross-sectional view).

exist, other than the only capacitive coupling to the ground plane (see Fig. 7). Each wire is coupled not only to the grounded substrate but also to the neighboring wires on the same layer and on adjacent layers. Not all capacitive components terminate at the grounded substrate; actually a large number of them connect to other wires. These (fringing, lateral, parallel, etc.) capacitors between wires not only form a source of noise (crosstalk among signal lines) but also can have a negative impact on the circuit performance.

To model the capacitance in the multilayered interconnect system with higher accuracy, 2D capacitance extraction methodology was developed. In 2D capacitance extraction, accurate geometry modeling and numerical techniques are implemented for the cross section of simulated structure (as in Fig. 7). For the 2D region of dielectrics, the electric field equation is solved with numerical techniques. 2D extraction ignores all three dimensional details and assumes that the geometries being modeled are uniform in one dimension, usually the signal propagation direction. Therefore, 2D capacitance extraction is only suitable only for some special cases, such as like the transmission line.

The details of numerical techniques for solving the electric field will be introduced in Section 3.3, albeit in a 3D manner.

3.2. 2.5D Method and Commercial Capacitance Extraction Tool

The 2.5D (also called *quasi-3D*) method goes a step further than 2D extraction. Its main idea is to calculate the capacitance of several cross sections (using the 2D method) and combine the 2-D results into the final capacitance value.

A typical 2.5D capacitance extraction method is also called the “(2 × 2)D method”, in which any 3D structure is swept in two perpendicular directions and by considering the geometry overlapping, 3D structure can be modeled more accurately (see Fig. 8).

In Fig. 8, an m_2 wire crosses an m_1 wire. Along direction A, a 2D cross-sectional view is shown in the middle. Along direction B, the other 2D cross section is shown to

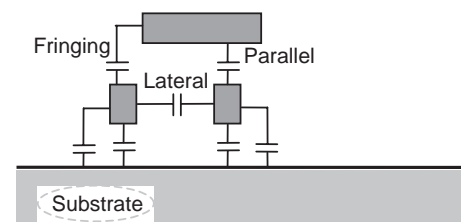


Figure 7. Capacitive coupling between wires in a multilayered interconnect system.

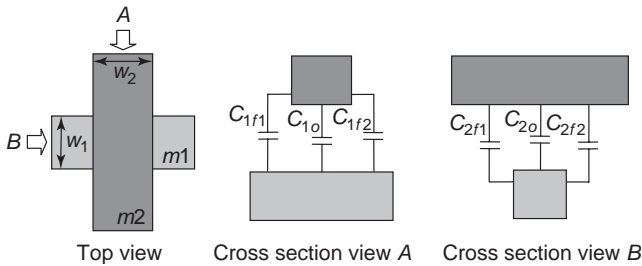


Figure 8. 2.5D capacitance for a crossover structure.

the right. Solving the two orthogonal strictly 2D problems numerically, we obtain $C_A = C_{1f1} + C_{1o} + C_{1f2}$, $C_B = C_{2f1} + C_{2o} + C_{2f2}$ (see Fig. 8). Then, $C_{m1,m2} = C_A \times w_1 + (C_B - C_{2o}) \times w_2$, where w_1, w_2 are the widths of wires m_1 and m_2 , respectively. However, this method is still not very accurate. The error could be more than 10%, especially for coupling capacitance, which is very important for signal integrity analysis.

Obviously, true 3D extraction is a straightforward method to achieve high precision. However, the 3D electrostatic Laplace equation must be solved numerically within a complicated 3D structure. This consumes extensive computational effort. 3D capacitance extraction (usually called the “field solver”) is actually not a trivial extension of the 2D case. This aspect is discussed further in Section 3.3.

For the current task of capacitance extraction in modern IC design, using the 3D extraction method directly is impossible because of its huge expense of memory and CPU time. To obtain a good tradeoff between accuracy and efficiency, modern capacitance extraction tools utilize special techniques for the full-chip extraction task, which is usually divided into three major steps [1]:

1. *Technology Precharacterization.* Given a description of the process cross sections, tens of thousands of test structures are enumerated and simulated with 2D and/or 3D field solvers. These structures are of medium dimensions. The resulting data are collected either to fit some empirical formulas or to build lookup tables (either type is called a “pattern library”). In Ref. 3, analytical equations are used for model fitting. A good fit would require fewer simulation points. The number of patterns can be reduced by pattern reduction techniques. Arora et al. [4] present a pattern compression technique that reduces the total number of precharacterization patterns. With this technology, the capacitance in some layout pattern can be extrapolated from the capacitance values in two simpler precharacterization patterns, without losing much accuracy. Capacitance field solvers employ different numerical algorithms, and they may give different answers for certain special layout structures depending on the problem setup and boundary conditions. Therefore, the precharacterization software should have the flexibility to incorporate any third-party field solvers. This first step should be performed only

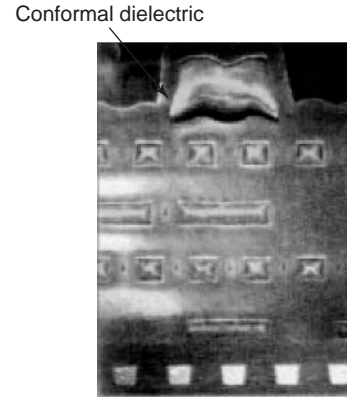


Figure 9. A realistic vertical cross section of IC interconnect. We see that conductors on layers 1–5 are trapezoidal, and there is a conformal dielectric on top of the top layer metal (passivation). (SEM photograph courtesy of IBM Corp. © Copyright IBM Corp. 1994, 1996.)

once per process technology. The challenge in this area includes the handling of increasingly complex processing technology, such as low- k dielectric, air-bubble dielectric, nonvertical conductor cross sections, conformal dielectric (see Fig. 9), and shallow trench isolations.

2. *Geometric Parameter Extraction.* This is also an integral part of precharacterization. If a geometric pattern requires 10 parameters to describe, there is a corresponding precharacterization of 1×5^{10} ($\sim 10,000,000$) patterns to simulate. This is assuming that five sample points are taken in each of the 10 parameters, resulting in a 10-dimensional (10D) table of the dimensions given above. This is clearly not feasible. On the other hand, if a geometric pattern can be described by very few parameters, then it is difficult for it to be accurate. In a full-chip situation, the runtime of geometric parameter extraction can be very time/space-consuming, with millions of interconnect polygons to analyze. Time/space-efficient geometric processing algorithms are very important. Habitz and Wemple [5] present a geometric parameter reduction technique in which geometric parameters can be dramatically reduced by taking advantage of the shielding effect. Conductors two layers away from the main conductor of interest do not require a precise description. This is particularly useful for the very-deep-sub-micrometer geometry, where a very distant conductor mesh behaves like a large airplane.
3. *Calculation of Capacitance from Geometric Parameters.* Here, the geometric parameters are matched to some entries in the pattern library. Usually a full-chip or full-path extraction task involves at least thousands of conductors. The whole structure is chopped into medium-size pieces first, which are then calculated with the pattern-matching approach described above. Finally, the capacitance values must be combined to get the desired result.

One major source of error is called the *pattern mismatch*, where extracted geometry parameters do not have an exact match in the pattern library. At this time, there are two remedies to perform the capacitance calculations. One method is to enhance the pattern library by running field solvers at the full-chip extraction time. The other method is to employ heuristics to synthesize a solution from closely matched precharacterization patterns. Even if all the geometric patterns match the library completely, there could still be discontinuities in the layout pattern decomposition, which is another source of error. This error is analyzed in Ref. 6, where the error bound was obtained by utilizing the “empty” and “full” boundary conditions.

3.3. Algorithms for 3D Field Solver

The 3D method can be used model the actual geometry accurately, so it behaves with the highest precision. 3D capacitance extraction becomes increasingly important under the DSM technology of VLSI circuit, although presently it is used widely only as a library-building tool in the industry. More recently, much research work has been devoted to improve the efficiency of the 3D extraction method. Related papers are published on the annually held conferences (*Design Automation Conf.*, *Int. Conf. Computer-Aided Design*, etc.) and many academic journals (*IEEE Trans. Microwave Theory Tech.*, *IEEE Trans. Comput. Aided Design*, etc.). To date, some 3D extraction algorithms have been developed to integrate with the commercial software of some electronic design automation (EDA) companies in the Silicon Valley (in California). Research on 3D capacitance extraction is still advancing very rapidly.

In this section, the principles and mainstream techniques of the 3D field solver are introduced. More cutting-edge techniques are mentioned with related references.

3.3.1. Overview. For a system involving multiple conductors (see Fig. 5), with one conductor setting 1V and others 0V, the electrostatic equation (called the *Laplace equation*) need to be solved with a homogenous dielectric region [7]:

$$\nabla^2 u = \frac{\partial^2 u}{\partial x^2} + \frac{\partial^2 u}{\partial y^2} + \frac{\partial^2 u}{\partial z^2} = 0 \quad (3)$$

where u is the electric potential. This equation can be transformed into different mathematical formulations. Then, various numerical methods are employed to solve it with different levels of efficiency.

According to the domain of the above Laplace equation (3), there are two models for capacitance extraction: (1) *the infinite-domain model*, in which the electrostatic field spreads to the infinite, resulting in an infinite problem space; and (2) *the finite-domain model*, where the electrostatic field is restricted within a finite domain, with the Neumann condition on the outer boundary [8]: $(\partial u / \partial n) = 0$. This means that electric field is not able to spread out of the finite problem domain. The Neumann condition is also called the *reflective boundary condition*, and is introduced as the “magnetic wall” in Ref. 9. It

should be pointed out that the infinite-domain model is ideal for simulating isolated structures, but for the on-chip application it is not accurate because of the influence of neighboring conductors. On the other hand, the finite-domain model considers a part cut from actual layout of VLSI circuit; it is suitable for the realistic capacitance extraction of VLSI interconnects [8]. Now, both models of capacitance extraction are used in different applications, and accordingly the numerical methods are also different. The problems a numerical algorithm usually encountered in modeling are discussed below.

Classifications of the 3D field solver methods include the domain discretization method, the boundary integral equation method, semianalytical approaches, and the stochastic method. The domain discretization method includes the finite-difference method (FDM) [10], finite-element method (FEM) [11], and the method of the measured equation of invariance (MEI) [13,14]. The boundary integral equation method includes the method of moment [15], indirect boundary element method (BEM) [8,17–27], and direct boundary element method [28–34]. The semianalytical approaches combine the analytical formulas and some traditional numerical methods [9,35–37]. The stochastic method is based on statistical theory [38].

FDM and FEM discretize the entire 3D domain, thus producing a linear algebra system with large order; hence the computational speed of these methods is greatly limited. However, since both methods are relatively well established, they are still used in the industry as a reference tool with accurate values calculated under fine grids. For example, the famous software of 2/3D capacitance extraction “Raphael” utilizes FDM, and the “SpiceLink” of Ansoft Corp. is based on FEM.

Since the mid-1990s, the boundary integral equation method has begun to replace the domain discretization method because of its high performance. In both indirect and direct BEM, only the boundary of 3D domain is discretized, and a smaller system of linear equations is obtained. Problems encountered with the complex boundary can be effectively handled with BEM, whose accuracy is superior to that of FEM as well. Thus, the BEM with rapid computing techniques has become the focus of research on the 3D field solver.

3.3.2. Indirect Boundary-Element Method. The indirect boundary method can be regarded as a variation of the method of moments (MoM). Because only the domain boundary needs to be discretized, the indirect BEM involves much fewer unknowns than does FDM or FEM. However, it leads to a dense coefficient matrix, whose formation and solution introduce many difficulties. The innovation of the multipole acceleration method, the singular-value decomposition (SVD) method, and the hierarchical method has made the indirect BEM more applicable. Now, indirect BEM combined with a fast computational technique has become a main choice for the 3D field solver.

The indirect BEM method is also called the *equivalent charge method*, whose boundary integral equation involves the surface charge density $\sigma(x')$ as an unknown

function

$$u(\mathbf{x}) = \int_{\Gamma} G(\mathbf{x}, \mathbf{x}') \sigma(\mathbf{x}') d\mathbf{a}' \quad (\mathbf{x} \in \Gamma) \quad (4)$$

where $G(\mathbf{x}, \mathbf{x}')$ is Green's function. For free space, $G(\mathbf{x}, \mathbf{x}') = 1/|\mathbf{x} - \mathbf{x}'|$; Γ is the boundary surface. After solving the surface charge density $\sigma(\mathbf{x}')$, the charge on conductor i can be calculated with

$$Q_i = \int_{S_d(i)} \sigma(\mathbf{x}') d\mathbf{a}' \quad (5)$$

where $S_d(i)$ is the surface of conductor i . We discretize the surfaces of m conductors into n constant elements (or panels); then the potential at the center of the k th panel \mathbf{x}_k can be expressed as a sum of the contributions of all the panels

$$u_k = \sum_{j=1}^n \int_{\Gamma_j} \frac{\sigma_j(\mathbf{x}')}{\|\mathbf{x}' - \mathbf{x}_k\|} d\mathbf{a}'$$

where $\sigma_j(\mathbf{x}')$ is the surface charge density of panel j (Γ_j). Substituting the known boundary conditions, we obtain a dense linear algebra equation.

$$\mathbf{P}q = b \quad (6)$$

where the coefficient matrix \mathbf{P} is dense and nonsymmetric. The Krylov subspace iterative method, such as the generalized minimal residual algorithm (GMRES) [2], is usually used to solve this equation.

For a problem involving multiple dielectrics, the polarization charge density on the dielectric interface needs to be introduced, which contributes to the potential distribution together with the free charge density on conductor surfaces. Therefore, the problem becomes equivalent to that in the free space and the simple free-space Green function is used to form Eq. (4). Except for Eq. (4) on each conductor panel, the normal derivative of the potential satisfies

$$\varepsilon_a \frac{\partial u_+(x)}{\partial \mathbf{n}_a} = \varepsilon_b \frac{\partial u_-(x)}{\partial \mathbf{n}_a} \quad (7)$$

with $\mathbf{x} \in$ interface of ε_a and ε_b at any point \mathbf{x} on a dielectric interface. Here \mathbf{n}_a is the normal to the dielectric interface at \mathbf{x} that points into dielectric a and ε_a and ε_b are the permittivities of the corresponding homogenous dielectric region; $u_+(x)$ is the potential at x approached from the side of the interface ε_a , and $u_-(x)$ is the analogous potential for the b side.

For the multielectric problem, the so-called total-charge Green function approach presented above involves more unknowns at the interfaces. Another choice to deal with the problem is to employ the multilayered Green function. Then, only the free charge density on the conductor surfaces needs to be considered as an unknown function. However, to evaluate the Green function for the multilayered medium, infinite summations are involved,

which is very time-consuming. Oh et al. [20] derived a closed-form expression of Green's function for the multilayered medium by approximating the Green function using a finite number of images in the spectral domain. This greatly reduces the computational task. Li et al. [22] presented for the first time the general analytical formulas for the static Green functions for shielded and open arbitrarily multilayered media. Zhao et al. [21] an efficient scheme for the generation of multilayered Green functions using a generalized image method presented. The multilayered Green function is much more complicated than the free-space Green function; it is applicable only to the simple stratified structure of multiple dielectrics, while for more complex structures, such as the conformal dielectric, the deduction of Green's function may be impossible.

More research work has been undertaken to accelerate the capacitance extraction using the total-charge Green's function approach. In 1991, Nabors et al. applied the multipole accelerated (MPA) method successfully, proposed earlier by Greengard and Rokhlin [16], to 3D capacitance extraction with the indirect BEM. In the MPA method, calculation of the interaction between charges [i.e., the coefficients in (6)] is divided into two parts: the near-field computation and the far-field computation. For the near-field computation, the coefficients are calculated directly; for the far-field computation, the multipole expansion and local expansion are used to expedite the computation. Therefore, the CPU time of forming and solving (6) with the iterative equation solver is greatly reduced. Figure 10 illustrates of the multipole expansion. Nabors and White [18], developed the adaptive, preconditioned MPA method. The corresponding software prototype FastCap is shared on the MIT Website, and has become a popular tool of capacitance extraction for relevant researchers. To date, the capacitance extraction using the MPA indirect BEM is still undergoing research [25].

In 1998, a fast hierarchical algorithm for 3D capacitance extraction was proposed at the *Design Automation Conference*, and was reprinted in a journal article [24]. Similar to the multipole algorithm, it is also based on fast computation of the "N-body" problem. For the singular integral kernel of $1/|\mathbf{x} - \mathbf{x}'|$, it can achieve high acceleration of computation, and only $O(N)$ operations are needed

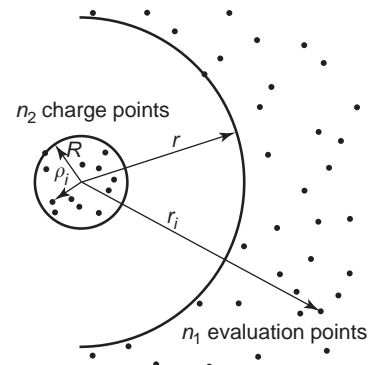


Figure 10. Evaluation point potentials are approximated with a multipole expansion [17].

for each iteration. For other weaker-singular kernels, the efficiency of this method may be reduced. In 1997, Kapur et al. and Long [19] proposed an accelerated method based on the singular-value decomposition (SVD) method that is independent of the kernel and based on the Galerkin method using the pulse function as the basis function. It requires an $O(N)$ times operation to construct the coefficient matrix and $O(N \log N)$ operations to perform an iteration. The precorrected fast Fourier transform (FFT) algorithm [23] has the same computational complexity, while it is based on the collocation method for discretization.

These studies on capacitance extraction with indirect BEM all handle the infinite-domain model. In 1996, Wang et al. [8] improved the multipole accelerated indirect BEM, enabling it to handle the finite-domain problem and also proposed a parallel multipole accelerated 3D capacitance simulation method based on nonuniformed cube partition.

Other fast computational methods for indirect BEM include those based on wavelets [26] and the multiscale method [27].

3.3.3. Direct Boundary-Element Method. The direct BEM is based on the direct boundary integral equation (BIE), and is suitable for solving the 3D Laplace equation with varied boundary conditions [12]. However, the direct BEM method is generally used to deal with the finite-domain model of capacitance extraction.

Within the finite domain that is involved in capacitance extraction (see Fig. 11), the electric potential u satisfies the following Laplace equation with mixed boundary conditions [32]

$$\begin{cases} \epsilon_i \nabla^2 u = 0, & \text{in } \Omega_i (i = 1, \dots, M) \\ u = u_0, & \text{on } \Gamma_u \\ q = \partial u / \partial \mathbf{n} = q_0 = 0, & \text{on } \Gamma_q \end{cases} \quad (8)$$

where the whole domain $\Omega = \bigcup \Omega_i$, where Ω_i stands for the space possessed by the i th dielectric. Γ_u represents the Dirichlet boundary (conductor surfaces), where u is known as the bias voltages; Γ_q represents the Neumann boundary (outer boundary of the simulated region), where the electric flux q is supposed to be zero. Here \mathbf{n} denotes the unit vector outward normal to the boundary. At the dielectric interface, the compatibility equation (7) holds.

With the fundamental solution as the weighting function, the Laplace equations in (8) are transformed into the

following direct BIEs by the Green identity [12]

$$c_s u_s^i + \int_{\partial \Omega_i} q^* u^i d\Gamma = \int_{\partial \Omega_i} u^* q^i d\Gamma \quad (i = 1, \dots, M)$$

where u_s^i is the electric potential at collocation point s (in dielectric region i) and c_s is a constant dependent on the boundary geometry near to the point s . $u^* = 1/4\pi r$ is the fundamental solution of the 3D Laplace equation, whose derivative along the outward normal direction \mathbf{n} is $q^* = \partial u^* / \partial \mathbf{n} = -(\mathbf{r}, \mathbf{n})/4\pi r^3$, r is the distance from the collocation point to the point on Γ , and $\partial \Omega_i$ is the boundary that surrounds dielectric region i .

Employing the collocation method after discretizing the boundary, such as that in the indirect BEM, we obtain system of linear equations [32]:

$$\mathbf{A}\mathbf{x} = \mathbf{f} \quad (9)$$

Finally, with the preconditioned Krylov iterative equation solver, such as the GMRES algorithm [2], the normal electric field intensity on the conductor surface is obtained [32].

In direct BEM, variables of both potential and field intensity are involved; thus two kinds of integral kernels are found. Although this is more complex than the indirect BEM method, direct BEM has its own advantages: (1) it is suitable for capacitance extraction within the finite domain since two variables are included, and (2) because the variables in each BIE are within the same dielectric region, it has a “localization” characteristic, which leads to a sparse linear system for problem with multiple dielectrics.

In direct BEM, a great deal of time and memory are consumed in forming and solving the system of discretized BEM equations. Wang et al. continued the research work of Fukuda [28] on 2D capacitance extraction using direct BEM, extending it to the 3D structure of VLSI interconnects [32]. An efficient analytical/semianalytical integration scheme was used to accurately calculate the boundary integrals under the VLSI planar process. This method achieves high computational speed and accuracy when forming Eq. (9) [32]. In 1996, Bachtold et al. [29] extended the multipole method to handle the “potential boundary integral” (whose kernel is $1/r^3$) in the direct BEM. They discussed the model of multiple dielectrics within the infinite domain. In 1999, Gu et al. extended the fast hierarchical method used in the indirect BEM and made it feasible to apply it for direct-BEM-based capacitance extraction [30].

In 2000, Yu et al. proposed a quasi-multiple medium (QMM) method, based on the localization characteristic of direct BEM [32]. The QMM method exploits the sparsity of the resulting coefficient matrix when handling the multi-dielectric problem. Together with the efficient equation organization and iterative solving technology, the QMM accelerated method has greatly reduced the computing time and memory usage. Figure 12 shows that a typical 3D interconnect capacitor with five dielectric layers is cut into $5 \times 3 \times 2$ fictitious medium regions. The QMM method has been successfully applied to actual 3D multidielectric

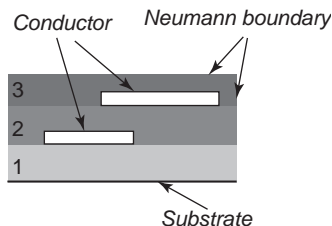


Figure 11. A structure with three dielectrics (cross-sectional view).

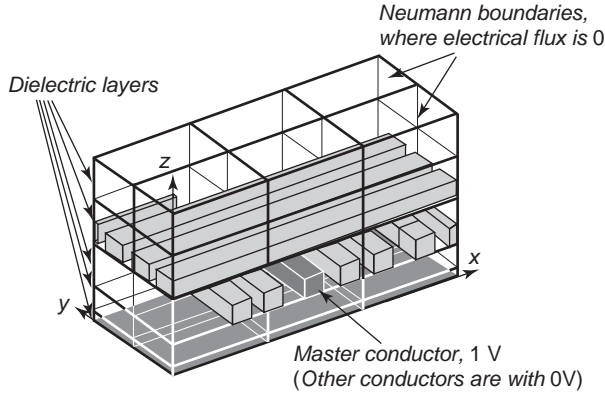


Figure 12. A typical 3D interconnect capacitor with five dielectric layers is cut into 3×2 structure.

capacitance extraction [32,34]. For the finite-domain multidielctric problem, the QMM-based method has shown a $10 \times$ higher computation speed and memory saving over the multipole approach (FastCap 2.0) with comparable accuracy [34].

Another kind of field solver, called the “global approach,” does not solve the resulting linear system in the usual way. The global approach discretizes the field equations and converts them to a circuit network of resistors or capacitors. Finally, with circuit reduction or matrix computation, the whole resistance or capacitance matrix can be obtained directly. In 1997, Dengi of Carnegie Mellon University proposed a global approach (called “macromodel” method) for 2D interconnect capacitance extraction based on direct BEM [31]. More recently, Lu et al. successfully extended the concept of boundary element macromodel to the 3D case, and developed a rapid hierarchical block boundary element method (HBBEM) for interconnect capacitance extraction [33].

3.3.4. Semianalytical Approaches. Semianalytical approaches have been proposed as a solution for 3D capacitance extraction. Basically, they take certain special procedures and reduce the original problem by one dimension, such as using domain decomposition. Since some subdomains with specific geometry symmetry can be handled using the analytical formula, these approaches have very high computational speed as well as much less memory usage. Another characteristic of these approaches is that the FDM is often used for the general and complicated subdomain. That is why these approaches are sometimes considered as improvements over the finite-difference method.

The semianalytical approaches include the dimension-reduction technique (DRT) [9] and techniques based on the domain decomposition method [35–37]. The principles of the latter two techniques will be briefly discussed as follows.

3.3.4.1. Dimension Reduction Technique. The DRT attempts to solve problems within the finite domain. Most VLSI interconnects have stratified structures, and every layer is homogeneous along the direction perpendicular to the interfaces of the layers (denoted as the z direction; see Fig. 13). The DRT takes full advantage of this fact. It first

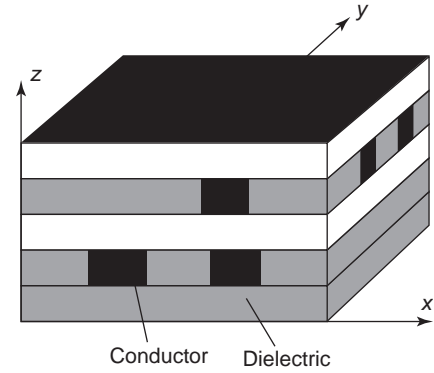


Figure 13. A 3D interconnect capacitor and the stratified layers.

partitions the whole structure according to these homogeneous layers. Then, for each layer the 3D Laplace equation can be reduced to a 2D Helmholtz equation, which is solved with the most efficient method (including the analytical formula) according to the arrangement of the conductors. Finally, the solutions for these cascading 2D problems are combined together to yield the final result.

For the finite-domain problem of the i th layer with Eq. (8), denote $W^{(i)}(x, y, V_c)$ as a linear function of x, y and the bias voltage setting on conductors (denoted by vector V_c), and let

$$u^{(i)} = v^{(i)} + W^{(i)}(x, y, V_c).$$

If there exists a function such as $W^{(i)}(x, y, V_c)$, that function $v^{(i)}$ satisfies

$$\begin{cases} \nabla^2 v^{(i)}(x, y, z) = 0 \\ v^{(i)}(x, y, z) = 0, & (x, y) \in \Gamma_u^{(i)} \\ \partial v^{(i)}(x, y, z) / \partial \mathbf{n} = 0, & (x, y) \in \Gamma_q^{(i)} \end{cases}$$

then from the method of separation of variables, the general solution of $v^{(i)}$ is

$$v^{(i)}(x, y, z) = \sum_{m=1} T_m^{(i)}(x, y) L_m^{(i)}(z)$$

where $T_m^{(i)}$ is the mode function fulfilling the Helmholtz equation and $L_m^{(i)}$ can be solved analytically [9].

According to the conductor arrangement in the layer and the preceding analysis, the layer slices are classified as follows:

1. An Empty layer or a layer containing some simple conductors (such as that involving straight lines penetrating the structure) for which the linear function W and the analytical solution of the Helmholtz equation both exist.
2. The layer for which the linear function W exists, allowing the corresponding 3D problem to be transferred into the 2D Helmholtz equation.
3. A complex layer for which the W function does not exist. The 3D Laplace equation must be solved, but

only the 2D finite-difference grid is utilized because of the geometry symmetry along the z direction.

The main drawback of the DRT is that the geometry it employs has some limitations; For instance, it is difficult to apply DRT to nonplanarized structures. So, for generalized and complicated interconnect structures using the DSM technology, the efficiency of DRT is not guaranteed.

3.3.4.2. Domain Decomposition Method. The domain decomposition method (DDM) is a newly developed numerical method. It can be subgrouped into the overlapping domain decomposition method (ODDM) and the nonoverlapping domain decomposition method (NDDM). The former is also called the *Schwarz alternating method* and the latter, the *Dirichlet–Neumann alternating method*. ODDM partitions the whole structures into some overlapped subdomains. Then, a global iteration is used for the solution. Its principles are discussed below [35].

Consider a 3D finite domain Laplace problem with the Dirichlet boundary condition

$$\begin{cases} \nabla^2 u = 0, & (x, y, z) \in \Omega \\ u|_{\Gamma} = g(x, y, z) \end{cases}$$

Assume that the problem domain Ω involves two overlapping subdomains Ω_1 and Ω_2 (see Fig. 14), and denote Γ_j and Λ_j as the outer boundary and fictitious boundary of Ω_j ($j=1, 2$), respectively. Then, the Schwarz alternating method is represented as

$$\begin{cases} \nabla^2 u_1^{i+1} = 0, & (x, y, z) \in \Omega_1 \\ u_1^{i+1} = u_2^i, & (x, y, z) \in \Lambda_1 \\ u_1^{i+1} = g(x, y, z), & (x, y, z) \in \Gamma_1 - \Lambda_1 \end{cases}$$

$$\begin{cases} \nabla^2 u_2^{i+1} = 0, & (x, y, z) \in \Omega_2 \\ u_2^{i+1} = u_1^{i+1}, & (x, y, z) \in \Lambda_2 \\ u_2^{i+1} = g(x, y, z), & (x, y, z) \in \Gamma_2 - \Lambda_2 \end{cases}$$

with $i=0, 1, 2, \dots$, where u^0 is the initial value for iteration. In each iterative step, the known values of u on Λ_1 are used to solve the field of subdomain Ω_1 . Then, the field of subdomain Ω_2 is resolved with the u obtained on Λ_2 . The discrepancy of u on Λ_1 between two adjacent iterative steps is used as the criterion of convergence. A relaxation factor ω can be introduced to these formulas to accelerate the convergence. It is also obvious that the convergence rate of the Schwarz alternating method is closely related to the size of the overlapping region. Usually the iteration

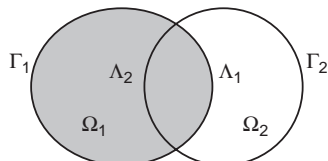


Figure 14. Two overlapping subregions.

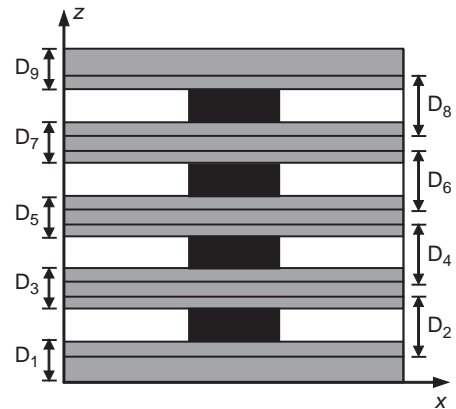


Figure 15. Four conductors embedded in nine dielectric layers.

error decreases exponentially with increase in the ratio of the overlapping domain over the subdomain [35].

It is straightforward to extend the preceding formulas of two subdomains to the generalized case with more subdomains. In each iterative step an analysis similar to that used in DRT can be employed to achieve high efficiency. In the actual application to capacitance extraction, the iteration sequence and selection of relaxation factor need to be considered. Figure 15 shows a cross-sectional view of an interconnect capacitor with nine layers, and the domain partition scheme is illustrated.

In the NDDM technique, the decomposed subdomains do not overlap each other, while the iteration algorithm is similar to that in ODDM; the difference is that in the adjacent subdomains the problem is solved with the Dirichlet boundary condition and the Neumann boundary condition, respectively, in the NDDM. In NDDM, there are fewer unknowns in the subdomain, and sometimes only 2D discretization is needed for a simple subdomain with homogeneous structure. However, the convergence rate of NDDM is slower than that of ODDM [36].

Research on capacitance extraction based on the domain decomposition method is still underway. More recent progress can be found in Ref. 37.

3.3.5. Other Methods. The measured equation of invariance (MEI) method can be considered as a variation of FDM. To solve the infinite-domain model of capacitance extraction, the MEI method terminates the meshes very close to the object conductors and still preserves the sparsity of the finite-difference (FD) equations. The geometry-independent measured equation of invariance (GIMEI) is proposed for the capacitance extraction of the general 2D and 3D interconnects by using the free-space Green function only [13]. The MEI method has now been developed to the on-surface level, where a surface mesh is used to minimize the number of unknowns [14]. The stochastic method is based on the random-walk theory and can effectively handle complex 3D structures. Its most recent progress can be found in Ref. 38.

4. PERSPECTIVE

In this article, we reviewed the state of the art in capacitance extraction techniques. These methods are discussed

mainly for the accurate analysis of VLSI interconnects. However, they can also be easily applied to computer-aided design of microwave ICs. With the development of IC technologies, the following issues related to capacitance extraction are important:

1. 3D capacitance extraction (i.e., 3D field solution) has the highest computational accuracy, and is suitable for complex interconnect structure under the DSM technologies. Many accelerating techniques have been developed to improve its speed. However, it is yet not feasible to use the 3D field solver directly in the full-chip extraction task. More effort should be devoted to improving the computational speed of the 3D field solver, or to develop special techniques for the full-chip task. The full-chip extraction method employing the 3D field solver would give both high computational speed and high accuracy.
2. Currently, few 3D capacitance extraction methods can be “tuned” for performance versus accuracy. The error estimation of the boundary-element method is also not established for practice. To make the 3D field solver suitable for various applications, its flexibility in tradeoff of accuracy versus computational performance must be improved. The adaptive algorithm and stable element partition scheme will be the focus of research in the future.
3. Mixed-signal integrated circuits have been demonstrated to provide high-performance system solutions for various applications such as wireless communications. Also, the silicon-based CMOS technology is increasingly widely used because of the fabrication cost advantage. To consider the significant impact of the lossy nature of the silicon substrate on the on-chip interconnects of the mixed-signal ICs, the frequency-dependent parameters of interconnects in high-speed circuits must be extracted accurately. Defining the complex permittivity of a material, the parasitic capacitance and conductance in a frequency-dependent model can be extracted using methods similar to that employed for traditional capacitance extraction. The most efficient algorithms for frequency-dependent capacitance extraction should be considered.

Acknowledgment

The authors would like to thank Prof. W. Hong, Southeast University, Nanjing, China, for much helpful advice.

BIBLIOGRAPHY

1. W. H. Kao, C. Lo, M. Basel, and R. Singh, Parasitic extraction: Current state of the art and future trends, *Proc. IEEE* **89**(5):729–739 (2001).
2. Y. Saad and M. H. Schultz, GMRES: A generalized minimal residual algorithm for solving nonsymmetric linear systems, *SIAM J. Sci. Stat. Comput.* **7**(3):856–869 (1986).
3. U. Choudhury and A. Sangiovanni-Vicentelli, Automatic generation of analytical models for interconnect capacitances, *IEEE Trans. Comput. Aided Design* **14**(4):470–480 (1995).
4. N. D. Arora, K. V. Raol, R. Schumann, and L. M. Richardson, Modeling and extraction of interconnect capacitances for multilayer VLSI circuits, *IEEE Trans. Comput. Aided Design* **15**(1): 58–67 (1996).
5. P. A. Habitz and I. L. Wemple, A simpler, faster method of parasitic capacitance extraction, *Electron. J.* 11–15 (Oct. 1997).
6. E. A. Dengi, *A Parasitic Capacitance Extraction Method for VLSI Interconnect Modeling*, Ph.D thesis, Carnegie Mellon Univ., March 1997.
7. J. D. Jackson, *Classical Electrodynamics*, Wiley, New York, 1975.
8. Z. Wang, Y. Yuan, and Q. Wu, A parallel multipole accelerated 3-D capacitance simulator based on an improved model, *IEEE Trans. Comput. Aided Design* **15**(12):1441–1450 (1996).
9. W. Hong, W. Sun, and Z. Zhu, A novel dimension-reduction technique for the capacitance extraction of 3-D VLSI interconnects, *IEEE Trans. Microwave Theory Tech.* **46**(8): 1037–1043 (1998).
10. A. Seidl, M. Svoboda, et al., CAPCAL-A 3-D capacitance solver for support of CAD systems, *IEEE Trans. Comput. Aided Design* **7**(5):549–556 (1988).
11. T. Chou and Z. J. Cendes, Capacitance calculation of IC packages using the finite element method and planes of symmetry, *IEEE Trans. Comput. Aided Design* **13**(9):1159–1166 (1994).
12. C. A. Brebbia, *The Boundary Element Method for Engineers*, Pentech Press, London, 1978.
13. W. Sun, W. W. Dai, and W. Hong, Fast parameter extraction of general interconnects using geometry independent measured equation of invariance, *IEEE Trans. Microwave Theory Tech.* **45**(5):827–835 (1997).
14. Y. W. Liu, K. Lan, and K. K. Mei, Computation of capacitance matrix for integrated circuit interconnects using on-surface MEI method, *IEEE Microwave Guided Wave Lett.* **9**(8): 303–304 (1999).
15. R. F. Harrington, *Field Computation by Moment Methods*, Macmillan, New York, 1968.
16. L. Greengard and V. Rokhlin, A fast algorithm for particle simulations, *J. Comput. Phys.* **73**:325–348 (1987).
17. K. Nabors and J. White, FastCap: A multipole accelerated 3-D capacitance extraction program, *IEEE Trans. Comput. Aided Design* **10**(11):1447–1459 (1991).
18. K. Nabors and J. White, Multipole-accelerated capacitance extraction algorithms for 3-D structures with multiple dielectrics, *IEEE Trans. Circ. Syst. I: Fund. Theory Appl.* **39**(11):946–954 (1992).
19. S. Kapur and D. Long, IES³: A fast integral equation solver for efficient 3-dimensional extraction, *Proc. IEEE/ACM Int. Conf. Comput. Aided Design* **34**:448–455 (1997).
20. K. S. Oh, D. Kuznetsov, and J. E. Schutt-Aine, Capacitance computations in a multilayered dielectric medium using closed-form spatial Green’s functions, *IEEE Trans. Microwave Theory Tech.* **42**(8):1443–1453 (1994).
21. J. Zhao, W. W. M. Dai, et al., Efficient three-dimensional extraction based on static and full-wave layered Green’s functions, *Proc. IEEE/ACM Design Automation Conf.* **35**:224–229 (1998).
22. K. Li, K. Atsuki, and T. Hasegawa, General analytical solution of static Green’s functions for shielded and open arbitrarily multilayered media, *IEEE Trans. Microwave Theory Tech.* **45**(1):2–8 (1997).

23. J. R. Phillips and J. K. White, A precorrected-FFT method for electrostatic analysis of complicated 3-D structures, *IEEE Trans. Comput. Aided Design* **16**(10):1059–1072 (1997).
24. W. Shi, J. Liu, N. Kakani, and T. Yu, A fast hierarchical algorithm for three-dimensional capacitance extraction, *IEEE Trans. Comput. Aided Design* **21**(3):330–336 (2002).
25. Y. C. Pan, W. C. Chew, and L. X. Wan, A fast multipole-method-based calculation of the capacitance matrix for multiple conductors above stratified dielectric media, *IEEE Trans. Microwave Theory Tech.* **49**(3):480–490 (2001).
26. N. Soveiko and M. S. Nakhla, Efficient capacitance extraction computations in wavelet domain, *IEEE Trans. Circ. Syst. I: Fund. Theory Appl.* **47**(5):684–701 (2000).
27. J. Tausch and J. White, A multiscale method for fast capacitance extraction, *Proc. IEEE/ACM Design Automation Conf.* **36**:537–542 (1999).
28. S. Fukuda, N. Shigyo, et al., A ULSI 2-D capacitance simulator for complex structures based on actual processes, *IEEE Trans. Comput. Aided Design* **9**(1):39–47 (1990).
29. M. Bachtold, J. G. Korvink, and H. Baltes, Enhanced multipole acceleration technique for the solution of large poisson computations, *IEEE Trans. Comput. Aided Design* **15**(12):1541–1546 (1996).
30. J. Gu, Z. Wang, and X. Hong, Hierarchical computation of 3-D interconnect capacitance using direct boundary element method. *Proc. IEEE Asia South Pacific Design Automation Conf.* 2000, Vol. 6, pp. 447–452.
31. E. A. Dengi and R. A. Rohrer, Boundary element method macromodels for 2-D hierarchical capacitance extraction, *Proc. IEEE/ACM Design Automation Conf.* **35**:218–223 (1998).
32. W. Yu, Z. Wang, and J. Gu, Fast capacitance extraction of actual 3-D VLSI interconnects using quasi-multiple medium accelerated BEM, *IEEE Trans. Microwave Theory Tech.* **51**(1):109–120 (2003).
33. T. Lu, Z. Wang, and W. Yu, Hierarchical block boundary-element method (HBBEM): A fast field solver for 3-D capacitance extraction, *IEEE Trans. Microwave Theory Tech.* **52**(1):10–19 (2004).
34. W. Yu and Z. Wang, Enhanced QMM-BEM solver for three-dimensional multiple-dielectric capacitance extraction within the finite domain, *IEEE Trans. Microwave Theory Tech.* **52**(2):560–566 (2004).
35. Z. Zhu, H. Ji, and W. Hong, An efficient algorithm for the parameter extraction of 3-D interconnect structures in the VLSI circuits: domain-decomposition method, *IEEE Trans. Microwave Theory Tech.* **45**(7):1179–1184 (1997).
36. Z. Zhu and W. Hong, A generalized algorithm for the capacitance extraction of 3-D VLSI interconnects, *IEEE Trans. Microwave Theory Tech.* **47**(10):2027–2030 (1999).
37. V. V. Veremey and R. Mittra, Domain decomposition approach for capacitance computation of nonorthogonal interconnect structures, *IEEE Trans. Microwave Theory Tech.* **48**(9):1428–1434 (2000).
38. A. Brambilla and P. Maffezzoni, A statistical algorithm for 3D capacitance extraction, *IEEE Microwave Guided Wave Lett.* **10**(8):304–306 (2000).
39. I. Bahl, *Lumped Elements for RF and Microwave Circuits*, Artech House, 2003.
40. L. Zhu and K. Wu, Accurate circuit model of interdigital capacitor and its application to design of new quasi-lumped miniaturized filters with suppression of harmonic resonance, *IEEE Trans. Microwave Theory Tech.* **48**(3):347–356 (2000).

CAVITY RESONATORS

ARVIND K. SHARMA
TRW
Redondo Beach, California

1. RESONANT STRUCTURES

Resonant structures are network elements that are used extensively in the development of various microwave components [1]. At low frequencies, resonant structures are invariably composed of lumped elements. As frequencies increase, lumped-element resonant circuits are attained by using transmission lines. Microwave resonant structures are almost invariably understood as cavity resonators. Conventional resonators consist of a bounded electromagnetic field in a volume enclosed by metallic walls. The electric and magnetic energies are stored in the electric and magnetic fields, respectively, of the electromagnetic fields inside the cavity and the equivalent lumped inductance and capacitance of the structure can be determined from the respective stored energy. It is important to note that cavity resonators, in contrast to lumped resonators, have an infinite number of resonant frequencies (or modes). In the vicinity of each resonant frequency, the cavity can be approximated by an associated lumped equivalent circuit.

Some energy is dissipated as finite conductivity of the metallic walls, and the equivalent resistance can therefore be determined from the currents flowing on the walls of the cavity resonator [2,3]. In this article, a brief description of the cavity resonators most commonly employed in various microwave components is presented. As far as possible, simple expressions have been provided for design applications. Basic parameters of microwave resonators are first presented because they describe a cavity. Then, various coaxial and waveguide resonators are described. Fabrication, coupling, measurements, and applications of cavity resonators are also included.

2. RESONATOR PARAMETERS

2.1. Resonant Frequency

The parameters of a resonator at microwave frequencies are essentially similar to those of a lumped-element resonator circuit at low frequencies. They can easily be described using an *RLC* series or parallel network. Consider, for instance, an *RLC* parallel network as shown in Fig. 1a. The input impedance of such a network as a function of frequency has both real and imaginary parts. At resonance, the input impedance is real and is equal to the resistance of the circuit. The electric and magnetic stored energies are also equal, leading to the expression for the resonant frequency as

$$\omega_0 = \frac{1}{\sqrt{LC}} \quad (1)$$

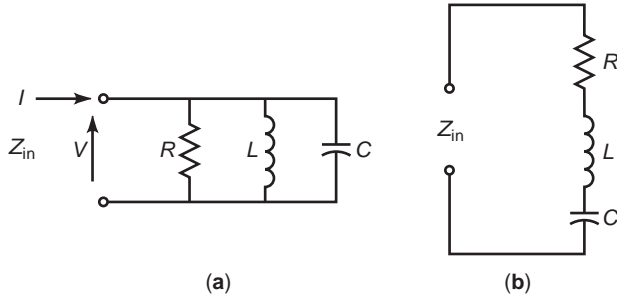


Figure 1. Lumped-element (a) parallel and (b) series resonant circuits.

2.2. Quality Factor

The performance of a resonant circuit is described in terms of the quality factor Q , and such features as frequency selectivity, bandwidth, and damping factors can be deduced from this. The quality factor is defined as

$$Q = \omega \frac{\text{time-averaged stored energy}}{\text{energy lost per second}} \quad (2)$$

for the lumped resonant circuits

$$Q = \omega RC = \frac{R}{\omega L} \quad (3)$$

for the parallel network in Fig. 1a, and

$$Q = \frac{1}{\omega CR} = \frac{\omega L}{R} \quad (4)$$

for the series network in Fig. 1b.

2.3. Fractional Bandwidth

The input impedance of the parallel resonant circuit of Fig. 1 is given by

$$Z_{\text{in}} = \left[\frac{1}{R} + \frac{1}{j\omega L} + j\omega C \right]^{-1} \quad (5)$$

At a frequency $\omega_0 \pm \Delta\omega$ in the vicinity of the resonant frequency, Eq. (5) reduces to

$$Z_{\text{in}} = \frac{R}{1 \pm j2Q(\Delta\omega/\omega_0)} \quad (6)$$

From Eq. (6), it is clear that at $\omega = \omega_0$ the input impedance is only resistive. However, when

$$\Delta\omega = \frac{\omega_0}{2Q} \quad (7)$$

the magnitude of the input impedance decreases to $R\sqrt{2}$ of its maximum value R , and the phase angle is $\pi/4$ for $\omega < \omega_0$ and $-\pi/4$ for $\omega > \omega_0$. From Eq. (7), the fractional band-

width BW is defined as

$$\text{BW} = \frac{2\Delta\omega}{\omega_0} = \frac{1}{Q} \quad (8)$$

2.4. Loaded Quality Factor

In practical situations, the resonant circuit is coupled to an external load R_L that also dissipates power, and the loaded quality factor Q_L is given by

$$\frac{1}{Q_L} = \frac{1}{Q} + \frac{1}{Q_e} \quad (9)$$

where Q_e is the external quality factor for a lossless resonator in the presence of the load.

2.5. Damping Factor

Another important parameter associated with a resonant circuit is the damping factor δ_d . It is a measure of the rate of decay of the oscillations in the absence of an exciting source. For high- Q resonant circuits, the rate at which the stored energy decays is proportional to the average energy stored. Consequently, the stored energy as a function of time is given by

$$W = W_0 e^{-2\delta_d t} = W_0 e^{-\omega_0 t/Q} \quad (10)$$

which implies that

$$\delta_d = \frac{\omega_0}{2Q} \quad (11)$$

Thus, we see that the damping factor is inversely proportional to the Q of the resonant circuit. In the presence of an external load, the Q should be replaced by Q_L .

Alternately, the input impedance in the vicinity of resonance Z_{in} given by Eq. (6) can be rewritten to take into account the effect of losses in terms of the complex resonant frequency

$$\omega_c = \omega_0 + j\delta_d = \omega_0 \left(1 + j\frac{1}{2Q} \right) \quad (12)$$

so that

$$Z_{\text{in}} = \frac{\omega_0 R / (2Q)}{j(\omega - \omega_c)} \quad (13)$$

In Eq. (13) the parameter R/Q is called the *figure of merit* and describes the effect of the cavity on the gain-bandwidth product. In terms of the lumped elements of the resonant circuit, we obtain

$$\frac{R}{Q} = \sqrt{\frac{L}{C}} \quad (14)$$

3. COAXIAL CAVITY RESONATORS

At microwave frequencies, the dimensions of lumped resonator circuits become comparable to the wavelength, and

this may cause energy loss by radiation. Therefore, resonant circuits at these frequencies are shielded to prevent radiation. Perfectly conducting enclosures, or cavities, provide a means of confining energy. Usually, cavities with the largest possible surface area for the current path are preferred for low-loss operation, and the energy is coupled to them by the various means described later in this article.

3.1. Coaxial Resonators

A coaxial cavity resonator (Fig. 2) supporting TEM (transverse electromagnetic) waves can easily be formed by a short section of coaxial line. Resonances appear whenever the length d of the cavity is an integral number of half-wavelengths. The resonance modes occur at

$$f = \frac{nc}{2d}, \quad n = 1, 2, \dots \quad (15)$$

where c is the speed of light. The lowest resonant frequency corresponds to $n = 1$, and the Q of the cavity for this mode is given by [4]

$$Q \frac{\delta}{\lambda_0} = \frac{1}{4 + 2(d/b)(1 + b/a) / \ln(b/a)} \quad (16)$$

where δ is the skin depth and a and b are inner and outer radii, respectively. It is also possible to have higher-order resonance modes, depending on the structural parameters of the coaxial line. The first higher-order mode appears when the average circumference is equal to the wavelength in the dielectric medium of the line. The cutoff frequency of this mode is

$$f_c = \frac{c}{\pi\sqrt{\epsilon_r}(a + b)} \quad (17)$$

where ϵ_r is the dielectric constant of the medium. Other higher-order modes correspond to TE (transverse electric) and TM (transverse magnetic) waves that exist in a circular waveguide with the radius of the center conductor approaching zero. The resonance condition is

$$k_{nml} = \left[p_{nm}^2 + \left(\frac{l\pi}{2d} \right)^2 \right]^{1/2} \quad (18)$$

where $k_{nml} = 2\pi f_{nml}/c$ and p_{nm} is the cutoff wavenumber that is obtained as the m th root of the transcendental

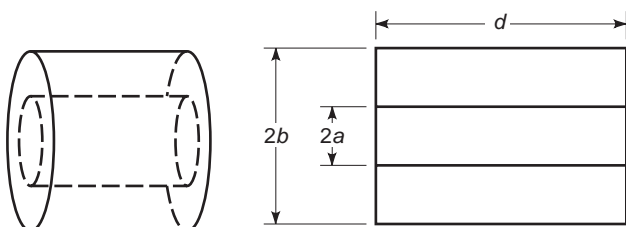


Figure 2. Coaxial cavity resonator and its cross section.

equations

$$J'_n(ka)N'_n(kb) - J'_n(kb)N'_n(ka) = 0 \quad (19)$$

for TE modes and

$$J_n(ka)N_n(kb) - J_n(kb)N_n(ka) = 0 \quad (20)$$

for TM modes. Here J_n and N_n are the n th-order Bessel functions of the first and second kinds, respectively, and the prime denotes their derivatives with respect to their arguments.

3.2. Reentrant Coaxial Resonators

Another coaxial cavity configuration consists of a short section of coaxial line with a gap in the center conductor. Figure 3a shows a capacitively loaded coaxial cavity. Radial cavity as shown in Fig. 3b is another possible variation. They are also referred to as *reentrant coaxial cavities* because the metallic boundaries extend into the interior of the cavity. They are widely used in microwave tubes. The resonant frequency of such a structure can be evaluated from the solution of the transcendental equation

$$\tan \beta l = \frac{dc}{\omega a^2 \ln(b/a)} \quad (21)$$

where d is the gap in the center conductor, and $2l + d$ is the length of the cavity. From Eq. (21), it is obvious that the capacitively loaded coaxial cavity can have an infinite number of modes. For the radial reentrant cavity of Fig. 3b, the resonant frequency can be evaluated by calculating the inductance and capacitance of the structure. The expression for the resonant frequency is

$$f = \frac{c}{2\pi\sqrt{\epsilon_r}} \left[al \left(\frac{a}{2d} - \frac{2}{l} \ln \frac{0.765}{\sqrt{l^2 + (b-a)^2}} \right) \ln \frac{b}{a} \right]^{-1/2} \quad (22)$$

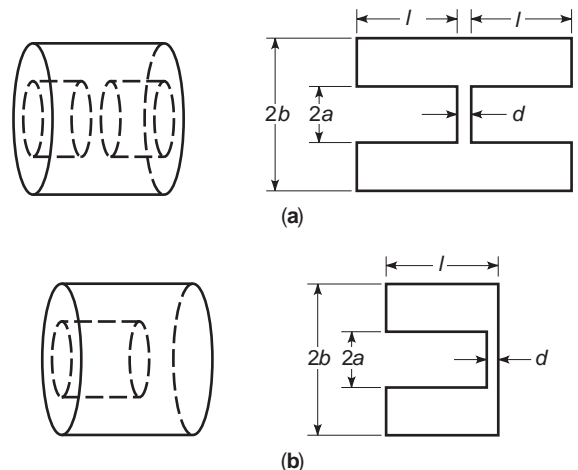


Figure 3. Reentrant coaxial cavity resonators: (a) capacitively loaded coaxial cavity resonator; (b) radial cavity resonators.

An approximate expression for the Q of the cavity is

$$Q \frac{\delta}{\lambda_0} = \frac{2l}{\lambda} \frac{\ln(b/a)}{2 \ln(b/a) + l[(1/a) + (1/b)]} \quad (23)$$

for a tunable reentrant cavity, d is large, and $(l - d)$ is also large compared with b . The resonances occur whenever the length of the center conductor is approximately a quarter-wavelength.

3.3. Annular Coaxial Resonator

An annular coaxial resonator is formed by a figure of revolution of a coaxial radial cavity resonator (refer to Fig. 3) about an axis that is offset from and parallel to the center conductor [5]. As shown in Fig. 4, the electric field in the plane containing the axis is similar to that of the radial cavity resonator. The electric field in the plane normal to the axis is radial and is same along the circumference. In effect, the annular resonator is equivalent to a half wavelength coaxial resonator with a small shunt capacitance in the middle. One of the important application of this type of resonator is that it can be coupled simultaneously with several sources. The electric field at the gap is quite high and results in good coupling to external sources.

4. WAVEGUIDE CAVITIES

4.1. Rectangular Waveguide Resonators

Rectangular resonant cavities are formed by a section of rectangular waveguide of length d . This cavity can also support an infinite number of modes. The field configura-

tion of the standing-wave pattern for the incident and reflected waves is not unique, that is, it depends on the assumed direction of propagation of the wave. In order to be consistent, we shall assume that wave propagation is in the positive z direction. The standing-wave pattern is then formed by the incident and reflected waves traveling in $+z$ and $-z$ directions, respectively. The cutoff wavenumber k_{cmn} is given by

$$k_{cmn}^2 = \left(\frac{m\pi}{a}\right)^2 + \left(\frac{n\pi}{b}\right)^2, \quad m=0, 1, 2, \dots, \quad n=0, 1, 2, \dots \quad (24)$$

where a and b are waveguide dimensions. The resonant wavenumber is then expressed as

$$k_{mnp} = \left[\left(\frac{m\pi}{a}\right)^2 + \left(\frac{n\pi}{b}\right)^2 + \left(\frac{p\pi}{d}\right)^2 \right]^{1/2}, \quad p=1, 2, \dots \quad (25)$$

and the resonant frequency is defined as

$$f_{mnp} = \frac{k_{mnp}c}{2\pi} \quad (26)$$

From the preceding discussion, we see that the resonant frequency is the same for TE and TM modes. Therefore, they are referred to as *degenerate modes*. The field configuration of the dominant TE_{101} mode is shown in Fig. 5b. The quality factor Q of the dominant TE_{101} mode in the rectangular resonant cavity having surface resistance R_s can be evaluated using the expression

$$Q = \frac{120\pi^2}{4R_s} \left[\frac{2b(a^2 + d^2)^{3/2}}{ad(a^2 + d^2) + 2b(a^3 + b^3)} \right] \quad (27)$$

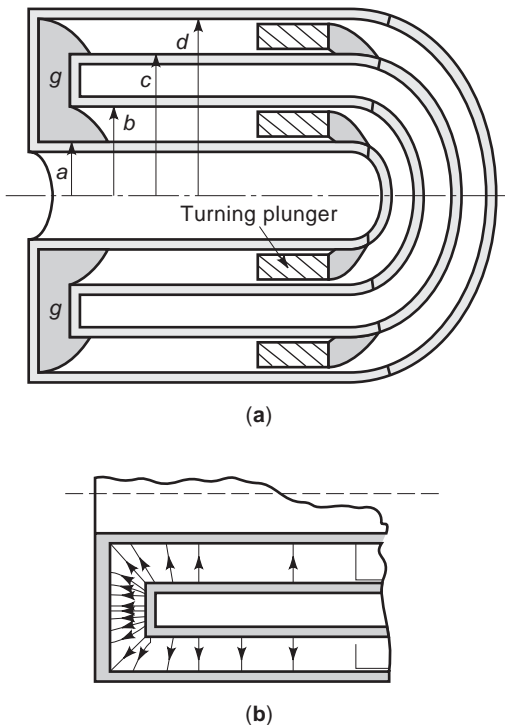


Figure 4. Two views of annular coaxial resonator structure.

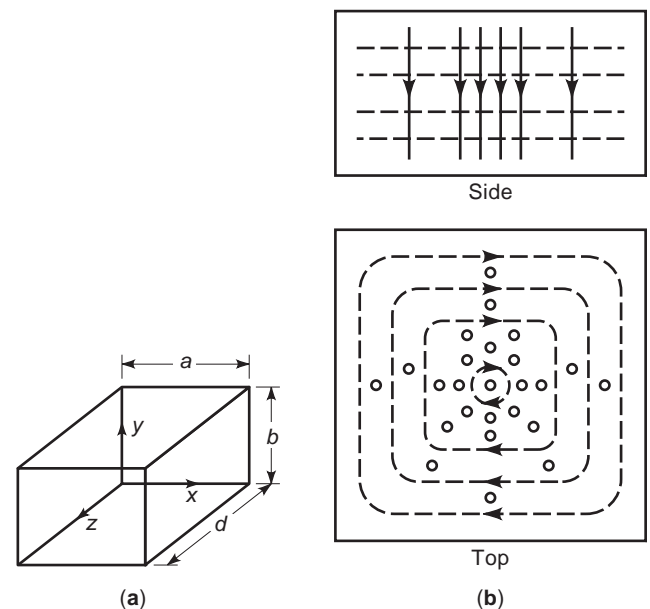


Figure 5. (a) Rectangular waveguide cavity resonator; (b) field configuration of the dominant TE_{101} mode.

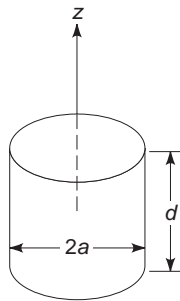
In rectangular cavities, the resonant frequency increases for higher-order modes, as does the Q at a given frequency. Higher-order mode cavity or “echo boxes” are useful in applications where a slow rate of decay of the energy stored in the cavity after it has been excited is required.

4.2. Circular Waveguide Resonators

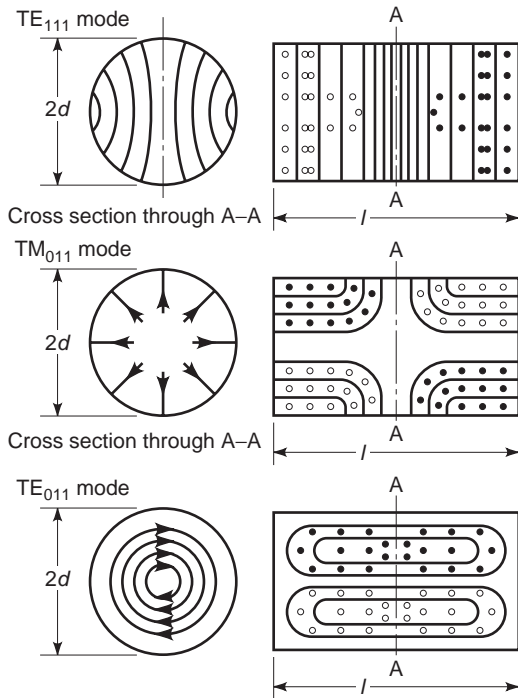
Circular waveguide cavities are most useful in various microwave applications. Most commonly, they are used in wavemeters to measure frequency, have a high Q factor, and provide greater resolution. These consist of a section of circular waveguides of radius a and length d as shown in Fig. 6.

The resonance wavenumber of the circular waveguide cavity is given by

$$k_{nml} = \left[\left(\frac{x_{nm}}{a} \right)^2 + \left(\frac{l\pi}{d} \right)^2 \right]^{1/2}, \quad l = 0, 1, 2, \dots \quad (28)$$



(a)



(b)

Figure 6. (a) Circular cylindrical waveguide cavity resonator; (b) field configurations for TE_{111} , TM_{011} , and TE_{011} modes in cylindrical cavities.

Table 1. Roots of the Transcendental Equation $J'_n(ka) = 0$

Modes		
n	m	p'_{nm}
0	1	0.0
1	1	1.841
2	1	3.054
0	2	3.832
3	1	4.201
4	1	5.318

where

$$x_{nm} = \begin{cases} p'_{nm} & \text{for TE modes} \\ p_{nm} & \text{for TM modes} \end{cases} \quad (29)$$

Values for p'_{nm} for various modes are given in Table 1. Field lines for TE_{111} , TM_{011} , and TE_{011} modes are shown in Fig. 6. Simplifying Eq. (28) yields

$$(2af_{nml})^2 = \left(\frac{cx_{nm}}{\pi} \right)^2 + \left(\frac{cl}{2} \right)^2 \left(\frac{2a}{d} \right)^2 \quad (30)$$

The Q of the circular cavity for TE_{nml} modes can be evaluated from

$$Q \frac{\delta}{\lambda_0} = \frac{[1 - (n/p'_{nm})^2][(p'_{nm})^2 + (l\pi a/d)^2]^{3/2}}{2\pi[(p'^2_{nm} + 2a/d(l\pi a/d)^2 + (1 - 2a/d)(nl\pi a/p'_{nm}d)^2]} \quad (31)$$

and for the dominant TE_{111} mode, Q can be obtained by substituting $n = m = l = 1$ in the preceding equation. Using Eq. (30), plots of $(2af)^2$ versus $(2a/d)^2$ can be used to construct mode charts, as shown in Fig. 7. From this it can be seen that, for the TE_{011} mode operation, the safe value of $(2a/d)^2$ is between 2 and 3. For TM model operation, the Q is given by

$$Q \frac{\delta}{\lambda_0} = \begin{cases} \frac{[p'^2_{nm} + (l\pi a/d)^2]^{1/2}}{2\pi(1 + 2a/d)} & \text{for } l > 0 \\ \frac{p_{nm}}{2\pi(1 + a/d)} & \text{for } l = 0 \end{cases} \quad (32)$$

As with rectangular cavity resonators, the Q is higher for higher-order modes.

4.3. Elliptic Waveguide Resonators

Elliptic resonant cavities that are formed using a section of an elliptic waveguide offer several advantages. There is no mode splitting caused by slight deformations in the cavity surface, and the electric field configuration in the transverse plane is fixed with respect to its axes. Also, the longitudinal electric field of the TM_{111} mode in an elliptic cavity with semi-major axis a is always greater than the circular cavity with radius a . This feature may be useful in the dielectric material characterization that uses perturbation techniques [6].

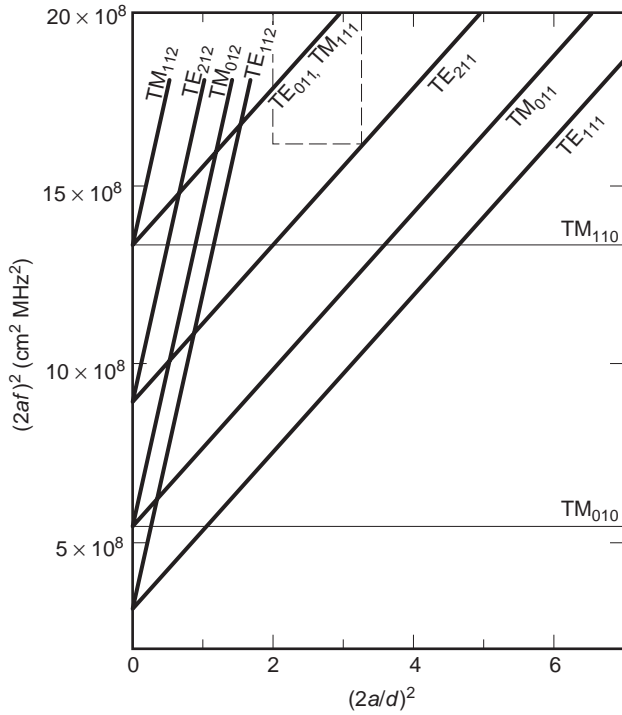


Figure 7. Mode chart of a circular cylindrical cavity resonator.

The elliptic waveguide supports four different types of modes, namely, even TE and TM modes and odd TE and TM modes. The TE modes have $E_z = 0$ and the TM modes have $H_z = 0$. From the solution of wave equations, there exist four different modes. The modes having cosine-type variation are called *even modes*, and modes having sine-type variation are called *odd modes*. The subscripts *c* and *s* are added to the mode designation to describe this variation.

The elliptic waveguide in Fig. 8a is shown along with the orthogonal elliptic coordinate system. As can be seen, the confocal elliptic cylinders are formed with constant ξ , and confocal hyperbolic cylinders are formed with constant η . The distance between the two foci, F and F' is $2h$. The outer wall of the elliptic waveguide is formed with $\xi = \xi_0$. The semi-major axis is then

$$2a = 2h \cosh \xi_0 \quad (33)$$

and, the semi-minor axis is

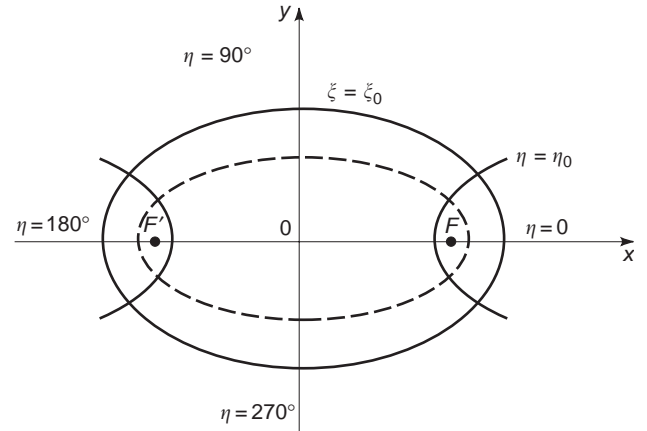
$$2b = 2h \sinh \xi_0 \quad (34)$$

Alternatively, the eccentricity e is

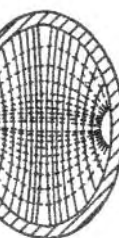
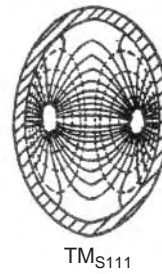
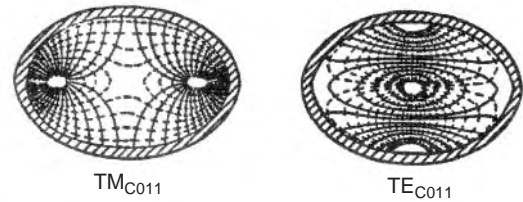
$$e = 1 / \cosh \xi_0 = \sqrt{1 - (b/a)^2} \quad (35)$$

The resonance wavenumber for elliptic cavity is given by

$$k_{rml} = \left[\left(\frac{2\sqrt{x_{rml}}}{ae} \right)^2 + \left(\frac{l\pi}{d} \right)^2 \right]^{1/2}, \quad l = 0, 1, 2, \dots \quad (36)$$



(a)



TE_{C111}

(b)

Figure 8. (a) Elliptic waveguide cavity resonator; (b) field configuration for some modes in elliptical cavities.

where

$$x_{rml} = \begin{cases} q'_{rml} & \text{for TE}_{rml} \text{ modes} \\ q_{rml} & \text{for TM}_{rml} \text{ modes} \end{cases} \quad (37)$$

In Eq. (37), r can be substituted with c and s to obtain even and odd modes, respectively. The parameter $q_{cmn}(q_{smn})$ is the n th parametric zero of the even (odd) modified Mathieu function of order m with argument ξ_0 and is used to calculate $\text{TM}_{cmn}(\text{TM}_{smn})$ modes. Similarly, for a $\text{TE}_{cmn}(\text{TE}_{smn})$ mode, the parameter $q'_{cmn}(q'_{smn})$ is the n th parametric zero of the first derivative of the even (odd)

modified Mathieu function of order m with argument ξ_0 and is used to calculate $TE_{cmn}(TE_{smn})$ modes. The equations used to find the parametric zeros are given next [7]:

$$\begin{aligned}
 \text{TM modes : } & Ce_m(\xi_0, q) = 0 \text{ even} \\
 & Se_m(\xi_0, q) = 0 \text{ odd} \\
 \text{TE modes : } & Ce'_m(\xi_0, q) = 0 \text{ even} \\
 & Se'_m(\xi_0, q) = 0 \text{ odd}
 \end{aligned}
 \tag{38}$$

Field lines for some modes are shown in Fig. 8b.

4.4. Annular Elliptic Resonator

The annular elliptic waveguide in Fig. 9a is shown along with the orthogonal elliptic coordinate system. The outer ellipse with eccentricity e_0 and the inner ellipse with eccentricity e_1 form a confocal annular elliptic waveguide. The distance between the two foci F and F' is $2h$ and is related to the other structural parameters via the relation

$$2h = 2a_0e_0 = 2a_1e_1 \tag{39}$$

where a_0 and a_1 are the semi-major axes of the outer and inner ellipses, respectively. Alternatively, the eccentricities e_0 and e_1 are also expressed as

$$e_0 = 1/\cosh \xi_0 = \sqrt{1 - (b_0/a_0)^2} \tag{40}$$

and

$$e_1 = 1/\cosh \xi_1 = \sqrt{1 - (b_1/a_1)^2} \tag{41}$$

where b_0 and b_1 are the semi-minor axes of the outer and inner ellipses, respectively. The axial coordinates of the outer and inner ellipses are ξ_0 and ξ_1 .

In a manner similar to the elliptic waveguide, the eigenvalue equation for annular elliptic waveguide was solved by Bräckelmann [8]. The relevant equations for TM and TE modes follow.

Even modes, TE_{cmn} :

$$\begin{aligned}
 Ce'_m(\xi_0, q_{cmn})Fe'y'_m(\xi_1, q_{cmn}) \\
 - Ce'_m(\xi_1, q_{cmn})Fe'y'_m(\xi_0, q_{cmn}) = 0
 \end{aligned}
 \tag{42}$$

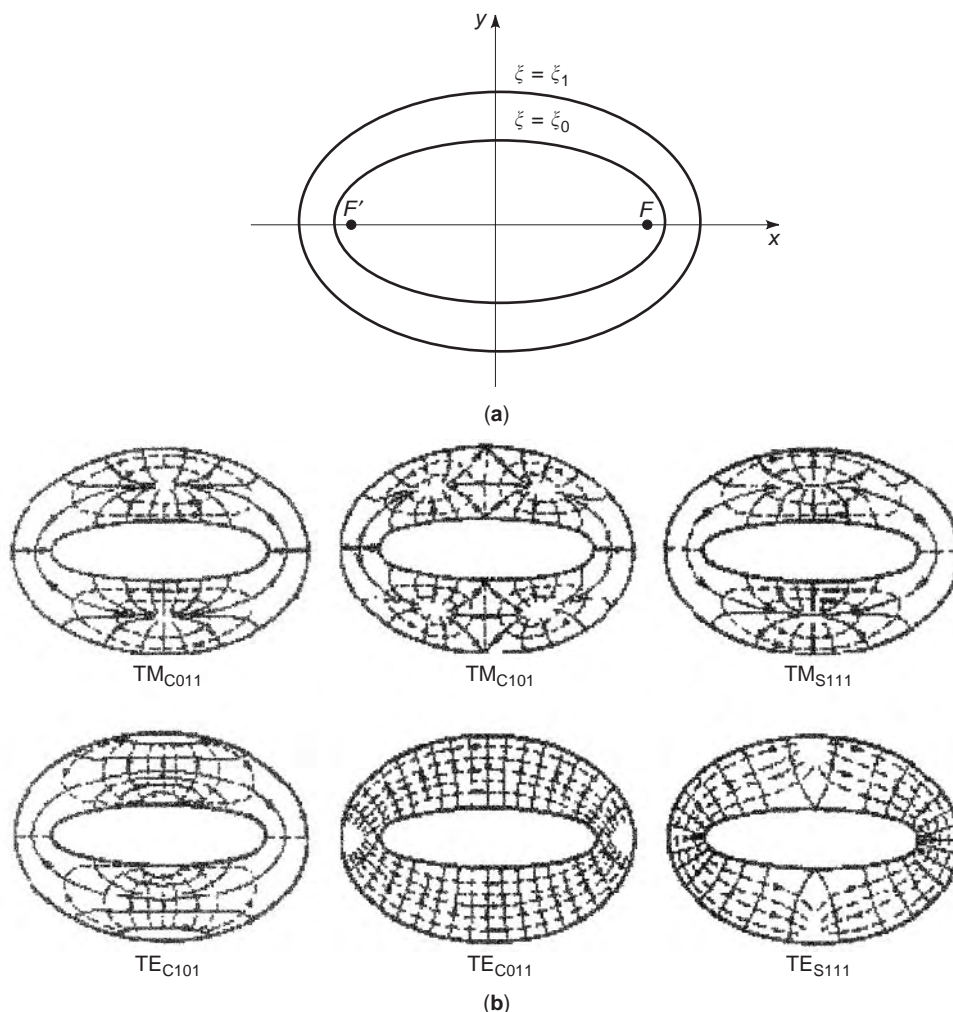


Figure 9. (a) Annular elliptic cavity resonator; (b) field configuration for some modes in annular elliptic cavities.

Odd modes, TE_{smn} :

$$\begin{aligned} Se'_m(\xi_0, q_{smn})Ge y'_m(\xi_1, q_{smn}) \\ - Se'_m(\xi_1, q_{smn})Fe y'_m(\xi_0, q_{smn}) = 0 \end{aligned} \quad (43)$$

Even modes, TM_{cmn} :

$$\begin{aligned} Ce_m(\xi_0, q_{cmn})Fe y_m(\xi_1, q_{cmn}) \\ - Ce_m(\xi_1, q_{cmn})Fe y_m(\xi_0, q_{cmn}) = 0 \end{aligned} \quad (44)$$

Odd modes, TM_{smn} :

$$\begin{aligned} Se_m(\xi_0, q_{smn})Ge y_m(\xi_1, q_{smn}) \\ - Se_m(\xi_1, q_{smn})Fe y_m(\xi_0, q_{smn}) = 0 \end{aligned} \quad (45)$$

In Eqs. (42)–(45), $Ce_m(\xi, q)$ and $Se_m(\xi, q)$ are the even and odd modified Mathieu functions of the first kind and order m . $Fe y_m(\xi, q)$ and $Ge y_m(\xi, q)$ are the even and odd modified Mathieu functions of the second kind and order m [9]. The primes in Eqs. (42)–(45) denote the derivative with respect to the argument ξ . The parameter q'_{cmn} is the n th parametric zero of Eq. (42), and q_{cmn} is the n th parametric zero of Eq. (44). Similar explanation applies for Eqs. (43) and (45) for the odd TE and TM modes.

The resonance wavenumber for annular elliptic cavity is given by

$$k_{rml} = \left[\left(\frac{2\sqrt{x_{rml}}}{ae} \right)^2 + \left(\frac{l\pi}{d} \right)^2 \right]^{1/2}, \quad l = 0, 1, 2, \dots \quad (46)$$

where

$$x_{rml} = \begin{cases} q'_{rml} & \text{for } TE_{rml} \text{ modes} \\ q_{rml} & \text{for } TM_{rml} \text{ modes} \end{cases} \quad (47)$$

The annular elliptic resonators also supports four different types of modes, namely, even TE and TM modes and odd TE and TM modes. Field lines for some modes are shown in Fig. 9b.

4.5. Spherical Resonators

Another cavity resonator shape is the spherical resonator. Based on the solution of Maxwell's equations in the spherical coordinate system, the axial symmetry results in TM modes containing E_r , E_θ , H_ϕ , and TE modes containing H_r , H_θ , E_ϕ . Because the origin is included inside the hollow spherical cavity, the resonance condition is easily obtained by setting $E_\theta = 0$ at $r = a$, where a is the radius of the sphere.

Solution of the transcendental equation

$$\tan ka = \frac{ka}{1 - (ka)^2} \quad (48)$$

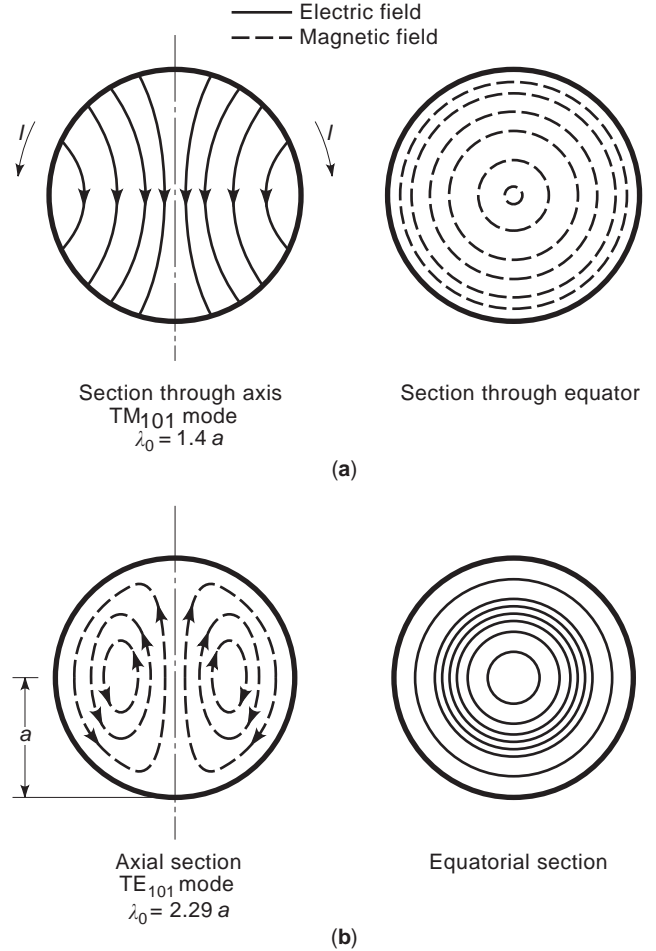


Figure 10. Fields in a spherical cavity resonator at the first and second resonant frequencies.

results in dominant TM_{101} resonance at

$$\lambda_0 = 2.29a \quad (49)$$

and the second TM_{102} resonance at a wavelength of

$$\lambda_0 = 1.4a \quad (50)$$

The modes in a spherical cavity are shown graphically in Fig. 10.

The Q of a spherical cavity operating in the dominant mode is

$$Q \frac{\delta}{\lambda_0} = 0.318 \quad (51)$$

and the equivalent shunt resistance is simply

$$R \frac{\delta}{\lambda_0} = 104.4 \quad (52)$$

4.5.1. Spherical Resonators with Reentrant Cones. Spherical resonators with reentrant cones were found to be suitable for realizing oscillators for klystrons [10].

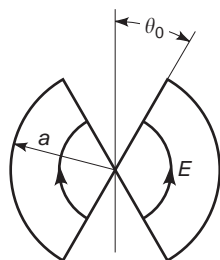


Figure 11. Spherical resonator with reentrant cones and fields in the fundamental modes.

It consists of a hollow conducting sphere of radius a and two cones whose apex is at the center of the sphere and subtends an angle of $2\theta_0$. Its structure and fundamental mode fields are shown in Fig. 11.

The resonant wavelength is not a function of θ , as is the case in spherical resonators. The resonant wavelength is

$$\lambda_0 = 4a \tag{53}$$

However, Q and R of the resonator are functions of the angle θ . The plots of $Q(\delta/\lambda_0)$ and $R(\delta/\lambda_0)$ [4] are given in Figs. 12 and 13, respectively.

As can be seen, the maximum Q is obtained at $\theta = 34^\circ$ and is given by

$$Q \frac{\delta}{\lambda_0} = 0.1095 \tag{54}$$

and the maximum R occurs at $\theta = 9^\circ$ and is given by

$$R \frac{\delta}{\lambda_0} = 32.04 \tag{55}$$

4.6. Ellipsoid–Hyperbolic Waveguide Resonators

Another cavity resonator suitable for klystrons is of ellipsoid–hyperboloid shape. This shape is a figure of revolution about the axis passing through its foci, as shown in

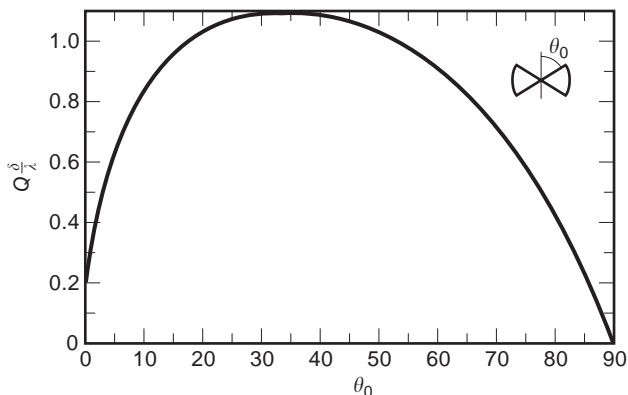


Figure 12. $Q(\delta/\lambda_0)$ for a spherical resonator with reentrant cones.

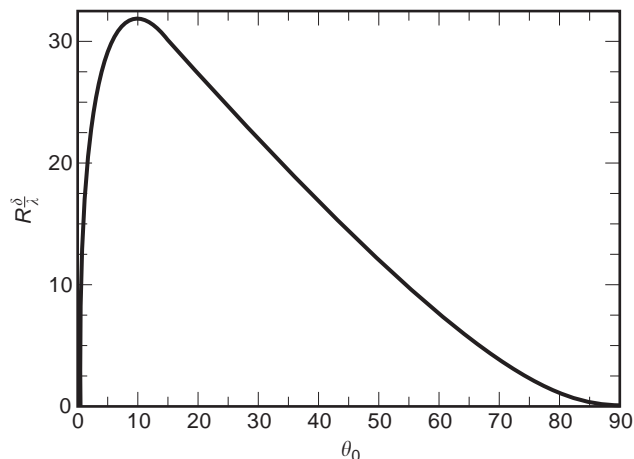


Figure 13. $R(\delta/\lambda_0)$ of a spherical resonator with reentrant cones.

Fig. 14. The distance between foci a as well as the hyperboloid that determines part of the resonator is held constant. The normalized resonant wavelength λ_0/b , where b is the equatorial radius, is plotted as a function of the shape factor $\sigma_0 = 2b/a$. Interestingly, the shape of the resonators vary widely as the shape factor is increased. Both the Q as well as the R are functions of the shape factor. The $Q(\delta/\lambda_0)$ and $R(\delta/\lambda_0)$ (given in Ref. 4) are plotted as a function of shape factor in Figs. 15 and 16, respectively.

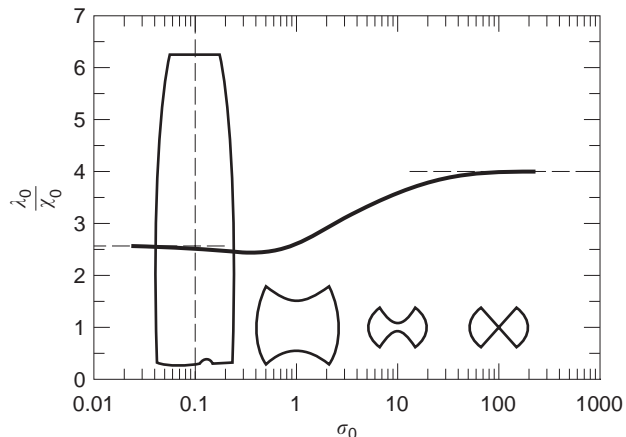
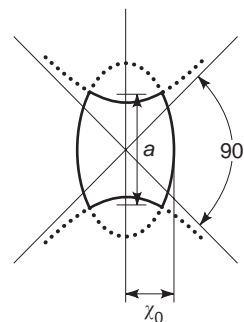


Figure 14. Ellipsoid–hyperboloid resonator and normalized resonant wavelength λ_0/b as a function of shape factor $\sigma_0 = 2b/a$.

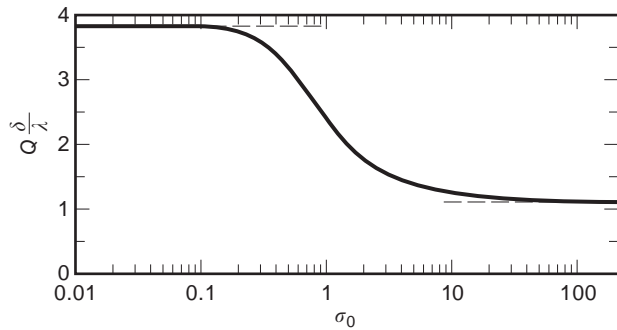


Figure 15. $Q(\delta/\lambda_0)$ of an ellipsoid–hyperboloid resonator as a function of shape factor $\sigma_0 = 2b/a$.

4.7. Arbitrarily Shaped Resonators

The early work in microwaves focused on analytical and numerical solutions of hollow waveguide problems. Most of the attempts were to solve them for TE and TM modes, either exactly or approximately. Ng [11] compiled the methods used to calculate the cutoff wavenumbers of hollow waveguides. As pointed out there, three basic cross-sectional shapes can be distinguished:

1. Convex shape
2. Nonconvex with smooth reentrant portion
3. Nonconvex with sharp reentrant portion

A resonant structure can be formed using any of these shapes by closing the hollow waveguide with endwalls. The cutoff wavenumbers can be found using references given in Table II of Ref. 11. The resonant frequency can be easily calculated. The basic equation to use is

$$k = \frac{2\pi f_0}{c} = \left[(k_c)^2 + \left(\frac{l\pi}{d} \right)^2 \right]^{1/2}, \quad l = 0, 1, 2, \dots \quad (56)$$

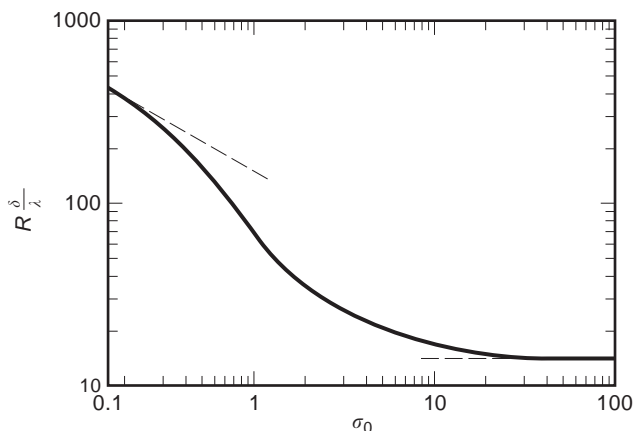


Figure 16. $R(\delta/\lambda_0)$ of an ellipsoid–hyperboloid resonator as a function of shape factor $\sigma_0 = 2b/a$.

5. FABRICATION

5.1. Materials

Microwave and millimeter-wave cavities are usually made from the same material used for the waveguide such as copper, brass, or aluminum. In order to provide low-loss characteristics, the interior (and exterior) is plated with low-loss materials such as silver and gold.

There exists a wide range of waveguide sizes to cover frequencies from as low as 400 MHz–200 GHz. The operating bandwidth of the waveguide increases as the frequency increases. Therefore, the method of fabrication is very important in realizing low-loss or high- Q cavities.

Cavities are formed using short sections of waveguides. There are various approaches used in their fabrication. The waveguide tubing formed using extrusion process generally provides various dimensional tolerances varying from 0.008 in. (0.2 mm) to 0.001 in. (0.025 mm). In order to realize accurate waveguide dimensions, particularly at millimeter wavelengths, the process of electroforming is generally used. A conducting or nonconducting mandrel is used as a starting material in the electroforming process. The mandrel is later removed to leave the electroformed waveguide. Special-grade stainless-steel mandrels with high surface finish can be used to electroform the waveguide. They are removed by heating and applying uniform force. Nonconducting mandrels formed using plastics or highly compressed wax can be used to form complicated cross sections. Such mandrels can be chemically dissolved to retain the final form of the electroformed waveguide.

In most applications, the waveguide must interact with cavities to realize the prescribed description of the component. Fabrication from a solid metal block using a milling process is preferred because it provides an integrated component for some complicated waveguide assemblies. This approach reduces reflections and spurious transmission by minimizing interfaces or flanges.

5.2. Cavity Perturbation

At resonance the cavity contains equal amounts of average electric and magnetic energy. Any perturbation in the structural dimensions or imperfections in the cavity wall will require readjustment in resonant frequency such that the electric and magnetic energies are equal. It is possible to measure accurately the frequency shift $\Delta\omega/\omega$, which can be used to determine other parameters of the cavity [2].

5.3. Effects of Temperature and Humidity

The resonant frequencies of a cavity resonator depend on the dimensional variations of the material used in the construction as well as on the variations in the dielectric constant.

As temperature changes, the dimensions of the cavity change in accordance with the thermal expansion coefficient of the material used in its construction. The change in the resonant frequency can be easily determined using the equation for the resonant frequency for a given cavity

structure. This change can be minimized by bimetals with a lower coefficient of thermal expansion.

Furthermore, the dielectric constant of the air within an unsealed cavity also varies depending on the temperature, atmospheric pressure, and humidity level.

5.4. Tunable Cavities

Various microwave and millimeter-wave applications require resonators that can be tuned frequently and at high speeds. Both contacting as well as noncontacting plungers are used to tune cavity resonators.

5.4.1. Contacting Plunger. A movable short circuit is provided by the direct contact between the plunger and the cavity walls. The plunger is typically a quarter wavelength long at the center frequency. In order to provide good electrical contact, the contacting plungers, as shown in Fig. 17, have axial serrations. These serrated fingers maintain sufficient pressure to scratch off any insulating film formed inside the cavity walls. Because the contact is made at or near a current node, the losses are minimized. In some cases, particularly for millimeter-wave applications, a metal shoulder is also added to move the short circuit reference plane forward. In this case, the actual contact is not at or near a current node.

Contacting resonators have several disadvantages, such as

- They provide erratic contact due to small metal particles and nonsmooth cavity interior walls.
- They are not repeatable because of the backlash in the mechanical driving mechanism as well as the friction between the contacting surfaces.
- The contact causes wear and produces an insulating film, which results in increased contact resistance. The increases losses will result in lower Q of the cavity.

5.4.2. Noncontacting Plunger. The disadvantages of the contacting plungers can be eliminated by using noncontacting plungers. These plungers provide a near short

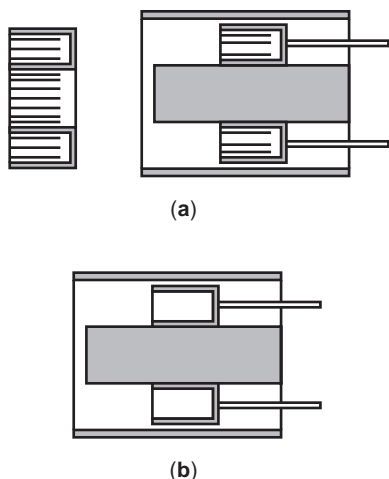


Figure 17. Contacting plunger.

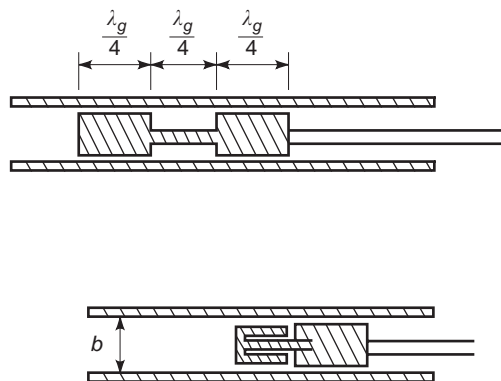


Figure 18. Noncontacting plunger.

circuit over a wider frequency range. The impedance at the face of the plunger is a complex impedance with a low value of resistance. The capacitive, choke, or bucket-type plungers, as shown in Fig. 18, provide reasonable performance [5]. Multisection plungers are formed by quarter-wavelength low-high-low impedance sections. The leakage through these sections may cause parasitic resonance; therefore, the back of the plunger section must be terminated in the characteristic impedance of the transmission line used to realize the cavity.

6. COUPLING INTO AND OUT OF CAVITIES

As we have seen, the cavities are essentially enclosed structures. In order to use them, we must couple them to transmission lines. We can use the coaxial line or any form of waveguide to couple power into and out of the cavities. In this sense, the input and output coupling structures act as a load on the cavity. The cavity parameters, such as resonant frequency and Q , are invariably affected by the presence of these structures. The resonant behavior of the cavities is exploited extensively in the realization of filters with prescribed functional forms.

6.1. General Coupling

Coupling structures provide a means of coupling energy into and/or out of the cavity. The excitation of the cavity can be accomplished by electric or magnetic coupling. In case of electric coupling, the electric field of the coupling structure is parallel to the electric field of the cavity. The magnetic coupling is provided when the magnetic field of the coupling structure is parallel to the magnetic field of the cavity.

The coaxial line can be used to provide either electric or magnetic coupling.

1. *Electric Probes.* The center conductor of the coaxial line acts as a probe. Its direction is parallel to the direction of the electric field in the cavity.
2. *Current Loops.* The center conductor of the coaxial line is terminated in a short circuit to form a loop. The loop produces a magnetic field perpendicular to the plane of the probe and in the same direction as the magnetic field in the cavity.

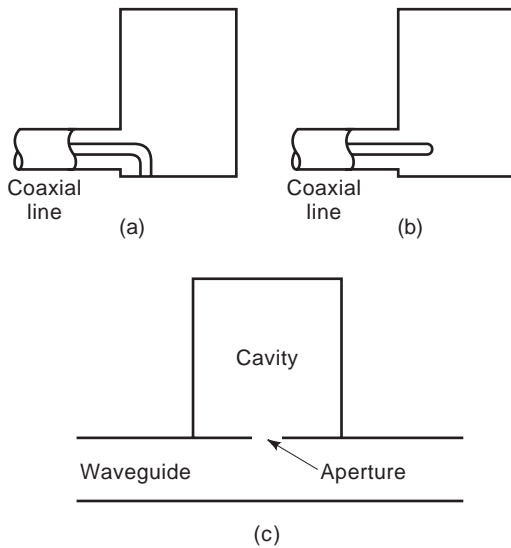


Figure 19. Cavity excitation using (a) loop coupling, (b) electric probe coupling, and (c) aperture coupling.

Cavities are also excited by waveguides through apertures formed by holes and slits (Fig. 19). The coupling mechanism can be of electric or magnetic type.

1. *Magnetic Coupling Apertures.* The aperture is located between the cavity and input waveguide such that the magnetic field in the waveguide is parallel to the magnetic field in the cavity. Round holes in the wall separating the waveguide and cavity provide magnetic coupling.
2. *Electric Coupling Apertures.* The aperture is located between the cavity and input waveguide such that the electric field in the waveguide is normal to the electric field in the cavity. A narrow slot in the wall separating the waveguide and cavity can provide electric coupling.

6.2. Coupling through Probes

One popular approach used to transfer energy from a coaxial line to a waveguide is by electric probes. In a typical configuration, the axis of the coaxial line is perpendicular to the broadside of the rectangular waveguide. The center conductor of the coaxial line protrudes through the waveguide wall and extends into the waveguide. The outer conductor of the coaxial line is terminated at the waveguide wall. The electric fields from the end of the center conductor terminate on the other broadside wall parallel to the dominant E field of the waveguide. They are, therefore, called electric probes. If the probe is shaped to form a circular loop and the end of the probe is terminated on the broad wall of the waveguide, the current flow through this loop will induce a magnetic field parallel to the dominant H field of the waveguide. In this case, the probe is a magnetic current loop.

In an electric probe, the center conductor of the coaxial line forms a radiating antenna. Depending on the length or depth of this section, the input impedance

at the interface can be inductive or capacitive. For optimum performance, the antenna should present a matched load at the interface. The probe excites waveguide modes that propagate in both directions; therefore, the energy is divided equally in both directions. In order to redirect the energy in the preferred direction, the other side is terminated in a short circuit. In the case of rectangular waveguide cavities, the placement of the probe is determined from one of the short-circuited ends. Invariably, a tunable short circuit will be required for optimum transfer of power. The probe can be constructed with various lengths and diameters. The distance between the probe and the short circuit is determined experimentally.

The bandwidth of the probe can be improved by providing a broadband match at the interface. This can be achieved by changing the length and diameter of the probe. Other approaches include making the end round, attaching a metal sphere at the end, or flaring the center conductor. If direct current (DC) return is desired, the probe can be terminated on the other broadwall, or it can rest on a crossbar across the waveguide broad dimension. Sometimes the probe is extended through the opposite side of the waveguide to form another section of shorted coaxial line. The position of the short circuit in this case provides an additional variable.

The input impedance of a short-diameter coaxial antenna is given by

$$Z_{\text{in}} \cong l^2 \cos^2 \frac{\pi x_0}{a} \sin^2 \frac{2\pi x_1}{\lambda_g} - jX \quad (57)$$

where l is length of the probe, x_0 is the distance from the center of the waveguide, and x_1 is the distance from the probe to the short circuit. The value of the reactance is large, implying that the input impedance has a large capacitive component.

6.3. Coupling Holes in Waveguides

The coupling from a waveguide to a cavity can be provided by apertures consisting of holes and slits. The aperture can be infinitesimally thin or with finite thickness. The insertion loss caused by a hole of finite thickness t is given by

$$\alpha_T = \alpha_b + \alpha_t \quad (58)$$

where α_b is the attenuation resulting from the susceptance of the hole and α_t is the attenuation in the below cutoff waveguide hole.

6.3.1. Holes in a Rectangular Waveguide. For a hole of diameter d in a rectangular waveguide normal to the direction of propagation, the normalized susceptance B is given by

$$\frac{B}{Y_0} \cong \frac{3}{2\pi} \frac{ab\lambda_g}{d^3} \quad (59)$$

where Y_0 is the characteristic admittance of the dominant waveguide mode and λ_g is the guide wavelength of a

waveguide having broadside dimension a and smaller dimension b .

The attenuation α_b resulting from the hole is

$$\alpha_b = 20 \log \frac{B}{2Y_0} \quad (60)$$

and the attenuation resulting from the finite thickness α_t is

$$\alpha_t = 32 \sqrt{1 - \left(1.706 \frac{d}{\lambda}\right)^2} \frac{t}{d} \cong 32 \frac{t}{d} \text{ dB} \quad (61)$$

where λ is the operating wavelength.

6.3.2. Holes in a Circular Waveguide. For a hole of diameter d normal to the direction of propagation in a circular waveguide of diameter $2a$, the normalized susceptance B is given by

$$\frac{B}{Y_0} = \frac{\lambda_g}{4a} \left(5.71 \frac{a^3}{d^3} - 2.344\right) \quad (62)$$

where Y_0 is the characteristic admittance of the dominant waveguide mode, and λ_g is the guide wavelength of the dominant mode.

The attenuation α_b resulting from the hole is

$$\alpha_b = 10 \log \left[\frac{(B/Y_0)^2}{4} - 1 \right] \text{ dB} \quad (63)$$

and the attenuation α_t resulting from the finite thickness is given by Eq. (61), and the total attenuation is calculated using Eq. (58).

7. RESONATOR MEASUREMENTS

As described earlier, the resonator is described fully in terms of the resonant frequency f_0 , the coupling coefficient, and the quality factors. The unloaded quality factor Q_u , loaded quality factor Q_L , and external quality factor Q_e are useful in various circuit analyses containing microwave cavities.

Experimental determination of the parameters is straightforward using modern microwave network analyzers. In Fig. 20, single-port and two-port cavity measurement setups are shown. The magnitude and phase of the reflection and transmission coefficients are measured to determine the resonator parameters.

7.1. Single-Port Resonator

The equivalent circuit of a single-port cavity resonator is shown in Fig. 1, where R , L , and C are the equivalent lumped resistance, inductance, and capacitance. The equivalent parallel and series circuits of Figs. 1a and 1b are also known as the detuned short and open configurations, respectively. The equivalence between series and

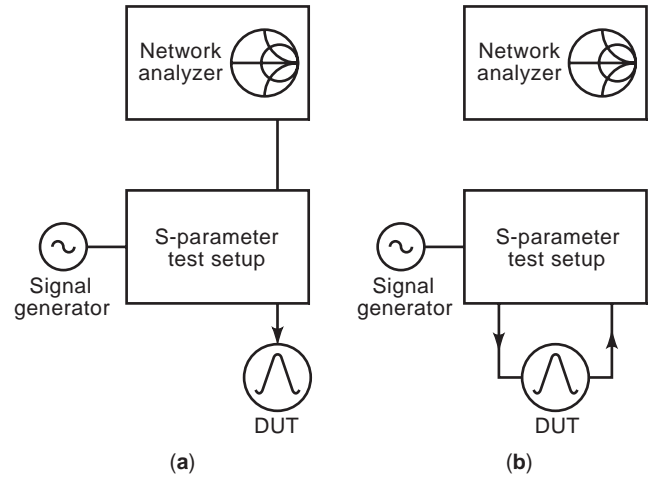


Figure 20. Measurement setup for (a) reflection and (b) transmission resonator.

shunt parameters of these resonant circuits is as shown in the following table:

Parameter	Series Tuned	Parallel Tuned
f_0	$\frac{1}{\sqrt{LC}}$	$\frac{1}{\sqrt{LC}}$
Q_u	$\frac{\omega L}{R}$	$\frac{R}{\omega L}$
β	$\frac{Z_0}{R}$	$\frac{R}{Z_0}$
Q_L	$\frac{Q_u}{1 + \beta}$	$\frac{Q_u}{1 + \beta}$

The input impedance of the circuit in Fig. 1a can be rewritten as

$$Z_{in} = \frac{R}{1 + j2Q_u\delta} \quad (64)$$

where $\delta = (\omega - \omega_0)/\omega_0$ represents the frequency detuning parameter [12]. By varying δ , the locus of the impedance given by Eq. (64) is determined. On a Smith chart, a circular locus, as shown in Fig. 21 is obtained depending on the coupling coefficient. For circle A, $R = Z_0$ and the locus passes through the origin. This condition is called *critical coupling* and corresponds to $\beta = 1$, implying that it provides a perfect match to the transmission line at resonance. The circle B with $R < Z_0$ is called undercoupled condition and $\beta < 1$. Finally, the circle C with $R > Z_0$ is an overcoupled condition with $\beta > 1$ [13].

The coupling coefficient for any cavity is calculated using the measurement of reflection coefficient S_{11,ω_0} at resonance. For the undercoupled case, we obtain

$$\beta = \frac{1 - S_{11,\omega_0}}{1 + S_{11,\omega_0}} \quad (65)$$

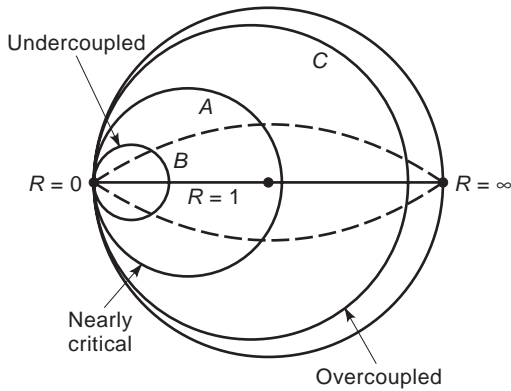


Figure 21. Input impedance of a single-port resonant cavity on the Smith chart for 3 degrees of coupling.

and for the overcoupled case, we obtain

$$\beta = \frac{1 + S_{11, \omega_0}}{1 - S_{11, \omega_0}} \quad (66)$$

The intersection of the impedance locus with the real axis provides the value of β as shown in Fig. 22.

Other quality factors can be determined from Eq. (64), which can be rewritten as

$$\begin{aligned} \bar{Z}_{in} = \frac{Z_{in}}{Z_0} &= \frac{\beta}{1 + j2Q_u \delta} \\ &= \frac{\beta}{1 + j2Q_L(1 + \beta)} = \frac{\beta}{1 + j2Q_e \beta} \end{aligned} \quad (67)$$

The Q_u , Q_L , and Q_e are related as

$$Q_u = Q_L(1 + \beta) = Q_e \beta \quad (68)$$

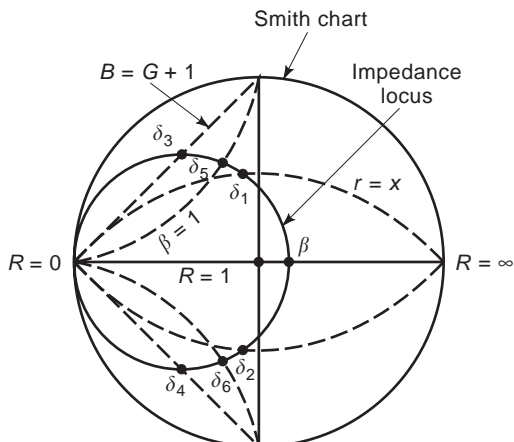


Figure 22. Determination of β and the half-power points from the Smith chart. Q_0 locus is given by $X=R(B=G)$; Q_L by $X=R+1$; Q_{ext} by $X=1$.

The normalized frequency deviations for unloaded, loaded, and external quality factors are given by

$$\delta_u = \pm \frac{1}{2Q_u}, \quad \delta_L = \pm \frac{1}{2Q_L}, \quad \delta_e = \pm \frac{1}{2Q_e} \quad (69)$$

From Eqs. (69) and (67), the impedance locus of Q_u is determined and is given by

$$(Z_{in})_u = \frac{\beta}{1 \pm j} \quad (70)$$

Equation (70) represents the points on the impedance locus where the real and imaginary parts of the impedance are the same. Figure 22 represents the locus of these points (corresponding to $R=X$) for all possible values of β . This locus is an arc whose center is at $Z=0 \pm j$, and the radius is the distance to the point $0 \pm j$. The intersection of this arc with the impedance locus determines the Q_u measurement points:

$$Q_u = \frac{f_0}{f_1 - f_2} \quad (71)$$

The frequencies f_1 and f_2 are called half-power points because these points correspond to $R=X$ on the impedance locus. The loaded and external Q values can be determined in a similar way. Equations (67) and (69), the impedances corresponding to Q_e and Q_L , are given by

$$(Z_{in})_e = \frac{\beta}{1 \pm j\beta} \quad (72)$$

and

$$(Z_{in})_L = \frac{\beta}{1 \pm j(1 + \beta)} \quad (73)$$

By using Eqs. (72) and (73), the Q_e and Q_L loci are easily determined. These loci are shown in Fig. 22.

7.2. Two-Port Resonator

The equivalent circuit of a two-port cavity resonator is shown in Fig. 23. In this case, the input and output coupling are represented as β_1 and β_2 . They are determined from

$$\beta_1 = \frac{Y_{01}}{n_1^2 G} \quad \text{and} \quad \beta_2 = \frac{Y_{02}}{n_2^2 G} \quad (74)$$

where Y_{01} and Y_{02} are the admittances seen at the input and output ports. The coupling coefficients are directly determined by measuring the VSWR at the input and output ports with the other port open-circuited.

The transmission response of such a resonant circuit measured using the setup of Fig. 20, is shown in Fig. 23. The coupling coefficients and the quality factors for two-port resonators determined from the measurement of the insertion loss T at resonant frequency and the 3 dB

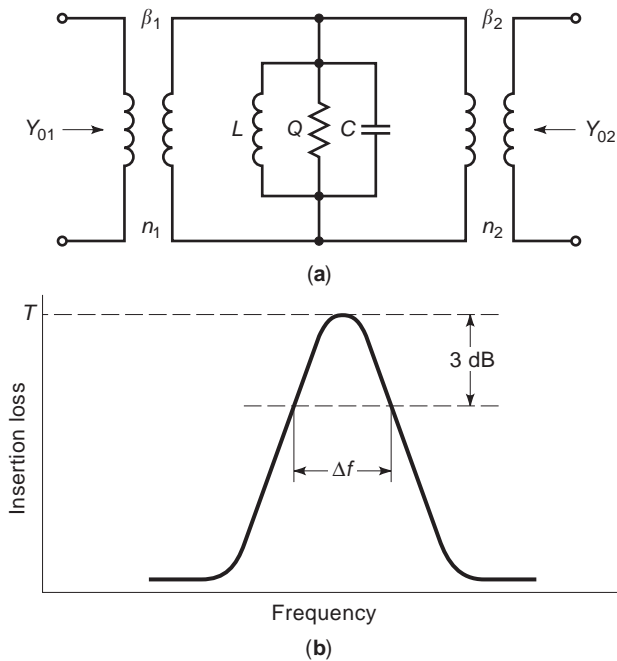


Figure 23. (a) Equivalent circuit of a two-port resonator with input and output transformers; (b) transmission response of a two-port resonator.

bandwidth Δf using the following well-known relations [14]

$$T = \frac{2\sqrt{\beta_1\beta_2}}{1 + \beta_1 + \beta_2} \tag{75}$$

$$Q_L = \frac{f_0}{\Delta f} \tag{76}$$

$$Q_u = Q_L(1 + \beta_1 + \beta_2) \tag{77}$$

8. APPLICATIONS

A development of the cavity resonators was an important milestone in microwave technology. Early work on cavity resonators focused on cavities of regular shapes. But the development of microwave oscillators and amplifiers required complex shapes to achieve the performance required in the development of klystrons, magnetrons, and traveling-wave tubes. Some of those shapes were covered in this article to illustrate the fact that different cavity structures are required to achieve the desired results.

Cavity resonators are also used extensively to measure frequency or wavelength. Tunable cavities are made to resonate at different frequencies by varying size and then calibrating size against frequency.

Cavity resonators are now most widely used to develop filters. Depending on the characteristics of the cavity, it can be used for narrowband as well as wideband filters. The applications of cavity resonators are concomitant with those of filters. In that sense, cavity resonators have

applications in lowpass, bandpass, bandstop, and high-pass filters. They are also used in duplexers, multiplexers, and directional filters.

In the following sections, the preceding applications will be reviewed and their key aspects will be highlighted. Additional information can be found in other relevant articles of this encyclopedia.

8.1. Applications in Microwave Tubes

There were many problems in the early development of microwave valves that were caused by circuit elements and their interconnections. The development of resonant cavities led to the invention of klystron. The cavity resonators were able to reduce the transit time. The capacitance between the cathode and grid was used to resonate with the low inductance provided by the cavity.

In klystron amplifiers, multiple cavities are used to allow bunching of electrons. Because the electromagnetic fields in a cavity are changing as a function of time, the alternating electric fields at the grid cause bunching of electrons. By using another cavity at an optimum distance, the electrons are further bunched to build up oscillations. The first “buncher” resonator is excited into resonance through external means, and the second “catcher” resonator takes out the power. In klystron amplifiers, internal feedback is also provided via openings in the cavities.

In the reflex klystron, the electron beam is bunched by passing through a single resonator. The reflector returns the electron beam to this cavity at an optimum bunched condition. At this time, the energy is extracted from the cavity.

Magnetrons use various shapes of cavities to build oscillations and power. The power is extracted from one of the resonators through a coupling loop or an iris.

In traveling wave tubes, cavities are used as part of the slow wave structure. For additional information, refer to the appropriate article in this encyclopedia.

8.2. Filters

In order to use cavity resonators in filter applications, a reactance or susceptance slope parameter is generally required. The reactance slope parameter for a series resonant structure is defined as

$$\chi = \left. \frac{\omega_0 dX}{2 d\omega} \right|_{\omega=\omega_0} \text{ ohms} \tag{78}$$

Similarly, the susceptance slope parameter for the parallel resonant structure is defined as

$$B = \left. \frac{\omega_0 dG}{2 d\omega} \right|_{\omega=\omega_0} \text{ siemens} \tag{79}$$

From Eqs. (78) and (79), it is straightforward to see that for a series resonant circuit at resonance

$$\chi = \omega_0 L = \frac{1}{\omega_0 C} \tag{80}$$

and

$$Q = \frac{\lambda}{R} \quad (81)$$

Similarly, for a parallel resonant circuit at resonance

$$B = \omega_0 C = \frac{1}{\omega_0 L} \quad (82)$$

and

$$Q = \frac{B}{G} \quad (83)$$

In a bandpass filter design, impedance or admittance inverters can be used with series or shunt-type resonant structures. The reactance or admittance slope parameter is related to filter prototype element values. The external Q and coupling coefficients are also expressed in terms of the reactance or admittance slope parameter. Inductive posts or irises with impedance inverters can be used to construct a bandpass filter. For details on waveguide filters, refer to the appropriate section in this encyclopedia.

8.3. Frequency Measurement

Both coaxial and waveguide resonators have been used in commercially available wavemeters. The main requirement in selecting cavity dimensions is to ensure that the cavity resonates in the fundamental mode, that there are no degenerate modes, and that they are easy to manufacture and calibrate.

These wavemeters are basically tunable cavities, and when the length is $\lambda_g/2$, the cavity resonates by taking in some energy from the transmission line, coaxial, or waveguide. This action will produce a dip in the transmitted power. When the length of the cavity is calibrated, the frequency or wavelength can be read off directly from the dial. The extent of the dip depends on the amount of coupling. The Q of wavemeter cavities is quite high, on the order of 5000–10,000 depending on the desired accuracy.

In a coaxial-line wavemeter, as shown in Fig. 24, the center conductor is used as a probe to couple energy to the resonator. Noncontacting plungers with chokes are used

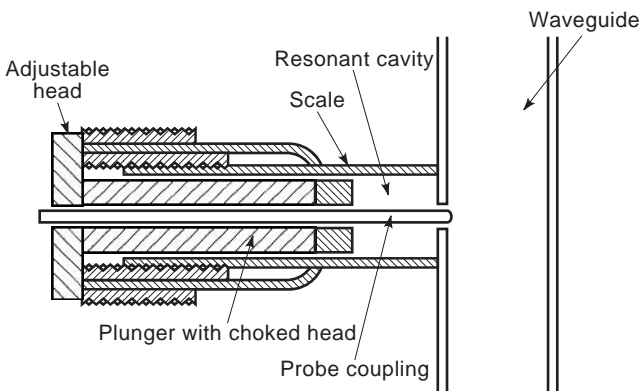


Figure 24. Coaxial cavity wavemeter.

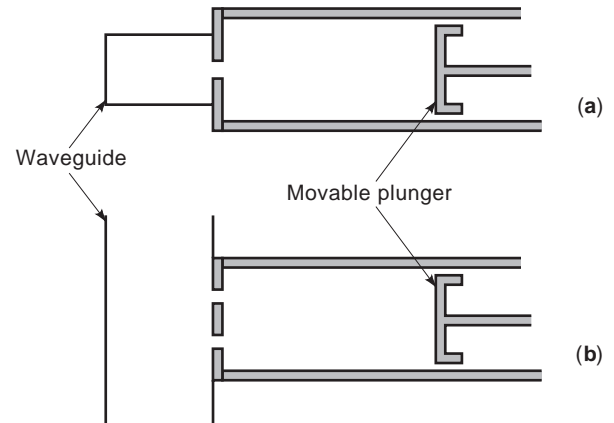


Figure 25. Cylindrical cavity wavemeter: (a) end view; (b) top view.

to provide a variable short position. The coaxial resonator will resonate whenever the cavity length is a half-wavelength. Measuring the change in plunger positions between two successive minima and multiplying by 2 will give the wavelength of operation. Because of the large surface area of the coaxial outer wall, the cavity Q is not very high.

Cylindrical cavities are generally used for wavemeters, as shown in Fig. 25. The currents in the TM_{01} mode flow circumferential to the cavity cross section. Therefore, the short-circuiting plunger does not need to have a good contact and provides easy manufacturability. Furthermore, other higher-order modes that require current flow in the endplates are not supported. In order to prevent other modes from being excited, two coupling holes in the side wall of a waveguide, which are a half-wavelength apart, are used. The bandwidth of the coupling structures can be increased by selecting an elongated hole.

BIBLIOGRAPHY

1. R. E. Collin, *Foundations of Microwave Engineering*, McGraw-Hill, New York, 1966, Chap. 7.
2. S. Ramo, J. Whinnery, and T. Van Duzer, *Fields and Waves in Communication Electronics*, Wiley, New York, 1965, Chap. 10.
3. R. N. Ghose, *Microwave Circuit Theory and Analysis*, McGraw-Hill, New York, 1963, Chap. 8.
4. T. Moreno, *Microwave Transmission Design Data*, Dover, New York, 1958, Chap. 18.
5. H. J. Reich et al., *Microwave Principles*, Van Nostrand, Princeton, NJ, 1960, Chap. 7.
6. J. G. Kretzschmar, Wave propagation in hollow conducting elliptic waveguide, *IEEE Trans. Microwave Theory Tech.* **MTT-18**:547–554 (1970).
7. J. G. Kretzschmar, Mode chart for elliptical resonant cavities, *Electron. Lett.* **6**:432–433 (1970).
8. W. Bräckelmann, Die Grenzfrequenzen von höheren Wellentypen im Koaxial Kabel mit elliptischem Querschnitt, *Arch. Elek. Übertragung.* **21**:421–426 (1967).
9. N. W. McLachlan, *Theory and Application of Mathieu Functions*, Clarendon Press, Oxford, UK, 1947.
10. W. W. Hansen and R. D. Richtmyer, On resonators suitable for klystron oscillators, *J. Appl. Phys.* **10**:189–199 (1939).

11. F. L. Ng, Tabulation of methods for the numerical solution of the hollow waveguide problem, *IEEE Trans. Microwave Theory Tech.* **MTT-22**:322–329 (1974).
12. E. L. Ginzton, *Microwave Measurements*, McGraw-Hill, New York, 1957, Chap. 9.
13. I. Bahl and P. Bhartia, *Microwave Solid State Circuit Design*, Wiley, New York, 1988, Chap. 3.
14. M. Sucher and J. Fox, *Handbook of Microwave Measurements*, 3rd ed., Vol. 2, Wiley, New York, 1963, Chap. 8.

FURTHER READING

- B. Lax and K. J. Button, *Microwave Ferrites and Ferromagnetics*, McGraw-Hill, New York, 1962, pp. 145–196.
- S. Y. Liao, *Microwave Devices and Circuits*, Prentice-Hall, Englewood Cliffs, NJ, 1980, Chap. 4.
- P. K. Mariner, *Introduction to Microwave Practice*, Academic Press, New York, 1961, Chap. 7.
- G. L. Matthaei, L. Young, and E. M. T. Jones, *Microwave Filters, Impedance Matching Networks and Coupling Structures*, McGraw-Hill, New York, 1964.
- S. R. Rengarajan and J. E. Lewis, Quality factor of elliptical cylindrical resonant cavities, *J. Microwave Power* **15**:53–57 (1980).
- A. K. Sharma, Spectral domain analysis of elliptic microstrip ring resonator, *IEEE Trans. Microwave Theory Tech.* **MTT-32**: 212–218 (1984).
- A. K. Sharma and B. Bhat, Spectral domain analysis of elliptic microstrip disk resonators, *IEEE Trans. Microwave Theory Tech.* **MTT-28**:573–576 (1980).

CELLULAR RADIO

WILLIAM C. Y. LEE
AirTouch Communication

The cellular radio system is sometimes called a *mobile phone system* or a *car phone system*. Due to the daily needs of subscribers, cellular systems have expanded considerably all over the world. This article discusses the history of cellular systems and the difficulty of deploying them in the mobile radio environment, elaborating on employing digital cellular systems, Personal Communication Services (PCS) mobile satellite systems, and the future IMT-2000 system.

1. HISTORY OF CELLULAR RADIO SYSTEMS

1.1. Analog System

1.1.1. Startup Period (1964–1987). In 1964, AT&T Bell Labs actively developed a high-capacity mobile radio phone system called Advanced Mobile Phone Service (AMPS) [1], which is an analog frequency modulation (FM) system. The system consists of many so-called cells.

Each cell has one or multiple transceivers. Because of the cell formation, the system is referred to as a cellular system. In the analog AMPS system, mobile units are compatible with all the cellular systems operating in the United States, Canada, and Mexico. A spectrum of 50 MHz (limited to 825–849 MHz for mobile transmissions and 869–896 MHz for base-station transmissions) is shared by two cellular system providers in each market (city). Each one provider operates over a bandwidth of 25 MHz in a duplex fashion (using 12.5 MHz in each direction between cell sites and mobile units). There are 416 channels, comprising 21 setup channels and 395 voice channels. The channel bandwidth is 30 kHz. Mobile cellular telecommunications systems [2] have two unique features:

1. First, they invoke the concept of frequency reuse for increasing spectrum efficiency. The same set of frequency channels can be assigned to many cells. These cells are called *cochannel cells*. The separation between two cochannel cells is engineered by the D/R ratio (see Fig. 1), where D is the cochannel cell separation and R is the cell radius. A 4-mi cell implies $R = 4$ mi. The D/R ratio is characteristic of a cellular system. If the D/R ratio is high, the voice quality is improved by reducing the system's user capacity.
2. A second feature, handing off communications from one frequency to another, occurs when a mobile unit enters a new cell. The scheme is called a handoff in North America and a handover in Europe. The system handles this operation automatically, and the users do not need to intervene. A good handoff

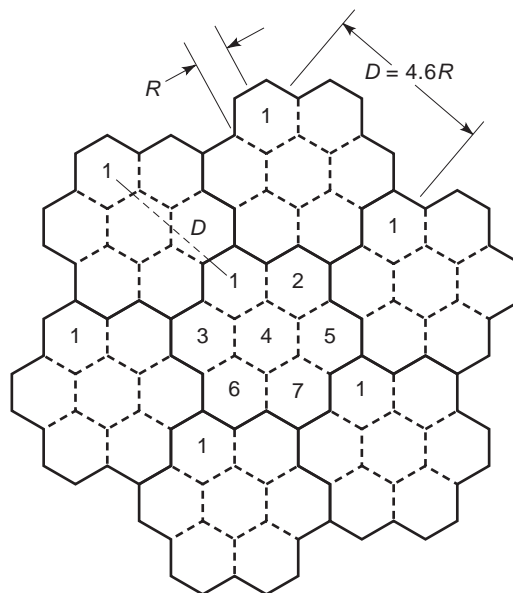


Figure 1. Hexagonal coils in an AMPS system: R = radius of cells, D = minimum separation of cochannel cells, $q = D/R = 4.6$, K = number of cells in a cluster = 7. Clusters are indicated, and the six cells that effectively interfere with cell 1 are numbered 2 through 7. The shaded cells are cochannel cells.

algorithm can reduce both the call drop rates and interference. In general, there are two kinds of handoffs: (1) soft handoffs, which implies making a new connection before breaking the old one; and (2) hard handoffs, which involves breaking the old connection before making the new one.

The first installation of a cellular system occurred in Tokyo in 1979, using a minor modification of AMPS. The first AMPS cellular system installed in the United States took place in Chicago in 1983. Analog cellular systems are in use over most of the world, employing different versions of AMPS: in Japan, the Nippon Telephone and Telegraph (NTT) AMPS system; in the UK, the Total Access Communications System (TACS); and in northern Europe, the Nordic Mobile Telephone (NMT). The major difference is their reduced channel bandwidths of 25 kHz instead of 30 kHz as in AMPS.

1.1.2. Mature Period (1987–1992). From 1987 to 1992, the 90 MSA (metropolitan statistical area) markets, as well as most of the 417 RSA (rural service area) markets, had cellular operations in the United States. The number of subscribers reached 1 million. The cell split (reducing the size of cells) technique and dynamic frequency assignment were applied to increase the user capacity.

When the cell radius R is less than half a kilometer, the cell is called a *microcell*. In such small cells it is harder to reduce the so-called cochannel interference in order to increase capacity, requiring special technological approaches called *microcell technology*. The world was also becoming more aware of the potential future markets. Suddenly, finding the means to increase capacity became urgent.

1.2. Digital System

1.2.1. Introduction Period. In 1987, the capacity of the AMPS cellular system started to show its limitations. The growth rate of cellular subscribers far exceeded expectations. In 1987, the Cellular Telecommunication Industry Association (CTIA) formed a Subcommittee for Advanced Radio Technology to study the use of a digital cellular system [3] to increase capacity. At that time, the Federal Communications Commission (FCC) had clearly stated that no additional spectrum would be allocated to cellular telecommunications in the foreseeable future. Therefore, the existing analog and forthcoming digital systems would have to share the same frequency band. In December 1989, a group formed by the Telecommunication Industry Association (TIA) completed a draft of a digital cellular standard.

The digital AMPS, which must share the existing spectrum with the analog AMPS, is a duplex time-division multiple-access (TDMA) system. The channel bandwidth is 30 kHz. There are 50 TDMA frames per second in each channel. Three or six timeslots per frame can serve three calls or six calls at the same time in one channel. The

speech coding rate is 8 kbps (kilobits) per second. An equalizer is needed in the receiver to reduce the intersymbol interference that is due to the spread in time delay caused by the dispersed time arrival of multipath waves. The North American TDMA system was first called IS-54 by the TIA. Later, the system was modified and renamed IS-136.

During this period, not all mobile telephone systems in Europe were compatible. A mobile phone unit working in one country could not operate in another country. In 1983, in response to the need for compatibility, a special taskforce, the Special Mobile Group [4], was formed among European countries to develop a digital cellular system called GSM (group of special mobile systems) in 1994, then renamed to stand for global system for mobile communications. The operating principles of the GSM system resemble those of the AMPS in radio operation, but the system parameters are different; this will be described later.

In the United States, in addition to the TDMA being considered above, another particularly promising technology is code-division multiple access (CDMA) [3]. It is a spread-spectrum technique with a bandwidth of 1.25 MHz. The maximum number of traffic channels is 55. This CDMA system is called IS-95 or cdmaone.

There are three mobile data systems in the United States: Ardis, operated by IBM/Motorola; Ram, operated by Ericsson; and CDPD (Cellular Digital Packet Data) system. The transmission rates for all data systems are around 8 kbps. Only CDPD operates in the cellular spectrum band.

1.2.2. The Future. Starting in 1996, the so-called PCS systems were deployed. They were cellular-like systems, but operated in the 1.8 GHz band in Europe and the 1.9 GHz range in North America. In Europe, the so-called DCS-1800 PCS systems were endorsed, which are based on the GSM system. In the United States, the PCS had three versions: DCS-1800 (a GSM version), TDMA-1900 (IS-136 version), and CDMA-1900 (IS-95 version). The PCS could have six operational licenses (A, B, C, D, E, F) in each city. Therefore, more competitors would be in the mobile phone services business.

In addition, the mobile satellite systems that use the LEO concept (low-Earth orbit) were deployed. Iridium (66 satellites) and Globalstar (48 satellites) were launched at 900 km and 400 km altitudes, respectively. These systems can integrate with cellular systems and enhance cellular coverage domestically and roam internationally as a global system. Other LEO systems are also in the development stage. There is a special LEO system called Teledesic that will be operating at 26 GHz with 840 satellites in orbit. This system is used for wideband data and video channels to serve subscribers in a high capacity network.

A future cellular system, called the International Mobile Telephone (IMT-2000) system, is now in the planning stage. A universal cellular standard (or PCS) system with high capacity and high transmission rate was realized by the year 2002.

2. MOBILE RADIO ENVIRONMENT: A DIFFICULT ENVIRONMENT FOR CELLULAR RADIO SYSTEMS

2.1. Understanding the Mobile Radio Environment

2.1.1. The Limitations of Nature. In the mobile radio environment, there are many attributes that limit the system performance for wireless communication. In the past, there were attempts to adapt digital equipment such as data modems and fax (facsimile) machines used for wireline to cellular systems. The data engineers at that time only realized the blanking and burst interruption in the voice channel as a unique feature of handoffs and power control. They modified data signaling by overcoming the impairments caused by blanking and burst signaling interruption. This modified data modem did not work as expected in the cellular system. Actually, the blanking and burst interruption scheme was not the sole cause of the inadequate data transmission and would have been relatively easy to handle. But without entirely understanding the impairments, the unexpected poor performance could not be offset by merely overcoming the blanking and burst signaling impairment.

2.1.2. Choosing the Right Technologies. In designing radiocommunication systems, there are many different technologies, and among them no single technology is superior to the others. Choosing a technology depends on real conditions in the environment of a particular communication. In satellite communication or microwave link transmission, the radio environments are different from that of the mobile radio environment. There are many good technologies that work in satellite communication and microwave link transmission, but they may not be suitable for the terrestrial mobile radio environment. Therefore, choosing the right technology must depend on the transmission environment.

2.2. Description of the Mobile Radio Environment

The mobile radio environment is one of the most complex ones among the various communication environments.

2.2.1. Nature Terrain Configuration. Because the antenna height of a mobile unit or a portable unit is very close to the ground, the ground-reflected wave affects the reception of the signal from the transmitting site via the direct path. The free-space loss is 20 dB/dec (dec stands for decade, a period of 10) or, in other words, it is inversely proportional to the distance d^{-2} . However, in the mobile radio environment, due to the existing ground-reflected wave and the small incident angle θ , as shown in Fig. 2, the total energy of the ground-reflected wave is reflected back to space. Due to the nature of electromagnetic waves, when the wave hits the ground, the phase of the wave changes by 180° . Therefore, at the mobile, the direct wave and reflected wave cancel each other instead of adding constructively. As a result, the signal that is received becomes very weak. A simple explanation is as follows. If the pathlength of the direct wave is d , the pathlength of the reflected wave is $d + \Delta d$. Then the received power of the two combined waves is proportional to d^{-4} as

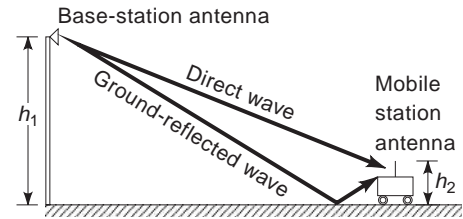


Figure 2. Two-wave propagation model.

demonstrated below

$$P_r \propto \left(\frac{1}{d} - \frac{1}{d + \Delta d} \right)^2 = \left(\frac{\Delta d}{d(d + \Delta d)} \right)^2 = \frac{(\Delta d)^2}{d^4} \quad (1)$$

where Δd is assumed to be much less than d and Δd is a function of the antenna height h_1 at the base station. From Eq. (1), the mobile radio path loss follows the inverse fourth-power rule or 40 dB/dec, and the antenna height gain follows the second-power rule or 6 dB/oct. In the mobile radio environment, the average signal strength at the mobile unit varies due to the effective antenna height h_e at the base station measured from the mobile unit location. Since the mobile unit is traveling, the effective antenna height is always changing as a function of terrain undulations, and so is the average signal strength. This phenomenon is shown in Fig. 3.

This two-wave (direct wave and ground-reflected wave) model is only used to explain the propagation loss of 40 dB/dec in the mobile radio environment, not the multipath fading.

2.2.2. Humanmade Effects

2.2.2.1. Humanmade Communities. These can be classified as metropolitan areas, urban areas, suburban areas, open areas, and so on. The distribution of buildings and homes depends on the population size. The reception of the signal is affected by the differences in humanmade communities and results in different propagation path loss.

2.2.2.2. Humanmade Structures. Different geographic areas use different construction materials, different types of construction frames, and different sizes of buildings.

Cities such as Los Angeles, San Francisco, and Tokyo are in earthquake zones and follow earthquake construction codes. The signal reception in those cities is different from that in others. Humanmade structures will affect the propagation path loss and multipath fading due

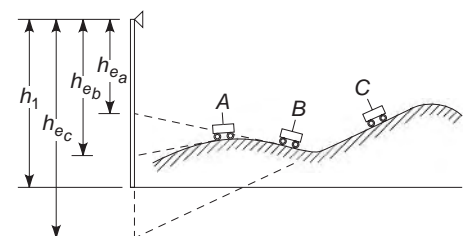


Figure 3. Effective antenna heights at base station based on different locations of mobile stations.

to reflection and the signal penetration through the buildings.

2.2.2.3. Humanmade Noise. This can be classified into two categories: industrial noise or automotive ignition noise. The high spikes in automotive ignition or in machines are like impulses in the time domain; their power spectrum density will cover a wide spectrum in the industrial frequency domain. At 800 MHz, automotive ignition noise is determined by the number of vehicles. For a traffic volume from 100 cars/h to 1000 cars/h, the noise figure increases 7 dB. As the application of ultra-high-frequency (UHF) devices and microwave systems increase, so does the noise pollution for cellular systems. As we will mention later, a communication system is designed to maintain the minimum required carrier-to-interference ratio (C/I_s). The interference I may, under certain circumstances, be included in noise the N . If the interference level is higher, the level of the carrier, C should also be higher in order to meet the $(C/I)_s$ requirement. This means that when the humanmade noise level is high, either the transmission power at the base station should be increased or the cell size must be reduced.

2.2.3. Moving Medium. If the mobile unit is in motion, the resulting signal from multipath waves at one location is not the same at another; thus the mobile receiver observes an instantaneous fluctuation in amplitude and phase. The amplitude change is called *Rayleigh phase*, and the phase change is a uniformly distributed process, or random FM in FM systems. The signal fading can be fast or slow depending on the speed of the vehicle. When the vehicle speed is slow, the average duration of fading is long. This average fading duration can be, for example, 7 ms at -10 dB below the average level when the vehicle speed is 24 km/h at a propagation frequency of 850 MHz. In an analog system, a fade duration of 7 ms does not affect the analog voice; the ear cannot detect these short fades. However, the fade duration of 7 ms is long enough to corrupt the digital (voice and data) transmissions. At a transmission rate of 20 kbps, 140 bits will sink in the fade. Furthermore, the vehicle speed of all the users is not constant, and the use of interleaving and channel coding to protect the information bits is very difficult. Furthermore, voice communication is operating in real time unlike data transmission which can be in any time-delay fashion. Many schemes used by data communication cannot be used for digital voice communication.

2.2.4. Dispersive Medium. Because of humanmade structures, the medium becomes dispersive. In a dispersive medium, two phenomena occur. One is time delay spread and the other is selective fading. The time delay spread is caused by a signal transmission from the base station reflected from different scatterers and arriving at the mobile unit at different times. In urban areas, the mean time-delay spread Δ is typically 3 μ s; in suburban areas, Δ is typically 0.5 μ s. In an open area, Δ is typically 0.2 μ s, and in an in-building floor, Δ is around 0.1 μ s or less. These time delay spreads do not affect the analog signal because the ear cannot detect the short delay

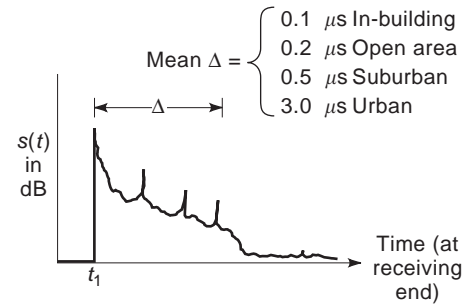


Figure 4. Time delay spread Δ at the receiving end when transmitting one bit in a dispersive medium.

spread. However, in a digital system when a symbol (bit) is sent, many echoes arrive at the receiver at different times. If the next symbol is sent out before the first one dies down, intersymbol interference occurs. The dispersive medium also causes frequency selective fading (Fig. 4).

The selective fading will not harm the moving receiver because when the mobile unit is moving, only the average power is considered. Then, in order to make a mobile phone call when the mobile unit is at a standstill, it usually requires that all the signal strengths from four frequencies have two strong setup channels and two strong voice channels. A pair of frequencies is formed by a channel carrying a call on both a forward link and a reverse link. When the mobile unit is moving, the average power of the four frequencies is the same. Then we base our quality estimates on one $(C/I)_s$ value. But when the mobile unit is still, the signals of four frequencies at one location are different due to frequency selective fading. Unless all four frequencies are above the acceptable threshold level, the call cannot be connected.

2.3. Concept of C/I

In designing high-capacity wireless systems, the most important parameter is the carrier-to-interference ratio (C/I). The C/I ratio and the D/R ratio are directly related. The D/R ratio is determined by the C/I ratio. Usually, with a given received signal level C , the lower the interference level, the higher the C/I ratio and hence the quality improves. There is a specific C/I level, namely $(C/I)_s$, that the system design criterion is based on. We may derive the relationship between C/I and D/R as follows. Assume that the first tier of six cochannel interference cells is the major cause for the interference I . Based on the 40 dB/dec propagation rule, we obtain

$$\frac{C}{I} = \frac{C}{\sum_{i=1}^6 I_i} \approx \frac{C}{6 \cdot I_i} = \frac{R^{-4}}{6 \cdot D^{-4}} = \frac{(D/R)^4}{6} \quad (2)$$

A general equation of the cochannel interference reduction factor q can be expressed, from Eq. (2), as

$$q = (D/R)_s = (6(C/I)_s)^{1/4} \quad (3)$$

where $(C/I)_s$ is obtained from a subjective test corresponding to the required voice (or data) quality level, as mentioned

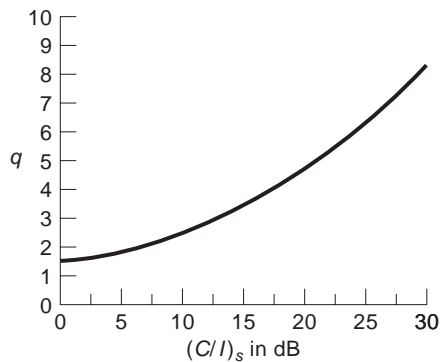


Figure 5. Relationship between q and $(C/I)_s$ [Eq. (3)].

previously. Equation (3) is plotted in Fig. 5. The $(C/I)_s$ ratio is chosen according to either the required voice or data channel quality.

2.4. The Predicted Signal Strength Models

Since the $(C/I)_s$ is a system design parameter, system planning engineers would like to use an effective model to predict both C and I in a given area. There are two different prediction models. One predicts the average signal strength along the radio path based on the path loss slope. The Okumura and Hata models [5,6] represent these types of models. The other predicts the local mean signal strength along a particular mobile path (street or road) based on the particular terrain contour. Lee's model [7] represents these types of models.

3. REASONS FOR DIGITAL CELLULAR

3.1. Compatibility in Europe

Again, due to the lack of a standard mobile radio system in Europe during the early 1980s, the mobile phone unit used in each country could not be used in other countries. Starting in 1982, ETSI (European Telecomms Standard Institute) formed a group called the Group of Special Mobile to construct an international mobile radio system called GSM for Europe. The system chosen was to be a digital system using TDMA for the access scheme. The GSM advanced intelligent network (AIN) was adopted from the wireline telephone network. GSM was the first digital mobile phone system in the world.

3.2. Capacity in North America

The frequency spectrum is a very limited resource commonly shared by all wireless communications. Among the wireless communications systems, cellular is the most spectral efficient system where the so-called spectral efficiency is related to the number of traffic channels per cell. From this number, we can derive the erlang/cell ratio, which translates to erlangs/km², or the number of traffic channels/km² based on the traffic model and the size of the cells.

However, a spectrum of only 50 MHz has been allocated to cellular operators in the United States. Furthermore, since two operators are licensed in each market, the spec-

trum of 50 MHz must be split in two. Therefore, system trunking efficiency is reduced and interference caused by an operator in one market often contaminates the other operator's allocated spectrum. Furthermore, manufacturing companies were always considering lowering the cost of cellular units and increasing sales volume. As a result, the specification of cellular units could not be kept tight, and thus more interference prevailed. Once interference increased and could not be controlled by cellular operators, both voice quality and system capacity decreased.

In 1987, the top 10 U.S. markets were already feeling the constraints of channel capacity; they would not be able to meet the market demand in the future. The solution for this increasing need for high capacity was to go digital [1-3]. Going digital was the best solution because of the nature of the digital waveform. If system compatibility is not an issue, the top 10 U.S. markets might and could go digital by themselves. However, for the sake of compatibility the United States needed one standard for the entire North American cellular industry.

3.3. The Advantages of a Digital System

Digital systems offer the following advantages:

1. The digital waveform is discrete in nature. Therefore, the digital waveform can be regrouped easily for transmission needs.
2. Digital transmission is less susceptible to noise and interference.
3. Digital modulation can confine the transmitted energy within the channel bandwidth.
4. Digital equipment may consume less battery power, and hence may reduce equipment weight.
5. Digital systems can provide reliable authentication and privacy (encryption).

4. REQUIREMENT FOR CELLULAR AND PCS

In 1996, the Telecommunications Act Bill was passed by the U.S. Congress and stated, in simple terms, that everyone could get into everyone's business. Cellular service is moving toward digital and is trying to compete with PCS. The PCS spectrum was auctioned in early 1996. There are wideband PCSs and narrowband PCSs (see Fig. 6). The spectrum of wideband PCS is allocated at 1900 MHz in order to operate the same technology as the cellular system. The spectrum of narrowband PCS is allocated at 900 MHz and is used for two-way paging. The joint requirements of both cellular and PCS are as follows:

From the end user's perspective—the PCS and cellular units should be light in weight and small in size, and have long talk-time capabilities without battery recharging and good quality in voice and data. The unit should be employable for initiating and receiving calls anywhere using any telephone feature. The important requirement of PCS and cellular is to please the vast majority of subscribers who always prefer to carry a single unit, not many units. This

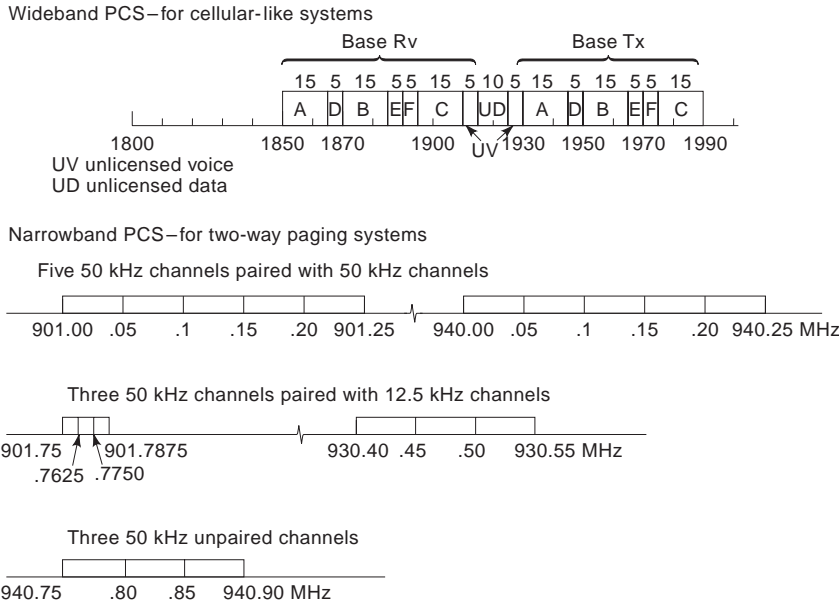


Figure 6. Spectrum allocated for wideband PCS and narrowband PCS.

unit can be classified according to the different grades of service.

From the system provider’s perspective—the PCS should provide full coverage and large system capacity to serve end users. An end user unit ideally should be serviced by one system with different grades of service and unless there are natural limitations by the various personal communication environments (such as mobile vehicle, pedestrian, and indoor public communication). Then one end user unit should be capable of accessing more than one system.

5. DIGITAL MODULATIONS AND MULTIPLE ACCESS

5.1. Digital Modulation Schemes

Digital modulation schemes can be selected to confine the transmitted energy of a digital voice signal in a given frequency bandwidth while transmitting in a mobile radio environment. The information may have to be modulated by signal phases or frequencies, rather than amplitudes, because the multipath fading impairs the signal amplitude.

5.2. Multiple Access

Digital transmission can use time-division multiple access (TDMA), frequency-division multiple access (FDMA), or code-division multiple access (CDMA), but in analog transmission only FDMA can be used. FDMA provides many different frequency channels, where each is assigned to support a call. TDMA means chopping a relatively broadband channel over time into many timeslots. Each timeslot is assigned to support a call. CDMA means generating many different code signatures over a long code-bitstream channel, where each code signature is assigned to convey a call. FDMA is a narrowband system. It

is a low-risk system to develop but was voted down by the industry in 1987. FDMA is not suitable for high-speed data transmission. TDMA was first developed in Europe and is called GSM. TDMA has been developed in North America. For the ADC (American Digital Cellular system), CDMA needs more advanced technology and is relatively harder to implement than the other two multiple-access schemes, especially in the mobile radio environment. However, the improved user capacity of CDMA has given the cellular industry the incentive to develop this system. Therefore, digital transmission in the mobile radio environment has only two competing multiple accesses. The North America selected TDMA based on the influence from the European GSM.

6. SPECIFICATIONS FOR DIFFERENT CELLULAR/PCS SYSTEMS

6.1. Analog Systems

Each traffic channel in an analog system uses two frequencies, one receiving and one transmitting frequency. In general, we often refer to “a 30-kHz channel” when we really mean a bandwidth of 30 kHz on one of two frequencies. Therefore, the total occupied spectrum for each traffic channel is 60 kHz. There are three analog systems: The AMPS from North America, the NTT system from Japan, and the TACS system from the UK. Their specifications are listed in Table 1.

6.2. TDMA Systems

The following TDMA systems can be grouped into two different duplexing techniques, FDD and TDD:

FDD. Frequency-division duplexing, where each traffic channel consists of two operational frequencies. The analog system can use only a FDD system, whereas the digital system has a choice.

Table 1. Large-Capacity Analog Cellular Telephones Used in the World

	Japan	North America	United Kingdom
System transmission frequency (MHz)			
Base station	870–885	869–894	917–950
Mobile station	925–940	824–849	872–905
Spacing between transmission and receiving frequencies (MHz)	55	45	45
Spacing between channels (kHz)	25, 12.5	30	25
Number of channels	600	832 (control channel 21 × 2)	1320 (control channel 21 × 2)
Coverage radius (km)	5 (urban area) 10 (suburbs)	2–20	2–20
Audio signal: type of modulation	FM	FM	FM
Frequency deviation (kHz)	±5	±12	±9.5
Data transmission rate (kbps)	0.3	10	8
Message protection	Transmitted signal is checked when it is sent back to the sender by the receiver.	Principle of majority decision is employed.	Principle of majority decision is employed.

Source: Report from International Radio Consultative Committee (CCIR) 1987.

GSM. The term GSM often implies DCS-1800 and DCS-1900 services. They are in the same family, only the carrier frequencies are different. We list the physical layer parameters in Table 2.

NA-TDMA (North American-TDMA). NA-TDMA, sometimes called ADC, is North America's standard system. It incorporates both 800 MHz and 1900 MHz system versions. The network follows philosophy of the GSM intelligent network. The physical layer is shown in Table 3.

The PDC (personal digital cellular) system. This system was developed in Japan and is very similar to the NA-TDMA system, but its radio carrier bandwidth is 25 kHz.

IDEN (integrated digital enhanced network). This system was developed by Motorola. It was called MIRS (mobile integrated radio system); then Motorola mod-

ified the system and renamed it IDEN. This system uses the SMR (Special Mobile Radio) band, which is specified by Part 90 of FCC CER (*Code of Federal Regulations*) in the private sector. The system now can be used cellularlike commercial services. The physical parameter system is as follows:

1. Full-duplex communication system
2. Frequency: 806–824 MHz (mobile transmitter), 851 MHz
3. Channel bandwidth: 25 kHz
4. Multiple access: TDMA
5. Number of timeslots: 6
6. Rate of speech coder: VSELP (vector sum excitation linear predicted)
7. No equalizer implemented
8. Handoff
9. Transmission rate: 6.5 kbps/slot
10. Forward error correction: 3 kbps
11. Dispatch capability

Table 2. Physical-Layer Parameters of GSM

Parameter	Specifications
Radio carrier bandwidth	200 kHz
TDMA structure	8 timeslots per radio carrier
Timeslot	0.577 ms
Frame interval	8 timeslots = 4.615 ms
Radio carrier number	124 radio carriers (935–960 MHz downlink, 890–915 MHz uplink)
Modulation scheme	Gaussian minimum shift keying with $BT^a = 0.3$
Frequency hopping	Slow frequency hopping (217 hops/s)
Equalizer	Equalization up to 16 μs time dispersion
Frequency hop rate	217 hops/s
Handover	Hard handover

^aBT = bandwidth × time.

Table 3. Physical Layer of NA-TDMA

Parameter	Specifications
Radio carrier bandwidth	30 kHz
TDMA structure	3 timeslots per radio carrier
Timeslot	6.66 ms
Frame interval	20 ms
Radio carrier number	2 × 416 (824–849 MHz reverse link, 869–894 MHz forward link)
Modulation scheme	$\frac{\pi}{4}$ -DQPSK
Equalizer	Equalization up to 60 μs time dispersion

TDD. Time-division duplexing, where transmission and reception are shared by one frequency. Certain timeslots are for transmission and certain timeslots are for reception.

CT-2 (Cordless Phone Two). CT-2 was developed by GPT Ltd. in the UK for so-called telepoint applications. Phone calls can be dialed out but cannot be received. The transmission parameters for CT-2 are as follows:

1. Full-duplex system
2. Voicocoder: 32 kbps adaptive differential pulse-code modulation (ADPCM).
3. Duplexing: TDD, where portable and base units transmit and receive on the same frequency but different timeslots
4. Multiple access: TDMA-TDD, up to four multiplexed circuits
5. Modulation: $\pi/4$ DQPSK differential QPSK, rolloff rate = 0.5
6. Data rate: 192 ksym/s (192 kilosymbols per second or 384 kbps)
7. Spectrum allocation: 1895–1918.1 MHz (this spectrum has been allocated for private and public use)
8. Carrier frequency spacing: 300 kHz

PHS (personal handy-phone system). It was developed in Japan. Now there are three operators: NTT, STEL, and DDI. The system serves for the low-tier subscribers, such as teenagers. There are around 7 million customers. The specifications for transmission parameters are as follows:

1. Full-duplex system
2. Voicocoder: 32 kbps adaptive differential pulse-code modulation (ADPCM)
3. Duplexing: TDD, where portable and base units transmit and receive on the same frequency but different timeslots
4. Multiple access: TDMA-TDD, up to four multiplexed circuits
5. Modulation: $\pi/4$ DQPSK, rolloff rate = 0.5
6. Data rate: 192 ksym/s (or 384 kbps)
7. Spectrum allocation: 1895–1918.1 MHz (this spectrum has been allocated for private and public use)
8. Carrier frequency spacing: 300 kHz.

Another system called PACS (personal access communication systems) [3] is in the same system family as PHS.

DECT (Digital European Cordless Telephone) [3]. DECT is a European standard system for slow-motion or in-building communications. Its system structure is as follows:

1. Duplex method: TDD
2. Access method: TDMA

3. RF (radiofrequency) power of handset: 10 mW
4. Channel bandwidth: 1.728 MHz/channel
5. Number of carriers: five (a multiple-carrier system)
6. Frequency: 1800–1900 MHz

DECT's characteristics are as follows:

1. Frame: 10 ms
2. Timeslots: 12
3. Bit rate: 38.8 kb/slot
4. Modulation: GFSK (Gaussian filtered FSK)
5. Handoff: yes

6.3. CDMA Systems

CDMA is another multiple-access scheme using different orthogonal code sequences to provide different call connections. It is a broadband system and can be classified by two approaches: (1) frequency-hopping system approach [3] and (2) direct-sequence system approach [3]. The commercial CDMA system applies the direct-sequence approach. Developed in the United States, it is called the IS-95 Standard System. The first CDMA system was deployed in Hong Kong and then in Los Angeles in 1995. CDMA is a high-capacity system. It has been proved, theoretically, that CDMA system capacity can be 20 times higher than analog capacity. In a CDMA system, all the cells share the same radio carrier in an operating system. The handoff from cell to cell is soft (i.e., not only is the frequency kept unchanged, but the cell is connected in both the old cell and the new cell in the handoff region). The IS-95 CDMA is now called cdmaone. The CDMA radio specifications are as follows:

1. CDMA shares the spectrum band with AMPS
2. Total number of CDMA radio carriers is 18.
3. Radio carrier bandwidth is 1.2288 MHz.
4. Pseudo noise (PN) chip rate is 1.2288 Mchips/s
5. Pilot channel is one per radio carrier.
6. Power control step is 1 dB in 1 ms.
7. Soft handoffs are used.
8. Traffic channels are 55 per each radio carrier.
9. Vocoder is qualcomm (quadrature) code-excited linear prediction (QCELP) at a variable rate.
10. Modulation is quaternary (quadrature) phase shift keying (QPSK).
11. Data frame size is 20 ms.
12. Orthogonal spreading is 64 Walsh functions.
13. Long PN code length is $2^{42} - 1$ chips.
14. Short PN code length is $2^{15} - 1$ chips.

6.4. Mobile Satellite Systems

Mobile satellite systems (MSSs) are used to enhance terrestrial radiocommunication, either in rural areas or in terms of global coverage. Therefore, MSS becomes, in a

Table 4. Comparative Low-Earth-Orbiting Mobile Satellite Service Applications

System Characteristics	Loral/ QUALCOMM	Motorola Iridium	TRW Odyssey	Constellation ARIES (b)	Ellipsat ELLIPSO
Number of satellites	48	66	12	48	24
Constellation altitude (North Meridian)	750	421	5600	550	1767 × 230
Unique feature	Transponder	Onboard processing	Transponder	Transponder	Transponder
Circuit capacity (U.S.)	6500	3835	4600	100	1210
Signal modulation	CDMA	TDMA	CDMA	FDMA/CDMA	CDMA
Gateways in USA	6	2	2	5	6
Gateway spectrum band	C band existing	New Ka band	New Ka band	Unknown	Unknown
Coverage	Global	Global	Global	Global	Northern Hemisphere

broad sense, a PCS system. By taking advantage of reduced transmitting power and short time delays, the low-Earth orbit (LEO) systems are being developed. However, there is a drawback. Each LEO system needs many satellites to cover the planet. There are many LEO systems, as shown in Table 4. There is also another LEO referred to as the *Teledesic system*, which will operate at 24 GHz with a spectrum band of 500 MHz. This LEO system is not just for enhancing cellular or PCS coverage, but also can replace the terrestrial long-distance telephone network in the future.

6.5. IMT-2000

Since the CDMA One system has been successfully deployed in Korea and the United States, in mid-1997 the European countries under the auspices of the so-called (ETSI) European Telecommunications Standard Institute, Japan (ARIB) Association of Radio Industrial and Business, and the United States (TIA) Telecom Industrial Assoc. began planning a universal single-standard system for the so-called IMT-2000 (International Mobile Telephone—Year 2000). There are three general proposals. The proposals disagree on many issues, but they do agree on the following general guideline principles:

1. Use wideband CDMA (WCDMA).
2. Use direct sequence as spread-spectrum modulation.
3. There should be a multiband, single mobile unit.
4. The standard band should be 5 MHz.
5. There is a need for international roaming.
6. There should be IPR (intellectual property right) issues in developing the new global system among all the international vendors.

The IMT-2000 system will require a great deal of compromise in selecting technologies due to the political differences in the international standards bodies. The formal IMT-2000 system will be adapted by the ITU (International Telecommunication Union). A single universal IMT-2000 was established by the year 2000.

BIBLIOGRAPHY

1. S. H. Blecher, Advanced mobile phone services, *IEEE Trans. Vehic. Technol.* **VT-29**:238–244 (1980).
2. W. C. Y. Lee, *Mobile Communications Design Fundamentals*, 2nd ed., Wiley, New York, 1993.
3. W. C. Y. Lee, *Mobile Cellular Telecommunications, Analog and Digital Systems*, McGraw-Hill, New York, 1995.
4. B. J. T. Malliner, An overview of the GSM system, *Proc. Digital Cellular Radio Conf.*, Hagen, FRG, Oct. 1988.
5. Y. Okumura et al., Field strength and its variability in VHF and UHF land-mobile radio service, *Rev. Electron. Commun. Lab.* **16**:825–873 (1968).
6. M. Hata, Empirical formula for propagation loss in land mobile radio services, *IEEE Trans. Vehic. Technol.* **VT-29**: 317–325 (1980).
7. W. C. Y. Lee, Spectrum efficiency in cellular, *IEEE Trans. Vehic. Technol.* **38**:69–75 (1989).

FURTHER READING

- J. Gabion, *The Mobile Comms Handbook*, IEEE Press, New York, 1985.
- M. Morly et al., *The GSM System*.

CHEBYSHEV FILTERS

ANTÔNIO CARLOS
M. DE QUEIROZ
Federal University of Rio de
Janeiro
Rio de Janeiro, Brazil

1. INTRODUCTION

Any signal can be considered to be composed of several sinusoidal components with different frequencies, amplitudes, and phases. *Filtering* is one of the fundamental methods in signal processing, where the signal is processed by a linear system that changes the amplitudes and

phases of these components, but not their frequencies. In the most usual form, filtering can be used to let pass or to reject selected frequency bands, ideally with no attenuation at the passbands and infinite attenuation at the stopbands. This article discusses a class of approximations to this kind of ideal filter, known as *Chebyshev filters*. It starts with a discussion on a technique for the derivation of optimal *magnitude filters*, then discusses the direct and inverse Chebyshev approximations for the ideal filtering operator, continuing with comments on extensions of the technique. Explicit formulas for *LC* ladder realizations for some cases, and tables with example filters that can be used to verify the properties of the filters and the formulas in the article, are listed at the end.

The magnitude approximation problem in *filter design* consists essentially in finding a convenient transfer function with the magnitude satisfying given attenuation specifications. Other restrictions can exist, such as structure for implementation, maximum order, and maximum Q of the poles, but in most cases the problem can be reduced to the design of a normalized continuous-time low-pass filter that can be described by a transfer function in Laplace transform. This filter must present a given maximum passband attenuation (A_{\max}), between $\omega = 0$ and $\omega = \omega_p = 1$ rad/s, and a given minimum stopband attenuation (A_{\min}) in frequencies above a given limit ω_r rad/s. From this prototype filter, the final transfer function can be obtained by frequency transformations [3,6,7], by continuous-time to discrete-time transformations in the case of a digital filter [1], or by a convenient transformation for realization by microwave structures [6].

A convenient procedure for the derivation of optimal magnitude filters is to start with the *transducer function* $H(s)$ and the *characteristic function* $K(s)$ [6]. $H(s)$ can also be called the *attenuation function*, which is the inverse of the filter transfer function, scaled to have the minimum of $|H(j\omega)|$ equal to 1. $K(s)$ is related to $H(s)$ by the equation, due to *FeldtKeller* [6]:

$$|H(j\omega)|^2 = 1 + |K(j\omega)|^2 \quad (1)$$

This greatly simplifies the problem, because $K(j\omega)$ can be a ratio of two real polynomials in ω , both with roots located symmetrically on both sides of the real axis, while $H(j\omega)$ is a complex function. $K(s)$ is obtained by replacing ω by s/j in $K(j\omega)$, and ignoring possible $\pm j$ or -1 multiplying terms resulting from the operation. The complex frequencies where $K(s) = 0$ are the attenuation zeros, and $K(s) = \infty$ corresponds to the transmission zeros. If $K(s)$ is a ratio of real polynomials in s , then $K(s) = F(s)/P(s)$, $H(s)$ is also a ratio of real polynomials, with the same denominator, $H(s) = E(s)/P(s)$, and $E(s)$ can be obtained by observing that for $s = j\omega$, Eq. (1) is equivalent to

$$\begin{aligned} H(s)H(-s) &= 1 + K(s)K(-s) \\ \therefore E(s)E(-s) &= P(s)P(-s) + F(s)F(-s) \end{aligned} \quad (2)$$

Because $E(s)$ is the denominator of the filter transfer function, which must be stable, $E(s)$ is constructed from the roots of the polynomial $P(s)P(-s) + F(s)F(-s)$ with nega-

tive real parts. The desired transfer function is then $T(s) = P(s)/E(s)$.

2. CHEBYSHEV POLYNOMIALS

Two important classes of approximations, the direct and inverse Chebyshev approximations, can be derived from a class of polynomials known as *Chebyshev polynomials*. These polynomials were first described by P. L. Chebyshev [2]. The Chebyshev polynomial of order n can be obtained from the following expression:

$$C_n(x) = \cos(n \cos^{-1} x) \quad (3)$$

It is simple to verify that this expression corresponds, for $-1 \leq x \leq 1$, to a polynomial in x . Using the trigonometric identity $\cos(a+b) = \cos a \cos b - \sin a \sin b$, we obtain

$$\begin{aligned} C_{n+1}(x) &= \cos[(n+1) \cos^{-1} x] \\ &= xC_n(x) - \sin(n \cos^{-1} x) \sin(\cos^{-1} x) \end{aligned} \quad (4)$$

Now applying the identity $\sin a \sin b = \frac{1}{2}[\cos(a-b) - \cos(a+b)]$ and rearranging, we obtain a recursion formula:

$$C_{n+1}(x) = 2xC_n(x) - C_{n-1}(x) \quad (5)$$

For $n = 0$ and $n = 1$, we have $C_0(x) = 1$ and $C_1(x) = x$. Using Eq. (5), the series of Chebyshev polynomials shown in Table 1 is obtained.

The values of these polynomials oscillate between -1 and $+1$ for x between -1 and $+1$, in a pattern identical to a stationary Lissajous figure [3]. For x out of this range, $\cos^{-1} x = j \cosh^{-1} x$, an imaginary value, but Eq. (3) is still real, in the form

$$C_n(x) = \cos(nj \cosh^{-1} x) = \cosh(n \cosh^{-1} x) \quad (6)$$

For high values of x , looking at the polynomials in Table 1, we see that $C_n(x) \approx 2^n x^n$, growing monotonically. The plots of some Chebyshev polynomials for $-1 \leq x \leq 1$ are shown in Fig. 1.

Table 1. Chebyshev Polynomials

n	$C_n(x)$
0	1
1	x
2	$2x-1$
3	$4x^3-3x$
4	$8x^4-8x^2+1$
5	$16x^5-20x^3+5x$
6	$32x^6-48x^4+18x-1$
7	$64x^7-112x^5+56x^3-7x$
8	$128x^8-256x^6+160x^4-32x^2+1$
9	$256x^9-576x^7+432x^5-120x^3+9x$
10	$512x^{10}-1280x^8+1120x^6-400x^4+50x^2-1$
11	$1024x^{11}-2816x^9+2816x^7-1232x^5+220x^3-11x$
12	$2048x^{12}-6144x^{10}+6912x^8-3584x^6+840x^4-72x^2+1$

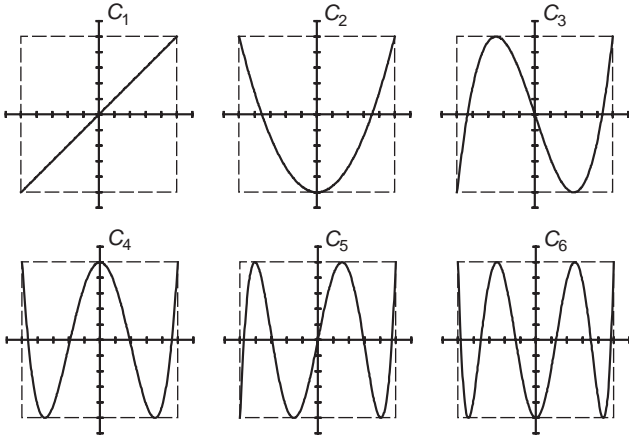


Figure 1. Plots of the first six Chebyshev polynomials $C_n(x)$. The squares limit the region $-1 \leq x \leq 1$, $-1 \leq C_n(x) \leq 1$, where the polynomial value oscillates.

3. THE CHEBYSHEV LOWPASS APPROXIMATION

The normalized *Chebyshev approximation* for lowpass filters is obtained by using

$$K(j\omega) = \epsilon C_n(\omega) \tag{7}$$

The result is a transducer function with the magnitude given by [from Eq. (1)]

$$|H(j\omega)|^2 = 1 + [\epsilon C_n(\omega)]^2 \tag{8}$$

The corresponding attenuation in decibels is

$$A(\omega) = 10 \log\{1 + [\epsilon C_n(\omega)]^2\} \tag{9}$$

The parameter ϵ controls the maximum passband attenuation, or the passband ripple. Considering that when $C_n(\omega) = \pm 1$ the attenuation $A(\omega) = A_{\max}$, Eq. (9) gives

$$\epsilon = (10^{0.1A_{\max}} - 1)^{1/2} \tag{10}$$

Figure 2 shows examples of the magnitude function $|T(j\omega)|$ in the passband and in the stopband obtained for some normalized Chebyshev lowpass approximations, with $A_{\max} = 1$ dB. The magnitude of the Chebyshev approximations presents uniform ripple in the passband, with the gain departing from 0 dB at $\omega = 0$ for odd orders and from $-A_{\max}$ dB for even orders.

The stopband attenuation is the maximum possible among filters derived from polynomial characteristic functions, with the same A_{\max} and degree [4]. This can be proved by assuming that there exists a polynomial $P_n(x)$ that is also bounded between -1 and 1 for $-1 \leq x \leq 1$, with $P_n(x) = \pm P_n(-x)$ and $P_n(+\infty) = +\infty$, but that exceeds the value of $C_n(x)$ for some value of $x > 1$. An approximation using this polynomial instead of $C_n(x)$ in Eq. (7) would be more selective. The curves of $P_n(x)$ and $C_n(x)$ will always cross n times for $-1 \leq x \leq 1$, due to the maximum oscillations of $C_n(x)$, but if $P_n(x)$ grows faster, they will

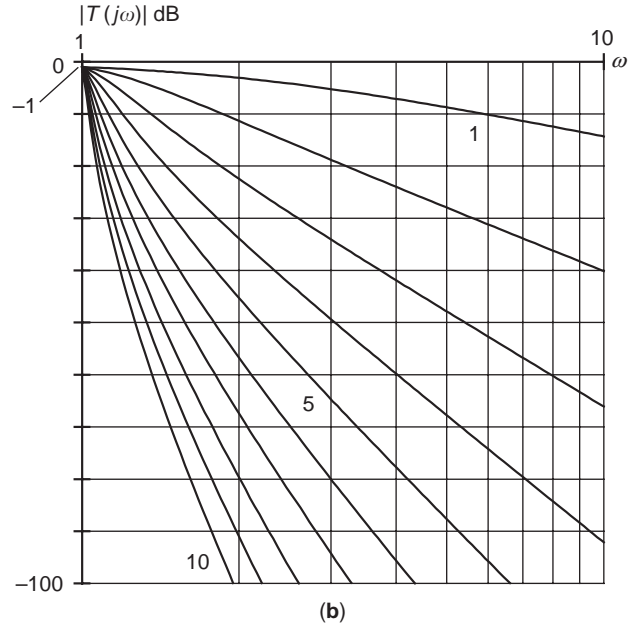
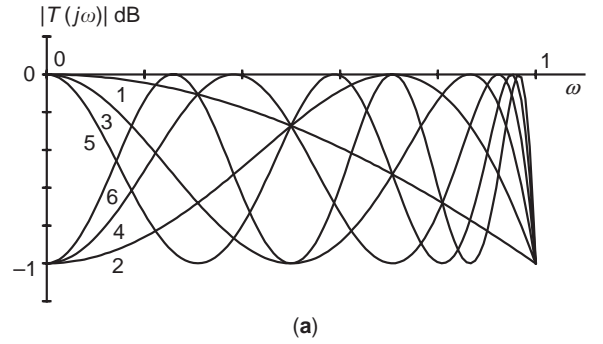


Figure 2. Passband gain (a) and stopband gain (b) for the first normalized Chebyshev approximations with 1 dB passband ripple. Observe the uniform passband ripple and the monotonic stopband gain decrease.

cross another 2 times for $x \geq 1$ and $x \leq -1$. This makes $P_n(x) - C_n(x)$ a polynomial of degree $n + 2$, because it presents $n + 2$ roots, what is impossible since both are of degree n .

The required approximation degree for given A_{\max} and A_{\min} can be obtained by substituting Eq. (6) in Eq. (9), with $A(\omega_r) = A_{\min}$ and solving for n . The result, including a denormalization for any ω_p is

$$n \geq \frac{\cosh^{-1} \gamma}{\cosh^{-1}(\omega_r/\omega_p)} \tag{11}$$

where it is convenient to define the following constant:

$$\gamma = \left(\frac{10^{0.1A_{\min}} - 1}{10^{0.1A_{\max}} - 1} \right)^{1/2} \tag{12}$$

The transfer functions for the normalized Chebyshev filters can be obtained by solving Eq. (2). For a polynomial

approximation, using $P(s) = 1$, from Eq. (7), it follows that

$$E(s)E(-s) = 1 + \left[\varepsilon C_n \left(\frac{s}{j} \right) \right]^2 \quad (13)$$

The roots of this polynomial are the solutions for s in

$$C_n \left(\frac{s}{j} \right) = \cos \left(n \cos^{-1} \frac{s}{j} \right) = \pm \frac{j}{\varepsilon} \quad (14)$$

Identifying

$$n \cos^{-1} \frac{s}{j} = a + jb \quad (15)$$

it follows that $\pm(j/\varepsilon) = \cos(a + jb) = \cos a \cos jb - \sin a \sin jb = \cos a \cosh b - j \sin a \sinh b$. Equating real and imaginary parts, we have $\cos a \cosh b = 0$ and $\sin a \sinh b = \mp(1/\varepsilon)$. Since $\cosh x \geq 1$, the equation of the real parts gives

$$a = \frac{\pi}{2}(1 + 2k) \quad k = 0, 1, \dots, 2n - 1 \quad (16)$$

and as for these values of a , $\sin a = \pm 1$, the equation of the imaginary parts gives

$$b = \mp \sinh^{-1} \frac{1}{\varepsilon} \quad (17)$$

Applying these results in Eq. (15), it follows that the roots of $E(s)E(-s)$ are

$$s_k = \sigma_k + j\omega_k \quad k = 0, 1, \dots, 2n - 1$$

$$\sigma_k = \sin \frac{\pi}{2} \frac{1 + 2k}{n} \sinh \left(\frac{1}{n} \sinh^{-1} \frac{1}{\varepsilon} \right) \quad (18)$$

$$\omega_k = \cos \frac{\pi}{2} \frac{1 + 2k}{n} \cosh \left(\frac{1}{n} \sinh^{-1} \frac{1}{\varepsilon} \right)$$

The roots s_k with negative real parts ($k \geq n$) are the roots of $E(s)$. By the expressions in Eq. (18), it is easy to see that the roots s_k are located in an ellipse with vertical semiaxis $\cosh[(1/n) \sinh^{-1}(1/\varepsilon)]$, horizontal semiaxis $\sinh[(1/n) \sinh^{-1}(1/\varepsilon)]$, and foci at $\pm j$. The location of the roots can be best visualized with the diagram shown in Fig. 3 [3].

4. REALIZATION OF CHEBYSHEV FILTERS

These approximations were originally developed for realization in passive form, and the best realizations were obtained as *LC* doubly terminated structures designed for maximum power transfer at the passband gain maxima [3,6,7]. These structures are still important today in high-frequency filters and as prototypes for active and digital realizations, due to the low sensitivity to errors in element values. At each attenuation zero, and the Chebyshev approximations have the maximum possible number of them distributed in the passband, maximum power

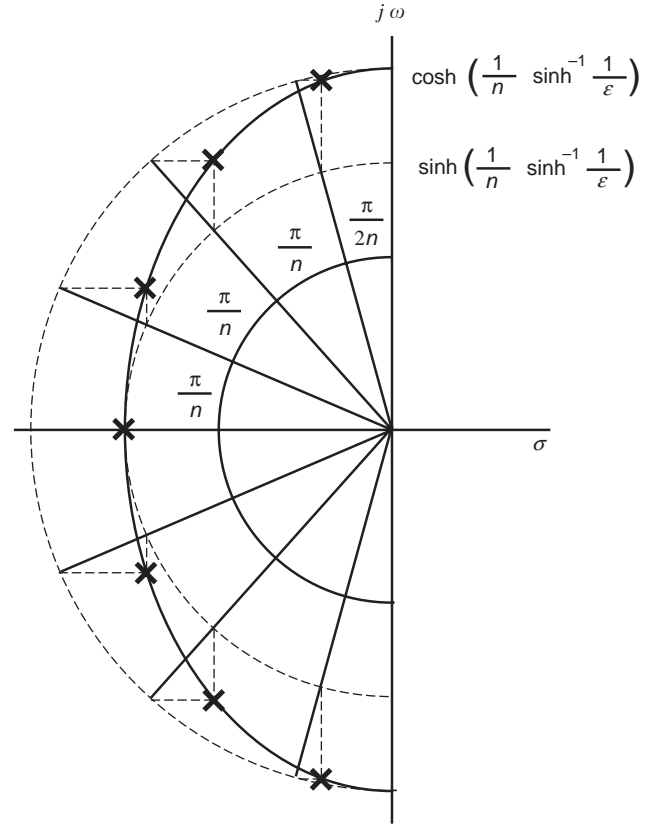


Figure 3. Localization of the poles in a normalized Chebyshev lowpass approximation (seventh order in this case). The pole locations can be obtained as shown.

transfer occurs between the terminations. In this condition, errors in the capacitors and inductors can only decrease the gain [5]. This causes zeros in the derivatives of $|T(j\omega)|$ in relation to all reactive element values at the attenuation zeros, and reduces the error throughout the passband. Table 2 lists polynomials, poles, frequency and Q of the poles, and *LC* doubly terminated ladder structures, with the structure shown in Fig. 4a, for some normalized Chebyshev lowpass filters. Note in the realizations that odd-order filters have identical terminations, but even-order filters require different terminations, because there is no maximum power transfer at $\omega = 0$, since the gain is not maximum there. With the impedance normalization shown, it is clear that the even-order realizations have antimetrical structure (one side is the dual of the other). The odd-order structures are symmetric.

5. THE INVERSE CHEBYSHEV LOWPASS APPROXIMATION

The *inverse Chebyshev approximation* is the most important member of the inverse polynomial class of approximations. The lowpass version is conveniently obtained by using the characteristic function obtained from

$$K(j\omega) = \frac{F(j\omega)}{P(j\omega)} = \frac{\varepsilon\gamma}{C_n(1/\omega)} = \frac{\varepsilon\gamma\omega^n}{\omega^n C_n(1/\omega)} \quad (19)$$

Table 2. Normalized Chebyshev filters with $A_{\max} = 1$ dB and $\omega_p = 1$ rad/s

Polynomials E(s)											
n	a_0	a_1	a_2	a_3	a_4	a_5	a_6	a_7	a_8	a_9	a_{10}
1	1.96523	1.00000									
2	1.10251	1.09773	1.00000								
3	0.49131	1.23841	0.98834	1.00000							
4	0.27563	0.74262	1.45392	0.95281	1.00000						
5	0.12283	0.58053	0.97440	1.68882	0.93682	1.00000					
6	0.06891	0.30708	0.93935	1.20214	1.93082	0.92825	1.00000				
7	0.03071	0.21367	0.54862	1.35754	1.42879	2.17608	0.92312	1.00000			
8	0.01723	0.10734	0.44783	0.84682	1.83690	1.65516	2.42303	0.91981	1.00000		
9	0.00768	0.07060	0.24419	0.78631	1.20161	2.37812	1.88148	2.67095	0.91755	1.00000	
10	0.00431	0.03450	0.18245	0.45539	1.24449	1.61299	2.98151	2.10785	2.91947	0.91593	1.00000
Poles											
n	re/im 1	ω/Q 1	re/im 2	ω/Q 2	re/im 3	ω/Q 3	re/im 4	ω/Q 4	re/im 5	ω/Q 5	
1	-1.96523										
2	-0.54887	1.05000									
	0.89513	0.95652									
3	-0.24709	0.99710	-0.49417								
	0.96600	2.01772									
4	-0.13954	0.99323	-0.33687	0.52858							
	0.98338	3.55904	0.40733	0.78455							
5	-0.08946	0.99414	-0.23421	0.65521	-0.28949						
	0.99011	5.55644	0.61192	1.39879							
6	-0.06218	0.99536	-0.16988	0.74681	-0.23206	0.35314					
	0.99341	8.00369	0.72723	2.19802	0.26618	0.76087					
7	-0.04571	0.99633	-0.12807	0.80837	-0.18507	0.48005	-0.20541				
	0.99528	10.89866	0.79816	3.15586	0.44294	1.29693					
8	-0.03501	0.99707	-0.09970	0.85061	-0.14920	0.58383	-0.17600	0.26507			
	0.99645	14.24045	0.84475	4.26608	0.56444	1.95649	0.19821	0.75304			
9	-0.02767	0.99761	-0.07967	0.88056	-0.12205	0.66224	-0.14972	0.37731	-0.15933		
	0.99723	18.02865	0.87695	5.52663	0.65090	2.71289	0.34633	1.26004			
10	-0.02241	0.99803	-0.06505	0.90245	-0.10132	0.72148	-0.12767	0.47606	-0.14152	0.21214	
	0.99778	22.26303	0.90011	6.93669	0.71433	3.56051	0.45863	1.86449	0.15803	0.74950	
Polynomials P(s)											
n	mult.	a_0									
1	1.96523	1.00000									
2	0.98261	1.00000									
3	0.49131	1.00000									
4	0.24565	1.00000									
5	0.12283	1.00000									
6	0.06141	1.00000									
7	0.03071	1.00000									
8	0.01535	1.00000									
9	0.00768	1.00000									
10	0.00384	1.00000									
Doubly terminated LC ladder realizations											
n	Rg/Rl	L/C 1	L/C 2	L/C 3	L/C 4	L/C 5	L/C 6	L/C 7	L/C 8	L/C 9	L/C 10
1	1.00000										
	1.00000	1.01769									
2	1.63087		1.11716								
	0.61317	1.11716									
3	1.00000		0.99410								
	1.00000	2.02359		2.02359							
4	1.63087		1.73596		1.28708						
	0.61317	1.28708		1.73596							
5	1.00000		1.09111		1.09111						
	1.00000	2.13488		3.00092		2.13488					
6	1.63087		1.80069		1.87840		1.32113				
	0.61317	1.32113		1.87840		1.80069					
7	1.00000		1.11151		1.17352		1.11151				
	1.00000	2.16656		3.09364		3.09364		2.16656			
8	1.63087		1.82022		1.93073		1.90742		1.33325		
	0.61317	1.33325		1.90742		1.93073		1.82022			
9	1.00000		1.11918		1.18967		1.18967		1.11918		
	1.00000	2.17972		3.12143		3.17463		3.12143		2.17972	
10	1.63087		1.82874		1.94609		1.95541		1.91837		1.33890
	0.61317	1.33890		1.91837		1.95541		1.94609		1.82874	

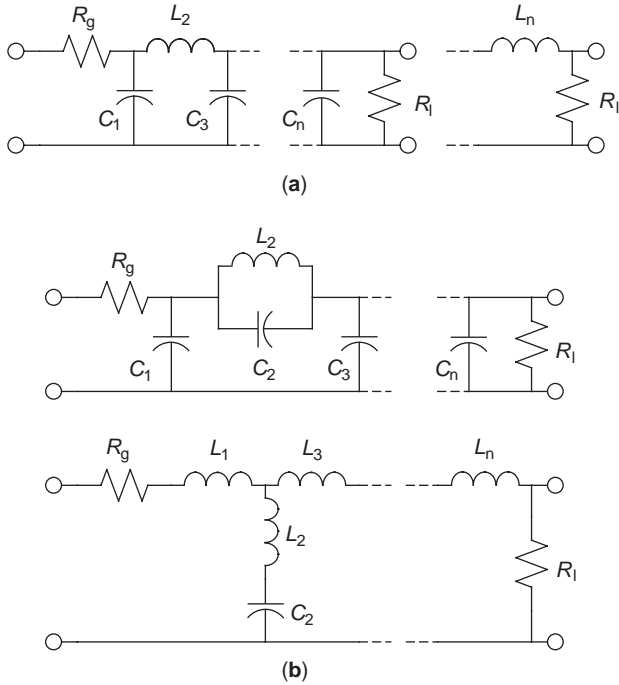


Figure 4. LC doubly terminated ladder realizations for Chebyshev filters, in the direct form (a) and in the inverse form (b). These classical realizations continue to be the best prototypes for active realizations, due to their low sensitivity to errors in the element values.

where ε and γ are as given by Eqs. (10) and (11). The polynomials $F(s)$ and $P(s)$ are then

$$F(s) = \varepsilon \gamma \left(\frac{s}{j} \right)^n \quad (20)$$

$$P(s) = \left(\frac{s}{j} \right)^n C_n \left(\frac{j}{s} \right)$$

Ignoring $\pm j$ or -1 , multiplying factors in Eq. (20), $F(s)$ reduces to $\varepsilon \gamma s^n$, and $P(s)$ reduces to a Chebyshev polynomial with all the terms positive and the coefficients in reverse order. The magnitude characteristic of this approximation is maximally flat at $\omega = 0$, due to the n attenuation zeros at $s = 0$, and thus is similar in the passband to a Butterworth approximation. In the stopband, it presents a series of transmission zeros at frequencies inverse to the roots of the corresponding Chebyshev polynomial. Between adjacent transmission zeros, there are gain maxima reaching the magnitude of $-A_{\min}$ dB. Without renormalization, the stopband starts at 1 rad/s, and the passband ends where the magnitude of the characteristic function, Eq. (19), reaches ε :

$$\omega_p = \frac{1}{C_n^{-1}(\gamma)} = \frac{1}{\cosh \left(\frac{1}{n} \cosh^{-1} \gamma \right)} \quad (21)$$

Odd-order filters present a single transmission zero at infinity, and even-order filters end with a constant gain

$-A_{\min}$ at $\omega = \infty$. From Eqs. (1) and (19), the attenuation in decibels for a normalized inverse Chebyshev approximation is

$$A(\omega) = 10 \log \left\{ 1 + \left[\frac{\varepsilon \gamma}{C_n(1/\omega)} \right]^2 \right\} \quad (22)$$

The gains for some normalized inverse Chebyshev approximations are plotted in Fig. 5. A frequency scaling by the factor given by Eq. (21) was applied, causing the passband to end at $\omega = 1$.

The selectivity of the inverse Chebyshev approximation is the same as the corresponding Chebyshev approximation, for the same A_{\max} and A_{\min} . This can be verified by calculating the ratio ω_p/ω_r for both approximations. For the normalized Chebyshev approximation, $\omega_p = 1$, and ω_r occurs when $\varepsilon C_n(\omega_r) = \gamma$. For the normalized inverse Chebyshev approximation, $\omega_r = 1$, and ω_p occurs when $(\varepsilon \gamma)/C_n(1/\omega_p) = \varepsilon$. In both cases, the resulting ratio is $\omega_r/\omega_p = C_n^{-1}(\gamma)$. Equation (11) can be used to compute the required degree.

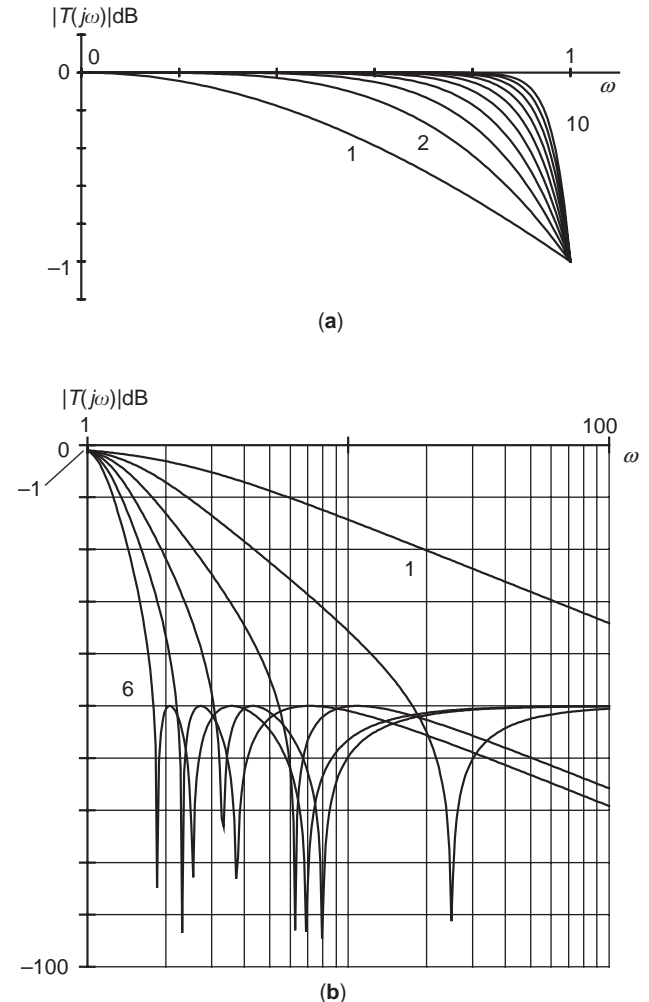


Figure 5. Passband gain (a) and stopband gain (b) for the first normalized inverse Chebyshev approximations with $A_{\max} = 1$ dB and $A_{\min} = 50$ dB. Observe the maximally flat passband and the uniform stopband ripple.

The transmission zero frequencies are the frequencies that make Eq. (19) infinite:

$$C_n\left(\frac{1}{\omega_k}\right) = \cos\left(n \cos^{-1}\left(\frac{1}{\omega_k}\right)\right) = 0$$

$$\therefore \omega_k = \frac{1}{\cos\left(\frac{\pi}{2} \frac{1+2k}{n}\right)}, \quad k=0, 1, \dots, n-1 \quad (23)$$

The pole frequencies are found by solving Eq. (2) with $F(s)$ and $P(s)$ as given by Eq. (20):

$$E(s)E(-s) = (\varepsilon\gamma)^2 \left(\frac{s}{j}\right)^{2n} + \left(\frac{s}{j}\right)^{2n} C_n\left(\frac{j}{s}\right)^2 \quad (24)$$

The roots of this equation are the solutions of

$$C_n\left(\frac{j}{s}\right) = \pm j\varepsilon\gamma \quad (25)$$

By observing the similarity of this equation to Eq. (14), the roots of $E(s)E(-s)$ can be obtained as the complex inverses of the values given by Eq. (18), with ε replaced by $1/(\varepsilon\gamma)$. They lie in a curve that is not an ellipse. $E(s)$ is constructed from the roots with negative real parts, which are distributed in a pattern that resembles a circle shifted to the left side of the origin.

Because of the similarity of the passband response to the Butterworth response, the phase characteristics of the inverse Chebyshev filters are much closer to linear than those of the direct Chebyshev filters, simplifying the task of a phase equalizer that may be cascaded with the magnitude filter. The maximum Q of the poles is also significantly lower for the same gain specifications.

6. REALIZATION OF INVERSE CHEBYSHEV FILTERS

The realization based on *LC doubly terminated ladder* structures is also convenient for inverse Chebyshev filters, by the same reasons mentioned for the direct approximation. In this case, the passband sensitivities are low because of the n th-order attenuation zero at $s=0$, which results in the nullification of the first n derivatives of the filter gain in relation to all the reactive elements at $s=0$, and keeps the gain errors small in all the passband. Stopband errors are also small, because the transmission zero frequencies depend only on simple *LC* series or parallel resonant circuits. The usual structures used are shown in Fig. 4b.

Those realizations are possible only for the odd-order cases, because those structures can't realize the constant gain at infinity that occurs in the even-order approximations (realizations with transformers or with negative elements, or with just one termination, are possible). Even-order modified approximations can be obtained by using, instead of the Chebyshev polynomials, polynomials obtained by the application, to the Chebyshev polynomials,

of the *Moebius transformation* [4,6]

$$x^2 \rightarrow \frac{x^2 - x_{z1}^2}{1 - x_{z1}^2}; \quad x_{z1} = \cos \frac{k_{\max}\pi}{2n} \quad (26)$$

where k_{\max} is the greatest odd integer that is less than the filter order n . This transformation moves the pair of roots closer to the origin of an even-order Chebyshev polynomial to the origin. If the resulting polynomials are used to generate polynomial approximations, starting from Eq. (7), the results are filters with two attenuation zeros at the origin that are realizable as a doubly terminated ladder filter with equal terminations, a convenience in passive realizations. If the same polynomials are used in inverse polynomial approximations, starting from Eq. (19), the results are filters with two transmission zeros at the infinity, which are now realizable by doubly terminated *LC* structures. The direct and inverse approximations obtained in this way have the same selectivity, slightly smaller than in the original case.

Table 3 lists polynomials, poles, zeros, frequency and Q of the poles, and *LC* doubly terminated realizations for some inverse Chebyshev filters. The filters were scaled in frequency to make the passband end at 1 rad/s instead of ω_p [Eq. (21)]. The even-order realizations were obtained from modified approximations with two transmission zeros at infinity, and are listed separately in Table 4. The structures are a mix of the two forms in Fig. 4b. Note that some realizations are missing. These are cases where the network would require negative elements, or transformers. For inverse Chebyshev filters, and other inverse polynomial filters, there is a minimum value of A_{\min} for each order that turns a pure *LC* doubly terminated realization possible [7].

7. OTHER SIMILAR APPROXIMATIONS

Different approximations with uniform passband or stopband ripple, somewhat less selective, can be generated by reducing the number or the amplitude of the oscillations in a Chebyshev-like polynomial, and generating the approximations starting from Eq. (7) or (19), numerically [8].

A particularly interesting case results if the last oscillations of the polynomial value end in 0 instead of ± 1 . This creates double roots close to $x = \pm 1$ in the polynomial. In a polynomial approximation, the higher-frequency passband minimum disappears, replaced by a second-order maximum close to the passband border. In an *LC* doubly terminated realization, the maximum power transfer at this frequency causes nullification of the first two derivatives of the gain in relation to the reactive elements, substantially reducing the gain error at the passband border. In an inverse polynomial approximation, this causes the joining of the first two transmission zeros, as a double transmission zero, which increases the attenuation and reduces the error at the stopband beginning, also allowing a symmetric realization for orders 5 and 7.

Other variations arise from the shifting of roots to the origin. This is also best done numerically. Odd- (even-) order polynomial approximations with any odd (even)

Table 3. Normalized Inverse Chebyshev Filters with $A_{\max} = 1$ dB, $A_{\min} = 50$ dB, and $\omega_p = 1$ rad/s

Polynomials E(s)											
n	a_0	a_1	a_2	a_3	a_4	a_5	a_6	a_7	a_8	a_9	a_{10}
1	1.96523	1.00000									
2	1.96838	1.98099	1.00000								
3	2.01667	3.14909	2.51015	1.00000							
4	2.19786	4.52937	4.90289	3.13118	1.00000						
5	2.60322	6.42983	8.61345	7.26320	3.81151	1.00000					
6	3.35081	9.35051	14.61162	14.91369	10.30744	4.54023	1.00000				
7	4.64002	14.09440	24.72451	29.03373	24.18372	14.09633	5.30979	1.00000			
8	6.82650	22.03426	42.29782	55.31092	52.89124	37.20009	18.68307	6.11268	1.00000		
9	10.54882	35.60372	73.49954	104.68294	111.48145	90.07839	54.81844	24.10445	6.94337	1.00000	
10	16.95789	59.19226	129.80937	198.24216	230.34722	207.44800	145.48766	77.89699	0.39330	7.79647	1.00000
Poles											
n	re/im 1	ω/Q 1	re/im 2	ω/Q 2	re/im 3	ω/Q 3	re/im 4	ω/Q 4	re/im 5	ω/Q 5	
1	-1.96523										
	0.00000										
2	-0.99049	1.40299									
	0.99363	0.70823									
3	-0.61468	1.25481	-1.28079								
	1.09395	1.02071									
4	-0.42297	1.18385	-1.14262	1.25229							
	1.10571	1.39945	0.51249	0.54799							
5	-0.30648	1.13993	-0.94418	1.23656	-1.31018						
	1.09795	1.85969	0.79849	0.65483							
6	-0.23016	1.10962	-0.75398	1.21506	-1.28598	1.35770					
	1.08549	2.41056	0.95283	0.80576	0.43545	0.52789					
7	-0.17794	1.08768	-0.59638	1.18959	-1.14085	1.36871	-1.47946				
	1.07303	3.05632	1.02930	0.99735	0.75619	0.59986					
8	-0.47425	1.16431	-0.14101	1.07137	-0.95398	1.34983	-1.48710	1.55173			
	1.06334	1.22752	1.06205	3.79891	0.95496	0.70747	0.44316	0.52173			
9	-0.38185	1.14152	-0.77805	1.31643	-0.11413	1.05899	-1.34453	1.56247	-1.70623		
	1.07575	1.49471	1.06189	0.84597	1.05282	4.63922	0.79596	0.58105			
10	-0.63221	1.27960	-0.31203	1.12193	-0.09407	1.04944	-1.13939	1.53032	-1.72054	1.78611	
	1.11252	1.01201	1.07766	1.79777	1.04521	5.57772	1.02161	0.67155	0.47954	0.51906	
Polynomials P(s)											
n	mult.	a_0	a_2	a_4	a_6	a_8	a_{10}				
1	1.96523	1.00000									
2	0.00316	622.45615	1.00000								
3	0.05144	39.20309	1.00000								
4	0.00316	695.02278	74.56663	1.00000							
5	0.03477	74.86195	19.34709	1.00000							
6	0.00316	1059.61979	494.96516	57.80151	1.00000						
7	0.03463	133.99401	95.81988	19.57753	1.00000						
8	0.00316	2158.72730	2130.49651	657.07341	64.84805	1.00000					
9	0.03786	278.65997	354.39519	150.23800	23.58892	1.00000					
10	0.00316	5362.55604	8380.91576	4584.36462	1023.53040	79.98165	1.00000				
Zeros											
n	ω_1	ω_2	ω_3	ω_4	ω_5						
1	∞										
2	24.94907										
3	6.26124	∞									
4	7.97788	3.30455									
5	3.74162	2.31245	∞								
6	6.92368	2.53424	1.85520								
7	3.60546	2.00088	1.60458	∞							
8	7.29689	2.56233	1.71209	1.45144							
9	3.88896	2.06927	1.53587	1.35062	∞						
10	8.08496	2.78589	1.78865	1.41948	1.28053						
LC doubly terminated realizations											
n	R_g/R_1	L/C 1	L/C 2	L/C 3	L/C 4	L/C 5	L/C 6	L/C 7			
1	1.00000										
	1.00000	1.01769									
3	1.00000		1.56153								
	1.00000	0.78077	0.01634	0.78077							
5	1.00000		1.16364		1.30631						
	1.00000	0.37813	0.16071	1.62010	0.05468	0.47172					
7	1.00000		0.72897		1.34370		0.96491				
	1.00000	0.09574	0.34265	1.32044	0.28905	1.32059	0.07972	0.30081			

Table 4. Normalized Even-Order Modified Inverse Chebyshev Filters with Two Transmission Zeros at Infinity, with $A_{\max} = 1$ dB, $A_{\min} = 50$ dB, and $\omega_p = 1$ rad/s

Polynomials E(s)											
n	a_0	a_1	a_2	a_3	a_4	a_5	a_6	a_7	a_8	a_9	a_{10}
2	1.96523	1.98254	1.00000								
4	2.12934	4.47598	4.86847	3.12041	1.00000						
6	3.14547	9.02141	14.23655	14.65051	10.18872	4.51414	1.00000				
8	6.32795	20.98707	40.68275	53.69811	51.69862	36.58972	18.48009	6.07949	1.00000		
10	15.69992	56.17036	124.1801	191.3464	223.6989	202.6490	142.8395	76.84994	30.12162	7.76165	1.00000
Poles											
n	re/im 1	ω/Q 1	re/im 2	ω/Q 2	re/im 3	ω/Q 3	re/im 4	ω/Q 4	re/im 5	ω/Q 5	
2	-0.99127	1.40187									
	0.99127	0.70711									
4	-0.43134	1.18419	-1.12886	1.23225							
	1.10284	1.37268	0.49409	0.54580							
6	-0.23626	1.11107	-0.76275	1.20632	-1.25806	1.32324					
	1.08566	2.35141	0.93457	0.79077	0.41016	0.52590					
8	-0.14421	1.07247	-0.48399	1.16315	-0.96075	1.33672	-1.45079	1.50858			
	1.06273	3.71848	1.05767	1.20162	0.92940	0.69566	0.41357	0.51992			
10	-0.64341	1.27784	-0.31781	1.12245	-0.09573	1.05011	-1.14584	1.51514	-1.67803	1.73625	
	1.10404	0.99303	1.07652	1.76590	1.04574	5.48452	0.99132	0.66115	0.44586	0.51735	
Polynomials P(s)											
n	mult.	a_0	a_2	a_4	a_6	a_8					
2	1.96523	1.00000									
4	0.16412	12.97454	1.00000								
6	0.11931	26.36278	10.89186	1.00000							
8	0.13145	48.13911	44.73326	12.54437	1.00000						
10	0.16119	97.39855	147.0191	76.50032	15.68797	1.00000					
Finite zeros											
n	ω_1	ω_2	ω_3	ω_4							
2	-										
4	3.60202										
6	2.69467	1.90542									
8	2.71078	1.74464	1.46706								
10	2.94484	1.82001	1.43081	1.28694							
Doubly terminated											
LC ladder realizations											
n	R_g/R_1	L/C 1	L/C 2	L/C 3	L/C 4	L/C 5	L/C 6	L/C 7	L/C 8		
2	1.00000		1.00881								
	1.00000	1.00881									
4	1.00000		1.51207	0.05275	0.58997						
	1.00000	0.64094		1.46110							
6	1.00000		0.87386		1.67233	0.13065	0.32187				
	1.00000	0.17880	0.31519	1.63514		1.05413					
8	1.00000		0.67581	0.32023	1.34317	0.38303	1.12998	0.18178	0.16760		
	1.00000	0.32898		1.02594		1.21303		0.74862			

number of attenuation zeros at $\omega=0$, up to the approximation's order (in the last case resulting a Butterworth approximation), can be generated. The same polynomials generate inverse polynomial approximations with any odd (even) number of transmission zeros at infinity.

In all cases, the maximum Q of the poles is reduced and the phase is closer to linear. Similar techniques can also be applied to elliptic approximations. For example, a lowpass elliptical approximation can be transformed into a Chebyshev approximation by the shifting all the transmission zeros to infinity, or into an inverse Chebyshev approximation by shifting all the attenuation zeros to the origin. There are many possibilities between these extremes.

8. EXPLICIT FORMULAS

The design of filter structures is simplified when *explicit formulas* for the element values are available. They also allow the design of very high-order filters (usually for digital implementation) without serious numerical problems. Explicit formulas for the element values of direct Chebyshev filters have been known since the 1950s, and are given below, in the version due to *Takahasi*, adapted for the notation used here. Their proof can be found in Ref. 7. The formulas apply to the structure in Fig. 4a, and solve not only the case where there is maximum power transfer, but also the mismatched cases where the terminations are

arbitrarily chosen. We start by redefining Eq. (8) to allow for mismatched terminations as

$$|H(j\omega)| = \frac{1 + [\varepsilon C_n(\omega)]^2}{A} \quad (27)$$

where $A \leq 1$. For degree n , with arbitrarily chosen terminations R_g and $R_1 \leq R_g$, the constant A is obtained (from the definition: $H(s)$ = actual attenuation/minimum possible attenuation) as

$$A = \frac{4R_g R_1}{(R_g + R_1)^2}, \quad \text{for odd } n \quad (28)$$

$$A = (1 + \varepsilon^2) \frac{4R_g R_1}{(R_g + R_1)^2}, \quad \text{for even } n$$

The matched case is obtained when $R_g = R_1$ for odd orders and, or for even orders, when

$$\frac{R_1}{R_g} = \frac{(1 + \varepsilon^2)^{1/2} - \varepsilon}{(1 + \varepsilon^2)^{1/2} + \varepsilon} \quad (29)$$

We then compute the two constants

$$k = \left[\left(\frac{1}{\varepsilon^2} + 1 \right)^{1/2} + \frac{1}{\varepsilon} \right]^{1/n} \quad (30)$$

$$h = \left[\left(\frac{1-A}{\varepsilon^2} + 1 \right)^{1/2} + \left(\frac{1-A}{\varepsilon^2} \right)^{1/2} \right]^{1/n} \quad (31)$$

The first capacitor C_1 is given by

$$C_1 = \frac{2s_1}{R_g[(k - k^{-1}) - (h - h^{-1})]} \quad (32)$$

and the other elements can be calculated by the recursion formulas

$$C_{2m-1}L_{2m} = \frac{4s_{4m-3}s_{4m-1}}{b_{2m-1}(k - k^{-1}, h - h^{-1})} \quad (33)$$

$$C_{2m+1}L_{2m} = \frac{4s_{4m-1}s_{4m+1}}{b_{2m}(k - k^{-1}, h - h^{-1})}$$

where $m = 1, 2, \dots$, to the last integer $\leq n/2$. The network ends at C_n for odd n , and in L_n for even n , which can be directly calculated, if convenient, as

$$C_n = \frac{2s_1}{R_1[(k - k^{-1}) + (h - h^{-1})]} \quad (34)$$

$$L_n = \frac{2R_1s_1}{(k - k^{-1}) + (h - h^{-1})}$$

The terms that appear in the formulas are

$$b_m(\zeta, \eta) = \zeta^2 - \mathbf{c}_{2m}\zeta\eta + \eta^2 + \mathbf{s}_{2m}^2 \quad (35)$$

$$\mathbf{s}_r = 2 \sin \frac{\pi r}{2n}, \quad \mathbf{c}_r = 2 \cos \frac{\pi r}{2n}$$

If it is desired to have $R_1 > R_g$, the network can be designed with the terminations interchanged and assembled inverted. A singly terminated network can be obtained by using a large R_g in the formulas. With $R_g = \infty$, the formulas give $A = 0$, $k = h$, and a limit in Eq. (32). An exact design can be obtained starting from the output end, with Eq. (34). The solutions for the matched cases ($A = 1$, $h = 1$) and singly terminating cases are unique. The solution given by the formulas for the mismatched cases are not the only solutions possible (see Ref. 7 for details). Explicit formulas for the element values of inverse Chebyshev LC ladder filters and for the variations discussed above are not known.

9. EXAMPLE

As an example of the application of the explicit formulas and the properties of the resulting filter, consider a fifth-order filter with 1 dB passband ripple, passband edge at 10 MHz, and terminations $R_g = 100 \Omega$ and $R_1 = 50 \Omega$. From Eq. (28) $A = 0.88888$, from Eq. (30) $k = 1.33055$, and from Eq. (31) $h = 1.13099$. The frequency-normalized element values are then obtained starting from Eq. (32), with Eq. (33) applied twice. The resulting values are then divided by $2\pi \times 10^7$, to place the passband edge at 10 MHz. The results are $C_1 = 592.2$ pF, $L_2 = 1.106$ μ H, $C_3 = 755.2$ pF, $L_4 = 1.058$ μ H, and $C_5 = 476.5$ pF.

Note that when the terminations are not matched, there is no special reason for the sensitivities of the filter magnitude in relation to the element values to be low. There is a continuous degradation of the sensitivity characteristics, with the matched case being the least sensitive and singly terminated case being the most sensitive. Figure 6 shows the normalized gain (scaled to a maximum of 0 dB), with expected error margins, for the example filter and for the two extreme cases. In the singly terminated case, with $R_g = \infty$, the input was assumed to be a current source. The expected errors were computed by sensitivity analysis [6], assuming uncorrelated 5% random variations in all the elements, including the terminations, using the formula for the gain statistical deviation

$$\Delta|T(j\omega)| = \frac{20}{\ln(10)} \left(\sum_i \left(\frac{\Delta x_i}{x_i} S_{x_i}^{[T(j\omega)]} \right)^2 \right)^{1/2} \text{ dB} \quad (36)$$

where $\Delta x_i/x_i$ is the tolerance of the element x_i , set to 0.05 to all the elements. Observe that for the matched case the error returns to ± 0.307 dB at all the gain peaks, what corresponds to the expected error due to the terminations alone. The example filter produces only slightly larger errors. There is a range where the singly terminated realization is the best, but it is much worse at the critical area of the passband border. Similar relations appear also for other orders.

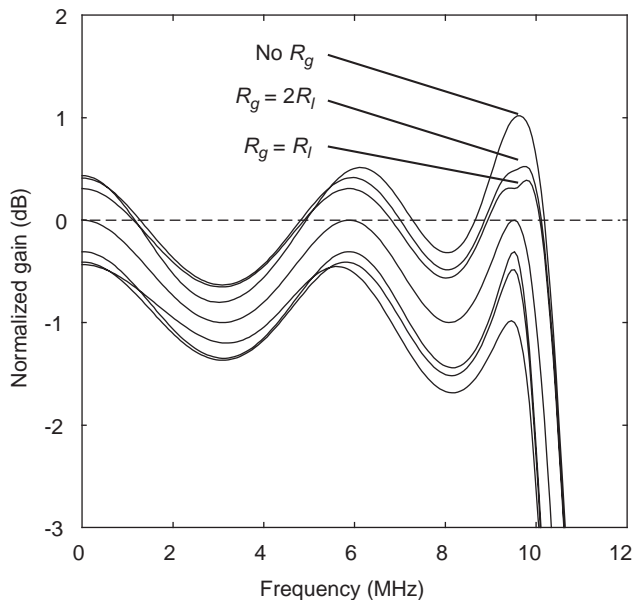


Figure 6. Expected passband errors for three 5th-order 1 dB Chebyshev filters, for 5% random variations on all the element values.

BIBLIOGRAPHY

1. A. Antoniou, *Digital Filters: Analysis, Design, and Applications*, McGraw-Hill, New York, 1993.
2. P. L. Chebyshev, Théorie des mécanismes connus sous le nom de parallélogrammes, *Oeuvres*, Vol. I, St. Petersburg, 1899.
3. M. E. Van Valkenburg, *Analog Filter Design*, Holt, Rinehart and Winston, New York, 1982.
4. R. W. Daniels, *Approximation Methods for Electronic Filter Design*, McGraw-Hill, New York, 1974.
5. H. J. Orchard, Inductorless filters, *Electron. Lett.* **2**:224–225 (Sept. 1966).
6. G. C. Temes and J. W. LaPatra, *Circuit Synthesis and Design*, McGraw-Hill Kogakusha, Tokyo, 1977.
7. L. Weinberg, *Network Analysis and Synthesis*, McGraw-Hill, New York, 1962.
8. A. C. M. de Queiroz and L. P. Calôba, An approximation algorithm for irregular-ripple filters, *Proc. IEEE Int. Telecommunications Symp.*, Rio de Janeiro, Brazil, Sept. 1990, pp. 430–433.

CHIRALITY

AKHLESH LAKHTAKIA
 Pennsylvania State University
 University Park, Pennsylvania

1. INTRODUCTION

Chiral media have the ability to discriminate between left-handed and right-handed electromagnetic (EM) fields.

These media can be classified into two types: (1) isotropic chiral media and (2) structurally chiral media. The molecules of a naturally occurring isotropic chiral medium are handed, while an artificial isotropic chiral medium can be made by randomly dispersing electrically small, handed inclusions (such as springs) in an isotropic achiral host medium. The molecules of a structurally chiral medium, such as a chiral nematic liquid crystal, are randomly positioned but have helicoidal orientational order. Structurally chiral media can also be artificially fabricated either as stacks of uniaxial laminae or using thin-film technology. Whereas considerable theoretical and experimental work on isotropic chiral media has been reported at microwave frequencies during the 1980s and the 1990s, microwave research on structurally chiral media remains in an embryonic stage at the time of this writing [1]. Therefore, the major part of this article is devoted to isotropic chiral media.

2. NATURAL OPTICAL ACTIVITY

Ordinary sunlight is split into its spectral components by a prism. A spectral component is monochromatic (i.e., it has one and only one wavelength λ_0 in vacuum). The wavelength λ_0 of one of the visible spectral components lies anywhere between 400 nm (violet) and 700 nm (red). A spectral component can be *almost* isolated from other spectral components by carefully passing sunlight through a series of filters. Although filtering yields quasi-monochromatic light, many experiments have been and continue to be performed and their results analyzed, assuming that the filtered light is monochromatic.

Light is an EM wave with spectral components to which our retinal pigments happen to be sensitive, and the consequent images, in turn, happen to be decipherable in our brains. All optical phenomena can be generalized to other electromagnetic spectral regimes.

Suppose that a monochromatic EM wave is propagating in a straight line in air, which is synonymous with vacuum (or free space) for our present purpose. Its electric field vector vibrates in some direction to which the propagation direction is perpendicular; the frequency of vibration is $f=c/\lambda_0$, where $c=3 \times 10^8$ m/s is the speed of light in vacuum. Its magnetic field vector also vibrates with the same frequency, but is always aligned perpendicular to the electric field vector as well as to the propagation direction. Suppose that we fix our attention on a certain plane that is transverse to the propagation direction. On this plane, the locus of the tip of the electric field vector is the so-called vibration ellipse, which is of the same shape as the locus of the tip of the magnetic field vector. A vibration ellipse is shown in Fig. 1. Its shape is characterized by a tilt angle as well as an axial ratio; in addition, it can be left-handed if the tip of the electric field vector rotates counterclockwise, or right-handed if otherwise. Similarly, an EM wave is said to be elliptically polarized, in general; however, the vibration ellipse can occasionally degenerate into a circle (circular polarization) or even a straight line (linear polarization).

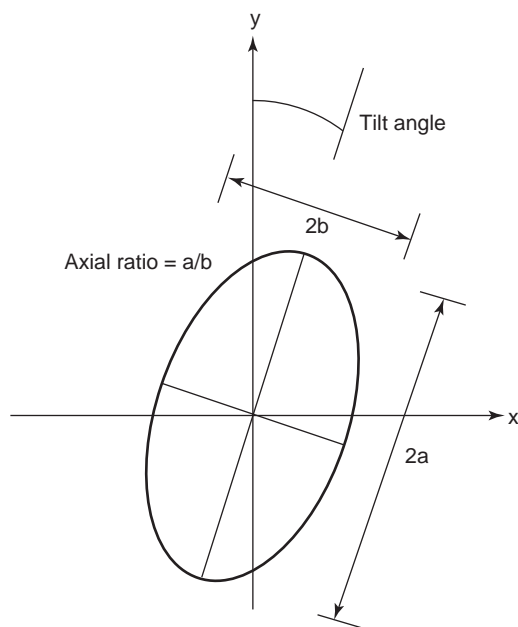


Figure 1. The tip of the electric field vector of a plane-polarized monochromatic electromagnetic wave traces the so-called vibration ellipse in a plane transverse to the propagation direction.

The shape of the vibration ellipse of monochromatic light is altered after traversal through a certain thickness of a so-called optically active medium. This phenomenon, known as *optical activity*, was discovered around 1811 by F. Arago while experimenting with quartz. Crystals are generally anisotropic, but J.-B. Biot observed around 1817 the optical activity of turpentine vapor, definitely an isotropic medium. Isotropic organic substances were believed to have exclusively biological provenances, and in 1860 L. Pasteur argued that turpentine vapor exhibited natural optical activity, but the optical activity of crystals could not be similarly qualified. Pasteur was unduly restrictive. Isotropic optically active media, of biological or other origin, are nowadays called *isotropic chiral media*, because EM fields excited in them necessarily possess a property called handedness (Greek *cheir* = hand). Facsimile reproductions of several early papers are available [2].

3. CHIRAL MEDIA: NATURAL AND ARTIFICIAL

The molecules of an isotropic chiral medium are mirror asymmetric (i.e., they are noncongruent with their mirror images). A chiral molecule and its mirror image are called *enantiomers* [3]. As examples, the two enantiomers of 2-butanol are shown in Fig. 2. Enantiomers can have different properties, although they contain identical atoms in identical numbers. One enantiomer of the chiral compound thalidomide may be used to cure morning sickness, during pregnancy, but its mirror image induces fetal malformation. Aspartame, a common artificial sweetener, is one of the four enantiomers of a dipeptide derivative. Of these four, one (i.e., aspartame) is sweet, another is bitter, while the remaining two are tasteless. Of the approxi-

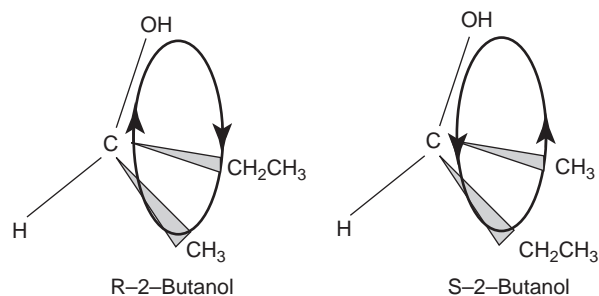


Figure 2. The two enantiomers of 2-butanol are mirror images of each other, as shown by the directed circular arrangements of the $-\text{OH}$, $-\text{CH}_2\text{CH}_3$, and $-\text{CH}_3$ groups.

mately 1850 natural, semisynthetic, and synthetic drugs marketed these days, no less than 1045 can exist as two or more enantiomers; but only 570 were being marketed in the late 1980s as single enantiomers, of which 61 were totally synthetic. But since 1992, the U.S. Food and Drug Administration (FDA) has insisted that only one enantiomer of a chiral drug be brought into the market. Biological chiroselectivity, once the subject of speculations by Pasteur on the nature of the life force (*vis viva*), is now the topic of conferences on the origin of life [4].

An isotropic chiral medium is circularly birefringent (i.e., both left-handed and right-handed circularly polarized light can propagate in a region filled with a homogeneous isotropic chiral medium, with different phase velocities and attenuation rates). Therefore, when monochromatic, elliptically polarized light irradiates an isotropic chiral slab, the tilt angle and the axial ratio of the transmitted light are different from those of the incident light. The change in the tilt angle is quantified as *optical rotation* (OR) and alteration of the axial ratio as *circular dichroism* (CD). Both OR and CD depend on the wavelength λ_0 , and the dependences are reasonably material-specific that spectroscopies based on their measurements have long had industrial importance. Biot himself had pioneered these attempts by cataloging the OR spectra of a large number of syrups and oils, and went on to found the science of saccharimetry for which he was awarded the Rumford Medal in 1840 by the Royal Society of London. The first edition of Landolt's tables on optical activity appeared in the German language in 1879; the English translation of the second edition of 1898 appeared in 1902.

Although Maxwell's unification of light with electromagnetism during the third quarter of the nineteenth century came to mean that natural optical activity is an EM phenomenon, the term *optical rotation* persisted. By the end of the nineteenth century, several empirical rules had evolved on OR spectrums of isotropic chiral mediums. Then, in the late 1890s, two accomplishments of note were reported:

1. J. C. Bose constructed several artificial chiral materials by twisting jute fibers and laying them end to end, and experimentally verified OR at millimeter wavelengths. These materials were anisotropic, but

Bose went on to infer from his experiments that isotropic chiral materials could also be constructed in the same way [5]. Thus, he conclusively demonstrated the geometric microstructural basis for optical activity, and he also constructed possibly the world's first artificial anisotropic chiral medium to alter the vibration ellipses of microwaves.

2. P. Drude showed that chiral molecules can be modeled as spiral oscillators and theoretically verified a rule Biot had given regarding OR spectra [6].

Experimental verification of Drude's spiral oscillator hypothesis had to wait for another two decades. As electromagnetic propositions can be tested at lower frequencies if the lengths are correspondingly increased and other properties proportionally adjusted, K. F. Lindman made 2.5-turn, 10-mm-diameter springs from 9-cm-long copper wire pieces of 1.2 mm cross-sectional diameter. Springs are handed, as illustrated in Fig. 3. Each spring was wrapped in a cotton ball, and about 700 springs of the same handedness were randomly positioned in a $26 \times 26 \times 26$ -cm cardboard box with an eye to achieving tolerable isotropy. Then the box was irradiated with 1–3-GHz ($30 \text{ cm} \geq \lambda_0 \geq 10 \text{ cm}$) microwave radiation and the OR was measured. Lindman verified Drude's hypothesis remarkably well. He also determined that (1) the OR was proportional to the number of (identically handed) springs in the box, given that the distribution of springs was rather sparse; and (2) equal amounts of left-handed or right-handed springs brought about the same OR, but in opposite senses [7]. Lindman's experiments were extensively repeated during the 1990s by many research groups in several countries [8,9], and several patents have even been awarded on making artificial isotropic chiral mediums with miniature springs.

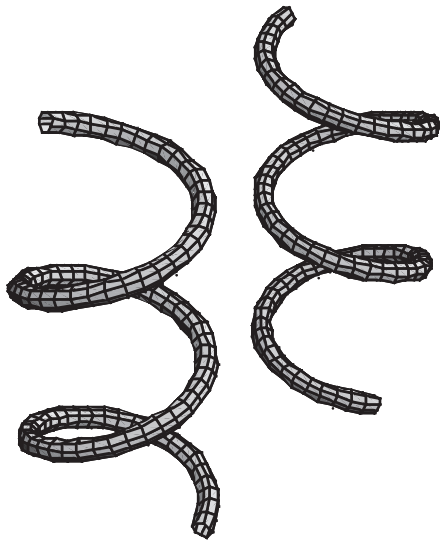


Figure 3. An enantiomeric pair of springs. An artificial isotropic chiral medium can be made by randomly dispersing springs in an isotropic achiral host medium, with more springs of one handedness than the springs of the other handedness.

4. CONSTITUTIVE RELATIONS OF AN ISOTROPIC CHIRAL MEDIUM

Electromagnetic fields are governed by the Maxwell postulates, in vacuum as well as in any material medium. These four postulates have a microscopic basis and are given in vacuum as follows:

$$\nabla \cdot \tilde{\mathbf{B}}(\mathbf{r}, t) = 0 \quad (1a)$$

$$\nabla \times \tilde{\mathbf{E}}(\mathbf{r}, t) = -\frac{\partial}{\partial t} \tilde{\mathbf{B}}(\mathbf{r}, t) \quad (1b)$$

$$\varepsilon_0 \nabla \cdot \tilde{\mathbf{E}}(\mathbf{r}, t) = \tilde{\rho}_{\text{tot}}(\mathbf{r}, t) \quad (1c)$$

$$\nabla \times \tilde{\mathbf{B}}(\mathbf{r}, t) = \mu_0 \varepsilon_0 \frac{\partial}{\partial t} \tilde{\mathbf{E}}(\mathbf{r}, t) + \mu_0 \tilde{\mathbf{J}}_{\text{tot}}(\mathbf{r}, t) \quad (1d)$$

Thus, $\tilde{\mathbf{E}}(\mathbf{r}, t)$ and $\tilde{\mathbf{B}}(\mathbf{r}, t)$ are the primitive or the fundamental EM fields, both functions of the three-dimensional position vector \mathbf{r} and time t ; $\varepsilon_0 = 8.854 \times 10^{-12}$ F/m and $\mu_0 = 4\pi \times 10^{-7}$ H/m are, respectively, the permittivity and the permeability of vacuum; $\tilde{\rho}_{\text{tot}}(\mathbf{r}, t)$ is the electric charge density and $\tilde{\mathbf{J}}_{\text{tot}}(\mathbf{r}, t)$ is the electric current density.

Equations (1) apply at any length scale, whereas the charge and the current densities must be specified not continuously but over a set of isolated points. Electromagnetically speaking, matter is nothing but a collection of discrete charged particles in vacuum. As per the Heaviside–Lorentz procedure to get a macroscopic description of continuous matter, spatial averages of all fields and sources are taken, while both $\tilde{\rho}_{\text{tot}}(\mathbf{r}, t)$ and $\tilde{\mathbf{J}}_{\text{tot}}(\mathbf{r}, t)$ are partitioned into matter-derived and externally impressed components. Then the Maxwell postulates at the macroscopic level can be stated as

$$\nabla \cdot \tilde{\mathbf{D}}(\mathbf{r}, t) = 0 \quad (2a)$$

$$\nabla \times \tilde{\mathbf{E}}(\mathbf{r}, t) = -\frac{\partial}{\partial t} \tilde{\mathbf{B}}(\mathbf{r}, t) \quad (2b)$$

$$\nabla \cdot \tilde{\mathbf{D}}(\mathbf{r}, t) = \tilde{\rho}(\mathbf{r}, t) \quad (2c)$$

$$\nabla \times \tilde{\mathbf{H}}(\mathbf{r}, t) = \frac{\partial}{\partial t} \tilde{\mathbf{D}}(\mathbf{r}, t) + \tilde{\mathbf{J}}(\mathbf{r}, t) \quad (2d)$$

Here, $\tilde{\rho}(\mathbf{r}, t)$ and $\tilde{\mathbf{J}}(\mathbf{r}, t)$ are the externally impressed source densities, while the new fields

$$\tilde{\mathbf{D}}(\mathbf{r}, t) = \varepsilon_0 \tilde{\mathbf{E}}(\mathbf{r}, t) + \tilde{\mathbf{P}}(\mathbf{r}, t) \quad (3a)$$

$$\tilde{\mathbf{H}}(\mathbf{r}, t) = \frac{\tilde{\mathbf{B}}(\mathbf{r}, t) - \tilde{\mathbf{M}}(\mathbf{r}, t)}{\mu_0} \quad (3b)$$

contain two matter-derived quantities: the polarization $\tilde{\mathbf{P}}(\mathbf{r}, t)$ and the magnetization $\tilde{\mathbf{M}}(\mathbf{r}, t)$.

Constitutive relations must be prescribed to relate the matter-derived fields $\tilde{\mathbf{D}}(\mathbf{r}, t)$ and $\tilde{\mathbf{H}}(\mathbf{r}, t)$ to the basic fields $\tilde{\mathbf{E}}(\mathbf{r}, t)$ and $\tilde{\mathbf{B}}(\mathbf{r}, t)$ in any material medium. The construction of these relations is primarily phenomenological, although certain epistemologically mandated proprieties

must be adhered to. The constitutive relations appropriate for a general, linear, homogeneous, material medium with time-invariant response characteristics may be stated as

$$\begin{aligned} \tilde{\mathbf{D}}(\mathbf{r}, t) = & \varepsilon_0 \tilde{\mathbf{E}}(\mathbf{r}, t) + \varepsilon_0 \int_0^\infty \tilde{\chi}^e(\tau) \cdot \tilde{\mathbf{E}}(\mathbf{r}, t - \tau) d\tau \\ & + \int_0^\infty \tilde{\chi}^{\text{em}}(\tau) \cdot \tilde{\mathbf{B}}(\mathbf{r}, t - \tau) d\tau \end{aligned} \quad (4a)$$

$$\begin{aligned} \tilde{\mathbf{H}}(\mathbf{r}, t) = & \frac{1}{\mu_0} \tilde{\mathbf{B}}(\mathbf{r}, t) - \frac{1}{\mu_0} \int_0^\infty \tilde{\chi}^{\text{m}}(\tau) \cdot \tilde{\mathbf{B}}(\mathbf{r}, t - \tau) d\tau \\ & + \int_0^\infty \tilde{\chi}^{\text{me}}(\tau) \cdot \tilde{\mathbf{E}}(\mathbf{r}, t - \tau) d\tau \end{aligned} \quad (4b)$$

Four constitutive property kernels appear in these equations; the dyadic $\tilde{\chi}^e(t)$ is the dielectric susceptibility kernel, $\tilde{\chi}^{\text{m}}(t)$ is the magnetic susceptibility kernel, while the dyadics $\tilde{\chi}^{\text{em}}(t)$ and $\tilde{\chi}^{\text{me}}(t)$ are called the *magnetolectric kernels*. Although a dyadic may be understood as a 3×3 matrix for the purpose of this article, Chen's textbook [10] is recommended for a simple introduction to the use of dyadics in EM theory.

All four dyadic kernels in Eqs. (4) are causal [i.e., $\tilde{\chi}^e(t) \equiv \mathbf{0}$ for $t \leq 0$, etc.], because all materials must exhibit delayed response. In addition, when we substitute Eqs. (4a) and (4b) in Eqs. (2c) and (2d), respectively, a redundancy emerges with respect to Eqs. (2a) and (2b). Elimination of this redundancy leads to the constraint [11]

$$\text{Tr}[\tilde{\chi}^{\text{em}}(t) - \tilde{\chi}^{\text{me}}(t)] \equiv 0 \quad (5)$$

which has never been known to be violated by a physical material. Finally, crystallographic symmetries may also impose additional constraints on the constitutive kernels. A medium described by Eqs. (4) is said to be *bianisotropic*, since the constitutive kernels indicate anisotropy, and both $\tilde{\mathbf{D}}(\mathbf{r}, t)$ and $\tilde{\mathbf{H}}(\mathbf{r}, t)$ depend on both $\tilde{\mathbf{E}}(\mathbf{r}, t)$ and $\tilde{\mathbf{B}}(\mathbf{r}, t)$.

Suppose next that the linear medium's constitutive properties are direction-independent. Equations (4) then simplify to

$$\begin{aligned} \tilde{\mathbf{D}}(\mathbf{r}, t) = & \varepsilon_0 \tilde{\mathbf{E}}(\mathbf{r}, t) + \varepsilon_0 \int_0^\infty \tilde{\chi}^e(\tau) \tilde{\mathbf{E}}(\mathbf{r}, t - \tau) d\tau \\ & + \int_0^\infty \tilde{\chi}^{\text{chi}}(\tau) \tilde{\mathbf{B}}(\mathbf{r}, t - \tau) d\tau \end{aligned} \quad (6a)$$

$$\begin{aligned} \tilde{\mathbf{H}}(\mathbf{r}, t) = & \frac{1}{\mu_0} \tilde{\mathbf{B}}(\mathbf{r}, t) - \frac{1}{\mu_0} \int_0^\infty \tilde{\chi}^{\text{m}}(\tau) \tilde{\mathbf{B}}(\mathbf{r}, t - \tau) d\tau \\ & + \int_0^\infty \tilde{\chi}^{\text{chi}}(\tau) \tilde{\mathbf{E}}(\mathbf{r}, t - \tau) d\tau \end{aligned} \quad (6b)$$

in consequence of Eq. (5), where the scalar $\tilde{\chi}^{\text{chi}}(t)$ is the chirality kernel. Equations (6a)–(6b) describe the *isotropic chiral medium*—the most general, isotropic, linear electromagnetic material known to exist [12,13].

Most commonly, EM analysis is carried out in the frequency domain, not the time domain. Let all time-depen-

dent quantities be Fourier-transformed; thus

$$\tilde{\mathbf{D}}(\mathbf{r}, t) = \frac{1}{2\pi} \int_{-\infty}^{\infty} e^{-i\omega t} \mathbf{D}(\mathbf{r}, \omega) d\omega \quad (7)$$

and so on, where $\omega = 2\pi f$ is the angular frequency. In the remainder of this article, phasors such as $\mathbf{D}(\mathbf{r}, \omega)$ are called *fields*, following normal practice. The four Maxwell postulates [Eqs. (2)] assume the form

$$\nabla \cdot \mathbf{B}(\mathbf{r}, \omega) = 0 \quad (8a)$$

$$\nabla \times \mathbf{E}(\mathbf{r}, \omega) = i\omega \mathbf{B}(\mathbf{r}, \omega) \quad (8b)$$

$$\nabla \cdot \mathbf{D}(\mathbf{r}, \omega) = \rho(\mathbf{r}, \omega) \quad (8c)$$

$$\nabla \times \mathbf{H}(\mathbf{r}, \omega) = -i\omega \mathbf{D}(\mathbf{r}, \omega) + \mathbf{J}(\mathbf{r}, \omega) \quad (8d)$$

while the constitutive equations [Eqs. 6] for an isotropic chiral medium simultaneously transform into

$$\mathbf{D}(\mathbf{r}, \omega) = \varepsilon_0 [1 + \chi^e(\omega)] \mathbf{E}(\mathbf{r}, \omega) + \chi^{\text{chi}}(\omega) \mathbf{B}(\mathbf{r}, \omega) \quad (9a)$$

$$\mathbf{H}(\mathbf{r}, \omega) = \frac{1}{\mu_0} [1 - \chi^{\text{m}}(\omega)] \mathbf{B}(\mathbf{r}, \omega) + \chi^{\text{chi}}(\omega) \mathbf{E}(\mathbf{r}, \omega) \quad (9b)$$

Using Eqs. (8b) and (8d) with $\mathbf{J}(\mathbf{r}, \omega) = \mathbf{0}$ in Eqs. (9a) and (9b), respectively, we obtain the Drude–Born–Fedorov (DBF) constitutive relations of an isotropic chiral medium:

$$\mathbf{D}(\mathbf{r}, \omega) = \varepsilon(\omega) [\mathbf{E}(\mathbf{r}, \omega) + \beta(\omega) \nabla \times \mathbf{E}(\mathbf{r}, \omega)] \quad (10a)$$

$$\mathbf{B}(\mathbf{r}, \omega) = \mu(\omega) [\mathbf{H}(\mathbf{r}, \omega) + \beta(\omega) \nabla \times \mathbf{H}(\mathbf{r}, \omega)] \quad (10b)$$

Their great merit is that the necessary mirror asymmetry is transparently reflected in them, because $\nabla \times \mathbf{E}(\mathbf{r}, \omega)$ and $\nabla \times \mathbf{H}(\mathbf{r}, \omega)$ are not true vectors but only pseudovectors. A chiral medium is thus described by three constitutive properties; the permittivity and permeability in Eqs. (10a) and (10b), respectively, may be formally defined as the ratios

$$\begin{aligned} \varepsilon(\omega) = & \frac{\mathbf{D}(\mathbf{r}, \omega) \cdot \mathbf{E}^*(\mathbf{r}, \omega)}{|\mathbf{E}(\mathbf{r}, \omega)|^2} \quad \text{if} \quad \mathbf{E}^*(\mathbf{r}, \omega) \\ & \cdot [\nabla \times \mathbf{E}(\mathbf{r}, \omega)] = 0 \end{aligned} \quad (11a)$$

$$\begin{aligned} \mu(\omega) = & \frac{\mathbf{B}(\mathbf{r}, \omega) \cdot \mathbf{H}^*(\mathbf{r}, \omega)}{|\mathbf{H}(\mathbf{r}, \omega)|^2} \quad \text{if} \quad \mathbf{H}^*(\mathbf{r}, \omega) \\ & \cdot [\nabla \times \mathbf{H}(\mathbf{r}, \omega)] = 0 \end{aligned} \quad (11b)$$

but the chirality parameter $\beta(\omega)$ can be regarded as either

$$\begin{aligned} \beta(\omega) = & \frac{\mathbf{D}(\mathbf{r}, \omega) \cdot [\nabla \times \mathbf{E}^*(\mathbf{r}, \omega)]}{\varepsilon(\omega) |\nabla \times \mathbf{E}(\mathbf{r}, \omega)|^2} \quad \text{if} \quad \mathbf{E}(\mathbf{r}, \omega) \\ & \cdot [\nabla \times \mathbf{E}^*(\mathbf{r}, \omega)] = 0 \end{aligned} \quad (11c)$$

or

$$\beta(\omega) = \frac{\mathbf{B}(\mathbf{r}, \omega) \cdot [\nabla \times \mathbf{H}^*(\mathbf{r}, \omega)]}{\mu(\omega) |\nabla \times \mathbf{H}(\mathbf{r}, \omega)|^2} \quad \text{if } \mathbf{H}(\mathbf{r}, \omega) \cdot [\nabla \times \mathbf{H}^*(\mathbf{r}, \omega)] = 0 \quad (11d)$$

where the asterisk denotes the complex conjugate. Equations (11) make it clear that while $\varepsilon(\omega)$ and $\mu(\omega)$ are true scalars, $\beta(\omega)$ has to be a pseudoscalar since the numerator in either of its two definitions contains a pseudovector. Other constitutive relations—equivalent to Eqs. (9) and Eqs. (10)—are also used in the frequency-domain EM literature, but this article is restricted to the DBF constitutive relations [Eqs. (10)], as they bring out the essence of chirality at the very first glance. An isotropic chiral medium and its mirror image share the same $\varepsilon(\omega)$ and $\mu(\omega)$, and their chirality parameters differ only in sign.

The time-averaged Poynting vector

$$\mathbf{S}(\mathbf{r}, \omega) = \frac{1}{2} \text{Re}[\mathbf{E}(\mathbf{r}, \omega) \times \mathbf{H}^*(\mathbf{r}, \omega)] \quad (12a)$$

denotes the direction of power flow. In any linear medium, the monochromatic Poynting theorem reads as

$$\begin{aligned} \nabla \cdot \mathbf{S}(\mathbf{r}, \omega) = & -\frac{1}{2} \text{Re}[\mathbf{E}(\mathbf{r}, \omega) \cdot \mathbf{J}^*(\mathbf{r}, \omega)] \\ & -\frac{1}{2} \text{Re}[i\omega[\mathbf{E}(\mathbf{r}, \omega) \cdot \mathbf{D}^*(\mathbf{r}, \omega) \\ & - \mathbf{B}(\mathbf{r}, \omega) \cdot \mathbf{H}^*(\mathbf{r}, \omega)]] \end{aligned} \quad (12b)$$

For specialization to an isotropic chiral medium, we have to substitute Eqs. (10) in Eq. (12b). The resulting expression is not particularly illuminating.

An isotropic chiral medium is Lorentz-reciprocal. Suppose that all space is occupied by a homogeneous isotropic chiral medium and all sources are confined to regions of bounded extent. Let sources labeled a radiate fields $\mathbf{E}_a(\mathbf{r}, \omega)$ and $\mathbf{H}_a(\mathbf{r}, \omega)$, while sources labeled b radiate fields $\mathbf{E}_b(\mathbf{r}, \omega)$ and $\mathbf{H}_b(\mathbf{r}, \omega)$, all at the same frequency. Then the relations [12]

$$\nabla \cdot [\mathbf{E}_a(\mathbf{r}, \omega) \times \mathbf{H}_b(\mathbf{r}, \omega) - \mathbf{E}_b(\mathbf{r}, \omega) \times \mathbf{H}_a(\mathbf{r}, \omega)] = 0 \quad (13a)$$

$$\begin{aligned} \nabla \cdot [\varepsilon(\omega)\mathbf{E}_a(\mathbf{r}, \omega) \times \mathbf{E}_b(\mathbf{r}, \omega) - \mu(\omega)\mathbf{H}_a(\mathbf{r}, \omega) \\ \times \mathbf{H}_b(\mathbf{r}, \omega)] = 0 \end{aligned} \quad (13b)$$

arise in a source-free region, in consequence of the Lorentz reciprocity of the medium.

5. ARTIFICIAL ISOTROPIC CHIRAL MEDIA

That matter is discrete has long been established. Furthermore, when we probe matter at length scales at which it appears continuous, whether the microstructure is molecular or merely comprises electrically small inclusions is of no consequence. The linear dimensions of an electrically

small inclusion are less than about a tenth of the maximum wavelength, in the media outside as well as inside the inclusion, at a particular frequency. Artificial isotropic chiral media—active at microwave frequencies—can be constructed with this thought in mind. Consider a random suspension of identical, electrically small, inclusions in a host medium, which we take here to be vacuum for simplicity. The number of inclusions per unit volume is denoted by N , and the volumetric proportion of the inclusions in the composite medium is assumed to be very small. Our objective is to *homogenize* this dilute particulate composite medium and estimate its effective constitutive properties [13]. Homogenization is much like blending apples into apple sauce or tomatoes into ketchup.

Any inclusion scatters the EM wave incident on it. Far away from the inclusion, the scattered EM field phasors can be conceptualized, equivalently, as being radiated by an ensemble of multipoles. Multipoles are necessarily frequency-domain entities; and adequate descriptions of electrically larger inclusions require higher-order multipoles, but homogenizing composite media with electrically large inclusions is fraught with conceptual perils.

The lowest-order multipoles are the electric dipole \mathbf{p} and the magnetic dipole \mathbf{m} . In formalisms for isotropic chiral media, both are accorded the same status. As all inclusions in our composite medium are electrically small, we can think that an inclusion located at position \mathbf{r}' is *equivalent* to the colocated dipoles characterized by the following relations:

$$\mathbf{p}_{\text{eqvt}}(\mathbf{r}', \omega) = \underline{\pi}_{\text{ee}}(\omega) \cdot \mathbf{E}_{\text{exc}}(\mathbf{r}', \omega) + \underline{\pi}_{\text{eh}}(\omega) \cdot \mathbf{H}_{\text{exc}}(\mathbf{r}', \omega) \quad (14a)$$

$$\mathbf{m}_{\text{eqvt}}(\mathbf{r}', \omega) = \underline{\pi}_{\text{he}}(\omega) \cdot \mathbf{E}_{\text{exc}}(\mathbf{r}', \omega) + \underline{\pi}_{\text{hh}}(\omega) \cdot \mathbf{H}_{\text{exc}}(\mathbf{r}', \omega) \quad (14b)$$

Here, $\mathbf{E}_{\text{exc}}(\mathbf{r}', \omega)$ and $\mathbf{H}_{\text{exc}}(\mathbf{r}', \omega)$ are the fields *exciting* the particular inclusion; while $\underline{\pi}_{\text{ee}}(\omega)$, $\underline{\pi}_{\text{eh}}(\omega)$, $\underline{\pi}_{\text{he}}(\omega)$, and $\underline{\pi}_{\text{hh}}(\omega)$ are the four linear polarizability dyadics that depend on the frequency, the constitution, and the dimensions of the inclusion. As the inclusions are randomly oriented and any homogenizable chunk of a composite medium contains a large number of inclusions, $\underline{\pi}_{\text{ee}}(\omega)$ and other terms in Eqs. (14) can be replaced by their orientationally averaged values. If the homogenized composite medium is isotropic chiral, this orientational averaging process *must* yield

$$\mathbf{p}_{\text{eqvt}}(\mathbf{r}', \omega) = N[\pi_{\text{ee}}(\omega)\mathbf{E}_{\text{exc}}(\mathbf{r}', \omega) + i\pi_{\text{chi}}(\omega)\mathbf{H}_{\text{exc}}(\mathbf{r}', \omega)] \quad (15a)$$

$$\mathbf{m}_{\text{eqvt}}(\mathbf{r}', \omega) = N[-i\pi_{\text{chi}}(\omega)\mathbf{E}_{\text{exc}}(\mathbf{r}', \omega) + \pi_{\text{hh}}(\omega)\mathbf{H}_{\text{exc}}(\mathbf{r}', \omega)] \quad (15b)$$

The polarizability dyadics of electrically small, handed inclusions (e.g., springs) may be computed either with standard scattering methods such as the method of moments [14] or using lumped-parameter circuit models [15]. Provided that dissipation in the composite medium can be ignored, at a certain angular frequency, $\pi_{\text{ee}}(\omega)$, $\pi_{\text{hh}}(\omega)$, and $\pi_{\text{chi}}(\omega)$ are purely real-valued.

On applying the Maxwell Garnett homogenization approach, the constitutive relations of the homogenized composite medium (HCM) are estimated as follows [12]:

$$\mathbf{D}(\mathbf{r}, \omega) = \tau_{ee}(\omega)\mathbf{E}(\mathbf{r}, \omega) + \tau_{chi}(\omega)\mathbf{H}(\mathbf{r}, \omega) \quad (16a)$$

$$\mathbf{B}(\mathbf{r}, \omega) = \tau_{hh}(\omega)\mathbf{H}(\mathbf{r}, \omega) - \tau_{chi}(\omega)\mathbf{E}(\mathbf{r}, \omega) \quad (16b)$$

where

$$\tau_{ee}(\omega) = \varepsilon_0 + \frac{[9\mu_0 N \tau_{ee} + 3N^2(\pi_{chi}^2 - \tau_{ee}\tau_{hh})]}{9\varepsilon_0\mu_0 - 3N(\varepsilon_0\pi_{hh} + \mu_0\tau_{ee}) - N^2(\pi_{chi}^2 - \tau_{ee}\tau_{hh})} \quad (16c)$$

$$\tau_{hh}(\omega) = \mu_0 + \frac{[9\varepsilon_0 N \tau_{hh} + 3N^2(\pi_{chi}^2 - \tau_{ee}\tau_{hh})]}{9\varepsilon_0\mu_0 - 3N(\varepsilon_0\pi_{hh} + \mu_0\tau_{ee}) - N^2(\pi_{chi}^2 - \tau_{ee}\tau_{hh})} \quad (16d)$$

$$\tau_{chi}(\omega) = \frac{i9\varepsilon_0\mu_0 N \pi_{chi}}{9\varepsilon_0\mu_0 - 3N(\varepsilon_0\pi_{hh} + \mu_0\tau_{ee}) - N^2(\pi_{chi}^2 - \tau_{ee}\tau_{hh})} \quad (16e)$$

Equivalently

$$\mathbf{D}(\mathbf{r}, \omega) = \varepsilon_{HCM}(\omega)[\mathbf{E}(\mathbf{r}, \omega) + \beta_{HCM}(\omega)\nabla \times \mathbf{E}(\mathbf{r}, \omega)] \quad (17a)$$

$$\mathbf{B}(\mathbf{r}, \omega) = \mu_{HCM}(\omega)[\mathbf{H}(\mathbf{r}, \omega) + \beta_{HCM}(\omega)\nabla \times \mathbf{H}(\mathbf{r}, \omega)] \quad (17b)$$

are the DBF constitutive relations of the HCM, with

$$\varepsilon_{HCM}(\omega) = \frac{\tau_{ee}(\omega)\tau_{hh}(\omega) + \tau_{chi}^2(\omega)}{\tau_{hh}(\omega)} \quad (17c)$$

$$\mu_{HCM}(\omega) = \frac{\tau_{ee}(\omega)\tau_{hh}(\omega) + \tau_{chi}^2(\omega)}{\tau_{ee}(\omega)} \quad (17d)$$

$$\beta_{HCM}(\omega) = -\frac{i}{\omega} \frac{\tau_{chi}(\omega)}{\tau_{ee}(\omega)\tau_{hh}(\omega) + \tau_{chi}^2(\omega)} \quad (17e)$$

as the constitutive parameters. Clearly, if $\pi_{chi}(\omega) \neq 0$, the composite medium has been homogenized into an isotropic chiral medium. In passing, other homogenization approaches are also possible for chiral composites [1,13].

6. BELTRAMI FIELDS IN AN ISOTROPIC CHIRAL MEDIUM

In a source-free region occupied by a homogeneous isotropic chiral medium, $\rho(\mathbf{r}, \omega) = 0$ and $\mathbf{J}(\mathbf{r}, \omega) = 0$. Equations (8a), (8c), and (10) then show that $\nabla \cdot \mathbf{E}(\mathbf{r}, \omega) = 0$ and $\nabla \cdot \mathbf{H}(\mathbf{r}, \omega) = 0$. Thus all four fields— $\mathbf{E}(\mathbf{r}, \omega)$, $\mathbf{H}(\mathbf{r}, \omega)$, $\mathbf{D}(\mathbf{r}, \omega)$, and $\mathbf{B}(\mathbf{r}, \omega)$ —are purely solenoidal. Next, Eqs. (8) and (10) together yield the following

vector Helmholtz-like equations:

$$\nabla^2 \begin{Bmatrix} \mathbf{E}(\mathbf{r}, \omega) \\ \mathbf{H}(\mathbf{r}, \omega) \\ \mathbf{D}(\mathbf{r}, \omega) \\ \mathbf{B}(\mathbf{r}, \omega) \end{Bmatrix} + 2 \frac{\omega^2 \varepsilon(\omega) \mu(\omega) \beta(\omega)}{1 - \omega^2 \varepsilon(\omega) \mu(\omega) \beta^2(\omega)} \nabla \times \begin{Bmatrix} \mathbf{E}(\mathbf{r}, \omega) \\ \mathbf{H}(\mathbf{r}, \omega) \\ \mathbf{D}(\mathbf{r}, \omega) \\ \mathbf{B}(\mathbf{r}, \omega) \end{Bmatrix} + \frac{\omega^2 \varepsilon(\omega) \mu(\omega)}{1 - \omega^2 \varepsilon(\omega) \mu(\omega) \beta^2(\omega)} \begin{Bmatrix} \mathbf{E}(\mathbf{r}, \omega) \\ \mathbf{H}(\mathbf{r}, \omega) \\ \mathbf{D}(\mathbf{r}, \omega) \\ \mathbf{B}(\mathbf{r}, \omega) \end{Bmatrix} = \begin{Bmatrix} \mathbf{0} \\ \mathbf{0} \\ \mathbf{0} \\ \mathbf{0} \end{Bmatrix} \quad (18)$$

In the limit $\beta(\omega) \rightarrow 0$, the medium becomes achiral and these equations reduce to the familiar vector Helmholtz equation, $\nabla^2 \mathbf{E}(\mathbf{r}, \omega) + \omega^2 \varepsilon(\omega) \mu(\omega) \mathbf{E}(\mathbf{r}, \omega) = \mathbf{0}$, and so on.

In lieu of the second-order differential equations [Eqs. (18)], first-order differential equations can be formulated. Thus, after defining the auxiliary fields

$$\mathbf{Q}_1(\mathbf{r}, \omega) = \frac{1}{2} \left[\mathbf{E}(\mathbf{r}, \omega) + i \sqrt{\frac{\mu(\omega)}{\varepsilon(\omega)}} \mathbf{H}(\mathbf{r}, \omega) \right] \quad (19a)$$

$$\mathbf{Q}_2(\mathbf{r}, \omega) = \frac{1}{2} \left[\mathbf{H}(\mathbf{r}, \omega) + i \sqrt{\frac{\varepsilon(\omega)}{\mu(\omega)}} \mathbf{E}(\mathbf{r}, \omega) \right] \quad (19b)$$

and using the wavenumbers

$$\gamma_1(\omega) = \frac{\omega \sqrt{\varepsilon(\omega) \mu(\omega)}}{1 - \omega \beta(\omega) \sqrt{\varepsilon(\omega) \mu(\omega)}} \quad (20a)$$

$$\gamma_2(\omega) = \frac{\omega \sqrt{\varepsilon(\omega) \mu(\omega)}}{1 + \omega \beta(\omega) \sqrt{\varepsilon(\omega) \mu(\omega)}} \quad (20b)$$

we get the two first-order differential equations

$$\nabla \times \mathbf{Q}_1(\mathbf{r}, \omega) = \gamma_1(\omega) \mathbf{Q}_1(\mathbf{r}, \omega) \quad (21a)$$

$$\nabla \times \mathbf{Q}_2(\mathbf{r}, \omega) = -\gamma_2(\omega) \mathbf{Q}_2(\mathbf{r}, \omega) \quad (21b)$$

which are easier to analyze than Eqs. (18). The denominators on the left sides of Eqs. (20) suggest that $\omega^2 \varepsilon(\omega) \mu(\omega) \beta^2(\omega) = 1$ is not permissible for an isotropic chiral medium, as both wavenumbers must have finite magnitudes.

According to Eqs. (21), $\mathbf{Q}_1(\mathbf{r}, \omega)$ and $\mathbf{Q}_2(\mathbf{r}, \omega)$ are Beltrami fields [12]. A Beltrami field is parallel to its own circulation. The concept arose early in the nineteenth century, and has often been rediscovered. The easiest way to think of a Beltrami field is as a spiral staircase or a tornado.

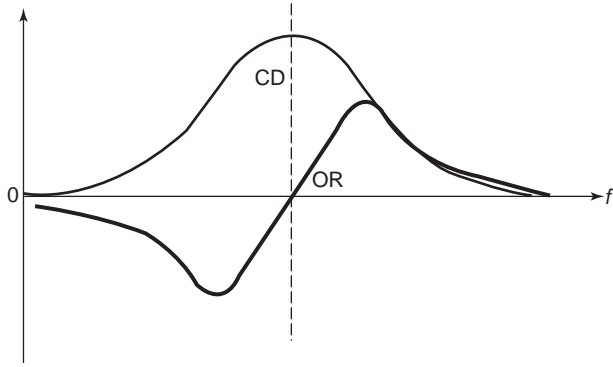


Figure 4. Optical rotation (OR) and circular dichroism (CD) spectra of a simple isotropic chiral medium. When the OR changes sign, the CD records either a maximum or a minimum, which phenomenon is called the *Cotton effect*.

While $\mathbf{Q}_1(\mathbf{r}, \omega)$ is a left-handed Beltrami field, the negative sign on the right side of Eq. (21b) means that $\mathbf{Q}_2(\mathbf{r}, \omega)$ is a right-handed Beltrami field, because the two complex-valued wavenumbers $\gamma_1(\omega)$ and $\gamma_2(\omega)$ must have positive real parts. Both wavenumbers also must have positive imaginary parts in a causal material medium, since causal materials must exhibit delayed response in the time domain and therefore must demonstrate EM loss (or attenuation) in the frequency domain.

As an isotropic chiral medium displays two distinct wavenumbers at a specific frequency, it is *birefringent*. More specifically, because $\mathbf{Q}_1(\mathbf{r}, \omega)$ and $\mathbf{Q}_2(\mathbf{r}, \omega)$ have plane-wave representations possible only in terms of circularly polarized plane waves, an isotropic chiral medium is often said to be *circularly birefringent*. The difference between $\gamma_1(\omega)$ and $\gamma_2(\omega)$ gives rise to *natural optical activity*. While OR is proportional to the *real* part of $[\gamma_1(\omega) - \gamma_2(\omega)]$, CD is proportional to the *imaginary* part of $[\gamma_1(\omega) - \gamma_2(\omega)]$. The OR and CD spectra must be consistent with the Kramers–Kronig relations [16]. The CD spectrum has a local maximum or minimum at the frequency where the sign of the OR changes; this feature is labeled as the *Cotton effect* after H. Cotton, who reported it in 1895 [2]. The OR and CD spectra of a simple chiral medium are illustrated in Fig. 4.

7. REPRESENTATION OF BELTRAMI FIELDS

A Beltrami field is represented in terms of toroidal and poloidal fields because the curl of a toroidal field is poloidal and vice versa [17]. Thus, the decomposition

$$\mathbf{Q}_v(\mathbf{r}, \omega) = \gamma_v(\omega) \nabla \times [\mathbf{r}\psi_v(\mathbf{r}, \omega)] + (-)^{v+1} \nabla \times \nabla \times [\mathbf{r}\psi_v(\mathbf{r}, \omega)]; \quad v = 1, 2 \quad (22)$$

is possible, as the first parts on the right sides of Eqs. (22) are toroidal and the second parts are poloidal. The scalar functions $\psi_v(\mathbf{r}, \omega)$ satisfy the scalar Helmholtz

equation as follows:

$$\nabla^2 \psi_v(\mathbf{r}, \omega) + \gamma_v^2(\omega) \psi_v(\mathbf{r}, \omega) = 0; \quad v = 1, 2 \quad (23)$$

Solutions of Eqs. (23) in the Cartesian, the circular cylindrical, and the spherical coordinate systems are commonplace [18].

Beltrami plane waves propagating in the $+z$ direction may be represented as

$$\mathbf{Q}_v(\mathbf{r}, \omega) = A_v 2^{-1/2} [\hat{\mathbf{x}} + (-)^{v+1} i \hat{\mathbf{y}}] \exp[i\gamma_v(\omega)z]; \quad v = 1, 2 \quad (24)$$

with A_v as the amplitudes, while $\hat{\mathbf{x}}$, $\hat{\mathbf{y}}$, and $\hat{\mathbf{z}}$ are the Cartesian unit vectors.

In the circular cylindrical coordinate system (ρ, φ, z) , Beltrami fields with an $\exp(iz)$ dependence may be expressed as the sums

$$\mathbf{Q}_v(\mathbf{r}, \omega) = \sum_{n=-\infty}^{\infty} A_{vn} [\mathbf{M}_n^{(3)}(\gamma_v(\omega)|\alpha, \mathbf{r}) + (-)^{v+1} \mathbf{N}_n^{(3)}(\gamma_v(\omega)|\alpha, \mathbf{r})]; \quad v = 1, 2 \quad (25a)$$

for regular behavior as $\rho \rightarrow \infty$, while the expansions

$$\mathbf{Q}_v(\mathbf{r}, \omega) = \sum_{n=-\infty}^{\infty} B_{vn} [\mathbf{M}_n^{(1)}(\gamma_v(\omega)|\alpha, \mathbf{r}) + (-)^{v+1} \mathbf{N}_n^{(1)}(\gamma_v(\omega)|\alpha, \mathbf{r})]; \quad v = 1, 2 \quad (25b)$$

are well behaved at $\rho = 0$, with A_{vn} and B_{vn} as the coefficients of expansion. The vector cylindrical wavefunctions are given as

$$\mathbf{M}_n^{(1)}(\sigma | \alpha, \mathbf{r}) = e^{i(\alpha z + n\varphi)} \left[\hat{\rho} \left(\frac{in}{\kappa\rho} \right) J_n(\kappa\rho) - \hat{\phi} \partial J_n(\kappa\rho) \right] \quad (26a)$$

$$\mathbf{M}_n^{(3)}(\sigma | \alpha, \mathbf{r}) = e^{i(\alpha z + n\varphi)} \left[\hat{\rho} \left(\frac{in}{\kappa\rho} \right) H_n^{(1)}(\kappa\rho) - \hat{\phi} \partial H_n^{(1)}(\kappa\rho) \right] \quad (26b)$$

$$\mathbf{N}_n^{(j)}(\sigma | \alpha, \mathbf{r}) = \frac{1}{\sigma} \nabla \times \mathbf{M}_n^{(j)}(\sigma | \alpha, \mathbf{r}); \quad j = 1, 3 \quad (26c)$$

where $\kappa = +(\sigma^2 - \alpha^2)^{1/2}$; $\hat{\rho}$, $\hat{\phi}$, and $\hat{\mathbf{z}}$ are the unit vectors in the cylindrical coordinate system; $J_n(\kappa\rho)$ are the cylindrical Bessel functions of order n , and $\partial J_n(\kappa\rho)$ are the respective first derivatives with respect to the argument; while $H_n^{(1)}(\kappa\rho)$ are the cylindrical Hankel functions of the first kind and order n , and $\partial H_n^{(1)}(\kappa\rho)$ are the first derivatives with respect to the argument. For quasi-two-dimensional problems, $\alpha = 0$ because $\partial/\partial z = 0$. Parenthetically, in this paragraph ρ denotes the radial distance in the xy plane and should not be confused with the use of ρ for charge density elsewhere in this article.

Finally, with A_{vsmn} and B_{vsmn} as the coefficients of expansion, in the spherical coordinate system (r, θ, φ) , we

have

$$\begin{aligned} \mathbf{Q}_v(\mathbf{r}, \omega) &= \sum_{s=1}^2 \sum_{n=1}^{\infty} \sum_{m=0}^n A_{vsmn} [\mathbf{M}_{smn}^{(3)}(\gamma_v(\omega)\mathbf{r}) \\ &+ (-)^{v+1} \mathbf{N}_{smn}^{(3)}(\gamma_v(\omega)\mathbf{r})]; \quad v=1, 2 \end{aligned} \quad (27a)$$

for fields regular as $r \rightarrow \infty$, and

$$\begin{aligned} \mathbf{Q}_v(\mathbf{r}, \omega) &= \sum_{s=1}^2 \sum_{n=1}^{\infty} \sum_{m=0}^n B_{vsmn} [\mathbf{M}_{smn}^{(1)}(\gamma_v(\omega)\mathbf{r}) \\ &+ (-)^{v+1} \mathbf{N}_{smn}^{(1)}(\gamma_v(\omega)\mathbf{r})]; \quad v=1, 2 \end{aligned} \quad (27b)$$

for fields regular at $r=0$. The well-known vector spherical wavefunctions, $\mathbf{M}_{smn}^{(j)}(\sigma\mathbf{r})$ and $\mathbf{N}_{smn}^{(j)}(\sigma\mathbf{r})$, are stated for $j=1, 3$ as

$$\mathbf{M}_{smn}^{(1)}(\sigma\mathbf{r}) = -[n(n+1)]^{1/2} j_n(\sigma\mathbf{r}) \hat{\mathbf{r}} \times \mathbf{B}_{smn}(\theta, \varphi) \quad (28a)$$

$$\mathbf{M}_{smn}^{(3)}(\sigma\mathbf{r}) = -[n(n+1)]^{1/2} h_n^{(1)}(\sigma\mathbf{r}) \hat{\mathbf{r}} \times \mathbf{B}_{smn}(\theta, \varphi) \quad (28b)$$

$$\mathbf{N}_{smn}^{(j)}(\sigma\mathbf{r}) = \frac{1}{\sigma} \nabla \times \mathbf{M}_{smn}^{(j)}(\sigma\mathbf{r}); \quad j=1, 3 \quad (28c)$$

where the angular functions

$$\begin{aligned} \mathbf{B}_{1mn}(\theta, \varphi) &= [n(n+1)]^{-1/2} \left[\hat{\boldsymbol{\theta}} \frac{d}{d\theta} P_n^m(\cos\theta) \sin m\varphi \right. \\ &\left. + \hat{\boldsymbol{\phi}} \frac{m}{\sin\theta} P_n^m(\cos\theta) \cos m\varphi \right] \end{aligned} \quad (29a)$$

$$\begin{aligned} \mathbf{B}_{2mn}(\theta, \varphi) &= [n(n+1)]^{-1/2} \left[\hat{\boldsymbol{\theta}} \frac{d}{d\theta} P_n^m(\cos\theta) \cos m\varphi \right. \\ &\left. - \hat{\boldsymbol{\phi}} \frac{m}{\sin\theta} P_n^m(\cos\theta) \sin m\varphi \right] \end{aligned} \quad (29b)$$

have been used. In these expressions, $\hat{\mathbf{r}}$, $\hat{\boldsymbol{\theta}}$, and $\hat{\boldsymbol{\phi}}$ are the unit vectors in the spherical coordinate system; $P_n^m(\cos\theta)$ are the associated Legendre functions of order n and degree m ; $j_n(\sigma r)$ are the spherical Bessel functions of order n ; and $h_n^{(1)}(\sigma r)$ are the spherical Hankel functions of the first kind and order n .

Boundary-value problems involving scattering by isotropic chiral half-spaces, cylinders, and spheres can be analytically solved using Eqs. (24)–(29). Boundary-value problems involving more complicated geometries generally require numerical treatment, which necessitates the use of Green functions.

Isotropic chiral waveguides for use at microwave frequencies have been theoretically studied extensively, although no practical realization thereof has yet come to light. Theoretical investigations on propagation in the so-called chirowaveguides generally consist of decomposing the Beltrami fields into axial and transverse

components as

$$\begin{aligned} \mathbf{Q}_v(\mathbf{r}, \omega) &= \mathbf{Q}_{vt}(\mathbf{r}, \omega) + \hat{\mathbf{z}} \mathbf{Q}_{vz}(\mathbf{r}, \omega), \\ \hat{\mathbf{z}} \cdot \mathbf{Q}_{vt}(\mathbf{r}, \omega) &\equiv 0; \quad v=1, 2 \end{aligned} \quad (30)$$

where the z coordinate is measured on the waveguide axis while two other mutually orthogonal coordinates are specified in the transverse plane. Assuming that all fields have an $\exp(izz)$ dependence on z , and making use of Eqs. (21), we get

$$\begin{aligned} \mathbf{Q}_{vt}(\mathbf{r}, \omega) &= \frac{1}{\gamma_v^2(\omega) - \alpha^2} [i\alpha \mathbf{I} + (-)^v \gamma_v(\omega) \hat{\mathbf{z}} \times \mathbf{I} \\ &\cdot \left[\nabla - \hat{\mathbf{z}} \frac{\partial}{\partial z} \right] \mathbf{Q}_{vz}(\mathbf{r}, \omega); \quad v=1, 2 \end{aligned} \quad (31)$$

where \mathbf{I} is the identity dyadic. The axial components satisfy the reduced scalar Helmholtz equations

$$\left[\nabla^2 - \frac{\partial^2}{\partial z^2} + \gamma_v^2(\omega) - \alpha^2 \right] \mathbf{Q}_{vz}(\mathbf{r}, \omega) = 0; \quad v=1, 2 \quad (32)$$

appropriate solutions of which are commonly worked out in many different ways for waveguides of different cross-sectional geometries [18].

8. SOURCES IN AN ISOTROPIC CHIRAL MEDIUM

Let us now assume the existence of a magnetic charge density $\rho_m(\mathbf{r}, \omega)$ and a magnetic current density $\mathbf{J}_m(\mathbf{r}, \omega)$, because they assist in the solution of dual problems [19]. In addition, let us define the intrinsic impedance $\eta(\omega) = \sqrt{\mu(\omega)/\varepsilon(\omega)}$ as well as the auxiliary wavenumber $k(\omega) = \omega \sqrt{\mu(\omega)\varepsilon(\omega)}$, and drop the explicit indication of dependences on ω for notational simplicity. Now Eqs. (8) may be written as

$$\nabla \cdot \mathbf{B}(\mathbf{r}) = \rho_m(\mathbf{r}) \quad (33a)$$

$$\nabla \times \mathbf{E}(\mathbf{r}) = i\omega \mathbf{B}(\mathbf{r}) - \mathbf{J}_m(\mathbf{r}) \quad (33b)$$

$$\nabla \cdot \mathbf{D}(\mathbf{r}) = \rho(\mathbf{r}) \quad (33c)$$

$$\nabla \times \mathbf{H}(\mathbf{r}) = -i\omega \mathbf{D}(\mathbf{r}) + \mathbf{J}(\mathbf{r}) \quad (33d)$$

which yield the relations

$$\nabla \times \mathbf{Q}_v(\mathbf{r}) + (-)^v \gamma_v \mathbf{Q}_v(\mathbf{r}) = \mathbf{W}_v(\mathbf{r}); \quad v=1, 2 \quad (34)$$

for a chiral medium, where

$$\mathbf{W}_1(\mathbf{r}) = \frac{\gamma_1}{2k} [i\eta \mathbf{J}(\mathbf{r}) - \mathbf{J}_m(\mathbf{r})] \quad (35a)$$

$$\mathbf{W}_2(\mathbf{r}) = \frac{\gamma_2}{2k} [\mathbf{J}(\mathbf{r}) + \frac{1}{i\eta} \mathbf{J}_m(\mathbf{r})] \quad (35b)$$

are the Beltrami source current densities [12].

Since Eqs. (34) are linear, they can be solved using standard techniques. Their complete solution can be compactly stated for all \mathbf{r} as

$$\mathbf{Q}_v(\mathbf{r}) = \mathbf{Q}_v^{\text{cf}}(\mathbf{r}) + \mathbf{Q}_v^{\text{rad}}(\mathbf{r}); \quad v = 1, 2 \quad (36)$$

where

$$\mathbf{Q}_v^{\text{rad}}(\mathbf{r}) = (-)^{v+1} \frac{2\gamma_1\gamma_2}{k} \int_{V_s} \underline{\mathbf{G}}_v(\mathbf{r}, \mathbf{r}_0) \cdot \mathbf{W}_v(\mathbf{r}_0) d^3\mathbf{r}_0; \quad (37)$$

$$v = 1, 2$$

are the particular solutions due to the source densities $\mathbf{W}_v(\mathbf{r})$, which are wholly confined to the region V_s , and $\mathbf{Q}_v^{\text{cf}}(\mathbf{r})$ are the complementary functions satisfying the relations

$$\nabla \times \mathbf{Q}_v^{\text{cf}}(\mathbf{r}) = (-)^{v+1} \gamma_v \mathbf{Q}_v^{\text{cf}}(\mathbf{r}); \quad v = 1, 2 \quad (38)$$

identically. Substituting Eqs. (36)–(38) in Eqs. (34), we obtain the dyadic differential equations

$$\nabla \times \underline{\mathbf{G}}_v(\mathbf{r}, \mathbf{r}_0) + (-)^v \gamma_v \underline{\mathbf{G}}_v(\mathbf{r}, \mathbf{r}_0) = (-)^{v+1} \left(\frac{2\gamma_1\gamma_2}{k} \right)^{-1} \underline{\mathbf{I}} \delta(\mathbf{r} - \mathbf{r}_0); \quad v = 1, 2 \quad (39)$$

where $\delta(\cdot)$ is the Dirac delta function.

The solutions of Eqs. (39) are the Beltrami–Green dyadic functions

$$\underline{\mathbf{G}}_v(\mathbf{r}, \mathbf{r}_0) = (-)^{v+1} \left(\frac{2\gamma_1\gamma_2}{k} \right)^{-1} [\nabla \times \underline{\mathbf{I}} + (-)^{v+1} \gamma_v \underline{\mathbf{I}}] \cdot \underline{\mathbf{G}}_{\text{fs}}(\gamma_v \mathbf{r}, \mathbf{r}_0); \quad v = 1, 2 \quad (40)$$

wherein

$$\underline{\mathbf{G}}_{\text{fs}}(\sigma | \mathbf{r}, \mathbf{r}_0) = \left(\underline{\mathbf{I}} + \frac{\nabla \nabla}{\sigma^2} \right) \frac{\exp(i\sigma |\mathbf{r} - \mathbf{r}_0|)}{4\pi |\mathbf{r} - \mathbf{r}_0|} \quad (41)$$

is the familiar dyadic Green function for free space. As the properties of $\underline{\mathbf{G}}_{\text{fs}}(\sigma; \mathbf{r}, \mathbf{r}_0)$ can be found in almost any graduate-level EM textbook [20,21], those of $\underline{\mathbf{G}}_v(\mathbf{r}, \mathbf{r}_0)$ can be easily determined, as illustrated in Ref. 12.

As an example of the use of Eqs. (37), let us consider an electric dipole moment \mathbf{p} located at the origin: $\mathbf{J}(\mathbf{r}) = -i\omega \mathbf{p} \delta(\mathbf{r})$ and $\mathbf{J}_m(\mathbf{r}) = \mathbf{0}$. The radiated Beltrami fields turn out be

$$\mathbf{Q}_1^{\text{rad}}(\mathbf{r}) = \frac{\omega^2 \mu}{k} \frac{\gamma_1 \gamma_2}{k^2} \gamma_1 \underline{\mathbf{G}}_1(\mathbf{r}, \mathbf{0}) \cdot \mathbf{p}; \quad r > 0 \quad (42a)$$

$$\mathbf{Q}_2^{\text{rad}}(\mathbf{r}) = i\omega \frac{\gamma_1 \gamma_2}{k^2} \gamma_2 \underline{\mathbf{G}}_2(\mathbf{r}, \mathbf{0}) \cdot \mathbf{p}; \quad r > 0 \quad (42b)$$

which show clearly that the radiation field of a point electric dipole in an isotropic chiral medium consists of left-handed as well as right-handed components. If we have instead a point magnetic dipole \mathbf{m} located at the origin,

the source current densities are specified as $\mathbf{J}(\mathbf{r}) = \mathbf{0}$ and $\mathbf{J}_m(\mathbf{r}) = -i\omega \mathbf{m} \delta(\mathbf{r})$, so that

$$\mathbf{Q}_1^{\text{rad}}(\mathbf{r}) = i\omega \frac{\gamma_1 \gamma_2}{k^2} \gamma_1 \underline{\mathbf{G}}_1(\mathbf{r}, \mathbf{0}) \cdot \mathbf{m}; \quad r > 0 \quad (43a)$$

$$\mathbf{Q}_2^{\text{rad}}(\mathbf{r}) = \frac{\omega^2 \varepsilon}{k} \frac{\gamma_1 \gamma_2}{k^2} \gamma_2 \underline{\mathbf{G}}_2(\mathbf{r}, \mathbf{0}) \cdot \mathbf{m}; \quad r > 0 \quad (43b)$$

are the corresponding radiated Beltrami fields. A major difference between isotropic chiral and achiral media is shown by the two sets of radiated fields, Eqs. (42) and (43). Without loss of generality, let the source dipole moments be aligned parallel to the z axis. Then, if the dipole moments are radiating in an achiral medium (i.e., $\beta = 0$), there is no magnetic field due to \mathbf{p} and there is no electric field due to \mathbf{m} at any point on the z axis. On the other hand, the wavenumber difference between the left-handed and the right-handed Beltrami fields guarantees that, in an isotropic chiral medium, both $\mathbf{E}^{\text{rad}}(\mathbf{r})$ and $\mathbf{H}^{\text{rad}}(\mathbf{r})$ are not generally null-valued on the z axis, regardless of which one of the two dipole moments is radiating.

Canonical sources of Beltrami fields are possible. If there is a source distribution such that $\mathbf{J}(\mathbf{r}) \equiv -(1/i\eta) \mathbf{J}_m(\mathbf{r})$ for all \mathbf{r} , then $\mathbf{Q}_2^{\text{rad}}(\mathbf{r}) \equiv \mathbf{0}$ from Eqs. (35) and (37). Likewise, a source distribution containing electric and magnetic current densities in the simple proportion $\mathbf{J}(\mathbf{r}) = (1/i\eta) \mathbf{J}_m(\mathbf{r})$ for all \mathbf{r} radiates only a right-handed field, because $\mathbf{Q}_1^{\text{rad}}(\mathbf{r}) \equiv \mathbf{0}$ emerges from the same equations.

Radiation by complex sources has to be generally treated using integral equations. Both the Maue and the Pocklington integral equations for radiation in a homogeneous isotropic chiral medium are available [12]. Cerenkov radiation in an isotropic chiral medium has also been described using Beltrami fields [12].

The foregoing developments make it clear that a description involving differentials of only the first order suffices for monochromatic radiation and propagation in an isotropic chiral medium. True, there are $\nabla \nabla$ terms in $\underline{\mathbf{G}}_1(\mathbf{r}, \mathbf{r}_0)$ and $\underline{\mathbf{G}}_2(\mathbf{r}, \mathbf{r}_0)$, but dyadic Green functions are not fields, being instead solutions of dyadic differential equations.

Finally, although the left-handed and the right-handed Beltrami fields are capable of being independently radiated and propagated as per Eqs. (34), they do indeed couple in an isotropic chiral medium. This coupling takes place only at bimedia boundaries where conditions on the tangential components of $\mathbf{E}(\mathbf{r})$ and $\mathbf{H}(\mathbf{r})$ must be satisfied; that is, the boundary conditions are specified not on $\mathbf{Q}_1(\mathbf{r})$ or $\mathbf{Q}_2(\mathbf{r})$ singly, but on the tangential components of the combinations $\mathbf{E}(\mathbf{r}) = \mathbf{Q}_1(\mathbf{r}) - i\eta \mathbf{Q}_2(\mathbf{r})$ and $\mathbf{H}(\mathbf{r}) = \mathbf{Q}_2(\mathbf{r}) + (1/i\eta) \mathbf{Q}_1(\mathbf{r})$.

9. THEOREMS FOR SCATTERING IN AN ISOTROPIC CHIRAL MEDIUM

Equations (36)–(39) suffice to set up certain often-used principles for monochromatic scattering and radiation problems, when all space is filled with a homogeneous isotropic chiral medium.

The source–region Beltrami fields can be obtained from Eqs. (37) using the Fikioris approach [22]. Let S be the

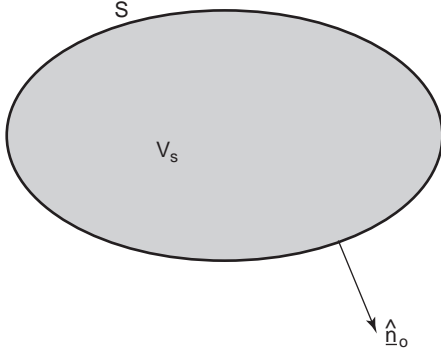


Figure 5. For the evaluation of fields in the region V_s , when the sources are also confined to the same region and all space is occupied by a homogeneous chiral medium.

surface of the convex-shaped source region V_s , where $\hat{\mathbf{n}}_0$ is the unit outward normal at $\mathbf{r}_0 \in S$ (see Fig. 5). Then, Eqs. (37) and (40) yield the following relations:

$$\begin{aligned} \mathbf{Q}_v^{\text{rad}}(\mathbf{r}) = & (-)^{v+1} \gamma_v \left\{ \int_{V_s} [\mathbf{G}_{\text{fs}}(\gamma_v | \mathbf{r}, \mathbf{r}_0) \cdot \mathbf{W}_v(\mathbf{r}_0) \right. \\ & - \mathbf{G}_{\text{p}}(\gamma_v | \mathbf{r}, \mathbf{r}_0) \cdot \mathbf{W}_v(\mathbf{r})] d^3 \mathbf{r}_0 \\ & \left. - \gamma_v^{-2} \mathbf{L}(\mathbf{r}) \cdot \mathbf{W}_v(\mathbf{r}) \right\} \\ & + \int_{V_s} [\nabla \times \mathbf{G}_{\text{fs}}(\gamma_v | \mathbf{r}, \mathbf{r}_0)] \cdot \mathbf{W}_v(\mathbf{r}_0) d^3 \mathbf{r}_0; \\ & v = 1, 2; \quad \mathbf{r} \in V_s \end{aligned} \quad (44)$$

The depolarization dyadic

$$\mathbf{L}(\mathbf{r}) = \frac{1}{4\pi} \int_S \frac{\hat{\mathbf{n}}_0 \mathbf{r}_0 - \hat{\mathbf{n}}_0 \mathbf{r}}{|\mathbf{r} - \mathbf{r}_0|^3} d^2 \mathbf{r}_0 \quad (45)$$

in Eqs. (44) is dependent on the shape of the region V_s , while

$$\mathbf{G}_{\text{p}}(\sigma | \mathbf{r}, \mathbf{r}_0) = \frac{\nabla \nabla}{\sigma^2} \frac{1}{4\pi |\mathbf{r} - \mathbf{r}_0|} \quad (46)$$

is an auxiliary dyadic function.

If the maximum linear extent of the region V_s times the magnitude of the greater of the two wavenumbers, γ_1 and γ_2 , is much smaller than unity, we may make the quasi-static approximation: $\mathbf{W}_1(\mathbf{r}_0) \cong \mathbf{W}_1(\mathbf{r})$ and $\mathbf{W}_2(\mathbf{r}_0) \cong \mathbf{W}_2(\mathbf{r})$ for all $\mathbf{r}_0 \in V_s$. Then, Eqs. (44) simplify to

$$\begin{aligned} \mathbf{Q}_v^{\text{rad}}(\mathbf{r}) \cong & \{ (-)^{v+1} \gamma_v [\mathbf{M}(\gamma_v | \mathbf{r}) - \gamma_v^{-2} \mathbf{L}(\mathbf{r})] \\ & + \mathbf{N}(\gamma_v | \mathbf{r}) \} \cdot \mathbf{W}_v(\mathbf{r}); \quad v = 1, 2; \quad \mathbf{r} \in V_s \end{aligned} \quad (47)$$

where the dyadics

$$\mathbf{M}(\sigma | \mathbf{r}) = \int_{V_s} [\mathbf{G}_{\text{fs}}(\sigma | \mathbf{r}, \mathbf{r}_0) - \mathbf{G}_{\text{p}}(\sigma | \mathbf{r}, \mathbf{r}_0)] d^3 \mathbf{r}_0 \quad (48a)$$

$$\mathbf{N}(\sigma | \mathbf{r}) = \int_{V_s} [\nabla \times \mathbf{G}_{\text{fs}}(\sigma | \mathbf{r}, \mathbf{r}_0)] d^3 \mathbf{r}_0 \quad (48b)$$

depend on the shape as well as on the size of V_s . Finally, the Rayleigh approximation requires that we ignore the dyadics $\mathbf{M}(\sigma | \mathbf{r})$ and $\mathbf{N}(\sigma | \mathbf{r})$ completely to obtain the estimates

$$\mathbf{Q}_v^{\text{rad}}(\mathbf{r}) \cong (-)^v \gamma_v^{-1} \mathbf{L}(\mathbf{r}) \cdot \mathbf{W}_v(\mathbf{r}); \quad v = 1, 2; \quad \mathbf{r} \in V_s \quad (49)$$

when V_s is an extremely small region. The right sides of Eqs. (47) and (49) are useful in homogenizing isotropic chiral composites as well as for devising the method of moments and the coupled dipole method for scattering by bianisotropic objects in isotropic chiral environments [12,23].

Turning now to the mathematical realizations of the Huygens principle and its progeny, we suppose that all space is divided into two regions, as shown in Fig. 6. The external region V_{ext} extends to infinity in all directions but is separated from an internal region V_{int} by the convex and once-differentiable surface S . Then the Huygens principle in a homogeneous isotropic chiral medium reads as follows [12]:

$$\begin{aligned} \mathbf{Q}_v(\mathbf{r}) = & (-)^{v+1} \frac{2\gamma_1 \gamma_2}{k} \int_S \mathbf{G}_v(\mathbf{r}, \mathbf{r}_0) \cdot [\hat{\mathbf{n}}_0 \times \mathbf{Q}_v(\mathbf{r}_0)] d^2 \mathbf{r}_0; \\ & v = 1, 2; \quad \mathbf{r} \in V_{\text{ext}} \end{aligned} \quad (50a)$$

$$\mathbf{0} = \int_S \mathbf{G}_v(\mathbf{r}, \mathbf{r}_0) \cdot [\hat{\mathbf{n}}_0 \times \mathbf{Q}_v(\mathbf{r}_0)] d^2 \mathbf{r}_0; \quad v = 1, 2; \quad \mathbf{r} \notin V_{\text{ext}} \quad (50b)$$

Thus, the Cauchy data for the fields in a chiral medium comprise the components of the Beltrami fields that are tangential to a boundary. When these data are prescribed on the surface S , we can find the Beltrami fields everywhere in the region V_{ext} .

The Huygens principle allows the enunciation of the exterior surface equivalence principle. Consider a problem in which surface Beltrami current densities $\mathbf{W}_1^s(\mathbf{r})$ and $\mathbf{W}_2^s(\mathbf{r})$ exist on the exterior side of the surface S (see Fig. 6). As per Eqs. (37), these surface current densities act as

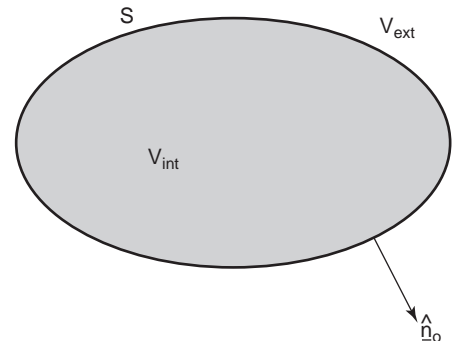


Figure 6. Relevant to the Huygens principle, the exterior surface equivalence principle, and the Ewald-Oseen extinction theorem, when all space is occupied by a homogeneous chiral medium.

sources of the radiated fields

$$\mathbf{Q}_v^{\text{rad}}(\mathbf{r}) = (-)^{v+1} \frac{2\gamma_1\gamma_2}{k} \int_S \mathbf{G}_v(\mathbf{r}, \mathbf{r}_0) \cdot \mathbf{W}_v^{\text{s}}(\mathbf{r}_0) d^2\mathbf{r}_0; \quad (51)$$

$$v = 1, 2; \quad \mathbf{r} \in V_{\text{ext}}$$

On comparing Eqs. (50a) and (51) to ensure the equivalence $\mathbf{Q}_v^{\text{rad}}(\mathbf{r}) \equiv \mathbf{Q}_v(\mathbf{r})$ for all $\mathbf{r} \in V_{\text{ext}}$, we obtain the relationships [12]

$$\mathbf{W}_v^{\text{s}}(\mathbf{r}_0) = \hat{\mathbf{n}}_0 \times \mathbf{Q}_v(\mathbf{r}_0); \quad v = 1, 2; \quad \mathbf{r}_0 \in S \quad (52)$$

as the exterior surface equivalence principle for Beltrami fields and sources, \mathbf{r}_0 in Eqs. (52) lying on the exterior side of S .

The Ewald–Oseen extinction theorem is a cornerstone of the extended-boundary-condition method [12,24]. For scattering in an isotropic chiral medium, this theorem may be stated as

$$\mathbf{0} = \mathbf{Q}_v^{\text{cf}}(\mathbf{r}) + (-)^{v+1} \frac{2\gamma_1\gamma_2}{k} \int_S \mathbf{G}_v(\mathbf{r}, \mathbf{r}_0) \cdot [\hat{\mathbf{n}}_0 \times \mathbf{Q}_v(\mathbf{r}_0)] d^2\mathbf{r}_0; \quad (53)$$

$$v = 1, 2; \quad \mathbf{r} \in V_{\text{int}}$$

where $\mathbf{Q}_v^{\text{cf}}(\mathbf{r})$ play the role of the incident Beltrami fields. Once $\mathbf{Q}_v(\mathbf{r}_0)$, $\mathbf{r}_0 \in S$, have been determined from Eqs. (53), the total fields in the exterior region may be determined as

$$\mathbf{Q}_v(\mathbf{r}) = \mathbf{Q}_v^{\text{cf}}(\mathbf{r}) + (-)^{v+1} \frac{2\gamma_1\gamma_2}{k} \int_S \mathbf{G}_v(\mathbf{r}, \mathbf{r}_0) \cdot [\hat{\mathbf{n}}_0 \times \mathbf{Q}_v(\mathbf{r}_0)] d^2\mathbf{r}_0; \quad (54)$$

$$v = 1, 2; \quad \mathbf{r} \in V_{\text{ext}}$$

From Eqs. (53) and (54), the plane-wave scattering dyadics for an object in an isotropic chiral environment can be derived, as can the forward plane-wave scattering amplitude theorems [12].

10. STRUCTURALLY CHIRAL MEDIA

The molecules of a naturally occurring isotropic chiral medium are mirror-asymmetric, and so are the inclusions in an artificial isotropic chiral medium. As a randomly dispersed and randomly oriented collection of mirror-asymmetric molecules or inclusions is also mirror-asymmetric, isotropic chiral media emerge with direction-independent constitutive properties. In contrast, the molecules or inclusions of a structurally chiral medium are not mirror-asymmetric, but their orientation is.

In chiral nematic liquid crystals (CNLCs)—also called *cholesteric liquid crystals*—needle-like molecules are randomly positioned on parallel sheets, with all molecules on any one sheet oriented parallel to one another and with the orientation rotating helicoidally as one moves across consecutive sheets. The situation is schematically depicted in Fig. 7. From 1850 to 1888, several scientists came across CNLCs but were unable to capitalize on their observations [25]. Then in 1888 the biochemist

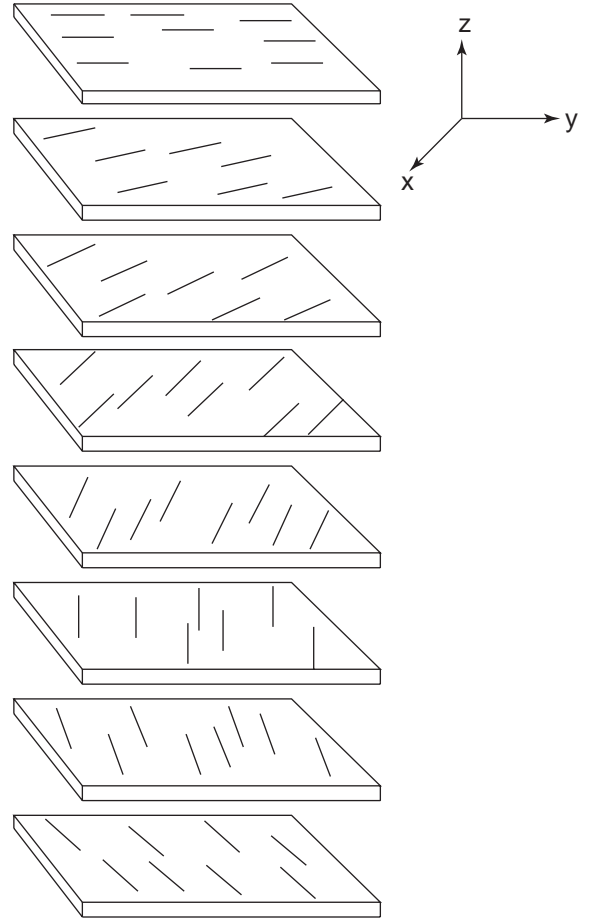


Figure 7. Schematic depiction of the arrangement of needle-like molecules in a chiral nematic liquid crystal. The gaps between the consecutive sheets as well as the sheets are fictitious, as they are merely aids to visualization. Only half of the electromagnetic period is shown.

F. Reinitzer observed that a CNLC named *cholesteryl benzoate* has two distinct melting points—it is a solid at temperatures below 145.5°C, a clear liquid at temperatures above 178.5°C, and a cloudy liquid in between. Reinitzer’s observation of the mesophase—when positional order is absent as in a liquid, but orientational order is still strong as in a solid—opened up the area of liquid crystal research in continuum mechanics as well as in optics [26–28].

Earlier, however, (in 1869), E. Reusch had anticipated the CNLC structure as a laminate of uniaxial dielectric sheets, with the crystallographic axes of any two adjacent sheets offset in the transverse plane by a fixed small angle. At a low enough frequency, this laminate appears as a continuously nonhomogeneous medium whose constitutive properties vary helicoidally. Thus

$$\mathbf{D}(\mathbf{r}, \omega) = \varepsilon_0 \underline{\mathbf{S}}(z) \cdot \underline{\boldsymbol{\varepsilon}}_{\text{ref}}(\omega) \cdot \underline{\mathbf{S}}^{-1}(z) \cdot \mathbf{E}(\mathbf{r}, \omega) \quad (55a)$$

$$\mathbf{H}(\mathbf{r}, \omega) = \frac{1}{\mu_0} \mathbf{B}(\mathbf{r}, \omega) \quad (55b)$$

are the frequency-domain constitutive relations of a CNLC, where

$$\underline{\epsilon}_{\text{ref}}(\omega) = \epsilon_a(\omega)[\mathbf{I} - \hat{\mathbf{x}}\hat{\mathbf{x}}] + \epsilon_b(\omega)\hat{\mathbf{x}}\hat{\mathbf{x}} \quad (56)$$

is the relative permittivity dyadic in a reference plane designated as $z=0$. The rotation dyadic

$$\underline{\mathbf{S}}(z) = [\hat{\mathbf{x}}\hat{\mathbf{x}} + \hat{\mathbf{y}}\hat{\mathbf{y}}] \cos \frac{\pi z}{\Omega} \pm [\hat{\mathbf{y}}\hat{\mathbf{x}} - \hat{\mathbf{x}}\hat{\mathbf{y}}] \sin \frac{\pi z}{\Omega} + \hat{\mathbf{z}}\hat{\mathbf{z}} \quad (57)$$

denotes that the CNLC structure varies helicoidally in the axial (i.e., z) direction with a period 2Ω ; however, the electromagnetic period is Ω . The upper sign in Eq. (57) applies for structural right-handedness; the lower, for structural left-handedness.

Reusch's model of a CNLC has been often implemented with either uniaxial crystals or fibrous laminae, and appears promising for microwave and RF applications as well [29]. More recently, thin-film technology has been pressed into service to realize the CNLC structure by releasing a directed evaporant flux toward a rotating substrate [30,31]. The reference permittivity dyadic of these chiral sculptured thin films (STFs) differs from Eq. (56), being

$$\begin{aligned} \underline{\epsilon}_{\text{ref}}(\omega) = & \epsilon_a(\omega)[\mathbf{I} - (\hat{\mathbf{x}} \cos \chi + \hat{\mathbf{z}} \sin \chi)(\hat{\mathbf{x}} \cos \chi + \hat{\mathbf{z}} \sin \chi) - \hat{\mathbf{y}}\hat{\mathbf{y}}] \\ & + \epsilon_b(\omega)(\hat{\mathbf{x}} \cos \chi + \hat{\mathbf{z}} \sin \chi)(\hat{\mathbf{x}} \cos \chi + \hat{\mathbf{z}} \sin \chi) + \epsilon_c(\omega)\hat{\mathbf{y}}\hat{\mathbf{y}}; \\ & \chi > 0^\circ \end{aligned} \quad (58)$$

instead, and the electromagnetic period is 2Ω .

The reference permittivity dyadics in Eqs. (56) and (58) are uniaxial and biaxial, respectively; that is, they have either one or two crystallographic axes. Biaxial $\underline{\epsilon}_{\text{ref}}(\omega)$ is displayed by chiral smectic liquid crystals also [26,27]. Thus in general $\underline{\epsilon}_{\text{ref}}(\omega)$ displays orthorhombic symmetry [32]. Moreover, particularly with advances in thin-film technology, there is no reason for a chiral STF to be

necessarily dielectric only. These considerations led to the proposal of the helicoidal bianisotropic medium (HBM), whose frequency-domain constitutive relations may be stated as [33]

$$\begin{aligned} \mathbf{D}(\mathbf{r}, \omega) = & \epsilon_0 \underline{\mathbf{S}}(z) \cdot [\mathbf{I} + \underline{\chi}_{\text{ref}}^e(\omega)] \cdot \underline{\mathbf{S}}^{-1}(z) \cdot \mathbf{E}(\mathbf{r}, \omega) + \underline{\mathbf{S}}(z) \\ & \cdot \underline{\chi}_{\text{ref}}^{\text{em}}(\omega) \cdot \underline{\mathbf{S}}^{-1}(z) \cdot \mathbf{B}(\mathbf{r}, \omega) \end{aligned} \quad (59a)$$

$$\begin{aligned} \mathbf{H}(\mathbf{r}, \omega) = & \frac{1}{\mu_0} \underline{\mathbf{S}}(z) \cdot [\mathbf{I} - \underline{\chi}_{\text{ref}}^m(\omega)] \cdot \underline{\mathbf{S}}^{-1}(z) \cdot \mathbf{B}(\mathbf{r}, \omega) + \underline{\mathbf{S}}(z) \\ & \cdot \underline{\chi}_{\text{ref}}^{\text{me}}(\omega) \cdot \underline{\mathbf{S}}^{-1}(z) \cdot \mathbf{E}(\mathbf{r}, \omega) \end{aligned} \quad (59b)$$

subject to the constraint

$$\text{Tr}[\underline{\chi}_{\text{ref}}^{\text{em}}(\omega) - \underline{\chi}_{\text{ref}}^{\text{me}}(\omega)] = 0 \quad (60)$$

The launching and propagation of EM waves in HBMs is best studied using a 4×4 matrix differential equation formalism [31,34].

Although chiral STFs made of fluorites, and single-frequency OR measurements on them, were reported in 1959 [35], systematic experimental studies—along with scanning electron microscopic verification of the microstructural geometry—appear to have begun only in 1995 [30]. Figure 8 shows the scanning electron micrograph of a chiral STF made of silicon oxide. As typical values of Ω realized today range from 30 nm to 10 μm , microwave applications of these films are yet not feasible, but are likely to become an active area of research once films with $\Omega \sim 100 \mu\text{m}$ become available. Many possible applications have been anticipated as the concept of STFs for biological, optical, electronic, chemical, and other applications is beginning to take root, while many optical and related applications have already been implemented [30,31].

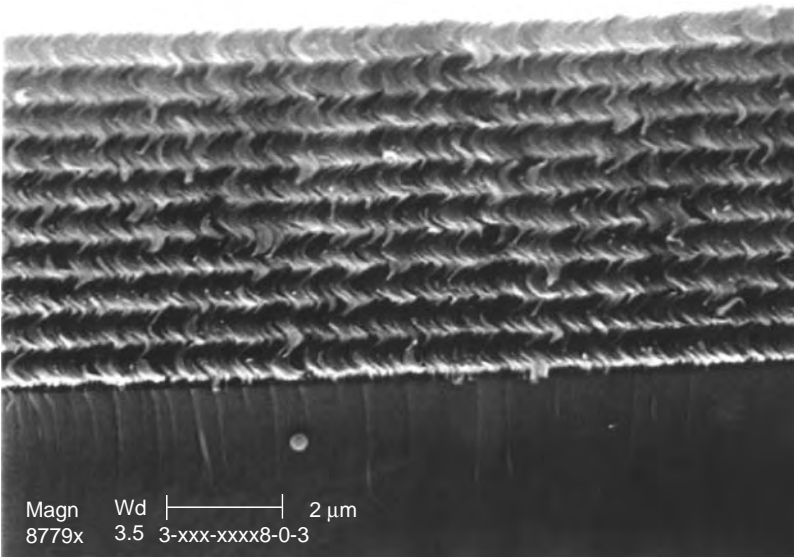


Figure 8. Scanning electron micrograph of a 10-period chiral sculptured thin film made of silicon oxide. (From Professor Russell Messier, Pennsylvania State University, with permission.)

Large-scale production appears feasible as well, with adaptation of ion-thruster technology [36].

BIBLIOGRAPHY

1. O. N. Singh and A. Lakhtakia, eds., *Electromagnetic Fields in Unconventional Materials and Structures*, Wiley, New York, 2000.
2. A. Lakhtakia, ed., *Selected Papers on Natural Optical Activity*, SPIE Optical Engineering Press, Bellingham, WA, 1990.
3. J. Jacques, *The Molecule and Its Double*, McGraw-Hill, New York, 1993.
4. B. Holmstedt, F. Hartmut, and B. Testa, eds., *Chirality and Biological Activity*, Alan R. Liss, New York, 1990.
5. J. C. Bose, On the rotation of plane of polarisation of electric waves by a twisted structure, *Proc. Roy. Soc. Lond.* **63**: 146–152 (1898).
6. P. Drude, *Lehrbuch der Optik*, S. Hirzel, Leipzig, 1900.
7. K. F. Lindman, Über eine durch ein isotropes system von spiralförmigen resonatoren erzeugte rotationspolarisation der elektromagnetischen wellen, *Ann. Phys. Leipzig.* **63**: 621–644 (1920).
8. R. Ro, *Determination of the Electromagnetic Properties of Chiral Composites, Using Normal Incidence Measurements*, Ph.D. thesis, Pennsylvania State Univ., University Park, PA, 1991.
9. F. Guérin, *Contribution à l'Étude Théorique et Expérimentale des Matériaux Composites Chiraux et Bianisotropes dans le Domain Microonde*, Ph.D. thesis, Univ. Limoges, Limoges, France, 1995.
10. H. C. Chen, *Theory of Electromagnetic Waves*, TechBooks, Fairfax, VA, 1993.
11. A. Lakhtakia and W. S. Weiglhofer, Constraint on linear, spatiotemporally nonlocal, spatiotemporally nonhomogeneous constitutive relations, *Int. J. Infrared Millim. Waves* **17**: 1867–1878 (1996).
12. A. Lakhtakia, *Beltrami Fields in Chiral Media*, World Scientific, Singapore, 1994.
13. A. Lakhtakia, ed., *Selected Papers on Linear Optical Composite Materials*, SPIE Optical Engineering Press, Bellingham, WA, 1996.
14. J. J. H. Wang, *Generalized Moment Methods in Electromagnetics*, Wiley, New York, 1991.
15. C. H. Durney and C. C. Johnson, *Introduction to Modern Electromagnetics*, McGraw-Hill, New York, 1969.
16. A. Moscowitz, Theoretical aspects of optical activity: small molecules, *Adv. Chem. Phys.* **4**:67–112 (1962).
17. S. Chandrasekhar, *Hydrodynamic and Hydromagnetic Stability*, Oxford Univ. Press, Oxford, UK, 1961.
18. P. Moon and D. E. Spencer, *Field Theory Handbook*, Springer, Berlin, 1988.
19. R. F. Harrington, *Time-Harmonic Electromagnetic Fields*, McGraw-Hill, New York, 1961, Chapter 3.
20. J. Van Bladel, *Electromagnetic Fields*, Hemisphere Publishing, New York, 1985.
21. W. C. Chew, *Waves and Fields in Inhomogeneous Media*, IEEE Press, New York, 1995.
22. J. G. Fikioris, Electromagnetic field inside a current-carrying region, *J. Math. Phys.* **6**:1617–1620 (1965).
23. B. Shanker and A. Lakhtakia, Extended Maxwell Garnett model for chiral-in-chiral composites, *J. Phys. D: Appl. Phys.* **26**:1746–1758 (1993).
24. P. C. Waterman, Scattering by dielectric obstacles, *Alta Frequenza (Speciale)* **38**:348–352 (1969).
25. P. J. Collings, *Liquid Crystals*, Princeton Univ. Press, Princeton, NJ, 1990, Chapter 2.
26. S. Chandrasekhar, *Liquid Crystals*, Cambridge Univ. Press, Cambridge, UK, 1992.
27. P. G. de Gennes and J. Prost, *The Physics of Liquid Crystals*, Clarendon Press, Oxford, 1993.
28. S. D. Jacobs, ed., *Selected Papers on Liquid Crystals for Optics*, SPIE Optical Engineering Press, Bellingham, WA, 1992.
29. A. Lakhtakia, G. Ya. Slepyan, and S. A. Maksimenko, Towards cholesteric absorbers for microwave frequencies, *Int. J. Infrared Millim. Waves* **22**:999–1007 (2001).
30. A. Lakhtakia, R. Messier, M. J. Brett, and K. Robbie, Sculptured thin films (STFs) for optical, chemical and biological applications, *Innov. Mater. Res.* **1**:165–176 (1996).
31. A. Lakhtakia, Sculptured thin films: accomplishments and emerging uses, *Mater. Sci. Eng. C* **19**:427–434 (2002).
32. J. F. Nye, *Physical Properties of Crystals*, Clarendon Press, Oxford, 1985.
33. A. Lakhtakia and W. S. Weiglhofer, Axial propagation in general helicoidal bianisotropic media, *Microwave Opt. Technol. Lett.* **6**:804–806 (1993).
34. A. Lakhtakia, Director-based theory for the optics of sculptured thin films, *Optik* **107**:57–61 (1997).
35. N. O. Young and J. Kowal, Optically active fluorite films, *Nature* **183**:104–105 (1959).
36. S. G. Bilén, M. T. Domonkos, and A. D. Gallimore, Simulating ionospheric plasma with a hollow cathode in a large vacuum chamber, *J. Spacecraft Rockets* **38**:617–621 (2001).

CIRCUIT STABILITY

JAMES A. SVOBODA
Clarkson University
Potsdam, New York

Stability is a property of well-behaved circuits and systems. Typically, stability is discussed in terms of feedback systems. Well-established techniques, such as Nyquist plots, Bode diagrams, and root locus plots, are available for studying the stability of feedback systems. Electric circuits can be represented as feedback systems. Nyquist plots, Bode diagrams, and root locus plots can then be used to study the stability of electric circuits.

1. FEEDBACK SYSTEMS AND STABILITY

Consider a feedback system such as the one shown in Fig. 1. This feedback system consists of three parts: a forward block, sometimes called the “plant”; a feedback block, sometimes called the “controller”; and a summer. The signals $v_i(t)$ and $v_o(t)$ are the input and output of the

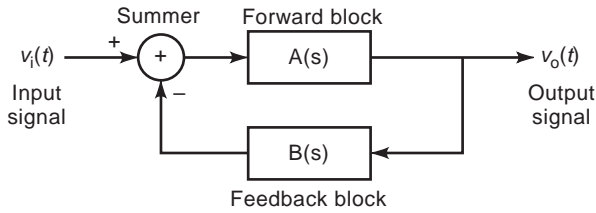


Figure 1. A feedback system.

feedback system. $A(s)$ is the transfer function of the forward block and $B(s)$ is the transfer function of the feedback block. The summer subtracts the output of the feedback block from $v_i(t)$. The transfer function of the feedback system can be expressed in terms of $A(s)$ and $B(s)$ as

$$T(s) = \frac{V_o(s)}{V_i(s)} = \frac{A(s)}{1 + A(s)B(s)} \tag{1}$$

Suppose that the transfer functions $A(s)$ and $B(s)$ can each be expressed as ratios of polynomials in s . Then

$$A(s) = \frac{N_A(s)}{D_A(s)} \quad \text{and} \quad B(s) = \frac{N_B(s)}{D_B(s)} \tag{2}$$

where $N_A(s)$, $D_A(s)$, $N_B(s)$, and $D_B(s)$ are polynomials in s . Substituting these expressions into Eq. (1) gives

$$\begin{aligned} T(s) &= \frac{\frac{N_A(s)}{D_A(s)}}{1 + \frac{N_A(s)N_B(s)}{D_A(s)D_B(s)}} = \frac{N_A(s)D_B(s)}{D_A(s)D_B(s) + N_A(s)N_B(s)} \\ &= \frac{N(s)}{D(s)} \end{aligned} \tag{3}$$

where the numerator and denominator of $T(s)$, $N(s)$, and $D(s)$ are both polynomials in s . The values of s for which $N(s) = 0$ are called the *zeros* of $T(s)$, and the values of s that satisfy $D(s) = 0$ are called the *poles* of $T(s)$.

Stability is a property of well-behaved systems. For example, a stable system will produce bounded outputs whenever its input is bounded. Stability can be determined from the poles of a system. The values of the poles of a feedback system will, in general, be complex numbers. A feedback system is stable when all of its poles have negative real parts.

The equation

$$1 + A(s)B(s) = 0 \tag{4}$$

is called the *characteristic equation* of the feedback system. The values of s that satisfy the characteristic equation are poles of the feedback system. The left-hand side of the characteristic equation, $1 + A(s)B(s)$, is called the *return difference* of the feedback system. Figure 2 shows how the return difference can be measured. First, the input, $v_i(t)$, is set to zero. Next, the forward path of the feedback system is broken. Figure 2 shows how a test signal, $V_T(s) = 1$, is applied and the response, $V_R(s) = -A(s)B(s)$, is

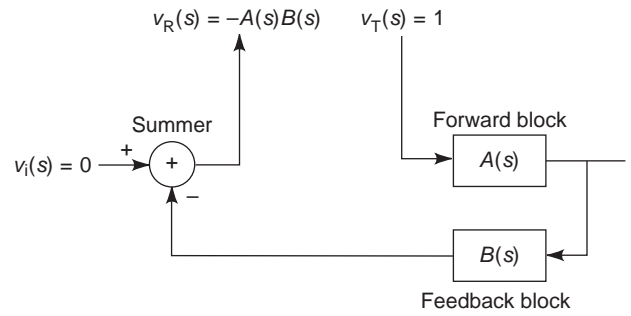


Figure 2. Measuring the return difference. The difference between the test input signal, $V_T(s)$, and the test output signal, $V_R(s)$, is the return difference.

measured. The difference between the test signal and its response is the return difference.

The calculation

$$\begin{aligned} \text{Return difference} &= 1 + A(s)B(s) = 1 + \frac{N_A(s)N_B(s)}{D_A(s)D_B(s)} \\ &= \frac{D_A(s)D_B(s) + N_A(s)N_B(s)}{D_A(s)D_B(s)} \end{aligned}$$

shows that

1. The zeros of $1 + A(s)B(s)$ are equal to the poles of $T(s)$.
2. The poles of $1 + A(s)B(s)$ are equal to the poles of $A(s)B(s)$.

Consider a feedback system of the form shown in Fig. 1 with

$$A(s) = \frac{s + 5}{s^2 - 4s + 1} \quad \text{and} \quad B(s) = \frac{3s}{s + 3} \tag{5}$$

The poles of the forward block are the values of s that satisfy $s^2 - 4s + 1 = 0$ (i.e., $s_1 = 3.73$ and $s_2 = 0.26$). In this case, both poles have real, rather than complex, values. The forward block would be stable if both poles were negative. They are not, so the forward block is itself an unstable system. To see that this unstable system is not well behaved, consider its step response [1,2]. The step response of a system is its zero state response to a step input. In other words, suppose that the input to the forward block was zero for a very long time. At some particular time, the value of input suddenly becomes equal to 1 and remains equal to 1. The response of the system is called the *step response*. The step response can be calculated by taking the inverse Laplace transform of $A(s)/s$. In this example, the step response of the forward block is

$$\text{Step response} = 5 + 0.675e^{3.73t} - 5.675e^{0.27t}$$

As time increases, the exponential terms of the step response get very, very large. Theoretically, they increase without bound. In practice, they increase until the system

saturates or breaks. This is typical of the undesirable behavior of an unstable system.

According to Eq. (3), the transfer function of the whole feedback system is

$$T(s) = \frac{\frac{s+5}{s^2-4s+1}}{1 + \frac{s+5}{s^2-4s+1} \times \frac{3s}{s+3}}$$

$$= \frac{(s+5)(s+3)}{(s^2-4s+1)(s+3) + (s+5)(3s)} = \frac{s^2+8s+15}{s^3+2s^2+4s+3}$$

The poles of the feedback system are the values of s that satisfy $s^3 + 2s^2 + 4s + 3 = 0$ —that is, $s_1 = -1$, $s_2 = -0.5 + j1.66$ and $s_3 = -0.5 - j1.66$. The real part of each of these three poles is negative. Since all of the poles of the feedback system have negative real parts, the feedback system is stable. To see that this stable system is well behaved, consider its step response. This step response can be calculated by taking the inverse Laplace transform of $T(s)/s$. In this example, the step response of the feedback system is

$$\text{Step response} = 5 - 11.09e^{-t} \cos(\sqrt{2}t + 63^\circ)$$

In contrast to the previous case, as time increases, e^{-t} becomes zero so the second term of the step response dies out. This stable system does not exhibit the undesirable behavior typical of unstable systems.

2. STABILITY CRITERIA

Frequently, the information about a feedback system that is most readily available is the transfer functions of the forward and feedback blocks, $A(s)$ and $B(s)$. Stability criteria are tools for determining whether a feedback system is stable by examining $A(s)$ and $B(s)$ directly, without first calculating $T(s)$ and then calculating its poles—that is, the roots of the denominator of $T(s)$. Two stability criteria will be discussed here: the Nyquist stability criteria and the use of Bode diagrams to determine the gain and phase margin.

The Nyquist stability criterion is based on a theorem in the theory of functions of a complex variable [1,3,4]. This stability criterion requires a contour mapping of a closed curve in the s plane using the function $A(s)B(s)$. The closed contour in the s plane must enclose the right half of the s plane and must not pass through any poles or zeros of $A(s)B(s)$. The result of this mapping is a closed contour in the $A(s)B(s)$ plane. Fortunately, the computer program MATLAB [5,6] can be used to generate an appropriate curve in the s plane and do this mapping.

Rewriting the characteristic equation, Eq. (4), as

$$A(s)B(s) = -1 \tag{6}$$

suggests that the relationship of the closed contour in the $A(s)B(s)$ plane to the point $-1 + j0$ is important. Indeed, this is the case. The Nyquist stability criterion involves

the number of encirclements of the point $-1 + j0$ by the curve in the $A(s)B(s)$ plane. Let

N = the number of encirclements, in the clockwise direction, of $-1 + j0$ by the closed curve in the $A(s)B(s)$ plane

Z = The number of poles of $T(s)$ in the right half of the s plane

P = The number of poles of $A(s)B(s)$ in the right half of the s plane

The Nyquist stability criterion states that N , Z , and P are related by

$$Z = P + N$$

A stable feedback system will not have any poles in the right half of the s plane, so $Z = 0$ indicates a stable system.

For example, suppose that the forward and feedback blocks of the feedback system shown in Fig. 1 have the transfer functions described by Eq. (5). Then

$$A(s)B(s) = \frac{3s^2 + 15s}{s^3 - s^2 - 11s + 3}$$

$$= \frac{3s^2 + 15s}{(s - 3.73)(s - 0.26)(s + 3)} \tag{7}$$

Figure 3 shows the Nyquist plot for this feedback system. This plot was obtained using the MATLAB commands

```
num = [0 3 15 0]; %Coefficients of the
              numerator of A(s) B(s)
den = [1 -1 -11 3]; %Coefficients of the
              denominator of A(s) B(s)
nyquist(num, den)
```

Since $A(s)B(s)$ has two poles in the right half of the s plane, $P = 2$. The Nyquist plot shows two counterclockwise encirclements of $-1 + j0$ so $N = -2$. Then $Z = P + N = 0$, indicating that the feedback system is stable.

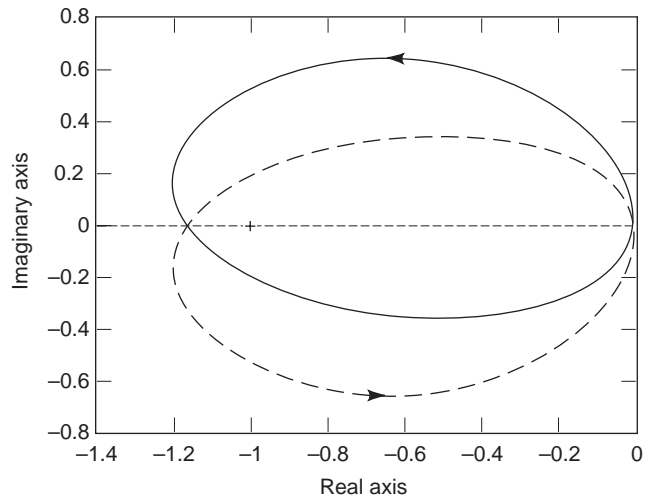


Figure 3. A Nyquist plot produced using MATLAB.

Feedback systems need to be stable in spite of variations in the transfer functions of the forward and feedback blocks. The gain and phase margins of a feedback system give an indication of how much $A(s)$ and $B(s)$ can change without causing the system to become unstable. The gain and phase margins can be determined using Bode diagrams. To obtain the Bode diagrams, first let $s = j\omega$ so that Eq. (6) becomes

$$A(j\omega)B(j\omega) = -1$$

The value of $A(j\omega)B(j\omega)$ will, in general, be complex. Two Bode diagrams are used to determine the gain and phase margins. The magnitude Bode diagram is a plot of $20 \log |A(j\omega)B(j\omega)|$ versus ω . The units of $20 \log |A(j\omega)B(j\omega)|$ are decibels. The abbreviation for decibel is dB. The magnitude Bode diagram is sometimes referred to as a plot of the magnitude of $A(j\omega)B(j\omega)$, in dB, versus ω . The phase Bode diagram is a plot of the angle of $A(j\omega)B(j\omega)$ versus ω .

It is necessary to identify two frequencies: ω_g , the gain crossover frequency; and ω_p , the phase crossover frequency. To do so, first take the magnitude of both sides of Eq. (7) to obtain

$$|A(j\omega)B(j\omega)| = 1 \quad (8)$$

Converting to decibels gives

$$20 \log |A(j\omega)B(j\omega)| = 0 \quad (9)$$

Equation (8) or (9) is used to identify a frequency, ω_g , the gain crossover frequency. That is, ω_g is the frequency at which

$$|A(j\omega_g)| |B(j\omega_g)| = 1$$

Next, take the angle of both sides of Eq. (4) to

$$\angle(A(j\omega)B(j\omega)) = 180^\circ \quad (10)$$

Equation (10) is used to identify a frequency, ω_p , the phase crossover frequency. That is, ω_p is the frequency at which

$$\angle A(j\omega_p) + \angle B(j\omega_p) = 180^\circ \quad (11)$$

The gain margin of the feedback system is

$$\text{Gain margin} = \frac{1}{|A(j\omega_p)| |B(j\omega_p)|} \quad (12)$$

The phase margin is

$$\text{Phase margin} = 180^\circ - (\angle A(j\omega_g) + \angle B(j\omega_g)) \quad (13)$$

The gain and phase margins can be easily calculated using MATLAB. For example, suppose the forward and feedback blocks of the feedback system shown in Fig. 1 have the transfer functions described by Eq. (3). Figure 4 shows the

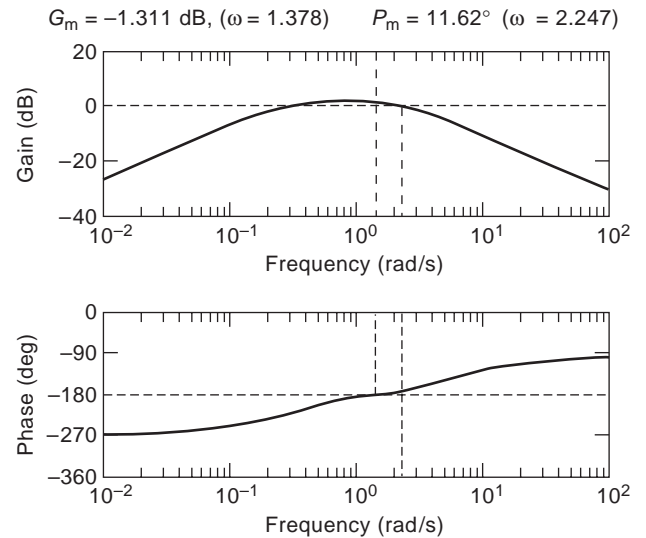


Figure 4. Bode plot used to determine the phase and gain margins. The plots were produced using MATLAB.

Bode diagrams for this feedback system. These plots were obtained using the MATLAB commands

```
num=[0 3 15 0]; %Coefficients of the
           numerator of A(s)B(s)
den=[1 -1 -11 3]; %Coefficients of the
           denominator of A(s)B(s)
margin(num,den)
```

MATLAB has labeled the Bode diagrams in Fig. 4 to show the gain and phase margins. The gain margin of -1.331 dB indicates that a decrease in $|A(s)B(s)|$ of 1.331 dB or, equivalently, a decrease in gain by a factor of 0.858 , at the frequency $\omega_p = 1.378$ rad/s, would bring the system the boundary of instability. Similarly, the phase margin of 11.6° indicates that an increase in the angle of $A(s)B(s)$ of 11.6° , at the frequency $\omega_g = 2.247$ rad/s, would bring the system the boundary of instability.

When the transfer functions $A(s)$ and $B(s)$ have no poles or zeros in the right half of the s plane, then the gain and phase margins must both be positive in order for the system to be stable. As a rule of thumb [7], the gain margin should be greater than 6 dB and the phase margin should be between 30 and 60° . These gain and phase margins provide some protection against changes in $A(s)$ or $B(s)$.

3. STABILITY OF LINEAR CIRCUITS

The Nyquist criterion and the gain and phase margin can be used to investigate the stability of linear circuits. To do so requires that the parts of the circuit corresponding to the forward block and to the feedback block be identified. After this identification is made, the transfer functions $A(s)$ and $B(s)$ can be calculated.

Figures 5–8 illustrate a procedure for finding $A(s)$ and $B(s)$ [8]. For concreteness, consider a circuit consisting of resistors, capacitors, and op amps. Suppose further that the input and outputs of this circuit are voltages. Such a circuit is shown in Fig. 5. In Fig. 6 one of the op amps has

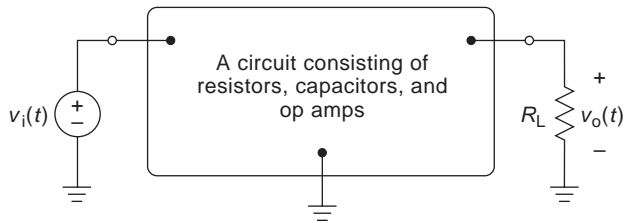


Figure 5. A circuit that is to be represented as a feedback system.

been separated from the rest of the circuit. This is done to identify the subcircuit N_B . The op amp will correspond to the forward block of the feedback system while N_B will contain the feedback block. N_B will be used to calculate $B(s)$. In Fig. 7, the op amp has been replaced by a model of the op amp (2). This model of the op amp indicates that the op amp input and output voltages are related by

$$V_B(s) = K(s)V_A(s) \quad (14)$$

The network N_B can be represented by the equation

$$\begin{pmatrix} V_o(s) \\ V_A(s) \end{pmatrix} = \begin{pmatrix} T_{11}(s) & T_{12}(s) \\ T_{21}(s) & T_{22}(s) \end{pmatrix} \begin{pmatrix} V_i(s) \\ V_B(s) \end{pmatrix} \quad (15)$$

Combining Eqs. (14) and (15) yields the transfer function of the circuit

$$T(s) = \frac{V_o(s)}{V_i(s)} = T_{11}(s) + \frac{T_{12}(s)K(s)T_{21}(s)}{1 - K(s)T_{22}(s)} \quad (16)$$

or

$$T(s) = \frac{V_o(s)}{V_i(s)} = \frac{T_{11}(s)(1 + K(s)T_{22}(s)) + T_{12}(s)K(s)T_{21}(s)}{1 + K(s)T_{22}(s)}$$

Equation (15) suggests a procedure that can be used to measure or calculate the transfer functions $T_{11}(s)$, $T_{12}(s)$, $T_{21}(s)$, and $T_{22}(s)$. For example, Eq. (15) says that when $V_i(s) = 1$ and $V_B(s) = 0$, then $V_o(s) = T_{11}(s)$ and $V_A(s) = T_{21}(s)$. Figure 8 illustrates this procedure for determining

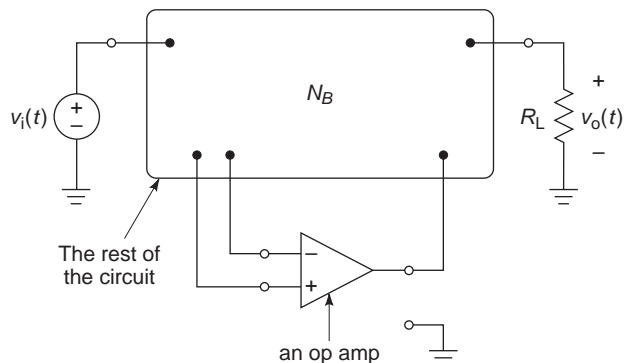


Figure 6. Identifying the subcircuit N_B by separating an op amp from the rest of the circuit.

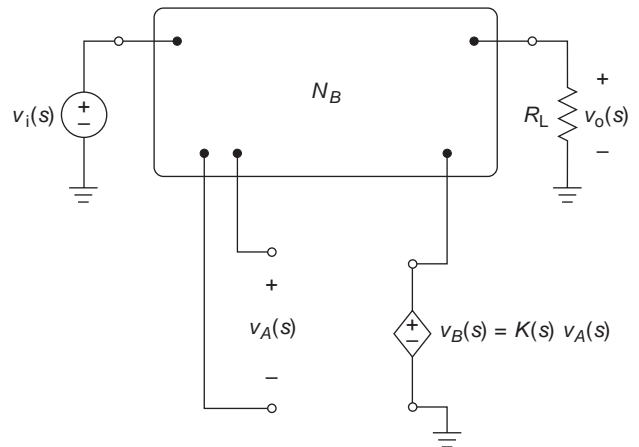


Figure 7. Replacing the op amp with a model of the op amp.

$T_{11}(s)$ and $T_{21}(s)$. A short circuit is used to make $V_B(s) = 0$ and the voltage source voltage is set to 1 so that $V_i(s) = 1$. Under these conditions the voltages $V_o(s)$ and $V_A(s)$ will be equal to the transfer functions $T_{11}(s)$ and $T_{21}(s)$. Similarly, when $V_i(s) = 0$ and $V_B(s) = 1$, then $V_o(s) = T_{12}(s)$ and $V_A(s) = T_{22}(s)$. Figure 9 illustrates the procedure for determining $T_{12}(s)$ and $T_{22}(s)$. A short circuit is used to make $V_i(s) = 0$, and the voltage source voltage is set to 1 so that $V_{B1}(s) = 1$. Under these conditions the voltages $V_o(s)$ and $V_A(s)$ will be equal to the transfer functions $T_{11}(s)$ and $T_{21}(s)$.

Next, consider the feedback system shown in Fig. 10. [The feedback system shown in Fig. 1 is part, but not all, of the feedback system shown in Fig. 10. When $D(s) = 0$, $C_1(s) = 1$ and $C_2(s) = 1$; then Fig. 10 reduces to Fig. 1. Considering the system shown in Fig. 10, rather than the system shown in Fig. 1, avoids excluding circuits for which $D(s) \neq 0$, $C_1(s) \neq 1$, or $C_2(s) \neq 1$.] The transfer function of this feedback system is

$$T(s) = \frac{V_o(s)}{V_i(s)} = D(s) + \frac{C_1(s)A(s)C_2(s)}{1 + A(s)B(s)} \quad (17)$$

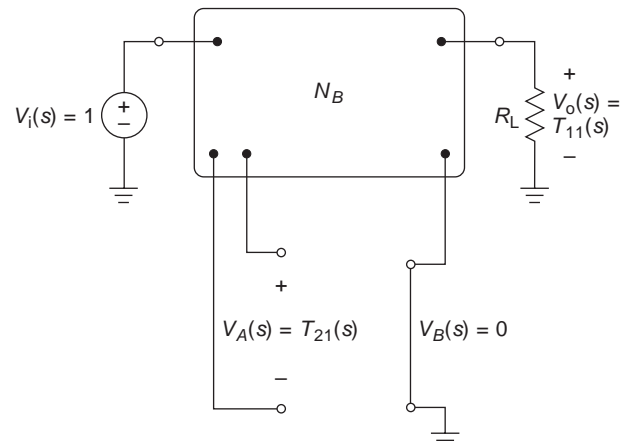


Figure 8. The subcircuit N_B is used to calculate $T_{12}(s)$ and $T_{22}(s)$.

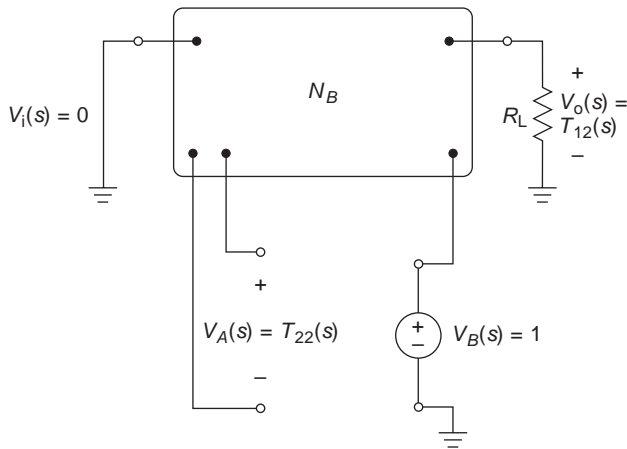


Figure 9. The subcircuit N_B is used to calculate $T_{11}(s)$ and $T_{21}(s)$.

or

$$T(s) = \frac{V_o(s)}{V_i(s)} = \frac{D(s)(1 + A(s)B(s)) + C_1(s)A(s)C_2(s)}{1 + A(s)B(s)}$$

Comparing Eqs. (16) and (17) shows that

$$A(s) = -K(s) \tag{18a}$$

$$B(s) = T_{22}(s)$$

$$C_1(s) = T_{12}(s) \tag{18b}$$

$$C_2(s) = T_{21}(s)$$

$$D(s) = T_{11}(s)$$

Finally, with Eqs. (18a) and (18b), the identification of $A(s)$ and $B(s)$ is complete. In summary

1. The circuit is separated into two parts: an op amp and N_B , the rest of the circuit.
2. $A(s)$ is open-loop gain of the op amp, as shown in Fig. 7.
3. $B(s)$ is determined from the subcircuit N_B , as shown in Fig. 9.

As an example, consider the Sallen–Key bandpass filter [9] shown in Fig. 11. The transfer function of this filter is

$$T(s) = \frac{V_o(s)}{V_i(s)} = \frac{5460s}{s^2 + 199s + 4 \times 10^6} \tag{19}$$

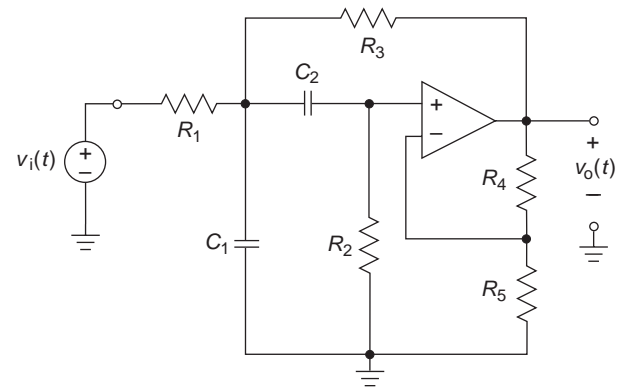


Figure 11. A Sallen–Key bandpass filter: $R_1 = R_2 = R_3 = R_5 = 7.07 \text{ k}\Omega$, $R_4 = 20.22 \text{ k}\Omega$, and $C_1 = C_2 = 0.1 \mu\text{F}$.

The first step toward identifying $A(s)$ and $B(s)$ is to separate the op amp from the rest of the circuit, as shown in Fig. 12. Separating the op amp from the rest of the circuit identifies the subcircuit N_B . Next, N_B is used to calculate the transfer functions $T_{11}(s)$, $T_{12}(s)$, $T_{21}(s)$, and $T_{22}(s)$. Figure 13 corresponds to Fig. 8 and shows how $T_{12}(s)$ and $T_{22}(s)$ are calculated. Analysis of the circuit shown in Fig. 13 gives

$$T_{12}(s) = 1 \text{ and } T_{22}(s) = \frac{0.259s^2 + 51.6s + 1.04 \times 10^6}{s^2 + 5660s + 4 \times 10^6} \tag{20}$$

[The computer program ELab [10] provides an alternative to doing this analysis by hand. ELab will calculate the transfer function of a network in the form shown in Eq. (16)—that is, as a symbolic function of s . ELab is free and can be downloaded from <http://sunspot.ece.clarkson.edu:1050/~svoboda/software.html> on the World Wide Web.]

Figure 14 corresponds to Fig. 9 and shows how $T_{11}(s)$ and $T_{21}(s)$ are calculated. Analysis of the circuit shown in Fig. 14 gives

$$T_{11}(s) = 0 \text{ and } T_{21}(s) = \frac{-1410s}{s^2 + 5660s + 4 \times 10^6} \tag{21}$$

Substituting Eqs. (20) and (21) into Eq. (16) gives

$$T(s) = \frac{K(s) \left(\frac{-1410s}{s^2 + 5660s + 4 \times 10^6} \right)}{1 - K(s) \left(\frac{0.259s^2 + 51.6s + 1.04 \times 10^6}{s^2 + 5660s + 4 \times 10^6} \right)} \tag{22}$$

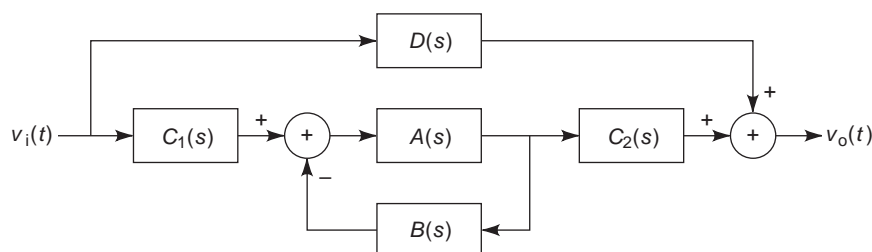


Figure 10. A feedback system that corresponds to a linear system.

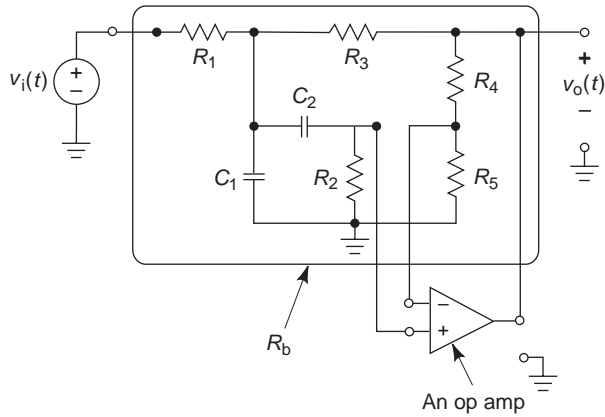


Figure 12. Identifying the subcircuit N_B by separating an op amp from the rest of the circuit.

When the op amp is modeled as an ideal op amp, $K(s) \rightarrow \infty$ and Eq. (22) reduces to Eq. (19). This is reassuring but only confirms what was already known. Suppose that a more accurate model of the op amp is used. A frequently used op amp model [2] represents the gain of the op amp as

$$K(s) = -\frac{A_o}{s + \frac{B}{A_o}} \quad (23)$$

where A_o is the DC gain of the op amp and B is the gain-bandwidth product of the op amp (2). Both A_o and B are readily available from manufacturers specifications of op amps. For example, when the op amp is a $\mu A741$ op amp, then $A_o = 200,000$ and $B = 2\pi \cdot 10^6$ rad/s, so

$$K(s) = -\frac{200,000}{s + 31.4}$$

Equation (18) indicates that $A(s) = -K(s)$ and $B(s) = T_{22}(s)$, so in this example

$$A(s) = \frac{200,000}{s + 31.4} \text{ and } B(s) = 0.259 \left(\frac{s^2 + 51.6s + 1.04 \times 10^6}{s^2 + 5600s + 4 \times 10^6} \right)$$

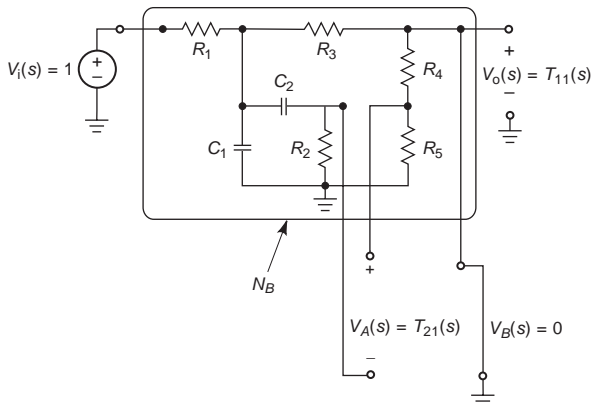


Figure 13. The subcircuit N_{B1} is used to calculate $T_{11}(s)$ and $T_{21}(s)$.

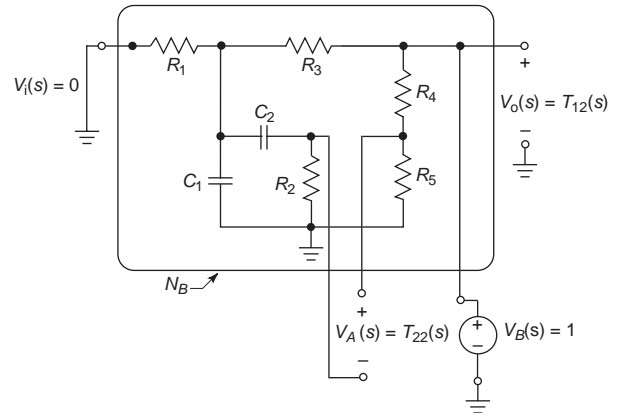


Figure 14. The subcircuit N_B is used to calculate $T_{12}(s)$ and $T_{22}(s)$.

To calculate the phase and gain margins of this filter, first calculate

$$A(s)B(s) = \frac{51,800(s^2 + 51.6s + 1.04 \times 10^6)}{s^3 + 5974s^2 + 5777240s + 1246 \times 10^6}$$

Next, the MATLAB commands

```
num = 20000*[0 0.259 51.6 1040000];
%Numerator Coefficients
den = [1 5974 5777240 1256*10^6];
%Denominator Coefficients
margin(num, den)
```

are used to produce the Bode diagram shown in Fig. 15. Figure 15 shows that the Sallen–Key filter will have an infinite-gain margin and a phase margin of 76.5° when a $\mu A741$ op amp is used.

4. OSCILLATORS

Oscillators are circuits that are used to generate a sinusoidal output voltage or current. Typically, oscillators have no input. The sinusoidal output is generated by the circuit itself. This section presents the requirements that a circuit must satisfy if it is to function as an oscillator and shows how these requirements can be used to design the oscillator.

To begin, recall that the characteristic equation of a circuit is

$$1 + A(s)B(s) = 0$$

Suppose that this equation is satisfied by a value of s of the form $s = 0 + j\omega_o$. Then

$$A(j\omega_o)B(j\omega_o) = -1 = 1e^{-j180^\circ} \quad (24)$$

In this case, the steady-state response of the circuit will contain a sustained sinusoid at the frequency ω_o (11). In other words, Eq. (24) indicates that the circuit will function as an oscillator with frequency ω_o when $A(j\omega_o)B(j\omega_o)$ has a magnitude equal to 1 and a phase angle of 180° .

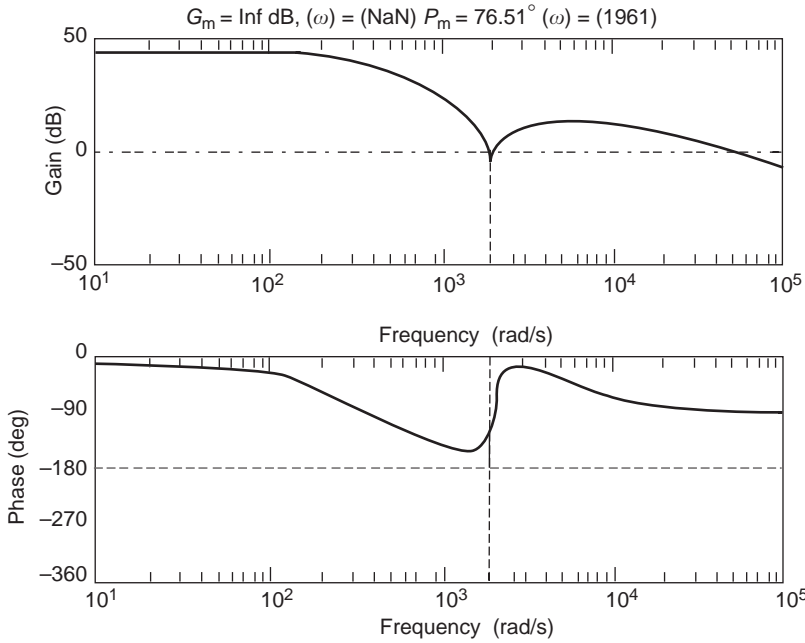


Figure 15. The Bode diagrams used to determine the phase and gain margins of the Sallen-Key bandpass filter.

As an example, consider using Eq. (24) to design the Wienbridge oscillator, shown in Fig. 16, to oscillate at $\omega_o = 1000$ rad/s. The first step is to identify $A(s)$ and $B(s)$ using the procedure described in the previous section. In Fig. 17 the amplifier is separated from the rest of the network to identify the subcircuit N_B . Also, from Eqs. (14) and (18), we have

$$A(s) = -K$$

Next, the subcircuit N_B is used to determine $B(s) = T_{22}(s)$, as shown in Fig. 18. From Fig. 18 it is seen that

$$T_{22}(s) = \frac{\frac{1}{C_s} * R}{\frac{1}{C_s} + R} = \frac{1}{\frac{1}{C_s} * R + \left(R + \frac{1}{C_s}\right)} = \frac{1}{1 + \left(R + \frac{1}{C_s}\right) \frac{\left(R + \frac{1}{C_s}\right)}{\left(R * \frac{1}{C_s}\right)}} = \frac{1}{1 + \left(R + \frac{1}{C_s}\right) \left(C_s + \frac{1}{R}\right)} = \frac{1}{3 + RCs + \frac{1}{RCs}}$$

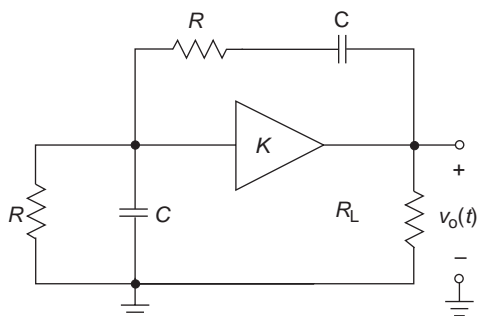


Figure 16. A Wien bridge oscillator.

So

$$A(s)B(s) = \frac{-K}{3 + RCs + \frac{1}{RCs}}$$

Now let $s = 0 + j\omega_o$ to get

$$A(j\omega_o)B(j\omega_o) = \frac{-K}{3 + j\omega_o RC - j\frac{1}{\omega_o RC}} \quad (25)$$

The phase angle of $A(j\omega_o)B(j\omega_o)$ must be 180° if the circuit is to function as an oscillator. That requires

$$j\omega_o RC - j\frac{1}{\omega_o RC} = 0 \Rightarrow \omega_o = \frac{1}{RC} \quad (26)$$

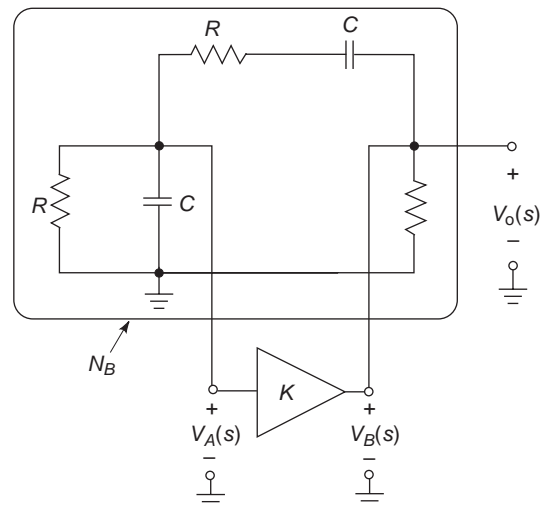


Figure 17. The amplifier is separated from the rest of the Wien bridge oscillator to identify the subcircuit N_B .

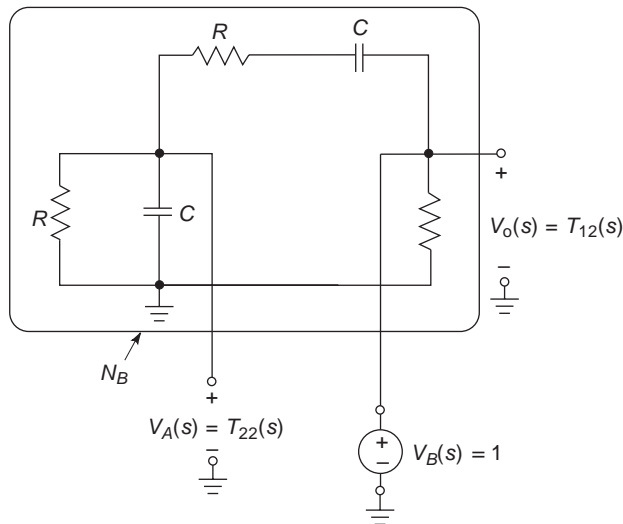


Figure 18. The subcircuit N_B is used to calculate $B(s) = T_{22}(s)$ for the Wien bridge oscillator.

Oscillation also requires that the magnitude of $A(j\omega_o)B(j\omega_o)$ be equal to 1. After substituting Eq. (26) into Eq. (25), this requirement reduces to

$$K = 3$$

That is, the amplifier gain must be set to 3. Design of the oscillator is completed by picking values of R and C to make $\omega_o = 1000$ rad/s (e.g., $R = 10$ k Ω and $C = 0.1$ μ F).

5. THE ROOT LOCUS

Frequently the performance of a feedback system is adjusted by changing the value of a gain. For example, consider the feedback system shown in Fig. 1 when

$$A(s) = \frac{N_A(s)}{D_A(s)} \text{ and } B(s) = K \tag{27}$$

In this case, $A(s)$ is the ratio of two polynomials in s and $B(s)$ is the gain that is used to adjust the system. The transfer function of the feedback system is

$$T(s) = \frac{N_A(s)}{D_A(s) + KN_A(s)} = \frac{N(s)}{D(s)} \tag{28}$$

The poles of feedback system are the roots of the polynomial

$$D(s) = D_A(s) + KN_A(s) \tag{29}$$

Suppose that the gain K can be adjusted to any value between 0 and ∞ . Consider the extreme values of K . When $K = 0$, $D(s) = D_A(s)$ so the roots of $D(s)$ are the same as the roots of $D_A(s)$. When $K = \infty$, $D_A(s)$ is negligible compared to $KN_A(s)$. Therefore $D(s) = KN_A(s)$ and the roots of $D(s)$ are the same as the roots of $N_A(s)$. Notice that the roots of $D_A(s)$ are the poles of $A(s)$ and the roots of $N_A(s)$ are the zeros of $A(s)$. As K varies from 0 and ∞ , the poles of $T(s)$

start at the poles of $A(s)$ and migrate to the zeros of $A(s)$. The root locus is a plot of the paths that the poles of $T(s)$ take as they move across the s plane from the poles of $A(s)$ to the zeros of $A(s)$.

A set of rules for constructing root locus plots by hand are available [1,4,7,13]. Fortunately, computer software for constructing root locus plots is also available. For example, suppose that the forward and feedback blocks in Fig. 1 are described by

$$A(s) = \frac{s(s - 2)}{(s + 1)(s + 2)(s + 3)} = \frac{s^2 - 2s}{s^3 + 6s^2 + 11s + 6} \text{ and } B(s) = K$$

The root locus plot for this system is obtained using the MATLAB [5,6] commands

```
num = ([0 1 -2 0]);
den = ([1 6 11 6]);
rlocus(num, den)
```

This root locus plot is shown in Fig. 19. After the root locus has been plotted, the MATLAB command

```
rlocfind(num, den)
```

can be used to find the value of the gain K corresponding to any point on the root locus. For example, when this command is given and the cursor is placed on the point where the locus crosses the positive imaginary axis, MATLAB indicates that gain corresponding to the point $0.0046 + j0.7214$ is $K = 5.2678$. For gains larger than 5.2678, two poles of $T(s)$ are in the right half of the s plane so the feedback system is unstable.

The bilinear theorem [12] can be used to make a connection between electric circuits and root locus plots. Consider Fig. 20, where one device has been separated from the rest of a linear circuit. The separated device could be a

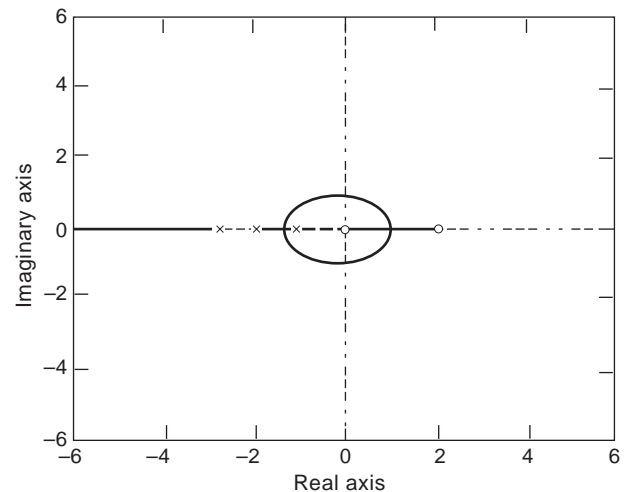


Figure 19. A root locus plot produced using MATLAB. The poles of $A(s)$ are marked by x 's and the zeros of $A(s)$ are marked by o 's. As K increases from zero to infinity, the poles of $T(s)$ migrate from the poles of $A(s)$ to the zeros of $A(s)$ along the paths indicated by solid lines.

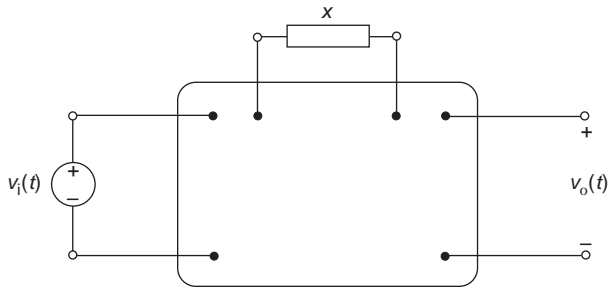


Figure 20. A single device is separated from the rest of the network. The parameter associated with this device is called x . The transfer function of the network will be a bilinear function of x .

resistor, a capacitor, an amplifier, or any two-terminal device [12]. The separated device has been labeled as x . For example, x could be the resistance of a resistor, the capacitance of a capacitor, or the gain of an amplifier. The bilinear theorem states that the transfer function of the circuit will be of the form

$$T(s) = \frac{V_o(s)}{V_i(s)} = \frac{E(s) + xF(s)}{G(s) + xH(s)} = \frac{N(s)}{D(s)} \quad (30)$$

where $E(s)$, $F(s)$, $G(s)$, and $H(s)$ are all polynomials in s . A transfer function of this form is said to be a bilinear function of the parameter x since both the numerator and denominator polynomials are linear functions of the parameter x . The poles of $T(s)$ are the roots of the denominator polynomial

$$D(s) = G(s) + xH(s) \quad (31)$$

As x varies from 0 to ∞ , the poles of $T(s)$ begin at the roots of $G(s)$ and migrate to the roots of $H(s)$. The root locus can be used to display the paths that the poles take as they move from the roots of $G(s)$ to the roots of $H(s)$. Similarly, the root locus can be used to display the paths that the zeros of $T(s)$ take as they migrate from the roots of $E(s)$ to the roots of $F(s)$.

For example, consider the Sallen–Key bandpass filter shown in Fig. 11. When

$$R_1 = R_2 = R_3 = 7.07 \text{ k}\Omega, \quad C_1 = C_2 = 0.1 \text{ }\mu\text{F}, \quad \text{and}$$

$$K = 1 + \frac{R_4}{R_5}$$

then the transfer function of this Sallen–Key filter is

$$T(s) = \frac{K(1414s)}{s^2 + (4 - K)(1414s) + 4 \times 10^6} = \frac{K(1414s)}{(s^2 + 5656s + 4 \times 10^6) + K(-1414s)} \quad (32)$$

As expected, this transfer function is a bilinear function the gain K . Comparing Eqs. (30) and (32) shows that $E(s) = 0$, $F(s) = 1414s$, $G(s) = s^2 + 5656s + 4 \times 10^6$, and

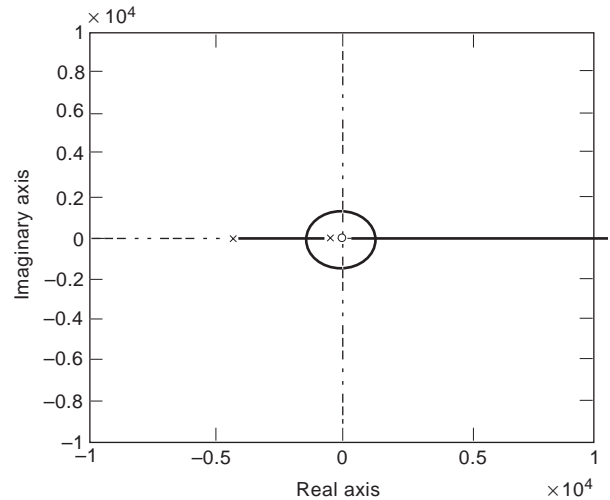


Figure 21. This root locus plot shows that the poles of the Sallen–Key bandpass filter move into the right of the s plane as the gain increases.

$H(s) = -1414s$. The root locus describing the poles of the filter is obtained using the MATLAB commands

```
G = ([1 5656 4*10^6]);
H = ([0 -1414 0]);
rlocus(H,G)
```

Figure 21 shows the resulting root locus plot. The poles move into the right half of the s plane, and the filter becomes unstable when $K > 4$.

BIBLIOGRAPHY

1. R. C. Dorf and R. H. Bishop, *Modern Control Systems*, 7th ed., Addison-Wesley, Reading, MA, 1995.
2. R. C. Dorf and J. A. Svoboda, *Introduction to Electric Circuits*, Wiley, New York, 1996.
3. R. V. Churchill, J. W. Brown, and R. F. Verhey, *Complex Variables and Applications*, McGraw-Hill, New York, 1974.
4. S. M. Shinnars, *Modern Control System Theory and Design*, Wiley, New York, 1992.
5. R. D. Strum and D. E. Kirk, *Contemporary Linear Systems Using MATLAB*, PWS, Boston, 1994.
6. N. E. Leonard and W. S. Levine, *Using MATLAB to Analyze and Design Control Systems*, Benjamin Cummings, Redwood City, CA, 1995.
7. K. Ogata, *Modern Control Engineering*, Prentice-Hall, Englewood Cliffs, NJ, 1970.
8. J. A. Svoboda and G. M. Wierzbza, Using PSpice to determine the relative stability of RC active filters, *Int. J. Electron.* **74**(4):593–604 (1993).
9. F. W. Stephenson, *RC Active Filter Design Handbook*, Wiley, New York, 1985.
10. J. A. Svoboda, ELab, A circuit analysis program for engineering education, *Comput. Appl. Eng. Educ.* **5**:135–149 (1997).
11. W.-K. Chen, *Active Network and Feedback Amplifier Theory*, New York, McGraw-Hill, 1980.
12. K. Gehler, *Theory of Tolerances*, Akademiai Kiado, Budapest, Hungary, 1971.

13. A. Budak, *Passive and Active Network Synthesis*, Waveland Press, Prospect Heights, IL, 1991, Chapter 6.

FURTHER READING

- P. Gray and R. Meyer, *Analysis and Design of Analog Integrated Circuits*, 3rd ed., Wiley, New York, 1993, Chapters 8 and 9.
A. Sedra and K. Smith, *Microelectronic Circuits*, 4th ed., Oxford Univ. Press, 1998, Chapter 8.

CIRCUIT TUNING

ROLF SCHAUMANN
Portland State University
Portland, Oregon

Circuit tuning refers to the process of adjusting the values of electronic components in a circuit to ensure that the fabricated or manufactured circuit performs to specifications. In digital circuits, where signals are switched functions in the time domain and correct operation depends largely on the active devices switching all the way between their ON and OFF states, tuning in the sense discussed in this article is rarely necessary. In analog continuous-time circuits, however, signals are continuous functions of time and frequency so that circuit performance depends critically on the component values. Consequently, in all except the most undemanding applications with wide tolerances, correct circuit operation almost always requires some form of tuning. Naturally, components could be manufactured with very tight tolerances, but the resulting fabrication costs would become prohibitive. In practice, therefore, electronic components used in circuit design are never or only rarely available as accurately as the nominal design requires, so we must assume that they are affected by fabrication and manufacturing tolerances. Furthermore, regardless of whether a circuit is assembled in discrete form with discrete components on a printed circuit board (as a hybrid circuit), or in integrated form on an integrated circuit chip, the circuit will be affected by parasitic components and changing operating conditions, all of which contribute to inaccurate circuit performance. Consider, for example, the requirement of implementing as a hybrid circuit a timer of 1 s for a timer circuit via an RC time constant $\tau = RC$ with an accuracy of 0.1%. Assume that R and C are selected to have the nominal values $R = 100 \text{ k}\Omega$ and $C = 10 \text{ }\mu\text{F}$, that inexpensive chip capacitors with $\pm 20\%$ tolerances are used, and that the desired fabrication process of thin-film resistors results in components with $\pm 10\%$ tolerances. The fabricated time constant can therefore be expected to lie in the range

$$0.68 \text{ s} \leq \tau = 100 \text{ k}\Omega(1 \pm 0.1)10 \text{ }\mu\text{F}(1 \pm 0.2) \leq 1.32 \text{ s}$$

In other words, the τ error must be expected to be $\pm 32\%$, which is far above the specified 0.1%. Tuning is clearly

necessary. Because capacitors are difficult to adjust and accurate capacitors are expensive, let us assume in this simple case that the capacitor was measured with 0.05% accuracy as $C = 11.125 \text{ }\mu\text{F}$ (i.e., the measured error was $+11.25\%$). We can readily compute that the resistor should be adjusted (trimmed) to the nominal value $R = \tau/C = 1 \text{ s}/11.125 \text{ }\mu\text{F} = 89.888 \text{ k}\Omega$ within a tolerance of $\pm 45 \text{ }\Omega$ to yield the correctly implemented time constant of 1 s with $\pm 0.1\%$ tolerances. Observe that tuning generally allows the designer to construct a circuit with less expensive wide-tolerance parts because subsequent tuning of these or other components permits the errors to be corrected. Thus, C was fabricated with 20% tolerances but measured with a 0.05% error to permit the resistor with fabrication tolerances of 10% to be trimmed to a 0.05% accuracy. Note that implied in this process is the availability of measuring instruments with the necessary accuracy.

Tuning has two main purposes. Its most important function is to correct errors in circuit performance caused by such factors as fabrication tolerances such as in the preceding example. Second, it permits a circuit's function or parameters, such as the cutoff frequency of a given lowpass filter, to be changed to different values to make the circuit more useful or to be able to accommodate changing operating requirements. But even the best fabrication technology together with tuning will not normally result in a circuit operating with *zero* errors; rather, the aim of tuning is to trim the values of one or more, or in rare cases of all, components until the circuit's response is guaranteed to remain within a specified *tolerance range* when the circuit is put into operation. Figure 1 illustrates the idea for a lowpass filter. Examples are a gain error that is specified to remain within $\pm 0.05 \text{ dB}$, the cutoff frequency f_c of a filter that must not deviate from the design value of, say, $f_c = 10 \text{ kHz}$ by more than 85 Hz, or the gain of an amplifier that must settle to, say, 1% of its final value within less than $1 \text{ }\mu\text{s}$. As these examples indicate, in general, a circuit's operation can be specified in the time domain, such as a transient response with a certain highest permissible overshoot or a maximal settling time, or in the frequency (s) domain through an input-output

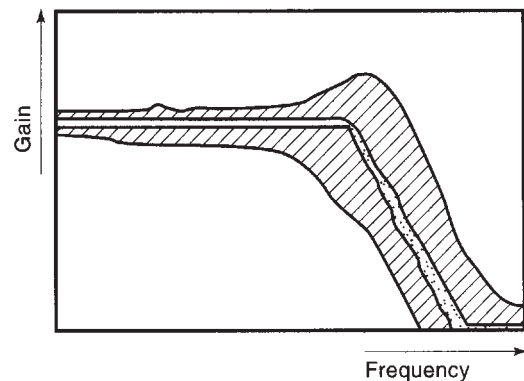


Figure 1. The shaded area in the gain–frequency plot shows the operating region for a lowpass filter that must be expected based on the basis of raw (untuned) fabrication tolerances; the dotted region is the acceptable tolerance range that must be maintained in operation after the filter is tuned.

transfer function with magnitude, phase, or delay specifications and certain tolerances (see Fig. 1). This article focuses on the tuning of *filters*, that is, of frequency-selective networks. Such circuits are continuous functions of components, described by transfer functions in the s domain, where tuning of design parameters (e.g., cutoff frequency, bandwidth, quality factor, gain), is particularly important in practice. The concepts discussed in connection with filters apply equally to other analog circuits. Obviously, in order to tune (adjust) a circuit, that circuit must be tunable; that is, its components must be capable of being varied in some manner (manually or electronically) by an amount sufficient to overcome the consequences of fabrication tolerances, parasitic effects, or other such factors.

An example will help to illustrate the discussion and terminology. Consider the simple second-order active bandpass circuit in Fig. 2. Its voltage transfer function, under the assumption of ideal operational amplifiers, can be derived to be

$$\begin{aligned} T(s) &= \frac{V_2}{V_1} = -\frac{b_1 s}{s^2 + a_1 s + a_0} \\ &= -\frac{\frac{1}{R_1 C_1} s}{s^2 + \frac{1}{R_2} \left(\frac{1}{C_1} + \frac{1}{C_2} \right) s + \frac{1}{R_1 R_2 C_1 C_2}} \end{aligned} \quad (1)$$

We see that $T(s)$ is a continuous function of the circuit components, as are all its coefficients that determine the circuit's behavior:

$$b_1 = \frac{1}{R_1 C_1}, \quad a_1 = \frac{C_1 + C_2}{R_2 C_1 C_2}, \quad a_0 = \frac{1}{R_1 R_2 C_1 C_2} \quad (2)$$

Just as in the earlier example of the RC time constant, the coefficients will not be implemented precisely if the component values have fabrication tolerances. If these component tolerances are “too large,” generally the coefficient errors will become “too large” as well, and the circuit will not function correctly. In that case, the circuit must be tuned. Furthermore, circuits are generally affected by parasitic components. Parasitic components, or *parasitics*, are physical effects that often can be modeled as “real components” affecting the circuit's performance but that frequently are not specified with sufficient accuracy and are not included in the nominal design. For instance, in the filter of Fig. 2, a parasitic capacitor can be assumed to

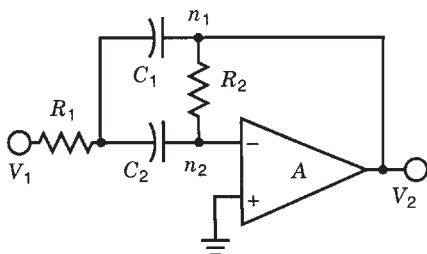


Figure 2. Active RC bandpass filter.

exist between any two nodes or between any individual node and ground; also, real “wires” are not ideal short-circuit connections with zero resistance but are resistive and, at high frequencies, even inductive. In the filter of Fig. 2, a parasitic capacitor C_p between nodes n_1 and n_2 would let the resistor R_2 look like the frequency-dependent impedance $Z_2(s) = R_2 / (1 + sC_p R_2)$. Similarly, real resistive wires would place small resistors r_w in series with C_1 and C_2 and would make these capacitors appear lossy. That is, the capacitors C_i , $i = 1, 2$, would present admittances of the form $Y_i(s) = sC_i / (1 + sC_i r_w)$. Substituting $Z_2(s)$ and $Y_i(s)$ for R_2 and C_i , respectively, into Eq. (1) shows that, depending on the frequency range of interest and the element values, the presence of these parasitics changes the coefficients of the transfer function, maybe even its type, and consequently the circuit's performance. Similarly, when changes occur in environmental operating conditions, such as bias voltages or temperature, the performance of electronic devices is altered, and as a result the fabricated circuit may not perform as specified.

As discussed by Moschytz [1, Section 4.4, pp. 394–425], and Bowron and Stevenson [2, Section 9.5, pp. 247–251], the operation of tuning can be classified into *functional* and *deterministic* tuning. In functional tuning, the designed circuit is assembled, and its performance is measured. By analyzing the circuit, we can identify which component affects the performance parameter to be tuned. These predetermined components are then adjusted in situ (i.e., with the circuit in operation), until errors in performance parameters are reduced to acceptable tolerances. The process is complicated by the fact that tuning is most often interactive, meaning that adjusting a given component will vary several circuit parameters; thus iterative routines are normally called for. As an example, consider again the active RC filter in Fig. 2. If its bandpass transfer function, Eq. (1), is expressed in the measurable terms of center frequency ω_0 , the pole quality factor $Q = \omega_0 / \Delta\omega$, the parameter that determines the filter's bandwidth $\Delta\omega$, and midband (at $s = j\omega_0$) gain K as

$$\begin{aligned} T(s) &= -\frac{\frac{1}{R_1 C_1} s}{s^2 + \frac{1}{R_2} \left(\frac{1}{C_1} + \frac{1}{C_2} \right) s + \frac{1}{R_1 R_2 C_1 C_2}} \\ &= -\frac{K \frac{\omega_0}{Q} s}{s^2 + s \frac{\omega_0}{Q} + \omega_0^2} \end{aligned} \quad (3)$$

These parameters are expressed in terms of the circuit components, and we arrive at the more meaningful and useful design equations

$$\omega_0 = \frac{1}{\sqrt{R_1 R_2 C_1 C_2}}, \quad Q = \sqrt{\frac{R_2 \sqrt{C_1 C_2}}{R_1 C_1 + C_2}}, \quad K = \frac{R_2}{R_1} \frac{C_2}{C_1 + C_2} \quad (4)$$

instead of Eq. (2). It is clear that varying any of the passive components will change all three filter parameters, so that expensive and time-consuming iterative tuning is

required. However, functional tuning has the advantage that the effects of all component and layout parasitics, losses, loading, and other hard-to-model or hard-to-predict factors are accounted for because the performance of the complete circuit is measured under actual operating conditions. In general, more accurate results are obtained by basing functional tuning on measurements of phase rather than of magnitude because phase tends to be more sensitive to component errors.

Deterministic tuning refers to calculating the needed value of a component from circuit equations and then adjusting the component to that value. We determined the resistor $R = \tau/C = 89.888 \text{ k}\Omega$ to set a time constant of 1 s at the beginning of this article in this manner. Similarly, from Eq. (4) we can derive the three equations in the four unknowns R_1 , R_2 , C_1 , and C_2

$$R_2 = \frac{Q}{\omega_0} \left(\frac{1}{C_1} + \frac{1}{C_2} \right), \quad R_1 = \frac{1}{R_2 \omega_0^2 C_1 C_2}, \quad C_1 = \frac{1}{KR_1 \omega_0} \quad (5)$$

with C_2 a free parameter. That there are more circuit components than parameters is normal, so the additional “free” elements may be used at will, for example, to achieve practical element values or element-value *spreads* (i.e., the difference between the maximum and minimum of a component type, such as $R_{\max} - R_{\min}$). Technology or cost considerations may place further constraints on tuning by removing some components from the list of tunable ones. Thus, in hybrid circuits with thin- or thick-film technology as in the preceding example, the capacitors will likely be fixed; only the two resistors will be determined as in Eq. (5) from the prescribed circuit parameters ω_0 and Q and the selected and measured capacitor values. This option leaves the midband gain fixed at the value $K = Q/(\omega_0 C_1 R_1)$. Precise deterministic tuning requires careful measurements and accurate models and design equations that, in contrast to the idealized expressions in Eq. (5), describe circuit behavior along with loss, parasitic, and environmental effects. As we saw in Eq. (5), the equations that must be solved are highly nonlinear and tend to be very complex, particularly if parasitic components also are involved. Computer tools are almost always used to find the solution. Typically, automatic laser trimming is employed to tune the resistors to the desired tolerances (e.g., 0.1%). A second tuning iteration using functional tuning may be required because the assembled circuit under power may still not meet the specifications as a result of further parasitic or loading effects that could not be accounted for in the initial deterministic tuning step.

1. SENSITIVITY

We mentioned earlier that a filter parameter P depends on the values k_i of the components used to manufacture a circuit, $P = P(k_i)$, and that real circuit components or parts can be realized only to within some tolerances $\pm \Delta k_i$; that is, the values of the parts used to assemble circuits are $k_i \pm \Delta k_i$. Clearly, the designer needs to know how much these tolerances will affect the circuit and whether the resulting errors can be corrected by adjusting (tuning) the

circuit after fabrication. Obviously, the parameter to be tuned must depend on the component to be varied. For example, Q in Eq. (4) is a function of the components R_1 , R_2 , C_1 , and C_2 , any one of which can be adjusted to correct fabrication errors in Q . In general, the questions of how large the adjustment of a component has to be, whether it should be increased or decreased, and what the best tuning sequence is are answered by considering the parameter’s *sensitivity* to component tolerances. How sensitive P is to the component-value tolerances—that is, how large the deviation ΔP of the parameter in question is—is computed for small changes via the derivative of $P(k_i)$ with respect to k_i , $\partial P/\partial k_i$, at the nominal value k_i :

$$\Delta P = \frac{\partial P(k_i)}{\partial k_i} \Delta k_i \quad (6)$$

Typically, designers are less interested in the absolute tolerances than in the relative ones

$$\frac{\Delta P}{P} = \frac{k_i}{P} \frac{\partial P}{\partial k_i} \frac{\Delta k_i}{k_i} = S_{k_i}^P \frac{\Delta k_i}{k_i} \quad (7)$$

where $S_{k_i}^P$ is the sensitivity, defined as “the relative change of the parameter divided by the relative change of the component”:

$$S_{k_i}^P = \frac{\Delta P/P}{\Delta k_i/k_i} \quad (8)$$

A detailed discussion of sensitivity issues can be found in many textbooks (see Schaumann et al. [3], Chapter 3, pp. 124–196). For example, the sensitivity of ω_0 in Eq. (4) to changes in R_1 is readily computed to be

$$\begin{aligned} S_{R_1}^{\omega_0} &= \frac{R_1}{\omega_0} \frac{\partial \omega_0}{\partial R_1} \\ &= \frac{R_1}{1/(R_1 R_2 C_1 C_2)^{1/2}} \left(-\frac{1}{2} \right) \frac{R_2 C_1 C_2}{(R_1 R_2 C_1 C_2)^{3/2}} = -\frac{1}{2} \end{aligned} \quad (9)$$

$S_{R_1}^{\omega_0} = -0.5$ means that the percentage error in the parameter ω_0 is one-half the size of the percentage error of R_1 and opposite in sign (i.e., if R_1 increases, ω_0 decreases). A large number of useful sensitivity relations that make sensitivity calculations easy can be derived (see, e.g., Moschytz [1], Section 1.6, pp. 103–105, 1.5, pp. 71–102, and 4.3, pp. 371–393, or Schaumann et al. [3], Chapter 3, pp. 124–196). Of particular use for our discussion of tuning are

$$\begin{aligned} S_k^{P(k^n)} &= n S_k^{P(k)}, \quad S_k^{P(\alpha k)} = S_k^{P(k)}, \\ S_k^{P(1/k)} &= -S_k^{P(k)}, \quad \text{and } S_k^{P(\sqrt{k})} = \frac{1}{2} S_k^{P(k)} \end{aligned} \quad (10)$$

where α is a constant, independent of k . The last two of these equations are special cases of the first one for $n = -1$ and $n = \frac{1}{2}$, respectively. The last equation generalizes the result obtained in Eq. (9). Equations (7) and (8) indicate that, for small differential changes, the

parameter deviation caused by a component error and, conversely from the point of view of tuning, the change in component value necessary to achieve a desired change in parameter can be computed if the sensitivity is known.

In Eqs. (6) and (7) we purposely used partial derivatives, $\partial P/\partial k_i$, to indicate that circuit parameters normally depend on more than one component [see Eq. (4)], all of which affect the accuracy of the parameter. To get a more complete picture of the combined effect of the tolerances and to gain insight into the operation of tuning involving several parameters, total derivatives need to be computed. Assuming P depends on n components, we find (see Schaumann et al. [3], Chapter 3, pp. 124–196)

$$\Delta P = \frac{\partial P}{\partial k_1} \Delta k_1 + \frac{\partial P}{\partial k_2} \Delta k_2 + \cdots + \frac{\partial P}{\partial k_n} \Delta k_n$$

that is

$$\begin{aligned} \frac{\Delta P}{P} &= \frac{k_1}{P} \frac{\partial P}{\partial k_1} \frac{\Delta k_1}{k_1} + \cdots + \frac{k_n}{P} \frac{\partial P}{\partial k_n} \frac{\Delta k_n}{k_n} \\ &= S_{k_1}^P \frac{\Delta k_1}{k_1} + \cdots + S_{k_n}^P \frac{\Delta k_n}{k_n} = \sum_{i=1}^n S_{k_i}^P \frac{\Delta k_i}{k_i} \end{aligned} \quad (11)$$

indicating that the sum of all relative component tolerances, weighted by their sensitivities, contributes to the parameter error. To illustrate the calculations, let us apply Eq. (11) to ω_0 in Eq. (4). Using Eqs. (9) and (10), the result is

$$\begin{aligned} \frac{\Delta \omega_0}{\omega_0} &= \frac{R_1}{\omega_0} \frac{\partial \omega_0}{\partial R_1} \frac{\Delta R_1}{R_1} + \frac{R_2}{\omega_0} \frac{\partial \omega_0}{\partial R_2} \frac{\Delta R_2}{R_2} \\ &\quad + \frac{C_1}{\omega_0} \frac{\partial \omega_0}{\partial C_1} \frac{\Delta C_1}{C_1} + \frac{C_2}{\omega_0} \frac{\partial \omega_0}{\partial C_2} \frac{\Delta C_2}{C_2} \\ &= S_{R_1}^{\omega_0} \frac{\Delta R_1}{R_1} + S_{R_2}^{\omega_0} \frac{\Delta R_2}{R_2} + S_{C_1}^{\omega_0} \frac{\Delta C_1}{C_1} + S_{C_2}^{\omega_0} \frac{\Delta C_2}{C_2} \quad (12) \\ &= -\frac{1}{2} \frac{\Delta R_1}{R_1} - \frac{1}{2} \frac{\Delta R_2}{R_2} - \frac{1}{2} \frac{\Delta C_1}{C_1} - \frac{1}{2} \frac{\Delta C_2}{C_2} \\ &= -\frac{1}{2} \left(\frac{\Delta R_1}{R_1} + \frac{\Delta R_2}{R_2} + \frac{\Delta C_1}{C_1} + \frac{\Delta C_2}{C_2} \right) \end{aligned}$$

The last expression gives insight into whether and how ω_0 can be tuned. Because the effects of the errors are additive, tuning just one component, say, R_1 , will suffice for given tolerances of R_2 , C_1 , and C_2 if ΔR_1 can be large enough. If we have measured the R_2 errors at -12% , and those of C_1 and C_2 at $+15\%$ and $+10\%$, respectively, Eq. (12) results in

$$\begin{aligned} \frac{\Delta \omega_0}{\omega_0} &= -\frac{1}{2} \left(\frac{\Delta R_1}{R_1} - 0.12 + 0.15 + 0.10 \right) \\ &= -0.5 \left(\frac{\Delta R_1}{R_1} + 0.13 \right) \end{aligned} \quad (13)$$

indicating that R_1 must be *decreased* by 13% to yield, within the linearized approximations made, $\Delta \omega_0 \approx 0$.

Inserting components with these tolerances into Eq. (4) for ω_0 confirms the result obtained.

To expand these results and gain further insight into the effects of tolerances, as well as beneficial tuning strategies and their constraints, we remember that a transfer function generally depends on more than one parameter. Returning to the example of Fig. 2 described by the function $T(s)$ in Eq. (3) with the three parameters ω_0 , Q , and K given in Eq. (4) and applying Eq. (11) leads to

$$\frac{\Delta \omega_0}{\omega_0} = S_{R_1}^{\omega_0} \frac{\Delta R_1}{R_1} + S_{R_2}^{\omega_0} \frac{\Delta R_2}{R_2} + S_{C_1}^{\omega_0} \frac{\Delta C_1}{C_1} + S_{C_2}^{\omega_0} \frac{\Delta C_2}{C_2} \quad (14a)$$

$$\frac{\Delta Q}{Q} = S_{R_1}^Q \frac{\Delta R_1}{R_1} + S_{R_2}^Q \frac{\Delta R_2}{R_2} + S_{C_1}^Q \frac{\Delta C_1}{C_1} + S_{C_2}^Q \frac{\Delta C_2}{C_2} \quad (14b)$$

$$\frac{\Delta K}{K} = S_{R_1}^K \frac{\Delta R_1}{R_1} + S_{R_2}^K \frac{\Delta R_2}{R_2} + S_{C_1}^K \frac{\Delta C_1}{C_1} + S_{C_2}^K \frac{\Delta C_2}{C_2} \quad (14c)$$

These equations can be expressed in matrix form as follows:

$$\begin{pmatrix} \frac{\Delta \omega_0}{\omega_0} \\ \frac{\Delta Q}{Q} \\ \frac{\Delta K}{K} \end{pmatrix} = \begin{pmatrix} S_{R_1}^{\omega_0} & S_{R_2}^{\omega_0} & S_{C_1}^{\omega_0} & S_{C_2}^{\omega_0} \\ S_{R_1}^Q & S_{R_2}^Q & S_{C_1}^Q & S_{C_2}^Q \\ S_{R_1}^K & S_{R_2}^K & S_{C_1}^K & S_{C_2}^K \end{pmatrix} \begin{pmatrix} \frac{\Delta R_1}{R_1} \\ \frac{\Delta R_2}{R_2} \\ \frac{\Delta C_1}{C_1} \\ \frac{\Delta C_2}{C_2} \end{pmatrix} \quad (15)$$

The *sensitivity matrix* in Eq. (15) (see Moschytz [1], Section 4.3, pp. 376–393, or Schaumann et al. [3], Section 3.3, pp. 161–188), a 3×4 matrix in this case, shows how the tolerances of all the filter parameters depend on the component tolerances. We see that adjusting any one of the circuit components will vary all filter parameters as long as *all* the sensitivities are nonzero, which is indeed the case for the circuit in Fig. 2. Thus, noninteractive tuning is not possible. To illustrate the form of the sensitivity matrix, we calculate for the circuit in Fig. 2

$$\begin{pmatrix} \frac{\Delta \omega_0}{\omega_0} \\ \frac{\Delta Q}{Q} \\ \frac{\Delta K}{K} \end{pmatrix} = \begin{pmatrix} -0.5 & -0.5 & -0.5 & -0.5 \\ -0.5 & 0.5 & -\frac{1}{2} \frac{C_1 - C_2}{C_1 + C_2} & \frac{1}{2} \frac{C_1 - C_2}{C_1 + C_2} \\ -1 & 1 & -\frac{C_1}{C_1 + C_2} & \frac{C_1}{C_1 + C_2} \end{pmatrix} \begin{pmatrix} \frac{\Delta R_1}{R_1} \\ \frac{\Delta R_2}{R_2} \\ \frac{\Delta C_1}{C_1} \\ \frac{\Delta C_2}{C_2} \end{pmatrix} \quad (16)$$

Note that the first line of Eq. (16) is equal to the last part of Eq. (12).

The tuning situation is simpler if the matrix elements above the main diagonal are zero as was assumed for an

arbitrary different circuit in Eq. (17a):

$$\begin{pmatrix} \frac{\Delta\omega_0}{\omega_0} \\ \frac{\Delta Q}{Q} \\ \frac{\Delta K}{K} \end{pmatrix} = \begin{pmatrix} S_{R_1}^{\omega_0} & 0 & 0 & S_{C_2}^{\omega_0} \\ S_{R_1}^Q & S_{R_2}^Q & 0 & S_{C_2}^Q \\ S_{R_1}^K & S_{R_2}^K & S_{C_1}^K & S_{C_2}^K \end{pmatrix} \begin{pmatrix} \frac{\Delta R_1}{R_1} \\ \frac{\Delta R_2}{R_2} \\ \frac{\Delta C_1}{C_1} \\ \frac{\Delta C_2}{C_2} \end{pmatrix}$$

$$= \begin{pmatrix} S_{R_1}^{\omega_0} & 0 & 0 \\ S_{R_1}^Q & S_{R_2}^Q & 0 \\ S_{R_1}^K & S_{R_2}^K & S_{C_1}^K \end{pmatrix} \begin{pmatrix} \frac{\Delta R_1}{R_1} \\ \frac{\Delta R_2}{R_2} \\ \frac{\Delta C_1}{C_1} \end{pmatrix} + \begin{pmatrix} S_{C_2}^{\omega_0} \\ S_{C_2}^Q \\ S_{C_2}^K \end{pmatrix} \frac{\Delta C_2}{C_2}$$

(17a)

Here the sensitivities to C_2 are irrelevant because C_2 is a free parameter and is assumed fixed so that the effects of C_2 tolerances can be corrected by varying the remaining elements. We see then that first ω_0 can be tuned by R_1 , next Q is tuned by R_2 without disturbing ω_0 because $S_{R_2}^{\omega_0}$ is zero, and finally K is tuned by C_1 without disturbing the previous two adjustments. Thus a sensitivity matrix of the structure indicated in Eq. (17a) with elements above the main diagonal equal to zero permits sequential “noninteractive” tuning if the tuning order is chosen correctly. Completely noninteractive tuning without regard to the tuning order requires all elements in the sensitivity matrix off the main diagonal to be zero as indicated for another circuit in Eq. (17b):

$$\begin{pmatrix} \frac{\Delta\omega_0}{\omega_0} \\ \frac{\Delta Q}{Q} \\ \frac{\Delta K}{K} \end{pmatrix} = \begin{pmatrix} S_{C_2}^{\omega_0} \\ S_{C_2}^Q \\ S_{C_2}^K \end{pmatrix} \frac{\Delta C_2}{C_2}$$

$$= \begin{pmatrix} S_{R_1}^{\omega_0} & 0 & 0 \\ 0 & S_{R_2}^Q & 0 \\ 0 & 0 & S_{C_1}^K \end{pmatrix} \begin{pmatrix} \frac{\Delta R_1}{R_1} \\ \frac{\Delta R_2}{R_2} \\ \frac{\Delta C_1}{C_1} \end{pmatrix}$$

(17b)

As can be verified readily, each component affects only one circuit parameter. Again, sensitivities to C_2 are irrelevant because C_2 is fixed, and the effects of its tolerances can be corrected by the remaining components.

An important observation on the effects of tolerances on circuit parameters and the resultant need for tuning can be made from Eq. (16). We see that the sensitivities of the dimensionless parameters (parameters with no physical unit) Q and K to the two resistors and similarly to the two capacitors are equal in magnitude but opposite in sign. Because dimensionless parameters are determined by ratios of like components [see Eq. (4)], we obtain from Eq. (4) with Eq. (10)

$$S_{R_1}^Q = -S_{R_2}^Q = S_R^Q = -0.5$$

$$S_{C_1}^Q = -S_{C_2}^Q = S_C^Q = -\frac{1}{2} \frac{C_1 - C_2}{C_1 + C_2}$$

(18)

Thus, the tolerances of Q are

$$\frac{\Delta Q}{Q} = S_R^Q \left(\frac{\Delta R_1}{R_1} - \frac{\Delta R_2}{R_2} \right) + S_C^Q \left(\frac{\Delta C_1}{C_1} - \frac{\Delta C_2}{C_2} \right)$$

(19)

with analogous expressions obtained for the gain K [see the last line of Eq. (16)]. Thus, if the technology chosen to implement the filter permits ratios of resistors and capacitors to be realized accurately (i.e., if all resistors have equal tolerances, as do all capacitors), tuning of dimensionless parameters will generally not be necessary. A prime example is integrated circuit technology, where absolute value tolerances of resistors and capacitors may reach 20–50%, but ratios, depending mainly on processing mask dimensions, are readily implemented with tolerances of a fraction of 1%. As an example, assume that the circuit in Fig. 2 was designed, as is often the case, with two identical capacitors $C_1 = C_2 = C$ with tolerances of 20% and that R_1 and R_2 have tolerances of 10% each

$$C_1 = C_2 = C_n + \Delta C = C_n(1 + 0.2)$$

$$R_1 = R_{1n} + \Delta R_1 = R_{1n}(1 + 0.1)$$

$$R_2 = R_{2n}(1 + 0.1)$$

(20)

where the subscript n stands for the nominal values. From Eq. (19), we find

$$\Delta Q = [S_R^Q(0.1 - 0.1) + S_C^Q(0.2 - 0.2)]Q = 0$$

Thus, the quality factor Q , depending only on ratios of like components, is basically unaffected because all like components have equal fabrication tolerances. This result can be confirmed directly from Eq. (4), where, for equal capacitors

$$Q = \frac{1}{2} \sqrt{\frac{R_2}{R_1}} = \frac{1}{2} \sqrt{\frac{R_{2n}(1 + 0.1)}{R_{1n}(1 + 0.1)}} \approx Q_n$$

(21)

Naturally, if R_1 and R_2 are selected from different manufacturing lots, or if R_1 and R_2 are from physically different fabrication processes (such as a carbon and a metal film resistor), tolerances cannot be assumed to be equal, Q errors are not zero, and tuning will be required.

The situation is quite different for any *dimensioned* circuit parameter, that is, a parameter with a physical unit (e.g., a frequency or time constant, or a voltage or a current). Such parameters are determined by *absolute* values of components, as seen for ω_0 in Eq. (4). Absolute values, depending on physical process parameters such as resistivity, permittivity, or diffusion depth, are very difficult to control and will usually suffer from large process variations. Thus, for the component tolerances in Eq. (20), sensitivity calculations predict from Eqs. (10) and (12) the realized center frequency error

$$\begin{aligned}\Delta\omega_0 &\approx -\frac{1}{2}\left(\frac{\Delta R_1}{R_1} + \frac{\Delta R_2}{R_2} + \frac{\Delta C_1}{C_1} + \frac{\Delta C_2}{C_2}\right)\omega_0 \\ &= -\frac{1}{2}(0.1 + 0.1 + 0.2 + 0.2) = -0.3\omega_0\end{aligned}\quad (22a)$$

that is, all individual component tolerances add to a -30% frequency error. Again, the validity of this sensitivity result can be confirmed directly from Eq. (4):

$$\begin{aligned}\omega_0 &= \frac{1}{\sqrt{R_1 R_2 C_1 C_2}} = \frac{1}{C\sqrt{R_1 R_2}} \\ &= \frac{1}{C_n(1+0.2)\sqrt{R_{1n}R_{2n}(1+0.1+0.1+0.01)}} \\ &\approx \frac{\omega_{0n}}{(1+.02)\sqrt{1+0.2}} \approx \frac{\omega_{0n}}{(1+0.2)(1+0.1)} \\ &= \frac{\omega_{0n}}{(1+0.32)} \approx \omega_{0n}(1-0.24)\end{aligned}\quad (22b)$$

The difference between the exact result in Eq. (22b) and the one obtained via the sensitivity approach in Eq. (22a) arises because the latter assumes *incremental* component changes whereas the former assumed the relatively large changes of 10 and 20%. The center frequency ω_0 is approximately 25–30% smaller than specified and must be corrected by tuning. This can be accomplished, for example, by trimming the two resistors to be 27% smaller than their *fabricated* values,

$$R_1 = R_{1n}(1+0.1)(1-0.27) \approx R_{1n}(1-0.2)$$

$$R_2 \approx R_{2n}(1-0.2)$$

so that sensitivity calculations yield

$$\Delta\omega_0 \approx -0.5(-0.2 - 0.2 + 0.2 + 0.2) = 0$$

More exact deterministic tuning requires the resistors to be trimmed to 24.2% smaller than the fabricated value as shown in Eq. (23):

$$\begin{aligned}\omega_0 &\approx \frac{1}{C_n(1+0.2)\sqrt{R_{1n}R_{2n}(1+0.1)(1-\delta)}} \\ &= \frac{\omega_{0n}}{1.32(1-\delta)} \Rightarrow \omega_{0n}\end{aligned}\quad (23)$$

where δ is the trimming change to be applied to the resistors as fabricated. Equation (23) results in $\delta = 0.242$. Of course, ω_0 tuning could have been accomplished by adjusting only one of the resistors by a larger amount; we trimmed both resistors by equal amounts to maintain *the value of their ratio* that determines Q according to Eq. (21), thereby avoiding the need to retune Q .

2. TUNING DISCRETE CIRCUITS

Whether implemented on a printed-circuit board, with chip and thin- or thick-film components in hybrid form, by use of wirewrapping, or in any other technology, an advantage of discrete circuits for the purpose of tuning is that circuit elements are accessible individually before or after assembly for deterministic or functional adjusting. Thus, after a circuit is assembled and found not to meet the design specifications, the circuit components (most commonly the resistors or inductors) can be varied until the performance is as required. All the previous general discussion applies to the rest of the article, so we shall present only those special techniques and considerations that have been found particularly useful or important for passive and active filters.

2.1. Passive Filters

Discrete passive filters are almost always implemented as lossless ladder circuits; that is, the components are inductors L and capacitors C as is illustrated in the typical circuit in Fig. 3. These LC filters are designed such that the maximum signal power is transmitted from a resistive source to a resistive load in the frequency range of interest; a brief treatment can be found in Schaumann et al. [3, Chapter 2, pp. 71–123]. As pointed out in our earlier discussion, accurate filter behavior depends on precise element values so that it is normally necessary to trim components. This tuning is almost always accomplished via variable inductors whose values are changed by screwing a ferrite slug (the “trimmer”) into or out of the magnetic core of the inductive windings. Variable discrete capacitors are hard to construct, expensive, and rarely used.

LC filters have the advantage of very low sensitivities to all their elements (see Schaumann et al. [3], Chapters 2 and 3, pp. 71–196), which makes it possible to assemble

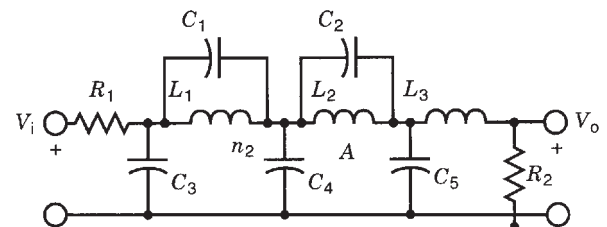


Figure 3. Sixth-order LC lowpass filter. The filter is to realize a maximally flat passband with a 2dB bandwidth of $f_c = 6$ kHz, minimum stopband attenuation $\alpha_s = 67.5$ dB with transmission zeros at 12 and 24 kHz. The nominal components are listed in Table 1. Note that at DC the filter has $-20 \log[R_2/(R_1 + R_2)] = 6.02$ dB attenuation.

the filter using less expensive wide-tolerance components. This property is further enhanced by the fact that lossless ladders are very easy to tune so that large tolerances of one component can be compensated by accurately tuning another. For example, the resonant frequency $f_0 = 1/\sqrt{LC}$ of an LC resonance circuit has $\pm 15\%$ tolerances if both L and C have $\pm 15\%$ tolerances; if L is then trimmed to $\pm 0.5\%$ of its correct value for the existing capacitor (with $\pm 15\%$ tolerances), f_0 is accurate to within 0.25% without requiring any narrower manufacturing tolerances. Without tuning, a 0.25% f_0 error would require the same narrow 0.25% tolerance in both components, which is likely more expensive than a simple tuning step.

It is well known that lossless ladders can be tuned quite accurately simply by adjusting the components to realize the prescribed transmission zeros (see Heinlein and Holmes [4], Section 12.3, pp. 591–604, and Christian [5], Chapter 8, pp. 167–176). Transmission zeros, frequencies where the attenuation is infinite, usually depend on only two elements: a capacitor and an inductor in a parallel resonant circuit (see Fig. 3) with the parallel tank circuits L_1, C_1 and L_2, C_2 in the series branches of the filter, or alternatively with series LC resonance circuits in the shunt branches. The resonant frequencies $f_{zi} = 1/\sqrt{L_i C_i}$, $i = 1, 2$, of the LC tank circuits are not affected by other elements in the filter, so that tuning is largely noninteractive. As mentioned, the effect of the tolerances of one component, say, C , are corrected by tuning L . It is performed by adjusting the inductors for maximum attenuation at the readily identified frequencies of zero transmission while observing the response of the complete manufactured filter on a network analyzer. Tuning accuracies of the transmission zeros of 0.05% or less should be aimed at. Such tuning of the transmission zeros is almost always sufficient even if the circuit elements have fairly large tolerances (see Heinlein and Holmes [4], Section 12.3, pp. 594–604). If even better accuracy is needed, adjustments of those inductors that do not cause finite transmission zeros, such as L_3 in Fig. 3, may need to be performed (see Christian [5], Chapter 8, pp. 167–176). For instance, consider the filter in Fig. 3 realized with unreasonably large tolerances of $\pm 15\%$, using the components shown in Table 1. This places the two resonant frequencies at 10.3 and 20.7 kHz, with the minimum stopband attenuation equal to only 56.7 dB; the 2-dB passband corner is reduced to 5.36 kHz. If we next tune the transmission zero frequencies to 12 and 24 kHz by adjusting *only* the inductors L_1 and L_2 to 23.5 and 40 mH, respectively, the minimum stopband attenuation is increased to 57.8 dB, and the 2 dB band-

width of the passband is measured as $f_c = 6.07$ kHz (refer to Table 1).

We still note that when functional tuning is performed, the filter must be operated with the correct terminations for which it was designed (see Christian [5], Section 8.2, pp. 168–173). Large performance errors, not just at DC or low frequencies, will result if the nominal terminations are severely altered. For example, an LC filter designed for 600- Ω terminations cannot be correctly tuned by connecting it directly without terminations to a high-frequency network analyzer whose input and source impedances are 50 Ω . Also, if maintaining an accurate narrow passband ripple is important, the tolerances of the untuned capacitors must not be too large. Finally, we observe that the tuning properties of passive LC ladders translate directly to active simulations of these filters via transconductance- C and gyrator- C circuits, which are widely used in high-frequency integrated circuits for communications (see the following discussion).

2.2. Active Filters

Several differences must be kept in mind when tuning active filters as compared to passive lossless filters, particularly to ladders:

1. Active filters are almost always more sensitive to component tolerances than LC ladders. Consequently, tuning is always required in practice.
2. Tuning in active filters is almost always interactive; that is, a filter parameter depends on many or all circuit components as discussed in connection with the circuit in Fig. 2 and the sensitivity discussion related to Eqs. (15) and (16). Consequently, tuning active filters usually requires computer aids to solve the complicated nonlinear tuning equations [see, e.g., the relatively simple case in Eq. (4)].
3. The performance of the active devices, such as operational amplifiers (op amps), and their often large tolerances almost always strongly affects the filter performance and must be accounted for in design and in tuning. Because active-device behavior is often hard to model or account for, functional tuning of the fabricated circuit is normally the only method to ensure accurate circuit performance.

In discrete active filters constructed with resistors, capacitors, and operational amplifiers on a circuit board or in thin- or thick-film form, tuning is almost always performed by varying the resistors. Variable resistors,

Table 1. LC Lowpass Filter (Elements in mH, nF, and k Ω)

Components	L_1	C_1	L_2	C_2	L_3	C_3	C_4	C_5	R_1	R_2
Nominal values	27.00	6.490	46.65	0.943	12.67	6.977	45.55	33.90	1.00	1.00
Performance	$f_c = 6.0$ kHz at $\alpha_p = 8.03$ dB; $f_{z1} = 12.0$ kHz, $f_{z2} = 24.0$ kHz, $\alpha_s = 57.5$ dB									
15% tolerance values	31	7.5	52	1.1	14	8	51	38	1.05	1.05
Performance untuned	$f_c = 5.36$ kHz at $\alpha_p = 8.01$ dB; $f_{z1} = 10.3$ kHz, $f_{z2} = 20.7$ kHz, $\alpha_s = 56.7$ dB									
Tuned values	23.5	7.5	40	1.1	14	8	51	38	1.05	1.05
Performance tuned	$f_c = 6.07$ kHz at $\alpha_p = 8.03$ dB; $f_{z1} = 12.0$ kHz, $f_{z2} = 24.0$ kHz, $\alpha_s = 57.8$ dB									

potentiometers, are available in many forms, technologies, and sizes required to make the necessary adjustments.

2.2.1. Second-Order Filters. The main building blocks of active filters are second-order sections, such as the bandpass circuit in Fig. 2. Many of the tuning strategies and concepts were presented earlier in connection with that circuit and the discussion of sensitivity. An important consideration when tuning an active filter is its dependence on the active devices as mentioned previously in point 3 (above). To illustrate the problem, consider again the bandpass filter in Fig. 2. The transfer function $T(s)$ in Eq. (1) is independent of the frequency-dependent gain $A(s)$ of the op amp only because the analysis assumed that the amplifier is ideal, that is, it has constant and very large (ideally infinite) gain, $A = \infty$. In practice, $T(s)$ is also a function of $A(s)$ as a more careful analysis shows:

$$T(s) = \frac{V_2}{V_1} = -\frac{\frac{1}{R_1 C_1} s \frac{A(s)}{1+A(s)}}{s^2 + \frac{1}{R_2} \left\{ \frac{1}{C_1} + \frac{1}{C_2} + \frac{1}{R_1 C_1 [1+A(s)]} \right\} s + \frac{1}{R_1 R_2 C_1 C_2}} \quad (24)$$

Evidently, for $A = \infty$, Eq. (24) reduces to Eq. (1), but finite and frequency-dependent gain can cause severe changes in $T(s)$ in all but the lowest-frequency applications. Consider the often used integrator model for the operational amplifier, $A(s) \approx \omega_t/s$, where ω_t is the unity gain frequency (or the *gain-bandwidth product*) of the op amp with the typical value $\omega_t = 2\pi \times f_t = 2\pi \times 1.5$ MHz. Using this simple model, which is valid for frequencies up to about 10–20% of f_t , and assuming $\omega_t \gg \omega$, the transfer function becomes

$$T(s) = \frac{V_2}{V_1} \approx -\frac{\frac{1}{C_1 R_1} s}{s^2 \left(1 + \frac{1}{\omega_t C_1 R_1} \right) + \frac{1}{R_2} \left(\frac{1}{C_1} + \frac{1}{C_2} \right) s + \frac{1}{R_1 R_2 C_1 C_2}} \quad (25)$$

To get an estimate of the resulting error, let the circuit be designed with $C_1 = C_2 = C = 10$ nF, $R_1 = 66.32 \Omega$ and $R_2 = 9.55$ k Ω to realize the nominal parameters $f_0 = 20$ kHz, $Q = 6$, and $K = 72$. Simulation (or measurement with a very fast op amp) shows that the resulting circuit performance is as desired. However, if the filter is implemented with a 741-type op amp with $f_t = 1.5$ MHz, the measured performance indicates $f_0 = 18.5$ kHz, $Q = 6.85$, and $K = 76.75$. Because of the complicated expressions involving a real op amp, it is appropriate to use functional tuning with the help of a network analyzer. Keeping C constant, the resulting resistor values, $R_1 = 68.5 \Omega$ and $R_2 = 8.00$ k Ω , lead to $f_0 = 20$ kHz and $Q = 6.06$. The midband gain for these element values equals $K = 62.4$ (remember from the

earlier discussion that K for the circuit in Fig. 2 cannot be separately adjusted if the capacitors are predetermined).

2.2.2. High-Order Filters. The two main methods for realizing active filters of order greater than two are active simulations of lossless ladders and cascading second-order sections. We mentioned in connection with the earlier discussion of LC ladders that tuning of active ladder simulations is completely analogous to that of the passive LC ladder: the electronic circuits that simulate the inductors are adjusted until the transmission zeros are implemented correctly. It remains to discuss tuning for the most frequently used method of realizing high-order filters, the cascading of first- and second-order sections. Apart from good sensitivity properties, relatively easy tuning is a main advantage of cascade implementations because each section performs in isolation from the others so that it can be tuned without interactions from the rest of the circuit. Remember, though, that each section by itself may require interactive tuning. Figure 4 shows the circuit structure where each of the blocks is a second-order section such as the ones in Figs. 2 and 5. If the total filter order is odd, one of the sections is, of course, of first order.

To illustrate this point, assume a fourth-order Chebyshev lowpass filter is to be realized with a 1-dB ripple passband in $0 \leq f \leq 28$ kHz with passband gain equal to $H = 20$ dB. The transfer function is found to be

$$T(s) = T_1(s) \times T_2(s) = \frac{1.66\omega_0^2}{s^2 + 0.279\omega_0 s + 0.987\omega_0^2} \frac{1.66\omega_0^2}{s^2 + 0.674\omega_0 s + 0.279\omega_0^2} \quad (26)$$

with $\omega_0 = 2\pi \times 28,000 \text{ s}^{-1} = 175.93 \times 10^3 \text{ s}^{-1}$ (see Schuermann et al. [3], Section 1.6, pp. 36–64). Let the function be realized by two sections of the form shown in Fig. 5. Assuming that the op amps are ideal, the transfer function of the lowpass section is readily derived as

$$\frac{V_2}{V_1} = \frac{K\omega_0^2}{s^2 + s \frac{\omega_0}{Q} + \omega_0^2} = \frac{\alpha_1 \alpha_2}{s^2 + s \left(\frac{1}{C_1 R_1} + \frac{1 - \alpha_1 \alpha_2}{C_2 R_2} \right) + \frac{1}{C_1 R_1 C_2 R_2}} \quad (27)$$

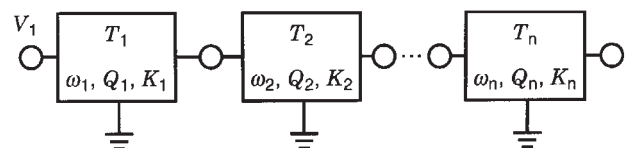


Figure 4. Cascade realization of $2n$ th-order filter. The n second-order sections do not interact with each other and can be tuned independently; that is, each section T_i can be tuned to its nominal values ω_i , Q_i , and H_i , $i = 1, 2, \dots, n$, without being affected by the other sections.

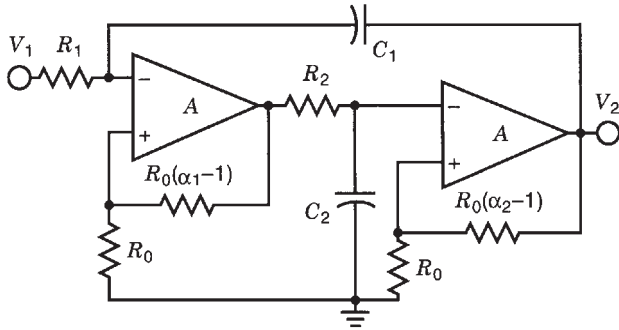


Figure 5. Two-amplifier active lowpass filter.

If the op amp gain is modeled as $A(s) = \omega_0/s$, α_i is to be replaced by

$$\alpha_i \Rightarrow \frac{\alpha_i}{1 + \alpha_i/A(s)} \approx \frac{\alpha_i}{1 + s\alpha_i/\omega_0} \quad (28)$$

We observe again that the circuit parameters ω_0 , Q , and gain K are functions of all the circuit elements so that design and tuning of each section will require iterative procedures, although Section 1 is independent of Section 2 as just discussed. Because there are six “components” (R_1 , R_2 , C_1 , C_2 , α_1 , and α_2) and only three parameters, some simplifying design choices can be made. Choosing $C_1 = C_2 = C$, $R_1 = R$, and $R_2 = k^2R$ (and assuming ideal op amps), Eq. (27) leads to in the expressions

$$\omega_0 = \frac{1}{kRC}, \quad Q = \frac{1}{k + \frac{1}{k}(1 - K)}, \quad K = \alpha_1\alpha_2 \quad (29)$$

The circuit is designed by first computing k from the given values Q and K ; next we choose a suitable capacitor value C and calculate $R = 1/(k\omega_0C)$. Finally, we determine the feedback resistors on the two op amps. Because only the product $\alpha_1\alpha_2$ is relevant, we choose $\alpha_1\alpha_2 = \alpha^2 = K$ (i.e., $\alpha = \sqrt{K} = \sqrt{1.66} = 1.288$). Working through the design equations and choosing all capacitors equal to $C = 150$ pF (standard 5% values) and $R_0 = 10$ k Ω results in $(\alpha - 1)R_0 = 2.87$ k Ω for both sections: $k = 0.965$, $R_1 = 40.2$ k Ω , $R_2 = 36.5$ k Ω for Section 1 and $k = 1.671$, $R_1 = 42.2$ k Ω , $R_2 = 120.1$ k Ω for Section 2. All resistors have standard 1% tolerance values. Building the circuit with 741-type op amps with $f_t = 1.5$ MHz results in a ripple width of almost 3 dB, the reduced cutoff frequency of 27.2 kHz, and noticeable peaking at the band edge. Thus, tuning is required. The errors can be attributed largely to the 5% capacitor errors and the transfer function changes as a result of the finite f_t in Eq. (28).

To accomplish tuning in this case, deterministic tuning may be employed if careful modeling of the op amp behavior, using Eq. (28), and of parasitic effects is used and if the untuned components (the capacitors) are measured carefully and accurately. Because of the many interacting effects in the second-order sections, using a computer program to solve the coupled nonlinear equations is unavoidable, and the resistors are trimmed to their computed values. Functional tuning in this case may

be more convenient, as well as more reliable in practice. For this purpose, the circuit is analyzed, and sensitivities are computed to help understand which components affect the circuit parameters most strongly. Because the sections do not interact, the high-order circuit is separated into its sections, and each section’s functional performance is measured and adjusted on a network analyzer. After the performance of all second-order blocks is found to lie within the specified tolerances, the sections are reconnected in cascade.

3. TUNING INTEGRATED CIRCUITS

With the increasing demand for fully integrated microelectronic systems, naturally, analog circuits will have to be placed on an integrated circuit (IC) along with digital ones. Of considerable interest are communication circuits where bandwidths may reach many megahertz. Numerous applications call for on-chip high-frequency analog filters. Their frequency parameters, which in discrete active filters are set by RC time constants, are in integrated filters most often designed with voltage-to-current converters (transconductors), $I_o = g_m V_i$, and capacitors (i.e., as $\omega = 1/\tau = g_m/C$). As discussed earlier, filter performance must be tuned regardless of the implementation method because fabrication tolerances and parasitic effects are generally too large for filters to work correctly without adjustment. Understandably, tuning in the traditional sense is impossible when the complete circuit is integrated on an IC because individual components are not accessible and cannot be varied. To handle this problem, several techniques have been developed. They permit tuning the circuits electronically by varying the bias voltages V_B or bias currents I_B of the active electronic components (transconductors or amplifiers). In the usual approach, the performance of the fabricated circuit is compared to a suitably chosen accurate reference, such as an external precision resistor R_e to set the value of an electronic on-chip transconductance to $g_m = 1/R_e$ or to a reference frequency ω_r to set the time constant to $C/g_m = 1/\omega_r$. This approach is indeed used in practice, where often the external parameters, R_e or ω_e , are adjusted manually to the required tolerances. Tuning can be handled by connecting the circuit to be tuned into an on-chip control loop, which automatically adjusts bias voltages or currents until the errors are reduced to zero or an acceptable level (see Schaumann et al. [3], Section 7.3, pp. 418–446, and Johns and Martin [6], Section 15.7, pp. 626–635). (A particularly useful reference is Tsvividis and Voorman [7]; it contains papers on all aspects of integrated filters, including tuning). Naturally, this process requires that the circuit be designed to be tunable, that is, that the components are variable over a range sufficiently wide to permit errors caused by fabrication tolerances or temperature drifts to be recovered. We also must try to keep the tuning circuitry relatively simple because chip area and power consumption are at a premium. Although digital tuning schemes are conceptually attractive, analog methods are often preferred. The reason is the need to minimize or eliminate generating digital (switching) noise, which

can enter the sensitive analog signal path through parasitic capacitive coupling or through the substrate, causing the dynamic range or the signal-to-noise ratio to deteriorate.

3.1. Automatic Tuning

Let us illustrate the concepts and techniques with a simple second-order example. Higher-order filters are treated in an entirely analogous fashion; the principles do not change. Consider the g_m - C filter in Fig. 6, which realizes the transfer function

$$T(s) = \frac{V_0}{V_1} = \frac{\alpha s^2 + s \left(\alpha \frac{g_{m1}}{C_1} - \beta \frac{g_{m2}}{C_2} \right) + \frac{g_{m0}g_{m2}}{C_1C_2}}{s^2 + s \frac{g_{m1}}{C_1} + \frac{g_{m1}g_{m2}}{C_1C_2}} \quad (30)$$

with pole frequency and pole Q equal to

$$\omega_0 = \sqrt{\frac{g_{m1}g_{m2}}{C_1C_2}}, \quad Q = \frac{\omega_0 C_1}{g_{m1}} = \sqrt{\frac{C_1/C_2}{g_{m1}/g_{m2}}} \quad (31)$$

Comparing Eq. (31) to Eq. (2) indicates that the filter parameters for this technology are determined in fundamentally the same way as for discrete active circuits: the frequency is determined by time constants (C_i/g_{mi}) and the quality factor, by ratios of like components. Analogous statements are true for the numerator coefficients of $T(s)$. We can conclude then that, in principle, tuning can proceed in a manner quite similar to the one discussed in the beginning of this article if we can just develop a procedure for varying the on-chip components. To gain an understanding of what needs to be tuned in an integrated filter, let us introduce a more convenient notation that uses the ratios of the components to some suitably chosen unit values g_m and C

$$g_{mi} = g_i g_m, \quad C_i = c_i C, \quad i = 1, 2 \quad \text{and} \quad \omega_u = \frac{g_m}{C} \quad (32)$$

where ω_u is a unit frequency parameter and g_i and c_i are the dimensionless component ratios. With this notation,

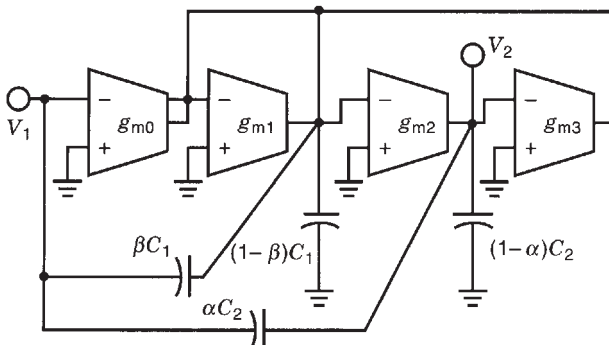


Figure 6. A general second-order transconductance- C filter. The circuit realizes arbitrary zeros by feeding the input signal into portions βC_1 and αC_2 of the capacitors C_1 and C_2 .

Eq. (30) becomes

$$T(s) = \frac{V_0}{V_1} = \frac{\alpha s^2 + s \left(\alpha \frac{g_1}{c_1} - \beta \frac{g_2}{c_2} \right) \omega_u + \frac{g_0 g_2}{c_1 c_2} \omega_u^2}{s^2 + s \frac{g_1}{c_1} \omega_u + \frac{g_1 g_2}{c_1 c_2} \omega_u^2} \quad (33)$$

Casting the transfer function in the form shown in Eq. (33) makes clear that the coefficient of s^i is proportional to ω_u^{n-i} , where n is the order of the filter, $n=2$ in Eq. (33); the constants of proportionality are determined by ratios of like components, which are very accurately designable with IC technology. The same is true for filters of arbitrary order. For example, the pole frequency for the circuit in Fig. 6 is determined as ω_u times a designable quantity, $\omega_0 = \omega_u \sqrt{g_1 g_2 / (c_1 c_2)}$. We may conclude therefore that it is only necessary to tune $\omega_u = g_m / C$, which, as stated earlier, as a ratio of two electrically dissimilar components will have large fabrication tolerances. In addition, the electronic circuit that implements the transconductance g_m depends on temperature, bias, and other conditions, so that ω_u can be expected to drift during operation. It can be seen from Eq. (33) that ω_u simply scales the frequency, that is, the only effect of varying ω_u is a shift of the filter's transfer function along the frequency axis.

We stated earlier that tuning a time constant, or, in the present case, the frequency parameter ω_u , is accomplished by equating it via a control loop to an external reference, in this case a reference frequency ω_R such as a clock frequency. Conceptually, the block diagram in Fig. 7 shows the method [8]. The control loop equates the inaccurate unit frequency $\omega_u = g_m / C$ to the accurate reference frequency ω_R in the following way: ω_R is chosen in the vicinity of the most critical frequency parameters of the filter (the band edge for a lowpass, midband for a bandpass filter), where sensitivities are highest. The transconductance g_m to be tuned is assumed to be proportional to the bias voltage V_B , such that $g_m = k V_B$, where k is a constant of proportionality with units of A/V^2 . g_m generates an output current $I = g_m V_R$, which results in the capacitor voltage $V_C = g_m V_R / (j \omega_R C)$. The two matched peak detectors PD convert the two signals V_R and V_C to their DC

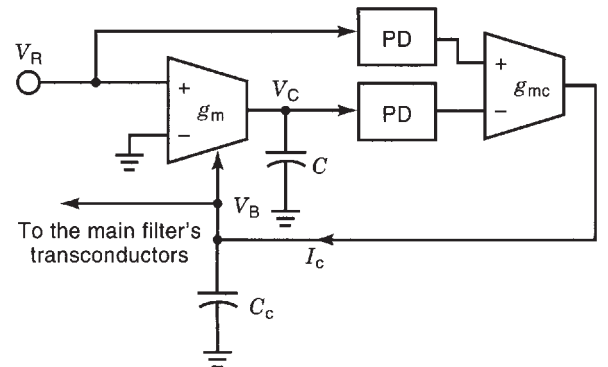


Figure 7. Automatic control loop to set $\omega_u = g_m / C$ via an applied reference signal V_R with frequency ω_R . The capacitor voltage equals $V_C = V_R (g_m / j \omega_R C)$, which makes the control current $I_c = g_{mc} V_R (1 - g_m / j \omega_R C)$. The operation is explained in the text.

peak values, so that any phase differences do not matter when comparing the signals at the input of g_{mc} . The DC output current $I_c = g_{mc}V_R\{1-[g_m/(j\omega_R C)]\}$ of the control-transconductance g_{mc} charges the storage capacitor C_c to the required bias voltage V_B for the transconductance g_m . The values g_{mc} and C_c determine the loop gain; they influence the speed of conversion but are otherwise not critical. If the value of g_m gets too large because of fabrication tolerances, temperature, or other effects, I_c becomes negative, C_c discharges, and V_B , that is $g_m = kV_B$, is reduced. Conversely, if g_m is too small, I_c becomes positive and charges C_c , and the feedback loop acts to increase V_B and g_m . The loop stabilizes when V_C and V_R are equal, that is, when $g_m(V_B)/C$ is equal to the accurate reference frequency ω_R . The g_{mc} - C_c combination is, of course, an integrator with ideally infinite DC gain to amplify the shrinking error signal at the input of g_{mc} . In practice, the open-loop DC gain of a transconductance of 35–50 dB is more than adequate. Note that the loop sets the value of ω_u to ω_R regardless of the causes of any errors: fabrication tolerances, parasitic effects, temperature drifts, aging, or changes in DC bias.

We point out that although the scheme just discussed only varies g_m , it actually controls the time constant C/g_m ; that is, errors in both g_m and C are accounted for. If one wishes to control only g_m , the capacitor C in Fig. 7 is replaced by an accurate resistor R_e , and the feedback loop will converge to $g_m = 1/R_e$.

Note that the feedback loop in Fig. 7 directly controls only the transconductance g_m (as does the frequency control circuit in Fig. 8) such that the unit frequency parameter ω_u within the control circuit is realized correctly. The actual filter is not tuned. However, good matching and tracking can be assumed across the IC because all g_m cells are on the same chip and subject to the same error-causing effects. This assumes that the ratios g , defined in Eq. (32) are not so large that matching problems will arise and that care is taken to account for

(model the effect of) filter parasitics in the control circuit. The same is true for the unit capacitor C in the control loop and the filter capacitors (again, if the ratios c_i are not too large). Consequently, the control bias current I_B can be sent to all the main filter's transconductance cells as indicated in Fig. 7 and thereby tune the filter. Clearly, this scheme depends on good matching properties across the IC chip. Accurate tuning cannot be performed if matching and tracking cannot be relied upon or, in other words, if the g_m - C circuit in the control loop is not a good representative model of the filter cells.

An alternative method for frequency tuning (see Schaumann et al. [3], Section 7.3, pp. 418–446, and Johns and Martin [6], Section 15.7, pp. 626–635) relies on phase-locked loops (see Johns and Martin [6], Chapter 16, pp. 648–695). The top half of Fig. 8 shows the principle. A sinusoidal reference signal V_R at $\omega = \omega_R$ and the output of a voltage-controlled oscillator (f -VCO) at ω_{vco} are converted to square waves by two matched limiters. Their outputs enter an XOR gate acting as a phase detector whose output contains a DC component proportional to the frequency difference $\Delta\omega = \omega_{vco} - \omega_R$ of the two input signals. The lowpass filter LPF 1 eliminates second- and higher-order harmonics of the XOR output and sends the DC component to the oscillator f -VCO, locking its frequency to ω_R . Just as the g_m - C circuit in Fig. 7, the oscillator is designed with transconductances and capacitors to represent (model) any frequency parameter errors of the filter to be tuned so that, relying on matching, the filter is tuned correctly by applying the tuning signal also to its g_m cells. The lowpass filter LPF 2 is used to clean the tuning signal V_f further before applying it to the filter.

We saw in Eq. (33) that all filter parameters depend, apart from ω_u , only on ratios of like components and are, therefore, accurately manufacturable and should require no tuning. This is indeed correct for moderate frequencies and filters with relatively low Q . However, Q is extremely sensitive (see Schaumann et al. [3], Chapter 7, pp. 410–486) to small parasitic phase errors in the feedback loops of active filters, so that Q errors may call for tuning as well, especially as operating frequencies increase. The problem is handled in much the same way as frequency tuning. One devises a model (the Q model in Fig. 8) that represents the Q errors to be expected in the filter and encloses this model circuit in a control loop where feedback acts to reduce the error to zero. Figure 8 illustrates the principle. In the Q control loop, a Q -VCO (tuned correctly by the applied frequency control signal V_f) sends a test signal to the Q model that is designed to represent correctly the Q errors to be expected in the filter to be tuned, and through a peak detector PD to an amplifier of gain K . K is the gain of an accurately designable DC amplifier. Note that the positions of PD and K could be interchanged in principle, but a switch would require that K is the less well-controlled gain of a high-frequency amplifier. The output of the Q model goes through a second (matched) peak detector. Rather than measuring Q directly, which is very difficult in practice, because it would require accurate measurements of two amplitudes and two frequencies, the operation relies on the fact that Q errors are usually proportional to magnitude errors. The

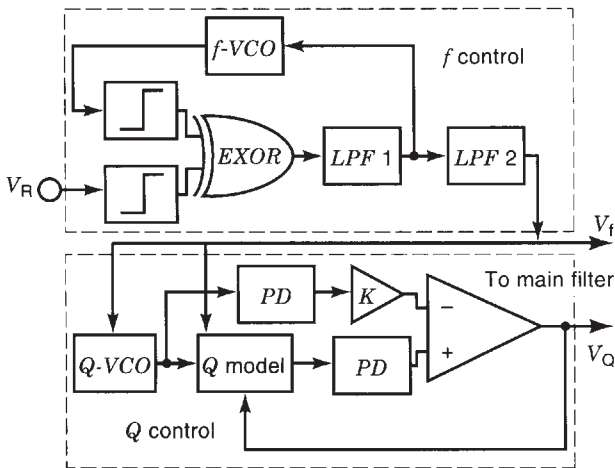


Figure 8. Dual-control loop-tuning system for tuning frequency parameters and quality factors of an integrated filter. Note that the frequency loop converges always, but for the Q loop to converge on the correct Q value, the frequency must be correct. Details of the operation are explained in the text.

diagram in Fig. 8 assumes that for correct Q the output of the Q model is K times as large as its input so that for correct Q the inputs of the comparator are equal. The DC error signal V_Q resulting from the comparison is fed back to the Q model circuit to adjust the bias voltages appropriately, as well as to the filter. In these two interacting control loops, the frequency loop will converge independently of the Q control loop, but to converge on the correct value of Q , the frequency must be accurate. Hence, the two loops must operate together. The correct operation and convergence of the frequency and Q control scheme in Fig. 8 has been verified by experiments (see Schaumann et al. [3], Chapter 7, pp. 410–486) but because of the increased noise, power consumption, and chip area needed for the control circuitry, the method has not found its way into commercial applications.

BIBLIOGRAPHY

1. G. Moschytz, *Linear Integrated Networks: Design*, Van Nostrand-Reinhold, New York, 1975.
2. P. Bowron and F. W. Stevenson, *Active Filters for Communications and Instrumentation*, McGraw-Hill, Maidenhead, UK, 1979.
3. R. Schaumann, M.S. Ghauri, and K.R. Laker, *Design of Analog Filters: Passive, Active RC and Switched Capacitor*, Prentice-Hall, Englewood Cliffs, NJ, 1990.
4. W. E. Heinlein and W. H. Holmes, *Active Filters for Integrated Circuits*, R. Oldenburg, Munich, 1974.
5. E. Christian, *LC Filters: Design, Testing and Manufacturing*, Wiley, New York, 1983.
6. D. A. Johns and K. Martin, *Analog Integrated Circuit Design*, Wiley, New York, 1997.
7. Y. Tividis and J. A. Voorman, eds., *Integrated Continuous-Time Filters: Principles, Design and Implementations*, IEEE Press, Piscataway, NJ, 1993.
8. J. F. Parker and K. W. Current, A CMOS continuous-time bandpass filter with peak-detection-based automatic tuning, *Int. J. Electron.* **1996**(5):551–564 (1996).

CIRCULAR WAVEGUIDES¹

CONSTANTINE A. BALANIS
Arizona State University
Tempe, Arizona
(edited by Eric Holzman
Northrop Grumman Electronic
Systems, Baltimore, Maryland)

1. INTRODUCTION

The circular waveguide is occasionally used as an alternative to the rectangular waveguide. Like other wave-

guides constructed from a single, enclosed conductor, the circular waveguide supports transverse electric (TE) and transverse magnetic (TM) modes. These modes have a cutoff frequency, below which electromagnetic energy is severely attenuated. Circular waveguide's round cross section makes it easy to machine, and it is often used to feed conical horns. Further, the TE_{0n} modes of circular waveguide have very low attenuation. A disadvantage of circular waveguide is its limited dominant mode bandwidth, which, compared to rectangular waveguide's maximum bandwidth of 2–1, is only 1.3. In addition, the polarization of the dominant mode is arbitrary, so that discontinuities can easily excite unwanted cross-polarized components.

In this article, the electromagnetic features of the circular waveguide are summarized, including the transverse and longitudinal fields, the cutoff frequencies, the propagation and attenuation constants, and the wave impedances of all transverse electric and transverse magnetic modes.

2. TRANSVERSE ELECTRIC (TE^z) MODES

The transverse electric to z (TE^z) modes can be derived by letting the vector potential \mathbf{A} and \mathbf{F} be equal to

$$\mathbf{A} = 0 \quad (1a)$$

$$\mathbf{F} = \hat{a}_z F_z(\rho, \phi, z) \quad (1b)$$

The vector potential \mathbf{F} must satisfy the vector wave equation, which reduces the \mathbf{F} of (1b) to

$$\nabla^2 F_z(\rho, \phi, z) + \beta^2 F_z(\rho, \phi, z) = 0 \quad (2)$$

When expanded in cylindrical coordinates, (2) reduces to

$$\frac{\partial^2 F_z}{\partial \rho^2} + \frac{1}{\rho} \frac{\partial F_z}{\partial \rho} + \frac{1}{\rho^2} \frac{\partial^2 F_z}{\partial \phi^2} + \frac{\partial^2 F_z}{\partial z^2} + \beta^2 F_z = 0 \quad (3)$$

whose solution for the geometry of Fig. 1 is of the form

$$F_z(\rho, \phi, z) = [A_1 J_m(\beta_\rho \rho) + B_1 Y_m(\beta_\rho \rho)] \\ \times [C_2 \cos(m\phi) + D_2 \sin(m\phi)] \\ \times [A_3 e^{-j\beta_z z} + B_3 e^{+j\beta_z z}] \quad (4a)$$

where

$$\beta_\rho^2 + \beta_z^2 = \beta^2 \quad (4b)$$

The constants $A_1, B_1, C_2, D_2, A_3, B_3, m, \beta_\rho$, and β_z can be found using the boundary conditions of

$$E_\phi(\rho = a, \phi, z) = 0 \quad (5a)$$

$$\text{The fields must be finite everywhere} \quad (5b)$$

$$\text{The fields must repeat every } 2\pi \text{ radians in } \phi \quad (5c)$$

¹This article is derived from material in *Advanced Engineering Electromagnetics*, by Constantine Balanis, Wiley, New York, 1989, Sect. 9.2.

diagram in Fig. 8 assumes that for correct Q the output of the Q model is K times as large as its input so that for correct Q the inputs of the comparator are equal. The DC error signal V_Q resulting from the comparison is fed back to the Q model circuit to adjust the bias voltages appropriately, as well as to the filter. In these two interacting control loops, the frequency loop will converge independently of the Q control loop, but to converge on the correct value of Q , the frequency must be accurate. Hence, the two loops must operate together. The correct operation and convergence of the frequency and Q control scheme in Fig. 8 has been verified by experiments (see Schaumann et al. [3], Chapter 7, pp. 410–486) but because of the increased noise, power consumption, and chip area needed for the control circuitry, the method has not found its way into commercial applications.

BIBLIOGRAPHY

1. G. Moschytz, *Linear Integrated Networks: Design*, Van Nostrand-Reinhold, New York, 1975.
2. P. Bowron and F. W. Stevenson, *Active Filters for Communications and Instrumentation*, McGraw-Hill, Maidenhead, UK, 1979.
3. R. Schaumann, M.S. Ghauri, and K.R. Laker, *Design of Analog Filters: Passive, Active RC and Switched Capacitor*, Prentice-Hall, Englewood Cliffs, NJ, 1990.
4. W. E. Heinlein and W. H. Holmes, *Active Filters for Integrated Circuits*, R. Oldenburg, Munich, 1974.
5. E. Christian, *LC Filters: Design, Testing and Manufacturing*, Wiley, New York, 1983.
6. D. A. Johns and K. Martin, *Analog Integrated Circuit Design*, Wiley, New York, 1997.
7. Y. Tividis and J. A. Voorman, eds., *Integrated Continuous-Time Filters: Principles, Design and Implementations*, IEEE Press, Piscataway, NJ, 1993.
8. J. F. Parker and K. W. Current, A CMOS continuous-time bandpass filter with peak-detection-based automatic tuning, *Int. J. Electron.* **1996**(5):551–564 (1996).

CIRCULAR WAVEGUIDES¹

CONSTANTINE A. BALANIS
 Arizona State University
 Tempe, Arizona
 (edited by Eric Holzman
 Northrop Grumman Electronic
 Systems, Baltimore, Maryland)

1. INTRODUCTION

The circular waveguide is occasionally used as an alternative to the rectangular waveguide. Like other wave-

guides constructed from a single, enclosed conductor, the circular waveguide supports transverse electric (TE) and transverse magnetic (TM) modes. These modes have a cutoff frequency, below which electromagnetic energy is severely attenuated. Circular waveguide’s round cross section makes it easy to machine, and it is often used to feed conical horns. Further, the TE_{0n} modes of circular waveguide have very low attenuation. A disadvantage of circular waveguide is its limited dominant mode bandwidth, which, compared to rectangular waveguide’s maximum bandwidth of 2–1, is only 1.3. In addition, the polarization of the dominant mode is arbitrary, so that discontinuities can easily excite unwanted cross-polarized components.

In this article, the electromagnetic features of the circular waveguide are summarized, including the transverse and longitudinal fields, the cutoff frequencies, the propagation and attenuation constants, and the wave impedances of all transverse electric and transverse magnetic modes.

2. TRANSVERSE ELECTRIC (TE^z) MODES

The transverse electric to z (TE^z) modes can be derived by letting the vector potential \mathbf{A} and \mathbf{F} be equal to

$$\mathbf{A} = 0 \tag{1a}$$

$$\mathbf{F} = \hat{a}_z F_z(\rho, \phi, z) \tag{1b}$$

The vector potential \mathbf{F} must satisfy the vector wave equation, which reduces the \mathbf{F} of (1b) to

$$\nabla^2 F_z(\rho, \phi, z) + \beta^2 F_z(\rho, \phi, z) = 0 \tag{2}$$

When expanded in cylindrical coordinates, (2) reduces to

$$\frac{\partial^2 F_z}{\partial \rho^2} + \frac{1}{\rho} \frac{\partial F_z}{\partial \rho} + \frac{1}{\rho^2} \frac{\partial^2 F_z}{\partial \phi^2} + \frac{\partial^2 F_z}{\partial z^2} + \beta^2 F_z = 0 \tag{3}$$

whose solution for the geometry of Fig. 1 is of the form

$$F_z(\rho, \phi, z) = [A_1 J_m(\beta_\rho \rho) + B_1 Y_m(\beta_\rho \rho)] \times [C_2 \cos(m\phi) + D_2 \sin(m\phi)] \times [A_3 e^{-j\beta_z z} + B_3 e^{+j\beta_z z}] \tag{4a}$$

where

$$\beta_\rho^2 + \beta_z^2 = \beta^2 \tag{4b}$$

The constants $A_1, B_1, C_2, D_2, A_3, B_3, m, \beta_\rho$, and β_z can be found using the boundary conditions of

$$E_\phi(\rho = a, \phi, z) = 0 \tag{5a}$$

$$\text{The fields must be finite everywhere} \tag{5b}$$

$$\text{The fields must repeat every } 2\pi \text{ radians in } \phi \tag{5c}$$

¹This article is derived from material in *Advanced Engineering Electromagnetics*, by Constantine Balanis, Wiley, New York, 1989, Sect. 9.2.

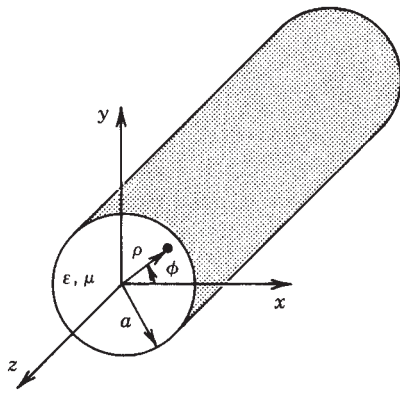


Figure 1. Cylindrical waveguide of circular cross section.

According to (5b), $B_1 = 0$ since $Y_m(\rho = 0) = \infty$. In addition, according to (5c)

$$m = 0, 1, 2, 3, \dots \tag{6}$$

Consider waves that propagate only in the +z direction. Then (4) reduces to

$$F_z^+(\rho, \phi, z) = A_{mn} J_m(\beta_\rho \rho) [C_2 \cos(m\phi) + D_2 \sin(m\phi)] e^{-j\beta_z z} \tag{7}$$

From Eq. (7), the electric field component of E_ϕ^+ can be written as

$$E_\phi^+ = \frac{1}{\epsilon} \frac{\partial F_z^+}{\partial \rho} = \beta_\rho \frac{A_{mn}}{\epsilon} J'_m(\beta_\rho \rho) [C_2 \cos(m\phi) + D_2 \sin(m\phi)] e^{-j\beta_z z} \tag{8a}$$

where

$$\beta_\rho = \frac{\partial}{\partial(\beta_\rho \rho)} \tag{8b}$$

Applying the boundary condition of (5a) in (8a), we then have that

$$E_\phi^+(\rho = a, \phi, z) = \beta_\rho \frac{A_{mn}}{\epsilon} J'_m(\beta_\rho a) [C_2 \cos(m\phi) + D_2 \sin(m\phi)] e^{-j\beta_z z} = 0 \tag{9}$$

which is satisfied only provided that

$$J'_m(\beta_\rho a) = 0 \Rightarrow \beta_\rho a = \chi'_{mn} \Rightarrow \beta_\rho = \frac{\chi'_{mn}}{a} \tag{10}$$

In (10) χ'_{mn} represents the n th zero ($n = 1, 2, 3, \dots$) of the derivative of the Bessel function J_m of the first kind of order m ($m = 0, 1, 2, 3, \dots$). An abbreviated list of the zeros χ'_{mn} of the derivative J'_m of the Bessel function J_m is found in Table 1. The smallest value of χ'_{mn} is 1.8412 ($m = 1, n = 1$).

Using (4b) and (10), β_z of the mn mode can be written as

$$(\beta_z)_{mn} = \begin{cases} \sqrt{\beta^2 - \beta_\rho^2} = \sqrt{\beta^2 - \left(\frac{\chi'_{mn}}{a}\right)^2} \\ \text{when } \beta > \beta_\rho = \frac{\chi'_{mn}}{a} \end{cases} \tag{11a}$$

$$(\beta_z)_{mn} = \begin{cases} 0 & \text{when } \beta = \beta_c = \beta_\rho = \frac{\chi'_{mn}}{a} \end{cases} \tag{11b}$$

$$(\beta_z)_{mn} = \begin{cases} -j\sqrt{\beta_\rho^2 - \beta^2} = -j\sqrt{\left(\frac{\chi'_{mn}}{a}\right)^2 - \beta^2} \\ \text{when } \beta < \beta_\rho = \frac{\chi'_{mn}}{a} \end{cases} \tag{11c}$$

Cutoff is defined when $(\beta_z)_{mn} = 0$. Thus, according to (11b)

$$\beta_c = \omega_c \sqrt{\mu\epsilon} = 2\pi f_c \sqrt{\mu\epsilon} = \beta_\rho = \frac{\chi'_{mn}}{a} \tag{12a}$$

$$(f_c)_{mn} = \frac{\chi'_{mn}}{2\pi a \sqrt{\mu\epsilon}} \tag{12b}$$

By using (12a) and (12b), we can write (11a)–(11c) as

$$(\beta_z)_{mn} = \begin{cases} \sqrt{\beta^2 - \beta_\rho^2} = \beta \sqrt{1 - \left(\frac{\beta_\rho}{\beta}\right)^2} = \beta \sqrt{1 - \left(\frac{\beta_c}{\beta}\right)^2} \\ = \beta \sqrt{1 - \left(\frac{\chi'_{mn}}{\beta a}\right)^2} = \beta \sqrt{1 - \left(\frac{f_c}{f}\right)^2} \\ \text{when } f > f_c = (f_c)_{mn} \end{cases} \tag{13a}$$

$$(\beta_z)_{mn} = \begin{cases} 0 & \text{when } f = f_c = (f_c)_{mn} \end{cases} \tag{13b}$$

Table 1. Zeros χ'_{mn} of Derivative $J'_m(\chi'_{mn}) = 0$ ($n = 1, 2, 3, \dots$) of Bessel Function $J_m(x)$

	$m = 0$	$m = 1$	$m = 2$	$m = 3$	$m = 4$	$m = 5$	$m = 6$	$m = 7$	$m = 8$	$m = 9$	$m = 10$	$m = 11$
$n = 1$	3.8318	1.8412	3.0542	4.2012	5.3175	6.4155	7.5013	8.5777	9.6474	10.7114	11.7708	12.8264
$n = 2$	7.0156	5.3315	6.7062	8.0153	9.2824	10.5199	11.7349	12.9324	14.1155	15.2867	16.4479	17.6003
$n = 3$	10.1735	8.5363	9.9695	11.3459	12.6819	13.9872	15.2682	16.5294	17.7740	19.0046	20.2230	21.4309
$n = 4$	13.3237	11.7060	13.1704	14.5859	15.9641	17.3129	18.6375	19.9419	21.2291	22.5014	23.7607	25.0085
$n = 5$	16.4706	14.8636	16.3475	17.7888	19.1960	20.5755	21.9317	23.2681	24.5872	25.8913	27.1820	28.4609

$$(\beta_z)_{mn} = \begin{cases} -j\sqrt{\beta_\rho^2 - \beta^2} = -j\beta\sqrt{\left(\frac{\beta_\rho}{\beta}\right)^2 - 1} = -j\beta\sqrt{\left(\frac{\beta_c}{\beta}\right)^2 - 1} \\ = -j\beta\sqrt{\left(\frac{\lambda'_{mn}}{\beta a}\right)^2 - 1} = -j\beta\sqrt{\left(\frac{f_c}{f}\right)^2 - 1} \\ \text{when } f < f_c = (f_c)_{mn} \end{cases} \quad (13c)$$

The guide wavelength λ_g is defined as

$$(\lambda_g)_{mn} = \frac{2\pi}{(\beta_z)_{mn}} \quad (14a)$$

which, according to (13a) and (13b), can be written as

$$(\lambda_g)_{mn} = \begin{cases} \frac{2\pi}{\beta\sqrt{1 - \left(\frac{f_c}{f}\right)^2}} = \frac{\lambda}{\sqrt{1 - \left(\frac{f_c}{f}\right)^2}} & \text{when } f > f_c = (f_c)_{mn} \\ \infty & \text{when } f = (f_c)_{mn} \end{cases} \quad (14b)$$

$$(\lambda_g)_{mn} = \{\infty \text{ when } f = (f_c)_{mn}\} \quad (14c)$$

In (14b) λ is the wavelength of the wave in an infinite medium of the kind that exists inside the waveguide. There is no definition of the wavelength below cutoff since the wave is exponentially decaying and there is no repetition of its waveform.

According to (12b) and the values of λ'_{mn} in Table 1, the order (lower to higher cutoff frequencies) in which the TE_{mn}^z modes occur is TE_{11}^z , TE_{21}^z , TE_{01}^z , and so on. It should be noted that for a circular waveguide, the order in which the TE_{mn}^z modes occur does not change, and the bandwidth between modes is also fixed. For example, the bandwidth of the first single-mode TE_{11}^z operation is $3.042/1.8412 = 1.6588 : 1$, which is less than $2 : 1$. This bandwidth is fixed and cannot be varied. A change in the radius only varies, by the same amount, the absolute values of the cutoff frequencies of all the modes but does not alter their order or relative bandwidth.

The electric and magnetic field components can be written from Eq. (7) as

$$\begin{aligned} E_\rho^+ &= -\frac{1}{\varepsilon\rho} \frac{\partial F_z^+}{\partial\phi} \\ &= -A_{mn} \frac{m}{\varepsilon\rho} J_m(\beta_\rho\rho) [-C_2 \sin(m\phi) \\ &\quad + D_2 \cos(m\phi)] e^{-j\beta_z z} \end{aligned} \quad (15a)$$

$$\begin{aligned} E_\phi^+ &= \frac{1}{\varepsilon} \frac{\partial F_z^+}{\partial\rho} \\ &= A_{mn} \frac{\beta_\rho}{\varepsilon} J'_m(\beta_\rho\rho) [C_2 \cos(m\phi) \\ &\quad + D_2 \sin(m\phi)] e^{-j\beta_z z} \end{aligned} \quad (15b)$$

$$E_z^+ = 0 \quad (15c)$$

$$\begin{aligned} H_\rho^+ &= -j \frac{1}{\omega\mu\varepsilon} \frac{\partial^2 F_z^+}{\partial\rho\partial z} \\ &= -A_{mn} \frac{\beta_\rho\beta_z}{\omega\mu\varepsilon} J'_m(\beta_\rho\rho) [C_2 \cos(m\phi) \\ &\quad + D_2 \sin(m\phi)] e^{-j\beta_z z} \end{aligned} \quad (15d)$$

$$\begin{aligned} H_\phi^+ &= -j \frac{1}{\omega\mu\varepsilon\rho} \frac{\partial^2 F_z^+}{\partial\phi\partial z} = -A_{mn} \frac{m\beta_z}{\omega\mu\varepsilon\rho} J_m(\beta_\rho\rho) \\ &\quad \times [-C_2 \sin(m\phi) + D_2 \cos(m\phi)] e^{-j\beta_z z} \end{aligned} \quad (15e)$$

$$\begin{aligned} H_z^+ &= -j \frac{1}{\omega\mu\varepsilon} \left(\frac{\partial^2}{\partial z^2} + \beta^2 \right) F_z^+ = -jA_{mn} \frac{\beta_\rho^2}{\omega\mu\varepsilon} J_m(\beta_\rho\rho) \\ &\quad \times [C_2 \cos(m\phi) + D_2 \sin(m\phi)] e^{-j\beta_z z} \end{aligned} \quad (15f)$$

where

$$\beta_\rho = \frac{\partial}{\partial(\beta_\rho\rho)} \quad (15g)$$

By using (15a)–(15f), the wave impedance (Z_w^{+z})^{TE} of the TE_{mn}^z (H_{mn}^z) modes in the $+z$ direction can be written as

$$Z_{mn}^h = (Z_w^{+z})_{mn}^{\text{TE}} = \frac{E_\rho^+}{H_\phi^+} = -\frac{E_\phi^+}{H_\rho^+} = \frac{\omega\mu}{(\beta_z)_{mn}} \quad (16a)$$

With the aid of (13a)–(13c) the wave impedance of (16a) reduces to

$$Z_{mn}^h = (Z_w^{+z})_{mn}^{\text{TE}} = \begin{cases} \frac{\omega\mu}{\beta\sqrt{1 - \left(\frac{f_c}{f}\right)^2}} = \frac{\sqrt{\frac{\mu}{\varepsilon}}}{\sqrt{1 - \left(\frac{f_c}{f}\right)^2}} = \frac{\eta}{\sqrt{1 - \left(\frac{f_c}{f}\right)^2}} \\ \text{when } f > f_c = (f_c)_{mn} \end{cases} \quad (16b)$$

$$Z_{mn}^h = (Z_w^{+z})_{mn}^{\text{TE}} = \begin{cases} \frac{\omega\mu}{0} = \infty & \text{when } f = f_c = (f_c)_{mn} \end{cases} \quad (16c)$$

$$Z_{mn}^h = (Z_w^{+z})_{mn}^{\text{TE}} = \begin{cases} \frac{\omega\mu}{-j\beta\sqrt{\left(\frac{f_c}{f}\right)^2 - 1}} = +j \frac{\sqrt{\frac{\mu}{\varepsilon}}}{\sqrt{\left(\frac{f_c}{f}\right)^2 - 1}} = +j \frac{\eta}{\sqrt{\left(\frac{f_c}{f}\right)^2 - 1}} \\ \text{when } f < f_c = (f_c)_{mn} \end{cases} \quad (16d)$$

By examining through (16b)–(16d), we can make the following statements about the impedance.

1. Above cutoff it is real and greater than the intrinsic impedance of the medium inside the waveguide.
2. At cutoff it is infinity.

3. Below cutoff it is imaginary and inductive. This indicates that the waveguide below cutoff behaves as an inductor that is an energy storage element.

3. TRANSVERSE MAGNETIC (TM^z) MODES

The transverse magnetic to z (TM ^{z}) modes can be derived in a similar manner as the TE ^{z} modes of Section 2 by letting

$$\mathbf{A} = \hat{a}_z A_z(\rho, \phi, z) \tag{17a}$$

$$\mathbf{F} = 0 \tag{17b}$$

The vector potential \mathbf{A} must satisfy the vector wave equation, which reduces for the \mathbf{A} of (17a) to

$$\nabla^2 A_z(\rho, \phi, z) + \beta^2 A_z(\rho, \phi, z) = 0 \tag{18}$$

The solution of (18) is obtained in a manner similar to that of (2), as given by (4), and it can be written as

$$\begin{aligned} A_z(\rho, \phi, z) = & [A_1 J_m(\beta_\rho \rho) + B_1 Y_m(\beta_\rho \rho)] \\ & \times [C_2 \cos(m\phi) + D_2 \sin(m\phi)] \\ & \times [A_3 e^{-j\beta_z z} + B_3 e^{+j\beta_z z}] \end{aligned} \tag{19a}$$

with

$$\beta_\rho^2 + \beta_z^2 = \beta^2 \tag{19b}$$

The constants $A_1, B_1, C_2, D_2, A_3, B_3, m, \beta_\rho$, and β_z can be found using the boundary conditions of

$$E_\phi(\rho = a, \phi, z) = 0 \tag{20a}$$

or

$$E_z(\rho = a, \phi, z) = 0 \tag{20b}$$

$$\text{The fields must be finite everywhere} \tag{20c}$$

$$\text{The fields must repeat every } 2\pi \text{ radians in } \phi \tag{20d}$$

According to (20c), $B_1 = 0$ since $Y_m(\rho = 0) = \infty$. In addition, according to (20d),

$$m = 0, 1, 2, 3, \dots \tag{21}$$

Considering waves that propagate only in the $+z$ direction, (19a) then reduces to

$$\begin{aligned} A_z^+(\rho, \phi, z) = & B_{mn} J_m(\beta_\rho \rho) [C_2 \cos(m\phi) \\ & + D_2 \sin(m\phi)] e^{-j\beta_z z} \end{aligned} \tag{22}$$

The eigenvalues of β_ρ can be obtained by applying either (20a) or (20b).

From Eq. (22), we can write the electric field component E_z^+ as

$$\begin{aligned} E_z^+ = & -j \frac{1}{\omega \mu \epsilon} \left(\frac{\partial^2}{\partial z^2} + \beta^2 \right) A_z^+ \\ = & -j B_{mn} \frac{\beta_\rho^2}{\omega \mu \epsilon} J_m(\beta_\rho \rho) [C_2 \cos(m\phi) \\ & + D_2 \sin(m\phi)] e^{-j\beta_z z} \end{aligned} \tag{23}$$

Application of the boundary condition of (20b) using (23) gives

$$\begin{aligned} E_z^+(\rho = a, \phi, z) = & -j B_{mn} \frac{\beta_\rho^2}{\omega \mu \epsilon} J_m(\beta_\rho a) \\ & \times [C_2 \cos(m\phi) + D_2 \sin(m\phi)] e^{-j\beta_z z} = 0 \end{aligned} \tag{24}$$

which is satisfied only provided that

$$J_m(\beta_\rho a) = 0 \Rightarrow \beta_\rho a = \chi_{mn} \Rightarrow \beta_\rho = \frac{\chi_{mn}}{a} \tag{25}$$

In (25) χ_{mn} represents the n th zero ($n = 1, 2, 3, \dots$) of the Bessel function J_m of the first kind of order m ($m = 0, 1, 2, 3, \dots$). An abbreviated list of the zeros χ_{mn} of the Bessel function J_m is found in Table 2. The smallest value of χ_{mn} is 2.4049 ($m = 0, n = 1$).

By using (19b) and (25), β_z can be written as

$$(\beta_z)_{mn} = \begin{cases} \sqrt{\beta^2 - \beta_\rho^2} = \sqrt{\beta^2 - \left(\frac{\chi_{mn}}{a}\right)^2} \\ \text{when } \beta > \beta_\rho = \frac{\chi_{mn}}{a} \end{cases} \tag{26a}$$

Table 2. Zeros χ_{mn} of $J_m(\chi_{mn}) = 0$ ($n = 1, 2, 3, \dots$) of Bessel function $J_m(x)$

	$m = 0$	$m = 1$	$m = 2$	$M = 3$	$m = 4$	$m = 5$	$m = 6$	$m = 7$	$m = 8$	$m = 9$	$m = 10$	$m = 11$
$n = 1$	2.4049	3.8318	5.1357	6.3802	7.5884	8.7715	9.9361	11.0864	12.2251	13.3543	14.4755	12.8264
$n = 2$	5.5201	7.1056	8.4173	9.7610	11.0647	12.3386	13.5893	14.8213	16.0378	17.2412	18.4335	19.6160
$n = 3$	8.6537	10.1735	11.6199	13.0152	14.3726	15.7002	17.0038	18.2876	19.5545	20.8071	22.0470	23.2759
$n = 4$	11.7915	13.3237	14.7960	16.2235	17.6160	18.9801	20.3208	21.6415	22.9452	24.2339	25.5095	26.7733
$n = 5$	14.9309	16.4706	17.9598	19.4094	20.8269	22.2178	23.5861	24.9349	26.2668	27.5838	28.8874	30.1791

$$(\beta_z)_{mn} = \begin{cases} 0 & \text{when } \beta = \beta_c = \beta_\rho = \frac{\chi_{mn}}{a} \end{cases} \quad (26b)$$

$$(\beta_z)_{mn} = \begin{cases} -j\sqrt{\beta_\rho^2 - \beta^2} = -j\sqrt{\left(\frac{\chi_{mn}}{a}\right)^2 - \beta^2} \\ \text{when } \beta < \beta_\rho = \frac{\chi_{mn}}{a} \end{cases} \quad (26c)$$

By following the same procedure as for the TE^z modes, we can write the expressions for the cutoff frequencies $(f_c)_{mn}$, propagation constant $(\beta_z)_{mn}$, and guide wavelength $(\lambda_g)_{mn}$ as

$$(f_c)_{mn} = \frac{\chi_{mn}}{2\pi a \sqrt{\mu\epsilon}} \quad (27)$$

$$(\beta_z)_{mn} = \begin{cases} \sqrt{\beta^2 - \beta_\rho^2} = \beta\sqrt{1 - \left(\frac{\beta_\rho}{\beta}\right)^2} = \beta\sqrt{1 - \left(\frac{\beta_c}{\beta}\right)^2} \\ = \beta\sqrt{1 - \left(\frac{\chi_{mn}}{\beta a}\right)^2} = \beta\sqrt{1 - \left(\frac{f_c}{f}\right)^2} \\ \text{when } f > f_c = (f_c)_{mn} \end{cases} \quad (28a)$$

$$(\beta_z)_{mn} = \begin{cases} 0 & \text{when } f = f_c = (f_c)_{mn} \end{cases} \quad (28b)$$

$$(\beta_z)_{mn} = \begin{cases} -j\sqrt{\beta_\rho^2 - \beta^2} = -j\beta\sqrt{\left(\frac{\beta_\rho}{\beta}\right)^2 - 1} = -j\beta\sqrt{\left(\frac{\beta_c}{\beta}\right)^2 - 1} \\ = -j\beta\sqrt{\left(\frac{\chi_{mn}}{\beta a}\right)^2 - 1} = -j\beta\sqrt{\left(\frac{f_c}{f}\right)^2 - 1} \\ \text{when } f < f_c = (f_c)_{mn} \end{cases} \quad (28c)$$

$$(\lambda_g)_{mn} = \begin{cases} \frac{2\pi}{\beta\sqrt{1 - \left(\frac{f_c}{f}\right)^2}} = \frac{\lambda}{\sqrt{1 - \left(\frac{f_c}{f}\right)^2}} & \text{when } f > f_c = (f_c)_{mn} \end{cases} \quad (29a)$$

$$(\lambda_g)_{mn} = \begin{cases} \infty & \text{when } f = f_c = (f_c)_{mn} \end{cases} \quad (29b)$$

According to (27) and the values of χ_{mn} of Table 2, the order (lower to higher cutoff frequencies) in which the TM^z modes occur is TM_{01} , TM_{11} , TM_{21} , and so forth. The bandwidth of the first single-mode TM_{01}^z operation is $3.8318/2.4059 = 1.5927:1$. Comparing the cutoff frequencies of the TE^z and TM^z modes, as given by (12b) and (27) along with the data of Tables 1 and 2, the order of the TE_{mn}^z and TM_{mn}^z modes is that of TE_{11} ($\chi'_{11} = 1.8412$), TM_{01} , ($\chi_{01} = 2.4049$), TE_{21} ($\chi'_{21} = 3.0542$), TE_{01} ($\chi'_{01} = 3.8318$) = TM_{11} ($\chi'_{11} = 3.8318$), TE_{31} ($\chi'_{31} = 4.2012$), and so forth. The dominant mode is TE_{11} and its bandwidth of single-mode operation is $2.4049/1.8412 = 1.3062:1$. Plots of the field configurations over a cross section of the waveguide,

both E and H , for the first 30 TE_{mn}^z and/or TM_{mn}^z modes are shown in Fig. 2 [1].

It is apparent that the cutoff frequencies of the TE_{0n} and TM_{1n} modes are identical; therefore they are referred to here also as *degenerate modes*.

The electric and magnetic field components can be written using (22) as

$$\begin{aligned} E_\rho^+ &= -j \frac{1}{\omega\mu\epsilon} \frac{\partial^2 A_z^+}{\partial\rho\partial z} \\ &= -B_{mn} \frac{\beta_\rho\beta_z}{\omega\mu\epsilon} J'_m(\beta_\rho\rho) \\ &\quad \times [C_2 \cos(m\phi) + D_2 \sin(m\phi)] e^{-j\beta_z z} \end{aligned} \quad (30a)$$

$$\begin{aligned} E_\phi^+ &= -j \frac{1}{\omega\mu\epsilon} \frac{1}{\rho} \frac{\partial^2 A_z^+}{\partial\phi\partial z} \\ &= -B_{mn} \frac{m\beta_z}{\omega\mu\epsilon\rho} J_m(\beta_\rho\rho) \\ &\quad \times [-C_2 \sin(m\phi) + D_2 \cos(m\phi)] e^{-j\beta_z z} \end{aligned} \quad (30b)$$

$$\begin{aligned} E_z^+ &= -j \frac{1}{\omega\mu\epsilon} \left(\frac{\partial^2}{\partial z^2} + \beta^2 \right) A_z^+ \\ &= -j B_{mn} \frac{\beta_\rho^2}{\omega\mu\epsilon} J_m(\beta_\rho\rho) \\ &\quad \times [C_2 \cos(m\phi) + D_2 \sin(m\phi)] e^{-j\beta_z z} \end{aligned} \quad (30c)$$

$$\begin{aligned} H_\rho^+ &= \frac{1}{\mu} \frac{1}{\rho} \frac{\partial A_z^+}{\partial\phi} = B_{mn} \frac{m}{\mu} \frac{1}{\rho} J_m(\beta_\rho\rho) \\ &\quad \times [-C_2 \sin(m\phi) + D_2 \cos(m\phi)] e^{-j\beta_z z} \end{aligned} \quad (30d)$$

$$\begin{aligned} H_\phi^+ &= -\frac{1}{\mu} \frac{\partial A_z^+}{\partial\rho} = -B_{mn} \frac{\beta_\rho}{\mu} J'_m(\beta_\rho\rho) \\ &\quad \times [C_2 \cos(m\phi) + D_2 \sin(m\phi)] e^{-j\beta_z z} \end{aligned} \quad (30e)$$

$$H_z^+ = 0 \quad (30f)$$

where

$$' = \frac{\partial}{\partial(\beta_\rho\rho)} \quad (30g)$$

By using (30a)–(30f), the wave impedance in the $+z$ direction can be written as

$$(Z_w^{+z})_{mn}^{\text{TM}} = \frac{E_\rho^+}{H_\phi^+} = -\frac{E_\phi^+}{H_\rho^+} = \frac{(\beta_z)_{mn}}{\omega\epsilon} \quad (31)$$

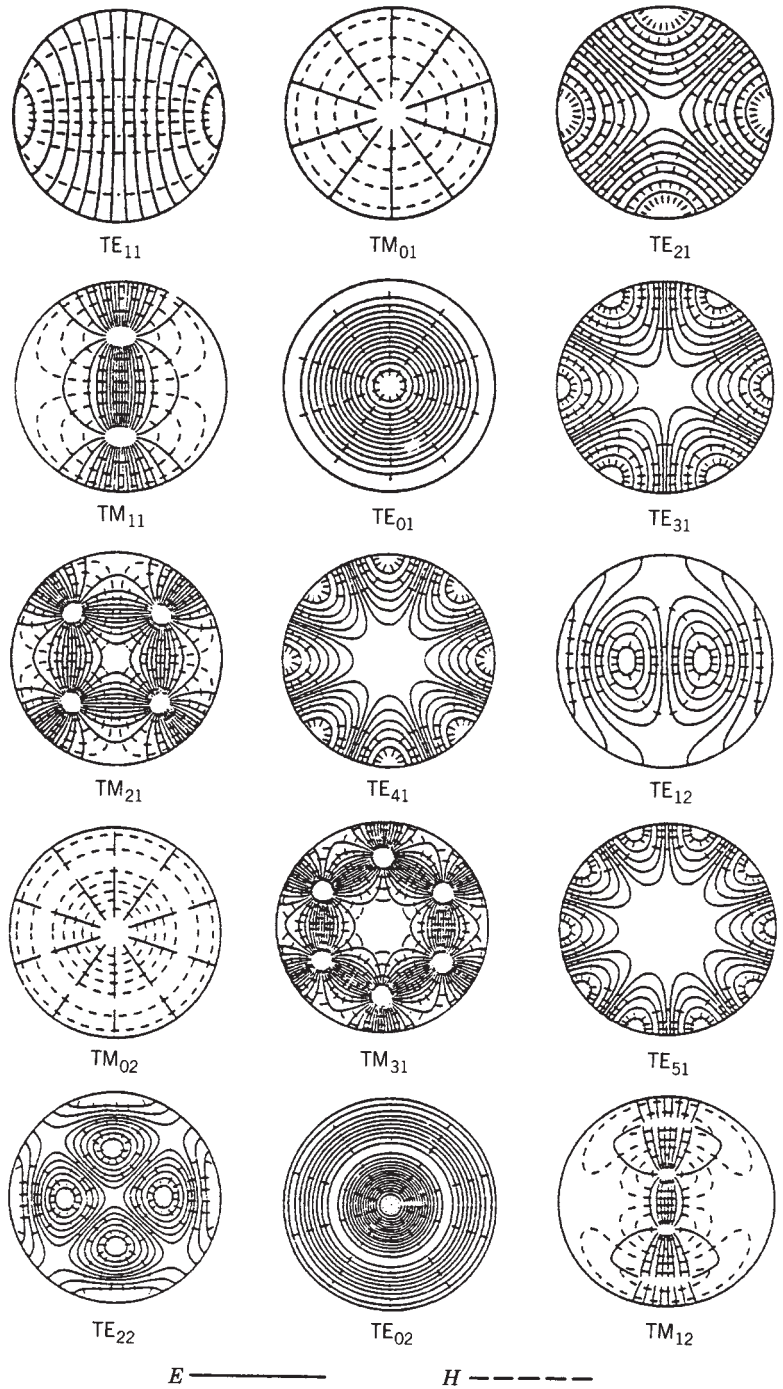


Figure 2. Field configurations of first 30 TE^z and/or TM^z modes in a circular waveguide. (Source: C. S. Lee, S. W. Lee, and S. L. Chuang, Plot of modal field distribution in rectangular and circular waveguides, *IEEE Trans. Microwave Theory Tech.*, © 1985, IEEE.)

With the aid of (28a)–(28c) the wave impedance of (31) reduces to

$$(Z_w^{+z})_{mn}^{TM} = \begin{cases} \frac{\beta \sqrt{1 - \left(\frac{f_c}{f}\right)^2}}{\omega \epsilon} = \sqrt{\frac{\mu}{\epsilon}} \sqrt{1 - \left(\frac{f_c}{f}\right)^2} = \eta \sqrt{1 - \left(\frac{f_c}{f}\right)^2} \\ \text{when } f > f_c = (f_c)_{mn} \end{cases} \quad (32a)$$

$$(Z_w^{+z})_{mn}^{TM} = \begin{cases} 0 \\ \frac{0}{\omega \epsilon} = 0 \end{cases} \text{ when } f = f_c = (f_c)_{mn} \quad (32b)$$

$$(Z_w^{+z})_{mn}^{TM} \left\{ \begin{aligned} \frac{-j\beta \sqrt{\left(\frac{f_c}{f}\right)^2 - 1}}{\omega \epsilon} &= -j\sqrt{\frac{\mu}{\epsilon}} \sqrt{\left(\frac{f_c}{f}\right)^2 - 1} \\ &= -j\eta \sqrt{\left(\frac{f_c}{f}\right)^2 - 1} \\ &\text{when } f < f_c = (f_c)_{mn} \end{aligned} \right. \quad (32c)$$

Examining (32a)–(32c) we can make the following statements about the wave impedance for the TM^z modes.

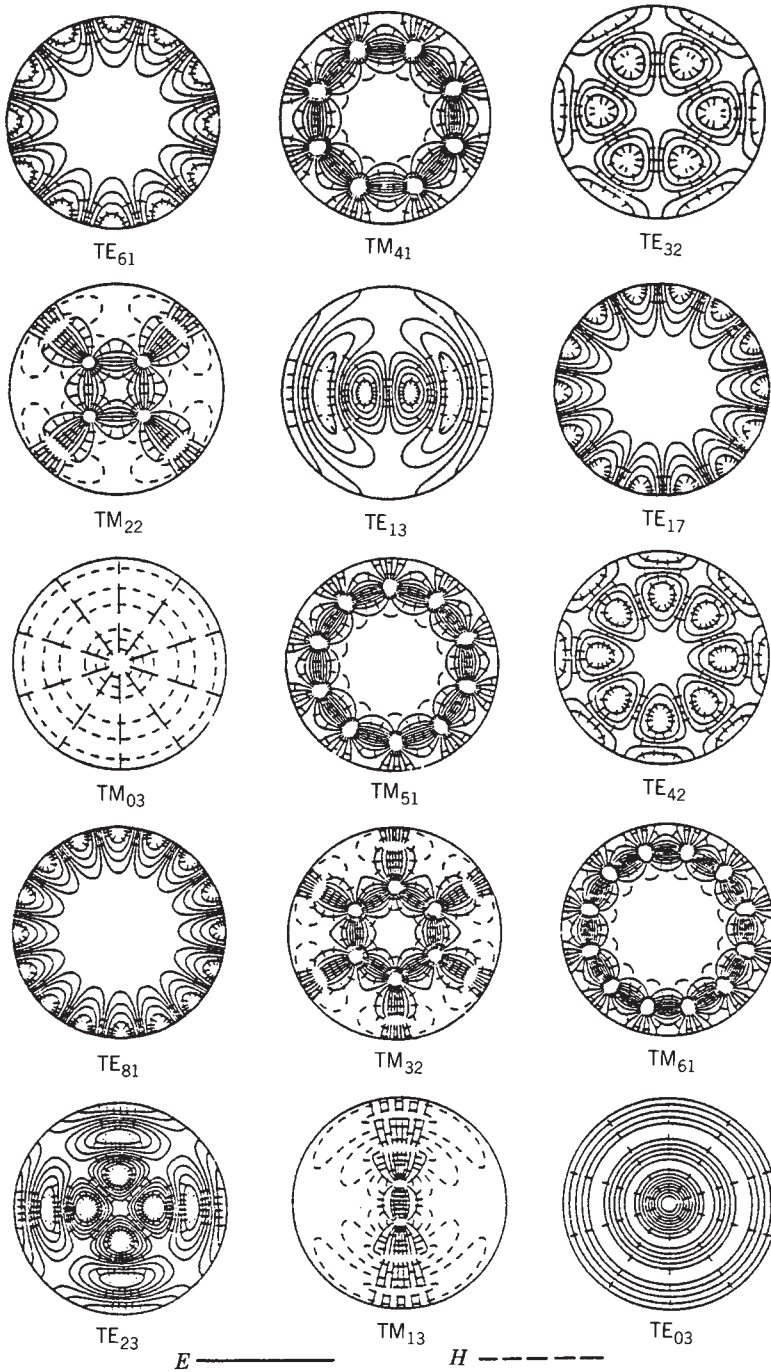


Figure 2. (Continued).

1. Above cutoff it is real and smaller than the intrinsic impedance of the medium inside the waveguide.
2. At cutoff it is zero.
3. Below cutoff it is imaginary and capacitive. This indicates that the waveguide below cutoff behaves as a capacitor that is an energy storage element.

Whenever a given mode is desired, it is necessary to design the proper feed to excite the fields within the waveguide and detect the energy associated with such modes. To maximize the energy exchange or transfer, this is accomplished by designing the feed, which is usually a probe

or antenna, so that its field pattern matches that of the field configuration of the desired mode. Usually the probe is placed near the maximum of the field pattern of the desired mode; however, that position may be varied somewhat in order to achieve some desired matching in the excitation and detection systems. Shown in Fig. 3 are suggested designs to excite and/or detect the TE_{11} and TM_{01} modes in a circular waveguide, to transition between the TE_{10} of a rectangular waveguide and the TE_{11} mode of a circular waveguide, and to couple between the TE_{10} of a rectangular waveguide and TM_{01} mode of a circular waveguide.

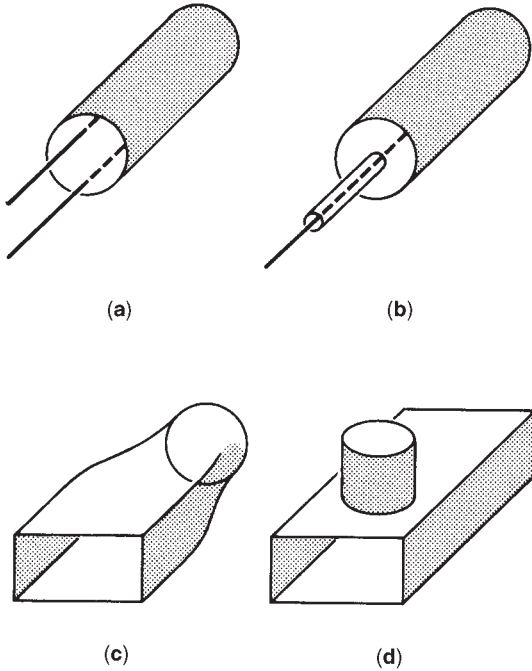


Figure 3. Excitation of TE_{mn} and TM_{mn} modes in a circular waveguide: (a) TE_{11} mode; (b) TM_{01} mode; (c) TE_{10} (rectangular)- TE_{11} (circular); (d) TE_{10} (rectangular)- TM_{01} (circular).

4. ATTENUATION FROM OHMIC LOSSES

It has been shown that the attenuation coefficients of the TE_{0n} ($n = 1, 2, \dots$) modes in a circular waveguide monotonically decrease as a function of frequency [2,3]. This is a very desirable characteristic, and because of this the excitation, propagation, and detection of TE_{0n} modes in a circular waveguide have received considerable attention. The attenuation coefficient for the TE_{mn}^z and TM_{mn}^z modes inside a circular waveguide are given, respectively, by

$$\begin{aligned}
 & TE_{mn}^z \\
 (\alpha_c)_{mn}^{TE^z} &= \frac{R_s}{a\eta \sqrt{1 - \left(\frac{f_c}{f}\right)^2}} \\
 & \times \left[\left(\frac{f_c}{f}\right)^2 + \frac{m^2}{(\gamma'_{mn})^2 - m^2} \right] \text{Np/m}
 \end{aligned} \tag{33a}$$

$$\begin{aligned}
 & TM_{mn}^z \\
 (\alpha_c)_{mn}^{TM^z} &= \frac{R_s}{a\eta} \frac{1}{\sqrt{1 - \left(\frac{f_c}{f}\right)^2}} \text{Np/m}
 \end{aligned} \tag{33b}$$

where

$$R_s = \sqrt{\frac{\omega\mu}{2\sigma}} \tag{34}$$

Plots of the attenuation coefficient versus the normalized frequency f/f_c , where f_c is the cutoff frequency of the dom-

inant TE_{11} mode, are shown for six modes in Fig. 4a and b for waveguide radii of 1.5 and 3 cm, respectively. Within the waveguide is free space and its walls are made of copper ($\sigma = 5.7 \times 10^7 \text{ S/m}$).

It is evident from the results of the preceding example that as f_c/f becomes smaller the attenuation coefficient decreases monotonically (as shown in Fig. 4), which is a desirable characteristic. It should be noted that similar monotonically decreasing variations in the attenuation coefficient are evident in all TE_{0n} modes ($n = 1, 2, 3, \dots$). According to (15a)–(15f), the only tangential magnetic field component to the conducting surface of the waveguide for all these TE_{0n} ($m = 0$) modes is the H_z component, while the electric field lines are circular. Therefore these modes are usually referred to as circular electric modes. For a constant power in the wave, the H_z component decreases as the frequency increases and approaches zero at infinite frequency. Simultaneously the current density and conductor losses on the waveguide walls also decrease and approach zero. Because of this attractive feature, these modes have received considerable attention for long-distance propagation of energy, especially at millimeter-wave frequencies. Typically attenuations as low as 1.25 dB/km (2 dB/mi) have been attained [2]. This is to be compared with attenuations of 120 dB/km for WR-90 copper rectangular waveguides, and 3 dB/km at $0.85 \mu\text{m}$, and less than 0.5 dB/km at $1.3 \mu\text{m}$ for fiberoptic cables.

Although the TE_{0n} modes are very attractive from the attenuation point of view, there are a number of problems associated with their excitation and retention. One of the problems is that the TE_{01} mode, which is the first of the TE_{0n} modes, is not the dominant mode. Therefore in order for this mode to be above its cutoff frequency and propagate in the waveguide, a number of other modes (such as the TE_{11} , TM_{01} , TE_{21} , and TM_{11}) with lower cutoff frequencies can also exist. Additional modes can also be present if the operating frequency is chosen well above the cutoff frequency of the TE_{01} mode in order to provide a margin of safety from being too close to its cutoff frequency.

To support the TE_{01} mode, the waveguide must be oversized and it can support a number of other modes. One of the problems faced with such a guide is how to excite the desired TE_{01} mode with sufficient purity and suppress the others. Another problem is how to prevent coupling between the TE_{01} mode and undesired modes. The presence of the undesired modes causes not only higher losses but also dispersion and attenuation distortion to the signal since each exhibits different phase velocities and attenuation. Irregularities in the inner geometry, surface, and direction (bends, nonuniform cross sections, etc.) of the waveguide are the main contributors to the coupling to the undesired modes. However, for the guide to be of any practical use, it must be able to sustain and propagate the desired TE_{01} and other TE_{0n} modes efficiently over bends of reasonable curvature. One technique that has been implemented to achieve this is to use mode conversion before entering the corner and another conversion when exiting to convert back to the desired TE_{0n} mode(s).

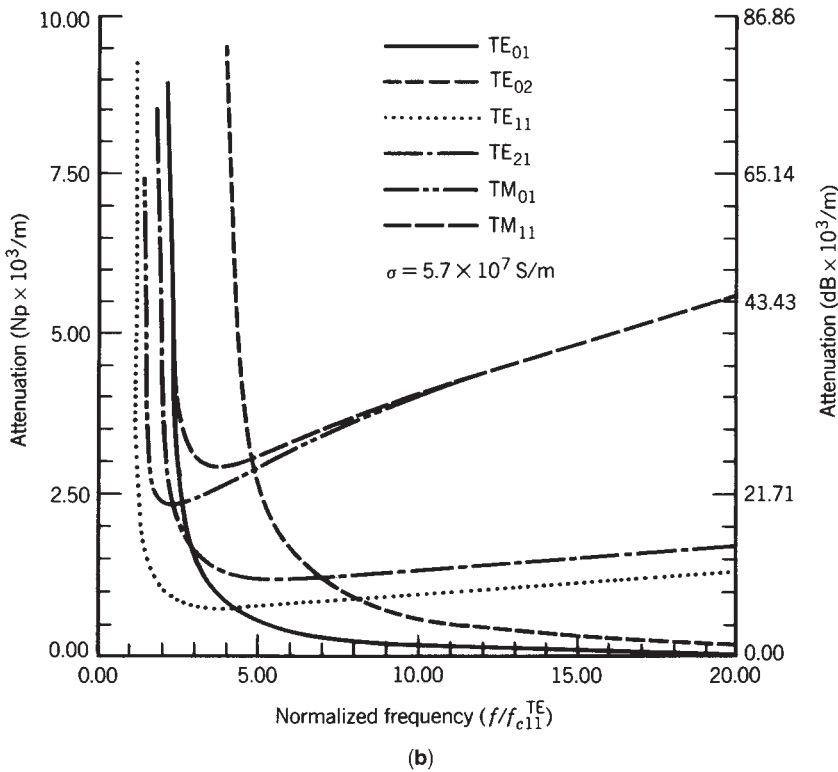
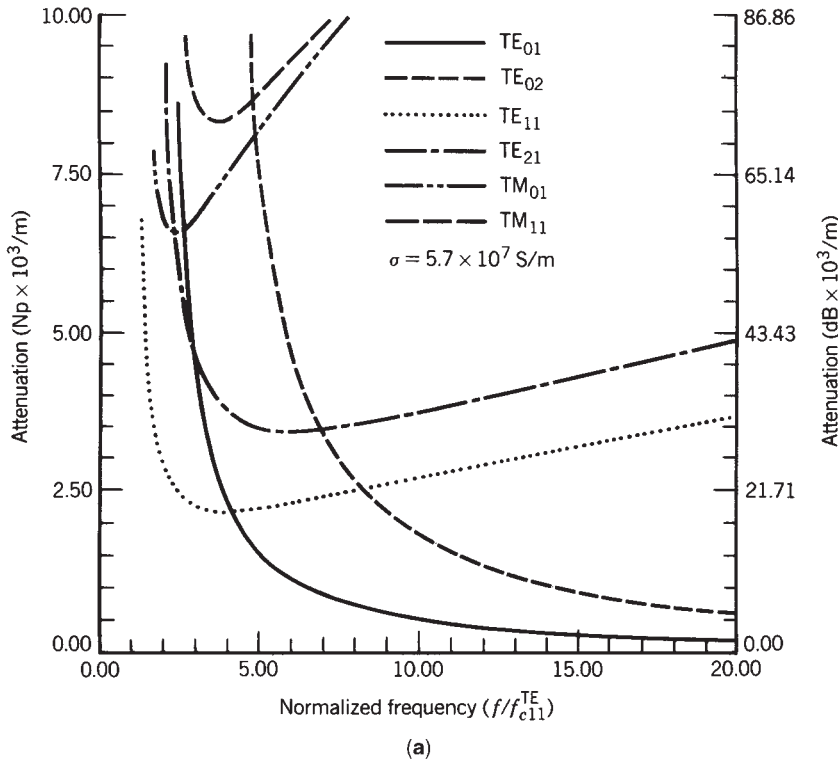


Figure 4. Attenuation for TE_{mn}^z and TM_{mn}^z modes in a circular waveguide: (a) $a = 1.5$ cm; (b) $a = 3$ cm.

Another method that has been used to discriminate against undesired modes and avoid coupling to them is to introduce filters inside the guide that cause negligible attenuation to the desired TE_{0n} mode(s). These filters introduce cuts that are perpendicular to the current paths of the undesired modes and parallel to the current direction

of the desired mode(s). Since the current path of the undesired modes is along the axis (z direction) of the guide and the path of the desired TE_{0n} modes is along the circumference (ϕ direction), a helical wound wire placed on the inside surface of the guide can serve as a filter that discourages any mode that requires an axial

Table 3. Summary of TE_{mn}^z and TM_{mn}^z Mode Characteristics of Circular Waveguide

	TE _{mn} ^z $\begin{pmatrix} m = 0, 1, 2, \dots \\ n = 1, 2, 3, \dots \end{pmatrix}$	TM _{mn} ^z $\begin{pmatrix} m = 0, 1, 2, 3, \dots \\ n = 1, 2, 3, 4, \dots \end{pmatrix}$
E_ρ^+	$-A_{mn} \frac{m}{\epsilon \rho} J_m(\beta_\rho \rho) [-C_2 \sin(m\phi) + D_2 \cos(m\phi)] e^{-j\beta_z z}$	$-B_{mn} \frac{\beta_\rho \beta_z}{\omega \mu \epsilon} J'_m(\beta_\rho \rho) [C_2 \cos(m\phi) + D_2 \sin(m\phi)] e^{-j\beta_z z}$
E_ϕ^+	$A_{mn} \frac{\beta_\rho}{\epsilon} J'_m(\beta_\rho \rho) [C_2 \cos(m\phi) + D_2 \sin(m\phi)] e^{-j\beta_z z}$	$-B_{mn} \frac{m \beta_z}{\omega \mu \epsilon \rho} J_m(\beta_\rho \rho) [-C_2 \sin(m\phi) + D_2 \cos(m\phi)] e^{-j\beta_z z}$
E_z^+	0	$-j B_{mn} \frac{\beta_\rho^2}{\omega \mu \epsilon} J_m(\beta_\rho \rho) [C_2 \cos(m\phi) + D_2 \sin(m\phi)] e^{-j\beta_z z}$
H_ρ^+	$-A_{mn} \frac{\beta_\rho \beta_z}{\omega \mu \epsilon} J_m(\beta_\rho \rho) [C_2 \cos(m\phi) + D_2 \sin(m\phi)] e^{-j\beta_z z}$	$B_{mn} \frac{m}{\mu \rho} J_m(\beta_\rho \rho) [-C_2 \cos(m\phi) + D_2 \sin(m\phi)] e^{-j\beta_z z}$
H_ϕ^+	$-A_{mn} \frac{m \beta_z}{\omega \mu \epsilon} \frac{1}{\rho} J_m(\beta_\rho \rho) [-C_2 \sin(m\phi) + D_2 \cos(m\phi)] e^{-j\beta_z z}$	$-B_{mn} \frac{\beta_\rho}{\mu} J'_m(\beta_\rho \rho) [-C_2 \cos(m\phi) + D_2 \sin(m\phi)] e^{-j\beta_z z}$
H_z^+	$-j A_{mn} \frac{\beta_\rho^2}{\omega \mu \epsilon} J_m(\beta_\rho \rho) [C_2 \cos(m\phi) + D_2 \sin(m\phi)] e^{-j\beta_z z}$	0
$\beta_c = \beta_\rho$	$\frac{\gamma'_{mn}}{a}$	$\frac{\gamma_{mn}}{a}$
f_c	$\frac{\gamma'_{mn}}{2\pi a \sqrt{\mu \epsilon}}$	$\frac{\gamma_{mn}}{2\pi a \sqrt{\mu \epsilon}}$
λ_c	$\frac{2\pi a}{\gamma'_{mn}}$	$\frac{2\pi a}{\gamma_{mn}}$
$\beta_z (f \geq f_c)$		$\beta \sqrt{1 - \left(\frac{f_c}{f}\right)^2} = \beta \sqrt{1 - \left(\frac{\lambda}{\lambda_c}\right)^2}$
$\lambda_g (f \geq f_c)$		$\frac{\lambda}{\sqrt{1 - \left(\frac{f_c}{f}\right)^2}} = \frac{\lambda}{\sqrt{1 - \left(\frac{\lambda}{\lambda_c}\right)^2}}$
$v_p (f \geq f_c)$		$\frac{v}{\sqrt{1 - \left(\frac{f_c}{f}\right)^2}} = \frac{v}{\sqrt{1 - \left(\frac{\lambda}{\lambda_c}\right)^2}}$
$Z_w (f \geq f_c)$	$\frac{\eta}{\sqrt{1 - \left(\frac{f_c}{f}\right)^2}} = \frac{\eta}{\sqrt{1 - \left(\frac{\lambda}{\lambda_c}\right)^2}}$	$\eta \sqrt{1 - \left(\frac{f_c}{f}\right)^2} = \eta \sqrt{1 - \left(\frac{\lambda}{\lambda_c}\right)^2}$
$Z_w (f \leq f_c)$	$j \frac{\eta}{\sqrt{\left(\frac{f_c}{f}\right)^2 - 1}} = j \frac{\eta}{\sqrt{\left(\frac{\lambda}{\lambda_c}\right)^2 - 1}}$	$-j \eta \sqrt{\left(\frac{f_c}{f}\right)^2 - 1} = -j \eta \sqrt{\left(\frac{\lambda}{\lambda_c}\right)^2 - 1}$
α_c	$\frac{R_s}{a \eta \sqrt{1 - \left(\frac{f_c}{f}\right)^2}} \left[\left(\frac{f_c}{f}\right)^2 + \frac{m^2}{(\gamma'_{mn})^2 - m^2} \right]$	$\frac{R_s}{a \eta} \frac{1}{\sqrt{1 - \left(\frac{f_c}{f}\right)^2}}$

component of current flow but propagates the desired TE_{0n} modes [3,4].

Another means to suppress undesired modes is to introduce within the guide very thin baffles of lossy material that will act as attenuating sheets. The surfaces of the baffles are placed in the radial direction of the guide so that they are parallel to the E_ρ and E_z components of the undesired modes (which will be damped) and normal to the E_φ component of the TE_{0n} modes that will remain unaffected. Typically two baffles are placed in a crossed pattern over the cross section of the guide.

A summary of the pertinent characteristics of the TE_{mn}^z and TM_{mn}^z modes of a circular waveguide are found listed in Table 3.

BIBLIOGRAPHY

1. C. S. Lee, S. W. Lee, and S. L. Chuang, Plot of modal field distribution in rectangular and circular waveguides, *IEEE Trans. Microwave Theory Tech.* **MTT-33**(3):271-274 (March 1985).
2. S. E. Miller, Waveguide as a communication medium, *Bell Syst. Tech. J.* **33**:1209-1265 (Nov. 1954).

3. S. P. Morgan and J. A. Young, Helix waveguide, *Bell Syst. Tech. J.* **35**:1347-1384 (Nov. 1956).
4. S. Ramo, J. R. Whinnery, and T. Van Duzer, *Fields and Waves in Communication Electronics*, Wiley, New York, 1965, pp. 429-439.

open-ended configuration, impedance steps, capacitive windows, T junctions, small elliptical and circular apertures, aperture coupling between two coaxial lines, and bifurcation of a coaxial line. The configurations and the equivalent circuits for some of the discontinuities are shown in Fig. 1. The mode-matching technique with variational formulation is the commonly used approach to arrive at the equivalent-circuit parameters of discontinuities. The available results for some of these discontinuities are summarized in the following sections.

COAXIAL LINE DISCONTINUITIES

R. GARG
 Indian Institute of Technology
 Kharagpur
 Kharagpur, India

Various types of coaxial-line discontinuities have been discussed in the literature [1-4], including: capacitive gaps,

1. CAPACITIVE GAPS IN COAXIAL LINES

A gap in the center conductor of a coaxial line, as shown in Fig. 1a, introduces mainly a series capacitance in the line. This type of discontinuity finds common use in microwave filters, DC blocks, and coaxial-line reentrant cavity.

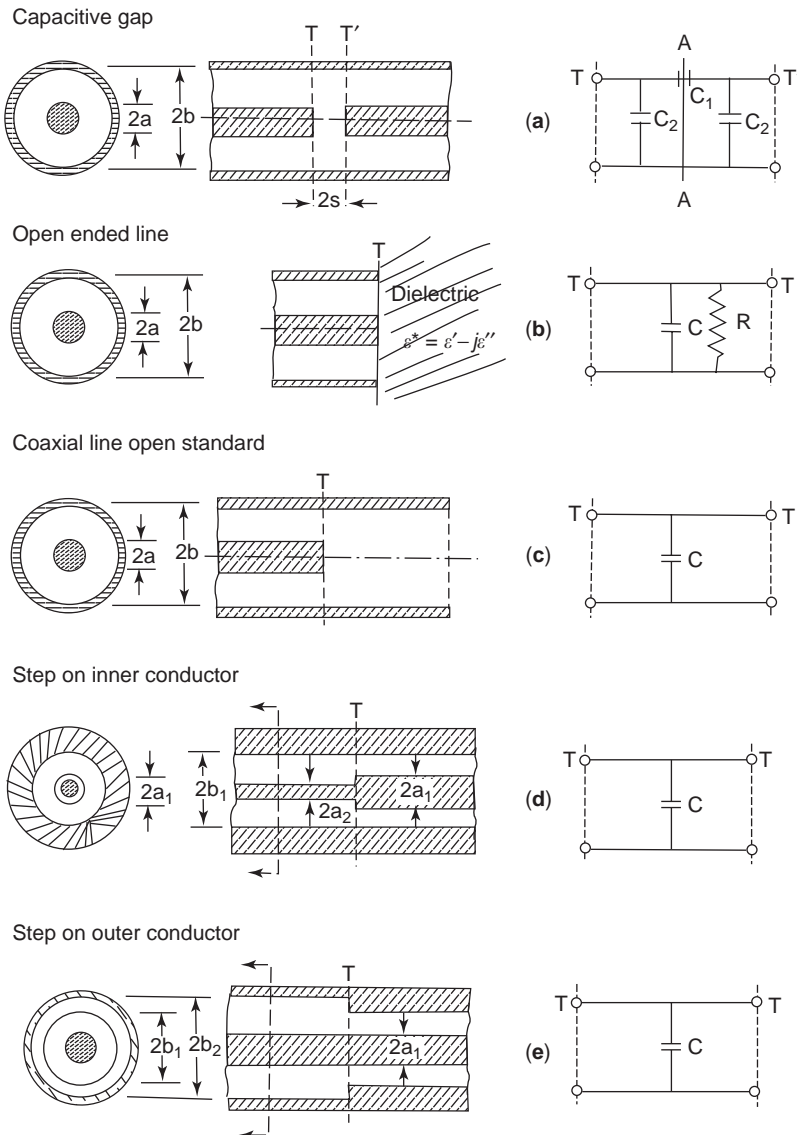


Figure 1. Discontinuities in coaxial lines and their equivalent circuits.

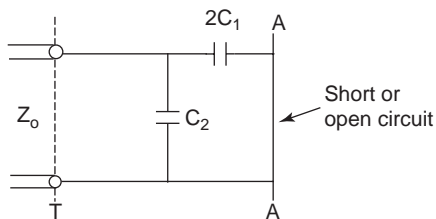


Figure 2. Equivalent circuit for the evaluation of capacitive gap discontinuities.

If the gap width is small compared to the wavelength, the problem can be treated electrostatically and the equivalent circuit of the gap discontinuity may be formulated as shown in Fig. 1a. For the purpose of analysis, the equivalent circuit may be written as shown in Fig. 2. The series and shunt capacitances are determined by computing three capacitances: total capacitances of a length of line (1) with a short circuit at plane AA, (2) with an open circuit at the plane AA, and (3) with no discontinuity. The section of line must be sufficiently long to ensure that an undisturbed field distribution is obtained at the end located away from the discontinuity. This condition is fulfilled if the linelength is equal to or greater than the diameter of the outer conductor. Numerical results for various gap widths and diameter ratios are given in Table 1 [3].

Gap capacitances for diameter ratios 5-1 and 7-1 are also given in Refs. 3 and 4. The values of capacitances C_1 and C_2 of Table 1 can also be utilized to determine capacitances for the open-end configuration and for the configuration shown in Fig. 3. The open-end capacitance is given by C_2 when $s \rightarrow \infty$. The capacitance with the short-circuiting plane at a distance s from the inner conductor is C , and is given by $(2C_1 + C_2)$. A closed-form expression for the capacitance C is written as follows [3,4]:

$$C = \frac{\pi a^2 \epsilon_0 \epsilon_r}{s} + 4a \epsilon_0 \epsilon_r \ln \left(\frac{b-a}{s} \right) \quad (1)$$

This equation is valid under the condition $\lambda_0 \gg (b-a) \gg s$. The first term in (1) is the parallel-plate capacitance between the face of the inner conductor and the short-circuiting plane. The second term is the fringing capacitance.

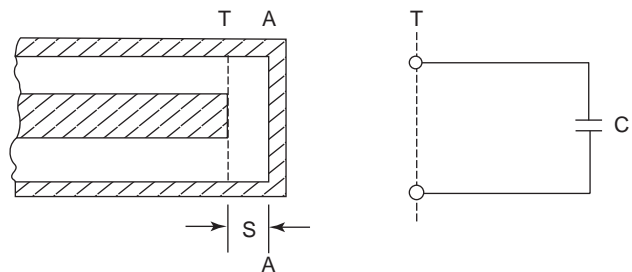


Figure 3. Coaxial line with short circuit (coaxial-line reentrant cavity) and its equivalent circuit.

It may be observed from Table 1 that C_2 approaches zero for vanishingly small gap width and therefore, the series capacitance C_1 is dominant in (1). As gap width increases, C_2 increases linearly but the decrease in C_1 is faster. Expression (1) is accurate to within 5% for small gaps ($s/a < 0.1$). For a 50-Ω line the error is less than 1.5%.

Variational analysis of the geometry of Fig. 2 shows that the capacitances C_1 and C_2 increase with frequency [5]. Variation of these capacitances with normalized frequency $k_0 b$ is shown in Fig. 4 for $s/a = 0.25$ and 0.025 in a 50-Ω line [5]. It is seen that while the shunt capacitance C_2 increases very slowly (almost negligibly) with frequency, the series capacitance C_1 increases much more rapidly and shows a sharp increase near the cutoff frequency of cylindrical waveguide TM_{01} mode. Variational analysis of a gap in the central conductor of a rectangular coaxial line has been reported [6]. The behavior of gap capacitances with gap width and frequency is similar to that in a cylindrical coaxial line. The gap capacitance in the coaxial line can also be described in terms of the associated reflection coefficient Γ . Eom et al. have used the mode-matching method to determine Γ for a coaxial line terminated in a gap [7]. A rapidly converging series for Γ has been obtained. The effect of dielectric inhomogeneity in the gap has been included.

2. OPEN-ENDED COAXIAL LINE

The schematic of an open-ended coaxial line with an infinite flange and its equivalent circuit are shown in Fig. 1b. The equivalent circuit consists of a parallel combination

Table 1. Capacitances C_1 and C_2 of Equivalent Circuit of Fig. 1a for Gaps in Coaxial Lines (pF/2πb, b in cm)

Gap Ratio (s/b)	Diameter Ratio (b : a)											
	10:9		4:3		5:3		2:1		2.3:1		3:1	
	C_1	C_2	C_1	C_2	C_1	C_2	C_1	C_2	C_1	C_2	C_1	C_2
0.05	0.367	0.0354	0.275	0.0143	0.188	0.0082	0.138	0.0061	0.109	0.00509	0.0702	0.0039
0.075	0.238	0.0486	0.183	0.0206	0.127	0.0120	0.0946	0.0089	0.0757	0.00746	0.0498	0.0057
0.100	0.173	0.0598	0.136	0.0265	0.0960	0.0156	0.0719	0.0116	0.0578	0.00972	0.0384	0.0074
0.150	0.106	0.0767	0.0858	0.0366	0.0623	0.0221	0.0474	0.0166	0.0384	0.0139	0.0259	0.0105
0.200	0.0718	0.0890	0.0598	0.0450	0.0443	0.0277	0.0340	0.0210	0.0277	0.0176	0.0188	0.0133
0.250	0.0516	0.0985	0.0436	0.0520	0.0328	0.0327	0.0254	0.0248	0.0217	0.0208	0.0143	0.0157
0.300	0.0383	0.1060	0.0328	0.0579	0.0249	0.0369	0.0194	0.0281	0.0161	0.0235	0.0109	0.0178

Source: Table 6 of H. E. Green, The numerical solution of some important transmission line problems, *IEEE Trans. Microwave Theory Tech.* MTT-13:676-692 (Sept. 1965) (© 1965 IEEE).

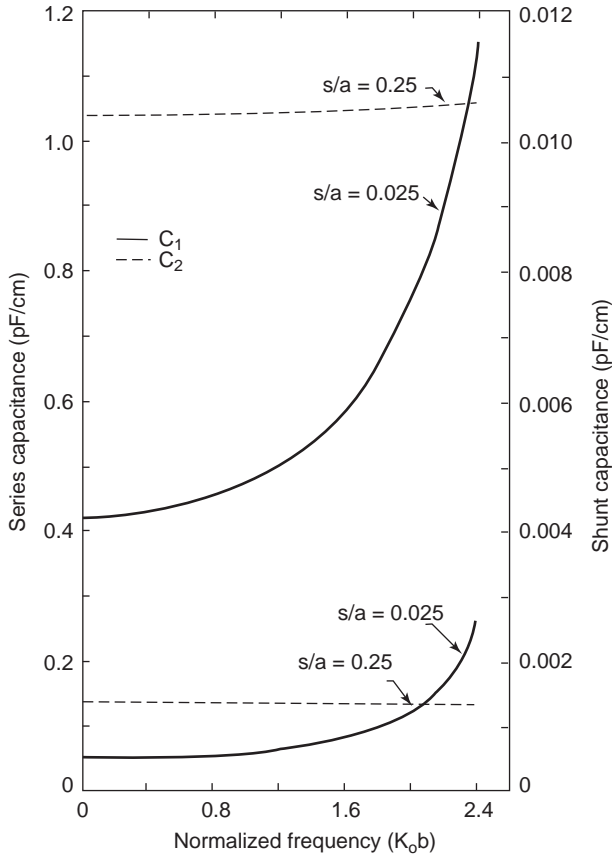


Figure 4. Frequency dependence of gap discontinuities of Fig. 2. [From Figure 3 of S. Sen and P. K. Saha, Equivalent circuit of a gap in the central conductor of a coaxial line, *IEEE Trans. Microwave Theory Tech.* **MTT-30**:2026–2029 (Nov. 1982) (© 1982 IEEE).]

of a capacitor C and a resistor R at the flange. The capacitance C arises from the fringing electric field between the center conductor and outer conductor of the coaxial line. The shunt resistance R represents the power loss due to radiation from the open end. Quasistatic analysis of the open-ended coaxial line has been described [8]. The aperture admittance at the flange may be written as [8]

$$Y_L = G_r + jB \quad (2)$$

where $G_r = 1/R$ and $B = \omega C$ and

$$B = \frac{2\omega\epsilon^*}{[\ln(b/a)]^2} \left[I_1 - \frac{k^2 I_2}{2} \right] \quad (3)$$

$$G_r = \frac{k^3 \pi \omega \epsilon^*}{12} \left[\frac{b^2 - a^2}{\ln(b/a)} \right]^2 \quad (4)$$

$$k^2 = \omega^2 \mu_0 \epsilon^*$$

where $\epsilon^* = \epsilon' - j\epsilon''$ represents the terminating medium at the flange. The coefficients I_1 and I_2 are defined as

Table 2. Value of Integrals I_1 and I_2 for a Few Coaxial Lines

Line (mm)	b (cm)	a (cm)	$I_1 (\times 10^{-3})$	$I_2 (\times 10^{-9})$
14 (air)	0.7145	0.3102	5.88293048	-103.784060
7 (air)	0.35	0.1520	2.88055348	-12.194870
8.3 (Teflon)	0.362	0.1124	4.21373732	-17.5606001
6.4 (Teflon)	0.2655	0.0824	3.09155881	-6.92967372
3.6 (Teflon)	0.1499	0.0455	1.77531131	-1.2618826
2.2 (Teflon)	0.0838	0.0255	0.99058927	-0.22018405

Source: Table 1 of D. K. Misra, A quasi-static analysis of open-ended coaxial lines, *IEEE Trans. Microwave Theory Tech.* **MTT-35**:925–928 (Oct. 1987) (© 1987 IEEE).

follows:

$$I_1 = \int_a^b \int_a^b \int_0^\pi \frac{\cos \phi'}{(\rho^2 + \rho'^2 - 2\rho\rho' \cos \phi')^{1/2}} \times d\phi' d\rho' d\rho \quad (5a)$$

$$I_2 = \int_a^b \int_a^b \int_0^\pi \cos \phi' (\rho^2 + \rho'^2 - 2\rho\rho' \cos \phi')^{1/2} \times d\phi' d\rho' d\rho \quad (5b)$$

Computed values of integrals I_1 and I_2 for a few commercially available coaxial lines are given in Table 2 [8].

It may be pointed out that the first term in (3) describes the upper bound for the static capacitance of the opening, while the second term gives the frequency-dependent part of the capacitance. Comparison with the data based on finite-element method (FEM) or method-of-moment (MoM) analysis shows good agreement [8].

Using the values of I_1 and I_2 from Table 2, the following expressions for the capacitance C may be derived from (3):

For a 3.6-mm Teflon-filled coaxial line in free space (f in MHz):

$$C(\text{pF}) = 0.0221 + 0.3453 \times 10^{-11} f^2 \quad (6a)$$

For a 6.4-mm Teflon-filled coaxial line in free space (f in MHz):

$$C(\text{pF}) = 0.03999 + 1.9687 \times 10^{-11} f^2 \quad (6b)$$

An open-ended coaxial line exciting a monopole probe (Fig. 5) has been used for permittivity measurements of biological materials. The biological tissues consist essentially of water; free ions such as Na^+ , K^+ , Ca^{2+} , Cl^- ; and a number of proteins. This composition makes the dielectric properties of the tissues similar to those of saline solutions, which are characterized by a high loss factor at microwave frequencies. The probe is used as a sensor for permittivity measurements. The sensor is placed in

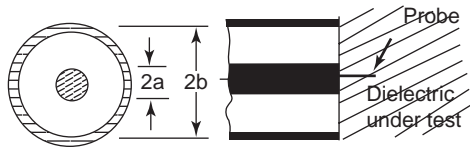


Figure 5. Coaxial-line-excited monopole probe for permittivity measurement.

contact with the material under test, and the reflection coefficient Γ is measured. Knowledge of the relationship between the measured Γ and the permittivity ϵ then allows one to determine the latter. A number of models have been developed to determine ϵ , including the capacitive model, the antenna model, the equivalent transmission-line model, and the rational function model. A comparative study of these models for a lossy material is available in Ref. 9, where it is concluded that the equivalent transmission-line model for biological tissue characterization is adequate.

3. REFLECTION STANDARD FOR COAXIAL LINES

A short-circuited coaxial line can be used as a reflection standard only at one frequency for which it is a quarter-wave long. However, an open-circuited coaxial line with extended outer conductor as shown in Fig. 1c, can be used as a broadband reflection standard with minimal losses. Also, this reflection standard can be fabricated easily using commercially available components. Variational analysis of this device has been reported elsewhere in the literature [2,10–12]. If the coaxial line/circular waveguide combination is operated below the cutoff frequency of the dominant mode in circular waveguide, the signal will get attenuated in the waveguide. In addition, if the waveguide is sufficiently long to attenuate the signal by ~ 50 dB, the radiation from the waveguide will be negligible. Therefore, the coaxial line/waveguide junction will be capacitive in nature. Bianco et al. [12] have computed the junction capacitance. The variation of junction capacitance with frequency for a 50- Ω 7-mm airline ($2b = 7$ mm, $\epsilon_r = 1.000640$) is given by the following expression [12]

$$C = \frac{C(0)}{(1 - (f_{\text{MHz}}/34450)^2)^{1/2}} \quad (7)$$

where $C(0)$ is the static capacitance and is 79.70 fF for the 7-mm line.

4. STEPS IN COAXIAL LINES

The step in a coaxial line can be due to (1) an abrupt change in the diameter of either the inner conductor (Fig. 1d) or the outer conductor (Fig. 1e) or (2) a simultaneous change in diameters of both the conductors. In other words, the step discontinuity may arise when two coaxial lines with different characteristic impedances are connected in cascade. Here, a_1 and b_1 are the radii of the inner and

outer conductors of one coaxial line and a_2 and b_2 represent the same for the other coaxial line. The step discontinuity may also result when a coaxial line is butt-terminated in a connector with the same impedance. The equivalent circuit of a step can be described by a shunt capacitance at the plane of the step as shown in Figs. 1d and 1e. The capacitance does not vary appreciably with frequency if the cross-sectional dimensions of the line at the plane of discontinuity are small fractions of the wavelength.

Discontinuity capacitance can be computed using the mode-matching technique for determining the difference in capacitances between that of the structure with the discontinuity, and that computed by adding the contributions of two single unperturbed lines with cross-sectional dimensions and lengths equal to the actual lines on each side of the step. The lines may be terminated by magnetic walls after a distance equal to one diameter on each side of the step. This technique has been used in Refs. 1 and 13. Gogioso et al. [14] have used the variational method to calculate the discontinuity capacitance. FEM has been used in Ref. 15 to analyze the double-step discontinuity; computed results for a butt transition between a coaxial line and a 7-mm precision connector are presented there.

Somlo [13] has obtained closed-form expressions for the discontinuity capacitance:

Step on the inner conductor (i.e., $b_1 = b_2 = b$; Fig. 1d):

$$\frac{C}{2\pi b} \text{ (F/m)} = \frac{\epsilon}{\pi} \left[\frac{\alpha^2 + 1}{\alpha} \ln \frac{1 + \alpha}{1 - \alpha} - 2 \ln \frac{4\alpha}{1 - \alpha^2} \right] + 1.11 \times 10^{-15} (1 - \alpha)(\tau - 1) \quad (8)$$

where $\alpha = (b - a_2)/(b - a_1)$ and $\tau = (b/a_1)$. The maximum error in (8) is ± 30 fF/m for $0.01 \leq \alpha \leq 1.0$ and $1.0 < \tau \leq 6.0$. In the limiting case when $a_1 \rightarrow 0$, $\tau \rightarrow \infty$, an expression for the step discontinuity obtained from Fig. 1 of Ref. 13 is given as follows:

$$\frac{C}{2\pi b} \text{ (F/m)} = \frac{2\epsilon}{\pi} (1.477 - \ln 4\alpha) \quad (9)$$

where $\alpha = (b - a)/b$. Equation (9) may be used to determine $C(0)$ for (7) [e.g., one obtains $C(0) = 80.7$ fF for 50- Ω 7-mm airline; this compares favorably with the computed value of 79.7 fF].

Step on the outer conductor (i.e., $a_1 = a_2 = a$; Fig. 1e):

$$\frac{C}{2\pi a} \text{ (F/m)} = \frac{\epsilon}{\pi} \left[\frac{\alpha^2 + 1}{\alpha} \ln \frac{1 + \alpha}{1 - \alpha} - 2 \ln \frac{4\alpha}{1 - \alpha^2} \right] + 4.12 \times 10^{-15} (0.8 - \alpha)(\tau - 1.4) \quad (10)$$

where $\alpha = (b_1 - a)/(b_2 - a)$ and $\tau = (b_2/a)$. The maximum error in (10) is ± 60 fF/m for $0.01 \leq \alpha \leq 0.7$ and $1.5 \leq \tau \leq 6.0$. The stepsize decreases as α increases from 0 to 1. For simultaneous steps in both the conductors, the discontinuity capacitance can be determined approximately from the discontinuity capacitances associated with step in either (inner or outer) conductor [3,4].

The frequency dependence of step capacitance has been included in Ref. 13 through a multiplier factor K that has been plotted for five different combinations of α and τ . This plot is included here as Fig. 6. The S matrix for a step discontinuity in the inner conductor of rectangular coaxial lines has been described by Xu et al. [16]. The mode-matching method in conjunction with FEM has been employed to improve accuracy and efficiency.

5. T JUNCTION OR STUB IN COAXIAL LINES

The configuration of a T junction and its equivalent circuit are shown in Fig. 7. The branchline can be viewed as a shunt circuit in parallel with the mainline. Experimental results for a specific set of parameters are available for $\lambda_0 = 10$ cm [17]. The T junction finds application in branchline couplers, filters, and other components and has been analyzed in a rectangular coaxial line [16] using mode matching, and FEM techniques. The analysis has been extended to a branchline directional coupler.

Other types of discontinuity in coaxial lines that occur less frequently, such as capacitive windows in a coaxial line, aperture coupling between two coaxial lines, bifurcation of a coaxial line, small elliptical and circular apertures in the outer conductor, and a coaxial line with infinite central conductor, are discussed in Ref. 1.

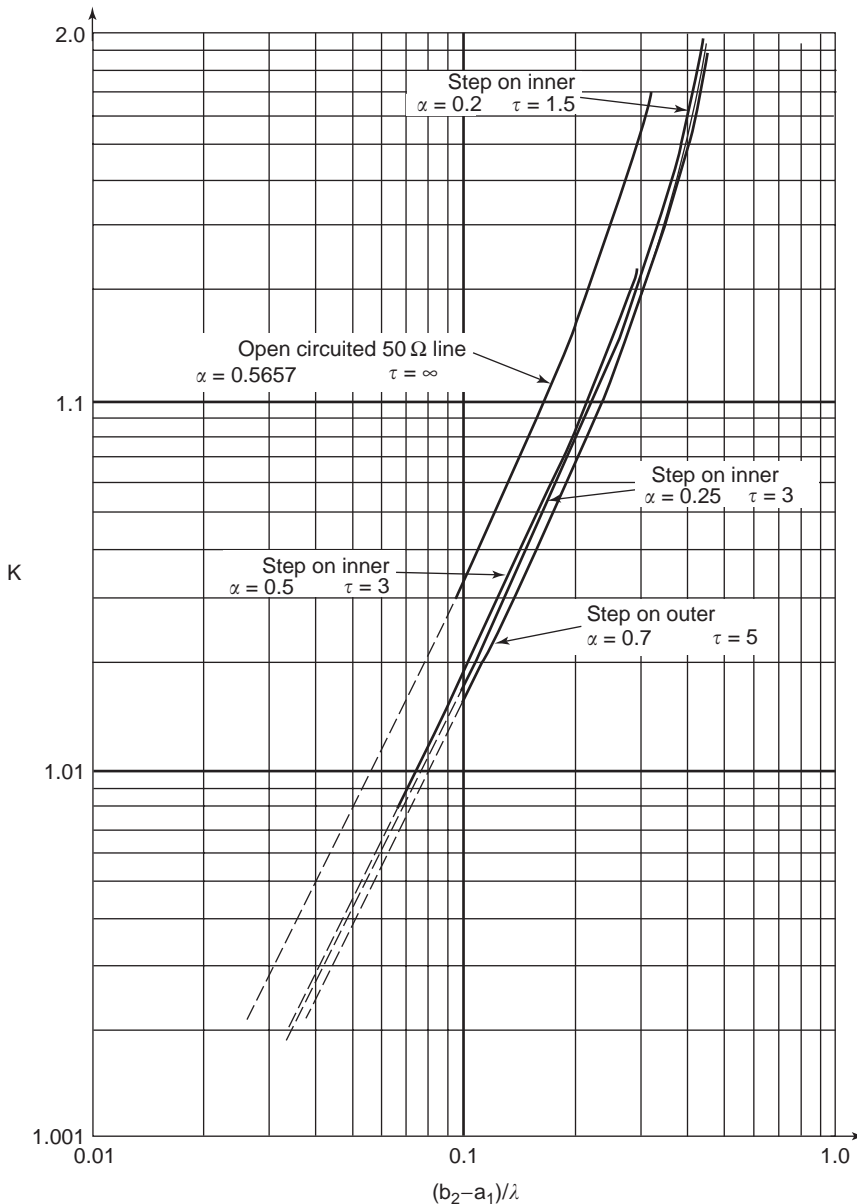


Figure 6. Frequency correction factor K for step capacitance versus $(b_2 - a_1)/\lambda$. [From Figure 3 of P. I. Somlo, Computation of coaxial-line step capacitance, *IEEE Trans. Microwave Theory Tech.* **MTT-15**:48-53 (Jan. 1967) (© 1982 IEEE).]

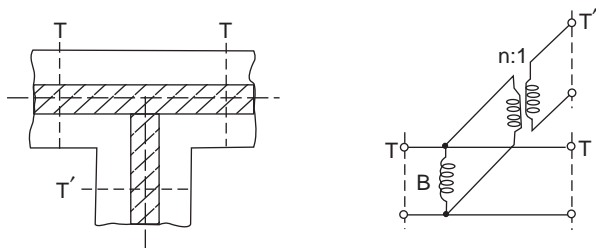


Figure 7. T junction and its equivalent circuit.

BIBLIOGRAPHY

- N. Marcuvitz, ed., *Waveguide Handbook*, Peter Peregrinus, London, 1986.
- J. R. Whinnery, H. W. Jamieson, and T. E. Robbins, Coaxial line discontinuities, *Proc. IRE* **32**:695–709 (Nov. 1944).
- H. E. Green, The numerical solution of some important transmission line problems, *IEEE Trans. Microwave Theory Tech.* **MTT-13**:676–692 (Sept. 1965).
- H. E. Green, The numerical solution of transmission line problems, in L. Young, ed., *Advances in Microwaves*, Vol. 2, Academic Press, New York, 1967, pp. 327–393.
- S. Sen and P. K. Saha, Equivalent circuit of a gap in the central conductor of a coaxial line, *IEEE Trans. Microwave Theory Tech.* **MTT-30**:2026–2029 (Nov. 1982).
- S. Chattopadhyay and P. K. Saha, Variational analysis of a gap in the central conductor of a rectangular coaxial line, *IEEE Trans. Microwave Theory Tech.* **47**:246–249 (Feb. 1999).
- H. J. Eom, Y. C. Noh, and J. K. Park, Scattering analysis of a coaxial line terminated by a gap, *IEEE Microwave Guided Wave Lett.* **8**:218–219 (June 1998).
- D. K. Misra, A quasi-static analysis of open-ended coaxial lines, *IEEE Trans. Microwave Theory Tech.* **MTT-35**:925–928 (Oct. 1987).
- D. Berube, F. M. Ghannouchi, and P. Savard, A comparative study of four open-ended coaxial probe models for permittivity measurements of lossy dielectric/biological materials at microwave frequencies, *IEEE Trans. Microwave Theory Tech.* **44**:1928–1934 (Dec. 1996).
- E. W. Risley, Jr., Discontinuity capacitance of a coaxial line terminated in a circular waveguide, *IEEE Trans. Microwave Theory Tech.* **MTT-17**:86–92 (Feb. 1969).
- E. W. Risley, Jr., Discontinuity capacitance of a coaxial line terminated in a circular waveguide: Part II—Lower bound solution, *IEEE Trans. Microwave Theory Tech.* **MTT-21**:564–566 (Aug. 1973).
- B. Bianco, A. Cosana, L. Gogioso, S. Ridella, and M. Parodi, Open-circuited coaxial lines as standards for microwave measurements, *Electron. Lett.* **16**:373–374 (May 8, 1980).
- P. I. Somlo, Computation of coaxial-line step capacitance, *IEEE Trans. Microwave Theory Tech.* **MTT-15**:48–53 (Jan. 1967).
- L. Gogioso, M. Marchesi, and M. Parodi, A variational approach to compute the equivalent capacitance of coaxial line discontinuities, *Proc. Int. Microwave Symp.* 1979, pp. 580–583.
- E. Marouby, M. Aubourg, and P. Guillon, Application of the finite element method to the design of transitions between coaxial lines, *IEE Proc. H* **137**:219–225 (Aug. 1990).
- S. Xu, X. Wu, W. Guo, and Z. Li, Scattering characteristics of rectangular coaxial line discontinuities, *IEE Proc. Microwave Anten. Propag.* **142**:257–264 (June 1995).
- C. G. Montgomery, R. H. Dicke, and E. M. Purcell, eds., *Principles of Microwave Circuits*, Peter Peregrinus, London, 1987, Sect. 9.6, p. 295.

COAXIAL LINES AND WAVEGUIDES

NEMAI CHANDRA KARMAKAR
Monash University
Clayton, Victoria, Australia
SHANTANU KUMAR PADHI
University of Queensland
St. Lucia, Queensland, Australia

1. INTRODUCTION

Starting with Maxwell's theoretical concept of wave propagation in the 1870s, followed by Heinrich Hertz' experimental proof of the transmission of electromagnetic wave energy in the 1890s, RF-microwave technologies saw extraordinary advances during the nineteenth and twentieth centuries. Progress in this field, particularly its application in high-frequency wired and wireless communications technology, has hinged most critically on the efficient transmission and reception of electromagnetic energy through various media. Without carefully designed transmission lines, RF and microwave technologies could not have undergone further development and modern civilization could certainly not have reached the present "information age." In everything from a handheld GPS receiver to a jumbo jet, transmission-line design is of crucial importance to proper operation. The sheer diversity of RF-microwave devices available today means that RF-microwave designers must spend most of their time tuning transmission lines, matching various sections, and designing controlled attenuation to other parts of the system. For example, while a mobile phone consists of high-frequency microstrip transmission lines in planar multilayered circuits, a jumbo jet has 275 km of cables of various forms, including low-frequency lighting, high-frequency navigation tools, and wireless terrestrial and satellite navigation and communication equipment. Just as High-frequency devices and gadgets such as radios, television sets, satellite ground stations, and satellite payloads are useless without efficient transmission lines, adapters, and assemblies in the same way that the main engine block in an automobile is useless without conduits, nuts, and bolts. Transmission lines are guiding structures that convey high-frequency electromagnetic energy from one block to another. Their careful design for amplitude and phase matching is therefore extremely important.

The high-frequency transmission line industry is a huge enterprise. According to <http://www.global-spec.com>, 186 coaxial cable manufacturing companies and 60 waveguide manufacturing companies operate in the United States alone. Moreover, 585 companies

manufacture cable assemblies, including connectors, adapters, and attenuators. In the year 2000, the market volume increased by about 25%. This is due to rapid growth of wireless mobile communications and other sectors. With the emergence of new innovative technologies in the twenty-first century, such growth is expected to continue at a still higher rate.

High-frequency cables, waveguides, and accessories are usually very expensive items because they require manufacturing to high standards and tolerances. The most common forms of such transmission lines are coaxial cables and waveguides. For RF–microwave frequencies, which span anything from a few MHz to 30 GHz, the coaxial line is the oldest and most widely used devices for transferring RF energy from one point to another. Heinrich Hertz used coaxial cables in his experiments to prove Maxwell’s theory of electromagnetic wave propagation. Hertz used coaxial lines to generate the standing waves. In the 1930s when radios became very popular, coaxial transmission lines were used exclusively at low frequencies such as VHF and UHF applications. The shielding properties of coaxial lines minimize the static interference of charge leakage at low frequencies. For higher-frequency applications such as 1 GHz and above, waveguide structures are generally used. The waveguide is preferred because of its low transmission losses and high power-handling capabilities. In 1897, Lord Rayleigh mathematically proved the concept of wave propagation through single-conductor rectangular and circular waveguides. He also proved the existence of a cutoff frequency below which no wave can propagate through the waveguide. Following the example of Lord Rayleigh, Sir Jagadish Chandra Bose invented waveguides and used these waveguides in his wireless experiments in 1894. He also invented waveguide horn antennas for millimeter-wave transmission and reception. Sir Jagadish Bose extensively used scientific demonstrations of EM wave propagations and detections in his teaching classes in the Presidency College of Kolkata, India. Also in 1894, Sir Oliver Lodge observed directional radiation when he surrounded a spark oscillator with a metal tube. Because high-frequency sources were not widely available, not much work was conducted on waveguides until about 1930. After this time, scientists from AT&T and MIT radiation laboratory rediscovered the waveguide and developed a theoretical framework to explain the cutoff frequencies and propagation modes. During and after World War II, the design and use of various coaxial cables and waveguides advanced with new thrusts for emerging applications in radars and wireless communications.

In this article we first describe the classical theory in which transmission lines are assumed to be a distributed section of series resistance and inductance, as well as shunt capacitance and conductance. This model is then evolved into the “telegrapher equation,” which explains the wave nature of electromagnetic energy guided by a two-conductor transmission line. Basic characteristic parameters such as the propagation constant, phase velocity, and characteristic impedance are derived. This generalized transmission line theory can be applied to any transmission-line type. Finally, the field theory of transmission

lines is used to derive coaxial transmission-line theory. Practical examples of various coaxial cables and cable assemblies available on the market are also presented. Different waveguide configurations such as parallel-plate, rectangular, circular, and elliptical waveguides are discussed and propagation modes in the waveguide are defined. Planar waveguides such as microstrip lines, slotlines, and coplanar waveguides are also presented.

2. CLASSIFICATION OF TRANSMISSION LINES

Most practical waveguide structures rely on single-mode propagation in a particular direction. They can consequently be conveniently classified according to the polarization properties of the electromagnetic waves they carry: transverse electromagnetic (TEM), transverse electric (TE), or transverse magnetic (TM) modes. TEM modes have both electric and magnetic fields transverse to the direction of propagation. In TM mode, the magnetic field is transverse to the direction of propagation and in TE mode, the electric field is transverse to the direction of propagation. Mathematically, these modes for a wave propagating in the z direction can be represented as follows:

1. TEM waves: $E_z = 0, H_z = 0$
2. TM waves: $E_z \neq 0, H_z = 0$
3. TE waves: $E_z = 0, H_z \neq 0$
4. Hybrid waves: $E_z \neq 0, H_z \neq 0$

Transmission lines can be classified with respect to polarization, as shown in the tree diagram in Fig. 1. TEM is the dominant mode of propagation in coaxial lines and parallel-plate transmission lines where two conductors are involved. TE and TM propagation modes are typically found in single-conductor waveguides, which have rectangular, circular, elliptical or ridge-type cross sections. Other than TEM, TE, or TM modes, hybrid modes are also known that contain all six components ($E_x, E_y, E_z, H_x, H_y, H_z$) of electric and magnetic fields. Examples of transmission lines that support hybrid modes of propagation include microstrip (MS) transmission line, slotline (SL), and coplanar waveguide (CPW) structure.

The various forms of transmission lines are shown in Fig. 2. Figure 2a illustrates the most typical such lines: a parallel, two-conductor transmission line in which the conductors are uniformly separated by an air dielectric. The evolution of waveguides away from the two-conductor transmission line can perhaps be best understood in terms of the theory of quarter-wave transformers. A quarter-wave section of a short-circuited transmission line is transformed by an operating frequency into an open circuit at the input end of the line. The waveguide is then considered to be two short-circuited, quarter-wave sections along the two-wire transmission line. The cutoff in the waveguide’s frequency dependence can be understood in terms of the behavior of the quarter-wave section of the line.

Figure 2b depicts a coaxial cable where the center conductor is concentric with the outer cylindrical conductor,

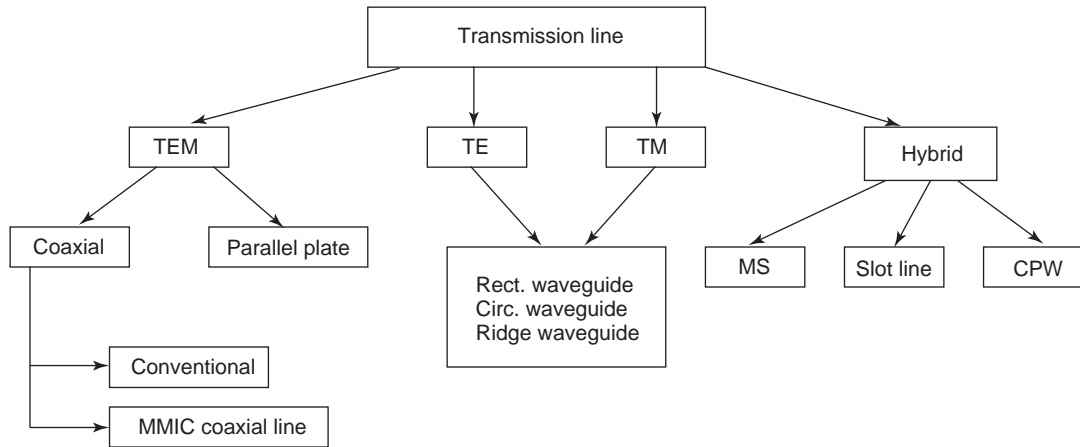


Figure 1. Classification of transmission lines based on a single mode of wave propagation.

which is usually the ground for the transmission line. As such, it acts as the shield for outside interference. The uniform gap between the two conductors is filled with a

dielectric material. The advantage of the coaxial cable is its high immunity to interfering signals due to the shielding provided by the outer conductor of the information-carrying signal.

Other forms of high-frequency transmission lines are dielectric waveguides (not shown here), parallel-plate waveguides (Fig. 2e), and planar transmission lines such as microstrip lines (Fig. 2f) and striplines (Fig. 2g).

Table 1 compares the three most popular transmission lines used in modern microwave circuits and systems: coaxial cables, waveguides, and microstrip lines. As can be seen, each line has its own advantages and disadvantages. While coaxial cables are popular in network-related, low- and medium-frequency operation, waveguides are preferred in high-frequency and high-power applications. At high frequencies, both coaxial cables and microstrip lines exhibit high power losses and signal distortions. Because of their better power-handling capability, waveguides are popular for radars and similar high-power, high-frequency applications in which their physical bulk is not a hindrance. For compact and portable, lightweight gadgets such as mobile phones, handheld GPS receivers, and some solid-state, high-power amplifier modules, microstrip lines are preferred. To compensate for the losses they suffer as a result of high attenuation, amplifiers are typically used. Transmission lines and circuit formats are therefore selected according to their specification requirements and applications.

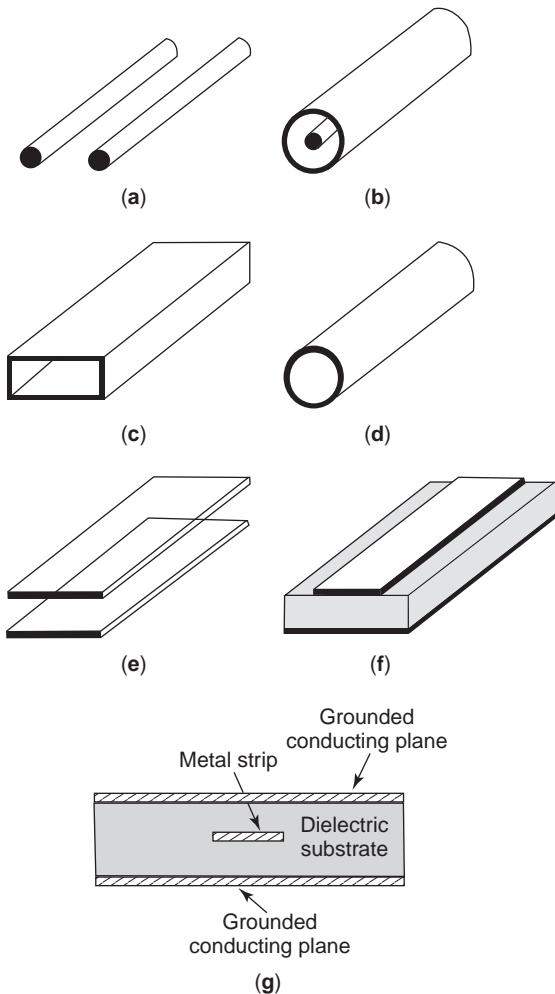


Figure 2. Commonly used waveguide structures: (a) open two-wire line; (b) coaxial line; (c) rectangular waveguide; (d) circular waveguide; (e) parallel-plate waveguide; (f) microstrip line; (g) stripline.

3. TRANSMISSION LINE THEORY: LUMPED-ELEMENT CIRCUIT MODEL

A transmission line is often schematically represented by a two-wire line, because transmission lines for TEM wave propagation always have at least two conductors. Figure 3 illustrates a differential length (Δz) of a two-conductor transmission line represented by a distributed parameter network. The voltages and currents vary in magnitude and phase over its length. The distributive parameters are

$$R = \text{resistance per unit length}$$

$$L = \text{inductance per unit length}$$

Table 1. Comparison of Common Transmission Lines and Waveguides

Characteristic	Coaxial line	Rectangular Waveguide	Microstrip line
Preferred mode	TEM	TE ₁₀	Quasi-TEM
Dispersion	None	Medium	Low
Bandwidth	High	Low	High
Power-handling capacity	Medium	High	Low
Loss/attenuation	Medium	Low	High
Physical size	Large	Large	Small
Ease of fabrication	Medium	Medium	Easy
Integration with other components	Hard	Hard	Easy

G = conductance per unit length

C = capacitance per unit length

Δz = incremental length

One can determine the current and voltage relations for the short length of line Δz . Kirchhoff's voltage and current laws are applied along the transmission line shown in Fig. 3. In the derivation, the line length of $\Delta z \rightarrow 0$ is assumed. Equations for the instantaneous voltages and currents and for time-harmonic equivalents are as follows:

Instantaneous equations

$$-\frac{\partial v}{\partial z} = Ri + L \frac{\partial i}{\partial t} \quad (1)$$

$$-\frac{\partial i}{\partial z} = Gv + C \frac{\partial v}{\partial t} \quad (2)$$

Time-harmonic equations where $e^{j\omega t}$ is assumed

$$-\frac{dV}{dz} = RI + j\omega LI \quad (3)$$

$$-\frac{dI}{dz} = GV + j\omega CV \quad (4)$$

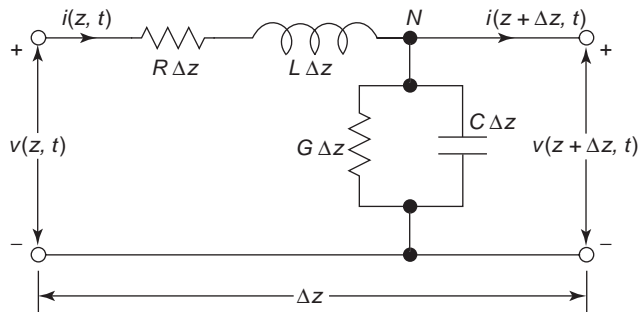


Figure 3. Lumped-element equivalent-circuit model of the differential length of a transmission line.

The solution for instantaneous voltages and currents is

$$v(z, t) = \text{Re}[V(z)e^{j\omega t}]; \quad i(z, t) = \text{Re}[I(z)e^{j\omega t}] \quad (5)$$

Wave equations for time-harmonic voltages and currents are rewritten as

$$\begin{aligned} -\frac{dV}{dz} &= (R + j\omega L)I \\ -\frac{dI}{dz} &= (G + j\omega C)V \\ \Rightarrow \begin{cases} -\frac{d}{dz} \left(\frac{dV}{dz} \right) = (R + j\omega L) \frac{dI}{dz} \\ \frac{d^2 V}{dz^2} = (R + j\omega L)(G + j\omega C)V \end{cases} \end{aligned} \quad (6)$$

The final expressions for time-harmonic voltage and current wave equations along the line are

$$\frac{d^2 V}{dz^2} = \gamma^2 V \quad (7)$$

$$\frac{d^2 I}{dz^2} = \gamma^2 I \quad (8)$$

The propagation constant γ for the line is defined as

$$\gamma = \sqrt{(R + j\omega L)(G + j\omega C)} = \alpha + j\beta \quad (9)$$

where α is the attenuation constant (Np/m) and β is the propagation constant (rad/m).

The traveling-wave solutions are

$$V(z) = V^+(z) + V^-(z) = V_0^+ e^{-\gamma z} + V_0^- e^{+\gamma z} \quad (10)$$

$$I(z) = I^+(z) + I^-(z) = I_0^+ e^{-\gamma z} + I_0^- e^{+\gamma z} \quad (11)$$

The plus sign indicates the forward-traveling wave, and the minus sign indicates the backward-traveling wave. Applying (11) to the voltage of (3) gives the current on the line:

$$I(z) = \frac{-1}{R + j\omega L} \frac{dV(z)}{dz} = \frac{\gamma}{R + j\omega L} [V_0^+ e^{-\gamma z} - V_0^- e^{+\gamma z}] \quad (12)$$

The characteristic impedance of the line is

$$Z_0 = \frac{V_0^+}{I_0^+} = \frac{R + j\omega L}{\gamma} = \sqrt{\frac{R + j\omega L}{G + j\omega C}} \quad (13)$$

To relate the voltage and current on the line; $Z_0 = (V_0^+ / I_0^+) = -(V_0^- / I_0^-)$. The wavelength of the wave along the line is

$$\lambda_g = \frac{2\pi}{\beta} \quad (14)$$

and the phase velocity of the wave along the transmission line is

$$v_p = \frac{\omega}{\beta} = \lambda f \tag{15}$$

For lossless transmission lines, $R = G = 0$; the propagation constant is $\gamma = j\omega\sqrt{LC} = \alpha + j\beta$. Therefore, the attenuation constant $\alpha = 0$ and $\beta = \omega\sqrt{LC}$. The characteristic impedance is

$$Z_0 = \sqrt{\frac{L}{C}} \tag{16}$$

The general solution of a lossless transmission line is

$$V(z) = V^+(z) + V^-(z) = V_0^+ e^{-j\beta z} + V_0^- e^{j\beta z} \tag{17}$$

$$I(z) = I^+(z) + I^-(z) = (V_0^+ / Z_0) e^{-j\beta z} - (V_0^- / Z_0) e^{j\beta z} \tag{18}$$

The wavelength of the wave along the line $\lambda_g = (2\pi/\beta) = (2\pi/\omega\sqrt{LC})$ and the phase velocity of the wave along the transmission line is $v_p = (\omega/\beta) = \lambda f$.

3.1. Coaxial Lines

The key feature of coaxial lines is that their characteristic impedance is very broadband. The fundamental mode of operation is TEM, where the electric and magnetic fields are transverse in the direction of propagation. A typical coaxial cable, shown in Fig. 4, consists of two concentric conductors of inner and outer radii a and b , respectively, with the space between them filled with a dielectric (ϵ_r) such as Teflon or polyethylene. In this section we perform a field analysis on a coaxial cable to calculate the equivalent circuit parameters such as $R, G, L,$ and C as defined earlier in the telegrapher equation.

Let the voltage between the conductors be $V_0 e^{\pm j\beta z}$ and the current $I_0 e^{\pm j\beta z}$. The fields of a traveling TEM wave inside the coaxial line along the $+z$ direction are then given as follows:

$$\mathbf{E} = \frac{V_0 \hat{\rho}}{\rho \ln(b/a)} e^{-\gamma z} \quad (\text{V/m}) \tag{19}$$

$$\mathbf{H} = \frac{I_0 \hat{\phi}}{2\pi\rho} e^{-\gamma z} \quad (\text{A/m}) \tag{20}$$

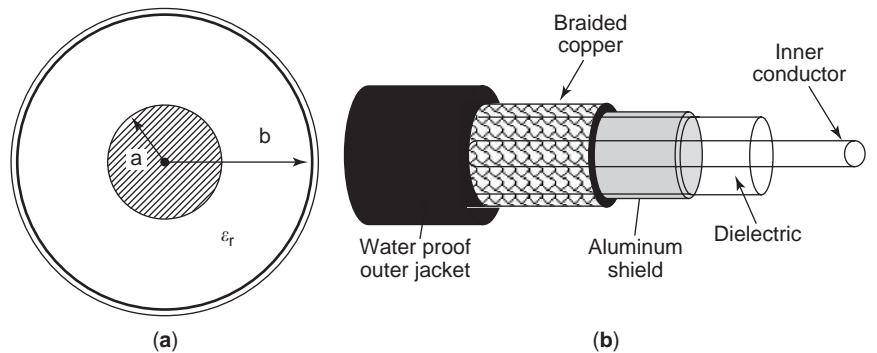


Figure 4. Coaxial cable: (a) cross-sectional view; (b) isometric view.

The conductors are assumed to have a surface resistivity R_s . The material filling the space between the conductors is assumed to have a complex permittivity $\epsilon = \epsilon' - j\epsilon''$, and the permeability is $\mu = \mu_0\mu_r$. We now determine the transmission line parameters $R, G, L,$ and C .

The time-average magnetic energy store is defined as

$$W_m = \frac{\mu}{4} \int_S \mathbf{H}\mathbf{H}^* ds = L|I_0|^2/4 \tag{21}$$

The self-inductance per unit length is

$$L = \frac{\mu}{|I_0|^2} \int_S \mathbf{H}\mathbf{H}^* ds \quad (\text{H/m}) \tag{22}$$

$$= \frac{\mu}{2\pi} \ln(b/a) \quad (\text{H/m})$$

The time-average electric energy stores is defined as

$$W_e = \frac{\epsilon}{4} \int_S \mathbf{E}\mathbf{E}^* ds = C|V_0|^2/4 \tag{23}$$

The self-capacitance per unit length is

$$C = \frac{\epsilon}{|V_0|^2} \int_S \mathbf{E}\mathbf{E}^* ds \quad (\text{F/m}) = \frac{2\pi\epsilon'}{\ln(b/a)} \quad (\text{F/m}) \tag{24}$$

The power loss per unit length due to the finite conductivity σ of the metallic conductor is

$$P_c = \frac{R_S}{2} \int_{C_1+C_2} \mathbf{H}\mathbf{H}^* dl = R|I_0|^2/2$$

where the surface resistivity is defined as $R_S = 1/\sigma\delta_S$, where δ_S is the skin depth of the conductor. The series resistance R per unit length of the line is

$$R = \frac{R_S}{|I_0|^2} \int_{C_1+C_2} \mathbf{H}\mathbf{H}^* dl \quad (\Omega/m) \tag{25}$$

$$= \frac{R_S}{2\pi} \left(\frac{1}{a} + \frac{1}{b} \right) \quad (\Omega/m)$$

Due to the “lossy” dielectric, the time-average power dissipated per unit length is

$$P_d = \frac{\omega \epsilon''}{2} \int_S \mathbf{E} \mathbf{E}^* ds = G |V_0|^2 / 2 \quad (26)$$

The conductance per unit length is

$$G = \frac{\omega \epsilon''}{|V_0|^2} \int_S \mathbf{E} \mathbf{E}^* ds \quad (\text{S/m}) = \frac{2\pi \omega \epsilon''}{\ln(b/a)} \quad (\text{S/m}) \quad (27)$$

So far we have calculated the equivalent-circuit model parameters of a coaxial cable with the radii of the outer and inner conductors of b and a , respectively. Now we opt to calculate the characteristic impedance of the coaxial line Z_0 , which is frequency-independent and can be calculated as

$$Z_0 = \frac{V_0}{I_0} = \sqrt{\frac{\mu}{\epsilon}} \ln\left(\frac{b}{a}\right) = \frac{60}{\sqrt{\epsilon_r}} \ln\left(\frac{b}{a}\right) \quad (\Omega) \quad (28)$$

The approximate cutoff frequency of the cable can be calculated from (29), at which point the first non-TEM mode of propagation begins. At a frequency above f_{cutoff} [5], other propagation modes dominate and the characteristic impedance becomes frequency-dependent:

$$f_{\text{cutoff}}(\text{GHz}) = \frac{7.51}{\sqrt{\epsilon_r}} \left(\frac{1}{a+b} \right) \quad (29)$$

The line parameters L , R , C , and G of coaxial lines can be calculated from

$$C = \frac{55.63 \epsilon_r}{\ln(b/a)} \quad (\text{pF/m}) \quad (30)$$

$$L = 200 \ln\left(\frac{b}{a}\right) \quad (\text{nH/m}) \quad (31)$$

$$R = 10 \left[\frac{1}{a} + \frac{1}{b} \right] \sqrt{\frac{f_{\text{GHz}}}{\sigma}} \quad (\Omega/\text{m}) \quad (32)$$

$$G = \frac{0.3495 \epsilon_r f_{\text{GHz}} \tan(\delta)}{\ln\left(\frac{a}{b}\right)} \quad (\text{S/m}) \quad (33)$$

where $\tan \delta$ is the loss tangent of the dielectric material, σ is the conductivity of the conductor in S/m, and f_{GHz} is the signal frequency in GHz.

3.1.1. Cable Losses. The losses in a coaxial cable arise from two sources: resistance of the conductors and the dielectric losses between the two conductors. The conductor losses are ohmic and increase with the square root of the frequency due to the skin effect. The dielectric loss is due to the finite conductivity of the dielectric material and increases linearly with the frequency. Figure 5a shows the attenuation per foot and power-handling capability of a MegaPhase TM Series test cable. As can be seen in Fig. 5a, the per unit length attenuation increases with frequency. In Fig. 5b the power-handling capacity of the cable reduces with frequency. The frequency dependence of the attenuation and the power-handling capability is explained in the following section.

The transmitted power can be expressed in terms of the voltage or maximum value of the electric field inside the line:

$$P_T = \frac{1}{2Z_0} |V|^2 = \frac{1}{\eta} |E_a|^2 (\pi a^2) \ln\left(\frac{b}{a}\right) \quad (34)$$

The attenuation coefficients due to conductor and dielectric losses are

$$\begin{aligned} P'_{\text{loss}} &= \frac{1}{2} R_s [(2\pi a) |H_a|^2 + (2\pi a) |H_b|^2] \\ &= \frac{R_s |I|^2}{4\pi} \left(\frac{1}{a} + \frac{1}{b} \right) \end{aligned} \quad (35)$$

$$\alpha_c = \frac{P'_{\text{loss}}}{2P_T} = \frac{R_s}{2\eta} \left(\frac{1}{a} + \frac{1}{b} \right) \frac{1}{\ln\left(\frac{b}{a}\right)} \quad (36)$$

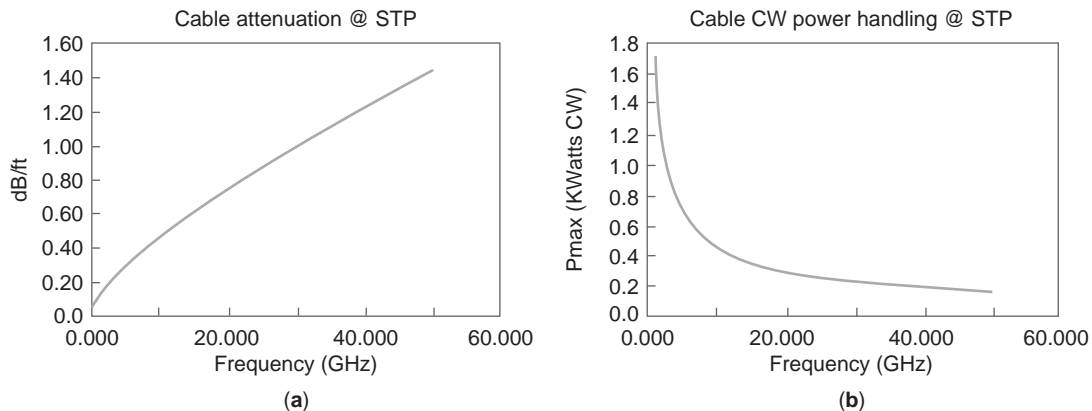


Figure 5. Attenuation per foot and power-handling capability of a coaxial cable as a function of frequency. (Source: <http://www.megaphase.com/html/test02.html>.)

$$\alpha_d = \frac{w}{2c} \tan(\delta) \quad (37)$$

Total losses will be

$$\alpha = \alpha_c + \alpha_d = \frac{R_s}{2\eta} \left(\frac{1}{a} + \frac{1}{b} \right) + \frac{\omega}{2c} \tan(\delta) \quad (38)$$

where the surface resistivity is

$$R_s = \sqrt{\frac{\omega\mu_0}{2\sigma}} \quad (39)$$

3.1.2. Types of Coaxial Cable. There are various types of coaxial cables available in the commercial market. They are broadly categorized as flexible cables and semirigid cables. Flexible cables are most widely used as measurement tools for test and characterization. There are two varieties of flexible cable available. The overall cable diameters vary from <0.25 in. to >1 in. depending on the power-handling capability of the wire. Some cables use a stranded inner conductor, while others employ solid wire with single braid or double-braided outer conductor. The outer jacket plays no part in the electrical performance of the cable—it simply holds everything together and supplies a waterproof covering. Selection of cable types depends primarily on the characteristic impedance of the cable, capacitance per unit length, power-handling capability, outer diameter, and attenuation per unit length at the specific frequency. Preference is also given to double-shielded/braided cable over the corresponding single-shielded cable due to the resilience against interference and physical ruggedness. Figure 6b shows an air-filled coaxial cable with spiral dielectric fin support. This cable displays low loss due to the air dielectric; the phase velocity is very close to that of the free space.

3.1.3. Semirigid Cables. Another popular transmission line is semirigid cable. Both inner and outer conductors are solid, and the two conductors are uniformly separated with dielectric material. Semirigid cables can be bent to moderate angles but, once bent, cannot be brought back to

their original shape. Cables of this type are neither rigid nor flexible; hence their name. Semirigid cables have better shielding capabilities and are more immune to outside interference than are flexible cables. Semirigid cables also have reduced attenuation and enhanced power-handling capabilities. Figure 7 shows various forms of semirigid cables soldered with SMA connectors at both ends. The inner conductors are made from various materials such as silver-coated copper, silver-plated copper-clad steel, and silver-plated aluminum. The dielectric filling is typically polyethylene, polytetrafluoroethylene (TFE Teflon), polytetrafluoroethylene-hexafluoropropylene (FEP Teflon), or kapton. The outer conductor is made of copper, aluminum, stainless steel, and special copper alloys. Selection of a particular type of semirigid cable involves consideration of factors such as power-handling capability, attenuation per unit length, size, higher-mode cutoff frequency, dielectric strength, and breakdown voltages (corona discharge voltage).

3.1.4. Coaxial Connectors. Coaxial cable is no use if interfacing with various components in a system is made. Various types of coaxial connectors and cable assemblies are used. Each type of connector can be attached to a cable in several ways: direct solder, crimp, and screw. Figure 7 shows various bent coaxial cable assemblies.

Interfacing cables with connectors and adapters need special care. Bending also requires special jigs to ensure minimum distortion of its regular shape. The cable must be cut to the exact length and then bent to the shape required. After shaping, the inner conductors are made in exact lengths such that they can be inserted into the inner conductor of a connector. Then solder is applied to the outer jacket to electrically connect the adapter and the cable. Adapter assemblies of this type are shown in Fig. 8.

3.1.5. More Recent Developments of Coaxial Line. Coaxial cables are nonplanar in nature, and compatibility with modern monolithic microwave integrated circuits (MMICs) and microelectromechanical structures (MEMS) is an issue. MMIC and MEMS support planar transmission lines such as microstrip lines, striplines, slotted lines, and coplanar waveguides (CPWs). More recently, with the advent of new processing techniques,

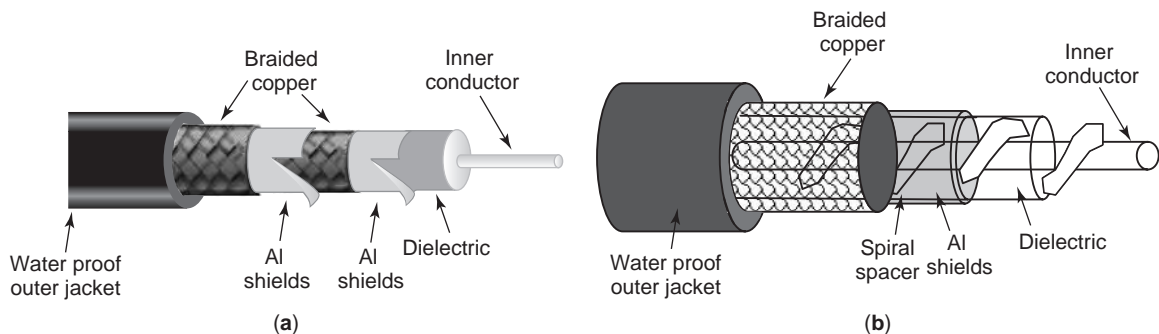


Figure 6. Flexible coaxial cable (coax) configurations: (a) double-braided solid-filled coax; (b) air-filled coax with spiral dielectric fin support.

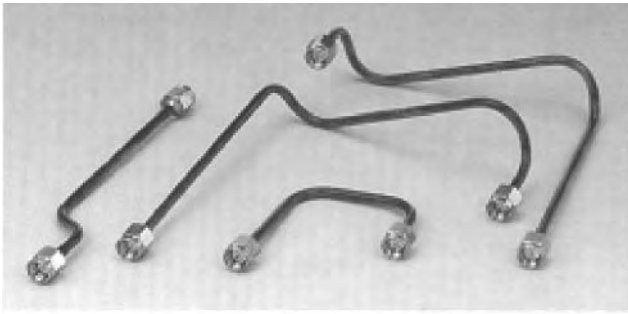


Figure 7. Various semirigid cable bends. (Source: http://www.shibata.co.jp/extt/3_g_g6.htm.)

MMIC and MEMS coaxial lines have been developed. These lines are designed for use in extremely wide frequency ranges from DC to THz. Monolithic implementation of coaxial lines in silicon and gallium arsenide (GaAs) substrate up to 40 GHz (c.f. Fig. 9a) has been reported [12]. The MMIC line is composed of a center conductor surrounded by a homogeneous dielectric (Polymide) covered entirely with a gold-plated ground plane. The pure TEM mode propagation of the proper mode is verified from the measurement. The authors also theoretically verify the losses up to 1000 GHz frequency band, and the transmission loss is about 15 dB/mm. The line has a measured maximum attenuation of 1.6 dB/mm at 40 GHz.

Developments in MEMS technology have made many breakthroughs in RF and microwave technologies. This state-of-the-art manufacturing technology supports IC batch processing on silicon wafers. A MEMS microcoaxial transmission line with inclined shields has been developed by the Korea Advanced Institute of Science and Technology [13]. With the removal of dielectric between the conductors, a very low attenuation of 0.03 dB/mm at 10 GHz has been obtained from the fabricated microcoaxial transmission line. Investigation reveals that the microcoaxial line fabricated on a glass line is less lossy than that fabricated on a silicon device. The MEMS microcoaxial line is shown in Fig. 9b.

Thus far, we have discussed the two main types of microwave transmission lines, namely, coaxial cables and waveguides, including their historical perspectives and more recent market statistics. The basic transmission-line theory of the telegrapher equation is presented. The theories of coaxial lines based on lumped elements as well as



Figure 8. Various coaxial cable assemblies. (Source: <http://www.gordontech.com.au/>.)

field theory have been presented. Two types of coaxial lines—flexible and semirigid cables—are discussed. Different connectors and adaptors of coaxial cables and cable assemblies are presented. Finally, the most recent development in MMIC and MEMS microcoaxial lines at higher frequencies are presented. In the following section, we will discuss waveguides.

3.2. Waveguide

In the preceding section, we discussed various types of coaxial transmission lines. In this section we shall discuss various nonplanar and planar waveguide structures and their modes of operations. Waveguides are extensively used to transfer electromagnetic energy efficiently from one point to another in a wide spectrum of frequency. Nonplanar waveguides are hollow tubes in which waves can propagate only at certain frequencies and cannot propagate below the cutoff frequencies. The cross section of the enclosed boundaries of the waveguide is transverse to the direction of propagation. Waveguides are used at microwave frequencies for two reasons: (1) they are often easier to fabricate than are coaxial lines and (2) they can be made to have less attenuation. Coaxial lines require the center conductor to be supported by the solid dielectric in the center of the outer cylindrical jacket. In contrast, a waveguide does not need any center conductor and its dielectric is air. Because of the high losses in a coaxial line over any distance (> 2 ft), along with the cable leakage at

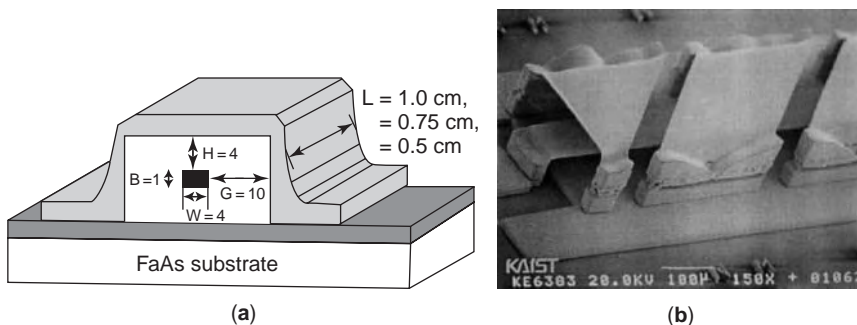
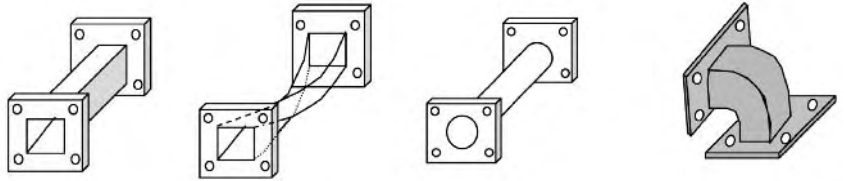


Figure 9. (a) MMIC rectangular coaxial line on GaAs [12]; (b) MEMS microcoaxial line [13].

Figure 10. Different forms of waveguides: (a) rectangular waveguide; (b) twist polarizer; (c) circular waveguide; (d) rectangular waveguide bend.



higher frequencies, the waveguide structure is preferred at higher frequencies. If the waveguide boundaries change direction within reasonable limits, the wave is bound to follow the changing direction without much distortion and discontinuity. In practice, such bends and junctions are very common in high-power radar systems where waveguides carry high-power high-frequency EM energy from the transmitter to the antenna. In waveguides, the waves are guided according to the distributions of the EM fields in the waveguide and their dependence on currents and charges on the conducting boundaries and the reflections of the fields in the conducting boundaries.

The most common hollow waveguides have rectangular or circular cross sections; however, the rectangular waveguides are preferred over circular ones for many applications. Figure 10 illustrates various forms of rectangular waveguides. Very often rectangular waveguides are designed such that one side of the rectangular wall is twice the length of the other side. This cross-sectional dimension has the advantage of enabling the operator to control the polarization of the wave to be transmitted. The electrical fields remain parallel to the smaller dimension of the waveguide cross section. If the dimension is made much larger, the electric field does not remain parallel to the side any more. On the other hand, if the dimension is made much smaller, then there will be considerable attenuation. The dimensions of the waveguide are generally designed such that only the fundamental or dominant mode can propagate. All other higher-order modes attenuate quite rapidly. Furthermore the dimensions are to be chosen such that there is a significant difference between the cutoff frequencies of the successive modes. This is necessary to ensure that only one designed mode may propagate.

Another popular type is the circular waveguide. In contrast to the rectangular waveguide, a circular waveguide lacks the sense of polarization of the wave that is being transmitted through. This is because there is no preferred direction across the circular cross-sectional plane. Furthermore, the cutoff frequencies of different modes are very close. As a consequence, it is very hard to determine an operating frequency that will yield a low attenuation for the dominant mode and high attenuation for the other higher-order modes. The advantage of the circular waveguide is exploited from its circular symmetry. Rotary joints use circular symmetry. For rotating antenna feeds used in radars, rotary joints are employed. The quality (Q) factor of the circular waveguide cavity is higher than that of the rectangular waveguide. This inherent characteristic is exploited in frequency meters.

Before proceeding further with the discussion of the hollow metallic waveguides, we shall first examine whether any wave can propagate within the waveguide (i.e., in a guide whose conducting boundaries form a simple connected region) and, if so, how the propagation takes place. As mentioned earlier with respect to coaxial cables, a TEM wave can propagate through the two-conductor transmission line. In contrast, in the single-conductor hollow waveguide such a TEM wave cannot propagate. This can be proved by field theory and solving the Helmholtz wave equation. Another very simple and interesting concept has been developed [14]. The waveguide can be perceived by a two-conductor transmission line supported by two quarter-wavelength short-circuited sections as shown in Fig. 11. Since the short-circuited quarter-wavelength section transforms into an open circuit (with infinity impedance, which is electrically invisible) at its input, there is no effect on power transmission. In many sections of this type, a rectangular waveguide such as that shown in Fig. 11 is used. To preserve the transmission-line property of the waveguide, the dimension d must not be less than one wavelength. Any frequency in the dimension a less than a half-wavelength (i.e., $< 0.5\lambda$) causes the circuit to become an inductive shunt ($j\omega L$), which prevents propagation. The frequency at which the a dimension is a half-wavelength is called the *cutoff frequency*.

Complete solutions to field equations are known for a limited number of structures with a well-defined geometry that is compatible with the coordinate system. Each mode

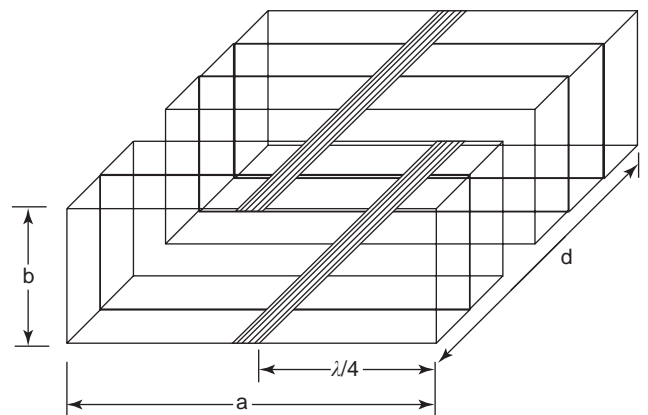


Figure 11. A rectangular waveguide derived from a two-wire transmission line supported by two quarter-wavelength short-circuited sections.

can be characterized by its electrical and magnetic components and can be visualized as field patterns by its electric and magnetic vectors.

In wave propagating structures, the transmission of microwave energy takes place in a region surrounded by boundaries, in most cases a metallic wall; and, for analytical purpose, these are assumed lossless. Other assumption is that, within the frequency of interest, a waveguide can support at least one propagating mode above its cutoff frequency, which is the function of waveguide geometry.

The time-harmonic electric and magnetic fields are assumed to have the following forms

$$E(x, y, z, t) = E(x, y)e^{j\omega t - j\beta z} \quad (40)$$

$$H(x, y, z, t) = H(x, y)e^{j\omega t - j\beta z} \quad (41)$$

where β is the propagation constant along the guide direction. The corresponding wavelength is the guide wavelength ($\lambda_g = 2\pi/\beta$):

$$\lambda_g = \frac{\lambda_0}{\sqrt{1 - \left(\frac{f_c}{f}\right)^2}} \quad (42)$$

where λ_0 is the wavelength of a plane wave propagating in an infinite medium. Two important features can be noted from this equation: (1) at higher operating frequency $\lambda = \lambda_0$ and (2) as f approaches f_c , λ_g becomes infinite and the corresponding mode does not propagate. Therefore, for a given mode of propagation, the operating frequency is always selected above the cutoff frequency.

3.2.1. Parallel-Plate Waveguide. The parallel-plate waveguide normally supports TM and TE modes. It can also support the TEM mode of propagation as it is formed with two flat plates or strips as shown in Fig. 2e. The stripwidth W is assumed to be much greater than the separation distance d so that the fringing field and any x components of the field can be ignored. A material with relative permittivity ϵ_r and permeability μ_0 is assumed to fill the region between the plates.

3.2.1.1. TEM Modes. The TEM mode solution can be obtained by solving Laplace's equation as in (43) for the electrostatic potential ϕ between the two plates:

$$\nabla_t^2 \phi(x, y) = 0 \text{ for } 0 \leq x \leq W \text{ and } 0 \leq y \leq d \quad (43)$$

The initial boundary conditions for potentials are

$$\begin{aligned} \phi(x, 0) &= 0 \\ \phi(x, d) &= V_0 \end{aligned} \quad (44)$$

Since there is no variation in the x plane, the equation can be solved with given boundary conditions and the transverse electric field and magnetic field components can be calculated. Once the electric field is derived, the voltage and the current on the top plate can be calculated from the

electric field component and the surface current density, respectively. The characteristic impedance of the parallel plate can be found as follows:

$$Z_0 = \frac{V}{I} = \frac{d\eta}{\omega} \quad (45)$$

The Z_0 depends only on geometry and the material parameter. The attenuation due to dielectric loss is given as follows:

$$\alpha_d = \frac{k \tan \delta}{2} \text{ (Np/m)} \quad (46)$$

The conductor attenuation for different mode of propagation can be calculated from the following equations:

$$\alpha_c = \frac{R_s}{\eta d} \text{ (Np/m) (for TEM mode)} \quad (47)$$

$$\alpha_c = \frac{2k_c^2 R_s}{k\beta\eta d} \text{ (Np/m) (for TE}_n \text{ mode)} \quad (48)$$

$$\alpha_c = \frac{2kR_s}{\beta\eta d} \text{ (Np/m) (for TM}_n \text{ modes)} \quad (49)$$

The cutoff frequency and propagation constant for TE_{*n*} and TM_{*n*} modes are

$$f_{c, \text{TM}} = \frac{\eta}{2d\sqrt{\mu\epsilon}} \quad (50)$$

and the propagation constant is

$$\beta_{\text{TE}} = \sqrt{k^2 - \left(\frac{n\pi}{d}\right)^2} \quad (51)$$

The wave impedance of TE_{*n*} and TM_{*n*} modes are frequency-dependent and are given as

$$Z_{\text{TM}} = \frac{-E_y}{H_x} = \frac{\beta\eta}{k} \quad (52)$$

$$Z_{\text{TE}} = \frac{E_x}{H_y} = \frac{k\eta}{\beta} \quad (53)$$

The attenuation due to conductor loss for TM₁, TE₁, and TEM modes in a parallel-plate waveguide is shown in Fig. 12. At the cutoff frequency the attenuation reaches infinity, prohibiting the propagation of modes.

3.2.2. Rectangular Waveguide. The rectangular waveguide can propagate TM or TE modes, but not TEM modes. The uniform rectangular waveguide structure is shown in Fig. 13. The propagation is in the z direction.

The cutoff frequency for TE_{*m*}_{*n*} modes can be calculated as follows:

$$f_{c, mn} = \frac{1}{2\pi\sqrt{\mu\epsilon}} \sqrt{\left(\frac{m\pi}{a}\right)^2 + \left(\frac{n\pi}{b}\right)^2} \quad (54)$$

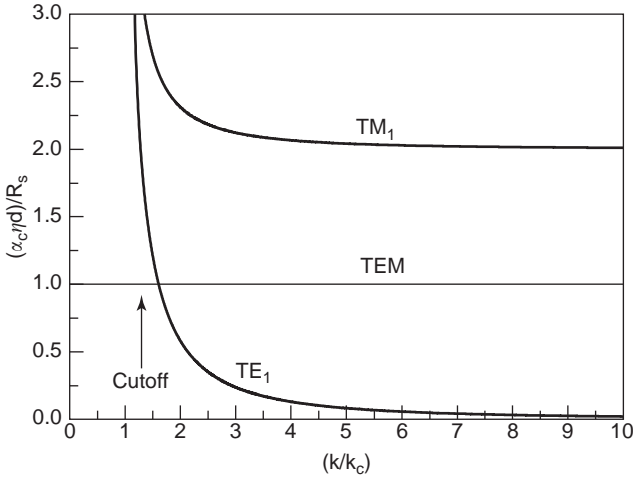


Figure 12. Attenuation due to conductor loss for TEM, TM_1 , and TE_1 modes of a parallel-plate waveguide.

The mode with the lowest cutoff frequency is called the *dominant mode*. As we have assumed previously that $a > b$, the lowest f_c occurs for the TE_{10} mode (for $m = 1$ and $n = 0$):

$$f_{c,10} = \frac{1}{2a\sqrt{\mu\epsilon}} \tag{55}$$

The propagation constant of TE mode is

$$\beta_{TE} = \sqrt{k^2 - k_c^2} = \sqrt{k^2 - \left(\frac{m\pi}{a}\right)^2 - \left(\frac{n\pi}{b}\right)^2} \tag{56}$$

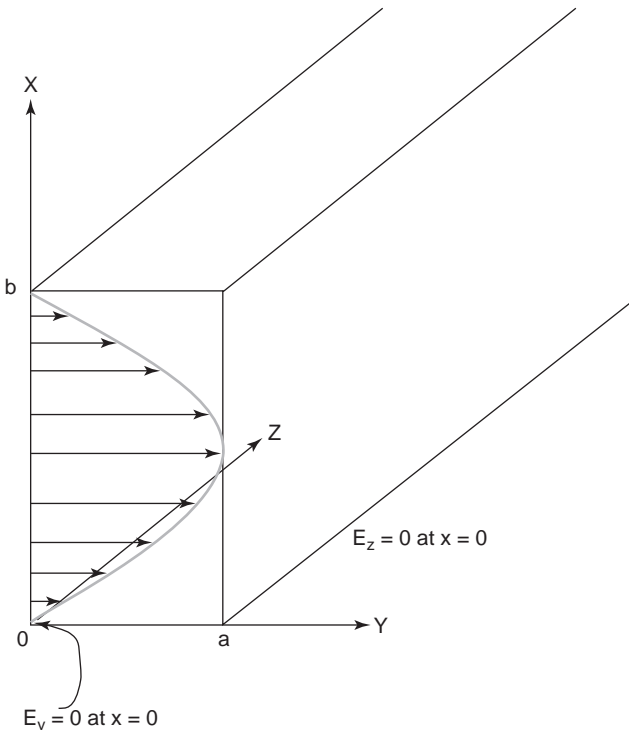


Figure 13. Coordinate system and electric field distribution in a rectangular waveguide.

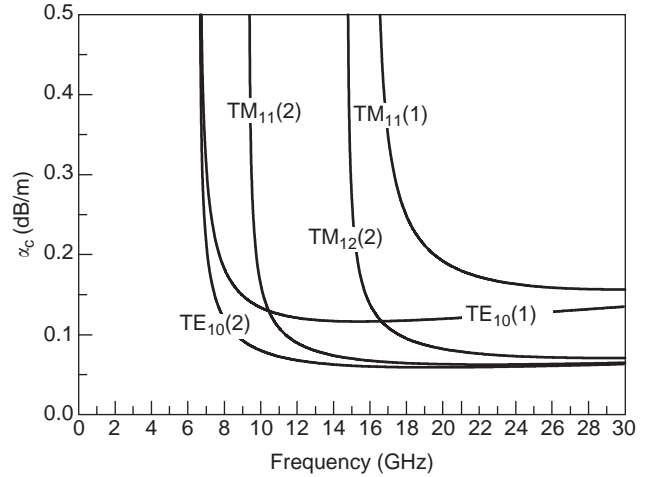


Figure 14. Attenuation of various modes of rectangular waveguide WR-90 with aluminum wall: (1) WR-90 waveguide; (2) WR-90 waveguide with $b = 2a$.

The wave impedance that relates the transverse electric and magnetic fields is

$$Z_{TE} = \frac{E_x}{H_y} = \frac{k\eta}{\beta} \tag{57}$$

where $\eta = \sqrt{\mu\epsilon}$, the intrinsic impedance of the material filling the waveguide.

The attenuation due to dielectric loss is shown in Fig. 14 for various TE and TM modes of rectangular waveguide WR-90 with an aluminum wall.

3.2.3. Circular Waveguide. The cross sectional view of a circular waveguide is shown in Fig. 15. Circular waveguides support TE and TM modes of propagation. Circular waveguides also used in many applications as guiding structures in the propagation of microwave energy.

The field equations are solved in cylindrical coordinates for both TE_{mn} and TM_{mn} modes as

$$\left(\frac{\partial^2}{\partial \rho^2} + \frac{1}{\rho} \frac{\partial}{\partial \rho} + \frac{1}{\rho^2} \frac{\partial^2}{\partial \phi^2} + k_c^2 \right) h_z(\rho, \phi) = 0 \tag{58}$$

where h_z and e_z respectively are electric and magnetic fields. The dominant mode in circular waveguide is TE_{11} mode. The propagation constant and cutoff frequency for TE_{mn} modes are expressed as follows:

$$\beta_{TE,nm} = \sqrt{k^2 - k_c^2} = \sqrt{k^2 - \left(\frac{\rho'_{nm}}{a}\right)^2} \tag{59}$$

$$f_{c,nm} = \frac{k_c}{2\pi\sqrt{\mu\epsilon}} = \frac{\rho'_{nm}}{2a\pi\sqrt{\mu\epsilon}} \tag{60}$$

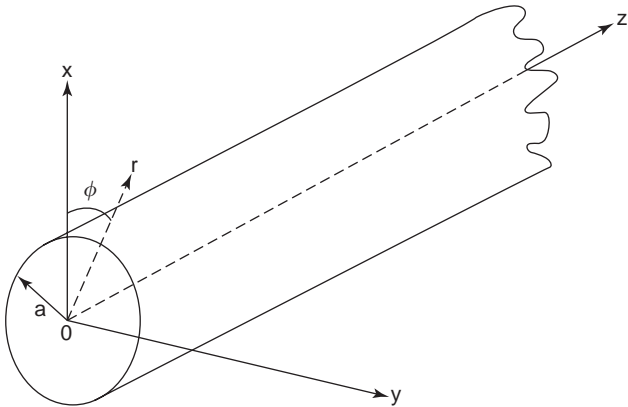


Figure 15. Cross sectional view of a circular waveguide.

For TM_{nm} modes the propagation constant and cutoff frequency are expressed as

$$\beta_{TM,nm} = \sqrt{k^2 - k_c^2} = \sqrt{k^2 - \left(\frac{\rho_{nm}}{a}\right)^2} \quad (61)$$

$$f_{c,nm} = \frac{k_c}{2\pi\sqrt{\mu\epsilon}} = \frac{\rho_{nm}}{2a\pi\sqrt{\mu\epsilon}} \quad (62)$$

where ρ and ρ' are the m th roots of Bessel's functions $J_n(x)$ and its first derivatives $J_n'(x)$ with order n , respectively. The attenuation due to conductor loss in an aluminum circular guide with radius 2.45 cm for different modes is shown in Fig. 16. As can be seen, the attenuation decreases to a very small quantity at higher frequency of operation. The transverse field patterns and the cutoff frequencies of various modes are shown in Figs. 17a and 17b, respectively.

3.2.4. Elliptic Waveguide. The elliptic waveguide is a cylindrical waveguide where the transverse section is of elliptical form, as shown in Fig. 18.

The readers are referred to other sources [1–3] for quantitative information on elliptic waveguides. The

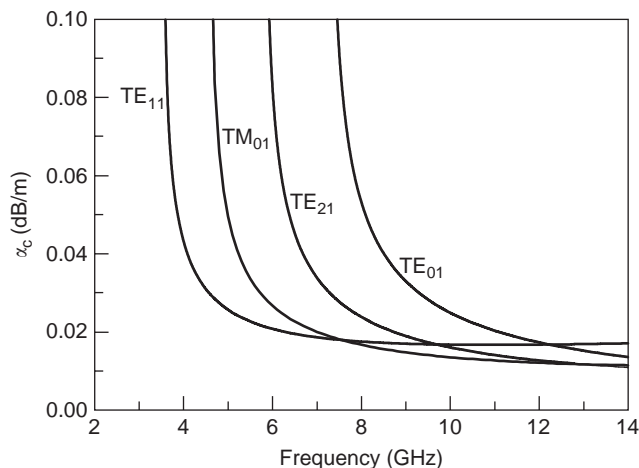


Figure 16. Attenuation due to metallic conductor of various modes of circular aluminum waveguide, with $a = 2.54$ cm.

dominant mode in elliptic waveguide is the eH_{11} mode. One major application of elliptical waveguide is impedance matching. The transverse electric and magnetic field patterns of several lower order modes in an elliptical waveguide with eccentricity $e = 0.75$ are shown in Fig. 19 [2].

3.2.5. Microstrip Line. The microstrip line is one of the most popular transmission lines [10] because it can be fabricated using the photolithography process and easily integrated with other active and passive microwave devices up to the millimeter-wave frequency band. The geometry of the microstrip transmission line is shown in Fig. 20.

The broad range of microwave components such as filters, resonators, diplexer, distribution networks, and matching circuits are made with microstrip lines. Although the microstrip structure is physically simple, the theoretical analysis is rather complex. A number of methods are employed to analyze the behavior of the microstrip line. However, there are closed-form analytical expressions for the characteristic impedance and propagation velocity [11]. The microstrip line supports quasi-TEM mode as the pure TEM mode is impossible because of the air-dielectric interface. Most of the power is confined to the region bounded by the width of the microstrip line, called the *fringing field*. Due to the presence of air in the fringing-field region, some of the power may radiate into free space. However, using a high-dielectric substrate and shielding the structure, the power loss due to radiation can be minimized. The microstrip medium is dispersive and supports higher-order modes. Nevertheless, its popularity is the result of the ease in integration with surface mountable chip components such as chip capacitors, chip resistors, and other lumped elements with good thermal dissipation properties of the medium without disturbing the RF propagation.

To design a basic microstrip line, it is important to know the characteristic impedance and effective permittivity, which is normally frequency-dependent. Many varieties of approximations have been reported in the literature [3]. However, the fairest and most accurate method in determining the characteristic impedance and effective permittivity [7] is outlined below:

$$Z_0 = \frac{\eta}{2\pi\sqrt{\epsilon_{re}}} \ln\left(\frac{8d}{W} + 0.25\frac{W}{d}\right) \quad \text{for } \left(\frac{W}{d} \leq 1\right)$$

$$Z_0 = \frac{\eta}{\sqrt{\epsilon_{re}}} \left(\frac{W}{d} + 1.393 + 0.667 \ln\left(1.444 + \frac{W}{d}\right)\right)^{-1} \quad (63)$$

$$\text{for } \left(\frac{W}{d} \geq 1\right)$$

where W is the width of the microstrip line, h is the height, and ϵ_{re} is the effective relative permittivity of the dielectric slab.

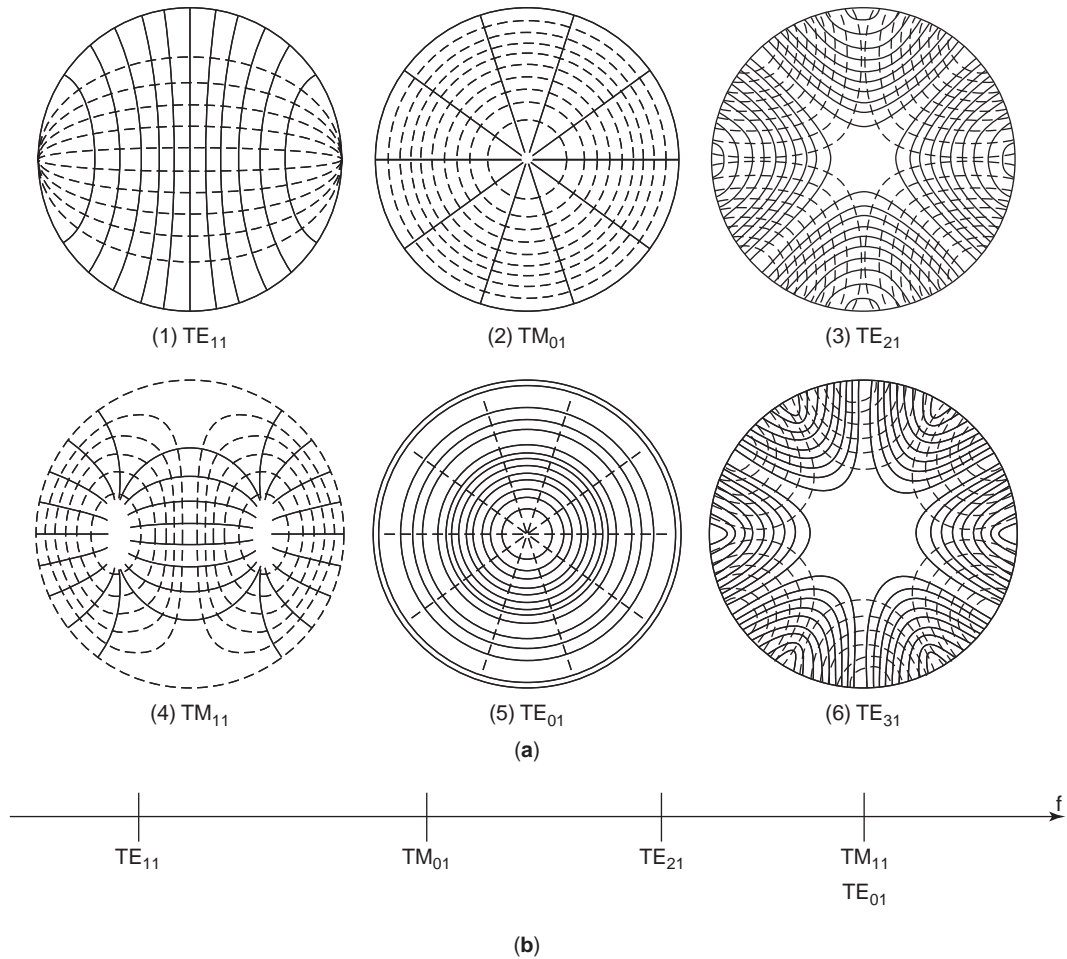


Figure 17. (a) Transverse field patterns of various modes in circular waveguide; (b) locations of cutoff frequencies of the first few TE and TM modes.

The effective permittivity can be expressed as

$$\epsilon_{re} = \frac{\epsilon_r + 1}{2} + \frac{\epsilon_r - 1}{2} F \frac{W}{d} \tag{64}$$

$$F \frac{W}{d} = \left(1 + 12 \frac{d}{W}\right)^{-0.5} + 0.04 \left(1 - \frac{W}{d}\right)^2 \text{ for } \left(\frac{W}{d} \geq 1\right)$$

$$F \frac{W}{d} = \left(1 + 12 \frac{d}{W}\right)^{-0.5} \text{ for } \left(\frac{W}{d} \leq 1\right) \tag{65}$$

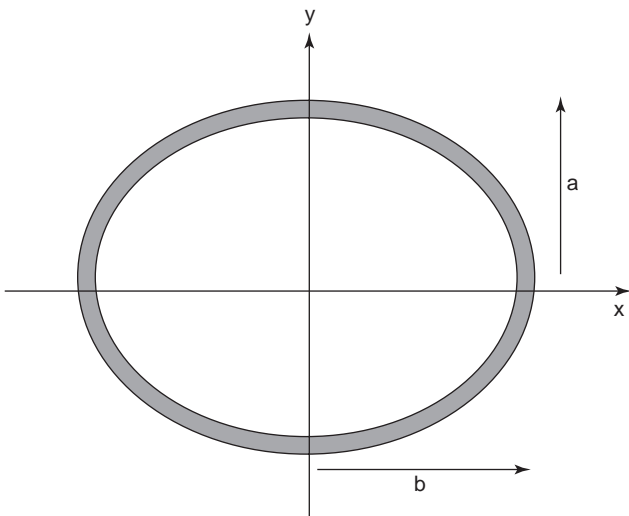


Figure 18. Geometry of the elliptical waveguide.

With these equations, the characteristic impedance and effective dielectric constant of a microstrip line can be evaluated. All modern microwave computer-aided design tools are equipped with these calculations for the characteristic impedance, linewidth, and effective dielectric constant of microstrip lines. At higher-frequency operation other factors such as decreased *Q* factors, radiation loss, surface-wave loss, and higher-order mode propagation are very critical in the design of microstrip lines. Figure 21 illustrates variation in the characteristic impedance and effective dielectric constants with respect to width for a microstrip line designed for two different substrates of

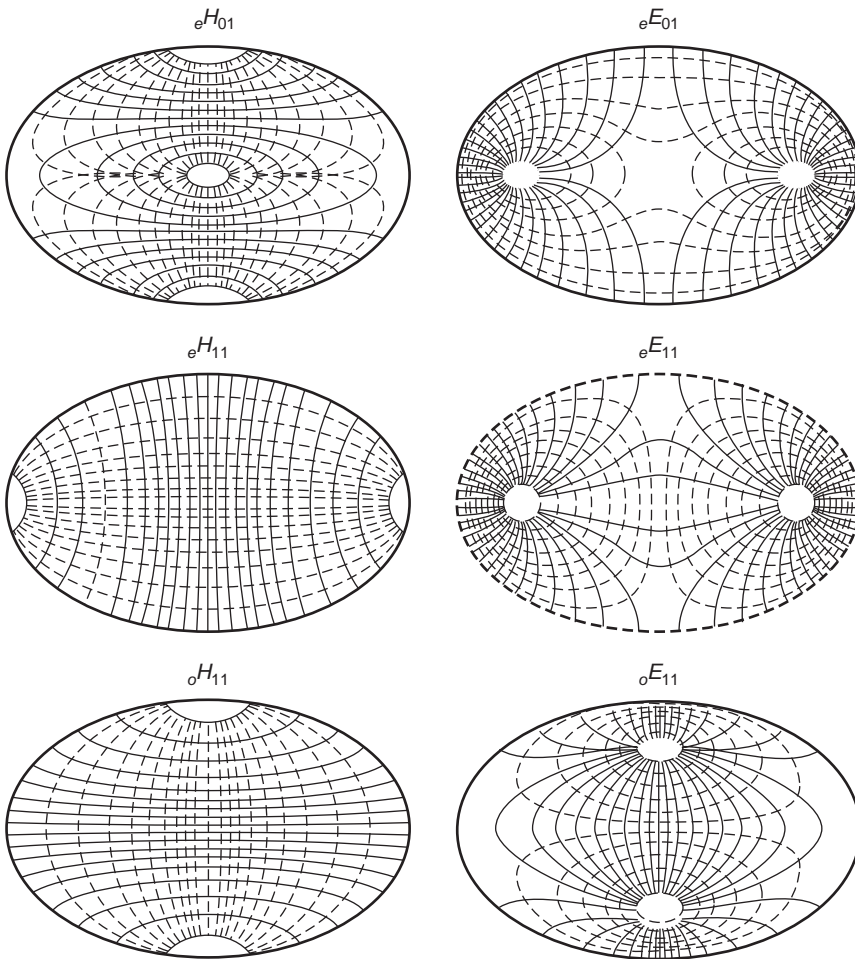


Figure 19. Field distribution of modes in elliptic waveguides [2].

dielectric constant of 2.0 and 10.5. As can be seen in Fig. 21a, the characteristic impedance decreases with the width–height ratio of the dielectric substrate. With higher dielectric constants the characteristic impedance is lower for the same dimension of line. As shown in Fig. 21b, the effective dielectric constant increases with the width–height ratio of microstrip lines. A microstrip realization of a quadrature direct conversion receiver [15] designed on RT Duroid substrate of dielectric constant of

10.5 and 0.635 mm thickness is presented in Fig. 22. As can be seen in the figure, all active and passive microwave devices such as quadrature hybrid coupler, asymmetric coupled-line bandpass filters, lowpass filters, Wilkinson power divider, and even harmonic mixer (EHMIX) are designed using photolithographic processes. The lumped components such as chip resistors, capacitors, and diode mixers are soldered on the microstrip lines. Thus microstrip lines have created a revolution in high-frequency and microwave circuits.

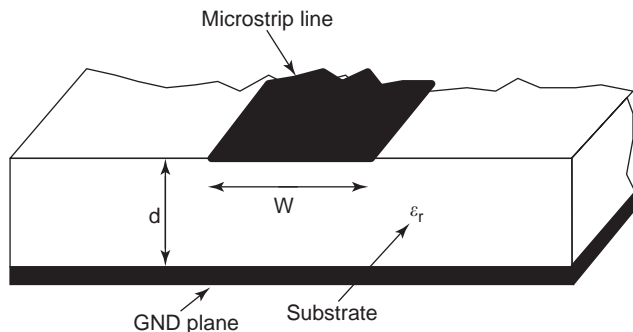


Figure 20. Structure of the microstrip line.

3.2.6. Slotline. Slotlines are planar transmission-line structures that are widely used in MMIC circuits. The basic slotline structure, shown in Fig. 23, consists of a dielectric slab with a narrow slot etched on the ground plane on only one side of the dielectric slab. This geometry is planar and well suited for MIC/MMIC designs. The wave propagates along the slot with the major electric field component oriented across the slot while the magnetic field is in the plane perpendicular to the slot. The mode of propagation in slotline is non-TEM in nature. Unlike the conventional waveguide, in the slotline there is no cutoff frequency and propagation occurs at all frequencies down to zero. Because of the slotline's non-TEM

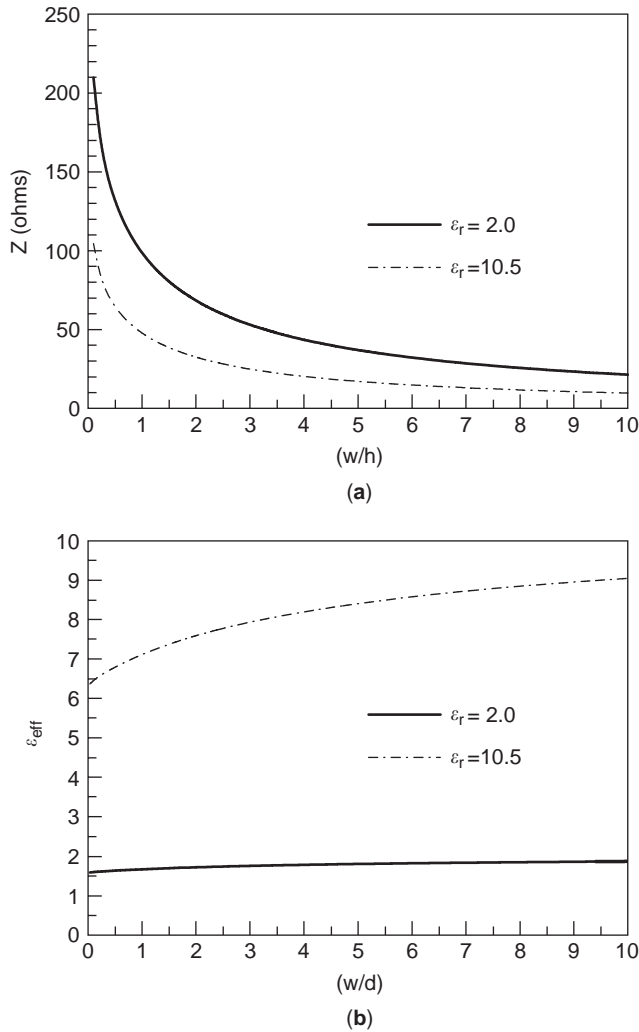


Figure 21. The characteristic of microstrip line. The variation of (a): characteristic impedance and (b): effective permittivity of the medium as a parameter of width.

nature, the characteristic impedance and phase velocity are not constant but vary with frequency at a slow rate. The characteristics of the slotline with regard to dielectric thickness are shown in Fig. 24 [6]. Readers are referred to

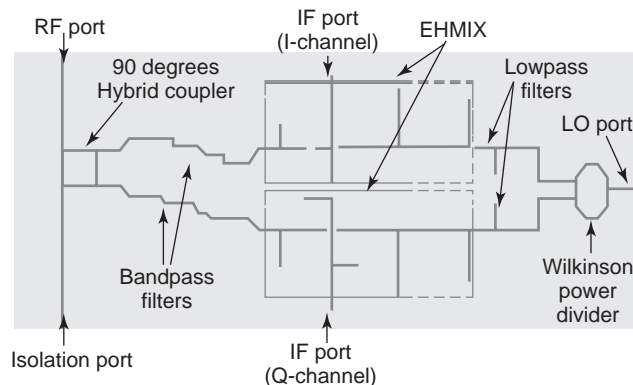


Figure 22. Microstrip realization of a mixer circuit.

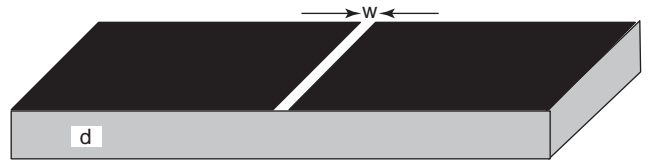


Figure 23. Slotline geometry.

the literature [3] for a detailed theoretical analysis of slotline structures.

3.2.7. Coplanar Waveguide Transmission Line. The geometry of coplanar waveguide (CPW), shown in Fig. 25, consists of two slots of width w etched on the ground plane of a dielectric substrate and separated by a spacing s . This structure is also referred to as a *uniplanar structure* as the signal-carrying line lies along with the ground plane in the same plane. This structure often demonstrates better dispersion behavior than does the microstrip line [4,5]. As a result of low parasitic effects, this structure is a good choice for higher-frequency operation. The characteristic impedance of the line depends primarily on the width of slots and their spacing for a given substrate.

The characteristic of a CPW line are shown in Fig. 26. The variation of effective dielectric constant and charac-

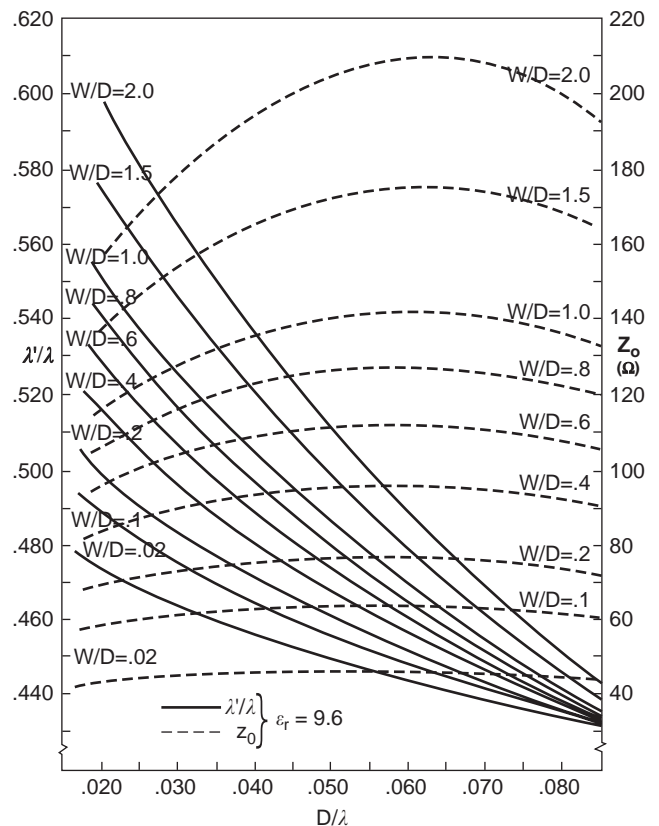


Figure 24. The dispersion characteristics of slotline from Ref. 6.

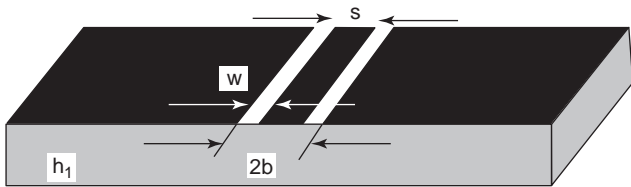


Figure 25. The geometry of a CPW line.

teristic impedance as line parameters can be a useful tool for the design of the CPW line and its associated components. A detailed analysis and closed-form expressions of CPWs are reported in Ref. 8.

Figure 27 is a photograph of various MMIC slot antennas on coplanar waveguides designed on GaAs substrate near 24 GHz. The slot dipole is fed through a CPW line, and the calculated and measured performances of

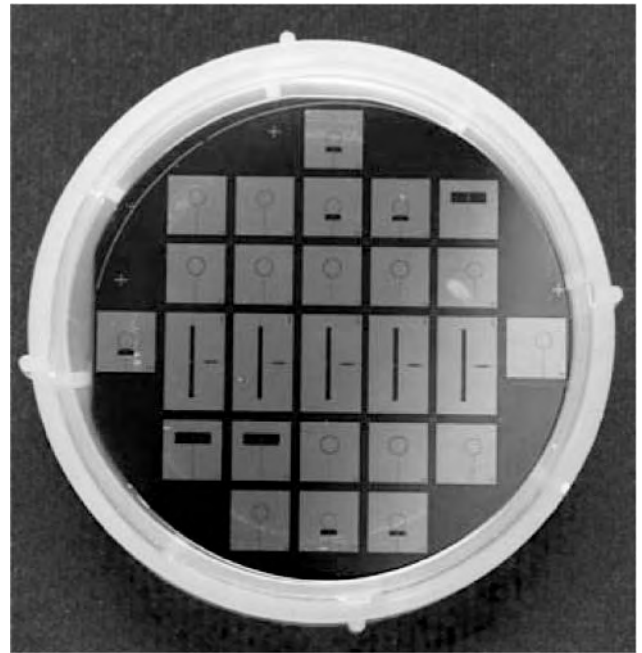


Figure 27. Photograph of a coplanar-waveguide-fed MMIC antenna on GaAs substrate near 24 GHz. (Courtesy PWTC, Nanyang Technological University, Singapore.)

the antenna is shown in Fig. 28. The details of antenna design are reported in Ref. 9.

4. CONCLUSION

This article has presented a historic perspective of coaxial cables and waveguides and has reviewed market potentials of coaxial cables, waveguides, and accessories. The classifications of various transmission lines according to the modes excited in the particular transmission lines have been shown. Two-wire transmission lines such as coaxial cables, parallel-plate waveguides, and microstrip lines support TEM mode fields. The single-conductor transmission lines support non-TEM mode fields such as TE and TM modes. Next, the classical transmission line theory has been derived in the “telegrapher” equation. Next, the coaxial cable has been discussed. The design parameters, higher-order mode cutoff frequency, and attenuation of coaxial cables were presented. The two main types of coaxial cable are flexible and semirigid coaxial cables. The most recent developments of extremely high-frequency coaxial cables exploiting MMIC and MEMS processing techniques were presented. It was shown that MEMS microcoaxial cable is low-loss even at very high frequencies such as in the millimeter-wave range.

Various waveguides in the form of parallel-plate waveguides and rectangular, circular, and elliptical waveguides were presented in terms of their cutoff frequencies and attenuation. Finally different planar waveguides such as microstrip lines, slotlines, and coplanar waveguides were presented. Their design formulas were also given for the benefit of designers.

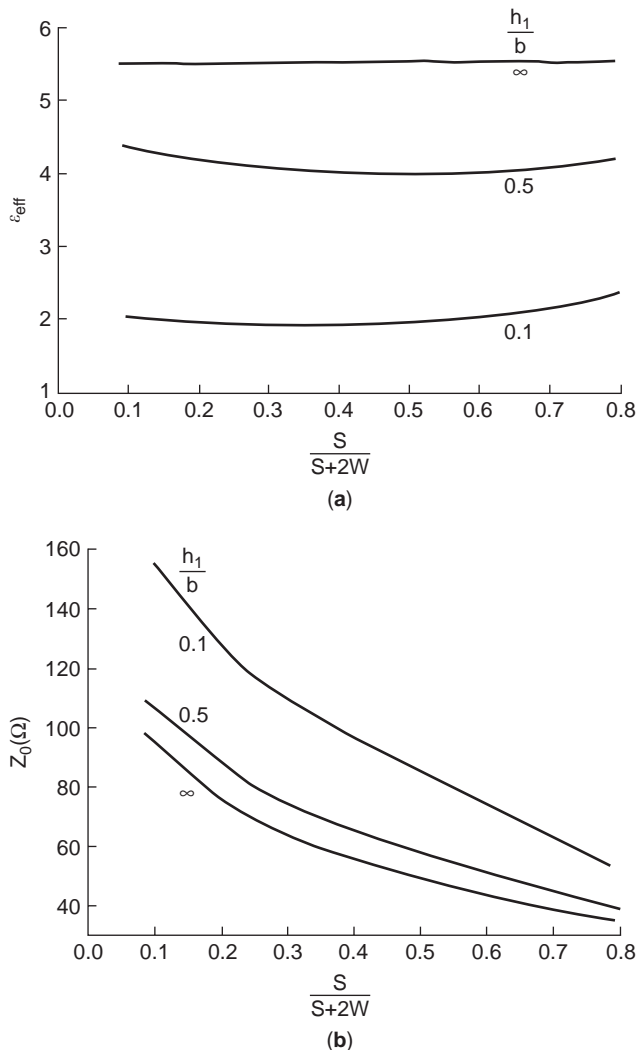


Figure 26. The characteristics of a CPW line: (a) variation of effective dielectric constant; (b) variation of characteristic impedance of Z_0 with CPW line parameters [8].

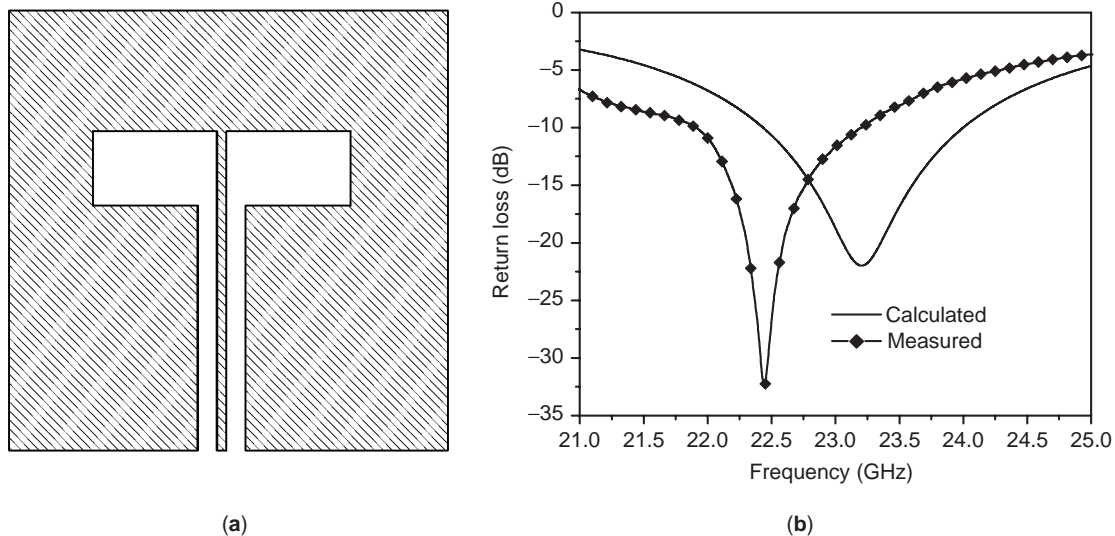


Figure 28. (a) CPW-fed slot dipole antenna at 24 GHz; (b) calculated and measured return loss of the antenna [9].

BIBLIOGRAPHY

1. D. M. Pozar, *Microwave Engineering*, Wiley, New York, 1998.
2. K. S. Packard, The origin of waveguides: A case of multiple rediscovery, *IEEE Trans. Microwave Theory Tech.* **MTT-32**:961–969 (Sept. 1984).
3. N. Marcuvitz, *Waveguide Handbook*, Peter Peregrinus, IEE, London, 1986.
4. R. N. Simons, *Coplanar Waveguide Circuits, Components and Systems*, J Wiley, New York, 2001.
5. R. E. Collins, *Foundation of Microwave Engineering*, 2nd ed., McGraw-Hill, New York, 1992.
6. E. A. Mariani et al., Slotline characteristics, *IEEE Trans. Microwave Theory Tech.* **MTT-17**:1091–1096 (1969).
7. M. Kobayashi, A dispersion formula satisfying recent requirements in microstrip CAD, *IEEE Trans. Microwave Theory Tech.* **MTT-36**:1246–1250 (Aug. 1998).
8. K. C. Gupta, R. Garg, I. Bahl, and R. Bhatia, *Microstripline and Slotlines*, Artech House, Norwood MA, 1996.
9. S. K. Padhi and N. C. Karmakar, Computer aided design of an CPW-fed slot antenna for MM-wave applications, *Int. J. RF Microwave Comput. Aided Design Eng.* **14**(1):4–14 (Jan. 2004).
10. I. J. Bahl and T. D. K. Trivedi, A designer's guide to microstrip line, *Microwaves* 174–182 (May 1977).
11. R. F. Harrington, *Time Harmonic Electromagnetic Field*, McGraw-Hill, New York, 1961.
12. J. A. Bishop, M. M. Hashemi, K. Kiziloglu, L. Larson, N. Dagli, and U. Mishra, Monolithic coaxial transmission lines for mm-wave ICs, *Proc. IEEE/Cornell Conf. Advanced Concepts in High Speed Semiconductor Devices and Circuits*, Aug. 1991, 5–7.
13. J.-B. Yoon, B.-I. Kim, Y.-S. Choi, and E. Yoon, 3-D construction of monolithic passive components for RF and microwave ICs using thick-metal surface micromachining technology, *IEEE Trans. Microwave Theory Tech.* **MTT-51**(1):279–288 (2003).
14. W. S. Cheung and F. H. Levien, *Microwaves Made Simple: Principles and Applications*, Artech House, Norwood, MA, 1985.
15. N. C. Karmakar, QPSK direct conversion receiver for wireless communications, *Int. J. RF Microwave Comput. Aided Eng.* (Jan. 2005).

COMBLINE FILTERS

CHI WANG
Orbital Sciences Corporation
Dulles, Virginia

1. INTRODUCTION

Comblines filters are one of the most widely used types of bandpass filters in many communication systems and other microwave applications because of many of their unique merits. The first comblines filter was introduced by Matthaei in 1963 [2]. The design equations and procedures of the rectangular bar comblines filter with narrow to moderate bandwidth, using the coupled rectangular bar design data from Getsinger [3], were also given by Matthaei [1,2]. Cristal [4,5] later presented the data for coupled circular cylindrical rods between parallel ground planes; thus, more manufacturing-advantageous and cost-effective cylindrical rod comblines filters can be designed with reasonable accuracy and excellent electrical performance. Although Matthaei's design equations were based on approximations, the results were shown to be reasonably good for narrow-to-octave bandwidth applications. Wenzel's exact analysis approach or full-wave electromagnetic simulations can be used for more accurate designs [9–11]. Comblines filters with elliptic function frequency responses, first presented by Rhodes and Levy, give great flexibility in their configuration and responses [6].

With the rapid development of satellite communications since the 1970s and mobile communications since the 1980s, generalized filters with elliptic function responses having cross-couplings between nonadjacent resonators are widely used [6–8,13,22–27]. Comblines filters are particularly suitable for achieving elliptic function response and for high-volume, low-cost production, because all the resonator rods can be mounted or built in on the common surface of the filter housing, while all the tuning

screws are mounted in a single cover. In addition, the resonator locations of the combline filter may be flexibly arranged according to the filter's coupling matrix and system mechanical requirement. The combination allows filters with large numbers of resonators and complicated cross-coupling configuration to be tuned nearly to theoretical performance without excessive cost.

In the physical realization of combline filters, the input and output couplings can be achieved by a short-circuited coupled line as part of an impedance transforming section, or an inductively coupled loop, a capacitive coupled probe, or by a direct, tapped-in line. The direct-tapped input/output configuration makes the combline filter more compact and easy to fabricate and therefore is more advantageous than other types of input/output structures [14–20]. This method was first described in the literature by Dishal [15] for small-percentage-bandwidth interdigital filters, and by Cohn [16] for combline filters. Cristal [17] gave exact general equivalent circuits for combline and interdigital arrays using graph transformations; thus the tapped line can be designed with high accuracy.

It is well known that the difference between the measured results and the design based on the conventional TEM combline theory can be as much as 30% depending on the filter's bandwidth [21]. Using full-wave electromagnetic computer-aided design (CAD) tools, combline filters can be designed in high accuracy with arbitrary resonator and coupling aperture dimensions [21,48]. The unloaded Q and the spurious responses of the resonators can be computed accurately from the electromagnetic simulators. Furthermore, the temperature characteristic and power handling capability of combline filters can be accurately determined [50–52].

Ceramic combline filters were introduced in the 1980s to satisfy the needs for miniature filters for mobile communications taking advantage of the development of high-dielectric-constant, low-loss dielectric materials. They have been widely used in many communication systems [40–47]. Ceramic combline filters can be manufactured using single or multiple solid ceramic blocks with a metallized exterior. The resonator rods are realized by a series of metallized holes that are grounded at one end of the block, where the opposite ends of the blocks are kept open. Therefore, the resonator lines are around a quarter-wavelength long at resonance. Couplings between adjacent resonators can be achieved by either series capacitors or apertures [42,48]. These ceramic combline filters can be designed and manufactured with high accuracy, and are very suitable for low-cost mass production.

Comblines are most suitable for applications requiring relatively low insertion loss in the frequency range between 500 MHz and 12 GHz, and they have following attractive features:

1. They are compact. The length of the resonator rods may be designed to be $\lambda_0/8$ or less at resonance. The unloaded Q of the resonator cavity is a function of its cross section. Therefore the size of the combline filter can be varied depending on the applications.
2. Combline filters possess the ability to be tuned over a wide range of frequencies without suffering significant degradation in performance [2,12]. The tuning range is a function of the amount of capacitance adjustment provided by the tuning screw.
3. The combline resonator has very high unloaded Q : volume ratio compared with other types of resonators, such as empty waveguide cavity and dielectric loaded resonators, although the combline resonator doesn't give the highest unloaded Q value.
4. They have strong stopbands, and the stopband above the primary passband can be made very broad. Combline filters may be designed to be spurious-free over 3–4 times the center frequency of the filter.
5. Adequate coupling can be maintained between resonator elements with sizable spacing between such resonator lines.
6. They are reliable, low in cost, and very suitable for manufacturing. All resonator rods can be mounted or built in to the filter housing, and all tuning screws can be directly attached to the housing or cover. In addition, all the materials are readily available and can be modified easily.

2. CONFIGURATIONS

A combline filter usually consists of a conductive enclosure and a number of parallel conductive rods serving as resonators, which are short-circuited at one end and open-circuited at the other end. The open ends of the resonator rods are usually close to one side of the enclosure in order to create sufficient capacitance between the rod and the ground. Coupling between resonators is achieved by way of the EM coupling between resonator lines. The input and output coupling may be achieved in several ways as stated in the introduction.

Figure 1 shows a combline bandpass filter in transmission-line form. The resonators of the filter consist of TEM-mode transmission-line elements that have a lumped capacitor C_b^s between the open end of each resonator line element and ground. Lines 1 through n and their associated capacitances C_1^s to C_n^s constitute resonators, while lines 0 and $n+1$ are not resonators but part of impedance transforming sections at both ends of the filter.

With the lumped capacitors present, the resonator lines will be less than a quarter-wavelength long at resonance, and the coupling between resonators will be predominantly magnetic in nature. It is usually desirable to make the capacitances of the combline filter sufficiently large so that the resonator lines will have a length of $\lambda_0/6$ or less at resonance.

The second passband of the combline filter occurs when the resonator line elements are somewhat over a half-wavelength long, so if the resonator lines are $\lambda_0/8$ long at the primary passband, the second passband will be centered at somewhat over 4 times the frequency of the first passband [2]. Therefore, the combline filters can have

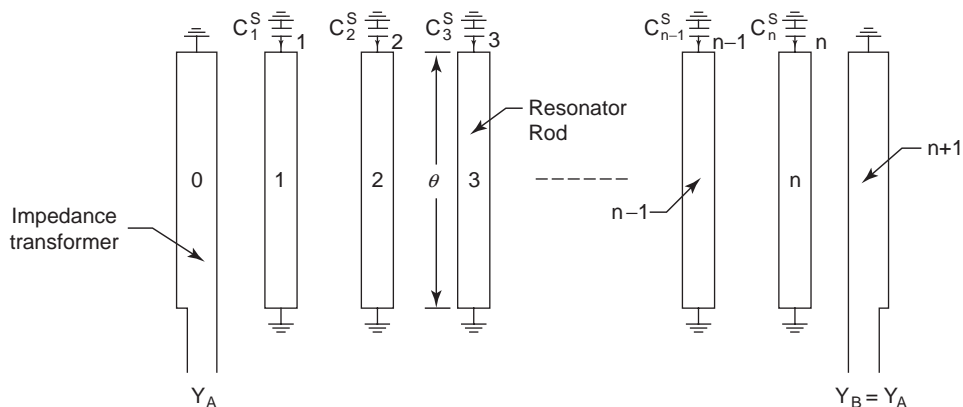


Figure 1. A combline filter with short-circuited input/output lines.

extremely broad spurious-free stopband compared with other types of filter.

Figure 2 shows the original four-pole combline filter having the configuration shown in Fig. 1 published by Matthaei in 1963 with its top cover removed. Figure 3 shows an alternate configuration of the combline filter that is currently widely used in the industry and is more favorable for manufacturing. The cross section of the resonator rods may be rectangular or circular; the circular configuration is more common because it is easier to manufacture. Each resonator rod has a counterbored hole at its open end. A tuning screw in the cover can be adjusted to penetrate in or out concentrically to the resonator rod to adjust the resonant frequency of the resonator to the desired value. The tuning screws between the resonator rods are used to adjust the coupling coefficient between the resonators.

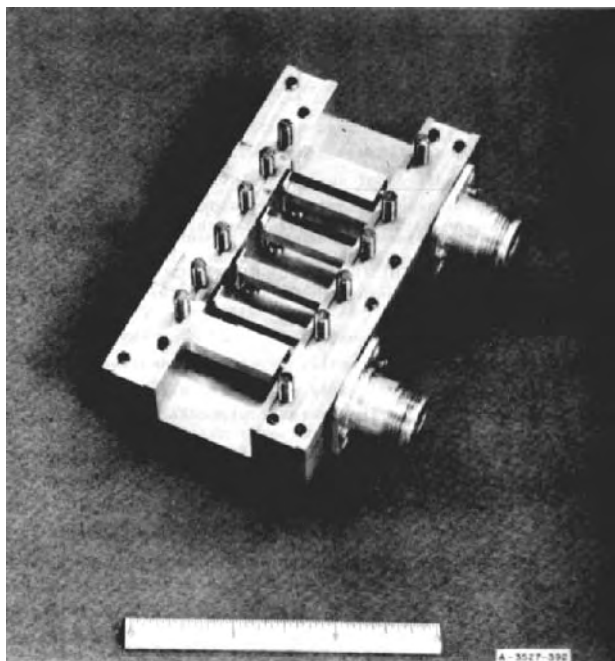


Figure 2. The original combline filter [1].

The input/output coupling can be achieved by short (or open)-circuited impedance transformer bars as shown in Matthaei's original configuration [2], or by direct tap as shown in Fig. 3. The input/output coupling can also be achieved by a coupling loop or probe. As the later input/output coupling methods do not need an extended transmission rod at each end of the combline filter, the filter is more compact.

The resonator rods can be separate parts mounted into the filter housing, using screws to achieve good contact, or can be built into the filter housing so that resonators and enclosure constitute a single piece, with only a top cover, tuning screws, and connectors needed to complete the filter. The couplings between resonators can be controlled by the spacing between them or by varying the aperture dimension on a conductive wall between two resonators. The resonators can be arranged in a row or in any desired layout depending on the coupling structure of the filter.

Significant progress in microwave filter technology has taken place since the 1970s, particularly the use of elliptic function responses using nonadjacent couplings between resonators together with compact filter configurations [6–8,13,22,23]. Transmission zeros can be achieved on the lower, higher side or both sides of the filter's passband depending on the attenuation requirements. The resultant filter may have sharper attenuation response; thus fewer resonators are required, which results in a more compact filter with lower insertion loss. Figure 4 shows an example of an elliptic function combline filter with built-in resonators and a very compact configuration [39].

There are several ways to design a combline filter, but the most popular method is to use a lowpass prototype filter. This is transformed into the desired bandpass filter, and then the physical dimensions are determined by either approximation or full-wave 3D electromagnetic simulations. Figure 5 shows the typical design procedure of a combline filter based on this approach. First, the specifications are used to determine the desired filter parameters, such as number of resonators, bandwidth, passband ripple, and the desired ideal frequency responses from the lowpass prototype filter. Then the filter topology and equivalent-circuit parameters, such as filter element values g_k , the admittance inverters $J_{k,k+1}$, impedance inverters $K_{k,k+1}$, or coupling matrix $M_{k,k+1}$, are

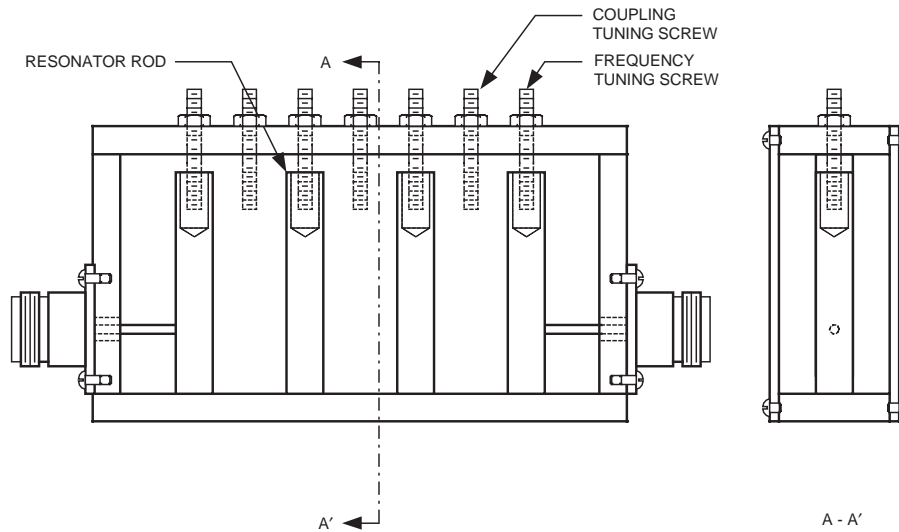


Figure 3. A combline filter with tapped-in input/output couplings.

determined. The required unloaded Q of the resonators is determined, and the basic cavity and rod dimensions can then be decided. Finally the rod, spacing, or aperture dimensions can be obtained from Matthaei's approximate design equations using Getsinger's or Cristal's design charts. A prototype is made to verify the correctness of the design and to perform some minor adjustments. Other practical issues such as temperature compensation and power handling capability should also be considered.

3. LOWPASS PROTOTYPE

Figure 6 shows a typical Chebyshev response of a lowpass prototype filter and that of the corresponding bandpass filter. The lowpass prototype filter is usually chosen to have unit bandwidth ω_1' for convenience, while the

bandwidth of the bandpass filter can be arbitrarily specified.

The relationship between the lowpass prototype response and the corresponding bandpass filter is given as [1,2]

$$L_A(\omega) = L'_A(\omega') \quad (1)$$

where

$$\omega' = \frac{\omega'_1}{\bar{\omega}} \left(\frac{\omega}{\omega_0} - \frac{\omega_0}{\omega} \right) \quad (2)$$

$$\bar{\omega} = \frac{\omega_2 - \omega_1}{\omega_0}, \quad \omega_0 = \sqrt{\omega_2 \omega_1} \quad (3)$$

The mapped lowpass prototype filter response has the same characteristics as that of the bandpass filter, or vice versa. Therefore, if the desired bandpass filter has n return loss poles in passband and m finite transmission zeros in stopband, the corresponding lowpass prototype filter will also have n poles in passband from $-\omega_1'$ to ω_1' at location a_i ($i = 1, 2, \dots, n$) and m zeros in stopband at location b_i ($i = 1, 2, \dots, m$). The insertion loss and return loss of the lowpass prototype filter versus frequency can be expressed in terms of the poles and zeros as

$$L_A = 10 \log \left(\frac{1}{1 + \varepsilon |\phi|^2} \right) \quad (4)$$

$$L_R = 10 \log \left(\frac{\varepsilon |\phi|^2}{1 + \varepsilon |\phi|^2} \right) \quad (5)$$

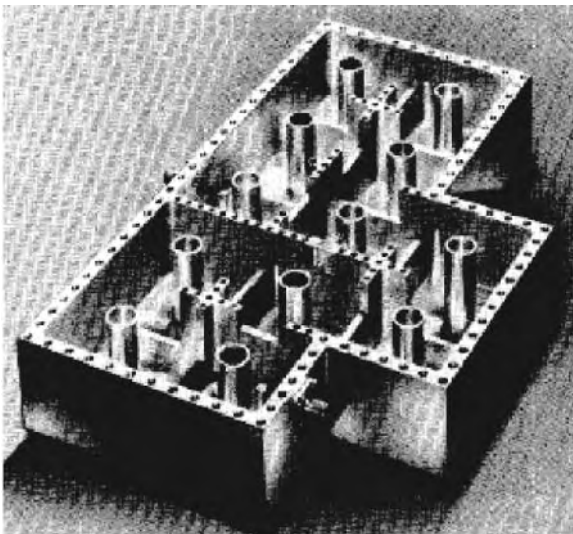


Figure 4. A 12-pole elliptic function combline filter [39].

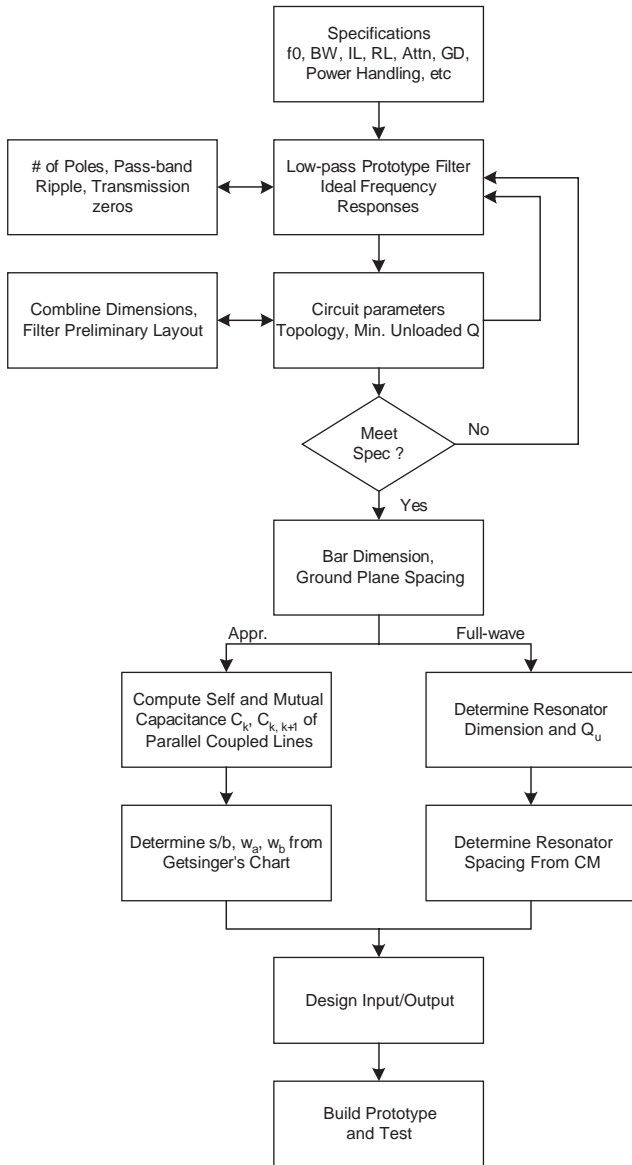


Figure 5. Typical combline filter design procedure.

where

$$\phi = \frac{P(\omega')}{Q(\omega')} = \frac{\prod_{i=1}^n (\omega' - a_i)}{\prod_{i=1}^m (\omega' - b_i)} \quad (6)$$

$$\varepsilon = 10^{L_{Ar}/10} - 1 \quad (7)$$

The approximation problem is to find the locations of the poles with locations of the given zeros to determine the equal-ripple passband response. The pole and zero locations of the transfer function can be determined by optimizing the polynomial function $P(\omega')$ through iterations [7] or by the recursive technique shown by Cameron [26]. For a Chebyshev response, all the transmission zeros are at infinity, and a closed-form expression for the pole loca-

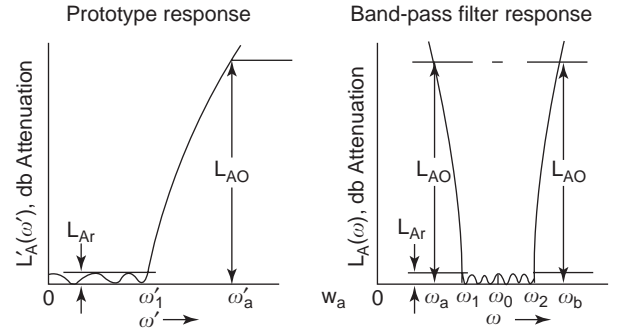


Figure 6. Lowpass prototype and corresponding bandpass filter responses.

tions exists, as follows:

$$a_i = \cos \left[\frac{(2i - 1)\pi}{2n} \right], \quad i = 1, 2, \dots, n \quad (8)$$

Figure 7 shows the attenuation characteristics for a 0.01-dB-ripple Chebyshev filter versus number of poles. The 0.01-dB passband ripple gives better than 25 dB return loss for the ideal case; therefore it is often used as the starting point for a practical filter design.

Given the transfer function and pole-zero locations of the lowpass prototype filter, the circuit element values of the lowpass and bandpass filters can be obtained by network synthesis. The commonly used forms for the prototype filter circuits are shown in Fig. 8 using g_k ($k = 0, 1, \dots, n, n + 1$) as the element values. The prototype filters in Fig. 8a using the shunt capacitor as the first element and in Fig. 8b using the series inductor as the first element have identical responses and g_k values; therefore, either form may be used depending on the applications. When converting a prototype filter to a bandpass filter, a lowpass prototype with n reactive elements leads to a bandpass filter with n resonators.

For Chebyshev filters having passband ripple L_{Ar} dB, $g_0 = 1$, and $\omega'_1 = 1$, the remaining g values can be obtained analytically as follows:

$$g_1 = \frac{2a_1}{\sinh \left(\frac{\beta}{2n} \right)} \quad (9)$$

$$g_k = \frac{4a_{k-1}a_k}{b_{k-1}g_{k-1}} \quad (10)$$

$$g_{n+1} = \begin{cases} 1 & \text{for } n \text{ odd} \\ \coth^2 \left(\frac{\beta}{4} \right) & \text{for } n \text{ even} \end{cases} \quad (11)$$

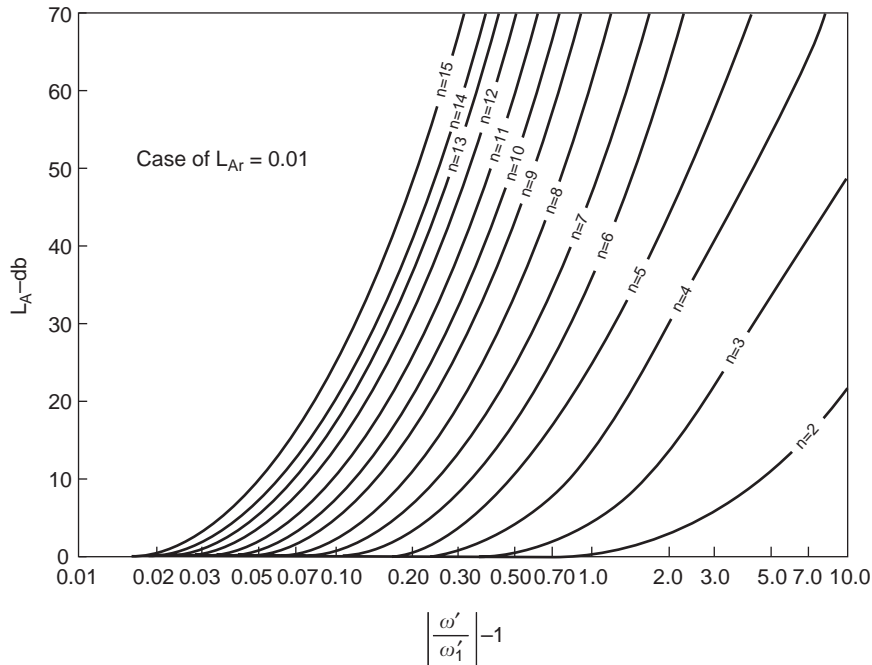


Figure 7. Attenuations of the 0.01-dB-ripple Chebyshev filters.

Here

$$\beta = \ln \left(\coth \frac{L_{Ar}}{17.37} \right) \tag{12}$$

$$a_k = \sin \left[\frac{(2k - 1)\pi}{2n} \right] \tag{13}$$

$$b_k = \sinh^2 \left(\frac{\beta}{2n} \right) + \sin^2 \left(\frac{k\pi}{n} \right) \tag{14}$$

Table 1 presents the computed g element values for Chebyshev filters for $n=1$ through 10 with 0.01- and 0.1-dB passband ripple levels.

The g values of the lowpass prototype filter given in Eqs. (9)–(11) are normalized to unit input impedance $g_0 = 1$ and unit bandwidth $\omega'_1 = 1$. For filters having different input port impedance and bandwidth, the desired inductance or capacitance values can be easily scaled from the normalized g values by the following equations

$$L = \frac{R_0}{\omega'} L' \tag{15}$$

$$C = \frac{C'}{R_0 \omega'} \tag{16}$$

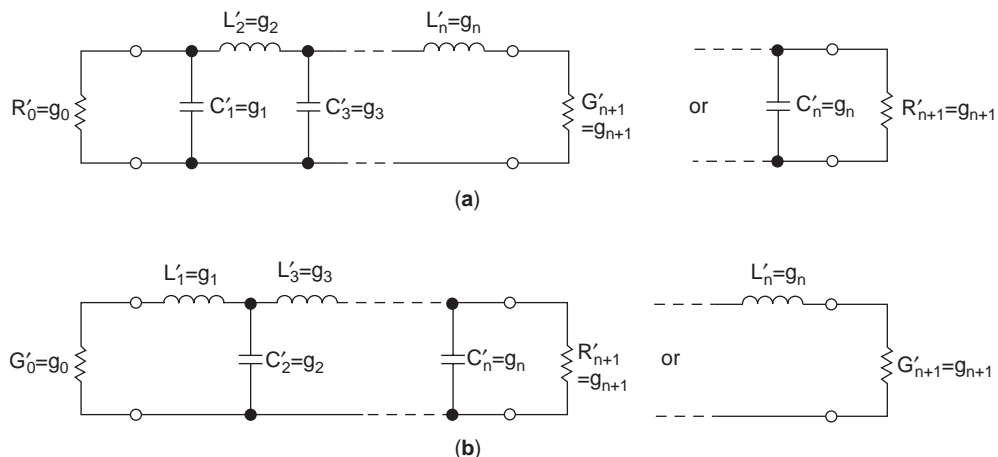


Figure 8. Lowpass filter circuit and parameters (a) a shunt capacitor as first element; (b) a series inductor as first element.

Table 1. Element Values for Chebyshev Filters Having $g_0 = 1, \omega_0' = 1$ for 0.01- and 0.1-dB Ripples

Value of n	g_1	g_2	g_3	g_4	g_5	g_6	g_7	g_8	g_9	g_{10}	g_{11}
0.01 dB ripple											
1	0.0960	1.0000									
2	0.4488	0.4077	1.1007								
3	0.6291	0.9702	0.6291	1.0000							
4	0.7128	1.2003	1.3212	0.6476	1.1007						
5	0.7563	1.3049	1.5773	1.3049	0.7563	1.0000					
6	0.7813	1.3600	1.6896	1.5350	1.4970	0.7098	1.1007				
7	0.7969	1.3924	1.7481	1.6331	1.7481	1.3924	0.7969	1.0000			
8	0.8072	1.4130	1.7824	1.6833	1.8529	1.6193	1.5554	0.7333	1.1007		
9	0.8144	1.4270	1.8043	1.7125	1.9057	1.7125	1.8043	1.4270	0.8144	1.0000	
10	0.8196	1.4369	1.8192	1.7311	1.9362	1.7590	1.9055	1.6527	1.5817	0.7446	1.1007
0.1 dB ripple											
1	0.3052	1.0000									
2	0.8430	0.6220	1.3554								
3	1.0315	1.1474	1.0315	1.0000							
4	1.1088	1.3061	1.7703	0.8180	1.3554						
5	1.1468	1.3712	1.9750	1.3712	1.1468	1.0000					
6	1.1681	1.4039	2.0562	1.5170	1.9029	0.8618	1.3554				
7	1.1811	1.4228	2.0966	1.5733	2.0966	1.4228	1.1811	1.0000			
8	1.1897	1.4346	2.1199	1.6010	2.1699	1.5640	1.9444	0.8778	1.3554		
9	1.1956	1.4425	2.1345	1.6167	2.2053	1.6167	2.1345	1.4425	1.1956	1.0000	
10	1.1999	1.4481	2.1444	1.6265	2.2253	1.6418	2.2046	1.5821	1.9628	0.8853	1.3554

where the values of the normalized inductor L' and capacitor C' are equal to the particular g value of the prototype filter.

The lowpass prototype filter circuits in Fig. 8 consist of both inductors and capacitors. However, in bandpass and bandstop filter designs, it is desirable to use the same type of resonator having all inductors or all capacitors in the prototype filters.

This can be achieved by using the impedance inverter (K inverter) or admittance inverter (J inverter) as shown in Fig. 9. The inverters act like frequency-independent quarter-wavelength lines, so that only inductors exist in the K -inverter prototype, and only

capacitors in the J -inverter prototype networks. Figure 9 also gives the equations for converting the g value of the lowpass filter prototype to these forms. The components value such as $R, L, C,$ or G in the prototype circuit using J or K inverters can be chosen arbitrarily. The frequency responses of the inverter circuits in Fig. 9 are identical to those of the original prototype filters.

Another commonly used analysis method in the cavity-type bandpass filter design is to use the coupling matrix. Figure 10 presents the equivalent circuit of a generalized coupled bandpass prototype filter using the coupling matrix [7,26].

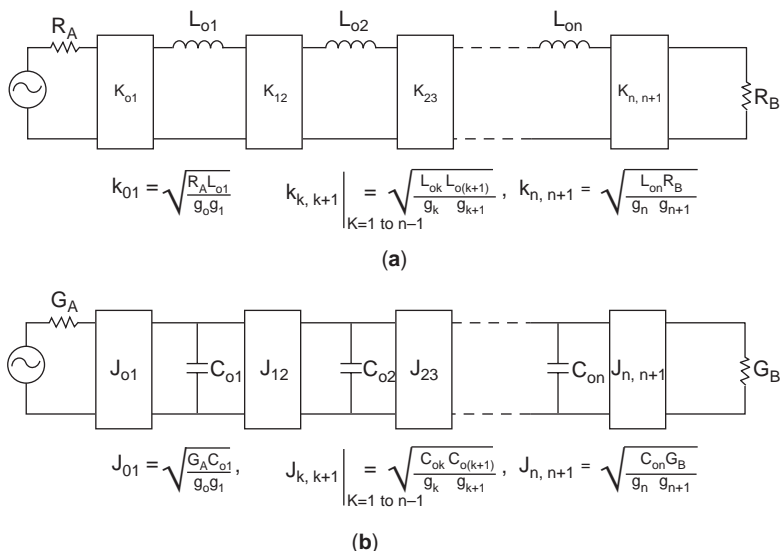


Figure 9. Modified prototype using impedance and admittance inverters.

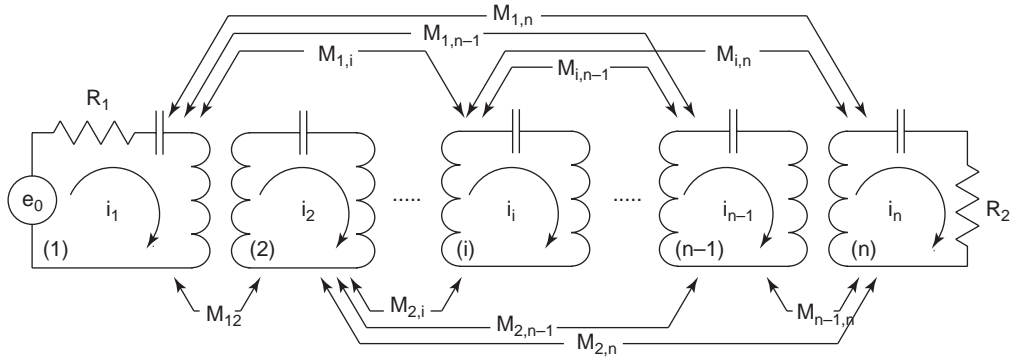


Figure 10. A bandpass filter equivalent circuit.

A general solution of the narrowband coupled cavity filter described above has been presented in a paper by Atia and Williams in the form of the loop equations as [7]

$$[Z] \cdot [I] = [V] \quad (17)$$

$$([R] + s[I] + j[M]) \begin{bmatrix} i_1 \\ i_2 \\ \vdots \\ i_{n-1} \\ i_n \end{bmatrix} = \begin{bmatrix} e_1 \\ 0 \\ \vdots \\ 0 \\ 0 \end{bmatrix} \quad (18)$$

where

$$s = j\omega' \quad (19)$$

$$[M] = \begin{bmatrix} \lambda_{11} & M_{12} & M_{13} & \cdots & M_{1,n-1} & M_{1n} \\ M_{12} & \lambda_{22} & M_{23} & \cdots & M_{2,n-1} & M_{2n} \\ M_{13} & M_{23} & \lambda_{33} & \cdots & M_{3,n-1} & M_{3n} \\ \vdots & \vdots & \vdots & \ddots & \vdots & \vdots \\ M_{1,n-1} & M_{2,n-1} & M_{3,n-1} & \cdots & \lambda_{n-1,n-1} & M_{n-1,n} \\ M_{1n} & M_{2n} & M_{3n} & \cdots & M_{n-1,n} & \lambda_{nn} \end{bmatrix} \quad (20)$$

The matrix R has all-zero entries except for the (1, 1) and (n, n) elements, which are R_1 and R_n , respectively. M is the so-called coupling matrix and has general entries of M_{ij} for $i \neq j$, and λ_{ii} for $i = j$. λ_{ii} gives the resonant frequency of each resonator mapped to the lowpass prototype domain according to Eqs. (2) and (3).

The coupling matrix of the bandpass filter can be determined by the network synthesis method as described in Refs. 7 and 26 or by optimization from the pole and zero locations of the filter's transfer function [24]. For the case of direct network optimization, the coupling matrix elements are the optimization variables and the objective error function can be established by determining the

difference between the transfer function frequency response of the prototype filter and the frequency response of the optimized filter. The Chebyshev coupling matrix of the same order can be used as the starting guess of the coupling matrix.

For filters with Chebyshev frequency responses, the coupling matrix of the filter can be obtained analytically from the g values of the prototype filter as

$$R_1 = \frac{1}{g_0 g_1} \quad (21)$$

$$M_{i,i+1} = \frac{1}{\sqrt{g_i g_{i+1}}} \quad (22)$$

$$R_n = \frac{1}{g_{n-1} g_n} \quad (23)$$

where the remaining elements in the coupling matrix are zero.

As in the case of the lowpass prototype filter, the coupling matrix shown in Eq. (20) is normalized to the passband from -1 to $+1$ and zero center frequency. For a bandpass filter with center frequency f_0 , and bandwidth BW, the required couplings of the filter are the normalized filter's coupling elements multiplied by the bandwidth with the unit same as that of the bandwidth.

4. DIRECT-COUPLED COMBLINE FILTER DESIGN

Matthaei gave the approximate design equations for the direct-coupled comblines filter shown in Fig. 1 in terms of the resonator rod's self-capacitance to ground C_j per unit length, and the mutual capacitance $C_{j,j+1}$ per unit length between neighboring resonator bars j and $j+1$ [1,2]. The design equations use the lowpass prototype filter parameters g_j ($i = 0, 1, \dots, n, n+1$) to achieve the desired frequency responses. The equations are sufficiently accurate for the applications of narrow bandpass filters with bandwidths up to octave.

By specifying the width of the filter enclosure and the resonator rod dimension, the admittance Y_{aj} of the resonator lines can be computed. It is usually desirable

to choose the ratio of enclosure width to resonator line-width in the range between 3 and 4 so that optimum unloaded Q can be achieved. In addition, the electrical length θ_0 of the resonator lines ranges between $\pi/4$ and $\pi/3$ at center frequency so that the filter will have both wide spurious-free stopband and less unloaded Q degradation due to excessive end loading in case shunt resonators are used.

4.1. Design Equations

The normalized J -inverter parameters of the combline filter can then be computed as

$$G_{T1} = \frac{(\omega_2 - \omega_1)b_1}{g_0g_1\omega_0\omega'_1} \tag{24}$$

$$J_{j,j+1} = \frac{(\omega_2 - \omega_1)}{\omega_0\omega'_1} \sqrt{\frac{b_j b_{j+1}}{g_j g_{j+1}}} \tag{25}$$

$$G_{Tn} = \frac{(\omega_2 - \omega_1)b_n}{g_n g_{n+1}\omega_0\omega'_1} \tag{26}$$

where

$$b_j = Y_{aj} \left(\frac{\cot \theta_0 + \theta_0 \csc^2 \theta_0}{2} \right) \tag{27}$$

The normalized self-capacitances per unit length between each resonator rod and ground are

$$\frac{C_0}{\epsilon} = \frac{Z_0 Y_A}{\sqrt{\epsilon_r}} \left(1 - \frac{G_{T1}}{Y_A} \right) \tag{28}$$

$$\frac{C_1}{\epsilon} = \frac{Z_0 Y_A}{\sqrt{\epsilon_r}} \left(\frac{Y_{a1}}{Y_A} - 1 + \frac{G_{T1}}{Y_A} - \frac{J_{12}}{Y_A} \tan \theta_0 \right) + \frac{C_0}{\epsilon} \tag{29}$$

$$\frac{C_j}{\epsilon} = \frac{Z_0 Y_A}{\sqrt{\epsilon_r}} \left(\frac{Y_{aj}}{Y_A} - \frac{J_{j-1,j}}{Y_A} \tan \theta_0 + \frac{G_{Tn}}{Y_A} - \frac{J_{j,j+1}}{Y_A} \tan \theta_0 \right), \tag{30}$$

$j = 2 \text{ to } n - 1$

$$\frac{C_n}{\epsilon} = \frac{Z_0 Y_A}{\sqrt{\epsilon_r}} \left(\frac{Y_{an}}{Y_A} - 1 + \frac{G_{Tn}}{Y_A} - \frac{J_{n-1,n}}{Y_A} \tan \theta_0 \right) + \frac{C_{n+1}}{\epsilon} \tag{31}$$

$$\frac{C_{n+1}}{\epsilon} = \frac{Z_0 Y_A}{\sqrt{\epsilon_r}} \left(1 - \frac{G_{Tn}}{Y_A} \right) \tag{32}$$

The normalized mutual capacitances per unit length between two adjacent resonator rods are

$$\frac{C_{01}}{\epsilon} = \frac{Z_0 Y_A}{\sqrt{\epsilon_r}} - \frac{C_0}{\epsilon} \tag{33}$$

$$\frac{C_{j,j+1}}{\epsilon} = \frac{Z_0 Y_A}{\sqrt{\epsilon_r}} \left(\frac{J_{j,j+1}}{Y_A} \tan \theta_0 \right), \quad j = 1 \text{ to } n - 1 \tag{34}$$

$$\frac{C_{n,n+1}}{\epsilon} = \frac{Z_0 Y_A}{\sqrt{\epsilon_r}} - \frac{C_{n+1}}{\epsilon} \tag{35}$$

The required lumped capacitances C_j^s between the open end of the resonator rod and ground are

$$C_j^s = Y_{aj} \frac{\cot \theta_0}{\omega_0}, \quad j = 1 \text{ to } n \tag{36}$$

Knowing the desired self- and mutual capacitances of the combline filter resonator rods, we can determine the spacing between the adjacent resonators from the Getsinger or Cristal's design curves for the parallel-coupled rectangular or circular bars as described in the following section.

4.2. Parallel-Coupled Bars

The resonator bars of a combline filter can be considered as an array of the parallel lines. The cross section of the bar is usually rectangular or circular. The dimensions of the lines can be related to the various line capacitances per unit length. The self- and mutual capacitances obtained from Eqs. (28)–(36) can be used to determine the bar dimensions from Getsinger's parallel-coupled rectangular line curves for the rectangular cross section resonator rod combline filters, or from Cristal's parallel-coupled cylindrical rod design data for the circular cross section resonator rod combline filters.

4.2.1. Coupled Rectangular Bars between Parallel Plates. The cross section of a parallel-coupled rectangular bars under consideration and various line capacitances are shown in Fig. 11. There are two parallel ground planes spaced a distance b apart, and a pair of rectangular bars located parallel to and midway between the ground planes. Assuming that C_a is the self-capacitance per unit length between line a and ground, C_{ab} is the mutual capacitance per unit length between lines a and b , and C_b is the capacitance per unit length between line b and ground, then, in terms of odd- and even-mode capacitances for lines a and b , respectively, we have

$$C_{oo}^a = C_a + 2C_{ab}, \quad C_{oe}^a = C_a \tag{37}$$

$$C_{oo}^b = C_b + 2C_{ab}, \quad C_{oe}^b = C_b \tag{38}$$

In Fig. 11, the capacitance per unit length of each line has been separated into component parts by their contributions. C_p is the parallel-plate capacitance per unit length from the top or bottom side of one bar to the adjacent ground plane, C'_{fe} is the fringing capacitance per unit length to ground from the inner corner when the bars

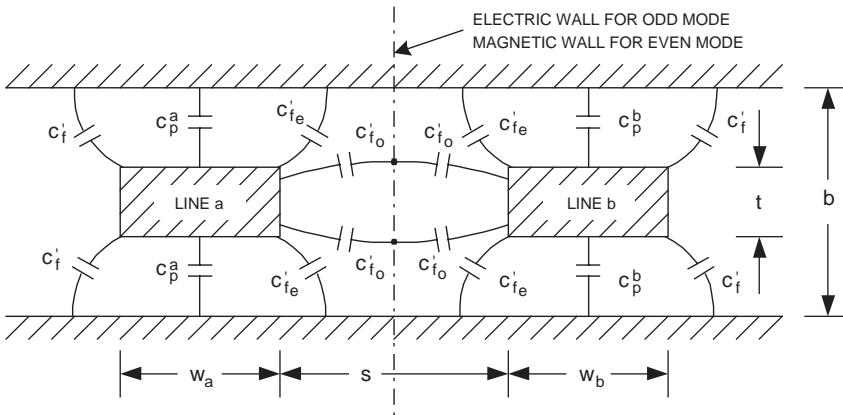


Figure 11. Cross section of parallel-coupled rectangular lines.

are excited in the even mode, and C'_{fo} is the fringing capacitance per unit length to ground from the inner corner when the bars are excited in the odd mode. The capacitance C'_f is the fringing capacitance per unit length for any of the outer corners of the rods. Assuming that all the coupled bars have the same height and thickness, so that the fringing capacitances are the same for both bars, the total self- and mutual capacitances of the coupled bars are

$$C_a = 2(C_p^a + C'_f + C'_{fe}) \tag{39}$$

$$C_{ab} = (C'_{fo} - C'_{fe}) \tag{40}$$

$$C_b = 2(C_p^b + C'_f + C'_{fe}) \tag{41}$$

Figures 12–14 give the normalized design charts by Getzinger [3], which relate $\Delta C/\epsilon$, C'_{fe}/ϵ , C'_{fo}/ϵ , and C'_f/ϵ to the rectangular bar dimensions, where

$$\Delta C = C_{ab} \tag{42}$$

To design a combline filter with rectangular cross section resonator bars, first compute the C_j and $C_{j,j+1}$ values of the filter using Eqs. (28)–(36), and then select a convenient value for t/b , and use Fig. 12 of $\Delta C/\epsilon$ and C'_{fe}/ϵ versus s/b to determine $s_{j,j+1}/b$ and also C'_{fe}/ϵ . Using t/b and Fig. 14 of C'_f/ϵ versus t/b , C'_f/ϵ can be determined. As the parallel-plate capacitance C_p/ϵ is given by

$$\frac{C_p}{\epsilon} = 2 \frac{w/b}{1 - t/b} \tag{43}$$

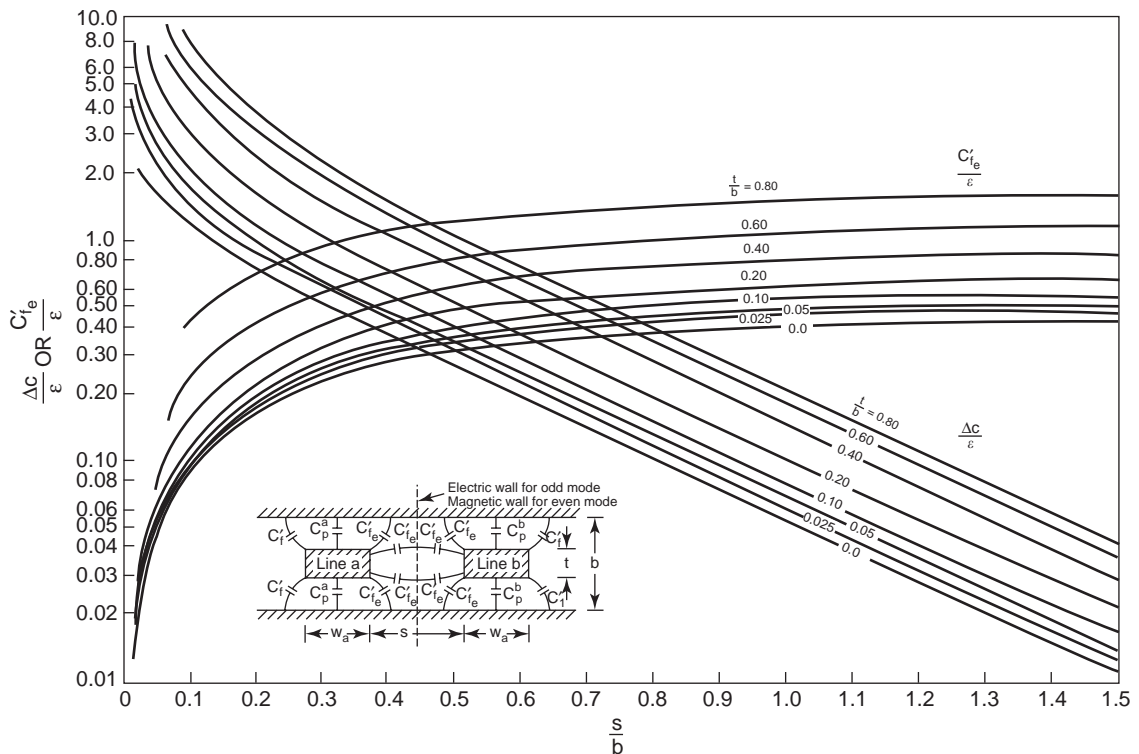


Figure 12. Fringing capacitances for coupled rectangular bars.

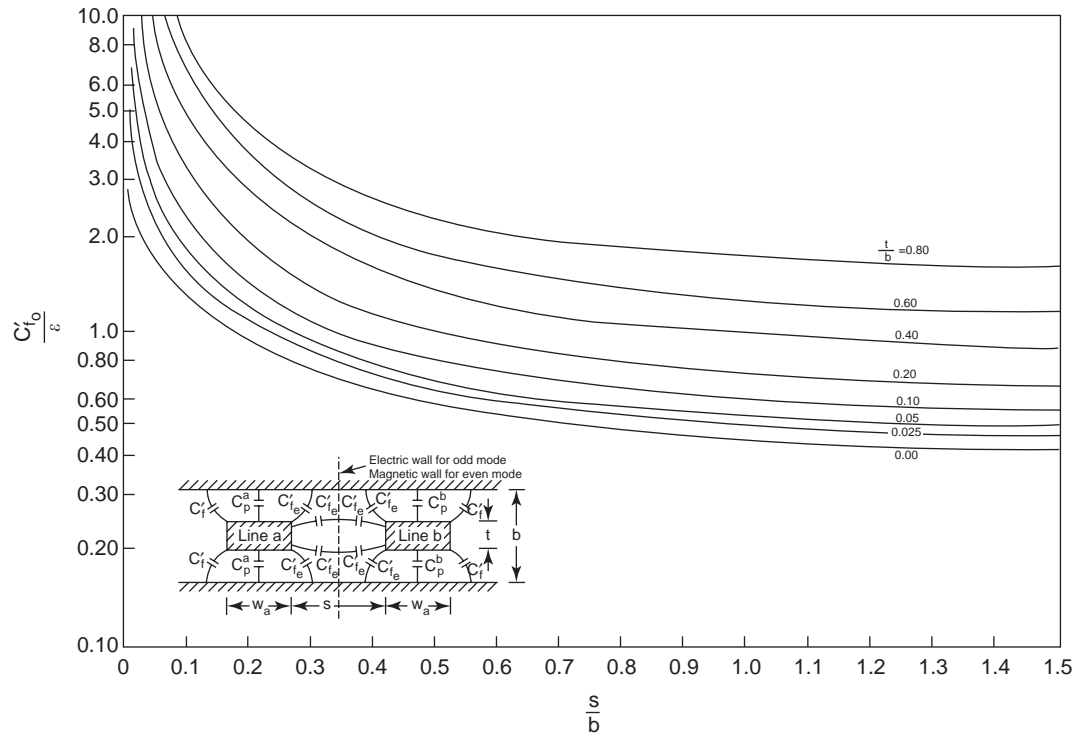


Figure 13. Odd-mode fringing capacitances for coupled rectangular bars.

when the ground-plane spacing b is specified, the desired bar width w_j can be determined as follows:

$$\frac{w_j}{b} = \frac{1}{2} \left(1 - \frac{t}{b} \right) \left[\frac{1}{2} \left(\frac{C_j}{\epsilon} \right) - \frac{(C'_{fe})_{j-1,j}}{\epsilon} - \frac{(C'_{fe})_{j,j+1}}{\epsilon} \right] \quad (44)$$

$$\frac{w_j}{b} = \frac{1}{2} \left(1 - \frac{t}{b} \right) \left[\frac{1}{2} \left(\frac{C_j}{\epsilon} \right) - \frac{C'_{fe}}{\epsilon} - \frac{C'_f}{\epsilon} \right] \quad (45)$$

4.2.2. Coupled Circular Rods between Parallel Plates. Comblines filters made from circular cylindrical

resonator rods can achieve the same excellent electrical performance and at the same time may offer manufacturing advantages. Cristal has given design data for coupled circular cylindrical rods between parallel ground planes [4] that can be used to accurately design a comblines filter with circular resonator rods. Figure 15 shows the geometry of the periodic, circular cylindrical rods between parallel ground planes under consideration. The circular rods have diameter d and are spaced periodically at a distance c . The ground planes are separated at distance b .

The spacing between adjacent rod surfaces is denoted by s and is given by

$$s = c - d \quad (46)$$

The total static capacitances of the rods are related to the mutual capacitance between two adjacent rods C_m and the self-capacitance C_g of each rod. The total capacitance measured between one rod and ground when the rods are driven in the odd mode is

$$C_o = C_g + 4C_m \quad (47)$$

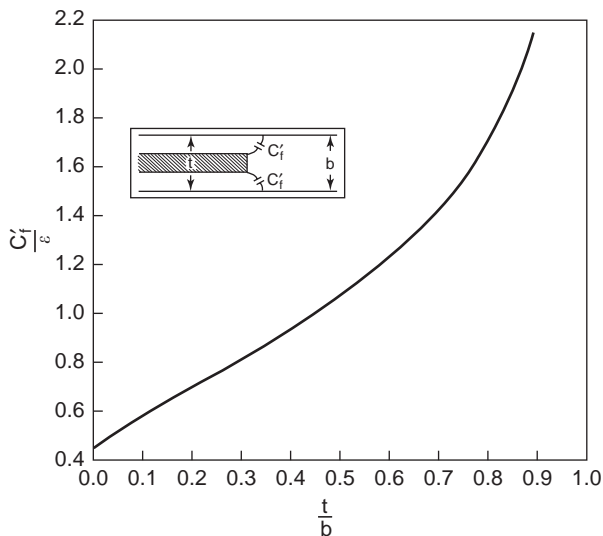


Figure 14. Fringing capacitance for an isolated rectangular bar.

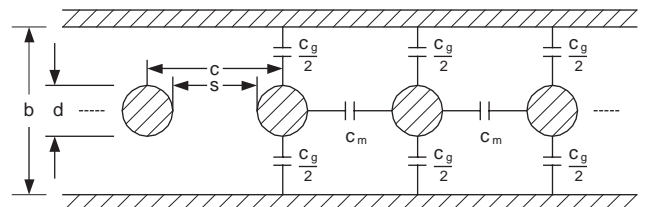


Figure 15. Cross section of parallel-coupled circular rods.

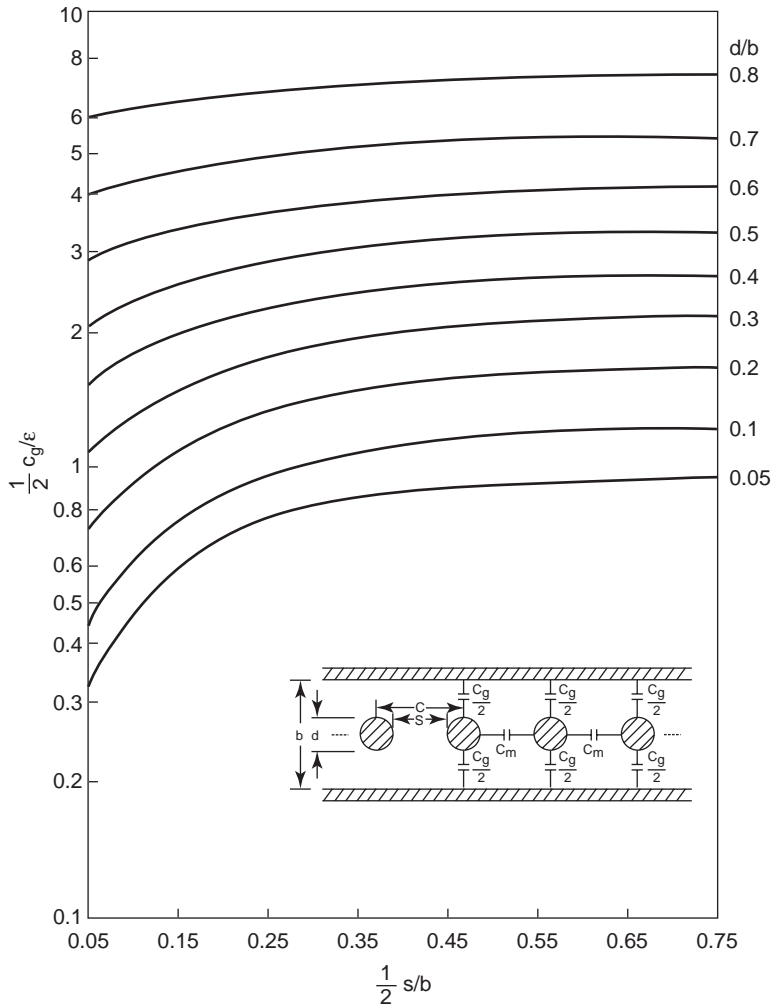


Figure 16. Graph of normalized mutual capacitance C_m/ϵ versus $\frac{1}{2}(s/b)$.

assuming that both sides of the rod are having the same potential conditions. The total capacitance measured between one rod and ground when the rods are driven in the even mode is

$$C_e = C_g \quad (48)$$

From Eqs. (47) and (48) we can obtain

$$C_m = \frac{1}{4}(C_o - 4C_e) \quad (49)$$

Cristal's design graphs of the normalized capacitance C/ϵ versus normalized spacing s/b are given in Fig. 16 for C_m/ϵ and in Fig. 17 for $\frac{1}{2}C_g/\epsilon$.

As in the rectangular cross section resonator bar case, to design a combline filter with circular cylindrical resonator rod, one first needs to compute the C_j and $C_{j,j+1}$ values of the filter using Eqs. (28)–(36), where

$$C_o = C_j \quad (50)$$

$$C_m = C_{j,j+1} \quad (51)$$

and then use Fig. 17 of C_m/ϵ to determine the rod spacing $s_{j,j+1}/b$ and use Fig. 16 of C_g/ϵ to determine the normalized rod diameter d/b .

4.3. Tapped-Line Input and Output

For a tap point located around the bottom 20% of a $\lambda/4$ -long resonator rod, the relationship between the tap point and the resulting loaded Q_e is given approximately by [15]

$$Q_e = \frac{\pi}{4} \left(\frac{R}{Z_o} \right) \left[\frac{1}{\sin^2[(\pi/2)(l/L)]} \right] \quad (52)$$

$$Q_e = \frac{f_o}{R_1 BW} \quad (53)$$

where l is the height of the tap point to the bottom of the resonator rod; L is the equivalent height of the resonator rod, which is equal to $\lambda/4$; R is the impedance of the input or output port; R_1 is the element of the filter's coupling matrix; and Z_o is the impedance of the resonator rod. Figure 18 shows the graph of the equation for the loaded Q .

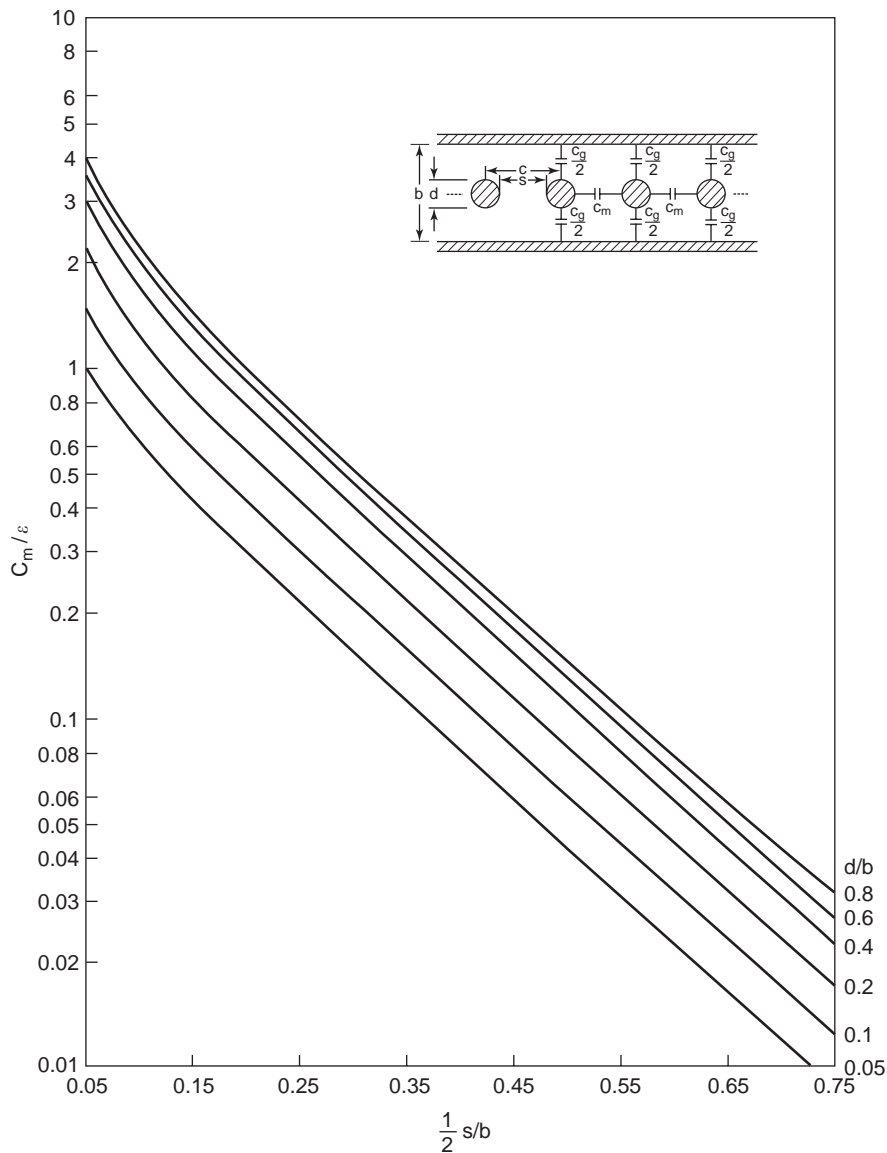


Figure 17. Graph of normalized half self-capacitance $\frac{1}{2} C_g/\epsilon$ versus $\frac{1}{2} (s/b)$.

Cristal [17] later presented a general open-wire equivalent circuit considering the effects of the coupled resonators using a graph transformation process for combline and interdigital filter designs. In previous papers he assumed that the input or output port will be directly connected to the tapped-in point. However, for practical applications, the tapped line will have an impedance different from that of the input/output port and resonator rod with a given electrical length. The tapped-line length and impedance can have significant effect and therefore should be included in the analysis of the combline filter input/output couplings. Figure 19 shows an equivalent circuit of the tapped-line input/output coupling neglecting the effect of the rest of the resonators. In Cristal’s approach, the graph transformation process or a circuit simulator can be used to solve the tapped-line coupling circuit.

5. FILTER TOPOLOGIES

The combline filter design equations presented in the previous sections are approximate and based on the direct-coupled filter type, typically exhibiting Chebyshev frequency responses. The stopband attenuation level is determined mainly by the number of stages of the filter. The use of nonadjacent or cross-couplings in the narrow-bandwidth bandpass filter with elliptic function response permits great flexibility in the choice of the frequency response. As a result, a smaller number of resonators are required to meet the attenuation specification.

Theoretically, cross-coupling can be applied between any two nonadjacent resonators of the filter, and also including the input and output ports. However, in practical applications the cross-couplings that can be applied are usually limited by the physical layout and complexity of

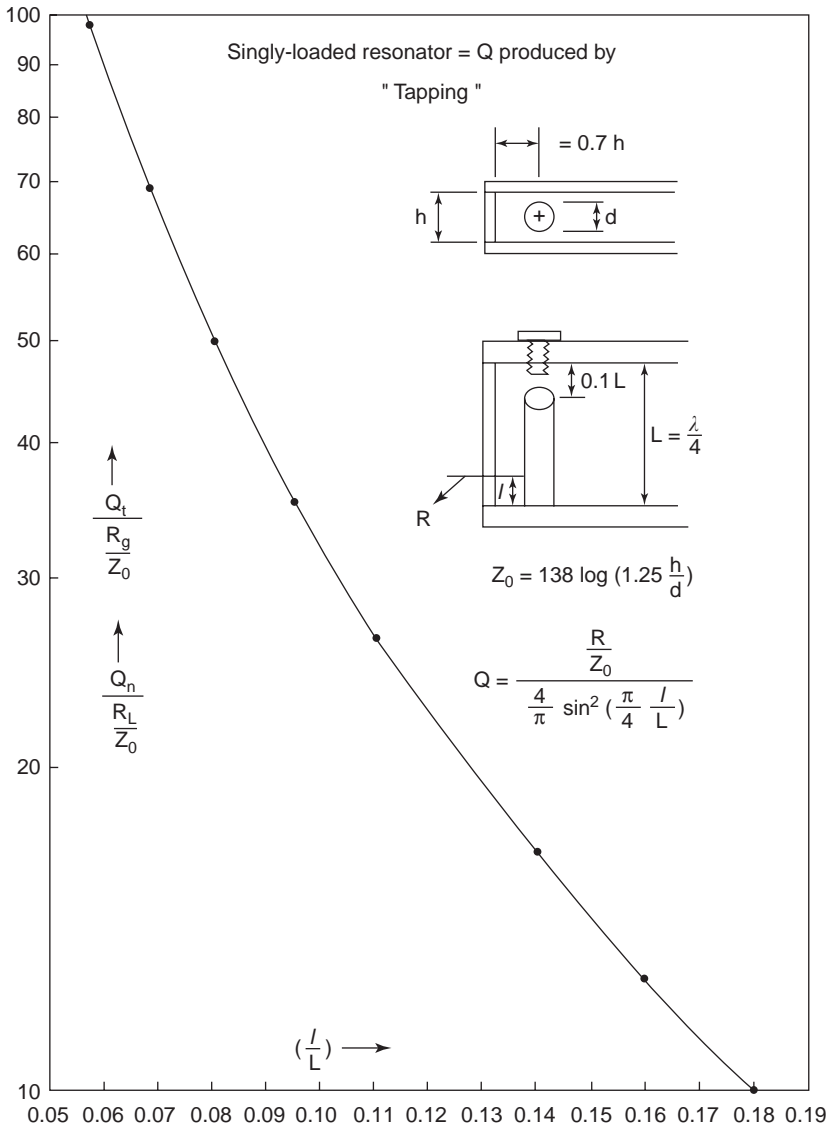


Figure 18. Loaded combline resonator Q versus tapped-line position.

the filters. The advantage of the filter with an extra number of cross-couplings may be offset by the layout limitation, with much more development effort and the sensitivity of the filter network, leading to longer tuning time and poorer temperature stability.

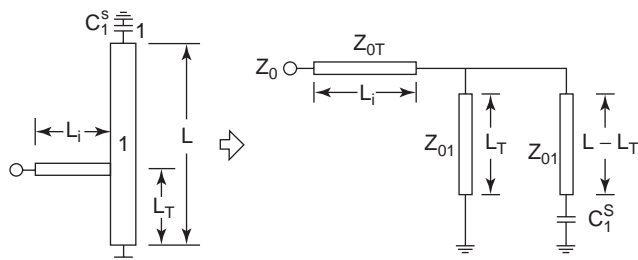


Figure 19. An equivalent circuit for the tapped-line input/output coupling geometry.

Comblines filters with either asymmetric or symmetric frequency response may be realized to meet the desired attenuation characteristics by applying the proper cross-coupling topology and values. For each desired filter transfer function, the configuration or topology that can achieve the targeted frequency response is not unique. However, it is usually preferable to achieve the desired frequency response by using known simple topologies. Figure 20 shows typical canonical-form coupled resonator filters with cross-couplings that can achieve the asymmetric frequency response in part (a), and symmetric frequency response in part (b) [13]. Topologies for so-called CQ and CT filters are shown in Fig. 21.

Filters having complicated cross-coupling structures as shown in Fig. 20 can achieve more transmission zeros using a minimum number of cross-couplings. However, each cross-coupling may affect more than one transmission zero location, which usually makes them more difficult to tune. For commercial applications when cost is a main concern,

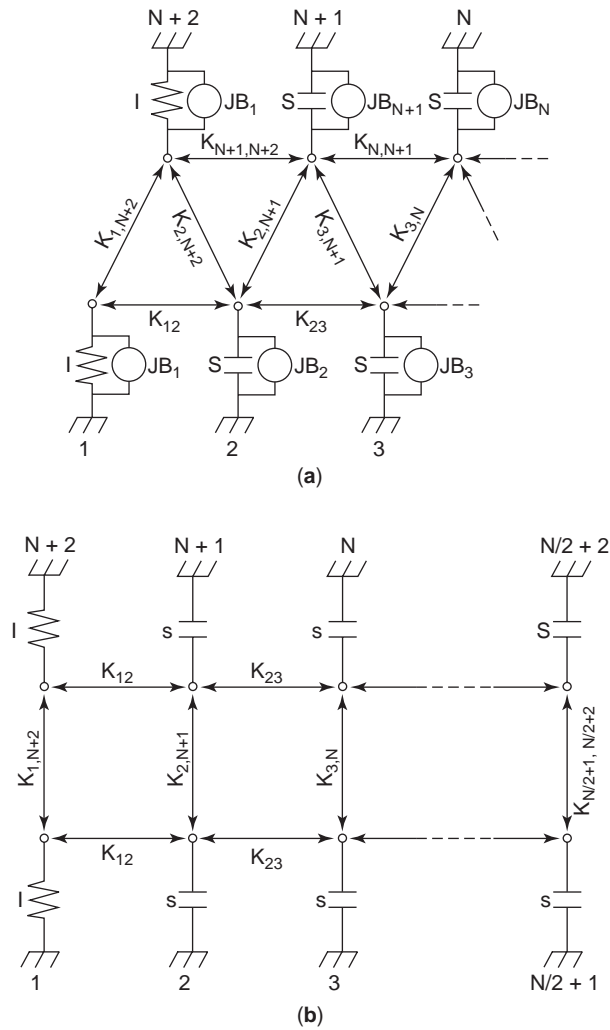


Figure 20. Canonical prototype networks having (a) asymmetric and (b) symmetric frequency responses.

the filter topology that makes the filter easy to design and to tune will be very attractive to filter designers.

The cascaded triplet (CT) or cascaded quadruplet (CQ) sections are relatively simple to tune. Each section is typically responsible only for the transmission zeros that it generates and therefore can be used as a basic building block to create more complicated filter structures. Figure 22 presents the examples using two CT or CQ sections in the cascaded filters.

A CT filter consists of cascaded groups of three cavities or nodes, each with one cross-coupling between first and third resonators in the CT section. The cross section will introduce one transmission zero at either the lower or the higher side of the passband depending on the sign of the cross-coupling. A cross-coupling with negative sign or capacitive-type coupling will generate the transmission zero at the lower side, while the positive or inductive cross-coupling will generate the transmission zero at the higher side. An aperture between two combline resonators usually achieves positive coupling unless the aperture is at the top of the cavity and the electrical length of the comb-

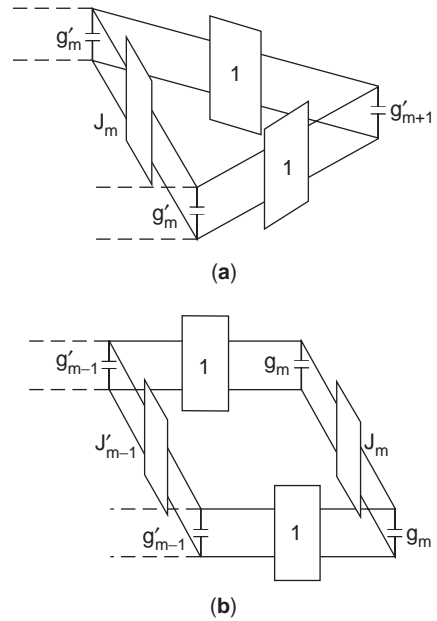


Figure 21. Typical filter building blocks: (a) cascaded triplet (CT) section; (b) cascaded quadruplet (CQ) section.

line rod is over 75° [48]. A coupling bar or probe between the top of the resonators can usually achieve the required capacitive coupling.

Similarly, a CQ filter consists of cascaded groups of four cavities or nodes, each with one cross-coupling between the first and fourth resonators in the CQ section. When the cross-coupling is capacitive, one symmetric pair of transmission zeros one at each side can be achieved. For inductive cross-coupling, a pair of zeros will be on the real axes, and as a result the group delay frequency response of the filter may be equalized.

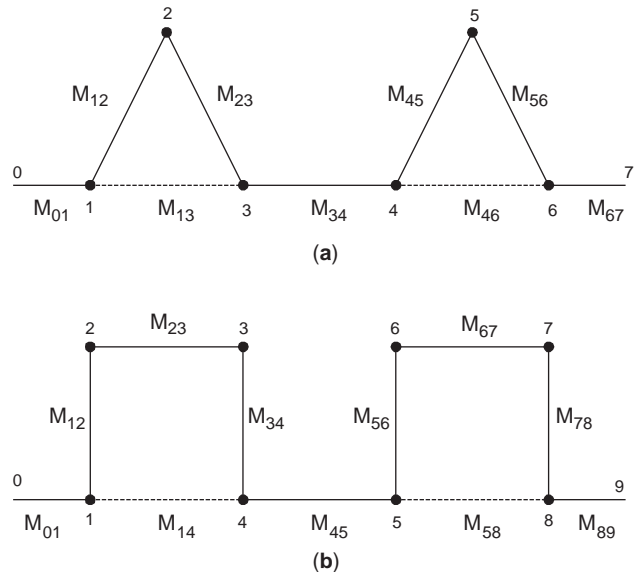


Figure 22. Cascaded coupling diagram: (a) a six-pole CT filter; (b) an eight-pole CQ filter.

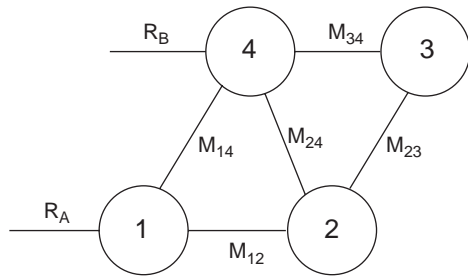


Figure 23. Generalized quadruplet section for two-transmission-zero implementation.

If the quadruplet section has two cross-couplings as shown in Fig. 23, two asymmetric transmission zeros may then be achieved. The locations of the zeros depend on the relative sign of the couplings. Assuming that all the adjacent couplings are inductive, Table 2 summarizes the locations of the zeros corresponding to the sign of the cross-couplings. Similarly, a general five-resonator section with three transmission zeros can be analyzed [25]. Figure 24 gives an example of an eight-pole combline filter having five transmission zeros using multiple cross-coupling four- and five-resonator sections. The three high-side zeros are realized by the 1–5 cross-coupled five-resonator section, while the two low-side zeros are realized by the 5–8 cross-coupled four-resonator section.

As a general rule, a simple Chebyshev response filter that meets the passband, but not the stopband, requirements would be used as the starting point of the design. By bringing transmission zeros from DC or infinity to finite frequencies, the desired stopband characteristics can be achieved. In most cases, the overall degree of the filter can be reduced compared with a Chebyshev design that meets the same requirements.

6. EM SIMULATIONS

To realize narrowband combline filters with relatively complex resonator topologies, all physical parameters such as cavity and aperture dimensions need to be determined from the given coupling matrix. Such filter designs are now increasingly dependent on accurate electromagnetic (EM) computer simulations, due to complexity of the filter structures. As a result, strong interaction

Table 2. Locations of Transmission Zeros for Generalized Quadruplet Section

Case	M_{14}	M_{24}	Number of Zeros ($<f_0, >f_0$)
1	= 0	< 0	1 (1, 0)
2	= 0	> 0	1 (0, 1)
3	< 0	= 0	2 (1, 1)
4	> 0	= 0	2 (j, j)
5	> 0	> 0	2 (0, 2)
6	> 0	< 0	2 (2, 0)
7	< 0	< 0	2 (1, 1)
8	< 0	> 0	2 (1, 1)

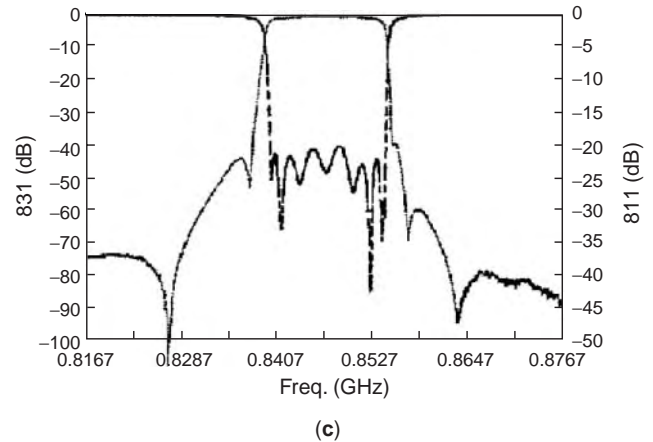
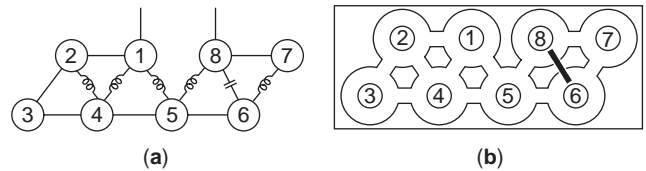


Figure 24. An eight-pole combline filter with five transmission zeros: (a) equivalent circuit; (b) layout; (c) measured frequency response.

between resonators cannot be neglected and should be considered in the design. These requirements usually can be satisfied only by EM simulation. As shown in Fig. 5, the approximate design equations from Eqs. (24)–(53) for space-coupled combline cases can be replaced completely by EM simulations.

6.1. EM Simulators and Methods

Three-dimensional (3D) EM simulation software is usually preferred for use in cavity-type combline filter design. The most commonly used numerical techniques for arbitrary structures are the finite-element method (FEM) and the finite-difference time-domain method (FDTD). These methods can analyze complex structures but usually require large amounts of memory and long computation time. Other computer software can solve some common structures very efficiently (using much less memory) by utilizing the properties of the structure, such as the mode-matching (MM) and transmission-line matrix (TLM) methods. For planar structure problems, the method of moment method (MoM) is usually used.

The commonly used commercial EM simulators are Ansoft or Agilent's HFSS using FEM, CST's Microwave Studio using the FDTD method for 3D arbitrary structures, Agilent's Momentum using FEM, Sonnet's Em, and Zeland's IE3D using MoM for 3D planar structures.

For narrow-bandwidth-coupled resonator filter design, it is usually convenient to divide the filter into individual pieces to determine the cavity and aperture dimension separately when using the EM simulation software to perform the design from the efficiency and memory usage point of view; otherwise too much simulation time will be

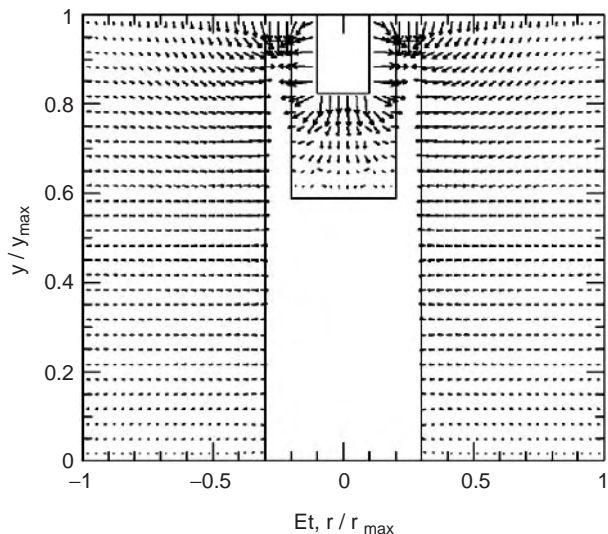


Figure 25. Typical electric field distributions of a combline cavity.

needed. Most of the parameters will be fine-tuned by tuning screws at the prototype stage and during production.

6.2. Resonant Frequency

An EM simulator can model the resonator and determine the resonant frequencies of both the fundamental and higher-order modes. In addition, the field distributions of the resonant cavity can be obtained, including the tuning screw as shown in Fig. 25. Figure 26 presents the typical higher-order mode chart of the combline resonators with the airgap between the rod and enclosure as a variable. It is shown that TM_{02} and HE_{11} are the first two higher-order modes of the typical combline resonator. For the small-gap case, a resonator with a shorter length has a larger mode separation. The resonant frequency of the first higher-order mode can be 3–5 times the dominant

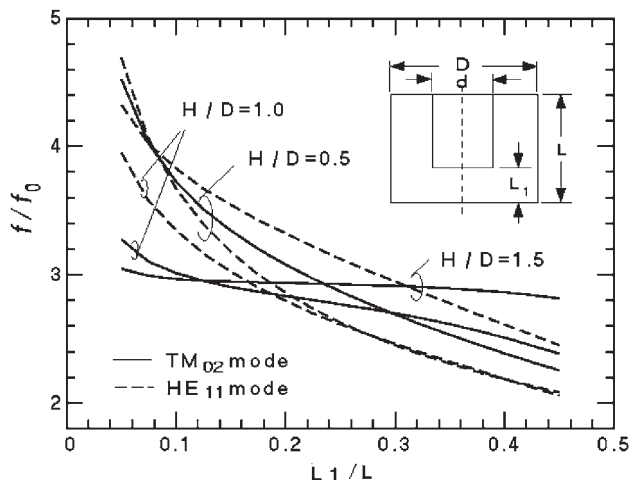


Figure 26. Typical mode chart of a combline resonator relative to dominant mode as a function of gap.

mode resonant frequency when the height of the cavity is 0.5–1.0 times the diameter of the cavity. The typical small-gap reentrant cavity bandpass filter can achieve a spurious-free range of more than twice the center frequency. This mode separation ratio decreases as the gap increases.

6.3. Unloaded Q

Accurate determination of the unloaded Q factor of the resonator is very important for combline filter design, since it directly relates to loss, size, and cost of the filter. Empirically, the unloaded Q of a combline resonator can be estimated from the measurements of many practical filters using the equation [21]

$$Q = Kb\sqrt{f_0} \tag{54}$$

where b is the width of the cavity in inches, f_0 is the resonant frequency in gigahertz, and K is a constant approximately equal to 1600 with b less than 0.08λ for a practical silver-plated combline resonator. However, when b is above 0.08λ , K increases, and can be as much as 2800 for $b = 0.18\lambda$. Figure 27 shows the measured unloaded Q of the combline resonator expressed in K values with b/λ in terms of K as a function of b/λ in the range between 0.12 and 0.20. The practical Q is dependent on factors such as surface roughness, plating quality, tuning screw penetration, and possible surface contact problems, which partially explains the spread in the K values of various designs having the same b/λ .

EM simulation software can compute the unloaded Q of a cavity accurately. Since a combline resonator has small

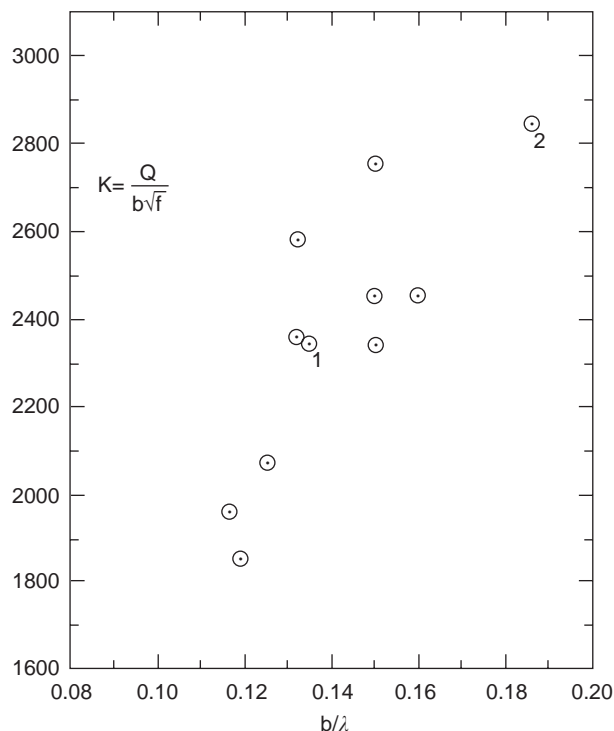


Figure 27. Measured normalized unloaded Q as a function of b/λ .

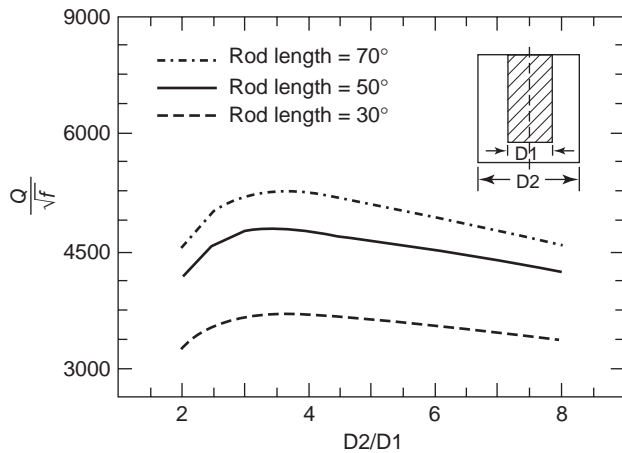


Figure 28. Computed unloaded Q of a combline resonator versus D_2/D_1 Ratio.

loss, a perturbation method is usually incorporated for this kind of computation. Figure 28 shows the computed unloaded Q of the combline resonators versus the ratio of the outer/inner diameter ratio D_2/D_1 with different rod lengths. It is shown that maximum unloaded Q of the resonators occurs when D_2/D_1 is approximately 3.6. Longer rod length yields higher unloaded Q for the same D_1 and D_2 .

Both the resonant frequency and unloaded Q decrease when the tuning screw penetrates into the cavity. The tuning screw may have a strong effect on unloaded Q of the combline resonator, which should be considered in the filter design. Figure 29 shows the computed unloaded Q of a combline resonator versus resonant frequency change by the tuning screw.

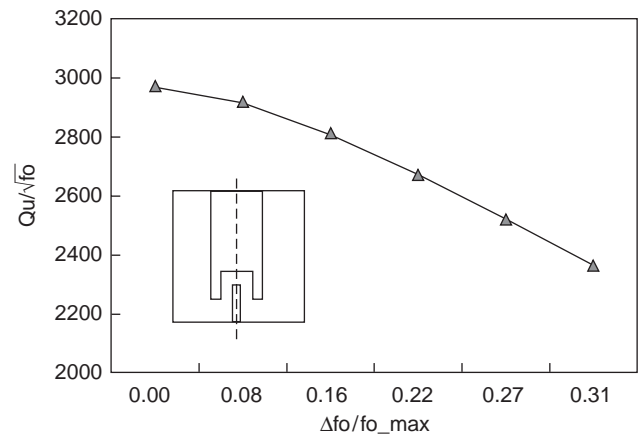


Figure 29. Unloaded Q of a combline resonator versus resonant frequency as an effect of the tuning screw.

7. TYPICAL APPLICATIONS

Comblines filters have been widely used in many communication systems and microwave applications. They have become more and more important for low-loss microwave filters in the 0.5–12 GHz frequency band for both narrow- and wideband applications. Applications of combline filters also include diplexers (duplexers), multiplexers, and delay-line filters. When a combline cavity is filled with a high dielectric constant material, it results in a dielectric resonator having significantly reduced dimensions.

Another application for combline filters is to replace the lowpass filter to achieve a very wideband spurious-free response in the system [49]. For this type of application, the bandwidth of the filter is usually relatively large and

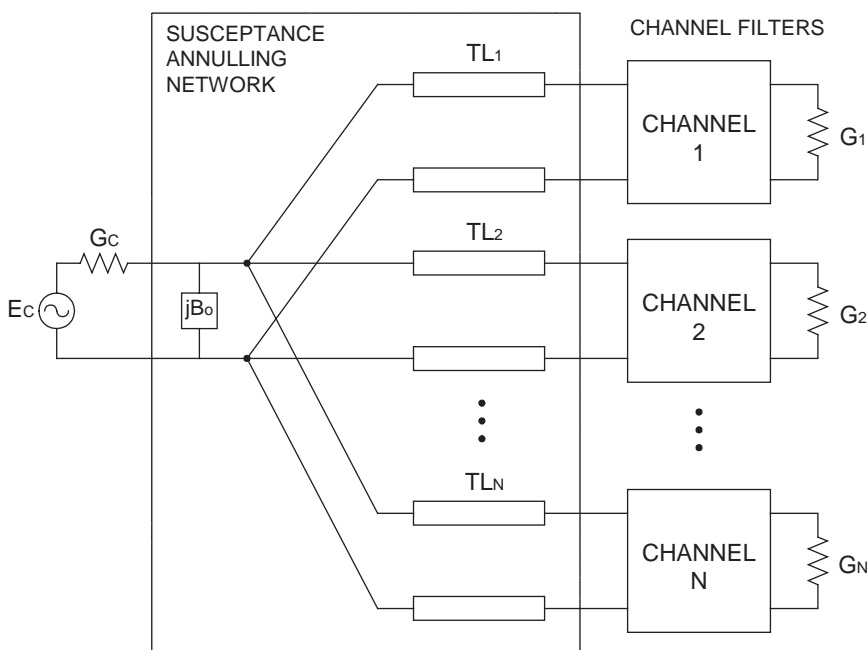


Figure 30. Schematic of a parallel-connected multiplexer.



Figure 31. A 1.8-GHz DCS duplexer.

therefore does not require very high unloaded Q ; thus the filter can be very small in size. As the combline resonator can have superior stopband performance, wideband spurious-free performance with a sharp rolloff skirt can be achieved easily with combline resonator filters.

Multiplexers, particularly duplexers, are frequently required by communication systems for RF front ends to separate or combine both transmit and receive signals [28–37]. A schematic drawing of a commonly used parallel-connected multiplexer with N channels is shown in Fig. 30. The multiplexer consists of channel filters and a susceptance annulling network, which in turn consists of transmission lines series-connected to each channel filter

and a shunt susceptance element at a common input port to help provide a nearly constant total input admittance [33–38]. The susceptance annulling network is achieved by optimizing the length and characteristic impedance of the transmission lines and the shunt susceptance element value to minimize the interaction among the channels. For narrowband applications, the susceptance jB_0 of the annulling network can be maintained by offsetting the resonant frequency of the first cavities of the channel filters to cancel the susceptance of the channel filters. Figure 31 is a photograph of a DCS (digital communication system) duplexer consisting of two 6-pole combline filters. Each channel filter has two CT sections having two transmission zeros at one side. Figure 32 presents the measured frequency response of the duplexer.

Acknowledgment

The author would like to thank reviewers for reviewing the article and many valuable suggestions.

BIBLIOGRAPHY

1. G. L. Matthaei, L. Young, and E. M. T. Jones, *Design of Microwave Filters, Impedance-Matching Networks and Coupling Structures*, McGrawHill, New York, 1964.
2. G. L. Matthaei, Combline bandpass filters of narrow or moderate bandwidth, *Microwave J.* **6**: 82–91 (Aug. 1963).
3. W. J. Getsinger, Coupled rectangular bars between parallel plates, *IEEE Trans. Microwave Theory Tech.* **MTT-10**:65–72 (Jan. 1962).
4. E. G. Cristal, Coupled circular cylindrical rods between parallel ground planes, *IEEE Trans. Microwave Theory Tech.* **MTT-12**:428–439 (July 1964).

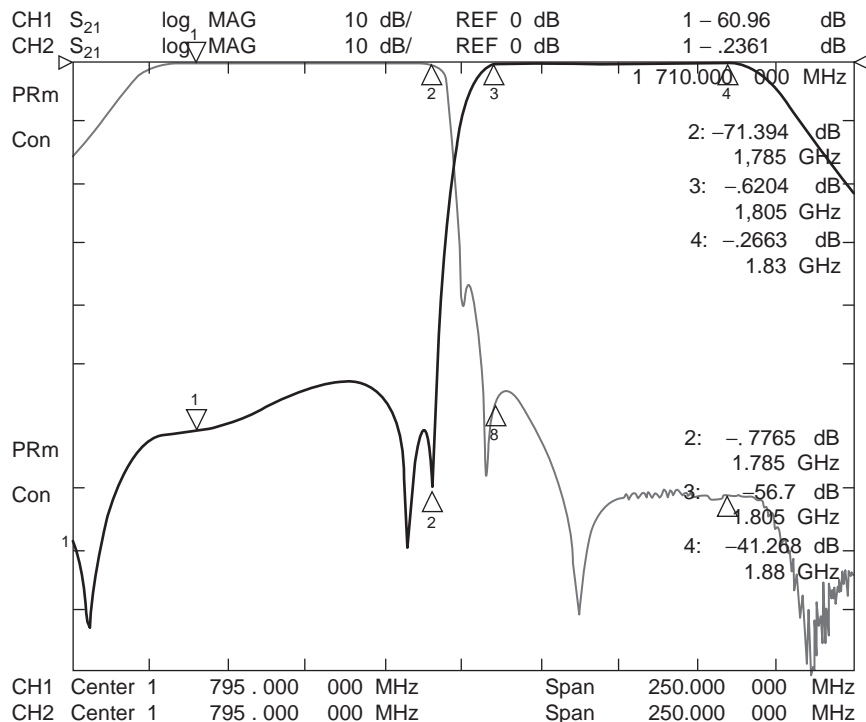


Figure 32. Measured frequency response of the duplexer.

5. E. G. Cristal, Data for partially decoupled round rods between parallel ground planes (corresp.), *IEEE Trans. Microwave Theory Tech.* **MTT-16**:311–314 (May 1968).
6. R. Levy and J. D. Rhodes, A combline elliptic filter, *IEEE Trans. Microwave Theory Tech.* **MTT-19**: 26–29 (Jan. 1971).
7. A. Atia, A. Williams, and R. Newcomb, Narrow-band multiple-coupled cavity synthesis, *IEEE Trans. Circ. Syst.* **MTT-21**: 649–655 (Sept. 1974).
8. R. Levy, Filters with single transmission zeros at real or imaginary frequencies, *IEEE Trans. Microwave Theory Tech.* **MTT-24**:172–181 (April 1976).
9. R. J. Wenzel, Synthesis of combline and capacitively loaded interdigital bandpass filters of arbitrary bandwidth, *IEEE Trans. Microwave Theory Tech.* **MTT-19**:678–686 (Aug. 1971).
10. R. J. Wenzel, Synthesis of combline and capacitively loaded interdigital bandpass filters of arbitrary bandwidth, *IEEE Trans. Microwave Theory Tech.* **MTT-19**:678–686 (Aug. 1971).
11. R. J. Wenzel, Exact design of wideband equal-ripple bandpass filters with non-adjacent resonator couplings, *IEEE MTT-S Int. Microwave Symp. Digest*, 1976, Vol. I, pp. 125–127.
12. G. D. O’Clock, Jr., Tunable frequency range and mismatch adjustment for combline bandpass filters, *IEEE Trans. Microwave Theory Tech.* **MTT-20**:238–239 (March 1972).
13. H. C. Bell, Canonical asymmetric coupled-resonator filters, *IEEE Trans. Microwave Theory Tech.* **MTT-30**:1335–1340 (Sept. 1982).
14. R. Levy and S. B. Cohn, A history of microwave filter research, design, and development, *IEEE Trans. Microwave Theory Tech.* **MTT-32**: 1055–1067 (Sept. 1984).
15. M. Dishal, A simple design procedure for small percentage bandwidth round-rod interdigital filters (corresp.), *IEEE Trans. Microwave Theory Tech.* **MTT-13**:696–698 (Sept. 1965).
16. S. B. Cohn, Generalized design of bandpass and other filters by computer optimization, *IEEE MTT-S Int. Microwave Symp. Digest*, 1974, Vol. I, pp. 272–274.
17. E. G. Cristal, Tapped-line coupled transmission lines with applications to interdigital and combline filters, *IEEE Trans. Microwave Theory Tech.* **MTT-23**:1007–1012 (Dec. 1975).
18. S. Caspi and J. Adelman, Design of combline and interdigital filters with tapped-line input, *IEEE Trans. Microwave Theory Tech.* **MTT-36**:759–763 (April 1988).
19. W.-T. Lo and C.-K. C. Tzuang, K-band quasi-planar tapped combline filter and diplexer, *IEEE Trans. Microwave Theory Tech.* **MTT-41**:215–223 (Feb. 1993).
20. C. Ernst and V. Postoyalko, Tapped-line interdigital filter equivalent circuits, *IEEE MTT-S Int. Microwave Symp. Digest*, 1997, Vol. II, pp. 801–804.
21. R. Levy, H.-W. Yao, and K. A. Zaki, Transitional combline/evanescent-mode microwave filters, *IEEE Trans. Microwave Theory Tech.* **MTT-45**:2094–2099 (Dec. 1997).
22. R. Levy, Direct synthesis of cascaded quadruplet (CQ) filters, *IEEE Trans. Microwave Theory Tech.* **MTT-43**:2940–2945 (Dec. 1995).
23. R. Hershtig, R. Levy, and K. Zaki, Synthesis and design of cascaded trisection (CT) dielectric resonator filters, *Proc. 27th European Microwave Conf. and Exhibition*, Sept. 1997, Vol. 2, pp. 784–791.
24. W. A. Atia, K. A. Zaki, and A. E. Atia, Synthesis of general topology multiple coupled resonator filters by optimization, *IEEE MTT-S Int. Microwave Symp. Digest*, 1998, Vol. II, pp. 821–824.
25. J.-F. Liang and D. Zhang, General coupled resonator filters design based on canonical asymmetric building blocks, *IEEE MTT-S Int. Microwave Symp. Digest*, 1999, Vol. III, pp. 907–910.
26. R. J. Cameron, General coupling matrix synthesis methods for Chebyshev filtering functions, *IEEE Trans. Microwave Theory Tech.* **MTT-47**:433–442 (April 1999).
27. R. Levy and P. Petre, Design of CT and CQ filters using approximation and optimization, *IEEE Trans. Microwave Theory Tech.* **MTT-49**:2350–2356 (Dec. 2001).
28. E. G. Cristal and G. L. Matthaei, A technique for the design of multiplexers having contiguous channels, *IEEE Trans. Microwave Theory Tech.* **MTT-12**:88–93 (Jan. 1964).
29. R. J. Wenzel and W. G. Erlinger, Narrowband contiguous multiplexing filters with arbitrary amplitude and delay response, *IEEE MTT-S Int. Microwave Symp. Digest*, 1976, Vol. I, pp. 116–118.
30. A. E. Atia, Computer-aided design of waveguide multiplexer, *IEEE Trans. Microwave Theory Tech.* **MTT-22**:332–336 (March 1974).
31. J. D. Rhodes, Design formulas for bandpass channel diplexers, *IEEE MTT-S Int. Microwave Symp. Digest*, 1976, Vol. I, pp. 112–115.
32. J. L. Haine and J. D. Rhodes, Direct design formulas for asymmetric bandpass channel diplexers, *IEEE Trans. Microwave Theory Tech.* **MTT-25**:807–813 (Oct. 1977).
33. J. D. Rhodes and R. Levy, A generalized multiplexer theory, *IEEE Trans. Microwave Theory Tech.* **MTT-27**:99–111 (Feb. 1979).
34. J. D. Rhodes and S. A. Alseyab, A design procedure for bandpass channel multiplexers connected at a common junction, *IEEE Trans. Microwave Theory Tech.* **MTT-28**:246–253 (March 1980).
35. P. M. LaTourrette, Multi-octave combline-filter multiplexer, *IEEE MTT-S Int. Microwave Symp. Digest*, 1977, Vol. I, pp. 298–301.
36. P. M. LaTourrette and J. L. Roberds, Extended-junction combline multiplexers, *IEEE MTT-S Int. Microwave Symp. Digest*, 1978, Vol. I, pp. 214–216.
37. P. M. LaTourrette, Wide-bandwidth combline filters with high selectivity, *IEEE MTT-S Int. Microwave Symp. Digest*, 1979, Vol. I, pp. 275–277.
38. W.-T. Lo and C.-K. C. Tzuang, K-band quasi-planar tapped combline filter and diplexer, *IEEE Trans. Microwave Theory Tech.* **MTT-41**:215–223 (Feb. 1993).
39. G. Pfitzenmaier, Synthesis and realization of narrow-band canonical microwave bandpass filters exhibiting linear phase and transmission zeros, *IEEE Trans. Microwave Theory Tech.* **MTT-30**:1300–1311 (Sept. 1982).
40. A. Fukasawa, Analysis and composition of a new microwave filter configuration with inhomogeneous dielectric medium, *IEEE Trans. Microwave Theory Tech.* **MTT-30**:1367–1375 (Sept. 1982).
41. M. Sagawa, M. Makimoto, and S. Yamashita, A design method of bandpass filters using dielectric-filled coaxial resonators, *IEEE Trans. Microwave Theory Tech.* **MTT-33**:152–157 (Feb. 1985).
42. K. Hano, H. Kohriyama, and K.-I. Sawamoto, A direct-coupled $\lambda/4$ -coaxial resonator bandpass filter for land mobile communications, *IEEE Trans. Microwave Theory Tech.* **MTT-34**:972–976 (Sept. 1986).

43. Y. Isota, M. Miyazaki, O. Ishida, and F. Takeda, A grooved monoblock combline filter suppressing the third harmonics, *IEEE MTT-S Int. Microwave Symp. Digest*, 1987, Vol. I, pp. 383–386.
44. R. Levy, Simplified analysis of inhomogeneous dielectric block combline filters, *IEEE MTT-S Int. Microwave Symp. Digest*, 1990, Vol. I, pp. 135–138.
45. T. Ishizaki and T. Uwano, A stepped impedance combline filter fabricated by using ceramic lamination technique, *IEEE MTT-S Int. Microwave Symp. Digest*, 1994, Vol. II, pp. 617–620.
46. H. Matsumoto, H. Ogura, and T. Nishikawa, A miniaturized dielectric monoblock bandpass filter for 800 MHz band cordless telephone system, *IEEE MTT-S Int. Microwave Symp. Digest*, 1994, Vol. I, pp. 249–252.
47. H. Matsumoto, T. Tsujiguchi, and T. Nishikawa, A miniaturized dielectric monoblock duplexer matched by the buried impedance transforming circuit, *IEEE MTT-S Int. Microwave Symp. Digest*, 1995, Vol. III, pp. 1539–1542.
48. H. -W. Yao, K. A. Zaki, A. E. Atia, and R. Hershtig, Full wave modeling of conducting posts in rectangular waveguides and its applications to slot coupled combline filters, *IEEE Trans. Microwave Theory Tech.* **MTT-43** (Part II):2823–2829 (Dec. 1995).
49. J.-F. Liang and W. D. Blair, High-Q TE₀₁ mode DR filters for PCS wireless base stations, *IEEE Trans. Microwave Theory Tech.* **MTT-46** (Part II):2493–2500 (Dec. 1998).
50. T. Olsson, P. Anderson, U. Jordan, M. Lisak, V. Semenov, and M. Ahlander, Microwave breakdown in air-filled resonators, *IEEE MTT-S Int. Microwave Symp. Digest*, June 1999, Vol. 3, pp. 915–918.
51. C. Wang and K. A. Zaki, Temperature compensation of combline resonators and filters, *1999 IEEE MTT-S Int. Microwave Symp. Digest*, June 1999, Vol. 3, pp. 1041–1044.
52. C. Wang and K. A. Zaki, Analysis of power handling capacity of bandpass filters, *2001 IEEE MTT-S Int. Microwave Symp. Digest*, May 2001, Vol. 3, pp. 1611–1614.

COMPLEX MEDIA

LE-WEI LI
WEN-YAN YIN
National University of
Singapore
Kent Ridge, Singapore

1. CONSTITUTIVE RELATIONS

For most media, the general form of constitutive relations that account for multiple effects resulting from interaction between electromagnetic waves and media can be expressed by [1]

$$D_i = \varepsilon_{ij} E_j + \gamma_{ij}^E \partial_t E_j + \zeta_{ij}^E \Delta_j E_k + \beta_{ij}^E B_j + \alpha_{ij}^E \partial_t B_j + \eta_{ijk}^E \Delta_j B_k + \dots \quad (1a)$$

$$H_i = \mu_{ij}^{-1} B_j + \gamma_{ij}^B \partial_t B_j + \eta_{ijk}^B \Delta_j B_k + \beta_{ij}^B E_j + \alpha_{ij}^B \partial_t E_j + \eta_{ijk}^B \Delta_j E_k + \dots \quad (1b)$$

where E_k and H_i are the electric and magnetic field components; D_i and B_k are electric and magnetic induction components; and ε_{ij} , γ_{ij}^B , η_{ijk}^E , and so on are constitutive tensors of different ranks. The space Δ_j and time ∂_t derivatives take into account spatial and temporal variations of the field.

For linear, stationary, and dispersive bianisotropic media in the frequency domain, their constitutive relations can be described by a set of equations as follows [2–25] ($e^{j\omega t}$):

$$\vec{D} = \varepsilon_0[\varepsilon(\omega)]\vec{E} + \sqrt{\mu_0\varepsilon_0}[\zeta(\omega)]\vec{H} \quad (2a)$$

$$\vec{B} = \mu_0[\mu(\omega)]\vec{H} + \sqrt{\mu_0\varepsilon_0}[\eta(\omega)]\vec{E} \quad (2b)$$

where ω is the operating angular frequency; the tensors $[\varepsilon(\omega)]$, $[\mu(\omega)]$, $[\zeta(\omega)]$ and $[\eta(\omega)]$ are the relative permittivity, permeability and magnetoelectric tensors, respectively. Apparently, Eqs. (2a) and (2b) are applicable for the constitutive description of electromagnetically anisotropic, biisotropic chiral, uniaxially, or biaxially bianisotropic media [26–45]. Therefore, Eqs. (2a), and (2b) can incorporate most practical applications of complex linear media used in RF engineering.

2. CLASSIFICATION OF BIANISOTROPIC¹ MEDIA

2.1. Continuous Groups of Symmetry (CGS)

In Eqs. (2a) and (2b), four constitutive tensors are usually described by a 3×3 matrix, respectively. However, according to the theory of continuous groups of symmetry (CGS) developed by Dmitriev [1,46–49], the number of independent elements in $[\varepsilon(\omega)]$, $[\mu(\omega)]$, $[\zeta(\omega)]$ and $[\eta(\omega)]$ for a given bianisotropic medium is completely governed by a certain magnetic group of symmetry. From CGS theory, we can understand the four constitutive tensors if the CGS of medium is known. Typically, these tensors correspond to the following CGSs:

$$D_{4h}(D_{2d}), D_{4h}(D_{2h}), C_{4h}(S_4), C_{4h}(C_{2h}),$$

$$D_4(D_2), D_{2d}(S_4), D_{2d}(D_2), D_{2d}(C_{2v}),$$

$$C_{4v}(C_{2v}), D_{2h}(D_2), D_{2h}(C_{2h}),$$

$$D_{2h}(C_{2v}), S_4(C_2), C_4(C_2), D_2(C_2), C_{2h}(C_i),$$

$$C_{2h}(C_2), C_{2h}(C_s), C_{2v}(C_2),$$

$$C_{2v}(C_s), C_i(C_1), C_2(C_1), C_s(C_1) \quad (3)$$

¹The term *bianisotropic* denotes the property of being biisotropic and/or anisotropic.

The constitutive tensors for these 23 linear complex media are given as follows [1]:

$$\begin{aligned}
 1^\circ(D_{4h}(D_{2d}); N_f = 5): [\varepsilon] &= \begin{bmatrix} \varepsilon_{xx} & 0 & 0 \\ 0 & \varepsilon_{xx} & 0 \\ 0 & 0 & \varepsilon_{zz} \end{bmatrix}, \\
 [\mu] &= \begin{bmatrix} \mu_{xx} & 0 & 0 \\ 0 & \mu_{xx} & 0 \\ 0 & 0 & \mu_{zz} \end{bmatrix} \quad (4a) \\
 [\xi] &= \begin{bmatrix} 0 & \xi_{xy} & 0 \\ \xi_{xy} & 0 & 0 \\ 0 & 0 & 0 \end{bmatrix}, \quad [\eta] = [\xi]
 \end{aligned}$$

$$\begin{aligned}
 2^\circ(D_{4h}(D_{2h}); N_f = 4): [\varepsilon] &= \begin{bmatrix} \varepsilon_{xx} & 0 & 0 \\ 0 & \varepsilon_{xx} & 0 \\ 0 & 0 & \varepsilon_{zz} \end{bmatrix}, \\
 [\mu] &= \begin{bmatrix} \mu_{xx} & 0 & 0 \\ 0 & \mu_{xx} & 0 \\ 0 & 0 & \mu_{zz} \end{bmatrix}, \quad (4b) \\
 [\xi] &= [\eta] = [0]
 \end{aligned}$$

$$\begin{aligned}
 3^\circ(C_{4h}(S_4); N_f = 6): [\varepsilon] &= \begin{bmatrix} \varepsilon_{xx} & 0 & 0 \\ 0 & \varepsilon_{xx} & 0 \\ 0 & 0 & \varepsilon_{zz} \end{bmatrix}, \\
 [\mu] &= \begin{bmatrix} \mu_{xx} & 0 & 0 \\ 0 & \mu_{xx} & 0 \\ 0 & 0 & \mu_{zz} \end{bmatrix} \quad (4c) \\
 [\xi] &= \begin{bmatrix} \xi_{xx} & \xi_{xy} & 0 \\ \xi_{xy} & -\xi_{xx} & 0 \\ 0 & 0 & 0 \end{bmatrix}, \\
 [\eta] &= [\xi]
 \end{aligned}$$

$$\begin{aligned}
 4^\circ(C_{4h}(C_{2h}); N_f = 4): [\varepsilon] &= \begin{bmatrix} \varepsilon_{xx} & 0 & 0 \\ 0 & \varepsilon_{xx} & 0 \\ 0 & 0 & \varepsilon_{zz} \end{bmatrix}, \\
 [\mu] &= \begin{bmatrix} \mu_{xx} & 0 & 0 \\ 0 & \mu_{xx} & 0 \\ 0 & 0 & \mu_{zz} \end{bmatrix}, \quad (4d) \\
 [\xi] &= [\eta] = [0]
 \end{aligned}$$

$$\begin{aligned}
 5^\circ(D_4(D_2); N_f = 7): [\varepsilon] &= \begin{bmatrix} \varepsilon_{xx} & 0 & 0 \\ 0 & \varepsilon_{xx} & 0 \\ 0 & 0 & \varepsilon_{zz} \end{bmatrix}, \\
 [\mu] &= \begin{bmatrix} \mu_{xx} & 0 & 0 \\ 0 & \mu_{xx} & 0 \\ 0 & 0 & \mu_{zz} \end{bmatrix} \quad (4e) \\
 [\xi] &= \begin{bmatrix} \xi_{xx} & 0 & 0 \\ 0 & \xi_{yy} & 0 \\ 0 & 0 & \xi_{zz} \end{bmatrix}, \\
 [\eta] &= -[\xi]
 \end{aligned}$$

$$\begin{aligned}
 6^\circ(D_{2d}(S_4); N_f = 8): [\varepsilon] &= \begin{bmatrix} \varepsilon_{xx} & \varepsilon_{xy} & 0 \\ -\varepsilon_{xy} & \varepsilon_{xx} & 0 \\ 0 & 0 & \varepsilon_{zz} \end{bmatrix}, \\
 [\mu] &= \begin{bmatrix} \mu_{xx} & \mu_{xy} & 0 \\ -\mu_{xy} & \mu_{xx} & 0 \\ 0 & 0 & \mu_{zz} \end{bmatrix} \quad (4f) \\
 [\xi] &= \begin{bmatrix} \xi_{xx} & \xi_{xy} & 0 \\ \xi_{xy} & -\xi_{xx} & 0 \\ 0 & 0 & 0 \end{bmatrix}, \\
 [\eta] &= \begin{bmatrix} \xi_{xx} & -\xi_{xy} & 0 \\ -\xi_{xy} & -\xi_{xx} & 0 \\ 0 & 0 & 0 \end{bmatrix}
 \end{aligned}$$

$$7^\circ(D_{2d}(D_2): N_f = \mathbf{6}): [\varepsilon] = \begin{bmatrix} \varepsilon_{xx} & 0 & 0 \\ 0 & \varepsilon_{xx} & 0 \\ 0 & 0 & \varepsilon_{zz} \end{bmatrix},$$

$$[\mu] = \begin{bmatrix} \mu_{xx} & 0 & 0 \\ 0 & \mu_{xx} & 0 \\ 0 & 0 & \mu_{zz} \end{bmatrix}$$

$$[\xi] = \begin{bmatrix} \xi_{xx} & 0 & 0 \\ 0 & \xi_{xx} & 0 \\ 0 & 0 & \xi_{zz} \end{bmatrix},$$

(4g)

$$8^\circ(D_{2d}(C_{2v}): N_f = \mathbf{6}): [\varepsilon] = \begin{bmatrix} \varepsilon_{xx} & 0 & 0 \\ 0 & \varepsilon_{xx} & 0 \\ 0 & 0 & \varepsilon_{zz} \end{bmatrix},$$

$$[\mu] = \begin{bmatrix} \mu_{xx} & 0 & 0 \\ 0 & \mu_{xx} & 0 \\ 0 & 0 & \mu_{zz} \end{bmatrix}$$

$$[\xi] = \begin{bmatrix} 0 & \xi_{xy} & 0 \\ \xi_{yx} & 0 & 0 \\ 0 & 0 & 0 \end{bmatrix},$$

(4h)

$$[\eta] = -[\xi]$$

$$9^\circ(C_{4v}(C_{2v}): N_f = \mathbf{6}): [\varepsilon] = \begin{bmatrix} \varepsilon_{xx} & 0 & 0 \\ 0 & \varepsilon_{xx} & 0 \\ 0 & 0 & \varepsilon_{zz} \end{bmatrix},$$

$$[\mu] = \begin{bmatrix} \mu_{xx} & 0 & 0 \\ 0 & \mu_{xx} & 0 \\ 0 & 0 & \mu_{zz} \end{bmatrix}$$

$$[\xi] = \begin{bmatrix} 0 & \xi_{xy} & 0 \\ \xi_{yx} & 0 & 0 \\ 0 & 0 & 0 \end{bmatrix}, [\eta] = [\xi]$$

(4i)

$$10^\circ(D_{2h}(D_2): N_f = \mathbf{9}): [\varepsilon] = \begin{bmatrix} \varepsilon_{xx} & 0 & 0 \\ 0 & \varepsilon_{yy} & 0 \\ 0 & 0 & \varepsilon_{zz} \end{bmatrix},$$

$$[\mu] = \begin{bmatrix} \mu_{xx} & 0 & 0 \\ 0 & \mu_{yy} & 0 \\ 0 & 0 & \mu_{zz} \end{bmatrix}$$

$$[\xi] = \begin{bmatrix} \xi_{xx} & 0 & 0 \\ 0 & \xi_{yy} & 0 \\ 0 & 0 & \xi_{zz} \end{bmatrix}, [\eta] = [\xi]$$

(4j)

$$11^\circ(D_{2h}(C_{2h}): N_f = \mathbf{8}): [\varepsilon] = \begin{bmatrix} \varepsilon_{xx} & \varepsilon_{xy} & 0 \\ -\varepsilon_{xy} & \varepsilon_{yy} & 0 \\ 0 & 0 & \varepsilon_{zz} \end{bmatrix},$$

$$[\mu] = \begin{bmatrix} \mu_{xx} & \mu_{xy} & 0 \\ -\mu_{xy} & \mu_{yy} & 0 \\ 0 & 0 & \mu_{zz} \end{bmatrix}$$

$$[\xi] = [\eta] = [0]$$

(4k)

$$12^\circ(D_{2h}(C_{2v}): N_f = \mathbf{8}): [\varepsilon] = \begin{bmatrix} \varepsilon_{xx} & 0 & 0 \\ 0 & \varepsilon_{yy} & 0 \\ 0 & 0 & \varepsilon_{zz} \end{bmatrix},$$

$$[\mu] = \begin{bmatrix} \mu_{xx} & 0 & 0 \\ 0 & \mu_{yy} & 0 \\ 0 & 0 & \mu_{zz} \end{bmatrix}$$

$$[\xi] = \begin{bmatrix} 0 & \xi_{xy} & 0 \\ \xi_{yx} & 0 & 0 \\ 0 & 0 & 0 \end{bmatrix},$$

$$[\eta] = \begin{bmatrix} 0 & \xi_{yx} & 0 \\ \xi_{xy} & 0 & 0 \\ 0 & 0 & 0 \end{bmatrix}$$

(4l)

$$\begin{aligned}
 13^\circ(S_4(C_2): N_f = \mathbf{9}): [\varepsilon] &= \begin{bmatrix} \varepsilon_{xx} & 0 & 0 \\ 0 & \varepsilon_{xx} & 0 \\ 0 & 0 & \varepsilon_{zz} \end{bmatrix}, \\
 [\mu] &= \begin{bmatrix} \mu_{xx} & 0 & 0 \\ 0 & \mu_{xx} & 0 \\ 0 & 0 & \mu_{zz} \end{bmatrix} \\
 [\zeta] &= \begin{bmatrix} \zeta_{xx} & \zeta_{xy} & 0 \\ \zeta_{yx} & \zeta_{yy} & 0 \\ 0 & 0 & \zeta_{zz} \end{bmatrix}, \\
 [\eta] &= \begin{bmatrix} \zeta_{yy} & -\zeta_{xy} & 0 \\ -\zeta_{yx} & \zeta_{xx} & 0 \\ 0 & 0 & \zeta_{zz} \end{bmatrix}
 \end{aligned}
 \tag{4m}$$

$$\begin{aligned}
 14^\circ(C_4(C_2): N_f = \mathbf{9}): [\varepsilon] &= \begin{bmatrix} \varepsilon_{xx} & 0 & 0 \\ 0 & \varepsilon_{xx} & 0 \\ 0 & 0 & \varepsilon_{zz} \end{bmatrix}, \\
 [\mu] &= \begin{bmatrix} \mu_{xx} & 0 & 0 \\ 0 & \mu_{xx} & 0 \\ 0 & 0 & \mu_{zz} \end{bmatrix} \\
 [\zeta] &= \begin{bmatrix} \zeta_{xx} & \zeta_{xy} & 0 \\ \zeta_{yx} & \zeta_{yy} & 0 \\ 0 & 0 & \zeta_{zz} \end{bmatrix}, \\
 [\eta] &= \begin{bmatrix} -\zeta_{yy} & \zeta_{xy} & 0 \\ \zeta_{yx} & -\zeta_{xx} & 0 \\ 0 & 0 & -\zeta_{zz} \end{bmatrix}
 \end{aligned}
 \tag{4n}$$

$$\begin{aligned}
 15^\circ(D_2(C_2): N_f = \mathbf{13}): [\varepsilon] &= \begin{bmatrix} \varepsilon_{xx} & \varepsilon_{xy} & 0 \\ -\varepsilon_{xy} & \varepsilon_{yy} & 0 \\ 0 & 0 & \varepsilon_{zz} \end{bmatrix}, \\
 [\mu] &= \begin{bmatrix} \mu_{xx} & \mu_{xy} & 0 \\ -\mu_{xy} & \mu_{yy} & 0 \\ 0 & 0 & \mu_{zz} \end{bmatrix} \\
 [\zeta] &= \begin{bmatrix} \zeta_{xx} & \zeta_{xy} & 0 \\ \zeta_{yx} & \zeta_{yy} & 0 \\ 0 & 0 & \zeta_{zz} \end{bmatrix}, \\
 [\eta] &= \begin{bmatrix} -\zeta_{xx} & \zeta_{yx} & 0 \\ \zeta_{xy} & -\zeta_{yy} & 0 \\ 0 & 0 & -\zeta_{zz} \end{bmatrix}
 \end{aligned}
 \tag{4o}$$

$$\begin{aligned}
 16^\circ(C_{2h}(C_i): N_f = \mathbf{12}): [\varepsilon] &= \begin{bmatrix} \varepsilon_{xx} & \varepsilon_{xy} & \varepsilon_{xz} \\ \varepsilon_{xy} & \varepsilon_{yy} & \varepsilon_{yz} \\ -\varepsilon_{xz} & -\varepsilon_{yz} & \varepsilon_{zz} \end{bmatrix}, \\
 [\mu] &= \begin{bmatrix} \mu_{xx} & \mu_{xy} & \mu_{xz} \\ \mu_{xy} & \mu_{yy} & \mu_{yz} \\ -\mu_{xz} & -\mu_{yz} & \mu_{zz} \end{bmatrix}
 \end{aligned}
 \tag{4p}$$

$$\begin{aligned}
 [\zeta] &= [\eta] = [0] \\
 17^\circ(C_{2h}(C_2): N_f = \mathbf{13}): [\varepsilon] &= \begin{bmatrix} \varepsilon_{xx} & \varepsilon_{xy} & 0 \\ \varepsilon_{xy} & \varepsilon_{yy} & 0 \\ 0 & 0 & \varepsilon_{zz} \end{bmatrix}, \\
 [\mu] &= \begin{bmatrix} \mu_{xx} & \mu_{xy} & 0 \\ \mu_{xy} & \mu_{yy} & 0 \\ 0 & 0 & \mu_{zz} \end{bmatrix} \\
 [\zeta] &= \begin{bmatrix} \zeta_{xx} & \zeta_{xy} & 0 \\ \zeta_{yx} & \zeta_{yy} & 0 \\ 0 & 0 & \zeta_{zz} \end{bmatrix}, \\
 [\eta] &= \begin{bmatrix} \zeta_{xx} & \zeta_{yx} & 0 \\ \zeta_{xy} & \zeta_{yy} & 0 \\ 0 & 0 & \zeta_{zz} \end{bmatrix}
 \end{aligned}
 \tag{4q}$$

$$18^\circ(C_{2h}(C_s): N_f = \mathbf{12}): [\varepsilon] = \begin{bmatrix} \varepsilon_{xx} & \varepsilon_{xy} & 0 \\ \varepsilon_{xy} & \varepsilon_{yy} & 0 \\ 0 & 0 & \varepsilon_{zz} \end{bmatrix},$$

$$[\mu] = \begin{bmatrix} \mu_{xx} & \mu_{xy} & 0 \\ \mu_{xy} & \mu_{yy} & 0 \\ 0 & 0 & \mu_{zz} \end{bmatrix}$$

(4r)

$$[\zeta] = \begin{bmatrix} 0 & 0 & \zeta_{xz} \\ 0 & 0 & \zeta_{yz} \\ \zeta_{zx} & \zeta_{zy} & 0 \end{bmatrix},$$

$$[\eta] = \begin{bmatrix} 0 & 0 & \zeta_{zx} \\ 0 & 0 & \zeta_{zy} \\ \zeta_{xz} & \zeta_{yz} & 0 \end{bmatrix}$$

$$19^\circ(C_{2v}(C_2): N_f = \mathbf{13}): [\varepsilon] = \begin{bmatrix} \varepsilon_{xx} & \varepsilon_{xy} & 0 \\ -\varepsilon_{xy} & \varepsilon_{yy} & 0 \\ 0 & 0 & \varepsilon_{zz} \end{bmatrix},$$

$$[\mu] = \begin{bmatrix} \mu_{xx} & \mu_{xy} & 0 \\ -\mu_{xy} & \mu_{yy} & 0 \\ 0 & 0 & \mu_{zz} \end{bmatrix}$$

(4s)

$$[\zeta] = \begin{bmatrix} \zeta_{xx} & \zeta_{xy} & 0 \\ \zeta_{yx} & \zeta_{yy} & 0 \\ 0 & 0 & \zeta_{zz} \end{bmatrix},$$

$$[\eta] = \begin{bmatrix} \zeta_{xx} & -\zeta_{yx} & 0 \\ -\zeta_{xy} & \zeta_{yy} & 0 \\ 0 & 0 & \zeta_{zz} \end{bmatrix}$$

$$20^\circ(C_{2v}(C_s): N_f = \mathbf{12}): [\varepsilon] = \begin{bmatrix} \varepsilon_{xx} & 0 & 0 \\ 0 & \varepsilon_{yy} & \varepsilon_{yz} \\ 0 & -\varepsilon_{yz} & \varepsilon_{zz} \end{bmatrix},$$

$$[\mu] = \begin{bmatrix} \mu_{xx} & 0 & 0 \\ 0 & \mu_{yy} & \mu_{yz} \\ 0 & -\mu_{yz} & \mu_{zz} \end{bmatrix}$$

(4t)

$$[\zeta] = \begin{bmatrix} 0 & \zeta_{xy} & \zeta_{xz} \\ \zeta_{yx} & 0 & 0 \\ \zeta_{zx} & 0 & 0 \end{bmatrix},$$

$$[\eta] = \begin{bmatrix} 0 & -\zeta_{yx} & \zeta_{zx} \\ -\zeta_{xy} & 0 & 0 \\ \zeta_{xz} & 0 & 0 \end{bmatrix}$$

$$21^\circ(C_i(C_1): N_f = \mathbf{21}): [\varepsilon] = \begin{bmatrix} \varepsilon_{xx} & \varepsilon_{xy} & \varepsilon_{xz} \\ \varepsilon_{xy} & \varepsilon_{yy} & \varepsilon_{yz} \\ \varepsilon_{xz} & \varepsilon_{yz} & \varepsilon_{zz} \end{bmatrix},$$

$$[\mu] = \begin{bmatrix} \mu_{xx} & \mu_{xy} & \mu_{xz} \\ \mu_{xy} & \mu_{yy} & \mu_{yz} \\ \mu_{xz} & \mu_{yz} & \mu_{zz} \end{bmatrix}$$

(4u)

$$[\zeta] = \begin{bmatrix} \zeta_{xx} & \zeta_{xy} & \zeta_{xz} \\ \zeta_{yx} & \zeta_{yy} & \zeta_{yz} \\ \zeta_{zx} & \zeta_{zy} & \zeta_{zz} \end{bmatrix},$$

$$[\eta] = \begin{bmatrix} \zeta_{xx} & \zeta_{yx} & \zeta_{zx} \\ \zeta_{xy} & \zeta_{yy} & \zeta_{zy} \\ \zeta_{xz} & \zeta_{yz} & \zeta_{zz} \end{bmatrix}$$

$$\begin{aligned}
 22^\circ(C_2(C_1): N_f = \mathbf{21}): [\varepsilon] &= \begin{bmatrix} \varepsilon_{xx} & \varepsilon_{xy} & \varepsilon_{xz} \\ \varepsilon_{xy} & \varepsilon_{yy} & \varepsilon_{yz} \\ -\varepsilon_{xz} & -\varepsilon_{yz} & \varepsilon_{zz} \end{bmatrix}, \\
 [\mu] &= \begin{bmatrix} \mu_{xx} & \mu_{xy} & \mu_{xz} \\ \mu_{xy} & \mu_{yy} & \mu_{yz} \\ -\mu_{xz} & -\mu_{yz} & \mu_{zz} \end{bmatrix} \\
 [\zeta] &= \begin{bmatrix} \zeta_{xx} & \zeta_{xy} & \zeta_{xz} \\ \zeta_{yx} & \zeta_{yy} & \zeta_{yz} \\ \zeta_{zx} & \zeta_{zy} & \zeta_{zz} \end{bmatrix}, \\
 [\eta] &= \begin{bmatrix} -\zeta_{xx} & -\zeta_{yx} & \zeta_{zx} \\ -\zeta_{xy} & -\zeta_{yy} & \zeta_{zy} \\ \zeta_{xz} & \zeta_{yz} & -\zeta_{zz} \end{bmatrix}
 \end{aligned} \tag{4v}$$

$$\begin{aligned}
 23^\circ(C_3(C_1): N_f = \mathbf{21}): [\varepsilon] &= \begin{bmatrix} \varepsilon_{xx} & \varepsilon_{xy} & \varepsilon_{xz} \\ \varepsilon_{xy} & \varepsilon_{yy} & \varepsilon_{yz} \\ -\varepsilon_{xz} & -\varepsilon_{yz} & \varepsilon_{zz} \end{bmatrix}, \\
 [\mu] &= \begin{bmatrix} \mu_{xx} & \mu_{xy} & \mu_{xz} \\ \mu_{xy} & \mu_{yy} & \mu_{yz} \\ -\mu_{xz} & -\mu_{yz} & \mu_{zz} \end{bmatrix} \\
 [\zeta] &= \begin{bmatrix} \zeta_{xx} & \zeta_{xy} & \zeta_{xz} \\ \zeta_{yx} & \zeta_{yy} & \zeta_{yz} \\ \zeta_{zx} & \zeta_{zy} & \zeta_{zz} \end{bmatrix}, \\
 [\eta] &= \begin{bmatrix} \zeta_{xx} & \zeta_{yx} & -\zeta_{zx} \\ \zeta_{xy} & \zeta_{yy} & -\zeta_{zy} \\ -\zeta_{xz} & -\zeta_{yz} & \zeta_{zz} \end{bmatrix}
 \end{aligned} \tag{4w}$$

It is obvious that the constitutive features of normal uniaxially anisotropic media such as microwave laminates can be represented by the CGSs of $C_{4h}(C_{2h})$ or $D_{4h}(D_{2h})$. Uniaxially bianisotropic media, such as chiroomega media, can be described by $D_{2d}(C_{2v})$ or $C_{4v}(C_{2v})$. For gyroelectric and gyromagnetic anisotropic media, their constitutive features can be represented by $D_{2h}(C_{2h})$. On the other hand, it should be pointed out that in these constitutive tensors, each element could be the function of operating frequency, or even a complex quantity. The interaction

features of electromagnetic waves with various composite bianisotropic structures can be found in the literature [50–54]. The constitutive tensors of some CGSs of bianisotropic media are described in detail below.

2.2. Ferroelectric Materials [55–57]

Ferroelectric thin films can be used as the substrate or superstrate of various microstrip- or coplanar-waveguide-based microwave devices (Fig. 1) that possess certain tunabilities in their electromagnetic features. When the crystalline principal axes of the ferroelectric film are oriented in the coordinate directions, the film is reduced to the simplified case of the CGS described above, namely, $D_{2h}(C_{2v})$ and $[\mu] = \mu_0 \bar{I}$, $\zeta_{xy} = \zeta_{yx} = 0$. The film's permittivity tensor $[\varepsilon_f]$ in the unbiased condition, the biasing electric field $\vec{E}_{\text{bias}} = 0$, can be expressed by

$$[\varepsilon_f(0)] = \begin{bmatrix} \varepsilon_{xx}(0) & 0 & 0 \\ 0 & \varepsilon_{yy}(0) & 0 \\ 0 & 0 & \varepsilon_{zz}(0) \end{bmatrix} \tag{5}$$

When the biasing DC electric field is applied, $[\varepsilon_f]$ becomes

$$[\varepsilon_f(\vec{E}_{\text{bias}})] = \begin{bmatrix} \varepsilon_{xx}(\vec{E}_{\text{bias}}) & 0 & 0 \\ 0 & \varepsilon_{yy}(\vec{E}_{\text{bias}}) & 0 \\ 0 & 0 & \varepsilon_{zz}(\vec{E}_{\text{bias}}) \end{bmatrix} \tag{6}$$

Here, each element $[\varepsilon_f(\vec{E}_{\text{bias}})]$ can be a function of each of the three bias field components $E_{x,y,z,\text{bias}}$. If we assume, for simplicity, diagonal functional projection of the bias field components onto the permittivity tensor $[\varepsilon_f]$ elements, then we have

$$[\varepsilon_f(\vec{E}_{\text{bias}})] = \begin{bmatrix} \varepsilon_{xx}(E_{x,\text{bias}}) & 0 & 0 \\ 0 & \varepsilon_{yy}(E_{y,\text{bias}}) & 0 \\ 0 & 0 & \varepsilon_{zz}(E_{z,\text{bias}}) \end{bmatrix} \tag{7}$$

Using the hexagonal perovskite crystalline form for $\text{Ba}_x\text{Sr}_{1-x}\text{TiO}_3$ (BSTO) thin film, with the c axis parallel to the y axis and having properties different from those in the a - and b -axis directions parallel to the xz plane and having the same effects, $[\varepsilon_f]$ takes an uniaxial form as

$$[\varepsilon_f(0)] = \begin{bmatrix} \varepsilon_{xx}(0) & 0 & 0 \\ 0 & \varepsilon_{yy}(0) & 0 \\ 0 & 0 & \varepsilon_{xx}(0) \end{bmatrix} \tag{8}$$

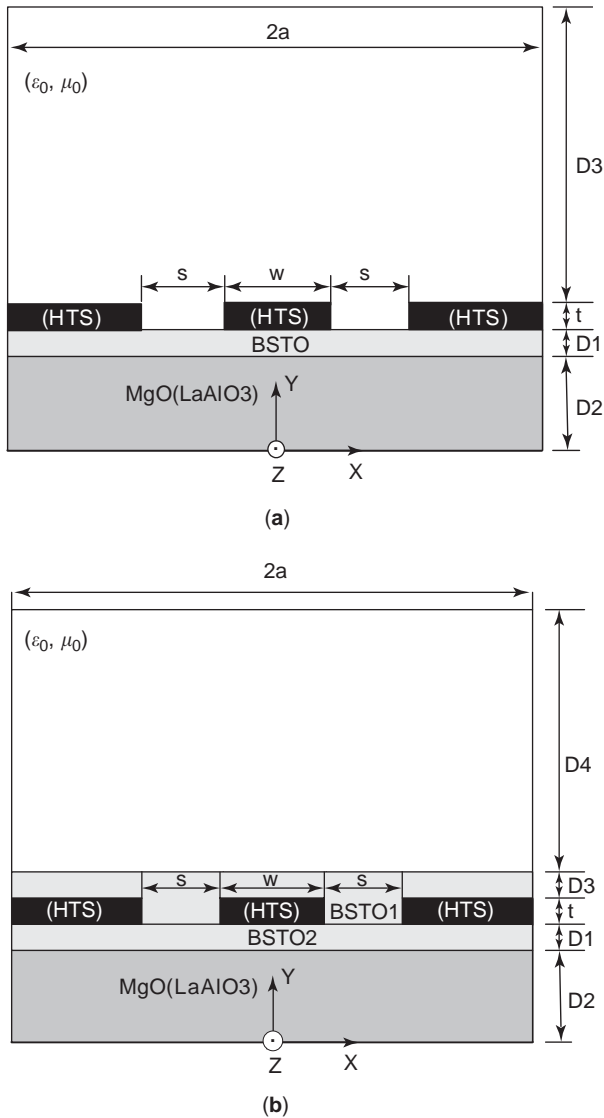


Figure 1. Cross-sectional views of two composite ferroelectric coplanar waveguides: (a) BSTO substrate; (b) BSTO superstrate-substrate.

In the case of $E_{\text{bias}} = E_x$, the ferroelectric effect renders $[\epsilon_f]$ as

$$[\epsilon_f(E_{\text{bias}})] = \begin{bmatrix} \epsilon_{xx}(E_{x,\text{bias}}) & 0 & 0 \\ 0 & \epsilon_{yy}(0) & 0 \\ 0 & 0 & \epsilon_{zz}(0) \end{bmatrix} \quad (9)$$

and $[\epsilon_f(E_{\text{bias}})]$ is biaxial.

It is understood that, as a rule, the losses in ferroelectrics decreases with decreasing temperature. So, after the discovery of high-temperature superconductivity (HTS), much effort has been devoted to combining HTS with ferroelectrics to realize the tunability of microwave devices in a low-loss situations. The modified microstrip structure in Fig. 1 consists of a dielectric substrate (LAO

or MgO, typically 254 μm thick), a ferroelectric thin-film layer with thickness ranging from 300 to 2000 nm for various applications, and a gold or YBCO thin film of 0.35 or 2 μm thick for the top strip, respectively.

On the other hand, in order to achieve the desired propagation characteristics of a ferroelectric microstrip line or coplanar waveguide, an additional ferrite layer can also be introduced in the substrate or superstrate-substrate structures presented above.

2.3. Sapphire

A nonmagnetic sapphire is also very important for high-frequency applications, and its relative permittivity tensor can be expressed by

$$[\epsilon] = \begin{bmatrix} \epsilon_{xx} & \epsilon_{xy} & 0 \\ \epsilon_{yx} & \epsilon_{yy} & 0 \\ 0 & 0 & \epsilon_{zz} \end{bmatrix} \quad (10a)$$

$$\epsilon_{xx} = \epsilon_x(T) \cos^2 \theta_e + \epsilon_y(T) \sin^2 \theta_e$$

$$\epsilon_{xy} = \epsilon_{yx}(T) = [\epsilon_y(T) - \epsilon_x(T)] \sin \theta_e \cos \theta_e$$

$$\epsilon_{yy} = \epsilon_x(T) \sin^2 \theta_e + \epsilon_y(T) \cos^2 \theta_e, \epsilon_{zz} = \epsilon_z(T) \quad (10b)$$

where θ_e ($0^\circ \leq \theta_e \leq 360^\circ$) is the misalignment angle between the coordinates of the line and principal axes of $[\epsilon]$ with respect to the x direction in x - y plane, $\epsilon_{x,y,z}(T)$ are the three principal-axis permittivities, and T is the operating temperature of sapphire.

2.4. Gyroelectric Media [58–61]

A great deal of attention has been paid to the microwave propagation in gyroelectric or solid-state magnetoplasmas in the past a few decades, since this type of medium ($[\zeta] = [\eta] = 0$) can be used to make various nonreciprocal devices for microwave and millimeter-wave applications, such as gyroelectric waveguides and planar microstrip transmission lines, as shown in Figs. 2a–2d. These models provide a basis for further developing planar integrated nonreciprocal devices, where the bulk gyroelectric media present the advantage of a very good coupling between the wave and the media. So, owing to the good mobility of the media, the losses are reduced.

In Fig. 2a, the longitudinal DC magnetic field is along the z -axis direction. On the other hand, if the DC magnetic field is wrapped around the z axis into a cylindrical shape, it forms an azimuthally magnetized solid-state plasma-filled coaxial waveguide that can support the cylindrically symmetric TM_{01} mode, and the corresponding permittivity tensor can be written as [61]

$$[\epsilon] = \begin{bmatrix} \epsilon_{xx} & 0 & \epsilon_{xz} \\ 0 & \epsilon_{yy} & 0 \\ -\epsilon_{xz} & 0 & \epsilon_{xx} \end{bmatrix} \quad (11)$$

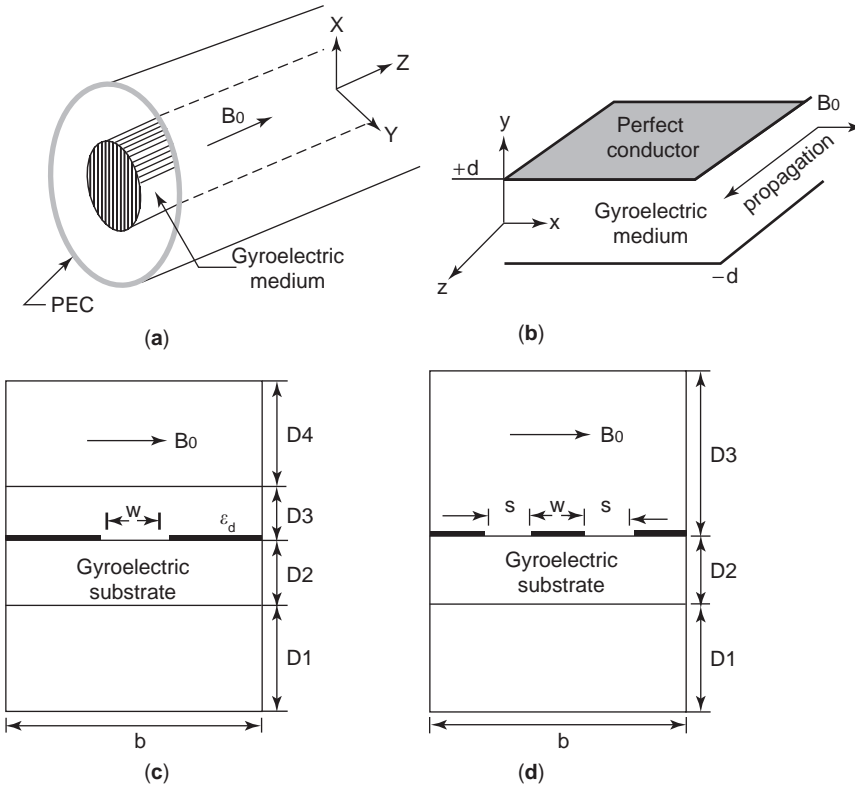


Figure 2. Schematic diagrams of gyroelectric waveguides and planar transmission lines: (a) circular; (b) planar; (c) slotline; (d) coplanar waveguide.

In Fig. 2b, there is a transversely magnetized plasma between two perfectly conducting parallel plates separated by a distance $2d$, where the static magnetic field is applied in the x direction and wave propagation is in the z direction. If the plasma is magnetized in the y direction, normal to the conducting plates, the modes are not, in general, separable into TE and TM modes. Here the relative permittivity tensor can be written in the form

$$[\varepsilon] = \begin{bmatrix} \varepsilon_{xx} & 0 & 0 \\ 0 & \varepsilon_{yy} & \varepsilon_{yz} \\ 0 & -\varepsilon_{yz} & \varepsilon_{zz} \end{bmatrix} \quad (12)$$

where each element in (12) is given in Ref. 61. Figure 2c shows a suspended single-slotline structure and Fig. 2d, a suspended coplanar waveguide.

When the biasing DC magnetic field \vec{B}_0 of the solid-state plasma in Fig. 2 is in an arbitrary direction (φ_0, θ_0) , its permittivity tensor can be described by $(e^{j\omega t})$

$$[\varepsilon(\omega)] = \begin{bmatrix} \varepsilon_{xx}(\omega) & \varepsilon_{xy}(\omega) & \varepsilon_{xz}(\omega) \\ \varepsilon_{yx}(\omega) & \varepsilon_{yy}(\omega) & \varepsilon_{yz}(\omega) \\ \varepsilon_{zx}(\omega) & \varepsilon_{zy}(\omega) & \varepsilon_{zz}(\omega) \end{bmatrix} \quad (13a)$$

$$\begin{aligned} \varepsilon_{xx}(\omega) &= \varepsilon_1(\omega) + [\varepsilon_2(\omega) - \varepsilon_1(\omega)] \sin^2 \nu \cos^2 \psi \\ \varepsilon_{xy}(\omega) &= -jg(\omega) \cos \nu + [\varepsilon_2(\omega) - \varepsilon_1(\omega)] \sin \psi \cos \psi \sin^2 \nu \\ \varepsilon_{xx}(\omega) &= \{jg(\omega) \sin \psi + [\varepsilon_2(\omega) - \varepsilon_1(\omega)] \cos \psi \cos \nu\} \sin \nu \\ \varepsilon_{yx}(\omega) &= jg(\omega) \cos \nu + [\varepsilon_2(\omega) - \varepsilon_1(\omega)] \sin \psi \cos \psi \sin^2 \nu \\ \varepsilon_{yy}(\omega) &= \varepsilon_1(\omega) + [\varepsilon_2(\omega) - \varepsilon_1(\omega)] \sin^2 \nu \sin^2 \psi \\ \varepsilon_{yz}(\omega) &= \{-jg(\omega) \cos \psi + [\varepsilon_2(\omega) - \varepsilon_1(\omega)] \sin \psi \cos \nu\} \sin \nu \\ \varepsilon_{zx}(\omega) &= \{-jg(\omega) \sin \psi + [\varepsilon_2(\omega) - \varepsilon_1(\omega)] \cos \psi \cos \nu\} \sin \nu \\ \varepsilon_{zy}(\omega) &= \{jg \cos \psi + [\varepsilon_2(\omega) - \varepsilon_1(\omega)] \sin \psi \cos \nu\} \sin \nu \\ \varepsilon_{zz}(\omega) &= \varepsilon_1(\omega) \sin^2 \nu + \varepsilon_2(\omega) \cos^2 \nu \end{aligned} \quad (13b)$$

In (13b), two consecutive rotations of angles ψ and ν are determined by the spherical angles φ_0 and θ_0 by

$$\cos \psi = \frac{\sin \theta_0 \cos \varphi_0}{\sqrt{(\sin^2 \theta_0 \cos^2 \varphi_0 + \cos^2 \theta_0)}} \quad (13c)$$

$$\cos \nu = \sin \theta_0 \sin \varphi_0 \quad (13d)$$

$$\varepsilon_1(\omega) = \varepsilon_s - \frac{\omega_p^2(\omega - j\tau^{-1})}{\omega \varepsilon_0 [(\omega - j\tau^{-1})^2 - \omega_c^2]} \quad (13e)$$

$$\varepsilon_2(\omega) = \varepsilon_s - \frac{\omega_p^2}{\omega \varepsilon_0 (\omega - j\tau^{-1})} \quad (13f)$$

$$g(\omega) = - \frac{\omega_p^2 \omega_c}{\omega \varepsilon_0 [(\omega - j\tau^{-1})^2 - \omega_c^2]} \quad (13g)$$

where $\omega_p = \sqrt{ne^2/\varepsilon_0 m^*}$ represents the plasma frequency; $\omega_c = eB_0/m^*$, the cyclotron frequency; n , the carrier concentration; e , the electron charge; m^* , the electron effective mass (kg) (i.e., $0.067 m_e$ for GaAs); m_e , the electron rest mass; B_0 , the DC magnetizing field; φ , the orientation angle of B_0 in the x - y plane; τ , the momentum relaxation time of the semiconductor material; and ε_s , the relative dielectric permittivity of the semiconductor.

2.5. Ferrites

Ferrites have been widely used as important elements in microwave and millimeter-wave devices, such as phase shifters, resonance isolators, circulators, and superstrates or substrates of microwave integrated circuits (MICs). One of the main advantages of using magnetized ferrites is that their characteristic parameters, as in Fig. 2, can be controlled by adjusting an applied DC magnetic bias field. Hence, various tunable microwave devices can also be designed when we combine ferrites with other materials, as shown in Fig. 3.

In Fig. 3b [62], a high-temperature superconductor (HTS) strip (2) of a width W is located on top of the dielectric substrate (1) and separated by a dielectric layer (3) from an epitaxial ferrite film (4) deposited on a dielectric substrate (5). The structure may contain either an HTS or metal bottom electrode (0), the microstrip resonator, or two HTS electrodes (Fig. 2a), placed at a distance W_1 from each other, the CPW resonator. The thickness of the HTS electrodes (2), ferrite layer (4), bottom electrode (0), and dielectric layers (1), (3), and (5) are t , t_f , t_0 and t_1 , t_3 , t_5 , respectively. An external DC biasing magnetic field H_e is applied parallel to the plane of the structure and makes an angle ϕ with the central stripline direction.

When the biasing DC magnetic field \vec{B}_0 takes an arbitrary orientation (φ_0, θ_0) , the permeability tensor $[\mu(\omega)]$ of ferrites can be written as [34]

$$[\mu(\omega)] = \begin{bmatrix} \mu_{xx}(\omega) & \mu_{xy}(\omega) & \mu_{xz}(\omega) \\ \mu_{yx}(\omega) & \mu_{yy}(\omega) & \mu_{yz}(\omega) \\ \mu_{zx}(\omega) & \mu_{zy}(\omega) & \mu_{zz}(\omega) \end{bmatrix} \quad (14a)$$

$$\mu_{xx}(\omega) = \mu(\omega) + [1 - \mu(\omega)] \sin^2 \theta_0 \cos^2 \varphi_0$$

$$\begin{aligned} \mu_{xy}(\omega) &= [1 - \mu(\omega)] \sin \varphi_0 \cos \varphi_0 \sin^2 \theta_0 \\ &\quad - j\kappa \cos \theta_0 \end{aligned}$$

$$\begin{aligned} \mu_{xz}(\omega) &= j\kappa \sin \varphi_0 \sin \theta_0 \\ &\quad + [1 - \mu(\omega)] \sin \theta_0 \cos \theta_0 \cos \varphi_0 \end{aligned}$$

$$\begin{aligned} \mu_{yx}(\omega) &= [1 - \mu(\omega)] \sin \varphi_0 \cos \varphi_0 \\ &\quad \times \sin^2 \theta_0 + j\kappa \cos \theta_0 \end{aligned}$$

$$\mu_{yy}(\omega) = \mu(\omega) + [1 - \mu(\omega)] \sin^2 \theta_0 \sin^2 \varphi_0$$

$$\begin{aligned} \mu_{yz}(\omega) &= -j\kappa \cos \varphi_0 \sin \theta_0 \\ &\quad + [1 - \mu(\omega)] \sin \theta_0 \cos \theta_0 \sin \varphi_0 \end{aligned}$$

$$\begin{aligned} \mu_{zx}(\omega) &= -j\kappa \sin \varphi_0 \sin \theta_0 + [1 \\ &\quad - \mu(\omega)] \sin \theta_0 \cos \theta_0 \cos \varphi_0 \end{aligned}$$

$$\begin{aligned} \mu_{zy}(\omega) &= j\kappa \cos \varphi_0 \sin \theta_0 + [1 \\ &\quad - \mu(\omega)] \sin \theta_0 \cos \theta_0 \sin \varphi_0 \end{aligned}$$

$$\mu_{zz}(\omega) = 1 - [1 - \mu(\omega)] \sin^2 \theta_0$$

$$\mu(\omega) = \mu_1(\omega) - j\mu_2(\omega) \quad (14b)$$

$$\mu_1(\omega) = 1 + \frac{\omega_0 \omega_m [\omega_0^2 - \omega^2 (1 - \alpha_m^2)]}{F_m}$$

$$\mu_2(\omega) = \frac{\omega \omega_m \alpha_m [\omega_0^2 + \omega^2 (1 + \alpha_m^2)]}{F_m}$$

$$\kappa(\omega) = \kappa_1(\omega) - j\kappa_2(\omega)$$

$$\kappa_1(\omega) = - \frac{\omega \omega_m [\omega_0^2 - \omega^2 (1 + \alpha_m^2)]}{F_m}$$

$$\kappa_2 = - \frac{2\omega_m \omega_0 \alpha_m \omega^2}{F_m}$$

$$F_m = [\omega_0^2 - \omega^2 (1 + \alpha_m^2)]^2 + 4(\omega \omega_0 \alpha_m)^2$$

where $\omega = |\gamma|H_0$, $\omega_m = |\gamma|M_s$, M_s is the saturation magnetization of the ferrite, γ denotes to the gyromagnetic ratio ($= -2.21 \times 10^5$ rad·m/C), α_m identifies the Landau damping coefficient, and the loss is taken into account.

2.6. Biisotropic Chiral Medium

Since the early 1990s many researchers have explored the diverse chirality effects in biisotropic chiral media on electromagnetic wave propagation, radiation, and scattering. Electromagnetic waves in chiral media show some very interesting features, such as optical rotatory dispersion (ORD), which causes the rotation of polarization; and circular dichroism, due to the different absorption coefficients of right- and left-handed circularly polarized waves. Some component models using chiral media have been proposed, such as chirowaveguides, chiro-lens, chiro-domes, chiro-strip antennas, chiral resonators, and chiral-mode transformers [63–83].

The constitutive equation for biisotropic chiral media can be easily obtained from Eqs. (2a) and (2b), as follows

$$\vec{D} = \varepsilon_0 \varepsilon_r \vec{E} + \sqrt{\mu_0 \varepsilon_0} \vec{\zeta} \vec{H} \quad (15a)$$

$$\vec{B} = \mu_0 \mu_r \vec{H} + \sqrt{\mu_0 \varepsilon_0} \vec{\eta} \vec{E} \quad (15b)$$

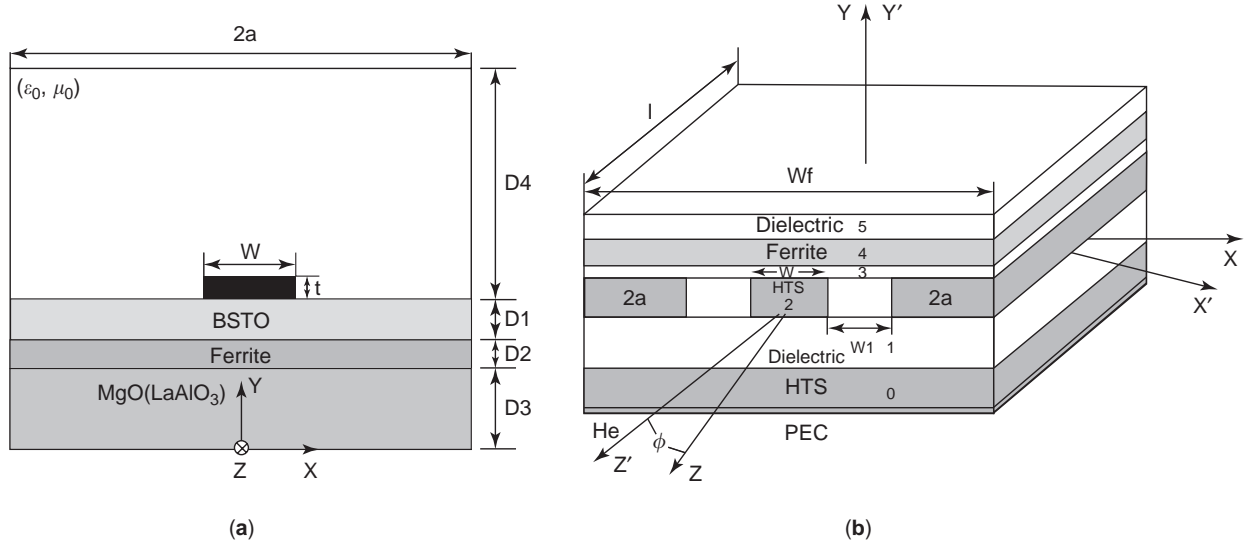


Figure 3. Geometries of ferrite-based tunable microstrip line and coplanar resonator: (a) BSTO-ferrite microstrip line; (b) multilayer composite HTS-ferrite coplanar resonator.

where we let $[\underline{\epsilon}] = \epsilon_r \bar{I}$, $[\underline{\mu}] = \mu_r \bar{I}$, $[\underline{\xi}] = \xi \bar{I} = j\kappa \bar{I}$, and $[\underline{\eta}] = \xi^* \bar{I} = -j\kappa \bar{I}$, where \bar{I} is the unit dyad, κ is the chirality parameter, and the frequency-dependent property of constitutive quantities should be understood but here ω is suppressed. In a chiral medium, the eigenmodes are the left- and right-handed circular polarized waves, as observed in ferrites. However, there is no biasing DC magnetic field needed. Some models of chiral devices are outlined as follows.

2.6.1. Chirowaveguides. Figure 4 shows the geometries of circular (a) and a rectangular (b) chirowaveguides, which have been extensively studied by some researchers.

The guided-mode characteristics in chirowaveguides in Fig. 4 are completely controlled by chirality parameter. It can be predicated that the ordinary modes of transverse electric TE_{nm} , transverse magnetic TM_{nm} , or transverse electromagnetic (TEM) modes cannot be supported in circular bianisotropic waveguides. The propagating modes along z axis are always hybrid, but they can be classified into hybrid modes HE_{nm} and EH_{nm} . The descriptor EH_{nm} is used here for hybrid modes originating in ordinary TM_{nm} modes, and HE_{nm} is used for hybrid modes stemming from ordinary TE_{nm} modes. Here $n(= -\infty, \dots, 0, \dots, \infty)$ and $m(= 1, \dots, \infty)$ respectively denote the azimuthal and radial quantum numbers, of which n implies an azimuthal variation $e^{-jn\phi}$ and m implies that the mode is number m when ordered after increasing cutoff frequency for given n .

The longitudinal components E_z and H_z are coupled with each other; however, E_z and H_z can be decoupled as follows

$$E_z = S_+ U_+ + S_- U_- \quad (16a)$$

$$H_z = q_+ U_+ + q_- U_- \quad (16b)$$

where U_{\pm} are determined by

$$\nabla_t^2 U_{\pm} + S_{\pm} U_{\pm} = 0 \quad (16c)$$

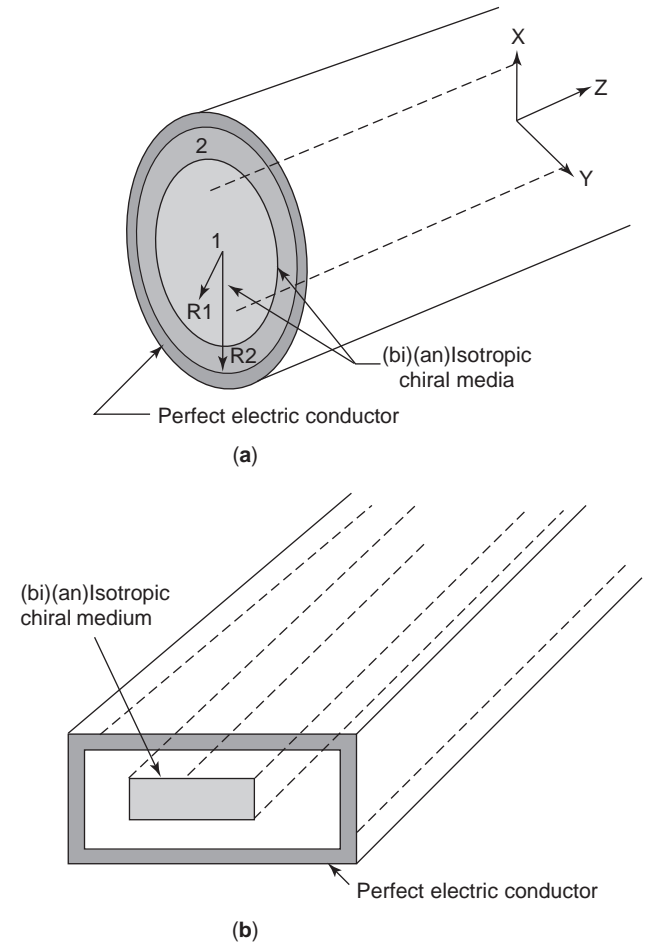


Figure 4. Geometries of chirowaveguides: (a) circular; (b) rectangular.

and more generally, by

$$S_{\pm} = \frac{-(C_1 + C_4) \pm \sqrt{(C_1 - C_4)^2 + 4C_2C_3}}{2} \quad (16d)$$

$$q_{\pm} = \frac{-S_{\pm}(S_{\pm} + C_1)}{C_2} \quad (16e)$$

$$C_1 = \frac{j\omega(A_{43}\eta_{zz} + A_{41}\varepsilon_{zz})}{\Delta_0}, \quad C_2 = \frac{j\omega(A_{43}\mu_{zz} + A_{41}\xi_{zz})}{\Delta_0}$$

$$C_3 = -\frac{j\omega(A_{21}\varepsilon_{zz} + A_{23}\eta_{zz})}{\Delta_0}, \quad C_4 = -\frac{j\omega(A_{21}\xi_{zz} + A_{23}\mu_{zz})}{\Delta_0}$$

$$\Delta_0 = A_{21}A_{43} - A_{23}A_{41} \quad (16f)$$

Further, the transverse components electric and magnetic fields inside the chiro-waveguide can be expressed in terms of E_z and H_z as follows [31,32,35,69–71]

$$\begin{bmatrix} E_x \\ E_y \\ H_x \\ H_y \end{bmatrix} = \begin{bmatrix} A_{22} & A_{21} & A_{42} & A_{41} \\ -A_{21} & A_{22} & -A_{41} & A_{42} \\ A_{24} & A_{23} & A_{44} & A_{43} \\ -A_{23} & A_{24} & -A_{43} & A_{44} \end{bmatrix} \begin{bmatrix} \frac{\partial E_z}{\partial x} \\ \frac{\partial E_z}{\partial y} \\ \frac{\partial H_z}{\partial x} \\ \frac{\partial H_z}{\partial y} \end{bmatrix} \quad (17a)$$

where

$$A_{21} = \frac{a_3b_2 + a_4b_3 - a_2b_1}{\Delta}, \quad A_{22} = \frac{a_1b_1 + a_4b_2 - a_3b_3}{\Delta}$$

$$A_{23} = \frac{a_1b_2 + a_2b_3 - a_4b_4}{\Delta}, \quad A_{24} = \frac{a_3b_4 - a_1b_3 - a_2b_2}{\Delta}$$

$$A_{41} = \frac{a_1b_5 + a_2b_8 - a_6b_9}{\Delta}, \quad A_{42} = \frac{a_2b_5 - a_3b_6 + a_4b_7}{\Delta}$$

$$A_{43} = \frac{a_1b_7 + a_3b_9 + a_2b_{10}}{\Delta}, \quad A_{44} = \frac{a_1b_6 + a_2b_8 + a_4b_9}{\Delta}$$

$$b_1 = a_7^2 + a_8^2, \quad b_2 = a_6a_7 - a_5a_8, \quad b_3 = a_6a_8 + a_5a_7,$$

$$b_4 = a_5^2 + a_6^2, \quad b_5 = a_3a_8 - a_4a_7$$

$$b_6 = a_1a_7 - a_3a_5, \quad b_7 = a_4a_5 - a_1a_8,$$

$$b_8 = a_2a_7 - a_3a_6, \quad b_9 = a_1a_6 - a_2a_5$$

$$a_1 = -(\gamma + \omega\eta_{xy}), \quad a_2 = j\omega\eta_{xx}, \quad a_3 = -\omega\mu_{xy},$$

$$a_4 = j\omega\mu_{xx}, \quad a_5 = \omega\varepsilon_{xy}, \quad a_6 = -j\omega\varepsilon_{xx}$$

$$a_7 = -(\gamma - \omega\xi_{xy}), \quad a_8 = -j\omega\xi_{xx}$$

$$\Delta = a_1(a_1b_1 + a_2b_4 - a_3b_3) + a_2(a_2b_1 - a_4b_3 - a_3b_2)$$

$$+ a_3(a_3b_4 - a_2b_2 - a_1b_3)$$

$$+ a_4(a_1b_2 - a_2b_3 + a_4b_4) \quad (17b)$$

where γ is the mode propagation constant. In Fig. 4a, six field components of the guided hybrid modes $HE(EH)_{nm}$ can be expressed in a set of closed-form equations. For example, in the inner chiral region ($\rho \leq R_1$) in Fig. 4a, the tangential field components are given by [69]

$$E_z^{(1)} = [D_1^{(1)}S_+^{(1)}J_n(\sqrt{S_+^{(1)}}\rho) + D_2^{(1)}S_-^{(1)}J_n(\sqrt{S_-^{(1)}}\rho)]e^{-jn\phi} \quad (18a)$$

$$E_{\phi}^{(1)} = \{D_1^{(1)}[-M_+^{(1)}J_n'(\sqrt{S_+^{(1)}}\rho) - \frac{jnN_+^{(1)}}{\rho}J_n(\sqrt{S_+^{(1)}}\rho)]$$

$$+ D_2^{(1)}[-M_-^{(1)}J_n'(\sqrt{S_-^{(1)}}\rho) - \frac{jnN_-^{(1)}}{\rho}J_n(\sqrt{S_-^{(1)}}\rho)]\}e^{-jn\phi} \quad (18b)$$

$$H_z^{(1)} = [D_1^{(1)}q_+^{(1)}J_n(\sqrt{S_+^{(1)}}\rho) + D_2^{(1)}q_-^{(1)}J_n(\sqrt{S_-^{(1)}}\rho)]e^{-jn\phi} \quad (18c)$$

$$H_{\phi}^{(1)} = \{D_1^{(1)}[-X_+^{(1)}J_n'(\sqrt{S_+^{(1)}}\rho) - \frac{jnY_+^{(1)}}{\rho}J_n(\sqrt{S_+^{(1)}}\rho)]$$

$$+ D_2^{(1)}[-X_-^{(1)}J_n'(\sqrt{S_-^{(1)}}\rho) - \frac{jnY_-^{(1)}}{\rho}J_n(\sqrt{S_-^{(1)}}\rho)]\}e^{-jn\phi} \quad (18d)$$

where $D_1^{(1)}$ and $D_2^{(1)}$ are unknown mode-expanding constants to be determined. Here, J_n and J_n' are the Bessel function of the first kind and its derivative, respectively. After some mathematical treatments, the mode dispersion and attenuation characteristics in chiro-waveguides can be understood.

As in normal waveguides, various discontinuities may also exist in chiro-waveguides, as shown in Fig. 5. This structure is symmetric in the z -axis direction, and the scattering of the guided mode may be analyzed in terms of the symmetric and asymmetric excitations as indicated in Ref. 79.

Figure 6 shows two cases of a normal waveguide partially filled with bianisotropic chiral media, and these may be easily met in the measurement of chiral parameter using some standard waveguide methods.

In the case of coaxial line filled with a biisotropic chiral medium, the influence of permittivity and length of chiral sample W on the amplitude of scattering parameters is depicted in Fig. 7, where $a = 3.04$ mm, $b = 7.0$ mm, $c = 6.0$ mm, $\zeta_c = 10^{-4}$ mho, and $\mu = \mu_0$.

2.6.2. Chiral Resonators. Chiral media can be used to produce circular cylindrical and spherical dielectric resonators that are further used in filters and antennas. Figure 8 shows the configurations of two chiral spherical resonators [81].

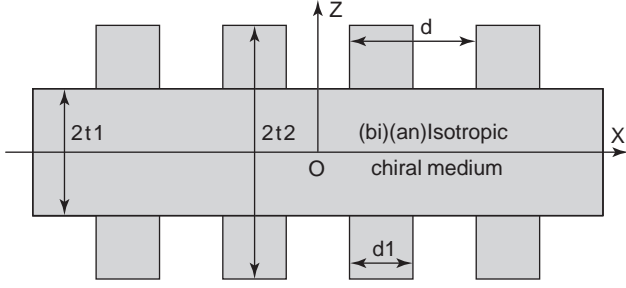


Figure 5. Cross-sectional view of a chirowaveguide grating [79].

The inner and outer electromagnetic fields of the chiral sphere shown in Fig. 8a can be expressed by

$$\begin{aligned} \vec{E}_{\text{chiral}}^{(1)} = & - \sum_{m,n} \{ ja_{mn} [\vec{N}_{e,mn}^{(1)}(k_+r) + \vec{M}_{e,mn}^{(1)}(k_+r)] \\ & + jb_{mn} [\vec{N}_{o,mn}^{(1)}(k_+r) + \vec{M}_{o,mn}^{(1)}(k_+r)] \\ & + c_{mn} [\vec{N}_{e,mn}^{(1)}(k_-r) - \vec{M}_{e,mn}^{(1)}(k_-r)] \\ & + d_{mn} [\vec{N}_{o,mn}^{(1)}(k_-r) - \vec{M}_{o,mn}^{(1)}(k_-r)] \} \end{aligned} \quad (19a)$$

$$\begin{aligned} \vec{H}_{\text{chiral}}^{(1)} = & \frac{1}{\eta_c} \sum_{m,n} \{ a_{mn} [\vec{N}_{e,mn}^{(1)}(k_+r) + \vec{M}_{e,mn}^{(1)}(k_+r)] \\ & + b_{mn} [\vec{N}_{o,mn}^{(1)}(k_+r) + \vec{M}_{o,mn}^{(1)}(k_+r)] \\ & + jc_{mn} [\vec{N}_{e,mn}^{(1)}(k_-r) - \vec{M}_{e,mn}^{(1)}(k_-r)] \\ & + jd_{mn} [\vec{N}_{o,mn}^{(1)}(k_-r) - \vec{M}_{o,mn}^{(1)}(k_-r)] \} \end{aligned} \quad (19b)$$

and

$$\begin{aligned} \vec{E}_{\text{free}} = & - \sum_{m,n} \{ je_{mn} \vec{N}_{e,mn}^{(4)}(k_0r) + jf_{mn} \vec{N}_{o,mn}^{(4)}(k_0r) \\ & + g_{mn} \vec{M}_{e,mn}^{(4)}(k_0r) + h_{mn} \vec{M}_{o,mn}^{(4)}(k_0r) \} \\ \vec{H}_{\text{free}} = & \frac{1}{\eta_0} \sum_{m,n} \{ -jg_{mn} \vec{N}_{e,mn}^{(4)}(k_0r) - jh_{mn} \vec{N}_{o,mn}^{(4)}(k_0r) \\ & + e_{mn} \vec{M}_{e,mn}^{(4)}(k_0r) + f_{mn} \vec{M}_{o,mn}^{(4)}(k_0r) \} \end{aligned} \quad (19c)$$

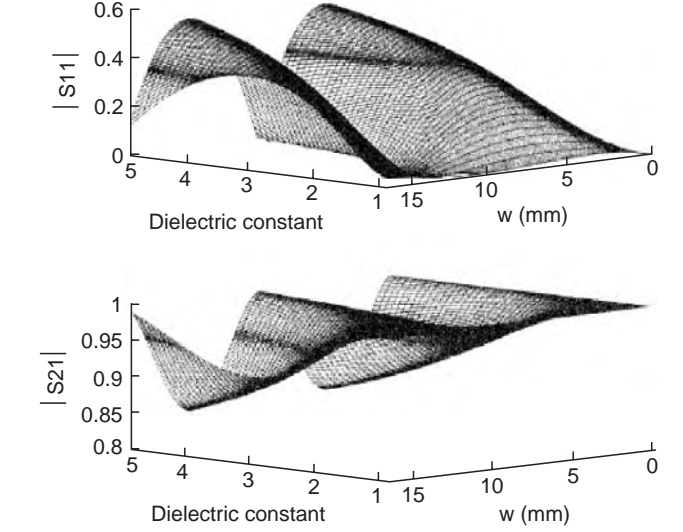
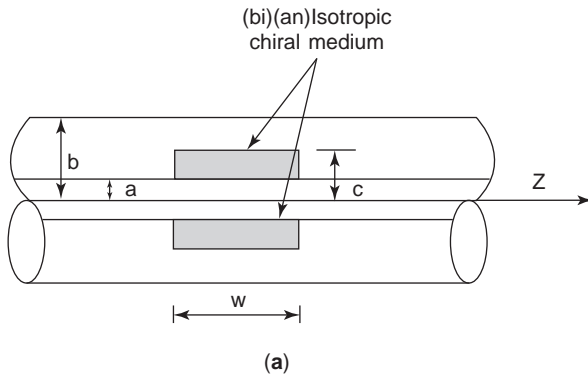


Figure 7. Influence of dielectric constant and length of chiral sample on the amplitude of scattering parameters for a coaxial line partially filled with case [80].

where a_{mn} , b_{mn} , c_{mn} , d_{mn} , e_{mn} , f_{mn} , g_{mn} , h_{mn} , are unknown coefficients that can be determined by boundary conditions at $r=R_1$; $\vec{M}_{e(o)mn}^{(1,4)}(k_{+(0)}r)$ and $\vec{N}_{e(o)mn}^{(1,4)}(k_{+(0)}r)$ are spherical vector wavefunctions. In the case of a multilayer chiral spherical resonator, as shown in Fig. 8b, the electromagnetic fields in each layer can be easily obtained as given in Refs. 72 and 73. Straightforwardly, a set of characteristic equations can be derived after some mathematical treatments, and the Q factor as a function of chirality parameter is shown in Fig. 9 for hybrid modes of different orders [81]. As an example, the Q factor of hybrid mode HE_{m22} varies from 30 to 500 as ξ_r increases from zero to one.

2.6.3. Chiral Striplines and Chiral Slotlines. A chiral medium can also be combined with other materials, such as ferrites, to form some novel nonreciprocal chirostrip transmission lines. Figure 10 shows the shielded chiralstripline and two chiral slotlines with chiral and ferrite substrates [42].

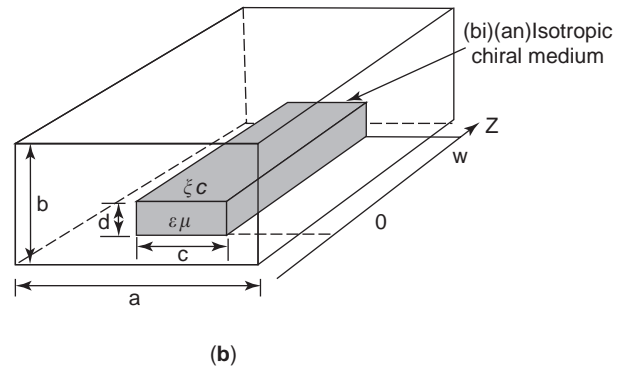


Figure 6. A waveguide partially filled with chiral media: (a) coaxial line; (b) rectangular waveguide.

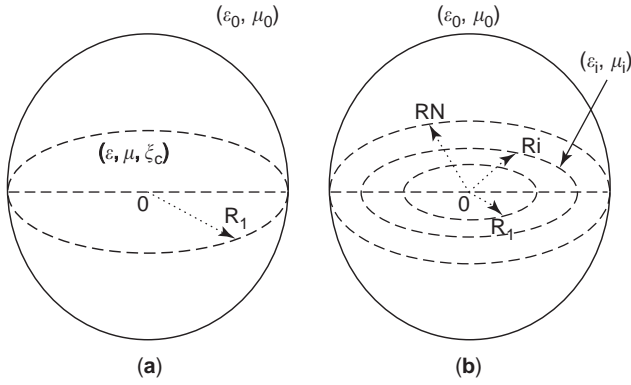


Figure 8. A single- (a) and a multilayer (b) chiral resonators.

Using the technique of exponential matrix in the spectral domain, together with the Galerkin MoM (method of moments) procedure, the mode dispersion characteristics in these structures can be understood. As an example, Fig. 11 shows the frequency dependence of effective permittivity $\epsilon_{\text{eff}+}$ in the structure shown in Fig. 10b, and both chirality and gyrotropy are considered here. The parameters chosen for calculation are assumed to be $f = 40$ GHz, $a = 3.556$ mm, $D_1 = D_4 = 3.3935$ mm, $D_2 = D_3 = 0.1625$ mm, $[\epsilon^{(2)}(\omega)] = 12.6 I$, $M_s^{(2)} \mu_0 = 0.275$, $\omega_0^{(2)}/\omega_m^{(2)} = 0.30$, $\alpha_m^{(2)} = 0.0$, $\theta_0^{(2)} = 90^\circ$, $\phi_0^{(2)} = 0^\circ$, $[\xi^{(2)}(\omega)] = [\eta^{(2)}(\omega)]^* = 10^{-6} I$, $[\epsilon^{(3)}(\omega)] = 2.2 I$, $[\mu^{(3)}(\omega)] = I$, $[\xi^{(3)}(\omega)] = [\eta^{(3)}(\omega)]^* = j0.5 I(a)$, and $j0.8 I(b)$.

In Fig. 11, the ferrite substrate is magnetically biased by a magnetic field fixed to the x -axis direction with saturation magnetization $M_s^{(2)} \mu_0 = 0.275$, $\omega_0^{(2)}/\omega_m^{(2)} = 0.3$. Physically, such a unilateral chiral ferrite slotline is a nonreciprocal structure, but only the effective dielectric constant of forward wave is demonstrated here. It is obvious that, at high frequency $f = 40$ GHz and for strong chirality, ϵ_{eff} decreases rapidly with increasing the slot width.

2.6.4. Faraday Chiral Media. Faraday chiral media are classified as chiropasmas or chiroferrites in which the effects of both gyrotropy and chirality are combined [49,84]. Corresponding to the CGS of C_∞ , their four constitutive tensors can be described by

$$[C] = \begin{bmatrix} C_{xx} & -jC_{xy} & 0 \\ jC_{xy} & C_{xx} & 0 \\ 0 & 0 & C_{zz} \end{bmatrix}, \quad C = \epsilon, \mu, \zeta, \eta \quad (20)$$

where these tensors contain a total of 12 scalar quantities. When a circular waveguide is filled with Faraday chiral media, as shown in Fig. 4a, the longitudinal components E_z and H_z can be decoupled and expressed by Eqs. (16a) and (16b). Following a procedure similar to that described in Refs. 32 and 35, the field distribution in each layer can be derived, and also the mode dispersion characteristics can be understood. Some hybrid analytical and numerical techniques, as proposed in Refs. 85–89, can be employed to

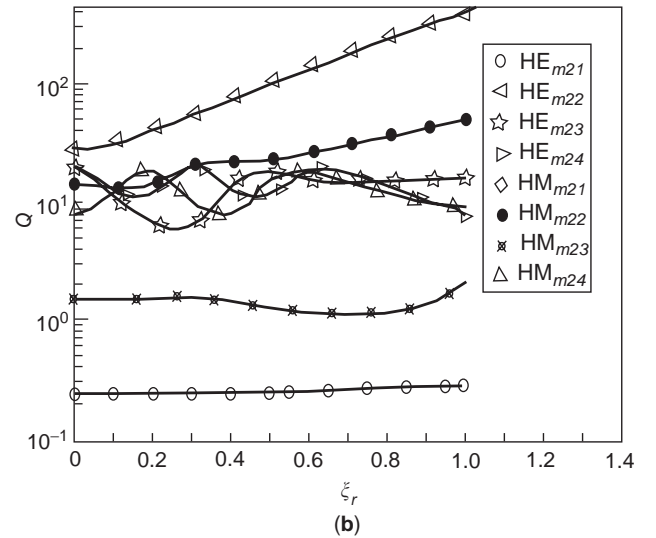
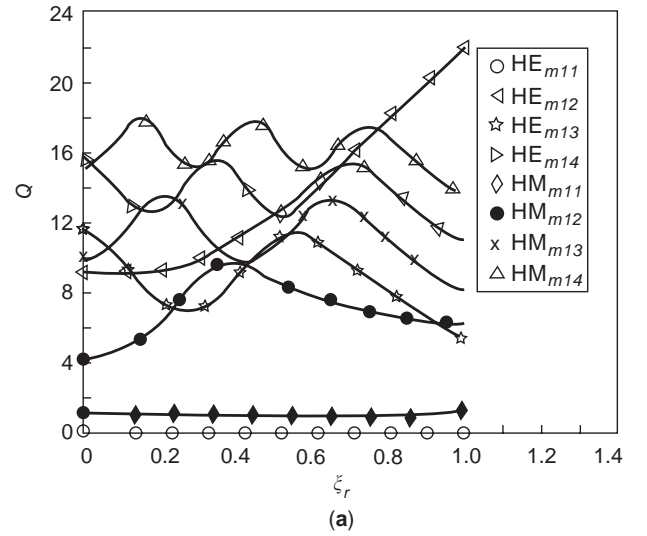


Figure 9. Q factor versus chirality parameter for hybrid modes of different orders: (a) $\epsilon_r = 10$, $\mu_r = 1$, $n = 1$; (b) $\epsilon_r = 10$, $\mu_r = 1$, $n = 2$.

study the combined effects of gyrotropy and chirality on the guided hybrid mode characteristics. On the other hand, it should be mentioned that to design and fabricate Faraday chiral media, and further to extract their constitutive parameters at microwave frequencies, is very challenging work. Although some methods have been proposed [90], many difficult problems need to be explored by the researchers in both material and microwave fields.

3. TYPICAL METHODOLOGIES

3.1. Exponential Matrix Technique in the Spectral Domain

Among the techniques used to deal with the interaction of an electromagnetic wave with multilayer bianisotropic media, we should mention the exponential matrix technique proposed by Tsalamengas [4], which has been successfully used to study source radiation and wave

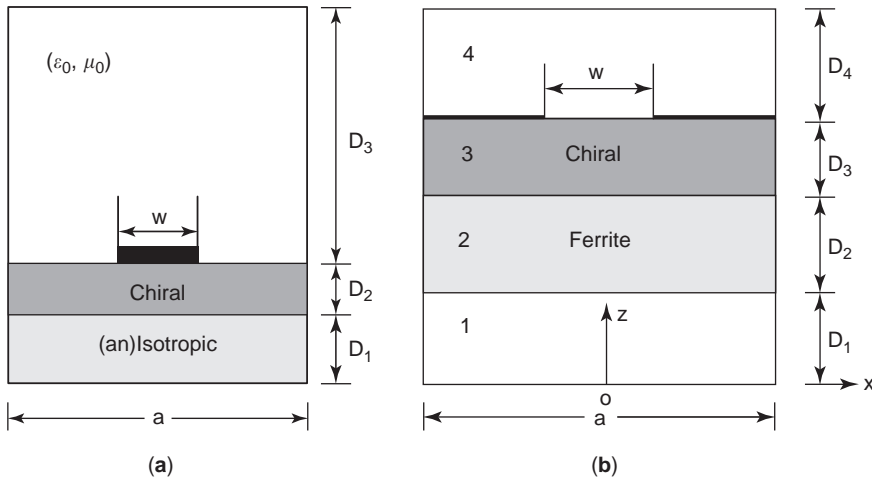


Figure 10. Cross-sectional views of three microstrip transmission lines with chiral and ferrite substrate: (a) chiral stripline; (b) unilateral chiral slotline; (c) bilateral chiral slotline.

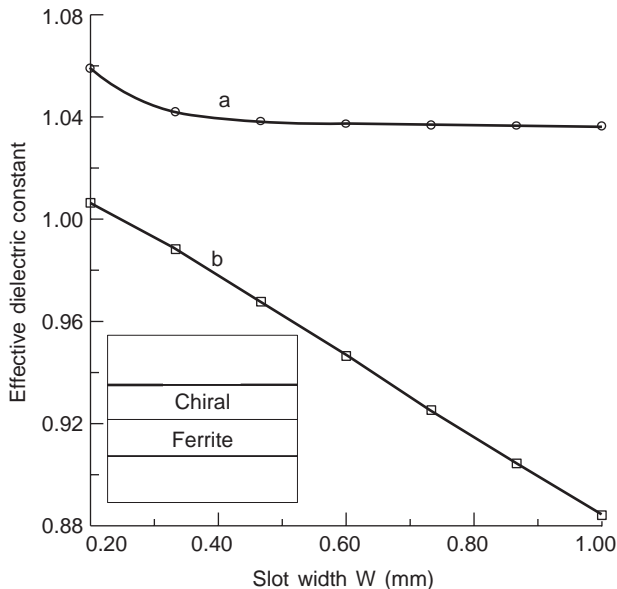


Figure 11. Slot width dependence of $\epsilon_{\text{eff}+}(\beta_+/k_0)^2$ in a unilateral slotline on a double-layer chiral-ferrite substrate.

propagation problems related to single-, double-, and multilayer bianisotropic structures [34,38–40,42,50–54] as shown in Fig. 12. Here, we let the z axis of a rectangular coordinate system be normal to all boundaries and the x and y axes lie in the plane of the top interface. In the z -axis direction, the geometry has discrete variation in material characteristics, and this structure may be with or without a backed plane at $z = -d^{(N)}$ ($d^{(N)} = \sum_{i=1}^N D^{(i)}$). For the nonbacked case the regions $z > 0$ and $z < -d^{(N)}$ are usually assumed to be free space (ϵ_0, μ_0) . The thickness of each layer is denoted by $D^{(1)}, \dots, D^{(i)} (|d^{(i)} - d^{(i-1)}|), \dots,$ and $D^{(N)}$. Mathematically, the four constitutive tensors $[\epsilon^{(i)}(\omega)], [\mu^{(i)}(\omega)], [\zeta^{(i)}(\omega)],$ and $[\eta^{(i)}(\omega)]$ ($i = 1, \dots, N$) of each layer may take any type of the above mentioned 23 CGSs or even another form [1].

Assuming that a linearly polarized electromagnetic wave is obliquely incident on a multilayer bianisotropic medium, as shown in Fig. 12, four propagating modes with different phase velocities can be generated in each layer. After propagation through the medium, the polarization of the transmitted field is rotated with respect to the polarization of the incident wave. Now we introduce the

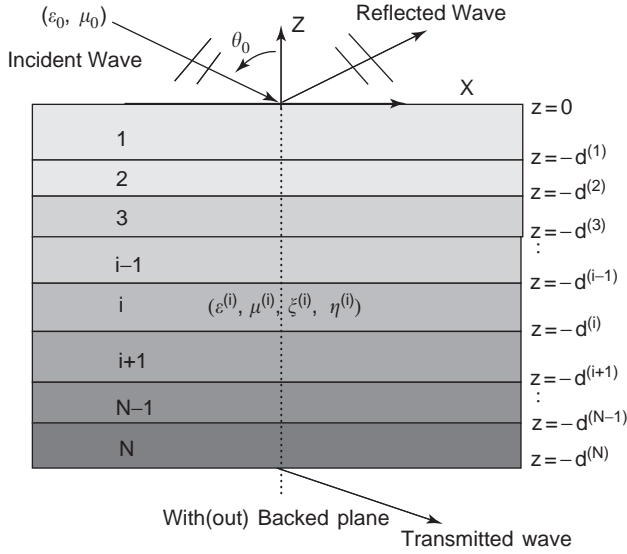


Figure 12. Cross section of multilayer bianisotropic medium with(out) backed plane.

one-dimensional Fourier transform domain defined by

$$\tilde{\psi}(k_x, z) = \frac{1}{2\pi} \int_{-\infty}^{+\infty} \psi(x; z) e^{jk_x x} dx \quad (21a)$$

$$\psi(x, z) = \int_{-\infty}^{+\infty} \tilde{\psi}(k_x; z) e^{-jk_x x} dk_x \quad (21b)$$

into the following Maxwell equations ($e^{j\omega t}$):

$$\begin{aligned} \nabla \times \tilde{\mathbf{H}}^{(i)} &= j\omega \{ \epsilon_0 [\epsilon^{(i)}(\omega)] \tilde{\mathbf{E}}^{(i)} \\ &+ \sqrt{\mu_0 \epsilon_0} [\zeta^{(i)}(\omega)] \tilde{\mathbf{H}}^{(i)} \}, \end{aligned} \quad (22a)$$

$$\begin{aligned} \nabla \times \tilde{\mathbf{E}}^{(i)} &= -j\omega \{ \mu_0 [\mu^{(i)}(\omega)] \tilde{\mathbf{H}}^{(i)} \\ &+ \sqrt{\mu_0 \epsilon_0} [\eta^{(i)}(\omega)] \tilde{\mathbf{E}}^{(i)} \} \end{aligned} \quad (22b)$$

Following a procedure similar to that proposed in Ref. 4, the transverse field components in each layer of multilayered bianisotropic slabs can be expressed as

$$\begin{aligned} \frac{d}{dz} \begin{bmatrix} \tilde{\mathbf{E}}_x^{(i)}(k_x; z) \\ \tilde{\mathbf{E}}_y^{(i)}(k_x; z) \\ \tilde{\mathbf{H}}_x^{(i)}(k_x; z) \\ \tilde{\mathbf{H}}_y^{(i)}(k_x; z) \end{bmatrix} &= \begin{bmatrix} q_{11}^{(i)} & q_{12}^{(i)} & q_{13}^{(i)} & q_{14}^{(i)} \\ q_{21}^{(i)} & q_{22}^{(i)} & q_{23}^{(i)} & q_{24}^{(i)} \\ q_{31}^{(i)} & q_{32}^{(i)} & q_{33}^{(i)} & q_{34}^{(i)} \\ q_{41}^{(i)} & q_{42}^{(i)} & q_{43}^{(i)} & q_{44}^{(i)} \end{bmatrix} \\ &\times \begin{bmatrix} \tilde{\mathbf{E}}_x^{(i)}(k_x; z) \\ \tilde{\mathbf{E}}_y^{(i)}(k_x; z) \\ \tilde{\mathbf{H}}_x^{(i)}(k_x; z) \\ \tilde{\mathbf{H}}_y^{(i)}(k_x; z) \end{bmatrix} \end{aligned} \quad (23)$$

where the matrix elements $q_{11}^{(i)} - q_{44}^{(i)}$ are functions of spectral variable k_x and material parameters (all the elements of $[\epsilon^{(i)}(\omega)]$, $[\mu^{(i)}(\omega)]$, $[\zeta^{(i)}(\omega)]$ and $[\eta^{(i)}(\omega)]$). After some mathematical manipulations, their exact expressions can be derived and presented [38]. Furthermore, the general solution to the vector differential Eq. (23) can be written as follows:

$$\begin{bmatrix} \tilde{\mathbf{E}}_x^{(i)}(k_x; z) \\ \tilde{\mathbf{E}}_y^{(i)}(k_x; z) \\ \tilde{\mathbf{H}}_x^{(i)}(k_x; z) \\ \tilde{\mathbf{H}}_y^{(i)}(k_x; z) \end{bmatrix} = \begin{bmatrix} T_{11}^{(i)}(\tilde{z}) & T_{12}^{(i)}(\tilde{z}) & T_{13}^{(i)}(\tilde{z}) & T_{14}^{(i)}(\tilde{z}) \\ T_{21}^{(i)}(\tilde{z}) & T_{22}^{(i)}(\tilde{z}) & T_{23}^{(i)}(\tilde{z}) & T_{24}^{(i)}(\tilde{z}) \\ T_{31}^{(i)}(\tilde{z}) & T_{32}^{(i)}(\tilde{z}) & T_{33}^{(i)}(\tilde{z}) & T_{34}^{(i)}(\tilde{z}) \\ T_{41}^{(i)}(\tilde{z}) & T_{42}^{(i)}(\tilde{z}) & T_{43}^{(i)}(\tilde{z}) & T_{44}^{(i)}(\tilde{z}) \end{bmatrix}_{\tilde{z} = -(z+d^{(i)})} \times \begin{bmatrix} \tilde{\mathbf{E}}_x^{(i)}(k_x; -d^{(i)}) \\ \tilde{\mathbf{E}}_y^{(i)}(k_x; -d^{(i)}) \\ \tilde{\mathbf{H}}_x^{(i)}(k_x; -d^{(i)}) \\ \tilde{\mathbf{H}}_y^{(i)}(k_x; -d^{(i)}) \end{bmatrix} \quad (24)$$

The matrix $[T^{(i)}(\tilde{z})]_{4 \times 4}$ in (24) is a transmission matrix, which physically relates to the tangential electromagnetic fields on one surface $z = -d^{(i)}$ to the tangential fields on another surface in the i th layer. Further, $[T^{(i)}(\tilde{z})]_{4 \times 4}$ can be expressed in the form of exponential matrix as follows:

$$[T^{(i)}(\tilde{z})]_{4 \times 4} = e^{z[q^{(i)}]_{4 \times 4}} \quad (25)$$

The procedure for calculating the exponential matrix in (25) can be followed as described in Ref. 4, and is omitted here.

The incident plane wave in the spectral domain can be expressed as a superposition of TM and TE (with respect to the y axis) as follows:

$$\begin{bmatrix} \tilde{\mathbf{E}}^{\text{inc}}(k_x; z) \\ \tilde{\mathbf{H}}^{\text{inc}}(k_x; z) \end{bmatrix} = \begin{bmatrix} -E_{\text{inc}}^{\text{TM}} \tilde{\mathbf{e}}_y - E_{\text{inc}}^{\text{TE}} \tilde{\mathbf{e}}_+ \\ [-E_{\text{inc}}^{\text{TM}} \tilde{\mathbf{e}}_+ + E_{\text{inc}}^{\text{TE}} \tilde{\mathbf{e}}_y] / \eta_0 \end{bmatrix} \times e^{-jk_0(x \sin \theta_0 - z \cos \theta_0)} \quad (26)$$

where θ_0 is the incident angle, $k_0 = \omega \sqrt{\mu_0 \epsilon_0}$, $k_x = k_0 \sin \theta_0$, $\eta_0 = \sqrt{\mu_0 / \epsilon_0}$, $\tilde{\mathbf{e}}_{\pm} = \pm \tilde{\mathbf{e}}_x \cos \theta_0 + \tilde{\mathbf{e}}_z \sin \theta_0$, and $\tilde{\mathbf{e}}_x$, $\tilde{\mathbf{e}}_y$, and $\tilde{\mathbf{e}}_z$ are the three unit vectors, respectively. The reflected wave fields in the spectral domain can be written as a superposition of TM and TE (to y)

$$\begin{bmatrix} \tilde{\mathbf{E}}^{(r)}(k_x; z) \\ \tilde{\mathbf{H}}^{(r)}(k_x; z) \end{bmatrix} = \begin{bmatrix} -E_0^{\text{TM}} \tilde{\mathbf{e}}_y - E_0^{\text{TE}} \tilde{\mathbf{e}}_- \\ [-E_0^{\text{TM}} \tilde{\mathbf{e}}_- + E_0^{\text{TE}} \tilde{\mathbf{e}}_y] / \eta_0 \end{bmatrix} \times e^{-jk_0 z \cos \theta_0} \quad (27)$$

where E_0^{TM} and E_0^{TE} refer to the TM and TE components in the reflected waves, respectively. In Fig. 12, if there is no backed plane at $z = -d^{(N)}$, the transmitted waves into region $z < -d^{(N)}$ are denoted by

$$\begin{bmatrix} \tilde{E}^{(t)}(k_x; z) \\ \tilde{H}^{(t)}(k_x; z) \end{bmatrix} = \begin{bmatrix} -E_2^{\text{TM}} \vec{e}_y - E_2^{\text{TE}} \vec{e}_+ \\ [-E_2^{\text{TM}} \vec{e}_+ + E_2^{\text{TE}} \vec{e}_y] / \eta_0 \end{bmatrix} \quad (28)$$

$$\times e^{jk_0(z+d^{(N)}) \cos \theta_0}$$

where E_2^{TM} and E_2^{TE} refer to the TM and TE components in transmitted waves, respectively. Furthermore, $E_{0,2}^{\text{TM}}$ and $E_{0,2}^{\text{TE}}$ above can be determined by enforcing the boundary conditions at each interface in Fig. 12. When the structure shown above is backed by a perfectly conducting backed plane, we have

$$\begin{bmatrix} E_0^{\text{TE}} \\ E_0^{\text{TM}} \end{bmatrix} = \begin{bmatrix} R_{11} & R_{21} \\ R_{12} & R_{22} \end{bmatrix} \begin{bmatrix} E_{\text{inc}}^{\text{TE}} \\ E_{\text{inc}}^{\text{TM}} \end{bmatrix} \quad (29)$$

where $R_{11,22}$ denotes for the copolarized reflection coefficients and $R_{12,21}$ represents the cross-polarized reflection coefficients [4]. In the no-backing case, the transmitted matrix is determined by

$$\begin{bmatrix} E_2^{\text{TE}} \\ E_2^{\text{TM}} \end{bmatrix} = \begin{bmatrix} T_{11} & T_{12} \\ T_{21} & T_{22} \end{bmatrix} \begin{bmatrix} E_{\text{inc}}^{\text{TE}} \\ E_{\text{inc}}^{\text{TM}} \end{bmatrix} \quad (30)$$

where $T_{11,12}$ and $T_{12,21}$ are the co- and cross-polarized transmission coefficients, respectively. A more detailed study on the co- and cross-polarized reflection and transmission characteristics of different layered omega(chiro)-ferrite geometries can be seen in Ref. 53. As an example, Fig. 13 shows the variations of the co(cross)-polarized reflection and transmission coefficients as a function of the incident angle for a chiroferrite slab in free space, and we let

$$\varepsilon_{xx}^{(1)} = \varepsilon_{yy}^{(1)} = 5.0, \quad \varepsilon_{zz}^{(1)} = 6.0, \quad \varepsilon_{xy}^{(1)} = -\varepsilon_{yx}^{(1)} = j0.3$$

$$\mu_{xx}^{(1)} = \mu_{yy}^{(1)} = 0.9, \quad \mu_{zz}^{(1)} = 1.5, \quad \mu_{xy}^{(1)} = -\mu_{yx}^{(1)} = j0.4$$

$$\zeta_{xx}^{(1)} = \eta_{xx}^{(1)} = \zeta_{yy}^{(1)} = \eta_{yy}^{(1)} = j0.5, \quad \zeta_{zz}^{(1)} = \eta_{zz}^{(1)} = j0.9$$

$$\zeta_{xy}^{(1)} = \eta_{xy}^{(1)} = j0.1, \quad \zeta_{yx}^{(1)} = \eta_{yx}^{(1)} = -j0.1$$

The biasing DC magnetic fields \vec{H}_0 of all chiroparticles are all along the z axis.

On the other hand, the technique described above, combined with the Galerkin MoM procedure, can also be extended to treat bianisotropic microstrip structures, as shown in the literature [39,40,42,54]. However, it should be mentioned that to deal with the mode dispersion characteristics in a microstrip transmission line with bianisotropic material, a general multilayer model is shown in Fig. 14. It is evident that this model can incorporate various applications [55–57]. However, we

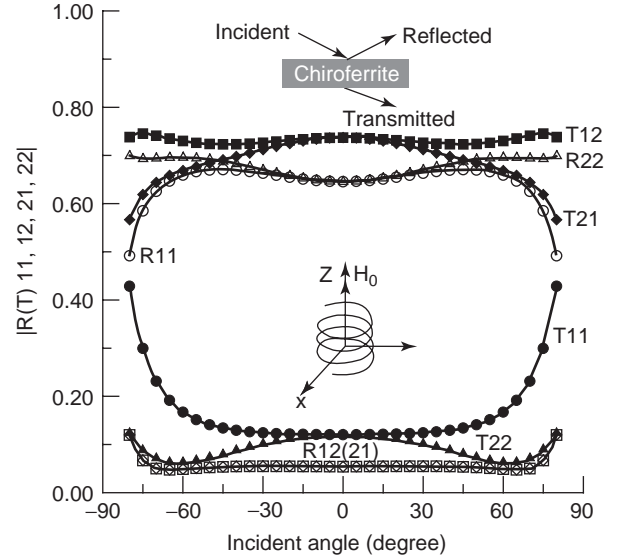


Figure 13. $R(T)_{pq}$ ($pq = 11, 22, 12, 21$) as a function of the incident angle θ_0 for a single-layer chiroferrite slab in free space (solid dotted lines— $T_{11;12;21;22}$; empty dotted lines— $R_{11;12;21;22}$), $D^{(1)}/\lambda = 0.5$ (where λ is the incident wavelength).

need to be careful about the destroy in image symmetry of the constitutive tensors [54,91].

3.2. Extended Finite-Element Method (FEM)

The extended FEM as well as the FEM–boundary-element method (FEM-BEM) is able to treat wave propagation and

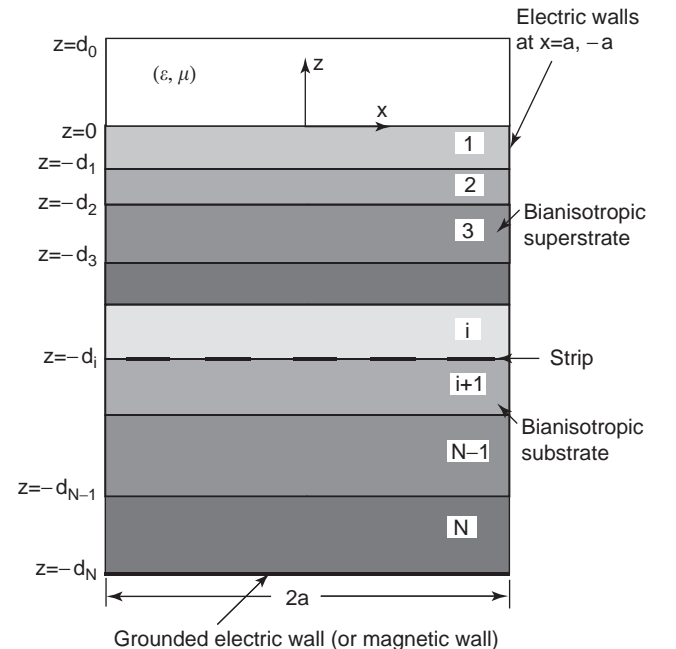


Figure 14. Cross-sectional view of a multiple microstrip transmission lines embedded in a multilayer bianisotropic superstrate–substrate.

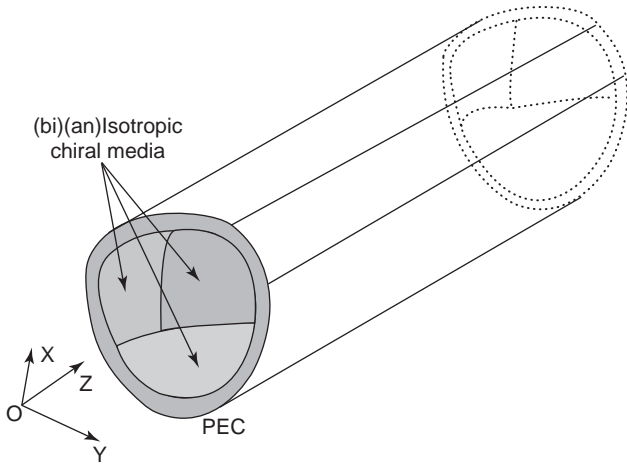


Figure 15. The bianisotropic waveguide with an arbitrary cross section.

radiation problems related to complex bianisotropic media [26,92,93]. Figure 15 shows the geometry of a bianisotropic waveguide with an arbitrary cross section, where the filled bianisotropic medium can be lossless or lossy. More generally, the bianisotropic region may consist of several types of bianisotropic media, but the structure must be homogeneous in the z -axis direction.

Following a procedure similar to that used in Refs. 92–94, for admissible test functions \vec{E}_{test} and \vec{H}_{test} , we must have

$$\sum_e \int \int_e \{ \vec{E}_{\text{test}}^* \cdot [j\nabla \times \vec{H} + \omega([\epsilon]\vec{E} + [\xi]\vec{H})] + \vec{H}_{\text{test}}^* \cdot [-j\nabla \times \vec{E} + \omega([\mu]\vec{H} + [\eta]\vec{E})] \} dx dy = 0 \quad (31)$$

where the appropriate interelement and boundary conditions are handled during the assembly \sum_e over all elements. Here, both the necessary continuity requirements on $\vec{n} \times \vec{E}$ and $\vec{n} \times \vec{H}$ and the additional requirements on $\vec{n} \cdot \vec{B}$ and $\vec{n} \cdot \vec{D}$ are, as described below, explicitly enforced on the test and expansion functions. The six components of the electric and magnetic test and expansion fields are approximated on each element in terms of the values at each nodal point according to

$$\begin{Bmatrix} \vec{E} \\ \vec{H} \end{Bmatrix} = [N]^T \begin{Bmatrix} \{E_x\} \\ \{E_y\} \\ \{E_z\} \\ \{H_x\} \\ \{H_y\} \\ \{H_z\} \end{Bmatrix} e^{-j\beta z} \quad (32a)$$

where

$$[N] = \begin{bmatrix} Z_0\{N\} & \{0\} & \{0\} & \{0\} & \{0\} & \{0\} \\ \{0\} & Z_0\{N\} & \{0\} & \{0\} & \{0\} & \{0\} \\ \{0\} & \{0\} & -jZ_0\{N\} & \{0\} & \{0\} & \{0\} \\ \{0\} & \{0\} & \{0\} & \{N\} & \{0\} & \{0\} \\ \{0\} & \{0\} & \{0\} & \{0\} & \{N\} & \{0\} \\ \{0\} & \{0\} & \{0\} & \{0\} & 0 & -j\{N\} \end{bmatrix} \quad (32b)$$

and $Z_0 = \sqrt{\mu_0/\epsilon_0}$. The real $m \times 1$ column vector $\{N\}$ is the element shape function vector, m is the number of nodal points on each element, $\{0\}$ is a $m \times 1$ null vector, and the superscript “T” denotes a matrix transposition. The column vectors $\{E_x\}$, $\{E_y\}$, $\{E_z\}$, $\{H_x\}$, $\{H_y\}$, and $\{H_z\}$ are $m \times 1$ complex field vectors representing the nodal point values of, respectively, E_x/Z_0 , E_y/Z_0 , jE_z/Z_0 , H_x , H_y , and jH_z on each element.

By employing the standard Galerkin procedure with the expansion in (32a) and (32b), we can obtain the following generalized eigenvalue equation

$$\{ \omega[P] + \beta[Q] + [R] \} \begin{Bmatrix} \{E_x\} \\ \{E_y\} \\ \{E_z\} \\ \{H_x\} \\ \{H_y\} \\ \{H_z\} \end{Bmatrix} = \{0\} \quad (33)$$

where the column vector is composed of all the nodal point variables used to represent \vec{E} and \vec{H} throughout the waveguide cross section. Note that both the complex propagation constant β and the real angular frequency ω may be treated as the eigenvalue, depending on which is numerically most advantageous or of primary interest.

By expanding (31) in component form, the quadratic sparse matrices $[P]$, $[Q]$, and $[R]$ take forms similar to those in Ref. 94, and

$$[Q] = -Z_0 \sum_e \iint_e \begin{bmatrix} \{0\} & \{0\} & \{0\} & \{0\} & -\{A\} & \{0\} \\ \{0\} & \{0\} & \{0\} & \{A\} & \{0\} & \{0\} \\ \{0\} & \{0\} & \{0\} & \{0\} & \{0\} & \{0\} \\ \{0\} & \{A\} & \{0\} & \{0\} & \{0\} & \{0\} \\ -\{A\} & \{0\} & \{0\} & \{0\} & \{0\} & \{0\} \\ \{0\} & \{0\} & \{0\} & \{0\} & \{0\} & \{0\} \end{bmatrix} dx dy \quad (34)$$

$$[R] = Z_0 \sum_e \iint_e \begin{bmatrix} \{0\} & \{0\} & \{0\} & \{0\} & \{0\} & -\{C\} \\ \{0\} & \{0\} & \{0\} & \{0\} & \{0\} & \{B\} \\ \{0\} & \{0\} & \{0\} & -\{C\} & \{B\} & \{0\} \\ \{0\} & \{0\} & \{C\} & \{0\} & \{0\} & \{0\} \\ \{0\} & \{0\} & -\{B\} & \{0\} & \{0\} & \{0\} \\ \{C\} & -\{B\} & \{0\} & \{0\} & \{0\} & \{0\} \end{bmatrix} dx dy \quad (35)$$

and

$$[A] = \{N\}\{N\}^T \quad (36a)$$

$$[B] = \{N\} \frac{\partial \{N\}^T}{\partial x} \quad (36b)$$

$$[C] = \{N\} \frac{\partial \{N\}^T}{\partial y} \quad (36c)$$

The continuity of $\vec{n} \times \vec{E}$, $\vec{n} \times \vec{H}$, $\vec{n} \cdot \vec{D}$, and $\vec{n} \cdot \vec{B}$, where \vec{n} is the unit normal vector perpendicular to an element side in the transversal x - y plane, is enforced. Also, the sample third-order triangular mesh is shown in Fig. 16, and in order to satisfy the interelement conditions, it is sufficient to apply the following at each nodal point along each internal side

$$\vec{n} \times (\vec{E}_p - \vec{E}_q) = 0 \quad (37)$$

$$\vec{n} \times (\vec{H}_p - \vec{H}_q) = 0 \quad (38)$$

$$\vec{n} \cdot ([\varepsilon_p] \vec{E}_p + [\xi_p] \vec{H}_p - [\varepsilon_q] \vec{E}_q - [\xi_q] \vec{H}_q) = 0 \quad (39)$$

$$\vec{n} \cdot ([\mu_p] \vec{H}_p + [\eta_p] \vec{E}_p - [\mu_q] \vec{H}_q - [\eta_q] \vec{E}_q) = 0 \quad (40)$$

where $\{\vec{E}_p, \vec{H}_p\}$ and $\{\vec{E}_q, \vec{H}_q\}$ represent unconnected field components in adjacent elements, p and q . To satisfy the external boundary conditions at each nodal point along each external side it is sufficient to enforce

$$\vec{n} \times \vec{E}_p = 0 \quad (41a)$$

$$\vec{n} \cdot ([\mu_p] \vec{H}_p + [\eta_p] \vec{E}_p) = 0 \quad (41b)$$

on electric walls and

$$\vec{n} \times \vec{H}_p = 0 \quad (42a)$$

$$\vec{n} \cdot ([\varepsilon_p] \vec{E}_p + [\xi_p] \vec{H}_p) = 0 \quad (42b)$$

on magnetic walls. From these equations, it can be found that the total number of unknown is $\leq 6N_p$, where N_p is the number of nodal points.

As indicated in Ref. 94, the most important property of the eigenvalue problem (30) now is the $O(1/N)$ density of the matrices $[P]$, $[Q]$, and $[R]$. This property ensures that

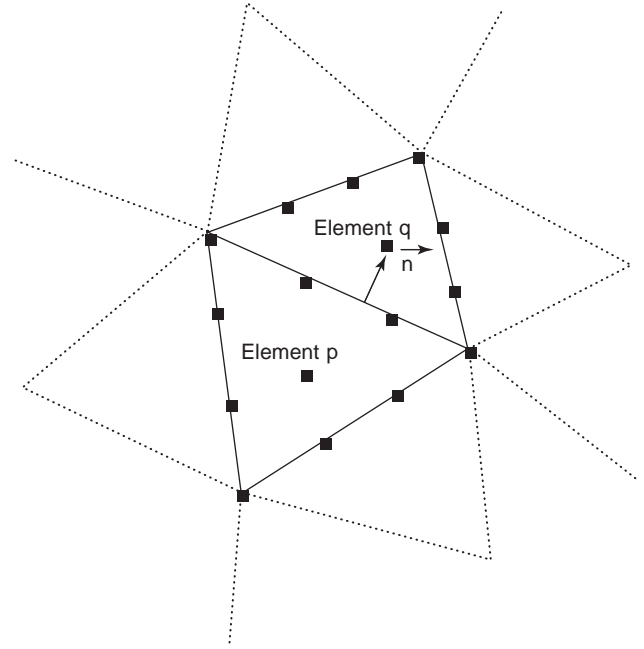


Figure 16. A portion of a sample of third-order mesh in the bianisotropic region.

the maximum number of nontrivial matrix elements on each row is independent of the dimension of the matrices. Thus an upper bound of the densities becomes $\rho = NN_z/N^2 \sim O(1/N)$, where N_z is the maximum number of nonzero elements on each row and N is the matrix dimension. Therefore, for large problems, sparse eigenvalue codes can be used to save significant amounts of computer time and memory.

3.3. Extended Method of Line (MoL)

The normal method of line (MoL) [28] is very useful in the analysis of planar radiative and transmissive microwave components. This method was developed by mathematicians and physicists in order to solve partial-differential equations in the electromagnetic analysis of optical and microwave devices, for the numerical solution of the partial-differential Helmholtz equation. Originally developed to study planar waveguides, MoL was also extended to study stratified microwave components with arbitrarily shaped cross sections and microstrip discontinuities, including one-dimensional and bidimensional resonators and antennas. The latest extensions of this method have been achieved to study gyrotropic media and microwave components mounted on cylindrical or spherical structures.

The standard version of MoL, does not allow for the study of elements with bianisotropic superstrate-substrates. More recently, an extended MoL numerical procedure, which allows for the analysis of components in the presence of any linear, inhomogeneous, or lossy bianisotropic medium, has been developed [28]. Such an extension is based on the generalization of the transmission-line equations for a general linear medium.

Applying the curl Maxwell equations in a sourceless bianisotropic region, and after some mathematical manipulations, a set of transmission-line equations for a bianisotropic medium in Cartesian coordinates can be derived as follows ($e^{j\omega t}$)

$$\frac{\partial[\mathbf{E}_t]}{\partial z} = \begin{bmatrix} A_{xx} & A_{xy} \\ A_{yx} & A_{yy} \end{bmatrix} [\mathbf{E}_t] + \begin{bmatrix} Z_{xx} & Z_{xy} \\ Z_{yx} & Z_{yy} \end{bmatrix} [\tilde{\mathbf{H}}_t] \quad (43a)$$

$$\frac{\partial[\mathbf{H}_t]}{\partial z} = \begin{bmatrix} Y_{xx} & Y_{xy} \\ Y_{yx} & Y_{yy} \end{bmatrix} [\mathbf{E}_t] + \begin{bmatrix} B_{xx} & B_{xy} \\ B_{yx} & B_{yy} \end{bmatrix} [\tilde{\mathbf{H}}_t] \quad (43b)$$

where $[\mathbf{E}_t] = \begin{bmatrix} E_x \\ E_y \end{bmatrix}$, $[\mathbf{H}_t] = \begin{bmatrix} H_x \\ H_y \end{bmatrix}$, $[\tilde{\mathbf{H}}_t] = \eta_0[\mathbf{H}_t]$, and $\eta_0 = \sqrt{\mu_0/\epsilon_0}$. The 16 operatorial tensor elements A_{ij} , B_{ij} , Y_{ij} , Z_{ij} , where $i, j = x, y, z$, involve both the constitutive tensor entries and the transverse derivatives and are given in Ref. 28 and omitted here, and are very similar to the expressions shown in Ref. 34.

It should be noted that Eqs. (43a) and (43b) can be decoupled only for particular bianisotropic media whose constitutive parameters allow the coupling matrices $[A]$ and $[B]$ to vanish. The necessary and sufficient condition on the medium constitutive tensors to obtain decoupled equations, independently from the excitation, can be written in the following form [28]

$$[\epsilon] = \begin{pmatrix} \epsilon_{xx} & \epsilon_{xy} & 0 \\ \epsilon_{yx} & \epsilon_{yy} & 0 \\ 0 & 0 & \epsilon_{zz} \end{pmatrix}, [\mu] = \begin{pmatrix} \mu_{xx} & \mu_{xy} & 0 \\ \mu_{yx} & \mu_{yy} & 0 \\ 0 & 0 & \mu_{zz} \end{pmatrix},$$

$$[\zeta] = \begin{pmatrix} 0 & 0 & \zeta_{xz} \\ 0 & 0 & \zeta_{yz} \\ \zeta_{zx} & \zeta_{zy} & 0 \end{pmatrix}, [\eta] = \begin{pmatrix} 0 & 0 & \eta_{xz} \\ 0 & 0 & \eta_{yz} \\ \eta_{zx} & \eta_{zy} & 0 \end{pmatrix} \quad (44)$$

which represents the CGS of $C_{2h}(C_s)$ above. Under such circumstances, a standard MoL procedure similar to that expressed in (43) can be used, and we have

$$\frac{\partial^2[\mathbf{E}_t]}{\partial z^2} = -[P_E][\mathbf{E}_t], \quad \frac{\partial^2[H_t]}{\partial z^2} = -[Q_E][H_t]. \quad (45a,b)$$

This set of equations can be easily discretized in two dimensions and then diagonalized, and the electromagnetic characteristics of the structure, as shown in Figs. 17a and 17b, can be further understood.

In the general case, an extended version of MoL needs to be developed, as discussed in Ref. 28. Starting from (43a) and (43b) and discretizing in the transverse plane as in the standard MoL, a set of equations involving trans-

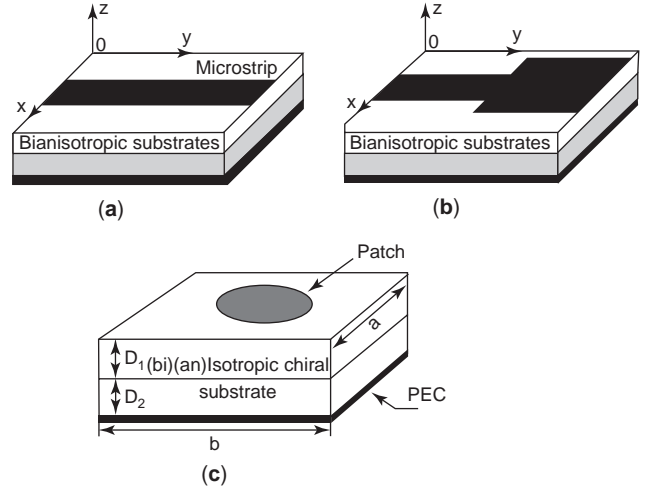


Figure 17. Microstrip transmission lines and antenna on bianisotropic substrates.

verse field components can be derived as follows

$$\frac{d[\hat{\mathbf{E}}_t]}{dz} = [\hat{\mathbf{A}}][\hat{\mathbf{E}}_t] + [\hat{\mathbf{Z}}][\hat{\mathbf{H}}_t] \quad (46a)$$

$$\frac{d[\hat{\mathbf{H}}_t]}{dz} = [\hat{\mathbf{Y}}][\hat{\mathbf{E}}_t] + [\hat{\mathbf{B}}][\hat{\mathbf{H}}_t] \quad (46b)$$

where the symbol $\hat{}$ stands for bidimensional discretization. Here $[\hat{\mathbf{E}}_t]$ and $[\hat{\mathbf{H}}_t]$ depend only on z , respectively, as shown in Fig. 18, where $\hat{\mathbf{E}}_x$ and $\hat{\mathbf{H}}_y$ are calculated on lines denoted by “o”, while $\hat{\mathbf{E}}_y$ and $\hat{\mathbf{H}}_x$ are sampled on lines denoted by \bullet . The other two sets, denoted by empty and solid square dots, respectively, contain the lines in which the central-difference derivatives are computed.

In Fig. 18, d_x and d_y are the discretization steps for the central-difference operators along x and y , respectively. The matrices $[\hat{\mathbf{A}}]$, $[\hat{\mathbf{Z}}]$, $[\hat{\mathbf{Y}}]$, and $[\hat{\mathbf{B}}]$ are obtained from Eqs. (4), given in Ref. 28, substituting their elements with discretized quantities. First of all, partial derivatives are substituted with central-difference matrices $[\hat{\mathbf{D}}]$, also including the boundary conditions.

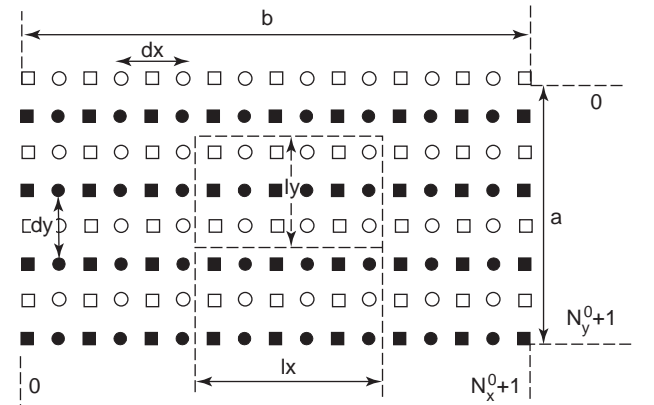


Figure 18. Rectangular patch with discretization lines.

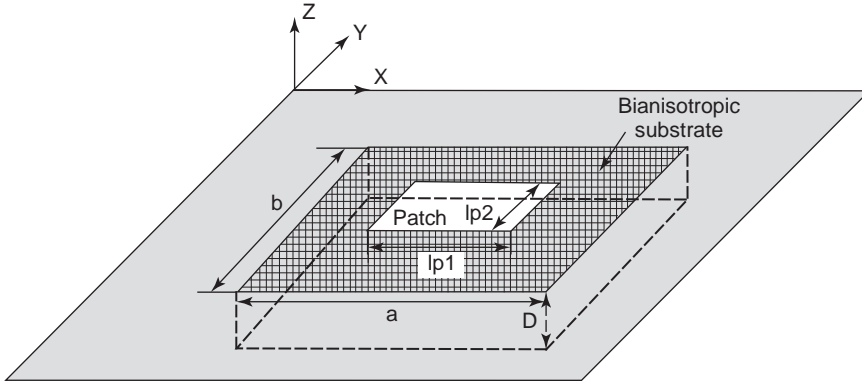


Figure 19. A patch cavity resonator loaded with a bianisotropic substrate.

Equations (46a) and (46b) are the algebraic discretized versions of the generalized transmission line equations, and they can be changed into

$$\frac{d[\hat{\psi}]}{dz} = \begin{bmatrix} \hat{\mathbf{A}} & \hat{\mathbf{Z}} \\ \hat{\mathbf{Y}} & \hat{\mathbf{B}} \end{bmatrix} [\hat{\psi}] \quad (47)$$

where $[\hat{\psi}] = [\hat{\mathbf{E}}_t \quad \hat{\mathbf{H}}_t]^T$ and the superscript “T” represents the transpose of matrix. It is evident that the solution to (47) is in the form of an exponential matrix, which is well documented in Ref. 4 and used elsewhere in the literature [34,38–40,50–54] by enforcing certain boundary conditions.

As a numerical example, Fig. 19 shows the geometry of a patch cavity resonator loaded with a bianisotropic substrate, and the resonant frequency versus patch side length is depicted in Fig. 20 for $\epsilon_r = 2.0$, $D = 0.8$ mm, and $a = b = 10$ cm.

In Fig. 18, the bianisotropic substrate is characterized by the CGS of $D_{2d}(C_{2v})$, and

$$[\epsilon] = \epsilon_0 \epsilon_r \begin{bmatrix} 1 & 0 & 0 \\ 0 & 1 & 0 \\ 0 & 0 & 1 \end{bmatrix}, \quad [\mu] = \mu_0 \begin{bmatrix} 1 & 0 & 0 \\ 0 & 1 & 0 \\ 0 & 0 & 1 \end{bmatrix}, \quad (48)$$

$$[\xi] = c_0^{-1} \begin{bmatrix} 0 & j\xi & 0 \\ j\xi & 0 & 0 \\ 0 & 0 & 0 \end{bmatrix}, \quad [\eta] = -[\xi]$$

where $c_0 = 3 \times 10^8$ m/s. It is seen that, compared to the isotropic case, the resonant frequency changes very little for a given patch width, and this is because the bianisotropic substrate is supposed to be very thin and the magnetoelectric coupling effect is very weak [28].

3.4. Finite-Difference Time-Domain Method (FDTD)

The finite-difference time-domain (FDTD) method [95] is the most popular three-dimensional full-wave numerical algorithm that has been used to model electromagnetic

phenomena and interactions in various fields. The simplicity and effectiveness of FDTD method stem from the utilization of a Cartesian grid from the discretization of the structure, with appropriate staggering of the unknown discrete values of the components of the electric and magnetic field vectors in such a manner that the curl operations in Maxwell’s equations can be approximated in terms of second-order accurate finite differences. The staggering of the fields is known as the *Yee lattice*. This discretization results in a state space representation of the discrete values of all six components of the electric and magnetic fields on the grid. The simplicity and versatility of the FDTD algorithm, combined with its suitability for parallel implementation, has prompted aggressive research and development toward its further enhancement.

In the time domain, the constitutive equations of biisotropic chiral media can be expressed by

$$\vec{D}(t) = \epsilon \vec{E}(t) + \frac{\chi}{c_0} \vec{H}(t) - \frac{1}{c_0} \int_0^t \kappa'(\tau) \vec{H}(t - \tau) d\tau \quad (49a)$$

$$\vec{B}(t) = \mu \vec{H}(t) + \frac{\chi}{c_0} \vec{E}(t) - \frac{1}{c_0} \int_0^t \kappa'(\tau) \vec{E}(t - \tau) d\tau \quad (49b)$$

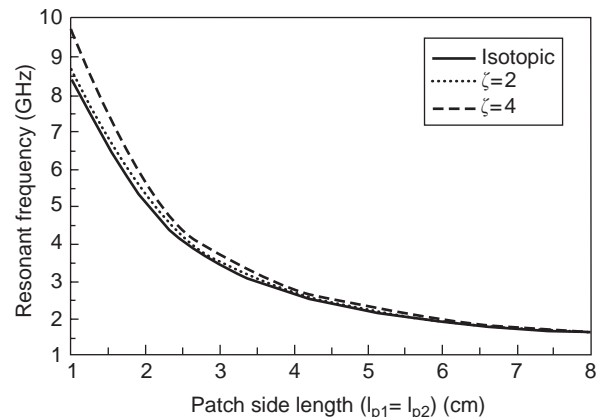


Figure 20. Resonant frequency versus patch side length [28].

and (49a) and (49b) respectively can be further discretized as

$$\begin{aligned} \vec{D}(n) = \varepsilon \vec{E}(n) + \frac{\chi}{c_0} \vec{H}(n) \\ - \frac{1}{c_0} \sum_{m=0}^{n-1} \vec{H}(n-m) \int_{m\Delta t}^{(m+1)\Delta t} \kappa'(\tau) d\tau \end{aligned} \quad (50a)$$

$$\begin{aligned} \vec{B}(n) = \mu \vec{H}(n) + \frac{\chi}{c_0} \vec{E}(n) \\ - \frac{1}{c_0} \sum_{m=0}^{n-1} \vec{E}(n-m) \int_{m\Delta t}^{(m+1)\Delta t} \kappa'(\tau) d\tau \end{aligned} \quad (50b)$$

The complex time-domain chirality parameter $\hat{\kappa}'(t)$ is defined as [95]

$$\hat{\kappa}'(t) = -j \frac{\tau \omega_0^2}{\sqrt{1-\xi^2}} e^{[-\xi \omega_0 t + j(\phi - \omega_0 \sqrt{1-\xi^2} t)]} \quad (51)$$

while the time-domain chirality parameter should be the real part of $\hat{\kappa}'(t)$, and

$$\kappa'(m\Delta t) = \int_{m\Delta t}^{(m+1)\Delta t} \kappa'(\tau) d\tau \quad (52a)$$

$$\hat{\kappa}'(m\Delta t) = \int_{m\Delta t}^{(m+1)\Delta t} \hat{\kappa}'(\tau) d\tau \quad (52b)$$

In the time domain, the time dependences of both permittivity and permeability are described by the following equations:

$$\varepsilon(t) = \varepsilon_0 \left[\varepsilon_\infty \delta(t) + \frac{(\varepsilon_s - \varepsilon_\infty) \omega_0 e^{-\omega_0 \xi_e t}}{\sqrt{1-\xi_e^2}} \sin(\omega_0 e \sqrt{1-\xi_e^2} t) \right] \quad (53a)$$

$$\mu(t) = \mu_0 \left[\mu_\infty \delta(t) + \frac{(\mu_s - \mu_\infty) \omega_0 m e^{-\omega_0 m \xi_m t}}{\sqrt{1-\xi_m^2}} \sin(\omega_0 m \sqrt{1-\xi_m^2} t) \right] \quad (53b)$$

Further, (50a) and (50b) respectively become [95]

$$\begin{aligned} \vec{D}(n) = \varepsilon_0 \varepsilon_\infty \vec{E}(n) + \frac{\chi}{c_0} \vec{H}(n) + \varepsilon_0 \text{Re}[\hat{\chi}_e(0)] \vec{E}(n) \\ + \varepsilon_0 \text{Re} \left[\hat{\psi}_{\chi_e}^E(n-1) e^{(-\xi_e + j\sqrt{1-\xi_e^2}) \omega_0 \Delta t} \right. \\ \left. - \frac{\text{Re}[\hat{\kappa}'(0)]}{c_0} \vec{H}(n) - \frac{1}{c_0} \text{Re}[\hat{\psi}_\kappa^H(n-1)] \right. \\ \left. \times e^{(-\xi - j\sqrt{1-\xi^2}) \omega_0 \Delta t} \right] \end{aligned} \quad (54a)$$

$$\begin{aligned} \vec{B}(n) = \mu_0 \mu_\infty \vec{H}(n) + \frac{\chi}{c_0} \vec{E}(n) + \mu_0 \text{Re}[\hat{\chi}_m(0)] \vec{H}(n) \\ + \mu_0 \text{Re} \left[\hat{\psi}_{\chi_m}^H(n-1) e^{(-\xi_m + j\sqrt{1-\xi_m^2}) \omega_0 \Delta t} \right. \\ \left. + \frac{\text{Re}[\hat{\kappa}'(0)]}{c_0} \vec{E}(n) + \frac{1}{c_0} \text{Re}[\hat{\psi}_\kappa^E(n-1)] \right. \\ \left. \times e^{(-\xi - j\sqrt{1-\xi^2}) \omega_0 \Delta t} \right] \end{aligned} \quad (54b)$$

where

$$\hat{\psi}_\phi^F(n) = \sum_{m=0}^{n-1} \vec{F}(n-m) \hat{\phi}(m) \quad (54c)$$

Finally, the general algorithm for dispersive biisotropic chiral media can be found, and in this algorithm [95], we must

1. Update the y component of the electric displacement $D_{i+(1/2)}^y(n+\frac{1}{2})$ and the magnetic flux density $B_{i+(1/2)}^y(n+\frac{1}{2})$ by

$$\begin{aligned} D_{i+1/2}^y \left(n + \frac{1}{2} \right) = \varepsilon_0 \varepsilon_\infty E_{i+1/2}^y \left(n + \frac{1}{2} \right) \\ + \varepsilon_0 \text{Re}[\hat{\chi}_e(0)] E_{i+1/2}^y \left(n + \frac{1}{2} \right) \\ + \varepsilon_0 \text{Re}[\hat{\psi}_{\chi_{e+(1/2)}}^E \left(n - \frac{1}{2} \right)] e^{(-\xi_e + j\sqrt{1-\xi_e^2}) \omega_0 \Delta t} \\ + \frac{\chi}{c_0} H_{i+(1/2)}^y \left(n + \frac{1}{2} \right) \\ - \frac{\text{Re}[\hat{\kappa}'(0)]}{c_0} H_{i+(1/2)}^y \left(n + \frac{1}{2} \right) \\ - \frac{1}{c_0} \text{Re}[\hat{\psi}_{\kappa_{i+(1/2)}}^H \left(n - \frac{1}{2} \right)] e^{(-\xi - j\sqrt{1-\xi^2}) \omega_0 \Delta t} \end{aligned} \quad (55a)$$

$$\begin{aligned} B_{i+1/2}^y \left(n + \frac{1}{2} \right) = \mu_0 \mu_\infty H_{i+1/2}^y \left(n + \frac{1}{2} \right) \\ + \mu_0 \text{Re}[\hat{\chi}_m(0)] H_{i+1/2}^y \left(n + \frac{1}{2} \right) \\ + \mu_0 \text{Re}[\hat{\psi}_{\chi_{m+(1/2)}}^H \left(n - \frac{1}{2} \right)] e^{(-\xi_m + j\sqrt{1-\xi_m^2}) \omega_0 \Delta t} \\ + \frac{\chi}{c_0} E_{i+1/2}^y \left(n + \frac{1}{2} \right) \\ + \frac{\text{Re}[\hat{\kappa}'(0)]}{c_0} E_{i+(1/2)}^y \left(n + \frac{1}{2} \right) \\ + \frac{1}{c_0} \text{Re}[\hat{\psi}_{\kappa_{i+(1/2)}}^E \left(n - \frac{1}{2} \right)] e^{(-\xi - j\sqrt{1-\xi^2}) \omega_0 \Delta t} \end{aligned} \quad (55b)$$

2. Update the x component of the electric displacement $D_i^x(n+1)$ and the magnetic flux density $B_{i+1}^x(n+1)$ by

$$\begin{aligned}
 D_i^x(n+1) = & \varepsilon_0 \varepsilon_\infty E_{i+1}^x(n+1) + \varepsilon_0 \operatorname{Re}[\hat{\gamma}_e(0)] E_{i+1}^x(n+1) \\
 & + \varepsilon_0 \operatorname{Re}[\hat{\psi}_{\lambda_{ei+1}}^{E^x}(n) e^{(-\xi_e + j\sqrt{1-\xi_e^2})\omega_0 \Delta t} + \frac{\chi}{c_0} H_i^x(n+1) \\
 & - \frac{\operatorname{Re}[\hat{\kappa}(0)]}{c_0} H_i^x(n+1) \\
 & - \frac{1}{c_0} \operatorname{Re}[\hat{\psi}_{\kappa_i}^{H^x}(n) e^{(-\xi - j\sqrt{1-\xi^2})\omega_0 \Delta t}]]
 \end{aligned} \tag{56a}$$

$$\begin{aligned}
 B_i^x(n+1) = & \mu_0 \mu_\infty H_i^x(n+1) \\
 & + \mu_0 \operatorname{Re}[\hat{\gamma}_m(0)] H_i^x(n+1) \\
 & + \mu_0 \operatorname{Re}[\hat{\psi}_{\lambda_{mi}}^{E^x}(n) e^{(-\xi_m + j\sqrt{1-\xi_m^2})\omega_0 \Delta t} \\
 & + \frac{\chi}{c_0} E_i^x(n+1) + \frac{\operatorname{Re}[\hat{\kappa}'(0)]}{c_0} E_i^x(n+1) \\
 & + \frac{1}{c_0} \operatorname{Re}[\hat{\psi}_{\kappa_i'}^{E^x}(n) e^{(-\xi - j\sqrt{1-\xi^2})\omega_0 \Delta t}]]
 \end{aligned} \tag{56b}$$

On the basis of (56a) and (56b), the interaction of a transient microwave signal with biisotropic media can be fully understood, in particular the material dispersion and loss effects.

To use biisotropic and bianisotropic chiral media to fabricate certain microwave devices, there are still many challenging problems that need to be explored further, such as the control or optimization of material parameters and their measurements.

BIBLIOGRAPHY

1. V. Dmitriev, Table of the second rank constitutive tensors for linear homogeneous media described by the point magnetic groups of symmetry, *Prog. Electromagn. Res.* **PIER-28**:43–95 (2000).
2. D. Graglia, P. L. E. Uslenghi, and R. E. Zich, Reflection and transmission for planar structures of bianisotropic media, *Electromagnetics* **11**:193–208 (1991).
3. F. L. Mesa, R. Marques, and M. Horno, A general algorithm for computing the bidimensional spectral Green's dyad in multilayered complex bianisotropic media: The equivalent boundary method, *IEEE Trans. Microwave Theory Tech.* **MTT-39**:1640–1649 (1991).
4. J. L. Tsalamengas, Interaction of electromagnetic waves with general bianisotropic slabs, *IEEE Trans. Microwave Theory Tech.* **MTT-40**:1870–1878 (1992).
5. I. V. Lindell, S. A. Tretyakov, and A. J. Viitanen, Plane-wave propagation in a uniaxial chiro-omega medium, *Microwave Opt. Technol. Lett.* **6**:517–520 (1993).
6. I. V. Lindell and A. J. Viitanen, Plane wave propagation in uniaxial bianisotropic medium, *Electron. Lett.* **29**:150–152 (1993).
7. A. Lakhtakia and W. S. Weiglhofer, Axial propagation in general helicoidal bianisotropic media, *Microwave Opt. Technol. Lett.* **6**:804–806 (1993).
8. S. A. Tretyakov and A. A. Sochava, Proposed composite materials for nonreflected shields and antenna radomes, *Electron. Lett.* **29**:1048–1049 (1993).
9. A. J. Viitanen and I. V. Lindell, Plane wave propagation in a uniaxial bianisotropic medium with an application to a polarization transformer, *Int. J. Infrared Millimeter Waves* **14**:1993–2010 (1993).
10. S. He and I. V. Lindell, Propagation eigenmodes for plane waves in a uniaxial bianisotropic medium and reflection from a planar interface, *IEEE Trans. Anten. Propag.* **AP-41**:1659–1664 (1993).
11. S. He, Wave propagation through dielectric-uniaxial bianisotropic interface and the computation of Brewster angles, *J. Opt. Soc. Am. A* **11**:2403–2409 (1993).
12. S. He, Y. Hu, and S. Strom, Electromagnetic scattering from a stratified bianisotropic slab, *IEEE Trans. Anten. Propag.* **AP-42**:856–858 (1994).
13. M. Norgren and S. He, General scheme for electromagnetic reflection and transmission for composite structures of complex materials, *IEE Proc. Microwave Anten. Propag.* **142**:52–56 (1995).
14. A. Lakhtakia and W. S. Weiglhofer, Influence of pitch on attenuation and handedness of axial propagation modes in helicoidal bianisotropic media, *Opt. Commun.* **111**:199 (1994).
15. A. Lakhtakia and W. S. Weiglhofer, On light propagation in helicoidal bianisotropic medium, *Proc. Roy. Soc. Lond. A* **438**:419–437 (1995).
16. A. Lakhtakia and W. S. Weiglhofer, Further results on light propagation in helicoidal bianisotropic mediums: oblique propagation, *Proc. Roy. Soc. Lond. A* **453**:93–105 (1997).
17. M. Norgren, Optimal design using stratified bianisotropic media: Application to anti-reflection coatings, *J. Electromagn. Waves Appl.* **12**:939–959 (1998).
18. D. Y. Khaliullin and S. A. Tretyakov, Reflection and transmission coefficients for thin bianisotropic layers, *IEE Proc. Microwave Anten. Propag.* **145**:163–168 (1998).
19. C. R. Simovski, M. S. Kondratjev, P. A. Belov, and S. A. Tretyakov, Interaction effects in two-dimensional bianisotropic arrays, *IEEE Trans. Anten. Propag.* **AP-47**:1429–1439 (1999).
20. V. Losada, R. R. Boix, and M. H. Horno, Full-wave analysis of circular microstrip resonators in multilayered media containing uniaxial anisotropic dielectric, magnetized ferrites, and chiral materials, *IEEE Trans. Anten. Propag.* **AP-48**:1057–1064 (2000).
21. A. Toscano and L. Vegni, Analysis of printed-circuit antennas with chiral substrates with the method of lines, *IEEE Trans. Anten. Propag.* **AP-49**:48–54 (2001).
22. E. O. Kamenetskii, Nonreciprocal microwave bianisotropic materials: Reciprocity theorem and network reciprocity, *IEEE Trans. Anten. Propag.* **AP-49**:361–366 (2001).
23. L. Vegni, F. Bilotti, and A. Toscano, Analysis of cavity backed rectangular patch antennas with inhomogeneous chiral substrates via a FEM-BEM formulation, *IEEE Trans. Magn.* **37**:3260–3263 (2001).
24. E. L. Tan, Vector wave function expansions of dyadic Green's functions for bianisotropic media, *IEE Proc. H, Microwaves Anten. Propag.* **149**:57–63 (2002).

25. W. S. Weiglhofer and A. Lakhtakia, Analytical investigation of electromagnetic waves in bianisotropic media, *IEE Proc. H, Microwaves Antenn. Propag.* **149**:138–139 (2002).
26. F. Bilotti, A. Toscano, and L. Vegni, FEM-BEM formulation for the analysis of cavity-backed patch antennas on chiral substrates, *IEEE Trans. Antenn. Propag.* **AP-51**:306–311 (2003).
27. F. Bilotti, L. Vegni, and A. Toscano, Radiation and scattering features of patch antennas with bianisotropic substrates, *IEEE Trans. Antenn. Propag.* **AP-51**:449–456 (2003).
28. A. Alu, F. Bilotti, and L. Vegni, Extended method of line procedure for the analysis of microwave components with bianisotropic inhomogeneous media, *IEEE Trans. Antenn. Propag.* **AP-51**:1582–1589 (2003).
29. W. Y. Yin, W. Wan, and W. B. Wang, Guided electromagnetic waves in parallel-plate gyroelectromagnetic biaxial chiro-waveguides, *J. Modern Opt.* **41**:59–65 (1994).
30. W. Y. Yin and W. Wan, Spectral-domain decoupling method of electromagnetic waves propagation and radiating in bianisotropic gyroelectromagnetic chiral media, *Microwave Opt. Technol. Lett.* **7**:187–193 (1994).
31. W. Y. Yin, W. Wan, and W. B. Wang, Mode characteristics in a circular uniaxial chiro-omega waveguide, *Electron. Lett.* **30**:1072–1073 (1994).
32. W. Y. Yin, W. Wan, and W. B. Wang, Guided electromagnetic waves in gyrotropic chiro-waveguides, *IEEE Trans. Microwave Theory Tech.* **42**:2156–2163 (1994).
33. W. Y. Yin and W. Wan, The combined effect of dispersion and damping on the scattering characteristics of Faraday chiral cylindrical scatterers, *Microwave Opt. Technol. Lett.* **10**:189–194 (1995).
34. W. Y. Yin, W. Wan, and W. B. Wang, Radiation from a dipole antenna on two-layer grounded Faraday chiral substrates, *J. Electromagn. Waves Appl.* **7**:1027–1044 (1995).
35. W. Y. Yin, W. Wan, and W. B. Wang, Mode bifurcation and attenuation in circular Faraday chiro-waveguide-summary, *J. Electromagn. Waves Appl.* **10**:1389–1394 (1996).
36. W. Y. Yin, Scattering by a linear array of uniaxial bianisotropic chiral cylinders, *Microwave Opt. Technol. Lett.* **12**:287–295 (1996).
37. W. Y. Yin, Scattering by two parallel cladged bianisotropic uniaxial chiral fibers, *J. Opt. Soc. Am. B* **13**:2833–2840 (1996).
38. W. Y. Yin, G. H. Nan, and I. Wolff, The combined effects of chiral operation in multilayered bianisotropic substrates, *Prog. Electromagn. Res. PIER-20*:153–178 (1998).
39. W. Y. Yin and I. Wolff, Bilateral coplanar waveguide and periodic microstrip line in bianisotropic superstrate-substrate structures, *J. Electromagn. Waves Appl.* **13**:259–275 (1999).
40. W. Y. Yin, L. W. Li, and I. Wolff, The compatible effects of gyrotropy and chirality in biaxially bianisotropic chiral- and chiro-ferrite microstrip line structures, *Int. J. Num. Model. Electron. Networks Devices Fields* **10**:209–227 (1999).
41. W. Y. Yin and L. W. Li, Multiple scattering from gyrotropic bianisotropic cylinders of arbitrary cross-sections using the modeling technique, *Phys. Rev. E* **60**:918–925 (1999).
42. W. Y. Yin, L. W. Li, and M. S. Leong, Hybrid effects of gyrotropic and chirality in ferrite fin-lines, *Microwave Opt. Technol. Lett.* **25**:40–44 (2000).
43. W. Y. Yin, L. W. Li, T. S. Yeo, and M. S. Leong, Effects of double helical conductances of surfaces on multiple scattering of eccentrically two-layered bianisotropic cylinder array: The case of TE_z -wave incidence, *Electromagnetics* **20**:369–382 (2000).
44. W. Y. Yin and L. W. Li, Effects of helical conductance of surfaces on multiple interaction of composite eccentrically bianisotropic cylinders: The case of TM_z -wave incidence, *Prog. Electromagn. Res. PIER-23*:221–236 (2001).
45. W. Y. Yin, L. W. Li, M. S. Leong, and T. S. Yeo, Indirect modeling of the scattering from two-dimensional composite uniaxial bianisotropic cylinders of arbitrary cross sections, *Int. J. Num. Model. Electron. Networks Devices Fields* **14**:237–256 (2001).
46. V. Dmitriev, Constitutive tensors and general properties of complex and bianisotropic media described by continuous groups of symmetry, *Electron. Lett.* **34**:532–534 (1998).
47. V. Dmitriev, Group theoretical approach to determine structure of complex and composite media constitutive tensors, *Electron. Lett.* **34**:743–745 (1998).
48. V. Dmitriev, Symmetry description of continuous homogeneous isotropic media under external perturbation, *Electron. Lett.* **34**:745–747 (1998).
49. V. Dmitriev, Constitutive tensor nomenclature of Kamenetskii's media, *Microwave Opt. Technol. Lett.* **18**:280–284 (1998).
50. W. Y. Yin and L. W. Li, Reflection and transmission characteristics of bianisotropic slabs with(out) a soft- and hard-surface: The clarification of the continuous magnetic group of symmetry, *Microwave Opt. Technol. Lett.* **21**:351–356 (1999).
51. W. Y. Yin and L. W. Li, Radiation patterns of a dipole antenna array on bianisotropic substrates with a soft- and hard-surface: The clarification of the continuous magnetic group of symmetry, *J. Electromagn. Waves Appl.* **13**:1173–1189 (1999).
52. W. Y. Yin, L. W. Li, T. S. Yeo, and M. S. Leong, The Muller matrix and scattering cross section of a linear array of eccentrically two-layered bianisotropic cylinders with double surface helical conductances: Clarifications of the magnetic symmetry groups—abstract, *J. Electromagn. Waves Appl.* **14**:1135–1137 (2000).
53. W. Y. Yin, B. Guo, and X. T. Dong, Comparative study on the interaction of electromagnetic waves with multi-layer omega(chiro)ferrite slabs, *J. Electromagn. Waves Appl.* **17**:15–29 (2003).
54. W. Y. Yin, B. Guo, L. W. Li, Y. B. Gan, and I. Wolff, Constitutive parameter effects in some multilayered bianisotropic microstrip lines: Clarification of magnetic groups of symmetry, *IEE Proc. Microwave Antenn. Propag.* **150**:18–22 (2003).
55. C. M. Krowne, Full-wave spectral Green's function integral equation calculation of coplanar ferroelectric thin film transmission structures, *Microwave Opt. Technol. Lett.* **26**:187–192 (2000).
56. C. M. Krowne, Theoretical considerations for finding anisotropic permittivity in layered ferroelectric/ferromagnetic structures from full-wave electromagnetic simulations, *Microwave Opt. Technol. Lett.* **28**:63–69 (2001).
57. C. M. Krowne, M. Daniel, S. W. Kirchoefer, and J. M. Pond, Anisotropic permittivity and attenuation extraction from propagation constant measurements using an anisotropic full-wave Green's function solver for coplanar ferroelectric thin-film devices, *IEEE Trans. Microwave Theory Tech.* **MTT-50**:537–548 (2002).
58. C. M. Krowne, Waveguiding structures employing the solid-state magnetoplasma effect for microwave and millimeter-wave propagation, *IEE Proc. Microwave Antenn. Propag.* **140**:147–164 (1993).
59. R. Pregla, Method of lines for the analysis of multilayered gyrotropic waveguide structures, *IEE Proc. Microwave Antenn. Propag.* **140**:183–192 (1993).

60. F. Mesa and M. Horno, Application of the spectral domain method for the study of surface slow waves in nonreciprocal planar structures with a multilayered gyrotropic substrate, *IEE Proc. Microwave Anten. Propag.* **140**:193–200 (1993).
61. L. E. Davis, R. Sloan, and D. K. Paul, TM_{0m} modes in transversely magnetized semiconductor-filled coaxial waveguide and parallel plates, *IEE Proc. Microwave Anten. Propag.* **140**:211–218 (1993).
62. T. Nurgaliev, S. Miteva, A. P. Jenkins, and D. D. Hughes, Investigation of MW characteristics of HTS microstrip and coplanar resonators with ferrite thin-film components, *IEEE Trans. Microwave Theory Tech.* **51**:33–40 (2003).
63. I. V. Lindell, Variational method for the analysis of lossless bi-isotropic (nonreciprocal chiral) waveguides, *IEEE Trans. Microwave Theory Tech.* **MTT-40**:402–405 (1992).
64. P. Pelet and N. Engheta, Modal analysis for rectangular chiro-waveguides with metallic walls using the finite-difference method, *J. Electromagn. Waves Appl.* **6**:1277–1285 (1992).
65. P. K. Koivisto, S. A. Tretyakov, and M. I. Oksanen, Waveguides filled with biisotropic media, *Radio Sci.* **28**:675–686 (1993).
66. H. Cory and S. Waxman, Coupling between chiral slabs, *J. Electromagn. Waves Appl.* **7**:1609–1622 (1993).
67. A. L. Topa and C. R. Pavia, New biorthogonality relations for inhomogeneous biisotropic planar waveguides, *IEEE Trans. Microwave Theory Tech.* **MTT-42**:629–634 (1994).
68. W. Y. Yin and W. B. Wang, Transverse coupling between two general biisotropic slabs, *Int. J. Infrared Millimeter Waves* **15**:1065–1072 (1994).
69. W. Y. Yin, W. Wan, and W. B. Wang, Hybrid mode characteristics in multilayered Faraday chiro-waveguides, *Prog. Electromagn. Res.* **PIER-13**:149–168 (1996).
70. L. W. Li, M. S. Leong, P. S. Kooi, T. S. Yeo, and K.-H. Tan, Rectangular modes and dyadic Green's functions in rectangular chiro-waveguides, I. Theory, *IEEE Trans. Microwave Theory Tech.* **MTT-47**:67–73 (1999).
71. L. W. Li, M. S. Leong, P. S. Kooi, T. S. Yeo, and K.-H. Tan, Rectangular modes and dyadic Green's functions in rectangular chiro-waveguides, II. Numerical results, *IEEE Trans. Microwave Theory Tech.* **MTT-47**:74–81 (1999).
72. W. Y. Yin and P. Li, The focal points of radially spherical chiro-lenses, *Microwave Opt. Technol. Lett.* **6**:561–564 (1993).
73. W. Y. Yin and P. Li, The theory of multilayered spherical chiro-dome, *Microwave Opt. Technol. Lett.* **7**:179–182 (1993).
74. P. Pelet and N. Engheta, Chirostrip antenna: Line source problem, *J. Electromagn. Waves Appl.* **6**:771–794 (1992).
75. W. Y. Yin and W. B. Wang, The analysis of the radiation characteristics of a two-layered chirostrip dipole antenna using dyadic Green's function, *Microwave Opt. Technol. Lett.* **6**:221–223 (1993).
76. A. Toscano and L. Vegni, A new efficient moment of method formulation for the design of microstrip antennas over a chiral grounded slab, *J. Electromagn. Waves Appl.* **11**:567–592 (1997).
77. A. J. Viitanen, Chiral soft-surface waveguide mode transformer, *Microwave Opt. Technol. Lett.* **27**:168–171 (2000).
78. A. J. Viitanen, Chiral hard surface waveguide mode transformer, *IEEE Trans. Microwave Theory Tech.* **MTT-48**:1077–1079 (2000).
79. X. Wu and D. L. Jaggard, Discontinuities in planar chiro-waveguides, *IEEE Trans. Microwave Theory Tech.* **MTT-45**:640–647 (2000).
80. X. Wu and D. L. Jaggard, A comprehensive study of discontinuities in chiro-waveguides, *IEEE Trans. Microwave Theory Tech.* **MTT-50**:2320–2330 (2002).
81. D. Worasawate, J. R. Mautz, and E. Arvas, Electromagnetic resonances and Q factors of a chiral sphere, *IEEE Trans. Anten. Propag.* **AP-52**:213–219 (2004).
82. M. Zhang, T. S. Yeo, L. W. Li, and M. S. Leong, Electromagnetic scattering by a multilayer gyrotropic bianisotropic circular cylinder, *Prog. Electromagn. Res.* **PIER-40**:91–111 (2003).
83. M. Zhang, L. W. Li, T. S. Yeo, and M. S. Leong, Scattering by a gyrotropic bianisotropic cylinder of arbitrary cross section: An analysis using generalized multipole technique, *Prog. Electromagn. Res.* **PIER-40**:315–333 (2003).
84. W. S. Weiglhofer and S. O. Hansen, Faraday chiral media revisited-I fields and sources, *IEEE Trans. Anten. Propag.* **AP-47**:807–814 (1999).
85. R. D. Graglia, M. S. Sarto, and P. L. E. Uslenghi, TE and TM modes in cylindrical metallic structures filled with bianisotropic materials, *IEEE Trans. Microwave Theory Tech.* **MTT-44**:1470–1477 (1996).
86. F. Olyslager, Properties of and generalized full-wave transmission line models for hybrid bianisotropic waveguides, *IEEE Trans. Microwave Theory Tech.* **MTT-44**:2064–2075 (1996).
87. V. Dmitriev, Comments on “Properties of and generalized full-wave transmission line models for hybrid bianisotropic waveguides”. *IEEE Trans. Microwave Theory Tech.* **MTT-47**:655–659 (1999).
88. Xu Yansheng and R. G. Bosisio, A study on the solutions of chiro-waveguides and bianisotropic waveguides with the used of coupled-mode analysis, *Microwave Opt. Technol. Lett.* **14**:308–311 (1997).
89. P. L. E. Uslenghi, TE-TM decoupling for guided propagation in bianisotropic media. *IEEE Trans. Anten. Propag.* **AP-45**:284–286 (1997).
90. E. O. Kamenetskii, On the technology of making chiral and bianisotropic waveguides or microwave propagation, *Microwave Opt. Technol. Lett.* **14**:103–107 (1996).
91. G. Plaza, F. Mesa, and F. Medina, On the use of SDA for the analysis of boxed planar lines with complex media, *IEEE Trans. Microwave Theory Tech.* **49**:1365–1368 (2001).
92. L. Valor and J. Zapata, An efficient finite element formulation to analyze waveguides with lossy inhomogeneous bi-anisotropic materials, *IEEE Trans. Microwave Theory Tech.* **MTT-44**:291–296 (1996).
93. L. Valor and J. Zapata, A simplified formulation to analyze inhomogeneous waveguide with lossy chiral media using the finite-element method, *IEEE Trans. Microwave Theory Tech.* **MTT-46**:185–187 (1998).
94. J. A. M. Svedin, Propagation analysis of chiro-waveguides using finite-element method, *IEEE Trans. Microwave Theory Tech.* **MTT-38**:1488–1496 (1990).
95. A. Grande, A. C. L. Cabeceira, J. Represa, P. P. M. So, and W. J. R. Hofer, FDTD modeling of transient microwave signals in dispersive and lossy bi-isotropic media, *IEEE Trans. Microwave Theory Tech.* **MTT-52**:773–784 (2004).

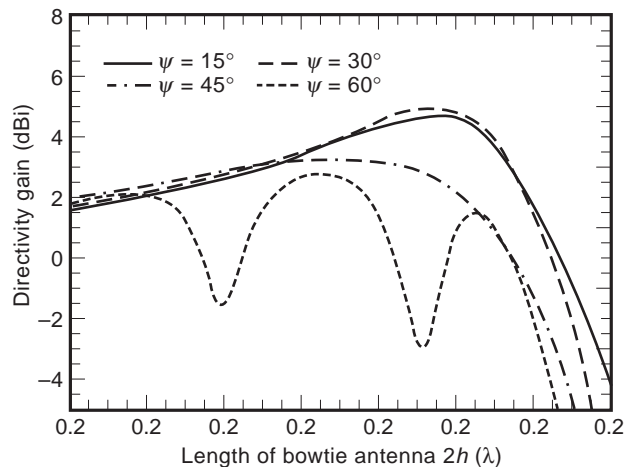


Figure 13. Directivity gain of a bowtie antenna in x direction (from Ref. 20).

lower-frequency regions, without affecting the radiation pattern.

3. TRIANGULAR (BOWTIE) ANTENNAS

A triangular plate antenna above a conducting ground plane and a bowtie antenna are shown in Figs. 10a and 10b. These antennas also possess broadband characteristics, though not as broad as a solid conical antenna. The theoretical characteristics of the bowtie antenna have been obtained numerically [20] by using the method of finite-difference time domain (FDTD). Figures 11a and 11b show the calculated input impedance. The input impedance of the triangular plate antenna above the ground plane is half of that of the bowtie antenna.

The far-zone electric field patterns in the x - y plane and in the x - z plane are shown in Figs. 12a and 12b, respectively. Note that the radiation is enhanced in the direction perpendicular to the antenna plate for the antenna length $2h \lesssim \lambda$, because the radiation from the antenna surface current is added in phase in that direction. The theoretical directivity gain of the bowtie antenna in the direction of the x axis is shown in dBi in Fig. 13 versus the antenna length $2h/\lambda$ for various cone angles [20]. It is noted here that the bowtie antenna can also be simulated by several radial wire rods as the solid biconical antenna.

BIBLIOGRAPHY

1. S. A. Schelkunoff, Principal and complementary waves in antennas, *Proc. IRE* **34**(1):23–32 (1946).
2. S. A. Schelkunoff, *Advanced Antenna Theory*, Wiley, New York, 1952.
3. P. D. P. Smith, The conical dipole of wide angle, *J. Appl. Phys.* **19**(1):11–23 (1948).
4. C. T. Tai, On the theory of biconical antennas, *J. Appl. Phys.* **19**(12):1155–1160 (1948).
5. C. T. Tai, Application of variational principle to biconical antennas, *J. Appl. Phys.* **20**(11):1076–1084 (1949).
6. C. H. Papas and R. W. P. King, Radiation from wide-angle conical antennas fed by a coaxial line, *Proc. IRE* **39**(1):49–51 (1951).
7. S. A. Saoudy and M. Hamid, Input admittance of a biconical antenna with wide feed gap, *IEEE Trans. Anten. Propag.* **38**(11):1784–1790 (1990).
8. V. Badii, K. Tomiyama, and D. M. Grimes, Biconical transmitting antennas, a numerical analysis, *Appl. Comput. Electromagn. Soc. J.* **5**(1):62–93 (1990).
9. J. G. Maloney, G. S. Smith, and W. R. Scott, Jr., Accurate computation of the radiation from simple antennas using the finite-difference time-domain method, *IEEE Trans. Anten. Propag.* **38**(7):1059–1068 (1990).
10. G. H. Brown and O. M. Woodward, Jr., Experimentally determined radiation characteristics of conical and triangular antennas, *RCA Rev.* **13**(4):425–452 (1952).
11. R. M. Bevens, *Handbook of Conical Antennas and Scatterers*, Gordon & Breach, New York, 1973.
12. C. Polk, Resonance and supergain effects in small ferromagnetically or dielectrically loaded biconical antennas, *IRE Trans. Anten. Propag.* **7**(special suppl.):414–423 (1959).
13. J. R. Wait, Electromagnetic radiation from conical structures, in R. E. Collin and F. J. Zucker, eds., *Antenna Theory*, McGraw-Hill, New York, 1969.
14. S. Adachi, A theoretical analysis of semi-infinite conical antennas, *IEEE Trans. Anten. Propag.* **8**:534–547 (1960).
15. C. E. Smith, C. M. Butler, and K. R. Umashanker, Characteristics of a wire biconical antenna, *Microwave J.* **22**(9):37–40 (1979).
16. O. Givati and A. P. C. Fourie, Analysis of skeletal wire conical antennas, *IEEE Trans. Anten. Propag.* **44**:844–858 (1996).
17. S. Adachi, R. G. Kouyoumjian, and R. G. Van Sickle, The finite conical antenna, *IEEE Trans. Anten. Propag.* **7**(special suppl.):S406–S411 (1959).
18. L. L. Bailin and S. Silver, Exterior electromagnetic boundary problem for sphere and cones, *IRE Trans. Anten. Propag.* **4**(1):5–16 (1956); corrections **4**(3):313 (1957).
19. A. G. Kandoian, Three new antenna types and their applications, *Proc. IRE* **70W-75W** (1946).
20. Private communication from Y. He, T. Uno, and S. Adachi, 1997.

COPLANAR STRIPLINE (CPS) COMPONENTS

YOUNG-HO SUH
Mimix Broadband Inc.
Houston, Texas

1. INTRODUCTION

Coplanar stripline (CPS) is an attractive uniplanar transmission line offering flexibility in the design of planar microwave and millimeter-wave circuits, especially in mounting the solid-state device in series or shunt with no via holes. Its balanced structure is useful in applications such as printed dipole antenna feeding, rectennas, uniplanar mixers [1], integrated optic traveling-wave

modulators [2], optical control microwave attenuators and modulators [3], and other optoelectric devices [4,5]. CPS characteristics include low loss, small dispersion, small discontinuity parasitics, comparable insensitivity to substrate thickness, and simple implementation of open-ended or short-ended strips.

A few studies regarding CPS components modeling and filter applications have been performed. In 1996, CPS discontinuities such as open and short circuits, series gap, spur slot, and spur strip were investigated [6]. In Ref. 6, each discontinuity was represented as an equivalent lumped element. The CPS open circuit was represented as a shunt capacitor, CPS short circuit was represented as a shunt inductor, and the CPS series gap was represented as a series capacitor. A quarter-wavelength spur slot and spur strip were represented as a series short circuit and a shunt open circuit, respectively. Simons et al. [6] also proposed CPS component measurement method using thru-reflect-line (TRL) calibration with CPS on-water standards for the first time. In 1997, CPS discontinuities and their applications to bandstop [7] and bandpass [8] filters were studied by using the spur-strip and the spur-slot resonators. Goverdhanam et al. [7] introduced various CPS components such as a narrow transverse slit, a symmetric step, a right-angle bend, and a tee junction. Fan et al. [9] proposed uniplanar hybrid ring couplers and a branchline hybrid coupler using an asymmetric CPS with 25% and 10% bandwidths, respectively, at a center frequency of 3 GHz in 1997. A lumped-element CPS lowpass filter was designed in 1998 [10] using spiral inductors and interdigital capacitors, and a CPS lowpass filter using a transverse slit and a parallel-coupled gap of CPS discontinuities was presented in 1999 [11]. Kim et al. introduced a CPS MEMS phase shifter that could be easily packaged or integrated into the waveguide in 2003 [12]. Lumped-element models of CPS circuits and discontinuities were extracted using a full-wave method of moments [13]. A new deembedding technique called a “short (circuit)/open(circuit) calibration scheme” is applied to calibrate these calculated models for accurate circuit model extraction.

Comparably extensive work has been reported in coplanar waveguide (CPW) components such as resonators and filters. Dib et al. investigated CPW discontinuities based on the solution of an appropriate surface integral equation in the space domain in 1991 [14]. In 1998, [15], Hettak et al. reported various types of CPW series resonators and their applications to filters and in 1999 they described CPW shunt stubs printed within the center conductor and implemented miniature filters were with these shunt stubs [16]. However, CPW shunt stub resonator requires additional airbridges or bonding wires, which might increase the fabrication cost and complexity. CPW series resonators require a large conductor area and, the structure of the CPW bandpass filter using CPW series resonators is comparably complex.

This article is organized into three major parts: (1) review and investigation of CPS characteristics; (2) introduction of CPS circuit components such as resonators, filters, and tee junction; and (3) CPS applications to antennas and wireless power transmission.

First, a CPS characteristics analysis using a quasi-TEM analytical equation derived by the conformal mapping method is described. The relationship between the characteristic impedance and CPS strip width and gap is analyzed. Transmission-line loss is analyzed as a function of characteristic impedance of CPS. Parameter variations due to change in substrate height are discussed. From the analysis, the design considerations for practical CPS component implementations are discussed. Following a brief analysis of CPS, new types of CPS components and their performances are presented. Six types of CPS resonator are first introduced and their performances are analyzed in terms of Q factor or bandwidth. CPS resonators are realized with open-ended and short-ended strips in various configurations, and lumped-element equivalent circuits for the resonators are presented. The appropriate circuit configuration for high Q factor is analyzed. The relationship between CPS characteristic impedance and CPS attenuation is briefly discussed for high Q factor. Two new classes of CPS bandpass filter are presented using the resonators discussed here for narrow- and wideband applications, and their lumped-element equivalent circuits are presented. A novel, simple CPS lowpass filter is presented using a CPS line loaded with interdigital capacitors. The lowpass filter is easily reproducible using a prototype of the desired filter type with the selected cut-off frequency.

A new method of microstrip-fed CPS tee junction is introduced without using bonding wires or via holes. For the tee junction, novel coupled CPS (CCPS) is presented and its performance is discussed. Tee-junction applications are demonstrated in a twin-dipole antenna and a dipole phased array with detailed illustrations and photographs.

Microstrip-to-CPS transition for CPS component measurements is briefly discussed. The transition presented in this article enables convenient CPS components measurement with a conventional network analyzer using the common short (circuit)/open (circuit) load-thru (SOLT) calibration method.

All the CPS components presented in this article is fabricated on the RT/Duroid 5870 substrate with 1 oz copper cladding, 20 mil substrate height, and the dielectric constant of 2.33.

2. CPS CHARACTERISTICS ANALYSIS FOR THE DESIGN CONSIDERATION

The structure of CPS on a finite substrate is illustrated in Fig. 1. Analytical techniques for calculating the characteristic impedance, the effective dielectric constant, and dielectric and conductor losses of the CPS are described in Refs. 12–14. Closed-form quasi-TEM parameters for the symmetric coplanar stripline on finite substrate thickness are necessary for practical purposes, which is extensively discussed in Ref. 20a. Loss mechanisms considered in this article are conductor (α_c) and dielectric (α_d) losses.

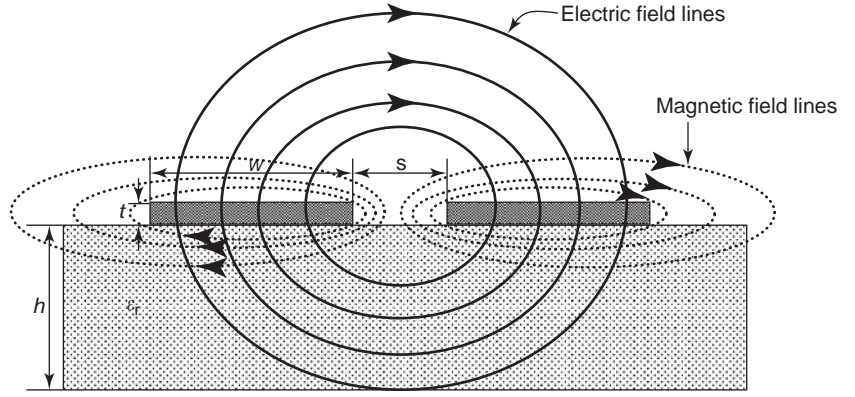


Figure 1. Coplanar stripline (CPS) structure (from Ref. 20b with permission from IEEE).

Dielectric loss (α_d) is independent of the geometry of the line and can be expressed as follows:

$$\alpha_d = 27.3 \frac{\epsilon_r}{\sqrt{\epsilon_{re}}} \frac{\epsilon_{re} - 1}{\epsilon_r - 1} \frac{\tan \delta}{\lambda_0} \quad (\text{dB/unit length}) \quad (1)$$

Effective dielectric constant (ϵ_{re}) is represented as

$$\epsilon_{re} = 1 + \frac{\epsilon_r - 1}{2} \frac{K'(k_1)}{K(k_1)} \frac{K(k_2)}{K'(k_2)} \quad (\text{F/unit length}) \quad (2)$$

where ϵ_r is the dielectric constant and $K(\bullet)$, $K'(\bullet)$ are the complete elliptic integrals of the first kind and its complement, respectively. k_1 and k_2 are expressed as

$$k_1 = \frac{s}{s + 2W} = \frac{a}{b} \quad (3)$$

$$k_2 = \frac{\sinh(\pi a/2h)}{\sinh(\pi b/2h)} \quad (4)$$

where h represents substrate thickness, s is the gap between the CPS strips, and W is the width of the CPS strip. $K(k)$ can be found with series expansion approximation as for $0 \leq k \leq 0.707$

$$K(k) = \frac{\pi}{2} \left\{ 1 + 2 \frac{k^2}{8} + 9 \left(\frac{k^2}{8} \right)^2 + 50 \left(\frac{k^2}{8} \right)^3 + 306.25 \left(\frac{k^2}{8} \right)^4 + \dots \right\} \quad (5)$$

and for $0.707 \leq k \leq 1$

$$K(k) = p + (p - 1) \left(\frac{k^2}{4} \right) + 9 \left(p - \frac{7}{6} \right) \left(\frac{k^4}{64} \right) + 25 \left(p - \frac{37}{30} \right) \left(\frac{k^6}{256} \right) + \dots \quad (6)$$

where

$$p = \ln \frac{4}{k'} \quad (7)$$

$$k' = \sqrt{1 - k^2} \quad (8)$$

$K'(k)$ can be obtained from $K'(k) = K(k')$ and applied to series expansions.

The conductor loss (α_c) of a CPS expression is given as

$$\alpha_c = \frac{8.68 R_s \sqrt{\epsilon_{re}}}{480 \pi K(k_1) K'(k_1) (1 - k_1^2)} \times \left\{ \frac{1}{a} \left[\pi + \ln \left(\frac{8 \pi a (1 - k_1)}{t (1 + k_1)} \right) \right] + \frac{1}{b} \left[\pi + \ln \left(\frac{8 \pi b (1 - k_1)}{t (1 + k_1)} \right) \right] \right\} \quad (\text{dB/unit length}) \quad (9)$$

a , b , and k_1 are as defined in (3). $K(\bullet)$ and $K'(\bullet)$ can be obtained from (5)–(8) with the property of $K'(\bullet) = K(\bullet')$. t is the strip thickness and R_s is the surface resistance, defined as

$$R_s = \sqrt{\frac{\omega \mu_0}{2 \sigma}} \quad (\Omega) \quad (10)$$

where σ is the metallic strip conductivity. These equations assume strip thickness $t > 3\delta$, $t \ll a$, and $t \ll (b - a)$, where δ is skin depth, expressed as

$$\delta = \sqrt{\frac{2}{\omega \mu \sigma}} \quad (\text{unit length}) \quad (11)$$

Total attenuation, including dielectric and conductor losses at 10 GHz, is plotted in Fig. 2 with a fixed strip width ($W = 1.5$ mm) and separation between the strips (s) increased from 0.1 to 20 mm. It is observed that the wider is the separation (s), the lower the total attenuation ($\alpha_c + \alpha_d$) and the higher the characteristic impedance (Z_0) are achieved. In other words, the higher the characteristic impedance of CPS, the lower the transmission-line

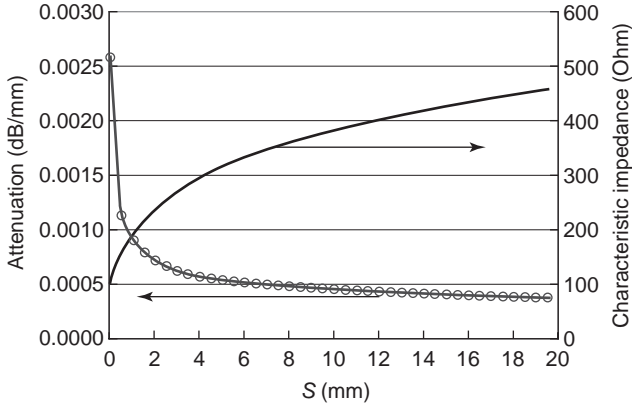


Figure 2. Total attenuation ($\alpha_c + \alpha_d$) of a CPS as a function of gap separation (s) at 10 GHz. The strip width (W) is fixed at 1.5 mm. A 20-mil-height, 2.33 dielectric constant, and 1-oz copper cladding substrate was used (from Ref. 20b with permission from IEEE).

attenuation that can be achieved. In the relationship between the dielectric constant of the substrate and the total attenuation, the higher is the dielectric constant, the higher is the total attenuation. For a practical design, moderate characteristic impedance with a proper dielectric constant substrate is used for low attenuation. Hence, Fig. 2 is useful for selecting CPS component design parameters.

3. CPS RESONATORS

3.1. Open-Ended T-Strip Resonators

Two types (A and B) of open-ended T-strip resonator are presented in this section. The structure of resonator type A and its lumped-element equivalent circuit are illustrated in Fig. 3. Resonator type A consists of open-ended T strips with 0.5 mm width and around $\lambda_g/2$ ($0.42 \lambda_g$) or 25.4 mm length, placed outside the strips designed to operate at a center frequency of ~ 4.28 GHz. As shown in

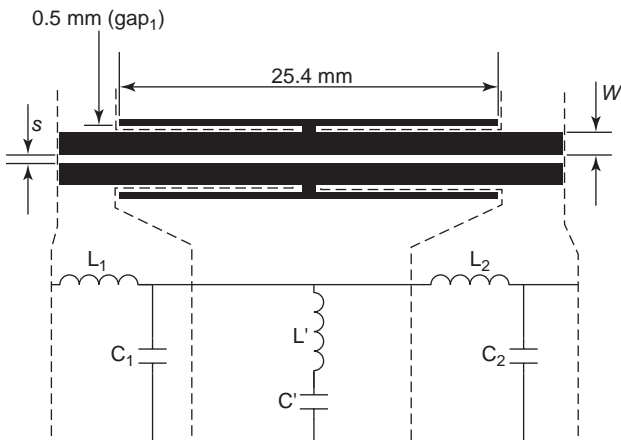


Figure 3. CPS resonator using open-ended T strips and its lumped-element equivalent circuit (type A) (from Ref. 20b with permission from IEEE).

Table 1. Simulated Loaded Q (Q_L) and Unloaded Q (Q_U) of Resonator Type A (from Ref. 20b with permission from IEEE)

Gap ₁ (mm)	s (mm)	Q_L	Q_U
0.25	0.6	113.6	114.7
	1.2	114.1	115.6
0.5	0.6	101.9	102.05
	1.2	104.7	105.2
1	0.6	62.6	72.8
	1.2	76.3	79.1

Fig. 3, the CPS transmission line is represented as lumped-element LC circuits. The T strips become inductor, and gap₁ induces coupling capacitance due to the coupling with CPS strips. Hence, T strips can be represented as a shunt series resonator ($L'C$ circuit), which exhibits bandstop behavior. The narrower is the gap₁, the higher is the loaded Q (Q_L) value, due to the strong coupling and the low loss at gap₁.

As discussed in Section 2, CPS transmission-line attenuation is reduced when the CPS strip separation (s) widens, as shown in Fig. 2. Accordingly, the narrower the gap₁, and greater the s will increase the loaded Q (Q_L). Computed loaded (Q_L) and unloaded Q (Q_U) values are displayed in Table 1 with various gap₁ and s values. The computation was performed using a commercial full-wave electromagnetic simulator, which uses the method of moments. Table 1 shows that the narrow gap₁ and the wide s configuration provide a high Q_L value, and Q_U values are similar in every configuration. Q_U calculation of the bandstop resonator [21] is expressed as

$$Q_U = \frac{Q_L}{\sqrt{(1 - 2 \times 10^{-L/20})}} \quad (12)$$

Where Q_L is the loaded Q , expressed as

$$Q_L = \frac{f_0}{\Delta f_{3 \text{ dB}}} \quad (13)$$

f_0 , $\Delta f_{3 \text{ dB}}$, and L represent the center frequency, the 3 dB insertion loss bandwidth, and the insertion loss at the center frequency, respectively.

Measured and simulated frequency responses of this type of resonator with 0.6 mm of s and 0.5 mm of gap₁ are shown in Fig. 4. A measured Q_L of 97.27 is achieved with a resonance frequency of 4.28 GHz with a 3 dB insertion loss bandwidth of 44 MHz. Q_U of 97.44 is obtained from (12) with the insertion loss (L) of -27.53 dB at the center frequency. Measured Q values agree with simulated result ($Q_L = 101.9$ and $Q_U = 102.05$) displayed in Table 1.

Resonator type B consists of open-ended T strips placed inside the CPS transmission line. The structure of resonator type B and lumped-element equivalent circuit are shown in Fig. 5.

Gap₂, gap₃, and the open-ended T-strip width are all 0.5 mm. To place the open-ended T strips between the narrowly spaced CPS strips, the transmission-line gap s is widened from 0.6 to 2.5 mm, which corresponds to the

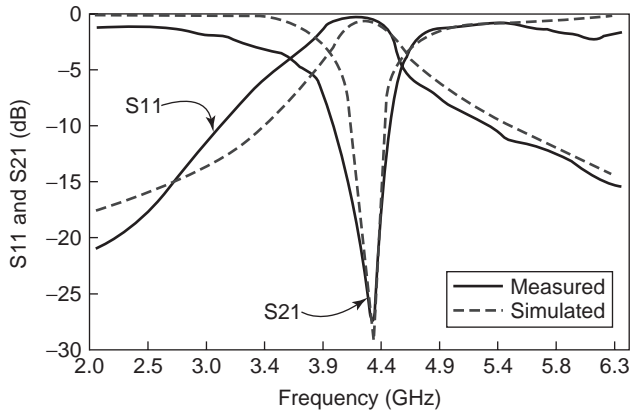


Figure 4. Simulated and measured frequency responses for open-ended T-strip resonator (type A) with gap_1 0.5 mm and s 0.6 mm (from Ref. 20b with permission from IEEE).

impedance value increase from 184 to 250 Ω . Despite this increase in impedance, little insertion loss deterioration occurs and the return loss response is better than 10 dB. The open-ended T-strip length is around $\lambda_g/2$ ($0.39\lambda_g$) or 25.4 mm at the center frequency of near 4.02 GHz. This type of resonator, similar to type A, has also coupling capacitance at gap_2 , and additional capacitance takes place at gap_3 .

Table 2 describes the simulated Q values of resonator type B with various gap_2 and gap_3 values. The gap_3 value corresponds to s value, which is the CPS separation between two strips. The narrower the gap_2 and the wider the s , the higher the Q_L values, due to the stronger coupling capacitance and, accordingly, the lower transmission-line attenuation, as shown in Fig. 2 from CPS analysis in Section 2. It can be concluded that the higher characteristic impedance corresponds to the higher Q_L values for CPS resonators as shown in Tables 1 and 2 and Fig. 2.

Simulated and measured frequency responses of the type B resonator are shown in Fig. 6. Measured Q_L and Q_U values of resonator type B, with 0.5 mm of gap_2 and gap_3 ,

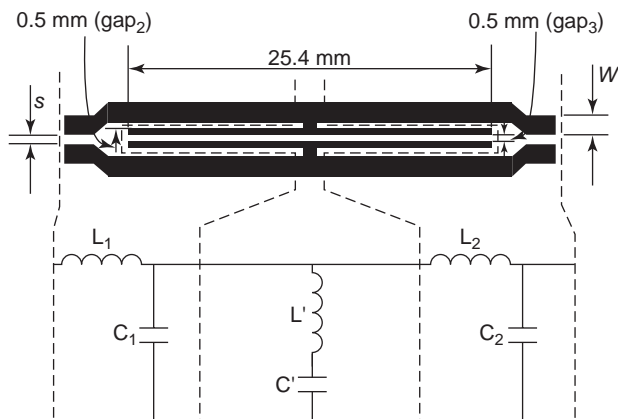


Figure 5. CPS resonator using open-ended T strips and lumped-element equivalent circuit (type B) (from Ref. 20b with permission from IEEE).

Table 2. Simulated Loaded Q (Q_L) and Unloaded Q (Q_U) of Resonator Type B (from Ref. 20b with permission from IEEE)

Gap ₂ (mm)	Gap ₃ (mm)	Q_L	Q_U
0.25	0.5	127.2	129.1
	1.0	129.7	130.6
	2.0	136.1	137.4
0.5	0.5	121.25	121.27
	1.0	124.3	125.2
	2.0	134.3	134.9

are 98.04 and 98.09, respectively. The 3 dB insertion loss bandwidth is 41 MHz, and the insertion loss (L) is -32.22 dB at the center frequency. The simulated Q_L and Q_U values are 121.25 and 121.27, respectively, as given in Table 2.

3.2. T-Slot Resonator

A T-slot resonator (type C) can be considered as a complementary structure of the type A resonator. Its structure is illustrated in Fig. 7. Similar to the spur-slot resonator in Ref. 7, a T slot can be considered as series short-ended stubs or shunt open-ended stubs where each arm measures a quarter-wavelength.

The frequency response of this resonator exhibits band-stop behavior and the lumped-element equivalent circuit is represented as a shunt-series resonator ($L'C'$ circuit). The length of the T slot is about $\lambda_g/2$ ($0.47\lambda_g$) or 25.4 mm at a center frequency of ~ 4.78 GHz. The width of the T slot (gap_4) is 0.5 mm, and s and W are 0.6 and 1.5 mm, respectively.

It is found that the T-slot resonator has a Q_L value much higher than that of open-ended T-strip resonators, mainly because the T-slot resonator's metallic area is much smaller than that of the T-strip resonator due to and thus the radiation loss of the former is much less. Simulated Q_L and its corresponding Q_U are described in Table 3.

Loaded Q (Q_L) of the T-slot resonator is ~ 262.93 with gap_4 0.5 mm and s 0.6 mm, while open-ended T-strip resonators such as types A and B have $Q_L < 150$. The T-slot resonator is also found to be less sensitive to gap_4 and s than is the open-ended T-strip resonator.

Similar to the case of two T-strip resonators, the value of Q_L increases when gap_4 is reduced and s is increased. This is due to the higher coupling at gap_4 and lower attenuation when s is increased. Wider s corresponds to higher characteristic impedance with fixed W for CPS as discussed in Section 2. While the relationship between the characteristic impedance and the value of Q_L follows the results of T-strip resonators, values of Q_L are not very sensitive to gap_4 and s or the characteristic impedances. This implies that the resonance energy is stored more effectively with the slot configuration than with the strip one.

It can be concluded that the higher characteristic impedance corresponds to the higher Q_L values for CPS resonators from the results of T-strip and T-slot resonators, and that the T-slot resonator has better performance in

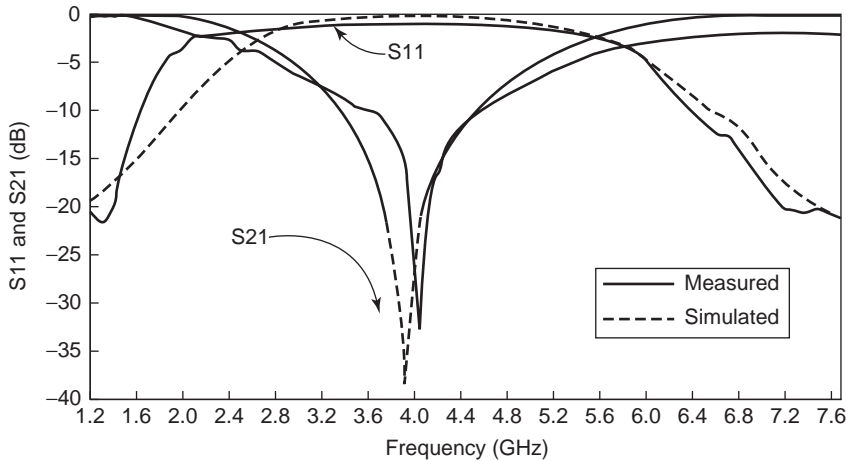


Figure 6. Simulated and measured frequency responses for open-ended T-strip resonator (type B) with gap_2 and gap_3 0.5 mm and s 0.6 mm (from Ref. 20b with permission from IEEE).

terms of the Q factors but insensitive to the characteristic impedance (see Tables 1–3 and Fig. 2).

Type C resonator simulated and measured frequency responses are shown in Fig. 8. Measured Q_L and its corresponding Q_U values of resonator type C, with 0.6 mm of s and 0.5 mm of gap_4 are 244.2 and 245.7, respectively. The 3 dB insertion loss bandwidth is 41 MHz, and the insertion loss (L) is -43.7 dB at the center frequency. These Q values are also close to simulated results ($Q_L=262.93$ and $Q_U=263.37$) given in Table 3.

3.3. Square-Ring-Shape Open-Ended Strip Resonator

The square-ring-shape open-ended strip resonator (type D) has two open-ended strips located outside the strips, similar to type A. These open-ended strips are bent to have square forms. The structure of square-ring-shape open-ended strip resonator is shown in Fig. 9.

The length of the open-ended strip is about $0.32\lambda_g$ (15.52 mm) at a center frequency of ~ 5.08 GHz. This resonator has a shorter coupling arm (4.625 mm) than do types A and B. Therefore, open-ended strips have loose coupling and induce high losses. Two open-ended strips are purposely located asymmetrically to prevent any pos-

sible radiation as does the dipole antenna. The asymmetric structure induces a spurious response around 6.1 GHz.

Measured and simulated return and insertion losses of this resonator are illustrated in Fig. 10. Measured Q_L and Q_U of this resonator are 23.51 and 23.87, respectively. The 3 dB insertion loss bandwidth is 216 MHz and the insertion loss (L) is -18.3 dB at the center frequency. Simulated Q_L and Q_U are 38.1 and 38.51, respectively.

Compared to resonators A and B, which consist of open-ended T strips, the type D resonator is compact but its Q_L is low. Hence, this resonator would be useful for applications requiring spatial efficiency with moderate bandstop purpose.

3.4. Short-Ended Strip Resonators

One merit of the uniplanar transmission line is the convenient implementation of the short-ended strips with no via holes. Two types of short-ended strip resonator (types E and F) are introduced and investigated. Resonator type E utilizes a short-ended strip, in contrast to resonator types A, B, and D as illustrated in Fig. 11.

The total length of the short-ended strip is about $0.44\lambda_g$ (13.7 mm), which is around $\lambda_g/2$, with 0.5 mm width at a center frequency of ~ 8 GHz. The transmission line is widened, similar to that of resonator type B, when the short-ended strip is placed between the CPS strips but little insertion loss deterioration occurs and return loss is >10 dB. The short-ended strip becomes an inductor and gap_4 induces coupling capacitance due to coupling with CPS strips. This short-ended strip and gap_4 consist of a

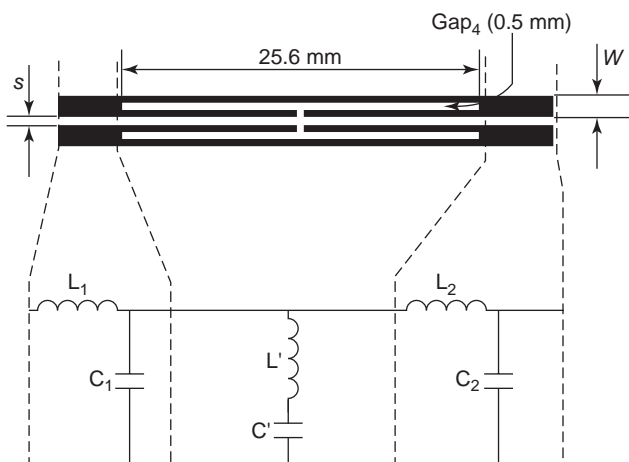


Figure 7. CPS resonator using T slots and its lumped-element equivalent circuit (type C).

Table 3. Simulated Loaded Q (Q_L) and Unloaded Q (Q_U) of Resonator Type C

Gap ₄ (mm)	s (mm)	Q_L	Q_U
0.25	0.6	265.00	265.52
	1.2	266.20	267.26
	1.8	267.24	267.97
0.5	0.6	262.93	263.37
	1.2	263.97	264.90
	1.8	264.37	266.55

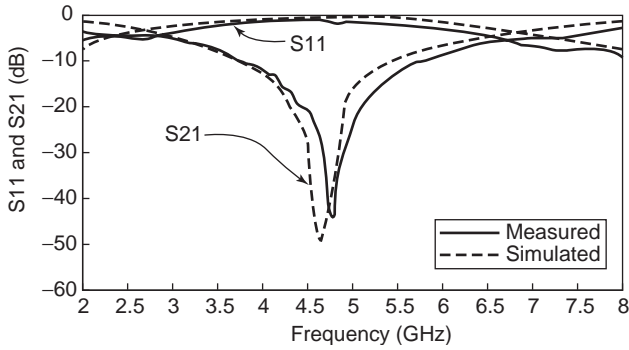


Figure 8. Simulated and measured frequency responses for a T-slot resonator (type C).

shunt-parallel resonator ($L''C''$ circuit), which acts as bandpass behavior.

Measured and simulated frequency responses of this resonator are illustrated in detail in Fig. 12. A measured insertion loss of 0.12 dB is achieved at a center frequency of 8.12 GHz. This type of resonator can be utilized for bandpass filter applications. The measured bandwidth of <3 dB insertion loss and >10 dB return loss is around 3 GHz (36.94%) with resonator type E.

For resonator type F, two short-ended strips are attached together in a closed polygon configuration as shown in Fig. 13. Similar to the type E resonator, coupling capacitance at gap₅ and the short-ended strip inductance consist in a shunt parallel resonator ($L''C''$ circuit), which exhibits bandstop behavior. The total length of the short-ended strip is about $1.1\lambda_g$ (48.1 mm) at a center frequency of ~5.4 GHz. The transmission-line gap s is widened similar to that of resonator types B and E.

Frequency responses of this resonator are illustrated in Fig. 14. The measured bandwidth of <3 dB insertion loss and >10 dB return loss is ~0.84 GHz (15.67%). A measured insertion loss of 0.5 dB was achieved at a center fre-

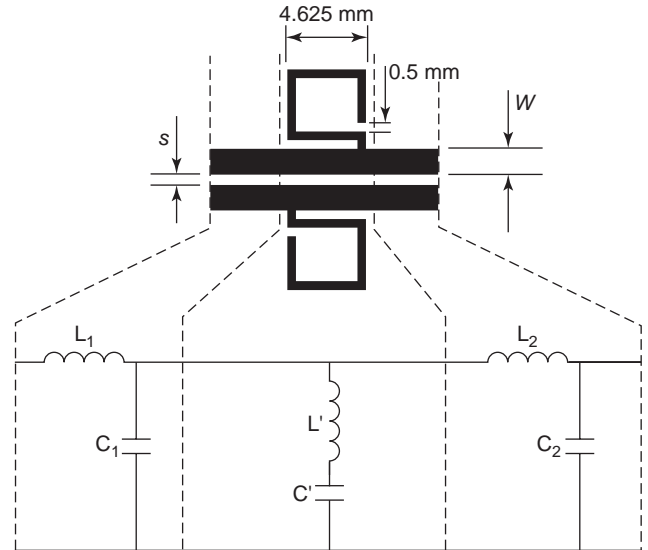


Figure 9. Square-ring-shape open-ended strip CPS resonator and its lumped-element equivalent circuit (type D) (from Ref. 20b with permission from IEEE).

quency of 5.36 GHz. The bandwidth of resonator type F is almost half that of resonator type E, which is due to the cascading of two identical resonators.

Six different types of resonator are presented, and their performances are analyzed. As discussed, the T-slot resonator (type C) has the highest Q_L among four different bandstop resonators and resonator type E has the widest passband bandwidth between the two different short-ended strip resonators. As shown in Tables 1-3 and Fig. 2, CPS resonators can have high Q_L when high characteristic impedance and strong coupling capacitance are employed. Many variations and combinations of these six resonators are possible. Therefore, these resonators would be very useful for designing CPS filters.

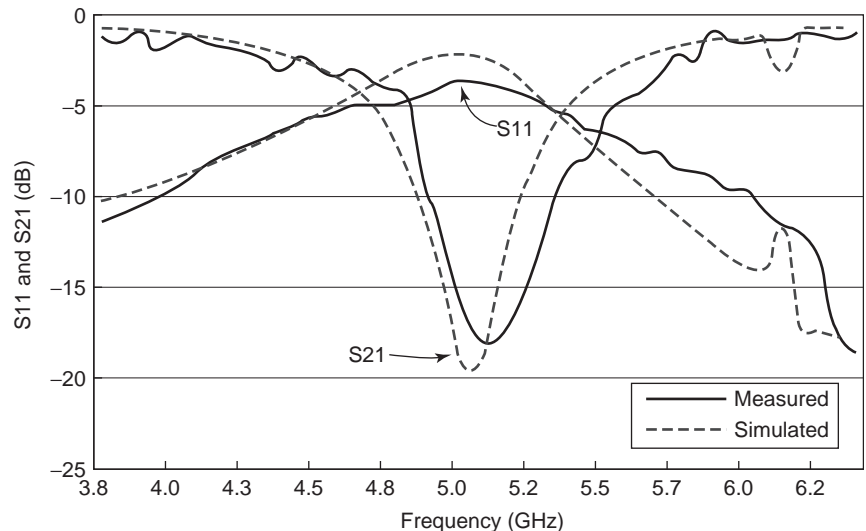


Figure 10. Simulated and measured frequency responses for square-ring-shape resonator (type D) (from Ref. 20b with permission from IEEE).

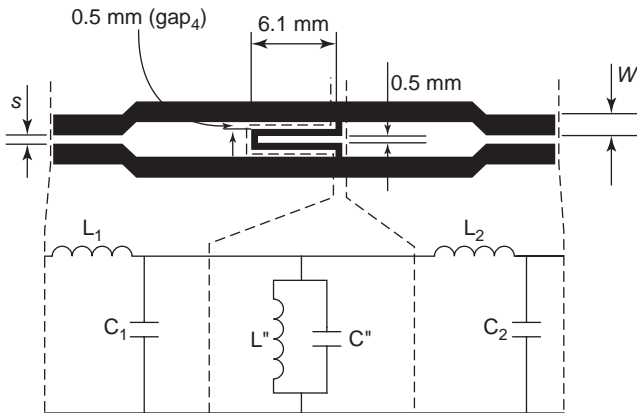


Figure 11. Short-ended strip CPS resonator and its lumped-element equivalent circuit (type E) (from Ref. 20b with permission from IEEE).

4. CPS FILTERS

This section describes two new classes of CPS bandpass filter that utilize combinations of the resonators presented in Section 3. Design methods for CPS bandpass filters are presented and discussed. These bandpass filters have good passband insertion loss and wide stopband suppressions. The simple CPS lowpass filter design method is also discussed with practical circuit implementation.

4.1. Bandpass Filter Realization Using Multiple Short-Ended Strips

This type of bandpass filter uses type E resonators presented in Section 3. The structure and the lumped-element equivalent circuit of this filter are shown in Fig. 15.

A transmission line with periodically loaded reactive cells has the characteristic of filters. One reactive cell can be formed with resonator type E, which exhibits bandstop behavior. The total length of the unit cell is around $\lambda_g/2$ ($0.41\lambda_g$) or 12.5 mm at a center frequency of 8 GHz. The spacing between neighboring cells is one of the most important factors for bandpass filter design in periodic structures.

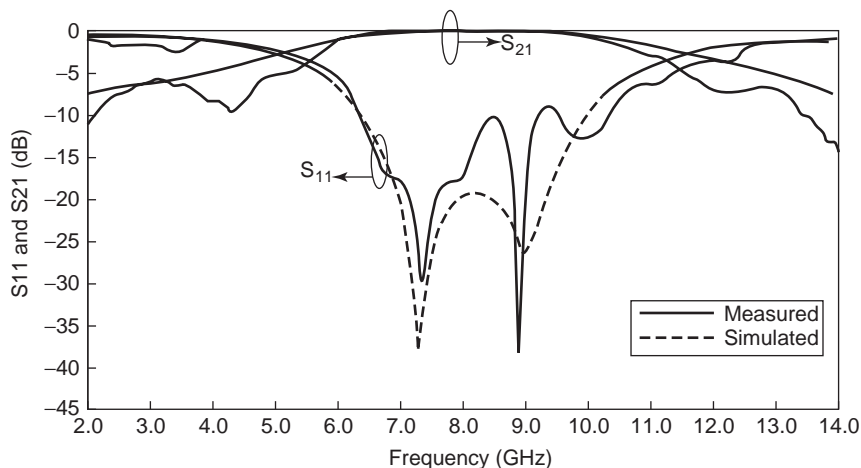


Figure 12. Simulated and measured frequency responses for short-ended strip resonator (type E) (from Ref. 20b with permission from IEEE).

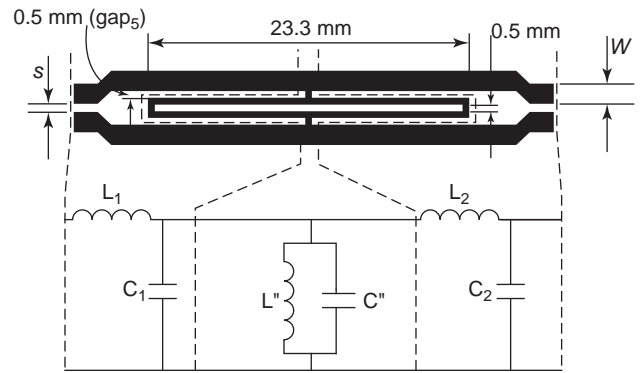


Figure 13. Closed polygon short-ended strip CPS resonator and its lumped-element equivalent circuit (type F) (from Ref. 20b with permission from IEEE).

Because of the structural dimension of the unit cell, uniform spacing between unit cells is impossible. Hence, two neighboring cells are grouped as a subcell. This bandpass filter, correspondingly, has two subcells. The inter-unit-cell spacing within the subcell is optimal at 2 mm; spacing under 2 mm manifests loose band rejection at stopbands, while spacing exceeding 2 mm exhibits sharper out-of-band rejection but shows unsatisfactory return loss at passband. A distance between subcells is about $\lambda_g/2$ ($0.46\lambda_g$) or 14 mm to ensure a good rejection at stopbands similar to conventional periodic structure. As shown in Fig. 15, CPS transmission-line sections are represented as the lumped-element LC circuits.

The short-ended strip consists a shunt parallel resonator ($L''C''$ circuits), discussed in Section 3 for resonator type E. The transmission-line gaps s is widened in the same way as in resonator types B, E, and F. For designing CPS components, transmission-line inductance and capacitance values play important roles and should be considered for CPS components modeling. Values of the capacitance and the inductance of CPS strips can be accurately extracted by the method of moments using commercial full-wave electromagnetic software.

Simulated and measured frequency responses of this filter are illustrated in Fig. 16. Measured insertion loss of 0.48 dB is achieved at a center frequency of 8.24 GHz. A

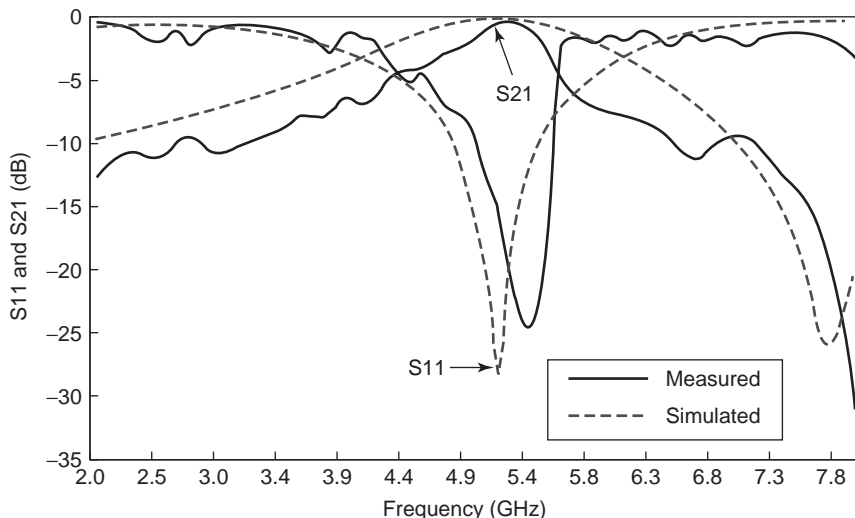


Figure 14. Simulated and measured frequency responses for closed polygon short-ended strip (type F) (from Ref. 20b with permission from IEEE).

wide bandwidth of 4.16 GHz (52%) is achieved with less than 3 dB insertion loss and better than 10 dB return loss, and the 1 dB insertion loss bandwidth ranges from 6.9 to 9.8 GHz. Stopbands range from 2 to 5.38 GHz in a lower stopband area and from 11.1 to 13.31 GHz in a higher stopband area.

4.2. Bandpass Filter Using Short-Ended Strips with T Strips

Figure 17 illustrates the bandpass filter structure using short-ended strips with T strips and shows its lumped-element equivalent circuit.

This type of filter consists of types A and F resonators and interdigital capacitors. Closed polygon short-ended strips (type F resonators) are represented as shunt-parallel resonators ($L''C''$ circuits) and T-strips (type A resonators) are represented as a shunt series resonator ($L'C'$ circuit). An interdigital capacitor (C) is placed inside each

type E resonator to provide higher capacitance. The interdigital capacitor is widely used as the microwave circuit's lumped-element component possessing tight coupling.

The capacitance of the interdigital capacitor is expressed as

$$C = \epsilon_0 \left(\frac{\epsilon_r + 1}{2} \right) \frac{K(k)}{K'(k)} Nl(F) \tag{14}$$

where $K(\bullet)$ is the complete elliptic integral of the first kind, which is expressed in (5)–(8). k is defined as

$$k = \sin \left(\frac{\pi W}{2d} \right) \tag{15}$$

where W is the width of the interdigital capacitor's finger and d is the distance between fingers; k' is as defined in (8).

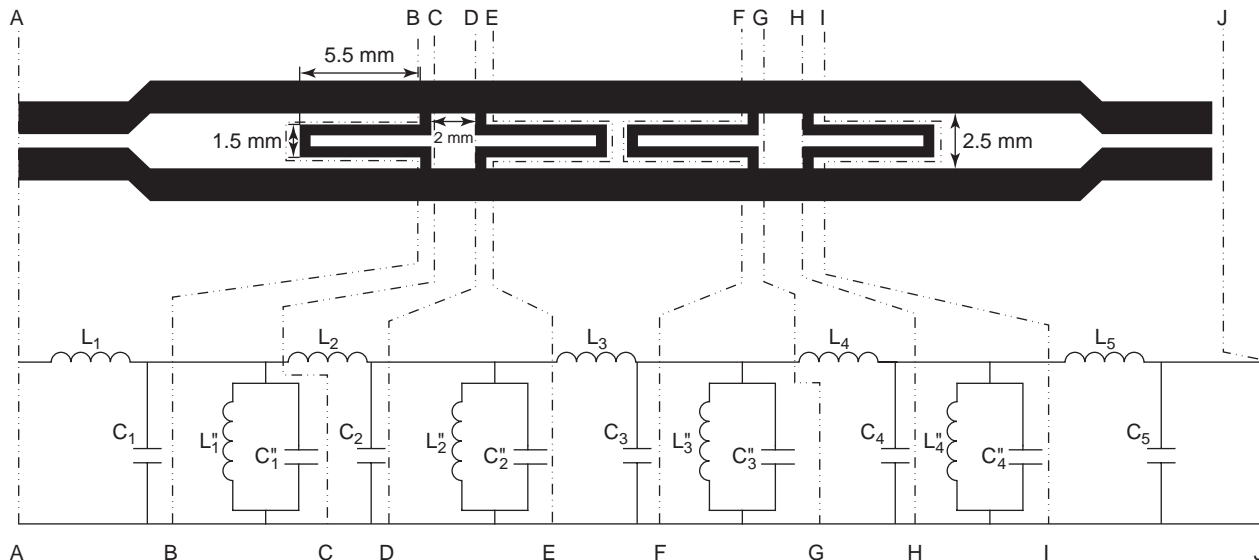


Figure 15. Bandpass filter structure using multiple short-ended strips and its lumped-element equivalent circuit (from Ref. 20b with permission from IEEE).

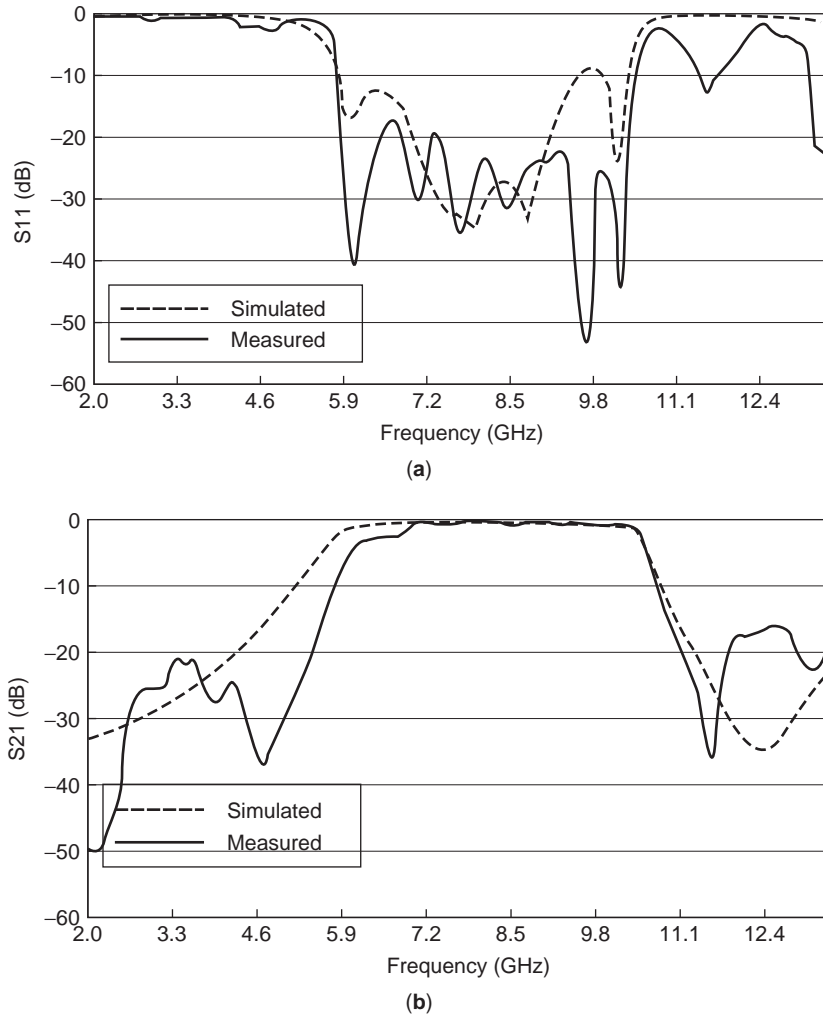


Figure 16. Simulated and measured frequency responses of a bandpass filter using multiple short-ended strips: (a) return loss; (b) insertion loss (from Ref. 20b with permission from IEEE).

The number and length of the interdigital capacitor fingers are $N = 3$ and $l = 2$ mm, respectively. All the interdigital capacitor gap distances are uniformly 0.5 mm, with a capacitance C of ~ 0.31 pF from full-wave electromagnetic simulation using the method of moments. Most of the capacitance takes place at the edges of the fingers. Hence, the gap distance between the fingers together with the number of fingers is important factor in determining the capacitance value.

The width of the short-ended strip is 0.5 mm and the length is $0.79 \lambda_g$ or 41.5 mm. The capacitance (C'') and inductance (L'') values of the short-ended strip are about 0.00563 pF/mm and 0.0763 nH/mm at 5 GHz, which can be found by simulation. The inductance (L'') and total capacitance, including interdigital capacitance ($C_T = C + C''$), can be found by the following equations

$$L'' = 0.0463 \times l(\text{nH}) \quad (16)$$

$$C_T = 0.31 + 0.00563 \times l(\text{pF}) \quad (17)$$

where l is the total length of the short-ended strip in millimeters. With (16) and (17), the approximate dimensions

of the short-ended strip can be found at the desired frequency.

Two unit cells are cascaded with a distance of $\sim \lambda_g/4$ ($0.28 \lambda_g$) or 13.6 mm. A type A resonator ($L'C'$ circuit) is combined with this filter to enhance the suppression at the lower stopband with a length of 29.1 mm ($0.48 \lambda_g$) at a center frequency of ~ 4 GHz. This is a good example an advantage of the uniplanar transmission line, namely, open-ended and short-ended strips together without any via holes.

Measured and simulated frequency responses are given in Fig. 18, showing good agreement between measured and simulated data. The measured bandwidth of < 1 dB insertion loss and > 10 dB return loss ranges from 4.82 to 5 GHz (3.64%). Stopbands with the suppression of less than -20 dB range from 3.56 to 3.98 GHz (0.42 GHz) at the lower band and from 5.48 to 6.08 GHz (0.6 GHz) at higher band. The low insertion loss of 0.61 dB was measured at a center frequency of 4.94 GHz.

Two types of bandpass filters are designed for wideband and narrowband applications using proposed resonators. Bandpass filters show low passband insertion loss and

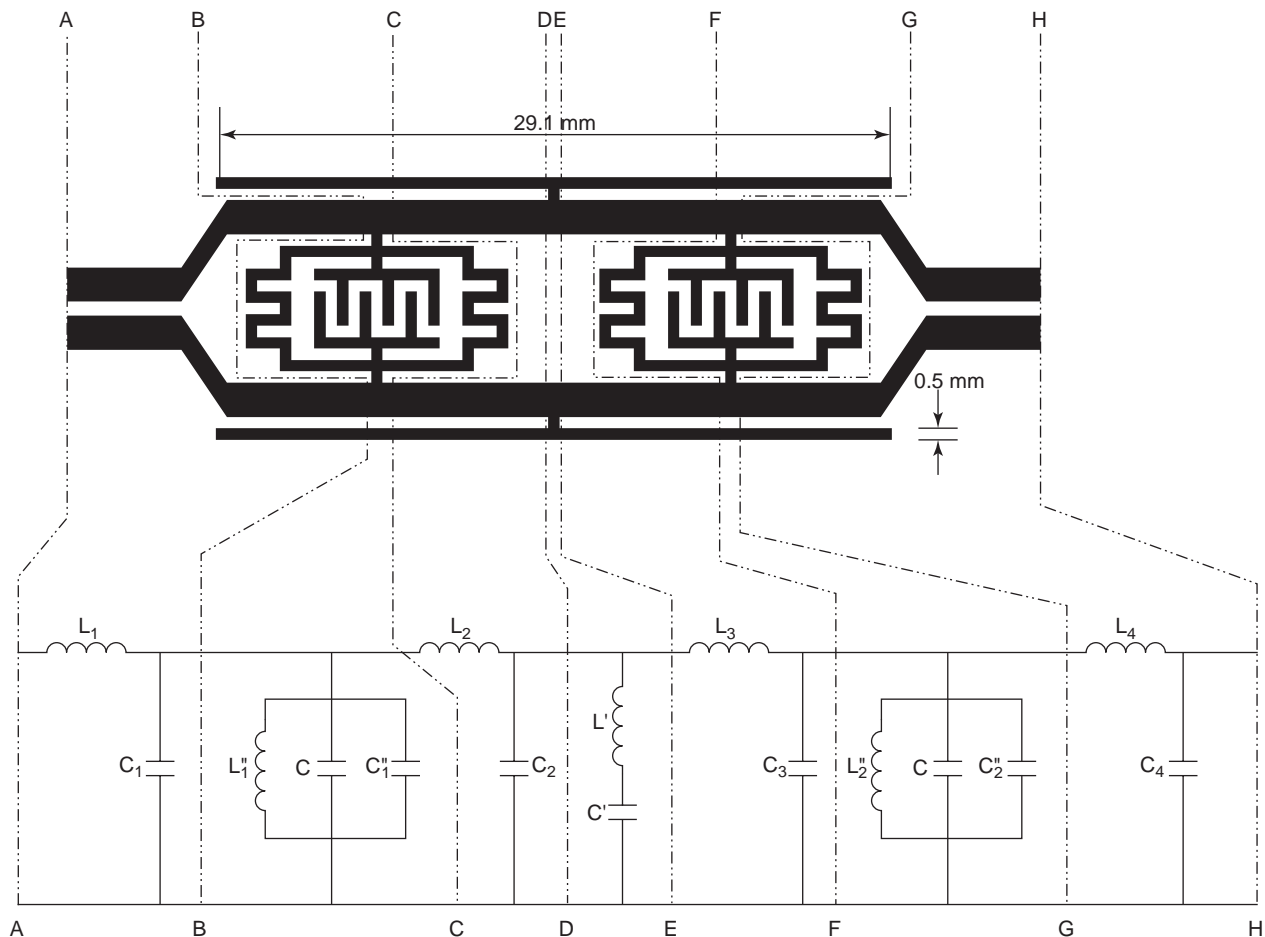


Figure 17. Structure of a bandpass filter using short-ended strips with T strips and its lumped-element equivalent circuit (from Ref. 20b with permission from IEEE).

good stopband suppression. These filters would be useful for uniplanar circuit implementations.

4.3. CPS Lowpass Filter

Few CPS lowpass filters have been reported. CPS lowpass filters are very useful in rectenna circuits [15–20a]. CPS lowpass filter design examples have been reported [5,6] with complex structures, the design methods are not clear. In this section, a novel lowpass filter with the lumped-element equivalent circuit is presented. The design method for the desired filter type is described. A simple 0.2 dB equal-ripple Chebyshev CPS lowpass filter is designed with a cutoff frequency of 7.4 GHz. The structure of the lowpass filter is illustrated in Fig. 19.

For designing the lowpass filter with the chosen specification, a ladder circuit and its element definitions should be first performed. Tabulated element values of the ladder circuit can be easily found in Ref. 28. With those element values, a prototype of the lowpass filter can be designed. After proper scaling in terms of impedance and frequency, lumped-element values of the lowpass filter can be found.

As shown in Fig. 19, capacitance is realized with the interdigital capacitor, and inductance is realized

with the CPS transmission line itself. Capacitance of the interdigital capacitors can be found by simulation or in (14).

As mentioned earlier, the CPS transmission line has its own inductance and capacitance, and those values should be considered for designing CPS components. This design demonstrates how the CPS line inherent inductance can be utilized in the design of the CPS components. At the design frequency, the capacitance and inductance of CPS per unit length can be found using a commercial simulator.

For inserting interdigital capacitors inside the narrowly spaced CPS strips, the CPS strip gap s is widened in the same way as in CPS resonator types B, E, and F, but little insertion loss deterioration occurs and return loss is better than 10 dB.

Simulated and measured frequency responses of the CPS lowpass filter are shown in Fig. 20. Measured data show sharp suppression after the cutoff frequency of 7.4 GHz and suppression better than 20 dB up to 13.8 GHz. A low passband insertion loss of 0.7 dB is achieved at passband. Measured and simulated data show good agreement. With this configuration, any kinds of CPS filters can be easily synthesized with desired specifications.

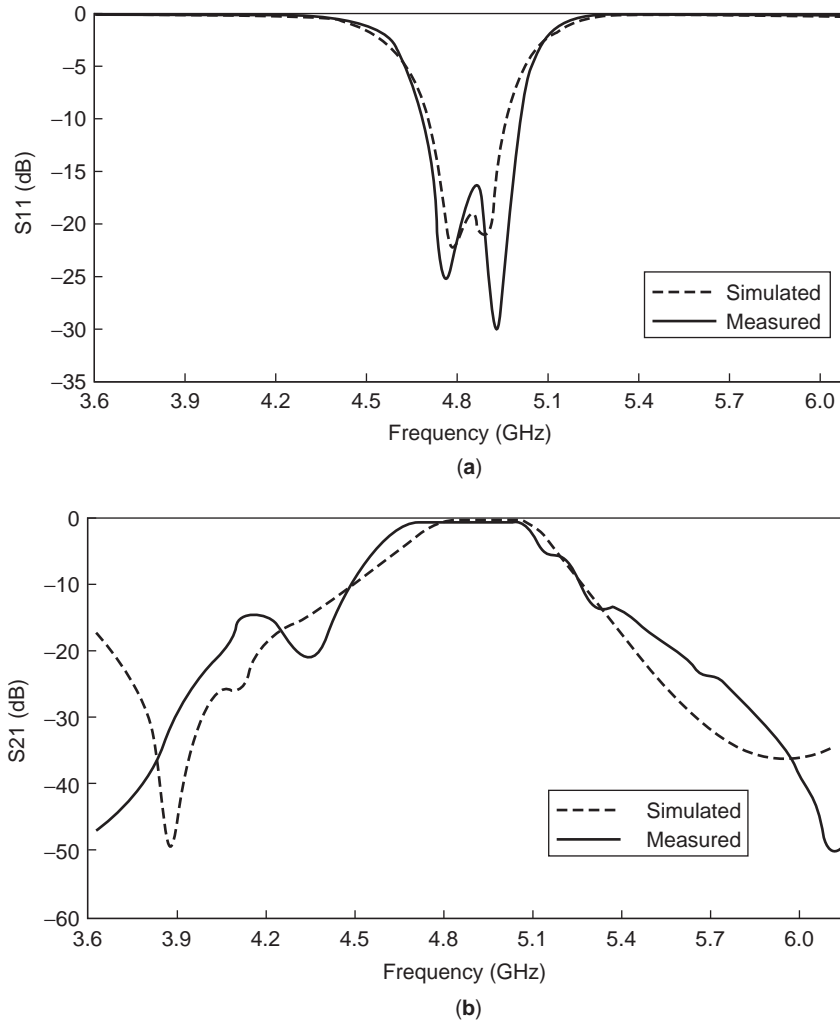


Figure 18. Simulated and measured frequency responses of a bandpass filter using short-ended strips with T strips: (a) return loss; (b) insertion loss.

5. MICROSTRIP-FED CPS TEE JUNCTION

Little work has been reported for CPS tee junctions. A CPS tee junction was introduced in 1997 [7], and a coplanar waveguide (CPW)-fed CPS tee junction was developed for the twin-dipole antenna feeding [29a]. Both methods require bonding wires.

In this section, a new microstrip fed CPS tee junction using a coupled CPS (CCPS) is introduced. Because of the inherent CPS structure as shown in Fig. 21a, it is almost impossible to build a CPS tee junction without having a discontinuity in the CPS structure. With the aid of the CCPS structure, which uses the coupling method, a physical discontinuity is introduced to the CPS structure while fields are continuous over the entire transmission line. Bonding wire is not required for constructing the CPS tee junction.

The structure of the coupled CPS is illustrated in Fig. 21b. One of the CPS strips is discontinued and is terminated with radial stubs with a rotation angle of 30° and a radius of 1.5 mm for coupling to the bottom-layer metallization. The bottom-layer metallization, which is coupled from the top layer's radial stubs, functions as a CPS strip as shown in Fig. 22. The radial stub is used to accomplish

a smooth field transition. Figure 22 compares metallization at different layers of the CPS with those of the conventional CPS shown in Fig. 1. A little insertion and return loss deterioration takes place because electric fields of the CCPS are not exactly normal to the strips.

Measured CCPS frequency responses are shown in Fig. 23, and its performance is compared with that of conventional CPS. Figure 23 also shows that the insertion loss of CCPS is around 0.5 dB deterioration compared with that of conventional CPS at 1.7–7.58 GHz and that the return loss is >10 dB. Insertion loss deterioration of <1 dB covers a wider frequency range, from 1.7 to 13.3 GHz.

The tee-junction configuration is illustrated in Fig. 24. Characteristic impedance of the CCPS is 184Ω , and the microstrip feedline has an input impedance of 50Ω . A quarter-wavelength transformer was used to transform the microstrip's impedance from 50Ω to 92Ω . Part of the microstrip feedline's ground plane forms the coupled CPS (CCPS).

The measured and simulated frequency responses of the tee junction are shown in Fig. 25. An ideal lossless tee junction equally splits the power between each output port with $S_{21} = S_{31} = -3$ dB. The measurements in Fig. 25 show an insertion loss of 0.7 dB and a return loss of

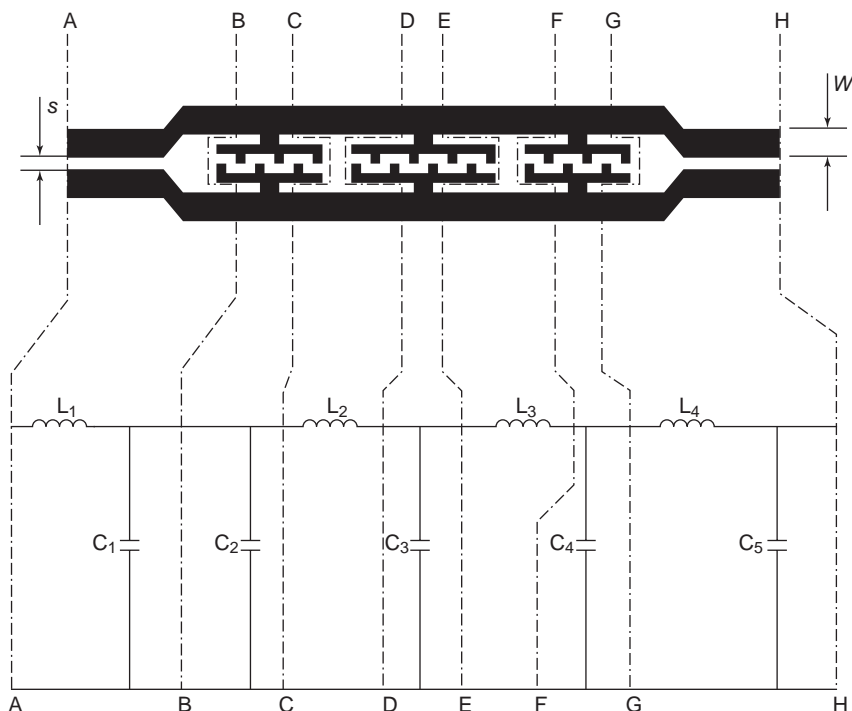


Figure 19. CPS lowpass filter and its lumped-element equivalent circuit.

> 10 dB at 2–4.15 GHz. It is expected that wider bandwidth can be achieved if a binomial or Chebyshev transformer is used instead of a quarter-wavelength transformer at the microstrip feeding.

Measured phases are almost identical at each output port as shown in Fig. 26.

6. CPS TRANSITION

For CPS component measurements, transition to other transmission lines, which enables convenient measurement with the conventional network analyzer, is required.

CPS-to-CPW, CPS-to-slotline, and CPS to-microstrip transitions have been reported.

In 1993 Ho et al. [30] developed a CPS-to-CPW transition. This transition included CPW-to-slotline transition as an intermediate transition. The measured frequency responses of the CPW-to-CPS-to-CPW back-to-back transition showed less than 1 dB insertion loss from 1.6 to 7 GHz (1–4.3), and the return loss was better than 13 dB.

Simons [31] developed a CPS-to-slotline transition with a bandwidth of 30% at 9.5 GHz in 1994. The measured insertion loss was 1.5 dB for the frequency range from 8 to 11.2 GHz (1–1.4) and a return loss of > 10 dB.

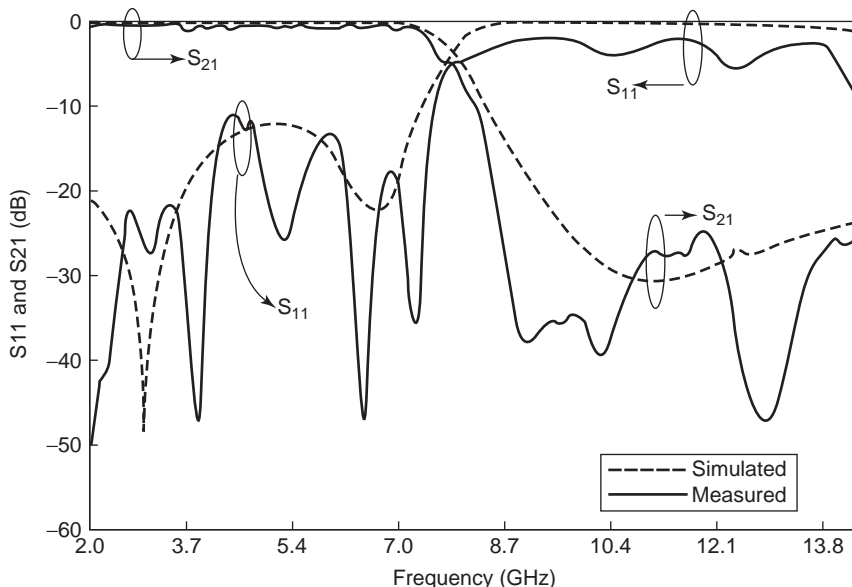


Figure 20. Simulated and measured frequency responses of CPS lowpass filter.

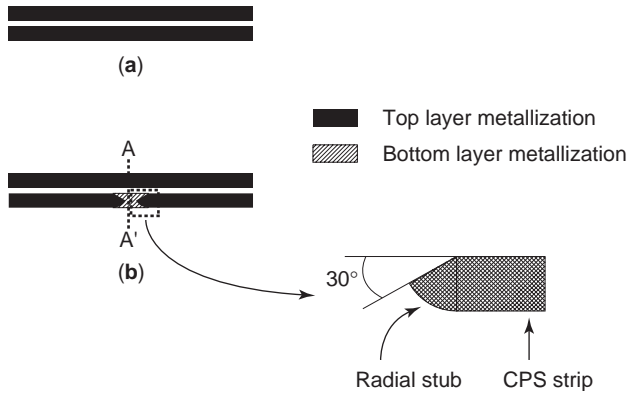


Figure 21. Coupled CPS (CCPS) structure: (a) conventional CPS; (b) CCPS (from Ref. 29b with permission from IEEE).

In 1994, Tilley et al. [32] presented a wideband CPW-to-CPS-to-CPW transition with 1 dB back-to-back insertion loss from 0.45 to 5 GHz (1–11). In 1995, Li et al. [33] proposed a CPW-to-CPS-to-CPW back-to-back transition with the bandwidth ranging from 0.4 to 3.6 GHz (1–9) using Chebyshev multisection impedance transformers in the CPW transmission line. In 2000, Mao et al. [34] demonstrated a CPS-to-CPW transition operating up to 20 GHz with an insertion loss of <0.5 dB and a return loss of >10 dB.

Various methods of designing CPS-to-microstrip transitions have been reported. In 1995, Dib et al. [35] reported a type of uniplanar transitions based on the concept of mode conversion with a 3 dB back-to-back insertion loss bandwidth from 7 to 11.5 GHz (1–1.6) for the CPS-to-microstrip transition. In 1997, Qian and Itoh [36] improved the performance with a 3 dB back-to-back insertion loss bandwidth from 6 to 13 GHz (1–2.1) by employing symmetric tee junction for the structure reported by Dib et al. [35]. Simons et al. [37] also proposed a CPS-to-microstrip transition using a coupling method with a 2.4 dB back-to-back insertion loss bandwidth from 5.1 to 6.1 GHz (1–1.2). However, this design used a CPS-to-microstrip-to-CPS back-to-back structure and required special CPS TRL (thru-reflect-line) on-wafer calibration standards with a National Institute of Standards and Technology (NIST) deembedding software program for a network analyzer calibration [37–39a]. Most of these CPS-to-microstrip

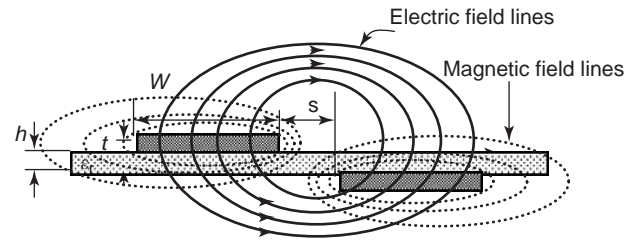


Figure 22. Cross-sectional view at A–A' with field distributions of CCPS for different layers of metallization (from Ref. 29b with permission from IEEE).

transitions used high-dielectric-constant substrate ($\epsilon_r > 10$) to reduce the CPS characteristic impedance [28–30].

This section introduces two types of broadband CPS-to-microstrip transitions. One operates from 1.3 to 13.3 GHz (1–10.2) with an insertion loss of <3 dB and a return loss of >10 dB for a back-to-back transition, and the other operates from 2 to 20 GHz (1–10) with an insertion loss of <3.5 dB and a return loss of >10 dB. Both have simple structures and can be easily fabricated using a low-dielectric-constant substrate ($\epsilon_r = 2.33$). Microstrip-to-CPS-to-microstrip back-to-back structures have been fabricated, which is convenient for CPS component measurement with a conventional network analyzer.

6.1. Transition with a Radial Stub Radius of 5.5 mm and its Performance

The structure of a back-to-back microstrip-to-CPS-to-microstrip transition is illustrated in Fig. 27. RT/Duroid 5870 is used as the substrate with a dielectric constant of 2.33 and a thickness of 20 mil.

The gap s and strip width W of the CPS are 0.6 and 1.5 mm, respectively. The CPS characteristic impedance is 184Ω , as was simulated with a commercial full-wave electromagnetic simulator, which uses the method of moments.

As shown in Fig. 1, electric field lines of CPS are directed from one strip conductor to the other on a layer. Electric field lines for microstrip are directed from top layer conductor to bottom layer ground-plane metallization. The radial stub is used to accomplish the rotation of the electric field lines and is rotated with an angle of ϕ to change electric field orientation from parallel to vertical

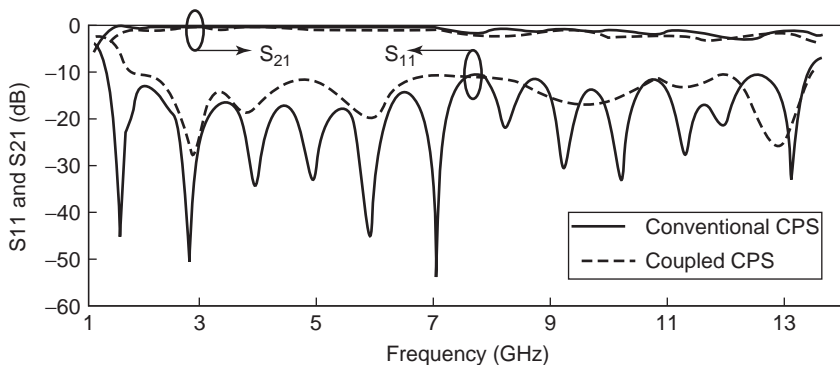


Figure 23. Frequency responses comparison between CPS and CCPS (from Ref. 29b with permission from IEEE).

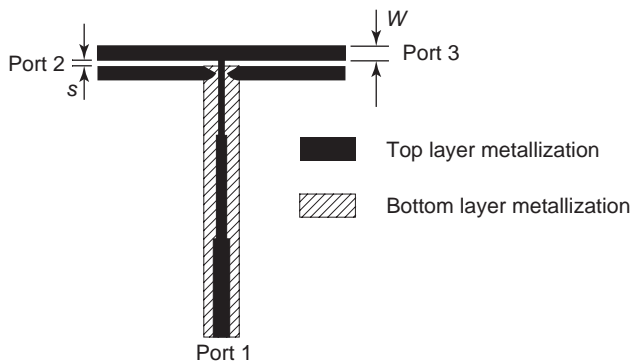


Figure 24. Structure of microstrip-fed CPS tee junction (from Ref. 29b with permission from IEEE).

against the substrate. The rotation angle ϕ is optimized at 30° for good coupling.

A broadband coupling can be accomplished by terminating one of the CPS strips with the radial stub as shown in Fig. 27.

The radius and the rotation angle (ϕ) were optimized at 5.5 mm and 30° , respectively. The width of microstrip line was optimized at 1.3 mm for $50\ \Omega$ matching. Length of the microstrip line is chosen as 40 mm. For the impedance transformation from the high characteristic impedance of CPS ($184\ \Omega$) to the microstrip line's impedance ($50\ \Omega$),

smooth insertion of the ground plane toward the microstrip line is important with the proper microstrip line width. Since this method does not employ any quarter-wavelength transformer, which would limit the bandwidth as seen in other methods [28,29a], broadband performance is achieved.

The radial stub length determines the highest operating frequency of the transition. This is because the radial stub creates a virtual short circuit to the bottom metallization with a quarter-wavelength, which is a ground plane of the transition. The shorter is the radial stub, the higher is the operating frequency. Therefore, factors such as radial stub length, rotation angle (ϕ), and length of microstrip determine performance of the transition.

The measured return and insertion loss of back-to-back transition, excluding the SMA (end launch assembly) connector loss, are illustrated in Fig. 28.

The measured $<3\ \text{dB}$ insertion loss bandwidth of back-to-back transition is from 1.3 to 13.3 GHz (1–10.2) with a return loss of better than 10 dB. The $<1\ \text{dB}$ insertion loss bandwidth for the back-to-back transition is from 1.4 to 7.3 GHz (1–5.2). For an insertion loss of less than 0.5 dB for the back-to-back transition, the bandwidth ranges from 1.5 to 6 GHz (1–4) with a return loss of $>10\ \text{dB}$.

The transition can be modified to operate at higher frequencies with shorter-radius radial stubs. Shorter-radius radial stubs enable higher frequency coupling between top

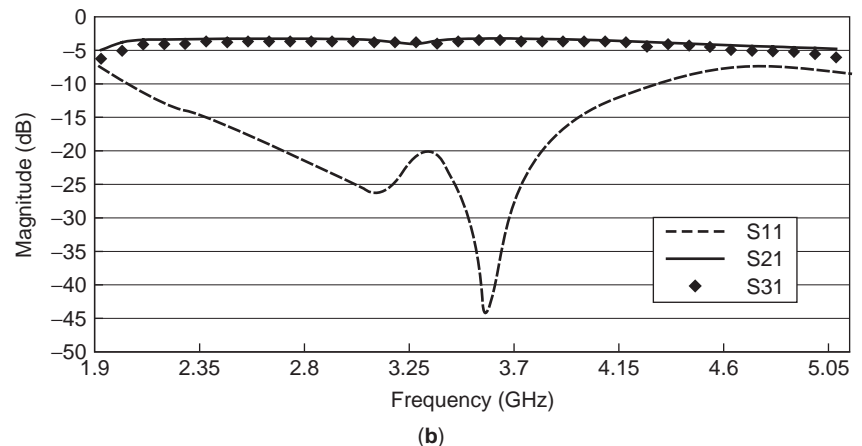
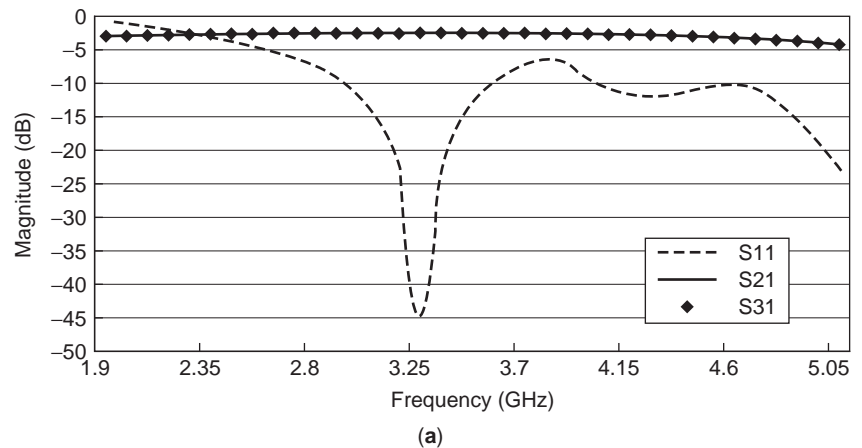
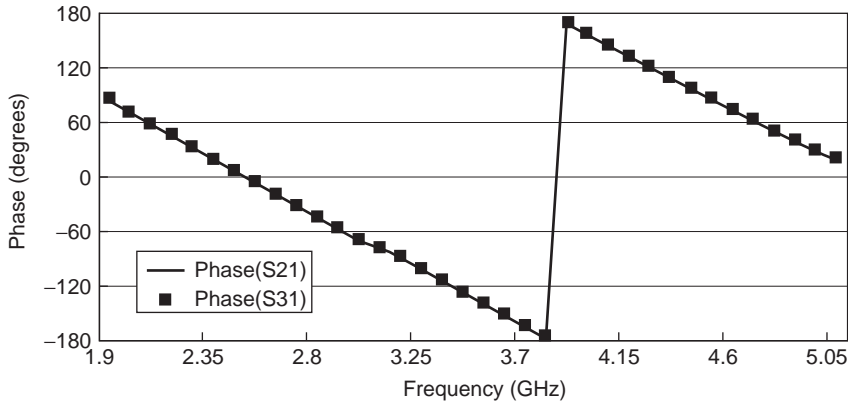
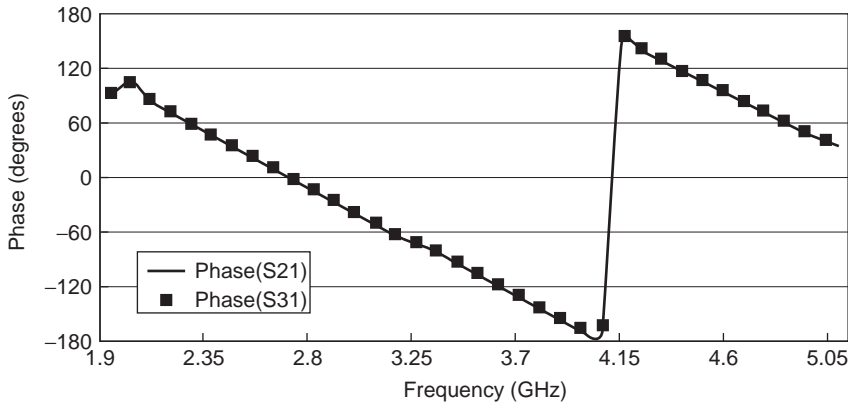


Figure 25. Frequency responses of tee junction: (a) simulated; (b) measured (from Ref. 29b with permission from IEEE).



(a)



(b)

Figure 26. Phase responses of tee junction: (a) simulated; (b) measured (from Ref. 29b with permission from IEEE).

and bottom metallization, but because of the smaller coupling area of the stub, insertion loss is increased. The transition with the radial stub radius of 2.5 mm has been designed and tested. The geometry of transition with a radial stub radius of 2.5 mm is illustrated Fig. 29.

Frequency responses of the transition are shown in Fig. 30. Measured back-to-back return loss is better than 10 dB from 2 to 20 GHz (1–10) with an insertion loss of

< 3.5 dB. Although the insertion loss is higher in the smaller radial stub structure than in the larger radial stub transition, the transition would be useful in feeding high-frequency dipole type antennas.

These transitions are convenient in measuring CPS components with the conventional network analyzer without any special on-wafer calibration standards for CPS TRL calibrations and should find many useful

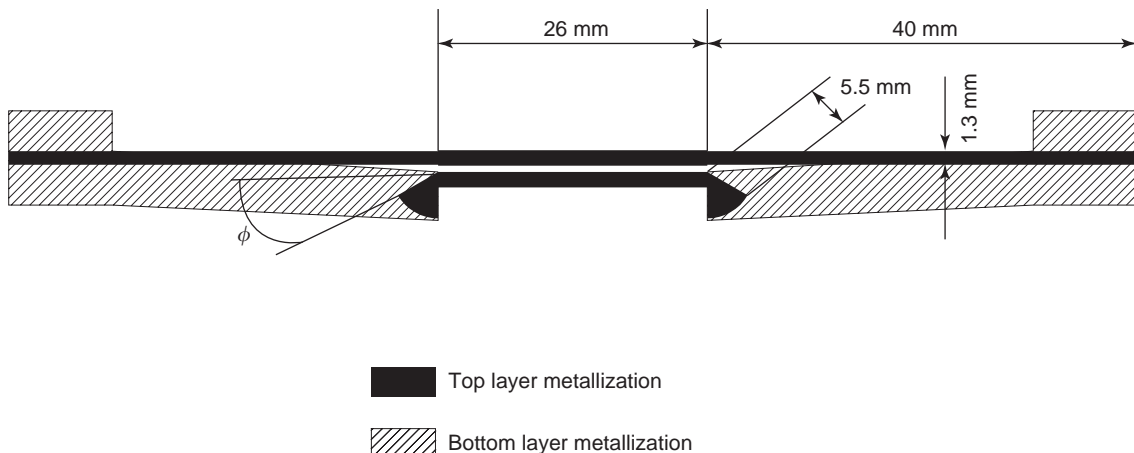


Figure 27. Microstrip-to-CPS-to-microstrip back-to-back transition structure with a radial stub radius of 5.5 mm (from Ref. 39b with permission from IEEE).

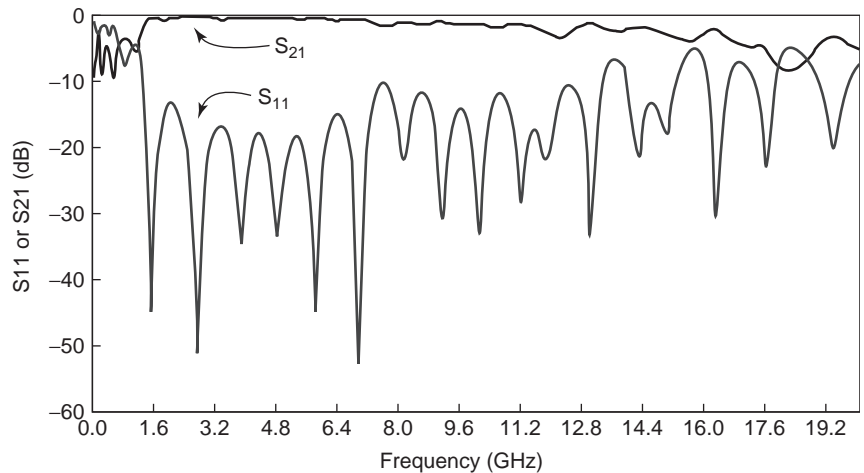


Figure 28. Measured return and insertion losses of the microstrip-to-CPS-to-microstrip back-to-back transition with a radial stub radius of 5.5 mm (from Ref. 39b with permission from IEEE).

applications for CPS components and circuits measurement as well as dipole type antenna feeding.

7. ANTENNA APPLICATION—A MILLIMETER-WAVE PRINTED DIPOLE PHASED-ARRAY ANTENNA FED BY A MICROSTRIP-TO-CPS TEE JUNCTION

A printed dipole antenna has the benefits of low profile, light weight, low cost, and compact size. To construct a printed dipole array, several configurations have been proposed. Nesic et al. [40] reported a one-dimensional printed dipole antenna array fed by microstrip at 5.2 GHz. Scott [41] introduced a microstrip-fed printed dipole array using a microstrip-to-CPS balun. In Refs. 40 and 41, the balun designs did not permit easy impedance matching, and the structures were too big and complicated. In 1998, a wide-band microstrip-fed twin-dipole antenna was introduced with a double-sided structure operating at the frequency range from 0.61 to 0.96 GHz [42]. Zhu and Wu [29a] developed a 3.5-GHz twin-dipole antenna fed by a hybrid finite ground coplanar waveguide (FGCPW)/CPS tee junction. An X-band monolithic integrated twin-dipole antenna

mixer was reported [43] with devices directly integrated into the antenna, so no feeding network was necessary.

In this section, a new planar printed dipole phased-array antenna using a multi-transmission-line tunable phase shifter controlled by a piezoelectric transducer (PET) [44,45a] is presented at 30 GHz. The phased array antenna uses a new twin-dipole antenna excited by a microstrip-fed CPS tee junction introduced in Section 5. The PET-controlled phase shifter does not require any solid-state devices or their driving circuits. The 1×8 twin-dipole phased-array antenna has compact size, low loss, low cost, light weight, and reduced complexity as well as good beam scanning with low sidelobe levels.

7.1. Microstrip-Fed CPS Tee Junction at Ka Band

The twin-dipole antenna is fed by a CPS. Since the conventional planar transmission line is a microstrip line, a microstrip-to-CPS transition is needed to feed the dipole. A microstrip-fed CPS tee junction without using bonding wires or airbridges was introduced in Section 5, where an operating frequency centered near 3.5 GHz with 0.7 dB insertion loss ranging from 2 to 4.15 GHz was described.

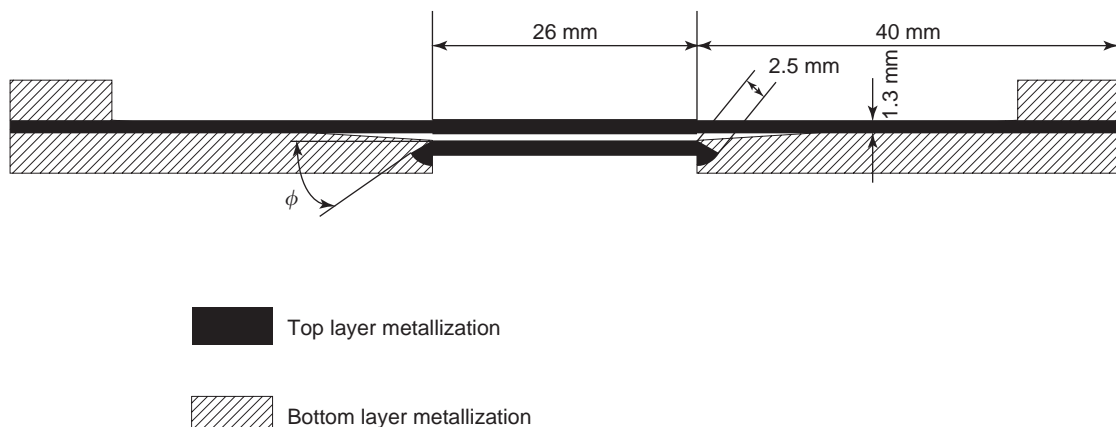


Figure 29. Microstrip-to-CPS-to-microstrip back-to-back transition with a radial stub radius of 2.5 mm.

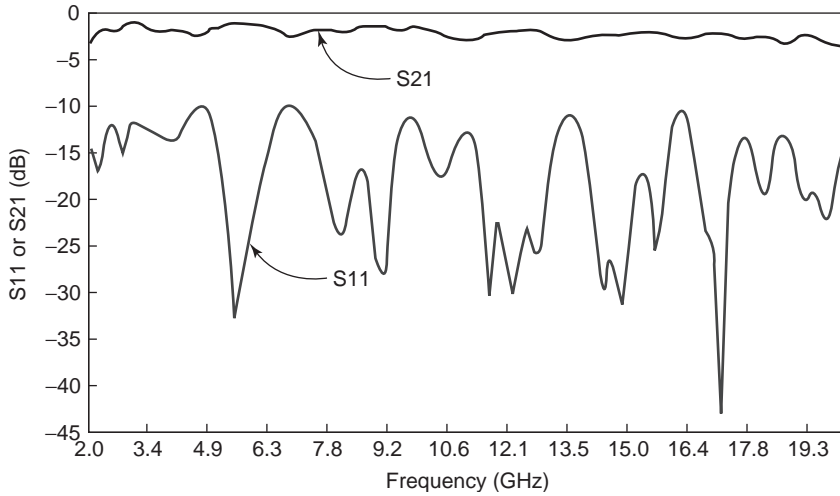


Figure 30. Measured return and insertion losses of the microstrip-to-CPS-to-microstrip back-to-back transition with a radial stub radius of 2.5 mm.

The tee junction utilized novel coupled CPS (CCPS). Using the CCPS, the transmission line can exhibit physical discontinuity while the fields are continuous over entire transmission line.

The structures of a conventional CPS and a CCPS at 30 GHz are identical to those in Fig. 21, but with different strip width W and gap s between strips. A 31-mil RT/Duroid 5870 substrate with a dielectric constant of 2.33 is used for the antenna and feeding network simulation and fabrication.

The width W of a CPS strip is 0.65 mm and the gap s between the strips is 0.5 mm, with a characteristic impedance of $202\ \Omega$. The wideband coupling performance of radial stubs is described in detail in the microstrip-to-CPS-to-microstrip back-to-back transition in Section 6, where the smaller radius of the radial stub is described as providing higher operating frequency with minimal insertion loss and return loss deterioration compared to the conventional CPS configuration.

Performances of CCPS are simulated and compared with those of conventional CPS as shown in Fig. 31. This figure shows that the insertion loss of CCPS deteriorates by ~ 1 dB compared with that of conventional CPS for the frequency range from 29.2 to 35 GHz and that the return loss is better than 10 dB. Insertion loss deterioration of less than 2 dB covers a wider frequency range, from 26.4 to

35 GHz. From the above mentioned results, CCPS shows that fields are continuous all over the transmission line with the aid of radial stub; however, a physical discontinuity is introduced at one of the CPS strips.

The structure of a microstrip-fed CPS tee junction at 30 GHz is shown in Fig. 32. The tee junction has the characteristic impedance of $202\ \Omega$ at each output port (ports 1 and 2). The input impedance to the microstrip feed at port 3 is about $101\ \Omega$, which is half of $202\ \Omega$. Radial stubs effectively rotate the electric fields from parallel to the normal to the substrate to ensure effective coupling to the bottom metallization, which provides the microstrip-line ground.

The tee junction is simulated to verify the performance at 30 GHz. Simulated performance of the tee junction, shown in Fig. 33, reveals that the tee junction splits the power equally to each CPS port with 1.2 dB insertion loss at 30 GHz. Simulated 2 dB insertion loss bandwidth of the tee junction is 27.2–34.8 GHz, and the return loss is > 20 dB.

7.2. Phased-Array Antenna with Multi-Transmission-Line PET-Controlled Phase Shifter

The structure of the twin-dipole antenna is illustrated in Fig. 34. The antenna array is placed in front of a reflector

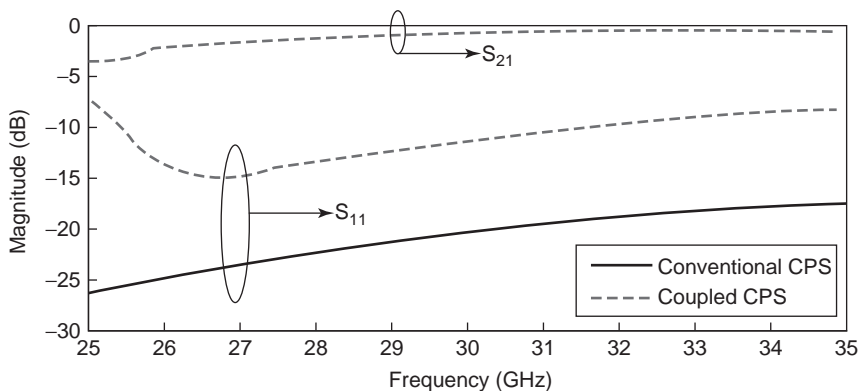


Figure 31. Simulated performance comparison at Ka band between conventional and coupled CPS (from Ref. 45b with permission from IEEE)

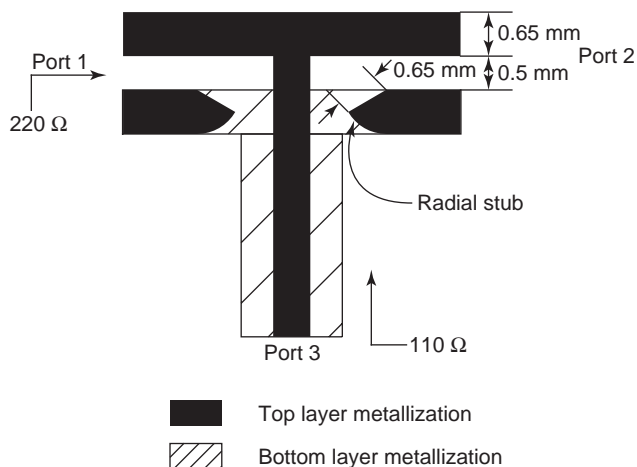


Figure 32. Structure of Ka-band microstrip-fed CPS tee junction for twin-dipole antenna feeding (from Ref. 45b with permission from IEEE).

for unidirectional radiation. The reflector is spaced from the antenna at the distance of 1.5 mm (60 mil), which is $\sim 0.15\lambda_0$.

The length of the dipole is 5.3 mm or $0.53\lambda_0$ and the distance between dipoles is optimized to 3.6 mm or $0.36\lambda_0$, which is less than a half-wavelength in order to provide low sidelobe and grating lobe levels as well as low insertion loss incurred from the CPS tee junction.

The input impedance of a single-dipole antenna is around 202Ω . The strip width W and gap s between strips of CCPS at the CPS tee junction are determined to have a CCPS characteristic impedance identical to the dipole antenna input impedance for good impedance matching.

The structure of the 1×8 printed twin-dipole phased array is shown in Fig. 35. The spacing d between the twin-dipole antennas is about 7.4 mm or $0.82\lambda_0$. A conventional microstrip power divider with binominal impedance transformers is used to cover the wide bandwidth. The bottom metallization provides good ground plane for the microstrip.

To obtain the required phase shift, the 101- Ω microstrip feeding lines to the antenna, which have the same input impedance as the twin dipole antenna, are perturbed with

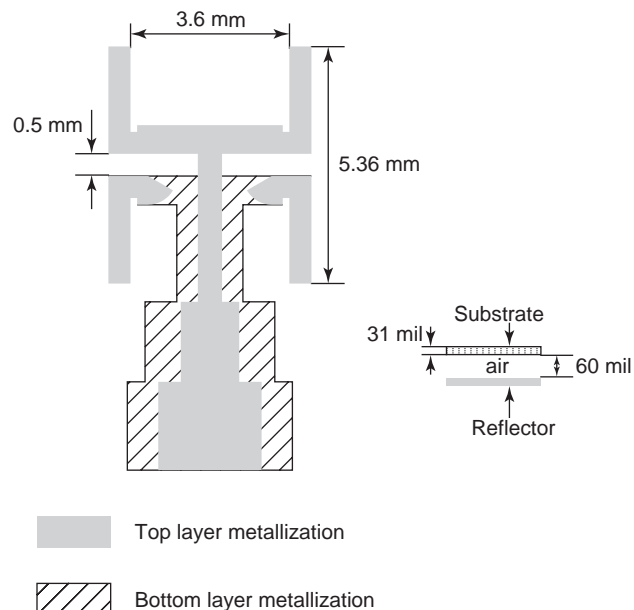


Figure 34. Structure of printed twin-dipole antenna fed by a microstrip-to-CPS tee junction (from Ref. 45b with permission from IEEE).

a dielectric perturber actuated by a piezoelectric transducer (PET). The length of dielectric perturber varies linearly from 5 to 35 mm on top of line 2 and on line 8. The first line is not perturbed. The PET is configured to have no deflection (no perturbation) when a DC voltage of 0 V is applied, and full deflection (full perturbation) when a DC voltage of 50 V is applied. A 50-mil RT/Duroid 6010 with a dielectric constant of 10.2 is used as the dielectric perturber.

The amount of differential phase shift ($\Delta\Phi_n$) is linearly proportional to the length of perturber [45a], which is expressed as

$$\Delta\Phi_n = L_{\text{perturber},n} \cdot \Delta\beta_n \tag{18}$$

where $L_{\text{perturber},n}$ is the perturber length along the n th transmission line. $\Delta\beta_n$ represents the differential

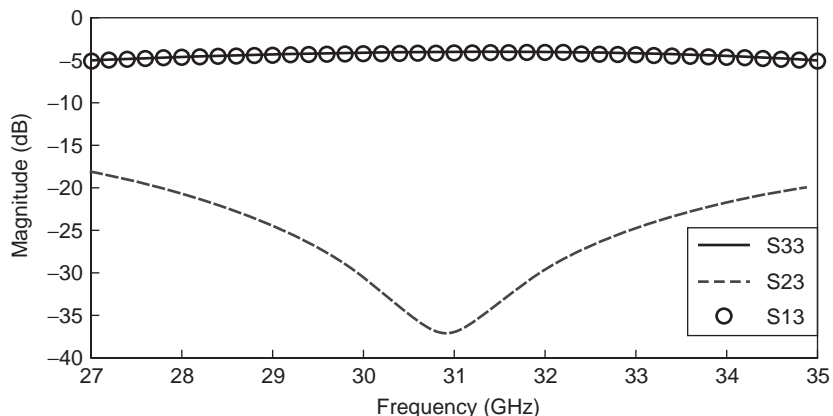


Figure 33. Simulated performance of tee junction near 30 GHz (from Ref. 45b with permission from IEEE).

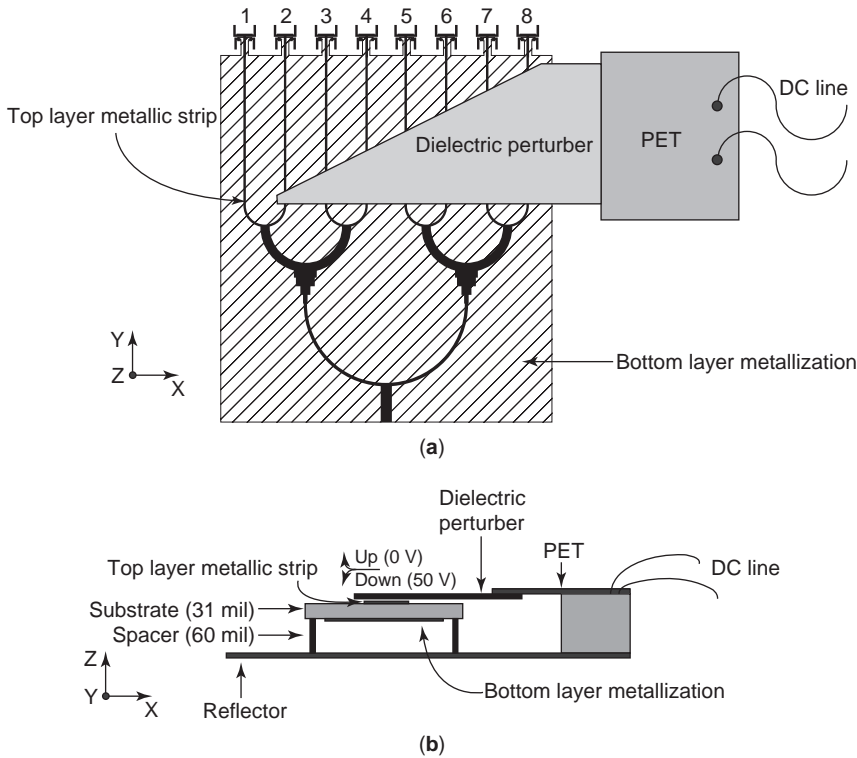


Figure 35. Structure of printed dipole phased-array antenna controlled by PET: (a) top view; (b) side view (from Ref. 45b with permission from IEEE).

propagation constant, expressed as

$$\Delta\beta_n = \beta_{\text{unperturbed}} - \beta_{\text{perturbed},n} \quad (19)$$

where $\beta_{\text{perturbed},n}$ represents the propagation constant of the n th perturbed transmission line, which is microstrip in this case. Since the first perturbed microstrip line (i.e., the second line) has the minimum perturbed length, the following relationship is obtained:

$$\Delta\Phi_2 = \Phi \quad (20)$$

With a dielectric perturber of 5 mm, the differential phase shift ($\Delta\Phi_n$) of 88.8° takes place with a 2 dB inser-

tion loss as shown in Fig. 36. The narrower microstrip line generates larger phase shift, but the insertion loss is increased. Hence, a proper microstrip line width should be chosen for having a good phase shift as well as low insertion loss.

Table 4 summarizes the design and measured parameters for the twin-dipole phased array. The parameters in Table 4 are useful in analytical calculations of the scan angle (θ_0), maximally achievable gain, and optimum element spacing d of the phased array.

According to (18) and (19), the perturber's length can be determined for a desired phase shift. A length of 5 mm dielectric perturber produces about 88.8° differential phase shift. Accordingly, the length of each neighboring

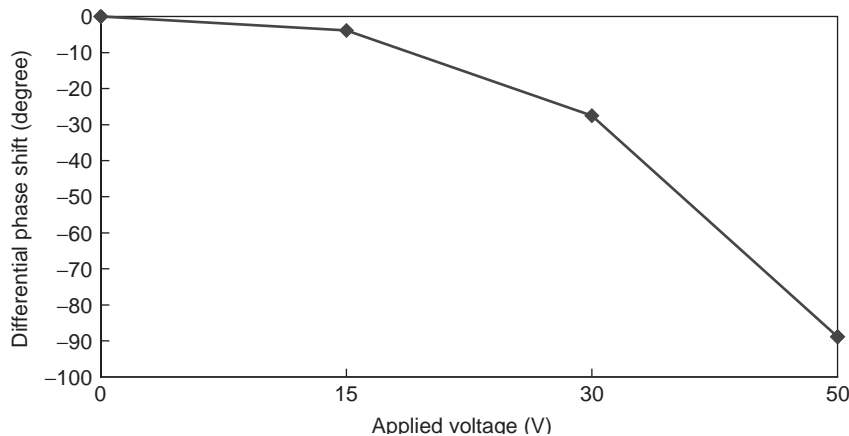


Figure 36. Measured differential phase shift for 5-mm dielectric perturber controlled by PET (from Ref. 45b with permission from IEEE).

Table 4. Parameter Values of Twin Dipole Phased Array (from Ref. 45b with permission from IEEE)

Frequency (GHz)	Single-Element Gain (dBi)	Progressive Phase Shift (Φ)	Element Spacing (d)	Number of Elements (N)
30	7.7	88.8°	7.4 mm	8

perturbed line is increased by 5 mm. The length of perturber for the final microstrip ($L_{\text{perturber,8th}}$) is ~ 35 mm, which gives a differential phase shift of 621.6° .

Measured return loss of the 1×8 twin dipole array is plotted in Fig. 37. The measured return loss is ~ 41.9 dB at 30.3 GHz for the unperturbed twin-dipole phased-array antenna. With perturbation by the dielectric perturber, the return loss is ~ 31.8 dB at 30.7 GHz, which shows a 0.4 GHz frequency shift compared with the unperturbed result. For a bandwidth from 30 to 31.5 GHz, a measured return loss is better than 15 dB.

7.3. Phased-Array Measurements

The phased array is measured in an anechoic chamber. As shown in Fig. 35, the antenna is arrayed for H -plane beam scanning. To accomplish bidirectional scanning, two triangular perturbers are used side by side [45a]. PET actuation for the dielectric perturber is configured as 0 V for no perturbation (no PET deflection) and 50 V for full perturbation (full PET deflection).

The measured twin-dipole phase-array antenna gain without perturbation (0 V for PET) is about 14.4 dB, with a 3 dB beamwidth of 6° as shown in Fig. 38. The fully perturbed antenna with a dielectric perturber controlled by PET shows about 42° ($-20^\circ \sim +22^\circ$) beam scanning with a gain of 12.2 dBi. Sidelobe levels of the steered beam are > 11 dB less than those of the mainbeam. The beam can be dynamically steered depending on the voltages applied to PET because the amount of phase shift changes according to the applied voltages on PET as shown in Fig. 36.

The comparison among analytical, simulation, and measured results of the phased array are exhibited in Table 5. The beam scanning angle follows closely among analytical, full-wave simulation, and measured results.

Measured unperturbed gain is about 2.3 dB lower than that found in analytical or simulated data. This is due to the insertion loss of the power divider and the mutual coupling effects among elements, which normally degrade antenna gain. The measured gains of steered beams are about 2.2 dB less than those of the unperturbed beam, due to the insertion loss incurred by dielectric perturbation.

8. CIRCUIT APPLICATION—A HIGH-EFFICIENCY DUAL-FREQUENCY RECTENNA FOR 2.45 AND 5.8 GHz WIRELESS POWER TRANSMISSION USING CPS TRANSMISSION LINE

As a circuit application of CPS, the dual-frequency rectenna is presented operating at both 2.45 and 5.8 GHz (ISM bands) simultaneously. The rectenna is an important element for wireless power transmission. Applications of the rectenna are mainly for receiving power where the physical connections are not possible. Various kinds of rectennas have been developed since Brown demonstrated the dipole rectenna using aluminum bars to construct the dipole and the transmission line [22]. He also presented a thin-film printed-circuit dipole rectenna [23] with an 85% conversion efficiency at 2.45 GHz. Linearly polarized printed dipole rectennas were developed at 35 GHz [25,46] with conversion efficiencies of 60% and 70%, respectively. A 5.8-GHz printed dipole rectenna was developed in 1998 [26] with a high conversion efficiency of 82%. Microstrip patch dual polarized rectennas were also developed at 2.45 GHz [27] and 8.51 GHz [47]. More recently, a circularly polarized rectenna, which does not require strict alignment between transmitting and receiving antennas, was developed at 5.8 GHz [48a] with a conversion efficiency of 60%. Strassner and Chang also developed a circularly polarized rectenna using dual-rhombic-loop antennas at 5.8 GHz in 2003 [49]. The 4×1 rectenna array showed a conversion efficiency of 82% operating at low power density.

Several rectenna operating frequencies have been considered and investigated. Components of microwave power transmission have traditionally focused at 2.45 GHz and have more recently moved up to 5.8 GHz, where the antenna aperture area is smaller than at 2.45 GHz. Both

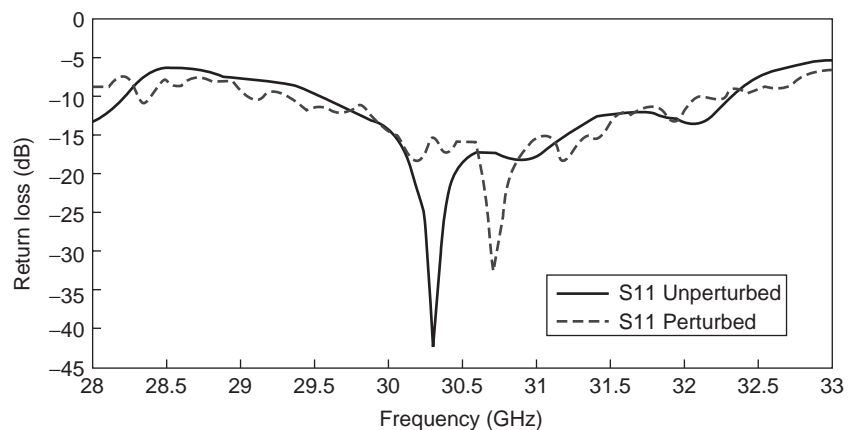


Figure 37. Measured return loss of printed twin-dipole phased-array antenna (from Ref. 45b with permission from IEEE).

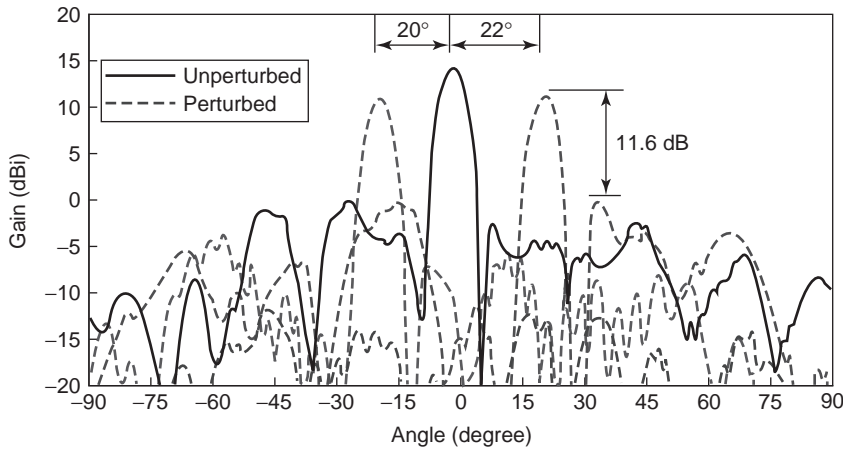


Figure 38. Measured H -plane radiation pattern for twin-dipole phased-array antenna at 30 GHz. Measured beam scanning is from -20° to $+22^\circ$ with full perturbation (from Ref. 45b with permission from IEEE). (This figure is available in full color at <http://www.mrw.interscience.wiley.com/erfme>.)

frequencies have comparably low atmospheric loss, cheap components availability, and reported high conversion efficiency.

If the rectenna operates at dual band, it can be used for wireless power transmission at either frequency depending on power availability. A rectifying diode is analyzed to obtain design parameters for high efficiencies at both frequencies. A diode parameter, that provides high conversion efficiency and insensitivity to operating frequency is discussed. To prevent the higher-order harmonics reradiation generated by the diode, a CPS lowpass filter integrated with two additional open-ended T-strip CPS bandstop filters is presented in this section.

8.1. Dual-Frequency Antenna Design

The structure of a rectenna is illustrated in Fig. 39. A schematic of the circuit is shown in Fig. 40. The rectenna consists of a receiving dual-frequency dipole antenna, a CPS input lowpass filter, two CPS bandstop filters, a rectifying diode, and a microwave block capacitor. The antenna receives the transmitted microwave power, and the input lowpass and the bandstop filters pass 2.45 and 5.8 GHz but block the higher-order harmonics from reradiation.

All microwave signals produced by the nonlinear rectifying diode, including fundamental and harmonics, are confined between the input filters and microwave block capacitor. Consequently, the conversion efficiency is improved.

As discussed in Section 2, a low-dielectric-constant substrate produces a low dielectric and conductor losses. Hence, a 20 mil RT/Duroid 5870 substrate with a low

Table 5. Comparison among Analytical, Simulation, and Measured Results of 1×8 Phased Array (from Ref. 45b with permission from IEEE)

Method	Beam Scanning θ_0 (deg)	Unperturbed Gain (dBi)	Element Spacing d (mm)
Analytical calculation	± 19.7	16.73	7.5
Full-wave simulation	± 20	16.48	7.4
Measured	$-20 \sim +22$	14.4	7.4

dielectric constant of 2.33 is used for the dual-frequency rectenna design to maximize conversion efficiency.

The CPS dipole dual-frequency antenna with a reflector plate is designed for 2.45 and 5.8 GHz (ISM bands). This type of dual-frequency antenna, introduced in 2000 [50], radiates bidirectionally and has a double-sided structure with a microstrip feed operating at 2.4 and 5.2 GHz. Double-sided dual-frequency printed dipole antennas were also reported [51,52] operating at 0.9 and 1.5 GHz.

The dual-frequency antenna presented in this section has a uniplanar structure, which has the advantage of convenient device mounting. A reflector plate is required for the unidirectional radiation/reception, and it also increases antenna gain.

As shown in Fig. 40, a long dipole is designed for operation at 2.45 GHz and a short dipole, at 5.8 GHz. The long dipole has a length of 126.7 mm or $1.072\lambda_0$ at 2.45 GHz, and the short dipole has a length of 45.04 mm or $0.812\lambda_0$ at 5.8 GHz. The feeding point has been moved about 0.8 mm from the edge of the short dipole for impedance matching. The coupling length and gap between the long and short dipole are around 6.32 and 4.2 mm, respectively.

The reflector plate is normally placed at a distance about a quarter-wavelength apart from the circuit at the design frequency for low sidelobes created from image sources. However, for dual-band operation, the reflector plate distance must be optimized in order to produce good radiation patterns and similar gains for both frequencies. The reflector plate distance is optimized at 17 mm, which is about $0.14\lambda_0$ of 2.45 GHz and $0.32\lambda_0$ of 5.8 GHz.

Measured frequency response of the antenna is shown in Fig. 41. This measurement was performed using the wideband CPS-to-microstrip transition presented in Section 6. Measured return losses for the antenna only are better than -30 and -25 dB at 2.45 and 5.8 GHz, respectively. Return losses at second-order harmonics of the antenna-only case are found to be around -8.6 and -3 dB at 4.9 and 11.6 GHz, respectively.

8.2. CPS Lowpass Filter Integrated with T-Strip Bandstop Filters

Filters are required for a rectenna to prevent all the harmonics from reradiating through the antenna. New simple

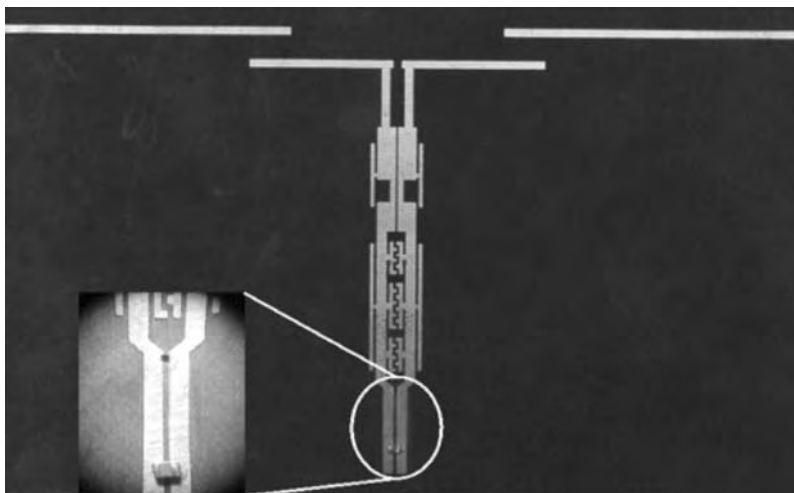


Figure 39. Circuit picture of dual-frequency rectenna. The circuit is separated from a reflector plate at a distance of 17 mm.

CPS lowpass filter integrated with bandstop filters are designed and shown in Fig. 42. As shown earlier at Fig. 19, the lowpass filter has a 0.2 dB ripple Chebyshev response with a cutoff frequency of 7 GHz to pass 2.45 and 5.8 GHz and to reject 11.6 GHz, which is the second-order harmonic of 5.8 GHz. However, the lowpass filter will pass the second-order harmonic of 2.45 GHz at 4.9 GHz, and the third-order harmonic level at 7.35 GHz will not be deeply suppressed.

Open-ended T-strip CPS bandstop filters, presented at Fig. 3, are placed outside the CPS strips for rejecting second- and third-order harmonics of 2.45 GHz at 4.9 and 7.35 GHz, respectively. The lengths of bandstop filters are 20.1 ($0.45\lambda_g$) and 10.5 ($0.35\lambda_g$) mm at 4.9 and 7.35 GHz, respectively.

The lowpass filter integrated with two additional open-ended T-strip bandstop filters needs to transform the antenna's input impedance of $95\ \Omega$ to the CPS characteristic

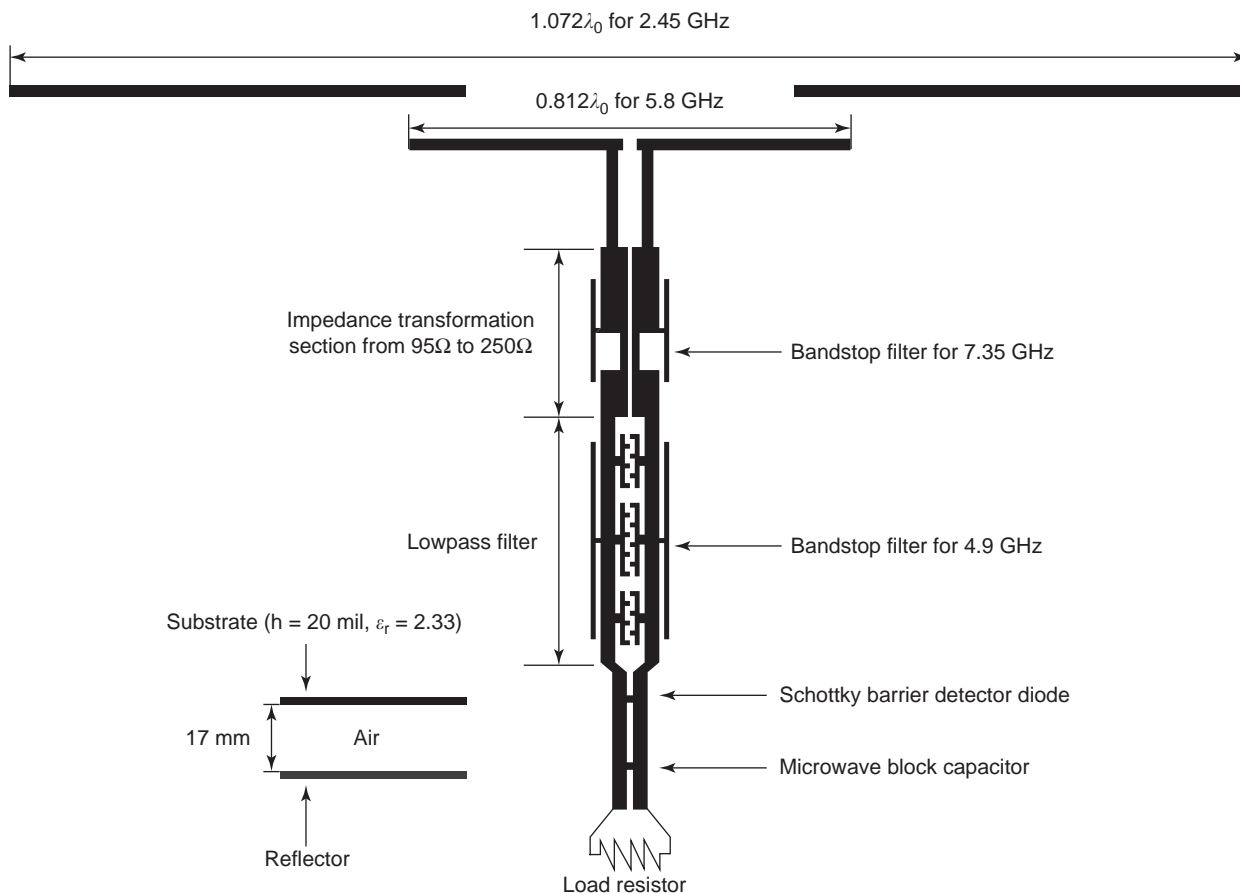


Figure 40. Dual-frequency rectenna circuit schematic (from Ref. 48b with permission from IEEE).

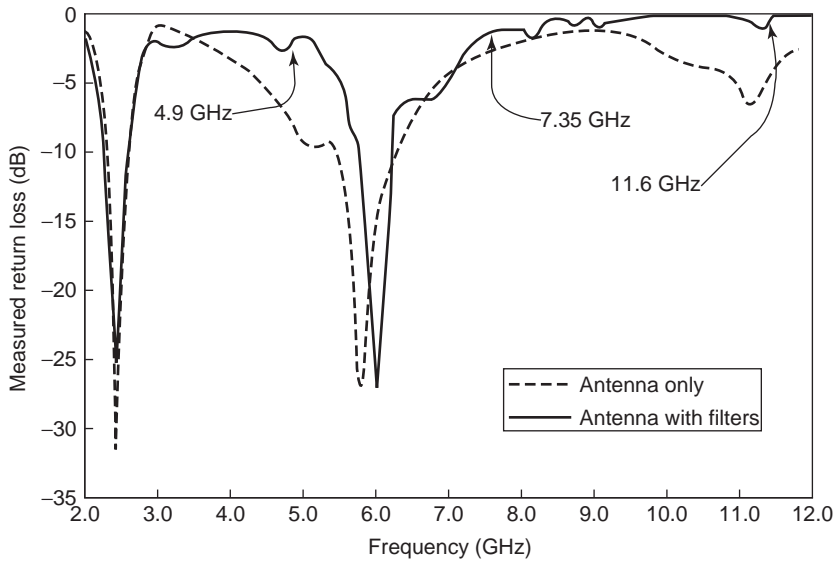


Figure 41. Measured frequency responses of the antenna and the antenna with filters. Good return loss is achieved at both 2.45 and 5.8 GHz (from Ref. 48b with permission from IEEE).

impedance of $250\ \Omega$ as well as blocking higher-order harmonics.

An impedance transformation section consisting of two CPS step discontinuities as shown in Fig. 42 is designed and optimized by a full-wave electromagnetic simulator.

The strip width W and the separation gap s of CPS, where the rectifying diode is placed, are designed as 1.5 and 0.6 mm, respectively, which corresponds to the $184\ \Omega$ of CPS characteristic impedance, (Z_0). The CPS characteristic impedance of $184\ \Omega$ is selective to ensure a high

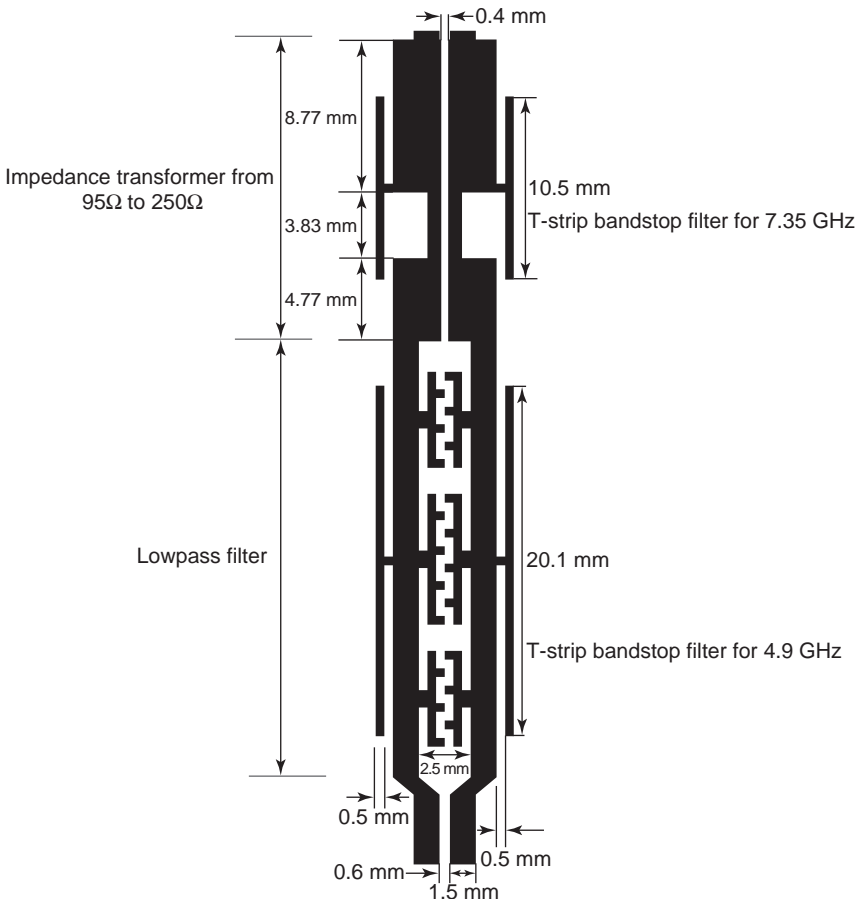


Figure 42. Structure of CPS lowpass filter with bandstop filters (from Ref. 48b with permission from IEEE).

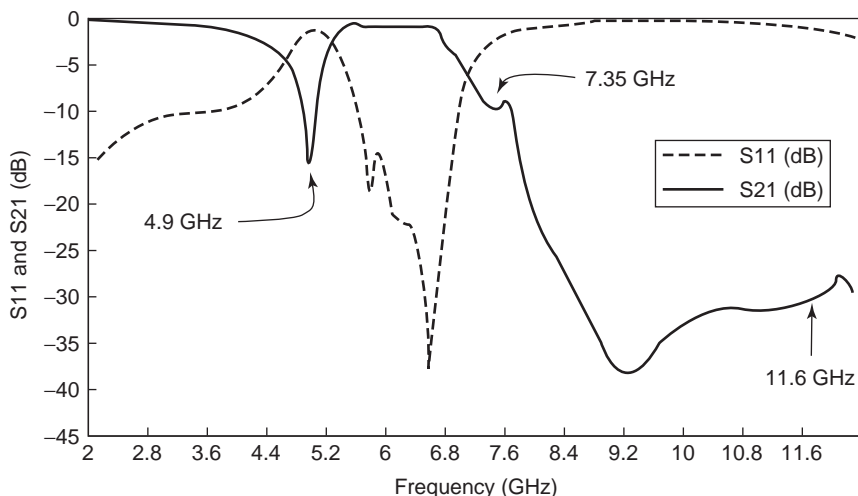


Figure 43. Measured frequency responses of CPS lowpass filter with bandstop filters. Low insertion losses of 0.15 and 0.75 dB are achieved at 2.45 and 5.8 GHz, respectively. Good band rejection performances are achieved at the second harmonics (4.9 and 11.6 GHz) of 2.45 and 5.8 GHz, and at the third harmonic (7.35 GHz) of 2.45 GHz (from Ref. 48b with permission from IEEE).

conversion efficiency according to the diode analysis, which will be discussed later.

Measured frequency responses of the lowpass filter integrated with bandstop filters are shown in Fig. 43. Low insertion losses of 0.15 and 0.75 dB are achieved at 2.45 and 5.8 GHz, respectively. Band rejections at the second (4.9 GHz) and the third (7.35 GHz) harmonics of 2.45 GHz are around 15 and 10 dB, respectively, and the band rejection at the second harmonic of 5.8 or 11.6 GHz is about 30 dB, which shows good bandstop performance for these harmonics.

8.3. Dual-Frequency Antenna Integrated with Filters

For comparison, the frequency response of the antenna integrated with filters is also shown in Fig. 41. Measured return losses of 15.1 and 18.2 dB are achieved at 2.45 and 5.8 GHz, respectively.

Measured return losses at the second-harmonic levels of 2.45 and 5.8 GHz are found to be 1.58 and 0.2 dB at 4.9

and 11.6 GHz, respectively. This shows that the lowpass filter integrated with two additional bandstop filters effectively block the second-order harmonics at both frequencies. The third-order harmonic level for 2.45 GHz is about 1.62 dB at 7.35 GHz. Higher-order harmonic levels are expected to be lower than second-order harmonics at both frequencies.

Radiation patterns of the antenna with filters are measured in the anechoic chamber. Measured radiation patterns at 2.45 and 5.8 GHz are shown in Figs. 44 and 45. Measured *E*-plane gains are 5 and 5.4 dBi with a 3 dB beamwidth of 31.5° and 36° at 2.45 and 5.8 GHz, respectively. Because the reflector's height has a longer wavelength at 5.8 GHz compared to that at 2.45 GHz, the radiation pattern for 5.8 GHz has a wider 3 dB beamwidth. It is possible to have an identical 3 dB beamwidth with similar radiation patterns for both frequencies by adjusting the reflector height, but the input impedances of the antenna for each frequency would be different. Hence, a tradeoff was made between the input impedance and the radiation pattern.

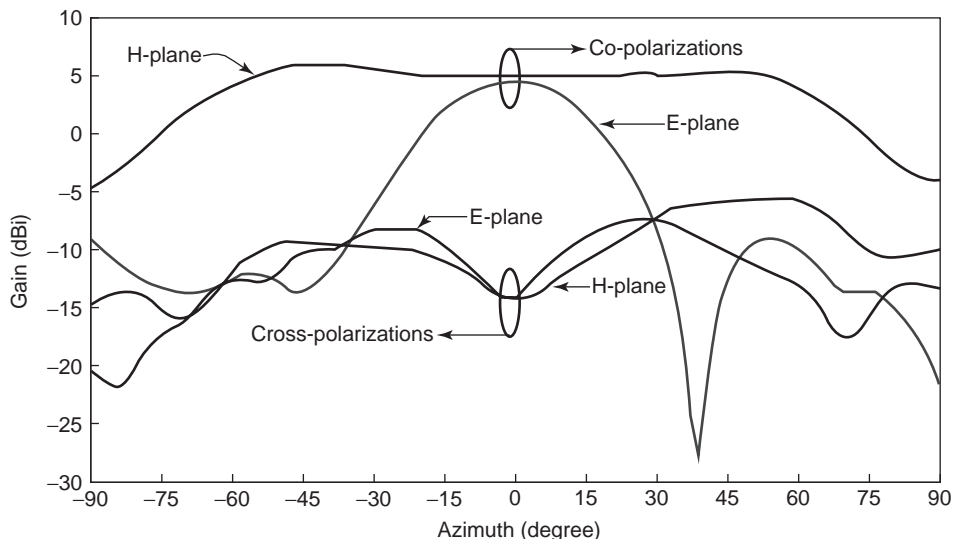


Figure 44. Radiation patterns of dual-frequency antenna at 2.45 GHz (from Ref. 48b with permission from IEEE). (This figure is available in full color at <http://www.mrw.interscience.wiley.com/erfme>.)

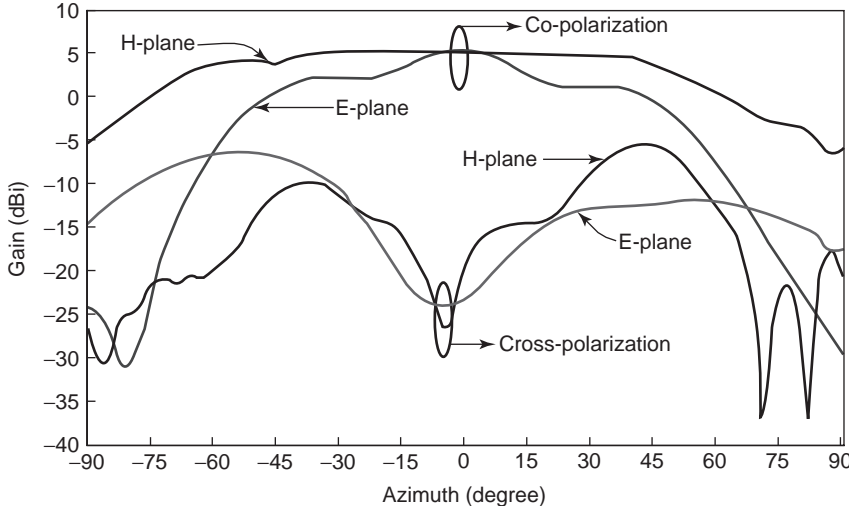


Figure 45. Radiation patterns of dual-frequency antenna at 5.8GHz (from Ref. 48b with permission from IEEE). (This figure is available in full color at <http://www.mrw.interscience.wiley.com/erfme>.)

At broadside, the cross polarization at 2.45 GHz is about 19.4 and 18.2 dB below the copolarizations in E and H planes, respectively. At 5.8 GHz, the cross-polarization is about 30.1 and 25 dB below the copolarizations in E and H planes, respectively. These low cross-polarization levels show good alignment between transmitting and receiving antennas. Relatively similar E -plane gains are achieved at both 2.45 and 5.8 GHz.

Second-order harmonic radiation patterns are measured and shown in Fig. 46. At broadside, the second-order harmonic radiation gains at 4.9 and 11.6 GHz are -10 and -15 dBi, respectively. Since the gains for the fundamental frequencies at 2.45 and 5.8 GHz are 5 and 5.4 dBi, the corresponding suppressions are about 15 and 20.4 dB, respectively.

8.4. Diode Analysis

A diode analysis is used to achieve high RF-to-DC conversion efficiencies at both frequencies. RF-to-DC conversion efficiency η_d and input impedance Z_d of the diode can be calculated from the closed-form equations in Ref. 26, which are expressed as

$$\eta_d = \frac{1}{1 + A + B + C} \quad (21)$$

where

$$A = \frac{R_L}{\pi R_s} \left(1 + \frac{V_{bi}}{V_0}\right)^2 \left[\theta_{on} \left(1 + \frac{1}{2 \cos^2 \theta_{on}}\right) - \frac{3}{2} \tan \theta_{on} \right] \quad (22)$$

$$B = \frac{R_s R_L (\omega C_j)^2}{2\pi} \left(1 + \frac{V_{bi}}{V_0}\right) \left(\frac{\pi - \theta_{on}}{\cos^2 \theta_{on}} + \tan \theta_{on} \right) \quad (23)$$

$$C = \frac{R_L}{\pi R_s} \left(1 + \frac{V_{bi}}{V_0}\right) \frac{V_{bi}}{V_0} (\tan \theta_{on} - \theta_{on}) \quad (24)$$

Diode input resistance is expressed as

$$R_d = \frac{\pi R_s}{\cos \theta_{on} \left(\frac{\theta_{on}}{\cos \theta_{on}} - \sin \theta_{on} \right)} \quad (25)$$

where R_L and R_s represent the load resistance and the series resistance of the diode, respectively. V_0 is an output

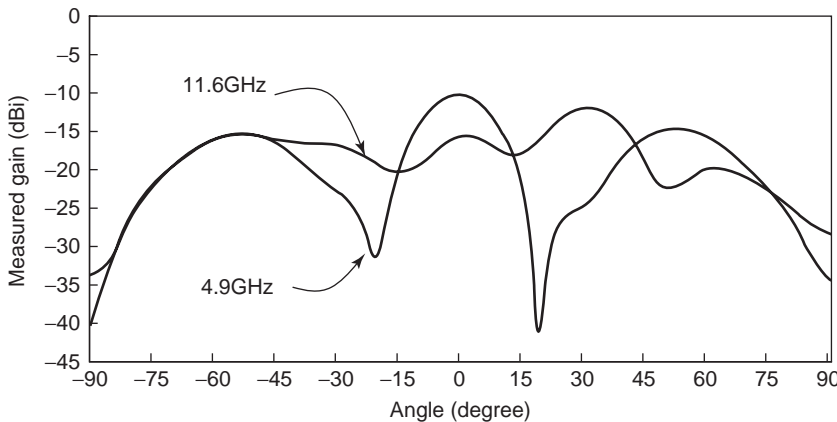


Figure 46. Second-harmonic radiation patterns. These patterns prove that the lowpass filter integrated with two open-ended T-strip bandstop filters effectively blocks higher-order harmonics. The second harmonics of 2.45 and 5.8 GHz are 4.9 and 11.6 GHz, respectively. (From Ref. 48b with permission from IEEE).

voltage produced at the load resistance, and V_{bi} is a diode's built-in voltage. θ_{on} is the diode conduction time in radians and C_j is the junction capacitance. The closed-form expression for θ_{on} and C_j is

$$\tan \theta_{on} - \theta_{on} = \frac{\pi R_s}{R_L \left(1 + \frac{V_{bi}}{V_0} \right)} \quad (26)$$

The junction capacitance C_j is defined as

$$C_j = C_{j0} \sqrt{\frac{V_{bi}}{V_{bi} + |V_0|}} \quad (27)$$

RF-to-DC conversion efficiency is frequency-dependent, as shown in parameter B in (23). To minimize the conversion efficiency dependence on the frequency, it is necessary to minimize the effect of parameter B . Since parameter B is proportional to the square of ωC_j , a small value of C_j will reduce the effect of parameter B on the conversion efficiency. For a small value of C_j , packaged diode is not suitable.

From the preceding analysis, a flip-chip-type GaAs Schottky barrier diode (MA4E1317) is selected as the rectifying device. The diode has a built-in voltage (V_{bi}) and a measured breakdown voltage (V_{br}) of 0.7 and 12 V, respectively. The maximum DC output voltage (V_0) is about 6 V. The zero-bias-junction capacitance (C_{j0}) is 0.02 pF with a series resistance (R_s) of a 4 Ω .

Using (21)–(27), RF-to-DC conversion efficiency η_d and input resistance of the diode R_d can be calculated in terms of load resistance R_L at 2.45 and 5.8 GHz, as shown in Fig. 47, where very little difference in conversion efficiency is observed between 2.45 and 5.8 GHz. This is due to the low zero-bias-junction capacitance (C_{j0}) of the diode. Since C_{j0} is low, the corresponding C_j is also low [26], and the value of parameter B is very small compared to those of parameters A and C . Consequently, parameter B , which is frequency-dependent, does not contribute much effect to the diode's conversion efficiency. From Fig. 47, the diode input resistance R_d and the load resistance R_L can be determined as design parameters for a desired target RF-to-DC conversion efficiency η_d .

Because of the diode dimension, the CPS strip width (s) is fixed at 0.6 mm and the corresponding characteristic impedance is 184 Ω . The diode input impedance is matched to this impedance of 184 Ω , which corresponds to a load resistance of 310 Ω as determined in Fig. 47. This gives $\sim 82\%$ target efficiency. To prevent the diode breakdown due to overload, determining the limit of output DC power is necessary.

Typically, the DC power level limit is determined by $P_{DC} < (V_{br}^2/4R_L)$ [26], where V_{br} is the breakdown voltage of the diode and R_L is the load resistance. Therefore, adequate load resistance R_L is required as well as adequate input resistance of the diode (R_d) to ensure a high efficiency and a high output DC power.

8.5. Rectenna Measurements

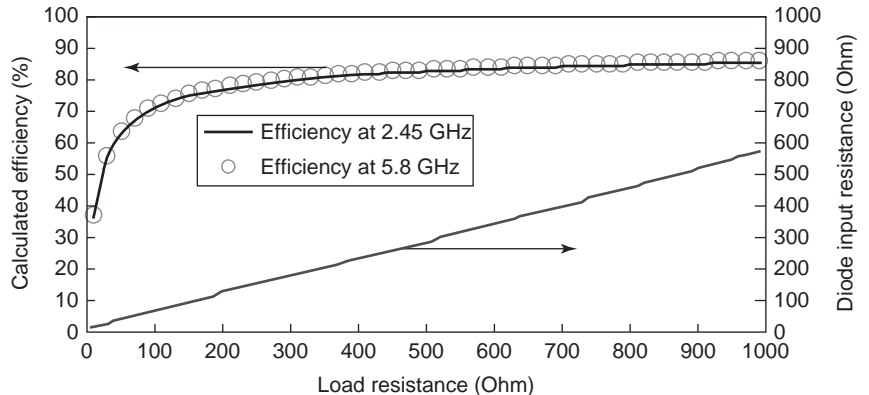
The rectenna is measured in free space. The measurement set up is shown in Fig. 48. Transmitting power is generated by a frequency synthesizer (HP 8341B) and amplified by power amplifiers. Two types of power amplifiers, L0203-42 and L0505-38 (Microwave Power Inc.), are used, which can produce up to +42 and +38 dBm at 2.45 and 5.8 GHz, respectively. For the transmitting power monitoring purpose, a directional coupler is used with 20 dB coupling along with a 20-dB attenuator for power meter (HP 437B) protection. Standard-gain horn antennas are used for transmitting power at 2.45 and 5.8 GHz, respectively. From the diode analysis described in Section 8.4, the load resistance R_L is taken as 310 Ω , for 82% target efficiency.

The microwave block capacitor not only bypasses the microwave signal to the diode but also cancels the capacitive reactance of the diode by selecting an appropriate distance from the diode at a specific frequency, which maximizes the RF-to-DC conversion efficiency [26]. For dual-band operation of the rectenna, the diode location is optimized at 7.5 mm to have high efficiencies at both frequencies.

Conversion efficiency of the rectenna is represented as

$$\eta = \frac{P_{DC}}{P_{received}} \times 100(\%) \quad (28)$$

Figure 47. Diode (MA4E1317) RF-to-DC conversion efficiency analyses in terms of the load resistance (R_L) and the diode input resistance (R_d) at 2.45 and 5.8 GHz. Diode parameter values of V_{bi} , V_0 , V_{br} are 0.7, 6, and 12 V, respectively. The zero bias junction capacitance (C_{j0}) of 0.02 pF, and a series resistance (R_s) of 4 Ω are used for the analyses (from Ref. 48b with permission from IEEE).



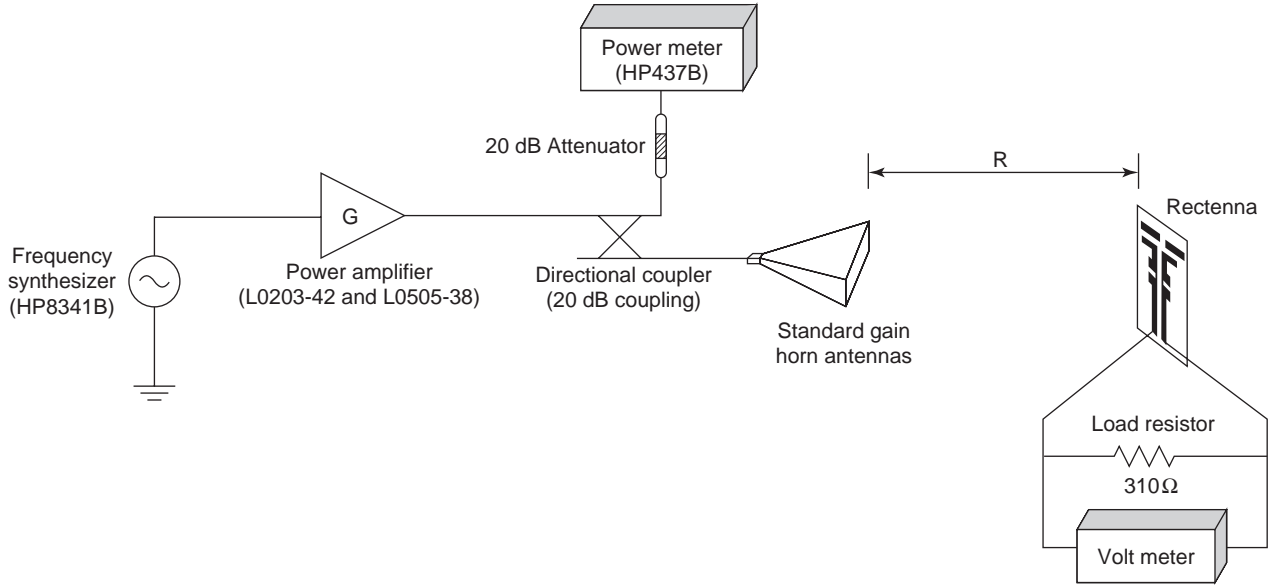


Figure 48. Rectenna measurement setup. Two different types of power amplifiers (L0203-42 and L0505-38) and transmitting standard-gain horn antennas are used for dual-frequency power transmissions (from Ref. 48b with permission from IEEE).

where P_{DC} is DC power produced at the load resistance (R_L) of the rectenna and $P_{received}$ is power received at antenna of the rectenna. $P_{received}$ is calculated from the Friis transmission equation expressed as

$$P_{received} = P_t \left(\frac{\lambda_0}{4\pi R} \right)^2 G_r G_t = P_t A_e \frac{G_t}{4\pi R^2} \quad (29)$$

where the effective area A_e is represented as

$$A_e = \frac{\lambda_0^2 G_r}{4\pi} \quad (30)$$

and where P_t represents transmitted power, G_t and G_r represent gains of transmitter and receiver antenna, respectively, and R is the distance between the transmitter and the receiver antennas.

For the rectenna measurements, R is taken to the edge of the far field. Parameters for calculating $P_{received}$ of the dual-frequency rectenna are displayed in Table 6. The efficiency is normally expressed as a function of power density. The power density is calculated by

$$P_D = \frac{P_r}{A_e} = \frac{P_t G_t}{4\pi R^2} \quad (31)$$

Table 6. Received Power Calculation parameters for Dual Frequency Rectenna (from Ref. 48b with permission from IEEE)

Frequency (GHz)	λ_0 (cm)	Far Field (cm)	G_r (dBi)	G_t (dBi)	A_e (cm ²)
2.45	12.2	87.1	5	14.5	37.7
5.8	5.1	48.5	5.4	17.6	7.4

Measured rectenna efficiencies are shown in Fig. 49. High efficiencies of 84.4% and 82.7% are measured at 2.45 and 5.8 GHz, respectively. Experimental efficiencies follow closely with the theoretical efficiency calculations. Received power at each highest efficiency points are 89.84 and 49.09 mW corresponding to power densities of 2.38 and 8.77 mW/cm² at 2.45 and 5.8 GHz, respectively, as shown in Fig. 49b.

At 80% efficiency points for both 2.45 and 5.8 GHz, the ideal received power levels at both frequencies are almost identical. Measurements show that received power levels at 80% efficiency points are 35.6 and 39.26 mW at 2.45 and 5.8 GHz, respectively. Considering the antenna's effective areas (A_e) listed in Table 6, the required power density of 5.8 GHz is around 5.1 times larger than that of 2.45 GHz to achieve 80% efficiency.

As shown in Fig. 46, the second-order harmonic radiations at 4.9 and 11.6 GHz are around 15 and 20 dB less than the fundamental frequency radiations at broadside. Therefore, second-order harmonic reradiations are quite small. Observing the return loss plot of the antenna integrated with filters in Fig. 41, higher-order harmonic reradiations are expected to be small.

9. CONCLUSION

In this article, the CPS transmission line was analyzed for practical components development. With this analysis, practical CPS components were developed, investigated, and their applications were implemented. It was found that a lower-dielectric-constant (ϵ_r) substrate and a higher CPS characteristic impedance (Z_0) are desired for lower CPS attenuation. Different CPS configurations such as varying s and W , can exhibit identical characteristic

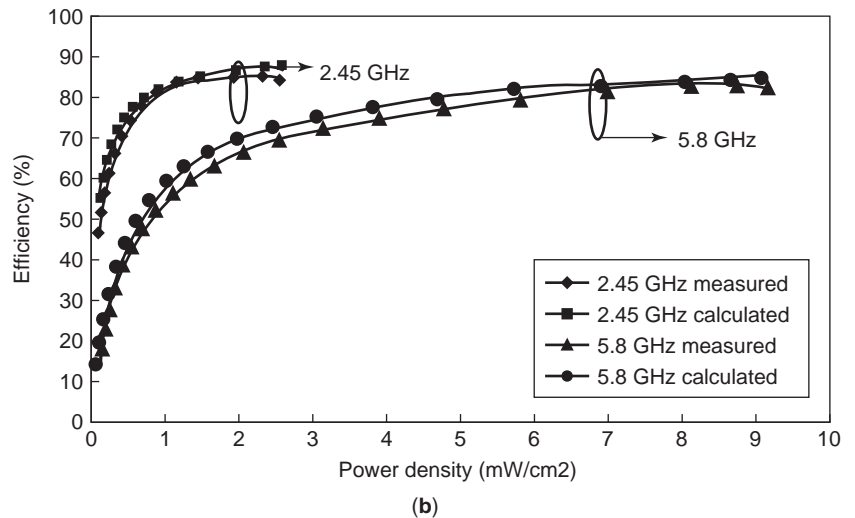
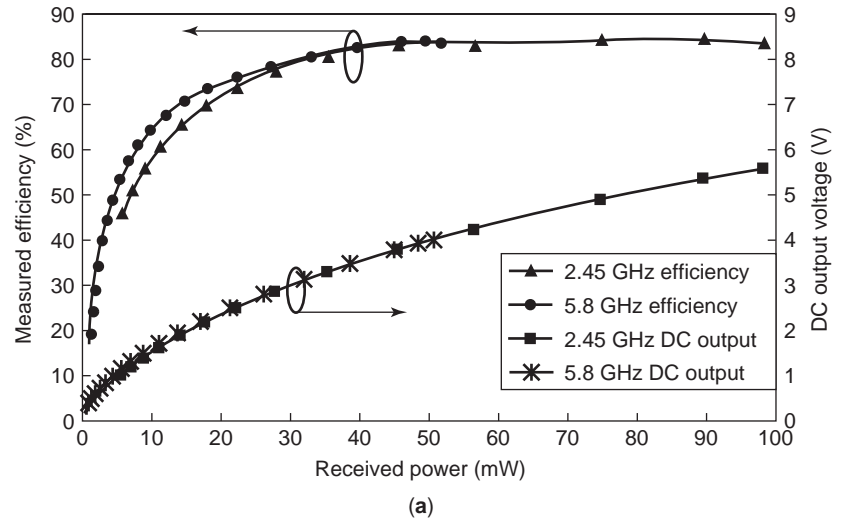


Figure 49. RF-to-DC conversion efficiency for dual-frequency rectenna: (a) efficiency and DC output voltage versus received power; (b) efficiency versus power density (from Ref. 48b with permission from IEEE).

impedance (Z_0). Although characteristic impedance values (Z_0) are identical with different CPS configurations, their attenuation values might be different. Therefore, attenuation should be verified by plotting in terms of s and W .

As for CPS components, six new types of CPS resonators were presented with open-ended T strip, short-ended strip, and T slots, and their performances were analyzed in terms of quality factor (Q factor) or bandwidth. We found that, while T-strip (types A, B, and D) and T-slot (type C) resonators exhibit bandstop behavior, short-ended strip resonators (types E and F) have bandpass frequency responses. The T-slot resonator (type C) has the highest Q factor among the resonators, which means that resonance energy is stored better in the slots than in the strips. As discussed earlier, CPS attenuation is reduced when the characteristic impedance (Z_0) is high, meaning that the higher is Z_0 , the higher is the Q factor. Lumped-element equivalent circuits of each resonator were presented. Two types of CPS bandpass filters were designed using the proposed resonators. Multiple short-ended strip bandpass filter exhibited a wide passband bandwidth, but the bandpass filter using short-ended strips with T strips showed narrow passband bandwidth. A simple CPS lowpass filter

was developed with a cutoff frequency of 7 GHz using interdigital capacitors and a CPS transmission line. The measured performance showed low insertion loss at passband and deep suppression at stopband.

A new CPS tee junction was introduced using a coupled CPS (CCPS). The CCPS developed does not require any bond wires or via holes to connect physically disconnected CPS lines. The performance of CCPS was compared with conventional CPS configuration, and its usefulness was discussed. Using the CCPS, a novel microstrip-fed CPS tee junction has been invented.

As an antenna application of CPS, a novel printed twin-dipole phase-array antenna was developed at 30 GHz using a multi-transmission-line tunable phase shifter controlled by a piezoelectric transducer (PET). The new twin-dipole antenna was designed using a microstrip-fed CPS tee junction. To construct the tee junction, CCPS was used for a physical discontinuity at CPS while fields were continuous over the entire transmission line. The tee junction effectively split power to each CPS output port with low insertion loss. The PET-actuated phase shifter required only one (unidirectional beam scanning) or two (bidirectional beam scanning) applied voltage sources to produce

the progressive phase shift (Φ). The twin dipole phased-array antenna demonstrated a 42° ($-20^\circ \sim +22^\circ$) beam scanning with more than 11 dB sidelobe suppression across the scan.

As a circuit application of CPS, a dual-frequency rectenna was presented operating at both 2.45 and 5.8 GHz (ISM bands) simultaneously. The rectenna has a dual-frequency dipole antenna integrated with CPS lowpass and bandpass filter. For high conversion efficiency, a diode analysis and transmission-line analysis were performed for low attenuation. Second-order harmonic reradiations were well suppressed with CPS filters without losing conversion efficiency.

Since little research has been done on CPS and its components, this article should provide some useful guidelines for designing and implementing CPS circuits and the practical aspects of printed dipole antennas.

BIBLIOGRAPHY

1. H. K. Chiou, C. Y. Chang, and H. H. Lin, Balun design for uniplanar broad band double balanced mixer, *Electron. Lett.* **31**(24):2113–2114 (Nov. 1995).
2. H. Haga, M. Izutsu, and T. Sueta, Travelling wave modulator switch with an etched grating, *IEEE J. Quantum Electron.* **QE-22**:902–906 (1986).
3. I. Hong and H. Park, Quasi-static analysis of travelling-wave electrodes with asymmetrical finite thickness for electro-optic modulators, *Optoelectron. IEE Proc.* **147**(2):120–122 (April 2000).
4. J. H. Son, H. H. Wang, J. F. Whitaker, and G. A. Mourou, Picosecond pulse propagation on coplanar striplines fabricated on lossy semiconductor substrates: Modeling and experiments, *IEEE Trans. Microwave Theory Tech.* **41**(9):1574–1580 (Sept. 1993).
5. S. S. Gevorgian and I. G. Mironenko, Asymmetric coplanar-strip transmission lines for MMIC and integrated optic applications, *Electron. Lett.* **26**(22):1916–1918 (Oct. 1990).
6. R. N. Simons, N. I. Dib, and L. P. B. Katehi, Modeling of coplanar stripline discontinuities, *IEEE Trans. Microwave Theory Tech.* **44**(5):711–716 (May 1996).
7. K. Goverdhanam, R. N. Simons, and L. P. B. Katehi, Coplanar stripline components for high-frequency applications, *IEEE Trans. Microwave Theory Tech.* **45**(10):1725–1729 (Oct. 1997).
8. K. Goverdhanam, R. N. Simons, and L. P. B. Katehi, Coplanar stripline propagation characteristics and bandpass filter, *IEEE Microwave Guided Wave Lett.* **7**(8):214–216 (Aug. 1997).
9. L. Fan, B. Heimer, and K. Chang, Uniplanar hybrid couplers using asymmetrical coplanar striplines, *IEEE Trans. Microwave Theory Tech.* **45**(12):2234–2240 (Dec. 1997).
10. S. G. Mao, H. K. Chiou, and C. H. Chen, Modeling of lumped-element coplanar-stripline low-pass filter, *IEEE Microwave Guided Wave Lett.* **8**(3):141–143 (March 1998).
11. S. Uysal and J. W. P. Ng, A compact coplanar stripline low-pass filter, *Proc. Asia Pacific Microwave Conf.*, Singapore, 1999, Vol. 2, pp. 307–310.
12. H. T. Kim, S. Lee, J. Kim, J. H. Park, Y. K. Kim, and Y. Kwon, A V-band cps distributed analog mems phase shifter, 2003 *IEEE MTT-S Digest*, Philadelphia June 2003, pp. 1481–1485.
13. L. Zhu and K. Wu, Field-extracted lumped-element models of coplanar stripline circuits and discontinuities for accurate radio-frequency design and optimization, *IEEE Trans. Microwave Theory Tech.* **50**(4):1207–1215 (April 2002).
14. N. Dib, L. Katehi, G. Ponchak, and R. Simons, Theoretical and experimental characterization of coplanar waveguide discontinuities for filter applications, *IEEE Trans. Microwave Theory Tech.* **39**(5):873–882 (May 1991).
15. K. Hettak, N. Dib, A. Sheta, and S. Toutain, A class of novel uniplanar series resonators and their implementation in original applications, *IEEE Trans. Microwave Theory Tech.* **46**(9):1270–1276 (Sept. 1998).
16. K. Hettak, N. Dib, A. Omar, G. Delisle, M. Stubbs, and S. Toutain, A useful new class of miniature CPW shunt stubs and its impact on millimeter wave integrated circuits, *IEEE Trans. Microwave Theory Tech.* **47**(12):2340–2349 (Dec. 1999).
17. G. Ghione, A CAD-oriented analytical model for the losses of general asymmetric coplanar lines in hybrid and monolithic MICs, *IEEE Trans. Microwave Theory Tech.* **41**(9):1499–1510 (Sept. 1993).
18. E. Chen and S. Y. Chou, Characteristics of coplanar transmission lines on multilayer substrates: Modeling and experiments, *IEEE Trans. Microwave Theory Tech.* **45**(6):939–945 (June 1997).
19. Z. Du, K. Gong, J. S. Fu, Z. Feng, and B. Gao, CAD model for asymmetrical, elliptical, cylindrical, and elliptical cone coplanar striplines, *IEEE Trans. Microwave Theory Tech.* **48**(2):312–316 (Feb. 2000).
- 20a. K. C. Gupta, R. Grag, I. Bhal, and P. Bhartia, *Microstrip Lines and Slotlines*, 2nd ed. Artech House, Norwood, MA, 1996.
- 20b. Y. H. Suh and K. Chang, Coplanar stripline resonators modeling and applications to filters, *IEEE Trans. Microwave Theory Tech.*, **50**(5):1289–1296 (May 2002).
21. J. Carroll, M. Li, and K. Chang, New technique to measure transmission line attenuation, *IEEE Trans. Microwave Theory Tech.* **43**(1):219–222 (Jan. 1995).
22. W. C. Brown, The history of power transmission by radio waves, *IEEE Trans. Microwave Theory Tech.* **32**(9):1230–1242 (Sept. 1984).
23. W. C. Brown and J. F. Triner, Experimental thin-film, etched-circuit rectenna, *IEEE MTT-S Digest*, 1982, pp. 185–187.
24. J. O. McSpadden, T. Yoo, and K. Chang, Theoretical and experimental investigation of a rectenna element for microwave power transmission, *IEEE Trans. Microwave Theory Tech.* **40**(12):2359–2366 (Dec. 1992).
25. T. Yoo and K. Chang, Theoretical and experimental development of 10 and 35 GHz rectennas, *IEEE Trans. Microwave Theory Tech.* **40**(6):1259–1266 (June 1992).
26. J. O. McSpadden, L. Fan, and K. Chang, Design and experiments of a high-conversion-efficiency 5.8-GHz rectenna, *IEEE Trans. Microwave Theory Tech.* **46**(12):2053–2060 (Dec. 1998).
27. J. O. McSpadden and K. Chang, A dual polarized circular patch rectifying antenna at 2.45 GHz for microwave power conversion and detection, *IEEE Int. Microwave Symposium Digest*, San Diego, CA, 1994, pp. 1749–1752.
28. G. L. Matthaei, L. Young, and E. M. Jones, *Microstrip Filters, Impedance-Matching Networks, and Coupling Structures*, Artech House, Boston, 1980.
- 29a. J. Zhu and K. Wu, Model-based characterization of CPS-fed printed dipole for innovative design of uniplanar integrated antenna, *IEEE Microwave Guided Wave Lett.* **9**(9):342–344 (Sept. 1999).

- 29b. Y. H. Suh and K. Chang, Microstrip fed coplanar stripline Tee junction using coupled coplanar stripline, *IEEE Int. Microwave Symposium Digest*, Phoenix, AZ, 2001 pp. 611–614.
30. C. H. Ho, L. Fan, and K. Chang, Broad-band uniplanar hybrid-ring and branch-line couplers, *IEEE Trans. Microwave Theory Tech.* **41**(12):2116–2125 (Dec. 1993).
31. R. N. Simons, Novel coplanar stripline to slotline transition on high resistivity silicon, *Electron. Lett.* **30**(8):654–655 (April 1994).
32. K. Tilley, X. D. Wu, and K. Chang, Coplanar waveguide fed coplanar strip dipole antenna, *Electron. Lett.* **30**(3):176–177 (Feb. 1994).
33. M.-Y. Li, K. Tilley, J. McCleary, and K. Chang, Broadband coplanar waveguide-coplanar strip-fed spiral antenna, *Electron. Lett.* **31**(1):4–5 (Jan. 1995).
34. S. Mao, C. Hwang, R. Wu, and C. Chen, Analysis of coplanar waveguide-to-coplanar stripline transitions, *IEEE Trans. Microwave Theory Tech.* **48**(1):23–29 (Jan. 2000).
35. N. I. Dib, R. N. Simons, and L. P. B. Katehi, New uniplanar transitions for circuit and antenna applications, *IEEE Trans. Microwave Theory Tech.* **43**(12):2868–2873 (Dec. 1995).
36. Y. Qian and T. Itoh, A broadband uniplanar microstrip-to-CPS transition, *Microwave Conf. Proc. AMPC*, 1992, Vol. 2, pp. 609–612.
37. R. N. Simons, N. I. Dib, and L. P. B. Katehi, Coplanar stripline to microstrip transition, *Electron. Lett.* **31**(20):1725–1726 (Sept. 1995).
38. G. F. Engen and C. A. Hoer, Thru-reflect-line: An improved technique for calibrating the dual six-port automatic network analyzer, *IEEE Trans. Microwave Theory Tech.* **MTT-27**(12):897–993 (Dec. 1979).
- 39a. R. B. Marks, A multilayer method of network analyzer calibration, *IEEE Trans. Microwave Theory Tech.* **39**(7):1205–1215 (July 1991).
- 39b. Y. H. Suh and K. Chang, A wideband coplanar stripline to microstrip transition, *IEEE Microwave and Wireless Communication Letters*, **11**(1):28–29 (Jan. 2001).
40. A. Nestic S. Jovanovic, and V. Brankovic, Design of printed dipoles near the third resonance, *IEEE Int. Antennas and Propagation Symp. Digest*, Atlanta, GA, Vol. 2, 1998, pp. 928–931.
41. M. Scott, A printed dipole for wide-scanning array application, *IEEE 11th Int. Conf. Antennas and Propagation*, Manchester, UK, 2001, Vol. 1, pp. 37–40.
42. G. A. Evtioushkine, J. W. Kim, and K. S. Han, Very wideband printed dipole antenna array, *Electron. Lett.* **34**(24):2292–2293 (Nov. 1998).
43. K. L. Deng, C. C. Meng, S. S. Lu, H. D. Lee, and H. Wang, A fully monolithic twin dipole antenna mixer on a GaAs substrate, *Asia Pacific Microwave Conf. Digest*, Sydney, NSW, Australia, 2000, pp. 54–57.
44. T. Y. Yun and K. Chang, A phased-array antenna using a multi-line phase shifter controlled by a piezoelectric transducer, *IEEE Int. Microwave Symp. Digest*, Boston, Vol. 2, 2000, pp. 831–833.
- 45a. T. Y. Yun and K. Chang, A low-cost 8 to 26.5 GHz phased array antenna using a piezoelectric transducer controlled phase shifter, *IEEE Trans. Antenna Propag.* **49**(9):1290–1298 (Sept. 2001).
- 45b. Y. H. Suh and K. Chang, A new millimeter-wave printed dipole phased array antenna using microstrip-fed coplanar stripline Tee junctions, *IEEE Trans. Anten. Propag.*, **52**(8): 2019–2026 (Aug. 2004).
46. P. Koert and J. T. Cha, Millimeter wave technology for space power beaming, *IEEE Trans. Microwave Theory Tech.* **40**(6):1251–1258 (June 1992).
47. L. W. Epp, A. R. Khan, H. K. Smith, and R. P. Smith, A compact dual-polarized 8.51-GHz rectenna for high-voltage (50 V) actuator applications, *IEEE Trans. Microwave Theory Tech.* **48**(1):111–120 (Jan. 2000).
- 48a. Y. H. Suh and K. Chang, A circularly polarised truncated-corner square patch microstrip rectenna for wireless power transmission, *Electron. Lett.* **36**(7):600–602 (March 2000).
- 48b. Y. H. Suh and K. Chang, A High-efficiency dual frequency rectenna for 2.45- and 5.8-GHz wireless power transmission, *IEEE Trans. Microwave Theory Tech.*, **50**(7):1784–1789 (July 2002).
49. B. Strassner and K. Chang, 5.8-GHz circularly polarized dual-rhombic-loop traveling-wave rectifying antenna for low power-density wireless power transmission application, *IEEE Trans. Microwave Theory Tech.* **51**(5):1548–1553 (May 2003).
50. Y. H. Suh and K. Chang, Low cost microstrip-fed dual frequency printed dipole antenna for wireless communications, *Electron. Lett.* **36**(14):1177–1179 (July 2000).
51. F. Tefiku and E. Yamashita Double-sided printed strip antenna for dual frequency operation, *IEEE Int. Antenna and Propagation Symp. Digest*, Baltimore, MD, 1996, Vol. 1, pp. 50–53.
52. F. Tefiku and C. A. Grimes, Design of broad-band and dual-band antennas comprised of series fed printed-strip dipole pairs, *IEEE Trans. Anten. Propag.* **48**(6):895–900 (June 2000).

COPLANAR STRIPLINE TRANSITIONS

RAINEE N. SIMONS
NASA Glenn Research Center
Cleveland, Ohio

1. INTRODUCTION

A *balun* is a circuit that is used to transform an unbalanced line to a balanced transmission line. In this article, the design of baluns, which transform an unbalanced line, such as a coplanar waveguide (CPW) and a microstrip line, to a balanced line, such as a coplanar stripline (CPS), is presented. The applications of these baluns include double-balanced mixers, balanced amplifiers, and feed network for dipole antennas. These baluns are also commonly referred to as “transitions between transmission lines.” The baluns are divided into two categories for the purpose of analysis: the Marchand baluns and the double-Y baluns. Almost all the baluns discussed in this article fall into the category of Marchand baluns.

2. COPLANAR STRIPLINE-TO-COPPLANAR WAVEGUIDE TRANSITION

2.1. Coplanar Stripline-to-Coplanar Waveguide Balun

Figure 1 shows a CPS to a CPW balun [1]. In this balun at the balanced end currents of equal magnitude but opposite

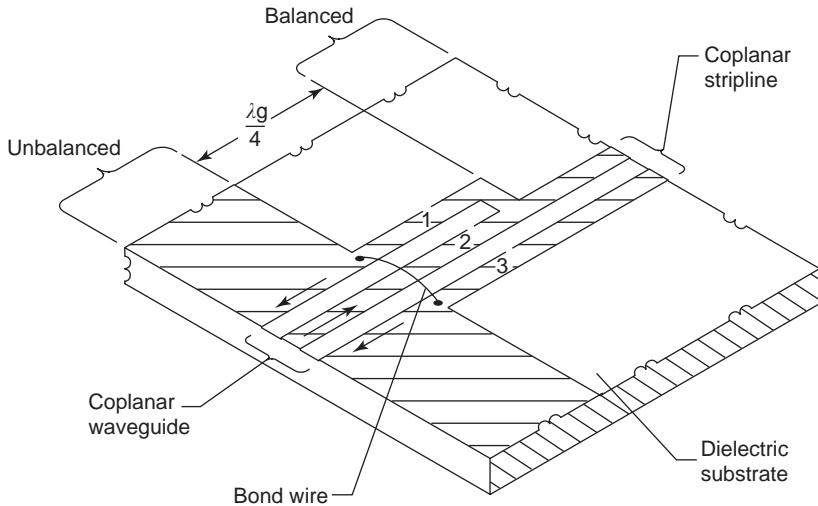


Figure 1. Coplanar stripline-to-coplanar waveguide transition with three strip transmission lines.

in direction flow along the two strip conductors. At the unbalanced end currents of equal magnitude but opposite in direction flow along the center strip conductor and the ground planes on either side. A short circuit placed between conductors 1 and 2 at the balanced end results in an open-circuit quarter-wavelength away at the unbalanced end, forcing all the currents to flow between conductors 2 and 3. Further, conductors 1 and 3 are short-circuited at the unbalanced end by a bond wire. This short circuit appears as an open-circuit quarter-wavelength at the balanced end, and therefore conductor 1 is isolated from the balanced end.

This transition, in addition to serving as a balun, also provides impedance transformation. Since RF energy propagates between conductors 2 and 3, the characteristic impedance between these conductors determines the impedance transformation over the quarter-wavelength section. In Ref. 2 the application of this transition to a CPW feed network for a dipole antenna array is demonstrated. A reduced-size lumped-element version of this transition is demonstrated in Ref. 3.

2.2. Coplanar Stripline-To-Coplanar Waveguide Balun With Slotline Radial Stub

Figure 2 shows a coplanar stripline (CPS)-to-coplanar waveguide (CPW) balun. In this balun one of the slots of the CPW is terminated in a broadband slotline radial open stub, while the other slot extends further to meet the CPS. In Ref. 4 the characteristics of an experimental balun are reported. The measured insertion loss and return loss of the balun are typically 1.0 dB and less than -13.0 dB, respectively, over the frequency range of 1.6–7.0 GHz. The balun has a bandwidth greater than 2 octaves. In Refs. 5 and 6 a variant of this balun is used for exciting a strip dipole and a spiral antenna, respectively.

2.3. Coplanar Stripline-to-Coplanar Waveguide Double-Y Balun

The double-Y junction in this balun [7] is formed by placing alternatively three coplanar striplines (CPSs) and three coplanar waveguides with finite-width ground planes (FW-CPWs) as shown in Fig. 3. The advantage

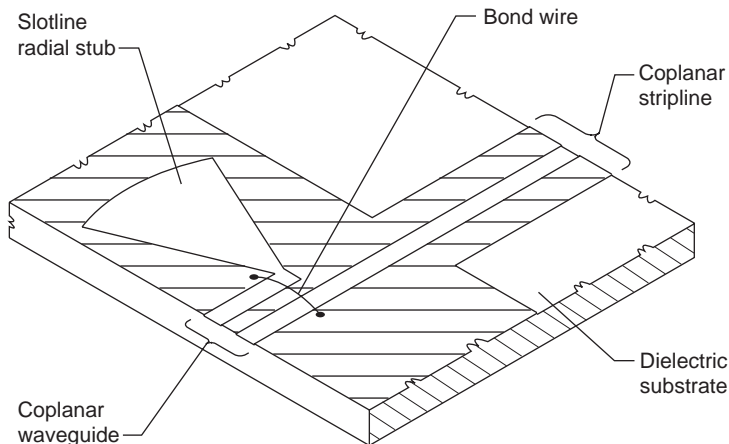


Figure 2. Coplanar stripline-to-coplanar waveguide transition with radial slotline stub.

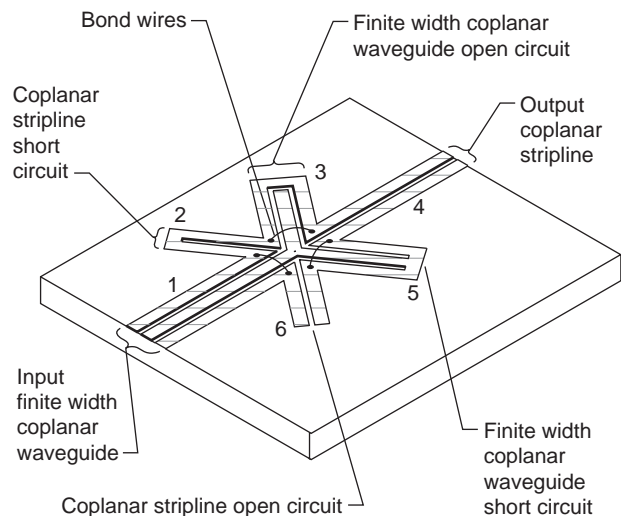


Figure 3. Coplanar stripline-to-coplanar waveguide double-Y balun or transition.

of FW-CPW over CPW in this design is the greatly reduced parasitics. Because of small parasitics the FW-CPW terminations behave almost like ideal open and short circuits, resulting in wider bandwidth. This balun is modeled as a six-port network as explained in Ref. 8. In Ref. 9 the characteristics of an experimental balun are reported. The geometry as well as typical measured characteristics are summarized in Table 1. These characteristics show that the balun has a bandwidth of several decades.

3. COPLANAR STRIPLINE-TO-MICROSTRIP TRANSITION

3.1. Coplanar Stripline-to-Microstrip Transition with an Electromagnetically Coupled Radial Stub

Coplanar stripline (CPS)-to-microstrip transitions [10] in a back-to-back arrangement are shown in Fig. 4. In each transition one of the CPS strip conductors is terminated in a microstrip radial stub of radius R and angle ϕ while the other strip conductor is extended forward to form the microstrip line. The CPS strip conductor width and separation are W and S , respectively. The width of the microstrip line is W_m . The resonance frequency of the radial stub depends on the radius R and angle ϕ . At resonance, the microstrip radial stub provides a virtual RF short circuit between the CPS strip conductor and the microstrip ground plane on the opposite side of the substrate. In the CPS, the electric field lines are across the strip conductors and parallel to the substrate. In the microstrip line, the electric field lines are normal to the substrate. Hence, to gradually rotate the electric field lines by 90° , the microstrip ground-plane edge is tapered at an angle θ . The electric field lines at various cross sections along the transition are illustrated in Fig. 5.

In Ref. 10, the characteristics of an experimental transition fabricated on a RT/Duroid 6010 substrate are reported. The measured insertion loss and return loss for

Table 1. Coplanar Waveguide with Finite-Width Ground Planes-to-Coplanar Stripline Double-Y Balun Or Transition

<i>Dimensions and Characteristics</i>	
<i>Substrate Material</i>	
ϵ_r and Thickness (mm)	Alumina 9.8, 0.635
<i>Coplanar Waveguide</i>	
S (mm)	0.12
W (mm)	0.04
g (mm)	0.1
$Z_{0(\text{CPW})}$ (Ω)	50.0
Stub length (mm)	0.996
<i>Coplanar Stripline</i>	
W (mm)	0.2
S (mm)	0.02
$Z_{0(\text{CPS})}$ (Ω)	50.0
Stub length (mm)	1.0
<i>Measured Characteristics</i>	
Frequency range (GHz)	DC – 12.0
S_{11} (dB)	≤ -13.0
S_{21} (dB)	2.0^a

^aFor two back-to-back transition.

Source: Ref. 9.

two back-to-back transitions over the frequency range of 5.1–6.1 GHz is 2.4 dB (max) and less than -10.0 dB, respectively. The -10.0 dB return loss bandwidth of both transitions is about 18% centered at 5.55 GHz. The numerical simulation of the transition carried out using the FDTD technique shows good agreement between measured and modeled results [10]. An optimized version of

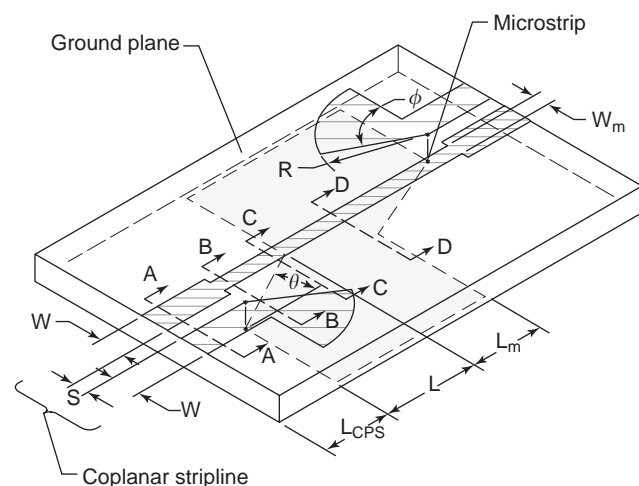


Figure 4. Two back-to-back coplanar stripline-to-microstrip transition: topside circuit pattern— $W = 0.69$ mm, $S = 0.19$ mm, $R = 5.08$ mm, $\phi = 60^\circ$, $W_m = 0.19$ mm, $L_{\text{CPS}} = 6.9$ mm; bottomside circuit pattern— $L = 7.1$ mm, $L_m = 12.7$ mm, $\theta \approx 7^\circ$. Substrate parameters: $h = 0.254$ mm, $\epsilon_r = 10.5$. Segments A-A, B-B, C-C, and D-D refer to the various cross sections along the transition.

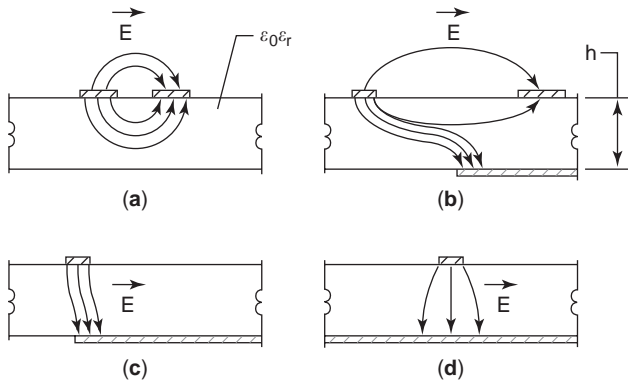


Figure 5. Electric field lines at various cross sections along the transition: (a) electric field between coplanar striplines at cross section A-A; (b) electric field between coplanar stripline and microstrip ground at cross section B-B; (c) electric field in cross section of asymmetric microstrip at C-C; (d) electric field in the cross section of the symmetric microstrip at D-D.

this transition has been demonstrated to have a decade bandwidth [11]. In addition, the radial stubs can be replaced by overlapping conductors as demonstrated in Ref. 12 to provide a virtual short circuit. In [13] and in [14] a transition from an asymmetric CPS (ACPS)-to-microstrip with radial stubs and with metal vias respectively, are demonstrated.

3.2. Uniplanar Coplanar Stripline-to-Microstrip Transition

A uniplanar coplanar stripline (CPS)-to-microstrip back-to-back transition [15] in a balanced arrangement is shown in Fig. 6. In this transition, a microstrip line of characteristic impedance $50\ \Omega$ is coupled to two orthogonal microstrip lines of characteristic impedance $70\ \Omega$ through a quarter-wave stepped impedance-matching transformer. The characteristic impedance of $70\ \Omega$ is chosen for ease of fabrication. In an ideal transition, the mean pathlength of the folded loop “a through b” is equal to $0.5\ \lambda_{g(\text{microstrip})}$, where $\lambda_{g(\text{microstrip})}$ is the guide wavelength in the microstrip of characteristic impedance $70\ \Omega$ at the center frequency f_0 . In a practical transition for wideband operation, the right-angle bend parasitic elements have to be compensated. A simple solution to this problem is to increase the mean pathlength of the microstrip. Hence, the mean pathlength is chosen as $0.638\ \lambda_{g(\text{microstrip})}$. This design ensures that the phase of the signals at the input locations a and b to the coupled microstrip line are 180° out of phase. The coupled microstrip lines are excited in the odd mode with the electric field lines predominantly across the gap S_2 . The dimensions of the gap S_2 is chosen such that the odd-mode characteristic impedance is $50\ \Omega$. The horizontal orientation of the electric field lines in the coupled microstrip makes the transition to a CPS simple. The width W and separation S of the CPS in the experimental transition is the same as the coupled microstrip width and separation.

In Ref. 15 the measured characteristics of the transition shown in Fig. 6 is reported. The transition is designed

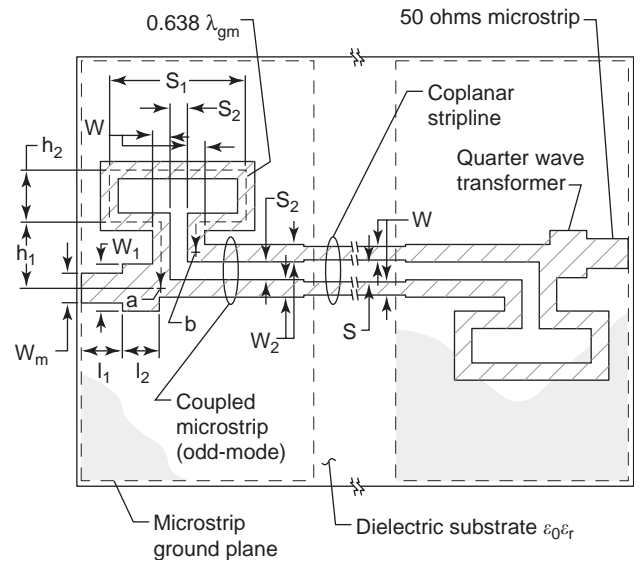


Figure 6. Two back-to-back balanced uniplanar coplanar stripline-to-microstrip transition. $W_m = 0.23\ \text{mm}$, $W_1 = 0.33\ \text{mm}$, $W_2 = W = S_2 = S = 0.1\ \text{mm}$, $l_1 = 4.9\ \text{mm}$, $l_2 = 2.8\ \text{mm}$, $S_1 = 2.1\ \text{mm}$, $h_1 = 0.54\ \text{mm}$, $h_2 = 1.34\ \text{mm}$. Substrate thickness $h = 0.254\ \text{mm}$, $\epsilon_r = 10.5$.

for operation at a center frequency $f_0 = 10.0\ \text{GHz}$; however, the measurements show that f_0 has shifted to $9.6\ \text{GHz}$. The measured insertion loss and return loss are about $2.0\ \text{dB}$ and less than $-10.0\ \text{dB}$, respectively, over 42% bandwidth centered at $9.6\ \text{GHz}$. The numerical simulation of the transition carried out using the FDTD technique shows that the measured and modeled results are in good agreement [15].

3.3. Stacked Coplanar Stripline-to-Microstrip Transition

Figure 7 shows a coplanar stripline (CPS)-to-microstrip transition [16] in a stacked configuration. In this transition the microstrip ground plane is attached using

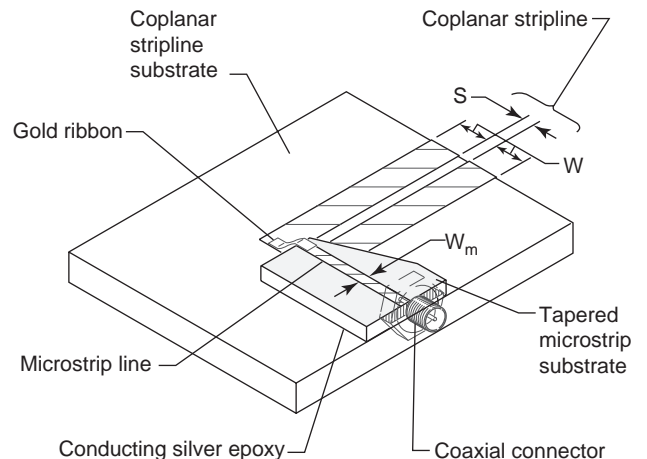


Figure 7. Coplanar stripline-to-microstrip transition using ribbon bond.

electrically conducting epoxy to one of the strip conductors of the CPS. The connection between the remaining strip conductors is by a gold ribbon. Lee and Itoh [16] describe the characteristics of an experimental transition. The geometry as well as the measured characteristics of the transition are summarized in Table 2. The transition has a wide bandwidth.

3.4. Microcoplanar Stripline-to-Microstrip Transition

Figure 8 shows a microcoplanar stripline (MCPS)-to-microstrip transition [17] in a back-to-back arrangement. In this transition, the width of the microstrip ground plane is abruptly reduced to form a symmetric parallel-plate line. The parallel-plate conductors are next flared out to form the MCPS. The cross section at three locations along the transition are shown in the inset in Fig. 8. Sections A-A, B-B, and C-C show the microstrip, the parallel plate, and the MCPS regions, respectively. The relevant parameters of the transition are as follows: $h_1 = 254 \mu\text{m}$, $\epsilon_{r1} = 10.5$, $\epsilon_{r2} \approx 1.0$, $W = 889 \mu\text{m}$, $W_m = 254 \mu\text{m}$, and the characteristic impedance $Z_{0(\text{microstrip})} = 50 \Omega$. In Ref. 17 the characteristics of an experimental transition are reported. The measured insertion loss and return loss are 1.0 dB and less than -16.0 dB , respectively, for two back-to-back transitions over the frequency range of 0.045–14.0 GHz. These losses also include the loss of the test fixture. The measurements show that the transition has a broad bandwidth.

Table 2. Coplanar Stripline-to-Microstrip Transition

<i>Dimensions and Characteristics</i>	
<i>Coplanar Stripline</i>	
Substrate thickness (μm)	3000
ϵ_r	10.0
W (μm)	490
S (μm)	58
$Z_{0(\text{CPS})}$ (Ω)	50
<i>Microstrip Line</i>	
Substrate thickness (μm)	127
ϵ_r	2.0
W_m (μm)	385
$Z_{0(m)}$ (Ω)	50
<i>Gold Ribbon</i>	
Width (μm)	350
Length (μm)	250
<i>Measured Characteristics</i>	
Frequency range (GHz)	DC – 18.0
S_{11} (dB)	$\leq -13.0^a$

^aFor two back-to-back transitions.

Source: Ref. 16.

4. COPLANAR STRIPLINE-TO-SLOTLINE TRANSITION

An electromagnetically coupled coplanar stripline (CPS)-to-slotline transition [18] in a back-to-back arrangement is shown in Fig. 9. The CPS and the slotline are on opposite sides of a dielectric substrate. To demonstrate the design

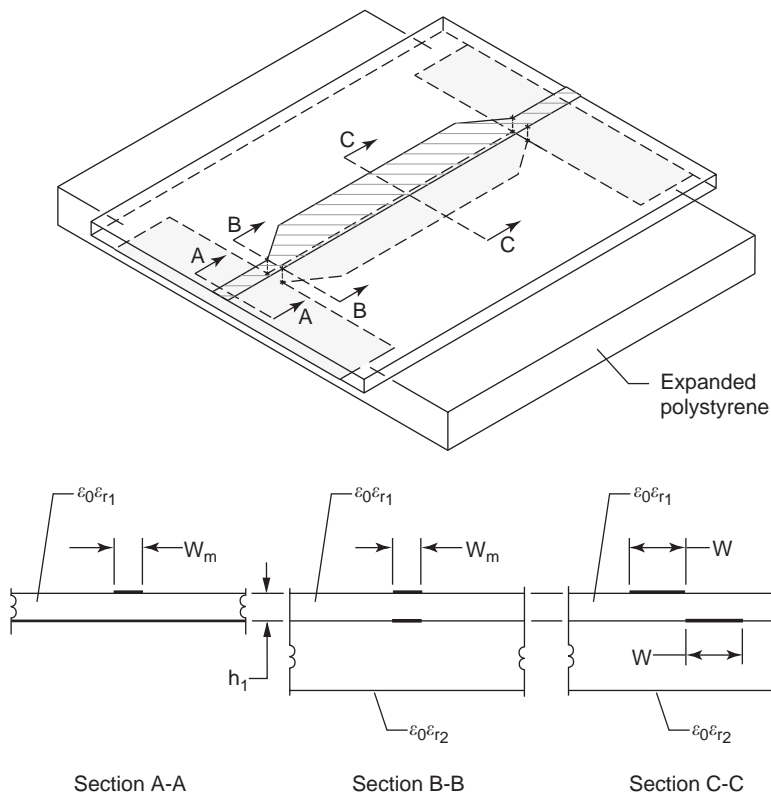


Figure 8. Two back-to-back micro-coplanar stripline-to-microstrip transition.

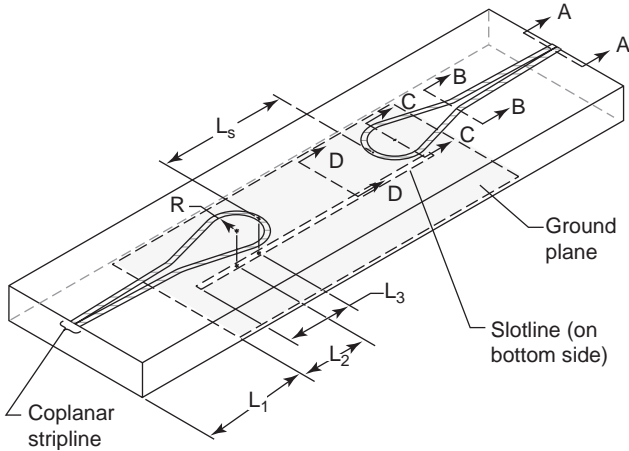


Figure 9. Two back-to-back electromagnetically coupled coplanar stripline-to-slotline transition. A-A, B-B, C-C, and D-D refer to the various cross-sections along the transition.

of the transition, the cross sections at four locations along the length are shown in Fig. 10. The input port at section A-A is a CPS with strip conductor width W_1 and separation S_1 . At section B-B the CPS overlaps the ground plane and transforms to coupled microstrip lines of width W_2 with odd-mode excitation. The separation S_2 between the coupled microstrip lines gradually diverges beyond B-B to C-C, but the strip width remains fixed at W_2 . At section C-C, the coupled microstrip lines are totally decoupled and behave as two independent lines. Beyond this plane, the CPS is terminated in a short circuit arc of radius R . Coupling between the CPS and the slotline takes place at the location where the short circuit arc crosses

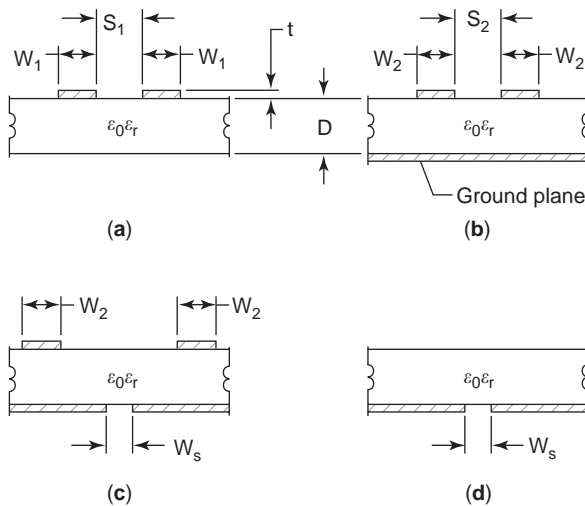


Figure 10. Cross-sectional view depicting transition between coplanar stripline to slotline: (a) at cross section A-A; coplanar stripline; (b) at cross section B-B; coupled microstrip lines; (c) at cross section C-C; decoupled microstrip lines; (d) at cross section D-D; slotline.

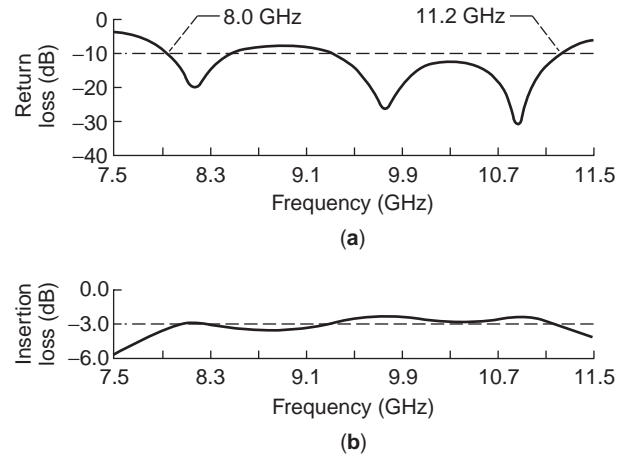


Figure 11. Measured characteristics: (a) return loss; (b) insertion loss.

the slotline at right angles. The slotline has a slot of width W_s .

Further, the slotline is terminated in a short circuit at a distance L_3 , which is approximately $\lambda_{g(\text{slotline})}/4$, where $\lambda_{g(\text{slotline})}$ is the guide wavelength in the slotline at the design frequency f_0 . The measured return loss and insertion loss characteristics of the transition are presented in Figs. 11a and 11b, respectively. Table 3 summarizes the transition performance.

Table 3. Coplanar Stripline-to-Slotline Transition

Dimensions and Characteristics	
Substrate	High-resistivity silicon ($\rho \approx 2500\text{--}3000 \Omega \text{ cm}$)
Thickness D (mm)	0.295
ϵ_r	11.7
t (μm)	≈ 2.5
Coplanar Stripline	
W_1 (mm)	0.28
S_1 (mm)	0.254
W_2 (mm)	0.24
S_2 (mm)	0.254
L_1 (mm)	6.35
L_2 (mm)	3.94
R (mm)	1.27
Slotline	
W_s (mm)	0.1143
L_s (mm)	7.13
L_3 (mm)	3.8
Measured Characteristics per Transition	
f_0 (GHz)	10.0
S_{11} (dB)	≤ -10.0
S_{21} (dB)	1.45
Bandwidth (%) at f_0	30.0

Source: Ref. 18.

BIBLIOGRAPHY

1. R. E. DeBrecht, Coplanar balun circuits for GaAs FET high-power push-pull amplifiers, *1973 IEEE G-MTT Int. Microwave Symp. Digest*, Boulder, CO, 1973, pp. 309–311.
2. R. N. Simons, G. E. Ponchak, R. Q. Lee, and N. S. Fernandez, Coplanar waveguide fed phased array antenna, *1990 IEEE Antennas and Propagation Symposium Digest*, Dallas, TX, May 1990, Vol. IV, pp. 1778–1781.
3. Y.-S. Lin and C. H. Chen, Novel lumped-element uniplanar transitions, *IEEE Trans. Microwave Theory Tech.* **49**(12):2322–2330 (Dec. 2001).
4. C.-H. Ho, L. Fan, and K. Chang, Broad-band uniplanar hybrid-ring and branch-line couplers, *IEEE Trans. Microwave Theory Tech.* **41**(12):2116–2125 (Dec. 1993).
5. K. Tilley, X.-D. Wu, and K. Chang, Coplanar waveguide fed coplanar strip dipole antenna, *Electron Lett.* **30**(3):176–177 (Feb. 1994).
6. M.-Y. Li, K. Tilley, J. McCleary, and K. Chang, Broadband coplanar waveguide-coplanar strip-fed spiral antenna, *Electron Lett.* **31**(1):4–5 (Jan. 1995).
7. V. Trifunovic and B. Jokanovic, Four decade bandwidth uniplanar balun, *Electron. Lett.* **28**(6):534–535 (March 1992).
8. R. N. Simons, *Coplanar Waveguide Circuits, Components, and Systems*, Wiley, New York, 2001, Sec. 10.6.3.
9. B. Jokanovic and V. Trifunovic, Double-Y baluns for MMICs and wireless applications, *Microwave J.* **41**(1):70–92 (Jan. 1998).
10. R. N. Simons, N. I. Dib, and L. P. B. Katehi, Coplanar stripline to microstrip transition, *Electron. Lett.* **31**(20):1725–1726 (Sept. 1995).
11. Y.-H. Suh and K. Chang, A wideband coplanar stripline to microstrip transition, *IEEE Microwave Wireless Compon. Lett.* **11**(1):28–29 (Jan. 2001).
12. T. Chiu and Y.-S. Shen, A broadband transition between microstrip and coplanar stripline, *IEEE Microwave Wireless Compon. Lett.* **13**(2):66–68 (Feb. 2003).
13. D. Jaisson, A single-balanced mixer with a coplanar balun, *Microwave J.* **35**(7):87–96 (July 1992) (corrections on p. 201, Sept. 1992).
14. D. Jaisson, Transition from a microstrip line to an asymmetrical coplanar waveguide, *Microwave J.* **37**(6):112–115 (June 1994).
15. R. N. Simons, N. I. Dib, R. Q. Lee, and L. P. B. Katehi, Integrated uniplanar transition for linearly tapered slot antenna, *IEEE Trans. Anten. Propag.* **43**(9):998–1002 (Sept. 1995).
16. H. Y. Lee and T. Itoh, Wideband and low return loss coplanar strip feed using intermediate microstrip, *Electron. Lett.* **24**(9):1207–1208 (Sept. 1988).
17. K. Goverdhanam, R. N. Simons, and L. P. B. Katehi, Micro-coplanar stripline—new transmission media for microwave applications, *1998 IEEE MTT-S Int. Microwave Symp. Digest*, Baltimore, MD, 1998, Vol. 2, pp. 1035–1038.
18. R. N. Simons, Novel coplanar stripline to slotline transition on high resistivity silicon, *Electron. Lett.* **30**(8):654–655 (April 1994).

COPLANAR WAVEGUIDE COMPONENTS

RAINEE N. SIMONS
 NASA Glenn Research Center
 Cleveland, Ohio

1. INTRODUCTION

Coplanar waveguide (CPW) is a type of planar transmission line suited for microwave integrated circuits (MICs) as well as for monolithic microwave integrated circuits (MMICs). The unique feature of this transmission line is that it is uniplanar in construction, which implies that all the conductors are on the same side of the substrate. This attribute simplifies realization of short- or open-circuited terminations and mounting of series and shunt lumped or active elements. In addition, it also circumvents the need for via holes. Furthermore, simplifies manufacturing and allows fast and inexpensive characterization using on-wafer techniques.

In this article, the design considerations for a CPW 3-dB hybrid coupler, 180° hybrid coupler, 3-dB magic-T, and aperture coupled patch antenna are presented. The hybrid couplers and the magic Ts are widely used in MICs as 90° and 180° power dividers and combiners that form the basic building blocks for subsystems such as balanced mixers, balanced upconverters, balanced modulators, balanced amplifiers, and balanced frequency multipliers. In addition, they are also used in the construction of image rejection mixers and upconverters. Furthermore, when hybrid couplers are integrated into the feed system of printed patch antennas and arrays, they can excite the radiator in the desired amplitude and phase to generate a linear or circular polarization. When magic Ts are integrated with antennas, they can form a comparator to produce the monopulse sum and difference signals needed in tracking radars.

In contrast with a Lange coupler, the above mentioned couplers do not require narrow strip conductors and slots, which impact tolerance and yield. To keep the chip size small and thus lower the cost, the designs presented here are for reduced-size hybrid couplers and magic Ts.

2. REDUCED-SIZE 3-dB BRANCHLINE HYBRID

Equivalent circuits of standard and reduced-size branchline hybrid are shown in Figs. 1a and 1b, respectively. In a standard hybrid the characteristic impedance of the branchline and the throughline are Z_0 and $Z_0/\sqrt{2}$, respectively. If in the reduced-size hybrid the characteristic impedance of the both the branchline and the throughline are Z , where Z is greater than Z_0 , then the electrical length of the branchline θ_1 , the electrical length of the throughline θ_2 , and the lumped capacitance C are given

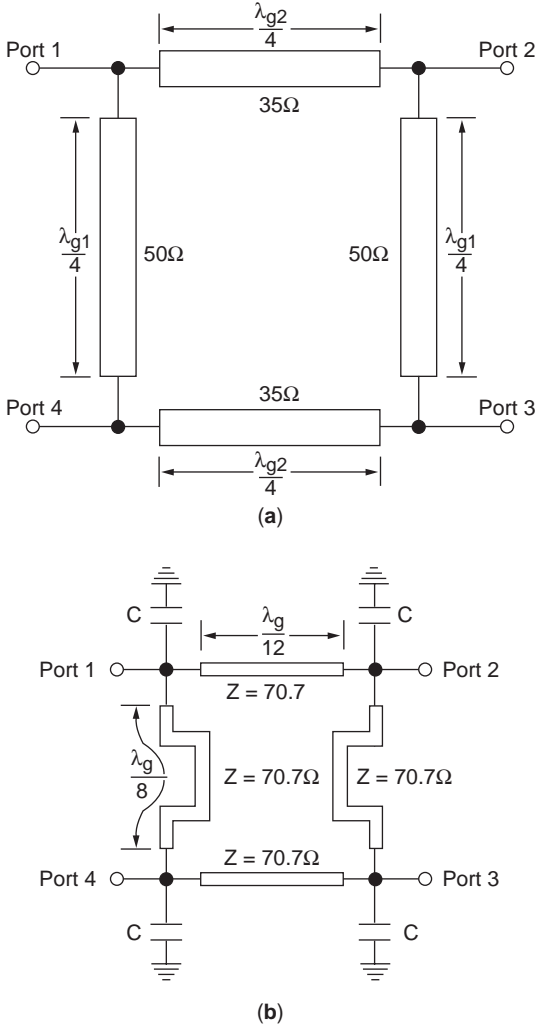


Figure 1. (a) Standard branchline hybrid; (b) reduced-size branchline hybrid. The guide wavelength on the line is denoted as λ_g .

by Ref. 1:

$$\theta_1 = \arcsin\left(\frac{Z_0}{Z}\right) \quad (1)$$

$$\theta_2 = \arcsin\left(\frac{Z_0}{\sqrt{2}Z}\right) \quad (2)$$

$$\omega CZ_0 = \sqrt{1 - \left(\frac{Z_0}{Z}\right)^2} + \sqrt{2 - \left(\frac{Z_0}{Z}\right)^2}. \quad (3)$$

As an example, when $Z_0 = 50\ \Omega$ and $Z = 70.7\ \Omega$, these three equations give $\theta_1 = 45^\circ$, $\theta_2 = 30^\circ$. This implies that the branchline and the throughline lengths θ_1 and θ_2 are $\lambda_g/8$ and $\lambda_g/12$, respectively, where λ_g is the guide wavelength.

The phase difference between the power to the direct port and the power to the coupled port, that is, the phase of (S_{21}/S_{31}) , is computed in Ref. 1 for the reduced-size hy-

brid and the standard quarter-wavelength hybrid. The results show that the bandwidth over which the phase difference is 90° is narrower in the case of the reduced-size hybrid.

In a coplanar waveguide (CPW) if the center strip conductor width is held fixed and the slot width increased, the characteristic impedance increases and the conductor loss reduces. Hence, the insertion loss of the reduced-size hybrid that has an impedance higher than that of the standard hybrid is not degraded by size reduction.

An experimental reduced-size hybrid fabricated on a semiinsulating GaAs is reported in Ref. 1. The constant-impedance transmission line is a CPW with a center strip width of $10\ \mu\text{m}$ and characteristic impedance of $70.0\ \Omega$. The lengths of the branchline and the throughline are $\lambda_{g(\text{CPW})}/8$ and $\lambda_{g(\text{CPW})}/12$, respectively, at 25 GHz. Air bridges are used at the CPW junctions to tie the ground planes at equal potential and suppress the coupled slotline even mode. Metal-insulator-metal (MIM) shunt capacitors are located at the corners of the inner ground metal. The insulator film is Si_3N_4 . The size of the fabricated hybrid is $500 \times 500\ \mu\text{m}$. This is more than 80% smaller than a standard branchline hybrid.

The measured performance of the hybrid in Ref. 1 over the frequency band of 24.0–26.0 GHz shows that the power coupled from port 1 to ports 2 and 3 is within $5.0 \pm 0.5\ \text{dB}$, return loss at port 1 is better than $-10.0\ \text{dB}$, and the isolation between ports 1 and 4 is better than $-12.0\ \text{dB}$. As a concluding remark, it may be mentioned that in Ref. 2 a small 90° hybrid coupler based on the Wheatstone bridge principle is demonstrated at a center frequency of 4.0 GHz.

3. REDUCED-SIZE 180° RING HYBRID

The equivalent-circuit representation of a standard 180° ring hybrid is shown in Fig. 2a. To reduce the size of the hybrid, first the quarter-wavelength lines of $70\ \Omega$ characteristic impedance are replaced by one-eighth wavelength lines of $100\ \Omega$ characteristic impedance with lumped capacitances at the ends. Then, the three-quarter wavelength line of $70\ \Omega$ characteristic impedance is replaced by a π -network consisting of lumped series capacitance and shunt inductances. The lumped shunt inductances and capacitances almost cancel each other, resulting in the equivalent circuit [1] shown in Fig. 2b.

Besides size reduction, the reduced-size ring hybrid has the advantage of being able to interchange ports at the location of the series metal-insulator-metal (MIM) capacitor [1] as illustrated in Fig. 3. In Fig. 3a, the output ports 2 and 3 are located on opposite sides of port 4. By interchanging the location of ports 2 and 4, the output ports 2 and 3 are located side by side as shown in Fig. 3b. Further, if port 4 is used as the input port, then the outputs at ports 2 and 3 are 180° out of phase as discussed in Ref. 3. This feature greatly simplifies balanced mixer construction using a ring hybrid [4].

An experimental reduced-size ring hybrid fabricated on a semiinsulating GaAs substrate with elevated CPW as the transmission line has been reported in Ref. 5. The

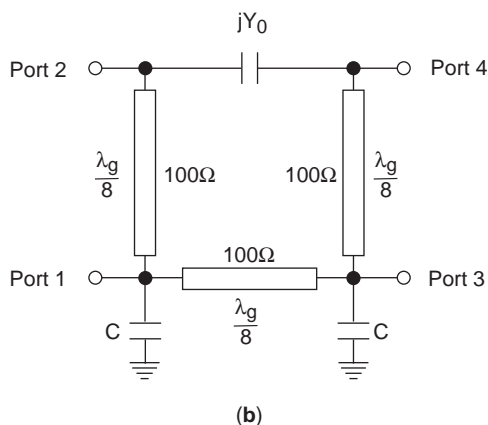
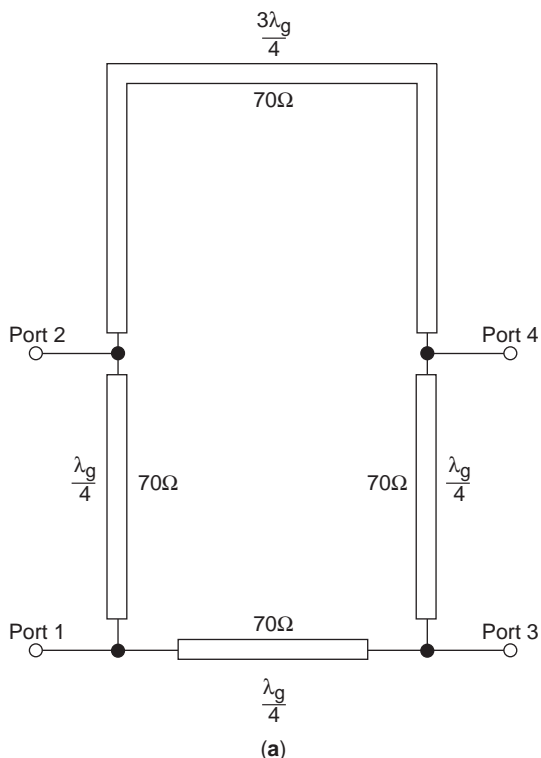


Figure 2. Representation of (a) standard 180° ring hybrid or rat race with transmission lines; (b) equivalent reduced-size 180° ring hybrid or ratrace with transmission lines and lumped elements. The wavelength on the line is denoted as λ_g .

elevated CPW has the advantage of reducing both the insertion loss as well as the chip area as discussed in Ref. 3. The hybrid consists of three $\frac{1}{8}$ th-wavelength 100- Ω elevated CPWs, a series capacitor and two shunt capacitors in place of the three $\lambda_g/4$, and a $3\lambda_g/4$ 70- Ω transmission line as in a standard ring hybrid. In the experimental hybrid, the elevated CPW is meandered to further reduce the overall size. The ring hybrid is schematically shown in Fig. 4.

The measurements show that the coupling loss ($|S_{12}|$, $|S_{42}|$) of the hybrid is on the order of 4.2 ± 0.8 dB, return loss ($|S_{22}|$) better than 17.0 dB, and isolation ($|S_{32}|$) better

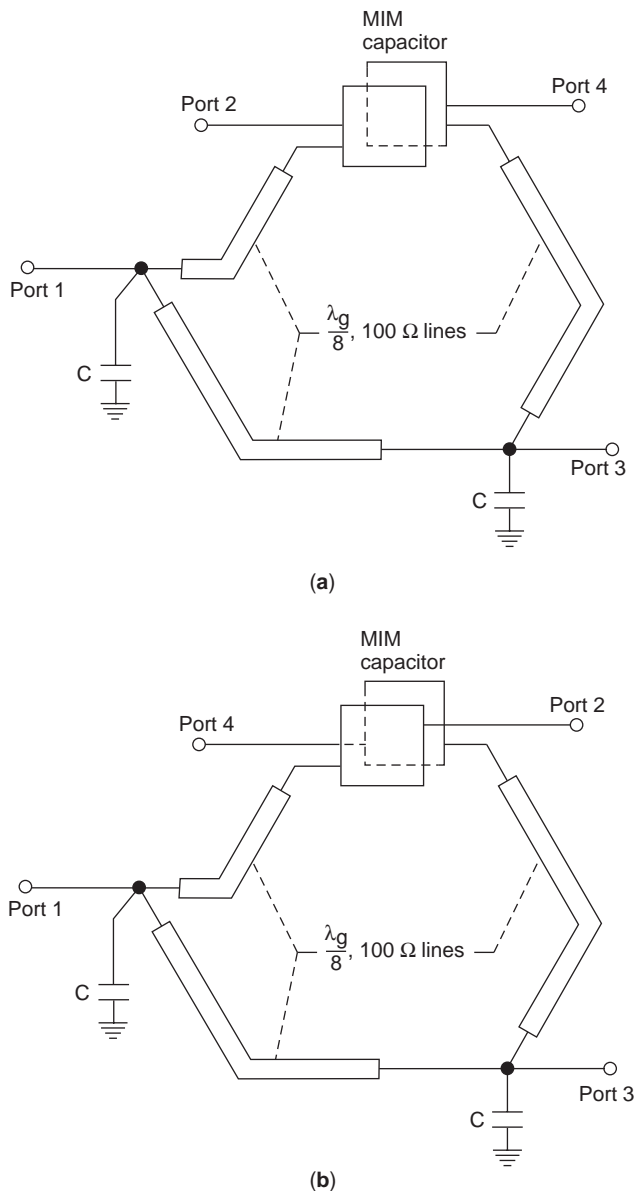


Figure 3. (a) Normal port layout; (b) port layout convenient for balanced mixer applications.

than 18.0 dB over the frequency range 15.0 ± 2.0 GHz. The chip size is on the order of 0.50×0.55 mm.

4. REDUCED-SIZE 3-dB MAGIC T

The circumference of a magic-T circuit is typically about one guide wavelength. To reduce the circumference and thereby the overall size, consider the hybrid ring topology [6] shown in Fig. 5. In this circuit it is assumed that the transmission lines in opposite ring arms are identical and that the hybrid ring is matched at all ports. The phase shifter may be located anywhere in any of the four arms. In this hybrid a signal fed to port 1 (*H* arm) will be split equally and be in phase between the two output ports 2

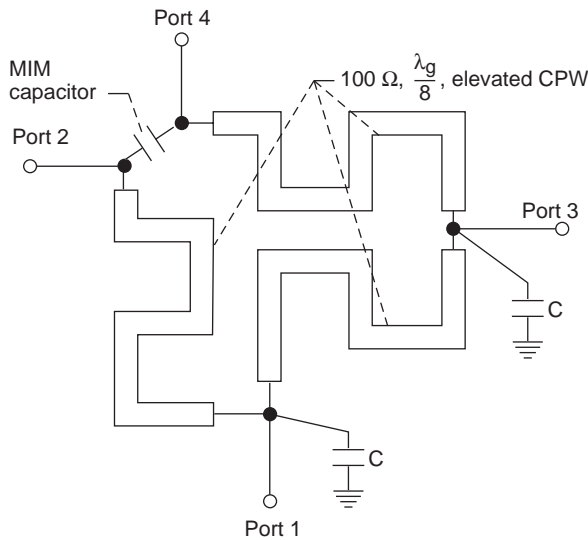


Figure 4. Reduced-size 180° ring hybrid with meandered elevated CPW.

and 3 (balanced arms). Similarly, a signal feed to port 4 (*E* arm) will be split equally and be out of phase between the two output ports 2 and 3. The following design equations hold good [6]:

$$Z_{c1}^2 = Z_0^2 \frac{\sin^2 \theta_1 + \sin^2 \theta_2 - 2 \cos \theta_1 \cos \theta_2}{\sin^2 \theta_1} \quad (4)$$

$$Z_{c2}^2 = Z_0^2 \frac{\sin^2 \theta_1 + \sin^2 \theta_2 - 2 \cos \theta_1 \cos \theta_2}{\sin^2 \theta_2} \quad (5)$$

where θ_i ($i = 1, 2$) is the electrical length of arm i at the center frequency f_0 . The impedances Z_{c1} and Z_{c2} are the

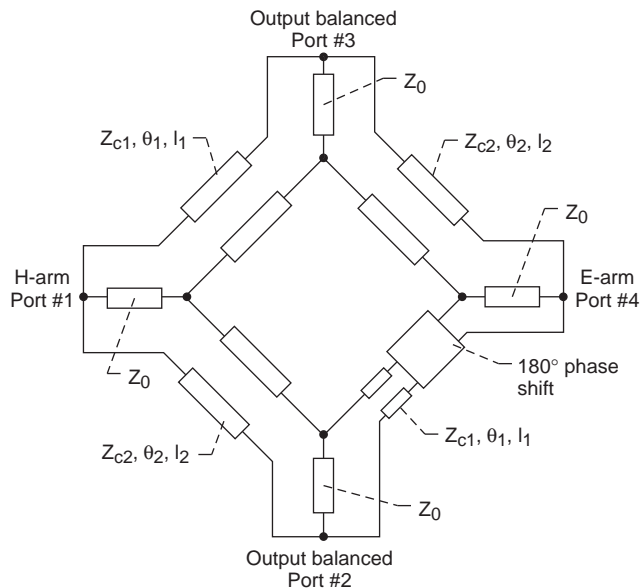


Figure 5. Generalized ring magic T.

characteristic impedances of the lines in the ring arms. The impedance Z_0 is the terminating impedance. To obtain real values for characteristic impedances, the following condition must be satisfied [6]:

$$\cos \theta_1 + \cos \theta_2 < \sqrt{2} \quad (6)$$

In a symmetric design all four ring arms are identical. In such a case Eqs. (4) and (5) reduces to [7]:

$$Z_c = Z_0 \sqrt{2} \sqrt{1 - \cot^2 \theta} \quad (7)$$

An experimental reduced-size magic T [6,7] realized with symmetric coplanar striplines is shown in Fig. 6a. Coplanar striplines are chosen because they allow easy crossover of the two strips to realize the 180° phase shifter needed at the *E* arm. The crossover may be placed at any position along the arm or at the T junction as shown in Fig. 6b.

In Ref. 7 θ is equal to 60° and for Z_0 equal to 50Ω, Z_c from (7) is equal to 57.6Ω. This design results in a ring circumference of 0.67 guide wavelength. The magic T is fabricated on a 254-μm-thick alumina substrate ($\epsilon_r = 9.9$),

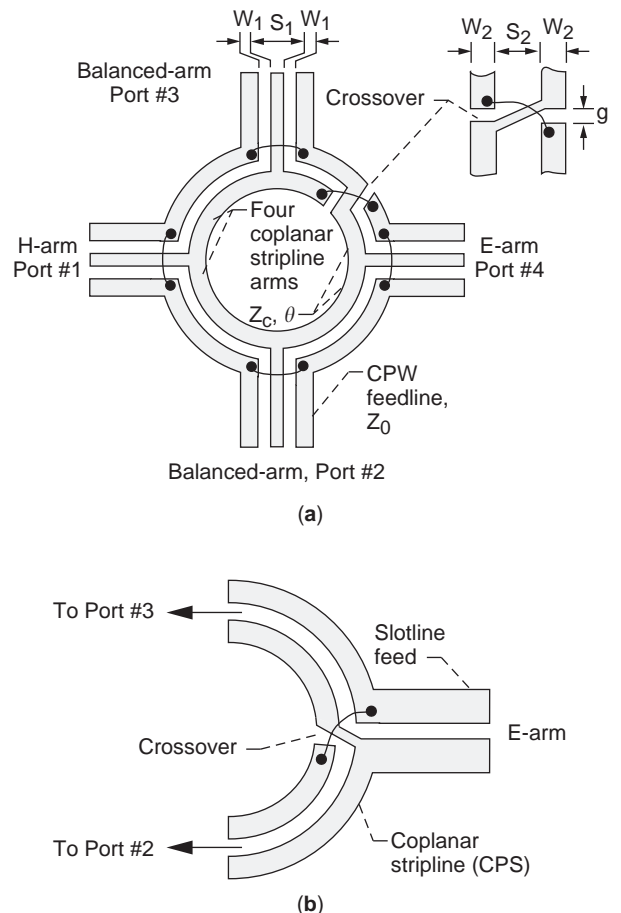


Figure 6. (a) Reduced-size ring magic T (from Ref. 7, copyright © IEE) (b) alternate implementation with slotline feed for *E*-arm (from Ref. 6, copyright © IEE).

Table 1. Reduced-Size 3-dB Ring Magic T

<i>Circuit Parameters and Measured Characteristics</i>	
Substrate (alumina) ϵ_r	9.9
Thickness (μm)	254
Metallization thickness (μm)	4.0
<i>Coplanar Waveguide</i>	
Strip width S_1 (μm)	50
Slot width W_1 (μm)	30
Z_0 (Ω)	50
<i>Coplanar Stripline</i>	
Strip width S_1 (μm)	300
Slot width S_2 (μm)	60
Z_c (Ω)	57.6
θ (deg)	60
Circumference λ_g	0.67
Ring radius (μm)	3478
Crossover gap g (μm)	100
<i>Measured Performance</i>	
Center frequency f_0 (GHz)	6
Frequency range (GHz)	4.5–9.2
Transmission when fed at <i>H</i> -arm mag (S_{21}), mag (S_{31}) (dB)	4.3 ± 0.3
Transmission when fed at <i>E</i> -arm mag (S_{24}), mag (S_{34}) (dB)	4.3 ± 0.3
Output magnitude balance when fed at <i>H</i> -arm mag (S_{21}/S_{31}) (dB)	0.3 ± 0.05
Output phase balance when fed at <i>H</i> -arm phase (S_{21}/S_{31}) (deg)	0 ± 4
Output magnitude balance when fed at <i>E</i> -arm mag (S_{24}/S_{34}) (dB)	0.4 ± 0.25
Output phase balance when fed at <i>E</i> -arm phase (S_{24}/S_{34}) (deg)	180 ± 4
Return loss mag (S_{22}) and mag (S_{33}) (dB)	< -10.0
Isolation mag (S_{EH}), mag (S_{32}) (dB)	< -23.0

and the conductor thickness is $4\mu\text{m}$. The geometric parameters and the measured performance of the magic T are summarized in Table 1. The magic T has a bandwidth slightly larger than 1 octave.

As a concluding remark, it may be mentioned that other designs for magic Ts can be found in Refs. 8–11 in the literature.

5. COPLANAR WAVEGUIDE APERTURE-COUPLED PATCH ANTENNA

Aperture-coupled feeding is attractive because of certain advantages, such as lack of physical contact between the feed and radiator, wider bandwidth, and better isolation between antennas and the feed network. Furthermore, aperture-coupled feeding allows independent optimization of antennas and feed networks by using substrates of different thickness or permittivity. A grounded coplanar waveguide (GCPW) aperture-coupled patch antenna is schematically illustrated in Fig. 7. In the experimental

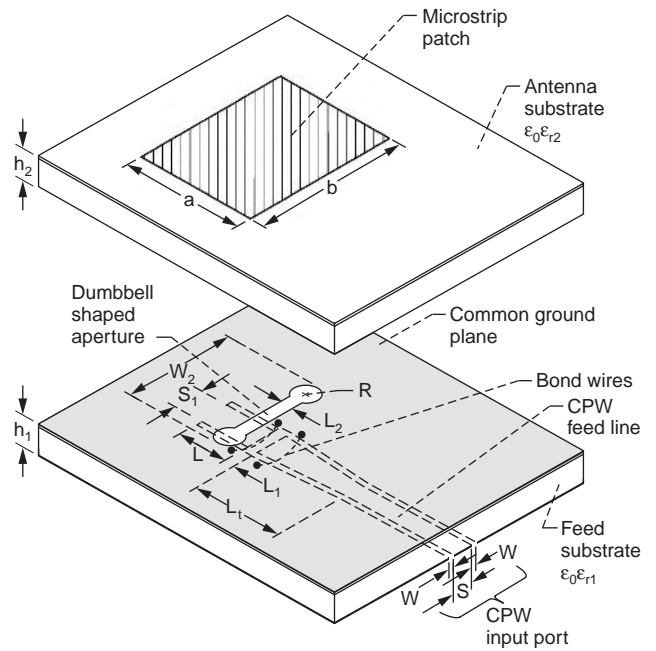
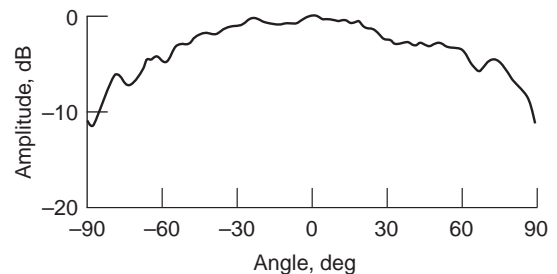
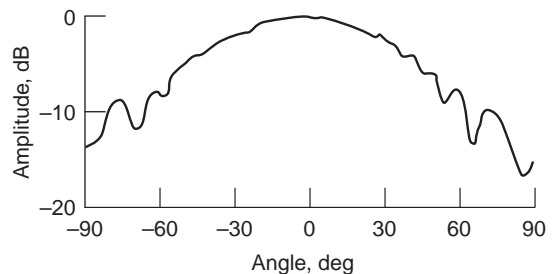


Figure 7. Grounded coplanar waveguide aperture-coupled patch antenna: $S = 0.076$ cm, $W = 0.025$ cm, $L = 0.711$ cm, $L_1 = 0.025$ cm, $L_2 = 0.205$ cm, $W_2 = 0.69$ cm, $a = 0.76$ cm, $b = 1.14$ cm, $h_1 = 0.051$ cm, $\epsilon_{r1} = 2.2$, $h_2 = 0.025$ cm, $\epsilon_{r2} = 2.2$, $L_t = 0.711$ cm, $S_1 = 0.355$ cm, $R = 0.0843$ cm.

antenna [12], the patch and the GCPW feed structure, with a series gap L_1 in the center conductor, are fabricated on separate substrates, and the aperture is etched in the common ground plane. The aperture is located directly



(a)



(b)

Figure 8. Measured radiation patterns for the grounded coplanar waveguide aperture-coupled patch antenna: (a) *E* plane; (b) *H* plane.

above the series gap. Thus, microwave power is coupled from the GCPW feedline to the patch through the aperture. In the experimental antenna, the patch is displaced by ~ 0.32 cm from the center of the aperture and the GCPW stub length L is adjusted to provide the best impedance match to the feedline. The radiation from the antenna is linearly polarized with the plane of polarization parallel to the patch side of dimension a .

The measured return loss is about -16.9 dB at the design frequency of 12.65 GHz as reported in Ref. 12. Typical measured E - and H -plane radiation patterns [12] for the GCPW aperture-coupled patch antenna are shown in Figs. 8a and 8b, respectively. The patterns look fairly symmetric and exhibit a 3 dB beamwidth of about 60° and 50° in the E and H planes, respectively. The measured front-to-back ratio is ~ 14.0 dB, which is typical for an aperture-coupled patch antenna. Finally, in Ref. 13 an aperture-coupled patch antenna with series slotline stubs in the CPW ground planes, instead of a series gap in the CPW center strip conductor, is demonstrated. The characteristics of this antenna are similar to those presented above.

BIBLIOGRAPHY

1. T. Hirota, A. Minakawa, and M. Muraguchi, Reduced-size branchline and rat-race hybrids for uniplanar MMIC's, *IEEE Trans. Microwave Theory Tech.* **38**(3):270–275 (March 1990).
2. M. -H. Murgulescu, P. Legaud, E. Penard, and I. Zaquine, New small 90° hybrid coupler, *Electron. Lett.* **30**(16):1289–1290 (Aug. 1994).
3. R. N. Simons, *Coplanar Waveguide Circuits, Components, and Systems*, Wiley, New York, 2001, Chap. 2, Sec. 11.4.
4. T. Hirota and M. Muraguchi, K-band frequency up-converters using reduced-size couplers and dividers, *1991 IEEE GaAs IC Symp.* Monterey, CA, Oct. 20–23, 1991, pp. 53–56.
5. H. Kamitsuna, A very small, low-loss MMIC rat-race hybrid using elevated coplanar waveguides, *IEEE Microwave Guided Wave Lett.* **2**(8):337–339 (Aug. 1992).
6. M. -H. Murgulescu, E. Penard, and I. Zaquine, Design formulas for generalized 180° hybrid ring couplers, *Electron. Lett.* **30**(7):573–574 (March 1994).
7. M. -H. Murgulescu, E. Moisan, P. Legaud, E. Penard, and I. Zaquine, New wideband, $0.67\lambda_g$ circumference 180° hybrid ring coupler, *Electron. Lett.* **30**(4):299–300 (Feb. 1994).
8. L. Fan, C.-H. Ho, S. Kanamaluru, and K. Chang, Wide-band reduced-size uniplanar magic-T, hybrid-ring, and deRonde's CPW-slot couplers, *IEEE Trans. Microwave Theory Tech.* **43**(12):2749–2758 (Dec. 1995).
9. M. Aikawa and H. Ogawa, A new MIC magic-T using coupled slot lines, *IEEE Trans. Microwave Theory Tech.* **MTT-28**(6): 523–528 (June 1980).
10. T. Hirota, Y. Tarusawa, and H. Ogawa, Uniplanar MMIC hybrids—a proposed new MMIC structure, *IEEE Trans. Microwave Theory Tech.* **MTT-35**(6):576–581 (June 1987).
11. M. Aikawa and H. Ogawa, Double-sided MIC's and their applications, *IEEE Trans. Microwave Theory Tech.*, **37**(2): 406–413 (Feb. 1989).
12. R. Q. Lee and R. N. Simons, Coplanar waveguide aperture-coupled microstrip patch antenna, *IEEE Microwave Guided Wave Lett.* **2**(4):138–139 (April 1992).
13. R. N. Simons and R. Q. Lee, Coplanar waveguide aperture coupled patch antennas with ground plane/substrate of finite extent, *Electron. Lett.* **28**(1):75–76 (Jan. 1992).

COPLANAR WAVEGUIDE (CPW) TRANSMISSION LINES

LEI ZHU
Nanyang Technological
University
Singapore

1. INTRODUCTION

The coplanar waveguide (CPW) was invented by Wen [1] in 1969 as a novel surface strip transmission line fabricated on a dielectric substrate. As the strip conductor is deposited on the same surface as the two ground planes in close proximity, the CPW transmission line has demonstrated several advantageous features over the conventional microstrip line, for instance, easy surface mounting of external devices, easy fabrication of both shunt and series passive elements, low-frequency dispersion, and easy adjustment of desirable characteristic impedance. Since its proposal, the CPW technology has been progressively gaining a tremendous application in exploration of advanced RF and microwave integrated circuits, modules, and subsystems. For this purpose, much effort has been carried out to construct a new variety of modified CPW transmission lines with varied cross-sectional configurations and accurately characterize their propagation performance in theory and experiment, as summarized in two relevant books [2,3]. In particular, various static and full-wave methods have been effectively developed to deal with these inhomogeneous transmission lines and derive the two per unit length transmission parameters, i.e., effective dielectric constant and characteristic impedance.

This article focuses on the fundamentals of various CPW transmission lines developed so far, including their geometric schematics, transmission characteristics, modeling techniques, and closed-form design formulas:

1. The three most popular CPW lines with infinite and finite ground widths as well as the backed conductor are comprehensively described to exhibit their transmission performance versus strip/slot dimension ratios, operating frequency, and strip conductor profile.
2. Low-transmission-loss shielded CPW, suspended CPW, nonleaky CPW, micromachined CPW, and cavity-assisted CPW are briefly investigated.
3. Various coupled CPW transmission lines and the extent of their weak and tight parallel coupling are discussed.

4. Various periodic slow-wave CPW transmission lines with series inductive and/or shunt capacitive loading in periodical intervals with the objective of miniaturization of CPW circuits are discussed, and their complete propagation characteristics in terms of effective per unit length transmission parameters are demonstrated.

2. BASIC CPW: GEOMETRY AND ANALYSIS

The conventional CPW transmission line [1] consists of the central strip conductor and the two infinite-width ground planes on two sides that are formed in close proximity on the same surface of a dielectric substrate with finite height, as illustrated in Fig. 1a. By equalizing the electric potentials at the two ground planes, only the even symmetric dominant CPW mode can be excited. At high frequencies, this CPW mode becomes non-TEM with a longitudinal component of magnetic field. In such a case, the tangential magnetic field, on the surface of the coupled slots between the strip conductor and two ground planes, becomes elliptically polarized. This conventional CPW was developed by Wen [1] for suitable applications in nonreciprocal ferrite devices. However, the CPW has been extensively utilized as a quasi-TEM transmission-line candidate for exploration of a variety of MMIC's circuits

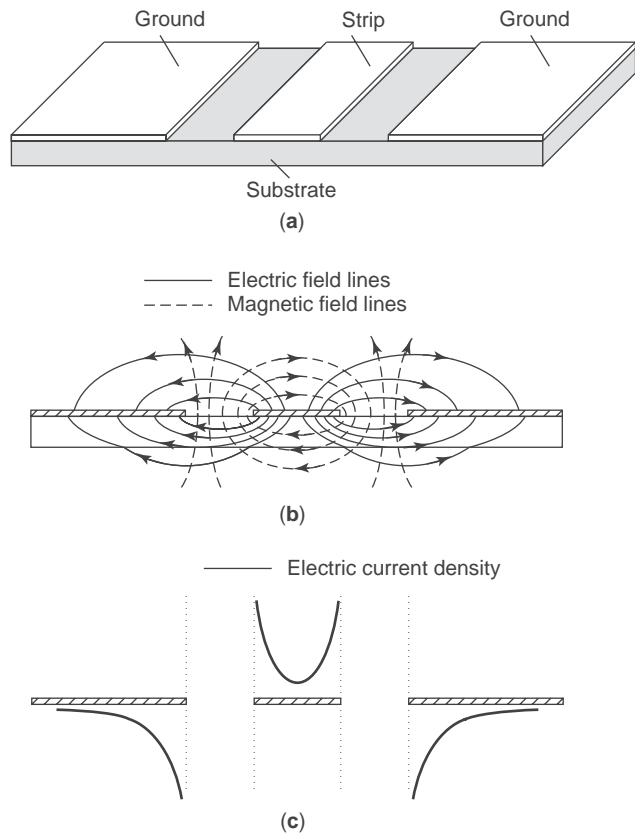


Figure 1. Schematic of infinite-ground coplanar waveguide (CPW) transmission line and distribution profiles of electromagnetic field and current density in cross section: (a) 3D schematic; (b) electric and magnetic field lines; (c) electric current density.

and modules. In this way, the cross-sectional dimensions, such as slot and strip widths, are readily selected electrically short in the frequency region of operation, so as to minimize the longitudinal magnetic field component.

Figure 1b shows the cross-sectional configurations of the electric and magnetic fields of the dominant quasi-TEM mode. The electric field lines start from the central conductor and then are symmetrically expanded with respect to the central plane toward the ground planes at two sides, whereas the magnetic field lines are perpendicular to their electric counterparts at any given location and surround the central conductor in terms of closed loops. Figure 1c illustrates the distribution of electric current densities on the strip conductor and ground planes, respectively, that are longitudinally oriented in an antiparallel pattern. The current density strength inherently tends to increase and then approach the infinity in an exponential function as the observed point moves to the metallic edges, regardless of either strip conductor or ground sides.

In Wen's work [1], the relative permittivity is assumed much larger than the unity ($\epsilon_r \gg 1$) so that the finite height of a substrate can be reasonably treated as the infinity ($h \rightarrow \infty$) for simplifying the theoretical analysis. But, in practice, ϵ_r and h have to be finite as shown in Fig. 2a. Also, the actual ground width of this CPW is usually finitely wide so as to formulate the call finite-ground CPW or FGCPW as shown in Fig. 2b. Further, an additional conductor plate is often formed on the opposite surface of a finite-height substrate in order to improve both the mechanical strength and power-handling capability, thus constructing the conductor-backed CPW (CBCPW) as illustrated in Fig. 2c. Moreover, many other modified CPW structures with dielectric multilayers and/or upper/lower

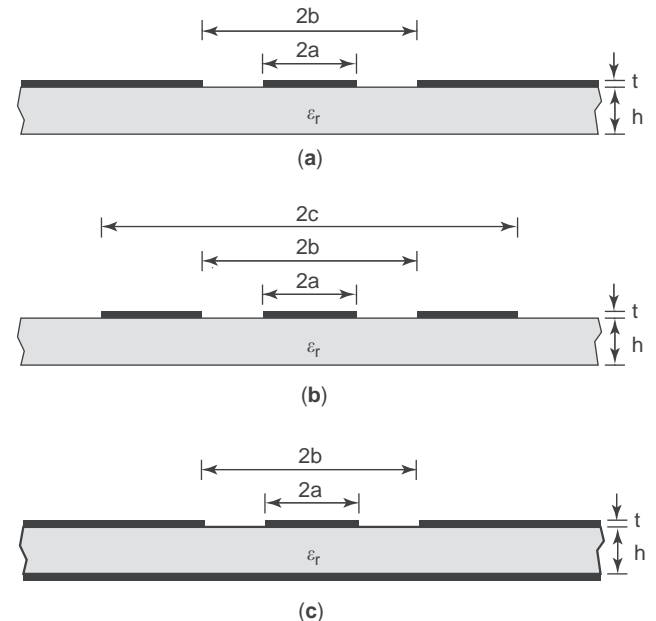


Figure 2. Cross-sectional view of three typical CPW transmission lines: (a) infinite-ground CPW; (b) finite-ground CPW; (c) conductor-backed CPW.

shielding conductors [2,3,5–7] are built on the basis of these three basic CPW in order to meet various requirements in realizing the preferred electrical performance and employing advanced fabrication techniques.

So far, extensive work in theory has been done to characterize a variety of CPW transmission lines in terms of per unit length characteristic impedance and propagation constants by developing the quasistatic and full-wave analysis approaches [2,3]. Assumption of quasi-TEM mode at low frequencies, the quasistatic conformal mapping technique was initially utilized to model the CPW line with infinite dielectric thickness [1] and then was significantly extended to consider a number of CPW structures with shielded and multilayered configurations [4–7]. In this way, the total per unit length capacitance can be derived as the algebraic sum of all the partial line capacitances [4–7] and separately calculated both above and below the slot interface. Generally speaking, this technique is strictly valid for the hypothesis that the interface of a substrate is considered as the magnetic wall or electric field lies on the dielectric interface. However, an accuracy of $>1\%$ for a wide range of physical dimensions and dielectric permittivity is achieved as compared with that of the full-wave spectral-domain method [6]. Of vital importance, this technique gives rise to analytical expressions for effective dielectric constants and characteristic impedance in terms of the ratio of complete elliptic integral of the first kind and its complement, $K(k)/K'(k)$, where k is the variable.

The detailed mathematics of this procedure can be found in the literature [e.g., 1–7] and are not discussed here. In this section, the three sets of closed-form design formulas are used to characterize three basic CPW structures in Figs. 2a–2c with respect to various physical dimensions. For the reader's convenience, the analytical expressions of the ratio $K(k)/K'(k)$, are provided below in two different regions of the variable k for infinite- and finite-width-ground CPWs:

$$\frac{K(k)}{K'(k)} = \frac{\pi}{\ln[2(1 + \sqrt[4]{1-k^2})/(1 - \sqrt[4]{1-k^2})]} \quad (0 \leq k \leq 0.707) \quad (1a)$$

$$\frac{K(k)}{K'(k)} = \frac{\ln[2(1 + \sqrt{k})/(1 - \sqrt{k})]}{\pi} \quad (0.707 \leq k \leq 1) \quad (1b)$$

2.1. Infinite-Ground CPW

For conventional CPW with infinite-width ground as in Fig. 2a, the two variables k_1 and k_2 are defined in terms of the dimensions a , b , and h , respectively, where the strip width $W = 2a$ and $S = b - a$:

$$k_1 = \frac{a}{b} \quad (2a)$$

$$k_2 = \frac{\sinh(\pi a/2h)}{\sinh(\pi b/2h)} \quad (2b)$$

As such, the per unit length effective dielectric constant and characteristic impedance can be deduced:

$$\epsilon_{re} = 1 + \frac{\epsilon_r - 1}{2} \frac{K(k_2) K'(k_1)}{K'(k_2) K(k_1)} \quad (3)$$

$$Z_0 = \frac{30\pi K'(k_1)}{\sqrt{\epsilon_{re}} K(k_1)} \quad (4)$$

Figures 3a and 3b show simulated results from Eqs. (3) and (4), respectively, with respect to the ratio of slot to strip widths (S/W in Fig. 3) under different h/W (height/width ratios). The impedance (Z_0) definitely increases as the slot is widened for all the four listed h/W because of reduced capacitive coupling between the strip conductor and two ground planes. As h/W increases, the Z_0 curve converges to that with very thick thickness ($h/W = 20$). Meanwhile, the effective dielectric constant (ϵ_{re}) falls down

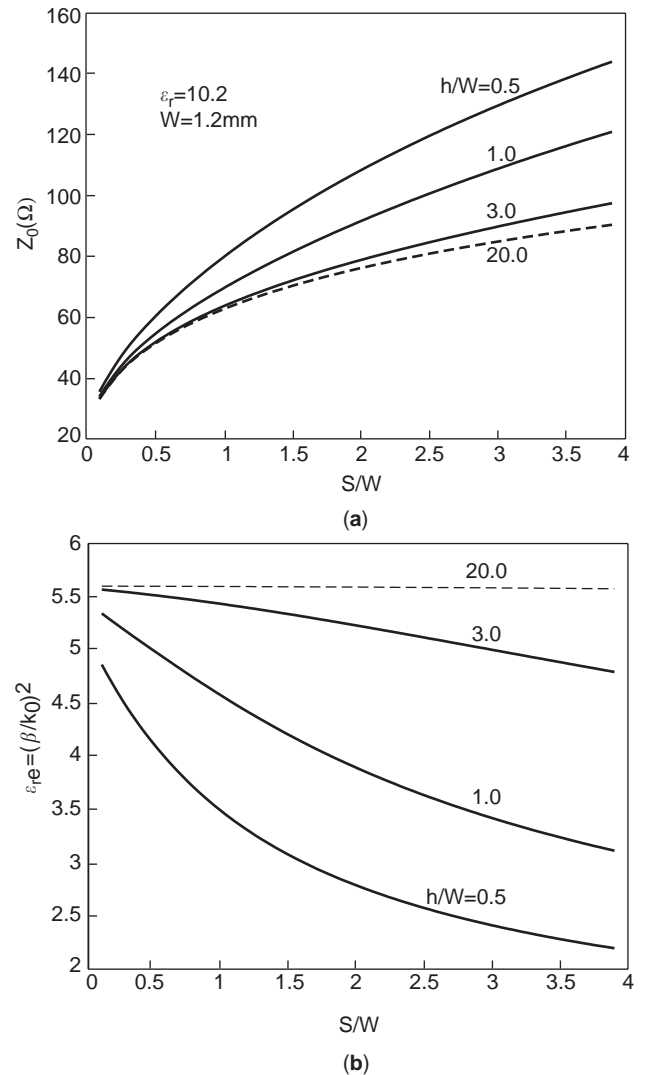


Figure 3. Per unit length transmission parameters of the infinite-ground CPW transmission line as a function of slot width (S/W) with varying substrate thickness (h/W): (a) characteristic impedance (Z_0); (b) effective dielectric constant (ϵ_{re}).

as the slot width is enlarged under the fixed finite thickness (h/W) and it eventually becomes almost independent of h if h/W is larger than 20 as can be seen in Fig. 3b. It can be further deduced from these results that the effect of finite dielectric substrate is almost ignorable if h exceeds $2b = W + 2S$.

2.2. Finite-Ground CPW

Practical CPW has finite-width ground planes as illustrated in Fig. 2b. In order to factor in the effect of finite ground, the two modified variables, k_3 and k_4 , are defined as below; thus Eqs. (3) and (4) are still valid for this finite-ground CPW by using k_3 and k_4 instead of k_1 and k_2 :

$$k_3 = \frac{a}{b} \sqrt{\frac{1 - b^2/c^2}{1 - a^2/c^2}} \quad (5a)$$

$$k_4 = \frac{\sinh(\pi a/2h)}{\sinh(\pi b/2h)} \sqrt{\frac{1 - \sinh^2(\pi b/2h)/\sinh^2(\pi c/2h)}{1 - \sinh^2(\pi a/2h)/\sinh^2(\pi c/2h)}} \quad (5b)$$

The calculated results are depicted in Figs. 4a and 4b, in which $W_1 = 2a$, $S = b - a$, and $W_2 = c - b$ indicate the strip, slot, and finite-ground widths, respectively. As the ground-to-strip width ratio of W_2/W_1 is reduced, Z_0 tends to increase and the effective ϵ_{re} also goes up slowly. This may be attributed to the weakened strip-to-ground coupling and partial transfer of field energy from the free space to dielectric substrate. Moreover, we can find that the effect of the two lateral finite grounds becomes much smaller as W_2 is widened beyond $2W_1$, especially for the narrow slot width (S).

2.3. Conductor-Backed CPW

An additional conductor plate is put on the lower interface of a substrate to form the *conductor-backed-CPW* (CBCPW) as shown in Fig. 2c. This CBCPW resembles a mixed coplanar-microstrip structure, thus supporting a parasitic microstriplike mode in addition to the dominant CPW mode. The CPW-mode characteristic impedance may be considerably reduced by the shunt connection of the two per unit length capacitances between strip and lateral ground as well as the strip and backed conductor. The performance of this CBCPW can also be characterized using the conformal mapping technique [2,3]. For this purpose, an alternative variable k_5 is defined as follows:

$$k_5 = \frac{\tanh(\pi a/2h)}{\tanh(\pi b/2h)} \quad (6)$$

As such, the two per unit length parameters can be calculated in terms of the two closed-form equations:

$$\epsilon_{re} = 1 + (\epsilon_r - 1) \frac{K(k_5)/K'(k_5)}{K(k_1)/K'(k_1) + K(k_5)/K'(k_5)} \quad (7)$$

$$Z_0 = \frac{60\pi}{\sqrt{\epsilon_{re}}} \frac{1}{K(k_1)/K'(k_1) + K(k_5)/K'(k_5)} \quad (8)$$

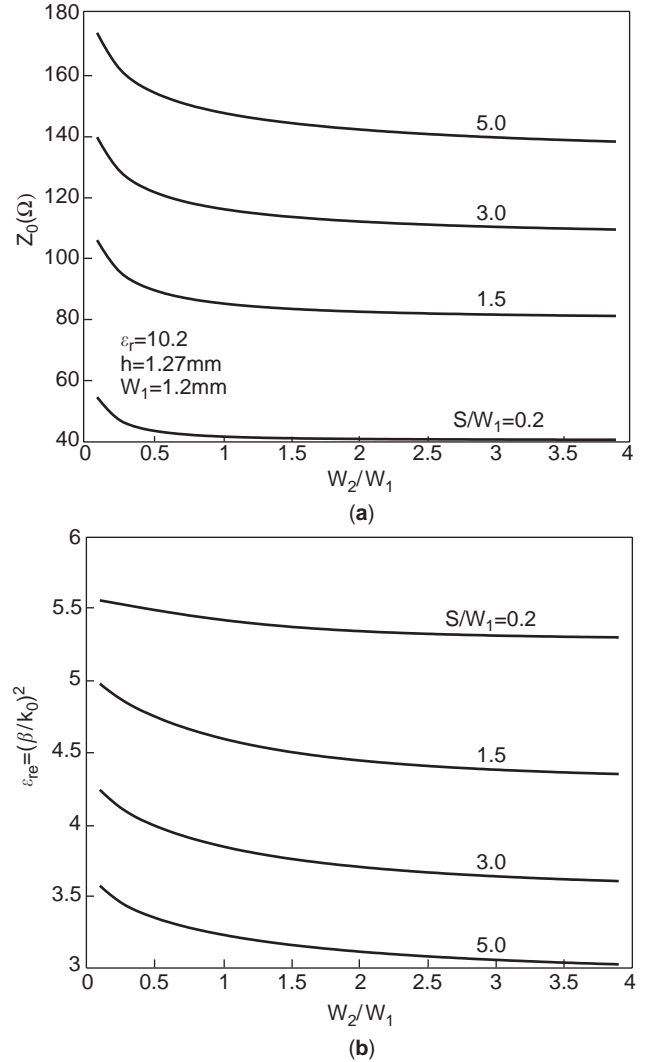


Figure 4. Per unit length transmission parameters of finite-ground CPW transmission line as a function of finite-ground width (W_2/W_1) with varying slot width (S/W_1): (a) characteristic impedance (Z_0); (b) effective dielectric constant (ϵ_{re}).

Figures 5a and 5b show the results of these two parameters versus the thickness-to-strip aspect ratio (h/W) under varied slot-to-strip aspect ratios (S/W). When the substrate is thin (i.e., with small h/W), the capacitive coupling between the strip and backed conductor is significantly tightened, causing this CBCPW to operate like a microstrip line with decreased characteristic impedance (Z_0), as can be observed in Fig. 5a. Meanwhile, the electromagnetic field is moved to the substrate region underneath the strip conductor, thereby enlarging the effective dielectric constant (ϵ_{re}) toward the dielectric permittivity (ϵ_r), as illustrated in Fig. 5b. At a narrow slot width of $S/W \leq 0.5$, the backed-conductor effect becomes negligibly small if the thickness (h) exceeds the strip width (W), implying that this CBCPW operates as a conventional CPW as in Fig. 2a. For the wide slot width ($S/W > 1.0$), both Z_0 and ϵ_{re} seem to depend on the substrate thickness (h/W) to some extent because of the concurrent existence of the strip-to-ground and strip-to-conductor coupling.

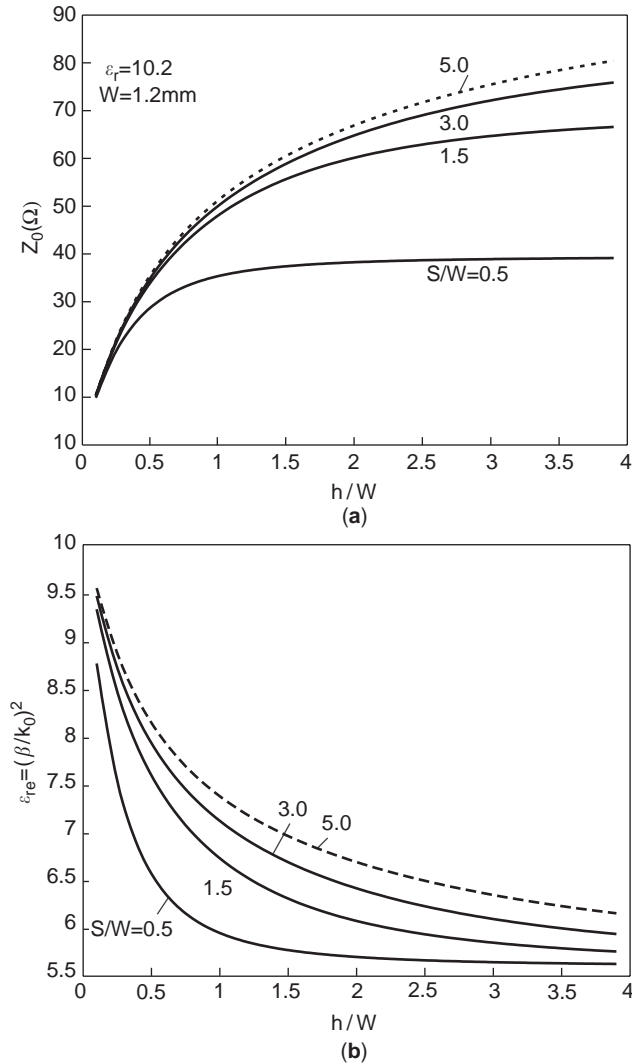


Figure 5. Per unit length transmission parameters of conductor-backed CPW transmission line as a function of substrate thickness (h/W) with varying slot width (S/W): (a) characteristic impedance (Z_0); (b) effective dielectric constant (ϵ_{re}).

Until now, the three basic CPW transmission lines have been characterized under the quasistatic assumption. The formulas presented above are well verified at low frequencies in comparison with the spectral-domain approach as discussed in Ref. 6. However, because of the inhomogeneous layers in these CPW, the two per unit length parameters become frequency-dispersive as the operating frequency increases as demonstrated extensively in the literature [2,3,8]. In addition, the higher-order modes may operate above their relevant cutoff frequencies and their parasitic effects cannot be taken into account in the design formulas above. Also, many other factors, such as the strip/ground conductor thickness and cross-sectional profiles, may seriously affect these two parameters. In order to rigorously model these CPW structures, a number of full-wave numerical approaches, such as the mode-matching method, spectral-domain method, method of lines, and the finite-element method, were successfully developed in

the 1970s–1990s. As the detailed procedures of these methods can be found in a contributed book [8], a lengthy and complicated formulation of these approaches in mathematics would be beyond the main objectives of this article and is not included here.

We nevertheless include some typical results using these full-wave approaches to demonstrate the electrical performance of CPW transmission lines with varied strip/conductor configurations [9,10]. Figures 6a and 6b show the calculated frequency-dispersive effective dielectric constants (ϵ_{re}) of the conductor-backed CPW, CBCPW, with rectangular or trapezoidal conductor configurations. In all these structures, ϵ_{re} seems to be frequency-independent at low frequencies ($f < 20 \text{ GHz}$) with a substrate thickness of $h = 100 \mu\text{m}$. This parameter increases sharply at the beginning and then more gradually as f increases, and eventually reaches to the relative permittivity of this substrate (i.e., $\epsilon_r = 12.9$), as f is beyond 100 GHz. In fact,

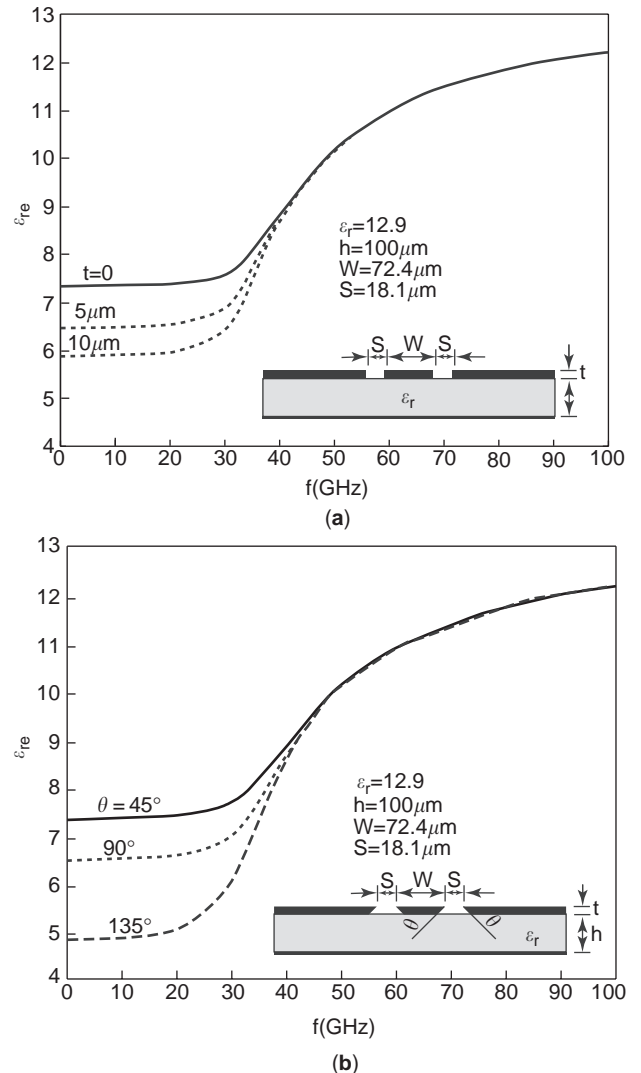


Figure 6. Frequency-dependent effective dielectric constant (ϵ_{re}) of conductor-backed CPW transmission line with rectangular or trapezoidal edge profile versus (a) conductor thickness (h) and (b) edge angle (θ).

all the electromagnetic (EM) fields definitely tend to be moved into the substrate region with high permittivity at high frequencies, thus causing the slow-wave propagation behavior with reduced velocity, which is the common frequency-dispersive feature for all CPW transmission lines. As can be observed in Fig. 6a, ϵ_{re} at low frequencies gradually decreases as the strip/ground thickness (t) increases from 0 to 10 μm . Because of tightened coupling between the central strip and two-side grounds for nonzero t , a small portion of EM fields in the substrate is moved to the free-space slot region. Figure 6b shows us that the varied angle (θ) of conductor edge wall affects the transmission properties. As θ increases, ϵ_{re} at low frequencies appears to drop because of the upward-oriented EM fields between the strip and ground.

3. MODIFIED CPW WITH ENHANCED PERFORMANCE

In this section, a variety of modified CPW transmission lines that have many promising features for applications in high-performance and millimeter-wave circuits will be overviewed. Figure 7a is the cross-sectional view of an initial CPW with metallic enclosure. This shielded CPW can completely avoid the unexpected radiation loss that occurs in the unbounded CPW discussed above. However, because of the high conductivity loss and serious frequency dispersion, the preferred construction for the CPW is suspension in a metallic enclosure as shown in Fig. 7b. This type of CPW was originally reported by Hatsuda [11], and the dominant-mode performance for this CPW is analyzed approximately using the relaxation method under the quasistatic assumption. To facilitate the mechanical installation, an improved CPW, the nonsymmetrically shielded CPW (NSCPW) [12] is shown in cross section Fig. 7c. This NSCPW is constructed by mounting the CPW in a nonsymmetric enclosure with respect to the upper and lower regions through the grooves. In addition to the low transmission loss and low frequency dispersion, this shielded NSCPW is best suited for mounting solid-state devices, constructing matching elements in series and shunt, and formulating the biasing circuits [12]. The propagation characteristics of the dominant and high-order modes are theoretically studied using full-wave methods [12,13], and the predicted phase constants of these modes are experimentally verified [12] by measuring the multiple transmission peaks of the two-port NSCPW resonator with coaxial launchers at two ends.

The theoretical characteristics of multilayered CPW transmission lines have been reported in the literature [5–7]. Three of these CPW structures that exhibit enhanced electrical performance, namely, elevated, insulated, and nonleaky CPW, are discussed here (see cross-sectional views in Fig. 8). The elevated CPW in Fig. 8a is proposed [14] for construction of a nonlinear transmission line fabricated with Schottky diodes on GaAs substrate. This CPW has several attractive features such as low loss, high wave velocity, and broad frequency bandwidth. Its propagation performance is characterized with respect to varied elevated heights [15] using the full-wave approach. The CPW is fabricated on silicon substrate for low-cost

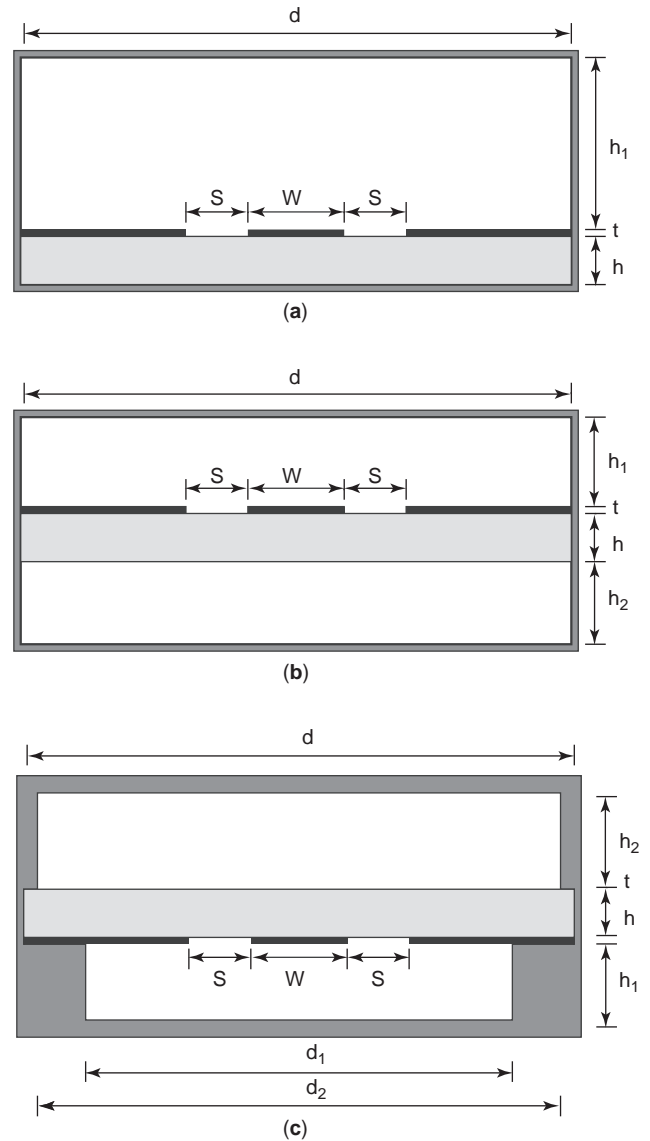


Figure 7. Cross-sectional view of enclosed CPW transmission lines: (a) shielded CPW; (b) suspended CPW; (c) suspended CPW with pedestal.

application in radiofrequency integrated circuits (RFICs). Due to high attenuation, the CPW is usually constructed by forming an insulated layer, such as low-loss polyimide [16] or SiO_2 [17], above the silicon substrate, as shown in Fig. 8b. The measured results show that attenuation can be reduced if the insulated layer is thick relative to the strip and slot widths [16]. Figure 8c shows the multilayered CBCPW with the upper metallic cover, and this CBCPW is one of two possible nonleaky CPW structures [18]. As demonstrated in the early literature, the presence of the backed conductor in the CBCPW causes unexpected power leakage into transverse directions in the form of a parallel-plate wave. As discussed by Liu et al. [18], this nonleaky CPW is established by forming an additional upper layer or insulated layer with higher permittivity above or below the strip/slot interface. Simulated results

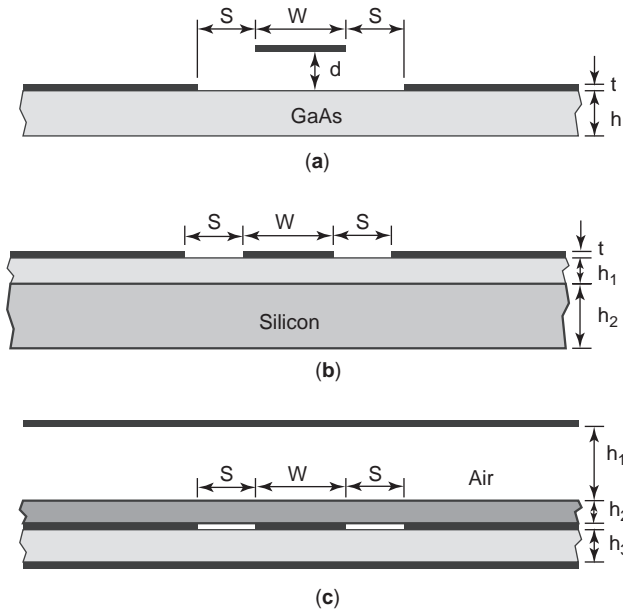


Figure 8. Cross-sectional view of unbounded CPW transmission lines: (a) elevated CPW; (b) insulated CPW; (c) nonleaky CPW.

show that the dominant CPW mode is purely bound without leakage over certain frequency ranges as verified by experiment [18].

Microshield line originated with Dib et al. [19] as a new type of monolithic transmission line. Figure 9a shows its cross-sectional geometry, in which the ground plane is deformed to totally or partially surround the inner conductor. By using the membrane technology, the inner conductor can be suspended in air, thus eliminating dielectric loss even at high frequencies. This line may be considered as an enhancement of the CPW or microstrip-line structure. As compared with the conventional CPW investigated above, this microshield line may have several advantages, such as no requirement for via holes or airbridges for ground equalization, reduced radiation loss, reduced electromagnetic interference, and a wide impedance range [19]. Since then, various types of microshield lines have been developed and analyzed using the efficient static or accurate full-wave methods. The V-shaped microshield line with triangular cavity profile is illustrated in Fig. 9b. Using the conformal mapping technique under the static assumption [20], a set of closed-form expressions is derived for characterization of symmetric and asymmetric V-shaped lines. In addition, Figs. 9c and 9d show the microshield lines with upward- and downward-oriented trapezoidal shapes, respectively, which may be the practical shape in fabrication. Their performances are studied in [21] with respect to positive or negative sidewall slope [i.e., angle (ϕ)], implying that the effect of these nonvertical sidewalls can be minimized by keeping these sidewalls away from the slot edges.

The silicon micromachining technique has been developed to effectively remove the lossy dielectric material below, above, or around the coupled apertures in CPW in an effort to minimize propagation loss and reduce frequency dispersion. Figure 10a shows the micromachined CPW

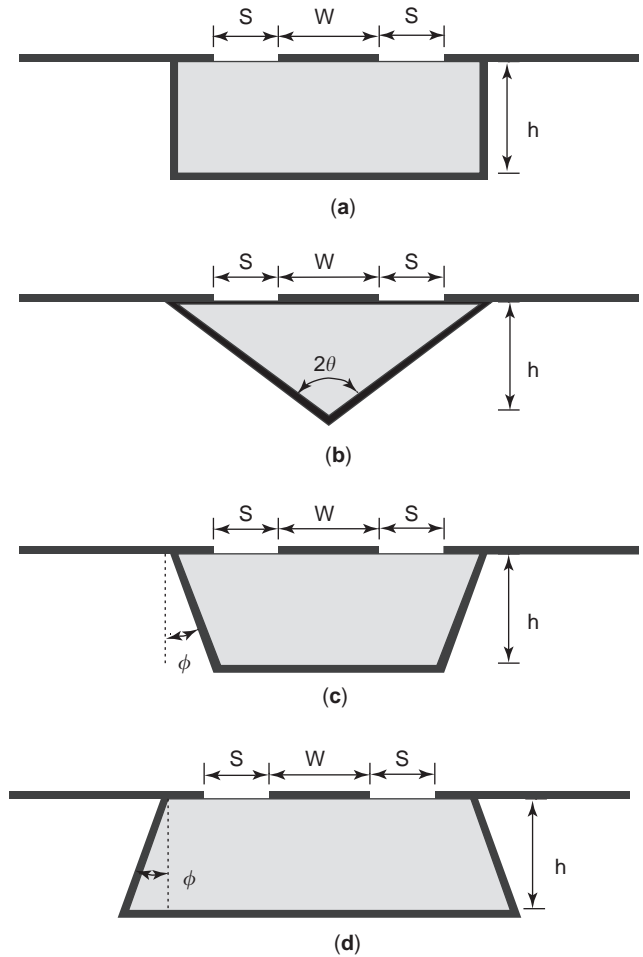


Figure 9. Cross-sectional view of microshielded CPW transmission lines with various cavity profiles: (a) rectangular shape; (b) triangular shape; (c,d) trapezoidal shape.

[22], where the material underneath the coupled apertures is partially removed for construction of the free-space V-shaped grooves. This resulting line minimizes the total propagation loss since the EM fields are distributed mainly in the lossless V-shaped region and current density flow on the conductor is reduced. Figure 10b shows a practical microshielded membrane CPW that is fabricated by attaching two silicon wafers together [3,22]. The upper wafer, with a metallized cavity, supports a membrane with the CPW. Because of an extremely thin electric membrane, the overlapping capacitances between the top ground planes and cavity sidewalls are very large in the microwave region, thus virtually short-circuiting the overlapped region. The lower wafer is metallized on the top surface and provides the bottom wall of the cavity. Figure 10c shows a micromachined overlay CPW [23]. By partially elevating the edges of the central conductor and further overlaying them with the two outer ground planes, this CPW has a lower propagation loss because the current density is redistributed on the conductors and the impedance range widens.

In practice, the CPW is usually placed on a ground plane for mechanical support, inadvertently giving rise to

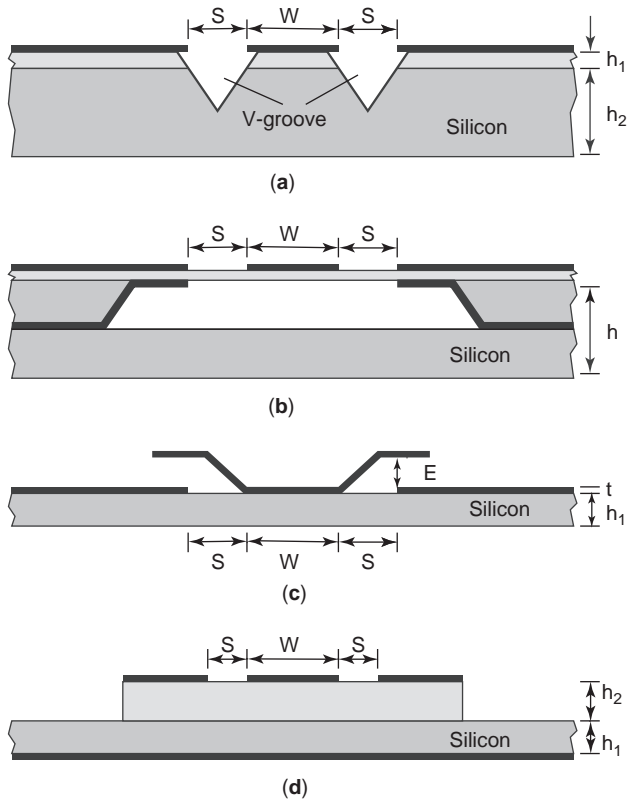


Figure 10. Cross-sectional view of silicon-based low-loss CPW transmission lines: (a) micromachined CPW with V-shaped groove; (b) microshielded membrane CPW; (c) micromachined overlay CPW; (d) Si-layer submounted CPW.

the conductor-backed CPW. In this CBCPW, the dominant CPW mode may be coupled to the parallel waveguide mode, which propagates transversally, causing the unwanted power leakage [24,25]. In addition, the substrate and side ground planes are always finitely widened, and this transversal leakage leads to substrate resonance and multiple-mode interference. In order to address this issue, the highly lossy silicon-doped substrate is inserted between the CPW and backed conductor as illustrated in Fig. 10d. This silicon submount layer operates as the absorbing layer to absorb this transversal leakage and eventually suppress the potentially harmful resonance. This suppression method is examined in numerical simulation and also verified by experimental characterization of the fabricated GaAs CBCPW [25]. Tien et al. [24] have shown that by laterally short-circuiting the side grounds with the lower ground, the electromagnetic field of the dominant CPW mode can be confined mostly within the surrounded conductor, thus alternatively suppressing this parasitic resonance.

4. COUPLED CPW

The traditional coupled CPW was originally presented [26] for design of directional couplers with improved isolation due to smaller difference between the even- and

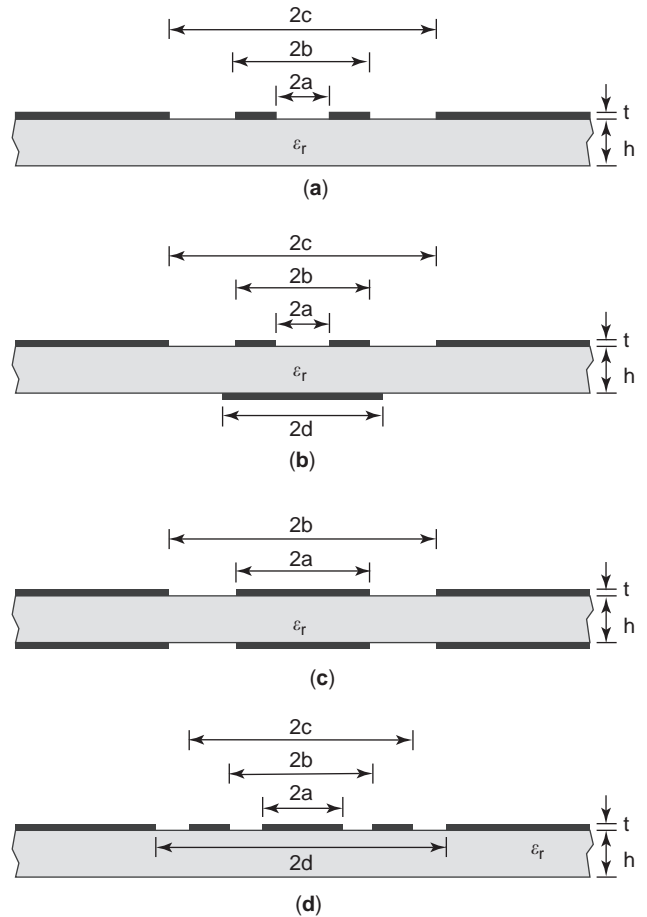


Figure 11. Cross-sectional view of various coupled CPW transmission lines: (a) edge-coupled; (b) backed-conductor-coupled; (c) broadside-coupled; (d) parallel-coupled.

odd-mode propagation velocities. As shown in Fig. 11a, it is constructed by placing the two parallel strip conductors in close proximity. Due to strong interaction between these two conductors, the EM power is coupled from one line to the other, and the amount of coupling depends mainly on the distance of separation $2a$ and longitudinal length of the coupling section. Under the approximate assumption of infinitely thick substrate, the static conformal mapping technique is applied to characterize the two per unit length capacitances in conjunction with the even and odd dominant modes. As a result, the two sets of closed-form formulas can be derived to calculate the characteristic impedance values and effective dielectric constants. Because the substrate is always electrically finite, the even- and odd-mode transmission parameters of the coupled CPW in Fig. 11a with finite thickness are obtained using the same static technique as employed by Wen [26]. The relevant analytical formulas can be found in Ref. 27. In the even-mode case, the two transmission parameters, $\epsilon_{re,e}$ and $Z_{0,e}$, can be obtained

$$\epsilon_{re,e} = 1 + \frac{\epsilon_r - 1}{2} \frac{K(k_{e2})K'(k_{e1})}{K'(k_{e2})K(k_{e1})} \quad (9)$$

$$Z_{0,e} = \frac{60\pi}{\sqrt{\epsilon_{re,e}}} \frac{K'(k_{e1})}{K(k_{e1})} \quad (10)$$

where

$$k_{e1} = \sqrt{\frac{b^2 - a^2}{c^2 - a^2}} \quad (11a)$$

$$k_{e2} = \sqrt{\frac{\sinh^2(\pi b/2h) - \sinh^2(\pi a/2h)}{\sinh^2(\pi c/2h) - \sinh^2(\pi a/2h)}} \quad (11b)$$

In the odd-mode case, the two corresponding parameters, $\epsilon_{re,o}$ and $Z_{0,o}$, can be given as

$$\epsilon_{re,o} = 1 + \frac{\epsilon_r - 1}{2} \frac{K'(k_{o1})}{K(k_{o1})} \left(\frac{K(k_{o2})}{K'(k_{o2})} + \frac{K(k_{o3})}{K'(k_{o3})} \right) \quad (12)$$

$$Z_{0,o} = \frac{60\pi}{\sqrt{\epsilon_{re,o}}} \frac{K'(k_{o1})}{K(k_{o1})} \quad (13)$$

in which the three variables k_{o1} , k_{o2} and k_{o3} can be analytically expressed as a function of the incomplete elliptical integral of the first kind with respect to all transverse dimensions [27]. These formulas are effectively verified by Cheng [27] in comparison with the results from the full-wave method.

In fact, the traditional coupled CPW in Fig. 11a usually has weaker coupling due to edge coupling, thus resulting in a limited operating bandwidth. In order to tighten the coupling to a certain degree, an extra finite-extent backed conductor is formed on the opposite surface of a dielectric substrate underneath the coupled strip conductors [28], as shown in Fig. 11b. This backed conductor is strongly coupled with each upper strip conductor in a surface-to-surface format, thus increasing the degree of coupling between the two strip conductors. Figure 11c shows the cross-sectional view of a broadside-coupled CPW [29], in which the two CPW lines are formed at the upper and lower surfaces of a thin substrate. Under the assumed upper and lower shielding covers, the even- and odd-mode characteristics of this substrate are studied using the quasi-static technique. Numerical results [29] demonstrate a significant increase in the ratio of the two impedances, causing the coupling enhancement. However, as was the case in the CBCPW, the parallel-plate mode may be excited in such a broadside-coupled CPW to transversally propagate in the substrate between the two ground planes. This unexpected mode raises some problematic issues, such as power leakage, EM interference, and increased power loss. Thus, this broadside-coupled CPW should be constructed in a metallic enclosure that maintains electrical contact with all the ground planes. In addition, a triple-line-coupled CPW has been characterized by Cheng [30], and its cross-sectional geometry is drawn in Fig. 11d. By equalizing the electrical potential in the central strip with those in the two side ground planes, this arrangement can effectively suppress spurious coupling between the two CPW lines so as to avoid any signal distortion. Also, this triple line constitutes a basic block for the parallel-coupled bandpass filter. Its coupling performance is

investigated using static and full-wave approaches such as conformal mapping [30].

5. PERIODIC SLOW-WAVE CPW

An infinite-extended CPW structure, loaded with identical obstacles at each periodic interval, may be considered as an effective uniform CPW transmission line [31]. This periodic CPW exhibits two fundamental properties: passband-stopband selectivity and slow-wave propagation. The passband performance is basically realized by periodically interrupting the uniform CPW with series capacitive or shunt inductive elements, in which the periodicity is comparable to the guided-wavelength operation in the passband. However, because of the unexpected occurrence of multiple ripples within the passband, this periodic CPW has rarely been studied for practical design of CPW circuits. On the contrary, various periodic CPW transmission lines with slow-wave and bandstop behaviors [32–40], have generated increasing interest since the early 1980s. Regardless of the various configurations and different terminologies, to my best knowledge, this class of periodic CPW commonly has two distinct features for the dominant mode: slow-wave propagation at low frequencies and stopband attenuation in the midfrequency range.

In order to reduce the loss in uniform slow-wave CPW with metal-insulator-semiconductor (MIS) and Schottky contact configurations, a crosstie conductor grating with a periodic pattern [32] is embedded underneath the uniform CPW surface to make up the initial periodic slow-wave CPW transmission line, as shown in Fig. 12a. Then, a modified crosstie overlay slow-wave CPW [33] is constructed by swapping the crosstie conductor with the CPW layer, as illustrated in Fig. 12b. Observing the cross section of the crosstie conductor in Fig. 12a or 12b, we see that the capacitive coupling between the central strip conductor and the two outer ground planes are significantly increased, thus reducing the characteristic impedance at this section. Actually, this crosstie conductor grating can be equivalently treated as extra shunt capacitive elements that are periodically loaded on the uniform CPW without a crosstie layer [40]. Alternatively, a slow-wave CPW is formed on periodically doped semiconductor substrate. Its schematic is shown in Fig. 12c, and Wang and Itoh [34] have shown that it can reduce the attenuation. In Refs. 32–34, these periodic CPW lines are approximately characterized by the well-known Floquet theorem as well as the approximation that the effects of each junction discontinuity between two constituent sections with and without crossties are neglected [32–34]. After these two sections are analyzed using the two-dimensional (2D) numerical technique, two effective per unit length transmission parameters of these periodic CPW lines are derived to explicitly demonstrate the fundamental guided-wave characteristics, namely, slow wave at low frequencies and bandstop or band rejection at certain midfrequencies.

To satisfy the requirements in miniaturizing millimeter-wave integrated circuits (MMICs), in a novel class of periodic slow-wave CPW lines [35–38], the strip conductor and/or ground-plane configurations are irregularly

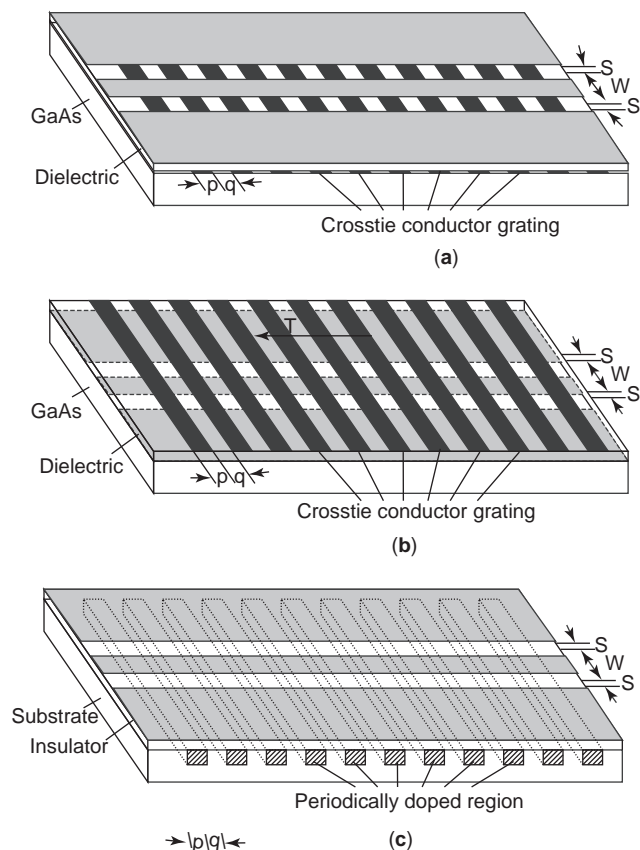


Figure 12. Schematic of traditional periodic slow-wave CPW transmission lines with (a) embedded crosstie grating; (b) overlaid crosstie grating; and (c) periodically doped substrate.

rearranged with periodically varied patterns. Figure 13a shows the periodic CPW with the central conductor in the form of a meanderline [35]. Because of an increased inductance per unit length, the slow-wave factor in the periodic CPW is at least twofold greater than that in the uniform CPW, resulting in a reduction in the longitudinal length. Figure 13b shows the shunt-capacitive-loaded slow-wave CPW [36] with interdigitated capacitors between the inner strip conductor and outer ground planes. Experimental study is performed to extract its complex propagation constant and characteristic impedance, thereby confirming the theoretically predicted slow-wave behaviors. By forming the periodic fingers in the two grounds and inserting them into the transversal slits of a central meander strip, a modified meanderline CPW [37] is constructed as illustrated in Fig. 13c. Its enhanced capacitance per unit lengths results in further lowering the velocity of propagation as exhibited in experiment. The work [38] describes the slow-wave CPW with periodic slots in the ground plane as shown in Fig. 13d. Since the uniform CPW is periodically loaded by these short-end slot-line stubs, the extra series inductance per unit length is increased so as to raise the slow-wave factor involved here. The calibration method in experiment has been utilized [38] to extract the velocity and characteristic impedance from the measured S parameters.

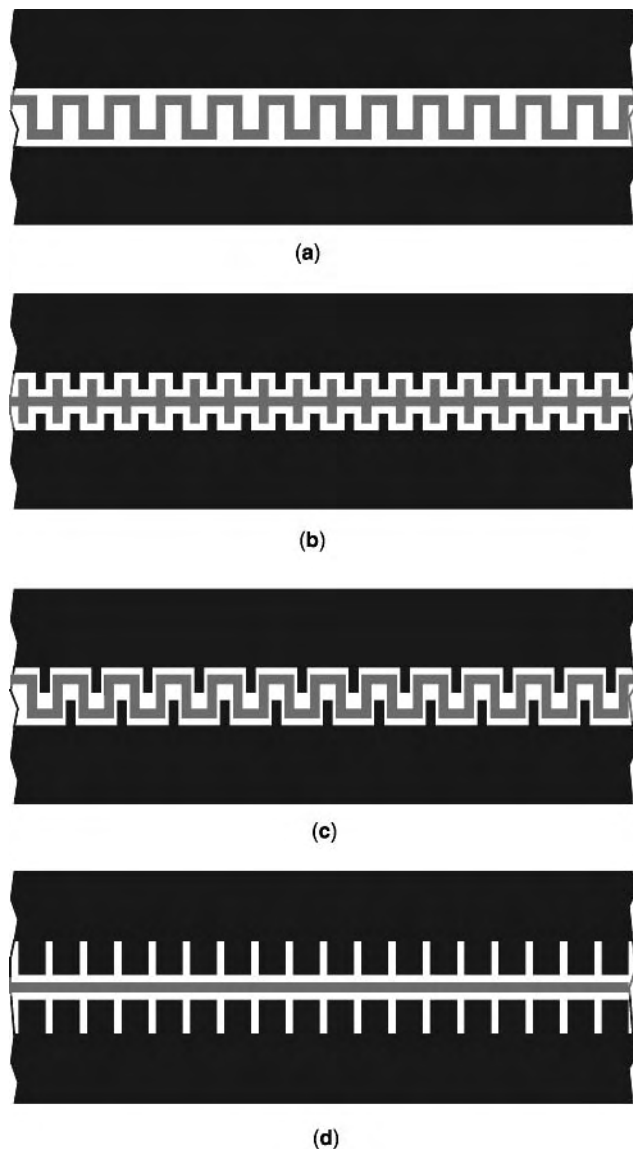


Figure 13. Top view of uniplanar slow-wave CPW transmission lines with series inductive and/or shunt inductive loading: (a) meanderline; (b) interdigitated capacitor; (c) modified meanderline; (d) periodically slotted ground.

The terms, *photonic* and *electromagnetic bandgap CPW*, introduced in 1999 [39], have again aroused significant interest in characterizing periodically loaded CPW transmission lines with nonuniform patterns on the backed conductor or CPW central strip/ground surface. In this aspect, the periodicity is selected to be electrically comparable to the CPW guided wavelength at high frequencies, thus inducing wave attenuation within a certain frequency range referred to as the *bandstop* [31], *band-reject* [33], or *bandgap* characteristic [39]. Extensive work has been undertaken in theory and experiment to characterize a large number of finite extended periodic CPW structures with varied unit configurations in terms of S parameters, thus illustrating the bandstop behavior of a two-port device [39]. Following the results in much of the

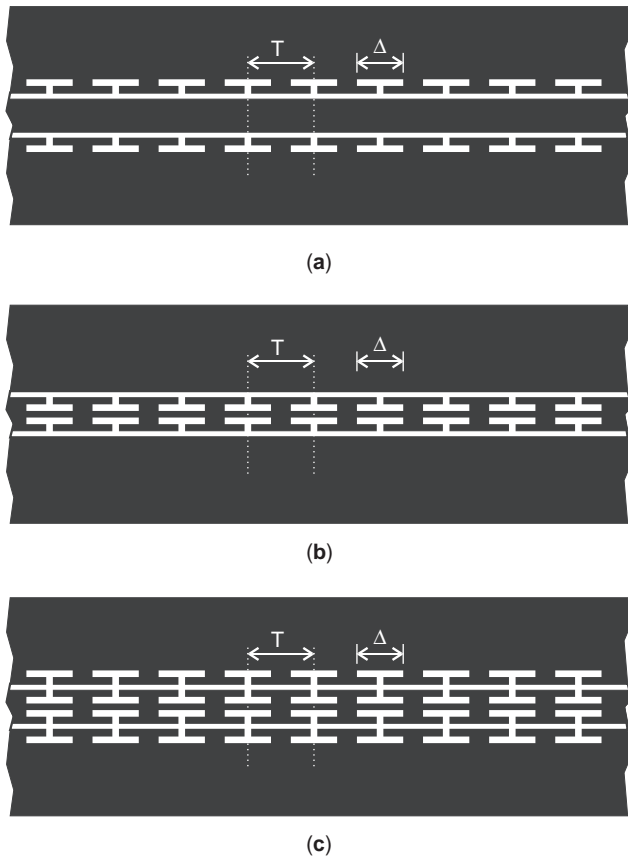


Figure 14. Top view of series inductively periodic CPW transmission lines with slow-wave and bandstop transmission behaviors: (a) T-slotted ground; (b) T-slotted strip; (c) T-slotted strip and ground.

early literature [31–38], one can deduce that the two per unit length transmission parameters are critically important in exposing the complete guided-wave characteristics of various periodic CPW transmission lines with infinite extension. Figure 14 illustrates the three modified periodic CPW transmission lines reported in Ref. 40, extended from the original structure described in Ref. 38. They are constructed by etching a pair of transverse slots on the ground planes and/or strip conductor so as to enhance the shunt inductive loading with low radiation loss.

With no hypothesis in theoretical modeling, the two per unit length transmission parameters of these infinite-extended periodic CPW lines [40] are directly extracted using the full-wave self-calibrated method of moments. Figure 15a plots the three relevant sets of extracted complex propagation constants (γ) normalized to the free-space wavenumber (k_0), specifically, $\gamma/k_0 = \alpha + j\beta$, where α and β are the attenuation and phase constants, respectively. Initially, the nonzero β/k_0 increases slowly and then rises rapidly while α/k_0 remains zero at low frequencies, regardless of the (varied) configurations. As the frequency further increases, β/k_0 begins to fall after peaking and α/k_0 appears, increasing and decreasing until it disappears again. These frequency ranges with nonzero α/k_0 are the so-called bandstop, band rejection, or bandgap for the guided wave propagating in these periodic CPW trans-

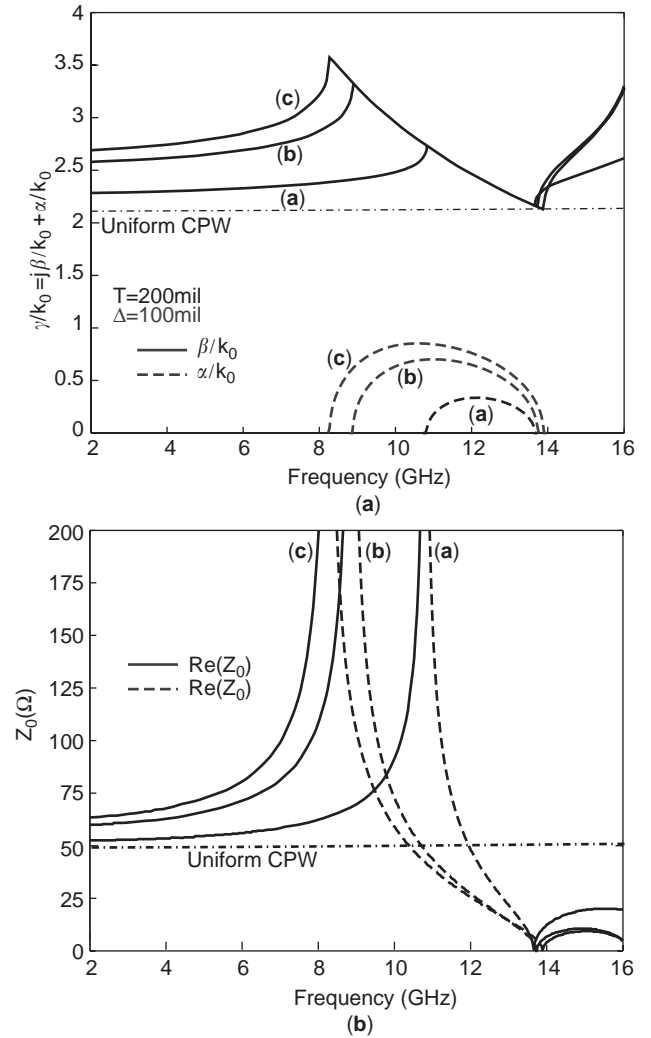


Figure 15. Per unit length transmission parameters of the three T-slotted periodic CPW transmission lines in Fig. 16: (a) complex propagation constant; (b) complex characteristic impedance.

mission lines. One of these lines, the periodic CPW (Fig. 15c) has the largest slow-wave factor at low frequencies and achieves the widest stop bandwidth because of inductive loading of paired slots on both inner and outer conductors. Figure 15b shows three sets of complex characteristic impedances, $Z_0 = \text{Re}(Z_0) + j \text{Im}(Z_0)$. In the lowpass frequency region, the real $\text{Re}(Z_0)$ tends to increase slowly and then exponentially rapidly to infinity, while the imaginary $\text{Im}(Z_0)$ remains zero. Then, $\text{Re}(Z_0)$ suddenly disappears and is converted to its infinity imaginary counterpart, $\text{Im}(Z_0)$, and this $\text{Im}(Z_0)$ drops off very quickly to zero. These nonzero $\text{Im}(Z_0)$ and zero $\text{Re}(Z_0)$ within the whole stopband provide an alternative physical view on the guided-wave bandstop behaviors of all the periodic slow-wave CPW transmission lines discussed here.

6. CONCLUSIONS

This article systematically describes the fundamental geometries and propagation characteristics of various

uniform CPW and periodic slow-wave CPW transmission lines. First, the three basic CPW lines with infinite or finite ground width and backed conductor are discussed, including detailed design formulas. Then, a variety of modified CPW lines, namely, shielded, suspended, and micromachined CPW, including their performance advantages such as low conductivity and low material and radiation losses, are briefly discussed. Next, four coupled CPW lines are roughly investigated in terms of relative coupling. Finally, several typical infinitely extended periodic CPW lines are characterized as an effective uniform CPW transmission line and their complete guided-wave performance, such as slow-wave propagation and stop-band attenuation, are demonstrated in terms of dispersive and complex propagation constants and characteristic impedance per unit length.

BIBLIOGRAPHY

1. C. P. Wen, Coplanar waveguide: A surface strip transmission line suitable for nonreciprocal gyromagnetic device applications, *IEEE Trans. Microwave Theory Tech.* **17**(12):1087–1090 (1969).
2. K. C. Gupta, R. Garg, I. Bahl, and P. Bhartia, *Microstrip Lines and Slotlines*, Artech House, Norwood, MA, 1996.
3. R. N. Simons, *Coplanar Waveguide Circuits, Components, and Systems*, Wiley, New York, 2001.
4. C. Veyres and V. F. Hanna, Extension of the application of conformal mapping technique to coplanar lines with finite dimension, *Int. J. Electron.* **48**(1):47–56 (1980).
5. G. Ghione and C. U. Naldi, Coplanar waveguides for MMIC applications: effect of upper shielding, conductor backing, finite-extent ground planes, and line-to-line coupling, *IEEE Trans. Microwave Theory Tech.* **35**(3):260–267 (1987).
6. S. S. Bedair and I. Wolff, Fast, accurate and simple approximate analytic formulas for calculating the parameters of supported coplanar waveguides for (M)MIC's, *IEEE Trans. Microwave Theory Tech.* **40**(1):41–48 (1992).
7. S. Gevorgian, L. J. P. Linner, and E. L. Kollberg, CAD models for shielded multilayered CPW, *IEEE Trans. Microwave Theory Tech.* **43**(4):772–779 (1995).
8. T. Itoh, *Numerical Techniques for Microwave and Millimeter-Wave Passive Structures*, Wiley, New York, 1989.
9. L. Zhu and E. Yamashita, Effects of conductor edge profile on transmission properties of conductor-backed coplanar waveguides, *IEEE Trans. Microwave Theory Tech.* **43**(4):847–853 (1995).
10. M. Goano, F. Bertazzi, P. Caravelli, G. Ghione, and T. A. Driscoll, A general conformal-mapping approach to the optimum electrode design of coplanar waveguides with arbitrary cross section, *IEEE Trans. Microwave Theory Tech.* **49**(9):1573–1580 (2001).
11. T. Hatsuda, Computation of coplanar-type strip-line characteristics by relaxation method and its application to microwave circuits, *IEEE Trans. Microwave Theory Tech.* **23**(5):795–802 (1975).
12. F. Alessandri, U. Goebel, F. Melai, and R. Sorrentino, Theoretical and experimental characterization of nonsymmetrical shielded coplanar waveguides for millimeter-wave circuits, *IEEE Trans. Microwave Theory Tech.* **37**(12):2020–2027 (1989).
13. L. Zhu and E. Yamashita, Full-wave boundary integral equation method for suspended planar transmission lines with pedestals and finite metallization thickness, *IEEE Trans. Microwave Theory Tech.* **41**(3):478–483 (1993).
14. U. Bhattacharya, S. Allen, and M. J. W. Rodwell, DC-725 GHz sampling circuits and subpicosecond nonlinear transmission lines using elevated coplanar waveguide, *IEEE Microwave Guided Wave Lett.* **5**(2):50–52 (1995).
15. S. Hofschien and I. Wolff, Simulation of an elevated coplanar waveguide using 2-D FDTD, *IEEE Microwave Guided Wave Lett.* **6**(1):28–30 (1996).
16. G. E. Ponchak and L. P. B. Katehi, Measured attenuation of coplanar waveguide on CMOS grade silicon substrates with polyimide interface layer, *IEE Electron. Lett.* **34**(13):1327–1329 (1998).
17. C. M. Nam and Y. S. Kwon, Coplanar waveguide on silicon substrate with thick oxidized porous silicon (OPS) layer, *IEEE Microwave Guided Wave Lett.* **8**(11):369–371 (1998).
18. Y. Liu, K. Cha, and T. Itoh, Non-leaky coplanar (NLC) waveguides with conductor backing, *IEEE Trans. Microwave Theory Tech.* **43**(5):1067–1072 (1995).
19. N. I. Dib, W. P. Harokopus, and P. B. Katehi, Study of a novel planar transmission line, *IEEE MTT-S Int. Microwave Symp. Digest*, 1991, pp. 623–626.
20. K. K. M. Cheng and I. D. Robertson, Simple and explicit formulas for the design and analysis of asymmetrical V-shaped microshield line, *IEEE Trans. Microwave Theory Tech.* **43**(10):2501–2504 (1995).
21. K. K. M. Cheng and I. D. Robertson, Quasi-TEM study of microshield lines with practical cavity sidewall profiles, *IEEE Trans. Microwave Theory Tech.* **43**(12):2689–2694 (1995).
22. K. J. Herrick, T. A. Schwarz, and L. P. B. Katehi, Si-micromachined coplanar waveguides for use in high-frequency circuits, *IEEE Trans. Microwave Theory Tech.* **46**(6):762–768 (1998).
23. H. T. Kim, S. Jung, J. H. Park, C. W. Baek, Y. K. Kim, and Y. Kwon, A new micromachined overlay CPW structure with low attenuation over wide impedance ranges and its application to low-pass filters, *IEEE Trans. Microwave Theory Tech.* **49**(9):1634–1639 (2001).
24. C. C. Tien, C. K. C. Tzuang, S. T. Peng, and C. C. Chang, Transmission characteristics of finite-width conductor-backed coplanar waveguide, *IEEE Trans. Microwave Theory Tech.* **41**(9):1616–1624 (1993).
25. S. J. Kim, H. S. Yoon, and H. Y. Lee, Suppression of leakage resonance in coplanar MMIC packages using a Si sub-mount layer, *IEEE Trans. Microwave Theory Tech.* **48**(12):2664–2669 (2000).
26. C. P. Wen, Coplanar-waveguide directional couplers, *IEEE Trans. Microwave Theory Tech.* **18**(6):318–322 (1970).
27. K. K. M. Cheng, Analysis and synthesis of coplanar coupled lines on substrate of finite thicknesses, *IEEE Trans. Microwave Theory Tech.* **44**(4):636–639 (1996).
28. C. L. Liao and C. H. Chen, Full-wave characterization of an edge-coupled coplanar-waveguide structure with backed conductor, *IEEE MTT-S Int. Microwave Symp. Digest*, 2000, pp. 1089–1092.
29. S. S. Bedair and I. Wolff, Fast and accurate analytic formulas for calculating the parameters of a general broadside-coupled coplanar waveguide for (M)MIC applications, *IEEE Trans. Microwave Theory Tech.* **37**(5):843–850 (1989).
30. K. K. M. Cheng, Analytical formula for calculating the coupling characteristics between parallel coplanar lines, *IEE Electron. Lett.* **32**(13):1208–1209 (1996).

31. R. E. Collin, Periodic structures and filters, in *Foundations for Microwave Engineering*, McGraw-Hill, New York, 1992, Chap. 8.
32. S. Seki and H. Hasegawa, Cross-tie-slow-wave coplanar waveguide on semi-insulating GaAs substrate, *IEE Electron. Lett.* **17**(25):940–941 (1981).
33. Y. Fukuoka and T. Itoh, Slow-wave coplanar waveguide on periodically doped semiconductor substrate, *IEEE Trans. Microwave Theory Tech.* **31**(12):1013–1017 (1983).
34. T. H. Wang and T. Itoh, Compact grating structure for application to filters and resonators in monolithic microwave integrated circuits, *IEEE Trans. Microwave Theory Tech.* **35**(12):1176–1182 (1987).
35. W. H. Haydl, Properties of meander coplanar transmission lines, *IEEE Microwave Guided Wave Lett.* **2**(11):439–441 (1992).
36. E. H. Bottcher, H. Pfitzenmaier, E. Droge, and D. Bimberg, Millimetre-wave coplanar slot transmission lines on InP, *IEE Electron. Lett.* **32**(15):1377–1378 (1996).
37. A. Gorur, C. Karpuz, and M. J. Lancaster, Modified coplanar meander transmission line for MMICs, *IEE Electron. Lett.* **30**(16):1317–1318 (1994).
38. R. Spickermann and N. Dagli, Experimental analysis of millimeter wave coplanar waveguide slow wave structures on GaAs, *IEEE Trans. Microwave Theory Tech.* **42**(10):1918–1924 (1994).
39. F. R. Yang, K. P. Ma, Y. Qian, and T. Itoh, A uniplanar compact photonic-bandgap (UC-PBG) structure and its applications for microwave circuits, *IEEE Trans. Microwave Theory Tech.* **47**(8):1509–1514 (1999).
40. L. Zhu, Guided-wave characteristics of periodic coplanar waveguides with inductive loading—unit-length transmission parameters, *IEEE Trans. Microwave Theory Tech.* **51**(10):2133–2138 (2003).

CORRUGATED HORN ANTENNAS

L. LUCCI
 G. PELOSI
 S. SELLERI
 University of Florence
 Florence, Italy
 R. NESTI
 National Institute for
 Astrophysics
 Florence, Italy

1. INTRODUCTION

Corrugated horns are microwave antennas commonly used as feeds for high-performance reflector antenna systems. Although rectangular corrugated horns have been successfully used, circular corrugated horns are used more frequently, and this type of radiation device is treated in detail in this article.

Corrugated horns are attractive as feeds as they possess several unique properties:

1. They have high beam symmetry and low sidelobes.
2. They show very low cross-polarization.
3. They exhibit high return loss over a quite broad band (30–40%).

Corrugated horn properties have been investigated since the 1950s, and the book by Clarricoats and Olver [1] gives an accurate analytical description of their electromagnetic features, introducing simple and powerful design tools, and thus so far is the major reference text on the subject of corrugated horn antennas.

These antennas are widely used in the field of radio astronomy, remote sensing, and telecommunications on both ground-based and satellite platforms, whenever simple and easy-to-fabricate solutions to efficiently feed reflector antennas are required.

More recently, research activity on corrugated horns has been devoted mainly to studying complex profiles for the corrugations. The effects of profiling the horns using an exponential taper are accurately described in Ref. 2, an exhaustive description of different methods for profiling the horn corrugations is given in Ref. 3, a profile specific for the electrical requirements typical of radio astronomy applications with reduced size and weight is shown in Ref. 4, and the effects of tuning the phase center position by shaping the exponential profile, without changing in practice other features such as beam size, sidelobe levels, return loss, and cross-polarization, have also been investigated [5].

This work is intended to give the reader a brief introduction to corrugated circular horns highlighting their electromagnetic features, analysis tools, and design aspects.

2. ELECTROMAGNETIC PROPERTIES OF CORRUGATED WAVEGUIDES

In this section we attempt to explain the theory of electromagnetic propagation in circular corrugated waveguides, with a short but thorough characterization of corrugated waveguides, highlighting their main aspects, as this knowledge is of great importance in understanding the features of corrugated horns.

Figure 1 shows a longitudinal section of a circular corrugated waveguide in a cylindrical coordinate system (O, ρ, φ, z) . The metallic corrugated boundary extends between an inner radius a and an outer radius b and is described in terms of a slot depth s , a slot width g , and a tooth width t , for a total longitudinal periodicity of period w . On the basis of this periodicity, the Floquet theorem ensures that if one knows the field within the period

$$[\mathbf{E}_{(p)}(\rho, \varphi, z), \mathbf{H}_{(p)}(\rho, \varphi, z)] \neq 0, \quad \text{for } z \in [0, w) \quad (1)$$

it is possible to obtain an arbitrary field configuration in the whole domain, $(0 \leq \rho < b, 0 \leq \varphi < 2\pi, -\infty < z < \infty)$, whose wave nature is characterized by means of a propagation constant β , as follows (propagation is assumed,

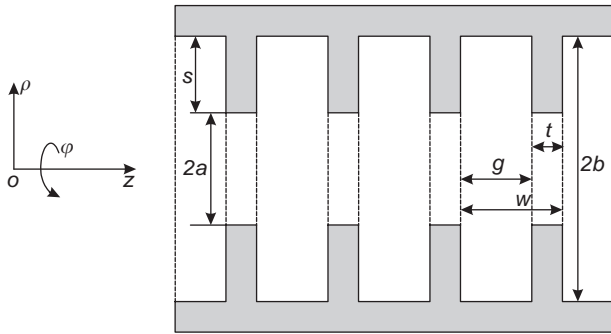


Figure 1. Corrugated waveguide geometry.

without loss of generality, in the +z-axis direction):

$$\begin{aligned} & [\mathbf{E}(\rho, \varphi, z), \mathbf{H}(\rho, \varphi, z)] \\ &= [\mathbf{E}_{(p)}(\rho, \varphi, z), \mathbf{H}_{(p)}(\rho, \varphi, z)]e^{-j\beta z} \end{aligned} \tag{2}$$

The periodical part of the field can be expanded in a Fourier series:

$$\begin{aligned} & [\mathbf{E}_{(p)}(\rho, \varphi, z), \mathbf{H}_{(p)}(\rho, \varphi, z)] \\ &= \sum_{n=0}^{\infty} [\mathbf{E}_n(\rho, \varphi), \mathbf{H}_n(\rho, \varphi)]e^{-j\beta_n z}, \end{aligned} \tag{3}$$

$$\beta_n = \frac{n\pi}{w}$$

From now on a series of assumptions will be performed largely to simplify the treatment. These assumptions are, however, justified as they relate to physical features of corrugated horns.

The first simplification is that the corrugation period is supposed to be very small compared to the wavelength, $w \ll \lambda$, so that in the Fourier spatial harmonic expansion (3) the term $n = 0$ is predominant and can be the only one considered. So the total field in the corrugated waveguide is reduced to the following:

$$\begin{aligned} & [\mathbf{E}(\rho, \varphi, z), \mathbf{H}(\rho, \varphi, z)] \\ &= [\mathbf{E}_0(\rho, \varphi), \mathbf{H}_0(\rho, \varphi)]e^{-j\beta z} \end{aligned} \tag{4}$$

The transverse function of the field representation in (4) $[\mathbf{E}_0(\rho, \varphi), \mathbf{H}_0(\rho, \varphi)]$ is assumed to be valid in the cylinder ($0 \leq \rho < a, 0 \leq \varphi < 2\pi$); the general form of the field solution is obtained by imposing the boundary condition in $\rho = a$. For the sake of simplicity, the subscript 0 will be omitted in the following equations. The solution appears to be similar to the one in the circular waveguide [6], but substantial differences emerge, especially for the eigenmode functions, due to the presence of the corrugations.

As in the more general case, such as, for example, optical fibers, in corrugated waveguides the boundary conditions at $\rho = a$ cannot be reduced to a perfect electric conductor or a perfect magnetic conductor; hence the field cannot be expanded in terms of only TE or only TM modes of a circular waveguide of radius a , but rather by a couple

of TE and TM modes. Such a combination can be seen as another couple of modes, which are called *hybrid modes*, each of which can propagate individually.

Thus, searching for the generic eigenmode solution, we proceed in a classical way [7] by considering the longitudinal components of the fields as scalar potentials; they have to satisfy the Helmholtz equation:

$$(\nabla_t^2 + k_t^2)[E_z(\rho, \varphi), H_z(\rho, \varphi)] = 0 \tag{5}$$

In this expression ∇_t^2 is a 2D operator on the variables (ρ, φ) and the transverse eigenvalue k_t is introduced; at this point it is unknown but must satisfy the relation

$$\left(\frac{2\pi}{\lambda}\right)^2 = k_0^2 = k_t^2 + \beta^2 \tag{6}$$

in which λ is the wavelength and k_0 is the free-space propagation factor; each eigenvalue will thus produce a different propagation constant β .

One should observe that the eigenvalue k_t in Eq. (5) is the same for both E_z and H_z , so that each mode of the associated pair TE and TM exhibits the same phase velocity and group velocity, hence producing a hybrid mode that is able to satisfy boundary conditions.

From a mathematical point of view, since the problem shows azimuthal symmetry, the solution to the Helmholtz equation (5) is the same as in a circular waveguide:

$$\left\{ \begin{aligned} E_z(\rho, \varphi) &= \sum_{m=0}^{\infty} J_m(k_t \rho) \\ [A_m \cos(m\varphi) + C_m \sin(m\varphi)] \\ H_z(\rho, \varphi) &= \sum_{m=0}^{\infty} J_m(k_t \rho) \\ \left[\frac{B_m}{Z_0} \sin(m\varphi) + \frac{D_m}{Z_0} \cos(m\varphi) \right] \end{aligned} \right. \tag{7}$$

where J_m is the m th-order first-kind Bessel function; A_m, B_m, C_m, D_m , are complex constants; and the characteristic impedance of the medium $Z_0 = \sqrt{\mu/\epsilon}$ is introduced, where μ is the magnetic permeability and ϵ is the electric permittivity of the medium. We must now point out the following observations:

- Equation (7) represents essentially the Fourier expansion of the potential in the azimuth coordinate φ for a given transverse eigenvalue k_t that has still to be determined by imposing boundary conditions.
- If a mode has no azimuth variation ($m = 0$), then it has a single polarization state, but, for each mode having $m > 0$, two linear polarizations exist and are associated to the two terms in the bracket on the right side of (7). Thus, given a generic mode with $m > 0$ (the eigenvalue k_t is also fixed), if $A_m = B_m = 0$, then one has one of the two possible field polarizations while if $C_m = D_m = 0$, one has the other one; the fields associated with each of these two polarization states are orthogonal, as can be easily seen by

computing the flux of the coupled Poynting vector $\mathbf{S} = \frac{1}{2} \mathbf{E}_{(A_m=B_m=0)} \times \mathbf{H}_{(C_m=D_m=0)}^*$ over an arbitrary circular section and verifying that it gives zero as result.

- Radial-type discontinuities excite modes having the same azimuth variation; thus the harmonic number m is preserved in a field propagating in a corrugated waveguide. We can also state that, in this kind of structure, there is no power transfer between fields characterized by a different harmonic number m .

Considering a corrugated waveguide excited by the circular waveguide TE₁₁ fundamental mode and choosing one of the two polarization states, a generic couple of hybrid mode potentials can be expressed as follows:

$$[E_z(\rho, \varphi), H_z(\rho, \varphi)] = J_1(k_t \rho) \left[A \cos(\varphi), \frac{B}{Z_0} \sin(\varphi) \right] \quad (8)$$

Before applying the boundary conditions, it is now useful to write the electromagnetic field generated by the potentials in (8), also expressing the z -variation terms:

$$\left\{ \begin{array}{l} E_z(\rho, \varphi, z) = A J_1(k_t \rho) \cos(\varphi) e^{-j\beta z} \\ H_z(\rho, \varphi, z) = \frac{B}{Z_0} J_1(k_t \rho) \sin(\varphi) e^{-j\beta z} \\ E_\varphi(\rho, \varphi, z) = j \frac{k_0}{k_t} \left[A \frac{\beta J_1(k_t \rho)}{k_0} + B J_1'(k_t \rho) \right] \sin(\varphi) e^{-j\beta z} \\ H_\varphi(\rho, \varphi, z) = -j \frac{k_0}{k_t Z_0} \left[A J_1'(k_t \rho) + B \frac{\beta J_1(k_t \rho)}{k_0} \right] \cos(\varphi) e^{-j\beta z} \\ E_\rho(\rho, \varphi, z) = -j \frac{k_0}{k_t} \left[A \frac{\beta J_1(k_t \rho)}{k_0} + B \frac{J_1(k_t \rho)}{k_t \rho} \right] \cos(\varphi) e^{-j\beta z} \\ H_\rho(\rho, \varphi, z) = -j \frac{k_0}{k_t Z_0} \left[A \frac{J_1(k_t \rho)}{k_t \rho} + B \frac{\beta J_1'(k_t \rho)}{k_0} \right] \sin(\varphi) e^{-j\beta z} \end{array} \right. \quad (9)$$

This set of expressions is a generic hybrid mode-field configuration with azimuth harmonic $m = 1$, in which the TM part ($A \neq 0, B = 0$) and the TE part ($A = 0, B \neq 0$) can be noted.

We now return to the particular problem under consideration here, namely, the corrugated waveguide geometry of Fig. 1. As already mentioned, in corrugated horns a small corrugation period, compared to the wavelength, is assumed; this fact allows us to further assume that inside the grooves of the corrugations ($a \leq \rho < b$) only a TEM wave propagating in the radial direction exists, with all higher-order modes in cutoff. In such a TEM wave (which is rigorously the exact solution in the asymptotic limit as the frequency and/or the radial co-ordinate approach infinity) all the field components are equal to zero except the z component of the electric field and the φ component of the magnetic field. Since the walls are perfect electric conductors, no power loss is present and the Poynting

vector in $\rho = a$ must be imaginary; hence

$$\frac{H_\varphi(a, \varphi)}{E_z(a, \varphi)} = -\frac{1}{jX_s} \quad (10)$$

where X_s assumes the meaning of a reactance.

The reactance of the total field at $\rho = a$ is given by two main contributions:

1. A contribution that holds for the portion of w of length g associated to the slot can be obtained by considering that the corrugation slot behaves like a transmission line of length s closed with a short circuit, thus having at the section $\rho = a$ a reactance value given by

$$X = Z_0 \tan(k_0 s) \quad (11)$$

2. A contribution that holds for the width t associated with the tooth is given by a short circuit at $\rho = a$, producing $X = 0$.

As a first approximation, the total reactance of the field at $\rho = a$ is given by considering both contributions according to their respective lengths of action. We can therefore apply the following boundary condition:

$$X_s = Z_0 \tan(k_0 s) \left(1 - \frac{t}{w} \right) \quad (12)$$

Thus, substituting (10) and (12) in the field representation (9) and also taking into account the following condition

$$E_\varphi(a, \varphi) = 0 \quad (13)$$

we obtain the following relations

$$\left\{ \begin{array}{l} \gamma = \frac{A}{B} = -\frac{k_0 u J_1'(u)}{\beta J_1(u)} \\ y \equiv -\frac{Z_0}{X_s} = \frac{k_0 J_1'(u)}{k_t J_1(u)} + \frac{\beta}{\gamma k_t u} \\ u \equiv k_t a \end{array} \right. \quad (14)$$

where γ is the hybrid factor, y represents the normalized susceptance, a new variable u is introduced, and $J_1'(u) = (d/du)J_1(u)$. Substituting these relations in (9), using some algebraic and trigonometric formulas, and neglecting the z dependence, a very interesting representation is found for the transverse component \mathbf{E}^t of the electric field, which is useful for analyzing the properties of corrugated waveguides:

$$\mathbf{E}^t(\rho, \varphi) = -j \frac{k_0 B}{k_t} \cdot \left\{ \left(\gamma \frac{\beta}{k_0} + 1 \right) J_0(k_t \rho) \hat{\mathbf{x}} + \left(1 - \gamma \frac{\beta}{k_0} \right) J_2(k_t \rho) [\cos(2\varphi) \hat{\mathbf{x}} + \sin(2\varphi) \hat{\mathbf{y}}] \right\} \quad (15)$$

Eliminating the hybrid factor γ in (14), the characteristic equation is obtained as follows:

$$\frac{y}{k_0 a} = \frac{J_1(u)}{u^3 J_1'(u)} \left[\left(u \frac{J_1'(u)}{J_1(u)} \right)^2 - \left(\frac{\beta}{k_0} \right)^2 \right] \quad (16)$$

Thus, solving this equation for the variable u , the eigenvalues k_t of the hybrid modes can be obtained. A detailed analysis of (16) is beyond the scope of this work; the reader is referred to the text by Clarricoats and Olver [1] for a more in-depth treatment of this topic. Here we are interested only in some cases of practical interest:

1. If we assume that the slot length s is a quarter-wavelength, then the normalized susceptance y is zero, and using the asymptotic limit $\beta \rightarrow k_0$, where the frequency is much greater than the cutoff frequency of the mode ($f \gg f_c$), we can approximate (16) by

$$\left(u \frac{J_1'(u)}{J_1(u)} \right)^2 - 1 = 0 \Rightarrow u \frac{J_1'(u)}{J_1(u)} = \pm 1 \quad (17)$$

2. In the same asymptotic limit $\beta \rightarrow k_0$, Eq. (17) is also obtained as an approximation of (16) independently from the slot length s , assuming that the radius a is large enough that the first side of (16) tends to zero.

These two cases are important in practice because in the region close to the throat (small a), corrugations are designed in order to satisfy condition 1, while condition 2 is satisfied in the region close to the aperture (large a).

Equation (17) can be easily solved using the recurrence formulas for Bessel functions

$$\begin{aligned} J_n(u) &= -J_{n-1}'(u) + \frac{(n-1)J_{n-1}(u)}{u} \\ &= J_{n+1}'(u) + \frac{(n+1)J_{n+1}(u)}{u} \end{aligned} \quad (18)$$

thus giving

$$\begin{cases} J_0(u) = 0 \\ J_2(u) = 0 \end{cases} \quad (19)$$

As can be noted from the first line of (14), in the asymptotic limit $\beta \rightarrow k_0$, the first line of (19) is equivalent to $\gamma = 1$ and the second, to $\gamma = -1$. The dual condition $\gamma = \pm 1$ is termed the *balanced hybrid condition*. If this condition is satisfied, the right side of (16) is always zero, thus producing a more general solution in the case in which the left side of (16) is zero.

In this particular case two sets of hybrid modes, *HE* and *EH*, corresponding to, respectively, $\gamma = 1$ and $\gamma = -1$, are simply given by analytical formulas.

The eigenvalues of these modes are

$$\begin{cases} HE_{1n} \Rightarrow k_t = k_{1n}^{HE} = \frac{u_{0n}}{a} \\ EH_{1n} \Rightarrow k_t = k_{1n}^{EH} = \frac{u_{2n}}{a} \end{cases} \quad (20)$$

where u_{0n} and u_{2n} are the well-known and tabulated zeros of the first-kind Bessel functions, the zero-order J_0 and the second-order J_2 , respectively.

Although these modes are approximated solutions of corrugated waveguides, in the sense explained above, they accurately describe wave propagation with the major advantage of a relatively simple analytical form.

Using solutions (20) in the electric field expression (15), with the asymptotic approximation $\beta \rightarrow k_0$, we obtain

- For the *EH*_{1n} modes ($\gamma = -1$) the transverse electric field is given by

$$\begin{aligned} \mathbf{E}_{1n}^t(\rho, \varphi) &\cong -j \frac{k_0 a}{u_{2n}} B J_2\left(\rho \frac{u_{2n}}{a}\right) \\ &[\cos(2\varphi)\hat{\mathbf{x}} + \sin(2\varphi)\hat{\mathbf{y}}] \end{aligned} \quad (21)$$

- For the *HE*_{1n} modes ($\gamma = 1$), we can use the following approximation for (16)

$$\begin{aligned} \frac{y}{k_0 a} &= \frac{1}{u^2} \frac{\beta}{k_0} \frac{1}{\gamma} (1 - \gamma^2) \\ &\cong \frac{2}{u^2} \left(1 - \gamma \frac{\beta}{k_0} \right) \\ &\Rightarrow \left(1 - \gamma \frac{\beta}{k_0} \right) = \frac{yu^2}{2k_0 a} \end{aligned} \quad (22)$$

thus leading to

$$\begin{aligned} \mathbf{E}_{1n}^t(\rho, \varphi) &\cong -j \frac{k_0 a}{u_{0n}} B \times \\ &\left\{ J_0\left(\frac{u_{0n}}{a} \rho\right) \hat{\mathbf{x}} + \frac{yu_{0n}^2}{4k_0 a} J_2\left(\frac{u_{0n}}{a} \rho\right) \right. \\ &[\cos(2\varphi)\hat{\mathbf{x}} + \sin(2\varphi)\hat{\mathbf{y}}] \left. \right\} \end{aligned} \quad (23)$$

While *EH* modes show undesired field configuration features, since there is no preferential direction for field polarization, as can be noted in the electric field configuration of the *EH*₁₁ mode of Fig. 2b, this is not the case for the *HE* modes. In fact, regarding the *HE*₁₁ fundamental hybrid mode, one should note that, in the case in which the first term inside the braces predominates over the second one, the field is essentially linearly polarized, as can be seen in Fig. 2a, and shows high azimuthal symmetry in amplitude. These features are of prime importance because they yield high beam symmetry and very low cross-polarization.

The second term inside the braces is highly undesired as it has the same negative polarization features as do *EH* modes. Its contribution should be as low as possible, and this may be achieved, as mentioned above, by keeping the susceptance y very small using quarter-wavelength slots.

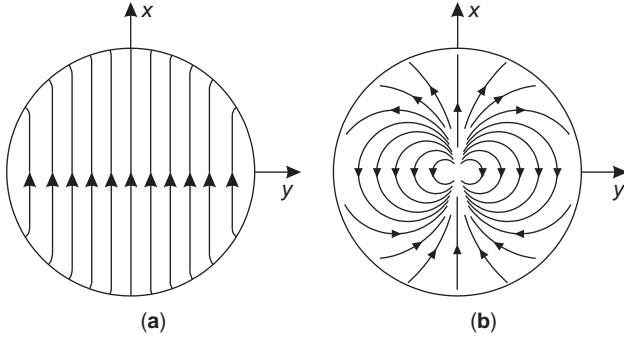


Figure 2. Corrugated waveguide—electric field distribution of hybrid modes: (a) HE_{11} ; (b) EH_{11} .

3. RADIATION PROPERTIES OF CORRUGATED CONICAL HORNS

A very useful method for accurate analytical description of the radiation properties of corrugated horns is the Gaussian beam approach, using the Gauss–Laguerre expansion of the electromagnetic field [8]. Although this approach is valid in the paraxial beam approximation [9] (i.e., for narrow beams), it is a very good tool for fast analysis and design of all the corrugated horns of practical interest. It enables accurate description of the main lobe shape, up to approximately -20 dB relative to the maximum, and accurate prediction of the phase center position. As a drawback sidelobes are not characterized and there is only a lower bound limit estimate for the cross-polarization level. These features can be taken into account, together with flange effects and other second-order phenomena, by resorting to numerical methods, as described later.

Referring to Fig. 3, let's consider a corrugated horn of conical shape excited by a perfectly azimuth symmetric fundamental HE_{11} hybrid mode that is assumed to be polarized in the y -axis direction. Thus the electric field contribution due to J_0 in (23) gives the amplitude distribution at the horn aperture, where it is also possible to accurately estimate the phase distribution. Indeed, using the same approximation usually applied to common conical waveguides, the radius of curvature of the aperture phase distribution is assumed equal to the height L of the

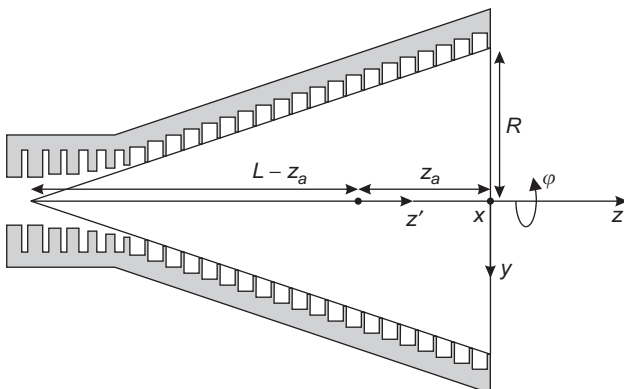


Figure 3. Conical corrugated horn geometry.

ideal triangle formed by the corrugated wall envelope and the aperture diameter (Fig. 3), which is approximately the horn length. This results in the following analytical expression for the field:

$$\mathbf{E}_{1n}^t(\rho, \varphi) \cong A_0 J_0\left(\rho \frac{u_{01}}{R}\right) e^{-j(k_0 \rho^2/2L)} \hat{\mathbf{y}} \quad (24)$$

The constant A_0 may be given an explicit value if, on the horn aperture surface S , the following power normalization rule is adopted:

$$\iint_S \mathbf{E}_{1n}^t(\rho, \varphi) \cdot [\mathbf{E}_{1n}^t(\rho, \varphi)]^* dS = 1 \quad (25)$$

leading to

$$A_0 = \frac{1}{\sqrt{\pi R J_1(u_{01})}} \quad (26)$$

The successive step is to expand the field in the space of the Gauss–Laguerre complete set ($0 \leq \rho < \infty$) of orthonormalized functions:

$$\begin{aligned} & \left[\frac{J_0\left(\frac{u_{01}}{R} \rho\right)}{\sqrt{\pi R J_1(u_{01})}} \right] e^{-j(k_0 \rho^2/2L)} \\ &= \left[\sum_{n=0}^{\infty} a_n \sqrt{\frac{2}{\pi w}} L_n^0\left(\frac{2\rho^2}{w^2}\right) \cdot e^{-(\rho^2/w^2)} \right] e^{-j(k_0 \rho^2/2L)} \end{aligned} \quad (27)$$

where a_n are the expansion coefficients and L_n^0 is the Laguerre zero-order n th polynomial. Of particular interest is the zero term of the expansion

$$G(\rho) = a_0 \sqrt{\frac{2}{\pi w}} \cdot e^{-(\rho^2/w^2)} e^{-j(k_0 \rho^2/2L)} \quad (28)$$

which represents the normalized fundamental *Gaussian beam mode*.

Neglecting a detailed analysis of the Gaussian beam, which can be found in Ref. 10, it is important to highlight that, in the expansion (27), w is an arbitrary parameter that can be chosen according to different objectives, each corresponding to different expansions. The most convenient choice for our purposes is the one maximizing the a_0 coefficient; thus, by taking the fundamental Gaussian beam mode only, the horn aperture field is already nicely approximated. Then, the expression

$$0 \leq a_0 = 2\sqrt{2} \int_0^1 \left[\frac{J_0(u_{01}u)}{p J_1(u_{01})} \right] e^{-(u^2/p^2)} u du \leq 1 \quad (29)$$

in which $p = w/R$ and $u = \rho/R$, must be maximized with respect to p .

Figure 4 shows the a_0 coefficient as a function of p . It has a maximum at $p = 0.6435$, with $a_0 = 0.99$, corresponding to a power coupling between the HE_{11} mode and the Gaussian beam mode (28) of $\sim 98\%$.

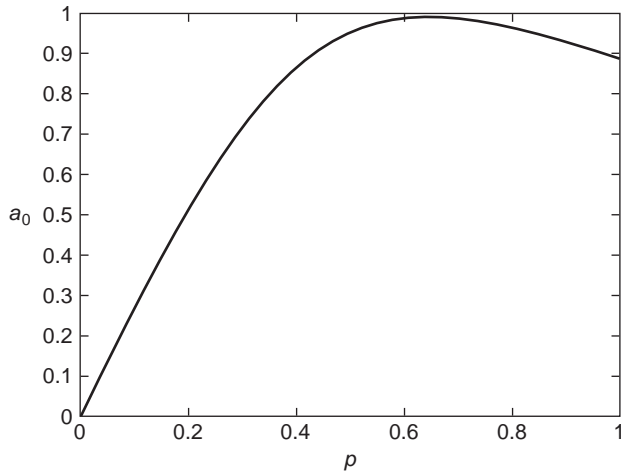


Figure 4. Coupling between the HE_{11} mode and the Gaussian beam mode.

Once the best-coupled Gaussian beam has been completely determined on the aperture ($z = 0$), the electromagnetic field is known, in our case, on the infinite half-space $z > 0$, thanks to the Gaussian beam propagation formula:

$$G(\rho, z') = \frac{w_0}{w(z')} \cdot e^{-[\rho^2/w^2(z')]} e^{-j[k_0 \rho^2/2H(z')]} e^{-jk_0 z'} \quad (30)$$

where a new coordinate $z' = z + z_a$ is introduced for convenience (Fig. 3), where z_a gives the horn aperture position with respect to z' . The term w_0 , termed “beam waist,” is a fundamental parameter governing all features of the Gaussian beam according to what is demonstrated in the following points:

1. The function $w(z')$ determines the transverse size of the beam; for each z' it gives the radial coordinate ρ at which the field has a e^{-1} ratio with the on-axis maximum. This size has a minimum value that is exactly w_0 at $z' = 0$, and its general expression is given analytically by

$$w(z') = w_0 \sqrt{1 + \left(\frac{z'}{z_c}\right)^2} \quad (31)$$

where z_c , the confocal distance, may be interpreted as the limit between near-field and far-field regions and is given by

$$z_c = \frac{\pi w_0^2}{\lambda} \quad (32)$$

where λ is the wavelength. From (31) we can see that in (30), the amplitude factor

$$A(z') = \frac{w_0}{w(z')} \quad (33)$$

decreases with a $1/z'$ law for large on-axis distances from the waist.

2. The term $H(z')$ gives the radius of curvature of the wavefronts and is a function of the beam waist, through the confocal distance z_c , according to

$$H(z') = \left(z' + \frac{z_c^2}{z'}\right) \quad (34)$$

This equation gives very important insights on Gaussian beam behavior. The radius of curvature is infinite in two cases: (1) in the near-field region at $z' = 0$, which means that the field has a planar phase front exactly at the waist, which is on the horn axis, commonly located in the inner corrugated region of the horn; and (2) while approaching infinity as z' tends to infinity, meaning that, since this occurs in the far region, the field has a spherical phase front. It must, however, be noted that the radius of curvature tends to infinity as z' , implying that the far-field phase center of the Gaussian beam is the beam waist position $z' = 0$. An even more important fact is that Eq. (34) gives the radius of curvature of the beam at every distance from the waist, so that, to the extent that the Gaussian beam is a good approximation of the field radiated by a corrugated horn, the phase center position of the horn is known simply and accurately everywhere, including the near-field region, with dramatic simplification in the design task of the optics of reflector antenna systems fed by corrugated horns.

It is now possible to characterize both phase center position and radiation patterns of corrugated horns. By considering the phase center position, the problem is to determine the horn aperture abscissa z_a , where the field expansion is completely known as a consequence of having determined the waist $w(z_a) = pR$, with $p = 0.6435$, and the radius of curvature $H(z_a) = L$.

To do this, the following inverse formulas, obtained by manipulating (31) and (34), are useful:

$$\begin{aligned} w_0 &= \frac{pR}{\sqrt{1 + \left(\frac{\pi(pR)^2}{\lambda L}\right)^2}}; \\ z_a &= \frac{L}{1 + \left(\frac{\lambda}{\pi(pR)^2}\right)^2} \end{aligned} \quad (35)$$

The relations in (35) are very important because they give analytically both the far-field phase center position with respect to the horn aperture (z_a from the aperture toward the throat) and the waist w_0 , which governs, as mentioned above, the Gaussian beam propagation. Thus, the field radiated by the horn ($z' > z_a$) can be analytically evaluated everywhere.

As a consequence, we can also characterize the corrugated horn radiation pattern. To do this, we approximate, in the far field, the expression (30) as follows:

$$w(z') \cong w(z) \cong w_0 \frac{z}{z_c} \quad (36)$$

Remembering the confocal distance expression (32) and passing to a spherical coordinate system

$$z = r \cos(\vartheta); \quad \rho = r \sin(\vartheta) \quad (37)$$

it is possible to rewrite the field radiated by the aperture distribution (24) with the Gaussian beam approximation (28) as follows

$$|E(r, \vartheta)| \cong \alpha_0 \sqrt{\frac{2}{\pi}} \left(\frac{\pi w_0^2}{\lambda} \right) \frac{1}{r \cos(\vartheta)} e^{-\tan^2(\vartheta)(\pi w_0/\lambda)^2} \quad (38)$$

which is assumed to be valid for $r > 0$ and $0 \leq \vartheta < \pi/2$.

Moreover, it is possible to use the inverse formulas (35) to express the radiated field in terms of the geometric parameters R and L and expand the $\hat{\mathbf{y}}$ versor in spherical coordinates, neglecting the radial component. Proceeding in this way, we have a full characterization of the radiated field, including its polarization, and obtain the following expression

$$\mathbf{E}(r, \vartheta, \varphi) = \frac{\alpha_0}{r} \exp \left[-\tan^2(\vartheta) \frac{1}{\left(\frac{\lambda}{R} \right)^2 \frac{1}{(\pi \cdot p)^2} + p^2 \left(\frac{R}{L} \right)^2} \right] \left[\sin(\varphi) \hat{\mathbf{i}}_\vartheta + \frac{\cos(\varphi)}{\cos(\vartheta)} \hat{\mathbf{i}}_\varphi \right]. \quad (39)$$

where

$$\alpha_0 = a_0 \sqrt{\frac{2}{\pi}} \left(\frac{\pi w_0^2}{\lambda} \right) \quad (40)$$

Figure 5 shows the accuracy that can typically be achieved with the Gaussian beam approximation. The plot gives the $\varphi = 45^\circ$ plane radiation pattern of a corrugated horn obtained by a full-wave analysis, which is assumed to be the reference, and by its best-fit Gaussian beam. The cut

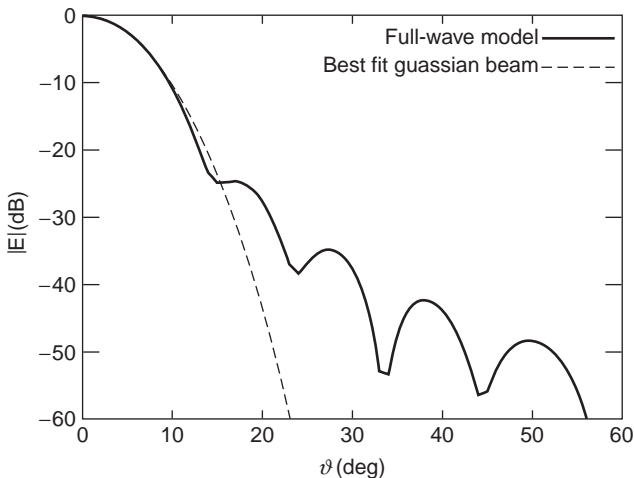


Figure 5. Corrugated horn radiation pattern at $\varphi = 45^\circ$: $L = 44\lambda$; $R = 3.4\lambda$.

chosen is representative of every φ cut, at least up to a level of approximately -35 dB, because of the high azimuthal symmetry of the horn. Thus we are led to the conclusion, which is more or less valid in general for standard corrugated horns, that the Gaussian beam approach gives high accuracy with respect to the beam pattern up to about -15 dB below the on-axis maximum.

4. DESIGN ASPECTS OF CORRUGATED HORNS

Thus far we have presented a quite general theory to help the reader understand the electromagnetic properties of corrugated horns. This knowledge is, however, sufficient only to a first step and rough design; for accurate design, further aspects are needed and are developed in the following paragraphs.

In particular, we intend to focus on arguments that constitute requirements for most applications. As seen above in (39), the mainbeam radiation is controlled by the aperture size and the horn length. A very important task is the design of the throat region because it controls primarily the input return loss and the proper excitation of the HE_{11} fundamental hybrid mode. Another important feature of corrugated horns is the cross-polarization, which is of importance mainly in modern dual-polarization applications. When the horn is used as a feed for a reflector, the phase center position must be accurately known; this, according to the Gaussian beam approximation, coincides in the far field with the waist position (35), while in near field it is given by the center of curvature of the phase front according to (34).

For a very accurate characterization of the properties mentioned above, numerical techniques are needed. A very accurate full-wave analysis method is presented below.

4.1. MainBeam Radiation of Corrugated Horns

As stated above, an accurate analytical characterization of the mainbeam pattern is given in (39). In practice, typical specifications related to the mainbeam are given in terms of *gain*, *edge taper*, or sometimes the *waist*, each of which may be used to determine the geometric parameters R and L of the horn.

When complex reflector arrangements are to be fed by a corrugated horn, the waist is typically given as a requirement because the design of the optics is efficiently done using the Gaussian beam approach.

If a waist w_0 is given, then the mainlobe can be determined. In particular, we can define the $1/e$ *half-beamwidth* as the angle at which the field intensity is $1/e$ down from the on-axis maximum. Neglecting the $\cos(\vartheta)$ term, from (38) we have the following approximation:

$$\vartheta_{1/e} = \tan^{-1} \left(\frac{\lambda}{\pi w_0} \right) \quad (41)$$

To obtain the geometric parameters of the horn, it is possible to proceed by fixing the phase shift on the horn

aperture

$$\beta = \frac{\pi R^2}{\lambda L} \tag{42}$$

to a maximum allowed value β_0 , where $\beta_0 = \pi/16$ is a practical choice.

Proceeding this way, it is possible to use the inverse formulas (35) to simply have

$$R = \frac{w_0}{p} \sqrt{1 + p^4 \beta_0^2};$$

$$L = \frac{\pi R^2}{\lambda \beta_0} \tag{43}$$

As already mentioned, the Gaussian model is valid in the paraxial beam approximation and, in practice, the wavelength can be regarded as the lower limit for the waist ($w_0 > \lambda$) in a design approach of this kind.

It is interesting to note that fixing the phase shift β is equivalent to fixing the wavelength-normalized radius R_λ and the half-flare angle α defined by

$$R_\lambda = \frac{R}{\lambda}; \quad \alpha = \tan^{-1} \left(\frac{R}{L} \right) \tag{44}$$

The *edge taper* is the level, relative to the on-axis maximum, at which the horn illuminates a certain elevation angle, usually individuated by the edge of the reflector that is fed directly.

For example, an edge taper of X dB at an angle ϑ_t may be necessary. This information may be used to directly obtain the waist by using (38), neglecting the $\cos(\vartheta)$ term again, yielding

$$10^{X/20} = e^{\tan^2(\vartheta_t)(\pi w_0/\lambda)^2} \tag{45}$$

leading to

$$w_0 = \frac{\lambda}{2.95\pi} \cdot \frac{\sqrt{X}}{\tan(\vartheta_t)} \tag{46}$$

Once the waist has been calculated, it is possible to proceed in the same way as in the previous case with the waist given directly.

In practice, because of the approximation in the Gaussian beam model, this method gives accurate results for edge taper levels X up to 20–25 dB and taper angles ϑ_t not greater than 30° .

If the gain is given as specification, an efficient way to proceed for simple, accurate, and fast design is as follows. First, it is more convenient to refer to the gain G_0 in the on-axis direction of the horn and, due to the high return loss and the low ohmic losses of corrugated horns, to approximate the gain with the

directivity D_0 :

$$G_0 \cong D_0 = 4\pi \frac{\text{power density in } \vartheta = 0}{\text{horn aperture outgoing power}} \tag{47}$$

$$= 4\pi \frac{U(\vartheta = 0)}{P_{\text{rad}}}$$

The power out from the aperture can be written as the flux of the real part of the Poynting vector:

$$P_{\text{rad}} = \frac{1}{2} \text{Re} \iint_S \mathbf{E} \times \mathbf{H}^* \cdot \hat{\mathbf{z}} dS$$

$$= \frac{1}{2} \text{Re}(Y_m) \iint_S |\mathbf{E}_t|^2 dS \tag{48}$$

where \mathbf{E}_t indicates the tangential component of the electric field, S is the horn aperture surface, and Y_m is the field admittance on the aperture. In the case of the hybrid HE_{11} fundamental mode, under the balanced hybrid condition (19), introducing the field impedance $Z_m = 1/Y_m$, we have $Z_m = \zeta$, the characteristic impedance of the medium.

The power density radiated in the free space on-axis direction is given by

$$U(\vartheta = 0) = \frac{r^2}{2\zeta} |\mathbf{E}_{\text{rad}}(\vartheta = 0)|^2 \tag{49}$$

The radiated electric field \mathbf{E}_{rad} in the far-field approximation (> 1) may be given as a function of the tangential electric field distribution \mathbf{E}_t on the horn aperture. This can be simply obtained by using the field expansion as a spectrum of plane waves, and this method is outlined in detail in Ref. 11.

Essentially, the far-field approximation can be obtained as the plane-wave spectrum

$$\mathbf{E}_{\text{rad}}(r, \vartheta, \varphi) = 2\pi j \frac{e^{-jk_0 r}}{r} k_0 \cos(\vartheta) \hat{\mathbf{E}}(\xi, \eta) \tag{50}$$

asymptotically evaluated at the stationary point $\xi = \sin(\vartheta) \cos(\varphi)$, $\eta = \sin(\vartheta) \sin(\varphi)$, where the spectrum is the 2D Fourier transform of the tangential electric field \mathbf{E}_t on the aperture:

$$\hat{\mathbf{E}}(u, v) = \frac{1}{(2\pi)^2} \iint_S \mathbf{E}_t(x, y) e^{-jux} e^{-jvy} dx dy \tag{51}$$

In the on-axis direction $\vartheta = 0$, we have

$$\hat{\mathbf{E}}(0, 0) = \frac{1}{(2\pi)^2} \iint_S \mathbf{E}_t dS \tag{52}$$

$$\mathbf{E}_{\text{rad}}(r, \vartheta = 0, \varphi) = j \frac{1}{\lambda} \frac{e^{-jk_0 r}}{r} \iint_S \mathbf{E}_t dS \tag{53}$$

$$U(\vartheta = 0) = \frac{1}{2\zeta} \frac{1}{\lambda^2} \left| \iint_S \mathbf{E}_t dS \right|^2 \tag{54}$$

Obviously, the traditional approach based on the auxiliary potential formulation according to the theory developed in Ref. 12 can be used, leading to the same results. It is thus possible to rewrite the on-axis gain expression (47) as a function of the tangential electric field distribution \mathbf{E}_t on the horn aperture alone

$$G_0 = \frac{4\pi}{\lambda^2} \frac{\left| \iint_S \mathbf{E}_t dS \right|^2}{Z_m \iint_S |\mathbf{E}_t|^2 dS} \quad (55)$$

where, in our case, $Z_m = \zeta$, as already stated.

We can use the *effective area* concept, in this case given by

$$A_e = \frac{\left| \iint_S \mathbf{E}_t dS \right|^2}{\iint_S |\mathbf{E}_t|^2 dS} \quad (56)$$

for

$$G_0 = 4\pi^2 R_\lambda^2 \eta_A \quad (57)$$

where the aperture radius normalized to the wavelength R_λ is as defined in (44) and $\eta_A = A_e/A$ is the *aperture efficiency*, where $A = \pi R^2$ is the geometric area of the aperture. The aperture efficiency, which is a measure of how much of the aperture is effectively used, can be expressed in a more useful way by using (24) (omitting the amplitude $A_0 = 1$)

$$\iint_S |\mathbf{E}_t|^2 dS = 2\pi \int_0^R J_0^2\left(u_{01} \frac{\rho}{R}\right) \rho d\rho \quad (58)$$

$$= \pi R^2 J_1^2(u_{01})$$

$$\left| \iint_S \mathbf{E}_t dS \right|^2 = 4\pi^2 R^4 \quad (59)$$

$$\left| \int_0^1 J_0(u_{01}x) e^{-j(\pi R_\lambda \tan(\alpha))x^2} x dx \right|^2$$

where we use the relation $\tan(\alpha) = R/L$.

Thus we obtain a useful aperture efficiency expression as a function only of the geometric parameters R and L :

$$\eta_A = \frac{4}{J_1^2(u_{01})} \left| \int_0^1 J_0(u_{01}x) e^{-j(\pi R_\lambda \tan(\alpha))x^2} x dx \right|^2 \quad (60)$$

This function is plotted against the parameter $R_\lambda \tan(\alpha)$ in Fig. 6. We observe that it has a maximum $\eta_A = 0.69$ in the origin, corresponding to the case of a corrugated waveguide with a null half-flare angle α . It has to be noticed that, in order to have the same efficiency, if we enlarge the aperture radius R , the horn length also has to be increased so that $R_\lambda \tan(\alpha)$ remains constant.

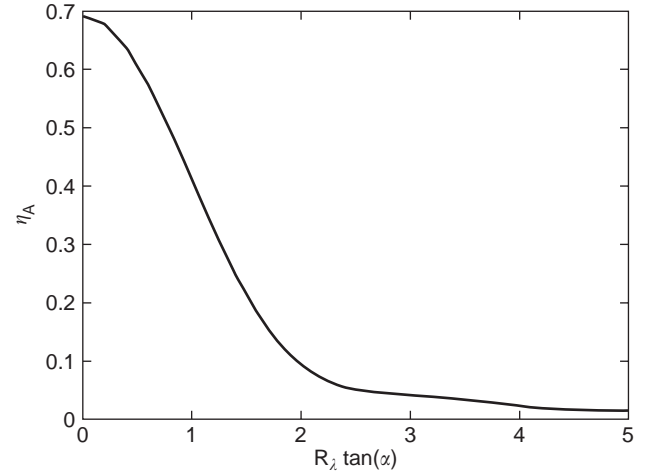


Figure 6. Corrugated feed horn aperture efficiency.

Concluding, according to (57) and (60), it is possible to express the on-axis gain as a function only of the geometric parameters R and L , which is the desired form, analogously to the other cases of the waist and edge taper specifications, in order to design corrugated horns. Together with the curve in Fig. 6, another useful design chart is given in Fig. 7, where parametric curves based on the on-axis gain expression (57), with the aperture efficiency given by (60), are plotted against R_λ , with the flare angle α used as a parameter. Given a particular on-axis gain specification, it is thus possible, both analytically and graphically, to obtain the most convenient solution in terms of R and L .

4.2. Design of the Throat Transition Region

The initial part of the corrugated horn, the throat region, is of primary importance because it directly determines the input matching and the excitation of the HE_{11} fundamental hybrid mode.

Because circular waveguides are the most convenient solutions to feed corrugated horns, the design of the throat is not straightforward. As mentioned previously, the ideal condition to support the propagation of the HE_{11} mode is that the widths of both the tooth and the slot be much smaller than the wavelength and that the slot depth be a quarter-wavelength. This latter condition would produce very poor input matching if applied directly to the initial corrugations connected to the circular waveguide. This is because a perfect magnetic wall results at a quarter-wavelength distance (the slot depth) from the metallic enclosure, constituting, with respect to the wave coming from the circular waveguide, an equivalent open circuit as a boundary condition at $\rho = a$. This produces abrupt discontinuities at the boundary, which presents, alternately, short circuits (tooth sections) and open circuits (groove sections) within a small fraction of the wavelength. This is the required boundary condition for the desired HE_{11} mode but is incompatible with the fundamental TE_{11} mode of the feeding circular guide; hence high reflection coefficients would be present.

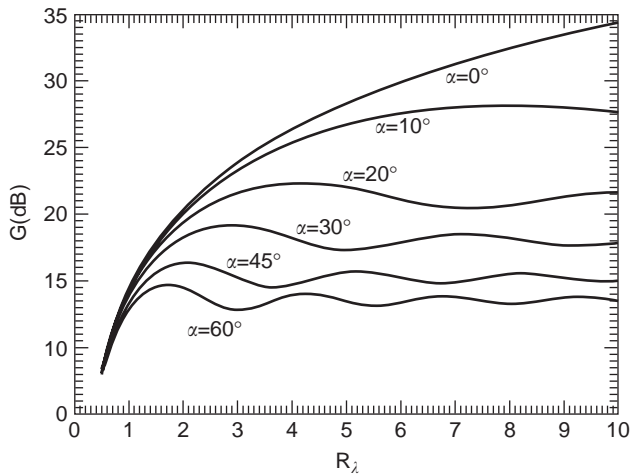


Figure 7. Corrugated horn gain versus aperture radius and half-flare angle.

The solution is a transition region where the corrugations begins with approximately half-wavelength slot depths and with the teeth thicker than the slots; the steady-state geometry is gradually reached with a few corrugations. Proceeding this way, two important objectives are obtained:

1. The equivalent boundary conditions for a half-wavelength-depth slot is a short circuit at $\rho = a$, and hence there is no abrupt discontinuity, with a gradual variation giving a good input matching.
2. A half-wavelength slot also ensures the proper propagating condition for the circular waveguide TM_{11} mode, thus producing an adequate condition to excite the hybrid HE_{11} mode of the corrugated waveguide (formed by the TM_{11} and TE_{11} modes).

This type of solution is given in Fig. 8, where typical values for the transition region geometry are explicitly given. In practice transition regions may be formed by 10–20 corrugations.

Problems associated with the design of the transition region have been encountered in the literature. Only an intuitive explanation of the proposed solution has been

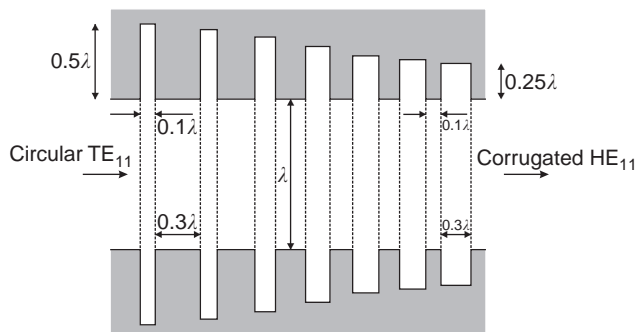


Figure 8. Corrugated horn throat: transition region typical geometry.

given here; a very detailed theoretical approach on this can be found, for example, in Ref. 13.

4.3. Cross-Polarization

A large part of modern applications is based on dual-polarization channels, where two channels exist at the same frequency in the same medium (free space or waveguide). This means that the transmitter and receiver subsystems, carrying the dual-polarized signal, need to keep the two polarizations separate, introducing negligible coupling between them.

Thus, a related figure of merit here is the extent to which the two polarizations may be kept uncoupled. With respect to corrugated horns, this parameter is given by the cross-polarization level and, instead of the ordinary ϑ and φ components of the radiated field, in these applications a more useful characterization is given in terms of copolar (CP) and cross-polar (XP) components.

According to the Ludwig definition [14], a Huygens source, (one electric and one magnetic elementary dipole, mutually orthogonal, in phase and whose amplitudes are in a ratio equal to the characteristic impedance of the medium) radiates a pure copolar field with null *cross-polarization*. Thus this source is taken as a reference, and the CP or XP pattern of any antenna is defined by projecting the antenna’s radiated field on the fields generated by two mutually orthogonal Huygens sources. The Huygens source reference for the copolar field is oriented so as to produce an electric field that is parallel to the one generated by the antenna in the far field and in the direction of maximum radiation. According to this definition, it is possible to demonstrate that, given the spherical coordinate components $E_\vartheta(\vartheta, \varphi)$, $E_\varphi(\vartheta, \varphi)$ of the radiated field, the copolar (E_{CP}) and cross-polar (E_{XP}) components are given by

$$\begin{bmatrix} E_{CP}(\vartheta, \varphi) \\ E_{XP}(\vartheta, \varphi) \end{bmatrix} = \underline{\underline{M}}(\varphi) \begin{bmatrix} E_\vartheta(\vartheta, \varphi) \\ E_\varphi(\vartheta, \varphi) \end{bmatrix} \quad (61)$$

where the conversion matrix $\underline{\underline{M}}(\varphi)$ depends on the direction of the far-region electric field vector; in the case of an y -directed or x -directed electric field, we have, respectively

$$\begin{aligned} \underline{\underline{M}}(\varphi) = \underline{\underline{M}}^y(\varphi) &= \begin{bmatrix} \sin(\varphi) & \cos(\varphi) \\ \cos(\varphi) & -\sin(\varphi) \end{bmatrix}, \\ \underline{\underline{M}}(\varphi) = \underline{\underline{M}}^x(\varphi) &= \begin{bmatrix} \cos(\varphi) & -\sin(\varphi) \\ \sin(\varphi) & \cos(\varphi) \end{bmatrix} \end{aligned} \quad (62)$$

As in a more general case of azimuth-symmetric feed, for a corrugated horn producing a field with a first-order harmonic variation in the azimuth coordinate ($m = 1$), the radiated field may be obtained once the E -plane and H -plane cut patterns, respectively $C_E(\vartheta)$ and $C_H(\vartheta)$, are given.

For example, in the case of an antenna radiating an y -polarized far-region electric field, the following relation

can be verified:

$$\begin{aligned} E_{\vartheta}(\vartheta, \varphi) &= C_E(\vartheta) \sin(\varphi); \\ E_{\varphi}(\vartheta, \varphi) &= C_H(\vartheta) \cos(\varphi) \end{aligned} \tag{63}$$

Combining these relations with (61), using the first row of (62), the following results are obtained

$$\begin{cases} E_{CP}(\vartheta, \varphi) = C_E(\vartheta) \sin^2(\varphi) + C_H(\vartheta) \cos^2(\varphi) \\ E_{XP}(\vartheta, \varphi) = [C_E(\vartheta) - C_H(\vartheta)] \sin(\varphi) \cos(\varphi) \\ = \frac{1}{2} [C_E(\vartheta) - C_H(\vartheta)] \sin(2\varphi) \end{cases} \tag{64}$$

and the same expression can be verified analogous [$C_E(\vartheta)$ and $C_H(\vartheta)$ are exchanged in the first expression] in the case of an x -axis polarization. From (64) it should be noted that, in general, the cross-polar component of the field has a maximum in the 45° plane cut.

Usually the level of cross-polarization is given as a level with respect to the maximum of the copolar; if we assume the copolar maximum in the direction $\vartheta = 0$, we can give the cross-polarization pattern, in decibels, as

$$XP(\vartheta) = 10 \log_{10} \frac{\frac{1}{4}|C_E(\vartheta) - C_H(\vartheta)|^2}{|C_E(\vartheta=0)|^2} \tag{65}$$

and the cross-polarization maximum can be found by searching for the maximum of this expression for all the allowed values of ϑ :

$$XP_{\max} = \max_{\vartheta \in (0, 180^\circ)} \left\{ 10 \log_{10} \frac{\frac{1}{4}|C_E(\vartheta) - C_H(\vartheta)|^2}{|C_E(\vartheta=0)|^2} \right\} \tag{66}$$

To obtain the cross-polarization characterization of corrugated horns, we can use the field expression (39).

Proceeding this way, we have the cross-polar features of the perfectly balanced hybrid HE_{11} mode that radiates unperturbed, according to the Gaussian beam model, thus neglecting contributions to cross-polarization coming from the nonideality of the fundamental mode itself, higher-order modes and flange effects.

From (39), we can readily find that

$$\begin{aligned} C_E(\vartheta) &= \exp \left[-\tan^2(\vartheta) \frac{1}{\left(\frac{1}{R_\lambda}\right)^2 \frac{1}{(\pi p)^2} + p^2 \tan^2(\alpha)} \right]; \\ C_H(\vartheta) &= \frac{C_E(\vartheta)}{\cos(\vartheta)} \end{aligned} \tag{67}$$

where $p = 0.6435$ and the wavelength-normalized aperture radius R_λ and the half-flare angle α are as already defined in (44), giving the following expression for the

cross-polarization pattern:

$$XP(\vartheta) = 10 \log_{10} \left\{ \frac{\left| 1 - \frac{1}{\cos(\vartheta)} \right|^2}{4} \exp \left[-\tan^2(\vartheta) \frac{2}{\left(\frac{1}{R_\lambda}\right)^2 \frac{1}{(\pi p)^2} + p^2 \tan^2(\alpha)} \right] \right\}. \tag{68}$$

This expression is plotted in Fig. 9, with R_λ as a parameter, for a corrugated waveguide ($\alpha = 0$).

Curves related to the maximum of cross-polarization are given in Fig. 10 as a function of R_λ , with α as a parameter.

Results shown in Figs. 9 and 10, even if obtained from an approximate theory, provide an important insight into the behavior of the cross-polar field of a corrugated horn, also giving the optimum limit for achievable cross-polarization performances. As we can see from both plots, the cross-polarization is only very slightly affected by R_λ and α , which, on the contrary, significantly influence the mainbeam pattern.

In fact, the geometry of the corrugations is of prime importance in maintaining the cross-polarization down at the levels given in Figs. 9 and 10. The corrugations must give the appropriate boundary conditions for propagation of the HE_{11} mode. As already stated regarding the transition region, typical optimum values, coming from a mix between theory and experimental data, are those given in the right side of Fig. 8, which are practically used for the steady-state corrugation geometry from the end of the transition region to the radiating aperture, consisting of a 0.25λ slot depth, a 0.1λ tooth width, and a 0.2λ slot width. These values, in practice, guarantee a cross-polarization level better than ~ 35 dB down the co-polar maximum, for bandwidth of about 30–40%.

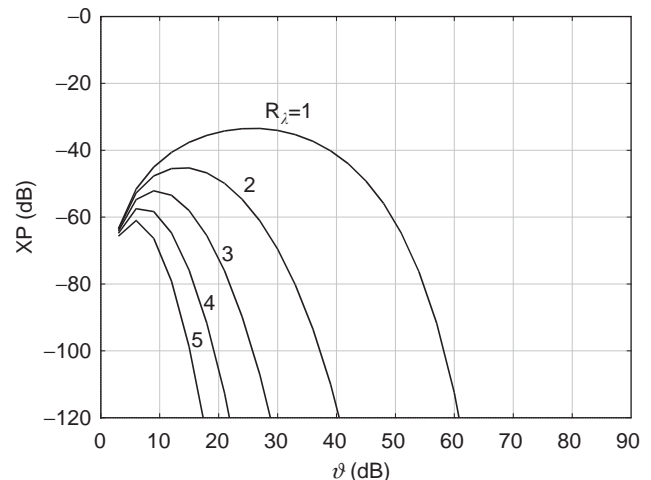


Figure 9. Corrugated waveguide cross-polar pattern for different values of the wavelength normalized aperture radius.

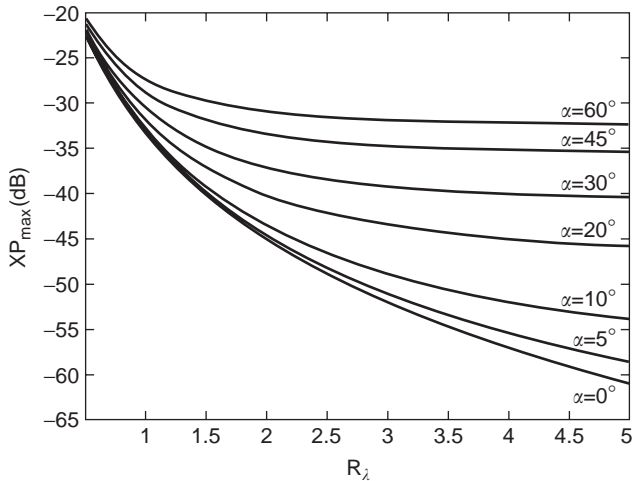


Figure 10. Cross-polarization maximum parametric curves for corrugated horns.

4.4. Phase Center

The *phase center* is theoretically defined as the origin in space of the spherical phase fronts of the radiated field. In general, for practical antennas, the definition holds only approximately, but corrugated horns are radiating structures for which a rather well-defined phase center exists.

In the Gaussian beam model, as we have seen, it is possible to predict the phase center position in both the near and far regions, by using (34) and (35). However, it is sometimes important to estimate a more accurate phase center position as a function of the radiating pattern. In particular, in the design of a corrugated horn, it is important to minimize the phase shift of the radiated field on a given spherical surface subregion (e.g., as delimited by the edges of the illuminated reflector). Thus the center of curvature of the phase-shift-minimized wavefront on that surface can be defined as the operative phase center of the antenna. Knowledge of this point is important in optimizing the position of a feed in a system of reflectors, to produce the best optical design.

Computation of the phase center, given the radiated phase pattern, can be carried out in different ways leading to different degrees of approximation in the evaluation. The one here shown is based on the minimization of a given phase pattern in the far-field region.

To better explain this method, we refer to Fig. 11, showing the geometry of a horn feeding a reflector antenna. The aim is to minimize the phase variation of the radiated far field inside the solid angle delimited by the elevation angle ϑ_0 (for sake of simplicity, a symmetric configuration is assumed), which is generally not necessarily associated with the reflector edges. Let's suppose that O and O' are two points separated by a distance d on the axis of the horn (where, by symmetry, the phase center is located); it can be shown that, in the far-field approximation, the phase patterns having the above mentioned points as phase reference are related by

$$\phi_{O'}^{P(\vartheta,\varphi)}(d) = \phi_O^{P(\vartheta,\varphi)} - k_0 d \cos(\vartheta) \quad (69)$$

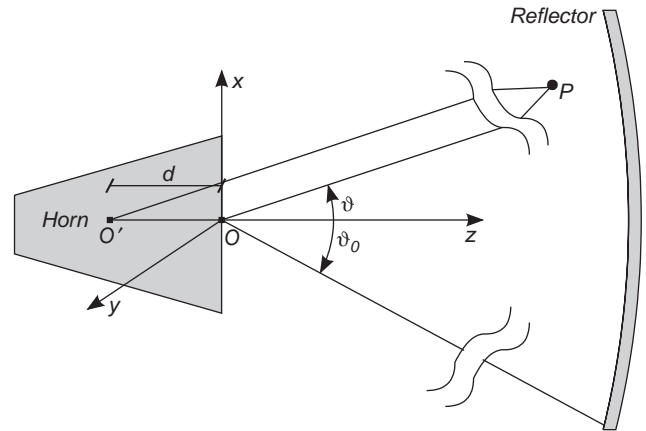


Figure 11. Reference geometry for phase center numerical evaluation.

in which $\phi_C^{P(\vartheta,\varphi)}$ is the phase at the observation point P with respect to the generic point C and k_0 is the wave-number. The right hand side of (69) can be seen as a function of the variable d ; thus the computation of the phase center can be mathematically formulated as the minimization of the function

$$f(d) = \sum_i \sum_j W_{ij} |\phi_{O'}^{P(\vartheta_i,\varphi_j)}(d) - \phi_O^{P(\vartheta=0)}(d)|^n \quad (70)$$

in which the absolute value of the phase shift, eventually powered to an arbitrary value n , is suitably weighted by W_{ij} coefficients, with the double summation extended over the samples (ϑ_i, φ_j) of the angular region of interest.

4.5. Profiled Horns

As stated in the introduction (Section 1), corrugated horns possessing profiles of corrugations consisting of complex curves have been studied extensively.

The effect of the curved profile is to excite an appropriate higher-order set of modes to add degrees of freedom with respect to standard linear profiled horns. These additional parameters can be used to control electrical requirements (the radiation pattern and the phase center location) or mechanical requirements (space occupation and weight reduction). In fact, using higher-order modes, it is possible to modify the standard corrugated horn aperture field in order to obtain a radiated mainbeam a bit closer to a rectangle, which is the optimum shape when feeding reflector antenna systems because both aperture and spillover efficiency are maximized. The same approach is also valid if low sidelobe levels are required, and in this case an exponential taper ending section is most appropriate to excite the correct set of higher-order modes; the longer is the exponential section, the lower is the sidelobe level. The property of exciting higher-order modes by varying the profile can be also used to satisfy requirements on the horn mainbeam and at the same time to reduce as much as possible the horn dimensions, which is an attractive feature especially in spacecraft applications. A further advantage of adopting curved profiles is

the possibility of controlling the phase center position and its stability versus frequency; for example, if the profile is quite flat in the region near the radiating aperture, resembling an open corrugated waveguide, the phase center is very close to the aperture itself, and is also very stable with respect to frequency. Thus phase center position and stability can be controlled by properly designing the slope and the shape of the end part of the profile. When dealing with optical systems, especially in those applications in which feed clusters are required, this feature gives some degree of freedom to the design of the geometric configuration of the feeds, which can be very critical because of mutual coupling, for example.

Typically, the design of profiled horns begins with the design of a standard linear horn, matching as closely as possible the specifications. Then, using numerical techniques performing the electromagnetic analysis and the optimization, the design is refined to fully satisfy all the requirements.

Here we discuss in analytical detail the so-called dual profile [5]. As shown in Fig. 12, it is formed by two elementary curves, the sine square r_s at the beginning and the exponential r_e at the end, according to the following rule

$$r_s(z) = R_i + (R_s - R_i) \left[(1 - A_s) \frac{z}{L_s} + A_s \sin^2 \left(\frac{\pi z}{2L_s} \right) \right], \quad 0 \leq z \leq L_s \quad (71)$$

$$\begin{aligned} r_e(z) &= R_s + e^{\alpha(z-L_s)} - 1, \\ L_s \leq z &\leq L_e + L_s, \\ \alpha &= \frac{1}{L_e} \ln(1 + R - R_s) \end{aligned} \quad (72)$$

where $0 \leq A_s \leq 1$ modulates the first region profile between a straight line and a pure sine square.

The principal effect of the sine square profile is the shaping of the mainlobe by properly exciting higher-order modes, while the exponential taper controls mainly the phase center position and the sidelobe levels.

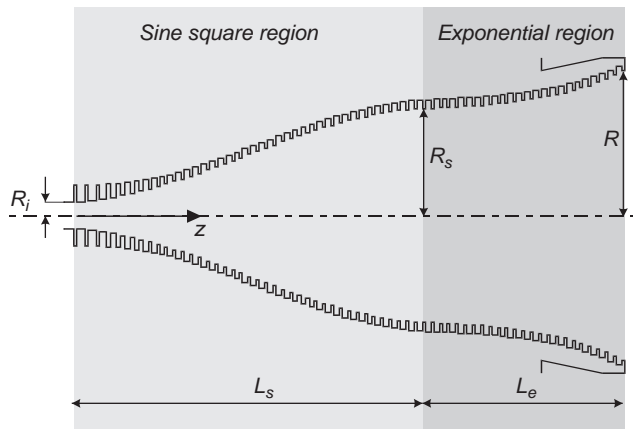


Figure 12. Dual-profile corrugated horn.

A more flexible version for the shaping of the horn corrugation profile can be obtained by using parametric curves. Among these the nonuniform rational B-splines (NURBS) are particularly versatile [15]. NURBS curves are generated by an ordered set of points $\{P_i\}$, $i=0, \dots, n$, defining the control polygon, through a function expressed as a ratio of vector-valued polynomials

$$\mathbf{P}(u) = \frac{\sum_{i=0}^n q_i \mathbf{P}_i N_{i,p}(u)}{\sum_{i=0}^n q_i N_{i,p}(u)} \quad (73)$$

where q_i are an assigned set of weights and $N_{i,p}(u)$ are the normalized B-spline basis functions of degree p . Design methods based on NURBS have already been successfully used [16], and a typical corrugated horn NURBS profile is shown in Fig. 13, where the upper part of the horn longitudinal cut is given and the control polygon is highlighted.

4.6. Numerical Techniques for Corrugated Horns

Thus far theoretical aspects of corrugated horns have been discussed on the basis of simple models. Formulas and graphs derived in this way are very useful in the design and, in general, are also sufficient if requirements are not too stringent. This is seldom the case in many modern applications, where high levels of accuracy are required in the design phase. Taking advantage of the computational power of modern computers, numerical techniques for the analysis of electromagnetic problems are now used successfully in microwave applications as a refinement of the simple design approach described above.

Regarding the analysis of circular corrugated horns, a hybrid numerical technique is the most efficient, using a combination of different methods according to their ability to accurately analyze different regions. This technique is presented in Ref. 17 and is based on the mode-matching method (MM) [18] and the method of moments (MoM) [19]. The internal part of the horn is best analyzed with MM

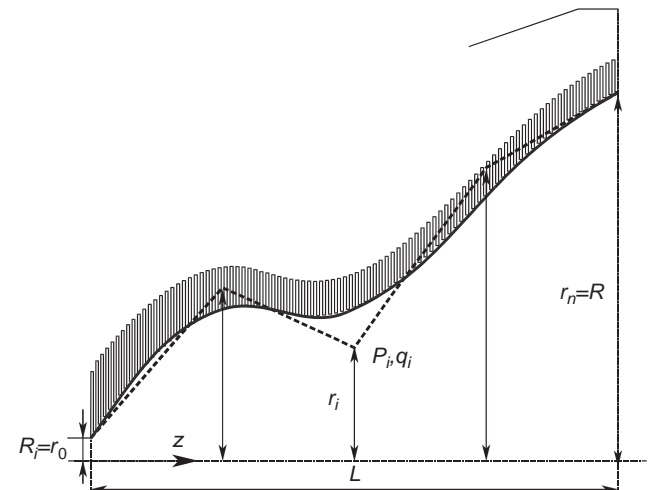


Figure 13. NURBS-profile corrugated horn.

making use of the generalized scattering matrix (GSM) concept. The horn can be seen as a cascade of single-step discontinuities in circular waveguide for which the MM method allows computation of the GSM. The overall horn geometry is analyzed by respectively cascading all the GSMs of the steps to find the overall GSM of the corrugated structure. MM is convenient for these structures because of its efficiency and small storage demand. In fact, whenever a new step is solved, it is immediately cascaded with the following step to form a partial GSM that includes all the steps solved thus far.

In the corrugated horn analysis only a particular subset of modes may be chosen. In the case of a circular waveguide TE_{11} excitation, the subset of TE_{1n}/TM_{1n} modes is sufficient to fully represent the field inside the horn if the azimuth symmetry is preserved everywhere. The rule for choosing the number N of modes in a single circular waveguide section for accurate numerical results and computation efficiency depends on the wavelength-normalized radius of the waveguide; typically, this is about $N=20R/\lambda$. The outer part of the horn, including the radiating aperture and the external metallization, is analyzed with the application of MoM to a combined field integral equation (CFIE). Formulating an equivalent problem in which the horn aperture and the external feed shape form a closed metallic surface, the CFIE enforces the boundary conditions for both the electric and magnetic fields. The axial symmetry of the structure is used to apply the body of revolution (BoR) formulation [20] to the MoM, so that an efficient expansion for electromagnetic sources and fields is possible. In particular, a subsectional basis function expansion is applied only along the generating curve of the BoR surface, while expansion in entire domain harmonic-type basis functions is used along the azimuth angle. In this way, CFIE may be solved easily for an unknown set of amplitudes of the basis functions used to expand electric surface current density on the external horn surface.

Finally, to complete the analysis, the coupling between the inner and the outer parts of the horn must be taken into account. This is done by applying the tangential field continuity over the horn aperture leading to a magnetic field integral equation (MFIE), which is solved by MoM.

Combination of MM and MoM allows us to compute the GSM of the horn in the presence of the actual outer feed shape. This also enables us, given the excitation, to estimate the input matching and calculate the external horn surface equivalent sources, allowing an easy computation of the radiated fields by means of the well-known free-space Green function. In conjunction with analysis techniques, numerical optimization procedures have been developed to produce complete tools for corrugated horn design.

Optimization techniques search for the optimum geometry satisfying a given set of specifications. Typically a cost is defined as a function of a particular set of electromagnetic performances so that the optimum solution is an extreme point of the cost function (a minimum or a maximum). Then the optimization procedure searches in the space of the allowed geometry parameters of the structure to be optimized to find this extreme point.

The existing used methods to search for the optimum geometry may be grouped into two categories: deterministic and stochastic.

A commonly used deterministic technique is the quasi-Newton method [21], while genetic algorithms [22] are an example of the stochastic type. The quasi-Newton method searching for the optimum value is governed mathematically by computing the differentiation, up to the second order, of the cost function. This is an iterative procedure where, at each computation step, the higher-order derivative information is used to directly evaluate the next point, in the space of the geometry to be optimized. Such a point is a potential candidate to be the optimum. This is quite a fast optimization method, performing very well if the iteration starting point is already within the basin of attraction of the optimum point itself; otherwise, as is well known, it remains confined to the nearest local minima.

Genetic algorithms are an evolutionary method producing successive populations of individuals according to their capabilities to adapt themselves to the environment. This capability is expressed in terms of a cost function, where individuals represent the codification of the space of the allowed geometric parameters. Individuals with higher capabilities (better cost functions) have a greater probability of reproducing themselves in successive generations (new sets of geometric parameters). In the genetic algorithm scheme, each successive generation is produced with genetic laws of crossover and mutation, yielding individuals that may have better capabilities, that is better cost functions.

From a practical point of view, genetic algorithms, like other stochastic methods, have complementary features with respect to direct searching techniques. They are generally more CPU-demanding and slower, but have the advantage of performing global searches for the optimum point without being trapped in local minima. A hybrid method based on genetic algorithms and the Quasi-Newton method has been successfully applied to corrugated horn design [23].

Artificial neural networks [24] (ANNs) are another useful approach for corrugated horn design. ANNs can be considered as universal approximators with the ability to model any given transfer function if properly instructed. On the basis of a given set of data related to horn geometry and performance, the network is able to "learn" how the horn operates. This learning process matures, generating an evolving model of the horn that may be perceived as a blackbox having geometric parameters such as input and electromagnetic performance such as output. The accuracy of the ANN model is refined by using the information coming from a cost function evaluating the distance, in terms of the performances, between the model and the real horn. The major advantage of this method is that, once the learning phase has produced, an accurate ANN model, the ANN-based horn analysis, is very fast, and thus is of prime interest in the horn design phase, where a very large number of simulations are commonly required. Examples of ANN applications to horn design can be found in Ref. 25.

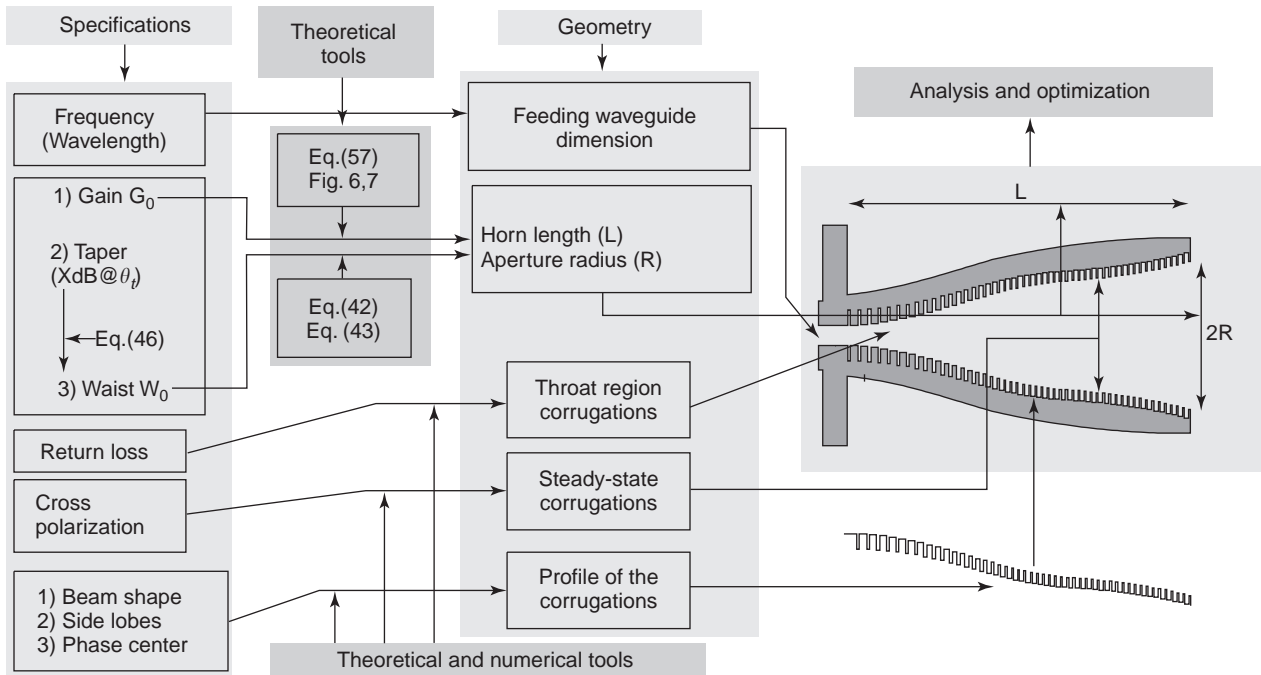


Figure 14. Schematic flow chart for corrugated horn design.

4.7. Summary of Corrugated Horn Design

To summarize the previous concepts, a practical design procedure is outlined, following the sketch in Fig. 14, showing a flowchart for corrugated horn design.

In the flowchart the design should be seen as a process linking a set of specifications (grouped under “specifications”) to a set of geometric parameters (geometry) that



Figure 15. High-gain feed horn at 32 GHz (Courtesy of the Institute of Radioastronomy of the Italian National Research Council.)

completely characterize the fundamental aspects of horn mechanics, at least from an electromagnetic perspective.

The frequency is the fundamental specification involved (by means of the wavelength) in all the horn geometry; however, from a design perspective, it directly fixes the dimension of the input waveguide feeding the horn once single fundamental mode propagation is imposed in the operative band.

Three equivalent specifications can be used to theoretically determine the horn length L and the aperture radius R ; if the horn gain G_0 is given, it is possible to use (57) and the graphs of Figs. 6 and 7 for best choice of L and R ; if the waist w_0 is given, then (42) and (43) can be

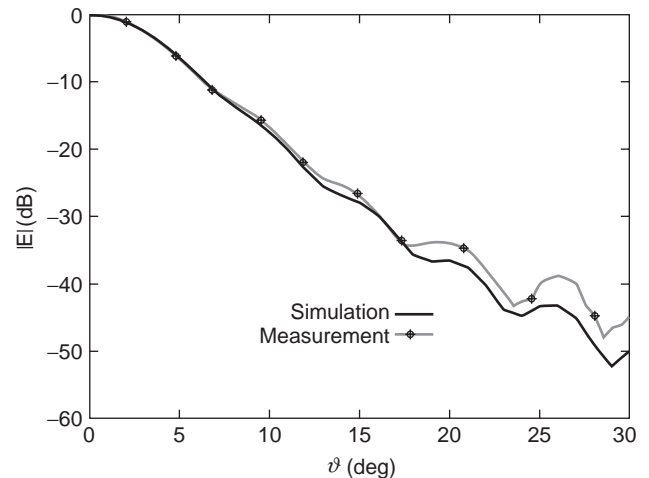


Figure 16. E -plane pattern cut of the 32-GHz high-gain corrugated horn.

used; if the taper X dB at θ_t is given, then the equivalent waist specification can be obtained from (46), proceeding as in the previous case.

Both theoretical and numerical tools should be used for the other specifications. Return loss is related mainly to the geometry of the throat region corrugations; cross-polarization affects the geometry of the steady-state region corrugations; and mainbeam shape, sidelobe, and phase center specifications should be used to design the curvature of the corrugation profile. The electromagnetic phenomena governing the preceding relations between specifications and horn geometry have been explained in the text above and values have been suggested to quantify these relations since this would be of greater help to the designer. However, those quantitative values should not be taken as an arbitrary rule; rather, they require further verification by analytical simulations according to the particular application, and this is the meaning of the term “numerical tools” introduced here. Once the horn geometry has been determined, analysis and optimization routines should be used to verify and refine the design.

5. CORRUGATED HORN DESIGN EXAMPLES

To give the reader an idea of the performances of corrugated horns, two examples are presented here.

Example 1. Assume a high-gain corrugated horn operating in Ka band at 32 GHz with gain of ~ 28 dB. Thus, according to the graph of Fig. 7, a 6λ aperture radius with an half-flare angle of $\sim 8^\circ$ has been chosen, leading to the prototype of Fig. 15 with an aperture diameter of ~ 11 cm and an overall length of ~ 38 cm.

The gain was verified to be correct by full-wave simulations, showing a ~ 1 dB variation in a 20% band, while the copolar radiation pattern is given in Fig. 16, highlighting results close to measurement data.

Particular attention in the design has been devoted to keep both the input reflection coefficient and the



Figure 18. Dual-profile corrugated horn at 22 GHz (Courtesy of the Institute of Radioastronomy of the Italian National Research Council.)

cross-polarization maximum as low as possible. As is shown in the plots of Fig. 17, the measured reflection coefficient is less than -30 dB with very good agreement with simulation data.

Example 2. Given a dual-profile corrugated horn at 22 GHz for use as a feed for a reflector antenna illuminated with an edge taper of 12 dB at 9.5° . The horn, whose prototype is given in Fig. 18, has been optimized for compactness, reducing about 20% space occupation with respect to a standard horn. It is interesting to observe the measured beam pattern of the horn that is compared in the plot of Fig. 19 with the results of the full-wave simulation.

Comparing the dual-profile horn pattern with the one of the standard horn in Fig. 16, we note the differences in the shape of the mainbeam and the secondary lobe due to the contribution to the radiation of higher-order modes, excited by the curved profile.

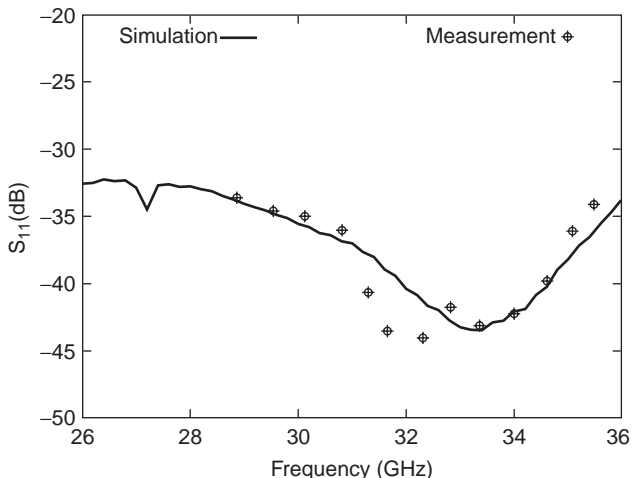


Figure 17. Reflection coefficient for the 32-GHz high-gain corrugated horn.

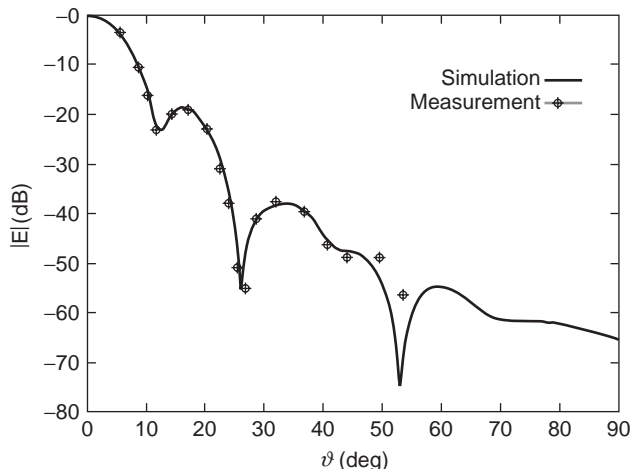


Figure 19. H -plane pattern cut of the 22-GHz dual-profile horn.

BIBLIOGRAPHY

1. P. J. B. Clarricoats and A. D. Olver, *Corrugated Horns for Microwave Antennas*, Peter Peregrinus, London; 1984.
2. C. Del Rio Bocio, R. Gonzalo, M. S. Ayza, and M. Thumm, Optimal horn antenna design to excite high-order Gaussian beam modes from TE_{0m} smooth circular waveguide modes, *IEEE Trans. Antenn. Propag.* **47**(9):1440–1448 (1999).
3. C. Granet, Profile options for feed horn design, *Proc. APMC'2000*, Dec. 2000, pp. 1448–1451.
4. G. G. Gentili, R. Nesti, G. Pelosi, and V. Natale, A new compact dual-profiled corrugated circular waveguide horn, *Electron. Lett.* **36**(6):486–487 (2000).
5. G. G. Gentili, E. Martini, R. Nesti, and G. Pelosi, Performance analysis of dual profile corrugated circular waveguide horns for radio astronomy antennas, *IEE Proc. Microwaves Antenn. Propag.* **148**(6):119–124 (2001).
6. C. A. Balanis, *Advanced Engineering Electromagnetics*, Wiley, New York, 1989, pp. 470–491.
7. R. E. Collin, *Advanced Engineering Electromagnetics*, Wiley, New York, 1989, pp. 100–104.
8. C. Aubry and D. Bitter, Radiation pattern of a corrugated conical horn in terms of Laguerre Gaussian functions, *Electron. Lett.* **11**(7):154–156 (1975).
9. D. H. Martin and J. W. Bowen, Long-wave optics, *IEEE Trans. Microwave Theory Tech.* **41**(10):1676–1690 (1993).
10. P. F. Goldsmith, *Quasioptical System: Gaussian Beam Quasioptical Propagation and Applications*, IEEE Press, Piscataway, NJ, 1989.
11. P. C. Clemmow, *The Plane Wave Spectrum Representation of Electromagnetic Fields*, Wiley–IEEE Press, New York, 1996.
12. C. A. Balanis, *Antenna Theory: Analysis and Design*, Wiley, New York, 1982, pp. 453–454.
13. X. Zhang, Design of conical corrugated feed horns for wide-band high frequency applications, *IEEE Trans. Microwave Theory Tech.* **41**(8):1263–1274 (1993).
14. A. C. Ludwig, The definition of cross-polarization, *IEEE Trans. Antenn. Propag.* **21**:116–119 (1973).
15. L. Piegl, On NURBS: A survey, *IEEE Computer Graph. Appl.* **11**(1):55–71 (1991).
16. L. Lucci, R. Nesti, G. Pelosi, and S. Selleri, Phase centre optimization in profiled corrugated circular horns with parallel genetic algorithms, *Prog. Electromagn. Res. PIER* **46**:127–142 (2004).
17. R. Cocioli, G. Pelosi, and R. Ravanelli, Combined mode matching-integral equation technique for feeders optimization, in P. P. Silvester, ed., *Software for Electrical Engineering Analysis and Design*, Computational Mechanics Publications, Southampton, UK, 1996.
18. T. Itoh, *Numerical Techniques for Microwave and Millimeter Wave Passive Structures*, Wiley, New York, 1989.
19. R. F. Harrington, *Field Computation by Moment Methods*, Macmillan, New York, 1968.
20. R. F. Harrington and J. R. Mautz, Radiation and scattering from bodies of revolution, *Appl. Sci. Res.* **20**:405–435 (1969).
21. R. Fletcher, *Practical Methods of Optimization*, Wiley, New York, 1981.
22. D. E. Goldberg, *Genetic Algorithms in Search, Optimization and Machine Learning*, Addison-Wesley, Reading, MA, 1989.
23. L. Lucci, R. Nesti, G. Pelosi, and S. Selleri, Design of an improved profiled corrugated circular horn at 320 GHz, *J. Electromagn. Waves Appl.* **18**(3):387–396 (2004).
24. J. M. Zurada, *Introduction to Artificial Neural System*, West, St. Paul, MN, 1992.
25. G. Fedi, S. Manetti, G. Pelosi, and S. Selleri, Profiled corrugated circular horns analysis and synthesis via an artificial neural network, *IEEE Trans. Antenn. Propag.* **21**:116–119 (1973).

COULOMB GAUGE IN ELECTROMAGNETICS, THE

ROBERT D. NEVELS
 KRZYSZTOF A. MICHALSKI
 Texas A&M University
 College Station, Texas

1. INTRODUCTION

Problems in high-frequency electromagnetic scattering and diffraction, where the fields are expressed in terms of magnetic vector (\mathbf{A}) and scalar (V) potentials, have in the past been solved almost exclusively with the Lorentz¹ gauge. However, in this article it will be shown that any wave guidance or scattering problem that can be found through an application of the Lorentz gauge can as well be solved subject to the Coulomb gauge. It will be shown that the Coulomb gauge formulation displays some unique mathematical characteristics that provide insight into the meaning and structure of potentials [1]. Also, the component parts of the mathematical expressions for the field arising from an application of the Coulomb gauge provide a way of directly determining how the field changes with a change in frequency.

The fact that the Lorentz and Coulomb gauges possess unique properties that correspond to physical aspects of the electromagnetic field suggests that the choice of gauge should depend on the kind of problem being solved or the physical parameters that are being sought. However, although gauge methods have existed for over 150 years, mathematical solutions for the electromagnetic field that include the region of the source current have been obtained only with these two gauges. Other gauges have been explored, but, without a solution that is valid in the source region, problems of practical interest, where objects can have any general shape, cannot be solved.

A comparison of the Lorentz and Coulomb gauges can best be displayed by incorporating the effects of some object such as a cylinder or wedge in the problem definition, thereby leaving the current distribution on a nearby arbitrary surface as the only unknown to be found. This approach is sometimes referred to as the “hybrid method

¹According to E. Whittaker’s *A History of the Theories of Aether and Electricity*, this gauge was first derived by L. Lorenz and not H. A. Lorentz. The interested reader is referred to Refs. 11 and 12 for more background on this historical oversight. Here we choose to continue to use the name by which the gauge has been known for over a century.

of moments (MM) Green's function method" [2,3]. From a purely mathematical point of view, a change in gauge means that the vector and scalar potentials will have Green functions [4,5] that differ significantly from those of the familiar Lorentz gauge. An important consequence of the hybrid MM/Green function method presented here is that the Green functions are in their most general dyadic form, incorporating all coordinate components in a few compact mathematical expressions. The advantage of the dyadic Green function formulation is that it provides a procedure for handling general three-dimensional boundary value problems in the Lorentz gauge, and yet it is uniquely suited for the Coulomb gauge owing to the particular solenoidal nature of the Coulomb vector potential and lamellar nature of the Coulomb scalar potential.

2. THE ELECTROMAGNETIC FIELD IN TERMS OF POTENTIALS

Maxwell's equations in time harmonic form are

$$\nabla \times \mathbf{E} = -j\omega \mathbf{B} \quad (1)$$

$$\nabla \times \mathbf{H} = \mathbf{J} + j\omega \mathbf{D} \quad (2)$$

$$\nabla \cdot \mathbf{D} = \rho \quad (3)$$

$$\nabla \cdot \mathbf{B} = 0 \quad (4)$$

where \mathbf{E} and \mathbf{H} are the electric and magnetic field intensities and \mathbf{D} and \mathbf{B} are the electric and magnetic field flux densities and ω is the radian frequency. Equation (3), when substituted into the divergence of (2), gives the continuity equation

$$\nabla \cdot \mathbf{J} = -j\omega \rho \quad (5)$$

a useful relationship between the electric current \mathbf{J} and charge ρ densities.

In this article all regions are assumed to be homogeneous, linear, and isotropic, which means that the permittivity ϵ and permeability μ of space are constant and the relationships between field intensities and the flux densities are given by the simple expressions

$$\mathbf{D} = \epsilon \mathbf{E} \quad \text{and} \quad \mathbf{B} = \mu \mathbf{H} \quad (6)$$

which are known as the *constitutive relations*. Also, in the mathematics of this article the time convention $\exp(j\omega t)$ is suppressed.

Because magnetic charge has never been observed, the right-hand side of the magnetic field divergence equation (4) is always zero. It also happens that the divergence of the curl of any vector \mathbf{U} is also always zero. This identity, expressed mathematically by $\nabla \cdot (\nabla \times \mathbf{U}) = 0$, when compared to (4) suggests the possibility that the flux density \mathbf{B} can be found by taking the curl of some other vector. In electromagnetism this vector has been assigned the sym-

bol \mathbf{A} and termed the *magnetic vector potential*:

$$\mathbf{B} = \nabla \times \mathbf{A} \quad (7)$$

At this point \mathbf{A} is not known, nor do we have an equation for it, but we do know a couple of facts. First, if the magnetic vector potential were known, then the magnetic field could be easily found with (7); second, because the electromagnetic fields must satisfy Maxwell's equations, it follows that the magnetic vector potential must also satisfy Maxwell's equations. The latter condition can be exploited in order to find the relationship between the vector potential \mathbf{A} and the electric field. To do this, Eq. (7) is substituted into (1) and the terms under the curl operation are collected, giving

$$\nabla \times (\mathbf{E} + j\omega \mathbf{A}) = 0 \quad (8)$$

By comparing (8) with another vector identity, $\nabla \times \nabla \psi = 0$, where ψ is any scalar function of position, it can be hypothesized that the term in the parenthesis can be expressed as the gradient of a scalar:

$$\mathbf{E} + j\omega \mathbf{A} = -\nabla V \quad (9)$$

The scalar, V , is referred to as the *electric scalar potential*. Equation (9) can be rearranged to display the electric field equivalent of (7):

$$\mathbf{E} = -j\omega \mathbf{A} - \nabla V \quad (10)$$

One obvious question to ask is why a negative sign is chosen in front of the gradient operation in (9) when an always less troublesome positive sign appears to be equally valid. One answer is that since the gradient produces a vector that is in the direction of increasing potential value, then the Lorentz force law, $\mathbf{F} = q\mathbf{E}$, holds true when $\omega = 0$ only if a negative sign is placed in front of the gradient of the potential.

2.1. Justification for Using Potentials

The fact that potentials save considerable effort when solving Maxwell's equations may not be immediately obvious. To see that potentials do indeed simplify electromagnetic field calculations, let us investigate what would happen if we were to attempt to directly solve for the electric or magnetic field. Taking the curl of Faraday's law (1) and substituting Ampere's law (2) into the result gives

$$\nabla \times \nabla \times \mathbf{E} + k^2 \mathbf{E} = j\omega \mu \mathbf{J} \quad (11)$$

or, with the vector identity

$$\nabla \times \nabla \times \mathbf{U} = -\nabla^2 \mathbf{U} + \nabla \nabla \cdot \mathbf{U} \quad (12)$$

and the continuity equation (5), Eq. (11) can be reduced to the Helmholtz equation

$$\nabla^2 \mathbf{E} + k^2 \mathbf{E} = \frac{j}{\omega \epsilon} (\nabla \nabla \cdot \mathbf{J} + k^2 \mathbf{J}) \quad (13)$$

Also, by taking the curl of (2), a similar set of vector operations leads to a Helmholtz equation for the magnetic field

$$\nabla^2 \mathbf{H} + k^2 \mathbf{H} = -\nabla \times \mathbf{J} \quad (14)$$

Although in some cases it is possible to find a Green function by directly solving Eqs. (11), (13), and (14), it is the complexity of these equations that encourages the use of potentials. For example, the $\nabla \times \nabla \times$ operator in (11) produces a set of three scalar equations in which E_x , E_y , and E_z are coupled. Similarly the $\nabla \nabla \cdot$ operator on the right-hand side of (13) leads to three scalar equations for the electric field, and $\nabla \times$ in (14) results in three scalar equations for the magnetic field that are in each of these cases coupled in terms of the current density components J_x , J_y , and J_z . It is very difficult to solve coupled sets of equations. However, it will be shown below that a mathematical relationship called a “gauge” can produce from one to three uncoupled equations from which all six electric and magnetic field components can be found. The use of gauges is therefore said to reduce the number of degrees of freedom, thereby simplifying the problem solution.

2.2. Nonuniqueness of Potentials

A potential is not unique even though it satisfies Maxwell’s equations and a given set of boundary conditions. However, potentials that satisfy the same boundary conditions differ from one another in definable ways. For instance, if the gradient of any scalar ψ is subtracted from a vector potential \mathbf{A} , then the result

$$\mathbf{A}' = \mathbf{A} - \nabla\psi \quad (15)$$

produces a different magnetic potential \mathbf{A}' , although the magnetic field will be the same as that obtained with the original \mathbf{A} . This can be shown by substituting (15) into (7)

$$\begin{aligned} \mathbf{B} &= \nabla \times \mathbf{A} + \nabla \times \nabla\psi \\ &= \nabla \times \mathbf{A}' \end{aligned} \quad (16)$$

and (15) into (4)

$$\nabla \cdot \mathbf{B} = \nabla \cdot \nabla \times \mathbf{A}' = 0 \quad (17)$$

and by observing, with the aid of (16), that

$$\nabla \times \mathbf{B} = \nabla \times \nabla \times \mathbf{A}' = \nabla \times \nabla \times \mathbf{A} \quad (18)$$

In other words, the magnetic flux density \mathbf{B} , as well as its divergence (17) and curl (18), are the same regardless of whether the vector potential used to define \mathbf{B} is \mathbf{A} or \mathbf{A}' , two expressions that differ by $\nabla\psi$. Equation (15) is referred to as a *vector potential gauge transformation*. The magnetic flux density \mathbf{B} is therefore said to be preserved under the gauge transformation between \mathbf{A} and \mathbf{A}' given in (15).

If the electric field is to be preserved under the gauge transformation, then the scalar potential in (10) must be modified so as to compensate for a change in the vector

potential. The electric field in terms of the new vector and scalar potentials is

$$\mathbf{E} = -j\omega \mathbf{A}' - \nabla V' \quad (19)$$

By substituting (15) into (19) it is clear that the electric field

$$\mathbf{E} = -j\omega \mathbf{A} - \nabla(-j\omega\psi + V') \quad (20)$$

will not change if the term in parentheses is equal to the original scalar potential V , that is

$$V' = V + j\omega\psi \quad (21)$$

This equation is known as the scalar potential gauge transformation.

The gauge transformations in (15) and (21) create a new set of potentials (\mathbf{A}', V') , yet the electric and magnetic fields produced with these new potentials are the same as those calculated with the original set (\mathbf{A}, V) . The fact that the electric and magnetic fields are the same, regardless of which set of potentials is used, is described as the gauge invariance property of the fields. From a historical prospective it is interesting that gauge transformations, after they were first discovered for the electromagnetic field, were incorporated into the mathematical description of many physical phenomena, which was a key to finding of a relationship between some of the fundamental forces of nature [12].

Although sets of potentials for a particular problem configuration are always related through the transformations in (15) and (21), the mathematical expression for ψ is seldom obvious. Each new set of potentials will give rise to a new ψ that, through (15) and (21), determines the relationship between the new potentials and the original set. An important use of the gauge transformations is suggested by rearranging (21) as follows:

$$\psi = \frac{V' - V}{j\omega} \quad (22)$$

This equation shows that the difference between the scalar potentials found with two different gauges produces ψ , which through (15) yields the remaining vector potential. This observation provides a valuable tool when deriving a new set of potentials since the equations from which scalar potentials are derived can be solved without resorting to complicated vector procedures. Once ψ is found we are relieved of the necessity of independently deriving the vector potential.

In the sections that follow the goal will not be to find the relationship between different sets of potentials, but rather to determine the link between a particular vector and scalar potential that form a single set. This relationship, called a “gauge”, leads to differential equations for the vector and scalar potentials and ultimately, by applying boundary conditions, to the potentials themselves.

2.3. Dyadic Green's Functions

In order to solve problems that involve current distributions or scattering structures that are encountered in practice, it is necessary to develop the dyadic Green function approach. Green's method is a systematic procedure for obtaining a mathematical expression in which the potential due to an elemental source is convolved with a particular current distribution in order to determine the potential caused by that current. The dyadic Green function method is the simplest method for finding the electromagnetic fields produced by a general-shaped structure via the Coulomb gauge. Here, as in most cases of practical interest, the potential is found first and then, by an application of Eqs. (7) and (10), the magnetic and electric fields. Limited space prevents a more thorough discussion of the topic of dyadics, so it is assumed that the reader has a working knowledge of the subject. If not, please refer to Appendix A for a brief introduction. Also the authors highly recommend the excellent text by Tai [4].

The vector potential is obtained in terms of a dyadic Green's function as follows. The current density forcing function on the right-hand side of Helmholtz potential equation

$$\nabla^2 \mathbf{A} + k^2 \mathbf{A} = -\mu \mathbf{J} \quad (23)$$

which will be derived later in this article, is replaced by a dyadic delta forcing function, resulting in

$$\nabla^2 \overline{\mathbf{G}} + k^2 \overline{\mathbf{G}} = -\overline{\delta}(\mathbf{r} - \mathbf{r}') \quad (24)$$

where $\overline{\mathbf{G}}$ is Green's function for an elemental source oriented in an arbitrary direction in free space and $\overline{\delta} = \overline{\mathbf{I}}\delta(\mathbf{r} - \mathbf{r}')$. $\overline{\mathbf{I}} = \hat{\mathbf{x}}\hat{\mathbf{x}} + \hat{\mathbf{y}}\hat{\mathbf{y}} + \hat{\mathbf{z}}\hat{\mathbf{z}}$ is the identity dyadic and $\delta(\mathbf{r} - \mathbf{r}')$ is the Dirac delta function. Equation (23) is postmultiplied by $\overline{\mathbf{G}}$ and (24) premultiplied by \mathbf{A} as follows:

$$(\nabla^2 \mathbf{A} + k^2 \mathbf{A} = -\mu \mathbf{J}) \cdot \overline{\mathbf{G}} \quad (25)$$

$$\mathbf{A} \cdot (\nabla^2 \overline{\mathbf{G}} + k^2 \overline{\mathbf{G}} = -\overline{\delta}(\mathbf{r} - \mathbf{r}')) \quad (26)$$

These two equations are subtracted and then integrated over a volume of space, yielding

$$\int_{\text{vol}} (\nabla^2 \mathbf{A} \cdot \overline{\mathbf{G}} - \mathbf{A} \cdot \nabla^2 \overline{\mathbf{G}}) dv = \int_{\text{vol}} (\mathbf{A} \cdot \overline{\delta}(\mathbf{r} - \mathbf{r}') - \mu \mathbf{J} \cdot \overline{\mathbf{G}}) dv \quad (27)$$

The volume integral on the left in (27) can be rewritten in terms of a surface integral bounding the volume as follows [6]

$$\begin{aligned} & \int_{\text{vol}} (\nabla^2 \mathbf{A} \cdot \overline{\mathbf{G}} - \mathbf{A} \cdot \nabla^2 \overline{\mathbf{G}}) dv \\ &= \int_{\text{surf}} [\nabla \cdot \mathbf{A}(\hat{\mathbf{n}} \cdot \overline{\mathbf{G}}) - (\hat{\mathbf{n}} \cdot \mathbf{A})\nabla \cdot \overline{\mathbf{G}} \\ &+ \nabla \times \mathbf{A} \cdot (\hat{\mathbf{n}} \times \overline{\mathbf{G}}) - (\hat{\mathbf{n}} \times \mathbf{A}) \cdot \nabla \times \overline{\mathbf{G}}] ds \end{aligned} \quad (28)$$

where $\hat{\mathbf{n}}$ is a unit vector normal to the bounding surface. If the surface extends to infinity, then this integral is zero due to the Sommerfeld radiation condition, which says that at infinity all fields, and therefore the potentials, must go to zero. If the bounding surface is a perfect conductor, then the conditions [7]

$$\hat{\mathbf{n}} \times \mathbf{A} = 0 \quad \nabla \cdot \mathbf{A} = 0 \quad \text{on surface} \quad (29)$$

hold for the vector potential and similarly for the vector potential Green's function $\overline{\mathbf{G}}$, so again the right hand side of (28) is zero. Equation (27) therefore reduces to

$$\mathbf{A}(\mathbf{r}') = \mu \int_{\text{vol}} \mathbf{J}(\mathbf{r}) \cdot \overline{\mathbf{G}}(\mathbf{r}|\mathbf{r}') dv \quad (30)$$

Interchanging \mathbf{r} and \mathbf{r}' and using the reciprocity theorem [7] of Green's functions $\overline{\mathbf{G}}(\mathbf{r}|\mathbf{r}') = \overline{\mathbf{G}}(\mathbf{r}'|\mathbf{r})$ gives

$$\mathbf{A}(\mathbf{r}) = \mu \int_{\text{vol}} \mathbf{J}(\mathbf{r}') \cdot \overline{\mathbf{G}}(\mathbf{r}|\mathbf{r}') dv' \quad (31)$$

A similar set of operations leads to the scalar potential equation

$$V(\mathbf{r}) = \frac{-1}{j\omega\epsilon} \int_{\text{vol}} G_V(\mathbf{r}|\mathbf{r}') \nabla' \cdot \mathbf{J}(\mathbf{r}') dv' \quad (32)$$

3. FREE-SPACE LORENTZ AND COULOMB GAUGE GREEN FUNCTION

In this section the scalar and vector potential Green functions for a general directed source in free space are derived in both the Lorentz and Coulomb gauges. It is shown that the Coulomb gauge vector potential Green function can be extracted from the well-known free-space Lorentz gauge vector potential Green function by taking advantage of a set of dyadic identities. The method presented here avoids the difficulties inherent in the vector eigenfunction approach, which will be used in the next section to derive Green's functions for a boundary value problem. In order to confirm the correctness of our expressions, the electric field mixed potential integral equation (MPIE) for the current on a straight finite-length wire scatterer is derived and solved by the method of moments [8]. The numerically computed Coulomb gauge current and an equation for the scattered far field are presented and compared in terms of numerical computation time and programming difficulty with that obtained via Lorentz for gauge potentials.

3.1. Analysis

The time-harmonic electric and magnetic fields are related to the magnetic vector potential \mathbf{A} and scalar potential V :

$$\mathbf{E} = -j\omega \mathbf{A} - \nabla V \quad (33)$$

$$\mathbf{H} = \frac{1}{\mu} \nabla \times \mathbf{A} \quad (34)$$

The differential equations that define the potentials and thereby give rise to Green's functions are obtained by

combining (33) and (44) with Maxwell's equations. For example (33) and (44) substituted into Maxwell's equation $\nabla \times \mathbf{H} = \mathbf{J} + j\omega\epsilon\mathbf{E}$, results in

$$\nabla^2 \mathbf{A} + k^2 \mathbf{A} = -\mu \mathbf{J} + \nabla(\nabla \cdot \mathbf{A} + j\omega\mu\epsilon V) \quad (35)$$

and (3) and (5) substituted into the divergence of (33) gives

$$\nabla^2 V + j\omega \nabla \cdot \mathbf{A} = \frac{\nabla \cdot \mathbf{J}}{j\omega\epsilon} \quad (36)$$

Equations (35) and (36) are as far as we can go in obtaining equations for the vector and scalar potentials without some additional information. This information is provided by the Helmholtz theorem, according to which a vector is completely specified by its divergence and curl. Another way of stating this is that if $\nabla \cdot \mathbf{A}$ and $\nabla \times \mathbf{A}$ are known, then there is an equation, the mathematical form of Helmholtz's equation, into which both can be placed that, when evaluated, will give \mathbf{A} . This equation, which is not necessary for our analysis because we will determine \mathbf{A} and V in a direct manner, can be found in many texts on vector analysis and field theory, for example, Collin [9]. The curl of the vector \mathbf{A} has already been defined in (34), so the determination of the divergence of \mathbf{A} is left entirely to our discretion. Does this mean that $\nabla \cdot \mathbf{A}$ can be defined to be any mathematical expression that can be written down? The answer is yes, but care must be taken to choose a divergence of \mathbf{A} that, when placed in (35) or (36), will lead to a differential equation that is solvable. Otherwise the vector potential and therefore the field given by (7) and (10) may not be found.

Two choices for the divergence of \mathbf{A} are presented in Sections 3.2 and 3.3, the first resulting in the Lorentz gauge and the second in the Coulomb gauge. The discovery of the vector potential is accredited to Franz Neumann; however, it was James Clerk Maxwell who first obtained a solution for \mathbf{A} by applying what is now known as the Coulomb gauge [10]. Although the difficulties presented by the Coulomb gauge vector potential differential equation prevented its general solution until recently, it is apparent that Maxwell distained the use of the Lorenz (please see footnote 1 on the first page of this article) gauge, for which a solution for the potentials already existed [11,12]. Likely Maxwell's reluctance to accept the Lorenz gauge arose because it produced what was thought to be nonphysical "retarded" fields. However, H. A. Lorentz rediscovered this gauge around the beginning of the twentieth century at a time when the concept of the retarded field was beginning to gain wide acceptance [11]. The simplicity of the Lorenz gauge vector potential differential equation and the fact that the Lorenz potentials are relativistically covariant led to its widespread use. The electromagnetic field has not been solved in general, including the source region, with any gauge other than these two.

3.2. Lorentz Gauge Green's Functions

With the definitions ($\mathbf{A} \equiv \mathbf{A}^L$) and ($V \equiv V^L$) we define the Lorentz gauge

$$\nabla \cdot \mathbf{A}^L = -j\omega\mu\epsilon V^L \quad (37)$$

where $k^2 = \omega^2\mu\epsilon$. Substitution of Eq. (37) in (35) and Eq. (37) in (36) leads to a set of decoupled potential equations:

$$\nabla^2 \mathbf{A}^L + k^2 \mathbf{A}^L = -\mu \mathbf{J} \quad (38)$$

$$\nabla^2 V^L + k^2 V^L = \frac{\nabla \cdot \mathbf{J}}{j\omega\epsilon} \quad (39)$$

As described above, Eq. (38) motivates the dyadic Green function equation

$$\nabla^2 \overline{\mathbf{G}}^L + k^2 \overline{\mathbf{G}}^L = -\overline{\delta}(\mathbf{r} - \mathbf{r}') \quad (40)$$

Equation (39) suggests a similar scalar Green function equation:

$$\nabla^2 G_V^L + k^2 G_V^L = -\delta(\mathbf{r} - \mathbf{r}') \quad (41)$$

Equations (40) and (41) have familiar solutions [13], respectively

$$\overline{\mathbf{G}}^L(\mathbf{r}|\mathbf{r}') = \begin{bmatrix} 1 & 0 & 0 \\ 0 & 1 & 0 \\ 0 & 0 & 1 \end{bmatrix} \frac{e^{-jkR}}{4\pi R} = \overline{\mathbf{I}}G(\mathbf{r}|\mathbf{r}') \quad (42)$$

$$G_V^L(\mathbf{r}|\mathbf{r}') = \frac{e^{-jkR}}{4\pi R} = G(\mathbf{r}|\mathbf{r}') \quad (43)$$

with $R = [(x - x')^2 + (y - y')^2 + (z - z')^2]^{\frac{1}{2}}$.

3.3. Coulomb Gauge Green's Functions

The Coulomb gauge

$$\nabla \cdot \mathbf{A}^C = 0 \quad (44)$$

in (35) and in (36) along with the definitions ($\mathbf{A} \equiv \mathbf{A}^C$) and ($V \equiv V^C$) leads to the set of Coulomb gauge potential equations

$$\nabla^2 \mathbf{A}^C + k^2 \mathbf{A}^C = -\mu \mathbf{J} + j\omega\mu\epsilon \nabla V^C \doteq -\mu \mathbf{J}^s \quad (45)$$

$$\nabla^2 V^C = \frac{1}{j\omega\epsilon} \nabla \cdot \mathbf{J} \quad (46)$$

At the beginning of this section we used the property of Helmholtz theorem that states that a vector is completely determined by its divergence and curl. The Helmholtz theorem in its mathematical form can also be viewed as expressing a vector \mathbf{J} solely in terms of its solenoidal (divergenceless) \mathbf{J}^s and lamellar (zero curl) \mathbf{J}^l parts [14]. Mathematically the properties of these two parts of a vector can be described by $\nabla \times \mathbf{J}^s \neq 0$, $\nabla \cdot \mathbf{J}^s = 0$, $\nabla \times \mathbf{J}^l = 0$, $\nabla \cdot \mathbf{J}^l \neq 0$. The superscript "s" in (45) which designates a solenoidal current density \mathbf{J}^s , results when the lamellar current \mathbf{J}^l is removed from the total current density $\mathbf{J} = \mathbf{J}^s + \mathbf{J}^l$. That $\mathbf{J}^l = j\omega\epsilon \nabla V^C$ can be shown by taking the

divergence of (45) and then applying the Coulomb condition (34).

It is important to note that the definition of the Coulomb gauge used here allows for $(\nabla \cdot \mathbf{A} = 0, V \neq 0)$, which encompasses far more territory than does that of a small but important class of problems where the divergences of both the magnetic vector potential \mathbf{A} and the current density \mathbf{J} are zero. In that case it is convenient to use what is commonly referred to as the “radiation gauge” [15].

The Green function equations pertaining to the Coulomb potential equations (45) and (46) respectively are

$$\nabla^2 \bar{\mathbf{G}}^C(\mathbf{r}|\mathbf{r}') + k^2 \bar{\mathbf{G}}^C(\mathbf{r}|\mathbf{r}') = -\bar{\delta}^s(\mathbf{r} - \mathbf{r}') \quad (47)$$

$$\nabla^2 G_V^C(\mathbf{r}|\mathbf{r}') = -\delta(\mathbf{r} - \mathbf{r}') \quad (48)$$

Note that because the dyadic delta function $\bar{\delta}^s$ is solenoidal, the Coulomb Green function $\bar{\mathbf{G}}^C$ must also be solenoidal. Equation (48) is simply the Poisson equation for a source in free space. The solution to (48) is

$$G_V^C(\mathbf{r}|\mathbf{r}') = \frac{1}{4\pi R} \quad (49)$$

As described in the introduction (Section 1), the vector eigenfunction method for solving (47) is in general formidable but in this particular case, where the source resides in free space, we can make some observations that will lead to a method for finding the Coulomb gauge Green function that is understandable to those readers with a basic knowledge of dyadic vector operations. First we observe that the solenoidal part of the Lorentz gauge vector potential Green function is equal to the Coulomb gauge vector potential Green function. This can be shown by first decomposing the dyadics on the left- and right-hand sides of (40) into solenoidal and lamellar parts and then equating just the solenoidal components. The result is Eq. (47). Therefore, since the Lorentz gauge Green function is already available (42), our strategy is to extract its solenoidal part. This can be done by first using the identity (12) in (40), which, on rearrangement of terms, becomes

$$\bar{\mathbf{G}}^L = \frac{1}{k^2} (\nabla \times \nabla \times \bar{\mathbf{G}}^L - \nabla \nabla \cdot \bar{\mathbf{G}}^L - \bar{\delta}(\mathbf{r} - \mathbf{r}')) \quad (50)$$

Identity (12) is next substituted into a second identity [13]

$$\bar{\delta}(\mathbf{r} - \mathbf{r}') = -\frac{1}{4\pi} \nabla^2 \left(\frac{\bar{\mathbf{I}}}{R} \right) \quad (51)$$

to get

$$\bar{\delta}(\mathbf{r} - \mathbf{r}') = \frac{1}{4\pi} \left[-\nabla \nabla \cdot \left(\frac{\bar{\mathbf{I}}}{R} \right) + \nabla \times \nabla \times \left(\frac{\bar{\mathbf{I}}}{R} \right) \right] \quad (52)$$

Finally, (52) is substituted into (50), yielding

$$\bar{\mathbf{G}}^L = \frac{-1}{k^2} \nabla \nabla \left(\frac{e^{-jkR} - 1}{4\pi R} \right) + \frac{1}{k^2} \nabla \times \nabla \times \bar{\mathbf{I}} \left(\frac{e^{-jkR} - 1}{4\pi R} \right) \quad (53)$$

The right-hand sides of (52) and (53) contain respectively the lamellar and solenoidal delta functions $\bar{\delta}^l$ and $\bar{\delta}^s$ and vector potential Green’s functions $\bar{\mathbf{G}}^l$ and $\bar{\mathbf{G}}^s$. The solenoidal term $\bar{\mathbf{G}}^s$ has been identified above as the Coulomb Green function $\bar{\mathbf{G}}^s = \bar{\mathbf{G}}^C$, which, by rearranging (53), can be written in a convenient form:

$$\bar{\mathbf{G}}^C = \bar{\mathbf{I}}G + \frac{1}{k^2} \nabla \nabla \left(\frac{e^{-jkR} - 1}{4\pi R} \right) \quad (54)$$

When the differentiation in (54) is performed, the result is

$$\bar{\mathbf{G}}^C(\mathbf{r}|\mathbf{r}') = \begin{bmatrix} S_{xx} & S_{xy} & S_{xz} \\ S_{yx} & S_{yy} & S_{yz} \\ S_{zx} & S_{zy} & S_{zz} \end{bmatrix} \frac{e^{-jkR}}{4\pi R} = \bar{\mathbf{S}}G(\mathbf{r}|\mathbf{r}') \quad (55)$$

$$\bar{\mathbf{S}} = \left[(1 - Q)\bar{\mathbf{I}} - (1 - 3Q)\frac{\mathbf{R}\mathbf{R}}{R^2} \right] \quad (56)$$

$$Q = \frac{1 + jkR - e^{jkR}}{(kR)^2} \quad (57)$$

$$\mathbf{R} = (x - x')\hat{\mathbf{x}} + (y - y')\hat{\mathbf{y}} + (z - z')\hat{\mathbf{z}} \quad (58)$$

This completes our presentation of the free-space Coulomb and Lorentz gauge Green functions. The potentials are found by employing Green’s method [13] as discussed above. Ordinarily, for a coordinate space (Euclidean) vector, one thinks of orthogonality as a property that requires the vector components to be mutually perpendicular. However, the solenoidal and lamellar parts of a vector can be shown to exhibit function orthogonality (see Appendix B). This property is used to resolve one of the apparent dilemmas of the Coulomb gauge integral equation formulation presented above, namely, that when Green’s method is applied to (45) and (47) the resulting vector potential integral contains a solenoidal current \mathbf{J}^s , rather than the desired surface current \mathbf{J} . This problem is resolved by simply replacing the solenoidal current with the total current:

$$\begin{aligned} \mathbf{A}^C(\mathbf{r}) &= \mu \int_{v'} \bar{\mathbf{G}}^C(\mathbf{r}|\mathbf{r}') \cdot \mathbf{J}^s(\mathbf{r}') dv' \\ &= \mu \int_{v'} \bar{\mathbf{G}}^C(\mathbf{r}|\mathbf{r}') \cdot \mathbf{J}(\mathbf{r}') dv' \end{aligned} \quad (59)$$

The replacement $\mathbf{J}^s(\mathbf{r}) \rightarrow \mathbf{J}(\mathbf{r})$ is allowed because solenoidal and lamellar vectors are orthogonal and since the Coulomb Green function is solenoidal, the integration process in (59) will automatically remove the lamellar part of the surface current. We emphasize that one can numerically solve only for the total current because the nonphysical solenoidal and lamellar currents cannot be numerically quantified since they exist throughout space. By analogy this last point is illustrated with Eq. (52), where the two terms on the right-hand side are respectively the lamellar and solenoidal delta functions. These terms are everywhere nonzero functions of position,

but together they collapse to a function that is nonzero only at $\mathbf{r} = \mathbf{r}'$.

Perhaps one of the most interesting controversies concerning the Coulomb gauge is the apparent instantaneous propagation of the scalar potential. Note that both the Lorentz and Coulomb gauge scalar potentials in (43) and (49) have the same static scalar potential owing to the fact that $k = \omega\sqrt{\mu\epsilon} = \omega/c \rightarrow 0$ as the frequency $\omega = 2\pi f \rightarrow 0$. However, the propagation factor $\exp(-jkr)$ that governs the velocity at which a wave propagates is absent from the Coulomb scalar potential (49). This seems to suggest that as soon as the source is turned on, the Coulomb scalar potential exists instantaneously throughout space. Although much has been written on this subject [16,17], it is important only that the electromagnetic field obey the speed-of-light law, which it does when the Coulomb vector and scalar potentials are combined in (33) to calculate the field. A summary of much of the literature on this subject is that, when a field is decomposed into component parts, there is no reason to expect that these components should each individually satisfy all the rules of physics. On the other hand, there is some interesting evidence, primarily associated with the Aharonov–Bohm experiment, that potentials may have some physical significance. However, these discussions are outside the context of this presentation and will not be pursued further.

The gauge invariance property of the electromagnetic field [15] ensures us that the fields given by (33) and (34) are unique, that is, independent of the choice of gauge. The equivalent current appearing in Eqs. (31) and (32) is also unique and can be used as a basis for comparing the Coulomb and Lorentz gauges. Below we present a method for solving for the current obtained with these two gauges.

3.4. Example: Scattering from a Straight Thin Wire

Some contrasting aspects of Eqs. (42) and (55) clearly indicate that the Lorentz gauge has a computational advantage over the Coulomb gauge. For example, the Coulomb gauge Green function contains a fully populated dyadic coefficient matrix $\bar{\mathbf{S}}$ while the Lorentz gauge coefficient is simply the diagonal identity dyadic $\bar{\mathbf{I}}$. This means, for example, that current flowing in the z direction will produce three (x , y , and z) dissimilar Coulomb vector potential components while the same z -directed current will produce only a single (z) Lorentz vector potential component. A general bent-wire scatterer solved by the method of moments MPIE technique would, for most of the moment matrix, require three calculations (a column of the $\bar{\mathbf{S}}$ dyadic) per matrix element with the Coulomb gauge and only one calculation with the Lorentz gauge.

On the other hand, for a straight wire, a Coulomb gauge analysis appears at first glance to have some advantages over the Lorentz gauge because of the simple mathematical form of the Coulomb scalar potential. Although this will not prove to be the case, we present below an MPIE analysis of a straight finite-length wire scatterer illuminated by a plane wave because it is a simple instructive problem for comparing our gauge formulations.

A straight wire of radius $a \ll \lambda$, length ℓ and lying along the z axis is illuminated by a plane wave with an electric field z component given by $E_z^i = E_0 \sin \theta e^{jkz \cos \theta}$ in a homogeneous free-space region (see Fig. 1). By enforcing the condition that the tangential component of the total electric field is zero on the wire surface one gets the MPIE

$$j\omega A_z^L + \frac{\partial}{\partial z} V^C = E_z^i \quad (60)$$

where in the Lorentz and Coulomb gauges the potentials are

$$A_z^L = \frac{\mu}{2\pi} \int_{z'} I(z') \int_{\phi'} \left\{ \begin{array}{l} G(z, z', \phi') \\ S_{zz} G(z, z', \phi') \end{array} \right\} d\phi' dz' \quad (61)$$

$$V^C = \frac{j}{2\pi\omega\epsilon} \int_{z'} \frac{d}{dz'} I(z') \int_{\phi'} \left\{ \begin{array}{l} G(z, z', \phi') \\ 1/4\pi R \end{array} \right\} d\phi' dz' \quad (62)$$

with

$$G(z, z', \phi') = \frac{e^{-jkR}}{4\pi R} \quad (63)$$

and $R = [(z - z')^2 + 2a^2 \sin^2 \phi']^{1/2}$.

3.5. Numerical Method

The method-of-moments (MM) procedure [8] is applied to solve Eqn. (60) for the unknown current $I(z)$ on a straight thin wire scatterer. The straight wire lying along the z axis is subdivided into N segments of length $\Delta z = \ell/N$. The

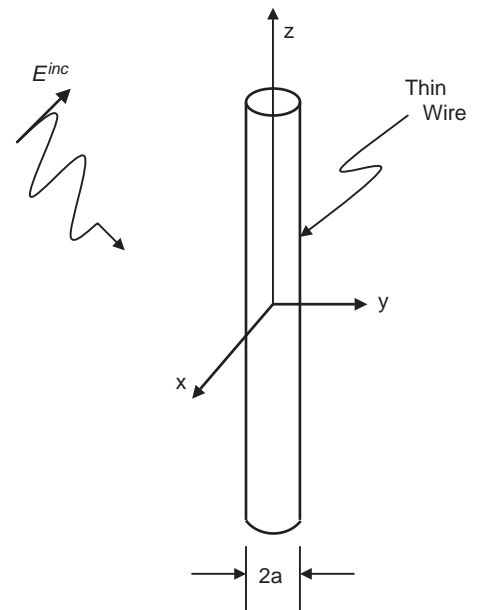


Figure 1. Plane wave incident on a thin straight wire.

current I is expanded as

$$I(z) = \sum_{n=1}^N I_n \Lambda_n(z) \quad (64)$$

where Λ_n are piecewise linear expansion functions defined as

$$\Lambda_n(z) = \begin{cases} \frac{z - z_{n-1}}{\Delta z}, & z_{n-1} \leq z \leq z_n \\ \frac{z_{n+1} - z}{\Delta z}, & z_n \leq z \leq z_{n+1} \\ 0, & \text{otherwise} \end{cases} \quad (65)$$

Note that (65) is piecewise differentiable, so the derivative with respect to z in (62) can be performed analytically. When the expansion (65) is used in (60) and the result “tested” with piecewise linear functions Λ_m , we arrive at a set of N simultaneous equations with N unknowns I_n expressed in matrix form:

$$[Z_{mn}][I_n] = [V_m], \quad m = 1, 2, \dots, N \quad (66)$$

The impedance matrix $[Z_{mn}]$ is inverted and multiplied by the voltage vector $[V_m]$. The resulting current amplitudes I_n are substituted into (64) giving the final current approximation. In our procedure we employed 21 rectangular basis and 21 testing functions.

3.6. Results

Figure 2 shows the current distributions on a three-quarter-wavelength (0.75λ) wire with a plane-wave excitation angle of incidence $\theta = 60^\circ$. The solid lines depict real and imaginary parts of the current due to a Coulomb gauge formulation while the overlying circles are from the Lorentz gauge analysis. The results for the two gauges are numerically indistinguishable. The computation time difference for each of these two results was 15% in favor of the Lorentz gauge.

A difference between the two gauges does emerge in the vector and scalar potential ϕ' integrations. The dyadic component S_{zz} is a regular non-singular function that presents no numerical difficulties. The singularity in $G(z, z', \phi')$ is evaluated by subtracting and adding $1/R$ as follows:

$$\int_{\phi'} G(z, z', \phi') d\phi' = \frac{1}{4\pi} \int_{\phi'=-\pi}^{\pi} \frac{e^{-jkR} - 1}{R} d\phi' + \frac{1}{4\pi} \int_{\phi'=-\pi}^{\pi} \frac{1}{R} d\phi' \quad (67)$$

Evaluation of the Lorentz scalar potential requires both integrals on the right-hand side (RHS) of (67) while only the second RHS integral is required for the Coulomb scalar potential. This advantage gained with the Coulomb gauge scalar potential calculation is not enough to

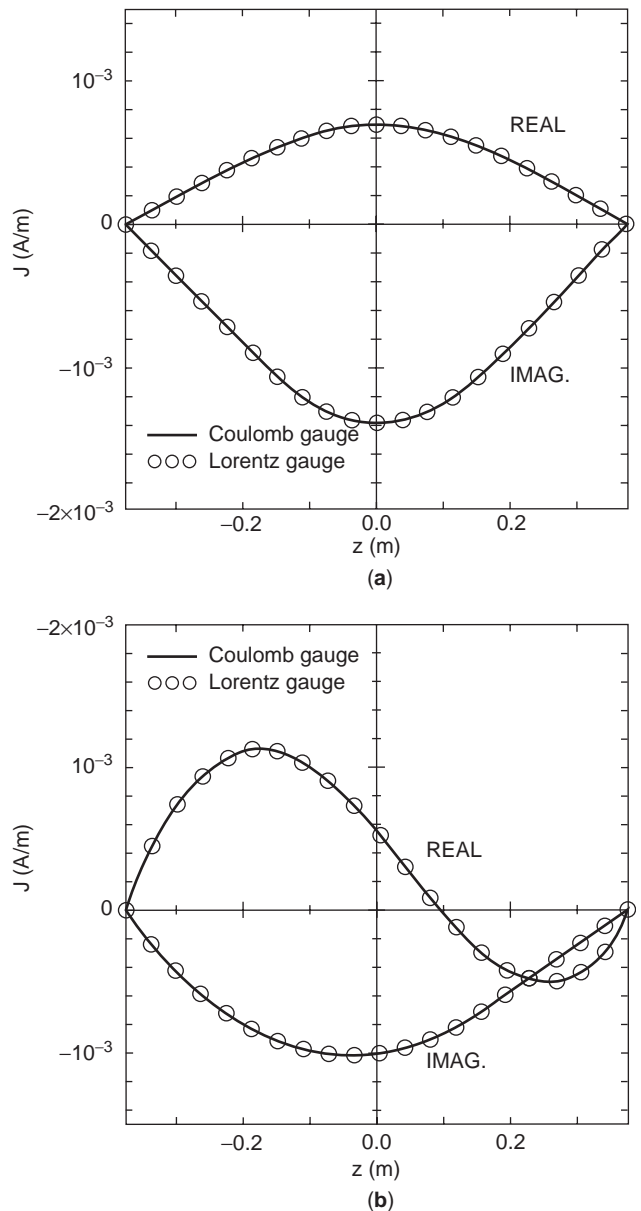


Figure 2. Comparison of Lorentz and Coulomb gauge current distributions on a $3/4$ dipole with plane-wave excitation at $\theta = 60^\circ$. The incident electric field amplitude is set to unity and $ka = 0.04$.

overcome the fact that the ϕ' integration in the Lorentz gauge can be carried out once and the result used in both the scalar and vector potentials [cf. (61) and (62)]. We can then conclude that the Lorentz gauge potentials can be computed more rapidly than the Coulomb gauge potentials for all thin-wire configurations and, it is safe to say, in any case for which a Green function can be derived. It should be pointed out, however, that the Coulomb scalar potential contains the static limit portion of the electromagnetic field. One can therefore isolate and observe the physical behavior of that part of the field (the Coulomb vector potential portion) that approaches zero as the excitation frequency decreases.

3.7. Far Field

The far-zone electric field can be found by letting $r \rightarrow \infty$ in (61) and (62) and then substituting the result into (10). The far electric field is

$$\mathbf{E}_\theta(\mathbf{r}) = j\omega\mu \frac{e^{-jkr}}{r} \int_{C'} I(z') e^{jkz' \cos\theta} dz' \sin\theta \quad (68)$$

in both gauges. Because, as was shown above, the currents and the far field expressions are the same, there is no difference in the far fields obtained by the two gauge formulations.

4. OPEN-REGION BOUNDARY VALUE PROBLEMS

As an example of a Coulomb gauge solution for an open-region boundary value problem, we present a two-dimensional surface of arbitrary shape in the presence of an infinite perfectly conducting wedge, subject to transverse electric excitation. The wedge/scatterer is analyzed by comparing mixed potential integral equations (MPIEs) that are constructed based on the Coulomb and Lorentz gauges. In each case the effect of the wedge is incorporated in the integral equation by means of the appropriate Green's functions, leaving the current distribution on the arbitrary surface as the only unknown. The Green functions are derived by the eigenfunction expansion technique [4]. A well-established moment method (MM) procedure [8] is adapted to numerically solve both gauge forms of the MPIE. Computed results are presented and the relative merits of the Coulomb and Lorentz gauge MPIEs are discussed. Zheng et al. [18] have provided more detailed presentation of this problem.

4.1. General Formulation of Integral Equations

Consider an infinitesimally thin surface that is in infinite extent and invariant along the z axis, but has an arbitrary (open or closed) cross-sectional profile C , and which resides near the edge of an infinite, perfectly conducting wedge of angle α , whose upper surface coincides with the ($x \geq 0, y = 0$) half-plane (see Fig. 3). The surrounding medium is homogeneous and is characterized by permittivity ε and permeability μ . The structure is illuminated by a plane-wave transverse electric (TE) to the z axis. Once the current distribution induced on the object C is found, other quantities of interest, such as the far field pattern, are easily determined.

In the case considered here (Fig. 3), \mathbf{J} is the unknown current induced on the perfectly conducting surface C by a known "incident" field $\mathbf{E}^i, \mathbf{H}^i$, which exists in the presence of the wedge. Enforcing the condition that the total tangential electric field, \mathbf{E} plus \mathbf{E}^i , is zero on C leads to the EFIE

$$\hat{\mathbf{t}} \times (j\omega\mathbf{A} + \nabla V) = \hat{\mathbf{t}} \times \mathbf{E}^i \quad (69)$$

where $\hat{\mathbf{t}}$ is a unit vector normal to C at $\boldsymbol{\rho}$, a position vector from the coordinate origin to a point on C . This equation is then solved for \mathbf{J} by the MM procedure.

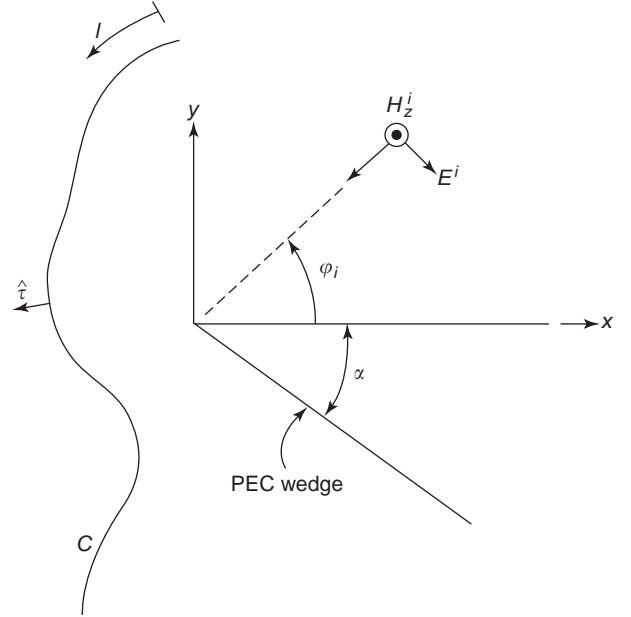


Figure 3. Scatterer of arbitrary cross-sectional profile C in the presence of an infinite wedge.

4.2. Lorentz Gauge Integral Equation

Choosing the Lorentz gauge

$$\nabla \cdot \mathbf{A} = -j\omega\mu\varepsilon V \quad (70)$$

in (35) leads to

$$\mathbf{A}(\boldsymbol{\rho}) = \mu \int_C \overline{\mathbf{G}}_A(\boldsymbol{\rho}|\boldsymbol{\rho}') \cdot \mathbf{J}(\boldsymbol{\rho}') dl' \quad (71)$$

where $\overline{\mathbf{G}}_A$ is the vector potential dyadic Green function, which satisfies

$$(\nabla^2 + k^2)\overline{\mathbf{G}}_A(\boldsymbol{\rho}|\boldsymbol{\rho}') = -\overline{\boldsymbol{\delta}}(\boldsymbol{\rho} - \boldsymbol{\rho}') \quad (72)$$

subject to the conditions $\hat{\mathbf{n}} \times \overline{\mathbf{G}}_A = 0, \nabla \cdot \overline{\mathbf{G}}_A = 0$ on the PC wedge, the radiation condition at infinity, and the edge condition [9]. In (72), $\overline{\boldsymbol{\delta}}$ is the dyadic delta function [19]. For later reference, we observe that \mathbf{A} , and thus $\overline{\mathbf{G}}_A$, can in general be represented as sums of their respective lamellar (irrotational) and solenoidal (divergenceless) parts. Hence, we may write

$$\overline{\mathbf{G}}_A(\boldsymbol{\rho}|\boldsymbol{\rho}') = \overline{\mathbf{G}}_A^l(\boldsymbol{\rho}|\boldsymbol{\rho}') + \overline{\mathbf{G}}_A^s(\boldsymbol{\rho}|\boldsymbol{\rho}') \quad (73)$$

It follows from (70) and (71) that V can be expressed as

$$V(\boldsymbol{\rho}) = \frac{1}{\varepsilon} \int_C G_V(\boldsymbol{\rho}|\boldsymbol{\rho}') q(\boldsymbol{\rho}') dl' \quad (74)$$

in which the scalar potential kernel G_V is related to $\bar{\mathbf{G}}_A^1$ through

$$\nabla \cdot \bar{\mathbf{G}}_A^1(\boldsymbol{\rho}|\boldsymbol{\rho}') = -\nabla' G_V(\boldsymbol{\rho}|\boldsymbol{\rho}') \quad (75)$$

where ∇' acts on the primed (source) coordinates.

When \mathbf{A} given by (71) and V given by (74) are used in (69), the Lorentz gauge MPIE is obtained.

4.3. Coulomb Gauge Integral Equation

In the Coulomb gauge $\nabla \cdot \mathbf{A} = 0$; hence the vector potential is solenoidal and may be obtained from (71) if $\bar{\mathbf{G}}_A^s$ is used in place of $\bar{\mathbf{G}}_A$. The Coulomb scalar potential can be found from (74), where G_V satisfies the Poisson equation

$$\nabla^2 G_V(\boldsymbol{\rho}|\boldsymbol{\rho}') = -\delta(\boldsymbol{\rho} - \boldsymbol{\rho}') \quad (76)$$

subject to the condition that $G_V = 0$ on the PC wedge, the edge condition, and the boundedness condition at infinity. As was already mentioned, (76) has a closed-form solution for the geometry of Fig. 3. When the Coulomb vector and scalar potentials are used in (69), the Coulomb gauge MPIE is obtained.

4.4. Green's Function Potentials

We begin by constructing two scalar eigenfunctions, $\psi_{n\kappa}$ and $\dot{\psi}_{n\kappa}$, which satisfy the equation

$$(\nabla_t^2 + \kappa^2) \begin{Bmatrix} \psi_{n\kappa}(\boldsymbol{\rho}) \\ \dot{\psi}_{n\kappa}(\boldsymbol{\rho}) \end{Bmatrix} = 0 \quad (77)$$

subject to, respectively, the Dirichlet and Neumann boundary conditions on the PC wedge. They must also satisfy the edge condition and be bounded as $\rho \rightarrow \infty$. In (77), ∇_t^2 is the transverse Laplacian in cylindrical coordinates (no z dependence). These eigenfunctions are easily obtained by, for example, the characteristic Green's function procedure [20]. For the problem of Fig. 3, the normalized eigenfunctions are

$$\begin{Bmatrix} \psi_{n\kappa}(\boldsymbol{\rho}) \\ \dot{\psi}_{n\kappa}(\boldsymbol{\rho}) \end{Bmatrix} = \sqrt{\frac{\varepsilon_n}{\beta}} J_{v_n}(\kappa\rho) \begin{Bmatrix} \sin v_n \varphi \\ \cos v_n \end{Bmatrix} \quad (78)$$

where ε_n is the Neumann number ($\varepsilon_n = 1$ for $n = 0$ and $\varepsilon_n = 2$ for $n > 0$), J_{v_n} is the Bessel function of fractional order $v_n = n\pi/\beta$, $\beta = 2\pi - \alpha$, $0 \leq \kappa < \infty$, and $n = 0, 1, 2, \dots$. These eigenfunctions possess the orthogonality properties

$$\int_0^\beta \int_0^\infty \begin{Bmatrix} \psi_{n\kappa} \\ \dot{\psi}_{n\kappa} \end{Bmatrix} \begin{Bmatrix} \psi_{n'\kappa'} \\ \dot{\psi}_{n'\kappa'} \end{Bmatrix} \rho d\rho d\varphi = \delta_{nn'} \frac{\delta(\kappa - \kappa')}{\kappa'} \quad (79)$$

where $\delta_{nn'}$ is the Kronecker delta ($\delta_{nn'} = 1$ when $n = n'$ and zero otherwise).

We now construct three species of vector eigenfunctions, $\mathbf{L}_{n\kappa}$, $\mathbf{M}_{n\kappa}$, and $\mathbf{N}_{n\kappa}$, as [4]

$$\mathbf{L}_{n\kappa} = \nabla \psi_{n\kappa} \quad (80)$$

$$\mathbf{M}_{n\kappa} = \nabla \times \hat{\mathbf{z}} \dot{\psi}_{n\kappa} = -\hat{\mathbf{z}} \times \nabla \dot{\psi}_{n\kappa} \quad (81)$$

$$\mathbf{N}_{n\kappa} = \frac{1}{\kappa} \nabla \times \nabla \times \hat{\mathbf{z}} \dot{\psi}_{n\kappa} = \hat{\mathbf{z}} \kappa \psi_{n\kappa} \quad (82)$$

Clearly, the $\mathbf{L}_{n\kappa}$ functions are lamellar and the $\mathbf{M}_{n\kappa}$ and $\mathbf{N}_{n\kappa}$ functions are solenoidal. It is easily confirmed that all of them satisfy (77) and the required boundary conditions. It also follows from (79) that the vector eigenfunctions possess the orthogonality properties

$$\int_0^\beta \int_0^\infty \begin{Bmatrix} \mathbf{L}_{n\kappa} \\ \mathbf{M}_{n\kappa} \\ \mathbf{N}_{n\kappa} \end{Bmatrix} \cdot \begin{Bmatrix} \mathbf{L}_{n'\kappa'} \\ \mathbf{M}_{n'\kappa'} \\ \mathbf{N}_{n'\kappa'} \end{Bmatrix} \rho d\rho d\varphi = \delta_{nn'} \kappa \delta(\kappa - \kappa') \quad (83)$$

We now expand $\bar{\mathbf{G}}_A$ in (72) in terms of the vector eigenfunctions and employ (77) and (83) to obtain

$$\bar{\mathbf{G}}_A^1(\boldsymbol{\rho}|\boldsymbol{\rho}') = \sum_{n=0}^{\infty} \int_0^\infty \frac{d\kappa}{\kappa(\kappa^2 - k^2)} \mathbf{L}_{n\kappa}(\boldsymbol{\rho}) \mathbf{L}_{n\kappa}(\boldsymbol{\rho}') \quad (84)$$

and

$$\bar{\mathbf{G}}_A^s(\boldsymbol{\rho}|\boldsymbol{\rho}') = \sum_{n=0}^{\infty} \int_0^\infty \frac{d\kappa}{\kappa(\kappa^2 - k^2)} [\mathbf{M}_{n\kappa}(\boldsymbol{\rho}) \mathbf{M}_{n\kappa}(\boldsymbol{\rho}') + \mathbf{N}_{n\kappa}(\boldsymbol{\rho}) \mathbf{N}_{n\kappa}(\boldsymbol{\rho}')] \quad (85)$$

Noting that the term in (85) comprising the $\mathbf{N}_{n\kappa}$ functions contributes only the $\hat{\mathbf{z}}\hat{\mathbf{z}}$ component of $\bar{\mathbf{G}}_A^s$, we separate it by writing

$$\bar{\mathbf{G}}_A^s = \bar{\mathbf{G}}_{At}^s + \hat{\mathbf{z}}\hat{\mathbf{z}} \bar{G}_{Azz}^s \quad (86)$$

where only $\bar{\mathbf{G}}_{At}^s$, the transverse part of $\bar{\mathbf{G}}_A^s$, is of consequence to the TE problem considered here.

Using (84) in (75), we easily find the Lorentz scalar potential Green's function as

$$G_V(\boldsymbol{\rho}|\boldsymbol{\rho}') = \sum_{n=1}^{\infty} \int_0^\infty \psi_{n\kappa}(\boldsymbol{\rho}) \psi_{n\kappa}(\boldsymbol{\rho}') \frac{\kappa d\kappa}{\kappa^2 - k^2} \quad (87)$$

(which, incidentally, is identical with G_{Azz}^s).

The eigenfunction expansion method can also be used to solve (76) for the Coulomb scalar potential Green function, with the result

$$G_V(\boldsymbol{\rho}|\boldsymbol{\rho}') = \sum_{n=1}^{\infty} \int_0^\infty \psi_{n\kappa}(\boldsymbol{\rho}) \psi_{n\kappa}(\boldsymbol{\rho}') \frac{d\kappa}{\kappa} \quad (88)$$

The integrations over the radial spectral variable κ in (84), (85) and in (87), (88) can be evaluated using

$$\int_0^\infty J_\nu(\kappa\rho)J_\nu(\kappa\rho')\frac{d\kappa}{\kappa} = \frac{1}{2\nu}\left(\frac{\rho_{<}}{\rho_{>}}\right)^\nu, \quad \nu > 0 \quad (89)$$

$$\begin{aligned} & \int_0^\infty J_\nu(\kappa\rho)J_\nu(\kappa\rho')\frac{\kappa d\kappa}{\kappa^2 - k^2} \\ &= -\frac{\pi j}{2} J_\nu(k\rho_{<})H_\nu^{(2)}(k\rho_{>}), \quad \nu \geq 0 \end{aligned} \quad (90)$$

and

$$\begin{aligned} & \int_0^\infty J_\nu(\kappa\rho)J_\nu(\kappa\rho')\frac{d\kappa}{\kappa(\kappa^2 - k^2)} \\ &= -\frac{\pi j}{2k^2} \left[J_\nu(k\rho_{<})H_\nu^{(2)}(k\rho_{>}) - \frac{j}{v\pi} \left(\frac{\rho_{<}}{\rho_{>}}\right)^\nu \right], \quad \nu > 0 \end{aligned} \quad (91)$$

where $\rho_{>}$ denotes the greater, and $\rho_{<}$ the lesser, of ρ and ρ' , and $H_\nu^{(2)}$ is the Hankel function of the second kind and order ν . In the above and henceforth, we omit the subscript n on ν for notational simplicity.

Using (91) in (86) and the notation

$$c_n^\pm = \cos \nu(\varphi - \varphi') \pm \cos \nu(\varphi + \varphi') \quad (92)$$

$$s_n^\pm = \sin \nu(\varphi - \varphi') \pm \sin \nu(\varphi + \varphi') \quad (93)$$

$$b_n^{\rho\rho'} = \frac{\nu}{k^2\rho\rho'} J_\nu(k\rho_{<})H_\nu^{(2)}(k\rho_{>}) - \nu\Omega_n \quad (94)$$

$$b_n^{\rho\rho'} = \begin{cases} \frac{\nu}{k\rho} J'_\nu(k\rho')H_\nu^{(2)}(k\rho) - \nu\Omega_n, & \rho > \rho' \\ \frac{\nu}{k\rho} J_\nu(k\rho)H_\nu^{(2)'}(k\rho') + \nu\Omega_n, & \rho < \rho' \end{cases} \quad (95)$$

$$b_n^{\varphi\rho'} = \begin{cases} -\frac{\nu}{k\rho'} J_\nu(k\rho')H_\nu^{(2)'}(k\rho) - \nu\Omega_n, & \rho > \rho' \\ -\frac{\nu}{k\rho'} J'_\nu(k\rho)H_\nu^{(2)}(k\rho') + \nu\Omega_n, & \rho < \rho' \end{cases} \quad (96)$$

$$b_n^{\varphi\rho'} = J'_\nu(k\rho_{<})H_\nu^{(2)'}(k\rho_{>}) + \nu\Omega_n \quad (97)$$

where J'_ν and $H_\nu^{(2)'}$ denote derivatives with respect to the arguments of the respective functions and

$$\Omega_n = \frac{j}{\pi k^2 \rho \rho'} \left(\frac{\rho_{<}}{\rho_{>}}\right)^\nu \quad (98)$$

we can express the elements of $\bar{\mathbf{G}}_{At}^s$ as

$$G_{A\rho\rho'}^s = \frac{\pi}{2j\beta} \sum_{n=1}^\infty c_n^- b_n^{\rho\rho'} \quad (99)$$

$$G_{A\rho\varphi'}^s = \frac{\pi}{2j\beta} \sum_{n=1}^\infty s_n^+ b_n^{\rho\varphi'} \quad (100)$$

$$G_{A\varphi\rho'}^s = \frac{\pi}{2j\beta} \sum_{n=1}^\infty s_n^- b_n^{\varphi\rho'} \quad (101)$$

$$G_{A\varphi\varphi'}^s = \frac{\pi}{4j\beta} \sum_{n=0}^\infty \varepsilon_n c_n^+ b_n^{\varphi\varphi'} \quad (102)$$

Finally, using (89) in (88) and summing the resulting series, we can express the Coulomb scalar potential as

$$G_V = -\frac{1}{2\pi} (\ln R^- - \ln R^+) \quad (103)$$

where

$$R^\pm = (1 - 2\xi \cos \zeta^\pm + \xi^2)^{1/2} \quad (104)$$

with

$$\zeta^\pm = \frac{\pi}{\beta} (\varphi \pm \varphi'), \quad \xi = \left(\frac{\rho_{<}}{\rho_{>}}\right)^{\pi/\beta} \quad (105)$$

The lamellar part of $\bar{\mathbf{G}}_A$ can also be transformed by a procedure analogous to that used to obtain Eqs. (99)–(102). When the corresponding components of $\bar{\mathbf{G}}_A^i$ and $\bar{\mathbf{G}}_{At}^s$ are added to form the transverse part of the Lorentz vector potential Green function, cancellations occur, resulting in the relatively simple expressions

$$G_{A\rho\rho'} = \frac{\pi}{2j\beta} \sum_{n=1}^\infty c_n^- a_n^+ \quad (106)$$

$$G_{A\rho\varphi'} = \frac{\pi}{2j\beta} \sum_{n=1}^\infty s_n^+ a_n^- \quad (107)$$

$$G_{A\varphi\rho'} = -\frac{\pi}{2j\beta} \sum_{n=1}^\infty s_n^- a_n^- \quad (108)$$

$$G_{A\varphi\varphi'} = \frac{\pi}{4j\beta} \sum_{n=0}^\infty \varepsilon_n c_n^+ a_n^+ \quad (109)$$

where

$$a_n^\pm = \frac{1}{2} [J_{\nu-1}(k\rho_{<})H_{\nu-1}^{(2)}(k\rho_{>}) \pm J_{\nu+1}(k\rho_{<})H_{\nu+1}^{(2)}(k\rho_{>})] \quad (110)$$

Finally, using (90) in (87), we express the Lorentz scalar potential as

$$G_V = \frac{\pi}{2j\beta} \sum_{n=1}^{\infty} c_n^- J_v(k\rho_<) H_v^{(2)}(k\rho_>) \quad (111)$$

4.5. Incident Field and Far-Field Pattern

The TE plane wave with amplitude E_0 impinging on the wedge at an angle φ_i (Fig. 3) produces in the absence of the arbitrary scatterer C the “incident” field \mathbf{E}^i, H_z^i . The components of \mathbf{E}^i , which appear as the driving function in the integral equation (69), are easily found as [21]

$$\begin{aligned} E_{\varphi}^i &= E_0 \frac{\pi}{\beta} \sum_{n=0}^{\infty} \varepsilon_n e^{j(v+1)\pi/2} J'_v(k\rho) \\ &\times [\cos v(\varphi - \varphi_i) + \cos v(\varphi + \varphi_i)] \end{aligned} \quad (112)$$

$$\begin{aligned} E_{\rho}^i &= E_0 \frac{\pi}{\beta} \sum_{n=1}^{\infty} \frac{2v}{k\rho} e^{j(v+1)\pi/2} J_v(k\rho) \\ &\times [\sin v(\varphi - \varphi_i) + \sin v(\varphi + \varphi_i)] \end{aligned} \quad (113)$$

When the scatterer is introduced near the wedge, the field \mathbf{E}^i, H_z^i is modified by the “scattered” field \mathbf{E}^s, H_z^s , whose source is the surface current (of density \mathbf{J}) induced on C . It can be shown that far from the edge

$$H_z^s = \left(\frac{2j}{\pi k\rho} \right)^{1/2} e^{-jk\rho} P(\varphi) \quad (114)$$

where

$$P(\varphi) = \frac{\pi k}{4\beta j} \int_C \mathbf{F}(\boldsymbol{\rho}', \varphi) \cdot \mathbf{J}(\boldsymbol{\rho}') d\ell' \quad (115)$$

is the far-field pattern, in which

$$\begin{aligned} F(\boldsymbol{\rho}', \varphi) &= \hat{\boldsymbol{\rho}}' \sum_{n=1}^{\infty} \frac{2v}{k\rho'} s_n^- e^{jv\pi/2} J_v(k\rho') \\ &- \hat{\boldsymbol{\phi}}' \sum_{n=0}^{\infty} \varepsilon_n c_n^+ e^{jv\pi/2} J'_v(k\rho') \end{aligned} \quad (116)$$

4.6. Numerical Method

To numerically solve the MPIEs in both gauges, we adapt the MM procedure developed in Ref. 22 for objects in free space. In this approach, the arbitrary contour C is modeled in terms of straight-line segments, as illustrated in Fig. 4, and the current \mathbf{J} is expanded as

$$\mathbf{J}(\rho) = \sum_{n=1}^N J_n \Lambda_n(l) \quad (117)$$

where Λ_n are piecewise linear expansion functions defined as

$$\Lambda_n(l) = \begin{cases} \frac{\boldsymbol{\rho}_n^+}{h_n^+} & l \text{ in } C_n^+ \\ \frac{\boldsymbol{\rho}_n^-}{h_n^-} & l \text{ in } C_n^- \\ 0, & \text{otherwise} \end{cases} \quad (118)$$

Here, l is the arclength along the contour approximating C , C_n^{\pm} denote segments which meet at the n th node, h_n^{\pm} are their respective lengths, $\boldsymbol{\rho}_n^+$ is a vector from the free node of C_n^+ to an arbitrary point on the segment, and $\boldsymbol{\rho}_n^-$ is a vector from an arbitrary point on segment C_n^- to its free node, as shown in Fig. 4. Observe that Λ_n is piecewise differentiable, so that we may take divergence of (117) to form an expansion for the charge density q , as dictated by (5).

When the expansion (117) is used in (69) and the resulting equation is “tested” with Λ_m , an algebraic system of simultaneous equations for the current expansion coefficients J_n is obtained, which may be written in matrix form:

$$[Z_{mn}][J_n] = [\Phi_m], \quad m = 1, 2, \dots, N \quad (119)$$

In (119), the elements of the $N \times N$ “impedance matrix” $[Z_{mn}]$ can be expressed as

$$Z_{mn} = j\omega\mu(A_{mn}^+ + A_{mn}^-) + \frac{1}{j\omega\varepsilon}(V_{mn}^+ - V_{mn}^-) \quad (120)$$

where

$$A_{mn}^{\pm} = \int_C \boldsymbol{\rho}_m^{\pm} \cdot \bar{\mathbf{G}}_{Ai}(l_m^{\pm}|l') \cdot \Lambda_n(l') dl' \quad (121)$$

and

$$V_{mn}^{\pm} = \int_C G_{\Phi}(l_m^{\pm}|l') \nabla' \cdot \Lambda_n(l') dl' \quad (122)$$

while the elements of the forcing vector are given as

$$\Phi_m = \boldsymbol{\rho}_m^{c+} \cdot \mathbf{E}^i(l_m^{c+}) + \boldsymbol{\rho}_m^{c-} \cdot \mathbf{E}^i(l_m^{c-}) \quad (123)$$

in which $\boldsymbol{\rho}_m^{c+}$ is a vector from the free node of segment C_m^+ to its midpoint and $\boldsymbol{\rho}_m^{c-}$ is a vector from the midpoint of segment C_m^- to its free node. The arclength coordinates of the middle points of C_m^{\pm} are denoted by l_m^{\pm} .

4.7. Sample Results

In this section we present sample numerical results for a simple structure near a wedge with an arbitrarily chosen angle α (see Fig. 5). In this case, $f = 300$ MHz, which corresponds to free-space wavelength $\lambda = 1$ m. The structure considered was that of a circular cylinder of radius $a = \lambda/2\pi$, enclosing the edge of a wedge with $\alpha = 30^\circ$, thus simulating a cylindrically tipped wedge, for which an exact solution is available [23]. The circular profile C of the cylinder was approximated by 30 straight-line segments. The current distribution on C for $\varphi_i = 45^\circ$ is shown in

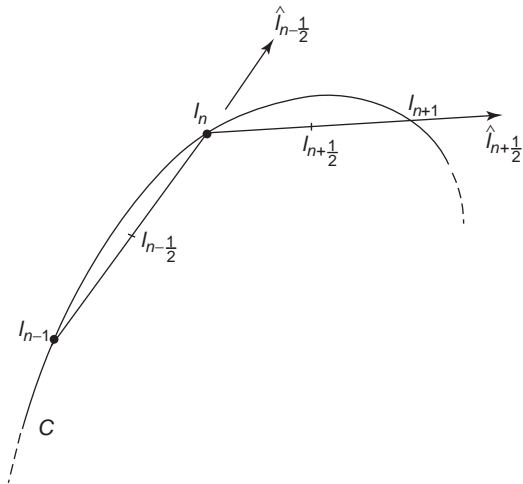


Figure 4. Contour C approximated by straight-line segments and local coordinates associated with the n th node.

Fig. 5a and the corresponding far-field pattern, in Fig. 5b. Since the Coulomb and Lorentz gauge-based programs produced graphically indistinguishable results, only the Lorentz gauge data are displayed here.

5. SUMMARY

Green's functions for the scalar and vector potentials are derived employing the Lorentz and Coulomb gauges. The two sets of gauge potentials are compared by constructing and solving integral equations for a straight wire in free space and for the two-dimensional problem of a conducting surface of arbitrary shape near an infinite wedge illuminated by a transverse electric plane wave. The attractive feature of the latter is the fact that the Coulomb scalar potential is available in closed form (rather than in series form, as in the Lorentz gauge) for the geometries considered here. However, this advantage of the Coulomb gauge formulation is offset by the fact that the resulting series converge slower than the corresponding series of the Lorentz gauge MPIE, and their acceleration is more involved. In the case of scattering from a wedge, we have observed on average a 15% savings in the impedance matrix fill time when the Lorentz gauge was used instead of the Coulomb gauge. However, the opposite is true in the case of the wire. Another advantage of the Coulomb gauge is that the scalar potential is identical to the static potential. This being the case, in the near zone the scalar potential entirely dominates the field, whereas in the far zone the vector potential dominates and the effect of the scalar potential can be neglected.

6. APPENDIX A

Dyadics are an alternative to the more usual matrix operations. For example, the matrix expression

$$\underline{\mathbf{B}} = \begin{bmatrix} b_{11} & b_{12} \\ b_{21} & b_{22} \end{bmatrix} \tag{A.1}$$

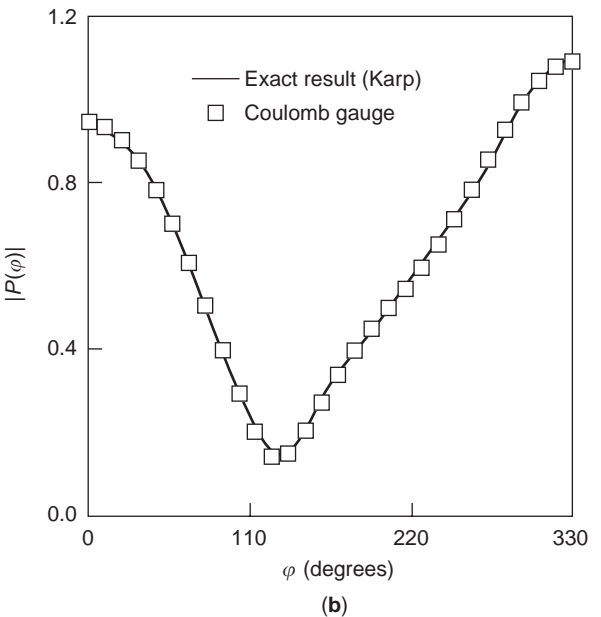
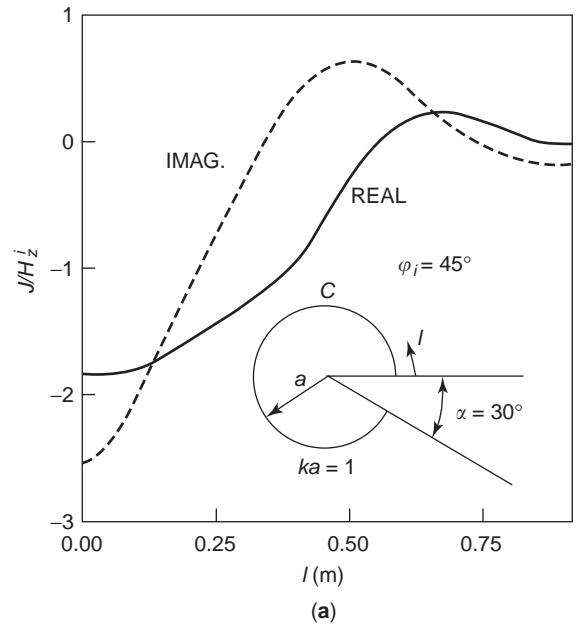


Figure 5. (a) Normalized current density on C and (b) far-field pattern for a cylindrically tipped wedge ($\alpha = 30^\circ$) illuminated by a plane wave with $\phi_i = 45^\circ$.

in dyadic notation becomes

$$\underline{\mathbf{B}} = b_{11}\hat{\mathbf{x}}\hat{\mathbf{x}} + b_{12}\hat{\mathbf{x}}\hat{\mathbf{y}} + b_{21}\hat{\mathbf{y}}\hat{\mathbf{x}} + b_{22}\hat{\mathbf{y}}\hat{\mathbf{y}} \tag{A.2}$$

where the product of two unit vectors, for example, $\hat{\mathbf{x}}\hat{\mathbf{y}}$, is a dyad and the sum of dyads, $\underline{\mathbf{B}}$ in this case, is a dyadic.

In this chapter the main operation that takes place between a vector and a dyadic is the dot product. The product of a vector and a matrix follows the usual rules of matrix multiplication; for example, multiplication of the vector $\mathbf{A} = a_{11}\hat{\mathbf{x}} + a_{12}\hat{\mathbf{y}}$ by the matrix $\underline{\mathbf{B}}$ in vector-matrix

notation is

$$\begin{aligned} \underline{\mathbf{A}}\underline{\mathbf{B}} &= [a_{11} \ a_{12}] \begin{bmatrix} b_{11} & b_{12} \\ b_{21} & b_{22} \end{bmatrix} \\ &= [(a_{11}b_{11} + a_{12}b_{21}) \ (a_{11}b_{12} + a_{12}b_{22})] \end{aligned}$$

or

$$\underline{\mathbf{A}}\underline{\mathbf{B}} = (a_{11}b_{11} + a_{12}b_{21})\hat{\mathbf{x}} + (a_{11}b_{12} + a_{12}b_{22})\hat{\mathbf{y}} \quad (\text{A.3})$$

The vector-dyadic dot product follows the rule that the dot product is taken between the two unit vectors in closest proximity to the dot. For example, $\hat{\mathbf{x}} \cdot \hat{\mathbf{x}}\hat{\mathbf{y}} = (\hat{\mathbf{x}} \cdot \hat{\mathbf{x}})\hat{\mathbf{y}} = \hat{\mathbf{y}}$, whereas $\hat{\mathbf{x}}\hat{\mathbf{y}} \cdot \hat{\mathbf{x}} = \hat{\mathbf{x}}(\hat{\mathbf{y}} \cdot \hat{\mathbf{x}}) = 0$. So, equivalent to the vector-matrix product (A.3) is the vector-dyadic dot product

$$\begin{aligned} \underline{\mathbf{A}} \cdot \underline{\mathbf{B}} &= a_{11}[b_{11}(\hat{\mathbf{x}} \cdot \hat{\mathbf{x}})\hat{\mathbf{x}} + b_{12}(\hat{\mathbf{x}} \cdot \hat{\mathbf{x}})\hat{\mathbf{y}} \\ &\quad + b_{21}(\hat{\mathbf{x}} \cdot \hat{\mathbf{y}})\hat{\mathbf{x}} + b_{22}(\hat{\mathbf{x}} \cdot \hat{\mathbf{y}})\hat{\mathbf{y}}] \\ &\quad + a_{12}[b_{11}(\hat{\mathbf{y}} \cdot \hat{\mathbf{x}})\hat{\mathbf{x}} + b_{12}(\hat{\mathbf{y}} \cdot \hat{\mathbf{x}})\hat{\mathbf{y}} \\ &\quad + b_{21}(\hat{\mathbf{y}} \cdot \hat{\mathbf{y}})\hat{\mathbf{x}} + b_{22}(\hat{\mathbf{y}} \cdot \hat{\mathbf{y}})\hat{\mathbf{y}}] \\ &= (a_{11}b_{11} + a_{12}b_{21})\hat{\mathbf{x}} \\ &\quad + (a_{11}b_{12} + a_{12}b_{22})\hat{\mathbf{y}} \end{aligned} \quad (\text{A.4})$$

Equations (A.3) and (A.4) show that the vector-matrix product is exactly equivalent to the vector-dyadic dot product.

Dyadic operations tend to be easier to perform and more systematic than operations with matrices. For example, it is not necessary to retain a dyad with a zero coefficient as must be done with terms of a matrix. More importantly, the fact that a dyadic can be readily decomposed into solenoidal and lamellar components is a crucial advantage in solving problems in the Coulomb gauge. For a more detailed discussion of dyadic operations the reader is referred to Tai [4].

7. APPENDIX B

The following example demonstrates function orthogonality between solenoidal and lamellar components of two dyadics, in which a dyadic delta function can be used to extract the solenoidal (or lamellar) component of a dyadic, and an alternative method can be employed to obtain the Coulomb gauge vector potential Green function. We evaluate [19]

$$\begin{aligned} \bar{\mathbf{G}}^{\text{C}}(\mathbf{r}|\mathbf{r}') &= \int_{v''} \bar{\delta}^{\text{S}}(\mathbf{r} - \mathbf{r}'') \cdot \bar{\mathbf{G}}^{\text{L}}(\mathbf{r}'' - \mathbf{r}') dv'' \\ &= \frac{1}{4\pi} \nabla \times \nabla \times \bar{\mathbf{I}} \int_{v''} \frac{\mathbf{G}(\mathbf{r}'' - \mathbf{r}')}{|\mathbf{r} - \mathbf{r}''|} dv'' \end{aligned} \quad (\text{B.1})$$

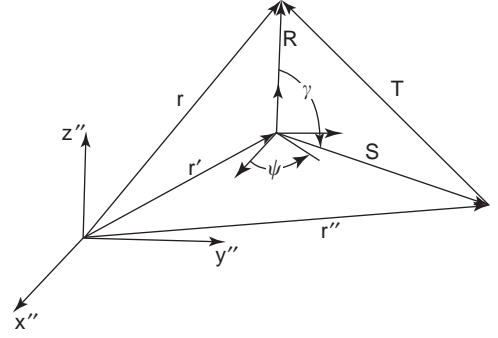


Figure 6. Coordinate transformation for volume integration.

The Lorentz gauge Green function $\bar{\mathbf{G}}^{\text{L}}$ contains both solenoidal and lamellar components while $\bar{\delta}^{\text{S}}$ is entirely solenoidal. An evaluation of this integral should yield the solenoidal component of $\bar{\mathbf{G}}^{\text{L}}$, which has been shown in the text to be the Coulomb Green function $\bar{\mathbf{G}}^{\text{C}}$.

Since the integration in (B.1) is over all space, the coordinate transformation shown in Fig. 6 can be made where \mathbf{r}' designates the new coordinate origin and

$$\begin{aligned} R &= |\mathbf{r} - \mathbf{r}'| \\ S &= |\mathbf{r}'' - \mathbf{r}'| \end{aligned} \quad (\text{B.2})$$

$$T^2 = S^2 + R^2 - 2SR \cos \gamma$$

giving

$$\begin{aligned} I &= \int_{v''} \frac{e^{-jk|\mathbf{r}'' - \mathbf{r}'|}}{|\mathbf{r}'' - \mathbf{r}'||\mathbf{r} - \mathbf{r}''|} dv'' \\ &= \int_{\psi=0}^{2\pi} \int_{\gamma=0}^{\pi} \int_{S=0}^{\infty} \frac{e^{-jkS}}{T} S \sin \gamma dS d\gamma d\psi \end{aligned} \quad (\text{B.3})$$

Integration in ψ is performed and a change of variables

$$U = (S^2 + R^2 - 2SR \cos \gamma)^{1/2} \quad (\text{B.4})$$

results in

$$\begin{aligned} I &= \frac{2\pi}{R} \int_{S=0}^{\infty} e^{-jkS} dS \int_{U=|R-S|}^{R+S} dU \\ &= \frac{4\pi}{R} \left\{ \int_{S=0}^R S e^{-jkS} dS + R \int_{S=R}^{\infty} e^{-jkS} dS \right\} \end{aligned} \quad (\text{B.5})$$

The first integral in (B.5) is evaluated by integration by parts. The second integral is evaluated by assuming that k contains a small loss factor so that as $S \rightarrow \infty$, $e^{-jkS} \rightarrow 0$.

Finally we arrive at

$$I = \frac{4\pi}{k^2} \left(\frac{e^{-jkR} - 1}{R} \right) \quad (\text{B.6})$$

which, when substituted into (B.1) yields the solenoidal part of the Lorentz gauge Green function given in (53).

BIBLIOGRAPHY

1. K. A. Michalski and R. D. Nevels, On the use of the Coulomb gauge in solving source excited boundary value problems in electromagnetics, *IEEE Trans. Microwave Theory Tech.* **36**(9):1328–1333 (1988).
2. E. H. Newman, An overview of the hybrid MM/Green's function method in electromagnetics, *Proc. IEEE* **76**:270–282 (1988).
3. L. N. Medgyesi-Mitschang and D. S. Y. Wang, Review of hybrid methods on antenna theory, *Digest Int. Symp. Anten.* **88**:15–24 (1988).
4. C.-T. Tai, *Dyadic Green's Functions in Electromagnetic Theory*, Intext Educational Publishers, Scranton, PA, 1971.
5. C.-T. Tai, On the eigenfunction expression of dyadic Green's functions, *Proc. IEEE* **61**:480–481 (1973).
6. J. Van Bladel, *Electromagnetic Fields*, Hemisphere Publishing, Washington DC 1985, Eq. 57, p. 509.
7. R. E. Collin, Radiation from simple sources, in Part 1, R. E. Collin and F. J. Zucker, eds., *Antenna Theory*, McGraw-Hill, New York; 1969, pp. 29–92.
8. R. F. Harrington, *Field Computation by Moment Methods*, Macmillan, New York; 1968.
9. R. E. Collin, *Field Theory of Guided Waves*, McGraw-Hill, New York; 1960, Sect. 5.6.
10. Edmund Whittaker, *A History of the Theories of Aether and Electricity*, Thomas Nelson and Sons Ltd., London, 1951.
11. R. D. Nevels and C.-S. Shin, Lorenz, Lorentz and the gauge, *IEEE Anten. Propag. Mag.* **43**(3):70–72 (June 2001).
12. J. D. Jackson and L. B. Okun, Historical roots of gauge invariance, *Rev. Mod. Phys.* **73**(3):(2001).
13. J. Van Bladel, *Electromagnetic Fields*, Hemisphere Publishing, 1985, A6.22, p. 542 and Eq. 28, p. 508.
14. R. Plonsey and R. E. Collin, *Principles and Applications of Electromagnetic Fields*, McGraw-Hill, New York, 1961, Chap. 1, Sect. 18.
15. J. D. Bjorken and S. D. Drell, *Relativistic Quantum Fields*, McGraw-Hill, New York, 1965, Sect. 14.2.
16. O. L. Brill and B. Goodman, Causality and the Coulomb gauge, *Am. J. Phys.* **35**:832–837 (1967).
17. R. D. Nevels and Z. Wu, Electromagnetic field and conduction current equivalence in the Lorentz and Coulomb gauges, *Electromagnetics* **12**(2):147–153 (April–June 1992).
18. D. Zheng, K. A. Michalski, K. J. Crowell, and R. D. Nevels, Transverse electric wave scattering by two-dimensional surfaces of arbitrary shape in the presence of a wedge, *Radio Sci.* **25**(3):721–730 (1990).
19. P. M. Morse and H. Feshbach, *Methods of Theoretical Physics*, McGraw-Hill, New York, 1953.
20. L. B. Felsen and N. Marcuvitz, *Radiation and Scattering of Waves*, Prentice-Hall, Englewood Cliffs, NJ, 1973.
21. R. F. Harrington, *Time-Harmonic Electromagnetic Fields*, McGraw-Hill, New York, 1961.
22. A. Glisson and D. R. Wilton, Simple and efficient numerical methods for problems of electromagnetic radiation and scattering from surfaces, *IEEE Trans. Anten. Propag.* **AP-28**:593–603 (1980).
23. S. N. Karp, *Diffraction by a Tipped Wedge with Application to Blunt Edges*, Report EM 52, Inst. Math and Science, New York Univ., May 1953.

COUPLED TRANSMISSION LINES

CLAYTON R. PAUL
Mercer University
Macon, Georgia

Two transmission lines whose electromagnetic fields are coupled induce signals from one line into the other. This coupling is either intentional as in directional couplers or unintentional, producing unwanted responses in the other line, which is referred to as *crosstalk*. This discussion of coupled transmission lines will concentrate on the analysis of coupled lines and can be used to design intentional coupling or to assess unintentional coupling as in crosstalk.

The study of two-conductor lines is standard in undergraduate electrical engineering courses [1]. The equations governing two-conductor lines and most of their properties have direct parallels in the case of multiconductor transmission lines (MTLs), which consist of $n + 1$ conductors, where $n > 1$. The equations and properties of the two-conductor line can be written for MTLs in a virtually identical form using matrix notation. We will focus on those parallels throughout this article in order to facilitate an understanding of MTLs. For a complete discussion of two-conductor lines and their properties, see Ref. 1. For a complete discussion of MTLs, see Ref. 2, which contains a large number of references on MTLs and their properties. See also Ref. 3 for an extensive list of references on MTLs.

Although a MTL can have any number of conductors (greater than two), we will concentrate here on a three-conductor line, $n = 2$. This will simplify the detail, and virtually all the discussion can be extended in a simple fashion to MTLs consisting of more than three conductors using matrix notation. Practical lines have losses in the finite, nonzero conductivities of the line conductors and in the losses in the surrounding dielectric medium. These losses complicate the analysis considerably. Their incorporation will be briefly discussed in Section 7, and the reader is referred to Ref. 2 for a more complete discussion.

In Section 1 we will investigate the transverse electromagnetic (TEM) mode of propagation on transmission lines. Although higher-order modes can exist at the higher frequencies, the dominant TEM mode has been shown to be sufficient for the analysis of transmission-line structures up to the low-gigahertz frequency range. As

digital clock speeds and the frequencies of analog systems continue to increase, seemingly without bound, the TEM-mode assumption will provide a simple but effective analysis tool for electronic systems in the near future. We will derive the MTL equations and discuss some general features of the problem.

In Section 2 we will briefly consider the all-important per unit length (PUL) parameters of inductance and capacitance through which the unique features that distinguish one specific type of line from another are contained. The MTL equations are the same for all MTLs, but these PUL parameters contain all the structural dimensions that distinguish one line from another. Without the ability to compute these PUL parameters for a specific line, solving the MTL equations would be fruitless.

In Section 3 we will investigate the time-domain solution of the MTL equations. We will show a useful SPICE model for coupled lines that allows complicated lines and terminations to be analyzed. The heart of the analysis is the ability to decouple the MTL equations. This separates the coupled lines into two uncoupled two-conductor lines for which we know the simple solution. Decoupling the MTL equations is discussed extensively in Refs. 2 and 3.

In Section 4 we will investigate the solution of the MTL equations in the frequency domain (single frequency, sinusoidal, steady state). Again, the heart of this solution process is the decoupling of the MTL equations.

In Section 5 we will present an approximate, lumped-circuit model of an MTL. This model is valid for lines that are electrically short, specifically, whose total length is less than, say, one-tenth of a wavelength at the highest significant frequency of the source. This approximate, lumped-circuit model bypasses the need to solve the MTL equations and is amenable to use in lumped-circuit analysis programs such as SPICE.

There are a few important classes of three-conductor MTLs for which a closed-form solution can be obtained. These are discussed in Section 6. For a three-conductor line in a homogeneous medium, the exact solution in the frequency domain can be readily obtained and shows considerable insight into its behavior, which is obscured in the numerical solution of the MTL equations. In some important instances, the line is electrically short, much less than a wavelength. In addition, the lines are not tightly coupled. This is said to be *weak coupling*. For a weakly coupled, electrically short line the solution reduces to the simple inductive-capacitive coupling model from which great insight and numerical results can be easily obtained. For lines in an inhomogeneous medium that are electrically long, the general solutions have not been obtained in closed form. However, for weak coupling a closed-form solution can be obtained, and the reader is referred to Ref. 5 for that solution.

1. THE MTL EQUATIONS

A generic three-conductor line ($n=2$) is shown in Fig. 1a. The line is parallel to the z axis. It consists of a total of

three ($n+1=3$) conductors. One conductor is chosen as the reference conductor to which the line voltages are referenced and through which the currents of the other two conductors “return.” The reference conductor is shown as a “ground plane” for illustration. However, the reference conductor can be of any type (wires, PCB lands, etc.). The dominant mode of propagation (extending from DC to the low-gigahertz frequency range) is the transverse electromagnetic (TEM) mode, wherein the electric and magnetic fields lie in the transverse or xy plane and are denoted by E^t , H^t , respectively. This assumption of the TEM field structure allows the unique definition of voltages and currents [1,2]. The line consists of a generator conductor that connects a source, characterized by an open-circuit voltage $V_S(t)$ and its source resistance R_S and a load characterized by a load resistance R_L . A receptor conductor connects two loads characterized by resistors R_{NE} and R_{FE} . The subscripts refer to “near end” and “far end,” respectively, with reference to the driving source of the generator line. Although we use resistive terminations, the analysis can be extended to dynamic and nonlinear terminations with the SPICE model to be developed. The voltages are defined with respect to the reference conductor and are functions of line position z and time t as $V_G(z, t)$ and $V_R(z, t)$. Similarly, the line currents are denoted as $I_G(z, t)$ and $I_R(z, t)$. We will assume throughout that the line is a *uniform* line wherein the conductors have uniform cross sections along their length and all conductors are parallel. The task will be to solve for the terminal voltages and currents of the line. The line is of total length L and extends from $z=0$ to $z=L$.

We next derive the differential equations governing these line voltages and line currents. We will use a lumped-circuit model to obtain these equations. The lumped-circuit model is not the only method for obtaining the governing equations. See Ref. 2 for alternative derivations directly from the electromagnetic field equations. Consider a differentially small section of length Δz as shown in Fig. 1b. Per unit length parameters of inductance and capacitance contain the structural dimensions of a particular line and will be discussed later. The PUL parameters of self-inductance are denoted as l_G , l_R , and the PUL parameters of self-capacitance are denoted as c_G , c_R . The PUL parameters of mutual inductance and capacitance are denoted by l_{GR} , c_{GR} , respectively. The inductance parameters have units of henries per meter (H/m), and the capacitance parameters have units of Farads per meter (F/m). We will assume that the line is lossless, that is, that the conductors are perfect conductors and the surrounding medium has zero conductivity. Hence the PUL parameters of conductor resistance and internal inductance as well as the conductance of the surrounding medium are absent from this PUL model. For a discussion of incorporating losses, see Section 7 and Ref. 2. Writing Kirchhoff’s voltage law around the loop consisting of the generator conductor and the reference conductor yields

$$V_G(z + \Delta z, t) = V_G(z, t) - l_G \Delta z \frac{\partial I_G(z, t)}{\partial t} - l_{GR} \Delta z \frac{\partial I_R(z, t)}{\partial t}$$

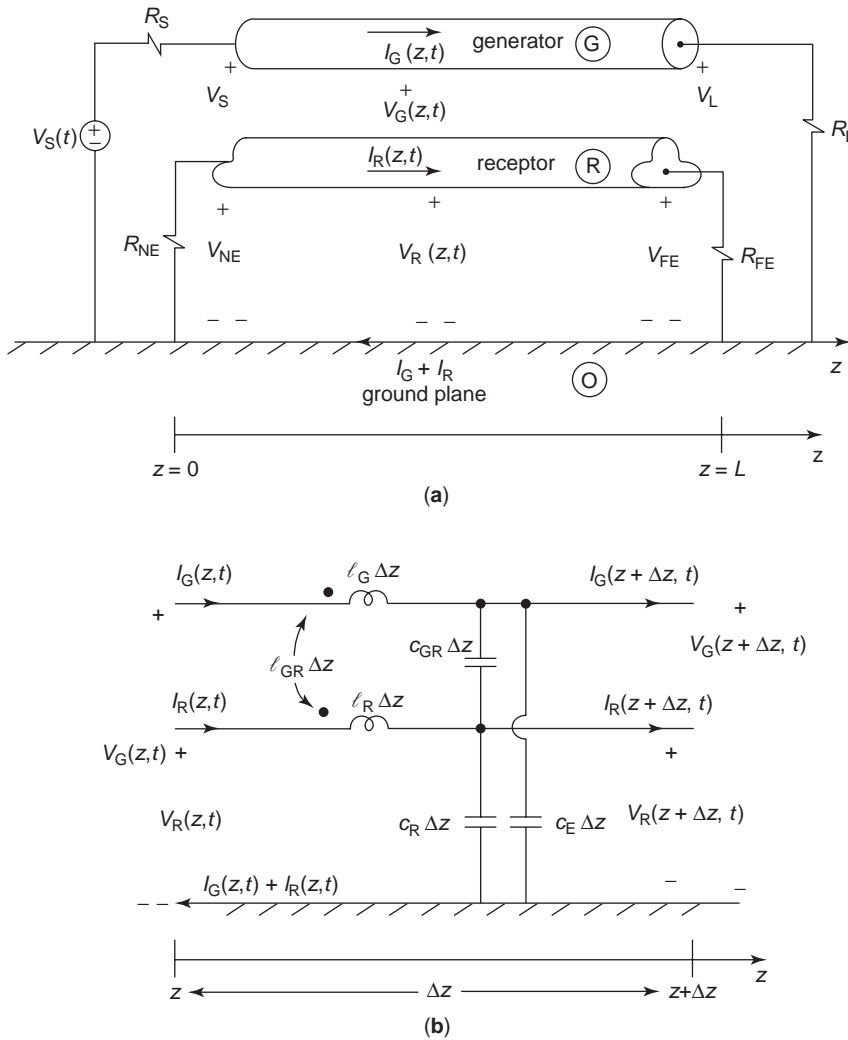


Figure 1. Illustration of coupled transmission lines; (a) the physical line with terminations, and (b) the per unit length equivalent circuit.

Similarly, writing Kirchhoff's current law at the node to the right of the inductor $l_G \Delta z$ yields

$$\begin{aligned} I_G(z + \Delta z, t) &= I_G(z, t) - c_G \Delta z \frac{\partial V_G(z + \Delta z, t)}{\partial t} \\ &\quad - c_{GR} \Delta z \frac{\partial (V_G(z + \Delta z, t) - V_R(z + \Delta z, t))}{\partial t} \end{aligned}$$

Dividing both sides by Δz and taking the limit as $\Delta z \rightarrow 0$ yield

$$\frac{\partial V_G(z, t)}{\partial z} = -l_G \frac{\partial I_G(z, t)}{\partial t} - l_{GR} \frac{\partial I_R(z, t)}{\partial t} \quad (1a)$$

$$\frac{\partial I_G(z, t)}{\partial t} = -(c_G + c_{GR}) \frac{\partial V_G(z, t)}{\partial t} + c_{GR} \frac{\partial V_R(z, t)}{\partial t} \quad (1b)$$

Similarly, for the receptor circuit we obtain

$$\frac{\partial V_R(z, t)}{\partial z} = -l_{GR} \frac{\partial I_G(z, t)}{\partial t} - l_R \frac{\partial I_R(z, t)}{\partial t} \quad (2a)$$

$$\frac{\partial I_R(z, t)}{\partial t} = c_{GR} \frac{\partial V_G(z, t)}{\partial t} - (c_R + c_{GR}) \frac{\partial V_R(z, t)}{\partial t} \quad (2b)$$

Combining (1) and (2) and writing them in matrix form yields the MTL equations to be solved as

$$\frac{\partial}{\partial z} \mathbf{V}(z, t) = -\mathbf{L} \frac{\partial}{\partial t} \mathbf{I}(z, t) \quad (3a)$$

$$\frac{\partial}{\partial z} \mathbf{I}(z, t) = -\mathbf{C} \frac{\partial}{\partial t} \mathbf{V}(z, t) \quad (3b)$$

where

$$\mathbf{V}(z, t) = \begin{bmatrix} V_G(z, t) \\ V_R(z, t) \end{bmatrix} \quad (4a)$$

$$\mathbf{I}(z, t) = \begin{bmatrix} I_G(z, t) \\ I_R(z, t) \end{bmatrix} \quad (4b)$$

and the PUL inductance and capacitance matrices are

$$\mathbf{L} = \begin{bmatrix} l_G & l_{GR} \\ l_{GR} & l_R \end{bmatrix} \quad (5a)$$

$$\mathbf{C} = \begin{bmatrix} (c_G + c_{GR}) & -c_{GR} \\ -c_{GR} & (c_R + c_{GR}) \end{bmatrix} \quad (5b)$$

The PUL parameter matrices \mathbf{L} and \mathbf{C} are symmetric, which is proved in Ref. 2. The MTL equations in (3) have considerable similarity to those for the two-conductor line, which is studied in all undergraduate electrical engineering curricula, where the quantities are scalars [1]. In fact, we will show that for a MTL the corresponding solutions and properties will have direct parallels to those for the two-conductor line but with matrix notation. Although we are studying a special case of the more general $(n+1)$ conductor MTL where $n=2$, the corresponding MTL equations for $n>2$ are in exactly the same form as in (3) [2]. The important point here is that if we can solve the MTL equations in (3) for a two-conductor line, we can readily obtain the solution for a general MTL where $n>2$.

Finally, the line is said to be a *uniform line* wherein the conductor cross sections and the cross sections of any inhomogeneous media surrounding the conductors are independent of z , and the line conductors are parallel to each other and the z axis. A *nonuniform line* would have the PUL parameter matrices as a function of z : $\mathbf{L}(z)$ and $\mathbf{C}(z)$. In this case the MTL equations would be quite difficult to solve except in certain special cases such as a line with exponential taper. Although there are several important cases of nonuniform lines, we will restrict our discussion to uniform lines, which represent the majority of the applications.

2. THE PER UNIT LENGTH PARAMETERS

The reader is once again reminded that all cross-sectional structural dimensions are contained in the PUL parameters in \mathbf{L} and \mathbf{C} . The MTL equations in (3) are identical for all lines. Hence, determining these parameters for a particular line is essential to the complete solution; solving the MTL equations would do little good without knowledge of the values of the PUL parameters for the specific line.

Because of the TEM mode assumption, the transverse electric and magnetic fields satisfy a static distribution in the two-dimensional (2D) xy cross-sectional plane [2]. In other words, the transverse electric and magnetic fields are the same as static field distributions in the xy plane

even though they vary with time. Hence a wide variety of commercially available 2D electrostatic and magnetostatic field solvers can be used to determine these PUL parameters. These field solvers use numerical solutions of Laplace's equation via the method of moments (MoM) or the finite-element method (FEM) [2].

Definition of these PUL parameters is very similar to the two-conductor case ($n=1$). Again, the TEM field structure is assumed to be present where the electric field intensity vector E^t and the magnetic field intensity vector H^t lie solely in the *transverse* or xy plane. There are two "circuits"; one is the loop formed between the generator conductor and the reference conductor, and the other loop is formed between the receptor conductor and the reference conductor. The PUL inductance matrix in (5a) relates the magnetic flux ψ penetrating these loops to the line currents as

$$\psi_G = l_G I_G + l_{GR} I_R \quad (6a)$$

$$\psi_R = l_{GR} I_G + l_R I_R \quad (6b)$$

In matrix form, these relations become

$$\Psi = \mathbf{L} \mathbf{I} \quad (7a)$$

where

$$\Psi = \begin{bmatrix} \psi_G \\ \psi_R \end{bmatrix} \quad (7b)$$

Each PUL parameter in (9) can be found in a fashion similar to that employed for two-port parameters, as follows:

$$l_G = \left. \frac{\psi_G}{I_G} \right|_{I_R=0} \quad (8a)$$

$$l_R = \left. \frac{\psi_R}{I_R} \right|_{I_G=0} \quad (8b)$$

$$l_{GR} = \left. \frac{\psi_G}{I_R} \right|_{I_G=0} = \left. \frac{\psi_R}{I_G} \right|_{I_R=0} \quad (8c)$$

This is illustrated in Fig. 2a. Similarly, the PUL capacitance matrix in (5b) relates the PUL charge on the conductors Q to the line voltages as

$$Q_G = (c_G + c_{GR})V_G - c_{GR}V_R \quad (9a)$$

$$Q_R = -c_{GR}V_G + (c_R + c_{GR})V_R \quad (9b)$$

In matrix form, these relations become

$$\mathbf{Q} = \mathbf{C} \mathbf{V} \quad (10a)$$

where

$$\mathbf{Q} = \begin{bmatrix} Q_G \\ Q_R \end{bmatrix} \quad (10b)$$

Each PUL parameter in (9) can be found in a fashion similar to that used for two-port parameters, as follows:

$$c_G + c_{GR} = \frac{Q_G}{V_G} \Big|_{V_R=0} \quad (11a)$$

$$c_R + c_{GR} = \frac{Q_R}{V_R} \Big|_{V_G=0} \quad (11b)$$

$$-c_{GR} = \frac{Q_G}{V_R} \Big|_{V_G=0} = \frac{Q_R}{V_G} \Big|_{V_R=0} \quad (11c)$$

This is illustrated in Fig. 2b.

There are several important properties of the PUL parameter matrices (see Ref. 2 for proofs of these properties):

1. The PUL parameters matrices \mathbf{L} and \mathbf{C} are real and symmetric, specifically, $\mathbf{L} = \mathbf{L}^t$ and $\mathbf{C} = \mathbf{C}^t$, where the superscript “t” on a matrix denotes its transpose.
2. The PUL parameter matrices \mathbf{L} and \mathbf{C} are positive-definite, meaning, among other things, that all their eigenvalues are nonzero and positive.

These important results will be used in the solution of the MTL equations.

We now discuss the important classes of lines seen in practice. First we consider typical lines in *homogeneous media* shown in Fig. 3. Figure 3a shows three bare wires

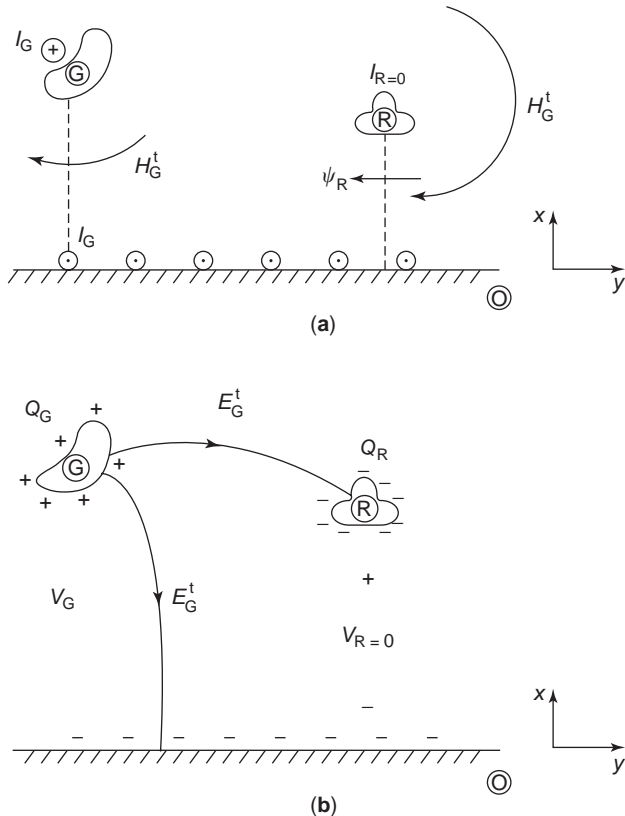


Figure 2. Illustration of the determination of the per unit length parameters of (a) mutual inductance, and (b) mutual capacitance.

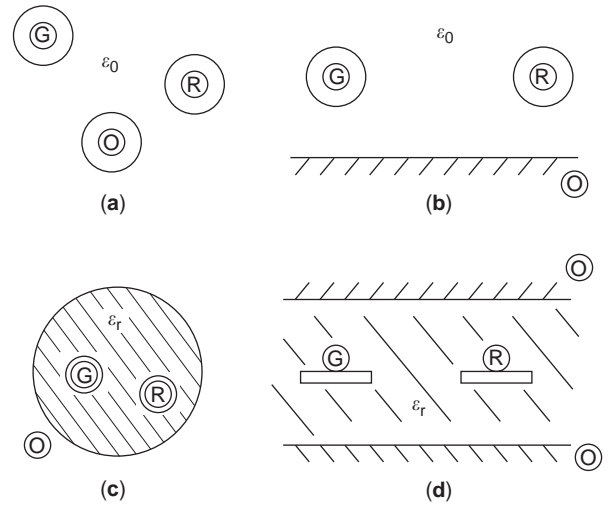


Figure 3. Cross sectional dimensions of lines in a homogeneous medium; (a) a three-wire line, (b) two wires above a ground plane, (c) two wires within an overall cylindrical shield, and (d) a coupled stripline.

(circular cross section conductors) immersed in free space. Wires typically have dielectric insulation such that the surrounding medium is inhomogeneous. In this illustration, we have removed (ignored) those insulations in order to make this a homogeneous medium problem. High-voltage transmission lines typically are bare. Figure 3b shows two bare wires above an infinite ground plane. Figure 3c shows two wires within a surrounding shield. The medium internal to the shield has a relative permittivity of ϵ_r . Figure 3d shows a typical structure occurring in printed circuit boards (PCBs): the coupled stripline. Two “lands” (rectangular cross section conductors) lie between two ground planes. This is typical of PCBs that have inner planes. The medium between the planes has a relative permittivity of ϵ_r where $\epsilon_r = 4.7$ for typical glass-epoxy (resin) (FR4) boards.

For the lines in a homogeneous medium having permeability $\epsilon = \epsilon_0 \epsilon_r$ and permeability μ_0 in Fig. 3, the velocity of propagation of the voltage and current waves is

$$v = \frac{1}{\sqrt{\mu\epsilon}} = \frac{v_0}{\sqrt{\epsilon_r}} \quad (12)$$

where $v_0 = 2.99792458 \times 10^8$ m/s is the speed of light. Perhaps the most important property of lines in a homogeneous medium is that the PUL parameter matrices are related as [2]

$$\mathbf{LC} = \mathbf{CL} = \mu\epsilon \mathbf{1}_2 = \frac{1}{v^2} \mathbf{1}_2 \quad (13)$$

where $\mathbf{1}_2$ is the 2×2 identity matrix:

$$\mathbf{1}_2 = \begin{bmatrix} 1 & 0 \\ 0 & 1 \end{bmatrix}$$

For the general $n + 1$ conductor MTL in a homogeneous medium, the PUL parameter matrices satisfy (13), where the identity matrix is $n \times n$ with ones on the main diagonal and zeros elsewhere. The property in (13) is the matrix counterpart to the familiar scalar result for two-conductor lines ($n = 1$) [1].

In general, numerical methods must be used to solve the 2D static field problem here. However, there exist some closed-form approximate solutions for these PUL parameters [2]. For the case of wires in a homogeneous medium as in Figs. 3a-c, these results can be obtained for wide separations. If the wires are sufficiently spaced so that the charge distributions around the peripheries of the wires are essentially uniform, simple formulas are obtainable [2].

Figure 4 shows several important cases of an *inhomogeneous surrounding medium*. Figure 4a shows the common case of a ribbon cable where wires with dielectric insulations are arranged in a linear array. Figure 4b shows the common coupled microstrip where two lands are etched on one side of a substrate and a ground plane on the other side constitutes the reference conductor. This commonly occurs in the outer layers of a PCB having innerplanes. Figure 4(c) shows a case where the three conductors lie on one side of the substrate. This occurs in PCBs that are single- or double-sided without inner planes.

For all these cases of an inhomogeneous medium surrounding the conductors, the electric field lies partly in the dielectric and partly in air. Hence the velocity of propagation is no longer given by (12). Furthermore, there are two velocities of propagation of the two “modes” on the line. In addition, the simple relation between the PUL \mathbf{L} and \mathbf{C} matrices given for a homogeneous medium in (13) no longer holds for an inhomogeneous medium.

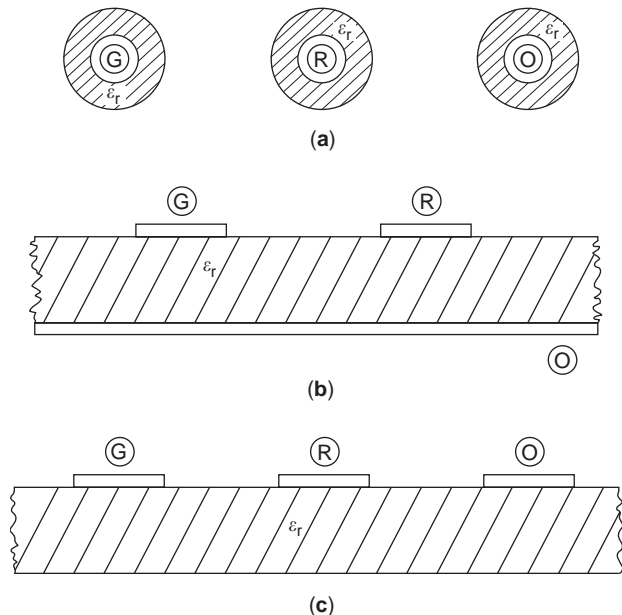


Figure 4. Cross sectional dimensions of lines in inhomogeneous media; (a) a three-wire ribbon cable, (b) a coupled microstrip, and (c) a printed circuit board (PCB).

For these cases of an inhomogeneous medium, numerical methods must be used to solve the electrostatic 2D problem. Reference 2 contains descriptions of several FORTRAN computer programs that can be used to compute, via numerical methods, the PUL parameter matrices \mathbf{L} and \mathbf{C} . Once the PUL capacitance matrix \mathbf{C} is determined, we can determine the PUL inductance matrix \mathbf{L} by first determining the PUL capacitance matrix *with the dielectric removed* \mathbf{C}_0 . Then the inductance matrix can be determined from the homogeneous medium relation in (13) as

$$\mathbf{L} = \frac{1}{v_0^2} \mathbf{C}_0^{-1} \tag{14}$$

Hence we only need to obtain the PUL capacitance matrix with the dielectric present and with the dielectric removed (and replaced with free space).

First consider the numerical solution of the ribbon cable in Fig. 4a. The solution method relies on the solution of a fundamental subproblem shown in Fig. 5a. A wire (cylindrical cross section conductor) of radius r_w is surrounded by a cylindrical dielectric insulation having permittivity ϵ . At the air-dielectric interface there is a bound charge distribution that we represent with a Fourier series in the angular variation θ as

$$\rho_b' = a_0' + \sum_{k=1}^{A'} a_k' \cos(\theta) + \sum_{k=1}^{B'} b_k' \sin(\theta) \text{ C/m}^2 \tag{15a}$$

Similarly, at the wire-dielectric interface there is a charge distribution consisting of a combination of free charge and a bound charge, which we represent with a Fourier series

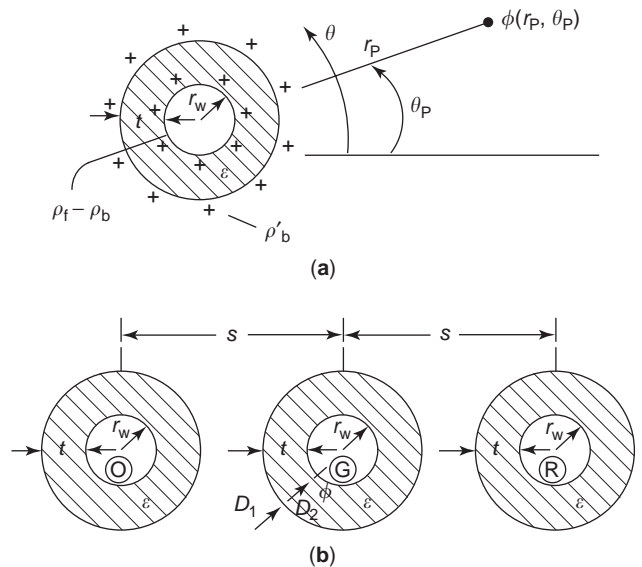


Figure 5. Illustration of the determination of capacitances of a ribbon cable; (a) illustrations of the expansion of charge distributions into bound and free charge, and (b) the physical dimensions of a three-wire ribbon cable.

in the angular variation θ as

$$\rho_f - \rho_b = a_0 + \sum_{k=1}^A a_k \cos(\theta) + \sum_{k=1}^B b_k \sin(\theta) \text{ C/m}^2 \quad (15b)$$

The constants in these expressions ($a'_0, a'_k, b'_k, a_0, a_k, b_k$) will be determined in the problem solution in order to satisfy the boundary conditions. We desire the potential $\phi(r_P, \theta_P)$ due to these charge distributions at a point that is a distance r_P from the wire center and an angle θ_P . Solutions for the potential and electric fields for this basic subproblem are given in Ref. 2. The total PUL charge distribution along the line is obtained from the constant terms in these distributions as

$$Q_f - Q_b = 2\pi r_w a_0 \text{ C/m} \quad (16a)$$

and

$$Q_b = 2\pi(r_w + t)a'_0 \text{ C/m} \quad (16b)$$

where the dielectric insulation is of thickness t . Hence the total PUL free charge distribution is

$$Q_f = 2\pi r_w a_0 + 2\pi(r_w + t)a'_0 \text{ C/m} \quad (17)$$

from which the PUL capacitances of the line can be found. For the three-wire ribbon cable in Fig. 5a, we choose the number of expansion terms around the wire–dielectric interface ($1 + A + B$), and around the air–dielectric interface ($1 + A' + B'$), and apply the boundary conditions. These are to match the potential at sufficient points on each wire (that is due to all charge distributions), and ensure continuity of the components of the electric flux density D_n that are normal to the air–dielectric interface at sufficient points around this interface (due to all charge distributions). This generates simultaneous equations of the form

$$\Phi = \mathbf{D}_{11}\mathbf{A} + \mathbf{D}_{12}\mathbf{A}' \quad (18a)$$

$$\mathbf{0} = \mathbf{D}_{21}\mathbf{A} + \mathbf{D}_{22}\mathbf{A}' \quad (18b)$$

Vector \mathbf{A} contains the expansion coefficients in (15b) for the bound plus free charge at the wire–dielectric interface, while \mathbf{A}' contains the expansion coefficients in (15a) for the bound charge at the air–dielectric interface. Equations (18a) enforce the potential at matchpoints on the wire surfaces, and equations (18b) enforce continuity of the normal components of the electric flux density vector across the air–dielectric interface at matchpoints on that surface. Putting these in matrix form gives

$$\begin{bmatrix} \Phi \\ \mathbf{0} \end{bmatrix} = \begin{bmatrix} \mathbf{D}_{11} & \mathbf{D}_{12} \\ \mathbf{D}_{21} & \mathbf{D}_{22} \end{bmatrix} \begin{bmatrix} \mathbf{A} \\ \mathbf{A}' \end{bmatrix} \quad (19)$$

Inverting this gives the solution for the expansion coefficients:

$$\begin{bmatrix} \mathbf{A} \\ \mathbf{A}' \end{bmatrix} = \begin{bmatrix} \mathbf{D}_{11} & \mathbf{D}_{12} \\ \mathbf{D}_{21} & \mathbf{D}_{22} \end{bmatrix}^{-1} \begin{bmatrix} \Phi \\ \mathbf{0} \end{bmatrix} \quad (20)$$

Once the expansion coefficients $a'_0, a'_k, b'_k, a_0, a_k, b_k$ are found from (20), the total free charge on each wire is obtained from (17), and hence we obtain the PUL capacitance matrix [2].

Reference 2 describes this process in greater detail and provides the implementation of the method in a FORTRAN computer code, RIBBON.FOR, which can be obtained from ftp://ftp.wiley.com/public/sci_tech_med/multiconductor_transmission/. As an example, consider the typical three-wire ribbon cable shown in Fig. 5b, where $s = 50$ mils (1.27 mm), the wires are AWG (American Wire Gauge) 28-gauge stranded having a radius of $r_w = 7.5$ mils (0.19 mm), an insulation thickness of $t = 10$ mils (0.254 mm), and PVC insulation having a relative permittivity of $\epsilon_r = 3.5$; we then obtain (with the reference conductor chosen as an outer wire)

$$\mathbf{C} = \begin{bmatrix} 37.432 & -18.716 \\ -18.716 & 24.982 \end{bmatrix} \text{ pF/m}$$

$$\mathbf{C}_0 = \begin{bmatrix} 22.494 & -11.247 \\ -11.247 & 16.581 \end{bmatrix} \text{ pF/m}$$

$$\mathbf{L} = \frac{1}{v_0^2} \mathbf{C}_0 = \begin{bmatrix} 0.7485 & 0.5077 \\ 0.5077 & 1.0154 \end{bmatrix} \mu\text{H/m}$$

and we used 10 expansion coefficients (the constant and 9 cosine terms) around the conductor–dielectric interface and around the dielectric–air interface for each of the three wires. Hence, the matrix to be inverted in Eq. (19) is 60×60 .

For conductors of rectangular cross section (lands) such as the coupled microstrip in Fig. 4b and the PCB in Fig. 4c, we use a similar numerical method. We first obtain the solution for the basic subproblem in Fig. 6a for the potential due to an infinitely long strip of width w along which the charge has a constant distribution ρ C/m². The solution of this basic subproblem is given in Ref. 2. For the coupled microstrip we divide each land into N subsections as shown in Fig. 6b. Instead of representing the free and bound charge as in the ribbon cable problem, we determine the subproblem potential by simply imaging across the air–dielectric interface and across the dielectric–ground plane interface and hence remove the dielectric and the ground plane (see Ref. 2 for details of this imaging). Then we choose N matchpoints at the center of each land subsection and determine the potential at that point due to all charge distributions of all the other subsections to yield

$$\Phi = \mathbf{D}\mathbf{A} \quad (21)$$

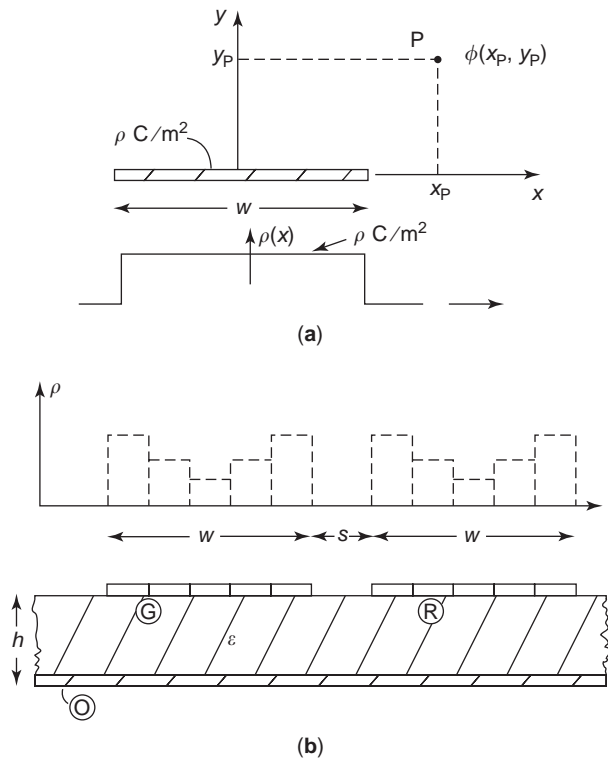


Figure 6. Illustration of the determination of capacitances of a coupled microstrip; (a) the basic subproblem of determining the potential due to a constant charge distribution, and (b) representation of the charge distribution on a coupled microstrip.

where **A** contains the (constant) charge distributions along the land subsections. Inverting this yields the charge distributions on each subdivision of each land. Once these charge distributions are obtained, the total PUL free charge distribution on each land is obtained by multiplying the charge distributions of each subdivision by the subdivision width and adding them for each land. The PUL capacitance matrix is then obtained [2].

Throughout this discussion we will show typical computed and experimental results confirming this theory. The structure to be used is a three-conductor ($n = 2$) coupled microstrip shown in Fig. 6b having dimensions $s = 100$ mils (2.54 mm) and $w = 100$ mils (2.54 mm) and a dielectric having a thickness of $h = 62$ mils (1.57 mm) and a relative permittivity of $\epsilon_r = 4.7$ (glass-epoxy or FR4). The method described above is implemented for the coupled microstrip in a FORTRAN computer program, MSTRP.FOR, described in Ref. 2, obtainable from ftp://ftp.wiley.com/public/sci_tech_med/multiconductor_transmission/. For this line we obtain the following equations, dividing each land into 30 subdivisions [hence the matrix in (21) is 60×60]:

$$\mathbf{C} = \begin{bmatrix} 115.511 & -4.927 \\ -4.927 & 115.511 \end{bmatrix} \text{ pF/m}$$

$$\mathbf{C}_0 = \begin{bmatrix} 33.593 & -3.722 \\ -3.722 & 33.593 \end{bmatrix} \text{ pF/m}$$

$$\mathbf{L} = \frac{1}{v_0^2} \mathbf{C}_0^{-1} = \begin{bmatrix} 335.327 & 37.153 \\ 37.153 & 335.327 \end{bmatrix} \text{ nH/m}$$

A FORTRAN code, PCB.FOR, for the PCB in Fig. 4c is also described in Ref. 2 and can be obtained from ftp://ftp.wiley.com/public/sci_tech_med/multiconductor_transmission/.

3. THE TIME-DOMAIN SOLUTION

The key to solving the coupled MTL equations in (3) is to transform the actual voltages and currents to “mode” voltages and currents with similarity transformations

$$\mathbf{V} = \mathbf{T}_V \mathbf{V}_m \tag{22a}$$

$$\mathbf{I} = \mathbf{T}_I \mathbf{I}_m \tag{22b}$$

where the real matrices \mathbf{T}_V and \mathbf{T}_I are 2×2 ($n \times n$ for the general $n + 1$ conductor MTL) with entries

$$\mathbf{T}_V = \begin{bmatrix} T_{VGG} & T_{VGR} \\ T_{VRG} & T_{VRR} \end{bmatrix} \tag{23a}$$

$$\mathbf{T}_I = \begin{bmatrix} T_{IGG} & T_{IGR} \\ T_{IRG} & T_{IRR} \end{bmatrix} \tag{23b}$$

and the 2×1 vectors \mathbf{V}_m and \mathbf{I}_m contain the mode voltages and currents, respectively, as

$$\mathbf{V}_m = \begin{bmatrix} V_{mG} \\ V_{mR} \end{bmatrix} \tag{24a}$$

$$\mathbf{I}_m = \begin{bmatrix} I_{mG} \\ I_{mR} \end{bmatrix} \tag{24b}$$

Substituting (22) into (3) yields

$$\frac{\partial}{\partial z} \mathbf{V}_m(z, t) = \underbrace{-\mathbf{T}_V^{-1} \mathbf{L} \mathbf{T}_I}_{\mathbf{L}_m} \frac{\partial}{\partial t} \mathbf{I}_m(z, t) \tag{25a}$$

$$\frac{\partial}{\partial z} \mathbf{I}_m(z, t) = \underbrace{-\mathbf{T}_I^{-1} \mathbf{C} \mathbf{T}_V}_{\mathbf{C}_m} \frac{\partial}{\partial t} \mathbf{V}_m(z, t) \tag{25b}$$

If transformations \mathbf{T}_V and \mathbf{T}_I can be found such that the mode PUL parameter matrices are diagonalized as

$$\begin{aligned} \mathbf{L}_m &= \mathbf{T}_V^{-1} \mathbf{L} \mathbf{T}_I \\ &= \begin{bmatrix} l_{mG} & 0 \\ 0 & l_{mR} \end{bmatrix} \end{aligned} \quad (26a)$$

$$\begin{aligned} \mathbf{C}_m &= \mathbf{T}_I^{-1} \mathbf{C} \mathbf{T}_V \\ &= \begin{bmatrix} c_{mG} & 0 \\ 0 & c_{mR} \end{bmatrix} \end{aligned} \quad (26b)$$

then the equations in terms of mode quantities in (25) are uncoupled. We will show methods of determining the transformations \mathbf{T}_V and \mathbf{T}_I that will simultaneously diagonalize \mathbf{L} and \mathbf{C} for any MTL.

The importance of this result is that the MTL equations in terms of the mode quantities are now uncoupled and consist of two uncoupled two-conductor lines:

$$\frac{\partial V_{mG}}{\partial z} = -l_{mG} \frac{\partial I_{mG}}{\partial t} \quad (27a)$$

$$\frac{\partial I_{mG}}{\partial z} = -c_{mG} \frac{\partial V_{mG}}{\partial t} \quad (27b)$$

$$\frac{\partial V_{mR}}{\partial z} = -l_{mR} \frac{\partial I_{mR}}{\partial t} \quad (28a)$$

$$\frac{\partial I_{mR}}{\partial z} = -c_{mR} \frac{\partial V_{mR}}{\partial t} \quad (28b)$$

The two-conductor line equations in (27) represent a two-conductor line with velocity of propagation

$$v_{mG} = \frac{1}{\sqrt{l_{mG} c_{mG}}} \quad (29a)$$

and characteristic impedance

$$Z_{CmG} = \sqrt{\frac{l_{mG}}{c_{mG}}} \quad (29b)$$

Similarly, the equations in (28) represent a two-conductor line with velocity of propagation

$$v_{mR} = \frac{1}{\sqrt{l_{mR} c_{mR}}} \quad (30a)$$

and characteristic impedance

$$Z_{CmR} = \sqrt{\frac{l_{mR}}{c_{mR}}} \quad (30b)$$

The solutions to the uncoupled-mode transmission-line equations in (27) are well known [1]:

$$V_{mG}(z, t) = V_G^+ \left(t - \frac{z}{v_{mG}} \right) + V_G^- \left(t + \frac{z}{v_{mG}} \right) \quad (31a)$$

$$\begin{aligned} I_{mG}(z, t) &= \frac{1}{Z_{CmG}} V_G^+ \left(t - \frac{z}{v_{mG}} \right) \\ &\quad - \frac{1}{Z_{CmG}} V_G^- \left(t + \frac{z}{v_{mG}} \right) \end{aligned} \quad (31b)$$

Similarly the solutions to the transmission line equations in (28) are:

$$V_{mR}(z, t) = V_R^+ \left(t - \frac{z}{v_{mR}} \right) + V_R^- \left(t + \frac{z}{v_{mR}} \right) \quad (32a)$$

$$\begin{aligned} I_{mR}(z, t) &= \frac{1}{Z_{CmR}} V_R^+ \left(t - \frac{z}{v_{mR}} \right) \\ &\quad - \frac{1}{Z_{CmR}} V_R^- \left(t + \frac{z}{v_{mR}} \right) \end{aligned} \quad (32b)$$

The functions V_G^+ , V_G^- , V_R^+ , V_R^- will be determined by the time history of the driving source, $V_S(t)$.

Hence, the original problem is transformed into two uncoupled two-conductor mode lines as shown in Fig. 7 with transformation networks representing the transformations \mathbf{T}_V and \mathbf{T}_I at the endpoints that transform out to the original line voltages and currents. We will show a simple SPICE implementation of Fig. 7.

Although we have two transformation matrices \mathbf{T}_V and \mathbf{T}_I , it can be shown that these can be chosen such that they are related as [3]

$$\mathbf{T}_V^t \mathbf{T}_I = \mathbf{1}_2 \quad (33)$$

where the superscript “t” denotes the transpose of the matrix $\mathbf{1}_2$ is the 2×2 identity matrix. Hence these transformation matrices are also related as

$$\mathbf{T}_V^t = \mathbf{T}_I^{-1} \quad (34)$$

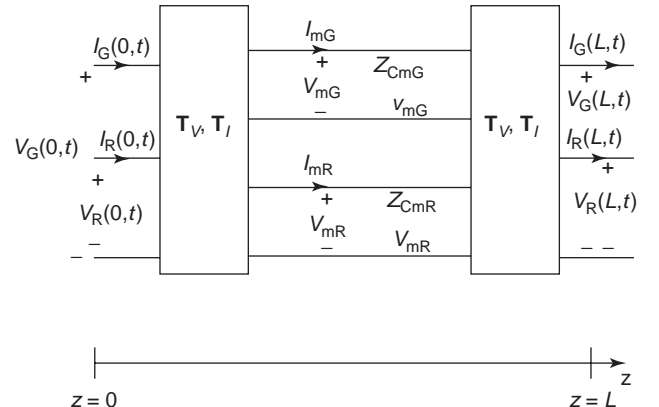


Figure 7. Illustration of the basic method for decoupling the MTL equations.

The implementation of the transformation networks in Fig. 7 is quite simple. Writing out the relation between the voltages and the mode voltages in (22a) and using (23a) gives

$$V_G = T_{VGG} V_{mG} + T_{VGR} V_{mR} \quad (35a)$$

$$V_R = T_{VRG} V_{mG} + T_{VRR} V_{mR} \quad (35b)$$

If we invert the relation between the currents and the mode currents in (22b) we obtain

$$\mathbf{I}_m = \mathbf{T}_I^{-1} \mathbf{I} \quad (36)$$

which becomes

$$\begin{bmatrix} I_{mG} \\ I_{mR} \end{bmatrix} = \underbrace{\begin{bmatrix} T_{IGG}^{-1} & T_{IGR}^{-1} \\ T_{IRG}^{-1} & T_{IRR}^{-1} \end{bmatrix}}_{\mathbf{T}_I^{-1}} \begin{bmatrix} I_G \\ I_R \end{bmatrix} = \underbrace{\begin{bmatrix} T_{VGG} & T_{VGR} \\ T_{VGR} & T_{VRR} \end{bmatrix}}_{\mathbf{T}_V^t} \begin{bmatrix} I_G \\ I_R \end{bmatrix} \quad (37)$$

where we have denoted the entries in the inverse of \mathbf{T}_I as T_{IXX}^{-1} . (The inverse of a matrix is not simply the inverse of each of its components. This notation for the entries in the inverse of \mathbf{T}_I was chosen for simplicity of notation.) Writing out (37) gives

$$I_{mG} = T_{IGG}^{-1} I_G + T_{IGR}^{-1} I_R = T_{VGG} I_G + T_{VGR} I_R \quad (38a)$$

$$I_{mR} = T_{IRG}^{-1} I_G + T_{IRR}^{-1} I_R = T_{VGR} I_G + T_{VRR} I_R \quad (38b)$$

The relations between the actual line voltage and the mode voltage in Eqs. (35) can be implemented using voltage-controlled voltage sources as shown in Fig. 8. The relations between the mode currents and the actual line currents in Eqs. (38) can be implemented using current-controlled current sources as shown in Fig. 8.

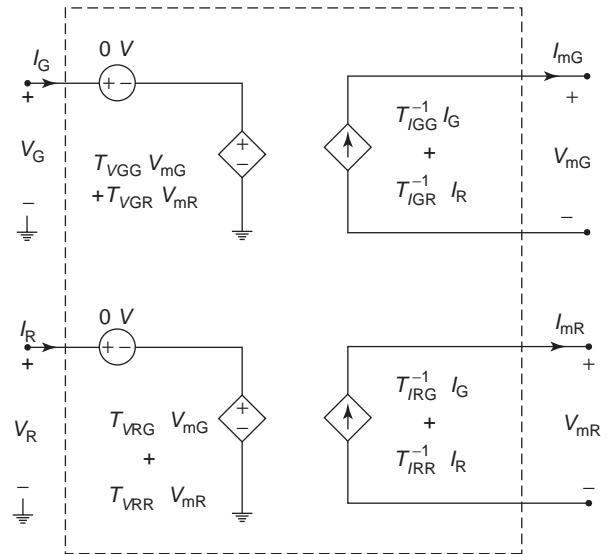


Figure 8. Implementation of the mode transformations in SPICE using controlled sources.

A SPICE (or the personal computer version, PSPICE) subcircuit model for transformations and mode transmission lines as shown in Fig. 9 can be generated by the FORTRAN program SPICEMTL.FOR that is described in Ref. 2 and can be obtained from ftp://ftp.wiley.com/public/sci_tech_med/multiconductor_transmission/. All that remains is to attach the terminations to that subcircuit model in order to give a complete SPICE solution model.

We will show results for a coupled microstrip shown in cross section in Fig. 10a. The PUL parameter matrices for this structure were computed in the previous section. The line is terminated in 50-Ω loads at each port, and the open-circuit voltage source is a 10-MHz, periodic, trapezoidal pulsetrain (representing a digital clock) having a voltage

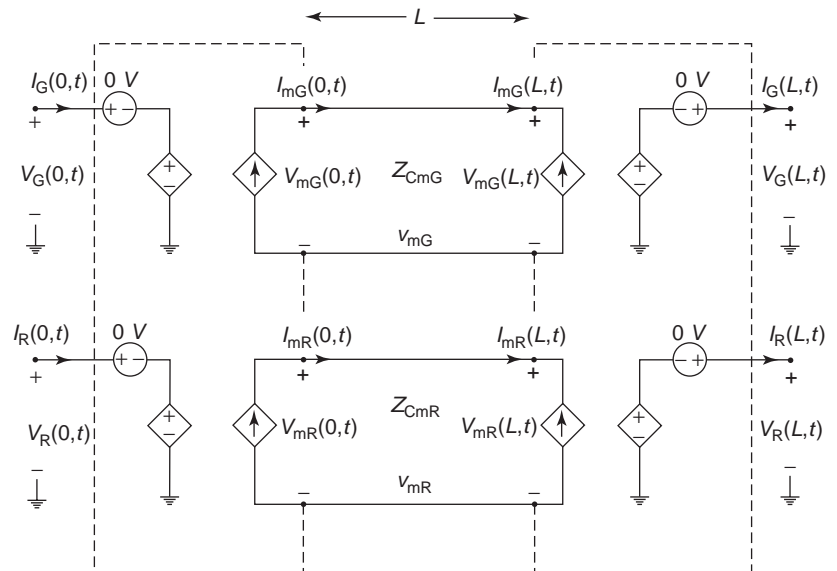


Figure 9. A complete SPICE model for a three-conductor coupled MTL.

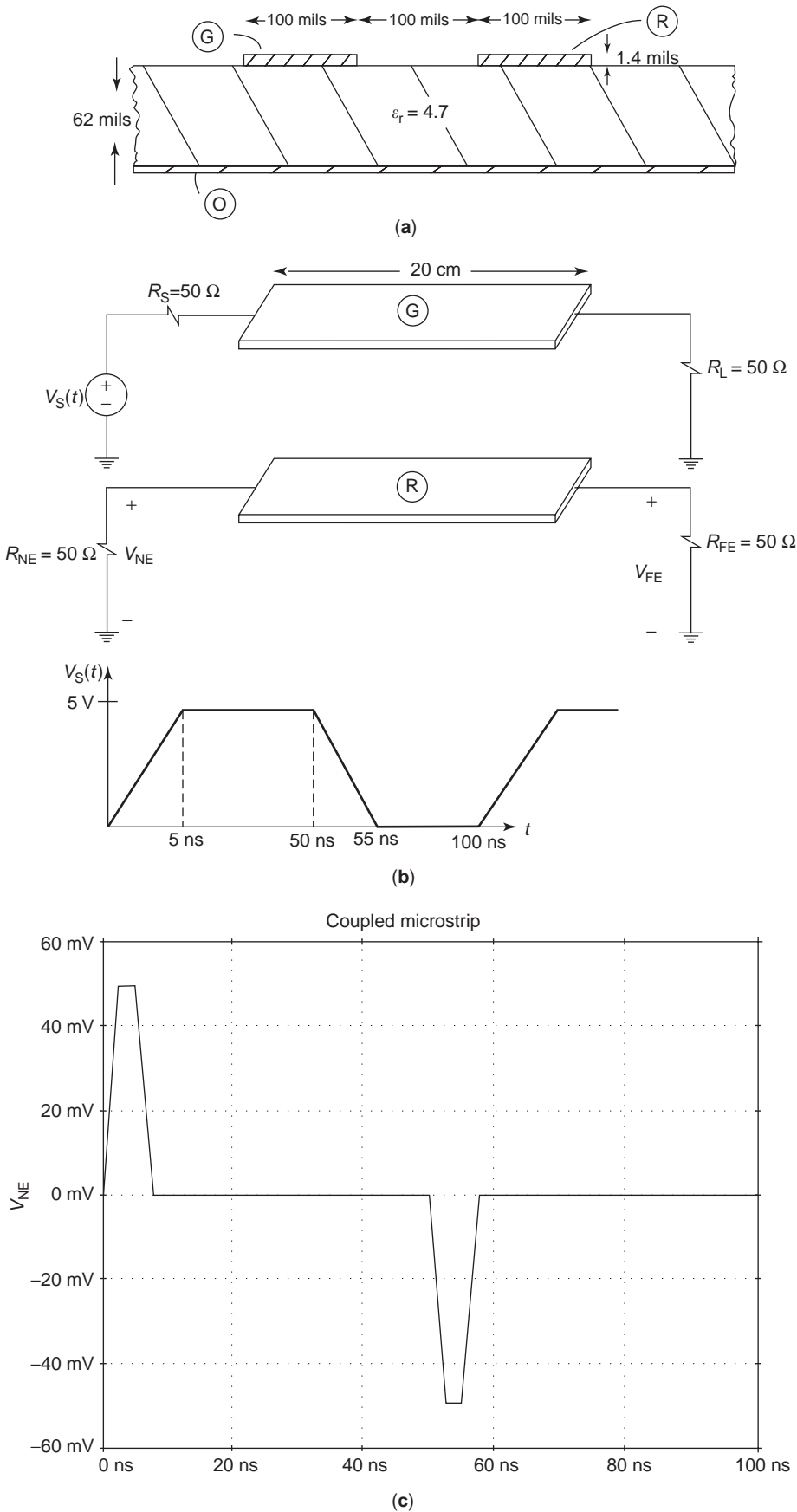


Figure 10. Illustration of a computational example; (a) the cross sectional dimensions of the coupled microstrip, (b) the longitudinal dimensions, terminations and source waveform, and (c) the SPICE predicted near-end cross-talk.

of 5 V, a rise/falltime of 5 ns, and a 50% duty cycle. The results of this PSPICE generated output for the near-end crosstalk voltage is shown in Fig. 10c. See Ref. 1 for experimental confirmation of these results.

For the coupled microstrip investigated, the transformations and mode velocities and characteristic impedances are

$$\mathbf{T}_V = \frac{1}{\sqrt{2}} \begin{bmatrix} 1 & -1 \\ 1 & 1 \end{bmatrix}$$

$$\mathbf{T}_I = \frac{1}{\sqrt{2}} \begin{bmatrix} 1 & -1 \\ 1 & 1 \end{bmatrix}$$

$$\mathbf{T}_I^{-1} = \frac{1}{\sqrt{2}} \begin{bmatrix} 1 & 1 \\ -1 & 1 \end{bmatrix}$$

Observe that (33) and (34) are satisfied. Because of the physical symmetry of this coupled microstrip (both lands have identical width and are at the same height above the ground plane), the transformations are simple. Inverting the voltage transformation to give \mathbf{T}_V^{-1} and writing out the transformation gives

$$V_{mG} = \frac{1}{\sqrt{2}} (V_G + V_R)$$

$$V_{mR} = \frac{1}{\sqrt{2}} (-V_G + V_R)$$

This is often referred to in the literature as the *even-mode/odd-mode transformation*. The characteristic impedances and one-way delays of the modes (the total line length is 20 cm) are

$$Z_{CmG} = 58.037 \Omega \quad T_{mG} = \frac{L}{v_{mG}} = 1.2836 \text{ ns}$$

$$Z_{CmR} = 49.757 \Omega \quad T_{mR} = \frac{L}{v_{mR}} = 1.1985 \text{ ns}$$

3.1. Determining the Mode Transformations

We now show how to determine the transformations \mathbf{T}_V and \mathbf{T}_I such that they simultaneously diagonalize the per unit parameter matrices, \mathbf{L} and \mathbf{C} , as in (26). We consider two separate cases: homogeneous media and inhomogeneous media.

3.1.1. Homogeneous Media. For the case of a homogeneous medium, we have the important identity

$$\mathbf{LC} = \mathbf{CL} = \frac{1}{v^2} \mathbf{1}_2 = \begin{bmatrix} 1 & 0 \\ 0 & 1 \end{bmatrix} \quad (39)$$

where $v^2 = v_0^2/\epsilon_r$. Because \mathbf{L} is real and symmetric, there always exists a transformation \mathbf{T} , such that [2]

$$\mathbf{T}^t \mathbf{L} \mathbf{T} = \mathbf{L}_m \quad (40a)$$

where \mathbf{L}_m is diagonal as

$$\mathbf{L}_m = \begin{bmatrix} l_{mG} & 0 \\ 0 & l_{mR} \end{bmatrix} \quad (40b)$$

and the inverse of \mathbf{T} is its transpose [2]:

$$\mathbf{T}^{-1} = \mathbf{T}^t \quad (41)$$

This diagonalization of a real, symmetric matrix is said to be an orthogonal transformation and is numerically accomplished with the stable and efficient Jacobi method [2]. In fact, for the special case of the three-conductor line considered here, we obtain

$$\mathbf{T} = \begin{bmatrix} \cos \theta & -\sin \theta \\ \sin \theta & \cos \theta \end{bmatrix} \quad (42a)$$

where

$$\tan 2\theta = \frac{2l_{GR}}{l_G - l_R} \quad (42b)$$

For MTLs with $n > 2$, a FORTRAN subroutine, JACOBI.SUB described in Ref. 2, is available to determine this orthogonal transformation in a stable and efficient manner. From the identity in (39), we obtain

$$\mathbf{C} = \frac{1}{v^2} \mathbf{L}^{-1} \quad (43)$$

Forming

$$\begin{aligned} \mathbf{T}^{-1} \mathbf{C} (\mathbf{T}^t)^{-1} &= \mathbf{T}^t \mathbf{C} \mathbf{T} \\ &= \frac{1}{v^2} \mathbf{T}^t \mathbf{L}^{-1} \mathbf{T} \\ &= \frac{1}{v^2} \mathbf{L}_m^{-1} \end{aligned} \quad (44)$$

Comparing (40a) and (44) to (26a) and (26b), we identify

$$\mathbf{T}_I = \mathbf{T} \quad (45a)$$

$$\mathbf{T}_V^{-1} = \mathbf{T}^t \quad (45b)$$

$$\mathbf{T}_V = \mathbf{T} \quad (45c)$$

Hence the mode characteristic impedances are

$$Z_{CmG} = vl_{mG} \quad (46a)$$

$$Z_{CmR} = vl_{mR} \quad (46b)$$

and all mode velocities are the same:

$$v_{mG} = v_{mR} = v \quad (47)$$

3.1.2. Inhomogeneous Media. For inhomogeneous media we no longer have the identity in (39). However, the transformations that simultaneously diagonalize \mathbf{L} and \mathbf{C} can still be obtained in a stable and numerically efficient manner. Since \mathbf{C} is real and symmetric, we can find an orthogonal transformation \mathbf{U} that diagonalizes it as [2]

$$\mathbf{U}^t \mathbf{C} \mathbf{U} = \theta^2 \quad (48a)$$

where θ^2 is diagonal as

$$\theta^2 = \begin{bmatrix} \theta_{mG}^2 & 0 \\ 0 & \theta_{mR}^2 \end{bmatrix} \quad (48b)$$

Because \mathbf{C} is also positive definite, its eigenvalues, θ_{mG}^2 and θ_{mR}^2 are real, positive, and nonzero [2]. In addition, since the transformation is an orthogonal one, we obtain

$$\mathbf{U}^{-1} = \mathbf{U}^t \quad (49)$$

Since the eigenvalues of \mathbf{C} in (48b) are real, positive, and nonzero, we can form the square root of θ^2 , θ , and form the product $\theta \mathbf{U}^t \mathbf{L} \mathbf{U} \theta$, which is real and symmetric. Hence we can obtain an orthogonal transformation that diagonalizes it as

$$\mathbf{S}^t (\theta \mathbf{U}^t \mathbf{L} \mathbf{U} \theta) \mathbf{S} = \Lambda^2 \quad (50a)$$

where Λ^2 is diagonal having real, positive, and nonzero eigenvalues on its diagonal as

$$\Lambda^2 = \begin{bmatrix} \Lambda_{mG}^2 & 0 \\ 0 & \Lambda_{mR}^2 \end{bmatrix} \quad (50b)$$

and

$$\mathbf{S}^{-1} = \mathbf{S}^t \quad (50c)$$

Define a transformation matrix as

$$\mathbf{T} = \mathbf{U} \theta \mathbf{S} \quad (51)$$

In order to minimize numerical errors, we normalize the columns of \mathbf{T} to a Euclidean length of unity as

$$\mathbf{T}_{\text{norm}} = \mathbf{T} \alpha \quad (52a)$$

where α is a 2×2 diagonal matrix:

$$\alpha = \begin{bmatrix} \alpha_{mG} & 0 \\ 0 & \alpha_{mR} \end{bmatrix} \quad (52b)$$

The desired transformations are

$$\mathbf{T}_I = \mathbf{U} \theta \mathbf{S} \alpha \quad (53a)$$

$$\mathbf{T}_V = \mathbf{U} \theta^{-1} \mathbf{S} \alpha^{-1} \quad (53b)$$

In addition, these transformations have the properties

$$\begin{aligned} \mathbf{T}_I^{-1} &= \alpha^{-1} \mathbf{S}^t \theta^{-1} \mathbf{U}^t \\ &= \mathbf{T}_V^t \end{aligned} \quad (54a)$$

$$\begin{aligned} \mathbf{T}_V^{-1} &= \alpha \mathbf{S}^t \theta \mathbf{U}^t \\ &= \mathbf{T}_I^t \end{aligned} \quad (54b)$$

To show that these in fact do simultaneously diagonalize \mathbf{L} and \mathbf{C} , we form

$$\begin{aligned} \mathbf{T}_V^{-1} \mathbf{L} \mathbf{T}_I &= \alpha \mathbf{S}^t \theta \mathbf{U}^t \mathbf{L} \mathbf{U} \theta \mathbf{S} \alpha \\ &= \alpha \Lambda^2 \alpha \end{aligned} \quad (55a)$$

$$\begin{aligned} \mathbf{T}_I^{-1} \mathbf{C} \mathbf{T}_V &= \alpha^{-1} \mathbf{S}^t \theta^{-1} \mathbf{U}^t \mathbf{C} \mathbf{U} \theta^{-1} \mathbf{S} \alpha^{-1} \\ &= \alpha^{-2} \end{aligned} \quad (55b)$$

Comparing (55) to (26) shows that

$$l_{mG} = \alpha_{mG}^2 \Lambda_{mG}^2 \quad (56a)$$

$$l_{mR} = \alpha_{mR}^2 \Lambda_{mR}^2 \quad (56b)$$

$$c_{mG} = \alpha_{mG}^{-2} \quad (56c)$$

$$c_{mR} = \alpha_{mR}^{-2} \quad (56d)$$

Hence the mode characteristic impedances and velocities of propagation become

$$Z_{CmG} = \alpha_{mG}^2 \Lambda_{mG}, \quad v_{mG} = \frac{1}{\Lambda_{mG}} \quad (57a)$$

$$Z_{CmR} = \alpha_{mR}^2 \Lambda_{mR}, \quad v_{mR} = \frac{1}{\Lambda_{mR}} \quad (57b)$$

4. THE FREQUENCY-DOMAIN SOLUTION

We now consider driving the line with a single-frequency, sinusoidal source: $V_S(t) = V_S \cos(\omega t + \theta)$. It is also assumed that the line is in steady state. The solution method is the phasor method used in the analysis of electric circuits where we replace the actual source with $\hat{V}_S = V_S e^{j\theta} = V_S \angle \theta$. We will denote all complex-valued phasor quantities with a caret ($\hat{\cdot}$) over them. This phasor method stems from the fact that, according to Euler's identity [1] $V_S(t) = \text{Re}[\hat{V}_S e^{j\omega t}] = \text{Re}[V_S e^{j(\omega t + \theta)}] = V_S \cos(\omega t + \theta)$. All time derivatives are replaced by $j\omega$ since $(d/dt) \Leftrightarrow j\omega$. Hence the

time-domain MTL equations in (3) become

$$\frac{d}{dz} \hat{\mathbf{V}}(z) = -j\omega \mathbf{L} \hat{\mathbf{I}}(z) \quad (58a)$$

$$\frac{d}{dz} \hat{\mathbf{I}}(z) = -j\omega \mathbf{C} \hat{\mathbf{V}}(z) \quad (58b)$$

We can once again transform to (phasor) mode quantities as

$$\hat{\mathbf{V}} = \mathbf{T}_V \hat{\mathbf{V}}_m \quad (59a)$$

$$\hat{\mathbf{I}} = \mathbf{T}_I \hat{\mathbf{I}}_m \quad (59b)$$

We showed that transformations can be found that simultaneously diagonalize \mathbf{L} and \mathbf{C} as in (26). Substituting the transformations into (58) again yields uncoupled, first-order differential equations as in (25). Hence little has changed from the time-domain case. We can use the SPICE model employed earlier with only a change in some control statements in order to solve for the magnitude and phase of the line phasor terminal voltages and currents [1,2]. In fact, for the coupled microstrip problem in Figs. 10a and 10b, we may use the SPICE code (developed with the FORTRAN code SPICEMTL.FOR [2]) to obtain the subcircuit model of the line. Changing the source to a 1-V sinusoid and running SPICE in the AC mode yields the magnitude plot for the near-end crosstalk voltage \hat{V}_{NE} (which is the transfer function since the source value is 1V) shown in Fig. 11.

An alternative to using SPICE to generate the frequency response, referred to as the *direct method*, is as follows. First we generate second-order differential equations from (58) by differentiating one and substituting the other to yield

$$\frac{d^2}{dz^2} \hat{\mathbf{V}}(z) = \hat{\mathbf{Z}} \hat{\mathbf{Y}} \hat{\mathbf{V}}(z) \quad (60a)$$

$$\frac{d^2}{dz^2} \hat{\mathbf{I}}(z) = \hat{\mathbf{Y}} \hat{\mathbf{Z}} \hat{\mathbf{I}}(z) \quad (60b)$$

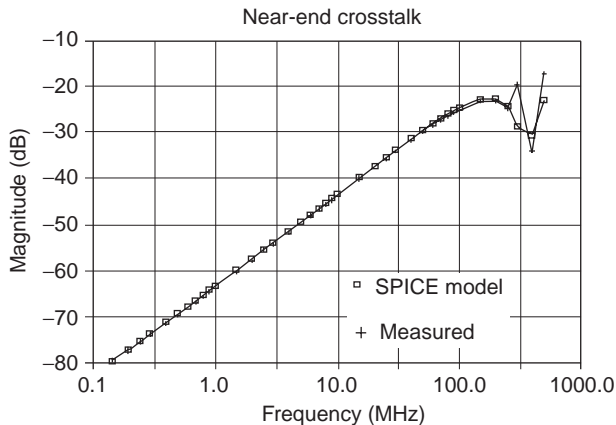


Figure 11. Predicted and experimentally measured frequency response of the near-end crosstalk.

where we have written the PUL impedance and admittance matrices compactly as

$$\hat{\mathbf{Z}} = j\omega \mathbf{L} \quad (61a)$$

$$\hat{\mathbf{Y}} = j\omega \mathbf{C} \quad (61b)$$

Again we seek to uncouple these equations by simultaneously diagonalizing the products $\hat{\mathbf{Z}} \hat{\mathbf{Y}}$ and $\hat{\mathbf{Y}} \hat{\mathbf{Z}}$. To do so, we arbitrary choose to diagonalize $\hat{\mathbf{Y}} \hat{\mathbf{Z}}$ as

$$\hat{\mathbf{T}}^{-1} \hat{\mathbf{Y}} \hat{\mathbf{Z}} \hat{\mathbf{T}} = \hat{\gamma}^2 = \begin{bmatrix} \hat{\gamma}_{mG}^2 & 0 \\ 0 & \hat{\gamma}_{mR}^2 \end{bmatrix} \quad (62)$$

Note that for a lossless line where $\hat{\mathbf{Z}}$ and $\hat{\mathbf{Y}}$ are as given by (61)

$$\hat{\mathbf{T}}^{-1} \hat{\mathbf{Y}} \hat{\mathbf{Z}} \hat{\mathbf{T}} = -\omega^2 \hat{\mathbf{T}}^{-1} \mathbf{C} \mathbf{L} \hat{\mathbf{T}} \quad (63)$$

and hence $\hat{\mathbf{T}} = \mathbf{T}_I$ and

$$\begin{aligned} \hat{\gamma}^2 &= \begin{bmatrix} -\omega^2 c_{mG} l_{mG} & 0 \\ 0 & -\omega^2 c_{mR} l_{mR} \end{bmatrix} \\ &= \begin{bmatrix} -\omega^2 / v_{mG}^2 & 0 \\ 0 & -\omega^2 / v_{mR}^2 \end{bmatrix} \end{aligned} \quad (64)$$

However, for the second-order equations in (60) there are many more choices for this transformation. For example, for a homogeneous medium, $\mathbf{L}\mathbf{C} = \mathbf{C}\mathbf{L} = (1/v^2)\mathbf{1}_2$ and the product is already uncoupled; hence we could choose $\hat{\mathbf{T}} = \mathbf{1}_2$.

Substituting the transformation

$$\hat{\mathbf{I}} = \hat{\mathbf{T}} \hat{\mathbf{I}}_m \quad (65)$$

into (60b) we obtain

$$\begin{aligned} \frac{d^2}{dz^2} \hat{\mathbf{I}}_m(z) &= \hat{\mathbf{T}}^{-1} \hat{\mathbf{Y}} \hat{\mathbf{Z}} \hat{\mathbf{T}} \hat{\mathbf{I}}_m(z) \\ &= \hat{\gamma}^2 \hat{\mathbf{I}}_m(z) \end{aligned} \quad (66)$$

whose general solution is

$$\hat{\mathbf{I}}_{mG} = \hat{\mathbf{I}}_{mG}^+ e^{-j\omega z/v_{mG}} - \hat{\mathbf{I}}_{mG}^- e^{j\omega z/v_{mG}} \quad (67a)$$

$$\hat{\mathbf{I}}_{mR} = \hat{\mathbf{I}}_{mR}^+ e^{-j\omega z/v_{mR}} - \hat{\mathbf{I}}_{mR}^- e^{j\omega z/v_{mR}} \quad (67b)$$

where the $\hat{\mathbf{I}}_{mG,R}^\pm$ are undetermined coefficients. These will be determined by the terminations of the line. Transforming to the total line currents, we obtain

$$\hat{\mathbf{I}} = \mathbf{T} (e^{-\hat{\gamma}z} \hat{\mathbf{I}}_m^+ - e^{\hat{\gamma}z} \hat{\mathbf{I}}_m^-) \quad (68a)$$

where

$$\hat{\mathbf{I}}_m^\pm = \begin{bmatrix} \hat{I}_{mG}^\pm \\ \hat{I}_{mR}^\pm \end{bmatrix} \quad (68b)$$

$$\mathbf{e}^{\pm\hat{\gamma}z} = \begin{bmatrix} e^{\pm j\omega z/v_{mG}} & 0 \\ 0 & e^{\pm j\omega z/v_{mR}} \end{bmatrix} \quad (68c)$$

The solution for the mode voltages can be obtained by substituting this into (58b):

$$\begin{aligned} \hat{\mathbf{V}}(z) &= -\hat{\mathbf{Y}}^{-1} \frac{d}{dz} \hat{\mathbf{I}}(z) \\ &= \underbrace{(\hat{\mathbf{Y}}^{-1} \hat{\mathbf{T}} \hat{\gamma} \hat{\mathbf{T}}^{-1})}_{\hat{\mathbf{Z}}_C} \hat{\mathbf{T}} (\mathbf{e}^{-\hat{\gamma}z} \hat{\mathbf{I}}_m^+ + \mathbf{e}^{\hat{\gamma}z} \hat{\mathbf{I}}_m^-) \end{aligned} \quad (69)$$

where the matrix of propagation constants is

$$\hat{\gamma} = \begin{bmatrix} j\omega/v_{mG} & 0 \\ 0 & j\omega/v_{mR} \end{bmatrix} \quad (70)$$

Note the definition of the characteristic impedance matrix $\hat{\mathbf{Z}}_C = \hat{\mathbf{Y}}^{-1} \hat{\mathbf{T}} \hat{\gamma} \hat{\mathbf{T}}^{-1}$ in (69). The characteristic impedance matrix is not diagonal. Hence, in order to “match” a MTL, we must obtain termination networks that represent this matrix rather than individually matching each line [2]. In other words, to match a MTL, we must have termination impedances between each line and the reference conductor and between each line.

The advantage of the direct method is that frequency-dependent losses can be readily incorporated into the solution. This will be discussed in Section 7. Losses cannot be readily incorporated into the SPICE model.

Alternatively, we may write the first-order equations in (58) in the form of state-variable equations commonly found in automatic control systems as well as the mathematical texts on the solution of ordinary differential equations. Hence we can draw from that enormous body of knowledge to obtain immediate solutions. We write the first-order equations in (58) as

$$\frac{d}{dz} \hat{\mathbf{X}}(z) = \hat{\mathbf{A}} \hat{\mathbf{X}}(z) \quad (71a)$$

where

$$\hat{\mathbf{X}}(z) = \begin{bmatrix} \hat{\mathbf{V}}(z) \\ \hat{\mathbf{I}}(z) \end{bmatrix} \quad (71b)$$

and

$$\hat{\mathbf{A}} = \begin{bmatrix} 0 & -\hat{\mathbf{Z}} \\ -\hat{\mathbf{Y}} & 0 \end{bmatrix} \quad (71c)$$

These are in identical form to state-variable equations [2]. The solution is well known:

$$\hat{\mathbf{X}}(L) = \hat{\Phi}(L) \hat{\mathbf{X}}(0) \quad (72a)$$

for a line of total length L that extends from $z = 0$ to $z = L$. Expanding (72a) gives

$$\begin{bmatrix} \hat{\mathbf{V}}(L) \\ \hat{\mathbf{I}}(L) \end{bmatrix} = \underbrace{\begin{bmatrix} \hat{\Phi}_{11} & \hat{\Phi}_{12} \\ \hat{\Phi}_{21} & \hat{\Phi}_{22} \end{bmatrix}}_{\hat{\Phi}(L)} \begin{bmatrix} \hat{\mathbf{V}}(0) \\ \hat{\mathbf{I}}(0) \end{bmatrix} \quad (72b)$$

This is said to be the *chain parameter matrix* of the line or the *ABCD* parameters. The chain parameter matrix $\hat{\Phi}(L)$ relates the voltages and currents at one end of the line to the voltages and currents at the other end. It is so called because a line can be broken into contiguous sections, and the overall chain parameter matrix of the entire line is the product of the chain parameter matrices of the adjacent sections (in the proper order). This is one way to represent a nonuniform line [2]. The chain parameter submatrices for a uniform line are [2]

$$\hat{\Phi}_{11}(L) = \frac{1}{2} \hat{\mathbf{Y}}^{-1} \hat{\mathbf{T}} (\mathbf{e}^{\hat{\gamma}L} + \mathbf{e}^{-\hat{\gamma}L}) \hat{\mathbf{T}}^{-1} \hat{\mathbf{Y}} \quad (73a)$$

$$\hat{\Phi}_{12}(L) = -\frac{1}{2} \hat{\mathbf{Z}}_C \hat{\mathbf{T}} (\mathbf{e}^{\hat{\gamma}L} - \mathbf{e}^{-\hat{\gamma}L}) \hat{\mathbf{T}}^{-1} \quad (73b)$$

$$\hat{\Phi}_{21}(L) = -\frac{1}{2} \hat{\mathbf{T}} (\mathbf{e}^{\hat{\gamma}L} - \mathbf{e}^{-\hat{\gamma}L}) \hat{\mathbf{T}}^{-1} \hat{\mathbf{Z}}_C^{-1} \quad (73c)$$

$$\hat{\Phi}_{22}(L) = \frac{1}{2} \hat{\mathbf{T}} (\mathbf{e}^{\hat{\gamma}L} + \mathbf{e}^{-\hat{\gamma}L}) \hat{\mathbf{T}}^{-1} \quad (73d)$$

In the general form of the solution in (68) and (69) there are four ($2n$ for a general MTL) undetermined constants in $\hat{\mathbf{I}}_m^+$ and $\hat{\mathbf{I}}_m^-$. In order to determine these undetermined constants, we need to apply the terminal constraints. With reference to Fig. 1a these are

$$\hat{\mathbf{V}}(0) = \hat{\mathbf{V}}_S - \hat{\mathbf{Z}}_S \hat{\mathbf{I}}(0) \quad (74a)$$

$$\hat{\mathbf{V}}(L) = \hat{\mathbf{Z}}_L \hat{\mathbf{I}}(L) \quad (74b)$$

where

$$\hat{\mathbf{V}}_S = \begin{bmatrix} \hat{V}_S \\ 0 \end{bmatrix} \quad (75a)$$

$$\hat{\mathbf{Z}}_S = \begin{bmatrix} R_S & 0 \\ 0 & R_{NE} \end{bmatrix} \quad (75b)$$

$$\hat{\mathbf{Z}}_L = \begin{bmatrix} R_L & 0 \\ 0 & R_{FE} \end{bmatrix} \quad (75c)$$

Substituting (68) and (69) into (74) yields [2]

$$\begin{bmatrix} (\hat{\mathbf{Z}}_C + \hat{\mathbf{Z}}_S) \hat{\mathbf{T}} & (\hat{\mathbf{Z}}_C - \hat{\mathbf{Z}}_S) \hat{\mathbf{T}} \\ (\hat{\mathbf{Z}}_C - \hat{\mathbf{Z}}_L) \hat{\mathbf{T}} \mathbf{e}^{-\hat{\gamma}L} & (\hat{\mathbf{Z}}_C + \hat{\mathbf{Z}}_L) \hat{\mathbf{T}} \mathbf{e}^{\hat{\gamma}L} \end{bmatrix} \begin{bmatrix} \hat{\mathbf{I}}_m^+ \\ \hat{\mathbf{I}}_m^- \end{bmatrix} = \begin{bmatrix} \hat{\mathbf{V}}_S \\ 0 \end{bmatrix} \quad (76)$$

Solving (76) for the four undetermined constants and substituting into (68) and (69) gives the solution for the line voltages and currents at any point along the line.

Reference 2 contains a description of the FORTRAN code MTL.FOR, which (1) diagonalizes $\hat{\mathbf{Y}}\hat{\mathbf{Z}}$ according to Eq. (62), (2) forms and solves Eq. (76), and (3) substitutes into Eqs. (68) and (69) to obtain the phasor terminal voltages. This code can be obtained from ftp://ftp.wiley.com/public/sci_tech_med/multiconductor_transmission/.

5. APPROXIMATE, LUMPED-CIRCUIT MODELS OF MTLs

If the line is electrically short at the highest frequency of the source, say, $L < \frac{1}{10}\lambda$, where $\lambda = v/f$ denotes a wavelength, then the line can be approximated with a lumped-circuit model and the solution of the MTL equations is bypassed. A useful such model is the so-called lumped- π model shown in Fig. 12. This name is in reference to its resemblance to the symbol π . The capacitances are split to give the circuit a reciprocal property. For the periodic, trapezoidal waveform with rise/falltimes τ_r/τ_f representing a digital signal, the highest significant frequency is approximately [2] $f_{\max} = 1/\tau_r$, where we assume the rise/falltimes to be equal. For example, for the 10-MHz pulsetrain with 5-ns rise/falltimes, which we have been investigating and shown in Fig. 10b, the maximum frequency is approximately 200 MHz. The total line length of 20 cm is $\frac{1}{4.44}\lambda$, where we have calculated the velocity of propagation as 1.777×10^8 m/s using an effective relative permittivity as the average of the board ($\epsilon_r = 4.7$) and air giving $\epsilon'_r = 2.85$. Figure 13a shows a comparison between the SPICE model and this lumped- π model for the source waveform in Fig. 10b. Some inaccuracy is caused by the inability of the lumped- π model to correctly process the high-frequency components of the source waveform. Figure 13b shows a similar comparison for the frequency response. Here we again see that the comparison is good up to only about 100 MHz, where the line length of 20 cm is about $\frac{1}{9}\lambda$.

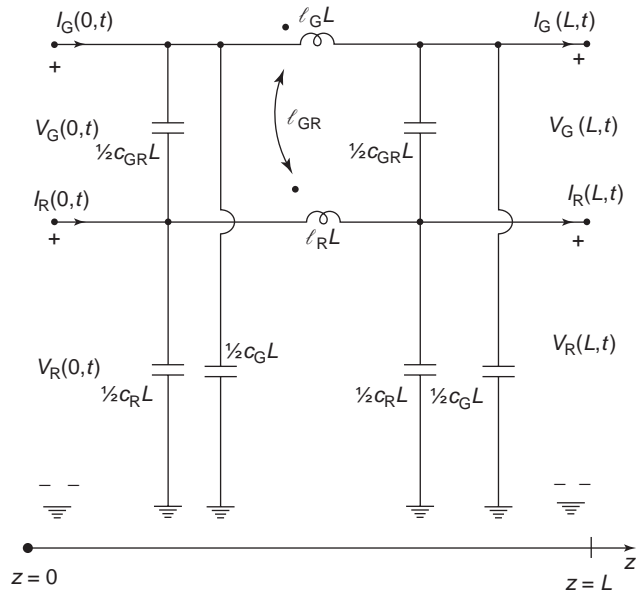


Figure 12. The lumped- π approximate model of the MTL.

6. CLOSED-FORM SOLUTIONS

In the previous discussions, the solution of the MTL equations in the time and frequency domains was obtained via numerical solution. There are some important cases where the solution of the MTL equations can be obtained in literal form (with symbols as opposed to numbers). These are (1) a three-conductor line ($n=2$) in a homogeneous medium and (2) a three-conductor line in an inhomogeneous medium assuming weak coupling.

For the case of a three-conductor line ($n=2$) in a homogeneous medium, the chain parameter submatrices in (73) simplify to [2]

$$\hat{\Phi}_{11}(L) = C\mathbf{1}_2 \tag{77a}$$

$$\hat{\Phi}_{12}(L) = -j\omega S\mathbf{L}\mathbf{L} \tag{77b}$$

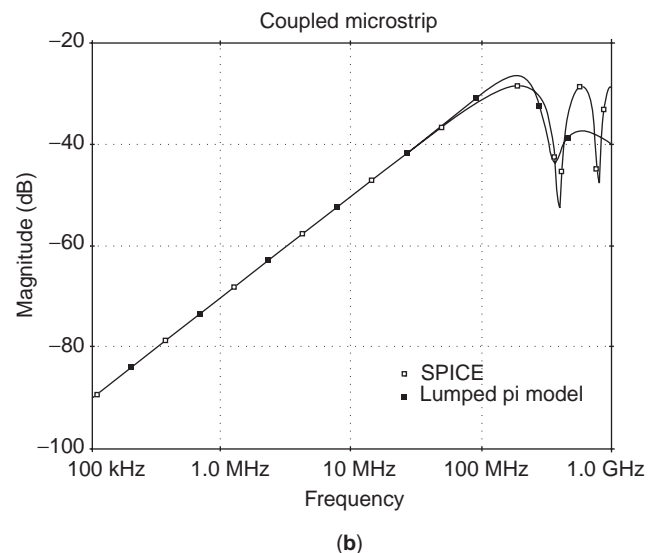
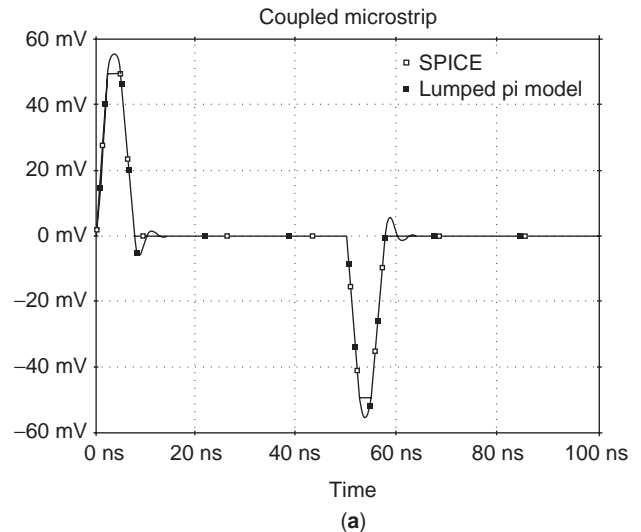


Figure 13. Comparison of the exact SPICE predictions to those of the lumped- π approximate model for the near-end crosstalk of the configuration of Figure 10; (a) time domain crosstalk, and (b) frequency response of the crosstalk.

$$\hat{\Phi}_{21}(L) = -j\omega SCL \quad (77c)$$

$$\hat{\Phi}_{22}(L) = C\mathbf{1}_2 \quad (77d)$$

where $\mathbf{1}_2$ is the 2×2 identity matrix and

$$C = \cos\left(2\pi \frac{L}{\lambda}\right) \quad (78a)$$

$$S = \frac{\sin\left(2\pi \frac{L}{\lambda}\right)}{2\pi \frac{L}{\lambda}} \quad (78b)$$

The velocity of propagation in this homogeneous medium is

$$v = \frac{1}{\sqrt{\mu\epsilon}} \quad (79)$$

and a wavelength is defined by

$$\lambda = \frac{v}{f} \quad (80)$$

The terminal conditions in (74) were incorporated, and the exact literal solutions for the near-end and far-end phasor voltages are [2]

$$\hat{V}_{NE} = \frac{S}{Den} [j\omega M_{NE}C + (j\omega)^2 TK_{NE}S] \hat{V}_S \quad (81a)$$

$$\hat{V}_{FE} = \frac{S}{Den} [j\omega M_{FE}] \hat{V}_S \quad (81b)$$

where

$$Den = C^2 + (j\omega)^2 S^2 \tau_G \tau_R P + j\omega CS(\tau_G + \tau_R) \quad (81c)$$

The various quantities in these expressions are defined by

$$M_{NE} = M_{NE}^{IND} + M_{NE}^{CAP} \quad (82a)$$

$$M_{FE} = M_{FE}^{IND} + M_{FE}^{CAP} \quad (82b)$$

$$M_{NE}^{IND} = \frac{R_{NE}}{R_{NE} + R_{FE}} l_{GR} L \frac{1}{R_S + R_L} \quad (82c)$$

$$M_{FE}^{IND} = -\frac{R_{FE}}{R_{NE} + R_{FE}} l_{GR} L \frac{1}{R_S + R_L} \quad (82d)$$

$$M_{NE}^{CAP} = M_{FE}^{CAP} = \frac{R_{NE} R_{FE}}{R_{NE} + R_{FE}} c_{GR} L \frac{R_L}{R_S + R_L} \quad (82e)$$

and

$$K_{NE} = M_{NE}^{IND} \frac{1}{\sqrt{1-k^2}} \frac{1 + \Gamma_{LG}}{1 - \Gamma_{LG}} \quad (82f)$$

where the superscripts ‘‘IND’’ and ‘‘CAP’’ denote inductive and capacitive, respectively, since those terms involve mutual inductance and mutual capacitance. The coupling coefficient between the two circuits is defined as

$$k = \frac{l_{GR}}{\sqrt{l_G l_R}} \quad (83)$$

the line one-way time delay is

$$T = \frac{L}{v} \quad (84)$$

and the reflections coefficients are

$$\Gamma_{SG} = \frac{R_S - Z_{CG}}{R_S + Z_{CG}} \quad (85a)$$

$$\Gamma_{LG} = \frac{R_L - Z_{CG}}{R_L + Z_{CG}} \quad (85b)$$

$$\Gamma_{SR} = \frac{R_{NE} - Z_{CR}}{R_{NE} + Z_{CR}} \quad (85c)$$

$$\Gamma_{LR} = \frac{R_{FE} - Z_{CR}}{R_{FE} + Z_{CR}} \quad (85d)$$

and the circuit characteristic impedances are defined by

$$Z_{CG} = v l_G \sqrt{1 - k^2} \quad (86a)$$

$$Z_{CR} = v l_R \sqrt{1 - k^2} \quad (86b)$$

The factor P in Den defined by

$$P = \left[1 - k^2 \frac{(\Gamma_S + \Gamma_{FE})(\Gamma_L + \Gamma_{NE})}{(1 + \Gamma_S \Gamma_L)(1 + \Gamma_{NE} \Gamma_{FE})} \right] \quad (87)$$

The circuit time constants are defined by

$$\tau_G = \frac{T}{\sqrt{1-k^2}} \frac{1 + \Gamma_S \Gamma_L}{1 - \Gamma_S \Gamma_L} \quad (88a)$$

$$\tau_R = \frac{T}{\sqrt{1-k^2}} \frac{1 + \Gamma_{NE} \Gamma_{FE}}{1 - \Gamma_{NE} \Gamma_{FE}} \quad (88b)$$

6.1. The Inductive/Capacitive Coupling Model

If the line is electrically short ($L \ll \lambda$), the terms C and S in (78) reduce to unity: $C \cong S \cong 1$. In addition, if the line is weakly coupled ($k \ll 1$), then P in Den becomes unity, $P = 1$.

These results simplify to [4]

$$\hat{V}_{NE} = j\omega \left[\underbrace{\frac{R_{NE}}{R_{NE} + R_{FE}} l_{GR} L \frac{1}{R_S + R_L}}_{\text{inductive coupling}} + \underbrace{\frac{R_{NE} R_{FE}}{R_{NE} + R_{FE}} c_{GR} L \frac{R_L}{R_S + R_L}}_{\text{capacitive coupling}} \right] \hat{V}_S \quad (89a)$$

$$\hat{V}_{FE} = j\omega \left[\underbrace{-\frac{R_{NE}}{R_{NE} + R_{FE}} l_{GR} L \frac{1}{R_S + R_L}}_{\text{inductive coupling}} + \underbrace{\frac{R_{NE} R_{FE}}{R_{NE} + R_{FE}} c_{GR} L \frac{R_L}{R_S + R_L}}_{\text{capacitive coupling}} \right] \hat{V}_S \quad (89b)$$

Observe that the frequency response has a phase of $\pm 90^\circ$ and the magnitude increases linearly with frequency (20 dB/decade). This behavior is evidenced in the lower frequencies of the transfer function in Figs. 11 and Fig. 13b. These results can be derived from the simple equivalent circuit shown in Fig. 14.

A simple time-domain extension of these results can be obtained by noting the equivalence

$$j\omega \Leftrightarrow \frac{d}{dt} \quad (90)$$

Hence the frequency-domain results in (89) become, in the time domain

$$V_{NE}(t) = \left[\underbrace{\frac{R_{NE}}{R_{NE} + R_{FE}} l_{GR} L \frac{1}{R_S + R_L}}_{\text{inductive coupling}} + \underbrace{\frac{R_{NE} R_{FE}}{R_{NE} + R_{FE}} c_{GR} L \frac{R_L}{R_S + R_L}}_{\text{capacitive coupling}} \right] \frac{dV_S(t)}{dt} \quad (91a)$$

$$V_{FE}(t) = \left[\underbrace{-\frac{R_{FE}}{R_{NE} + R_{FE}} l_{GR} L \frac{1}{R_S + R_L}}_{\text{inductive coupling}} + \underbrace{\frac{R_{NE} R_{FE}}{R_{NE} + R_{FE}} c_{GR} L \frac{R_L}{R_S + R_L}}_{\text{capacitive coupling}} \right] \frac{dV_S(t)}{dt} \quad (91b)$$

Hence the time-domain crosstalk voltages depend on the instantaneous slope of the source voltage waveform.

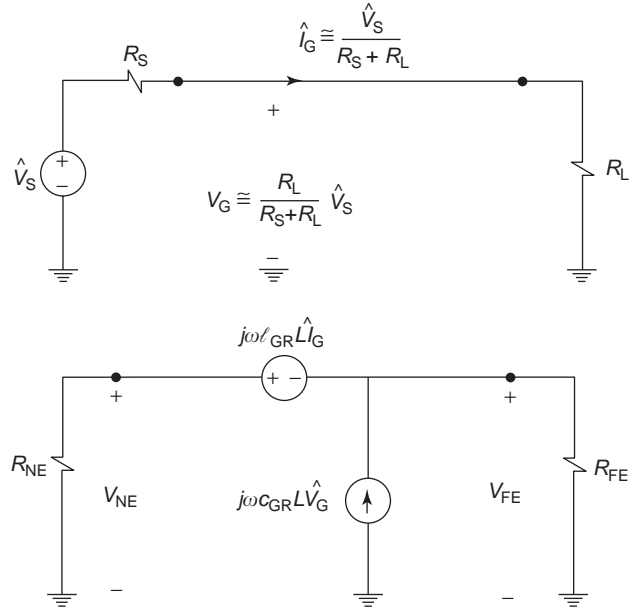


Figure 14. The inductive-capacitive coupling model for weakly coupled, electrically short lines.

Hence, the crosstalk occurs during the transition (rise/falltimes) of the pulse waveform as illustrated in Fig. 15. For the situation in Fig. 10, this model predicts that the crosstalk pulses would have magnitude of 49 mV and the full SPICE exact model predicts a level of 50 mV. Hence, the structure in Fig. 10a is evidently “weakly coupled.”

This previous exact literal solutions were for a homogeneous medium. If we relax this requirement, we can obtain the literal solution for an inhomogeneous medium. However, the solution is quite complicated, and in order to make it feasible, we must assume weak coupling from the outset. The reader is referred to Ref. 5 for the details of that solution.

7. INCORPORATION OF LOSSES

The previous results have ignored losses. Losses occur in the finite, nonzero conductor resistance and in the nonzero conductivity of the surrounding medium. Typically at frequencies in the low-GHz range, the losses in the surrounding dielectric are negligible. As operating frequencies of digital and analog systems continue to increase, this may no longer be true. The losses in the conductors are due to the finite nonzero conductivity of the conductor material. In addition, when the conductor cross-sectional dimensions become on the order of a skin depth, the current crowds to the conductor surfaces and the PUL resistance increases as the square root of frequency, \sqrt{f} (see Ref. 2 for computed resistances vs. frequency for wires and PCB lands). The conductors possess, in addition to a PUL resistance r , an internal PUL inductance l_{int} , due to magnetic flux internal to the conductor, which decreases as the square root of frequency.

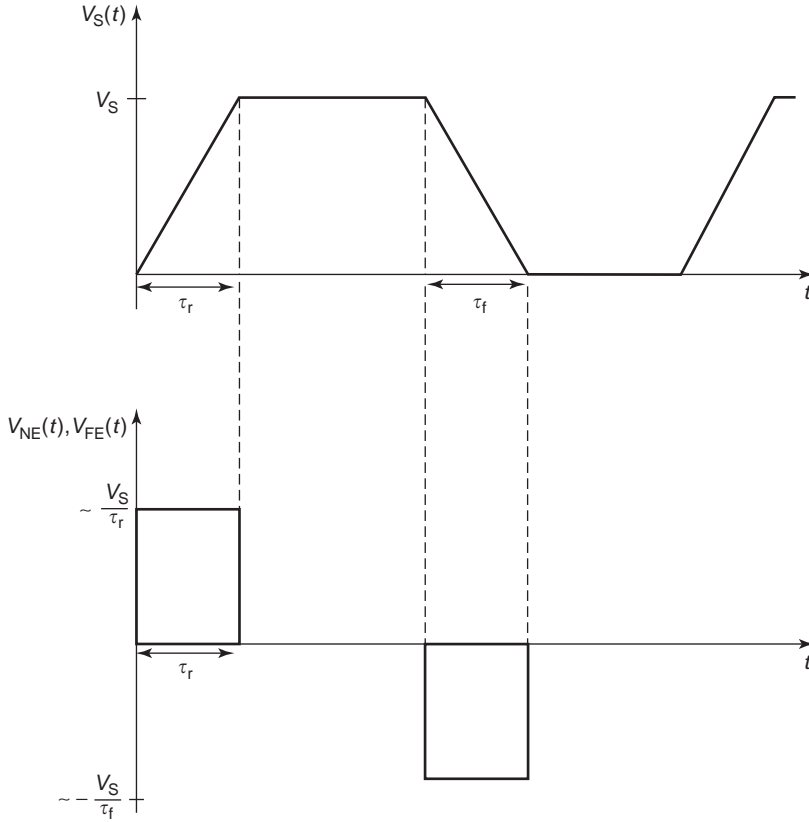


Figure 15. Time-domain crosstalk predictions of the inductive-capacitive coupling model for weakly coupled, electrically short lines.

The MTL equations with losses included can be written in the frequency domain as

$$\frac{d}{dz} \hat{\mathbf{V}}(z) = -\hat{\mathbf{Z}}(\omega) \hat{\mathbf{I}}(z) \quad (92a)$$

$$\frac{d}{dz} \hat{\mathbf{I}}(z) = -\hat{\mathbf{Y}}(\omega) \hat{\mathbf{V}}(z) \quad (92b)$$

where

$$\hat{\mathbf{Z}}(\omega) = \mathbf{R}(\omega) + j\omega \mathbf{L}_{\text{int}}(\omega) + j\omega \mathbf{L} \quad (93a)$$

$$\hat{\mathbf{Y}}(\omega) = \mathbf{G}(\omega) + j\omega \mathbf{C} \quad (93b)$$

The matrices \mathbf{R} and \mathbf{L}_{int} contain the conductor losses, while the matrix \mathbf{G} contains the losses in the surrounding medium. The PUL parameter matrices \mathbf{L} and \mathbf{C} remain as before. The frequency-domain or phasor solution for sinusoidal steady-state excitation of the line can be solved using the direct method of Section 4. Those results were written in terms of a general $\hat{\mathbf{Z}}$ and $\hat{\mathbf{Y}}$, and the method is unchanged when losses are added to the MTL equations as in (92) and (93). We must now find a transformation that diagonalizes the product $\hat{\mathbf{Y}}(\omega)\hat{\mathbf{Z}}(\omega)$ as in (62). This is a straightforward problem and is computed in the FORTRAN code MTL.FOR described in Ref. 2. However, here the diagonalization is frequency-dependent [$\hat{\mathbf{T}}(\omega)$] and must be repeated at each frequency. Nevertheless, the re-

maining solution process is identical to that described in Section 4.

Incorporation of losses into the time-domain solution is much more difficult and is the subject of much present research. If we represent (92) via the Laplace transform, where s represents the Laplace transform variable, we have

$$\frac{d}{dz} \mathbf{V}(z, s) = -\mathbf{Z}(s) \mathbf{I}(z, s) \quad (94a)$$

$$\frac{d}{dz} \mathbf{I}(z, s) = -\mathbf{Y}(s) \mathbf{V}(z, s) \quad (94b)$$

If we can find the inverse Laplace transform of $\mathbf{Z}(s)$ and $\mathbf{Y}(s)$ as $\mathbf{z}(t)$ and $\mathbf{y}(t)$, then Eqs. (94) become, in the time domain

$$\frac{d}{dz} \mathbf{V}(z, t) = -\mathbf{z}(t) * \mathbf{I}(z, t) \quad (95a)$$

$$\frac{d}{dz} \mathbf{I}(z, t) = -\mathbf{y}(t) * \mathbf{V}(z, t) \quad (95b)$$

where $*$ denotes convolution. The requirement for performing convolution in the time domain can be mathematically intensive. A method known as *recursive convolution* provides a computationally efficient implementation [2]. One of the more popular ways of inc-

orporating losses into the time-domain solution is to use the finite-difference, time-domain (FDTD) method [2]. The MTL equations are discretized in space and time, and a bootstrapping method of solution is implemented [2]. The recursive convolution method for implementing losses fits the FDTD method very well. See Ref. 2 for a description of this method.

8. SUMMARY

We have investigated the solution of the transmission-line equations for multiconductor transmission lines (MTLs). The discussion concentrated on lossless lines. Numerical methods for determining the per unit length (PUL) parameter matrices \mathbf{L} and \mathbf{C} , which contain the line PUL inductances and capacitances were discussed. All cross-sectional dimensions that distinguish one line from another are contained in these parameter matrices. Solution of the MTL equations without the solution for the PUL parameter matrices would be a waste of time. An exact time-domain SPICE model for lossless MTLs was developed according to the ability to decouple the MTL equations. This SPICE model could also be used to compute the frequency-domain solution for the terminal voltages and currents. The frequency-domain solution can also be directly obtained by decoupling the MTL equations. Finally, some important classes of weakly coupled lines allow closed-form, literal solutions. These literal solutions allow considerable insight into the coupling mechanism, whereas a numerical solution does not give this insight.

BIBLIOGRAPHY

1. C. R. Paul, *Electromagnetics for Engineers: with Applications to Digital Systems and Electromagnetic Interference*, Wiley, Hoboken, NJ, 2004.
2. C. R. Paul, *Analysis of Multiconductor Transmission Lines*, Wiley-Interscience, New York, 1994.
3. C. R. Paul, Decoupling the multiconductor transmission line equations, *IEEE Trans. Microwave Theory Tech.* **44**(8):1429–1440 (Aug. 1996).
4. C. R. Paul, *Introduction to Electromagnetic Compatibility*, Wiley-Interscience, New York, 1992.
5. C. R. Paul, Solution of the transmission-line equations under the weak-coupling assumption, *IEEE Trans. Electromagn. Compat.* **EMC-44**(3):413–423 (Aug. 2002).

CRYOGENIC ELECTRONICS

A. R. JHA
JHA Technical Consulting
Services
Cerritos, California

1. INTRODUCTION

Integration of cryogenic electronics involving high-temperature superconductor (HTS) technology or low-temper-

ature superconductor (LTS) technology in conjunction with microstrip circuit technology has created a new class of low-loss microwave, MM-wave, and infrared (IR) components for possible applications in high-performance commercial, industrial, military, and space systems. Planar microstrip HTS circuits and cryogenically cooled microwave and MM-wave devices have demonstrated significant performance improvements in insertion loss, reliability, power consumption, and packaging. A variety of HTS and LTS microwave and MM-wave components such as thin-film bandpass filters (BPFs), high- Q resonators, high-quantum-efficiency laser diodes, precision solid-state phase shifters, low-noise GaAs MESFET and HEMT amplifiers, low-phase-noise solid-state MM-wave sources, and IR focal planar arrays (FPAs) have been developed with minimum power consumption, high reliability, high device efficiency, and stable performance over wide instantaneous bandwidth. Significant performance improvement in widely used cryogenic electronic and RF components or devices will be identified with particular emphasis on reliability, power consumption, and cost. Integration of cryogenic electronic technology will result in cost-effective design of satellite communication systems, terrestrial communication equipment, missile guidance sensors, unmanned air vehicles (UAVs), high-altitude reconnaissance drones, underwater sonar transmitters, high-power missile tracking radars, and space-based IR surveillance sensors.

Studies performed by the author indicate that integration of cryogenic electronic (CE) technology offers the potential of a 10-fold miniaturization of payload electronic equipment, leading to significant reduction in cost and rapid development of small or microsatellite systems. The studies further indicate that the major system cost is due to the cryogenic cooler required to maintain a specified operating temperature within the system. Performance capabilities and limitations of potential cryogenic coolers and microcoolers are briefly summarized. Applications of cryogenic electronics in various commercial, industrial, military, and space systems will be described identifying significant performance improvements. Performance capabilities and limitations of CE devices are identified wherever applicable.

2. CE TECHNOLOGY FOR COMMUNICATION AND SPACE SYSTEMS

Recent (as of 2004) studies indicate that record-level performance improvements have been observed in cryogenically cooled electronic switches, laser diodes, RF/IR detectors, GaAs amplifiers, Josephson driver circuits, ADCs, low-noise mixers, thin-film tunable filters, and other RF and MM-wave devices. Furthermore, research and development (R&D) activities are vigorously pursued to demonstrate the feasibility of cryogenic electronics, including both HTS and LTS devices, in satellite communication systems, base transceiver stations (BTSs) for terrestrial mobile communication, medical diagnostic equipment, and space sensors. Deployment of noise reduction filter technology for spatial and spectral filtering and

input multiplexing channel filters in the front end of the multicarrier BTS receiver (Fig. 1) will result in significant improvement in power consumption, channel isolation, skirt selectivity, insertion loss, and overall system reliability. Integration of fast switching filters in the system will introduce the antijam capability to a satellite communication (satcom) system, thereby providing the most effective and secured communication capability required by law enforcement agencies.

Cryogenic electronic (CE) components or devices have been deployed in a 60-channel HTS multiplexer that duplicates the requirements of the Intelsat-8 satellite communication system and in a Ka-band beam link subsystem that defines the critical requirements of the multimedia satellite communication system. In addition, the use of CE components in the HTS-satellite communication system provides reduction in launch cost, increase in payload capacity, improvement in noise figure and receiver figure-of-merit (G/T), increase in ground station effective radiated power, reduction in antenna size, improved gain margin

needed under rainy and fading conditions, reduction in prime power requirements, and smaller satellite bus architecture due to miniaturization provided by the cryogenic electronic technology. These CE components are best suited for deployment in second- and third-generation BTS-based digital mobile communication systems capable of providing GSM and wideband CDMA (WCDMA) capabilities. The BTS transceiver architecture shown in Fig. 1 permits several cryogenic electronic components including the ADC devices, BPFs, preselectors, preamplifiers (LNAs), and mixers to share a common cooling system, leading to significant reduction in operating cost and system weight.

2.1. Cryogenically Cooled Analog-to-Digital Converter (ADC) Devices

Superconducting ADC architectures using rapid single-quantum-flux (RSQF) technology are best suited for military systems that demand excellent linearity of 16 bits or

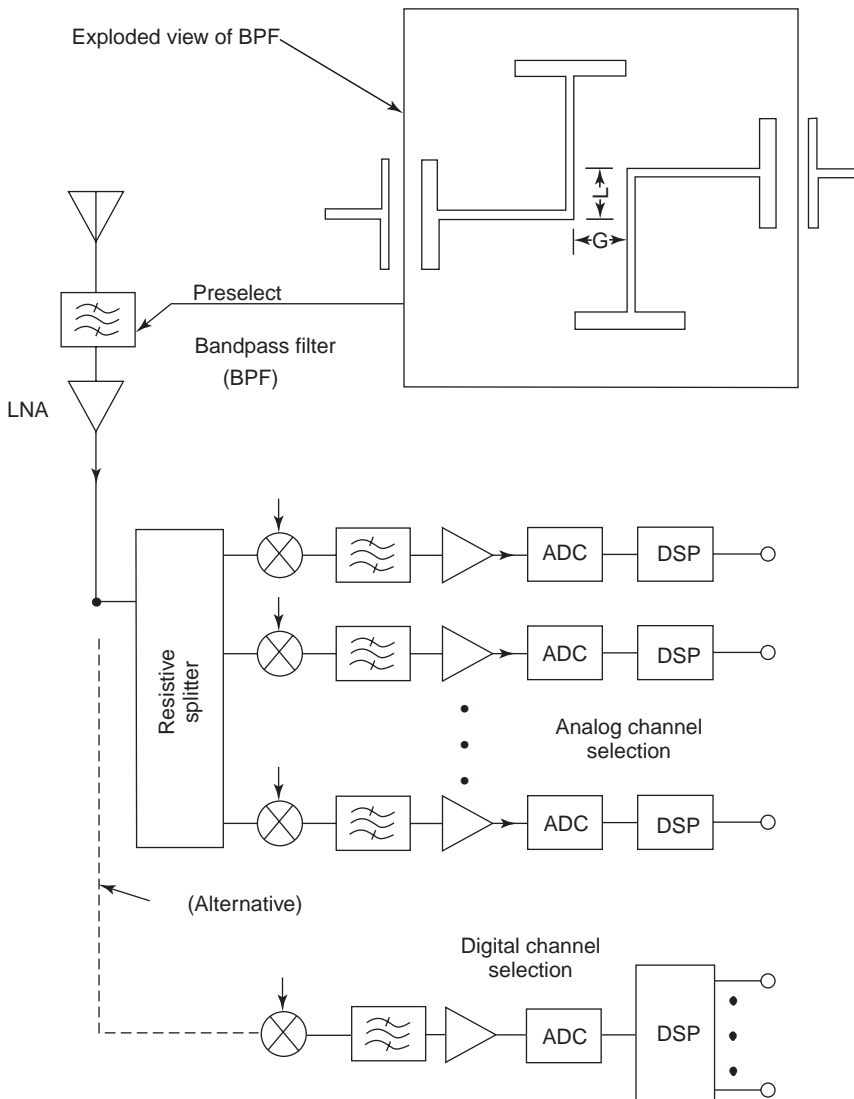


Figure 1. Cryogenic electronic components for applications in communication satellites and base transceiver stations (BTSs) for terrestrial mobile communications.

more, spurious-free dynamic range greater than 78 dB, and third-order intermodulation products better than 65 dB. An innovative ADC design developed by Hpress Corp. (NY) for a 10-bit ADC unit consisting of more than 800 Josephson junction (JJ) devices has demonstrated a dynamic range equivalent to that of a 14-bit ADC, while operating at a cryogenic temperature of 4.2 K. An ADC design with LTS microelectronic technology offers high sensitivity, improved reliability, high resolution, wide instantaneous bandwidth, and power consumption as low as 5 mW/chip at 4.2 K. Further improvement in dynamic range and instantaneous bandwidth in an ADC can be achieved through a combination of oversampling and flux quantization feedback techniques. It is important to point out that superconducting ADC design based on LTS technology at 4.2 K appears to be the only way to achieve simultaneously low aperture time, high internal clock frequency, high data rate, lowest power consumption, and optimum accuracy.

2.2. Cryogenically Cooled Microwave and MM-Wave Mixers

Superconducting microwave and MM-wave mixers using JJ devices and stable solid-state sources have demonstrated sensitivities better than -90 dBm/MHz over a 10–13 GHz frequency range, including the losses in the microwave structures. Performance requirements for microwave mixers are not stringent compared to those for MM-wave mixers. Lower noise figure, conversion loss, and LO (local-oscillator) power requirement are possible only at lower cryogenic temperatures. Typical noise figure and LO power requirements for MM-wave mixers as a function of cryogenic temperature are summarized in Table 1.

The data in Table 1 indicate that the LO power requirement is reduced by a factor of 3 and the noise figure (NF) is reduced close to 2 dB when the mixer is operated at 77 K. It is important to mention that lower noise figure and higher gain are possible from superconductor–insulator–superconductor (SIS) mixers employing LTS Nb-based tunnel junctions in waveguide cavities integrated with SIS chips. SIS mixers are widely used at sub-millimeter-wave frequencies exceeding 200 GHz. Note that an SIS mixer using Josephson junction (JJ) devices has to be biased above a specified threshold voltage to avoid instabilities caused by the Josephson currents at low bias levels. Furthermore, lowest LO power (~ 1 nW) is required for a single-junction SIS mixer, thereby making this mixer design most cost-effective. SIS mixers are limited to small-signal applications and have instantaneous bandwidth of < 3 GHz, which is adequate for astronomic applications but insufficient for radar and communications systems.

Table 1. Noise Figure and LO Power as a Function of Cryogenic Temperature

Frequency (GHz)	300 K		77 K	
	NF (dB)	LO Power (dBm)	NF (dB)	LO Power (dBm)
75–110	5.08	0.60	2.68	0.20
90–140	5.51	0.62	3.06	0.22
110–170	6.12	0.73	3.44	0.25
140–220	6.45	0.92	4.10	0.32

2.3. Cryogenically Cooled Low-Noise Amplifier (LNA)

Significant performance improvements have been achieved by lowering the operating temperature (T) of the RF and MM-wave amplifiers, regardless of whether the amplifiers use GaAs MESFET or AlGaAs HEMT or Si HBT devices. Optimum improvement in performance has been observed at lower cryogenic temperatures as illustrated by data summarized in Tables 2–4.

All the data summarized in Tables 2–4 demonstrate that lower operating temperatures yield significant improvement in gain, noise figure (NF), power-added efficiency, and power consumption. Note the gain of the amplifier is also dependent on the bias level. Furthermore, in all solid-state amplifiers higher gain is possible with higher values of transconductance and lower gate and source resistances. Furthermore, integration of feedback technique tends to minimize gain fluctuations over the band of interest. In a C-band GaAs LNA, significant improvement is observed when the operating temperature is reduced to 4.2 K. In a C-band amplifier operating over the 3200–4200 MHz region, noise figures as low as 1.2, 0.62, and 0.32 dB have been observed at operating temperatures of 300, 77, and 4.2 K, respectively.

2.4. Cryogenically Cooled Microwave Filters and Their Applications

In all satellite communications systems, channel filters play a key role in performance optimization. These filters are required to meet stringent passband and stopband performance requirements. In these filters, sharp skirt selectivity is of critical importance. The multipole self-equalized, quasielliptic HTS planar filter configuration is best suited to satisfy the required performance specifications. The most efficient and cost-effective way to realize both the elliptic function response and the self-realization is to use a dual-mode resonator configuration as shown in

Table 2. Performance Improvement in GaAs MESFET Amplifiers

T (K)	Wideband Amplifier (8–18 GHz)		Narrowband Amplifier (9.5–10.5 GHz)	
	Gain (dB)	NF (dB)	Gain (dB)	NF (dB)
300	22	2.08	23	1.25
200	24	1.59	26	0.98
77	27	0.87	29	0.35
10	29	0.73	32	0.26

Table 3. Performance Improvement in Pseudomorphic HEMT Amplifiers

Parameter	12 GHz Amplifier		18 GHz Amplifier	
	300 K	20 K	300 K	20
Gain (dB)	7	12	5	11
Noise figure (dB)	2.8	0.59	3.7	0.97
Power required (mw)	68	45	93	63

Fig. 1. This resonator configuration allows coupling between the nonadjacent resonators with minimum complexity. Dual-mode patch resonators have been used to design HTS filters with elliptic response in the passband. However, elimination of undesired coupling between the various resonator elements is a serious design problem. This problem can be overcome by using a lumped-element HTS filter with a basic resonator configuration as illustrated in Fig. 1. This resonator configuration permits easy control of coupling between the two modes by adjusting the spacing G and the offset parameter L . In brief, this resonator configuration allows ease of realization and controlling the cross-coupling between the resonators, which is necessary to achieve both the quasielliptic and self-equalization functions with minimum cost and complexity. The 10-pole self-equalized input channel filter using the dual-mode resonator configuration is an integral part of the multichannel HTS multiplexer subsystem. This filter design can be integrated with an input circulator for channel dropping and output isolator to isolate the filter from backreflections. The drop-in ferrite components are fully qualified to operate at cryogenic temperatures. Such a filter designed for operation in a C-band satellite communication system exhibited low insertion loss, symmetric bandpass response, and sharp skirt selectivity.

Significant improvement in mass reduction of electronics payload and satellite mission life has been observed due to integration of cryogenic electronic technology in the satellite communication systems. In a 60-channel multimedia satellite design, a mass reduction of 10 kg and mission life extension of 2 years are noted because of the integration of cryogenic electronic technology-based components.

It is important to mention that performance requirements such as insertion loss, instantaneous bandwidth, stopband rejection, and in-band phase linearity for microwave filters vary from application to application. In general, filter performance requirements for military and space systems are more stringent in terms of weight, size, and reliability. These requirements dictate the filter design parameters for the architecture and resonators

Table 4. Power-Added Efficiency (%) for HBT Amplifiers Operating at X Band

T (K)	Common-base Design	Common-Emitter Design
300	31	43
77	43	55

best suited for the architecture selected. In case of satellite communications filters, microstrip or stripline or coplanar waveguide resonator structures could meet the performance requirements with minimum cost and complexity. Long-dispersive-HTS, tapped-delay-line chirp filters are most attractive for use in wideband compressive receivers. Long-dispersive-HTS, tapped-delay-line chirp filters fabricated from HTS thin films of yttrium barium calcium oxide (YBCO) on magnesium oxide (MgO) substrate or lanthanum aluminate (LaAlO_3) are best suited for military warfare applications, where high sensitivity is of critical importance for spectral analysis and remote sensing. In case of satellite communications and terrestrial mobile communications, miniature superconducting filters with unique filter geometry, minimum size, low insertion loss, excellent skirt selectivity, linear phase response over wideband, and maximum stopband rejection are considered the most desirable features.

Optimum filter performance requires low insertion loss and high resonator Q_0 (unloaded Q), which are possible only at lower cryogenic operations. A superconducting filter design using a thin film of YBCO on MgO substrate demonstrated a stopband rejection of -40 dB at 86 K, -60 dB at 77 K, and -80 dB at 15 K. The same filter while operating at 5 GHz demonstrated a reduction in insertion loss by 2% at 77 K, 16% at 15 K, and 35% at 4.2 K operation. A 60-channel superconducting multiplexer integrated with pulsetube cryocooler and 10-pole channel filters using HTS planar structures has demonstrated a reduction in mass of $>50\%$ and in size of $>65\%$ using HTC YBCO film on LaAlO_3 substrate.

2.4.1. Resonator Requirements for Nb-Based and YBCO-Based Filters. Printed circuit resonator, microstrip resonator, and coplanar technologies will provide significant reduction in insertion loss, weight, and size when cooled down to lower cryogenic temperatures. Studies performed by the author on microwave filters indicate that significant reduction in insertion loss can be realized using HTS YBCO-based (77-K) or LTS Nb-based (4.2-K) filter elements. Resonator parameters can be selected to meet specific system performance requirements. The resonators described above have demonstrated unloaded Q (Q_0) greater than 150,000 at 10 GHz, a bandwidth in excess of 10,000 MHz, amplitude accuracy of 0.05 dB, and filter passband loss of <1.65 dB at 77 K temperature. Filter performance characteristics are strictly dependent on resonator type and its unloaded Q , substrate parameters, and the operating temperature. Resonators with higher electrical conductivity, with polished and even surfaces tend to offer higher unloaded Q_0 . Higher the Q_0 , the lower will be the insertion loss and the sharper will be the skirt selectivity. However, all these benefits come with additional cost, size, weight, and complexity.

2.4.1.1. Unloaded Q for Resonators. Superconducting filter resonators must use appropriate substrate technology for the deposition of the thin film of superconducting compound materials, namely, yttrium barium calcium oxide (YBCO) compound on low-loss magnesium oxide (MgO) or lanthanum aluminate substrate (LaAlO_3) for

77 K operation. Nb-based alloy films must be deposited on sintered-alumina substrate (Al_2O_3) to achieve best performance at 4.2 K operation. The low-temperature Nb-based resonators demonstrated a Q close to 10^6 at 14.5 GHz frequency when operating at a cooling temperature between 4.2 and 1.8 K. Computed values of unloaded Q of resonators made from YBCO thin films on lanthanum aluminate substrate and Nb-based films on alumina substrate as a function of frequency are summarized in Table 5.

The computations listed in Table 5 indicate that the higher the operating frequency, the lower will be the unloaded Q and the lower the cryogenic temperature, the higher will be the Q_0 . Unloaded Q_0 of the resonator is dependent on the operating frequency, cryogenic temperature, superconductor film properties, substrate thickness, surface conditions of the film, and RF surface resistance of the film. The unloaded Q of a superconducting microstrip is dependent on the operating frequency and cryogenic temperature and can be defined as

$$Q_0 = [(0.00395)(f)(h)/R_s] \quad (1)$$

where f is the operating frequency (GHz), h is the dielectric substrate thickness (μm), and R_s is the surface resistance of the superconducting thin film (Ω). Assuming a surface resistance of $10^{-7} \Omega$ at 4.2 K for a 10- μm LTS niobium (Nb) film deposited on silicon substrate, the unloaded Q comes to 3.9×10^5 at 1 GHz frequency. HTS resonators have potential applications in fixed-tune filters, tunable filters, oscillators, and tuners. A HTS tunable filter using an LC circuit with a Q factor in excess of 10^5 at 77 K demonstrated a tuning range of 17–1, while operating over the frequency range of 1–23 GHz. A solid-state source using a high- Q superconductor resonator will exhibit significantly improved frequency stability at lower cryogenic temperatures.

2.4.1.2. Insertion Loss in Resonators. The insertion loss (IL) in a superconducting microstrip resonator can be given as

$$\text{IL} = [20 \log(1 + Q_{\text{ex}}/Q_0)] \quad (2)$$

where Q_{ex} is the Q for the external circuit with typical values generally less than 1000 and Q_0 is the unloaded Q as defined by Eq. (1), whose value can run into a few million at higher frequencies and lower cryogenic temperatures. The insertion loss for the HTS YBCO microstrip resonator on LaAlO_3 substrate at 77 K cryogenic temperature can be computed using an empirical formula given

as

$$\text{IL} = [1.59 \times 10^{-5} f^2] \text{ dB/mm} \quad (3)$$

where the frequency is expressed in GHz.

2.4.1.3. RF Surface Resistance of Superconductor Films. The RF surface resistance of a superconductor film is the most important parameter, which determines the unloaded Q and insertion loss in the resonator. As stated earlier, the lower the surface resistance, the higher will be the unloaded Q and the lower will be the insertion loss. It is important to mention that the RF surface resistance is dependent on the operating frequency, cryogenic temperature, intensity of the RF field, properties of superconductor compound and dielectric substrate, and thickness and surface finish of the superconductor film. Furthermore, minimum film thickness must be used to allow a few RF penetration depths to shield the substrate from the RF field.

Studies performed by the author on a variety of high-temperature superconductors in bulk, single crystal, polycrystalline, and film indicate that the RF field intensity, operating frequency, and cryogenic temperature have significant impact on the RF surface resistance R_s . These studies further indicate that R_s increases monotonically with field amplitude through a transition region characterized by a strong field dependence, and then saturates to a value of a few percentage of the normal state surface resistance just above the critical temperature T_c . Lower surface resistance is possible only at low cryogenic temperatures and low RF surface fields ($< 0.1 \text{ G}$). The same studies also reveal that at high fields ($> 30 \text{ G}$) the R_s values of polycrystalline samples can increase by several orders of magnitude, although the samples remain in the superconducting state up to the highest fields. In the presence of low RF field, the frequency dependence of R_s in the transition region is approximately quadratic, but at high fields R_s shows only a weak dependence on frequency and temperature. Specifically, f^2 scaling is not universally valid under high field conditions. More recent studies on superconductor-oriented films and single crystals show a significant improvement in RF properties, leading to achievement of lower R_s values under similar operating parameters.

2.4.1.3.1. Surface Resistance Computation for Normal Conductor Film. The RF surface resistance of a normal conductor film at cryogenic temperatures can be expressed

Table 5. Unloaded Q Values for Superconducting Resonators as a Function of Frequency and Cryogenic Temperature (Millions, M)

Frequency α (GHz)	Nb-Based Resonators		YBCO-Based Resonators		
	$T = 4.2 \text{ K}$		$T = 90 \text{ K}$	$T = 77 \text{ K}$	$T = 50 \text{ K}$
1	0.08 M		0.7 M	1.8 M	3.9 M
10	0.05 M		0.08 M	0.5 M	1 M
100	0.04 M		0.07 M	0.4 M	0.8 M

as

$$R_s = [\pi \rho f \mu_0]^{0.5} \quad (\Omega) \quad (4)$$

where ρ is the resistivity ($\Omega \cdot \text{cm}$), f is the frequency (Hz/s), and μ_0 is the permeability of the medium, with a value of 1.258×10^{-8} (H/cm). For the copper film, the resistivity is $1.72 \mu\Omega \cdot \text{cm}$ at 300 K, $0.8 \mu\Omega \cdot \text{cm}$ at 77 K, and $0.25 \mu\Omega \cdot \text{cm}$ at 4.2 K. Computed values of surface resistance for the copper film at 4.2 K temperature are 0.0028Ω at 1 GHz, 0.0088Ω at 10 GHz, and 0.028Ω at 100 GHz. These computations indicate that the surface resistance for normal conductor films is proportional to the square root of the RF frequency.

2.4.1.3.2. Surface Resistance Computation for Superconductor Films. The surface resistance for the superconductor films, including HTS-based YBCO and TBCCO films and LTS-based Nb alloy films, is a function of operating frequency, intensity of RF field, cryogenic temperature, properties of superconductor material, film thickness, and surface conditions of the film. Several empirical formulas exist to compute the surface resistance under low RF field environments. The most accurate expression for computation of surface resistance can be written as

$$R(f, T) = [Cf^n \exp(-E_g/kT)] \quad (\Omega) \quad (5)$$

where C is a constant function of frequency, f is the operating frequency (Hz), T is the cryogenic temperature (K), n is the exponent parameter (which varies from 1 to 2 depending on the RF field intensity), E_g is the energy gap ($1.76 \times kT_c$), T_c is the critical temperature for the superconductor (111 K for TBCCO film, 91 K for YBCO film, and 9.4 K for Nb alloy film), and k is Boltzmann's constant. The exact value of constant C is dependent on the RF field intensity and is not readily available.

However, the most practical and reliable expression for the surface resistance, which is widely used by the research scientists, can be given as

$$R(f, T) = [(0.5)(\omega^2)(\mu_0)^2 \lambda(T)] \quad (\Omega) \quad (6)$$

where ω is the angular frequency ($2\pi f$) and $\lambda(T)$ is the London penetration depth for the superconductor film, which is a function of operating frequency and critical temperatures and can be written as

$$\lambda(T) = [\lambda_0 / 1 - (T/T_c)^4] \quad (7)$$

For a LTS-Nb-based film (4.2 K), the surface resistance comes to about $10^{-7} \Omega$ at 1 GHz, $10^{-5} \Omega$ at 10 GHz, and $10^{-3} \Omega$ at 100 GHz. Surface resistance values for HTS YBCO films as a function of temperature and frequency have been computed and are summarized in Table 6. These computed values [which agree with those in *Proc. IEEE* 1252 (Aug. 1989)] show the surface resistance dependence as the square of the frequency for the superconductor films under low RF fields. As stated earlier, this

Table 6. Values of Surface Resistance for Various Superconductor Films (Ω)

Frequency (GHz)	Nb Film ($T=4.2$ K)	YBCO Film ($T=4.2$ K)	YBCO Film ($T=77$ K)
1	10^{-7}	2×10^{-6}	8×10^{-6}
10	10^{-5}	2×10^{-4}	8×10^{-4}
100	10^{-3}	2×10^{-2}	8×10^{-2}

square law may not be valid under high RF field environments.

A superconductor oxypolished cavity employing thin films offers much higher values of unloaded Q and lower values of surface resistance. The surface resistance for a cavity-based superconductor films can be written as

$$R(f, T) = [G/Q_0(f, T)] \quad (\Omega) \quad (8)$$

where G is a constant that has a value of 780Ω for a TE_{011} mode cavity and Q_0 is the quality factor for the cavity function frequency (f) and temperature (T).

3. CRYOGENIC ELECTRONIC COMPONENTS FOR MILITARY SYSTEMS

Cryogenic electronic technology has potential applications in missile electronics, high-performance radar systems, electronic countermeasure systems (ECMs), UAVs, reconnaissance drones, battlefield sensors, transmit/receive (T/R) modules, battlefield aerial surveillance sensors, electronically steerable phased-array antennas, and electronic support measure (ESM) receivers. Superconducting signal processing components such as tapped-delay-line structures for matched filtering, convolution, correlation, and Fourier analysis are best suited for precision tracking radars, satellite communication systems, and space surveillance sensors with stringent performance specifications. Microwave delay lines using superconducting meanderline structures are most attractive for deployment in electronic warfare (EW) systems.

3.1. Digital Radiofrequency Memory (DRFM) using cryogenically-cooled devices

Cryogenically cooled components including ADCs, DACs, mixers, solid-state LOs, and stripline technology-based delay lines with meanderline configuration are best suited for effective integration in the design of DRFM, which offers real-time performance simulation of high-performance radars using complex waveforms and sophisticated EW systems incorporating advanced ECM techniques. Simulation techniques such as these will be able to define the requirements for a EW system capable of providing effective ECM capability against enemy radars without undertaking extensive field tests. It is important to mention that low spurious levels over wide instantaneous bandwidth is the principal requirement for a DRFM-based system, a condition that cannot be met by uncooled

microwave components. The ADC device is the heart of the DRFM system, and an uncooled ADC will not be able to meet stringent system requirements. Studies performed by the author indicate that incorporating an Nb-based RSQF superconductive logic in the ADC architecture will meet these stringent performance requirements. The high-resolution requirements can be satisfied only with cryogenically cooled electronic circuits with ultralow time constants and with the correct threshold levels. Cryogenically cooled devices and components used in the DRFM system can be enclosed in a common cryogenic chamber shown by the dotted rectangle in Fig. 2. In this way only one cryogenic cooler can provide cooling to all the cryogenic electronics involved with minimum cost.

Design of the meanderline delay line requires the use of a London two-fluid model to derive the slow mode propagation velocity in the meanderline structure, which is dependent on the ratio of dielectric substrate thickness to superconductor film thickness to penetrate the depth. The propagation velocity in the delay medium is strictly dependent on the coherence length, mean-free path, surface reflection, cryogenic temperature, and magnetic field. However, the effective penetration depth is given by the modified London penetration depth (λ_L), which takes into account the superconductor Nb-based or YBCO-based film thickness. The phase velocity of the dominant slow-wave E mode is a function of velocity of light in the dielectric and the penetration depth in the superconductor thin film. Any superconductor alloy impurity will increase the delay per unit length without increasing the insertion loss or degrading the pulse shape. A delay line using a superconductor meanderline structure offers significant improvements in size, weight, and insertion loss over a conventional uncooled delay line made from coaxial transmission lines. It is important to mention that the wave interaction produces slight nonlinear dispersion; therefore, both the linear and nonlinear dispersive performance levels are possible with this unique delay-line structure.

This geometry is very useful as a dispersive delay-line element for a pulse compression filter widely used in high-performance, long-range missile detection radars.

3.2. Cryogenically Cooled Local-Oscillator (LO) or Solid-State RF Source

A stable solid-state RF source with low phase noise can be used as a LO source to provide power to RF mixers shown in Fig. 2. Phase noise and frequency stability are the most critical performance parameters for a LO. Small LO power requirements can be met with a solid-state source comprising of one or two solid state devices such as HBTs or MESFETs or HEMTs or Gunn diodes. The frequency stability of such sources is dependent on bias level, fluctuation in supply voltage, and operating environments. In cases where frequency stability is of paramount importance, thermal stabilization circuit, regulated voltage power supply, and cryogenic cooling must be considered for the LO design. An X-band superconducting oscillator using lead-plated cavity with $Q = 10,000$ demonstrated a frequency stability of 10^{-8} at 6.7 K. A superconducting monotron oscillator using a reflex klystron stabilized with a superconducting cavity achieved a frequency stability of $> 10^{-12}$ at 10 K operating temperature. Of course, high stability sources do suffer slightly from higher weight and cost.

The solid-state sources are generally used to provide LO power in the microwave and MM-wave regions. However, when LO frequencies are in sub-millimeter-wave regions, frequency multipliers using varactors or step recovery diodes are used to achieve sufficient power levels. The conversion efficiencies of these frequency multipliers can be significantly improved using cryogenic cooling as shown in Table 7.

The phase noise of an uncooled frequency multiplier source is relatively high, as shown in Table 7, but it can be reduced at least by 20 dBc/Hz under CW operation

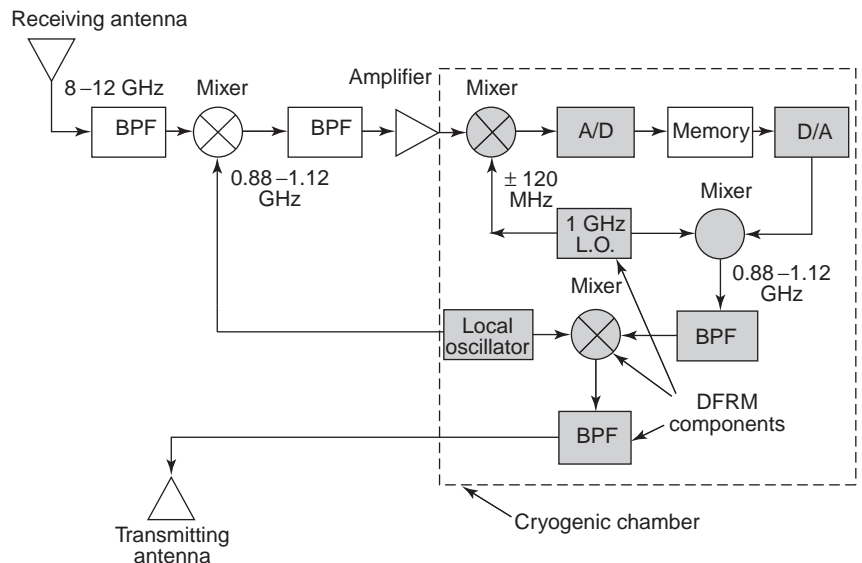


Figure 2. Cryogenic electronic components deployed by an electronic warfare system.

Table 7. Conversion Efficiency of Cryogenically Cooled Frequency Multipliers^a

Multiplier Type and Cutoff Frequency (GHz)	300 K	77 K
Doubler (1000 GHz)	39%	87%
Tripler (500 GHz)	32	54
Quadrupler (800 GHz)	23	42
Quintupler (1000 GHz)	9	21
Sextupler (1500 GHz)	18	29

^aAn input frequency of 10 GHz is assumed in each case.

through cryogenic cooling at 77 K. Cryogenic cooling also improves the conversion efficiency of the multiplier, thereby increasing the output power. Under pulse operations, the intrapulse phase change across a 10- μ s pulse is 2.5° at 300 K, which can be reduced well under 0.8° at 77 K. Studies performed by the author indicate that higher conversion efficiencies have been observed when integrated series IMPATT structure (ISIS) diodes are used in the design of microwave frequency multipliers. In brief, cryogenic cooling does improve the frequency stability and phase noise of the source irrespective of LO design.

3.3. Detectors and Focal Planar Arrays (FPAs) for Target Tracking and Imaging

High-performance detectors and cryogenically cooled FPAs are widely used by airborne IR sensors to track targets and by high-resolution digital cameras to achieve high quality of images of the objects. RF detectors are used to monitor microwave and MM-wave signals. Earlier bolometer IR detectors using temperature-dependent resistances were used to detect IR and MM-wave signals. Direct detectors are characterized in terms of dark current, noise equivalent power (NEP), responsivity, quantum efficiency, detectivity, and dynamic range. Significant improvement in dark current, responsivity, and detectivity is noticed at a cryogenic temperature optimized over a specific spectral region (see Tables 8 and 9 and Fig. 3). IR FPAs are widely used by military IR search-and-tracking (IRST) sensors for target tracking and IR line scanners (IRLSs) for battlefield thermal imaging with high resolution. Photoconductive (PC) and photovoltaic (PV) detectors using Hg:Te: Cd alloy structure when cooled to 77 K offer low dark current and high quantum efficiency at operating wavelengths up to 17 μ m. For an 8- μ m detector junction, the dark current is reduced from 700 nA at 77 K to much less than 1 nA at 40 K cryogenic temperature (Tables 8 and 9 and Fig. 3). Such detectors are best suited for detection and tracking of long-range ballistic missiles during launch, boost, and cruise phases.

Table 8. Performance of Hg:Te: Cd Detectors for Various IR Bands

Hg _{1-x} :Cd _x :Te	T (K)	Spectral Region (μ m)	Maximum Detectivity (cm Hz ⁻¹ W ⁻¹)
0.39	80	1.5–3.5	1.8×10^{11} at 1.8 μ m
0.27	80	4.5–5.0	5×10^{10} at 5 μ m
0.20	80	7–11	3×10^{11} at 11 μ m
0.18	80	14–17	5.6×10^{10} at 17 μ m

3.4. Microcooler Requirements for Military and Space Sensors

Cryogenic cooler requirements are more stringent at lower cryogenic temperatures. For cooling military and space system components and devices, lower weight, size, and power consumption and higher cooling efficiency and reliability are the most critical performance requirements. For certain military applications cooling time is of paramount importance to the life of the cooler. For space applications minimum weight, size, and power consumption are the principal requirements. The word greater reliability are the principal requirements. Studies performed by the author on various cooler configurations indicate that miniaturized microcoolers have potential applications to space sensors, IR missile seeker, airborne IR thermal imaging radiometers, and mini-IRST sensors. A microcooler using a stirling cycle engine takes less than 3 min to reach a liquid nitrogen temperature of 77 K. This type of cryocooler is deployed in military missions where short cooling time is the principal requirement. A microcooler designed for NASA thermal imaging sensor weighs only 15 oz, consumes power less than 3 W, has a shelf life more than 5 years, and has demonstrated a continuous operation over 8000 h with no compromise in reliability or cooling performance. High-reliability coolers require improved materials with self-lubrication features, very-low-friction clearance seals, and linear drive mechanisms. A microcooler can provide a cooling capacity of > 150 mW at 77 K with a heat load of 150 mW and a cooling time ranging from 1.5 min at 120 K to 4 min at 77 K from a room temperature of 25 °C. Research studies performed by the author on cryogenic coolers reveal that reduction in the Intelsat-8 multiplexer's mass and size by 50–65% is possible by using pulsetube cryocoolers. Research studies further reveal that closed-cycle cryocoolers are best suited for high-resolution imaging, MRI, and NMR applications.

4. APPLICATION OF CRYOGENIC ELECTRONIC TECHNOLOGY IN MEDICAL AND SCIENTIFIC RESEARCH FIELDS

Cryogenic electronic technology has played a key role in the development of medical diagnostic equipment and scientific research instrumentation. Integration of low-temperature superconductor (LTS) technology in early 1960s allowed the design and development of high-power magnetic resonance imaging (MRI) magnets to achieve high-resolution images of human organs. LTS technology has also played a key role in the design and development of

Table 9. Detector Dark-Current Levels as a Function of Temperature

Temperature (K)	8 μm Diameter at		1000 μm Diameter at	
	– 100 mV ^a	– 50 mV	– 100 mV	– 50 mV ^a
40	5×10^{-9}	10^{-9}	5×10^{-4}	10^{-4}
63	10^{-9}	10^{-7}	8×10^{-5}	5×10^{-5}
78	7×10^{-7}	5×10^{-7}	10^{-4}	9×10^{-5}

^aWavelength 17 μm.

nuclear magnetic resonance (NMR) equipment best suited for medical diagnosis and scientific research.

4.1. Application of Cryogenic Electronic Technology for Medical Diagnosis

The MRI provides physicians, veterinarians, and surgeons with precision diagnostic tools to locate and diagnose medical problems in the body with high reliability. MRI demands superconducting windings of topological precision greater than that provided by crystalline conductors. Magnets with storage capacity of 40 MJ of energy can be developed with adiabatic windings, in which the conductors are locally uncooled. Availability of improved magnetic components and state-of-the art cryogenic electronic technology has significantly improved the design of the MRI equipment with major emphasis on enhanced resolution and patient comfort. The latest MRI equipment contains couple of openings in the cylindrical structure to eliminate patient fear.

The use of high-resolution nuclear magnetic resonance (NMR) in the critical medical analysis and diagnosis of human organs is now considered the state-of-the art technique involving proton frequencies exceeding 850 MHz, which is possible only with superconducting ribbons of high quality. LTS or HTS technology can be applied to the design and development of accelerators widely used in fusion and other scientific research activities. Both NMR

and accelerator magnets demand superconducting windings with high current density ratings. The magnet configuration can be optimized for high-resolution capability and to meet state-of-the art performance levels. The dipole magnets with superconducting windings are deployed in the design of superconducting supercollider (SSCs) for industrial, military, and space research applications. Niobium–titanium (4.2 K) filament wires with high current density are used in the SSC program to achieve exceptionally high performance capability.

4.2. Requirements for Superconducting Windings or Coils

Characterizations of superconductor materials and superconducting windings indicate that windings or coils must stringent requirements in terms of uniformity, pitch, and spacing between the layers. These superconducting windings or coils are designed to produce very high magnetic fields, which are necessary for high-energy physics experiments, controlled thermonuclear fusion, magnetohydrodynamic power generators, magnetic resonance imaging equipment, and levitated high-speed ground vehicles such as the bullet train in Japan with a speed capability of 550 km/h.

Winding or coil materials must be selected with lower critical temperatures (T_c) to meet the specified performance requirements for a particular system. Intermediate superconducting compounds such as Nb₃Sn, Nb₃Al, and Nb₃(Al_{0.8}, Ge_{0.2}) are best suited for high-magnetic-field applications because of their lower critical temperatures, ranging from 17 to 21 K. These coils use superconducting wires or filaments or multifilaments capable of generating high flux levels with minimum insertion loss and heat generation. Both MRI and NMR equipment require liquid helium (4.2 K) refrigeration systems using either rotary or reciprocating compressors and expansion engines to provide the required cooling capacity.

4.3. Josephson Junction (JJ) Devices for Medical and Scientific Applications

As stated earlier, JJ devices are widely used for detection and mixing at MM-wave and sub-millimeter-wave levels, but their potential application was first explored in the design and development of the magnetic sensors such as superconducting quantum interference devices (SQUIDS). JJ devices can be fabricated using various configurations, including tunnel junction, multijunction, bridge junction, and point contact. Selection of a particular configuration depends on the type of parameters to be detected and resolution accuracy requirements.

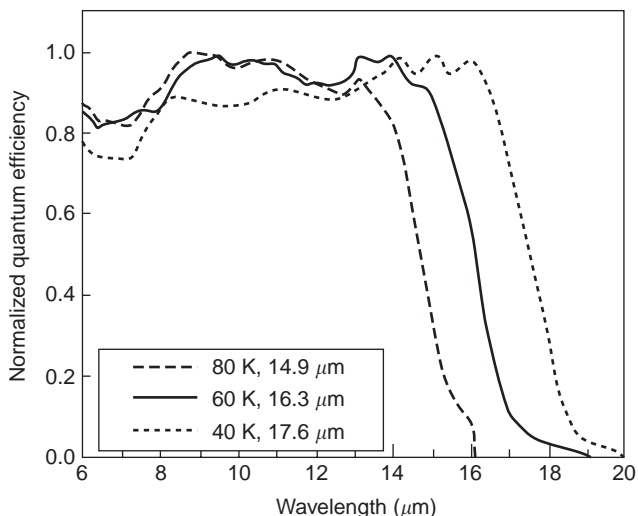


Figure 3. Quantum efficiency as a function of wavelength and temperature.

Critical elements of the magnetometer, the first-derivative gradiometer, and the second-derivative gradiometer with different pickup loop orientations are shown in Figs. 4a, 4b, and 4c, respectively. Noise energy levels for various DC and RF SQUID devices operating at different cryogenic temperatures are shown in Fig. 4d. A cooling temperature of 4.2 or lower is used for Nb-based thin films, while temperatures at 77 K and 28 K are preferred for YBCO thin films. The lowest noise energy levels occur for DC Nb-based SQUID devices operating at 4.2 K. It is evident from Fig. 4d that the noise energy level RF commercial SQUID devices remains flat at 4.2 K.

These devices are used to measure magnetic field with an accuracy of $10^{-14} \text{ T Hz}^{-1}$ (T stands for tesla, which is equal to 10,000 G) and magnetic field gradient with an accuracy of $10^{-12} \text{ T/m}^{-1} \text{ Hz}^{-1}$. Superconducting SQUID is widely used in the design of the magnetic anomaly detection (MAD) device, which is best suited for anti-submarine warfare (ASW) reconnaissance missions. Note the sensor resolution is limited by the Josephson noise developed in the low-temperature circuit resistance at 4.2 K.

4.4. Critical Elements of SQUID-Based Sensors

Cryogenically cooled flux transformers and pickup loops are used in the design of SQUID-based sensors. A pickup loop is connected across the input coil to fabricate a superconducting flux transformer, which is made from Nb wire. The orientation of the pickup loop and the number of loops deployed determine the type of SQUID-based sensor, namely, a magnetometer or first-derivative gradiometer or second-derivative gradiometer. The SQUID device and the

input coil are enclosed in a superconducting enclosure. A fraction of the applied magnetic energy in the pickup loop is transferred to the SQUID. Magnetometer loop has a typical sensitivity of 0.01 pT/Hz. Magnetometers are widely used in geophysics research applications such as active electromagnetic (EM) sounding, piezomagnetism, and tectonomagnetism. The axial first-derivative gradiometer with two pickup loops wound in opposite directions measures the quantity (dB/dz) along the z axis, where B is the magnetic flux density. The second-derivative gradiometer employs three pickup loops and measures the quantity (d^2B/dz^2) along the z axis. The first-derivative gradiometers are operated in a shielded room made from mumetal magnetic material that attenuates the ambient magnetic noise. However, the second-derivative gradiometer can be operated in an unshielded environment. In cases where ultrahigh sensitivity is required, an array containing 50–100 gradiometers incorporating integrated thin-film devices can be used to design a most sensitive clinical viable system.

4.5. Various Applications of SQUID-Based Gradiometers

The most important application of a gradiometer is in field of neuromagnetism. This sensor detects the weakest magnetic signals emanating from the human brain. Two basic kinds of measurements are made on human brain. In the first, the sensors detect spontaneous activity of the brain based on the magnetic pulses coming out of patient brain suffering from local epilepsy. The second kind of measurement involves evoked response of the brain such as the

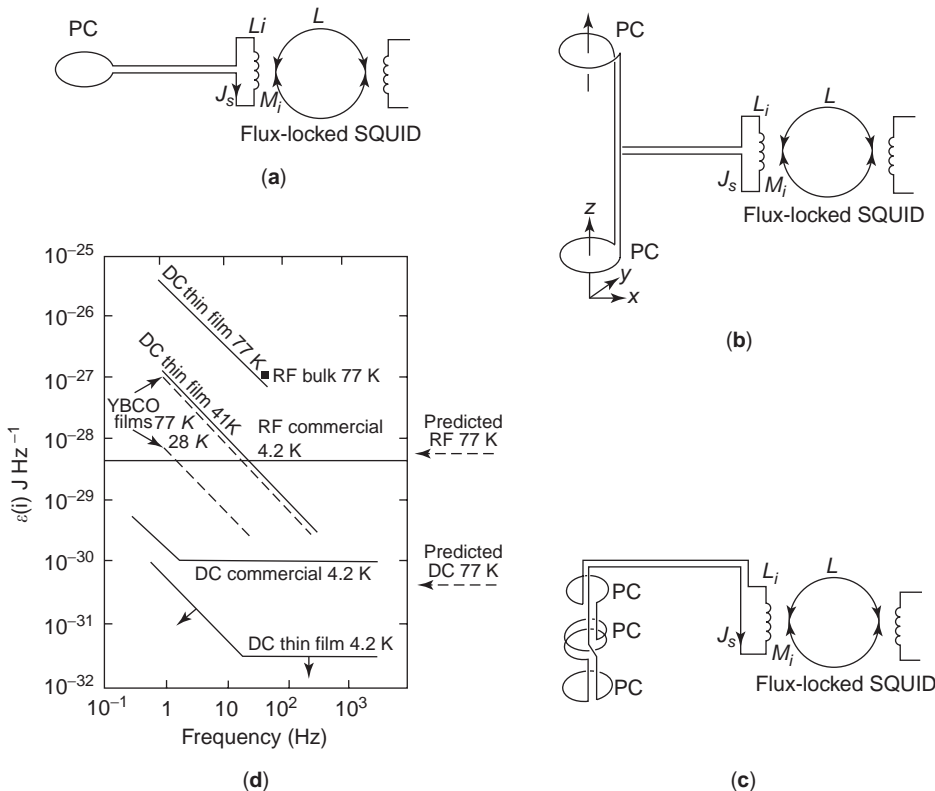


Figure 4. Low-temperature Josephson junction devices used in a (a) SQUID magnetometer, (b) first-derivative gradiometer, and (c) second-derivative gradiometer and (d) noise energy levels in Nb-based (4.2 K) and YBCO-based (77 and 28 K) thin films (PC = pick coil or loop).

magnetic field from the auditory cortex generated by different frequency tones.

Besides medical diagnostic applications, SQUID gradiometers are widely employed in the research studies of corrosion and location of fractures in the underground pipelines and other structures not easily accessible. These gradiometers can be deployed to locate fine cracks in the building structures or metallic posts affected by earthquakes.

5. APPLICATION OF CRYOGENIC ELECTRONICS IN COMPUTER AND HIGH-SPEED SIGNAL PROCESSING

High-speed switching capability (1–5 ps), low power consumption (3–5 μ Watt/chip), and low dispersion feature of the JJ devices are the most desirable parameters to meet the operational requirements of the digital circuits for use in high-speed computing systems and complex signal processing equipment used by radar and ECM systems. Josephson digital logic circuits made from niobium alloy operating at 4.2 K have demonstrated improved process reliability, high-speed capability, and extremely low power consumption. These logic circuits are capable of meeting the performance requirements for large-scale integration (LSI) circuit and very-large-scale integrated (VLSI) circuit applications. Both the LSI and VLSI circuits are best suited for ultrafast Josephson microprocessors, which are the backbone of complex signal processors or supercomputers. The Josephson microprocessor is capable of operating at clock frequencies much greater than 800 MHz. Josephson circuits use a variety of cryogenic electronic integrated circuits as Josephson logic gates such as JJ tunnel logic, current injection device (CID) logic, resistive coupled JJ logic, and modified variable threshold logic (MVTL). Among all these logic devices, the fastest gate delay (<1.5 ps) is observed in the MVTL OR gate. The JJ shift register, OR gate, and AND gates are the critical components of the high-speed Josephson microprocessors and are widely used in the design of high-power computing systems. OR-type and AND-type decoders have been developed using Nb-based Josephson IC technology with access time far below 0.5 ns for 1–4-kb (kilobit) memories using improved architectures. A \geq 4-kb multiplier can be fabricated using LTS-Nb-based threshold logic circuits with multiplication time far below 150 ps and power consumption not exceeding 1 mW. A 16-bit multiplier consisting of 828 MVTL gates demonstrated a multiplication time of <1 ns with power consumption <25 mW and with a gate delay not exceeding 6 ps. Josephson logic gates made from

HTS YBCO films at 77 K can be as fast as Nb-based devices, but they suffer from power dissipation as high as 200 μ W/gate compared to 1–8 μ W/gate for Nb-based logic gates.

LSI and VLSI circuits are widely used in semiconductor chips to design very high-speed complex digital computers for possible applications in advanced radars with multiple target tracking capability, ECM systems to mitigate threats posed by hostile missiles, and space MM-wave radiometers for high-quality imaging. The use of these Josephson devices has also allowed several military and scientific research laboratories to maintain a primary Josephson voltage standard with high-speed instrumentation capability. In addition, JJ devices are best suited for high-performance waveform acquisition and display equipment, leading to development of precision measurement instruments for scientific and industrial research applications.

6. SUMMARY

This article is devoted to cryogenic electronics. Performance capabilities of most widely used cryogenic electronic components and devices using HTS and LTS technologies are summarized with emphasis on reliability, power consumption, and weight. Performance improvements due to integration of cryogenic electronic technology in RF, microwave, and millimeter-wave components, including RF detectors, ADCs, MESFET and HEMT amplifiers, mixers, filters, solid-state sources, frequency multipliers, and laser diodes are identified. Applications of cryogenic electronic technology in satellite communication systems, terrestrial mobile communication systems, space sensors, missile seeking systems, and long-range, missile tracking radars are discussed. Benefits due to deployment of cryogenic electronic components in the design and development of medical diagnostic equipment such as MRI and NMR, scientific and industrial instruments, space sensors, and battlefield systems are summarized. Performance requirements and applications of low-temperature SQUIDs and Josephson junction (JJ) devices such as JJ shift registers, decoders, and logic gates in high-speed computers and sophisticated digital signal processors generally used by missile tracking radar, ECM, and high-resolution imaging sensors are identified. Despite several benefits of cryogenic cooling technology, high-power cryocooler reliability and procurement cost remain the major drawbacks, which can be eliminated by using highly efficient pulsetube cryogenic cooler technology.

COMPUTATIONAL ELECTROMAGNETIC SCATTERING MODELS FOR MICROWAVE REMOTE SENSING

KUNG-HAU DING
Air Force Research Laboratory
Hanscom AFB, Massachusetts
LEUNG TSANG
University of Washington
Seattle, Washington
QIN LI
University of Washington
Seattle, Washington

1. INTRODUCTION

Modeling of electromagnetic wave scatterings by random discrete scatterers and rough surfaces play an important role in geoscience and remote sensing research. Since the 1970s, considerable theoretical efforts have been made to elucidate and understand the scattering processes involved in such problems, and various models have been developed for microwave active and passive remote sensing applications [1–7]. With the rapid advances in computer technology and fast computational electromagnetics algorithms, numerical simulations of scattering by random media allow us to solve Maxwell's equations exactly without the limitations of analytical approximate models. The numerical models can provide a valuable means for evaluating the validity regimes of analytical scattering theories; in addition, they can potentially aid in the future development of extended analytical models. These theoretical and numerical models, which are commonly used for tackling electromagnetic wave scattering problems and for remote sensing applications, have been presented in three volumes of books [5–7]. In this article, we will update the development in the numerical scattering models for discrete random scatterers, with emphasis on the applications of microwave remote sensing in snowcover, seafoam, and vegetation canopy.

The frequency dependence of scattering by geophysical media at microwave frequencies is an important topic because multifrequency measurements are used in remote sensing applications. In Section 2, we investigate rigorously the frequency dependence of scattering by dense media [7–9]. The approach used is based on the Monte Carlo simulations where the three-dimensional solutions of Maxwell's equations are pursued [6]. The particle positions are generated by deposition and bonding techniques. The properties of absorption, scattering, and extinction are calculated for dense media consisting of sticky and nonsticky particles. Numerical solutions of Maxwell's equations indicate that the frequency dependence of densely packed sticky small particles is much weaker than that of independent scattering. Numerical results are illustrated using parameters of snow in microwave remote sensing. Comparisons are made with extinction measurements as a function of frequency.

In Section 3, polarimetric microwave emissions from foam-covered ocean surfaces are studied. The foam is

treated as densely packed air bubbles coated with thin seawater coating [10–12]. The absorption, scattering, and extinction coefficients are computed from the Monte Carlo solutions of Maxwell's equations for a collection of coated particles. These quantities are then applied in the dense media radiative transfer (DMRT) theory [2,7] to calculate the polarimetric microwave emissivities of ocean surfaces with foam cover. The theoretical results of Stokes brightness temperatures with typical parameters of foam in passive remote sensing at 10.8 and 36.5 GHz are illustrated and compared with experimental measurements [10–12].

We present an efficient computational model for computing tree scattering at VHF/UHF frequencies in Section 4. A structure model with dielectric cylinders is used to simulate trees with bare branches. The method of moments (MoM) is applied to solve the volume integral equation for the tree scattering signatures. An efficient numerical algorithm based on the sparse matrix iterative approach (SMIA) is applied in solving the matrix equation iteratively [13–15]. The SMIA decomposes the impedance matrix into a sparse matrix for the near interactions, and a complementary matrix for the far interactions among the cylindrical sub-cells of the tree structure. The SMIA tree scattering model is applied to calculate scattering from various simulated trees with up to several hundreds of branches using a laptop computer. Solutions obtained from the SMIA method agree very well with the solutions obtained using exact matrix inversion and the conjugate gradient method (CGM). The key feature of the SMIA approach is that very little iteration is required to obtain convergent solutions, compared to the CGM, the SMIA approach may reduce the number of iterations by a factor of >100 [16].

In Section 5, a UV multilevel partitioning (UV-MLP) method is presented for solving the volume scattering problem [17–20]. The method consists of setting up a rank table of transmitting and receiving block sizes and their separations. The table can be set up speedily using coarse-coarse sampling. For a specific scattering problem with given geometry, the scattering structure is partitioned into multilevel blocks. By looking up the rank in the pre-determined table, the impedance matrix for a given transmitting and receiving block is expressed by a product of U and V matrices. We demonstrate the method for two-dimensional volume scattering by discrete scatterers. Multiple scattering is cast into the Foldy-Lax equations of partial waves [2,5–7]. We show that the UV decomposition can be applied directly to the impedance matrix of partial waves of higher order than the usual lowest-order Green function. Numerical results are illustrated for randomly distributed cylinders with diameter of 1 wavelength. For scattering by 1024 cylinders on a single PC processor with 2.6-GHz CPU and 2 GB (gigabytes) of memory, only 14 CPU minutes is needed to obtain the numerical solution and, for 4096 cylinders, only 7.34 s is needed for one matrix-vector multiplication.

2. FREQUENCY DEPENDENCE OF SCATTERING BY DENSE MEDIA WITH APPLICATIONS TO SNOW

For remote sensing applications, the measurements are generally taken at multiple frequencies [21–25] because

each frequency contains information. For instance, the special sensor microwave/imager (SSM/I) radiometer measures at 19, 22, 37, and 85 GHz. Backscattering data are usually measured at L, C, and X bands in the active remote sensing case [1–4]. These multiple frequency measurements are used in many applications, such as the snow parameter retrievals, the surface type classification, and metamorphism signature of snow. Thus, the frequency dependence of scattering is an important issue for making a better use of multifrequency data in remote sensing. The extinction of dry snow is due primarily to scattering rather than absorption. Since the snow grain sizes are much smaller than wavelength, classical Rayleigh scattering theory indicates that the dependence on scattering is frequency to the fourth power. The important question of dense media is whether the scattering still exhibits frequency to the fourth power when these small particles are densely packed. Several approaches have been used in studying the frequency dependence of scattering. The first is based on experimental measurements and empirical fitting. Hallikainen et al. [22] measured the extinction coefficients of snow at 18, 35, 60, and 90 GHz. The second approach is based on analytical modeling using effective medium theories [2,7]. Analytical approaches that account for correlations between particles, such as the quasicrystalline approximation (QCA) and quasicrystalline approximation with coherent potential (QCA-CP) [2,7], have been used to simulate the densely packed media. The Percus–Yevick (PY) pair distribution functions are used to model the relative location of particles. The dense media radiative transfer equations have been derived based on QCA for sticky particles and found useful applications in microwave remote sensing of snow [7,26]. At higher frequencies, particles become comparable to wavelength and higher-order multipoles have to be included [27–29]. The third approach is a rigorous approach based on Monte Carlo (MC) simulations of exact solutions of Maxwell equations that govern microwave interactions exactly [6]. The method consists of generating the positions of the particles on a computer on the basis of prescribed rules. Once the positions are generated, the Maxwell equations are solved numerically. Numerical methods include the T -matrix method [2,7], the finite-difference time-domain (FDTD) method [30], and the volume integral equation method [6]. Monte Carlo simulations have been applied to study the extinction coefficients and the effective permittivities for dense media [27–35]. In 2001–2003, we conducted two- and three-dimensional Monte Carlo simulations to investigate the frequency dependence of scattering by dense media [7–9].

In this section, we describe the three-dimensional dense medium scattering simulations for media with small and moderate size particles. Particles with (sticky) and without interparticle force (nonsticky) are both used in simulations to study the frequency dependence of the extinction coefficient. The T -matrix method is used, and the effects of absorption are included. For typical snow grains, the diameters are in millimeter ranges, and the size parameter ka values are ranging from 0.2 to 1 depending on the frequencies. It is shown that densely

packed sticky particles exhibit a frequency dependence of scattering coefficient weaker than that of independent scattering. The methodology of dense media study consists of studying the pair distribution functions of particle positions, computer growth of dense media, and three-dimensional solutions of Maxwell equations for the computer-grown dense media. Section 2.1 briefly describes the pair distribution functions and the computer creation of discrete random media with sticky particles. The three types of formulations of Foldy–Lax multiple scattering equations, based on exciting field, scattered field, and internal field, for spheres are presented in Section 2.2. We also describe how to calculate scattering and absorption coefficients. Convergence tests are performed using various numerical parameters to show that the results are accurate. In Section 2.3, simulation convergence with respect to the number of particles used, the number of multipoles used, the box size used, and the number of realizations are demonstrated. In Section 2.4, we present results based on Monte Carlo simulations of densely packed sticky and nonsticky dielectric spheres. The Monte Carlo simulation results are compared with independent scattering and QCA results. The results of Monte Carlo simulations are in good agreement with QCA results. Simulated results are shown for various size parameter ka and stickiness parameter τ for the four microwave frequencies at 18, 35, 60, and 90 GHz using typical parameters in snow. Comparisons are also made with extinction measurements [22] as a function of frequency.

2.1. Pair Distribution Functions and Computer Generation of Ensemble of Particle Positions for Finite-Size Sticky Particles

The pair distribution functions for various types of materials, which can be classified as gas, crystal, and liquid/glass, are described in detail in three other texts [2,6,36]. The key observation is that liquid is a “dynamical” system with moving molecules while glass is amorphous solid that is “static.” Yet they have same probability density function (pdf) and joint pdf of particle positions. They both have short-range order with the same class of pair distribution functions. Another comparison is using the Bernal random closed-packed sphere model, which is a macroscopic “static” situation, because in this model the spheres are dropped into the container. On the other hand, the Percus–Yevick (PY) hard-sphere model is based on molecular “dynamics” of liquids using a hard-sphere potential. Yet the Bernal random closed-packed sphere model and the PY model give very similar pair distribution functions. In practice, the Bernal random packing is of limited use, due to its fixed volume fraction at about 63%. From these studies one can see that static situations can be generated from dynamic situations because one can view the dynamics as merely random walk or shuffling of particles to create realizations of random positions of particles. In other words, shuffling of particle positions creates the static situation of various statistical ensembles. The particles do not actually move in a natural snow medium.

To understand the scattering of waves by dense discrete random media, it is important to systematically

generate the ensemble of random positions of particles using the procedure of computer growth. To generate the “static” case of dense random media with fractional volume between 20% and 50%, we have been using shuffling, which is viewed as a means of creating different realizations rather than viewing particles as actually moving in real life. The particles are first placed periodically, which is possible up to 70%. Then the particles are shuffled, by random walk, to attain the random positions. The results of particle positions actually look quite realistic.

Aggregation is introduced by allowing particles to bond. The diffusion-limited aggregation methods [37] are not useful as they are limited to low fractional volume, and the structure created is quite sparse not dense as in snow grain. The fractional volume decreases as the number of particles increases for fractals generated by diffusion limited aggregation. The manner in which bonding is done is actually “static.” The probabilities are constructed based on the exposed surface area of the particles. Then bonding is decided on the basis of these probabilities [6,38–40]. We call these particles “sticky” because they bear similarities to the Percus–Yevick liquid model of a sticky potential; the pair functions are also similar.

Sticky particle models are used to consider cases when the particles can have surface adhesion [6]. This means that when the particles are randomly packed together, they tend to form clusters and bonds with each other. The adhesive force is parameterized using a variable τ that governs the degree of clustering. Analytic solutions of the pair distribution functions can be calculated for particles of the same size [41] and for medium with multiple sizes of particles [42]. They have distinct pair distribution functions that are different from those of nonsticky particles. To generate the positions of particles in the sticky particle model, a two-step procedure is used. First, the Metropolis shuffling technique is used to provide random positions of the particles in a box. Next we follow the work of Seaton and Glandt [38] and Kranendonk and Frenkel [39], to allow the particles to form bonds. There are four binding states for each particle: unbonded, single bond, double bond, and triple bond. Transition probabilities are calculated. The particles are then selected to form bonds on the basis of these transition probabilities [6,38–40]. The sequence of bonds can be formed by different particles resulting in aggregates.

The sticky particle model is useful to describe snow because the ice grains in snow are adhesive. Furthermore, as metamorphism occurs, the ice grains form bridges. The appropriateness of the sticky particle model can be verified by reexamining the pair distribution functions in snow and comparing them with the sticky particle model. It has been observed that grain size in snow follows a lognormal size distribution [43]. The large size grain can be viewed as a result of aggregates. The study of relation between particle size distribution and the alternative viewpoint of aggregation of small particles to form larger size grains will be studied in the future.

In the following simulations, all the particles are assumed to have the same size. However, since the particles can form bonds and aggregates, the effective sizes of the particles can be much larger. Furthermore, the aggregates consist of a varying number of particles. This gives an effective size distribution when the medium is viewed as aggregates of particles. The particle positions are generated for both nonsticky and sticky particles. After the particle positions are generated, the conjugate gradient method is used to solve the Foldy–Lax multiple scattering matrix equations described in Section 2.2.

2.2. Numerical Solution of Maxwell Equations Based on Foldy–Lax Formulation

The final step of simulation is to solve Maxwell equations of these realizations to study the coherent wave and incoherent waves by averaging the electromagnetic fields and intensities over realizations. In the dispersion relation for the coherent wave, the coherent wave has an effective propagation constant that has a real part and an imaginary part. The real part corresponds to effective permittivity. The imaginary part accounts for loss due to absorption and scattering. The scattering loss is due to the conversion of coherent waves to incoherent waves. It can be calculated by angular integration of the incoherent wave intensities. In the simulations, Maxwell equations are solved exactly. Then we calculate incoherent waves by subtracting the coherent wave from the scattered wave. Absorption is calculated by finding the absorption loss of each particle, based on the solution of internal fields of each particle. Combining scattering and absorption give the extinction of the dense random media. However, for dry snow, the extinction is crucial and the results of extinction are shown in Section 2.4. The procedures are used for the four frequencies: 18, 37, 60, and 90 GHz.

Consider a medium consisting of N spheres, with radii a and permittivities ϵ_p , centered at $\vec{r}_1, \vec{r}_2, \dots, \vec{r}_N$. An incident wave with wavevector \vec{k}_i is impinging onto the medium. The solution of Maxwell’s equations can be cast into the Foldy–Lax multiple scattering equations. In matrix form [2,6,9]

$$\vec{w}^{(q)} = \sum_{p=1, p \neq q}^N \overline{\sigma}(k\vec{r}_q\vec{r}_p) \overline{T}^{(p)} \vec{w}^{(p)} + e^{i\vec{k}_i \cdot \vec{r}_q} \vec{a}_{\text{inc}} \quad (1)$$

where $\vec{w}^{(q)}$ are the exciting field coefficients, $q = 1, 2, \dots, N$, $\overline{\sigma}(k\vec{r}_q\vec{r}_p)$ is the vector spherical wave transformation matrix, $\overline{T}^{(p)}$ the T matrix representing scattering from the scatterer p , and \vec{a}_{inc} the incident field coefficients. The physical interpretation of Eq. (1) is that the exciting field at particle q is equal to the incident field plus the scattered fields from all other particles except itself.

The relationships between exciting field coefficients $w_{mn}^{(M)}$ and $w_{mn}^{(N)}$, scattered field coefficients $\alpha_{mn}^{S(M)}$ and $\alpha_{mn}^{S(N)}$,

and internal field coefficients $c_{mn}^{(M)}$ and $c_{mn}^{(N)}$ are as follows [6,9]

$$a_{mn}^{S(M)} = T_n^{(M)} w_{mn}^{(M)} \quad (2)$$

$$a_{mn}^{S(N)} = T_n^{(N)} w_{mn}^{(N)} \quad (3)$$

$$\begin{aligned} a_{mn}^{S(M)} &= S_n^{(M)} c_{mn}^{(M)} \\ a_{mn}^{S(N)} &= S_n^{(N)} c_{mn}^{(N)} \\ c_{mn}^{(M)} &= B_n^{(M)} w_{mn}^{(M)} \\ c_{mn}^{(N)} &= B_n^{(N)} w_{mn}^{(N)} \end{aligned} \quad (4)$$

with $T_n^{(M)}$, $T_n^{(N)}$, $S_n^{(M)}$, $S_n^{(N)}$, $B_n^{(M)}$, and $B_n^{(N)}$ as given by

$$T_n^{(M)} = -\frac{j_n(k_p a)[ka j_n(ka)]' - j_n(ka)[k_p a j_n(k_p a)]'}{j_n(k_p a)[ka h_n(ka)]' - h_n(ka)[k_p a j_n(k_p a)]'}$$

$$T_n^{(N)} = -\frac{(k_p a)^2 j_n(k_p a)[ka j_n(ka)]' - (ka)^2 j_n(ka)[k_p a j_n(k_p a)]'}{(k_p a)^2 j_n(k_p a)[ka h_n(ka)]' - (ka)^2 h_n(ka)[k_p a j_n(k_p a)]'} \quad (5)$$

$$\begin{aligned} S_n^{(M)} &= -ika [j_n(ka)[k_p a j_n(k_p a)]' - j_n(k_p a)[ka j_n(ka)]'] \\ S_n^{(N)} &= \frac{i}{k_p a} [(k_p a)^2 j_n(k_p a)[ka j_n(ka)]' \\ &\quad - (ka)^2 j_n(ka)[k_p a j_n(k_p a)]'] \end{aligned} \quad (6)$$

$$B_n^{(M)} = \frac{i}{ka} \frac{1}{j_n(k_p a)[ka h_n(ka)]' - h_n(ka)[k_p a j_n(k_p a)]'}$$

$$B_n^{(N)} = \frac{1}{(k_p a)^2 j_n(k_p a)[ka h_n(ka)]' - (ka)^2 h_n(ka)[k_p a j_n(k_p a)]'} \quad (7)$$

The unknowns in (1) are exciting field coefficients. We can rewrite the equation for $w_{mn}^{(M)}$ and $w_{mn}^{(N)}$ as

$$\begin{aligned} w_{mn}^{(M)(q)} &= e^{i\vec{k}_i \cdot \vec{r}_q} a_{mn}^{(M)} + \sum_{p=1, p \neq q}^N \sum_{\mu\nu} [A_{\mu\nu mn}(k\vec{r}_q \vec{r}_p) \\ &\quad \times T_v^{(M)} w_{\mu\nu}^{(M)(p)} + B_{\mu\nu mn}(k\vec{r}_q \vec{r}_p) T_v^{(N)} w_{\mu\nu}^{(N)(p)}] \end{aligned} \quad (8)$$

$$\begin{aligned} w_{mn}^{(N)(q)} &= e^{i\vec{k}_i \cdot \vec{r}_q} a_{mn}^{(N)} + \sum_{p=1, p \neq q}^N \sum_{\mu\nu} [B_{\mu\nu mn}(k\vec{r}_q \vec{r}_p) \\ &\quad \times T_v^{(M)} w_{\mu\nu}^{(M)(p)} + A_{\mu\nu mn}(k\vec{r}_q \vec{r}_p) T_v^{(N)} w_{\mu\nu}^{(N)(p)}] \end{aligned}$$

where $a_{mn}^{(M)}$ and $a_{mn}^{(N)}$ are the incident field coefficients and $A_{\mu\nu mn}$ and $B_{\mu\nu mn}$ are the spherical wave transformation between two particles [2,6,9]. Equation (8) is the exciting field formulation of multiple scattering equations.

We can also derive multiple scattering equations for the scattered and internal fields. Multiplying T -matrix coefficients $T_n^{(M)}$ or $T_n^{(N)}$ on both sides of (8) and applying the relationship between exciting field and scattered field, we then have the Foldy–Lax equations for scattered field

coefficients:

$$\begin{aligned} a_{mn}^{S(M)(q)} &= e^{i\vec{k}_i \cdot \vec{r}_q} T_n^{(M)} a_{mn}^{(M)} + T_n^{(M)} \sum_{p=1, p \neq q}^N \sum_{\mu\nu} \\ &\quad [A_{\mu\nu mn}(k\vec{r}_q \vec{r}_p) a_{\mu\nu}^{S(M)(p)} + B_{\mu\nu mn}(k\vec{r}_q \vec{r}_p) a_{\mu\nu}^{S(N)(p)}] \end{aligned} \quad (9)$$

$$\begin{aligned} a_{mn}^{S(N)(q)} &= e^{i\vec{k}_i \cdot \vec{r}_q} T_n^{(N)} a_{mn}^{(N)} + T_n^{(N)} \sum_{p=1, p \neq q}^N \sum_{\mu\nu} \\ &\quad [B_{\mu\nu mn}(k\vec{r}_q \vec{r}_p) a_{\mu\nu}^{S(M)(p)} + A_{\mu\nu mn}(k\vec{r}_q \vec{r}_p) a_{\mu\nu}^{S(N)(p)}] \end{aligned}$$

The unknowns of (9) are the scattered field coefficients. Thus, it is called the *scattered field formulation*. Replacing $T_n^{(M)} w_{mn}^{(M)}$ and $T_n^{(N)} w_{mn}^{(N)}$ with $S_n^{(M)} c_{mn}^{(M)}$ and $S_n^{(N)} c_{mn}^{(N)}$, respectively, in (9) and multiplying respective $B_n^{(M)}$ and $B_n^{(N)}$ on both sides, we then have the internal field formulation of Foldy–Lax equations:

$$\begin{aligned} c_{mn}^{(M)(q)} &= e^{i\vec{k}_i \cdot \vec{r}_q} B_n^{(M)} a_{mn}^{(M)} + B_n^{(M)} \sum_{p=1, p \neq q}^N \sum_{\mu\nu} \\ &\quad [A_{\mu\nu mn}(k\vec{r}_q \vec{r}_p) S_\mu^{(M)} c_{\mu\nu}^{(M)(p)} + B_{\mu\nu mn}(k\vec{r}_q \vec{r}_p) S_\nu^{(N)} c_{\mu\nu}^{(N)(p)}] \\ c_{mn}^{(N)(q)} &= e^{i\vec{k}_i \cdot \vec{r}_q} B_n^{(N)} a_{mn}^{(N)} + B_n^{(N)} \sum_{p=1, p \neq q}^N \sum_{\mu\nu} \\ &\quad [B_{\mu\nu mn}(k\vec{r}_q \vec{r}_p) S_\mu^{(M)} c_{\mu\nu}^{(M)(p)} + A_{\mu\nu mn}(k\vec{r}_q \vec{r}_p) S_\nu^{(N)} c_{\mu\nu}^{(N)(p)}] \end{aligned} \quad (10)$$

We have studied the condition numbers of the various types of Foldy–Lax formulations [8,9]. The scattered and exciting field formulations have similar condition numbers; however, the matrices based on scattered field formulations have much larger condition number than do those based on internal field formulations for the same set of parameters. Thus, the internal field formulation is applied in the three-dimensional scattering simulations.

After solving the multiple scattering equations, the scattered field coefficients $a_{mn}^{S(M)}$ and $a_{mn}^{S(N)}$ can be calculated, and the scattered far-field coefficients in the scattering direction $\hat{\mathbf{k}}_s = \hat{\mathbf{x}} \sin \theta_s \cos \phi_s + \hat{\mathbf{y}} \sin \theta_s \sin \phi_s + \hat{\mathbf{z}} \cos \theta_s$ are given by

$$\begin{aligned} \bar{\mathbf{E}}_s(\theta_s, \phi_s) &= \frac{e^{ikr}}{kr} \sum_{q=1}^N e^{-i\vec{k}_s \cdot \vec{r}_q} \sum_{mn} \gamma_{mn} [a_{mn}^{S(M)(q)} \bar{\mathbf{C}}_{mn}(\theta_s, \phi_s) i^{-n-1} \\ &\quad + a_{mn}^{S(N)(q)} \bar{\mathbf{B}}_{mn}(\theta_s, \phi_s) i^{-n}] \end{aligned} \quad (11)$$

where $\bar{\mathbf{B}}_{mn}(\theta, \phi)$ and $\bar{\mathbf{C}}_{mn}(\theta, \phi)$ are vector spherical wavefunctions and γ_{mn} is a coefficient [2,6].

The scattered field can be further decomposed into coherent and incoherent parts. The scattering coefficient arises from the incoherent fields because the coherent wave propagates in the forward transmitted direction and does not contribute to scattering or extinction. For Monte Carlo simulation with N_r realizations, the coherent

scattered field ($\bar{\mathbf{E}}_s$) is calculated by averaging over realizations

$$\langle \bar{\mathbf{E}}_s(\theta_s, \phi_s) \rangle = \frac{1}{N_r} \sum_{\sigma=1}^{N_r} \bar{\mathbf{E}}_s^\sigma(\theta_s, \phi_s) \quad (12)$$

where $\bar{\mathbf{E}}_s^\sigma$ is the scattered field for realization σ and angular brackets represent averaging over realizations. The incoherent scattered field is given by

$$\bar{\mathbf{E}}_s^\sigma(\theta_s, \phi_s) = \bar{\mathbf{E}}_s^\sigma(\theta_s, \phi_s) - \langle \bar{\mathbf{E}}_s(\theta_s, \phi_s) \rangle \quad (13)$$

The bistatic scattering cross section is proportional to the averaged incoherent intensity:

$$\sigma_b(\hat{\mathbf{k}}_s, \hat{\mathbf{k}}_i) = r^2 \frac{\langle |\bar{\mathbf{E}}_s^\sigma(\theta_s, \phi_s)|^2 \rangle}{|\bar{\mathbf{E}}_{\text{inc}}|^2} \quad (14)$$

The scattering cross section is the result of integrating the bistatic cross section over solid angles. The scattering coefficient is the scattering cross section per unit volume

$$\kappa_s = \frac{\sigma_s}{V} = \frac{1}{V} \int_0^\pi d\theta_s \sin\theta_s \int_0^{2\pi} d\phi_s \sigma_b(\hat{\mathbf{k}}_s, \hat{\mathbf{k}}_i) \quad (15)$$

where V is the sample volume in the simulation. The power absorbed by particle q can be written as [5]

$$W_a^{(q)} = -\frac{1}{2\eta k^2} \sum_{mn} [|w_{mn}^{(M)(q)}|^2 (\text{Re } T_n^{(M)} + |T_n^{(M)}|^2) + |w_{mn}^{(N)(q)}|^2 (\text{Re } T_n^{(N)} + |T_n^{(N)}|^2)] \quad (16)$$

The absorption coefficient is expressed as

$$\kappa_a = \frac{1}{V} \sum_{q=1}^N \frac{W_a^{(q)}}{W_{\text{inc}}} = -\frac{1}{Vk^2 |\bar{\mathbf{E}}_{\text{inc}}|^2} \sum_{q=1}^N \sum_{mn} [|w_{mn}^{(M)(q)}|^2 (\text{Re } T_n^{(M)} + |T_n^{(M)}|^2) + |w_{mn}^{(N)(q)}|^2 (\text{Re } T_n^{(N)} + |T_n^{(N)}|^2)] \quad (17)$$

2.3. Results of Using Different Number of Particles

In Monte Carlo simulations, it is important to demonstrate convergence of the results with respect to the numbers of particles used. Physically, this means that the simulated extinction coefficients are extinction per unit volume and should not be dependent on the number of particles used. The number of particles used in the simulations is chosen on the basis of frequencies, volume fractions, and particle diameters. The particle positions are first generated within a unit cube for selected fractional volume and number of particles. The positions are then scaled according to the actual particle size. It has the following relationship

$$f_v = \frac{N_{\text{part}}}{V} \frac{4}{3} \pi a^3 \quad (18)$$

Table 1. Scattering Coefficients and Box Sizes for Different Number of Particles

Number of Particles	L in λ Units	κ_e/k
10	0.189	6.754639×10^{-5}
100	0.407	1.605086×10^{-4}
1000	0.877	1.963294×10^{-4}
2000	1.105	1.998608×10^{-4}

where f_v is the fractional volume, N_{part} the number of particles within the simulated volume V , a the radius of particle, and $V=L^3$. In general, to ensure that a sufficient amount of incoherent fields is generated as a result of scattering in the sample volume, L has to be larger than (or at least close to) one wavelength λ . Table 1 lists the results of extinction coefficients for $ka=0.2$, $f_v=20\%$, and $\epsilon_p=(3.2+i0.01)\epsilon_0$ with different numbers of particles. The simulated box size L is also shown in the table in the unit of wavelength. As illustrated in the table, results show convergence with respect to the number of particles and with respect to box size.

Monte Carlo simulations are performed for different frequencies and physical parameters, including particle size, permittivity, and stickiness. Results based on independent scattering are also shown. The numerical parameters, such as N_{max} , number of particles, and number of realizations, are chosen such that results converge. The maximum number of particles used in simulations is 2000, and up to 50 realizations are used. The simulation results for permittivities ϵ_p with different loss tangents, $\epsilon_p = \epsilon'_p + i\epsilon''_p$, are shown in Fig. 1. Nonsticky particles (i.e., lacking interparticle forces) with diameter 1.2 mm occupying 20% of volume fraction are used in Fig. 1. Results of scattering coefficient κ_s for $\epsilon_p=(3.2+i0.01)\epsilon_0$ and $\epsilon_p=(3.2+i0.02)\epsilon_0$ are quite similar, as shown in Fig. 1a. The scattering coefficient based on independent scattering assumption is larger than that calculated based on QCA or Monte Carlo (MC) simulations. The absorption rate κ_a varies because of the difference in the imaginary part of ϵ_p , as indicated in Fig. 1b, where κ_a is larger for larger ϵ''_p . MC simulations predict higher absorption rate than do the other methods. Generally, independent scattering gives the largest extinction coefficient while QCA predicts the smallest.

2.4. Frequency Dependence of Sticky and Nonsticky Particles

Figure 2 shows the results for different stickiness parameter τ . Particles with diameter 1.2 mm occupying 20% of volume with permittivity $\epsilon_p=3.2\epsilon_0$ are used. The extinction coefficient and scattering coefficient are the same because there is no absorption in this case. The smaller the τ is, the larger the interparticle forces are. Three stickiness parameters are used in the simulations: $\tau=0.1$, $\tau=0.5$, and nonsticky, which corresponds to $\tau=\infty$. For $\tau=0.1$, however, the scattering coefficient is larger than independent scattering at 18, 35, and 60 GHz. It is smaller than independent scattering at 90 GHz. This is because for small τ , the particles strongly tend to adhere

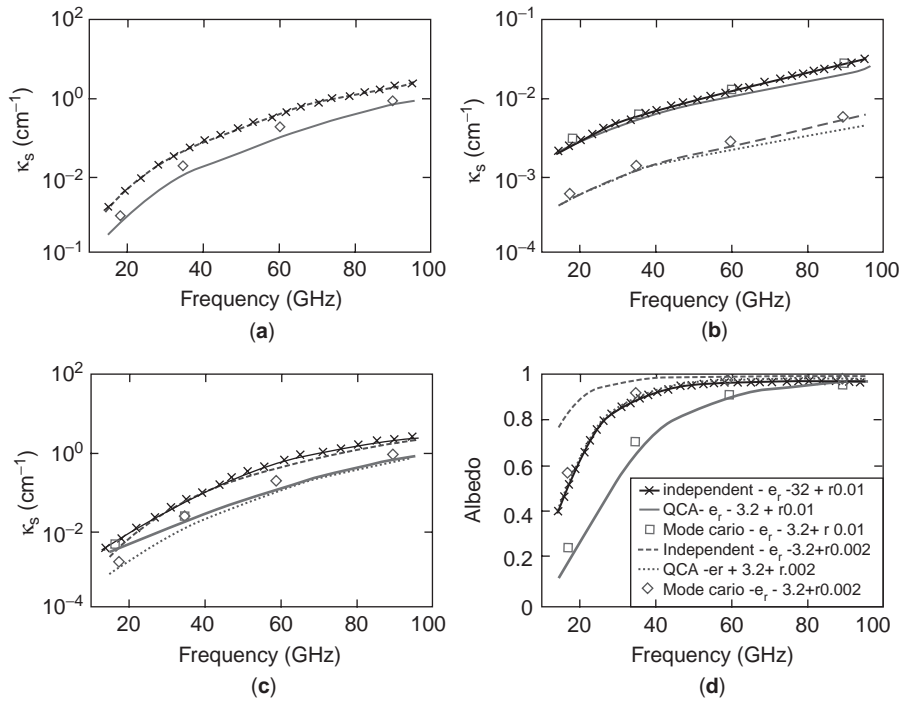


Figure 1. Results of different particle permittivities: $\epsilon_p = (3.2 + i0.01)\epsilon_0$ and $\epsilon_p = (3.2 + i0.02)\epsilon_0$ —particles occupy 20% of volume fraction with diameter 1.2mm: (a) scattering coefficient; (b) absorption rate; (c) extinction coefficient; (d) albedo ($\hat{\omega}$) as a function of frequency. (This figure is available in full color at <http://www.mrw.interscience.wiley.com/erfme>.)

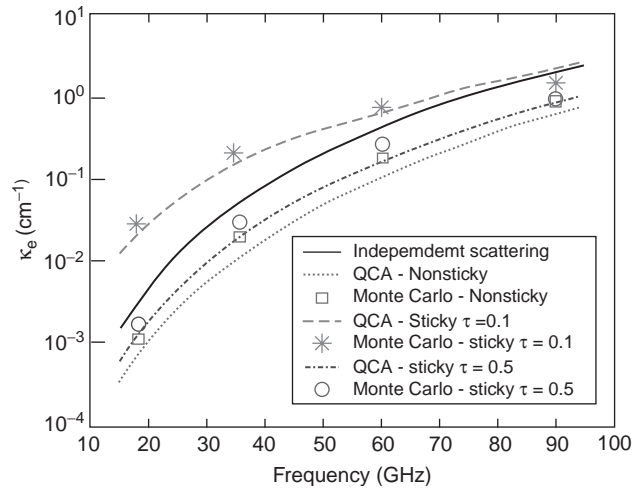


Figure 2. Extinction coefficient in reciprocal centimeters (cm⁻¹) as a function of frequency in gigahertz (GHz) of different stickiness parameter $\tau = 0.1, \tau = 0.2,$ and ∞ . Particles occupy 20% of volume fraction with diameter 1.2mm and $\epsilon_p = 3.2\epsilon_0$. (This figure is available in full color at <http://www.mrw.interscience.wiley.com/erfme>.)

and form clusters. The result is that the particles have larger effective sizes. The effect of the property is exhibited at low frequencies. At higher frequency, the clustering effect of scattering declines and the particles scatter more like the usual dense media. Therefore, the frequency dependence decreases as τ gets smaller. Results for $\tau = 0.5$ and non-sticky particles are about the same. This means that the stickiness represents little difference in scattering except for small stickiness parameter τ . Table 2 lists the scattering coefficients for various stickiness parameters at selected frequencies. The scattering coefficient at 18GHz is used as reference. To study the frequency dependence, we define n such that

$$\frac{\kappa_s(\text{at } f_2)}{\kappa_s(\text{at } f_1)} = \left(\frac{f_2}{f_1}\right)^n \tag{19}$$

where f_1 and f_2 are the two frequencies and κ_s is the scattering coefficient at a specific frequency and n is a power law to be determined. On the basis of the simulated

Table 2. Scattering Coefficients in (dB/m) for Various Stickiness Parameters at Selected Frequencies

Frequency (GHz)	Monte Carlo		QCA		Independent Scattering
	$\tau = 0.1$	$\tau = 0.5$	$\tau = 0.1$	$\tau = 0.5$	
18	12.051	0.738	9.450	0.571	1.376
35	82.761	13.203	63.856	8.172	20.359
60	326.643	116.167	297.824	72.251	185.546
90	707.985	443.461	957.044	354.834	862.510

Table 3. Frequency Dependence n Based on Scattering Coefficients from Table 2

Frequency (GHz)	Monte Carlo		QCA		Independent Scattering
	$\tau = 0.1$	$\tau = 0.5$	$\tau = 0.1$	$\tau = 0.5$	
18	—	—	—	—	—
35	2.898	4.338	2.873	4.001	4.038
60	2.741	4.202	2.866	4.020	4.063
90	2.531	3.976	2.869	3.996	4.051

results, the frequency dependence n is calculated by

$$n = \frac{\log \left[\frac{\kappa_s(atf_2)}{\kappa_s(atf_1)} \right]}{\log \left(\frac{f_2}{f_1} \right)} \tag{20}$$

The results for $f_1 = 18$ GHz are shown in Table 3. The frequency dependence n for stickiness $\tau = 0.1$ is less than that of nonsticky particles and $\tau = 0.5$. For nonsticky particles, dense media scattering is less than independent scattering. This reduction of scattering for dense media becomes a smaller effect at higher frequency. Thus results in Table 3 can exhibit index larger than 4. Note that a least-square fit with snow extinction measurements gives an index n between 2 and 3 [22]. The index is consistent with the simulated index n of sticky particles.

Figure 3 shows the results for nonsticky particle with different sizes. Particles occupying 20% of volume with permittivity $\epsilon_p = 3.2\epsilon_0$ are used. The extinction coefficients versus frequency are plotted. We note that scattering increases with particle size, and the scattering by Monte Carlo simulation is less than independent scattering. However, the difference gets smaller at high frequencies. Figure 4 shows results for a sticky particle with $\tau = 0.1$, and the diameters of particles are 1, 1.2, and 1.5 mm. These represent typical ice grain sizes in snow. Note that

scattering increases with particle size. For sticky particles, the simulation results are larger than independent scattering at low frequencies and are smaller than independent scattering at high frequencies. At 90 GHz, the extinction is large. Thus at such high frequency, passive remote sensing will not be useful to determine snow depth.

We next compare Monte Carlo simulation results with that of QCA. For nonsticky particles, the extinction coefficient calculated from QCA is smaller than that from MC at low frequencies while the extinction coefficients of MC and QCA are comparable at higher frequency. For sticky particles, larger particles generally have higher extinction coefficients. We note that the QCA results are generally much closer to simulations than independent scattering. The QCA formulation has been used in dense media formulation and applied to passive remote sensing of spaceborne sensors [7,26].

In the results described above, we have not taken into account the dependence of loss tangent on frequency because the computed results of extinction are dominated by scattering rather than absorption. However, in comparison with experimental data in Fig. 5, we include the dependence of loss tangent on frequency. The permittivity of ice as a function of frequency can be found in Ref. 5. In Fig. 5 we compare Monte Carlo simulation, independent scattering, and snow extinction measurement data at 18, 35, 60, and 90 GHz [22]. We use ground truth mean grain diameter of 1 mm and snow density of 0.315 g/cm^3 [22].

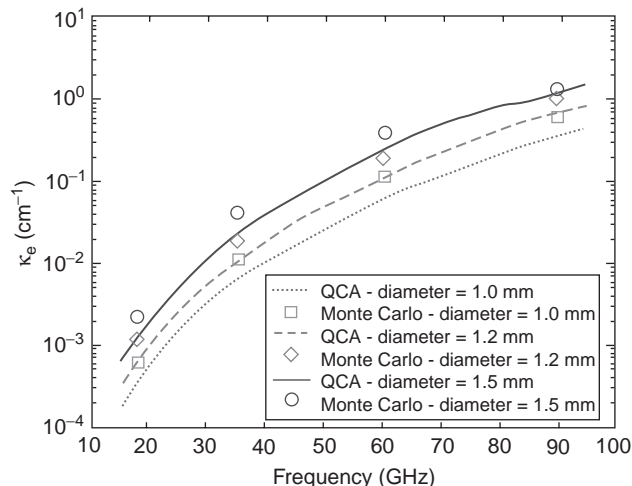


Figure 3. Extinction coefficient in cm^{-1} of different particle sizes as a function of frequency in GHz for nonsticky particles. Particles occupy 20% of volume with permittivity $\epsilon_p = 3.2\epsilon_0$. (This figure is available in full color at <http://www.mrw.interscience.wiley.com/erfme>.)

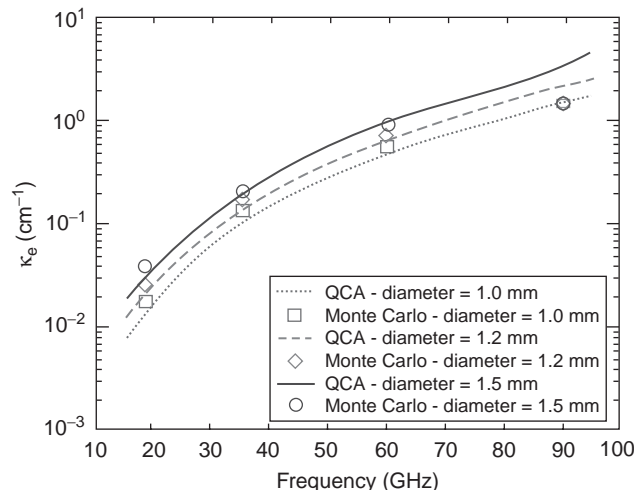


Figure 4. Extinction coefficient in cm^{-1} of different particle sizes as a function of frequency in GHz for sticky particles ($\tau = 0.1$). Particles occupy 20% of volume with permittivity $\epsilon_p = 3.2\epsilon_0$. (This figure is available in full color at <http://www.mrw.interscience.wiley.com/erfme>.)

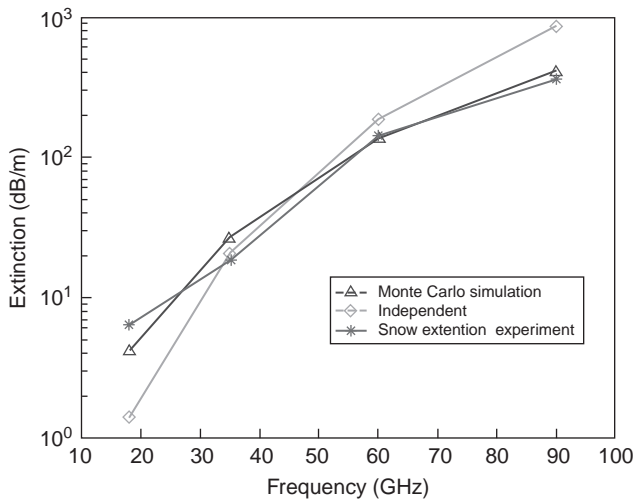


Figure 5. Comparison of Monte Carlo simulation results with experimental data and independent scattering. (This figure is available in full color at <http://www.mrw.interscience.wiley.com/erfme>.)

The simulation is based on a volume fraction of 0.4134. The permittivity of ice grains chosen is $\epsilon_p = 3.2\epsilon_0 + i\epsilon_s''$. The loss tangent depends on frequency and $\epsilon_s''/\epsilon_0 = 0.007, 0.009, 0.011, \text{ and } 0.014$, respectively, at 18, 35, 60, and 90 GHz, which correspond to a salinity of 0.12 parts per thousand [44]. The frequency dependence as exhibited by Monte Carlo simulation is in reasonable agreement with experiment and is much better than that of independent scattering.

In this section we present the Monte Carlo simulations performed for various frequencies, particle sizes, particle permittivities, and cases with different stickiness parameters τ . Monte Carlo simulation results compare well with QCA results. Scattering based on the sticky particle assumption has a much weaker frequency dependence than does that of independent scattering of frequency to the fourth power. This frequency dependence has been shown to better match the observed frequency dependence of snow terrain [7,26]. For problems of very complicated geometry, Monte Carlo simulations provide the correct solutions for Maxwell equations. The results of simulations can be tabulated and further combined with dense media radiative transfer theory. The dense media radiative transfer theory has been used extensively for mapping of snow depth using spaceborne radiometer.

3. POLARIMETRIC PASSIVE MICROWAVE REMOTE SENSING OF WIND VECTORS WITH FOAM-COVERED OCEAN SURFACE

Fully polarimetric microwave remote sensing means that all four Stokes parameters are measured [45]. There has been an increasing interest in the applications of polarimetric microwave radiometers for ocean wind remote sensing [46–49]. It is known that the presence of foam on the ocean surface has a profound effect on the brightness temperatures measured by microwave radiometers. Although foam typically covers only a few percent of sea

surfaces, increasing foam coverage on the sea surface can substantially increase the sea surface emissivity [50–52]. However, there is a great concern on the impact of foam on the retrieval of the ocean surface wind vector from satellite-mounted microwave instruments, which is due in large part to the difficulty in making measurements at high-wind conditions when significant foam coverage is present. In the past, empirical microwave emissivity models [48,50,51,53–55] were used to estimate the effect of the foam above the ocean surface on the passive microwave remote sensing measurements. These are empirical fitting procedures using experimental data and the empirical models do not take into account the physical microstructure of foam and the foam-layer thickness. The subject of foam dynamics has also attracted great attention. Huang and Jin discussed a composite model of foam scatterers and two-scale wind-driven rough sea surface [52]. Controlled field experiments were performed to measure foam dynamics and the microwave emissivity of calm seawater [56,57].

More recently, physically based approaches, based on the quasicrystalline approximation (QCA) dense media model or Monte Carlo simulations, have been developed to account for the microstructure of foam [10–12]. The model treats the foam as densely packed air bubbles coated with thin seawater coating. In order to model high-density packing, a face-centered-cubic (fcc) structure is used to place the air bubbles. It was shown that the polarization and frequency of the brightness temperatures depend on the physical microstructure properties of foam and the foam-layer thickness. In this section, we present the polarimetric microwave emission model for foam-covered ocean surfaces. The dense media model of foam is applied to calculate the values of the complex effective propagation constants, the extinction coefficients, and the albedo. These are used to describe the characteristics of the foam layer. In Section 3.1, we describe the physical and geometric model of foam. The Monte Carlo simulation by solving Maxwell's equations and DMRT theory are summarized in Sections 3.2 and 3.3, respectively. In the Monte Carlo simulations, the volume integral equation has been used. The absorption, scattering, and extinction coefficients are calculated, and the simulation results for emissivity with typical foam parameters at 10.8 and 36.5 GHz are presented in Section 3.4. Comparisons are also made with experimental data [57] for vertical and horizontal polarizations. The Monte Carlo simulation results with those based on QCA are compared in Section 3.5. The effects of boundary roughness of ocean surface can be included in the boundary conditions of dense media radiative transfer (DMRT) theory by using the second-order small perturbation method (SPM) [2,7,46]. A fully polarimetric passive model for wind-generated and foam-covered rough sea surfaces, using the empirical Durden–Vesecy spectrum [58], is presented in Ref. 12.

3.1. Description of Foam Model

Figure 6 shows a video micrograph of the bubble structure of artificially generated foam on the surface of Chesapeake Bay [57]. Analysis of this and similar images shows that

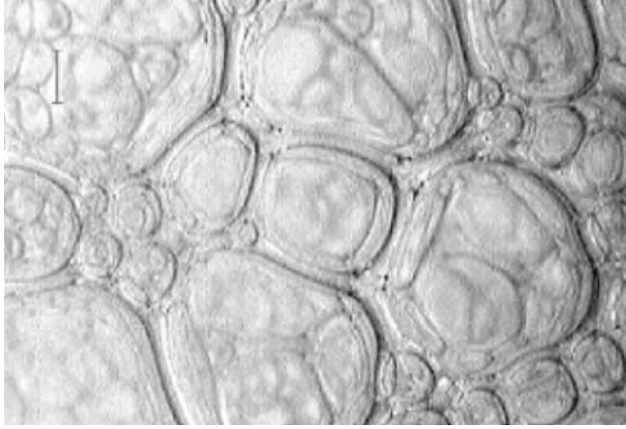


Figure 6. Videomicrograph of artificially generated bubbles in foam on the surface of Chesapeake Bay. The scale in the upper left corner shows a distance of 1 mm.

the void fraction of this foam is 80–90% in most cases. To simplify the foam model, the foam is assumed to be composed of densely packed spherical air bubbles with thin seawater coating [10–12]. The physical and geometric structure of a spherical dielectric-coated particle is illustrated in Fig. 7, where s_j denotes that the coated particle is of the j th species, $s_j = 1, 2, \dots, L$. The core of the coated particle is air, and the shell is seawater. It is assumed that all the particles have the same outer radius a_{s_j} , but need not be identical in coating thicknesses ($a_{s_j} - b_{s_j}$). $\epsilon_{a_{s_j}}$ and $\epsilon_{b_{s_j}}$ are permittivities within the shell and in the core of the coated particle, respectively.

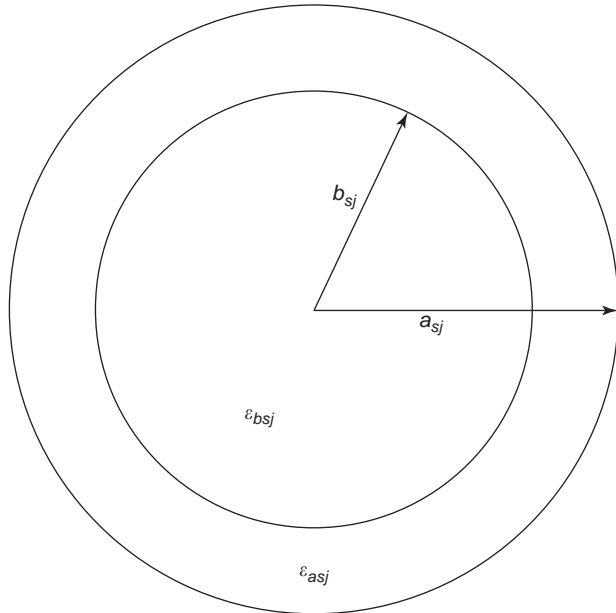


Figure 7. Spherical dielectric-coated particle; a_{s_j} and b_{s_j} are the outer and inner radii of the spherical shells, respectively, and $\epsilon_{a_{s_j}}$ and $\epsilon_{b_{s_j}}$ are permittivities within the shell and in the core of the coated particle, respectively.

To achieve high-density packing, the coated particles are arranged in a FCC lattice structure that has a packing density of $\pi/\sqrt{18} \approx 74\%$ [11,12]. The air regions include the core regions of the coated particles and the interstitial space between the coated particles. For example, let V be the total volume of the foam and N be the number of coated particles. The j th coated particles has a inner radius b_j and outer radius a_j . The fractional volume of coated particles is about 74%; the fractional volume of seawater f_w is then

$$f_w = \frac{1}{V} \sum_{j=1}^N \frac{4\pi}{3} (a_j^3 - b_j^3) \quad (21)$$

By choosing values for the inner and outer radii, the foam void fraction ($1.0 - f_w$) can be on the order of 90%, which is in agreement with experimental measurements of artificially generated foam [57].

3.2. Absorption and Extinction Based on Monte Carlo Simulation by Solving Maxwell's Equations

Consider the thermal emission from a layered medium with coated particles embedded in a background medium of air, as indicated in Fig. 8. The layer consists of coated particles (region 1), and covers a half-space of ocean (region 2). The scattering coefficient and absorption coefficient of a collection of N coated particles are defined respectively as scattering cross section per unit volume and absorption cross section per unit volume. In the Monte Carlo simulation approach, we place N particles in volume V , and calculate the absorption and scattering of these N particles collectively by solving Maxwell's equations and then averaging over realizations and dividing them by the volume V . These are done for large N and the results of the scattering and absorption coefficients computed in this manner converge for large N .

A volume integral equation derived from Maxwell's equations is used to solve scattering and absorption for the N particles [6,11,12]. The volume integral equation has the internal electric field in the coated region as the unknown. The internal field $\vec{E}_i(\vec{r})$ in the seawater coating

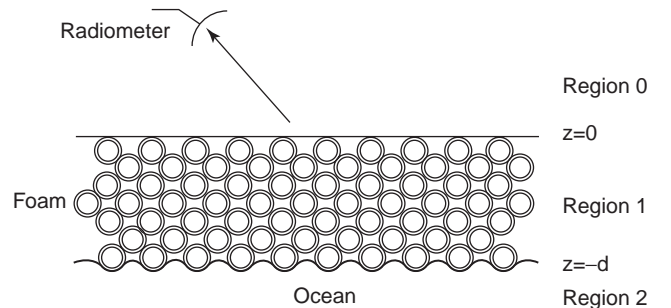


Figure 8. Geometric configuration for thermal emission from foam-covered ocean. The foam layer is region 1 and is absorptive and scattering. Region 2 is the ocean.

region of particle i , $\bar{r} \in V_i$, is given by

$$\begin{aligned} \bar{\mathbf{E}}_i(\bar{r}) = & \bar{\mathbf{E}}^e(\bar{r}) + k^2 \sum_{j=1}^N \int_{V_j} d\bar{r}' g(\bar{r}, \bar{r}') (\epsilon_{vj} - 1) \bar{\mathbf{E}}_j(\bar{r}') \\ & - \sum_{j=1}^N \nabla \int_{V_j} d\bar{r}' \nabla' g(\bar{r}, \bar{r}') (\epsilon_{vj} - 1) \bar{\mathbf{E}}_j(\bar{r}') \end{aligned} \quad (22)$$

where $\bar{\mathbf{E}}^e(\bar{r})$ is the incident field, $g(\bar{r}, \bar{r}')$ the free space scalar Green's function, ϵ_{vj} the relative permittivity of particle within the coating, V_j the volume occupied by particle j , and $i = 1, 2, \dots, N$. We expand the internal field in the coating region of particle j , $\bar{\mathbf{E}}_j(\bar{r})$, into three basis functions. The basis functions are from the electrostatic solutions of the coating region of a coated sphere [11]. The subscript j is suppressed in Eqs. (23) and (24)

$$\bar{\mathbf{E}}_j(\bar{r}) = \sum_{\alpha=1}^3 c_{\alpha}(\bar{r}) \bar{f}_{\alpha}(\bar{r}) \quad (23)$$

$$\begin{aligned} \bar{f}_1(\bar{r}) = & \frac{1+2\epsilon_r}{3\epsilon_r} \hat{x} + \frac{1-\epsilon_r}{3\epsilon_r} b^3 \\ & \times \left[\hat{r} \frac{2}{r^3} \sin \theta \cos \phi - \frac{1}{r^3} (\hat{\theta} \cos \theta \cos \phi - \hat{\phi} \sin \phi) \right] \\ \bar{f}_2(\bar{r}) = & \frac{1+2\epsilon_r}{3\epsilon_r} \hat{y} + \frac{1-\epsilon_r}{3\epsilon_r} b^3 \\ & \times \left[\hat{r} \frac{2}{r^3} \sin \theta \sin \phi - \frac{1}{r^3} (\hat{\theta} \cos \theta \sin \phi + \hat{\phi} \cos \phi) \right] \\ \bar{f}_3(\bar{r}) = & \frac{1+2\epsilon_r}{3\epsilon_r} \hat{z} + \frac{1-\epsilon_r}{3\epsilon_r} b^3 \left[\hat{r} \frac{2}{r^3} \cos \phi + \hat{\theta} \frac{1}{r^3} \sin \theta \right] \end{aligned} \quad (24)$$

where $\bar{r} \in V_j$. Letting

$$\begin{aligned} \bar{q}_{j\alpha}(\bar{r}) = & k^2 \int_{V_j} d\bar{r}' g(\bar{r}, \bar{r}') (\epsilon_{vj} - 1) \bar{f}_{j\alpha}(\bar{r}') \\ & - \nabla \int_{V_j} d\bar{r}' \nabla' g(\bar{r}, \bar{r}') (\epsilon_{vj} - 1) \bar{f}_{j\alpha}(\bar{r}') \end{aligned} \quad (25)$$

we can express the integral equation (22) as

$$\begin{aligned} \sum_{\alpha=1}^3 c_{i\alpha} \bar{f}_{i\alpha}(\bar{r}) = & \bar{\mathbf{E}}^{\text{ex}}(\bar{r}) + \sum_{j=1, j \neq i}^N \sum_{\alpha=1}^3 c_{j\alpha} \bar{q}_{j\alpha}(\bar{r}) \\ & + \sum_{\alpha=1}^3 c_{i\alpha} \bar{q}_{i\alpha}(\bar{r}) \end{aligned} \quad (26)$$

We then apply the Galerkin method to rewrite (26) in a linear system of equations for the coefficients

$$\begin{aligned} & \sum_{\alpha=1}^3 c_{i\alpha} \int_{V_i} d\bar{r} \bar{f}_{i\alpha}(\bar{r}) \cdot [\bar{f}_{i\alpha}(\bar{r}) - \bar{q}_{i\alpha}(\bar{r})] \\ = & \int_{V_i} d\bar{r} \bar{f}_{i\beta}(\bar{r}) \cdot \bar{\mathbf{E}}^e(\bar{r}_i) \\ & + \sum_{j=1, j \neq i}^N \sum_{\alpha=1}^3 c_{j\alpha} \int_{V_j} d\bar{r} \bar{f}_{i\beta}(\bar{r}) \cdot \bar{q}_{j\alpha}(\bar{r}) \end{aligned} \quad (27)$$

with $i = 1, 2, \dots, N$ and $\beta = 1, 2, 3$. Taking the small particle assumption into account, we can make approximations of (27):

$$\begin{aligned} & \sum_{\alpha=1}^3 c_{i\alpha} \int_{V_i} d\bar{r} \bar{f}_{i\alpha}(\bar{r}) \cdot [\bar{f}_{i\alpha}(\bar{r}) - \bar{q}_{i\alpha}(\bar{r})] \\ = & \int_{V_i} d\bar{r} \bar{f}_{i\beta}(\bar{r}) \cdot \bar{\mathbf{E}}^e(\bar{r}_i) + \sum_{j=1, j \neq i}^N \sum_{\alpha=1}^3 k^2 (\epsilon_{rj} - 1) c_{j\alpha} \\ & \times \int_{V_i} d\bar{r} \bar{f}_{i\beta}(\bar{r}) \cdot \bar{\mathbf{G}}(\bar{r}_i, \bar{r}_j) \int_{V_j} d\bar{r}' \bar{f}_{j\alpha}(\bar{r}') \end{aligned} \quad (28)$$

After simplifications, (28) can be written as

$$\begin{aligned} c_{i\beta} \bar{K}_i = & \bar{s}_{i\beta} \cdot \bar{\mathbf{E}}^e(\bar{r}_i) + \sum_{j=1, j \neq i}^N \sum_{\alpha=1}^3 k^2 (\epsilon_{rj} - 1) \\ & \times c_{j\alpha} \bar{s}_{i\beta} \cdot \bar{\mathbf{G}}(\bar{r}_i, \bar{r}_j) \cdot \bar{s}_{j\alpha} \end{aligned} \quad (29)$$

where

$$\begin{aligned} \bar{K}_i = & \frac{2\epsilon_{ri} + 1}{3\epsilon_{ri}} \cdot \frac{1}{9\epsilon_{ri}} \cdot \frac{4\pi}{3} (a_i^3 - b_i^3) \\ & \times \frac{(2\epsilon_{ri} + 1)(2 + \epsilon_{ri}) - 2b_i^3(\epsilon_{ri} - 1)^2}{a_i^3} \end{aligned} \quad (30)$$

and

$$\begin{aligned} \bar{s}_{i1} = & \int_{V_i} d\bar{r} \bar{f}_{i1}(\bar{r}) = \frac{2\epsilon_{ri} + 1}{3\epsilon_{ri}} \cdot \frac{4\pi}{3} (a_i^3 - b_i^3) \hat{x} \\ \bar{s}_{i2} = & \int_{V_i} d\bar{r} \bar{f}_{i2}(\bar{r}) = \frac{2\epsilon_{ri} + 1}{3\epsilon_{ri}} \cdot \frac{4\pi}{3} (a_i^3 - b_i^3) \hat{y} \\ \bar{s}_{i3} = & \int_{V_i} d\bar{r} \bar{f}_{i3}(\bar{r}) = \frac{2\epsilon_{ri} + 1}{3\epsilon_{ri}} \cdot \frac{4\pi}{3} (a_i^3 - b_i^3) \hat{z} \end{aligned} \quad (31)$$

After solving the matrix equations, the power absorbed by N coated particles can be calculated by

$$P_{\text{abs}} = \frac{1}{2} \omega \sum_{j=1}^N \int_{V_j} d\bar{r} \epsilon_{vj}'(\bar{r}) |\bar{\mathbf{E}}_j(\bar{r})|^2 \quad (32)$$

and the absorption coefficient is the absorption per unit volume

$$\kappa_{\text{abs}} = \frac{P_{\text{abs}}}{\frac{1}{2\eta} |\bar{\mathbf{E}}^e|^2 V} \quad (33)$$

where η is the free-space wave impedance. The scattered far field can be calculated as following

$$\begin{aligned} \bar{\mathbf{E}}_s(\bar{\mathbf{r}}) = & \frac{k^2 e^{ikr}}{4\pi r} (\hat{v}_s \hat{v}_s + \hat{h}_s \hat{h}_s) \sum_{j=1}^N \int_{V_j} d\bar{\mathbf{r}} \\ & \times (\epsilon_{vj} - 1) \bar{\mathbf{E}}_j(\bar{\mathbf{r}}) e^{-ik\hat{s} \cdot \bar{\mathbf{r}}_j} \end{aligned} \quad (34)$$

Then the scattered power is

$$P_s = \frac{1}{2\eta} \int_0^{2\pi} d\phi_s \int_0^\pi d\theta_s \sin \theta_s (|E_{vs}|^2 + |E_{hs}|^2) \quad (35)$$

where E_{vs} and E_{hs} are vertical and horizontal polarized components of the scattering fields, respectively. The scattering coefficient is scattering cross section per unit volume

$$\kappa_s = \frac{P_s^{\text{inco}}}{\frac{1}{2\eta} |\bar{\mathbf{E}}^{\text{ex}}|^2 V} \quad (36)$$

where P_s^{inco} is the incoherent part of the scattered power.

The coherent wave is obtained by averaging the scattered field over the Monte Carlo realizations [6,11]. To obtain the incoherent power, we have to subtract the coherent intensity. Thus

$$\begin{aligned} P_s^{\text{inco}} = & \frac{1}{2\eta} \int_0^{2\pi} d\phi_s \int_0^\pi d\theta_s \sin \theta_s \{ \langle |E_{vs}|^2 \rangle \\ & - \langle E_{vs} \rangle \langle E_{vs} \rangle^* + \langle |E_{hs}|^2 \rangle \\ & - \langle E_{hs} \rangle \langle E_{hs} \rangle^* \} \end{aligned} \quad (37)$$

where the angular brackets represent averaging over realizations. The extinction coefficient is $\kappa_e = \kappa_s + \kappa_{\text{abs}}$, and the albedo is $\tilde{\omega} = \kappa_s / \kappa_e$. The effective permittivity can be calculated as follows. In the forward direction $\bar{k}_s = \bar{k}_i$, the scattered field in the incident polarization can be written as $E_s = F e^{ikr} / r$. Then the effective propagation constant K is given by

$$K = \text{Re} \left(\sqrt{k^2 + \frac{4\pi F}{V}} \right) + i \left(\frac{\kappa_e}{2} \right) \quad (38)$$

The effective permittivity is expressed as

$$\epsilon_{\text{eff}} = \frac{K^2}{k^2} \quad (39)$$

The effective permittivity of foam will be used in the Fresnel reflection coefficients for the air-foam flat interface and the foam-ocean flat interface in the dense media radiative transfer theory. The calculated scattering and

absorption coefficients are then substituted into dense media radiative transfer equations. A Rayleigh phase matrix is used in the dense media radiative transfer equations [2,7].

3.3. Dense Media Radiative Theory

Consider the thermal emission problem of a foam layer covered wind-roughened ocean surfaces, as indicated in Fig. 8. The foam layer consists of coated dielectric particles in region 1. The DMRT equations for passive remote sensing in region 1 can be written as follows

$$\begin{aligned} \frac{d}{dz} \bar{I}_u(z, \mu, \phi) = & -\kappa_{\text{es}} \bar{I}_u(z, \mu, \phi) \\ & + \kappa_{\text{as}} C \bar{T} + \bar{\mathbf{F}}_u(z, \mu, \phi) \end{aligned} \quad (40)$$

$$-\frac{d}{dz} \bar{I}_d(z, \mu, \phi) = -\kappa_{\text{es}} \bar{I}_d(z, \mu, \phi)$$

$$+ \kappa_{\text{as}} C \bar{T} + \bar{\mathbf{F}}_d(z, \mu, \phi)$$

$$\begin{aligned} \bar{\mathbf{F}}_u(z, \mu, \phi) = & \frac{\kappa_{\text{ss}}}{4\pi} \int_0^1 d\mu' \int_0^{2\pi} d\phi' \\ & \times [\bar{\mathbf{P}}(\mu, \phi; \mu', \phi') \bar{I}_u(z, \mu', \phi') \\ & + \bar{\mathbf{P}}(\mu, \phi; -\mu', \phi') \bar{I}_d(z, \mu', \phi')] \end{aligned} \quad (41)$$

$$\begin{aligned} \bar{\mathbf{F}}_d(z, \mu, \phi) = & \frac{\kappa_{\text{ss}}}{4\pi} \int_0^1 d\mu' \int_0^{2\pi} d\phi' \\ & \times [\bar{\mathbf{P}}(-\mu, \phi; \mu', \phi') \bar{I}_u(z, \mu', \phi') \\ & + \bar{\mathbf{P}}(-\mu, \phi; -\mu', \phi') \bar{I}_d(z, \mu', \phi')] \end{aligned}$$

where $\bar{I}_u(z, \mu, \phi)$ and $\bar{I}_d(z, \mu, \phi)$ represent, respectively, upward- and downward-going specific intensities and 4×4 matrices containing the four Stokes parameters; $\mu = \cos \theta$, $\mu' = \cos \theta'$, $\kappa_{\text{es}} = \kappa_e / \cos \theta$, $\kappa_{\text{ss}} = \kappa_s / \cos \theta$; κ_a and κ_s are the absorption and scattering coefficient matrices taken to be diagonal respectively; $C = K_b K'^2 / (\lambda^2 k^2)$, where K_b is the Boltzmann's constant [2,5]; $\bar{\mathbf{P}}(\mu, \phi; \mu', \phi')$ is the Rayleigh scattering phase matrix; and \bar{T} is the temperature profile in the layer. The boundary condition at $z = 0$ is

$$\bar{I}_d(z = 0, \theta, \phi) = \bar{\mathbf{R}}(\theta) \bar{I}_u(z = 0, \theta, \phi) \quad (42)$$

where $\bar{\mathbf{R}}(\theta)$ is a reflection matrix of the flat surface at the air-foam interface

$$\begin{aligned} & \bar{\mathbf{R}}(\theta) \\ = & \begin{bmatrix} |R_v(\theta)|^2 & 0 & 0 & 0 \\ 0 & |R_h(\theta)|^2 & 0 & 0 \\ 0 & 0 & \text{Re}(R_v(\theta) R_h^*(\theta)) & -\text{Im}(R_v(\theta) R_h^*(\theta)) \\ 0 & 0 & \text{Im}(R_v(\theta) R_h^*(\theta)) & \text{Re}(R_v(\theta) R_h^*(\theta)) \end{bmatrix} \end{aligned} \quad (43)$$

in which R_v and R_h are the Fresnel reflectivities with effective propagation constant K and effective relative permittivity ϵ_{eff} for dense media.

The rough surface boundary condition at $z = -d$ is bistatic and is determined by the second-order SPM

$$\begin{aligned} \bar{\mathbf{I}}_u(z = -d, \mu, \phi) &= \bar{\bar{\mathbf{G}}}_c(\theta, \phi) \bar{\mathbf{I}}_d(z = -d, \mu, \phi) \\ &+ \frac{K^2}{\mu} \int_0^1 d\mu' \int_0^{2\pi} d\phi' \mu'^2 W(\bar{\mathbf{k}}_\perp - \bar{\mathbf{k}}'_\perp) \\ &\times \bar{\bar{\mathbf{G}}}_{\text{ic}}(\mu, \phi; -\mu', \phi') \bar{\mathbf{I}}_d(z = -d, \mu', \phi') + \bar{e}CT_g \end{aligned} \quad (44)$$

where $\bar{\bar{\mathbf{G}}}_c$ and $\bar{\bar{\mathbf{G}}}_{\text{ic}}$ respectively are the coherent and incoherent scattering phase matrixes of the rough surface at $z = -d$.

$$\bar{\bar{\mathbf{G}}}_{\text{c,ic}} = \begin{bmatrix} \langle |f_{vv}|^2 \rangle & \langle |f_{vh}|^2 \rangle & \text{Re}(f_{vv}f_{vh}^*) & -\text{Im}(f_{vv}f_{vh}^*) \\ \langle |f_{hv}|^2 \rangle & \langle |f_{hh}|^2 \rangle & \text{Re}(f_{hv}f_{hh}^*) & -\text{Im}(f_{hv}f_{hh}^*) \\ 2\text{Re}(f_{vv}f_{vh}^*) & 2\text{Re}(f_{vh}f_{hh}^*) & \text{Re}(f_{vv}f_{hh}^* + f_{vh}f_{hv}^*) & \text{Im}(f_{vh}f_{hh}^* - f_{vv}f_{hh}^*) \\ 2\text{Im}(f_{vv}f_{vh}^*) & 2\text{Im}(f_{vh}f_{hh}^*) & \text{Im}(f_{vv}f_{hh}^* + f_{vh}f_{hv}^*) & \text{Re}(f_{vv}f_{hh}^* - f_{vh}f_{hv}^*) \end{bmatrix} \quad (45)$$

For $\bar{\bar{\mathbf{G}}}_c$, $f_{\alpha\alpha} = f_{\alpha\alpha}^{(0)} + f_{\alpha\alpha}^{(2)}$, $f_{\alpha\beta} = f_{\alpha\beta}^{(2)}$, and for $\bar{\bar{\mathbf{G}}}_{\text{ic}}$, $f_{\alpha\beta} = f_{\alpha\beta}^{(1)}$. Here, symbols α and β represent vertical and horizontal. $f_{vv}^{(0)}$ and $f_{hh}^{(0)}$ are Fresnel reflection coefficients for vertical and horizontal polarizations with the zeroth-order fields considered. $f_{\alpha\beta}^{(1)}$ and $f_{\alpha\beta}^{(2)}$ are scattering coefficients of the α -polarized component of the first- and second-order scattered fields with β -polarized incident field, respectively, which are given in Ref. 7. The zeroth- and second-order fields give the coherent reflection coefficients of the surfaces. $f_{\alpha\beta}^{(1)}$ gives the incoherent polarimetric bistatic scattering coefficient due to the first-order scattered field. They are derived using the second-order small-perturbation method (SPM) [2, 7]. T_g is the temperature of the half-space below the foam and \bar{e} are the emissivities of the lower boundary. The differential equations in (40) have standard solutions of the form

$$\begin{aligned} \bar{\mathbf{I}}_u(z) &= \bar{\mathbf{I}}_u(-d)e^{-\kappa_{\text{es}}(z+d)} + \int_{-d}^z dz' [\bar{\mathbf{F}}_u(z') \\ &+ \kappa_{\text{as}}C\bar{\mathbf{T}}]e^{-\kappa_{\text{es}}(z-z')} \end{aligned} \quad (46)$$

$$\begin{aligned} \bar{\mathbf{I}}_d(z) &= \bar{\mathbf{I}}_d(0)e^{\kappa_{\text{es}}z} + \int_z^0 dz' [\bar{\mathbf{F}}_d(z') \\ &+ \kappa_{\text{as}}C\bar{\mathbf{T}}]e^{\kappa_{\text{es}}(z-z')} \end{aligned} \quad (47)$$

Next, we incorporate the rough surface boundary conditions into a form suitable for iterative solutions. Substituting the boundary conditions into (46) and (47), we

have

$$\begin{aligned} \bar{\mathbf{I}}_u(z) &= e^{-\kappa_{\text{es}}(z+d)} \bar{\bar{\mathbf{G}}}_c(\mu, \phi) \bar{\mathbf{I}}_d(z = -d, \mu, \phi) \\ &+ e^{-\kappa_{\text{es}}(z+d)} \frac{K^2}{\mu} \int_0^1 d\mu' \int_0^{2\pi} d\phi' \mu'^2 W(\bar{\mathbf{k}}_\perp - \bar{\mathbf{k}}'_\perp) \\ &\times \bar{\bar{\mathbf{G}}}_{\text{ic}}(\mu, \phi; -\mu', \phi') \bar{\mathbf{I}}_d(z = -d, \mu', \phi') \\ &+ \bar{e}CT_g e^{-\kappa_{\text{es}}(z+d)} + \int_{-d}^z dz' [\bar{\mathbf{F}}_u(z') + \kappa_{\text{as}}C\bar{\mathbf{T}}] e^{-\kappa_{\text{es}}(z-z')} \end{aligned} \quad (48)$$

$$\begin{aligned} \bar{\mathbf{I}}_d(z) &= \bar{\bar{\mathbf{R}}}(\theta) \bar{\mathbf{I}}_u(z = 0, \theta, \phi) e^{\kappa_{\text{es}}z} + \int_z^0 dz' \\ &\times [\bar{\mathbf{F}}_d(z') + \kappa_{\text{as}}C\bar{\mathbf{T}}] e^{\kappa_{\text{es}}(z-z')} \end{aligned} \quad (49)$$

The source terms in (48) are the upward temperature originating from the layer temperature profile. We assume a temperature profile $T = T_g$

$$\int_{-d}^z dz' \kappa_{\text{as}}CTe^{-\kappa_{\text{es}}(z-z')} = C \frac{\kappa_a}{\kappa_e} T_g [1 - e^{-\kappa_{\text{es}}(z+d)}] \quad (50)$$

The contribution from the lower half-space is $\bar{e}CT_g \exp[-\kappa_{\text{es}}(z+d)]$. The source term in (49) is the downward temperature:

$$\int_z^0 dz' \kappa_{\text{as}}CTe^{\kappa_{\text{es}}(z-z')} = C \frac{\kappa_a}{\kappa_e} T_g [1 - e^{\kappa_{\text{es}}z}] \quad (51)$$

All other terms in (48) that depend on the upward and downward temperatures can be evaluated using these three source terms. Using (41), (50), and (51), and after taking integration over z , we have

$$\begin{aligned} \bar{\mathbf{V}}(z=0) &= \int_{-d}^0 dz' \bar{\mathbf{F}}_u(z') e^{\kappa_{\text{es}}z'} \\ &\approx \frac{1}{4\pi} \frac{\kappa_s \kappa_a}{\kappa_e \kappa_e} \int_0^1 d\mu' \int_0^{2\pi} d\phi' \bar{\bar{\mathbf{P}}}(\mu, \phi; \mu', \phi') \\ &\times \left[c_0 \bar{\mathbf{T}} + \left(\bar{e}CT_g \frac{\kappa_e}{\kappa_a} - \bar{\mathbf{T}} \right) c_1 e^{-\kappa_e d / \mu'} \right] \\ &+ \frac{1}{4\pi} \frac{\kappa_s \kappa_a}{\kappa_e \kappa_e} \int_0^1 d\mu' \int_0^{2\pi} d\phi' \bar{\bar{\mathbf{P}}}(\mu, \phi; \\ &- \mu', \phi') c_0 \bar{\mathbf{T}} + \bar{\mathbf{T}}(c_0 - c_2) \end{aligned} \quad (52)$$

where $c_0 = 1 - \exp(-\kappa_{\text{es}}d)$, $c_1 = \{1 - \exp[-\kappa_{\text{es}}d(1 - \mu/\mu')]\} / (1 - \mu/\mu')$, and $c_2 = \{1 - \exp[-\kappa_{\text{es}}d(1 + \mu/\mu')]\} / (1 + \mu/\mu')$. Another term in (48) accounting for upward scattering of

the downward temperature by the lower boundary at $z = -d$ can be evaluated using the source term given by (51) as

$$\begin{aligned}
 \overline{SG}(z=0) &= \overline{G}_c(\mu, \phi) \bar{I}_d(z = -d, \theta, \phi) e^{-\kappa_{es}d} \\
 &+ \frac{K'^2}{\mu} \int_0^1 d\mu' \int_0^{2\pi} d\phi' \mu'^2 W(\bar{\mathbf{k}}_{\perp} - \bar{\mathbf{k}}'_{\perp}) \overline{G}_{ic}(\mu, \phi; \\
 &- \mu', \phi') \bar{I}_d(z = -d, \mu', \phi') e^{-\kappa_{es}d} \\
 &\approx C \frac{\kappa_a}{\kappa_e} \overline{G}_c(\mu, \phi) \bar{T}(1 - e^{-\kappa_{es}d}) e^{-\kappa_{es}d} \\
 &+ C \frac{\kappa_a}{\kappa_e} \frac{K'^2}{\mu} \int_0^1 d\mu' \int_0^{2\pi} d\phi' \mu'^2 W(\bar{\mathbf{k}}_{\perp} - \bar{\mathbf{k}}'_{\perp}) \\
 &\times \overline{G}_{ic}(\mu, \phi; -\mu', \phi') \bar{T}(1 - e^{-\kappa_{es}d/\mu'}) e^{-\kappa_{es}d}
 \end{aligned} \tag{53}$$

Thus the complete expression for the upward temperature at $z=0$ within the layer is

$$\begin{aligned}
 \bar{I}_u^{(1)}(z=0) &= C \frac{\kappa_a}{\kappa_e} \bar{T}(1 - e^{-\kappa_{es}d}) + \bar{e}CT_g e^{-\kappa_{es}d} \\
 &+ \bar{V}(z=0) + \overline{SG}(z=0)
 \end{aligned} \tag{54}$$

This is the first-order solution of \bar{I}_u . The second order solution for the upward temperature at $z=0$ is

$$\begin{aligned}
 \bar{I}_u^{(2)}(z=0) &= C \frac{\kappa_a}{\kappa_e} \bar{T}(1 - e^{-\kappa_{es}d}) + \bar{e}CT_g e^{-\kappa_{es}d} \\
 &+ \bar{V}(z=0) + \overline{SG}^{(2)}(z=0)
 \end{aligned} \tag{55}$$

where

$$\begin{aligned}
 \overline{SG}^{(2)}(z=0) &= \overline{G}_c(\mu, \phi) \bar{I}_d(z = -d, \theta, \phi) e^{-\kappa_{es}d} \\
 &+ \frac{K'^2}{\mu} \int_0^1 d\mu' \int_0^{2\pi} d\phi' \mu'^2 W(\bar{\mathbf{k}}_{\perp} - \bar{\mathbf{k}}'_{\perp}) \\
 &\times \overline{G}_{ic}(\mu, \phi; -\mu', \phi') \bar{I}_d(z = -d, \mu', \phi') e^{-\kappa_{es}d}
 \end{aligned} \tag{56}$$

The brightness temperatures \bar{T}_B in the direction (θ_0, ϕ_0) , where $\theta_0 = \sin^{-1}(K' \sin \theta/k)$ as related to θ by Snell's law,

are given by

$$\bar{T}_B(\theta_0, \phi_0) = \overline{\bar{T}}(\theta) \bar{I}(z=0, \theta, \phi) \tag{57}$$

$\overline{\bar{T}}(\theta) =$

$$\begin{bmatrix}
 1 - |R_v(\theta)|^2 & 0 & 0 & 0 \\
 0 & 1 - |R_h(\theta)|^2 & 0 & 0 \\
 0 & 0 & \frac{\cos \theta_0}{\cos \theta} \text{Re}(T_v(\theta)T_h^*(\theta)) - \frac{\cos \theta_0}{\cos \theta} \text{Im}(T_v(\theta)T_h^*(\theta)) \\
 0 & 0 & \frac{\cos \theta_0}{\cos \theta} \text{Im}(T_v(\theta)T_h^*(\theta)) & \frac{\cos \theta_0}{\cos \theta} \text{Re}(T_v(\theta)T_h^*(\theta))
 \end{bmatrix} \tag{58}$$

where $T_v(\theta) = 1 + R_v(\theta)$, and $T_h(\theta) = 1 + R_h(\theta)$.

3.4. Numerical Simulations of Emissivities for Foam-Covered Flat Ocean Surfaces

In this section, we illustrate the numerical results of the emissivity, based on a model of coated particles in a FCC structure, for a foam-covered flat ocean surface and compare with these results some experimental measurements. The absorption rate, scattering rate, and effective permittivity are first calculated using the Monte Carlo simulation. Subsequently, these quantities are used to compute the emissivity. The foam parameters are summarized as follows: a_j and b_j , the respective outer and inner radii of air bubble j ; N , number of air bubbles; V , total sample volume in the Monte Carlo simulations; f_w , the volume fraction of seawater in foam; ϵ_w , the permittivity of seawater; and θ , the observation angle. Note that the permittivity of seawater ϵ_w is a function of frequency and other physical parameters, such as the temperature and salinity. In the following simulations, the permittivities of seawater at 10.8 and 36.5 GHz are $49.149 + i40.105$ and $13.448 + i24.784$, respectively [60]. The experimental measurements are conducted at the Chesapeake Bay Detachment at 10.8 and 36.5 GHz. The diameter of air bubble ranges from 500 to 5000 μm with median between 900 and 1000 μm [57].

In the Monte Carlo simulations, different realizations of the sample of spheres are obtained by rotations of the sample volume. From the results of the different realizations, the coherent fields and the incoherent fields are calculated. The parameters used for Monte Carlo simulations are summarized in Table 4. The total number of coated air bubbles, which are arranged in a face-centered-cubic structure, is $N = N' + N'' = 500$, where two species of coated air bubbles are used. They have the same outer radii but have different inner radii, b' and b'' . We choose N' bubbles randomly of inner radii b' , and the rest have inner radii of b'' . Seven realizations are generated by rotations of the sample. The respective absorption rate, scattering rate, extinction rate, albedo, and effective permittivity calculated from Monte Carlo simulations are given in Tables 5–7. Figures 9 and 10 plot the microwave emissivity dependence on the observation angle at 10.8 and

Table 4. Parameters for Monte Carlo Simulations Shown in Figs. 9–13

	a (mm)	b' (mm)	N'	b'' (mm)	N''	V (mm ³)	f_w (%)
Figures 9–11	1.0	0.4472	75	0.99795	425	2828	10.5
Figure 12	0.5	0.2271	75	0.49885	425	353.6	10.5
Figure 13	0.25	0.1285	75	0.24945	425	44.19	10.5

36.5 GHz for vertical and horizontal polarizations, respectively. The foam parameters are listed in Table 4. As the size of the bubbles increases, the scattering coefficient increases, and the albedo also increases. The increase in albedo causes the corresponding brightness temperatures to decrease.

The microwave emissivities, at 10.8 and 36.5 GHz and for vertical and horizontal polarizations, as a function of the thickness of foam layer with different sizes of coated air bubbles are plotted in Figs. 11–13. In actual foam, the air bubbles have a size distribution with mean diameter about 1 mm. However, scattering increases with particle sizes and the effective scattering mean size can be substantially larger than the mean size. In our simulations, we use single size particles. Three radii of air bubbles, 1.0, 0.5, and 0.25 mm, are used and represent the effective scattering mean. In actual foam, the coating thicknesses vary and also vary as a function of depth. For convenience, we have used two coating thicknesses. The observation angle is $\theta = 53^\circ$. From these figures, we can see that as the foam layer thickness increases, the emissivity increases correspondingly and then saturates at a particular thickness of the foam layer, for both horizontal and vertical polarizations. The saturation point of horizontal polarization is slightly larger than that of vertical polarization. For layer thickness larger than the saturation thickness, the *difference* of emissivity between the two frequencies increases as the size of coated air bubbles increases.

In Figs. 14 and 15, the simulation results of microwave emissivities are compared with the experimental data as a function of observation angle. An average foam layer thickness 2.8 cm is used. The parameters used for Monte Carlo simulation are the same as those used in Figs. 9–11, with a coated air bubble radius of 1.0 mm. In the experiment, the emissivities of horizontal and vertical polarizations are measured, at 10.8 and 36.5 GHz, for a foam layer with a mean thickness of 2.8 cm. To facilitate the comparisons, we list in Table 8, the experimental data, the DMRT model results, and the air–ocean half-space results for the emissivities at 10.8 and 36.5 GHz. From Figs. 14 and 15, we see that Monte Carlo simulations produce results in

reasonably good agreement with experimental measurements. Both simulations and experiments indicate that absorption at 10.8 GHz is appreciable. In addition, the simulations show that emissivities at 10.8 and 36.5 GHz are comparable. The absorption coefficient at 36.5 GHz is larger than that at 10.8 GHz. However, scattering has a significant effect at 36.5 GHz. The results are in good agreement at small angles of incidence. At large incidence angles, the difference increases. We are presently studying the refinement of the model by investigating realistic foam generation algorithms that can improve the model.

3.5. Comparison with Quasicrystalline Approximation

In this section, we compare the Monte Carlo results with those based on QCA, in which wave scattering and emission in a medium consisting of densely packed coated particles are solved by using QCA in combination with the DMRT theory [10]. It is assumed that there are two species of air bubbles that have the same outer radius a , but have different coating thickness with inner radii of b_1 and b_2 . The parameters of the foam model are given in Table 9. Emissivities of horizontal and vertical polarizations are simulated at 10.8 and 36.5 GHz.

The quantities for foam layer calculated by QCA and by Monte Carlo simulations are shown in Tables 10 and 11, respectively. Figure 16 is based on Monte Carlo simulations. We can see that the emissivities at 10.8 and 36.5 GHz are comparable. This feature is consistent with experimental measurements [57]. On the other hand, as shown in Fig. 17, which is based on QCA, the emissivities at 36.5 GHz are higher than at 10.8 GHz. For dense media consisting of particles densely packed, there are two different cases. They are differentiated by a large loss tangent and small loss tangent where the loss tangent is $\sigma/(\omega\epsilon)$ and σ is the conductivity of the medium. A large loss tangent represents the case where the conductive current is much larger than the displacement current, while the reverse is true for the small loss tangent case. It has been shown by extensive simulations [27] that QCA is valid for the small loss tangent case. The QCA theory has been

Table 5. Numerical Results from Monte Carlo Simulations for Figs. 9–11

Parameter	At 10.8 GHz	At 36.5 GHz
Absorption rate κ_{abs} (cm ⁻¹)	0.2849	0.8854
Scattering rate κ_{s} (cm ⁻¹)	0.01201	0.5738
Extinction rate κ_{e} (cm ⁻¹)	0.2969	1.4592
Albedo	0.04045	0.3933
Effective permittivity ϵ_{eff}	$1.448 + i0.158$	$1.158 + i0.206$

Table 6. Numerical Results from Monte Carlo Simulations for Fig. 12

Parameter	At 10.8 GHz	At 36.5 GHz
Absorption rate κ_{abs} (cm ⁻¹)	0.3009	0.9150
Scattering rate κ_{s} (cm ⁻¹)	2.552×10^{-3}	0.1380
Extinction rate κ_{e} (cm ⁻¹)	0.3035	1.0530
Albedo	8.403×10^{-3}	0.1310
Effective permittivity	$1.508 + i0.165$	$1.284 + i0.156$

Table 7. Numerical Results from Monte Carlo Simulations for Fig. 13

Parameter	At 10.8 GHz	At 36.5 GHz
Absorption rate κ_{abs} (cm^{-1})	0.2686	0.9042
Scattering rate κ_s (cm^{-1})	6.521×10^{-5}	0.01553
Extinction rate κ_e (cm^{-1})	0.2686	0.9197
Albedo	2.427×10^{-4}	0.01689
Effective permittivity ϵ_{eff}	$1.478 + i0.144$	$1.356 + i0.140$

successful in dry snow [7,26]. However, the QCA theory is less successful when conductive current dominates [59]. The conductive current can go through several connected particles. On the other hand, QCA is limited to pair distribution functions. Thus the applicability of QCA is also dependent on frequency through the dependence on $\sigma/(\omega\epsilon)$. We can see that the results of QCA are in better agreement with those of Monte Carlo simulations at high frequency of 36.5 GHz, and less successful at low frequency of 10.8 GHz. However, the experiment reported in Refs. 11 and 57 was at 19.0 GHz and QCA was reasonably successful. Since Monte Carlo simulations provide the exact solution of Maxwell equations, this model will be applied to calculate the four Stokes parameters in the next section.

Four Stokes parameters of brightness temperature for foam-covered rough ocean surface are theoretically analyzed. Important features are shown by the results at 10.8, 19.0, and 36.5 GHz for the four Stokes parameters. It is important to determine, with respect to these Stokes parameters, how the foam affects brightness temperatures and retrieval of the ocean surface wind vector. The first two Stokes parameters are increased with the presence of foam, and the third and fourth parameters are reduced. The azimuthal variations of polarimetric brightness temperature are also illustrated. The first two Stokes parameters are even functions of ϕ ; the last two parameters are odd functions. Emissions with various windspeeds and foam layer thickness are also studied. The four Stokes

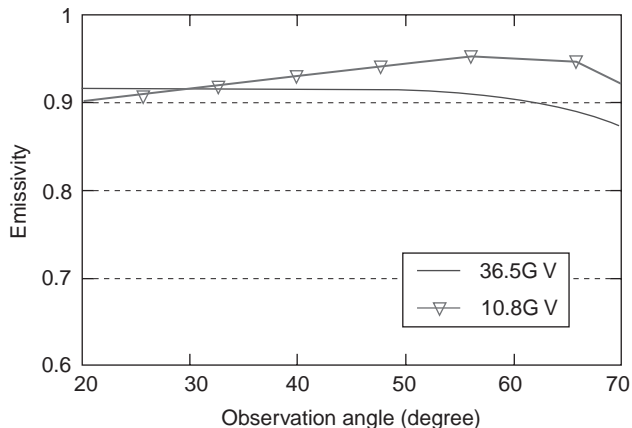


Figure 9. Emissivity as a function of observation angle for vertical polarization. The radius of the coated air bubble is 1.0 mm. (This figure is available in full color at <http://www.mrw.interscience.wiley.com/erfme>.)

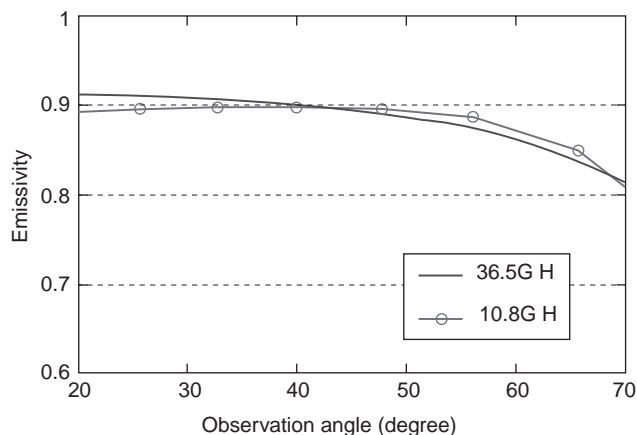


Figure 10. Emissivity as a function of observation angle for horizontal polarization. The radius of the coated air bubble is 1.0 mm. (This figure is available in full color at <http://www.mrw.interscience.wiley.com/erfme>.)

parameters of brightness temperature are dependent on windspeeds and foam thickness.

4. TREE SCATTERING MODEL AT UHF/VHF USING SPARSE MATRIX ITERATIVE APPROACH

Electromagnetic wave interaction with plants plays an important role in microwave remote sensing applications. Various scattering models have been developed to study wave propagation and scattering in vegetation canopy [1–7]. In the past, vector radiative transfer theory was used extensively to compute the backscattering coefficients of forests for comparison with microwave backscatter measurements [1–4]. While the radiative transfer approach can handle complicated geophysical structures, it ignores coherent wave interactions within the tree structure. A coherent addition approximation (CAA) scattering model has been applied to take into account the effects of coherent scattering and branching structure

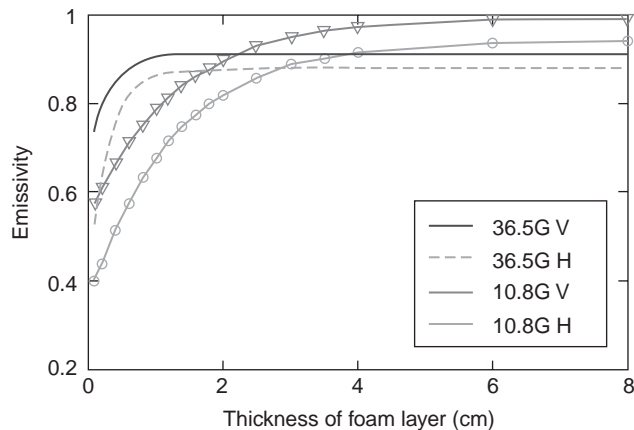


Figure 11. Emissivity as a function of the thickness of the foam layer at observation angle 53° . The radius of the coated air bubble is 1.0 mm. (This figure is available in full color at <http://www.mrw.interscience.wiley.com/erfme>.)

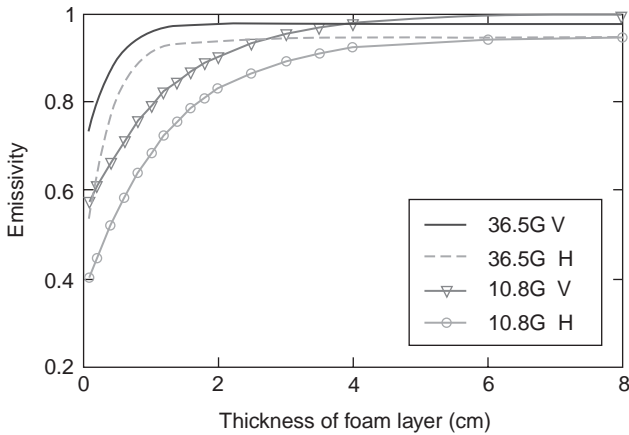


Figure 12. Emissivity as a function of the thickness of the foam layer at observation angle 53° . The radius of the coated air bubble is 0.5 mm. (This figure is available in full color at <http://www.mrw.interscience.wiley.com/erfme>.)

[6,61]. The volume and surface integral equation formulations with the method of moments computational models have also been employed to investigate tree scattering [6,62–64]. Monte Carlo simulations and tree geometric models based on Lindenmayer systems [65] have also been applied to take into account the random nature of trees [6,16,63]. Foliage attenuation has driven the application of radar frequency down to the VHF/UHF region. At these low frequencies, it is useful to have a clear understanding of the coherent interaction effects of tree branches and trunk of a single tree or a small group of trees. In this section we describe a computationally efficient model for computing tree scattering at VHF/UHF frequencies. At these low frequencies, the effects of scattering by tree leaves can be neglected. A structure model with dielectric cylinders is employed to simulate trees with bare branches. The method of moments is used to calculate tree scattering signatures by discretizing the volume integral equation and transforming it into a matrix equation [6]. An efficient numerical algorithm based on the

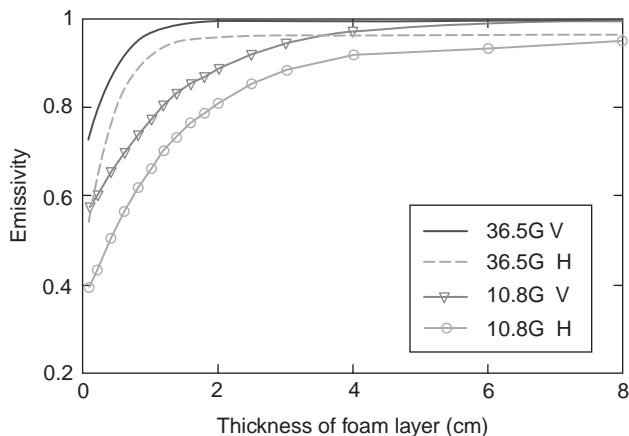


Figure 13. Emissivity as a function of the thickness of the foam layer at observation angle 53° . The radius of the coated air bubble is 0.25 mm. (This figure is available in full color at <http://www.mrw.interscience.wiley.com/erfme>.)

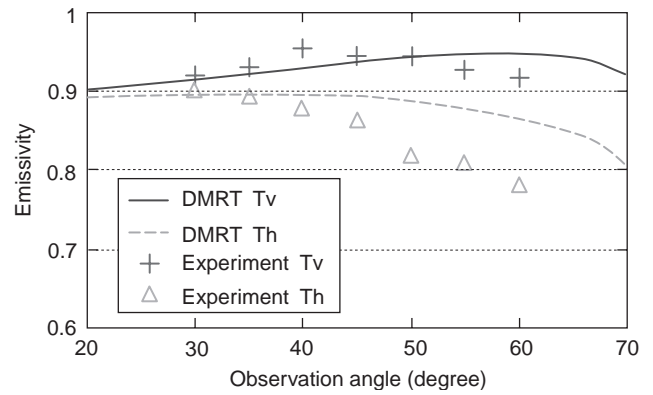


Figure 14. Comparison between the simulation results and measurements of microwave emissivity at 10.8 GHz for horizontal polarization and vertical polarization, respectively. (This figure is available in full color at <http://www.mrw.interscience.wiley.com/erfme>.)

sparse matrix iterative approach (SMIA) [13–16] is used to solve the matrix equation. In the SMIA method, the impedance matrix of the resultant matrix equation is decomposed into a sparse matrix for the near interactions and a complementary matrix, for the far interactions among the cylindrical subcells of the tree structures. Using a direct sparse solver to estimate the strong interaction part, we iteratively included the weak interaction contribution to update the solution. The key feature of this approach is that very little iteration is required to obtain convergent solutions. The SMIA technique has been applied in combination with the canonical grid method to solve rough surface scattering [6,13] and analyze microstrip interconnects [14,15]. Section 4.1 gives the volume integral equation formulation and the MoM treatment for the tree scattering problem, and describes the SMIA method. In Section 4.2, some numerical results are illustrated for scattering from simulated trees and demonstrate that the SMIA method can significantly reduce the number of iterations when compared to the conventional conjugate gradient method (CGM).

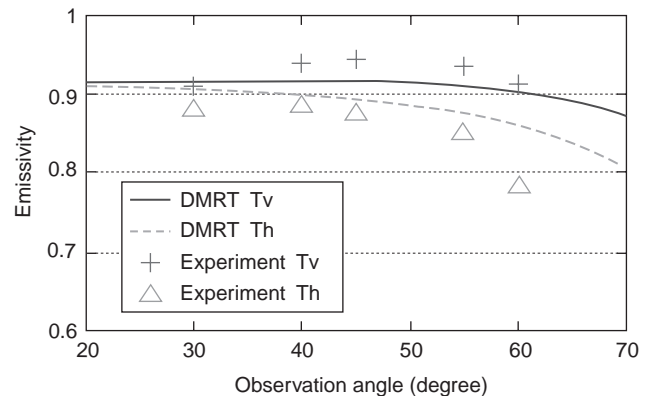


Figure 15. Comparison between the simulation results and measurements of microwave emissivity at 36.5 GHz for horizontal polarization and vertical polarization, respectively. (This figure is available in full color at <http://www.mrw.interscience.wiley.com/erfme>.)

Table 8. Emissivities of Experimental Data, DMRT Model, and Air-Ocean Half-Space Results

$\theta(^{\circ})$	Experiment		DMRT Model		Air-Ocean Half Space Results	
	V	H	V	H	V	H
<i>a. Results at 10.8 GHz</i>						
30	0.920	0.900	0.915	0.897	0.422	0.337
35	0.930	0.890	0.923	0.898	0.440	0.322
40	0.955	0.875	0.930	0.899	0.462	0.305
45	0.945	0.860	0.939	0.898	0.489	0.285
50	0.945	0.815	0.946	0.894	0.523	0.263
55	0.929	0.805	0.950	0.885	0.564	0.239
60	0.919	0.780	0.951	0.871	0.615	0.211
<i>b. Results at 35.6 GHz</i>						
30	0.910	0.880	0.916	0.908	0.526	0.429
40	0.940	0.885	0.916	0.900	0.570	0.391
45	0.945	0.875	0.915	0.895	0.599	0.367
55	0.935	0.850	0.911	0.877	0.676	0.310
60	0.912	0.785	0.905	0.863	0.725	0.276

4.1. Formulation and Sparse Matrix Iterative Approach

The discrete-dipole approximation (DDA) has been applied to calculate electromagnetic scattering and absorption by trees [6,16,63]. At VHF/UHF frequencies, the tree trunks and branches can be modeled as thin dielectric circular cylinders. In the discretization process, each tree branch is divided into cylindrically shaped subcells with the same radius. The volume integral equation for the electric field is given by

$$\bar{\mathbf{E}}(\bar{\mathbf{r}}) = \bar{\mathbf{E}}^{\text{inc}}(\bar{\mathbf{r}}) + \frac{k_0^2}{\varepsilon_0} \int_V \bar{\mathbf{G}}_0(\bar{\mathbf{r}}, \bar{\mathbf{r}}') \cdot [\varepsilon_p(\bar{\mathbf{r}}') - \varepsilon_0] \bar{\mathbf{E}}(\bar{\mathbf{r}}') d\bar{\mathbf{r}}' \quad (59)$$

where $\bar{\mathbf{E}}^{\text{inc}}(\bar{\mathbf{r}})$ is the incident field, $\varepsilon_p(\bar{\mathbf{r}})$ is the permittivity distribution within region V and k_0 , ε_0 , and $\bar{\mathbf{G}}_0(\bar{\mathbf{r}}, \bar{\mathbf{r}}')$ are the wavenumber, permittivity, and free-space dyadic Green function, respectively. If we subdivide the volume into small elemental volumes ΔV_i , each centered at $\bar{\mathbf{r}}_i$, $i = 1, 2, \dots, N$, the discretized version of (59) becomes

$$\bar{\mathbf{p}}_i = \bar{\alpha}_i \cdot \bar{\mathbf{E}}_i^{\text{inc}} - \bar{\alpha}_i \cdot \frac{k_0^2}{\varepsilon_0} \sum_{j=1, j \neq i}^N \frac{\int_{\Delta V_j} d\bar{\mathbf{r}}' \bar{\mathbf{G}}_0(\bar{\mathbf{r}}_i, \bar{\mathbf{r}}')}{\Delta V_j} \cdot \bar{\mathbf{p}}_j \quad (60)$$

where $\bar{\mathbf{E}}_i^{\text{inc}}$, $\bar{\mathbf{p}}_i = \Delta V_i (\varepsilon_{pi} - \varepsilon_0) \bar{\mathbf{E}}_i$, and $\bar{\mathbf{E}}_i$ are the respective vectors of the incident field, dipole moment, and electric field at the center $\bar{\mathbf{r}}_i$ of the i th elemental volume ΔV_i . The summation over j runs over all the subcells ($j \neq i$) that form the tree structure. ε_{pi} is the permittivity of the i th elemental volume, which is assumed to be constant within ΔV_i . In (60), the dyad $\bar{\alpha}_i = \hat{\mathbf{x}}\hat{\mathbf{x}}\alpha_{ix} + \hat{\mathbf{y}}\hat{\mathbf{y}}\alpha_{iy} + \hat{\mathbf{z}}\hat{\mathbf{z}}\alpha_{iz}$ is a diagonal matrix whose elements, for a vertical circular cylindrical cell of radius

a_i and length ℓ_i , are given by [6]

$$\begin{aligned} \alpha_{ix} &= \Delta V_i (\varepsilon_{pi} - \varepsilon_0) \frac{1}{1 + \left(\frac{\varepsilon_{pi}}{\varepsilon_0} - 1\right) (L_{ix} - k_0^2 D_{ix})} \\ \alpha_{iy} &= \Delta V_i (\varepsilon_{pi} - \varepsilon_0) \frac{1}{1 + \left(\frac{\varepsilon_{pi}}{\varepsilon_0} - 1\right) (L_{iy} - k_0^2 D_{iy})} \\ \alpha_{iz} &= \Delta V_i (\varepsilon_{pi} - \varepsilon_0) \frac{1}{1 + \left(\frac{\varepsilon_{pi}}{\varepsilon_0} - 1\right) (L_{iz} - k_0^2 D_{iz})} \end{aligned} \quad (61)$$

where

$$\begin{aligned} L_{ix} &= L_{iy} = \frac{\ell_i}{2\sqrt{\ell_i^2 + 4a_i^2}} \\ L_{iz} &= 1 - \frac{\ell_i}{2\sqrt{\ell_i^2 + 4a_i^2}} \end{aligned} \quad (62)$$

and

$$\begin{aligned} D_{ix} &= D_{iy} = \frac{a_i^2}{8} \ln \frac{\sqrt{\ell_i^2 + 4a_i^2} + \ell_i}{\sqrt{\ell_i^2 + 4a_i^2} - \ell_i} + \frac{\ell_i}{8} \\ &\quad \times \left(\sqrt{\ell_i^2 + 4a_i^2} - \ell_i \right) + i \frac{k_0 a_i^2 \ell_i}{6} \\ D_{iz} &= \frac{a_i^2}{4} \ln \frac{\sqrt{\ell_i^2 + 4a_i^2} + \ell_i}{\sqrt{\ell_i^2 + 4a_i^2} - \ell_i} + i \frac{k_0 a_i^2 \ell_i}{6} \end{aligned} \quad (63)$$

Table 9. Parameters of Foam Model for Simulation Results in Figs. 16 and 17

d	$2a$	$2b_1$	$2b_2$	f	f_w	f_1	f_2
3 cm	2000 μm	1220 μm	1995.9 μm	74%	10.3%	12.9%	61.1%

Table 10. Quantities of Foam Based on QCA from Fig. 18

Parameter	At 10.8 GHz	At 36.5 GHz
Absorption rate κ_{abs} (cm^{-1})	0.1763	0.9042
Scattering rate κ_{s} (cm^{-1})	0.0567	0.01553
Extinction rate κ_{e} (cm^{-1})	0.2330	0.9197
Albedo	0.2435	0.01689
Effective permittivity ϵ_{eff}	$1.4573 + i0.1245$	$1.356 + i0.140$

As can be seen from (59), we need to consider only those volumes that have $\epsilon_{\text{pi}} \neq \epsilon_0$. The matrix equation (60) is of dimension $3N \times 3N$, where N is the total number of small cylindrical cells. The factor 3 arises from the Cartesian components of the polarization vector.

Equation (60) is the DDA matrix equation, which can be expressed as

$$\bar{\bar{Z}} \cdot \bar{X} = \bar{C} \quad (64)$$

where the vector \bar{C} corresponds to the known incident field and \bar{X} is the unknown polarization vector to be solved numerically. In general, the impedance matrix $\bar{\bar{Z}}$ resulting from the discretization of the volume integral equation is large, dense, and complex. Its elements are proportional to the integrals of the Green dyad as shown in (60). Usually an iterative solver, such as conjugate gradient method (CGM), is coupled with some kind of preconditioning strategy to improve the spectral properties of the impedance matrix $\bar{\bar{Z}}$ such that the matrix equation (64) can be solved much more rapidly [66]. Several preconditioners, such as blockdiagonal [67], sparse approximate inverse (SPAI) [68], and incomplete LU (ILU) factorization [69], have been considered in the electromagnetic wave scattering problem.

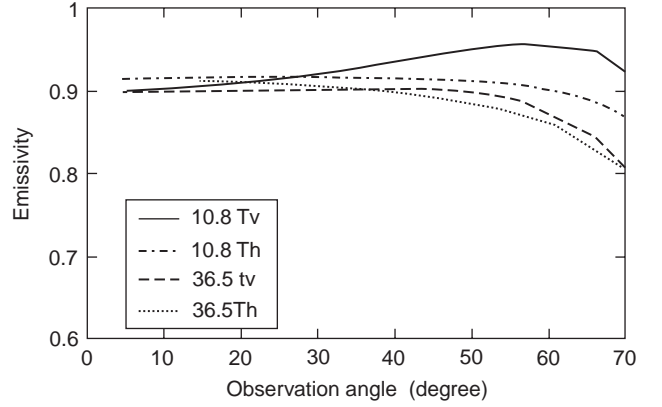
The sparse matrix iterative approach (SMIA) technique [6,13–16] has been applied to solve the matrix equation (64). Equation (64) is solved iteratively by decomposing the impedance matrix $\bar{\bar{Z}}$ into two parts

$$\bar{\bar{Z}} = \bar{\bar{Z}}^{(s)} + \bar{\bar{Z}}^{(w)} \quad (65)$$

where $\bar{\bar{Z}}^{(s)}$, which is a sparse matrix, includes the near or strong interactions among the close-by cylindrical sub-cells, and $\bar{\bar{Z}}^{(w)}$, which is a complementary matrix accounting for the far or weak interactions, contains the remaining elements of the impedance matrix $\bar{\bar{Z}}$.

Table 11. Quantities of Foam Based on Monte Carlo Simulations from Fig. 16

Parameter	At 10.8 GHz	At 36.5 GHz
Absorption rate κ_{abs} (cm^{-1})	0.2686	0.9042
Scattering rate κ_{s} (cm^{-1})	6.521×10^{-5}	0.01553
Extinction rate κ_{e} (cm^{-1})	0.2686	0.9197
Albedo	2.427×10^{-4}	0.01689
Effective permittivity ϵ_{eff}	$1.478 + i0.144$	$1.356 + i0.140$


Figure 16. Emissivities as a function of observation angle for vertical and horizontal polarizations at 10.8 and 36.5 GHz, using the model based on Monte Carlo simulations.

The numerical procedure uses a sparse solver to estimate the first-order solution $\bar{X}^{(1)}$

$$\bar{\bar{Z}}^{(s)} \cdot \bar{X}^{(1)} = \bar{C} \quad (66)$$

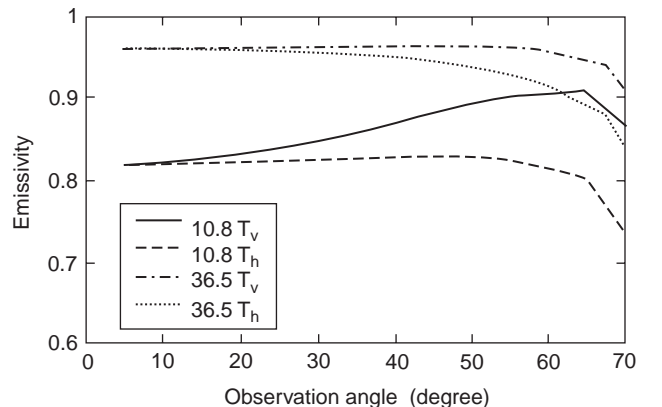
and iteratively includes the weak interaction contribution to update the higher-order solution $\bar{X}^{(n+1)}$:

$$\bar{\bar{Z}}^{(s)} \cdot \bar{X}^{(n+1)} = \bar{C} - \bar{\bar{Z}}^{(w)} \cdot \bar{X}^{(n)} \quad (67)$$

The iterations are carried out until the error norm criterion

$$\frac{\|\bar{\bar{Z}} \cdot \bar{X}^{(n)} - \bar{C}\|}{\|\bar{C}\|} \leq \delta \quad (68)$$

is satisfied. δ has been set equal to 1×10^{-4} for the numerical computations presented in Section 4.2.


Figure 17. Emissivities as a function of observation angle for vertical and horizontal polarizations at 10.8 and 36.5 GHz, using the model based on QCA.

4.2. Numerical Results

As shown in Fig. 18, six trees are generated on the basis of the Lindenmayer systems [6,65]. The tree characteristics are given in Table 12. We can see that the tree height varies from 2.67 to 5.65 m, and the total number of branches, including the trunk, can be as much as several hundreds. The total number of discretized cylindrical subcells N and the total number of unknown polarizations $3N$ are also given. The total number of unknowns ranges from several hundreds for a simpler tree to several thousands for a more complicated tree. We can see that the number of unknowns is much smaller when compared to using a surface integral equation approach for calculating the tree scattering [64]. In addition, Table 12 includes the expansions of the trees in the x and y directions, the variations of the radii and lengths of branches for each tree, and the woody volume of each tree.

A number of numerical examples for the polarimetric bistatic scattering from the simulated trees are presented in the following. The permittivities used are $\epsilon_p = 9.62 + i4.332$ and $\epsilon_p = 33.357 + i21.408$, which are calculated from the formula developed by Ulaby et al. [3]. The two permittivities are for gravimetric moisture contents of $M_g = 26\%$ and $M_g = 68\%$ at 300 MHz, respectively. The radiowavelength is $\lambda = 1$ m, and the incidence angle is $\theta_i = 45^\circ$. The bistatic scattering cross sections of trees 5 and 6 for $\epsilon_p = 9.62 + i4.332$ are shown in Figs. 19 and 20, respectively. We also use the solutions for an exact full matrix inversion (INV) and the conjugate gradient method (CGM) as baselines to illustrate the accuracy of the SMIA approach. We can see that solutions of the SMIA method agree very well with the solutions of exact matrix inversion and CGM.

Figure 21 shows the number of iterations required to achieve convergence, and compares the convergence rates for solving the scattering from trees 5 and 6 using the CGM and SMIA techniques. Note that CGM requires thousands of iterations for the percentage error to reduce to $10^{-2}\%$ while the SMIA requires only about 10 iterations. In Table 13 we present a comparison of the condition number of the impedance matrix \bar{Z} , the number of iterations for horizontal and vertical-polarization incidence, matrix filling, solving, and total computation time for the scattering solutions of six trees. The computational time is based on a Dell Latitude C800 with a 512 M RAM memory and 848 MHz microprocessor. It is noted that, because of their large condition numbers, trees 3 and 4 require a large number of iterations to converge by using the conventional CGM, while the SMIA method takes only a few iterations to reach a convergent solution. It is clear from Table 13 that, compared to the CGM, the SMIA technique reduces the number of iterations by a factor of >100 and provides a much faster numerical solution scheme for computing tree scattering while keeping the sufficient accuracy.

In Figs. 22 and 23 we plot the respective bistatic scattering cross sections of trees 5 and 6 for a larger tree permittivity $\epsilon_p = 33.357 + i21.408$. These plots show that solutions based on the SMIA method agree very well with the exact matrix inversion for this high-dielectric-constant case. As shown in Table 14, because of the large matrix condition numbers in this high-dielectric-contrast case, scattering results for the CGM are not computed. Compared to Table 13, the SMIA method requires more iteration to converge for scattering from trees with larger permittivities. However, SMIA is still more efficient than the full matrix inversion in matrix solving.

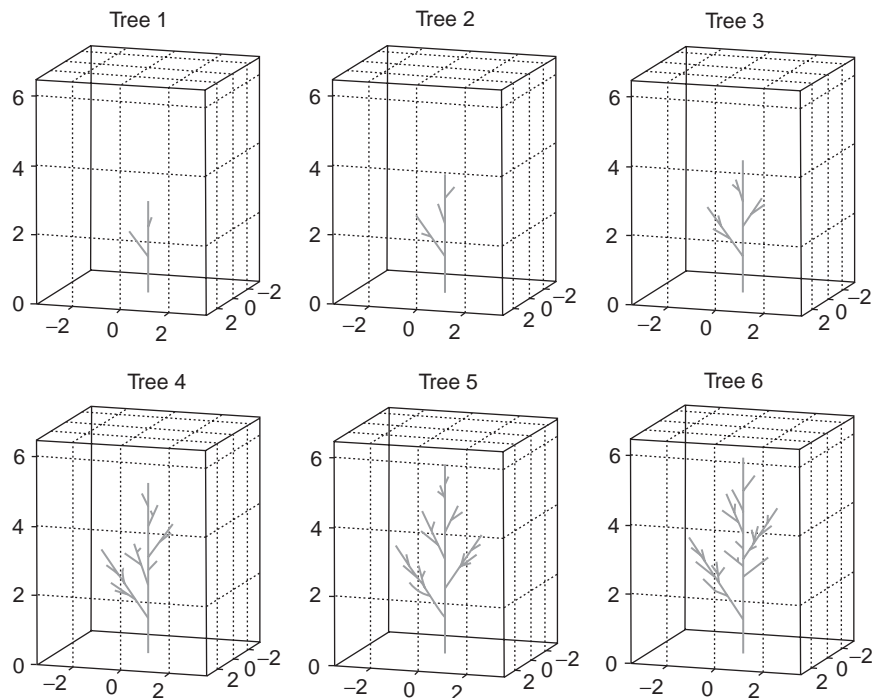


Figure 18. Simulated tree samples using the Lindenmayer systems. (This figure is available in full color at <http://www.mrw.interscience.wiley.com/erfme>.)

Table 12. Simulated Tree Characteristics

	Tree 1	Tree 2	Tree 3	Tree 4	Tree 5	Tree 6
Number of cylinders	7	15	31	63	127	255
Tree height (m)	2.66996	3.47377	3.83806	4.93697	5.48677	5.65101
Minimum x coordinate (m)	0	-0.2577	-0.4513	-0.7715	-0.8045	-1.1348
Maximum x coordinate (m)	0.27391	0.7793	0.72995	1.51781	1.05277	1.74531
Minimum y coordinate (m)	-0.7967	-1.2325	-1.4731	-1.9889	-2.0793	-2.2819
Maximum y coordinate (m)	0.25491	0.36842	0.95329	1.07843	1.618	1.29136
Maximum cylinder length (m)	1	1	1	1	1	1
Minimum cylinder length (m)	0.34548	0.25109	0.15404	0.11553	0.04543	0.03565
Maximum cylinder radius (m)	0.05	0.05	0.05	0.05	0.05	0.05
Minimum cylinder radius (m)	0.03782	0.03244	0.03281	0.02636	0.03074	0.02448
Total cylinder volume (m ³)	0.02636	0.03935	0.05961	0.0812	0.13313	0.14928
Number of cells	58	120	191	433	554	1077
Number of unknowns	174	360	573	1299	1662	3231

We have illustrated the use of SMIA numerical tree scattering model to calculate scattering from simulated trees with up to several hundred branches. We use the solutions of an exact full matrix inversion and the conjugate gradient method (CGM) as baselines to illustrate the accuracy and efficiency of the SMIA algorithm. Solutions based on the SMIA method agree very well with the exact matrix inversion and the CGM. Compared to the CGM, the SMIA approach can significantly reduce the number of iterations and provides a much faster numerical scheme for computing tree scattering.

5. WAVE SCATTERING BY DISCRETE SCATTERERS USING UV MULTILEVEL PARTITION METHOD

With the advent of modern computers and the development of fast numerical methods, Monte Carlo simulations

of volume scattering problems have become an attractive approach. A common method that has been used in numerical simulations is the volume integral equation method and its solution by the method of moments (MoM). Conventional implementation of the MoM requires $O(N^3)$ operations and $O(N^2)$ computer memory storage. Several fast numerical methods have been used, such as the sparse matrix canonical grid (SMCG) method [6,70–72] and the fast multipole method (FMM) [73,74], and a characteristic basis function has been used to solve volume scattering problems [75]. In all these approaches, subsectional basis functions and the lowest-order Green function or the lowest-order partial wave are used to construct the impedance matrix. In Ref. 71, small circular discrete scatterers were used for the SMCG method and the matrix multiply operation was extended to partial waves higher than the lowest order.

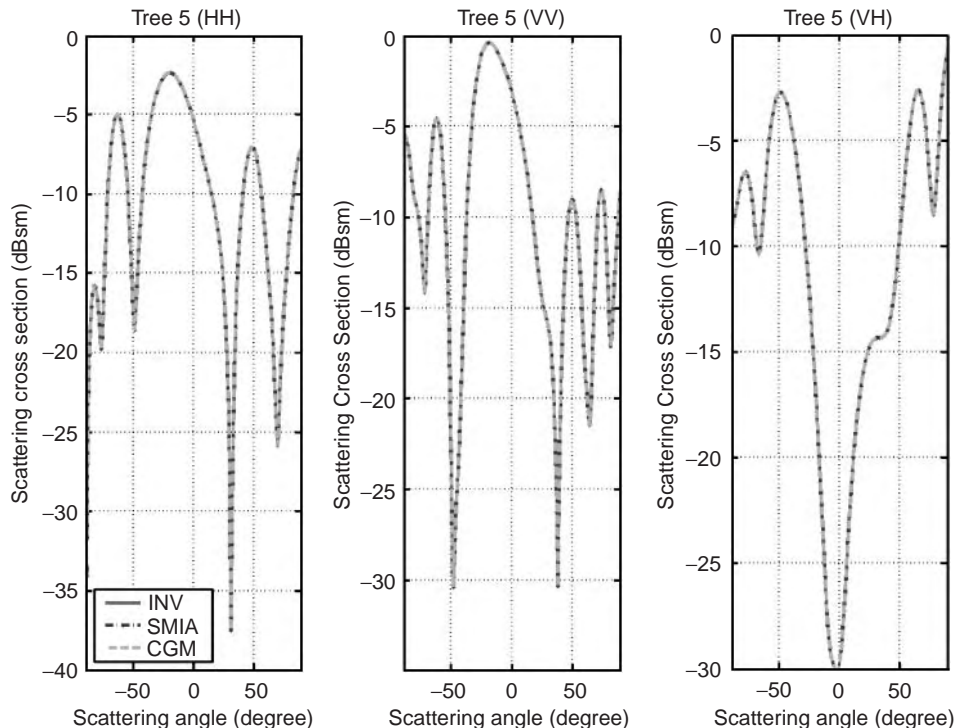
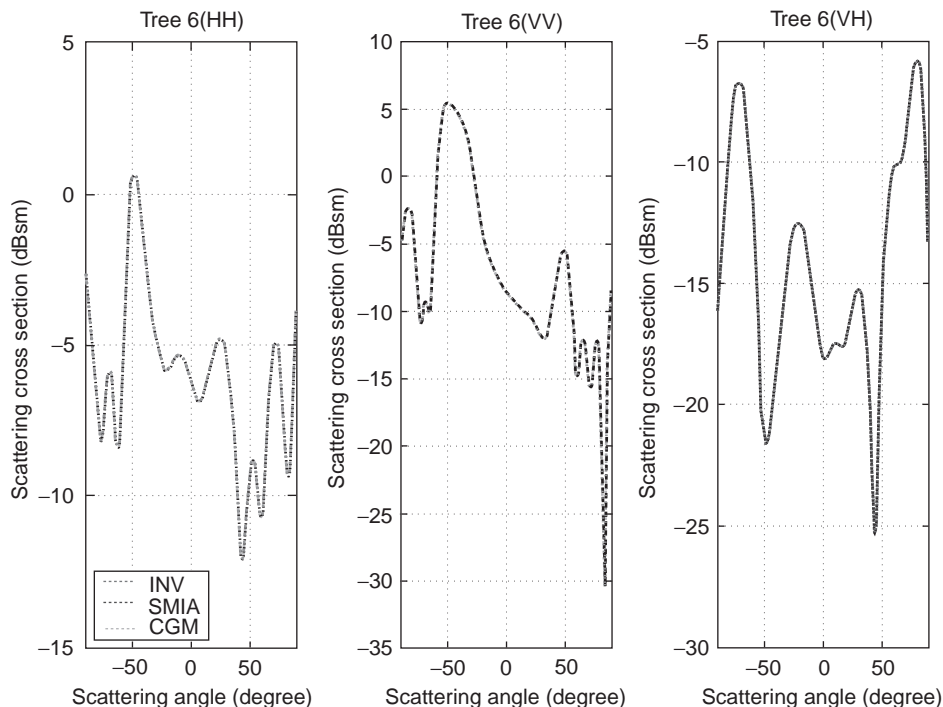


Figure 19. Comparison of the bistatic scattering cross sections of tree 5 calculated by the full matrix inversion (INV), conjugate gradient method (CGM), and sparse matrix iterative approach (SMIA). The wavelength is $\lambda = 1$ m, the incidence angle $\theta_i = 45^\circ$, and the permittivity $\epsilon_p = 9.62 + i4.332$. (This figure is available in full color at <http://www.mrw.interscience.wiley.com/erfme>.)

Figure 20. Comparison of the bistatic scattering cross sections of tree 6 calculated by the full matrix inversion (INV), conjugate gradient method (CGM) and sparse matrix iterative approach (SMIA). The wavelength is $\lambda=1$ m, the incidence angle $\theta_i=45^\circ$, and the permittivity $\epsilon_p=9.62+i4.332$. (This figure is available in full color at <http://www.mrw.interscience.wiley.com/erfme>.)



In this section, we present a UV method using multi-level partitioning (UV-MLP) to solve volume scattering problems [20]. The UV method has also been used to solve rough surface scattering problems [18,19]. The method consists of setting up a table of transmitting and receiving block sizes and their separations. For a specific scattering problem with given geometry, the scattering structure is partitioned into multilevel blocks. We will illustrate the

UV method for the case of scattering by a large number of circular cylinders. The cylinders are moderate in size with diameter comparable to wavelength. The problem has many physical applications, such as interesting resonant scattering and weak and strong localization occur when particles of wavelength sizes are densely packed together [7]. For this kind of problems, the Foldy-Lax multiple scattering equations can be used with higher-order partial waves as basis functions. The impedance matrices are thus in terms of Green functions of higher-order partial waves. It is shown that the UV decomposition can be applied directly to the impedance matrix of partial waves of higher order. We also apply the multilevel matrix partitioning (MLP) to partition the partial waves impedance matrix \bar{Z} . By looking up the rank in the predetermined table, the partial waves impedance matrix for a given transmitting and receiving block of discrete scatterers is expressed into a $U \times V$ matrix product. In Section 5.2, we describe the problem of independent rank determination. We give the Foldy-Lax equations of scattering by a conglomeration of circular cylinders in Section 5.3. In Section 5.4, we describe the multilevel partitioning process and the UV method, in Section 5.5. In Section 5.6, the computational complexity of the proposed algorithm is derived. In Section 5.7, we demonstrate the technique for a problem with up to 4096 cylinders, each with diameter equal to 1 wavelength. If a volumetric subsectional element is used with MoM for the problem of 1024 cylinders, using 100 points per square wavelength, the number of unknowns will be approximately 80,425. Using the present method of multilevel UV, the solution is completed in 14 min using a single PC processor of 2.6 GHz. The numerical results are illustrated and discussed.

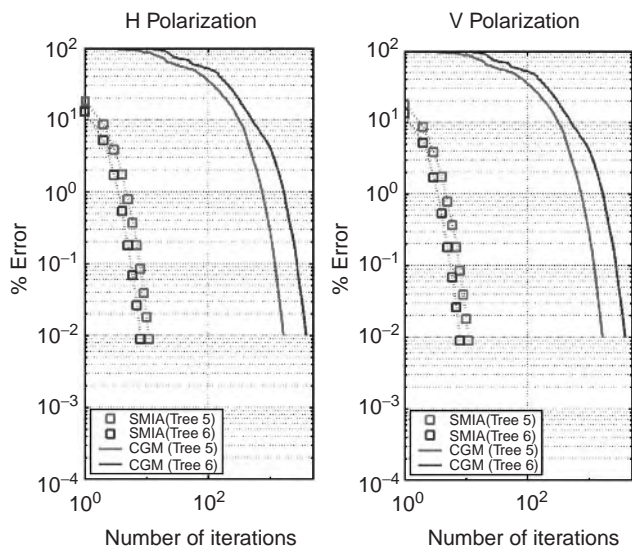


Figure 21. Comparison of the convergence rates for calculating scattering from trees 5 and 6 using the conjugate gradient method (CGM) and sparse matrix iterative approach (SMIA). (This figure is available in full color at <http://www.mrw.interscience.wiley.com/erfme>.)

Table 13. SMIA and CGM Compared

	Tree 1		Tree 2		Tree 3		Tree 4		Tree 5		Tree 6	
Number of unknowns	174		360		573		1299		1662		3231	
Condition number	53127.99		4084.755		521019.4		165276.5		1975.732		1481.116	
Method	CGM	SMIA	CGM	SMIA	CGM	SMIA	CGM	SMIA	CGM	SMIA	CGM	SMIA
Matrix filling (s)	12.77	10.30	31.60	25.85	57.29	49.43	169.64	139.31	238.80	196.23	715.84	591.04
Number of iterations (H)	750	6	1207	6	10586	7	11454	7	1634	11	3783	8
Number of iterations (V)	788	6	1209	6	216	7	11471	6	1648	11	3616	8
Matrix solving (s)	17.05	0.173	118.50	0.769	2620.7	2.374	14437.	13.628	3403.2	30.673	28906.	124.98
Total time (s)	29.89	10.53	150.19	27.06	2678.1	51.95	14607.	153.56	3642.4	227.26	29623.	717.08

5.1. Problem Independent Rank Table

We describe two methods of predetermination of rank used in volume scattering problems. Consider two square blocks each of side S . The center is separated by distance R as shown in Fig. 24. Because of multilevel partitioning, we have $2S \leq R \leq C_D S$, where C_D is a constant depending on the dimension of the problem.

5.1.1. Method of Volume Discretization or Boundary Discretization

5.1.1.1. Volume Discretization. We discretize the blocks by 100 points per square wavelength. Let there be N points in the transmitting block and N points in the receiving block. Let receiving points be denoted by $\bar{\rho}_p$, $p = 1, 2, \dots, N$, and the transmitting points denoted by $\bar{\rho}_q$, $q = 1, 2, \dots, N$. The Green function in a two-dimensional problem is given by

$$Z_{pq} = \frac{i}{4} H_0^{(1)}(k|\bar{\rho}_p - \bar{\rho}_q|) \quad (69)$$

Then the impedance matrix is of dimension $N \times N$. We can use the singular value decomposition (SVD) method to determine the rank. Let σ_1 be the largest singular value, and let the singular values be arranged in decreasing magnitude. Given a threshold ε , the rank r is such that $|\sigma_{r+1}/\sigma_1| \leq \varepsilon$.

5.1.1.2. Enclosing Boundary Radiation. By Huygen's principle, the equivalent sources are the boundary surfaces that are the four sides of the block. By choosing the boundary radiation, it will reduce the number of points and yet get similar rank for the impedance matrix.

5.1.1.3. Coarse Sampling. As block size increases, the method described becomes prohibitive. However, we know from previous experience that the rank is much smaller than the size of the matrix. Thus we can use much coarser sampling. We use the terminology in which *dense* sampling is the usual 10 points per wavelength for boundary or volume sampling and *coarse* sampling

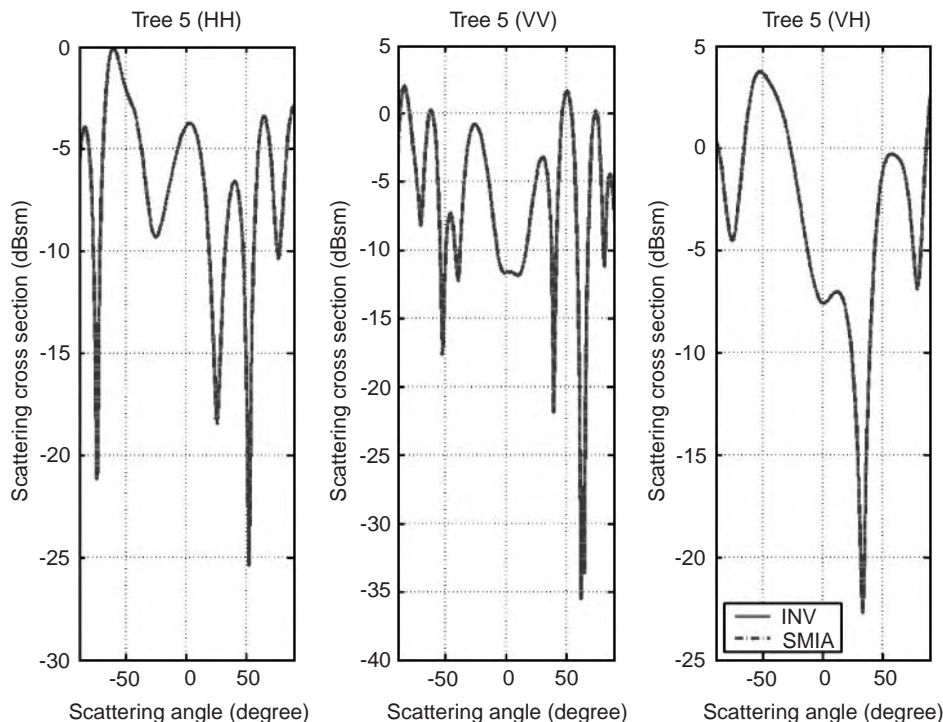
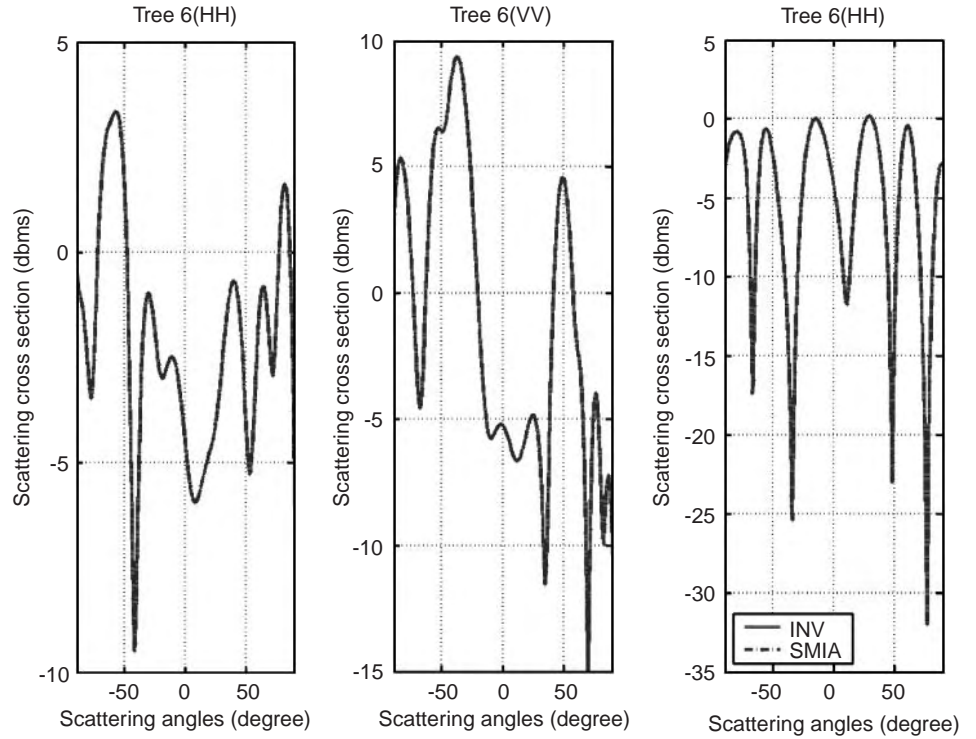


Figure 22. Comparison of the bistatic scattering cross sections of tree 5 calculated by the full matrix inversion (INV) and sparse matrix iterative approach (SMIA). The wavelength is $\lambda = 1$ m, the incidence angle $\theta_i = 45^\circ$, and the permittivity $\varepsilon_p = 33.357 + i21.408$. (This figure is available in full color at <http://www.mrw.interscience.wiley.com/erfme>.)

Figure 23. Comparison of the bistatic scattering cross sections of tree 6 calculated by the full matrix inversion (INV) and sparse matrix iterative approach (SMIA). The wavelength is $\lambda = 1$ m, the incidence angle $\theta_i = 45^\circ$, and the permittivity $\epsilon_p = 33.357 + i21.408$. (This figure is available in full color at <http://www.mrw.interscience.wiley.com/erfme>.)



means that we pick the number of points to be slightly greater than the rank. This means that we have a priori knowledge of roughly what the rank is on the basis of the numerical experiments carried out. *Coarse* sampling means that we pick the number of points several times larger than the rank. In forming a matrix, we need to select the number of points in the receiving region and a set of points in the transmitting region. Thus we have (receiving sampling)–(transmitting sampling). This means that we can have *dense-coarse sampling*, meaning dense in the receiving region and coarse in the transmitting region etc. To establish the rank of a matrix, we find that it is sufficient to have coarse-coarse sampling.

5.1.2. Method of Using Two Circular Cylinders. We can replace the transmitting and receiving blocks by two cylinders of diameter $D_b = 2S/\sqrt{\pi}$, as illustrated in Fig. 25, where both the cylinder and the square will have the same area. The centers of the receiving cylinder

and the transmitting cylinder are respectively $\bar{\rho}_r$ and $\bar{\rho}_t$. If partial waves are used to describe the waves from the transmitting cylinder to the receiving cylinder, we can truncate the partial waves at $N_c^b = 0.75kD_b$. We use the subscript “b” to denote *block*, reflecting the fact that the purpose of these two large equivalent cylinders is only to set up the rank table and not the physical size of the many cylinders in the multiple scattering problems. From Foldy–Lax equations [6], for two equivalent receiving and transmitting cylinders, the interaction matrix has the following form

$$w_m^{(r)} = \text{incidence wave} + \sum_{n=-N_c^b}^{N_c^b} H_{(m-n)}^{(1)} \times (k|\bar{\rho}_r - \bar{\rho}_t|) e^{i(m-n)\phi_{\bar{\rho}_r\bar{\rho}_t}} T_n w_n^{(t)} \quad (70)$$

where $m = -N_c^b, -N_c^b + 1, \dots, N_c^b$. Then the Foldy–Lax partial wave impedance matrix $\bar{\bar{Z}}_b$ is of dimension

Table 14. SMIA and INV Compared

	Tree 1		Tree 2		Tree 3		Tree 4		Tree 5		Tree 6	
Number of unknowns	174		360		573		1299		1662		3231	
Condition number	130733.0		10351.14		1161364.0		706516.4		5229.153		26051.72	
Method	INV	SMIA	INV	SMIA	INV	SMIA	INV	SMIA	INV	SMIA	INV	SMIA
Matrix filling (s)	10.32	10.28	26.03	25.84	47.30	47.16	139.89	139.25	196.96	196.24	590.67	596.81
Number of iterations (H)	0	10	0	11	0	15	0	19	0	22	0	68
Number of iterations (V)	0	10	0	13	0	15	0	19	0	20	0	60
Matrix solving (s)	0.200	0.250	2.245	1.541	9.085	4.116	104.93	25.106	220.46	45.667	1612.0	442.72
Total time (s)	10.56	10.57	28.35	27.47	56.84	51.44	245.10	164.64	417.77	242.27	2203.3	1040.2

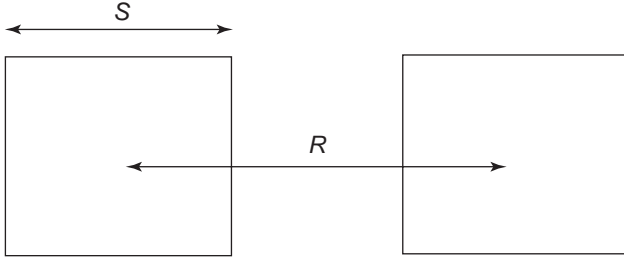


Figure 24. Illustration of rank determination.

$(2N_c^b + 1) \times (2N_c^b + 1)$ and the elements are given by

$$(\bar{\bar{Z}}_b)_{mn} = H_{(m-n)}^{(1)}(k|\bar{\rho}_r - \bar{\rho}_t|) e^{i(m-n)\phi_{r\bar{\rho}_t}} \quad (71)$$

where $m, n = -N_c^b, -N_c^b + 1, \dots, N_c^b$. We can apply the SVD to determine the rank of $\bar{\bar{Z}}_b$. This is a fast method because $N_c^b \ll N$. This has a slightly larger rank because their smallest separation is slightly less.

On the basis of the two techniques described above, a rank table is given in Table 15, where the superscripts 1, 2, 3, and 4 are used to indicate the different cases of (1) area sampling (100 points per square wavelength), (2) boundary (line) dense sampling (10 points per wavelength), (3) boundary (line) coarse sampling (4 points per wavelength), and (4) cylindrical wave expansion, respectively. The threshold chosen for rank determination is 1×10^{-5} . It is seen that all of them gives essentially same rank for same physical problem.

5.2. Foldy-Lax Partial-Wave Equation

Consider N_p cylinders of permittivity ε_p and radius a distributed arbitrarily in a square, as illustrated in Fig. 26. Let a plane TM wave be incident on them. The Foldy-Lax multiple scattering equation in terms of partial wave expansions is expressed as [6,20]

$$\begin{aligned} c_n^{(N)(q)} = & \frac{-i^n e^{-in\phi_i}}{k} e^{i\bar{k}_i \cdot \bar{\rho}_q} E_{vi} B_n^{(N)} \\ & + B_n^{(N)} \sum_{n'=-N_c}^{N_c} \sum_{p=1, p \neq q}^{N_p} H_{(n-n')}^{(1)}(k|\bar{\rho}_p - \bar{\rho}_q|) \\ & \times e^{-i(n-n')\phi_{p\bar{\rho}_q}} S_{n'}^{(N)} c_{n'}^{(N)(p)} \end{aligned} \quad (72)$$

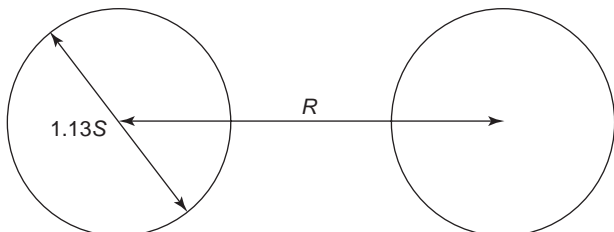


Figure 25. Illustration of rank determination with Foldy-Lax equation.

Table 15. Rank Table of Volume Scattering

$L_x = L_y$ (λ)	Points in Block	Distance (λ)	Rank
1.0	100	2.00	$9^1, 9^2, 9^3, 8^4$
1.0	100	4.24	6, 6, 6, NA
2.0	400	4.00	10, 11, 11, 11
2.0	400	8.48	7, 7, 7, NA
4.0	1,600	8.00	12, 13, 13, 15
4.0	1,600	17.0	8, 9, 9, NA
8.0	6,400	16.0	NA, 18, 18, 23
16.0	25,600	32.0	NA, 26, 26, 37
32.0	102,400	64.0	NA, 41, 41, 63

where $c_n^{(N)(q)}$ is internal field coefficient, $\bar{\rho}_q$ is the position of the q th cylinder and $B_n^{(N)}$ and $S_{n'}^{(N)}$ are given by [6,20]

$$\begin{aligned} B_n^{(N)} = B_{-n}^{(N)} = & -\frac{2ik}{\pi a k_p} \\ & \times \frac{1}{k_p H_n^{(1)}(ka) J_n'(k_p a) - k H_n^{(1)'}(ka) J_n(k_p a)} \end{aligned} \quad (73)$$

$$\begin{aligned} S_n^{(N)} = S_{-n}^{(N)} = & -\frac{i\pi a k_p}{2k} [k_p J_n(ka) J_n'(k_p a) \\ & - k J_n'(ka) J_n(k_p a)] \end{aligned} \quad (74)$$

Parameter k_p is wavenumber inside the particle. Each particle has N_c partial waves. Note that the number N_c is different from N_c^b , which denotes rank determination for block structure. For each particle, the partial wave is truncated at $N_c = 1.5ka$.

The Foldy-Lax equation is a matrix equation with the dimension of $N = N_p (2N_c + 1)$. Each particle has $(2N_c + 1)$ coefficients. The impedance matrix for the particle with itself is a $(2N_c + 1) \times (2N_c + 1)$ unit matrix. The impedance matrix for two different particles p and

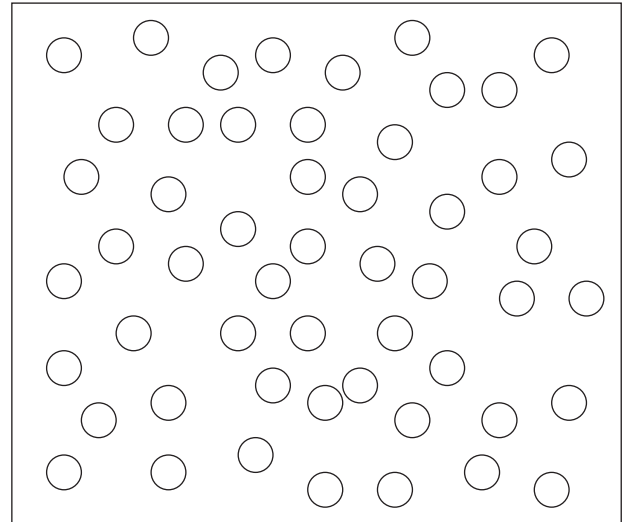


Figure 26. Illustration of many random distributed cylinders.

q , $\bar{\bar{Z}}_{pq}$, is of dimension $(2N_c + 1) \times (2N_c + 1)$, and the matrix elements are given by $-B_n^{(N)} H_{(n-n')}^{(1)}(k|\bar{\rho}_p - \bar{\rho}_q|) \exp[-i(n - n')\phi_{\bar{\rho}_p \bar{\rho}_q}] S_n^{(N)}$.

5.3. Matrix Compression for Partial Waves

Suppose that the cylinders are of diameter 1 wavelength and are densely packed as in Fig. 26. Then $N_c = 0.75(2\pi) = 4$, so that there are nine partial waves for each particle. Consider two blocks of side S wavelengths, with the distance separated by distance R , as shown in Fig. 27, the number of cylinders in each block is approximately S^2 . The dimension of the impedance matrix using partial waves between the two blocks is $S^2(2N_c + 1) = 9S^2$.

For example, if $S = 32$ wavelengths, then the impedance matrix of the blocks is of dimension $(9)(32 \times 32) = 9216$. However, the rank is only 41 from Table 15. We observe the following:

1. If volume discretization is used, and assuming 100 volumetric elements per square wavelength over the areas of the cylinders, the dimension of the impedance matrix between the two blocks is 80,425.
2. Since the particles of the physical problem are of 1 wavelength diameter, using partial wave expansion, the dimension of the impedance matrix between these two blocks is only 9216, which is substantially less than that of volume discretization. This reduction is even more for three-dimensional problems.
3. Whether volume discretization or partial wave expansion for the 1λ cylinders, the rank is the same and is 41.
4. Since the use of partial waves reduces the dimension of the matrix, it is advantageous to use partial waves.
5. It is important to recognize that UV method can directly be applied to the compression of the partial wave impedance matrix of dimension 9216.
6. The impedance matrix is of the form of $-B_n^{(N)} H_{(n-n')}^{(1)}(k|\bar{\rho}_p - \bar{\rho}_q|) \exp[-i(n - n')\phi_{\bar{\rho}_p \bar{\rho}_q}] S_n^{(N)}$. Only the factor $H_{(n-n')}^{(1)}(k|\bar{\rho}_p - \bar{\rho}_q|) \exp[-i(n - n')\phi_{\bar{\rho}_p \bar{\rho}_q}]$ depends on both particles. Thus the compression needs be done only for this term. After the compression is done, we can postmultiply by $-B_n^{(N)}$ and premultiply by $S_n^{(N)}$.

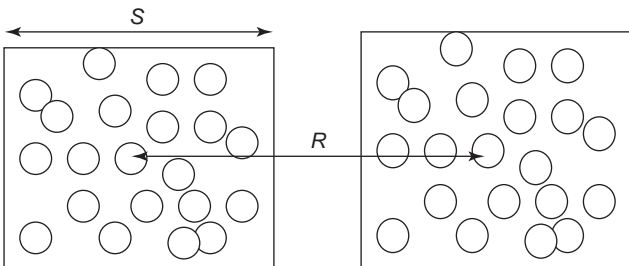


Figure 27. Illustration of interactions of many cylinders within two blocks.

After the internal field coefficients are determined, the scattered field in direction ϕ_s is

$$E_s = \sqrt{\frac{2k}{\pi\rho}} e^{i(k\rho - \pi/4)} \sum_{q=1}^{N_p} \sum_{n=-N_c}^{N_c} S_n^{(N)} c_n^q e^{in(\phi_s - \pi/2)} e^{-i\bar{k}_s \cdot \bar{\rho}_q} \quad (75)$$

The bistatic scattering coefficient as defined in Ref. 2 can be calculated.

5.4. Multilevel Partition Process

For the physical problem of the cylinders distributed in Fig. 28, we use the same techniques to do multilevel partitioning as in the case of three-dimensional rough surface scattering [19]. However, the matrix equation is in terms of partial waves form and there are $(2N_c + 1)$ partial waves for each cylinder. If there are M_r cylinders in the receiving group and M_t cylinders in the transmitting groups, the size of the interaction matrix is $M_r(2N_c + 1) \times M_t(2N_c + 1)$.

Assuming that we have a square area as shown in Fig. 28a, we first split it into four blocks as shown in Fig. 28b. Each of the four blocks is a subgroup at the P th level, which has the largest group size. Then we split each subblock into another four small groups as shown in Fig. 28c. This splitting process is continued until we reach the smallest group size, which is at the first level. We decompose the full impedance matrix in Eq. (76) as the sum of P sparse matrices as follows:

$$\bar{\bar{Z}} = \bar{\bar{Z}}^{(0)} + \bar{\bar{Z}}^{(1)} + \bar{\bar{Z}}^{(2)} + \dots + \bar{\bar{Z}}^{(P-1)} \quad (76)$$

Matrix $\bar{\bar{Z}}^{(0)}$ includes all the interactions among neighboring groups (including the self group) at the first level. Matrix $\bar{\bar{Z}}^{(1)}$ includes all the interactions among neighboring groups at the second level and consists of blocks in the first level. Similarly, matrix $\bar{\bar{Z}}^{(i)}$ includes all the interactions among neighboring groups at the $(i + 1)$ th level, but these consist of blocks in the i th level.

To facilitate understanding of the multilevel partitioning process, we give an example that has 64 subgroups at the first level. Assume each group has M elements. For this example, the highest level is $P = 3$. Thus $\bar{\bar{Z}} = \bar{\bar{Z}}^{(0)} + \bar{\bar{Z}}^{(1)} + \bar{\bar{Z}}^{(2)}$ and the impedance matrix of $\bar{\bar{Z}}$ is $64M \times 64M$ and has $4096 M \times M$ blocks.

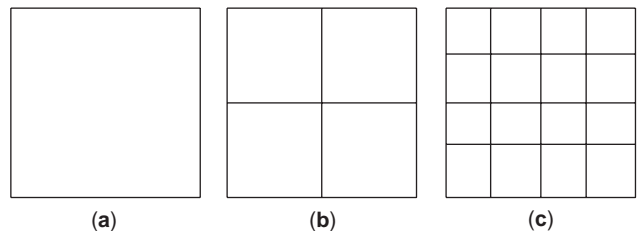


Figure 28. Illustration of multilevel partitioning process.

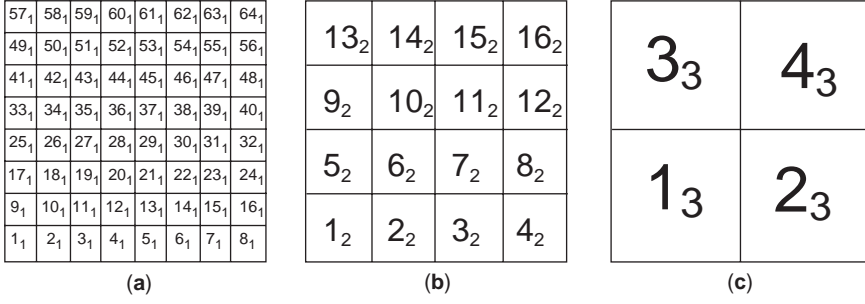


Figure 29. Illustration of multilevel partitioning process with 64 subgroups at the first level.

In Fig. 29a, the 64 subgroups of the first level are expressed as $1_1, 2_1, \dots, 64_1$. E. In Fig. 29b, the level 2 groups are shown and are represented as $1_2, 2_2, \dots, 16_2$. Each of the level 2 groups has four level 1 groups. For example, the group 3_2 has 4 groups of $5_1, 6_1, 13_1$, and 14_1 . In Fig. 29c, the level 3 groups are shown, denoted as $1_3, 2_3, 3_3$, and 4_3 . Each of the level 3 groups has four level 2 groups. For example, the group 2_3 has four groups of $3_2, 4_2, 7_2$, and 8_2 .

We use m_i to represent the group m of the level i . Then the matrix \bar{Z}_{m_i, n_i} represents the interactions between the receiving group m and the transmitting group n of the i th level. Since the four level 1 groups form a level 2 group and four level 2 groups form a level 3 group, the dimension of \bar{Z}_{m_1, n_1} is $M \times M$, and the dimension of \bar{Z}_{m_2, n_2} is $4M \times 4M$. Examples are as follows:

$$\bar{Z}_{3_2, 5_2} = \begin{bmatrix} \bar{Z}_{5_1, 17_1} & \bar{Z}_{5_1, 18_1} & \bar{Z}_{5_1, 25_1} & \bar{Z}_{5_1, 26_1} \\ \bar{Z}_{6_1, 17_1} & \bar{Z}_{6_1, 18_1} & \bar{Z}_{6_1, 25_1} & \bar{Z}_{6_1, 26_1} \\ \bar{Z}_{13_1, 17_1} & \bar{Z}_{13_1, 18_1} & \bar{Z}_{13_1, 25_1} & \bar{Z}_{13_1, 26_1} \\ \bar{Z}_{14_1, 17_1} & \bar{Z}_{14_1, 18_1} & \bar{Z}_{14_1, 25_1} & \bar{Z}_{14_1, 26_1} \end{bmatrix} \quad (77)$$

$$\bar{Z}_{6_2, 5_2} = \begin{bmatrix} \bar{Z}_{19_1, 17_1} & \bar{Z}_{19_1, 18_1} & \bar{Z}_{19_1, 25_1} & \bar{Z}_{19_1, 26_1} \\ \bar{Z}_{20_1, 17_1} & \bar{Z}_{20_1, 18_1} & \bar{Z}_{20_1, 25_1} & \bar{Z}_{20_1, 26_1} \\ \bar{Z}_{27_1, 17_1} & \bar{Z}_{27_1, 18_1} & \bar{Z}_{27_1, 25_1} & \bar{Z}_{27_1, 26_1} \\ \bar{Z}_{28_1, 17_1} & \bar{Z}_{28_1, 18_1} & \bar{Z}_{28_1, 25_1} & \bar{Z}_{28_1, 26_1} \end{bmatrix} \quad (78)$$

$$\bar{Z}_{1_3, 2_3} = \begin{bmatrix} \bar{Z}_{1_2, 3_2} & \bar{Z}_{1_2, 4_2} & \bar{Z}_{1_2, 7_2} & \bar{Z}_{1_2, 8_2} \\ \bar{Z}_{2_2, 3_2} & \bar{Z}_{2_2, 4_2} & \bar{Z}_{2_2, 7_2} & \bar{Z}_{2_2, 8_2} \\ \bar{Z}_{5_2, 3_2} & \bar{Z}_{5_2, 4_2} & \bar{Z}_{5_2, 7_2} & \bar{Z}_{5_2, 8_2} \\ \bar{Z}_{6_2, 3_2} & \bar{Z}_{6_2, 4_2} & \bar{Z}_{6_2, 7_2} & \bar{Z}_{6_2, 8_2} \end{bmatrix} \quad (79)$$

In $\bar{Z}^{(0)}$, we select interactions of the level 1 groups with their nearest neighbors. For example, 20_1 has eight neighbors of $11_1, 12_1, 13_1, 19_1, 21_1, 27_1, 28_1$, and 29_1 . Thus $\bar{Z}^{(0)}$ includes $\bar{Z}_{11_1, 20_1}, \bar{Z}_{12_1, 20_1}, \bar{Z}_{13_1, 20_1}, \bar{Z}_{19_1, 20_1}, \bar{Z}_{20_1, 20_1}, \bar{Z}_{21_1, 20_1}, \bar{Z}_{27_1, 20_1}, \bar{Z}_{28_1, 20_1}$, and $\bar{Z}_{29_1, 20_1}$, a total of nine matrices. Note that self-interaction is also included here. We note that (1) block size of \bar{Z}_{m_1, n_1} is $M \times M$, (2) there are 36 interior

first-level 1 groups of blocks $= 36 \times 9 = 324$ ($M \times M$) blocks, (3) 24 edge first-level groups of six blocks $= 24 \times 6 = 144$ ($M \times M$) blocks, and (4) four corner first-level groups of four blocks $= 4 \times 4 = 16$ ($M \times M$) blocks. Thus $\bar{Z}^{(0)}$ has total of $324 + 144 + 16 = 484$ ($M \times M$) blocks.

In $\bar{Z}^{(1)}$, we select the interactions between level 2 groups and their nearest neighbors. For example, we need to include $\bar{Z}_{6_2, 5_2}$. However, we need to exclude those that have been included $\bar{Z}^{(0)}$. We define the impedance matrix primes, for example

$$\bar{Z}'_{6_2, 5_2} = \begin{bmatrix} \bar{Z}_{19_1, 17_1} & \bar{0}_1 & \bar{Z}_{19_1, 25_1} & \bar{0}_1 \\ \bar{Z}_{20_1, 17_1} & \bar{Z}_{20_1, 18_1} & \bar{Z}_{20_1, 25_1} & \bar{Z}_{20_1, 26_1} \\ \bar{Z}_{27_1, 17_1} & \bar{0}_1 & \bar{Z}_{27_1, 25_1} & \bar{0}_1 \\ \bar{Z}_{28_1, 17_1} & \bar{Z}_{28_1, 18_1} & \bar{Z}_{28_1, 25_1} & \bar{Z}_{28_1, 26_1} \end{bmatrix} \quad (80)$$

where $\bar{0}_1$ is the zero matrix of dimension ($M \times M$). Thus $\bar{Z}^{(1)}$ includes the entire \bar{Z}'_{m_2, n_2} where m_2 and n_2 are neighbors. As shown in Eq. (80), the matrix \bar{Z}'_{m_2, n_2} consists of blocks with size of $M \times M$, and each block consists of a transmitting region and a receiving region that are not neighbors of each other. For example, in $\bar{Z}_{19_1, 17_1}$, the receiving region is 19_1 and the transmitting region is 17_1 , and the two are not neighbors of each other; also, the separation R between the transmitting and the receiving regions is at a minimum of $2S$ for $\bar{Z}_{19_1, 17_1}$, where S is the block size. It is at a maximum of $R = 3\sqrt{2}S$ for $\bar{Z}_{44_1, 17_1}$ that is in $\bar{Z}'_{10_2, 5_2}$. Thus $\bar{Z}^{(1)}$ includes (1) four interior level 2 groups that have eight neighbors, four of which have 12 blocks and four of which have 15 blocks [the total number of blocks is $4 \times (4 \times 12 + 4 \times 15) = 432$]; (2) eight edge level 2 groups that have five neighbors, three of which have 12 blocks, while two of them have 15 blocks [the total number of blocks is $8 \times (3 \times 12 + 2 \times 15) = 528$]; and (3) four corner level 2 groups that have three neighbors, two of which have 12 blocks and one that has 15 blocks [the total number of blocks is $4 \times (2 \times 12 + 1 \times 15) = 156$]. Thus matrix $\bar{Z}^{(1)}$ includes $432 + 528 + 156 = 1116$ ($M \times M$) blocks.

In $\bar{Z}^{(2)}$, we select the interactions between level 3 groups and their nearest neighbors. For example, we need to include $\bar{Z}_{1_3, 2_3}$. However, some of the interactions have already been included in $\bar{Z}^{(0)}$ and $\bar{Z}^{(1)}$ and therefore

need to be excluded. We define the prime impedance matrices, for example

$$\bar{\bar{Z}}'_{1_3 2_3} = \begin{bmatrix} \bar{\bar{Z}}_{1_2 3_2} & \bar{\bar{Z}}_{1_2 4_2} & \bar{\bar{Z}}_{1_2 7_2} & \bar{\bar{Z}}_{1_2 8_2} \\ \bar{\bar{0}}_2 & \bar{\bar{Z}}_{2_2 4_2} & \bar{\bar{0}}_2 & \bar{\bar{Z}}_{2_2 8_2} \\ \bar{\bar{Z}}_{5_2 3_2} & \bar{\bar{Z}}_{5_2 4_2} & \bar{\bar{Z}}_{5_2 7_2} & \bar{\bar{Z}}_{5_2 8_2} \\ \bar{\bar{0}}_2 & \bar{\bar{Z}}_{6_2 4_2} & \bar{\bar{0}}_2 & \bar{\bar{Z}}_{6_2 8_2} \end{bmatrix} \quad (81)$$

Note that the building blocks of $\bar{\bar{Z}}'_{1_3 2_3}$ are level 2 blocks and are of size $(4M \times 4M) = 16M \times M$. This is important, as it indicates that as the level increases, the block size will grow by 4 times as we go up each level. We have four level 3 groups, and each of them has two neighbors with 12 level 2 blocks and one neighbor with 15 level 2 blocks. Thus, we have $4 \times (2 \times 12 + 1 \times 15) = 156$ level 2 blocks. Since each level 2 block has 16 level 1 blocks, we then have a total of $16 \times 156 = 2496$ level 1 blocks in $\bar{\bar{Z}}^{(2)}$.

Thus the total count is $484 + 1116 + 2496 = 4096$, and all the level 1 blocks are counted exactly once. To summarize, the block size in $\bar{\bar{Z}}^{(0)}$ is of $M \times M$, in $\bar{\bar{Z}}^{(1)}$ is of $M \times M$, and in $\bar{\bar{Z}}^{(2)}$ is of $4M \times 4M$. In applying UV decomposition, the UV is applied to each block for that level. Each block consists of a transmitting region and a receiving region that are not neighbors of each other. However, their separations are within a restricted range as indicated before.

5.5. UV Method

The matrix $\bar{\bar{Z}}_{m_i n_i}$, which represents the interactions of two nonneighbor groups m_i and n_i , can be represented by UV decomposition. The matrix $\bar{\bar{Z}}_{m_i n_i}$ is of dimensions $4^{(i-1)}M(2N_c + 1) \times 4^{(i-1)}M(2N_c + 1)$. The rank of $\bar{\bar{Z}}_{m_i n_i}$, r , is much smaller than $4^{(i-1)}M(2N_c + 1)$. For simpler notation, we denote $\bar{\bar{Z}}_{m_i n_i}$ by $\bar{\bar{A}}$, which has dimension of $N \times N$ and rank of r with $r \ll N$. To decompose $\bar{\bar{A}}$ by the SVD and Gram-Schmidt processes will be CPU and memory-intensive because N is large. Note that in Section 5.6, the SVD is applied to find r . But because of coarse-coarse sampling, the selected matrices are roughly of dimension $r \times r$ only. To perform UV decomposition, we need only r independent columns of $\bar{\bar{A}}$ and r independent rows of $\bar{\bar{A}}$.

Let the column of $\bar{\bar{A}}$ be denoted by $\bar{\bar{a}}_l$, where $l = 1, 2, \dots, N$, where $N = 4^{(i-1)}M(2N_c + 1)$. The matrix element A_{mn} is the m th element of the column vector $\bar{\bar{a}}_n$, $A_{mn} = (\bar{\bar{a}}_n)_m$. Note that the N columns are the number of cylinders $4^{(i-1)}M$ times the number of partial waves $(2N_c + 1)$ in the transmitting region. However there are only r independent columns. In the transmitting region, we select r columns from the N columns. The r elements must be uniformly distributed in the transmitting region. If the rank r is less than the number of cylinders inside the transmitting area, we select the zeroth-order partial wave of r cylinders uniformly distributed. If the rank r is larger than the number of cylinders $4^{(i-1)}M$, we select the zeroth-order harmonics of all the cylinders first, and then select the first-order partial wave of $4^{(i-1)}M$ uniformly distributed cylinders.

We compute the r columns $\bar{\bar{u}}_l$, $l = 1, 2, \dots, r$. Each column is of dimension of N and coincides with a column of $\bar{\bar{A}}$

$$U_{ml} = (\bar{\bar{u}}_l)_m = A_{mp(l)} \quad (82)$$

where $m = 1, 2, \dots, N$ and $p(l)$ is a column index of $\bar{\bar{A}}$ that depends on l . Note that to get U_{ml} , one needs to go through all the N elements in the receiving region. Thus the matrix $\bar{\bar{U}}$ has rN elements.

Because of linear independence, any general column $\bar{\bar{a}}_m$ of $\bar{\bar{A}}$ is a linear combination of $\bar{\bar{u}}_l$, that is

$$\bar{\bar{a}}_m = \sum_{l=1}^r v_{lm} \bar{\bar{u}}_l \quad (83)$$

where $m = 1, 2, \dots, N$, and v_{lm} are the coefficients to be determined.

We pick r rows of $\bar{\bar{A}}$, which has total of rN elements. The r rows correspond to r elements in the receiving group. The criterion for picking up elements is the same as in the transmitting area. We first put these rows in a matrix of $\bar{\bar{R}}$, its matrix elements are given as $R_{m_a p} = A_{m(m_a)p}$, with $p = 1, 2, \dots, N$ and $m_a = 1, 2, \dots, r$. We next pick the m_a rows in $\bar{\bar{u}}_l$, $l = 1, 2, \dots, r$. That will give us an $r \times r$ matrix named $\bar{\bar{U}}$ with $\bar{\bar{U}}_{m_a n_a} = (\bar{\bar{u}}_{n_a})_{m(m_a)}$. Then we set

$$R_{m_a l} = \sum_{n_a=1}^r \bar{\bar{U}}_{m_a n_a} v_{n_a l} \quad (84)$$

with $l = 1, 2, \dots, N$. In matrix notation, $\bar{\bar{V}}$ is of dimension $r \times N$, $\bar{\bar{R}}$ is of dimension $r \times N$, $\bar{\bar{U}}$ is of dimension $r \times r$, $\bar{\bar{R}} = \bar{\bar{U}}\bar{\bar{V}}$, and $\bar{\bar{V}} = \bar{\bar{U}}^{-1}\bar{\bar{R}}$. This completes the UV decomposition of $\bar{\bar{A}}$, and

$$\bar{\bar{A}} = \bar{\bar{U}}\bar{\bar{V}} \quad (85)$$

To summarize, we take r columns of $\bar{\bar{A}}$ and then r rows of N , representing a total of $2rN$ elements. We need to take the inverse of an $r \times r$ matrix $\bar{\bar{U}}$, and a matrix multiplication of an $r \times r$ matrix with an $r \times N$ matrix. The computational and memory efficiency is achieved when $r \ll N$.

5.6. Computational Complexity Analysis

5.6.1. Multilevel Group Sizes and Number of Groups.

The centers of the cylinders are generated in a square area with $\sqrt{N_p}$ points in both x and y directions, such that the total number of cylinders is N_p . Note that each cylinder has a finite radius of a . We use various subgroup sizes at P level to partition the whole area as follows:

1. At the P th level, split the whole area as four groups. Each group has $N_p/4$ cylinders. Let L_P be the number of groups and M_P be the number of cylinders of each group at the P th level. Thus, $L_P = 4 = 2^{2(P-P+1)}$, and $M_P = N_p/4 = N_p/L_P$.
2. Split each group into four subgroups and continuing this partitioning, at the i th level, we have

$L_i = 2^{2(P-i+1)}$ subgroups and $M_i = N_p/L_i$ cylinders of each subgroup at the i th level, respectively.

- At the first level, we have respectively $L_1 = 2^{2P}$ level 1 subgroups and $M_1 = N_p/L_1$ cylinders of each subgroup.

5.6.2. Cost Function at i th Level. In $\bar{\bar{Z}}^{(i)}$, we select the interactions between level $(i+1)$ groups and their nearest neighbors. However, some of the interactions have already been included in the lower-level groups and must be excluded from them. There are five kinds of neighboring groups:

- Groups Sharing Only One Common Point.** As shown in Fig. 30a, for the neighboring groups of $m_{(i+1)}$ and $n_{(i+1)}$, only one common point is shared between them. The impedance matrix that will be calculated is

$$\bar{\bar{Z}}'_{m_{(i+1)}n_{(i+1)}} = \begin{bmatrix} \bar{\bar{Z}}_{m_i^{(1)}n_i^{(1)}} & \bar{\bar{Z}}_{m_i^{(1)}n_i^{(2)}} & \bar{\bar{Z}}_{m_i^{(1)}n_i^{(3)}} & \bar{\bar{Z}}_{m_i^{(1)}n_i^{(4)}} \\ \bar{\bar{Z}}_{m_i^{(2)}n_i^{(1)}} & \bar{0}_i & \bar{\bar{Z}}_{m_i^{(2)}n_i^{(3)}} & \bar{\bar{Z}}_{m_i^{(2)}n_i^{(4)}} \\ \bar{\bar{Z}}_{m_i^{(3)}n_i^{(1)}} & \bar{\bar{Z}}_{m_i^{(3)}n_i^{(2)}} & \bar{\bar{Z}}_{m_i^{(3)}n_i^{(3)}} & \bar{\bar{Z}}_{m_i^{(3)}n_i^{(4)}} \\ \bar{\bar{Z}}_{m_i^{(4)}n_i^{(1)}} & \bar{\bar{Z}}_{m_i^{(4)}n_i^{(2)}} & \bar{\bar{Z}}_{m_i^{(4)}n_i^{(3)}} & \bar{\bar{Z}}_{m_i^{(4)}n_i^{(4)}} \end{bmatrix} \quad (86)$$

The dimension of matrix $\bar{\bar{Z}}_{m_i n_i}$ is of $M_i(2N_c+1) \times M_i(2N_c+1)$. The computational steps for $\bar{\bar{Z}}_{m_i n_i} \cdot \bar{\mathbf{b}}_{M_i}$ through the UV is of $2(2N_c+1)M_i r_i$, where r_i is the rank of $\bar{\bar{Z}}_{m_i n_i}$. In here we assume that the rank r_i of $\bar{\bar{Z}}_{m_i n_i}$ is the same for all block interactions at the same level. There are 15 nonzero matrices of $\bar{\bar{Z}}_{m_i n_i}$ in the $\bar{\bar{Z}}'_{m_{(i+1)}n_{(i+1)}}$. The total computational steps for $\bar{\bar{Z}}'_{m_{(i+1)}n_{(i+1)}} \cdot \bar{\mathbf{b}}'_{M_{(i+1)}}$ are $30(2N_c+1)M_i r_i$.

- Groups Sharing One Common Edge.** As shown in Fig. 30b, for the neighboring groups of $m_{(i+1)}$ and

$n_{(i+1)}$, one common edge is shared between them. The impedance matrix that will be calculated is

$$\bar{\bar{Z}}'_{m_{(i+1)}n_{(i+1)}} = \begin{bmatrix} \bar{\bar{Z}}_{m_i^{(1)}n_i^{(1)}} & \bar{0}_i & \bar{\bar{Z}}_{m_i^{(1)}n_i^{(3)}} & \bar{0}_i \\ \bar{\bar{Z}}_{m_i^{(2)}n_i^{(1)}} & \bar{\bar{Z}}_{m_i^{(2)}n_i^{(2)}} & \bar{\bar{Z}}_{m_i^{(2)}n_i^{(3)}} & \bar{\bar{Z}}_{m_i^{(2)}n_i^{(4)}} \\ \bar{\bar{Z}}_{m_i^{(3)}n_i^{(1)}} & \bar{0}_i & \bar{\bar{Z}}_{m_i^{(3)}n_i^{(3)}} & \bar{0}_i \\ \bar{\bar{Z}}_{m_i^{(4)}n_i^{(1)}} & \bar{\bar{Z}}_{m_i^{(4)}n_i^{(2)}} & \bar{\bar{Z}}_{m_i^{(4)}n_i^{(3)}} & \bar{\bar{Z}}_{m_i^{(4)}n_i^{(4)}} \end{bmatrix} \quad (87)$$

There are 12 nonzero matrices of $\bar{\bar{Z}}_{m_i n_i}$ in $\bar{\bar{Z}}'_{m_{(i+1)}n_{(i+1)}}$. The total computational steps for $\bar{\bar{Z}}'_{m_{(i+1)}n_{(i+1)}} \cdot \bar{\mathbf{b}}'_{M_{(i+1)}}$ are $24(2N_c+1)M_i r_i$.

- Interior Groups.** Interior groups have eight neighbors, four of which share only one common point and four others that share one common edge. There are $(\sqrt{L_{(i+1)}}-2)^2$ interior groups at the $(i+1)$ th level. Thus computational steps for the interior groups at the i th level are $(\sqrt{L_{(i+1)}}-2)^2[4 \times 30(2N_c+1)M_i r_i + 4 \times 24(2N_c+1)M_i r_i] = 216(\sqrt{L_{(i+1)}}-2)^2(2N_c+1)M_i r_i$.
- Edge Groups.** Edge groups have five neighbors; two of them share only one common point and three of them share one common edge. There are $4(\sqrt{L_{(i+1)}}-2)$ edge groups at the $(i+1)$ th level. Thus computational steps for the edge groups at the i th level are $4(\sqrt{L_{(i+1)}}-2)(2 \times 30M_i r_i + 3 \times 24M_i r_i)(2N_c+1) = 528(\sqrt{L_{(i+1)}}-2)(2N_c+1)M_i r_i$.
- Corner Groups.** Corner groups have three neighbors. One of them shares only one common point and two of them share one common edge. There are four corner groups at the $(i+1)$ th level. Thus computational steps for the corner groups at the i th level are $4(1 \times 30M_i r_i + 2 \times 24M_i r_i)(2N_c+1) = 312(2N_c+1)M_i r_i$.

Thus the total computational step at the i th level is the sum of $216(\sqrt{L_{(i+1)}}-2)^2 M_i r_i (2N_c+1)$ for the interior groups, $528(\sqrt{L_{(i+1)}}-2) M_i r_i (2N_c+1)$ for the edge groups,

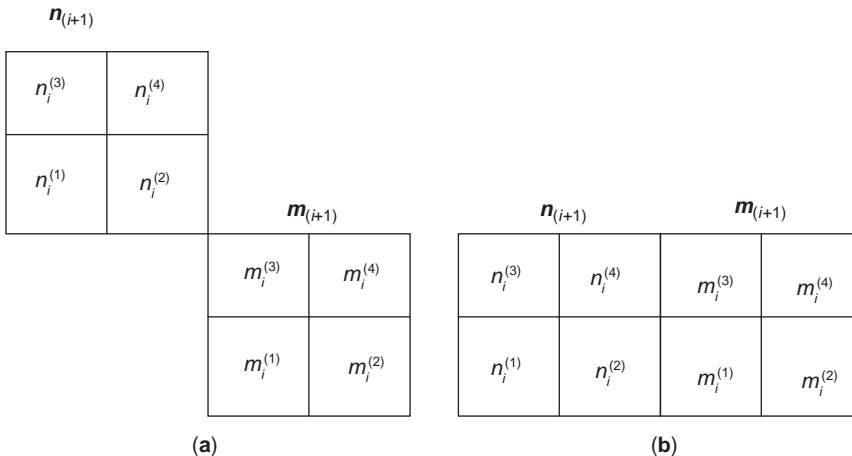


Figure 30. Illustration of interactions of multiple cylinders within two blocks.

and $312M_i r_i (2N_c + 1)$ for the corner groups, which is equal to

$$2M_i r_i \left(108L_{(i+1)} - 168\sqrt{L_{(i+1)}} + 60 \right) (2N_c + 1) \quad (88)$$

5.6.3. Cost Function for the Multilevel UV Method (Non-near). The total computational steps for nonneighbor block interactions through the multilevel UV decomposition are

$$\sum_{i=1}^{P-1} 2r_i M_i \left[108L_{(i+1)} - 168\sqrt{L_{(i+1)}} + 60 \right] (2N_c + 1) \quad (89)$$

Generally speaking, the rank of each level block will increase with increase in block size. For simplicity, we assume $r_i = r$ to be a constant here, and substituting this r in Eq. (89), we have

$$27rN(2N_c^b + 1) \log_2 \left(\frac{N}{M_1} \right) + 60rN(2N_c^b + 1) - 120rM_1(2N_c + 1) \quad (90)$$

5.6.4. Cost Function for Near-Field Interactions in $\bar{Z}^{(0)}$. All the near-field interactions are included in the matrix $\bar{Z}^{(0)}$, which is computed directly as the original impedance matrix. The block size in $\bar{Z}^{(0)}$ is of dimension of $(2N_c + 1)M_1 \times (2N_c + 1)M_1$. The computational steps for the block and block interaction are $(2N_c + 1)^2 M_1^2$.

1. *Interior Group.* The interior group has nine blocks (including self-interaction). There are $(\sqrt{L_1} - 2)^2$ interior groups at the first level. Thus the computational steps for the interior groups at the first level are $9(\sqrt{L_1} - 2)^2 M_1^2 (2N_c + 1)^2$.
2. *Edge Groups.* Each edge group has six blocks (including self-interaction). There are $4(\sqrt{L_1} - 2)$ edge groups at the first level. Thus the computational steps for the edge groups at the first level are $6(\sqrt{L_1} - 2)M_1^2 (2N_c + 1)^2$.
3. *Corner Groups.* Each corner group has four blocks (including self). There are four corner groups at the first level. Thus the computational steps for the corner groups at the first level are $4M_1^2 (2N_c + 1)^2$.

The total computational step for near-field interaction is then the sum of $9(\sqrt{L_1} - 2)^2 M_1^2 (2N_c + 1)^2$ for the interior groups, $6(\sqrt{L_1} - 2)M_1^2 (2N_c + 1)^2$ for the edge groups, and $4M_1^2 (2N_c + 1)^2$ for the corner groups, which is equal to

$$(9NM_1 - 12N^{1/2}M_1^{3/2} + 4M_1^2)(2N_c + 1)^2 \quad (91)$$

5.6.5. Cost Function. The total computational step for multilevel partitioning UV is sum of the near and nonnear

interactions and is given by

$$\left[27rN \log_2 \frac{N}{M_1} + 60rN - 120rM_1 \right] (2N_c + 1) + (9NM_1 - 12N^{1/2}M_1^{3/2} + 4M_1^2)(2N_c + 1)^2 \quad (92)$$

5.7. Numerical Results and Discussion

The numerical simulation results are presented and compared in terms of the matrix–vector product and solutions of the Foldy–Lax equation with an iterative solver. Simulations are based on the periodic distributions of many cylinders and the random distribution of many cylinders. We assume that all the cylinders have the same diameter of 1 wavelength. The horizontal and vertical separations between the centers of two neighboring cylinders are taken as 1.3 wavelengths for periodic distribution. For the case of random distribution, the center of each cylinder is moved randomly within the range from -0.15 to 0.15 wavelength in both horizontal and vertical directions. The relative dielectric constant of all the cylinders is 3.2 in Fig. 29 and is equal to 1.5 in Figs. 30 and 31. The computer used in the simulations is a Pentium single processor of 2.6 GHz with 2 GB (gigabyte) memory.

5.7.1. Rank Determination for Foldy–Lax Equation. First, we illustrate the rank determination for the problem. The cylinders are first grouped with the multilevel partitioning process, and then we know the size of each group. On the basis of the coarse–coarse boundary sampling, we can calculate the ranks of interaction groups with the SVD method. Since the UV is not as strict as the SVD method, we actually use a rank a little bit higher than that calculated when constructing the UV matrix.

5.7.2. CPU for the UV. In Table 16, we list the CPU time based on the UV method for different numbers of cylinders. The diameter of each cylinder is 1 wavelength, and the number of partial waves is 9. This means that there are nine partial waves unknowns to be determined for each cylinder. The numbers of cylinders are 64, 256, 1024, and 4096. The preprocessing time of the UV method is the time used to construct $U \times V$ matrix and also the time for rank determination. The CPU time for matrix–vector multiplication means the CPU time spent for one time matrix–vector multiplication. For the case of 4096 cylinders, which corresponds to 36,864 partial wave unknowns, it takes less than ~ 7.34 s for the matrix–vector multiplication. This case corresponds to 321,700 equivalent numbers of volumetric unknowns.

5.7.3. Comparisons of the Matrix–Vector Product. The results for 4096 cylinders are shown in Fig. 31. Because of the limited computer resource, the direct multiplication is not possible for this case. Thus we make comparison between the SVD-based QR method and the UV method. We use the product from the SVD method as the horizontal values and the product from the UV method as the vertical

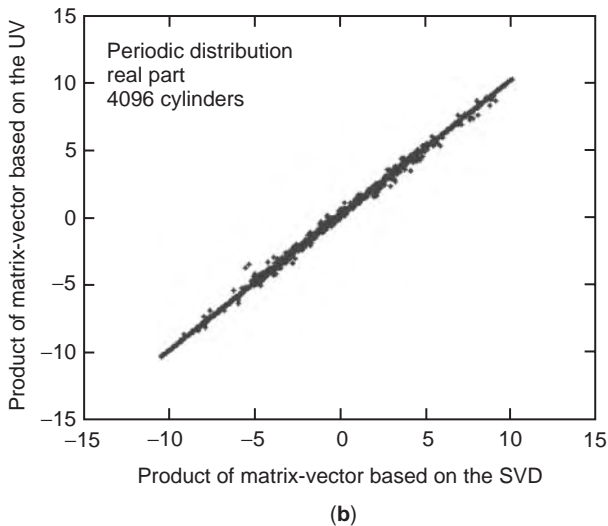
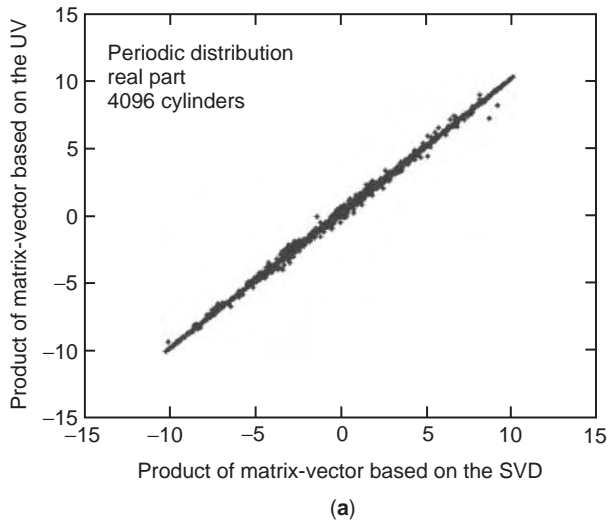


Figure 31. Comparisons of the matrix–vector products calculated by the SVD-based QR method and the UV method. The number of cylinders is 4096 with a diameter of 1.0 wavelength. (This figure is available in full color at <http://www.mrw.interscience.wiley.com/erfme>.)

values. Figure 31a shows results for the real part and Fig. 31b, is for the imaginary part. We can see that all the points are along a 1–1 line, which means that the products from both methods are matched well for this case.

In Table 16, we also list the relative norm errors for the matrix–vector product compared with direct matrix–vector multiplication for all the cases cited above. The errors inside parentheses for 1024 cylinders indicate random

Table 16. CPU for the UV Method and Norm Error

Number of Cylinders	Preprocessing Time (s)	Matrix–Vector Product (s)	Norm Error
64	1	0.02	0.0033
256	14	0.13	0.0020
1024	115	1.03	0.0015 (0.0017)
4096	999	7.34	0.0127

distribution. It can be seen that the errors are pretty small. This means that an accurate matrix–vector product can be reached through the UV method.

5.7.4. Comparisons of the Solutions of Foldy–Lax Equation for Different Numbers of Cylinders. Using the proposed UV method, we have solved the Foldy–Lax equation with an iterative solver for randomly distributed cylinders. The relative dielectric constant of all the cylinders is 1.5 and the convergent condition for the iterative approach is set up at 1×10^{-3} . We have done this for 1024 cylinders. For this case, we have made comparisons with the solutions from the SVD-based QR method. Good agreement was obtained.

In Table 17, we list the CPU time and relative norm errors for each solution. We also show the number of CG iterations and CPU time for the rank determination. The CPU time for rank determination is included in the second column in brackets. The numbers of iterations are listed in column 3 and in parentheses. The total CPU for 64 cylinders is 3 s with a total of 36 s for 256 cylinders. For 1024 cylinders, preprocessing time is 121 s, taking only 32 s for rank determination based on the coarse–coarse sampling. The CPU for iteration method is 711 s, which needs 330 iterations to reach the convergence. The relative errors are 0.0014 for 64 cylinders, 0.0078 for 256 cylinders, and 0.0189 for 1024 cylinders. Thus, using the UV method, we can solve the partial wave equation very efficiently and accurately. However, the number of CG iterations grows with the number of cylinders. This property of the Foldy–Lax partial wave equation needs to be investigated further.

5.7.5. Bistatic Scattering Coefficients for Different Numbers of Cylinders. After the solutions of the Foldy–Lax equation, we can calculate the scattering coefficients. Figure 32 shows the bistatic scattering coefficients for cylinders totaling 1024. The incidence angle is 30° . The diameter of all cylinders is 1.0 wavelength and the

Table 17. CPU for the UV-CG Method and Norm Error

Number of Cylinders	Preprocessing Time (s)	CG Time (s)	Total CPU Time (s)	Norm Error
64	2 ($<1^a$)	1 (21^b)	3	0.0014
256	15 (4)	21 (75)	36	0.0078
1024	121 (32)	711 (330)	832	0.0189

^aCPU time for rank determination.

^bNumber of iterations for the conjugate gradient method.

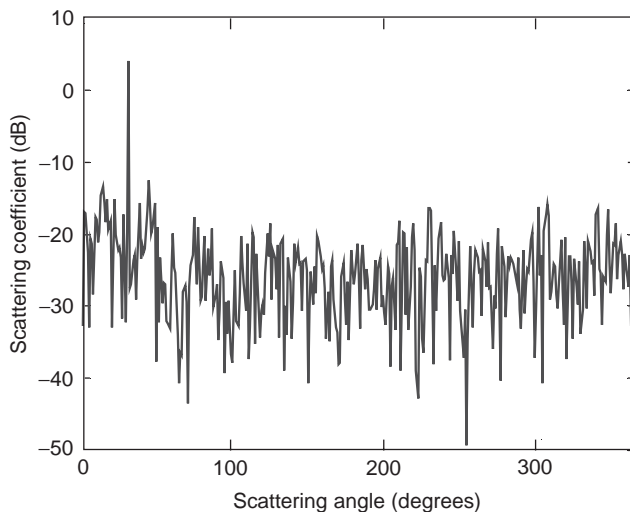


Figure 32. Bistatic scattering coefficients based on the UV method. The number of cylinders is 1024, with radius of 1.0 wavelength. The incidence angle is 30° . (This figure is available in full color at <http://www.mrw.interscience.wiley.com/erfme>.)

relative permittivity is 1.5. The cylinders are randomly distributed.

The UV-MLP method is presented for the rapid solution of integral equation. Like SMCG and FMM methods, the UV-MLP method emphasizes on the reduction of both CPU and memory requirements for matrix–vector multiplication. On the other hand, the method of characteristic basis functions [75] emphasizes the drastic reduction in basis functions.

BIBLIOGRAPHY

1. F. T. Ulaby, R. K. Moore, and A. K. Fung, *Microwave Remote Sensing: Active and Passive*, Vols. 1 and 2, Addison-Wesley, Reading, MA, 1981.
2. L. Tsang, J. A. Kong, and R. T. Shin, *Theory of Microwave Remote Sensing*, Wiley-Interscience, New York, 1985.
3. F. T. Ulaby, R. K. Moore, and A. K. Fung, *Microwave Remote Sensing: Active and Passive*, Vol. 3, Artech House, Norwood, MA, 1986.
4. A. K. Fung, *Microwave Scattering and Emission Models and Their Applications*, Artech House, Norwood, MA, 1994.
5. L. Tsang, J. A. Kong, and K. H. Ding, *Scattering of Electromagnetic Waves*, Vol. 1: *Theory and Applications*, Wiley-Interscience, New York, 2000.
6. L. Tsang, J. A. Kong, K. H. Ding, and C. O. Ao, *Scattering of Electromagnetic Waves*, Vol. 2: *Numerical Simulations*, Wiley-Interscience, New York, 2001.
7. L. Tsang and J. A. Kong, *Scattering of Electromagnetic Waves*, Vol. 3: *Advanced Topics*, Wiley-Interscience, New York, 2001.
8. J. Guo, L. Tsang, K. H. Ding, A. T. C. Chang, and C. T. Chen, Frequency dependence of scattering by dense media of small particles based on Monte Carlo simulation of Maxwell's equations, *IEEE Trans. Geosci. Remote Sens.* **40**:153–161 (Jan. 2002).
9. C. T. Chen, L. Tsang, J. Guo, A. T. C. Chang, and K. H. Ding, Frequency dependence of scattering and extinction of dense media based on three-dimensional simulations of Maxwell's equations with applications to snow, *IEEE Trans. Geosci. Remote Sens.* **41**:1844–1852 (Aug. 2003).
10. J. Guo, L. Tsang, W. Asher, K. H. Ding, and C. T. Chen, Applications of dense media radiative transfer theory for passive microwave remote sensing of foam covered ocean, *IEEE Trans. Geosci. Remote Sens.* **39**:1019–1027 (May 2001).
11. D. Chen, L. Tsang, L. Zhou, S. C. Reising, W. Asher, L. A. Rose, K. St Germain, K. H. Ding, and C. T. Chen, Microwave emission and scattering of foam based on Monte Carlo simulations of dense media, *IEEE Trans. Geosci. Remote Sens.* **41**:782–790 (April 2003).
12. L. Zhou, L. Tsang, and D. Chen, Polarimetric microwave remote sensing of wind vectors with foam covered rough ocean surfaces, *Radio Sci.* **38**(4):12-1–12-14 (DOI: 10.1029/2002RS002764) (Aug. 2003).
13. K. Pak, L. Tsang, and J. T. Johnson, Numerical simulations and backscattering enhancement of electromagnetic waves from two-dimensional dielectric random rough surfaces with the sparse matrix canonical grid method, *J. Opt. Soc. Am. A* **14**:1515–1529 (1997).
14. C. H. Chan, C. M. Lin, L. Tsang, and Y. F. Leung, A sparse-matrix/canonical grid method for analyzing microstrip structures, *IEICE Trans. Electron.* **E80-C**:1354–1359 (1997).
15. S. Q. Li, Y. Yu, C. H. Chan, K. F. Chan, and L. Tsang, A sparse-matrix/canonical grid method for analyzing densely packed interconnects, *IEEE Trans. Microwave Theory Tech.* **MTT-49**:1221–1228 (2002).
16. K. H. Ding and L. Tsang, A sparse matrix iterative approach for modeling tree scattering, *Microwave Opt. Technol. Lett.* **38**(1):198–202 (Aug. 2003).
17. H. G. Wang, C. H. Chan, L. Tsang, and V. Jandhyala, An improved multi-level matrix QR factorization for large-scale simulations on magnetoquasistatic analysis of integrated circuits over multi-layered lossy substrates (in press).
18. L. Tsang, D. Chen, Q. Li, and V. Jandhyala, A fast numerical solutions of wave scattering problem: Part I: 2D problem of PEC surface scattering, *Radio Sci.* (2004).
19. L. Tsang, Q. Li, D. Chen, and V. Jandhyala, Wave scattering with UV multi-level partitioning method Part II: 3D problem of non-penetrable surface scattering, *Radio Sci.* (2004).
20. L. Tsang and Q. Li, Wave scattering with UV multi-level partitioning method, wave scattering by discrete scatterers, *Microwave Opt. Technol. Lett.* **41**(5):354–361 (June 2004).
21. A. T. C. Chang, J. L. Foster, and D. K. Hall, Nimbus-7 SMMR derived global snow cover parameters, *Ann. Glaciol.* **9**:39–44 (1987).
22. M. T. Hallikainen, F. T. Ulaby, and T. E. V. Deventer, Extinction behavior of dry snow in the 18- to 90- GHz range, *IEEE Trans. Geosci. Remote Sens.* **25**:737–745 (June 1987).
23. L. Wilson, L. Tsang, J. N. Hwang, and C. T. Chen, Mapping snow water equivalent in mountainous areas by combining a spatially distributed snow hydrology model with passive microwave remote sensing data, *IEEE Trans. Geosci. Remote Sens.* **37**:690–704 (March 1999).
24. S. Rosenfeld and N. C. Grody, Metamorphic signature of snow revealed in SSM/I measurements, *IEEE Trans. Geosci. Remote Sens.* **38**:53–63 (Jan. 2000).
25. C. T. Chen, B. Nijssen, J. Guo, L. Tsang, A. Wood, J. N. Hwang, and D. P. Lettenmaier, Passive microwave remote sensing of snow constrained by hydrological simulations, *IEEE Trans. Geosci. Remote Sens.* **39**:1744–1756 (Aug. 2001).
26. L. Tsang, C. T. Chen, A. T. C. Chang, J. Guo, and K. H. Ding, Dense media radiative transfer theory based on

- quasicrystalline approximation with applications to passive microwave remote sensing of snow, *Radio Sci.* **35**(3):731–749 (2000).
27. L. Tsang, C. E. Mandt, and K. H. Ding, Monte Carlo simulations of the extinction rate of dense media with randomly distributed dielectric spheres based on solution of Maxwell's equations, *Opt. Lett.* **17**(5):314–316 (1992).
28. L. M. Zurk, K. H. Ding, L. Tsang, and D. P. Winebrenner, Monte Carlo simulations of the extinction rate of densely packed spheres with clustered and nonclustered geometries, *J. Opt. Soc. Am. A* **12**(8):1772–1781 (1995).
29. L. M. Zurk, L. Tsang, and D. P. Winebrenner, Scattering properties of dense media from Monte Carlo simulations with applications to active remote sensing of snow, *Radio Sci.* **31**:803–819 (1996).
30. K. Karkkainen, A. Sihvola, and K. Nikoskinen, Analysis of a three-dimensional dielectric mixture with finite difference method, *IEEE Trans. Geosci. Remote Sens.* **39**:1013–1018 (May 2001).
31. C. Mandt, Y. Kuga, L. Tsang, and A. Ishimaru, Microwave propagation and scattering in a dense distribution of spherical particles: experiment and theory, *Waves Random Media* **2**:225–234 (1992).
32. C. C. Lu, W. C. Chew, and L. Tsang, The application of recursive aggregate T-matrix algorithm in the Monte Carlo simulations of the extinction rate of random distribution of particles, *Radio Sci.* **30**(1):25–28 (1995).
33. Y. Nanbu and M. Tateiba, A comparative study of the effective dielectric constant of a medium containing randomly distributed dielectric spheres embedded in a homogeneous background medium, *Waves Random Media* **6**(4):347–360 (1996).
34. B. E. Barrowes, C. O. Ao, F. L. Teixeira, J. A. Kong, and L. Tsang, Monte Carlo simulation of electromagnetic wave propagation in dense random media with dielectric spheroids, *IEICE Trans. Electron.* **E83-C**:1797–1802 (2000).
35. P. R. Siqueira and K. Sarabandi, T-matrix determination of effective permittivity for three-dimensional dense random media, *IEEE Trans. Anten. Propag.* **48**:317–327 (2000).
36. S. M. Allen and E. L. Thomas, *The Structure of Materials*, Wiley, New York, 1999.
37. T. Vicsek, *Fractal Growth Phenomena*, World Scientific Publishers, Singapore, 1992.
38. N. A. Seaton and E. D. Glandt, Monte Carlo simulation of adhesive spheres, *J. Chem. Phys.* **87**(3):1785–1790 (1987).
39. W. G. T. Kranendonk, and D. Frenkel, Simulation of the adhesive-hard-sphere model, *Mol. Phys.* **64**(3):403–424 (1988).
40. K. H. Ding, L. Tsang, and S. E. Shih, Monte Carlo simulation of particle positions for densely packed multispecies sticky particles, *Microwave Opt. Technol. Lett.* **30**:187–192 (2001).
41. R. J. Baxter, Ornstein-Zernike relation and Percus-Yevick approximation for fluid mixtures, *J. Chem. Phys.* **52**:4559–4562 (1970).
42. J. W. Perram and E. R. Smith, A model for the examination of phase behavior in multicomponent systems, *Chem. Phys. Lett.* **35**:138–140 (1975).
43. J. Shi, R. E. Davis, and J. Dozier, Stereological determination of dry snow parameters for discrete microwave modeling, *Ann. Glaciol.* **17**:295–299 (1993).
44. C. Matzler and U. Wegmuller, Dielectric properties of fresh-water ice at microwave frequencies, *J. Phys. D* **20**:1623–1630 (1987).
45. L. Tsang, Polarimetric passive microwave remote sensing of random discrete scatterers and rough surfaces, *J. Electromagn. Waves Appl.* **5**(1):41–57 (1991).
46. S. H. Yueh, R. Kwok, F. K. Li, S. V. Nghiem, W. J. Wilson, and J. A. Kong, Polarimetric passive remote sensing of ocean wind vector, *Radio Sci.* **29**:799–814 (1994).
47. J. T. Johnson, J. A. Kong, R. T. Shin, S. H. Yueh, S. V. Nghiem, and R. Kwok, Polarimetric thermal emission from rough ocean surfaces, *J. Electromagn. Waves Appl.* **8**:43–59 (1994).
48. S. H. Yueh, Modeling of wind direction signals in polarimetric sea surface brightness temperatures, *IEEE Trans. Geosci. Remote Sens.* **35**:1400–1418 (1997).
49. D. B. Kunkel and A. J. Gasiewski, Simulation of passive microwave wind direction signatures over the ocean using an asymmetric-wave geometrical optics model, *Radio Sci.* **32**:59–78 (1997).
50. A. Stogryn, The emissivity of sea foam at microwave frequencies, *J. Geophys. Res.* **77**:1658–1666 (1972).
51. P. M. Smith, The emissivity of sea foam at 19 and 37 GHz, *IEEE Trans. Geosci. Remote Sens.* **26**:541–547 (1988).
52. X. Z. Huang and Y. Q. Jin, Scattering and emission from two-scale randomly rough sea surface with foam scatterers, *IEE Proceedings - Microwaves, Antennas and Propagation* **142**:109–114 (April 1995).
53. G. F. Williams, Microwave emissivity measurements of bubbles and foam, *IEEE Trans. Geosci. Electron.* **GE-9**:221–224 (1971).
54. T. T. Wilheit Jr, A model for the microwave emissivity of the ocean's surface as a function of wind speed, *IEEE Trans. Geosci. Electron.* **GE-17**:244–249 (1979).
55. P. C. Pandey and R. K. Kakar, An empirical microwave emissivity model for a foam-covered sea, *IEEE J. Ocean. Eng.* **OE-7**(3):135–140 (1982).
56. W. Asher, Q. Wang, E. C. Monahan, and P. M. Smith, Estimation of air-sea gas transfer velocities from apparent microwave brightness temperature, *Mar. Technol. Soc. J.* **32**(2):32–40 (1998).
57. L. A. Rose, W. Asher, S. C. Reising, P. W. Gaiser, K. M. St. Germain, D. J. Dowgiallo, K. A. Horgan, G. Farquharson, and E. J. Knapp, Radiometric measurements of the microwave emissivity of foam, *IEEE Trans. Geosci. Remote Sens.* **40**:2619–2625 (Dec. 2002).
58. S. P. Durden and J. F. Vesecky, A physical radar cross section model for a wind driven sea with swell, *IEEE J. Ocean. Eng.* **OE-10**:445–451 (1985).
59. W. C. Chew, J. A. Friedrich, and R. Geiger, A multiple scattering solution for the effective permittivity of a sphere mixture, *IEEE Trans. Geosci. Remote Sens.* **28**:207–214 (1990).
60. L. A. Klein and C. T. Swift, An improved model for the dielectric constant of sea water at microwave frequencies, *IEEE Trans. Anten. Propag.* **25**(1):104–111 (1977).
61. S. H. Yueh, J. A. Kong, J. K. Jao, R. T. Shin, and T. Le Toan, Branching model for vegetation, *IEEE Trans. Geosci. Remote Sens.* **30**:390–402 (1992).
62. W. C. Au, L. Tsang, and J. A. Kong, Absorption enhancement of scattering electromagnetic waves by dielectric cylinder clusters, *Microwave Opt. Technol. Lett.* **7**:454–457 (1994).
63. Z. Chen, L. Tsang, and G. Zhang, Scattering of electromagnetic waves by vegetation based on the wave approach and the stochastic Lindenmayer system, *Microwave Opt. Technol. Lett.* **8**:30–33 (1995).

64. J. He, N. Geng, L. Nguyen, and L. Carin, Rigorous modeling of ultrawideband VHF scattering from tree trunks over flat and sloped terrain, *IEEE Trans. Geosci. Remote Sens.* **39**: 2182–2193 (2001).
65. P. Prusinkiewicz and A. Lindenmayer, *The Algorithmic Beauty of Plants*, Springer, New York, 1990.
66. G. H. Golub and C. F. Van Loan, *Matrix Computations*, 3rd ed., Johns Hopkins Univ. Press, Baltimore, 1996.
67. G. Alleon, M. Benzi, and L. Giraud, Sparse approximate inverse preconditioning for dense linear systems arising in computational electromagnetics, *Num. Algorithms* **16**:1–15 (1997).
68. J. M. Song, C. C. Lu, and W. C. Chew, Multilevel fast multipole algorithm for electromagnetic scattering by large complex objects, *IEEE Trans. Anten. Propag.* **AP-45**:1488–1493 (1997).
69. K. Sertel and J. L. Volakis, Incomplete LU preconditioner for FMM implementation, *Microwave Opt. Technol. Lett.* **26**:265–267 (2000).
70. C. H. Chan and L. Tsang, A sparse-matrix canonical grid method for scattering by many scatterers, *Microwave Opt. Technol. Lett.* **8**(2):114–118 (Feb. 1995).
71. J. Guo, L. Tsang, A. T. C. Chang, Q. Li, C. C. Huang, and K. H. Ding, Bistatic phase function and fast solution of scattering by 2-dimensional random distributed scatterers, *Microwave Opt. Technol. Lett.* **38**(4):313–317 (Aug. 2003).
72. B. E. Barrowes, C. Ao, F. L. Teixeira, and J. A. Kong, Sparse matrix/canonical grid Method applied to 3-D dense medium simulations, *IEEE Trans. Anten. Propag.* **51**:48–58 (2003).
73. C. C. Lu, J. M. Song, and W. C. Chew, A multi-level fast multipole algorithm for solving 3D volume integral equations of electromagnetic scattering, *Proc. IEEE Antennas Propagation Int. Symp.*, 2000, pp. 1864–1867.
74. C. C. Lu, Site specific propagation modeling by multilevel fast multipole algorithm, in B. Beker and Y. Chen, eds., *Recent Research Development in Microwave Theory and Techniques*, Research Signpost, Kerala, India, 2003.
75. Y. F. Sun, C. H. Chan, R. Mittra, and L. Tsang, Characteristic basis function methods for solving large problems arising from dense medium scattering, *Proc. IEEE Antennas Propagation Int. Symp.*, Columbus, OH, 2003.

CONFORMAL ANTENNAS

DIPAK L. SENGUPTA
University of Detroit Mercy
Detroit, Michigan

A conformal antenna may be defined as an antenna whose radiating aperture conforms to the surface of the body on which it is mounted. Ideally, such antennas are flush mounted or low profile (i.e., they do not protrude appreciably out of the mounting surface). Basic slot and microstrip (patch) antennas are typical examples of conformal antenna elements. The term *conformal array* has no unique definition. Kummer [1] defines it as an array that is nonplanar. We shall assume here that a conformal

array consists of conformal (or low-profile) antenna elements placed on a nonplanar surface. The array surface is not generally at the disposal of the antenna designer and is often dictated by the specific application. For ground-based application, a conformal phased array requiring coverage over 360° in azimuth (omnidirectional coverage) or coverage over a hemisphere the array surface may be cylindrical or spherical, respectively. For conformal arrays on aircraft, missiles, satellites, and surface ships, the array shape may assume another form dictated by the contour of the vehicle. Basic slot and microstrip antennas are extensively discussed in the literature—for example, the textbook by Balanis [2] is a typical reference. These antennas provide ideal performance only when they are mounted on planar surfaces. During conformal application the curvature of the mounting surface can affect their impedance and radiation properties; such effects must be taken into account during the design of such antennas.

The need for conformal phased arrays for aircraft and missile applications, and for ground-based arrays with omnidirectional coverage in azimuth or complete hemispherical coverage in space, has grown continually with requirements that emphasize maximum utilization of available space and minimum cost. Many of the developments in conformal arrays have been extensions of the concepts for planar phased arrays, which are extensively discussed in the literature (for example, in Ref. 2). However, there are significant differences between planar and conformal arrays that must be taken into account during the design of the latter. The individual elements on curved bodies point in different directions that make it necessary to turn off those elements that radiate primarily away from the desired beam direction. For this reason also, one cannot factor out the element pattern out of the total radiation pattern—this makes the conformal array analysis and synthesis more difficult. The element orientation may also cause severe crosspolarization. In addition, the mutual coupling effects between the elements can be severe in some cases.

Within the limitations of space allowed, it is not possible to describe here every aspect of conformal antennas and antenna arrays. Instead, we shall at first describe briefly certain aspects of a few basic antennas that are commonly used either singly or as array elements for conformal applications. Then we give brief descriptions of a selected number of conformal antennas and antenna arrays. Specifically, this article describes the following:

1. The specific considerations that must be given to the performance of basic slot and microstrip or patch antenna elements when mounted on nonplanar conducting surfaces
2. A selected number of conformal antennas: for example, microstrip conformal antennas and dielectric-filled edge slot (DFES) antennas
3. A class of wraparound antennas and antenna arrays
4. Cylindrical and spherical phased arrays used for omnidirectional and hemispherical coverage, respectively.

All of these antennas have found practical applications. Detailed descriptions of their development, design procedures, and analysis of their performance are described in the references cited at appropriate places.

Literature on conformal antennas is vast and ranges from technical journal articles to numerous textbooks and specialized books, of which Refs. 2–8 are typical.

1. BASIC ANTENNA ELEMENTS

Elementary slot and microstrip patch antennas are commonly used singly or as array elements for conformal application. However, these radiators provide ideal performance only when they use plane conducting surfaces. Ideal theory can be used when the radii of curvature of the surfaces are large compared to the operating wavelength. In other cases both the impedance and radiation characteristics may be affected significantly.

1.1. Slots on Curved Surfaces

The radiation patterns of slot antennas can be significantly altered by the curved mounting surface. Pathak and Kouyoumjian [9] give a convenient extension of the geometric theory of diffraction (GTD) for apertures in curved surfaces. Figure 1, taken from Ref. 9, shows the patterns of an axial slot element on perfectly conducting circular cylinders of various radii; the results indicate the accuracy of the approximate theory. The effects of the cylinder radius on the patterns shown in Fig. 1 should be noticed. A similar slot on a flat ground plane would have a constant pattern from $\phi = 0$ to 180° . Radiation patterns of slots on a variety of other generalized surfaces are discussed in Refs. 10–12. Mailloux [13] summarizes some of the results of Pathak and Kouyoumjian [9] shown in Fig. 2, which gives the radiated power pattern in the upper half-plane ($\theta \leq 90^\circ$) for an infinitesimal slot in a cylinder of radius a . The angular extent of the transition zone is on the order of $(k_0 a)^{-1/3}$ on each side of the shadow boundary, where

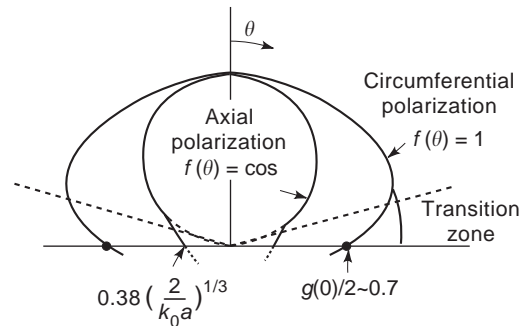


Figure 2. Approximate pattern of a thin slot on a conducting cylinder of radius a ; k_0 is the free-space propagation constant. (After Ref. 6.)

$k_0 = 2\pi/\lambda_0$ is the propagation constant in free space. The results indicate that above the transition zone (i.e., the illuminated zone) the circumferentially polarized radiation is nearly constant but the axially polarized radiation has a $\cos \theta$ pattern. Compared with the field strength in the $\theta = 0^\circ$ direction, the field strengths in the $\theta = 90^\circ$ area are found to be about 0.7 and $0.4(2/k_0 a)^{1/3}$ for circumferential and axial polarizations, respectively. It should be noted that in the case of flat surface the field reduces to zero in the $\theta = 90^\circ$ area.

1.2. Slots on Metallic Cones

Slots and slot arrays on metallic cones are found advantageous to use for missile or missilelike bodies. For efficient design of such arrays, the self- and mutual admittances must be taken into account. Theoretical and experimental investigation of slot antennas on metallic cones are discussed in Ref. 14, where the effects of scattering from a sharp tip on the mutual admittances have been investigated for pairs of circumferential and radial slots on a semi-infinite metallic cone. The base of the conical model used in the experimental study was terminated in a spherical cap to minimize scattering from the finite length of the apparatus. The two slot antennas configurations considered are shown in Fig. 3. Self- and mutual admittance expressions for pairs of slots shown in Fig. 3 have been derived by Golden et al. [14], and the results have been confirmed by measurements. These admittance results can be immediately applied to determine the aperture voltages required for the analysis of N -element slots on cones.

In Ref. 14 the circumferential slot results illustrate interference effects between the direct coupling from slot to slot via the geodesic path over the conical surface and the tip backscattering. For the radial slot configuration, the results indicate negligible tip scattering effects. Golden and Stewart [15] have found that the current distribution near a slot for a sharp cone can be approximated by the distribution on an equivalent cylinder if scattering from the apex (on tip) is small. Thus, the mutual admittance between two slots can be approximately calculated by using a cylindrical model with the same local radii of curvature as the cone, provided the wave scattering from either

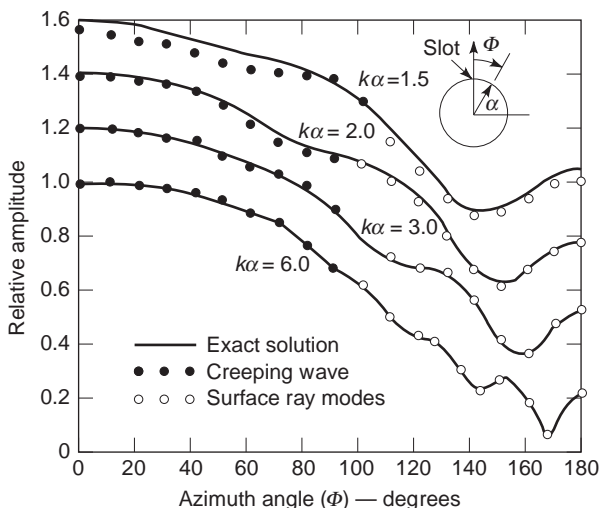


Figure 1. Patterns of a thin axial slot on a perfectly conducting cylinder. (After Ref. 9.)

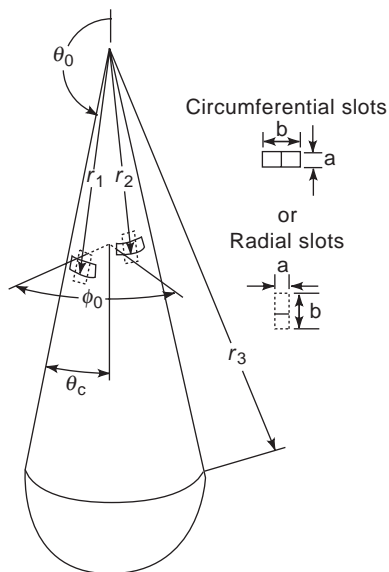


Figure 3. Slotted-cone geometry.

the tip or the base region of the vehicle is negligible. The slotted cone and equivalent cylinder are shown in Fig. 4, which reveals that the cylinder has a radius equal to the radius of the circular cross section of the cone midway between the two slots antennas. For small-angle cones ($\theta_0 \sim 180^\circ$), the radial separation of the slots on the cone can be equated to the axial separation of the slots on the equivalent cylinder.

Mutual coupling ($|S_{12}|$ parameter) results versus azimuthal separation for two circumferential and axial slots on a cylinder are shown in Figs. 5 and 6, respectively. The mutual coupling between two radial slots on a 12.2° half-angle cone is shown in Fig. 7 as a function of frequencies. Figure 8 shows the mutual coupling versus frequencies for circumferential slots on a 12.2° (half-angle) cone. The

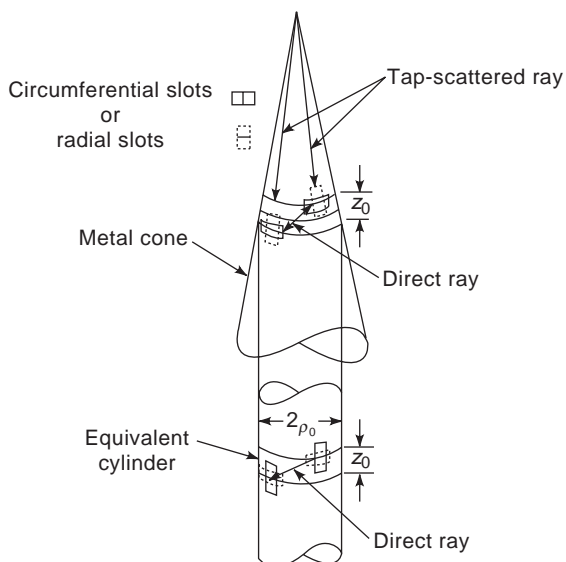


Figure 4. Slotted cone and equivalent cylinder.

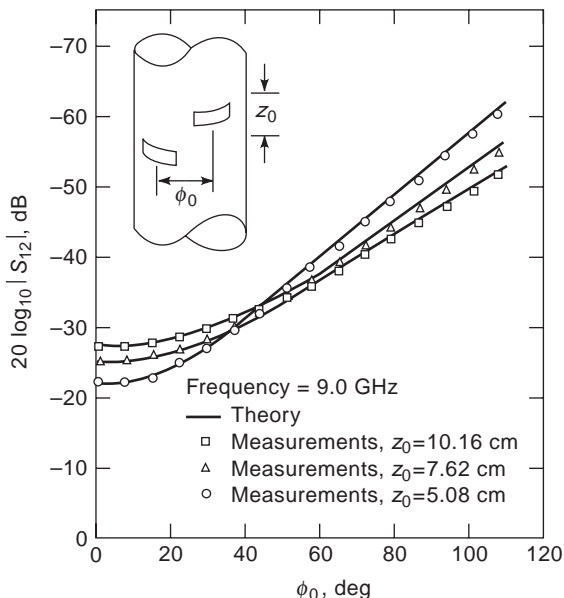


Figure 5. Mutual coupling for circumferential slots on cylinder, $\rho_0 = 5.057$ cm. (After Ref. 14.)

results illustrate the interference effects between the direct and tip-scattered components. The mutual coupling between circumferential slots on an 11° (half-angle) cone is shown in Fig. 9. Using the results given in Ref. 14, it may be concluded that for the case of circumferential slots (radial electric fields) the tip-scattered portion of the azimuthal magnetic field at the slot aperture can be expressed in terms of an appropriate diffraction coefficient; in the case of radial slots (azimuthal electric fields) there is no radial component of the magnetic field in the far field of tip and therefore no contribution to the mutual admittance. More detailed results and discussions are given in Refs. 14 and 15.

1.3. Microstrips on Curved Surfaces

Microstrip or patch is a popular low-profile, flush-mounted antenna developed in the 1970s. Detailed descriptions of

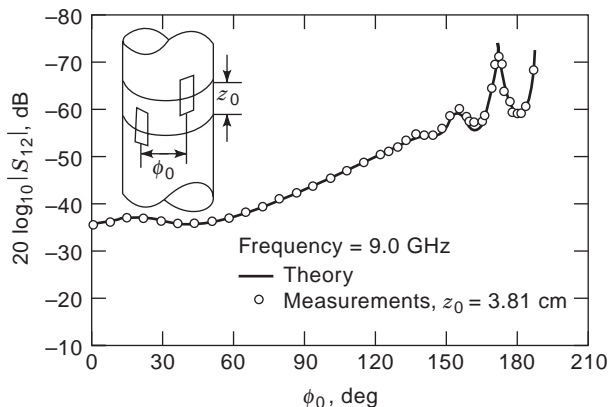


Figure 6. Mutual coupling for axial slots on cylinder, $\rho_0 = 5.057$ cm. (After Ref. 14.)

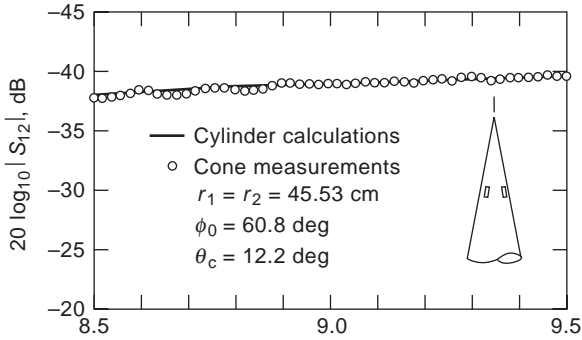


Figure 7. Mutual coupling for radial slots versus frequency, $\rho_0 = 9.622$ cm. (After Ref. 14.)

the research and development of microstrip antennas can be found in Refs. 16 and 17. Such antennas generally use a metallic patch on a dielectric substrate backed by a planar ground plane, and they are excited either by a stripline or a coaxial line. The shape of the patch can be rectangular, circular, or some other shape, in general, of which the first two are the most popular. We shall mostly describe the basic rectangular patch antenna whose one dimension is $\lambda/2$ at the operating wavelength in the substance and the other dimension is slightly less than the former. Ideally, such antennas produce similar E - and H -plane patterns that have maxima in the broadside direction; generally, the polarization is linear and parallel to the patch plane but they can be designed to produce circular polarization also. For conformal applications, it is necessary to take into account the effects of nonplanar surfaces on the performance of such antennas.

1.4. Cylindrical–Rectangular Patch Antenna

The geometry of a rectangular microstrip patch antenna mounted on a conducting cylinder is shown in Fig. 10. Resonant frequencies and radiation characteristics of this antenna are discussed in Refs. 18 and 19. For thin substrate satisfying $h \ll a$, Luk et al. [19] give the following expression for the (transverse magnetic mode with respect

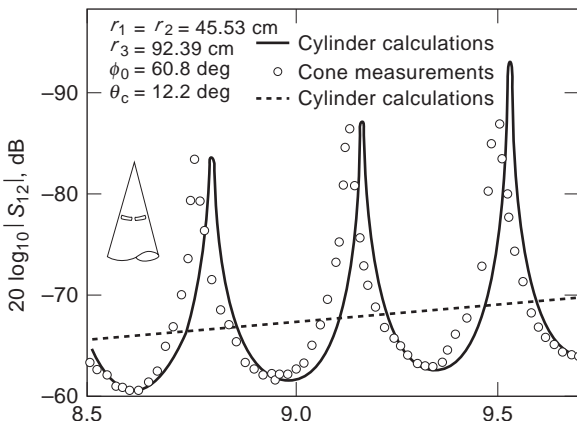


Figure 8. Mutual coupling for circumferential slots versus frequency, $\rho_0 = 9.622$ cm. (After Ref. 14.)

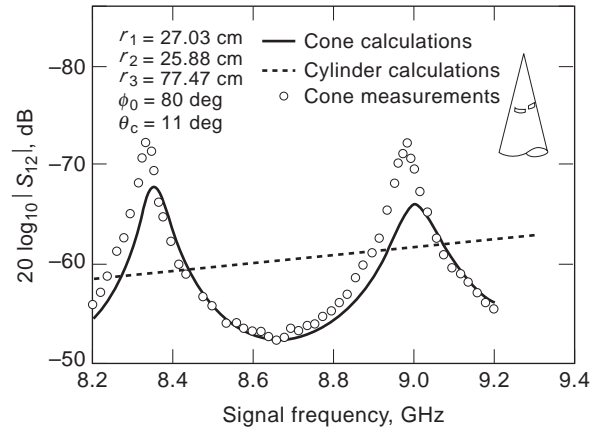


Figure 9. Mutual coupling for circumferential slots versus frequency; $\rho_0 = 5.041$ cm. (After Ref. 14.)

to ρ) TM_ρ resonant frequencies for the antenna

$$f_{mn} = \frac{c}{2\sqrt{\epsilon_r}} \left[\left(\frac{m}{2(a+h)\theta_1} \right)^2 + \left(\frac{n}{2b} \right)^2 \right]^{1/2} \quad (1)$$

where c is the velocity of light in free space, ϵ_r is the dielectric constant of the substrate, and $m, n = 0, 1, 2, \dots$, but $m = n \neq 0$. Equation (1) indicates that if the dimensions of the patch—that is, $2(a+h)\theta$ and $2b$ —are fixed, the resonant frequencies of the TM_ρ modes are not affected by the curvature of the thin substrate. However, to account for fringing fields, effective values of the dimensions are to be used in Eq. (1), as mentioned by Carver and Mink [20]. Luk et al. [19] discuss the E - and H -plane radiation patterns produced by the antenna using $\epsilon_r = 1.06$, $\epsilon_r = 2.32$, and different values a . It is found that the patterns are not sensitive to the thickness. For a curved patch, there is significant radiation in the lower hemisphere for the TM_{01} mode; the deviation from the flat patch results increases for larger value of ϵ_r . Compared to the TM_{10} mode, there is less radiation in the lower hemisphere for the TM_{01} mode. Wong and Ke [21] describe the design of this antenna for

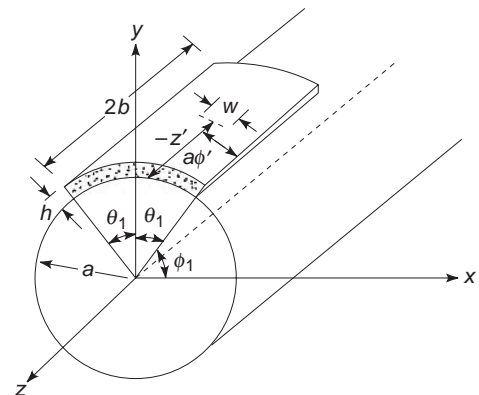


Figure 10. Geometry of a cylindrical–rectangular microstrip patch antenna.

circular polarization by using the TM_{01} and TM_{10} modes excited by a single coaxial feed located on a diagonal line and the operating frequency chosen between the two lowest frequencies f_{01} and f_{10} given by Eq. (1).

Kashiwa et al. [22] describe the application of a strip-line-fed cylindrically curved rectangular patch antenna as a small, portable antenna for mobile communication. It has been found that near the resonant frequency the real part of the input impedance approaches $50\ \Omega$. The radiation patterns near the broadside direction are found to be similar to those of the equivalent planar antenna; however, significant differences have been found in large off-broadside directions.

Radiation patterns of a cavity-backed microstrip patch antenna on a cylindrical body of arbitrary cross section have been investigated theoretically and experimentally by Jin et al. [23]. The finite-element method is used to characterize the microstrip patch antennas, and then the reciprocity theorem is applied in conjunction with a two-dimensional method of moments to calculate the radiated field. The method can be extended to characterize the radiation patterns of conformal microstrip patch antennas on general three-dimensional bodies.

1.5. Microstrip Patch Antennas on Conical Surfaces

The use of microstrip antennas on conical surfaces is of interest for aerospace vehicles with portions of their bodies conically shaped. Performance of a basic rectangular patch antenna on a metallic cone has been investigated theoretically by Descardecì and Giarola [24]. In the analysis the substrate thickness is assumed to be very small compared with the distance of the patch to the cone apex, and the curvature radius of the cone surface large compared with the operating wavelength. The capacitive effects and losses associated with surface waves have been neglected. Except for these assumptions, the cavity model analysis used is general and applies to any conical surface. Within the approximations made, the resonant frequency is not significantly affected by the conical surface. However, the radiation pattern is affected, with a consequent influence on the input impedance and the total quality factor. Details can be found in Ref. 24.

2. CONFORMAL ANTENNAS

2.1. The Omnidirectional Microstrip Antenna

The omnidirectional (also known as *nondirectional* or “omni”) microstrip or spiral slot antenna discussed in Refs. 25–27 is essentially a short-circuited quarter-wavelength microstrip patch wrapped around a cylindrical surface to form a spiral, as shown in Fig. 11. The cylinder is an epoxy fiberglass dielectric, and the copper conduction is added using an electroless plating–masking–electroplating technique. The lower end and the insider of the patch are similarly plated to form a short circuit and ground plane. The spiral slot antenna has a height and diameter of $0.06\lambda_0$ but, unlike conventional small antennas, has well-matched input voltage standing-wave ratio (VSWR) of less than 2:1 over a 2% bandwidth at 238 MHz. The

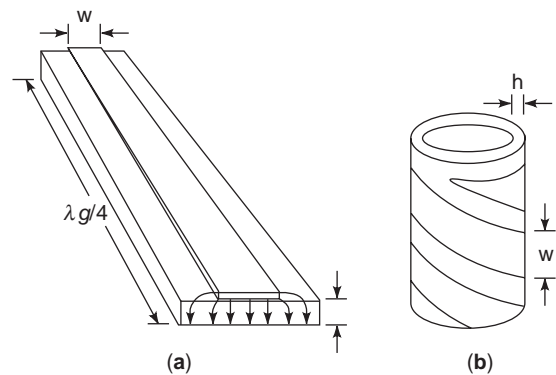


Figure 11. (a) Linear short-circuited $\lambda_g/4$ microstrip resonator; (b) omnidirectional microstrip antenna: a cylindrical $\lambda/4$ microstrip resonator. (After Ref. 27.)

radiation patterns are similar to those of a dipole oriented parallel to the cylinder axis, and the +1 dB gain indicates an efficiency of better than 50%. The spiral slot has also been developed for 42-MHz application in which the antenna has to be contained in a $0.04\lambda_0 \times 0.15\lambda_0$ cylindrical volume.

2.2. Dielectric-Filled Edge Slot Antenna

A class of circumferential slot antennas, called the DFES antennas, that are ideally suited for conformal mounting on conducting bodies of revolution has been described by Schaubert et al. [28]. As shown in Fig. 12, the simplest form of the antenna consists of a disk of dielectric substrate that is copper-coated on both sides and mounted between the two halves of a conducting body so that the radiating aperture coincides with the surface. The antenna is excited at the center by a coaxial line whose outer conductor is connected to the lower conducting surface, and the inner conductor is extended through the dielectric and finally connected to the conducting surface at the upper end of the substrate. The input reflection coefficients of the antenna are found to assume minimum values at some discrete frequencies, called the *operating frequencies*,

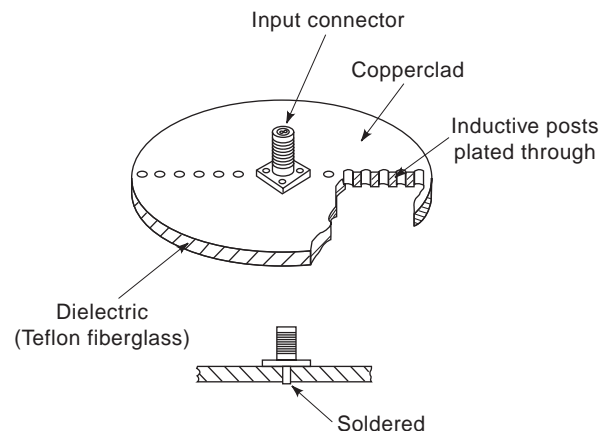


Figure 12. Two-element edge slot antenna.

where the antenna also radiates most efficiently. The DFES antenna can be tuned for a desired operating frequency by using a number of axially oriented passive metallic posts. The antenna without the tuning posts is referred to as the “basic” DFES antenna, which generally provides the highest operating frequency. By varying the number and location of the inductive posts, the operating frequency of the antenna can be tuned over a 6:1 range; instantaneous bandwidths of 3% are typical. The theory and design of basic and tuned DFES antennas mounted on a conducting cylinder have been developed and discussed by Sengupta and Martins-Camelo [29]. The radiation patterns of edge slot excited conducting bodies of revolution display a high degree of azimuthal symmetry. The radiation pattern of DFES antennas is strongly influenced by the body on which it is mounted. The patterns in Fig. 13 are typical of the performance of the antenna when mounted on a conducting cylinder.

Sometimes it is not possible to place a flat disk across the body, and at times the antenna must be mounted near the top of a conical body where the diameter is not sufficient to build an antenna operating at the desired frequency. In such cases the planar disk can be deformed (symmetrically) to fit in the available space and to operate at the required frequency. A conical edge slot antenna is described in Ref. 28, and its radiation patterns are shown

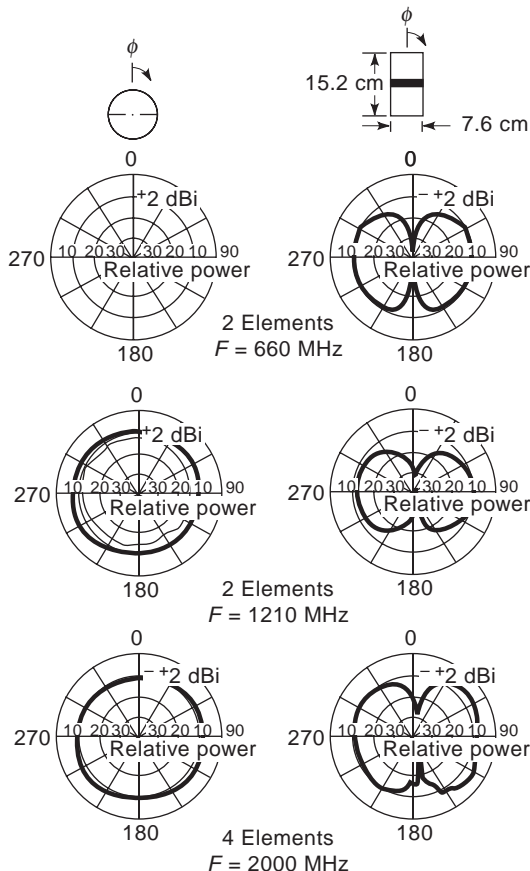


Figure 13. Radiation patterns of a 7.6-cm DFES antenna mounted on a cylinder. (After Ref. 28.)

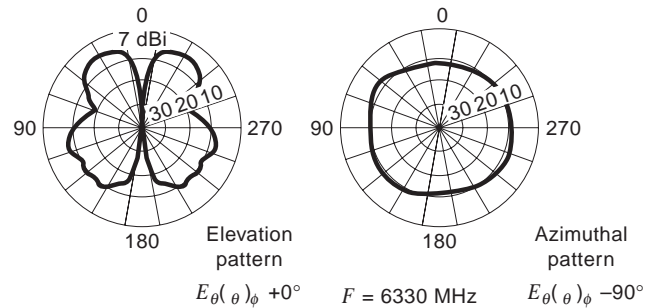


Figure 14. Radiation patterns of four-element edge slot antenna mounted on conical base. (After Ref. 28.)

in Fig. 14. The DFES antenna is a versatile and useful radiator. Because the azimuthal symmetric radiation pattern can be obtained at any desired frequency within a very wide range, system designers are not restricted in their choice of operating frequency. Also, DFES antennas can be integrated into a variety of structures because their shape can be varied to conform to the body and the available space.

2.3. Microstrip Wraparound Antennas

Microstrip wraparound antennas consisting of continuous metal strips that wrap around missiles, rockets, and satellites can provide omnidirectional coverage. Various forms of such antennas are described in Refs. 30–34. Munson [30] proposes a continuous radiator for linear polarization, as shown in Fig. 15, which shows that the microstrip feed network is a parallel (or corporate) feed network where two-way power splits are equal phase to all of the feedpoints. The number of power divisions can be 2, 4, 8, 16, and so on. The specific number of feeds and power divisions required is dictated by the microstrip radiator. The number of feedpoints N_F must exceed the number of wavelengths in the dielectric in the L direction (i.e., N_F). The following design relations can be used for the antenna shown in Fig. 15:

$$\lambda = \frac{\lambda_0}{\sqrt{\epsilon_r}} \quad (2)$$

$$w = \frac{\lambda_0}{2\sqrt{\epsilon_r}} = \frac{\lambda}{2} \quad (3)$$

$$L = \pi D \quad (4)$$

$$L_D = \frac{L(\epsilon_r)^{1/2}}{\lambda_0} \quad (5)$$

$$N_F > L_D \quad (6)$$

$$\text{With } \lambda_0 = \text{wavelength in free space} \quad (7)$$

The pattern coverage of the omnidirectional antenna shown in Fig. 15 depends on the diameter of the missile. A

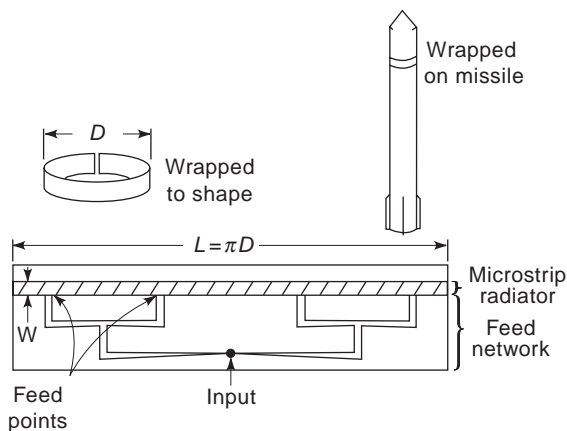


Figure 15. Microstrip wraparound antenna. (After Ref. 30.)

typical measured E -plane pattern of a wraparound antenna mounted on an 8-in. (203-mm) cylinder given in Ref. 31 is reproduced in Fig. 16. The limiting factor in the omnidirectional coverage is a hole at the tip and tail of the missile that gets narrower as the diameter of the missile increases.

Reference 33 studies radiation patterns of wraparound microstrip antenna on a spherical body for different radii of the conducting sphere, frequencies, dielectric constant, and thickness of the dielectric. Specifically, the antenna studied consists of a metal strip of width d wrapped around a conducting sphere of radius a covered with a dielectric substrate of chosen thickness d . A φ -symmetric transverse electromagnetic mode of excitation is used. The parameter d is kept equal to half a wavelength (λ) inside the dielectric for constructive interference to occur in the

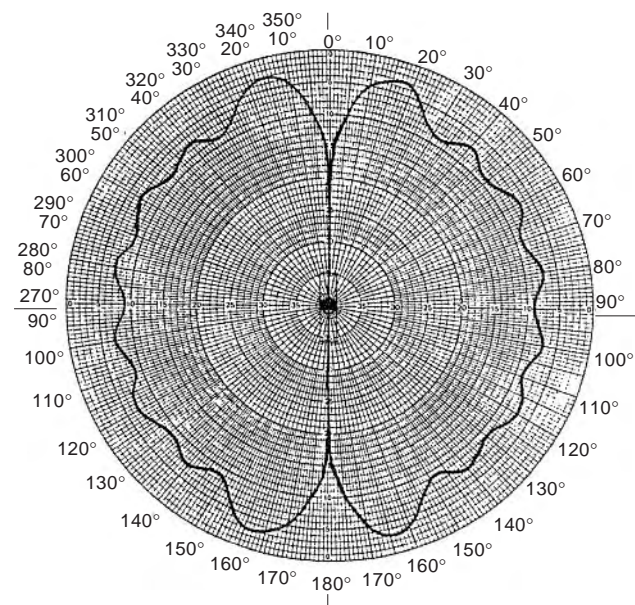


Figure 16. Measured E -plane pattern of the 8-in. (203-mm) wraparound microstrip antenna. The antenna pattern is a figure of revolution about the missile axis. (After Ref. 31.)

broadside direction. The following comments summarize the findings of the investigation reported in Ref. 33:

1. Radiation patterns are almost independent of the pressure of the patch when the radius of the sphere is much larger than the strip width.
2. The larger the radius of the sphere ($a \gg \lambda_0$), the better the omnidirectional pattern.
3. The dielectric constant ϵ_r does not have significant influence on the pattern shape. The radiation intensity tends to increase with increase of the dielectric constant.
4. The shape of the radiation patterns remains almost unchanged for different substrate thickness (h) for $h \ll \lambda_0$. However, sidelobe levels increase with increase of ϵ_r .

Radiation patterns of rectangular microstrip patches arrayed circumferentially on a circular cylinder (wrap-around array) have been computed in Ref. 34. Both axial and circumferential patches, using axial and circumferential modes of excitation, respectively, have been used. In general, it has been found that the number of circumferential patches required for a given ripple in the gain pattern is considerably less than that required in the axial case, thus simplifying the feed network for the former case. Results given in Ref. 34 compared favorably with reported measurements.

2.4. A Patch Array for Aircraft

A patch array designed for an aircraft to satellite communication link is described by Sanford [35] and is shown in Fig. 17. Eight patches are mounted together with the phase shifting and feeding circuitry to scan the beam in the elevation direction. Designed for operation at 1.5 GHz, the array, including the radome, is 3.6 mm thick. Element phasing was optimized for maximum multipath rejection at low scan angles and to account for the curvature of the mounting surface. Each element was pointed in a different direction and has an inherent phase error relative to the center elements. A digital computer was used to determine how the design parameters actually affect the performance of the array. The spacing of the array elements must be greater than 0.32λ (in free space) because the physical size of the radiating element on Teflon fiberglass requires thin space. The spacing required to prevent the

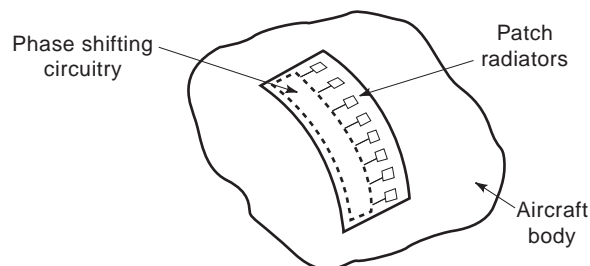


Figure 17. Conformal array for aircraft application. (After Ref. 35.)

formation of grating lobes is given by

$$D \leq \frac{\lambda}{1 + \sin \theta} \quad (8)$$

where D is the separation distance between the patch element, λ is the wavelength in free space, and θ is the maximum beamsteering angle. For a 50° maximum steering angle, D must be less than 0.57λ .

2.5. Concentric Microstrip Ring Arrays

Bhattacharyya and Garg [36] describe the design of a concentric annular ring microstrip antenna array that can be excited by means of a single feed by interconnecting two consecutive rings with an impedance transformer. The feasibility of such an antenna is based on the observation that annular rings with different mean radii can be designed to resonate at the same frequency for the TM_{12} mode. An impedance bandwidth of about 5% for $VSWR \leq 2$ has been reported in Ref. 36. It has been found possible to control the principal plane patterns for concentric arrays independently of each other by appropriately designing the feed system.

Saha-Misra and Chowdhury [37] describe electromagnetically fed concentric microstrip ring arrays using the log-periodic principle that have been reported to have increased impedance and radiation pattern bandwidths. Specifically, circular, square, and triangular concentric rings have been investigated. Generally, these antennas work at multiple bands of frequencies with some bands having larger bandwidths than standard microstrip antennas. With a nonuniformly spaced concentric annular ring array, almost 20% bandwidth for $VSWR \leq 2$ has been reported. A planar, wideband feed for a slot spiral antenna has been described by Nurnberger and Volakis [38]. The antenna has been developed for operation at very high frequency (VHF) frequencies. In contrast to most traditional printed spiral antenna designs, the one reported in Ref. 38 incorporates a completely planar spiral microstrip balun feed, thereby making it attractive for a variety of conformal applications.

3. CONFORMAL ARRAYS

Antenna arrays conforming to a nonplanar surface are suitable and may even be a requirement for a number of applications. For example, phased arrays of flush-mounted elements conformally mounted on the surface of an aircraft or missile reduce the aerodynamic drag and hence are preferable. Also, in some cases a nonplanar array surface may provide some natural advantage for broad-beam coverage in space. Spherical, cylindrical, and conical arrays have been developed for ground, airborne, and missile applications. We shall consider here the class of conformal arrays where the radiating surface is nonplanar with a radius of curvature large compared to the operating wavelength. Conformal arrays that are highly curved are generally difficult to design because of the following reason [1,3,4,8]:

1. Array elements point in different directions, and so it is often necessary to switch off those elements that radiate primarily away from the desired direction of radiation. This, in turn, requires more sophisticated switching mechanisms for activation of elements.
2. The fact that element patterns cannot be factored out of the total radiation pattern makes the analysis and synthesis of such antennas more complicated.
3. Mutual coupling effects can be very severe and difficult to ascertain.
4. Nonplanar arrangement of elements may give rise to severe cross-polarization effects.

3.1. Spherical Arrays

Certain applications require phased arrays capable of steering the beam over a complete hemisphere. For this requirement a spherical array surface seems to provide some natural advantage for beam steering. Schrank [39] discusses the manner in which an array of radiating elements placed on a sphere provides a natural configuration for obtaining hemispherical coverage with nearly identical highly directive beams. A spherical phased array consisting of circularly polarized flat spiral antenna elements has been developed by Sengupta et al. [40,41]. Theoretical design and other considerations are given in Ref. 42, and experimental fabrication and results are given in Ref. 41. As described in Ref. 40, a special element distribution was obtained from the consideration of icosahedron geometry resulting in a best possible uniformity of element spacing. It was found that the array could operate with widely spaced elements. The special element distribution developed for this purpose considerably suppressed the grating lobes in the pattern and thereby made the array significantly broadband. Figure 18 shows the icosahedron geometry of element locations on a spherical surface. The choice of circularly polarized elements made the antenna beam retain its circular polarization fairly well over the entire range of beam steering directions [39,40]. Experimental results given in Ref. 41 demonstrate the capability of a spherical array of 16 flat spiral antennas over a frequency range of 0.6–3 GHz. The work reported in Ref. 41 used manual control of phase and illuminated aperture area; consequently, the results obtained were limited in scope. However, with the availability of modern sophisticated

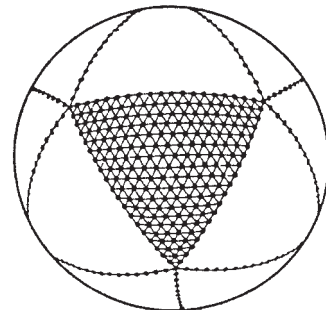


Figure 18. Icosahedron geometry of element locations. (After Ref. 39.)

computer control mechanisms, it seems that such spherical arrays could provide almost complete hemispherical phased coverage over a broad band.

3.2. Cylindrical Arrays

Conformal elements such as microstrips and slots arrayed around the circumference of large metal cylinders have been used to obtain omnidirectional pattern coverage. Such coverage may also be obtained with the help of wrap-around antenna, as discussed earlier. References 42–46 show that an array of slots equally spaced around the circumference of a cylinder can produce a pattern with very low ripple. Crosswell and Knop [43] have obtained extensive numerical data using realistic patterns for slots on perfectly conducting planes. In such arrays the design parameters are the numbers of elements, radiating elements, and feed network. The number of elements is chosen to provide a nearly omnidirectional pattern; the minimum number of elements is determined by the allowed amplitude ripple. The evaluation of the amplitude ripple can be given in terms of the fluctuation, which is defined as the ratio of maximum $|F|$ to minimum $|F|$, where F is the total far-field pattern of an S -element circular array and is given by [42]

$$F = S \sum_{n=0}^N A_n (-j)^n \frac{d^n}{dz^n} [J_0(z) + 2(j)S J_S(z) \cos S\phi] \quad (9)$$

where $J_S(z)$ is the Bessel function of the first kind of order S , $z = k_0 a \sin \theta$; k_0 is the free-space wavenumber; a is the radius of the circular array; θ, ϕ are the usual coordinates; the z axis is the axis of the cylinder; and $N \leq S$.

The preceding expression assumes that the single element pattern $f(\phi^1)$ can be expressed by a Fourier cosine series

$$f(\phi') = \sum_{n=0}^{\infty} A_n \cos^n \phi' \quad (10)$$

A practical single-element pattern can be approximated by

$$f(\phi') = \begin{cases} \frac{1 + \cos \phi'/2}{2} \\ \frac{2 + 3 \cos \phi' + \cos 2\phi'}{6} \end{cases} \quad (11)$$

Pattern fluctuations as a function of size of cylinder and number of elements for the preceding two single-element patterns are given in Ref. 43. Cylindrical phased arrays, where selected sections are illuminated to provide a beam in a certain direction, are sometimes found advantageous to use for some requirements. Sophisticated types of electronic switches for such circular arrays are based on a concept originally proposed by Shelton [45] and developed by Sheleg [46]. The antenna uses a Butler matrix-fed circular array with fixed phase shifters to execute current modes around the array and variable phase shifters to provide continuous scanning of the radiated beam over

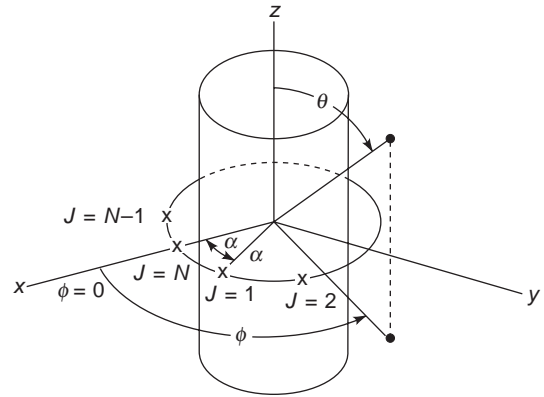


Figure 19. Coordinates for continuous cylindrical sheet of vertical current elements.

360°. The operation was experimentally demonstrated with a 32-dipole circular array.

The principles involved in scanning a multimode array are readily seen by considering a continuous distribution of current, as described by Sheleg [46]. Figure 19 shows the configuration of a continuous cylindrical sheet of vertical current elements around a vertical conducting cylinder of radius a . Referring to Fig. 19, consider a current distribution $I(x)$ to be the sum of a finite number of continuous current modes $I_n e^{jn\alpha}$ with $-N \leq n \leq N$. The radiation pattern for $I(x) = I_n e^{jn\alpha}$ is then given by

$$E(\phi) = \sum_{n=-N}^N C_n e^{jn\phi} \quad (12)$$

where C_n are complex constants given by

$$C_n = 2\pi K j^n I_n J_n \left(\frac{2\pi a}{\lambda} \right) \quad (13)$$

where K is a constant, λ is the wavelength of operation, and J_n is the Bessel function defined earlier. If, in the antenna being considered, it is desired that the pattern mode be equal in magnitude and be in phase at $\phi = 0$, the excitation of the current modes must be

$$I_n = \frac{1}{2\pi K j^n J_n \left(\frac{2\pi a}{\lambda} \right)} \quad (14)$$

Under this condition, the radiation pattern is given by

$$E(\phi) = \sum_{n=-N}^N e^{jn\phi} = \sin \left(\frac{2N+1}{2} \phi \right) / \sin \frac{\phi}{2} \quad (15)$$

If the phase difference between the adjacent modes is ϕ_0 (i.e., multiply I_n by $e^{-jn\phi_0}$), the resultant radiation

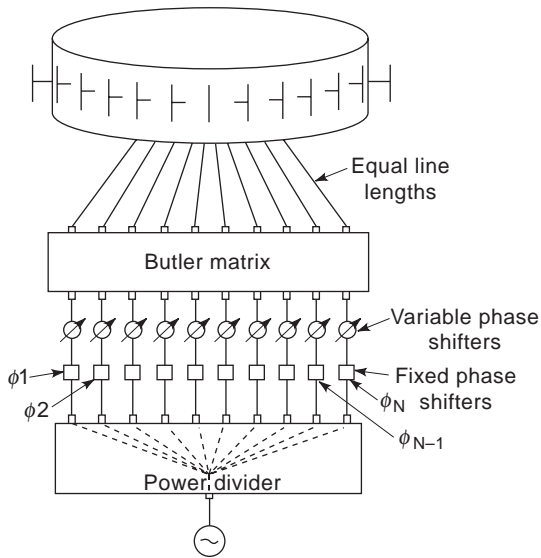


Figure 20. Schematic diagram of scanning multimode array. (After Ref. 46.)

pattern is

$$E(\varphi) = \frac{\sin[(2N+1)(\varphi - \varphi_0)/2]}{\sin[(\varphi - \varphi_0)/2]} \quad (16)$$

which indicates a beam in the φ_0 direction. As described by Sheleg [46], it was possible to excite simultaneously and independently all the modes both positive and negative n , from 0 to $N/2$, by connecting a single ring on N elements to the outputs of a Butler matrix. A schematic diagram of a scanning multimode array is shown in Fig. 20. The desired phase and amplitude distribution is established over the inputs of the Butler matrix by fixed phase shifts and a corporate structure. Once the pencil-beam pattern is formed at some azimuth angle, it is scanned just as in a linear array; the mode amplitudes are held fixed and a linear phase progression is set up on the mode inputs by operating the variable phase shifters.

3.3. Conical Array

Kummer [1] discusses a number of difficulties associated with antenna pattern synthesis utilizing conical surfaces. An array on a conical surface generally looks different at different aspect angles; also, the geometry is such that all elements do not contribute equally to the main beam direction, thereby causing cross-polarization problems. In spite of this, for their obvious applications to missile and other similar vehicles, conical arrays have been considered for conformal array development. Theoretical and experimental investigations of various aspects of conical arrays are discussed in Refs. 15, 47, and 48. The experimental studies of Munger et al. [48] provide some data on the characteristics of several conical arrays. Balzano and Dowling [47] developed an effective method to evaluate the pattern of elements in a conical array. The method takes into account the mutual coupling between array

elements and aperture matching conditions. By properly matching the array aperture, the radiation in a certain direction can be substantially increased, thus allowing the designer to meet specific design goals in the application of conical arrays to airborne or missileborne systems. Moreover, it has been shown that in some cases, the element pattern can be approximated by much simpler planar and cylindrical models.

BIBLIOGRAPHY

1. W. H. Kummer, Preface, *IEEE Trans. Antennas Propag.* **AP-22**:1-3 (1974).
2. C. A. Balanis, *Antenna Theory*, 2nd ed., Wiley, New York, 1997.
3. R. C. Johnson and H. Jasik, eds., *Antenna Engineering Handbook*, 2nd ed., McGraw-Hill, New York, 1984.
4. R. C. Hansen, *Significant Phased Array Papers*, Artech House, Dedham, MA, 1973.
5. Y. T. Lo and S. W. Lee, eds., *Antenna Handbook: Theory, Applications, and Design*, Van Nostrand Reinhold, New York, 1988.
6. R. J. Mailloux, *Phased Array Antenna Handbook*, Artech House, Boston, 1994.
7. W. H. Kummer, guest editor, special issue on conformal arrays, *IEEE Trans. Antenn. Propag.* **AP-22**:1-150 (1974).
8. R. C. Hansen, *Microwave Scanning Antennas*, Vols. I-III, Academic Press, New York, 1964.
9. P. H. Pathak and R. G. Kouyoumjian, An analysis of the radiation from aperture in curved surfaces by the geometrical theory of diffraction, *Proc. IEEE* **62**:1438-1447 (1974).
10. P. H. Pathak et al., A uniform GTD solution for the radiation from sources on a curvex surface, *IEEE Trans. Antenn. Propag.* **AP-29**:602-622 (1981).
11. W. D. Burnside, R. J. Marhefka, and C. L. Yu, Roll plane analysis of on-aircraft antennas, *IEEE Trans. Antenn. Propag.* **AP-21**:780-786 (1973).
12. W. D. Burnside et al., A study of KC-135 aircraft antenna patterns, *IEEE Trans. Antenn. Propag.* **AP-23**:309-316 (1975).
13. R. J. Mailloux, Conformal and low-profile arrays, in Ref. 3.
14. K. E. Golden, G. E. Stewart, and D. C. Pridmore-Brown, Approximation techniques for the mutual admittance of slot antennas on metallic cones, *IEEE Trans. Antenn. Propag.* **AP-22**:43-48 (1974).
15. K. E. Golden and G. F. Stewart, Self and mutual admittance of rectangular slot antennas in the presence of inhomogeneous plasma layer, *IEEE Trans. Antenn. Propag.* **AP-17**:763-771 (1969).
16. D. C. Chang, *IEEE Trans. Antenn. Propag.* **AP-29**:1-182 (1981).
17. I. J. Bahl and P. Bhartia, *Microstrip Antennas*, Artech House, Norwood, MA, 1980.
18. C. M. Krowne, Cylindrical-rectangular microstrip antenna, *IEEE Trans. Antenn. Propag.* **AP-31**:194-199 (1983).
19. K.-M. Luk, K.-F. Lee, and J. S. Dahele, Analysis of the cylindrical-rectangular patch antenna, *IEEE Trans. Antenn. Propag.* **AP-37**:143-147 (1989).
20. K. R. Carver and J. W. Mink, Microstrip antenna technology, *IEEE Trans. Antenn. Propag.* **AP-29**:2-24 (1981).

21. K.-L. Wong and S.-Y. Ke, Cylindrical-rectangular microstrip for circular polarization, *IEEE Trans. Anten. Propag.* **AP-41**: 246–249 (1993).
22. T. Kashiwa, T. Onishi, and I. Fukai, Analysis of microstrip antennas on a curved surface using the conformal grids FDTD method, *IEEE Trans. Anten. Propag.* **AP-42**:423–427 (1994).
23. J. M. Jin et al., Calculation of radiation patterns of microstrip antennas on cylindrical bodies of arbitrary cross section, *IEEE Trans. Anten. Propag.* **AP-45**:126–132 (1997).
24. J. R. Descardecı and A. J. Giarola, Microstrip antenna on a conical surface, *IEEE Trans. Anten. Propag.* **AP-40**:460–463 (1992).
25. H. S. Jones, *Design of Dielectric-Loaded Circumferential Slot Antennas of Arbitrary Size for Conical and Cylindrical Bodies*, Report HDL-TR-1684, Harry Diamond Laboratories, Adelphi, MD, 1974.
26. D. H. Schaubert, A. R. Sindons, and F. G. Farrar, The spiral slot: A unique microstrip antenna, *Proc. 1978 Antenna Applic. Symp.*, Univ. of Illinois Allerton Conf., Harry Diamond Laboratories, Oct. 1978.
27. A. D. Krall et al., The omni microstrip antenna: A new small antenna, *IEEE Trans. Anten. Propag.* **AP-27**:850–853 (1979).
28. D. H. Schaubert, H. S. Jones, and F. Reggia, Conformal dielectric-filled edge-slot antennas with inductive-post turning, *IEEE Trans. Anten. Propag.* **AP-27**:713–716 (1979).
29. D. L. Sengupta and L. F. Martins-Camelo, Theory of dielectric-filled edge-slot antennas, *IEEE Trans. Anten. Propag.* **AP-28**:481–490 (1980).
30. K. F. Munson, Conformal microstrip antennas and microstrip phased arrays, *IEEE Trans. Anten. Propag.* **AP-22**:74–78 (1974).
31. R. F. Munson, Omnidirectional microstrip arrays, pp. 7–19, 7–21 of Ref. 3.
32. S. B. D. A. Fonseca and A. J. Giarola, Analysis of microstrip wraparound antennas using dyadic Green's functions, *IEEE Trans. Anten. Propag.* **AP-31**:248–253 (1983).
33. A. Das, S. K. Das, and M.-S. Narasimhan, Radiation characteristics of wraparound microstrip antenna on spherical body, *IEEE Trans. Anten. Propag.* **AP-39**:1031–1034 (1991).
34. I. Jayakumar et al., A conformal cylindrical microstrip array for producing omnidirectional radiation pattern, *IEEE Trans. Anten. Propag.* **AP-34**:1258–1261 (1986).
35. G. G. Sanford, Conformal microstrip phased array for aircraft tests with ATS-6, *IEEE Trans. Anten. Propag.* **AP-26**:642–646 (1978).
36. A. K. Bhattacharyya and R. Garg, Input impedance of annular ring microstrip antenna using circuit theory approach, *IEEE Trans. Anten. Propag.* **AP-33**:369–374 (1985).
37. I. Saha-Misra and S. K. Chowdhury, Concentric microstrip ring antenna: Theory and experiment, *J. Electromagn. Wave Appl.* **10**:439–450 (1996).
38. M. W. Nurnberger and J. L. Volakis, A new planar feed for slot spiral antennas, *IEEE Trans. Anten. Propag.* **AP-44**:130–131 (1996).
39. H. E. Schrank, Basic theoretical aspects of spherical phased arrays, in A. A. Oliner and G. H. Knitted, eds., *Phased Array Antennas*, Artech House, Dedham, MA, 1972, pp. 323–327.
40. D. L. Sengupta, T. M. Smith, and R. W. Larson, Radiation characteristics of spherical array of circularly polarized elements, *IEEE Trans. Anten. Propag.* **AP-16**:1–7 (1968).
41. D. L. Sengupta, J. E. Ferris, and T. M. Smith, Experimental study of a spherical array of circularly polarized elements, *Proc. IEEE* **56**:2048–2051 (1968).
42. T. S. Chu, On the use of uniform circular arrays to obtain omnidirectional patterns, *IEEE Trans. Anten. Propag.* **AP-7**:436–438 (1959).
43. W. F. Croswell and C. M. Knop, On the use of an array of circumferential slots on a large cylinder as an omnidirectional antenna, *IEEE Trans. Anten. Propag.* **AP-14**:394–396 (1966).
44. W. F. Croswell and C. R. Cockrell, An omnidirectional microwave antenna for use on spacecraft, *IEEE Trans. Anten. Propag.* **AP-17**:459–466 (1969).
45. P. Shelton, Application of hybrid matrices to various multi-mode and multibeam antenna systems, *Proc. IEEE Washington Chapter P GAP Meeting*, March 1965.
46. B. Sheleg, A matrix-fed circular array for continuous scanning, *Proc. IEEE* **56**:2016–2027 (1968).
47. Q. Balzano and T. B. Dowling, Mutual coupling analysis of arrays of apertures on cones, *IEEE Trans. Anten. Propag.* **AP-22**: 92–97 (1974).
48. A. D. Munger et al., Conical array studies, *IEEE Trans. Anten. Propag.* **AP-22**:35–42 (1974).

CONFORMAL MAPPING TECHNIQUES

ERDEM YAZGAN

VOLKAN AKAN

Hacettepe University

Beytepe, Ankara, Turkey

1. INTRODUCTION

Conformal mapping (MP) is the transformation of a region defined in a complex plane to a distinct region in the reference plane of another complex variable by using a proper transformation function. Since 1867, conformal mapping techniques (CMTs) have been used by many mathematicians and engineers. Many engineering applications such as boundary value problems and electromagnetic field problems in which the components of the fields are confined in a defined plane can be tackled by using CMTs. Here the crucial point is that a complex and cumbersome structure can be transformed into a simpler and well-known one. When the transformation is done, an important characteristic is retained: the angle between lines of flux and equipotential lines or transversity of fields (e.g., electric and magnetic fields). Also, there is a wide area for CMT applications such as heat, fluid flow problems, and electromagnetic problems. According to the known general literature as reviewed in detail by Schinzinger [1]. Routh [2] has transformed vibrating membrane structure into simpler configurations, and in 1900. Carter [3] published a note on airgap and interpolar induction as the first application of conformal mapping to a real engineering problem. After then, usage of CMTs began to spread in

very large areas such as wave propagation between irregular boundaries [4–7], acoustic channels [8], radio propagation around Earth [9,10], reflection from waveguide corners [11], calculation of quasistatic parameters of coplanar striplines, coplanar waveguides, and microstrip lines, electrooptical applications, and also resonance frequency calculations of microstrip patch antennas and resonators [12–34].

Potential and flux functions are defined below with related mathematical equations, followed by a detailed definition and discussion of the basic properties of conformal mapping.

In Section 4, the Schwarz–Christoffel transformation, which is used widely for quasistatic models, is defined. Finally, examples of CM applications in electromagnetic problems are illustrated and explained.

2. POTENTIAL FUNCTION AND FLUX FUNCTION AS CONJUGATE FUNCTIONS

The basic mathematical definitions are presented below in order to introduce the potential function and the flux function as conjugate functions.

If two complex numbers are considered

$$\begin{aligned} z &= x + jy \\ r &= x - jy \end{aligned} \tag{1}$$

where

$$j = \sqrt{-1}$$

it is very simple to show that z and r satisfy Laplace equation. The real parts and the imaginary parts of these numbers satisfy the Laplace equation.

If $F = u + jv$ is a function of $z = x + jy$ as

$$\begin{aligned} F &= G(x + jy) \\ F &= G(z) \end{aligned} \tag{2}$$

This can be rewritten as

$$\begin{aligned} \frac{\partial F}{\partial x} &= \frac{\partial G(z)}{\partial z} \frac{\partial z}{\partial x} \\ \frac{\partial F}{\partial x} &= G'(z) \end{aligned} \tag{3}$$

Then

$$\frac{\partial^2 F}{\partial x^2} = G''(z) \tag{4}$$

and for the imaginary part

$$\begin{aligned} \frac{\partial F}{\partial y} &= \frac{\partial G(z)}{\partial z} \frac{\partial z}{\partial y} \\ \frac{\partial F}{\partial y} &= jG'(z) \end{aligned} \tag{5}$$

and

$$\begin{aligned} \frac{\partial^2 F}{\partial y^2} &= j \frac{\partial G'(z)}{\partial z} \frac{\partial z}{\partial y} \\ \frac{\partial^2 F}{\partial y^2} &= j^2 \frac{\partial G'(z)}{\partial z} \\ \frac{\partial^2 F}{\partial y^2} &= -G''(z) \end{aligned} \tag{6}$$

From Eqs. (4) and (6) one can obtain

$$\frac{\partial^2 F}{\partial x^2} + \frac{\partial^2 F}{\partial y^2} = 0 \tag{7}$$

Examination of these in terms of u and v yields

$$\frac{\partial^2 F}{\partial x^2} = \frac{\partial^2 u}{\partial x^2} + j \frac{\partial^2 v}{\partial x^2} \tag{8}$$

and

$$\frac{\partial^2 F}{\partial y^2} = \frac{\partial^2 u}{\partial y^2} + j \frac{\partial^2 v}{\partial y^2} \tag{9}$$

If Eqs. (8) and (9) are summed, and using Eq. (7), the following equation is obtained:

$$\frac{\partial^2 u}{\partial x^2} + \frac{\partial^2 u}{\partial y^2} + j \left(\frac{\partial^2 v}{\partial x^2} + \frac{\partial^2 v}{\partial y^2} \right) = 0 \tag{10}$$

Equation (10) shows that

$$\frac{\partial^2 u}{\partial x^2} + \frac{\partial^2 u}{\partial y^2} = 0 \tag{11}$$

and

$$\frac{\partial^2 v}{\partial x^2} + \frac{\partial^2 v}{\partial y^2} = 0 \tag{12}$$

From these equations it can be seen that real and imaginary parts of any function of a complex variable $x + jy$ satisfy Laplace's equation.

Briefly, if F is a function of z where $F = u + jv$ and $z = x + jy$, this leads to

$$\nabla^2 u = 0, \quad \nabla^2 v = 0 \tag{13}$$

where \mathbf{u} is the *potential function* and the conjugate function \mathbf{v} is the *flux function*.

The relations between potential and flux functions, known as the *Cauchy–Riemann* equations, are very important.

Again

$$F = u + jv \quad (F = G(z))$$

$$z = x + jy$$

and

$$\frac{\partial F}{\partial x} = \frac{\partial u}{\partial x} + j \frac{\partial v}{\partial x} \tag{14}$$

Also, one can write

$$\frac{\partial F}{\partial x} = \frac{\partial G(z)}{\partial z} \frac{\partial z}{\partial x}$$

$$\frac{\partial F}{\partial x} = \frac{\partial G(z)}{\partial z} \tag{15}$$

from which

$$\frac{\partial u}{\partial x} + j \frac{\partial v}{\partial x} = \frac{\partial G(z)}{\partial z} \tag{16}$$

and

$$\frac{\partial F}{\partial y} = \frac{\partial u}{\partial y} + j \frac{\partial v}{\partial y}$$

$$\frac{\partial F}{\partial y} = \frac{\partial G(z)}{\partial z} \frac{\partial z}{\partial y}$$

$$\frac{\partial F}{\partial y} = j \frac{\partial G(z)}{\partial z}$$

so

$$\frac{\partial u}{\partial y} + j \frac{\partial v}{\partial y} = j \frac{\partial G(z)}{\partial z} \tag{17}$$

If Eq. (17) is multiplied by j and then summed with Eq. (16), the following equation is obtained:

$$\left(\frac{\partial u}{\partial x} - \frac{\partial v}{\partial y}\right) + j\left(\frac{\partial u}{\partial y} + \frac{\partial v}{\partial x}\right) = 0 \tag{18}$$

Then

$$\frac{\partial u}{\partial x} = \frac{\partial v}{\partial y} \tag{19}$$

$$\frac{\partial v}{\partial x} = -\frac{\partial u}{\partial y} \tag{20}$$

Equations (19) and (20) are Cauchy–Riemann equations. It must be emphasized that these equations are crucial points of conjugate functions.

3. CONFORMAL MAPPING

After explaining the conjugate functions for CM, we can now define conformal mapping. Kreyszig [35] defined CM as “The mapping defined by an analytic function $f(z)$ is conformal, except at critical points, that is, points at which the derivative $f'(z)$ is zero.” In other words, if the function is analytic at point z and $f'(z) = df/dz \neq 0$, then the transformation is said to be conformal. The most important property of CM is illustrated in Fig. 1.

As seen in Fig. 1, following CM, curves 1 and 2 form the same angle ψ , the angle between their oriented tangents at the intersection point. Note that this is the same angle in both magnitude and direction. One also determine whether a mapping function is analytic using the Cauchy–Riemann equations. If these equations [(19) and (20)] are satisfied by a complex function, this complex function is analytic.

As mentioned in Ref. 1 for CM, scaled factors must be taken into account. For this case, examination of infinitesimal displacements between p and w planes, where $p = x + jy$ and $w = \phi + j\theta$, will be beneficial:

$$d\phi \leftrightarrow dl_\phi \text{ or } dl_\phi = h_\phi(\phi, \theta)d\phi \tag{21}$$

$$d\theta \leftrightarrow dl_\theta \text{ or } dl_\theta = h_\theta(\phi, \theta)d\theta \tag{22}$$

For the static case we can use constant lines F and V (see Fig. 2) as flux lines and equipotentials, and for wave propagation E and H fields can be parallel to these constant lines. As shown in Ref. 1 for relating curl and divergence between planes p and w , regardless of time, the curvilinear squares are helpful. So in p plane dl_ϕ, dl_θ is written as $d\phi, d\theta$, where $dl_\phi = dl_\theta = dp/\sqrt{2}$ and $d_\phi = d_\theta = dw/\sqrt{2}$:

$$h_\phi = \left|\frac{dl_\phi}{d\phi}\right| = h_\theta = \left|\frac{dl_\theta}{d\theta}\right| = h = \left|\frac{dp}{dw}\right| \tag{23}$$

Here h is a function of p or w and h can be written as

$$h = \left|\frac{dp}{dw}\right| = \left|g'_{w-p}(w)\right| \tag{24}$$

$$\frac{1}{h} = \left|\frac{dw}{dp}\right| = \left|g'_{p-w}(p)\right| \tag{25}$$

It must be noted that CM requires that scaling factors be equal in all directions because of the Cauchy–Riemann

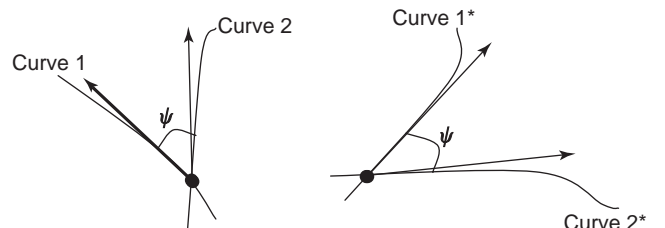


Figure 1. Conformal mapping for curves 1 and 2 and their images after transformation.

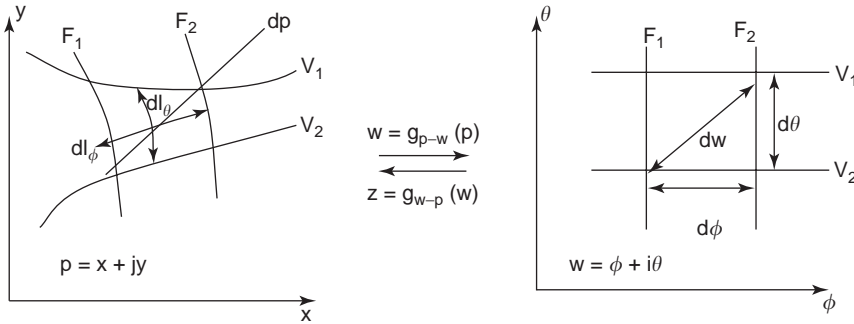


Figure 2. Transformation between p and w planes.

equations. In order to obtain equal scaling factors in all directions, m is introduced instead of h as in Ref. 1. For instance, transformation from the Cartesian coordinates to the cylindrical coordinates r, ϕ, z (not the same as ϕ with $w = \phi + j\theta$ plane) is $x = r \cos \phi$ $y = r \sin \phi$ $z = z$ $h_r, h_\phi,$ and h_z are expressed as $h_r = 1, h_\phi = r$ and $h_z = 1$. Now, let's write $m_r, m_\phi,$ and m_z such that m directly assigns for $d\phi$ a factor $1/r$:

$$m_r = h_r, \quad m_\phi = \frac{h_\phi}{r} \quad (26)$$

$$m_z = h_z$$

If axially uniform configuration is taken into account, then

$$m_z = 1 \quad (27)$$

and

$$m_r = m_\phi = m \quad (28)$$

This is also the general case for any coordinate transformations in CM. This generalization is shown in Table 1.

Table 1. Field Equations

Equation	p Plane, with x, y, z as Coordinates	w Plane, with ξ, η, ζ as coordinates
Metric coefficient	$m_x = 1$ $m_y = 1$ $m_z = 1$	$m_\xi = m$ $m_\eta = m$ $m_\zeta = 1$
$\nabla \times \vec{E}$	$\frac{\partial E_z}{\partial y} - \frac{\partial E_y}{\partial z} = -\mu \frac{\partial H_x}{\partial t}$ $\frac{\partial E_x}{\partial z} - \frac{\partial E_z}{\partial x} = -\mu \frac{\partial H_y}{\partial t}$ $\frac{\partial E_y}{\partial x} - \frac{\partial E_x}{\partial y} = -\mu \frac{\partial H_z}{\partial t}$	$\frac{\partial E_\zeta}{\partial \eta} - \frac{\partial (mE_\eta)}{\partial \zeta} = -\mu m \frac{\partial H_\xi}{\partial t}$ $\frac{\partial (mE_\xi)}{\partial \zeta} - \frac{\partial E_\zeta}{\partial \xi} = -\mu m \frac{\partial H_\eta}{\partial t}$ $\frac{\partial (mE_\eta)}{\partial \xi} - \frac{\partial (mE_\xi)}{\partial \eta} = -\mu m^2 \frac{\partial H_\zeta}{\partial t}$
$\nabla \times \vec{H}$	$\frac{\partial H_z}{\partial y} - \frac{\partial H_y}{\partial z} = \sigma E_x + \epsilon \frac{\partial E_x}{\partial t}$ $\frac{\partial H_x}{\partial z} - \frac{\partial H_z}{\partial x} = \sigma E_y + \epsilon \frac{\partial E_y}{\partial t}$ $\frac{\partial H_y}{\partial x} - \frac{\partial H_x}{\partial y} = \sigma E_z + \epsilon \frac{\partial E_z}{\partial t}$	$\frac{\partial H_\zeta}{\partial \eta} - \frac{\partial (mH_\eta)}{\partial \zeta} = \sigma m E_\xi + \epsilon m \frac{\partial E_\xi}{\partial t}$ $\frac{\partial (mH_\xi)}{\partial \zeta} - \frac{\partial H_\zeta}{\partial \xi} = \sigma m E_\eta + \epsilon m \frac{\partial E_\eta}{\partial t}$ $\frac{\partial (mH_\eta)}{\partial \xi} - \frac{\partial (mH_\xi)}{\partial \eta} = \sigma m^2 E_\zeta + \epsilon m^2 \frac{\partial E_\zeta}{\partial t}$
$\nabla \cdot \vec{D}$	$\epsilon \frac{\partial E_x}{\partial x} + \epsilon \frac{\partial E_y}{\partial y} + \epsilon \frac{\partial E_z}{\partial z} = 0$	$\epsilon \frac{\partial (mE_\xi)}{\partial \xi} + \epsilon \frac{\partial (mE_\eta)}{\partial \eta} + \epsilon m^2 \frac{\partial E_\zeta}{\partial \zeta} = 0$
$\nabla \cdot \vec{B}$	$\mu \frac{\partial H_x}{\partial x} + \mu \frac{\partial H_y}{\partial y} + \mu \frac{\partial H_z}{\partial z} = 0$	$\mu \frac{\partial (mH_\xi)}{\partial \xi} + \mu \frac{\partial (mH_\eta)}{\partial \eta} + \mu m^2 \frac{\partial H_\zeta}{\partial \zeta} = 0$

Source: Ref. 1.

If Table 1 is examined carefully, an important point is seen, namely, that the field components can be rearranged as follows after transformation:

$$\begin{aligned} E_\phi &= mE_\xi, & H_\phi &= mH_\xi \\ E_\theta &= mE_\eta, & H_\theta &= mH_\eta \end{aligned} \quad (29)$$

where $\phi = \xi, \theta = \eta,$ and $q = \zeta$. It is understood (see Fig. 3) that the effect of transformation has been reflected to fields and a new set of coordinates have been formed as ϕ, θ, q . As demonstrated in Ref. 1, the new medium obtained has characteristics $\sigma, \mu,$ and ϵ that remain unchanged in the w plane, but along the z direction they are seen as (see also Table 1)

$$\sigma_z = m^2 \sigma, \quad \mu_z = m^2 \mu, \quad \epsilon_z = m^2 \epsilon_z \quad (30)$$

On the basis of this equation, the new medium introduced is anisotropic. Moreover, it can be inhomogeneous if m is a function of coordinates [$m_{(x,y)}$ or $m_{(\phi,\theta)}$]. Some complexities occur because for this reason. These complexities can be resolved by simplification of the boundary. In addition,

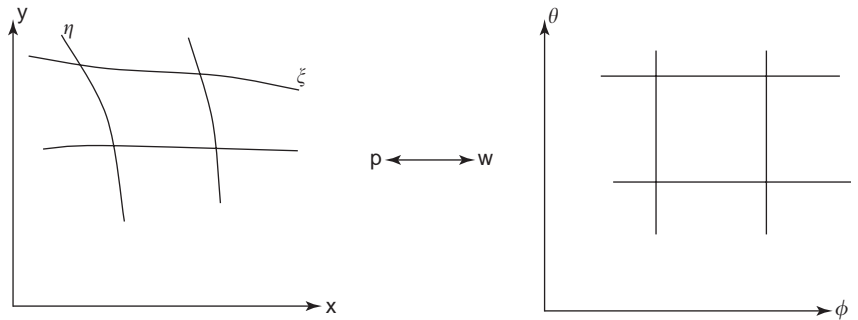


Figure 3. Demonstration of changing fields and coordinates after transformation.

depending on the features of m , some approximations can be used in many applications.

If wave propagation is considered, one can write again the equations in phasor form as shown in Table 1. They can also be written for TE, TM, and TEM cases. Table 2 shows these equations and also includes wave equations.

If Table 2 is examined carefully, the vanishing anisotropy (note that there is no change along the z direction) can be seen, and this leads to a simplification.

In many problems the main purpose is to find the characteristic impedance of a transmission line or propagation constant. For these cases, application of local boundary conditions will be adequate. There is no need to obtain the entire solution for the wave propagation. As is known, m is generally variable but an effective m can be used in such problems.

4. SCHWARZ-CHRISTOFFEL TRANSFORMATION

The Schwarz-Christoffel transformation opens out the interior of a polygon in a defined plane into half of another plane, obtaining a simpler structure with a known solution. It's a powerful method and is often used in transmission-line problems (coplanar stripline and waveguide). This method involves a procedure between two structures

(the original structure and a transformed simpler one) in order to obtain the transformation equation. As shown in Fig. 4, the polygon has been opened between points A and B . One must note that the opening point is not one of the corners. If opening is required at a corner, then this corner is not taken into account for transformation. Here, the conformal transformation equation is

$$w = f(z) \tag{31}$$

The transformation equation is obtained by using the well-known relation [36]

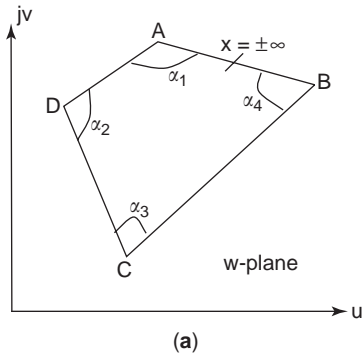
$$\frac{dw}{dz} = M(z - x_1)^{(\alpha_1/\pi)-1} (z - x_2)^{(\alpha_2/\pi)-1} (z - x_3)^{(\alpha_3/\pi)-1} \dots \tag{32a}$$

where M is a complex constant, x_n are real number representing points on the x axis of the z plane in Fig. 4b and satisfying $x_1 < x_2 < \dots < x_{N-1} < x_N$, and α_N are interior angles of the polygon in Fig. 4a. Note that the number of factors must be equal to the number of sides of the polygon plus constant M (as a factor). Integrating Eq. (32a) with

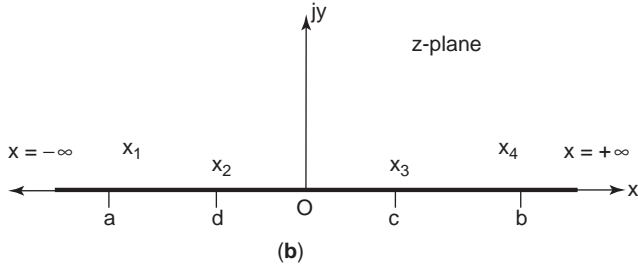
Table 2. Basic Equations for Propagating Wave in Transformed Plane^a

TM Wave	TE Wave	TEM Wave
$E_z = H_\phi = H_\theta = 0$	$H_z = E_\phi = E_\theta = 0$	$H_\phi = E_\phi = 0$
$\frac{\partial H_z}{\partial \theta} = (\sigma + jw\epsilon)E_\phi$	$\frac{\partial E_z}{\partial \theta} = -jw\mu H_\phi$	$\frac{\partial E_z}{\partial \theta} = 0 \quad \frac{\partial H_z}{\partial \theta} = 0$
$\frac{\partial H_z}{\partial \phi} = -(\sigma + jw\epsilon)E_\theta$	$\frac{\partial E_z}{\partial \phi} = jw\mu H_\phi$	$\frac{\partial E_z}{\partial \phi} = jw\mu H_\phi \quad \frac{\partial H_z}{\partial \phi} = -(\sigma + jw\epsilon)E_\theta$
$\frac{\partial E_\phi}{\partial \phi} + \frac{\partial E_\theta}{\partial \theta} = 0$	$\frac{\partial H_\phi}{\partial \phi} + \frac{\partial H_\theta}{\partial \theta} = 0$	$\frac{\partial E_\theta}{\partial \theta} = 0 \quad \frac{\partial H_\theta}{\partial \theta} = 0$
$\frac{\partial E_\theta}{\partial \phi} - \frac{\partial E_\phi}{\partial \theta} = -jw\mu m^2 H_z$	$\frac{\partial H_\theta}{\partial \phi} - \frac{\partial H_\phi}{\partial \theta} = (\sigma + jw\epsilon)m^2 E_z$	$\frac{\partial E_\theta}{\partial \phi} = -jw\mu m^2 H_z \quad \frac{\partial H_\theta}{\partial \phi} = (\sigma + jw\epsilon)m^2 E_z$
Wave equation:	Wave equation:	Wave equation:
$\frac{\partial^2 H_z}{\partial \phi^2} + \frac{\partial^2 H_z}{\partial \theta^2} - jw\mu(\sigma + jw\epsilon)m^2 H_z = 0$	$\frac{\partial^2 E_z}{\partial \phi^2} + \frac{\partial^2 E_z}{\partial \theta^2} - jw\mu(\sigma + jw\epsilon)m^2 E_z = 0$	$\frac{\partial^2 H_z}{\partial \phi^2} - jw\mu(\sigma + jw\epsilon)m^2 H_z = 0$
$m = m(\phi, \theta)$	$m = m(\phi, \theta)$	$m = (\phi, \theta)$

Source: Ref. 1.
^aWith no variation in z plane.



(a)



(b)

Figure 4. The Schwarz–Christoffel transformation, (a) polygon in w plane; (b) transformed structure in z plane.

respect to z gives

$$w = f(z) = M \int \prod_{n=1}^N (z - x_n)^{\alpha_n/\pi - 1} dz + Q \quad (32b)$$

where Q is an arbitrary constant. It determines the position of the polygon in the w plane. This mapping is known as the *Schwarz–Christoffel transformation*. Briefly, as seen from Fig. 4, the interior region of the polygon in the z plane is transformed into the upper half-plane in the p plane. Afterward, using another transformation, the simpler structure can be obtained.

5. APPLICATIONS OF CM

Some CM applications in electromagnetic problems are given below, such as effective resistance calculation, calculation of quasistatic parameters of asymmetric coplanar waveguide, elliptical and cylindrical striplines, calculation of resonant frequency of rectangular patch antennas, Earth-flattening procedures for radiowave propagation, and, finally, bent rectangular waveguides.

5.1. Effective Resistance Calculation of a Current Path between Two Planar Electrodes

In the example given by Gibbs [36], two electrodes are semiinfinite (longitudinally). Also, between these electrodes there exists a known voltage value. Here the problem is to find the effective resistance of the current path per unit length. This problem is illustrated in Fig. 5.

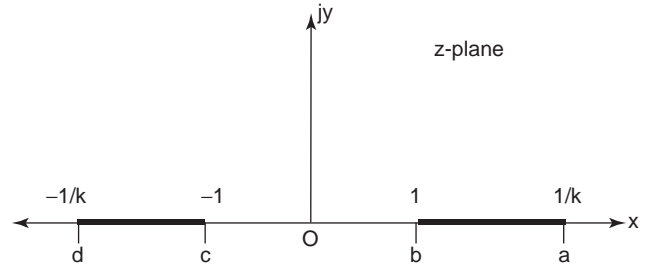


Figure 5. Cross-sectional view of semiinfinite conductors in z plane.

After transformation the region shown in Fig. 6 is obtained. The points a' , b' , c' , and d' are obtained via the Schwarz–Christoffel transformation relation

$$\begin{aligned} \frac{dw}{dz} &= M(z - a)^{\alpha_{a'}/\pi - 1} \\ &\times (z - 1)^{\alpha_{b'}/\pi - 1} \\ &\times (z + 1)^{\alpha_{c'}/\pi - 1} \\ &\times (z - d)^{\alpha_{d'}/\pi - 1} \end{aligned} \quad (33)$$

where

$$\begin{aligned} d &= -a \text{ and } a = \frac{1}{k} \\ \alpha_{a'} &= \alpha_{b'} = \alpha_{c'} = \alpha_{d'} = \frac{\pi}{2} \end{aligned} \quad (34)$$

so

$$\begin{aligned} \frac{dw}{dz} &= M(z - a)^{-(1/2)} \\ &\times (z - 1)^{-(1/2)} \\ &\times (z + 1)^{-(1/2)} \\ &\times (z + a)^{-(1/2)} \end{aligned} \quad (35)$$

and

$$w = M \int \frac{dz}{(z^2 - 1)^{1/2}(z^2 - a^2)^{1/2}} \quad (36)$$

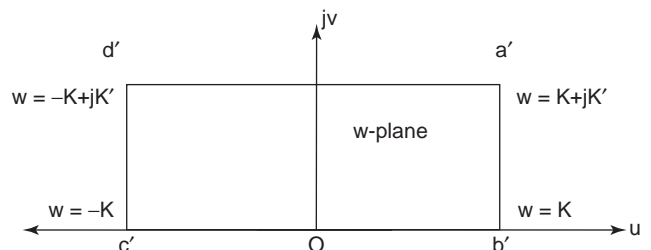


Figure 6. Mapping of electrodes using the Schwarz–Christoffel transformation.

Then, letting $k = 1/a$, the integral can be formed as follows

$$w = C \int \frac{dz}{(1 - z^2)^{1/2}(1 - k^2z^2)^{1/2}} \quad (37)$$

where $C = -kM$. Equation (37) is the elliptic integral. From definition of the complete elliptic integral and its complementary value, the following equations can formulated:

At

$$b' \quad w = \int_0^1 \frac{dz}{(1 - z^2)^{1/2}(1 - k^2z^2)^{1/2}} = K$$

At

$$\begin{aligned} a' \quad w &= \int_0^{1/k} \frac{dz}{(1 - z^2)^{1/2}(1 - k^2z^2)^{1/2}} \\ w &= \int_0^1 \frac{dz}{(1 - z^2)^{1/2}(1 - k^2z^2)^{1/2}} \\ &+ j \int_1^{1/k} \frac{dz}{j(1 - z^2)^{1/2}(1 - k^2z^2)^{1/2}} \\ w &= K + jK' \end{aligned} \quad (38)$$

Also, points c' and d' can be expressed as

$$\begin{aligned} w &= -K \quad \text{for } c' \\ w &= -K + jK' \quad \text{for } d' \end{aligned} \quad (39)$$

If points a , b , c , and d are chosen as $a = 2$, $b = 1$, $c = -1$, and $d = -2$, then, from $1/k = 2$, we see that k is equal to 0.5.

In the w plane the resistance between $|b'a'|$ and $|c'd'|$ per unit length is

$$R = \rho \frac{|c'b'|}{|b'a'|} \quad (\Omega) \quad (40)$$

The effective resistance between electrodes is invariant under CM, so

$$\begin{aligned} R &= \rho \frac{|c'b'|}{|b'a'|} \\ R &= \rho \frac{2K}{K'} \quad (\Omega) \end{aligned} \quad (41)$$

where K is the complete elliptic integral of first kind and K' is complementary to K . For $k = 0.5$, we obtain

$$R = 1.56 \times \rho(\Omega) \quad (42)$$

The application of CM has been shown above for the calculation of effective resistance.

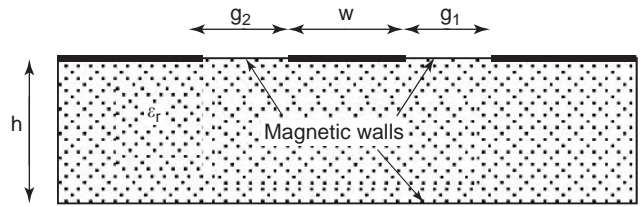


Figure 7. The original ACPW.

5.2. Calculations of quasistatic parameters of asymmetric coplanar waveguide

In this section we consider another example, which has been studied via the quasi-TEM approximation [24]. In this study, the characteristic impedance and the effective permittivity relations of ACPW (asymmetric coplanar waveguide) have been derived by the authors. The cross section of ACPW is shown in Figs. 7 and 8.

In Fig. 7 dielectric–air interfaces are assumed to be magnetic walls. Figure 8 shows a detailed version of Fig. 7 (coordinates have been defined).

Using the method of superposition of partial capacitances, analytical expressions for the total line capacitance C , the characteristic impedance Z_0 , and the effective dielectric constant ϵ_{eff} of quasi-TEM lines can be obtained. We can begin with calculation of total capacitance per unit length:

$$\begin{aligned} C &= C_a + C_d \\ &= C_a + \epsilon_r C_{0\epsilon_r} \\ &= (C_a + C_{0\epsilon_r}) + \epsilon_r C_{0\epsilon_r} - C_{0\epsilon_r} \\ &= C_0 + C_{0\epsilon_r}(\epsilon_r - 1) \end{aligned} \quad (43)$$

Here, C_a is the air capacitance, C_d refers to capacitance of the dielectric part, $C_{0\epsilon_r}$ refers to capacitance of the dielectric part without substrate, and C_0 refers to summation of capacitances C_a and $C_{0\epsilon_r}$. Now we can calculate C_0 by first transforming the upper half-plane of Fig. 8 into the rectangular region as shown in Fig. 9. This mapping was done by the Schwarz–Christoffel transformation, the integral equation of which is

$$W = \int_{t_0}^t \frac{dt}{\sqrt{(t - t_1)(t - t_2)(t - t_3)(t - t_4)}} \quad (44)$$

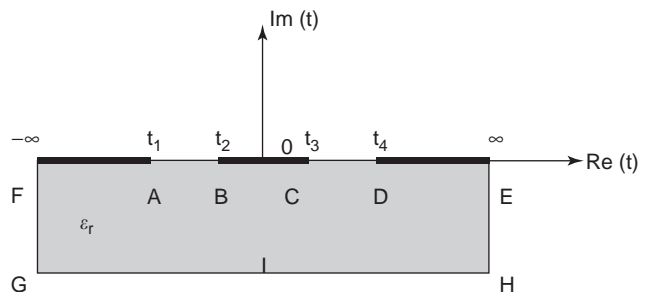


Figure 8. Cross section of the original ACPW in t plane.

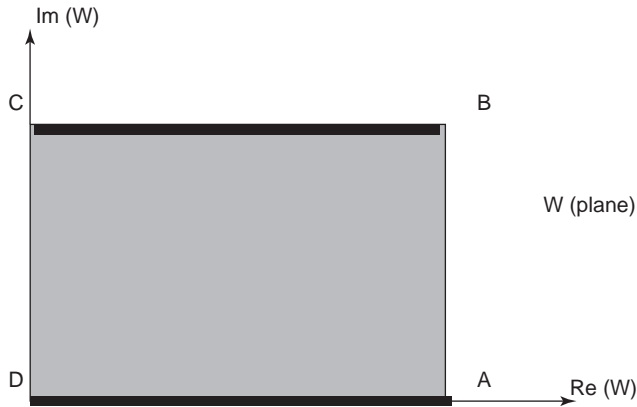


Figure 9. Transformation into a parallel-plate capacitor.

Then C_0 is given by

$$C_0 = 2\epsilon_0 \frac{K(k_0)}{K(k'_0)} \quad (45)$$

and

$$k_0 = \sqrt{\frac{1 + [(g_1 + g_2)/w]}{[1 + (g_1/w)][1 + (g_2/w)]}} \quad (46)$$

As a second step, the calculation of the dielectric capacitance is given.

Since the dielectric part of the structure is finite, we first transform the dielectric region (shaded area) in Fig. 8 is transformed into the lower-half region of Fig. 10 using the mapping function

$$z = \sinh\left(\frac{\pi t}{2h}\right) \quad (47)$$

We can then transform the lower half-plane shown in Fig. 10 into the parallel-plate capacitor using the Schwarz-Christoffel transformation in the same way

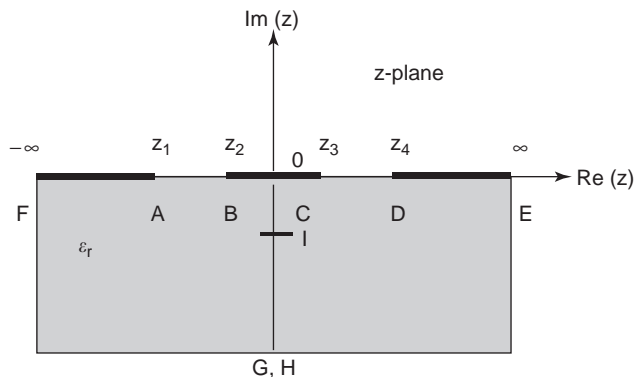


Figure 10. Intermediate mapping for the dielectric region (into z plane).

as we did earlier. The integral equation for this transformation is

$$w = \int_{z_0}^z \frac{dz}{\sqrt{(z - z_1)(z - z_2)(z - z_3)(z - z_4)}} \quad (48)$$

Then

$$C_{0\epsilon_r} = \epsilon_0 \frac{K(k_d)}{K(k'_d)} \quad (49)$$

where

$$k_d = \sqrt{\frac{2(G_1 + G_2)/W}{(1 + G_1/W)(1 + G_2/W)}} \quad (50)$$

and

$$\begin{aligned} W &= \sinh\left(\frac{\pi w}{4h}\right) \\ G_1 &= \sinh\left(\frac{\pi(w + 2g_1)}{4h}\right) \\ G_2 &= \sinh\left(\frac{\pi(w + 2g_2)}{4h}\right) \end{aligned} \quad (51)$$

Now, the total line capacitance relation per unit length can be written

$$\begin{aligned} C &= C_0 + C_{0\epsilon_r}(\epsilon_r - 1) \\ C &= 2\epsilon_0 \frac{K(k_0)}{K(k'_0)} + \epsilon_0(\epsilon_r - 1) \frac{K(k_d)}{K(k'_d)} \end{aligned} \quad (52)$$

and the effective permittivity is given by

$$\epsilon_{\text{eff}} = \frac{C}{C_0} = 1 + \frac{\epsilon_r - 1}{2} \frac{K(k_d)}{K(k'_d)} \frac{K(k'_0)}{K(k_0)} \quad (53)$$

and as seen from Eq. (53), the filling factor is

$$q = \frac{K(k_d)}{K(k'_d)} \frac{K(k'_0)}{K(k_0)} \quad (54)$$

Also, the characteristic impedance can be calculated easily by using the quasistatic approximation as follows:

$$Z_0 = \frac{60\pi}{\sqrt{\epsilon_{\text{eff}}}} \frac{K(k'_0)}{K(k_0)} \quad (55)$$

One must note that the quasi-TEM approximation is valid only at low frequencies. But, because of their dispersion characteristics, CPWs and CPSSs with cross-sectional dimensions that do not exceed the substrate thickness are slightly sensitive to changes in frequency for almost the entire microwave region.

Thus, the accuracy of this method shows good agreement with other methods and experimental results that

Table 3. Comparison of Characteristic Impedance (in Ω) Results^a

ACPW	Cross Section Dimensions			Calculated		Measured
	w (μm)	$g1$ (μm)	$g2$ (μm)	Ref. 24	Ref. 15	Ref. 15
1	747	123	1060	51.77	51.78	51.5
2	737	257	991	59.88	59.88	57.5
3	735	356	843	62.96	62.96	61.1
4	1250	196	1756	53.51	53.53	52.0
5	1248	406	1548	62.37	62.38	62.4
6	1244	575	1386	67.16	67.17	66.3

Source: Ref. 24.
^aObtained in Refs. 15 and 24, where $\epsilon_r = 9.9$ and $h = 635$ mm.

are available in the literature. The results can be seen in Table 3.

Having completed these basic planar problems, we now study more complicated geometries such as elliptical and cylindrical transmission lines.

5.3. Calculations of Quasistatic Parameters of Elliptical, Cylindrical, and Asymmetrical Coplanar Striplines

In Fig. 11, a cross section of an elliptical coplanar stripline (ECPS) with infinitely small arc strips on the outer surface of a dielectric substrate (having relative dielectric ϵ_r) is shown. As seen, the two ellipses are given as confocal. Semi-major and semi-minor axes of the elliptical cylinders are $a_1, a_2, b_1,$ and $b_2,$ respectively.

The focal distance of the two confocal elliptical cylinders is given as follows:

$$c = [a_1^2 - b_1^2]^{1/2} = [a_2^2 - b_2^2]^{1/2} \tag{56}$$

In order to transform the ECPS in the ξ plane in Fig. 11 into a cylindrical coplanar stripline (CCPS) in the z plane as shown in Fig. 12, the following formula is used:

$$z = \frac{1}{c}(\xi \mp \sqrt{\xi^2 - c^2}) \tag{57}$$

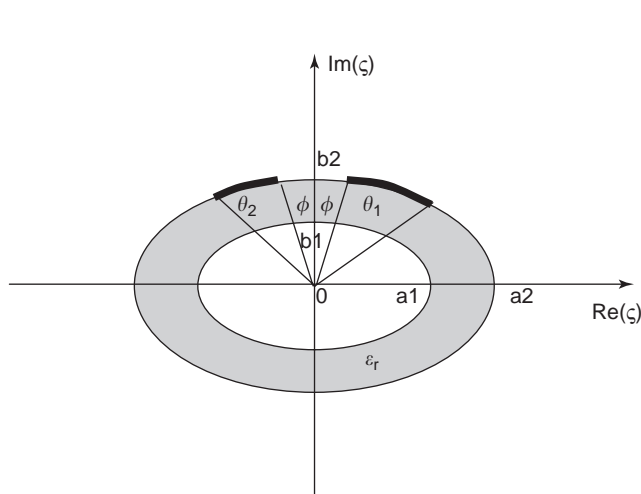


Figure 11. Cross-sectional illustration of ECPS.

The radii of the cylindrical structure in Fig. 12 are

$$r_1 = \left[\frac{a_1 + b_1}{a_1 - b_1} \right]^{1/2}, \quad r_2 = \left[\frac{a_2 + b_2}{a_2 - b_2} \right]^{1/2} \tag{58}$$

By using the mapping function

$$u = j \ln \frac{z}{r_2} + \frac{\pi}{2} \tag{59}$$

the CCPS is transformed into the asymmetric coplanar striplines (ACPS) with a finite-boundary dielectric substrate on the u plane as seen in Fig. 13.

After the finite boundary substrate ACPS is obtained as shown in Fig. 13, the total capacitance per unit length of this structure is equal to the sum of the free-space capacitance C_0 after replacing the dielectric substrate by air and the capacitance C_d of the substrate having dielectric constant $(\epsilon_r - 1)$ as done in the previous example. Thus, the structure without the substrate in Fig. 13 is transformed into the rectangular region in Fig. 14 using the

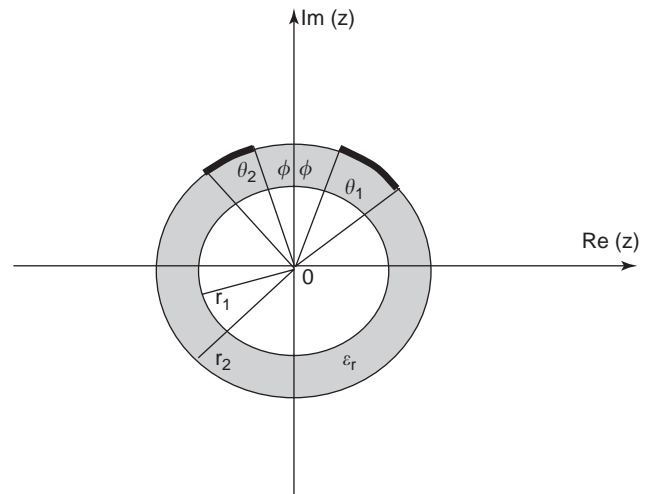


Figure 12. Cross-sectional illustration of CCPS.

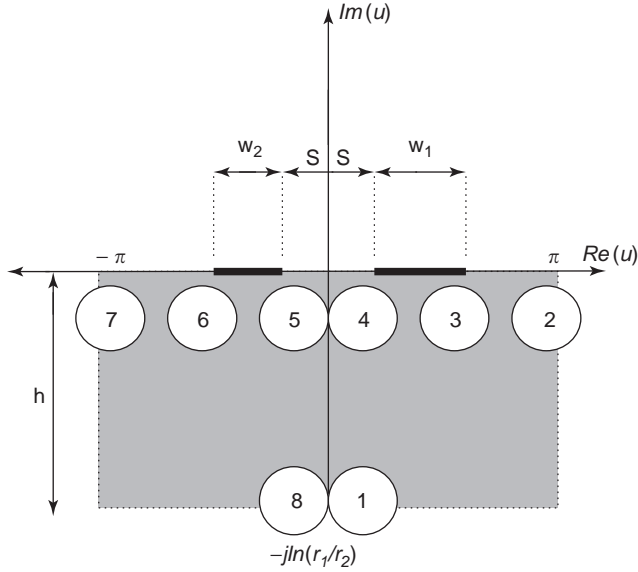


Figure 13. Cross-sectional illustration of ACPS.

Schwarz–Christoffel transformation as given in Ref. 26. Here

$$W = \int_{u_0}^u \frac{du}{\sqrt{(u - u_3)(u - u_4)(u - u_5)(u - u_6)}} \quad (60)$$

$$C_0 = 2\varepsilon_0 \frac{K(k'_0)}{K(k_0)} \quad (61)$$

and modular k_0 can be written as

$$k_0 = \left[\frac{2s(2s + w_1 + w_2)}{(2s + w_1)(2s + w_2)} \right]^{\frac{1}{2}} \quad (62)$$

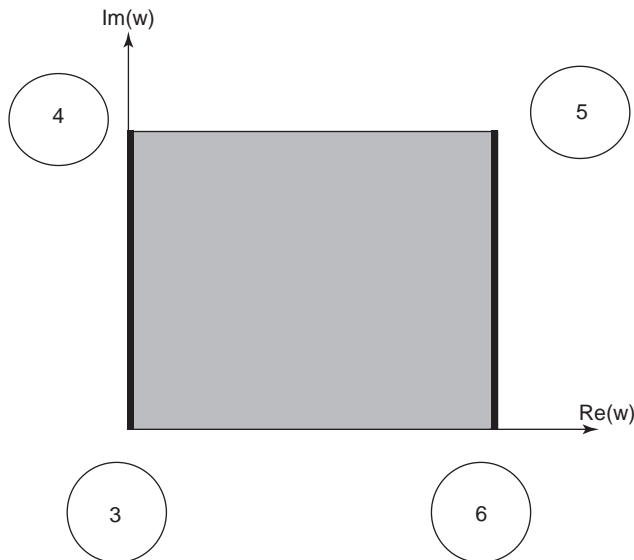


Figure 14. Transformation into a parallel-plate capacitor.

$K(k_0)$ is the complete elliptic integral of the first kind with modulus k_0 and $k'_0 = (1 - k_0^2)^{1/2}$.

In order to compute the dielectric capacitance C_d , the dielectric region in Fig. 13 is first transformed into the lower-half region in Fig. 15 by using the mapping function as seen in Ref. 26:

$$t = sn \left(\frac{K(k)}{\pi} \mu, k \right) \quad (63)$$

Then, the structure obtained in Fig. 15 is again mapped into the rectangular region in Fig. 14 using the Schwarz–Christoffel transformation

$$W = \int_{t_0}^t \frac{dt}{\sqrt{(t - t_3)(t - t_4)(t - t_5)(t - t_6)}} \quad (64a)$$

where

$$t_3 = s_t + w_{t2}, \quad t_4 = s_t \quad (64b)$$

$$t_5 = -s_t, \quad t_6 = -s_t - w_{t1}$$

So

$$C_d = \varepsilon_0(\varepsilon_r - 1) \frac{K(k'_d)}{K(k_d)} \quad (65)$$

where

$$k_d = \left[\frac{2t_4(t_3 - t_6)}{(t_3 + t_4)(t_4 - t_6)} \right]^{\frac{1}{2}} \quad (66a)$$

and

$$t_3 = s_t + w_{t2}, \quad t_4 = s_t \quad (66b)$$

$$t_5 = -s_t - w_{t1}$$

After this, the total line capacitance C and the characteristic impedance Z_0 per unit length can be

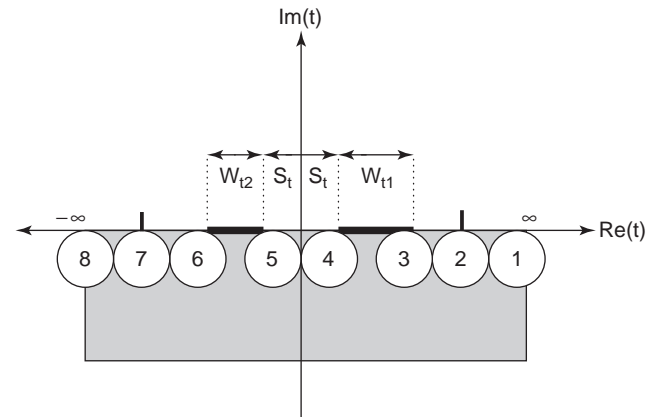
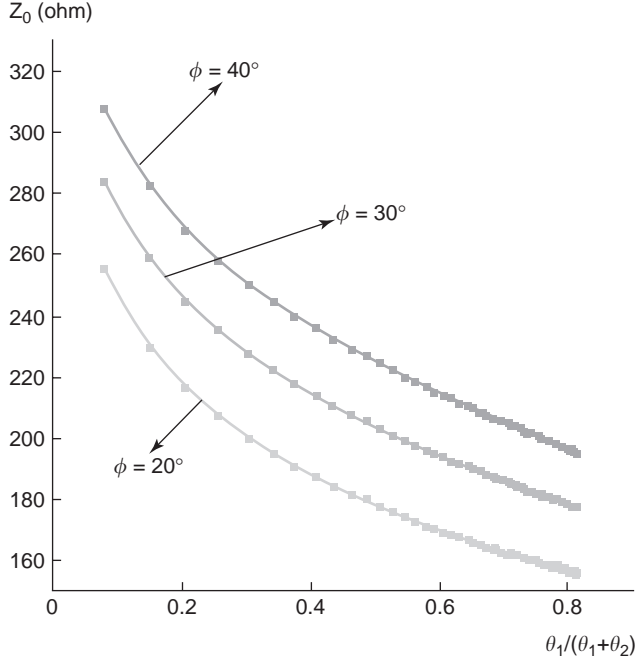


Figure 15. The intermediate transformation for the dielectric region.

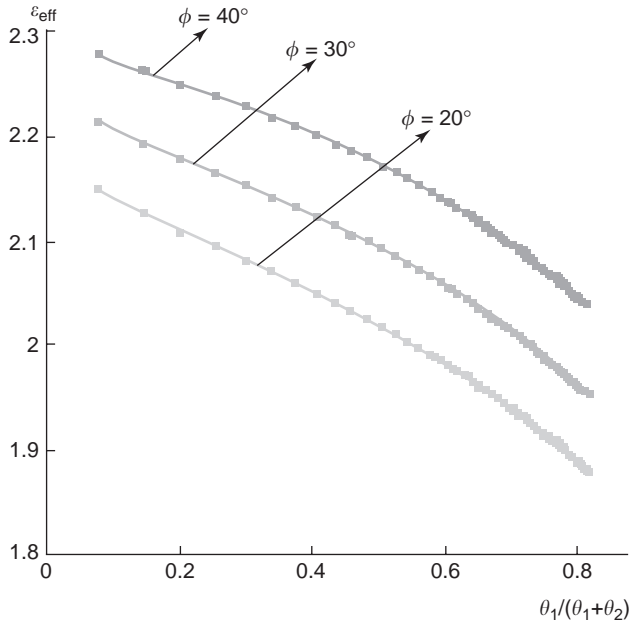
obtained as

$$C = 2\epsilon_0\epsilon_{\text{eff}} \frac{K(k'_0)}{K(k_0)} \quad (67)$$

$$Z_0 = \frac{60\pi}{\sqrt{\epsilon_{\text{eff}}}} \frac{K(k_0)}{K(k'_0)} \quad (68)$$



(a)



(b)

Figure 16. Z_0 and ϵ_{eff} for ECPS and CCPS versus $\theta_1/(\theta_1 + \theta_2)$ [$\epsilon_r = 3.78$, $\theta_2 = 30^\circ$, $(a_2 + b_2)/(a_1 + b_1) = 3$]: (a) characteristic impedance; (b) effective dielectric constant (from Ref. 26).

where the effective permittivity ϵ_{eff} is given by

$$\epsilon_{\text{eff}} = 1 + \frac{\epsilon_r - 1}{2} \frac{K(k_0)}{K(k'_0)} \frac{K(k'_d)}{K(k_d)} \quad (69)$$

The formulation derived is used to see the effect of w , s , h in the variation of ϵ_{eff} and Z_0 of ECPS, CCPS, and ACPS.

Some results for the characteristic impedance and the effective dielectric constants can be seen in Figs. 16a and 16b, where finally, the variation of the characteristic impedance and the effective dielectric constant with respect to $\theta_1/(\theta_1 + \theta_2)$ is seen for ECPS and CCPS, respectively.

5.4. Resonant Frequency Calculation of Rectangular Patch Antennas with Multidielectric Layers

Zhong et al. [31] have reported that the longlasting problem of analyzing rectangular patch antennas with multidielectric layers has been solved (for calculation of resonant frequency) by CMT and the transmission-line model. According to this approach, the microstrip patch antenna is taken up as a microstrip line. In addition, when the quasi-TEM wave propagates in this line, a quasistatic value of ϵ_e or ϵ_{eff} (effective dielectric constant) can be obtained by using CMT [31]. The rectangular patch is shown in Fig. 17. Using the Wheeler transformation [32] the z plane in Fig. 17 is mapped into Fig. 18.

After one transformation and approximation (shown in Figs. 18 and 19, respectively), the quasistatic effective permittivity is obtained as follows

$$\epsilon_e = \epsilon_{r1}\epsilon_{r2} \frac{(q_1 + q_2)^2}{\epsilon_{r1}q_2 + \epsilon_{r2}q_1} + \epsilon_{r3} \frac{(1 - q_1 - q_2)^2}{\epsilon_{r3}(1 - q_1 - q_2 - q_3) + q_3} \quad (70)$$

where q_1 , q_2 , and q_3 are the filling factors, which are defined by the ratio of partial areas S_1 , S_2 , and S_3 to the total area S_c , respectively, as shown in Figs. 18 and 19.

These can be written for $\frac{w}{h} \geq 1$ (wide microstrip line) as

$$q_1 = \frac{S_1}{S_c} = \frac{h_1}{2h_{12}} \left\{ 1 + \frac{\pi}{4} - \frac{h_{12}}{w_e} \times \ln \left[\frac{2w_e}{h_1} \sin \left(\frac{\pi h_1}{2h_{12}} \right) + \cos \left(\frac{\pi h_1}{2h_{12}} \right) \right] \right\} \quad (71)$$

$$q_2 = \frac{S_2}{S_c} = 1 - q_1 - \frac{h_{12}}{2w_e} \ln \left(\frac{\pi w_e}{h_{12}} - 1 \right) \quad (72)$$

$$q_3 = \frac{S_3}{S_c} = 1 - q_1 - q_2 - \frac{h_{12} - v_e}{2w_e} \times \ln \left(\frac{2w_e}{2h_{13} - h_{12} + v_e} \cdot \cos \left(\frac{\pi v_e}{2h_{12}} \right) + \sin \left(\frac{\pi v_e}{2h_{12}} \right) \right) \quad (73)$$

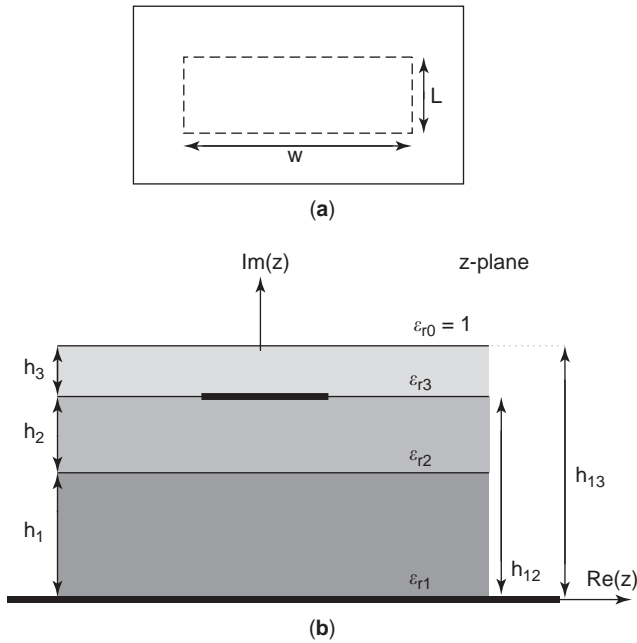


Figure 17. The original structure: (a) top view; (b) cross-sectional view (from Ref. 31).

where the w_e (effective linewidth) and the quantity V_e are given [32] by

$$w_e = w + \frac{2h_{12}}{\pi} \ln \left[17.08 \left(\frac{w}{2h_{12}} + 0.92 \right) \right] \quad (74)$$

$$v_e = \frac{2h_{12}}{\pi} \tan^{-1} \left[\frac{2\pi}{\pi w_e - 4h_{12}} (h_{13} - h_{12}) \right] \quad (75)$$

and ϵ_{eff} can be determined as mentioned by Zhong et al. [31] by

$$\epsilon_{\text{eff}} = \epsilon'_r - \frac{\epsilon'_r - \epsilon_e}{1 + P(f)} \quad (76)$$

This last equation (76) has been developed for a microstrip line on one substrate, but here the multilayer line is

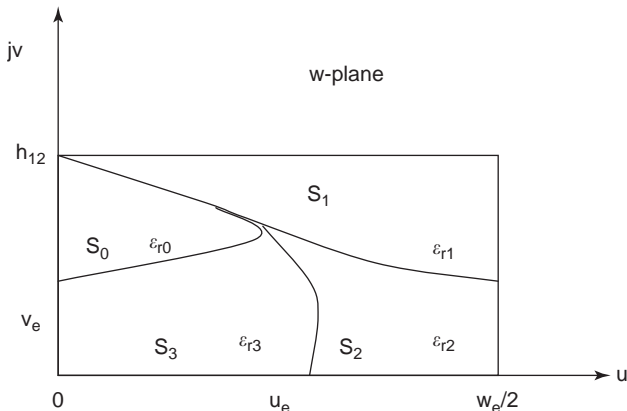


Figure 18. The boundary curves after transformation (from Ref. 31).

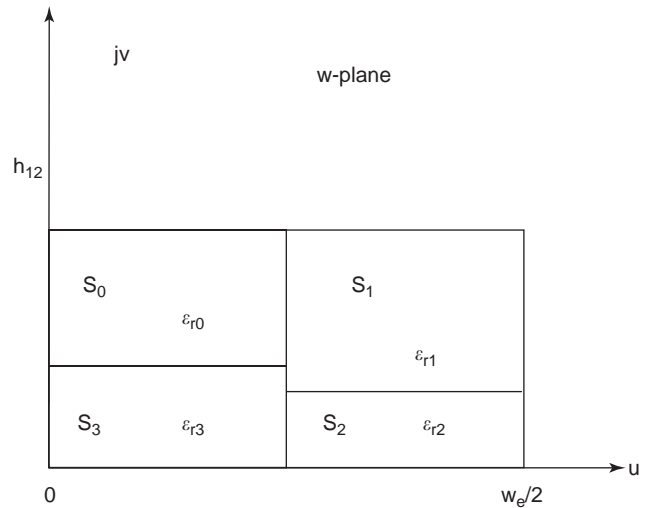


Figure 19. Approximation of the individual dielectric areas in Fig. 18 (from Ref. 31).

taken as a normal line having substrate with ϵ_e and equivalent relative dielectric constant ϵ'_r . The relation between ϵ_e and ϵ'_r is as below

$$\epsilon_e = \frac{1}{2} [\epsilon'_r + 1 + (\epsilon'_r - 1) A] \quad (77)$$

$$A = \left(1 + \frac{12h_{12}}{w} \right)^{-1/2} \quad (78)$$

and

$$\epsilon'_r = \frac{2\epsilon_e - 1 + A}{1 + A} \quad (79)$$

and $P(f)$, which depends on frequency, is given [33] as

$$P(f) = P_1 P_2 [(0.1844 + P_3 P_4) 10 f h_{12}]^{1.5763} \quad (80)$$

in which

$$\begin{aligned} P_1 &= 0.27488 \\ &+ \left[0.6315 + \frac{0.525}{(1 + 0.157 f h_{12})^{20}} \right] \\ &\times u' - 0.065683 \exp(-8.7513 u') \\ P_2 &= 0.33622 [1 - \exp(-0.03442 \epsilon'_r)] \\ P_3 &= 0.0363 \exp(-4.6 u') \\ &\times \left\{ 1 - \exp \left[- \left(\frac{f h_{12}}{3.87} \right)^{4.97} \right] \right\} \\ P_4 &= 1 + 2.751 \\ &\times \left\{ 1 - \exp \left[- \left(\frac{\epsilon_r}{15.916} \right)^8 \right] \right\} \end{aligned} \quad (81)$$

Table 4. Comparison between Experimental Results and Results of Present Method Where $L = 33.25$, $h_1 = 0$, $h_2 = 3.18$, $w = 32.25$, $\epsilon_{r2} = \epsilon_{r3} = 2.32$

Cover Thickness h_3 (mm)	Experiment f_r (GHz)	Calculated f_{r0} (GHz)
3.18	2.749	2.718
6.36	2.704	2.701
9.54	2.682	2.688
12.72	2.670	2.678

Source: Ref. 31.

Eventually, the resonant frequency f_r can be written as

$$f_r = \frac{c}{2(L + 2\Delta L)\sqrt{\epsilon_{\text{eff}}}} \quad (82)$$

Experimental and reported methods [31] are compared in Table 4.

The comparison of results between calculation and experiments indicates the evaluation accuracy of CMT application in calculation of the resonance frequency.

5.5. The Earth-Flattening Procedures in Radiowave Propagation via CMT

Another application of CM that has been used for Earth-flattening procedures in radio propagation problems by Richter [9] is discussed here. In this example wave propagation along the spherical Earth is the main subject, but Earth is assumed to be a cylinder; that is, Earth's curvature transverse to the direction of propagation can be neglected. Also, it is mentioned in this article that this is a frequently valid assumption in practice. The mapping function for the cylinder can be applied to the spherical geometry, thus significantly simplifying the differential equations. Figures 20 and 21 illustrate this transformation.

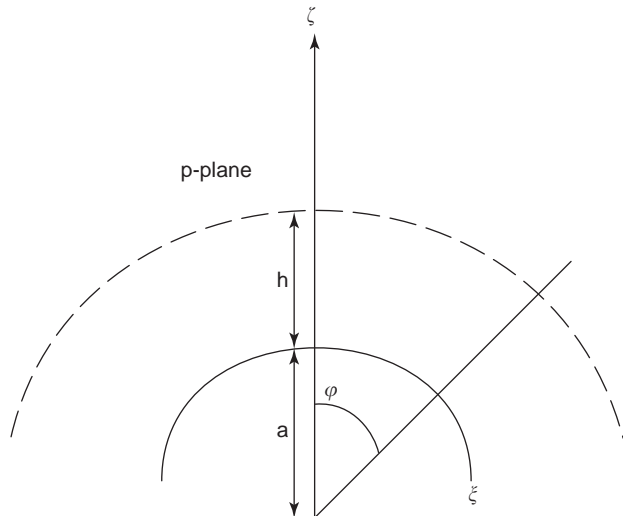


Figure 20. Polar coordinate system (original structure) (from Ref. 9).

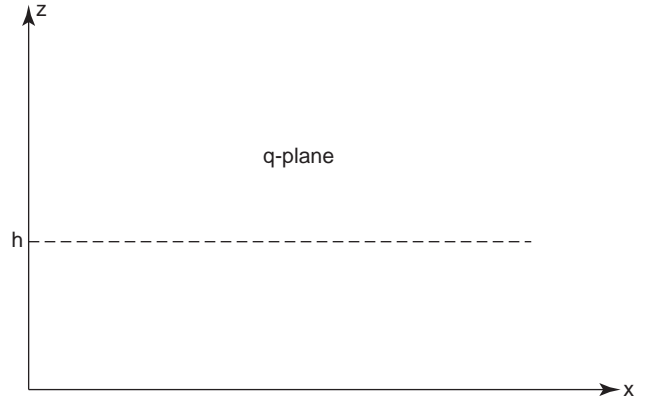


Figure 21. Cartesian coordinate system after transformation (from Ref. 9).

Specifically, this mapping is the transformation from the polar into the Cartesian coordinate system by

$$q = jb_2 \ln\left(\frac{p}{b_1}\right) \quad \text{or} \quad p = b_1 \exp\left(-\frac{jq}{b_2}\right) \quad (83)$$

where

$$j = [-1]^{1/2}, \quad p = \zeta e^{-j\varphi}, \quad \xi = \zeta\varphi \quad (84)$$

and

$$q = x + jz \quad (85)$$

Then

$$z = b_2 \ln \frac{\zeta}{b_1} \quad \text{and} \quad x = b_2\varphi \quad (86)$$

For $\zeta = a$, $z = 0$, so $b_1 = a$, and if $\zeta = h + a$ for $z = h$, then

$$b_2 = \frac{h}{\ln\left(1 + \frac{h}{a}\right)} \quad (87)$$

In Fig. 20 the p plane is considered as a Riemann surface and its range is $0 \leq \varphi \leq 2\pi$; in the q plane the range is $0 \leq x < 2\pi b_2$. The CM relation between p and q is

$$F(x, z) = \frac{d\zeta}{dz} = \frac{d\xi}{dx} \quad (88)$$

and

$$F(z) = \frac{a}{h} \left[\ln\left(1 + \frac{h}{a}\right) \right] \left(1 + \frac{h}{a}\right)^{z/h} \quad (89)$$

Here, it must be noted that F is only a function of z and is independent of x . Therefore this case simplifies the solution for wave propagation.

In Eq. (89) $F(z)$ has been expanded for $(\frac{h}{a}) \ll 1$ in Ref. 9 as follows:

$$F(z) = 1 + \frac{z}{a} - \frac{h}{2a} \quad (90)$$

Now, TE and TM waves, which are guided by Earth, can be examined by using CM. Here, Earth is assumed to be a perfectly conducting cylinder surrounded by an isotropic, nonconducting medium, and its permittivity $\varepsilon(\zeta)$ is a function of only ζ .

5.5.1. TM Case. In p plane the (Fig. 20) one can express the components of the TM wave as E_ζ, E_ξ and H_η and in the q plane (Fig. 21) after transformation these components can be written as E_z, E_x , and H_y , respectively. It must be noted that the coordinates η and y are perpendicular to these planes (p plane and q planes, respectively). The following partial-differential equation can be reached using Maxwell equations for E_ζ, E_ξ, H_η :

$$\begin{aligned} F^2(z) &= \mu(z), \quad \varepsilon(\zeta) = \varepsilon'(z) \\ H_\eta &= H_y, \quad F(z)E_\xi = E_x, \quad F(z)E_\zeta = E_z \end{aligned} \quad (91)$$

Then

$$\begin{aligned} \frac{d^2 H_y(z)}{dz^2} - \frac{1}{\varepsilon'(z)} \frac{d\varepsilon'(z)}{dz} \frac{dH_y(z)}{dz} \\ + [\beta_0^2 \varepsilon'(z) F^2(z) - \beta^2] H_y(z) = 0 \end{aligned} \quad (92)$$

where

$$\beta = \frac{2\pi}{\lambda}, \quad \beta_0^2 = \omega^2 \mu_0 \varepsilon_0, \quad \text{and } \lambda = \text{wavelength} \quad (93)$$

5.5.2. TE Case. The TE wave components are H_ζ, H_ξ , and E_η in p plane and H_z, H_x , and E_y in the q plane. Using the following relations for the TE wave

$$\begin{aligned} \varepsilon(\zeta) &= \varepsilon'(z), \quad F^2(z) = \varepsilon''(z) \\ E_y &= E_\eta, \quad H_x = F(z)H_\xi, \quad H_z = F(z)H_\zeta \end{aligned} \quad (94)$$

then similarly

$$\frac{d^2 E_y(z)}{dz^2} + [\beta_0^2 \varepsilon'(z) F^2(z) - \beta^2] E_y(z) = 0 \quad (95)$$

Equation (92) indicates that following transformation in Fig. 21, the permeability $\mu(z) = K^2(z)$ and permittivity $\varepsilon'(z)$ are space-dependent.

Richter [9] has explained the meaning of $K^2(z)$, in which the elements of volume of both systems are different; however, the magnetic field strengths are equal. Thus, there exists a fictitious permeability so that the total magnetic energy would be equal in both coordinate systems. In addition, in Eq. (95) there is space-dependent permittivity [i.e., $\varepsilon'(z) \cdot \varepsilon''(z)$]. Here again, the reason is the

same as the previous one for introducing a fictitious permittivity.

If Eqs. (92) and (95) are written in another form where

$$\beta = \beta_0 F(h) \cos \theta_h \quad (96)$$

then θ_h is the angle of the wave normal to the x axis at height h . Therefore, Eqs. (92) and (95) can be written as follows:

$$\frac{d^2 f}{dz^2} + B_0^2 t^2 f = 0 \quad (97)$$

It must be noted that $\varepsilon^l(z)$ is assumed to be a constant. Here t is

$$\begin{aligned} t^2 &= F^2(z) - \left(\frac{\beta}{\beta_0}\right)^2 \\ &= F^2(z) - F^2(h) \cos^2 \theta_h \end{aligned} \quad (98)$$

Finally, the differential equations can be solved by using different methods as mentioned in Ref. 9.

5.6. Bent Rectangular Waveguide

The procedure of analyzing bent rectangular waveguide has been summarized [9] by using CM. The analyzed waveguide geometry in $z = x + jy$ plane is seen in Fig. 22. As mentioned in this article, in one case the wave travels in the plane of irregularity. The transformed structure in the $w = u + jv$ plane is shown in Fig. 23.

The wave equation in the transformed plane is

$$\frac{\partial^2 Q}{\partial u^2} + \frac{\partial^2 Q}{\partial v^2} + m^2 k^2 Q = 0 \quad (99)$$

where Q represents the electrical or magnetic components of the wave and the metric coefficient m (see Section 3) is

$$\begin{aligned} m &= 1 + g(u, v) = |f'(u + jv)|^2 \pi^2 / b^2 \\ 1 + g(u, v) &= [\cosh u + \cos v]^{2\alpha} [\cosh(u - t)]^{-\alpha} \\ &\quad \times [\cosh(u + t) - \cos \theta]^{-\alpha} \end{aligned} \quad (100)$$

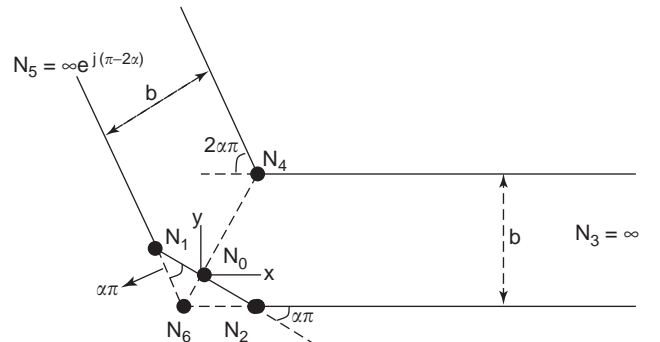


Figure 22. The original bent waveguide in z plane (from Ref. 9).

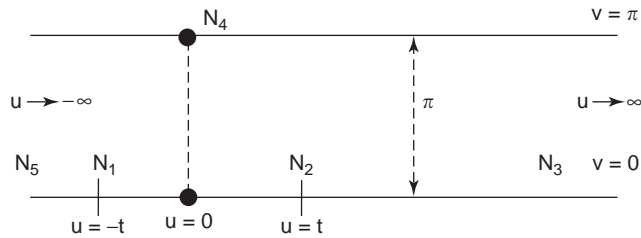


Figure 23. The waveguide after transformation [$z = x + jy = f(u + jv) = f(w)$] in w plane (from Ref. 9).

Here $f'(u + jv)$ denotes the first derivative of the transformation function $f(w)$ (obtained using the Schwarz–Christoffel transformation in Ref. 9), $2\pi\alpha$ is the total angle of the bend, and t is a parameter that depends on α and the ratio $|N_4 - N_0|/|N_4 - N_6|$. Also, k can be written as

$$k = \frac{2b}{\lambda} \left\{ 1 - \left(\frac{\lambda_0}{2a} \right)^2 \right\}^{1/2} = -j\Gamma \frac{b}{\pi} \quad (101)$$

$$\Gamma = j2\pi \lambda_0^{-1} (1 - \lambda_0^2 a^{-2} / 4)^{1/2}$$

$$\gamma_i^2 = i^2 - k^2, \quad i = 0, 1, 2, 3, \dots, \gamma_0 = jk$$

where λ_0 is the free-space wavelength and a is the largest of the rectangular cross section of the waveguide. This application method can be used in other irregularities such as inserts in the channel as argued in Ref. 34.

6. SUMMARY

A limited number of examples of conformal mapping techniques (CMTs) have been presented in this article. However, as seen from each example, analytical closed-form expressions have been obtained easily via these CMTs. These equations can be implemented in CAD tools accurately. Other methods such as the finite-difference method, integral equation method, and full-wave analysis are unwieldy, since they require excessive amounts of computer memory and calculation time.

As shown from a comparison of the results of conformal mapping with other methods and measured values from experiments reported in the general literature, accuracy of the CM techniques is very good. Also, it has been mentioned many articles that since this method is analytical, the relation between parameters to be calculated and physical parameters can be interpreted easily.

BIBLIOGRAPHY

1. R. Schinzinger, Conformal transformations in the presence of field components along a third axis—part I, *Int. J. Electric. Eng. Educ.* **13**:76–89 (1976).
2. E. J. Routh, The advanced part of a treatise on the dynamics of a system of rigid bodies, Part II of a Treatise on the Whole Subject, 6th ed., Dover, 1905, pp. 461–467.

3. F. W. Carter, A note on airgap and interpolar induction, *J. Inst. Electric. Eng.* **29**:925 (1900).
4. H. H. Meinke, Die Anwendung der konformen abbildung auf Wellenfelder, *Z. Angew. Physik.* **1**:245–252 (1949).
5. H. H. Meinke, Ein allgemeines Lösungsverfahren fuer inhomogene Zylindersymmetrische Wellenfelder, *Z. Angew. Physik.* **1**:509–516 (1949).
6. R. Piloty Jun, Die Anwendung der konformen Abbildung auf die Feldgleichungen in inhomogenen Rechteckrohren, *Z. Angew. Physik.* **1**:441–448 (1949).
7. H. H. Meinke, Das Verhalten elektromagnetischer Wellen instark inhomogenen Leitungsbauerelementen, *Z. Angew. Physik.* **2**:473–478 (1950).
8. P. A. Laura, Calculations of eigenvalues for uniform fluid waveguides with complicated cross sections, *J. Acoust. Soc. Am.* **42**:21–26 (1967).
9. J. H. Richter, Application conformal mapping to Earth-flattening procedures in radio propagation problems, *Radio Sci.* **1**:1435–1438 (1966).
10. R. A. Pappert, A numerical study of VLF mode structure and polarization below an anisotropic ionosphere, *Radio Sci.* **3**:219–233 (1968).
11. S. O. Rice, Reflection from corners in rectangular wave guides—conformal transformation, *Bell Syst. Tech. J.* **28**:104–135 (1949).
12. W. Hilberg, From approximations to exact relations for characteristic impedances, *IEEE Trans. Microwave Theory Tech.* **MTT-17** (5):259–265 (May 1969).
13. C. Veyres and V. F. Hanna, Extension of the application of conformal mapping technique to coplanar lines with finite dimensions, *Int. J. Electron.* **48**(1):47–56 (1980).
14. V. F. Hanna and D. Thebault, Analysis of asymmetrical coplanar waveguides, *Int. J. Electron.* **50** (3):221–224 (1981).
15. V. F. Hanna and D. Thebault, Theoretical and experimental investigation of asymmetric coplanar waveguides, *IEEE Trans. Microwave Theory Tech.* **MTT-32**(12):1649–1651 (Dec. 1984).
16. G. Ghione and C. Naldi, Analytical formulas for coplanar lines in hybrid and monolithic MICs, *Electron. Lett.* **20**(4): 179–181 (Feb. 1984).
17. G. Ghione and C. Naldi, Coplanar waveguides for MMIC applications: Effect of upper shielding, conductor backing, finite extent ground planes, and line-to-line coupling, *IEEE Trans. Microwave Theory Tech.* **MTT-35**(3):260–267 (March 1987).
18. G. H. Owyang and T. T. Wu, The approximate parameters of slot lines and their complement, *IRE Trans. Anten. Propag.* **49**–55 (Jan. 1958).
19. G. Ghione, A CAD-oriented analytical model for the losses of general asymmetric coplanar lines in hybrid and monolithic MICs, *IRE Trans. Microwave Theory Tech.* **41**(9):1499–1510 (Sept. 1993).
20. L. Zeng, Y. Wang, Accurate solutions of elliptical and cylindrical striplines and microstrip lines, *IEEE Trans. Microwave Theory Tech.* **MTT-34**(2):259–264 (Feb. 1986).
21. J. Svacina, Analysis of multilayer microstrip lines by a conformal mapping method, *IEEE Trans. Microwave Theory Tech.* **40**(4):769–772 (April 1992).
22. S. Rawal, D. R. Jackson, An exact TEM calculation of loss in a stripline of arbitrary dimensions, *IEEE Trans. Microwave Theory Tech.* **39**(4):694–699 (April 1991).
23. R. N. Simons, Coplanar Waveguide Circuits, Components, and Systems, Wiley, New York, 2001.

24. C. Karpuz, A. Görür, H. Görür, and M. Alkan, Fast and simple analytical expressions for quasistatic parameters of asymmetric coplanar lines, *Microwave Opt. Technol. Lett.* **9**(6): 334–336 (Aug. 20, 1995).
25. A. Görür, C. Karpuz, and M. Alkan, Quasistatic TEM characteristics of overlaid supported asymmetric coplanar waveguides, *Int. J. Microwave Millimeter Wave Comput. Aided Eng.* **6** (5):297–304 (1996).
26. V. Akan and E. Yazgan, A simple formulation for quasistatic parameters of elliptical, cylindrical and asymmetrical coplanar strip lines, *Microwave Opt. Technol. Lett.* **41**(1):18–21 (April 5, 2004).
27. V. Akan and E. Yazgan, Quasistatic TEM characteristics of multilayer elliptical and cylindrical coplanar waveguides, *Microwave Opt. Technol. Lett.* **42**(4):317–322 (Aug. 20, 2004).
28. G. Ghione, M. Goana, G. Madonna, G. Omega, M. Pirola, S. Boss, D. Frassati, and A. Perasso, Microwave modelling and characterization of thick coplanar waveguides on oxide-coated lithium niobate substrates for electrooptical applications, *IEEE Trans. Microwave Theory Tech.* **47**(12):2287–2293 (Dec. 1999).
29. M. Goana, F. Bertazzi, P. Caravelli, G. Ghione, and T. A. Driscoll, A general conformal-mapping approach to the optimum electrode design of coplanar waveguides with arbitrary cross section, *IEEE Trans. Microwave Theory Tech.* **49**(9):1573–1580 (Sept. 2001).
30. J. T. Bernhard, and C. J. Tousignant, Resonant frequencies of rectangular microstrip antennas with flush and spaced dielectric superstrates, *IEEE Trans. Anten. Propag.* **47**(2) (Feb. 1999).
31. S. S. Zhong, G. Liu and G. Qasim, Closed form expressions for resonant frequency of rectangular patch antennas with multilayer dielectric layers, *IEEE Trans. Anten. Propag.* **42**(9):1360–1363 (Sept. 1994).
32. H. A. Wheeler, Transmission-line properties of parallel wide strips by a conformal-mapping approximation, *IEEE Trans. Microwave Theory Tech.* **MTT-12**:280–287 (March 1964).
33. M. Kirschning, R. H. Jansen, Accurate model for effective dielectric constant of microstrip with validity up to millimeter-wave frequencies, *Electron. Lett.* **18**:272–273 (March 1982).
34. R. Schinzinger, Conformal transformations in the presence of field components along a third axis—part II, *Int. J. Electric. Eng. Educ.* **13**:127–131 (1976).
35. E. Kreyszig, *Advanced Engineering Mathematics*, Wiley, Singapore, 1993.
36. W. J. Gibbs, *Conformal Mappings in Electrical Engineering*, Chapman & Hall, London, 1958.

CONICAL ANTENNAS

SABURO ADACHI
Tohoku Institute of Technology
Sendai, Japan

This article describes characteristics such as input impedance, radiation pattern, and directivity gain of conical antennas consisting of solid conducting cones, conducting conical plates, or their modifications. Conical conducting

structures on which simple antenna elements such as dipole and a slot are mounted are also described. An important general feature of conical antennas is their lack of sensitivity to frequency variation, that is, their broadband characteristics. Note that a conical horn antenna is described in HORN ANTENNAS.

The history of the practical use of conical antennas is long. Sir Oliver Lodge constructed a biconical antenna in 1897 and made a wireless communication experiment, while a single cone antenna on the ground and a fan (flat triangular) antenna were used by Marconi and others. The history of the theory of conical antennas is also long. The spherical coordinate is one of the few coordinates for which the method of variable separation in electromagnetic field problems can be applied. The conical surface is defined by a constant polar angle $\theta = \psi$ in the spherical coordinate system. For this reason conical antennas and biconical antennas, in particular, have been extensively investigated by Schelkunoff [1,2], Smith [3], Tai [4,5], Papas and King [6], and many others.

In the limit as $\psi \rightarrow 0$ and π , the biconical antenna is reduced to a vanishingly thin linear antenna that is very sensitive to frequency (that is, of narrow bandwidth). As the cone angle increases, the antenna shows broadband characteristics that make it useful for practical applications.

Figure 1 shows an infinitely long, symmetric biconical conductor with a half-cone angle ψ and an infinitesimally small feeding gap (δ gap). The antenna is assumed to be located in free space. This structure can support the transverse electromagnetic (TEM) transmission line mode, that is, the outward-propagating principal spherical-wave mode expressed by

$$H_\phi = \frac{1}{r \sin \theta} H_0 e^{-j\beta r} \quad (1)$$

$$E_\phi = \eta H_\phi \quad (2)$$

where $\beta = 2\pi/\lambda$ (λ : wavelength) is the free-space wavenumber and $\eta = \sqrt{\mu_0/\epsilon_0}$ is the free-space wave impedance. The

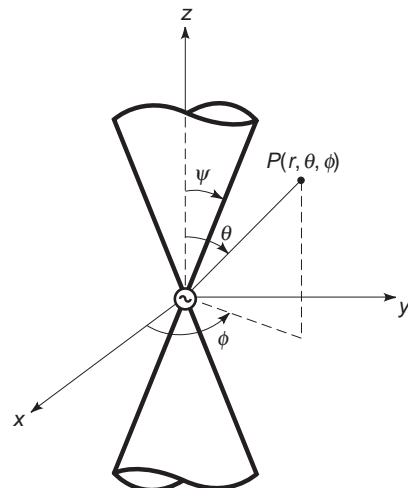


Figure 1. Infinite biconical conductor fed by a δ -gap generator.

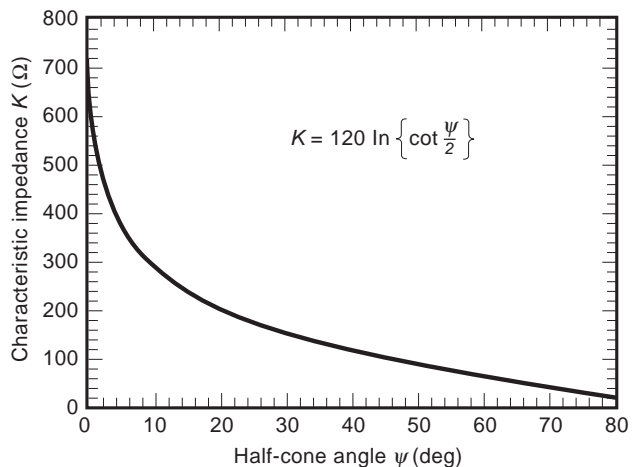


Figure 2. Characteristic impedance of a biconical transmission line.

characteristic impedance K of the biconical transmission line is given by the ratio of the transmission voltage (i.e., the integral of E_θ along the cone meridian) to the conduction current along the cone as follows:

$$K = \frac{\eta}{\pi} \ln \left[\cot \frac{\psi}{2} \right] \tag{3}$$

Figure 2 shows the characteristic impedance K versus the half-cone angle ψ .

1. BICONICAL ANTENNAS

Figure 3 shows the geometry of the biconical antenna. The conducting antenna surfaces are defined by the conical surfaces $\theta = \psi$ and $\theta = \pi - \psi$, and the two spherical end surfaces at $r = a$. The analytical procedure of the biconical antenna will be outlined below. In region I, the electric and magnetic fields are represented as a sum of the outward- and inward-traveling TEM principal modes and an infi-

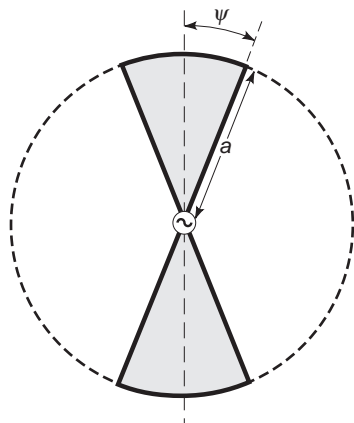


Figure 3. Symmetric biconical antenna.

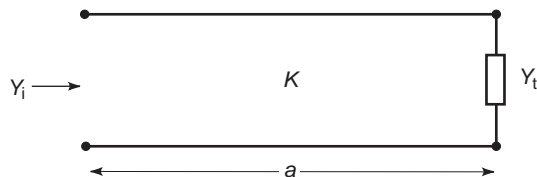


Figure 4. Equivalent circuit of a symmetric biconical antenna.

nite number of complementary (higher) transverse magnetic (TM) modes. In region II, the fields are represented by an infinite series of complementary radiating modes. Boundary conditions on the aperture indicated by the dashed lines in Fig. 3 and the end surfaces of the cone at $r = a$ are used to obtain an infinite set of linear algebraic equations from which the amplitudes of the complementary modes and the principal mode reflected back at the aperture are determined.

The input admittance of the biconical antenna is represented by the equivalent transmission line circuit as shown in Fig. 4, where K is the characteristic impedance given by Eq. (3). The terminal admittance Y_t represents the effect of the truncation of the biconical transmission line at $r = a$, that is, the transformation of the outward-traveling TEM mode into the complementary modes in both regions and the reflected TEM mode, which eventually determines the input admittance of the biconical antenna Y_i .

Schelkunoff [2] has formulated the abovementioned boundary value problem rigorously and has discussed in detail special cases of a vanishingly thin antenna and a very wide-angle cone, or a spherical antenna with a very narrow equatorial gap. Tai [4] has obtained the exact analytical solution of the terminal admittance of the vanishingly thin antenna, which has been found to be identical to the expression obtained ingeniously by Schelkunoff. Tai [5] has also made an important contribution to the development of the theory for biconical antennas by applying Schwinger’s variational method. He has given the first-order variational numerical solution for the specific wide cone angles $\psi = 39.23^\circ, 57.43^\circ,$ and 66.06° .

The more recent development of computers has made feasible the numerical solution of Schelkunoff’s formulation. However, it is still not easy to solve the infinite set of linear determining equations with reasonable accuracy because of slow convergence of the infinite series when the cone-angle decreases. For example, 15 or more modes for $\psi = 5^\circ$ [7], and 13 modes for $\psi = 5^\circ$ [8] are necessary for computation of the input impedance. A conical monopole above an image plane driven by a coaxial line has been numerically analyzed by using the finite difference time domain method [9].

When the upper half-cone of the biconical antenna is mounted on an infinite conducting plane (ground plane), the antenna forms a conical unipole having one half of the input impedance of the biconical antenna. Figures 5 and 6 (from Brown and Woodward, Jr. [10]) show respectively the measured input resistance and reactance of a conical unipole having flat caps instead of spherical caps. It is clear that the antenna tends to have a constant input

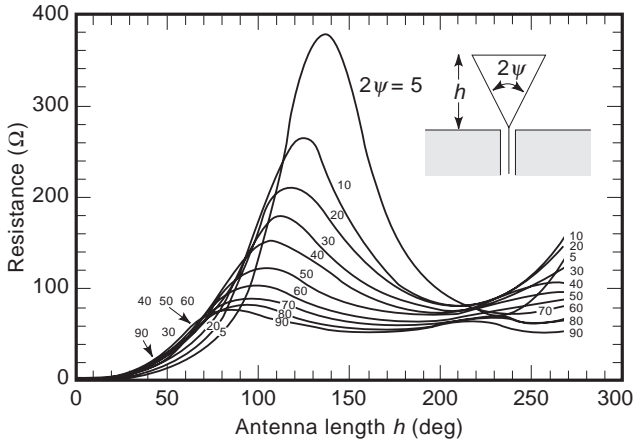


Figure 5. Measured input resistance of a conical unipole versus length in electrical degrees showing broadband characteristics with increasing cone angle (from Ref. 10).

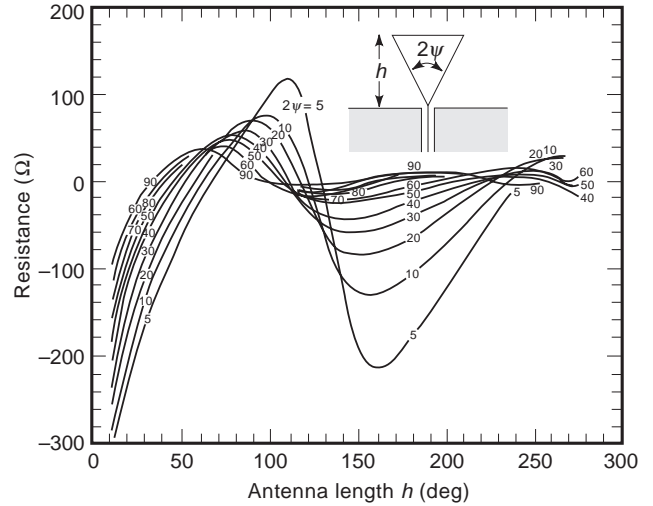


Figure 6. Measured input reactance of a conical unipole versus length in electrical degrees showing broadband characteristics with increasing cone angle (from Ref. 10).

resistance and a small reactance around zero versus frequency, showing broadband characteristics as the cone angle is increased.

The radiation pattern of the biconical antenna has been computed by Papas and King [6] and by Bevensee [11]. Figure 7 shows the far-zone electric field pattern [6] for

the cone angle of $\psi = 30^\circ$. It is found that the patterns are not much different from those of a straight wire antenna.

Theoretical analysis of biconical antennas loaded with and/or immersed in dielectric, lossy, and ferromagnetic materials has been provided by Schelkunoff [2], Tai [4],

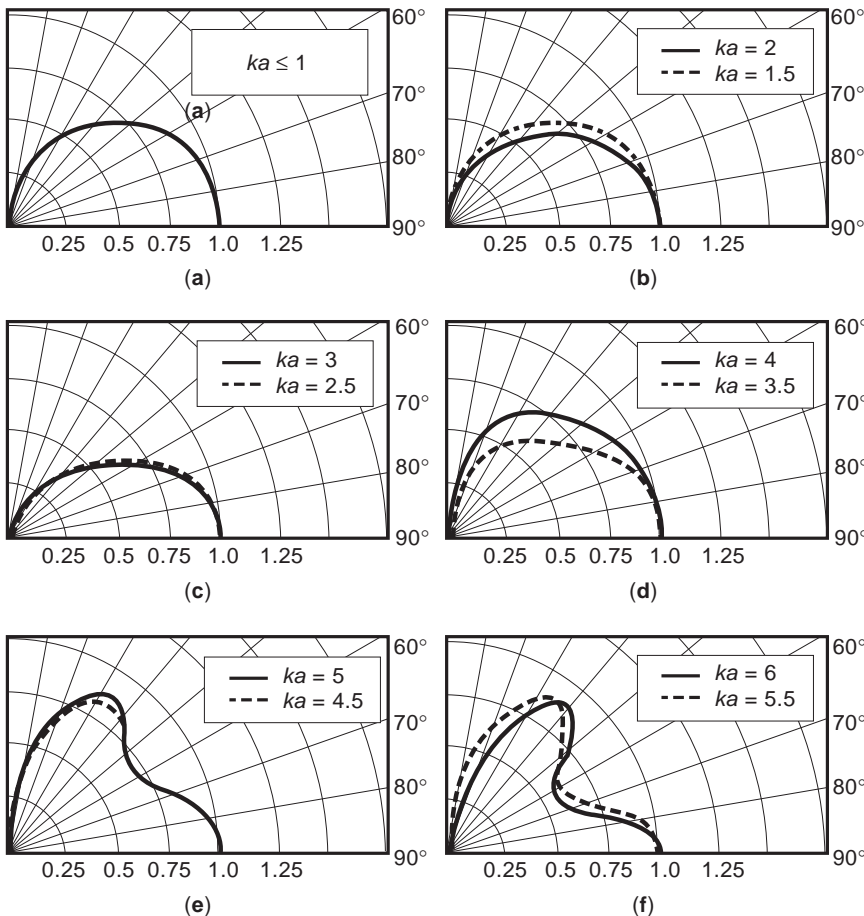


Figure 7. Far-zone electric field patterns of a biconical antenna, $\psi = 30^\circ$. Patterns do not change very much from $ka = 0$ to $ka \approx \pi$.

Polk [12], and others. These topics are reviewed by Wait [13]. The theory of an asymmetric biconical antenna was also discussed by Schelkunoff [2]. The variational approach by Tai was extended to a semiinfinite asymmetric conical antenna consisting of an infinite cone and a finite cone [14].

To reduce wind resistance and/or weight, a solid biconical antenna can be replaced by a skeletal conducting wire structure using several radial rods [15,16]. It has been found, however, by analysis using the moment method that a considerable number of wires (e.g., 16) is required to approximate the solid biconical antenna.

2. ANTENNAS ON CONICAL STRUCTURE

In practice, a conical structure on which simple antenna elements such as dipole, disk, cone, slot, or patch are mounted to excite a cone is often used. The infinite cone excited with an axial dipole at the tip has shown [14] that the strong radiation occurs along the small-angle cone unless the dipole length is about a half-wavelength. Figure 8 shows a finite wide-angle cone excited with a quarter-wavelength long and a half-wavelength long dipole [17]. Note that the maximum radiation can be directed toward the horizontal plane by proper choice of a and θ_0 at a desired frequency. A cone excited with an axially symmetric circumferential slot close to the tip [18] shows radiation characteristics similar to those of a dipole-excited cone, since a small circumferential slot (magnetic current loop) is equivalent to a small axial electric dipole. When the circumferential slot is not too close to the tip, that is, apart by 2.5 wavelength ($2\psi = 30^\circ$), the radiation pattern shows a rather complicated lobe structure [18]. The cone excited with a circular disk at the tip is called a *discone antenna* [19]. This antenna is fed with a coaxial

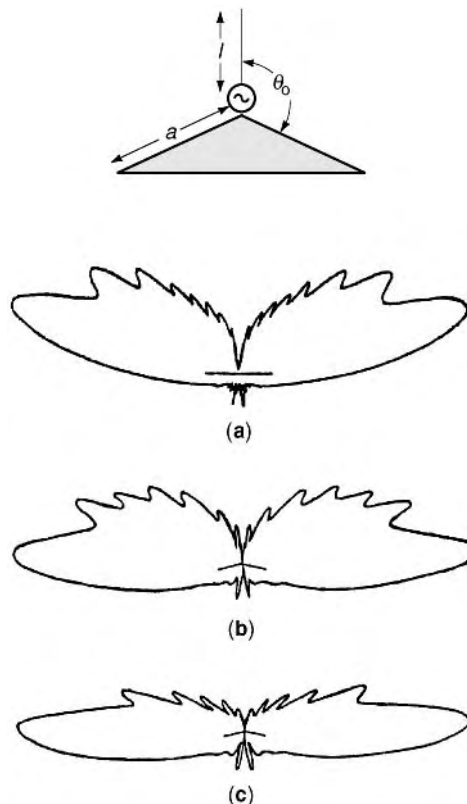


Figure 8. Far-zone electric field pattern of a tip-excited conical antenna, $\beta a = 50$: (a) $\theta_0 = 90^\circ$, $l = \lambda/4$; (b) $\theta_0 = 103.8^\circ$, $l = \lambda/4$; (c) $\theta_0 = 103.8^\circ$, $l = \lambda/2$; radiation beam can be directed to horizon by slanting a cone downward (from Ref. 17).

cable whose inner conductor terminates on the center of the disk and whose outer conductor terminates on the tip of the cone. The radiation pattern of the discone is similar

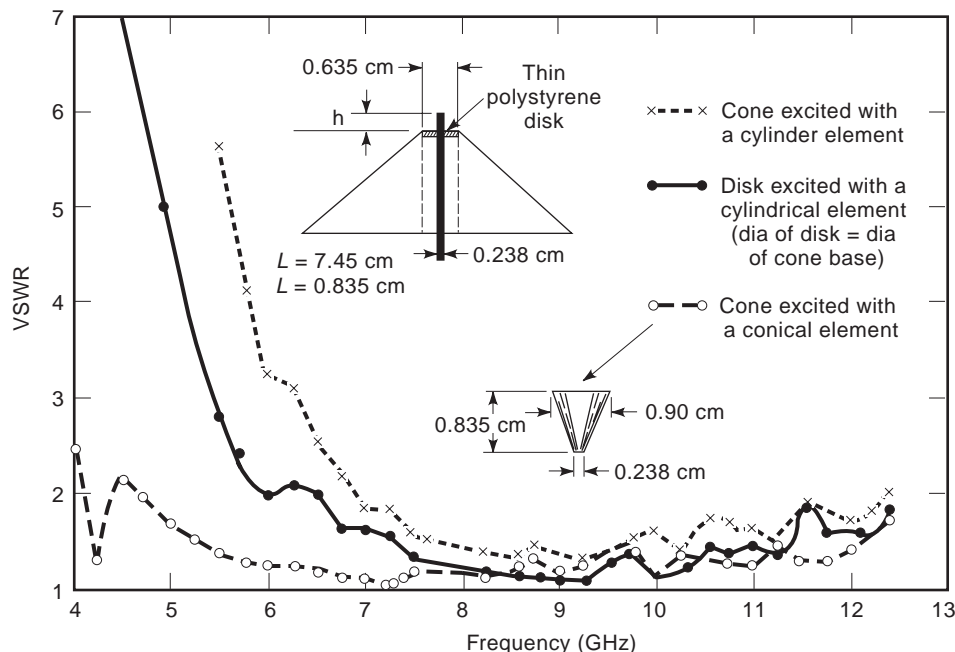


Figure 9. VSWR versus frequency of a disk and a cone excited with a cylindrical element or a conical element showing that a cone excited with a conical element is most broadband (from Ref. 17).

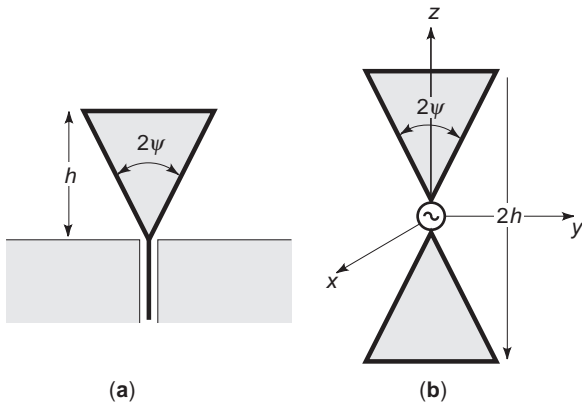


Figure 10. (a) Triangular plate antenna and (b) bowtie antenna.

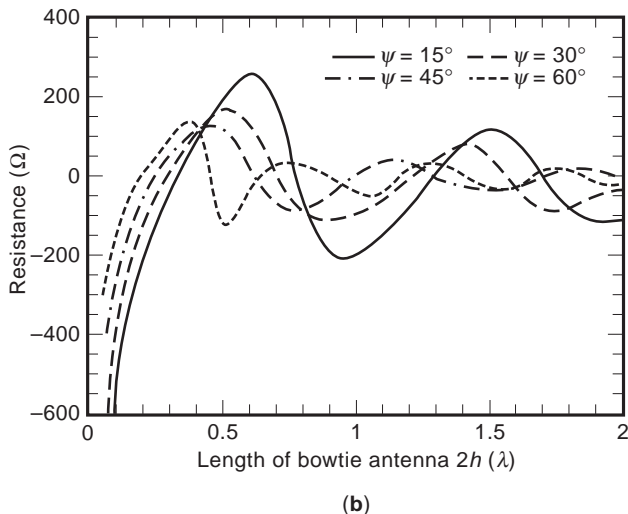
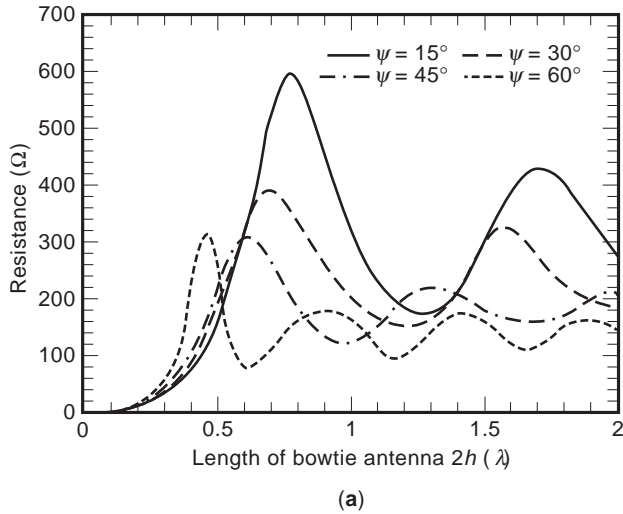
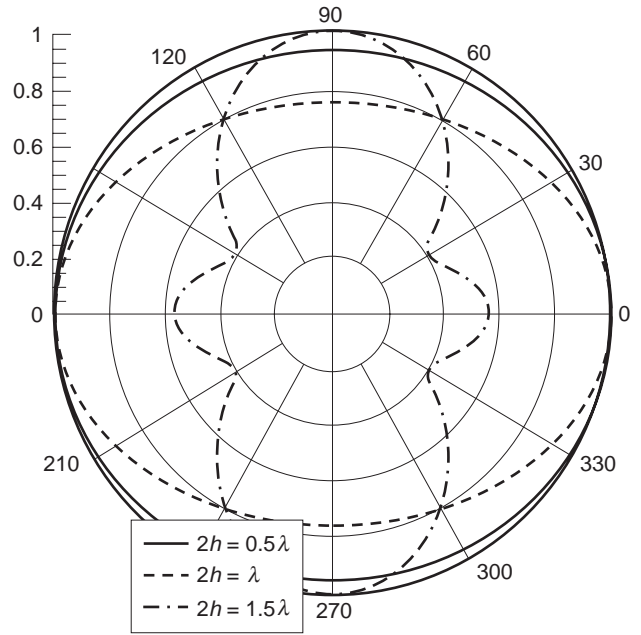
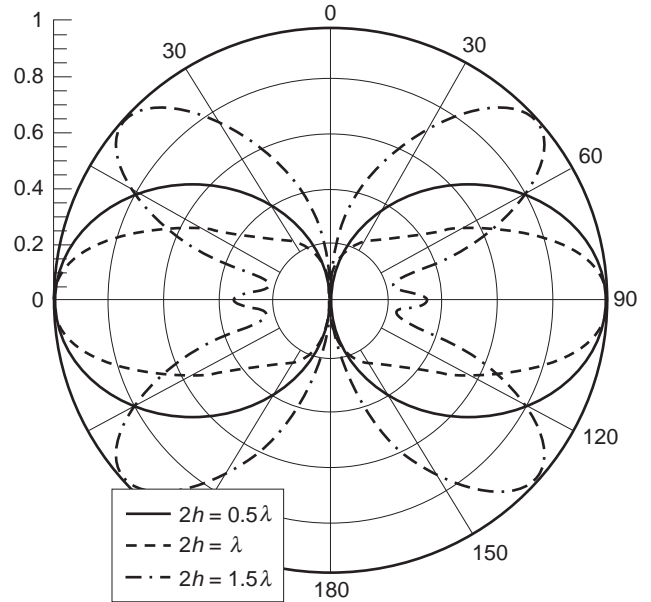


Figure 11. Input impedance of a bowtie antenna showing the broadband characteristics with increasing flare angle (from Ref. 20).



(a) x-y plane



(b) x-z plane

Figure 12. Far-zone electric field pattern of a bowtie antenna, $\psi = 30^\circ$; (a) x-y plane (b) x-z plane (from Ref. 20).

to that of a dipole antenna, but its input impedance bandwidth is exceedingly broad compared with an ordinary dipole antenna.

Figure 9 shows the measured input VSWR (for 57.6-Ω-cable) versus frequency of the finite conical antenna with different exciting elements at its tip [17]. The cone excited with a conical element (an asymmetric biconical antenna) indicates very broadband characteristics, particularly in

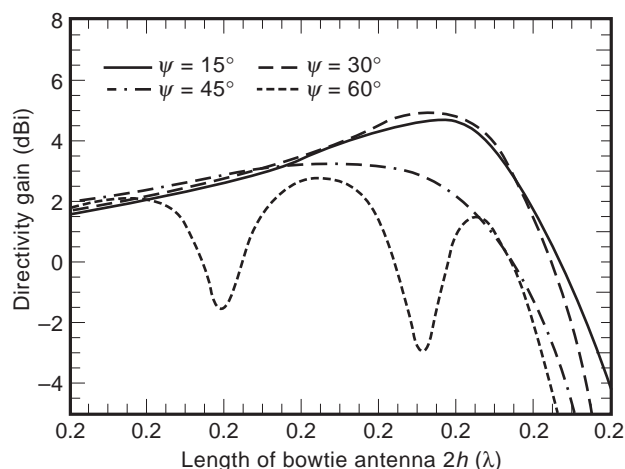


Figure 13. Directivity gain of a bowtie antenna in x direction (from Ref. 20).

lower-frequency regions, without affecting the radiation pattern.

3. TRIANGULAR (BOWTIE) ANTENNAS

A triangular plate antenna above a conducting ground plane and a bowtie antenna are shown in Figs. 10a and 10b. These antennas also possess broadband characteristics, though not as broad as a solid conical antenna. The theoretical characteristics of the bowtie antenna have been obtained numerically [20] by using the method of finite-difference time domain (FDTD). Figures 11a and 11b show the calculated input impedance. The input impedance of the triangular plate antenna above the ground plane is half of that of the bowtie antenna.

The far-zone electric field patterns in the x - y plane and in the x - z plane are shown in Figs. 12a and 12b, respectively. Note that the radiation is enhanced in the direction perpendicular to the antenna plate for the antenna length $2h \lesssim \lambda$, because the radiation from the antenna surface current is added in phase in that direction. The theoretical directivity gain of the bowtie antenna in the direction of the x axis is shown in dBi in Fig. 13 versus the antenna length $2h/\lambda$ for various cone angles [20]. It is noted here that the bowtie antenna can also be simulated by several radial wire rods as the solid biconical antenna.

BIBLIOGRAPHY

1. S. A. Schelkunoff, Principal and complementary waves in antennas, *Proc. IRE* **34**(1):23–32 (1946).
2. S. A. Schelkunoff, *Advanced Antenna Theory*, Wiley, New York, 1952.
3. P. D. P. Smith, The conical dipole of wide angle, *J. Appl. Phys.* **19**(1):11–23 (1948).
4. C. T. Tai, On the theory of biconical antennas, *J. Appl. Phys.* **19**(12):1155–1160 (1948).
5. C. T. Tai, Application of variational principle to biconical antennas, *J. Appl. Phys.* **20**(11):1076–1084 (1949).
6. C. H. Papas and R. W. P. King, Radiation from wide-angle conical antennas fed by a coaxial line, *Proc. IRE* **39**(1):49–51 (1951).
7. S. A. Saoudy and M. Hamid, Input admittance of a biconical antenna with wide feed gap, *IEEE Trans. Anten. Propag.* **38**(11):1784–1790 (1990).
8. V. Badii, K. Tomiyama, and D. M. Grimes, Biconical transmitting antennas, a numerical analysis, *Appl. Comput. Electromagn. Soc. J.* **5**(1):62–93 (1990).
9. J. G. Maloney, G. S. Smith, and W. R. Scott, Jr., Accurate computation of the radiation from simple antennas using the finite-difference time-domain method, *IEEE Trans. Anten. Propag.* **38**(7):1059–1068 (1990).
10. G. H. Brown and O. M. Woodward, Jr., Experimentally determined radiation characteristics of conical and triangular antennas, *RCA Rev.* **13**(4):425–452 (1952).
11. R. M. Bevensee, *Handbook of Conical Antennas and Scatterers*, Gordon & Breach, New York, 1973.
12. C. Polk, Resonance and supergain effects in small ferromagnetically or dielectrically loaded biconical antennas, *IRE Trans. Anten. Propag.* **7**(special suppl.):414–423 (1959).
13. J. R. Wait, Electromagnetic radiation from conical structures, in R. E. Collin and F. J. Zucker, eds., *Antenna Theory*, McGraw-Hill, New York, 1969.
14. S. Adachi, A theoretical analysis of semi-infinite conical antennas, *IEEE Trans. Anten. Propag.* **8**:534–547 (1960).
15. C. E. Smith, C. M. Butler, and K. R. Umashanker, Characteristics of a wire biconical antenna, *Microwave J.* **22**(9):37–40 (1979).
16. O. Givati and A. P. C. Fourie, Analysis of skeletal wire conical antennas, *IEEE Trans. Anten. Propag.* **44**:844–858 (1996).
17. S. Adachi, R. G. Kouyoumjian, and R. G. Van Sickle, The finite conical antenna, *IEEE Trans. Anten. Propag.* **7**(special suppl.):S406–S411 (1959).
18. L. L. Bailin and S. Silver, Exterior electromagnetic boundary problem for sphere and cones, *IRE Trans. Anten. Propag.* **4**(1):5–16 (1956); corrections **4**(3):313 (1957).
19. A. G. Kandoian, Three new antenna types and their applications, *Proc. IRE* **70W-75W** (1946).
20. Private communication from Y. He, T. Uno, and S. Adachi, 1997.

COPLANAR STRIPLINE (CPS) COMPONENTS

YOUNG-HO SUH
Mimix Broadband Inc.
Houston, Texas

1. INTRODUCTION

Coplanar stripline (CPS) is an attractive uniplanar transmission line offering flexibility in the design of planar microwave and millimeter-wave circuits, especially in mounting the solid-state device in series or shunt with no via holes. Its balanced structure is useful in applications such as printed dipole antenna feeding, rectennas, uniplanar mixers [1], integrated optic traveling-wave

DIELECTRIC LOADED ANTENNAS

L. SHAFI
University of Manitoba
Winnipeg, Manitoba, Canada

1. INTRODUCTION

A transmit antenna converts the energy of a guided wave in a transmission line into the radiated wave in an unbounded medium. The receive antenna does the reverse. The transmission lines such as waveguides and coaxial and microstrip lines use conductors mostly to confine and guide the energy, but antennas use them to radiate it. Because the radiated energy is in unbounded region, phase control is often used to direct the radiation in the desired direction. Dielectrics play an important role in this process, and this article discusses a few representative cases. An important antenna parameter is its *directivity*, which is the measure of its control over the energy flow. To increase the directivity, the antenna size must be increased, and the influence of dielectrics on their performance changes considerably. Thus, in this article, the use of dielectrics in antenna applications is divided into two categories of large high-gain and small low-gain antenna applications.

In high-gain antenna applications, reflectors and lenses are used extensively [1]. They are passive and operate principally on the basis of their geometry. Consequently, they are relatively low-cost, reliable, and wide-band. Reflectors are usually made of good conductors, and thus have lower loss, and because of their high strength, can be made light. But reflectors suffer from limited scan capability. Lenses, on the other hand, because of their transparency, have more degree of freedom, specifically, two reflecting surfaces and the relative permittivity or refractive index. They also do not suffer from aperture blockage. However, lenses have disadvantages in large volume and high weight.

In microwave antenna applications, lenses have numerous and diverse applications, but in most cases they are large in size with respect to wavelength. Thus, physical and geometric optics apply, and most of the lens design techniques can be adopted from optics to microwave applications. The aperture theory and synthesis techniques can also be used effectively to facilitate designs. In addition, the use of an optical ray path in lens design makes the solution frequency-independent. In practice, however, the lens size in microwave frequencies is finite with respect to the wavelength, and the feed antenna is frequency-sensitive. Thus, the performance of the lens antenna also becomes frequency-dependent.

Natural dielectrics at microwave frequencies have reflective indices larger than unity and for collimation, require convex surfaces. However, artificial media using guiding structures, such as waveguides, are equivalent to

dielectrics with refractive index less than unity, and result in concave lenses. They are usually dispersive, resulting in variation of the refractive index with frequency, and have narrower operating bandwidths.

In small antennas dielectrics are used often to improve the radiation efficiency and polarization of the antennas, such as waveguides and horns. This is important in telecommunication applications, where polarization control is required to implement frequency reuse and minimize interference, especially in satellite and wireless communications. Horn antennas and reflector feeds are examples that incorporate dielectrics or lens loading to improve performance [2].

Another area of important dielectric use is insulated antennas in biological applications and remote sensing with buried or submerged antennas. The use of dielectric loading eliminates direct RF energy leak into the lossy environments, and ensure radiative coupling into the target objects. Often a full-wave analysis is needed to provide a proper understanding of their resonance property and coupling mechanism to the surrounding media.

The dielectric loading is also used for antenna miniaturization. Low-loss dielectrics with medium to high relative permittivities are now available and are used increasingly to reduce the antenna size. A number of important areas include dielectric-loaded waveguides and horn, and dielectric resonator and microstrip antennas. By aperture loading of waveguides and small horns, excellent pattern symmetry and low cross-polarization can be obtained, which are essential features of reflector and lens feeds. In addition, the dielectric loading reduces the size of the antennas and makes them useful candidates for multibeam applications, using reflectors and lenses. Miniaturization of the antenna is also an important requirement in wireless communications. Microstrip patch or slot antennas with high-relative-permittivity substrates play an important role in this area, and their derivatives are used in most applications. In dipole and monopole cases the dielectric loading is external and used for size reductions.

Finally, dielectric loading can also be used for gain enhancement, without shaping them such as lenses. Planar dielectrics can be used as radomes or covers to protect the antennas. By proper selection of the radome parameters, the antenna gain can also be increased significantly, while protecting the antennas from the environment.

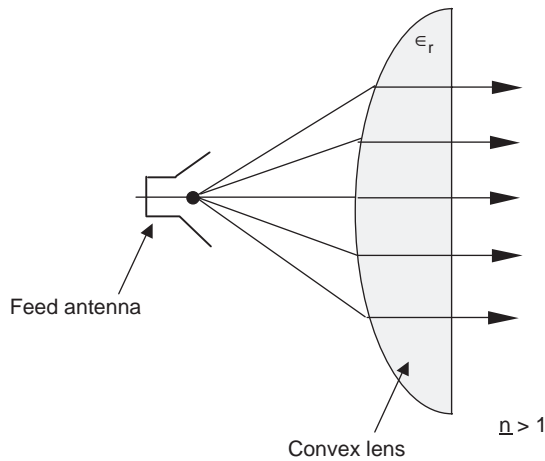
2. DIELECTRIC LENS ANTENNAS

In optical terms, a lens produces an image of a source point at the image point, and lenses could be located anywhere in the space. As an antenna, this property means that the source and image points are focused at each other and the lens has two focal points. In turn, these focal points signify locations in the space, where rays emanating from the lens arrive at equal phases. This

property provides a mathematical relationship for describing the lens operation, and therefore its design.

To simplify the mathematics, the lens configuration is assumed to be rotationally symmetric, and the focal points are placed on its axis. A further simplification can be made for antenna applications, where the image point moves to infinity; that is, the lens focuses a nearby source point, on its axis, to another axial point at infinity. In such a case, all rays leaving the lens travel parallel to its axis, and their phasefronts are planes normal to the lens axis. This is shown in Fig. 1, where ϵ_r is the relative permittivity of the lens material, and $n = \sqrt{\epsilon_r}$ is its refractive index.

To design the lens, one is required to determine the geometry of its two faces, front and back, or the coordinates x_1, y_1 , and x_2, y_2 of points P_1 and P_2 (Fig. 2). There



$$n = \sqrt{\epsilon_r} \quad (a)$$

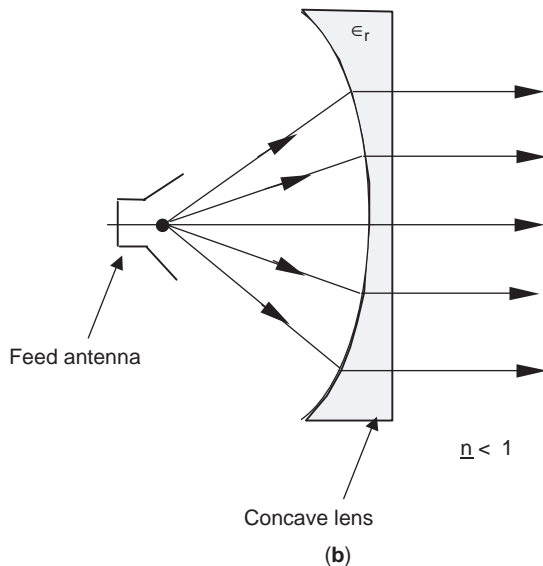


Figure 1. Geometry of lens antennas showing the feed and influence of lens on ray direction.

are four unknowns to be determined. The equality of the phase on the phasefronts requires that the electrical length between the focal points and the phasefronts be independent of the pathlengths. This provides one equation. Two other equations can be obtained from the ray optics at the lens interface points P_1 and P_2 , namely, the Fermat principle of minimum pathlengths. This enforces the well-known Snell law of refraction at the lens surface points. An additional relationship must be generated from the required lens properties, to enable a unique solution for the lens design.

To enforce the invariance of the ray pathlength, the central ray passing through points A, B , and C is selected as the reference and its length from S to C is compared with that of the ray passing through points P_1, P_2 , and P_3 . This provides the following equation

$$\overline{SP_1} + n\overline{P_1P_2} + \overline{P_2P_3} = \overline{SA} + n\overline{AB} + \overline{BC} \quad (1)$$

or

$$r_1 + nr_3 + L_1 = F + nT + L_0 \quad (2)$$

where in terms of P_1 and P_2 coordinates each length is given by

$$\begin{aligned} r_1 &= (x_1^2 + y_1^2)^{1/2} \\ r_3 &= [(x_2 - x_1)^2 + (y_2 - y_1)^2]^{1/2} \\ L_1 &= (x_3 - x_2) \\ L_0 &= x_3 - (F + T) \end{aligned} \quad (3)$$

and F and T are the lens focal length and axial thickness, and are therefore constant lengths defining the lens.

Enforcing the Fermat principle at points P_1 and P_2 results in differentiation of the pathlength in Eq. (1) in terms of its variables x_1, y_1 and x_2, y_2 and setting it to zero. This provides the slope of the lens surface profiles at each point P_1 and P_2 .

At point P_1 one obtains

$$\frac{d}{dx_1} [r_1 + nr_3 + L_1] = \frac{d}{dx_1} [F + nT + L_0] = \frac{d}{dx_1} L_0 \quad (4)$$

where the constants F and T are dropped and after simplifications one finds

$$\frac{dy_1}{dx_1} = \frac{x_1 r_3 - (x_2 - x_1) n r_1}{(y_2 - y_1) n r_1 - y_1 r_3} \quad (5)$$

At point P_2 , a similar differentiation in terms of x_2 gives

$$\frac{dy_2}{dx_2} = \frac{(x_2 - x_1) n - r_3}{(y_2 - y_1) n} \quad (6)$$

Equations (2), (5), and (6) are three fundamental equations to design the required lens. Without another relationship, x_1 may be selected as the independent variable. Then others, namely, x_2, y_1 , and y_2 , become dependent

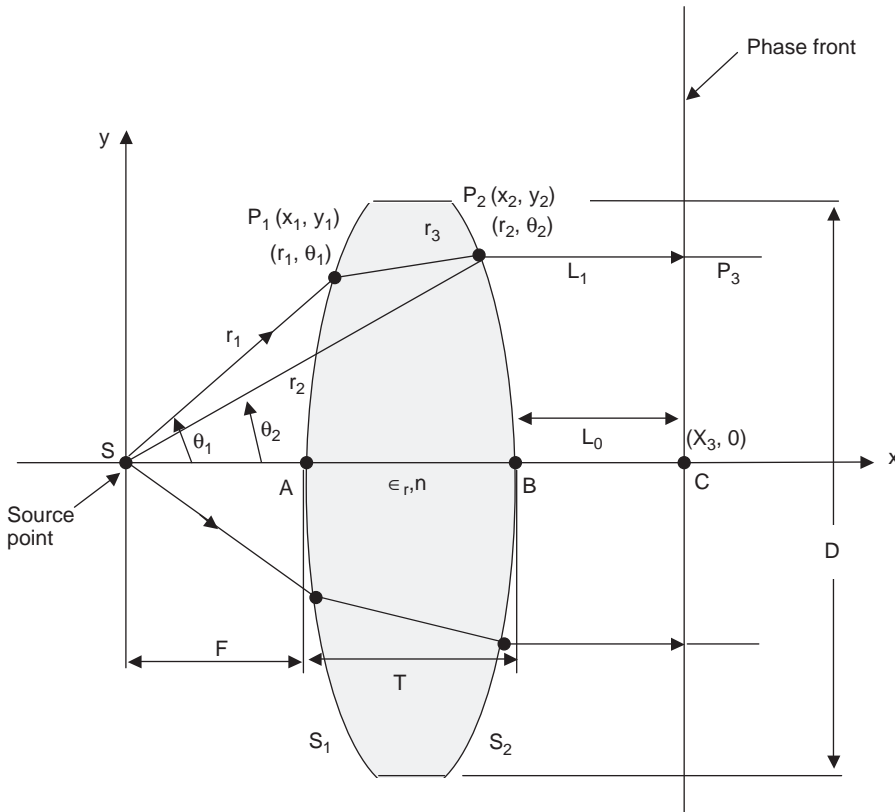


Figure 2. Geometry of a lens indicating ray and surface coordinates.

variables to be determined in terms of x_1 . The solutions give the lens profiles in rectangular coordinates. If the lens profiles in polar coordinates are required, Eqs. (2), (5), and (6) can be obtained in terms of r_1, θ_1 and r_2, θ_2 , the polar coordinates of P_1 and P_2 . Differentiating Eq. (2) in terms of θ_1 and θ_2 gives

$$\frac{dr_1}{d\theta_1} = \frac{nr_1r_2 \sin(\theta_2 - \theta_1)}{r_3 - n[r_2 \cos(\theta_2 - \theta_1) - r_1]} \quad (7)$$

and

$$\frac{dr_2}{d\theta_2} = \frac{nr_1r_2 \sin(\theta_2 - \theta_1) + r_2r_3 \sin \theta_2}{r_3 \sin \theta_2 - n[r_2 - r_1 \cos(\theta_2 - \theta_1)]} \quad (8)$$

where use is made of the following polar coordinate relationships:

$$\begin{aligned} x_1 &= r_1 \cos \theta_1 \\ y_1 &= r_1 \sin \theta_1 \\ x_2 &= r_2 \cos \theta_2 \\ y_2 &= r_2 \sin \theta_2 \\ r_3 &= |r_1 - r_2| = [r_1^2 + r_2^2 - 2r_1r_2 \cos(\theta_2 - \theta_1)]^{1/2} \end{aligned} \quad (9)$$

Solutions of Eqs. (7) and (8) give the lens profiles in polar coordinates, which are often more compact in form. Also, for some simple lens configurations, they result in well-

known and easily recognizable parametric equations of the conic sections, generalizing the solution.

2.1. Examples of Simple Lenses

The lens design becomes considerably easier, if one of the lens surfaces is predetermined. This eliminates one of the differential equations, as the surface profile is already known. Among many surfaces to select the simpler ones are the planar and spherical surfaces, with the planar normal to the lens axis. Such selections give simple profile equations. The planar surface is described by a constant x coordinate and the spherical one by a constant polar coordinate r . These simplifications also assist in solutions of the other lens profile, for which an analytic solution can also be determined. Since either of the lens profiles can be predetermined as planar or spherical, four possible solutions exist. Only two, however, result in simple conical sections.

If the second surface S_2 is assumed to be planar, normal to the lens axis, the rays arriving from the right-hand side, parallel to the lens axis x , enter the lens unaffected and change direction only after the first lens surface S_1 . Then they focus at S ; that is, only the S_1 surface of the lens collimates the beam. Looking from the left side, spherical rays originating from the focal point S , enter the lens at S_1 and become parallel to its axis. Thus, after leaving the lens at S_2 , since they are normal to S_2 , their direction remains unchanged. In this case, the active surface S_1 of the lens is a hyperbola in cylindrical lens, and hyperboloid in rotationally symmetric lens.

If the surface S_1 is spherical, it becomes inactive, since the focal point is a point source and rays emanating from

it constitute spherical waves. Thus, when S_1 is predetermined as a spherical surface, they enter the lens unaffected. Their collimation is done entirely by the lens' second surface S_2 . Its surface is again a conic section, and its cross section is elliptic. In the other two cases, both surfaces S_1 and S_2 of lens participate in beam collimation and consequently are interdependent and more complex.

2.1.1. Lens with Planar S_2 . On S_2 , x is constant and slope is infinite (Fig. 3) and the surface is defined by

$$\begin{aligned} x_2 &= F + T \\ y_2 &= y_1 \end{aligned} \tag{10}$$

A consequence of this is $L_1 = L_0$ in Eq. (2), and using Eq. (10) it becomes

$$r_1 + nr_3 = F \tag{11}$$

which, using Eqs. (10), becomes a function of x_1 and y_1 . It can be solved directly to yield the profile of S_1 as

$$y_1^2 - (n^2 - 1)(x_1 - F)^2 = 2(n - 1)F(x_1 - F) \tag{12}$$

or in polar coordinates

$$r_1 = \frac{(n - 1)F}{n \cos \theta_1 - 1} \tag{13}$$

They represent rectangular and polar equations of a hyperbola, which is the lens profile on S_1 . They can also be used to determine the lens thickness on the axis. For this, one can use two extreme rays, passing through the lens tip and the axis. The equality of the electrical lengths gives

$$F + nT = r_1(\theta_{1 \max}) = \left[\left(\frac{D}{2} \right)^2 + (F + T)^2 \right]^{1/2} \tag{14}$$

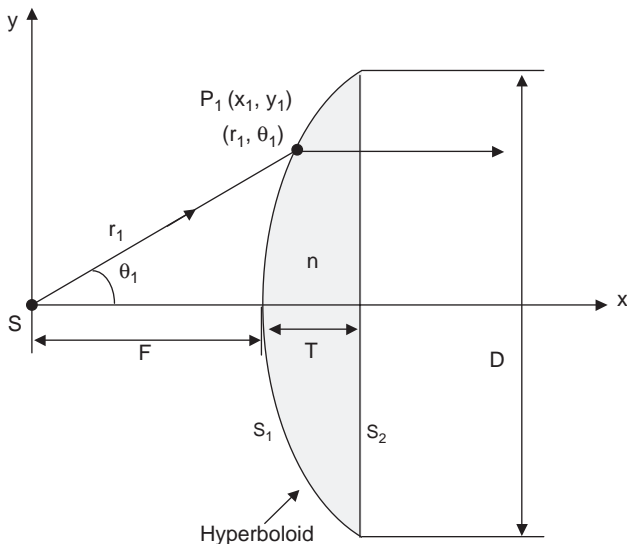


Figure 3. Geometry of lens with a planar surface S_2 .

A solution of this equation gives the lens thickness T as

$$T = (n + 1)^{-1} \left[\left(\frac{(n + 1)D^2}{4(n - 1)} + F^2 \right)^{1/2} - F \right] \tag{15}$$

and

$$\begin{aligned} \theta_{1 \max} &= \cos^{-1} \left(\frac{1}{n} \right) \\ &= \tan^{-1} \left(\frac{(D/2)}{F + T} \right) \end{aligned} \tag{16}$$

Equation (16) shows that, for a given dielectric, the lens aperture angular size is limited by its refractive index n . In other words, with common dielectrics there is a limit on the compactness of the lens. That is, the focal length F cannot be reduced beyond the limit specified by Eq. (16).

2.1.2. Lens with Planar S_1 . In this case, both lens surfaces contribute to the beam collimation. Its surface can be determined similar to the case (in Section 2.1.1) by enforcing $x_1 = F$ and infinite slope for S_1 (Fig. 4). The results are [3]

$$x_1 = F$$

$$x_2 =$$

$$\frac{\{[(n-1)T - [F^2 + y_1^2]^{1/2}][(n^2-1)y_1^2 + n^2F^2]^{1/2} + n^2F[F^2 + y_1^2]^{1/2}\}}{[n^2(F^2 + y_1^2)]^{1/2} - [(n^2-1)y_1^2 + n^2F^2]^{1/2}}$$

$$y_2 = y_1 \left[1 + \frac{(x_2 - F)}{[(n^2 - 1)y_1^2 + n^2F^2]^{1/2}} \right]$$

$$T = \frac{1}{2} (n - 1)^{-1} [(4F^2 + D^2)^{1/2} - 2F] \tag{17}$$

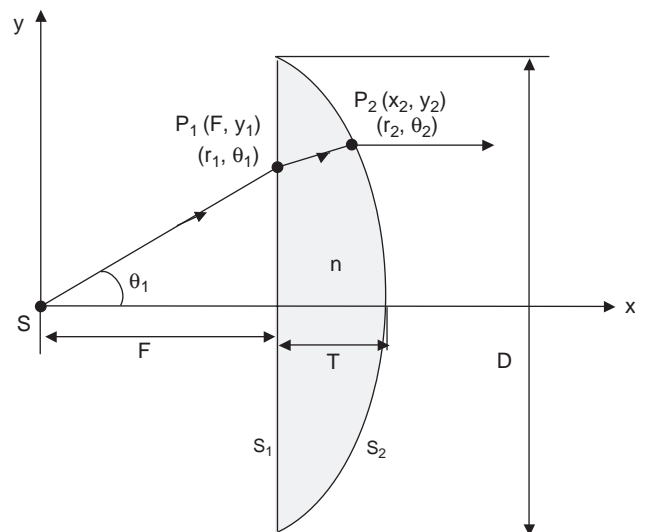


Figure 4. Geometry of lens with a planar surface S_1 .

Note that, since the beam collimation is due to both surfaces, the coordinates of S_2 are now dependent on those of S_1 .

2.1.3. Lens with One Spherical Surface. When S_1 is a spherical surface, all spherical wave originating at the focal point S pass through it unaffected. The second surface, S_2 , collimates the beam. The geometry is shown in Fig. 5, and S_2 is an ellipse given as

$$r_2 = \frac{(n - 1)R}{n - \cos \theta_2} \tag{18}$$

where $R = F + T$ and other parameters are as defined in Fig. 5. Its equation in rectangular coordinates has the form

$$y_2 = \left[\left[\frac{x_2 + (n - 1)R}{n} \right]^2 - x_2^2 \right]^{1/2}$$

and

$$T = \frac{1}{2} (n - 1)^{-1} [2F - (4F^2 - D^4)^{1/2}] \tag{19}$$

$$\theta_{2 \max} = \cos^{-1} \left(\frac{1}{n} \right)$$

the last equation again sets a limit for the peak angular aperture of the lens for a given dielectric material.

When the surface S_2 is assumed to be spherical, then both lens surfaces participate in collimating the beam. The inner surface S_1 can be obtained from [3]

$$n^2 [r_2^2 + r_1^2 - 2r_1 r_2 \cos(\theta_1 - \theta_2)] = [(n - 1)T + r_2 \cos \theta_2 - r_1]^2$$

$$n^2 r_1 \sin(\theta_1 - \theta_2) = \sin \theta_2 [(n - 1)T + r_2 \cos \theta_2 - r_1] \tag{20}$$

$$T = \left[\frac{4(n - 1)F^2 - (n - 3)D^2}{4(n - 1)(n - 3)^2} \right]^{1/2} + \frac{F}{n - 3}$$

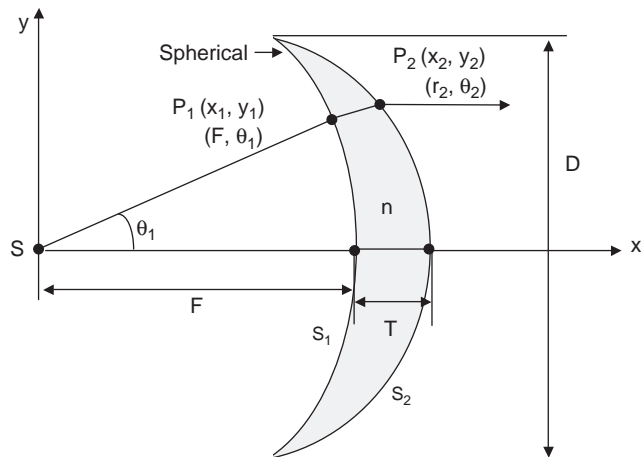


Figure 5. Geometry of lens with a spherical surface S_1 .

3. EFFECT OF LENS ON AMPLITUDE DISTRIBUTION

The lens equations (1) to (6) were based on the ray path analysis, or in antenna terms, the *phase relationships*. The amplitude distributions were not considered. In practical applications, however, the amplitude distributions are also important and will influence the aperture efficiency of the lens, sidelobe levels, and cross-polarization. To state it briefly, a uniform aperture distribution gives the highest directivity, but has high sidelobes because of its high edge illumination. Sidelobes can be reduced by tapering the field toward the edge. Excessive tapering, however, rapidly reduces the lens directivity. It is therefore useful to know the influence of the lens on the field amplitude as well.

Assume that $A(\theta)$ is the angular dependence of the wave amplitude radiating from the focal points and $A(\rho)$, with $\rho = r \sin \theta$, the amplitude distribution of the collimated beam. Then, using the conservation of power, and neglecting the reflection at the lens surface, the following amplitude relationships can be obtained [1].

Hyperbolic lens of case in Section 2.1.1

$$\frac{A(\rho)}{A(\theta_1)} = \frac{1}{F} \left[\frac{(n \cos \theta_1 - 1)^3}{(n - 1)^2(n - \cos \theta_1)} \right]^{1/2} \tag{21}$$

Elliptic lens of case in Section 2.1.3

$$\frac{A(\rho)}{A(\theta_1)} = \frac{1}{F} \left[\frac{(n - \cos \theta_1)^3}{(n - 1)^2(n \cos \theta_1 - 1)} \right]^{1/2} \tag{22}$$

An inspection of these equations shows that in Eq. (21) the amplitude ratio decreases with θ_1 ; that is, after leaving the lens the field is concentrated near its axis. The amplitude, in fact, drops to zero at the angle $\theta_{1 \max}$, given by Eq. (16). This lens, therefore, enhances the field taper of the source and is a good candidate for low-sidelobe applications. However, its aperture efficiency will be low. In contrast, the amplitude ratio in Eq. (22) increases with θ_1 ; that is, this lens corrects the amplitude taper of the source and enhances the aperture efficiency, but in the process, raises the sidelobe levels. Thus, it may be used in applications in which the aperture efficiency is more critical than the sidelobe levels.

For most common dielectrics the refractive index is $n = 1.6$, (i.e., $\epsilon_r \cong 2.55$). For these materials the limit of the aperture angle is $\theta_{1 \max} = 51.3^\circ$. Within this limit the amplitude ratios of Eqs. (21) and (22), normalized to axial values, are shown in Table 1. The amplitude tapering of hyperbolic lenses is clearly evident. A 35° lens adds another 10 dB to the aperture field taper, and beyond 40° , the lens is practically useless. For large-angle-lens applications, higher-dielectric-constant materials must be used. Table 1 also shows the amplitude enhancement of elliptic lens. A 35° lens improves the aperture field uniformity by as much as 6.3 dB. It increases rapidly thereafter and yields about 10 and 20 dB improvements for lens angles of 45° and 50° , respectively. These amplitude enhancements, however, must be accepted as theoretical

Table 1. Amplitude Distributions^a for the Hyperbolic and Elliptic Lenses of Figs. 3 and 5

Amplitude ratio $\frac{A(\rho)}{A(\theta_1)}$		Ray Angle θ_1 (degrees)							
		0	10	20	30	35	40	45	50
Hyperbolic lens equation [Eq. (21)]	Relative value (dB)	1.0	0.928	0.733	0.466	0.328	0.196	0.084	0.008
		0.0	-0.65	-2.70	-6.64	-9.70	-14.17	-21.5	-41.75
Elliptic lens equation [Eq. (22)]	Relative value (dB)	1.0	1.060	1.26	1.69	2.06	2.67	3.17	9.25
		0.0	0.51	2.01	4.55	6.29	8.54	10.03	19.33

^aWhere $n = 1.6$, $\epsilon_r = 2.55$, $\theta_{1\max} = 51.3^\circ$.

limits, since at these wide angles the lens surface reflectivity will reduce the practically attainable levels. Surface matching layers must be used to minimize the reflections.

3.1. General Lens Design

In the general lens of Fig. 2, both surfaces are profiled and participate in collimating the beam. Thus, a more versatile lens can be obtained. However, Eqs. (1)–(6) showed that there are at least four unknown coordinates, x_1, y_1 and x_2, y_2 , to be determined. But, the optical relationships provided only three equations, which are not sufficient to determine uniquely the coordinates of both surfaces S_1 and S_2 . Another relationship must be generated, which may be imposed on the amplitude distribution $A(\rho)$, to control the directivity or sidelobes. Alternatively, one may impose conditions on the aperture phase errors. An important case is the reduction of phase errors due to the source lateral defocusing. This will allow beam scanning without excessive degradation in efficiency and sidelobe levels. In most cases, however, the problem is too complex for analytic solution and a numerical approval must be used.

4. ABERRATIONS

The term *aberration*, which originated in optics, refers to the imperfection of lens in reproduction of the original image. In antenna theory, the performance is measured in terms of the aperture amplitude and phase distributions. The phase distribution, however, is the most critical parameter and influences the far field significantly. It is therefore used in evaluating the performance of aperture antennas such as lenses and reflectors. With a perfect lens and a point source at its focus, the phase error should not exist. However, there are fabrication tolerances, and misalignments can occur that will contribute to aberrations. Even without such imperfections, lens antennas can suffer from aberrations. Practical lens feeds are horn antennas and small arrays. Both have finite sizes and deviate from the point source [2]. This means that part of the feed aperture falls outside the focal point, and rays emanating from them do not satisfy the optical relationships. Thus, on the lens aperture, the phase distribution is not uniform. Similar situations also occur when the feed is moved off axis laterally to scan the beam. Again, aperture phase error occurs as a result of pathlength differences. A somewhat different situation arises when the feed is moved

axially, front or back. In this case, the phase error is symmetric, as all the rays leaving the source with equal angles travel equal distances and arrive at the aperture at an equal radial distance from the axis, that is, on a circular ring. But the length of the ray increases, or decreases, with radial distance on the aperture. The phase error is, therefore, quadratic on the aperture and reduces the aperture efficiency, while raising the sidelobes.

The general aberration (i.e., the lens aperture phase error) can depend implicitly on both feed and lens coordinates and be difficult to comprehend. However, like all other phase-error-related problems, it can also be represented as the pathlength difference with a reference ray. For rotationally symmetric rays, the natural reference is the axial ray. The pathlength difference can then be obtained by a Taylor-type expansion of the general ray length in terms of the axial one. For small aberrations the first few terms in the expansion will be sufficient to describe the length accurately. In terms of the aperture polar coordinates ρ and ϕ , the expansion becomes

$$L(\rho, \phi) = L_{\text{axial}} + \alpha\rho \cos \phi + \beta\rho^2[1 + \cos^2 \phi] + \gamma\rho^3 \cos \phi + \dots \quad (23)$$

where α , β , and γ are constants indicating the magnitude of each phase error. The leading term is linear in ρ and ϕ , then becomes quadratic, cubic, and so on, and the magnitude of each depends on the nature of imperfection causing the phase error. The even terms are caused by either an axial defocusing or an axially symmetric error. The odd terms can be due to a lateral displacement of the feed, or asymmetric errors.

The effects of each error can be investigated by its introduction in the aperture field and determining the far field using a Fourier transformation or diffraction integral. For one-dimensional errors (i.e., $\rho = x$ and $\phi = 0$), the effect can be understood easily, and has been investigated by Silver [1]. The first term is linear and in a Fourier integral shifts, the transform variable. It thus causes a tilt of the beam, but the gain remains the same. Using Silver's notation, if $f(x)$ is the aperture distribution and $g(u)$ the far field, that is, its Fourier transform with a linear phase error, one finds, with no phase error

$$g_0(u) = \frac{a}{2} \int_{-1}^1 f(x) \exp[jux] dx \quad (24)$$

and with phase error

$$g(u) = \frac{a}{2} \int_{-1}^1 f(x) \exp[j(ux - \alpha x)] dx = g_0(u - \alpha) \quad (25)$$

where $u = (\pi a/\lambda) \sin \theta$ and a is the aperture length. Equation (25) shows that the beam peak is moved from the $\theta = 0$ direction to θ_0 calculated by

$$u - \alpha = 0$$

or

$$\theta_0 = \sin^{-1} \left(\frac{\alpha \lambda}{\pi a} \right) \quad (26)$$

A quadratic phase error is symmetric on the aperture and does not tilt the beam, but reduces its gain. For small values of β , it can be calculated analytically [1] and is given by

$$\begin{aligned} g(u) &= \frac{a}{2} \int_{-1}^1 f(x) \exp[j(ux - \beta x^2)] dx \\ &\cong \frac{a}{2} [g_0(u) + j\beta g_0''(u)] \end{aligned} \quad (27)$$

where $g_0''(u)$ is the second derivative of $g_0(u)$. Because of this phase error, the gain decreases progressively with increasing β , and eventually the beam bifurcates and maxima appear on either side of the axis. It also raises the sidelobe levels. Figure 6 shows typical pattern degradation due to this error.

The next important phase error is the cubic one that has odd power dependence on the aperture coordinate. However, this error not only tilts the beam but also reduces the gain, and asymmetrically affects the sidelobes, raising them on one side while reducing them on the opposite side. Its effect is therefore a combination of the effects of linear and quadratic phase errors. For small

errors its far field is given by [1]

$$\begin{aligned} g(u) &= \frac{a}{2} \int_{-1}^1 f(x) \exp[j(ux - \delta x^3)] dx \\ &\cong \frac{a}{2} [g_0(u) + \delta g_0'''(u)] \end{aligned} \quad (28)$$

where $g_0'''(u)$ is the third derivative of $g_0(u)$. For a few small phase errors the far fields of this phase error are shown in Fig. 7. They show clearly the beam tilt, the gain loss, and raising the sidelobes toward the beam tilt. They are known as *coma lobes*, after the corresponding aberration in optics. Also, because this phase error causes more severe pattern degradation than others, it should be eliminated, especially as it manifests mostly in beam scanning. Feed lateral displacements to scan the beam can readily cause coma lobes. Fortunately, a number of lens surface modifications have been found to reduce the effects of this error [3].

5. ZONED LENSES

So far, the equations used for lens designs equalized the ray path lengths. The frequency of operation, or its wavelength, did not enter the equations. Thus, in principle, they should function at all frequencies. However, the directivity of a lens depends on the lens aperture size D , and is often used for high gain applications. This results in large lens sizes in wavelength, and at microwave frequencies, in large physical sizes, both the aperture diameter D and thickness T . It can, therefore, become excessively heavy and difficult to use. Since the thickness of the lens can be several wavelengths, it can be reduced along the ray path in multiple wavelengths without altering the relative phase change. The process starts at the edge, where the thickness is zero. Moving down toward the axis, the thickness increases progressively until it becomes one wavelength. This thickness can be made zero without

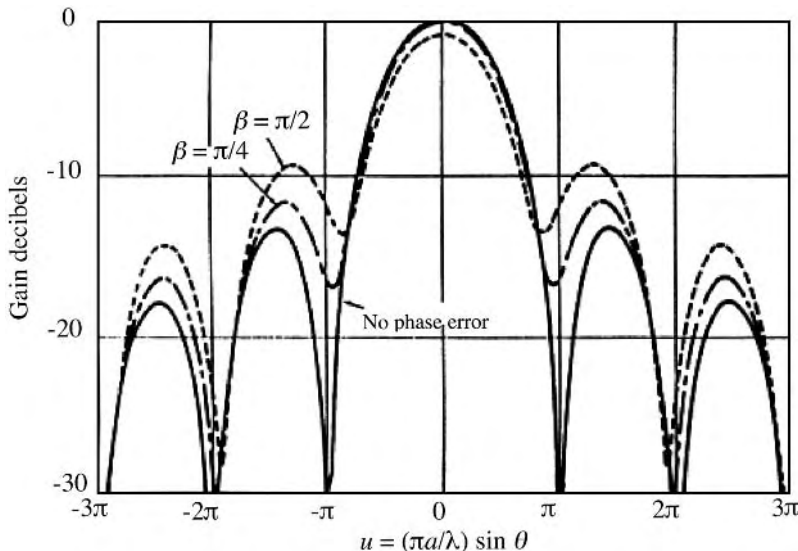


Figure 6. Effect of quadratic phase error on the far-field pattern, reducing the mainbeam and raising the sidelobes.

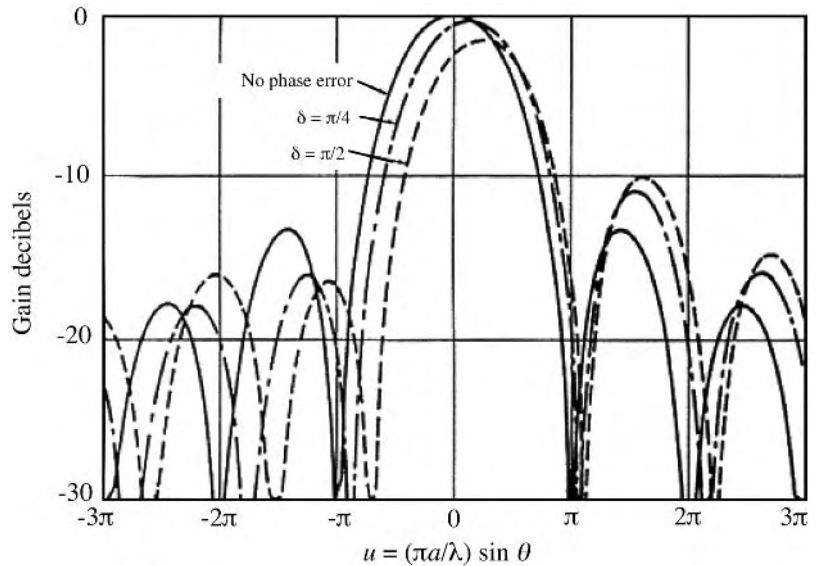


Figure 7. Effect of cubic phase error on the far-field pattern, causing beam tilt and asymmetry in the sidelobes.

altering the phase. The process can be continued K times until one arrives at the lens axis. In practice, one must maintain a small thickness t_m to provide adequate mechanical strength, the value of which will depend on the lens size, the material strength, and the application type.

With zoned lenses, and neglecting t_m , because the thickness does not exceed one electrical wavelength, its thickness is limited to $\lambda/(n-1)$. Including the minimum thickness t_m , the total thickness is limited to $t_m + l/(n-1)$ regardless of the number of zones. The pathlengths in wavelength, however, are not equal. With K zones, the ray path at the edge will be longer by a length equal to $(K-1)\lambda$. This causes the frequency dependence of lens operation, limiting its bandwidths. Enforcing the commonly used Silver criterion for this aperture phase error [1] (i.e. $> 0.125\lambda$), the useful bandwidth of a lens with K zones can be calculated from [1]

$$\text{Bandwidth} \cong \frac{25}{K-1} \text{ percent} \quad (29)$$

Equation (29) is valid for small variations of λ and uniform aperture distributions. For taper distributions, the effect of phase errors is smaller and the actual bandwidth can exceed that of Eq. (29).

Zoning the lens can cause one additional and severe problem due to shadowing. Two adjacent rays from the focus can travel through two separate zones, resulting in a dark ring zone on the aperture. This occurs in the transmit mode, and causes a loss of directivity and increased sidelobe levels. In the receive mode, the energy falling on the shadow zones never reaches the lens focus and diffracts into the space, again causing reduction of gain and increased noise temperature. Figure 8 shows the geometry of a three-zone lens and shadowing due to R_1 and R_2 rays.

Zoning without shadowing is also possible, but should be done on the nonrefracting surface of the lens. In a hyperbolic lens, this should be done on the planar

backsurface. Shadowing will be eliminated, but phase errors still occur at the transition lines due to diffraction effects.

6. REFLECTION FROM LENS SURFACE

Because the wave impedance in air and the dielectric medium of lens are different, reflections occur for all the rays. The reflection coefficient depends on both the wave polarization and the angle of incidence, namely, the angle of ray with the local normal on the lens surface. Neither can be avoided. With a linearly polarized wave, the relative polarization, with respect to the plane of incidence, changes from perpendicular to parallel, as the ray direction rotates on the lens surface. However, their reflection coefficient behaves differently. For perpendicular polarization, it increases progressively with the incidence angle but for parallel polarization, it decreases initially, and after vanishing at the Brewster angle, increases rapidly. Consequently, incidence angles must be kept small, less than 30° , to minimize the polarization effects on the lens aperture distribution.

The surface reflection effects can be reduced, when warranted, by utilizing an impedance-matching layer between the lens and free space. At normal and small angles of incidence, the refractive index of the matching layer can be found using a quarter-wavelength transformer rule. It is the geometric means of the refractive index of the lens dielectric and that of air. In practice, a different dielectric material may be used as the matching layer, or it may be synthesized by preferentially removing a fraction of the dielectric material from the lens surface, such as drilling $\lambda/4$ holes or cutting grooves [4]. However, care must be taken to determine their polarization effects.

The surface reflections also influence the impedance mismatch at its feed. The problem is most severe in cases where the lens surface is coincident with one of the

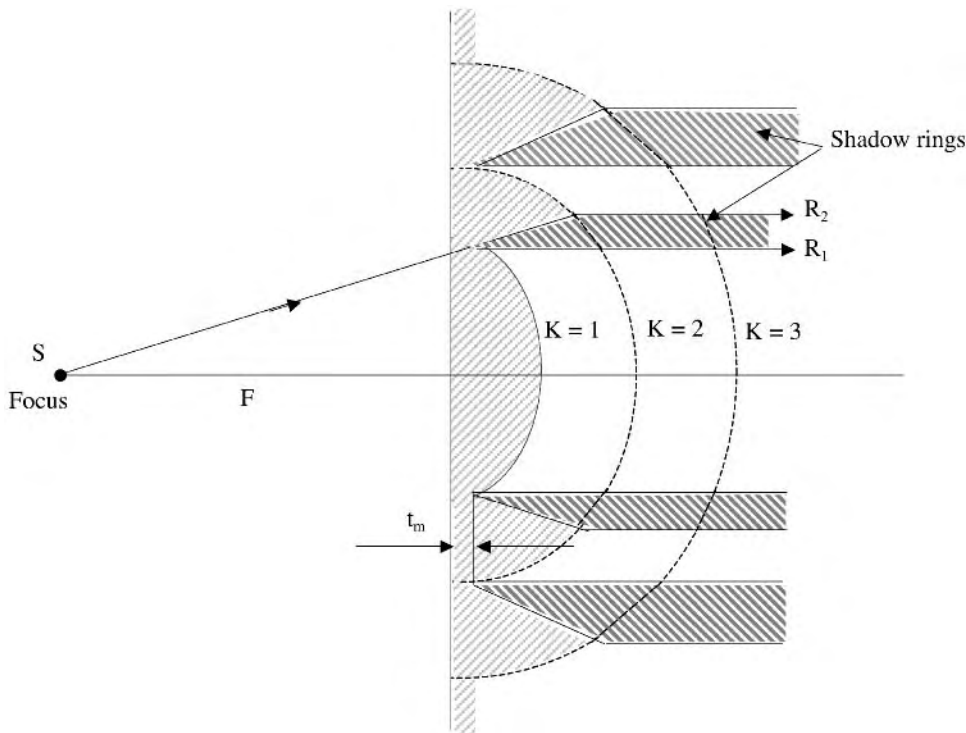


Figure 8. Geometry of a zoned lens with shadowing effects.

equiphase surfaces, namely, the wavefront. Then, the entire reflected wave travels back to the feed, the degree of which depends on the lens refractive index. At normal incidence, since the reflection coefficient is $|R| = (n - 1)/(n + 1)$, the reflected power is unacceptably large for all common dielectrics, and a matching surface should be used. In the event that a matching layer cannot be used, the reflection effects on the feed can be minimized by lateral defocusing of the feed, or retuning of the feed over a narrow bandwidth.

7. LENSES WITH $n < 1$

Lens equations (1) to (6) were developed without specifying the value of the refractive index, and are therefore valid for $n < 1$ cases as well. However, the lens surface becomes inverted. For instance, the hyperbolic lens equation [Eq. (13)] for $n < 1$ modifies to

$$r_1 = \frac{(1 - n)F}{1 - n \cos \theta_1} \quad (30)$$

and the lens surface becomes elliptical, concave toward the focus, similar to Fig. 1b. On the inner region a minimum thickness t is required to provide mechanical strength. Zoning is also possible and will cause shadowing when incorporated on the actively refracting surface. The bandwidth limitations due to n remains the same as the dielectric lenses with $n > 1$. However, the lens media for $n < 1$ such as metal plates and waveguides are usually frequency-sensitive and exhibit narrower bandwidths.

8. CONSTRAINED LENSES

The function of a lens is to modify the phasefront of an incident wave, say, from spherical to planar. In practice, this may be accomplished by means other than the dielectric lenses. In most general cases, the lens surfaces consist of a plurality of receiving and radiating elements, interconnected by processing elements. The received signals on one surface are modified in amplitude and phase and reradiated from the elements of the next surface. In passive designs, the interconnection is due to transmission lines, such as parallel plates, waveguides, and even coaxial lines. The design process is similar to the dielectric lenses and is governed by the pathlength equation. Snell's law, however, is not satisfied at all surfaces, and the problem of surface reflection and transmission must be solved using the wave equation. Nevertheless, lenses can be designed with similar surfaces, but with inverted curvature, as the dielectric lenses [3].

The simplest case uses parallel plates, with spacing a , between 1λ and 0.5λ . When the electric field is parallel to the plates, a non-TEM waveguide mode is excited and has a wavelength λ_p given, in terms of the free-space wavelength λ , by

$$\lambda_p = \frac{\lambda}{\left[1 - \left(\frac{\lambda}{2a}\right)^2\right]^{1/2}} \quad (31)$$

which can be used to define an equivalent refractive index as

$$n = \frac{\lambda}{\lambda_p} = \left[1 - \left(\frac{\lambda}{2a} \right)^2 \right] < 1 \tag{32}$$

In cylindrical lenses, when the plates and electric field are normal to the cylinder axis, Snell’s law of refraction governs the transition between the lens and outside media. But when they are parallel to the cylinder axis, the incident rays are constrained to pass between the plates and Snell’s law is not satisfied [1].

An example of the rotationally symmetric constrained lens is the planar-elliptic surface lens of Eq. (30). It is usually zoned to reduce its size and weight [4]. Other useful transmission media are the rectangular and square waveguides, operating in TE₁₀ or TE₀₁ modes. The waveguide dimensions must be such that only these modes can propagate and higher-order modes are suppressed. The square waveguide can be used for circularly polarized applications, otherwise, must be avoided to reduce cross-polarization.

9. INHOMOGENEOUS LENSES

In the lenses studied so far, the refractive index *n* was constant and the shape was profiled to satisfy the ray path condition. On the other hand, if the lens shape is kept fixed, then another parameter, such as the refractive index, must be allowed to change in order to help in collimating the beam. This is achieved in a family of lenses, the most important ones of which are spherical in shape, such as Luneberg lens, Maxwell’s fish-eye, and Eaton lenses. Their spherical shape provides a perfect three-dimensional symmetry, useful in applications such as the wide-angle scanning. They also have only a radial inhomogeneity, making them both physically and electrically symmetric.

9.1. Luneberg Lenses

The term *Luneberg lens* refers to a family of lenses with two axial foci. They can be both outside the lens or one inside and the other outside. The most useful case, however, is the lens with one focus on its surface, while the second one is at infinity. Thus, an axial point on the lens surface is focused to an axial point at infinity, on the opposite side of the lens. The refractive index of this lens is given by

$$n(r) = \left[2 - \left(\frac{r}{a} \right)^2 \right]^{1/2} \tag{33}$$

where *a* is the lens radius and *r* is the radial distance of a point inside the lens. At the origin, the refractive index is *n*(0) = √2, and on its surface it becomes unity. Both are practically significant. The refractive index values and variations are in reasonable range, and the lens can be synthesized. Moreover, the unity of its refractive index on the surface eliminates the impedance mismatch and, consequently, the surface reflections. The geometry and

ray paths of this lens are shown in Fig. 9, with a feed horn on its surface. Scanning the feed on its surface scans the radiated beam, without alteration. The scan limit is set only by the mechanical limitation of the feed horn motion. With a spherical conducting cap on its surface the lens also acts as a perfect reflector (i.e., a back-scatterer; Fig. 10). The main difficulty with this lens is its fabrication problems. Multilayer shells are normally used to synthesize the refractive index inhomogeneity. Figure 11 shows one case, where 10 layers are used to construct an 18-in. diameter lens. While the approximation to a continuously variable refractive index is reasonable, the wave scattering at the layer transitions reduces the lens efficiency.

With the abovementioned refractive index, the Luneberg lens performance is ideal at the geometric optics limits, when the lens diameter in wavelength is large. At microwave frequencies, the wavelength is large and the lens diameter in wavelength may not be large. Its performance, namely, directivity, and sidelobe levels deteriorate rapidly. In such cases, the refractive index profile can be modified to improve its performance. This can be done by determining the excitation efficiencies of various spherical modes and calculating its far field and directivity [5]. The new dielectric permittivity profile is defined as

$$\epsilon_r = n^2 = 2B - A^2 \left(\frac{r}{a} \right)^2 \tag{34}$$

the constant parameters *A* and *B* are determined to maximize the gain. Three different cases are identified and investigated. Their refractive index profiles are shown

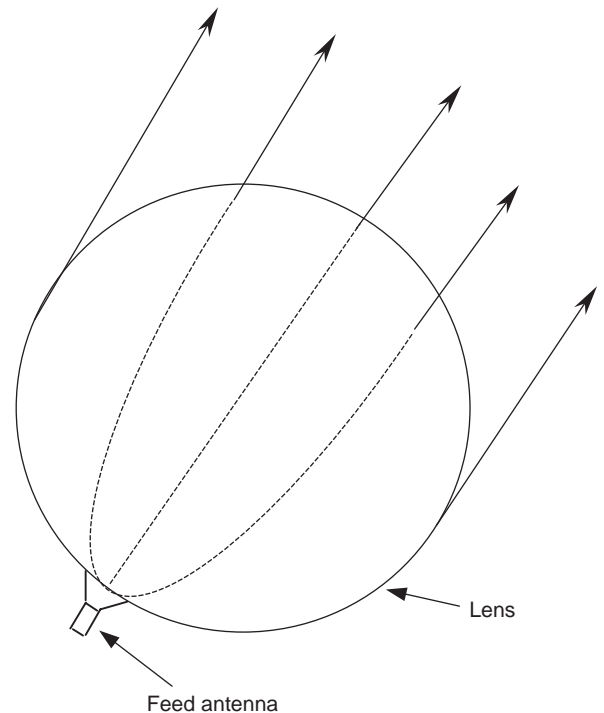


Figure 9. Typical ray paths in a Luneberg lens.

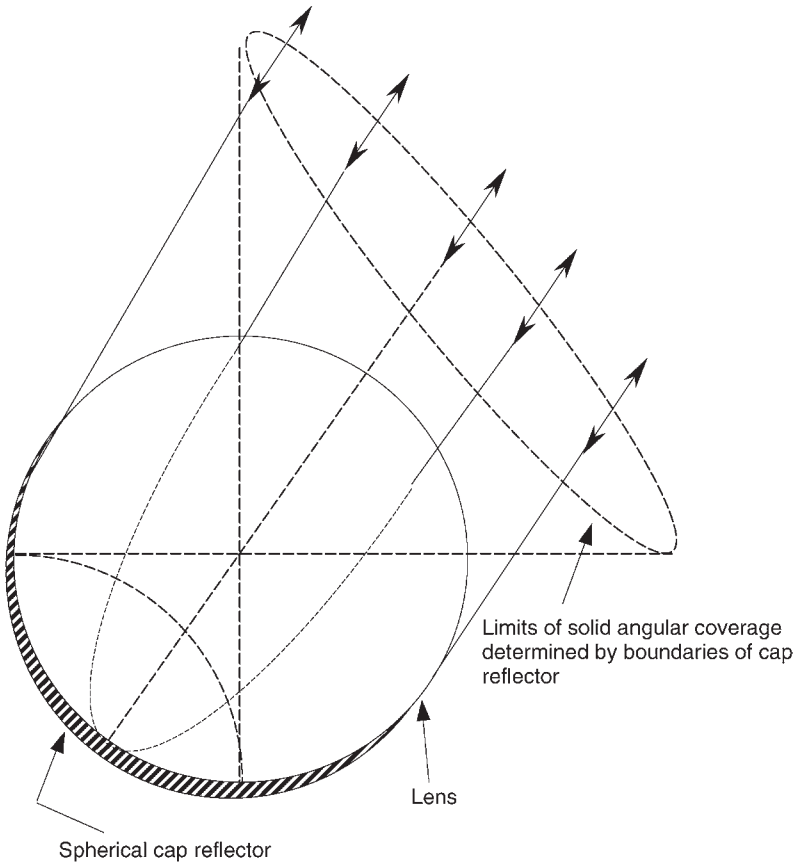


Figure 10. A passive Luneberg lens reflector returning the incident rays.

in Fig. 12. For case (a), $A=B=1$, which is the ordinary Luneberg lens. For profile *b*, $A=1$ and $B>0$, and the dielectric profile is the same as Luneberg lens with a constant increase given by $(2B - 2)$. In Fig. 12 profile *b* is for $B = 1.1$. For profile *c*, $B = 1$ and $A < 1$, which increases the lens permittivity at its surface ($A^2 = 0.95$ in Fig. 12). For profile *d* $A^2 = B$, and the dielectric profile falls between profiles *a* and *b*: ($A^2 = B = 1.1$ in Fig. 12). It gives a lens permittivity close to unity at its surface, which will

improve its impedance match to free surface. Profiles *b* and *c* give larger refractive indexes and are expected to perform better at lower frequencies. This is investigated

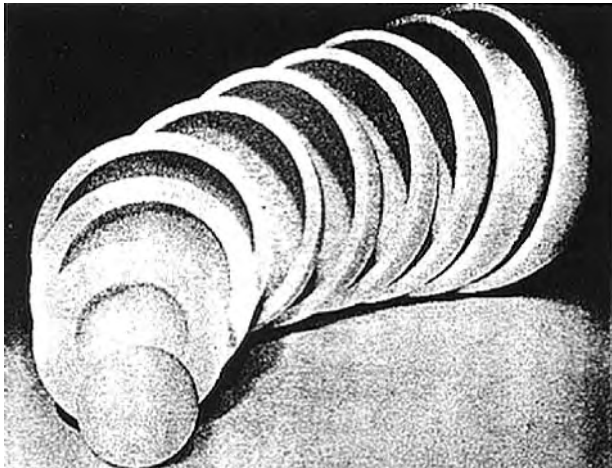


Figure 11. Multilayer spherical shell construction of a Luneberg lens.

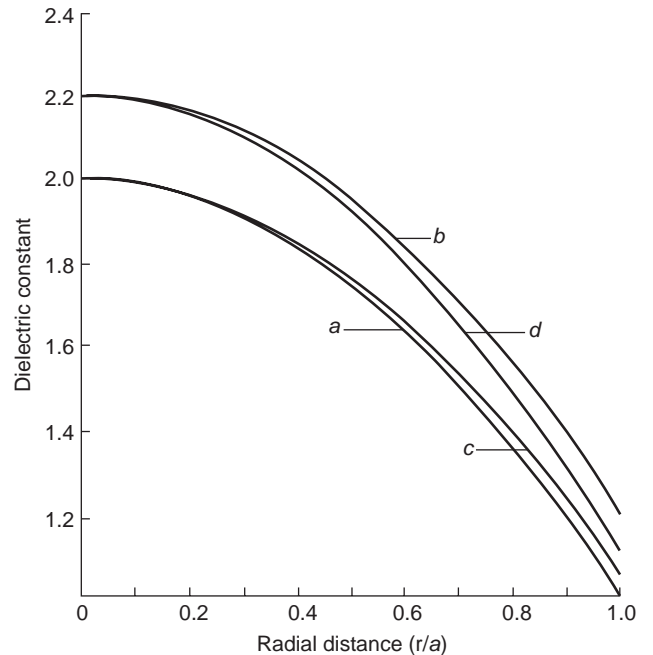


Figure 12. Refractive index of modified Luneberg lenses to improve low-frequency performance.

Table 2. Performance Parameters of Modified Luneberg Lens

Diameter (λ)	Luneberg Lenses				Modified Luneberg Lenses					
	B Value	$A=B=1$			$A=1$		$A^2=B$			
		Gain (dBi)	Beamwidth (deg)	First Sidelobe Level (dBi)	Gain (dB)	Beamwidth (deg)	First Sidelobe Level (dB)	Gain (dBi)	Beamwidth (deg)	First Sidelobe Level (dB)
2	1.4	14.79	30.2	-14.41	17.56	23.5	-17.15	16.85	24.0	14.79
4	1.16	20.761	15.1	-16.05	22.70	13.0	-16.9	22.0	13.25	-16.1
6	1.1	24.34	9.8	-16.9	25.75	9.0	16.97	25.17	9.1	-16.4
8	1.075	26.90	7.3	-17.1	27.98	6.7	-17.01	27.56	7.0	-16.6
10	1.04	28.78	5.8	-16.35	29.35	5.5	-15.97	29.26	5.6	-16.81

using the spherical harmonics, and the results for the directivity, sidelobe levels, and beamwidths are shown in Table 2.

9.2. Constant n Spherical Lens

The difficulty with fabrication of the inhomogeneous lenses encouraged investigators to search for quasi-ideal spherical lenses with constant refractive index. An interesting case is a lens with $\epsilon_r \cong 3$, studied earlier by Bekefi and Farnell [6] and more recently by Mason [7]. With a Huygen source feed at its surface, the computed phase distribution across its aperture, for different relative permittivities, is shown in Fig. 13. For $\epsilon_r \cong 3$, the phase error is below 10° , across about 60% of the aperture. It remains within acceptable range for gain calculated over at least 70% of the aperture, resulting in excellent gain performance over a wide range of frequencies. The only drawback seems to be the excitation of internal modes at their resonance. Their effect reduces with the loss tangent of the dielectric material.

10. DIELECTRIC-LOADED HORNS

Horn antennas are among the most useful and versatile antennas. They have a relatively simple shape and are easy to fabricate and use. They are used as test antennas, feeds for reflector and lens antennas, or independently as communication antennas. Because of their diverse applications, their electrical specifications vary considerably. As test antennas, they are used as gain standards and required to have good polarization isolation in the principal E and H planes. Rectangular horns are commonly used for this application to simplify the polarization definition and gain calculation. As a feed for reflector and lens antennas, the requirements are significantly different. While having a finite aperture size, they must behave as a point source, have small sidelobes and backlobes to minimize power spillovers, and have negligible cross-polarization in the entire radiation zone. To achieve such stringent requirements, their design must be precise and an accurate solution must be known to assess their performance. This is more so with circular horns and consequently have found more widespread applications as feeds than rectangular ones.

Electromagnetic analysis, however, has shown that conventional smooth-walled horns cannot provide radiation patterns with acceptable polarization purity and low spillover. Corrugated horns are developed for these applications, but are costly and narrowband. Dielectric loading of the horn has been shown to improve the performance and in certain applications may be used to replace corrugated ones.

In applications where horn antennas are used as independent communication antennas, gain and aperture efficiency may be the fundamental parameters to optimize. However, to obtain high gain, the horn aperture size must increase, which also increases the aperture phase errors. The phase errors can be maintained low by using small

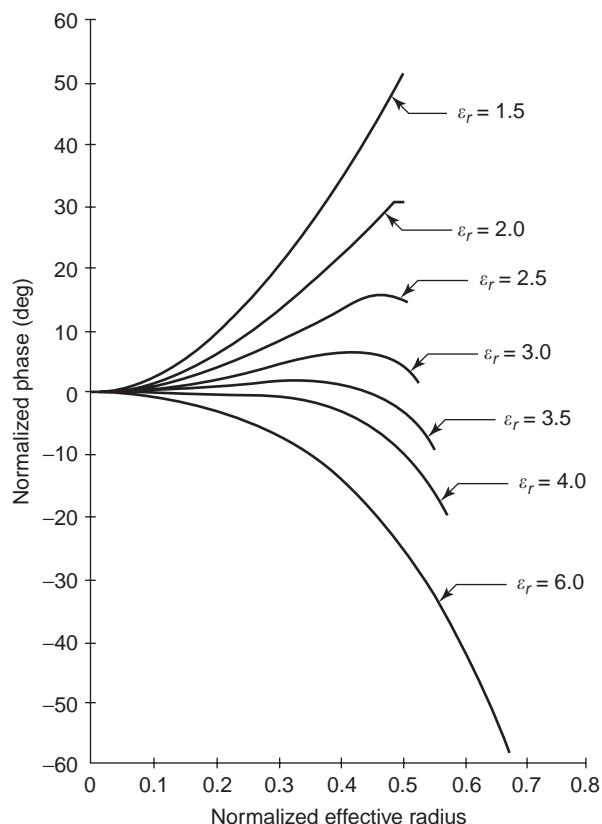


Figure 13. Phase across aperture of a constant n spherical lens.

cone angles, but this increases the horn size. A convenient solution is then to use a lens at the horn aperture to reduce or eliminate the phase errors, by collimating the beam. Consequently, compact high-gain horns can be designed with controlled aperture phase and amplitude distributions, to improve the aperture efficiency and horn gain. Alternatively, lenses can be used to suitably modify the aperture distribution in both amplitude and phase to shape the radiation patterns.

In this section, initially the dielectric-loaded and lens-corrected horns will be discussed. Then, the use of dielectric in small antennas such as waveguides, microstrip antennas, and dipoles, will be considered, to improve their operation in specific applications.

10.1. Dielectric Loading

Historically, dielectric-cone loading inside smooth-walled conical horns was used by Clarricoats et al. [8], and Lier [9] to simulate the effect of corrugations. Corrugated horns, with quarter-wavelength corrugation depths, can support hybrid HE₁₁ mode. This mode radiates with low cross-polarization and can be designed to have negligible sidelobes. Introduction of the cone dielectric, with an airgap as shown in Fig. 14 inside a smooth-walled horn, was also shown to support hybrid modes and improve the performance. Clarricoats et al. [8] used low-dielectric-constant materials, such as foams with a relative permittivity of 1.13. But, in Lier’s work [9], solid-dielectric cones with a relative permittivity of 2.5 was used, again showing good performance. Both groups of investigators also analyzed these dielectric-loaded horns using modal expansions, and studied the effects of the airgap, horn permittivity, aperture diameter, flare angle, and the throat region. Airgap size was found to be strongly dependent

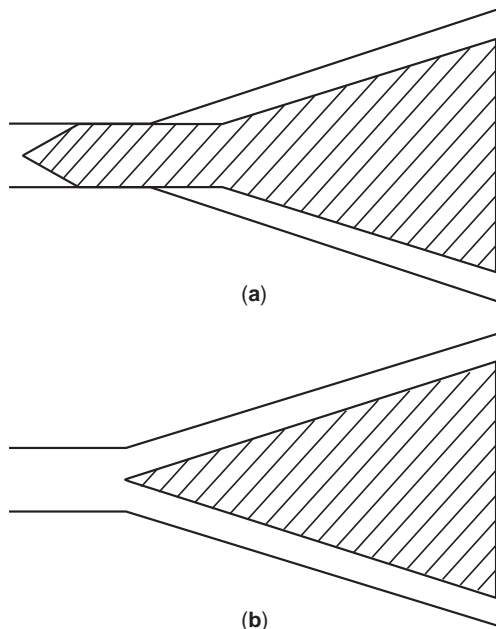


Figure 14. Geometry of a dielectric-loaded horn showing two possible dielectric insertions.

on the aperture diameter, and both are dependent on the dielectric permittivity. The airgap size generally increases with the horn diameter, and for a given diameter there is a minimum relative permittivity of dielectric to support the hybrid mode to minimize the cross-polarization. Both flare angle and the throat region have similar influences. Large flare angles, and asymmetric throat region design, excite higher-order modes and thus increase cross-polarization.

A variation of the conical dielectric-loaded horn is shown in Fig. 15. Its wall is profiled. A large flare angle near its throat reduces its axial length and results in a compact horn. Then, its small flare angle near the aperture improves the cross-polarization. The profile is described by the following equation

$$r(z) = r_{th} + 3\Delta r \left(1 - \frac{2z}{3L}\right) \left(\frac{z}{L}\right)^2 \tag{35}$$

$$\Delta r = r_{ap} - r_{th}$$

where r_{ap} and r_{th} are the horn radii at the antenna’s aperture and throat. A profile horn of this type was designed and optimized. Its performance is compared with the linear horn in Table 3. Its cross-polarization is improved by 4 dB. The effect of length reduction on the performance of the abovementioned profile horn is also shown in Table 4. It shows that the performance remains steady and comparable to a linear horn for length reductions by as much as 22%.

10.2. Lens-Corrected Horns

In high-gain horns, the aperture diameter in wavelength is large, and the horn length can be excessive, unless its flare angle is made large. But the combination of large aperture size and large flare angle can cause severe

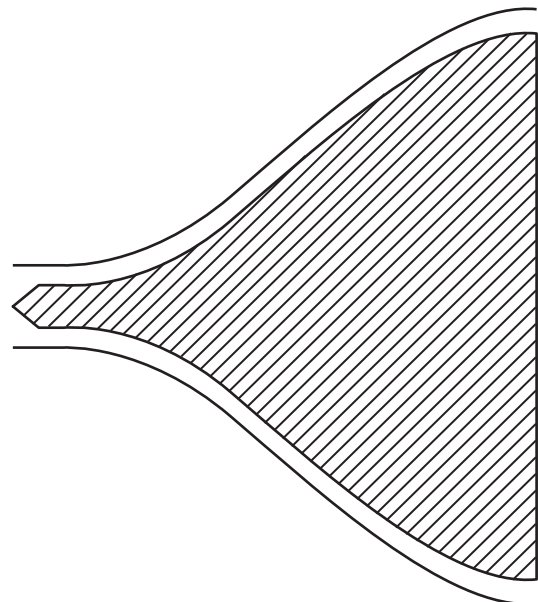


Figure 15. Geometry of a dielectric-loaded profile horn.

Table 3. Performance^a of Dielectric Loaded Linear and Profiled Horns

Parameter	Linear Horn	Profiled Horn
3 dB beamwidth (deg)	14.8	13.7
10 dB beamwidth (deg)	26.9	24.8
Directivity (dBi)	22.1	22.5
Efficiency (%)	61.8	68.1
Peak cross polar (dB)	-32.2	-36.0
VSWR	1.04	1.03

^aWhere $R_{th} = 1.14$ cm, $r_{up} = 27.7$ cm, $L = 30.9$ cm, $\epsilon_r = 1.13$, airgap = 1.2 cm.

aperture phase error. This problem can be remedied by using a lens at the horn aperture. Figure 16 shows three possible options. These simple lenses and others, including zoned lenses, may be used, and would correct the horn aperture phase distributions. But each lens will have different influences on the aperture amplitude distribution. The properties of the first two lenses were investigated earlier, and Table 1 showed their effect on the amplitude distribution. Type (a) (in Fig. 16) increases the amplitude taper according to Eq. (21) and will reduce both sidelobes and the aperture efficiency. Type (b) will compensate for the amplitude taper, and according to Eq. (22), the lens permittivity can be used to control the aperture distribution, and thus the horn efficiency and the pattern sidelobes. For type (c), an analytic expression is not available and a numerical procedure must be used. However, as was indicated earlier with respect to this lens, both surfaces help in collimating the beam, but its second surface is similar to type (b) lens and its influence on the aperture distribution will be similar as well. With a hybrid-mode horn, corrugated or dielectric-loaded, the resulting aperture distributions for different lens relative permittivities are shown in Fig. 17, which shows that for ϵ_r around 1.22, the aperture amplitude distribution is nearly uniform.

11. DIELECTRIC-LOADED WAVEGUIDES

Waveguides have small aperture size and are not as efficient radiators as horns. Part of the energy leaks out and induces current on the outside wall, which radiates laterally and backward, causing large backlobes. The wave impedances of waveguide modes are also different from the free-space intrinsic impedance, and strong reflections can occur on the aperture, causing poor input impedance match. These problems can be partly overcome by

Table 4. Performance of Profile Horn with Length Reduction

Length (cm)	Peak Cross-Polarization (dB)	3 dB Beamwidth (deg)	Efficiency (%)
30.9	-36.0	13.7	68.1
27.5	-36.8	13.8	64.4
24.0	-31.6	14.0	57.1
15.0	-27.6	16.1	32.0

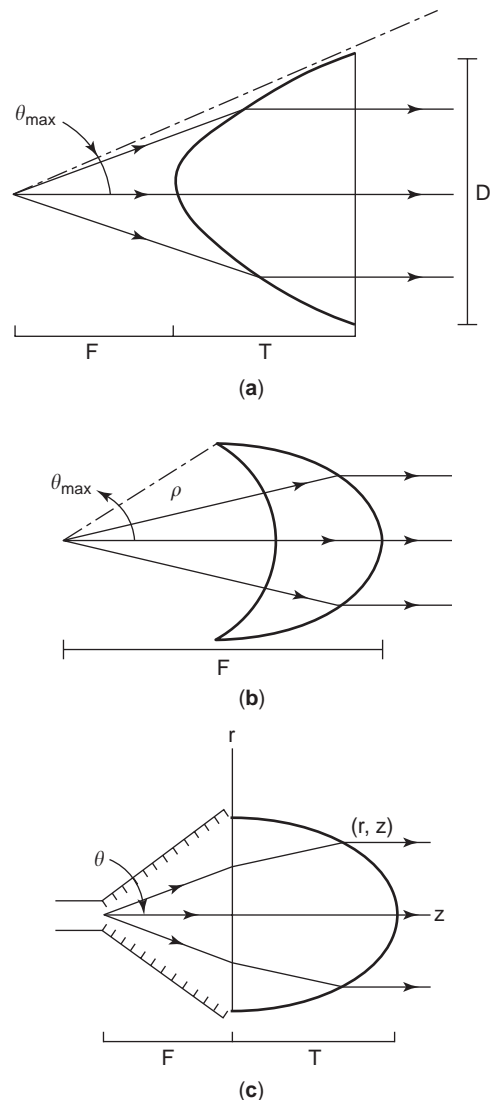


Figure 16. Three examples of lens types for loading horn aperture.

flaring the waveguide at its aperture. However, similar and even better performance can be obtained by loading the waveguide by a short section of a dielectric. The size and shape of the dielectric constant provide several parameters that can be used to shape the radiation patterns and tailor them to the desired specifications. Table 5 shows the results for three different end loadings, and the type of performance variations one could achieve [2]. Two other examples are shown in Figs. 18 and 19, with combinations of dielectric and cavity loadings [2]. In Fig. 18, the end geometry is optimized for nearly perfect pattern symmetry, with negligible cross-polarization. Figure 20 shows its copolar and cross-polar radiation patterns. In Fig. 19, the combination was again optimized for a heavily shaped radiation pattern, again with negligible cross-polarization in the forward direction. It is an ideal feed for deep parabolic reflectors with small $f/D = 0.25$. It provides high aperture efficiency of 81% due to its front pattern null, very low cross-polarization, and extremely

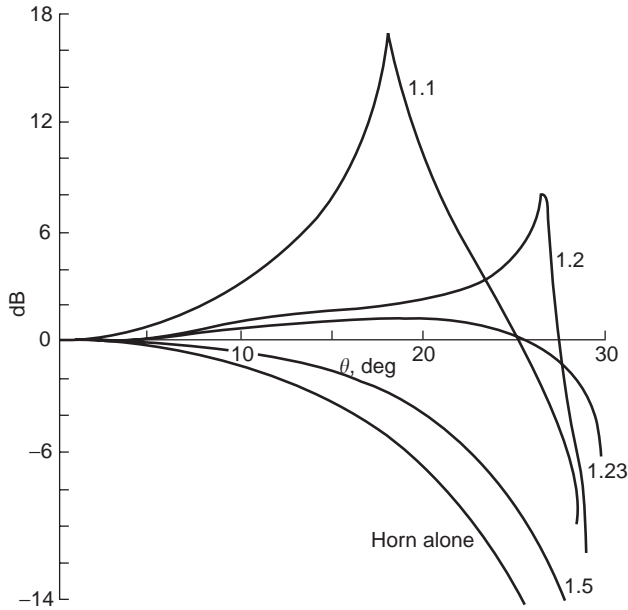


Figure 17. Aperture amplitude distribution for a lens corrected horn 30° semiflare angle hybrid-mode horn, type *c* lens.

low noise temperatures due to small f/D , the focal length : diameter ratio.

12. MICROSTRIP AND DIELECTRIC RESONATORS

Microstrip antennas are discussed in a separate article (see MICROSTRIP ANTENNAS), and usually consist of a conducting patch separated from a ground plane by a dielectric substrate. They are low-profile and increasingly popular antennas for practically any type of application. Their radiation patterns, however, are asymmetric with unequal *E*- and *H*-plane patterns. But, with careful optimization, the pattern symmetry can be achieved to

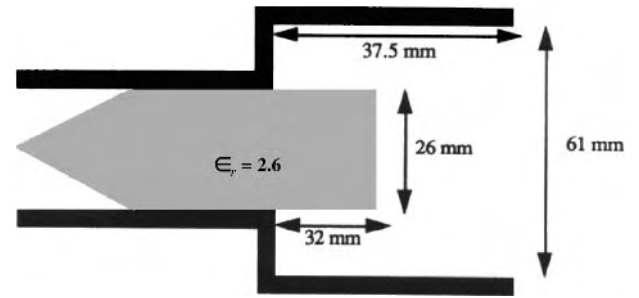


Figure 18. Geometry of a dielectric cavity-loaded waveguide feed.

minimize cross-polarization. Figure 21 shows a case of stacked patches with a side choke for equalizing the principal-plane pattern, low backradiation, and cross-polarization. Similar performance can also be obtained using a dielectric resonator in lieu of a microstrip patch. The dimensions of the dielectric resonator are related to the wavelength by

$$d = \frac{1.841\lambda}{4n\pi} \left[16 + \left(\frac{\pi d}{1.841h} \right)^2 \right]^{1/2} \tag{36}$$

The excited mode is the TM_{110} mode, and produces radiation similar to that of a microstrip patch. In Fig. 22, the resonator and the cavity are optimized for symmetric pattern in the principal planes to reduce the cross-polarization. They are shown in Fig. 23, with excellent symmetry. Both the microstrip and resonator antennas can be used as efficient reflectors and lens feeds with high aperture efficiency and low cross-polarization.

13. INSULATED ANTENNAS

Practically all antennas have conducting parts, but in certain families of antennas, especially small resonant

Table 5. Performance of Dielectric-Loaded Waveguide with Shaped Dielectrics

Geometry	Peak Cross-Polarization $0 \leq \theta \leq 90^\circ$ (dB)	Gain (dBi)	Half-Beamwidths			
			3 dB		10 dB	
			<i>E</i> plane	<i>H</i> plane	<i>E</i> plane	<i>H</i> plane
a	-33.95	8.28	36.82	36.18	71.47	72.51
b	-24.74	8.11	37.21	38.32	73.42	71.35
c	-24.43	13.47	19.43	20.25	33.13	35.17

$d = 0.6\lambda, \epsilon_r = 2.5$

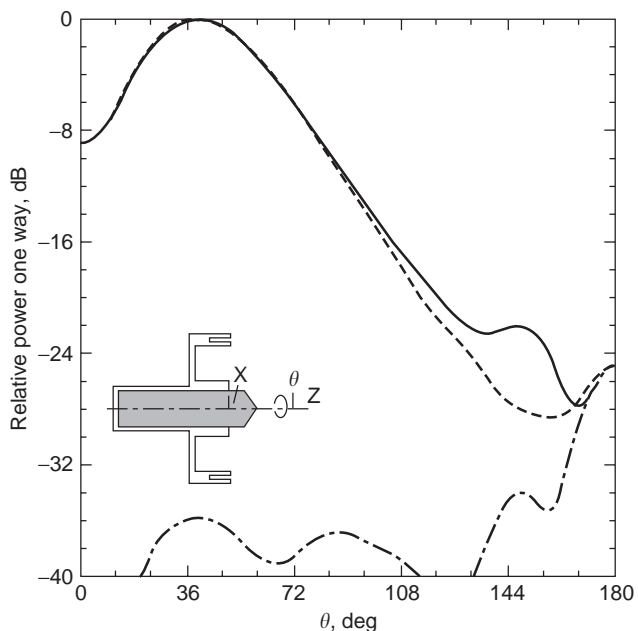


Figure 19. Geometry and radiation pattern of a shaped dielectric and cavity loaded waveguide feed.

ones, the conduction current radiates directly. Typical examples are the wire antennas and microstrip antennas that are often half-wavelength resonators. In wire antennas, the current is excited by the applied voltage directly on the wire, which radiates in the surrounding space. In microstrip antennas, the currents are both on the patch and its ground plane, which are separated by a dielectric substrate. For this reason, only the patch current is

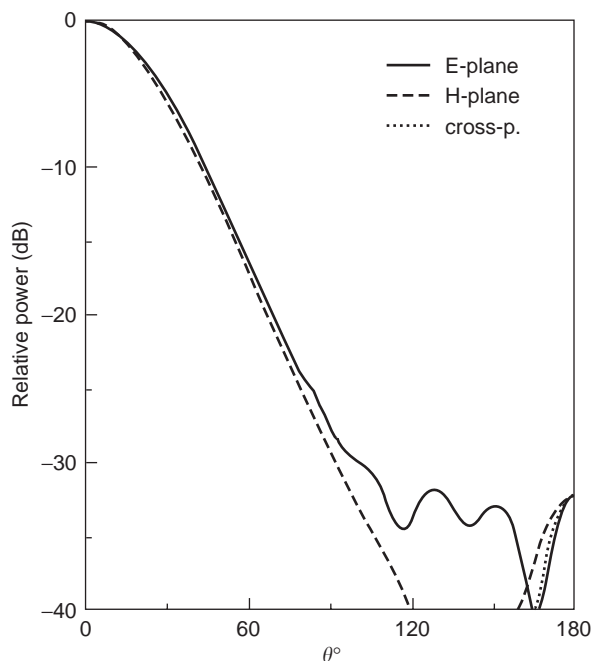


Figure 20. Radiation patterns of the waveguide feed of Fig. 18, showing perfect pattern symmetry and near negligible cross-polarization.

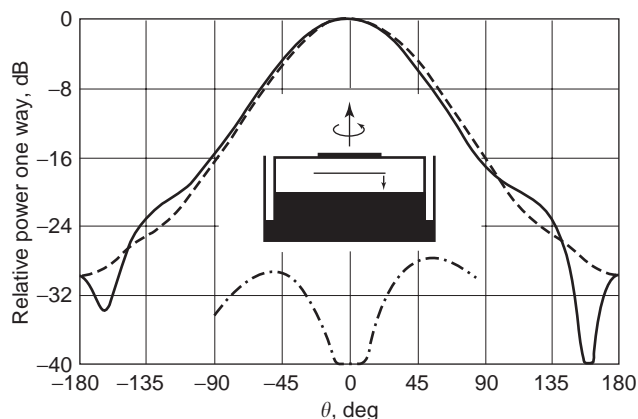


Figure 21. Geometry and radiation patterns of a stacked microstrip feed, with peripheral choke to minimize back radiation.

exposed to the surrounding medium. However, in either case, the physical constants of the medium are excessively lossy, and can short-circuit the antenna current and prevent its operation. In practice, this problem can occur in remote sensing and biological applications. In the former case, the antennas may be buried underground, or submerged in sea and ocean waters that have high electrical conductivities. In the latter case, the antennas are implanted into various types of body tissues that can have excessively high conductivities. In such cases, to ensure antenna operation, the conduction currents must be insulated from the surrounding conducting medium. A simple but effective method is to use a thin dielectric coating on the antenna conductor carrying the radiating currents. The coating will provide insulation between the

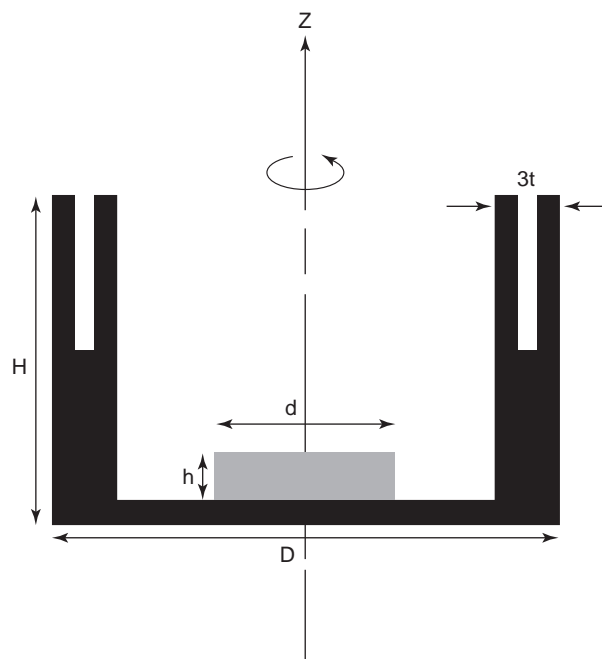


Figure 22. Geometry of a dielectric resonator antenna, showing a conducting cavity of height H and diameter D , with a dielectric disk of height h and diameter d .

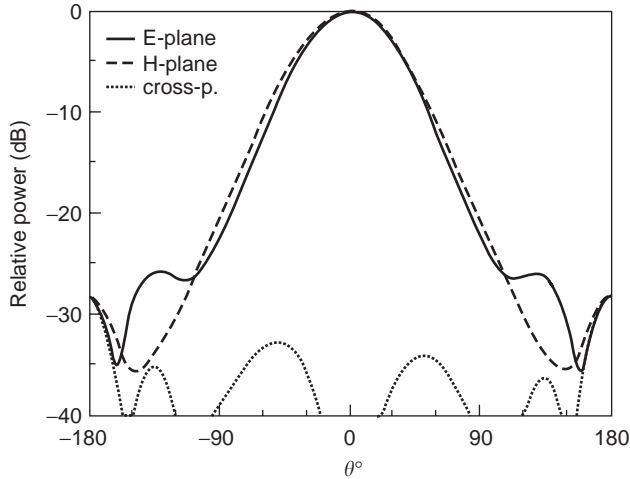


Figure 23. Radiation patterns of the dielectric resonator antenna.

conducting antenna and the medium, thereby eliminating the conduction current. The excitation energy will then transfer into the pointing vector, leaving the antenna.

The behavior of the insulated antennas in a medium of complex permittivity differs considerably from that in free space, and should be analyzed carefully. For instance, consider a conventional dipole of length $2h$, as shown in Fig. 24. The wire is a good conductor and has a diameter of

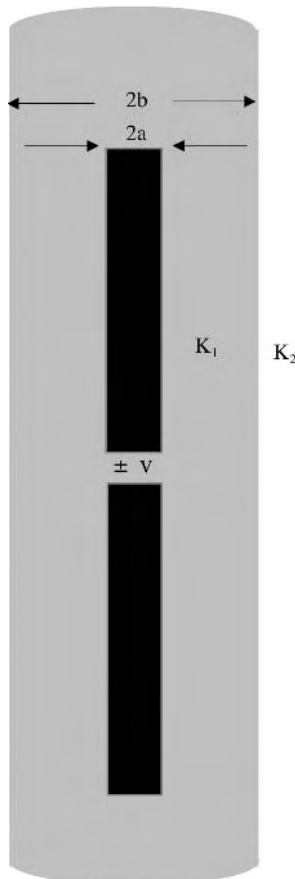


Figure 24. Geometry of an insulated dipole antenna.

$2a$, insulated by a cylindrical dielectric region of diameter $2b$ and propagation constant k_1 , located in an infinite exterior region of k_2 . With a thin-wire approximation, the dipole current can be represented by a sinusoidal distribution of the form described in Ref. 10. The time factor is assumed to be $\exp(j\omega t)$

$$I(z) = \frac{-jV \sin k_L(h - |z|)}{2Z_{ca} \cos k_L h} \quad (37)$$

where

$$k_L = k_1 \left[1 + \frac{H_0^{(2)}(k_2 b)}{k_2 b H_1^{(2)}(k_2 b) \ln \frac{b}{a}} \right]^{1/2} \quad (38)$$

$$Z_{ca} = \frac{\varsigma_1 k_L}{2\pi k_1} \ln \left(\frac{b}{a} \right) \quad (39)$$

$$\varsigma_1 = \frac{\omega \mu_0}{k_1} \quad (40)$$

$$k_1 = \omega [\mu_1 \epsilon_1]^{1/2} \quad (41)$$

and $H_0^{(2)}$ and $H_1^{(2)}$ are Hankel functions of zero and first order. Note that with a perfect insulation dielectric k_1 is real but k_2 is complex due to the presence of Hankel functions in Eq. (38). It reduces to k_1 when b , the radius of the insulation, becomes infinitely large. In view of Eq. (38), the dipole current distribution, input impedance, as well as the radiation resistance, and the resonance frequency can depend strongly on the radius b and propagation constant k_1 , and k_2 , the propagation constant of the exterior region. The latter may not be fully known, or constant, during the application because of variations in moisture content and other variables. Thus, the insulation parameters should be selected appropriately to minimize the dependence of k_1 on k_2 .

14. MEDICAL AND BIOLOGICAL ANTENNAS

Another area in which insulated antennas play an important role is the biological and medical applications. They can be noninvasive (i.e., not penetrating the body) or invasive. In either case, the properties of insulated antennas can be significantly different from those in free space. Thus, care must be taken in their design and analysis to ensure adequate power transfer to the right tissue. Non-invasive radiators are often dielectric-loaded waveguides and horns, discussed in the previous section. The dielectric loading in this case is used to improve impedance matching and coupling to the body. Their design is not significantly different from those of other dielectric-loaded waveguides, except that the end shaping must prevent hotspots and improve penetration.

Microstrip antennas and arrays are other types of radiators suitable for noninvasive applications. However, their resonance property and power coupling to the body can be sensitive to the extent and nature of contact to the

skin. Dielectric coating over the radiating patch or slot can insulate the antenna and minimize the body's influence. This is due to the fact that, in microstrip antennas, the resonance depends on the effective dielectric constant, and not the actual substrate permittivity. With single-layer substrates of thickness h , this effective permittivity, for a conductor linewidth of W , is given by

$$\epsilon_{\text{eff}} = \frac{\epsilon_r + 1}{2} + \left(\frac{\epsilon_r - 1}{2}\right) \left(1 + \frac{12h}{w}\right)^{-1/2} \quad (42)$$

However, it can change significantly by introducing a higher permittivity layer over the substrate. Consequently, in biological applications, where the tissue relative permittivity can be excessively high due to the water content having $\epsilon_r \cong 80$, the nature of the proximity or contact with the body can alter ϵ_{eff} significantly [11]. Since microstrip antennas are narrowband, or at best not wide-band, the efficiency of their radiation and coupling to the body can be deteriorated. The effect can be reduced by introducing a superstrate layer over the microstrip antenna, to control the relative permittivity variations.

Invasive-type radiators can produce more uniform and controllable heating patterns, but they require implantation in the tissue. The most convenient types are the insulated needle radiator, basically the end of the coaxial line. However, this type of antenna can generate strong currents on the outer coaxial conductor and cause tissue heating behind the antenna. An improvement can be obtained by introduction of a quarter-wavelength choke over the coaxial conductor to form a sleeve antenna. Their analysis and sensitivity study can be carried out similar to the insulated dipole antennas. Figure 25 shows the geometry of needle and sleeve antennas.

15. NRD WAVEGUIDE ANTENNAS

A nonradiative dielectric (NRD) waveguide, shown in Fig. 26, consists of a dielectric slab sandwiched between two parallel conducting plates. It is known to have low resistive losses at high frequencies and useful structure for

design of low-loss circuit components, such as couplers, filters, and even amplifiers [12]. If an antenna can be designed using an NRD guide, it will be low-loss, and can be integrated with other NRD components. The resulting system of circuit-antenna combination will therefore be compact and provide high operating efficiency, useful in many high-frequency applications. However, in an NRD the field propagates within the dielectric slab and is cut off between the parallel plates outside the dielectric, where it attenuates exponentially. To cause radiation, therefore, one must expose its guided field to the external region. This can be accomplished in three different ways: (1) by cutting a slot on one of the conductors over the dielectric slab, (2) by terminating the parallel plates a short distance from the dielectric slab, and (3) by terminating the dielectric slab in free space.

In the first antenna type, cutting an aperture or slot on one of the conducting plates over the dielectric disturbs its guided field and causes the radiation [12,13]. However, the slot also causes discontinuities in the NRD guide that excites the dominant parallel-plate mode, which is not low-loss. In the second antenna type, the attenuating field between parallel plates leaks outside and radiates like a leaky-wave antenna [14,15]. This is a continuous radiation along the guide, and its radiation beam squints with frequency. The third antenna type radiates from the open end of the guide, and provided its termination geometry does not differ from that of the guide's cross section, it does not generate other modes [16]. It is therefore a well-behaved antenna and its radiation is due primarily to the guided mode of the dielectric. Its operation is discussed below.

Figure 26 shows the cross-sectional and end views of a conventional NRD guide [12]. The principal transverse field distributions are shown in Fig. 27, and in region I, which is the dielectric region, these fields are given by

$$E_{y1} = \frac{(K^2 \epsilon_r - \beta_y^2)}{j\omega\mu_0\epsilon_0\epsilon_r} \cos \frac{\pi x}{a} \cos(\beta_y y) e^{-j\beta_g z} \quad (43)$$

$$H_{x2} = \frac{j\beta_g}{\mu_0} \cos \frac{\pi x}{a} \cos(\beta_y y) e^{-j\beta_g z} \quad (44)$$

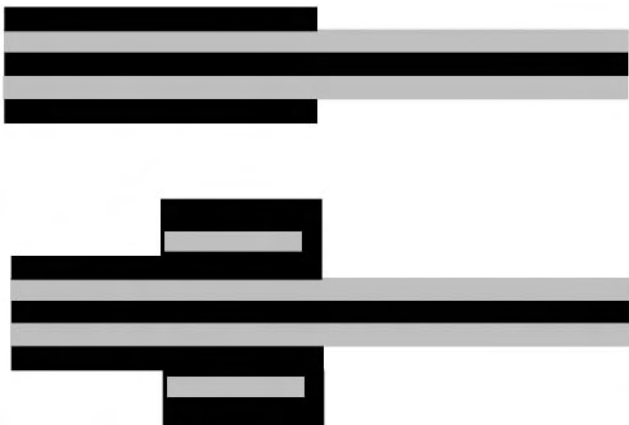


Figure 25. Implantable radiator types: (a) needle radiator; (b) sleeve antenna.

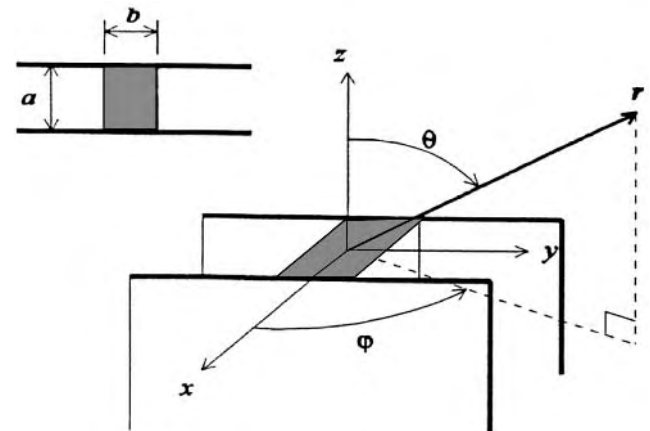


Figure 26. Geometry of NRD guide.

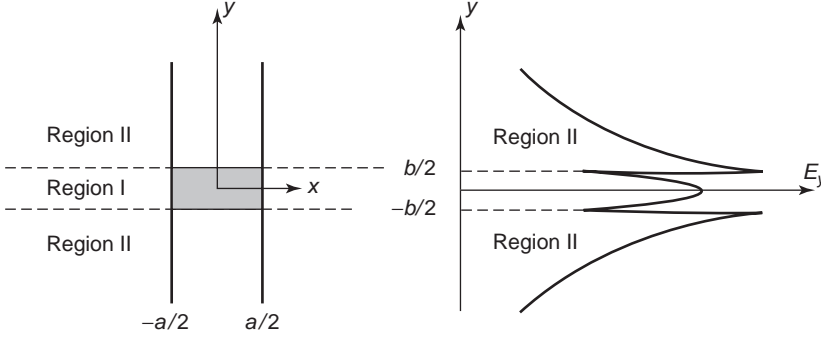


Figure 27. Fields in dielectric and air regions of NRD guide.

Between the parallel plates, in region II, the corresponding fields are

$$E_{y_2} = \cos\left(\frac{\beta_y b}{2}\right) \frac{(k^2 + \alpha_y^2)}{j\omega\mu_0\epsilon_0} \cos\left(\frac{\pi x}{a}\right) e^{-\alpha_y(|y|-b/2)} e^{-j\beta_g z} \quad (45)$$

$$H_{x_2} = j\cos\left(\frac{\beta_y b}{2}\right) \frac{\beta_g}{\mu_0} \cos\left(\frac{\pi x}{a}\right) e^{-\alpha_y(|y|-b/2)} e^{-j\beta_g z} \quad (46)$$

The guided field parameters in these equations are computed from the following transcendental equations:

$$\beta_g^2 = k_0^2 \epsilon_r - (\pi a)^2 - \beta_y^2 \quad (47)$$

$$= k_0^2 \epsilon_r - (\pi a)^2 + \alpha_y^2 \quad (48)$$

$$\beta_y \tan \frac{1}{2} \beta_y b = \epsilon_r \alpha_y \quad (49)$$

$$k^2 - \beta_y^2 = k_0^2 + \alpha_y^2 \quad (50)$$

Equations (43) to (46) can be used to define the equivalent electric and magnetic currents on the truncated aperture of Fig. 26, which can then be used to determine the radiation integrals [17]. The resulting far radiated fields in the principal planes are

$$\begin{aligned} E_{\theta(\phi=\pi/2)} &= E_{\theta}^0 [1 + \zeta_1 \cos \theta + \Gamma(1 - \zeta_1 \cos \theta)] \\ &\times \frac{b}{2} \left\{ \frac{\sin(b/2k \sin \theta + \beta_y b/2)}{b/2k \sin \theta + \beta_y b/2} \right. \\ &+ \left. \frac{\sin(b/2k \sin \theta - \beta_y b/2)}{b/2k \sin \theta - \beta_y b/2} \right\} \\ &+ E_{\theta}^0 [1 + \zeta_2 \cos \theta \\ &+ \Gamma(1 - \zeta_2 \cos \theta)] \left\{ \frac{2\epsilon_r \cos(\beta_y b/2)}{\alpha_y^2 + k^2 \sin^2 \theta} \right\} \\ &\times \left\{ \alpha_y \cos\left(\frac{b}{2k \sin \theta}\right) - k \sin \theta \sin\left(\frac{b}{2k \sin \theta}\right) \right\} \end{aligned} \quad (51)$$

$$\begin{aligned} E_{\phi(\phi=\pi/2)} &= E_{\phi}^0 \left\{ [\cos \theta + \zeta_1 + \Gamma(\cos \theta - \zeta_1)] \frac{1}{\beta_y} \sin\left(\frac{\beta_y b}{2}\right) \right. \\ &+ \left. [\cos \theta + \zeta_2 + \Gamma(\cos \theta - \zeta_2)] \frac{2\epsilon_r}{\alpha_y} \cos\left(\frac{\beta_y b}{2}\right) \right\} \\ &\times \left\{ \frac{\cos(ka/2 \sin \theta)}{(ka/2 \sin \theta)^2 - (\pi/2)^2} \right\} \end{aligned} \quad (52)$$

with

$$Z_{g1} = \frac{(k^2 \epsilon_r - \beta_y^2)}{k \epsilon_r \beta_g} \eta = \frac{\eta}{\zeta_1} \quad (53)$$

$$Z_{g2} = \frac{(k^2 + \alpha_y^2)}{k \beta_g} \eta = \frac{\eta}{\zeta_2} \quad (54)$$

where η is the free-space impedance. The parameter Γ is the reflection coefficient of the NRD guide radiating aperture, calculated using its wave impedance in Eqs. (53) and (54) and the free-space impedance.

An example of the radiation patterns is shown in Fig. 28. The dielectric region dimensions are 15×10.16 mm, and the relative permittivity is 2.55. At 9.5 GHz the impedance of the open-ended NRD guide is $z = 0.5940 + j0.5520$, which gives a reflection coefficient of $\Gamma = -0.1203 + j0.3380$. Other propagation parameters are shown in Table 6 [16]. Figure 28 shows an excellent agreement between the computed and measured radiation patterns, indicating that the single-mode operation of the NRD guide for this antenna type is a good assumption. The radiation patterns are also well defined and have a beam peak in the forward direction. The antenna is therefore a suitable candidate for single-element use or high-gain array applications.

16. ANTENNA MINIATURIZATION

Antenna miniaturization is an important issue in certain communication and mobile applications. Dielectric loading can be a useful tool for such applications, because for natural dielectrics the relative permittivity of the material is larger than unity. The velocity of electromagnetic waves

Table 6. Propagation Constants of NRD Guide

k_0	198.97
α_y	138.40
β_y	205.44
β_z	121.98

and their wavelengths within the dielectric medium, therefore, reduce by the square root of the relative permittivity. Since the waveguide and antenna dimensions are in terms of the wavelengths, they also become smaller inside dielectrics. Thus, the phenomenon can be used effectively for reducing the dimensions of the antennas. In certain applications, such as microstrip antennas, this is common knowledge, and for the case of dielectric resonators, it was discussed in Section 12. For other applications the case must be handled accordingly. An important issue is realization of the fact that the normal wavelength reduction by the square root of the relative permittivity occurs only inside infinite dielectric regions. In other cases, the effect is less and consequently an effective dielectric constant ϵ_{eff} is normally defined. For microstrip substrates this has been determined analytically, and was provided in Eq. (42). In most cases, however, the problem must be solved numerically. Here the case of a dielectric-coated monopole is discussed. Monopoles have a simple geometry and are important antenna candidates, but must be installed vertically, making them a tall structure. A reduction of their length can be very desirable in many applications.

Figure 29 shows the geometry of a dielectric coated monopole [18]. The dielectric material is a cylindrical ceramics of relative permittivity of $\epsilon_r = 38$, covering a conducting tube of diameter d_{in} and height 6.4 mm. The configuration is placed over an infinite ground plane and solved numerically using a finite-element method to determine its resonant frequency, impedance, return loss, and the bandwidth. The computed results are compared with measurements in Fig. 30 for the resonant frequency, and in Fig. 31 for the return loss.

Aside from a small frequency shift, the agreement is good. Figure 30 shows that, as the coating thickness

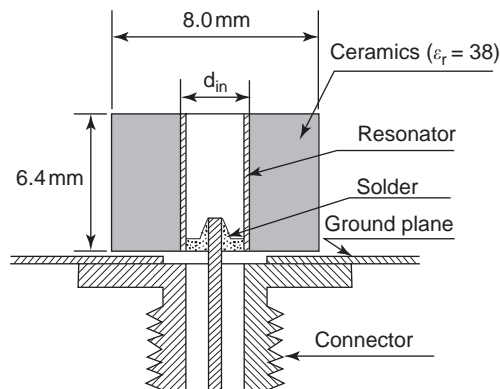


Figure 29. A cross section of the dielectric-coated antenna.

increases, the effect of the dielectric increases. This is manifested in the form of reduced resonant frequency as the monopole diameter is decreased, while keeping the coating diameter constant. In the limit of smallest monopole diameter, the resonant frequency is about 4.7 GHz, a reduction of about 2.4, as compared to its resonant frequency in free space. The effective permittivity is therefore about 5.8, which is much smaller than 38, the actual relative permittivity of the dielectric material. For larger effective permittivity values, one must either increase the dielectric thickness or increase its length beyond the monopole end. Since both of these solutions result in an increased size of the overall structure, a compromise must be made in any practical application.

17. GAIN ENHANCEMENT

Dielectric loading, when used judiciously, can be an effective means for increasing the gain of an antenna. The focusing effect of dielectric lenses was discussed in Section 2. This section addresses the case of planar dielectric loading. Lenses are not desirable solutions in some applications because of the high cost of fabrication or manufacturing tolerances at millimeter-wave frequencies. Simple planar dielectric layers are more desirable to

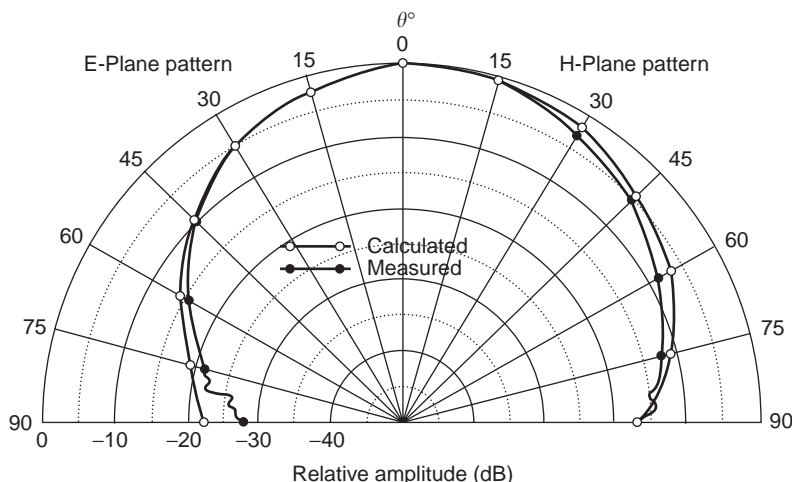


Figure 28. Measured and calculated radiation patterns of NRD guide.

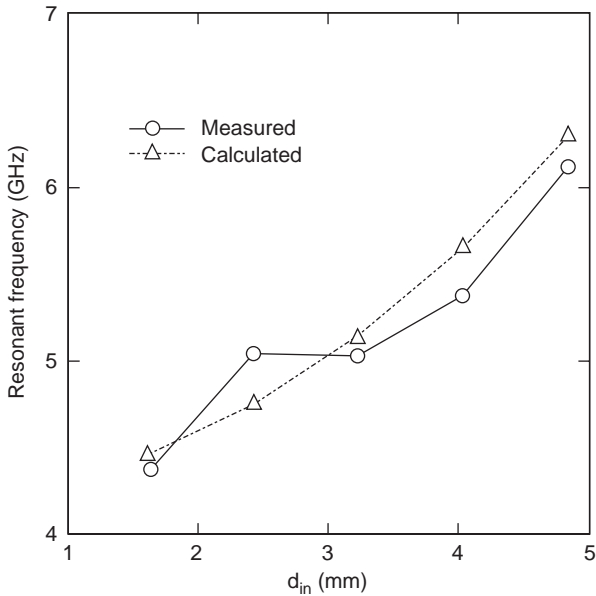


Figure 30. Comparison of the calculated and measured resonant frequencies of antenna in Fig. 29.

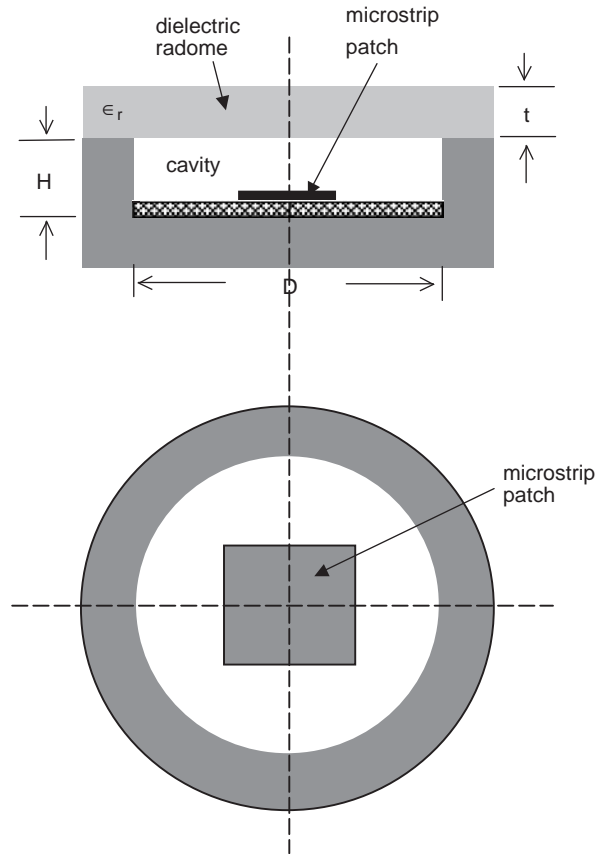


Figure 33. Geometry of a radome-covered cavity antenna.

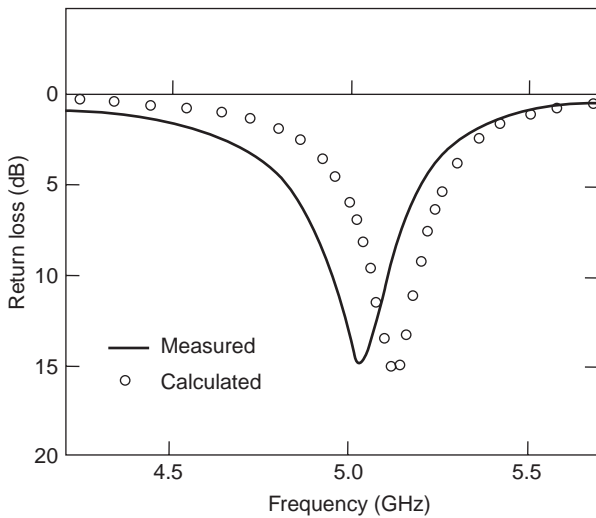


Figure 31. Return loss of the dielectric-coated monopole antenna ($d_{in} = 3.2$ mm) plotted against frequency.

use. They are natural in microstrip structures and cost-effective forms in most radome applications. When used properly, they can increase the antenna gain in proportion to their relative permittivity, compared to adjacent regions.

Figure 32 shows the geometry of a typical dielectric covered region. A planar dielectric layer of thickness t in region II is placed over another layer of thickness H in region I, which is over a conducting ground plane. Inside region I an antenna element is represented by an electric current I_0 , parallel to the ground plane and at a distance h . This problem was investigated by Jackson and

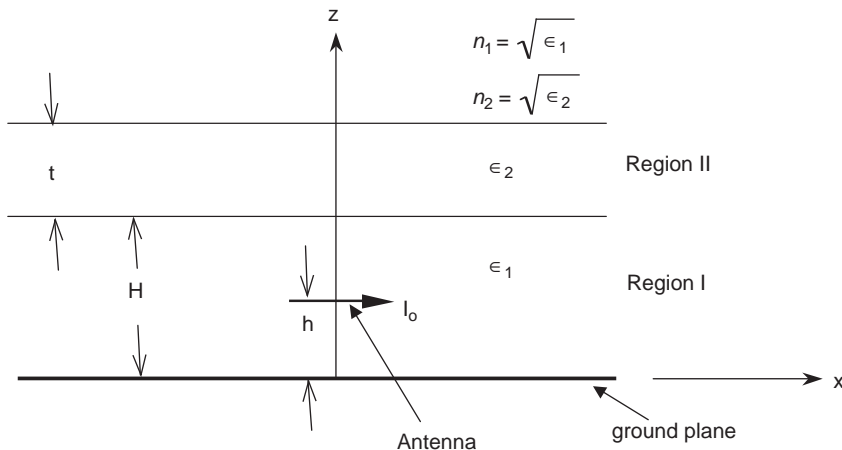


Figure 32. Antenna embedded in a two-layer planar dielectrics.

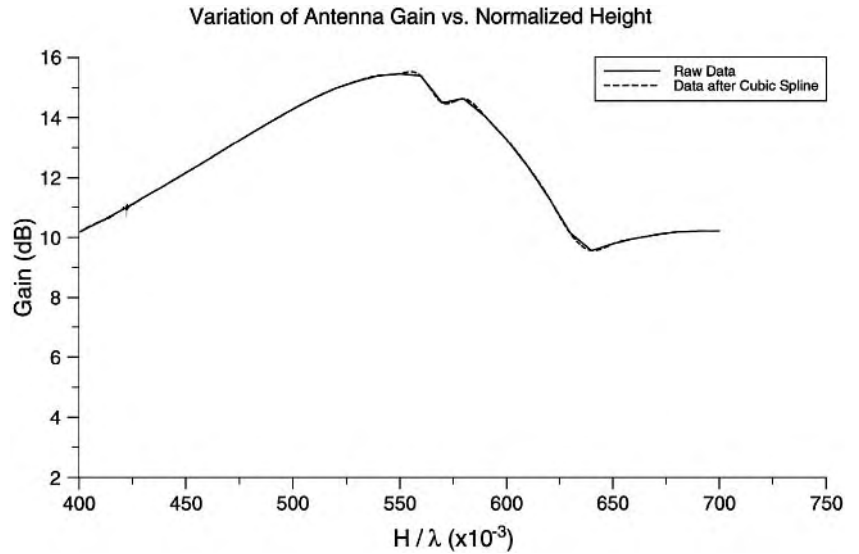


Figure 34. Variation of the cavity gain with its height H , $D = 2.0\lambda$, $\sqrt{\epsilon_r t} = 0.25$, $\epsilon_r = 10$.

Alexopoulos [18] using a transmission-line approximation. They have shown that the optimum thicknesses for maximizing the gain are given by

$$\frac{n_1 H}{\lambda_0} = \frac{m}{2}, \quad m = 1, 2, 3, \dots \quad (55)$$

$$\frac{n_2 t}{\lambda_0} = \frac{2n - 1}{4}, \quad n = 1, 2, \dots \quad (56)$$

$$\frac{n_1 h}{\lambda_0} = \frac{2p - 1}{4}, \quad p = 1, 2, \dots \quad (57)$$

and for this optimum thickness relationships the gain is approximately

$$\text{Gain} = 8 \frac{H}{\lambda_0} \left(\frac{\epsilon_2}{\epsilon_1} \right) \quad (58)$$

This indicates that, if region I is an air medium, then the antenna gain increases proportionally to the relative

permittivity of region II. For example, if the relative permittivity of region II is selected to be 100, then the antenna gain will increase by about 20 dB, over its gain without the presence of the dielectric layer. However, this gain increase is at the expense of the antenna gain bandwidth, which decreases inversely in terms of the relative permittivity.

The antenna spacing of Eq. (57) is not a hard rule and can be relaxed without a significant gain degradation. This allows the use of the other two parameters in Eqs. (55) and (56) to design radomes for gain enhancements. In an earlier study [19], the author placed a microstrip antenna at the bottom of a cavity that had a diameter $D = 2\lambda$. A radome was used to cover the cavity. From Eqs. (55) and (56) the optimum radome thickness is a quarter of a dielectric wavelength, and the optimum cavity height must be half-wavelengths. Figure 33 shows the antenna geometry, and Figs. 34 and 35 provide the variation of its gain with the cavity and radome thicknesses. The microstrip antenna gain without the radome was about 6 dBi, and the computed peak gains, in Figs. 34

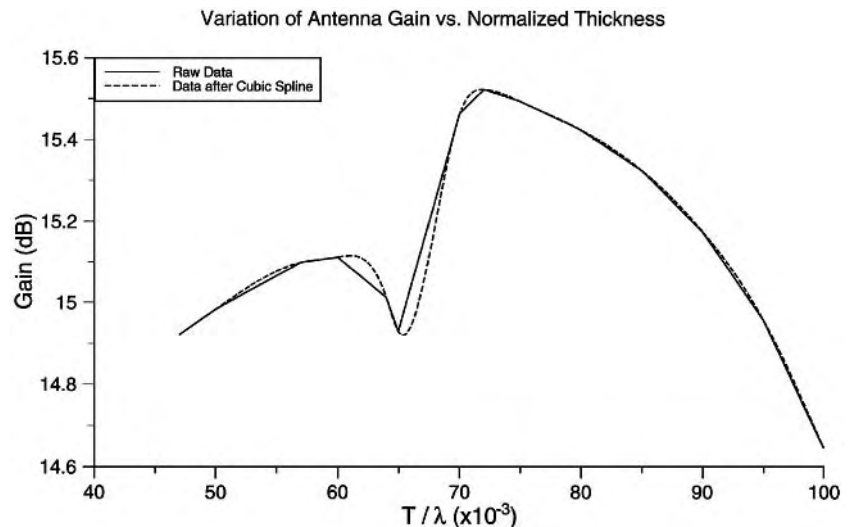


Figure 35. Dependence of the cavity gain on radome thickness, $D = 2.0\lambda$, $H = 0.55\lambda$, $\epsilon_r = 10$.

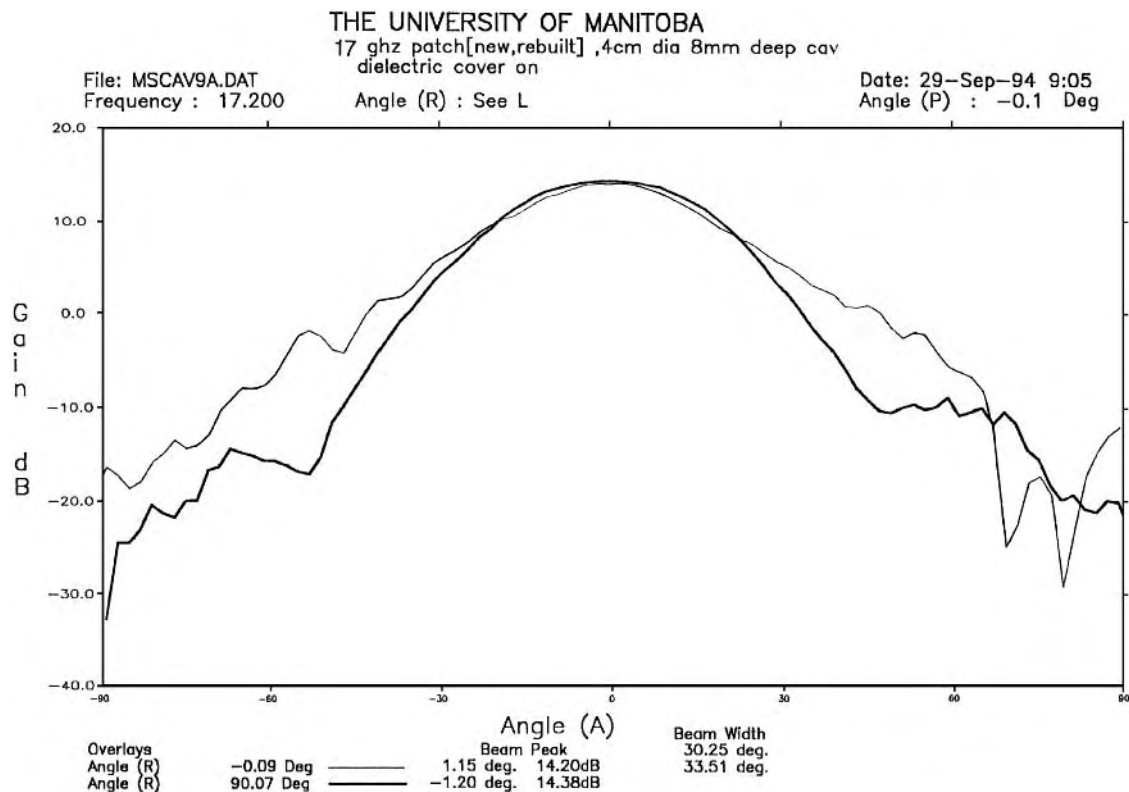


Figure 36. Measurement of principal plane patterns of cavity antenna, $D=4$ cm, $H=0.9$ cm, $t=1.27$ mm, $\epsilon_r=10.2$, $f=17.2$ GHz.

and 35, are about 15.7 dBi, indicating an increase of about 9.7 dB, which is in good agreement with the prediction of Eq. (58). A set of measured gain patterns, in the principal E and H planes, are shown in Fig. 36. They confirm the predicted gain enhancement.

BIBLIOGRAPHY

1. S. Silver, *Microwave Antenna Theory and Design*, Peter Peregrinus, London, 1984.
2. A. D. Oliver, P. J. B. Clarricoats, A. Kishk, and L. Shafai, *Microwave Horns and Feeds*, Peter Peregrinus, London, 1994.
3. Y. T. Lo and S. W. Lee, *Antenna Handbook, Theory Applications and Design*, Van Nostrand Reinhold, New York, 1988, Chapter 16.
4. R. C. Johnson and H. Jasik, *Antenna Engineering Handbook*, 2nd ed., McGraw-Hill, New York, 1984.
5. M. Barakat and L. Shafai, Studies on certain modified Luneberg lenses, *IEE Proc.* **130** (Part H)(5):363–368 (Aug. 1983).
6. G. Bekefi and G. W. Farnell, A homogeneous dielectric sphere as a microwave lens, *Can. J. Phys.* **34**:790–803 (1956).
7. V. B. Mason, *The Electromagnetic Radiation from Simple Sources in the Presence of a Homogeneous Dielectric Sphere*, Ph.D. dissertation, Univ. Michigan, 1972.
8. P. J. B. Clarricoats, A. D. Oliver, and M. Rizk, A dielectric loaded conical feed with low cross-polar radiation, *Proc. URSI Symp. EM Theory*, Spain, Aug. 1983, pp. 351–354.
9. E. Lier, A dielectric hybrid mode antenna feed, a simple alternative to the corrugated horn, *IEEE Trans.* **AP-34**: 21–29 (1986).
10. R. W. P. King, S. R. Mishra, K. M. Lee, and G. S. Smith, The insulated monopole: admittance and junction affect, *IEEE Trans. Anten. Propag.* **AP-23**(2):172–177 (March 1975).
11. I. J. Bahl and S. S. Stuchly, Analysis of a microstrip covered with a lossy dielectric, *IEEE Trans. Microwave Theory Tech.* **MTT-28**:104–109 (Feb. 1980).
12. J. A. G. Malherbe, The design of a slot array in nonradiating dielectric waveguide, Part I, theory, *IEEE Trans. Anten. Propag.* **AP-32**(12):1335–1340 (Dec. 1984).
13. A. Sanchez and A. A. Oliner, A new leaky waveguide for millimeter waves using nonradiative dielectric (NRD) waveguide, Part I: Accurate theory, *IEEE Trans. Microwave Theory Tech.* **MTT-35**(8):737–747 (Aug. 1987).
14. J. A. G. Malherbe, A leaky-wave antenna in nonradiative dielectric waveguide, *IEEE Trans. Anten. Propag.* **AP-36**(9): 1231–1235 (Sept. 1988).
15. J. A. G. Malherbe, Radiation from an open-ended nonradiative dielectric waveguide, *Microwave Opt. Technol. Lett.* **14**(5):266–268 (April 1977).
16. R. E. Collin and F. J. Zucker, *Antenna Theory*, Part I, McGraw-Hill, New York, 1969.
17. N. Bamba et al., Finite-element analysis of dielectric coated antenna, *Int. Symp. Antennas and Propagation*, Sapporo, Japan, Sept. 1992, Vol. 2, pp. 433–436.
18. D. R. Jackson and N. G. Alexopoulos, Gain enhancement methods for printed circuit antennas, *IEEE Trans. Anten. Propag.* **AP-33**(9):976–987 (Sept. 1985).
19. L. Shafai, D. J. Roscoe, and M. Barakat, Simulation and experimental study of microstrip fed cavity antennas, *Int. Symp. Antennas and Applied Electromagnetics, ANTEM'96*, Aug. 1996, pp. 549–554.

DIELECTRIC MEASUREMENT

R. BARTNIKAS
IREQ/Institut de Recherche
d'Hydro-Québec
Varenes, Québec
Canada

Dielectric measurements are concerned with the characterization of solid, liquid, and gaseous insulating materials over a wide range of DC and AC conditions at different frequencies, temperatures, field strengths, and pressures, under differing environments. The frequency range covered extends downward from the power frequency of 50 or 60 Hz through the ultralow frequency range from 10^{-2} to 10^{-6} Hz to DC and upward into the audiofrequency (AF), radiofrequency (RF), and microwave ranges and, finally, into the optical region for optically transparent dielectrics. It can be appreciated that a variety of specimen cells are required to suit the nature of the test and to act as containment vessels or holders for the specimens undergoing evaluation. The test methods and specimen containers used over the lower frequency spectrum differ substantially from those employed over the higher frequency spectrum (>300 MHz), because, at lower frequencies, the dielectric specimen behaves as a lumped circuit element, as opposed to its distributed parameter behavior over the higher frequency region, where the physical dimensions of the specimen become of the same order as the wavelength of the electric field. This delimiting difference necessarily requires other test procedures to be utilized at high frequencies, and constitutes perhaps the main reason for the bifurcation and the unfortunate, but often attending, isolation of the two fields of endeavor—even though the aim over the lower and upper frequency regions is identical, namely, the characterization of dielectric materials.

Space does not permit a detailed description of all the dielectric measurement procedures and, consequently, only a cursory presentation is made. Nor is it possible, within the given constraints, to delve into the various dielectric conduction and loss mechanisms in order to discuss the interpretative aspects of the measurement methods. Accordingly, the presentation is necessarily confined to a concise description of the most common methods of dielectric measurement employed currently. Wherever feasible, the methods given attempt to comply with the general guidelines of those specified in national and international standards, such as those by ASTM (American Society for Testing and Materials) and IEC (International Electrotechnical Commission), in order to put methods forward that are universally accepted and have withstood the test of time. The dielectric measurement methods presented here will deal principally with those of dc conductivity, dielectric constant and loss as a function of frequency, and voltage breakdown or dielectric strength.

1. DC CONDUCTIVITY MEASUREMENTS

1.1. Volume Resistivity (ρ_v)

Insulating materials employed on electrical equipment usually characterized by a high insulation resistance

and thus provide an isolating medium between adjacent components that are maintained at different potentials. In certain applications, such as for capacitor components, bushings, and cables, they must exhibit extremely low leakage current. In other applications, where partially conducting polymers are of interest, the insulation resistance values are substantially reduced. Insulation resistance measurements, which are generally carried out under DC conditions, yield not only data on the electrical conduction characteristics of a material, but may also provide an indication of the uniformity or impurity content of the insulating material. It is thus of considerable practical interest to classify the various insulating materials in terms of their DC insulation resistance, which can then be related to their DC electrical conductivity. The DC conductivity σ_{DC} of an insulating or dielectric material, is more fundamental property, as it bears a direct relationship to the conduction mechanisms taking place in the dielectric. It is defined as [1]

$$\sigma_{DC} = \frac{J_{iDC}}{E} \quad (1)$$

where J_{iDC} is the DC leakage or conduction current density in A/cm² and E is the direct electrical field in V/cm; the units of σ_{DC} are S/cm. If it is assumed that the DC conductivity arises from a drift of singly charged carriers e in the field direction, having a charge concentration n per cm³ and a mobility of μ in cm²V⁻¹s⁻¹, then Eq. (1) may be expressed as

$$\sigma_{DC} = e\mu n \quad (2)$$

The measured DC volume insulation resistance, R_v , is related to the DC volume resistivity of dielectric ρ_v by

$$\rho_v = \frac{A}{d} R_v \quad (3)$$

where A is the area of the measuring electrodes in cm² and d denotes the thickness of the dielectric specimen in cm; by definition, the DC conductivity is inversely related to the DC volume resistivity as

$$\sigma_{DC} = 1/\rho_v \quad (4)$$

such that the units of volume resistivity are in $\Omega \cdot \text{cm}$.

There are various specimen holder electrode systems and measurement techniques available for determining the volume insulation resistance R_v in terms of which the volume resistivity ρ_v may be computed, employing Eq. (3) [2–4]. For illustrative purposes, only the most prevalent ones in use will be considered. Figure 1 depicts a typical three-terminal electrode system with the dielectric specimen held between circular parallel-plane metallic electrodes. The electrodes are usually made of stainless steel, with the low-potential (guarded) electrode of diameter D_1 , having a diameter size less than the high-potential electrode, whose diameter D_3 is equal to that of the guarding electrode. The separation between the latter and the low-potential guarded electrode is equal to g , such that $g \leq 2d$,

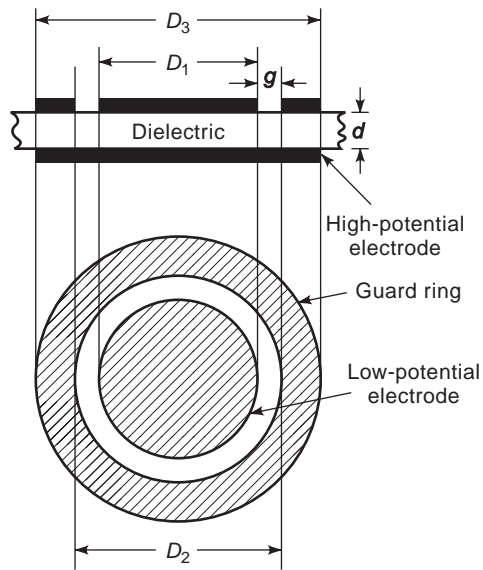


Figure 1. Three-terminal electrode system for the measurement of volume resistivity (after ASTM D257) [3].

where d denotes the thickness of the dielectric specimen. The gap g between the low-potential and guard electrodes must be sufficiently large to prevent leakage over the surface of the dielectric from influencing the volume resistivity measurement; this is particularly important with high-input-impedance electrometers. A value of $g = 2d$ is most expedient, since it permits the measurement of both volume and surface insulation resistance with an identical electrode configuration.

The fringing of the flux lines essentially extends the guarded electrode edge into the gap region bounded by the measuring or low-potential electrode and the guard ring. Hence the area, A , in Eq. (3) is not the geometrical area of the low-potential electrode, but is approximately given [2] by

$$A = \frac{\pi(D_1 + g)^2}{4} \quad (5)$$

The determination of specimen thickness d in Eq. (3), does not present itself as a trivial problem [5]. Exact parallelism between the two opposite sides of a solid dielectric specimen is difficult to achieve, in practice. With polymers, it is common to make several thickness measurements along the specimen surface, either with a micrometer or a dial gauge, and then determine the average value of d . With most polymeric materials, the dielectric specimens will tend, in general, to conform to the surface of the measuring electrodes. However, with hard materials, the optically flat electrodes will generally not be contiguous with every portion of the surface of the dielectric. In such circumstances, the three-terminal electrodes must be either paint or vapor deposited on the rigid surfaces of the specimen. For this purpose, silver or aluminum is frequently employed, although aluminum is less desirable, because of its propensity to form nonconducting oxide films. Alternatively, tinfoil electrodes may be utilized, in conjunction

with a minute thickness of silicone grease, applied to ensure their adhesion to the specimen's surface. When liquid dielectrics are evaluated, permanently mounted three-terminal electrodes are employed, in conjunction with a cell container into which the liquid specimen submerges the measurement electrodes.

Figure 2 portrays a schematic three-terminal circuit diagram for the measurement of the volume insulation resistance R_v . Perhaps one of the most important considerations in the measurement of R_v is the time at which, following the application of the electric field, the actual measurement is made. When the voltage is suddenly applied across the specimen, the observed initial charging current is associated with the polarization of the dielectric; both the induced and permanent dipoles in the dielectric become aligned in the direction of the electrical field. Once this very rapid process is completed, the current commences a monotonic decline with time, as surplus free charge carriers are gradually swept out of the dielectric by the electric field. The nature of these charge carriers and their mobility are directly associated with the structure of the dielectric material. If the dielectric has an open structure, such as glass, the charge carriers may be ions; similarly, in a dielectric liquid such as an oil, where electrolytic contamination may be the source of the charge carriers, ions may be also responsible for the conduction current. In polymers, where the latitude of ionic motion is greatly restricted, the conduction process is frequently governed by electrons. Ideally, the R_v value should be measured when the conduction or the so-called leakage current attains a constant value, which is a function of the dielectric under test. For example, in a polymer, the value of constant current may be achieved when all excess free electrons have been removed from the dielectric and the residual leakage current is entirely determined by the trapping and detrapping rates of the electrons at the various traps (principally shallow traps). Thus, the number of migrating electrons at any one time approaches a constant value when an equilibrium is attained between the time each electron resides trapped in a well and the time it is free to migrate before it again becomes re-trapped. Since the complexity of the conduction process virtually ensures that different dielectrics are characterized by different times necessary for the leakage current to attain a constant value, it has been agreed *ad arbitrium* that all insulation resistance measurements should be made following a one-minute application of the electrical field.

Since the volume resistivity ρ_v of good insulating materials falls in the range from 10^{12} to $>10^{18} \Omega \text{ cm}$, the leakage current I_1 for such materials must be measured with a picoammeter, as indicated in Fig. 2. The guard circuit improves the accuracy of the measurement by reducing the influence of the leakage resistance. The effects of the coaxial cable resistance connected across the DC power supply can be greatly decreased by shunting the input of the coaxial cable to its shield, by means of an operational amplifier with unity gain; this feature is often incorporated in commercially available electrometer/ohmmeter instruments [6].

The volume insulation resistance R_v , in addition to being contingent on the time of the voltage application, is

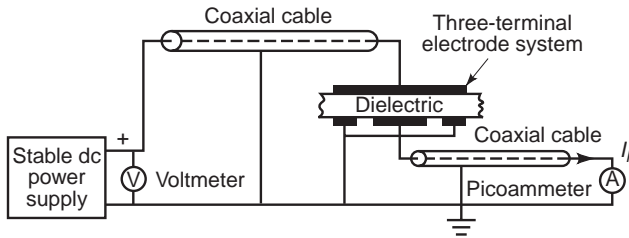


Figure 2. Schematic circuit diagram for a three-terminal measurement of the volume insulation resistance.

also a function of the applied voltage V ; it is temperature-dependent as well. Thus, the value of V and the temperature must be specified; in general, the values of 100 and 500 V are most commonly employed [2,3]. Following one minute of voltage application, the value of R_v then calculated from

$$R_v = \frac{V}{I_1} \tag{6}$$

In the measurement of R_v an accuracy of 5% may be readily obtained. However, as the volume resistivity ρ_v is subsequently obtained in terms of Eq. (3), the accuracy of the ρ_v value is somewhat degraded, as a result of errors inherent in the measurement of the specimen thickness d and the estimation of the electrode area A [refer to Eq. (5)] when compensation for the field fringing effects is made.

1.2. Surface Resistivity (ρ_s)

Surface resistance R_s of solid insulating materials is, to a large extent, determined by the state of cleanliness or contamination of the surface of the dielectric under test. It is, as well, a strong function of surface moisture, particularly if the moisture film contains electrolytic impurities either intrinsic to the liquid film itself or as a result of solid ionic contaminants originally present on the solid dielectric surface. Surface resistance is thus a measure of the material's propensity to surface contamination and constitutes a useful indicator as concerns the surface tracking resistance of insulators when subjected to electric fields. It is common practice to condition the specimens prior to measurement in a dry atmosphere, before

performing the actual measurement at 50% relative humidity.

Surface resistance measurements may be carried out, either with two- or three-terminal electrode systems, although three-terminal electrodes are usually employed to eliminate stray leakage effects. The units of surface resistance are ohms or ohms per square. The latter refers to the arrangement of the electrodes, the configuration of a square, on the surface of the specimen, as depicted in Fig. 3 [2].

It is evident from the electrode arrangement in Fig. 3 that the surface resistance measurement also includes a contribution of the volume resistance. The magnitude of this contribution diminishes as the surface conductivity becomes increasingly greater than the volume conductivity. The procedure followed in measuring the surface resistance R_s is identical to that of R_v . The surface resistance is given by

$$R_s = \frac{V}{I_{s1}} \tag{7}$$

where I_{s1} is the surface leakage current and V is the voltage across the high-potential (H) and low-potential (L) electrodes. In Fig. 3, G represents the guard electrodes and g denotes the separation between the guard (G) and low-potential (L) electrodes. The surface resistivity ρ_s in ohms or ohms per square, is then determined from [2]

$$\rho_s = \frac{y}{x} R_s \tag{8}$$

where y denotes the length of the low-potential electrode (L) and x is the separation between the high- (H) and low- (L) potential electrodes. The electrodes may be applied with silver paint; alternatively, silver or aluminum electrodes may be deposited upon the surface under vacuum. Frequently, tinfoil electrodes are utilized with an extremely thin-layer film of silicone jelly applied on their underside, in order to provide adhesion on the specimen's surface.

Another approach is to employ the circular three-terminal electrode system of Fig. 2, but with the connections changed as portrayed in Fig. 4. Note that with this arrangement, the high potential is applied to the circular electrode (H) encompassing the center electrode, which

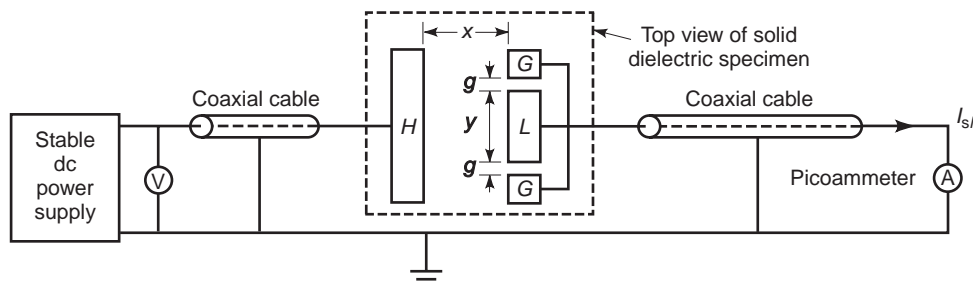


Figure 3. Schematic circuit diagram for the measurement of surface resistance with a three terminal electrode arrangement on the dielectric's surface [2].

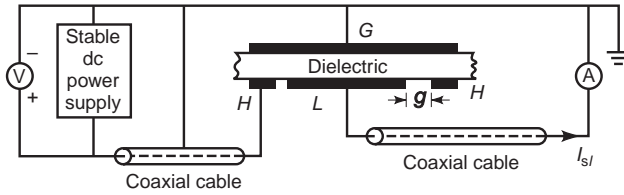


Figure 4. Schematic circuit diagram of a three-terminal circular electrode arrangement for the measurement of the surface insulation resistance [3,6].

acts as the low-potential electrodes (L), while the upper electrode is connected to ground. In contradistinction to Fig. 2 (for volume resistivity measurements), the gap distance $g \geq 2d$; in analogy to Fig. 3, g is equivalent to the electrode separation distance, x . With circular electrode symmetry, the surface resistivity becomes [2,3]

$$\rho_s = \frac{\pi D_1}{g} R_s \quad (9)$$

where D_1 is the diameter of the low-potential electrode (L). The diameter of the upper grounded electrode (G) may be equal to or greater than that of the encompassing circular high-potential electrode (H).

2. PERMITTIVITY AND LOSS MEASUREMENTS ON LUMPED CAPACITANCE SPECIMENS

Under alternating voltages, dielectric materials are employed either as supports to insulate electrical components from each other and ground, or as dielectrics in capacitors. Some applications require dielectrics of low loss and low dielectric constant, while in others, high-dielectric-constant materials are desirable, to provide the highest possible capacitance for a given physical size. Thus two of the most important electrical properties of dielectric materials, in terms of which their use and application suitability at either low or high frequencies are assessed, are those of dielectric loss and dielectric constant.

The capacitance C of a parallel-plate capacitor containing a dielectric material having a relative real permittivity, ϵ'_r , may be expressed as

$$C = \epsilon'_r C_0 \quad (10)$$

where C_0 is the capacitance in vacuo and is given by

$$C_0 = \frac{\epsilon_0 A}{d} \quad (11)$$

where A is the area of the capacitor's plates in cm^2 , d the thickness of the dielectric, and ϵ_0 the permittivity in vacuo equal to 8.854×10^{-14} F/cm. By definition, ϵ'_r is equal to the ratio ϵ'/ϵ_0 , where ϵ' is the real value of the permittivity. Frequently, the relative real value of the permittivity ϵ'_r is simply referred to as the *dielectric constant*. The occurrence of loss in dielectrics, which may be associated with the migration of free charge carriers, space charge po-

larization, or the orientation of permanent dipoles, is manifest externally by a phase shift between the electric field (\mathbf{E}) and the displacement (\mathbf{D}) vectors [1]; consequently, the permittivity, ϵ , becomes a complex quantity of the form

$$\epsilon = \epsilon' - j\epsilon'' \quad (12)$$

where ϵ'' denotes the imaginary value of the permittivity. The total current density vector \mathbf{J} through the dielectric, composed of the leakage current density \mathbf{J}_l and capacitative or displacement current density \mathbf{J}_c vectors, may be expressed in terms of ϵ' and ϵ'' as

$$\begin{aligned} \mathbf{J} &= \mathbf{J}_l + \mathbf{J}_c \\ &= (\omega\epsilon'' + j\omega\epsilon')\mathbf{E} \end{aligned} \quad (13)$$

The phasor relationship between the current density vectors \mathbf{J}_l , \mathbf{J}_c , and \mathbf{J} is delineated in Fig. 5a with its corresponding RC equivalent circuit in Fig. 5b, in terms of which the dissipation factor ($\tan \delta$) of the dielectric specimen may be defined as

$$\tan \delta = \frac{J_l}{J_c} = \frac{I_l}{I_c} \quad (14)$$

where I_l and I_c are the corresponding current vectors. From Eqs. (14) and (15), it follows that

$$\tan \delta = \frac{\epsilon''}{\epsilon'} \quad (15)$$

Since the AC conductivity σ_{AC} is by definition, equal to \mathbf{J}_l/\mathbf{E} , then, in terms of Eq. (13), we obtain

$$\sigma_{AC} = \omega\epsilon'' \quad (16)$$

and

$$\tan \delta = \frac{\sigma_{AC}}{\omega\epsilon'} \quad (17)$$

The AC conductivity σ_{AC} must be distinguished from its DC value σ_{DC} because it may include permanent dipole

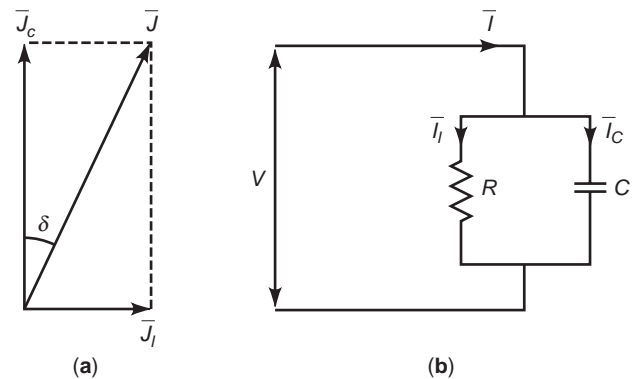


Figure 5. Current density phasor relationship in a dielectric (a) with its corresponding equivalent parallel RC circuit (b).

orientation losses, as well as frequency-dependent space charge polarization controlled carrier migration processes, which do not arise under DC conditions. It is readily apparent from the equivalent-circuit diagram, which represents the lossy part of a dielectric by an equivalent resistance, that

$$\begin{aligned} \tan \delta &= \frac{I_1}{I_c} \\ &= \frac{1}{\omega RC} \end{aligned} \tag{18}$$

where V is the applied voltage vector and I_1 is given by V/R and I_c by $j\omega CV$. It must be borne in mind that, the parallel equivalent RC circuit representation in Fig. 5b is valid only at one particular frequency, since both R and the capacitance C of the specimen are functions of frequency, as well as temperature and electric field. It must be further emphasized that, whereas some dielectric measurement circuits view the dielectric specimen as a parallel equivalent circuit with a large equivalent parallel insulation resistance R , others consider the dielectric as a series RC circuit, where the series resistance $R_s \ll R$. The $\tan \delta$ value for the series RC circuit representation becomes

$$\tan \delta = \omega R_s C \tag{19}$$

It is apparent that one can derive the primary dielectric parameters of σ_{AC} , ϵ'' , and ϵ' from the measured values of C and $\tan \delta$ by means of Eqs. (10), (15), and (17).

2.1. Measurements at Low Frequencies (from 10^{-6} to 10 Hz)

In studies related to the identification of charge carriers and space charge effects, it is desirable to carry out measurements in the frequency range between 10^{-6} and 10 Hz. For measurements below 10^{-1} Hz, it is common practice to apply a rapid risetime voltage step pulse across the specimen and subsequently observe the form of the charging or decay current. The arrangement for this measurement is very similar to that of the volume resistivity measurement in Fig. 2, with the exception that a switch is employed in conjunction with the DC power supply to abruptly apply a voltage step across the specimen [7,8]. Since the total charging current comprises all the frequency components contained within the voltage excitation step, Fourier transformation procedures can be utilized to derive the individual current distributions at the discrete frequencies. This procedure may be utilized irrespective of whether the specimen is charged or discharged. The relative real and imaginary permittivities ϵ'_r and ϵ''_r , respectively, may be expressed in terms of the resulting current as

$$\epsilon'_r(\omega) = \frac{1}{C_0 V} \int_0^\infty i(t) \cos \omega t \, dt + \frac{C_\infty}{C_0} \tag{20}$$

and

$$\epsilon''_r(\omega) = \frac{1}{C_0 V} \int_0^\infty i(t) \sin \omega t \, dt + \frac{G}{\omega C_0} \tag{21}$$

where V is the magnitude of the voltage step, C_∞ represents the lumped capacitance of the specimen at infinite frequency, and G is the DC conductance. Practical implications impose the upper and lower integration limits on Eqs. (20) and (21); the lower limit is fixed by the risetime of the electrometer employed (usually about 1 s) and the upper limit by the smallest value of current that the electrometer can measure (about 10^{-16} A) in the presence of extraneous noise. A numerical procedure is normally followed, to carry out these types of measurement [9]. For each frequency of measurement, the computer performs a numerical integration between the two integration limits to determine the values of ϵ'_r and ϵ''_r .

An automated precision time-domain reflectometer procedure is available that permits rapid measurements down to 10^{-4} Hz with an accuracy of 0.1% and a resolution of 10^{-5} in the $\tan \delta$ value [10,11]. Its schematic circuit diagram is depicted in Fig. 6.

Positive and negative voltage steps are applied across the specimen and the reference capacitors, C and C_{ref} respectively. The operational amplifier, in conjunction with the feedback capacitor C_f constitute a charge detector, providing an output that is proportional to the net charge injected [$Q_{ref} - Q(t)/C_f$] by the two opposite-polarity voltage steps of amplitude ΔV and $-\Delta V$, respectively. As the voltage across the specimen changes from 0 to ΔV , the charge $Q(t)$ flowing through the specimen is determined from

$$C(t) = \frac{Q(t)}{\Delta V} \tag{22}$$

where $C(t)$ denotes a time-dependent capacitance. Hence the complex capacitance of the specimen $C^*(\omega)$, as a function of frequency, may be expressed as

$$\begin{aligned} C^*(\omega) &= C'(\omega) - jC''(\omega) \\ &= \int_0^\infty C(t)' \exp[-j\omega t] dt \end{aligned} \tag{23}$$

where $C(t)'$ is the time derivative of $C(t)$. The relative real and imaginary permittivities, ϵ' and ϵ'' , are then deduced from

$$C'(\omega) \simeq \int_0^\infty C(t) \cos \omega t \, dt + C(0) + C_{ref} \tag{24}$$

and

$$C''(\omega) \simeq \int_0^\infty C(t) \sin \omega t \, dt \tag{25}$$

where $C'(\omega)$ and $C''(\omega)$ are the real and imaginary capacitances corresponding to $\epsilon'_r C_0$ and $\omega \epsilon''_r C_0$, respectively; $C(0)$ is the initial capacitance and the integration is

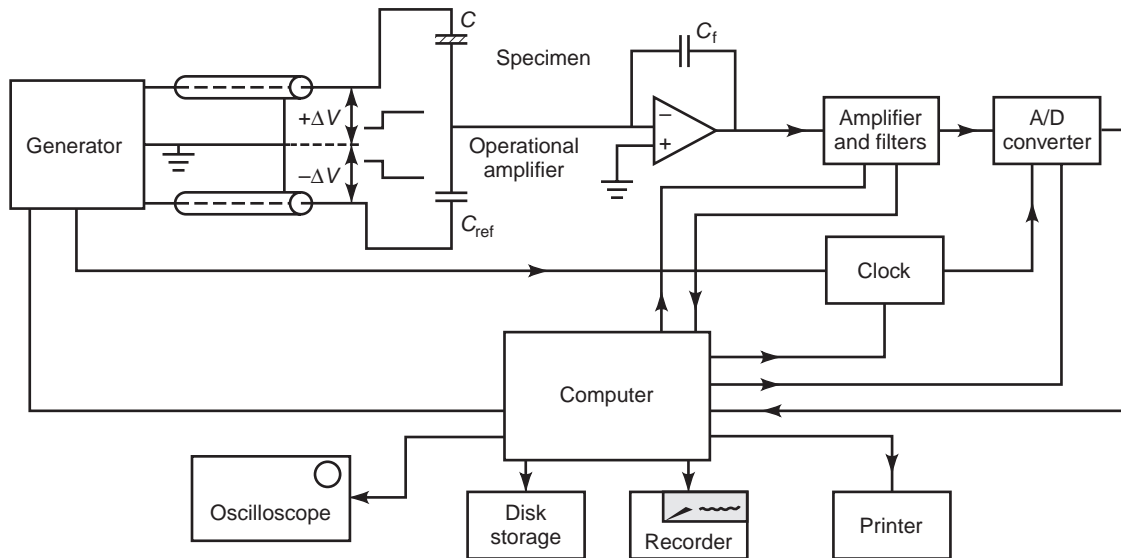


Figure 6. Schematic circuit diagram of time-domain system for measurements down to 10^{-4} Hz [10].

carried out for all times following the application of the voltage step at $t=0$. The minimum and the maximum feasible measurement times t_{\max} and t_{\min} determine the minimum and maximum measurement frequencies $\omega_{\min}/2\pi$ and $\omega_{\max}/2\pi$, respectively. The entire measurement is completed in less than one cycle at $\omega_{\min}/2\pi$.

A most useful instrument, which is frequently employed in the range from 10^{-2} to 10^2 Hz and occasionally up to 10^4 Hz, is the Thompson–Harris bridge [12,13]. A two-terminal specimen cell is utilized in conjunction with the bridge, so that a correction must be made to take into account fringing effects at the electrode edges. The schematic circuit diagram of the bridge, portrayed in Fig. 7, incorporates a specimen biasing feature [14], which is included to permit the determination of the depth of charge traps in the dielectric bulk and adjacent to the measuring electrodes.

The highly regulated frequency generator used in conjunction with the Thompson–Harris bridge must provide

exact in-phase and quadrature voltage outputs of V and jV , respectively. Operational amplifiers delineated in Fig. 7 provide the necessary voltage, phase, and impedance relationships. The capacitive current of the specimen is balanced by the injection of an out-of-phase voltage $-\beta V$ across a variable capacitor C_c ; injection of a quadrature voltage of αjV across C_R compensates for the conduction or leakage current in the specimen conductance G_x . Balance of the bridge is achieved by manipulating the capacitors C_C and C_R and observing the null point, in terms of the Lissajous figures displayed on the long-persistence oscilloscope. At balance, the conductance of the specimen G_x is given by

$$G_x = \omega \alpha C_R \quad (26)$$

and the capacitance of the specimen C_x is

$$C_x = \beta C_c \quad (27)$$

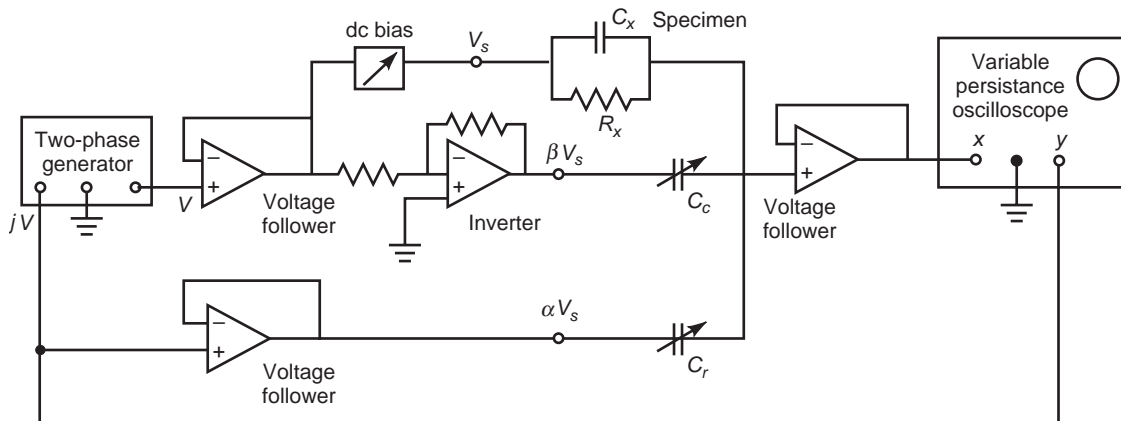


Figure 7. Thompson–Harris low-frequency bridge with specimen bias control feature [14].

from which the dissipation factor of the dielectric ($\tan \delta$) is obtained as

$$\begin{aligned}\tan \delta &= \frac{G_x}{\omega C_x} \\ &= \frac{\alpha C_R}{\beta C_c}\end{aligned}\quad (28)$$

Note that α and β are dimensionless quantities, representing the fraction of the voltage, V_s injected across C_R and C_c , respectively.

Not indicated in Fig. 7 is a zero-offset feature, which is utilized in routine measurements to compensate for the DC coupling circuitry, in order to prevent erratic shifts in the Lissajous figures while balancing is being carried out. The accuracy of the bridge is 0.1% with resolution ordinarily better than 0.1%.

Frequency response analyzer methods may also be employed for low-frequency measurements. These computerized techniques perform adequately well within the range from 10^{-4} to 10^4 Hz [15].

2.2. Power and Intermediate-Frequency Methods (10 Hz–1 MHz)

A considerable portion of the electrical insulating materials manufactured for use in electrical apparatus and cables are evaluated within the frequency range from 50 Hz to 1 MHz, employing primarily bridge type circuits. A further substantial portion of tests at high voltages are carried out at fixed power frequencies of 50, 60, and 400 Hz. The bridge circuits designed for power frequency applications, where measurements are normally made as a function of voltage, differ significantly from those involving measurements as a function of frequency at low voltage. Since most of these tests are performed by means of either Schering or transformer ratio arm bridges, the discussion here will be essentially confined to these types of bridges.

A common low-voltage Schering bridge arrangement, which employs the parallel substitution technique recommended in ASTM D150 [16], is depicted in Fig. 8 for the case where measurements are carried with a two-terminal specimen cell.

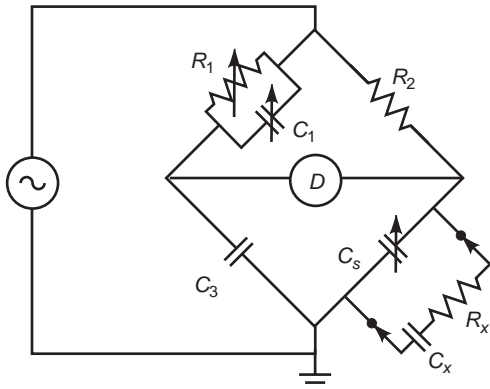


Figure 8. Low-voltage Schering bridge, employing the parallel substitution technique in accordance with ASTM D150 [16].

The capacitance C_3 is selected such that its negligibly small dielectric losses are approximately equal to those of the intrinsically low-loss standard capacitor C_s . Note that the Schering bridge views the specimen as an equivalent series $R_x C_x$ device, so that the variable arm composed of the parallel combination of R_1 and C_1 must be capable of compensating for the losses in the small series resistance R_x of the specimen. The null detector, which is normally an amplifier, is tuned to the frequency of the measurement, $f = \omega/2\pi$. Balance is first obtained by an adjustment of the capacitors C_1 and C_s , with the specimen disconnected. Then, with the specimen placed in parallel with the standard capacitor C_s , the bridge is rebalanced. The specimen capacitance C_x is thus determined from

$$C_x = C'_s - C''_s \quad (29)$$

and the dissipation factor from

$$\tan \delta_x = \frac{\omega R_1 C'_s (C''_1 - C'_1)}{(C'_s - C''_s)} \quad (30)$$

where C'_1, C'_s , and C''_1, C''_s denote the values of the variable capacitors C_1 and C_s at balance with the specimen disconnected and reconnected, respectively. The substitution technique eliminates the errors introduced by the coupling effects of the various stray capacitances, but it does not circumvent errors arising from connecting lead influences.

The procedures for the correction of lead and stray capacitance effects have been standardized and are explicitly enumerated in ASTM D150 [16]. It is the inductance, L_s , and the resistance R_s the leads, which contribute to the apparent increase of the capacitance ΔC and the dissipation factor $\Delta \tan \delta$ in accordance with the relations [16]

$$\Delta C = \omega^2 L_s C^2 \quad (31)$$

and

$$\Delta \tan \delta = \omega R_s C \quad (32)$$

where C is the true capacitance of the specimen; it is to be emphasized that, as the skin effect increases with frequency, the lead resistance R_s increases significantly with the square root of the frequency, $f = \omega/2\pi$. A standard practice for assessing the effect of the leads is to perform a measurement on a miniature sized capacitor, where the latter is first directly connected to the bridge terminals and then inserted across the far end of the leads. The difference between the two readings permits the calculations of ΔC and $\Delta \tan \delta$.

The appearance of an edge capacitance C_e and a ground capacitance C_g will lead to an increase in the measured apparent capacitance

$$C_a = C + C_e + C_g \quad (33)$$

and an apparent dissipation factor

$$\tan \delta_a = \frac{C \tan \delta}{C_a} \quad (34)$$

The relative real and imaginary permittivity ϵ'_r and ϵ''_r will then be given by

$$\begin{aligned} \epsilon'_r &= \frac{C}{C_0} \\ &= \frac{C_a - (C_e + C_g)}{C_0} \end{aligned} \quad (35)$$

and

$$\epsilon''_r = C_a \tan \delta_a / C_0 \quad (36)$$

For the normal type of specimen dimensions, where the parallel-plane cylindrical electrodes are smaller than the diameter of the specimen, the capacitance in vacuo C_0 with edge effect correction, may be expressed empirically in pF as [16]

$$C_0 = 0.006954 \frac{D^2}{d} \quad (37)$$

where d is the thickness of the specimen and D the diameter of the electrodes in mm. Exact formulas for the edge correction may be found in Ref. 17; the use of the exact formulas does not result in a significant difference for the correction. As with all dielectric measurements, the accuracy attainable is contingent not only upon the accuracy of the observed capacitance and $\tan \delta$ values, but also on the stray and edge effects of the electrodes employed, as well as the calculated interelectrode vacuum capacitance C_0 . In general, the permittivity is determinable to within $\pm 1\%$ and the $\tan \delta$ value to within $\pm(5\% + 0.0005)$ [16].

The circuit of a power frequency high-voltage Schering bridge, portrayed in Fig. 9, represents essentially an inverse arrangement of its sibling low-voltage bridge equivalent. The lower bridge arms of R_4 , C_4 , and R_3 constitute

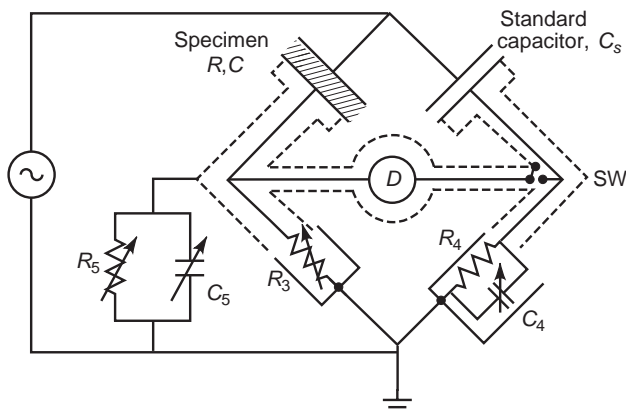


Figure 9. Classical power frequency circuit of high-voltage Schering bridge with Wagner's Earth [2].

the balancing elements, while the upper arms of the series representation of the specimen, R, C , together with the standard capacitor, C_s , which have a high impedance in comparison with the lower resistive arms, assume the major portion of the voltage drop. This arrangement provides the bridge with an inherent safety feature, since the lower arms where balance manipulation of the bridge is carried out, remain at low potential. Figure 9, which represents the classical Schering bridge circuit, delineates also the guard circuit's balancing elements R_5 and C_5 , arranged in accordance with the so-called Wagner's Earth method. The guard circuit, which is implemented in order to eliminate the stray capacitance to ground, necessarily entails the use of a three-terminal measurement procedure. The solid dielectric slab specimen is placed in a three-terminal cell of the type depicted in Fig. 1, or if the specimen is a liquid dielectric, a concentric coaxial electrode cell [18] may be employed. Frequently, the specimen undergoing test may be a high-voltage power cable or stator bar, whose high-voltage terminated ends must also incorporate a guard circuit [19]. The standard capacitor C_s , which must be partial-discharge-free up to the maximum measurement voltage, is normally a 100 pF compressed-gas-filled unit with negligible dielectric loss. Note that the low-voltage arms are enveloped in grounded shields; the shield, screening the low-potential electrodes of the specimen and standard capacitor, including the detector that normally comprises an amplifier tuned to the power frequency, eliminates the stray capacitances to ground and between the components themselves. Thus, any capacitance current, which may develop between the detector and the high-voltage portion of the bridge, flows directly to ground via the auxiliary bridge arm of R_5 and C_5 . Since the latter are interposed between the shield and the bridge ground, their manipulation balances the guard or shield circuit. The switch SW , shown in Fig. 9, permits the necessary independent balancing steps for the bridge guard circuit and the bridge itself. At balance, the capacitance of the specimen [2] is given by

$$C = \frac{C_s R_4}{R_3} \quad (38)$$

and for equal self-inductances inherent with the resistive elements R_3 and R_4 , the dissipation factor reduces to

$$\tan \delta = \omega R_4 C_4 \quad (39)$$

Since high-voltage Schering bridges are normally designed to operate at one fixed power frequency, the dials of R_3 and C_4 are calibrated to read directly the capacitance and $\tan \delta$ values of the specimen, respectively. It is to be emphasized that, under high voltage conditions, should the specimen under test undergo partial discharge, then the indicated $\tan \delta$ value will reflect the power losses due to partial discharges, in addition to the dielectric losses occurring in the solid, liquid, or solid-liquid insulating system of the specimen [20].

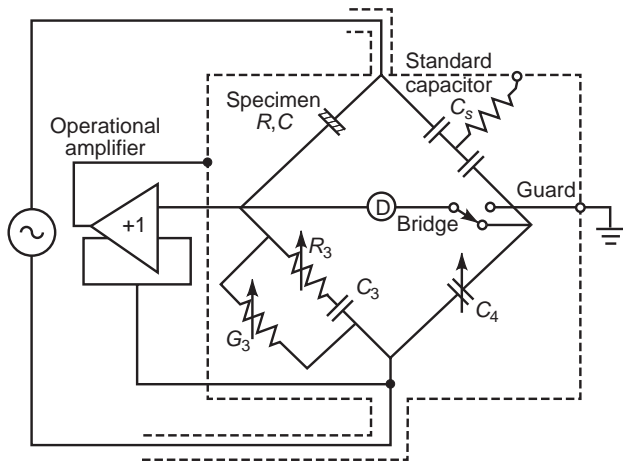


Figure 10. Schematic diagram of precision Tettex Schering bridge for measurements at power frequency [21].

Present high-voltage fixed power frequency Schering bridges employ a driven or active guard technique for balancing of the guard circuit in lieu of the classical Wagner’s Earth method. In this approach, the guard circuit and the detector, *D*, are maintained automatically, at the same potential, by means of a unit gain operational amplifier, whereby only a single balance step is required for the bridge. This feature, together with other improvements in the Schering bridge, is well exemplified in the Tettex precision Schering bridge, which has been designed for use on thin dielectric specimens up to 2 kV; its circuit is depicted in Fig. 10.

The bridge is limited in voltage, since now the lower arms are capacitive in nature, in order to attain a higher sensitivity as the stray capacitances are thus greatly reduced. The capacitance of the specimen, *C*, is obtained by

an adjustment of *C*₄ to yield

$$C = \frac{C_s C_3}{C_4} \tag{40}$$

and the value of $\tan \delta$ at the null is obtained by adjustment of *R*₃; the already low dielectric loss standard capacitor *C*_s is artificially reduced to zero, such that the $\tan \delta$ value of the specimen becomes

$$\tan \delta = \omega R_3 C_3 + \frac{G_3}{\omega C_3} \tag{41}$$

In the measurements carried out with Schering bridges, the capacitance and $\tan \delta$ values of the dielectric specimens are obtained in terms of the resistance and capacitance elements of the bridge. Hence, the precision and accuracy of the measurements are determined by the accuracy of these resistances and capacitances themselves. Precise dielectric measurements may also be performed by means of an inductively coupled voltage divider, utilizing a transformer arrangement, thereby circumventing some of the accuracy and stability constraints associated with resistive and capacitive elements [2,22]. Perhaps one of the finest precision/accuracy commercially available transformer ratio arm bridges for variable-frequency measurements in the range from 10 Hz to 100 kHz is that of Gen Rad, under the designation type 1621 transformer ratio arm bridge. Its schematic circuit diagram is delineated in Fig. 11. A 12-digit readout of the specimen capacitance *C*_x with a 10 ppm accuracy is provided within the range from 10⁻⁷ to 10 μF. A basic accuracy of 0.1% is attainable for conductance *G*_x measurements within the range of 10⁻¹⁰–10³ μS—that is, a $\tan \delta$ value of 10⁻⁷ at 1 kHz may be determined with a four-figure resolution.

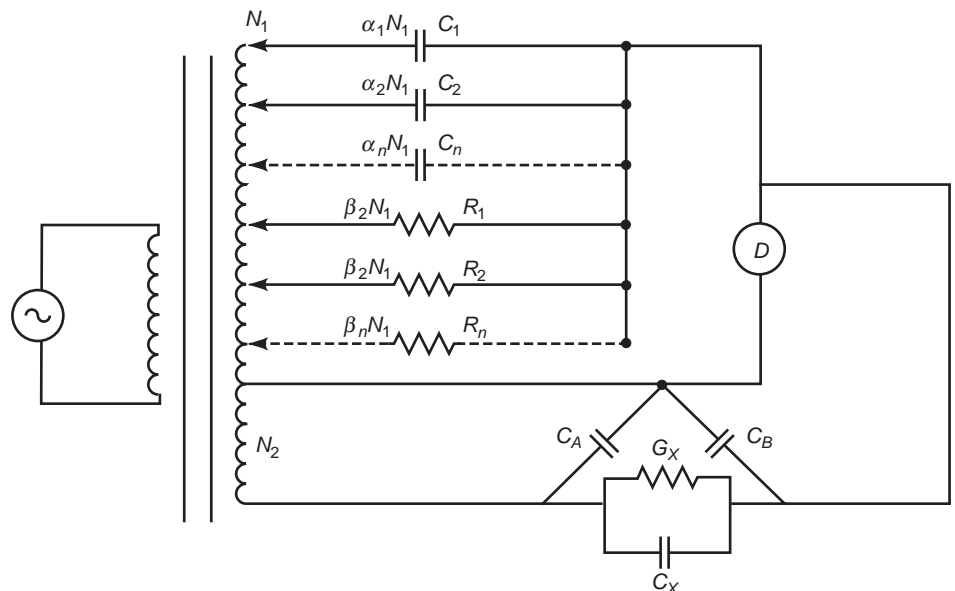


Figure 11. Basic circuit of Gen Rad type 1621 precision transformer ratio arm bridge [23].

The capacitances C_A and C_B shunting the transformer winding and the specimen, respectively, do not introduce any error into the measurement, since the former produces only a reduction of the voltage across the specimen, while the latter causes only a decrease in the sensitivity of the detector D . In balancing the bridge, the multiple tapped transformer principle is utilized in the course of the resistive and capacitive decade adjustments. Accordingly, the balance equation at the null of the bridge is given by

$$N_2(G_x + j\omega C_x) = N_1[(\beta_1 G_1 + \beta_2 G_2 + \dots + \beta_n G_n) + j\omega(\alpha_1 C_1 + \alpha_2 C_2 + \dots + \alpha_n C_n)] \quad (42)$$

Equating the real and imaginary terms yields the capacitance of the specimen

$$C_x = \frac{N_1}{N_2}[\alpha_1 C_1 + \alpha_2 C_2 + \dots + \alpha_n C_n] \quad (43)$$

and the conductance

$$G_x = \frac{N_1}{N_2}[\beta_1 G_1 + \beta_2 G_2 + \dots + \beta_n G_n] \quad (44)$$

The dissipation factor of the specimen as a function of frequency is obtained as

$$\begin{aligned} \tan \delta &= \frac{G_x}{\omega C_x} \\ &= \frac{[\beta_1 G_1 + \beta_2 G_2 + \dots + \beta_n G_n]}{\omega[\alpha_1 C_1 + \alpha_2 C_2 + \dots + \alpha_n C_n]} \end{aligned} \quad (45)$$

Note that the transformer ratio arm bridge views the dielectric specimen as an RC parallel equivalent circuit.

A computer-controlled automatic transformer ratio arm has been developed for measurements at power frequencies under high-voltage conditions [24]. The bridge circuit is delineated schematically in Fig. 12, in which the

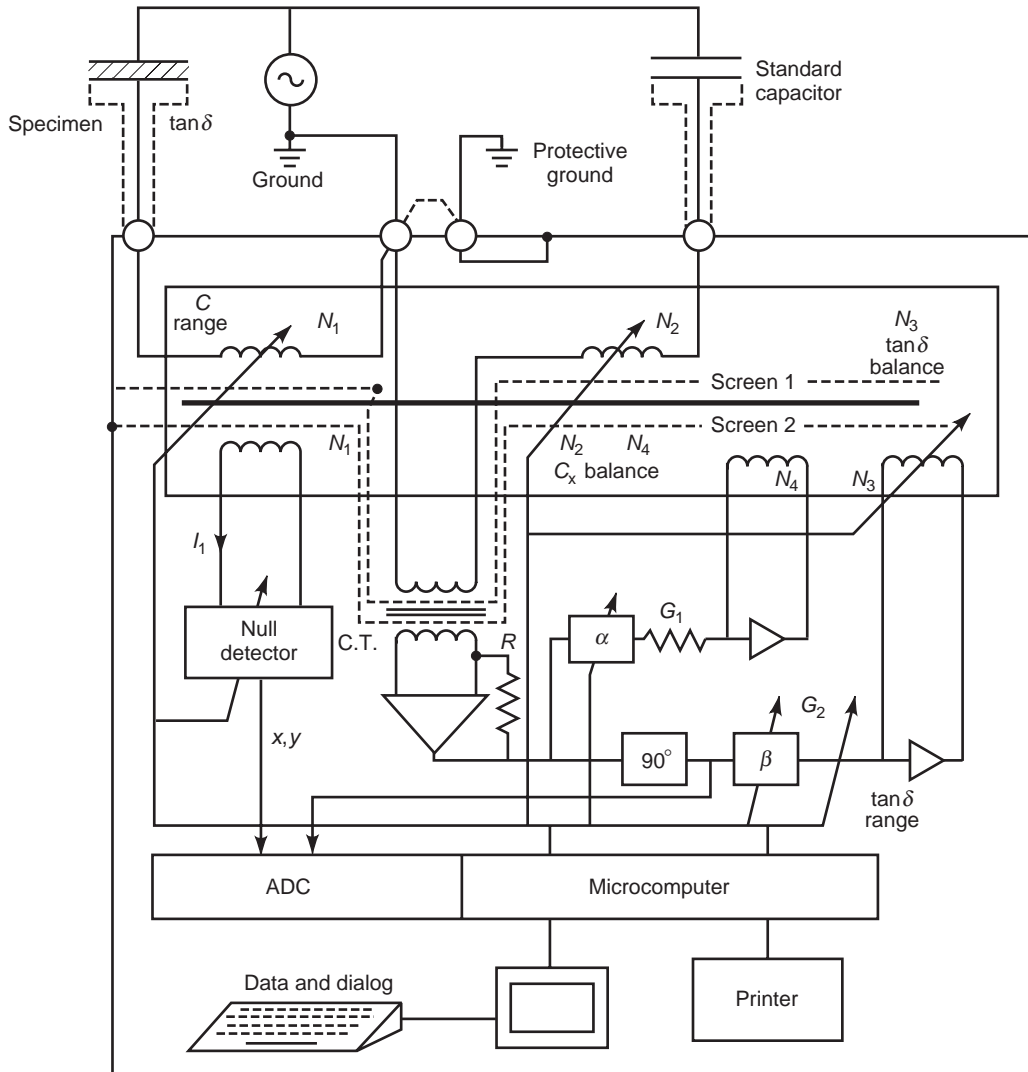


Figure 12. Automated power frequency transformer ratio arm bridge with computer control for measurements at high voltages [24].

coarse and fine balances are obtained by variation of the current comparator windings N_1, N_2 and N_3, N_4 , respectively. The currents in N_3 and N_4 are controlled by the multiplying analog-to-digital converters (ADCs), α and β , respectively, and are proportional to the current in the standard high-voltage capacitor C_s . The ampere turns equation for the balance condition at an applied voltage V across the specimen when the current I is equal to zero in the winding of the null detector N_1 is given by

$$V(G_x + j\omega C_x)N_1 = j\omega C_s V(N_2 + \alpha R G_1 N_4 - j\beta R G_2 N_3) \quad (46)$$

Equating the real and imaginary terms leads to the approximate expressions for the parallel, equivalent capacitance C_x and dissipation factor $\tan \delta$ of the dielectric [18,24]:

$$C_x = \frac{(N_2 + \alpha)C_s}{N_1} \quad (47)$$

$$\tan \delta = \frac{\beta R G_2}{1 + \frac{\alpha}{N_2}} \quad (48)$$

The automation of the power frequency transformer ratio arm bridge results in a reduction of the accuracy of the $\tan \delta$ measurement from $\pm 1 \times 10^{-7}$ to $\pm 1 \times 10^{-5}$.

2.3. Radiofrequency Methods (1–200 MHz)

Bridge techniques become unsuitable for measurements at frequencies beyond 1 MHz, because of the onset of inductance effects and, as a consequence, within the radio-frequency region of 1–200 MHz, resonance rise (Q meter) or susceptance variation methods must be employed [2,18]. Within these frequencies, three-terminal techniques become inapplicable cable and measurements must be carried out using two-terminal specimen holders.

The basic Q -meter circuit is shown in Fig. 13, in which the capacitance and $\tan \delta$ values of the specimen are determined in terms of a variable standard capacitor C_s and

the quality factor Q of the circuit. The coil L denotes a range of shielded fixed-inductance coils that are employed to establish resonance of the circuit with the specimen (G_x, C_x) inserted and removed. By definition, the Q value of the circuit is equal to the ratio of the peak voltage V_0 across the oscillator to that across the inductance, V_L such that

$$\begin{aligned} \frac{V_0}{V_L} &= \left(1 + \frac{\omega^2 L^2}{R^2}\right)^{1/2} \\ &= (1 + Q) \\ &\simeq Q \end{aligned} \quad (49)$$

for $Q \gg 1$. The voltmeter (V) of the Q meter is calibrated to read the Q values directly, since Q is given by V/IR . Representing the values of C'_s, Q' and C_s, Q as those obtained with the specimen disconnected and connected, respectively, yields the capacitance C_x and $\tan \delta$ values of the specimen as

$$C_x = C'_s - C_s \quad (50)$$

and

$$\tan \delta = \frac{1}{Q_x} \quad (51)$$

where

$$Q_x = \frac{C'_s - C_s}{C'_s} \frac{Q' Q}{Q' - Q} \quad (52)$$

When the measurements are carried out at high frequencies, a stiff short copper connecting wire should be employed between the specimen and the high-potential terminal of the Q meter, so that when disconnected, its same geometrical position, and configuration, a short

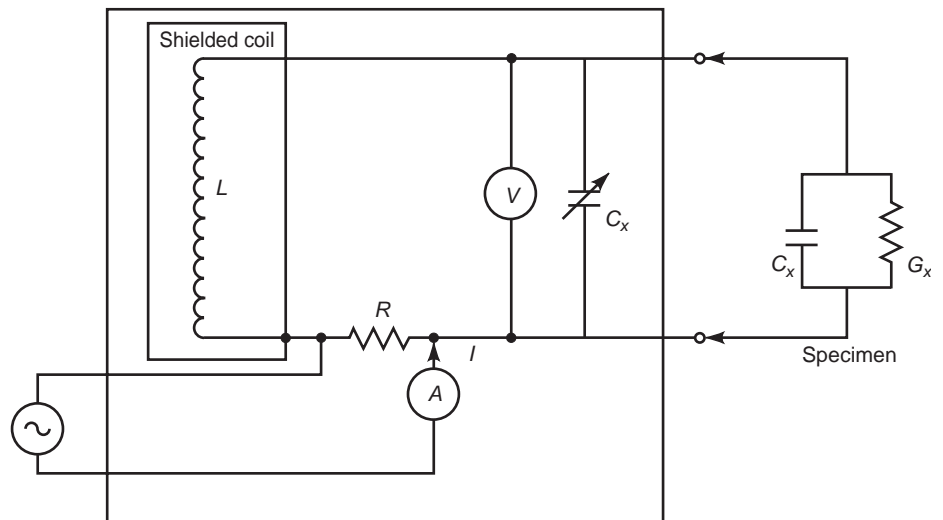


Figure 13. Q -meter circuit.

distance removed from the high-potential terminal, may be maintained, to ensure negligible change in the stray effects of the two positions of the connecting wire. With parallel-plane micrometer electrode specimen holders, accuracies of $\pm(0.1\% + 0.02 \text{ pF})$ and $\pm(2\% + 0.00005 \text{ pF})$, for the respective capacitance and $\tan \delta$ values of solid dielectric specimens may be achieved [16]. For solid specimens, an excellent precision reproducibility of $\pm 0.05\%$ and $\pm 5 \times 10^{-5}$ for C_x and $\tan \delta$, respectively, may be obtained by means of liquid displacement-type specimen holders [25]. A fluid displacement cell for use at 1 MHz, consisting of a fixed-plate, two-terminal, self-shielding capacitor, in which the edge and ground effects are taken into account, is depicted in Fig. 14.

The cell is most frequently employed for measurements at 1 MHz on polyethylene, although cell designs for frequencies up to 100 MHz are available. The fluid that is used in conjunction with polyethylene specimens is silicone with a kinematic viscosity of 1.0 cSt ($1 \times 10^{-6} \text{ m}^2/\text{s}$) at 23°C , whose dielectric constant matches that of polyethylene, and whose $\tan \delta$ value between 100 kHz and 1 MHz is negligibly small (about 5×10^{-5}). The separation between the fixed measuring electrodes of the cell design in Fig. 14 is $1.52 \pm 0.05 \text{ mm}$, thereby restricting the specimen thickness 1.27 mm , in order to allow for the formation of a finite liquid film thickness on both sides of the solid dielectric specimen adjacent to the central (high-potential) and outer (ground potential) plate electrodes or terminals. Two identical sizes ($68.3 \times 100 \text{ mm}$) of polyethylene sheet or slab specimens are employed, and measurements are made on the specimens inserted in the silicone fluid and then on the silicone fluid itself with the specimens removed.

The real value of the permittivity or dielectric constant of the polyethylene specimen ϵ' is obtained from the relation

$$(\epsilon' - \epsilon'_1) = \frac{\Delta C}{C_0} \left(\frac{d_0}{d} \right) \quad (53)$$

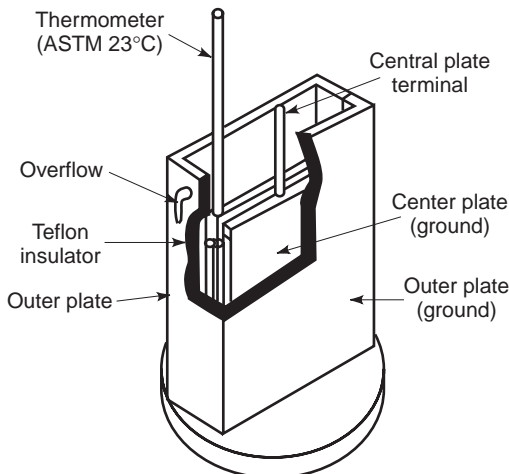


Figure 14. Fluid displacement cell with a fixed electrode separation equal to $1.52 \pm 0.05 \text{ mm}$ after ASTM Test Standard D1531 [25].

where ϵ'_1 is the real value of the permittivity of the silicone fluid at the measurement temperature, d_0 denotes the electrode separation, d represents the average thickness of the two specimens, and C_0 is the capacitance in vacuo of the double-plated capacitor within the fluid displacement cell, given by

$$C_0 = 2 \left[\frac{\epsilon_0 A}{d_0} \right] \quad (54)$$

where ϵ_0 is the permittivity of free space, A is the area of the center capacitor plate or electrode; the value of ΔC is obtained from

$$\Delta C = (C_2 - C_1) \quad (55)$$

where C_2 is the measured capacitance with the two solid dielectric specimens immersed in the silicone fluid and C_1 the corresponding value with the two specimens removed.

The dissipation factor, $\tan \delta$, of the two polyethylene specimens is defined by

$$\tan \delta = \tan \delta_1 + (\tan \delta_c - \tan \delta_1)[d_0/d] \quad (56)$$

where $\tan \delta_1$ the dissipation factor of the silicone fluid itself and is given by

$$\tan \delta_1 = C_T(Q_c - Q_1)/C_1 Q_0 Q_1 \quad (57)$$

where C_T represents the total capacitance of the tuned Q -meter resonant circuit prior to the connection of the specimen cell, Q_0 denotes the quality factor of the circuit at resonance prior to the connection of the ungrounded lead to the cell terminal, and Q_1 is the quality factor of the measuring circuit at resonance following the connection of the lead to the terminal of the cell containing the silicone fluid only, and C_1 the capacitance of the silicone fluid determined from the relation

$$C_1 = (C'_1 - C_1) \quad (58)$$

where C'_1 is equal to the capacitance reading following the connection of the leads to the circuit terminals before the connection of the ungrounded lead to the cell terminal. The value of the dissipation factor $\tan \delta_c$ obtained with the polyethylene specimens immersed in the cell, is determined from

$$\tan \delta_c = C_T(Q_0 - Q_2)/(\epsilon'_1 C_0 + \Delta C) Q_0 Q_2 \quad (59)$$

where Q_2 is the quality factor with the two solid specimens inserted in the cell.

The susceptance variation method originally propounded by Hartshorn and Ward [26] with subsequent refinements [27,28] is perhaps the most common method utilized for permittivity and loss measurements over the frequency region extending from 100 kHz to 200 MHz. The technique is based on the half-power point measurements of voltage across an LC resonant circuit, with the solid or liquid specimen inserted and removed from the test cell. A

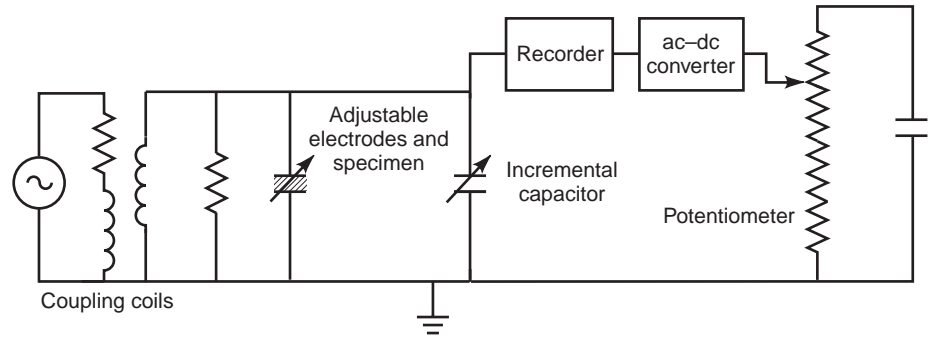


Figure 15. Schematic circuit diagram of modified Hartshorn-Ward susceptance variation circuit [27].

modified susceptance variation circuit and a cross-sectional profile view of the associated micrometer adjustable holder for solid specimens are depicted in Figs. 15 and 16, respectively. For liquids, the specimen holder is similar to that depicted in Fig. 16, except that two parallel concave electrodes are employed to permit containment of the liquid specimen.

The micrometer adjustable electrode system depicted in Fig. 16 portrays a solid dielectric specimen between plane-parallel electrodes. In the measurement procedure, resonance is first established with the specimen inserted between the electrodes and the maximum value of the voltage e_1 of the AC-DC converter is recorded. Thereafter, the specimen is removed and the separation of the electrodes is reduced until resonance is reestablished; this resonance point is characterized by a larger output voltage e_0 of the AC-DC converter. The capacitance of this air gap spacing is numerically equal to the capacitance of the specimen C_x and is obtained directly from the calibrated reading of the main micrometer setting. Manipulation of the main micrometer head, in conjunction with the small vernier or incremental capacitor, yields the half-power points of the resonance curve; the resulting width of the resonance curve is equivalent to a capacitance change, designated as ΔC_0 . It is the square law detection feature of the instrument that relates the ΔC_0 value directly to the recorded change of reading in the incremental capacitor. Hence the dissipation factor of the specimen [27] is

given by

$$\tan \delta = \left[\left(\frac{e_0}{e_1} \right)^{1/2} - 1 \right] \frac{\Delta C_0}{2C_x} \quad (60)$$

The real value of the permittivity ϵ'_r is normally obtained in terms of the thickness of the specimen d_s and the quantity, Δd

$$\epsilon'_r = \frac{d_s}{d_s - \Delta d} \quad (61)$$

where Δd represents the decrease in separation of the main electrodes in air required to restore the same capacitance as that obtained with the specimen placed between the electrodes. An accuracy of 1% is achievable on permittivity measurements and $\tan \delta$ may be determined to within $\pm 1.0 \times 10^{-6}$.

3. PERMITTIVITY AND LOSS MEASUREMENTS ON DISTRIBUTED PARAMETER SPECIMENS

Dielectric specimens behave as distributed parameter systems when the wavelength of the electromagnetic field becomes comparable to or is less than the physical dimensions of the specimen. The transition from lumped to distributed parameter behavior occurs generally within the frequency range from 300 MHz to 600 MHz. The high-frequency dielectric measurements represent a vast area of endeavor, which involves the use of resonant cavities of cylindrical and rectangular shapes, waveguides, or transmission lines, including quasioptical procedures, as well as optical methods requiring the use of spectrometers and interferometers. Since it would not be feasible within the space constraints to cover, even in a cursory manner, all test method variations over the millimeter and submillimeter wavelengths, the test procedures followed over this range of frequencies will be illustrated by a number of widely used and representative test methods.

3.1. Reentrant Cavity Method (300-600 MHz)

The reentrant cavity measurement technique constitutes, in essence, an extension of the Hartshorn-Ward method; it uses the same specimen cell arrangement, with the

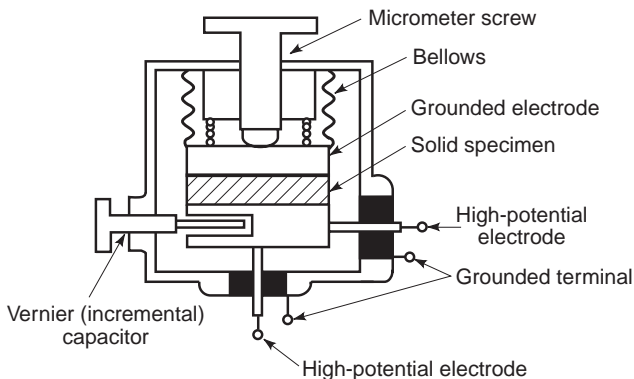


Figure 16. Micrometer adjustable electrode for use in conjunction with the susceptance variation circuit [26].

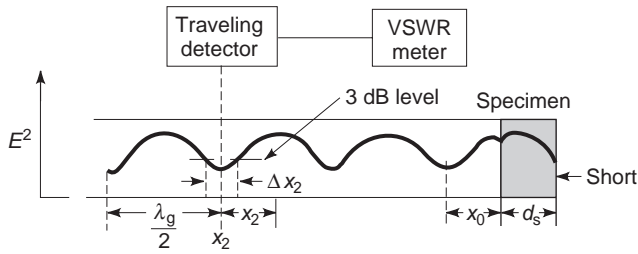


Figure 17. Standing voltage wave pattern in a short-circuited coaxial waveguide containing a solid dielectric specimen [2].

exception that the inner walls are silver-plated, and the oscillator signal is admitted into the cell cavity via a coupling loop with a detector loop situated on the opposite wall of the concentric coaxial cell cavity [29]. The reentrant cavity is calibrated as a wavemeter, with the main micrometer adjustable specimen capacitor acting as the prime frequency control device and the vernier capacitor as an incremental control device (refer to Fig. 16). As in the case of the Hartshorn–Ward technique, the dielectric parameters are determined in terms of the width of the resonance curve with the specimen inserted between the measurement electrodes and then removed.

3.2. Coaxial Line–Waveguide Methods (500 MHz–50 GHz)

Waveguide or transmission-line methods are based on the shorted coaxial-line technique developed by Roberts and von Hippel [30]. Although for low loss dielectric solids and liquids, the technique yields optimum performance for microwave frequencies up to 50 GHz; the method has been used up to 95 GHz [31]. The confinement of the electrical field within the hollow waveguide’s circular or rectangular geometry eliminates stray capacitance and inductance effects. A standing-wave pattern results within the waveguide, from a reflection of the incident wave at the short-circuit termination adjacent to where the solid specimen is inserted as depicted in Fig. 17. When liquid specimens are tested, the waveguide is mounted in a vertical position [18]. Figure 17 indicates the position of the electrical nodes (position of the interference minima), with the width of the nodes, Δx , as indicated at the 3-dB points.

In terms of Δx , the voltage standing-wave ratio, abbreviated as VSWR, or r , may be expressed as

$$r = \lambda_{gs} / \pi \Delta x \tag{62}$$

where λ_{gs} is the wavelength of the slotted coaxial line; it is along the slot that a traveling probe is displaced to determine the VSWR. Since the value of Δx changes when the specimen is removed from the waveguide, the VSWR (r) also changes accordingly.

Perhaps one of the most common shorted coaxial transmission line arrangements in use is that described in ASTM D2520 [32], which is suitable for temperature-controlled measurements up to 1650°C, when utilized in conjunction with a platinum alloy with 20% rhodium as the material for the specimen holder; its schematic diagram is delineated in Fig. 18. A micrometer adjustable specimen capacitor acting as the prime frequency control device and the vernier capacitor as an incremental control device (refer to Fig. 16). As in the case of the Hartshorn–Ward technique, the dielectric parameters are determined in terms of the width of the resonance curve with the specimen inserted between the measurement electrodes and then removed.

$$\begin{aligned} \lambda_{gh}^{-2} &= \lambda_0^{-2} - \lambda_c^{-2} \\ &= \lambda_0^{-2} - (2a)^{-2} \end{aligned} \tag{63}$$

where λ_0 is the wavelength of the radiation in free space and is equal to c/f , where c is the velocity in free space and f is the frequency.

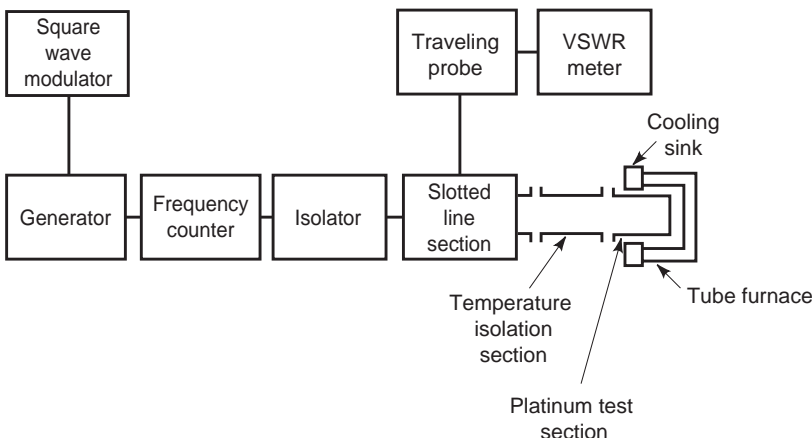


Figure 18. Schematic diagram of short-circuited rectangular waveguide with a temperature-controlled test specimen section (after ASTM D2520) [32].

With the specimen of thickness d_s inserted adjacent to the short in the waveguide, the impedance of the line at the specimen–air interface [33] is given by

$$Z_{in} = (j\omega\mu_0/\gamma_2) \tanh(\gamma_2 d_s) \quad (64)$$

where μ_0 is the permeability of the nonmagnetic dielectric material, which is identical to that in free space. Assuming negligible losses in the walls of the waveguide, the propagation constant of the coaxial waveguide γ_2 containing the specimen is given by

$$\gamma_2 = 2\pi(\lambda_c^{-2} - \epsilon'_r \lambda_0^{-2})^{1/2} \quad (65)$$

The load impedance at a phase distance φ from the observed electrical node for the value of the VSWR r given by Eq. (62), (34) is

$$Z_{meas} = f\mu_0\lambda_g[(1 - jr \tan \varphi)/(r - j \tan \varphi)] \quad (66)$$

where λ_g is the wavelength of the guide and is equal to $2\pi/\beta_2$; here β_2 is the phase coefficient of the waveguide with the specimen inserted; φ is the corrected phase distance, defined by

$$\varphi = 2\pi[(N/2) - (d_s/\lambda_{gh}) \pm (x_2 - x_1)\lambda_{gs}] \quad (67)$$

where N represents the smallest integer for which φ is positive, x_2 is the position of the traveling detector with the specimen inserted, as indicated in Fig. 17, and x_1 is the equivalent distance with the specimen removed.

Equating the impedances Z_{in} and Z_{meas} yields

$$\frac{\tanh \lambda_2 d_s}{\gamma_2} = \frac{\lambda_{gh}(1 - jr \tan \varphi)}{2\pi j(r - j \tan \varphi)} \quad (68)$$

Equating the real and imaginary terms yields the relative real value of the permittivity ϵ'_r of the specimen as

$$\epsilon'_r = [(\beta_2/2\pi)^2 + \lambda_c^{-2}]/\lambda_0^{-2} \quad (69)$$

and, for low-loss specimens [34], the dissipation factor simplifies to

$$\tan \delta = \frac{\Delta x(1 - \lambda_0^2/\epsilon'_r \lambda_c^2)(1 + \tan^2 \varphi)}{d_s\{[1 + \tan^2 \beta_2 d_s] - [(\tan \beta_2 d_s)/\beta_2 d_s]\}} \quad (70)$$

where the width of the node Δx that would be measured at the face of the specimen is given by

$$\Delta x = \Delta x_2 - \Delta x_1 \quad (71)$$

The principal factors affecting the accuracy of the measurements are associated with the assumption that losses at the walls of the waveguide are negligible and that the finite airgap between the solid specimen and the walls of the waveguide does not influence appreciably the results; evidently, the latter error does not arise with liquid specimens [18]. However, accuracies of $\pm 1\%$ for ϵ'_r and ± 200 radians for the loss angle δ are achievable.

3.3. Resonant Cavity Methods (about 500 MHz–60 GHz)

A resonating cavity may be viewed as a transmission line, which is shortened at both ends that are separated by an arbitrary multiple of one-half the operating wavelength. The insertion of a dielectric specimen into the cavity alters the wavelength and, as a consequence, the change in the quality factor Q of the cavity with the specimen inserted and removed can be used to derive the dielectric parameters of the specimen. Since resonant cavities have intrinsically high values of Q , they constitute an effective means for measuring low-loss dielectric materials. The specimens may have different geometrical configurations such as spheres, sheets, disks, rods, and so forth, and may fill the cross section of the beam, if necessary. The required specimen size becomes smaller as the cavity size diminishes with frequency, thereby also necessitating a redesign of the cavity with each octave increase in frequency. For frequencies above 60 MHz, the reduced cavity sizes, irrespective of their shape, rapidly approach a practical limit. Although open resonant cavities or interferometers may exceed substantially the frequency of 60 MHz [35] their applicability is confined to specimens having dielectric constants in excess of 5.

A coaxial waveguide shorted at one end becomes a resonant cavity when shorted at both ends. It may be resonated either by varying the frequency of the externally applied field or by varying the radial or axial dimensions of the cavity itself. A very widely used rectangular microwave cavity design for operation in the transverse electric field, TE_{10N} mode, is depicted in Fig. 19. Note that, in the mode designation code, the first subscript denotes the number of half-waves across the short-circuited waveguide, the second subscript refers to the number of half-waves from top to bottom of the waveguide, and the third subscript represents the odd number of half-waves along the waveguide. The closed cavity arrangement in Fig. 19 is identical to that given in the test method described in ASTM D2520 [32]. It is of paramount importance that the diameter of the iris holes in the transmitting and detecting ends be small to achieve high Q values. The particular design of the shown resonant cavity is intended for use with solid rod-shaped specimens, which are held suspended between the top and bottom holes that are drilled into the waveguide (refer to Fig. 19). The resonant frequency of

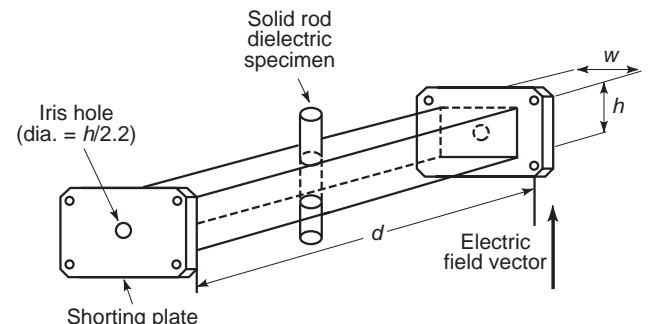


Figure 19. Closed rectangular resonant cavity for tests on solid rod-shaped dielectric specimens (after ASTM D2520) [32].

the specimen is defined by

$$f_0 = 15[(1/w)^2 + (N/d)^2]^{1/2} \quad (72)$$

where d is the physical length of the closed cavity and w its width (both in cm), N denotes the odd number of half-waves along the cavity, and the resonant frequency is in GHz. It is palpably evident, from Eq. (72), that higher test frequencies require closed cavities with increasingly reduced physical dimensions.

The measurements may be carried out either by means of the traditional VSWR meter utilizing a point-by-point approach or, for more rapidly obtainable results, a frequency sweep generator may be employed, as portrayed in the schematic test circuit of Fig. 20, in accordance with an IEC method [36]. The latter method may be computerized, in order to minimize errors, by recording simultaneously dual outputs from the signal generator and the cavity.

The measurements are carried out with the empty cavity and then with the specimen inserted. The quality factor Q_0 of the empty cavity is given by

$$Q_0 = \frac{f_0}{\Delta f_0} \quad (73)$$

where the half-power bandwidth of the empty resonant cavity is

$$\Delta f_0 = f_{02} - f_{01} \quad (74)$$

and f_{01} and f_{02} are the lower and upper frequency half-power (3 dB) points; the 3 dB points are established by means of a variable precision attenuator. When the specimen is inserted into the cavity, the quality factor Q_s becomes

$$Q_s = \frac{f_s}{\Delta f_s} \quad (75)$$

where f_s the new resonant frequency of the closed cavity containing the specimen and the half power bandwidth is

$$\Delta f_s = f_{s2} - f_{s1} \quad (76)$$

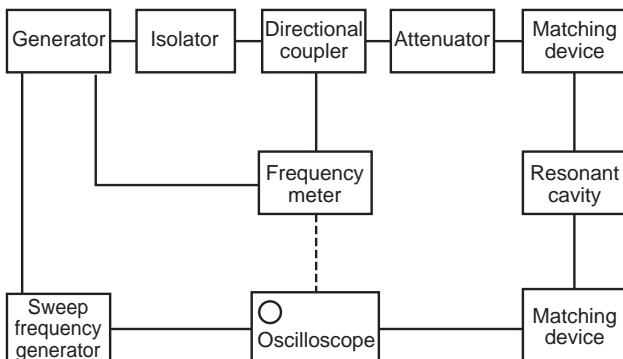


Figure 20. Microwave closed resonant cavity measurement system, using a sweep frequency generator technique (after IEC Publ. 377-2) [36].

where f_{s2} and f_{s1} are respectively, the upper and lower 3 dB point frequencies. The value of the relative real permittivity ϵ'_r and the dissipation factor $\tan \delta$ may now be determined from

$$\epsilon'_r = \left[\left(\frac{V_0(f_0 - f_s)}{2V_s f_s} \right) + 1 \right] \quad (77)$$

and

$$\tan \delta = \frac{\left[\frac{V_0}{4V_s} \left(\frac{1}{Q_s} - \frac{1}{Q_0} \right) \right]}{\left[\left(\frac{V_0(f_0 - f_s)}{2V_s f_s} \right) + 1 \right]} \quad (78)$$

where V_s and V_0 are respectively, the volumes of the specimen and the empty cavity. Note that the measured quantities are not contingent on the dimensions of the closed cavity. An accuracy to within 0.5% for the permittivity and approximately 5% for the dissipation factor are attainable. The specimen size and location within the cavity plays an important role; these two parameters influence the magnitude of the difference between Q_s and Q_0 on which the precision and accuracy depend. A high Q value for the cavity is thus important, since the 3 dB point frequencies become more clearly defined.

3.4. Quasioptical and Optical Methods (30–3000 GHz)

Dielectric measurements at microwave frequencies in excess of 60 GHz become increasingly arduous, as a result of the unduly small size of resonant cavity required. The difficulty is circumvented by employing for the microwave frequency range the same methods as those that are utilized in lightwave optics; such procedures are commonly referred to as *quasioptical* or *free-space techniques*. In analogy to an optical spectrometer, the collimator in a quasioptical microwave-type instrument consists of a parabolic reflector connected to a microwave generator, with the plane-wave source directed toward the dielectric specimen [37]. The latter is in sheet form and is mounted upon an object table, as in the case of an optical spectrometer. Another parabolic reflector (substituting an optical telescope), connected to a detector, receives the signal, which is either reflected from or transmitted through the sheet specimen. Thus, the resulting attenuation in the path between the transmitting and receiving parabolic reflectors constitutes a measure of the dielectric loss in the intervening dielectric sheet [38].

Quasioptical techniques also include the use of optical cavity resonators, which are suitable for measurements within the millimeter and submillimeter wavelengths of the electromagnetic spectrum. This differs from the usual closed cavity microwave resonator, in that the length of the resonator corresponds to a length number of wavelengths, while the specimen (in sheet form) assumes only a small fraction of the overall length [2]. There are three types of quasioptical resonator: the classical Fabry–Perot interferometer, the confocal resonator, and the semiconfocal resonator. The confocal resonator has the advantage that the electric field is more confined to the axis of the

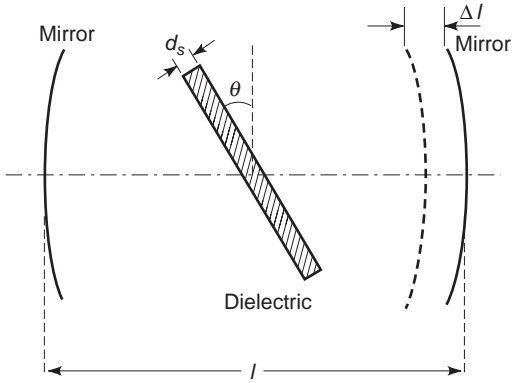


Figure 21. Quasioptical confocal resonator arrangement [39].

resonator, resulting in Q values generally higher than 10^5 and lower diffraction losses. The Q of a semiconfocal resonator is approximately equal to half that of the confocal resonator.

For illustrative purposes, the measurement procedure followed with a quasioptical confocal resonator [39], delineated in Fig. 21, will be described, which has been successfully used at frequencies up to 343 GHz. As with any resonant cavity, the resonant frequency of the quasi-optical cavity is perturbed by the insertion of the specimen. The specimen is intentionally mounted at an angle, θ , to the vertical axis of the cavity, in order to eliminate standing-wave phenomena. The angle permits the waves reflected from the air–dielectric interface to escape from the resonator. The resonance is restored by reducing the distance ℓ between the two mirrors by an amount equal to $\Delta\ell$. The real value of the index of refraction n' of the specimen (39) is then given by

$$n' = (\epsilon'_r)^{1/2} = \left(1 + \frac{\Delta\ell}{d_s} - \frac{\varphi}{\beta_0 d_s}\right) \tag{79}$$

where d_s is the thickness of the dielectric specimen, β_0 is the phase factor in free space and is equal to $2\pi/\lambda_0$, and the angle φ is defined by

$$\varphi = \tan^{-1} \left[\frac{\sin 2n'\beta_0 d_s}{\left(\frac{n'+1}{n'-1}\right) - \cos 2n'\beta_0 d_s} \right] \tag{80}$$

For $\tan \delta$ measurements, the length of the empty quasioptical confocal resonator must be adjusted to an odd number of half-wavelengths at the resonant frequency for which the Q value is to be determined. The specimen must then be inserted at a position vertical to the axis of the resonator—that is, with $\theta = 0$, the Q value is maximized as the escape of the power from the resonator is minimized. With the resonant frequency restored as each mirror is moved inward a distance, $\Delta\ell/2$, the quality factor, Q_s , with the specimen inserted is then determined. The expression

for the dissipation factor [39] follows as

$$\tan \delta = \frac{\beta_0 \ell - \beta(\Delta\ell + d_s) \left[1 + \frac{\sin \beta_0(\Delta\ell + d_s)}{\beta_0(\Delta\ell + d_s)}\right]}{Q_s \eta^2 (\epsilon'_r)^2 \beta_s d_s \left[1 + \frac{\sin \beta_s d_s}{\beta_s d_s}\right]} + \frac{1}{Q_s} - \left\{ \frac{Q_0 \lambda_0 / 2\pi \ell}{\eta^2 (\epsilon'_r)^2 \beta_s d_s \left[1 + \frac{\sin \beta_s d_s}{\beta_s d_s}\right]} \right\} \tag{81}$$

where β_s is the phase constant in the dielectric medium and is equal to $2\pi/\lambda_s$; the value of η is

$$\eta = \left\{ \frac{[(n')^2 + \omega t^2 \beta_0 x_1] / (n')^2}{1 + \omega t^2 \beta_0 x_1} \right\} \tag{82}$$

where x_1 denotes the distance from the reflector to the dielectric sheet.

In the frequency range from 300 to 3000 GHz (wavelengths of 1 mm–100 μ m), true optical measurement techniques are employed. As this wavelength range overlaps the infrared region, infrared sources and detectors are utilized. If a broadband radiation source is employed, the component measurement frequencies, appearing at the output of an interferometer, are selected by means of a computer in terms of their Fourier components. Broadband radiation sources require more sensitive detectors; it is for this reason that laser sources, although monochromatic, appear to be more popular.

Figure 22 depicts an arrangement for the measurement of dielectric absorption at optical frequencies, utilizing a laser source [40]. The attenuation of the transmitted signal is obtained by comparing the amplitude of the signal transmitted through the specimen V with a monitored incident signal V_m . The method entails the use of different specimen thicknesses d_s , which requires adjustment of the polarizing attenuator, in order to maintain a constant transmission loss.

The dissipation factor is related to the absorption coefficient a_p , which obtained from the relation [40]

$$\ln A = a_p d_s + \text{constant} \tag{83}$$

the units of a_p are in nepers per cm; A is the reading of the attenuator, which is equal to $(\cos \varphi)^4$; here φ is the central polarizer angle of the attenuator. From the nature of Eq. (83), it is apparent that the absorption coefficient a_p can be obtained directly from a linear plot of $\ln A$ versus the specimen thickness d_s . The imaginary part of the index of refraction is equal to $ca_p/4\pi f$, where f is the frequency. Hence, the relative real value of the permittivity is given by

$$\epsilon'_r = (n')^2 - \left(\frac{ca_p}{4\pi f}\right)^2 \tag{84}$$

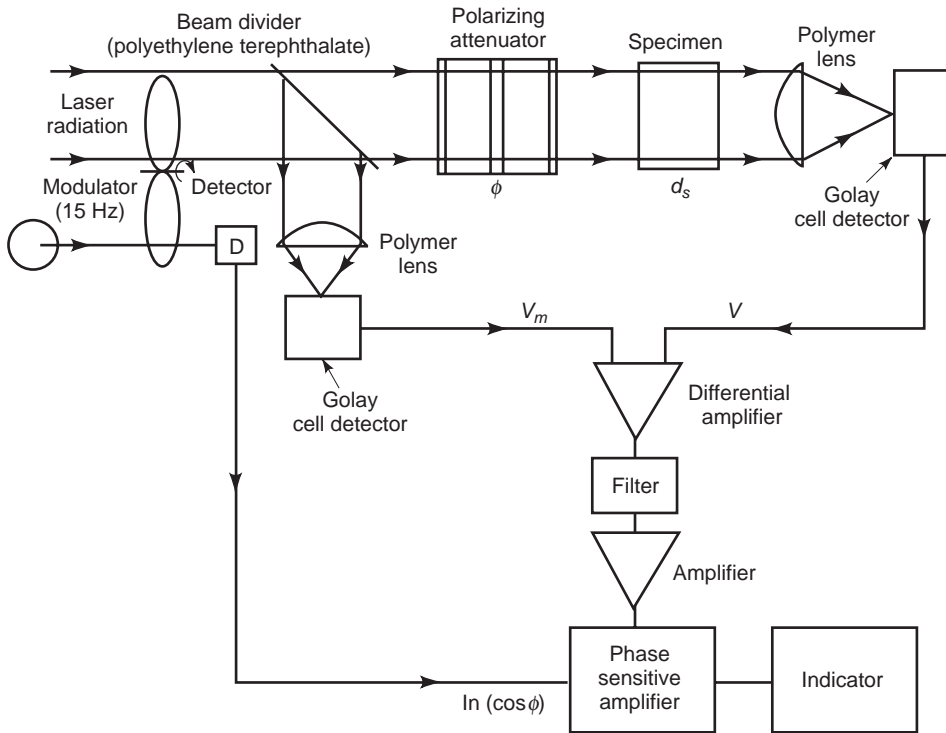


Figure 22. Dielectric absorption measurement system at optical frequencies with a laser radiation source [40].

and the relative imaginary value of the permittivity is

$$\varepsilon''_r = \frac{cn' a_p}{4\pi f} \quad (85)$$

The dissipation factor, which is equal to the ratio $\varepsilon''_r/\varepsilon'_r$ is then

$$\tan \delta = \frac{8\pi f n' c a_p}{(4\pi f n')^2 - (c a_p)^2} \quad (86)$$

The foregoing approach is based on transmission techniques, but laser source reflection arrangements are also available. It should be observed that there are a number of variations in the types of interferometers available for dielectric measurements, including the classical Michelson interferometer, which, in conjunction with a broadband radiation source, is suitable for measurements up to 3000 GHz. Laser, refraction measurements, based on the Mach-Zehnder approach, may also be employed to derive dielectric data. A comparison of the various optical measurement techniques at a large number of laboratories indicates that, whereas the real value of the index of refraction, n' , may be determined to an accuracy of 1%, the errors in the measurement of the absorption coefficient, a_p , may be as high as 37% [41].

4. VOLTAGE BREAKDOWN STRENGTH MEASUREMENTS

Voltage breakdown strength measurements are carried out on insulating materials to determine whether these materials can withstand certain operating stresses without failure. Since voltage failure is frequently initiated at

fault sites within solid insulating materials, the dielectric strength serves as an indicator of the homogeneity of the material. In liquid dielectrics, low dielectric strength values may be associated with moisture content, electrolytic contamination, and a high particle content. With gases for which the dielectric strength is a definite function of the composition of the gas (pure or mixture), dielectric strength data may be used to detect contamination from other gases, as well as determine the breakdown characteristics of intentionally combined gas mixtures.

The dielectric strength of insulating materials is highly contingent on the geometry of the test electrodes utilized. Sharp accentuated electrode edges lead to electrical field concentrations at the edges, which cause initiation of voltage breakdown of the material at voltages substantially below those that can be achieved under more uniform electrical field conditions. Thus voltage breakdown data are inextricably associated with the specific geometry of the test electrodes employed.

The true value of the breakdown strength or, more specifically, the intrinsic breakdown strength of the dielectric is obtained when the applied electric field is perfectly uniform. A uniform field can be achieved by means of Rogowski-Rengier profile electrodes; however, the application of such recessed-type electrodes to solid specimens requires the embedding of the electrodes into the solid dielectric by means of a suitable molding process when plastic dielectrics specimens are tested. Several relatively simple recessed electrode systems have been developed, which do not entirely produce a uniform field, but that improve the electrical field configuration appreciably, thereby permitting the attainment of dielectric strengths approaching the intrinsic value. One such simplified arrangement is depicted in Fig. 23 [42].

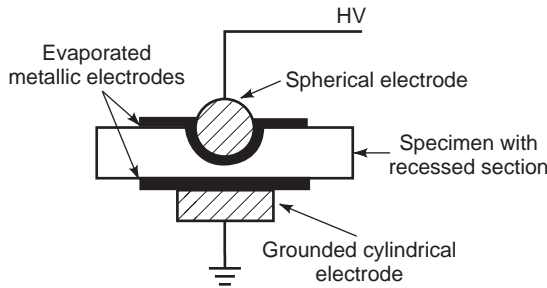


Figure 23. Spherical HV electrode with recessed solid specimen [42].

The recess in the rigid solid dielectric may be machined to form a highly stressed region in the specimen, with the electrodes vapor deposited on the dielectric to preclude any air gaps between the electrodes on the specimen. Alternatively, with nonporous solid dielectrics, conducting silver paint may be applied. Should sparkover occur at the edges prior to dielectric breakdown, the entire electrode assembly may be immersed in a mineral or silicone oil bath, provided the solid specimen is a nonporous material. The conductivity σ_m and dielectric constant ϵ'_m of the immersing medium must be selected such that under DC test voltages [43]

$$\sigma_m E_m > \sigma_s E_s \tag{87}$$

where E is the electric field and the subscripts “m” and “s” refer, respectively, to the oil medium and the solid specimen. Under alternating test voltages, we obtain

$$\epsilon'_m E_m > \epsilon'_s E_s \tag{88}$$

If the liquid is partially conducting, then

$$\epsilon'_m E_m \sec \delta_m > \epsilon'_s E_s \sec \delta_s \tag{89}$$

where δ is the loss angle.

Although the intrinsic strength of a dielectric material provides information on the maximum breakdown strength attainable for that material and thus is used to ascertain the nature of the mechanism responsible for the breakdown, it is, per se, of little consequence in practice. In fact, the intrinsic breakdown strength is usually one to several orders of magnitude higher than the electrical breakdown stress obtained with regular parallel-plane electrodes, or with the various electrical insulation configurations existing in different electrical apparatus. For this reason, the type of electrodes used in standard routine breakdown tests on materials are relatively simple to use, and are designed to provide reproducible results primarily for comparison purposes.

4.1. Electrode Systems for Routine Breakdown Tests on Solid Specimens

Present practice in assessing the breakdown strength and the quality of solid, liquid, and gaseous dielectric materials for use in electrical apparatus and cables involves the

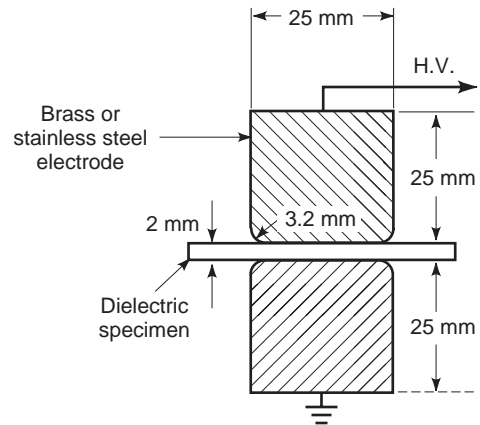


Figure 24. Equal-diameter electrode system for dielectric strength measurement on sheet materials (after ASTM D149) [44].

use of a number of electrode systems, in accordance with national and international standards. For solid materials, the most commonly employed electrode system is the one-inch or 25-mm two-cylindrical electrode equal-diameter system portrayed in Fig. 24 [44]. The edges of the electrodes are rounded to a radius of 3.2mm, to minimize stress enhancement. In all dielectric strength tests, the thickness of the specimen must be specified, because the voltage stress, at which breakdown occurs, increases with a reduction of the specimen’s thickness. Thus, although very thin solid dielectric films may break down at low voltages, the corresponding breakdown stresses are appreciably higher than those for thick films of the same material, even though the latter may undergo breakdown at much higher applied voltages.

It is evident that equal-diameter electrodes systems must be concentric. This requirement may be circumvented by the use of two electrodes with different diameters, in accordance with IEC Publication 243, as depicted in Fig. 25 [45]. Note that the IEC (International Electrotechnical Commission) standard specifies dielectric specimen thicknesses equal to or less than 3.0 ± 0.2 mm. If tapes of reduced width are tested, then rod electrodes of the geometry delineated in Fig. 26 are utilized. When

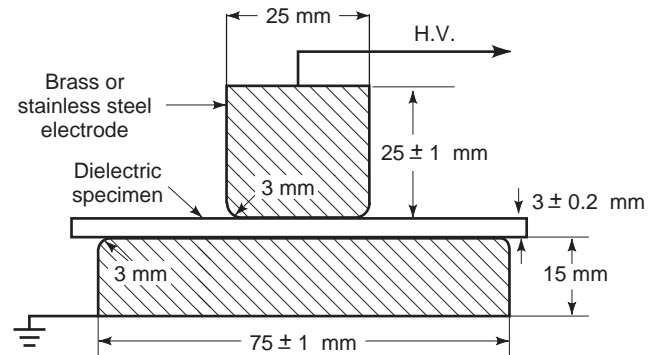


Figure 25. Unequal-diameter electrode system for dielectric strength measurements on sheet materials (after IEC Publication 243) [45].

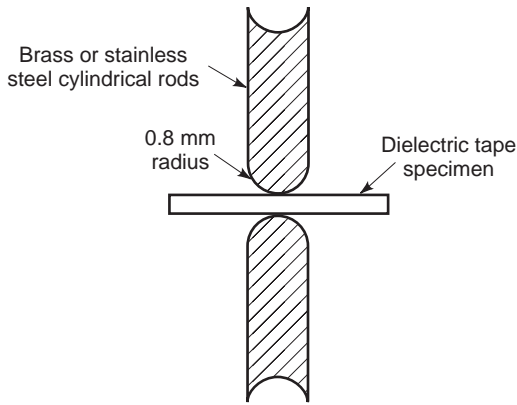


Figure 26. Cylindrical rod electrodes for dielectric strength measurements on thin narrow plastic tape or other narrow specimens (after ASTM D149) [44].

breakdown tests are carried out on thin inorganic films with application to electron devices, miniature counter electrodes are vapor deposited onto the surface of the specimen. For the evaluation of embedding compounds or greases, the standard procedure of ASTM D149 requires hemispherical electrodes, having an equivalent diameter of 12.7 mm [44].

The foregoing described electrode systems for solid dielectric specimens are suitable for tests under AC power frequency, DC, and impulse conditions. The electrode systems, for routine determination of the dielectric strength of liquids, differ from those described for solids. Routine acceptance tests on oils of petroleum origin for electrical apparatus and cables are carried out with an oil cup containing parallel-plane polished brass electrodes, with an interelectrode spacing of 2.5 ± 0.01 mm. The electrodes have a diameter of 25 mm and a thickness of 3 mm; they are square at the edges and are separated from the inner wall of the oil test cup by a distance of not less than 13 mm. The oil test cup assembly is shown in Fig. 27 [46]. The electrodes within the cell must be cleaned with a dry hydrocarbon solvent following each breakdown test; particular care must be taken to remove any carbonization

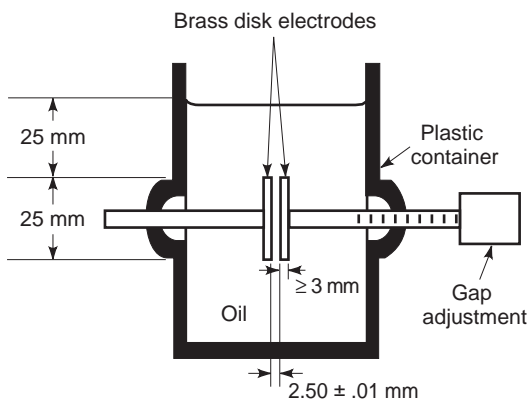


Figure 27. Parallel-plane square-edge electrode system for dielectric strength measurements on mineral oils (after ASTM D877) [46].

deposits on the electrodes, and the electrodes must be re-polished should any pitting of the surface manifest. Prior to admitting the liquid specimen into a cleaned test cell, the latter must be rinsed by the same liquid to remove any residues of the cleaning compound.

It is palpably evident from the geometric configuration of the square-edge electrodes in Fig. 27, that electrical stress enhancement occurs at the edges of the electrodes and that, therefore, breakdown is likely to occur there. For lower viscosity dielectric liquids (< 19 cSt or mm^2/s at 40°C), test electrodes, with the geometrical contour depicted in Fig. 28, have been found to be particularly effective in detecting decreases in the breakdown strength as a result of cellulose fiber contamination and absorbed moisture [47]. These electrodes are normally referred to as VDE (Verband Deutscher Electrotechniker)-type electrodes. Measurements of dielectric strength are performed with electrode separations of either 1 or 2 mm, with a gentle downward oil flow at the electrodes created by means of a rotating impeller located beneath the electrodes in the test cell.

Since oil-filled and impregnated electrical power equipment is subjected to lightning and switching impulses, it is important to assess the quality of the oil in terms of its impulse breakdown strength. Under nonuniform electrical field conditions, the dielectric strength of the oil is contingent on the polarity of the impulse in contradistinction to negligible differences observed under uniform fields. For this reason, nonuniform field electrode systems are frequently utilized for impulse tests. The electrodes may typically consist of either two 12.7 mm diameter brass or steel spheres or, for highly nonuniform fields, one such sphere and a steel needle point with a 0.06 mm radius of curvature at the needle tip [48].

The breakdown strength of gases is normally determined under quasiuniform AC field conditions. Typical electrodes utilized for this purpose consist of a sphere-to-plane geometry, wherein the electrical field is uniform directly underneath the sphere adjacent to the plane, becoming increasingly less uniform as the separation between the sphere and the plane increases. With a sphere-to-plane geometry, electrical breakdown tends to always occur in the uniform field region—that is, at the point where the separation between the sphere and the plane is least. The high-potential sphere electrode may

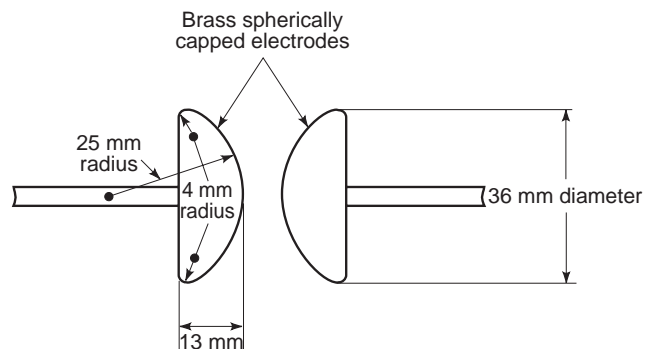


Figure 28. VDE electrode system for dielectric breakdown strength measurements on low-viscosity liquids [47].

be of steel with a diameter of 0.75 in. or 19.1 mm, and the ground potential electrode may be a cylindrical brass plane with a 1.5 inch or 38.1 mm diameter [49]. The tests are performed at 25°C at a standard pressure of 760 torr.

4.2. Voltage Breakdown Test Conditions and Procedures

The presence of lethal voltages in breakdown voltage tests necessitates strict adherence to high-voltage safety practices. Since the breakdown voltage may be a function of the ambient temperature, pressure, and humidity, depending on where solid, liquid, or gas specimens are tested, these parameters should be recorded at the time of the test; solid insulating materials should be conditioned prior to the breakdown test, so that they may reach thermal and moisture equilibrium with the environment. For more lossy solid and liquid specimens, the application of intense alternating electrical fields may result in cumulative heat generation due to dielectric losses, thereby leading to a thermal instability induced breakdown. Solid specimens may contain gas cavity inclusions, within which intense recurring partial discharges at elevated alternating fields may cause rapid deterioration of the adjacent solid insulation, thus leading to conspicuously lower breakdown strengths. Both thermal and discharge mechanism associated breakdowns account for the lower observed AC breakdown strengths, as opposed to those measured under DC and impulse conditions. Where the breakdown strength is controlled by the thermal and partial discharge mechanism, the breakdown process is a strong function for the time of voltage application. Accordingly, the rate of voltage rise in any voltage breakdown test is an important parameter.

For solid dielectrics, the rate of ac sinusoidal voltage rise is fixed usually at 500 V/s, though more rapid or slower rise rates may also be used. Breakdown or rupture of the dielectric is indicated by an audible voltage collapse across the specimen, as well as a visual burn at the tip of the breakdown. In order to minimize stress-induced aging effects in the insulation undergoing the voltage breakdown test, ASTM D149 stipulates that the duration of a short-time breakdown must not exceed 20 s. In the past, a voltage step test was employed, whereby the voltage was raised in steps; at each step it was maintained for a preset time, prior to the next-step increment in voltage, until the ensuence of dielectric breakdown event—that is, an abrupt voltage collapse across the specimen. The use of the step procedure was required in the absence of voltage sources with automatically regulated rate of voltage rise controls.

In DC dielectric breakdown strength determinations on dielectric material specimens, a single rate of voltage rise of 500 V/s is employed [50]. Under direct voltages, the initial breakdown event produces a minute channel in the volume of the solid dielectric, whose trace is not readily discernible. Reapplication of the direct voltage results in successively lower breakdown voltages, which confirm that a DC breakdown has already occurred. Also, the additional damage and burning produced within the breakdown channel renders it more visible.

Impulse tests on solid dielectric specimens are performed by increasing the peak voltage of the impulse gradually, from an initial peak value of 0.7 times the anticipated breakdown voltage [45,50]. The lightning impulse is simulated with an impulse waveform having a time to peak of 1.2 μ s and a decay time of 50 μ s to 50% of its initial peak value. Impulse breakdown is indicated by a voltage collapse at any point of the impulse waveform [2]; the peak voltage value of this impulse wave is considered as the impulse breakdown voltage. Location of the actual breakdown channel caused by an impulse may require, as in the DC case, several reapplications of the voltage pulse, to cause additional carbonization within the breakdown channel.

In the measurement of dielectric strength of liquid specimens at AC power frequencies using the parallel-plane square-edge electrodes, a fixed voltage rise of 3 kV/s is generally specified [46]. To avoid pitting of the test electrode surfaces, the short-circuit current at breakdown in the specimen is not permitted to exceed 10 mA/kV. For tests with the same electrode system under direct voltages, the same rate of voltage rise should be adequate. When the VDE-type electrodes are employed for low-viscosity liquids at power frequency, a much lower rate of voltage rise of 0.5 kV/s is preferred. Impulse breakdown tests performed on dielectric liquids are often carried out with both the simulated lightning impulse of the 1.2 by 50 μ s form and a switching surge impulse form with a 100 μ s risetime to peak and a decay time >1000 μ s. The impulse breakdown tests are carried out either at positive or negative polarities; often the measurements may be performed at both polarities. The measurement sequence at either polarity is begun at a voltage substantially below the expected impulse voltage breakdown level. Normally, three impulse waves are applied at each selected impulse voltage test level; it is an accepted practice to traverse at least three test levels prior to breakdown, with a fixed minimum time interval between each voltage level test. ASTM D3300 recommends a time interval of 30 s. The peak impulse voltage at breakdown is measured oscillographically across a calibrated resistive voltage divider. Whenever needle electrodes are employed, the geometry of the needle tip is altered, due to the energy released by the breakdown spark; this necessitates a change of the needle electrodes after each breakdown event.

Routine voltage breakdown strength measurements on insulating gases are normally performed under AC power frequencies, using a standard rate of voltage rise of 500 V/s [49]. The breakdown strength of gases is a function of gap spacing and gas pressure; since the value of the latter varies with the ambient temperature, both the pressure and temperature must be recorded for breakdown results obtained with a fixed gap setting.

It should be emphasized that, when the breakdown voltages are determined for solid, liquid, and gas specimens, the gap length or specimen thickness must be stated in each case. Even when the value of the voltage breakdown strength is provided in the units of voltage per unit specimen thickness, the specimen thickness must still be specified, because the breakdown strength is a function of the specimen thickness. Also, the dispersion in

the voltage breakdown data requires some form of statistical analysis. Breakdown strength data ordinarily refer to a mean measured value on 10 specimens. A low ratio (about 0.1) of the standard deviation to the mean value, derived from the ten measurements, is usually considered as an indicator of an acceptable probable error in the test results.

5. CONCLUDING REMARKS

The foregoing presentation of the measurement of conductivity, permittivity, and dielectric loss, and dielectric strength of electrical insulating materials has attempted to provide a concise cursory description of a number of the most common measurement techniques in use. Space limitations prevented a discussion on the various conduction and breakdown mechanism and their influence on the measured quantities. For a more in-depth discussion on the mechanisms involved and their determining inference on the measured quantities obtained with a variety of different test methods, the reader is referred to other literature [2,18,20,42].

BIBLIOGRAPHY

1. R. Bartnikas, Dielectrics and insulators, in R. Dorf, ed., *The Electrical Engineering Handbook*, CRC/IEEE Press, Boca Raton, FL, 1997, Chap. 55.
2. R. Bartnikas, ed., *Engineering Dielectrics*, Vol. IIB, *Electrical Properties of Solid Insulating Materials: Measurement Techniques*, STP926, ASTM, Philadelphia, 1987.
3. ASTM D257, *Standard Test Methods for D-C Resistance or Conductance of Insulating Materials*, *Annual Book of ASTM Standards*, Vol. 10.01, Philadelphia, 1997.
4. IEC Publication 93, *Methods of Test for Volume Resistivity and Surface Resistivity of Solid Electric Insulating Materials*.
5. ASTM D374, *Standard Test Methods for Thickness of Solid Electric Insulation*, *Annual Book of ASTM Standards*, Vol. 10.01, Philadelphia, 1997.
6. *Low Level Measurements*, 4th ed., Keithley Instruments, Cleveland, OH, 1993.
7. B. V. Hamon, An approximate method for deducing dielectric loss factor from direct current measurements, *Proc. IEE* **99**:151–155 (1952).
8. H. Block et al., Treatment of data in step-response, dielectric relaxation measurements, *J. Chem. Soc. Faraday Trans. II* **68**:1890–1896 (1972).
9. H. St-Onge, Electrical conduction in 3-percent carbon filled polyethylene—Part I: Low field results, *IEEE Trans. Electric Insul.* **EI-11**:20–27 (1976).
10. P. J. Hyde, Wide-frequency range dielectric spectrometer Part II, *Proc. IEE* **117**:1891–1901 (1970).
11. F. I. Mopsik, Precision time-domain dielectric spectrometer, *Rev. Sci. Instrum.* **55**:79–87 (1984).
12. A. M. Thompson, A bridge for the measurement of permittivity, Parts B and C, *Proc. IEE* **103**:705–709 (1955).
13. W. P. Harris, *Operators Procedures Manual for the Harris Ultra-Low Frequency Impedance Bridge*, National Bureau of Standards Report 9627, Washington, DC, 1968.
14. R. J. Krieglger and R. Bartnikas, Dielectric loss and current-voltage measurements in sodium-contaminated Si-SiO₂-Cr structures, *IEEE Trans. Electron. Devices* **ED-20**:722–731 (1973).
15. J. Pugh, *Proc. 4th Int. Conf. Dielectr. Mater. Meas. Appl.*, IEE Conf. Publ. 239, Lancaster, UK, Sept. 10–13, 1984, pp. 247–249.
16. ASTM D150, *Standard Test Methods for AC Loss Characteristics and Permittivity (Dielectric Constant) of Solid Electrical Insulating Materials*, *Annual Book of ASTM Standards*, Vol. 10.01, 1998.
17. H. J. Wintle and S. Kurylowicz, Edge corrections for strip and disc capacitors, *IEEE Trans. Instrum. Meas.* **IM-34**:41–47 (1985).
18. R. Bartnikas, ed., *Engineering Dielectrics*, Vol. III, *Electrical Insulating Liquids*, Monograph 2, ASTM, Philadelphia, 1994.
19. R. Bartnikas and K. D. Srivastava, eds., *Power Cable Engineering*, Sandford Fleming, Waterloo, Ontario, 1987.
20. R. Bartnikas and E. J. McMahon, eds., *Engineering Dielectrics*, Vol. I, *Corona Measurement and Interpretation*, STP 669, ASTM, Philadelphia, 1979.
21. A.G. Tettex, *Präzisions-Verlustfaktor und Kapazitäts MeBrücke Typ 2821*, Prospekt 2821, Blatt 103, Zürich 1980.
22. O. Petersons, A self-balancing high voltage capacitance bridge, *IEEE Trans. Instrum. Meas.* **IM-13**:216–224 (1964).
23. *Bridges/Standards*, Gen Rad Bulletin JN 4240-681, Gen Rad, Boston, MA.
24. P. Osvath and S. Widmer, A high-voltage high-precision self-balancing capacitance and dissipation factor-measuring bridge, *IEEE Trans. Instrum. Meas.* **IM-35**:19–23 (1986).
25. ASTM D1531. *Test for Dielectric Constant and Dissipation Factor of Polyethylene by Liquid Displacement Procedure*, *Annual Book of ASTM Standards*, Vol. 10.01, 1997.
26. L. Hartshorn and W. H. Ward, The measurement of the permittivity and power factor of dielectrics at frequencies from 10⁴ to 10⁸ cycles per second, *J. IEE* **79**:597–609 (1936).
27. W. Reddish et al., Precise measurement of dielectric properties at radio frequencies, *Proc. IEE* **118**: 255–265, (1971).
28. K. A. Buckingham and J. W. Billing, *Proc. 3rd Int. Conf. Dielectric Measurement Applications*, Birmingham, England, Sept. 10–13, 1979, pp. 392–395.
29. T. V. L. Parry, The measurement of permittivity and power factors of dielectrics at frequencies from 300 to 600 c/s, part III, *J. IEE* **98**:303–311 (1951).
30. S. Roberts and A. von Hippel, A new method for measuring dielectric constant and loss in range of centimeter waves, *J. Appl. Phys.* **17**:610–616 (1946).
31. W. B. Bridges, M. B. Klein, and E. Schweigh, Measurement of dielectric constant and loss tangent of thallium mixed halide crystals KRS-5 and KRS-6 at 95 GHz, *IEEE Trans. Microwave Theory Tech.* **MTT-30**:286–292 (1982).
32. ASTM D2520, *Test Methods for Complex Permittivity of Solid Electrical Insulating Materials at Microwave Frequencies and Temperatures to 1650°C*, *Annual Book of ASTM Standards*, Vol. 10.01, 1998.
33. W. B. Westphal, Distributed circuits, in A. von Hippel, ed., *Dielectric Materials and Applications*, Wiley, New York, 1954, Chap. 2, Sect. A2.
34. T. W. Dakin and C. Works, Microwave dielectric measurements, *J. Appl. Phys.* **18**:789–796 (1947).
35. A. C. Lynch, Transmission methods for measurement of dielectric loss, *Conf. High Frequency Dielectr. Meas.*, Natl. Physical Laboratory, Teddington, UK, March 27–29, 1972.
36. IEC Publication 377-2, *Measurement of Permittivity and Loss at Frequencies above 300 MHz*.

37. A. H. Sharbough and S. Roberts, Dielectric measurement procedures, in K. Lark-Horowitz and V. A. Johnson, eds., *Solid State Physics*, Vol. VI, Part B, Academic Press, New York, 1959, Chap. 7, Sect. 71.
38. W. Culshaw, A spectrometer for millimetre wavelengths, *Proc. IEE*, Part IIA, **100**:5–14 (1953).
39. J. E. Degenford, A quasi-optic technique for measuring dielectric loss tangents. *IEEE Trans. Instrum. Meas.* **IM-17**:413–417 (1968).
40. J. Chamberlain, Submillimetre-wave techniques, Conf. High Frequency Measurement, Natl. Physical Laboratory, Teddington, UK, March 27–29, 1972.
41. J. R. Birch et al., An intercomparison of measurement techniques for the determination of the dielectric properties of solids at near millimeter wavelengths, *IEEE Trans. Microwave Theory Tech.* **42**:956–965 (1994).
42. J. K. Nelson, in R. Bartnikas and R. M. Eichhorn, eds., *Engineering Dielectrics*, Vol. IIA, *Electrical Properties of Solid Insulating Materials: Molecular Structure and Electrical Behavior*, STP 783, ASTM, Philadelphia, 1983.
43. S. Whitehead, *Dielectric Breakdown of Solids*, Clarendon Press, Oxford, 1953.
44. ASTM D149, *Test Method for Dielectric Breakdown Voltage and Dielectric Strength of Electrical Insulating Materials at Commercial Power Frequencies*, *Annual Book of ASTM Standards*, Vol. 10.01, 1997.
45. IEC Publication 60, 243, Parts 1–3, *Electric Strength of Insulating Materials—Test Methods*.
46. ASTM D877, *Standard Test Method for Dielectric Breakdown Voltage of Insulating Liquids Using Disk Electrodes*, *Annual Book of ASTM Standards*, Vol. 10.03, 1997.
47. ASTM, D1816, *Standard Test Method for Dielectric Breakdown Voltage of Insulating Oils of Petroleum Origin Using VDE Electrodes*, *Annual Book of ASTM Standards*, 1997, Vol. 10.03; see also VDE (Verband Deutscher Elektrotechniker) Specification 0370.
48. ASTM D3300, *Standard Test Method for Dielectric Breakdown Voltage of Insulating Oils of Petroleum Origin under Impulse Conditions*, *Annual Book of ASTM Standards*, Vol. 10.03, 1997.
49. ASTM D2477, *Standard Test Method for Dielectric Strength of Insulating Gases at Commercial Power Frequencies*, *Annual Book of ASTM Standards*, Vol. 10.03, 1997.
50. ASTM D3755, *Test Method for Dielectric Breakdown Voltage and Dielectric Strength of Solid Electrical Insulating Materials under Direct Voltage Stress*, *Annual Book of ASTM Standards*, Vol. 10.02, 1997.

DIELECTRIC PERMITTIVITY AND LOSS

D. K. DAS-GUPTA
University of Wales
Bangor, Wales

Dielectrics can be defined as materials with high electrical resistivities that conduct virtually no electricity at low DC electric fields. A large group of materials, including gases, liquids, semiconductors, ceramics, and organic and inorganic polymers, are classified as dielectrics. There are, however, no perfect dielectric materials.

The study of the electrical properties of dielectrics arises from their practical need for efficient electrical insulation requirements for long operational life. Many dielectric materials are classified by their electrical breakdown strength, dielectric loss, permittivity, and polarization, and these macroscopic properties are related to their atomic and molecular structures. Although dielectrics are widely employed in diverse applications (e.g., capacitors, cables, transformers, motors), the study of dielectrics has progressed very little since the early investigation of ferroelectric phenomena. However, the advent of microelectronics and complex control devices and components in defense and industrial applications has made dielectric research important in its own right.

The present article briefly reviews the electrostatic concepts that lead to time- and frequency-dependent dielectric phenomena together with the models of dielectric relaxation behavior in various materials. It also includes some explanations for the dielectric aging of insulating materials under high fields in humid environments.

1. DIELECTRIC POLARIZATION

1.1. Static Field

When an electric field is applied to a dielectric material, three processes can occur:

1. A steady flow of direct current (due to the DC conductivity σ_0) may occur if free charges are capable of moving throughout the volume without restraint.
2. Bound charges can form dipoles by aligning with the field and provide *polarization*. On removal of the field the dipoles may return to their original random orientations with the help of thermal energy, giving rise to *dielectric relaxation*.
3. Electronic and ionic charges may hop through the defect sites. These charges are neither free nor bound, and they give rise to an intermediate form of polarization, which involves finite charge storage.

Dielectrics may broadly be divided into nonpolar and polar materials. In nonpolar materials in an external field a dielectric polarization occurs when the positive and negative charges experience an electrical force that causes them to move apart in the direction of the external field. As a result, the centers of positive and negative charges no longer coincide. The molecules are then said to be *polarized*, and each molecule forms a dipole and acquires a dipole moment \mathbf{p} , defined thus

$$\mathbf{p} = e \mathbf{dl} \quad (1)$$

where e is the electronic charge and \mathbf{dl} the displacement ($\sim 10^{-10}$ – 10^{-11} m in magnitude) between the two charge centers. Note that \mathbf{dl} is a vector that points from the negative to the positive charge. Such dipoles are called *induced* dipoles. On removal of the field, the charges are redistributed and the dipole moment vanishes.

With polar dielectrics, which lack structural symmetry, the charge centers of opposite polarities do not coincide for a molecule even in the absence of an electric field. However, these molecular dipoles may be randomly distributed, thus summing to a zero dipole moment over any macroscopic volume element [1–9]. In the presence of an appropriate electric field, the molecules may align themselves in the field direction and thus provide a net dipole moment.

Macroscopically, the electric field in a dielectric is described [2] by the electric field strength \mathbf{E} (V/cm) and the electrical displacement density, also known as the electric flux density, \mathbf{D} (C/m²), where both \mathbf{D} and \mathbf{E} are vector quantities. Now the polarization can be defined as the dipole moment per unit volume, namely

$$\mathbf{P} = \sum_{i=1}^N \mathbf{p}_i / \Delta v \quad (2)$$

and is also a vector quantity. It should be noted that the normal component of \mathbf{P} at the surface equals the surface charge density per unit area. These three vectors, \mathbf{D} , \mathbf{E} , and \mathbf{P} , in a material medium other than vacuum, are related thus

$$\mathbf{D} = \epsilon_0 \mathbf{E} + \mathbf{P} \quad (3)$$

or

$$\mathbf{D} = \epsilon \mathbf{E} \quad (4)$$

where

$$\epsilon = \epsilon_0 \epsilon_r \quad (5)$$

where ϵ_0 is the permittivity in free space (8.85×10^{-12} F/m) and ϵ_r is the relative permittivity (dimensionless) or the dielectric constant of the material, which takes into account the polarization effect and is defined as

$$\epsilon_r = \frac{C}{C_0} \quad (6)$$

where C_0 is the capacitance of a capacitor with a vacuum between two conductors and C the capacitance when the same region is filled with the dielectric. ϵ_r is independent of the shape or size of the conductors and is entirely a characteristic of the particular dielectric medium. Table 1 [4] gives the values of ϵ_r for static or low-frequency (<1-kHz) fields of several materials. ϵ_r , which is a macroscopic and directly measurable parameter, is connected with the microscopic structure of a dielectric material and with its polarization behavior.

From Eq. (3), we have

$$\begin{aligned} \mathbf{D} &= \epsilon_0 \left(1 + \frac{\mathbf{P}}{\epsilon_0 \mathbf{E}} \right) \mathbf{E} \\ &= \epsilon_0 (1 + \chi) \mathbf{E} \\ &= \epsilon_0 \epsilon_r \mathbf{E} \end{aligned} \quad (7)$$

Table 1. The Relative Permittivity of Some Solid Dielectrics at 25°C

Dielectric	ϵ_r
Vacuum	1 (by definition)
Air (atmospheric pressure, 0°C)	1.0006
Amber	2.7
Borosilicate glass	4.0
Corning glass 0010	6.68
Corning glass 0014	6.78
Pyrex glass	4–5
Quartz (fused)	3.8
Diamond	5.5
Porcelain	5.5
Marble	10–15
Mica	6–11
Steatite	6
Polyethylene	2.25
Polyvinylchloride (PVC)	6
Epoxy resin	3.6–11
Rubber	3–4
Neoprene	7
Beeswax (white)	2.65
Beeswax (yellow)	2.73
Paraffin wax	2.3
Barium titanate	1200

Source: Ref. 4.

where

$$\epsilon_r = 1 + \chi \quad \text{and} \quad \chi = \frac{\mathbf{P}}{\epsilon_0 \mathbf{E}} \quad (8)$$

and χ is the dielectric susceptibility. Thus the parameter χ also provides a link between the macroscopic properties and the atomic molecular theory of dielectric materials.

We may also write a general relation between \mathbf{P} and \mathbf{E} thus (8)

$$\mathbf{P} = \epsilon_r \chi \mathbf{E} + \text{higher terms in } \mathbf{E} \quad (9)$$

where the higher terms in \mathbf{E} are applicable to the phenomenon of hyperpolarization. It should be noted that χ is the ratio of bound charge density to free charge density of a capacitor. A measurement of ϵ_r and hence χ provides the magnitude of the polarization \mathbf{P} of a dielectric material at any particular field \mathbf{E} .

One of the most useful methods of determining \mathbf{P} is to measure the current density $\mathbf{J}(t)$ as a function of time, as [8]

$$\mathbf{J}(t) = \frac{d\mathbf{D}}{dt} \quad (10)$$

It may be shown [3,8] that for noninteracting dipoles, χ is given by

$$\chi(0) = \frac{NP^2}{3\epsilon_0 kT} \quad (11)$$

where $\chi(0)$ is the static susceptibility in the zero-frequency limit, N the number density of polarizable molecules, k the Boltzmann constant, and T the temperature. χ is a dimensionless and scalar quantity in an isotropic medium.

2. MICROSCOPIC CONCEPTS OF POLARIZATION

We shall consider here the three cases of electronic, ionic, and orientational polarizations.

An isolated neutral atom in an electric field acquires a dipole moment when an external electric field produces a separation of the charge centers of opposite polarities. This is known as the *electronic polarization*, and it provides an induced dipole moment

$$p_{\text{ind}} = \alpha_e \mathbf{E} \quad (12)$$

where α_e is the electronic polarizability of an atom and is given by

$$\alpha_e = 4\pi \epsilon_0 r_0^3 \quad (13)$$

where r_0 is the radius of the spherical of an electron cloud surrounding an atomic nucleus. The molar polarizability Π of a monoatomic gas is given by

$$\Pi = N_0 \frac{4\pi}{3} r_0^3 \quad (14)$$

where N_0 is the number of molecules in a gram molecule (Avogadro's number). The lowest polarizability belongs to the noble gases with their completely filled outer electronic shells, which screen the nuclei from the effect of the external electric field. For hydrogen, with $r_0 = 0.53 \times 10^{-10}$ m, α_e is 1.66×10^{-41} F/m². Hence for a field E of 10^5 V/m¹, $\alpha E = 10^{-36}$ C/m. The length l of this induced dipole is $p/e = 10^{-17}$ m (where e is the electronic charge), which is indeed an extremely small distance compared with atomic dimensions [6].

Ionic polarization occurs in ionic substances, such as alkali halides, whose molecules are formed of atoms that have excess charges of opposite polarities. In an external field the relative positions of the positive and negative ions of a molecule may shift, thus introducing the dipole moment in addition to the induced electronic polarization. The ionic polarization p_i is given by

$$p_i = \alpha_i \mathbf{E} \quad (15)$$

where α_i is the ionic polarizability of the molecule, which arises from the ionic displacement. The alkali halides (halides of the group I elements) have the highest polarizabilities, possibly because of the single electron in their outermost shells. Table 2 [6] provides a list of values of contribution of ions to the molar polarization of typical alkali halides.

The third type of polarization, known as the *orientational polarization*, is associated with permanent dipoles in dipolar materials that possess a dipole moment even in the absence of an externally applied electric field. However,

Table 2. Ionic Polarization as a Fraction of the Total Polarization for Alkali Halides, and (in Parentheses) the Ionic Polarization of Each Compound Relative to that of LiF

	F	Cl	Br	I
Li	0.68 (1.0)	0.53 (3.22)	0.49 (1.96)	0.40 (2.09)
Na	0.65 (1.12)	0.50 (3.38)	0.44 (1.82)	0.39 (2.13)
K	0.65 (1.95)	0.49 (4.25)	0.46 (2.38)	0.38 (2.34)
Rb	0.62 (2.19)	0.52 (5.14)	0.44 (2.46)	0.38 (2.62)

Source: Ref. 6.

such a moment may not be observed macroscopically, as the thermal energy will randomize the dipoles so that the average moment will be zero over a small physical volume. On an application of an external electric field the dipoles will experience a torque, which will orient them in the field direction so that the average dipole moment will no longer be zero. It may be shown [3] that the orientational polarizability α_0 is given by

$$\alpha_0 = \frac{p^2}{3kT} \quad (16)$$

By adding the three polarizabilities mentioned above, the total polarization P can now be written as the sum of the three components

$$\mathbf{P} = p_e + p_i + p_0 = N \left(\alpha_e + \alpha_i + \frac{p_0^2}{3kT} \right) \mathbf{E} \quad (17)$$

where N is the number of contributing molecules or particles per unit volume.

Of course, not all atoms or molecules need display each of these three types of polarizability. Only the orientational polarization is temperature-dependent. Equation (17) is known as the *Langevin-Debye* formula, and we have

$$\chi = \epsilon_r - 1 = \frac{\mathbf{P}}{\epsilon_0 \mathbf{E}} = \frac{N}{\epsilon_0} \left(\alpha_e + \alpha_i + \frac{p_0^2}{3kT} \right) \quad (18)$$

Thus a measurement of ϵ_r as a function of temperature may help to distinguish the orientational polarization contribution from the sum of the components α_e and α_i , which are practically independent of temperature.

Figure 1 shows (9) a plot of $\epsilon_r - 1$ as a function of $1/T$ for the molecule of methyl amine (CH₅N). The intercept for the line at $1/T = 0$ and its slope are approximately 8×10^{-4} and 0.6 K^{-1} , respectively. From Eqs. (8), (9), and (17), we have (9)

$$\alpha_e + \alpha_i = \frac{8 \times 10^{-4} \epsilon_0}{N} \approx 6 \times 10^{-4} \text{ F/m}^2 \quad (19)$$

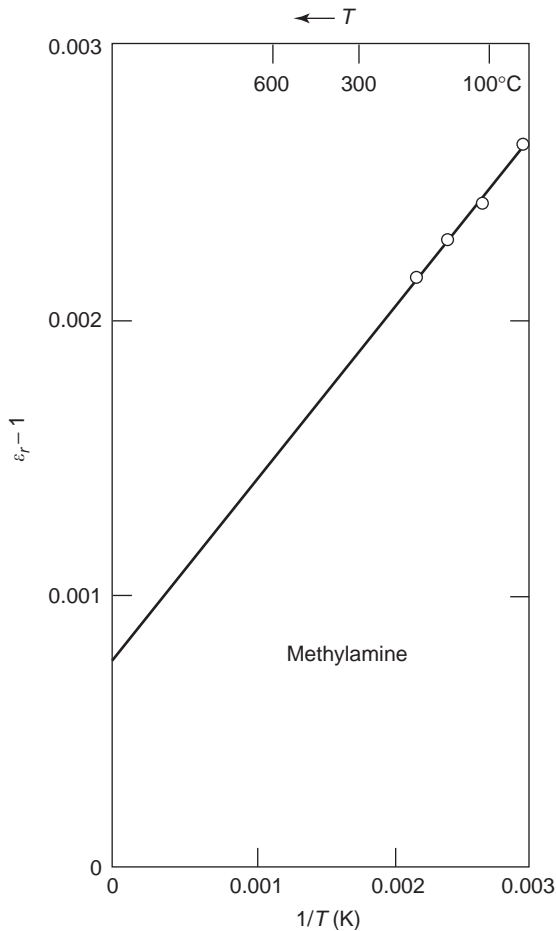


Figure 1. A plot of $\epsilon_r - 1$ as a function of $1/T$ for a molecule of methylamine (CH_5N) [9,10].

and

$$p_0^2 = \frac{0.6\epsilon_0 3k}{N} \approx 4.2 \times 10^{-30} \text{ C/m} \quad (20)$$

The further separation of α_e and α_i is not possible using this technique alone.

Table 3 gives the electric dipole moments of some molecules. The commonly used unit of dipole moment is the debye; $1 \text{ D} = 3.33 \times 10^{-30} \text{ C/m}$.

Table 3. Electric Dipole Moments of Some Molecules

Molecule	Dipole moment	
	(10^{-30} C/m)	(D)
HCl	3.5	1.05
CsCl	35.0	10.5
H ₂ O	6.2	1.87
D ₂ O	6.0	1.80
NH ₃	4.9	1.47
HgCl ₂	0.0	0
CCl ₄	0.0	0
CH ₄ O	5.7	1.71

Space charge (interfacial) polarization generally arises from a presence of electrons and/or ions that have limited macroscopic motions in the bulk of a dielectric material. Eventually these charge carriers are localized at lattice defect sites, metal–electrode interfaces, impurity centers, and voids. As a result, the electric field in the dielectric may become distorted, thus producing an apparent increase in the dielectric constant. Space charge polarization is particularly evident in multiphase and inhomogeneous dielectrics, and its effect is dominant, particularly at low frequencies, in practical dielectrics such as impregnated paper, polymers, and sintered ceramics.

The study of dielectric polarization and susceptibility in liquids and solids is more complicated than in gases because of the interactions between the atoms and molecules in the condensed phase. These atoms and molecules will still exhibit electronic, ionic, and orientational polarizations. However, the effective local field E_1 on an atom or molecule in a liquid or a solid dielectric may not be the same as the externally applied field E . It is difficult to calculate the effective local field E_1 in the condensed phase except for the most symmetric crystals.

Since $P = \epsilon_0 (\epsilon_r - 1) E$, for the simplest case of a cubic crystal, the Lorentz equation for the local field E_1 (6) is

$$E_1 = (\epsilon_r + 2)E/3 \quad (21)$$

and $P = N\alpha E_1$, where α is the total polarizability and N the number of molecules per unit volume. Hence

$$P = (\epsilon_r + 2)NE/3 \quad (22)$$

and

$$\frac{N\alpha}{3\epsilon_0} = \frac{\epsilon_r - 1}{\epsilon_r + 2} \quad (23)$$

Equation (23) is the Clausius–Mossotti equation, which relates the microscopic property of the polarizability α with the macroscopic property of the relative permittivity or dielectric constant ϵ_r . Now we have

$$N = \frac{N_0\rho}{M} \quad (24)$$

where N_0 is the Avogadro number, M the molecular weight, and ρ the density. Substituting Eq. (24) into Eq. (23), we obtain the molar polarizability per mole:

$$\frac{N_0\alpha}{3\epsilon_0} = \frac{M}{\rho} \frac{\epsilon_r - 1}{\epsilon_r + 2} \quad (25)$$

Equation (25) should be used with caution, as it does not take dipolar interactions into account properly. Equation (23) may, however, be used to calculate the electronic polarizability α_e from the measured values of ϵ_r for dilute gases, for which $\epsilon_r \approx 1$ and $\epsilon_r + 2 \approx 3$. For such cases, we have

$$\alpha_r = \frac{\epsilon_0(\epsilon_r - 1)}{N} = \frac{\epsilon_0\chi}{N} \quad (26)$$

Table 4. Polarizability of Argon

Form	T (K)	Pressure (atm)	ϵ_r	$\alpha_e (10^{-40} \text{ F/m}^2)$
Gas	293	1	1.000517	1.83
Liquid	83	1	1.53	1.86

Source: Ref. 9.

Table 4 shows that the polarizability of the element argon does not vary significantly [9] between its dilute gas and liquid states. That may not be true for other gases with more extensive electronic structure when condensed to liquid or solid form.

The polarizabilities of α_e and α_i may be determined independently for ionic crystals in the solid state. The relative permittivities ϵ_r of ionic crystals are frequency-dependent. For an applied field at low frequencies the value of ϵ_r will be dependent on both α_e and α_i , whereas in the optical frequency range the lattice ions will not be able to follow the applied field and ϵ_r will only be ϵ_e . Table 5 shows the static (low-frequency) and optical (high-frequency) values of ϵ_r for some ionic crystals [9]. The difference between the values of ϵ_r in the second and the third columns is the contribution of the ionic polarization alone, whereas those in the third column characterize the contribution due to α_e .

The behavior of orientational polarization in dipolar molecules in the gas and liquid phases may be quite large if rotation of the dipoles is possible [10]. For such a case, the polarizability will have contributions from α_e , α_i , and α_0 , where the α_0 contribution will be temperature-dependent, where ϵ_r increases with decreasing temperature. However, as the temperature is lowered and the material solidifies, the value of ϵ_r will drop abruptly when the molecules can no longer rotate, and thus rotation cannot contribute to the polarization. Figure 2a [9,11] illustrates such behavior of ϵ_r for nitromethane. It may be observed that at 244 K, nitromethane freezes and ϵ_r drops abruptly from 45 to just under 5. At this temperature α_0 is zero for nitromethane and its polarizability arises from the α_e and α_i contributions, which are independent of temperature. However, there are some solids, such as HCl, that do not show this type of behavior. For HCl in the liquid state ϵ_r is large and increases with decreasing temperature, indicating rotational behavior of the molecules (see Fig. 2b). However, below 165 K, where HCl freezes, ϵ_r still continues to increase [9,12] because of the increase in the den-

Table 5. Static and Infinite-Frequency Capacitivity of Some Ionic Crystals

Material	ϵ_r	
	Static	Optical
LiF	9.27	1.90
LiC	11.05	2.68
NaCl	5.62	2.32
KCl	4.64	2.17
RbCl	5.10	2.18
NaI	6.60	2.96

Source: Ref. 9.

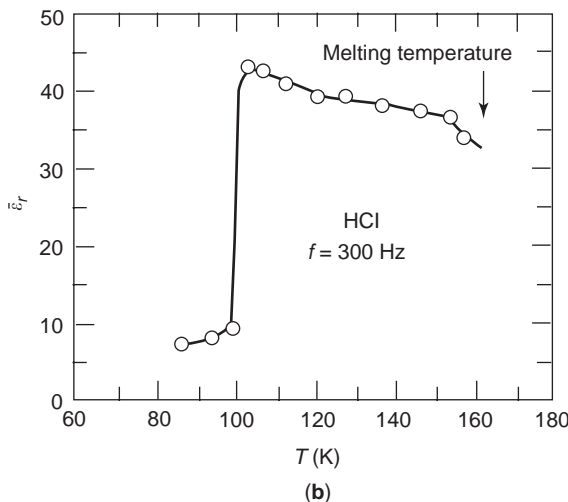
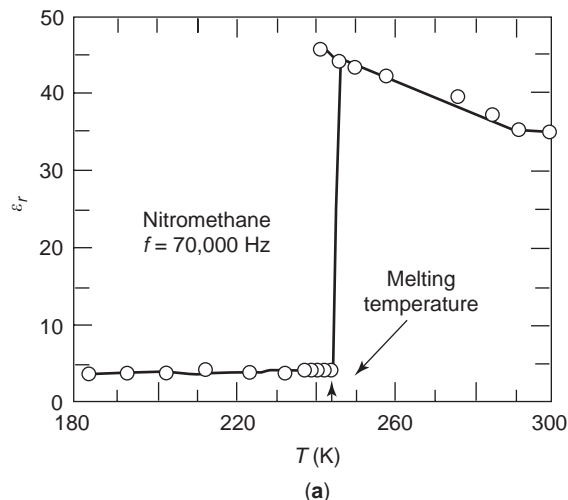


Figure 2. The behavior of ϵ_r versus T for completely hindered (a) and partly hindered (b) rotation of dipoles in the solid: (a) nitromethane [9,11]; (b) hydrogen chloride [9,12].

sity of the material. At 100 K, the molecular rotation finally ceases and α_0 virtually becomes zero. The polarization contribution at this temperature in HCl originates from α_e and hindered rotation [9,12].

3. DIELECTRIC LOSS

3.1. Time-Dependent Dielectric Response

The dielectric behavior has been represented in the previous section by three vectors, \mathbf{D} , \mathbf{E} , and \mathbf{P} , which are assumed to be collinear in space and in the same phase in time. However, neither of these two assumptions is necessarily valid. We shall only consider the nature of the dielectric behavior with time for nonpolar materials and those containing permanent dipoles. Regarding the spatial collinearity, extensive treatment of crystal symmetry is necessary and will not be discussed here.

The time-dependent dielectric response may be synthesized [8] from three fundamental time dependences of the electric field: the delta function $\delta(t)$, the step function $1(t)$,

and the harmonic function $\sin \omega(t)$ or $\cos \omega(t)$, where ω is the angular frequency ($= 2\pi f$). Equation (3) may now be represented thus

$$\mathbf{D}(t) = \varepsilon_0 \mathbf{E} + \mathbf{P}(t)$$

where the first term on the right-hand side provides the instantaneous free-space contribution and the second the delayed polarization. We define a dielectric response function $\phi(t)$. The polarization response to a delta function excitation of strength $E \Delta t$ is [8]

$$\mathbf{P}(t) = \varepsilon_0 (\mathbf{E} \Delta t) \phi(t) \quad (27)$$

where E is the electric field, acting over a time period ΔT . From the principle of causality, we have

$$\phi(t) = 0 \quad \text{for } t < 0 \quad (28)$$

In the absence of any permanent polarization, we obtain

$$\lim_{t \rightarrow \infty} \phi(t) = 0 \quad (29)$$

Furthermore, from the principle of superposition, we have [8]

$$\mathbf{P}(t) = \varepsilon_0 \int_{-\infty}^t \phi(t - \tau) \mathbf{E}(\tau) dT \quad (30)$$

Equation (30) implies that the magnitude of polarization at a time t in a dielectric will depend on its past value; in other words, the material has a memory. On an application of an elementary step function field $E1(t)$, the dielectric polarization is given by

$$\mathbf{P}(t) = \varepsilon_0 \mathbf{E} \int_0^t \phi(\tau) d\tau \quad (31)$$

The charging current $I_c(t)$ is given by [8]

$$I_c(t) = \frac{d\mathbf{D}(t)}{dt} + \sigma_0 \mathbf{E} \quad (32)$$

$$\begin{aligned} &= \varepsilon_0 \frac{d\mathbf{E}(t)}{dt} + \frac{d\mathbf{P}(t)}{dt} + \sigma_0 \mathbf{E} \\ &= \varepsilon_0 \mathbf{E} [\delta(t) + \phi(t)] + \sigma_0 \mathbf{E} \end{aligned} \quad (33)$$

where the delta function $\delta(t)$ represents the instantaneous free-space response of the step function field, followed by the polarization current $d\mathbf{P}(t)/dt$ of the material. σ_0 is the DC conductivity, if any, of the dielectric at infinitely long time. Thus, we have [8]

$$\mathbf{P}(\infty) = \varepsilon_0 \mathbf{E} \int_0^{\infty} \phi(t) dt = \varepsilon_0 \chi(0) \mathbf{E} \quad (34)$$

where $P(\infty)$ is the polarization with a steady electric field E after an infinitely long time when the polarizing elements tend to be oriented along the field direction. On

removal of this step function field, a depolarization current $I_d(t)$ will follow as the thermal agitation randomizes the orientation of the dipoles with time. For this latter case there will be no contribution of σ_0 at $E = 0$.

3.2. Frequency-Dependent Dielectric Response

The polarization response to a harmonic field is known as the *frequency-domain response*. Taking the Fourier transform of both sides of Eq. (34), we get

$$\mathbf{P}(\omega) = \varepsilon_0 \chi(\omega) \mathbf{E}(\omega) \quad (35)$$

where $P(\omega)$ and $E(\omega)$ are the Fourier transforms of the time-dependent polarization and field, respectively. $\chi(\omega)$ is the frequency-dependent complex susceptibility, and it is the Fourier transform of the time-dependent response function $\phi(t)$:

$$\chi(\omega) = \chi'(\omega) - i\chi''(\omega) = \int_0^{\infty} \phi(t) e^{i\omega t} dt \quad (36)$$

The real part $\chi'(\omega)$ provides the magnitude of polarization in phase with the harmonic driving field $E(\omega)$ and does not contribute to the power loss, whereas the imaginary part $\chi''(\omega)$, which is in quadrature with the field, is referred to as the *dielectric loss*. $\chi'(\omega)$ and $\chi''(\omega)$ may be represented as odd and even functions of frequency, respectively:

$$\chi'(\omega) = \int_0^{\infty} \phi(t) \cos \omega t dt \quad (37)$$

$$\chi''(\omega) = \int_0^{\infty} \phi(t) \sin \omega t dt \quad (38)$$

In terms of permittivity, we may write

$$\mathbf{D}(\omega) = \varepsilon(\omega) \mathbf{E}(\omega) = \varepsilon_0 [1 + \chi'(\omega) - i\chi''(\omega)] \mathbf{E}(\omega) \quad (39)$$

For zero frequency, namely, the static case, we have

$$\chi'(0) = \int_0^{\infty} \phi(t) dt \quad (40)$$

and

$$\chi''(0) = 0 \quad (41)$$

Equation (36) shows that both $\chi'(\omega)$ and $\chi''(\omega)$ are functions of the dielectric response function $\phi(t)$, and these two parameters are Hilbert transforms of each other, through what are referred to as the *Kramers–Kronig relations*:

$$\chi'(\omega) = \frac{1}{\mathbf{P}} C \int_{-\infty}^{\infty} \frac{\chi''(x)}{x - \omega} dx \quad (42)$$

$$\chi''(\omega) = -\frac{1}{\mathbf{P}} C \int_{-\infty}^{\infty} \frac{\chi'(x)}{x - \omega} dx \quad (43)$$

where C denotes the Cauchy principal value of the integral. For the static case

$$\chi'(0) = \frac{2}{\pi} \int_{-\infty}^{\infty} \chi''(x) d \ln x \quad (44)$$

Equation (44) indicates that the variation of the dielectric parameters with frequency, specifically, the dielectric dispersion, is an essential property of dielectric materials [8]. It also shows that any mechanism that can lead to a strong polarization in a dielectric material must also lead to large losses in some frequency range. In other words, it is not possible to have a loss-free dielectric with a finite susceptibility [8]. In most dielectrics the loss is significant only in limited frequency ranges. Figure 3 [8] shows schematically two nonoverlapping loss processes at the low frequencies and a resonance process in the optical frequency range. In a limited frequency region we may define a *high-frequency permittivity* ϵ_{∞} , accounting for all the processes occurring at higher frequencies; thus [see Eq. (39)]

$$\epsilon(\omega) = \epsilon_{\infty} + \epsilon_0[\chi_x'(\omega) - i\chi_x''(\omega)] \quad (45)$$

from which we get

$$\epsilon_x'(\omega) = \epsilon_{\infty} + \epsilon_0\chi_x'(\omega) \quad (46)$$

and

$$\epsilon_x''(\omega) = \epsilon_0\chi_x''(\omega) \quad (47)$$

For an alternating voltage the frequency-dependent complex capacitance $C(\omega)$ is

$$C(\omega) = C'(\omega) - iC''(\omega) \quad (48)$$

where $C'(\omega)$ and $C''(\omega)$ are the real and imaginary parts of the complex capacitance. The loss angle δ is the angle between the electric field and the dielectric polarization. The

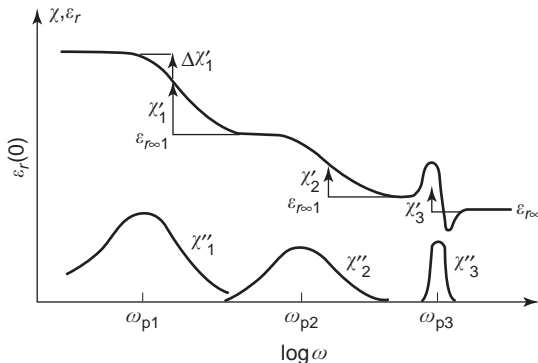


Figure 3. Schematic diagram of the frequency dependence of the real and imaginary parts of the complex susceptibility, showing three processes; the last one is a resonance process [8].

loss tangent

$$\tan \delta = \frac{C''(\omega)}{C'(\omega)} = \frac{\epsilon''(\omega)}{\epsilon'(\omega)} \quad (49)$$

is independent of the geometry of the dielectric material.

The existence of the polarization with respect to the field leads to the energy dissipation in the dielectric. Now the power dissipation \mathbf{P} per unit volume is

$$\mathbf{P} = I_{\text{phase}} \mathbf{E}$$

where I_{phase} is the part of the current in phase with \mathbf{E} , and is given by

$$\mathbf{P} = \omega \mathbf{E}^2 \epsilon_0 \epsilon' \tan \delta = \omega \mathbf{E}^2 \epsilon_0 \epsilon'' \quad (50)$$

Table 6 gives (6) typical values of the permittivity and loss factor of various dielectric materials at room temperature for different frequencies. Generally polar materials have larger permittivities and loss tangents than do non-polar materials. For many liquids the frequency at which maximum energy loss occurs at room temperature is approximately 1000 MHz (wavelength $\lambda \approx 0.3$ m), as shown [1] for three typical liquids in Table 7, where τ is the relaxation time ($= 1/f$).

Another type of energy loss occurs in a resonance absorption process at very high (i.e., IR, visible, and UV) frequencies. Although the real and imaginary parts of the complex permittivity vary in a manner similar to that for dipole relaxation, the origin of the energy loss is different in this process. At optical frequencies the permittivity of the dielectric is due almost entirely to the electronic polarization. In the absence of any external field a vibrating electron of charge e and mass m is elastically bound to its nucleus by a restoring force, and its equation of motion is

$$m \frac{d^2x}{dt^2} + kx = 0 \quad (51)$$

where k is the restoring-force constant and x is the displacement of the electron. This equation represents a simple harmonic motion, and its solution is

$$x = x_0 \sin \omega_0 t + A \quad (52)$$

where $\omega_0 = (k/m)^{1/2}$, A is the integration constant, x_0 the amplitude of oscillation, and ω_0 the natural resonance angular frequency of the oscillation. When an external alternating electric field is applied to this system, the resulting motion is a forced oscillation, represented by

$$m \frac{d^2x}{dt^2} + m\omega_0^2 x = e \mathbf{E} \cos \omega t \quad (53)$$

where \mathbf{E} is the amplitude of the field \mathbf{E} and ω is its frequency. Clearly the response of the oscillating system will now depend on both ω and ω_0 . The oscillations might be expected to build up without limit when $\omega = \omega_0$, although they are expected to be small at frequencies far away from

Table 6. Dielectric Properties of Materials

Material	Direction	Relative permittivity ϵ_r				Loss tangent $\tan \delta$
		$f = 60 \text{ Hz}$	100 kHz	1 MHz	100 MHz	
<i>Crystals</i>						
Rutile, TiO_2	\parallel_c	—	170	170	—	10^{-4}
	\perp_c	—	90	90	—	2×10^{-4}
Aluminum oxide, Al_2O_3	\parallel_c	—	10.6	10.6	10.6	—
	\perp_c	—	8.6	8.6	8.6	—
Lithium niobate, LiNbO_3	\parallel_c	—	—	30	—	0.05
	\perp_c	—	—	75	—	—
<i>Ceramics</i>						
BaTiO ₃	—	—	—	1600	—	150×10^{-4}
Alumina	—	—	—	4.5–8.5	—	0.0002–0.01
Steatite	—	—	—	5.5–7.5	—	0.0002–0.004
Rutile	—	—	—	14–110	—	0.0002–0.005
Porcelain	—	—	—	6–8	—	0.003–0.02
<i>Polymers</i>						
Polyethylene	—	—	2.3	2.3	—	$10^{-4} - 10^{-3}$
Polypropylene	—	2.1	—	—	—	2.5×10^{-4}
PTFE	—	2.1	2–3	2–3	—	2×10^{-4}
Polystyrene	—	2.55	—	—	—	5×10^{-5}
PVC	—	3–6	3–5	3.5	3.0	10^{-4}
Polycarbonate	—	—	—	2.8	—	3×10^{-2}
Polyester	—	—	—	4–5	—	0.02
Nylon 66	—	—	3.5	3.33	3.16	0.02
<i>Glasses</i>						
Pyrex	—	—	—	—	4–6	0.008–0.025
Quartz	—	—	—	4	—	2×10^{-4}
Vycor	—	—	—	—	3.8	9×10^{-4}
<i>Miscellaneous</i>						
Mica	—	—	—	5	—	3×10^{-4}
Neoprene	—	—	—	6.3	—	—

Source: Ref. 6.

ω_0 . However, at resonance (i.e. $\omega = \omega_0$), the oscillations will in fact be limited (damped) by the emission of electromagnetic radiation by the oscillating charges, which dissipates energy. It may be shown that in a resonance absorption process [6]

$$\epsilon'(\omega) = \epsilon_0 + \frac{Ne^2}{m} \frac{\omega_0^2 - \omega^2}{(\omega_0^2 - \omega^2) + r^2\omega^2} \tag{54}$$

and

$$\epsilon''(\omega) = \frac{Ne^2}{m} \frac{r\omega}{(\omega_0^2 - \omega^2) + r^2\omega^2} \tag{55}$$

Table 7. Typical Relaxation Times of Three Liquids

Material	Temperature (°C)	τ (10^{-11} s)
H ₂ O	19	1
CH ₃ OH	19	6
C ₂ H ₅ OH	20	13

Source: Ref. 9.

where r is a constant of the material, called the *dissipation constant*. These quantities have the form shown in Fig. 3 at very high frequencies. For $\omega = 0$, which is the static case, we have

$$\epsilon'(0) = \epsilon_0 + \frac{Ne^2}{m\omega_0^2} \tag{56}$$

$\epsilon''(\omega)$ approaches zero for both $\omega \gg \omega_0$ and $\omega \ll \omega_0$, and it goes through a maximum value of $Ne^2/(mr\omega)$. Again $\epsilon''(\omega)$ represents an energy loss and the power loss \mathbf{P} is given again by

$$\mathbf{P} = \omega \epsilon''(\omega) \epsilon_0 \mathbf{E}^2 \tag{57}$$

As the characteristic values of ω_0 for electron clouds are very high, the resonance absorptions and their corresponding energy losses occur at very high frequencies in the IR-UV range.

For pure nonpolar dielectrics, whether solid, liquid, or gas, the polarization is of an essentially electronic nature. Some polar materials with a highly symmetric structure, like carbon tetrachloride (CCl₄), may also

Table 8. A Comparison of ϵ' and n^2 Values for Several Nonpolar Materials

Material	n^2	ϵ'	Frequency of measurement of ϵ' (Hz)
Hydrogen (liquid, -253°C)	1.232	1.228	
Diamond	5.66	5.68	
Nitrogen (liquid, -197°C)	1.453	1.454	
Oxygen (liquid, -190°C)	1.491	1.507	
Chlorine (liquid)	1.918	1.910	
Bromine	2.66	3.09	
Paraffin (liquid)	2.19	2.20	10^3
Benzene	2.25	2.284	10^3
Polystyrene	2.53	2.55	10^2 to 10^{10}
Polyethylene	2.28	2.30	10^2 to 10^{10}
Carbon tetrachloride	2.13	2.238	
PTFE	1.89	2.10	10^2 to 10^{10}

Source: Refs. 13,14.

exhibit electronic polarization. The presence of electronic polarizability may be verified with the Maxwell relation, $\epsilon^1 = n^2$, where n is the refractive index of the dielectric. Table 8 compares the ϵ^1 and n^2 values for a few marginally nonpolar materials [13,14].

4. MODELS OF DIELECTRIC RELAXATION

4.1. Models

The first model of the dielectric relation is due to Debye [3]. According to this model, the susceptibility function $\chi(\omega)$ for noninteracting polar molecules is given by [7]

$$\chi(\omega) \propto \frac{1}{1 + i(\omega/\omega_p)} \tag{58}$$

where ω_p is the angular frequency at which the maximum loss peak occurs. The real and imaginary parts of $\chi(\omega)$ are

$$\chi'(\omega) \propto \frac{1}{1 + \omega^2\tau^2} \tag{59}$$

and

$$\chi''(\omega) \propto \frac{\omega\tau}{1 + \omega^2\tau^2} \tag{60}$$

The corresponding time-domain response $\phi(t)$ follows the exponential function (15)

$$\phi t \propto e^{-t/\tau} \tag{61}$$

The loss peak occurs here at $\omega = \omega_p = 1/\tau$. Figure 4 shows the dependence of $\chi'(\omega)$, $\chi''(\omega)$, and $\phi(t)$ of Eqs. (59)–(61) [16] in log-log representation. The loss peak is symmetric about ω_p , and its width at half-height is 1.144 decades on the frequency scale. The Debye behavior has been observed in gases and in some polar liquids. The relaxation behavior of water and deuterium oxide closely

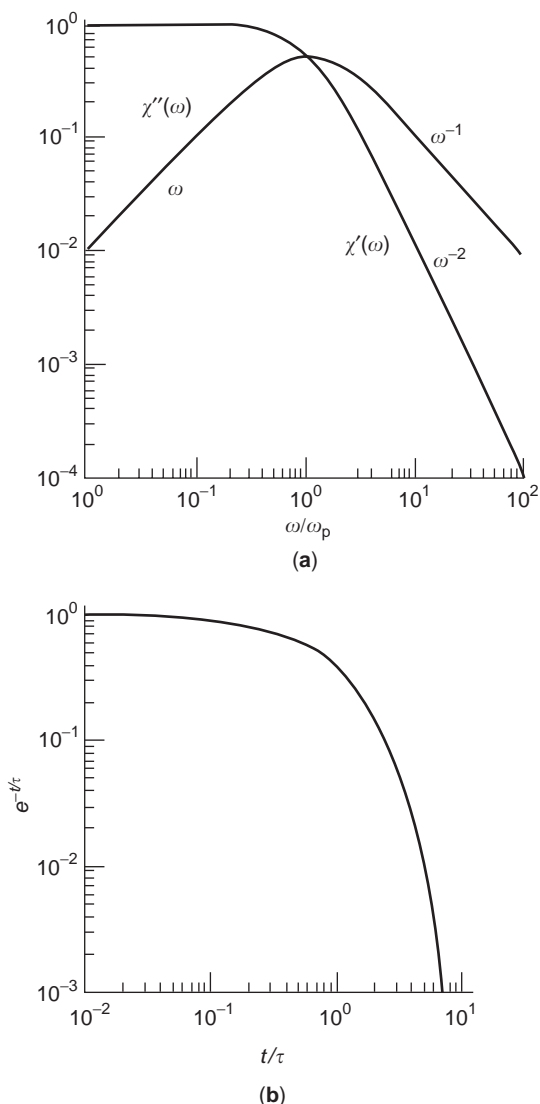


Figure 4. (a) The ideal Debye response in the frequency domain, with its characteristic frequency dependence of $\chi'(\omega) \propto \omega^{-2}$ and $\chi''(\omega) \propto \omega^{-1}$ above the loss peak. (b) The corresponding time-domain response, which is purely exponential, is plotted here in the somewhat unfamiliar log-log representation [16].

approximates that of the Debye form [17–19]. However, it is generally nonexistent in solids.

To account for the departure of the observed dielectric behavior, the following empirical expressions have been proposed. The Cole–Cole equation (20) is

$$\chi(\omega) \propto \frac{1}{1 + (i\omega/\omega_p)^{1-\alpha}} \tag{62}$$

where α is a fitting parameter in the range $0 < \alpha \leq 1$. Equation (62) provides a broader and symmetric relaxation spectrum than the Debye type. Furthermore, for $\omega > \omega_0$, $\chi'(\omega)$ and $\chi''(\omega)$ show parallelism in the log-log plot.

The Davidson–Cole equation has the form [21]

$$\chi(\omega) \propto \frac{1}{(1+i\omega/\omega_p)^\beta} \tag{63}$$

where β is yet another curve-fitting parameter in the range $0 < \beta \leq 1$. Equation (63) provides asymmetric relaxation profiles at $\omega \leq \omega_0$, whereas $\chi'(\omega)$ and $\chi''(\omega)$ remain parallel at $\omega > \omega_0$.

The Fuoss–Kirkwood model [22] for the imaginary part of the susceptibility is

$$\chi''(\omega) \propto \frac{2(\omega/\omega_p)^\gamma}{1 + (\omega/\omega_p)^{2\gamma}} \tag{64}$$

Another relaxation model is given by

$$\chi(\omega) \propto \sum_{s=1}^{\infty} \frac{\Gamma(\Delta s)}{(s-1)!} \left(\frac{\exp(-i\Delta\pi/2)}{\omega^\Delta \omega_p^{-\Delta}} \right)^s \tag{65}$$

This is an expansion into the frequency domain of the Kolrauch–Williams–Watts function [15] of time: $\exp[-(t/\tau)^\Delta]$. The parameter Δ in Eq. (65) has no physical

significance and is not based on the physics of dielectric interactions.

So far the models have had only one fitting parameter, namely, α for the Cole–Cole equation, β for the Davidson–Cole equation, γ for the Fuoss–Kirkwood equation, and Δ for the Kolrauch–Williams–Watt equation. The model due to Havriliak and Negami [23,24], the first one with two parameters, is given by

$$\chi(\omega) \propto \frac{1}{[1 + (i\omega/\omega_p)^{1-\alpha}]^\beta} \tag{66}$$

It should be stressed again that the fitting parameters α and β in this equation have no physical significance.

A classical form of presentation of the dielectric data is to plot $\chi'(\omega)$ or $\epsilon'(\omega)$ against $\chi''(\omega)$ or $\epsilon''(\omega)$, namely, the so-called Cole–Cole plot [20]. Figure 5 shows the shapes of the Debye, Cole–Cole, and Davidson–Cole equations for the susceptibility functions in Cole–Cole plots. It has been shown [20] that with the Debye model, a graph of $\chi'(\omega)$ against $\chi''(\omega)$ over the entire frequency range will be a semicircle and $\chi(\infty)$ or ϵ_∞ is obtained from the intercept at the horizontal axis (see Fig. 5a). Thus the relaxation time τ may be obtained from the slope of a straight line from the

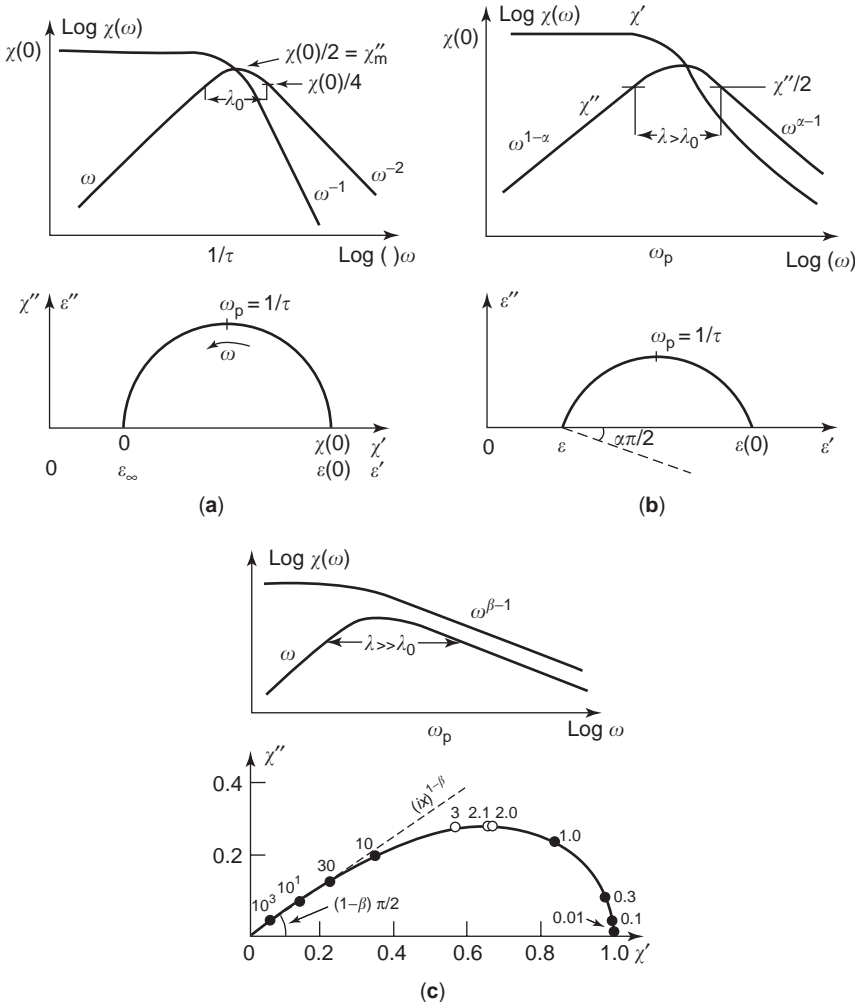


Figure 5. The frequency dependence of the real and imaginary parts of the susceptibility and the Cole–Cole presentation for (a) Debye, (b) Cole–Cole, and (c) Davidson–Cole systems [8].

origin to a point on the semicircle for which ω is known. Now the Cole–Cole relaxation model provides a symmetric but broader relaxation spectrum, and the corresponding Cole–Cole plot is still a semicircle. However, its center is depressed below the χ' or ϵ' horizontal axis (see Fig. 5b) with the angle $\alpha\pi/2$ between the radius of the circle and χ' or ϵ' axis. There is no molecular interpretation of this factor α , and it has been interpreted as a “spreading factor” of the actual relaxation time about a certain mean value. The magnitude of α must lie between zero and unity. The Cole–Cole plot for the Davidson–Cole model is a skewed plot (see Fig. 5c), representing a severe departure from the Debye relaxation behavior.

The Havriliak–Negami function [23,24] with two parameters, α and β [Eq. (66)], appears to provide the best results for the fitting of the measured dielectric data for most materials. However, none of these mathematical models that invoke a distribution of relaxation energies (25) or times offer any physical interpretation of material properties [26–29].

It has been suggested that a dielectric loss spectrum may be regarded as a mathematical summation of a distribution function $g(\tau)$ of Debye responses corresponding to a distribution of relaxation times [30]; thus

$$\chi(\omega) = \int_0^\infty \frac{g(\tau)}{1+i\omega\tau} d\tau \tag{67}$$

The distribution functions are always positive, and curves of $\chi''(\omega)$ or $\epsilon''(\omega)$ can be formed from them by the superposition of many single relaxation-time or frequency curves [31]. It has been shown [32] that the product of the elapsed time and the depolarization current is a convolution of the distribution function of relaxation frequencies with a weight function of an asymmetric bell shape. A similar relationship is also shown to exist for the imaginary part of the permittivity. The same work [32] also proposes a deconvolution procedure to determine the distribution function of relaxation frequencies from experimental data. A distribution of relaxation times from the frequency dependence of the real part of the complex permittivity has also been made with the inverse Fourier transformation [33]. As stated earlier, however, no distribution of relaxation times that can claim physical reality can be associated with relaxation systems in condensed matter [8,26,27].

A two-parameter model for the complex susceptibility function $\chi(\omega)$, known as the *universal relaxation law*, has been proposed [8,16], which states that all solid dielectrics follow fractional power laws in frequency. It is of interest to note that $\chi(\omega)$ may be expressed by a simple empirical expression [16,23]

$$\chi(\omega) = A[1 + (ix)^m]^{(n-1)/m} \tag{68}$$

where the exponents m and n lie between zero and unity and x is the normalized frequency. Equation (68) indicates that the experimental state of dielectric susceptibility can be fitted with two power-law exponents. The Debye function is a limiting form of this equation for $m = 1$ and $n = 0$.

For the symmetric loss peak at ω_p and $x=1$, we have $m = 1 - n$. Furthermore, the ratio $\chi''(\omega)/\chi'(\omega)$ decreases as m and $1 - n$ become smaller, thus providing broader peaks as in the case of the Cole–Cole function. This leads to the universal law, characterized by two fractional power laws in frequency respectively below and above the loss peak frequency ω_p [8,16]

$$\chi''(\omega) = \tan\left(\frac{m\pi}{2}\right)[\chi(0) - \chi'(\omega)] \propto \omega^m \quad \text{for } \omega \ll \omega_p \tag{69}$$

for $\omega \ll \omega_p$ and

$$\chi''(\omega) = \cot\left(\frac{n\pi}{2}\right)\chi'(\omega) \propto \omega^{n-1} \quad \text{for } \omega \gg \omega_p \tag{70}$$

where the exponents are in the ranges $0 < n < 1$ and $0 < m < 1$.

As a result, in the high-frequency range of the loss peak, the ratio of the imaginary to the real part of the complex susceptibility is a frequency-independent constant:

$$\frac{\chi''(\omega)}{\chi'(\omega)} = \cot\left(\frac{n\pi}{2}\right) \tag{71}$$

Hence, in a log–log plot $\chi''(\omega)$ and $\chi'(\omega)$ appear as parallel lines for $\omega \gg \omega_p$. It should be noted that for the Debye process this ratio is $\omega\tau$ and thus increases linearly with frequency, which is consistent with the idea that the process is a “viscous” phenomenon in which the dielectric loss is linearly related to the angular velocity [16].

For the low-frequency part of the loss peak ($\omega < \omega_p$), we have [8,15]

$$\frac{\chi''(\omega)}{\Delta\chi'(\omega)} = \tan\left(\frac{m\pi}{2}\right) \tag{72}$$

where $\Delta\chi'(\omega) = \chi(0) - \chi'(\omega)$ is known as the *dielectric decrement* and is the extent to which the polarization at any particular frequency falls short of the value of the equilibrium polarization in a static field. Equations (69) and (70) may be represented by the empirical law combining the two fractional power laws above and below ω_p [8]:

$$\chi''(\omega) \propto \frac{1}{(\omega/\omega_p)^{-m} + (\omega/\omega_p)^{1-n}} \tag{73}$$

The Fourier transforms of fractional power laws correlate the frequency-domain dielectric parameters with their time-domain behavior thus (16):

$$\omega^m \propto t^{-m-1} \quad \text{for } t \gg \tau \tag{74}$$

$$\omega^{n-1} \propto t^{-n} \quad \text{for } t \ll \tau \tag{75}$$

In the carrier-dominated low-frequency dispersion (LFD) or quasi-DC (QDC) systems, mobile charge carriers, such as ions and electrons, act as polarizing species and provide a broad dielectric response [16,34–36] in which no loss peak is observed. The LFD (or QDC)

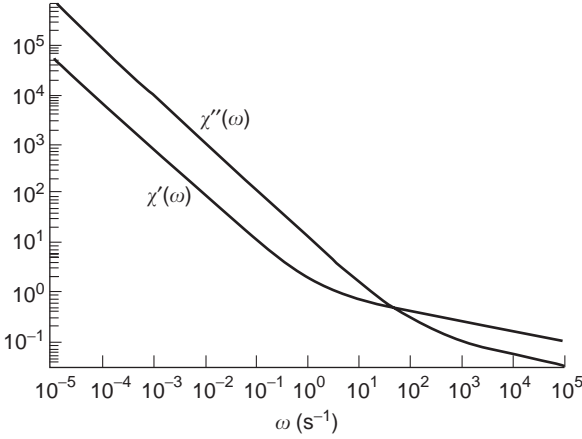


Figure 6. The frequency dependence of a system dominated by LFD or QDC with $n_1 = 0.8$ at high frequencies and $n_2 = 0.5$ at low frequencies. The crossover point is deliberately shifted to high frequencies to show the LFD or QDC region [16].

relaxation is characterized by two independent processes, below and above a certain critical frequency ω_c , which may be represented by Eq. (70). The real and imaginary parts of the complex dielectric susceptibility steadily increase with decreasing frequency for small values of n_2 , at frequencies less than ω_c . This is followed by a flat loss behavior above ω_c with $n_1 \approx 1$ [8,16,28]. The frequency ω_c plays a role analogous to that for ω_p in a dipolar system.

Figure 6 shows [16] typical behavior of $\chi(\omega)$ for the LFD (or QDC) system. Figure 7 shows schematically the typical time-domain behavior of a dipolar LFD (or QDC) system together with the flat loss response corresponding to $n \rightarrow 1$ [15]. Note that the flat loss behavior is the limiting case of the dielectric response that occurs in low-loss materials with a very small value of the ratio $\chi''(\omega)/\chi'(\omega)$. The value

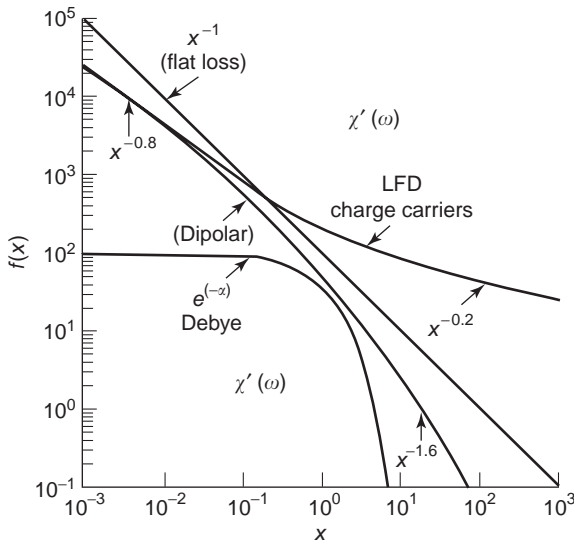


Figure 7. The time-domain response $\phi(t/\tau)$ of typical dielectric systems, including the Debye exponential response; the dipolar response with $n = 0.8$, $m = 0.6$; the carrier-dominated LFD response with $n_1 = 0.8$, $n_2 = 0.2$; and the flat loss with $n = 1$ [16].

of n_2 can never be zero, and hence n cannot actually have a value of 1, although nearly flat loss behavior has been observed experimentally.

There are few examples of solids, including single crystals of ferroelectrics, that show pure Debye relaxation behavior. A variety of solids (viz., low-loss dielectrics, dipolar materials, semiconductor p-n junctions, and biological materials) are known to show dielectric dispersions that may be fitted with the universal fractional power law [Eq. (73)]. Furthermore, dipolar systems exhibit loss peaks, whereas the carrier-dominated systems exhibit LFD (or QDC) behavior [8,34,35].

A stochastic model for the universal dielectric dispersion has also been proposed [37–39]. This probabilistic model is based on the assumption that individual dipoles and their environments interact during the process of relaxation and the dielectric response function is given by [37]

$$\phi(t) = \phi_0 \alpha \omega_p (\omega_p t)^{\alpha-1} [1 + k(\omega_p t)^\alpha] \quad (76)$$

where ϕ_0 is a constant of the relaxation function $\phi(t)$, and k is a positive real number. In the short-time limit this function is

$$\phi(t) \approx (\omega_p t)^{\alpha-1} = (\omega_p t)^{-n} \quad (77)$$

where $n = 1 - \alpha$ and $0 < n < 1$. The corresponding long-time limit is

$$\phi(t) \approx (\omega_p t)^{-(\alpha+k)/k} = (\omega_p t)^{-m-1} \quad (78)$$

where $m = \alpha/k$ and $0 < m < 1$ if $\alpha < k$. The exponents m and n of the universal fractional law [8] are thus related by [37]

$$m = \frac{1-n}{k} \quad (79)$$

where $k > 1 - n$ and $0 < n < 1$. If $1 - n < k \leq 1$, then $1 - n \leq m < 1$, and this is observed in most analyzed experimental results. For $k = 1$ we have $m = 1 - n$, and this is the Cole–Cole response. For $k = 1 - n$ we have $m = 1$, which is the Davidson–Cole response. If $k > 1$, then $0 < m < 1$, which is observed only in a small number of analyzed data [21,33,38]. In this case, $k \rightarrow 0$ and the Williams–Watts response is observed [15,40]. The probabilistic model [37–39] thus suggests a relation between the empirical parameters m and n , defining the low- and high-frequency regions of the complex dielectric susceptibility. It has been suggested [37] that the parameter (k) may be related to the waiting-time distribution of the relaxing dipoles, which may follow a Weibull distribution, namely

$$R(s) = \exp(-ks^\delta) \quad (80)$$

where $R(s)$ is the waiting-time distribution, k is a positive real number, and $0 < \delta < 1$. It has been shown [37] that for a particular waiting-time distribution function, the

solution for $\phi(t)$ can be obtained in a simple analytical form:

$$\phi(t) = \phi(t, 1-n, k), \quad 0 < 1-n < 1 \quad \text{and} \quad k > 0 \quad (81)$$

The relatively recent model [41,42] based on a cluster theory is perhaps the most sophisticated approach to the explanation of relaxation phenomena observed in imperfect materials. The theory has been derived in the framework of quantum mechanics and takes into account the manybody interactions present in condensed matter.

The dipoles in the condensed phase may be regarded as connected with other dipoles through their morphological structure, and it is unlikely that they can act independently as in the Debye model. Both solids and liquids are composed of spatially limited regions possessing partially regular structural order, and such regions may be called *clusters* [41]. In any material many clusters may exist, and in the presence of coupling between them an array may form displaying partial long-range order. Absence of coupling in the limit may lead to a *cluster gas*. In contrast, systems with strong coupling between these arrays will produce an almost perfect crystal. The model also considers two kinds of interactions—*intracluster* and *intercluster* exchanges—and each of these makes its own contributions to the final behavior of the complex susceptibility function.

A dipole in the intracluster motion may first relax exponentially ($d^{-t/\tau}$) as suggested in the Debye model. In doing so, it will affect the field experienced by other neighboring dipoles in the cluster. These neighboring dipoles, in turn, may also relax exponentially, thereby affecting the field experienced by the first dipole, and so on. As a result, the overall effect will be a process with an exponential single dipole relaxation of the form $e^{-t/\tau}$ and concomitant t^{-n} behavior for the relaxation of the cluster dipole moment. The intercluster exchange will have a range larger than that for the intracluster motion, and its origin will be in dipoles near the edge of the cluster interconnecting to a neighboring cluster [29,36,40]. It has been shown [41] that with the intracluster motion and with the progressive involvement of an increasing number of elements with the progress of time, a fractional power law (i.e., ω^{n-1} behavior) for the susceptibility function may be obtained. Furthermore, the parameter n ($0 < n < 1$) is related to the average cluster structure. Highly ordered structure has n values approaching unity, thus indicating an existence of completely correlated clusters. On the other hand, $n \rightarrow 0$ would signify a large degree of disorder, and the limit $n = 0$ would yield Debye-like relaxation behavior.

The intracluster-coupled mode may change to an intercluster mode as the spatial extent of the coupling (wavelength) increases beyond the cluster size. The mathematical derivation of the susceptibility function for the intercluster exchanges is similar to that of the intracluster motion, as the intercluster exchanges are now the perturbation of an ideal state. The result is also a fractional power law [41], giving an ω^m behavior for the susceptibility function. Once again the value of m is in the range $0 < m < 1$, and m represents the degree of structural order, this time on the larger scale of the cluster, namely,

the degree of ordering in the cluster array. Hence, $m \rightarrow 0$ indicates an almost ideal lattice structure, whereas $m \rightarrow 1$ may give rise to a wide distribution of clusters. The intracluster motion and the intercluster exchange mechanisms are schematically represented in Fig. 8 [28].

For the intracluster motion the susceptibility function is given by [41]

$$\chi(\omega) \propto \left(1 + i \frac{\omega}{\omega_p}\right)^{1-n} {}_2F_1\left(1-n, 1-m \frac{\omega_p}{\omega_p + i\omega}\right) \quad (82)$$

where ${}_2F_1$ is the Gaussian hypergeometric function. It should be noted that the asymptotic limits of Eq. (82) are the universal relaxation law [i.e., Eqs. (69) and (70)] [8].

The Dissado–Hill quantum-mechanical model [41] describes a QDC phenomenon as a partial conduction process that is equivalent to the LFD phenomenon [8] described above. In the QDC process considerations similar to those for the dipoles are given to systems containing charge carriers. The difference between a QDC process and DC conduction at low frequencies is that the latter phenomenon is characterized by

$$\chi(\omega) \rightarrow \text{constant} \quad (83)$$

and

$$\chi''(\omega) \propto \frac{\sigma_{dc}}{\omega} \quad (84)$$

where σ_{dc} is the frequency-independent DC conductivity. For the high frequencies, the Maxwell–Wagner interfacial polarization effect [1] may be used to predict a limiting

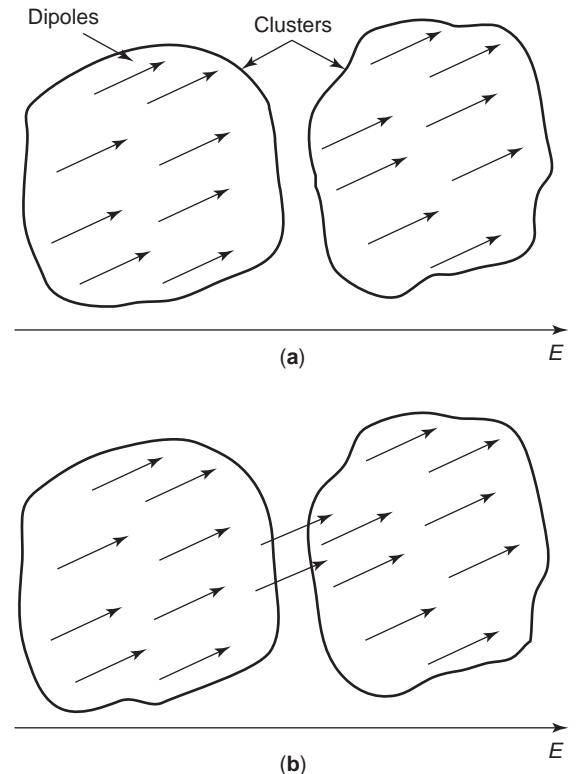


Figure 8. Schematic diagram of (a) intracluster motion and (b) intercluster exchange mechanism of Dissado–Hill model of dielectric relaxation [29,36].

behavior of the form

$$\chi'(\omega) \propto \omega^{-2} \quad (85)$$

$$\chi''(\omega) \propto \omega^{-1} \quad (86)$$

and

$$\chi''(\omega) \quad (87)$$

$$\chi'(\omega) \propto \omega$$

The Dissado–Hill model [41] suggests that the motion of all charge carriers within a cluster of correlation length is cooperative, that is, that the motion of a charge carrier to a neighboring site is limited to the vacancy of such sites and by other charges surrounding it. The model [41] divides the response into high-frequency (short-time) behavior above a critical frequency ω_c , where intracluster motion occurs, and low-frequency (long-time) behavior below ω_c , where intracluster motion exchange occurs. The intracluster motion, which is analogous to the flipping of dipoles, is now replaced by the hopping of charges between available sites within a correlation length ξ , which reduces the overall polarization of the cluster. The high-frequency response has the same functional form as for the dipoles: ω^{n-1} , $0 < n < 1$. Again the physical meaning of the exponent n is the average degree of structural ordering within a cluster, and small values of n will correspond to irregularities in a cluster such as might occur when an interstitial ion or a dislocation is present. The parameter n may also be related to the entropy density per cluster constituent. The value of n may be independent of temperature for thermally stable cluster structuring [41].

In the intercluster exchange there is a physical transport of charges between the clusters. The charge motion is no longer correlated with the available sites of the donor cluster, but rather with those of the acceptor cluster. For this case the susceptibility function is shown to be a fractional power law of the form ω^{-p} , with $0 < p < 1$ [41]. A small value of p indicates a set of clusters that are almost identical to each other, while a large value of p is associated with a broader distribution of clusters in which intercluster exchanges can carry the effective charge through many clusters over a long distance. In the presence of both the intracluster hopping and intercluster charge transport, the susceptibility function of the system is given by [42]

$$\chi(\omega) \propto \left(\frac{\omega_c}{\omega_c + i\omega} \right)^{1-n} {}_2F_1 \left(1-n, 1+p, 2-n; \frac{\omega_c}{\omega_c + i\omega} \right) \quad (88)$$

The asymptotic forms of $\chi(\omega)$ at high and low frequencies with respect to ω_c are [42]

$$\chi'(\omega) \propto \chi''(\omega) \approx \chi'(\omega_c) \left(\frac{\omega}{\omega_c} \right)^{-p} \quad \text{for } \omega \ll \omega_c \quad (89)$$

$$\chi'(\omega) \propto \chi''(\omega) \propto \chi'(\omega_c) \left(\frac{\omega}{\omega_c} \right)^{n-1} \quad \text{for } \omega > \omega_c \quad (90)$$

Once again, it may be noted that the asymptotic values of this model [41,42] are the same as those of the universal law model [8,15]. The relations between the exponents n and p of these two models are

$$p = 1 - n_2 \quad (91)$$

$$n = n_1 \quad (92)$$

where n_1 and n_2 refer to the values of the parameters of the universal law above and below ω_c , respectively [41]:

$$\chi'(\omega) \propto \chi''(\omega) \propto \omega^{n_2-1} \quad \text{for } \omega \ll \omega_c \quad (93)$$

$$\chi'(\omega) \propto \chi''(\omega) \propto \omega^{n_1-1} \quad \text{for } \omega > \omega_c \quad (94)$$

Summarizing the above, it appears that all dielectric materials commonly investigated have the following characteristics in terms of the indices n and m (41):

$n = 0, m = 1$ express the Debye limit of an ideal liquid with independent cluster constituents in the system.

$n = 1, m = 0$ occurs in an ideal crystal with no internal relaxation and zero loss.

For real liquids $n \rightarrow 0, m \rightarrow 1$, and the average clusters are weakly bound.

For plastic crystals, waxes, and viscous liquids, $n \approx \frac{1}{2}$ and $m \approx \frac{1}{2}$. These materials have clusters with restricted structural range.

For solids with interstitial impurities and ferroelectrics, $n \rightarrow 0$ and $m \rightarrow 1$. Ferroelectrics have weakly bound clusters of dipole reversals, thus yielding a small value of n .

For imperfectly crystallized materials with topographical impurities, glasses, and vitreous polymer systems, $n \rightarrow 1$ and $m \rightarrow 0$.

It may be noted that $n + m = 1$ will occur only when the intra- and intercluster displacements lie along the same coordinates, as in Lennard–Jones liquids [43] and hydrogen-bonded systems [44].

The cluster model [41,42] is in many ways the most rigorous description of relaxation of defects in a dielectric system, and it offers an ab initio derivation of the entire spectral shape of the frequency dependence of the susceptibility function.

Table 9 lists the theoretical concepts of dielectric relaxation models, discussed above.

4.2. Electric Equivalent Circuits for Dielectric Loss

A dielectric capacitor can be represented by an electrical circuit where the dielectric loss is reproduced mainly by an equivalent resistance R in series or in parallel with the capacitor and, occasionally, an inductance. A Debye system can be represented, for example, by a resistance and a capacitance in series, while non-Debye behavior of dielectric susceptibility may be constructed with more complex circuits.

Table 9. Theoretical Concepts of Relaxation Models

Function	Equation		Parameters
Debye	$\chi''(\omega) \propto \frac{1}{(\omega/\omega_p)^{-1} + (\omega/\omega_p)}$	(26)	$\alpha = 0$ $\beta = 1$
Cole–Cole	$\chi''(\omega) \propto \frac{1}{(\omega/\omega_p)^{\alpha-1} + (\omega/\omega_p)^{1-\alpha}}$	(27)	$0 < \alpha < 1$ $\beta = 1$
Davidson–Cole	$\chi''(\omega) \propto \frac{1}{(\omega/\omega_p)^{-1} + (\omega/\omega_p)^\beta}$	(28)	$\alpha = 0$ $0 < \beta < 1$
Havriliak–Negami	$\chi''(\omega) \propto \frac{1}{(\omega/\omega_p)^{\alpha-1} + (\omega/\omega_p)^{\beta(1-\alpha)}}$	(29)	$0 < \alpha < 1,$ $0 < \beta < 1$
Jonscher, Dissado, and Hill (dipolar peak)	$\chi''(\omega) \propto \frac{1}{(\omega/\omega_p)^{-m} + (\omega/\omega_p)^{n-1}}$	(21)	$0 < m < 1$ $0 < n < 1$
Jonscher, Dissado, and Hill (QDC process)	$\chi'(\omega) \propto \chi''(\omega) \propto \omega^{n_2-1}$ for $\omega \ll \omega_c$	(24)	$0 < n_2 < 1$ $0 < n_1 < 1$
	$\chi'(\omega) \propto \chi''(\omega) \propto \omega^{n_2-1}$ for $\omega \gg \omega_c$	(25)	
Weron (stochastic model)	$\phi(t) = \phi_0 \alpha \omega_p (\omega_p t)^{\alpha-1} [1 + k(\omega_p t)^\alpha]^{-(1+k)/k}$	(41)	$m = (1 - n)/k$ $1 - n < m < 1$

Source: Refs. 29,36.

For such cases, the concept of a *universal* capacitor [8] has been proposed, and the resulting frequency dependence of the dielectric parameters is

$$\chi(\omega) \propto C_n(\omega) = \beta(i\omega)^{n-1} = \beta \left(\sin \frac{n\pi}{2} - i \cos \frac{n\pi}{2} \right) \omega^{n-1} \quad (95)$$

It should be noted that for nonideal dielectric responses, the circuit elements will have frequency-dependent dispersive properties. Figure 9 shows schematic representations of simple circuit combinations of ideal, frequency-independent elements and some forms of presentation of dielectric data. The frequency response of lossy capacitors of the type represented by Eq. (89) is shown in Fig. 10 [8,36,45]. The association of universal capacitors and dispersive circuit elements is schematically represented in Table 10 [29].

4.3. Relaxation Behavior in Materials

The relaxation phenomena have been studied for a wide range of materials, from covalent, ionic, and van der Waals crystals at one extreme through glasses, liquids containing suspensions, solid synthetic polymers, and p-n junctions at the other [41].

The permittivity of nonpolar gases at normal pressure is close to unity, and the Clausius–Mossotti equation [23]

adequately describes its variation with moderate density changes [46]. At high pressures the molar polarization of gases deviates from the Clausius–Mossotti equation. The molecular polarizability is enhanced by the attractive forces between the molecules, whereas the repulsive forces decrease it.

Centrosymmetric molecules do not possess dipole or octupole moments, but quadrupole moments may be present in some gases, such as hydrogen, carbon dioxide, carbon disulfide, oxygen, nitrogen, benzene, and ethylene. Tetrahedral molecules, on the other hand, have zero dipole and quadrupole moments (e.g., methane and carbon tetrachloride) [46]. The presence of higher dipole moments in a molecule induces moments on its neighbors and produces deviations from the Clausius–Mossotti equation. Polar gases display temperature dependence of the orientational polarization, and their dielectric loss spectra follow the Debye relaxation behavior in which partial orientation of the permanent dipoles occurs under an externally applied field. Polar gases absorb energy in the microwave region through two processes: rotational absorption and unquantized molecular collision. The high-frequency dielectric properties of gases have been well reviewed [47,48] and will not be discussed further here.

There is as yet no exact theory of liquids, which have been treated either as dense gases or as disordered solids.

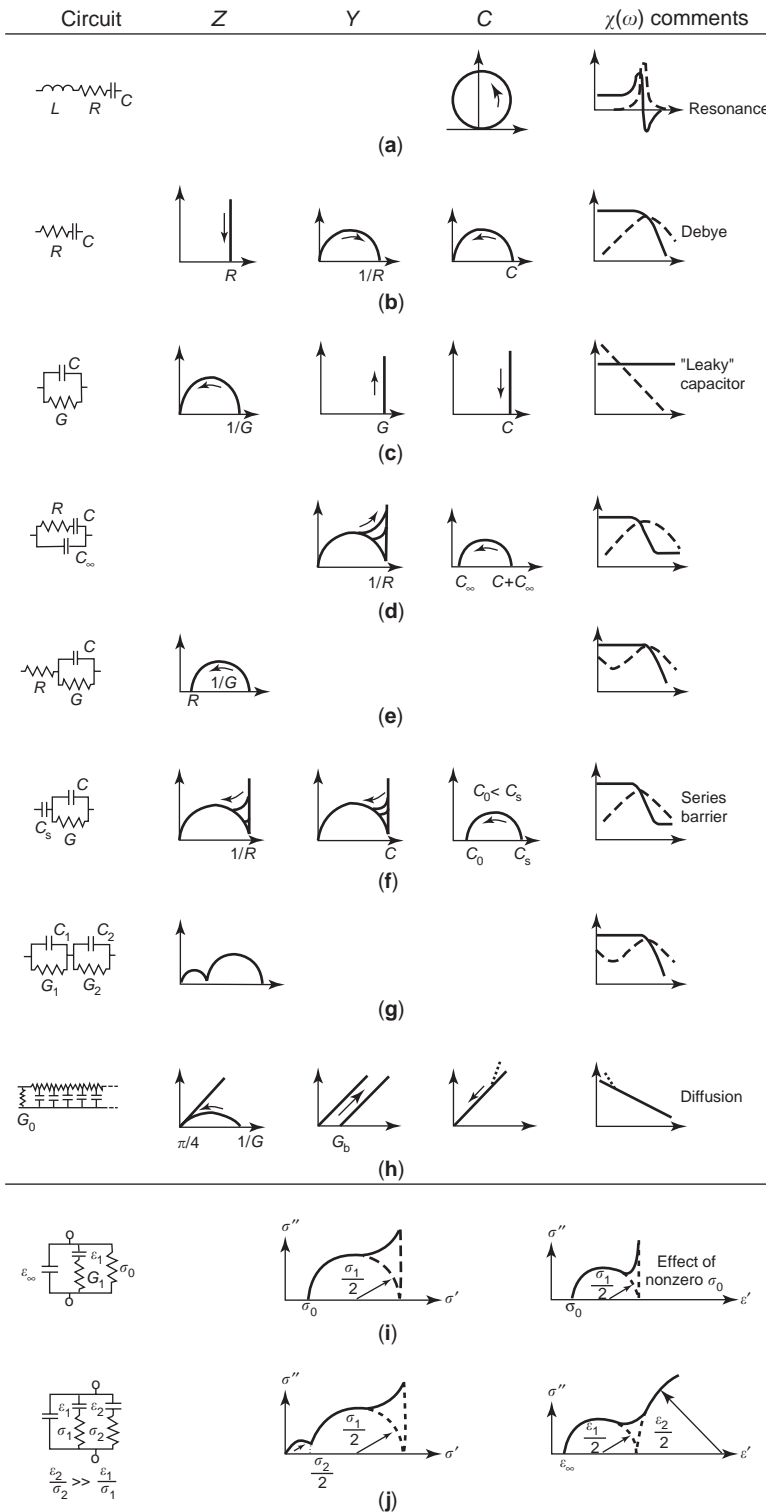


Figure 9. Schematic representation of simple circuits formed as a combination of ideal, frequency-independent elements (a-h) and some forms of presentation of dielectric data (i,j) [8,36,45].

The dielectric relaxation in polar liquids (dilute solutions) with spherical dipolar molecules can be interpreted in terms of the orientation of individual dipoles. In the Debye process, it is assumed that a spherical dipolar molecule obeys Stokes' law, which states that the relaxation time is proportional to the shear viscosity of the liquid and to r^3 , where r is the radius of the sphere. However, the relax-

ation time must depend on the viscosities of both the solvent and the solute. The molecular radius calculated from the relaxation time with the Debye model is usually too small. Improved fit to the relaxation behavior of liquids may be obtained with empirical formulas (Cole-Cole [20], Davidson-Cole [21], Havriliak-Negami [23,24]) and the universal law [8].

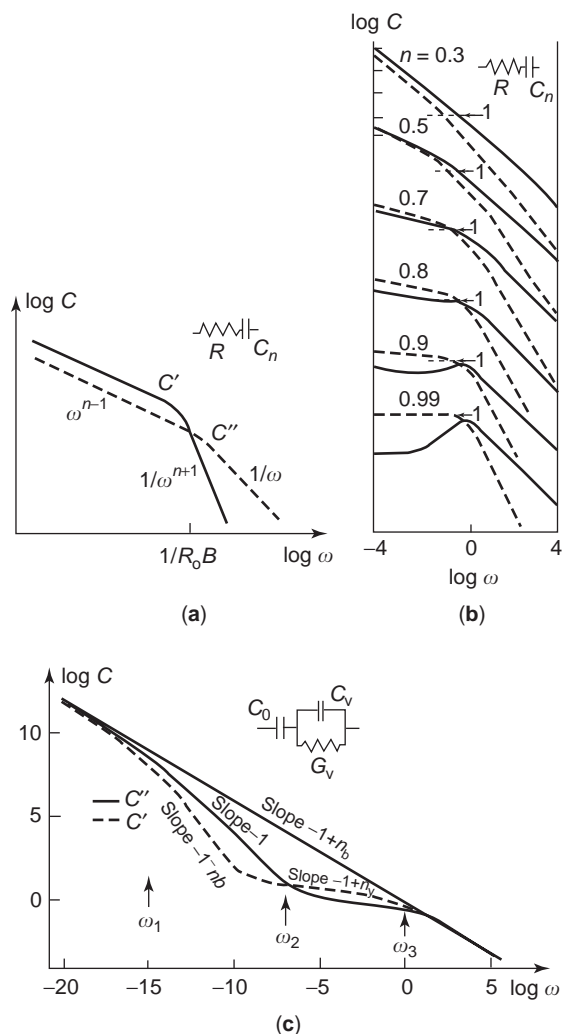


Figure 10. The frequency response of circuits involving universal lossy capacitors of the type $C_n = B(i\omega)^{n-1}$: (a) response of a series combination of C_n with a resistor R ; (b) calculated frequency dependences for a range of values of the exponent n ; (c) the response of the series-parallel circuit shown, with two universal capacitors, one of which corresponds to a series barrier region, while the other forms the equivalent of a volume region with its parallel conductance G_v . The values of parameters assumed in the calculation are as follows: $B_v = 1$, $G_v = 10^{-6}$, $n_v = 0.85$, $B_s = 1$, $n_s = 0.4$. At very low frequencies the volume behavior is dominated by the conductance, and the response is that of a series combination of C_b and G_v , which is therefore closely similar to that seen in (a) [8].

The intermolecular forces in associated liquids are stronger and perhaps more directional in some cases than in other liquids. Water is probably the most important associated liquid. The dielectric relaxation behavior of water agrees well with the Cole-Cole model [20] with $\alpha = 0.02 \pm 0.007$ [45,49]. It has been suggested [50] that the kinetic process responsible for the dielectric relaxation in water is cluster formation. Water is composed of fluctuating clusters of bonded molecules with unbonded molecules between them. Individual molecules are able to move frequently from one cluster to another, and their dipole orientation will depend on the number of hydrogen bonds they form [45,50]. It should be noted that the clustering is a

Table 10. Electrical Analog Equivalent Circuits

Circuit	Function
	Debye [Eq. (52)]
	Dipolar relaxation
	[Eq. (67)] QDC process
	[Eqs. (87), (88)] Flat loss [Eq. (87)]

Source: Ref. 29.

random process and that it is not possible to subdivide water molecules into groups that remain the same over a period of time longer than the average relaxation time, $\approx 9.6 \times 10^{-12}$ s, which is perhaps related to the OH stretching vibration at 1.10×10^{13} Hz. This vibration is affected by the hydrogen bonding. Alcohols have a wide distribution of relaxation times, which tend to follow the empirical Cole-Cole [20] and Davidson-Cole [21] models. The dielectric properties of liquids have been comprehensively reviewed elsewhere [45,50] and will not be discussed further here.

A perfect alkali halide ionic crystal such as NaCl can be polarized only by perturbing its thermal vibrations. However, in practice all crystals contain dislocations, specifically, polarizable flaws, which do not always distort the lattice, particularly when the ionic radii are similar [45]. The dielectric relaxation behavior in such materials is complicated by the presence of their ionic and electronic conductivities. For these materials the relaxation time τ tends to be long (≈ 1 s) at room temperature, and it obeys

$$\tau = Ae^{E_a/kT} \tag{96}$$

where E_a is the thermal activation energy and A is a constant. It is of interest to note that the mechanical relaxation time of these materials is often half the dielectric one, neglecting electrostatic interactions. This implies that the shear modes of polarization relax twice as fast as do the tensile ones [45]. The dielectric behavior of alkali halides with divalent cations has been reviewed extensively by Meakins [51].

Organic semicrystalline and amorphous polymers are practical electrical insulating materials that consist of macromolecules. Such molecular solids have both covalent and van der Waals bonds, which facilitate molecular motion in comparison with entirely covalently bonded solid dielectrics. The activation process in these materials also follows an Arrhenius relationship of the form of Eq. (90) except at the glass transition temperature T_g . The relaxation process at T_g is approximated by the William-Landel-Ferry relationship [52],

$$\tau(T) = \tau_0 \exp\left(\frac{C_1(T - T_g)}{C_2 + T - T_g}\right) \tag{97}$$

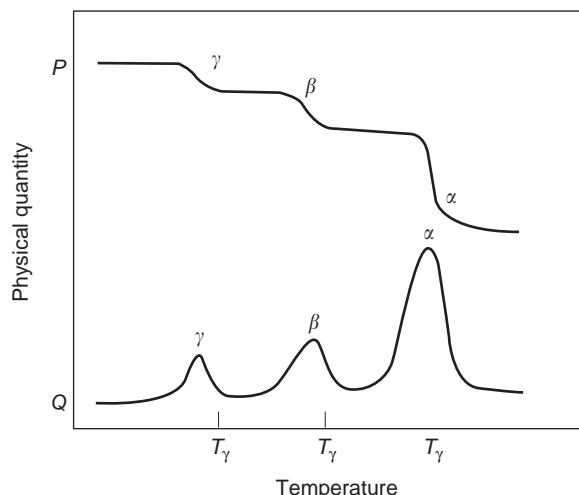


Figure 11. Schematic diagram of the temperature dependence of complex properties of polymers [54].

where τ_0 is a constant, and C_1 and C_2 are also constants with values ≈ 17 and ≈ 51 , respectively [46]. The relaxation time τ decreases with increasing temperature, as may be observed in isochronal plots of depolarizing current against temperature [53].

The relaxation behavior of polymers is related to several complex physical parameters—shear modulus, heat capacity, permittivity, and refractive index—which exhibit transitions with increasing temperature [54] (see Fig. 11). In an amorphous polymer the principal transition is the glass transition at a temperature T_g , which is labeled as the α transition at T_α in Fig. 11. Above T_g the free volume decreases to a critical value, thus severely restricting the segmental motions of the polymer chains. In a semicrystalline polymer there will be an additional transitional phenomenon at the melting temperature T_m . There are other secondary transitions, β and γ in order of decreasing temperature (i.e., $T_\alpha > T_\beta > T_\gamma$). For example, in polyethylene, the α , β , and γ relaxations at 1 kHz occur at 77, -13 , and -113°C , respectively. The α relaxation is attributed to motions in the crystalline phase, and the β relaxation arises from primary motions of the chain branches in the amorphous phase. The γ relaxation may be associated with a combination of processes including defect migration and the reorientation motion in the amorphous phase [55]. The α , β , and γ relaxations in polypropylene occur at 80, 0, and -80°C . Table 11 gives the glass transition temperatures T_g of some common polymers [54].

4.4. Experimental Evidence of Frequency Response and a Comparison with the Cluster Models

Although ideal Debye response in ferroelectric single crystals has been observed [56], there exist, in general, very few examples of such responses in condensed matter. Although water may be regarded as a classic dielectric, its dielectric behavior displays a broadened relaxation peak that departs from a true Debye relation [8,57]. Near-Debye relaxation responses have also been observed in silicon p-n junctions [8]. It may not be appropriate to

Table 11. Glass Transition Temperature T_g of Common Polymers^a

Polymer	T_g ($^\circ\text{C}$)
PE	$-90, -35$
PP	-10
Polymethylpentene	30
PS	95
PAN	105
PVC	85
PVF	$-20, 45$
PVDC	-15
PA 6	50
PA 66	90
PA 610	40
PMMA	105
POM	$-90, -10$
Poly(phenylene oxide)	210
PC	150
PETP	65
CA	105
NR	-75
CR	-45
NBR	-20

Source: Ref. 54.

^aThese are approximate values; where two temperatures are given, the assignment of the glass transition remains doubtful. T_m is independent of chain length for high-molar-mass polymers, but falls somewhat as the chains become very short.

discuss experimentally observed dielectric dispersion data with the Cole–Cole, Davidson–Cole, and Havriliak–Negami models, which are basically empirical in nature. However, relaxation spectroscopy can provide considerable information on dielectric materials from the measurement of the shape of the loss peak as well as the relaxation rate and amplitude. The shape of a loss peak is clearly characterized by the parameters m and n of the Dissado–Hill [41,42] and universal law [8] models. This procedure has been employed to demonstrate the presence of cluster structure in (1) the viscous liquid produced from the glassy state above a glass transition [58], (2) plastic crystal phases [59], and (3) ferroelectrics [60,61]. The cluster size becomes strongly temperature-dependent in ferroelectrics near the Curie temperature [61]. The amplitude and the relaxation rate are related [60–62]. These considerations also hold true for liquid crystals [60,61,63]. Figures 12a and 12b show the observed dielectric response of poly-*r*-benzyl-L-glutamate (PBLG) and poly-*r*-methyl-L-glutamate (PMLG), respectively [42]. The loss peaks in both cases are broad with values of n and m in conformity with the cluster model [41]. Table 12 gives the values of shape indices n and m for PBLG in different states, from which it may be observed that as the local order decreases in solution, the value of n decreases, and that of m increases [41,63]. These examples cover some typical cluster structures with different values of m and n [41].

It is suggested that the quantum-mechanical cluster model provides explanations for the relaxation dynamics in materials that show non-Debye susceptibility behavior over a wide frequency range. The cluster model shows that the free energy of a cluster is held constant and its entropy

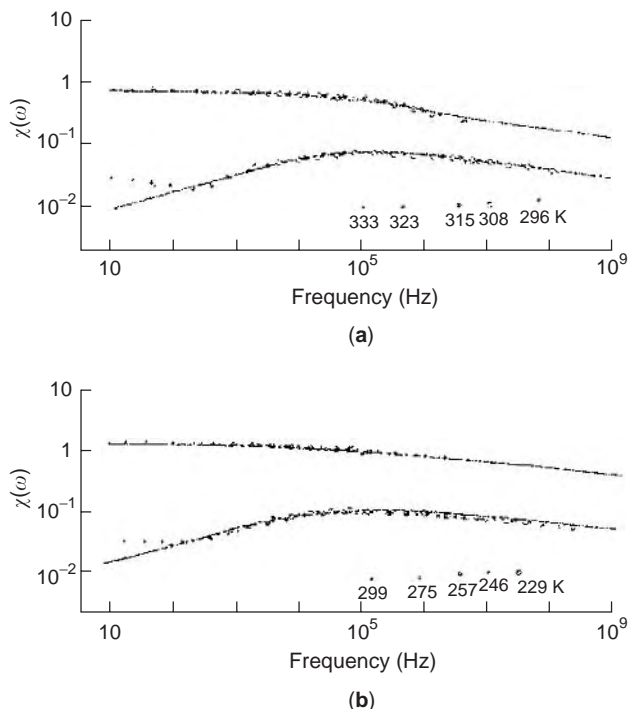


Figure 12. Master curves for the dielectric response of oriented films of (a) PBLG and (b) PMLG. The theoretical spectral shape in the plots has been determined with the values (a) $m = 0.28$, $n = 0.87$; (b) $m = 0.24$, $n = 0.92$. Plot (a) is scaled at 333 K; (b), at 299 K. In both, the small magnitude of the dispersion has limited the accuracy with which the real part of the susceptibility could be determined for the higher frequency values [42].

evolves at the expense of its internal energy (i.e., enthalpy), resulting in a power-law relaxation process.

5. APPLICATION OF DIELECTRIC SPECTROSCOPY IN DETECTING AGING IN INSULATING POLYMERS

5.1. Dielectric Aging and Treeing

Polymers experience aging when subjected to a mechanical or electric stress over an extended period of time. The aging produces irreversible deterioration of physical, chemical, and dielectric and other electrical properties, which may eventually lead to electrical breakdown of an

Table 12. Spectral Shape Indices Observed in Dielectric Response of PBLG in Different Physical States

Sample	m	n
Solid, orientationally ordered film	0.28	0.87
Solid, prepared by the Leuch method	0.42	0.81
Solution in benzene with ϵ -caprolactam	0.78	0.50
Solution in <i>trans</i> -1,2-dichloroethylene containing <i>NN</i> -formidemethylamide	1.0	0.50
Solution in purified ethylene dichloride	0.78	0.49
Solution in ethylene dichloride	0.61	0.49
Solution in dioxan	—	0.44
Solution in dioxan with DMF	0.76	0.51
Solution in dioxan	0.81	0.54

Source: Refs. 41,63.

insulating polymer. It must be stressed that physical and chemical aging may occur independently without the application of an external electric field. However, the aging process may be accelerated by the field in conjunction with other factors.

The mechanisms for electrical breakdown have been extensively reviewed [64]. The chemical aging models have also been reviewed [65] and will not be discussed in detail here. The present section provides in brief the results of a study of aging of polyethylene under an AC field in humid environment by dielectric spectroscopy.

Dielectric aging in a dry environment at moderate to high electric field appears to begin mostly at imperfections in materials where the local field tends to be enhanced. At such locations, treelike electrical channels may form and propagate due to the occurrence of partial discharges. Space charges play a significant role in the initiation and growth of electrical trees [66]. Water trees in polymeric insulators with AC fields in humid environments may arise from microphase separation in partially oxidized polymers as a result of field-induced electrochemical processes [67]. It has been shown that water trees in cross-linked polyethylene consist of tracks of hydrophilic carboxylate salts in the amorphous phase of the polymer [68–70]. The dielectric aging and the water tree growth incorporate electrochemical processes following the electrophysical process of water and ion diffusion in the polymer [68]. It has been suggested that the electrochemical degradation of polyolefins associated with aging and water treeing involve five fundamental steps: (1) electrolysis of water, in which oxygen and hydrogen peroxide radicals are formed, as both are oxidizing agents; (2) initiation of degradation; (3) catalysis of degradation by metal ions; (4) chain scission, resulting in the formation of ketones and carboxylate ions; and (5) conversion of ketones to carboxylate ions [71]. Electric-field-driven oxidation has also been proposed by other workers [64,72–74].

The electrooxidation occurs in the local field direction, and water tree tracks are formed by chain scission in the amorphous regions of the polymer. The track region is hydrophilic. As a result, water molecules in the polymer matrix condense to form liquid water in the track, which then transports ions to provide further oxidation at the tip of the track. Thus a track propagates itself in a similar manner to that of a self-propagating electrical tree or a gas breakdown channel, although at a different rate [71].

It may thus be expected that aging and its progress due to the electrooxidation of a polymer in a humid environment may be detected by a study of its dielectric behavior over a wide frequency range.

5.2. Evidence of Aging in Frequency Response

Figure 13 shows the frequency response of the real and the imaginary parts [$\chi'(\omega)$ and $\chi''(\omega)$, respectively] of the complex susceptibility $\chi(\omega)$ of unaged and crosslinked polyethylene (XLPE) cable samples and samples AC-aged (6 kV/mm, 50 Hz) for up to 6000 h in water at room temperature [36,75]. It may be observed from the fitted response that there are three relaxation processes: (1) a high-frequency (HF) loss peak at $\sim 5 \times 10^5$ Hz, (2) a

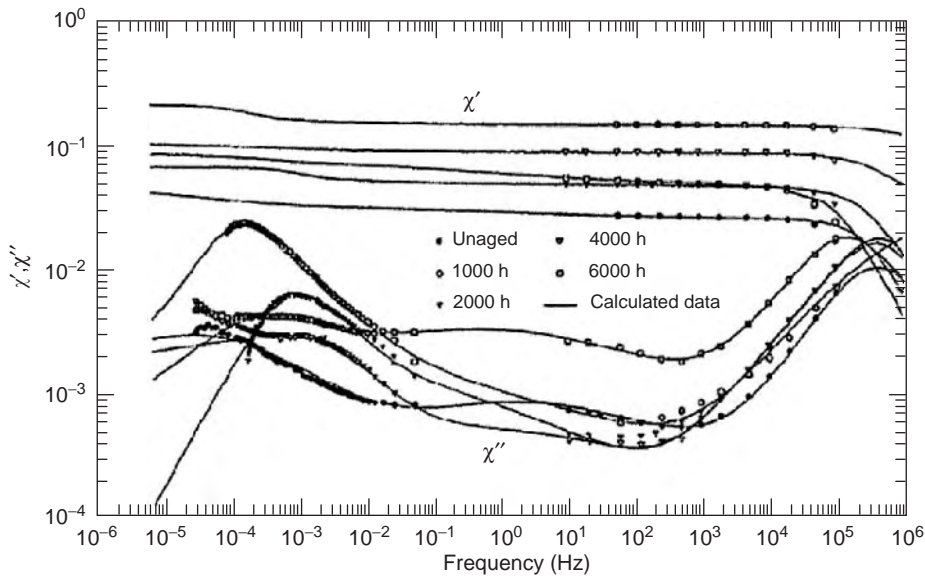
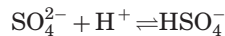


Figure 13. Dielectric behavior of XLPE cable samples, unaged and AC-aged ($6 \times 10^6 \text{ V m}^{-1}$, 50 Hz, room temperature, water) up to 6000 h [36].

medium-frequency (MF) loss peak at ~ 1 Hz, and (3) a low-frequency (LF) loss peak at $\sim 10^{-4}$ Hz. It is suggested that the HF loss peak is due to bound water containing ions. It has been stated that in principle there are two relaxations in water: the fluctuations in polarization and the dissociation of water into ions. The latter relaxation occurs in the gigahertz range, whereas the former one may be observed at $\sim 10^5$ Hz. For example, for a solution of MgSO_4 in water at 20°C [76], the following chemical reactions of the electrolyte may occur, each possessing its own relaxation characteristic:



The first process is slower than the second, for which the relaxation peak occurs at $\sim 2 \times 10^5$ Hz, which is in agreement with the location of the HF peak in Fig. 13 [45,76]. The second chemical reaction is more rapid and is outside the experimental range of Fig. 13. The HF peak (Fig. 13) is observed to be fairly independent of the aging time. It has also been shown that the diffusion coefficient of water vapor in polyethylene is $\approx 1.4 \times 10^{-6} \text{ m}^2/\text{s}$ and is independent of electrical stress [77,78]. Furthermore, polar impurities in polyethylene have been alleged to attract water [70], which will be bound in the polymer. In view of these observations, the origin of the observed HF peak (Fig. 13) may be attributed to the ions in bound water, as stated before [28,29,36].

XLPE cable samples contain crosslinking byproducts (such as cumyl alcohol and acetophenone, as well as antioxidants), which may diffuse out of the cable with the progress of time. In addition, antioxidants react chemically with the oxidation products in the sample. The MF loss peak at ~ 1 Hz appears to increase slightly (Fig. 13) with continued aging. It also becomes broader, overlapping with the LF peak. It is suggested that the MF peak may

originate from the presence of the polar moieties discussed above [28,29,36].

The LF loss peak (Fig. 13), occurring at 10^{-4} Hz, changes significantly with aging. It may be noticed that the magnitude of this peak at first rises sharply, up to an aging time of 1000 h. Subsequently it decreases progressively, although its magnitude is still greater after 6000 h of aging than that of the unaged sample. Furthermore, the LF loss peak becomes broader with increasing aging time.

The LF loss peak amplitude increases initially because of the formation of free radicals. It may be argued that a competitive process involving the production of polar moieties due to electrochemical reactions and injected space charges establishes itself with increasing aging time. Eventually, the space charge component becomes dominant as the polymer becomes more conductive. The relaxation loss behavior thus shows the presence of intracluster interaction in the MF-HF region and of intercluster charge motion in the low-frequency region; the latter phenomenon becomes dominant with continued aging [29,36].

Figure 14 [28,36,75] shows a possible electrical equivalent circuit for the unaged and electrically aged XLPE samples in a humid environment. The dielectric relaxation behavior of the unaged XLPE cable sample of Fig. 13 may be represented by a parallel-connected network of (1) three series-connected frequency-dependent resistances R_1 , R_2 , and R_3 and (2) three dissipative capacitances C_1 , C_2 , and C_3 , giving three dipolar peaks in the LF, MF, and HF regions, respectively. The QDC response in the LF region with progressive aging has been taken into account by removing the resistance R_3 from the circuit. The observed broadening of the MF peak with aging will cause R_2 to diminish with aging, although it will still have a nonzero value. The values of R_1 and C_1 for the HF peak should not change significantly, as the HF peak remains unaffected by field aging. Figure 14 also incorporates the very high-frequency capacitance C_∞ and G_0 in parallel. The latter parameter represents any DC conduction mechanism in the dielectric [75].

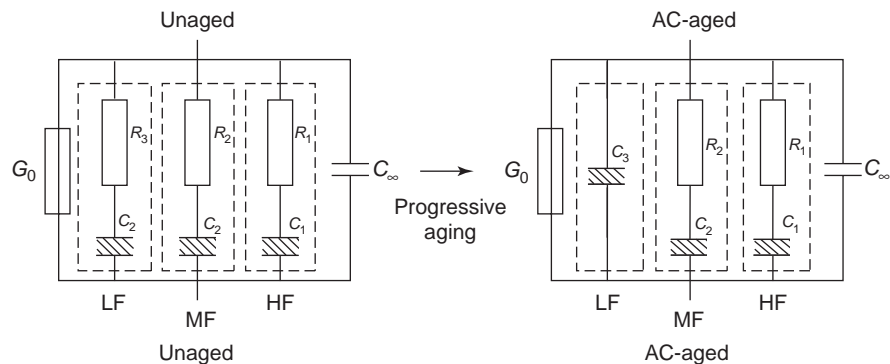


Figure 14. Analog equivalent circuits of unaged and AC-aged XLPE cable samples [28,36,75].

It is thus suggested that the dielectric spectroscopy, particularly in the LF range, may be a convenient tool in identifying aging [79]. Furthermore, the Debye relaxation model [3] and the intracuster and intercluster manybody interaction model [41,42] may provide explanations for the relaxation behavior observed at a molecular level.

BIBLIOGRAPHY

- C. J. F. Böttcher and P. Bordewijk, *Theory of Electric Polarization*, 2nd ed., Vol. 1, Elsevier, Amsterdam, 1973, Chaps. 1, 2, pp. 9–90.
- H. Fröhlich, *Theory of Dielectric Constant and Dielectric Loss*, Clarendon, Oxford; 1958, Chap. 1, pp. 1–14.
- P. Debye, *Polar Molecules*, Dover, New York, 1929, Chap. 5.
- A. A. Zaky and R. Hawley, *Dielectric Solids*, Routledge, Kegan & Paul, London; 1970, Chaps. 1, 2, pp. 2–25.
- A. R. Von Hippel, ed., *Dielectric Materials and Applications*, MIT Press, Cambridge, MA; 1954, Chaps. 1–3, pp. 3–36.
- M. C. Lovell, A. J. Avery, and M. E. Vernon, *Physical Properties of Materials*, Van Nostrand Reinhold, New York; 1976, Chap. 8, pp. 153–184.
- A. Schönhals, Dielectric properties of amorphous polymers, in J. P. Runt and J. J. Fitzgerald, eds., *Dielectric Spectroscopy of Polymer Materials*, Washington: American Chemical Society (ACS), Washington, DC, 1997, Chap. 3, pp. 81–106.
- A. K. Jonscher, *Dielectric Relaxation in Solids*, Chelsea Dielectric Press, London; 1983, Chap. 2, pp. 13–61.
- C. A. West and R. M. Thomson, *Physics of Solids*, McGraw-Hill, New York; 1970, Chaps. 18, 19, pp. 388–421.
- R. Sängler, O. Steiger, and K. Gächter, Temperature effect der Molekularpolarisation einiger Gase und Dämpfe, *Helv. Phys. Acta* **5**:200–210 (1932).
- C. Smyth and W. Walls, Dielectric investigation of nitromethane and chloropicrid, *J. Chem. Phys.* **3**, 557–559 (1935).
- C. Smyth and C. Hitchcock, Dipole rotation and the transition in the crystalline hydrogen halides, *J. Am. Chem. Soc.* **55**:1830–1840 (1933).
- J. C. Anderson, *Dielectrics*, Chapman & Hall, London; 1964, Chap. 7, pp. 83–97.
- L. Hartshorn and J. A. Saxton, *Handb. Phys.*, **26**:640 (1958).
- G. Williams and D. C. Watts, Non-symmetrical aspects of multiple dielectric relaxation in behaviour arising from a single empirical decay function, *Trans. Faraday Soc.* **66**:80–85 (1970).
- A. K. Jonscher, *Universal Relaxation Law*, Chelsea Dielectric Press, London; 1996, Chap. 1, pp. 1–44.
- J. M. Alison, *A Dielectric Study of Lossy Materials over the Frequency Range of 4-82 GHz*, Ph.D. thesis, Univ. London, 1990.
- R. M. Hill and A. K. Jonscher, The dielectric behaviour of condensed matter and many body interpretation, *Contemp. Phys.* **24**:75–110 (1983).
- J. M. Alison and R. J. Sheppard, A precision wave-guide system for the measurement of complex permittivity of lossy liquids and solid tissues in the frequency range 29 GHz–90 GHz, 1: The liquid system for 29–45 GHz—an investigation in water, *Meas. Sci. Technol.* **1**:1093–1098 (1993).
- K. S. Cole and R. H. Cole, Dispersion and absorption in dielectrics, 1. Alternating current characteristics, *J. Chem. Phys.* **9**:341–351 (1941).
- D. W. Davidson and R. H. Cole, Dielectric relaxation in glycerol, propylene, and *n*-propanol, *J. Chem. Phys.* **12**:1484–1490 (1951).
- R. M. Fuoss and J. G. Kirkwood, Electrical properties of solids. VIII. Dipole moments in polyvinyl chloride diphenyl systems, *J. Am. Chem. Soc.* **63**:385–394 (1941).
- S. Havriliak and S. Negami, A complex plane analysis of α -dispersion in some polymer systems, *J. Polym. Sci. C* **14**: 99–117 (1966).
- S. Havriliak and S. Negami, A complex plane representation of dielectric and mechanical relaxation processes in some polymers, *Polymer* **8**:161–210 (1967).
- J. R. Macdonald, Transient and temperature response of a distributed, thermally activated system, *J. Appl. Phys.* **34**:538–552 (1963).
- B. Gross, Electret research—stages in development, *IEEE Trans. Electric. Insul.* **EI-21**(3):249–269 (1986).
- B. Gross, Distribution functions in linear viscoelastic theory, *J. Appl. Phys.* **62**:2763–2770 (1987).
- D. K. Das-Gupta and P. C. N. Scarpa, Polarization and dielectric behaviour of ac-aged polyethylene, *IEEE Trans. Dielectrics Electric. Insul.* **3**:366–374 (1996).
- D. K. Das-Gupta and P. C. N. Scarpa, Modelling of dielectric relaxation spectra of polymers in the condensed phase, *IEEE Electric. Insul. Mag.* **15**:23–32 (1999).
- G. C. Garton, The distribution of relaxation times in dielectrics, *Trans. Faraday Soc. A* **42**:55–60 (1946).
- N. G. McCrum, B. E. Read, and G. Williams, Phenomenological theories of mechanical and dielectric relaxations, in *Anelastic and Dielectric Effects in Polymer Solids*, Wiley, New York; 1967, Chap. 4, pp. 102–237.

32. C. J. Dias, Determination of a distribution relaxation frequency, *Phys. Rev. B* **53**:14212–14222 (1996).
33. K. Liedermann, The calculation of a distribution of relaxation times from the frequency dependence of the real permittivity with the inverse Fourier transformation, *J. Non-cryst. Solids* **175**:21–30 (1994).
34. A. K. Jonscher, Dielectric response of polar materials, *IEEE Trans. Electric. Insul.* **25**:622–629 (1990).
35. A. K. Jonscher, The universal dielectric response and its physical significance, *IEEE Trans. Electric. Insul.*, **EI-19**:567–577 (1992).
36. P. C. N. Scarpa, *Polarization and Dielectric Behaviour of AC Aged Polyethylene*, Ph.D. thesis, Univ. Wales, 1995.
37. K. Weron, A probabilistic mechanism hidden behind the universal power law for dielectric relaxation, *J. Phys. Condens. Matt.* **3**:9151–9162 (1991).
38. K. Weron and A. Jurlewicz, Two forms of self-similarity as a fundamental feature of the power-law dielectric response, *J. Phys. A Math. Gen.* **26**:395–410 (1993).
39. A. Weron, K. Weron, and W. A. Wyoczynski, Relaxation functions in dipolar materials, *J. Stat. Phys.* **78**:1027–1038 (1995).
40. J. T. Bender and M. F. Shlesinger, Derivation of the Kohlrausch-Williams/Watts decay law from activation energy dispersion, *Macromolecules* **18**:591–592 (1985).
41. L. A. Dissado and R. M. Hill, A cluster approach to the structure of imperfect materials and their relaxation spectroscopy, *Proc. Roy. Soc. Lond.* **390**:131–180 (1983).
42. L. A. Dissado and R. M. Hill, Anomalous low frequency dispersion, *J. Chem. Soc. Faraday Trans. 2* **80**:291–319 (1984).
43. R. M. J. Cotterill and J. C. Tallon, Melting and the liquid glassy state, *J. Chem. Soc. Faraday Disc.* **69**:241–260 (1980).
44. H. P. Schwan, R. J. Sheppard, and E. H. Grant, Complex permittivity of water at 25°C, *J. Chem. Phys.* **64**:2257–2258 (1976).
45. V. V. Daniel, *Dielectric Relaxation*, Academic Press, London; 1967, Chap. 7, pp. 95–109.
46. N. E. Hill, W. E. Vaughan, and M. Davies, *Dielectric Properties and Molecular Behaviour*, Van Nostrand Reinhold, London; 1969, Chaps. 3–5, pp. 191–461.
47. K. H. Illinger, Dispersion and absorption of microwaves in gases and liquids, in J. B. Birks and J. Hart, eds., *Progress in Dielectrics*, Academic Press, London; 1962, Vol. 4, pp. 37–101.
48. H. G. Sutter, Dielectric polarization in gases, in M. Davies, ed., *Dielectric and Related Molecular Processes*, Chemical Society, London; 1972, Vol. 1, Chap. 3, pp. 64–99.
49. E. H. Grant, T. J. Buchanan, and H. F. Cook, Dielectric behaviour of water at microwave frequencies, *J. Chem. Phys.* **26**:156–161 (1957).
50. J. B. Hasted, Dielectric properties of water and of aqueous solutions, in M. Davies, ed., *Dielectric and Related Molecular Processes*, Chemical Society, London; 1972, Vol. 1, Chap. 5, pp. 121–161.
51. R. J. Meakins, Mechanism of dielectric absorption in solids, *Progr. Dielectr.* **3**:151–202 (1961).
52. M. L. Williams, R. F. Landel, and J. D. Ferry, The temperature dependence of relaxation mechanisms in amorphous polymers and other glass-forming liquids, *J. Am. Chem. Soc.* **77**:3701–3707 (1955).
53. D. K. Das-Gupta and R. S. Brockley, A study of absorption currents in polypropylene, *J. Phys. D Appl. Phys.* **11**:955–962 (1978).
54. C. Hall, *Polymer Materials: An Introduction for Technologists and Scientists*, 2nd ed., Macmillan Education, London; 1989, Chap. 2, pp. 34–54.
55. R. T. Baily, A. M. North, and R. A. Pethrick, *Molecular Motions in High Polymers*, Clarendon, Oxford; 1981.
56. K. Deguchi, E. Okaane, and E. Nakamura, Effects of deuteration on the dielectric properties of ferroelectric CsH₂PO₄, 1. Static dielectric properties, *J. Phys. Soc. Japan* **51**:3569–3574 (1969).
57. P. R. Mason, J. B. Hasted, and L. More, The use of statistical theory in fitting equations to dielectric dispersion data, *Adv. Mol. Rel. Proc.* **6**:217–232 (1974).
58. M. Shablakh, R. M. Hill, and L. A. Dissado, Dielectric examination of glass-forming system, *J. Chem. Soc. Faraday Trans. 2* **78**:639–655 (1982).
59. M. Shablakh, L. A. Dissado, and R. M. Hill, Structure and dielectric relaxation mechanisms in the cyclic alcohols, cyclopentanols for cyclo-octanol, *J. Chem. Soc. Faraday Trans. 2* **79**:369–417 (1983).
60. L. A. Dissado and R. M. Hill, Dielectric behaviour of materials undergoing dipole alignment transitions, *Phil. Mag. B* **41**:625–642 (1980).
61. L. A. Dissado and R. M. Hill, Dynamic scaling and the first order character of ferroelectric transitions, *J. Phys. C* **16**:4023–4039 (1983).
62. P. C. Hohenberg and B. I. Halperin, Theory of dynamic critical phenomena, *Rev. Mod. Phys.* **49**:435–479 (1977).
63. L. A. Dissado and R. M. Hill, Examination of the dielectric susceptibility of poly-*r*-benzyl-L-glutamate, *J. Chem. Soc. Faraday Trans. 2* **78**:81–93 (1982).
64. L. A. Dissado and J. C. Fothergill, *Electrical Degradation and Breakdown in Polymers*, Peter Peregrinus, London; 1992, pp. 74–116.
65. L. Reich and S. A. Stivala, *Elements of Polymer Degradation*, McGraw-Hill, New York; 1971, pp. 1–275.
66. T. Hibma and H. R. Zeller, Direct measurement of space charge injection from a needle electrode into dielectrics, *J. Appl. Phys.* **59**:1614–1620 (1986).
67. H. R. Zeller, Thermodynamics of water treeing, *IEEE Trans. Electric. Insul.* **EI-22**:677–681 (1987).
68. R. Ross and J. J. Smit, Composition on growth of water trees in XLPE, *IEEE Trans. Electric. Insul.* **27**:519–530 (1992).
69. E. F. Steenis, *Water Treeing in Polymer Cable Insulations*, KEMA Scientific Technical Report, 1990, Vol. 8, pp. 149–208.
70. E. F. Steenis and F. H. Kruger, Water treeing in polyethylene cables, *IEEE Trans. Electric. Insul.* **5**:989–1028 (1990).
71. J. J. Xu and S. A. Boggs, The chemical nature of water treeing: theories and evidence, *IEEE Electric. Insul. Mag.* **10**(5):29–37 (1994).
72. H. J. Henkel et al., Relationship between the chemical structure and the effectiveness of additives in inhibiting water-trees, *IEEE Trans. Electric. Insul.* **EI-22**:157–161 (1987).
73. A. Garton et al., Oxidation and water tree formation in service-aged XLPE cable insulation, *IEEE Trans. Electric. Insul.* **22**:405–412 (1987).
74. R. J. Densley et al., Water treeing and polymer oxidation, *Conf. Record, Int. Symp. Electrical Insulation*, IEEE Publication 90-CH2727-6, 1990, pp. 178–182.
75. P. C. N. Scarpa, A. Svatik, and D. K. Das-Gupta, Dielectric spectroscopy of polyethylene in the frequency range of 10⁵ Hz to 10⁶ Hz, *Polym. Eng. Sci.* **36**:1072–1080 (1996).

76. M. Eigen, G. Kurtze, and K. Tamm, Zum Reaktionsmechanismus der Ultraschallabsorption in Wässrigen Electrolytlösungen, *Electrochemistry* **57**:103–118 (1957).
77. J. C. Chan and S. M. Jaczek, The moisture absorption of XLPE cable insulation under simulated service condition, *IEEE Trans. Electric. Insul.* **EI-13**:194–197 (1978).
78. H. Li, *The Association of Ions and Electrical Properties with Water Treeing in Low Density Polyethylene*, Ph.D. thesis, Univ. Strathclyde, UK, 1993.
79. D. K. Das-Gupta, Conduction mechanisms and high field effects in synthetic insulating polymers, *IEEE Trans. Electric. Insul.* **4**:149–156 (1997).

DIELECTRIC RESONATOR ANTENNAS

H. K. NG
K. W. LEUNG
City University of Hong Kong
Kowloon, Hong Kong SAR

1. INTRODUCTION

1.1. Background

Traditionally, a dielectric resonator (DR) was used as an oscillator or a filter [1], which was treated as a source of energy storage rather than as an antenna. The DR was first proposed as an effective radiator in 1983 by Long et al. [2]. They demonstrated the radiation capability of the DR with different shapes [3,4]. Henceforward, DRs were widely accepted as efficient antennas.

Researchers look for a compact, low-loss, and low-cost antenna. A DR is simple in construction; it consists of dielectric material and, therefore, has no metallic loss. This is a prominent feature especially for operation in the millimeter-wave region, where the radiation efficiency of conventional metallic antennas is usually limited by metallic loss. In addition, the wavelength inside the DR is smaller than that in free space by a factor of $1/\sqrt{\epsilon_r}$, where ϵ_r is the dielectric constant of the DR. Therefore, by increasing ϵ_r , it is possible to obtain a smaller antenna.

For many years, researchers have studied different DR shapes, such as cylindrical [2,5], rectangular [3], hemispherical [4], triangular [6,7], spherical cap [8], and cylindrical ring [9,10]. Various shapes of the dielectric resonator antenna (DRA) are shown in Fig. 1. In general, in fundamental mode a DRA radiates like a magnetic dipole, a functions that is independent of antenna shape. Although DRAs are well suited for high-frequency applications, only a few of them have been examined through limited theoretical work.

Early studies of the DRA concentrated on linear polarization (LP) [11–16]. Figure 2 shows the coaxial-probe-fed DRA, which was widely used for excitation of LP DRAs. However, it introduces ohmic loss and large probe self-reactance at high frequencies. Furthermore, a hole must be drilled in the superhard DR to accommodate the probe. This inadvertently creates undesirable airgaps [17] between the probe and the DR, causing measured results to

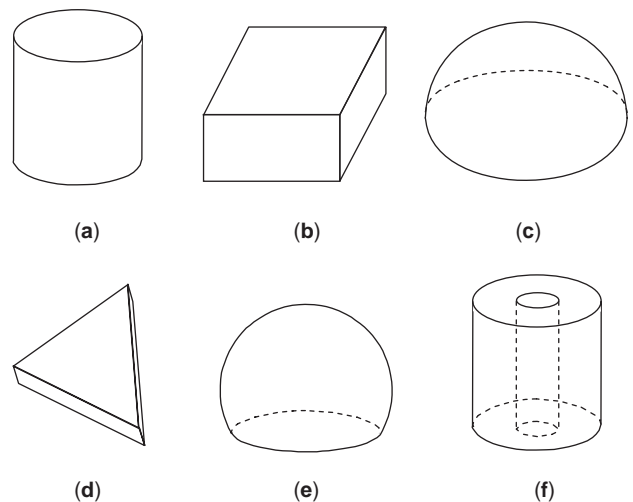


Figure 1. Various DRA configurations: (a) cylindrical; (b) rectangular; (c) hemispherical; (d) triangular; (e) spherical cap; (f) cylindrical ring.

deviate from the theoretical design. More recently, an LP DRA has been investigated using a new excitation scheme [18]: the conformal strip excitation (Fig. 3). The strip is simply cut from an adhesive conducting tape and then mounted on the DRA surface. Since the strip does not penetrate inside the DRA, the strip length can be adjusted very easily. This greatly facilitates postmanufacture trimmings of the antenna. Moreover, using this excitation method, the undesirable airgap between the feeding probe and the DRA [19] can be avoided. This article focuses on the proposed conformal-strip-fed DRA. We will introduce an angular displacement for the strip to have one more degree of freedom for matching the impedance.

The circularly polarized (CP) DRA [20–24] has been a very attractive topic because, it allows a more flexible orientation between the transmitting and receiving antennas than does the LP system. In addition, CP fields are less sensitive to the propagation effect than are LP fields, and the CP system is therefore widely used in satellite communications. A simple and straightforward CP DRA design utilizes a quadrature feed [5,25,26], but this substantially increases the size and complexity of the feed network. Petosa et al. [27] shifted the complexity from the feed network to the DRA, but the cross-shaped DRA may

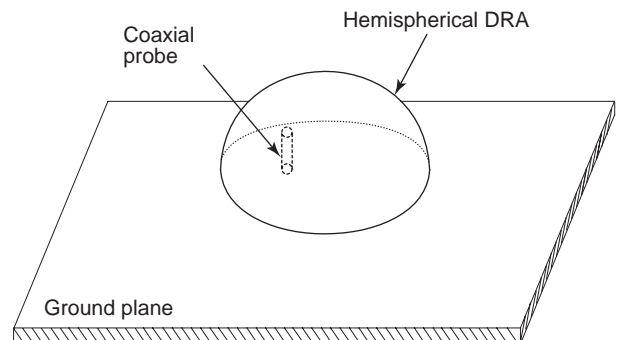


Figure 2. Configuration of coaxial-probe-fed DRA.

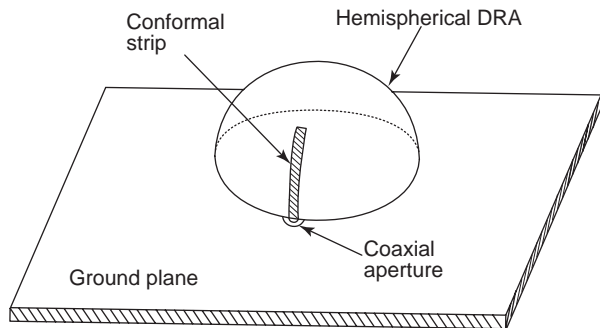


Figure 3. Configuration of conformal-strip-fed DRA.

not be available in the commercial market. To avoid these problems, a parasitic patch has been applied to the conformal-strip-fed DRA [20,24]. The use of a parasitic patch on the DRA was first considered by Li et al. [28] and later by Chen et al. [29]. In their work, the parasitic patch was placed on top of a DRA, mainly to tune the operating frequency instead of exciting CP fields. More recently, the use of a parasitic patch for the excitation of CP fields has been extended to aperture-coupled sources [30,31]. In this article, we will also demonstrate a CP DRA with a parasitic patch.

1.2. Methodology

In the analyses, the mode-matching method is used to find the various Green's functions, from which the integral equations for the conformal strip and parasitic patch currents are formulated. The equations are then solved using the method of moments (MoM).

To speed the numerical computation, the impedance integrals are evaluated either using newly obtained recurrence formulas or by direct analytical integration. It is well known that evaluating self-impedance integrals numerically is difficult because of the singularity problem of Green's functions. Around the singular points, excessive modal terms of the DRA Green's functions are required for accurate calculation of the functions. However, the amplitudes of high-order Hankel functions are so large that they are difficult to handle numerically. In addition, the integrands will fluctuate very sharply around these points and therefore very dense sampling points will be required to evaluate the integrals accurately, leading to considerable programming effort and computation time. The singularity problem was previously solved using the recurrence approach [18]. Since low-order integrals can be evaluated analytically, all the impedance integrals can be calculated without the need for any numerical integration. The same approach will be used in this article. The recurrence formulas [18] can be used only for a constant latitude current around the equatorial plane. Although they can be generalized for pulse-mode basis functions at any latitude angles, new recurrence formulas for piecewise sinusoidal (PWS) basis functions are discussed in this article instead to accelerate the MoM convergence rate.

2. CONFORMAL-STRIP-EXCITED DRA

2.1. Introduction

The conformal strip described in Ref. 18 was placed along a meridian plane of the hemispherical DRA. Virtually, the strip length is the only strip parameter used for tuning the impedance (the width of a slender strip has a relatively small effect on the input impedance). We extend the previous theory [18] to include an arbitrary angular strip displacement θ_0 . The strip begins at the base of the hemisphere and then bends back, as shown in Fig. 4. By doing so, we can desirably obtain one more degree of freedom in designing the DRA. The effect of strip displacement on input impedance was investigated, and it was found that impedance matching can easily be achieved by varying this parameter. The far fields of the new configuration were also studied. Measurements were carried out to verify the calculations, and reasonable agreement between theory and experiment was found.

2.2. Theory

To simplify the formulation, the coordinate system shown in Fig. 4 is used. With this coordinate system, the unknown strip current can be expanded using sinusoidal functions and, thus, the related MoM integrals can be evaluated in closed form. A hemispherical DRA of radius a and dielectric constant ϵ_r is excited by a conformal strip of length l and width W . The conformal strip has angular displacement θ_0 from the z axis.

2.2.1. Green's Functions. Nevels and his collaborators [33,34] have presented the modal Green's function as the sum of particular and homogeneous solutions. The potentials associated with the source in unbounded regions correspond to the particular part, whereas the boundary discontinuities are taken into account by the homogeneous part. As both the excitation strip and the parasitic element are on the DR surface in the present problem, it is unnecessary to use the previous approach. In the following formulation, the fields are assumed to vary harmonically as $e^{j\omega t}$. The field and source points are denoted by $\vec{r}(r, \theta, \phi)$ and $\vec{r}'(r', \theta', \phi')$, respectively. The Green functions ($r=r'=a$) of \hat{E}_ϕ due to a $\hat{\phi}$ -directed point current is

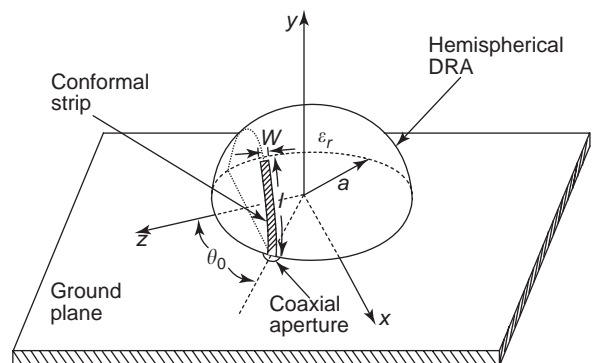


Figure 4. Configuration of the conformal-strip-excited hemispherical DRA with an angular strip displacement θ_0 .

found as follows

$$G_{J_\phi}^{E_\phi} = \frac{j\eta_0}{2\pi ar} \sum_{n=0}^{\infty} \frac{2n+1}{n(n+1)} \sum_{m=1}^n m \frac{(n-m)!}{(n+m)!} \sin m(\phi - \phi') \cdot \left\{ \frac{1}{\Delta_n^{\text{TE}}} \frac{d}{d\theta'} P_n^m(\cos \theta') \frac{P_n^m(\cos \theta)}{\sin \theta} \Phi_n - \frac{1}{\Delta_n^{\text{TM}}} \frac{P_n^m(\cos \theta')}{\sin \theta'} \frac{d}{d\theta} P_n^m(\cos \theta) \Psi_n \right\} \quad (1a)$$

$$G_{J_\phi}^{E_\phi} = \frac{j\eta_0}{2\pi ar} \sum_{n=0}^{\infty} \frac{2n+1}{n(n+1)} \sum_{m=1}^n \frac{(n-m)!}{(n+m)!} \cos m(\phi - \phi') \cdot \left\{ \frac{1}{\Delta_n^{\text{TE}}} \frac{d}{d\theta'} P_n^m(\cos \theta') \frac{d}{d\theta} P_n^m(\cos \theta) \Phi_n - \frac{m^2}{\Delta_n^{\text{TM}}} \frac{P_n^m(\cos \theta')}{\sin \theta'} \frac{P_n^m(\cos \theta)}{\sin \theta} \Psi_n \right\} \quad (1b)$$

where

$$\Phi_n = \begin{cases} \hat{H}_n^{(2)}(k_0 a) \hat{J}_n(kr) & r < a \\ \hat{J}_n(ka) \hat{H}_n^{(2)}(k_0 r) & r > a \end{cases} \quad (1c)$$

$$\Psi_n = \begin{cases} \hat{H}_n^{(2)}(k_0 a) \hat{J}'_n(kr) & r < a \\ \hat{J}'_n(ka) \hat{H}_n^{(2)'}(k_0 r) & r > a \end{cases} \quad (1d)$$

It should be mentioned that the functions Φ_n and Ψ_n have different forms for the E field inside ($r < a$) and outside ($r > a$) the DR. All other symbols were defined in Refs. 35 and 36.

2.2.2. MoM. Enforcing the boundary condition that the total tangential electric fields should vanish on the strip surface, we have

$$E^s + E^i = 0 \quad (2)$$

where E^s and E^i are defined as the scattered and impressed fields due to the current density $J_{\phi s}$ and the excitation source, respectively. Using a delta gap source model, the impressed field can be written as $(V_0/a)\delta(\phi)$. Then Eq. (2) can be rewritten as

$$\frac{-1}{W} \iint_{S_0} G_{J_\phi}^{E_\phi} J_{\phi s}(\phi) dS' = \frac{V_0}{a} \delta(\phi) \quad (3)$$

where S_0 is the strip surface. Let $I(\phi) = J_{\phi s} W$ be the strip current, which is expanded as follows using the MoM

$$I(\phi) = \sum_{q=1}^N I_q f_q(\phi) \quad (4)$$

where I_q are unknown expansion coefficients to be determined, and $f_q(\phi)$ are PWS basis functions given by

$$f_q(\phi) = \begin{cases} [\sin k_e(h - a|\phi - \phi_q|)] / \sin k_e h & a|\phi - \phi_q| < h \\ 0 & \text{elsewhere} \end{cases} \quad (5)$$

where $h = 2l/(N+1)$, $\phi_q = (-l + qh)/a$, and $k_e = \sqrt{(\epsilon_r + 1)/2} k_0$ are the PWS-mode half-length, the center-point of the q th expansion mode, and the effective wave-number at the DRA-air interface, respectively. The expansion coefficients are found via the matrix equation $[Z_{pq}][I_q] = [f_p(0)]$, where Z_{pq} are given by

$$Z_{pq} = \frac{-ja^2 \eta_0}{4\pi W^2} \sum_{n=1}^{\infty} \frac{2n+1}{n(n+1)} \left\{ \frac{\hat{J}_n(ka) \hat{H}_n^{(2)}(k_0 a)}{\Delta_n^{\text{TE}}} \times \sum_{m=0}^n \frac{2}{\Delta_m} \cdot \frac{(n-m)!}{(n+m)!} [\Theta_1(n, m)]^2 \Phi(p, q, m) \right. \quad (6)$$

$$\left. - \frac{\hat{J}'_n(ka) \hat{H}_n^{(2)'}(k_0 a)}{\Delta_n^{\text{TM}}} \sum_{m=1}^n 2m^2$$

$$\cdot \frac{(n-m)!}{(n+m)!} [\Theta_2(n, m)]^2 \Phi(p, q, m) \right\}$$

$$\Theta_1(n, m) = \int_{\theta_0 - W/(2a)}^{\theta_0 + W/(2a)} \frac{dP_n^m(\cos \theta)}{d\theta} \sin \theta d\theta \quad (7)$$

$$\Theta_2(n, m) = \int_{\theta_0 - W/(2a)}^{\theta_0 + W/(2a)} P_n^m(\cos \theta) d\theta \quad (8)$$

$$\Phi(p, q, m) = \left[\frac{2k_e a (\cos k_e h - \cos m \phi_h)}{(m - k_e a)(m + k_e a) \sin k_e h} \right]^2 \quad (9)$$

$$\times \cos m(\phi_p - \phi_q)$$

where

$$\phi_h = \frac{h}{a \sin \theta_0} \quad (10)$$

Since recurrence formulas exist for the integrals Θ_1 and Θ_2 , the integrals can be calculated very easily and quickly. Consequently, the solution (3) is a regular modal series that can be implemented very straightforwardly. As the solution can be calculated without need for any numerical integration, it is computationally very efficient. After the strip current is obtained, the input impedance can be readily calculated from

$$Z_{\text{in}} = \frac{1}{2 \sum_{q=1}^N I_q f_q(0)} \quad (11)$$

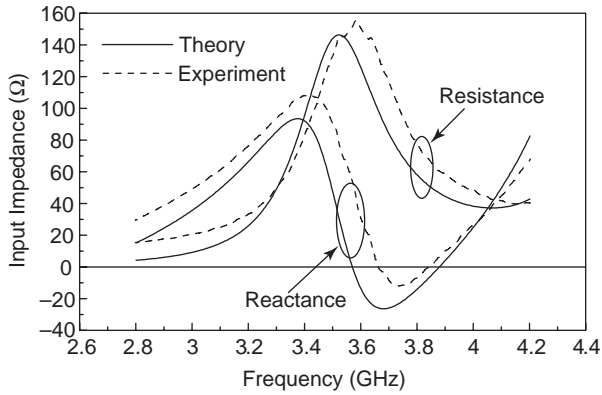


Figure 5. Measured and calculated input impedances for the configuration $a = 12.5$ mm, $\epsilon_r = 9.5$, $l = 12.0$ mm, $W = 1.2$ mm, and $\theta_0 = 80^\circ$. (From Leung and Ng [32], © 2001 John Wiley & Sons, Inc.)

where the factor of 2 accounts for the image effect of the ground plane. From the strip current the radiation can be found easily.

2.3. Results and Discussion

To verify the theory, a hemispherical DRA of $a = 12.5$ mm and $\epsilon_r = 9.5$ was measured using an HP8510C network analyzer. A conformal strip of length $l = 12.0$ mm and width $W = 1.2$ mm was cut from an adhesive conducting tape. For the calculation part, two basis functions and 60 modal terms were used. Figure 5 shows the measured and calculated input impedances for $\theta_0 = 80^\circ$, and reasonable agreement between theory and experiment is observed. The measured and calculated resonant frequencies are 3.52 and 3.58 GHz, respectively, with error 1.7%. The results are consistent with the source-free value of 3.68 GHz [36].

Figure 6 displays the calculated input impedance for $\theta_0 = 60^\circ, 70^\circ$, and 80° . It is observed that the impedance increases with θ_0 , showing that θ_0 can be used as a new parameter to match the impedance.

The measured and calculated far fields at 3.56 GHz for $l = 12.0$ mm, $W = 1.2$ mm, and $\theta_0 = 80^\circ$ are shown in Fig. 7, where reasonable agreement between theory and experiment is observed. The fields are of a broadside mode, as expected. It is found that the copolarized field is stronger than the cross-polarized field by more than 16 dB in the

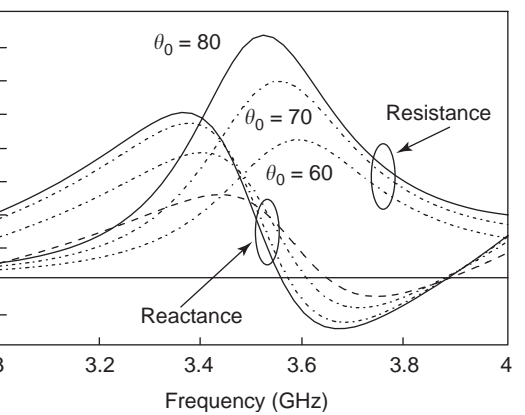
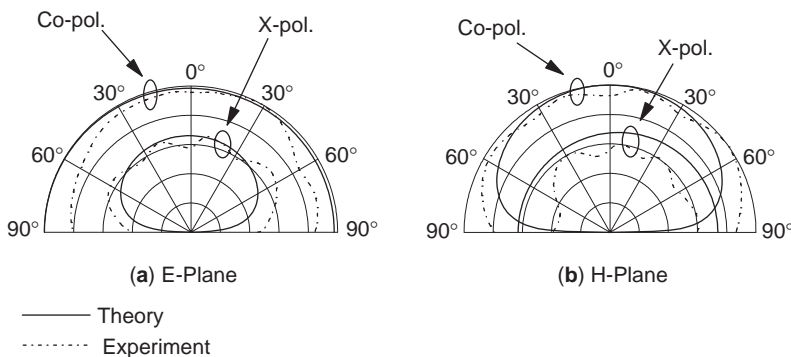


Figure 6. Calculated input impedances for $\theta_0 = 60^\circ, 70^\circ$, and 80° , with $a = 12.5$ mm, $\epsilon_r = 9.5$, $l = 12.0$ mm, $W = 1.2$ mm. (From Leung and Ng [32], © 2001 John Wiley & Sons, Inc.)

broadside direction ($\theta_0 = 0^\circ$), which is sufficient for many practical applications. Note that the H -plane cross-polarized field is not symmetric about the center, due to the angular displacement of the excitation strip.

3. CIRCULARLY POLARIZED DRA EXCITED BY A CONFORMAL STRIP WITH A PARASITIC PATCH

3.1. Introduction

Thus far, the work on CP DRAs has been mainly experimental. The first theoretical work was carried out by Esselle [21], who used the finite-difference time-domain (FDTD) method to study the CP rectangular DRA. The FDTD method can handle a large class of problems, but since it is purely numerical, a very long computation time is required. Moreover, no physical insights into the problem can be obtained through the numerical formulation. In this section, a CP DRA excitation method that employs a single parasitic patch is presented [24]. The conformal-strip-excited hemispherical DRA [18] is used for the demonstration. Nevertheless, the CP technique can be used with other excitation methods and DRAs.

3.2. Theory

The configuration of the DRA is shown in Fig. 8, where a hemispherical DRA of radius a and dielectric constant ϵ_r is

Figure 7. Measured and calculated co- and cross-polarized field patterns at $f = 3.5$ GHz, with $a = 12.5$ mm, $\epsilon_r = 9.5$, $l = 12.0$ mm, $W = 1.2$ mm. (From Leung and Ng [32], © 2001 John Wiley & Sons, Inc.)

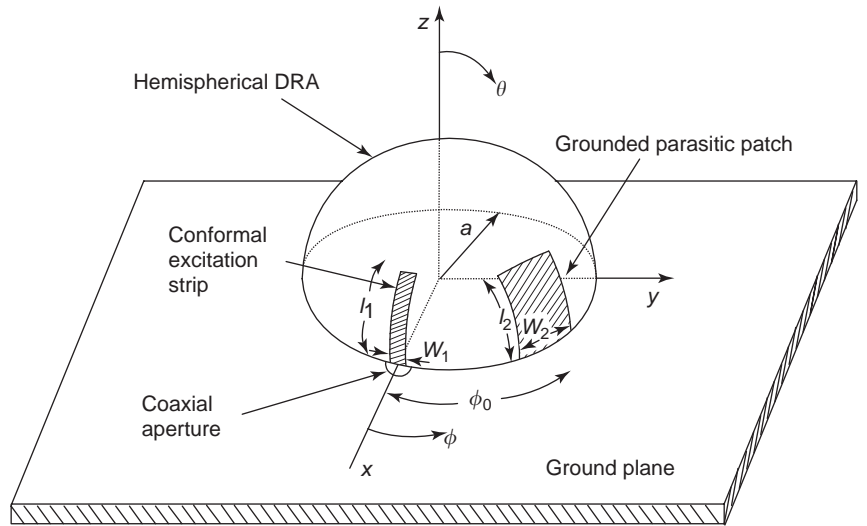


Figure 8. Configuration of conformal-strip-excited DRA with a parasitic patch. (From Leung and Ng [24], 2003 © IEEE.)

fed by the conformal strip of length l_1 and width W_1 . The parasitic patch of length l_2 and width W_2 is displaced at ϕ_0 from the excitation strip. Since the patch current involves both θ and ϕ components, in this case, integrals of associated Legendre functions will inevitably encountered. Therefore, a convectional coordinate system is used in this section.

Image theory is used to remove the ground plane. The equivalent imaged configuration, shown in Fig. 9, is a spherical DRA with the strip and patch lengths doubled: $L_1 = 2l_1$ and $L_2 = 2l_2$.

3.2.1. Green's Functions. Since the excitation strip is assumed to be slender, it has only a longitudinal current. For the parasitic patch, however, the length-to-width ratio is arbitrary. Therefore, both the latitude and azimuthal currents have to be considered. The current distributions are shown in Fig. 9. In the formulation, the superscripts A

and B refer to the excitation strip and the parasitic patch, respectively. The $\hat{\theta}$ -directed current J_θ^A flows on the surface of the excitation strip. For the parasitic patch, the $\hat{\theta}$ - and $\hat{\phi}$ -directed patch currents are defined as J_θ^B and J_ϕ^B , respectively.

The $\hat{\theta}$ - and $\hat{\phi}$ -directed E -field Green's functions due to a $\hat{\phi}$ -directed point current J_ϕ have been obtained in (1a) and (1b). Now, two more Green's functions in (12a) and (12b) are found that are due to a $\hat{\theta}$ -directed point current J_θ :

$$G_{J_\theta}^{E_\theta} = \frac{j\eta_0}{2\pi ar} \sum_{n=0}^{\infty} \frac{2n+1}{n(n+1)} \sum_{m=0}^n \frac{(n-m)!}{(n+m)!} \cos m(\phi - \phi') \cdot \left\{ \frac{m^2}{\Delta_n^{TE}} \frac{P_n^m(\cos \theta')}{\sin \theta'} \frac{P_n^m(\cos \theta)}{\sin \theta} \Phi_n - \frac{1}{\Delta_n^{TM} \Delta_m} \frac{d}{d\theta'} P_n^m(\cos \theta') \frac{d}{d\theta} P_n^m(\cos \theta) \Psi_n \right\} \quad (12a)$$

$$G_{J_\theta}^{E_\phi} = \frac{j\eta_0}{2\pi ar} \sum_{n=0}^{\infty} \frac{2n+1}{n(n+1)} \sum_{m=1}^n m \frac{(n-m)!}{(n+m)!} \sin m(\phi - \phi') \cdot \left\{ \frac{1}{\Delta_n^{TE}} \frac{P_n^m(\cos \theta')}{\sin \theta'} \frac{d}{d\theta} P_n^m(\cos \theta) \Phi_n - \frac{1}{\Delta_n^{TM}} \frac{d}{d\theta'} P_n^m(\cos \theta') \frac{P_n^m(\cos \theta)}{\sin \theta} \Psi_n \right\} \quad (12b)$$

3.2.2. MoM. With the Green's functions presented above, the strip and patch currents can be solved by using the MoM. Enforcing the boundary condition that the total E field should vanish on the conducting excitation strip, we have

$${}^A E_{J_\theta}^0 + {}^B E_{J_\theta}^0 + {}^B E_{J_\phi}^0 + E^i = 0 \quad (13)$$

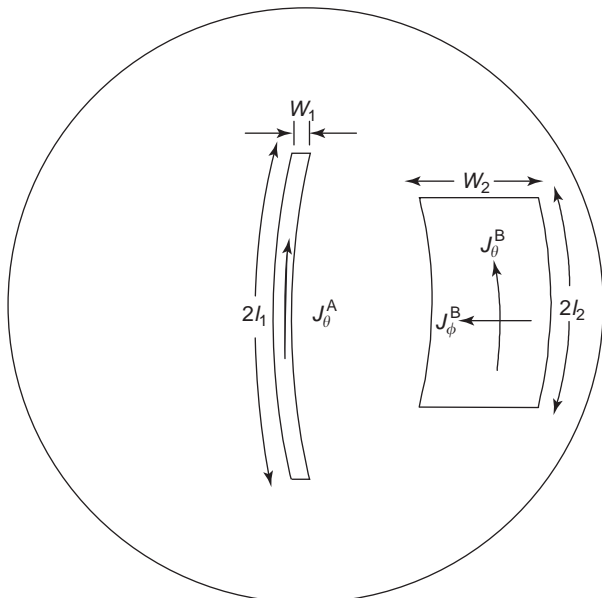


Figure 9. Equivalent geometry of the DRA configuration.

where E^i is the impressed E field on the excitation strip. Equation (13) can be rewritten in terms of Green's functions,

$$\iint_{S_A} G_{J_0}^{E_0} J_0^A dS' + \iint_{S_B} G_{J_0}^{E_0} J_0^B dS' + \iint_{S_B} G_{J_\phi}^{E_0} J_\phi^B dS' + E^i = 0 \quad (14)$$

where S_A and S_B are the surfaces of the excitation strip and parasitic patch, respectively. For simplicity, the delta gap source is used again to model the excitation, $E^i = (V_0/\alpha)\delta(\theta)$, where V_0 is the excitation voltage and is set to unity for convenience. Let $I_\theta^A = J_\theta^A W_1$ be the excitation strip current and $I_\theta^B = J_\theta^B W_2$, $I_\phi^B = J_\phi^B L_2$; then (14) becomes

$$\begin{aligned} & \frac{-1}{W_1} \iint_{S_A} G_{J_0}^{E_0} I_\theta^A dS' + \frac{-1}{W_2} \iint_{S_B} G_{J_0}^{E_0} I_\theta^B dS' \\ & + \frac{-1}{L_2} \iint_{S_B} G_{J_\phi}^{E_0} I_\phi^B dS' = \frac{1}{\alpha} \delta(\theta) \end{aligned} \quad (15)$$

The next step is to expand the currents using the MoM as follows

$$I_\theta^A(\theta) = \sum_{p_1=1}^{N_1} I_{p_1}^{0A} f_{p_1}^{0A}(\theta) \quad (16)$$

$$I_\theta^B(\theta) = \sum_{p_2=1}^{N_2} I_{p_2}^{0B} f_{p_2}^{0B}(\theta) \quad (17)$$

$$I_\phi^B(\phi) = \sum_{p_3=1}^{N_3} I_{p_3}^{\phi B} f_{p_3}^{\phi B}(\phi) \quad (18)$$

where $f_{p_1}^{0A}(\theta)$, $f_{p_2}^{0B}(\theta)$, and $f_{p_3}^{\phi B}(\phi)$ are PWS basis functions given by

$$f_{p_1}^{0A}(\theta) = \begin{cases} \frac{\sin(\theta_h^A - |\theta - \theta_{p_1}^A|)}{\sin \theta_h^A}, & a|\theta - \theta_{p_1}^A| < h_1 \\ 0 & \text{elsewhere} \end{cases} \quad (19)$$

$$f_{p_2}^{0B}(\theta) = \begin{cases} \frac{\sin(\theta_h^B - |\theta - \theta_{p_2}^B|)}{\sin \theta_h^B}, & a|\theta - \theta_{p_2}^B| < h_2 \\ 0 & \text{elsewhere} \end{cases} \quad (20)$$

$$f_{p_3}^{\phi B}(\phi) = \begin{cases} \frac{\sin k_e(h_3 - a|\phi - \phi_{p_3}^B|)}{\sin k_0 h_3}, & a|\phi - \phi_{p_3}^B| < h_3 \\ 0 & \text{elsewhere} \end{cases} \quad (21)$$

in which

$$\theta_h^A = \frac{h_1}{a}, \quad \theta_{p_1}^A = \frac{\pi}{2} - \frac{L_1}{2a} + p_1 \theta_h^A, \quad h_1 = \frac{L_1}{N_1 + 1} \quad (22)$$

$$\theta_h^B = \frac{h_2}{a}, \quad \theta_{p_2}^B = \frac{\pi}{2} - \frac{L_2}{2a} + p_2 \theta_h^B, \quad h_2 = \frac{L_2}{N_2 + 1} \quad (23)$$

$$\phi_h^B = \frac{h_3}{a}, \quad \phi_{p_3}^B = \phi_0 - \frac{W_2}{2a} + p_3 \phi_h^B, \quad h_3 = \frac{W_2}{N_3 + 1} \quad (24)$$

and $k_e = \sqrt{(\epsilon_r + 1)/2} k_0$ is the effective wavenumber at the DRA-air interface. By employing the Galerkin procedure, we multiply both sides of (15) by $f_{q_1}^{0A}(\theta)$ ($1 \leq q_1 \leq N_1$) and integrate the result over the strip surface, yielding

$$\begin{aligned} & \frac{-1}{W_1^2} \sum_{p_1=1}^{N_1} I_{p_1}^{0A} \iint_{S=S_A} \iint_{S'=S_A} f_{q_1}^{0A}(\theta) G_{J_0}^{E_0} f_{p_1}^{0A}(\theta') dS' dS \\ & + \frac{-1}{W_1 W_2} \sum_{l=1}^{N_2} I_{p_2}^{0B} \iint_{S=S_A} \iint_{S'=S_B} f_{q_1}^{0A}(\theta) G_{J_0}^{E_0} f_{p_2}^{0B}(\theta') dS' dS \\ & + \frac{-1}{W_1 L_2} \sum_{v=1}^{N_3} I_{p_3}^{\phi B} \iint_{S=S_A} \iint_{S'=S_B} f_{q_1}^{0A}(\theta) G_{J_\phi}^{E_0} f_{p_3}^{\phi B}(\theta') dS' dS \\ & = \int_{\pi/2-L_1/a}^{\pi/2+L_1/a} f_{q_1}^{0A}(\theta) \delta(\theta) d(\theta) \end{aligned} \quad (25)$$

Similarly, two more integral equations can be obtained by enforcing the following boundary conditions on the parasitic patch:

$${}^A \mathbf{E}_{J_0}^\phi + {}^B \mathbf{E}_{J_0}^\phi + {}^B \mathbf{E}_{J_\phi}^\phi = 0 \quad (26a)$$

$${}^A \mathbf{E}_{J_0}^0 + {}^B \mathbf{E}_{J_0}^0 + {}^B \mathbf{E}_{J_\phi}^0 = 0 \quad (26b)$$

Applying the Galerkin procedure again, we multiply the two equations by $f_{q_2}^{0B}(\theta)$ ($1 \leq q_2 \leq N_2$) and $f_{q_3}^{\phi B}(\phi)$ ($1 \leq q_3 \leq N_3$), respectively. Totally, there are three sets of equations with three sets of unknowns, which can be solved via the following matrix equation

$$\begin{bmatrix} [Z_{\theta\theta}^{AA'}(p_1, q_1)]_{N_1 \times N_1} & [Z_{\theta\theta}^{AB'}(p_1, q_2)]_{N_1 \times N_2} & [Z_{\theta\phi}^{AB'}(p_1, q_3)]_{N_1 \times N_3} \\ [Z_{\theta\theta}^{BA'}(p_2, q_1)]_{N_2 \times N_1} & [Z_{\theta\theta}^{BB'}(p_2, q_2)]_{N_2 \times N_2} & [Z_{\theta\phi}^{BB'}(p_2, q_3)]_{N_2 \times N_3} \\ [Z_{\phi\theta}^{BA'}(p_3, q_1)]_{N_3 \times N_1} & [Z_{\phi\theta}^{BB'}(p_3, q_2)]_{N_3 \times N_2} & [Z_{\phi\phi}^{BB'}(p_3, q_3)]_{N_3 \times N_3} \end{bmatrix} \cdot \begin{bmatrix} [I_{p_1}^{0A}]_{N_1 \times 1} \\ [I_{p_2}^{0B}]_{N_2 \times 1} \\ [I_{p_3}^{\phi B}]_{N_3 \times 1} \end{bmatrix} = \begin{bmatrix} [V_{q_1}^A]_{N_1 \times 1} \\ [0]_{N_2 \times 1} \\ [0]_{N_3 \times 1} \end{bmatrix} \quad (27)$$

where, for $X, Y = A$ or B and $\alpha, \beta = \theta$ or ϕ , we obtain

$$Z_{\alpha\beta}^{XY'}(p, q) = \frac{-1}{\Gamma_\alpha^X \Gamma_\beta^Y} \iint_{S=S_X} \iint_{S'=S_Y} f_p^{\alpha X}(\alpha) G_{\beta}^{E_z} f_{q'}^{\beta Y}(\beta') dS' dS \quad (28)$$

$$V_{q_1}^A = \int_{\pi/2-L_1/a}^{\pi/2+L_1/a} f_{q_1}^{\theta A}(\theta) \delta(\theta) d\theta \quad (29)$$

with $\Gamma_\theta^{A,B} = W_{1,2}$ and $\Gamma_\phi^B = L_2$. For the voltage matrix $[V_{q_1}^A]$, the center element is equal to unity but all the other elements are zero. After the current vector $[I_{p_1}^{\theta A}]$ is obtained from (27), the input impedance can be calculated from $Z_{in} = \gamma / \sum_{p_1=1}^{N_1} I_{p_1}^{\theta A} f_{p_1}^{\theta A}(0)$, where $\gamma = 1$ for the equivalent spherical structure and $\frac{1}{2}$ for the original hemispherical structure. The other two current vectors $[I_{p_2}^{\phi B}]$, $[I_{p_3}^{\phi B}]$, together with $[I_{p_1}^{\theta A}]$, will be used to calculate the radiation fields of the antenna. To this end, the key step is to evaluate the various impedance elements $Z_{\alpha\beta}^{XY'}$, which will be discussed next.

3.2.3. Evaluation of Z Matrix. Numerical evaluation of $Z_{\alpha\beta}^{XY'}$ will be very difficult when $X = Y$, since the field and source points may coincide in this case, causing the singular problem to occur. Using the previous approach [18], all $Z_{\alpha\beta}^{XY'}$ can be calculated without the need for any numerical integration. Thus, the computation time and programming effort are greatly reduced. To begin with, the Green's functions (1) and (12) are substituted into (29) to get nine different expressions:

$$\begin{aligned} Z_{\theta\theta}^{AA'}(p_1, q_1) &= -\frac{ja^2\eta_0}{2\pi W_1^2} \sum_{n=1}^{\infty} \\ &\cdot \left\{ \sum_{m=0}^n \rho_{TE}(n, m) \cdot m^2 \cdot \Theta_1^A(p_1, n, m) \right. \\ &\Theta_1^A(q_1, n, m) \cdot \Phi_1(m, \phi_A, \phi_A) \\ &- \sum_{m=0}^n \frac{\rho_{TM}(n, m)}{\Delta_m} \cdot \Theta_2^A(p_1, n, m) \\ &\left. \Theta_2^A(q_1, n, m) \cdot \Phi_1(m, \phi_A, \phi_A) \right\} \end{aligned} \quad (30)$$

$$\begin{aligned} Z_{\theta\phi}^{AB'}(p_1, q_2) &= -\frac{ja^2\eta_0}{2\pi W_1 W_2} \sum_{n=1}^{\infty} \\ &\cdot \left\{ \sum_{m=0}^n \rho_{TE}(n, m) \cdot m^2 \cdot \Theta_1^A(p_1, n, m) \right. \\ &\Theta_1^B(q_2, n, m) \cdot \Phi_1(m, \phi_A, \phi_B) \\ &- \sum_{m=0}^n \frac{\rho_{TM}(n, m)}{\Delta_m} \cdot \Theta_2^A(p_1, n, m) \\ &\left. \Theta_2^B(q_2, n, m) \Phi_1(m, \phi_A, \phi_B) \right\} \end{aligned} \quad (31)$$

$$\begin{aligned} Z_{\phi\phi}^{AB'}(p_1, q_3) &= -\frac{ja^2\eta_0}{2\pi W_1 L_2} \sum_{n=1}^{\infty} \\ &\cdot \left\{ \sum_{m=0}^n \rho_{TE}(n, m) \cdot m \cdot \Theta_1^A(p_1, n, m) \right. \\ &\Theta_4^B(n, m) \cdot \Phi_2(q_3, m, \phi_A, \phi_B) \\ &- \sum_{m=0}^n \rho_{TM}(n, m) \cdot m \cdot \Theta_2^A(p_1, n, m) \\ &\left. \Theta_3^B(n, m) \cdot \Phi_2(q_3, m, \phi_A, \phi_B) \right\} \end{aligned} \quad (32)$$

$$\begin{aligned} Z_{\phi\theta}^{BA'}(p_2, q_1) &= -\frac{ja^2\eta_0}{2\pi W_1 W_2} \sum_{n=1}^{\infty} \\ &\cdot \left\{ \sum_{m=0}^n \rho_{TE}(n, m) \cdot m^2 \cdot \Theta_1^B(p_2, n, m) \right. \\ &\Theta_1^A(q_1, n, m) \cdot \Phi_1(m, \phi_B, \phi_A) \\ &- \sum_{m=0}^n \frac{\rho_{TM}(n, m)}{\Delta_m} \Theta_2^B(p_2, n, m) \\ &\left. \Theta_2^A(q_1, n, m) \cdot \Phi_1(m, \phi_B, \phi_A) \right\} \end{aligned} \quad (33)$$

$$\begin{aligned} Z_{\theta\theta}^{BB'}(p_2, q_2) &= -\frac{ja^2\eta_0}{2\pi W_2^2} \sum_{n=1}^{\infty} \\ &\cdot \left\{ \sum_{m=0}^n \rho_{TE}(n, m) \cdot m^2 \cdot \Theta_1^B(p_2, n, m) \right. \\ &\Theta_1^B(q_2, n, m) \cdot \Phi_1(m, \phi_B, \phi_B) \\ &- \sum_{m=0}^n \frac{\rho_{TM}(n, m)}{\Delta_m} \Theta_2^B(p_2, n, m) \\ &\left. \Theta_2^B(q_2, n, m) \cdot \Phi_1(m, \phi_B, \phi_B) \right\} \end{aligned} \quad (34)$$

$$\begin{aligned} Z_{\phi\phi}^{BB'}(p_2, q_3) &= -\frac{ja^2\eta_0}{2\pi W_2 L_2} \sum_{n=1}^{\infty} \\ &\cdot \left\{ \sum_{m=0}^n \rho_{TE}(n, m) \cdot m \cdot \Theta_1^B(p_2, n, m) \right. \\ &\Theta_4^B(n, m) \cdot \Phi_2(q_3, m, \phi_B, \phi_B) \\ &- \sum_{m=0}^n \rho_{TM}(n, m) \cdot m \cdot \Theta_2^B(p_2, n, m) \\ &\left. \Theta_3^B(n, m) \cdot \Phi_2(q_3, m, \phi_B, \phi_B) \right\} \end{aligned} \quad (35)$$

$$\begin{aligned}
Z_{\phi\theta}^{BA'}(p_3, q_1) = & -\frac{ja^2\eta_0}{2\pi W_1 L_2} \sum_{n=1}^{\infty} \\
& \cdot \left\{ \sum_{m=0}^n \rho_{TE}(n, m) \cdot m \cdot \Theta_4^B(n, m) \right. \\
& \Theta_1^A(q_3, n, m) \cdot \Phi_2(p_1, m, \phi_B, \phi_A) \\
& - \sum_{m=0}^n \rho_{TM}(n, m) \cdot m \cdot \Theta_3^B(n, m) \\
& \left. \Theta_2^A(q_3, n, m) \cdot \Phi_2(p_1, m, \phi_B, \phi_A) \right\}
\end{aligned} \quad (36)$$

$$\begin{aligned}
Z_{\phi\theta}^{BB'}(p_3, q_2) = & -\frac{ja^2\eta_0}{2\pi W_2 L_2} \sum_{n=1}^{\infty} \\
& \cdot \left\{ \sum_{m=0}^n \rho_{TE}(n, m) \cdot m \cdot \Theta_4^B(n, m) \right. \\
& \Theta_1^B(q_2, n, m) \Phi_2(p_3, m, \phi_B, \phi_B) \\
& - \sum_{m=0}^n \rho_{TM}(n, m) \cdot m \cdot \Theta_3^B(n, m) \\
& \left. \Theta_2^B(q_2, n, m) \cdot \Phi_2(p_3, m, \phi_B, \phi_B) \right\}
\end{aligned} \quad (37)$$

$$\begin{aligned}
Z_{\phi\phi}^{BB'}(p_3, q_3) = & -\frac{ja^2\eta_0}{2\pi L_2^2} \sum_{n=1}^{\infty} \\
& \cdot \left\{ \sum_{m=0}^n \frac{\rho_{TE}(n, m)}{\Delta_m} \Theta_4^B(n, m) \right. \\
& \Theta_4^B(n, m) \cdot \Phi_3(p_3, q_3, m, \phi_B, \phi_B) \\
& - \sum_{m=0}^n \rho_{TM}(n, m) \cdot m^2 \cdot \Theta_3^B(n, m) \\
& \left. \Theta_3^B(n, m) \cdot \Phi_3(p_3, q_3, m, \phi_B, \phi_B) \right\}
\end{aligned} \quad (38)$$

where

$$\begin{aligned}
\rho_{TE}(n, m) = & \frac{2n+1}{n(n+1)} \cdot \frac{\hat{J}_n(ka)\hat{H}_n^{(2)}(k_0a)}{\Delta_n^{TE}} \\
& \cdot \frac{(n-m)!}{(n+m)!}
\end{aligned} \quad (39)$$

$$\begin{aligned}
\rho_{TM}(n, m) = & \frac{2n+1}{n(n+1)} \cdot \frac{\hat{J}_n(ka)\hat{H}_n^{(2)'}(k_0a)}{\Delta_n^{TM}} \\
& \cdot \frac{(n-m)!}{(n+m)!}
\end{aligned} \quad (40)$$

$$\begin{aligned}
\Phi_1(m, \phi_X, \phi_Y) \\
= \int_{\phi_{X1}}^{\phi_{X2}} \int_{\phi_{Y1}}^{\phi_{Y2}} \cos m(\phi - \phi') d\phi' d\phi
\end{aligned} \quad (41)$$

$$\begin{aligned}
\Phi_2(p, m, \phi_X, \phi_Y) \\
= \int_{\phi_{X1}}^{\phi_{X2}} \int_{\phi_{Y1}}^{\phi_{Y2}} \sin m(\phi - \phi') f_p^{\phi_Y}(\phi) d\phi' d\phi
\end{aligned} \quad (42)$$

$$\begin{aligned}
\Phi_3(p, q, m, \phi_B) \\
= \int_{\phi_{B1}}^{\phi_{B2}} \int_{\phi_{B1}}^{\phi_{B2}} f_p^{\phi_B}(\phi) \cos m(\phi - \phi') \\
f_q^{\phi_B}(\phi') d\phi' d\phi
\end{aligned} \quad (43)$$

$$\begin{aligned}
\Theta_1^X(p, n, m) \\
= \int_{\theta_p^X - \theta_h^X}^{\theta_p^X + \theta_h^X} P_n^m(\cos \theta) f_p^{\theta X}(\theta) d\theta
\end{aligned} \quad (44)$$

$$\begin{aligned}
\Theta_2^X(p, n, m) \\
= \int_{\theta_p^X - \theta_h^X}^{\theta_p^X + \theta_h^X} \frac{dP_n^m(\cos \theta)}{d\theta} \sin \theta f_p^{\theta X}(\theta) d\theta
\end{aligned} \quad (45)$$

$$\Theta_3^B(n, m) = \int_{\pi/2 - l_2/a}^{\pi/2 + l_2/a} P_n^m(\cos \theta) d\theta \quad (46)$$

$$\Theta_4^B(n, m) = \int_{\pi/2 - l_2/a}^{\pi/2 + l_2/a} \frac{dP_n^m(\cos \theta)}{d\theta} \sin \theta d\theta \quad (47)$$

and

$$\begin{aligned}
\phi_{A1} = -W_1/2a, \quad \phi_{A2} = W_1/2a, \quad \phi_{B1} = \phi_0 - W_2/2a, \\
\text{and } \phi_{B2} = \phi_0 + W_2/2a
\end{aligned} \quad (48)$$

The integrals will be evaluated by either using the recurrence technique or analytical integration. This will be discussed in the following paragraphs.

3.2.3.1. $\Theta_1^X(p, n, m)$ and $\Theta_2^X(p, n, m)$. To evaluate $\Theta_1^X(p, n, m)$ and $\Theta_2^X(p, n, m)$ ($X=A$ or B) analytically, the absolute sign of the PWS functions $f_p^{\theta A}(\theta)$ (19) and $f_p^{\theta B}(\theta)$ (20) is first removed by breaking each integral into two parts. After several mathematical manipulations, the

following results are obtained

$$\begin{aligned} \Theta_1^X(p, n, m) = & \frac{1}{\sin \theta_h^X} [\sin(\theta_h^X - \theta_p^X) I_1(n, m) \\ & + \cos(\theta_h^X - \theta_p^X) I_1'(n, m) \\ & + \sin(\theta_h^X + \theta_p^X) I_2(n, m) \\ & - \cos(\theta_h^X + \theta_p^X) I_2'(n, m)] \end{aligned} \quad (49)$$

$$\begin{aligned} \Theta_2^X(p, n, m) = & \frac{1}{\sin \theta_h^X} [\sin(\theta_h^X - \theta_p^X) I_3(n, m) \\ & + \cos(\theta_h^X - \theta_p^X) I_3'(n, m) \\ & + \sin(\theta_h^X + \theta_p^X) I_4(n, m) \\ & - \cos(\theta_h^X + \theta_p^X) I_4'(n, m)] \end{aligned} \quad (50)$$

where

$$\begin{aligned} I_{1,2}(n, m) = & \left[x \sqrt{1 - x^2} P_n^m(x) \right]_{x_1}^{x_2} + K(m, n) - \frac{2}{2n + 1} \\ & \cdot \left\{ \frac{1}{2n + 3} K(n + 2, m + 2) \right. \\ & - \left(\frac{1}{2n + 3} + \frac{1}{2n - 1} \right) K(n, m + 2) \\ & \left. + \frac{1}{2n - 1} K(n - 2, m + 2) \right\} \end{aligned} \quad (51)$$

$$\begin{aligned} I_{1,2}'(n, m) = & \frac{-n(n - m + 1)}{(2n + 1)(2n + 3)} K(n + 2, m + 1) \\ & + \left\{ \frac{(n + 1)(n + m)}{(2n + 1)(2n - 1)} + \frac{n(n - m + 1)}{(2n + 1)(2n + 3)} \right\} \\ & \cdot K(n, m + 1) - \frac{(n + 1)(n + m)}{(2n + 1)(2n - 1)} K(n - 2, m + 1) \end{aligned} \quad (52)$$

$$\begin{aligned} I_{3,4}(n, m) = & \frac{-(n - m + 1)}{2n + 1} K(n + 1, m) \\ & - \frac{m + n}{2n + 1} K(n - 1, m) \end{aligned} \quad (53)$$

$$\begin{aligned} I_{3,4}'(n, m) = & \frac{-1}{2n + 1} \{ K(n + 1, m + 1) \\ & - K(n - 1, m + 1) \} \end{aligned} \quad (54)$$

in which

$$K(n, m) = \int_{x_1}^{x_2} \frac{P_n^m(x)}{\sqrt{1 - x^2}} dx \quad (55)$$

with $[f(x)]_{x_1}^{x_2} = f(x_2) - f(x_1)$, $x_1 = \cos(\theta_p^X - \theta_h^X)$, $x_2 = \cos \theta_p^X$ for $I_{1,3}, I_{1,3}'$ and $x_1 = \cos \theta_p^X$, $x_2 = \cos(\theta_p^X + \theta_h^X)$ for $I_{2,4}, I_{2,4}'$. For $K(n, m)$, the recurrence formulas with arbitrary x_1, x_2

have been obtained [37] as follows

$$\begin{aligned} K(n + 1, m) = & \frac{-(2n + 1)}{(n + 1)(n - m + 1)} \left[\sqrt{1 - x} P_{n+1}^m(x) \right]_{x_1}^{x_2} \\ & + n(n + m) K(n - 1, m) \end{aligned} \quad (56)$$

$$\begin{aligned} K(n, m + 1) = & -2[P_n^{m+1}(x)]_{x_1}^{x_2} \\ & + (n + m)(n - m + 1) K(n, m - 1) \end{aligned} \quad (57)$$

with initial values given by

$$\begin{aligned} K(0, 0) = & [\sin^{-1}(x)]_{x_1}^{x_2}, \quad K(1, 0) = -[1 - x^2]_{x_1}^{x_2}, \\ K(n, 1) = & [P_n(x)]_{x_1}^{x_2} \end{aligned} \quad (58)$$

3.2.3.2. $\Theta_3^B(n, m)$ and $\Theta_4^B(n, m)$. The integrals $\Theta_3^B(n, m)$ and $\Theta_4^B(n, m)$ were studied in [18, Eqs. (11) and (12)], and the results are given by

$$\begin{aligned} \Theta_3^B(n + 1, m) = & \frac{1}{(n + 1)(n - m + 1)} \\ & \left\{ -(2n + 1)[1 - (-1)^{n+m}] \right. \\ & \left. \sqrt{1 - x_b^2} P_n^m(x_b) + n(n + m) \Theta_3^B(n - 1, m) \right\} \end{aligned} \quad (59)$$

$$\begin{aligned} \Theta_3^B(n, m + 2) = & -2[1 - (-1)^{n+m}] P_n^{m+1}(x_b) \\ & + (n + m + 1)(n - m) \Theta_3^B(n, m) \end{aligned} \quad (60)$$

where

$$x_b = \cos\left(\frac{\pi}{2} - \frac{l_2}{a}\right) = \sin \frac{l_2}{a} \quad (61)$$

and the initial values are

$$\Theta_3^B(n, 0) = \Theta_3^B(n, 1) = [(-1)^n - 1] P_n(x_b) \quad (62)$$

The integral $\Theta_3^B(n, m)$ can be expressed in terms of $\Theta_4^B(n, m)$, which is given by

$$\begin{aligned} \Theta_4^B(n, m) = & [(-1)^{n+m} - 1] \sqrt{1 - x_b^2} P_n^m(x_b) \\ & - \frac{1}{2n + 1} [(n + m) \Theta_3^B(n - 1, m) \\ & - (m - n - 1) \Theta_3^B(n + 1, m)] \end{aligned} \quad (63)$$

3.2.3.3. $\Phi_2(p, m, \phi_X, \phi_Y)$. The integrals $\Phi_2(p, m, \phi_X, \phi_Y)$ are zero when $m = 0$. When $m \neq 0$, the integration can be

performed analytically. The result is given by

$$\Phi_2 = \frac{-2k_e a}{\sin k_e h} \cdot \frac{[\cos m(\phi_{X2} - \phi_p) - \cos m(\phi_{X1} - \phi_p)](\cos k_e h - \cos m\phi_h^B)}{(m - k_e a)(m + k_e a)} \quad (64)$$

The last integral $\Phi_3(p, q, m, \phi_B)$ is given by (9). Now all the integrals can be evaluated analytically. Note that $Z_{\alpha\beta}^{XY}$ are simply regular series that can be implemented easily in a straightforward manner.

3.2.4. Evaluation of Radiation Field Patterns. The far field of the antenna comprises radiation from the excitation strip current I_θ^A and parasitic patch current components I_θ^B, I_ϕ^B . The electric far field is given by

$$\begin{aligned} E_{\theta,\phi}(r, \theta, \phi) &= \frac{j\eta_0 a}{2\pi W_1} \cdot \frac{e^{-jk_0 r}}{r} \sum_{p_1=1}^{N_1} I_{p_1}^{\theta A} \cdot \mathbf{E}_{\theta\theta,\theta\phi}^{A'}(p_1, \theta, \phi) \\ &+ \frac{j\eta_0 a}{2\pi W_2} \cdot \frac{e^{-jk_0 r}}{r} \sum_{p_2=1}^{N_2} I_{p_2}^{\theta B} \cdot \mathbf{E}_{\theta\theta,\theta\phi}^{B'}(p_2, \theta, \phi) \\ &- \frac{j\eta_0 a}{2\pi L_2} \cdot \frac{e^{-jk_0 r}}{r} \sum_{p_3=1}^{N_3} I_{p_3}^{\phi B} \cdot \mathbf{E}_{\theta\phi,\phi\phi}^{B'}(p_3, \theta, \phi) \end{aligned} \quad (65)$$

in which

$$\begin{aligned} E_{\theta\theta}^{X'}(p, \theta, \phi) &= \sum_{n=1}^{\infty} j^n \frac{2n+1}{n(n+1)} \\ &\times \left\{ \frac{j\hat{J}_n(ka)}{\Delta_n^{\text{TE}}} \sum_{m=0}^n m^2 \frac{(n-m)!}{(n+m)!} \frac{P_n^m(\cos \theta)}{\sin \theta} \right. \\ &\Theta_1^X(p, n, m) \Phi_4(m, \phi) \\ &- \frac{\hat{J}_n'(ka)}{\Delta_n^{\text{TM}}} \sum_{m=0}^n \frac{1}{\Delta_m} \frac{(n-m)!}{(n+m)!} \frac{dP_n^m(\cos \theta)}{d\theta} \\ &\left. \Theta_1^X(p, n, m) \Phi_4(m, \phi) \right\} \end{aligned} \quad (66)$$

$$\begin{aligned} E_{\theta\phi}^{X'}(p, \theta, \phi) &= \sum_{n=1}^{\infty} j^n \frac{2n+1}{n(n+1)} \\ &\times \left\{ \frac{j\hat{J}_n(ka)}{\Delta_n^{\text{TE}}} \sum_{m=0}^n m \frac{(n-m)!}{(n+m)!} \frac{dP_n^m(\cos \theta)}{d\theta} \right. \\ &\Theta_2^X(p, n, m) \Phi_5(m, \phi) \\ &- \frac{\hat{J}_n'(ka)}{\Delta_n^{\text{TM}}} \sum_{m=0}^n m \frac{(n-m)!}{(n+m)!} \frac{P_n^m(\cos \theta)}{\sin \theta} \\ &\left. \Theta_5^X(p, n, m) \Phi_5(m, \phi) \right\} \end{aligned} \quad (67)$$

$$\begin{aligned} E_{\phi\theta}^{B'}(p, \theta, \phi) &= \sum_{n=1}^{\infty} j^n \frac{2n+1}{n(n+1)} \\ &\times \left\{ \frac{j\hat{J}_n(ka)}{\Delta_n^{\text{TM}}} \sum_{m=0}^n m \frac{(n-m)!}{(n+m)!} \frac{dP_n^m(\cos \theta)}{d\theta} \right. \\ &\Theta_3^B(n, m) \Phi_6(p, m, \phi) \\ &- \frac{\hat{J}_n'(ka)}{\Delta_n^{\text{TE}}} \sum_{m=0}^n m \frac{(n-m)!}{(n+m)!} \frac{P_n^m(\cos \theta)}{\sin \theta} \\ &\left. \Theta_3^B(n, m) \Phi_6(p, m, \phi) \right\} \end{aligned} \quad (68)$$

$$\begin{aligned} E_{\phi\phi}^{B'}(p, \theta, \phi) &= \sum_{n=1}^{\infty} j^n \frac{2n+1}{n(n+1)} \\ &\times \left\{ \frac{j\hat{J}_n(ka)}{\Delta_n^{\text{TM}}} \sum_{m=0}^n m^2 \frac{(n-m)!}{(n+m)!} \frac{P_n^m(\cos \theta)}{\sin \theta} \right. \\ &\Theta_4^B(n, m) \Phi_7(p, m, \phi) \\ &- \frac{\hat{J}_n'(ka)}{\Delta_n^{\text{TE}}} \sum_{m=0}^n \frac{1}{\Delta_m} \frac{(n-m)!}{(n+m)!} \frac{dP_n^m(\cos \theta)}{d\theta} \\ &\left. \Theta_4^B(n, m) \Phi_7(p, m, \phi) \right\} \end{aligned} \quad (69)$$

where, for $X=A$ or B

$$\Phi_4^X(m, \phi) = \int_{\phi_{X1, X1}}^{\phi_{X2, X2}} \sin m(\phi - \phi') d\phi' \quad (70)$$

$$\Phi_5^X(m, \phi) = \int_{\phi_{X1, X1}}^{\phi_{X2, X2}} \cos m(\phi - \phi') d\phi' \quad (71)$$

$$\Phi_6^B(p, m, \phi) = \int_{\phi_{B1}}^{\phi_{B2}} \sin m(\phi - \phi') f_p^{\phi B}(\phi') d\phi' \quad (72)$$

$$\Phi_7^B(p, m, \phi) = \int_{\phi_{B1}}^{\phi_{B2}} \cos m(\phi - \phi') f_p^{\phi B}(\phi') d\phi' \quad (73)$$

The integrals $\Phi_4^X(m, \phi)$ (70) and $\Phi_5^X(m, \phi)$ (71) can easily be evaluated in a single step. For $\Phi_6(p, m, \phi)$ and $\Phi_7(p, m, \phi)$, the results were obtained previously [38, p. 302] and are summarized here:

$$\Phi_4^X(m, \phi) = \begin{cases} \frac{1}{m} [\cos m(\phi - \phi_{X2}) - \cos m(\phi - \phi_{X1})] & m \neq 0 \\ 0 & m = 0 \end{cases} \quad (74)$$

$$\Phi_5^X(m, \phi) = \begin{cases} -\frac{1}{m} [\sin m(\phi - \phi_{X2}) - \sin m(\phi - \phi_{X1})] & m \neq 0 \\ 0 & m = 0 \end{cases} \quad (75)$$

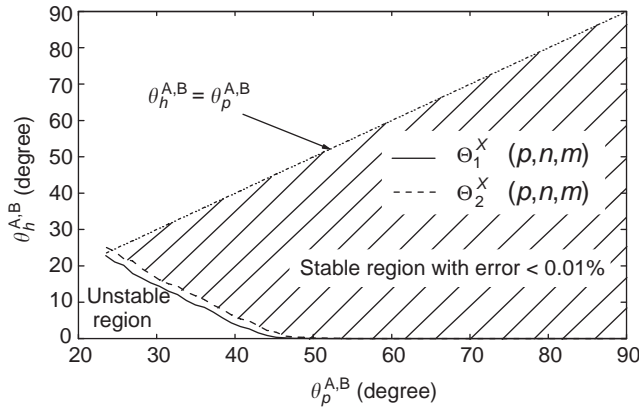


Figure 10. The range of PWS-mode half-angle $\theta_h^{A,B}$ for stable calculations of $\Theta_1^X(p, n, m)$ and $\Theta_2^X(p, n, m)$, with $n=60$ and $m=60$. (From Leung [37], © 2001 IEEE.)

$$\Phi_6^B(p, m, \phi) = \frac{2k_e a}{\sin k_e h} \cdot \frac{\sin m(\phi - \phi_p)(\cos k_e h - \cos m\phi_h^B)}{(m - k_e a)(m + k_e a)} \quad (76)$$

$$\Phi_7^B(p, m, \phi) = \frac{2k_e a}{\sin k_e h} \cdot \frac{\cos m(\phi - \phi_p)(\cos k_e h - \cos m\phi_h^B)}{(m - k_e a)(m + k_e a)} \quad (77)$$

It should be mentioned that, by using $\vec{H} = (1/\eta_0)\hat{r} \times \vec{E}$, the magnetic far fields can be found easily.

3.3. Results and Discussion

3.3.1. Convergence Check. The convergence checks for the modal solution and MoM were done. In the following calculations, 60 modal terms and $N_1=N_2=5$, $N_3=3$ were used.

The numerical stability of the integrals $\Theta_{1,2}^X(p, n, m)$ ($X=A$ or B) that utilize the new recurrence formulas has also been studied. Although these results are analytically exact, their numerical accuracy may be unsatisfactory because of the finite precision of the computer. It was found that the stability of the results decreased with increasing order and degree of $P_n^m(x)$, and therefore the worst cases of $\Theta_{1,2}^X(p, 60, 60)$ are considered, where p is a dummy parameter in the stability check. The usable range for the PWS half-mode angles $\theta_h^{A,B}$ as a function of the PWS center angles $\theta_p^{A,B}$ is shown in Fig. 10. Only the range $0^\circ \leq \theta_p^{A,B} \leq 90^\circ$ is shown because the results are symmetric for $90^\circ \leq \theta_p^{A,B} \leq 180^\circ$. Since $0^\circ \leq \theta \leq 180^\circ$ for the adopted coordinate system, only the region $\theta_h^{A,B} \leq \theta_p^{A,B}$ (below the straight line $\theta_h^{A,B} = \theta_p^{A,B}$) should be considered for $0^\circ \leq \theta_p^{A,B} \leq 90^\circ$. It is seen that Θ_2^X has a slightly smaller stable region than does Θ_1^X and, hence, the overall stable region is limited by Θ_1^X . The shaded area in the figure shows the overall stable region, outside which the results will become unstable. Note that care has to be taken for $\theta_p^{A,B} < 46^\circ$, as the half-mode angles $\theta_h^{A,B}$ in this case should

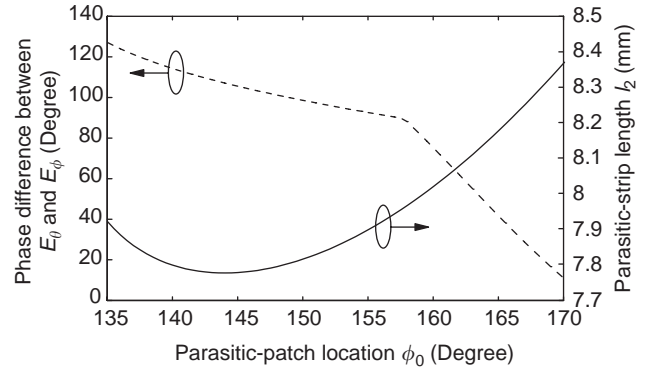


Figure 11. Phase difference between far-field E_θ and E_ϕ as a function of parasitic patch location, with $|E_\theta| = |E_\phi|$, $\epsilon_r=9.5$, $a=12.5$ mm, $l_1=14$ mm, $W_1=1.2$ mm, and $W_2=2$ mm. (From Leung and Ng [24], 2003 © IEEE.)

not be too small or unstable results will be obtained. In this article, all results are calculated within the stable region, and thus the accuracy is ensured. For $\Theta_3^B(n, m)$ (46) and $\Theta_4^B(n, m)$ (47), the recurrence results [18] are very stable and can therefore be used directly.

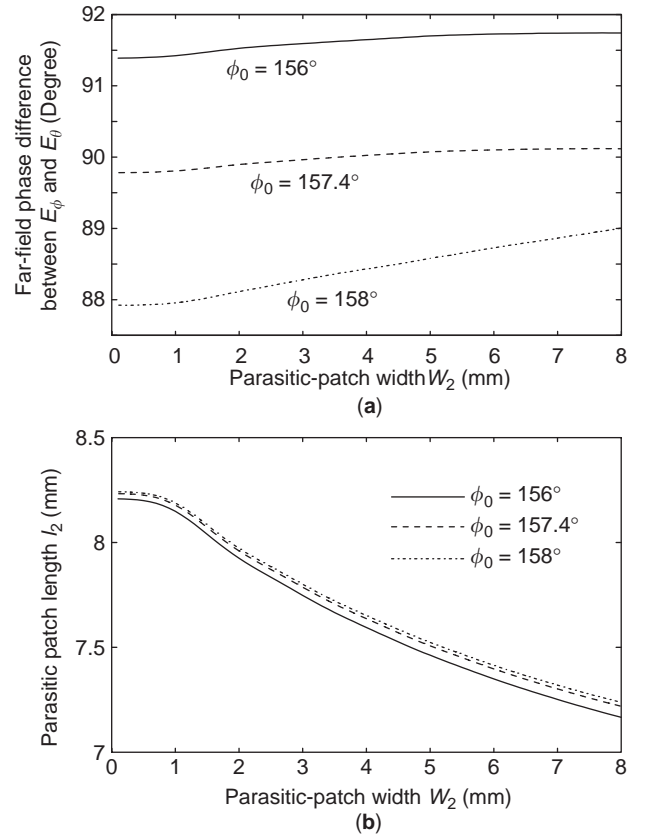


Figure 12. (a) Far-field phase difference as a function of parasitic patch width, with $|E_\theta| = |E_\phi|$, $\epsilon_r=9.5$, $a=12.5$ mm, $l_1=14$ mm, $W_1=1.2$ mm; (b) parasitic patch length as a function of parasitic patch width, with $|E_\theta| = |E_\phi|$, $\epsilon_r=9.5$, $a=12.5$ mm, $l_1=14$ mm, and $W_1=1.2$ mm. (From Leung and Ng [24], 2003 © IEEE.)

3.3.2. Circularly Polarized DRA. It is well known that the far fields E_θ and E_ϕ have to be equal in amplitude but different in phase by 90° for ideal CP fields. The angular positions of the patch ϕ_0 , patch length l_2 , and patch width W_2 are tuned to meet these two requirements. The roles of the parasitic patch and excitation strip will be discussed.

3.3.2.1. Effects of Parasitic Patch. To demonstrate the results, a DR of dielectric constant $\epsilon_r=9.5$ and radius $a=12.5$ mm is used. The excitation strip has length $l_1=14$ mm and width $W_1=1.2$ mm. Figure 11 shows the far-field phase difference between E_θ and E_ϕ as a function of the parasitic patch position ϕ_0 with $|E_\theta|=|E_\phi|$. The condition $|E_\theta|=|E_\phi|$ is maintained in the curve by adjusting the length l_2 of the parasitic patch. With reference to the figure, the 90° phase difference is obtained when $\phi_0=157.4^\circ$. The corresponding patch length l_2 is also given in the figure, where it is found that l_2 should be equal to 7.96 mm in order to excite CP fields.

The effect of the patch width W_2 on the phase difference is shown in Fig. 12(a) for different ϕ_0 values. It is found that the phase difference only increases slightly with W_2 . Again, the condition $|E_\theta|=|E_\phi|$ is maintained by adjusting

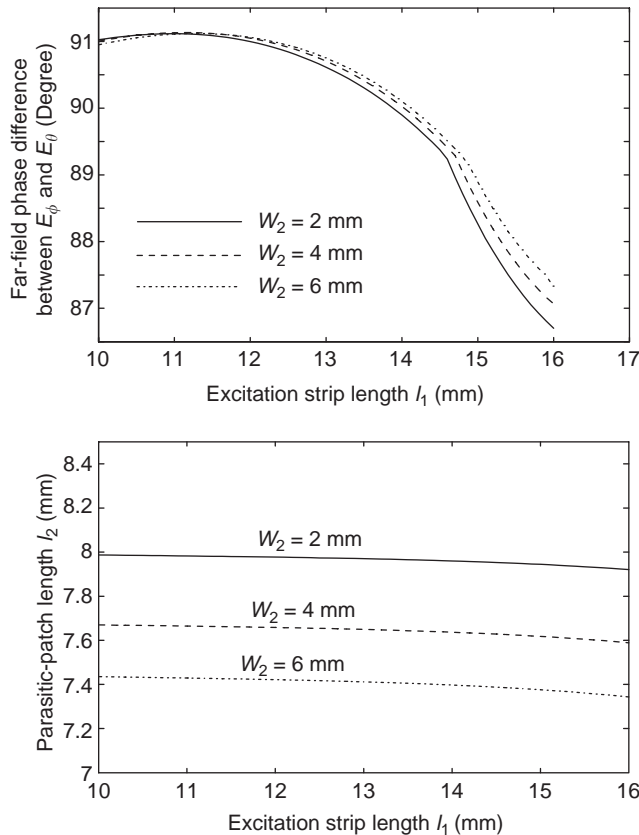


Figure 13. (a) Far-field phase difference as a function of excitation strip length, with $|E_\theta|=|E_\phi|$, $\epsilon_r=9.5$, $a=12.5$ mm, $W_1=1.2$ mm, and $\phi_0=157.4^\circ$; (b) parasitic patch length as a function of excitation strip length, with $|E_\theta|=|E_\phi|$, $\epsilon_r=9.5$, $a=12.5$ mm, $W_1=1.2$ mm and $\phi_0=157.4^\circ$. (From Leung and Ng [24], 2003 © IEEE.)

l_2 , shown in Fig. 12(b). It is seen that in order to keep $|E_\theta|=|E_\phi|$, l_2 should decrease when W_2 increases. Note that the length-to-width ratio (l_2/W_2) is almost the same for different ϕ_0 . From the results, it can be deferred that the patch location is more important than the patch width in the CP design.

3.3.2.2. Effects of the Excitation Strip. The effect of the conformal strip length l_1 on the phase difference for different W_2 is shown in Fig. 13(a). The corresponding patch length l_2 for keeping $|E_\theta|=|E_\phi|$ is shown in Fig. 13(b). It can be observed from Fig. 13(a) that by increasing l_1 by 60% (from 10 to 16 mm) the phase angle is reduced by only 4.2% (from 91° to 87.2°) for $W_2=4$ mm. This shows that the strip length l_1 has only a small effect on CP operation. Moreover, with reference to Fig. 13(b), the patch length l_2 remains almost unchanged as l_1 varies, meaning that virtually no adjustments of the parasitic patch dimensions are required to maintain CP operation. These are very favorable results, as this suggests that once the antenna generates CP fields, the length of the excitation strip can be varied alone in order to change the

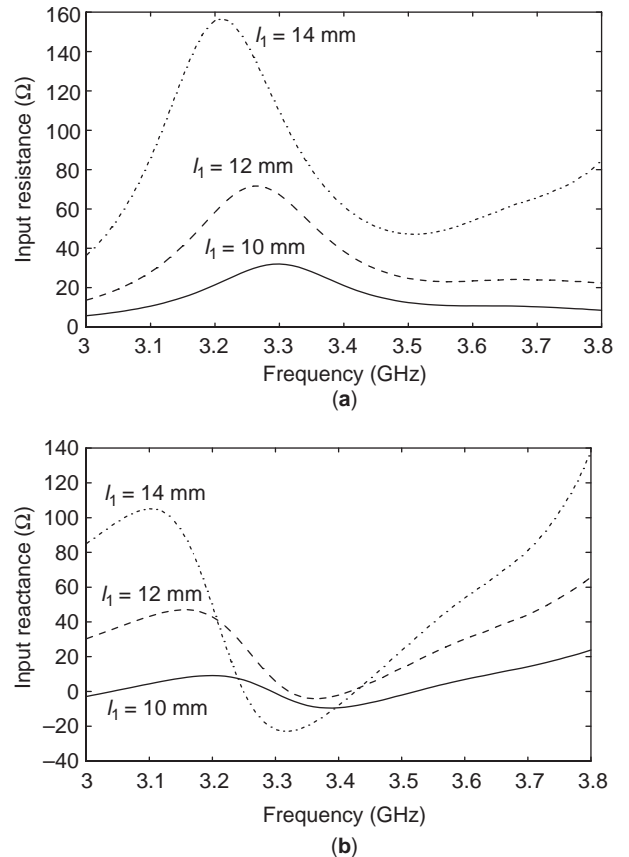


Figure 14. Calculated input impedance as a function of frequency with 0-dB AR at $f=3.56$ GHz: $\epsilon_r=9.5$, $a=12.5$ mm, $W_1=1.2$ mm, and (—) $l_1=10$ mm, $l_2=7.89$ mm, $W_2=2.73$ mm, $\phi_0=158.5^\circ$; (---) $l_1=12$ mm, $l_2=7.88$ mm, $W_2=2.73$ mm, $\phi_0=158.5^\circ$; (- - - -) $l_1=14$ mm, $l_2=7.91$ mm, $W_2=2.26$ mm, $\phi_0=157.4^\circ$: (a) input resistance; (b) input reactance. (From Leung and Ng [24], 2003 © IEEE.)

input impedance, without significantly disturbing CP operation. This greatly facilitates the impedance tuning of the CP antenna. It is noted from Fig. 13(b) that the wider the patch width W_2 is, the smaller the patch length l_2 is required.

Figure 14 shows the calculated input impedance for $l_1 = 10, 12, 14$ mm. For each l_1 , the parameters of the parasitic patch are adjusted to give the 0-dB AR at $f = 3.56$ GHz. With reference to the figure, the input impedance can be altered by changing l_1 and, thus, the impedance matching can be achieved for practical designs. The parameters of the parasitic patch for each case are shown in the figure caption. Note that the patch sizes and locations for different l_1 are almost the same, which is consistent with the discussion above. Since it is futile to change the strip and patch parameters iteratively, the design process is very simple.

3.3.3. Measured and Calculated Results. To verify the theory, an experiment was carried out using a hemispherical DR of dielectric constant $\epsilon_r = 9.5$ and radius $a = 12.5$ mm. The excitation strip has length $l_1 = 14$ mm and width $W_1 = 1.2$ mm, whereas the parasitic patch has length $l_2 = 7.9$ mm, width $W_2 = 2.2$ mm, and angular position $\phi_0 = 157.4^\circ$. Both the excitation strip and parasitic patch were cut from a conducting adhesive tape. Measurements were done with an HP8510C network analyzer, and the reference place was set at the coaxial aperture by using the port extension. To reduce possible errors introduced by airgaps between the ground plane and DR, the DR was first put on the adhesive side of a conducting tape [18]. Figure 15 shows the measured and calculated input impedance for the DRA. The measured and calculated resonant frequencies (zero reactance) are 3.25 and 3.27 GHz with only 0.62% error. The return loss (minimum $|S_{11}|$) was also studied. It was found that the measured and calculated matching frequencies ($|S_{11}| < -20$ dB) are operated at 3.42 and 3.43 GHz, respectively, which are higher than the

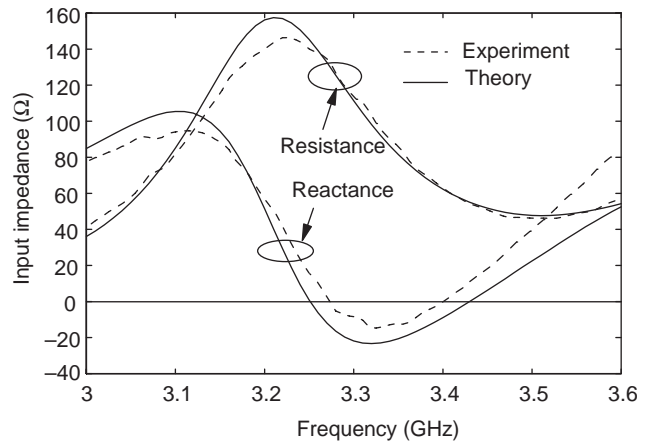


Figure 15. Measured and calculated input impedance for the DRA, with $\epsilon_r = 9.5$, $a = 12.5$ mm, $l_1 = 14$ mm, $l_2 = 7.9$ mm, $W_1 = 1.2$ mm, $W_2 = 2.2$ mm, and $\phi_0 = 157.4^\circ$. (From Leung and Ng [24], 2003 © IEEE.)

zero-reactance values. A similar phenomenon was observed in Ref. 36.

Figure 16 shows the measured and calculated ARs as a function of frequency. Again, reasonable agreement between theory and experiment is obtained. The ripple in the measured result is caused mainly by the finite ground-plane diffraction. It is found that the calculated 3-dB AR bandwidth is 2.4%, which is typical for a singly fed DRA.

The measured and calculated $x-z$ and $y-z$ plane radiation patterns are shown in Figs. 17a and 17b, respectively. Again, reasonable agreement between theory and experiment is obtained. As expected, the radiation fields are of a broadside mode. It is observed that the antenna is operated in a right-hand CP mode, with more than 27 dB difference between the right-hand and left-hand fields in the broadside direction ($\theta = 0^\circ$). It should be mentioned that the antenna can be operated in a left-hand CP mode by symmetrically displacing the parasitic patch on the opposite side, that is, by changing ϕ_0 from 157.4° to 202.6° .

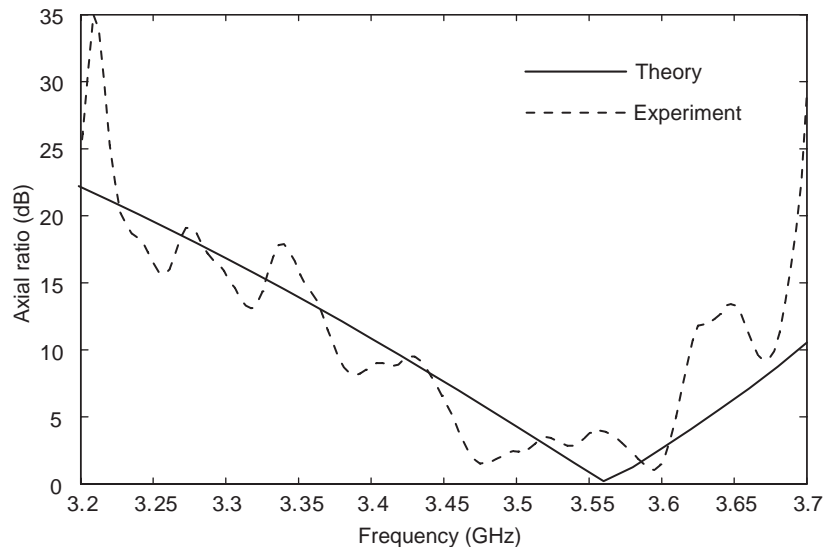


Figure 16. Measured and calculated ARs as a function of frequency in the broadside direction, with $\epsilon_r = 9.5$, $a = 12.5$ mm, $l_1 = 14$ mm, $l_2 = 7.9$ mm, $W_1 = 1.2$ mm, $W_2 = 2.2$ mm, and $\phi_0 = 157.4^\circ$. (From Leung and Ng [24], 2003 © IEEE.)

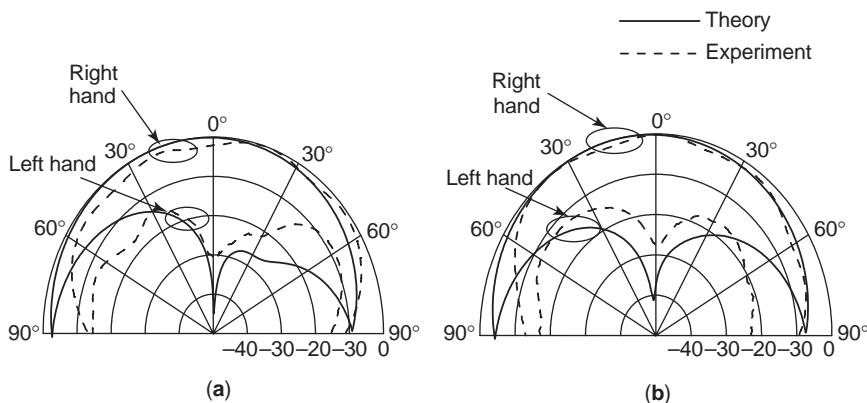


Figure 17. Measured and calculated right-hand and left-hand field patterns at $f = 3.52$ GHz, with $\epsilon_r = 9.5$, $a = 12.5$ mm, $l_1 = 14$ mm, $l_2 = 7.9$ mm, $W_1 = 1.2$ mm, $W_2 = 2.2$ mm, and $\phi_0 = 157.4^\circ$: (a) x - y plane; (b) y - z plane. (From Leung and Ng [24], 2003 © IEEE.)

4. CONCLUSION

Conformal-strip-excited LP and CP hemispherical DRAs has been studied theoretically and experimentally. In the analysis, the MoM has been applied to find the strip currents. To reduce computation time and complexity, the integrals associated with the associated Legendre functions have been evaluated by virtue of recurrence formulas. Linearly Polarized DRA has been introduced as an angular strip displacement to facilitate impedance matching. By adding a parasitic patch on the sidewall of the DRA, a CP DRA can be excited. The parasitic patch has been displaced at 157.4° from the excitation strip to give the optimum AR around the design frequency. It has been found that the AR and input impedance of the antenna are controlled predominantly by the parasitic patch and excitation strip, respectively. Because each part can be designed independently, the design of the CP DRA is quite an easy task.

Acknowledgements

This work was supported by a grant from the Research Grant Council of the Hong Kong Special Administrative Region, China (Project CityU 1178/01E).

BIBLIOGRAPHY

1. D. Kajfez and P. Guillon, eds., *Dielectric Resonators*, Artech House, Norwood, MA, 1986.
2. S. A. Long, M. W. McAllister, and L. C. Shen, The resonant cylindrical dielectric resonator antenna, *IEEE Trans. Anten. Propag.* **AP-31**:406–412 (May 1983).
3. M. W. McAllister, S. A. Long, and G. L. Conway, Rectangular dielectric resonator antenna, *Electron. Lett.* **19**:218–219 (March 1983).
4. M. W. McAllister and S. A. Long, Resonator hemispherical dielectric antenna, *Electron. Lett.* **20**:657–658 (Aug. 1984).
5. G. Drossos, Z. Wu, and L. E. Davis, Circular polarized cylindrical dielectric resonator antenna, *Electron. Lett.* **32**:281–283 (Feb. 1996).
6. A. Ittipiboon, R. K. Mongia, Y. M. M. Antar, P. Bhartia, and M. Cuhaci, Aperture-fed rectangular and triangular dielectric resonators for use as magnetic dipole antennas, *Electron. Lett.* **29**:2001–2002 (Nov. 1993).
7. H. Y. Lo, K. W. Leung, K. M. Luk, and E. K. N. Yung, Low profile equilateral-triangular DRA of very high permittivity, *Electron. Lett.* **35**:2164–2166 (1999).
8. K. W. Leung, K. M. Luk, and E. K. Yung, Spherical cap dielectric resonator antenna using aperture coupling, *Electron. Lett.* **29**:1530–1531 (Aug. 1993).
9. R. K. Mongia, A. Ittipiboon, P. Bhartia, and M. Cuhaci, Electric-monopole antenna using a dielectric ring resonator, *Electron. Lett.* **29**:1530–1531 (Aug. 1993).
10. K. W. Leung, K. Y. Chow, K. M. Luk, and E. K. N. Yung, Excitation of dielectric resonator antenna using a soldered-through probe, *Electron. Lett.* **33**:349–350 (Feb. 1997).
11. Y. M. M. Antar and Z. Fan, Theoretical investigation of aperture-coupled rectangular dielectric resonator, *IEEE Proc. Microwave Anten. Propag.* **143**:113–118 (April 1996).
12. N. C. Chen, K. L. Wong, and K. W. Leung, Input impedance of inclined printed slot antennas and inclined-slot-coupled dielectric resonator antennas, *Microwave Opt. Technol. Lett.* **12**:47–50 (May 1996).
13. K. W. Leung, K. Y. Chow, K. M. Luk, and E. K. N. Yung, Offset dual-disk dielectric resonator antenna of very high permittivity, *Electron. Lett.* **32**:2038–2039 (Oct. 1996).
14. K. W. Leung, Z. N. Chen, K. M. Luk, and E. K. N. Yung, Aperture-coupled dielectric resonator antenna with a thick ground plane, *IEEE Trans. Anten. Propag.* **AP-46**:1242–1243 (Aug. 1998).
15. H. Y. Lo, K. W. Leung, K. M. Luk, and E. K. N. Yung, Low profile equilateral-triangular dielectric resonator antenna of very high permittivity, *Electron. Lett.* **35**:2164–2166 (Dec. 1999).
16. K. Y. Chow and K. W. Leung, Theory and experiment of the cavity-backed slot-excited dielectric resonator antenna, *IEEE Trans. Electromagn. Compat.* **42**:287–290 (Aug. 2000).
17. G. P. Junker, A. A. Kish, A. W. Glisson, and D. Kajfez, Effect of an air gap around the coaxial probe exciting a cylindrical dielectric resonator antenna, *Electron. Lett.* **30**:177–178 (Feb. 1994).
18. K. W. Leung, Conformal strip excitation of dielectric resonator antenna, *IEEE Trans. Anten. Propag.* **AP-48**:961–967 (June 2000).
19. G. P. Junker, A. A. Kishk, A. W. Glisson, and D. Kajfez, Effect of fabrication imperfections for ground-plane-backed dielectric resonator antennas, *IEEE Anten. Propag. Mag.* **37**:40–46 (1995).
20. R. T. Long, R. J. Dorris, S. A. Long, M. A. Khayat, and J. T. Williams, Use of parasitic strip to produce circular

- polarization and increased bandwidth for cylindrical dielectric resonator antenna, *Electron. Lett.* **37**:406–408 (March 2001).
21. K. P. Esselle, Circularly polarized higher-order rectangular dielectric resonator antenna, *Electron. Lett.* **32**:1742–1743 (Sept. 1996).
 22. C. Y. Huang, J. Y. Wu, and K. L. Wong, Cross-slot-coupled microstrip antenna and dielectric resonator antenna for polarization, *IEEE Trans. Anten. Propag.* **AP-47**:605–609 (1999).
 23. M. T. Lee, K. M. Luk, E. K. N. Yung, and K. W. Leung, Microstripline feed circularly polarized cylindrical dielectric resonator antenna, *Microwave Opt. Technol. Lett.* **24**:206–207 (March 2000).
 24. K. W. Leung and H. K. Ng, Theory and experiment of circularly polarized dielectric resonator antenna with a parasitic patch, *IEEE Trans. Anten. Propag.* **AP-51**:405–412 (March 2003).
 25. R. K. Mongia, A. Ittipiboon, M. Cuhacim, and D. Rosecoe, Circularly polarized dielectric resonator antenna, *Electron. Lett.* **30**:1361–1362 (Aug. 1994).
 26. K. W. Leung, W. C. Wong, K. M. Luk, and E. K. N. Yung, Circular-polarised dielectric resonator antenna excited by dual conformal strips, *Electron. Lett.* **36**:484–486 (March 2000).
 27. A. Petosa, A. Ittipiboon, and M. Cuhaci, Array of circular-polarised cross dielectric resonator antennas, *Electron. Lett.* **32**:1742–1743 (Sept. 1996).
 28. Z. Li, C. Wu, and J. Litva, Adjustable frequency dielectric resonator antenna, *Electron. Lett.* **32**:606–607 (March 1996).
 29. Z. N. Chen, K. W. Leung, K. M. Luk, and E. K. N. Yung, Effect of parasitic disk on a coaxial probe-fed dielectric resonator antenna, *Microwave Opt. Technol. Lett.* **15**:166–168 (June 1997).
 30. H. K. Ng and K. W. Leung, Excitation of CP aperture-coupled dielectric resonator antenna with a parasitic patch, *IEEE Antennas and Propagation Soc. Int. Symp. Digest*, Boston, July 2001, Vol. 4, pp. 202–205.
 31. K. W. Leung, W. C. Wong, and H. K. Ng, Circularly polarized slot-coupled dielectric resonator antenna with a parasitic patch, *IEEE Anten. Wireless Propag. Lett.* **1**:57–59 (2002).
 32. K. W. Leung and H. K. Ng, Dielectric resonator antenna fed by a displaced conformal strip, *Microwave Opt. Technol. Lett.* **29**:185–187 (May 2001).
 33. R. D. Nevels, The annular aperture antenna with a hemispherical center conductor extension, *IEEE Trans. Anten. Propag.* **AP-35**:41–45 (Jan. 1987).
 34. R. D. Nevels and J. E. Wheeler, Radiation from a dielectric coated hemispherical conductor fed by a coaxial transmission line, *IEEE Trans. Electromagn. Compat.* **31**:16–20 (Feb. 1989).
 35. K. W. Leung, K. M. Luk, K. Y. A. Lai, and D. Lin, Theory and experiment of coaxial probe fed dielectric resonator antenna, *IEEE Trans. Anten. Propag.* **AP-41**:1390–1398 (1993).
 36. K. W. Leung, K. M. Luk, K. Y. A. Lai, and D. Lin, Theory and experiment of an aperture-coupled hemispherical dielectric resonator antenna, *IEEE Trans. Anten. Propag.* **AP-43**:1192–1198 (1995).
 37. K. W. Leung, Analysis of zonal and rectangular slot on a conducting spherical cavity, *IEEE Trans. Anten. Propag.* **49**:1739–1745 (Dec. 2001).
 38. K. M. Luk and K. W. Leung, eds., *Dielectric Resonator Antennas*, Baldock, Hertfordshire, England; Philadelphia: Research Studies Press Ltd., 2003.

DIELECTRIC RESONATOR FILTERS

S. BILA
 D. BAILLARGEAT
 S. VERDEYME
 P. GUILLON
 IRCOM
 Limoges, France

Because microwave filtering is an important function required to keep a number of different systems in working order, the specifications of a filter are varied. We can, however, try to classify some of them as presented in Table 1. The constraints are electrical, mechanical, thermal, and commercial.

The objective in this article is to show the advantages of the dielectric resonator (DR) technique to satisfy some of these functions, along with its disadvantages, in comparison with some other well-known solutions.

DRs are suitable for bandpass filtering. DR filters are classified as three-dimensional (3D) devices, in opposition to two-dimensional (2D) planar ones.

The main advantages of 2D solutions are their relative bycompact dimensions, their easier integration in circuit or module environment, and their well-known design and manufacturing procedures. They are, however, limited in their applications to the processing of low power, sizable relative bandwidth signal, in relation to the poor unloaded quality factor of localized microwave elements or planar resonators. Some solutions are proposed to restrict losses, such as applying supraconductors or active-element techniques, but they remain inadequate to replace 3D devices, in particular for high-power requirements.

In the class of 3D devices, designers have first chosen waveguides or metallic empty cavities to satisfy their very narrow bandwidth filtering requirements. However, since the mid-1980s, high-dielectric-constant materials, having low loss tangent and good thermal stability, have become available. The DR solution has been preferred for a number of applications, in particular spatial ones. This technique allows us to reduce significantly the cavities and waveguide device sizes, for equivalent electrical and increased thermal performances. Some average ratios can be given for dual-mode resonators (DR compared with cavity):

1 : 4 in volume
 1 : 2 in mass

Moreover, the DR shape and the mode in which it is excited can be chosen to give a response to particular requirements, as we will see later in this article. A number of DR shapes and filter topologies have, however, been proposed. Our work here is limited to the presentation of the most popular ones.

In this article, we present some characteristic parameters of DR filters, which are generally introduced

- polarization and increased bandwidth for cylindrical dielectric resonator antenna, *Electron. Lett.* **37**:406–408 (March 2001).
21. K. P. Esselle, Circularly polarized higher-order rectangular dielectric resonator antenna, *Electron. Lett.* **32**:1742–1743 (Sept. 1996).
 22. C. Y. Huang, J. Y. Wu, and K. L. Wong, Cross-slot-coupled microstrip antenna and dielectric resonator antenna for polarization, *IEEE Trans. Anten. Propag.* **AP-47**:605–609 (1999).
 23. M. T. Lee, K. M. Luk, E. K. N. Yung, and K. W. Leung, Microstripline feed circularly polarized cylindrical dielectric resonator antenna, *Microwave Opt. Technol. Lett.* **24**:206–207 (March 2000).
 24. K. W. Leung and H. K. Ng, Theory and experiment of circularly polarized dielectric resonator antenna with a parasitic patch, *IEEE Trans. Anten. Propag.* **AP-51**:405–412 (March 2003).
 25. R. K. Mongia, A. Ittipiboon, M. Cuhacim, and D. Rosecoe, Circularly polarized dielectric resonator antenna, *Electron. Lett.* **30**:1361–1362 (Aug. 1994).
 26. K. W. Leung, W. C. Wong, K. M. Luk, and E. K. N. Yung, Circular-polarised dielectric resonator antenna excited by dual conformal strips, *Electron. Lett.* **36**:484–486 (March 2000).
 27. A. Petosa, A. Ittipiboon, and M. Cuhaci, Array of circular-polarised cross dielectric resonator antennas, *Electron. Lett.* **32**:1742–1743 (Sept. 1996).
 28. Z. Li, C. Wu, and J. Litva, Adjustable frequency dielectric resonator antenna, *Electron. Lett.* **32**:606–607 (March 1996).
 29. Z. N. Chen, K. W. Leung, K. M. Luk, and E. K. N. Yung, Effect of parasitic disk on a coaxial probe-fed dielectric resonator antenna, *Microwave Opt. Technol. Lett.* **15**:166–168 (June 1997).
 30. H. K. Ng and K. W. Leung, Excitation of CP aperture-coupled dielectric resonator antenna with a parasitic patch, *IEEE Antennas and Propagation Soc. Int. Symp. Digest*, Boston, July 2001, Vol. 4, pp. 202–205.
 31. K. W. Leung, W. C. Wong, and H. K. Ng, Circularly polarized slot-coupled dielectric resonator antenna with a parasitic patch, *IEEE Anten. Wireless Propag. Lett.* **1**:57–59 (2002).
 32. K. W. Leung and H. K. Ng, Dielectric resonator antenna fed by a displaced conformal strip, *Microwave Opt. Technol. Lett.* **29**:185–187 (May 2001).
 33. R. D. Nevels, The annular aperture antenna with a hemispherical center conductor extension, *IEEE Trans. Anten. Propag.* **AP-35**:41–45 (Jan. 1987).
 34. R. D. Nevels and J. E. Wheeler, Radiation from a dielectric coated hemispherical conductor fed by a coaxial transmission line, *IEEE Trans. Electromagn. Compat.* **31**:16–20 (Feb. 1989).
 35. K. W. Leung, K. M. Luk, K. Y. A. Lai, and D. Lin, Theory and experiment of coaxial probe fed dielectric resonator antenna, *IEEE Trans. Anten. Propag.* **AP-41**:1390–1398 (1993).
 36. K. W. Leung, K. M. Luk, K. Y. A. Lai, and D. Lin, Theory and experiment of an aperture-coupled hemispherical dielectric resonator antenna, *IEEE Trans. Anten. Propag.* **AP-43**:1192–1198 (1995).
 37. K. W. Leung, Analysis of zonal and rectangular slot on a conducting spherical cavity, *IEEE Trans. Anten. Propag.* **49**:1739–1745 (Dec. 2001).
 38. K. M. Luk and K. W. Leung, eds., *Dielectric Resonator Antennas*, Baldock, Hertfordshire, England; Philadelphia: Research Studies Press Ltd., 2003.

DIELECTRIC RESONATOR FILTERS

S. BILA
 D. BAILLARGEAT
 S. VERDEYME
 P. GUILLON
 IRCOM
 Limoges, France

Because microwave filtering is an important function required to keep a number of different systems in working order, the specifications of a filter are varied. We can, however, try to classify some of them as presented in Table 1. The constraints are electrical, mechanical, thermal, and commercial.

The objective in this article is to show the advantages of the dielectric resonator (DR) technique to satisfy some of these functions, along with its disadvantages, in comparison with some other well-known solutions.

DRs are suitable for bandpass filtering. DR filters are classified as three-dimensional (3D) devices, in opposition to two-dimensional (2D) planar ones.

The main advantages of 2D solutions are their relative bycompact dimensions, their easier integration in circuit or module environment, and their well-known design and manufacturing procedures. They are, however, limited in their applications to the processing of low power, sizable relative bandwidth signal, in relation to the poor unloaded quality factor of localized microwave elements or planar resonators. Some solutions are proposed to restrict losses, such as applying supraconductors or active-element techniques, but they remain inadequate to replace 3D devices, in particular for high-power requirements.

In the class of 3D devices, designers have first chosen waveguides or metallic empty cavities to satisfy their very narrow bandwidth filtering requirements. However, since the mid-1980s, high-dielectric-constant materials, having low loss tangent and good thermal stability, have become available. The DR solution has been preferred for a number of applications, in particular spatial ones. This technique allows us to reduce significantly the cavities and waveguide device sizes, for equivalent electrical and increased thermal performances. Some average ratios can be given for dual-mode resonators (DR compared with cavity):

1 : 4 in volume
 1 : 2 in mass

Moreover, the DR shape and the mode in which it is excited can be chosen to give a response to particular requirements, as we will see later in this article. A number of DR shapes and filter topologies have, however, been proposed. Our work here is limited to the presentation of the most popular ones.

In this article, we present some characteristic parameters of DR filters, which are generally introduced

Table 1. Microwave Filter Specifications

Electrical	Mechanical	Thermal	Commercial
Central frequency	Mass and volume	Temperature range of use	Components and materials costs
Passband width	Vibration resistance	Maximum dissipated power	Machining cost
Passband ripple	Machining tolerances	Sensitivity of electrical response to temperature variations	Design cost
Out-of-band selectivity and rejection	Manufacturing difficulties		Delay for design and realization of filter
Response isolation			
Insertion losses			
SWR			
Group delay			
Power capabilities			

during the synthesis procedure. These definitions are helpful in explaining the choices of filter designers, in particular the DR shapes and arrangements in multipole devices.

In Section 1, the class of devices loaded by cylindrical DRs is investigated. This is a common shape for the DR. It can be excited on a symmetric mode (TE_{0n} or TM_{0m}) or on a first hybrid mode (HEM_{11}). Different DR arrangements in the filter are presented and discussed.

For particular applications in microwave filtering, we can fit the DR shape or the DR mode. For high-power applications, it is important to put the high-dielectric-constant material in contact with a metallic enclosure, to improve the thermal dissipation. DRs of a quarter-cut cylinder, a cylindrical rod, or a dielectric plate shielded in a metallic cavity are investigated. Solutions are also given to optimize the isolation of the filter response on the frequency axis, or to apply DR to the millimeter wave filtering. These particular applications are included in Section 2.

Approaches developed to design DR filters are discussed in Section 4. A four-pole DR filter synthesis is proposed as an example.

1. ELECTRICAL CHARACTERISTIC PARAMETERS OF A DR FILTER

Applying conventional methods, the design of microwave filters starts with the selection of an ideal transfer function that fulfills the electrical objectives of the specifications. The synthesis of this ideal transfer function leads to an equivalent lumped-element circuit. This circuit is characterized by a coupling matrix that depends on the lumped-element values. A number of studies have been devoted to this task [1,2]. Different circuit topologies can be chosen. However, for the DR filters presented in this article, the equivalent circuit is close to the one presented in Fig. 1 (canonical symmetric design). Nevertheless, if another solution is chosen, the same characteristic parameters may have to be computed.

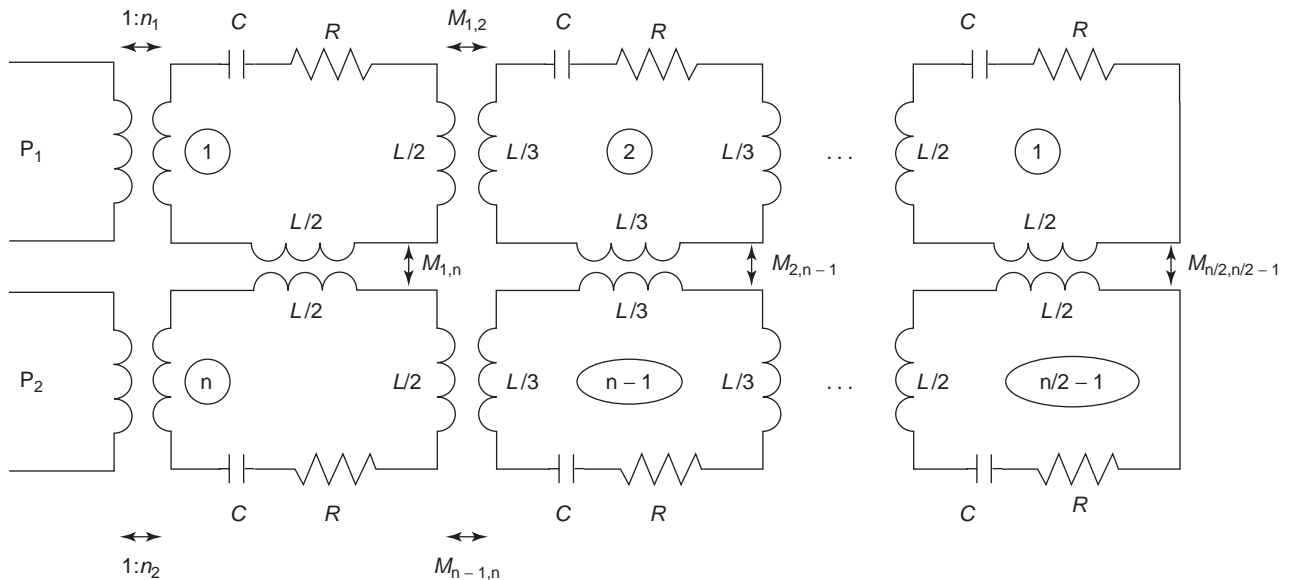


Figure 1. Equivalent circuit of a symmetric n -pole filter.

From the circuit presented Fig. 1, we define the following:

- The central frequency of the filter:

$$f_0 = \frac{1}{2\pi\sqrt{LC}} \quad (1)$$

- The unloaded quality factor of each resonator:

$$Q_0 = \frac{L\omega_0}{R}, \quad \omega_0 = 2\pi f_0 \quad (2)$$

- The input and output coupling coefficients. In the electrical scheme, the coupling levels between the excitation access (P_1 and P_2) and the first and last resonators (1 and n) are characterized, respectively, by the ratios $1/n_1$ and $1/n_2$. It is however generally preferred to define external quality factors Q_{ei} [1] at port i , ($i \in \{1, 2\}$), by

$$Q_{ei} = \frac{2\pi L f_0}{R_{ei}} \quad \text{with} \quad (3)$$

$$R_{ei} = R_0 n_i^2 \quad (4)$$

as the external loading resistance at port P_i . Coupling coefficients α_i are also defined at port i by

$$\alpha_i = \frac{Q_0}{Q_{ei}} \quad (5)$$

- The coupling coefficient between resonators. The resonators are intercoupled, longitudinally and crosswise, in the general case. We define a coupling coefficient K_{ij} between resonators i and j by

$$K_{ij} = \frac{M_{ij}}{L} \quad (6)$$

The crosswise coupling coefficients (except $K_{n/2,n/2-1}$) may cancel to obtain conventional Butterworth or Chebyshev responses. Some of them are different from zero and can be negative for elliptic bandpass function realizations, including transmission zeros in the out-of-band part of the transmission response.

These parameters help the designer perform the third synthesis step, the computation of the device dimensions. The topology of the filter, in particular the DR arrangement, is easily directly deduced from the equivalent-circuit one, which, in fact, justifies this approach. In Section

3, we explain how the dimensions of the filter are computed from knowledge of the parameters f_0 , M_{ij} , and Q_{ei} .

2. FILTERS COMPOSED OF CYLINDRICAL DRs

Cylindrical DRs are more often used to realize multipole filters. We discuss this class of solutions here. The DR is generally shielded in a metallic box, to avoid radiation losses. It can then be excited on transverse electric TE_{0n} modes, transverse magnetic TM_{0m} modes, or hybrid HEM_{nm} modes. The natures of the transmission lines or waveguides used to couple the filter, the nature of the DRs arrangement in the device, and the nature of the electrical, mechanical, and thermal characteristics of the filter depend on the choice of the DR mode. Table 2 compares the performance levels of the TE_{01} , TM_{01} , and HEM_{11} modes. The dimensions are optimized to obtain a resonant frequency equal to 4 GHz. We notice that the DR acting on the TE_{01} mode is the less bulky one. Even if the electrical performances are comparable, the TM_{01} mode is more radiative in the cavity, which increases the metallic losses on the enclosure. The HEM_{11} mode is in fact very interesting for reduction of filter size. The filter performance of each particular TE, TM, or hybrid mode is discussed below.

2.1. Monomode Filter

The DRs are excited on the symmetric TM_{01} or TE_{01} modes. An n -pole “monomode” filter is then composed of n DRs. The dimensions of each DR and of the metallic enclosure are generally chosen to optimize, at the filter center frequency, the dielectric and metallic losses and the device sizes, as well as to avoid spurious responses around the filter bandpass.

Different topologies of the TE_{01} mode, have been reported in the literature. The DRs can be placed side by side on the same plane. To obtain good isolation on this mode, the ratio between diameter and height of each DR is generally chosen to be 2. Then the radial radiation of each DR is small and the DRs can be coupled directly; a metallic iris does not have to be placed systematically between the DRs to limit the filter size.

Two examples of realization are presented in Figs. 2 and 3. Different techniques can be employed to couple the filter. Propagative rectangular waveguides can be connected to both ends of a waveguide section above cutoff, which contains the DR. The TE_{01} mode of the DRs is excited if their axis are positioned along the wide dimension of the monomode waveguide (Fig. 2). The distances between the first (and respectively last) DR and the junctions between

Table 2. Comparison between TE_{01} , TM_{01} , HEM_{11} , and DR^a Mode Performance Levels

	f_0 (GHz)	Q_0	D_{RD} (mm)	H_{RD} (mm)	D_C (mm)	H_C (mm)
TE_{01}	4	8600	14	5.5	28	19.5
TM_{01}	4	7500	28	8.3	52	56
HEM_{11}	4	9600	19.3	6	40	20

^aCylindrical DR (diameter D_{RD} , height H_{RD} , permittivity $\epsilon_r = 36$, loss tangent 10^{-4}) enclosed in a cylindrical metallic cavity (diameter D_C , height H_C , metallic conductivity 1.7×10^7 S/m).

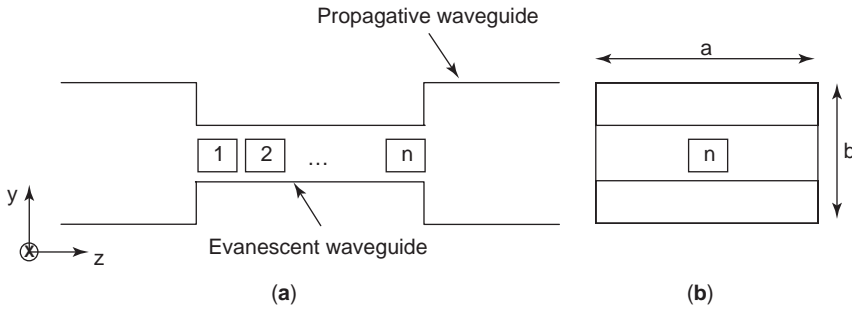


Figure 2. DRs excited on a TE_{01} mode through rectangular waveguides.

the waveguide sections enable us to tune the level of the input (respectively output) coupling coefficient. This technique is suitable for high-power applications.

To improve the integration of the filter in its environment, we must couple the first and last DRs to microstrip lines (Fig. 3). Nevertheless, the metallic losses of such a structure increases, as the DR must be placed near the metallic strip and ground plane to obtain the required coupling levels. The evolution of the coupling coefficient as a function of the distance between the line and the DR is given in Ref. 3.

Dielectric resonators might also be coupled through coaxial probes [4] or loops [5]. Particular attention to the positioning of the excitation systems around the DR enable us to obtain a good isolation of the bandpass response on the frequency axis.

From the devices shown in Figs. 2a and 2b [4–6], we obtain narrow-bandpass Chebyshev or Butterworth responses. Stopband filters can also be realized easily using these DR coupling techniques, coupling the DR to a propagative waveguide or a transmission line [7].

Coupling the DRs side by side enables us to maintain them easily, such as on a dielectric substrate, whose material is chosen to improve the temperature stability of the filter. Moreover, some tuning elements can be integrated around the DRs; some metallic or dielectric screws are generally placed along the DRs axis to tune the filter resonant frequency, as well as between the DRs to adjust the coupling coefficients.

On the TE_{01} , TM_{01} , and TM_{02} modes, DRs have also been mounted axially on a cylindrical dielectric rod. To

obtain an elliptic response on these symmetric modes, in the same device we can combine axial and side-by-side mounting configurations. A two-stage device is constructed. The transversal coupling M_{ij} can then be achieved, as it has been done for empty metallic cavities. A negative coupling is obtained by setting some upper and lower cavity axis; the resulting transmission zeros placed around the passband response increase the filter selectivity [8].

Different techniques, including those mentioned previously, have been developed for the mounting of DRs in their enclosure; for instance, the DRs can be glued on a dielectric support. This technique may, however, be critical because of the generation of parasitic gaps between the glued materials and the poor glue loss tangent. A mounting based on a differential dilatation phenomenon between each DR and its environment is more suitable for obtaining high electrical performance. The capability of the filter to withstand vibration is fundamental for space applications. Some test measurements are given, for example, in Ref. 9.

2.2. Dual-Mode Filters

Dual-mode filters [10] are now widely used because they offer equivalent electrical performance levels, smaller size, and less mass than do classical fundamental TE or TM-mode filters. A metallic screw, or another perturbation is placed around the DR to break the rotational symmetry. Then, on the first or second hybrid mode, the two polarizations sections are imposed, and their frequencies differ in relation to the perturbation dimension. Figure 4 presents a two-pole dual-mode filter, composed of only one DR. Two monomode DRs would be coupled to obtain the same electrical response. The DR is excited through coaxial probes. Two tuning screws are generally added in the excitation probe axis to tune the central resonant frequency.

The coupling screw is placed at an angle of 45° from the excitation axis. In this case, the symmetry of the structure suffices to fix the direction of the two polarizations. The electromagnetic environment of each mode differs; thus the resonant frequencies f_1 and f_2 of the two polarizations differ. The power combining is constructive between f_1 and f_2 at the output access, which explains the bandpass response obtained from this device. Some transmission zeros are also observed, due to the combination of opposite phases between the two polarizations, and between these phases and a higher-order mode of the DR [11].

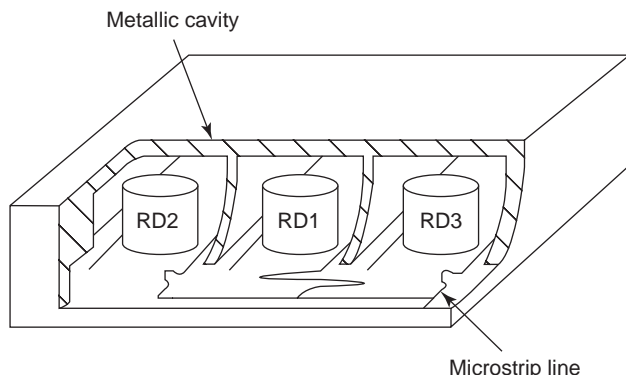


Figure 3. DR lines excited on a TE_{01} mode through microstrip lines.

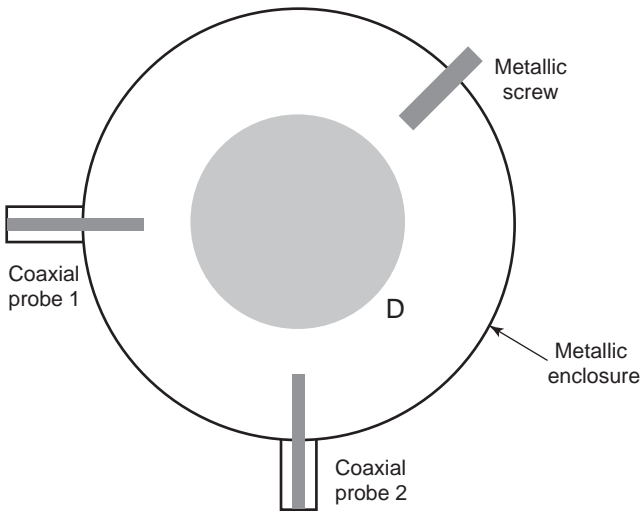


Figure 4. Dual-mode DR excited by two coaxial probes.

For n -pole elliptic realization, with $n > 2$ and n as an odd number, we need to couple parallel modes in adjacent DRs (longitudinal coupling) and to avoid extra coupling between orthogonal modes of different DRs. Three screws are placed around each DR as shown in Fig. 4, and adjacent DRs are generally iris-coupled. Two orthogonal rectangular apertures machined in a metallic plate enable us to impose the required coupling level between each set of parallel polarizations. To obtain a negative sign on some crosswise coupling coefficients, the different screws are not positioned at the same angle with the excitations in the different cavities. This technique is well known for metallic cavity realizations [12]. An example of four-pole topology is presented in Fig. 5, where the DRs are coupled to input-output coaxial probes.

The excitation can also take the form of rectangular waveguides, coupled to the input-output cavities through

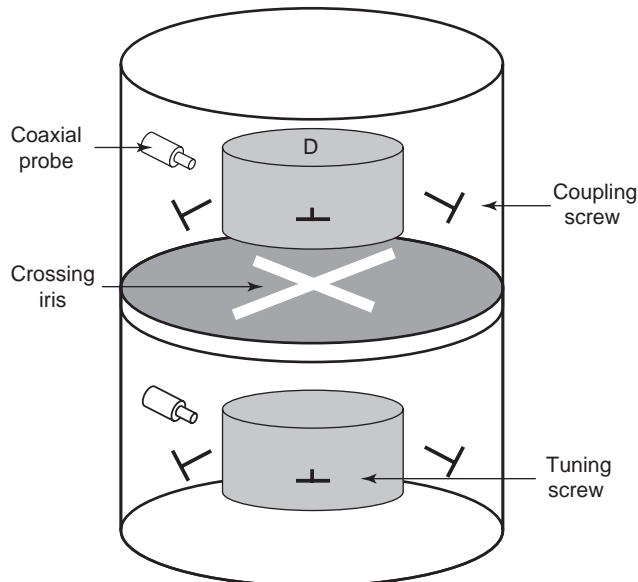


Figure 5. Example of four-pole dual-mode DR filter.

rectangular irises, for power applications. These irises are then generally placed in a plane perpendicular to the DR axis.

Adjacent DRs can also be coupled directly, rather than iris coupled [13]. Then realizations of small coupling levels may require large separation between adjacent DRs, and may consequently require significant sizes. However, the introduction of evanescent waveguide sections between DRs enable us to reduce the device dimensions [14]. The drawbacks of this method are the filter spurious characteristics and the dependent coupling level between the mode sets of adjacent DRs. In the same way as monomode realizations, dual-mode DRs can be mounted in a planar relationship to one another. Each DR is again enclosed in a metallic cavity. The DR intercouplings are controlled independently by a metallic iris that contains two rectangular noncrossing apertures placed in an appropriate manner [15]. This solution is interesting for its flexibility in the arrangement of the DR cavities.

More than two modes have also been coupled in the same DR cavity, to conserve weight and size in comparison with the previous solutions. The two polarizations of the HEM_{11} modes and the TM_{01} mode have been simultaneously excited in a planar DR-mounted cavity. Two of these three-pole modules have been coupled through an iris composed of two separate T-shaped apertures [16].

3. PARTICULAR APPLICATIONS OF DRS IN MICROWAVE FILTERING

3.1. DR for High-Power Applications

The dual-mode devices we have presented above are interesting for their high electrical performance levels and limited sizes. But even if the filter dissipated power is small, the resulting thermal dissipation remains critical for certain applications, such as space applications, because the thermal conductivity of most dielectric material is poor.

A solution consists of positioning the high permittivity resonators in contact with the metallic enclosure, to improve the thermal dissipation efficiency, and then to improve the power-handling capability of the filter.

We can first take advantage of the electromagnetic field symmetry of a cylindrical DR. It can be divided into two or more parts, without modifying the resonant frequency and field repartition of some modes, if the physical metallic walls are placed in planes in which electrical wall conditions are naturally verified [17,18]. In this way a cylindrical DR excited on a TE_{01} mode can be split, for example, into four parts. If each of the cut planes are in contact with a metallic wall (Fig. 6), all quarter-cut DRs will resonate at the same frequency.

The improvement of the power-handling capability is not the sole purpose of this technique. A number of cylindrical DR modes do not satisfy the electrical wall condition in the planes where they are imposed on the quarter-cut DR. They are then suppressed in the “image” DR. Hence the out-of-band rejection performances of the filter is improved, suppressing spurious responses.

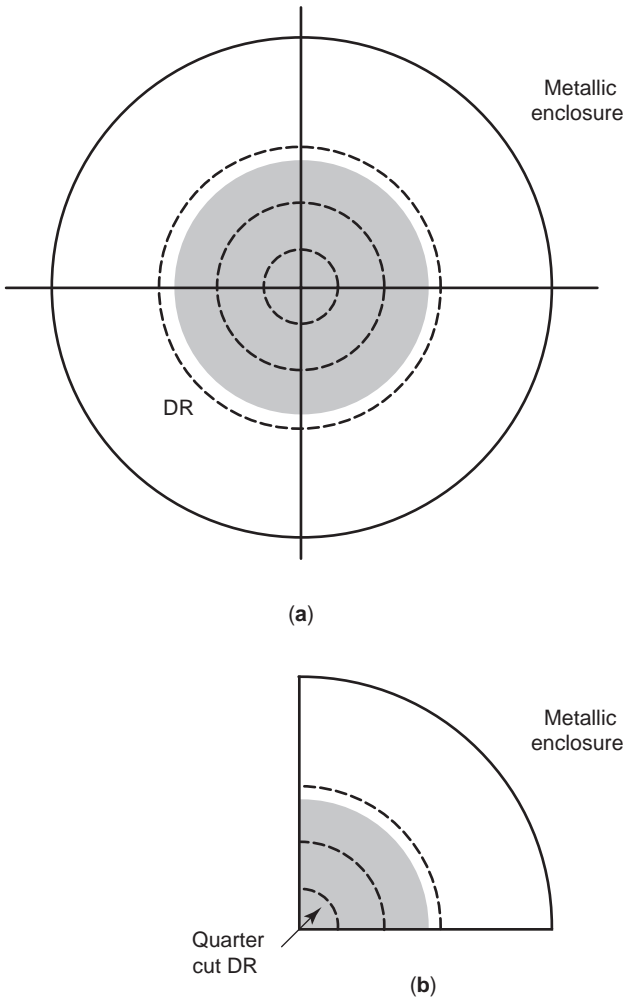


Figure 6. Equivalent cylindrical (a) and quarter-cut (b) DRs excited on a TE_{01} mode (— electric field lines).

This technique also provides very compact structures, reducing the size not only of the DR but also of the metallic enclosure. This is an important advantage, particularly for 900-MHz–3-GHz applications. Nevertheless, the metallic losses on the metallic plane in contact with the DR increase dramatically, resulting in a poor unloaded

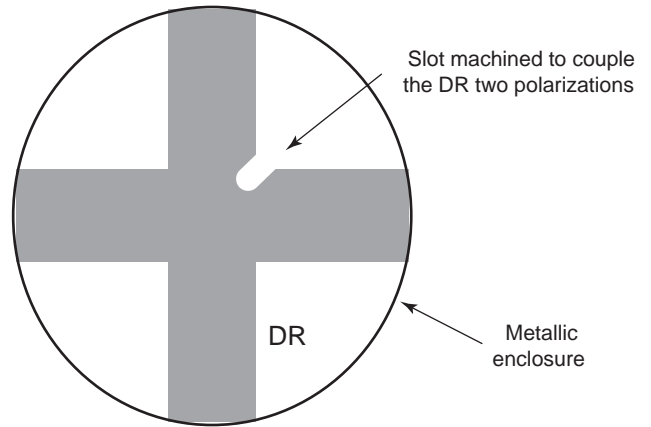


Figure 8. TM dual-mode resonator.

quality factor Q_0 of the DR. We can note, however, that the image resonator might be preferred to coaxial dielectric field resonators, considering the sizes and losses at the same frequency. Figure 7 presents a possible arrangement of the DRs to realize an elliptic five-pole function [17].

Different techniques have been proposed to increase the unloaded quality factor of the split DR. TM dual-mode DRs have been developed for use in the L and C frequency bands for mobile communication applications. A cross is formed as shown in Fig. 8, by two parallelepipedic DRs excited on a TM_{01} mode [19]. The tuning element required to couple the two degenerated modes is not a metallic screw, but a perturbation directly machined near the center of the cross. An unloaded quality factor equal to 9000 has been obtained at 1.9 GHz, for a dielectric loss tangent equal to 5×10^{-5} [20]. A high-permittivity dielectric plate has also been placed in a metallic enclosure to provide a good compromise between the unloaded quality factor level and the thermal dissipation capability [21]. The corners of a thin parallelepipedic plate have been cut to provide a good contact between the resonator and a cylindrical metallic cavity (Fig. 9).

The dimensions are optimized to limit the metallic and dielectric losses on the first TE mode that has degenerated. It has been shown that the electrical performance of this resonator is not far from that of the cylindrical

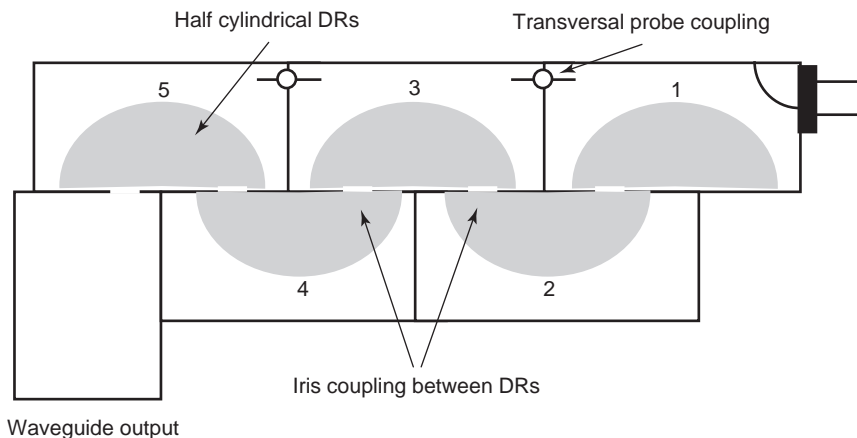


Figure 7. Five-pole elliptic filter using the split-DR technique.

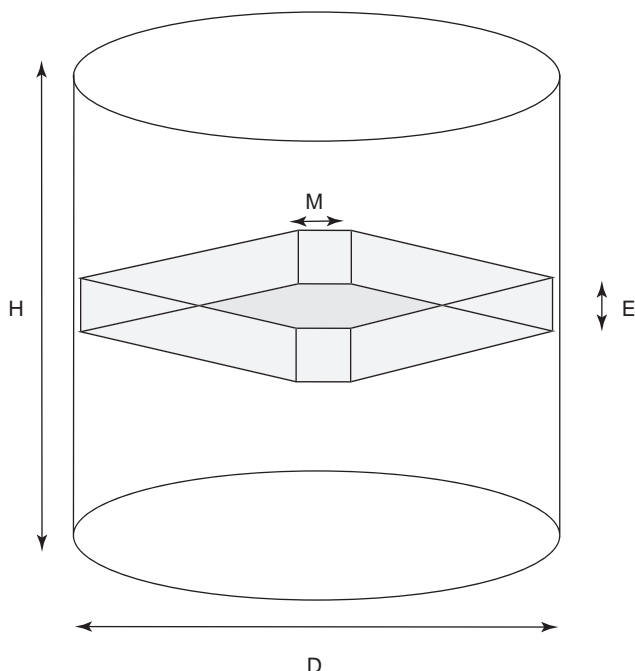


Figure 9. High-permittivity dielectric plate resonator technique.

dual-mode one, and this solution is more suitable for power applications. Metallic screws are generally placed around the dielectric plate to couple the first TE polarizations. Slots are then machined in the plate, both to couple these polarizations and to optimize the out-of-band rejection of the filter. Superimposed cavities are coupled through metallic cross irises. The topology of an eight-pole autocorrected quasielliptic filter is presented in Fig. 10. The transmission and reflection responses, along with the group delay of the filter, are presented in Fig. 11.

Some other studies have been performed to optimize the DR shape to increase the unloaded quality factor of the resonators, in particular by choosing adequate forms of the DR dielectric support in contact with the metallic enclosure [22].

3.2. Filter Configurations for Optimization of Out-of-Band Rejection

Conventional DR filters have relative poor stopband rejection performance, due to the excitation of higher-order mode resonances. A lowpass filter, placed at the output of the bandpass DR filter, might solve this problem, but the bulk and the electrical performance of the cascaded filter suffer from this solution. Different filter configurations have, however, been proposed to increase the out-of-band rejection.

We have already underlined that the quarter-cut DR, or the TM_{01} DR, which are of interest for power applications, are also efficient techniques for elimination of some of the spurious responses.

Coupling structures have been designed to suppress the excitation of some modes. A single-mode TE_{01} filter realization is, for example, presented in Ref. 23. The diameter: height ratio of the DR is generally chosen to optimize the mode isolation. A hole can be machined in the cylindrical DR, along its axis [24,25], and the DR shape can be matched [26] to increase this isolation. A more sophisticated solution consists of mixing DRs excited on different modes in a same filter. To obtain part of the ring DR isolation, and part of the compactness of dual-mode devices, TE_{01} ring DRs and a HEM_{11} dual-mode DR have been coupled to realize six-pole elliptic filters, combining four DRs. DRs can be mounted axially [27] or side by side [28] in their metallic enclosures. As an example, the center frequency of the realized filter is equal to 1.23 GHz; its passband is 20 MHz, and the out-of-band rejection is better than -40 dB in the 1–1.9 GHz frequency band [27].

3.3. DR for High-Frequency Applications

When the frequency increases, the dimensions of cylindrical DRs excited on the first TE_{01} , TM_{01} , and HEM_{11} modes become too small. The limit of conventional DR applications can be set around 20 GHz. To solve the manufacturing problem, spherical DRs have been proposed. But the critical mechanical stability of the devices, along with the spurious modes around the bandpass limits their applications.

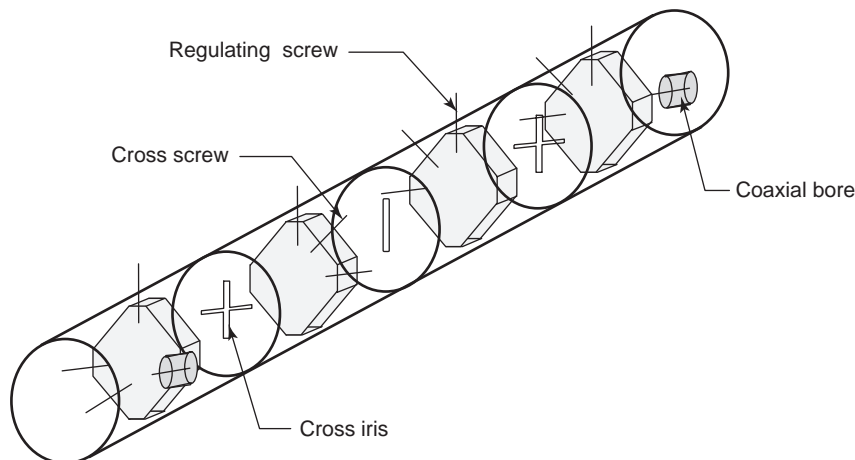


Figure 10. Dielectric plate eight-pole connected elliptic filter.

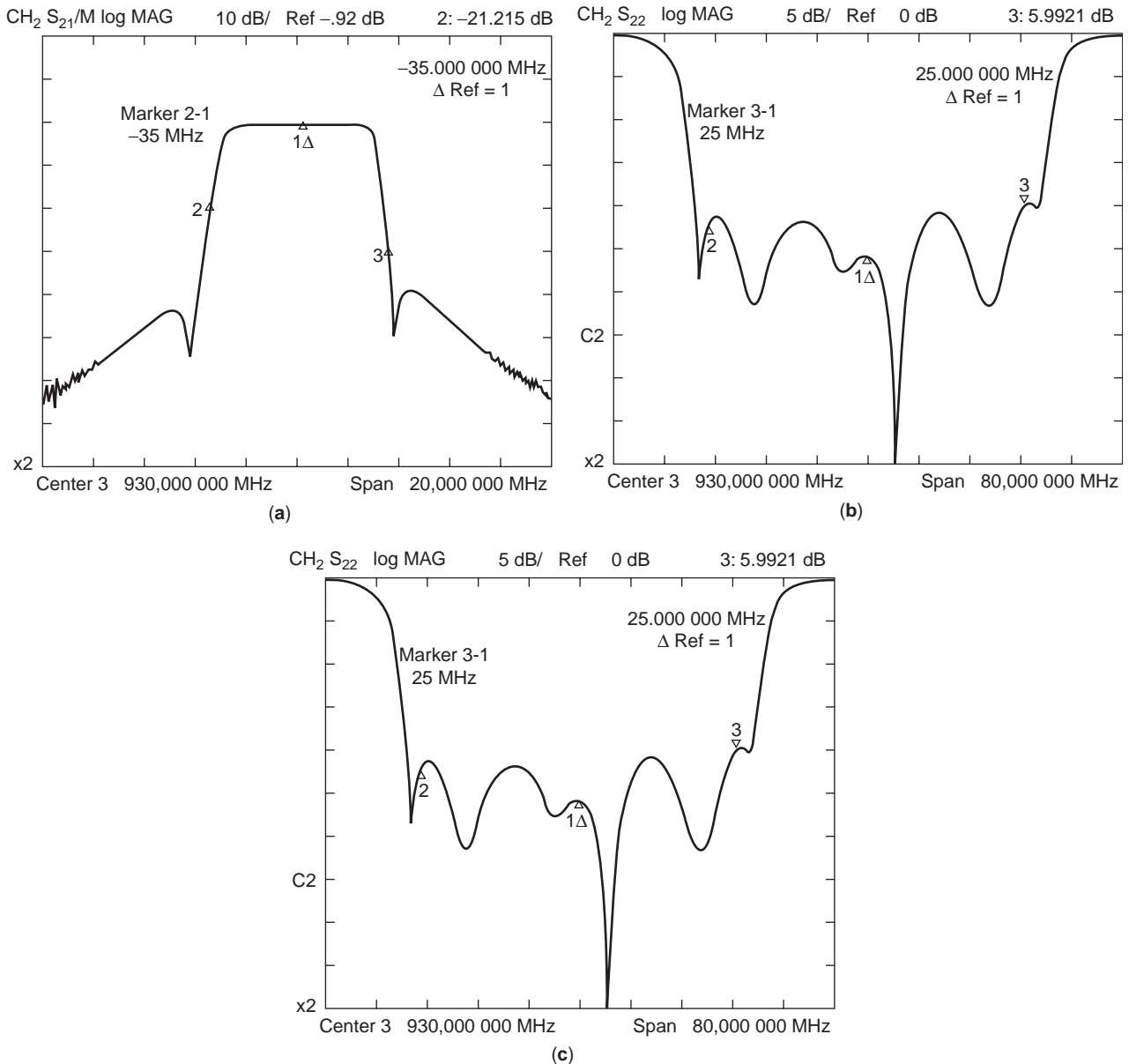


Figure 11. (a,b) Transmission and reflection coefficient variations as a function of the frequency; (c) group delay variation in filter passband.

We can, however, use cylindrical DRs on whispering gallery modes [29]. For important azimuthal variation number, the DR can be used easily up to 100 GHz. Moreover, the field is very effectively stored in with the DR, and the unloaded quality factor, which thus depends only on the material loss tangent, is important. Examples of filter realizations are given in Ref. 30.

4. THEORETICAL DESIGN OF MICROWAVE DR FILTERS

4.1. Introduction

DRs are used for the realization of narrowband filters up to 0.01% relative bandwidth. The electrical responses of such devices are then very sensitive to their geometric and

physical characteristics, and particular attention must be paid to their design.

The purpose of the theoretical design can be not only to optimize the filter performances but also to reduce the cost of the product. If the design is not efficient, the time required for the tuning can be important; different devices are manufactured, and even in the phase when the dimensions are known, an experimenter must spend time and effort to tune each filter.

However, DR structures are difficult to analyze, because their geometries are very complex. We have seen that the filter topologies are diverse; DRs can be intercoupled or coupled through a metallic iris; they may be excited by coaxial probes, metallic waveguides, and microstrip lines; their shapes are not systematically

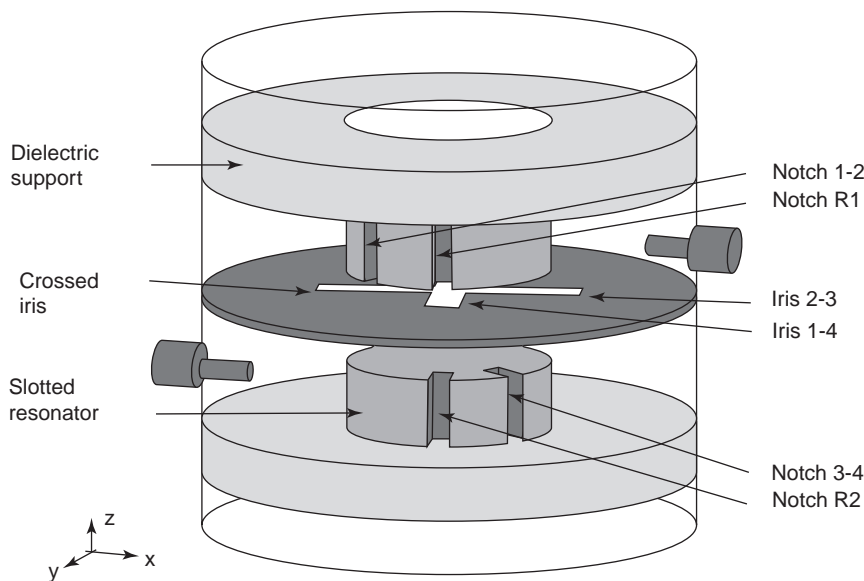
cylindrical; and they can be maintained in their metallic enclosures through a wide variety of systems. Moreover, the structures are very compact, and if we can define different segments in its composition, strong couplings are generated between the DRs through high-order modes. Thus the classical approach that is applied in the circuit software, namely, the segmentation method, is not efficient here; we cannot characterize each segment independently from the others, and we cannot connect the different contributions to obtain the device response.

Analytical-approach models were initially developed to assist designers. These methods are described in Ref. 31. Since the late 1980s, rigorous analyses have been performed, first on some parts of the DR filter. Examples include application of modal methods [32,33], the finite-element method [34], or the method of lines [35] to characterize axisymmetric dielectric-loaded metallic cavities, computing the resonant frequencies of these devices. Some other studies have been performed on the design of three-dimensional resonator, which is nonsymmetrical in structure. The resonant frequency of a DR shielded in a parallelepipedic enclosure has been computed applying the modal method [36] and the finite-element method [37,38]. From these computations we can easily deduce the coupling coefficient between two DRs for symmetric structures. The coupling coefficient between a DR and a waveguide or a transmission line has been computed by

applying the finite-element method [39,40]. Now, with the evolution of computer capabilities, a number of research teams are interested in the electromagnetic optimization of DR devices applying numerical simulation. A number of articles deal with the rigorous design of multipole filters. In this section we will describe a solution for the rigorous design of a multipole DR filter using the finite-element method [40].

4.2. Method for Optimized Design of a DR Filter

The procedure generally applied to determine the geometric dimensions of a multipole filter is deduced from the lumped-element synthesis presented in Section 1. To explain this approach, we have chosen here to design a dual-mode four-pole DR filter because this design groups together some problems found in a large variety of DR filter topologies. In the dual-mode DR presented in Section 1, the metallic screws are replaced by slots directly machined in the DR. The four-pole filter, shown in Fig. 12, consists of a metallic cavity, two input/output coaxial probes, and two slotted DRs coupled through metallic cross irises. Because the experimental filter will not be tuned, the synthesis procedure has to be performed rigorously. To compute the filter dimensions that satisfy given electrical characteristics, we develop the approach presented in Fig. 13.



Metallic cavities :	Dielectric resonators :	Crossed iris :
$H_C = 14.1 \text{ mm}$	$H_{DR} = 3.4 \text{ mm}$	$L_{14} = 5.20 \text{ mm}$
$R_C = 15.5 \text{ mm}$	$R_{DR} = 7.6 \text{ mm}$	$L_{23} = 7.70 \text{ mm}$
	$\epsilon_{DR} = 37$	$w = 1.00 \text{ mm}$
		$t = 1.00 \text{ mm}$
Tuning notches :	Coupling notches :	Notch-DR distances :
$D_{DR1} = 0.62 \text{ mm}$	$D_{12} = 0.93 \text{ mm}$	$d_{DR1} = 1.10 \text{ mm}$
$D_{DR2} = 0.62 \text{ mm}$	$D_{34} = 0.93 \text{ mm}$	$d_{DR2} = 1.10 \text{ mm}$
$w = 1.00 \text{ mm}$	$w = 1.00 \text{ mm}$	

Figure 12. Four-pole slotted DR filter.

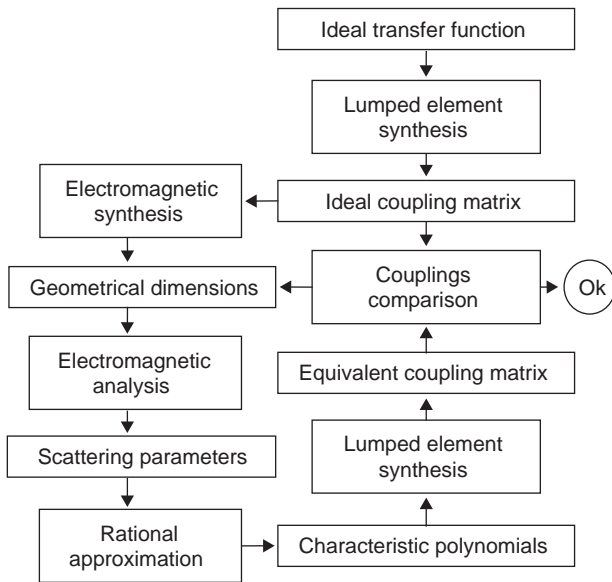


Figure 13. Design method of multipole filter.

In the first stage, an equivalent lumped-element circuit is synthesized from the ideal transfer function. The synthesis leads to a coupling matrix that characterizes the ideal equivalent circuit. This objective coupling matrix gives all the information about the ideal electrical characteristic parameters of the filter.

Applying the 3D finite-element method [40], we can then compute the initial dimensions of the structure with respect to the previous electrical parameters. An electromagnetic synthesis allows us to determine the following:

1. The DR and metallic cavity dimensions required to satisfy the center frequency f value.
2. The probe depth penetration, computed to obtain the required input/output coupling coefficient levels.
3. The dimension of the cross iris to obtain the required coupling coefficient between the parallel polarizations of the two DRs. The theoretical synthesis method is generally interrupted here for classical applications. Screws are then placed around the filter to couple the polarizations and to account for the resonant frequencies of the filter. Then a set of irises are manufactured, and each experimental device has to be tuned. Choosing the slotted DR solution, we can continue with the synthesis computations.
4. The coupling notch dimensions, which impose the coupling coefficient between the two polarizations of each DR.
5. The dimensions of a second notch, which are introduced to compensate for the influence of the probes and the iris on the resonant frequency of the excited polarization.

Then, all the dimensions of the device presented in Fig. 12 are known, but only approximately because of the segmentation approach applied in these initial steps, which does not account for the indirect dependence between the different elements.

In the third stage, an electromagnetic optimization loop is performed applying the following procedure:

1. The 3D finite-element method is applied in order to compute the scattering parameters between the access ports of the whole structure.
2. The scattering parameters are approximated as rational functions in the frequency domain.
3. From the approximated rational functions, an equivalent circuit, namely, a coupling matrix, of the simulated filter is synthesized.
4. By comparing the extracted coupling matrix and the ideal one, the filter dimensions are corrected according to the dimension sensitivities from the electromagnetic synthesis.

The loop is performed as long as the electrical objective is not attained.

This procedure is detailed in Refs. 40 and 41. The ideal transfer function and the electromagnetic response at the

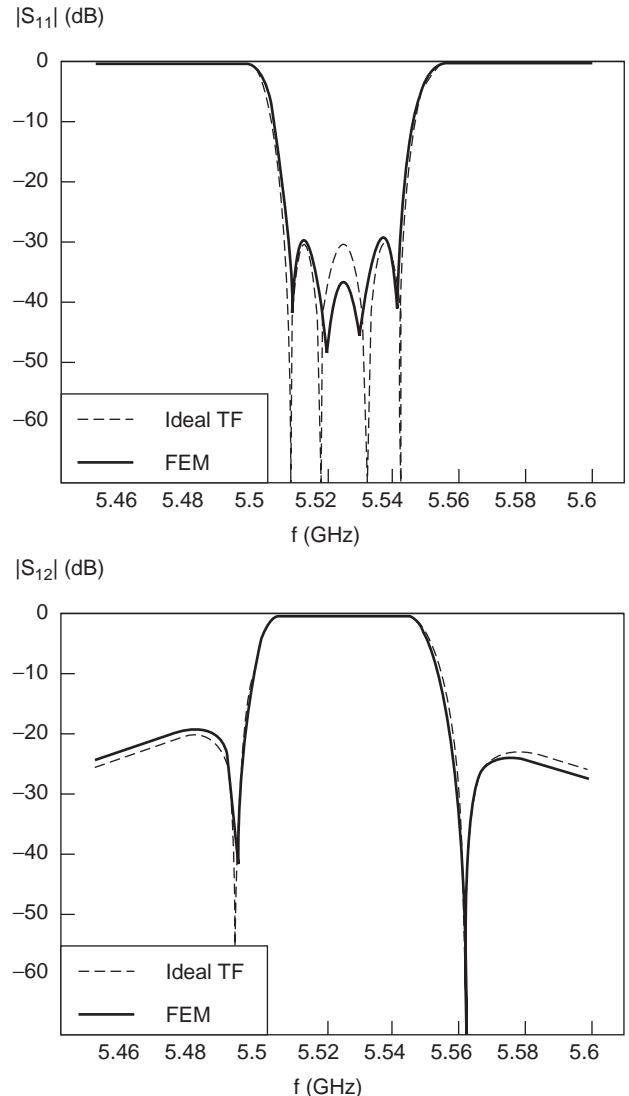


Figure 14. Comparison of ideal and electromagnetic results.

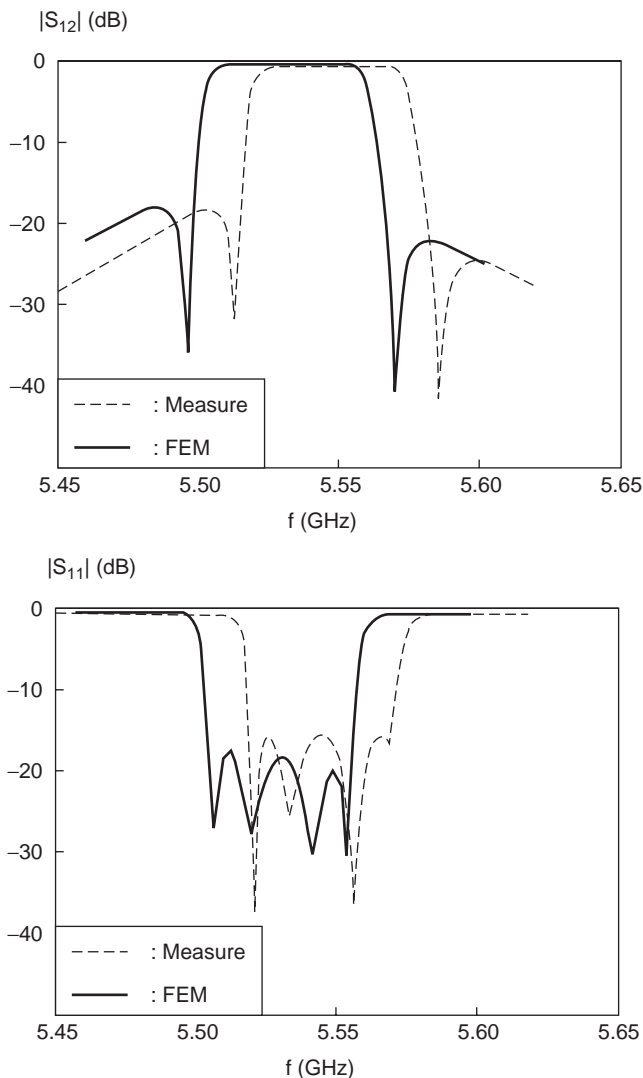


Figure 15. Comparison of theoretical and measured results.

end of the optimization are compared in Fig. 14. We can note the good convergence of the electromagnetic model response with a return loss of > 30 dB in the passband. In Ref. 40, the filter is designed with a slightly different filtering pattern. The electromagnetic response along with the experimental results are presented in Fig. 15. The filter is realized and measured without tuning elements. The difference between the computed and measured center frequencies is less than 0.2%, and the difference between the bandwidths is less than 5%. The theoretical and experimental standing-wave ratios are in good agreement.

5. CONCLUSION

DRs are currently placed in a number of devices, especially in microwave filters. The topologies of these filters are diverse, and they are a function of the system in which they are placed. Their main applications are found in the treatment of power signals and very narrow bandwidth filtering.

In this article, we have described different topologies proposed in recent years (as of 2004). A number of research teams are still working to increase the performance of DR filters, and to widen their domain of applications. Some of the topics under consideration are the following:

- The realization of filters in the millimeter wavelength band
- The work performed to decrease the volume and weight of DR devices
- The realization of DR filters without mechanical tuning for mass production
- The design of reconfigurable DR filters for multifrequency band applications
- The development of advanced synthesis techniques for simplified design of DR filters [42], for example, with a minimum number of elements

BIBLIOGRAPHY

1. G. Matthaei, L. Young, and E. M. T. Jones, *Microwave Filters, Impedance Matching and Coupling Structures*, Artech House, Dedham, MA, 1963.
2. A. E. Atia, A. E. Williams, and M. W. Newcomb, Narrowband multiple coupled cavity synthesis, *IEEE Trans. Circ. Syst. CAS-21*(5):649–655 (Sept. 1974).
3. D. Chaimbault, S. Verdeyme, and P. Guillon, Rigorous design of the coupling between a dielectric resonator and a microstrip line, *Proc. 24th European Microwave Conf. (EMC)*, Cannes, Sept. 5–8, 1994.
4. Y. Kobayashi and M. Minegishi, A low loss band pass filter using electrically coupled high Q $TM_{01\delta}$ dielectric rod resonators, *IEEE Trans. Microwave Theory Tech.* **36**(12):1727–1732 (Dec. 1988).
5. T. Nishikawa et al., *Microwave Bandpass Filter Provided with Dielectric Resonators*, U.S. Patent 4,143,344 (March 6, 1979).
6. S. B. Cohn, Microwave band pass filters containing high Q dielectric resonators, *IEEE Trans. Microwave Theory Tech.* **16**:218–277 (April 1968).
7. C. V. Ren, Waveguides band stop filter utilizing $Ba_2 Ti_9 O_{20}$ resonators, *Proc. 1978 Int. Microwave Symp.* June 1978, p. 227.
8. A. E. Atia and A. E. Williams, General TE_{011} mode waveguide band pass filters, *IEEE Trans. Microwave Theory Tech.* **24**(10):640 (Oct. 1976).
9. S. Vigneron, B. Theron, V. Madrangeas, F. Tounsi, and P. Guillon, Dielectric resonators filters for space applications, *Proc. ESA-ESTEC Workshop on Microwave Filters for Space Applications*, June 1990, pp. 71–80.
10. S. J. Fiedziusko, Dual mode dielectric resonator loaded cavity filters, *IEEE Trans. Microwave Theory Tech.* **30**(9):1311–1316 (Sept. 1982).
11. D. Baillargeat, S. Verdeyme, and P. Guillon, Symmetrical quasi elliptic two pole dielectric resonator filter, *Electron. Lett.* **31**(11):893–895 (May 25, 1995).
12. A. E. Atia and A. E. Williams, New types of waveguide band pass filters satellite transponders, *Comsat Tech. Rev.* **1**(1): 21–43 (1971).
13. K. A. Zaki, C. Chen, and A. E. Atia, Canonical and longitudinal dual mode dielectric resonator without iris,

- IEEE Trans. Microwave Theory Tech.* **35**(12):1130–1135 (Dec. 1987.)
14. S. C. Chen and K. A. Zaki, A novel coupling method for dual mode dielectric resonators and waveguide filters, *IEEE Trans. Microwave Theory Tech.* **38**(12):1885–1892 (Dec. 1990).
 15. W. C. Tang, D. Siu, B. C. Beggs, and J. Sferazza, *Planar Dual Mode Cavity Filters including Dielectric Resonators*, U.S. Patent 4,652,843, March 24, 1987.
 16. W. C. Tang, D. Siu, B. C. Beggs, and J. Sferazza, Triple Mode Dielectric Loaded Band Pass Filter, U.S. Patent, 4,675,630 (June 23, 1987).
 17. T. Nishikawa, K. Wakino, K. Tsunoda, and Y. Ishikawa, Dielectric high power band pass filter using quarter cut TE_{015} image resonator for cellular base structures, *IEEE MTT-S Digest*, 1987, pp. 133–136.
 18. R. J. Cameron, W. C. Tang, and L. M. Kudsia, Advances in dielectric loaded filters and multiplexers for communications satellites, *Proc. ESA/ESTEC Workshop on Microwave Filters for Space Applications*, Noordwijk June 1990.
 19. K. Wakino, T. Nishikawa, and Y. Ishikawa, Miniaturization technologies of dielectric resonator filters for mobile communications, *Proc. MTT Workshop on Filters and Multiplexers for Mobile Communications*, June 17, 1993.
 20. Y. Ishikawa, J. Hattori, S. Abe, E. Kobayashi, and T. Nishiyawa, 1.9 GHz compact low loss dielectric diplexer designer by dual mode waveguide transmission line method, *Proc. 24th European Microwave Conf. (EMC)*, Sept. 1994, Vol. 2, pp. 1179–1184.
 21. S. Moraud, S. Verdeyme, P. Guillon, Y. Latouche, S. Vigneron, and B. Theron, A new dielectric loaded cavity for high power microwave filtering, *IEEE MTT-S Digest*, 1996, Vol. 2, pp. 615–618.
 22. S. Gendraud, S. Moraud, S. Verdeyme, P. Guillon, S. Vigneron, and B. Theron, New miniaturized dielectric loaded cavity microwave resonators, *Proc. 25th European Microwave Conf. (EMC)*, Bologne, Sept. 1995, pp. 691–695.
 23. R. V. Snyder, Dielectric resonator filter with wide stop bands, *IEEE Trans. Microwave Theory Tech.* **40**:2100–2102 (Nov. 1992).
 24. Y. Kobayashi and M. Miura, Optimum design of shielded dielectric rod and ring resonators for obtaining the best mode separation, *IEEE MTT-S Digest*, 1984, Vol. 1, pp. 184–186.
 25. S. W. Chen and K. A. Zaki, Dielectric ring resonators loaded in waveguide and on substrate, *IEEE Trans. Microwave Theory Tech.* **39**:2069–2076 (Dec. 1991).
 26. R. M. Mansour, Dual mode dielectric resonator filter with improved spurious performance, *IEEE MTT-S Digest*, 1993, pp. 443–446.
 27. J. F. Liang, K. A. Zaki, and A. E. Atia, Mixed modes dielectric resonator loaded cavity filters, *IEEE MTT-S Digest*, 1994, pp. 731–734.
 28. C. Wang, H. W. Yao, and K. A. Zaki, Mixed modes cylindrical planar dielectric resonator filters with rectangular enclosure, *IEEE MTT-S Digest*, 1995, Vol. 2, pp. 501–504.
 29. X. H. Jiao, P. Guillon, L. A. Bermudez, and P. Auxemery, Whispering gallery modes of dielectric structures: Application to millimeter wave bandstop filters, *IEEE Trans. Microwave Theory Tech.* **35**(12):1169–1175 (Dec. 1987).
 30. D. Cros, F. Nigon, P. Besnier, M. Aubourg, and P. Guillon, Whispering gallery dielectric resonator filters, *IEEE MTT-S Digest*, 1996, Vol. 2, pp. 603–606.
 31. D. Kajfez and P. Guillon, *Dielectric Resonators*, Artech House, Dedham, MA, 1986.
 32. W. K. Hui and I. Wolff, A multicomposite, multilayered cylindrical dielectric resonator for applications in MMIC's, *IEEE Trans. Microwave Theory Tech.* **2**(3):415–423 (March 1994).
 33. K. A. Zaki, Electromagnetic simulation of dielectric resonator devices using mode matching technique, *Proc. MTT-S Workshop WFFA, Dielectric Resonators in Microwave Active and Passive Circuits*, San Francisco, 1996.
 34. P. S. Kooi et al., Finite element analysis of the shielded cylindrical dielectric resonators, *IEE Proc.* **132**(Part H)(1):7–16 (Feb. 1995).
 35. D. Kremer and R. Pregla, The method of lines for the hybrid analysis of multilayered dielectric resonators, *IEEE MTT-S Digest*, Orlando, 1995, Vol. 2, pp. 491–494.
 36. X. P. Liang and K. A. Zaki, Modeling of cylindrical dielectric resonators in rectangular waveguides and cavities, *IEEE Trans. Microwave Theory Tech.* **41**(12):2174–2181 (Dec. 1993).
 37. R. Ferrari and G. Maille, Three dimensional finite element method for solving electromagnetic problems, *Electron. Lett.* **14**(15):467–468 (July 1978).
 38. S. Verdeyme, M. Aubourg, and P. Guillon, Three dimensional finite element method applied to dielectric resonators devices, *IEEE MTT-S*, Los Angeles, 1989.
 39. J. P. Cousty, S. Verdeyme, M. Aubourg, and P. Guillon, Finite element for microwave device simulations: Applications to microwave DRs filters, *IEEE Trans. Microwave Theory Tech.* **40**(5):925–932 (May 1992).
 40. D. Baillargeat, S. Verdeyme, P. Guillon, and M. Guglielmi, New dual mode coupling using slotted dielectric resonator, *Microwave Opt. Technol. Lett.* (Jan. 1993).
 41. S. Bila, D. Baillargeat, S. Verdeyme, M. Aubourg, P. Guillon, F. Seyfert, J. Grimm, L. Baratchart, C. Zanchi, and J. Sombrin, Direct electromagnetic optimization of microwave filters, *IEEE Microwave Mag.* **2**(1):46–51 (March 2001).
 42. S. Bila, D. Baillargeat, S. Verdeyme, F. Seyfert, L. Baratchart, C. Zanchi, and J. Sombrin, Simplified design of microwave filters with a symmetric transfer functions, *Proc. 33rd European Microwave Conf. (EuMW 03)*, Munich, Germany, Oct. 2003.

DIELECTRIC RESONATOR OSCILLATORS

VINCENT F. FUSCO
 Queen's University of Belfast
 Belfast, Northern Ireland
 ANDREW DEARN
 Plextek Ltd.
 Gear Chesterford, United
 Kingdom

Oscillators producing energy at microwave frequencies are an essential component in most microwave communication systems, such as communication links, radar, and frequency synthesizers. There are significant commercial pressures to improve the performance of oscillators with respect to giving them lower noise characteristics, higher DC-to-RF efficiency, better temperature and frequency stability, and so on. The dielectric resonator when coupled with two/three-terminal active devices provides a vehicle for producing high-quality fixed-frequency or narrowband

tunable oscillators. Low-loss temperature-stable dielectric materials with high-quality Q factors mean that miniature resonators can be formed that have physical compatibility with microwave integrated circuits [1]. A dielectric resonator (DR) can be used to form the stabilizing element in an oscillator. Dielectric resonator oscillators (DROs) are characterized by the following properties: high-frequency stability, high efficiency, and low manufacturing cost. They also can be made to provide good temperature stability.

Two- and three-terminal active devices exhibit phase noise characteristics at microwave frequencies. Oscillators constructed using these devices can have their phase noise behavior improved by the addition of a DR element.

For a three-terminal device the dielectric resonator for first-order feedback topologies [2] can occupy one of several positions within the circuit, as illustrated in Fig. 1.

In Fig. 1a the DR is mounted in order to provide parallel feedback to the three-terminal active device. Here the coupling action is between device ports [3].

In Fig. 1b the DR is located so that energy produced as a result of negative resistance obtained at the device port is reflected back with correct phasing into the active device by the DR, which presents a high impedance at the device port. The DR acts as a bandstop filter, and in this way an oscillation is set up. This configuration has good phase noise characteristics. However, it is sensitive to load variation and tends to mode-jump in the presence of two resonant circuits [4]. The configuration in Fig. 1c generally provides superior performance compared to the other two methods and is compatible with the off-chip bonding processes required for stabilizing monolithic microwave integrated circuit (MMIC) oscillators. Here the DR acts as a very high- Q resonator element for the series feedback oscillator, giving good frequency stability and low phase noise. In a field-effect transistor (FET) realization, where the DR is coupled to the gate circuit and the feedback is a common source, the operating point is very insensitive to load variation, due to intrinsic isolation between the input and output provided by the low gate-to-drain capacitance of the active device. A varactor diode can be added for tuning purposes. Higher-order feedback implementations [5], for example, shunt feedback DRO configurations such as those given in Fig. 2, are also possible [6]. Multiple DR and push-push frequency doubling oscillator configurations are also possible [7].

In Fig. 2 the DR behaves as a high- Q filter in the positive feedback path. In Fig. 2a part of the output signal is coupled back to the input port. By adjusting lengths l_1 and l_2 , the Barkhausen oscillation condition can be satisfied. In Fig. 2b the DR is coupled between two ports and the

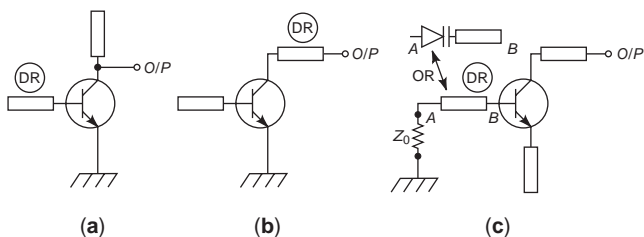


Figure 1. Typical DRO topologies.

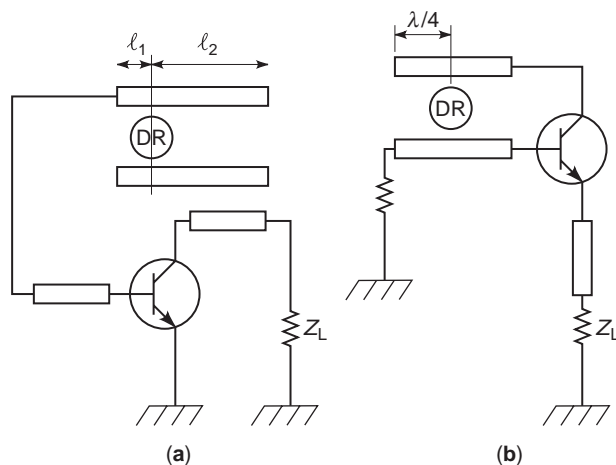


Figure 2. Shunt feedback topologies.

output is taken from the third. Here the position of the DR is adjusted in order to maximize the negative resistance at the output port of the active device.

In the shunt feedback configurations the two coupling coefficients in the parallel feedback case cannot be adjusted separately. Also, since the coupling is to an open-circuit line, these types of circuits tend to be very sensitive to the lateral position of the DR.

The selection of the active device for oscillator applications depends on the frequency of operation. Below 12 GHz, bipolar junction transistors (BJTs) and HBT find application due to their superior flicker $1/f$ and noise levels [8]. A 4-GHz, 21-dBm series feedback bipolar transistor DR oscillator with a phase noise spectral density of -130 dBc/Hz at 10 kHz from the carrier was reported [9]. Values of -89 dBc/Hz at 10 kHz offset have been reported at 21.4 GHz for a reflection type DRO producing 10 dBm output power [10]. Stabilized Gunn oscillators operating at 35 GHz [11] and HBT DROs at 25 GHz have also been reported [12].

It is significant to note that generally as frequency increases, output power can be maintained only at the expense of increased phase noise, since the DR must be coupled more tightly to the circuit.

The key elements to be optimized with respect to oscillator performance are

- Output power
- Startup stability
- Phase noise
- DC-RF efficiency
- Tuning range
- Sensitivity to DR placement
- Frequency pushing/pulling

For a very high-frequency operation into the millimeter-wave region, or for very high Q -factor operation in the centimeter wavelength region, DRs operated in whispering gallery mode [13] are employed [14–16]. Here the important dimension is the circumference rather than the diameter of the DR. This leads to more practical-sized DRs for higher-frequency circuits.

1. DIELECTRIC RESONATORS

A dielectric resonator (DR) is a high-dielectric-constant ceramic material formed into a regular geometric shape, usually a solid or hollow cylindrical or cuboid shape. The material usually has a relative dielectric constant of around 30–40 (but can be as high as 92) and exhibits low-loss characteristics. The high permittivity of the material means that energy can be stored within the DR. The DR can resonate in various modes that are governed by the dimensions, geometry, and electrical properties of the DR itself and by the physical environment in which it is to operate. The development of temperature-stable high-dielectric-constant dielectric materials means that it is now possible to construct resonators that exhibit minimum change in resonant frequency with temperature.

The most commonly used DR shape is a solid cylinder. Here the most common mode of operation is denoted the $TE_{01\delta}$ or dipole mode (Fig. 3).

For a dielectric constant of 40, only 5% of the electric field and 40% of the magnetic field exist outside the DR. This energy decays rapidly as the distance from the DR surface increases [17]. The resonant frequency of an isolated cylindrical DR is given approximately by Gisson [18] as

$$f_{\text{GHz}} = \frac{34}{a\sqrt{\epsilon_r}} \left[\frac{a}{\ell} + 3.45 \right] \quad (1)$$

where a, ℓ are in millimeters and $0.5 < a/\ell < 2$, while $30 < \epsilon_r < 50$.

For operation in fundamental mode the dimensions of the DR are approximately one guide wavelength: $\lambda g = \lambda_0 / \sqrt{\epsilon_r}$.

The lowest frequency of operation is limited by tolerable DR size; typically this is 1 GHz, while the highest frequency, about 100 GHz, is governed by internal losses and minimum resonator dimensions [19]. In order to avoid spurious modes, the length of the DR is usually restricted to lie between $0.175a \leq \ell \leq 0.225a$.

2. DIELECTRIC RESONATOR MATERIAL PROPERTIES

The Q factor and temperature stability provided by dielectric resonators are invariably impaired by imperfect material parameters. The material from which the resonator is constructed will have losses produced by its finite

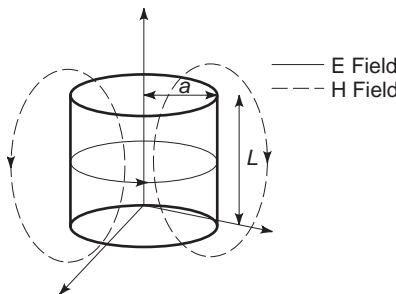


Figure 3. Cylindrical dielectric resonator $T_{01\delta}$ mode.

conductivity and also by polarization-induced damping under radiofrequency (RF) excitation conditions [20].

If dielectric loss within the resonator is denoted Q_d , then

$$Q_d = \frac{W}{W_d \tan \delta} \quad (2)$$

where $\tan \delta$ is the loss tangent of the resonator material, W is the total energy stored in the cavity, and W_d is the energy stored in the dielectric resonator. Q_d is often quoted as

$$Q_d = \frac{C}{f} \quad (3)$$

where C is a constant quoted by the resonator manufacturer.

Sometimes the loss tangent is given as

$$\tan \delta = A + Bf \quad (4)$$

where A and B are constants quoted by the manufacturer.

A more complete description of the losses in the resonator yields the total dissipated power in the resonator P_{tot} to be

$$P_{\text{tot}} = P_d + P_c + P_r + P_{\text{ext}} \quad (5)$$

where

P_d = power dissipated in the dielectric material

P_c = power dissipated in the surrounding enclosed metal

P_r = radiation loss

P_{ext} = power coupled to the external circuit

From this, Q factors for each term can be related to

Dielectric loss

$$Q_d = \frac{\omega W_e}{P_d} \quad (6)$$

Conductor loss

$$Q_c = \frac{\omega W_e}{P_c} \quad (7)$$

Radiation loss

$$Q_r = \frac{\omega W_e}{P_r} \quad (8)$$

External Q factor

$$Q_{\text{ext}} = \frac{\omega W_e}{P_{\text{ext}}} \quad (9)$$

where W_e is the total electric energy stored in the cavity defined by the shield enclosing the dielectric resonator.

The total loaded Q factor for the enclosed DR is

$$\frac{1}{Q_L} = \frac{1}{Q_d} + \frac{1}{Q_c} + \frac{1}{Q_r} + \frac{1}{Q_{ext}} \quad (10)$$

while the unloaded Q factor is

$$\frac{1}{Q_u} = \frac{1}{Q_d} + \frac{1}{Q_c} + \frac{1}{Q_r} \quad (11)$$

Techniques for measuring these quantities have been suggested in Refs. 21–23.

Temperature-dependent effects that cause a change in the DRs stabilizing function within an oscillator also need to be quantified.

The *linear coefficient of expansion* for a material is defined as the change in length of a rod of the material $\Delta\ell$, divided by its length L such that

$$\frac{\Delta\ell}{L} = \alpha T \quad (12)$$

where α (ppm/°C) is the linear expansion coefficient. As a DR puck expands or contracts, its resonant frequency will vary such that

$$\frac{\Delta f}{f_o} = -\alpha \Delta T \quad (13)$$

The negative sign indicates that as the DR puck becomes longer, its resonant frequency decreases.

With a DR, its relative permittivity ϵ_r is also a function of temperature. This variation is expressed very approximately as

$$\frac{\Delta\epsilon_r}{\epsilon_r} = \tau_E \Delta T \quad (14)$$

where τ_E is the temperature coefficient of the dielectric resonator (ppm/°C).

By combining these relationships together, we obtain an approximate equation for the temperature stability of a DR:

$$\frac{\Delta f}{f} = \frac{\partial f}{\partial L} \frac{\Delta L}{f} + \frac{\partial f}{\partial \epsilon_r} \frac{\Delta \epsilon_r}{f} \quad (15)$$

By denoting the temperature coefficient of the resonant frequency of the DR as τ_{DR} , we obtain

$$\tau_{DR} = -\alpha - \frac{T \tau_E}{2} \quad (16)$$

This equation implies that by making τ have twice the magnitude of α and giving it an opposite sense of operation, τ_E can be reduced to zero; that is, the DR can be temperature-compensated. Note, however, that since the DR will expand as temperature is increased, τ must always be negative for temperature compensation to occur.

Now consider the effect that these temperature changes have on the stability of a DRO. If an unstabilized oscillator

has a negative frequency drift with temperature, then a DR with a positive temperature coefficient is required so that temperature–frequency stabilization can be achieved. The frequency stability τ_f of a DRO has been modeled in Ref. 24 as

$$\tau_f = \tau_{DR} + \left(\frac{k+2}{4Q_u}\right) \frac{\partial\phi}{\partial\tau} \quad (17)$$

where $\partial\phi/\partial\tau$ is the temperature-induced phase variation of the active-circuit one-port measurement

$$\tau_{DR} = \frac{1}{f_o} \frac{df_o}{dT}$$

The second term just stated indicates that for a free-running oscillator the frequency drift is amplified by an amount proportional to the coupling coefficient of the DR.

By arranging Eq. (17), it is possible to find the desired value for τ_{DR} that yields zero τ_f

$$\tau_{DR} = -\left(\frac{k+2}{4Q_u}\right) \frac{\partial\phi}{\partial\tau} \quad (18)$$

Here $\partial\phi/\partial\tau$ and τ_{DR} are unknown. The in situ value for τ_{DR} when placed in its operating configuration can be found using a load-pull technique.

Alternatively if $\partial\phi/\partial\tau$ is assumed to be constant for a small change in coupling coefficient k , then Eq. (17) can be used to form two simultaneous equations from which the in situ τ_{DR} can be obtained directly. This second method should be used with caution since $\partial\phi/\partial\tau$ is nonlinear.

From this discussion it is clear that judicious selection of τ_{DR} and coupling coefficient can be used to compensate for temperature-induced DRO frequency drift [24].

3. QUALITY FACTOR

Quality or Q factor relates energy stored to average power loss. In a DR-based circuit, this is of critical importance since it is a measure of the resonator bandwidth, which is inversely proportional to the Q factor. Temperature stability and AM/FM noise performance of dielectric resonator oscillator circuits also depend on the Q factor:

$$Q = \omega_0 \frac{\text{energy stored}}{\text{average power loss}} \quad (19)$$

$$\omega_0 = \text{resonant frequency rad/s}$$

A second equation for quality factor that relates to group delay through a resonant circuit is useful for oscillator work [25]. This is the loaded quality factor Q_L :

$$Q_L = \omega_0 \frac{\tau}{2} = -\frac{\omega_0}{720} \frac{d\phi}{df} \quad (20)$$

Here, τ = group delay(s) and ϕ = phase of the open-loop voltage transfer function (degrees). The loaded Q is used in oscillator design to express the width of the phase slope

and resonance curve, including the effects of external components. As a consequence, Q_L is dominated by components external to the DR that have their own Q factor, called, Q_{ext} .

The unloaded Q factor Q_u is used when the Q of the resonant circuit is determined only by dissipation losses in the resonator. These various Q factors are related as follows:

$$\frac{1}{Q_L} = \frac{1}{Q_u} + \frac{1}{Q_{\text{ext}}} \quad (21)$$

For oscillator design Q_L can be used in the determination of single-sideband noise prediction.

4. LUMPED-ELEMENT COUPLING MODELS

By assuming that the aspect ratio of the DR and the frequency of operation have been selected such that only a single mode is excited then an isolated DR can be represented as a series resonant circuit with equivalent-circuit components R_r , C_r , and L_r [26].

Figure 4 shows a DR coupled to a short section of microstrip line, at reference plane pp^1 , which is represented by R_1 , C_1 , and L_1 . When the resonator is excited in $TE_{01\delta}$ mode, the coupling can be represented by a mutual inductance term L_m , which is proportional to the separation distance d , between the microstrip line and the DR (Fig. 4) [27].

If the microstrip line is assumed to have zero loss in the coupling region, R_1 can be neglected. By neglecting the microstrip-line capacitance, the resulting simplified equivalent circuit can be expressed close to resonance as a parallel resonant circuit (Fig. 5) where [28]

$$R = \frac{\omega^2 L_m^2}{R_r}$$

$$C = \frac{L_r}{\omega^2 L_m^2}$$

$$L = \omega^2 L_m^2 C_r$$

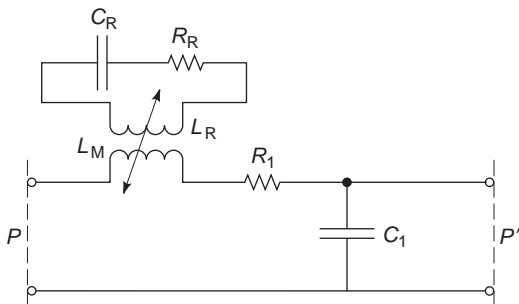


Figure 4. Equivalent circuit of DR coupled to microstrip line.

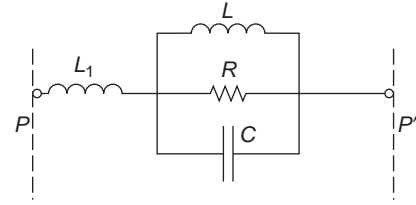


Figure 5. Simplified model of DR coupled to microstrip line.

The general expression for a parallel resonant circuit is

$$Z = \frac{R}{1 + j2Q_0\delta} \quad (22)$$

Hence

$$Q_u = \frac{\omega_0 L_r}{R_r} = \omega_0 R C \quad (23)$$

$$\omega_0^2 = \frac{1}{L_r C_r} = \frac{1}{LC} \quad (24)$$

$$\delta = \frac{\omega - \omega_0}{\omega} \quad (25)$$

Thus the equivalent circuit impedance (Fig. 4) can be written as

$$Z_T = j\omega L_1 + \frac{R}{1 + j2Q_u\delta} \quad (26)$$

These results are valid close to the fundamental resonance $TE_{01\delta}$ mode of the DR where δ^2 tends to zero. Outside this frequency range other DR modes exist, which can be modeled by a Foster-type equivalent circuit consisting of a series cascade of parallel tuned circuits [29]. With this approach characterization of the i th resonant circuit requires the i th resonant frequency, unloaded Q factor, and effective coupled resistance to be determined. In addition, when the resonant frequencies of several modes occur in close proximity the individual modal performances cannot be easily established because of mode interaction [30,31]. It is useful to note that $TE_{01\delta}$ mode can be well separated from other modes by correct selection of DR and enclosure dimensions.

When integrating the DR into an oscillator by means of a microstrip connecting line, the parallel tuned circuit in Fig. 5 becomes externally loaded as shown in Fig. 6.

Here the DR is loaded by the internal impedance of the generator and the load. If Z_g and Z_L are assumed to be real with line lengths ℓ_1 and ℓ_2 reduced to zero at resonance, the parallel structure reduces to R . From Eq. (27) the value of R depends on the amount of coupling between the DR and the line. A coupling coefficient term observed at the input port is defined as the ratio of the resonator coupled resistance k at the resonator frequency to the resistance external to the resonator [32]

$$k = \frac{R}{R_{\text{ex}}} \quad (27)$$

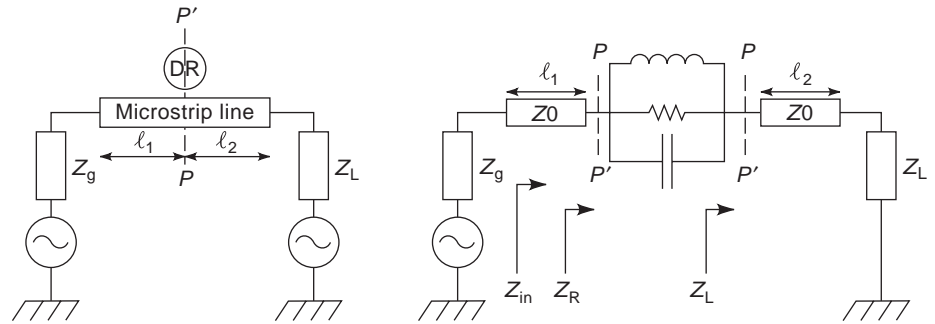


Figure 6. Oscillator DR coupling.

or

$$k = \frac{Q_u}{Q_e} \tag{28}$$

for a DR coupled to a matched line $R_g = R_L = Z_0$, here

$$k = \frac{R}{2Z_0} \tag{29}$$

for a DR coupled to a short-circuited load $R_L = 0$, here

$$k = \frac{R}{Z_0} \tag{30}$$

When a reactive termination loads the resonant circuit, this presents itself in series with the parallel equivalent circuit. This will cause an imperfect match and will also cause an additional reactive load to appear in series with the equivalent circuit [33].

If x_1 is the normalized reactance appearing in series with the parallel resonant circuit, then the definition for the coupling coefficient observed at the input port becomes

$$k = \frac{R}{Z_N(1+x_1^2)} \tag{31}$$

and for a short circuit

$$k = \frac{R}{Z_0(1+x_1^2)} \tag{32}$$

here

$$x_1 = \frac{\omega L_1}{Z_N} \tag{33}$$

where Z_N is the total impedance loading the DR.

Also under these conditions the resonant frequency shifts to a new frequency f_L where

$$f_L = f_0 \left[1 + \frac{x_1 k}{2Q_u} \right] \tag{34}$$

and

$$Q_u = Q_L(1+k) \tag{35}$$

When coupled to a matched microstrip line, x_1 is usually much less than one.

When the microstrip-line lengths l_1, l_2 are not equal to zero, then the DR is coupled to the generator and load terminations Z_L, Z_g via microstrip-line segments l_1, l_2 (Fig. 6).

For a matched line Eq. (28) is valid. For a short-circuit load and assuming lossless line

$$k = \frac{R}{Z_0(1 + \tan^2(\beta l_2))} \tag{36}$$

Here maximum coupling occurs at

$$l_2 = \frac{n\lambda_g}{4}, \quad n = 0, 2, 4 \tag{37}$$

while minimum coupling occurs at

$$l_2 = \frac{m\lambda_g}{4}, \quad m = 1, 3, 5 \tag{38}$$

where λ_g = effective wavelength of the microstrip line.

The same result occurs when considering the impedance presented at the input port under similar conditions.

Terminating the line in an arbitrary reactance shifts the maxima and minima of the magnetic field along the line. Since the $TE_{01\delta}$ mode couples to the magnetic field, line coupling will be maximized at peaks in the magnetic field standing wave and minimized at troughs. Coupling to the maximum point on the standing wave will present the coupling coefficient given by Eq. (29) at $n = 0, 2, 4$, and so on. The maximum coupling coefficient is reported experimentally to consistently occur at a distance $d = 0.7a$, where a is the radius of the DR puck [33].

5. MEASUREMENT OF DR COUPLING COEFFICIENT

The most convenient method for experimentally estimating coupling coefficient k involves a measurement of loaded quality factor Q_L , which is related to k as

$$Q_L = \frac{Q_u}{1+k} \tag{39}$$

However, Q_u is not normally known and has to be determined by the losses at ω_0 . From Ginzton [34] and Khanna

[35], Q_L can be established from the phase of the input impedance locus obtained by a one-port measurement made on the DR

$$Q_L = \frac{f_0}{f_4 - f_3} \quad (40)$$

where f_0 is the center frequency, f_3 is the frequency at which the phase is lagging that at f_0 by 45° , and f_4 is the frequency at which the phase is leading that at f_0 by 45° . The results obtained by this method are typically 10% greater than those obtained by the method of deembedded S parameters shown next.

By assuming zero radiation loss at the DR microstrip junction, it can be shown from scattering parameter theory that for a matched system

$$k = \frac{1 - [S_{11}]^2 - [S_{21}]^2}{2[S_{21}]^2} \quad (41)$$

A number of useful computer source codes for computing the resonant frequency and unloaded Q factor for shielded DRs are given in Ref. 36.

6. DIELECTRIC RESONATOR COUPLED TO A MICROSTRIP LINE

The most frequently used method of integrating a DR into a microwave integrated circuit is to couple it to a microstrip line. Here the problem is confined to the $TE_{01\delta}$ mode of a cylindrical DR (Fig. 1). Here the suffixes refer to the standing-wave pattern in the azimuthal, radial, and axial directions, respectively, for the fundamental TE mode $\delta = 1$.

A typical coupling configuration is shown in Fig. 7. An approximate representation of the H -field lines is given in order to illustrate the inductive nature of the coupling between a DR in $TE_{01\delta}$ mode and the quasi-TEM mode of microstrip line.

Here the magnetic field lines match each other principally on the radial direction of the DR field directly under the microstrip line. The coupling between the DR and the line is inversely proportional to the separation and, between them, is defined by a mutual inductance coupling coefficient term k . With this type of coupling a proportion

of energy is radiated away from the DR. Therefore the effect of losses in the microstrip substrate, signal line, and enclosure act to perturb the electromagnetic field and alter the Q factor of the DR [37,38]. For oscillator design an equivalent circuit model for the line DR coupled arrangement is required. The DR may be fixed to the line using a low-loss adhesive [39,40]. If the adhesive has a slow setting time, then reworking of the DR position for tuning can be made.

7. DIELECTRIC RESONATOR TUNING

For optimum phase noise designs the oscillator center frequency should be equal to that of the dielectric resonator. For many circuits it is useful to have a DR tuning facility. One way of achieving this is to use mechanical tuning (Fig. 8).

Here a metal [41], dielectric [42], or DR [43] plunger is inserted in either the topwall or the sidewall of the structure. The presence of the tuning element causes a localized distortion of the electromagnetic fields. With a metal plunger, the additional losses in the plunger lower the Q_u of the resonator as the coupling between DR and plunger becomes tighter, that is, as L is reduced. For a metal plunger as L is reduced, the frequency of operation is increased, while the reverse is true for a dielectric plunger. Generally a DRO used with the metal plunger tuning arrangement also produces a reduced output power as L decreases. With this arrangement, about a 3% tuning range can be made.

With a second DR replacing the plunger topcap in Fig. 8, the resultant change in Q_u is smaller than for the metal tuner case. This arrangement yields about an 8% tuning range.

Electronic tuning of the DR is also possible using a varactor diode as the tuning element. This can be mounted internally to the DR [44] or more usually as the termination on a line coupled to the DR (Fig. 1). A large tuning range requires tight coupling between the DR and the varactor, which inevitably leads to a reduction in Q_u .

If Q_u is the unloaded Q of the varactor, then [45]

$$Q_{ur} = \frac{Q_u}{2} \left(\frac{f_0}{\Delta f} \right) \quad (42)$$

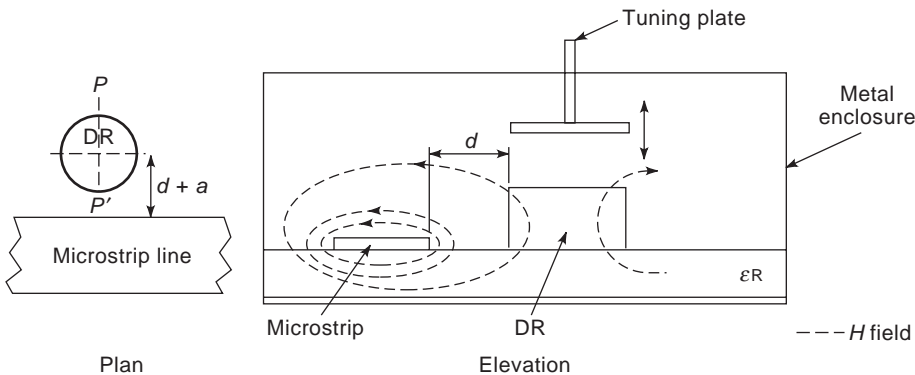


Figure 7. DR coupled to microstrip line, physical and electrical equivalent.

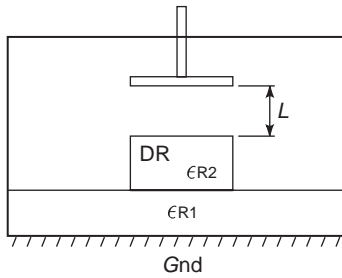


Figure 8. Mechanical DR tuning arrangement.

where Q_{ur} is the unloaded Q of the varactor tuned DR and Δf is the change in resonance frequency. According to Ref. 45, an approximately 0.5% tuning bandwidth can be obtained with this arrangement.

Other techniques such as optical tuning [46], magnetic tuning [47], and segmented disk tuning also exist [48].

8. OSCILLATOR BASIC THEORY

8.1. Negative Resistance

In order for microwave oscillation to begin, a means to overcome the resistive losses in the circuit has to be provided. These losses include undesired stray and parasitic resistances, and also the load into which the oscillator must operate (usually 50Ω). To do this, the concept of *negative resistance* is introduced. To illustrate the concept, consider the simple equivalent circuit of Fig. 9. If the amount of negative resistance exactly cancels the sum of the positive resistances, then the circuit will have a resonant or oscillation frequency where the inductive reactance is equal to the capacitive reactance; that is

$$2\pi fL = \frac{1}{2\pi fC} \tag{43}$$

where f = resonant frequency, L = inductance, and C = capacitance. This condition is known as the *steady-state oscillation condition*. In order for oscillation to build up, an excess of negative resistance is required. Then, any small perturbation in the circuit, such as electrical noise, will kickstart a resonance. As oscillation builds, the amount of negative resistance decreases until the steady-state condition is met. A negative resistor can be formed from an unstable active device with suitable feedback applied. Consider a transistor with feedback such that the magnitude of the input reflection coefficient (S_{11})

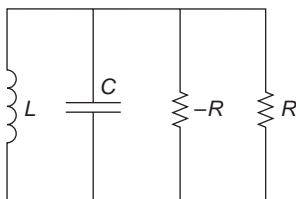


Figure 9. Simple equivalent circuit of a microwave oscillator.

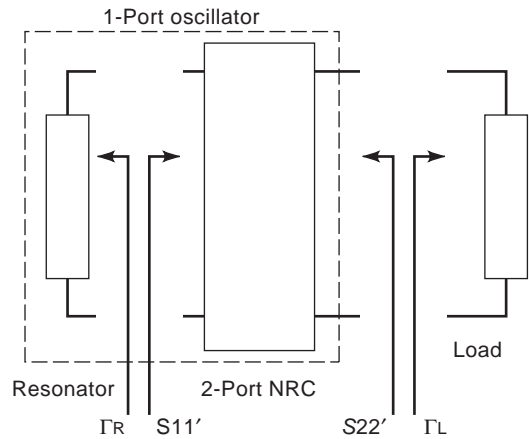


Figure 10. Negative-resistance oscillator schematic showing port definitions.

is greater than one. This means that when an AC signal is incident on the port, more energy is reflected than is actually incident. This can be regarded as a negative resistance.

8.2. Oscillator Equation

The one-port negative-resistance oscillator schematic is illustrated in Fig. 10. The oscillator can be considered as a two-port negative-resistance circuit and a one-port resonator. The resulting oscillator then operates into a one-port load. The large-signal steady-state oscillation condition is given by

$$\Gamma_r \cdot S'_{11} = 1 \tag{44}$$

where Γ_r is the reflection coefficient of the resonator and S'_{11} is the large-signal input reflection coefficient of the negative-resistance circuit, when terminated in the load. The reflection coefficients stated immediately above are complex numbers, and so the equation can be expanded into its magnitude and angle parts:

$$|\Gamma_r| \cdot |S'_{11}| = 1 \tag{45}$$

$$\text{Ang}(\Gamma_r) + \text{Ang}(S'_{11}) = 0 \tag{46}$$

If the equations are now expanded into impedance forms, then we obtain

$$R + R_n = 0 \tag{47}$$

$$X_L + X_C = 0 \tag{48}$$

where R is the sum of positive resistances, R_n is the negative resistance, X_L is the inductive reactance, and X_C is the capacitive reactance. Equation (48) simply expands to Eq. (43) and determines the resonant frequency.

We have already stated that before steady-state oscillation can be achieved, there must be an excess negative resistance to enable resonance to start. At the buildup of

oscillation, Eqs. (47) and (48) can be approximated to

$$r + r_n < 0 \tag{49}$$

$$x_L + x_C = 0 \tag{50}$$

where the resistances and reactances are now small-signal values. In terms of reflection coefficients, the small-signal approximation to the oscillation condition becomes

$$|\Gamma_r| \cdot |S'_{11}| > 1 \tag{51}$$

$$\text{Ang}(\Gamma_r) + \text{Ang}(S'_{11}) = 0 \tag{52}$$

where the reflection coefficients are now the more easily measurable small-signal values. It should be noted here that Γ_r depends on the value of characteristic impedance Z_0 used to calculate it. Hence it is possible with this approach to find a startup condition in terms of Γ in one port but not in another for a given Z_0 .

8.3. Oscillator Graphical Analysis

The solving of the small-signal *oscillation condition* is illustrated graphically in Fig. 11 with reference to Fig. 10. Here the Z (complex) represents the overall impedance of the closed-loop oscillator, including the load. The frequency at which the imaginary part goes through zero (i.e., resonance) is clear, and at this frequency there is an excess negative resistance.

8.4. N-Port Oscillation Condition

It can be shown that the condition for oscillation is also present at the output port of the previously discussed negative-resistance circuit. This means that we could also solve

$$\Gamma_L \cdot S'_{22} = 1 \tag{53}$$

where Γ_L is the reflection coefficient of the load and S'_{22} is the large-signal output reflection coefficient of the negative resistance circuit, when terminated in the resonator. This condition can be shown to hold at all ports of an N -port oscillator [49].

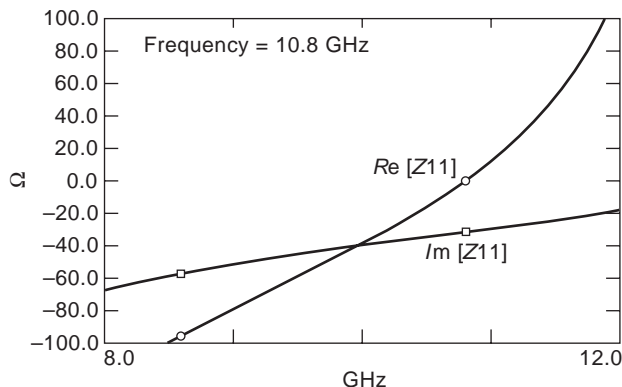


Figure 11. Graphical oscillator solution showing one-port oscillation condition.

8.5. Oscillator Figures of Merit

8.5.1. Frequency Pulling. As the reflection coefficient of the load Γ_L forms a vital part of Eq. (53) and influences the input reflection coefficient S'_{11} in Eq. (44), it is obvious that any change in its phase will affect the oscillation frequency. The change in oscillation frequency due to a change in the load reflection coefficient is known as *frequency pulling*. This is usually determined by first measuring the frequency of an oscillator into a load of known reflection coefficient (often -12 dB). The phase of the load is then varied from 0 to 360° by means of a phase shifter or sliding load. The maximum deviation from the nominal frequency is the pulling figure. Pulling can be greatly reduced by isolating the oscillator’s output from the load. This is usually achieved by use of a buffer amplifier with high reverse isolation.

8.5.2. Frequency Pushing. The basic function of the DRO is to convert DC energy to RF. The scattering parameters of the active device are dependent on the applied bias voltages and currents. Even regulated power supply voltages can experience fluctuations which lead to minute changes in output frequency. The change in oscillation frequency with respect to DC supply voltage is known as *frequency pushing*. The parameter is measured by first noting the nominal oscillator frequency. The applied DC supply voltage is then varied (by one volt, for example) and the frequency deviation measured. Frequency pushing is then expressed in units of frequency per volt. In practical circuits pushing is minimized by using well-regulated supply voltages.

8.6. Oscillator Stability

An oscillator is said to be stable if the output frequency (and power) do not vary with temperature and time. Dielectric resonators are good for producing stable oscillators because of their high Q factors. Dielectric resonators may be used in oscillators in two distinct ways:

1. As a high- Q passive element coupled to a free-running oscillator. Here the DR is not used as the oscillator’s main resonator, but is “locked” to this resonance. Such an oscillator is known as a *dielectrically stabilized oscillator* (DSO).
2. As a circuit element in the oscillator, whereby the DR actually determines the oscillation frequency.

It is known that free-running oscillators generally have a negative temperature coefficient. Thus the oscillator’s frequency falls as temperature is increased. The temperature coefficient of a DR can be made positive by careful choice of material composition. Thus the DR can be made to compensate for free-running oscillator drift. The temperature stability of a complete DRO is dependent on [50]

- The coupling coefficient between the DR and the rest of the circuit
- The Q of the oscillator

- The rate of change of the active device's reflection coefficient phase with temperature

Typical variations in oscillator frequency with temperature in DROs are of the order of 4 ppm/°C. This value can be reduced, to values as low as 1 ppm/°C, by several techniques, including

- *Phase Locking.* A high-frequency voltage-controllable DRO is phase-locked to a low-frequency crystal oscillator of superior phase noise and stability; this improves long-term frequency stability.
- *Digital Compensation.* Here the performance of an oscillator with temperature is measured and the information stored in programmable read-only memory. A temperature sensor circuit is then used, in conjunction with a lookup table, to apply a correction voltage to the oscillator in order to hold it at constant frequency.
- By stabilizing the DRO in a temperature-controlled localized oven [51].

The primary properties of a dielectric resonator oscillator, that is, frequency and output power, can be measured using the test setup illustrated in Fig. 12. The frequency of oscillation is measured on a high-frequency spectrum analyzer, or RF counter. The power can also be read from the analyzer display, but is often more accurately determined using a separate RF power meter.

Frequency pushing can now be determined by observing the shift in oscillation frequency as the supply voltage is varied. Pulling is measured by replacing the power meter with a tunable load of known return loss (usually 12 dB). The phase of this load is then varied through 360°, and the resulting maximum excursion from the nominal frequency are noted.

Phase noise can be measured on the analyzer display at suitable offset frequencies. A correction has to be made for the filter (resolution) bandwidth of the measuring instrument. More accurate phase noise measurement (especially close to the carrier) requires a dedicated phase noise testset.

The abovementioned oscillator parameters are usually determined over a range of temperatures. This enables the variation of the frequency and output power with temperature to be determined.

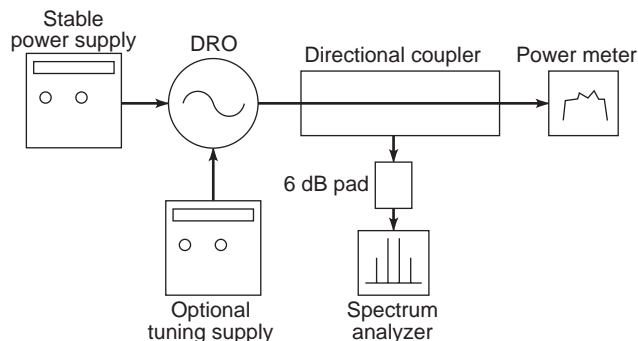


Figure 12. Typical DRO test setup for measuring power output and frequency spectrum.

9. OSCILLATOR PHASE NOISE

The phase noise of an oscillator is an important quantity. Ultimately phase noise limits adjacent-channel selectivity in a receiver. The output signal from a physical oscillator is not monochromatic. In a real oscillator, noise sidebands arise since the frequency of the signal can vary with time as a result of phase noise created by phase modulation of the signal [52]. The usual method for characterizing the noise is to determine the single-sideband (SSB) phase noise power spectral density at a given frequency offset from the carrier (dBc/Hz). A frequency offset figure of 10 kHz is often quoted.

The phase noise comes from the various noise sources available in the circuit as well as the active-device intrinsic noise sources. These noise sources induce phase noise by nonlinear device mechanisms causing upconversion of the baseband noise to the oscillator frequency. Noise sources that are due to white noise generally contribute $1/f^2$ to the spectrum of the phase noise, while $1/f$ noise adds $1/f^3$ to the phase noise spectrum. Individual noise sources are to a first approximation considered uncorrelated. In practice, up/downconversion can occur, leading to correlated amplitude-modulated (AM) and frequency-modulated (FM) noise effects. The $1/f$ noise acts to alter the frequency of the oscillation.

When designing a DRO with low phase noise, the unloaded Q factor of the resonator should be as high as possible. The $1/f$ noise of the active device should be as low as possible. JFETs, then bipolar transistors and HBTs, have the lowest $1/f$ noise with GaAs FETs having the worst $1/f$ performance. Also the center frequency of oscillation of the DR is usually equal to that of the oscillator. Here the DR acts to select the frequency of oscillation. Under these conditions the center frequency of the DR will have a maximum rate of change of phase with respect to frequency; that is, the resonator will have its highest Q . Noise power density is split between AM and PM noise by equal amounts. In addition, AM noise is usually much more dominant than PM noise at offset frequencies far removed from the carrier [53]. Close to the carrier PM noise is the dominant factor. Methods for simulating oscillator phase noise are given in Refs. 54 and 55.

Leeson's Eq. (52) and Eq. (54) describe the expected single-sideband (SSB) phase noise power density at a frequency f_m offset from the carrier for an oscillator using a single resonator; here

$$L_{\text{pm}} \approx 10 \log_{10} \left[\frac{NRkT}{A} \frac{1}{8Q_L^2} \left(\frac{f_0}{f_m} \right)^2 \right] \text{dBc/Hz} \quad (54)$$

where NR is the device noise ratio, A = oscillator output power, Q_L = loaded Q , f_0 = oscillator center frequency (Hz), and f_m = carrier offset (Hz).

Equation (54) shows that the oscillator SSB phase noise is affected by the loaded Q squared, namely, 6 dB improvement per Q_L doubling, hence the incentive for using a DR with as high a Q as possible. Leeson's equation shows that the SSB phase noise reduces at 6 dB/octave over the range it applies. This range is for f_m greater than frequency f_1 ,

the $1/f$ flicker noise corner frequency, and less than below the frequency f_2 , where $f_2 = f_0/2Q_L$. Above f_2 the oscillator upconverted white noise dominates. To correctly apply this equation, the $1/f$ noise for the device must be known a priori. In addition, the device noise ratio at its operating power level (assumed to be in the linear range of operation) and loaded Q for the circuit are also required. A detailed discussion of low-noise oscillator design and measurement methods can be found in Ref. 56.

10. DESIGN EXAMPLE—10.8-GHz DRO

Consider the schematic of Fig. 13. The circuit consists of a common-source MESFET-based negative-resistance circuit (NRC), with series capacitive feedback. The DR is coupled to the gate via a $50\text{-}\Omega$ -terminated microstrip transmission line. The substrate for the transmission line is chosen to be $254\text{-}\mu\text{m}$ -thick alumina ($\epsilon_r = 9.9$). The width of the line is $238\text{ }\mu\text{m}$, which corresponds to a characteristic impedance of $50\text{ }\Omega$.

The first step is to choose a suitable DR size. As a practical example, consider the Murata TE_{01 δ} DRD series [57]. The most suitable dimensions for a 10.8-GHz circuit are a diameter of 6.5 mm and a thickness of 2.9 mm. It can be shown that this puck will resonate at approximately 10.34 GHz when enclosed in a well-spaced metallic environment. In a practical circuit the resonator will operate at a higher frequency, due to the presence of the thin substrate. The shift in frequency can be approximated by the

analytical formula in Ref. 50. Final tuning to 10.89 Hz by use of a metal tuning screw can then be achieved.

Step 2 involves choice of a suitable transistor and bias condition. For this example a GMMT 0.5- μm -gate-length/300- μm -gate-width GaAs MESFET is used. When biased at $+5\text{ V } V_{ds}$ and $I_{ds} = 50\% I_{dss}$, the transistor exhibits some 12 dB of available gain at this frequency. This is more than adequate for this type of oscillator design.

Next the two-port NRC is designed. To do this, the series capacitive feedback is varied until the magnitude of the input reflection coefficient (S_{11}) is greater than one, indicating negative resistance. In practice a value greater than 1.2 should be used. This is generally enough to ensure sufficient excess negative resistance to kickstart an oscillation. For this transistor a value of 0.24 pF results in $|S_{11}|$ being of the order of 1.4 at 11 GHz, as illustrated in Fig. 14.

Next the complete oscillator is simulated to solve the small-signal approximation to the complex condition for oscillation, that is, $\Gamma \cdot S_{11} > 1$. A model for the coupled DR can be developed using the mutually coupled parallel LCR model and coupling factor k , as discussed previously. In practice the equivalent circuit is merely an RF open circuit at resonance. Therefore the circuit can be simplified to the circuit shown in Fig. 15. To complete the oscillator design, the transmission-line length l_1 , at which point the center of the DR is placed, is calculated. For this example a value of 4.427 mm is determined. The resulting oscillation frequency, in terms of real and imaginary parts of the overall impedance, is shown in Fig. 16. The angle goes through zero at 10.8 GHz, with the resulting magnitude

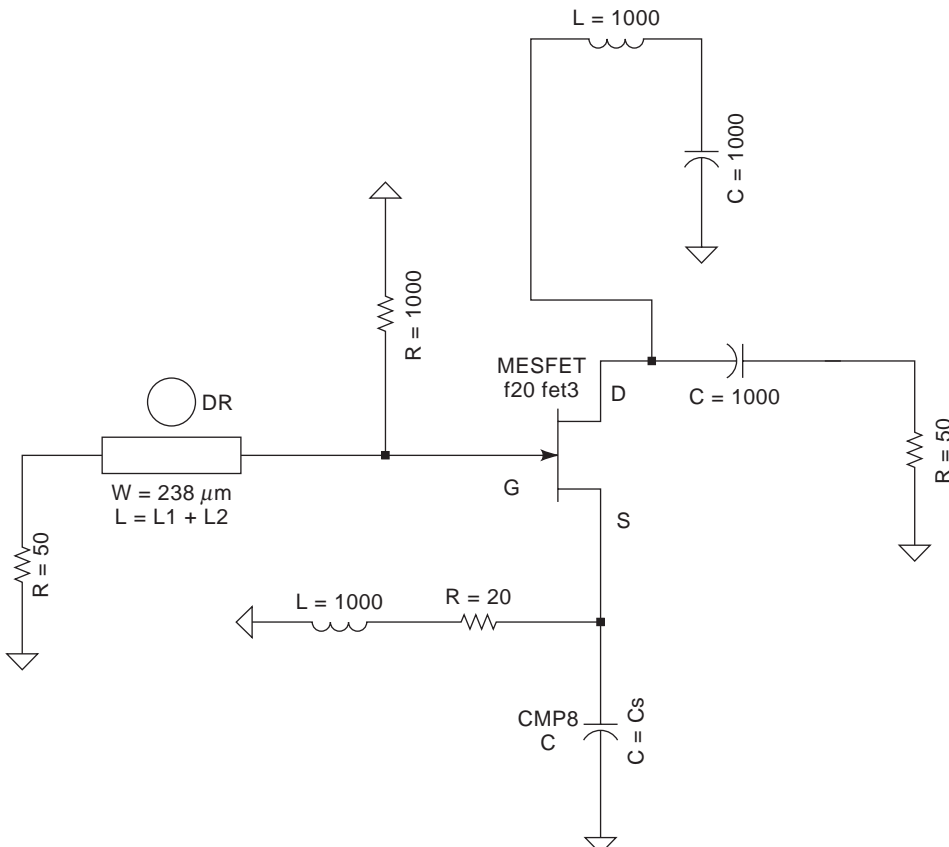


Figure 13. Circuit schematic for 10.8-GHz DRO example design ($\epsilon_r = 10.0$, $h = 254\text{ }\mu\text{m}$).

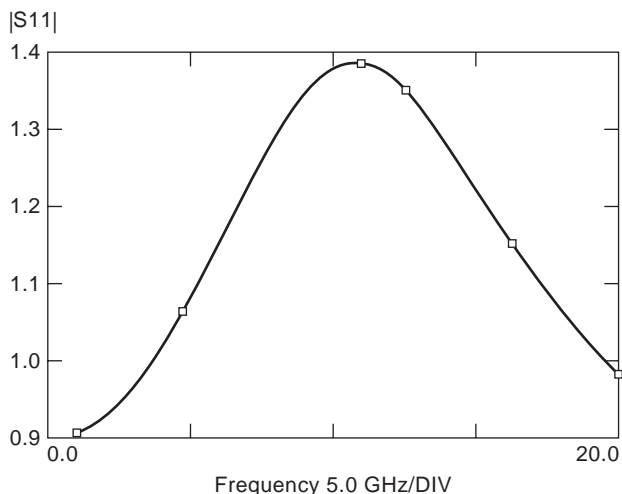


Figure 14. One-port input reflection plot.

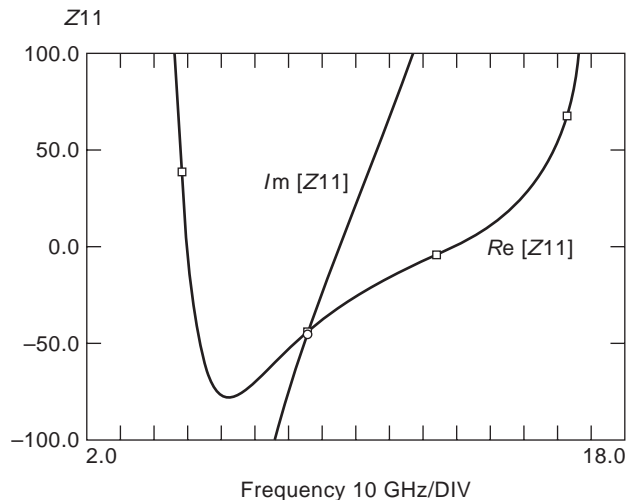


Figure 16. One-port oscillation condition.

simultaneously exceeding 1.2. A large-signal simulation can be performed using a harmonic balance technique to predict output power and other important oscillator parameters. For this example +11 dBm output power was predicted, with a DC-to-RF conversion efficiency of approximately 13%. In addition the phase noise was predicted as -80 dBc/Hz at 10 kHz offset. This is achieved by including important noise parameter values in the non-linear device model.

In practice the circuit is now fabricated by using an arbitrary length for l_2 , and suitably terminating the line in the characteristic impedance, 50 Ω. The circuit is biased as required and the DR placed on the alumina in approximately the correct position. The puck is then moved around until oscillation of suitable magnitude, Q factor, and phase noise is obtained. The resonator is then fixed into position, and mechanically tuned to the exact required frequency.

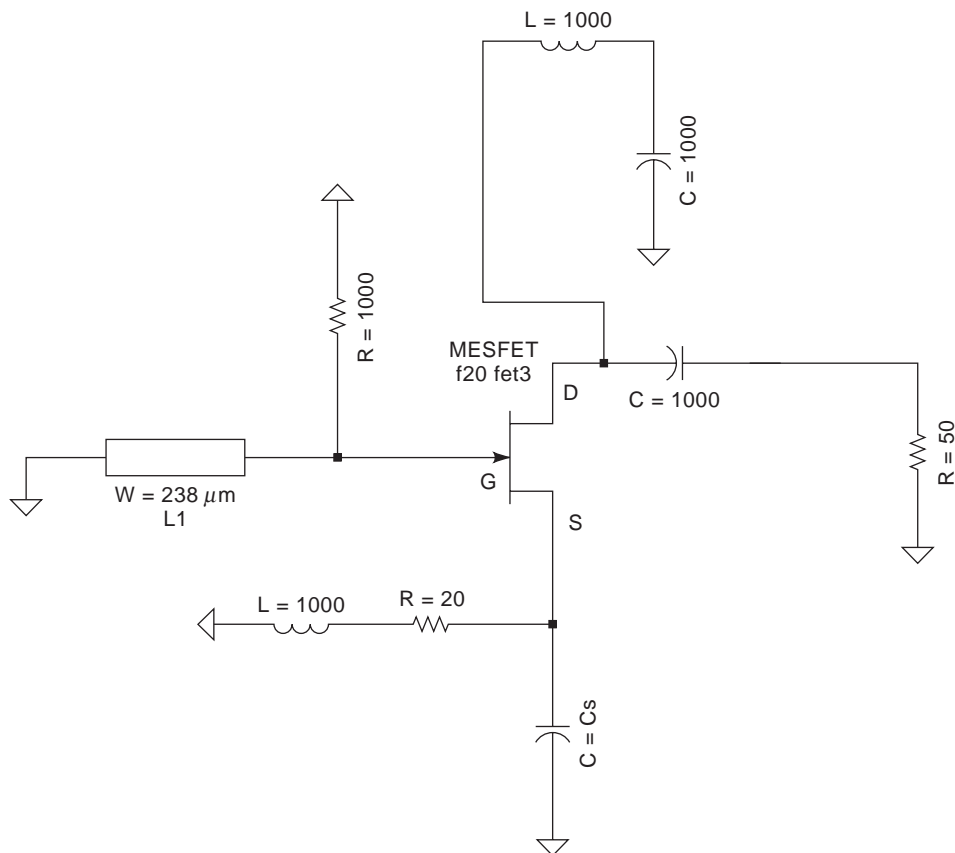


Figure 15. Simplified equivalent circuit for 10.8 GHz DRO example design.

Electronic tuning of the circuit to enable phase locking to a crystal reference is possible. To achieve this, a $\lambda/4$ length of transmission line incorporating a tuning varactor is also coupled to the resonator. Tuning the varactor capacitance changes the phase of the coupled line, resulting in pulling of the DR frequency.

11. DRO CAD TECHNIQUES

The practical realization of dielectric resonator oscillators DROs can be assisted by the use of linear and nonlinear CAD tools. Linear scattering parameters can be used to represent the active device and feedback network [3,58–61]. Important DRO performance features such as output power, efficiency, steady state stability and tuning range, have been simulated [62–64].

Series feedback DROs have been designed using S-parameter methods whereby a topology is selected to yield maximum negative resistance at one port while maintaining small-signal startup conditions [50,65]. When parallel feedback topology is used, a more complex design procedure is required [66]. Here, when the DR is coupled between two of the device terminals, the reflection coefficient at the third terminal Γ_3 is expressed in terms of the DR and active device scattering parameters. The position of the DR and hence the coupling coefficient are optimized to maximize Γ_3 and a matching circuit designed to maximize the startup condition [61].

Small-signal techniques do not necessarily lead to maximum power oscillators, nor do they ensure stability of operation. Nonlinear large signal techniques are needed to do this. Broadly two classes exist here: time domain [67] and harmonic balance [68]. The former method uses numerical integration of state space equations describing the active device and the embedding circuit. All circuit elements must be represented in the time variable as voltage-dependent current equations. There are no constraints on the harmonic content; hence highly nonlinear circuits can be examined. The time-domain approach is well suited to oscillator simulation because oscillation startup, transient, and steady response can all be obtained on a single analysis run. However, each timestep must be small enough to ensure numerical convergence of the integration routine. This is a severe limitation when high- Q resonators such as DRs are used [69].

With the harmonic balance approach, nonlinear circuit elements are analyzed in the time domain and transformed into the frequency domain, where they are represented by a finite number of harmonic currents. Linear elements are solved directly in the frequency domain. Where linear and nonlinear components are joined, current continuity forms the boundary condition for the harmonic balance algorithm. With this approach the high- Q circuits are solved by numerically efficient algorithms directly in the frequency domain. However, in order to simulate circuits with strong nonlinearities, many harmonics are needed for accurate representation of the nonlinear waveforms, thus increasing computational time. In addition, the harmonic balance approach yields only steady-state information about the oscillator's behavior.

In a DRO the DR dampens higher harmonics; thus the harmonic balance approach is attractive here [63]. In Ref. 63 the device topology was fixed a priori and the circuit element values were numerically optimized to satisfy a prescribed set of electrical specifications. An alternative approach is to synthesize from the maximum added power condition the general device terminations [70]. This approach has been adapted for DRO synthesis [71,72]. Most commercially available industrial circuit simulators for microwave use such as a Hewlett-Packard model [73] will handle time-domain and harmonic balance simulation with embedded large-signal active-device models.

BIBLIOGRAPHY

1. C. L. Ren and J. K. Ploude, Application of dielectric resonators in microwave components, *IEEE Trans. Microwave Theory Tech.* **MTT-29**:754–759 (1981).
2. S. J. Fiedziuszko, Microwave dielectric resonators, *Microwave J.* 189 (Sept. 1986).
3. A. Khanna, Parallel feedback FET DRO using 3-port S-parameters, *IEEE Int. Microwave Symp. Digest*, San Francisco, 1984, pp. 181–183.
4. H. Abe et al., A highly stabilized low-noise GaAs FET integrated oscillator with a dielectric resonator in the C-band, *IEEE Trans. Microwave Theory Tech.* **MTT-26**(3):156–162 (1978).
5. R. S. Pengelly, *Microwave FETs—Theory, Design and Applications*, 2nd ed., Wiley, New York, 1986.
6. O. Ishikora et al., A highly stabilized GaAs FET oscillator using a dielectric resonator feedback circuit in the 9–14 GHz range, *IEEE Trans. Microwave Theory Tech.* **MTT-28**(8):817–824 1980.
7. K. W. Lee et al., Push-push, frequency doubling, *MMIC Oscillators, IEEE GaAs IC Symp.*, 1987, pp. 227–230.
8. S. Chen et al., U-Band MMIC HBT DRO, *IEEE Microwave Guided Wave Lett.* **4**(2):50–52 (1994).
9. K. Borst, N. Loechel, and K. Wacker, Low noise synthesized microwave local oscillator for high capacity digital radio systems using a dielectric resonator and a SAW reference, *Proc. 19th European Microwave Conf.*, London, 1989, pp. 555–560.
10. K. Imai and H. Nakakita, A 22 GHz band low noise down converter for satellite broadcast receivers, *Proc. 19th European Microwave Conf.*, London, 1989, pp. 549–554.
11. C. D. Prasad, S. S. Serin, and D. Singh, 35 GHz dielectric resonator stabilized gunn oscillator, *Int. J. Infrared Millimeter Waves* **17**(2):393–402 (1996).
12. K. Ogawa et al., 25 GHz dielectric resonator oscillator using an Al GaAs/GaAs HBT, *Electron. Lett.*, **26**(18):1514–1516 (1990).
13. D. Cros and P. Guillon, Whispering gallery dielectric resonator modes for W-band devices, *IEEE Microwave Theory Tech.* **38**(11):1036 (1990).
14. A. Bermadez et al., A 94 GHz low noise GaAs FET oscillator using whispering gallery dielectric resonator modes and a new push-push configuration reducing 1/f converted noise, *IEEE MTT-S Int. Microwave Symp. Digest*, 1988, pp. 481–484.
15. S. Kharkovsky, A. Kirichenko, and A. Kogut, Solid-state oscillators with whispering-gallery mode dielectric resonators, *Microwave Opt. Technol. Lett.* **12**(4):210–213 (1996).

16. I. U. Khairuddin and I. C. Hunter, Whispering-gallery dielectric resonator mode GaAs FET oscillator, *IEE Proc. Microwave Anten. Propag.* **143**(5):441–443 (1996).
17. D. Kajfez, Simple models, in D. Kajfez and P. Guillon, eds., *Dielectric Resonators*, Artech House, Dedham, MA, 1986.
18. A. W. Gisson, Integrated equation methods, in D. Kajfez and P. Guillon, eds., *Dielectric Resonators*, Artech House, Dedham, MA, 1986.
19. M. R. Stieglitz, Dielectric resonators: Past, present and future, *Microwave J.* 121–126 (April 1989).
20. R. E. Collin, *Foundations for Microwave Engineering*, McGraw-Hill, New York, 1966, pp. 17–20.
21. B. W. Hakki and P. D. Coleman, A dielectric resonator method of measuring inductive capacities in the millimetre range, *IRE Trans. Microwave Theory Tech.* **MTT-8**:402–410 (1960).
22. W. E. Courtney, Analysis and evaluation of a method of measuring the complex permittivity and permeability of microwave insulators, *IEEE Trans. Microwave Theory Tech.* **MTT-18**:476–485 (1970).
23. C. Tsironis, Highly stable dielectric resonator FET oscillators, *IEEE Trans. Microwave Theory Tech.* **MTT-33**(4):1011–1025 (1985).
24. M. Massias, M. J. Howes, and V. Postoyalko, A novel analysis and design technique for temperature stable DROs, *Proc. 19th European Microwave Conf.*, London, 1989, pp. 418–423.
25. K. Kurokawa, Microwave solid state oscillator circuits, in M. J. Howes and O. V. Morgan, eds., *Microwave Devices – Device Circuit Interactions*, Wiley, New York, 1976.
26. R. R. Bonetti and A. E. Atia, Generalized dielectric resonator filters, *COMSAT Tech. Rev.* **11**(2):321–343 (1981).
27. P. Guillon and S. Mekerta, A bandstop dielectric resonator filter, *IEEE MTT-S Int. Microwave Symp. Digest*, 1981, pp. 170–173.
28. B. Ginzton, *Microwave Measurements*, McGraw Hill, New York, 1957, pp. 391–427.
29. D. Kajfez and E. J. Hwan, Q-Factor measurement with a network analyser, *IEEE Trans. Microwave Theory Tech.* **MTT-32**(7):666–670 (1984).
30. T. Hammersley, J. Richardson, and V. Postoyalko, Varactor tuning of dielectric resonator oscillators, *Microwave Eng. Europe* 25–28 (May/June 1990).
31. W. P. Wheless and D. Kajfez, Experimental characterization of multi-moded microwave resonators using an automated network analyser, *IEEE Trans. Microwave Theory Tech.* **MTT-35**(12):1263–1270 (1987).
32. A. Khanna and Y. Gorault, Determination of loaded, unloaded and external quality factors of a dielectric resonator coupled to a microstrip line, *IEEE Trans. Microwave Theory Tech.* **MTT-31**(3):261–264 (1983).
33. Alpha Industries, The tuning and exciting of DR modes, *Mickrowelster Mag.* **11**(Part 6):550–552 (1985).
34. B. Ginzton, *Microwave Measurements*, McGraw Hill, New York, 1957, pp. 391–427.
35. A. P. S. Khanna, Q measurement of microstrip coupled dielectric resonators, *Microwaves RF* **23**(1):81–86 (1984).
36. L. A. Trinogga, G. Kaizhou, and F. C. Hunter, *Practical Microstrip Circuit Design*, Ellis Horwood, Chichester, UK, 1991.
37. P. Guillon, B. Byser, and M. Chaubet, Coupling parameters between a dielectric resonator and a microstrip line, *IEEE Trans. Microwave Theory Tech.* **MTT-33**(3):222–226 (1985).
38. P. Guillon and Y. Garault, Coupling between a microstrip transmission line and a dielectric resonator, *IEEE MTT-S Int. Microwave Symp. Digest*, 1976, pp. 200–202.
39. Trans-Bond, Trans-Tech., Inc., *Dielectric Resonator Mounting Adhesive*, Alpha Industries, 19/21 Chapel St., Marlow, Bucks, SL7 3HN, UK.
40. *Araldite Epoxy Resin*, Ciba-Geigy, Plastics, Duxford, Cambridge, CB2 4QA, UK.
41. D. Kajfez, Simple models, in D. Kajfez and P. Guillon, eds., *Dielectric Resonators*, Artech House, Dedham, MA, 1986.
42. Alpha Industries, *A Designer's Guide to Microwave Dielectric Ceramics*, Trans-Tech, Inc., Marlow, Bucks, UK, 1990, Publication 5008040, Rev. 2.
43. K. Wada, E. Nagata, and I. Haga, Wideband tunable DR VCO, *Proc. 15th European Microwave Conf.* 1985, pp. 407–412.
44. L. A. Trinogga and A. J. Fox, Inclusive varactor tuning of dielectric resonator filters, *Proc. 26th European Microwave Conf.*, Prague, Sept. 1996, pp. 162–164.
45. O. Y. Chan and S. Kazeminejad, Voltage controlled oscillator using dielectric resonator, *Electron. Lett.* **24**(13):407–412 (1988).
46. P. R. Herczfeld and A. S. Daryoush, Optically tuned and FM modulated x-band dielectric resonator oscillator, *Proc. 14th European Microwave Conf.*, Liege, Belgium, 1984, pp. 268–273.
47. J. Krupka, Magnetic tuning of cylindrical Ho_{1δ}-mode dielectric resonators, *IEEE Trans. Microwave Theory Tech.* **MTT-37**:743–747 (1989).
48. A. Nestic, A new method for frequency modulation of dielectric resonator oscillators, *Proc. 15th European Microwave Conf.*, 1985, pp. 403–406.
49. K. Kurokawa, Microwave solid state oscillator circuits, in M. J. Howes and O. V. Morgan, eds., *Microwave Devices – Device Circuit Interactions*, Wiley, New York, 1976.
50. D. Kajfez and P. Guillon, eds., *Dielectric Resonators*, Artech House, Dedham, MA, 1986.
51. *Fundamentals of Quartz Oscillators*, Hewlett-Packard Application Note 200-2, Electronic Counter Series, Santa Rosa, CA, 1980.
52. D. B. Leeson, A simple model of feedback oscillation noise spectrum (Letters), *Proc. IEEE* 329–330 (Feb. 1996).
53. S. Hamilton, FM and AM noise in microwave oscillators, *Microwave J.* 105–109 (June 1978).
54. Hewlett-Packard, *Simulating Noise in Nonlinear Circuits Using the HP Microwave and RF Design Systems*, Santa Rosa, CA, 1993, Product Note 85150-4.
55. A. Howard, Simulate oscillator phase noise, *Microwaves RF* 64–70. (Nov. 1993).
56. G. D. Vendelin, *Design of Amplifiers and Oscillators by the S-parameter Method*, Wiley, New York, 1982, pp. 145–162.
57. Data Sheet, *Microwave Ceramic Resonator Catalogue*, Murata-Erie Publication 58-04C, Tokyo, Japan, 1994.
58. K. Borst, N. Loechel, and K. Wacker, Low noise synthesized microwave local oscillator for high capacity digital radio systems using a dielectric resonator and a SAW reference, *Proc. 19th European Microwave Conf.*, London, 1989, pp. 555–560.
59. P. G. Wilson and R. D. Carver, An easy-to-use FET DRO design procedure suited to most CAD programs, *IEEE MTT-S Int. Microwave Symp. Digest*, 1989, pp. 1033–1036.
60. C. Y. Ho and T. Kajiba, DRO state of the art, *Appl. Microwave, Microwave Symp. Digest*, Vol. 3, Long Beach, CA, spring 1990.

61. A. C. Murphy and P. J. Murphy, Computer program aids dielectric resonator feedback oscillator design, *Microwave J.* 131 (Sept. 1988).
62. A. M. Pavio and M. A. Smith, A 20-40 GHz push-push dielectric resonator oscillator, *IEEE Trans. Microwave Theory Tech.* **MTT-33**(12):1346–1349 (1985).
63. V. Rizzoli, A. Costanzo, and A. Neri, Analysis and optimization of DROs using a general-purpose CAD program, *Alta Freq.* **57**(7):389–398 (1988).
64. F. Filicori, V. A. Monaco, and G. Vannini, A design method for parallel feedback dielectric oscillators, *19th European Microwave Conf.*, London, 1989, pp. 412–417.
65. A. Sweet, *MIC and MMIC Amplifier and Oscillator Circuit Design*, Artech House, Dedham, MA, 1990.
66. A. Podocomeni and L. Conrado, Design of microwave oscillators and filters using transmission mode dielectric resonators coupled to microstrip lines, *IEEE Trans. Microwave Theory Tech.* **MTT-33**:1324–1332 (1985).
67. M. I. Sobhy and A. K. Jastrzebski, Computer-aided design of microwave integrated circuits, *Proc. 14th European Microwave Conf.*, Liege, Belgium, 1984, pp. 705–710.
68. V. Rizzoli, A. Lipperini, and E. Menazzi, A general purpose program for non-linear microwave circuit design, *IEEE Trans. Microwave Theory Tech.* **MTT-31**:762–770 (1983).
69. I. Kipinis and A. S. Khanna, Large signal computer-aided analysis and design of silicon bipolar MMIC oscillators and mixers, *IEEE Trans. Microwave Theory Tech.* **MTT-37**(3):558–564 (1989).
70. Y. Xuan and C. Snowden, A generalized approach to the design of microwave oscillators, *IEEE Trans. Microwave Theory Tech.* **MTT-35**(12):1340–1347 (1987).
71. S. W. J. Seawright et al., Optimum DRO synthesis, *Proc. 19th European Microwave Conf.*, London, 1989, pp. 406–411.
72. S. W. J. Seawright et al., Computer-aided design of a microwave MESFET DRO, *Proc. 19th European Conf. Circuit Theory and Design*, 1989, pp. 561–565.
73. Hewlett-Packard, *Microwave and RF Design System*, MDS, Vols. 1–8, Brighton, England, 1989.

DIELECTRIC RESONATORS

ANDREW R. WEILY
 KARU P. ESSELLE
 Macquarie University
 Sydney, New South Wales,
 Australia
 ANANDA SANAGAVARAPU
 MOHAN
 University of Technology
 Sydney, New South Wales,
 Australia

1. INTRODUCTION

The widespread use of the dielectric resonator (DR) in microwave engineering is due to four main attributes: price, performance, size, and versatility. The price of a DR is low, particularly when manufactured in large quantities. As a resonant element in microwave circuits they give very high performance in terms of Q factor and temperature

stability. The DR is smaller and lighter than conventional air-filled cavity resonators, enabling significant miniaturization; the reduction in size being proportional to $\sqrt{\epsilon_r}$, where ϵ_r is the relative permittivity of the DR material. DRs are also extremely versatile components, finding important applications over a wide range of frequency bands in microwave filters, oscillators, and antennas in both microwave integrated circuit (MIC) and monolithic microwave integrated circuit (MMIC) environments. They are also used in measurement techniques for determining the relative permittivity and loss tangent of dielectric materials and the surface resistance of superconductors.

The most common shape for the DR is a cylinder with its diameter greater than its length, where the $TE_{01\delta}$ (transverse electric) mode is dominant. This mode is similar to a magnetic dipole that is aligned with the axis of the cylinder, with the azimuthal E fields forming concentric circles about the axis. Other DR shapes that also find use are dielectric ring resonators, spheres, and parallelepipeds. The resonator is usually placed in a cylindrical or rectangular cavity, or on top of a substrate within a cavity as shown in Fig. 1. The use of the substrate allows external coupling of the DR mode to a nearby microstrip line, while the cavity enclosure prevents radiation losses and shields the resonator from external fields. The air-dielectric interfaces of the DR form the walls of a cavity that support resonant modes, similar to the configuration for a conventional cavity resonator. However, in a DR evanescent fields exist in the air region outside the dielectric material, due to imperfect confinement of the field by the DR walls. For large dielectric constants the DR walls can be approximated as perfect magnetic conductors (PMC), or open circuits, that require the magnetic field tangential to the wall to be zero. The accuracy of this approximation improves as the dielectric constant increases in value.

Richtmeyer pioneered the concept of the “dielectric resonator” in 1939 showing that suitably shaped dielectric objects such as spheres and circular rings could act as high-frequency resonators [1]. This seminal work received little further attention until 1962, when Okaya and Barash described theory and experimental results on rectangular DRs made from TiO_2 (rutile) and $SrTiO_3$ (strontium titanate) [2]. They introduced an approximate second-order analysis of the modes in rectangular DRs that gave reasonably accurate results when compared with measurements, and observed the poor temperature stability of the available high-dielectric-constant materials. In 1968 Cohn published a second-order analysis of the cylindrical DR operating in the $TE_{01\delta}$ mode and equations for DR interresonator coupling [3], which enabled high- Q bandpass filters to be designed using high-purity TiO_2 ($\epsilon_r \approx 100$) [4]. Unfortunately the high sensitivity of TiO_2 to changes in temperature made these DR filters impractical, but led Cohn to throw down a challenge to material scientists to develop high-dielectric-constant materials with improved temperature sensitivity.

This challenge was met when Raytheon developed the first barium tetratitanate ceramics that were both low loss and temperature stable [5], which were further improved on by researchers at Bell Laboratories [6]. At around the same time it was shown that a dielectric resonator placed

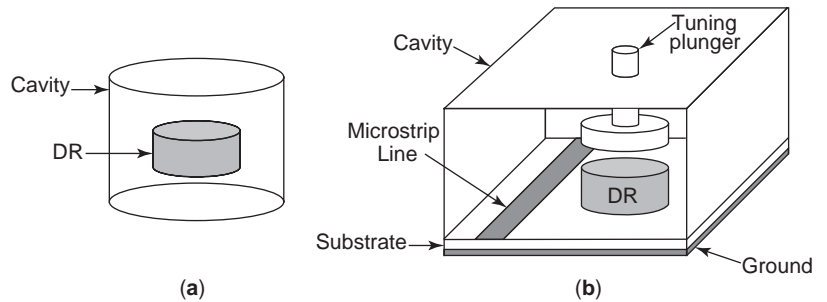


Figure 1. (a) Configuration of a cylindrical dielectric resonator loaded in a cavity; (b) dielectric resonator on a substrate coupled to a microstrip line.

between two parallel conducting plates could be used to accurately measure complex permittivity and permeability [7]. The next advance was the development of ceramic materials with adjustable temperature coefficients [8], enabling the value of temperature coefficient to be chosen to minimize or cancel out the material thermal expansion, leading to DR components with high temperature stability. These breakthroughs in material science technology paved the way for a large number of new temperature-stable filter and oscillator circuits based on DRs [9].

The first dual-mode axial-mounted DR-loaded cavity filter, introduced in 1982 [10], used hybrid-mode DRs and was able to match the performance of conventional dual-mode waveguide filters. Dual-mode filters have the advantage of reduced size and weight over monomode devices. Because of these advantages, the filter became popular for space applications. Dual-mode filters in planar cavities [11] and triple-mode filters were introduced soon after [12]. Advances in the mode-matching technique also led to the precise design of $TE_{01\delta}$ [13], $TM_{01\delta}$ [14], and $EH_{11\delta}$ mode filters [15,16].

In recent years, more emphasis has been placed on techniques for improving the spurious performance of DRs and DR filters, to overcome limitations imposed by the crowded mode spectrum of DRs. Several methods have arisen to achieve this goal. The simplest method involves optimization of the DR dimensions [17]. Mode suppression devices also can provide a small improvement. In $TE_{01\delta}$ -mode DR filters the use of resonant irises [18] or quarter-cut resonators [19] has shown a good suppression of higher-order modes. Quarter-cut resonators can also give extremely good heat dissipation and are suitable for use in high-power filters.

More effective methods involve using “composite” resonators [20,21], exciting combinations of different modes of the same type of resonator [22,23], or mixing two completely different types of resonators, for example, combine and $TE_{01\delta}$ DRs [24–26], or conductor- and dielectric-loaded resonators [27]. Since the higher-order modes of the different resonators occur at different frequencies, the spurious performance is enhanced considerably. Improved performance can also be achieved with filters containing rectangular DRs [28], dielectric combines [29], conductor-loaded DRs [30], and sandwiched conductor DRs [31]. The development of the hybrid dielectric/high-temperature superconductor (HTS) resonator is a further innovation that has the benefit of extremely low losses and reduced size [32]. Another advance was the introduction of a resonator

that uses slots in the DR for tuning and coupling dual-mode DR filters, thus replacing the tuning and coupling screws traditionally used [33]. Filters constructed using slotted DRs have the advantage that they require very little tuning. An excellent reference on the topic of DRs, DR filters, and DR oscillators is the book edited by Kajfez and Guillon [34].

2. ANALYSIS OF DIELECTRIC RESONATORS

As mentioned previously, early analysis methods for DRs modeled the resonator walls as perfect magnetic conductor (PMC) surfaces [2]. Cohn [3] improved on this approach by setting only the curved DR surfaces to be PMC walls, with the flat surfaces modeled as air–dielectric interfaces, allowing fields to leak out into an infinite circular waveguide with magnetic walls. Kobayashi derived analytical solutions for dielectric rod resonators short-circuited at both ends [35,36]. Regions not accounted for in the PMC wall model were gradually included through the use of perturbation and variational techniques and can be described as approximate techniques [37–51]. The resonant frequencies calculated using perturbational techniques or variational methods are more accurate than the simple PMC wall models, but are usually limited to the axially symmetric modes. The approximate methods have limitations since in some of the regions they may not satisfy Maxwell’s equations or exact boundary conditions. To increase the accuracy of prediction and for applicability to more general structures, rigorous analysis and numerical methods are required.

The finite-difference frequency-domain (FDFD) method is one numerical technique that has been successfully applied to rotationally symmetric DRs [52–55]. This technique discretizes the fields inside the DR and then, by imposing boundary conditions, formulates a matrix eigenvalue problem that is solved to obtain the resonant frequency, field distribution, and unloaded Q for any given mode. The powerful finite-element method (FEM) has also been applied to DRs [56–59]. In this method the solution region is discretized into subregions or elements. Governing equations are then derived, assembled over the elements of the solution region and the resulting system of equations solved. FEM is a versatile method as it can handle complex geometries and inhomogeneous media much better than can the finite-difference method owing to the use of highly flexible adaptive meshing schemes.

Early FEM formulation solutions were plagued by the appearance of nonphysical “spurious” modes, but by using “mixed” elements these modes may be eliminated [59]. Integral equation (IE) formulations [60,61] and the method of moments (MoM) have also been applied to DRs, to accurately compute resonant frequencies, unloaded Q , and field distributions. IE formulations and MoM use Green’s functions and hence are ideally suited to modeling resonators in open regions; their use can become quite complicated for cavity-type applications.

Mode matching combines analytical solutions and computational models for closed-region problems, and has been extensively applied to analyze DRs in cylindrical and rectangular cavities [62–74]. This technique divides the DR into subregions and may be classified as either radial or longitudinal mode-matching, depending on the way the subregions of the DR are divided and matched. The fields in each subregion are expressed as a linear combination of the appropriate eigenmode fields of an infinite waveguide with unknown coefficients. Fields of the adjacent regions are then “matched” to satisfy boundary conditions, from which an infinite system of linear equations is obtained in terms of the unknown coefficients. The zeros of the determinant of the system yield the resonant frequencies of the DR. The number of modes used in the generation of the system must be increased until relative convergence is achieved. Solution of the resonant frequencies also gives the modal field distributions, and hence the unloaded Q may be calculated for any given mode. Because of the appearance of complex modes in the longitudinal mode-matching technique [70] as well as computational difficulties, the radial mode-matching technique has emerged as the more popular method. Radial mode matching has been successfully applied to analyze DRs in rectangular cavities by using a Bessel–Fourier series to match the fields between two different coordinate systems at a fictitious boundary [72]. Resonant frequencies of uniaxial anisotropic DRs [73] and generalized multilayer anisotropic DRs [74] have also been analyzed using radial mode matching. For the multilayer anisotropic DRs, whispering gallery modes and unloaded Q were also calculated. Although mode matching is very accurate and computationally efficient, it is limited in the number of inhomogeneous regions and resonator shapes it can model. The problem size may also be limited when using FEM and MoM by the excessive time it takes to fill and solve a matrix, as the number of unknowns increases.

The finite-difference time-domain (FDTD) method [75] has been widely used to solve a broad range of electromagnetic problems. In this method Maxwell’s time-dependent curl equations are solved directly. The time-domain fields are calculated using explicit update equations. This approach has several advantages over the frequency-domain methods mentioned previously. Broadband results may be obtained from a single simulation, arbitrary structures may be analyzed, and the problem size is not limited by the size of the matrix to be inverted, a limitation encountered in frequency-domain methods. Frequency-domain parameters may be obtained by Fourier-transforming time-domain values obtained from the FDTD algorithm. Nonlinear materials and devices may

also be modeled. FDTD has been applied to dielectric resonators using the 2D rotationally symmetric (RS) FDTD algorithm coupled with the discrete Fourier transform (DFT) [76,77]. To improve computational efficiency as well as computing Q values, digital filtering coupled with Prony’s method [78] or the matrix–pencil technique [79] has been used instead of the DFT. Computational efficiency has also been improved by using digital filtering and the MUSIC (multiple signal classification) algorithm [80], and the Pade interpolation method [81]. These techniques reduce the number of timesteps required to obtain accurate resonant frequencies from time-domain samples. A nonorthogonal FDTD method has also been used to model DRs [82]. An effective dielectric constant was used with a 3D rectangular FDTD algorithm [83] to increase the accuracy in modeling the curved surfaces of a DR for hybrid modes in rectangular enclosures. A locally conformal FDTD method has also been used to model both open and closed DRs [84]. Resonant frequencies for selected higher-order modes have been calculated using FDTD [85,86], as have unloaded Q using perturbation techniques [87,88].

3. MODES AND MODE CHARTS

The modes of a cylindrical DR of the type shown in Fig. 1a may be classified as transverse electric (TE), transverse magnetic (TM), or hybrid electromagnetic (HEM). Three subscripts are used to differentiate between the different modes of a given classification. The first subscript is an integer m denoting the azimuthal field variation of the mode, while the second integer n refers to the number of radial variations. Usually, the third subscript p of a resonator mode refers to the integer number of half-wavelength variations in the axial or z direction. However, the imperfect walls of the DR leads to a field variation smaller than half a wavelength and so is denoted by [34]

$$p = l + \delta \quad \text{for } l = 0, 1, 2, 3, \dots \quad (1)$$

A further property of cylindrical DRs is the circular symmetry of the TE and TM modes, that is, $m = 0$ for all TE and TM modes. The hybrid modes are further classified into EH and HE modes according to the function P , defined as the ratio of the H_z to E_z field components of the hybrid mode [89]. For $|P| < 1$, the mode is classified as HE and is TM-like in its characteristics. When $|P| > 1$, the mode is classified as EH and is TE-like. The modes that exist in the cylindrical DR and their appropriate subscripts are summarized in Table 1.

A number of authors have used different notations in the literature to designate hybrid modes. Notations such as HE_{mnp} [60] or simply HE_{mn} [64] have been used but do not differentiate between the TE-like and TM-like nature of the hybrid modes. This distinction is important when determining the appropriate method for (1) external coupling to the mode, (2) interresonator coupling, and (3) spurious mode suppression. The HE/EH notation also includes more information about the field distribution of the mode.

Table 1. Mode Classifications for Cylindrical DRs

Mode	Mode Classification	m	n	p
TE_{0np}	Transverse electric (TE)	$m = 0$	$n = 1, 2, 3, \dots$	$p = \delta, 1 + \delta, 2 + \delta, 3 + \delta, \dots$
TM_{0np}	Transverse magnetic (TM)	$m = 0$	$n = 1, 2, 3, \dots$	$p = \delta, 1 + \delta, 2 + \delta, 3 + \delta, \dots$
EH_{mnp}	Hybrid (TE-like)	$m = 1, 2, 3, \dots$	$n = 1, 2, 3, \dots$	$p = \delta, 1 + \delta, 2 + \delta, 3 + \delta, \dots$
HE_{mnp}	Hybrid (TM-like)	$m = 1, 2, 3, \dots$	$n = 1, 2, 3, \dots$	$p = \delta, 1 + \delta, 2 + \delta, 3 + \delta, \dots$

To understand the nature of the modes more clearly, the field distributions of several lower-order modes have been calculated for the generic structure of Fig. 2 using the FDTD method. This figure shows the parameters used to characterize the DR. These parameters were set to $D_x = 0$, $d/D = 2.0$, $L/D = 0.4$, $M = L$, $\epsilon_r = 38.0$, and $\epsilon_3 = 1$ for the field calculations. The results of these calculations are plotted for $TE_{01\delta}$, $TM_{01\delta}$, $EH_{11\delta}$, and $HE_{11\delta}$ modes in Fig. 3a and the $EH_{21\delta}$, $HE_{21\delta}$, $EH_{31\delta}$, and $HE_{31\delta}$ modes in Fig. 3b. Each plot represents the transverse fields of the resonator taken as a slice through the center of the DR. It should be noted that the field patterns within the dielectric material for the HE_{mnp} and EH_{mnp} modes have a strong resemblance to the respective TM_{mnp} and TE_{mnp} modes in a PMC wall cylindrical resonator. This is further confirmation of the TM-like nature of the HE modes and TE-like characteristics of the EH modes.

Each mode of the cylindrical DR can be characterized by either an electric (P) or magnetic dipole (M) moment. These dipole moments are shown for some of the lower-order modes in Fig. 4. For a given mode, a comparison between the dipole moment and the field plot of Fig. 3 confirms that the E field (or H field) does indeed align with the electric (or magnetic) dipole moment. This dipole moment characterization is useful for determining the best way to externally couple energy to a particular mode. It is usually best to couple to electric dipole modes via the E field using an electric field probe. For magnetic dipole modes, it is best to couple through the H field using a loop-type probe that intercepts the magnetic field lines. These recommendations serve as a rough guide for coupling to the modes of the DR, but are not the only methods possible.

Mode charts for the resonator configuration of Fig. 2 have been calculated using the commercial software CST Microwave Studio [90], and are presented in Figs. 5–8. Mode charts are important for determining the spurious performance of a DR, enabling the frequency spacing between adjacent modes to be analyzed. This knowledge allows the dimensions of the DR and cavity to be designed to give optimal spurious separation. The charts also show the effect that the proximity of the cavity to the DR has on the resonant frequency of each mode. This information is useful for determining the appropriate location of tuning elements in the cavity. Figure 5 shows the effect of the cavity height on several lower-order modes. Over the range plotted almost all the mode resonant frequencies decrease as the cavity height increases; only the TM_{0np} modes increase in frequency. For $M/D > 0.7$, the cavity height has little or no effect on the modes, and the resonant frequencies approach a constant value.

A plot of normalized frequency versus DR aspect ratio (D/L) is given in Fig. 6. This shows that the $TE_{01\delta}$ mode is dominant (lowest in frequency) for $D/L > 1$, while the $HE_{11\delta}$ mode is dominant for $D/L < 1$. In practice D/L is typically set to approximately 2.5, so that the $TE_{01\delta}$ mode is dominant and there is good separation between the $TE_{01\delta}$ and $HE_{11\delta}$ modes. Figure 7 is a mode chart for the ratio between the cavity diameter and DR diameter (d/D). Similar to the configuration shown in Fig. 5, once the cavity diameter is greater than a certain value, this ratio no longer influences the resonant frequency of the modes, and they converge to a constant value. Kobayashi showed that by using a dielectric ring resonator, a DR with a concentric hole in its center, the mode separation is improved [17]. This property is illustrated in the mode chart of Fig. 8. It shows that increasing the diameter of the hole (D_x) has little effect on the $TE_{01\delta}$ mode, while the higher-order modes tend to increase in frequency.

4. SIMPLIFIED ANALYSIS OF THE $TE_{01\delta}$ MODE

This section examines a simplified method for calculating the resonant frequency of a $TE_{01\delta}$ mode in a DR. It is more accurate than the magnetic wall models and provides intuition into the nature of the fields in and around the DR. Although the accuracy is less than that of variational [46] and mode-matching solutions [62], the formulation has the advantage of low complexity. This method was first presented by Itoh and Rudokas in 1977 [41] and was expanded on by Kajfez [34].

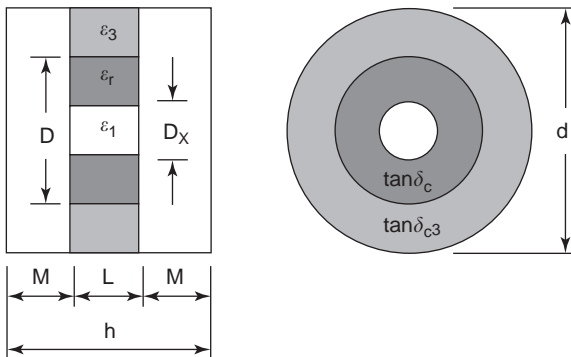


Figure 2. Configuration of a dielectric ring resonator (DRR) in a cylindrical cavity. The DRR is supported in the cavity by a low dielectric constant material (ϵ_3). (From Kobayashi and Miura [17], © 1984 IEEE.)

The configuration under analysis is shown in Fig. 9 and consists of a cylindrical DR with radius a and height L , separated by M_1 and M_2 from the lower and upper ground planes, respectively. This structure is analyzed using a cylindrical coordinate system (r, ϕ, z) and is divided into six regions as shown in the figure. At resonance most of the energy of the DR is stored in region 1, while the fields decay exponentially in regions 2–4. Regions 5 and 6 are ignored since very little energy is stored there. This approximation introduces a small error, but greatly simplifies the solution of the equations that define the structure. Since the $TE_{01\delta}$ mode is circularly symmetric, only the E_ϕ , H_r , and H_z fields exist. To satisfy the boundary conditions and ensure the continuity of the tangential fields, E_ϕ in each region is

$$E_{\phi 1} = A_1 J_1(k_{r1}r) \cos(\beta z - \theta) \quad (2)$$

$$E_{\phi 2} = A_2 J_1(k_{r1}r) \sinh(\alpha_2(z + M_1)) \quad (3)$$

$$E_{\phi 3} = A_3 J_1(k_{r1}r) \sinh(\alpha_3(z - L - M_2)) \quad (4)$$

$$E_{\phi 4} = A_4 K_1(k_{r4}r) \cos(\beta z - \theta) \quad (5)$$

where

$$A_2 = A_1 \frac{\cos(\theta)}{\sinh(\alpha_2 M_1)}, \quad A_3 = A_1 \frac{\cos(\beta L - \theta)}{\sinh(\alpha_3 M_2)},$$

$$A_4 = A_1 \frac{J_1(k_{r1}a)}{K_1(k_{r4}a)}$$

and

$$\beta^2 = k_0^2 \epsilon_{r1} - k_{r1}^2 = k_0^2 \epsilon_{r4} + k_{r4}^2, \quad \alpha_2^2 = k_{r1}^2 - k_0^2 \epsilon_{r2}, \quad (6)$$

$$\alpha_3^2 = k_{r1}^2 - k_0^2 \epsilon_{r3}$$

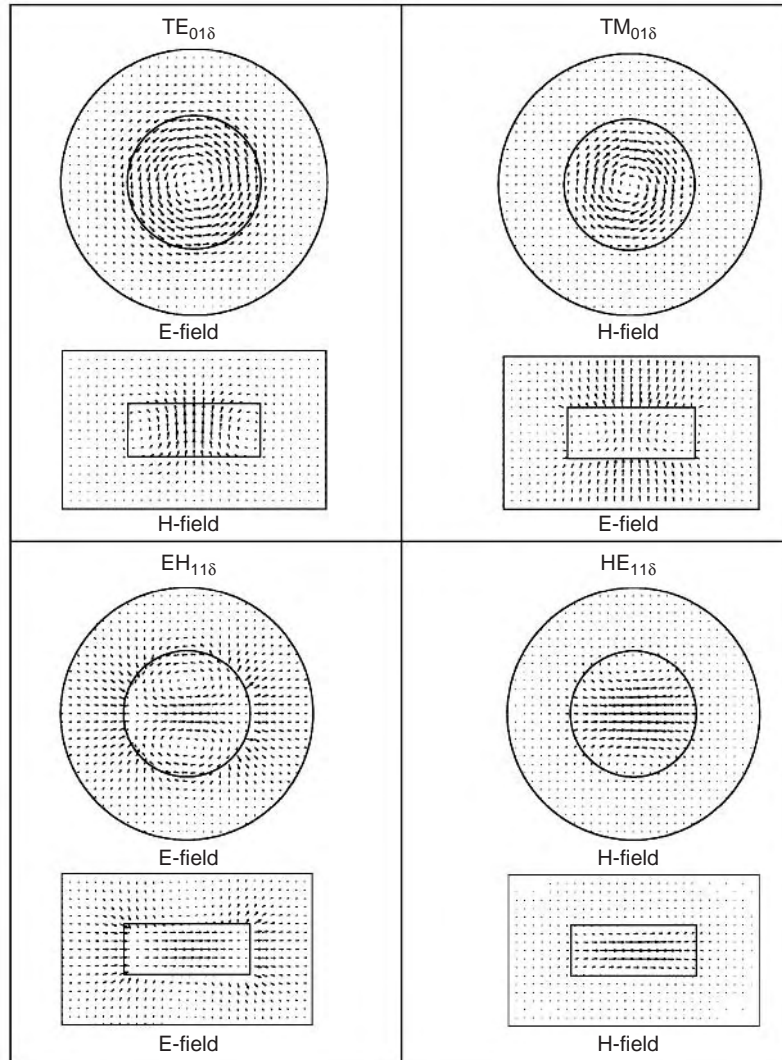
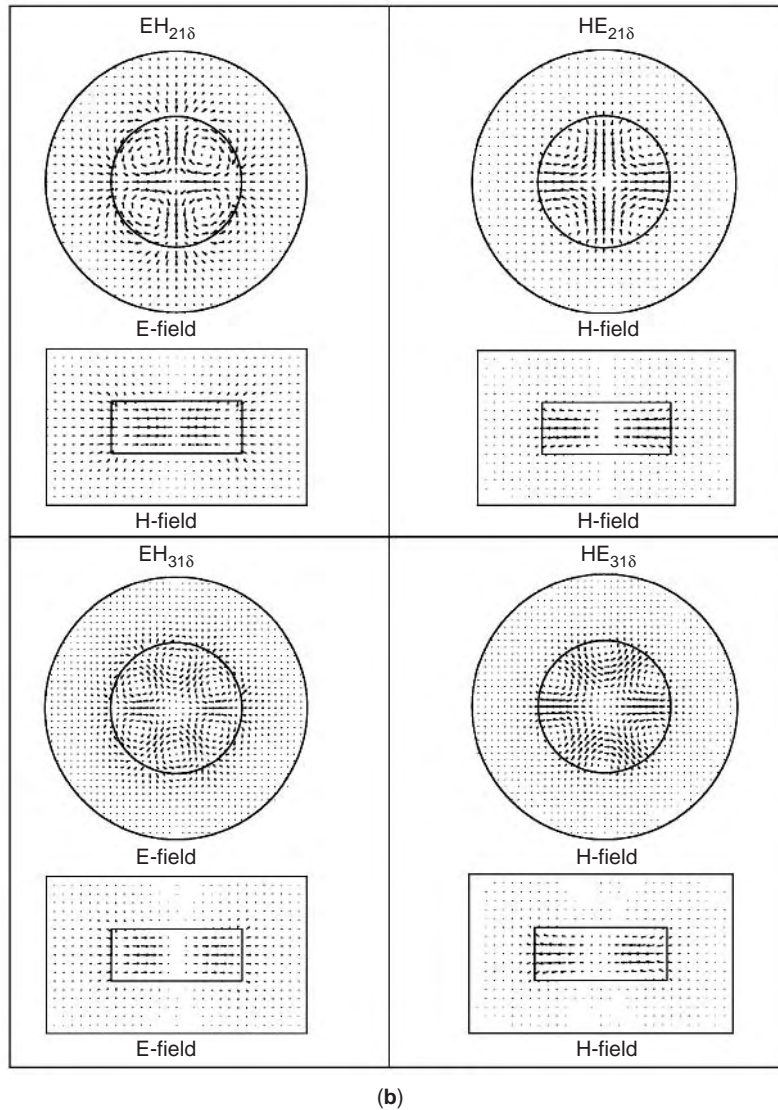


Figure 3. Field distributions for the (a) $TE_{01\delta}$, $TM_{01\delta}$, $EH_{11\delta}$, and $HE_{11\delta}$ modes and (b) $EH_{21\delta}$, $HE_{21\delta}$, $EH_{31\delta}$, and $HE_{31\delta}$ modes.



(b) Figure 3. (Continued).

In Eqs. (2)–(5) and those that follow $J_n(k_r r)$ is the Bessel function of the first kind, order n , while $K_n(k_r r)$ is the modified Bessel function of the second kind, order n .

From Maxwell's equations H_r is derived from E_ϕ as follows

$$H_{r1} = \frac{j\beta}{\omega\mu_0} A_1 J_1(k_{r1}r) \sin(\beta z - \theta) \quad (7)$$

$$H_{r2} = -\frac{j\alpha_2}{\omega\mu_0} A_2 J_1(k_{r1}r) \cosh(\alpha_2(z + M_1)) \quad (8)$$

$$H_{r3} = -\frac{j\alpha_3}{\omega\mu_0} A_3 J_1(k_{r1}r) \cosh(\alpha_3(z - L - M_2)) \quad (9)$$

$$H_{r4} = \frac{j\beta}{\omega\mu_0} A_4 K_1(k_{r4}r) \sin(\beta z - \theta) \quad (10)$$

while H_z is obtained in a similar manner:

$$H_{z1} = \frac{jk_{r1}}{\omega\mu_0} A_1 J_0(k_{r1}r) \cos(\beta z - \theta) \quad (11)$$

$$H_{z2} = \frac{jk_{r1}}{\omega\mu_0} A_2 J_0(k_{r1}r) \sinh(\alpha_2(z + M_1)) \quad (12)$$

$$H_{z3} = \frac{jk_{r1}}{\omega\mu_0} A_3 J_0(k_{r1}r) \sinh(\alpha_3(z - L - M_2)) \quad (13)$$

$$H_{z4} = -\frac{jk_{r4}}{\omega\mu_0} A_4 K_0(k_{r4}r) \cos(\beta z - \theta) \quad (14)$$

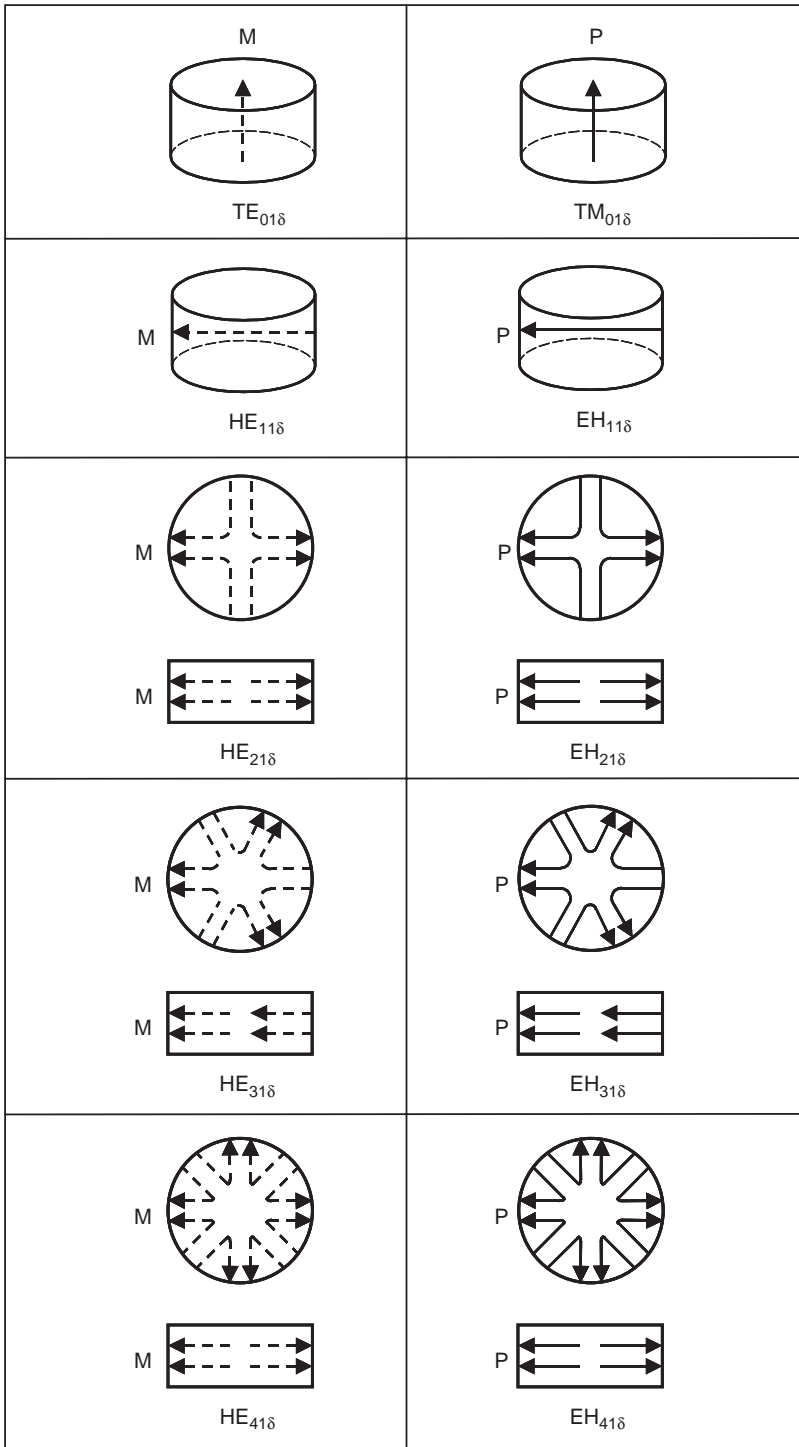


Figure 4. Magnetic (M) and electric (P) dipole moments for several modes of the cylindrical DR. (From Kobayashi and Miura [17], © 1984 IEEE.)

Applying continuity conditions to H_{z1} and H_{z4} at $r = a$ gives the first eigenvalue equation

$$\frac{J_1(k_{r1}a)}{k_{r1}J_0(k_{r1}a)} = -\frac{K_1(k_{r4}a)}{k_{r4}K_0(k_{r4}a)} \quad (15)$$

where

$$k_{r4}^2 = k_0^2(\epsilon_{r1} - \epsilon_{r4}) - k_{r1}^2 \quad (16)$$

The continuity conditions for H_{r1} and H_{r2} at $z = 0$ give

$$\tan(\theta) = \frac{\alpha_2}{\beta} \coth(\alpha_2 M_1) \quad (17)$$

while the continuity conditions for H_{r1} and H_{r3} at $z = L$ give

$$\tan(\beta L - \theta) = \frac{\alpha_3}{\beta} \coth(\alpha_3 M_2) \quad (18)$$

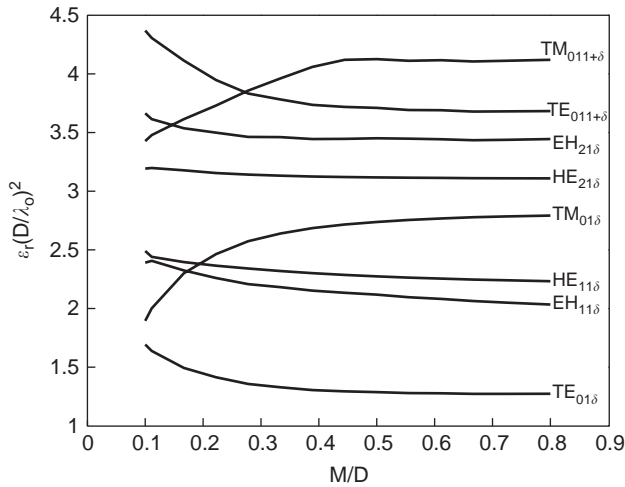


Figure 5. Mode chart of normalized frequency versus M/D (with $D/L=2.5$, $d/D=2$, $D_x=0$).

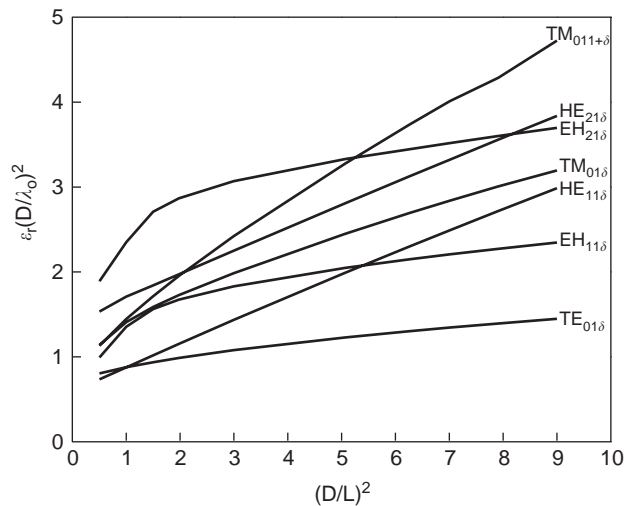


Figure 6. Mode chart of normalized frequency versus $(D/L)^2$ (with $d/D=2$, $M/D=0.4$, $D_x=0$).

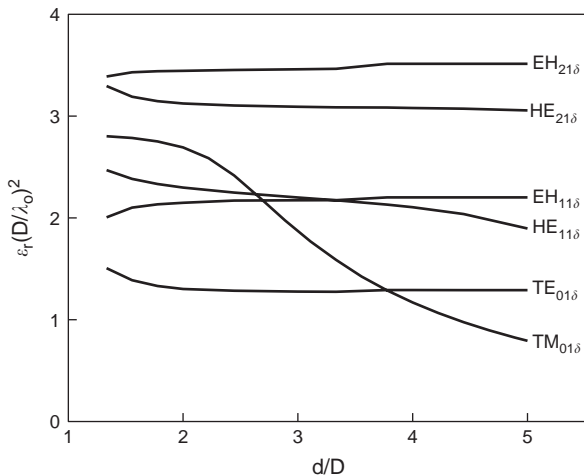


Figure 7. Mode chart of normalized frequency versus d/D (with $D/L=2.5$, $M/D=0.4$, $D_x=0$).

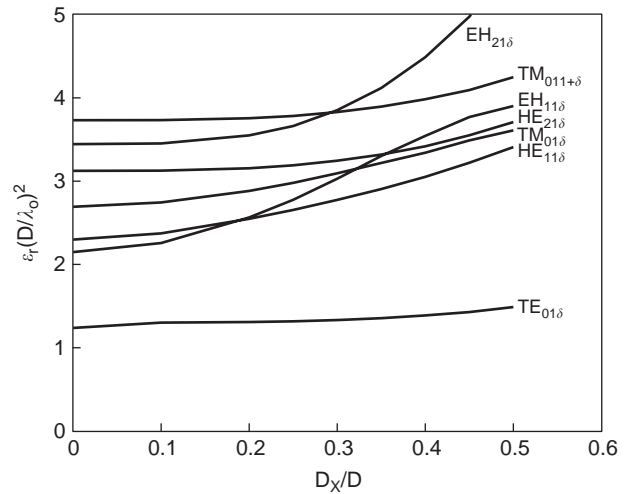


Figure 8. Mode chart of normalized frequency versus D_x/D (with $D/L=2.5$, $d/D=2$, $M/D=0.4$).

Combining Eqs. (17) and (18) by eliminating θ yields the second eigenvalue equation

$$\beta L = \tan^{-1} \left(\frac{\alpha_2}{\beta} \coth(\alpha_2 M_1) \right) + \tan^{-1} \left(\frac{\alpha_3}{\beta} \coth(\alpha_3 M_2) \right) + p\pi, \quad (19)$$

$p = 0, 1, 2, 3, \dots$

For the $TE_{01\delta}$ mode $p=0$. Solving the coupled Eqs. (6), (15), and (19) gives k_0 , from which the resonant frequency is calculated

$$f_0 = \frac{k_0 c}{2\pi} \quad (20)$$

where c is the speed of light in a vacuum, or 2.99792458×10^8 m/s. In practice, Eqs. (6), (15), and (19) are solved numerically using a zero-finding computer program or subroutine such as Broyden's method. Several example configurations from the literature as well as their computed and measured resonant frequencies are given in Table 2. These results show that when M_1 and M_2 are

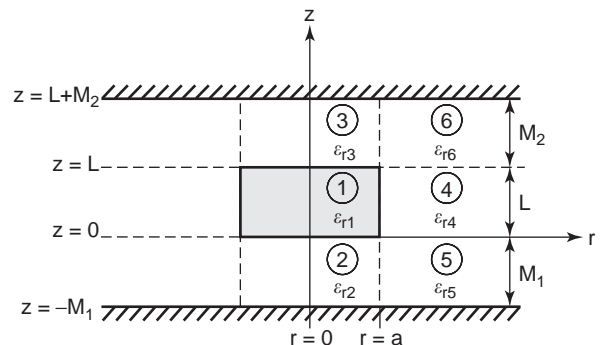


Figure 9. Configuration of the DR used in the simplified analysis of a $TE_{01\delta}$ mode. (From Itoh and Rudokas [41], © 1977 IEEE.)

Table 2. Comparison of Simplified Method with Measured Values for TE_{01δ} Mode

ϵ_{r1}	ϵ_{r2}	ϵ_{r3}	ϵ_{r4}	a (mm)	L (mm)	M_1 (mm)	M_2 (mm)	f_0 (GHz) Measured	f_0 (GHz) Computed
36.2	1.0	1.0	1.0	3.015	4.16	3.41	3.41	7.94 [46]	8.311 (+4.7%)
34.19	9.6	1.0	1.0	7.49	7.48	0.7	0.72	4.348 [34]	4.355 (+0.2%)
63.7	1.0	1.0	1.0	14.29	11.25	0.0	0.0	2.131 [7]	2.131 (0%)

large, which corresponds to an open DR, the accuracy of the method worsens. The accuracy increases as the PEC walls get closer to the resonator. When $M_1 = M_2 = 0$, the analysis is exact. This leads to the conclusion that the method is best suited to DRs placed on thin substrates with the PEC cavity enclosure close to the topface of the DR, such as would be seen in an MIC or MMIC environment. It also works well for DRs sandwiched between two PEC plates, a configuration typically used to measure relative permittivity and loss tangent of dielectric materials [7].

5. Q FACTOR

The quality factor is an important figure of merit for assessing the performance of a DR, or any microwave resonator. It characterizes both the dielectric and conductor losses for closed resonators, as well as radiation losses for open resonators. In this section, only closed resonators are considered. Filter insertion loss is inversely proportional to the resonator unloaded Q . Design objectives require a low insertion loss, which in turn necessitates high- Q resonators. Narrow bandwidth filters also require high- Q resonators, particularly in today's crowded electromagnetic spectrum where communications receivers need high cochannel and spurious signal rejection.

General Q calculations will be described for the structure shown in Fig. 2. It consists of a cylindrical cavity made out of metal, a high-permittivity dielectric ring resonator, and its dielectric supporting structure. The unloaded quality factor Q_u of a resonator is defined as [91]

$$Q_u = \omega_0 \frac{\text{stored energy}}{\text{average power dissipated}} \quad (21)$$

$$= \omega_0 \frac{W}{P_c + P_d + P_{\text{sup}}}$$

where ω_0 is the resonant frequency of the DR; W is the stored energy; and P_c , P_d , and P_{sup} are the power dissipated due to losses in the conductor, dielectric resonator, and dielectric support, respectively. The unloaded Q may be expressed in terms of the individual Q factors of the conductor Q_c , the dielectric resonator Q_d , and dielectric support Q_{sup} as follows:

$$\frac{1}{Q_u} = \frac{1}{Q_c} + \frac{1}{Q_d} + \frac{1}{Q_{\text{sup}}} \quad (22)$$

The stored energy, W may be written as [92]

$$W = W_e + W_m \quad (23)$$

where W_e and W_m denote the energies stored in the electric and magnetic fields, respectively. The stored electric energy is defined as

$$W_e = \frac{1}{4} \int_V \epsilon |\mathbf{E}|^2 dV \quad (24)$$

and the stored magnetic energy is

$$W_m = \frac{1}{4} \int_V \mu |\mathbf{H}|^2 dV \quad (25)$$

However, at resonance, the stored magnetic energy equals the stored electric energy, or $W_e = W_m$; hence

$$W = 2W_e = 2W_m = \frac{1}{2} \int_V \epsilon |\mathbf{E}|^2 dV = \frac{1}{2} \int_V \mu |\mathbf{H}|^2 dV \quad (26)$$

So, from Eq. (26) it is clear that the stored energy may be calculated from either the electric field or the magnetic field.

The conductor power dissipation is calculated from the tangential magnetic fields at the surface of the conducting enclosure as

$$P_c = \frac{1}{2} \oint_S R_S |\mathbf{H}_{\text{tan}}|^2 dS \quad (27)$$

where R_S is the surface resistance of the conductor, \mathbf{H}_{tan} is the magnetic field tangential to the enclosure walls, and S denotes the surface area of the enclosure walls. Introducing the skin depth, $\delta = 1/\sqrt{\pi f_0 \mu \bar{\sigma} \sigma_0}$, where f_0 is the resonant frequency, σ_0 is the conductivity of the enclosure, and $\bar{\sigma}$ is a relative conductivity, which accounts for the surface roughness of the conductor, the power dissipation due to the conducting walls may be redefined as

$$P_c = \omega_0 \frac{\delta}{4} \oint_S \mu |\mathbf{H}_{\text{tan}}|^2 dS \quad (28)$$

Then from Eqs. (26) and (28) we can now define the conductor Q as [85]

$$Q_c = \omega_0 \frac{W}{P_c} = \frac{2}{\delta} \frac{\int_V \mu |\mathbf{H}|^2 dV}{\oint_S \mu |\mathbf{H}_{\text{tan}}|^2 dS} \quad (29)$$

To model both damping and ohmic losses within the dielectric resonator material, a complex permittivity

is introduced:

$$\varepsilon_c = \varepsilon - j \frac{\sigma}{\omega} \quad (30)$$

The loss tangent is the ratio between the imaginary and real parts of the complex permittivity and is a measure of the power loss in the dielectric. The loss tangent is defined as

$$\tan \delta_c = \frac{\sigma}{\omega \varepsilon} \quad (31)$$

Rearranging Eq. (31), we can obtain the effective conductivity to account for the losses in the dielectric resonator:

$$\sigma_{\text{eff}} = 2\pi f_0 \varepsilon_r \varepsilon_0 \tan \delta_c \quad (32)$$

Then the dielectric resonator power dissipation may be calculated as

$$P_d = \frac{1}{2} \int_{V'} \sigma_{\text{eff}} |\mathbf{E}|^2 dV' \quad (33)$$

where V' denotes the volume of the dielectric resonator only. From Eqs. (26) and (33) the dielectric resonator Q is [85]

$$Q_d = \omega_0 \frac{W}{P_d} = \omega_0 \frac{\int_V \varepsilon |\mathbf{E}|^2 dV}{\int_{V'} \sigma_{\text{eff}} |\mathbf{E}|^2 dV'} \quad (34)$$

where V is the volume of the entire resonator and ε is a function of position for inhomogeneous resonators. Using a similar approach we may define the Q factor for the dielectric support

$$Q_{\text{sup}} = \omega_0 \frac{W}{P_{\text{sup}}} = \omega_0 \frac{\int_V \varepsilon |\mathbf{E}|^2 dV}{\int_{V''} \sigma_{\text{eff}_3} |\mathbf{E}|^2 dV''} \quad (35)$$

where σ_{eff_3} is the effective conductivity of the dielectric support and V'' is the volume of the dielectric support only. The effective conductivity of the dielectric support may be found using Eq. (32).

Q factors as a function of M/D for the resonator configuration of Fig. 2 have been calculated using the commercial software CST Microwave Studio [90], and are presented in Figs. 10–13 for the $\text{TE}_{01\delta}$, $\text{EH}_{11\delta}$, $\text{HE}_{11\delta}$, and $\text{TM}_{01\delta}$ modes. The metallic walls of the cavity are modeled as copper, with $\sigma = 5.8 \times 10^7 \text{ S/m}$, while the loss tangent of the dielectric material is set to $\tan \delta = 5 \times 10^{-5}$. Each of these figures show the effect of the cavity height on Q_c , Q_d , and Q_u . In general, as the cavity height increases so does the value of Q_c , which leads to a greater value of Q_u . This is to be expected since the fields outside the DR walls are evanescent, so increasing the height of the cavity reduces the size of the tangential fields induced on the metallic walls. In practice, the cavity size cannot be increased indefinitely to increase the Q factor, because the overall volume of the cavity needs to be kept small. For filter applications, the cavity size cannot be made too large

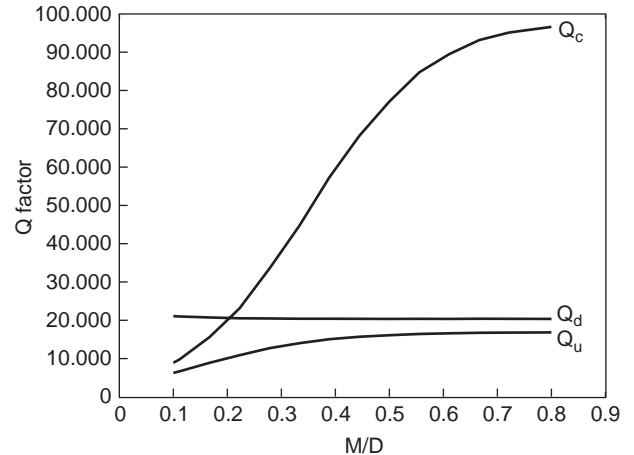


Figure 10. Q factor versus M/D for the $\text{TE}_{01\delta}$ mode (with $\varepsilon_r = 38$, $\varepsilon_3 = 1$, $D/L = 2.5$, $d/D = 2$, $D_x = 0$).

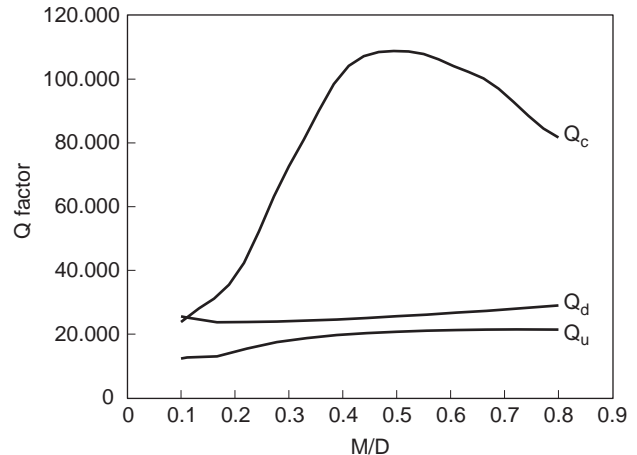


Figure 11. Q factor versus M/D for the $\text{EH}_{11\delta}$ mode (with $\varepsilon_r = 38$, $\varepsilon_3 = 1$, $D/L = 2.5$, $d/D = 2$, $D_x = 0$).

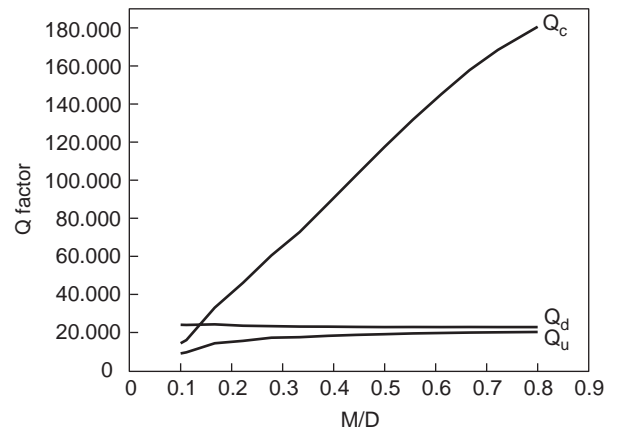


Figure 12. Q factor versus M/D for the $\text{HE}_{11\delta}$ mode (with $\varepsilon_r = 38$, $\varepsilon_3 = 1$, $D/L = 2.5$, $d/D = 2$, $D_x = 0$).

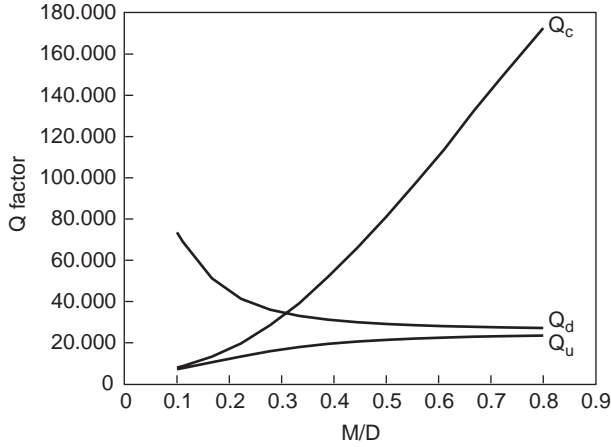


Figure 13. Q factor versus M/D for the $TM_{01\delta}$ mode (with $\epsilon_r = 38$, $\epsilon_3 = 1$, $D/L = 2.5$, $d/D = 2$, $D_x = 0$).

because substantial field strength is required on the cavity walls to generate interresonator coupling. Cavity design should take into consideration Q_u , cavity volume, and spurious performance; it usually requires a compromise between these parameters and is further influenced by the intended DR application.

6. MATERIAL PARAMETERS

An important parameter for evaluating the temperature stability of a dielectric resonator is the temperature coefficient of resonant frequency τ_f . This parameter takes into account the thermal linear expansion of the DR material and its enclosure, as well as the variation in the relative permittivity ϵ_r of the DR material as a function of temperature. The temperature coefficient is expressed as the ratio of the change in frequency to the original frequency divided by the change in temperature:

$$\tau_f = \frac{\Delta f_0}{f_0 \Delta T} \quad (36)$$

Units of the temperature coefficient are parts per million per degree Celsius (ppm/°C). The temperature coefficient for the structure in Fig. 2, which includes the effect of the dielectric support, is [13]

$$\tau_f = A_r \tau_r + A_3 \tau_3 + (A_D + A_x + A_L) \tau_x + A_C \tau_C \quad (37)$$

where

$$\begin{aligned} \tau_r &= \frac{\Delta \epsilon_r}{\epsilon_r \Delta T}, & \tau_3 &= \frac{\Delta \epsilon_3}{\epsilon_3 \Delta T}, \\ \tau_x &= \frac{\Delta D}{D \Delta T} = \frac{\Delta D_x}{D_x \Delta T} = \frac{\Delta L}{L \Delta T}, & (38) \\ \tau_C &= \frac{\Delta d}{d \Delta T} \end{aligned}$$

and

$$\begin{aligned} A_r &= \frac{\epsilon_r}{f_0} \frac{\Delta f_0}{\Delta \epsilon_r}, & A_3 &= \frac{\epsilon_3}{f_0} \frac{\Delta f_0}{\Delta \epsilon_3}, & A_D &= \frac{D}{f_0} \frac{\Delta f_0}{\Delta D}, \\ A_x &= \frac{D_x}{f_0} \frac{\Delta f_0}{\Delta D_x}, & A_L &= \frac{L}{f_0} \frac{\Delta f_0}{\Delta L}, & A_C &= \frac{d}{f_0} \frac{\Delta f_0}{\Delta d} \end{aligned} \quad (39)$$

In Eq. (38) τ_r and τ_3 represent the temperature coefficients of the dielectric constants of the resonator and support, while τ_x and τ_C are the coefficients of thermal linear expansion for the dielectric material and conductor enclosure, respectively. The constants A_r , A_3 , A_D , A_x , A_L , and A_C can be determined accurately by calculating the small resonant frequency shifts Δf_0 caused by the small changes $\Delta \epsilon_r$, $\Delta \epsilon_3$, ΔD , ΔD_x , ΔL , or Δd , respectively. In practice, temperature compensation of the dielectric resonator configuration can be obtained by choosing τ_r to cancel out τ_x and τ_C . Manufacturers usually supply materials with a range of τ_r values to choose from. Some typical values of dielectric constant, loss tangent, temperature coefficient, and thermal expansion for DR materials from two different manufacturers are given in Tables 3 and 4.

7. EXTERNAL AND INTERRESONATOR COUPLING

For a DR to be useful in a microwave circuit, it must be coupled to an external transmission line, another resonator, or both. One of the simplest ways to externally couple the $TE_{01\delta}$ mode in an MIC environment is to place it next to a microstrip line, as shown in Fig. 1b. Since the $TE_{01\delta}$ mode behaves like a magnetic dipole, its magnetic field loops link with the transverse field of the microstrip line. The coupling structure and field lines of the DR and microstrip are illustrated in Fig. 14a [93]. By simply changing the distance d between the DR and microstrip line, the coupling value is varied. The equivalent circuit of the coupling structure is a parallel resonant circuit placed in series with the microstrip line [94], as shown in Fig. 14b.

Table 3. Typical Parameters of DR Materials Available from Trans-Tech

Series	Dielectric Constant	Q (1/tan δ)	Available τ_f (ppm/°C)	τ_x (ppm/°C)	Composition
2900	29–30.7	> 50,000 at 2 GHz	4/2/0/–2	> 10	BaZnTa oxide
3500	34.5–36.5	> 35,000 at 2 GHz	6/3/0/–3	10	BaZnCoNb
4300	43	> 9500 at 4.3 GHz	6/3/0/–3/–6	6.5	Zrtitanium-based
4500	44.7–46.2	> 9500 at 4.3 GHz	6/3/0/–3/–6	6.5	Zrtitanium-based
8300	35–36.5	> 9500 at 4.3 GHz	9/6/3/0/–3	10	Titanate-based
8700	29.5–31	> 10,000 at 10 GHz	4/2/0	10	BaZnTa oxide

Table 4. Typical Parameters of Resomics DR Materials Available from Murata

Material Code	Dielectric Constant	Q ($1/\tan \delta$)	Available τ_f (ppm/ $^{\circ}$ C)	τ_z (ppm/ $^{\circ}$ C)
U	36–40	>6000 at 7 GHz	–4–10	6–7
M	37–40	>7000 at 7 GHz	0–6	6–7
V	33–36	>10,000 at 10 GHz	0–8	12–13
R	29–31	>12,000 at 10 GHz	0–6	10.7
B	27–29	>15,000 at 10 GHz	0–6	11
E	24–25	>20,000 at 10 GHz	0–6	10.7
F	23–24	35,000 at 10 GHz	0–4	11

The external coupling, characterized by the external coupling factor Q_e , may be calculated using a magnetic field flux method. This procedure relates Q_e to the energy stored in the resonator and the magnetic flux linking the microstrip and DR together [93]

$$Q_e = 4 \frac{Z_c}{\omega_0 \mu_0^2} \frac{W}{\left\{ \int \int_S \mathbf{H} \cdot d\mathbf{S} \right\}^2} \quad (40)$$

where

$$W = \frac{1}{4} \epsilon_0 \epsilon_i \int_{V_i} |\mathbf{E}_i|^2 dV_i \quad (41)$$

In these equations, Z_c is the characteristic impedance of the microstrip, \mathbf{H} is the magnetic field vector, S is the cross section of the microstrip substrate, \mathbf{E}_i is the electric field

vector in medium i , ϵ_i is the relative permittivity of medium i , and V_i is the volume of medium i . Details of an analytical expression for Q_e that gives good agreement with measured results are presented in Ref. 93.

The analysis of interresonator coupling coefficients between two DRs in a waveguide will now be examined. A typical coupling structure for this situation is shown in Fig. 15. It consists of two identical DRRs placed coaxially within a cutoff circular waveguide of diameter d . The spacing between the two DRRs is $2M$, and the spacing to the PEC walls enclosing the cylindrical waveguide at each end is M_1 . This structure supports many different modes, but for this analysis we are only interested in the modes that couple magnetically through a dominant TE evanescent mode in the cutoff waveguide such as the $TE_{01\delta}$ and $EH_{11\delta}$ modes. The derivation of the coupling coefficient presented follows the approach of Zaki and Chen [95]. The equivalent circuit for a magnetically coupled mode near resonance, shown in Fig. 16a, consists of two series-resonant circuits coupled by a mutual inductance M . Defining the coupling coefficient k in terms of the equivalent-circuit parameters gives

$$k = \frac{M}{L} \quad (42)$$

Since this analysis will exploit the structural symmetry of the configuration given in Fig. 15, we define an equivalent circuit with a symmetry plane as shown in Fig. 16b. Replacing the symmetry plane with a PEC yields a single resonant circuit. The resonant frequency of the circuit f_e may be related to its equivalent-circuit parameters to obtain

$$f_e = \frac{1}{2\pi\sqrt{(L-M)C}} \quad (43)$$

Repeating the procedure for the PMC wall yields a circuit with a resonant frequency f_m that may be given in terms of the equivalent-circuit parameters as

$$f_m = \frac{1}{2\pi\sqrt{(L+M)C}} \quad (44)$$

Solving Eqs. (42)–(44) for the coupling coefficient k yields

$$k = \frac{M}{L} = \frac{f_e^2 - f_m^2}{f_e^2 + f_m^2} \quad (45)$$

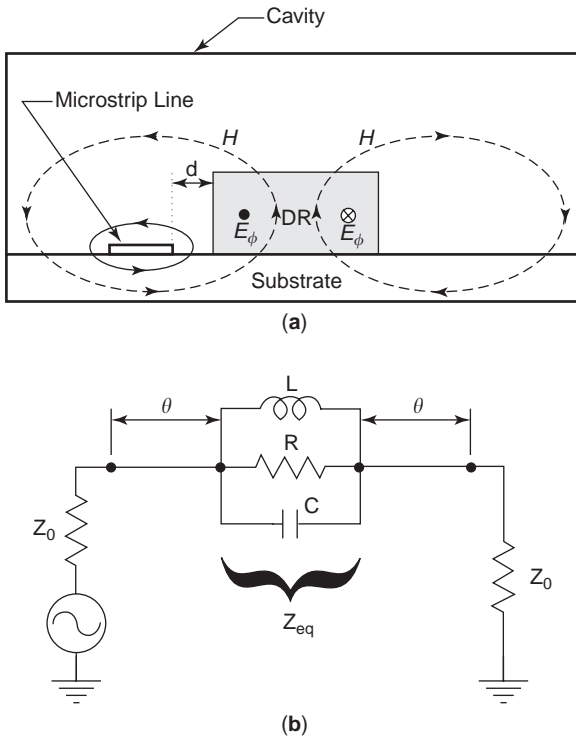


Figure 14. (a) Configuration of $TE_{01\delta}$ mode DR coupled to a microstrip line (from Guillon et al. [93], © 1981 IEEE); (b) equivalent circuit of the coupled DR (from Khanna and Garault [94], © 1983 IEEE).

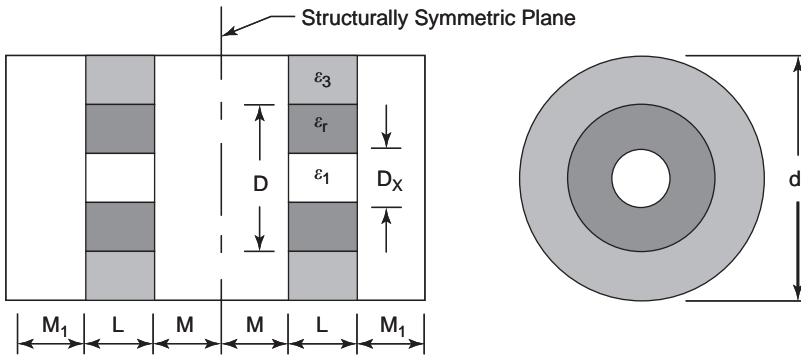


Figure 15. Configuration of coupled dielectric ring resonators (DRRs) showing the position of the structurally symmetric plane. (From Kobayashi and Minegishi [13], © 1987 IEEE.)

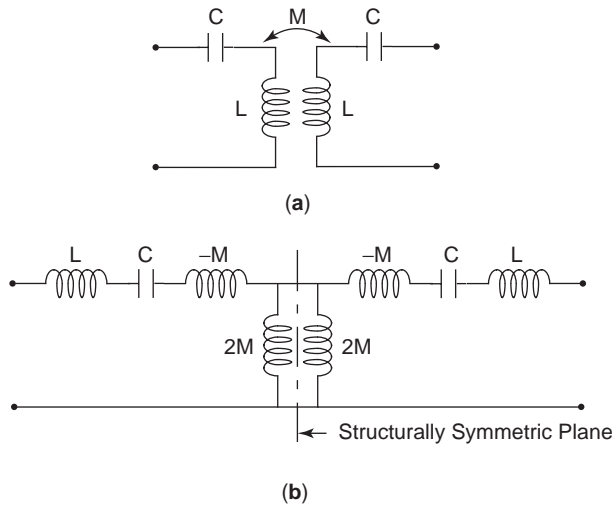


Figure 16. Equivalent circuit of two magnetically coupled resonators: (a) in conventional form; (b) including a structural symmetry plane. (From Zaki and Chen [95], © 1987 IEEE.)

The computation of inter-resonator coupling has been reduced to the problem of calculating the resonant frequencies of two different structures that have a PEC or PMC wall at the plane of structural symmetry. A similar equation may be derived for electric coupling, only the signs of the numerator values are reversed [14]. A more general equation for both electric and magnetic coupling is

$$k = \frac{|f_e^2 - f_m^2|}{f_e^2 + f_m^2} \tag{46}$$

The resonant frequencies f_e and f_m may be calculated using an approximate analysis method, mode matching, or numerical techniques such as FDTD, FEM, or FIT. Each method has been used in the literature to accurately calculate DR interresonator coupling coefficients. This technique may also be used to calculate interresonator coupling through a slot in a conducting wall, as long as the configuration has a structural symmetry plane similar to that shown in Fig. 15. Measured and computed coupling coefficients for two $EH_{11\delta}$ DRRs coupled via a slot are compared in Fig. 17 [96]. The inset of the figure shows the configuration of the coupling structure.

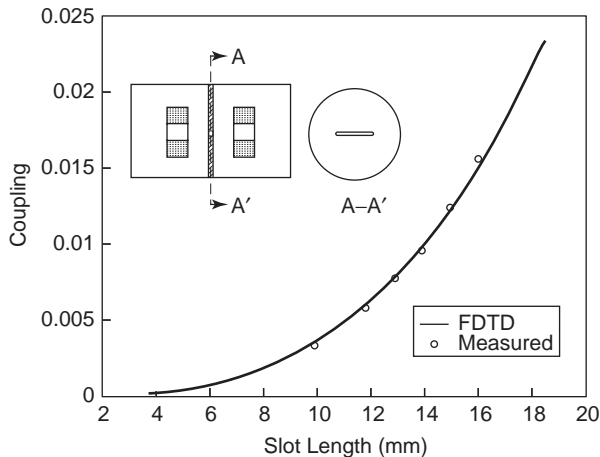


Figure 17. Measured and calculated slot coupling coefficients of an $EH_{11\delta}$ DRR for a slot width of 1.6 mm and a slot thickness of 1 mm (dimensions $d = 37.4$ mm, $D = 21$ mm, $D_x = 8.4$ mm, $L = M = 7.4$ mm, $\epsilon_r = 35$, $f_0 = 4.030$ GHz). Inset shows configuration of the structure. (From Weily et al. [96]; this material is used by permission of John Wiley and Sons, Inc. Copyright © 2001 by John Wiley and Sons, Inc.)

BIBLIOGRAPHY

1. R. D. Richtmeyer, Dielectric resonators, *J. Appl. Phys.* **10**: 391–398 (June 1939).
2. A. Okaya and L. F. Barash, The dielectric microwave resonator, *Proc. IRE* **50**:2081–2092 (Oct. 1962).
3. S. B. Cohn, Microwave filters containing high-Q dielectric resonators, *IEEE Trans. Microwave Theory Tech.* **16**:218–227 (April 1968).
4. W. H. Harrison, A miniature high-Q bandpass filter employing dielectric resonators, *IEEE Trans. Microwave Theory Tech.* **16**:210–218 (April 1968).
5. D. J. Masse et al., A new low-loss high- κ temperature-compensated dielectric for microwave applications, *Proc. IEEE* **59**:1628–1629 (Nov. 1971).
6. J. K. Plourde, D. F. Linn, H. M. O’ Bryan Jr., and J. Thomson Jr., $Ba_2Ti_3O_{20}$ as a microwave dielectric resonator, *J. Am. Ceramic Soc.* **58**:418–420 (Sept.–Oct. 1975).
7. W. E. Courtney, Analysis and evaluation of a method of measuring the complex permittivity and permeability of microwave insulators, *IEEE Trans. Microwave Theory Tech.* **18**:476–485 (Aug. 1970).

8. K. Wakino, T. Nishikawa, S. Tamura, and Y. Ishikawa, Microwave bandpass filters containing dielectric resonators with improved temperature stability and spurious response, *IEEE MTT-S Int. Microwave Symp. Digest*, 1975, pp. 63–65.
9. J. K. Plourde and C. L. Ren, Application of dielectric resonators in microwave components, *IEEE Trans. Microwave Theory Tech.* **29**:754–770 (Aug. 1981).
10. S. J. Fiedziuszko, Dual-mode dielectric resonator loaded cavity filters, *IEEE Trans. Microwave Theory Tech.* **30**:1311–1316 (Sept. 1982).
11. W. C. Tang et al., *Planar Dual-Mode Cavity Filters Including Dielectric Resonators*, U.S. Patent 4,652,843 (March 24, 1987).
12. W. C. Tang, An 8-pole quasi-elliptic function filter realized in 3 dielectric resonator cavities, *IEEE MTT-S Int. Microwave Symp. Digest*, 1986, pp. 349–351.
13. Y. Kobayashi and M. Minegishi, Precise design of a bandpass filter using high-Q dielectric ring resonators, *IEEE Trans. Microwave Theory Tech.* **35**:1156–1160 (Dec. 1987).
14. Y. Kobayashi and M. Minegishi, A low-loss bandpass filter using electrically coupled high-Q $TM_{01\delta}$ dielectric rod resonators, *IEEE Trans. Microwave Theory Tech.* **36**:1727–1732 (Dec. 1988).
15. K. A. Zaki, C. Chen, and A. E. Atia, Canonical and longitudinal dual-mode dielectric resonator filters without iris, *IEEE Trans. Microwave Theory Tech.* **35**:1130–1135 (Dec. 1987).
16. Y. Kobayashi and K. Kubo, Canonical bandpass filters using dual-mode dielectric resonators, *IEEE MTT-S Int. Microwave Symp. Digest*, 1987, pp. 137–140.
17. Y. Kobayashi and M. Miura, Optimum design of shielded dielectric rod and ring resonators for obtaining best mode separation, *IEEE MTT-S Int. Microwave Symp. Digest*, 1984, pp. 184–187.
18. R. V. Snyder, Dielectric resonator filters with wide stopbands, *IEEE Trans. Microwave Theory Tech.* **40**:2100–2103 (Nov. 1992).
19. T. Nishikawa, K. Wakino, K. Tsunoda, and Y. Ishikawa, Dielectric high-power bandpass filter using quarter-cut $TE_{01\delta}$ image resonator for cellular base stations, *IEEE Trans. Microwave Theory Tech.* **35**:1150–1155 (Dec. 1987).
20. K. Wakino, T. Nishikawa, H. Matsumoto, and Y. Ishikawa, Miniaturized bandpass filters using half wave dielectric resonators with improved spurious response, *IEEE MTT-S Int. Microwave Symp. Digest*, 1978, pp. 230–232.
21. Y. Kobayashi and C. Inoue, Bandpass and bandstop filters using dominant $TM_{01\delta}$ mode dielectric rod resonators, *IEEE MTT-S Int. Microwave Symp. Digest*, 1997, pp. 793–796.
22. J.-F. Liang, K. A. Zaki, and A. E. Atia, Mixed modes dielectric resonators filters, *IEEE Trans. Microwave Theory Tech.* **42**:2449–2454 (Dec. 1994).
23. C. Wang, H.-W. Yao, K. A. Zaki, and R. R. Mansour, Mixed modes cylindrical dielectric resonator filters with rectangular enclosure, *IEEE Trans. Microwave Theory Tech.* **43**:2817–2823 (Dec. 1995).
24. H. Y. Hwang, N. S. Park, H. Y. Cho, S. W. Yun, and I. S. Chang, The design of bandpass filters made of both dielectric and coaxial resonators, *IEEE MTT-S Int. Microwave Symp. Digest*, 1997, pp. 805–808.
25. J. F. Liang and W. D. Blair, High-Q TE_{01} mode DR filters for PCS wireless base stations, *IEEE Trans. Microwave Theory Tech.* **46**:2493–2500 (Dec. 1998).
26. A. R. Weily and A. S. Mohan, Design and wideband spurious performance prediction for a mixed resonator combine/ TE_{01} -mode DR filter using FDTD, *Microwave Opt. Technol. Lett.* **23**(5):266–273 (Dec. 5, 1999).
27. C. Wang, K. A. Zaki, and A. E. Atia, Dual-mode combined dielectric and conductor loaded cavity filters, *IEEE MTT-S Int. Microwave Symp. Digest*, 1997, pp. 1103–1106.
28. A. Abdelmonem, J.-F. Liang, H.-W. Yao, and K. A. Zaki, Full wave design of spurious free DR TE mode band pass filter, *IEEE Trans. Microwave Theory Tech.* **43**:744–752 (April 1995).
29. C. Wang, K. A. Zaki, A. E. Atia, and T. G. Dolan, Dielectric combine resonators and filters, *IEEE Trans. Microwave Theory Tech.* **46**:2501–2506 (Dec. 1998).
30. I. C. Hunter, J. D. Rhodes, and V. Dassonville, Dual-mode filters with conductor loaded dielectric resonators, *IEEE Trans. Microwave Theory Tech.* **47**:2304–2311 (Dec. 1999).
31. A. R. Weily and A. S. Mohan, Microwave filters with improved spurious performance based on sandwiched conductor dielectric resonators, *IEEE Trans. Microwave Theory Tech.* **49**:1501–1507 (Aug. 2001).
32. J. A. Curtis, S. J. Fiedziuszko, and S. C. Holme, Hybrid dielectric/HTS resonators and their applications, *IEEE MTT-S Int. Microwave Symp. Digest*, 1991, pp. 447–450.
33. D. Baillargeat, S. Verdeyme, M. Aubourg, and P. Guillon, CAD applying the finite-element method for dielectric-resonator filters, *IEEE Trans. Microwave Theory Tech.* **46**:10–17 (Jan. 1998).
34. D. Kajfez and P. Guillon, eds., *Dielectric Resonators*, 2nd ed., Noble Publishing, Tucker, GA, 1998.
35. Y. Kobayashi and S. Tanaka, Resonant modes of a dielectric rod resonator short-circuited at both ends by parallel conducting plates, *IEEE Trans. Microwave Theory Tech.* **28**:1077–1085 (Oct. 1980).
36. Y. Kobayashi, K. Kojima, and S. Yoshida, Shielded TM_{010} dielectric rod resonator, *Electron. Commun. Japan* **64-B**:65–71 (Feb. 1981).
37. J. S. Fiedziuszko and A. Jelenski, The influence of conducting walls on resonant frequencies of the dielectric microwave resonator, *IEEE Trans. Microwave Theory Tech.* **19**:778–780 (Sept. 1971).
38. J. Van Bladel, On the resonances of a dielectric resonator of very high permittivity, *IEEE Trans. Microwave Theory Tech.* **23**:199–208 (Feb. 1975).
39. Y. Konishi, N. Hoshino, and Y. Utsumi, Resonant frequency of a $TE_{01\delta}$ dielectric resonator, *IEEE Trans. Microwave Theory Tech.* **24**:112–114 (Feb. 1976).
40. M. Verplanken and J. Van Bladel, The electric-dipole resonances of ring resonators of very high permittivity, *IEEE Trans. Microwave Theory Tech.* **24**:108–112 (Feb. 1976).
41. T. Itoh and R. S. Rudokas, New method for computing the resonant frequencies of dielectric resonators, *IEEE Trans. Microwave Theory Tech.* **25**:52–54 (Jan. 1977).
42. M. W. Pospieszalski, On the theory and application of the dielectric post resonator, *IEEE Trans. Microwave Theory Tech.* **25**:228–231 (March 1977).
43. P. Guillon and Y. Garault, Accurate resonant frequencies of dielectric resonators, *IEEE Trans. Microwave Theory Tech.* **25**:916–922 (Nov. 1977).
44. M. W. Pospieszalski, Cylindrical dielectric resonators and their applications in TEM line microwave circuits, *IEEE Trans. Microwave Theory Tech.* **27**:233–238 (March 1979).
45. M. Verplanken and J. Van Bladel, The magnetic-dipole resonances of ring resonators of very high permittivity, *IEEE Trans. Microwave Theory Tech.* **27**:328–333 (April 1979).

46. M. Jaworski and M. W. Pospieszalski, An accurate solution of the cylindrical dielectric resonator problem, *IEEE Trans. Microwave Theory Tech.* **27**:639–643 (March 1979).
47. R. R. Bonetti and A. E. Atia, Design of cylindrical dielectric resonators in inhomogeneous media, *IEEE Trans. Microwave Theory Tech.* **29**:323–326 (April 1981).
48. J. Krupta, Optimization of an electrodynamic basis for determination of the resonant frequencies of microwave cavities partially filled with a dielectric, *IEEE Trans. Microwave Theory Tech.* **31**:302–305 (March 1983).
49. D. Maystre, P. Vincent, and J. C. Mage, Theoretical and experimental study of the resonant frequency of cylindrical dielectric resonator, *IEEE Trans. Microwave Theory Tech.* **31**:844–848 (Oct. 1983).
50. M. Tsuji, H. Shigesawa, and K. Takiyama, Analytical and experimental investigations on several resonant modes in open the dielectric resonators, *IEEE Trans. Microwave Theory Tech.* **32**:628–633 (June 1984).
51. J. Krupta, Computations of frequencies and intrinsic Q factors of TE_{0nm} modes of a dielectric resonators, *IEEE Trans. Microwave Theory Tech.* **33**:274–277 (March 1985).
52. P. Guillon, J. P. Balabaud, and Y. Garault, TM_{01p} tubular and cylindrical are dielectric resonator mode, *IEEE MTT-S Int. Microwave Symp. Digest*, 1981, pp. 163–166.
53. J. E. Lebaric and D. Kajfez, Analysis of dielectric resonator cavities using the finite integration technique, *IEEE Trans. Microwave Theory Tech.* **37**:1740–1747 (Nov. 1989).
54. C. C. Su and J. M. Guan, Finite difference analysis of dielectric-loaded cavities using the simultaneous iteration of the power method with the Chebyshev acceleration technique, *IEEE Trans. Microwave Theory Tech.* **42**:1998–2006 (Oct. 1994).
55. J. Mielewski, A. Cwikla, and M. Mrozowski, Accelerated FD analysis of dielectric resonators, *IEEE Microwave Guided Wave Lett.* **8**:375–377 (Nov. 1998).
56. F. H. Gil and J. P. Martinez, Analysis of dielectric resonators with tuning screw and supporting structure, *IEEE Trans. Microwave Theory Tech.* **33**:1453–1457 (Dec. 1985).
57. P. S. Kooi, M. S. Leong, and A. L. S. Parakash, Finite element analysis of the shielded dielectric resonator, *Proc. IEE* **132**(Part H):7–16 (Feb. 1985).
58. M. Taheri and D. Mirshekar-Syahkal, Accurate determination of modes in dielectric-loaded cylindrical cavities using a one-dimensional finite element method, *IEEE Trans. Microwave Theory Tech.* **37**:1536–1541 (Oct. 1989).
59. V. Madrangeas, M. Aubourg, P. Guillon, S. Vigneron, B. Theron, and D. Parise, A new finite element method formulation applied to D. R. microwave filter design, *IEEE MTT-S Int. Microwave Symp. Digest*, 1990, pp. 415–418.
60. A. W. Glisson, D. Kajfez, and J. James, Evaluation of modes in dielectric resonators using a surface integral equation formulation, *IEEE Trans. Microwave Theory Tech.* **31**:1023–1029 (Dec. 1983).
61. D. Kajfez, A. W. Glisson, and J. James, Computed modal field distributions for isolated dielectric resonators, *IEEE Trans. Microwave Theory Tech.* **32**:1609–1616 (Dec. 1984).
62. Y. Kobayashi, K. Kojima, and S. Yoshida, Resonant modes for a shielded dielectric resonator, *Electron. Commun. Japan* **64-B**:44–51 (Oct. 1981).
63. U. S. Hong and R. H. Jansen, Numerical analysis of shielded dielectric resonators including substrate, support disk, and tuning post, *Electron. Lett.* **18**(23):1000–1002 (Nov. 11, 1982).
64. K. A. Zaki and A. E. Atia, Modes in dielectric-loaded waveguides and resonators, *IEEE Trans. Microwave Theory Tech.* **31**:1039–1045 (Dec. 1983).
65. Y. Kobayashi, T. Aoki, and Y. Kabe, Influence of conductor shields on the Q-factors of a TE_0 dielectric resonator, *IEEE Trans. Microwave Theory Tech.* **33**:1361–1366 (Dec. 1985).
66. K. A. Zaki and C. Chen, Intensity and distribution of hybrid-mode fields in dielectric-loaded waveguides, *IEEE Trans. Microwave Theory Tech.* **33**:1442–1447 (Dec. 1985).
67. K. A. Zaki and C. Chen, Loss mechanisms in dielectric-loaded resonators, *IEEE Trans. Microwave Theory Tech.* **33**:1448–1452 (Dec. 1985).
68. K. A. Zaki and C. Chen, New results in dielectric-loaded resonators, *IEEE Trans. Microwave Theory Tech.* **34**:815–824 (July 1986).
69. Y. Kobayashi and S. Nakayama, Design charts for shielded dielectric rod and ring resonators, *IEEE MTT-S Int. Microwave Symp. Digest*, 1986, pp. 241–244.
70. C. Chen and K. A. Zaki, Resonant frequencies of dielectric resonators containing guided complex modes, *IEEE Trans. Microwave Theory Tech.* **36**:1455–1457 (Oct. 1988).
71. S.-W. Chen and K. A. Zaki, Dielectric ring resonators loaded in waveguide and on substrate, *IEEE Trans. Microwave Theory Tech.* **39**:2069–2076 (Dec. 1991).
72. X.-P. Liang and K. A. Zaki, Modeling of cylindrical dielectric resonators in rectangular waveguides and cavities, *IEEE Trans. Microwave Theory Tech.* **41**:2174–2181 (Dec. 1993).
73. Y. Kobayashi and T. Senju, Resonant modes of shielded uniaxial-anisotropic dielectric rod resonators, *IEEE Trans. Microwave Theory Tech.* **41**:2198–2205 (Dec. 1993).
74. C. Wang and K. A. Zaki, Generalized multilayer anisotropic dielectric resonators, *IEEE MTT-S Int. Microwave Symp. Digest*, 1998, pp. 233–236.
75. K. S. Yee, Numerical solution of initial boundary value problems involving Maxwell's equations in isotropic media, *IEEE Trans. Antennas Propag.* **14**:302–307 (May 1966).
76. A. Navarro, M. J. Nuñez, and E. Martin, Study of TE_0 and TM_0 modes in dielectric resonators by a finite difference time-domain method coupled with the discrete Fourier transform, *IEEE Trans. Microwave Theory Tech.* **39**:14–17 (Jan. 1991).
77. Y. Chen, R. Mittra, and P. Harms, Finite-difference time-domain algorithm for solving Maxwell's equations in rotationally symmetric geometries, *IEEE Trans. Microwave Theory Tech.* **44**:832–839 (June 1996).
78. J. A. Pereda, L. A. Vielva, A. Vegas, and A. Prieto, Computation of resonant frequencies and quality factors of open dielectric resonators by a combination of the finite-difference time-domain (FDTD) and Prony's methods, *IEEE Microwave Guided Wave Lett.* **2**:431–433 (Nov. 1992).
79. A. R. Weily and A. S. Mohan, Mode-chart calculation for dielectric- and conductor-loaded resonators using modal extraction and FDTD, *Microwave Opt. Technol. Lett.* **21**(6):405–411 (June 20, 1999).
80. Z. Bi, Y. Shen, K. Wu, and J. Litva, Fast finite-difference time-domain analysis of resonators using digital filtering and spectrum estimation techniques, *IEEE Trans. Microwave Theory Tech.* **40**:1611–1619 (Aug. 1992).
81. Z. Ma and Y. Kobayashi, Analysis of dielectric resonators using the FDTD method combined with the Pade interpolation technique, *IEICE Trans. Electron.* **E-84C**:973–976 (July 2001).
82. P. Harms, J.-F. Lee, and R. Mittra, A study of the non-orthogonal FDTD method versus the conventional FDTD technique

for computing resonant frequencies of cylindrical cavities, *IEEE Trans. Microwave Theory Tech.* **40**:741–746 (April 1992).

83. N. Kaneda, B. Houshmand, and T. Itoh, FDTD analysis of dielectric resonators with curved surfaces, *IEEE Trans. Microwave Theory Tech.* **45**:1645–1649 (Sept. 1997).
84. S. Dey and R. Mittra, A conformal finite-difference time-domain technique for modeling cylindrical dielectric resonators, *IEEE Trans. Microwave Theory Tech.* **47**:1737–1739 (Sept. 1999).
85. C. Wang, H.-W. Yao, and K. A. Zaki, An improved FDTD method for analysis of higher order modes high Q dielectric resonators, *IEEE AP-S Int. Symp. Digest*, 1995, pp. 236–239.
86. D. Kajfez, A. Elsherbeni, and A. Mokaddem, Higher order modes in dielectric resonators, *IEEE AP-S Int. Symp. Digest*, 1996, pp. 306–309.
87. C. Wang, B.-Q. Gao, and C.-P. Deng, Q factor of a resonator by the finite-difference time-domain method incorporating perturbation techniques, *Electron. Lett.* **29**(21):1866–1867 (Oct. 14, 1993).
88. C. Wang, B.-Q. Gao, and C.-P. Deng, Accurate study of Q-factor of a resonator by a finite-difference time-domain method, *IEEE Trans. Microwave Theory Tech.* **43**:1524–1529 (July 1995).
89. E. Snitzer, Cylindrical dielectric waveguide modes, *J. Opt. Soc. Am.* **51**:491–498 (May 1961).
90. *CST Microwave Studio 5.0 User Manual*, CST Darmstadt, Germany, 2004.
91. R. F. Harrington, *Time Harmonic Electromagnetic Fields*, McGraw-Hill, New York, 1961.
92. D. K. Cheng, *Field and Wave Electromagnetics*, Addison-Wesley, Reading, MA, 1989.
93. P. Guillon, B. Byzery, and M. Chaubet, Coupling parameters between a dielectric resonator and a microstripline, *IEEE Trans. Microwave Theory Tech.* **33**:222–226 (March 1985).
94. A. P. S. Khanna and Y. Garault, Determination of loaded, unloaded, and external quality factors of a dielectric resonator coupled to a microstrip line, *IEEE Trans. Microwave Theory Tech.* **31**:261–264 (March 1983).
95. K. A. Zaki and C. Chen, Coupling of non-axially symmetric hybrid modes in dielectric resonators, *IEEE Trans. Microwave Theory Tech.* **35**:1136–1142 (Dec. 1987).
96. A. R. Weily and A. S. Mohan, Time domain CAD of dual-mode HE_{11} dielectric resonator microwave filters, *Microwave Opt. Technol. Lett.* **29**(1):6–11 (April 5, 2001).

DIGITAL MICROWAVE RECEIVERS

JOHANN F. LUY
TH. MUELLER
DaimlerChrysler Research
Ulm, Germany

1. INTRODUCTION

The general tasks of a receiver are amplification, channel selection, and demodulation of a signal. The kind of channel selection may be used to distinguish between analog and digital receiver architectures. In a superheterodyne receiver (Fig. 1), the problem of image frequency suppres-

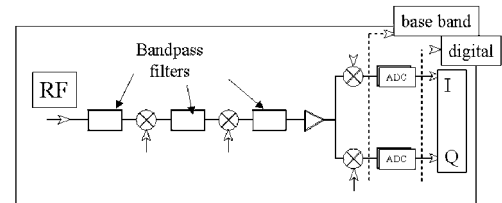


Figure 1. Analog receiver: superheterodyne principle.

sion can be solved quite well by proper selection of the IF frequencies and bandpass filters. Channel selection is determined by the analog filters, and reconfiguration by software is not supported.

Quadrature direct-conversion architecture is obtained if the RF and first IF mixer stages are dropped and the RF signal is fed directly to the analog in-phase and quadrature downconversion mixers (Fig. 2). The reduced complexity of this zero-IF receiver is the advantage of this concept. The disadvantages are the problems with static and dynamic offsets and corresponding errors in amplitude and phase of the received signals.

The simplified principle of a digital receiver is shown in Fig. 3, where the analog signal passes an antialiasing filter (AAF) and a sample-and-hold (S/H) unit. The sampled values of the signal are then converted into the digital domain by an analog-to-digital converter (ADC) and fed into an accumulator (ACCW) for further digital signal processing. Digital signal processing of the received signal provides high flexibility and opens new possibilities regarding diversity techniques. By broadband sampling of the FM band between 87 and 108 MHz, it has been shown that coherent superposition of different channels containing the same information can lead to significantly improved signal quality [1]. Channel diversity and MIMO signal processing techniques become possible with digital front ends [2].

2. RF AND IF SAMPLING ARCHITECTURE

By sampling the radio frequency (RF) or intermediate frequency (IF), the number of input stages and therefore the hardware effort can be reduced. The architectures of both receiver types are shown in Fig. 4. The performance of the ADC with respect to bandwidth and resolution [3] is decisive for the choice of the receiver architecture. The ADC performs a quantization in time and in value of the input RF or IF signal.

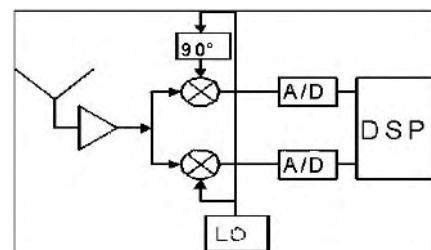


Figure 2. Analog receiver: direct-conversion architecture.

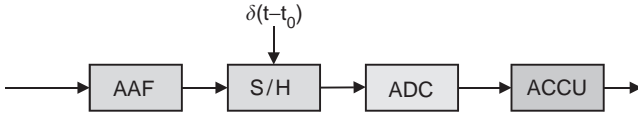


Figure 3. Digital receiver illustrating the bandpass-limited sampling concept.

The sampling process with the sampling frequency f_S can be understood in frequency domain by folding the input signal with a series of diracs with distance f_S (see Fig. 5). The input signal at frequency f_{IF} is shifted by the sampling process to $f_{IF} - kf_S$, where k is an integer value. A filter has to select a frequency band so that only the desired signal is sampled and all the other frequency components are suppressed to avoid aliasing [4]. The requirements on the slope of the filter are minimal if the input frequency is an odd multiple of $f_S/4$ because the distance to the next possible interferer becomes maximal. The complex downconversion is usually realized in the digital domain. This enables the use of high-order modulation schemes, and ensures exact gain and phase matching in in-phase and quadrature branches. Especially for a fixed IF frequency, the digital downconversion can be realized by multiplying the sampled signal with $+1s$ and $-1s$ (see Fig. 4b).

By choosing a high sampling rate, the achievable signal-to-noise ratio in the desired channel can be calculated by the formula

$$\text{SNR}_{\text{CH}} = \text{SNR}_{\text{ADC}} + 10 \log_{10} \left(\frac{f_S}{2B_{\text{CH}}} \right)$$

with the channel bandwidth B_{CH} , the sampling frequency f_S , and the signal-to-noise ratio of the ADC SNR_{ADC} in decibels. It can be seen that with increasing sampling rate the SNR also increases. The state of the art is about 72 dB SNR_{ADC} at a sampling rate of 105 MHz [5].

The highest flexibility can be reached with broadband RF sampling receivers [6]. Here all channels are available in parallel, and the channel bandwidth and demodulation are defined by digital signal processing so that the radio is fully software-defined. In contrast to IF sampling receivers, the dynamic range that has to be handled by the ADC becomes critical. To calculate the necessary dynamic range, we have to accumulate the power of all interferers and noise in the digitized frequency band. As an example, the specification of GSM¹ defines a maximum interferer power of -23 dBm, whereas noise and interferers in the desired channel with a bandwidth of 200 kHz have to keep below -112 dBm. If we perform IF sampling, the IF filter will be able to suppress most of the interferers so that the interfering power will be below -43 dBm.

The second important factor when defining receivers is intermodulation. The state of the art is about 90 dB spurious-free dynamic range [5]. To compare this with traditional downconverting architectures, we should remember

¹European Telecommunication Standard, ETS 300-577, FTS 300 577, *Radio Transmission and Reception*, Dec. 1999, European Telecommunication Standards Institute, Valbonne, France.

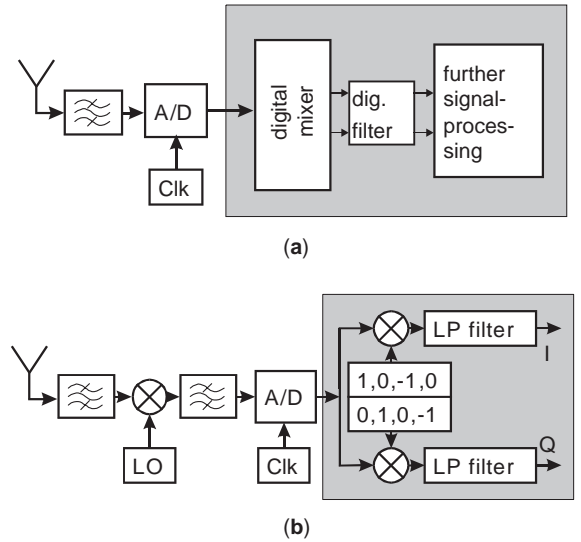


Figure 4. (a) RF sampling receiver; (b) IF sampling receiver.

that the spurious-free dynamic range (SFDR) of an amplifier or mixer can be calculated out of the third-order interception point ICP3_{out} and the output noise power N_{out} :

$$\text{SFDR} = \frac{2}{3}(\text{ICP3}_{\text{out}} - N_{\text{out}}).$$

A standard monolithic integrated mixer [7] will show an SFDR of about 82 dB referring to a channel bandwidth of 200 kHz.

The selection of the sampling frequency also depends on the technical feasibility of the antialiasing filter. Choosing a frequency plan where the input signal with bandwidth B is centered on f_{SIG} an odd multiple of $f_S/4$, a filter margin on each side of $f_S/2 - B$ is allowed to reach the specified suppression of interferers. In practice [8], bandwidth B should be maintained below $f_S/4$, which corresponds to a minimum oversampling ratio of 2.

An important issue for the implementation of RF or IF sampling ADCs is sampling jitter [9]. The sources of sampling jitter are mainly the clock generator phase noise and the aperture jitter of the sampling unit. The slope of the input signal will transform the error $\Delta\tau$ of the sampling time in an amplitude error Δy as shown in Fig. 6:

$$\Delta y = \Delta\tau \cdot \left. \frac{\partial y}{\partial t} \right|_{t_s}$$

In broadband sampling receivers the input signal consists of the desired signal and a couple of interferers. The slope of the signal can be calculated by the sum of the slopes of each partial signal, weighted with its amplitude. If one signal is dominant, it will define the slope of the input signal. If the signal amplitude is much lower than the amplitude of the interferer, then the slope of the input signal will be defined by the interferer. If the sampled signal is independent of the sampling frequency, then we have to look on the statistical properties of the input signal.

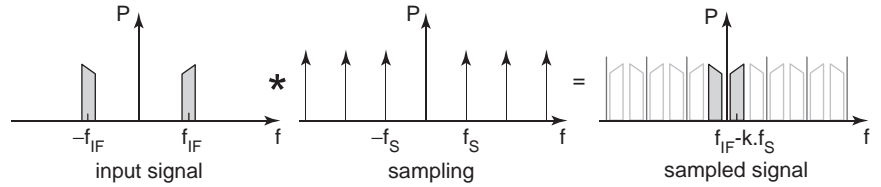


Figure 5. General six-port architecture.

For a sinusoidal input signal y with amplitude A_{sin} , we obtain the variance of the slope

$$\begin{aligned} \text{Var}\left(\frac{\partial y}{\partial t}\right) &= \int p_{\text{slope}}(y)y^2 dy \\ &= 2A_{\text{sin}}^2 f^2 \pi^2 \end{aligned}$$

Finally we can calculate the achievable signal to noise ratio in decibels when sampling a sinusoid signal with a nonideal sampling circuit:

$$\begin{aligned} \text{SNR}_{\text{dB}} &= 10 \log\left(\frac{P_{\text{SIG}}}{P_{\text{noise}}}\right) \\ &= 10 \log\left(\frac{\frac{1}{2}A_{\text{sin}}^2}{2A_{\text{sin}}^2 f^2 \pi^2 \Delta\tau^2}\right) \\ &= -20 \log(2f\pi\Delta\tau) \end{aligned}$$

3. SIX-PORT ARCHITECTURE

The six-port direct-conversion technique is another promising approach toward software configurable receivers at millimeter-wave carrier frequencies. The crucial advantage over the sampling architecture is its simple construction requiring only the reference oscillator as an active RF component, making this technology particularly attractive for future low-cost and broadband RF front ends operating at millimeter-wave frequencies.

The six-port technology traces back to the 1970s, when it was developed as an alternative network analyzer [10]. By means of a six-port reflectometer, it is possible to mea-

sure the complex reflection coefficient of a device under test (DUT). Furthermore, by the application of 2 six-ports—one on each side of the unknown DUT—it is possible to determine the complete set of the S-parameters [11]. Starting in the mid-1990s the six-port principle was investigated for use as a direct-conversion receiver [12,13]. Complete receivers were realized, and signals that were modulated by quadrature phase shift keying (QPSK) and quadrature amplitude modulation (QAM) schemes have since been received and demodulated successfully. Sony has verified the concept for a multicarrier system based on HIPERLAN/2 (High-Performance Local Area Network/2) and UMTS-FDD (Universal Mobile Telecommunication System–Frequency-division duplex) standards [14,15], and Nokia has found the six-port direct-conversion technique in a receiver a viable concept for mobile terminals [16]. Other applications include anticollision radars [17], very accurate short-range distance measurement [18], and direction finding systems [19].

The functional principle of six-port devices is based on the measurement of four independent output powers corresponding to the complex ratio between two superposed electromagnetic waves under different phase angles. While in reflectometers used for the measurement of the complex reflection coefficient, a leakage from the LO port to the test port of the DUT is essential, six-port circuits for receivers require a very large isolation of the LO and the RF ports. Carrier recovery (Fig. 7) is a possible approach to avoid the need for an independent LO in a six-port direct digital receiver [22].

To describe this principle, the six-port in Fig. 8 is considered together with two input signals, one from a local oscillator (LO)

$$a_{\text{LO}}(t) = |a_{0,\text{LO}}| \cdot e^{j(2\pi f_{\text{LO}}t + \phi_{\text{LO}})}$$

and the other from the RF port

$$a_{\text{RF}}(t) = |a_{0,\text{RF}}| \cdot e^{j(2\pi f_{\text{RF}}t + \phi_{\text{RF}})}$$

which is the RF signal to be detected, that is, measured by the six-port receiver.

Ideally, the six-port circuit represents a nondissipative network and the frequencies of the RF and LO signal are identical. For example, at port 3, the RF signal is attenuated twice by 3 dB and 90° phase-shifted. This signal is added to the LO signal, which is also attenuated twice by 3 dB although it does not receive a phase shift. For zero phase shift between the LO and the RF signal and the same amplitudes at the input ports, this leads to a resulting amplitude of $\sqrt{2}/2$ for the superposed wave to be detected at port 3. During a 360° phase shift of the RF signal, the amplitudes resulting at the output ports are sine functions.

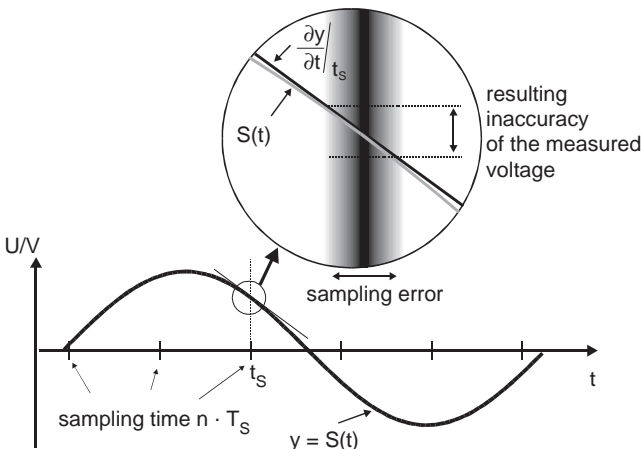


Figure 6. Transformation of sampling error in amplitude error.

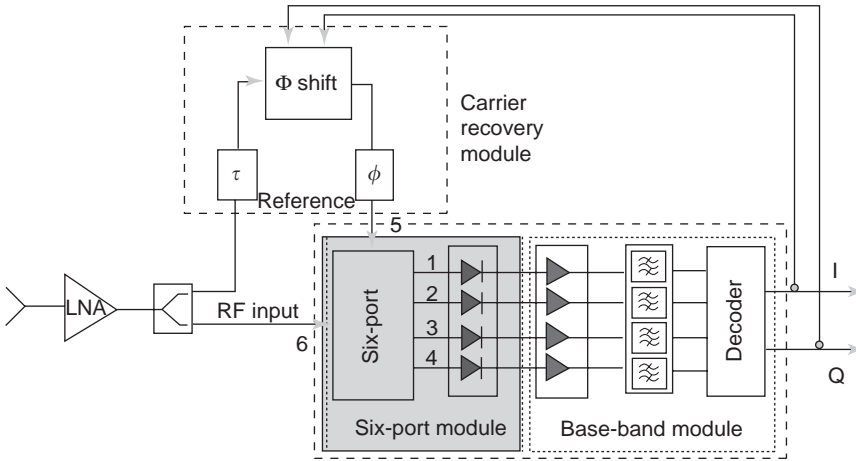


Figure 7. Architecture of hardware six-port direct digital receiver with carrier recovery from QPSK signal (from Ref. 22).

At each output port (ports 3–6) the signal passes through detector circuits. A diode is used to rectify the signal, and a subsequent lowpass filter (LPF) outputs the amplitude of the signal, which is amplified and A/D-converted. It becomes clear that the diode is the most critical block in this receiver chain that has to be operated in its quadratic region where the output voltage depends linearly on the power to be detected. However, minor deviations from the square law can be compensated in the digital domain by suitable calibration methods.

From at least three linearly independent output powers, the complex ratio between the two input signals

$$\Gamma(t) = \left| \frac{a(t)_{0,RF}}{a(t)_{0,LO}} \right| \cdot e^{j(2\pi \Delta f t + \Delta\phi)}$$

can be determined. Furthermore, it can be shown that if the leakage from the LO signal to the RF port is neglected, the following linear relationship exists between the I and Q components of the RF waveform and the power ratios P_i/P_3 ($i = 3 \dots 6$):

$$I(t) = \sum_{i=3}^6 A_i \frac{P_i(t)}{P_3(t)}$$

$$Q(t) = \sum_{i=3}^6 B_i \frac{P_i(t)}{P_3(t)}$$

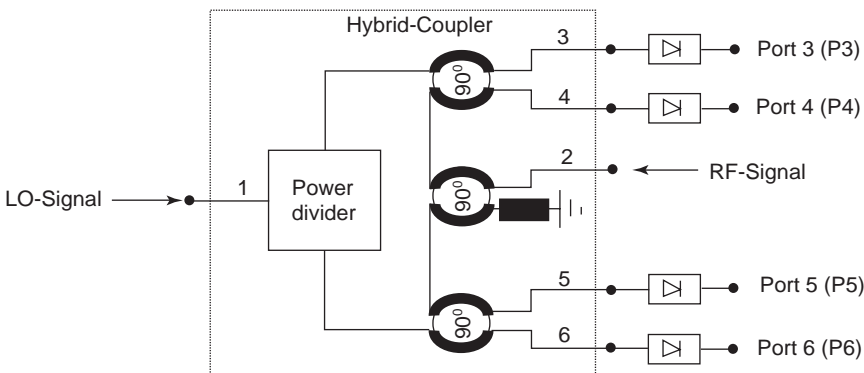


Figure 8. Sampling process in the frequency domain.

where A and B are calibration coefficients to be determined by a suitable method. In the case of QPSK modulation, this can be done by solving eight equations from four known different states. As real six-ports are dependent on the operating frequency, a calibration has to be done for each frequency. Simulation and measurement results for QPSK modulation from 2 to 20 GHz using the same circuit and the described calibration method confirm the broadband operation of the six-port technology [20].

Apart from the described simple method, the so-called dual-tone calibration method is often used [21]. This method has to be applied if there is a relevant leakage from the LO to the RF port as, for example, in reflection coefficient measurements or radar applications.

The advantages and disadvantages of the six-port technology, when compared to conventional heterodyne or zero-IF (ZIF) architectures, strongly depend on the application of interest. First to mention are the additional output paths, which require more LNAs, filters, and ADCs. In real communication standard environments, a DC offset is caused by second-order nonlinearities, which are also present in ZIF receivers and require an additional compensation circuit in each path. In comparison to heterodyne receivers, an image rejection filter and one LO can be saved in a six-port architecture. It should also be mentioned that three output ports in suitable five-port architecture are in principle sufficient to explicitly determine the amplitude and phase. The additional sixth port serves a way as a cyclic redundancy check and extends the

operation bandwidth. This can reduce the hardware effort further with respect to cost of accuracy and bandwidth.

However, the main advantage of the six-port technology is its broadband capability and the possibility for software configuration and calibration. The six-port technology also becomes very attractive when extremely high carrier frequencies at millimeter wavelengths are used. The trend toward higher data rates will make use of new bands: 17, 24, and 60 GHz have been considered. The intrinsic broadband property makes it in principle possible to design RF front-ends operation over more than three decades of bandwidth. Additionally, the same hardware can in general be used for different standards simply by loading suitable baseband processing algorithms. When these software algorithms also become available in the future, extremely broadband six-port RF front-ends might be the technology of choice for SDR platforms. This can help support a certain quality of service (QoS) as different bands and standards can be probed and selected to transmit information in harsh side conditions.

The six-port technique is very well suited for accurately measuring the phase difference of two waves. This makes the principle very attractive for determining the angle of an incident wavefront, which is essential for multiple-input/single-output (MISO) and multiple-input/multiple-output (MIMO) systems. In a simple approach as described in Ref. 19, the LO is replaced by a second antenna and can lead to accurate results in the case where a plane wave at a fixed frequency has to be detected. Modifications including an optimization of the number of input antennas and output ports as well as frequency selection mechanisms are considered and might offer smart six-port-based antennas for digital beamforming, MISO, MIMO, and space diversity compatibility.

4. HIGH-Q MILLIMETER-WAVE FILTERS WITH INTEGRATION CAPABILITY

Important issues in digital microwave receivers are the design and the realization of high-Q filters for planar

integration. Several approaches are known from the literature (Fig. 9):

- Dielectric resonators attain the highest possible Q values but have poor integration capability.
- Use of multiple wafers that are glued or bonded may lead to unloaded Q values up to several hundred. Integration capability depends on the possible use of multiple wafers.
- Use of a single wafer with planar filters usually results in unloaded Q-values that are quite low. If the substrate is 3D-structured, unloaded Q values up to 400 are feasible at center frequencies around 20 GHz.

Three-dimensional structuring of silicon substrates can help provide enough “volume” to obtain high quality factors. In order to avoid multiple wafer bonding or gluing techniques, a tilted waveguide resonator concept is applied with feeding structures of an inductive type. The concept of a microelectromechanical system antialiasing filter (MEMS AAF) is illustrated in Fig. 10. In one realization scheme the silicon material itself is used as dielectric fill material whereas the cavity surrounding is realized by subsequent placing of metallized via holes [23]. Q values of 100 are possible at center frequencies of 22 GHz if high-resistivity silicon is used as the dielectric fill material for the resonator.

An air-filled cavity concept leads to still higher Q values: ≤400 are obtained from a microstrip-coupled resonator operated in a H_{101} resonance. Figure 11 gives an impression from the layout and the realization of a 22.4-GHz microstrip-coupled filter [24].

5. APPLICATIONS: SOFTWARE-DEFINED MULTIPLE-STANDARD TUNER PLATFORM

The number of different audio and video standards is actually increasing. Beside analog audio and video, we have to cope with different digital audio standards such as DAB [Digital Audio Broadcasting (European standard)], IBOC

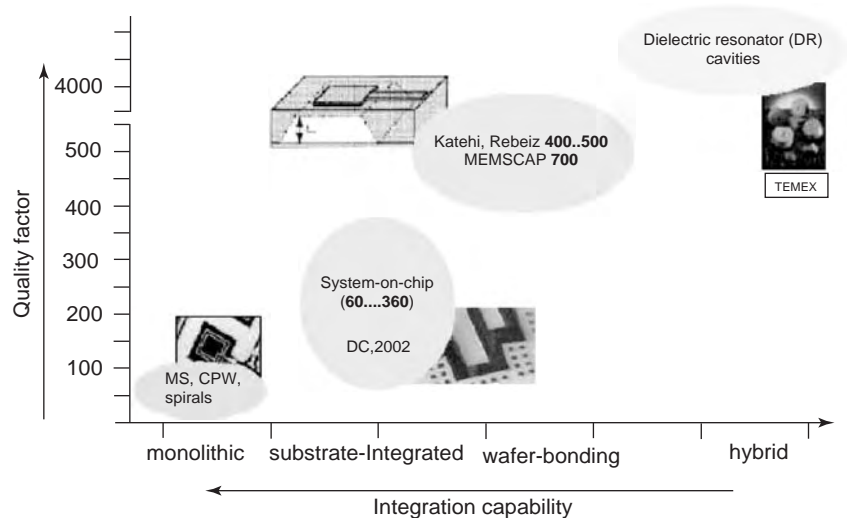


Figure 9. Quality factor versus integration capability of several filter techniques.

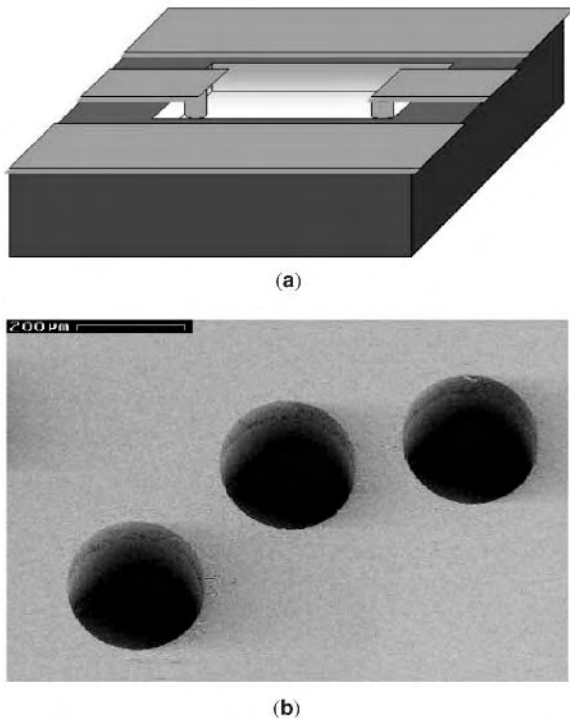


Figure 10. Concept of inductively coupled 90° tilted resonator (a) and part of realized version with metallized via holes (b) in high resistivity silicon.

[in-band/on-channel (radio)], DRM [Digital Radio Mondial (international consortium)]. Sirius Satellite Radio, and XM Satellite Radio, beside the new digital video standards such as DVB-T (Digital Video Terrestrial Broadcasting). A realization by parallel implementation of all standards is no longer practical because of size, weight, and power consumption [25]. Therefore a fully software reconfigurable receiver has to handle these standards and be capable of making updates during the receiver lifetime. The principal block diagram is shown in Fig. 12. Two receiver paths are realized to enable antenna diversity for all frequency ranges.

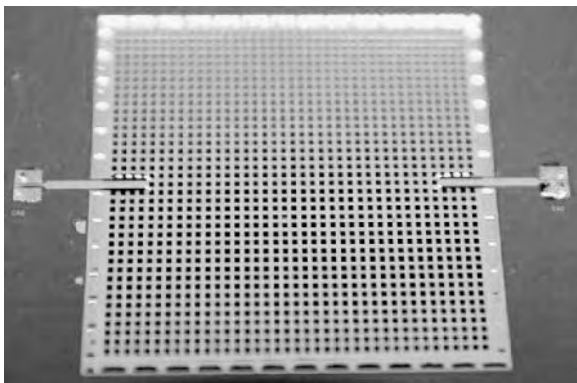


Figure 11. Microstrip-coupled resonator. The length of each side is 9.45 mm.

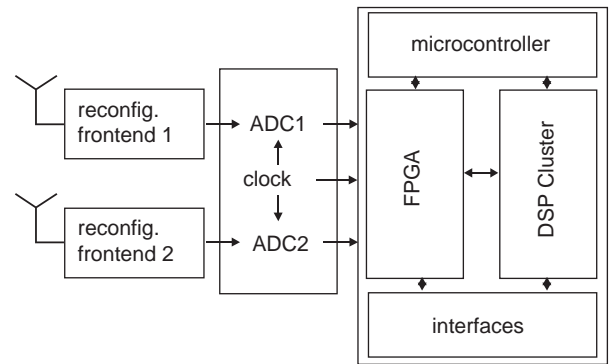


Figure 12. Block diagram of a reconfigurable receiver for automotive applications.

Two independent frontends amplify the signal and realize, if necessary, the downconversion on an IF frequency. In a first realization step the front end is able to handle the FM frequency range from 88 to 108 MHz and the DVB-T frequency range between 470 and 861 MHz. It is possible to extend it to AM/DRM (0.1–10 MHz), DAB (174–230 MHz), and the satellite based digital audio broadcasting services Sirius/XM Sat Radio at 2.3 GHz.

The sampling clock is about 76.8 MHz, so the FM spectrum can be sampled directly and channel selection is performed in the digital domain. Because of limited signal processing power for DVB-T and FM, two different sampling rates are used. For FM the signal is directly sampled so that the wanted signal between 88 and 108 MHz appears at 11.2–31.2 MHz after sampling. The DVB-T signal is mixed down to an IF frequency of 155 MHz and sampled after IF filtering with a sample rate of 48 MHz. The signal will finally appear at 11 MHz.

Direct sampling of the FM signal requires that the ADC be able to handle the whole dynamics of the FM band. Slow fading of the input signal is adapted by digital programmable amplifiers, whereas fast fading must be handled in digital domain.

The main task of the input stages is to suppress out-of-band interferers that may appear in the wanted signal band after sampling. A four-stage filter based on low-cost printed LC resonators is built up and realizes a suppression higher than 80 dB of out-of-band interferers. For FM the highest signal levels can be expected in the wanted signal band so that the filtering fulfills the requirements.

The requirement for the ADC is a signal-to-noise ratio of about 90 dB related to a signal bandwidth of 400 kHz and a spurious-free dynamic range (SFDR) of 95 dB. Particularly regarding the SFDR, care has to be taken when designing the ADC driver stages.

For DVB-T reception, an analog downconverter stage is implemented to achieve a fixed intermediate frequency of 155 MHz. To avoid IF disturbance by the image frequency, an adjustable analog input filter is used. It is based on LC resonators with varactor diodes and can be controlled over a digital to analog converter by the microcontroller. A suppression of more than 80 dB of the image frequency 310 MHz above the used channel is realized. The frequency response is depicted in Fig. 5. After downconversion the

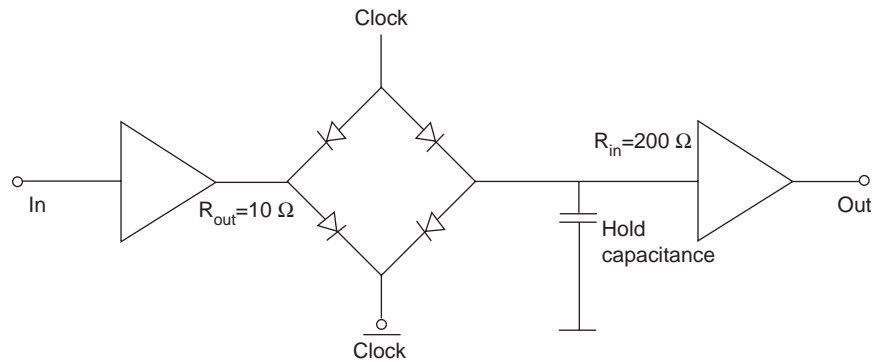


Figure 13. High-frequency sample-and-hold circuit.

amplification can be directly set by the digital signal processing unit to achieve an optimum amplitude at the input of the analog to digital converter.

By using an IF bandwidth of about 10 MHz, all standards in this frequency range can be handled, so it is only a question of digital signal processing to process them.

Because DVB-T uses an 8-channel OFDM modulation scheme, the influence of phase noise of the local oscillator is critical [26,27]. At 100 kHz offset a phase noise of -110 dBc is achieved, which conforms to simulations sufficient for DVB-T.

The complex downconversion and channel filtering is realized in a FPGA (field-programmable gated array). Further signal processing tasks, including demodulation, channel estimation, interleaving, and decoding, are implemented partly in the FPGA and in an array of DSPs.

6. A MILLIMETER-WAVE SAMPLING HEAD

The basic components of a millimeter-wave sampling head are shown in Fig. 13 [28]. The analog RF input signal passes the high- Q MEMS AAF and is then converted to a low impedance level ($<10 \Omega$). The impedance transformer and amplifiers can be realized in commercial SiGe technology for operation frequencies up to 24 GHz [29]. As a switch stage, a silicon millimeter wave integrated circuit (SIMMWIC) Schottky diode quadruple bridge is used [30]. The Schottky diodes have a cutoff frequency of 1.5 THz. The impedance transformer II is again realized in SiGe technology and has to provide a high input impedance level.

7. CONCLUSIONS

Two kinds of digital receivers are discussed in this article: the direct bandpass-limited sampling receiver and the six-port configuration. The sampling architecture poses the highest requirements for the analog-to-digital converter. Bandpass limitation can be used to relax these requirements or to trade against higher resolution of the converter. The bandpass filter makes this approach basically a narrowband solution. The six-port digital receiver is based on a scalar measurement technique that uses multiple detection channels at different points during the

period of a signal, which consists of the signal to be received and a reference signal of the same frequency. As this is an additive rather than a multiplicative mixing process, the system dynamics of a six-port receiver are inferior to, for example, those of a heterodyne or direct conversion receiver. The six-port receiver, however, is basically broadband-capable and does not have to cope with image rejection problems.

Direct narrowband sampling of millimeter-wave signals becomes feasible with silicon-based high-speed integration technologies and high- Q MEMS approaches. If a sampling and clock frequency of 10.66 GHz is applied to a carrier frequency of 24 GHz and a signal with 250 MHz bandwidth is used a resolution of 3 bits is obtained if noise shaping is not applied.

Acknowledgments

The authors acknowledge the contributions of Torsten Mack, Dr. Karl Strohm, and Dr. Franz Schmückle.

BIBLIOGRAPHY

1. H. Schnepf, Th. Müller, and J.-F. Luy, Channel diversity in a software autoradio, *Proc. IEEE Vehic. Technol. Conf.*, Rhodes, Greece, May 2001, pp. 190–194.
2. J. Lindner, Advanced modelling of wireless digital transmission: From scalars to vectors, *Proc. Frequenz* 55, 2001, pp. 296–300.
3. R. H. Walden, Analog to digital converter survey and analysis, *IEEE J. Select. Areas Commun.* 17(4):539–550 (April 1999).
4. J. H. Reed, *Software Radio: A Modern Approach to Radio Engineering*, Prentice-Hall, Englewood Cliffs, NJ, 2002.
5. http://www.analog.com:AD6645_datasheet.
6. J. Tsui, *Digital Techniques for Wideband Receivers*, Artech House, Norwood, MA, 1995.
7. http://www.analog.com:AD8345_datasheet.
8. T. Müller, J. Hao, and J.-F. Luy, A fully software configurable receiver for automotive applications, *Proc. Software Defined Radio Technical Conf.*, San Diego, Nov. 11, 2002.
9. T. Müller, S. Herter, and J.-F. Luy, Clock generator phase noise in RF sampling receivers, *Proc. 2nd Karlsruhe Workshop on SDR*, Karlsruhe, Germany, March 2003.
10. G. F. Engen and C. A. Hoer, Application of an arbitrary 6-port junction to power measurement problems, *IEEE Trans. Instrum. Meas.* **IM-21**:470–474 (Nov. 1972).

DIGITAL RADIO

VALENTINE A. AALO
Florida Atlantic University
Boca Raton, Florida

11. G. F. Engen, The six-port reflectometer: An alternative network analyzer, *IEEE Trans. Microwave Theory Tech.* **MTT-25**: 1075–1080 (Dec. 1977).
12. B. Huyart et al., A MMIC six-port reflectometer, *Proc. 35th Midwest Symp. Circuits and Systems*, Washington, DC, Aug. 12, 1992, pp. 1485–1488.
13. Ji. Li, R. G. Bosisio, and K. Wu, A six-port direct digital receiver, *IEEE MTT Symp. Digest*, San Diego, May 1994, Vol. 3, pp. 1659–1662.
14. M. Ratni, D. Krupezevic, Z. Wang, and J.-U. Jürgensen, Broadband digital direct down conversion receiver suitable for SDR, *Proc. PIMRC*, 2002.
15. J.-U. Jürgensen, D. Krupezevic, M. Ratni, and Z. Wang, Baseband aspects of a direct conversion receiver concept utilizing five-port technology, *Proc. 2nd Karlsruhe Workshop on Software Radio*, 2002.
16. J. Hyyryläinen, L. Bogod, S. Kangasmaa, H.-O. Scheck, and T. Ylämurto, Six-port direct conversion receiver, *Proc. 27th European Microwave Conf. and Exhibition*, Jerusalem, 1997.
17. C. G. Migelez, B. Huyart, E. Bergeault, and L. P. Jallet, A new automobile radar based on the six-port phase/frequency discriminator, *IEEE Trans. Vehic. Technol.* **49**(4):1416–1423 (July 2000).
18. A. Stelzer, C. G. Diskus, R. Weigel, and H. W. Thim, Using a six-port device in an FM-CW radar, *Proc. 8th Int. Symp. Microwave and Optical Technology ISMOT 2001*, Montreal, Quebec, Canada, June 19–23, 2001, Polytechnic International Press, pp. 323–326.
19. B. Huyart, J.-J. Laurin, R. G. Bosisio, and D. Roscoe, A direction-finding antenna system using an integrated six-port circuit, *IEEE Trans. Anten. Propag.* **43**(12):1508–1512 (Dec. 1995).
20. T. Mack, A. Honold, and J.-F. Luy, An extremely broadband software configurable six-port receiver platform, *European Microwave Week 2003*, Oct. 6–10, Munich, pp. 623–626.
21. G. F. Engen, Calibrating the six-port reflectometer by means of sliding terminations, *IEEE Trans. Microwave Theory Technol.* **MTT-26**:951–957 (1978).
22. R. G. Bosisio, Six-port receivers, *Proc. Workshop on Software Radios, RAWCON 2003*, Boston.
23. K. M. Strohm, F.-J. Schmückle, B. Schauwecker, J.-F. Luy, and W. Heinrich, Silicon micromachined RF MEMS resonators, *Proc. IEEE MTT-S*, Seattle, 2002, pp. 1209–1212.
24. K. M. Strohm, F.-J. Schmückle, O. Yaglioglu, J.-F. Luy, and W. Heinrich, 3D silicon micromachined resonators, *Proc. IEEE MTT-S*, Philadelphia, 2003, pp. 1801–1804.
25. T. Müller, M. Sliskovic, J.-F. Luy, and H. Schöpp, An automotive broadband sampling receiver for analog and digital broadcasting standards, *Proc. 2003 Software Defined Radio Technical Conf.*, Orlando, FL, Nov. 17–19, 2003.
26. C. Muschallik, Influence of RF oscillators on an OFDM signal, *IEEE Trans. Consum. Electron.* **31**(1):3 (Aug. 1995).
27. M. S. El-Tanany and Y. Wu, L. Házy, Analytical modeling and simulation of phase noise interference in OFDM-based digital television terrestrial broadcasting systems, *IEEE Trans. Broadcast.* **47**(1) (March 2001).
28. E. Biebl, Sampling architectures, *Proc. IEEE MTT-S*, Philadelphia, 2003, pp. 1055–1058.
29. <http://www.atmel.com/atmel/products/prod45.htm>
30. Datasheet, *SIMMVIC Schottky diodes*, DaimlerChrysler, 2002.

This article presents an overview of digital radiocommunications with emphasis on wireless personal communications. Digital radio consists of two main processes: speech coding (and video coding for future systems) and modulation. In speech coding, the continuous analog voice signal is converted into a discrete digital form. In communication systems that provide digital voice services, it is necessary to encode the analog speech into a digital stream for transmission over the channel and at the receiver, to reconstruct the signal with acceptable fidelity. Modulation, on the other hand, is the process of impressing the discrete digital signal onto a radio signal, by varying some parameter or parameters in combination (usually the amplitude, frequency, or phase) of the radio signal. Digital transmission systems exist in a wide variety of forms, mainly determined by the nature of the channel over which the system operates. A process which is common to many digital transmission systems is regeneration. Typically, the received signal at the input of a repeater (receiver) arrives attenuated and dispersed by the channel and corrupted by noise. The first operation of the receiving repeater, therefore, is to preamplify and shape the weakened signal to a level and form from which a reliable threshold detection may be performed. In a wireless channel, the transmitted signal also undergoes multipath fading and shadowing due to obstructions in the transmission path. To combat the effect of multipath fading, the receiver may employ diversity reception, channel coding, and equalization.

The main objective of wireless personal communication is to allow the user access to the capabilities of the global network at any time and without regards to location and mobility. There has been a tremendous growth in the number of subscribers to wireless services in the last decade. As a result, it became very difficult to operate and maintain the quality of the original first-generation analog cellular systems. As the number of subscribers increases in these systems, call quality diminishes. To handle the increasing traffic, the cellular concept in which identical frequencies at noninterfering distances are reused, was adopted giving rise to more interference in the system. Digital radio, used extensively in second-generation and the evolving third-generation systems, considerably improves the quality of the cellular system and enhances the services available to the mobile subscribers. Some advantages of digital cellular radio include [1,2]:

1. More efficient use of the limited radiofrequency (RF) spectrum to improve system capacity
2. Improving the voice quality beyond what is possible with analog cellular systems, especially maintaining voice quality in heavy traffic conditions and use of voice activity detection to save power and increase throughput

3. Providing support for a wider array of services and features
4. Simplifying the task of frequency planning, operating, and maintaining the cellular system
5. Providing a smooth transition from the analog systems to digital radio systems.

Cordless and cellular telephony have gained widespread user acceptance. Cordless telephones are low-power, low-range phones that enable the user to move around the home or office and still place and receive phone calls. The handsets typically operate within 100 m of the user's base station, which is connected to the public switched telephone network (PSTN). Cordless telephony has evolved from being a simple home appliance to sophisticated systems in applications for universal low-power cordless and telepoint systems aimed at pedestrians, and cordless private branch exchange (PBX). Digital cordless telephone systems (such as CT2, DECT, PHS) are optimized for low-complexity equipment and high-quality speech in a quasistatic (with respect to user mobility) environment. They can support higher data rates and more sophisticated applications.

On the other hand, digital cellular radio, originally targeted at vehicular users in urban areas, was developed to maximize bandwidth efficiency and frequency reuse in a macro-cellular, high-speed fading environment. The first-generation cellular systems are analog systems based mostly on frequency-division multiple access (FDMA) and have very limited capacity and poor to average speech quality. The second-generation cellular systems (e.g., IS-54, GSM, IS-95) are all-digital systems and use more efficient multiple access techniques to share the available spectrum among the users. Although personal communications services (PCS) may be regarded as a third-generation system, its implementation uses modified versions of the cellular protocols used in the second-generation systems. While the first-generation analog and second-generation digital systems are designed to support voice communication with limited data communication capabilities, third-generation systems will focus on providing a wide variety of services which include wireless extensions of integrated services digital network (ISDN) and broadband asynchronous transfer mode (ATM). These systems will concentrate on service quality, system capacity, and terminal and personal mobility issues. They will use a variety of cell structures ranging from the conventional macrocells to microcells for urban areas, picocells for indoor applications, and supercells for satellite-based systems.

1. DIGITAL CELLULAR RADIO

1.1. The Cellular Concept

The continuous increase in the demand for telecommunications services and systems has resulted in spectral congestion. Thus the original one cell system with a high-power transmitter to provide good coverage in a wide service area has quickly become limited in capacity. The cellular concept in which the geographic service area

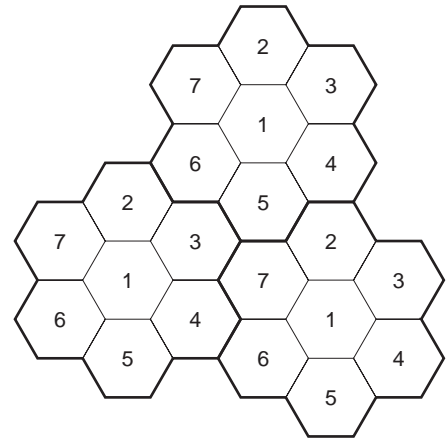


Figure 1. Frequency reuse.

is divided into small regions (called *cells*), each of which is served by a low-power transmitter (base station), has provided a solution to the spectral congestion problem. Adjacent cells are assigned different frequency channels so that the frequencies can be reused throughout the coverage area, leading to a considerable improvement in system capacity. Figure 1 shows a seven-cell frequency reuse pattern. Although frequency reuse increases system capacity, it also increases the amount of adjacent-channel and co-channel interference present in the system. Therefore, for the efficient utilization of the radio spectrum, the frequency allocation scheme must be optimized to increase capacity and minimize interference. As the traffic grows in the coverage area, new cells and channels can be added to the system. The hexagonal cell structure is usually employed in the design of a cellular system; however, in practice the actual cell coverage area (footprint) is irregular and depends on the terrain and multipath characteristics of the radio channel [3]. As such, there may be some regions within the coverage region where there is exceptionally high likelihood of deep signal fades (called *blindspots*) due to shadowing, tunnels, and other obstructions in the signal path. Blindspots can be overcome by using repeaters that receive the signals selectively in one direction, amplify them, and then retransmit exact replicas of the signals in the required direction. Three types of repeaters may be identified, namely: broadband repeaters, frequency-band-selective repeaters, and channel-selective repeaters [4]. Signal degradation at the cell boundaries is handled by handoff operation.

1.2. Handoff

Handoff encompasses a set of functions that are supported between a mobile user and the cellular network that allows the user to move from one cell to another or one radio channel to another, within or between cells, while a call is in progress. When a mobile user is engaged in a call, it will frequently move out of the coverage area of the base station with which it is communicating, and unless the call is passed to another base station, the call will be lost. Thus, the system continuously monitors the quality of the

signals received from the active mobile users. When the signal falls below a preset threshold the system checks whether another base station can receive the mobile user at a better signal level, and if so, the mobile user is commanded by a control signal to switch to the new frequency (corresponding to the new base station). Although the process of measuring the signal quality, channel allocation, and handoff may take a few seconds, there should not be any noticeable break in conversation of the mobile user. Effective and reliable handoff is essential in controlling cochannel interference, especially for microcellular systems.

1.3. The Cellular Network

The structure of all cellular networks is essentially similar. Being complete telephone networks, they have dedicated exchanges within the interconnected system with base stations connected to the exchanges. In practice, however, there are different ways of planning the network depending on the capacity requirement, implementation cost, and capabilities of the chosen manufacturer's equipment. As shown in Fig. 2, a typical cellular system consists of mobile stations, base stations, and a mobile switching center (MSC). Each mobile unit contains a transceiver, antenna, and control circuitry and may be handheld or mounted in a vehicle. The communication between the mobile station and the base station is defined by a standard *air interface*. Each cell in the coverage area is served with one or more base stations that are connected to the MSC. The MSC, in turn, coordinates the activities of the

base stations and connects them via microwave or fiber links to the public switched telephone network (PSTN) which forms the global telecommunications network that connects wireline telephone switching centers (called central offices) to MSCs throughout the world.

1.4. Multiple-Access Schemes

Multiple-access techniques are utilized to accommodate multiple users in the available channels. The multiple access scheme controls the allocation of the channel capacity to the users. The allocation scheme is chosen to maximize the spectral efficiency and minimize transmission delay in the system. Other desirable properties of the multiple-access scheme include fairness of the allocation process, stability of the system, robustness with respect to equipment failure and changing conditions of other users in the system, and flexibility in allowing the integration of voice and data traffic. In addition, in a wireless mobile communication environment, the hidden terminal problem and near-far effect, the effects of multipath fading and shadowing, as well as the effects of cochannel and adjacent channel interference must also be considered. The commonly used multiple-access schemes in cellular systems are frequency-division multiple access (FDMA), time-division multiple access (TDMA), and code-division multiple access (CDMA). In FDMA, the available bandwidth is divided into channels that are assigned to the users on demand and each user uses the channel for the entire duration of the transmission. Frequency guardbands are provided at the edges of the band to minimize crosstalk. Although FDMA has relatively low complexity, requires few overhead bits (for synchronization and framing), and usually does not require equalization since the effect of intersymbol interference (ISI) is minimal, it is wasteful because only a fixed number of users (channels) can be supported and when a channel is not being used it remains idle. Furthermore, FDMA requires very tight filtering to minimize adjacent channel interference and intermodulation. In TDMA systems, the usage of each frequency channel is partitioned into multiple time slots, and each user is assigned a specific frequency-timeslot combination. Thus, in a given cell only a single mobile user uses the entire frequency at any given time. Although TDMA has the disadvantages of requiring synchronization (as well as overhead for guard timeslots) and equalization and can also be wasteful, it permits the use of flexible bit rates and may be used for bursty transmission to save power. Another major advantage of TDMA (over FDMA) arises from the fact that by transmitting and receiving in different time slots it may be possible to eliminate the duplexer circuitry in the mobile unit, replacing it with a fast-switching circuit that turns the transmitter and the receiver on and off at the appropriate times, thus prolonging the battery life of the handsets. Also, TDMA-based systems tend to be more flexible and more open to technological change. Thus, with improvements in speech coding algorithms, a TDMA channel is more easily reconfigurable to accept new techniques supporting higher, lower, or variable bit rates, without disrupting the frequency plan of the cellular network. With CDMA (which uses direct-sequence

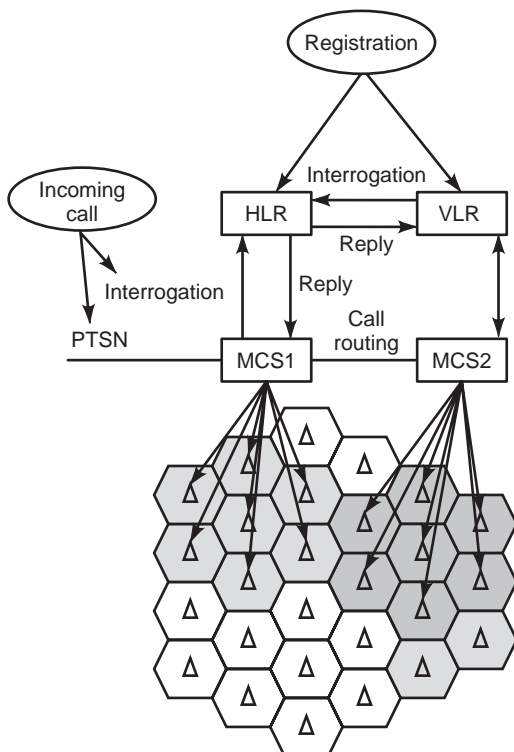


Figure 2. The cellular network.

spreading), a frequency channel is shared simultaneously by multiple users in a given cell, and the signals are distinguished by spreading them with different codes. CDMA has the advantage of offering multipath immunity and interference rejection and provides a graceful performance degradation as the number of users in the system increases. However, CDMA is susceptible to the near-far problem and requires power control [3]. Figure 3 illustrates the three commonly used multiple access schemes in cellular networks.

In general, digital systems can support more users per base station per megahertz of spectrum, allowing wireless system operators to provide service in high-density areas more economically. The use of TDMA or CDMA digital architecture provides the additional advantage of sharing the radio hardware in the base station among the multiple users. It offers flexibility for mixing voice/data communication and the support of new services. A potential for further capacity increases is also possible with the use of reduced-rate speech coders. Furthermore, reduced RF transmit power (increasing battery life of handsets) and the use of encryption for communication privacy, are possible. It offers a more natural integration with the evolving digital wireline network and reduced system complexity (mobile-assisted handoffs, fewer radio transceivers, etc.). While the second-generation cellular systems are based on digital transmission, some of them are designed to coexist with their analog counterparts, while all the evolving third-generation cellular and PCS systems use digital transmission.

In wireless communications systems, it is usually desirable for the subscriber to simultaneously send information to the base station while receiving information from the base station. The process whereby the subscriber can transmit and receive information simultaneously is known as *duplexing*. The two most commonly used duplexing techniques are frequency-division duplexing (FDD) and time-division duplexing (TDD). In FDD, the forward link (base-to-mobile station) and the reverse link (mobile-to-base station) transmissions are done simultaneously on different frequency channels. In this case, a

device called a *duplexer* is used inside each subscriber unit and base station to allow the simultaneous signal transmission and reception on the duplex channel pair. In TDD systems, the same frequency band is used in both the forward and the reverse links but it is required that the transmissions in different directions occur in different time slots.

A performance measure that is commonly used to characterize a digital radio system is the spectral efficiency. The spectral efficiency of a digital radio system E_s is defined as [5]

$$E_s = \frac{\eta_c}{WCA_c} \text{ (erlangs/MHz/km}^2\text{)} \quad (1)$$

where η_c is the carried traffic per channel in erlang, W is the channel bandwidth in MHz, A_c is the cell area in km^2 , and C is the cluster size (number of cells in a reuse cluster).

1.5. Speech Coding

In wireless systems that provide digital voice services, there is the need to encode the analog speech signal into a digital stream for transmission over the channel (air interface). At the receiver, the signal is reconstructed with acceptable fidelity. There are several major parameters to consider in choosing a speech coding scheme for wireless application. These include the transmitted bit rate (kbps), the delivered speech quality, robustness to transmission errors, and complexity of implementation of the chosen scheme. Available speech coding techniques may be classified into three main categories: waveform coding, model-based coding, and hybrid techniques. Waveform coding techniques are usually the simplest to implement and their implementation may be done in either the time domain or the frequency domain. At the transmitter, the analog speech is sampled, quantized, and encoded into digital stream for transmission. At the receiver, a decoder reconstructs the original speech signal. The coder-decoder combination is commonly referred to as a *codec*. Waveform

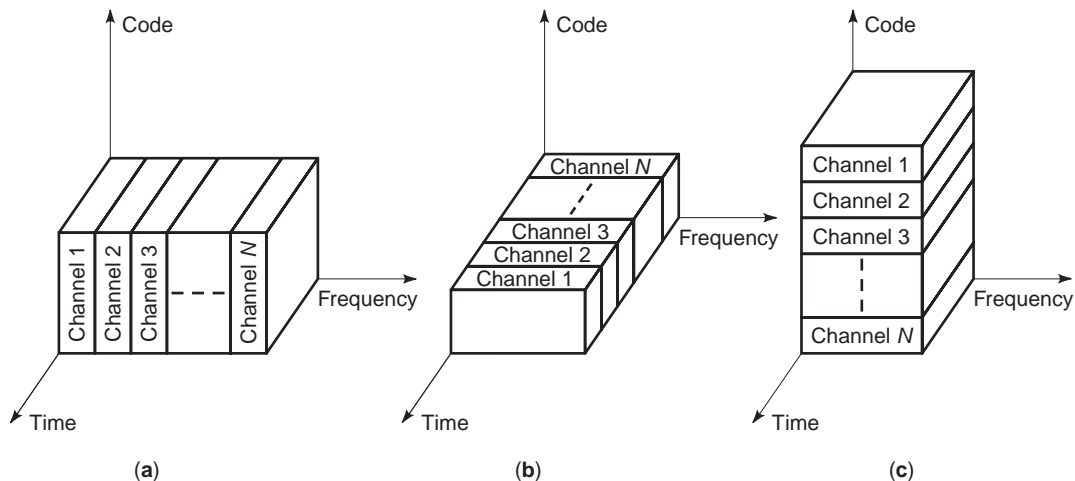


Figure 3. Multiple-access techniques: (a) FDMA; (b) TDMA; (c) CDMA.

speech coding techniques implemented in the time domain include pulse-code modulation (PCM), differential PCM (DPCM), delta modulation (DM), and adaptive predictive coding (APC). One form of delta modulation known as digitally variable slope delta modulation (DVSDM) is used in the second-generation UK cordless telephone system (CT2) because of its implementational simplicity and low cost, but to some extent sacrificing voice quality. When waveform coding is implemented in frequency-domain, the speech signal is filtered into contiguous, nonoverlapping sub-bands encoded independently using time-domain techniques. Examples include subband coding (SBC) and adaptive transform coding (ATC) schemes. In model-based speech coding techniques, signal processing algorithms are used to extract and transmit certain parameters from the analog speech waveform that correspond to the actual time-varying parameters of the speech production mechanism in the human vocal tract (modeled as an electric filter). Thus the algorithms, which are usually called *vocoders*, attempt to describe the speech production mechanism in terms of a few independent parameters used as the information-bearing signals. At the receiver, the received parameters are decoded and used to control a speech synthesizer that is an algorithmic representation of the speech generation model, thereby approximating the original speech signal. Vocoders are medium complexity systems and operate at low bit rates. Their poor speech quality may be attributed to the oversimplified source models used and the assumption that the source and the filter are independent. The poor and synthetic quality of speech vocoders has led to the speech coding approach known as *residual excitation*. In this approach, the speech is synthesized, but a small part is transmitted as a coded waveform part and another as a vocoded part; hence the name *hybrid*. The penalty is the higher bit rate of transmission required, but now a very much improved speech quality is realized. Examples of model-based speech coding schemes that are often used in wireless applications include linear predictive coder (LPC) which usually requires some form of error correction coding when used in wireless channels, long term predictors that include multipulse excitation (MPE-LPT) and regular pulse excitation (RPE-LPT), code-excited linear predictive (CELP) coder and quadrature code-excited linear predictive (QCELP) speech coding schemes, and residual-excited linear predictive coding (RELPC). Table 1 summarizes the

speech coding specification for some cordless and cellular systems [3].

1.6. Modulation Techniques

Many modern mobile communications systems use digital modulation techniques as they offer the advantages of greater noise immunity and robustness to channel impairments, easier multiplexing and integration of different types of information (e.g., voice, data, and video), and greater security over their analog counterparts. Digital modulation also allows the use of source coding, error control coding, encryption, and equalization to improve the performance of the overall system. New advances in very-large-scale integration (VLSI) and digital signal processing (DSP) technology have also improved the effectiveness of the digital modulation schemes used in wireless communications systems. The choice of a digital modulation scheme for use in a wireless environment is influenced by several factors. A desirable modulation scheme provides low bit error rates at low received signal-to-noise ratios, occupies a minimum bandwidth, performs well in a multipath fading environment, and is easy and cost-effective to implement. Since the existing modulation techniques do not simultaneously possess all of these qualities, tradeoffs are often made in a modulation scheme for a particular wireless application. The performance of a digital modulation scheme is usually measured in terms of power efficiency and bandwidth efficiency. *Power efficiency* describes the ability of the modulation scheme to preserve the fidelity of the digital message at low power levels. It is usually expressed as the amount of power (usually given as the ratio of the signal energy per bit to noise power spectral density, E_b/N_0) required at the input of the receiver to achieve a specified probability of error. *Bandwidth efficiency* describes the ability of the modulation scheme to accommodate data within a limited bandwidth. It is defined as the ratio of the throughput data rate per hertz in a given bandwidth and directly reflects how effectively the allocated bandwidth is utilized. While power and bandwidth considerations are very important, other factors must also be considered in choosing a modulation scheme for a wireless application. For example, cellular systems are usually interference-limited and the performance of the modulation scheme in an interference environment is also important. The sensitivity of the receiver to timing

Table 1. Speech Coder Used in Various Digital Radio Systems

Standard	Service Type	Speech Coder Type Used	Bit Rate (kbps)
GSM	Cellular	RPE-LTP	13
CD-900	Cellular	SBC	16
USDC (IS-54)	Cellular	VSELP	8
IS-95	Cellular	CELP	1.2, 2.4, 4.8, 9.6
IS-95 PCS	PCS	CELP	14.4
PDC	Cellular	VSELP	4.5, 6.7, 11.2
CT2	Cordless	ADPCM	32
DECT	Cordless	ADPCM	32
PHS	Cordless	ADPCM	32
DCS-1800	PCS	RPE-LTP	13
PACS	PCS	ADPCM	32

jitters caused by the time-varying channel is an important consideration. For personal communications systems that serve a large number of subscribers in the service area, a modulation scheme that allows a simple yet efficient detector is desirable in order to minimize the cost and complexity of the subscriber receiver unit. Digital modulation schemes may be classified as linear or nonlinear.

In a linear modulation scheme, the transmitted signal may be expressed as

$$\begin{aligned} \phi(t) &= \text{Re}\{A f(t) \exp(j\omega_c t)\} \\ &= A[f_a(t) \cos(\omega_c t) - f_b(t) \sin(\omega_c t)] \end{aligned} \tag{2}$$

where A is the amplitude, $\omega_c = 2\pi f_c$ is the angular carrier frequency, f_c is the carrier frequency, and $f(t) = f_a(t) + j f_b(t)$ is the complex envelope representation of the modulating signal. Linear modulation techniques have good bandwidth efficiency and are attractive for wireless communication systems where there is increasing demand to accommodate more and more subscribers within a limited bandwidth. However, linear modulation schemes are usually transmitted using RF amplifiers, which have poor power efficiency. The use of power efficient amplifiers leads to the regeneration of filtered sidelobes causing severe adjacent-channel interference. A number of techniques have been developed to handle this problem in practice. Examples of linear modulation schemes that are commonly used in practical mobile applications include binary phase shift keying (BPSK), quadrature phase shift keying (QPSK), offset QPSK, and $\pi/4$ QPSK. Coherent detection uses the carrier frequency and phase information to provide optimum detection. It is well known that when coherent detection is used at the receiver the bit error rate performance of BPSK in an additive white Gaussian noise (AWGN) channel is given by

$$P_{E,BPSK}(\gamma) = Q(\sqrt{2\gamma_b}) \tag{3}$$

where

$$Q(t) = \frac{1}{\sqrt{2\pi}} \int_t^\infty \exp(-x^2/2) dx$$

$\gamma_b = \gamma^2(E_b/N_0)$ and γ is the random attenuation factor due to channel fading. The average bit error rate is then obtained by averaging Eq. (3) over the probability density function of γ^2 , $p(\gamma)$:

$$\int_0^\infty P_{E,BPSK}(\gamma) p(\gamma) d\gamma \tag{4}$$

In a Rayleigh fading environment, we have

$$p(\gamma) = \frac{1}{\gamma} e^{-\gamma/\bar{\gamma}} \tag{5}$$

and the average bit error rate can be shown to be given by

$$\bar{P}_{E,BPSK} = \frac{1}{2} \left(1 - \sqrt{\frac{\bar{\gamma}}{1+\bar{\gamma}}} \right) \tag{6}$$

where $\bar{\gamma} = E(\gamma_b) = (E_b/N_0)E(\gamma^2)$ is the average signal-to-noise ratio. In practice, the carrier phase information may not be known precisely or may be random (due to channel fluctuations). In such cases, differentially coherent detection may be employed. The probability of error for differential PSK in AWGN is

$$P_{E,DPSK} = \frac{1}{2} \exp(-\gamma_b) \tag{7}$$

while the average bit error rate can be shown to be given by

$$\bar{P}_{E,DPSK} = \frac{1}{2(1+\bar{\gamma})} \tag{8}$$

The bit error rate performance of QPSK is similar to that of BPSK. However, QPSK comprises two orthogonal BPSK signals and thus has the advantage of providing twice the spectral efficiency of BPSK with the same energy. As such, twice as much data can be transmitted in the same bandwidth. QPSK ideally has a constant amplitude property but occasional π -radian phase shifts momentarily cause the signal envelope of filtered QPSK to pass through zero. This causes serious problems when QPSK is used in mobile/satellite applications with nonlinear amplification because of interference from the sidelobes. OQPSK is a modified version of QPSK in which π -radian phase shifts do not occur. Although OQPSK has the same signal constellation and, therefore, same bit error performance as QPSK, it is not susceptible to adjacent channel interference caused by the regeneration of sidelobes. In $\pi/4$ QPSK the maximum phase transition of 135° is a compromise between the 180° phase transition of QPSK and 90° for OQPSK. Noncoherent detection can be used to demodulate a $\pi/4$ QPSK signal and can provide better performance in a multipath fading environment than OQPSK. Thus $\pi/4$ QPSK has the same performance (bit error rate and spectral efficiency) as QPSK but has less amplitude fluctuation. $\pi/4$ QPSK has been adopted in the North American digital standard (IS-54), the Japanese digital cellular and the Trans European Trunked Radio [3].

Nonlinear modulation techniques have constant envelope so that power efficient class C amplifiers can be used without introducing degradation in the spectrum occupied by the transmitted signal, but they usually occupy larger bandwidths than do linear modulation schemes. Examples of constant-envelope modulation schemes that are frequently used in mobile communication applications are frequency shift keying (FSK), minimum shift keying (MSK), and Gaussian minimum shift keying (GMSK). In binary FSK, the transmitted signal of bit duration T_b may be expressed as

$$f_k(t) = \sqrt{\frac{2E_b}{T_b}} \cos \omega_k t, \quad 0 \leq t \leq T_b \tag{9}$$

when the binary digit $k(k=0, 1)$ is transmitted, where $\omega_0 - \omega_1 = 2n\pi/T_b$ and n is an integer. The average probability of error of the optimum coherent detector in a Rayleigh fading channel corrupted by AWGN can be shown to be given by

$$\bar{P}_{E,\text{CFSK}} = \frac{1}{2} \left(1 - \sqrt{\frac{\bar{\gamma}}{2 + \bar{\gamma}}} \right) \quad (10)$$

while it is

$$P_{E,\text{NCFSK}} = \frac{1}{2 + \bar{\gamma}} \quad (11)$$

for a noncoherent detector. The phase information in FSK signal is not properly utilized at the receiver except for synchronization. MSK is a special case of *continuous phase* FSK (CPFSK) in which the peak frequency deviation is half the bit rate. Thus, MSK may be regarded as a special case of OQPSK with the rectangular pulseshaping replaced by half-sinusoidal pulse shaping. Thus, like OQPSK, MSK has a constant envelope but the phase transitions are continuous. Also, an MSK signal (like an FSK signal) can be demodulated coherently or noncoherently. Finally, GMSK may be regarded as a special case of MSK in which the sinusoidal weighting function is replaced by a Gaussian shaped pulse. GMSK also has constant envelope and excellent spectral efficiency. The average bit error rate of coherently demodulated MSK (and GMSK) in Rayleigh fading channel may be shown to be given by [3]

$$P_{E,\text{MSK}} = \frac{1}{2} \left(1 - \sqrt{\frac{\eta\bar{\gamma}}{1 + \eta\bar{\gamma}}} \right) \quad (12)$$

where η is a constant that depends on the product of the demodulator 3 dB bandwidth and the symbol duration (BT) and is given by

$$\eta \cong \begin{cases} 0.68, & \text{for GMSK (BT} = 0.25) \\ 0.85, & \text{for MSK (BT} = \infty) \end{cases} \quad (13)$$

GMSK has been adopted for use in GSM, DECT, and U.S. cellular packet data (CDPD).

2. CHANNEL PROPAGATION

The performance of a wireless communications system is limited by the nature of the mobile radio channel. The transmission path between the transmitter and the receiver usually varies as a result of obstructions from buildings, mountains, and foliage and also as a result of variations in the atmosphere. Thus, electromagnetic wave propagation is usually influenced by the mechanisms of reflection, refraction, and scattering. Multiple reflections cause the transmitted signal to travel along different paths of varying lengths and attenuations, and the interactions of these waves at the receiver location causes multipath fading. Notwithstanding the multipath

fading, the long-term average strength of the received signal decreases as the separation between the transmitter and the receiver increases.

2.1. Channel Propagation Models

Propagation models to characterize the mobile channel can usually be classified into two groups, depending on whether they focus on predicting the average received signal strength (*large-scale* models) or the variability of the received signal (*small-scale* models) at a given distance from the transmitter. Large-scale propagation models based on measurements of actual channels indicate that the mobile radio channel may be characterized by the fourth-power loss model [6]:

$$P_r = \frac{P_t V}{d^\alpha} \quad (14)$$

where P_r is the average received power, P_t is the average transmitted power, d is the distance between the mobile and the base station, α is the exponent of power attenuation ($\alpha \approx 4$, for macrocells), and V is a random variable whose decibel value can be modeled by a zero-mean Gaussian variable (i.e., V is *lognormal*) with standard deviation in the range of 6–12 dB. The propagation in an urban microcellular channel with a line-of-sight (LoS) may be characterized by the following dual-slope path loss model [6]

$$P_r = \frac{P_t V}{d^{\alpha_1} \left(1 + \frac{d}{d_0} \right)^{\alpha_2}} \quad (15)$$

where α_1 and α_2 are the attenuation exponents, and $d_0 = 4h_t h_r / \lambda$, where λ is the transmission wavelength and h_t and h_r are the transmitting and receiving antenna heights, respectively. The decibel standard deviation of the lognormal random variable V is now on the order of 3 dB. Measurements in several urban environments indicate that for small transmitting and receiving antenna heights ($h_t = h_r \approx 3.7$ m), $\alpha_1 \approx 2.2$ and $\alpha_2 \approx 3.3$. For medium antenna heights (about 8.5 m), $\alpha_1 \approx 2.2$ and $\alpha_2 \approx 3.4$ and for large antenna heights, $\alpha_1 \approx 2.1$ and $\alpha_2 \approx 4.2$ [3].

On the other hand, small-scale multipath propagation causes rapid fluctuations in signal strength (fading) over small distances or time intervals. Small-scale propagation is also influenced by Doppler shifts caused by relative motion between the transmitter and the receiver, and by the time dispersion caused by the multipath propagation delays. Time dispersion due to multipath propagation causes the transmitted signal to undergo either *flat* or *frequency-selective* fading. The Rayleigh and Rice probability density functions are commonly used to model envelope fluctuations in a flat-fading channel when there is no direct transmission path between the transmitter and the receiver and when a LoS component is present, respectively. The Nakagami m distribution is a more general model that has been shown to provide a better match to envelope measurements in different mobile radio environments than the Rayleigh and Rice distributions. The Rayleigh

distribution is a special case of the Nakagami distribution, while the Rice distribution can be approximated by the Nakagami distribution for a large range of mean signal-to-noise ratio values.

2.2. Combating Multipath Fading

Two major causes of performance degradation in wireless systems are multipath fading and shadowing. There are three ways to combat the effects of fading in these systems: diversity reception, channel coding, and equalization. Diversity reception techniques are used extensively on multipath fading radio channels to reduce the effect of fading on system performance, including both fixed and mobile terminals. In diversity reception, several replicas of the transmitted signal, each carrying the same information and undergoing independent fading, are combined at the receiver. The diversity may be obtained in time, frequency, or space. There are several ways that the receiver may combine the received diversity signals for optimum performance. Three of the commonly used linear combining schemes are maximal-ratio combining (MRC), equal-gain combining (EGC), and selection diversity combining (SDC). *Microscopic diversity* reduces the effect of instantaneous short-term (or small-scale) fading by combining several uncorrelated signals received at the radio port using any of the combining methods. *Macroscopic diversity* mitigates the effect of long-term (or large-scale) shadowing by using several geographically distributed base stations to serve each cell. The base station with the largest average local mean signal power is usually selected [5,7]. Figure 4 shows the diversity gain obtained by using MRC microscopic diversity reception in detecting BPSK signals in a Rayleigh fading channel. We observe from the figure that with a coherent detector at the receiver, in order to obtain an error rate of 10^{-3} , the receiver requires a signal-to-noise ratio (SNR) of 24 dB when there is no diversity ($L=1$), but only 11 dB with dual-branch diversity ($L=2$) and 4 dB with fourth-order ($L=4$) diversity. The

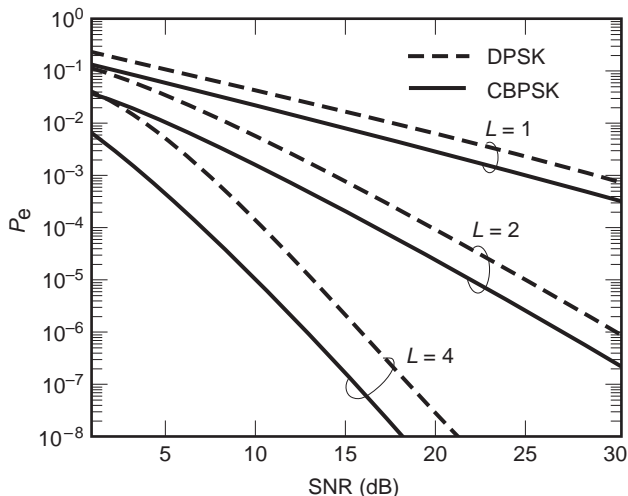


Figure 4. Average bit error rate for a BPSK system with L -branch microscopic MRC diversity in a Rayleigh fading channel.

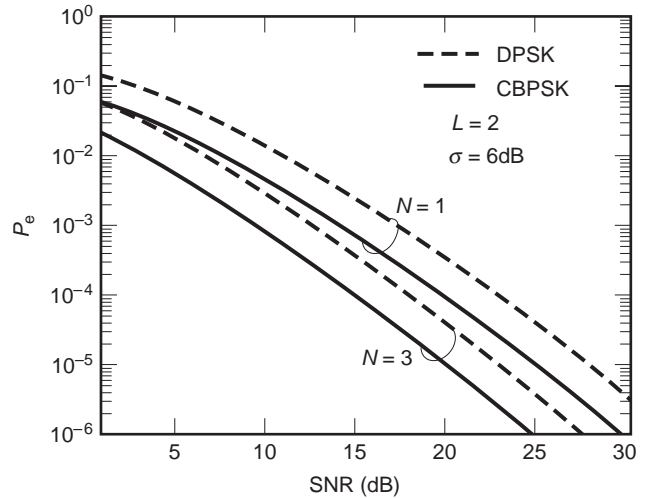


Figure 5. Average bit error rate for a BPSK system with macroscopic selection diversity (and dual-branch microscopic MRC diversity) in a shadowed Rayleigh fading channel.

performance of DPSK is about 3 dB inferior to that of coherent PSK. In Fig. 5, the effect of macroscopic selection diversity is shown, with the lognormal shadowing assumed to have a decibel standard deviation of 6 dB. At a bit error rate of 10^{-3} and with dual order microscopic diversity, macroscopic diversity of order 3 ($N=3$) provides about 5 dB improvement over the system with no macroscopic diversity ($N=1$).

In channel coding schemes, extra bits (with no message) are added to the information bitstream before being transmitted over the channel. At the receiver, the added redundant bits are used to detect/correct errors that may have occurred in the bitstream. Channel error control techniques used in wireless channels may be classified into three groups, namely: error detection coding (the most commonly used error detection scheme is the cyclic redundancy check (CRC) codes because they are very easy to implement using shift registers), forward error correction (FEC) coding (using block or convolutional codes), and automatic repeat request (ARQ) transmission protocols. The amount of diversity gain introduced by channel coding depends on the minimum distance of the code. The addition (and interleaving) of redundant bits into the data bitstreams in the channel coding process gives rise to time or frequency diversity and improves the resistance of the system to multipath fading.

The time-variant multipath channel after exhibits bursty error characteristics. By the process of interleaving, the bursty channel can be transformed into a channel having independent errors by spreading the coded data over several timeslots. Interleaving is used extensively in the second-generation digital cellular systems.

A very serious problem in high-data-rate transmission systems is intersymbol interference (ISI) caused by frequency-selective multipath fading. In this case, increasing the transmission power worsens the problem because the interference power increases. Signal processing techniques (known as equalization) may be used to minimize

the effect of ISI. In wireless applications, *adaptive* equalization is used since the mobile channel is random and time-varying. The operation of an equalizer usually involves the transmission of a known, fixed-length training sequence to set the parameters of the equalizer at the receiver. New algorithms, called "blind equalization," which do not require training sequences, are currently under research. During data transmission, the adaptive equalizer uses recursive algorithms to evaluate the channel and estimate the filter coefficients that are used to compensate for the channel distortions. Adaptive equalizers can be classified as linear or nonlinear depending on how the equalizer output is used for subsequent control (feedback) of the equalizer.

3. WIRELESS TRANSCEIVER STRUCTURE

The complexity of radiocommunication systems is increasing significantly with the application of more sophisticated multiple access and digital modulation techniques that are necessary in order to accommodate the tremendous growth in the number of subscribers of wireless communication services. Advances in wireless technology and new applications for wireless systems and services have given rise to a variety of portable voice, data, and messaging systems. The development of low-rate digital speech coding techniques and the continuous increase in the device density of integrated circuits have led to completely digital second-generation cellular systems. Also, the evolving third-generation cordless, cellular, and PCS systems are all expected to be fully digital. Digital signal processing (DSP) techniques traditionally used for speech and channel codecs are presently being used extensively for advanced digital communications transceiver design. In addition to speech and channel codecs, these techniques are also being used for detection and demodulation, equalization, frequency synthesis, and channel filtering.

3.1. Radio Receiver Principles

A considerable amount of computing resources are necessary to achieve the performance desired for personal communication systems and the required power needed to drive the constituent units of the system may be prohibitive for portable applications. Thus, the key requirements for wireless portable terminals are performance, cost, power consumption, and size. Low power consumption may be achieved through technology and system-level tradeoffs. The receiver power is consumed by the RF components, baseband DSP, digital application-specific integrated circuits (ASICs), and mixed signal devices. At the system level, power consumption may be optimized by proper choice of system operations such as time-division multiplexing and voice-activity detection. For example, many digital processors feature powerdown modes that allow turning off peripheral and certain computational units. One drawback of such method, however, is that it does not always allow for fast rampups. In a wireless environment, the receiver may have to process very low desired signal levels in the presence of large levels of

unwanted signals. Therefore, the architecture used in the receiver front end must satisfy requirements such as sensitivity, dynamic range, selectivity, and manufacturability. Radio receiver principles that may be used include the superheterodyne principle, digital receivers with DSP techniques, and direct-conversion receivers [8].

In a direct-conversion receiver, the received RF signal is filtered in a duplexer, and passed through a low-noise amplifier followed by a bandpass filter. The output of the filter is then split and, along with two local oscillators in phase quadrature at the carrier frequency, are fed to a quadrature mixer. The outputs of the quadrature mixer are then passed through a lowpass filter followed by analog-digital (A/D) conversion to produce the in-phase (I) and quadrature (Q) samples. Since the receiver processes the full RF spectrum at baseband, this architecture requires high dynamic range, high sensitivity, low noise, as well as proper amplitude and phase balancing between the I and Q branches. The main advantage of the direct-conversion architecture is its simplicity as it has a low component count. It also has a wide tuning range and high selectivity. However, a number of challenges are present in its realization. For example, a high-gain low-noise mixer is necessary to combat the $1/f$ amplifier noise at baseband as well as a technique to cancel the associated large DC-offset. The direct-conversion receiver architecture is used in a number of cellular and wireless products. For example, a radio receiver that incorporates direct-conversion into an integrated circuit in a way that avoids the need for discrete intermediate frequency filters and is particularly suitable for use in wireless devices has been proposed [9]. Also, FSK paging receivers at 450 MHz and 930 MHz as well as some 900 MHz wireless LAN products are available.

3.2. Miniaturization

Wireless personal communication devices such as pagers and cellular and cordless telephones are becoming more compact and more light weight as a result of improvements in device-mounting technology and development of different kinds of devices. By using advanced very large-scale integration (VLSI) technology, the implementation of complex algorithms is economically feasible. The use of complementary metal-oxide semiconductor (CMOS) device scaling technology has facilitated the employment of denser and faster memory chips as well as digital microprocessors. Rapid advances in solid-state integrated circuit technology have fueled the growth of commercial wireless communication systems with the desire to produce high-performance, low-power, small-size, low-cost, and high-efficiency devices. The increasing use of integrated circuits in radio designs has resulted in significant improvements in the reliability and performance of the digital receivers. Rapid advances in packaging technology resulting in compact designs of wireless terminals as well as considerable drops in manufacturing costs resulting from improved procedures in assembly and testing have also increased the deployment of these devices.

3.3. Design Tools

The lifecycles of many cellular and cordless products are very short. As such, in order to compete successfully, companies must turn system concepts into silicon VLSI very rapidly. High-quality computer-aided design tools are therefore very important for efficient design, simulation, and realization of the systems. The design methodology used in these tools must be chosen to allow different levels of abstraction at different points in the timescale. The algorithms used in these design tools are usually comprehensively specified with block diagrams that are specified hierarchically, with each block representing a signal processing operation. The blocks are usually parameterized so that automatic evaluation of the different simulations can be done based on the block diagrams. Depending on the digital communication system involved, multirate and variable-rate processing may be supported. Two simulation approaches that are available in practical design tools are the data-flow-oriented approach (e.g., COSSAP from Synopsys) and the time-driven approach (e.g., SPW from Candence) [10]. In addition to the algorithmic simulations, the architecture of the digital communication system also needs to be simulated. The simulation of the architecture may be software-based or hardware-based.

4. OVERVIEW OF DIGITAL RADIO SYSTEMS

4.1. Digital Cellular Systems

Digitization allows the use of TDMA and CDMA over FDMA as multiple-access alternatives. The North American Digital Cellular systems have evolved into two *Interim Standards*, one based on TDMA (IS-54) and the other based on CDMA (IS-95). The Global System for Mobile communication (GSM) as well as the Japanese Pacific Digital Cellular (PDC) system (which is very similar to the IS-54 system) are also based on TDMA while the Broadband-CDMA (IS-665) system is a specialized CDMA system [3,5,11].

4.1.1. North American Digital Cellular Systems. The development of a digital cellular standard in North America came as a result of tremendous increase in the demand for cellular services. The capacity of the first-generation analog advanced mobile phone system (AMPS) was limited, and there was no new spectrum available to meet the increased demand. Therefore, the objective of the second-generation systems was not only to increase the capacity of the existing spectrum but also to provide additional services. The Cellular Telecommunications Industry Association (CTIA) which consists mainly of cellular service providers and the Telecommunication Industry Association (TIA) consisting of equipment manufacturers established a technical committee to develop a digital standard. Finally, in 1989, the industry adopted the dual-mode transmission standard, which is referred to as the Electronics Industry Association Interim Standard 54.

4.1.2. TDMA System (IS-54). This is an all-digital second-generation cellular system that was designed to

coexist with and eventually replace the first-generation analog cellular system. On the forward link, the spectrum allocation for IS-54 is 824–849 MHz while on the reverse link it is 869–894 MHz. The modulation scheme used is differential quadrature phase shift keying (DQPSK) with $\pi/4$ radians phase shift between successive symbols, to reduce amplitude fluctuations in the signal envelope. However, as it is a linear modulation scheme, it has poor power efficiency resulting in larger size and weight of the handset. Each TDMA frame has 6 timeslots of 324 bits each, with a framelength of 40 ms, giving a bit rate of 48.6 kbps. Since the channel spacing is 30 kHz, the resulting bandwidth efficiency of 1.62 bps/Hz is relatively high. The speech coder is VSELP operating at 7.95 kbps and produces a speech frame every 20 ms (or 159 bits every second). Of these, the leading 77 bits of each frame are protected with error control coding and the remaining 82 bits are unprotected, resulting in 260 channel bits per frame. Thus the full-rate coder results in a transmitted data rate of 13 kbps.

4.1.3. CDMA System (IS-95). This system is based on direct-sequence CDMA (DSSSS) and was proposed by Qualcomm in 1989 and adopted in 1993. IS-95 was also designed to be compatible with the AMPS. The spectrum allocation for IS-95 on the forward link is 824–849 MHz, while it is 869–894 MHz on the reverse link. With an allowable bandwidth of 1.25 MHz, it uses a direct-sequence spread-spectrum signal with chip rate 1.228 Mbps. The speech coder used is QCELP with variable rates (ranging from 1200 to 9600 bps) determined by the accompanying voice activity detector. Block interleaving with duration 20 ms provides time diversity while the wide bandwidth allows for frequency diversity and multipath (rake) diversity, making the system robust to multipath fading. Different modulation and spreading techniques are employed on the forward and reverse links. On the forward link, BPSK modulation is used with QPSK spreading. For a single user, either form of modulation yields the same performance, but in a multiple-access environment the use of QPSK spreading randomizes the phase of the desired user relative to the other users in the system giving rise to much less phase degradation for the desired user. Although the 64×64 Hadamard matrix used may allow 64 users in a cell, only 61 Walsh codes are available since the remaining codes are reserved for the pilot, synchronization, and paging channels. Also, on the forward channel, many user signals are multiplexed and transmitted to multiple users, allowing a common pilot signal to be inserted for all the users. Therefore, coherent demodulation is possible on the forward link. On the reverse link, on the other hand, since the users operate asynchronously and are power controlled, no pilot signal is transmitted by the mobile users. Therefore, noncoherent M -ary ($M=64$) orthogonal modulation/demodulation, which is power efficient, is employed on the reverse link.

IS-95 is modified in the following ways in order to support higher data rates for better speech quality at PCS

frequencies:

1. On the reverse link, the convolutional code rate is changed from $\frac{1}{3}$ to $\frac{1}{2}$.
2. On the forward link, the convolutional code rate is changed from $\frac{1}{2}$ to $\frac{3}{4}$.
3. The standard QCELP speech coder is replaced by QCELP13, which also has variable rate and is designed to provide improvements in spectral quantization, voice activity detection, and pitch prediction. It operates in several modes (which includes QCELP).
4. The data rate is changed from (1200, 2400, 4800, 9600 bps) to (1800, 3600, 7200, 14400 bps).

4.1.4. Broadband CDMA System (IS-665). The wideband CDMA standard supports several bandwidths (5, 10, or 15 MHz) at PCS frequencies. The forward link is similar to that of IS-95 with a few exceptions. There is a pilot signal, a synchronization signal, and up to seven paging signals and several traffic signals are supported as options. Also, unlike IS-95, where the chip rate is 1.228 Mbps, in IS-665, several chip rates (of 4.096, 8.192, and 12.288 Mbps) may be used. On the reverse link, the mobile users transmit pilot signals to the base station. Therefore, coherent detection (of the QPSK modulated signal) is possible. Both the CDMA (IS-95) and the Broadband CDMA (IS-665) systems are synchronized by the Global Position Satellite (GPS) time. The speech coding scheme used is ADPCM.

4.1.5. European Digital Cellular—GSM (DCS 1800). The GSM standard was developed as a joint initiative by members of the Conference of European Posts and Telecommunications Administration (CEPT) with the initial objective of building a unified pan-European network, giving the subscribers a uniform service and easy roaming throughout all of Europe. The GSM technical standard makes full use of currently available technology, incorporating features such as low bit rate speech, convolutional channel coding with bit interleaving, and frequency hopping. Services supported by GSM may be classified into three types: telephone services, data services, and supplementary ISDN services. The spectrum allocation for GSM at 900 MHz is categorized into the *standard* or the *extended* GSM band while the allocation for GSM at 1800 MHz is referred to as *Digital Cellular System 1800* (DCS 1800) band. The frequency assignments for these bands are as follows: for forward link, 935–960 MHz standard GSM, 925–960 MHz extended GSM, and 1805–1880 MHz DCS 1800; for reverse link, 890–915 MHz standard GSM, 880–915 MHz extended GSM, and 1710–1785 MHz DCS 1800.

With a spacing of 200 kHz, the standard GSM has 124 channels, the extended GSM has 174 channels, and DCS 1800 has 374 channels. Each GSM channel supports eight simultaneous users using TDMA of framelength 4.615 ms. The modulation is GMSK with $BT = 0.3$ and slow frequency-hopping every frame at 217 hops per second is used to provide additional protection against frequency-selective fading and cochannel interference. Interleaving is also used to minimize the effect of deep fades. The speech coder

is a regular pulse-excited linear predictive coder (RPE-LPC) with long-term prediction with voice detection capability (voice activity detection factor of 40%) and provides a net bit rate of 13 kbps. It operates in discontinuous transmission mode to prolong battery life. Presently, GSM networks have been deployed in over 60 countries in Europe, the Middle East, Asia, and Africa. In North America, GSM is deployed as PCS 1900.

4.1.6. Japanese Personal Digital Cellular. Established in 1991, the Japanese Personal Digital Cellular (PDC) system is very similar to the North American IS-54 system in terms of their operational characteristics and in the requirement that they replace an existing analog cellular system. The frequency allocation for the PDC represents the main difference between the two systems. PDC has two small frequency bands in the 800/900 and the 1400 MHz band. On the forward link, the frequency assignments are 810–826 MHz and 1477–1501 MHz, while on the reverse link, they are 940–956 MHz and 1429–1453 MHz. With a channel spacing of 25 kHz to be compatible with the existing analog system, PDC uses TDMA to multiplex three slots for three users in a 20-ms frame onto a carrier. The modulation is $\pi/4$ DQPSK with a channel data rate of 422 kbps, and the VSELP voice coder uses error correction coding. Mobile-assisted handoff facilitates the use of small cells, and with the use of space diversity, reduces the required carrier-to-interference ratio. The system provides high quality services, high security, and long handset battery life.

4.2. Digital Cordless Telephony

Cordless telephones are low-power, low-range, full-duplex communication systems that use radio to extend the handset to a dedicated base station with a specific telephone number that is connected to the public switched telephone network. Cordless telephone systems provide the user with limited mobility and it is seldom possible to maintain a call if the user travels outside the coverage range of the base unit. In the first-generation cordless telephone systems, the handset typically operates with localized mobility within a very limited range (on the order of 10 m) of the base unit and is used in the home or in the office. They use analog frequency modulation and operate mainly as extension telephone to a transceiver connected to the public wired network. Because of its analog nature and limited operating range, it has limited traffic-carrying capacity, which in turn limits the full development potential of these systems. Second-generation cordless telephone systems are based on digital transmission format and provide wider coverage ranges, offer good speech quality, provide better security, are more resistant to interference and noise, and use compact handsets with built-in antenna [2].

4.2.1. Cordless Telephone—CT2. This is a second-generation cordless telephone standard introduced in Great Britain in 1989 and designed for residential and office use. It is also used to provide *telepoint services*. Telepoint is a service that is provided to cordless handset owners from

cordless base stations located in public places, such as railway stations and shopping centers. This is a basic public communication service for the less migratory, more localized sector of the traveling market and does not compete directly with the wide roaming mobile cellular network. Thus, the handset purchased for residential or office use can also be used to access the telepoint service while the user is in transit between the home and the office. In CT2, speech waveforms are coded using ADPCM with a bit rate of 32 kbps. Two-way full-duplex conversation is achieved using time-division duplexing (TDD). The modulation used is Gaussian filtered FSK with bandwidth-bit period product $BT = 0.3$. A Canadian enhancement of CT2 is called CT2+ and provides additional mobility management functions.

4.2.2. Digital European Cordless Telecommunication (DECT). DECT is a pan-European standard for cordless telephone that was designed to provide cost-effective communication to high user densities in picocells. Intended applications of DECT include residential cordless telephony, telepoint services, and cordless PBX. Although DECT is functionally closer to a cellular system than a standard cordless telephone system, the interface of DECT to the PSTN or ISDN network remains the same as for a corded telephone. DECT uses TDMA with TDD and the base station can support multiple handsets simultaneously with a single transceiver. The modulation and speech coding techniques used in DECT are similar to those in CT2.

4.2.3. Personal Handyphone System (PHS). PHS is a Japanese air interface standard with the design objective of providing service not only for home and office use but also for public access capability. PHS uses TDMA and TDD, with each TDMA frame of 5 ms duration. The speech coding used is ADPCM with data rate of 32 kbps in conjunction with CRC error detection (with no error correction) and the modulation used is $\pi/4$ DQPSK. Since PHS uses dynamic channel assignment the base stations can allocate channels based on the signal strength seen at both the base station and the portable, and handoffs are supported only at walking speeds as the system is designed for microcell/indoor PCS use.

4.2.4. Personal Access Communication Systems (PACS). PACS is a third-generation personal communications system designed to support voice, data, and video images for low-speed portable applications in microcell/indoor environments. The PACS interface provides wireless connectivity to a local exchange carrier (LEC) and it uses TDMA, with frequency-division duplexing (FDD). The modulation used is $\pi/4$ QPSK, with coherent demodulation, which provides substantially better performance than do other digital cordless telephone systems with discriminator-based receivers. Two-branch polarization diversity with feedback at both the base station, and the handset gives an improvement that approaches a four-branch diversity reception system. The subscriber unit uses adaptive power

control to minimize battery drains during transmission and to reduce cochannel interference on the reverse link.

4.3. Paging Systems

A traditional paging system is a one-way, wireless communication device that sends brief messages (usually a numeric message, an alphanumeric message, or a voice message) to notify a subscriber of the need to call a particular telephone number or to receive further instruction from another location. There are two types of paging systems: the radio common carrier (or a *subscriber* system) and the *private* paging systems. The subscriber paging system is a licensed, public paging company providing paging services to the public and the coverage area may be local, statewide, nationwide, or international. The private paging system involves a customer-owned transmission system and paging receivers for private paging use. When multiple transmitters broadcast a page (known as *simulcast*), the subscribers can roam from the home area to anywhere the paging system is networked. The traditional definition of paging has evolved from the one-way communication device to a two-way device that sends and receives data with services including customized response functions, connection to online information services, e-mail messaging, etc. A number of signaling standards for paging systems have also evolved. Examples include POCSAG, which is a one-way paging system; ERMES, which is the European paging system; Motorola's FLEX family of paging products; and AT&T's P-act, which is a narrowband PCS paging system [12].

5. PERSONAL COMMUNICATION SERVICES

Wireless personal communication services (PCS) is a concept that extends wireless communications beyond the limitations of the current cellular system to provide users with the ability to communicate with anyone, anywhere, and at any time. A number of characteristics are generally associated with PCS in order to provide reliable service on demand anywhere, any time. The handsets must be portable and easy to use with a long battery life, each user must have a single personalized number that can be reached anywhere, and the system must provide an individualized feature profile that follows the user and provides service at any location. PCS must support various user mobility patterns and provide wide user roaming ability to provide for universal accessibility. Consequently, different cell sizes must be used depending on the type of application and user density. In general, four types of cells can be distinguished for PCS: the picocell (for low-power indoor applications), the microcell (for low-power indoor or outdoor pedestrian applications in high-population-density areas), the macrocell (for high-power vehicular applications), and supermacro cells (for use with satellite systems). Radio systems for PCS must have a variety of operating power levels, and the users should be able to use the service in diverse environments with a wide variation in the radio propagation properties. The system must allow easy integration of the wireless system with the

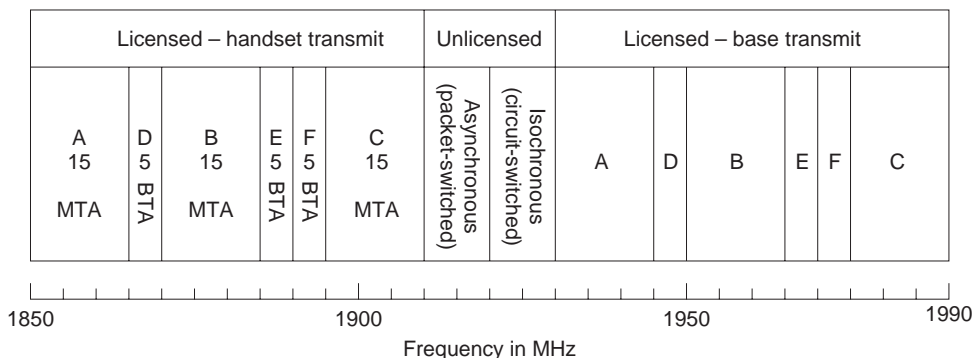


Figure 6. The US PCS frequency plan.

wireline system and ubiquitous deployment of the radio systems.

The services that can be offered by PCS and cellular are identical, except that the operating frequencies are different. The subscriber is indifferent to the frequency band as long as the services are not affected. Thus, the main forces that influence the PCS and the cellular industries are similar. Some of these forces are the regulators, PCS operators, equipment vendors, subscribers, and competing products. The service area in the United States and its territories are divided into 51 major trading areas (MTAs) and 493 basic trading areas (BTAs) according to the Rand McNally 1992 *Commercial Atlas and Marketing Guide*, 123rd ed. Based on FCC regulation, each area in the United States can be served by at least six PCS operators, in addition to the existing two cellular operator and one specialized mobile radio (SMR) service operators [12].

One of the most important defining elements of PCS is the FCC's allocation of 120 MHz of spectrum around the 1200 MHz frequency band for licensed operation and another 20 MHz for unlicensed operation, resulting in a total of 140 MHz for PCS. This is about three times the 50 MHz spectrum currently used by the cellular system, indicating the resolve to make PCS more widely available. Figure 6 shows the frequency allocation for PCS.

No specific technology has been mandated by the FCC for the PCS market. As such, a number of competing technologies have been chosen by the major PCS carriers. Presently, seven PCS standards can be identified. These include GSM (PCS 1900), a derivative of the GSM/DCS 1800 standard; CDMA, a modification of IS-95; DAMPS; PACS, air interface for pedestrian applications; CDMA/TDMA, a composite hybrid that uses TDMA within cells and CDMA between cells; DECT-based TDMA; and broadband CDMA [12]. Of these, the four most widely deployed systems at the present time are GSM, CDMA, TDMA, and PACS.

BIBLIOGRAPHY

1. T. B. Bursh et al., Digital radio for mobile applications, *AT&T Tech. J.* **72**:19-26 (1993).
2. J. E. Padgett, C. G. Gunther, and T. Hattori, Overview of wireless personal communications, *IEEE Commun. Mag.* **33**:28-41 (1995).

3. T. S. Rappaport, *Wireless Communications: Principles & Practice*, Prentice-Hall, Upper Saddle River, NJ, 1996.
4. R. C. Macario, *Cellular Radio: Principles and Design*, 2nd ed., McGraw-Hill, New York, 1997.
5. V. K. Garg and J. E. Wilkes, *Wireless and Personal Communications Systems*, Prentice-Hall, Upper Saddle River, NJ, 1996.
6. M. V. Clarke, V. Erceg, and L. J. Greenstein, Reuse efficiency in urban microcellular networks, *IEEE Trans. Vehic. Technol.* **46**:279-288 (1997).
7. A. Abu-Dayya and N. C. Beaulieu, Micro- and macrodiversity NCFSK (DPSK) on shadowed Nakagami-fading channels, *IEEE Trans. Commun.* **42**:2693-2702 (1994).
8. H. Meyr and R. Subramanian, Advanced digital receiver principles and technologies for PCS, *IEEE Commun. Mag.* **33**: 68-78 (1995).
9. T. Okanobu, D. Yamazaki, and C. Nishi, A new radio receiver system for personal communications, *IEEE Trans. Consum. Electron.* **41**:795-803 (1995).
10. K. S. Shanmugam, Simulation and implementation tools for signal processing and communication systems, *IEEE Commun. Mag.* **32**:36-40 (1994).
11. A. Fukasawa et al., Wideband CDMA system for personal radio communications, *IEEE Commun. Mag.* **34**:116-123 (1996).
12. R. Kuruppillai, M. Dontamsetti, and F. J. Cosentino, *Wireless PCS*, McGraw-Hill, New York, 1997.

DIODES

KONSTANTINOS MISIAKOS
 NCSR "Demokritos"
 Athens, Greece

The word *diode* originates from the Greek word Δίοδος, meaning passage or way through. In electronics terminology, in fact, diode refers to a two-terminal device that allows current to flow in one direction while it blocks the flow of current in the opposite direction. Such devices usually employ semiconductor junctions or metal-semiconductor junctions. There are also diodes made of vacuum tubes or metal—purely ionic crystal contacts. This article deals with semiconductor p-n-junction diodes because they are the most widely used in practice because of their versatility, reproducibility, stability, and compatibility with integrated circuit technology. Additionally, an

insight into the operation of the p-n-junction diode is the basis for understanding the device physics of other semiconductor devices, the majority of which use the p-n-junction as the building block. The semiconductor of our choice will be silicon because almost all diodes, discrete or integrated, are made of this element. Extensions to other semiconductors will be made to generalize theoretical results or to set limits to the validity of certain equations.

Figure 1a shows the electrical symbol of a diode. The arrow-type symbol indicates the conduction direction. For a diode to conduct an appreciable electric current, the voltage on the left side of the symbol must be a little higher than the voltage on the right side. If this polarity is reversed, the current drops to negligible values even for a large bias. The two previous polarity modes are known as *forward bias* and *reverse bias*, respectively. In Fig. 1b the very basic material structure of a diode is shown. The starting material is a high-purity silicon crystal, the properties of which are properly modified by selectively introducing dopants (elements) from either the third or the fifth column of the periodic table. The third-column elements, when introduced into the silicon lattice, behave as acceptors: they trap electrons from the valence band, thereby creating positively charged holes in the valence band and negatively charged immobile acceptor ions. The acceptor-doped part of the diode is called the p side. On the other hand, fifth-column elements behave as donors; they give up their fifth electron, creating a population of conduction band electrons and positively charged immobile donor ions. The donor-doped part of the device is the n side. The introduction of acceptor and donor dopants into silicon creates the two polarity sides of the diode, as shown in Fig. 1a. Schematically speaking, when applying a forward bias, the higher voltage on the p side makes the electron and hole gases move into each other. Thus, an electric current is created through electron-hole pair recombination. On the contrary, a lower voltage on the p side moves the charge carriers away, thus preventing recombination and eliminating the current. In terms of dopants, the previous account of how the p-n diode is formed also holds for germanium diodes, which also is a fourth-column elemental semiconductor. For compound semiconductors (e.g., GaAs, InP, CdTe), the chemical origin of donor and acceptor dopants is more complex in relation to the semiconductor elements themselves.

In Fig. 2 the current-voltage (I - V) characteristic of an ideal diode as well as a realistic one is shown. The ideal

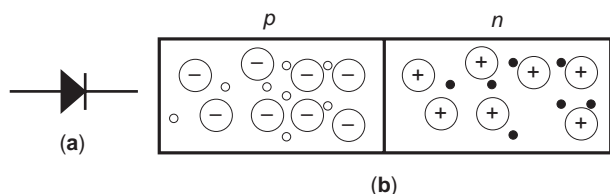


Figure 1. Electrical symbol of a diode (a) and illustration of a semiconductor p-n junction (b). In (b) the large circles with the minus and the plus signs are the acceptor and the donor ions, whereas the small circles are the holes (empty) and the electrons (dark).

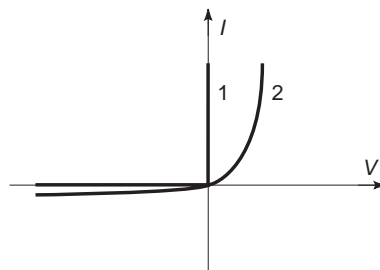


Figure 2. The current-voltage characteristics of an ideal diode (curve 1) and a realistic one (curve 2).

diode would behave as a perfect switch when forward-biased; unlimited current flows without any voltage drop across the device. The same ideal diode would allow no current in the reverse direction, no matter what the magnitude of the reverse bias is. Now, a realistic semiconductor diode would exhibit a resistance to current flow in the forward direction, whereas in reverse bias a small current would always be present due to leakage mechanisms. The disagreement between the ideal and the actual electrical behavior is not restricted only to the static I - V characteristics shown in Fig. 2. It extends to the transient response obtained when applying a time-dependent terminal excitation. The response of a realistic diode cannot follow at exactly the same speed as the terminal excitation of an ideal diode would. When designing a diode to be used as a switching device, care is taken to bring the device electrical characteristics as close to the ideal ones as possible. This is done by choosing both the geometric features and the fabrication process steps in a way to suppress the parasitic components of the diode. As a result of the semiconductor electronic band structure as well as technological constraints, material limitations impose certain basic restrictions on the device performance and create the subsequent deviation from the ideal performance. In the following sections, these restrictions will be investigated, and the deviation from the ideal performance will be analyzed in terms of the basic device physics, material constants, and geometry considerations.

Before considering the device physics of the diode, we will briefly discuss the steps in the basic fabrication process employed when making a silicon diode. These steps determine its basic geometric and technological characteristics, which in turn determine the device electrical behavior. Today, almost all silicon diodes are made through the standard planar process of the silicon integrated circuit technology. A silicon wafer is first oxidized at temperatures in the vicinity of 1000°C . Such oxidation creates a silicon dioxide (SiO_2) cover layer with a thickness on the order of a micrometer. This layer is used as a mask for the subsequent technological steps. The SiO_2 film is then patterned by lithographic techniques and through etching, which allows windows of exposed silicon to be opened. Then, either by diffusion or by ion implantation, dopants are introduced into the exposed areas. The dopants are of a type opposite to the one already existing in the original wafer. In this way, p-n junctions are created in the exposed areas. In the rest of the wafer, the SiO_2 layer stops the ions

and prevents diffusion into the silicon bulk. On the back surface, another diffusion or implantation of the same dopants as in the bulk is usually applied for reasons that will become clear in the next sections. At the end, metal contacts are evaporated on the front and the back. Lithography, again, on the frontside defines the contacts of the individual diodes. The metal contacts are required for the diodes to interact with the external world in terms of terminal excitation (voltage or current) and terminal response (current or voltage, respectively). Similar methods are used for germanium diodes, whereas the compound semiconductor devices are usually made by epitaxial growth on proper substrates and by in situ doping.

1. FUNDAMENTALS OF P-N JUNCTIONS

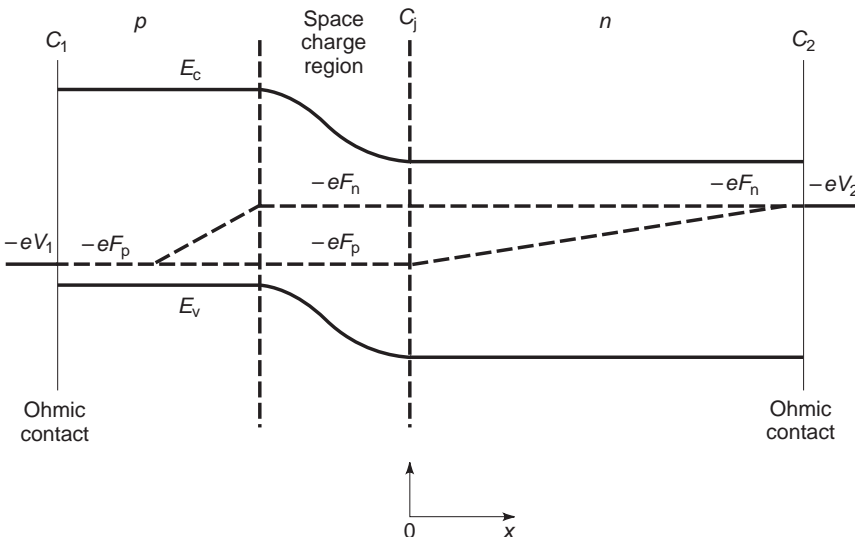
The basic p-n-junction device physics was proposed by Shockley [1]. He derived the current-voltage characteristics, considering the electron and hole current continuity equations and the relationship between the carrier quasi-Fermi levels and the externally applied potentials. Here, we rederive the general current-voltage relation of a p-n junction based on Shockley's classic work [1] and its later extension [2].

1.1. Basic Equations and Assumptions

To formulate the electron-hole transport in a semiconductor device mathematically, we can always start by expressing the carrier densities and currents in terms of the carrier quasi-Fermi potentials under uniform temperature conditions:

$$J_n = -e\mu_n n \nabla F_n \quad (1a)$$

$$J_p = e\mu_p p E + eD_p \nabla n \quad (1b)$$



$$n = n_i \exp\left(\frac{-eF_n - E_i}{kT}\right) \quad (1c)$$

$$J_p = -e\mu_p p \nabla F_p \quad (2a)$$

$$J_p = e\mu_p p E - eD_p \nabla p \quad (2b)$$

$$p = n_i \exp\left[\frac{-(-eF_p) + E_i}{kT}\right] \quad (2c)$$

In Eqs. (1a) and (2a), J_n and J_p are the electric current densities of electrons and holes, respectively. Equations (1b) and (2b) express the currents in terms of drift and diffusion, where μ_n , D_n , n and n_p , D_p , p are the mobilities, diffusivities, and volume densities of electrons and holes, respectively. Finally, F_n and F_p are the electron and hole quasi-Fermi potentials, E_i is the intrinsic energy level, and E the electric field density. Figure 3 shows the energy band diagram of a p-n junction under forward bias and illustrates the space dependence of the quasi-Fermi potentials, of the bottom of the conduction band E_c , and of the top of the valence band E_v . Equations (1c) and (2c) hold provided that the differences $E_c - (eF_n)$ and $(eF_p) - E_v$ are positive and at least several times the thermal energy kT . Equations (1a) and (2a) are borrowed from thermodynamics and hold provided that the bias is such that perturbations from equilibrium are small. "Small" here implies that the energy distribution of electrons and holes in the conduction and the valence band, respectively, continue (within a good approximation) to follow the Boltzmann statistics. Additionally, we assume that the mean free paths of the carriers are negligible compared to the physical dimensions of the device. Finally, Eqs. (1) and (2) hold provided quantum-mechanical tunneling of carriers across potential barriers is not important. Such a constraint is relaxed in the last section of nonconventional transport diodes.

Figure 3. The band diagram of a forward-biased p-n junction. Boundaries C_1 and C_2 are the ohmic contacts, whereas C_j is the base-injecting boundary.

The second set of equations to be considered is the electron and hole continuity equations:

$$\frac{\partial n}{\partial t} = \frac{1}{e} \nabla \cdot \mathbf{J}_n - U(n,p) + G \quad (3)$$

$$\frac{\partial p}{\partial t} = \frac{1}{e} \nabla \cdot \mathbf{J}_p - U(n,p) + G \quad (4)$$

where U is the electron–hole net recombination rate either by band-to-band transitions or through traps, whereas G is the band-to-band generation rate resulting from ionizing radiation or impact ionization processes. For the sake of simplicity, we assume that U and G are the same for both carriers. Equations (3) and (4) are more general than the previous ones because they do the “bookkeeping” by equating the increase in the rate of carrier density to minus the carrier losses resulting from carrier out-fluxing ($\nabla \mathbf{J}_p/e$ and $-\nabla \mathbf{J}_n/e$) and recombination.

Next is the Poisson equation, which relates the electric field to the charge density caused by both mobile and immobile charges:

$$\nabla \cdot \mathbf{E} = \frac{e}{\varepsilon} [-n + p + N_D - N_A] \quad (5)$$

where ε is the semiconductor dielectric constant and N_D and N_A are the donor and acceptor densities, respectively. The charge density resulting from donors and acceptors is not carrier density dependent, unless the temperature drops to the cryogenic region.

The final equation to be considered is the one that equates the electric field to the gradient of the electrostatic potential:

$$\mathbf{E} = \frac{1}{e} \nabla E_c = \frac{1}{e} \nabla E_v = \frac{1}{e} \nabla E_i \quad (6)$$

Equation (6) implies that the electrostatic potential is determined by conduction and the valence band edges because the carriers there have only potential energy. The last equation assumes that the separation in the energy scale of the three levels (E_c , E_v , and E_i) is space-independent. So, in Eq. (6), as well as in Eqs. (1b,c) and (2b,c), we neglect band distortion resulting from heavy doping or other effects (e.g., mechanical strain). This is discussed in a later section on heavy doping effects.

1.1.1. Boundary Conditions. Equations (1)–(6) form a system of six relations with six unknown variables: F_n , F_p , E_i , J_n , J_p , and E . They apply, within the range of their validity, to any semiconductor device. In this sense, any semiconductor device understanding, design, operation, and performance is based on this set of six equations. What distinguishes a device of a particular kind is its boundary conditions, as well as the doping and trap density and type.

1.1.2. Ohmic Contacts. For a diode, a two-terminal device, the boundary conditions necessarily include two ohmic contacts that will supply the charge to be trans-

ported through the device. The voltage across and the current through the two ohmic contacts are, interchangeably, the excitation or the response of the device. The ohmic contacts are realized by depositing metals (e.g., Ti or Al) on heavily doped regions of the semiconductor. An ideal ohmic contact should, by definition, establish thermodynamic equilibrium between the metal and the semiconductor at all the contact points. In analytical terms, this is expressed by equating the carrier quasi-Fermi potentials to the metal Fermi potential

$$F_n(C_1) = F_p(C_1) = V_1 \quad (7a)$$

$$F_n(C_2) = F_p(C_2) = V_2 \quad (7b)$$

where V_1 and V_2 are the voltages of the metal contacts ($V_1 - V_2$ is the terminal voltage), whereas C_1 and C_2 are the contact areas of the first and the second ohmic contact, respectively. The pinning of the Fermi potentials at the externally applied voltages is illustrated in Fig. 3. If $V_1 = V_2$ and G in Eqs. (3) and (4) were zero, the device would be in equilibrium. Then the solution of the previous system of six equations would be zero currents and equal and flat Fermi potentials throughout the diode. When an external voltage is applied, the splitting of the Fermi potential values between the two ohmic contacts drives the device out of equilibrium. Such a boundary value split enforces a separation of the electron and hole quasi-Fermi potentials through the device, as shown in Fig. 3. The separation of the two potentials implies that the nonequilibrium conditions mainly refer to the interaction between electrons and holes. At any point, excluding ohmic contacts, electrons are out of equilibrium with respect to holes because the relaxation time of interband transitions (recombination and generation mechanisms) required to bring them into equilibrium are too slow (milliseconds or microseconds for germanium and silicon and nanoseconds for most compound semiconductors). On the contrary, the intra-band transitions resulting from scattering have short relaxation times (picoseconds) so that electrons or holes are nearly in equilibrium within their band. This is required for the carrier Fermi potentials to have a meaning, as mentioned in the discussion following Eqs. (1) and (2).

1.1.3. Semiconductor–Insulator Interfaces. The surface that bounds the device includes, in addition to the ohmic contact, the semiconductor–vacuum or semiconductor–insulator interface. The exposed semiconductor surface is usually covered by an insulating film (SiO_2 in silicon) to reduce recombination. If we assume that there is no injection in the insulator, then at the interface the boundary conditions for Eqs. (3) and (4) are

$$\frac{\partial n_s}{\partial t} = -\frac{1}{e} J_n^n - U_s \quad (8)$$

$$\frac{\partial p_s}{\partial t} = -\frac{1}{e} J_p^n - U_s \quad (9)$$

where the subscript “s” refers to surface densities and the superscript “n” refers to the normal component looking

into the insulator. The boundary conditions for Eq. (5) are dictated by the laws of electrostatics. The discontinuity of the normal component of the dielectric displacement vector must be equal to the surface charge density, whereas the tangential component of the electric field must be continuous.

Because the boundary conditions have been set, the system of six equations [Eqs. (1)–(6)] can be solved, in principle. As it turns out, the solution of such a nonlinear system of coupled equations can be found only numerically even for one-dimensional p-n junctions with uniform acceptor and donor densities. To derive analytical approximations, we need to make certain assumptions regarding the physical makeup of the device and the degree of bias. These analytical expressions help predict the device response under reasonable bias, whereas the appreciation of their validity range provides an insight into the diode device physics.

2. DOPING CARRIER PROFILES IN EQUILIBRIUM AND THE QUASINEUTRAL APPROXIMATION

As mentioned earlier, a p-n-junction diode consists of an acceptor-doped p region in contact with a donor-doped n region. The two-dimensional area where the donor and acceptor densities are equal is called the *metallurgical junction*. Let's assume, for the moment, equilibrium conditions. In such a case, the currents are zero and the quasi-Fermi potentials are equal and spatially independent, $F_n = F_p = F$. Therefore, from Eqs. (1c) and (2c), $pn = n_i^2$, where n_i is the intrinsic carrier density. Now, the six equations reduce to the Poisson equation, which, with the help of Eqs. (1c), (2c), and (6), takes the form

$$\nabla^2[E_i - (-eE)] = \frac{e^2}{\epsilon} \left[-n_i \exp\left(\frac{(-eF) - E_i}{kT}\right) + n_i \exp\left(\frac{E_i - (-eF)}{kT}\right) + N_D + N_A \right] \quad (10)$$

The last equation is known as the *Boltzmann–Poisson* equation. Approximate analytical solutions are possible when the donor and acceptor densities are uniform in the n and p regions, respectively. In this case, the field is zero, and the bands are flat everywhere except at and near the metallurgical junction. The finite field region around the metallurgical junction is called the *space charge region*, whereas the zero-field regions are called *quasineutral regions*, for reasons to be explained shortly. In the n and p quasineutral regions, electrons and holes are the majority carriers, respectively. The majority-carrier densities are equal to the respective doping densities. With reference to the metallurgical junction, the space charge region extends W_A and W_D within the p and the n regions. At zero bias, and in one dimension, an approximate solution of

Eq. (10) gives

$$W_A = \sqrt{\frac{2\epsilon}{e} V_{bi} \frac{N_D}{N_A(N_A + N_D)}} \quad (11a)$$

$$W_D = \sqrt{\frac{2\epsilon}{e} V_{bi} \frac{N_A}{N_D(N_A + N_D)}} \quad (11b)$$

$$V_{bi} = \frac{kT}{e} \ln\left(\frac{N_A N_D}{n_i^2}\right) \quad (11c)$$

In Eq. (11c) V_{bi} is the zero bias electrical potential difference, or barrier, between the p and the n sides reflected in the level differences of the flat bands of each side. Such a barrier prevents majority carriers from diffusing into the other side. These approximations result by assuming that the electron and hole densities are zero in the space-charge region. This is the depletion approximation, which reduces Eq. (10) to a linear second-order differential equation with constant terms and coefficients.

The zero-field condition for the rest of the n and p sides, outside the space charge region, apparently justifies the term quasi-neutral regions. This term also applies when the n and p regions have gradually changing dopant profiles in the sense that the net space charge is much less than the majority-carrier charge. Here, by gradually changing we mean that the doping profile $N(x)$ in the quasineutral region must be such that [3]

$$\frac{ekT}{e^2} \left| \nabla^2 \left[\ln \frac{N(x)}{n_i} \right] \right| \ll N(x) \quad (12)$$

In such regions, the zero-bias majority-carrier density continues to be nearly the same as the net dopant density, but the electric field is not zero as in the uniform doping case.

3. FORWARD AND REVERSE BIAS CONDITIONS

The quasineutrality condition of the n and p regions is preserved even under bias, but now the boundaries with the space charge region move appropriately to accommodate the new boundary conditions. This neutrality condition can be expressed as

$$n \approx p + N_D - N_A \quad (13)$$

Under a small forward bias, the applied voltage changes the electric field preferentially at the space charge region, because it is the region with the fewest carriers, has the highest resistance, and is in series with more conductive n and p regions. The equilibrium barrier height V_{bi} lowers under forward bias, and the majority electrons overcoming the repulsive field diffuse from the n side to the p side, whereas the holes are doing the opposite. The carrier quasi-Fermi potentials are no longer equal, as shown in Fig. 3. The diffusion process, through the space charge region and inside the quasineutral regions, increases dramatically

the minority-carrier population on either side and gives rise to an appreciable electric current.

For forward voltages, the degree of bias defines three injection-level regimes distinguished by how the minority-carrier density compares to the majority one in the quasineutral regions. These regimes are the low-level, the moderate-level, and the high-level injection condition. In the low-level injection regime, the minority-carrier density is well below the majority-carrier density, and the electric field in the quasineutral regions is practically unaffected by the bias. As a result, the applied voltage drops across the space charge region and reduces the barrier height from V_{bi} to $V_b = V_{bi} - V$. Provided the depletion approximation still holds, Eq. (11) still applies and V_{bi} is replaced by V_b . In low-level injection, the majority-carrier density is the same as at zero bias, as Eq. (13) points out, and is nearly equal to the net doping density. In the high-level injection regime, the minority-carrier injection is so intense that the injected carriers have densities far exceeding the dopant densities. Now, both carrier densities are about the same, $n = p$, to preserve neutrality in the quasineutral region. In other words, there is no real distinction between minority and majority carriers in terms of concentrations, but we obtain an electron-hole plasma having densities well above those of the dopant densities instead. In the moderate injection, the minority-carrier density approaches the order of magnitude of the majority-carrier density causing the majority-carrier density to start to increase, as Eq. (13) implies.

Under reverse bias, the built-in barrier increases in the space charge region, the repulsive forces on the majority carriers coming from the quasineutral regions increase, and injection of minority carriers is not possible. The space charge region is now totally depleted from both carriers, and a small leakage current exists as a result of thermal generation of electron-hole pairs in the depletion region.

3.1. Recombination Currents in the Steady State

Here, we will introduce the base and emitter terms as well as a general expression for the terminal current as the sum of recombination components. Between the two quasineutral regions, the emitter is the one that is heavily doped, usually by diffusion or implantation, whereas the base is more lightly doped and occupies most of the substrate on which the device is made, at least in silicon. The heavy doping of the emitter excludes the possibility of moderate- or high-level injection conditions in this region. At forward bias, majority carriers from the emitter diffuse as minority carriers to the base where they recombine. Simultaneously, recombination occurs in the emitter, because minority carriers are backinjected from the base, as well as in the space charge region. At steady state, $\partial n/\partial t = \partial p/\partial t = 0$, and in the dark $G = 0$. Now, the continuity equations [Eqs. (3) and (4)] become after volume integration:

$$I_D = I_e + I_b + I_{SCR} \quad (14)$$

where I_D is the terminal current and I_e , I_b , and I_{SCR} are the net recombination currents in the emitter, the base, and the space charge region, respectively. Equation (14)

expresses the total current as the sum of the recombination currents in the three regions of the device. Therefore, excess carrier recombination along with diffusion are the two basic transport mechanisms that determine the diode current at a given bias. The carrier recombination occurs either at the ohmic contacts, at the surface, or in the bulk. The minority carriers that arrive at the ohmic contact are supposed to recombine simultaneously there, to preserve the boundary condition, Eq. (7). The bulk recombination occurs either through traps or through band-to-band transitions. In terms of trap-mediated recombination, the Shockley-Read-Hall mechanism [4,5] is the most common:

$$U_{SRH} = \frac{(pn - n_i^2)N_t}{\frac{1}{\sigma_p v_{th}} \left[n + n_i \exp\left(\frac{E_t - E_i}{kT}\right) \right]} + \frac{1}{\sigma_n v_{th}} \left[p + n_i \exp\left(-\frac{E_t - E_i}{kT}\right) \right] \quad (15)$$

In Eq. (15), N_t is the trap density, σ_n and σ_p are the electron and hole capture cross sections, respectively, E_t is the trap energy level in the gap, and v_{th} is the carrier thermal velocity. The band-to-band recombination is discussed in Section 6.

4. APPROXIMATE ANALYTICAL EXPRESSIONS IN THE STEADY STATE

As mentioned previously, the set of Eqs. (1)–(6) has no analytical solution in the general case. Approximate closed-form expressions, though, are possible when low-level injection conditions dominate in the quasineutral base region. Without loss of generality, we assume that we are dealing with a p-n diode with a heavily doped p emitter and an n base. The steady-state situation results when a terminal bias, say, a terminal voltage V , is steadily applied on the terminals, and we wait long enough for the initial transient to disappear. The steady-state version of the continuity equations [Eqs. (3) and (4)] is simplified because the time derivatives are set equal to zero. First, we will derive the expressions for the base current, and then extensions will be made for the recombination current in the emitter and the space charge regions. If low-level injection conditions prevail in the base, then, to a good approximation, the original system of equations [Eqs. (1)–(6)] reduces to the minority-carrier equations [Eqs. (2) and (4)], which are now decoupled from Eq. (5) (the Poisson equation). This decoupling results because, as mentioned earlier, at low-level injection the electric field is practically bias-independent. Any small field variations would affect only the drift current of the majority carriers because of their high density; the minority carriers would not be influenced. That is why we focus on the minority-carrier transport to exploit the Poisson equation decoupling. Another reason for focusing on the minority carriers is the fact that the recombination in low-level injection, where $p \ll n$, can always be written as a linear function of their

density:

$$U = (p - p_0)/\tau \quad (16)$$

In Eq. (16), p_0 is the equilibrium carrier density, whereas the variable τ , the minority-carrier lifetime, is the inverse of the derivative of the recombination rate with respect to the minority-carrier density. In the case of Shockley–Read–Hall recombination, $\tau = 1/\sigma_p v_{\text{th}} N_t$. Therefore, from Eqs. (2b), (4), and (16), we end up with

$$-\nabla \cdot (\mathbf{E} \mu_p p' - D_p \nabla p') - p'/\tau + G = 0 \quad (17)$$

where $p' = p - p_0$ is the excess minority-carrier density. Because of the field independence on p' , Eq. (17) is linear and becomes homogenous if $G = 0$. In the latter case, the solution is proportional to $p'(C_j)$, the excess minority-carrier density at the injecting boundary (Fig. 3).

4.1. Forward Bias and Low-Level Injection

Under forward bias, a basic assumption will be made. This assumption allows the coupling of the minority-carrier density to the externally applied terminal voltage; the Fermi levels are flat in the regions where the carriers are a majority and also in the space charge region. Under this condition and from Eqs. (1c), (2c), and (7), we obtain

$$p(C_j)n(C_j) = n_i^2 \exp(eV/kT) \quad (18)$$

$$p'(C_j) = \frac{n_i^2 [eV/kT - 1]}{N_D(C_j)} \quad (19)$$

Equation (18) holds under any injection level, provided that the flat Fermi potential assumption holds, whereas Eq. (19) for the excess minority-carrier density holds only in low-level injection. The proportionality of the solution with respect to $p'(C_j)$ forces all carrier densities and currents to become proportional to the term $\exp(eV/kT) - 1$. Here, we note that the surface recombination is also a linear function of the excess minority-carrier density when $p \ll n$. More analytically, Eq. (9) becomes

$$J_p^n = eS_p p' \quad (20)$$

where S_p is the surface recombination velocity. Therefore, the total base recombination current in Eq. (14) is proportional to the term $\exp(eV/kT) - 1$. The same is true for the quasineutral emitter recombination. Thus, Eq. (14) becomes

$$I_D = (I_{0e} + I_{0b})[\exp(eV/kT) - 1] + I_{\text{SCR}} \quad (21)$$

where the preexponential factors I_{0b} and I_{0e} are the base and emitter saturation currents, respectively. Equation (19) points out that the saturation currents are proportional to n_i^2 .

The space charge region recombination is a current component that is hard to express in analytical terms. This difficulty arises because in this region the field

depends on the bias and there is no such entity as a minority carrier. Consequently, the linearity conditions that allowed us to derive Eq. (21) no longer hold. To derive an approximate expression for the bias dependence of I_{SCR} , certain simplifications must be made throughout the space charge region regarding the integral of Eq. (15). These simplifications result in a bias dependence of the form $\exp(eV/nkT) - 1$, where n , the ideality or slope factor, takes values from 1 to 2 [2]. The specific value depends on the trap position in the energy gap, the doping profiles, and the cross section for hole capture relative to the cross section for electron capture. This range for n holds provided that the capture coefficients do not depend on the electric field. Now the preexponential factor I'_{SCR} is proportional to n_i . Finally, the expression for the forward current of a diode in the base of which low-level injection conditions prevail becomes

$$I_D = (I_{0e} + I_{0b})[\exp(eV/kT) - 1] + I'_{\text{SCR}}[\exp(eV/nkT) - 1] \quad (22)$$

For voltages higher than $3nkT/e$, the unity can be dropped from Eqs. (21) and (22). Because of a better slope factor, the emitter and base recombination will dominate the diode current for voltages above a certain level. Below this level, the space charge region recombination must also be considered.

Such trends are seen in Fig. 4. Curve 1 is the $I-V$ characteristic of a diode with a base doping of

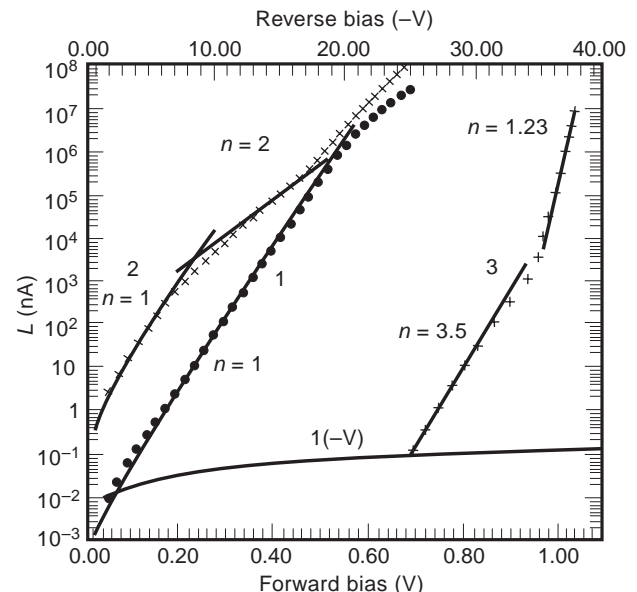


Figure 4. The experimental $I-V$ characteristics of two different diodes. Diode 1 has a base thickness of $250 \mu\text{m}$, a base-doping density of $5.5 \times 10^{14} \text{cm}^{-3}$, and an area of $2.9 \times 2.9 \text{mm}^2$. Diode 2 has a base thickness of $300 \mu\text{m}$, a base-doping density of $4.5 \times 10^{11} \text{cm}^{-3}$, and an area of $5 \times 5 \text{mm}^2$. The base in both devices is of n type. Plot 3 is the $I-V$ characteristic of diode 2 at 78K . The other plots are at 300K . Curve 1 ($-V$) is the reverse bias characteristic, with reversed sign, of diode 1 (top axis). The straight lines in curves 1, 2, and 3 are the exponential $\exp(eV/nkT) - 1$ fits to the experimental points. The slope factor n is also shown.

$5.5 \times 10^{14} \text{ cm}^{-3}$ and has an ideality factor of 1 in the bias range from 0.2 up to 0.4 V. For lower voltages, the space charge region recombination slightly increases the ideality factor and makes the measured current deviate from the $\exp(eV/kT) - 1$ dependence. The ideality factor also increases for voltages above 0.4 V because of high-injection effects, which are discussed in the next subsection. The device of curve 2 has a very light doping density in the base, $4.5 \times 10^{11} \text{ cm}^{-3}$ and is driven in high injection at even smaller bias. As discussed in the next subsection, curve 2 exhibits unity slope factor even at very low voltages.

Curve 3 shows what happens if the temperature is reduced to 78 K. The sharp reduction of the intrinsic carrier density due to its $\cong \exp(-E_g/2kT)$ dependence requires much higher voltages to reach the same current as at 300 K. In fact, to reach a current density of 10 mA/cm^2 , a voltage in excess of 1 V is required. The reduction of n_i reduces the recombination in the base and the emitter is much faster than in the space charge region because the proportionality constants are n_i^2 and n_i , respectively. Therefore, at low temperatures, the bias regions with higher than 1 ideality factor are expected to be wider. This is evidenced in curve 3 of Fig. 4, where the ideality factor is 3.5 for voltages below 950 mV. The increase of the ideality factor above 2 is a result of the Poole-Frenkel effect, which reduces the effective energy separation of the traps from the bands [6]. The influence of small values of n_i on the ideality factor is evident not only when the temperature drops but also when the bandgap increases. In several compound semiconductor devices, their large bandgap, compared to 1.1 eV of silicon, results in an intrinsic carrier density, which is several orders of magnitude smaller than the 10^{10} cm^{-3} value for silicon at 300 K [7,8]. Consequently, their $I - V$ characteristics show slope factors substantially larger than 1 for the entire range of bias. On the contrary, germanium diodes have slope factors of 1 even at reduced temperatures because of the smaller gap, 0.66 eV, of the semiconductor.

4.1.1. The One-Dimensional Case. Equation (22) holds for any three-dimensional geometry and doping profiles because no assumption, except for low-level injection, was made so far regarding doping profiles and device topology. If, however, we want to express in closed form the saturation values of the emitter and base recombination currents, then one-dimensional devices with uniform doping profiles must be considered. In such a case, the one-dimensional, homogenous, and constant-coefficient version of Eq. (17) becomes

$$\frac{d^2 p'}{dx^2} = \frac{p'}{L_p^2} \quad (23)$$

where $L_p = \sqrt{D_p \tau}$ is the minority-carrier diffusion length. The first boundary condition for Eq. (23) is Eq. (19) applied at the injecting boundary. The other one refers to the ohmic contact. If it is an ideal ohmic contact deposited directly on the uniformly doped base, then the second boundary condition becomes, from Eq. (7), $p'(l) = 0$. Here,

l is the base length and the coordinate origin is at the injecting boundary, as shown in Fig. 3. In many cases, between the ohmic contact and the uniformly doped base, a thin and heavily doped region intervenes.

This region has a thickness on the order of a micrometer and a doping of the same type as the rest of the base. The purpose of such a layer, called the "backsurface field," is to provide a better ohmic contact and to isolate the contact from the lightly doped base so that carrier recombination-generation is reduced [9]. Such a backsurface field terminates the lightly doped base of diode 2 in Fig. 4 making it a p-i-n diode, where "i" stands for intrinsic. Therefore, in the presence of this contact layer, the base ends at a "low/high" n-n⁺ junction. In terms of minority-carrier recombination, this interface is characterized by an effective recombination velocity S_{pe} , experienced by the minority carriers at the low side of the junction. The expression for S_{pe} is

$$S_{pe} = \frac{I_{0c} N_D}{en_i^2 S} \quad (24)$$

where I_{0c} is the saturation value of the recombination current in the backsurface field and S is the device cross section. Equation (24) can be derived from Eq. (20), by applying Eq. (19) at the n-n⁺ junction and by equating the minority current at the low/high junction to the recombination in the heavily doped region.

Under the previous boundary conditions, the solution of Eq. (23) yields for the base saturation current:

$$I_{0b} = S \frac{en_i^2 D_p}{N_D L_p} \frac{1 + \frac{D_p}{S_{pe} L_p} \tanh(\ell/L_p)}{\tanh(\ell/L_p) + \frac{D_p}{S_{pe} L_p}} \quad (25)$$

Equation (25) shows that, in terms of the one-dimensional geometry, the quantity that matters is the ratio ℓ/L_p . Values of this ratio much less than one define the short base, whereas values above 3 define the long base. In the long-base case, Eq. (25) becomes $I_{0b} = Sen_i^2 D_p / (N_D L_p)$. Similar equations hold for a uniform emitter, too, but now the heavy-doping effects could modify the value of n_i^2 , as will be discussed in Section 6. If the base doping is very light, as in a p-i-n diode, then the increased value of I_{0b} will make the base recombination dominate the current components in Eq. (22). Accordingly, the influence of space charge region recombination current on the slope factor will be suppressed even for voltages as low as a few kT/e , as shown in Fig. 4, curve 2. Also, by extrapolating the $\exp(eV/kT)$ fit of curve 2 at zero voltage, a base recombination current of 0.7 nA is obtained. This corresponds to a 300 K saturation current density of 2.8 nA/cm^2 compared to emitter saturation current densities on the order of pA/cm^2 . On the other hand, diode 1, with a base doping density three orders of magnitude higher than that in diode 2, exhibits a saturation current of 24 pA/cm^2 . This saturation current comes mainly from the base recombination as a result of its relatively light doping density and the absence of a backsurface field, which gives S_{pe} very high values.

Equation (25) applies to uniformly doped regions. If the doping is nonuniform, closed-form expressions are not possible, in the general case. This is the case because the one-dimensional version of Eq. (17) is still an ordinary differential equation with nonconstant coefficients. However, analytical approximations based on iterative techniques can be derived [10].

4.1.2. Diffusion in Three Dimensions. Equation (23) holds provided the cross-sectional dimensions of the diode are much larger than the diffusion length. Otherwise, lateral diffusion of minority carriers in the base becomes important. In such a case, the three-dimensional version of Eq. (23) takes the form

$$\nabla_{p'}^2 = \frac{p'}{L_p^2} \quad (26)$$

The last equation can be solved very accurately by semi-analytical techniques based on the two-dimensional Fourier transform [11]. Simulation results are as shown in Fig. 5. As illustrated, in the case of a point contact diode having emitter dimensions of $0.1 L_p$, the base recombination is expected to increase by a factor of 25 as a result of the lateral carrier diffusion.

4.2. High-Level Injection

So far, our analytical approaches were based on the low-level injection assumption. In high-level injection, where

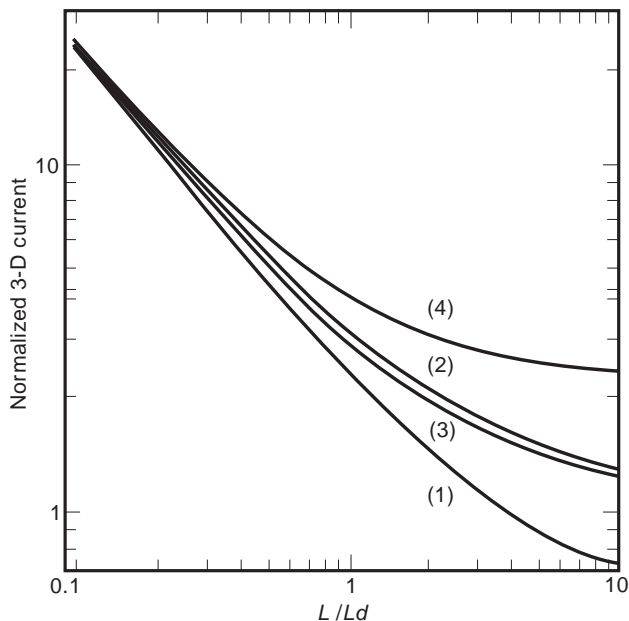


Figure 5. Three-dimensional diffusion base saturation current of a planar p-n junction with a square emitter having a sidelength L . The top surface of the base is supposed to have zero recombination velocity. The current is normalized with respect to the one-dimensional diffusion current $I_{0b} = en_i^2 L^2 D_p / N_D L_p$. In curve 2, $S_{pe} = 0$ and $l = L_p/2$. In curve 2, l is assumed to be infinite. In curve 3, $S_{pe} = D_p/L_p$ and $l = L_p/2$, whereas in curve 4, S_{pe} is assumed to be infinite and $l = L_p/2$.

$n = p$, an equation similar to Eq. (23) can be derived where now the hole diffusion length is replaced by the ambipolar diffusion length [12]. The boundary conditions, however, are not linear and depend on the electric field, which, now, is a function of bias. If the quasi-Fermi potentials are flat in the quasineutral base, then the electron-hole plasma density p is space independent and equals $n_i \exp(eV/2kT)$, as can be derived from Eq. (18). In such a case, by integrating the recombination current in the emitter, the base, and the backsurface field, we obtain

$$I_D = (I_{0e} + I_{0c}) \exp(eV/kT) + (eSl/\tau') \exp(eV/2kT)n_i \quad (27)$$

In Eq. (27), τ' is the high-injection lifetime defined as the ratio of the recombination rate divided by the plasma density. The flat Fermi level condition can easily be satisfied in p-i-n diodes where the light base doping density makes the high-level injection possible even at a bias of 0.4 V. In Fig. 4, curve 2 shows the $\exp(eV/2kT)$ dependence, or slope factor of 2, for voltages of about 0.4 V, which drive the p-i-n device to high-level injection. For even higher voltages, the emitter and backsurface field recombination in Eq. (27) starts dominating the current, and the slope factor drops again. For higher base doping densities, as in curve 1 of diode 1, the required voltage for high-level injection conditions could exceed 0.5 V at 300 K. Now, the heavily doped region recombination in Eq. (27) competes with the bulk recombination, and the slope factor of 2 does not appear. The bent of both curves 1 and 2 at voltages near 0.6 V is a result of series resistance effects, which invalidate the assumption of flat Fermi levels across the base. In such a case, the simulation is possible only by device simulators that solve the complete system of the transport equations.

4.3. Reverse Bias

Under reverse bias where $V < 0$, the assumption of flat Fermi levels across the space charge region that led to Eq. (22) no longer hold. On the other hand, however, the space charge region can be considered to be fully depleted from free carriers. In such a case, Eq. (11) holds with V_{bi} replaced by $V_{bi} + |V|$. Therefore, the depleted space charge region will expand toward the base according to the square root of the bias for $|V| > 5$ V. In this region, the Shockley-Read-Hall Eq. (15) predicts a negative recombination or generation of electron-hole pairs. This generation current is the basic component of the leakage current in reverse bias. The contribution of the diffusion components from the base and the emitter, $-I_{0b} - I_{0e}$, is usually negligible unless the base is very lightly doped. The bottom line in Fig. 4 shows the reverse-bias current for diode 1. The square-root dependence on voltage is not exactly obeyed because of the Poole-Frenkel effect, which increases the generation rate at higher fields.

5. TRANSIENT RESPONSE OF DIODES

If a diode is subjected to a transient terminal bias, then in addition to currents due to carrier diffusion and

recombination, we also have the dielectric displacement current resulting from the time dependence of the electric field. If low-level injection is observed in the quasineutral regions, the displacement current is restricted in the space charge region. At the same time, low-level injection ensures that linearity holds in the base and the emitter, and Eq. (17) still applies with $\partial p'/\partial t$ replacing zero in the right-hand side of the relation. The solution of the time-dependent edition of Eq. (17) provides the minority-carrier currents at the injecting boundaries of the base and the emitter, $I_b(t)$ and $I_e(t)$, respectively. These currents have now two components: the minority-carrier recombination and the minority-carrier storage current $\partial Q'/\partial t$, where Q' is the total excess minority-carrier charge. To calculate the total transient current, reconsider Eq. (14) in its transient version. Therefore, in addition to $I_b(t)$ and $I_e(t)$, the transient space charge region current is required. Unlike the base and the emitter, this current in addition to the recombination and storage component also includes the displacement current [13]. Insofar as the displacement current is concerned, the space charge region behaves as a parallel-plate capacitor with a plate distance $W = W_A + W_D$, Eq. (11), a dielectric constant ϵ , and a capacitance $C_{SCR} = \epsilon S/W$. During transit, the dielectric displacement current is supplied by the majority carriers from either side of the junction.

To calculate the transient currents in the base and the emitter, the boundary conditions must be defined. Boundary condition Eq. (20) holds because of linearity. The other condition at the injecting boundary depends on the kind of transient to be considered [14]. Here we will assume that the device is in equilibrium for $t < 0$, whereas at $t = 0$ a constant voltage V is applied. We can now assume that Eq. (19) applies with $p'(C_j)$ replaced by $p'(C_j, t)$ for $t > 0$. This assumption has a validity range depending on how fast the flat quasi-Fermi potential condition can be established across the space charge region. In fact, even in the absence of series resistance effects, it takes a short time for this condition to be established. This short time relates to the dielectric response time of the majority carriers and the minority-carrier diffusion time across the space charge region [14]. For almost all practical cases, the delay in establishing a fixed minority-carrier density at the edge of the quasineutral region will not exceed the limit of a few tens of a picosecond [14], in the absence of series resistance effects. Therefore, if the time granularity used in solving the time-dependent version of Eq. (17) is restricted to about a nanosecond, then the solutions will be accurate. In practical cases, however, the very first part of the transient current, following the sudden application of a voltage, will be determined by charging C_{SCR} through the series resistance of the majority carriers in the base and the emitter. The respective time constant could be on the order of a nanosecond. In such a case, the minority-carrier transport in the base will determine the transient only after several nanoseconds have elapsed since the application of the voltage. The transient base transport can be expressed in semianalytical forms using Laplace transform techniques [14], especially in the case of uniform and one-dimensional quasineutral regions. In a long-base diode, the transition will last for about a minority-carrier

lifetime. In a short-base device with an ohmic contact at the base end, the transient will last approximately $l^2/2D_p$, which is the minority-carrier diffusion time through the base.

5.1. Small-Signal Response

In many cases, the device operates under sinusoidal small-signal excitation superimposed on a steady-state excitation. In such cases, Eq. (17) still holds, but now $1/\tau$ will have to be replaced by $1/\tau + j\omega$, where j is the imaginary unit and ω is the angular frequency of the excitation. This is the case because the time derivative of the small-signal carrier density is the carrier density amplitude times $j\omega$. Having done the complex lifetime replacement, the analysis that followed Eq. (17) still holds. Now, however, the small-signal value of the excess minority-carrier density at the injecting boundary will be the steady-state value in Eq. (19) times ev/kT . Here, v is the small-signal terminal voltage, which is supposed to be much less than kT/e . Under low-level injection and in view of the previous transient response discussion, the small-signal version of Eq. (22) will refer to a terminal current I_D^* having a real and an imaginary component:

$$\begin{aligned} I_D^* &= (I_{0e}^* - I_{0b}^*) \frac{ev}{kT} \left[\exp\left(\frac{eV}{kT}\right) - 1 \right] \\ &+ I_{SCR}^* \frac{ev}{nkT} \left[\exp\left(\frac{eV}{nkT}\right) - 1 \right] \\ &+ j\omega C_{SCR} v = v(G + j\omega C) \end{aligned} \quad (28)$$

The star exponents denote the complex values of the saturation currents as a result of the complex lifetime. In Eq. (28), G and C are the diode small-signal parallel conductance and capacitance, respectively. These two components are of great importance because their frequency dependence can reveal minority-carrier properties, such as diffusivity and lifetime [15], and allow the device circuit representation when the diode is part of a greater small-signal circuit. For uniformly doped quasineutral regions, I_{0e}^* and I_{0b}^* can be obtained from Eq. (25) by replacing the diffusion length $L = (D\tau)^{1/2}$ with the complex diffusion length $L^* = L/(1 + j\omega\tau)^{1/2}$. For frequencies sufficiently high, the magnitude of the complex diffusion length will become much shorter than the base thickness. Then, the complex version of Eq. (25) predicts that the base current would change as $1/L^*$. If the base component in Eq. (28) were to dominate, then beyond a certain frequency, C would change as $\omega^{-1/2}$ while G would change as $\omega^{1/2}$.

This frequency dependence is confirmed in Fig. 6, which shows the frequency response of diode 1, from Fig. 4, at two bias points. The theoretical fit to the experimental results was obtained on the basis of the diode equivalent circuit shown in Fig. 7. This circuit includes all the components relating to carrier injection and storage in the device's three regions in accordance with Eq. (28). It also includes the base resistance R_N , which has been ignored in Eq. (28). In Fig. 6, the square root law is better obeyed at the higher bias point and for frequencies less than 1 MHz,

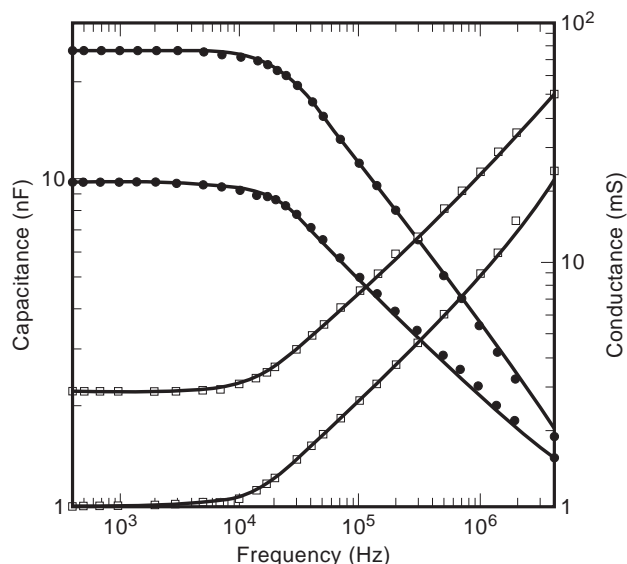


Figure 6. Experimentally measured capacitance (dots) and conductance (squares) at 300 K for diode 1. The bottom and the top curves correspond to two different bias points: 420 mV and 450 mV, respectively. The solid curves are the theoretical fits from the equivalent circuit of Fig. 7.

especially for the capacitance. This is a combined result of the space charge region capacitance, the relative contribution of which increases at lower bias, and the series resistance, the influence of which is stronger at high frequencies. The corner frequencies of the conductance and the capacitance depend on the base thickness and the lifetime. The fit shown in Fig. 6 gave a minority-hole lifetime in the n-type base of about 30 μ s. Such a lifetime and Eq. (25) imply that the saturation current density of 24 pA/cm² at 300 K, as shown in Fig. 4, is 90%, due to base recombination. The emitter contribution of 10% is discussed in Section 6.

The series resistance R_N becomes the bulk majority-carrier resistance under reverse bias or even under forward bias, provided that the frequency is high ($|L^*| \ll l$). The capacitance C_{QNR}^N in parallel with R_N , as shown in Fig. 7, is the geometric capacitance of the quasineutral base [16,17]. For ordinary resistivity devices, it can be ignored unless the frequency is in the gigahertz range. However, for diodes made on high resistivity substrates, this capacitance must be considered especially at reverse bias and high frequencies [17]. From Fig. 7 and in the limit of very high frequencies under forward bias, the parallel conductance saturates at $1/R_N$ whereas the parallel capacitance does so at C_{QNR}^N . This is because of the combination of the increasing injection conductances and the space charge region capacitance. Then, the product $R_N C_{QNR}^N$ becomes the dielectric response time of the majority carriers in a uniform base. At high injection, the parallel conductance will saturate at the sum of the two carrier conductances [18]. Under reverse bias, the circuit of Fig. 7 reduces to the space charge region capacitance in series with the parallel combination of C_{QNR}^N and R_N . Unlike the forward-bias case, where the circuit parameters depend

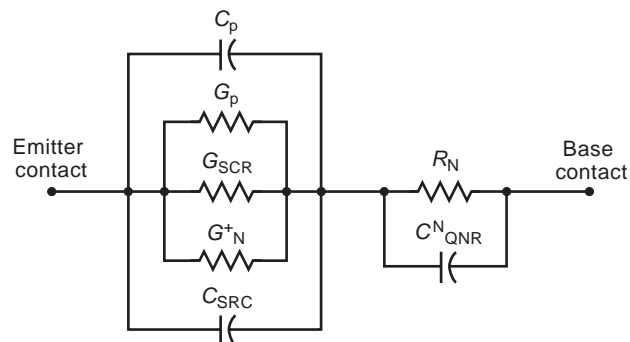


Figure 7. The equivalent-circuit model of a diode. The base injection currents in Eq. (28) correspond to C_p , imaginary part, and G_p , real part. The injection in the emitter is represented by G_N^+ . The space charge region recombination is represented by G_{SCR} , whereas C_{SRC} is the space charge region capacitance. The rest of the components are accounted for in the text.

roughly exponentially on the terminal voltage V , in reverse bias the voltage dependence would be restricted to $V^{-1/2}$. In the sense of the voltage dependence, the circuit of Fig. 7 is the circuit of a varactor.

6. HEAVY-DOPING EFFECTS IN THE EMITTER

In the previous subsection, the emitter saturation current density was estimated to be about 2 pA/cm². From Eq. (25) and by assuming microsecond lifetimes, we would expect saturation currents on the order of a fA/cm² from an emitter doped in the range 10^{19} – 10^{20} cm⁻³. Such a discrepancy by three orders of magnitude is due to the heavy-doping effects, namely, the short lifetime resulting from Auger recombination and the effective increase of n_i due to bandgap narrowing. In the Auger recombination process, a minority carrier recombines directly with a majority one, and the energy is transferred to another majority carrier. Because of such kinetics, the Auger minority-carrier lifetime is inversely proportional to the square of the majority-carrier density. The proportionality constant is $\sim 10^{-31}$ cm⁶/s for minority electrons in p⁺ emitters and 3×10^{-31} cm⁶/s for minority holes in n⁺ emitters [19]. In heavily doped regions, the Auger recombination rate is by far higher than the Shockley–Read–Hall rate and determines the lifetime. Therefore, nanosecond lifetimes are expected, especially for holes, in emitters doped in the vicinity of 10^{20} cm⁻³.

In a heavily doped region, every minority carrier interacts strongly with the majority carriers because of their high density. The minority-majority carrier attraction along with the carrier–dopant interaction and the semiconductor lattice random disruption by the dopant atoms reduces the bandgap and changes the density of states in both bands [20,21]. The net result is an effective shrinkage of the gap depending on the doping type and density [22–24]. This shrinkage changes the intrinsic carrier density n_i to a much higher effective n_{ie} . The result of the band distortion is that the original system of transport equations [Eqs. (1)–(6)] no longer holds. More specifically,

Eqs. (1b,c) and (2b,c) are not valid for the majority carriers even if n_{ie} substitutes n_i because Boltzmann statistics must be replaced by Fermi–Dirac statistics. Also, Eq. (6) no longer holds in a nonuniform region because the band edges are not parallel any more and each carrier experiences a different field. However, the minority carriers still follow the Boltzmann statistics, and Eq. (17) holds for the minority carriers. Now E is the minority-carrier field ($1/e\nabla E_c$ for electrons), and the boundary condition Eq. (19) is valid with n_i replaced by n_{ie} . Therefore, Eq. (25) still applies for the minority-carrier recombination in a uniformly doped emitter. For an emitter doped at about 10^{20} cm^{-3} , a gap narrowing of about 100 meV is expected [22–24], which makes n_{ie} several tens higher than n_i . If such an n_{ie} as well as nanosecond lifetimes replace n_i and microsecond lifetimes in Eq. (25), an emitter saturation current on the order of pA/cm^2 is predicted, in accordance with the experimental results of the previous section.

7. DIODES OF NONCONVENTIONAL TRANSPORT

So far in this article, devices based on the drift and diffusion model of Eqs. (1) and (2) were studied. Charge carriers can be transported from one region to another by tunneling. Also, they can be temporarily trapped in energy gap states, atom clusters, or crystallites imbedded in insulating films, thereby affecting the tunneling or the conventional transport of the free carriers.

In this respect, the first device to be examined is p-i-n diode 2 of Fig. 4, operating at cryogenic temperatures. Around 4.2 K, the equilibrium Fermi level in the lightly doped n⁻ region is pinned at the donor level. These levels, now, are not ionized except for a fraction to compensate the charge of the unintentionally introduced acceptor ions. At such low temperatures, there are no free carriers in the base, and no measurable conduction is possible unless the voltage is raised enough to achieve the flatband condition [25,26]. For silicon, this voltage V_0 would be about 1.1 V. For even higher voltages, conduction is possible only if electrons and holes can be injected in the frozen substrate from the n and p regions, respectively. In this sense, Eq. (24) based on the assumption of flat majority-carrier Fermi levels no longer holds. For $T < 10 \text{ K}$, injection is possible by carrier tunneling through the small potential barrier existing at each of the p-i and i-n interfaces [26]. These barriers exist because of the band distortion in the heavily doped regions and the smaller gap there, as outlined in the previous section. For $V > V_0$, electrons tunnel in the i layer, and the higher the forward bias, the higher the current due to a field-induced effective lowering of the barriers.

As shown in Fig. 8, for temperatures below 10 K it takes at least several volts to establish a current of few nanoamperes. The injected electrons in the i layer are trapped by the ionized donors and built a space charge and a subsequent potential barrier. For even higher voltages approaching 10 V, the barrier at the i-p interface lowers, holes now enter the i layer in large numbers. Their charge neutralizes the trapped electron charge and causes the voltage breakdown and the negative differential resistance that appears in Fig. 8 for $T < 10 \text{ K}$. The negative

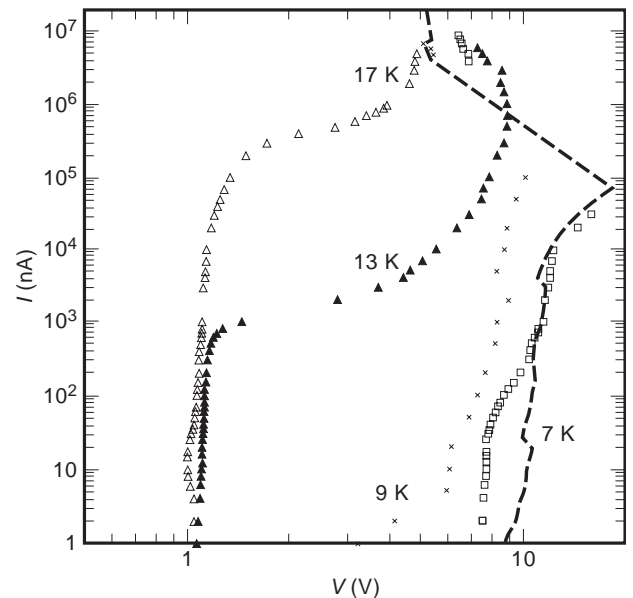


Figure 8. Measured $I - V$ characteristics of diode 2 at cryogenic temperatures. The square points correspond to 4.2 K. The $T < 10 \text{ K}$ plots exhibit a distinct voltage breakdown. [Reprinted from K. Misiakos, D. Tsamakis, and E. Tsoi, Measurement and modeling of the anomalous dynamic response of high resistivity diodes at cryogenic temperatures, *Solid State Electron.* **41**:1099–1103 (1997), with kind permission from Elsevier Science Ltd, The Boulevard, Langford Lane, Kidlington OX5 1GB, UK.]

resistance persists and beyond breakdown as a result of new carrier generation by the impact ionization of occupied shallow donors by the injected carriers. The interaction of free and trapped carriers through impact ionization gives rise to a negative dynamic conductance and capacitance that for frequencies high enough change as ω^{-2} [27]. For $T > 10 \text{ K}$ the injection mechanism changes to thermion emission over the interface potential barriers, whereas the space charge effects are now less pronounced.

Another example of tunneling injection mechanism is the breakdown effect in zener diodes. Here, the base is quite heavily doped ($\approx 10^{18} \text{ cm}^{-3}$), and the strong electric field in the space charge region increases even further by applying a reverse bias. For fields approaching 10^6 V/cm , a valence band electron can tunnel to a conduction band state of the same energy. This way, electron–hole pairs are created, and the reverse current sharply increases. Another diode structure based on tunneling is a new metal–insulator–semiconductor device having silicon nanocrystals imbedded in the thin insulating film [28]. One way to realize such diodes is by depositing an aluminum electrode on a thin (on the order of 10 nm) SiO_2 layer containing silicon nanocrystals. The substrate is n-type crystalline silicon. The silicon nanocrystals can be created either by oxidizing deposited amorphous silicon layers [28] or by low-energy silicon-ion implantation in the SiO_2 film [29]. In the absence of the nanocrystals, by applying a negative voltage of a few volts on the aluminum electrode relative to the n-type silicon substrate, only a small tunneling current would be present.

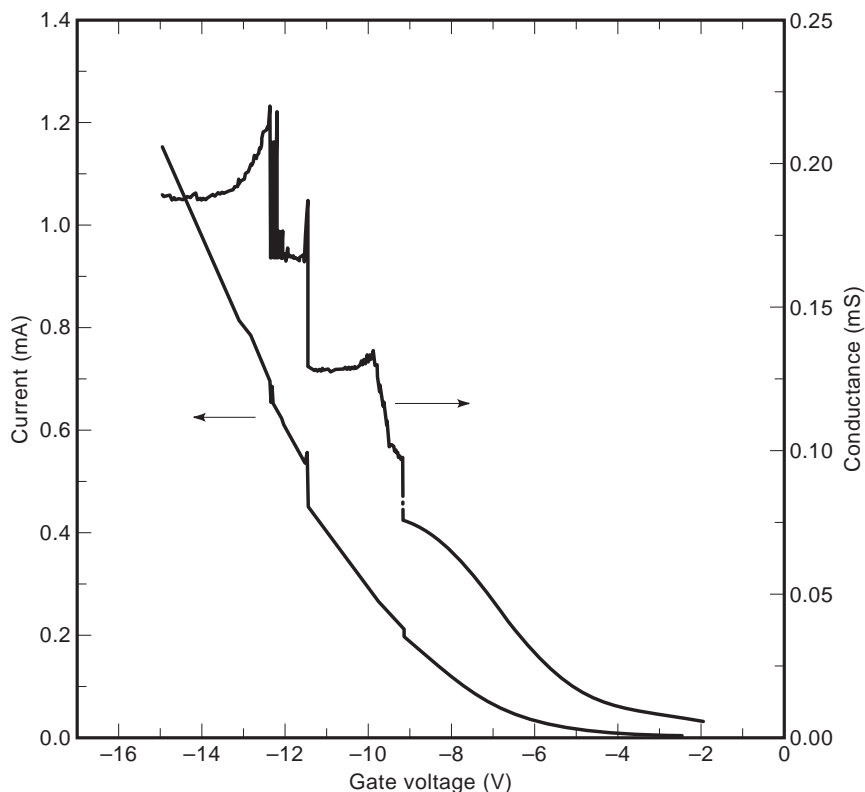


Figure 9. Current and conductance plots of a reverse-biased quantum dot diode. The conductance peaks correspond to steps in current curve. [Reprinted from P. Normand et al., Silicon nanocrystal formation in thin thermal-oxide films by very low energy Si^+ ion implantation, *Microelectron. Eng.* **36**(1–4): 79–82 (1997) with kind permission of Elsevier Science-NL, Sara Burgerhartstraat 25, 1055 KV Amsterdam, The Netherlands.]

When the nanocrystals are introduced, much higher currents are observed while the conductance curve exhibits characteristic peaks. Such peaks are shown in Fig. 9 showing the reverse current and conductance of a quantum dot diode formed by low-energy implantation of silicon in a 10-nm SiO_2 layer [29]. The conductance peaks appear when the metal Fermi level is swept across the discrete energy states of the nanocrystals, thus enabling resonant tunneling from the metal to the semiconductor [28]. The three-dimensional confinement of electrons in the quantum box crystallites creates a large separation between energy states, which along with the Coulomb blockade effect of the occupied states explains the large voltage separation of the three first conductance peaks in Fig. 9 [28,29]. Such quantum dot devices hold the promise of single-electron transistors [30] and silicon-based light emitting diodes [31].

Ending this article, we would like to mention the basic uses of the diode as a device. The most frequent use of the diode is the protection of complementary metal oxide semiconductor (CMOS) integrated circuits from electrostatic discharges by clamping the output pads to the power-supply voltages through reverse-biased p-n junctions. In analog integrated circuits, forward-biased diodes are used for voltage shifting. Such diodes usually come from properly wired bipolar transistors (e.g., emitter–base diodes with base–collector short-circuited). Diodes, as discrete devices, find applications mainly as rectifying elements in power circuits. The breakdown effect of zener diodes makes these devices useful as voltage reference sources in power supplies. Photodiodes are widely used for detecting photons or charge particles. Finally, large area

diodes with exposed front surface and proper design and engineering can efficiently convert solar light into electricity and are used as solar cells [32].

BIBLIOGRAPHY

1. W. Shockley. *Electrons and Holes in Semiconductors*, Van Nostrand, Princeton, NJ, 1950.
2. C. T. Sah, R. N. Noyce, and W. Shockley, Carrier generation and recombination in p-n junction and p-n junction characteristics, *Proc. IRE* **45**:1228–1243 (1957).
3. J. A. del Alamo, Charge neutrality in heavily doped emitters, *Appl. Phys. Lett.* **39**:435–436 (1981).
4. W. Shockley and W. T. Read, Statistics of the recombination of holes and electrons, *Phys. Rev.* **87**:835–842 (1952).
5. R. N. Hall, Electron-hole recombination in germanium, *Phys. Rev.* **87**:387 (1952).
6. J. C. S. Woo, J. D. Plummer, and J. M. C. Stork, Non-ideal base current in bipolar transistors at low temperatures, *IEEE Trans. Electron. Devices* **34**:131–137 (1987).
7. A. B. Sproul and M. A. Green, Intrinsic carrier concentration and minority carrier mobility from 77 K to 300 K, *J. Appl. Phys.* **74**:1214–1225 (1993).
8. K. Misiakos and D. Tsamakis, Accurate measurements of the intrinsic carrier density from 78 to 340 K, *J. Appl. Phys.* **74**:3293–3297 (1993).
9. J. G. Fossum, Physical operation of back surface field solar cells, *IEEE Trans. Electron. Devices* **24**:322–325 (1977).
10. J. S. Park, A. Neugroschel, and F. A. Lindholm, Systematic analytical solution for minority-carrier transport in semiconductors with position dependent composition with application

- to heavily doped silicon, *IEEE Trans. Electron. Devices* **33**:240–249 (1986).
11. S. Kavadias and K. Misiakos, Three-Dimensional simulation of planar semiconductor diodes, *IEEE Trans. Electron. Devices* **40**:1875–1878 (1993).
 12. S. M. Sze, *Physics of Semiconductor Devices*, 2nd ed., Wiley, New York, 1981, p. 87.
 13. F. A. Lindholm, Simple phenomenological model of transition region capacitance of forward biased p-n junction diodes or transistor diodes, *J. Appl. Phys.* **53**:7606–7608 (1983).
 14. T. Jung, F. A. Lindholm, and A. Neugroschel, Unifying view of transient responses for determining lifetime and surface recombination velocity in silicon diodes and back-surface field solar cells with application to experimental short circuit current decay, *IEEE Trans. Electron. Devices* **31**:588–595 (1984).
 15. A. Neugroschel et al., Diffusion length and lifetime determination in p-n junction solar cells and diodes by forward biased capacitance measurements, *IEEE Trans. Electron. Devices* **25**:485–490 (1978).
 16. B. M. Vul and E. I. Zavattitskaya, The capacitance of p/n junctions at low temperatures, *Sov. Phys.-JETP (Engl. transl.)* **11**:6–11 (1960).
 17. S. Kavadias et al., On the equivalent circuit model of reverse biased diodes made on high resistivity substrates, *Nucl. Instrum. Methods Phys. Res.* **A322**:562–565 (1992).
 18. K. Misiakos and D. Tsamakis, Electron and hole mobilities in lightly doped silicon, *Appl. Phys. Lett.* **64**:2007–2009 (1994).
 19. J. Dziewior and W. Schmid, Auger coefficients for lightly doped and highly excited silicon, *Appl. Phys. Lett.* **31**:346–348 (1977).
 20. G. D. Mahan, Energy gap in Si and Ge: Impurity dependence, *J. Appl. Phys.* **51**:2634–2646 (1980).
 21. P. T. Landsberg et al., A model for band-p shrinkage in semiconductors with application to silicon, *Phys. Status Solidi B* **130**:255–266 (1985).
 22. J. W. Slotboom and H. C. de Graaff, Measurements of band gap narrowing in Si bipolar transistors, *Solid-State Electron* **19**:857–862 (1976).
 23. A. W. Wieder, Emitter effects in shallow bipolar devices: measurements and consequences, *IEEE Trans. Electron. Devices* **27**:1402–1408 (1980).
 24. J. A. del Alamo and R. M. Swanson, Measurement of steady-state minority-carrier recombination in heavily doped n-type silicon, *IEEE Trans. Electron. Devices* **34**:1580–1589 (1987).
 25. A. K. Jonscher, p-n junctions at very low temperatures, *Br. J. Appl. Phys.* **12**:363–371 (1961).
 26. Y. N. Yang, D. D. Coon, and P. F. Shepard, Thermionic emission in silicon at temperatures below 30 K, *Appl. Phys. Lett.* **45**:752–754 (1984).
 27. K. Misiakos, D. Tsamakis, and E. Tsoi, Measurement and modeling of the anomalous dynamic response of high resistivity diodes at cryogenic temperatures, *Solid-State Electron.* **41**:1099–1103 (1997).
 28. E. H. Nicollian and R. Tsu, Electrical properties of a silicon quantum dot diode, *J. Appl. Phys.* **74**:4020–4025 (1993).
 29. P. Normand et al., Silicon nanocrystal formation in thin thermal-oxide films by very-low energy Si⁺ ion implantation, *Microelectron. Eng.* **36**(1–4):79–82 (1997).
 30. K. Yano et al., Room-temperature single-electron memory, *IEEE Trans. Electron. Devices* **41**:1628–1638 (1994).
 31. D. J. Dimaria et al., Electroluminescence studies in silicon dioxide films containing tiny silicon islands, *J. Appl. Phys.* **56**:410 (1984).
 32. F. Zhang, S. Wenham, and M. A. Green, Large area, concentrator buried contact solar cells, *IEEE Trans. Electron. Devices* **42**:145–149 (1995).

DIPOLE ANTENNAS AND ARRAYS*

CYNTHIA M. FURSE
 OM P. GANDHI
 University of Utah
 Salt Lake City, Utah
 GIANLUCA LAZZI
 North Carolina State University

1. INTRODUCTION

A dipole antenna is most commonly a linear metallic wire or rod with a feedpoint at the center as shown in Fig. 1. Most often, this type of antenna has two symmetric radiating arms. Because of the symmetry of the antenna relative to the x - y plane containing the feedpoint, the resultant radiation is independent of ϕ (rotationally symmetric about the z axis). Dipole antennas and arrays of dipoles are commonly used for HF and UHF broadcasting, TV, and FM communications, and as electric field probes. This article describes the basic nature and applications of dipole antennas and some of their variations such as biconical and bowtie antennas, slot dipoles, folded dipoles, sleeve dipoles, and shunt-fed dipoles. The commonly used broadband log periodic and Yagi-Uda dipole arrays are also discussed.

2. DIPOLE ANTENNA TYPES

2.1. Infinitesimal Dipole (Hertzian Dipole)

An infinitesimal dipole ($L \ll \lambda$) is a small element of a linear dipole that is assumed to be short enough that the current (I) can be assumed to be constant along its length L . This is also called a *Hertzian dipole*. The electric and magnetic field components of this dipole are [6]

$$\bar{H} = \frac{1}{4\pi} IL \sin \theta e^{-j\beta_0 r} \left(\frac{j\beta_0}{r} + \frac{1}{r^2} \right) \alpha_\phi \quad (1)$$

$$\begin{aligned} \bar{E} = & \frac{j\eta_0 IL}{2\pi\beta_0} \cos \theta \left(\frac{j\beta_0}{r^2} + \frac{1}{r^3} \right) e^{-j\beta_0 r} \alpha_r \\ & - \frac{j\eta_0 IL}{4\pi\beta_0} \sin \theta \left(-\frac{\beta_0^2}{r} + \frac{j\beta_0}{r^2} + \frac{1}{r^3} \right) e^{-j\beta_0 r} \alpha_\theta \end{aligned} \quad (2)$$

where $\eta_0 = (\mu_0/\epsilon_0)^{1/2}$ is the intrinsic impedance ($= 377 \Omega$) for free space and $\beta_0 = \omega(\mu_0\epsilon_0)^{1/2}$ is the propagation constant ($= \omega/c$, where c is the velocity of light). The fields are

*See also Section on Monopole Antennas

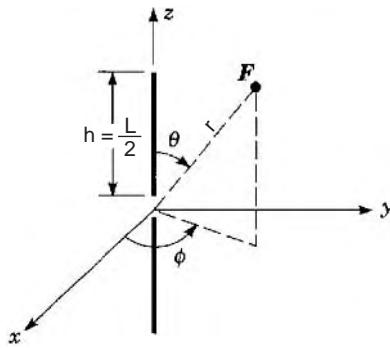


Figure 1. Dipole antenna.

seen to decay rapidly ($1/r^3$ and $1/r^2$ variation) very near the antenna, and less rapidly ($1/r$ variation) farther away. The fields with terms $1/r^2$ and $1/r^3$ (the *induction terms*) provide energy that is stored near the antenna. The fields with $1/r$ variation (the *radiation terms*) provide actual energy propagation away from the antenna. The distance away from the antenna where the induction and radiation terms are equal is $d = \lambda/2\pi$. When $d < \lambda/2\pi$, this is the *near field* of the antenna, and the induction terms dominate. When $d > \lambda/2\pi$, this is the *far field*, and the radiation terms dominate. In the far field, the wave propagation is in the transverse electromagnetic (TEM) mode, which is characteristic of far-field radiation from finite structures.

The far-zone radiated fields of the Hertzian dipole follow from (1) and (2) by retaining the $1/r$ varying terms:

$$\bar{H} = \frac{j}{4\pi r} IL \sin \theta e^{-j\beta_0 r} a_\phi \tag{3}$$

$$\bar{E} = \frac{j\eta_0}{4\pi r} IL \sin \theta e^{-j\beta_0 r} a_\theta \tag{4}$$

As expected for TEM wave propagation, the \mathbf{E} and \mathbf{H} fields are perpendicular to each other and to the outward propagation in the \mathbf{r} direction. Also the ratio of $\mathbf{E}/\mathbf{H} = \eta_0 = (\mu_0/\epsilon_0)^{1/2}$, which is the intrinsic impedance of free space.

The radiation pattern of this short dipole is shown in Fig. 2, and exhibits the classical symmetry expected of dipole antennas, which is both independent of ϕ and symmetric about the x - y plane through the center (feedpoint)

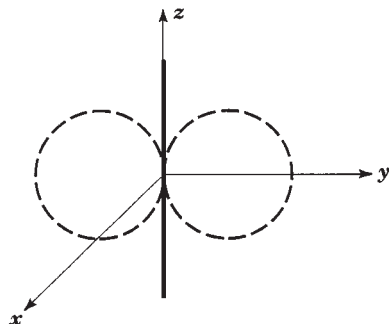


Figure 2. Radiation pattern for an infinitesimal (or Hertzian) dipole.

of the dipole. The magnitude of the total radiated power is $P_{\text{rad}} = 40 \pi^2 I_0^2 (L/\lambda)^2$. From Eqs. (3) and (4) it is interesting to note that even for this constant-current infinitesimal dipole, the radiated power density is proportional to $\sin^2 \theta$. Hence, it is maximum for $\theta = 90^\circ$ (i.e., in the x - y plane normal to the orientation of the dipole) and zero for the directions along the length of the dipole ($\theta = 0^\circ$ and 180°). The latter property for zero radiation along the length of the dipole will be seen for all linear dipoles regardless of length. It follows from the fact that a linear antenna may be considered to be composed of infinitesimal dipoles that do not create \mathbf{E} and \mathbf{H} fields or radiated power density for the $\theta = 0^\circ$ and 180° directions.

2.2. Linear Dipole Antennas

The geometry of a linear dipole antenna of length $L = 2h$ is shown in Fig. 1. The current distribution is sinusoidal, and is given by

$$I(z') = \frac{I(0)}{\sin kh} \sin k(h - |z'|) \text{ for } -h < z' < h \tag{5}$$

where $I(0)$ is the current at the feedpoint of the antenna, h is the half-length of the antenna, and $k = \omega(\mu\epsilon)^{1/2}$ is the propagation constant in the material surrounding the dipole. The current distributions for several lengths of dipole antennas are shown in Fig. 3.

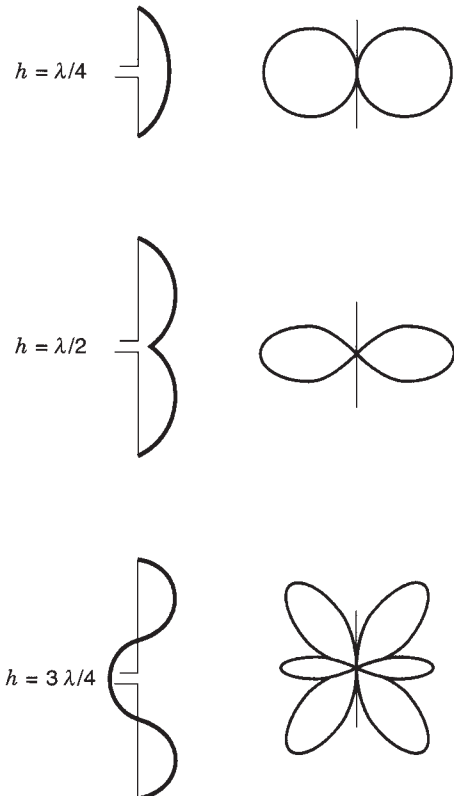


Figure 3. Current distributions and associated radiation patterns for several different lengths of dipole antennas.

The electric and magnetic fields around the dipole are calculated by modeling the antenna as a series of Hertzian or elemental dipoles and integrating the fields from each of these elements. The resultant fields far from the antenna at a distance r are

$$\vec{E} = \frac{j\eta I(0)}{2\pi r \sin(kh)} F(\theta) e^{j(\omega t - kr)} \vec{\theta} \quad (6)$$

and

$$\vec{H} = \frac{jI(0)}{2\pi r \sin(kh)} F(\theta) e^{j(\omega t - kr)} \vec{\phi} \quad (7)$$

where $\eta = (\mu/\epsilon)^{1/2}$, and where the θ dependence of the radiated fields $F(\theta)$ is called the *pattern factor* and is given by the following:

$$F(\theta) = \frac{\cos(kh \cos(\theta)) - \cos kh}{\sin \theta} \quad (8)$$

The radiation power density (*radiation pattern*) is given by

$$P(\theta) = \frac{\vec{E} \bullet \vec{E}^*}{2\eta} \vec{r}_0 = \frac{\eta I^2(0)}{8\pi^2 r_0^2 \sin^2(kh)} F^2(\theta) \quad (9)$$

Using $\eta = \eta_0 = 120\pi$, this can also be expressed in terms of the total radiated power $W (= I^2(0)R_a/2)$ and the feedpoint resistance R_a as follows:

$$P(\theta) = \frac{30}{\pi r^2} \frac{W}{R_a} \frac{F^2(\theta)}{\sin^2 kh} \quad (10)$$

The normalized radiation patterns are shown in Fig. 3b for several different lengths of dipoles.

The directivity of a dipole antenna related to the maximum power density that an antenna can create at a distance r is given by

$$D = \frac{P_{\max}}{P_0} = \frac{F^2(\theta)_{\max}}{\frac{1}{2} \int_0^\pi F^2(\theta) \sin \theta d\theta} \quad (11)$$

$$= \frac{120}{R_a} \frac{F^2(\theta)_{\max}}{\sin^2 kh}$$

where $P_0 = W/(4\pi r^2)$ is the isotropic power density that would have been created at the field point if the antenna had a directivity of one and radiated isotropically for all angles (clearly a mathematical possibility but not physically realizable).

The input resistance R_a of a center-fed dipole antenna of length $2h$ is twice that of an end-fed monopole of length h . This may therefore be obtained by using the graphs given in the related encyclopedia article, *MONOPOLE ANTENNAS*.

The ohmic losses of a dipole antenna [given by $I^2(0)R_{\text{ohmic}}/2$] are quite small, particularly for $h/\lambda > 0.1$. The resultant antenna radiation efficiencies (given by $R_a/(R_a + R_{\text{ohmic}})$) are on the order of 90–99%.

Two effects cause the behavior of physical dipoles to slightly differ from that of ideal dipoles: (1) realistic antennas have some finite thickness, and (2) the ends of the dipole capacitively couple to air, effectively making the dipole electrically longer by 2–9% than its physical length. For a half-wave dipole (length = $2h = \lambda/2$), for instance, the physical length must be slightly shortened in order to create a resonant length antenna ($X_a = 0$). Table 1 shows the wire lengths required to produce a resonant half-wave dipole. This shortening varies from 2% to 9%, depending on the thickness of the dipole.

Since a dipole antenna is a physically resonant structure, its feedpoint impedance (particularly the reactance X_a) varies greatly with frequency. Thus, these antennas have a fairly narrow bandwidth. The VSWR of a dipole antenna as a function of frequency and wire thickness is shown in Fig. 4 for an antenna that would be half-wave resonant at 300 MHz. Using a measure of “usable bandwidth” that the measured VSWR should be less than 2–1, this antenna has bandwidths of $310 - 262 = 48$ MHz for the thicker wire and $304 - 280 = 24$ MHz for the thinner wire. As fractions of the design frequency (300 MHz), the bandwidths are 16 and 8%, respectively.

2.3. Slot Dipole

A slot dipole antenna is a dual to the linear dipole antenna. The radiation pattern of a slot antenna is identical to that of the linear dipole of the same length (see Fig. 3) except that orientations of the \mathbf{E} and \mathbf{H} are interchanged. Also the feedpoint impedance Z_s of a slot antenna is related to that of the dual linear antenna by the following equation

$$Z_s = \frac{\eta^2}{4Z_a} \quad (12)$$

where Z_s is the impedance of the slot and Z_a is the impedance of the dual linear antenna.

2.4. Biconical Dipoles

A biconical dipole such as that shown in Fig. 5a is commonly used for broadband applications when the flare angle θ is between 30° and 60° . The exact flare angle is not

Table 1. Wire Lengths Required to Produce a Resonant Half-Wave Dipole for a Wire Diameter of $2a$ and a Length L

Length : diameter ratio $L/(2a)$	Percent Shortening Required	Resonant Length L	Dipole Thickness Class L
5000	2	0.49λ	Very thin
50	5	0.475λ	Thin
10	9	0.455λ	Thick

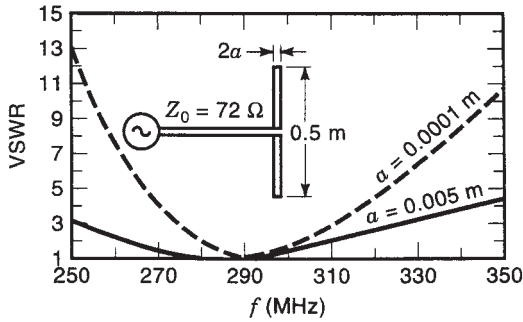


Figure 4. VSWR of a dipole antenna as a function of frequency and wire thickness (from Ref. 3).

critical, so it is generally chosen so that the impedance of the dipole nearly matches the impedance of the feedline to which it is connected. The impedance of the biconical dipole varies as a function of wavelength and flare angle, with a relatively flat impedance response for wide flare angles. Hence, this antenna is of broader bandwidth than a simple linear dipole.

Some variations of this method of using flaring to increase bandwidth are the flat bowtie antenna (which may be built on a printed circuit board) and the wire version of the biconical antenna shown in Figs. 5b and 5c, respectively.

2.5. Folded Dipole Antennas

A folded dipole antenna is shown in Fig. 6. The dipole is created by joining two cylindrical dipoles at the ends and driving the entire structure by a transmission line (often a two-wire transmission line) at the center of one arm as shown. The feedpoint impedance of a folded dipole of two identical-diameter arms is 4 times larger than that for an unfolded dipole of the same length. This can actually be advantageous, since the feedpoint resistance may now be comparable to the characteristic impedance Z_0 of the transmission line or feedline. The reactance of the antenna may easily be compensated by using a lumped element with a reactance that is negative of the reactance at the terminals of the folded dipole antenna or else by using a foreshortened antenna length to resonant length arms so that $X_a = 0$ (see Table 1).

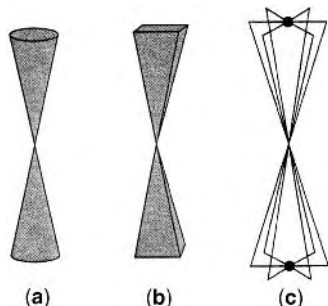


Figure 5. Biconical dipole antenna and variations: (a) biconical dipole antenna; (b) flat bowtie antenna; (c) wire version of biconical dipole antenna.

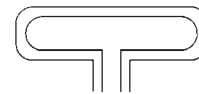


Figure 6. Folded dipole antenna.

2.6. Shunt-Fed Dipoles

Matching networks of reactive elements are generally required to match the feedpoint impedance ($R_a + jX_a$) of center-fed dipoles to transmission lines. Typically these lines have characteristic impedance on the order of 300–600 Ω . To alleviate the need for matching networks, the antennas are at times shunt-fed at symmetric locations off the centerpoint as shown in Fig. 7. This procedure using either the delta match (Fig. 7a) or the T-match (Fig. 7b) is often used for half-wave dipoles ($2h = \lambda/2$) with A and B dimensions that are typically on the order of 0.10–0.15 λ .

2.7. Sleeve Dipole

The sleeve dipole antenna and its equivalent electrical model are shown in Fig. 8. In practice, this antenna is built from a coaxial line with the outside conductor and insulation stripped away from the center conductor, which is left protruding. The outer conductor is connected to the ground plane, and the image produced by the ground plane creates an equivalent sleeve dipole antenna. These dipoles are useful, because they have a broadband VSWR over nearly an octave of bandwidth.

3. APPLICATIONS

Dipole antennas and arrays of dipole antennas are used for shortwave (3–30 MHz) and for VHF and UHF (30–900 MHz) radio and TV broadcasting. If directional communication is desired such as for shortwave radio transmission via the ionosphere, a phased array of horizontal dipoles may be used mounted above a ground plane. The spacing is chosen to send the major lobe of radiation toward the sky at a suitable angle to reflect off the ionosphere and provide broadcast coverage over the desired service area.

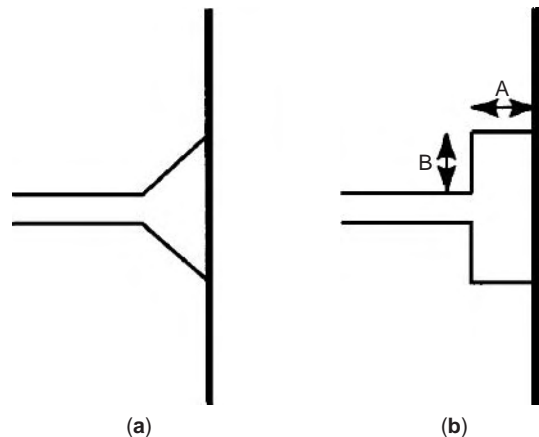


Figure 7. Shunt-fed dipoles: (a) delta match; (b) T-match.

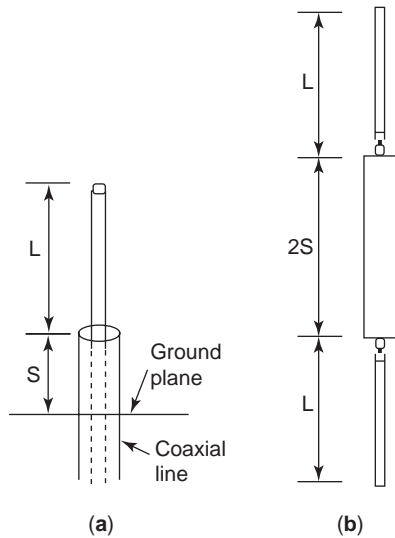


Figure 8. Sleeve dipole antenna: (a) physical model; (b) equivalent electrical model.

For VHF and UHF radio and TV broadcasting over a 360° azimuthal angle, collinearly mounted vertical dipoles that are excited in phase with each other are often used. Two examples of this are shown in Figs. 9a and 9b. An example variation of this is a three- to eight-bay turnstile antenna used for TV broadcasting shown in Fig. 10a. Each turnstile is made of two perpendicular slot antennas as shown in Fig. 10b.

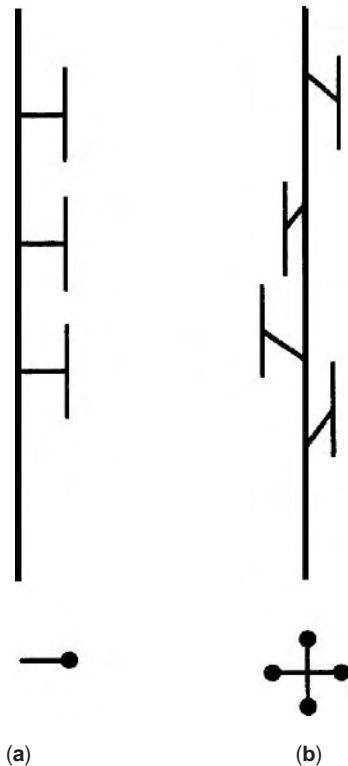


Figure 9. Collinearly mounted vertical dipoles for VHF and UHF radio and TV broadcasting: (a) pole-mounted array of collinear dipoles; (b) vertical dipoles spaced around a pole.

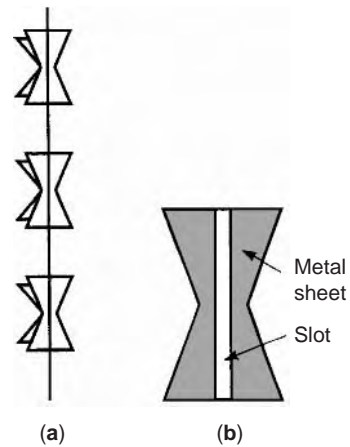


Figure 10. Variation on collinearly mounted vertical dipoles: (a) turnstile antenna used for TV broadcasting; (b) two perpendicular slot antennas constituting each turnstile.

3.1. Log periodic Antennas

For broadband applications log periodic antennas are commonly used as both transmitting and receiving antennas. The bandwidth is easily controlled by adjusting the relative lengths of the longest and shortest elements in the array. The geometry of a log periodic array is shown in Fig. 11a, which shows how the “phase reversal” feed system for this antenna is constructed. The equivalent antenna model of this array is shown in Fig. 11b. The elements of the array are dipole antennas that increase in both length and spacing according to the formula

$$\tau = \frac{R_{n+1}}{R_n} = \frac{d_{n+1}}{d_n} \tag{13}$$

where $\tau = f_n/f_{n+1}$ is the ratio of the resonant frequencies f_n and f_{n+1} of the adjacent dipole elements. Since lengths and spacings are interrelated, the choice of one initial value controls the design of the remaining elements. The spacing between one half-wave dipole and its adjacent shorter neighbor is given by

$$\sigma = \frac{d_n}{2L_n} = \frac{(1 - \tau)}{4} \cot \alpha \tag{14}$$

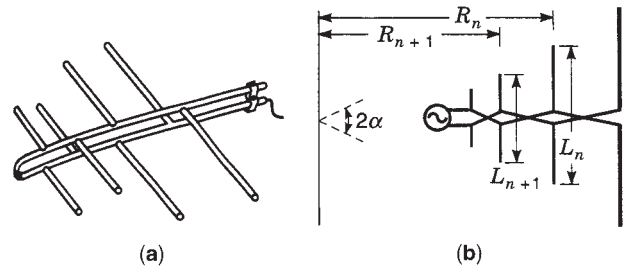


Figure 11. Log periodic dipole array: (a) geometry of a log periodic array showing how the “phase reversal” feed system for this antenna is constructed (from Ref. 6); (b) equivalent antenna model of the log periodic array.

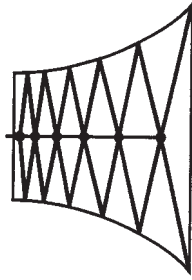


Figure 12. LPA with sawtooth wire elements for increased bandwidth. Dots indicate feedpoint locations; heavy wires indicate dipole elements; light wires indicate wires for structural support only.

Log periodic arrays are generally constructed with small values of α ($10^\circ \leq \alpha \leq 45^\circ$ [5]) and large values of τ ($0.95 \leq \tau \leq 0.7$ [5]), which essentially gives a traveling wave propagating to the left in the backfire direction, away from the antenna array. The nature of this array is that only the elements that are approximately half-wavelength long radiate, and since they are radiating to the left, the smaller elements do not interfere with them. This is accomplished by the phase reversal of the feeds. An array that is built without the phase reversal radiates in the endfire direction. The interference of the longer elements to the right of radiating elements results in spurious reflections and erratic impedance behavior, known as “end effect.”

An effective way to further increase the bandwidth of a log periodic antenna is to change from dipole elements to elements with individual broader bandwidths, similar to changing from a dipole antenna to a biconical antenna. This is accomplished for log periodic arrays by using a configuration of wires such as shown in Fig. 12, where each element is a sawtooth element and therefore has broader bandwidth than the individual dipole elements.

3.2. Broadband Dipole Curtain Arrays

A broadband dipole curtain such as shown in Fig. 13 is commonly used for high-power (100–500-kW) HF ionospheric broadcasting and shortwave broadcasting stations. The curtain is composed of several dipoles, usually a half-wavelength long, mounted horizontally or vertically in a rectangular or square array, often backed by a reflecting plane or wire mesh. This array has several desirable features, including high gain, broad bandwidth, independent control of horizontal and vertical radiation patterns, ease of matching (low VSWR), and the ability to efficiently broadcast efficiently. Using a phased-feeds system, this array allows beamsteering of the radiation

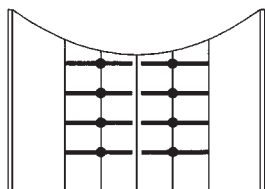


Figure 13. A broadband dipole curtain. Dots indicates feedpoint locations.

pattern in both the azimuthal and elevation planes, providing a very high degree of flexibility.

3.3. VHF/UHF Communication Applications:

3.3.1. Yagi–Uda Dipole Array. Yagi–Uda arrays are commonly used as general-purpose antennas from 3 to 3000 MHz, in particular as home TV antennas. They are inexpensive, have reasonable bandwidth, and have gains up to 17 dBi or more if multiple arrays are used. They have unidirectional beams with moderate sidelobes [6].

A typical Yagi–Uda array is shown in Fig. 14. This array is a simple endfire array of dipole antennas where only one of the elements is driven and the rest are parasitic. The parasitic elements operate as either reflectors or directors. In general [6], the longest antenna, which is about $\lambda/2$ in length, is the main reflector, and is generally spaced $\lambda/4$ in back of the driven dipole. The feed element is commonly a folded dipole antenna $0.45\text{--}0.49\lambda$ long. Adding directors, which are generally $0.4\text{--}0.45\lambda$ long, to the front of the driven element increases the gain of the array. The directors are not always of the same length, diameter, or spacing. Common arrays have 6–12 directors and at most two reflectors. Additional improvements in gain by adding more elements are limited; however, arrays have been designed with 30–40 elements [5]. A gain (relative to isotropic) of 5–9 per wavelength of array length is typical for Yagi–Uda arrays, for an overall gain of 50–54 (14.8–17.3 dB).

The Yagi–Uda array is characterized by a main lobe of radiation in the direction of the director elements and small sidelobes. The beamwidth is small, generally $30\text{--}60^\circ$ [5]. Typical *E*- and *H*-plane patterns of a Yagi–Uda array are shown in Fig. 15. Typically, the performance of a Yagi–Uda array is computed using numerical techniques [5, Ref. 17]. For the simple case where all the elements are approximately the same size, the electric field pattern can be computed from the array factors of the various elements.

The input impedance of a Yagi–Uda array is often small. For example, for a 15-element array with reflector length = 0.5λ , director spacing = 0.34λ , and director length = 0.406λ , the input impedance is 12, 22, 32, 50, or 62Ω for reflector spacings of $0.10, 0.13, 0.15, 0.18,$ and 0.25λ , respectively. This can make matching to typical transmission lines (50, 75, or 300Ω) difficult. Folded dipoles used for the driven element are therefore used to boost the input impedance by a factor of ≥ 4 .

Extensive studies of the design of Yagi–Uda arrays have been made [5, Ref. 20], and tables are provided to optimize the Yagi–Uda array for a desired gain.

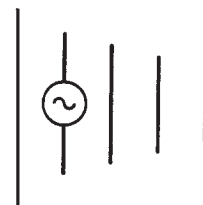


Figure 14. Yagi–Uda array.

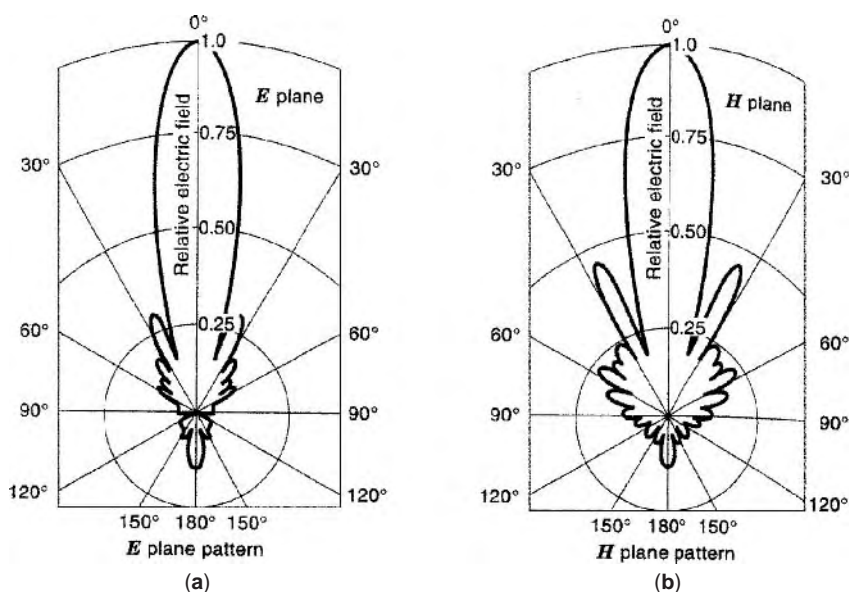


Figure 15. Typical *E*- and *H*-plane patterns of a Yagi-Uda array; total number of elements = 27, number of directors = 25, number of reflectors = 1, number of driven elements = 1, total length of reflector = 0.5λ , total length of feeder = 0.47λ , total length of each director = 0.406λ , spacing between reflector and feeder = 0.125λ , spacing between adjacent directors = 0.34λ , radius of wires = 0.003λ (from Ref. 7).

3.3.2. Dipoles for Circular Polarization. For applications that require a circularly polarized antenna such as TV and FM broadcasts and space communications, at least two dipoles, each of which has a linear polarization, must be combined in an array, often referred to as *crossed dipoles*. In a crossed dipole configuration, dipoles are mounted perpendicular to each other for circular polarization or at other angles for elliptical polarization. Currents are fed 90° out of phase between the two dipoles. These can also be used as probes for sensing vector fields to isolate individual components of the electric field. Adaptations of the crossed dipole are shown in Figs. 16a and 16b. Dipole arrays such as the Yagi-Uda can also be combined to provide circular polarization, as shown in Fig. 16c.

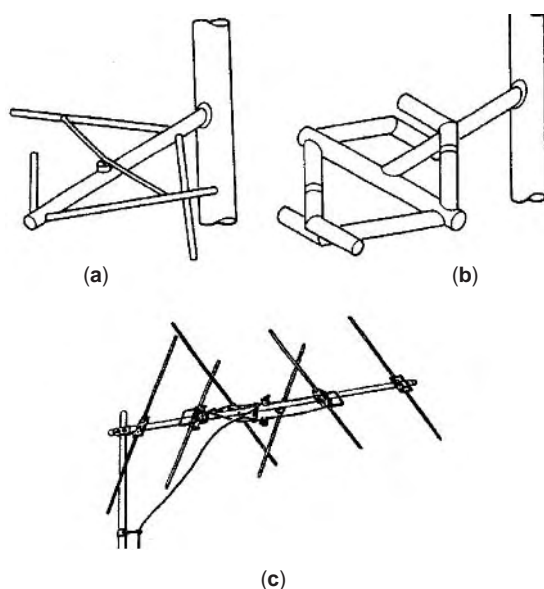


Figure 16. Cross-dipole applications for circular or elliptical polarization (from Ref. 6): (a) two shunt-fed slanted V dipoles; (b) series-fed slanted dipoles; (c) circularly polarized Yagi-Uda array.

BIBLIOGRAPHY

1. J. D. Kraus, *Antennas*, 2nd ed., McGraw-Hill, New York, 1988.
2. M. F. Iskander, *Electromagnetic Fields and Waves*, Prentice-Hall, Englewood Cliffs, NJ, 1992.
3. W. L. Stutzman and G. A. Thiele, *Antenna Theory and Design*, J Wiley, New York, 1991.
4. O. P. Gandhi, *Microwave Engineering and Applications*, Pergamon Press, New York, 1985.
5. C. A. Balanis, *Antenna Theory—Analysis and Design*, J Wiley, New York, 1982.
6. R. C. Johnson, *Antenna Engineering Handbook*, 3rd ed., McGraw-Hill, New York, 1993.
7. G. A. Theile, Analysis of Yagi-Uda antennas, *IEEE Trans. Anten. Propag.* **17** (1969).

DIRECT SATELLITE TELEVISION BROADCASTING

JOHN P. GODWIN
DirecTV

Direct-to-home (DTH) satellite television broadcasting has no strict technical or legal definition. Since the late 1970s the term has been used to delineate commercial systems that deliver television directly to consumer homes using communication satellites in geosynchronous orbit. Systems originally intended for DTH applications have operated at downlink frequencies above 11 GHz and with antennas of 1 m or less. Certain systems operated at 4 GHz were planned for cable television distribution and became, secondarily, DTH systems with customer parabolic antennas in the 2.5–3.0 m range. Most systems have been supported primarily from subscription and pay-per-view revenues rather than advertising revenues. In the

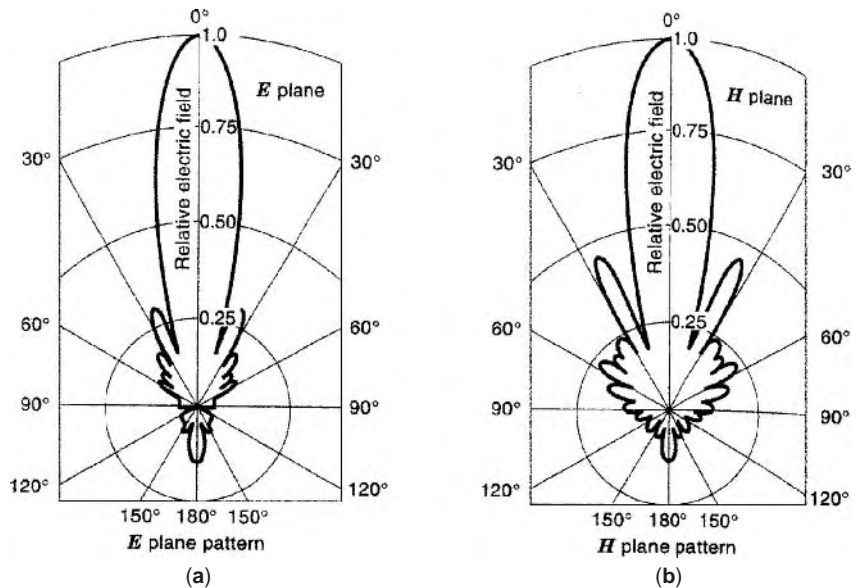


Figure 15. Typical *E*- and *H*-plane patterns of a Yagi-Uda array; total number of elements = 27, number of directors = 25, number of reflectors = 1, number of driven elements = 1, total length of reflector = 0.5λ , total length of feeder = 0.47λ , total length of each director = 0.406λ , spacing between reflector and feeder = 0.125λ , spacing between adjacent directors = 0.34λ , radius of wires = 0.003λ (from Ref. 7).

3.3.2. Dipoles for Circular Polarization. For applications that require a circularly polarized antenna such as TV and FM broadcasts and space communications, at least two dipoles, each of which has a linear polarization, must be combined in an array, often referred to as *crossed dipoles*. In a crossed dipole configuration, dipoles are mounted perpendicular to each other for circular polarization or at other angles for elliptical polarization. Currents are fed 90° out of phase between the two dipoles. These can also be used as probes for sensing vector fields to isolate individual components of the electric field. Adaptations of the crossed dipole are shown in Figs. 16a and 16b. Dipole arrays such as the Yagi-Uda can also be combined to provide circular polarization, as shown in Fig. 16c.

BIBLIOGRAPHY

1. J. D. Kraus, *Antennas*, 2nd ed., McGraw-Hill, New York, 1988.
2. M. F. Iskander, *Electromagnetic Fields and Waves*, Prentice-Hall, Englewood Cliffs, NJ, 1992.
3. W. L. Stutzman and G. A. Thiele, *Antenna Theory and Design*, J Wiley, New York, 1991.
4. O. P. Gandhi, *Microwave Engineering and Applications*, Pergamon Press, New York, 1985.
5. C. A. Balanis, *Antenna Theory—Analysis and Design*, J Wiley, New York, 1982.
6. R. C. Johnson, *Antenna Engineering Handbook*, 3rd ed., McGraw-Hill, New York, 1993.
7. G. A. Theile, Analysis of Yagi-Uda antennas, *IEEE Trans. Anten. Propag.* **17** (1969).

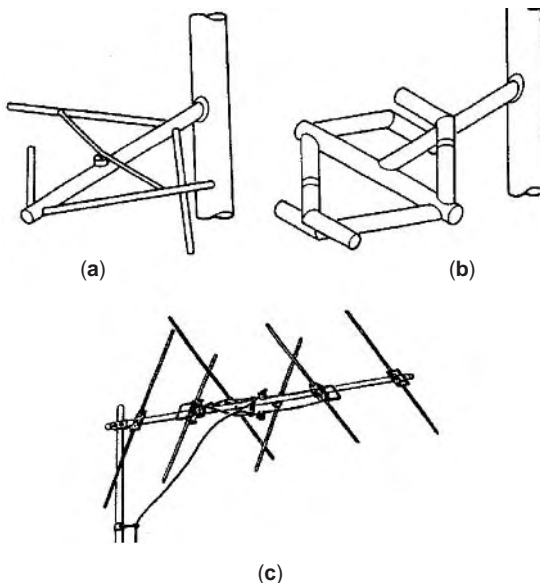


Figure 16. Cross-dipole applications for circular or elliptical polarization (from Ref. 6): (a) two shunt-fed slanted V dipoles; (b) series-fed slanted dipoles; (c) circularly polarized Yagi-Uda array.

DIRECT SATELLITE TELEVISION BROADCASTING

JOHN P. GODWIN
DirecTV

Direct-to-home (DTH) satellite television broadcasting has no strict technical or legal definition. Since the late 1970s the term has been used to delineate commercial systems that deliver television directly to consumer homes using communication satellites in geosynchronous orbit. Systems originally intended for DTH applications have operated at downlink frequencies above 11 GHz and with antennas of 1 m or less. Certain systems operated at 4 GHz were planned for cable television distribution and became, secondarily, DTH systems with customer parabolic antennas in the 2.5–3.0 m range. Most systems have been supported primarily from subscription and pay-per-view revenues rather than advertising revenues. In the

various direct-to-home systems deployed worldwide, a variety of technologies has been used, including analog and digital modulations and both standard and high-definition television formats. Certain systems have been entirely national in scope, while others have broadcast on a regional basis. From a regulatory viewpoint, both fixed satellite service (FSS) bands and broadcasting satellite service (BSS) bands have been used. Direct-to-home systems are sometimes also referred to as direct broadcast satellite (DBS) systems. This article describes the broadcasting and reception systems of a typical digital DTH broadcasting system, but does not cover the substantial infrastructure necessary for customer service and billing.

1. EVOLUTION AND EXISTING SYSTEMS

Although DTH satellite television was a dream of satellite engineers since the early 1960s, little progress was made until the early 1980s. Satellite technology steadily improved in generating high-radiofrequency (RF) power levels, and ground electronics improved by the introduction of low-cost, low-noise microwave transistors. Through 1994 these early systems used analog frequency modulation.

During the 1980s in the Americas, the earliest major system was the Satellite Technology Corporation project in the United States. This plan intended to deliver five channels to each time zone with a dedicated satellite for each. The user terminals were to employ parabolic dishes of 85 cm diameter. This project was abandoned, primarily for economic reasons. Also, in the United States during the 1980s, home reception began of satellite transmissions intended for delivery to cable television systems. The transmissions were at C band in the frequency range 3.7–4.2 GHz. These early home dishes were 2.5–3.0 m in diameter and cost several thousands of dollars, but increased satellite power permitted new C-band home dishes to drop in size to about 1.5 m by the early 1990s. This United States C-band DTH marketplace peaked at about 3.9 million homes in 1994. In Japan the quasigovernment broadcaster NHK utilized satellite delivery to 45-cm dishes for both standard National Television Systems Committee (NTSC) and multiple sub-Nyquist encoding (MUSE) high-definition television. By 1993 this service, called BS for broadcasting satellite, was received by 4.5 million homes. The inexpensive analog BS receivers also became a typical feature of new television sets for the Japanese marketplace. In Europe the early use of satellites was for delivery of state-owned television networks. In the early 1990s, the Astra satellites became a major vehicle for DTH delivery of private, commercial channels. Multiple television broadcasters utilized Astra, including British Sky Broadcasting (BSkyB), which was providing over 40 analog channels to 6.4 million homes at the end of 1997 [1]. Other European satellites are also providing DTH services, including Eutelsat and Hispasat.

During 1994 the era of multichannel, all-digital DTH satellite delivery began with two systems in the United States, the Primestar system owned by a consortium of

cable firms, and a system operated primarily by DirecTV, Inc., a unit of Hughes Electronics. The Primestar system used “medium-power” satellites and approximately 0.75–1.0 m dishes; the DirecTV broadcast used “high-power” satellites and 45-cm dishes. By late 1997 the Primestar system delivered more than 160 channels to nearly 2 million homes in the United States by year end 1997. The DirecTV service delivered more than 175 channels to 3.3 million homes in the United States by year end 1997. In 1995 another DTH business using “high-power” satellites entered this marketplace; this new entrant, EchoStar, reached approximately 1 million homes by year end 1997. AlphaStar, a short-lived DTH service, acquired only about 51,000 subscribers in the United States before filing for bankruptcy in 1997. Elsewhere in the Americas, three DTH services to Latin America were initiated in the early 1990s. One of these ventures, Galaxy Latin America, began broadcast operations in June 1995. Galaxy Latin America is a joint venture of Hughes and major media firms from Mexico, Venezuela, and Brazil. (The general company information given above was found at the World Wide Web sites listed in the Further Reading list.)

In Japan in 1996, the joint venture PerfectV started multichannel, all-digital broadcasting with approximately a half-million subscribers by year-end 1997 [2]. This firm was joined in the marketplace by DIRECTV JAPAN in December 1997. A third entrant, Japan Sky Broadcasting (JSkyB), announced in 1997 that it would merge with the first broadcaster, PerfectV. All three firms use a Japanese industry variant of the digital videobroadcasting (DVB) format, and all three use medium-power FSS satellites. Within Japan the category of service provided by these three competitors is called *digital communications satellite*, or *digital CS*, in contrast to the high-power broadcasting satellite or BS service by NHK.

By early 1998 in Europe there were plans underway to convert existing analog systems, for example, BSkyB in the United Kingdom, and to launch new digital satellite platforms. New digital satellite systems in operation include DF1 in Germany; Telepiu in Italy; Via Digital (Hispasat) and Canal Satellite in Spain; TPS, AB-sat, and Canal Satellite Numerique in France [3].

2. REFERENCE ARCHITECTURE

Figure 1 shows a simplified diagram of an all-digital multichannel satellite DTH system. Figure 2 shows the exterior of a typical DTH broadcasting site including four 13-m uplink antennas.

2.1. Broadcasting Facility

Most existing DTH systems have been used as delivery systems for existing programs, for example, broadening the market exposure of existing programming or delivering the programming with improved quality or convenience. As a delivery or rebroadcast system, a substantial portion of programming typically arrives at the DTH broadcasting or uplink facility via other “backhaul” satellites or terrestrial fiber. Programming, such as theatrical films, arrives at the facility as prerecorded

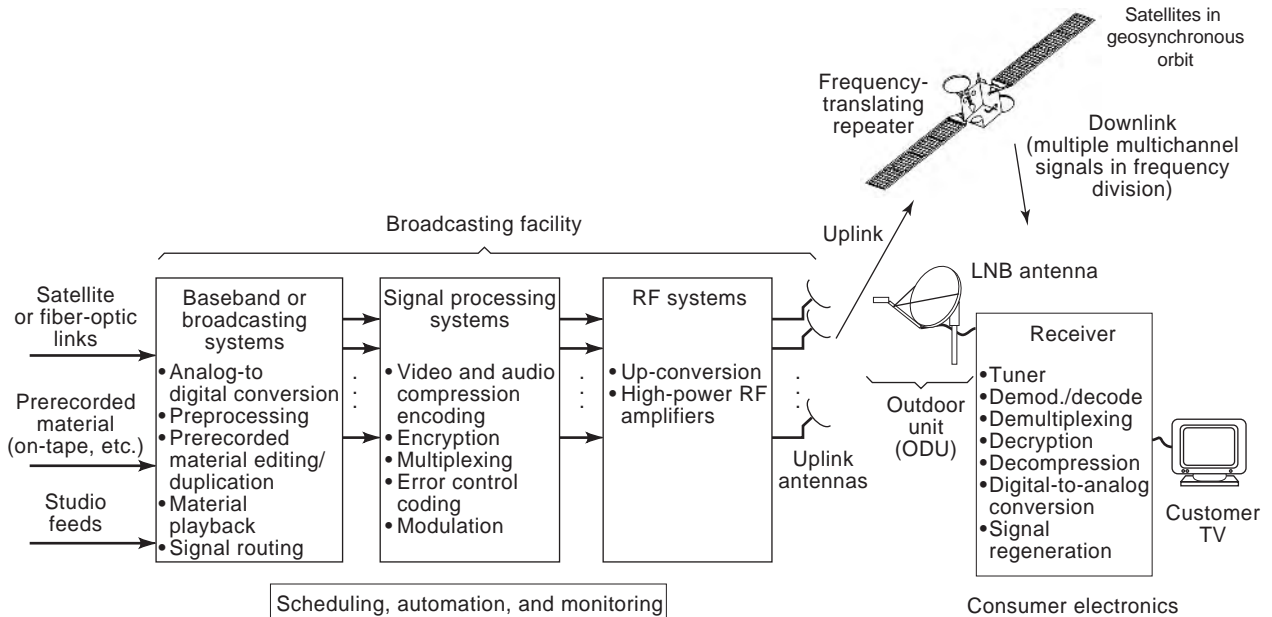


Figure 1. Simplified diagram of an all-digital multichannel satellite DTH system. Major broadcasting and transmission equipment groups are shown but not customer service and billing systems.

digital tapes. In a limited number of systems, the broadcasting facility also includes studios for the creation of unique programming.

The broadcasting facility provides a number of functions common to any broadcasting facility, such as incoming signal monitoring, adjustment, and resynchronization, signal routing within the facility, and for prerecorded material, quality control, cloning, and playback. For playback, broadcast-quality tape players are utilized or, more recently, the material is stored on and played from video file servers using redundant arrays of independent disks (RAID) technology.

Large, multichannel “pay” DTH broadcasting also requires that the broadcast site provide *conditional access*



Figure 2. This DTH site in Colorado uses four 13-m antennas for uplink operations and numerous smaller dishes for programming reception. Courtesy of DirecTV, Inc.

equipment, service information/electronic program guide (SI/EPG) equipment, compression encoders, and multiplexing, error control, and modulation equipment. The conditional access system, which includes equipment within the home, permits customer access to programming services only when certain *conditions* have been met—for example, the customer account is in good standing or the customer is located outside a program blackout area. The SI/EPG equipment prepares specialized broadcast streams that provide the consumer equipment with technical attributes of each view channel (the service information), along with program content information for display by the home receivers. The EPG data typically include program title, start and stop time, synopsis, parental rating, etc. The signal compression equipment performs *redundancy reduction* processing on the television video and separately the audio to reduce the total information rate. A typical digital studio signal at 270 Mbps (megabits per second) is reduced to the range of 2–10 Mbps before broadcast. This dynamically reduces the investment needed to put the transmission path in service (i.e., the satellites) and, conversely, greatly increases the number of available viewer channels for a given satellite investment. Most operational digital DTH systems have utilized the Motion Picture Experts Group (MPEG) MPEG1 or MPEG2 compression standards [4,5], or proprietary systems with similar characteristics. (See Section 4). The *compressed* streams from multiple channels are typically multiplexed into a single high-speed stream. This multiplexing process may be “fixed” in that peak bit rates are allocated to each video channel or, in certain systems, the individual channel rates may vary dynamically depending on their instantaneous bit rate need—the latter approach is called *statistical multiplexing*. The composite bitstream is then coded by error control to add

selective redundancy for error detection and correction. The error control coding permits systems to be designed that offer high-quality operation with a threshold level lower than that possible in previous analog systems. The modulation utilized is commonly a constant envelope modulation such as quadrature phase shift keying (QPSK), which is typical of a satellite system for which the satellite repeater has a limiting final output stage.

2.2. Transmission Path

The transmission path includes the error control coding and modulation described above, the uplink site’s upconverters, transmitters, and antennas, the uplink propagation path, the relay satellite, and the downlink transmission path including the subscriber antenna and receiver front end. In all existing DTH systems, the satellite has been a frequency translating microwave repeater. The expense of generating high satellite RF transmitter levels has caused these systems to be “downlink limited,” meaning that the composite uplink and downlink carrier-to-noise ratio (CNR) is dominated by the downlink CNR. The downlink CNR is determined primarily by the satellite effective isotropic radiated power (EIRP) per transponder, carrier attenuation by rain along the line of sight, and the subscriber antenna gain. The subscriber electronics equipment completing the transmission path consists of a small-aperture antenna, a low-noise block downconverter, tuner, demodulator, and error control decoder. The “error corrected” information stream out of the error control decoder is passed to the remainder of the digital circuitry within the receiver. (See Section 5.)

2.3. Home Electronics

The home electronics in a typical all-digital system include the antenna, low-noise block (LNB) converter, tuner-demodulator-decoder circuitry and other digital circuitry for demultiplexing, decryption under conditional access control, video and audio decompression, and video and audio output signal generation. For example, in digital receivers for the United States marketplace the

final output circuitry recreates an analog composite NTSC or S-video signal for delivery to a standard television set. In a typical digital satellite receiver, a removable device, often in the form of an International Organization for Standardization (ISO) smart card, provides the conditional access control function. (See Section 6.)

3. THEORETICAL MODELS

3.1. Information Theory

Figure 3 shows a theoretical model useful in DTH system design, and the corresponding system elements used to implement the theoretical model. A text such as Ref. 6 describes an “ultimate” system design in which *source encoding* is used to remove redundancy information in the bitstream representing the source, that is, the television signal, and then *channel encoding* to protect the encoded source by carefully adding redundancy. Information theory tells us that source codes exist that can drive the number of bits necessary to encode the source toward a theoretical minimum. MPEG2, shown in the lower portion of Fig. 3, provides a practical realization of the information theory by a complex set of transform, run-length, and other source codes. The MPEG algorithm further reduces the information content by selective removal of detail not subjectively important. Channel-coding theory indicates that channel codes exist that can drive the error rate toward zero while not driving the useful throughput toward zero. In 1966 Forney [7] demonstrated a path to realization of this theory by showing that concatenating multiple, simpler channel codes can create a powerful channel code. Figure 3 illustrates a DTH implementation using concatenated convolutional and Reed–Solomon (RS) codes. A bit interleaver is also used to “smooth” burst error sequences entering the RS decoder.

3.2. Layered Model

Figure 4 provides a “layered” or “protocol” model for DTH systems [8]. The layers shown are for the consumer

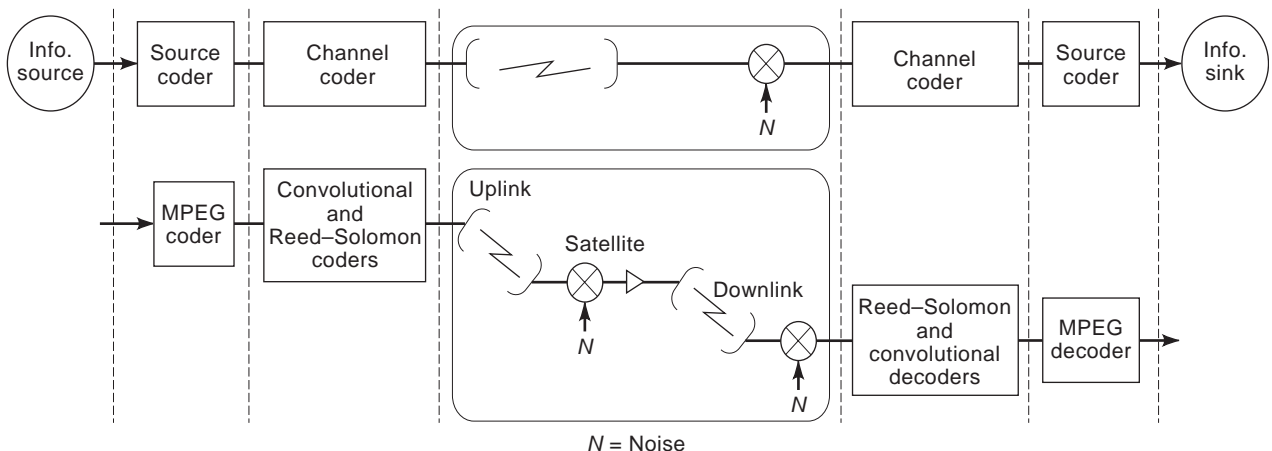


Figure 3. Theoretical source and channel coding are currently implemented by distinct source and channel coding processing.

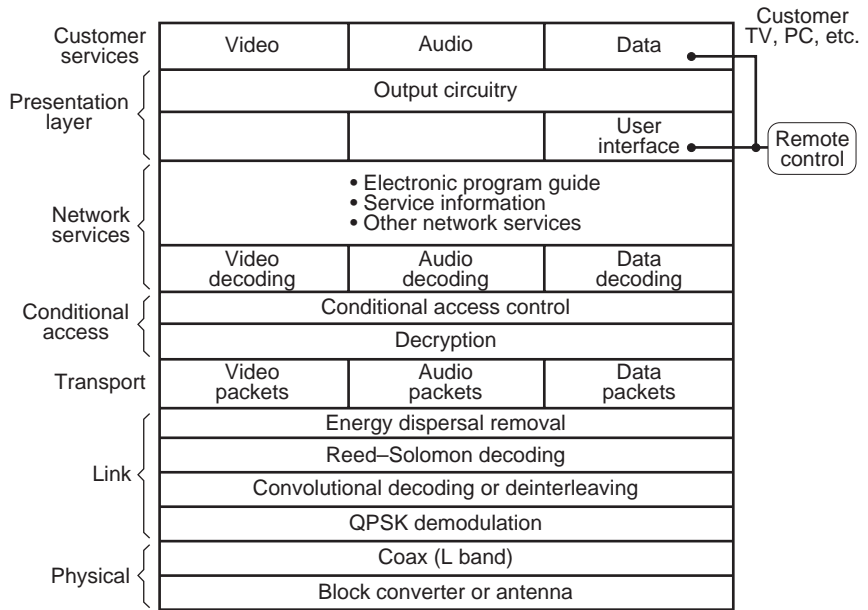


Figure 4. Layered or protocol model provides a practical decomposition of functions in a generic DTH integrated receiver decoder. (Source: International Telecommunication Union, Document 10-11S/TEMP/18, Fig. 1.)

electronics part of the system, but of course the same layers are necessary within the broadcasting facility equipment. As in layered, communications protocols, it is intended that the design tradeoffs of one layer do not interact with the design tradeoffs of the adjoining layers. For example, the design of MPEG decoder chips is largely independent of the design of the video output circuitry, which may be targeted for either NTSC, phase alternation line (PAL), or sequential couleur avec memoire (SECAM) television receivers. As another example, the MPEG coder to decoder syntax was largely designed without great concern about the specific error characteristics of the channel. However, to improve recovery in the event of channel errors, the MPEG standard does include a Macro Block Slice structure that generally limits error propagation to a portion of a frame.

Each layer is discussed in the following and in Sections 4 and 5. The realization of these protocol layers is discussed in Section 6.

3.2.1. Physical Layer. The physical layer at the bottom of Fig. 4 presents the RF to an intermediate-frequency (IF) LNB converter and the resulting IF interface to the digital receiver itself. An IF frequency starting at 950 MHz is typical but not required [8].

3.2.2. Link Layer. This layer is discussed in detail later in Section 5.

3.2.3. Transport Layer. The transport layer is a multiplexing layer or, for example, the systems layer of the MPEG2 standard. In each format given in Ref. 8, this layer provides common, fixed-length packets for all service types including video, audio, data, or overhead data such as electronic program guide information. Fixed-length

packets ease high-speed processing and use of direct memory access.

3.2.4. Conditional Access Layer. This layer provides decoding of specialized conditional access (CA) packets, sometimes called *entitlement management messages* (EMMs) and *entitlement control messages* (ECMs) [9]. The EMMs give instructions to the subscriber electronics regarding the authorized *entitlements*, for example, current subscriptions or pay per view status. The ECMs indirectly provide cryptographic keys for decryption of the individual services. In several systems these packets are passed from the receiver to a smart card with an embedded secure microprocessor. The microprocessor decodes ECMs and returns the corresponding keys. A decryption circuit within the receiver uses the keys and provides decrypted packets for each service to the network services layer. The receiver to microprocessor interface is often similar to the ISO standard [10].

3.2.5. Network Services Layer. This layer delivers the underlying DTH technical services. These services include video plus audio or “television,” standalone audio services, and data delivery services. Separate processes handle the decompression of each service type. For example, video decompression algorithms are quite distinct from those used for audio decompression. Video compression is discussed in greater detail later in Section 4. Other network services include decoding of the electronic program guide and service information syntax.

3.2.6. Presentation Layer. This layer puts the network services in final form for the end user. The layer includes the NTSC or PAL encoders and output circuitry and the on-screen user interface. Although the electronic program guide information delivered by the network is common to all receiver types, each receiver designer may choose a unique user interface concept. For example, for a typical

television program schedule grid, the grid extent (that is, numbers of view channels and time extent) and the color scheme are entirely up to the designer. The presentation layer also receives inputs from the user remote control, which is typically linked to the receiver using infrared or RF.

3.2.7. Customer Services Layer. In most DTH systems the customer provides the final display device such as the television or personal computer. This key assumption bounds the complexity of the satellite receiver and defines the characteristics of its output circuitry. For example, although a typical all-digital DTH system can deliver a three-component television signal, most existing televisions in the United States accept only a composite NTSC input. Since many new sets in the United States also accept a “separate chroma/luma” S-video signal, many satellite receivers in the American marketplace have supplied an S-video output in addition to the composite output. Figure 4 shows the remote control interfacing with both the presentation layer (user interface) and the customer services layer. The latter interface permits control of the display device by the same remote control device—for example, the remote may control the television volume level.

4. COMPRESSION

4.1. Fundamentals

Source coding may be lossless and permit a complete reconstruction by the source decoder, or source coding may be lossy and trade the quality of the reconstructed signal against the bits needed to transmit or store the signal. The nature of the compression algorithms vary with the signal type, its intended audience, and the cost relationship between the value of “saving bits” versus the value of the codec development and production. Reference 11 provides an excellent overview of the television compression state of the art through 1994.

The MPEG1 [4] and MPEG2 standards [5] have been broadly deployed in consumer products. The MPEG1 standard is intended for noninterlace video and data rates up to about 1.5 Mbps. The MPEG2 standard accommodates both noninterlace and interlace video, standard definition applications up to about 10 Mbps, and high-definition formats at bit rates up to about 15–50 Mbps. Note that while these standards provide details on the syntax and semantics between the encoder and decoder and are specific to a standard decoder, they say very little about the encoder. They are very abstract and do not dictate the technology of implementation. Both standards utilize two distinct processes in tandem to achieve high compression levels: discrete cosine transform (DCT) coding and

motion-compensated interframe prediction. The MPEG2 standard makes more complex algorithms available for motion compensation with interlace video. The discussion that follows provides a very simplified description of MPEG processing.

4.2. Discrete Cosine Transform Coder

Figure 5 illustrates the first major MPEG process, a DCT of pixel element values, the *lossy* quantization of these values, and then the *lossless* encoding of the result. Consumer television signals are acquired and displayed as linescan images, but since substantial spatial redundancy exists, the linescan images are first converted to 8×8 pixel blocks for MPEG processing. The DCT represents the horizontal and vertical information in the block using cosine functions as the basis vectors. The quantization step ignores the near-zero coefficients and tends to concentrate the energy in the transform domain into the low-frequency components. The “zigzag” readout of the coefficients starts with the DC coefficient and proceeds in zigzag fashion toward the highest frequency vertical and horizontal component. If insufficient bits are available, the higher-frequency coefficients may not be encoded. The next processing steps use tables of run-length and variable-length codes, which, based on experiment, will require the lowest average number of bits to represent the coefficients. The run-length codes use short codes for very likely bit sequences and long codes for less likely sequences. The variable-length codes are created such that no codeword is the prefix of another codeword. The buffer feedback path recognizes that image redundancy varies substantially across the blocks of a given image, but that for most applications the required output bit rate must be constant. As buffer fullness approaches, quantization can be increased, the bit rate reduced and, unfortunately, the quality will be reduced as well. Note that in multichannel systems, the output of a single encoder need not be at a fixed bit rate. In a DTH system, when a buffer strategy is used across all the video channels carried in a single stream, the technique is called *statistical multiplexing*.

In MPEG the spatial DCT coder described above is supplemented with an interframe predictor to also exploit the temporal redundancy of a given pixel block. Since motion within the image will cause the pixel values to “move” across the frame, the MPEG algorithms also include the technique discussed in the following.

4.3. Motion-Compensated Interframe Prediction

In MPEG, *motion compensation* determines the translation vector of 16×16 pixel blocks of luminance (called *macroblocks*) across multiple frames. Redundancy reduction is achieved by transmitting the vectors and quantized

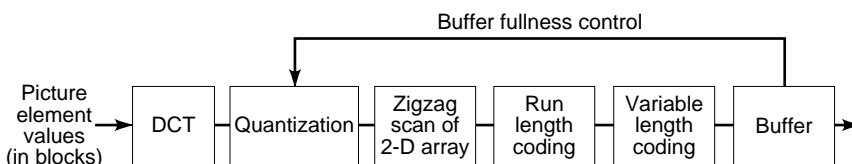


Figure 5. The discrete cosine transform (DCT) encoder path with its buffer control feedback loop is one of two major elements of the MPEG encoding process.

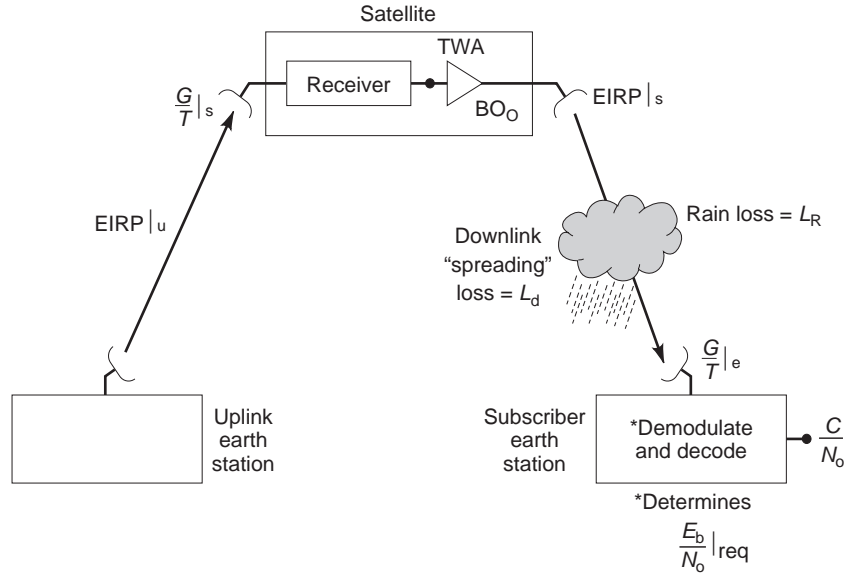


Figure 6. For design analysis purposes, the end-to-end DTH link is often split into “uplink” and “downlink” models. The downlink model assumes a noiseless uplink with the desired signal injected at the satellite TWTA input.

prediction errors, rather than the blocks, and further efficiencies are achieved by differentially encoding the vectors and also using variable length codes. The vectors are determined by finding the best macroblock match in the previous (and possibly also the future) reference frame. These searches generally are restricted in horizontal and vertical extent and can be very computationally intensive.

The MPEG2 algorithm is more sophisticated than MPEG1 in several areas, particularly motion compensation modes. Both compression schemes permit forward prediction, backward prediction, and interpolated prediction between images. The images may be either video frames or fields. MPEG1 can use only frame-based prediction; however, MPEG2 optionally can use field-based prediction, which allows increased coding efficiency for interlaced video. From video material in which the motion is slow, frame prediction is more efficient and MPEG2 performs similarly to MPEG1. As motion increases, field prediction coding becomes more efficient.

The MPEG2 toolkit is very complex. It is impractical to recreate the entire toolkit in every application. The MPEG2 group has therefore defined a handful of subsets or profiles of the full syntax. Also, within a profile, sets of parameter constraints have been identified as levels, with each higher level including all constraints from the lower levels.

5. TRANSMISSION (OR LINK LAYER)

5.1. Link Equation, Antenna Size, and Coverage

The most fundamental design equation in a DTH satellite system is the communications link equation. Ignoring uplink noise and interference contributions, the downlink carrier power (*C*) to noise power density (*N*₀) ratio is, in decibels, as follows [12]:

$$\frac{C}{N_0} = \text{EIRP}|_s - \text{BO}_0 - L_d + \frac{G}{T}|_e - k - L_r \text{ dB} \cdot \text{Hz} \quad (1)$$

where the $\text{EIRP}|_s$ is the effective power of the satellite with respect to an isotropic radiator, BO_0 is the backoff of the satellite transmitter with respect to saturation, L_d is the free space loss at the carrier frequency, $G/T|_e$ is a receive figure of merit for the DTH subscriber terminal, k is Boltzmann’s constant ($-228.6 \text{ dB} \cdot \text{W/K} \cdot \text{Hz}$), and L_r is the link loss due to rain. Figure 6 illustrates the definition of these link parameters. For a typical DTH design, each satellite transmitter handles a single carrier, so carrier intermodulation is not a concern and the transmitter output backoff is nominally zero. As a reference case, assume a downlink frequency of 12 GHz, a path loss of -205.8 dB , and a clear weather situation with $L_r = 0.0 \text{ dB}$. Equation (1) then becomes simplified to

$$\frac{C}{N_0} = \text{EIRP}|_s + \frac{G}{T}|_e + 22.8 \text{ dB} \cdot \text{Hz} \quad (2)$$

Using the parameters of Ref. 13 as an example, the typical edge of coverage EIRP is 52.0 dB·W and the subscriber terminal G/T is 11.3 dB/K for a 45-cm dish. The clear-weather, edge-of-coverage performance is then

$$\frac{C}{N_0} = 86.1 \text{ dB} \cdot \text{Hz} \quad (3)$$

The required C/N_0 is determined by the information bit rate and the required E_b/N_0 , energy per information bit over the noise density, for the system’s modulation and coding with an implementation margin. The equation relating the two ratios is

$$\frac{C}{N_0}|_{\text{req}} = \frac{E_b}{N_0}|_{\text{req}} + r + R \text{ dB} \cdot \text{Hz} \quad (4)$$

where r is the coding rate and R is the transmission rate in dB·Hz. The information bit rate is the product of the code

rate and transmission rate, which is expressed as a sum in decibels.

Using $r = \frac{49}{64}$ and $R = 40$ Mbps (for an information rate of 30.6 Mbps or 74.9 dB · Hz), and a threshold E_b/N_0 value of 7.8 dB · Hz, then

$$\frac{C}{N_0} \Big|_{\text{req}} = 82.7 \text{ dB} \cdot \text{Hz} \quad (5)$$

The clear-weather, edge-of-coverage performance is then the difference of Eqs. (3) and (5), or 3.4 dB. This is the clear-weather margin for a 45 cm dish for the parameters of Ref. 13. Below a 30 cm diameter (for BSS systems in the Americas), intersystem interference sources due to adjacent satellites cause the simplified analysis used above to become quite inappropriate. Above about 90 cm, the narrow beam of the subscriber antenna may actually be detrimental to satisfactory performance. For narrowbeam subscriber antennas, small satellite stationkeeping errors may cause the line of sight to move outside the subscriber antenna’s main beam.

5.2. Propagation Effects at 12 GHz

In the preceding link example, the value L_r is a link margin against rain and other propagation phenomena. In fact, a system design is typically based on statistical and geometric models to predict the rain degradation along the line of sight. Although a variety of propagation-related impairments can occur, the dominant effects are due to rain and wet snow and result in signal attenuation and attendant increases in the received “sky” noise. Experimentation work, as described in Ref. 14, has compared the rain attenuation along a given path with the rain rate measured on the path and found that the specific attenuation (dB/km) can be approximated by the expression

$$\text{Specific attenuation} = a\mathbb{R}^b \quad (6)$$

where \mathbb{R} is the rain rate in the millimeters per hour and a and b are frequency- and temperature-dependent constants.

With this fundamental model, worldwide environmental information and a geometric model of the “rain cylinder” along the line of sight, comprehensive models have been developed for DTH system design. Figure 7 shows the rain regions assumed by the International Telecommunication Union (ITU) for BSS planning for the Americas. Figure 8 illustrates the attenuation predicted by the ITU model for Region K of the Americas. The outage value assumed in Fig. 8 (1% of the worst-case month) is a requirement that should be reevaluated by the designer in each new application.

5.3. Interference

In addition to rain degradations, DTH designs must consider intrasystem and intersystem interference. Interference into the subscriber dish is a primary concern. Received interference includes cross-polarized, cofrequency, intrasystem interference, interference from other

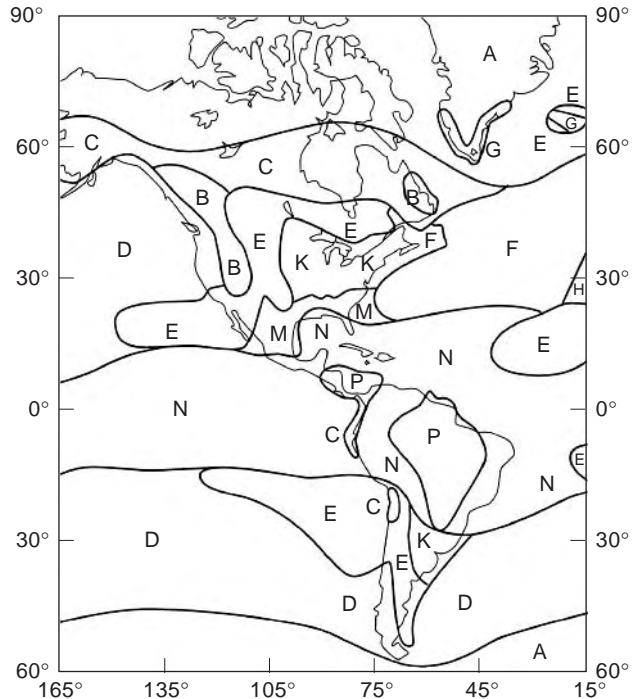


Figure 7. The ITU rain attenuation model for the Broadcasting Satellite Service (12.2–12.7 GHz) has divided the Americas into a number of zones. The model assumes the same rain rate statistics across all areas of a given zone. [Source: International Telecommunication Union, *Radio Regulations*, Vol. 2, App. 30, Fig. 3 (see Ref. 16).]

satellites operating at adjacent orbit locations, and emissions from terrestrial users of the same frequency band. The Broadcasting Satellite Service was carefully planned to separate orbital “slot” assignments for satellites with beams with common coverage [15–17], for example, for the United States the primary orbital assignments have 9° of longitude separation. In the Federal Communications Commission’s (FCC’s) Fixed Satellite Service assignments at 11.7–12.2 GHz, the satellites are separated by as little as 2° of longitude; the 2° separation causes dishes of less than 60 cm in diameter, with relatively little spatial isolation, to have generally unacceptable adjacent satellite interference. In the BSS in the United States, the use of 45-cm dishes is a common practice and one service provider has announced plans to use 30-cm dishes.

5.4. Satellite Design

Figure 9 illustrates a typical DTH satellite platform. All operational DTH systems have used satellites in geosynchronous orbit (GSO) with microwave frequency translation repeaters. After placement in a GSO, the satellite orbital period is equal (synchronous) with the rotational period of Earth, and the satellite appears to be stationary over a given longitude at the equator. This greatly simplifies the design of the millions of receive terminals that point toward the satellite.

A frequency translating repeater typically receives an uplink carrier via the receive coverage antenna beam,

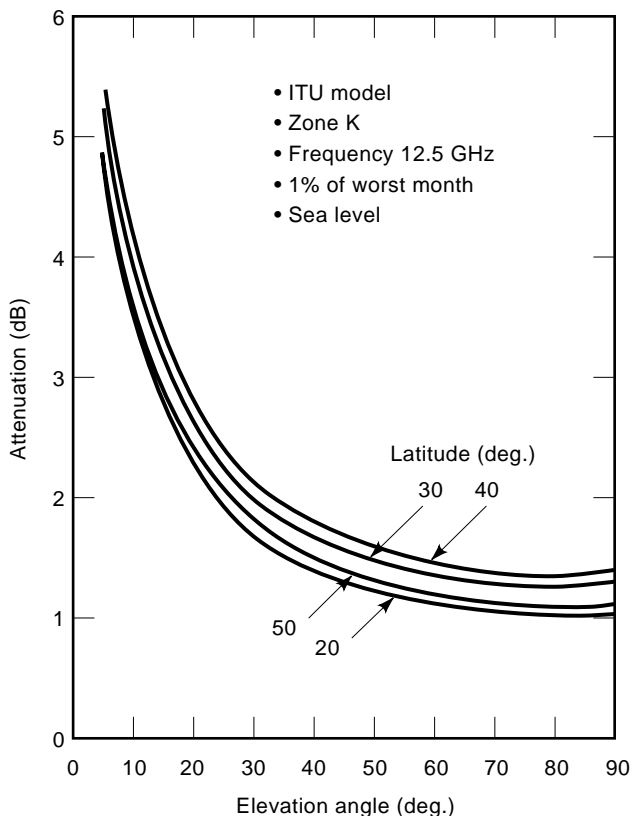


Figure 8. Rain-related downlink attenuation decreases as the elevation angle above the horizon increases but the attenuation does not increase monotonically with latitude. These curves are based on the ITU propagation model and apply to rain zone K. [Source: International Telecommunication Union, *Radio Regulations*, Vol. 2, App. 30, Fig. 4h (see Ref. 16).]

mixes the signal to the downlink frequency, and then amplifies it for transmission to the transmit coverage beam. This type of translating design is highly reliable and flexible. The receive and transmit coverages need not

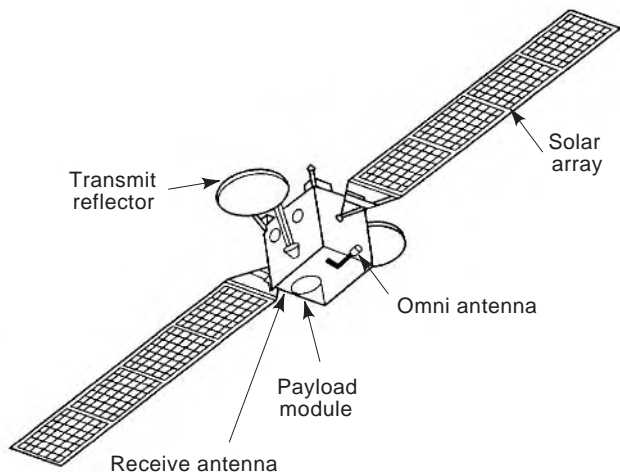


Figure 9. The deployed configuration of DTH satellites is dominated by the solar panels used for power generation. (Courtesy of DirecTV, Inc.)

be identical—for example, for a typical national system the receive beam coverage may be the 48 contiguous states while the transmit beam coverage may consist of all 50 states. (See *SATELLITE ANTENNAS*.) The DTH satellite’s total DC and total RF power levels are key attributes since most of the satellite weight and hence cost are involved in generating high power levels. This relationship between weight and cost is largely due to the high cost and relative unreliability of launch vehicles. As one example, the Galaxy Latin America satellite launched at the end of 1997 had an end-of-life solar array power capability of about 8.0 kW. (See Ref. 18.)

The satellite electronics associated with processing and amplifying a single carrier, such as a multiplexed digital television carrier, is called a satellite *transponder*. The final output stage or transmitter is normally a traveling-wave-tube amplifier (TWTA), a device with very high gain, high efficiency, perhaps in excess of 50%, and wide bandwidth. Although high-power TWTA reliability was a DTH design issue through 1990, dozens of transmitters with power levels above 100 W have operated without apparent incident for more than three years during the 1990s.

5.5. Regulatory Considerations

Direct-to-home systems are typically regulated at the national level. Until relatively recently virtually all nations had a government-owned post, telephone, and telegraph (PTT) or quasigovernment agency that owned and operated all national telecommunication facilities. With the worldwide trend toward commercialization and competition, the government role is tending toward regulation of DTH businesses via RF and business licensing. For example, in Japan, the Ministry of Post and Telecommunications (MPT) has allowed three new commercial DTH businesses to compete with the traditional quasigovernment broadcaster NHK. Each of these businesses has required MPT approval over multiple aspects including the provider (consignor) of each programming channel, the content of the channel, the business viability of each channel, the RF licensing of the uplink site, and the RF licensing of the satellite.

The situation in the United States is somewhat unique in that competing private telecommunication businesses have existed since the 1970s. The FCC licenses and regulates satellite systems primarily via licensing of the satellites themselves. Small receive-only antennas do not require licensing, and the FCC has ordered that, in general, dishes smaller than 1 m cannot be regulated by state or local authorities [19].

Broadcasting from one nation into another commonly requires official *landing rights* in the distant nation, particularly if the broadcaster intends to collect subscriber fees. Issues of frequency use and coordination between nations are handled by an agency of the United Nations, the International Telecommunication Union [20]. The regulatory agency, that is, the PTT, MPT, or FCC, of each UN nation sends representatives to various ITU working groups to establish mutually agreed international regulations. In general, each agency makes the international

regulations a part of their national regulations; the ITU itself has no powers of enforcement. The ITU has established a number of frequency bands for satellite communications; for DTH applications the bands utilized have been both in the FSS and BSS. The FSS name comes from the fact that, for frequency coordination purposes, the transmitters and receivers are assumed to be at fixed locations, that is, not mobile. The BSS bands also assume “fixed” RF sources but with the added assumption that the primary usage is direct broadcast. In the early 1980s, when the international BSS arrangements were completed, this distinction was quite important since the representatives to the ITU sessions wished to be sure that their nations would someday have the benefit of DTH service. Thus the use of the BSS band (around 12 GHz) has been strictly planned such that every nation existing at the time of the agreement has a specific set of assigned frequencies, polarizations, and satellite antenna coverage. Note that the difference between the FSS and BSS bands is entirely regulatory, not technical—in fact, the BSS band in the United States is the same frequency as the FSS band in Japan and vice versa.

The ITU regulations are based on dividing the world into three regions with specific geographic boundaries. These regions are roughly defined as follows: Region 1 consists of Europe, Africa, and the former Soviet Union; Region 2 consists of the Americas; and Region 3 consists of Asia, excluding the former Soviet Union. Among these different regions the specific regulations can vary substantially, and within a given country the national administration may impose additional regulations. For example, under ITU auspices the BSS frequency bands vary by region, the frequency assignments vary by country, and each country assigns frequencies to a system or company. The downlink plan for all regions is contained in App. 30 of the ITU Radio Regulations [16]. The uplink or “feeder” link plan is contained in Appendix 30A of the ITU Regulations [17]. The 1997 World Radio Conference made changes to certain parameters for Regions 1 and 3 only.

Traditionally, telecommunications standardization has been performed by international groups such as the ITU, International Organization for Standardization (ISO), International Electrotechnical Committee (IEC), and the Joint Technical Committee (JTC1) of the ISO and IEC [21]. As a growing trend, standards are being addressed by regional groups such as the European Telecommunications Institute (ETSI) or the T1 committee in the United States, an organization accredited by the American National Standards Institute. Additionally, specialized, ad hoc groups have been formed to address certain areas of technology, for example, the Asynchronous Transfer Mode (ATM) Forum, the Internet Engineering Task Force (IETF), and the Digital Audio Visual Council (DAVIC).

The ITU has developed a standard for “Digital multi-programme television emissions by satellite” [8], but this is an international recommendation, not a requirement, unless implemented by a national agency as a national standard. This ITU recommendation includes three closely related broadcast formats that can be decoded by the same or similar receiver circuitry. Table 1 compares the characteristics of the three formats. All three utilize

QPSK modulation, concatenated convolutional and Reed–Solomon coding, MPEG compression, and fixed-length transport packets.

In Europe the Digital Video Broadcasting (DVB) Project to develop specifications for all aspects of digital television broadcasting was launched in 1993, following a two-year effort. Since producing its first digital satellite standard, the DVB Project has developed specifications, guidelines, and recommendations for the many ancillary parts of digital broadcasting. These have been accepted as standards for DTH systems by more than 200 broadcasters, manufacturers, network operators, and by regulatory bodies in over 30 countries [9].

In Japan, the Association of Radio Industries and Businesses (ARIB) has selected a DVB variant as the standard for digital CS systems [22]. In the United States, the FCC has not required specific requirements for DTH services.

In general, these various standards have dealt with the link, transport, and network services layers, but not the conditional access layer. Certain governments have standards to restrict or specify the encryption method controlled by the conditional access system. For example, Japan’s MPT has specified the encryption algorithm for the new digital CS systems. Recently, DVB, DAVIC, and the Advanced Television Systems Committee (ATSC) in the United States have begun work on conditional access standardization. (See also TELEVISION BROADCAST TRANSMISSION STANDARDS.)

6. CONSUMER ELECTRONICS

Consumer electronics equipment for DTH applications has achieved very low cost, high performance, and excellent perceived value by carefully designed very-large-scale integration (VLSI) and mass production. By use of standards, for example, MPEG2, and standard techniques, many VLSI have been used in more than one platform and thus achieved greater economies of scale.

6.1. Outdoor Electronics

The offset fed parabolic reflector continues to be the dominant antenna type due to its simplicity and high gain for a given aperture size. The offset geometry achieves an aperture efficiency greater than 60% by eliminating the “feed blockage” present in a focus fed geometry. Figure 10 shows a 45 cm parabolic dish, digital receiver, and remote control produced by Panasonic in 1997 for the CS market in Japan. Single-polarization, fixed-scan, phased array antennas are also used, but generally not where their size would be greater than 60 cm × 60 cm, when distribution losses become significant.

6.2. Receivers

In the design shown in Fig. 10, the receiver supplies DC power to the outdoor electronics via the coaxial cable delivering the digital signals to the receiver. Additionally, biasing this supply voltage above or below the nominal value implements polarization selection at the feed. Figure 11 gives a reference architecture for a digital

Table 1. Summary of ITU Direct-to-Home Formats

Function	System A	System B	System C
Randomization for energy dispersal	Yes	Explicit	Yes
Reed-Solomon outer code	(204, 188, $T=8$)	(146, 130, $T=8$)	(204, 188, $T=8$)
RS field generator polynomial		$X^8 + X^4 + X^3 + X^2 + 1$	
Interleaving	Forney	Ramsey II	Forney
Inner coding		Convolutional, $K=7$	
Basic code		$\frac{1}{2}$	$\frac{1}{3}$
Generator polynomial		171, 133 (octal)	117, 135, 161 (octal)
Forward error correction (FEC)	$\frac{1}{2}$, $\frac{2}{3}$, $\frac{3}{4}$, $\frac{5}{6}$, and $\frac{7}{8}$	$\frac{1}{2}$, $\frac{2}{3}$, and $\frac{6}{7}$	$\frac{1}{2}$, $\frac{2}{3}$, $\frac{3}{4}$, $\frac{4}{5}$, $\frac{5}{6}$, $\frac{11}{11}$, and $\frac{7}{8}$
Signal modulation		QPSK	
Symbol rate	Variable	20 Mbaud	19.5 and 29.3 Mbaud
Transport layer	MPEG2	System B	MPEG2
Packet size (bytes) [payload]	188 [184]	130 [127]	188 [184]
Identification ID (bit)	13	12	13
Statistical multiplexing	Not restricted	Capable	Capable
Method of synchronization for video and audio		Timestamping (27 MHz reference)	
Video source decoding			
Syntax		MPEG2	
Levels		At least main level	
Profiles		At least main profile	
Audio source decoding	MPEG2 layers I and II	MPEG1 layer II (included in MPEG2)	ATSC A/53 or MPEG2 layers ^b I and II
Typical transponder bandwidth (MHz)	Not specified	24 or 27 MHz	24, 27, or 36 MHz
Selectable conditional access		Yes	
Service information	ETS 300 468 ^c	System B	ATSC A/56 + [†] SCTE ^c DVS/011 ^b
Electronic program guide	ETS 300 707 ^c	System B	User-selectable
Teletext	Supported		Not specified
Subtitling		Supported	
Closed caption	Not specified		Yes
Delivered TV standards	Not specified	NTSC and PAL M	NTSC and PAL
Aspect ratios	4:3 and 16:9 (2.21:1 optionally)	4:3 and 16:9	4:3 and 16:9
Video resolution formats	Not restricted	MPEG subset	MPEG subset
Frame rates (frames/s)	Not specified	29.97	25 (PAL) 29.97 (NTSC)
Compatibility with other MPEG2 delivery systems	ISO/IEC 13818 ^d	Some processing required	ISO/IEC 13818 ^d

^aEuropean Telecommunications Standards

^bAdvanced Television Systems Committee (standards)

^cSociety of Cable Television Engineers

^dSee Ref. 5.

DTH receiver [8]. This common architecture can be applied to any of the three digital formats contained within the reference.

6.2.1. Hardware. In implementing the reference hardware architecture of Fig. 11, the underlying large-scale integrated circuits (LSI) have since 1994 undergone multiple stages of evolutionary development. As an example, Table 2 summarizes the LSI evolution of the RCA-brand receivers produced for the United States marketplace. Each generation has seen greater levels of integration [23] with the fourth generation being a "two-chip" receiver.

Similar levels of LSI integration are also expected with the availability of such chips as the Texas Instruments Series AV 7000 shown in Fig. 12. This chip provides the

equivalent of 2.5×10^6 transistors using 0.35 μm complementary metal oxide semiconductor (CMOS) technology. Advance information [24] indicates that this circuit will incorporate the following:

- 32-bit reduced instruction set computer (RISC) central processing unit (CPU) [40 million instructions per second (mips)]
- Advanced graphics accelerator
- Memory manager
- Transport/decryption (DES)
- MPEG2 video decoder (MPEG1 and MPEG2)
- Audio decoder (MPEG1)
- NTSC/PAL encoder



Figure 10. Direct-to-home consumer electronics includes a *mini-dish*, a receiver, and remote control. This Panasonic equipment for the DIRECTV JAPAN system went on sale in December 1997. Courtesy of Matsushita Electric Industrial Co., Ltd.

To complete a typical receiver, the designer will add the following:

- Tuner
- Link integrated chip
- Memory [read-only memory (ROM), random-access memory (RAM), dynamic RAM (SDRAM)]
- Smart card
- Telephone modem
- Other peripherals

The AV 7000 chip also provides an interface to external consumer electronics or computer devices using the IEEE 1394 aerial digital protocol.

6.2.2. Software. Software architectures have been driven by the functionality of the major VLSI. The “transport” chips have provided some degree of logical filtering of the high-speed data streams—and hence not required filtering by the primary processor. The MPEG chips have, in general, relied on the processor to perform group of pictures (GOP) and picture sequence-level processing. The primary processor also typically handles program guide and user interface tasks.

From a subscriber standpoint new product generations have exhibited faster response times and improved graphical interfaces. As a point of reference for 1998 technology, the Texas Instruments AV 7000 chip [24] was designed to provide graphics support for up to eight windows, 8 bit color depth, 16 levels of blending and transparency, overlapping windows, and other features.

More recent products have also included *interactive* or *multimedia* software layers, which include, for example, Panasonic’s DVX for DIRECTV JAPAN and Thomson Sun Interactive LLC’s OpenTV. The latter, a forerunner of an emerging interactive services industry, began in 1994 as an alliance of Thomson Multimedia and Sun Microsystems. OpenTV supplies interactive operating systems and services for digital receivers used by pay television services, among other activities [25].

7. MORE RECENT DEVELOPMENTS

7.1. Technology

Technological progress continues in most disciplines important to DTH digital systems. Satellite manufacturers have announced platforms with total DC power levels of at least 15 kW [26]. With a power generation capability 4 times that of DTH satellites launched in 1995, these newer platforms were in orbit before the year 2001.

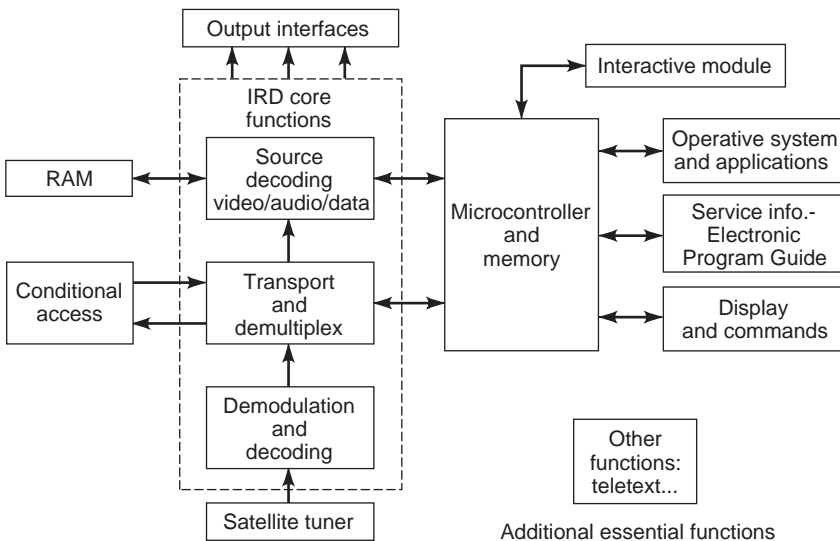


Figure 11. The ITU generic reference model for a satellite integrated receiver decoder. (Source: International Telecommunication Union, Document 10-11S/TEMP/18, Fig. 2.)

Table 2. Evolution of LSI in RCA-Brand DSS

	First Generation	Second Generation	Third Generation	Fourth Generation
Initial retail availability	June 1994	Jan. 1996	Jan. 1997	1998/99
Major large scale integrated circuits (LSI)	Microprocessor	Microprocessor	} ARM IC	} DXX ^a
	Transport/decrypt	Transport/decrypt		
	QPSK demodulator	} Link IC	} Link IC	} Link IC
	Convolutional decoder			
	RS decoder			
	Video decompression	} MPEG A/V	} MPEG A/V	} DXX ^a
	Audio decompression			
	NTSC encoder	NTSC encoder	NTSC encoder	} Telephone modem
	Telephone modem	Telephone modem	Telephone modem	
	Video DRAM	Video DRAM	Video DRAM	

^aSingle chip
 Source: Information courtesy of Thomson Consumer Electronics, Inc.

Modulation and coding show continuing improvements, particularly in turbo coding [27], and advanced modulation formats with higher information content per unit bandwidth (bps/Hz) [28] are under consideration in newer system designs. Compression standards development continued with the MPEG4 standard [29], finally approved in late 1998 for version 1 and late 1999 for version 2. The MPEG4 architecture permits different compression algorithms to be applied to different source material. The proposed inventory of algorithms includes image decomposition into multiple objects and the existing transform-based algorithms such as MPEG2.

7.2. Proposed Systems and Services

New system filings in 1997 at the FCC included a DTH system [30] operating at a downlink frequency of

17.3–17.8 GHz, a band commonly referred to as the *Ka band*. This system filing proposed to accelerate initial use of this frequency band as a new *BSS expansion band*, planned by the ITU to first come into operation in 2007. Also in 1997 a group proposed a system called Skybridge [31], which would reuse the existing BSS band but with nongeosynchronous satellites. The system design uses 64 satellites in 1457 km altitude orbits for a variety of telecommunications services. The plan suggests that frequency reuse can be achieved by not broadcasting from a particular Skybridge satellite to a particular region unless, as seen from the user location, the separation angle is sufficiently large between the line of sight to Skybridge and to the geosynchronous satellite arc. According to the Skybridge plan, if the separation angle is large, and certain other conditions are met, the discrimination of the user antenna will lower the Skybridge interference to an acceptable level.

In the area of new service offerings, the Hughes DirecPC service is one example of DTH satellite broadcasting to a personal computer platform. This service, available in the United States, Japan, and Europe, utilizes a small, outdoor dish and, installed in a conventional PC, a digital satellite receiver card. During 1998 in the United States, the DirecPC services included both *pull* (two-way) and *push* (one way) Internet access. In early 1998, DirecTV, Inc., demonstrated high-definition DTH broadcasting with delivery of 1280 × 1080 picture elements (pixels) in interlaced signals to a television provided by Thomson Consumer Electronics. DirecTV announced that it would initiate nationwide high-definition (HD) broadcasts before the end of 1998 and coincident with the first terrestrial digital broadcasts [32].

BIBLIOGRAPHY

1. News Corporation, 1997 Annual Report.
2. BBC Worldwide Monitoring (online), Japan PerfecTV and JSkyB to merge, Dec. 25, 1997. Dow Jones Interactive online wire service Dec. 29, 1997.
3. C. Bulloch, Current state of play—satellite broadcasting in Europe, *Via Satellite*, July 8, 1997.
4. International Organization for Standardization and International Electrotechnical Committee, ISO/IEC 11172-x, Information technology—generic coding of moving pictures

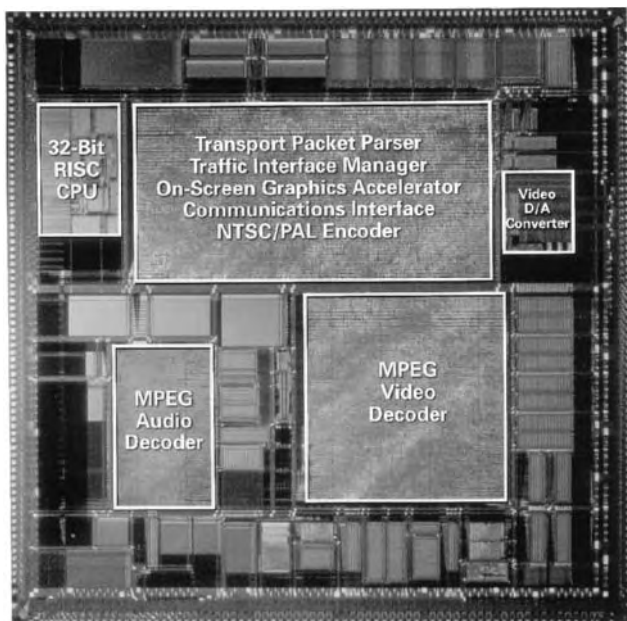


Figure 12. Rapid VLSI progress now permits a single chip to provide all DTH receiver core functions and many secondary functions, such as a microprocessor. (Copyright © 1998, Texas Instruments Incorporated.)

- and associated audio: parts 1-3, video, audio and systems MPEG1.
5. International Organization for Standardization and International Electrotechnical Committee, ISO/IEC 13818-x, Information technology—generic coding of moving pictures and associated audio: parts 1-3, video, audio and systems MPEG2.
 6. B. Sklar, *Digital Communications, Fundamentals and Applications*, Prentice-Hall, Englewood Cliffs, NJ, 1988, pp. 4–9.
 7. G. D. Forney, Jr., *Concatenated Coding*, MIT Press, Cambridge, MA, 1966.
 8. International Telecommunication Union (ITU) Radiocommunication Assembly, Common functional requirements for the reception of digital multiprogramme television emissions by satellites operating in the 11/12 GHz frequency range, recommendation no. 1294, Geneva, Oct. 1997.
 9. Digital Video Broadcasting (DVB), ETS 300 421, Digital satellite transmission systems; Framing structure, channel coding and modulation for 11/12 GHz satellite services, Dec. 1994.
 10. International Organization for Standardization, ISO 7816-3: 1989, Identification cards—Integrated circuit cards with contact. Part 3: Electronic signals and transmission protocols.
 11. A. N. Netravali and B. G. Haskell, *Digital Pictures Representation, Compression, and Standards*, 2nd ed., Plenum, New York, 1995.
 12. V. K. Bhargava et al., *Digital Communications by Satellite, Modulation, Multiple Access and Coding*, Wiley, New York, 1981, pp. 10–18.
 13. EchoStar DBS Corporation, Application for authority to construct a direct broadcast satellite system at 148 deg. W. long., before the Federal Communications Commission, Feb. 28, 1996.
 14. L. J. Ippolito, Jr., *Radiowave Propagation in Satellite Communications*, Van Nostrand-Reinhold, New York, 1986, pp. 38–63.
 15. E. E. Reinhart, An introduction to the RARC '83 plan for DBS systems in the Western Hemisphere, *IEEE J. Select. Areas Commun.* **SAC-3**(1):13–19 (1985).
 16. International Telecommunication Union (ITU), *Radio Regulations*, 1982 ed., rev. 1985, 1986, 1988, Vol. 2, App. 30.
 17. International Telecommunication Union (ITU), *Radio Regulations*, 1982 ed., rev. 1985, 1986, 1988, Vol. 2, App. 30A.
 18. Hughes Communications Galaxy, Inc., Application for authority to construct, launch and operate one separate international fixed communications satellite, before the Federal Communications Commission, July 13, 1994.
 19. Federal Communications Commission, *Code of Federal Regulations*, Part 47, Sect. 1.4000.
 20. L. Taylor, Winners and losers in the scramble for spectrum, *Satellite Commun.* 28–32 (Feb. 1998).
 21. K. Asatani and S. Nogami, Trends in standardization on multimedia communications, *IEEE Commun. Mag.* **35**(7):112–116 (July 1997).
 22. Association of Radio Industries and Businesses (ARIB). *Receivers for CS Digital Broadcasting*, ARIB STD-B1, 1.0 ed., Tokyo, Japan, Aug. 1996.
 23. W. H. Mengel, personal communication to author, March 11, 1998; information courtesy of Thomson Consumer Electronics, Inc.
 24. Texas Instruments, product preview, integrated set-up digital signal processor TMS320AV7100, 1997.
 25. OpenTV, Inc., World Wide Website (online), 1998.
 26. News breaks, *Aviation Week Space Technol.* 18–19 (Feb. 16, 1998).
 27. S. Benedetto, D. Divsalar, and J. Hagenauer, guest editorial, Concatenated coding techniques and iterative decoding: Sailing toward channel capacity, *IEEE J. Select. Areas Commun.* **16**:137–139 (1998).
 28. Y. Hara, Japan sets broadcast-satellite digital TV standards, *EE Times* (Feb. 13, 1998) (online); available at <http://www.eet.com>.
 29. ISO/IEC 14496-x, Information technology—coding of audiovisual objects (MPEG4).
 30. DirecTV Enterprises, Inc., Application for authority to construct, launch and operate an expansion system of direct broadcast satellites, before the Federal Communications Commission, June 5, 1997.
 31. Skybridge L.L.C., Application for authority to launch and operate a global network of low earth orbit communications satellites providing broadband services in the fixed satellite service, file nos. 48-SAT-P/LA-97, 89-SAT-AMEND-97.
 32. F. Biddle, DirecTV unit will offer HDTV programs in fall, Dow Jones & Co. wire service, Jan. 7, 1998.

FURTHER READING

For further reading and current information and general information about the major systems in the United States, please consult the World Wide Websites listed below:

DirecTV <http://www.directv.com/>
 EchoStar <http://www.dishnetwork.com/>
 PrimeStar <http://www.primestar.com/>
 USSB <http://www.ussb.com/>

Information about evolving standards can be found at the following:

ATSC <http://www.atsc.org/>
 DAVIC <http://www.davic.org/>
 DVB <http://www.dvb.org/>

DIRECTION OF ARRIVAL ESTIMATION AND ADAPTIVE PROCESSING USING A CONFORMAL PHASED ARRAY

TAPAN K. SARKAR
 Syracuse University
 Syracuse, New York
 MAGDALENA SALAZAR-PALMA
 Madrid Polytechnic University
 Madrid, Spain

1. INTRODUCTION

The phased arrays are used to sort out signals in space specifically when there are coherent multipaths of the

signal, as the information about the multipaths does not exist in the temporal domain. A more sophisticated form of phased arrays is an adaptive array which spatially filters out the signal of interest in the midst of clutter, jammer, and interference. The science of adaptive phased arrays, which started in the early 1950s, was implemented primarily through analog processing, as during that period of time the analog correlation processing was the only way. However, with the advent of digital signal processing we are currently using the same algorithms in the digital scenario without taking a critical look at whether such a methodology is really meaningful. For example, when using an analog adaptive algorithm, it is imperative that the adaptive weights can never be greater than unity as that would be equivalent to using an amplifier for the weights. Hence, the antenna array pattern for analog systems has a great physical significance. Therefore, with analog processing the array resolution is essentially limited by the size of the aperture and how closely one can resolve spatially spaced signals are dictated by the Rayleigh resolution criteria. So with the advent of digital signal processing one can go beyond the Rayleigh resolution and resolve signals within the width of the mainbeam of the array. Moreover, the adaptive weights can take any complex value numerically as we are now processing the signals digitally, and the purpose of the weights is equivalent to multiplying the voltages at the antenna feed points by some numbers. In such scenarios, the antenna array pattern loses to have any special significance at all.

The second shortcoming of the current phased-array methodology is that the mathematical description of the adaptive problem is set up as a detection problem rather than as an estimation problem. To illustrate this point, when we are dealing with radars, we are sending out a waveform, and the assumption is that we are trying to detect the same transmitted waveform delayed in time and attenuated, since the radar signal is not getting dispersed as it is propagating through free space. Hence, in such a situation we only want to know whether the transmitted radar signal reflected from the target exists. If the radar return exists then we know how far is the target from the time delay and from the Doppler shift, the velocity of the target. The optimum way to detect the existence of a particular waveshape we transmitted is to use a matched filter whose transfer function is the complex conjugate of the Fourier transform of the transmitted radar waveform. However, in a multi-path-rich mobile communication, detection is not the problem that we want to address, because we know that the signal is there; what we want to do is to estimate its correct amplitude, as that will correct for fading. The current mathematical approach of adaptive filtering is to use a Wiener filter-based model where a pilot signal is transmitted before every transmission and the channel along with the array is calibrated before the actual signal is sent. This leads to serious problems for real-time transmission as the assumption that the environments are identical when the pilot signal was sent and when the actual transmission is arriving may not be the same in a mobile environment. That is why a direct data domain least-squares approach based on a single snapshot of the voltages measured at the feedpoint of the

antenna elements at a particular instance of time has been used to solve the estimation problem directly [1].

In this article we are going to extend the single-snapshot-based direct-data-domain approach to deal with conformal adaptive phased arrays. In the current way of thinking one wants to use essentially an antenna element that has as close to an omnidirectional pattern as possible and then derive the gain by using hundreds and even thousands of them to get any significant gain from the array. Now one has to put a receiver channel at each of these antenna elements and that exponentially increases the cost. So, in order to minimize the cost, one then defines a subaperture and then sums up all the voltages in an analog fashion at the feedpoint of these antennas. Then either (1) a sum-and-difference beam pattern is formed to resolve the target or (2) digital beamforming using these summed up voltages is employed. This is not a sound procedure as it defeats the entire purpose of digital beamforming. It can easily be seen that this sub aperture summation negates the basic fundamental model of any adaptive signal processing algorithm! What is proposed in this section is to use directive elements on a conformal surface to perform adaptive processing. Use of directive elements will significantly reduce the number of antenna elements, and then, if one places these directive elements on a conformal surface to do adaptive processing, a significantly smaller number of antenna elements will be required, without sacrificing the gain. Such a methodology is illustrated here.

2. DOA ESTIMATION USING A CONFORMAL MICROSTRIP PATCH ARRAY ON THE SIDE OF AN AIRCRAFT

Estimation of direction of arrival (DoA) is one of the primary applications of phased arrays. One DoA estimation algorithm that deals with nonuniformly spaced antenna array elements is the MUSIC (multisignal classification) algorithm [1,2]. However, the performance of this signal processing technique deteriorates if the mutual coupling between the antenna elements and the effect of near-field scatterers are not accounted for in the analysis. Through this example we illustrate how to merge the electromagnetic analysis with the signal processing. In addition, we use a complex antenna element such as a microstrip patch antenna to illustrate how the antenna effects can be taken into account.

In this example, we estimate the DoA of the various signals impinging on a conformal microstrip patch array on the side of a Fokker aircraft. As seen in Fig. 1, the elements of the 11-element microstrip patch array are not placed uniformly, as the two groups of six and five elements are separated much more widely than those in a uniform interelement spacing, nor do they lie on a flat surface. A detailed view of the microstrip patch antenna element is also shown in Fig. 1. The half-wave rectangular microstrip patch element is fed by a probe and is situated on a high-dielectric-constant substrate so that it resonates at an operating frequency of 100 MHz. The thickness of the dielectric substrate is 0.01λ and has an $\epsilon_r = 32$. There is a strong mutual coupling between the antenna elements, including the wings and fuselage of the

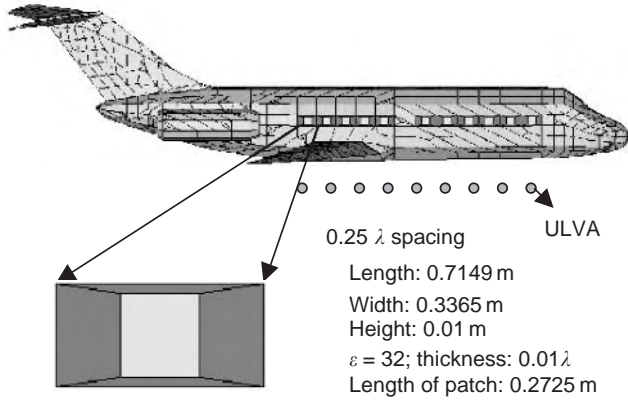


Figure 1. Geometry of a microstrip patch array on the side of an aircraft and an equivalent ULVA representing the microstrip patch array mounted on a conformal surface.

aircraft. To account for the effects of the mutual coupling between the antenna elements and the various near-field scatterers, we take the actual electromagnetic field scenario containing the 11-element patch array and then transform and interpolate the actual voltages that exist at the feedpoint of the antenna elements to an equivalent set of antenna voltages that would exist in a uniform linear virtual array (ULVA) containing isotropic omnidirectional radiators radiating in free space. The real 11-element array is interpolated into a virtual array consisting of 11 uniformly spaced omnidirectional point sources separated by 0.25λ at 100 MHz as shown in Fig. 1. We consider three signals arriving from 139° , 99° , and 60° , and impinging at the microstrip patch array from the side of the aircraft. The azimuthal angle is defined from the nose of the aircraft. The intensities and associated DoAs of the three signals to be simulated for this real case are summarized in Table 1. The simulation is done using the electromagnetic simulation tool WIPL-D as described in Ref. 3. In this example the elevation dimension has been neglected as there was only one layer of the microstrip array. Later on we will illustrate how DoA estimation can be done in both azimuth and elevation.

Hence, our problem can be stated as follows. Given the complex array manifold matrix $[A(\varphi)]$ of a nonuniformly spaced array in the presence of mutual coupling between the elements of the array and near-field coupling effects between the platform and other electromagnetic obstacles, our first objective will be to transform the voltages induced in an actual array to a set of voltages that would be induced in ULVA consisting of omnidirectional isotropic point radiators radiating in free space. This is numerically carried out by using a transformation matrix $[\mathfrak{A}_q]$, which,

when operating on $[A(\varphi)]$, produces numerically a modified manifold $[A_v(\varphi)]$, which is due to a ULVA manifold matrix. The elements of this virtual array are isotropic omnidirectional point radiators radiating in free space. Thus, we compensate not only for the lack of nonuniformity but also for the presence of mutual coupling between the elements in the real array in addition to near-field coupling effects between the elements of the array and the aircraft.

After we account for the strong electromagnetic coupling effects between the elements of the microstrip patch array and the aircraft at 100 MHz, such as the effects of nonuniformity in the spacing between the elements on a conformal nonplanar surface and the effects of mutual coupling between the elements of the patch array and their interactions with the wings and fuselage by using the approach described in Chap. 6 of Ref. 1, we first transform the 11 voltages available at the terminals of the antennas to that induced in a ULVA as explained in Ref. 1. Then the matrix pencil approach [1,4,5] is applied to the processed voltages to estimate their DoAs and their complex amplitudes. The matrix pencil approach is also a direct data domain approach to estimate the DoAs of the signals and had been shown to have the least Cramer–Rao bound in the estimation of the poles as compared to various other contemporary methods. Since no covariance matrix is formed from the data, the matrix pencil approach can resolve coherent signals and is computationally very efficient as the poles are found in a direct fashion as the solution of a generalized eigenvalue problem. The simulation results from the two-step process is presented in Table 2. First, the electromagnetic analysis is carried out to compensate for the mutual coupling and near-field effects and then the matrix pencil method is applied to estimate the DoA of the three signals and their complex amplitudes. From Table 2 it is seen that not only the DoAs but also the complex amplitudes of the coherent signals have been recovered with engineering accuracy using a conformal phased array consisting of nonuniformly spaced microstrip patch elements.

3. ADAPTIVE PROCESSING USING A SINGLE SNAPSHOT FROM A NONUNIFORMLY SPACED ARRAY OPERATING IN THE PRESENCE OF MUTUAL COUPLING AND NEAR-FIELD SCATTERERS

In this section, we illustrate how to employ the same interpolation technique of Chap. 6 in Ref. 1 to carry out adaptive processing using a single snapshot of the data using a nonuniformly spaced array in the presence of mutual coupling and near-field scatterers. In all the

Table 1. Complex Amplitudes of all Signals and Their DoAs Incident on Aircraft

	Magnitude (V/m)	Phase	DoA
Signal 1	1	0°	139°
Signal 2	1	0°	99°
Signal 3	1	0°	60°

Table 2. Estimated DoAs and Strengths of the Three Signals Incident on Phased Array

	Magnitude (V/m)	Phase	DoA
Signal 1	1.04	-0.05°	139.71°
Signal 2	0.91	0.06°	101.86°
Signal 3	1.08	-0.01°	61.75°

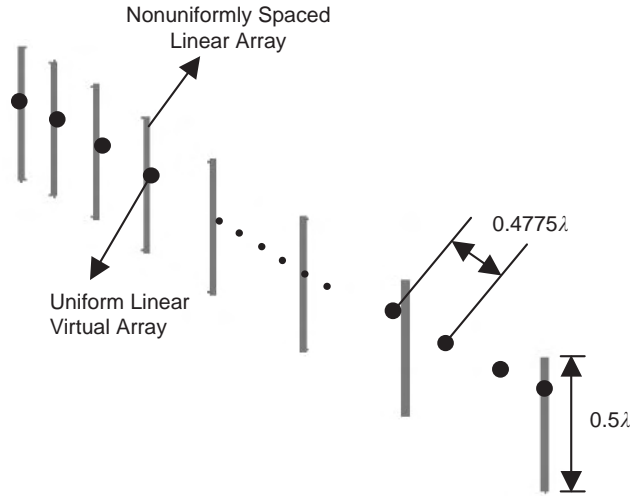


Figure 2. Geometry of a nonuniformly spaced linear array (NLA) and a ULVA (shown by dots) electromagnetically representing the NLA.

examples, we are basically interested in three different kinds of antenna configurations. The three different arrangements we have used are as follows:

1. A nonuniformly spaced linear array (NLA) (as shown in Fig. 2)
2. A semicircular array (SCA) (as shown in Fig. 3)
3. A spatially sinusoidally modulated array (SSA) (as shown in Fig. 4)

In all the antenna configurations, as shown in Figs. 2–4, the antenna elements of the real array are considered to be half-wavelength-long thin-wire dipoles. Each element of the array is identically point loaded by 50 Ω at the center. The dipoles are all z-directed and hence are parallel to each other. They are of length $L = \lambda/2$ and radius $r = \lambda/200$. The details of the antenna array elements are presented in Table 3.

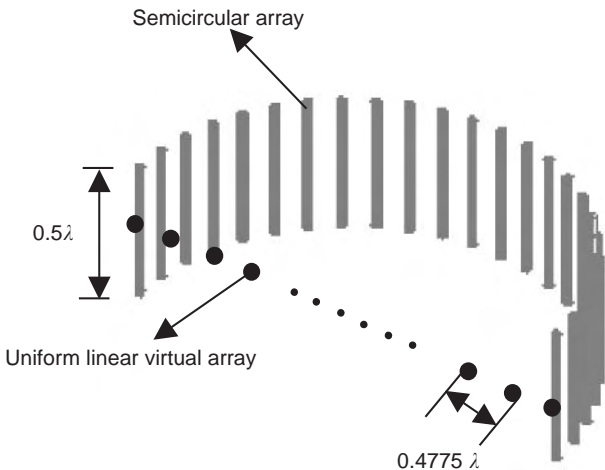


Figure 3. Geometry of a semicircular array (SCA) and a ULVA (shown by dots) electromagnetically representing the SCA.

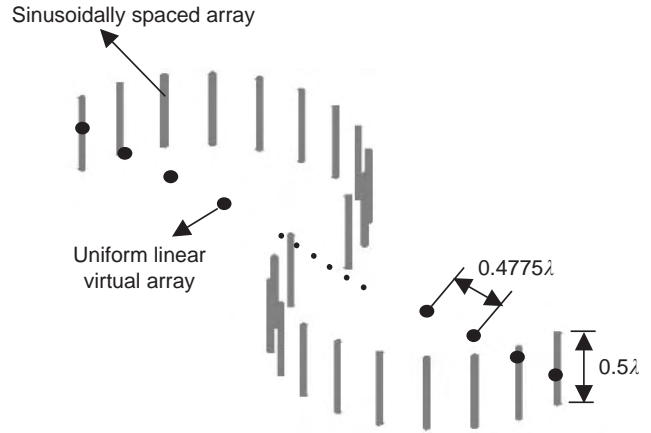


Figure 4. Geometry of a sinusoidally spaced array (SSA) and a ULVA (shown by dots) electromagnetically representing the SSA.

As described in Ref. 1, all the real arrays operating in the three different configurations mentioned above are interpolated into a similar ULVA consisting of 17 uniformly spaced omnidirectional point sources separated by a distance d/λ . Typically d is chosen to be close to $\lambda/2$. By choosing the reference point at the center of the real array in configuration 2 for the SCA and configuration 3 for the sinusoidally modulated array, the steering vectors associated with the virtual array is given by the following equation:

For configuration 1 (NLA = a nonuniformly spaced linear array), we choose the first element in the array as a reference point. Then the steering vectors for the ULVA are given by

$$[A_v(\varphi)] = \{[1, e^{[j2\pi\Delta/\lambda]\cos\varphi}, e^{[j2\pi2\Delta/\lambda]\cos\varphi}, \dots, e^{[j2\pi(2k)\Delta/\lambda]\cos\varphi}]^T\}_{(2k+1) \times 1} \tag{1}$$

Here the number $(2k + 1)$ of elements of the virtual array is considered to be odd and equal to 17, and λ is the wavelength of the signal located in the far-field region of the array, and the distance Δ between the elements in the virtual array is 0.4775λ . Here we want to correct for all the electromagnetic effects in the azimuth sector of $[\Phi] = [\varphi_q, \varphi_{qq}] = [30, 150^\circ]$. The incremental angle ϕ for the computation of the transformation matrix is chosen to be 1° . The sector chosen here is of width 120° symmetrically located around the broadside. Then, a set of voltages induced at the antenna elements are measured and computed for far-field sources located at each of the angles $\varphi_q, \varphi_q + \phi, \varphi_q + 2\phi, \dots, \varphi_{qq}$. The measured/computed vector $A(\varphi)$ is then distorted from the ideal steering vector defined by (1), due to the presence of mutual coupling between the elements of

Table 3. Physical Sizes for Dipole Antenna Elements in all Three Antenna Arrays

Number of elements in the three arrays	24
Length of z-directed wires	$\lambda/2$
Radius of wires	$\lambda/200$
Loading at center of element	50 Ω

Table 4. Complex Amplitudes of Signals and Their DoAs

	Magnitude (V/m)	Phase	DoA
Signal	1.0	0.0°	80°
Jammer 1	1.0	0.0°	70°
Jammer 2	1.0–500.0	0.0°	60°

the real array. The actual steering vectors having all the undesired electromagnetic effects are computed using the electromagnetic analysis code WIPL-D [3]. We compute the transformation matrix to compensate for the effects of non-uniformity in spacing and the presence of mutual coupling between the elements of the real array. The induced voltages at the elements of the antenna array result in a compensated set of input voltages in which the nonuniformity in spacing and mutual coupling effects are eliminated from the actual measured/computed voltages. We then apply the direct-data-domain least-squares approach described in Ref. 1 to estimate the complex amplitude of the signal of interest (SoI) given its DoA. Next we illustrate the performance of these three complex arrays through numerical electromagnetic simulations.

3.1. Constant Signal

First, we consider a case where we have two jammers arriving at the array along with the SoI. The interference-to-signal ratio for the jammers impinging on the array from an angle of 60° is varied from 0 to 54 dB. The other jammer arrives at the array at an angle of 70° with respect to the x axis. The SoI is incident at an angle of 80° at a frequency of 300 MHz. The various electrical parameters of the signals are summarized in Table 4. The received signal-to-thermal-noise ratio (SNR) at the antenna elements is set at 20 dB in this example. For this input, the signal strength is estimated while rejecting jammers. This estimation is applied to all the three antenna configurations.

The output signal-to-interference-plus-noise ratio (SINR) is an indicator of the accuracy of our estimate. It is defined as

$$\text{SINR}_{\text{out}} = 20 \log \left| \frac{\alpha}{\alpha - \alpha_{\text{est}}} \right| \quad (2)$$

where α is the amplitude of the desired signal and α_{est} is the estimate of the amplitude of the reconstructed signal.

The results are shown in Figs. 5 and 6 for all the three configurations. The thermal noise is ignored in Fig. 5, while the signal-to-noise ratio is set at 20 dB in Fig. 6. The noise is additive and is modeled as a Gaussian random variable. The x axis of the graph corresponds to the second jammer-to-SoI power level (as defined in Table 4), while the y axis corresponds to the output signal-to-interference-plus-noise ratio, as defined in (2). It can be observed in these figures that the interpolation technique using measured/computed steering vector shows proper compensation for all the electromagnetic effects of the real arrays to estimate the magnitude of the SoI based on the direct-data-domain approach.

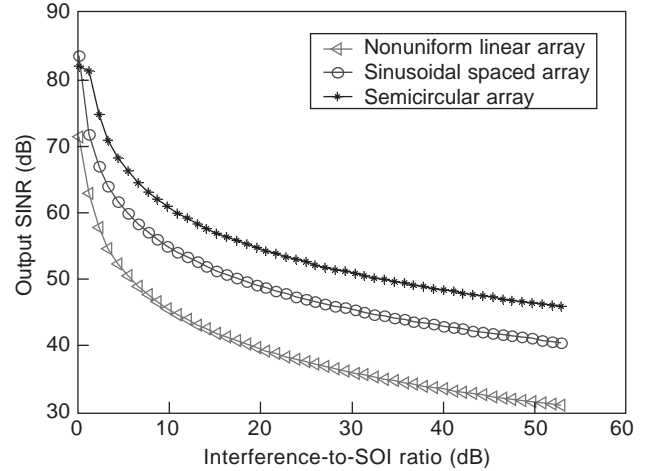


Figure 5. Output SINR as a function of interference-to-SoI ratio in decibels (dB) without noise.

3.2. Effect of Variation of Angular Separation between Signal and Jammer

Next we consider the fidelity in the performance for various angular separations between a signal and a closely spaced jammer inside the mainlobe for all three antenna configurations. We consider a case where we have one jammer signal arriving at the array along with the SoI. The DoA of the jammer is varied from 101° to 110° while the SoI is arriving from 100° with respect to the x axis. The signal-to-interference ratio is fixed at 0 dB, as shown in Table 5.

The results are shown in Fig. 7 for the three antenna configurations. The x axis corresponds to the angular separation between the SoI and the jammer, while the y axis corresponds to the output signal-to-interference-plus-noise ratio. These plots indicate that, after compensation of the various unwanted electromagnetic effects, good estimates for the amplitude of the SoI based on a direct-data-domain approach have been obtained. It is seen from the figures that the performance of a semicircular array

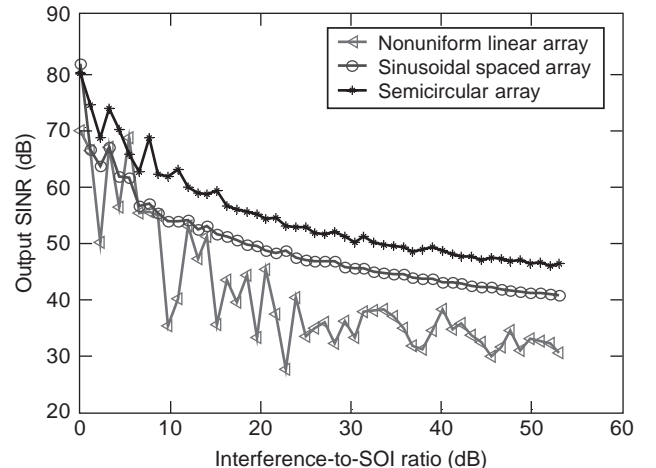


Figure 6. Output SINR as a function of interference-to-SoI ratio in dB with additive thermal noise.

Table 5. Complex Amplitudes of Various Signals and Their DoAs

	Magnitude (V/m)	Phase	DoA
Signal	1.0	0.0°	100°
Jammer	1.0	0.0°	$101\text{--}110^\circ$

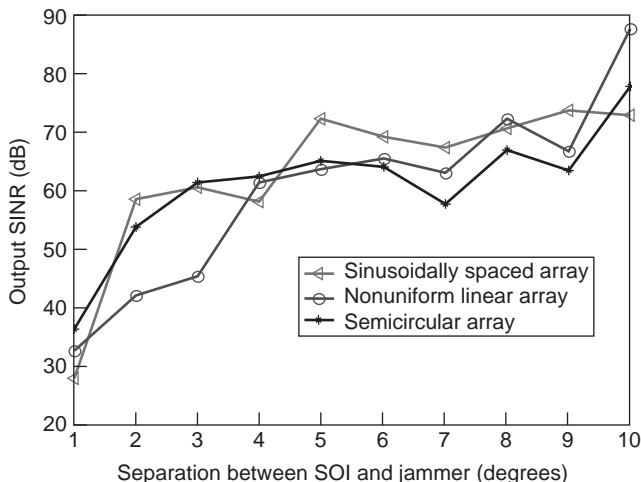
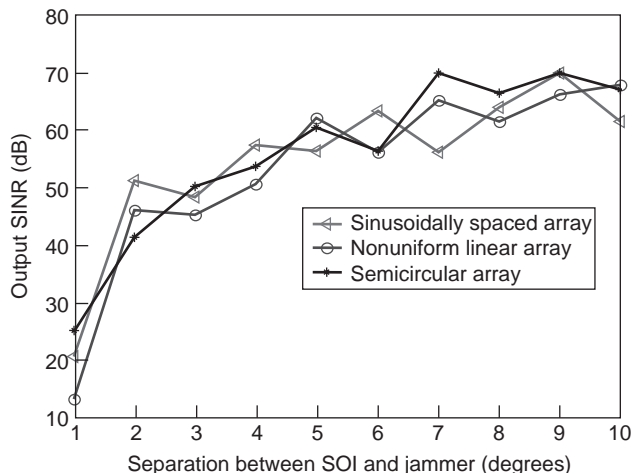
and a spatially sinusoidally modulated array in estimating the DoA when the interferer is in the mainlobe is better than that for a nonuniform linearly spaced array.

3.3. Effects of Blockage Produced by Near-Field Scatterers

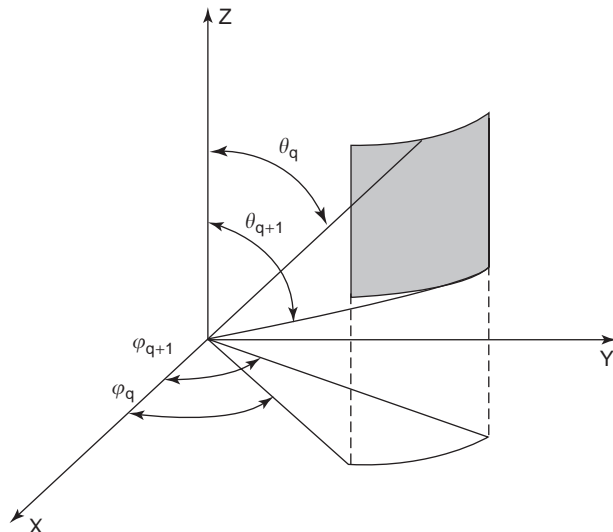
Next, we consider the effects of a near-field scatterer located near each array configuration. The near-field scatterer is located within a distance that is twice the radius of the array and is located along the direction of 60° in such a way that this near-field scatterer interferes with the direct line of sight of the SoI. The length and width of this square cylindrical near-field scatterer are 1.26 wavelengths, and the height of the scatter is 3.28 wavelengths. The desired signal and the jammers are as summarized in Table 5. The results are shown in Fig. 8 for the three different array configurations. It can be observed in these figures that the output signal-to-interference-plus-noise ratio is much lower than where there was no blockage of the SoI, due to a near-field scatterer. However, one can still obtain a proper estimate for the complex amplitude of the SoI after compensating for the various unwanted effects even when the jammer is in the mainlobe and operating in the presence of a large near-field scatterer.

4. DOA ESTIMATION USING A PHASED ARRAY LOCATED ON A CONFORMAL HEMISPHERICAL SURFACE

In this section, we describe how to carry out DoA estimation using directive antenna elements over a conformal surface like a hemisphere. We consider the use of three

**Figure 7.** Output SINR as a function of separation between SoI and jammer.**Figure 8.** Output SINR as a function of separation between SoI and jammer with blockage.

directive antenna elements, such as a short-circuited dual-patch antenna, a dielectric resonator antenna, and a horn antenna as elements in a conformal array. The surface selected for the implementation is a hemisphere. The procedure is to carry out the analysis to obtain the steering vectors over a conical scan subtended by the azimuth angles $[\varphi_q, \varphi_{q+1}]$ and from elevation angles spanning $[\theta_q, \theta_{q+1}]$. This is illustrated by Fig. 9. In the examples to follow, we transform the real array where the antenna elements are located over a hemispherical surface into a two-dimensional uniform planar linear virtual array (2D ULVA) lying in the x - y plane containing the projection of the hemisphere, as shown in Fig. 10. The 2D ULVA have been formulated in the form of a cross, a L-shaped, or a two-dimensional grid configuration. Here, in this methodology, the one-dimensional transformation matrix, for azimuth angles is extended to two dimensions to handle both elevation and azimuth angles [1]. Through

**Figure 9.** Parameters of the sector in which the signals of interest lie.

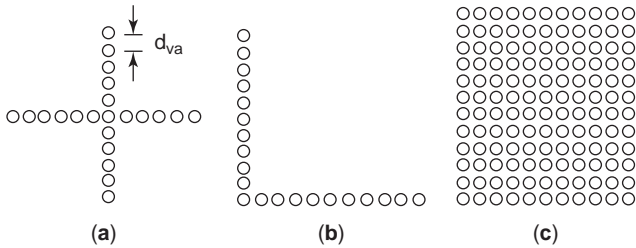


Figure 10. Different configurations of the two-dimensional uniform linear virtual arrays (d_{va} = distance between the virtual elements): (a) cross-configuration; (b) L configuration; (c) grid configuration.

this 2D transformation matrix, we map the voltages that are induced at the feedpoint of these real antenna elements operating in the presence of mutual coupling and other near-field scatterers to a planar 2D ULVA.

4.1. Short-Circuited Dual-Patch Antenna on a Hemispherical Surface

The first structure to be considered in this technique is the application of a short-circuited dual-patch antenna (SDPA) to form an array over a hemispherical surface. An antenna element representing a SDPA is shown in Fig. 11, and the specific dimensions are given in Fig. 12 [6]. A SDPA consists of two layers, in which the upper patch, which is of trapezoidal shape, is connected along one edge to the ground by a vertical metal wall and the other edge is connected to the lower patch by another vertical wall. These novel features produce a significant reduction in the resonant frequency of the antenna. The numerical results obtained by using a dynamic electromagnetic simulator such as WIPL-D [3] are very similar to the experimental results described in Ref. 6. The actual geometry of the SDPA is shown in Fig. 12, and the input impedance for this geometry as a function of frequency is given in Fig. 13. For this structure the resonant frequency occurs at about 2.41 GHz, as shown in Fig. 13. Finally, the radiation pattern of the SDPA along the E plane is shown in Fig. 14, illustrating that the element pattern has some directivity and the frontlobe is larger than the backlobe. These results are close to the measured ones given in Ref. 6. The SDPA is considered to be fabricated over a finite square ground plane of size G centimeters on each side. We now consider a 48-element array consisting of an SDPA that is distributed over a hemisphere of radius 1.4λ . The elements are placed in a star configuration as seen in Fig. 15. We now transform the actual voltages that are induced at the feedpoint of these antenna elements located on the surface of a hemi-

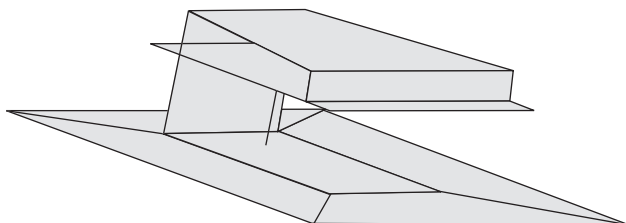


Figure 11. A short-circuited dual-patch antenna element.

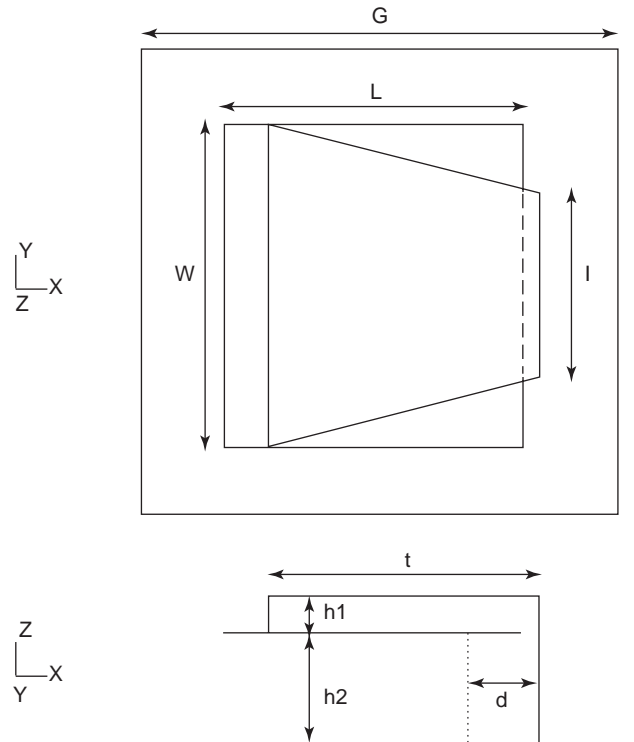


Figure 12. Geometry of the short-circuited dual-patch antenna: $h^1 = 2$ mm; $h^2 = 6$ mm; $d = 4$ mm; $t = 15$ mm; $l = 10$ mm; $L = 16.5$ mm; $W = 17.5$ mm; $G = 27.4$ mm.

isphere to a 16-element planar 2D ULVA located on the x - y plane with $z = 0$. The 2D ULVA consists of omnidirectional point antennas radiating in free space as shown in Fig. 16. The spacing between the virtual elements is 0.5λ at 2.41 GHz, and all the omnidirectional point sources are placed as a 4×4 array located within the base of the hemisphere as seen in Fig. 16.

For all the examples that we will present, the azimuth scan angle φ varies from φ_q to φ_{qq} with an angular step of 1° (i.e., $\varphi = 1$). The step size for the elevation angle is also

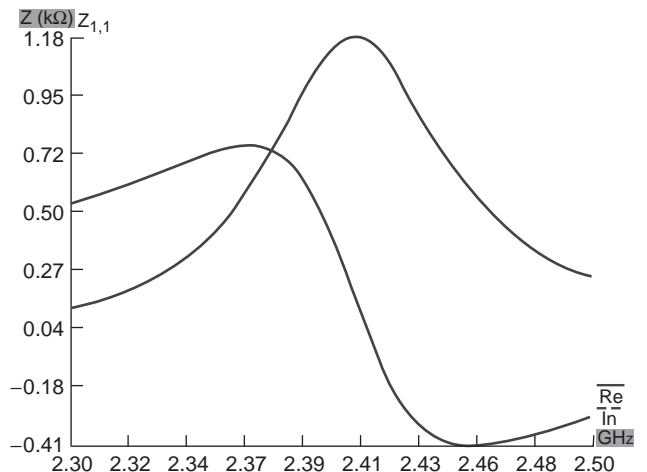


Figure 13. Impedance versus frequency of a SDPA; resonance frequency = 2.41 GHz. (This figure is available in full color at <http://www.mrw.interscience.wiley.com/erfme>.)

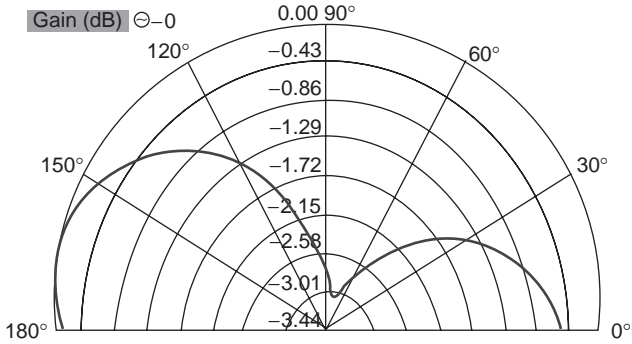


Figure 14. Radiation pattern of the short-circuited dual-patch antenna; normalized; E plane.

1° (i.e., $\theta = 1^\circ$). This information is now used to calculate the transformation matrix $[\mathfrak{S}_q]$.

We next define a transformation error to check the accuracy of this interpolation in both φ and θ . The error is defined by

Interpolation error

$$= \sqrt{\frac{1}{IJ} \sum_{i=1}^I \sum_{j=1}^J |[A_v(\Phi_q; \Theta_q)]_{i,j} - [\mathfrak{S}_q][A(\Phi_q; \Theta_q \Theta)]_{i,j}|^2} \quad (3)$$

The interpolation error and the condition number of the transformation matrix for different values of the sectors q are given in Table 6. The condition number is defined as the ratio of the largest singular value to the smallest singular value of the transformation matrix. It is an indicator of how sensitive is the solution to changes of the physical dimensions of the antenna array. As observed from Table 6, the error in the transformation to a ULVA remains more or less constant until $0^\circ \leq \theta \leq 50^\circ$. The azimuth scan is the entire 360° . We do not present results beyond $\theta \leq 50^\circ$ because all the SDPA elements on the hemisphere do not see the signal, and hence the transformation matrix $[\mathfrak{S}_q]$ becomes undefined. In that case we restrict the azimuth angle scan, as will be seen later on in this section. Therefore this procedure works if the interpolation error is reasonably small. This can be determined a priori for the structures of interest.

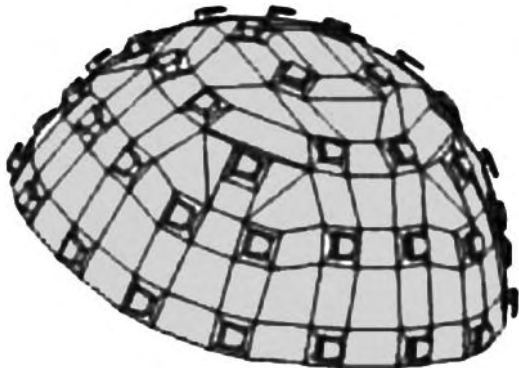


Figure 15. Short-circuited dual-patch antenna array.

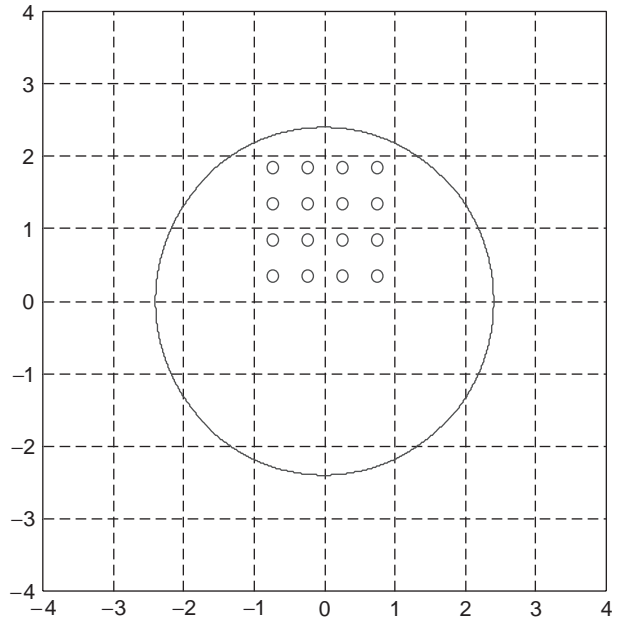


Figure 16. Location of the 16-element virtual array when the scanned sector is defined by the azimuth angle $(\varphi_q, \varphi_{qq}) = (30^\circ, 150^\circ)$ and elevation angle $(\theta_q, \theta_{qq}) = (0^\circ, 40^\circ)$.

For this example, the goal here is to estimate the directions of arrival and the amplitudes of three signals that are incident on the array, from $(\varphi, \theta)_1 = (50^\circ, 5^\circ)$, $(\varphi, \theta)_2 = (80^\circ, 20^\circ)$, and $(\varphi, \theta)_3 = (140^\circ, 30^\circ)$. The amplitudes of all the signals are 1V with zero phase. The scan for the transformation matrix is carried out spanning over all the azimuth angles $(\varphi_q, \varphi_{qq}) = (30^\circ, 150^\circ)$ and the elevation angles $(\theta_q, \theta_{qq}) = (0^\circ, 40^\circ)$. The scan for the transformation matrix is carried out spanning over all the azimuth angles $(\varphi_q, \varphi_{qq}) = (30^\circ, 150^\circ)$ and the elevation angles $(\theta_q, \theta_{qq}) = (0^\circ, 40^\circ)$. We now use the matrix pencil method [1,4,5] in two dimensions to estimate the DoA of three signals impinging on the 48-element array, which has been interpolated to a 16-element 2D ULVA as shown in Fig. 16. The distance between the elements of the virtual array is 0.5λ and is centered at a distance $R/2$, where R is the radius of the hemisphere and is oriented along the direction shown in Fig. 16.

To solve this problem, we first generate the transformation matrix that electromagnetically maps the voltages induced on a 16-element SDPA situated on a hemisphere as shaded in Fig. 17 situated over a quadrant of a hemispherical surface to a 16-element 2D ULVA as shown by

Table 6. Interpolation Error and Condition Number for Transformation Matrix $[\mathfrak{S}_q]$ When Interpolating to a 16-Element ULVA

Elevation Scan Angle (θ)	Interpolation Error (%)	Condition Number
$0^\circ \rightarrow 10^\circ$	0.2	2.7×10^8
$0^\circ \rightarrow 20^\circ$	0.36	5×10^5
$0^\circ \rightarrow 30^\circ$	2.4	8×10^5
$0^\circ \rightarrow 40^\circ$	5.9	17,191
$0^\circ \rightarrow 50^\circ$	10.2	15,368

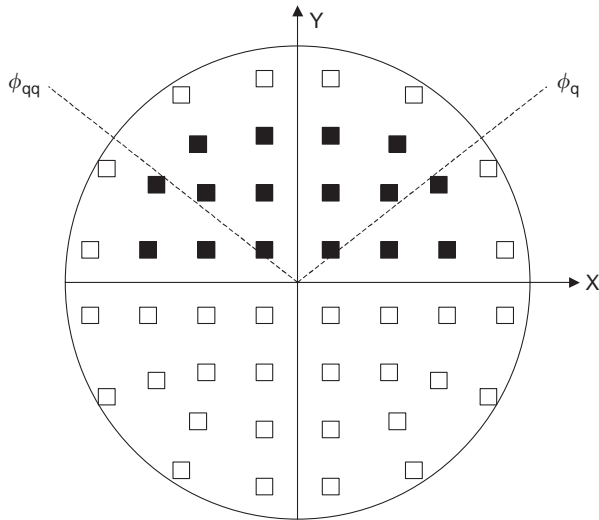


Figure 17. Top view of the hemispherical array. The black squares represent the 16 active elements for processing, and the white squares represent the rest of the real elements mounted over the hemispherical surface.

Fig. 16. Here the real elements are short-circuited dual-patch antennas placed over the hemispherical array in a star configuration. The estimated DoAs of all the three signals given by the matrix pencil method using the voltages induced in the 2D ULVA are given in Table 7. The estimated amplitudes of all three signals are also shown in Table 7.

4.2. Dielectric Resonator Antennas on a Hemispherical Surface

The next example deals with an antenna array consisting of rectangular dielectric resonator (RDRs) antennas as antenna elements located on a hemispherical surface. The reason that the dielectric resonators are chosen as antenna elements is because they have a high radiation efficiency, typically greater than 98%.

An antenna element representing a RDR is shown in Fig. 18, where the specific dimensions of the RDR are as given in Fig. 19 [7]. The coaxial probe extends into a dielectric of relative permittivity of 8.9. The antenna element is situated over a square finite ground plane of dimension $G = 6.0$ cm along each side. The input impedance as a function of frequency is shown in Fig. 20 and was obtained using WIPL-D [3]. The results are similar to those in Ref. 7. The actual resonant frequency of this RDR occurs at 3.07 GHz, as in Fig. 20. Finally, the radiation pattern along the E plane is shown in Fig. 21.

Table 7. Estimation of DoA of Three Signals: $(\varphi, \theta)_1 = (50^\circ, 5^\circ)$, $(\varphi, \theta)_2 = (80^\circ, 20^\circ)$, $(\varphi, \theta)_3 = (140^\circ, 30^\circ)$

φ	θ	Estimation of φ	Estimation of θ	Estimation of Amplitude
50°	5°	51.91°	5.83°	1.03
80°	20°	78.80°	18.84°	0.87
140°	30°	141.38°	30.51°	0.93

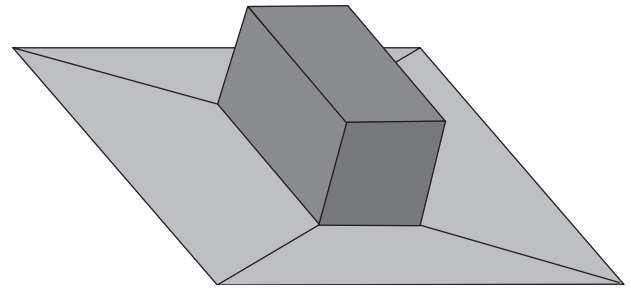


Figure 18. A rectangular dielectric resonator antenna element.

A total of 48 RDR elements are placed on a hemisphere of radius 2.1λ , as shown in Fig. 22, in order to create an RDR hemispherical array (RDR HA). We now transform the voltages induced in these real antenna elements to those that will be induced by the same incident fields if they were to illuminate the ULVA. The 18 antenna elements that are used in this transformation are represented by the black squares in Fig. 23. The sector over which the transformation is carried out is covered by the azimuth angle of $(\varphi_q, \varphi_{qq}) = (30^\circ, 150^\circ)$, and the elevation scan angle varies from 10° to 50° . The actual voltages induced in the 18 real elements are mapped to the voltages induced that will be induced in the 16-element 2D ULVA, as shown in Fig. 16. For the ULVA the elements are point radiators radiating in free space. These virtual elements are separated by 0.5λ . The results of the accuracy and stability of this transformation are given in Table 8. To carry out an estimation of DoA for three signals impinging on this 48-RDR-element array, we transform the voltages induced in the real 18-element array (as shown by the black squares in Fig. 23) to a 16-element ULVA. The goal here is to estimate the directions of arrival and the amplitudes of three signals that are incident on the array from $(\varphi, \theta)_1 = (50^\circ, 5^\circ)$, $(\varphi, \theta)_2 = (80^\circ, 20^\circ)$, and $(\varphi, \theta)_3 = (140^\circ, 30^\circ)$. The amplitude of all the signals is 1 V with a zero phase angle. The scan to generate the transformation matrix is carried

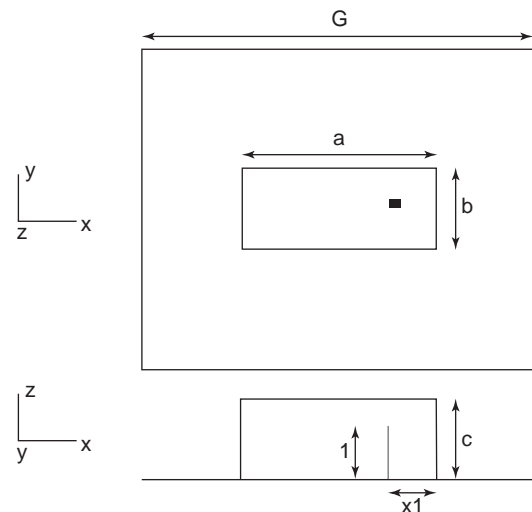


Figure 19. Geometry of a rectangular dielectric resonator antenna: $a = 30$ mm; $b = 15$ mm; $c = 15$ mm; $l = 10.3$ mm; $x_1 = 7.5$ mm; $G = 60$ mm.

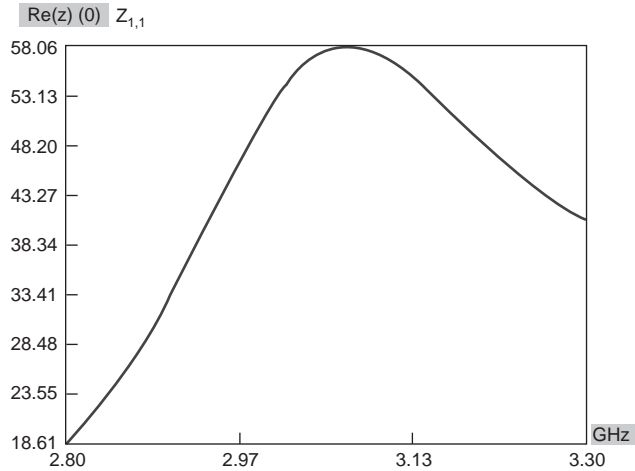


Figure 20. Impedance versus frequency resonant of the RDR antenna element at a frequency of 3.07 GHz.

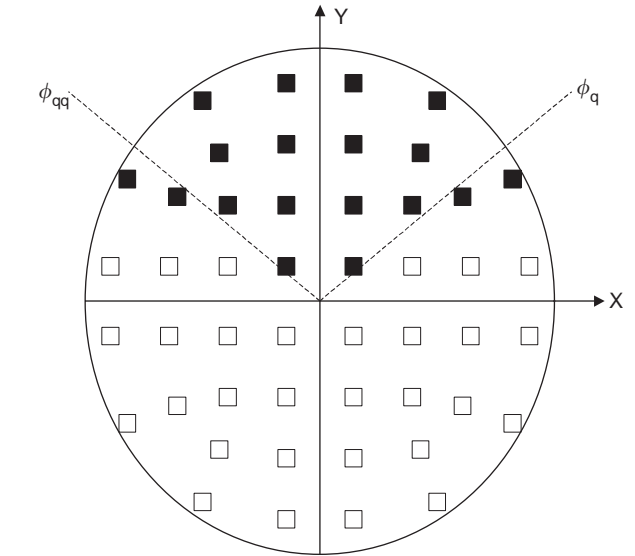


Figure 23. Top view of the hemispherical array. The black squares represent the 18 active elements in the processing, and the white squares represent the rest of the real elements mounted over the hemispherical surface.

Table 8. Interpolation Error and Condition Number for a RDR HA Using a 16-Grid Virtual Array ($d_{va} = 0.5$)

Elevation Scan Angle (θ)	Interpolation Error (%)	Condition Number
$0^\circ \rightarrow 10^\circ$	0.2	1.3×10^7
$0^\circ \rightarrow 20^\circ$	0.22	5.1×10^5
$0^\circ \rightarrow 30^\circ$	0.4	22,763
$0^\circ \rightarrow 40^\circ$	1.1	7029
$0^\circ \rightarrow 50^\circ$	4.2	2970

Table 9. Estimation of DoA of Three Signals: $(\varphi, \theta)_1 = (50^\circ, 5^\circ)$, $(\varphi, \theta)_2 = (80^\circ, 20^\circ)$, $(\varphi, \theta)_3 = (140^\circ, 30^\circ)$

φ	θ	Estimation of φ	Estimation of θ	Estimation of Amplitude
50°	5°	51.7°	5.9°	1.2
80°	20°	78.3°	18.3°	1.3
140°	30°	140.8°	29.2°	1.0

out over the azimuth angles of $(\varphi_q, \varphi_{qq}) = (30^\circ, 150^\circ)$ and the elevation angles of $(\theta_q, \theta_{qq}) = (0^\circ, 40^\circ)$.

The estimated DoAs of all the three signals given by the matrix pencil method using the voltages induced in the 2D ULVA are given in Table 9. The estimated amplitudes of all three signals are also shown in Table 9.

4.3. An Array of Horn Antennas on a Hemispherical Surface

Finally, we consider an array of horn antennas located on a hemispherical surface. The probe-fed horn antenna is shown in Fig. 24, and its dimensions are shown in Fig. 25. The input impedance at the probe feed is shown in Fig. 26, as a function of frequency demonstrating that the resonant frequency of the horn occurs at 2.41 GHz. At that frequency the element radiation pattern is given by Fig. 27.

A nonplanar conformal array on a hemispherical surface is formed by using 48 horn antennas placed on a

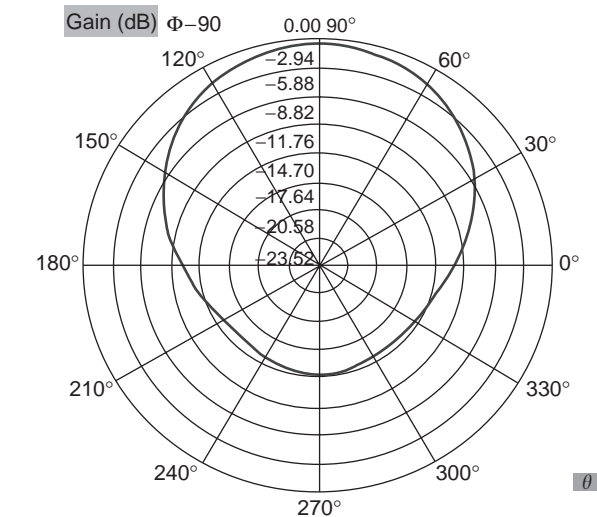


Figure 21. Radiation pattern of the rectangular dielectric resonator antenna element; normalized.

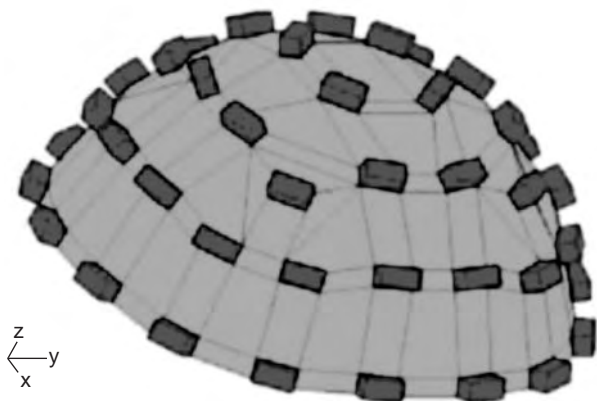


Figure 22. Rectangular dielectric resonator arrays on a hemispherical surface.

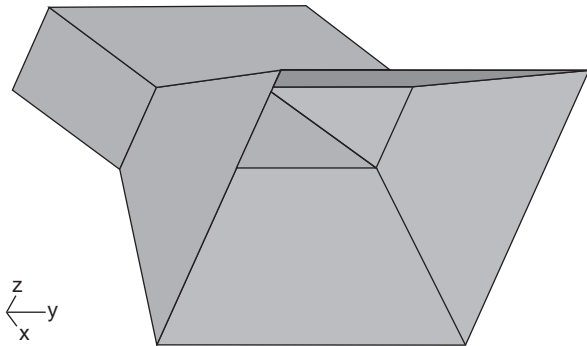


Figure 24. A horn antenna.

hemispherical surface of radius 2.4λ as shown in Fig. 28. The properties of the transformation matrix when we transform the voltages induced in the actual array consisting of 18 elements (see Fig. 28) to the voltages that will be induced in a 16-element planar ULVA (see Fig. 16) are given in Table 10. The sector scan in azimuth and in elevation is limited by $(\varphi_q, \varphi_{qq}) = (30^\circ, 150^\circ)$ and $(\theta_q, \theta_{qq}) = (0^\circ, 40^\circ)$, respectively. The interpolation error and the condition number of the transformation matrix $[\mathfrak{S}_q]$ for different sectors q are shown in Table 10.

To carry out DoA estimation of the three signals $(\varphi, \theta)_1 = (50^\circ, 5^\circ)$, $(\varphi, \theta)_2 = (80^\circ, 20^\circ)$, and $(\varphi, \theta)_3 = (140^\circ, 30^\circ)$ impinging on the hemispherical horn array, we transform the voltages that are induced on the shaded 18-horn antenna elements as shown in Fig. 17 to the 2D ULVA of Fig. 16. The amplitude of all the signals is 1 V.

The estimated DoAs of all three signals given by the matrix pencil method using the voltages induced in the 2D ULVA are given in Table 11. The estimated amplitudes of all

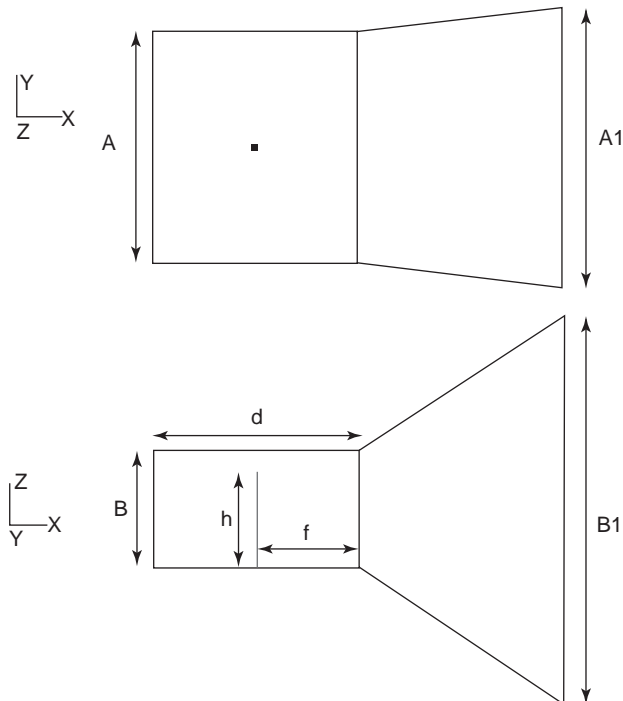


Figure 25. Geometry of the horn antenna: $A = 6$ cm; $d = 5$ cm; $f = 2.5$ cm; $h = 2.5$ cm; $B = 3$ cm; $A_1 = 7.2$ cm; $B_1 = 10$ cm.

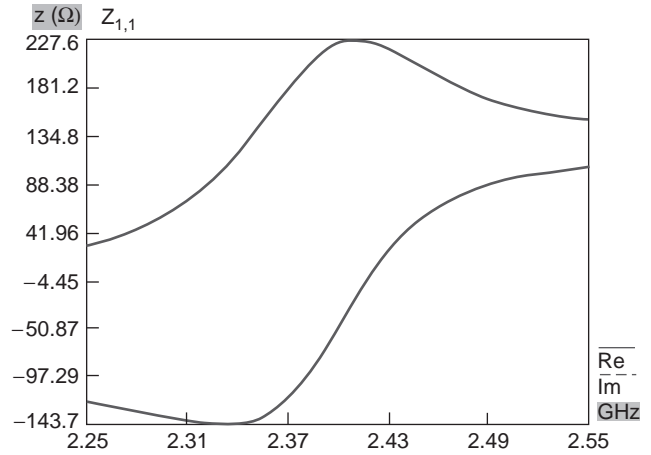


Figure 26. Impedance response of the horn antenna. (This figure is available in full color at <http://www.mrw.interscience.wiley.com/erfme>.)

three signals are also shown in Table 11. The estimates using a single snapshot of the data voltages are quite accurate. It is important to note that the error in the transformation matrix increases as we increase the azimuth angle θ toward 90° because the increase in degrees of freedom is not commensurate with the number of antenna elements. The error can be controlled either by adding additional arrays or by reducing the scan angle for the group of active elements.

It is seen that it is possible to carry out a DoA estimation by using directive antenna elements located on a hemispherical surface. The 2D matrix pencil method is applied to the outputs from the 2D ULVA to estimate the DoAs of the various signals illustrates that the results can be obtained with engineering accuracy. The use of directive elements is made possible through this methodology, which increases the efficiency of the system, as we now have a larger signal-to-noise ratio to operate in. In addition, such a

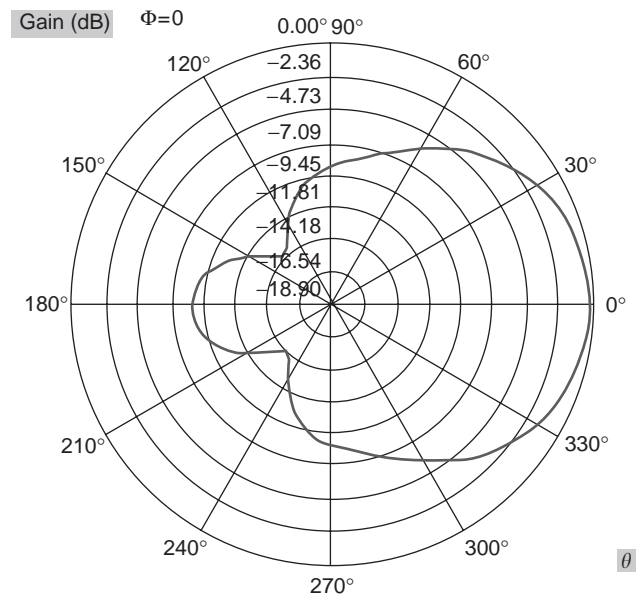


Figure 27. Radiation pattern of a single-horn antenna; normalized.

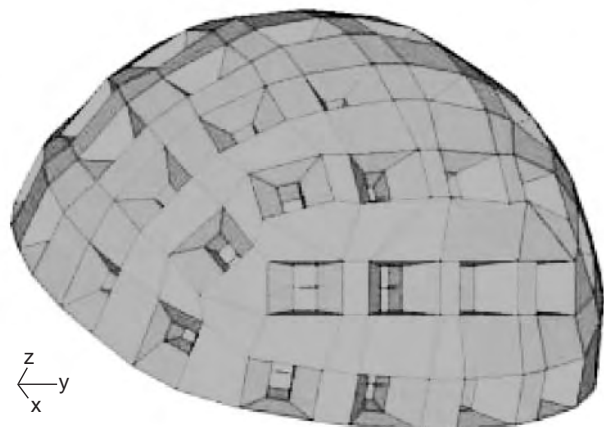


Figure 28. An array of conformal horn antenna aligned on a hemispherical surface.

Table 10. Interpolation Error and Condition Number for Transformation Matrix [3] When Interpolating to a 16-Element ULVA (Star Configuration with a Conformal Shape)

Elevation Scan Angle (θ)	Error Interpolation (%)	Condition Number
$0^\circ \rightarrow 10^\circ$	0.2	5.7×10^7
$0^\circ \rightarrow 20^\circ$	0.27	2.7×10^7
$0^\circ \rightarrow 30^\circ$	0.73	20,512
$0^\circ \rightarrow 40^\circ$	2.4	4767

Table 11. Estimation of DoA of Three Signals: $(\varphi, \theta)_1 = (50^\circ, 5^\circ)$, $(\varphi, \theta)_2 = (80^\circ, 20^\circ)$, and $(\varphi, \theta)_3 = (140^\circ, 30^\circ)$

φ	θ	Estimation of φ	Estimation of θ	Estimation of Amplitude
50°	5°	47.5°	4.4°	1.1
80°	20°	80.4°	18.1°	1.0
140°	30°	141.6°	29.5°	1.1

system significantly reduces the cost of a phased-array system, as there are fewer antenna elements and hence fewer receiver channels and therefore fewer number of A/Ds are required to carry out digital beamforming.

5. CONCLUSION

This article has presented a preprocessing technique that transforms a nonuniformly spaced array operating in the presence of mutual coupling between the elements of the array and near-field scatterers into a virtual array of omnidirectional isotropic point elements operating in free space that is suitable to the application of a direct data domain algorithm. Through such a transformation formulated using an interpolation technique, we have shown that one can not only compensate for the effects of mutual coupling in a nonuniformly spaced array but also eliminate the effects of strong near-field scatterers. Since the transformed output voltages are those of a uniformly spaced linear array consisting of omnidirectional point

radiators, a conventional adaptive algorithm can easily be applied to extract the SoI in the presence of jammers. Finally, it is shown how to use directive antenna elements located on a conformal hemispherical surface is used to perform DoA estimation using a single snapshot of the data.

BIBLIOGRAPHY

1. T. K. Sarkar, M. Wicks, M. Salazar-Palma, and R. Bonnaeu, *Smart Antennas*, Wiley, Hoboken, NJ, 2003.
2. B. Friedlander, The root-MUSIC algorithm for direction finding with interpolated arrays, *Signal Process.* **30**: 15–29 (1993).
3. B. M. Kolundzija, J. S. Ognjanovic, and T. K. Sarkar, *WIPL-D: Electromagnetic Modeling of Composite Metallic and Dielectric Structures*, Artech House, Norwood, MA, 2000 (<http://wipl-d.com>).
4. T. K. Sarkar and O. Pereira, Using matrix pencil for estimating parameters of exponentially damped/undamped sinusoids in noise, *IEEE Anten. Propag. Mag.* **37**(1): 48–55 (February 1995).
5. Y. Hua and T. K. Sarkar, Generalized pencil of functions method for extracting poles of an EM system from its transient response, *IEEE Trans. Anten. Propag.* **37**(2) (1989).
6. R. Chair, K. M. Luk, and K. F. Lee, Miniature shorted dual-patch antenna, *IEEE Proc. Microwave Anten. Propag.* **147**(4): 273–276 (August 2000).
7. M. W. McAllister, S. A. Long, and G. L. Conway, Rectangular dielectric resonator antenna, *Electron. Lett.* **19**: 218–219 (March 1983).

DIRECTIONAL COUPLERS

TULLIO ROZZI
ANTONIO MORINI
Università di Ancona
Ancona, Italy

The directional coupler (DC) is the most useful four-port microwave device. Substantially, it consists of a four-port device, where a wave entering any port excites two other ports with prescribed amplitudes, whereas the remaining port is isolated. This property makes the DC an essential component when dealing with microwave devices, as it allows to distinguish reflected waves from incident ones. After a definition of the ideal DC, the typical parameters and the electrical characteristics of actual devices are illustrated, then, the main applications of DC are considered and, finally, some common realizations of DC are shown, particularly focusing the attention on different coupling mechanisms and technologies.

1. DEFINITION

An ideal directional coupler is a linear, reciprocal, and lossless four-port device, often indicated as in Fig. 1, with the following properties [1]:

1. The ports are matched.
2. Each port is only coupled to other two ports, the fourth one being isolated.



Figure 1. Schematic representations of a directional coupler.

Therefore, the scattering matrix of an ideal directional coupler takes the form

$$S = \begin{bmatrix} 0 & s_{12} & s_{13} & 0 \\ s_{12} & 0 & 0 & s_{24} \\ s_{13} & 0 & 0 & s_{24} \\ 0 & s_{24} & s_{34} & 0 \end{bmatrix} \quad (1)$$

apart from an insignificant permutation of the port indices. Thus, a wave incident at port 1, not being reflected at all, splits between ports 2 and 3, while port 4 is isolated. Conversely, a wave incident at port 2 is coupled to ports 1 and 4, with port 3 isolated under that excitation (hence the name directional coupler). The fundamental parameter characterizing the ideal directional coupler is the so-called coupling C , defined as the reciprocal of the magnitude of the transmission coefficient between ports 1 and 3 (i.e., $C = -20 \log |s_{13}|$).

It is also shown that any linear, reciprocal, lossless, and matched four-port must be a directional coupler. Its scattering matrix S is in fact

$$S = \begin{bmatrix} 0 & s_{12} & s_{13} & s_{14} \\ s_{12} & 0 & s_{23} & s_{24} \\ s_{13} & s_{23} & 0 & s_{24} \\ s_{14} & s_{24} & s_{34} & 0 \end{bmatrix} \quad (2)$$

Since losslessness implies the unitarity of the scattering matrix, $SS^+ = I$, where I is the unit matrix, the following equations must be satisfied:

$$|s_{12}|^2 + |s_{13}|^2 + |s_{14}|^2 = 1 \quad (3)$$

$$|s_{12}|^2 + |s_{23}|^2 + |s_{24}|^2 = 1 \quad (4)$$

$$|s_{13}|^2 + |s_{23}|^2 + |s_{34}|^2 = 1 \quad (5)$$

$$|s_{14}|^2 + |s_{24}|^2 + |s_{34}|^2 = 1 \quad (6)$$

$$s_{13}s_{23}^* + s_{14}s_{24}^* = 0 \quad (7)$$

$$s_{12}s_{23}^* + s_{14}s_{34}^* = 0 \quad (8)$$

$$s_{12}s_{24}^* + s_{13}s_{34}^* = 0 \quad (9)$$

By multiplying Eq. (7) by s_{12} and Eq. (8) by s_{13} and subtracting one from the other, one obtains the equation

$$s_{14}(s_{12}s_{24}^* - s_{13}s_{34}^*) = 0 \quad (10)$$

whose solutions are

$$s_{14} = 0 \quad (11)$$

$$s_{12}s_{24}^* = s_{13}s_{34}^* \quad (12)$$

Let us consider the first solution. From Eq. (7) it also follows that $s_{23} = 0$ [otherwise we would have $s_{12} = s_{13} = 0$, in contradiction with Eq. (3)]. Moreover, by subtracting Eq. (4) from Eq. (3) and Eq. (5) from Eq. (3), one obtains $|s_{13}| = |s_{24}| = \alpha$ and $|s_{12}| = |s_{34}| = \beta$. By setting $\phi_{ij} = \angle S_{ij}$, from Eq. (9) one obtains the relationship linking the phases:

$$(\phi_{12} - \phi_{13}) + (\phi_{34} - \phi_{24}) = \pi \quad (13)$$

Therefore, the scattering matrix of the device takes the form

$$S = \begin{bmatrix} 0 & \beta e^{j\phi_{12}} & \alpha e^{j\phi_{13}} & 0 \\ \beta e^{j\phi_{12}} & 0 & 0 & \alpha e^{j\phi_{24}} \\ \alpha e^{j\phi_{13}} & 0 & 0 & \beta e^{j\phi_{34}} \\ 0 & \alpha e^{j\phi_{24}} & \beta e^{j\phi_{34}} & 0 \end{bmatrix} \quad (14)$$

Note that when $\phi_{12} - \phi_{13} = \phi_{34} - \phi_{24}$, as often occurs in practical cases when the coupler is symmetric ($s_{13} = s_{24}$ and $s_{12} = s_{34}$), we obtain

$$\phi_{12} - \phi_{13} = \pi/2 \quad (15)$$

Therefore, the outputs from ports 2 and 3 are in quadrature. In this case, it is always possible to choose the reference planes in such a way that the scattering matrix takes the form

$$S = \begin{bmatrix} 0 & j\beta & \alpha & 0 \\ j\beta & 0 & 0 & \alpha \\ \alpha & 0 & 0 & j\beta \\ 0 & \alpha & j\beta & 0 \end{bmatrix} \quad (16)$$

When we consider Eq. (12), we note immediately that the solutions $s_{12} = 0$ and $s_{34} = 0$, or $s_{13} = 0$ and $s_{24} = 0$, respectively, are the same as that obtained previously, after exchanging the coupled ports with the isolated ones. For instance, under excitation of port 1, the isolated port becomes port 2 while port 3 and port 4 are coupled. Therefore, the first case examined can be taken as typical.

An alternative picture representing a directional coupler commonly used in measurement benches is shown in Fig. 2. The figure emphasizes that port 4 of the DC is terminated on a matched load. Actually, in many applications, port 4 is not used at all. Nevertheless, this port must be loaded in order to suppress the secondary line signals due to its mismatch. Moreover, the sketch suggests an intuitive idea of the realization of a directional coupler: two parallel transmission lines electromagnetically coupled to each other. A portion of the wave traveling from port 1 toward port 2 couples to port 3. According to common

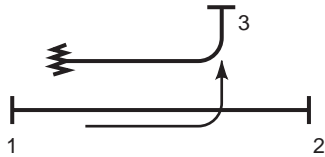


Figure 2. Schematic representations of a directional coupler in the configuration commonly used in microwave measurements.

parlance, the branch connecting ports 1 and 2 is called the “main arm,” while the one linking ports 3 and 4 is called the “secondary arm.”

2. REAL DIRECTIONAL COUPLERS

Of course, it is impossible to obtain both perfect match at the four ports and full isolation of the uncoupled ports [2,3]. Therefore, in order to characterize an actual coupler, it is necessary to define, in addition to the coupling, the directivity D

$$D = 20 \log \frac{|s_{13}|}{|s_{14}|} \tag{17}$$

which represents the ratio between the power flowing from 1 to 3 and that from 1 to 4. In the ideal case the directivity is infinite. Sometimes it is preferred to use another parameter, the isolation I , defined by

$$I = 20 \log \frac{1}{|s_{14}|} = C + D \tag{18}$$

Additionally, actual devices are typically characterized by the following quantities:

- *Frequency range*—operational band of the coupler. Typically, commercial waveguide couplers operate over the whole waveguide band. Over that band the following parameters are defined:
- *The nominal coupling C* —typical values are 3, 6, 10, 20, 30, and 40 dB.
- *Coupling sensitivity/deviation*—the maximum deviation C with respect to its nominal value.
- *Minimum directivity D* —typically between 30 and 50 dB.
- *Insertion loss*—the maximum insertion loss on the main path (ports 1–2).
- *Primary-arm VSWR*—the VSWR on the main path.
- *Secondary-arm VSWR*—that of the secondary path.
- *Power-handling capability (cw)/(peak)*—the maximum continuous or peak power that can be carried by the coupler.
- *Connectors*—indicate the connectors by which the coupler is fed.

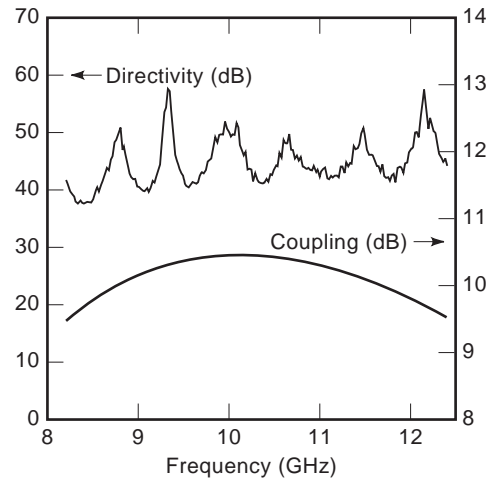


Figure 3. Coupling and directivity of a commercial 10 dB multi-hole waveguide directional coupler.

3. MEASUREMENT OF THE COUPLER PARAMETERS

Since a directional coupler is a linear four-port device, its characteristic parameters C and D are commonly deduced by measuring the scattering parameters with the help of a network analyzer. This is very easy in coaxial and rectangular waveguides, where analyzer flanges are the same as those of the device under test. In microstrip and in planar circuits, some attention must be paid to the feed transitions. Such transitions could noticeably alter the response of the coupler. Figure 3 shows the typical measured parameters of a commercial 10-dB directional coupler in a rectangular waveguide.

4. APPLICATIONS

The main feature of the coupler is its ability to detect whether a wave traveling along the main branch is propagating from 1 to 2 or in the opposite direction. That makes the coupler an essential component in telecommunication and measurement systems. A few of the most important applications are discussed next.

4.1. Reflectometer

From the detection of the propagation direction of a wave follows the possibility of measuring the reflection of an unknown device. This is achieved by arranging the measurement bench as depicted in Fig. 4.

In the ideal case [i.e., when the scattering matrix of the directional coupler is given by Eq. (1), and assuming port 4 to be perfectly matched], the signal detected at port 3, b_3 , is proportional to ρ_1 , the reflectivity of the device under test (DUT) loading port 1, while port 2 is fed by a microwave generator (4). In fact

$$b_3 = s_{13}s_{12}\rho_1 \tag{19}$$

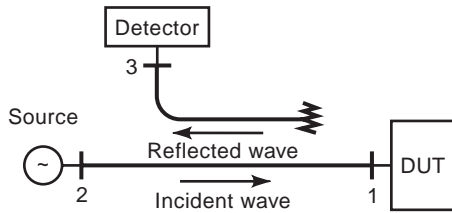


Figure 4. Bench for reflectometry measurements. By means of the DC, part of the signal reflected by the device under test flows to port 3, where it is detected and measured.

The measurement requires knowledge of the term $s_{13}s_{12}$, which can be easily measured by substituting the unknown load ρ_1 with a known one, typically a totally reflecting load, as a short circuit ($\rho_k = -1$). Under such a condition, the signal delivered at port 3 is

$$b_{3k} = -s_{13}s_{12} = -s_{13}s_{12} \quad (20)$$

Once this step, commonly referred to as the calibration, has been completed, one can find the reflection ρ_1 as

$$\rho_1 = -b_3/b_{3k} \quad (21)$$

4.2. Monitoring, Feedback, and Power Measurements

In the configuration of Fig. 5 the coupler is used for the purpose of monitoring the output level of a given source. The signal at port 3 can also be used as a feedback for the source itself—for instance, when a leveled output power is required (see FEEDBACK AMPLIFIERS).

The use of coupler with large coupling is very useful when dealing with measurements of high power signals, which could destroy power meters. The typical bench for such measurements is shown in Fig. 6.

4.3. Couplers as Part of More Complex Systems

The coupler often represents an essential part of more complex devices, such as the mixer or the four-way circulator, shown in Figs. 7 and 8, respectively. In the first case the coupler provides a strong separation between the local oscillator (LO), while in the second case two 3 dB couplers, connected as shown in Fig. 8, permit one to obtain (in the

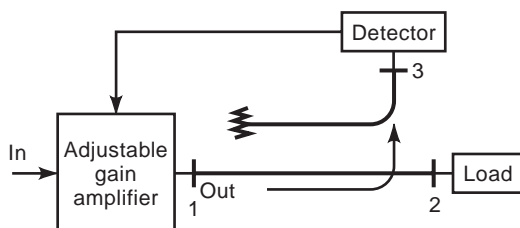


Figure 5. Monitoring and feedback of a source output. Part of the signal outgoing from the amplifier is coupled into the detector and used to control the gain of the amplifier.

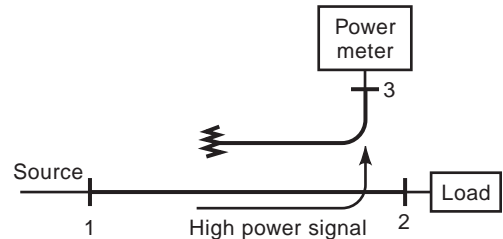


Figure 6. Measurement of power signals. Only a small amount of the power signal is delivered to the power meter in order to prevent damage.

ideal case) the following scattering matrix:

$$S = \begin{bmatrix} 0 & 0 & 0 & e^{j\phi_{14'}} \\ 0 & 0 & e^{j\phi_{41'}} & 0 \\ 0 & e^{j\phi_{1'4}} & 0 & 0 \\ e^{j\phi_{4'1}} & 0 & 0 & 0 \end{bmatrix} \quad (22)$$

When port 1 is fed, the power equally splits between ports 2 and 3, while port 4 is isolated. Then, thanks to the phase shifter, the signal traveling from port 3 to port 3' is shifted by 180° with respect to the signal directly arriving at port 2'. The output of the combination of the two signals 180° out of phase is different from zero only at port 4'. Therefore, $s_{14} = 0$, $s_{14'} \neq 0$ and $s_{11'} = 0$. Analogously, when port 4 is fed, ports 1 and 4' are isolated, while port 1' is coupled. It is easy to repeat the same reasoning when ports 1' and 4' are fed and to recover the scattering matrix of Eq. (22).

5. COUPLING MECHANISMS

The two lengths of transmission line forming the coupler can be coupled to each other by different mechanisms. Schematically, a first distinction can be made between lumped and distributed coupling [5].

Considering that at microwave frequencies purely lumped coupling does not exist, since propagation effects occur, we will consider the coupling as lumped if the region where the coupling physically takes place is much shorter

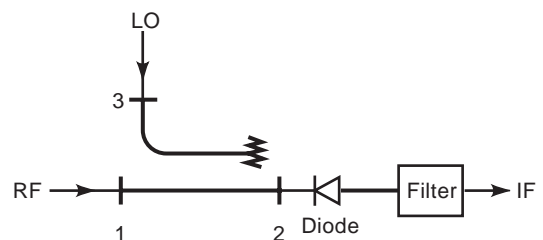


Figure 7. Microwave mixer. The radiofrequency (RF) low power signal, coming from the antenna, is mixed with the one generated by the local oscillator (LO) via a nonlinear device (diode). The filter separates the intermediate frequency (IF) while the directional coupler provides a strong isolation between RF and LO channels.

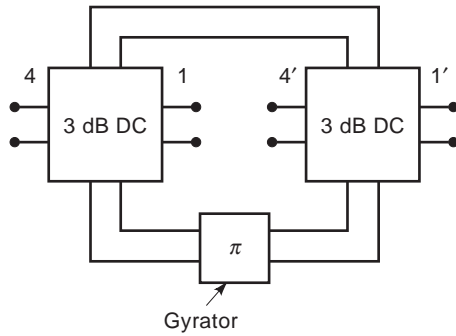


Figure 8. A four-way circulator is supposed to feed one port at a time. For instance port 1: In that case port 4 is uncoupled and the signal is split equally among the remaining ports of the first junction. At the second junction, the two signals combine 180° out of phase because of the phase shifter inserted in the lower pattern. Therefore, due to the symmetry, they can couple only to port 4', while port 1' is isolated. The same reasoning applies when port 4' is being fed. In that case, however, the phase shifter does not operate as the signal flows counterclockwise in the lower pattern. Therefore, the signals arriving at the first coupler are in phase and combine only to port 1. Analogous reasoning holds for ports 1' and 4.

than the wavelength. Lumped coupling can be achieved in both waveguide and planar technology.

In the first case, a further distinction can be made as to whether the coupling is directive. Coupling may be made directive by shaping the coupling region in such a way that on the secondary guide it produces two waves that are in phase opposition in one direction. The double aperture invented by Saad and Riblet [6] (Fig. 9a) provides a clear example of such a mechanism. In fact, in the secondary guide the thin vertical slot produces two waves 180° out of phase, propagating in opposite direction, while the thin horizontal slot produces two waves in phase. It is therefore possible to choose the dimensions and the positions of the two slots so that the amplitudes of the waves that are separately excited are almost the same. Thus, in one direction the two waves sum in phase, while in the opposite direction they cancel. Note that the bandwidth of this coupler is wide enough since the aforementioned mechanism does not take advantage of resonance effects. The same mechanism can be exploited by collapsing the two thin apertures into an elliptical one and adjusting eccentricity

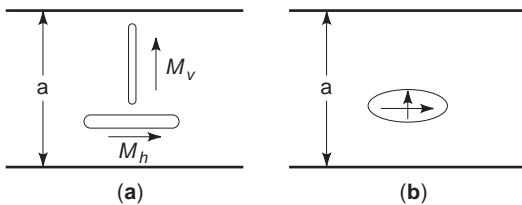


Figure 9. Riblet and Saad directional aperture. In the second arm, the magnetic current M_v excites two waves whose amplitudes are 180° out of phase and propagating in opposite directions. On the contrary, the waves excited by the magnetic current M_h are in phase. Hence, it is possible to adjust the dimensions of the apertures in such a way that the two scattered waves cancel in one direction and sum in the opposite over a broad band.

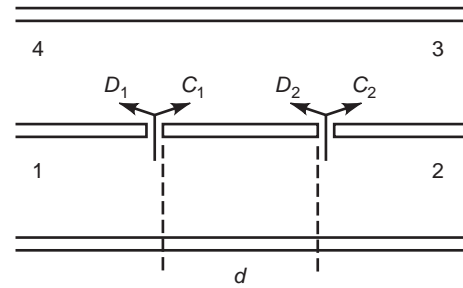


Figure 10. Waveguides coupled via two circular holes spaced by a distance $d = \lambda_g/4$. At the resonant frequency the waves propagating toward the right, C_1 and C_2 , coupled to the secondary arm by the holes, sum in phase while those propagating toward the left, D_1 and D_2 , cancel, because of the 180° phase shift due to the different pattern.

and the position according to the preceding criteria [7,8], as shown in Fig. 9b.

Of course, coupler performance can be strongly improved by cascading several properly spaced apertures. To understand the principle of operation, let us consider two lengths of rectangular waveguides positioned side by side and coupled via two apertures drilled in the broad wall, as illustrated in Fig. 10. We want to couple them in such a way that a fraction of the power traveling from port 1 to port 2 is delivered to port 3 while port 4 is isolated. On the contrary, a wave traveling from 2 to 1 must couple only to port 4. If C_k and D_k denote the fraction of signal delivered to ports 3 and 4, respectively, when a wave travels from port 1 to 2, then the amplitude of the wave at port 3 is given by

$$A_3 \approx |(C_1 + C_2)| \tag{23}$$

while at port 4 we have

$$A_4 \approx |(D_1 + D_2 e^{-j2\beta d})| \tag{24}$$

Therefore, if $D_1 \approx D_2$, $C_1 \approx C_2$, and $2\beta d = \pi$ (that is, the apertures are equal and spaced by $\lambda_g/4$), $A_4 = 0$. Hence, the structure shows, at least at one frequency, the characteristics we are looking for. It is apparent that the design of a directional coupler providing given performance over almost the whole waveguide band is quantitatively much more complicated and requires the use of an appropriately dimensioned array of apertures, as schematically sketched in Fig. 11.

Under the hypothesis that the power coupled by a single aperture to the secondary waveguide is small, let us assume C_n and D_n to be the coupling coefficients of the n th aperture in the forward and reverse directions. Let us also suppose to separate the apertures by a distance d . Hence, the whole coupling into port 3 (B_3), computed in correspondence of the last aperture, is

$$B_3 = A e^{-j\beta N d} \sum_{n=0}^N C_n e^{-j\beta(N-n)d} \tag{25}$$

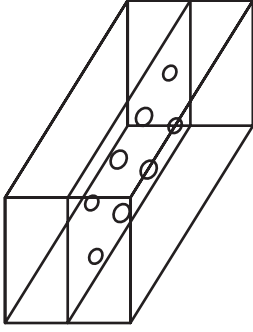


Figure 11. Multiaperture waveguide directional coupler. Dimensions and positions of the coupling holes are chosen so as to optimize DC performance over the whole waveguide band.

The whole coupling coefficient into port 4, B_4 , computed in correspondence of the first aperture is

$$B_4 = A \sum_{n=0}^N D_n e^{-j2\beta nd} \quad (26)$$

Coupling and directivity are given by the following formulas [2]:

$$C = -20 \log \left| \sum_{n=0}^N C_n \right| \quad (27)$$

$$D = -C - 20 \log \left| \sum_{n=0}^N D_n e^{-j2\beta nd} \right| \quad (28)$$

Bethe showed that the forward and the reverse couplings between two waveguides via a circular aperture of radius r_n , normalized with respect to the waveguide width a , are, respectively, $C_n = T_f r_n^3$ and $D_n = T_b r_n^3$. Under the hypothesis that the wall separating the two waveguides is infinitesimally thin, the coefficients T_f and T_b assume closed-form expressions [9]. Therefore, we can rewrite C and D in terms of the latter

$$C = -20 \log |T_f| - 20 \log \left| \sum_{n=0}^N r_n^3 \right| \quad (29)$$

$$D = -C - 20 \log |T_b| - 20 \log |F| \quad (30)$$

where we have used the array factor F , defined as $F = \sum_{n=0}^N r_n^3 e^{-j2\beta nd}$.

The radii r_n are then chosen in such a way as to obtain C and D over the prescribed band. This is analogous to the design of filters and impedance transformers. As in those cases, a Chebyshev characteristic often represents the best tradeoff in terms of performance/number of array elements. Apertures are chosen in such a way as to equate the coefficients of the array factor to those of the

Chebyshev polynomial of order N , T_N :

$$F = \left| \sum_{n=0}^N r_n^3 e^{-j2n\theta} \right| \quad (31)$$

$$= K |T_N(\sec \theta_m \cos \theta)| \quad \text{where } \theta = \beta d$$

The midband frequency is $\theta = \pi/2$ and corresponds to $d = \lambda_g/4$, and θ_m is the value of βd at the band edges. The positive constant K is chosen to obtain the desired coupling at the midband frequency:

$$C = -20 \log K |T_f| |T_N(\sec \theta_m)| \quad (32)$$

When $\theta = 0$, $F = |\sum_{n=0}^N r_n^3| = |T_N(\sec \theta_m)|$. Therefore, the directivity is given by the formulas

$$D = 20 \left[\log \left| \frac{T_f}{T_b} \right| + \log \left| \frac{T_N(\sec \theta_m)}{T_N(\sec \theta_m \cos \theta)} \right| \right] \theta \neq \frac{\pi}{2} \quad (33)$$

$$D = 20 \left[\log \left| \frac{T_f}{T_b} \right| + \log |T_N(\sec \theta_m)| \right] \theta = \frac{\pi}{2} \quad (34)$$

Although T_f/T_b depends on frequency and the characteristic is, in principle, different from the Chebyshev one, nevertheless such a shift is almost negligible, except very close to the midband frequency. Therefore, in the wide-band case that contribution is negligible in the band where $\beta d = \theta_m$. Correspondingly

$$D = D_m = 20 \log |T_N(\sec \theta_m)| \quad (35)$$

where D_m is the minimum directivity in the passband, due to the array factor. Hence, once the coupler specifications are set in terms of midband frequency f_0 , bandwidth Δ_f , coupling, and directivity, the distance d separating two adjacent apertures is given by

$$d = \frac{\pi}{2\beta(f_0)} \quad (36)$$

It is immediate to compute $\cos \theta_m \approx d\beta(f_0 \pm \Delta f)$ and, from Eq. (35), the degree N of the Chebyshev polynomial yielding the specifications on directivity. Because of the non-linearity of $\beta(f)$, $\cos \theta_m$ is only approximately calculated.

The constant K is obtained from Eq. (32):

$$K = 10^{-C/20} |T_f| |T_N(\sec \theta_m)| \quad (37)$$

Once the coefficients T_f are properly computed, either by means of an electromagnetic analysis or by Bethe's more accurate closed formulas, one has only to equate the coefficients of the array factor to those of T_N and to determine the aperture radii. The preceding theory could be further improved with the help of a more accurate analysis of the coupling mechanisms, as the one proposed by Levy [10,11]. At present, however, thanks to the availability of efficient and accurate field theory based computer-aided design (CAD), it seems to be more convenient to improve the design by performing an optimization directly on the

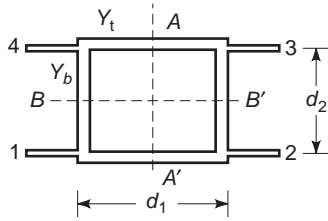


Figure 12. The branchline coupler.

electromagnetic model of the actual physical structure. The resulting design is exact, and device tuning is unnecessary [12] (see ELECTROMAGNETIC FIELD MEASUREMENT) [13].

In planar technology, lumped coupling is often obtained by physically connecting two lines. In the preceding configuration, coupling due to electromagnetic induction can be considered negligible with respect to direct coupling. The main couplers employing such a coupling mechanism are the branchline coupler and the hybrid ring coupler. Both permit one to obtain large coupling values easily, since the lines are electrically connected. In particular, the electromagnetic analysis of the first one (Fig. 12) is difficult to carry out rigorously; a circuit analysis, however, is simple if one takes advantage of the four-fold symmetry. In fact, it is easy to study the equivalent circuit under four independent excitations: (1,1,1,1), (1, -1, -1,1), (1, -1,1, -1), (1,1, -1, -1). The corresponding reflections at the port 1, $\Gamma_a, \Gamma_b, \Gamma_c, \Gamma_d$ are given by [5]

$$\Gamma_a = \frac{1 - jY_t t_t - jY_b t_b}{1 + jY_t t_t + jY_b t_b} \tag{38}$$

$$\Gamma_b = \frac{t_t + jY_t - jY_b t_t t_b}{t_t - jY_t + jY_b t_t t_b} \tag{39}$$

$$\Gamma_c = \frac{t_b - jY_t t_t t_b + jY_b}{t_b + jY_t t_t t_b - jY_b} \tag{40}$$

$$\Gamma_d = \frac{t_t t_b + jY_t t_b + jY_b t_t}{t_t t_b - jY_t t_b - jY_b t_t} \tag{41}$$

where $t_t = \tan \beta_t d_1/2$, $t_b = \tan \beta_d d_2/2$, and Y_t and Y_b are the normalized characteristic admittances of the throughline and the branchlines, respectively. The characteristic admittance of the input line is normalized to 1.

It is immediate to combine Eqs. (38)–(41), thus finding the scattering parameters of the branchline coupler:

$$S_{11} = \frac{1}{4}(\Gamma_a + \Gamma_b + \Gamma_c + \Gamma_d) \tag{42}$$

$$S_{12} = \frac{1}{4}(\Gamma_a - \Gamma_b + \Gamma_c - \Gamma_d) \tag{43}$$

$$S_{13} = \frac{1}{4}(\Gamma_a - \Gamma_b - \Gamma_c + \Gamma_d) \tag{44}$$

$$S_{14} = \frac{1}{4}(\Gamma_a + \Gamma_b - \Gamma_c - \Gamma_d) \tag{45}$$

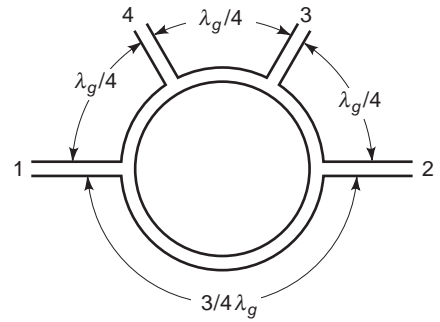


Figure 13. Ring coupler. A wave entering port 1 is split into two waves that recombine in phase at ports 2 and 4. On the other hand, port 3 is isolated, since the waves propagating clockwise and counterclockwise respectively are 180° out of phase. The same reasoning applies to the remaining ports.

If $t_t = t_b = 1$ (i.e., the electrical lengths of the throughline and the branchline are the same) and also $Y_t^2 - Y_b^2 = 1$, the four ports are matched, $S_{14} = 0$, and

$$S_{31} = -\frac{Y_b}{Y_t} \tag{46}$$

$$S_{21} = -j\frac{1}{Y_t} \tag{47}$$

S_{31} and S_{21} are in quadrature, which is predictable because of the symmetry of the coupler. The coupling $C = 20 \log 1/|S_{31}|$ depends on the ratio between the two characteristic impedances. When $Y_t/Y_b = \sqrt{2}$, $C = 3$ dB. In that case a coupler, also having the outputs in quadrature, is commonly called “hybrid.” The preceding characteristics hold exactly only in a narrow interval around of the working frequency. However, it is possible to enlarge considerably the bandwidth of the coupler by cascading sections [14,15].

The principal of operation of the hybrid ring (Fig. 13) is similar to that of the branch coupler. When port 1 is fed, the signal splits equally into two signals traveling clockwise and counterclockwise that recombine at the remaining ports. At ports 2 and 3 the signals sum in phase, while at port 4 they are 180° out of phase and their combination is negligible. Therefore, ports 2 and 3 are coupled while port 4 is isolated. The reasoning can be easily extended to the other ports, thus recovering the characteristic of a DC.

6. DISTRIBUTED COUPLING

In planar structures (e.g., microstrip, stripline, finline, slotline, which are the most common), as well as in TEM lines (e.g., coaxial cables), the coupling is often obtained by placing the two lines parallel and close to each other over a certain length, in such a way that a portion of the field wave traveling along the first guide couples by electromagnetic induction into the second one in contraflow, as schematically sketched in Fig. 14 [16–18]. The coupling depends mainly on the gap separating the two strips: The wider the gap, the weaker the coupling.

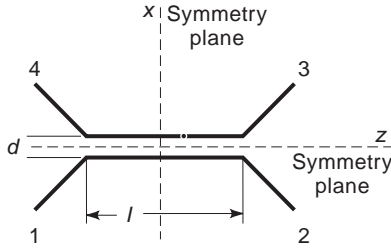


Figure 14. Distributed coupling between strips on the same substrate: A wave traveling on a line couples electromagnetically to the other one. Coupling depends both on the distance between the lines and on their length.

We take as typical the coupler shown in Fig. 14 consisting of two parallel strips of length l placed on a grounded substrate and separated by a distance d . The twofold symmetry of the circuit with respect to the planes $x = 0$ and $z = 0$ enforces the following relationships linking the scattering parameters:

$$s_{11} = s_{22} = s_{33} = s_{44} \quad (48)$$

$$s_{12} = s_{34} \quad (49)$$

$$s_{13} = s_{24} \quad (50)$$

$$s_{14} = s_{23} \quad (51)$$

Hence, the scattering matrix takes the form

$$S = \begin{bmatrix} s_{11} & s_{12} & s_{13} & s_{14} \\ s_{12} & s_{11} & s_{14} & s_{13} \\ s_{12} & s_{14} & s_{11} & s_{14} \\ s_{14} & s_{13} & s_{12} & s_{11} \end{bmatrix} \quad (52)$$

The scattering parameters can be calculated by considering two independent sets of excitations. The first is $a_1 = 1$, $a_2 = 0$, $a_3 = 0$, $a_4 = 1$ and corresponds to a magnetic wall on the symmetry plane $x = 0$. The second is $a_1 = 1$, $a_2 = 0$, $a_3 = 0$, $a_4 = -1$ and corresponds to an electric wall on the same symmetry plane. The reflected waves at ports 1 and 2 are given by

a under the first excitation

$$b_1^e = s_{11} + s_{13} \quad (53)$$

$$b_2^e = s_{12} + s_{14} \quad (54)$$

b under the second excitation

$$b_1^o = s_{11} - s_{13} \quad (55)$$

$$b_2^o = s_{12} - s_{14} \quad (56)$$

It is immediate to calculate the parameters of the four-port:

$$s_{11} = \frac{b_1^e + b_1^o}{2} \quad (57)$$

$$s_{12} = \frac{b_2^e + b_2^o}{2} \quad (58)$$

$$s_{13} = \frac{b_1^e - b_1^o}{2} \quad (59)$$

$$s_{14} = \frac{b_2^e - b_2^o}{2} \quad (60)$$

The preceding two situations can be modeled by two transmission lines having normalized characteristic impedances Z_0^e and Z_0^o and, correspondingly, electrical lengths θ^e and θ^o . Although the physical lengths of the lines are the same, their electrical lengths are different in the non-TEM case, and the propagation constants are different in the two cases. Let us suppose both lines are fed by transmission lines with unit characteristic impedance. The transmission matrices are given by

$$T = \begin{bmatrix} \cos \theta^{e/o} & jZ_0^{e/o} \sin \theta^{e/o} \\ \frac{j}{Z_0^{e/o}} \sin \theta^{e/o} & \cos \theta^{e/o} \end{bmatrix} \quad (61)$$

As observed previously, losslessness implies that the condition under which the device is a directional coupler is $s_{11} = 0 = b_1^e + b_1^o$. Such a condition is satisfied when

$$\frac{\left(Z_0^e - \frac{1}{Z_0^e}\right)j \sin \theta^e}{2 \cos \theta^e + \left(Z_0^e + \frac{1}{Z_0^e}\right)j \sin \theta^e} = \frac{\left(Z_0^o - \frac{1}{Z_0^o}\right)j \sin \theta^o}{2 \cos \theta^o + \left(Z_0^o + \frac{1}{Z_0^o}\right)j \sin \theta^o} \quad (62)$$

An immediate solution is obtained when $\theta^e = \theta^o = \theta$, as occurs when the strips are embedded in a homogeneous medium, and $Z_0^o = 1/Z_0^e$. The more immediate solution is therefore to place over the strip a dielectric layer that has the same permittivity as the substrate. This particular case pertains to TEM couplers. In such a case, the coupling C is given by the formula

$$C = 20 \log \frac{[1 - c^2 \cos^2 \theta]^{1/2}}{c \sin \theta} \quad (63)$$

where $c = Z_0^e - Z_0^o/Z_0^e + Z_0^o$. Since in microstrip technology $c_{\max} \approx \frac{1}{2}$, the maximum coupling achievable by the ordinary photolithographic technique is about 6 dB and occurs when $\theta = \pi/2$. Moreover, its bandwidth is rather narrow and the directivity moderate. Much better performances are obtained by the Lange interdigitated coupler, shown in Fig. 15 [19].

This configuration permits one to achieve 3 dB coupling easily, as well as an octave bandwidth and a good

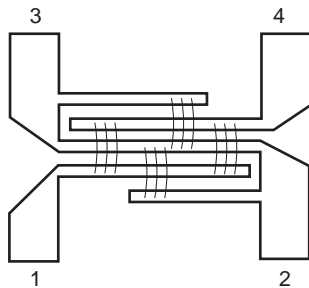


Figure 15. Lange interdigitated coupler. Bond wire connects strips to suppress the propagation of unwanted modes.

directivity. This coupler is, however, difficult to realize and the bond wires are critical at the higher frequencies. Moreover, the higher the frequency, the more difficult it is to equalize the phase velocities of the even and odd modes. Nevertheless, its good electrical characteristics and compactness make the Lange coupler suitable for applications up to 30 GHz with standard technology, but the gallium arsenide (GaAs) monolithic version is used up to 100 GHz. A comprehensive and accurate analysis of the interdigitated coupler is reported in Ref. 20.

The compensation of the different phase velocities over a wide band is one of the more difficult tasks in microstrip couplers. At present, designers often adopt one of the following strategies:

1. Placing two capacitances across the lines at the input and the output
2. Using nonuniform planar transmission lines
3. Shaping the two strips in a serpentine form or in a shark teeth form (wiggly coupler) as shown in Fig. 16
4. Combining the preceding techniques (for instance, by shaping as shark teeth the strips of a nonuniform coupler)

Similar to waveguide couplers, bandwidth and directivity can be much improved by cascading many coupled line sections, as indicated in Fig. 17 [21–23].

A detailed description of planar directional couplers can be found in Ref. 24. Planar couplers are also affected

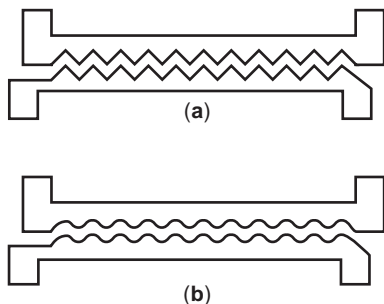


Figure 16. The wiggly and serpentine coupler. These configurations are meant to equalize even the odd phase velocities, in order to optimize the coupler response over a wide band.

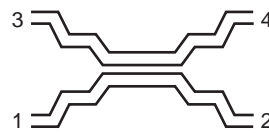


Figure 17. An example of a multisection microstrip coupler.

by high conductor losses. In this regard, the use of superconductor technology is attractive, though unfortunately not mature enough for large-scale production. Microstrip couplers do not achieve performances comparable to the ones realized in waveguide; therefore, they are hardly employed in measurement benches, where high directivity and low losses are required. However, their use in civil telecommunication systems is widespread.

BIBLIOGRAPHY

1. S. B. Cohn and R. Levy, History of microwave passive components with particular attention to directional couplers, *IEEE Trans. Microwave Theory Tech.* **32**:1046, 1054 (1984).
2. R. Collin, *Field Theory of Guided Waves*, 2nd ed., IEEE Press, Piscataway, NJ, 1992.
3. K. Chang, *Handbook of Microwave Components, Microwave Passive Components and Antennas*, Vol. 1, Wiley, New York, 1990.
4. T. S. Laverghetta, *Modern Microwave Measurements and Techniques*, Artech House, Norwood, MA, 1988.
5. R. Collin, *Foundations for Microwave Engineering*, 2nd ed., McGraw-Hill, New York, 1992.
6. H. J. Riblet and T. S. Saad, A new type of waveguide directional coupler, *Proc. IRE* **36**:61–64 (1948).
7. R. Levy, Directional couplers. In *Advances in Microwaves*, Vol. 1, Academic Press, New York, 1966, pp. 115–206.
8. G. L. Matthaei, L. Young, and E. M. T. Jones, *Microwave Filter, Impedance Matching Networks and Coupling Structures*, McGraw-Hill, New York, 1964.
9. H. Bethe, Theory of diffraction by small holes, *Phys. Rev.* **66**:163–182 (1944).
10. R. Levy, Analysis and synthesis of waveguide multi-aperture directional couplers, *IEEE Microwave Theory Tech.* **16**:995–1006 (1968).
11. R. Levy, Improved single and multi-aperture waveguide coupling theory, including explanation of mutual interactions, *IEEE Microwave Theory Tech.* **28**:331–338 (1980).
12. P. Arcioni et al., Wideband modeling of arbitrarily shaped E-plane waveguide components by the boundary integral-resonant mode expansion method, *IEEE Microwave Theory Tech.* **44**:1017–1023 (1996).
13. J. Uher, J. Bornemann, and U. Rosenberg, *Waveguide Components for Antenna Feed Systems: Theory and CAD*, Artech House, Norwood, MA, 1993.
14. R. Levy and L. F. Lind, Synthesis of symmetrical branch guide directional couplers, *IEEE Microwave Theory Tech.* **16**:80–89 (1968).
15. R. Levy, Zolotarev branch guide directional couplers, *IEEE Microwave Theory Tech.* **21**:95–99 (1973).

16. J. A. G. Malherbe, *Microwave Transmission Line Couplers*, Artech House, Norwood, MA, 1988.
17. B. Bhat and S. K. Koul, *Analysis Design and Applications of Fin Lines*, Artech House, Norwood, MA, 1987.
18. K. C. Gupta et al., *Microstrip Lines and Slotlines*, Artech House, Norwood, MA, 1996.
19. J. Lange, Interdigitated stripline quadrature hybrid, *IEEE Trans. Microwave Theory Tech.* **17**:1150–1151 (1969).
20. V. Rizzoli and A. Lippardini, The design of interdigitated couplers for MIC applications, *IEEE Trans. Microwave Theory Tech.*, **26**:7–15, 1978.
21. R. Levy, General synthesis of asymmetrical multi-element coupled-transmission-line directional couplers, *IEEE Microwave Theory Tech.* **11**:226–237 (1963).
22. E. G. Crystal and L. Young, Theory and tables of optimum symmetrical TEM-mode directional couplers, *IEEE Microwave Theory Tech.* **13**:544–558 (1965).
23. P. P. Toullos and A. C. Todd, Synthesis of symmetrical TEM-mode directional couplers, *IEEE Microwave Theory Tech.* **13**:536–543 (1965).
24. S. Uysal, *Nonuniform Line Microstrip Directional Couplers and Filters*, Artech House, Norwood, MA, 1993.

DIRECTIVE ANTENNAS

IGOR ALEXEFF
 MARK RADER
 WENG LOCK KANG
 The University of Tennessee
 Knoxville, Tennessee

Radio antennas that are directive have many advantages over stationary antennas. They can observe in one direction while ignoring much larger signals coming in from the sides. In addition, as transmitting antennas, they can direct a small amount of radiation directly to the proper receiver. Conventional directive antennas use large mirrors for short waves, such as are used in radar. For longer-wave antennas, they use reflector and director elements aligned with the antenna. The basic problem with such arrays is that they are mechanically steered, which is slow and difficult to do with large antennas, especially in the presence of wind, ice, or snow.

One way of having a large steerable antenna with no moving parts is to use a phased array. A phased array is based on Huygen's principle, which states that a wavefront can be determined at a point in time by constructing a surface tangent to a collection of secondary waves. Thus, if one has a large number of small antennas located on a line, and if the antennas are excited in phase, the resultant wavefront is normal to the line. If each small antenna is excited with a small phase shift relative to the next antenna, the wave propagates at an angle to the line. Conversely, if the array is used for reception, the small antenna signals, combined with the individual phase shifts, allow the array to scan in azimuth. The principle can be improved by using a two-dimensional array located on a plane to scan in altitude as well as azimuth. In fact, by properly adjusting the

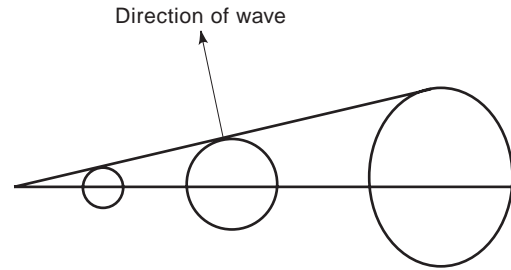


Figure 1. Three sources of waves giving a directed wavefront. The phase of the middle and left sources have been delayed.

phase shifts, such an antenna can be located on a curved surface, such as the nose or wing of an aircraft. The basic principle is shown in Fig. 1. Since the subject of directive antennas is so large, Professor Herb Neff, UTK Emeritus (an antenna specialist), recommends using Refs. 1 and 2 for reference.

Newer antennas being developed include the “agile mirror” [3,4] designed by Dr. Wallace M. Manheimer of the US Naval Research Laboratory. In this concept, a sheet of ionized air or other gas forms a reflecting surface. Since the sheet is not a mechanical body, it can be tilted and re-formed in a very short span of time. Thus, the direction of transmission or reception can be varied extremely rapidly. A magnetic field is used to help direct the sheet electron beam that forms the plasma. A second advantage of such an antenna is that it vanishes when the electrical discharge is terminated. This is a great advantage for stealth technology, because a mechanical antenna presents a large scattering cross section to radar signals near the antenna resonant frequency. One disadvantage of the “agile mirror” is that it must be formed in a gas at reduced pressure.

A second new type of antenna is the “stealth antenna,” which is being developed by the Patriot Scientific Corporation in San Diego, California. The idea, originally developed by Dr. Igor Alexeff at the University of Tennessee [5], uses glow discharge tubes to comprise elements of an antenna. When the tubes are energized, the antenna is a complete conducting structure. When the tubes are deenergized, the antenna becomes either a large number of separate, nonresonant conducting components or just a nonconducting structure of glass tubing. By selectively energizing various tubes, the antenna also can be directed.

BIBLIOGRAPHY

1. C. A. Balanis, *Antenna Theory: Analysis and Design*, Harper & Row, New York, 1982.
2. R. S. Elliott, *Antenna Theory and Design*, Prentice-Hall, Englewood Cliffs, NJ, 1981.
3. J. Matthew et al., *Phys. Rev. Lett.* **77**:1982 (1996).
4. R. A. Meger et al., *Phys. Plasmas* **2**(6):2532 (1995).
5. W. L. Kang, M. Rader, and I. Alexeff, A conceptual study of stealth plasma antenna, *Proc. IEEE Conf. Plasma Science*, Boston, MA, 1996, p. 261.

DISTRIBUTED AMPLIFIERS

T. KORYU ISHII
Marquette University
Milwaukee, Wisconsin

1. DEFINITION AND STRUCTURE

The objective of this article is to present various aspects of distributed amplifiers. Distributed amplifiers are by definition, electronic amplifiers consisting of distributed circuit parameters. However, in practice, amplifier systems that consist of a number of discrete amplifiers associated with distributed parameter circuits are often termed *distributed amplifiers*; this latter amplifier is actually a pseudodistributed amplifier.

In practice, the distributed parameter circuit often takes the form of a transmission line. The circuit parameters, the inductance, the capacitance, and the resistance are distributed throughout the transmission line. If the transmission line is a conventional passive transmission line, the electrical output power of the transmission line is either equal to or less than the electrical input power depending on the power loss of the transmission line.

If the transmission line is active, then the output power is greater than the input. In this case, the transmission line is considered as an amplifier; this is actually a distributed amplifier.

For example, an ordinary optical fiber cable is a passive transmission line for lightwaves. The output light of the optical cable is always less than the input light because of the cable loss. But an erbium-doped optical fiber cable is different. The lightwave output of the cable is greater than the lightwave input. The input lightwaves (which are electromagnetic waves) are amplified. The erbium-doped optical fiber cable is an active transmission line and is one form of distributed amplifier. A schematic diagram of a generic distributed amplifier is shown in Fig. 1a. In this distributed amplifier, the transmission line is continuously loaded by the continuously distributed power-pumping active substrate.

In a pseudodistributed amplifier, a number of discrete amplifiers are periodically loaded as shown in Fig. 1b. The input power is amplified by these discrete amplifiers; therefore the output of the transmission line is greater than the input power.

The objective of the distributed amplifiers is to obtain a high-frequency bandwidth with high-gain amplification. The operating frequency ranges are in RF, microwaves, and lightwaves. Depending on the operating frequency range, the amplifier configurations are markedly different. The transmission line can be a two-wire line, a coaxial ("coax") line, a waveguide, a microstripline, a coplanar waveguide, or an optical fiber cable.

The term "distributed amplifier" contrasts against "discrete amplifier" or "lumped amplifier." A lumped amplifier is represented in a block diagram as shown in Fig. 2. In a lumped or discrete amplifier, where point *A* is the input and point *B* is the output, the geometric distance between

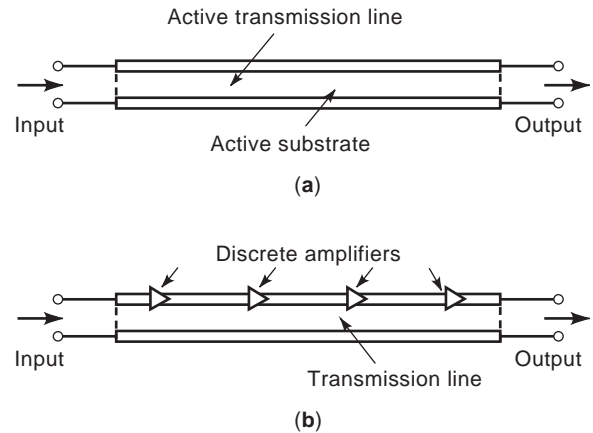


Figure 1. Generic configuration of distributed amplifiers. Signals to be amplified are fed at the left terminal. The signals are amplified during propagation on the line. The amplified signals exit from the right. (a) Distributed amplifier. The amplifier consists of a continuous active transmission line. (b) Pseudodistributed amplifier. Lumped amplifiers are periodically loaded on a passive transmission line.

these two points is negligibly small in comparison with the operating wavelength. A distributed amplifier can also be represented by a block diagram as shown in Fig. 2, but the geometric distance between the actual point *A* and the actual point *B* is comparable to the operating wavelength.

1.1. Continuous Active-Diode Distributed Amplifiers

Activated tunnel diodes, Gunn diodes, and varactor diodes are considered as active diodes. When tunnel diodes and Gunn diodes are properly biased, these diodes exhibit negative resistance. Ordinarily a resistance is positive. A positive resistance consumes electrical energy. A negative resistance generates electrical energy. Therefore, if the amount of negative resistance is adjusted by material composition, configuration, and the bias current and if the circuit impedance of the transmission line is properly adjusted, then the active-diode-loaded transmission line can amplify propagating electromagnetic waves on the transmission line. One possible biasing method is illustrated in Fig. 3a. The transmission line is most likely a microstripline or a coplanar coupled waveguide. The microstripline is DC-biased through a RF choke. If the active substrate is a tunnel diode of long degenerate pn junction, the properly forward-biased pn junction exhibits negative resistance by the tunnel effect [1]. If the active substrate is a long Gunn diode of properly doped n-type GaAs, the substrate exhibits negative resistance by the carrier momentum transfer effect [2].

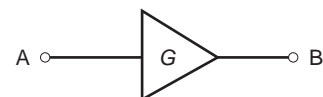
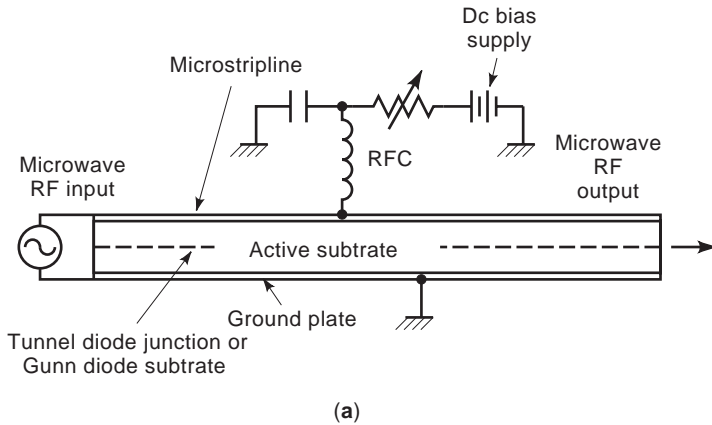
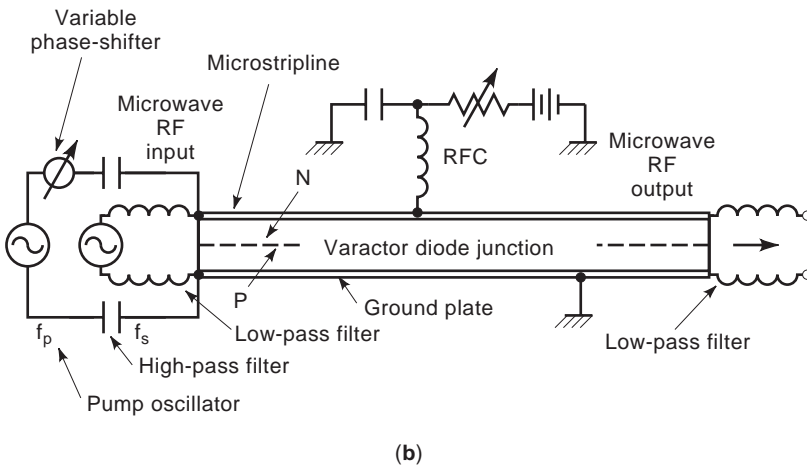


Figure 2. A block diagram representation of a discrete amplifier, a lumped amplifier, or a distributed amplifier. Generic symbols of a generic amplifier: *G* represents the gain of the amplifier (which can be the voltage, current, or power gain); *A* is the input, and *B* is the output terminal.



(a)



(b)

Figure 3. Continuous diode distributed amplifiers. Electromagnetic waves to be amplified are fed from the left end, and amplified signals exit at right. (a) Continuously loaded tunnel diode or Gunn diode transmission-line distributed amplifier. The entire transmission line consists of a long and narrow section of tunnel diode junction or Gunn diode active region. (b) Continuously loaded varactor diode transmission-line parametric distributed amplifier. The entire section of the transmission line consists of a reverse-biased variable capacitance pn junction.

The negative resistance can also be created by a properly biased and pumped long varactor diode junction. The varactor diode is a reverse-biased pn-junction diode. This is a variable-capacitance diode, and the junction capacitance is varied depending on the bias voltage across the diode. The junction capacitance in the case of Fig. 3b is controlled by the DC bias and the pump oscillator voltage launched on the microstripline transmission line. Some varactor diodes work without DC bias. The pump oscillator frequency f_p is approximately twice of the signal frequency f_s for the best results. When the pump oscillator frequency and phase are properly adjusted, the energy of the pump oscillator transfers to the signal through the variable-junction capacitance and the signal waves are amplified as the waves propagate on the microstripline. The amplifier that functions by use of a junction capacitance is termed a *varactor parametric amplifier* [1]. The type of parametric amplifier shown in Fig. 3b is a traveling-wave varactor parametric amplifier. Since the junction capacitance is continuously distributed along the microstripline, this is a distributed amplifier.

1.2. Periodically Loaded Active-Diode Distributed Amplifiers

A schematic diagram of a periodically loaded active-diode microstripline distributed amplifier is shown in Fig. 4a. The active diodes are either discrete tunnel diodes or

Gunn diodes. The periodicity L is usually less than a quarter-wavelength to avoid resonance. When the periodicity is made equal to either a quarter-wavelength or a half-wavelength, the amplifier will be at resonance. In such cases, the frequency bandwidth becomes narrow and it may also become unstable and oscillate; therefore the resonance should be avoided. One objective of the distributed amplifier is to obtain a wide frequency bandwidth; thus it is safe to keep the periodicity L less than a quarter-wavelength. The diodes must be DC-biased properly at the middle of the negative-resistance region.

A schematic diagram of a periodically loaded variable-capacitance diode (varactor diode) parametric distributed amplifier is shown in Fig. 4b. As seen from the diagram, varactor diodes are reverse-biased by the DC bias supply and are pumped by the pump oscillator. The pump frequency f_p is approximately twice of the signal frequency f_s to be amplified. The pump wave on the line must be synchronized with the signal wave. The synchronization is accomplished using a variable phase shifter as shown in the pump oscillator circuit. The pump oscillator power is transferred into the signal through the varactor, and the signal wave is amplified [1,2]. The varactor diodes are pumped so that when and where the signal waves crest the junction, the capacitance becomes minimum. This phasing makes the microwave signal voltage amplified. The transmission line can be a microstripline as shown or

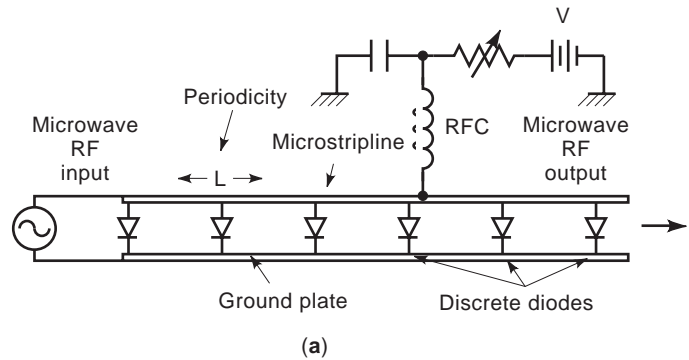
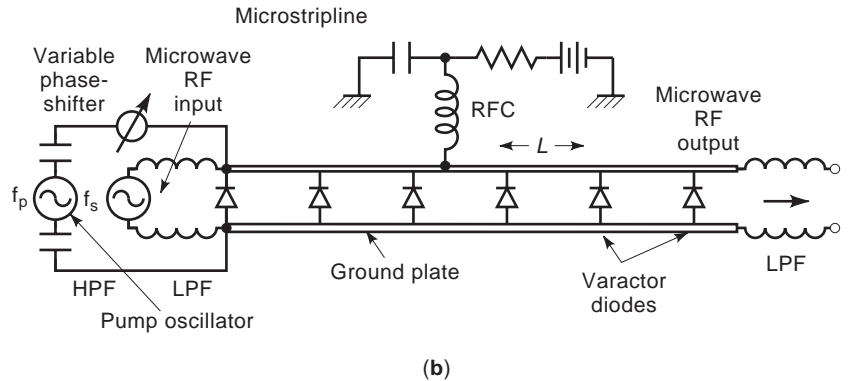


Figure 4. Periodically loaded active-diode distributed amplifiers. (a) Periodically loaded active-diode microstripline distributed amplifier. A microstripline is periodically loaded by active diodes with periodicity L . A properly biased active diode is capable of amplifying electromagnetic signals. (b) Periodically loaded active capacitive parametric distributed amplifier. A microstripline is loaded periodically by properly biased and pumped varactor diodes with periodicity L . Such a varactor diode acts as a lumped amplifier.



a coplanar coupled waveguide. An example of a coplanar coupled waveguide distributed amplifier is sketched in Fig. 5. As seen from this figure, fabrication of a coplanar coupled waveguide amplifier is easier than fabrication of a microstripline amplifier.

1.3. Continuous Transistor Distributed Amplifiers

A schematic diagram of a continuous transistor distributed amplifier is shown in Fig. 6. This is a FET (field-effect transistor) of long configuration. The length of lines must be greater than a wavelength of the operating carrier signals. The microwave input signals are fed into the coplanar coupled waveguide that consists of a gate strip and a source strip. As the input microwaves propagate along

this input gate–source coplanar coupled waveguide, the amplified signal waves appear on the drain–gate coplanar coupled waveguide. Then the amplified microwaves exit at the end of the drain–gate coplanar coupled waveguide. The long transistor must be properly DC-biased as shown in Fig. 6.

1.4. Periodically Loaded Transistor Distributed Amplifiers

A schematic diagram of a periodically loaded transistor distributed amplifier is shown in Fig. 7. To qualify as a distributed amplifier, the length of the coplanar coupled waveguide must be longer than a wavelength of operating microwaves. If the length is very short, this is a simple

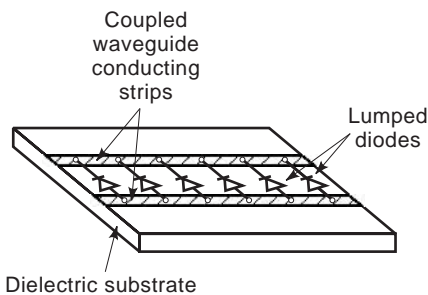


Figure 5. An example of coplanar coupled waveguide distributed amplifier. This is an example of a case in which the transmission line is a coplanar coupled waveguide. Lumped diodes are mounted on it periodically.

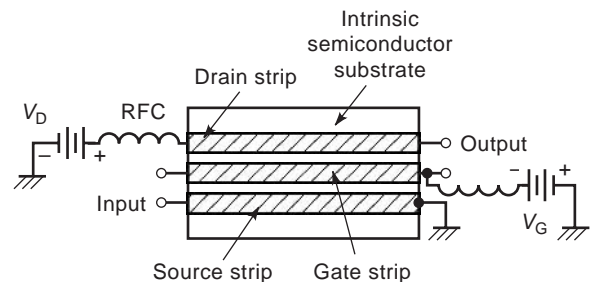


Figure 6. A schematic diagram of a continuous transistor distributed amplifier. This is a case of extremely long gate field-effect transistor. The length of the gate can be several wavelengths longer than the operating wavelength. As the input signals propagate on the gate–source line, the amplified output signals travel on the drain–gate line. The amplified signals exit at the right.

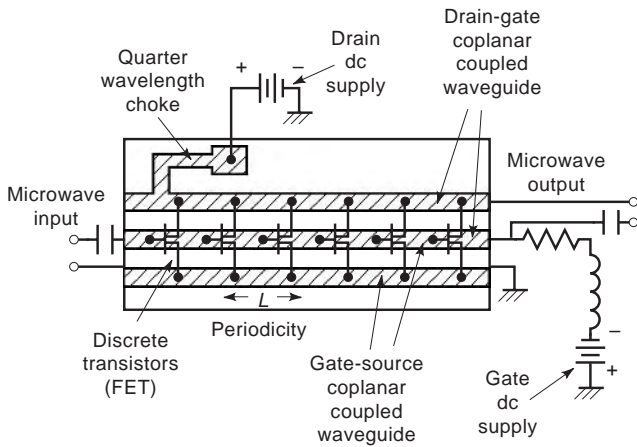


Figure 7. A schematic diagram of a periodically loaded transistor distributed amplifier. Discrete transistors are periodically loaded on a coplanar coupled waveguide. The input signals fed on the gate-source coplanar waveguide are amplified as the signals propagate on the line. The amplified output appears on the drain-gate coplanar coupled waveguide. The output propagates on the line and exit from the right.

parallel operation of the transistors. The input microwave signals are fed to the input of the gate-source coplanar coupled waveguide as shown in Fig. 7. As microwaves propagate down the gate-source waveguide, the amplified microwaves appear on the drain-gate coplanar coupled waveguide. The amplified microwaves propagate toward the output and exit from there. The coplanar coupled waveguides are periodically loaded by discrete FETs. The periodicity L must be less than a quarter-wavelength to avoid resonance. Otherwise, $n(\lambda_l/2) < L < (2n + 1)(\lambda_l/4)$, where λ_l is the transmission line wavelength and $n = 0, 1, 2, 3, \dots$

1.5. Thermionic Traveling-Wave Distributed Amplifiers

A thermionic traveling-wave amplifier is a vacuum tube [2]. Electrons are emitted from an electron gun into a vac-

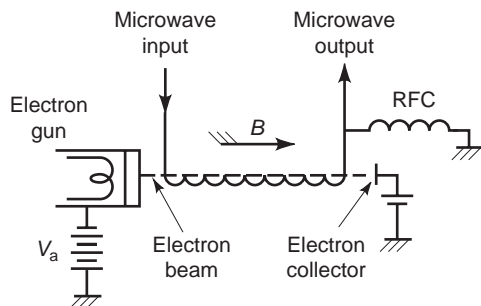


Figure 8. A schematic diagram of a thermionic traveling-wave distributed amplifier. The pitch of the helical transmission line is adjusted so that the axial speed of microwave propagation on the line is almost equal to the speed of electrons in the electron beam. Under this condition, The kinetic energy of electrons is transferred into the traveling microwaves on the line, and the propagating microwaves are amplified.

uum as shown in Fig. 8. The emitted electrons are pulled by the anode, which is a helical transmission line focused by the longitudinally applied DC magnetic flux B . The electron beam is shot through the helix line and hits at an endplate termed the *electron collector*. The electron collector collects used (“spent”) electrons. The helix transmission line is a distributed parameter transmission line. The pitch angle of the helix transmission line, the diameter of the helix, and the electron acceleration voltage are adjusted in such a way that the speed of the electron beam is equal to the axial propagation speed of microwaves on the helical line. Then the kinetic energy of the electron beam is transferred to the microwave energy on the helical line through the distributed capacitance between the electron beam and the helical line. As the microwaves on the line and the electrons in the beam travel together, the microwaves are amplified and exit from the output of the tube as shown in Fig. 8 [2]. The helical transmission line is replaced by a meander line or an interdigital transmission line (2).

1.6. Fiberoptic Distributed Amplifiers

A schematic diagram of a fiberoptic distributed amplifier is shown in Fig. 9. The main part of this amplifier is a section of erbium-doped optical glass fiber cable [3]. As seen from this figure, if a lightwave of proper wavelength is pumped into the fiber cable through a directional coupler from a pump laser, and the lightwave signal to be amplified is fed into the input of the fiber cable thorough an isolator, then, while the signal lightwave is propagating in the fiber cable, the signal lightwave is intensified by the emission of radiation from the erbium atoms that are pumped by the lightwave that is propagating in the fiber cable from the pump laser. The pump lightwave travels with the signal lightwave and pumps energy into the signal lightwaves through the stimulated emission of radiation from erbium atoms. The particular optical fiber is considered to be a distributed parameter transmission-line amplifier for propagating optical electromagnetic wave signals.

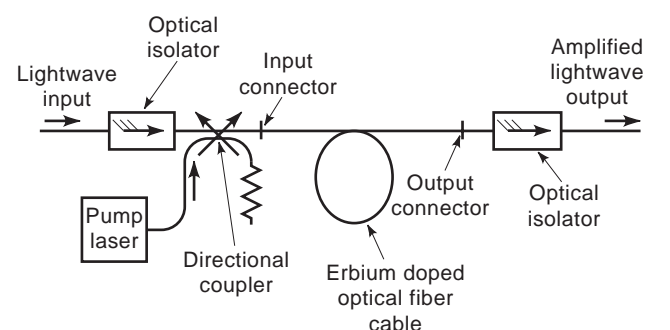


Figure 9. A schematic diagram of a fiber cable lightwave distributed amplifier. The active part is a long section of erbium-doped fiber cable. The erbium atoms are pumped by a light from the pump laser at left. The input lightwave signals are amplified by the stimulated emission of radiation from the pumped erbium atoms in the active fiber cable.

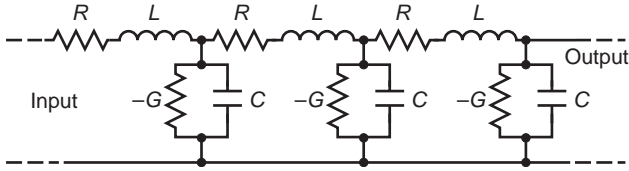


Figure 10. An equivalent circuit of a generic distributed amplifier. The negative conductance $-G$ generates energy and amplifies signals that are traveling on this line.

2. GENERAL GOVERNING EQUATIONS

2.1. Gain

A generic configuration of a distributed amplifier transmission circuit is shown in Fig. 10. In this diagram, R is

$$G(f) = \alpha(f)l$$

$$= \frac{(2\pi f)(C(f)R(f) - L(f)G(f))l}{\sqrt{2} \left\{ ((2\pi f)^2 L(f)C(f) + R(f)G(f)) + \sqrt{(2\pi f)^2 (C(f)R(f) - L(f)G(f))^2 + (R(f)G(f) + (2\pi f)^2 L(f)C(f))^2} \right\}^{1/2}} \tag{5}$$

the series resistance per meter of the distributed amplifier, L is the series inductance per meter of the distributed amplifier, $-G$ is the negative conductance per meter of the distributed amplifier, and C is the capacitance per meter of the distributed amplifier. The amplification constant of this amplifier is [1]

$$\alpha = \frac{\omega(CR - LG)}{\sqrt{2} \left\{ (\omega^2 LC + RG) + \sqrt{\omega^2 (CR - LG)^2 + (RG + \omega^2 LC)^2} \right\}^{1/2}} \tag{1}$$

[nepers (napiers)/meter (Np/m)]

where G is the magnitude of the negative conductance parameter. In a distributed amplifier, if the propagating power increase per meter is ΔP (W/m) and the propagating voltage increase parameter is ΔV (V/m), the magnitude of the negative conductance per meter is $G = 2\Delta P/(\Delta V)^2$ (S/m).

The phase constant of this amplifier is [1]

$$\beta = \frac{\left\{ (\omega^2 LC + RG) + \sqrt{\omega^2 (CR - LG)^2 + (\omega^2 LC + RG)^2} \right\}^{1/2}}{\sqrt{2}} \tag{2}$$

If the length of the active region of the amplifier is l meters long, then the voltage gain of the amplifier

is

$$A = \alpha l \text{ (Np)} \tag{3}$$

The total phase shift across the active region of the amplifier is

$$\Delta l = \beta l \text{ [radians (rad)]} \tag{4}$$

2.2. Frequency Bandwidth

In a generic distributed amplifier, the circuit parameters R , L , C , and G are functions of operating frequency f . Therefore, the gain of the amplifier is

At the edge of the frequency bandwidth at a frequency f'

$$G(f') = \frac{1}{\sqrt{2}} G(f_0) \tag{6}$$

where f_0 is the center frequency of the amplifier. Usually Eq. (6) is at least the second-order equation of f' . One root is f'_H , which is greater than f_0 and the other is f'_L , which is less than f_0 . Then the frequency bandwidth is

$$\Delta f = f'_H - f'_L \tag{7}$$

2.3. Sensitivity

According to the *IEEE Standard Dictionary* [4], sensitivity is defined as “the minimum input signal required to produce a specified output signal having a specified signal to noise ratio.” This means that

$$\frac{P_s A}{KTBAF} = \frac{S_0}{N_0} \tag{8}$$

where A is the power gain of an amplifier, K is the Boltzmann constant (1.38054×10^{-23} J/K), T is the absolute temperature of the input circuit to the amplifier, B is the overall frequency bandwidth of the amplifier, P_s is the input signal power, F is the noise figure of the amplifier, and S_0/N_0 is the signal-to-noise power ratio of the amplifier at

the output. Then

$$P_s = KTBF \frac{S_0}{N_0} \quad (9)$$

As “a specified signal to noise ratio,” often

$$\frac{S_0}{N_0} = 1 \quad (10)$$

is used for the definition of the sensitivity of the amplifier. Then, the sensitivity is

$$P_s |_{S_0/N_0=1} = KTBF \quad (11)$$

For a distributed amplifier, the value of B is obtained using Eq. (7). The value of the noise figure F can be obtained from the next section. Then the sensitivity is

$$P_s |_{S_0/N_0=1} = \frac{N_0}{A} \quad (12)$$

where A is given by

$$A = e^{2\alpha l} \quad (13)$$

where αl is given by Eq. (5).

2.4. Noise Figure

The noise figure F of an amplifier is given by [1]

$$F = \frac{N_0}{KTBA} \quad (14)$$

where N_0 is the noise output of the amplifier (W). For a distributed amplifier, both the frequency bandwidth B and the power amplification A are given by Eqs. (7) and (5), respectively.

2.5. Dynamic Range

A range of input signal level in which the gain of the amplifier is constant is termed the *dynamic range* of the amplifier. Usually, the gain of an amplifier is less at an extremely small input signal level or at a large input signal level.

In the semiconductor distributed amplifiers, thermionic distributed amplifiers or even in fiberoptic distributed amplifiers, the values of L , C , R , and G are inherent functions of operating signal levels V_s . (Therefore, in Eq. (1)

If the gain constant in the linear region of the distributed amplifier is α_0 , then the power gain of the amplifier is

$$A_0 = e^{2\alpha_0 l} \quad (16)$$

where l is the length of the active region of the distributed amplifier. In a large-signal level V_s , the gain will be compressed by saturation and

$$A(v_s) = e^{2\alpha(v_s)l} \quad (17)$$

where $\alpha(V_s)$ is as given in Eq. (15).

If the gain compression of $-n$ dB is chosen, then

$$-n \text{ (dB)} = 10 \log_{10} \frac{A(v_s)}{A_0} \quad (18)$$

or

$$n \text{ (dB)} = 10 \log_{10} e^{2[\alpha_0 - \alpha(v_s)]l} \quad (19)$$

or

$$n \text{ (dB)} = 8.686\{\alpha_0 - \alpha(v_s)\}l \quad (20)$$

In practice, $n = 1$ is often chosen, and the value of the input voltage for $n = 1$ is termed the *input signal voltage* at 1 dB compression point. The 1 dB compression point input signal voltage is then

$$\alpha(v_s) = \alpha_0 - \frac{1}{8.686l} \quad (21)$$

2.6. Stability

As seen from Eq. (1), a generic distributed amplifier is inherently stable. A controlling parameter in Eq. (1) is the magnitude of the negative conductance per meter G . Equation (1) does not show any singularity due to the size of G within the range of practical operation.

3. PERIODICALLY LOADED ACTIVE-DIODE DISTRIBUTED AMPLIFIERS

3.1. Periodically Loaded Tunnel Diode Distributed Amplifiers

In a periodically loaded tunnel diode disturbed amplifier, a number of discrete tunnel diodes are periodically loaded on a RF transmission line as shown in Fig. 4a. A generic volt-

$$\alpha(v_s) = \frac{\omega(C(v_s)R(v_s) - L(v_s)G(v_s))}{\sqrt{2} \left\{ (\omega^2 L(v_s)C(v_s) + R(v_s)G(v_s)) + \sqrt{\omega^2(C(v_s)R(v_s) - L(v_s)G(v_s))^2 + (R(v_s)G(v_s) + \omega^2 L(v_s)C(v_s))^2} \right\}^{1/2}} \quad (15)$$

ampere curve of a tunnel diode is shown in Fig. 11. This is a plot of the diode current and the voltage across the diode. When the diode is biased in a negative-conductance region, the amount of the negative conductance is given by

$$G = \frac{\partial I}{\partial V} < 0 \tag{22}$$

An equivalent circuit of a discrete tunnel diode is shown in Fig. 12, where L is the lead inductance, R_s is the spreading resistance, C_j is the junction capacitance, C_p is the package capacitance, and $-G$ is the negative conductance of the tunnel junction created by the tunnel effect. With the help of additional impedance matching components, it is possible to tune out the inductances and capacitances, and under a matched and tuned condition, the tunnel diode can be represented by a negative conductance of magnitude G_D .

The RF power gain due to a discrete negative conductance G_D that is matched to a characteristic impedance of the transmission line Z_0 is [3]

$$A = \frac{1}{1 - G_D Z_0} \tag{23}$$

At any diode in Fig. 4a, half of the amplified power goes back to the input and only another half of the power amplified continues to travel toward the output. So, the actual power gain of traveling waves toward the output is

$$A^+ = \frac{1}{2(1 - G_D Z_0)} \tag{24}$$

If N diodes are used in a distributed amplifier as shown in Fig. 4a, after matching and tuning, the total power gain of the amplifier is

$$A_T = (A^+)^N = \frac{1}{2^N(1 - G_D Z_0)^N} \tag{25}$$

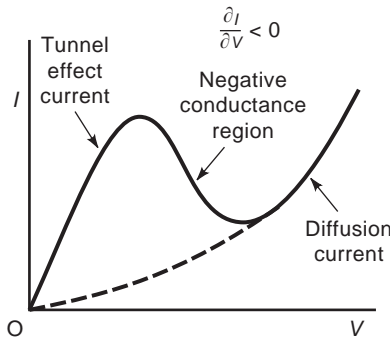


Figure 11. Generic voltampere (V - A) curve of a tunnel diode. Note that the V - A curve does not follow Ohm's Law. Note also the negative differential conductance at the midvoltage region. This is a plot of the diode current versus the diode bias voltage.

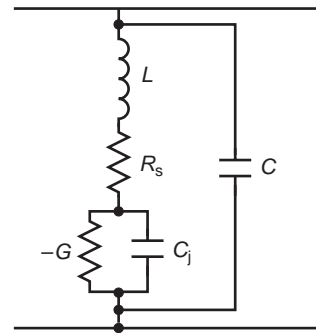


Figure 12. Equivalent circuit of a tunnel diode for a packaged diode that is properly biased. *Key:* C is the package capacitance, C_j is the junction capacitance; R_s is the spreading resistance, L is the lead inductance, and $-G$ is the negative conductance of the packaged tunnel diode.

For the impedance matching and tuning, in addition to attaching the impedance-matching circuit components to the diode mount, the adjustment of periodicity together with the diode biasing must be done properly.

3.2. Periodically Loaded Gunn Diode Distributed Amplifiers

A voltampere characteristic of a generic Gunn diode is in a similar shape as shown in Fig. 11, except that the negative conductance is smaller than that of a tunnel diode. The negative conductance of Gunn diode is created by the transfer of the electronic momentum between a high-electric-field domain and a low-field domain in the bulk of a semiconductor diode. The equivalent circuit of a Gunn diode is similar to the circuit shown in Fig. 12. Therefore the principle of periodically loaded Gunn diode distributed amplifiers is similar to the principle of periodically loaded tunnel diode distributed amplifiers. Then the power gain equation of a Gunn diode distributed amplifier consists of N Gunn diodes in the negative conductance G_D with the characteristics impedance Z_0 is

$$A_T = \frac{1}{2^N(1 - G_D Z_0)^N} \tag{26}$$

3.3. Periodically Loaded Varactor Diode Distributed Parametric Amplifiers

When discrete variable capacitance diodes (varactor diodes) are periodically mounted on a transmission line as shown in Fig. 4b, RF voltage is amplified by the parametric effect of the junction capacitance. The voltage gain across a single parametric capacitance diode is given by [5]

$$A = \frac{v_p \sqrt{Q_i}}{4(V_0 + V_{r0})} + \sqrt{Q_s} \tag{27}$$

where v_p is the pump voltage across the junction capacitance of the varactor diode, V_0 is the magnitude of the contact potential barrier of the diode, V_{r0} is the DC reverse bias voltage, and Q_i and Q_s are the quality factors of the idler circuit and the signal circuit per diode, respectively.

In a parametric amplifier, the idler frequency in Fig. 4b is usually

$$f_i = f_p - f_s \quad (28)$$

and

$$f_p \simeq 2f_s \quad (29)$$

for a high gain [5]. So

$$Q_i \simeq Q_s \quad (30)$$

Applying the same concept expressed in Eqs. (25) and (26), the total voltage gain of N -diode distributed parametric amplifier is, after matching and tuning

$$A_{vT} = \left\{ \frac{v_p \sqrt{Q_i}}{4(V_0 + V_{r0})} + \sqrt{Q_s} \right\}^N \quad (31)$$

4. PERIODICALLY LOADED TRANSISTOR DISTRIBUTED AMPLIFIERS

Similar concepts of Eqs. (25), (26), and (31) are applicable to a periodically loaded discrete-transistor amplifier. The transistors can be either junction transistors or field-effect transistors. If the s parameter of the discrete transistor from the gate (or base) to the drain (or collector) is S_{21} , then, after impedance matching and tuning, the voltage gain of N -transistor distributed amplifier is given by

$$A_{vT} = S_{21}^N \quad (32)$$

5. THERMIONIC DISTRIBUTED AMPLIFIERS

Thermionic distributed amplifiers are vacuum tubes referred to as *traveling-wave tubes* (TWTs). A schematic diagram of a generic TWT is shown in Fig. 8, and the principle of the TWT distributed amplifier was briefly explained earlier in this article. While microwaves travel along the helical transmission line with the axial propagation speed approximately equal to the speed of electron beam, the kinetic energy of the electron beam is gradually transferred to the propagating microwaves in the transmission circuit and hence the microwaves are amplified. The propagation constant of a TWT is given by [1,2]

$$\dot{\gamma} = \beta_e \left[-\frac{\sqrt{3}}{2} C + j \left(1 + \frac{C}{2} \right) \right] (m^{-1}) \quad (33)$$

where β_e is the phase constant associated with the DC electron beam and

$$\beta_e \equiv \frac{\omega}{u_0} \quad (34)$$

where ω is the operating angular frequency and u_0 is the speed of the electrons in the beam. C in Eq. (33) is termed the *gain parameter* [1,2] and is given by

$$C^3 = \frac{Z_0 I_a}{4V_a} \quad (35)$$

where Z_0 is the characteristic impedance of the helical line, I_a is the DC electron-beam current, and V_a is the acceleration anode voltage of the traveling-wave tube.

If the length of the active interaction region on the helical transmission line is l meters long, then the voltage gain of this TWT is [2]

$$A = e^{(\sqrt{3}/2)C\beta_e l} \quad (36)$$

6. QUANTUM ELECTRONIC DISTRIBUTED AMPLIFIERS

A quantum electronic distributed amplifier can be a continuous configuration as shown in Fig. 9. If the signal to be amplified is a lightwave, then this distributed amplifier is a traveling-wave laser. If the signal to be amplified is a microwave, then this distributed amplifier is a traveling-wave maser. For a traveling-wave maser, instead of the optical fiber cable, a microwave transmission line that is continuously loaded with maser material such as a ruby or a rutile crystal, and instead of the pump laser, a microwave local pump oscillator is used.

At any rate, the gain constant of a traveling-wave maser or laser distributed amplifier is given by [6]

$$\alpha = \frac{\omega}{2Q_{m0}v_g} \quad (37)$$

where ω is the angular frequency of the signal to be amplified, Q_{m0} is the quality factor/meter of the active cable, and v_g is the group velocity of the signal in the cable. The quality factor Q_{m0} is given by

$$Q_{m0} = \omega \frac{W_{s0}}{\Delta P} \quad (38)$$

where W_{s0} is the electromagnetic energy of the signal stored per meter of the cable and ΔP is the signal power loss per meter of the cable.

The voltage gain of this continuously loaded distributed laser or maser amplifier is

$$A = e^{\omega l / (2Q_{m0}v_g)} \quad (39)$$

where l is the length of active part of the cable.

A quantum electronic distributed amplifier can be a periodical loading configuration as shown in Fig. 13. A

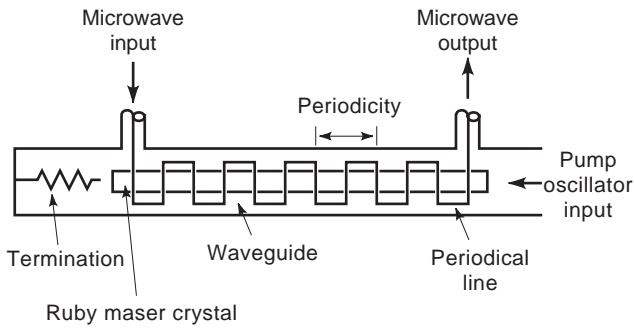


Figure 13. A schematic diagram of a periodically loaded quantum electronic maser distributed amplifier. The ruby maser crystal is pumped by the pump oscillator input in the waveguide. Microwave input signals are amplified by the stimulated emission of radiation from the pumped maser crystal, while propagating down the meander line. The meander line is structured to lengthen the interaction time between the input signals and the stimulated emission of radiation.

microwave transmission line of a periodical structure is continuously loaded with an activated maser crystal and placed in a rectangular microwave waveguide. The pump power from a pump oscillator is fed to the rectangular waveguide to activate the maser crystal. The pumped-up maser crystal emits radiation when stimulated by the input microwave signals.

In a manner similar to the case of continuously loaded quantum electronic distributed amplifier, the voltage gain of the periodically loaded quantum electronic distributed amplifier is given by

$$A = e^{(\omega l / 2Q_{mp} v_g)} \tag{40}$$

where Q_{mp} is the quality factor within the periodicity of the periodical structure. Then

$$Q_{mp} = \omega \frac{W_{sp}}{\Delta P} \tag{41}$$

where W_{sp} is the signal energy stored within the periodicity of the structure of the transmission line and ΔP is the signal power loss within the periodicity.

7. EXAMPLES OF DISTRIBUTED AMPLIFIERS

7.1. RF Distributed Amplifiers

In practice, at RF < 300 MHz, a distributed amplifier can be built using discrete components or surface-mountable discrete components. An example of such distributed amplifiers is shown schematically in Fig. 14 [3,6,20,23,24]

Discrete FETs are sequentially excited through the gate delay line or the gate artificial transmission line consisting of $C_g, \frac{1}{2}L_g, L_g, L_{gg},$ and R_g . These are discrete components. C_g is a DC blocking input coupling capacitor, L_g is an inductor to produce the desired phase delay between stages of the FET amplifiers, and R_g is the matched terminating resistor for the artificial transmission line. The idea is to generate RF traveling waves on the gate artificial transmission line. L_{gg} is a stray inductance of the gate lead. In most cases L_{gg} is negligibly small at most RF frequencies. R_s and C_s are the source bias resistor and bypass capacitor, respectively. L_{dd} is the stray inductance of the drain of the FET. By making the drain lead as short as possible, it is possible to make L_{dd} negligibly small at RF frequencies.

The drain delay line or the drain artificial transmission line is formed by $R_d, L_d,$ and C_d . R_d is an impedance-matched resistor to the drain artificial transmission line,

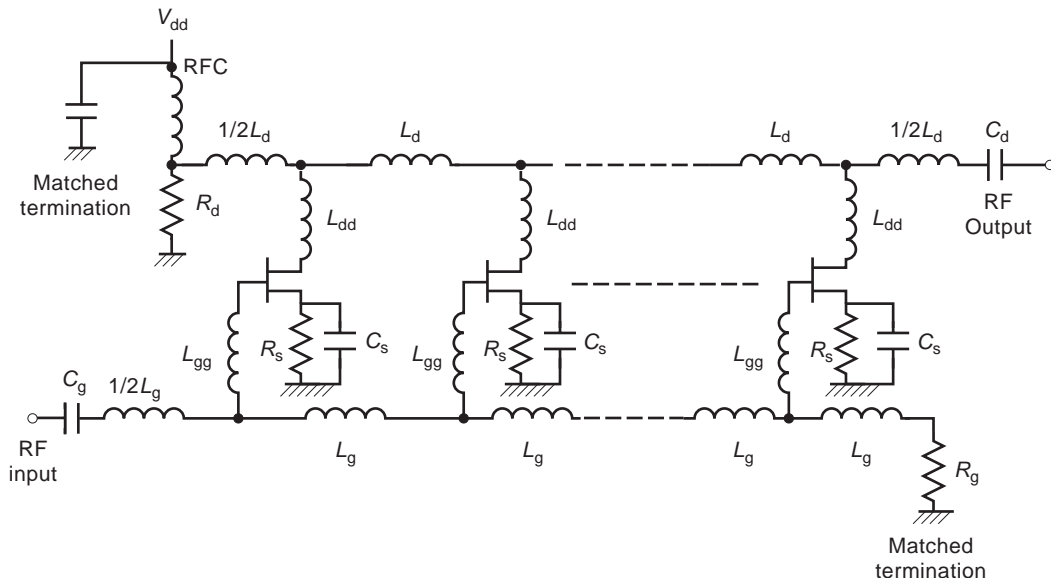


Figure 14. A schematic diagram of an example of an RF distributed amplifier. The input signals are successively and sequentially amplified by properly phased multistage FET amplifiers.

and L_d is the phase-delaying inductor between stages. The value of L_d must be determined so that the phase of waves on the drain artificial transmission line synchronize with the phase of waves on the gate artificial transmission line. C_d is a DC blocking RF coupling capacitor to the output load. The transistors are biased through a RF choke coil and a decoupling capacitor.

7.2. Microwave Distributed Amplifiers

Various types of distributed amplifiers in microwave frequency have been built in the past [7–9]. In microwave frequencies, the distributed amplifiers take forms of monolithically developed integrated circuits as shown in Fig. 15 as an example. As is the case in Fig. 14, the microwave input signals to be amplified are fed to the gate microstripline with impedance-matched terminating resistance R_g through a DC blocking coupling capacitor C_{cg} . The gate of each FET that is properly biased is sequentially excited. Amplified microwave drain current propagates along the drain microstripline toward the output and is coupled out to the output circuit through a DC blocking coupling capacitor C_{dd} . The drain microstripline is terminated with an impedance-matched resistor R_d . The drain microstripline is biased through a RF choke coil and a bypass capacitor with V_{DD} .

Most microwave monolithic integrated-circuit (MMIC) distributed amplifiers have extremely wide frequency bands even though the total gain is not so high. They are extremely compact. For example, Kimura and Imai [11] monolithically integrated a seven stage distributed amplifier on a 1.5×2.5 -mm IC substrate and reported a flat gain of 9 dB over the frequency range 0–55 GHz with a 6 dB noise figure. Further examples can be found in the literature [11–19,25–27].

7.3. Lightwave Distributed Amplifiers

Actual configuration of a lightwave distributed amplifier is shown in Fig. 9. These amplifiers are actually deployed to boost lightwave signals for a long-haul lightwave signal transmission such as transoceanic lightwave cables. For example [3], the lightwave input signal to be amplified has a wavelength of 1500 nm. The pump laser is a 980-nm

solid-state laser diode that feeds the pump power through a directional coupler to the main cable. The directional coupler is a pair of lightwave waveguides placed in proximity to each other so that the lightwaves can couple with one waveguide to another. The end of the lightwave guide for the pump laser that is the primary waveguide of the directional coupler is reflectionlessly terminated using a lightwave-absorbing component. The pump laser light is fed into the main lightwave waveguide, which is an erbium-doped optical fiber. The pump laser light excites or “pumps up” the atoms of erbium to prepare for emission of radiation at 1500 nm. When these pumped-up erbium atoms receive stimulating radiation at 1500 nm by the input lightwaves, they emit radiation at the same wavelength 1500 nm. This is a laser amplifier. The emission of radiation continues as the input lightwave travels in the erbium-doped optical fiber. The emitted wave travels together with the stimulating lightwave. The amplified lightwave exits from the output connector. The lightwave gain of 15 dB is reported for several-meters-long erbium-doped plastic optical fiber cable.

The amplifier cable can be a praseodymium-doped fluoride fiberglass cable for a wavelength of 1300 nm [3]. A gain of 40 dB for several-meters-long cable has been reported [3].

8. CONTINUOUS DISTRIBUTED AMPLIFIERS

8.1. Continuous Active-Diode Distributed Amplifiers

In Fig. 5, by removing all discrete diodes and using an intrinsic semiconductor substrate instead of the dielectric substrate, it is possible to monolithically develop a continuous tunnel diode junction or Gunn effect diode contact between the two strips of metallization. Then, if the conducting strips form a coplanar waveguide that is properly biased at the negative resistance of the diode, the microwaves fed into one end of the coplanar waveguide will be amplified by the distributed negative resistance as it travels along the coplanar waveguide, and the amplified microwave will exit from the other end of the coplanar waveguide.

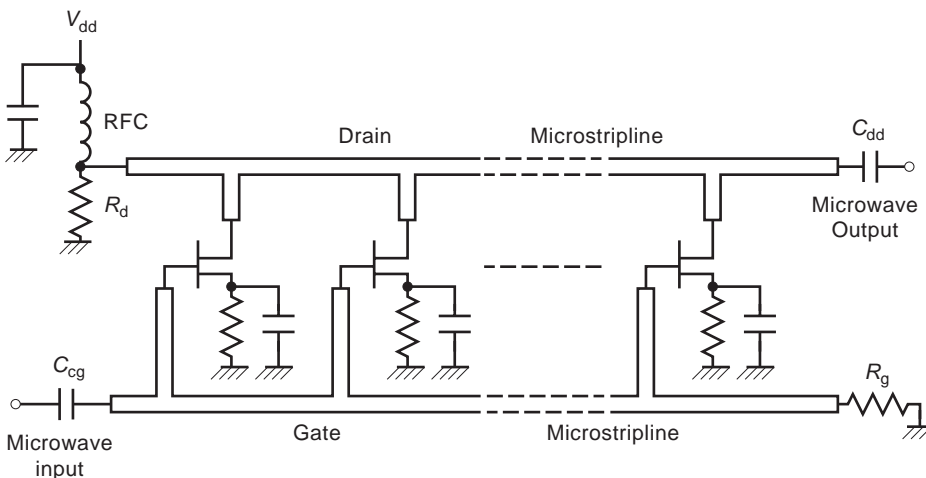


Figure 15. A schematic diagram of a microwave monolithic distributed amplifier. Both the gate and drain lines are microstriplines. The gate line feeds the FET sequentially. On the drain microstripline, the amplified signals are sequentially combined and propagate out at right.

8.2. Continuous Transistor Distributed Amplifiers

A conceptual diagram of a continuous transistor distributed amplifier is shown in Fig. 6. The length of the microstrips must exceed several wavelengths of the transmission-line wavelength. The transmission-line wavelength on the coplanar waveguide is smaller than the free-space wavelength and is inversely proportional to the square root of the effective relative permittivity of the substrate in the gap between the conducting strips. For a semiconductor substrate, it is not uncommon for the effective relative permittivity to be 10 or higher.

8.3. Continuous Parametric Varactor Diode Distributed Amplifier

A conceptual schematic diagram of a continuous parametric varactor diode distributed amplifier is shown in Fig. 3b. Here, the concept is the same and as that for an MMIC amplifier, but an alternate method and a more convenient approach to MMIC technology is shown. Instead of using the microstripline as shown in Fig. 3b, the configuration is changed to a coplanar waveguide as shown in Fig. 5. A long junction varactor diode is monolithically developed flatly between the gap of long parallel metallization strips of a coplanar waveguide.

8.4. Continuous Ferrimagnetic Distributed Amplifiers

The space between the long gap of metallization strips of either the microstripline as shown in Fig. 3b or the coplanar waveguide as shown in Fig. 5 can be filled with a magnetized ferrimagnetic material or a ferrite. This constitutes a ferrimagnetic continuous distributed amplifier [1,10]. The nonlinear magnetism of a ferrite renders the system as a variable-inductance parametric amplifier when both the pump oscillator power and the signal power are launched into a same transmission line; then the pump oscillator power gradually transfers into the signals through the distributed nonlinear inductance of the ferrites as both signals and the pump oscillator power travel together along the ferrite-loaded transmission line.

9. TRENDS OF DISTRIBUTED AMPLIFIER TECHNOLOGY

One of the most common concepts of a distributed amplifier consists in a number of amplifier units distributed along a transmission line [6,7,16,20–22]. An alternate approach to obtain the wide frequency bandwidth and higher gain is to use the concept of matrix amplifiers [27]. A generic concept of a matrix amplifier is illustrated in Fig. 16. As seen from this figure, a matrix amplifier consists of several tiers of distributed amplifiers. Each tier is connected by bleeder lines. The bleeder lines connect the

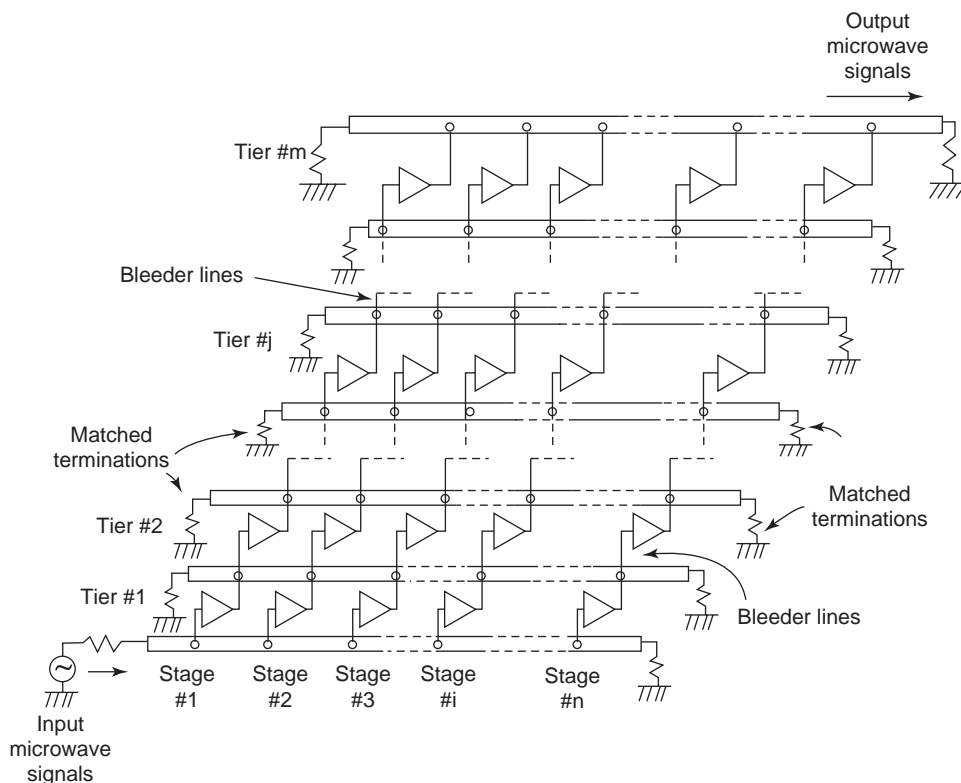


Figure 16. A schematic diagram of a generic n -stage \times m -tier matrix distributed amplifier. Types of stage amplifiers in each tier are not necessarily identical. This feature gives flexibility in design to meet given requirements on amplifier performance. The RF or microwave input signals to be amplified are fed at the lower left corner of this diagram. The amplified output is taken out at the upper right corner of this diagram.

output points of each (amplification) stage of a distributed amplifier and the input points of each stages of the next tier distributed amplifier. Thus, when the signal travels down the first tier of the distributed amplifier, each stage of the amplifiers of the second tier are successively excited. This process is repeated until the output signal reaches the output point of the final stage of the amplifier unit in the final tier. In a matrix amplifier, a part of the signal travels in a longitudinal direction along the direction of the transmission line of each distributed amplifier. The remainder of the signal travels in a transverse direction along the amplifier tiers through bleeder lines.

In a matrix amplifier, the amplifiers in each tier need not be identical in type. This feature gives design flexibility for the required performance of an amplifier.

Another, unorthodox, type of distributed amplifier is the transversely distributed amplifier. In a transversely distributed amplifier a number of amplifier units are distributed on a screen that is oriented in transversely to the direction of the incoming microwave propagation. Incoming microwave signals are amplified by the amplifier units distributed throughout the screen and reradiated from the other side of the screen. This structure may be considered simply as an array of amplifiers rather than a distributed amplifier. But the spacing among amplifier units is comparable in distance to the operating wavelengths for proper phasing. Therefore, the transversely distributed amplifiers are distributed amplifiers of a special kind.

A schematic diagram of a generic transversely distributed amplifier is shown in Fig. 17. Incoming microwave or

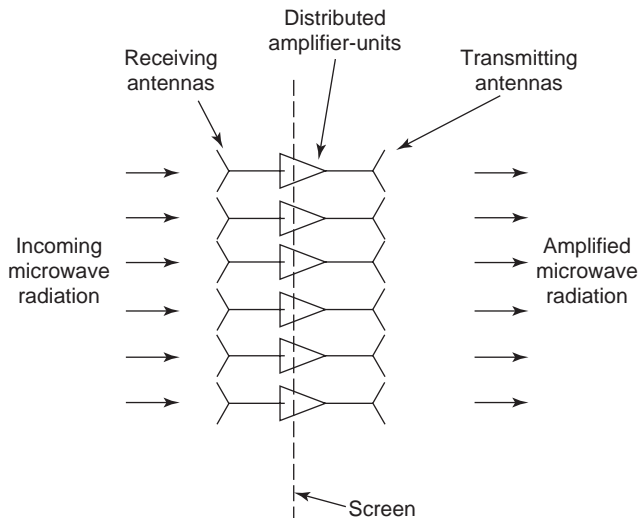


Figure 17. A schematic diagram of a generic transversely distributed amplifier. A number of amplifier units are distributed on a transversely extended screen against incident microwave radiation. Incident microwave radiation is received by receiving antennas and amplified by the amplifier units. The amplified microwaves are reradiated from the transmitter antennas toward the other side or the same side of the screen in a desired direction. The frequency of the output may be identical to the frequency of the input signals. The output frequency may be different from the input by mixing or regeneration.

RF signals are amplified by a properly distributed amplifier on a screen and reradiated to space in the other side of the screen in the required direction [28–30]. Usually the transversely distributed amplifier is placed at a midpoint in a microwave transmission beam between the transmitter and the receiver for the microwave signal booster [28], with microwave signal booster and microwave beam steering [29], or in accordance with microwave distribution analysis within the beam [30]. Usually, the direction of the output reradiation is the same as or collinear with that of the incoming radiation. But the direction of the output radiation can be at any desired direction by proper phasing of the distributed amplifier units.

Research and development trends for the traditional distributed amplifier are pushing the already extremely broad frequency band even wider [24], in a search for a new design approach to obtain optimal amplifier performance [26,31,32], and for ultra-high-speed digital signal-processing amplification [33]. For example, an ultrabroadband distributed amplifier designed to cover 100 MHz–20 GHz has been reported by Virdee and Birdee [24]. In MMIC technology, beside the traditional silicon, gallium nitride [26] and indium phosphide [32] technologies are developing and producing good results. In the digital signal processing, a distributed amplifier capable of handling 40 Gbps has been reported by Shigematsu et al. [33].

Today, the technology of conventional distributed amplifiers is a mature one. Commercial products of distributed amplifiers are available on the market [34,35].

10. CONCLUSION

Distributed amplifiers are electrical transmission lines with periodically or continuously loaded amplifiers. The main feature of the distributed amplifier is the wide frequency bandwidth. Wide-bandwidth amplifiers have a large channel capacity and are also capable of handling extremely short or fast pulses. Distributed amplifiers are useful for fast digital data transmission systems of gigabit rates. Distributed amplifiers can be made compact by the use of the monolithic integrated-circuit technology.

BIBLIOGRAPHY

1. T. K. Ishii, *Microwave Engineering*, Harcourt Brace Jovanovich, San Diego, CA, 1989.
2. T. K. Ishii, *Practical Microwave Electron Devices*, Academic Press, San Diego, CA, 1990.
3. Editorials, *Lightwaves* 26, (Nov. 1993).
4. IEEE, *IEEE Standard Dictionary of Electrical and Electronics Terms*, Wiley-Interscience, New York, 1972.
5. J. T. Coleman, *Microwave Devices*, Reston Publishing Co., Reston, VA, 1982.
6. J. B. Beyer et al., MESFET distributed amplifier design guidelines, *IEEE Trans. Microwave. Theory Tech.*, **32**:268–275 (1984).
7. K. B. Niclas et al., On theory and performance of solid-state microwave distributed amplifiers, *IEEE Trans. Microwave. Theory Tech.* **31**:447–456 (1983).

8. W. Kennan and N. K. Osbrink, Distributed amplifiers: Their time comes again, *Microwaves RF* **23**:119–125 (1984) (Part I); **23**:126–153 (1984) (Part II); **24**:13 (1985) (correction).
9. T. K. Ishii, *Maser and Laser Engineering*, Robert E. Krieger, Huntington, NY, 1980.
10. K. W. Kobayashi et al., Extending the bandwidth performance of heterojunction bipolar transistor-based distributed amplifiers, *IEEE Trans. Microwave Theory Tech.* **44**:739–748 (1996).
11. S. Kimura and Y. Imai, 0–40 GHz GaAs MESFET distributed baseband amplifier IC's for high-speed optical transmission, *IEEE Trans. Microwave Theory Tech.* **44**:2076–2082 (1996).
12. A. H. Barea and I. D. Robertson, Monolithic MESFET distributed baluns based on the distributed amplifier gate-line termination technique, *IEEE Trans. Microwave Theory Tech.*, **45**:188–195 (1997).
13. J. L. B. Walker, Improving operation of classic broadband balanced amplifiers, *Microwaves RF* **26**:175–182 (1987).
14. J. L. B. Walker, ed., *High-Power GaAs FET Amplifiers*, Artech House, Boston, 1993, pp. 264–281.
15. Y. Ayasli et al., 2–20 GHz travelling wave power amplifiers, *IEEE 1998 Microwave and Millimeter-Wave Monolithic Circuits Symp. Digest*, Boston, May 31–June 1, 1998, pp. 67–70.
16. B. Kim and H. Q. Tserung, 0.5W 2–21 GHz monolithic GaAs distributed amplifier; *Electron. Lett.* 288–289 (March 1984).
17. Y. Ayasli et al., Capacitively coupled-travelling-wave power amplifier, *IEEE Trans. Microwave Theory Tech.* **32**:1704–1711 (1984).
18. E. M. Chase and W. Keenan, A power distributed amplifier using constant-R networks, *IEEE 1986 Microwave and Millimeter-Wave Monolithic Circuits Symp. Digest*, Baltimore, MD, June 4–5, 1986, pp. 13–17.
19. M. J. Schindler et al., A K/Ka-band distributed power amplifier with capacitive drain coupling, *IEEE 1988 Microwave and Millimeter-Wave Monolithic Circuit Symp. Digest*, New York, May 24–25, 1988, pp. 5–8.
20. E. L. Ginzton et al, Distributed amplification, *Proc. IRE* **36**:956–969 (1948).
21. K. E. Jones, G. S. Barta, and G. C. Herrick, A1 to 10 GHz tapered distributed amplifier in a hermetic surface mount package, *Proc. IEEE GaAs IC Symp.*, Montrey, CA, Nov. 12–14, 1985, pp. 137–140.
22. P. K. Tien, Parametric amplification and frequency mixing in propagating circuits, *J. Appl. Phys.* **29**:1347–1357 (Sept. 1958).
23. B. Y. Banyamin and M. Berwick, Analysis of the performance of four cascaded single-stage distributed amplifiers, *IEEE Trans. Microwave Theory Tech.* **48**:2657–2663 (2000).
24. A. S. Virdee and B. S. Birdee, Computer-aided design of ultraband 100 MHz to 20 GHz amplifiers, *Microwave J.* **43**: 76–88 (2000).
25. D. R. Webster, G. Ataei, and D. G. Haigh, Low-distortion MMIC power amplifier using a new form of derivative superposition, *IEEE Trans. Microwave Theory Tech.*, **49**:328–332 (2001).
26. B. M. Green et al., High efficiency monolithic gallium nitride distributed amplifier, *IEEE Microwave Guided Wave Lett.* **10**:267–269 (2000).
27. C. Paoloni, HEMT-HBT matrix amplifier, *IEEE Trans. Microwave Theory Tech.* **48**:1308–1312 (2000).
28. R. Bashivullah and A. Mortazawi, A slotted waveguide power amplifier for spatial power combining applications, *IEEE Trans. Microwave Theory Tech.* **48**:1142–1147 (2000).
29. A. B. Yokovlev et al., A waveguide-based aperture-coupled patch amplifier array-full wave system analysis and experimental validation, *IEEE Trans. Microwave Theory Tech.* **48**:2692–2699 (2000).
30. K. Yang et al., Active-amplifier-array diagnostics using high-resolution electron optic field mapping, *IEEE Trans. Microwave Theory Tech.* **49**: 849–857 (2001).
31. F. Centurelli et al., Synthesis oriented approach to design microwave multi-device amplifiers with prefixed stability margin, *IEEE Microwave Guided Wave Lett.* **10**:102–104, 2000.
32. J. W. Archer et al., An indium phosphide MMIC for 180–205 GHz, *IEEE Microwave Wireless Comput. Lett.* **11**:4–6 (2001).
33. H. Shigematsu et al., A distributed amplifier for 40 GBPS fiber optic communication systems, *Microwave J.* **45**:78–90 (2002).
34. FSY Microwave Inc., A duplexer, combiner and distribution amplifier for wireless application, *Microwave J.* **43** (6): 156–158 (2000).
35. Amplifier Research, A broadband hybrid solid-state and TWT amplifier, *Microwave J.* **45**(9):184–186 (2002).

DUAL- AND MULTI-FREQUENCY MICROSTRIP ANTENNAS

K. F. LEE
 The University of Mississippi
 Oxford, Mississippi
 K. M. LUK
 Y. H. SHUM
 City University of Hong Kong
 Kowloon, Hong Kong

1. INTRODUCTION

There are many applications in wireless communications that involve two or more distinct frequencies. Because of the attractive features of the microstrip patch antenna, such as planar profile, ruggedness, and low cost, there has been considerable interest in the development of these antennas to meet the dual- or multifrequency specifications. It is sometimes possible that a broadband microstrip antenna can cover the frequencies of interest. However, the disadvantage of using a broadband antenna is that it also receives undesired frequencies unless some kind of filtering network is introduced to reject such frequencies. On the other hand, the advantage of a dual- or multifrequency design is that it focuses only on the frequencies of interest and is thus more desirable. It is the purpose of this article to present several such designs. Dual-frequency designs will be emphasized since they are much more developed than multifrequency designs, which have become a topic of current interest.

In Section 2, dual-frequency single and stacked patches are reviewed. Section 3 presents dual-frequency designs obtained by loading the patch with either a reactive load or with slots. Section 4 describes a more recent design introduced by the present authors using the proximity

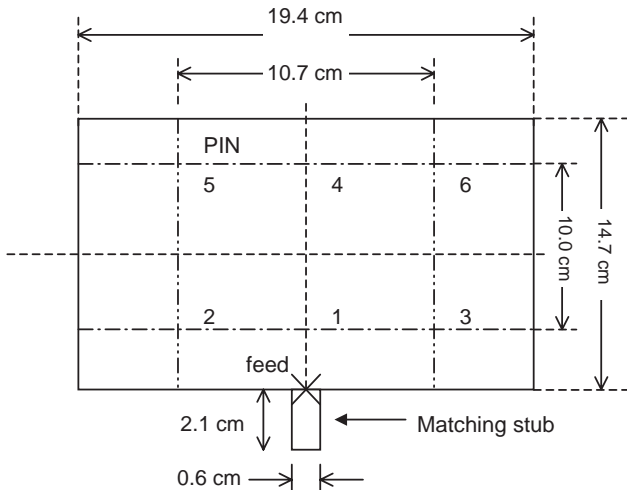


Figure 1. Geometry (in centimeters) of a rectangular patch antenna with six possible short-circuiting pins and a short circuit matching. (From Zhong and Lo [1], reproduced with permission from IEE.)

coupling of a U-shaped patch with unequal arms and a wideband E-shaped patch. Dual-frequency wideband patches using a L-probe feed, also introduced by the present authors, are presented in Section 5. Section 6 discusses two methods of designing multi-frequency patch antennas. The article ends with some concluding remarks.

2. DUAL-FREQUENCY SINGLE AND STACKED PATCHES

2.1. Single-Element Dual-Frequency Microstrip Antennas

It is possible for a single-element microstrip antenna to operate at many frequencies corresponding to the various resonant modes pertaining to the structure. However, for most applications, it is required that the radiation pattern, the polarization, and the impedance be similar, if not identical, in all the frequency bands of operation. This immediately rules out many modes. Furthermore, for a given geometry, all the resonant frequencies are related in fixed ratios.

If for a particular patch shape two modes can be found that produce similar radiation patterns with the same polarization, dual frequency is possible with a single patch.

Table 1. Resonant Frequencies of the TM_{01} and TM_{03} Modes against Short-circuiting Pins Used

Number of Pins	Pin Position	f_{01} (MHz)	f_{03} (MHz)	f_{03}/f_{01}
0	—	613	1861	3.04
1	(1)	664	1874	2.82
2	(1)(2)	706	1865	2.64
3	(1)(2)(3)	792	1865	2.36
4	(1)(2)(3)(6)	813	1865	2.29
5	(1)(2)(3)(5)(6)	846	1865	2.20
6	(1) to (6)	891	1865	2.09

Source: From Zhong and Lo [1], reproduced with permission from IEE.

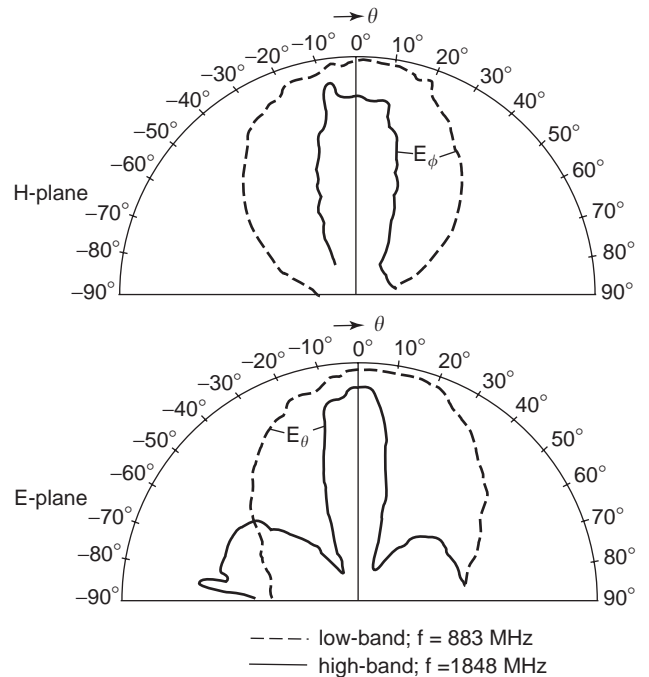


Figure 2. Typical radiation patterns in H and E planes for antennas shown in Fig. 1 with six pins inserted. (From Zhong and Lo [1], reproduced with permission from IEE.)

For the rectangular patch, the two modes TM_{01} and TM_{03} satisfy this requirement. However, their resonant frequencies are related by a ratio of approximately 3; the exact value is dependent on the edge effect. It has been

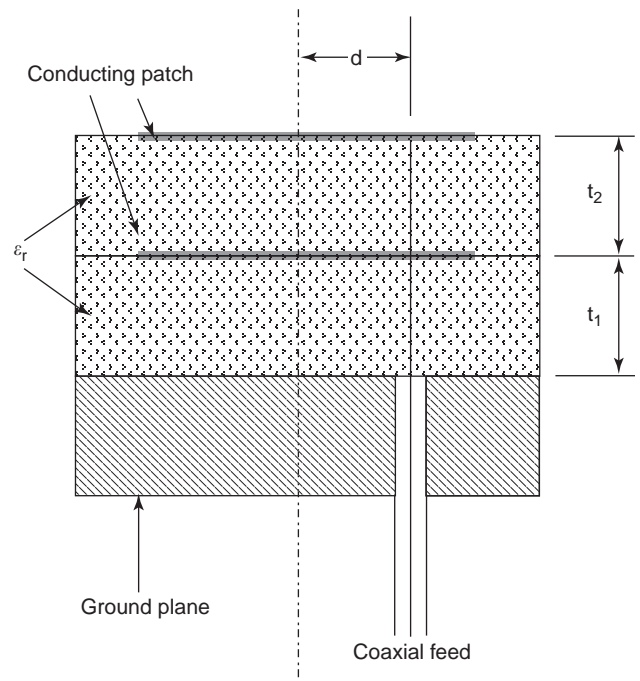


Figure 3. Dual-frequency stacked microstrip antenna. (From Long and Walton [2], © 1979 IEEE.)

shown that placement of short-circuiting pins on the nodal lines of the TM_{03} mode field has little effect on this mode but a strong effect on the TM_{01} mode. Zhong and Lo [1] demonstrated that this offers a way of altering not only the separation of the two frequency bands but also the input impedance of the TM_{01} mode. The geometry of the rectangular patch in their experiment is shown in Fig. 1. It is made of $\frac{1}{8}$ -in. copper-cladded Rexolite 2200 with six short-circuiting pin positions. The effects of successively adding more and more pins (each approximately 0.05 cm in diameter) at the positions indicated in Fig. 1 are shown in Table 1. It is seen that the ratio of the two operating frequencies f_{03}/f_{01} can be varied from approximately 3 to 2. Since all these pins are located on the TM_{03} mode null lines, f_{03} remains constant at about 1865 MHz while f_{01} is varied from 613 to 891 MHz. In order for the impedances of the two bands to be close to 50Ω at resonance, it is necessary to

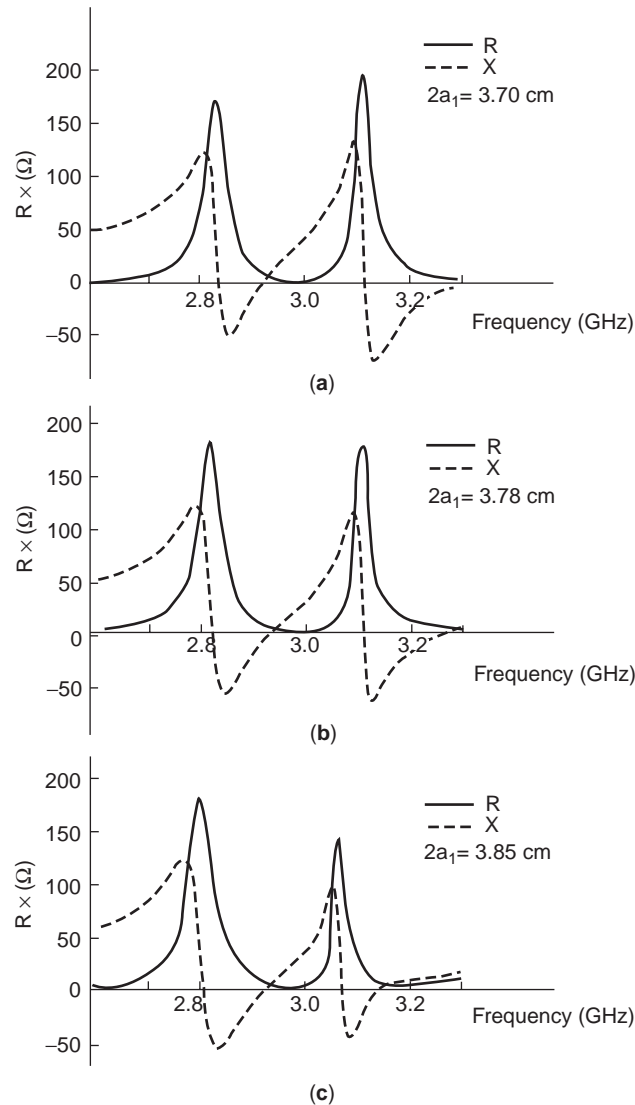


Figure 4. Real and imaginary parts of impedance of stacked circular patches etched on a dielectric with $\epsilon_r = 2.47$: (a) $2a_1 = 3.70$ cm; (b) $2a_1 = 3.78$ cm; (c) $2a_1 = 3.85$ cm. (From Long and Walton [2], © 1979 IEEE.)

attach a short capacitive stub of 0.6×2.1 cm. With the stub added, the bandwidth with reference to a standing-wave ratio (SWR) of 3:1 is about 2% for the lowband and almost 8% for the highband. Typical low- and highband patterns in both E and H planes are shown in Fig. 2. It is seen that, while the two modes radiate strongest in the broadside, the directivities of the two modes are quite different.

The rectangular patch is not the only geometry capable of providing dual-frequency operation. It will be shown in Section 6 that the TM_{01} , TM_{20} , and TM_{21} modes of the equitriangular patch are all broadside modes with similar polarizations in the broadside direction (refer to Fig. 31 for a detailed radiation pattern). By choosing the location of the feed properly, the impedances of these modes do not vary greatly. Section 6 discusses the utilization of the equitriangular patch for dual- or triple-frequency operations.

2.2. Dual-Frequency Stacked Patches

By using a stacked geometry consisting of two patches on two substrate layers, dual-frequency operation is obtained. The first experiment, reported by Long and Walton [2], utilized two stacked circular patches. The geometry is shown in Fig. 3.

The disks were photoetched on separate substrates and aligned so that their centers were along the same line. The sizes of the two disks and their spacings were varied and the resultant behavior of the antenna characteristics measured. The antenna was fed by means of a coaxial line. The center conductor passes through a clearance hole in the lower disk and is connected electrically to the upper disk. If one considers the two regions under the patch as two resonant cavities, it is clear that the system behaves as a pair of coupled cavities. Since the fringing fields are

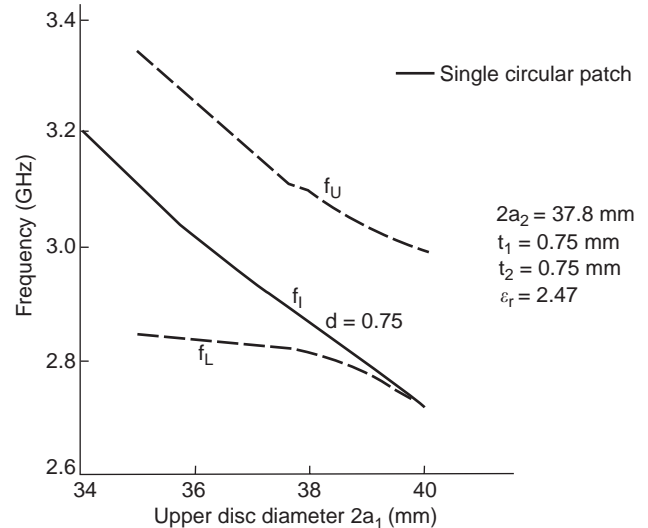


Figure 5. Resonant frequencies versus upper disk diameter of stacked circular patches etched on a dielectric with $\epsilon_r = 2.47$, $2a_2 = 3.78$ cm, $t_1 = t_2 = 0.75$ mm. (From Long and Walton [2], © 1979 IEEE.)

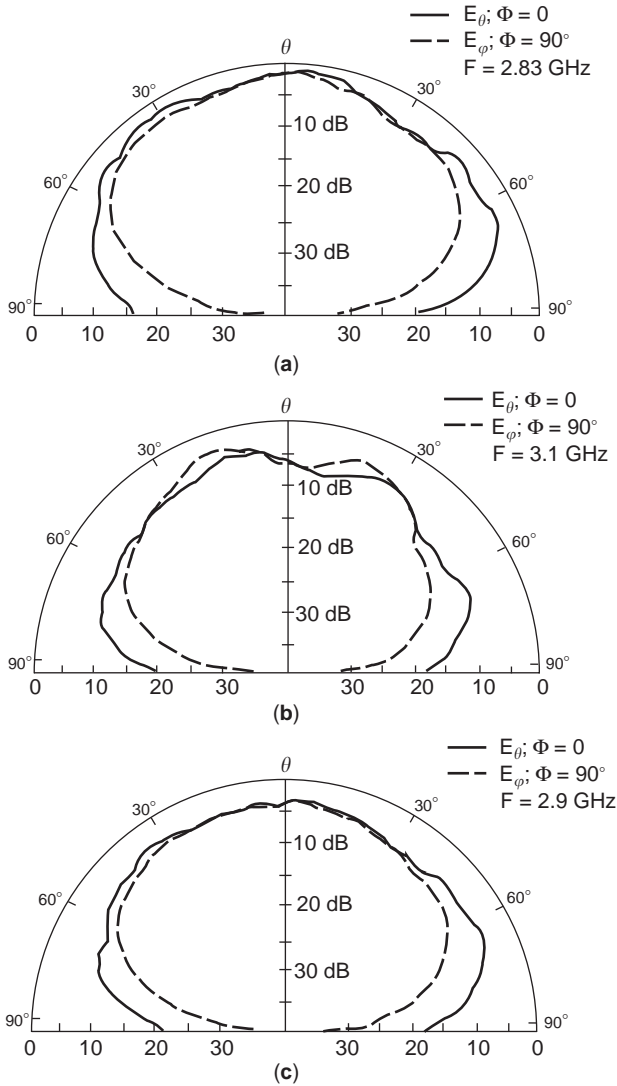


Figure 6. Radiation pattern of stacked circular patches antenna: (a) $f = 2.83$ GHz; (b) $f = 3.1$ GHz; (c) $f = 2.9$ GHz. (From Long and Walton [2], © 1979 IEEE.)

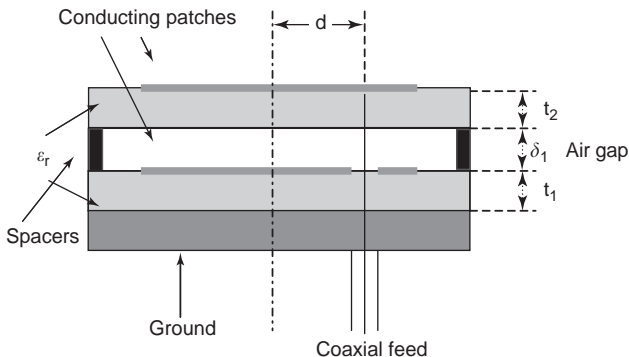


Figure 7. Tunable dual-frequency stacked microstrip antenna utilizing the airgap concept. (From Dahele and Lee [3], © 1982 IEEE.)

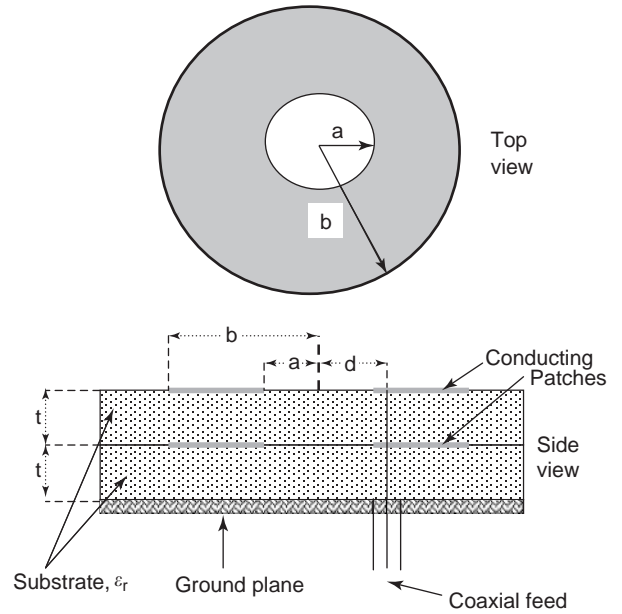


Figure 8. Geometry of the stacked annular ring antenna. (From Dahele et al. [4], © 1987 IEEE.)

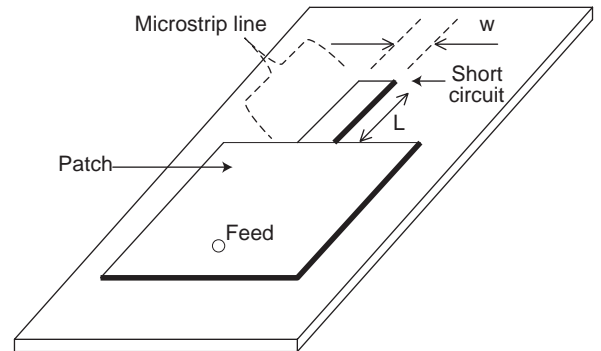


Figure 9. Dual-frequency rectangular patch antenna with monolithic reactive loading. (From Davidson et al. [6], reproduced with permission from IEE.)

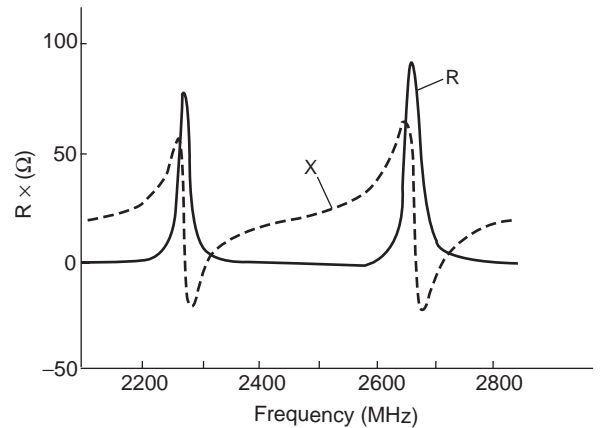


Figure 10. Impedance of edge-loaded, 4×6 cm-patch antenna with $L = 4.0$ cm, $W = 0.33$ cm, $\epsilon_r = 2.17$, $t = 0.079$ cm; coaxially fed near the edge end at the center of the 6-cm side. (From Davidson et al. [6], reproduced with permission from IEE.)

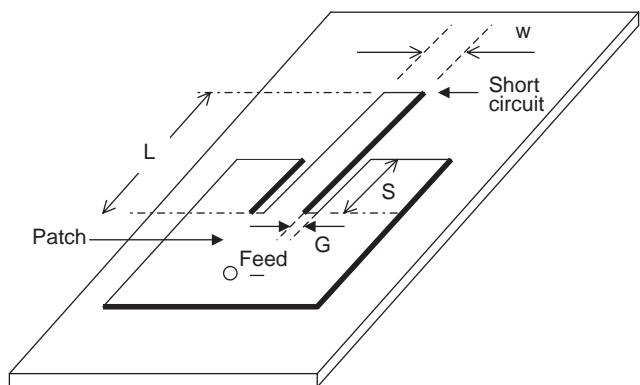


Figure 11. Geometry incorporating an insert dimension S and a gap spacing G . (from Davidson et al. [6], reproduced with permission from IEEE.)

Table 2. Resonant Frequencies of Dual-Frequency Rectangular Patch with Reactive Loading

W (cm)	L (cm)	G (cm)	S (cm)	f_L (GHz)	f_U (GHz)	f_U/f_L
0.33	4.0	1.0	1.5	2.356	2.494	1.054
0.33	4.0	0	0	2.275	2.666	1.172
0.33	8.4	0	0	2.339	2.628	1.124
0.33	4.0	0.7	1.5	2.437	2.494	1.023
0.33	4.0	0.3	1.5	2.471	2.514	1.017

Source: From Davidson et al. [6], reproduced with permission from IEEE.

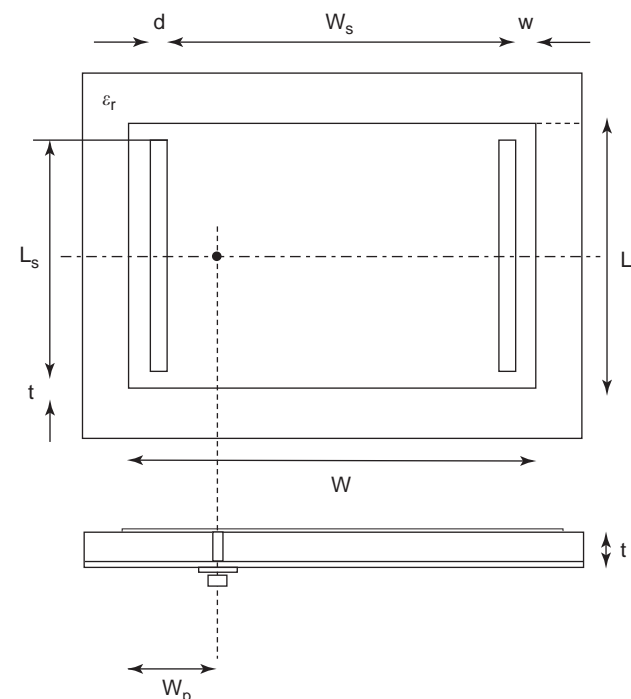
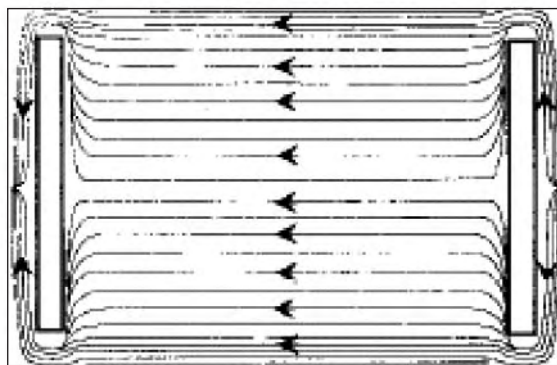
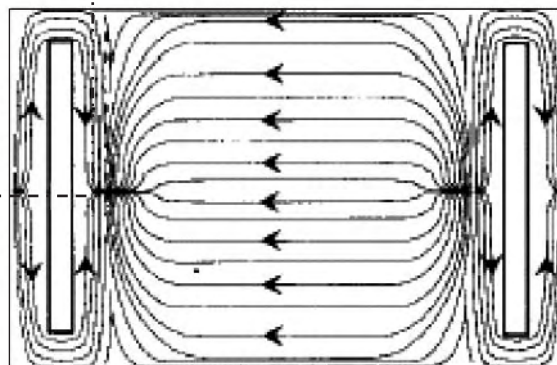


Figure 12. Geometry of probe feed SPA. (From Maci et al. [7], reproduced with permission from IEEE.)



(a)



(b)

Figure 13. Current distributions on slotted patch ($W = 40$ mm; $L = 30$ mm; $d = 1$ mm; $L_s = 28$ mm; $W_s = 36$ mm): (a) TM_{10} mode; (b) TM_{30} mode. (From Maci et al. [7], reproduced with permission from IEEE.)

different for the upper and lower cavities, two resonant frequencies are expected even if the diameters of the two disks are the same. Long and Walton [2] showed that,

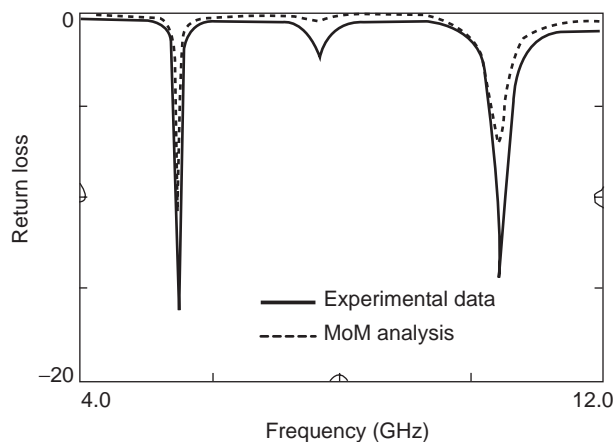


Figure 14. Return loss of SPA without tuning resonators fed by 50- Ω coaxial probe ($W = 15.5$ mm; $L = 11.5$; $l = 0.5$ mm; $w = 1$ mm; $d = 1$ mm; $W_p = 5.5$ mm; $\epsilon_r = 2.2$; $t = 0.8$ mm) (— experimental data; - - - MoM analysis). (From Maci et al. [7], reproduced with permission from IEEE.)

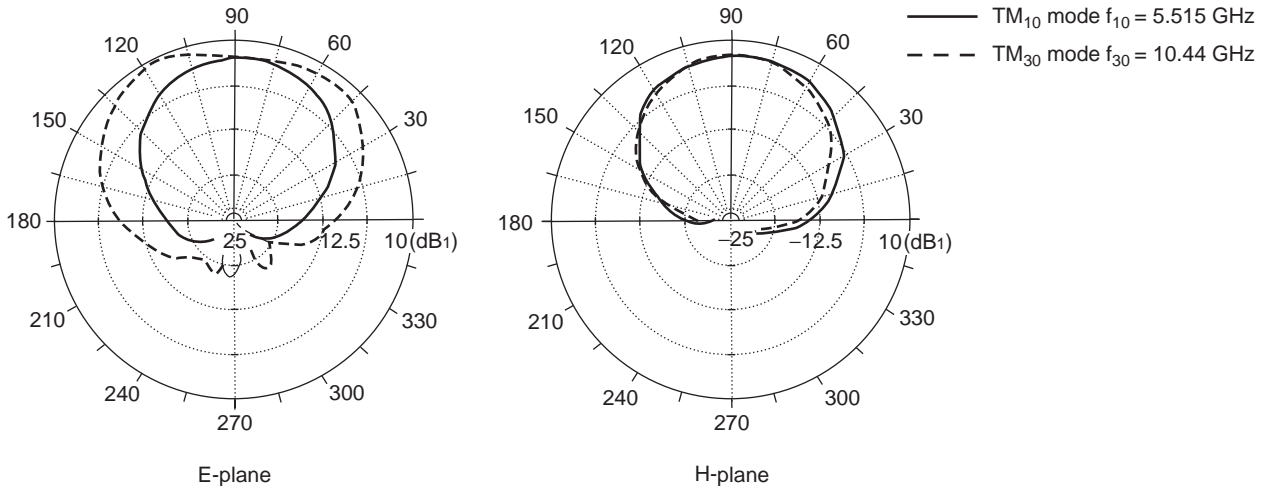


Figure 15. Measured patterns for SPA ($W = 15.5$ mm; $L = 11.5$ mm; $l = 0.5$ mm; $w = 1$ mm; $d = 1$ mm; $W_p = 5.5$ mm; $\epsilon_r = 2.2$; $t = 0.8$ mm) (— TM_{10} mode, $f_{10} = 5.515$ GHz; - - - TM_{30} mode, $f_{30} = 10.44$ GHz). (From Maci et al. [7], reproduced with permission from IEE.)

unlike the single-element dual-frequency rectangular patch operated in the TM_{01} and TM_{03} modes, in which the frequency ratio is approximately 3 when no short-circuiting pins are used, this design can produce resonant frequencies that are considerably closer. A typical frequency ratio is 1.2; the exact value is determined by the relative diameters of the upper and lower disks, the thicknesses of the substrate layers, and the relative permittivities of the substrates.

Figure 4 shows the real and imaginary parts of the input impedance for $2a_2 = 3.78$ cm, $t_1 = t_2 = 0.075$ cm, and three values of $2a_1$. The relative permittivity of both layers is 2.47. The resonant frequencies as a function of the

upper disk diameter are shown in Fig. 5. Also shown is the resonant frequency of the lowest mode for a single disk of diameter $2a$ and substrate thickness $t = 0.075$ cm, taking into account the fringing field through the effective diameter. It is seen that the lower resonant frequency is relatively constant, remaining near the value of a single disk with $2a = 3.78$ cm and $d = 0.075$ cm. The upper resonance, on the other hand, is highly dependent on the size of the upper disk. Radiation patterns were also given in Ref. 2, which showed that they were similar to the radiation pattern of the lowest mode of the single circular patch. The radiation pattern is shown in Fig. 6.

Dahele and Lee [3] have applied the airgap concept to the design of dual-frequency stacked disks. The geometry is shown in Fig. 7, in which an airgap between the two substrates is introduced. By increasing the width of the airgap, the upper resonant frequency increases, accompanied by a broadening of the bandwidth of the lower resonance.

Dahele et al. [4] also studied a structure consisting of two stacked annular ring patches as shown in Fig. 8. This structure was also found to exhibit dual-frequency behavior. As in the case of circular disks, an upper airgap was found to be a convenient method of altering the separation between the frequency bands. A theoretical analysis of the stacked circular disks and stacked annular rings using Hankel transforms was given by Fan and Lee [5]. The predicted resonant frequencies showed excellent agreement with the measurements in Refs. 2 and 4.

In the two designs discussed in this section, the stacked geometry is suitable when the frequency ratio is in the range of 1.1–1.2, while the single element incorporating short-circuiting pins yields frequency ratios in the range of 2–3. In the next section, two additional designs are presented: patch with reactive loading and patch with slots. The former also yields similar frequency separation as the stacked patches, while loading a rectangular patch with slots can reduce the frequency ratio from about 3 to as low as 1.57.

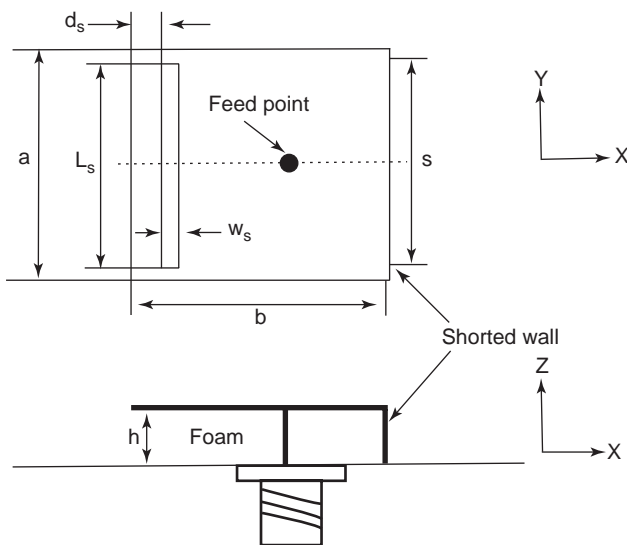


Figure 16. Geometry of dual-band short-circuited patch antenna ($a = 38$ mm; $b = 25$ mm; $L_s = 36$ mm; $W_s = 1$ mm; $d_s = 2$ mm; $h = 3$ mm). (From Guo et al. [9], reproduced with permission from IEE.)

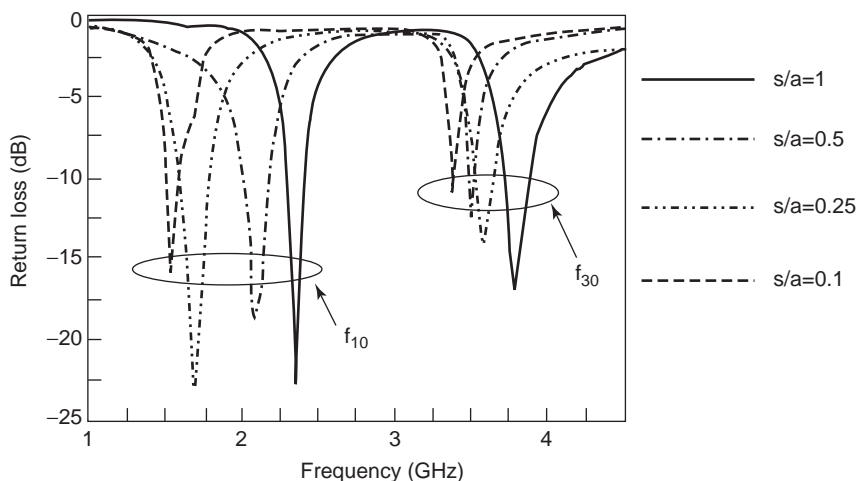


Figure 17. Measured return loss for different short-circuited plane widths (— $s/a=1$; - · - · $s/a=0.5$; · · · $s/a=0.25$; - - - $s/a=0.1$). (From Euo et al. [9], reproduced with permission from IEE.)

3. DUAL-FREQUENCY LOADED PATCHES

3.1. Patch with Reactive Loading

A dual-frequency microstrip antenna can be obtained by loading it with a reactive load, such as a short-circuited

coaxial line or a short-circuited microstrip line. The latter preserves the low-profile characteristics of the microstrip patch antenna. Such a structure, shown in Fig. 9, was demonstrated experimentally by Davidson et al. [6]. In the experiment, a rectangular patch of dimensions 6×4 cm etched on a substrate with $\epsilon_r=2.17$ and thickness

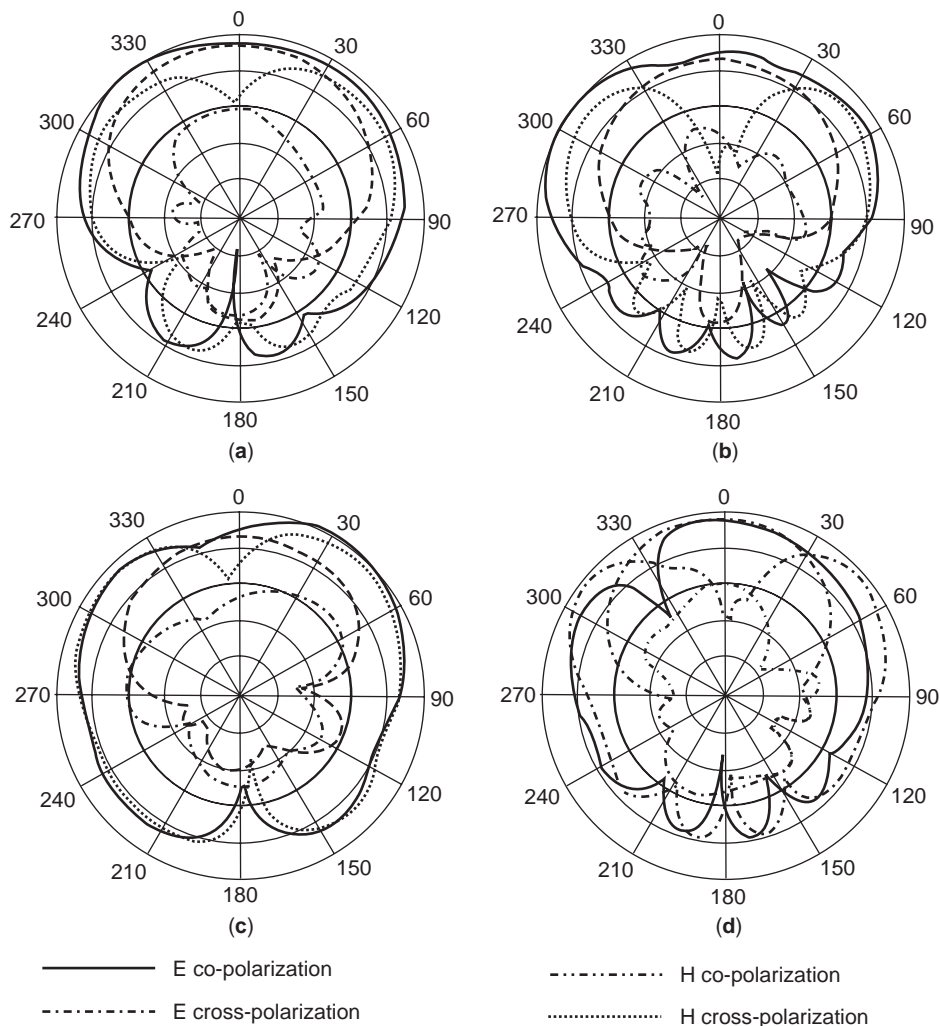


Figure 18. Measured field patterns: (a) $s/a=1$, $f_{10}=2.355$ GHz; (b) $s/a=1$, $f_{30}=3.785$ GHz; (c) $s/a=0.1$, $f_{10}=2.355$ GHz; (d) $s/a=0.1$, $f_{30}=3.785$ GHz (— E copolarization; - · - · E cross-polarization; - · · H copolarization; · · · H cross-polarization). (From Guo et al. [9], reproduced with permission from IEE.)

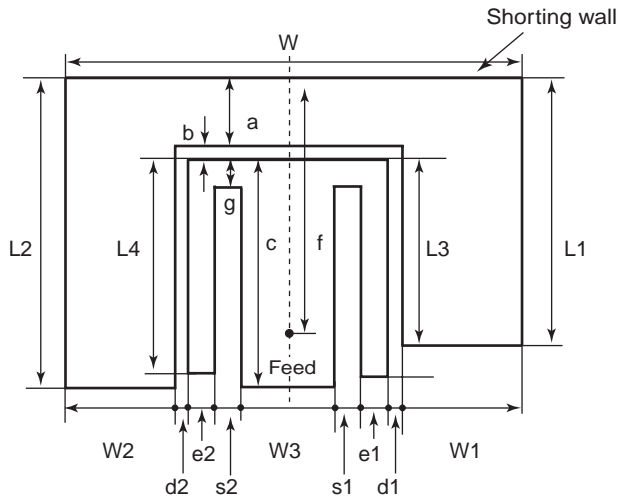


Figure 19. Dual-band patch antenna at 900 and 1800 MHz with $h = 11$ mm. (From Guo et al. [10], © 2002 IEEE.)

0.079 cm. It is coaxially fed near the edge and at the center of the 6-cm side. For a linelength of $L = 4.0$ cm and linewidth $w = 0.33$ cm, the measured real and imaginary parts of the input impedance are as shown in

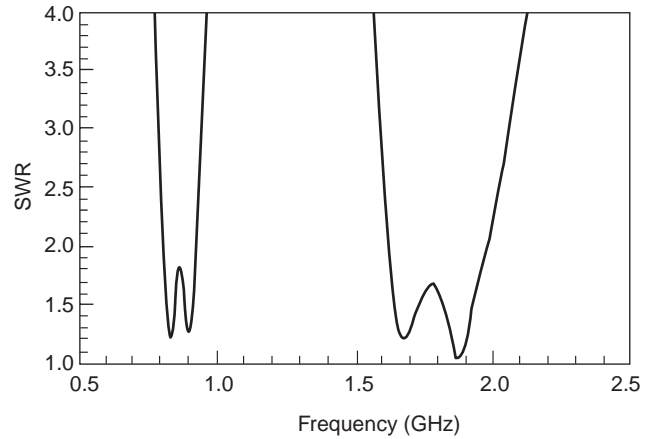


Figure 20. Measured SWR of the antenna in Fig. 19 (From [10], © 2002 IEEE.)

Fig. 10. Good pattern characteristics were observed at each of the resonant frequencies, 2.275 and 2.666 GHz, respectively.

The separation of the resonances can be varied by (1) changing the length of the microstrip line and (2) introducing an inset dimension S with an accompanied gap

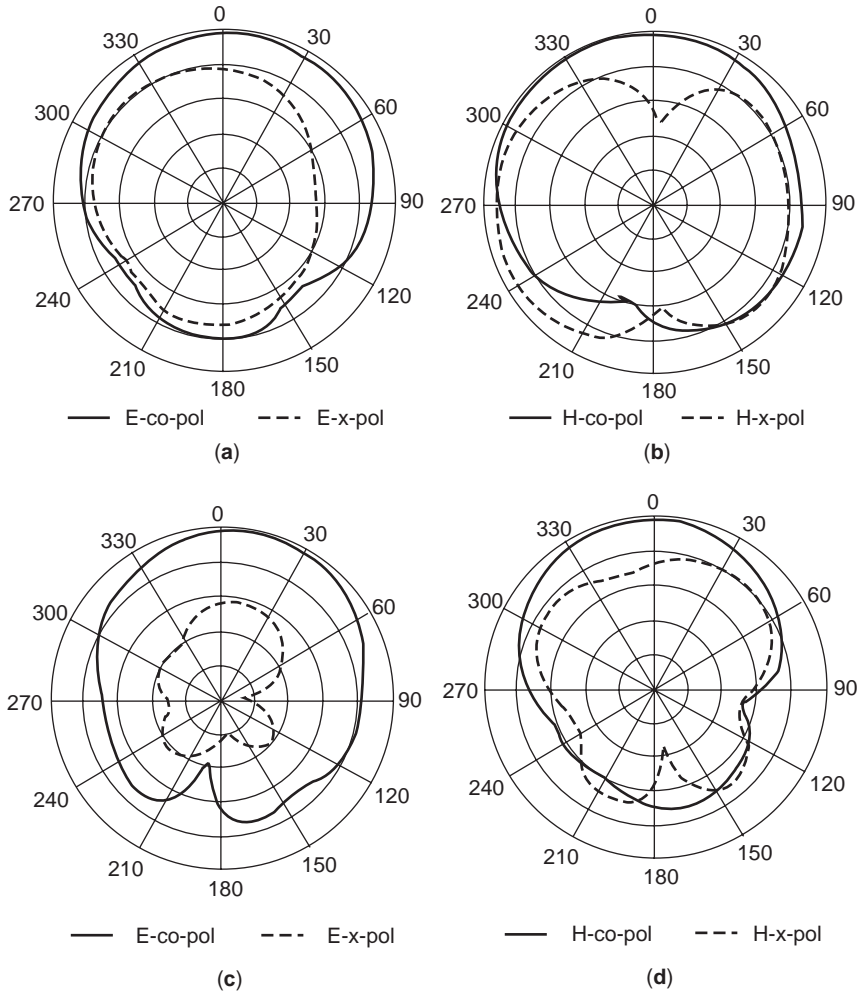


Figure 21. Radiation patterns of the antenna in Fig. 19, 10 dB/div: (a) E plane at 900 MHz; (b) H plane at 900 MHz, (c) E plane at 1800 MHz (d) H plane at 1800 MHz (From Guo et al. [10], © 2002 IEEE.)

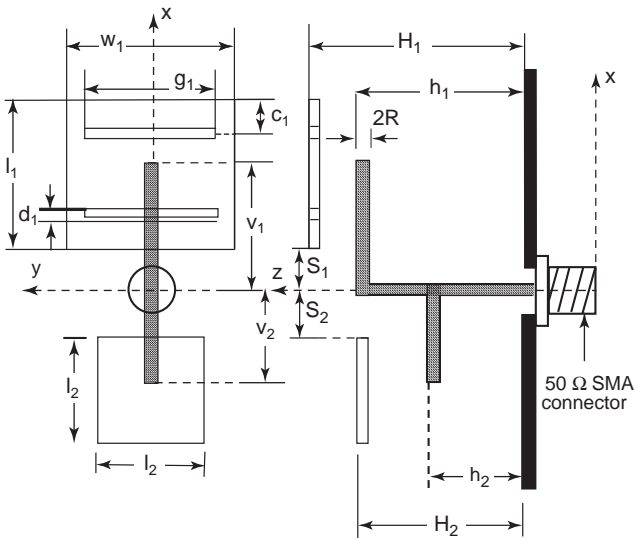


Figure 22. Geometry of the basic L-probe dual-band antenna. (From Luk et al. [15], reproduced with permission from IEE.)

spacing G between the line and the patch, as shown in Fig. 11. The results for the resonant frequencies are shown in Table 2. It is seen that the frequency ratio varies between 1.017 and 1.172.

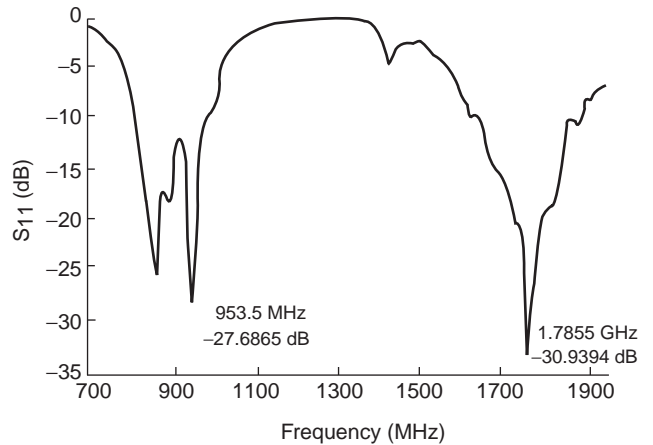


Figure 23. Measured return loss S_{11} . (From Luk et al. [15], reproduced with permission from IEE.)

3.2. Patch with Slots

A dual-band rectangular patch antenna with a frequency ratio of < 2 can be obtained by loading the patch with two narrow slots etched inside the patch, which are close to and parallel to the radiating edges [7]. Such a slotted patch antenna (SPA) is shown in Fig. 12.

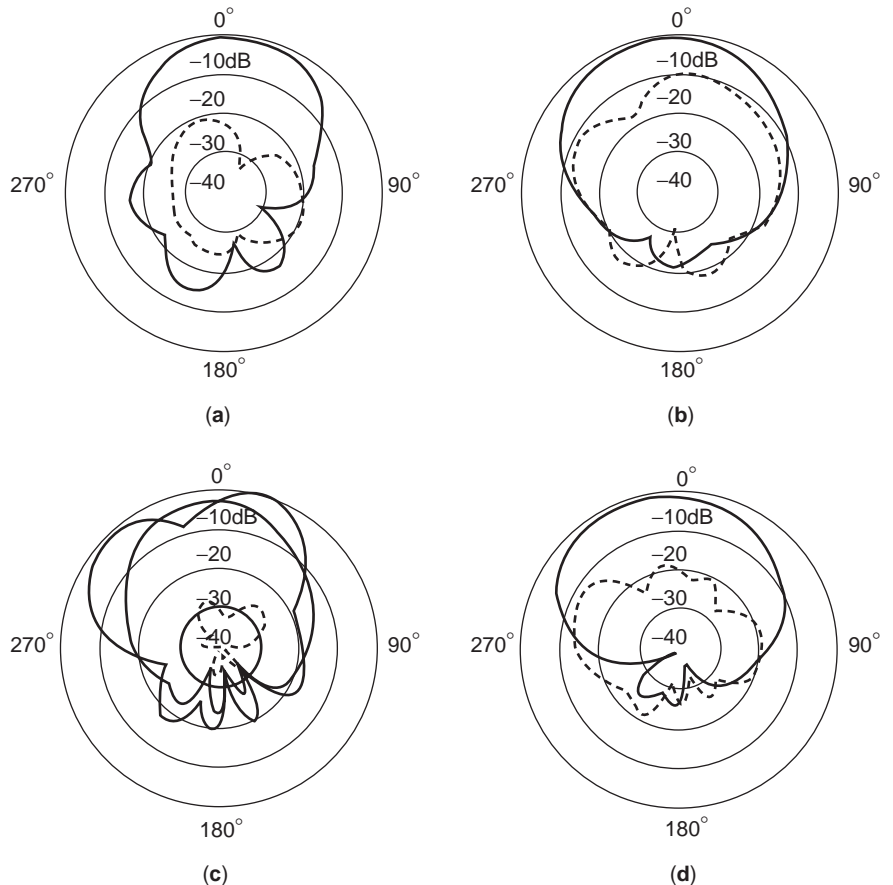


Figure 24. Radiation pattern: (a) E plane at 953.5 MHz; (b) H plane at 953.5 MHz; (c) E plane at 1.7855 GHz; (d) H plane at 1.7855 GHz (— copolarization; ···· copolarization; ——— copolarization without slots—for (c) only). (From Luk et al. [15], reproduced with permission from IEE.) (This figure is available in full color at <http://www.mrw.interscience.wiley.com/erfme>.)

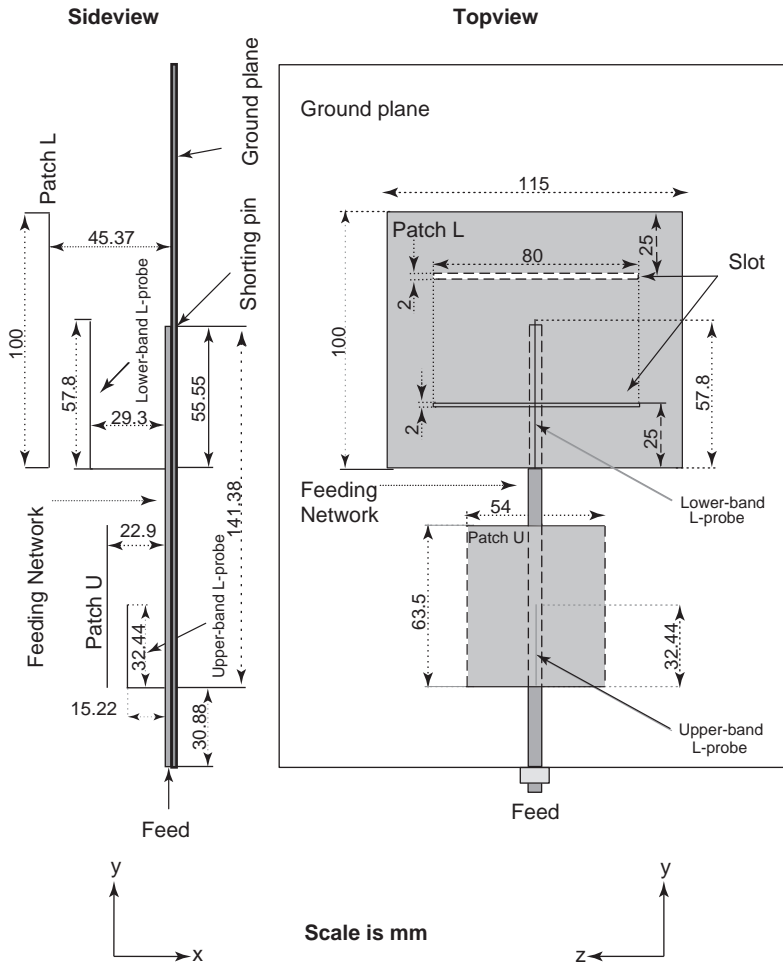


Figure 25. Geometry of L-probe dual-band antenna with DC ground.

The reduction in frequency separation can be explained as arising from the perturbation of the TM_{10} and TM_{30} modes, as shown in Figs. 13a and 13b. These narrow slots are placed close to the radiating edges, where the current is nearly minimum for the TM_{10} mode. Consequently, the

current distribution for this mode is only slightly perturbed. Hence, its resonant frequency is only slightly different from that of the rectangular patch without a slot. For the TM_{30} mode, slots are located where the current of the unperturbed TM_{30} mode is significant, leading to

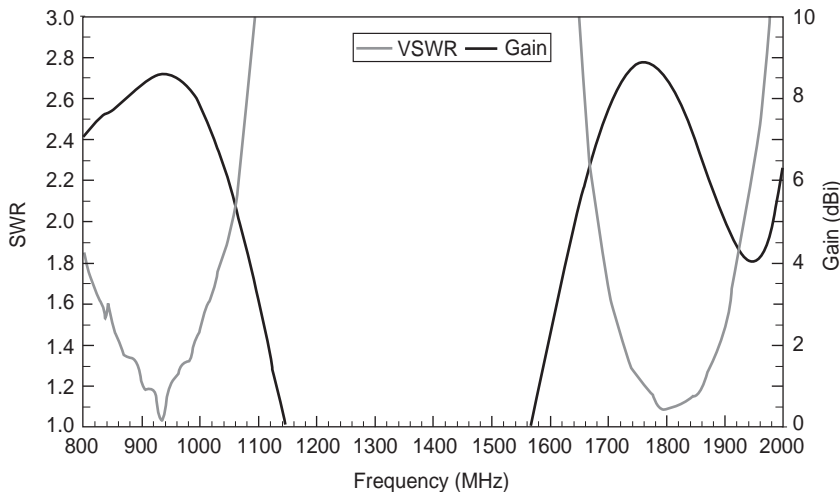


Figure 26. Measured standing-wave ratio and gain of the dual-band antenna. (This figure is available in full color at <http://www.mrw.interscience.wiley.com/erfme>.)

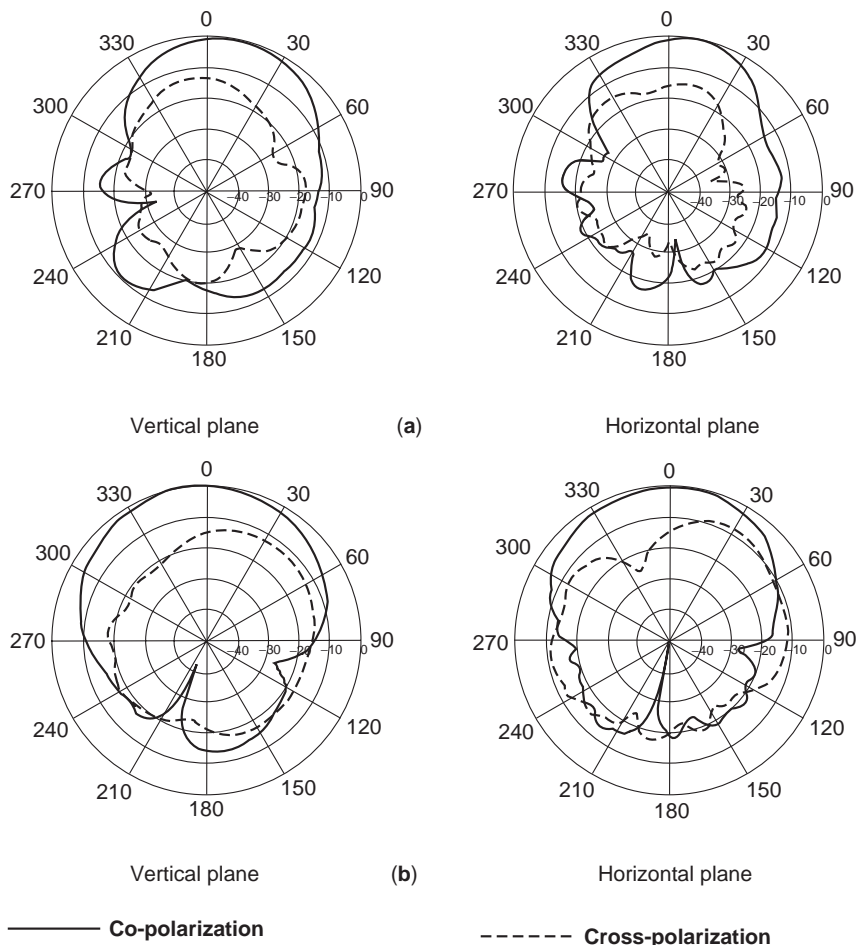


Figure 27. Measured radiation patterns of the antenna of Fig. 25 at 0.9 GHz (a) and 1.8 GHz (b). (— copolarization; - - - cross polarization).

strong modification of the current distribution. As a result, the resonance frequency decreases, due to the increase in the current pathlength introduced by the slot.

Maci et al. [7] performed numerical analysis based on the method of moments (MoM) and fabricated several prototypes at C and X bands. Design criteria were obtained from the MoM analysis. Figure 14 shows the amplitude of the reflection coefficient for a patch with the dimensions shown in the caption. Two resonances were obtained at $f_{10} = 5.515$ GHz and $f_{30} = 10.446$ GHz. The frequency ratio was 1.89. The experimental curve (continuous line) compares well with the results obtained by MoM analysis (dashed line). The central resonance of lower amplitude that appears in the Fig. 14 is associated with the TM_{20} mode that is excited in the structure owing to the asym-

metric feed. The measured radiation patterns of this antenna in the E and H planes are shown in Fig. 15. The dashed and continuous lines correspond to the lower and the upper frequencies, respectively. A gain of 6.5 dB was found for the lower frequency and 6.8 dB for the upper frequency. The *E*-plane radiation pattern at the upper frequency is broader than that for the lower frequency.

Maci et al. also showed that, by introducing resonant tuning stubs, the frequency ratio can be further reduced to about 1.57 [7].

3.3. Slot-Loaded Short-Circuited Patch Antenna

It is well known that the size of a rectangular patch can be reduced by short-circuiting along the vertical central axis,

Table 3. Summary of Radiation Characteristics

	Vertical Plane			Horizontal Plane			
	Frequency (GHz)	3 dB Beamwidth	Cross-polarization (dB)	Backlobe (dB)	3 dB Beamwidth	Cross-polarization (dB)	Backlobe (dB)
Lower band	0.9	56.3°	-13	-12	83.0°	-15	-13
Upper band	1.8	40.4°	-12	-15	74.9°	-9	-19

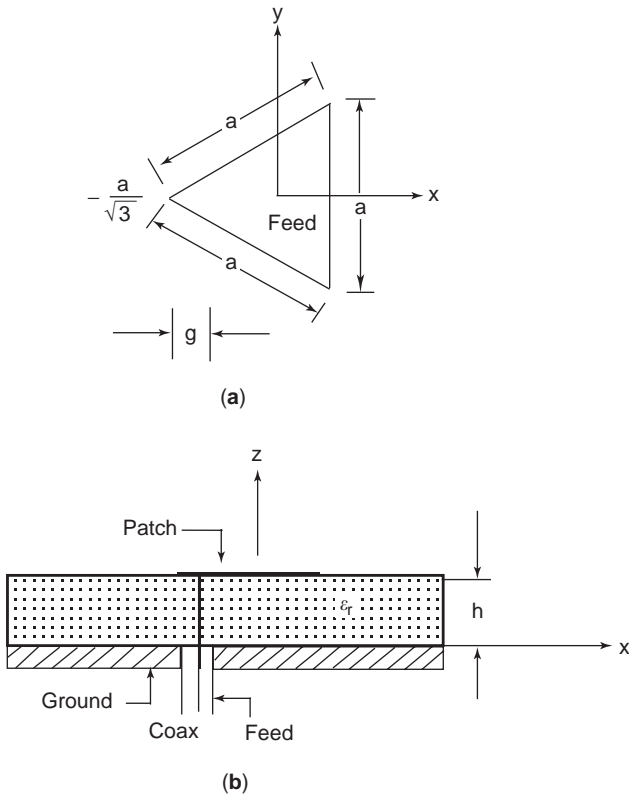


Figure 28. Geometry of equilateral triangular patch antenna. (From Lee et al. [16], © 1988 IEEE.)

which corresponds to the zero-potential plane for the TM_{10} and TM_{30} modes, and by using only one-half of the patch. The size of the antenna can be further reduced by decreasing the short-circuiting plane width [8]. Guo et al. [9] showed that this technique can be applied to reduce the size of the dual-frequency slot-loaded patch antenna.

The geometry of this antenna is shown in Fig. 16. A single slot with dimensions $L_s \times W_s$ is cut in a rectangular patch with dimensions $a \times b$ with a short-circuited plane with width s placed at its other side. The patch is separated from the ground plane by a foam substrate of thickness h . The slot is placed a small distance d_s from the radiating edge of the patch. The parameters of the slot were selected using the design criteria given in Ref. 7. It is found that, by controlling the short-circuiting plane width, both the TM_{10} and TM_{30} modes are strongly perturbed.

Many designs of the proposed antenna with various short-circuiting plane widths were fabricated and measured by Guo et al. [9]. Figure 17 shows typical results of the measured return loss for the cases with $s/a = 1, 0.5, 0.25,$ and 0.1 for the dimensions shown in the caption. It is seen that the perturbed TM_{10} and TM_{30} modes are excited with good impedance matching. However, when $s/a < 0.1$, no feedpoint can be found for exciting the two frequencies with good matching. This indicates that there are limitations to the present dual-band design. It is seen that the frequency ratio f_{30}/f_{10} varies in the range $\approx 1.6 - 2.2$. For the case $s/a = 0.1$, the frequency f_{10}

occurred at 1.535 GHz, which is about 0.29 times the frequency f_{10} (5.35 GHz) for a regular half-wavelength patch of the same patch size. The partial shorting plane therefore significantly reduces the resonant length of the patch.

Typical measured far-field radiation patterns at the two operating frequencies for the case with $s/a = 1$ and $s/a = 0.1$ are shown in Fig. 18. For the experiment, the shorted patch was mounted on a large ground plane (a circular disk with diameter $= 3\lambda_0$) to reduce diffraction off the edges. Similar radiation patterns and polarizations for the two operating frequencies f_{10} and f_{30} are observed. It can be seen that for $s/a = 1$, there is a mainbeam squint of about 32° and 43° in the E plane for f_{10} and f_{30} , respectively. For $s/a = 0.1$, the corresponding mainbeam squint is about 30° and 6° . For $s/a = 1$, the measured gain in the maximum direction is 2.2 and 2.75 dBi for f_{10} and f_{30} , respectively, while for $s/a = 0.1$, the corresponding gain is 0.4 and 1.9 dBi. It should be noted that although the H -plane cross-polarization level is quite high, it may not be a disadvantage in some applications, such as indoor mobile communications.

4. DUAL-FREQUENCY COUPLED PATCHES

In this section, we present a dual-frequency design that makes use of the concept of a low-frequency (outer) patch coupled to a high-frequency (inner) patch [10]. The low-frequency element is a U-shaped patch with unequal arms, while the high-frequency element is a E-shaped patch [11], which is a variation of the wideband U-slot patch [12]. The geometry is shown in Fig. 19. The inner patch is fed by a coaxial probe, and the outer patch is excited through proximity coupling to the inner patch.

It is noted that the two arms of the U patch are not equal. This introduces two closely spaced resonances at the lower frequency, making the bandwidth of the low-band wider than the case when the arms are of equal length. Moreover, a short-circuiting wall is introduced in the U patch to reduce the size of the patch. An antenna of this type was designed to operate at both 900 and 1800 MHz, using FR4 substrate material with relative permittivity equal to 4.4 [10]. It has the following parameters: $W = 40$ mm, $W_1 = 5$ mm, $W_2 = 5$ mm, $W_3 = 16$ mm, $L_1 = 45$ mm, $L_2 = 50$ mm, $L_3 = 42.5$ mm, $L_4 = 42.5$ mm, $a = 4$ mm, $b = 2$ mm, $c = 44$ mm, $d_1 = 2$ mm, $d_2 = 2$ mm, $e_1 = 3.5$ mm, $e_2 = 3.5$ mm, $s_1 = 1.5$ mm, $s_2 = 1.5$ mm, $f = 41$ mm, $g = 10$ mm, and $h = 11$ mm.

The measured SWR of the dual-band antenna is shown in Fig. 20. The bandwidth of the lower-frequency element is 13.3% with a frequency range of 807–922 MHz, and that of the upper band is 20% with a frequency range of 1625–1982 MHz when $SWR \leq 2$. The substrate thickness corresponds to 0.033 free-space wavelength at 900 MHz, while the length L_2 and the width W are $0.15\lambda_0$ and $0.12\lambda_0$, respectively. Figure 21 shows the copolarization E - and H -plane radiation patterns at 900 and 1800 MHz, respectively. At 900 MHz, the 3 dB beamwidth in the E plane is 109° and in the H plane, 127° . At 1800 MHz, the 3 dB beamwidth in the E plane is 72° and

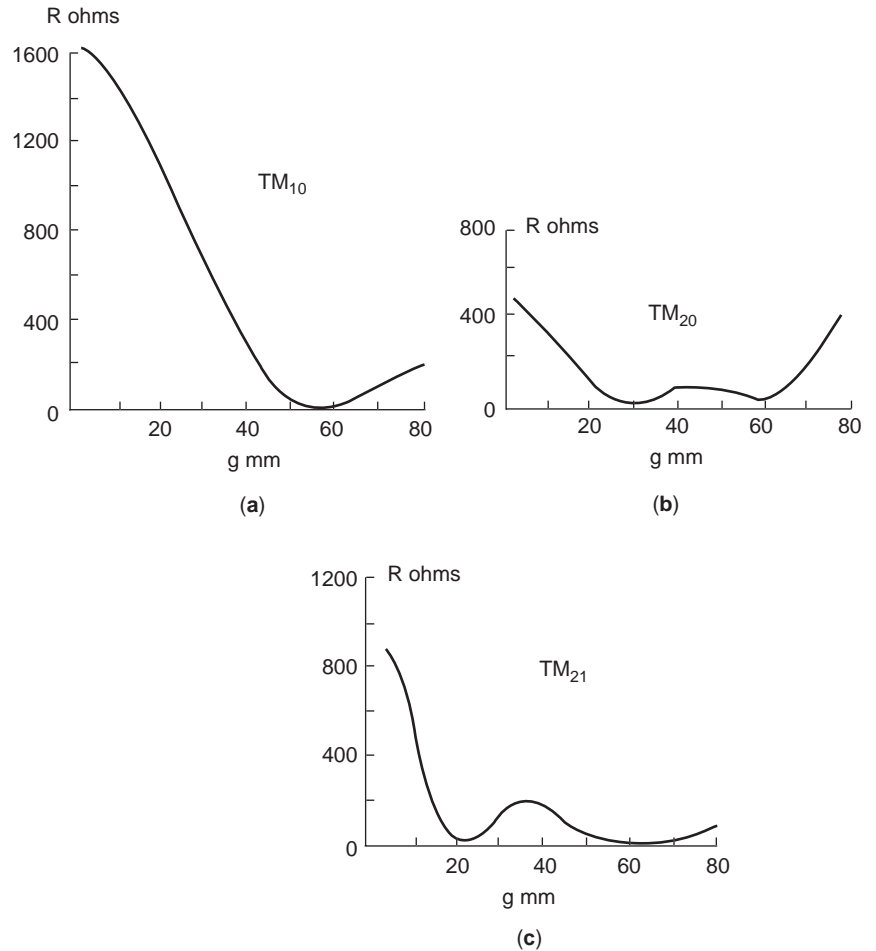


Figure 29. Theoretical input impedance at resonance as function of feed position. (From Lee et al. [16], © 1988 IEEE.)

in the H plane, 73° . The beamwidth in the lower band is larger than that in the upper band. The measured gain of the antenna was 2 ± 1.5 dBi and 4.5 ± 1.8 dBi at the lower and upper bands, respectively. The measured results confirm that the lower band is due to the short-circuited U-shaped patch with two unequal arms and the upper one is due to the inner coaxially fed E-shaped patch. Note that the cross-polarization was significantly higher than with the single-patch antenna. However, for indoor mobile communications, this would lead to better transmission capabilities in a multipath environment.

5. DUAL-FREQUENCY WIDEBAND L-PROBE PATCH

5.1. Basic L-Probe Dual-Band Antenna

The L-probe patch [13,14] is a wideband patch antenna. This technique can be further extended to dual-band operation [15]. For ease of operation and to reduce cost, the antenna should have only one input for both frequency bands. In this section, the design of a dual-band patch antenna excited by two L probes through one feed is described.

The geometry of a dual-band band patch antenna [15] consisting of two L probes is shown in Fig. 22. The

antenna operates at 900 MHz (λ_1 , lower-band operation) and 1.8 GHz (λ_2 , upper-band operation). The probes are combined together to form a feed structure. The lower-band patch has length $l_1 = 102$ mm ($0.312\lambda_1$) and width, $w_1 = 110$ mm ($0.336\lambda_1$) and is 45.4 mm ($0.139\lambda_1$) above the ground. Two slots with width = 2 mm and length = 90 mm are etched l_1 away from the radiation edge of the lower-band patch. These two slots are used to suppress the excitation of the TM_{20} mode that would influence the upper-band radiation pattern. The upper-band patch with sides $l_2 = 37$ mm ($0.227\lambda_1$) is 21.5 mm ($0.128\lambda_1$) above the ground. Because of the coupling effect of the lower-band patch, the resonant length of this patch is less than that of an isolated patch operated at the same frequency.

The measured return loss S_{11} is as shown in Fig. 23. The impedance bandwidth ($S_{11} < -10$) of 20.8 and 17.9% was found for the lower and upper bands, respectively. It is wide enough to cover GSM 900 and 1800 cellular phone systems. The maximum gain of 8.4 dBi was found in the upper band. The measured radiation patterns are shown in Fig. 24. The 3 dB beamwidths of lower and upper bands are 71° and 75° in the H plane and are 56° and 60° , in the E plane. The cross-polarization is -10 and -13 dB in the lower and upper bands, respectively.

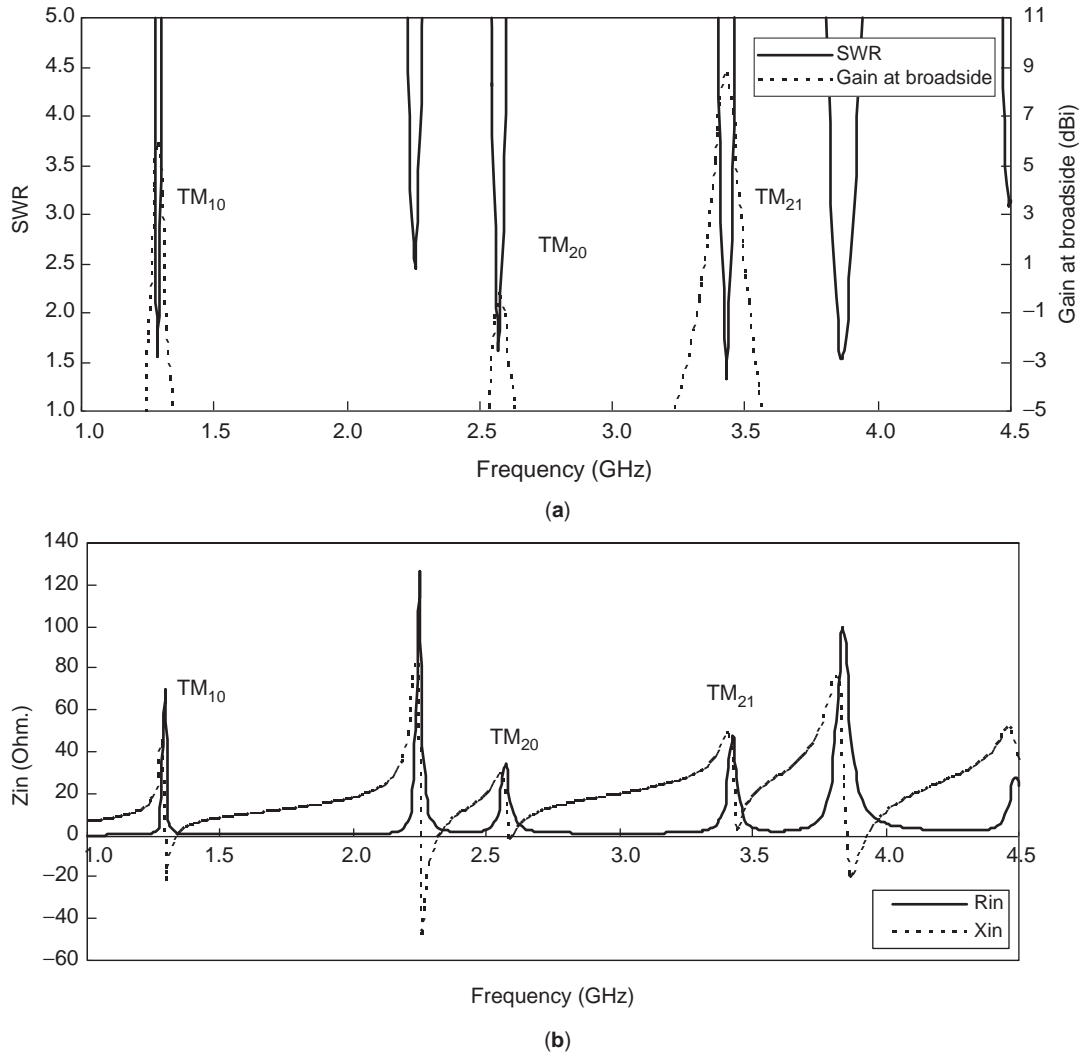


Figure 30. Standing-wave ratio and gain (a) and input impedance (b) of triangular patch antenna.

5.2. Advanced Design For L-Probe Dual-Band Antenna Bandwidth

The L-probe dual-band patch antenna can be modified to have a DC grounded feature, which protects the antenna against the lightning hazard. This is accomplished by adding a short-circuit stub in the feeding network of the antenna. Such a design is presented in this section.

The geometry of the antenna, which operates at both 900 MHz (f_1) (lower band) and 1800 MHz (f_2) (upper band), is shown in Fig. 25. The antenna consists of two rectangular patches of different sizes. The thickness of each aluminum patch is 1 mm. The lower-band patch (patch L) with dimensions 100 mm ($0.33\lambda_1$) \times 15 mm ($0.35\lambda_1$) is supported 45.37 mm above the ground by plastic pins. The height and length of the larger probe are 29.265 and 57.8 mm, respectively, and the antenna is located 55.55 mm (about $1/4\lambda_1$) away from the short-circuiting pin. In order to suppress the TM_{02} mode of the larger patch, two slots with sides 80×2 mm are etched on the

patch. The upper-band patch (patch U) with dimensions 63.5 mm ($0.381\lambda_2$) \times 54 mm ($0.324\lambda_2$) is located 22.9 mm ($0.137\lambda_2$) above the ground. The height and length of the smaller probe are 15.22 and 32.44 mm, respectively, and the probe is located at 141.38 mm (about $0.75\lambda_2$) away from the short-circuiting pin. The thickness and dielectric constant of the microwave substrate are, respectively 1.5 mm and 2.65. The characteristic impedance transmission line is 50 Ω . The size of the ground plane is 200×275 mm.

Figure 26 shows the measured standing-wave ratio (SWR) and gain of the dual-band patch antenna. For $SWR < 2$, the impedance bandwidth of 27.5% was found for lower-band operation and 14.1% for the upper-band operation. The results show the antenna is wide enough to cover the GSM 900 and 1800 mobile phone systems. An average gain of 8 dBi was found for the lower band and 7.5 dBi for the upper band. The measured radiation patterns of the antenna are shown in Fig. 27. The characteristics of the vertical and horizontal planes are summarized in Table 3.

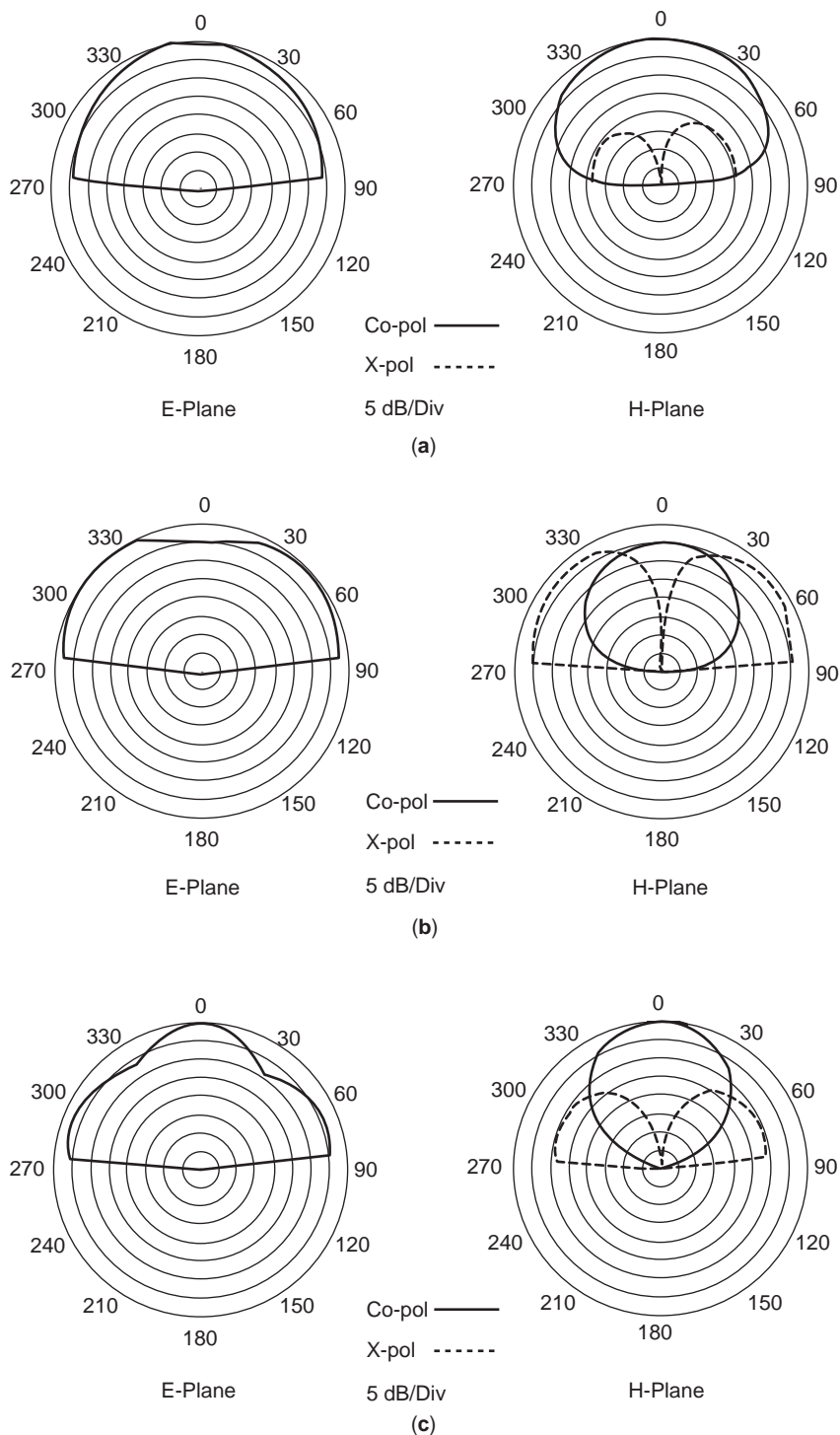


Figure 31. Radiation patterns of triangular patch antenna: (a) TM_{10} mode; (b) TM_{20} mode; (c) TM_{21} mode.

6. MULTIFREQUENCY PATCH ANTENNAS

6.1. Single-Element Triple-Frequency Triangular Patch Antennas

As mentioned in Section 2.1, it is possible for a single-element patch antenna to operate at several frequency bands corresponding to the various resonant modes

pertaining to the patch structure. For dual-band operation, we can simply select the rectangular patch, which can be operated at the TM_{01} and TM_{03} broadside modes with a single feed. For triband operation, other patch shapes have to be considered.

From the cavity model analysis of equilateral triangular patch antennas [16], it appears that we can excite the three broadside modes, namely, TM_{10} , TM_{20} , and TM_{21}

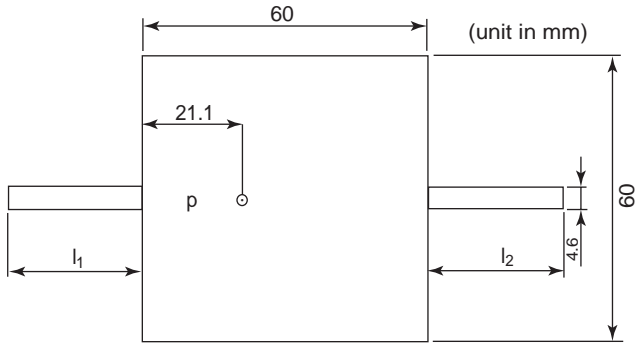


Figure 32. A coaxially fed square patch antenna loaded with stubs (substrate thickness = 0.79 mm, dielectric constant = 2.17).

modes, with a single feed. In particular, if we select the length of each edge of an equilateral triangular patch to be 10 cm, as shown in Fig. 28, we can ensure that the antenna matches at the three modes by choosing the feed position $g = 50$ mm (Fig. 29) from an edge of the triangle.

Using the IE3D¹ simulation tool, we have analyzed the performance of the triangular patch antenna. The gain, SWR, input impedance, and radiation pattern are shown in Figs. 30 and 31. It can be observed that the antenna does resonate at the TM_{10} , TM_{20} , and TM_{21} modes with resonant frequencies of 1299, 2599, and 3499 MHz, respectively. The three modes basically have broadside radiation patterns.

6.2. Multifrequency Stub-Loaded Patch Antennas

As described in Section 3.1, a patch antenna can be operated in dual frequency if the patch is loaded with a single stub. The technique can be generalized for designing patch antennas with triple-band operation. As demonstrated by Daniel and Kumar [17], it is possible to design a square patch antenna with the triband characteristic by loading the two radiating edges with two open-circuited stubs of unequal lengths, as shown in Fig. 32.

To confirm the results presented in Ref. 17, we have employed the IE3D software to simulate the performance of this antenna. The simulated SWRs of the antenna with and without the two stubs are shown in Fig. 33. It can be observed that without the stubs, only one resonant mode is found within the frequency range 1.2–2 GHz. With the addition of the two stubs, three modes are generated. The antenna can now be operated at around 1.252, 1.540, and 1.935 GHz. This antenna has a frequency ratio of 1:1.23:1.55, which indicates that the three operating bands are more closely packed than those of triangular patch antenna with multimode operation. The radiation patterns of the antenna are shown in Fig. 34. It can be observed that the three modes radiate strongly in the broadside direction.

¹IE3D is a tradename for the MoM full-wave electromagnetic simulator manufactured by Zeland Software.

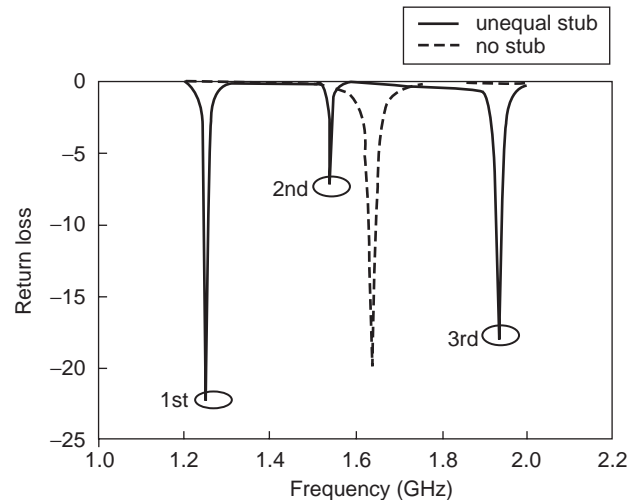


Figure 33. Return loss of square patch antennas.

6.3. Multifrequency Microstrip Antenna Consisting Of Parallel Microstrip Dipoles

Although the two designs presented in Sections 6.1 and 6.2 can be operated at three frequency bands, the gain varies substantially between different bands. In particular, a very low gain is observed at the middle frequency. Also, in these techniques, it is difficult to generate more than three broadside modes with a single feed. Alternatively, multifrequency operation can be realized by using electromagnetically coupled parallel microstrip dipoles of different lengths excited by the aperture-coupling technique [18]. As shown in Fig. 35, six dipoles and the feed-line are centered on the coupling aperture. To achieve a uniform excitation of the dipoles, the longest pair of dipoles is located closer to the center of the aperture and the shortest closer to the edges of the aperture. With appropriate selection of dimensions [18], a triple-band patch antenna operated at $f_1 = 5.3$ GHz, $f_2 = 6.28$ GHz, and $f_3 = 7.19$ GHz was successfully designed. The bandwidth at bands 1, 2, and 3 are respectively 4%, 4.5%, and 2.1%. This is an attractive feature as the difference between the bandwidths at the different frequency bands is small. Moreover, the antenna has similar broadside radiation patterns at the three bands.

6.4. Multifrequency Microstrip Antenna Using Multiple Stacked Elements

Another technique has been proposed for the design of a multifrequency patch antenna with similar bandwidth and gain at different frequency bands. As shown in Fig. 36, the antenna consists of a driven patch and four parasitic patches placed underneath the driven patch [19].

The driven patch, which has dimensions of 51×51 mm, is fed by capacitive coupling in order to mitigate the mismatching due to the probe inductance. It is etched on a thin dielectric substrate of thickness 0.8 mm and dielectric constant 3.38. The parasitic patches are supported by foam layers and are slightly larger than the driven patch. Their dimensions are adjusted for optimum

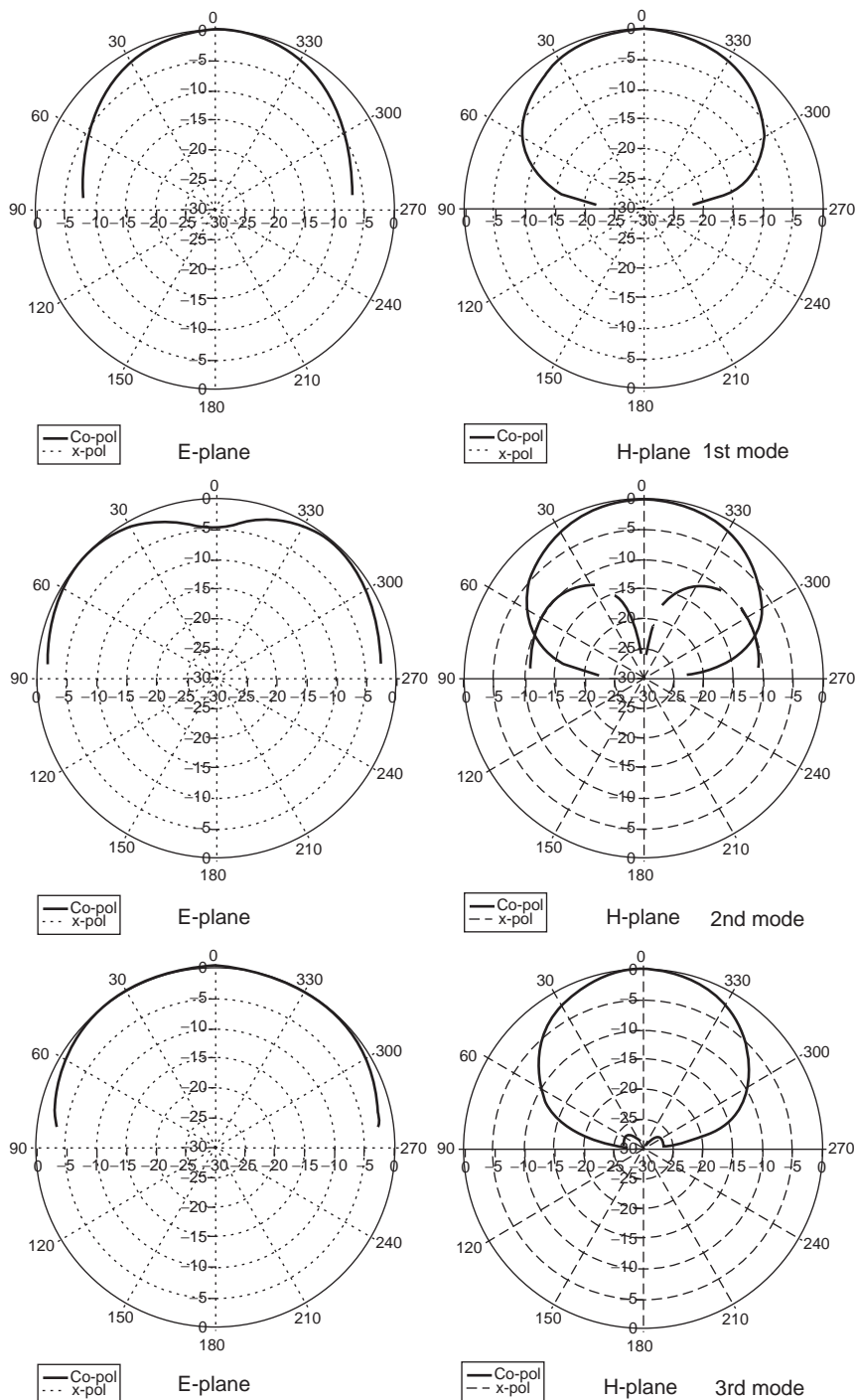


Figure 34. Radiation patterns of square patch antenna. (This figure is available in full color at <http://www.mrw.interscience.wiley.com/erfme>.)

performance based on simulation. The total thickness of the antenna is 15.6 mm. Measured results of the antenna are listed in Table 4.

It was found that the antenna could be operated at five frequency bands with gains varying from 7 to 9 dB, and bandwidth varying from 1.5% to 5.5%. The operating bands are closely packed in this design (small frequency ratios). Moreover, the radiation patterns at different frequencies are similar and stable. The radiation pattern is shown in Fig. 37.

7. CONCLUDING REMARKS

Many present-day wireless applications demand aesthetically pleasing devices operating at dual- or triple-frequency bands. Examples include triband GSM mobile phones, integrated GPS/GSM receivers, and dual-band wireless local-area networks. Because of its low-profile characteristic, multiband microstrip antennas are becoming the most popular choice as an embedded or conformal antenna in modern wireless devices or systems.

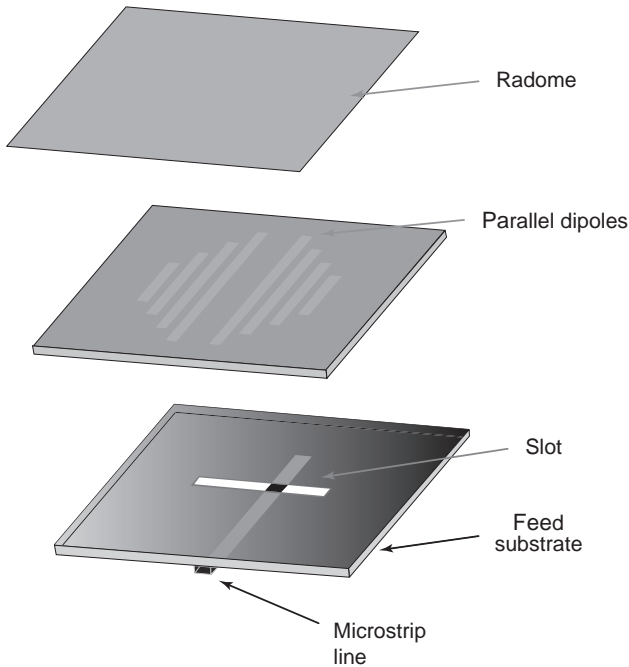


Figure 35. Geometry of microstrip antenna with parallel microstrip dipoles. (From Croq and Pozar [18], © 1992 IEEE).

Table 4. Bandwidth and Gain Experimental Data

Band	Frequency (GHz)	Bandwidth (%)	Gain (dB)
1	1.634	5.5	9.2
2	1.819	2.0	8.4
3	1.954	2.7	7.6
4	2.092	1.5	6.9
5	2.289	5.3	7.3

In this article, major techniques available in the literature for designing dual-band and multiband microstrip antennas have been reviewed, with emphasis on the principles of operation and design guidelines. It has been demonstrated that if a large frequency ratio is required, the multimode technique is preferable, whereas if a small frequency ratio is required, the multiple-resonator techniques, including the stacked patch or coplanar patch geometry, are good choices.

BIBLIOGRAPHY

1. S. S. Zhong and Y. T. Lo, Single-element rectangular microstrip antenna for dual-frequency operation, *Electron. Lett.* **19**:298–300 (1983).
2. S. A. Long and W. D. Walton, A dual frequency stacked circular disk antenna, *IEEE Trans. Anten. Propag.* **27**:270–273 (1979).
3. J. S. Dahele and K. F. Lee, A dual-frequency stacked microstrip antenna, *IEEE AP-S Int. Symp. Digest*, 1982, pp. 308–311.
4. J. S. Dahele, K. F. Lee, and D. P. Wong, Dual-frequency stacked annular-ring microstrip antenna, *IEEE Trans. Anten. Propag.* **35**:1281–1285 (1987).
5. Z. Fan and K. F. Lee, Hankel transform domain analysis of dual-frequency stacked circular-disk and annular-ring microstrip antennas, *IEEE Trans. Anten. Propag.* **39**(6):867–870 (1991).
6. S. E. Davidson, S. A. Long and W. F. Richards, Dual-band microstrip antennas with monolithic reactive loading, *Electron. Lett.* **21**:936–937 (1985).

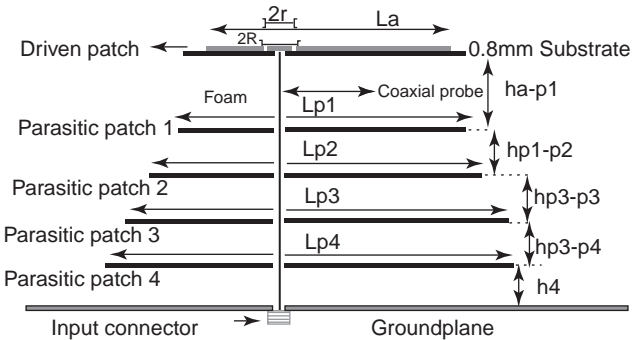


Figure 36. Geometry of microstrip antenna with stacked elements. (From Anguera et al. [19], © 2003 IEEE).

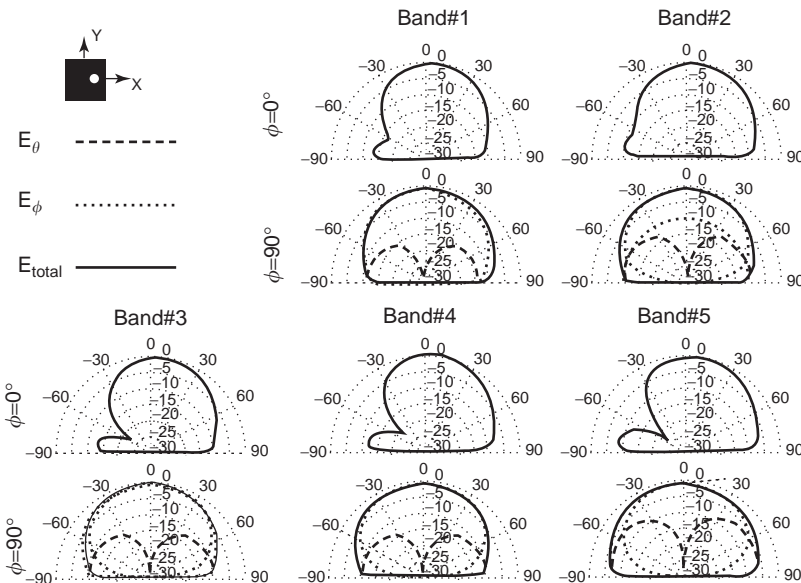


Figure 37. Radiation pattern of microstrip antenna with stacked elements (From Anguera et al. [19], © 2003 IEEE).

7. S. Maci, G. Biffi Gentili, P. Piazzesi, and C. Salvador, Dual band slot loaded patch antenna, *IEE Proc. Microwaves Anten. Propag. H* **142**:225–232 (1995).
8. K. F. Lee, Y. X. Guo, J. A. Hawkins, R. Chair, and K. M. Luk, Theory and experiment on microstrip patch antennas with shorting walls, *IEE Proc. Microstrip Anten. Propag.* **147**(6):521–525 (2000).
9. Y. X. Guo, K. M. Luk, and K. F. Lee, Dual-band slot-loaded short circuited patch antenna, *Electron. Lett.* **36**:289–291 (2000).
10. Y. X. Guo, K. M. Luk, K. F. Lee, and R. Chair, A quarter-wave U-shaped patch antenna with two unequal arms for wideband and dual-frequency operations, *IEEE Trans. Anten. Propag.* **50**:1082–1087 (2002).
11. F. Yang and Y. Rahmat-Samii, Wideband dual parallel slot patch antenna (DPSPA) for wireless communications, *IEEE AP-S Int. Symp. Digest*, 2000, 1650–1653.
12. T. Huynh and K. F. Lee, Single-layer single-patch wideband microstrip antenna, *Electron. Lett.* **31**:1310–1312 (1995).
13. K. M. Luk, C. L. Mak, Y. L. Chow, and K. F. Lee, Broadband microstrip patch antenna, *Electron. Lett.* **34**:1441–1443 (1998).
14. C. L. Mak, K. M. Luk, K. F. Lee, and Y. L. Chow, Experimental study of a microstrip patch antenna with an L-shaped probe, *IEEE Trans. Anten. Propag.* **48**:777–783 (2000).
15. K. M. Luk, C. H. Lai, and K.F. Lee, Wideband L-probe-feed patch antenna with dual-band operation for GSM/PCS base stations, *Electron. Lett.* **35**:1123–1124 (1999).
16. K. F. Lee, K. M. Luk, and J. S. Dahele, Characteristics of the equilateral triangular patch antenna, *IEEE Trans. Anten. Propag.* **36**(11):1510–1518 (1988).
17. A. E. Daniel and G. Kumar, Tuneable dual and triple frequency stub loaded rectangular microstrip antenna, *IEEE Antennas Propagation Symp. Digest*, June 1995 pp. 2140–2143.
18. F. Croq, and D. M. Pozar, Multifrequency operation of microstrip antennas using aperture coupled parallel resonators, *IEEE Trans. Anten. Propag.* **40**(11):1367–1374 (1992).
19. J. Anguera, G. Font, C. Puente, C. Borja, and J. Soler, Multifrequency microstrip patch antenna using multiple stacked elements, *IEEE Microwave Wireless Compon. Lett.* **13**(3):123–124 (March 2003).

ELECTROMAGNETIC-BANDGAP-ASSISTED BANDPASS FILTERS

NEMAI C. KARMAKAR
Monash University
Clayton, Victoria, Australia

MOHAMMAD NURUNNABI
MOLLAH
Khulna University of
Engineering and Technology
Khulna, Bangladesh

1. INTRODUCTION

The new millennium has brought many broadband design challenges, with the memory-hungry multimedia contents and new-generation wireless mobile communications demand for larger ever bandwidth to satisfy very high data rates. The demand can be met with the design with high functionality per unit volume. Naturally frequency agile and unwanted frequency immune responses from RF and microwave devices are needed. Electromagnetic bandgap structures (EBGSs) are playing a vital role in enhancing the performance of microwave devices. EBG materials are periodic structures, that exhibit wide bandpass and band-rejection properties at microwave frequencies. The introduction of periodic perturbation such as dielectric rods, holes, and patterns in waveguides and PCB substrates has resulted in the development of EBGSs, which are also termed *photonic bandgap* (PBG) materials. As in a photonic crystal (PC), photon propagation is impeded by electrons and the electromagnetic (EM) waves in a EBG material are impeded by the periodic discontinuity, hence resulting in a slow-wave structure. Because of their unique properties of distinct passband and stopband characteristics, planar PBG materials find potential applications in antennas, amplifiers, waveguides, filters, power dividers/combiners, phased arrays, electromagnetic compatibility (EMC) measurements, and many other microwave devices [1–18]. The passband characteristic of the PBG structure (PBGs) is used as a slow wave medium, which reduces the size of electronics boards. The wide stopband is applied to suppress spurious transmission and leakage in guided structures such as conductor-backed coplanar waveguides (CPWs) and striplines. Careful design of the PBGS can improve antenna matching and hence bandwidth, and can suppress spurious harmonics, sidelobes, and backlobes of antenna elements and arrays. In filters PBGSs are used for harmonic suppressions such that in a filterbank the interference with other filters can be minimized.

This article investigates PBG-assisted asymmetric coupled-line bandpass filters (BPFs). Both conventional circular patterned PBGs and defected ground structures (DGSs) are used to suppress the harmonics of the filter. Since PBG is a periodic structure, the theory of periodic structures is reviewed first. The passband and stopband phenomena are explained with the help of capacitively

loaded transmission line. The formulation for full-wave analysis of 1D PBG structure is also reported. The transmission-line model of a modified uniplanar compact PBG structure (UCPBGS) is analyzed and a dispersion diagram of the UCPBGS is presented. The calculated stopband and passband properties of the modified UCPBGS validate the model. This structure is used in harmonic suppression of a hairpin filter [37].

Before presenting the PBG-assisted BPF design, we will analyze a PBG-engineered 50- Ω transmission line realized by 2D and 1D circular patterned uniform PBGSs (UPBGSs). A comparison of the 1D and 2D UPBGSs shows that there is no significant difference in passband and stopband properties between the two. Next, UPBGSs are used to suppress the harmonics of a four-section asymmetric coupled-line BPF. Different designs of UPBG-assisted BPFs are investigated and the *S*-parameter performance is described to investigate the effectiveness of harmonic suppression. This comprehensive investigation reveals that a careful design procedure is required to achieve the optimum suppression of harmonics without affecting the passband performance of PBG-assisted BPFs. The strong interaction between the poles and zeros of PBGS and BPFs drastically distorts the passband performance of BPF.

We investigated nonuniform PBGSs in 2003 [15]. Nonuniform PBGSs provide better passband return loss (RL) and minimum passband ripples compared with those for the conventional UPBGSs. We also observe that the nonuniform PBGSs yield better harmonic suppression compared with the UPBGSs. In our investigation nonuniform *binomially* distributed PBGSs are used for significant harmonic suppression. Few designs are investigated to observe the effects of different numbers and positions of the unit cells of binomially distributed PBGSs on the harmonic suppression and passband performances.

Finally, DGS has been used in the BPF. The wide stopband property of the DGS is exploited to suppress both second and third harmonics of the BPF. The uniform and nonuniform PBGSs are designed at a single stopband frequency, which is the second- or third-harmonic frequency of BPFs. Therefore, two sets of PBGSs are needed to suppress the second and third harmonics. The new dumbbell-shaped DGS reported in the open literature [19] is more compact and yields very wide stopband performance [20]. These DGS assisted BPFs are investigated for simultaneous second- and third-harmonic suppressions of BPF. Detailed investigations into DGS-assisted BPFs are presented toward the end of the article, followed by the conclusion.

2. THEORY OF PBG STRUCTURES

PBGSs have occupied significant portions of the microwave engineering literature. PBGSs enhance the performance of many microwave devices and components. The acronym PBG is actually used in optical communication.

More recently, PBG-related terminology has been scaled down for RF engineering applications. PBGSs are old concepts because they generate stopband- and passband-like periodic structures. To understand the stopband and passband phenomena of PBGSs, we first review the conventional periodic structure [21].

Waveguides and transmission lines loaded at periodic intervals with identical reactive elements are referred to as *periodic structures* [21]. This type of period structure yields two distinct properties:

1. Passband–stopband characteristics
2. Stemming waves with phase velocity lower than the velocity of light in free space

In the passband EM waves does not attenuate along the structure. There is some incidental conductor loss only. On the other hand, in the stopband the EM waves are totally attenuate so that they cannot propagate throughout the structure. Stopband characteristics are very important to suppress surface waves. EM waves having the velocity lower than the velocity of light in free space are called *slow waves*. Periodic perturbation in the ground plane provides periodic discontinuity. Thus the slow-wave property of the EM waves is achieved. Slow-wave structures (SWSs) are promising candidates for compact design.

2.1. Periodic Structures

2.1.1. **Capacitively Loaded Transmission Line.** A simple capacitively loaded transmission line can be analyzed to conceive the idea of periodic structures. The velocity of EM wave in a physically smooth transmission line can be written as

$$V_p = \frac{1}{\sqrt{LC}} = \frac{1}{\sqrt{\mu_0 \epsilon_0 \epsilon_r}} \tag{1}$$

where V_p is the phase velocity of EM wave, L is the series inductance per unit length, C is the shunt capacitance per unit length, ϵ_r is the dielectric constant of the medium surrounding the conductor, and ϵ_0 and μ_0 are free-space values of the permeability and permittivity, respectively.

From Eq. (1) it is seen that with the value of the dielectric constant (ϵ_r), the phase velocity of EM waves reduces. One problem arises from this simple way of reducing the phase velocity. If we increase the value of dielectric constant, then higher-order modes propagate. To avoid this propagation, the cross-sectional dimensions of the line must be reduced accordingly. This is the limitation of increasing the value of dielectric constant to get the reduced value of the phase velocity of EM waves.

We know $LC = \mu_0 \epsilon_r \epsilon_0$ for dielectric media, so any attempt of increasing the value of C to reduce the phase velocity is restricted here, because if we increase the value of C , the value of L will automatically reduce to maintain the relation $LC = \mu_0 \epsilon_r \epsilon_0$ in a physically smooth transmission line. Under this circumstance, we can relax the restriction of a physically smooth transmission line instead of an electrically smooth line. An effective increase in the shunt capacitance per unit length (C) can be

achieved without disturbing the value of inductance per unit length (L) by loading lumped shunt capacitance at periodic intervals where the spacings between the loaded shunt capacitance are small compared with the wavelength. At this stage, although the line is not physically smooth, it will be an electrically smooth line. Under this condition the capacitance will increase, which can be observed from the following equation of the phase velocity

$$V_p = \frac{1}{\sqrt{(C + C_0/d)L}} = \frac{\omega}{\beta} \tag{2}$$

where C_0/d is the loaded lumped capacitance per unit length, ω is the angular frequency, and β is the phase constant.

There are many ways of obtaining periodic structures. One of the simplest ways is to load a thin diaphragm at a regular interval in a coaxial transmission line. The diaphragm may be machined as the integral part of the center conductor. The fringing electric field in the vicinity of the diaphragm increases the local storage of electric energy and gives more extra shunt capacitance.

2.1.2. **Circuit Analysis of a Periodic Structure.** We may assume a transmission line to be a combination of the finite unit cell of the structure. Figure 1a illustrates the equivalent circuit of a basic unit cell of a capacitively loaded coaxial line, and Fig. 1b shows the complete transmission line composed of the basic unit cells.

The unit cell may be divided into three parts: two transmission lines of length $d/2$ on either side of a normalized shunt susceptance B .

2.1.2.1. **Relationship between Input and Output Variables.** Let V_n and I_n be the input voltage and current variables, respectively, and let V_{n+1} and I_{n+1} be the output voltage and current variables, respectively.

The relationship can be found by using the *ABCD* transmission matrix. Overall, the *ABCD* parameters of a unit cell can be written as

$$\begin{bmatrix} A & B \\ C & D \end{bmatrix} = \begin{bmatrix} \cos \theta/2 & j \sin \theta/2 \\ j \sin \theta/2 & \cos \theta/2 \end{bmatrix} \begin{bmatrix} 1 & 0 \\ j\bar{B} & 1 \end{bmatrix} \tag{3}$$

$$\begin{bmatrix} \cos \theta/2 & j \sin \theta/2 \\ j \sin \theta/2 & \cos \theta/2 \end{bmatrix}$$

where $\theta = k_0 d$ and k_0 is the free-space wavenumber.

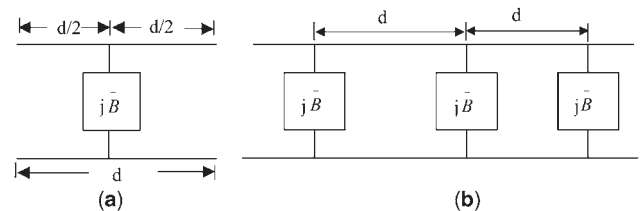


Figure 1. (a) Equivalent-circuit model of a unit cell of capacitively loaded line; (b) a transmission line cascaded by unit cells.

Our unit cells are symmetric where $A=D$. When an EM wave propagates through periodic structures, the voltage and current at the $(n+1)$ th terminal are equal to the values of the voltage and current of the n th terminal except for the phase delay. Please note that we assume the transmission lines to be lossless. Therefore, the relations of V and I are as follows:

$$V_{n+1} = e^{-\gamma d} V_n \quad (4)$$

$$I_{n+1} = e^{-\gamma d} I_n \quad (5)$$

Using Eqs. (4) and (5), we find that Eq. (6) generates a matrix eigenvalue equation for the solution of V_{n+1} and I_{n+1} :

$$\begin{bmatrix} V_n \\ I_n \end{bmatrix} = \begin{bmatrix} A & B \\ C & D \end{bmatrix} \begin{bmatrix} V_{n+1} \\ I_{n+1} \end{bmatrix} = e^{\gamma d} \begin{bmatrix} V_{n+1} \\ I_{n+1} \end{bmatrix} \quad (6)$$

Nontrivial solutions for V_{n+1} and I_{n+1} are obtained if the determinant of this matrix vanishes:

$$\begin{bmatrix} A - e^{\gamma d} & B \\ C & D - e^{\gamma d} \end{bmatrix} = 0 \quad \text{or} \\ AD - BC + e^{2\gamma d} - e^{\gamma d}(A+D) = 0$$

Assuming reciprocal circuit and letting $AD - BC = 1$, we have $1 + e^{2\gamma d} - e^{\gamma d}(A+D) = 0$ or

$$\cosh \gamma d = \frac{A+D}{2} \quad (7)$$

Expansion of (3) shows that $A=D = \cos \theta - (\bar{B}/2) \sin \theta$. Substituting these values in Eq. (7), we have

$$\cosh \gamma d = \cos \theta - \frac{\bar{B}}{2} \sin \theta \quad (8)$$

Equation (8) is a very vital equation for understanding passband and stopband phenomena created by periodic structure.

2.1.2.2. Explanation. We can explain the phenomena with the following cases.

Case 1. When the right-hand side (RHS) of Eq. (8) is less than 1, $\cosh \gamma d = \cos \theta - (\bar{B}/2) \sin \theta < 1$, then, under these circumstances $\gamma = j\beta$ and

$$\cos \beta d = \cos \theta - \frac{\bar{B}}{2} \sin \theta \quad (9)$$

Case 2. When $\cos \theta - (\bar{B}/2) \sin \theta > 1$, we have $\cosh \gamma d = \cos \theta - (\bar{B}/2) \sin \theta > 1$. Under these circumstances $\gamma = \alpha$, $\beta = 0$, and

$$\cosh \alpha d = \cos \theta - \frac{\bar{B}}{2} \sin \theta \quad (10)$$

Case 3. When $\cosh \gamma d = \cos \theta - (\bar{B}/2) \sin \theta < -1$, then $\gamma d = j\pi + \alpha$ and $\cosh \gamma d = \cosh(j\pi + \alpha d) = -\cosh \alpha d$ or

$$-\cosh \alpha d = \cos \theta - \frac{\bar{B}}{2} \sin \theta < -1 \\ \cosh \alpha d = - \left(\cos \theta - \frac{\bar{B}}{2} \sin \theta \right) \quad (11)$$

Equations (9)–(11) are very important for understanding the propagation of EM waves through periodic structures. It is apparent that there will be frequency bands for which unattenuated wave propagation is possible, separated by frequency bands in which the wave is attenuated. Fully attenuated waves yield stopband, and unattenuated waves generate passband. Thus these equations help us understand stopband and passband phenomena of PBGS.

Let us consider $d \ll \lambda_0$ in our case. So the electrical length $\theta = k_0 d$ will be small and βd will also be small. Under these conditions

$$\cos \theta = 1 - \frac{\theta^2}{2} \quad (12)$$

$$\cos \beta d = 1 - \frac{\beta^2 d^2}{2} \quad (13)$$

Equation (9) then assumes either of the following forms:

$$\Rightarrow 1 - \frac{\beta^2 d^2}{2} = 1 - \frac{k_0^2 d^2}{2} - \frac{B k_0 d}{2} \\ \beta^2 d^2 = k_0^2 d^2 + \bar{B} k_0 d \quad (14)$$

$$\beta^2 = k_0^2 + \frac{\bar{B} k_0}{d}$$

We have the relations:

$$k_0^2 = \omega^2 \mu_0 \epsilon_0 = \omega^2 LC \quad (15)$$

$$\bar{B} = \frac{B}{Y_c} = \omega C_0 \sqrt{\frac{L}{C}} \quad (16)$$

(where characteristic impedance $Z_c = \sqrt{L/C} = 1/Y_c$). Substituting k_0 and \bar{B} from (15) and (16) in Eq. (14), we have

$$\beta^2 = \omega^2 LC + \omega^2 \frac{LC_0}{d}$$

or

$$\beta = \omega \sqrt{L \left(C + \frac{C_0}{d} \right)} \quad (17)$$

Equation (17) is very important in understanding the slow-wave effect of periodic structures. We can observe new value of capacitance $C + C_0/d$ in which capacitance has been increased by C_0/d . Therefore, we find that at low frequencies where $d \ll \lambda_0$, the loaded line has a shunt

capacitance $C + C_0/d$ per unit length. Increased β value results in reduction of the phase velocity.

2.2. Full-Wave Analysis of One-Dimensional PBG Structure

2.2.1. Fundamental Equation. Maxwell's equations are fundamental equations to form the foundation for electromagnetic theory. These equations can be written in differential form as follows:

$$\nabla \times \mathbf{E} = -\frac{\partial \mathbf{B}}{\partial t} \quad (18)$$

$$\nabla \times \mathbf{H} = \mathbf{J} + \frac{\partial \mathbf{D}}{\partial t} \quad (19)$$

$$\nabla \cdot \mathbf{D} = \rho \quad (20)$$

$$\nabla \cdot \mathbf{B} = 0 \quad (21)$$

where \mathbf{E} is the electric field intensity, \mathbf{B} is the magnetic flux density, \mathbf{H} is the magnetic field intensity, and \mathbf{D} is the electric flux density. The electric current density \mathbf{J} and electric charge density ρ are the sources of the electromagnetic fields.

The constitutive relations are

$$\mathbf{D} = \epsilon_r \epsilon_0 \mathbf{E} \quad (22)$$

$$\mathbf{B} = \mu_r \mu_0 \mathbf{H} \quad (23)$$

where ϵ_r and ϵ_0 are the relative permittivity and free-space permittivity, respectively and μ_r and μ_0 are the relative permeability and free-space permeability, respectively. The relation between the electric charge density and electric current density is defined as the continuity equation

$$\nabla \cdot \mathbf{J} = -\frac{\partial \rho}{\partial t} \quad (24)$$

Finally, Lorentz' force equation determines the total electromagnetic force on a charge q to be

$$\mathbf{F} = q(\mathbf{E} + \mathbf{u} \times \mathbf{B}) \quad (25)$$

where \mathbf{u} is the velocity of the moving charge.

Equations (18)–(25) provide the necessary framework for predicting all macroscopic electromagnetic interactions.

2.2.2. Analytical Techniques. The use of Maxwell's equations in the wave equation and the understanding of Floquet's principle yield the eigenvalue equation for the periodic structure. The solution of the eigenvalue equation for the periodic structure can be obtained by the use of Fourier series. The EM wave may be transverse electric (TE) or transverse magnetic (TM) depending on the orientation of the structure. We present a mathematical model for a rectangular patterned UPBGS. The structure of rectangular patterned uniform PBGSs is shown in Fig. 2.

2.2.2.1. Transverse Electric (TE_x) Case. The electric field can be expanded [22] as a periodic function of plane waves

in x with period d and prescribed propagation constant of k_{x0} as follows

$$\mathbf{E}(x, y) = \hat{z}E_z(x, y) = \hat{z}E_p(x)e^{-jk_{x0}x}e^{-jk_y y} \quad (26)$$

where $E_p(x)$ is the periodic electric field that propagates only in the xy plane, that is, $k_z = 0$. The electric field must satisfy the wave equation, so applying the operator $(\nabla_{xy}^2 + k^2)$ to $E_z(x, y)$ of Eq. (26) and noting that the dielectric constant is a function of x , we obtain

$$\nabla_{xy}^2 E_z(x, y) + k_0^2 \epsilon_r(x) E_z(x, y) = 0 \quad (27)$$

Assuming the parallel slabs to be infinite in the y and z directions, Eq. (27) can be simplified to

$$\begin{aligned} -\frac{d^2}{dx^2} E_z(x, y) + k_y^2 E_z(x, y) \\ = k_0^2 \epsilon_r(x) E_z(x, y) \end{aligned} \quad (28)$$

The periodic electric field is expanded in a Fourier series in x with unknown coefficients a_n , which serves to represent the dependence on y :

$$E_p(x) = \sum_n a_n e^{-j(2\pi n/d)x} \quad (29)$$

Since the dielectric function is also periodic, it is appropriate to expand it in another Fourier series with coefficient b_m :

$$\epsilon_r(x) = \sum_m b_m e^{-j(2\pi m/d)x} \quad (30)$$

Substituting the Fourier expansions for the field and the dielectric into Eq. (28) and carrying out the algebraic

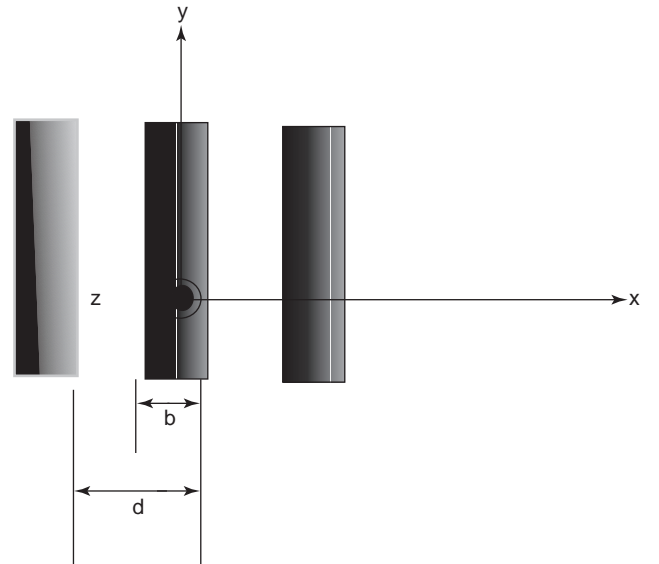


Figure 2. One-dimensional lattice of dielectric slabs having width b and period d .

operations, we obtain

$$\begin{aligned} & \sum_n \left[\left(\frac{2\pi n}{d} + k_{x0}^2 \right)^2 + k_y^2 \right] a_n e^{-j(2\pi n/d)x} \\ &= k_0^2 \sum_n \sum_m a_n b_m e^{-j(2\pi m/d)x} e^{-j(2\pi n/d)x} \end{aligned} \quad (31)$$

In order to determine the unknown coefficients a_n and b_m , Eq. (31) is multiplied by an orthogonal function and integrated over one unit cell, which produces a Krönecker delta function for a specific index:

$$\begin{aligned} & \sum_n \left[\left(\frac{2\pi n}{d} + k_{x0} \right)^2 + k_y^2 \right] a_n \delta \left(\frac{2\pi p}{d} - \frac{2\pi n}{d} \right) \\ &= k_0^2 \sum_n \sum_m a_n b_m \delta \left(\frac{2\pi p}{d} - \frac{2\pi m}{d} - \frac{2\pi n}{d} \right) \end{aligned} \quad (32)$$

The convolution in Eq. (32) is easily cast into the following general matrix form

$$\left[\left(\frac{2\pi n}{d} + k_{x0} \right)^2 + k_y^2 \right] a_n = k_0^2 \sum_m b_{n-m} a_m \quad (33)$$

where

$$\begin{aligned} b_{n-m} &= \frac{1}{d} \int_{-(b/2)}^{b/2} (\epsilon_r - 1) \exp \left[-j \frac{2\pi(n-m)}{d} x \right] dx \\ &+ \frac{1}{d} \int_{-(d/2)}^{d/2} (1) \exp \left[-j \frac{2\pi(n-m)}{d} x \right] dx \\ &= \frac{b}{d} (\epsilon_r - 1) \text{sinc} \frac{\pi(n-m)b}{d} + \delta_{n-m} \end{aligned} \quad (34)$$

A generalized linear eigensystem problem is represented by $Ax = \lambda Bx$, where A and B are $n \times n$ matrices. The value λ is an eigenvalue and $x \neq 0$ is the corresponding eigenvector. The propagating modes in the TE_x case are solutions of the generalized linear eigensystem in (33).

The solution of Eq. (33) is obtained [22] using the commercial software Matlab. The resulting eigenvalues of the matrix are the squares of the frequencies of the propagating modes in the structure. The solutions of the frequencies of the propagating modes in the structure are obtained for the specific values of phase shift. The band structures for a 1D lattice of dielectric slabs with filling factor (b/d) of 0.5 is shown in Fig. 3 for $k_{x0}a \in [-\pi, \pi]$. The dielectric constant of the dielectric slab is 13.

Figure 3 shows the dispersion diagram of a square patterned PBGSs. It can be seen that a stopband is present from normalized frequencies of 0.15–0.255 GHz.

2.2.3. Transmission-Line Model of PBG Structures. This section presents the analytical approach of the bandgap performance of UCPBG. The mathematical formulation of UCPBGs is described that has been developed using a transmission-line model [23].

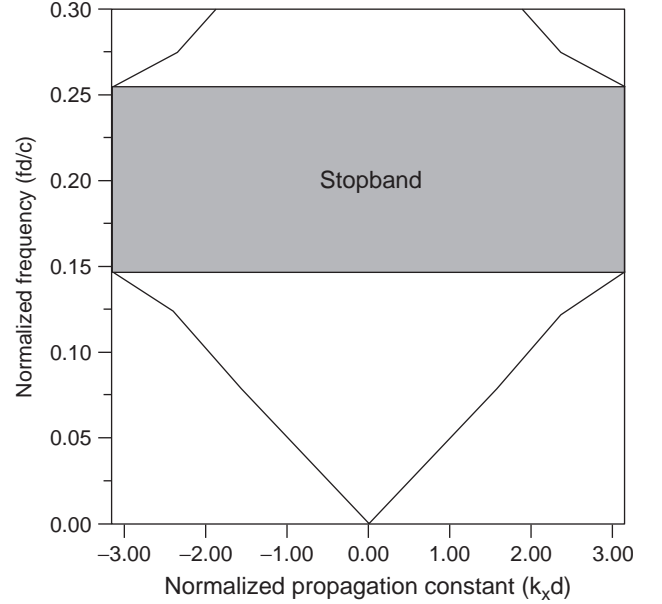


Figure 3. Band structure for 1D lattice of dielectric slabs with Filling Factor of 0.5 having dielectric constant of 13.

Basically, a unit UCPBGS consists of a square metallic patch with four connecting branches. The period of each cell is approximately a half-wavelength of the center frequency of the attenuation pole. The slow-wave effect of the periodic structures causes contraction of the transmission-line wavelength; the period is no longer a half-wavelength of the same center frequency. Hence, the slow-wave effect gives rise to a unique compact device structure. Yang and Itoh [10] designed a periodic UCPBGS using a complex finite-difference time-domain (FDTD) method. The method requires numerous numeric codes to be written for analysis of the specific frequency characteristic of a LPF (lowpass filter) response. The slow-wave factor (SWF) of the UCPBG structure is approximately 1.2–2.4 times higher than that for the unperturbed line at passband. Rahman and Stuchly [23] proposed a transmission-line model to calculate the impedance of each section followed by analysis of the whole structure. The following section presents the transmission-line model of a unit UCPBG cell and the dispersion diagrams.

2.2.3.1. UCPBG Theory. The analytic models of two high-impedance surfaces of UCPBGS are shown in Figs. 4a and 4b. The lattice in Fig. 4a consists of a distribution of square metal patches; each patch is short-circuited to the ground plane by a thin pin. The lattice in Fig. 4b consists of square patches; each is indented with four narrow connecting branches. The circuits can be considered as the arrays of reactively loaded resonators coupled by gap capacitors. If the short-circuiting pins or the connecting branches are disregarded, the period of each cell would be a half-wavelength of the resonant frequency. However, the additional short-circuiting pins or connecting branches increase the reactive loading of the cell and consequently cause a lower resonant frequency. This agrees with the slow-wave effect of the PBG structure. Thus, the 2D

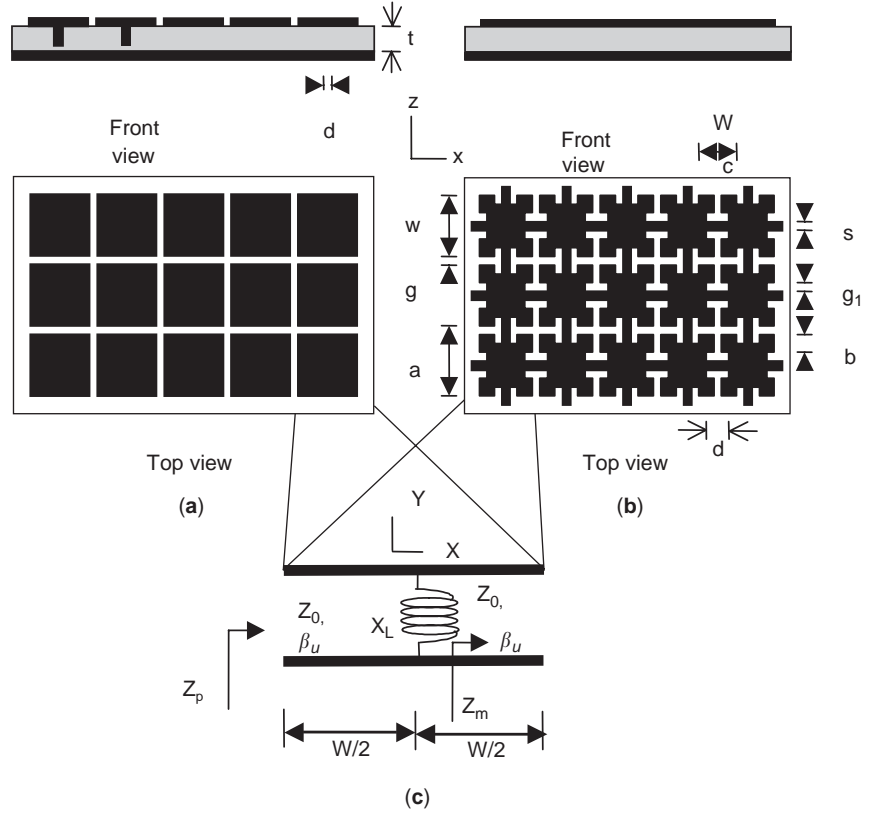


Figure 4. (a) Array of square metal plates with short-circuiting pins; (b) array of square metal plates with connecting branches; (c) equivalent circuit of each resonator section.

UCPBGs arrays shown in Figs. 4a and 4b can be considered as structures periodically loaded with gap capacitances and inductances provided by either the short-circuiting pins or the connecting branches.

The equivalent circuit of the reactive loading part for Figs. 4a and 4b can be represented by Fig. 4c, where Z_p is the reactance of the resonator. The capacitive reactance X_c represents the coupling gap capacitance between the neighboring resonators.

With reference to Fig. 4c, the impedance Z_p of each resonator section is calculated in two steps using the following transmission-line formula (where subscript u is for unloading conditions, l is the length of the transmission line):

$$Z_{in} = Z_0 \frac{Z_1 + jZ_0 \tan(\beta_u l)}{Z_0 + jZ_1 \tan(\beta_u l)} \quad (35)$$

Step 1: Taking $Z_1 = \infty$ at $l = 0$ and calculating Z_m at $l = w/2$ using Eq. (35), we obtain

$$Z_m = -jZ_0 \cot \frac{\beta_u w}{2} \quad (36)$$

Step 2: Taking $Z_1 = X_L/Z_m$ at $l = w/2$, including the reactance X_L represented by a coil, Z_p can be calculated using Eq. (35) as follows:

$$Z_p = Z_0 \frac{Z_1 + jZ_0 \tan(\beta_u w/2)}{Z_0 + jZ_1 \tan(\beta_u w/2)} \quad (37)$$

For each cell in Fig. 4a, using the numerical method given, we can express the inductive loading X_L of the

central short-circuiting pin, with inductance equal to [24]

$$L = 2 \times 10^{-7} t \left[\ln \left(\frac{4t}{d} \right) + 0.5 \left(\frac{d}{t} \right) - 0.75 \right] \quad (38)$$

where t and d are the length and diameter of the pin, respectively.

The coupling capacitance between resonators can be written as [24]

$$C = \frac{w\epsilon_0(1 + \epsilon_r)}{\pi} \cosh^{-1} \left(\frac{a}{g} \right) \quad (39)$$

where a, w, g denote the dimensions as shown in Fig. 4. In Fig. 4 Z_0 is the characteristic impedance of the line and β_u is the phase constant of a lossless line.

Similarly, considering each cell in Fig. 4b, using the numerical method given, the total inductance provided by the four connecting branches, can be calculated as [24]

$$L = 0.25 \times 10^{-7} d \left[\ln \left(\frac{d}{s} \right) + 0.2235 \left(\frac{s}{d} \right) + 1.193 \right] k_g \quad (40)$$

where k_g is a correction factor for the ground plane, which is given as [24]

$$k_g = 0.57 - 0.145 \ln \left(\frac{s}{t} \right) \quad (41)$$

and the coupling capacitance between resonators is [24]

$$C = \frac{2b\epsilon_0(1 + \epsilon_r)}{\pi} \cosh^{-1}\left(\frac{w_c}{g}\right) \quad (42)$$

Both Z_p from Eq. (37) in parallel with reactance of the coupling capacitor X_c of Fig. 4c contributed to the impedance of unit PBG. Hence, the UCPBG array in Figs. 4a and 4b can be treated as a transmission line periodically loaded with lumped impedance Z consisting of Z_p in parallel with X_c with a period of a :

$$Z = \frac{Z_p X_c}{Z_p + X_c} \quad (43)$$

The equivalent circuit for the wave propagation in the x direction shown in Fig. 5 is also an analogous circuit corresponding to the propagation in the y direction. According to Shumpert [22], the $ABCD$ matrix of a cascade of unit UCPBG cell, consisting of a transmission-line section of length $a/2$, series impedance Z as defined in Eq. (43) and another transmission-line section of length $a/2$ is

$$\begin{aligned} \begin{bmatrix} A & B \\ C & D \end{bmatrix} &= \begin{bmatrix} \cos \frac{\beta_u a}{2} & jZ_0 \sin \frac{\beta_u a}{2} \\ jY_0 \sin \frac{\beta_u a}{2} & \cos \frac{\beta_u a}{2} \end{bmatrix} \begin{bmatrix} 1 & Z \\ 0 & 1 \end{bmatrix} \\ &= \begin{bmatrix} \cos \frac{\beta_u a}{2} & jZ_0 \sin \frac{\beta_u a}{2} \\ jY_0 \sin \frac{\beta_u a}{2} & \cos \frac{\beta_u a}{2} \end{bmatrix} \\ &= \begin{bmatrix} \cos \beta_u a + j \frac{Z}{2Z_0} \sin \beta_u a \\ \frac{Z_0}{2} \cos \beta_u a + jZ_0 \sin \beta_u a + \frac{Z}{2} \\ \frac{Z}{2Z_0} \cos \beta_u a + \frac{j}{Z_0} \sin \beta_u a - \frac{Z}{2Z_0^2} \\ \cos \beta_u a + j \frac{Z}{2Z_0} \sin \beta_u a \end{bmatrix} \end{aligned} \quad (44)$$

For the conditions of a reciprocal network, $AD - BC = 1$ and nontrivial solution, the determinant of the matrix must vanish. We derived the following equation of propagation constant γ along with the infinite periodic UCPBGS as

$$\cosh(\gamma a) = \cos(\beta_u a) + j \frac{Z}{2Z_0} \sin(\beta_u a) \quad (45)$$

where Z_0 is the characteristic impedance and β_u is the phase constant of the unloaded line; they are the same as those of the resonators.

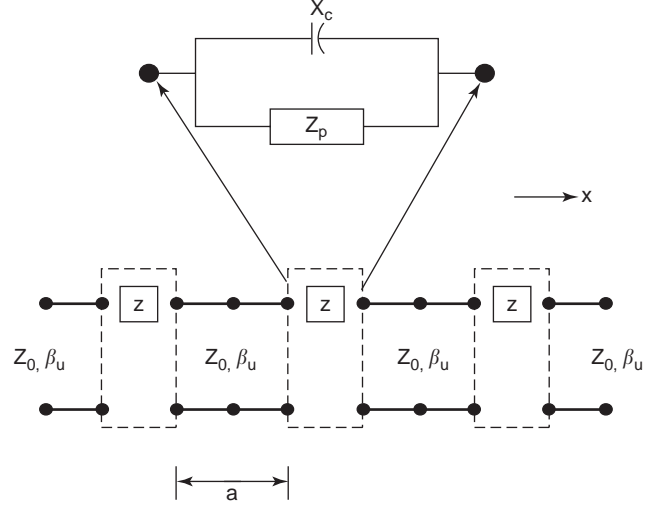


Figure 5. Equivalent circuit of a periodic structure.

With $\gamma = \alpha + j\beta$, Eq. (45) can be rearranged as follows

$$\begin{aligned} &\cosh(\alpha a) \cos(\beta a) + j \sinh(\alpha a) \sin(\beta a) \\ &= \cos(\beta_u a) + j \frac{Z}{2Z_0} \sin(\beta_u a) \end{aligned} \quad (46)$$

where α denotes attenuation of the wave propagation.

Since Z is purely reactive for lossless (ideal-case) resonators, thus rendering the RHS of Eq. (46) a real value, a purely real value is produced for the left-hand side (LHS) of Eq. (46) with the condition of either $\alpha = 0$ or $\beta = 0$, $n\pi/a$. This corresponds to passband and stopband conditions, which are considered below for the wave propagation in PBG structures:

1. The passband condition of the periodic structure $\alpha = 0$ and $\beta \neq 0$, $n\pi/a$, in Eq. (46) is reduced to

$$\cos(\beta a) = \cos(\beta_u a) + j \frac{Z}{2Z_0} \sin(\beta_u a) \quad (47)$$

2. The stopband condition of the periodic structure $\alpha \neq 0$ and $\beta = 0$, $n\pi/a$, in Eq. (46) is reduced to

$$\cosh(\alpha a) = \cos(\beta_u a) + j \frac{Z}{2Z_0} \sin(\beta_u a) \quad (48)$$

We have designed the UCPBGS and simulated the structure using Matlab software. The dimensions of the UCPBGS presented here are $w = 15.0$ mm, $a = 15.13$ mm, $g = 0.13$ mm, $g_1 = 2.615$ mm, $b = 1.885$ mm, $d = 3.8$ mm, $s = 6.0$ mm, and $W_c = 9.1$ mm. The geometry of a modified UCPBG structure is shown in Fig. 6. This type of UCPBG structure can find applications in harmonic suppression of hairpin filters [25–33,37].

The bandgap performance is shown in Fig. 7. As can be seen in the dispersion diagram in Fig. 7, the first stopband is created at 2–2.8 GHz, followed by a passband.

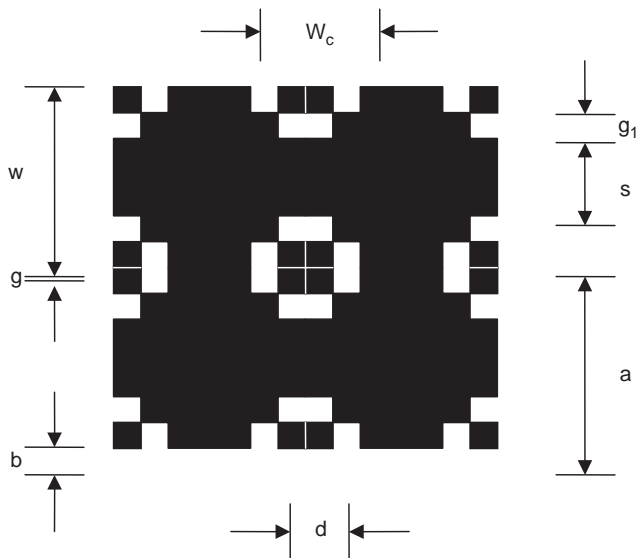


Figure 6. Geometry of a modified UCPBG structure to yield stopband at lower frequency. Dimensions: $w = 15.0$ mm, $a = 15.13$ mm, $g = 0.13$ mm, $g_1 = 2.615$ mm, $b = 1.885$ mm, $d = 3.8$ mm, $s = 6.0$ mm, $W_c = 9.1$ mm.

2.3. Uniform PBG Configurations Applied to Microstrip Lines

In the preceding sections the theory and analysis of periodic structures followed by UCPBG configurations are presented. In modern microwave devices, microstrip transmission lines are commonplace. Therefore, in the following sections, we shall concentrate our investigation only on PBG-assisted microstrip transmission lines. To derive the characteristic performance of PBG-assisted lines, it is more logical to use scattering parameters

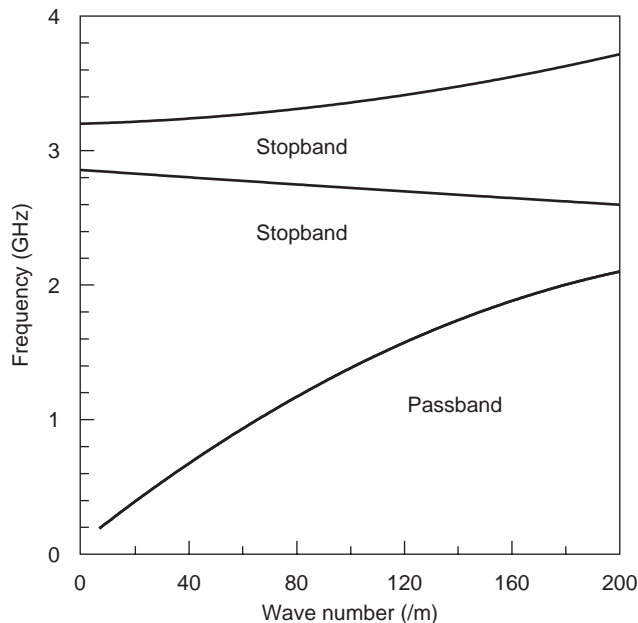


Figure 7. Plot of propagation wavenumber, passband, and stopband frequency range of the 2D UCPBG array. (This figure is available in full color at <http://www.mrw.interscience.wiley.com/erfme>.)

(S parameters) instead of showing the K - β diagram. S parameters are the universally accepted format for device characterization. Moreover, we shall use the commercially available software tool IE3D (from Zeland Software, Inc.) to design and extract S parameters for all designs due to the flexibility of IE3D. IE3D is a method-of-moment (MoM)-based full-wave analysis tool and hence is very accurate.

The perturbation in the ground plane of any microstrip transmission line in the form of PBGS creates stopband. This stopband is useful for suppression of surface waves, leakage, and spurious transmission and to improve the performance of antennas, filters, and other microwave devices and components. The stopband characteristic is significantly influenced by the shape, size, and period of the PBGS located on the ground plane. Therefore it is useful to investigate the performance of the standard 50- Ω microstrip transmission line on PBGSs. We will investigate the PBG-assisted line to verify the performance of three rows of uniform PBGSs as reported by Radisic et al. [33]. In this section we will investigate uniform circular patterned PBGSs (UPBGSs). It is well known that the EM field is highly concentrated under the microstrip line. We will investigate one-dimensional (1D) uniform PBGS (one row) and compare the results with those for two-dimensional (2D) structures (three rows).

2.3.1. Design of Microstrip Transmission Line over Uniform PBGS (UPBGS). With the inclusion of PBGSs, the dispersion characteristics of a transmission line change. First we design a microstrip transmission line with unperturbed ground plane that does not provide any stopband characteristics. Then we observe the effect on the dispersion characteristics in the form of scattering matrices versus frequency by perturbing the ground plane with UPBGSs.

Bragg’s condition is used [34] in the PBGS design to calculate the central stopband frequency. Under this condition, intercell separation (we call it “period”) is approximately equal to half a wavelength of the stopband center frequency. From the intercell separation, the size of the PBG element is calculated on the basis of the filling factor (FF).

The center frequency of the stopband is calculated approximately with the following expression:

$$\beta a = \pi \tag{49}$$

where a is the period of the PBG pattern and β is the wavenumber in the dielectric slab and is defined by the following expression:

$$\beta = \frac{2\pi f_0}{c} \sqrt{\epsilon_e} \tag{50}$$

where f_0 is the center frequency of the stopband, ϵ_e is the effective relative permittivity of the dielectric slab, and c denotes the speed of light in free space.

On the basis of Eqs. (49) and (50), we designed three-row and one-row circular PBGSs in the ground plane of a 50- Ω microstrip transmission line. The geometries of the

two designs are shown in Fig. 8. The S -parameter performances are shown in Fig. 9. It can be seen that both designs provide identical S -parameter performances. Impressive agreement between the two results justifies the fact that the EM field is highly concentrated under the microstrip transmission line. The two side rows in three-row PBGSs have a minimal effect on the dispersion characteristics of the line. This finding motivates us to use 1D PBGSs under only the lines of BPF for harmonic suppression. PBG-assisted BPF will be discussed in the next section.

2.4. PBGSs in Harmonic Suppression of BPF

Nowadays microstrip BPFs are extensively used in modern microwave integrated circuits. The performance of the overall RF system is affected by the spurious transmission of a conventional BPF. Yang et al. [1] propose the use of UCPBGS to suppress the spurious transmission. The UCPBGS is a complex design on a 2D plane and occupies more space in a circuit. On the other hand, classical circular-patterned PBGSs are simple in design and can be made 1D. 1D PBGSs need less space and create fewer problems in electronic packaging. We have shown in Fig. 9 that 1D UPBGS provides stopband performance very similar to that of 2D UPBGS. Therefore 1D UPBGS is used in a filter to suppress harmonics. The numbers of PBG elements have significant influence on S -parameter performance [35]. In this section we will investigate the effect of the number of PBG elements on harmonic suppression of a BPF.

Nonuniform PBGSs realized by the implementation of binomial and Chebyshev distributions yield better S -parameter performance [15]. We will determine whether the configuration of nonuniform PBGSs can improve harmonic suppression. We will use only binomially distributed PBG elements.

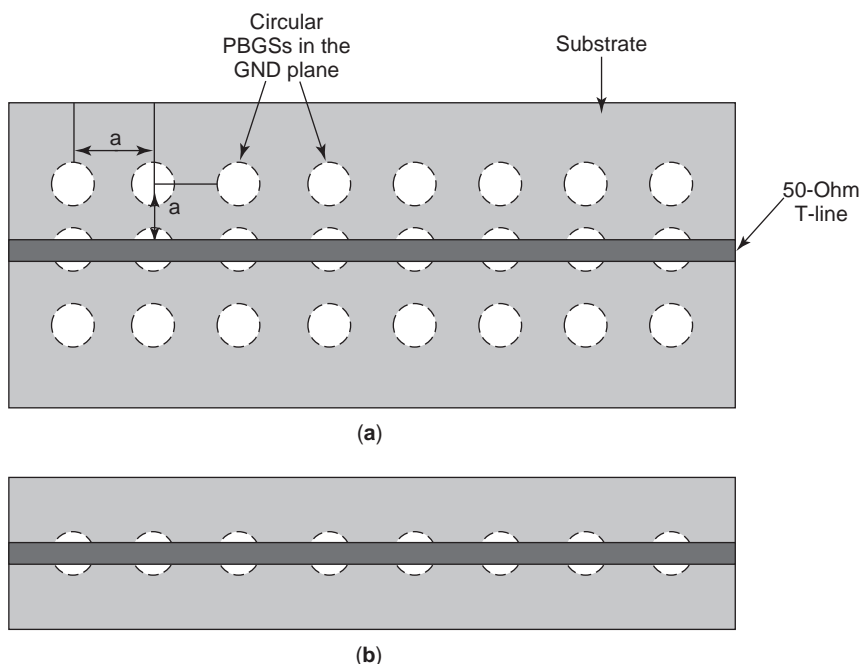


Figure 8. Uniform circular PBG-engineered microstrip transmission lines: (a) three rows; (b) one row.

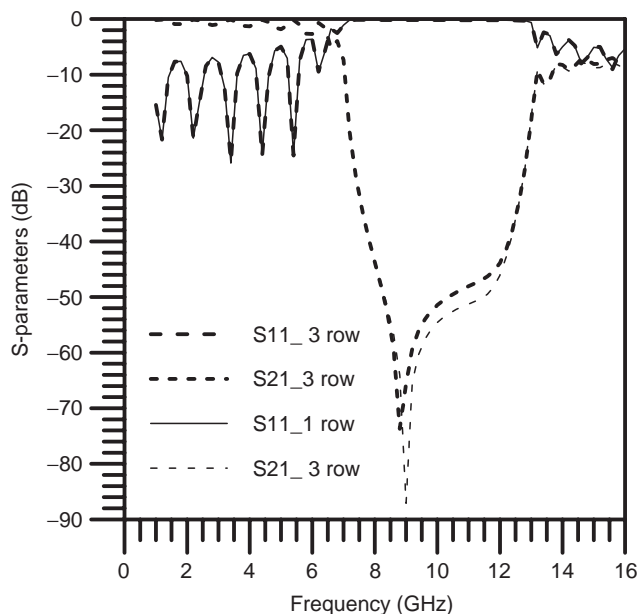


Figure 9. S parameters versus frequency of PBG-assisted transmission lines as shown in Fig. 7.

The harmonics are the multiplication of the fundamental frequency. 1D and 2D PBGSs generate distinct stopbands at a single frequency; therefore it is not possible to achieve significant multiple harmonic suppression by 1D or 2D PBGSs. DGS can yield wider stopbands [19]. We will use this unique property of DGSs to suppress second and third harmonics of a filter simultaneously.

2.4.1. Design of UPBGSs for Harmonic Suppression. We investigate five UPBGSs assisted BPFs with different lattices and numbers of UPBGSs: (1) BPF on a 2D array

of UPBGSs with square lattice (Fig. 10b), (2) BPF on dense 2D UPBGSs of rectangular lattice (Fig. 10c), (3) BPF on 1D UPBGSs located exactly under the two extreme 50-Ω lines and the central coupled line (Fig. 10d), (4) BPF on UPBGSs that are located under two extreme 50-Ω lines only (Fig. 10e), and finally (5) BPF on UPBGSs that are located under all the lines of a BPF (Fig. 10f). As periodic structures, both PBGSs and BPFs have their own poles and zeros. Theoretical formulation of the combined structure is not a trivial task. Only full-wave analyses of some structures are reported in the open literature. So far no thorough investigations into the effect of the position, number, and lattice structures of UPBGS on BPFs have been reported. The design investigation of UPBGS-assisted BPF reveals that PBGS drastically degrades the

passband performance. The design objective of simultaneous excellent passband and harmonics suppression is not fulfilled. Although many PBGS-assisted BPFs have been reported in the open literature, this problem has been overlooked. The motivation of thorough full-wave analysis has been derived to address this issue. In this section we investigate these effects on BPF with the aid of IE3D. These thorough investigations are very useful in understanding the behavior of BPFs in the presence of PBGSs.

2.4.1.1. Standard BPF. We first designed a four-section asymmetric coupled-line BPF (shown in Fig. 10a) on RT/Duroid with $\epsilon_r = 10.2$ and $h = 0.635$ mm. The dimensions of the coupled lines were $W_1 = 0.425$ mm, $W_2 = 0.525$ mm,

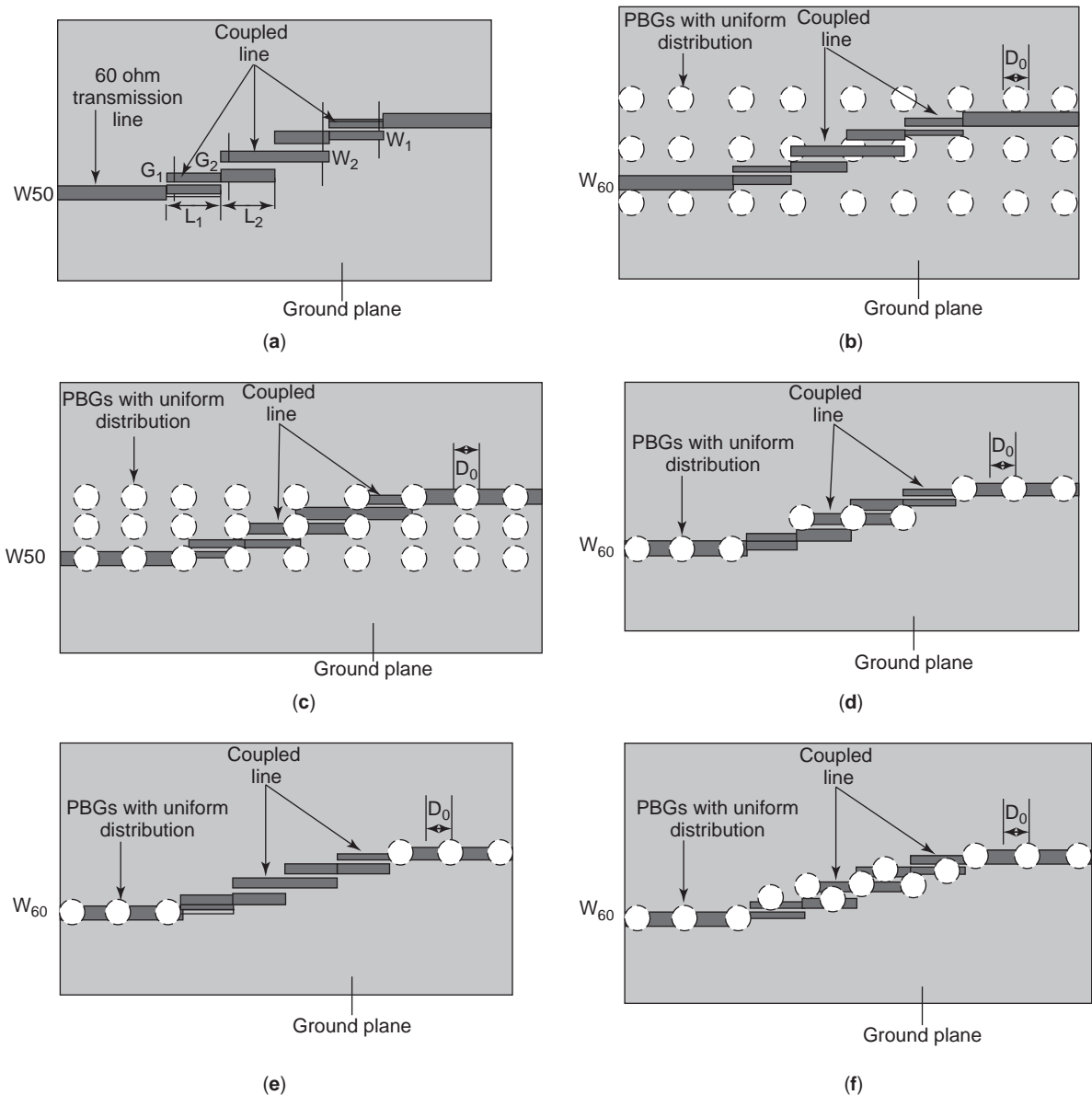


Figure 10. Various designs of BPFs assisted by uniform circular PBGSs: (a) standard four-section asymmetric coupled-line BPF; (b) BPF on 2D square lattice PBGSs; (c) BPF with dense 2D PBGSs (rectangular lattice); (d) BPF with PBGSs under 50-Ω and central coupled lines; (e) BPF with PBGSs under two extreme 50-Ω lines only; (f) BPF with PBGSs under all lines only.

$G_1 = 0.2$ mm, $G_2 = 0.7$ mm, $L_1 = L_2 = 3.625$ mm, and $W_{50} = 0.6$ mm. The passband design frequency was 7.5 GHz.

2.4.1.2. BPF on 2D Array of UPBGs. In this design the UPBGs are etched in the ground plane of the BPF and their periodicities in the X and Y directions form a square-patterned lattice structure. The geometry, shown in Fig. 10b, consists of three rows of nine PBG elements. The UPBGs generate the first stopband at 15 GHz to suppress the second harmonics of the filter.

2.4.1.3. BPF with Dense 2D UPBGs. Next a 2D array of UPBGs is situated beneath all the lines of BPF having rectangular lattice structures. The Bragg's condition is applied in the x direction to create a stopband at 15 GHz. The geometry is shown in Fig. 10c.

2.4.1.4. BPF with PBGs under 50- Ω and Central Coupled Lines. In this design PBG elements are etched under 50- Ω and central coupled lines only. This design consists of nine PBG elements total. The geometry of this design is shown in Fig. 10d. The objective of the design is to eliminate redundant PBG cells.

2.4.1.5. BPF with PBGs under 50- Ω Lines Only. In this design, PBG elements are located under 50- Ω lines only. There are six PBG elements in this design as shown in Fig. 10e.

2.4.1.6. BPF with UPBGs under All Lines. UPBGs are under all the microstrip lines of BPF, based on the assumption that the field is confined below the lines. Beyond the lines there are no PBG elements. The geometry is shown in Fig. 10f.

2.4.2. Results. All the designs are simulated with the EM Zeland IE3D software. The ground plane has been assumed to be infinite. We used the RT/Duroid substrate having a dielectric constant of 10.2 and a height of 0.635 mm. We produced theoretical results for different geometries of UPBGs-assisted BPF. To see the effect of UPBGs in harmonic suppression, we show the performance of the reference BPF. Finally, the results of the measured insertion loss (IL) performances of a standard BPF and a UPBGs-assisted BPF are compared in Sections 2.4.2.1–2.4.2.7.

2.4.2.1. Performance of Reference BPF. An IE3D-simulated S -parameter/frequency plot of a standard asymmetric coupled-line BPF is shown in Fig. 11. The presence of spurious transmission around 15 GHz is obvious in the reference BPF. At this frequency the maximum value of return loss (RL) is found to be 9 dB and IL is found to be 2.5 dB. At 7.5 GHz, which is the passband, the maximum value of return loss (RL) is -22.5 dB and IL is 0.5 dB. At third harmonic, the IL is 0 dB.

2.4.2.2. Performance of BPF on 2D Array of UPBGs. For harmonics suppression we applied a 2D array of UPBG in the ground plane of a reference BPF. The harmonic is suppressed by application of 2D array of UPBGs as

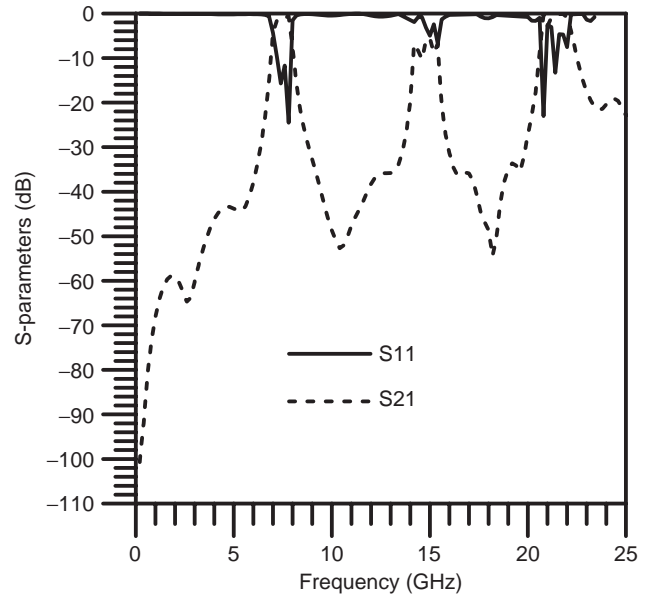


Figure 11. IE3D-simulated S -parameter performance of a standard coupled-line BPF as shown in Fig. 10a. Substrate is RT/Duroid having dielectric constant 10.2 and height 0.635 mm.

shown in Fig. 12. The RL performance at second harmonic should ideally be zero for proper harmonic suppression. But the maximum value of RL is here 2 dB and the value of the transmission coefficient is 9 dB. The IL at third harmonic is 0 dB. We understand that the UPBGs are not exact under the lines, so they are not sufficiently effective to suppress the transmission at second-harmonic frequency.

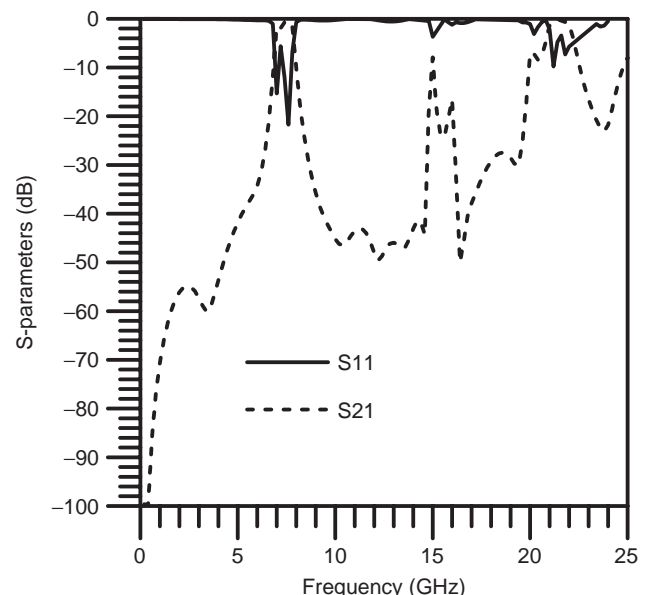


Figure 12. Theoretical S -parameter performances of a BPF with square lattice 2D UPBGs (Fig. 10b). Substrate is RT/Duroid having dielectric constant 10.2 and height 0.635 mm.

2.4.2.3. Performance of BPF on Dense 2D Array of UP-BGSs. Figure 13 shows the simulation result of a BPF with 2D PBGSs that are denser than the conventional 2D square lattice structure. In this case they conform to a rectangular lattice. We see that at 7.5 GHz the maximum RL is 25 dB and the maximum RL at 15 GHz is about 0 dB. The IL at 15 GHz is about 40 dB. Significant second-harmonic suppression is achieved here. The third-harmonic value of IL is 0 dB.

2.4.2.4. Performance of BPF with Three-Line UP-BGSs. We simulated the BPF where the PBGSs are under two 50-Ω lines and the central coupled lines. The performance is shown in Fig. 14. In this design (Fig. 10d), two sides of the UPBGSs are situated under two 50-Ω lines and three UPBGSs are under the central coupled line. From the simulation results it can be seen that at 15 GHz the maximum value of RL is about 1 dB; only and the transmission coefficient is found to be approximately 14 dB. The third-harmonic value of IL is 2 dB. Harmonic suppression is not satisfactory. In addition to this, the passband performance at fundamental frequency is distorted significantly.

2.4.2.5. Performance of BPF with UPBGSs under Two Extreme 50-Ω Lines. Considering the possibility that EM propagation takes place through the 50-Ω line, we first used UPBGSs under two 50-Ω lines only to see their effects on harmonic suppression. The simulation result, shown in Fig. 15, does not seem promising at all; rather, at fundamental, second, and third harmonic frequencies, the performances are poor.

2.4.2.6. Performance of BPF with UPBGSs under All Lines. Finally we used PBG under all the lines. The design

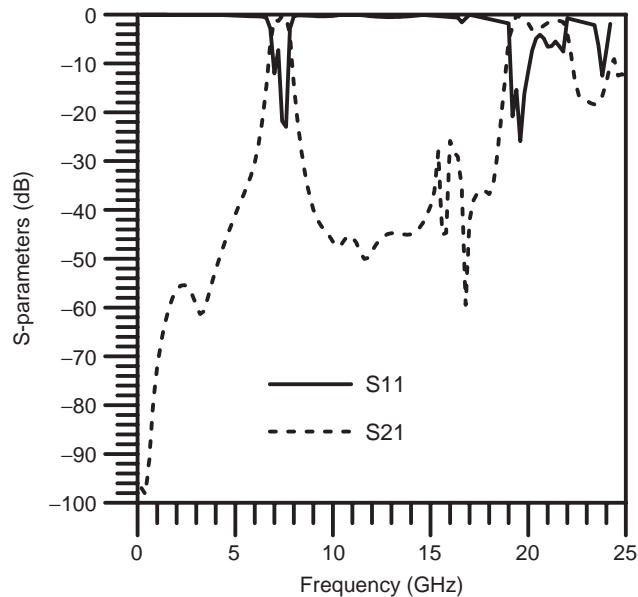


Figure 13. Simulated S-parameter performance of BPF with dense rectangular lattice 2D UPBGSs (Fig. 10c). Substrate is RT/Duroid having dielectric constant of 10.2 and height 0.635 mm.

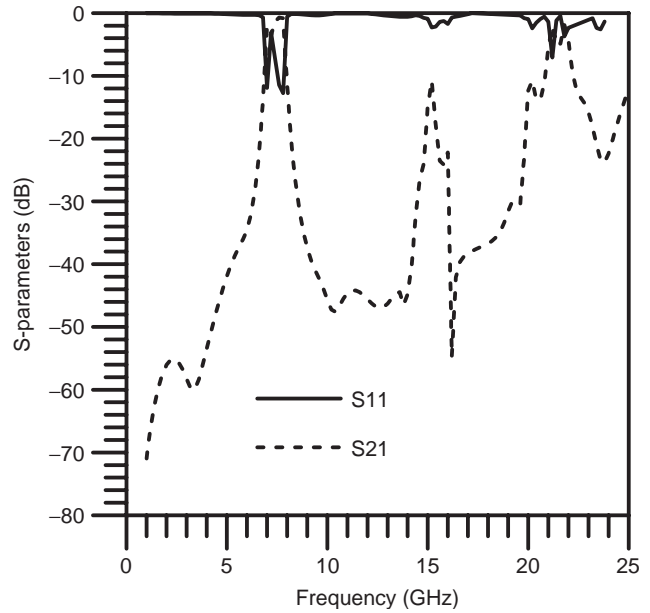


Figure 14. Simulated S-parameter performance of a BPF with UPBGSs on 50-Ω lines and central coupled line (Fig. 10d). Substrate is RT/Duroid having dielectric constant 10.2 and height 0.635 mm.

provides S-parameter performances as shown in Fig. 16. It can be seen that at 7.5 GHz the maximum RL is more than 30 dB. At 15 GHz the maximum RL is approximately 0 dB and IL is approximately 30 dB. In this case significant improvements in fundamental and second harmonic frequencies are achieved. Only a small ripple in the transmission band is noticed, and this can be controlled by resizing the UPBGS elements.

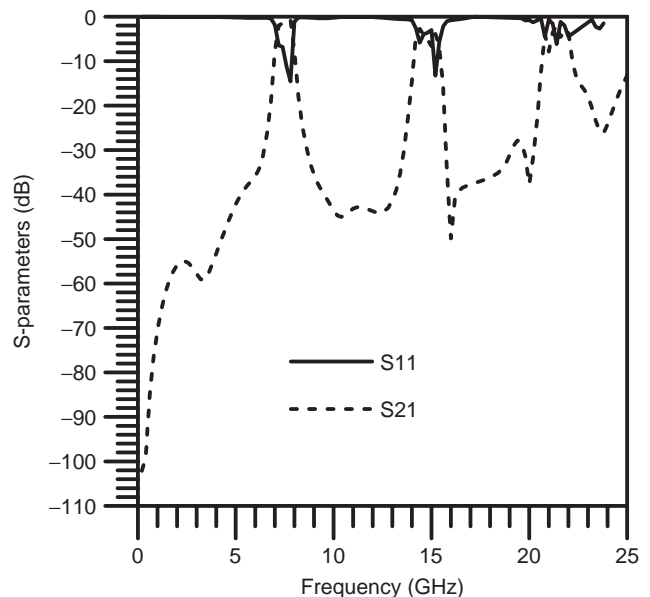


Figure 15. Simulated S-parameter performances of a BPF with PBGSs on two 50-Ω lines only (Fig. 10e). Substrate is RT/Duroid having dielectric constant of 10.2 and height of 0.635 mm.

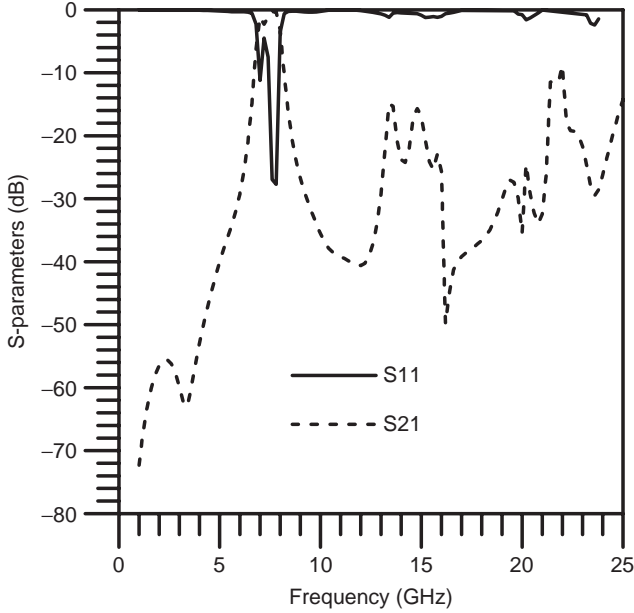


Figure 16. Theoretical S -parameter performances of a BPF when UPBGSs are situated under all the lines (Fig. 10f). Substrate is RT/Duroid having dielectric constant 10.2 and height 0.635 mm.

2.4.2.7. Comparison of S_{21} Performances. Finally we fabricated the optimized reference BPF and UPBGS-assisted BPF. The measured IL performances up to 20 GHz are shown in Fig. 17. Compared to the simulation results in Fig. 11, the measured results in Fig. 17 have shifted in both fundamental frequencies; this frequency shift may be due to the fabrication errors. For the reference BPF the average 3-dB IL bandwidth (IL BW) is 7.18%. Average IL at second harmonic is found to be 10 dB for the reference

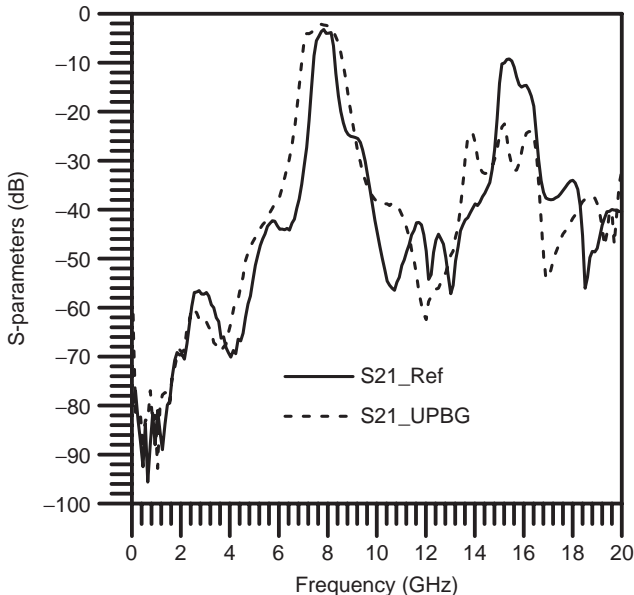


Figure 17. Measured IL performances of an optimized BPF. Substrate is Taconic, having dielectric constant of 10 and height 0.635 mm.

Table 1. Performance of UPBGS-Assisted BPF

Designs	IL at 2nd Harmonic (dB)	IL at 3rd Harmonic (dB)
Reference BPF	2.5	0
BPF on 2D array of UPBGSs	9	0
BPF on dense 2D array of UPBGSs	40	0
BPF on 3-line UPBGS (PBGSs on two 50- Ω lines + central coupled line)	14	2
BPF on two-line UPBGS (UPBGSs on two 50- Ω lines)	5	2
BPF on 1D UPBGS (UPBGSs on all lines)	30	15

BPF. UPBGS-assisted BPF provides an average IL of 30 dB. The 3 dB IL BW is found to be 16.02%. It can be concluded that UPBGS-assisted BPF improves performance in terms of IL BW and second-harmonic suppression.

The performance levels of UPBGS-assisted BPF are shown in Table 1.

2.4.3. Designs of B-PBGs for Harmonic Suppression. We have designed BPFs with *binomially* distributed PBGSs (B-PBGSs). We investigate harmonic suppression due variation in the number of PBG elements in B-PBG-assisted BPF (B-BPF). Various designs of B-BPFs are shown in Fig. 18.

In Fig. 16, the B-PBGSs have a FF of 0.4 (0.4 is the optimum FF for binomially distributed PBGSs [36]). Using conducting copper Foil to vary the number of PBG elements, we compare the IL performances for B-BPF in several different designs:

Design 1. The ground plane of the reference BPF is perturbed by PBGSs with binomial distribution. In this design three lines (consisting of two extreme 50- Ω lines and one central coupled line) are perturbed by B-PBGSs having an FF of 0.4. The rests are loaded with uniform PBGSs having FF 0.25. The total number of PBG elements in B-BPFs is 13. The geometry is shown in Fig. 18a.

Design 2. In this design we use only two PBG elements from the two extremes and PBG elements of B-BPF are closed as shown in Fig. 18b.

Design 3. In this case the two 50- Ω lines of BPF are loaded by four PBG elements. The remaining PBG elements are closed. The geometry is shown in Fig. 18c.

Design 4. In this design the BPF is loaded by six PBG elements from the two extremes. The PBG elements are under 50- Ω lines only as shown in Fig. 18d.

Design 5. In this design 10 PBG elements of B-BPF are used. The design is shown in Fig. 18e. No PBG elements are situated under the central coupled line.

Design 6. This design consists of 12 PBG elements in the ground plane of a BPF. Here the central PBG

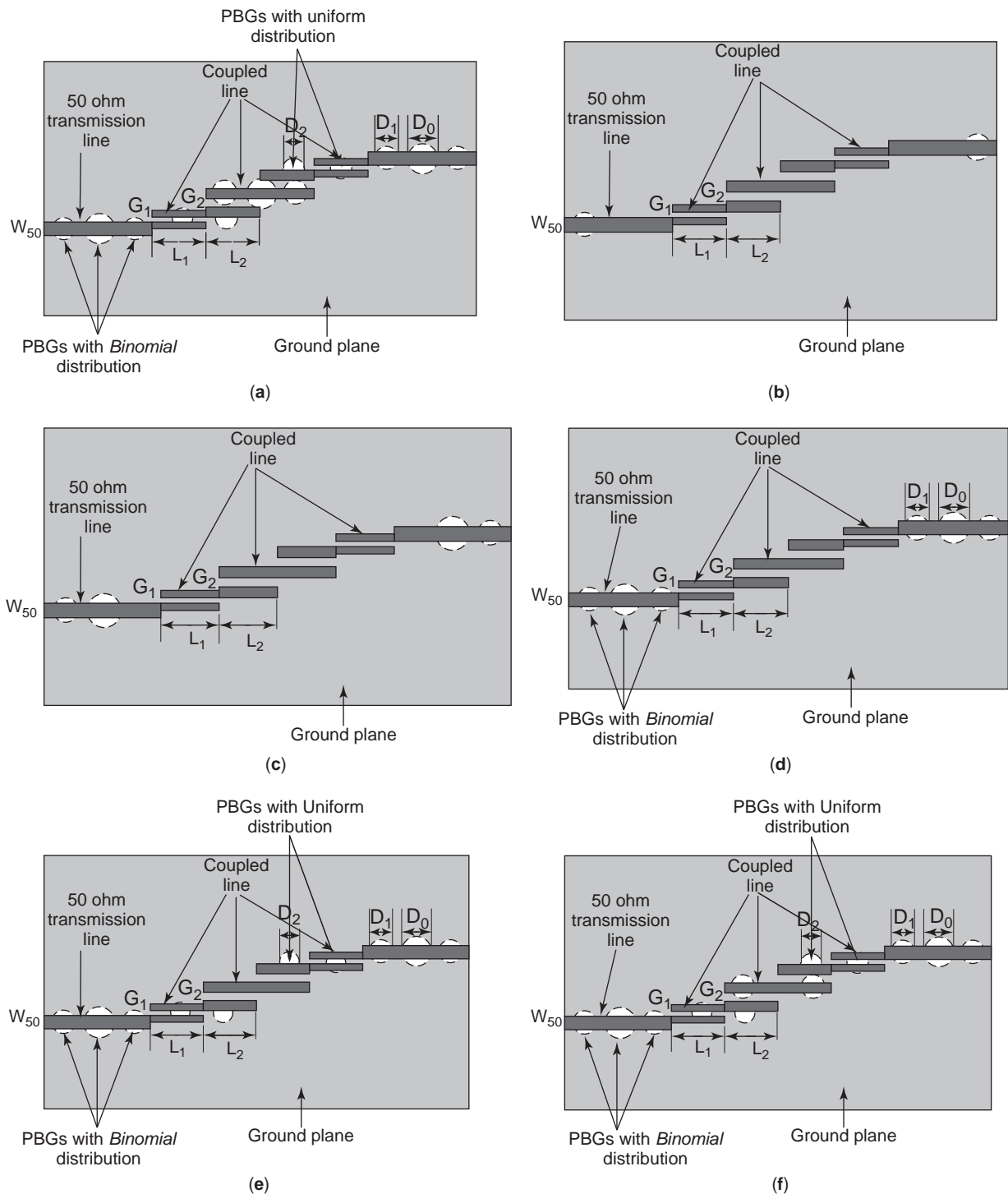


Figure 18. Various designs of B-BPFs with B-PBGSs: (a) elements under all lines; (b) two elements under 50-Ω lines only; (c) four elements under 50-Ω lines; (d) six elements under 50-Ω lines; (e) elements under all lines except central coupled lines; (f) elements under all lines except the central larger PBG elements in the central coupled line.

element of the central coupled line is omitted. The design is shown in Fig. 18f.

We present the RL performances for other designs below. We show only IL performances to indicate harmonic suppression.

2.4.3.1. Reference Optimized BPF. The experimental S -parameter performance of a standard BPF is shown in Fig. 19. We are investigating the harmonics (second and third harmonics) by varying the number of PBG elements. For standard BPF the measured second and third harmonics are found to be 13 and 8 dB, respectively.

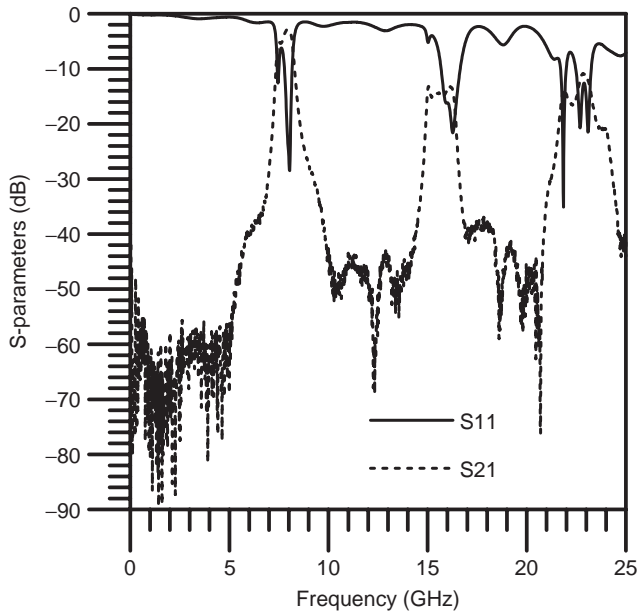


Figure 19. Measured S -parameter performance of a standard BPF. Substrate is Taconic having dielectric constant 10 and height 0.635 mm.

2.4.4. Performance of B-BPF. We fabricated all the designs and measured performance by vector network analyzer (VNA). The measured IL and RL performances of a BPF loaded by binomially distributed PBGS are as follows:

Design 1. The IL performance of the B-BPF (Fig. 18a) is shown in Fig. 20. In this design a total of 13 PBG

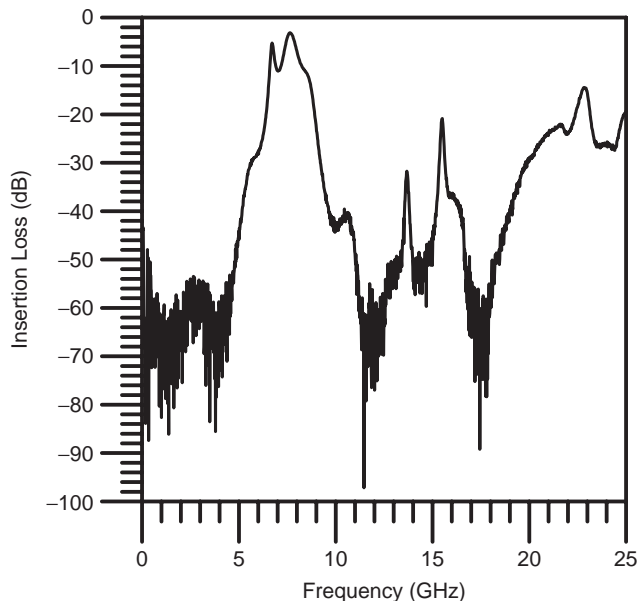


Figure 20. Measured IL performance of a B-BPF shown in Fig. 18a where PBG elements are periodically loading under all the lines. Substrate is Taconic having dielectric constant 10 and height 0.635 mm.

elements are used to suppress the harmonics. B-BPF provides second and third harmonics as 32 and 20 dB; the harmonics are suppressed by 19 and 12 dB, respectively. However, the IL performance in the transmission band is seen to be poor. Under these circumstances we will investigate the influence of different numbers of PBG elements on the performance of BPF.

Design 2. We investigate the BPF as shown in Fig. 18b with two PBG elements. During the measurement the IL performances show second and third harmonics to be 30 and 17.5 dB, respectively (the graph is not shown here).

Design 3. Four PBG elements etched in the ground plane of a BPF as shown in Fig. 18d yields the IL performance, providing second and third harmonics as 37 and 16 dB, respectively (the graph is not shown here).

Design 4. During measurement of the IL performance of a BPF (Fig. 18d) loaded by six PBG elements, second and third harmonics are found to be 34 and 14 dB, respectively. It is worthwhile to mention that this configuration hold completely *binomially* distributed PBGS under two 50- Ω lines of a BPF (the graph is not shown here).

Design 5. The design in Fig. 18e provides 40 and 22 dB IL as second and third harmonics. The transmission band at the fundamental frequency is also seen to be improved. The IL performance for 10 PBG elements is shown in Fig. 21.

Design 6. As can be seen from Fig. 22, design 5 (Fig. 18f) yields ILs of 38 and 21 dB at second and third harmonics. The transmission band at the fundamental frequency is similar to that for design 5.

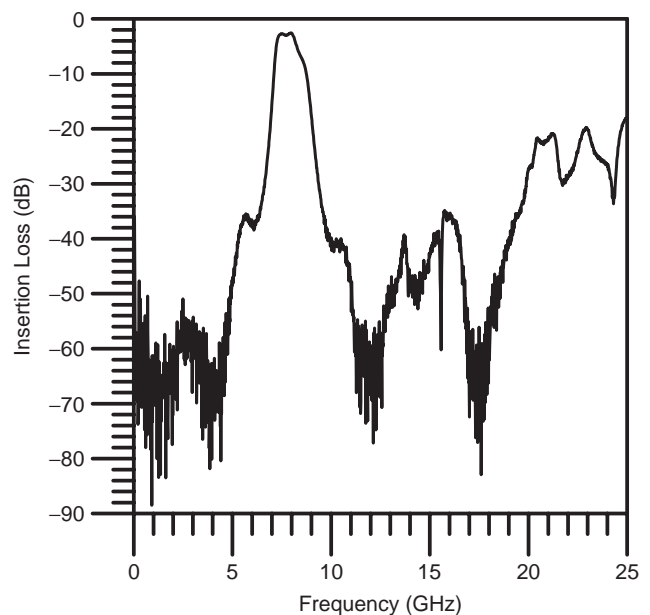


Figure 21. Measured IL performance of BPF when 10 PBG elements are under all lines except the central coupled line.

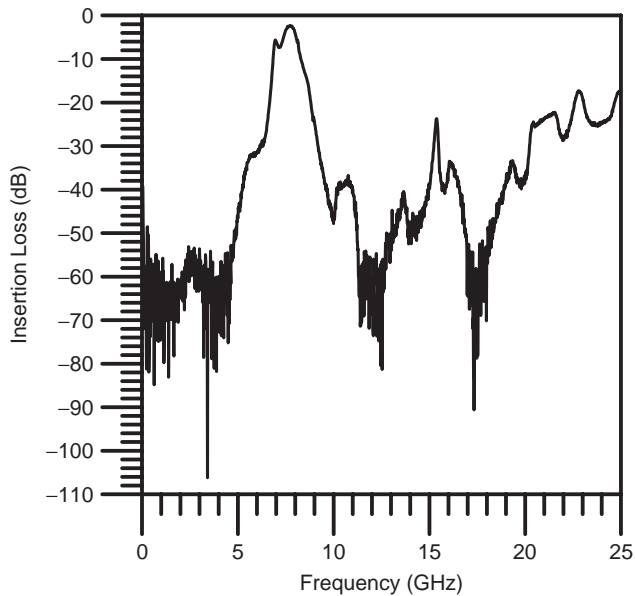


Figure 22. Measured IL performance of a BPF loaded by 12 PBG elements. Only one larger element under the central coupled line is closed.

The IL performances for all the designs are compared in Table 2, where it can be seen that the 10-PBG element provides the best performance. 12-PBG elements also provide almost similar performance. It is also clear from the investigation that suppressions of second and third harmonics do not follow the number of PBG elements; rather, their position and size are the important issues in harmonic suppression of coupled-line BPF. The important finding is the role of larger PBG elements of the central coupled line. Comparing results from Figs. 21 and 22, it can be concluded that the middle larger element under the central coupled line degrades the performance.

2.4.4.1. Binomially/Uniformly Assisted BPF Comparison.

In order to investigate the improved performance of B-BPF over the UPBG-assisted BPF, the combined performances are shown in Fig. 23. It can be seen in Fig. 23 that the average 10 dB RL BW at fundamental frequency for both B-BPF and U-BPF is 16.2%. The 3 dB IL BW is found to be 19.56%. The average isolation at second

Table 2. Performance of a Coupled-Line BPF with Binomially Distributed PBGS along with Different Numbers of PBG Elements

Number of PBG Elements	Insertion loss (IL) (dB)	
	2nd Harmonics	3rd Harmonics
0 (reference BPF)	13	8
2	30	17.5
4	37	16
6	34	14
10	42.5	22
12	38	21
13	20	17.5

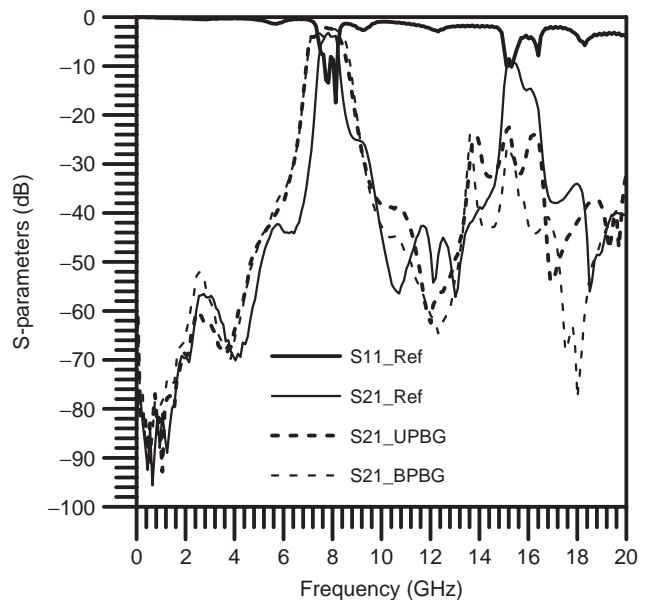


Figure 23. Measured S-parameter performance of an optimized BPF along with the IL performances of B-BPF and UPBGs-assisted BPF.

harmonic is -39 dB for B-BPF, compared to the U-BPF of -29 dB. The performances of an optimized BPF, UPBGs-assisted BPF, and B-BPF are compared in Table 3.

2.5. DGS for Harmonic Suppression

2.5.1. Design. In this subsection we report the novel idea for simultaneous suppression of second- and third-order harmonics generated in a conventional BPF. We have already reported that the dumbbell-shaped DGS can yield a wider stopband [20]. Now we implement this unique property in an asymmetric four-section coupled-line BPF to suppress the second- and third-order harmonics. We propose using 1D EBGSs (dumbbell-shaped DGSs) that are located just under standard $50\text{-}\Omega$ lines. No DGS will be used under the coupled lines. We also present a novel idea that the dumbbell-shaped DGSs, which are designed at two different frequencies, are to be located under two end $50\text{-}\Omega$ lines only. This design is sufficient to suppress the second- and third-order harmonics. We investigate a few different designs. Figure 24 shows one of the various designs investigated. It is noted

Table 3. Performance of an Optimized BPF with UPBGs and B-PBGS

Type	Average	Average	Average
	3 dB IL BW (%)	10 dB RL BW (%)	2nd Harmonics (dB)
Standard BPF	7.18	5.96	6
UPBGs-assisted BPF	16.02	15.2	29
B-BPF (with omission of central PBG elements)	19.56	16.2	39

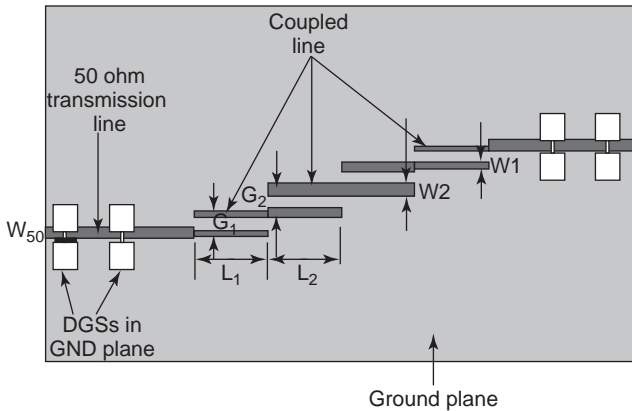


Figure 24. Geometry of a DGS-assisted BPF; four DGSs are located under two 50- Ω lines.

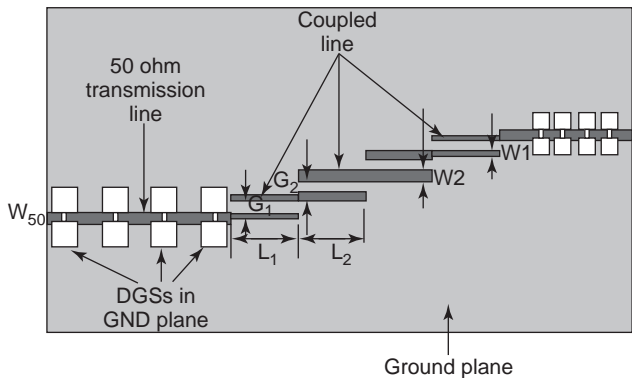


Figure 25. Geometry of a DGS-assisted BPF having four larger DGSs under LHS 50- Ω line and four smaller DGSs under RHS 50- Ω line.

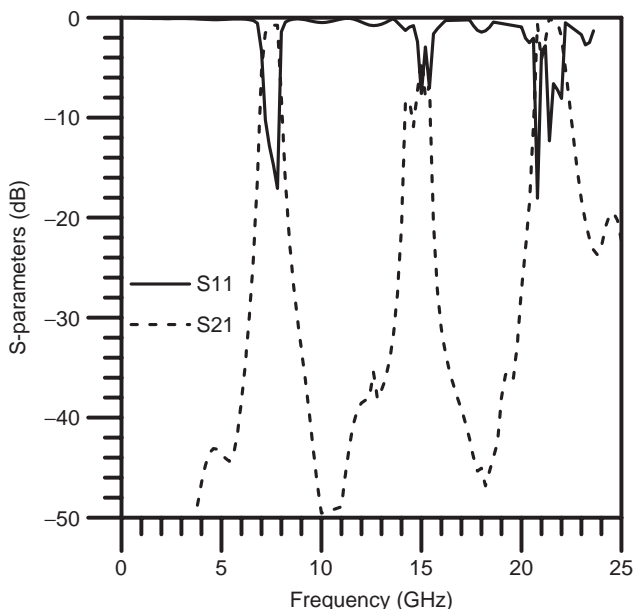


Figure 26. S -parameter performances of an optimized reference BPF.

that the designs differ from each other with respect to the number of DGSs only. The designs are as follows:

Design 1. Here we use a total of four DGSs under two 50- Ω lines. Two DGSs will be located under each 50- Ω line. The larger square slot of the DGS unit measures $52 \times 52 \text{ mm}^2$, and the vertical narrow slot is $20 \times 15 \text{ mm}^2$. The geometry of a BPF with four DGSs in the ground plane is shown in Fig. 24.

Design 2. In this case we use four DGSs under only the left-side 50- Ω line. There are no DGS elements under the right-side 50- Ω line. The geometry is identical to Fig. 24, with the exception that DGS elements are located only on the left side rather than on both left and right.

Design 3. Four DGSs are located under the left 50- Ω line designed for second-harmonic suppression. Another set of four DGSs is located under the right 50- Ω line, which is suitable for third-harmonic suppression. The RHS (right-hand-side) DGSs are smaller in size than the LHS DGSs. This is obvious, as they are designed at higher frequency to suppress third harmonics. The geometry is shown in Fig. 25.

Design 4. Four DGSs are located under the LHS 50- Ω line and eight DGSs are placed under the RHS 50- Ω line. The eight DGS elements are designed for significant third-harmonic suppression. The geometry is identical to that in Fig. 25.

2.5.2. Results. Theoretical investigations have been carried out on DGS-assisted BPFs for effective suppression of second (at 15 GHz) and third (at 22.5 GHz) harmonics. The S -parameter performances for the various designs are given below (theoretical performances of the standard optimized BPF used in all designs are shown in

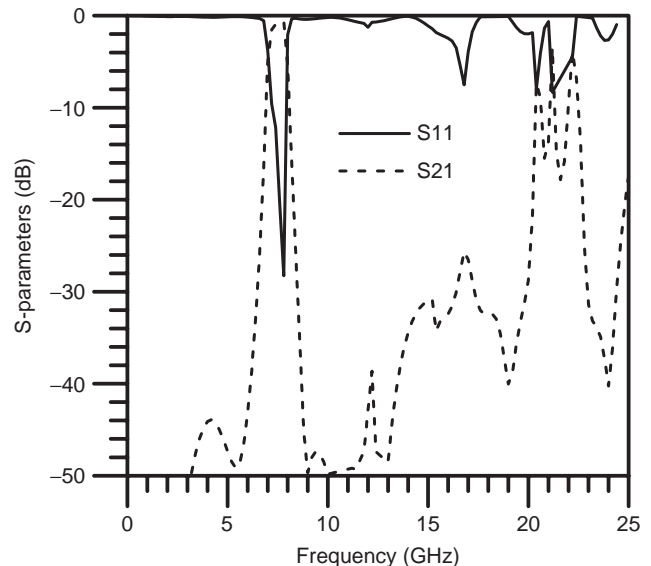


Figure 27. S -parameter performances of a DGS-assisted BPF having a total of four DGSs (2 + 2) lying under two 50- Ω lines.

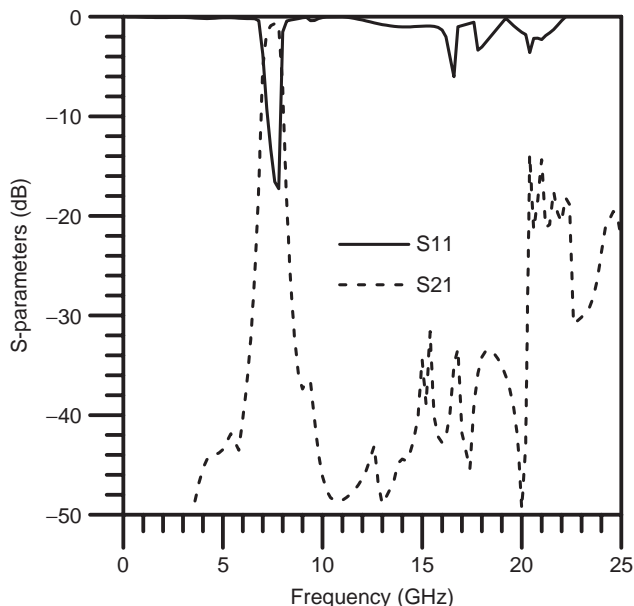


Figure 28. S-parameter performances of a BPF assisted by four DGSs lying under the LHS 50-Ω transmission line.

Fig. 26; the second and third harmonics are 6 and 0 dB, respectively):

Design 1. The S-parameter performances for four DGS (2+2) located under two 50-Ω lines are shown in Fig. 27. From the IL performance it can be seen that the ILs at second and third harmonics are 28 and

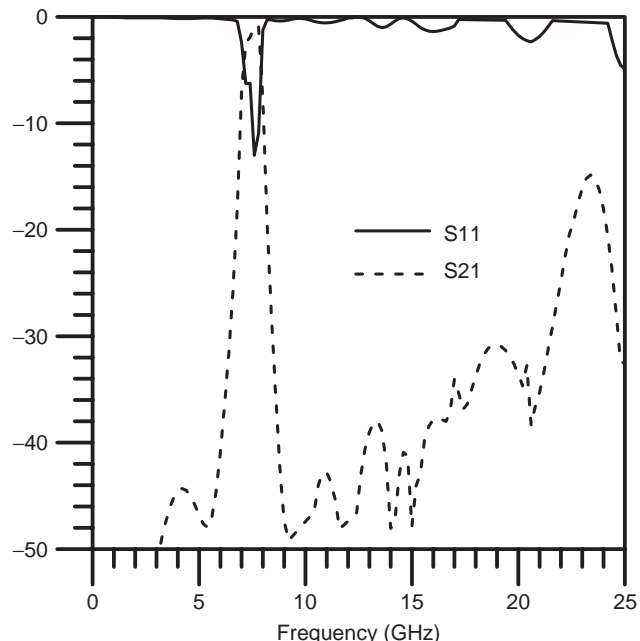


Figure 29. S-parameter performances of DGS-assisted BPF where two sets of four (i.e., total eight) DGSs have been placed under two 50-Ω lines.

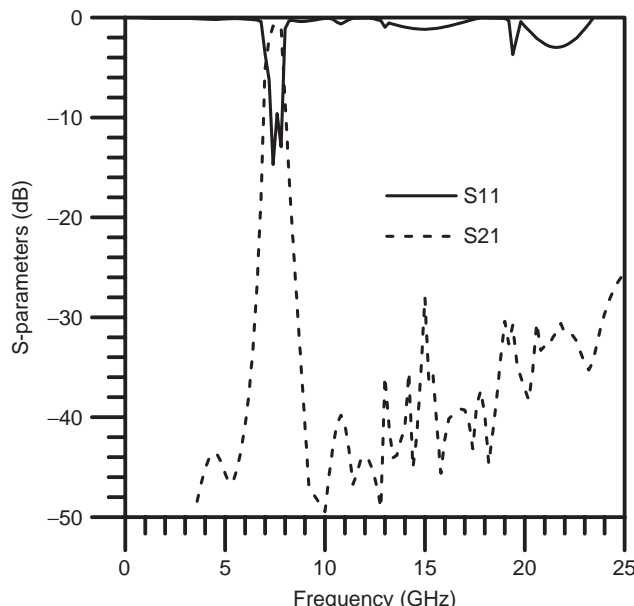


Figure 30. S-parameter performances of DGS-assisted BPF where four DGSs are used under the LHS 50-Ω line and eight DGSs are designed for third-harmonic suppression and placed under the RHS 50-Ω line.

6 dB, respectively. Input matching is seen to be improved.

Design 2. The S-parameter performances of a BPF assisted by four DGSs under the LHS 50-Ω line are shown in Fig. 28. It can be seen that this design provides the ILs at second and third harmonics of 38 and 20 dB, respectively.

Design 3. In this design we have placed four DGSs under the LHS 50-Ω line for use in second-harmonic suppression, and four other DGSs are placed under the RHS 50-Ω line, designed for use in third-harmonic suppression. This is a new technique, in which we have designed DGSs at two frequencies for effective harmonic suppression. The S-parameter performances of this design are shown in Fig. 29. It can be seen that this design provides second and third harmonics as 40 and 20 dB, respectively.

Design 4. In this case we attempted to suppress the third harmonic significantly. For this purpose eight DGSs are used under the RHS 50-Ω lines to generate deeper and wider stopbands to suppress the third harmonics. The S-parameter performances of this design are shown in Fig. 30. It can be seen that the suppression at third harmonic has improved significantly to 30 dB.

3. CONCLUSIONS

We have reviewed the theory of periodic structures to understand the passband and stopband phenomena of PBGSs. The dispersion diagram of a modified UCPBG

structure is presented, based on the transmission-line model [23] of PBGSs. We have compared the S -parameter performances of three rows with those of one row of PBG-assisted transmission lines. It can be seen that they provide almost identical performances. Therefore we have placed 1D PBG elements just under the lines of BPF for the suppression of higher-order harmonics.

We have theoretically investigated BPF for UPBGSs with different conditions. From all the results it can be seen that the performance improves if the PBG elements are located just under the lines. We have also fabricated optimized reference BPF and a BPF with UPBGS. It can be seen that, due to inclusion of PBG elements in a conventional BPF, the IL performance improves significantly in terms of passband performance and harmonic suppression.

We designed binomially distributed PBGSs for the suppression of spurious transmission in a BPF. A compact microstrip BPF with intrinsic spurious suppression was reported [1] in which 2D UC-PBGSs are used. 2D UC-PBGSs are more complex and take more space to describe; thus we have proposed BPBGSs that yield ripple-free transmission with wider stopband in microstrip lines. We investigated IL performances of a BPF with a variable number of PBG elements. It can be seen that BPBGSs suppress second harmonics significantly; they also suppress third harmonics. It is very interesting to note that in a microstrip transmission line the stopband scales with the number of PBG elements. But our present study reveals that it does not hold true for harmonic suppression of a BPF. This can be explained as the coupling phenomenon of the poles of BPF and PBG elements. The PBG elements situated under the central coupled line may provide significant coupling of PBGS and BPFs and may drastically degrade the passband performances.

Random usage of PBGS under BPF does not always lead to descent passband and harmonic suppression. In most cases, passband performance is drastically distorted; therefore careful design and investigation is required. In our investigation we observed that the strong coupling between the central coupled line of BPF and the central PBG element under the coupled line destroys the bandpass performance of BPF. After careful design of elimination of central PBG elements, the designs with both 10 and 12 PBG elements provide better IL performance.

Finally, we have investigated DGS-assisted BPF. Of the few designs that we have investigated, all suppress both second and third harmonics significantly. A new technique of using two sets of DGSs designed at two different frequencies works well in second- and third-harmonic suppression.

BIBLIOGRAPHY

1. F.-R. Yang, K.-P. Ma, Y. Qian, and T. Itoh, A uniplanar compact photonic-bandgap (UC-PBG) structure and its applications for microwave circuits, *IEEE Trans. Microwave Theory Tech.* **47**(8):1509–1514 (Aug. 1999).
2. Y. Qian, D. Sievenpiper, V. Radisic, Y. Yablonovitch, and T. Itoh, A novel approach for gain and bandwidth enhancement of patch antenna, *Proc. Radio and Wireless Conf.*, 1998 (RAWCON98), 1998.
3. Y. Qian, R. Coccioli, D. Sievenpiper, V. Radisic, E. Yablonovitch, and T. Itoh, Microstrip patch antenna using novel photonic band-gap structures, *Microwave J.* **42**(1):66–76 (Jan. 1999).
4. R. Coccioli, F.-R. Yang, K.-P. Ma, and T. Itoh, Aperture-coupled patch antenna on UC-PBG substrate, *IEEE Trans. Microwave Theory Tech.* **47**(11):2123–2130 (Nov. 1999).
5. R. Gonzalo, P. D. Maagt, and M. Sorolla, Enhanced patch antenna performance by suppressing surface waves using photonic-bandgap substrates, *IEEE Trans. Microwave Theory Tech.* **47**(11):2131–2138 (Nov. 1999).
6. K. M. Shum, Q. Xue, C. H. Chan, and K. M. Luck, Investigation of microstrip reflectarray using a photonic bandgap structure, *Microwave Opt. Technol. Lett.* **28**(2):114–116 (Jan. 20, 2001).
7. P. S. Hui and A. Alphones, Microstrip patch antenna with annular ring PBG, *Proc. Asia Pacific Microwave Conf. 2000*, Sydney, Australia, Dec. 2000, pp. 1347–1351.
8. R. Gonzalo, B. Martinez, P. D. Maagt, and M. Sorolla, Patch antennas on photonic crystal structures (online), <http://www.ecs.umass.edu/ece/allerton/99/34/>.
9. Y. Qian, R. Coccioli, F.-R. Yang, and T. Itoh, Passive and active component design using PBG, *Proc. 6th Int. Conf. Terahertz Electronics*, 1998, pp. 42–45.
10. F.-R. Yang, Y. Qian, and T. Itoh, A novel uniplanar compact PBG structure for filter and mixer applications, *IEEE MTT-S (Microwave Theory and Techniques Symp.) Int. Digest*, Anaheim, CA, June 13–19, 1999, Vol. 3, pp. 919–922.
11. E. R. Brown, C. D. Parker, and E. Yablonovitch, Radiation properties of a planar antenna on a photonic-crystal substrate, *J. Opt. Soc. Am. B. Opt. Phys.* **10**(2):404–407 (Feb. 1993).
12. A. Harvey, Periodic and guiding structures at microwave frequencies, *IRE Trans. Microwave Theory Tech.* **8**:30–61 (June 1959).
13. D. Nestic and A. Nestic, Bandstop microstrip PBG filter with sinusoidal variation of the characteristic impedance and without etching in the ground plane, *Microwave Opt. Technol. Lett.* **29**(6) (June 20, 2001).
14. S. K. Sharma and L. Shafai, Enhanced performance of an aperture-coupled rectangular microstrip antenna on a simplified unipolar compact photonic bandgap (UC-PBG) structure, *IEEE-APS (Antennas and Propagation Symp.)*, Boston, July 8–13, 2001, Vol. 2, 498–501.
15. N. C. Karmakar and M. N. Mollah, Investigation into non-uniform photonic bandgap microstripline lowpass filters, *IEEE-Trans. Microwave Theory Tech.* **51**(2):564–572 (Feb. 2003).
16. V. Radisic et al., Novel architectures for high-efficiency amplifiers for wireless applications, *IEEE Trans. Microwave Theory Tech.* **46**(11):1901–1909 (Nov. 1998).
17. C. Y. Hang, W. R. Deal, Y. Qian, and T. Itoh, High efficiency transmitter front-ends integrated with planar antennas and PBG, *Proc. 2000 Asia-Pacific Microwave Conf.*, Australia.
18. N. C. Karmakar and M. N. Mollah, Harmonic suppression of a bandpass filter using binomially distributed photonic bandgap structures, *Proc. IEEE-APS*, Columbus, OH, July 22–27, 2003, pp. 883–886.

19. D. Ahn, J.-S. Park, C.-S. Kim, J. Kim, Y. Qian, and T. Itoh, A design of the low-pass filter using novel microstrip defected ground structure, *IEEE Trans. Microwave Theory Tech.* **49**(1):86–93 (Jan. 2001).
20. M. N. Mollah and N. C. Karmakar, A novel hybrid defected ground structure as low pass filter, *Proc. IEEE APS-S Int.* 2004, Monterey, CA, June 20–26, 2004.
21. D. M. Pozar, *Microwave Engineering*, Addison-Wesley, Reading, MA, 1990.
22. J. D. Shumpert, *Modeling of Periodic Dielectric Structures (Electromagnetic crystal)*, Ph.D. dissertation, Univ. Michigan, 2001.
23. M. Rahman and M. A. Stuchly, Transmission line-periodic circuit representation of planar microwave photonic bandgap structures, *Microwave Opt. Technol. Lett.* **30**(1) (July 5, 2001).
24. I. J. Bahl and P. Bhartia, *Microwave Solid State Circuit Design*, New York, Wiley, 1998.
25. G. L. Larkins, R. Socorregut, and Y. A. Vlasov, Superconducting microstrip hairpin filter with BaTiO₃ patches, *IEEE Trans. Appl. Superconduct.* **13**(2):724–726 (June 2003).
26. C.-M. Tsai, S.-Y. Lee, and C.-C. Tsai, Hairpin filters with tunable transmission zeros, 2001 *IEEE MTT-S Int. Microwave Symp. Digest*, May 2001, Vol. 3, pp. 2175–2178.
27. R. R. Bonetti, and A. E. Williams, Preliminary design steps for thin-film superconducting filters, *IEEE MTT-S Int. Microwave Symp. Digest*, May 8–10, 1990, Vol. 1, pp. 273–276.
28. Y. Di, P. Gardner, P. S. Hall, H. Ghafouri-Shiraz, and J. Zhou, Multiple-coupled microstrip hairpin-resonator filter, *IEEE Microwave Wireless Compon. Lett.* **13**(12):532–534 (Dec. 2003).
29. A. N. Deleniv, M. S. Gashinova, I. B. Vendik, and A. Eriksson, “Design of an interdigital hairpin bandpass filter utilizing a model of coupled slots, *IEEE Trans. Microwave Theory Tech.* **50**(9):2153–2158 (Sept. 2002).
30. G. L. Matthaei, N. O. Fenzi, R. J. Forse, and S. M. Rohlfing, Hairpin-comb filters for HTS and other narrow-band applications, *IEEE Trans. Microwave Theory Tech.* **45**(8):1226–1231 (Aug. 1997).
31. G. L. Matthaei, N. O. Fenzi, R. Forse, and S. Rohlfing, Narrow-band hairpin-comb filters for HTS and other applications, *IEEE MTT-S Int. Microwave Symp. Digest*, 1996, Vol. 2, pp. 457–460.
32. Y. Di, P. Gardner, P. S. Hall, and H. Ghafouri-Shiraz, Multiple-coupled microstrip hairpin-resonator filter, *Proc. 3rd Int. Microwave and Millimeter Wave Technology Conf.*, 2002, pp. 1051–1054.
33. V. Radisic, Y. Qian, R. Coccioli, and T. Itoh, Novel 2-D photonic bandgap structures for microstrip lines, *IEEE Microwave Guided Wave Lett.* **8**(2):69–71 (Feb. 1998).
34. P. J. Schields, *Bragg’s Law and Diffraction*, Center for High Pressure Research, State Univ. New York, Stony Brook, NY; available online at <http://www.eserc.stonybrook.edu/Project-Java/Bragg/>.
35. M. N. Mollah and N. C. Karmakar, Effect of number of uniform photonic bandgap (U-PBG) elements on the performance of microstrip transmission lines, *Proc. PACRIM-2003*, Victoria, Canada.
36. M. N. Mollah and N. C. Karmakar, Optimum filling factor and performance of a transmission line at X-band perturbed by binomially distributed photonic bandgap (PBG) structure, *Proc. PACRIM-2003*, Victoria, Canada.
37. R. L. L. Ling, *Improved Performance of Planar Filters on Photonic Bandgaps*, M.Sc. thesis, Nanyang Technological Univ., Singapore, May 2004.

ELECTROMAGNETIC COMPATIBILITY

CLAYTON R. PAUL
Mercer University
Macon, Georgia

1. INTRODUCTION

Electromagnetic compatibility (EMC) concerns the reduction of interference in electronic systems. For a more complete discussion of EMC, see Ref. 1. All figures in this article are taken from that reference. Interference has occurred when an electromagnetic emission causes the unintended operation of a device. A typical interference scenario consists of a *source* (or emitter), a *transfer* (or coupling) *path*, and a *receptor* (or receiver) as shown in Fig. 1. Hence there are three ways to reduce the interference in the receptor: (1) reduce the level of the source, (2) increase the attenuation of the transfer path, and (3) reduce the susceptibility of the receptor. Generally the optimal procedure is to work from left to right, that is, first reduce the level of the source, then increase the attenuation of the transfer path, and finally, if needed, reduce the susceptibility of the receptor. The source and the receptor may be intended or unintended. Examples of intended sources are the emissions from an FM radio transmitter or an airport surveillance radar. Arcing at the brushes of a DC motor and the radiated emissions from a digital computer are examples of unintended emissions. Generally, the transfer path is either through air or via metallic conduction as in wires. An unintended receptor for the energy might be a television set that has received the emissions from a digital computer. In the case of unintended sources such as the clock in a digital computer, the levels of emission can be reduced, as we will see, by increasing the rise/falltimes of the clock pulses. This serves to reduce the levels of the high-frequency components without affecting the functionality of the computer. The levels of intended sources such as an FM radio transmission can rarely be reduced. Shielding and filtering are common ways of increasing the attenuation of the transfer path. Separating the source and receptor, when possible, also accomplishes this. In some cases the susceptibility of the receptor can be reduced by use of error correcting codes.

Generally interference occurs through radiated emissions or conducted emissions. Susceptibility also occurs through these two mechanisms. Hence there are four basic EMC subproblems shown in Fig. 2. These are radiated emissions, radiated susceptibility, conducted emissions, and conducted susceptibility. It should be pointed out that *time-varying currents radiate*. Hence currents, whether on cables or on metallic cabinets cause radiated

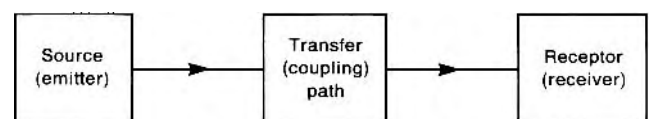


Figure 1. The basic decomposition of the EMC coupling problem.

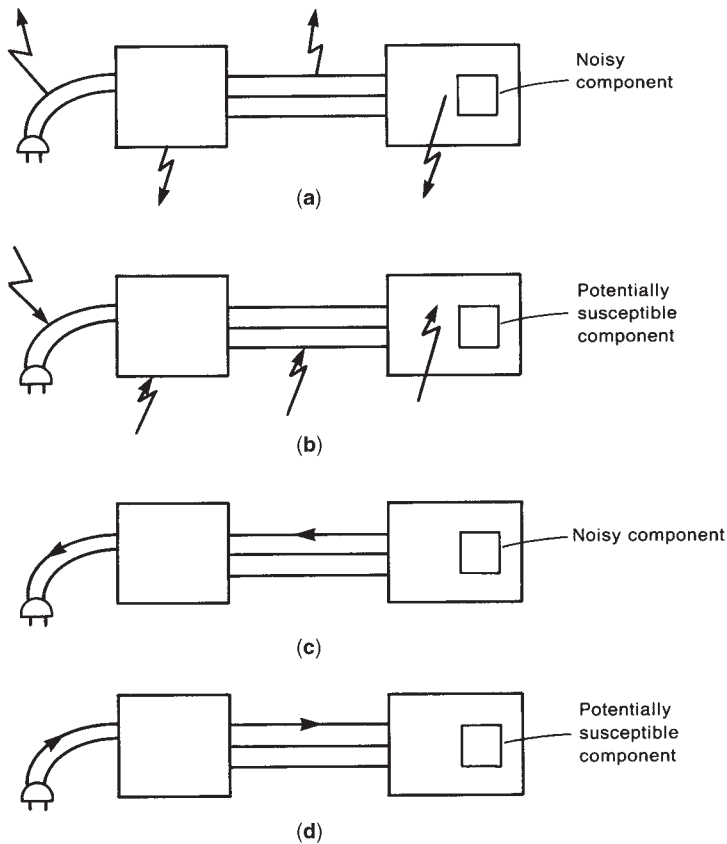


Figure 2. The four basic EMC subproblems: (a) radiated emissions; (b) radiated susceptibility; (c) conducted emissions; and (d) conducted susceptibility.

emissions. Typically long cables in the systems that carry high-frequency noise currents are the primary mechanisms for radiated emissions. These radiated emissions may cause interference with adjacent electronic systems. External sources such as the emissions from an FM radio transmitter or an airport surveillance radar may impinge on an electronic product. These emissions induce unintended currents on the metallic cabinets or cables of the systems that may create interference with the system. This is referred to as a *radiated susceptibility problem*. The power cord of an electronic device carries, in addition to the necessary 60-Hz power signal, other higher-frequency signals. For example, the harmonics of a digital clock in a product frequently show up on the power cord. These “noise” signals are then conducted onto the power net of the installation. The power net of an installation is in essence a large antenna in that the phase wires, and the neutral wires are “hardwired” together. When high-frequency noise is conducted out of the product via the power cord and placed on this large power net, they then radiate which can cause interference. A frequent example of this is the interference with a TV set caused by the arcing at the commutator of a motor as in a vacuum cleaner. These noise signals, in addition to radiating, also proceed out the power cord of the vacuum cleaner and hence onto the power net. These are examples of conducted emissions. And finally high-frequency signals are conducted along wires and the metallic cabinets of a device. Hence they may appear in unintended places within the device causing interference. A common such case is where noise on

the AC power net is conducted into the product via the device power cord. Switching on a motor such as in an air conditioner somewhere in the building will induce noise on the power net, which can be conducted into a product via the power cord. Lightning during thunderstorms induces signals on the power transmission lines. These also may be conducted into the product, causing interference. These scenarios constitute conducted susceptibility problems.

In addition to these primary concerns in EMC, there are also other aspects of EMC shown in Fig. 3. Electrostatic discharge or ESD is becoming a frequent mechanism for causing interference in digital systems. When a human wearing rubber-soled shoes walks across a nylon carpet, charge is deposited on the person’s body. When the person approaches a digital device such as a computer keyboard, this accumulation of charge on the finger creates an intense electric field that may be of sufficient magnitude to break down the air, resulting in an intense discharge much like a miniature lightning discharge. This discharge can cause improper operation of the device such as loss of data or permanent destruction of some of the electronic components in the device. The detonation of a nuclear device creates an intense radiated electric field that can damage or destroy electronic systems. This is referred to as an *electromagnetic pulse (EMP)*. Even though a communication center does not receive direct blast damage, this intense electromagnetic field can damage the communication electronics and prevent a retaliatory action. Lightning occurs frequently and can result in large

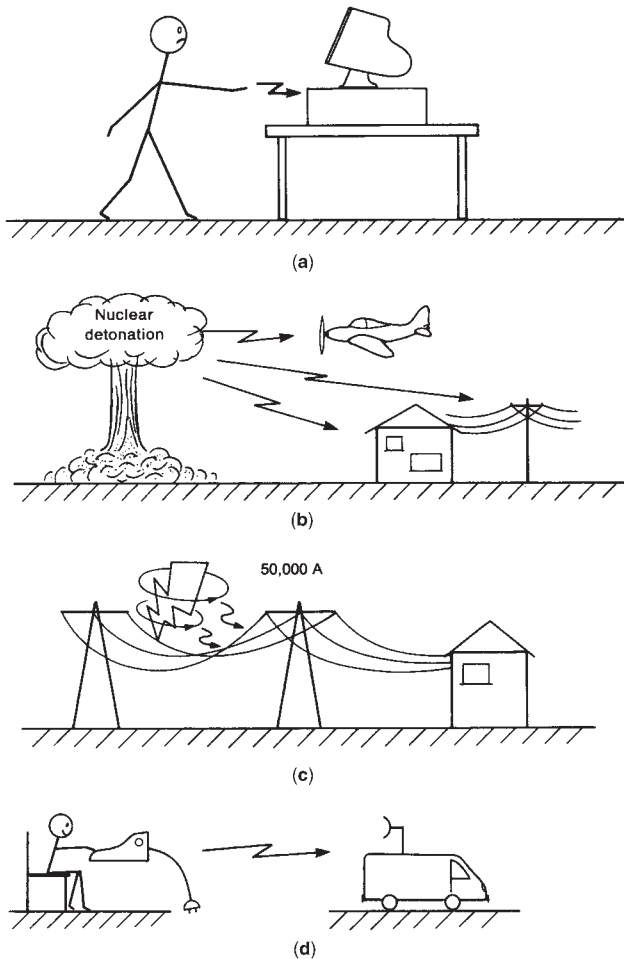


Figure 3. Other aspects of EMC: (a) electrostatic discharge (ESD); (b) electro-magnetic pulse (EMP); (c) lightning; (d) TEM-PEST (secure communication and data processing).

current channels. Although a direct strike can cause severe damage, indirect strikes can also induce damaging currents in electronic devices. And finally, it has been shown that it is possible to indirectly determine information being transmitted by monitoring the electromagnetic emissions. Communication security is obviously of extreme importance in the military context, but it is also important in the business world in order to protect trade secrets.

2. REGULATORY REQUIREMENTS FOR ELECTRONIC SYSTEMS

In the United States, the Federal Communications Commission (FCC) has regulatory authority over wire and radio communications, and has the responsibility for limiting interference with communications. Around 1979, the personal computer was being introduced to consumers in the United States. Residents of apartments began complaining to the FCC about interference being caused in their television receivers by a personal computer in an adjacent apartment. In order to limit the

interference potential of these personal computers, the FCC instituted regulations in Title 47 of the *Code of Federal Regulations*, Part 15, Subpart J which limited the radiated and conducted (exiting the power cord) emissions of all “digital devices” that are intended to be sold in the United States. (Look on the back of your calculator, personal computer, or laser printer to see the FCC compliance notice.) The FCC defines a “digital device” rather broadly as “Any unintentional radiator (device or system) that generates and uses timing pulses at a rate in excess of 9000 pulses (cycles) per second and uses digital techniques.” This definition is rather broad and covers, in addition to personal computers, virtually anything “digital” such as electronic typewriters and laser printers. These regulations prescribe limits on the maximum radiated and conducted emissions of a “digital device.” The conducted emissions are defined as those exiting the power cord of the digital device, and the frequency of the regulation ranges from 150 kHz to 30 MHz. The radiated emission limits extend from 30 MHz to well over 1 GHz, with this upper limit depending on the fifth harmonic of the system clock. See Ref. 1 for a discussion of these specific limits. For example, for a digital device intended for residential use (as opposed to business use), the limit on noise current exiting the power cord is on the order of $5\ \mu\text{A}$, whereas the limit on the electric field of radiated emissions is on the order of $100\text{--}500\ \mu\text{V/m}$ when measured at a distance of 3 m.

It is very important to emphasize that if the conducted or radiated emissions of a “digital device” exceed the FCC limits at any frequency within the regulation frequency range, *it cannot be legally sold in the United States!* The FCC has the statutory authority for imposing fines and/or jail sentences if anyone intentionally violates the regulation. Hence, even though a company develops, for example, a revolutionary device (e.g., a laser printer that has the dimensions of a laptop computer, prints 50 pages per minute in color, and can be sold for under \$50 U.S.), this is all for naught if the device fails to meet the FCC limits. Even if the device fails the FCC limits, additional suppression measures can be taken to bring those emissions into compliance. However, adding the suppression measures such as filters and shielding will add to the cost of the product yet not enhance its functionality and hence will affect its marketability. Therefore, one of the most important design goals of electronic products today is to design the system to comply with the FCC limits.

Virtually all other countries in the world have similar and sometimes more stringent limits on the emissions of digital products. Hence EMC is a global concern. For example, prior to the institution of the FCC limits in the United States, most countries in Europe had individual limits on radiated and conducted emissions of digital devices that were similar to those instituted later in the United States. Most of these limits were those developed by CISPR (the French translation meaning International Special Committee on Radio Interference). CISPR is a committee of the International Electrotechnical Commission (IEC), an international body that promulgates standards in order to facilitate trade between countries. CISPR published a recommended standard known as CISPR 22 that concerns information technology equipment

(ITE) which also includes digital devices. Many countries in Europe and throughout the world have adopted the CISPR 22 standard. The CISPR 22 limits are quite similar to the FCC limits. In recent years many countries in Europe have come together to form the European Economic Community or European Union in order to facilitate trade between the member nations. They have essentially adopted the CISPR 22 standard for radiated and conducted emissions of digital devices that are to be sold in those countries. This is called a *European Norm*, and the standard is EN 55022. Hence, complying with limits on radiated and conducted emissions of digital devices is a worldwide concern. In addition, the European standards impose additional regulatory requirements on digital devices that limit the *susceptibility* of a digital device to electromagnetic emissions. This requirement has not yet been imposed by the FCC but has created considerable concern for manufacturers of digital products that are intended for sale in Europe.

The measurement of these levels must be conducted by strict rules that are described in related standards. The measurement of radiated emissions is generally conducted in a semianechoic chamber as illustrated in Fig. 4. A shielded room encloses the test and prevents external emissions from contaminating the test results. The walls are lined with materials (carbon-impregnated foam or more recent ferrite tiles) that absorb electromagnetic waves in the frequency range of the regulations. This is done to prevent reflections from the shielded room walls and hence to simulate free space. The floor is a ground plane; hence the prefix “semi” in the chamber name. The conducted emissions are noise currents exiting the power cord of the device. These are routinely measured with a

line impedance stabilization network (LISN) as shown in Fig. 5. The digital product under test has its power cord plugged into the LISN, and the LISN is plugged into the commercial power outlet. The purposes of the LISN are twofold:

1. The impedance seen between phase and ground and between neutral and ground of the commercial power net *over the regulatory frequency range of 150 kHz–30 MHz* varies widely; thus the first purpose of the LISN is to present a constant $50\ \Omega$ impedance between phase and ground and between neutral and ground over the regulatory frequency range.
2. The second purpose of the LISN is to prevent noise on the commercial power net from contaminating the test. Inductors L1 are present to block this, and capacitors C2 are present to divert this noise to ground. Of course, the LISN must also pass the 60 Hz commercial power to the product. At 60 Hz, L1 is essentially a low impedance and C2 is essentially a high impedance. Hence the LISN is transparent to the 60 Hz power but appears as shown in Fig. 6 at the regulatory frequencies of 150 kHz–30 MHz.

These EMC regulatory requirements *cannot be waived*. If a digital device fails to meet these limits at any frequency, it cannot be legally sold in that country! There are certain other EMC requirements that can be relaxed if deemed necessary. These are for military products, commercial aircraft and automobiles, and other commercial

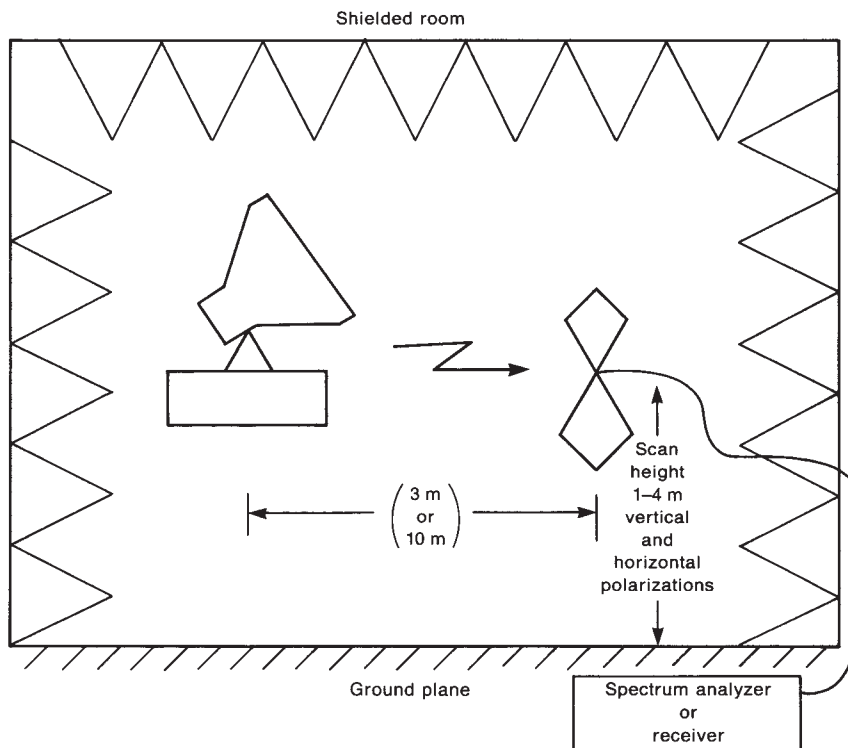


Figure 4. Illustration of the use of a semianechoic chamber for the measurement of radiated emissions.

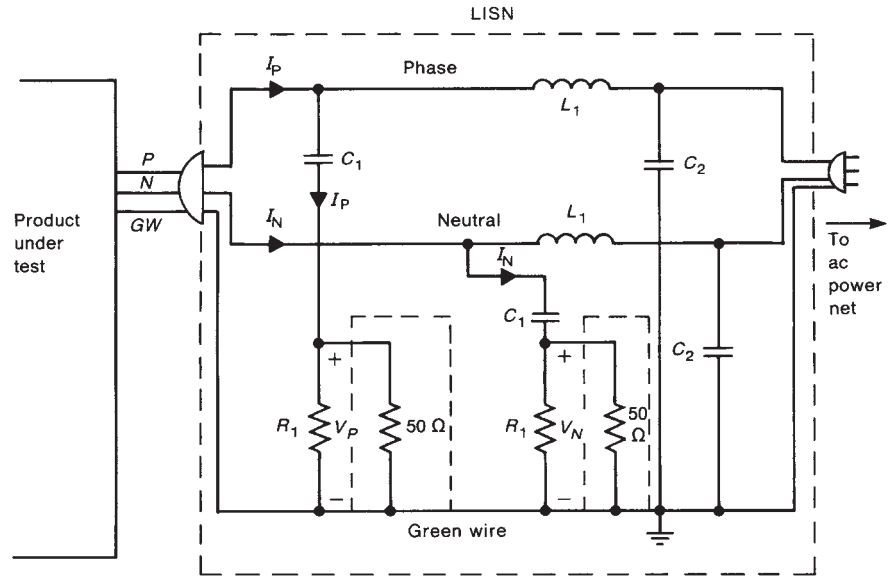


Figure 5. The line impedance stabilization network (LISN) for the measurement of conducted emissions.

vehicles. In the United States, in the early 1960s the Department of Defense (DoD) instituted a broad range of EMC requirements concerning, among other things, limits on the radiated and conducted emissions from virtually all electronic products that are sold to DoD units (U.S. Army, Navy, Coast Guard, etc.) These are military standards and the EMC regulation is MIL-STD-461E. The frequency range of regulation of the emissions is drastically greater than the FCC or CISPR 22 regulations, extending in some cases from 30 Hz to 40 GHz. However, the project officer for the contract has the authority to “tailor” these limits to fit the particular requirements of the system in which the electronic device is to be installed. In addition to the military, commercial aircraft manufacturers in the United States voluntarily comply with a standard on radiated and conducted emissions of commercial aircraft known as DO-160D. These voluntary standards prescribe limits on radiated and conducted emissions (on cables) as well as susceptibility in order to prevent or reduce the potential for interference with critical flight systems on the aircraft. Manufacturers of commercial automobiles and trucks in the United States also voluntarily comply with a standard such as SAE J551-2, which provides, among other things,

limits on the radiated and conducted emissions of the vehicle as well as its susceptibility to external electromagnetic emissions. Again these limits are intended to prevent or reduce the potential for interference with electronic systems on the vehicle from either internal or external sources. Once again, these are voluntary but manufacturers generally comply because introduction into the market of an airplane or vehicle that is susceptible to everyday emissions from radio towers and other ambient emitters that the airplane or vehicle routinely encounters would create a devastating loss of confidence with consumers.

3. TIME-DOMAIN VERSUS FREQUENCY-DOMAIN DESCRIPTION OF DIGITAL SIGNALS

The abovementioned regulatory requirements on digital devices are given in the frequency domain, that is, at each frequency within a frequency range. Hence it is important to investigate the relation between the time-domain waveforms of digital signals and their spectral content. The primary waveform in a digital device is its clock(s) signals. These are periodic, pulses with period T that are approximately trapezoidal in shape and have risetimes and

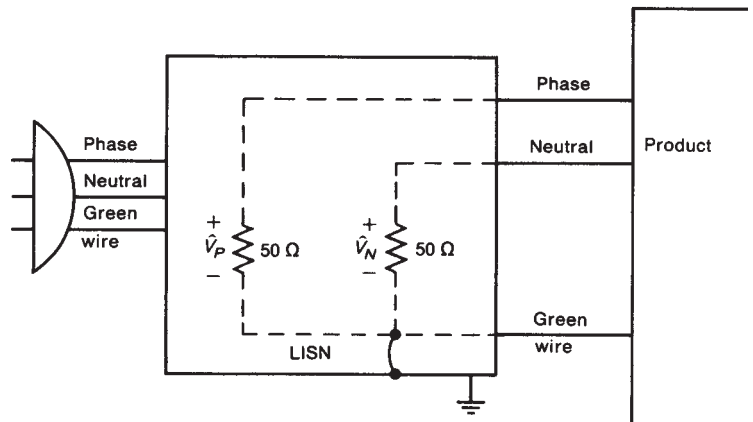


Figure 6. Equivalent circuit of the LISN as seen by the product over its intended frequency range of use.

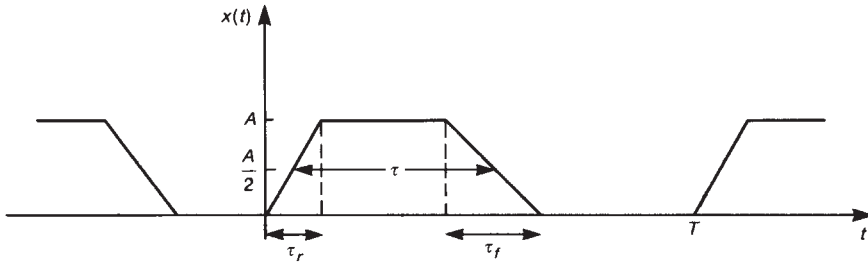


Figure 7. The periodic, trapezoidal pulse-train representing clock and data signals of digital systems.

falltimes of τ_r and τ_f , respectively, as illustrated in Fig. 7. Typical clock signals have equal risetimes and falltimes or approximately so. Digital data signals have a similar waveform but are random in occurrence as opposed to the deterministic clock signal. Since the clock is periodic, we may decompose it into its spectral components with the Fourier series, giving the representation [1]

$$\begin{aligned} x(t) = & X_0 + X_1 \cos(\omega_0 t + \theta_1) \\ & + X_2 \cos(2\omega_0 t + \theta_2) \\ & + X_3 \cos(3\omega_0 t + \theta_3) + \dots \end{aligned} \quad (1)$$

Hence, the signal consists of the sum of a DC or average value X_0 , plus an infinite number of harmonics having magnitude X_n and phase θ_n and frequencies $n\omega_0$, where $\omega_0 = (2\pi/T)$ and the fundamental (repetition) frequency is $f_0 = (1/T)$. For the trapezoidal waveform in Fig. 7 having equal risetimes and falltimes, the magnitudes of these spectral components are [1]

$$X_n = 2AD \left| \frac{\sin(n\pi D)}{n\pi D} \right| \left| \frac{\sin(n\pi\tau f_0)}{n\pi\tau f_0} \right| \quad (2)$$

where the duty cycle is

$$D = \frac{\tau}{T} = \tau f_0 \quad (3)$$

and the pulsewidth between 50% points is τ .

In order to facilitate an understanding of how the time-domain properties affect the spectral content, it is possible

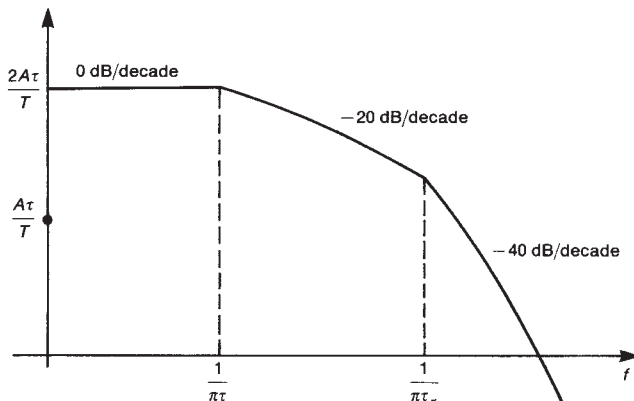


Figure 8. Bounds on the one-sided magnitude spectrum of a trapezoidal pulse-train.

to obtain spectral bounds on the magnitude as shown in Fig. 8 [1]. This Bode plot shows that the magnitudes of the spectral components fall off with increasing frequency as 0 dB/decade out to the first breakpoint, which occurs at $1/\pi\tau = f_0/\pi D$. Above this breakpoint the levels fall off as 20 dB/decade up to the next breakpoint, which is $1/\pi\tau_r$. Above this the levels fall off as 40 dB/decade. Hence, *to reduce the high-frequency spectral content, we must increase the pulse rise/falltimes*. This is a primary method of *reducing the source*. Figure 9 shows a comparison between the exact levels and the spectral bounds for a 1-V, 1-MHz clock having a rise/falltime of 20 ns, a 50% duty cycle, and a 30% duty cycle. Figure 10 shows a spectrum analyzer display of a 1-V, 10-MHz, 50% duty cycle digital clock signal having rise/falltimes of 20 and 5 ns illustrating the considerable reduction of the high-frequency spectral content achieved by increasing the rise/falltimes of the pulse.

4. METHODS FOR REDUCING EMISSIONS FOR COMPLIANCE

4.1. Radiated Emissions

We first describe methods for reducing radiated emissions. Again, time-varying currents radiate whether they are on cables or metallic cabinets. However, the predominant radiated emissions for digital products seem to emanate from wires or printed circuit board (PCB) traces in the system. The PCB traces are also referred to as “lands” because of their rectangular cross sections. There are two possible types of current. Consider a two-conductor (wire or PCB land) transmission line as shown in Fig. 11. *Differential-mode* currents are the usual functional currents on these conductors, and these phasor currents are denoted as \hat{I}_D in Fig. 11a. At a line cross section these are equal in magnitude but opposite in phase. These are the functional or desired currents that are designed for. If we view each conductor current as a Hertzian dipole (assuming that the conductor is electrically short and the observation point is in the far field at this frequency), then the radiated electric fields, \hat{E}_1 and \hat{E}_2 , subtract. Since the two currents are not collocated, they do not cancel. Conversely, there also exist *common-mode* currents on the conductors and these phasor currents are denoted as \hat{I}_C . At a cross section of the line the two currents have the same magnitude and are in phase as shown in Fig. 11b. Again viewing these as Hertzian dipoles, we see that their radiated electric fields add. Common-mode currents are sometimes referred to as *antenna-mode currents*. One way of viewing

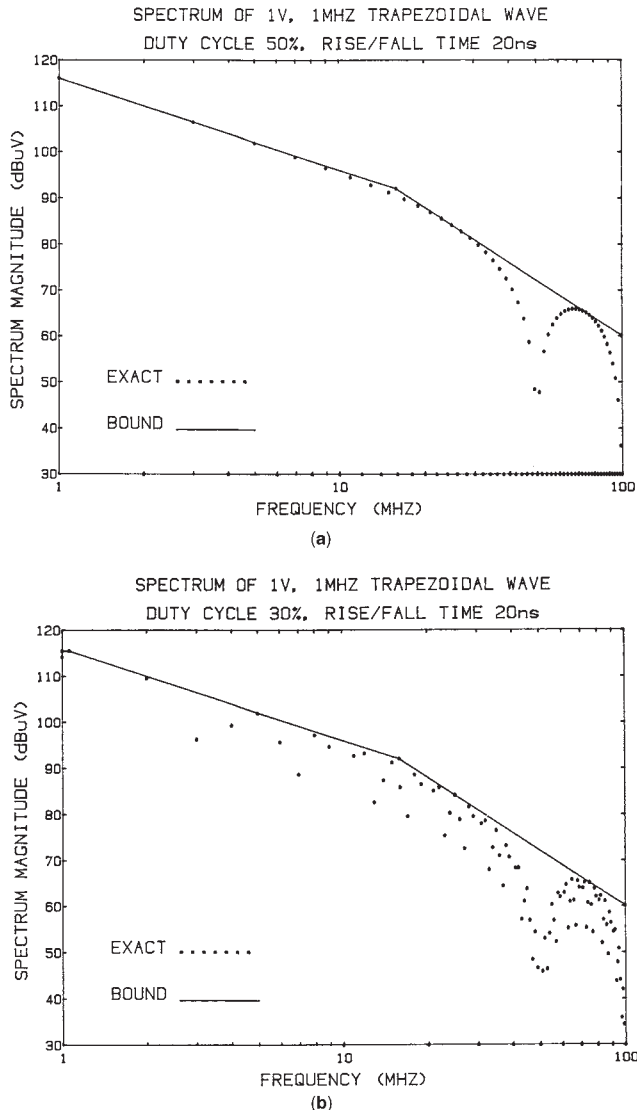


Figure 9. Examples illustrating the spectral bounds for various duty cycles of a 1-V, 1-MHz, trapezoidal pulsetrain having rise/falltimes of 20 ns: (a) 50% duty cycle; (b) 30% duty cycle.

them is as having a return path to their source consisting of, for example, parasitic capacitances to a third adjacent conductor (which is always present). The differential-mode currents are easily calculated, but the common-mode currents are not easily calculated (if at all). The common-mode currents are usually measured with a current probe [1]. The important observation here is that, because the differential-mode current emissions subtract but the common-mode emissions add, a common-mode current of magnitude much smaller than that of the differential-mode current can cause equal or greater emission levels. Radiated emissions from common-mode currents can be devastating in terms of radiated emissions and tend to be one of the major causes (if not the sole cause) of radiated emission and product noncompliance with the regulations for digital products today. For example, one can compute that for a 1 m length of ribbon cable (wire separation of 50 mils or 1.27 mm) a level of

differential-mode current at 30 MHz of some 20 mA will cause radiated emissions at 3 m that will exceed the FCC limit, whereas only 8 μ A of common-mode current will cause the same level of emission at 30 MHz.

Suppressing the emissions of these two currents requires different techniques. In the case of differential-mode currents, capacitors can be placed between the two wires to divert the current and keep it off the cable. In general, the longer the cable, the greater the potential for the current to radiate. The value of the capacitor is chosen to give a relatively low impedance (relative to the cable termination impedance) at the frequency of the emission current. In addition to the technique of current diversion, as with a parallel capacitor, there is the technique of current blocking where inductors or ferrite beads are inserted in series with each line to block the differential-mode currents of each line. In this case the value of the series impedance must be chosen to give a large impedance (relative to the cable termination impedance). It must be remembered that these differential-mode currents are required for the product to operate properly. Hence these suppression measures must be chosen with care so that these intended currents are not corrupted to the point that functionality of the product is impaired.

Suppressing the radiated emissions of common-mode currents requires a different technique. The common technique is to use common-mode chokes as illustrated in Fig. 12. A common-mode choke can take many forms. We have shown a toroid where the two cable wires are wound the same direction. In the case of differential-mode currents as shown in Fig. 12b, the magnetic fluxes of the differential-mode currents tend to cancel, and hence the choke is transparent to these currents. However, the magnetic fluxes of the common-mode currents add in the core, and hence the common-mode currents see a net impedance inserted in each line. These chokes are constructed of ferrite materials such as manganese-zinc or nickel-zinc materials with additional materials added to produce high-frequency losses. In addition to inserting inductances selectively in the lines as shown in Fig. 12c, these ferrite chokes also insert high-frequency resistances (not shown) and provide selective loss, thus dissipating the energy in the common-mode currents. There are also chokes consisting of a ferrite core that is clamped around both wires such as is frequently seen in personal computer systems on the keyboard and video cables.

We now will derive a simple model for these emissions that will illustrate the factors that can be controlled in order to reduce their emissions. First consider the case of differential-mode currents on the two wires as shown in Fig. 13, where the wires are separated by a distance s and are a total length \mathcal{L} . If we assume that the line length is much less than a wavelength and the observation point is in their far field (typically a wavelength or more), then we may view these as Hertzian dipoles and simply superimpose their fields. The resulting maximum electric field is then [1]

$$|\hat{E}_{D,\max}| = 1.316 \times 10^{-14} \frac{|\hat{I}_D| f^2 \mathcal{L} s}{d} \quad (4)$$

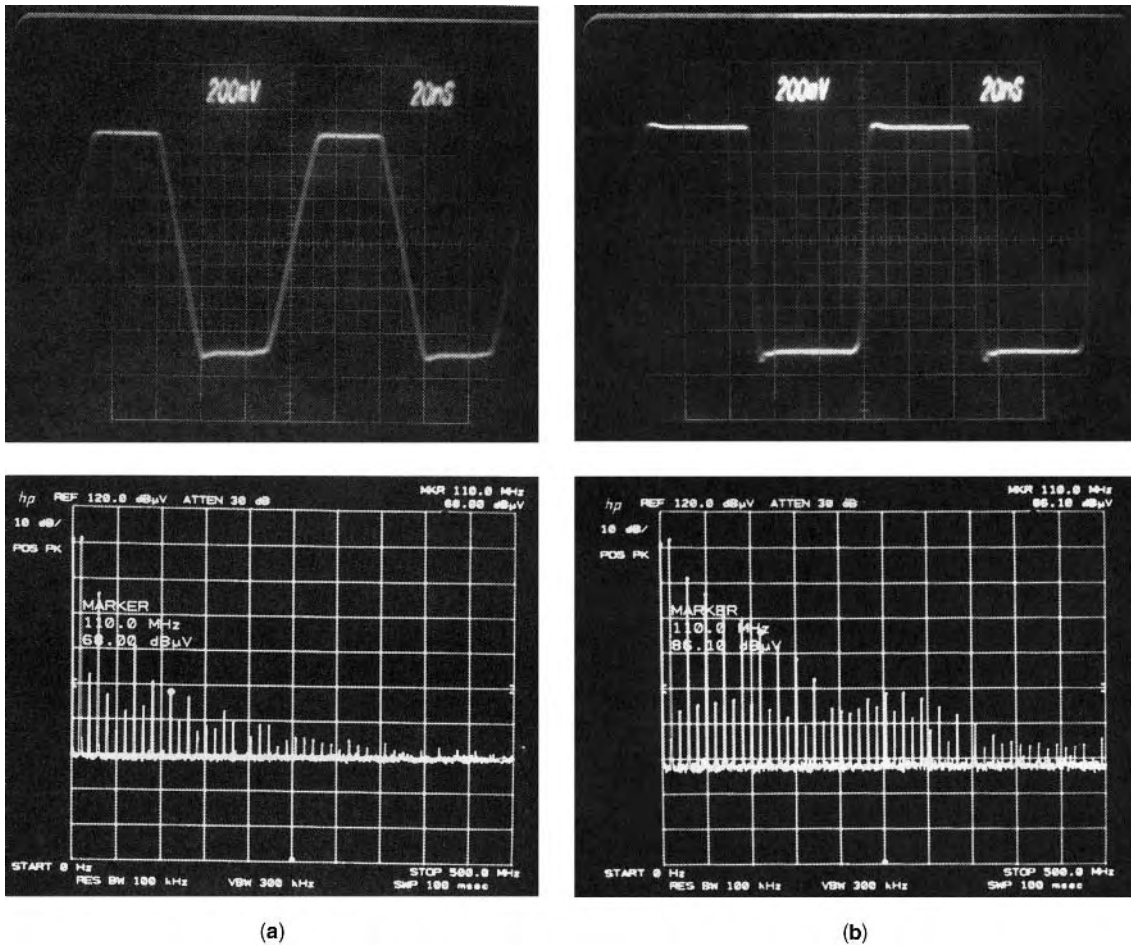


Figure 10. Experimentally measured spectra of 1-V, 10-MHz, 50% duty cycle trapezoidal pulse-trains for rise/falltimes of (a) 20 ns; (b) 5 ns.

where d is the distance to the observation point. For residential digital devices in the United States, this is the regulatory measurement distance of 3 m. At 30 MHz, the FCC limit is $100 \mu\text{V}/\text{m}$ at 3 m. We can calculate from this that a level of about 20 mA on a 1 m length of ribbon cable at this frequency will just exceed this limit. The reason we derive a simple result such as in (4) is not so much to calculate emission levels but more importantly to determine the factors that control the emission. For example,

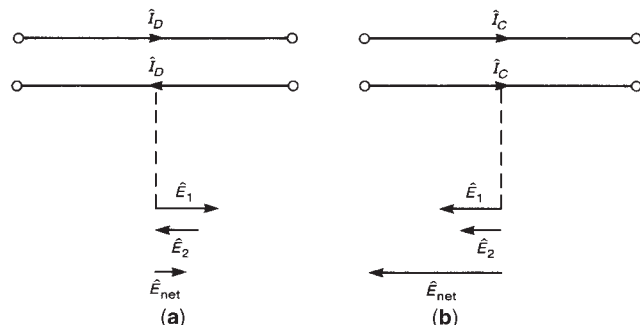


Figure 11. Illustration of the relative radiated emission potential of (a) differential-mode currents and (b) common-mode currents.

(4) shows that the factors affecting the level of the radiated field are (1) the level of the current (the level of the Fourier *component* of this current) at this frequency, (2) the frequency (squared), and (3) the loop area formed by the conductors, $A = \mathcal{L}s$. The level of the current (perhaps a high-frequency component of a clock signal) can be reduced by increasing pulse rise/falltimes. These can be reduced only up to a point where the functionality of the product becomes impaired. Usually there is considerable latitude in doing this in the original design. The frequency here is the frequency of the emission (and the regulation), which cannot be changed. The final item, loop area formed by the two conductors can be easily controlled. Two cases are illustrated in Fig. 14. Figure 14a shows a digital clock that serves an application-specific integrated circuit (ASIC). The loop area of the two connection leads must be kept to a minimum. This can be easily done by (1) placing the clock as close as possible to the device being served and (2) placing the two connection leads as close together as possible. In the layout of a PCB, this would be the initial order of business. Figure 14b shows a ribbon cable attached to a stepper motor. The pin assignments in the connectors are as shown. The prime items, such as A' , are the returns for the currents on the unprimed wires, such as A . Because of the pin assignments, each return

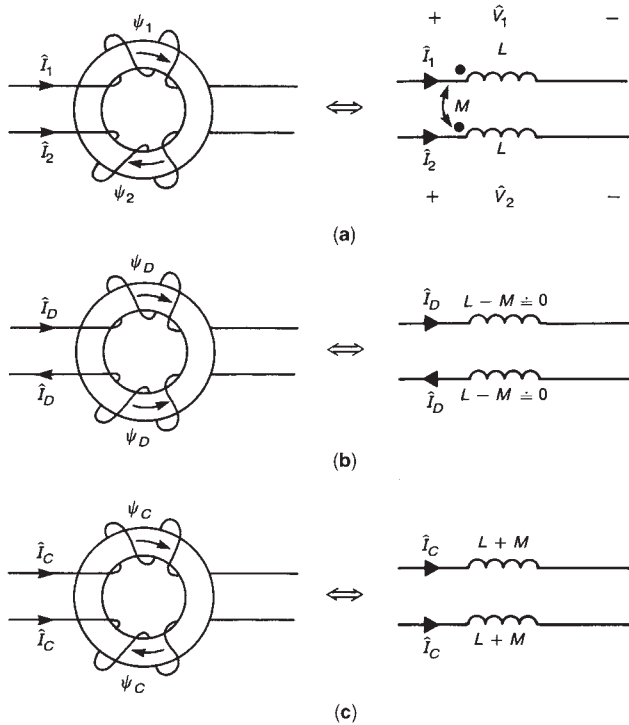


Figure 12. Modeling the effect of a common-mode choke on (a) the currents of a two-wire line, (b) the differential-mode components, and (c) the common-mode components.

encompasses three loop areas between wires. If the pin assignments had been as shown in Fig. 14c, then the individual loop areas would be reduced by one-third and the radiated emissions would be, according to the model in Fig. 14, reduced by about 10 dB. Simple understanding of the basic mechanisms will often lead to “cost-free” EMC suppression.

Next we consider a simple model for the emissions from common-mode currents shown in Fig. 15. Once again considering the two conductors as Hertzian dipoles and

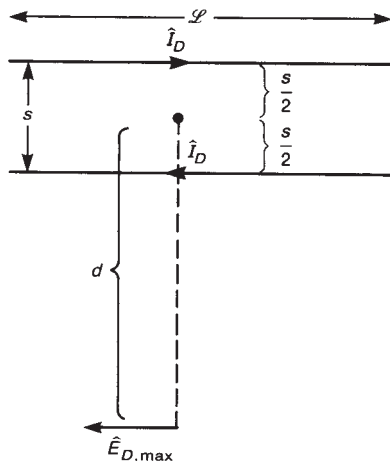


Figure 13. A simplified estimate of the maximum radiated emissions due to differential-mode currents with constant distribution.

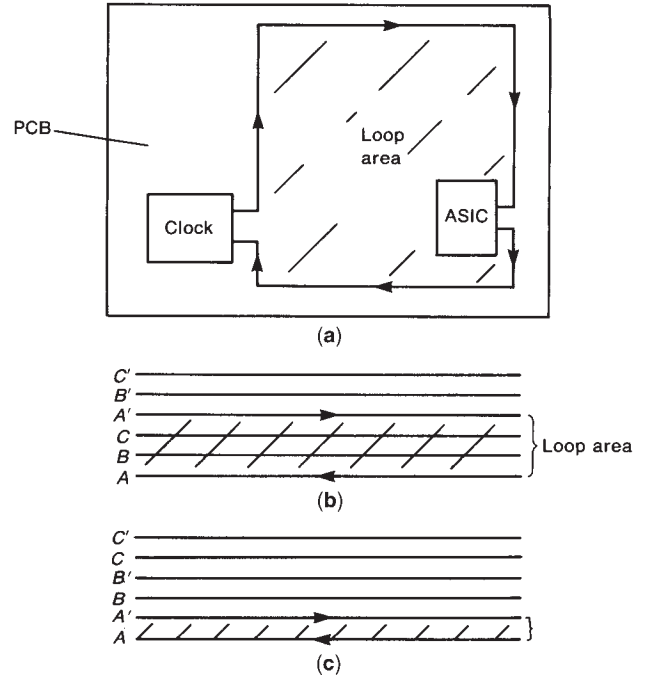


Figure 14. Common mistakes that lead to unnecessarily large differential-mode emissions: (a) large clock land areas; (b,c) choices of connector pin assignments in ribbon cables to minimize loop area.

superimposing their fields gives [1]

$$|\hat{E}_{C,max}| = 1.257 \times 10^{-6} \frac{|\hat{I}_D| f \mathcal{L}}{d} \quad (5)$$

For a 1 m length of ribbon cable at 30 MHz, we can calculate that a level of common-mode current of some 8 μA will cause an electric field at the regulatory measurement distance of 3 m that exceeds the FCC limit. Hence very small levels of common-mode currents can be devastating from the standpoint of complying with the regulatory limits. In (5) we observe that the two factors that control these

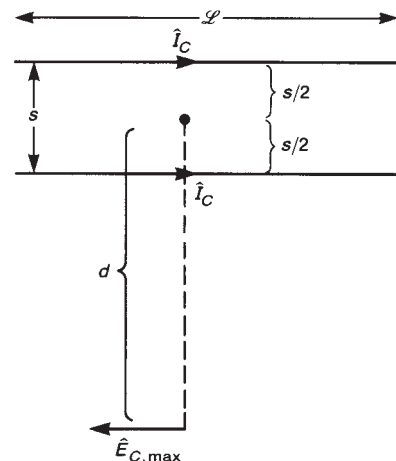


Figure 15. A simplified estimate of the maximum radiated emissions due to common-mode currents with constant distribution.

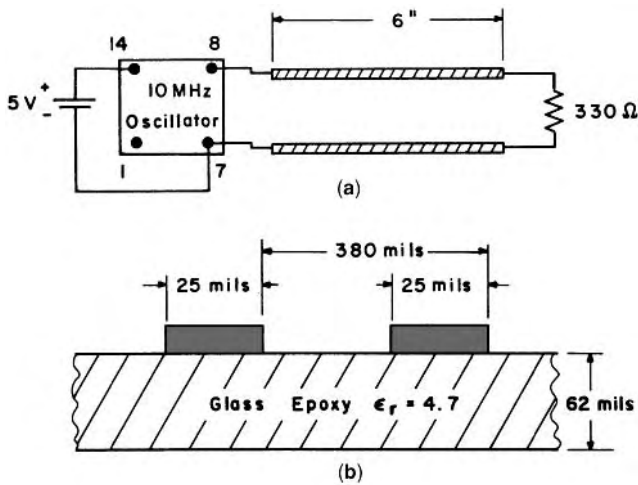


Figure 16. An experiment illustrating common-mode currents on PCBs: (a) device schematic; (b) PCB cross-sectional dimensions.

emission levels are (1) the level of the current and (2) the *length* of the cable. Reducing the levels of the differential-mode currents tends to also reduce the levels of the common-mode currents, although the precise relationship is not clear. Also, we should endeavor to make all connections (wires and PCB lands) as short as possible.

In order to illustrate the devastating nature of common-mode currents, we investigate the simple experiment shown in Fig. 16. Two PCB lands of width 25 mils (0.635 mm) and length 6 in (15.2 cm) are mounted on a typical PCB substrate. A 10-MHz dual-inline package (DIP) oscillator is powered by a 5-V battery (no connection to the commercial power system) and is connected to the two lands. The two lands are terminated in a 330-Ω

resistor. The characteristic impedance of this line is about 330 Ω, and hence the line is matched. The radiated electric fields measured in a typical semianechoic chamber at 3 m are shown in Fig. 17. On these measured emissions are superimposed the predictions of the common-mode model in (5) denoted as “x.” The common-mode currents used in this model were measured with a current probe. In addition, the emissions of the differential-mode currents were measured on each individual wire and also predicted with a transmission-line model. The emissions computed with the measured differential-mode currents with (4) are shown as “o” and the emissions computed with the computed differential-mode currents with (4) are shown as “+.” These results show that (1) the emissions of common-mode currents greatly exceed those from differential-mode currents and are dominant, and (2) the simple models in (4) and (5) are sufficiently accurate to illustrate the factors that affect these emissions.

4.2. Conducted Emissions

Now we turn to the suppression of conducted emissions. As stated earlier, the standard regulatory test for conducted emissions of a digital product is to plug the product’s power cord into a LISN and the LISN into the commercial power outlet. Again the noise currents (150 kHz–30 MHz) exiting the phase and neutral conductors of the power cord consist of differential-mode and common-mode currents. The differential-mode currents flow out of the phase conductor and return on the neutral conductor. The common-mode currents flow out of the phase and neutral conductors and return on the safety or green wire of the product. The primary method of suppressing these emissions is with a power supply filter shown in Fig. 18. Ordinarily the power supply filter is at the last point of exit of the power cord from the product. The important components in the filter are (1) a

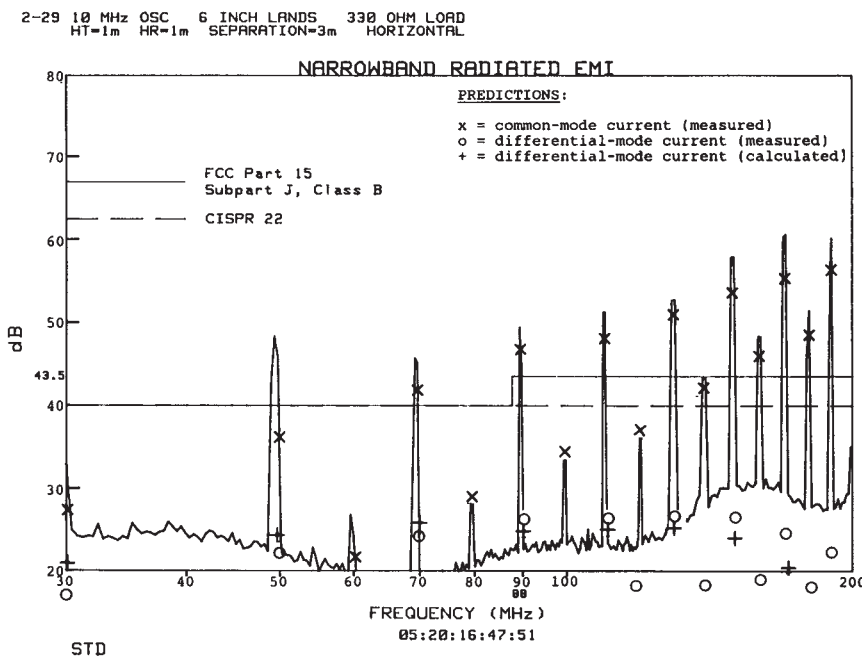


Figure 17. Measured and predicted emissions of the device of Fig. 16.

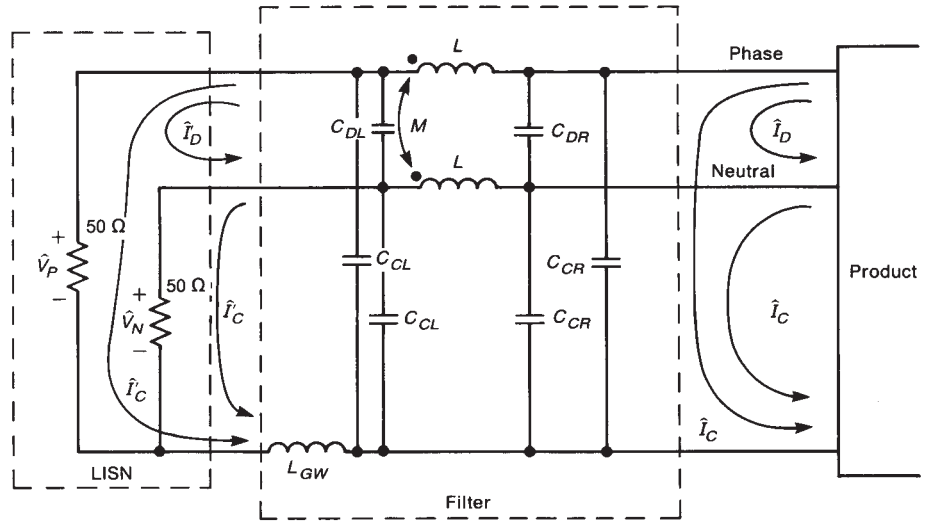


Figure 18. A typical power supply filter topology.

common-mode choke denoted by self- and mutual inductances L and M , (2) line-to-line capacitors denoted as C_{DR} and C_{DL} , and (3) line-to-ground capacitors denoted as C_{CR} and C_{CL} . The subscripts “L” and “R” denote left and right, respectively. The common-mode choke acts as described before; it selectively blocks the common-mode noise current and is transparent to the differential-mode noise current. It is necessary to use a common-mode choke rather than individual inductors here since the differential-mode current contains the important 60 Hz power current. The 60 Hz power current has a very large magnitude, on the order of 1–10 A in typical digital products and hence would saturate the ferrite cores of individual inductors. The common-mode choke is transparent to the high-level 60 Hz current, and hence the core of the common-mode choke is not saturated by it. The line-to-line capacitors are present to divert the differential-mode noise currents, and the line-to-ground capacitors are present to divert the common-mode noise currents.

4.3. Shielding

Another suppression measure is obtained with *shielding*. Generally, shielding should be used as a last resort for suppression since (1) it is difficult to implement in its ideal form (shielding effectiveness values of > 200 dB can easily be calculated but are impossible or too costly to implement), and (2) shielding is generally quite expensive compared to other simple methods. A shield is a contiguous

metal enclosure. There are two purposes for shields as illustrated in Fig. 19. One is to keep internal fields from being radiated (possibly causing noncompliance with radiated emission levels) and the other is to keep external fields from interfering with internal electronics (preventing susceptibility to, for example, a FM radio transmitter or an airport surveillance radar).

The simplest model of a shield is a large, conducting plane of conductivity σ and thickness t as shown in Fig. 20. The most common measure of shielding effectiveness (SE) is the ratio of the electric field that is incident on the shield to the electric field that exits the shield. In decibels this is [1]

$$SE_{dB} = 20 \log_{10} \left| \frac{E_{incident}}{E_{transmitted}} \right| \tag{6}$$

This gives the shielding effectiveness as a positive value. For example, a SE of 100 dB means that the electric field is reduced by a factor of 100,000 as it transits the shield wall. If we assume that (1) the shield is in the far field of the source (such as a radar) so that the incident field is a uniform plane wave and (2) the incident wave strikes the shield wall normal to its surface, then a simple result for the shielding effectiveness can be obtained as [1]

$$SE_{dB} = \underbrace{20 \log_{10} \left| \frac{\eta_0}{4\eta} \right|}_{R_{dB}} + \underbrace{20 \log_{10}(e^{t/\delta})}_{A_{dB}} \tag{7}$$

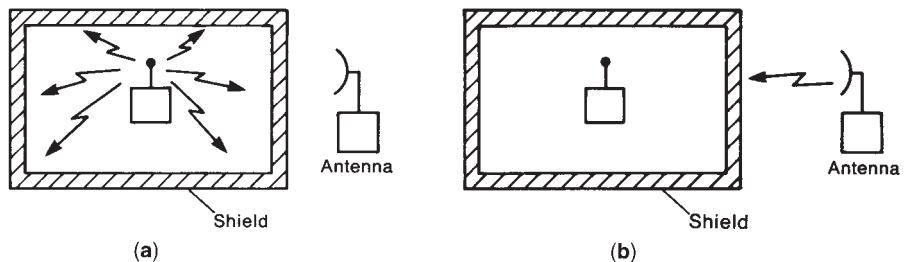


Figure 19. Illustration of the use of a shielded enclosure to (a) contain radiated emissions and (b) exclude radiated emissions.

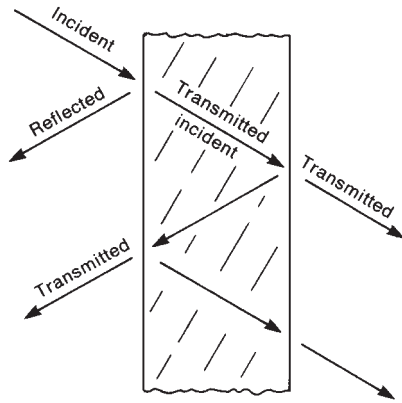


Figure 20. Illustration of multiple reflections within a shield.

where the intrinsic impedance of free space is $\eta_0 = 377 \Omega$, the intrinsic impedance of the conducting shield is $\hat{\eta} = \sqrt{j\omega\mu/(\sigma + j\omega\epsilon)}$, and $\delta = 1/\sqrt{\pi f\mu\sigma}$ is the skin depth. The first term in (7) is said to be the reflection loss and accounts for the reflection at the left and right interfaces of the shield walls. The second term is said to be the absorption loss and accounts for attenuation of the waves as they pass through the shield. This absorption term can be written as $A_{dB} = 8.69(t/\delta)$. Hence a shield thickness of one skin depth gives ~ 9 dB of absorption loss, and a shield thickness of five skin depths gives ~ 44 dB.

From this result one can compute shielding effectiveness values on the order of 100–500 dB. Rarely will these be realized in actual systems because of the inevitable penetrations of the shield by openings to allow for cooling and by cables that must exit the shield. These penetrations must be properly treated (such as placing gratings with many small, closely spaced holes over openings or placing filters in every exiting cable), or else the shielding effectiveness will be drastically reduced.

Other types of “shielding” act to divert rather than reflecting magnetic fields. Ferromagnetic materials have relative permeabilities greater than unity. For example, sheet steel has $\mu_r = 2000$, and mumetal has $\mu_r = 30,000$. These materials present a low reluctance path for the magnetic fields and hence divert them away from electronics that may be susceptible to them.

4.4. Crosstalk

There is another aspect to EMC that is often overlooked: the ability of the system to interfere with itself. A common such situation is crosstalk between adjacent transmission lines. Consider a three-conductor line shown in Fig. 21. One conductor is called the *generator* conductor and forms, with the *reference* conductor (a ground plane, a wire, a PCB land, or an overall shield), the generator circuit. It is driven by a source that has an open-circuit voltage $V_S(t)$ and source resistance R_S , and is terminated by a resistor R_L . Another conductor, the receptor conductor, with the reference conductor forms the receptor circuit. This circuit is terminated at the near end (with reference to the source on the generator circuit) with a resistor R_{NE} and at the far end with a resistor R_{FE} . The line has total length of \mathcal{L} . The electric and magnetic fields of the generator circuit interact with the receptor circuit and cause induced voltages, V_{NE} and V_{FE} , at the terminals of the receptor circuit. These induced voltages may cause interference with the devices that are represented by R_{NE} and R_{FE} . This is referred to as *crosstalk*.

Computing this crosstalk is generally a formidable task. (See COUPLED TRANSMISSION LINES in this Encyclopedia). We may, however, obtain a simple model for this crosstalk as long as (1) the line length is much less than a wavelength at the highest significant frequency of the source, that is, electrically short, and (2) the two circuits are weakly coupled [1]. This simple model is shown in Fig. 22. The electric field and voltage of the generator circuit induce a current source in the receptor circuit, via a per unit length (PUL) mutual capacitance c_m , whose value is $j\omega c_m \mathcal{L} \hat{V}_{G,DC}$ where $\hat{V}_{G,DC}$ is the phasor voltage between the conductors of the generator circuit. Because the line length is assumed electrically small, this voltage is approximately constant along the line and can be computed as though it were DC as

$$\hat{V}_{G,DC} \cong \frac{R_L}{R_S + R_L} \hat{V}_S \tag{8a}$$

Similarly, the magnetic field and current of the generator circuit induce a voltage source (according to Faraday’s law) in the receptor circuit, via a PUL mutual inductance l_m , whose value is $j\omega l_m \mathcal{L} \hat{I}_{G,DC}$ where $\hat{I}_{G,DC}$ is the phasor

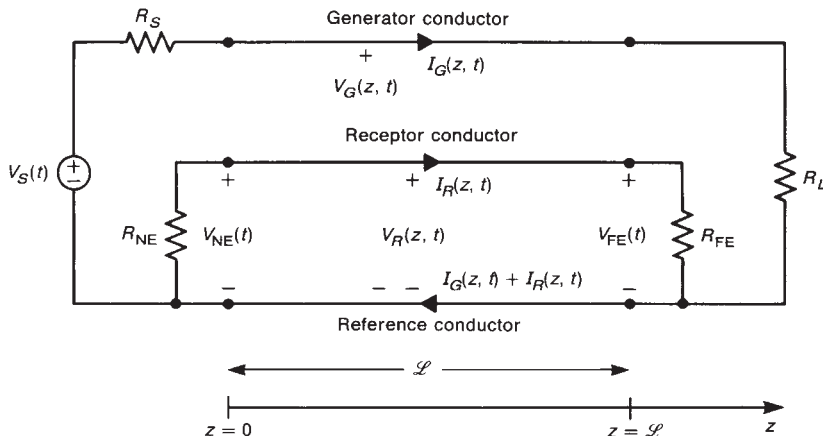


Figure 21. The general three-conductor transmission line, illustrating crosstalk.

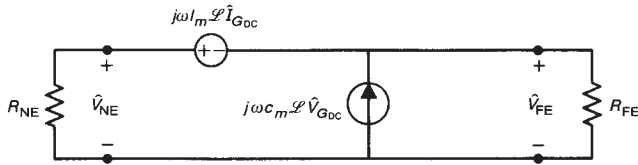


Figure 22. The simple inductive–capacitive coupling model of the receptor circuit for sinusoidal excitation.

current along the conductors of the generator circuit. Because the line length is assumed electrically short, this current is also approximately constant along the line and can be computed as though it were DC as

$$\hat{I}_{G,DC} \cong \frac{1}{R_S + R_L} \hat{V}_S \quad (8b)$$

Hence the near-end and far-end phasor crosstalk voltages can be computed from this circuit as

$$\begin{aligned} \hat{V}_{NE} = & \underbrace{\frac{R_{NE}}{R_{NE} + R_{FE}} j\omega l_m \mathcal{L} \hat{I}_{G,DC}}_{\text{inductive coupling}} \\ & + \underbrace{\frac{R_{NE} R_{FE}}{R_{NE} + R_{FE}} j\omega c_m \mathcal{L} \hat{V}_{G,DC}}_{\text{capacitive coupling}} \end{aligned} \quad (9a)$$

$$= j\omega \left[\frac{R_{NE}}{R_{NE} + R_{FE}} \frac{1}{R_S + R_L} l_m \mathcal{L} + \frac{R_{NE} R_{FE}}{R_{NE} + R_{FE}} c_m \mathcal{L} \frac{R_L}{R_S + R_L} \right] \hat{V}_S$$

$$\begin{aligned} \hat{V}_{FE} = & - \underbrace{\frac{R_{FE}}{R_{NE} + R_{FE}} j\omega l_m \mathcal{L} \hat{I}_{G,DC}}_{\text{inductive coupling}} \\ & + \underbrace{\frac{R_{NE} R_{FE}}{R_{NE} + R_{FE}} j\omega c_m \mathcal{L} \hat{V}_{G,DC}}_{\text{capacitive coupling}} \end{aligned} \quad (9b)$$

$$= j\omega \left[- \frac{R_{FE}}{R_{NE} + R_{FE}} \frac{1}{R_S + R_L} l_m \mathcal{L} + \frac{R_{NE} R_{FE}}{R_{NE} + R_{FE}} c_m \mathcal{L} \frac{R_L}{R_S + R_L} \right] \hat{V}_S$$

These phasor crosstalk voltages are the sum of an inductive coupling term due to the mutual inductance and the current of the generator circuit, and a capacitive coupling term due to the mutual capacitance and the voltage of the generator circuit. Observe that the final results in (9) vary directly with the frequency ($\omega = 2\pi f$) of the source. Hence the magnitudes of the crosstalk “transfer functions” $|\hat{V}_{NE}/\hat{V}_S|$ and $|\hat{V}_{FE}/\hat{V}_S|$ increase with frequency at 20 dB/decade while the phase is 90° . A substantial amount of experimental as well as computed data given in Ref. 1 confirm this behavior and the predictions of this simple model.

The model presented above is for single-frequency, sinusoidal source waveforms. For more general time-

domain waveforms we may substitute

$$j\omega \Leftrightarrow \frac{d}{dt} \quad (10)$$

to give the time-domain crosstalk as

$$\begin{aligned} V_{NE}(t) = & \underbrace{\left[\frac{R_{NE}}{R_{NE} + R_{FE}} \frac{1}{R_S + R_L} l_m \mathcal{L} + \frac{R_{NE} R_{FE}}{R_{NE} + R_{FE}} c_m \mathcal{L} \frac{R_L}{R_S + R_L} \right]}_{M_{NE}} \\ & \times \frac{dV_S(t)}{dt} \end{aligned} \quad (11a)$$

$$\begin{aligned} V_{FE}(t) = & \underbrace{\left[- \frac{R_{FE}}{R_{NE} + R_{FE}} \frac{1}{R_S + R_L} l_m \mathcal{L} + \frac{R_{NE} R_{FE}}{R_{NE} + R_{FE}} c_m \mathcal{L} \frac{R_L}{R_S + R_L} \right]}_{M_{FE}} \\ & \times \frac{dV_S(t)}{dt} \end{aligned} \quad (11b)$$

Hence the near-end and far-end crosstalk voltages depend on the derivative of the source voltage waveform, also known as its “slew rate.” Consider the source waveform to be that of a digital clock or data signal. The resulting crosstalk waveforms are shown in Fig. 23. Observe that (1) the crosstalk pulses occur during the transitions of the clock or data pulses and (2) their levels depend, in addition

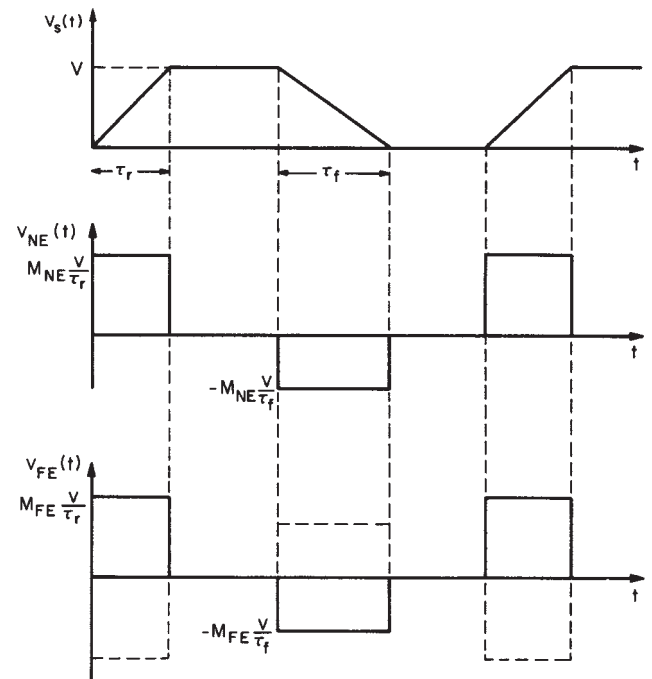


Figure 23. Time-domain crosstalk prediction of the inductive–capacitive coupling model for a trapezoidal pulsetrain excitation.

to the mutual inductance and capacitance, on the rise/fall-times of the source waveforms. Hence again we see that in order to reduce the crosstalk magnitudes, we should increase the rise/falltimes of the clock and data pulses. This rule of thumb also applied to radiated emissions.

We now turn to other methods of reducing crosstalk useful for wire-type conductors. Clearly, since the crosstalk depends on the PUL mutual inductance and capacitance between the two circuits, we can reduce the crosstalk by (1) separating the two circuits further and (2) orienting the two circuits so that they are orthogonal to each other. When these methods along with increasing the rise/falltimes fail to reduce the crosstalk to acceptable levels, we have two other options: (1) enclosing the generator and/or receptor wires with a shield and (2) twisting the two wires of the generator circuit together and/or twisting the two wires of the receptor circuit together to form twisted pairs. First we address the use of shielded wires. Suppose that we enclose, for example, the receptor wire with a concentric shield as shown in Fig. 24. The mutual capacitance between the generator wire and the receptor wire will be eliminated, and we obtain the capacitive coupling model shown in Fig. 24. From this we see that the capacitive coupling can be eliminated if we make the shield voltage (with respect to the reference conductor, e.g., a ground plane) zero. Since the line is assumed to be electrically short, we can “ground” the shield at only one end and make the voltage all along it approximately zero. In order to eliminate inductive coupling with a shield, the shield must be “grounded” at both ends as shown in Fig. 25. The process is as follows. The current of the generator circuit induces a magnetic field that threads the shield-reference conductor loop thereby inducing a current flowing back along the shield \hat{I}_S , which produces its own magnetic flux that tends to cancel the original flux penetrating this loop. If the shield were not connected to the reference conductor (“grounded”) at both ends, no shield current could flow and hence no counteracting mag-

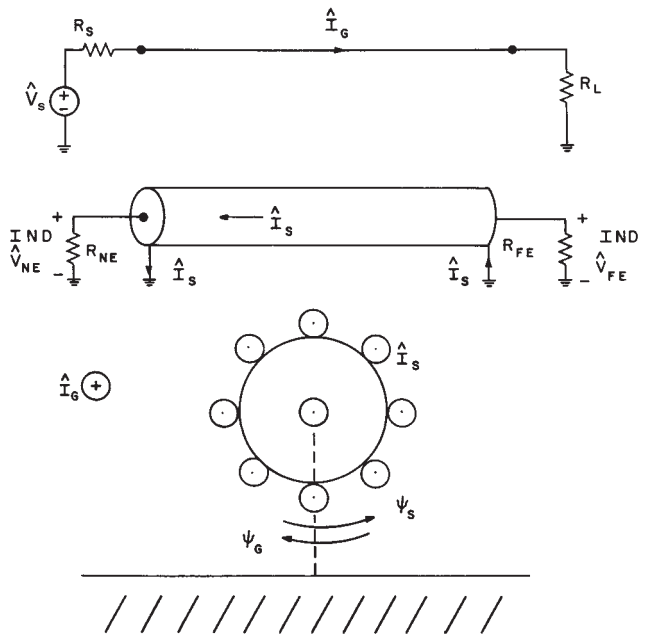


Figure 25. Illustration of the effect of placing a shield around a receptor wire on inductive coupling.

netic field would be produced. Hence, surrounding the generator wire and/or the receptor wire with a concentric shield will ideally eliminate (1) capacitive coupling as long as it is grounded at at least one end and (2) inductive coupling as long as it is grounded at both ends.

The other alternative is to replace the receptor wire with two wires (a dedicated return) and twist them together to form a twisted pair. A similar scheme can be applied to the generator wire producing the same effect. The basic process whereby a twisted wire eliminates magnetic field or inductive coupling is illustrated in Fig. 26. The current of the generator circuit causes magnetic fluxes to penetrate the loops of the twisted pair, inducing in them, by Faraday’s law, voltage sources. When we “untwist” this twisted pair, we see that the Faraday voltage sources in adjacent twists cancel out. Suppose, for example, that the reference conductor is a ground plane and the receptor wires are twisted together as shown in Fig. 27. Although a twisted pair is truly a bifilar helix, we have shown an approximate model consisting of

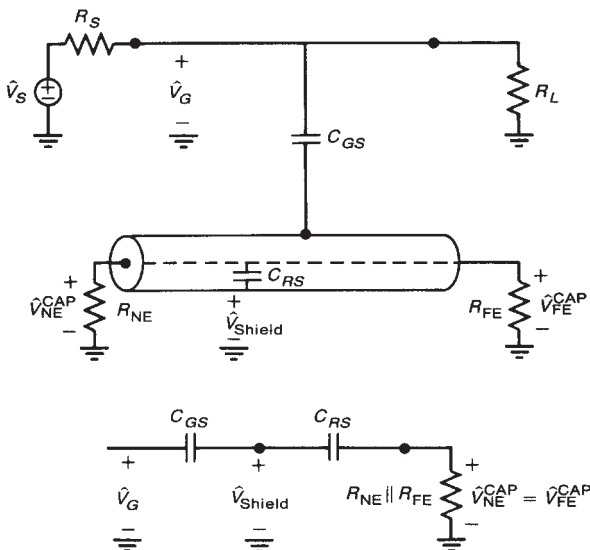


Figure 24. A lumped equivalent circuit for capacitive coupling for the shielded receptor wire.

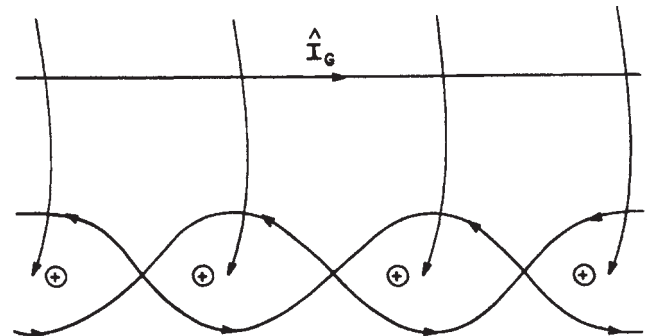


Figure 26. Illustration of the effect of a twisted pair of receptor circuit wires on magnetic field (inductive) coupling.

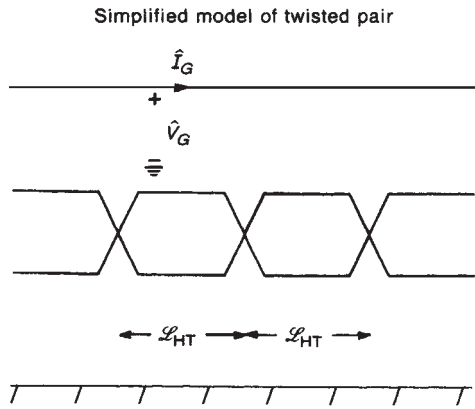


Figure 27. A simple “abrupt loop” model of a twisted pair of receptor circuit wires.

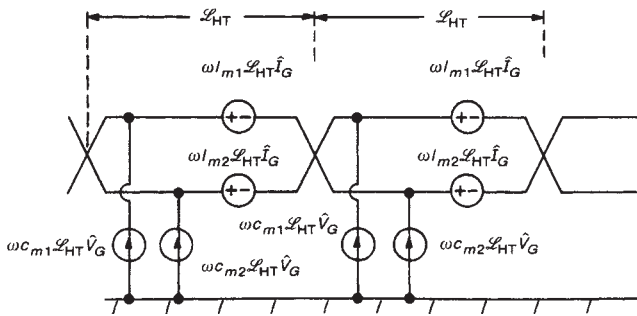
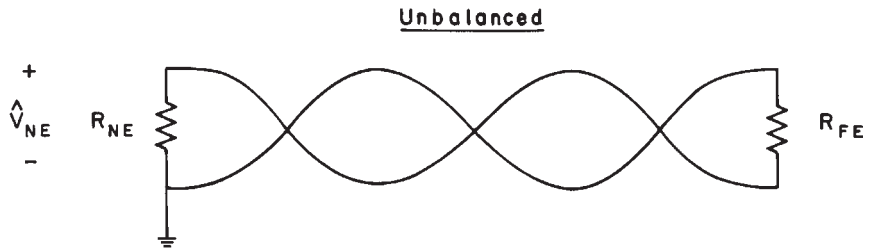


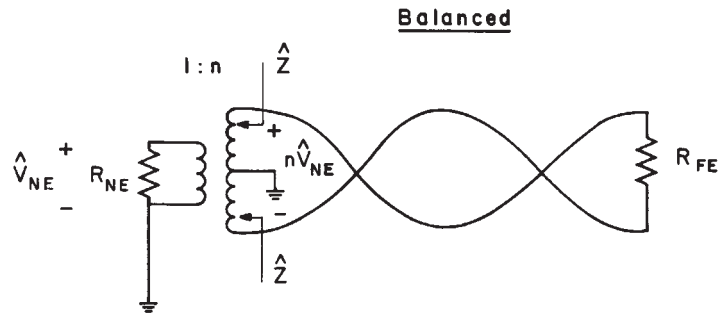
Figure 28. The simple inductive-capacitive coupling model for the twisted pair of receptor circuit wires.

adjacent loops abruptly interchanged. The length of each half-twist is denoted by \mathcal{L}_{HT} . We can view this as superimposing two of our previous generator-receptor coupling circuits; that is, we may view the twisted receptor pair as being two receptor wire-ground plane circuits. Hence the induced sources are as shown in Fig. 28. There are two ways of “terminating” a two-wire line as shown in Fig. 29. In the unbalanced case, one end is single-ended while the other is floating. In the balanced case, either center-tapped transformers or balanced line drivers and receivers are used to terminate the line. For the unbalanced case, “untwisting” the two wires gives the equivalent circuit of Fig. 30. The Faraday law-induced sources again tend to cancel. However, the induced current sources of the lower wire are short-circuited out but those attached to the upper wire do not cancel. Hence the inductive coupling portion of the crosstalk is canceled out and the capacitive coupling portion is approximately the same as before the wires were twisted together. For the balanced termination case, “untwisting the pair of receptor wires” gives the equivalent circuit in Fig. 31. Observe that the Faraday law-induced voltage sources are again canceled out by the twist but more importantly, the balancing of the terminations causes the capacitive-coupling-induced current sources to also cancel out. Hence, (1) a twisted pair eliminates inductive coupling by virtue of the twist but (2) the capacitive coupling can be eliminated only by using balanced terminations. See Ref. 1 for extensive experimental and computed data that confirm these observations about shielded wires and twisted pairs in the reduction of crosstalk.



Note: Grounded at only one end to avoid ground loops.

(a)



Each wire of twisted pair sees same impedance to ground at each end.

(b)

Figure 29. Terminating a twisted pair: (a) unbalanced; (b) balanced.

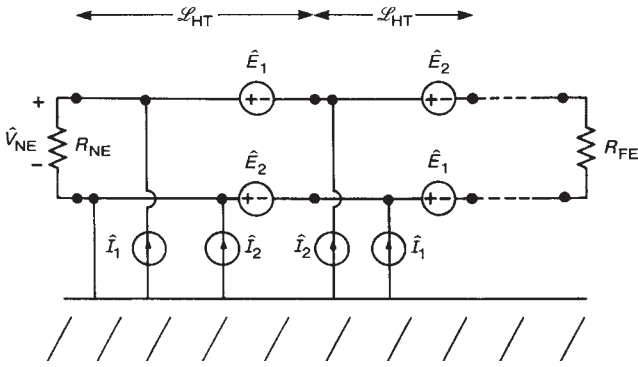


Figure 30. The inductive–capacitive coupling model for the unbalanced twisted receptor wire pair obtained by “untwisting” the wires.

5. SUMMARY

Interference in electronic systems is increasing in importance because of the necessity to use higher clock speeds in digital systems and to use the GHz frequency spectrum for analog systems. For these reasons, the electromagnetic compatibility (EMC) of electronic systems is rapidly becoming an important design criterion. Susceptibility of electronic systems to electromagnetic emissions as well as the unintended generation of electromagnetic emissions by those electronic systems can create loss of consumer confidence if the operation of those devices is impaired.

Perhaps more importantly, virtually all countries throughout the world now limit the unintended electromagnetic emissions of digital devices, and some limit the susceptibility of digital devices to electromagnetic emissions. Hence EMC of digital devices has become a legal issue. It does little good to produce a novel digital device if it cannot be legally sold in a country because of its inability to comply with the legal requirements on its electromagnetic emissions and/or its susceptibility to them. Hence EMC will no doubt steadily increase as an important design criterion for digital products. The majority of electrical engineering curricula do not address this problem today, although the number of curricula that do is steadily increasing [2]. Hence the majority of those graduating engineers have little, if any, knowledge of this important aspect of design until they enter the job place. It has become imperative that universities begin to incorporate EMC into their curricula so that engineers will be better prepared to design future electronic products.

BIBLIOGRAPHY

1. C. R. Paul, *Introduction to Electromagnetic Compatibility*, Wiley-Interscience, New York, 1992.
2. C. R. Paul, *Electromagnetics for Engineers: with Applications to Digital Systems and Electromagnetic Interference*, Wiley, New York, 2004.

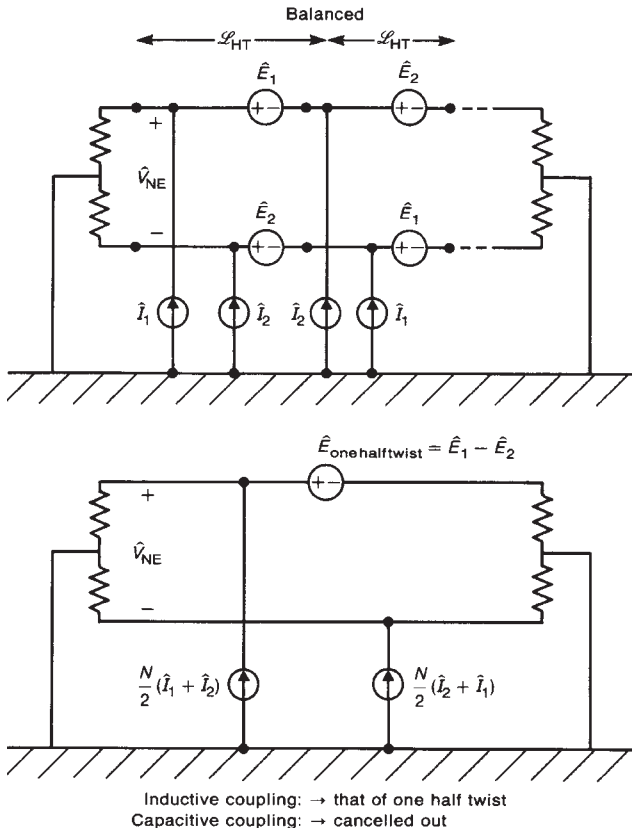


Figure 31. The inductive–capacitive coupling model for a twisted receptor wire pair and balanced terminations.

ELECTROMAGNETIC FERRITE TILE ABSORBER

CHRISTOPHER L. HOLLOWAY
 JAMES R. BAKER-JARVIS
 ROBERT T. JOHNK
 RICHARD G. GEYER
 U.S. Department of Commerce
 Boulder Laboratories
 Boulder, Colorado

Anechoic chambers have been used for over forty years to simulate different operating environments for a wide range of frequencies [1–3]. These chambers provide an accurate and convenient environment for electromagnetic compatibility (EMC) testing and are important cost-effective tools for achieving EMC compliance. To perform tests in anechoic chambers in the 30 MHz to 1000 MHz frequency range, good low-frequency electromagnetic absorbers are needed. Magnetic materials, such as ferrite tile absorbers, offer the type of low-frequency performance needed for EMC testing inside shielded rooms (or chambers).

The first anechoic chambers were constructed in the early 1950s for antenna measurements. These chambers were equipped with bats of loosely spun animal hair coated with carbon. This broadband “hair” absorber was 5.08 cm (2 in) thick and provided –20 dB of reflectivity (20 log [reflected wave/incident wave]) at normal incidence from 2.4 GHz to 10 GHz. Later in the decade, the hair absorber was replaced by a new generation of absorber that

offered -40 dB of reflectivity at normal incidence. Unlike the hair absorber, the new absorber was equipped with a shaped or convoluted front surface. Commercially manufactured absorbers emerged in the 1960s and boasted less than -60 dB of reflectivity at normal incidence. This low reflectivity was obtained at high microwave frequencies, however, where the thickness (tip-to-base dimension) of the pyramids was at least several wavelengths.

The multiple reflections between the electrically thick pyramids account for the excellent performance. Because the individual pyramids are relatively large compared with a wavelength, the sides of the pyramids reflect and re-reflect the incident wave many times. Upon each reflection, a portion of the wave is absorbed by the pyramid. Hence, an extremely small portion of the incident wave energy survives the many reflections that occur before it arrives at the solid absorber base located between the pyramids and the metal chamber wall. Then the remaining wave is absorbed further as it travels through the base until it is reflected by the chamber wall. The reflected wave is absorbed as it proceeds through the absorber base and again experiences the multiple reflections between adjacent pyramids before emerging from the plane defined by the pyramid tips.

Semi-anechoic chambers were first used for emission measurements during the 1970s as an alternative to an open area test site (OATS), a ground-plane facility for emission measurements performed from 30 MHz to 1000 MHz. These chambers were equipped with a conducting floor to simulate the large ground plane employed on the OATS. Because it obviously was impractical to construct a chamber with absorbers several wavelengths long at 30 MHz, the early chambers typically were equipped with 0.91 to 1.83 m (3 to 6 ft) thick absorber. Originally intended to be operated at higher frequencies, this absorber restricted the use of these chambers to approximately the 90 MHz to 1000 MHz frequency range [4].

With the promulgation of emission requirements during the late 1970s, absorber manufacturers were confronted with a growing demand for a compact wideband absorber to operate over the entire 30 to 1000 MHz frequency range. The evolution of compact wideband absorbers was catalyzed in the mid 1980s when techniques to calculate and measure its reflectivity were developed. The first computationally efficient, accurate calculation of absorber reflectivity became possible when the method of homogenization was used in a theoretical model [5–7]. Soon afterward, the reflectivity of compact, wideband absorbers was measured directly with large test fixtures [8–11].

To achieve small reflectivities over the entire 30 to 1000 MHz frequency range, compact wideband absorbers must use tapered structures (like pyramids or wedges) that not only operate at frequencies where they are electrically thick, but at the frequencies where they are electrically thin. When an incident wave encounters electrically thin absorbers, it does not “see” the fine structure of the pyramids or wedges. Instead, the incident wave behaves as though it encountered a solid medium whose effective conductivity and permittivity vary with the distance into the medium. These effective material properties differ from the conductivity and permittivity of the actual material used to construct the absorber.

An optimized electrically thin absorber provides a transition from the wave impedance of free space to the wave impedance of the absorber base. With the correct carbon loading, most of the incident wave penetrates the tapered structure (pyramids or wedges) and is absorbed as it travels through their solid base. Moreover, the carbon loading can be adjusted further to obtain cancellation between the portion of the incident wave reflected by the tapered structure and the wave that emerges from the absorber after reflection by the metal wall. This cancellation causes an extremely small reflectivity, albeit over a relatively narrow frequency range. In general, the carbon loading selected for electrically thin, tapered structures differs from the loading employed for electrically thick structures [7].

Although it is possible to achieve good low-frequency performance of carbon-loaded, tapered structures, they are physically large and require large metal enclosures to house them. An alternative to these large carbon-loaded, tapered structures is the ferrite-tile absorber. Electrically thin ferrite tiles were developed in Japan during the early 1960s [12–14] as an alternative to urethane pyramids and wedges. Because they have a wave impedance close to the impedance of free space, the tiles allow direct penetration of the incident wave without significant reflection at the air-to-tile interface. Furthermore, the tiles are magnetically lossy absorbing the penetrating wave almost completely as it travels through the tile. Subsequently, the wave is reflected by the metal wall behind the ferrite and travels toward the ferrite/air interface. As with the electrically thin urethane absorber, the thickness of the ferrite can be selected to achieve narrowband cancellation from the portion of the incident wave reflected at the air-to-tile interface and from the wave that emerges from the ferrite tile after reflection by the metal wall.

Recently, thin urethane pyramids or wedges that operate from about 200 MHz to 1000 MHz have been combined with ferrite tiles that are effective from 30 MHz to 600 MHz. The combination of these two absorbers, along with properly chosen dielectric layers, results in an ultra-compact wideband “hybrid” absorber that exhibits excellent performance from 30 MHz to 1000 MHz [15,16]. These “hybrid” absorbers are discussed in detail in [3].

In this chapter, we discuss the ferrite tile, ferrite grids, and hybrid combinations of urethane and ferrite absorbers typically used in electromagnetic test chambers for the 30 MHz to 1000 MHz frequency range. We present formulas and calculated reflectivities (or reflection coefficients). We also discuss how material properties and reflectivities are measured for the ferrite-tile absorbers.

1. MODELING FERRITE TILES

The performance of absorbers is determined by comparing the magnitudes of incident and reflected plane waves, where the absorber is assumed to be an infinite plane. One such comparison is the reflection coefficient Γ , defined as

$$\Gamma = \frac{E_r}{E_i} \quad (1)$$

where E_r is the reflected electric field and E_i is the incident electric field. Alternatively, absorber performance is expressed as reflectivity R in decibels as

$$R = 20 \cdot \log_{10}(|\Gamma|) [\text{dB}] \quad (2)$$

The smaller the value of R in dB, the better the performance of the absorber.

It is very straightforward to model a ferrite tile theoretically with the aid of classical transmission-line equations. The reflectivity of a solid ferrite tile backed by a metal wall is given by

$$\Gamma = \frac{Z_f - \eta}{Z_f + \eta} \quad (3)$$

where η is defined as

$$\eta = \sqrt{\frac{\mu}{\varepsilon}} \quad (4)$$

and

$$Z_f = \eta \frac{1 - e^{-2\gamma d}}{1 + e^{-2\gamma d}} \quad (5)$$

where d is the ferrite thickness and γ is the propagation constant defined by

$$\gamma = j\omega\sqrt{\mu\varepsilon} \quad (6)$$

In these expressions ε and μ are the complex permittivity and permeability of the ferrite tile. While Eq. (3) is for a normal incident plane wave, it can be modified to handle off-normal incidence by incorporating the angular dependence into the impedance and propagation constant (for details, see [3,6,17]).

Figure 1 shows the reflectivity of a solid ferrite tile and the material properties are given in Table 1. The figure shows that the tile performs very well below 600 MHz, but above 600 MHz, the tile performance deteriorates.

The higher frequency (>600 MHz) performance is improved by using so-called "ferrite grids." A ferrite grid (or waffle) is shown in Fig. 2. The grid is a two-dimensional array of square air sections cut into a ferrite-tile matrix. This structure is modeled with an averaging technique known as homogenization and the transverse material properties are approximated by the following expressions [3]:

$$\varepsilon_t = \varepsilon_a + \frac{1 - g}{\frac{1}{\varepsilon_0 - \varepsilon_a} + \frac{g}{2\varepsilon_a}}$$

and

$$\mu_t = \mu_a + \frac{1 - g}{\frac{1}{\mu_0 - \mu_a} + \frac{g}{2\mu_a}} \quad (7)$$

The longitudinal permittivity and permeability are known exactly [18] as

$$\varepsilon_z = (1 - g)\varepsilon_0 + g\varepsilon_a$$

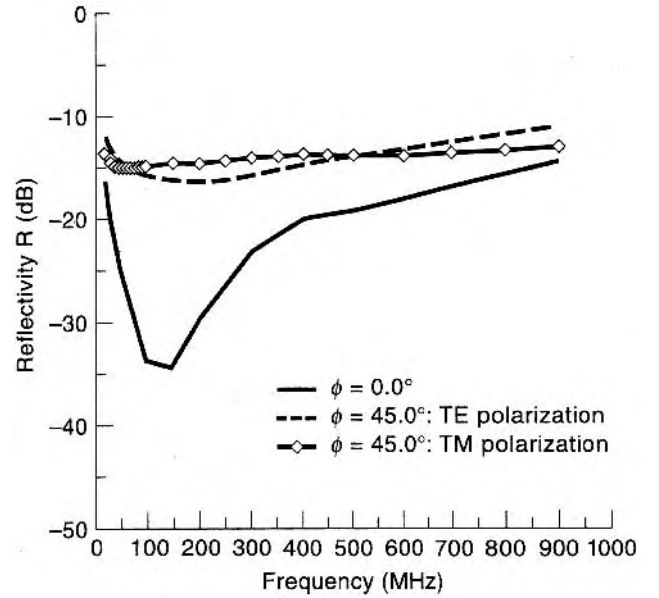


Figure 1. Reflectivity of a 6.38 mm (0.25 in) solid ferrite tile at 0° and 45° incident angles.

and

$$\mu_z = (1 - g)\mu_0 + g\mu_a \quad (8)$$

In these expressions, $g = a^2/p^2$ is the fraction of space occupied by the absorber, and ε_a and μ_a are complex parameters of the bulk ferrite. These material properties then are substituted into Eq. (5) to obtain the reflectivity of the ferrite grid.

The reflectivity of the ferrite grid strongly depends on the filling factor g . One of the advantages of this ferrite

Table 1. Data on Ferrite Tiles

Frequency (MHz)	Ferrite Tiles			
	Permittivity		Permeability	
	ε'_r	ε''_r	μ'_r	μ''_r
30	10.88	0.16	52.31	236.17
40	10.93	0.37	31.26	181.36
50	11.04	0.50	21.05	147.02
60	11.24	0.51	15.59	123.51
70	11.39	0.27	12.32	106.32
80	11.41	0.09	9.96	93.56
90	11.37	0.07	8.16	83.57
100	11.19	0.04	6.74	75.52
150	11.29	0.53	3.39	51.64
200	10.97	0.07	1.85	38.77
250	11.37	0.26	1.40	31.38
300	10.93	0.18	0.52	26.23
400	11.00	0.17	0.12	19.82
500	11.03	0.02	0.47	15.66
600	10.95	0.19	0.59	12.93
700	10.99	0.28	0.59	11.07
800	11.18	0.23	0.48	9.69
900	11.31	0.14	0.38	8.55
1000	11.36	0.04	0.29	7.69

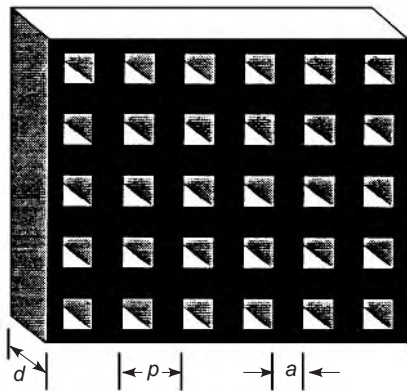


Figure 2. Illustration of the grid or waffle ferrite tile geometry.

grid geometry over the standard solid tile is that there is an additional parameter, the filling factor g , that can be varied to place the nulls (or minimum) of the reflectivity at a desired frequency. The ferrite grid can be designed for wider frequency band performance over that of the standard solid tiles by appropriately choosing the tile thickness, filling factor g , and the material properties of the ferrite. Figure 3 shows results of the reflectivity of a ferrite grid for various values of the filling factor g . The optimum reflectivity of an 18-mm thick ferrite grid with a filling factor of $g = 0.725$ was calculated using the material properties in [19]. The results are shown in Fig. 4 for normally and obliquely incident waves.

Small, tapered, electric-absorbing structures boast very low reflectivities above about 200 MHz [3], whereas ferrite tiles perform best below 600 MHz. Hence, compact wideband absorbers can be designed by combining tapered electrical absorbers with ferrite tiles. The reflectivity in the 600 MHz to 1000 MHz range is also reduced by simply adding a dielectric layer between the ferrite and the metal chamber wall. The performance advantages of these so-called “hybrids” are presented in [3].

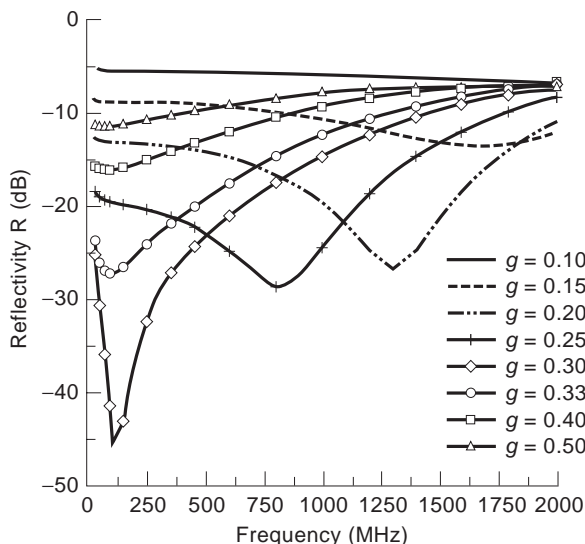


Figure 3. Reflectivity of a 16 mm ferrite grid for various values of the volume fraction g for an incident angle of 0° .

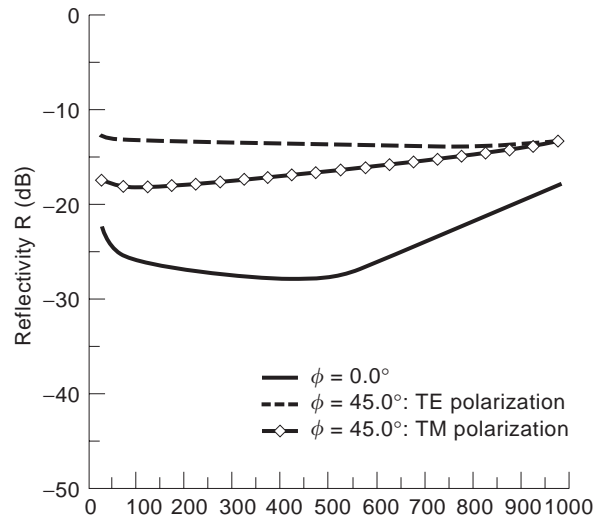


Figure 4. Reflectivity of a ferrite grid at 0° and 45° incident angles for filling factor $g = 0.725$ and a thickness of $d = 18$ mm (0.71 in).

In the following sections, we discuss how the material properties and the reflectivities of the ferrite tiles are measured.

2. MEASUREMENTS OF MATERIAL PROPERTIES

Accurate measurements of the high-frequency dispersive magnetic properties of ferrite materials are important for optimally designing a ferrite tile absorber. Magnetic loss mechanisms are strongly frequency-dependent and generally behave nonlinearly. At very low frequencies hysteretic effects (or braking forces acting on Bloch walls in motion) dominantly influence magnetic loss. Eddy currents also produce an *apparent* reduction of permeability and an *apparent* increase of magnetic loss tangent associated with attenuation of the magnetic field inside a ferrite material at low frequencies. However this remains small in most ferrite materials with low dielectric loss.

At RF and microwave frequencies, domain wall movement and domain rotation contribute to magnetic loss. The initial permeability spectrum is usually considered to be that part of the permeability spectrum due to domain wall motion. As the RF excitation frequency increases, domain wall rotation no longer fully responds to the excitation. At this point, magnetization does not move in phase with the excitation, and losses occur. Then the real part μ' of the magnetic permeability decreases with increased frequency. The imaginary part, or magnetic loss index μ'' , goes through a broad absorptive relaxation.

One characteristic constant of ferrites is the product $f_0 = |\mu_d^*|f_c$, where $\mu_d^* = \mu'_d - j\mu''_d$ is the demagnetized scalar initial permeability and f_c is the corner frequency above which $|\mu_d^*|$ falls off with frequency as $1/f$. For some polycrystalline ferrites, this product represents the frequency at which the relative permeability becomes 1 [20]. This rule is only a first-order approximation that depends on the spectral overlap of domain wall and domain rotation relaxation phenomena in the ferrite under test. Another characteristic

of ferrite materials is that the peak in the magnetic loss index usually occurs at the frequency where the real permeability has decreased to one-half its static value [21].

Generally, the absorptive window applications of ferrite materials are at frequencies below natural gyromagnetic resonance $\gamma_{gr}M_s$, where M_s is saturation magnetization (T) and γ_{gr} is the gyromagnetic ratio (28 GHz/T or 35.19 MHz · m/kA). At frequencies less than $\gamma_{gr}M_s$, magnetic losses in ferrite materials are high, whereas at frequencies greater than natural gyromagnetic resonance, magnetic losses rapidly decrease. With increasing saturation magnetization, (1) natural gyromagnetic resonance shifts to higher frequencies, (2) f_c increases, and (3) the low-frequency static initial permeability decreases. The absorptive window, similarly, shifts to higher frequencies.

With an applied static magnetic field in the z direction, ferrite materials become uniaxially anisotropic and non-reciprocal, and the magnetic permeability is described by the well-known nondiagonalized tensor

$$\bar{\mu} = \mu_0 \begin{bmatrix} \mu^* & j\kappa^* & 0 \\ -j\kappa^* & \mu^* & 0 \\ 0 & 0 & \mu_z^* \end{bmatrix} \quad (9)$$

where $\mu^* = \mu' - j\mu''$ is the principal direction transverse component of the magnetic permeability, $\mu_z^* = \mu'_z - j\mu''_z$ is the parallel component, and $\kappa^* = \kappa' - j\kappa''$ is the off-diagonal transverse component. All components of the magnetic permeability tensor are complex because of ferrite magnetic losses. Particular tensor components depend on ferrite composition, porosity, grain size, saturation magnetization, and RF frequency, temperature, and applied static magnetic field strength. Near ferromagnetic resonance (with an applied static field) saturated ferrite losses are expressed by the resonance line width. Without an applied static field, the ferrite in the demagnetized state is isotropic and reciprocal. In this case the permeability tensor reduces to the scalar frequency-dependent permeability, $\mu_d^* = \mu'_d - j\mu''_d$.

Regardless of general spectral characteristics, the magnetic properties of ferrite materials must be measured at microwave frequencies. Experimental procedures for accurate magnetic permeability measurements on demagnetized ferrites, therefore, depend spectrally on which side of the natural gyromagnetic resonance the magnetic characterization is desired. At frequencies lower than $\gamma_{gr}M_s$, one-port permeameter and two-port coaxial transmission line measurements provide accurate magnetic permeability characterization of ferrite materials. At microwave frequencies above $\gamma_{gr}M_s$, resonant cavity or dielectric resonator techniques must be used.

2.1. Transmission Line Measurement

The goal of this section is to present transmission line measuring methods for permeability [22]. In the measurement, a sample is inserted into a waveguide or a coaxial line, and the sample is subjected to an incident electromagnetic field. In developing the scattering equations, usually only the fundamental waveguide mode is assumed

to exist. At low frequencies, the impedance of the sample is measured. At microwave frequencies, the two-port scattering matrix is measured. Reflection coefficient and scattering equations are found from an analysis of the magnetic field in the sample holder. Both high- and low-frequency measurements are considered. The first technique, the permeameter, is a low-frequency technique. When lumped circuit parameters (LCR) are used as data, this method is limited to frequencies below 50 MHz. The method is extended to a higher frequency by using reflection coefficient data from a network analyzer. As the operating frequency increases to the point where there is an appreciable electric field in the sample, however, then knowledge of the permittivity is required. The second technique is the transmission line scattering parameter technique. This technique is limited to microwave frequencies, because the measured phase change across the sample becomes inaccurate below 1 MHz. Previous work using the coaxial line for magnetic measurements has been done, for example, by Von Hippel [23], Bussey [24], Geyer and Baker-Jarvis [25], and Hoer [26].

2.1.1. Permeameters. The permeameter consists of a short-circuited coaxial sample holder (see Fig. 5) with a sample on the inner conductor of a coaxial line terminated in a short circuit. The advantages of this approach are the ease of sample installation and the broad frequency capability. An air-gap correction is not necessary for permeability measurements because the magnetic field is tangential to air gaps. In this technique, a LCR meter is used to measure admittance Y in the frequency range of 100 Hz to 1 MHz. Then this admittance is converted to a reflection coefficient by $\Gamma = (Y_0 - Y)/(Y_0 + Y)$, where Y_0 is the admittance without the sample. The reflection coefficient for a sample positioned next to a short-circuited termination is given by

$$\Gamma = \exp[-2(\gamma_a L_a + \gamma_t L_t)] \frac{\tanh(\gamma L) - \frac{\mu_0 \gamma}{\mu \gamma_0}}{\tanh(\gamma L) + \frac{\mu_0 \gamma}{\mu \gamma_0}} \quad (10)$$

where γ is the propagative constant in the material given by

$$\gamma = j \sqrt{\frac{\omega^2 \mu_r^* \epsilon_r^*}{c_{vac}^2} - \left(\frac{2\pi}{\lambda_c}\right)^2} \quad (11)$$

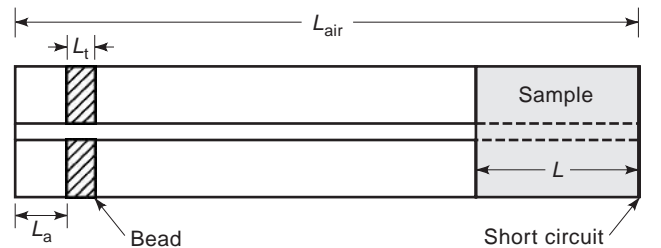


Figure 5. Measurement setup for one-port coaxial line permeameter. Sample resides adjacent to the short circuit.

Also, c_{vac} is the speed of light in a vacuum; L is the sample length, the subscripts a and t denote air-line section in the connector and support bead; λ_c is the cutoff wavelength; and ϵ_0 and μ_0 are the permittivity and permeability of vacuum, respectively, $\epsilon_r^* = \epsilon_r' - j\epsilon_r''$ and $\mu_r^* = \mu_r' - j\mu_r''$ are the complex permittivity and permeability relative to a vacuum, respectively. This equation is useful for both microwave and low-frequency measurements. At low frequencies the permittivity of the sample does not contribute to the determination of permeability. We have shown the frequency limitation for applying the permeability technique is given by

$$f \ll \frac{c}{4\pi\mu L} \quad (12)$$

where c is the speed of light in a vacuum.

2.1.2. Two-Port Permeability and Permittivity Determination. The two-port scattering parameter technique is used from approximately 50 MHz to microwave frequencies and yields both permittivity and permeability (see Fig. 6). The scattering parameters are defined in terms of the reflection coefficient Γ and the transmission coefficient z by

$$S_{11} = R_1^2 \left[\frac{\Gamma(1 - z^2)}{1 - \Gamma^2 z^2} \right] \quad (13)$$

$$S_{22} = R_2^2 \left[\frac{\Gamma(1 - z^2)}{1 - \Gamma^2 z^2} \right] \quad (14)$$

$$S_{21} = R_1 R_2 \left[\frac{z(1 - \Gamma^2)}{1 - \Gamma^2 z^2} \right] \quad (15)$$

and

$$\gamma_0 = j \sqrt{\left(\frac{\omega}{c_{lab}} \right)^2 - \left(\frac{2\pi}{\lambda_{nc}} \right)^2} \quad (16)$$

where γ_0 is the propagation constant in a vacuum, c_{lab} is the speed of light, and ω is the radian frequency.

$$R_1 = \exp(-\gamma_0 L_1) \quad (17)$$

and

$$R_2 = \exp(-\gamma_0 L_2) \quad (18)$$

are the respective reference plane transformations. Equations (13) through (15) are derived in detail by Hoer and

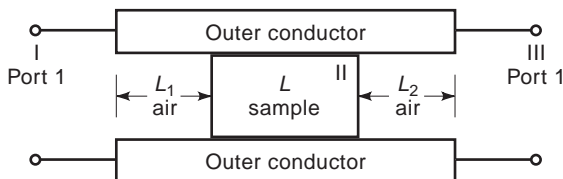


Figure 6. A dielectric sample in a transmission line. Port 1 and Port 2 denote positions of calibration reference planes.

Rasmussen [26]. The transmission coefficient z is expressed as

$$z = \exp(-\gamma L) \quad (19)$$

and the reflection coefficient is defined as

$$\Gamma = \frac{\frac{\mu}{\gamma} - \frac{\mu_0}{\gamma_0}}{\frac{\mu}{\gamma} + \frac{\mu_0}{\gamma_0}} \quad (20)$$

For a coaxial line, the cutoff frequency approaches 0 ($\omega_c \rightarrow 0$).

To obtain both the permittivity and the permeability from the scattering parameter relationships, at least two independent measurements are necessary. In the full scattering parameter solution, a solution of the equations is obtained that is invariant to reference planes for ϵ_r^* and μ_r^* . A set of equations for single-sample magnetic measurements for an air line of length L_{air} is

$$S_{11}S_{22} - S_{21}S_{12} = \exp(-2\gamma_0(L_{air} - L)) \frac{\Gamma^2 - z^2}{1 - \Gamma^2 z^2} \quad (21)$$

and

$$(S_{21} + S_{12})/2 = \exp(-\gamma_0(L_{air} - L)) \frac{z(1 - \Gamma^2)}{1 - \Gamma^2 z^2} \quad (22)$$

It is possible to obtain an explicit solution to Eqs. (21) and (22). If $x = (S_{21}S_{12} - S_{11}S_{22}) \exp[2\gamma_0(L_{air} - L)]$ and $y = [(S_{21} + S_{12})/2] \exp[\gamma_0(L_{air} - L)]$, then the physical roots for the transmission coefficient are given by

$$Z = \frac{x+1}{2y} \pm \sqrt{\left(\frac{x+1}{2y} \right)^2 - 1} \quad (23)$$

and the reflection coefficient is expressed as

$$\Gamma_2 = \pm \sqrt{\frac{x - Z^2}{xZ^2 - 1}} \quad (24)$$

The ambiguity in the \pm sign in Eq. (24) is resolved by considering the reflection coefficient calculated from S_{11} alone:

$$\Gamma_3 = \frac{\alpha(Z^2 - 1) \pm \sqrt{\alpha^2 Z^4 + 2Z^2(2S_{11} - \alpha^2) + \alpha^2}}{2S_{11}Z^2} \quad (25)$$

where $\alpha = \exp(-2\gamma_0 L_1)$. The correct root for Γ_3 is chosen by requiring that $|\Gamma_3| \leq 1$. An estimate of L_1 is needed in Eq. (25). If Γ_2 is compared with Γ_3 , then the \pm sign ambiguity is resolved and therefore Γ_2 is determined. Then the permeability and permittivity are

$$\mu_r^* = -\frac{1 + \Gamma_2}{1 - \Gamma_2} \frac{1}{\gamma_0 L} (\ln Z + 2\pi j n) \quad (26)$$

and

$$\varepsilon_r^* = \frac{c^2}{\omega^2} \left[\left(\frac{2\pi}{\lambda_c} \right)^2 - \frac{1}{L^2} (\ln Z + 2\pi jn)^2 \right] / \mu_r^* \quad (27)$$

where $n = 0, \pm 1, \pm 2, \dots$. The correct value of n is chosen by using a group-delay comparison test. At low frequencies, the correct roots are identified more easily because they are more widely spaced.

Equations (26) and (27) have an infinite number of roots for magnetic materials, because the logarithm of a complex number is multivalued. To choose the correct root, it is necessary to compare the measured group delay with the calculated group delay. The calculated group delay is related to the change of the wave number k with respect to the angular frequency by

$$\tau_{\text{calc.group}} = -L \frac{d}{df} \sqrt{\frac{\varepsilon_r^* \mu_r^* f^2}{c^2} - \frac{1}{\lambda_c^2}} \quad (28)$$

$$= -\frac{1}{c^2} \frac{f \varepsilon_r^* \mu_r^* + f^2 \frac{1}{2} \frac{d(\varepsilon_r^* \mu_r^*)}{df}}{\sqrt{\frac{\varepsilon_r^* \mu_r^* f^2}{c^2} - \frac{1}{\lambda_c^2}}} L \quad (29)$$

The measured group delay is given by

$$\tau_{\text{meas.group}} = \frac{1}{2\pi} \frac{d\phi}{df} \quad (30)$$

where ϕ is the phase of Z . To determine the correct root, the calculated group delays are found from Eq. (29) for various values of n in the logarithm term, where $\ln Z = \ln |Z| + j(\theta + 2\pi n)$. The calculated and measured group delays are compared to yield the correct value of n . When there is no loss in the sample under test, the solution is divergent at integral multiples of one-half wavelength in the sample. This occurs because the phase of S_{11} cannot be measured accurately for small $|S_{11}|$. In the low loss limit, both of the scattering equations reduce to the relationship $Z^2 \rightarrow 1$, which is a relationship only for the phase velocity, and therefore solutions for ε_r^* and μ_r^* are not separable. This singular behavior is minimized in cases where permeability is known a priori, as shown in previous work performed by Baker-Jarvis [22].

A measurement on a ferrite material is given in Fig. 7 using both the permeameter and two-port techniques. This figure indicates that the permeameter method breaks down around 50 MHz.

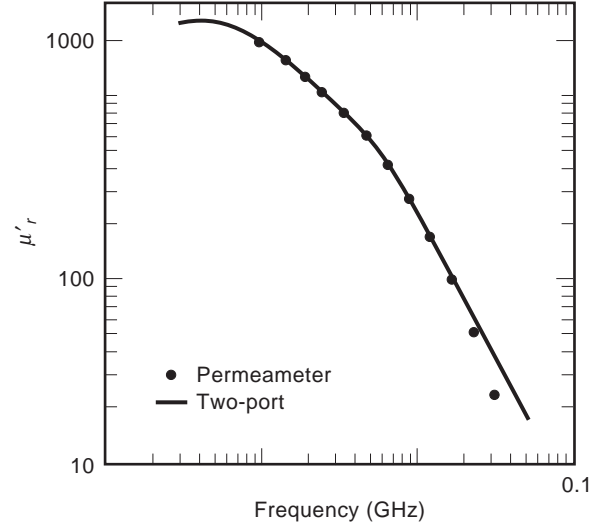


Figure 7. The measured real part of the permeability using both the permeameter and scattering techniques.

2.2. Dielectric-Resonator Measurements

At frequencies above $\gamma_{gr} M_s$, resonant-cavity [27–31] or dielectric-resonator techniques [32–36] must be used to accurately characterize ferrite magnetic properties. Commonly used fixtures for determining the demagnetized scalar permeability μ_d^* are either a H_{011} mode cavity for measuring one cylindrical sample or a rectangular cavity operating in the TE_{102} mode with a small spherical sample placed at the center [37]. Both of these techniques generally employ perturbation theory, which restricts sample size and, accordingly, allowable magnetic energy partial filling factors and sensitivity to measure small changes in the Q -factor. More recently, Latrach, Le Roux, and Jecko [31] have used a TM_{mn0} cavity for permeability measurements of ferrite disk samples from 2 GHz to 8 GHz. By dielectrically loading the TM_{mn0} cavity, the measured resonant frequency was changed. The method presented here, discussed in more detail in [34–36], uses low-loss H_{011} dielectric resonators, containing the ferrite sample under test, whose complex permittivity is given by $\varepsilon_f^* = \varepsilon_f' - j\varepsilon_f''$. The aspect ratios and permittivities of the dielectric resonators are chosen to spectrally characterize a *single* sample over a broad frequency range. The H_{011} resonant system used in these measurements is illustrated in Fig. 8. The resonators are coupled to the external microwave source through two loop-terminated coaxial cables,

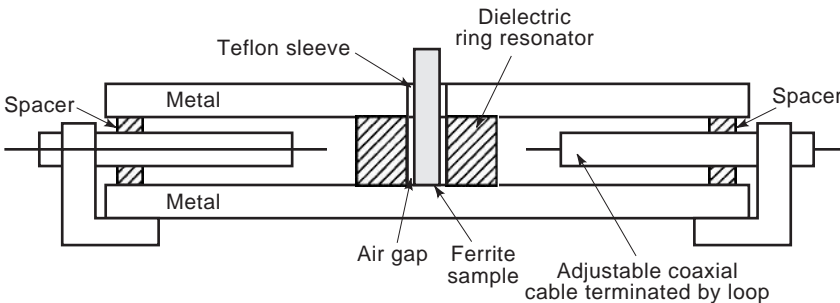


Figure 8. Parallel-plate H_{011} resonant configuration used to measure magnetic permeability.

and these are adjusted so that the measured loaded Q -factor is equal to the unloaded Q -factor within any prescribed accuracy.

Formulations for the electromagnetic fields in a ferrite rod and in coaxial cylindrical dielectric layers surrounding the rod are found in several papers and textbooks [38–52]. At the boundaries between the cylindrical interfaces, the well-known continuity conditions between tangential electric and magnetic field components must be satisfied. At the conductive ground planes, tangential electric fields must vanish. These well-known boundary conditions create a system of linear equations with respect to the constant coefficients in the field expressions, which have nontrivial solutions only if the corresponding determinant vanishes. For fixed values of dimensions and material properties of the resonant system, it is possible to find eigenvalues as roots of the determinant equation. Material properties are determined by measuring resonant frequencies and unloaded Q factors of the dielectric ring resonators with and without the ferrite sample.

The H_{011} resonant frequencies of a ring resonator with a ferrite sample are determined by ϵ'_{rr} , ϵ'_f , and μ'_d , where ϵ'_{rr} is the relative permittivity of the dielectric ring resonator. For ferrite sample diameters less than one-quarter of the external ring resonator diameter, these resonant frequencies are primarily determined by ϵ'_{rr} and μ'_d .

The first step in the measurement process is to verify the complex permittivity of the ferrite sample under test with a TM_{0n0} cavity. Second, the complex permittivities of each dielectric ring resonator are found from measurements of the resonant frequencies and unloaded Q factors of the empty ring resonators operating in the H_{011} mode, given the geometrical dimensions of the resonators and taking into account conductive microwave losses of the upper and lower ground planes. Then values of the imaginary parts of ϵ_f^* and ϵ_r^* are calculated, assuming a linear increase with frequency. Next, the scalar permeability μ'_{db} computed from measurements of the resonant frequency of these resonators, which contain a completely demagnetized sample and operate in the H_{011} mode, is evaluated from the H_{011} eigenvalue equation in determinant form:

$$F(\epsilon'_f, \mu'_d, f_0) = 0 \quad (31)$$

where f_0 is the measured resonant frequency of the H_{011} mode for a resonator containing the demagnetized ferrite sample.

After μ'_d is determined, the imaginary part of the permeability, $\mu''_f = \mu'_f \tan \delta_{m,f}$, is found as a solution to the equation

$$Q^{-1} = Q_c^{-1} + p_{e,r} \tan \delta_{e,r} + p_{e,f} \tan \delta_{e,f} + p_{\mu'_d} \tan \delta_{m,f} \quad (32)$$

where Q is the unloaded Q factor for the H_{011} mode; Q_c is the Q factor representing conductor losses in the metal plates for the H_{011} mode; $p_{e,r}$ is the electric-energy-filling factor for the dielectric ring resonator; $p_{e,f}$, $p_{\mu'_d}$ are the ferrite sample electric- and magnetic-energy-filling factors; $\tan \delta_{e,r}$ and $\tan \delta_{e,f}$ are the dielectric loss tangents of the

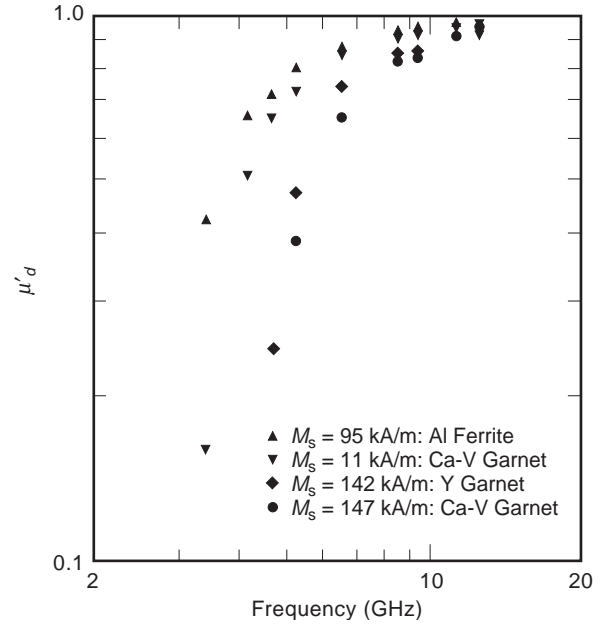


Figure 9. Measured relative permeability μ'_d of several aluminum-doped, calcium-vanadium, and yttrium garnet ferrites with $9 \text{ kA/m} \leq M_s \leq 147 \text{ kA/m}$ as a function of frequency.

ring resonator and the ferrite sample under test; and $\tan \delta_{m,f}$ is the magnetic loss tangent of the ferrite.

Typical measurement data for bulk ceramic ferrites by this technique are given in Figs. 9 and 10. Uncertainties in μ'_d for typical dimensional uncertainties in the geometric parameters of the dielectric ring resonators and the ferrite sample under test are estimated to be $\pm 0.8\%$, that is, μ'_d is $\pm 1 \times 10^{-5}$. Combined complex permeability data of two ferrites with differing saturation magnetizations over greater than four frequency decades, where both

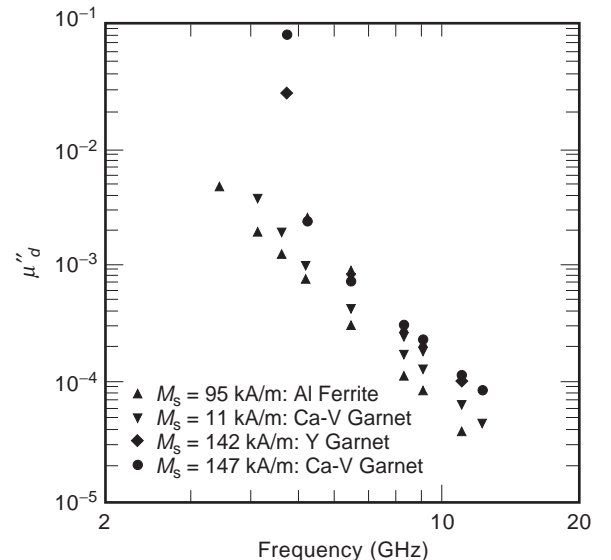


Figure 10. Measured relative magnetic loss index μ''_d of several aluminum-doped, calcium-vanadium, and yttrium garnets with $95 \text{ kA/m} \leq M_s \leq 147 \text{ kA/m}$ as a function of frequency.

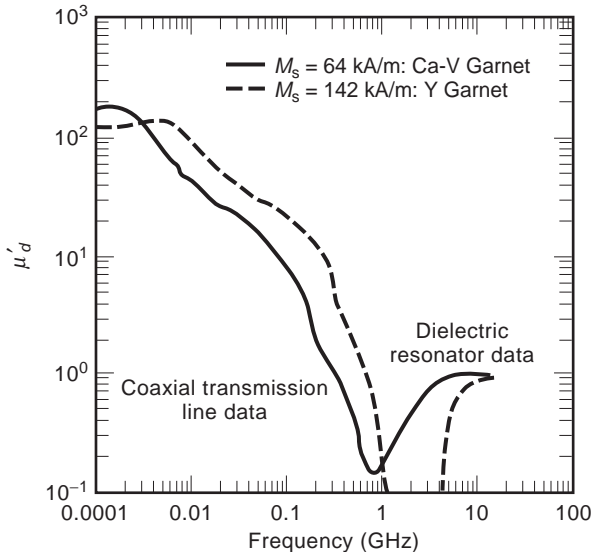


Figure 11. Combined two-port coaxial transmission line and dielectric resonator relative permeability measurements for yttrium and calcium-vanadium garnet ferrites from 1 MHz to 10 GHz.

two-port coaxial transmission line and dielectric resonator data have been combined, are shown in Figs. 11 and 12. The rapid increase in magnetic loss, as natural gyromagnetic resonance is approached, is clearly seen. In addition, the large differences in nonlinear magnetic loss behavior over a broad frequency range are apparent.

The total attenuative losses of ferrite-tile absorbers should include both the dielectric and magnetic properties of the ferrite materials under examination. For a

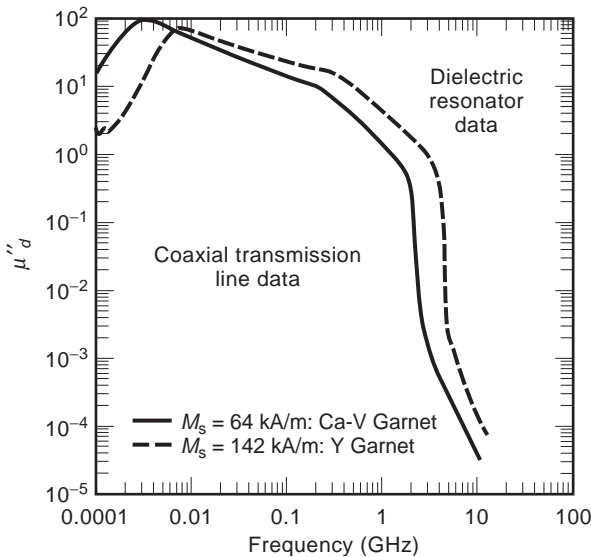


Figure 12. Combined two-port coaxial transmission line and dielectric resonator measurements of relative magnetic loss index for yttrium and calcium-vanadium garnet ferrites from 1 MHz to 10 GHz.

plane-wave TEM field, the attenuative loss α is given by

$$\alpha = \frac{\sqrt{2\omega}}{2c} \sqrt{\epsilon_f \mu_f' [(1 + \tan^2 \delta_{e,f})^{1/2} (1 + \tan^2 \delta_{m,f})^{1/2} + \tan \delta_{e,f} \tan \delta_{m,f}]}$$
(33)

where c is the speed of light.

3. REFLECTIVITY MEASUREMENTS

In designing a ferrite absorber that performs well over a selected frequency range, it is important to measure the reflectivity of the absorber for normal and oblique incidence. However, the large test fixtures currently used to characterize an absorber from 30 MHz to 1000 MHz allow measuring reflectivities only at normal incidence [8–11]. Although an arch is used to measure reflectivities at oblique angles, it is useful only at frequencies above approximately 600 MHz [53,54]. An alternative to these techniques is a method under development at the National Institute of Standards and Technology (NIST) in Boulder, CO. This alternative technique uses time-frequency methods to measure reflectivity at arbitrary angles and polarization [55–57].

A block diagram of the bistatic free-space reflectivity measurement system at NIST is depicted in Fig. 13. The measurement system consists of a time- or frequency-domain network analyzer, two TEM horn antennas, and interconnecting RF/microwave cables with a 50 Ω characteristic impedance. More detailed descriptions of time- and frequency-domain versions of this measurement system are given in [55–59]. A rectangular ferrite-tile sample (or metal plate reference) is placed in the plane of the two TEM horn antennas at a distance of 1 to 4 m. The level of the sample center is adjusted to match the antenna aperture centers, and the normal to the sample surface bisects the angle between the two horn antenna apertures. The measurements are performed in an ordinary room (laboratory, warehouse, etc.) or in an absorber-lined chamber (semi- or fully anechoic). To minimize the effects of floor,

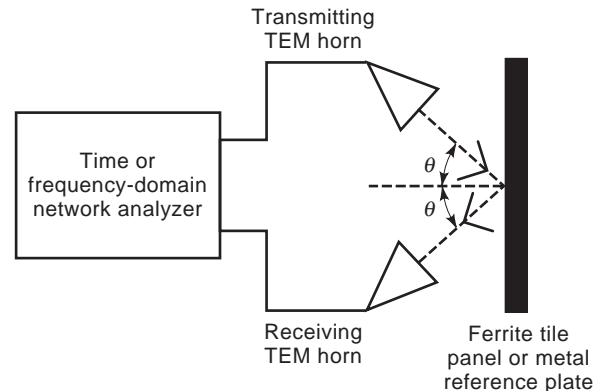


Figure 13. Bistatic free-space RF absorber reflectivity measurement system.

ceiling, and wall reflections, the sample under test should be situated centrally within the room volume.

Obtaining the scattering characteristics of the ferrite tile sample under test requires the following steps:

1. A time-domain waveform is obtained for the ferrite-tile sample under test by placing it close to the TEM horn antennas (typically from 1 to 4 m from the antenna apertures).
2. The sample is removed and a background time-domain waveform is obtained.
3. The waveform of step (2) is subtracted from that of step (1). The resulting waveform consisted of the ferrite-tile sample response plus a component that emanates from the shadow region behind the sample. This process removes significant systematic effects due to antenna-to-antenna coupling and spurious environmental reflections.
4. The shadow-region waveform component is readily eliminated by time-gating, which deletes the undesired waveform component(s). Time-gating works only if there is sufficient separation between the sample and the wall directly behind it, which allows the absorber response to die out before the shadow-region component arrives.
5. Steps (1)–(4) are repeated for a rectangular (or square) metal reference plate. The NIST system employs a 3 m × 3 m metal plate.
6. The time-gated absorber and metal reference plate waveforms obtained in steps (5) and (6) are each Fourier transformed to obtain scattering amplitude spectra.
7. Then the amplitude spectra are divided to obtain the backscatter coefficient which is given by

$$BC(f, \theta) = \frac{|FT(\text{gated absorber waveform})|}{|FT(\text{gated reference waveform})|} \quad (34)$$

where f is the frequency, θ is the angle of incidence, FT denotes the Fourier transform, and BC is the

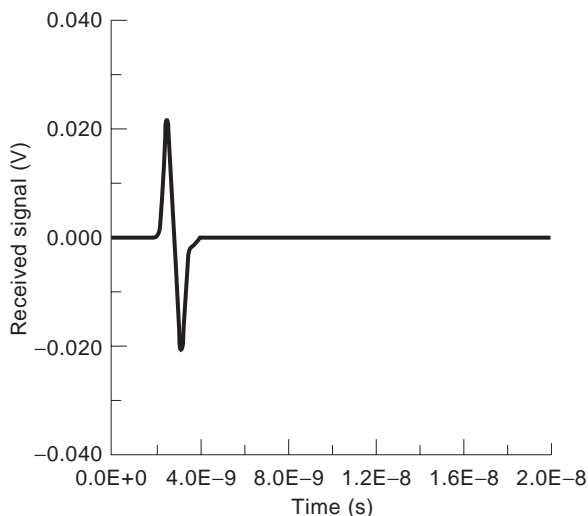


Figure 14. Gated time-domain metal reference plate waveform.

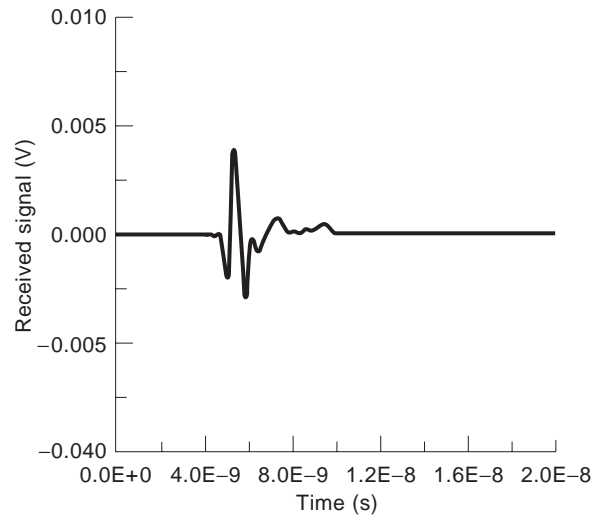


Figure 15. Gated time-domain ferrite-tile waveform.

backscatter coefficient. The backscatter coefficient is a real, frequency-domain quantity that directly compares the reflection characteristics of the ferrite-tile absorber system under test with that of the metal plate reference signal. The smaller the backscatter coefficient, the better the performance of the ferrite-tile system.

Examples of gated time-domain reference and ferrite-tile-panel waveforms are shown in Figs. 14 and 15, respectively. These waveforms are obtained from a bistatic measurement at a 30° angle of incidence with both the receiving and transmitting antennas horizontally polarized. A synthetic time-domain method is used [59] in which the acquired frequency-domain data are Fourier transformed into time-domain waveforms. The reference waveform of Fig. 14 is obtained from a 3 m × 3 m

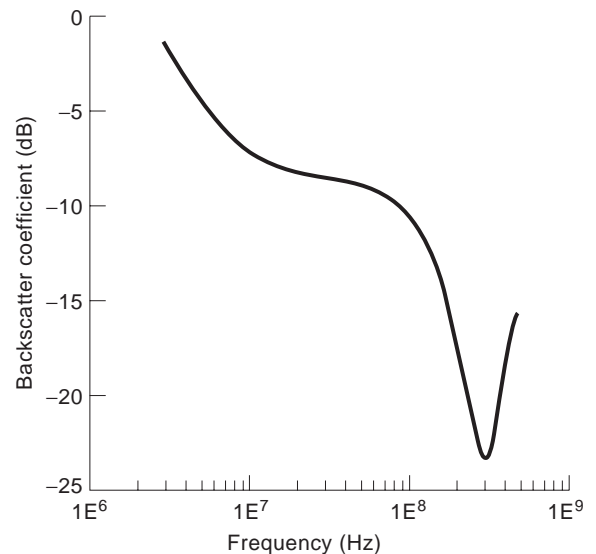


Figure 16. Backscatter coefficient results obtained from the waveforms of Figs. 14 and 15 in conjunction with Eq. (34).

metal reference plate, located 3.0 m from the antenna aperture centers. It is interesting to note that the reference waveform is nearly a perfect doublet, a result of the differentiating properties of TEM horns in the transmitting mode [60]. The corresponding waveform obtained for a 2.4 m × 2.4 m ferrite-tile panel backed by a plywood layer and metallic ground plate is depicted in Fig. 15. Reflections from the front and back surfaces of the ferrite tiles produce the initial triplet (5 ns to 7 ns). Wavefront curvature and finite sample size are responsible for the portion of the waveform that occurs after 7 ns. The frequency-domain back-scatter coefficient characteristics from these gated waveforms are depicted in Fig. 16 for a frequency range of 3 MHz to 500 MHz. The characteristic notch that occurs slightly above 300 MHz is a phenomenon typical for ferrite tile systems backed by a ground plane.

4. CONCLUSION

In this article, ferrite tile electromagnetic absorbing materials were discussed. Methods to model performance, measure material properties, and measure the reflectivity of this type of absorbing material were presented. The advantages of the ferrite-tile absorber are that they are small and offer very low reflectivity in the frequency range of 30 MHz to 600 MHz. However, above 600 MHz the performance of these ferrite tiles begins to degrade. Dielectric layers behind the ferrite tiles and tapered electric absorbing structures in front of the tiles are used to improve the high-frequency performance of the ferrites. A discussion on how well these hybrid absorbers work is found in [3]. The next generation of ferrite-tile absorbers, consisting of thin magnetic layers [61–64] and a combination of ferrite layers with chiral materials [3], is currently being developed.

BIBLIOGRAPHY

1. A. J. Simmons and W. H. Emerson, An anechoic chamber making use of a new broadband material. *Convention Record of the IRE 1953 National Convention: Part 2-Antennas and Communications*, pp. 31–41.
2. W. H. Emerson, Electromagnetic wave absorbers and anechoic chambers through the years. *IEEE Trans. Antennas Propagat.*, **21**: 484–490, 1973.
3. C. L. Holloway et al., Comparison of electromagnetic absorber used in anechoic and semi-anechoic chambers for emissions and immunity testing of digital devices. *IEEE Trans. Electromag. Compat.*, **39**: 33–47, 1997.
4. R. F. German, Comparison of semi-anechoic chambers and open-field site attenuation measurements. *Proc. 1982 IEEE International Symposium on Electromagnetic Compatibility*, Santa Clara, CA, September 8–10, 1982, pp. 260–265.
5. E. F. Kuester and C. L. Holloway, Improved low-frequency performance of pyramid-cone absorbers for application in semi-anechoic chambers. *Proc. 1989 IEEE National Symposium on Electromagnetic Compatibility*, Denver, CO, May 23–25, 1989, pp. 394–399.
6. E. F. Kuester and C. L. Holloway, A low-frequency model for wedge or pyramid absorber arrays-I: theory. *IEEE Trans. Electromagn. Compat.*, **36**: 300–306, 1994.
7. C. L. Holloway and E. F. Kuester, A low-frequency model for wedge or pyramid absorber arrays-II: computed and measured results. *IEEE Trans. Electromagn. Compat.*, **36**: 307–313, 1994.
8. N. Ari, D. Hansen, and H. Garbe, Analysis and measurements of electromagnetic scattering by pyramidal absorbers. *8th Int. Zurich Symp. Technical Exhibition Electromagnetic Compatibility*, Zurich, March 7–9, 1989, pp. 301–304.
9. D. Hansen, N. Ari, and H. Garbe, An investigation into the scattering and radiation characteristic of RF-absorbers. *Proc. 1988 IEEE International Symposium on Electromagnetic Compatibility*, Seattle, WA, August 2–4, 1988, pp. 99–105.
10. S. Takeya and K. Shimada, New measurement method of RF absorber characteristics by large square coaxial line. *Proc. 1988 IEEE International Symposium on Electromagnetic Compatibility*, Dallas, TX, August 9–13, 1993, pp. 397–402.
11. P. Pues, Electromagnetic wave absorber measurement in a large coax. *9th Int. Zurich Symp. Technical Exhibition Electromagnetic Compatibility*, Zurich, March 1991, pp. 541–546.
12. Y. Naito et al., Characteristics of the ferrite absorbing wall. *Trans. I.E.C.E., Japan*, **52-B** (1): 26, 1969 (available in English in *Electronics and Communication in Japan*, p. 76, 1969).
13. Y. Natio and E. Fujiwara, Thickness of electromagnetic wave absorber utilizing ferrite. *Trans. I.E.C.E., Japan*, **53-B** (9): 537, 1970 (available in English in *Electronics and Communication in Japan*, p. 94, 1970).
14. Y. Natio, On the permeability dispersion of a spinel ferrite. *Electronics and Communication in Japan*, **56-C** (2): 118–123, 1973.
15. T. Ellam, An update on the design and synthesis of compact absorber for EMC chamber applications. *Proc. 1994 IEEE International Symposium on Electromagnetic Compatibility*, Chicago, August 22–26, 1994, pp. 408–412.
16. K. Ishino et al., Realization of compact semi- and fully anechoic chambers using a new developed composite absorber. *Proc. 1994 IEEE International Symposium on Electromagnetic Compatibility*, Chicago, August 22–26, 1994, pp. 413–418.
17. L. M. Brekhovskikh, *Waves in Layered Media*, New York: Academic Press, 1960, ch. 1.
18. E. F. Kuester and C. L. Holloway, Comparison of approximations for effective parameters of artificial dielectrics. *IEEE Trans. Microwave Theory Techn.*, **38** (11): 1752–1755, 1990.
19. M. Takahashi, *A new structure of electromagnetic wave absorber*, Toyo Corporation, Technical Report, October 1991.
20. R. G. Geyer et al., Spectral characterization of ferrites for use as magnetic reference materials. *Conf. Precision Electromag. Meas. Dig.*, 1992, pp. 107–108.
21. J. L. Snoek, Dispersion and absorption in magnetic ferrites at frequencies above one Mc/s. *Physica XIV*, **4**: 207–217, 1948.
22. J. Baker-Jarvis et al., Transmission/reflection and short-circuit line methods for measuring permittivity and permeability. *Natl. Inst. Stand. Technol., Tech. Note 1355*, May, 1992.
23. A. R. V. Hippel, *Dielectric Materials and Applications*, Cambridge, MA: M.I.T. Press, 1954.
24. R. B. Goldfarb and H. E. Bussey, Method for measuring complex permeability at radio frequencies. *Rev. Sci. Instrum.*, **58** (4): 624–627, 1987.

25. R. G. Geyer and J. Baker-Jarvis, Spectral characterization of ferrites for use as magnetic reference materials. *CPEM'92 Digest*, Conference on Precision Electromagnetic Measurements, 1992, pp. 107–108.
26. C. A. Hoer and A. L. Rasmussen, Equations for the radiofrequency magnetic permeameter, *NBS Journal of Research*, **67C**:69–76, 1963.
27. R. C. LeCraw and E. G. Spencer, Tensor permeabilities of ferrites below magnetic saturation, *IRE Conv. Rec.* New York, pt. 5, 1956, pp. 66–74.
28. J. J. Green and T. Kohane, Testing of ferrite materials for microwave applications, *Semicond. Prod. Solid State Technol.*, **7**:46–54, 1964.
29. H. E. Bussey and L. A. Steinert, Exact solution for a gyromagnetic sample and measurements on a ferrite, *IRE Trans. Microwave Theory Tech.*, **6**: 72–76, 1958.
30. W. Muller-Gronau and I. Wolff, A microwave method for the determination of the real parts of the magnetic and dielectric material parameters of premagnetized microwave ferrites. *IEEE Trans. Microwave Theory Tech.*, **32**:377–382, 1983.
31. M. Latrach, P. LeRoux, and F. Jecko, Accurate method for experimental determination of real part of initial permeability of demagnetized ferrite samples. In *Proc. 10eme Colloque Optique Hertzienne et Dielectriques*, Rennes, September 6–8, 1989, pp. 339–342.
32. N. Ogasawara et al., Highly sensitive procedures for measuring permeabilities (μ_{\pm}) for circularly polarized fields in microwave ferrites. *IEEE Trans. Magnetics*, **12**:256–269, 1976.
33. J. Krupka, Resonant modes in shielded cylindrical ferrite and single crystal resonators. *IEEE Trans. Microwave Theory Tech.*, **37**:691–697, 1989.
34. R. G. Geyer and J. Krupka, Microwave behavior of ferrites: theory and experiment. *Conf. Digest on Precision Electromagnetic Measurements*, June 17–20, 1996, pp. 206–207.
35. R. G. Geyer and J. Krupka, Complex permeability measurements of microwave ferrites. In *Microwave Processing of Materials V, Materials Research Society Symposium Proceedings*, **430**:257–262, 1996.
36. J. Krupka and R. G. Geyer, Complex permeability of demagnetized microwave ferrites near and above gyromagnetic resonance, *IEEE Trans. Magnetics*, **32** (3):1924–1933, 1996.
37. J. J. Green and F. Sandy, Microwave characterization of partially magnetized ferrites. *IEEE Trans. Microwave Theory Tech.*, **22**:641–645, 1974.
38. M. L. Kales, Modes in waveguides containing ferrites, *J. Appl. Phys.*, **24**:604–608, 1953.
39. H. Suhl and L. R. Walker, Topics in guided wave propagation through gyromagnetic media. Pt. I-The completely filled cylindrical guide, *Bell Syst. Tech. J.*, **33**:579–659, 1954.
40. E. Snitzer, Cylindrical dielectric waveguide modes. *J. Opt. Soc. Amer.*, **51**:491–498, 1961.
41. R. A. Waldron, Electromagnetic wave propagation in cylindrical waveguides containing gyromagnetic media, *J. Brit. IRE*, **18**: 597–612, 677–690, and 733–746, 1958.
42. R. A. Waldron, Theory of the mode spectra of cylindrical waveguides containing gyromagnetic media. *J. Brit. IRE*, **19**: 347–356, 1959.
43. R. A. Waldron, Features of cylindrical waveguides containing gyromagnetic media. *J. Brit. IRE*, 695–706, 1960.
44. R. A. Waldron, Loss properties of ferrite-loaded cylindrical waveguides containing gyromagnetic media. *J. Brit. IRE*, 321–334, 1963.
45. R. A. Waldron, Properties of ferrite-loaded cylindrical waveguides in the neighborhood of cutoff. *Proc. IEEE*, **109B** (suppl. no. 21): 90–94, 1962.
46. R. A. Waldron, Properties of inhomogeneous cylindrical waveguides in the neighborhood of cutoff, *J. Brit. IRE*, **25**: 547–555, 1963.
47. J. E. Tompkins, Energy distribution in partially ferrite-filled waveguides, *J. Appl. Phys.*, **29**:399–400, 1958.
48. R. A. Waldron, *Ferrites*, New York: Van Nostrand, 1961.
49. P. J. B. Clarricoats, *Microwave Ferrites*, London: Chapman and Hall, 1961.
50. A. J. Baden-Fuller, *Ferrites at Microwave Frequencies*, London: Peter Peregrinus, 1987, Chap. 3.
51. H. D. Godtman and W. Hass, Magnetodynamic modes in axially magnetized rods between two parallel conducting sheets. *IEEE Trans. Microwave Theory Tech.*, **15**:478–480, 1967.
52. A. M. Duputz and A. C. Priou, Computer analysis of microwave propagation in a ferrite circular waveguide-optimization of phase-shifter longitudinal field section, *IEEE Trans. Microwave Theory Tech.*, **22**:601–613, 1974.
53. E. F. Knott, J. F. Shaeffer, and M. T. Tuley, *Radar Cross Section: Its Prediction, Measurement and Reduction*, Dedham, MA: Artech House, Inc., 1985, Chap. 10.
54. R. E. Hiatt, E. F. Knott, and T. B. A. Senior, *A study of VHF absorber and anechoic rooms*, College of Engineering, Department of Electrical and Computer Engineering, Radiation Laboratory, University of Michigan, Ann Arbor, Michigan, Tech. Report No. 5391-1-F, February, 1963.
55. S. Tofani, A. Ondrejka, and M. Kanda, Time-domain method for characterizing the reflectivity of absorbing materials from 30 to 1000 MHz, *IEEE Trans. Electromagn. Compat.*, **33**:234–240, 1991.
56. S. Tofani et al., Bistatic scattering of absorbing materials from 30 to 1000 MHz, *IEEE Trans. Electromagn. Compat.*, **34**: 304–307, 1992.
57. R. Johnk et al., Time-domain measurements of the electromagnetic backscatter of pyramidal absorbers and metallic plates, *IEEE Trans. Electromagn. Compat.*, **35**:429–433, 1993.
58. R. T. Johnk and A. R. Ondrejka, Electrical material properties from a freespace time-domain RF absorber reflectivity measurement system, *Proc. 1997 IEEE International Symposium on Electromagnetic Compatibility*, August 11–22, 1997, Austin, TX.
59. IEEE standard PAR-1128, Recommended practice for RF absorber evaluation, to be published.
60. R. A. Lawton and A. R. Ondrejka, Antennas and the associated time-domain range for the measurement of impulsive fields, Nat. Bur. Stand. (U.S.) Tech. Note 1008, 1978.
61. H. W. Helberg and V. Kose, Die breitbandige absorption elektromagnetischer wellen durch dünne ferritschichten, *Zeitschrift für Angewandte Physik*, **19**:509–514, 1965.
62. F. Mayer and J. P. Chaumat, Dielectromagnetic materials for absorber-lined chambers (ALC). *Proc. 9th International Zurich Symposium on Electromagnetic Compatibility*, Zurich, March 12–14, 1991, pp. 569–572.
63. H. Komori and Y. Konishi, Wideband electromagnetic wave absorber with thin magnetic layers, *IEEE Trans. Broadcasting*, **40**:219–222, 1994.
64. Z. Cohn, J. Daly, and C. Parker, Advanced ferrite materials for anechoic chambers, *Ceramics Trans.*, **47**:269–284, 1995.

ELECTROMAGNETIC FIELD COMPUTATION IN PLANAR MULTILAYERS

KRZYSZTOF ARKADIUSZ
MICHALSKI
Texas A&M University
College Station, Texas

1. INTRODUCTION

In a variety of applications, such as geophysical prospecting, remote sensing, detection of landmines and unexploded ordnance, noninvasive testing, planning of hyperthermia, modeling of wave propagation in wireless communication, design of microstrip circuits and antennas, modeling of integrated circuit interconnects, characterization of silicon wafer defects, interpretation of near-field scanning optical microscopy, modeling of nano- and extreme-ultraviolet (EUV) lithography, and other emerging technologies, it is necessary to compute electromagnetic fields in planar, layered media. The purpose of this article is to present a succinct yet reasonably complete introduction to this topic. The emphasis is on the development of dyadic Green functions (DGFs), which make it possible to compute the fields due to any configuration of sources. In particular, a complete set of electric and magnetic DGFs is derived for planar, multilayered media, in an efficient and convenient-to-use form, based on a transmission-line equivalent circuit along the axis normal to the stratification. Attention is limited to media with at most uniaxial anisotropy, which, although important in practice, still allow the simple transmission-line representation of the electromagnetic fields. Also, the analysis is restricted to multilayers of infinite lateral extent, although a large part of the presented material can also be adapted for laterally shielded geometries.

2. STATEMENT OF THE PROBLEM

Consider a plane-stratified medium excited by arbitrary electric and magnetic currents (\mathbf{J} , \mathbf{M})¹ occupying a volume V , as illustrated in Fig. 1a. It is desired to determine the resulting electric and magnetic fields (\mathbf{E} , \mathbf{H}) at an arbitrary location \mathbf{r} . Of interest are also the far-zone radiation fields and the fields excited in the multilayer by an obliquely incident plane wave.

We assume that the stratification is perpendicular to the z axis and of infinite lateral extent along x and y . The layers are numbered from 1 to N in the direction of increasing z , where the number of layers N is arbitrary. The n th layer, with interfaces at $z = z_n$ and $z = z_{n+1}$, is filled with a homogeneous, linear, uniaxial medium [1, p. 5], characterized by permittivity and permeability dyadics,²

¹Throughout this article, vectors are denoted by boldface letters, unit vectors are distinguished by carets, and dyadics (i.e., second-rank Cartesian tensors) are denoted by doubly underlined boldface letters.

²A symbol \mathbf{ab} is called a *dyad*, and a sum of dyads is called a *dyadic* [2, App. 3]. A dot product of a dyad and a vector is defined as follows: $\mathbf{ab} \cdot \mathbf{c} = \mathbf{a}(\mathbf{b} \cdot \mathbf{c})$, $\mathbf{c} \cdot \mathbf{ab} = (\mathbf{c} \cdot \mathbf{a})\mathbf{b}$.

$\underline{\underline{\epsilon}}_n$ and $\underline{\underline{\mu}}_n$, respectively. The optical axis of the medium is assumed to be normal to the interfaces. The multilayer may be shielded from below and/or above by plates that present three possible boundary conditions: (1) $\hat{\mathbf{n}} \times \mathbf{E} = Z_s \hat{\mathbf{n}} \times (\hat{\mathbf{n}} \times \mathbf{H})$, where $\hat{\mathbf{n}}$ is the interface normal vector and Z_s is a specified surface impedance; (2) $\hat{\mathbf{n}} \times \mathbf{E} = 0$, which defines a perfect electric conductor (PEC); and (3) $\hat{\mathbf{n}} \times \mathbf{H} = 0$, which defines a perfect magnetic conductor (PMC).

We approach this problem in the frequency domain, which means that all field quantities are phasors evaluated at an implicitly understood radian frequency ω . Once a phasor [e.g., $\mathbf{E}(\mathbf{r})$] is found, the corresponding physical, time-domain field can be obtained by the inverse Fourier transform [3, p. 9]³

$$\begin{aligned} \mathbf{E}(\mathbf{r}, t) &= \frac{1}{2\pi} \int_{-\infty}^{\infty} \mathbf{E}(\mathbf{r}) e^{j\omega t} dt \\ &= \Re e \frac{1}{\pi} \int_0^{\infty} \mathbf{E}(\mathbf{r}) e^{j\omega t} dt \end{aligned} \quad (1)$$

Also, we will initially assume that the medium properties may vary along the z direction, which will obviate the use of layer subscripts. Only at a later stage will we restrict the medium to have piecewise-constant parameters along the z axis. Under these assumptions, the fields are governed by Maxwell's equations [4, p. 745]

$$\nabla \times \mathbf{E} = -j\omega \underline{\underline{\mu}}_0 \underline{\underline{\mu}} \cdot \mathbf{H} - \mathbf{M}, \quad (2)$$

$$\nabla \times \mathbf{H} = j\omega \underline{\underline{\epsilon}}_0 \underline{\underline{\epsilon}} \cdot \mathbf{E} + \mathbf{J}$$

where ϵ_0 and μ_0 are the free-space permittivity and permeability, respectively, and where

$$\underline{\underline{\epsilon}} = \underline{\underline{I}}_t \epsilon + \hat{\mathbf{z}} \hat{\mathbf{z}} \epsilon_z, \quad \underline{\underline{\mu}} = \underline{\underline{I}}_t \mu + \hat{\mathbf{z}} \hat{\mathbf{z}} \mu_z \quad (3)$$

In the above, $\underline{\underline{I}}_t = \hat{\mathbf{x}} \hat{\mathbf{x}} + \hat{\mathbf{y}} \hat{\mathbf{y}}$ is the transverse unit dyadic and ϵ and μ denote the transverse, and ϵ_z and μ_z the longitudinal permittivities and permeabilities, respectively, all relative to free space. For lossy media, the dyadics $\underline{\underline{\epsilon}}$ and $\underline{\underline{\mu}}$ become complex-valued.

To solve the problem before us, it will be helpful to introduce the concept of a dyadic Green function (DGF),⁴ as follows. Consider a Hertzian dipole with moment $\mathbf{I}\ell$ placed at \mathbf{r}_0 in a layered medium, as illustrated in Fig. 2. The current density of this point source is given as

$$\mathbf{J}(\mathbf{r}) = \mathbf{I}\ell \delta(\mathbf{r} - \mathbf{r}_0) \quad (4)$$

where δ denotes the Dirac delta function [3, p. 568]. The electric field due to this dipole at any point \mathbf{r} can be

³The $e^{j\omega t}$ time convention adopted here is prevalent in engineering disciplines. In physics, the alternative $e^{-i\omega t}$ convention is almost exclusively employed. The formulas presented here can be converted to that convention by the substitution $j \rightarrow -i$.

⁴Also referred to as *Green's tensor*.

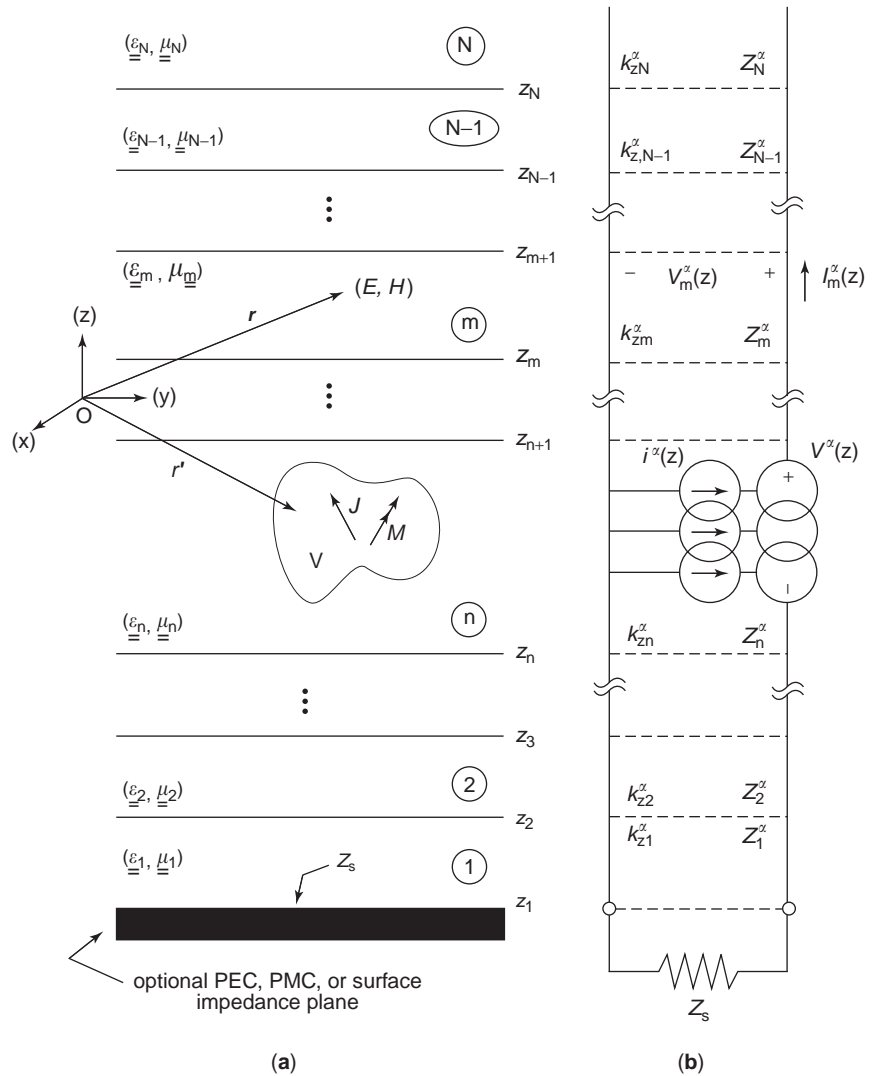


Figure 1. Electric and magnetic currents in a layered medium: (a) physical configuration; (b) transmission-line analog.

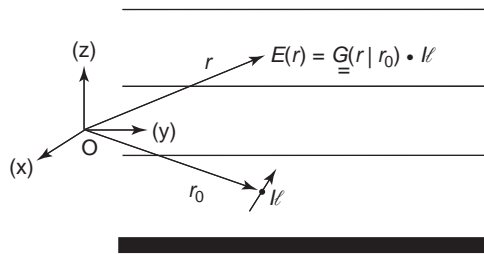


Figure 2. Hertzian dipole with moment $I\ell$ located at \mathbf{r}_0 in a layered medium. The field at \mathbf{r} is determined by the dyadic Green function $\underline{\underline{\mathbf{G}}}(\mathbf{r}|\mathbf{r}_0)$ and the orientation and amplitude of the dipole.

expressed as⁵

$$\mathbf{E}(\mathbf{r}) = \underline{\underline{\mathbf{G}}}(\mathbf{r}|\mathbf{r}_0) \cdot I\ell = \langle \underline{\underline{\mathbf{G}}}(\mathbf{r}|\mathbf{r}'); \mathbf{J}(\mathbf{r}') \rangle \quad (5)$$

⁵The notation \langle , \rangle is used for integrals of products of two functions separated by the comma over their common spatial support, with a dot over the comma indicating a dot product. Source coordinates are distinguished by primes.

where $\underline{\underline{\mathbf{G}}}(\mathbf{r}|\mathbf{r}')$ is the (electric) DGF of the layered medium. When expressed in Cartesian coordinates, $\underline{\underline{\mathbf{G}}}(\mathbf{r}|\mathbf{r}')$ can be thought of as a 3×3 matrix, whose columns render the x , y , and z components of the electric field at \mathbf{r} , due to an x -, y -, and z -oriented unit-strength dipole at \mathbf{r}' [2, p. 17]. For example, the x component of $\mathbf{E}(\mathbf{r})$, due to a unit-strength y -oriented dipole at \mathbf{r}' , is given as $G_{xy}(\mathbf{r}|\mathbf{r}') = \hat{\mathbf{x}} \cdot \underline{\underline{\mathbf{G}}}(\mathbf{r}|\mathbf{r}') \cdot \hat{\mathbf{y}}$. The DGF fully characterizes the influence of the layered medium on the field of the dipole. Hence, it rigorously includes all physical effects, such as multiple reflections and transmissions at the interfaces [5].

The DGF concept can be extended in an obvious way to magnetic fields and also to magnetic currents. The magnetic current concept is useful in the modeling of small coils [6], coaxial antenna feeds [7,8], as well as via holes and slots in printed-circuit boards (PCBs) [9,10]. Since we consider linear media, superposition applies,⁶ and the electric and magnetic fields due to arbitrary current

⁶The superposition principle states that, in a linear system, the effect due to an aggregate of causes is the sum of the effects due to all causes taken individually [11, p. 481].

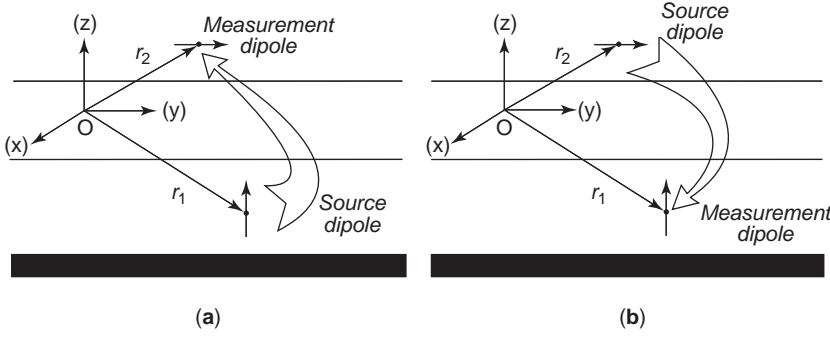


Figure 3. Illustration of reciprocity. The field measurements in situations (a) and (b) are identical.

distributions (\mathbf{J} , \mathbf{M}) may be expressed as

$$\mathbf{E}(\mathbf{r}) = \langle \underline{\underline{\mathbf{G}}}^{EJ}(\mathbf{r}|\mathbf{r}'); \mathbf{J}(\mathbf{r}') \rangle + \langle \underline{\underline{\mathbf{G}}}^{EM}(\mathbf{r}|\mathbf{r}'); \mathbf{M}(\mathbf{r}') \rangle \quad (6)$$

$$\mathbf{H}(\mathbf{r}) = \langle \underline{\underline{\mathbf{G}}}^{HJ}(\mathbf{r}|\mathbf{r}'); \mathbf{J}(\mathbf{r}') \rangle + \langle \underline{\underline{\mathbf{G}}}^{HM}(\mathbf{r}|\mathbf{r}'); \mathbf{M}(\mathbf{r}') \rangle \quad (7)$$

where $\underline{\underline{\mathbf{G}}}^{PQ}(\mathbf{r}|\mathbf{r}')$ is the DGF relating P -type fields at \mathbf{r} and Q -type currents at \mathbf{r}' . In view of the translational symmetry of the medium with respect to the transverse coordinates, these DGFs can also be expressed as

$$\underline{\underline{\mathbf{G}}}^{PQ}(\mathbf{r}|\mathbf{r}') \equiv \underline{\underline{\mathbf{G}}}^{PQ}(\boldsymbol{\rho} - \boldsymbol{\rho}'; z|z') \quad (8)$$

where $\boldsymbol{\rho}$ is the projection of \mathbf{r} on the xy plane. Note that this property does not hold in laterally shielded environments.

Let $(\mathbf{J}_a, \mathbf{M}_a)$ and $(\mathbf{J}_b, \mathbf{M}_b)$ be two separate source distributions, which give rise to the fields $(\mathbf{E}_a, \mathbf{H}_a)$ and $(\mathbf{E}_b, \mathbf{H}_b)$, respectively. From the Maxwell's equations (2), the following reciprocity theorem can be established⁷ [12, p. 50; 13, p. 22]:

$$\langle \mathbf{M}_a; \mathbf{H}_b \rangle - \langle \mathbf{J}_a; \mathbf{E}_b \rangle = \langle \mathbf{M}_b; \mathbf{H}_a \rangle - \langle \mathbf{J}_b; \mathbf{E}_a \rangle \quad (9)$$

By substituting various combinations of dipole sources and their corresponding responses (6) and (7) into the above, the reciprocity properties of the DGFs can be derived. For example, if we postulate $\mathbf{M}_a = \mathbf{J}_b = 0$, $\mathbf{M}_b = \hat{\mathbf{y}} \delta(\mathbf{r} - \mathbf{r}_1)$, and $\mathbf{J}_a = \hat{\mathbf{x}} \delta(\mathbf{r} - \mathbf{r}_2)$, we obtain $G_{xy}^{EM}(\mathbf{r}_2|\mathbf{r}_1) = -G_{yx}^{HJ}(\mathbf{r}_1|\mathbf{r}_2)$. Proceeding in a similar fashion, we can show that

$$\underline{\underline{\mathbf{G}}}^{EJ}(\mathbf{r}|\mathbf{r}') = [\underline{\underline{\mathbf{G}}}^{EJ}(\mathbf{r}'|\mathbf{r})]^T \quad (10)$$

$$\underline{\underline{\mathbf{G}}}^{HM}(\mathbf{r}|\mathbf{r}') = [\underline{\underline{\mathbf{G}}}^{HM}(\mathbf{r}'|\mathbf{r})]^T \quad (11)$$

$$\underline{\underline{\mathbf{G}}}^{EM}(\mathbf{r}|\mathbf{r}') = -[\underline{\underline{\mathbf{G}}}^{HJ}(\mathbf{r}'|\mathbf{r})]^T \quad (12)$$

One important use of reciprocity in electromagnetics is as a check of equations and their computer implementation. For example, from (10) we obtain $G_{yz}^{EJ}(\mathbf{r}_2|\mathbf{r}_1) = G_{zy}^{EJ}(\mathbf{r}_1|\mathbf{r}_2)$,

⁷This holds provided the permittivity and permeability dyadics are symmetric, $\underline{\underline{\boldsymbol{\epsilon}}} = \underline{\underline{\boldsymbol{\epsilon}}}^T$ and $\underline{\underline{\boldsymbol{\mu}}} = \underline{\underline{\boldsymbol{\mu}}}^T$, where the superscript "T" indicates a transposed dyadic. This condition is clearly satisfied for the uniaxial media considered here.

which means that the y component of the electric field "measured" at \mathbf{r}_2 , due to a unit-strength z -oriented dipole at \mathbf{r}_1 , is equal to the z component of the electric field "measured" at \mathbf{r}_1 , due to a y -oriented unit-strength dipole at \mathbf{r}_2 (see Fig. 3). Reciprocity can also be used to obviate some derivations and to reduce the programming effort. For example, we note that in view of (12), $\underline{\underline{\mathbf{G}}}^{EM}$ can be computed from $\underline{\underline{\mathbf{G}}}^{HJ}$.

It should now be clear that the problem stated at the beginning of this section, and illustrated in Fig. 1a, can be reduced to that of finding the four DGFs of the layered medium. In what follows, we will show that these DGFs can be conveniently expressed in terms of the scalar Green functions of the transmission line analogue of the medium, illustrated in Fig. 1b, whose parameters will be defined in due course. This transmission-line equivalent circuit will also prove useful in the derivation of the far-zone radiated fields, as well as the fields excited in the multilayer by an incident plane wave.

3. TRANSMISSION-LINE ANALOG

Let the currents (\mathbf{J}, \mathbf{M}) radiate in a region filled with a medium characterized by z -dependent parameters $\underline{\underline{\boldsymbol{\epsilon}}} = \underline{\underline{\boldsymbol{\epsilon}}}(z)$ and $\underline{\underline{\boldsymbol{\mu}}} = \underline{\underline{\boldsymbol{\mu}}}(z)$, as illustrated in Fig. 4a. For this problem, we will derive a transmission-line equivalent circuit depicted in Fig. 4b. Since the medium is homogeneous and of infinite extent in any transverse (to z) plane, the analysis is facilitated by the Fourier transformation of all fields with respect to the transverse coordinates, defined as follows

$$\mathcal{F}f(\mathbf{r}) \equiv \tilde{f}(\mathbf{k}_\rho; z) = \int_{-\infty}^{\infty} \int_{-\infty}^{\infty} f(\mathbf{r}) e^{j\mathbf{k}_\rho \cdot \boldsymbol{\rho}} dx dy \quad (13)$$

$$\mathcal{F}^{-1}\tilde{f}(\mathbf{k}_\rho; z) \equiv f(\mathbf{r}) = \frac{1}{(2\pi)^2} \int_{-\infty}^{\infty} \int_{-\infty}^{\infty} \tilde{f}(\mathbf{k}_\rho; z) e^{-j\mathbf{k}_\rho \cdot \boldsymbol{\rho}} dk_x dk_y \quad (14)$$

where

$$\boldsymbol{\rho} = \hat{\mathbf{x}}x + \hat{\mathbf{y}}y, \quad \mathbf{k}_\rho = \hat{\mathbf{x}}k_x + \hat{\mathbf{y}}k_y \quad (15)$$

Hence, we apply (13) to Maxwell's equations (2), noting that the operator nabla transforms as $\nabla \rightarrow -j\mathbf{k}_\rho + \hat{\mathbf{z}}d/dz$. Furthermore, we separate the transverse and longitudinal

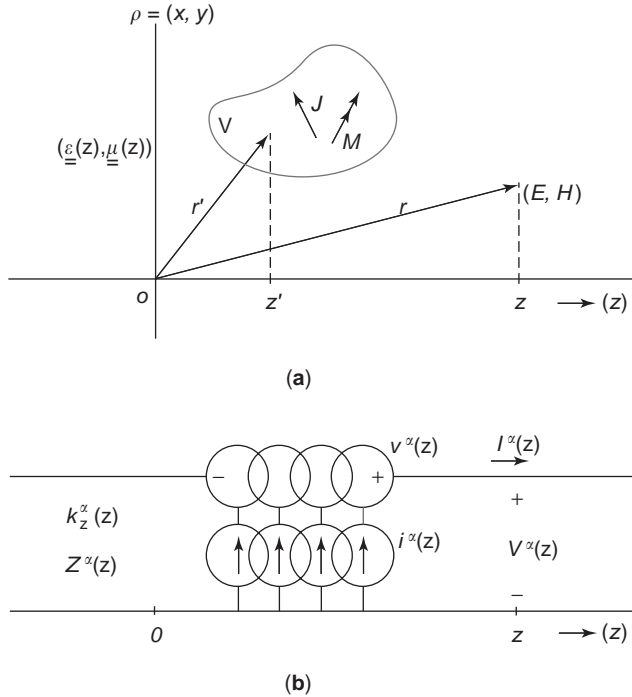


Figure 4. Currents in a uniaxial medium with z -dependent parameters: (a) physical configuration; (b) transmission-line analog.

parts of the resulting equations, to obtain [14]

$$\begin{aligned} \frac{d}{dz} \tilde{\mathbf{E}}_t &= \frac{1}{j\omega\epsilon_0\epsilon} \left(k^2 - \frac{1}{v^e} \mathbf{k}_\rho \mathbf{k}_\rho \cdot \right) (\tilde{\mathbf{H}}_t \times \hat{\mathbf{z}}) \\ &+ \mathbf{k}_\rho \frac{\tilde{\mathbf{J}}_z}{\omega\epsilon_0\epsilon_z} - \tilde{\mathbf{M}}_t \times \hat{\mathbf{z}} \end{aligned} \quad (16)$$

$$\begin{aligned} \frac{d}{dz} \tilde{\mathbf{H}}_t &= \frac{1}{j\omega\mu_0\mu} \left(k^2 - \frac{1}{v^h} \mathbf{k}_\rho \mathbf{k}_\rho \cdot \right) (\hat{\mathbf{z}} \times \tilde{\mathbf{E}}_t) \\ &+ \mathbf{k}_\rho \frac{\tilde{\mathbf{M}}_z}{\omega\mu_0\mu_z} - z \times \tilde{\mathbf{J}}_t \end{aligned} \quad (17)$$

$$-j\omega\epsilon_0\epsilon_z \tilde{\mathbf{E}}_z = j\mathbf{k}_\rho \cdot (\tilde{\mathbf{H}}_t \times \hat{\mathbf{z}}) + \tilde{\mathbf{J}}_z \quad (18)$$

$$-j\omega\mu_0\mu_z \tilde{\mathbf{H}}_z = j\mathbf{k}_\rho \cdot (\hat{\mathbf{z}} \times \tilde{\mathbf{E}}_t) + \tilde{\mathbf{M}}_z \quad (19)$$

where

$$\begin{aligned} k &= k_0 \sqrt{\epsilon\mu}, \\ v^e &= \frac{\epsilon_z}{\epsilon}, \\ v^h &= \frac{\mu_z}{\mu} \end{aligned} \quad (20)$$

and where $k_0 = \omega\sqrt{\mu_0\epsilon_0}$ is the free-space wavenumber, k is the medium wavenumber, and v^e and v^h are the electric and magnetic anisotropy ratios, respectively. It is understood that all media parameters may be z -dependent.

The subsequent analysis is greatly simplified if one defines a spectral-domain coordinate system based on

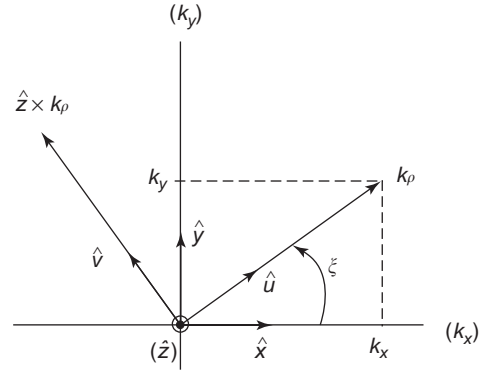


Figure 5. Spectral-domain coordinate system.

$(\mathbf{k}_\rho, \hat{\mathbf{z}} \times \mathbf{k}_\rho)$, as illustrated in Fig. 5, with the unit vectors $(\hat{\mathbf{u}}, \hat{\mathbf{v}})$ given by [15]

$$\begin{aligned} \hat{\mathbf{u}} &= \frac{\mathbf{k}_\rho}{k_\rho} = \hat{\mathbf{x}} \cos \xi + \hat{\mathbf{y}} \sin \xi, \\ \hat{\mathbf{v}} &= \frac{\hat{\mathbf{z}} \times \mathbf{k}_\rho}{k_\rho} = -\hat{\mathbf{x}} \sin \xi + \hat{\mathbf{y}} \cos \xi \end{aligned} \quad (21)$$

where ξ is the angle the vector \mathbf{k}_ρ makes with the positive x axis and $k_\rho = \sqrt{k_x^2 + k_y^2}$. In this system, the transverse electric and magnetic fields can be expressed as [16,17]

$$\tilde{\mathbf{E}}_t = \hat{\mathbf{u}} V^e + \hat{\mathbf{v}} V^h, \quad \hat{\mathbf{z}} \times \tilde{\mathbf{E}}_t = -\hat{\mathbf{u}} V^h + \hat{\mathbf{v}} V^e \quad (22)$$

$$\tilde{\mathbf{H}}_t \times \hat{\mathbf{z}} = \hat{\mathbf{u}} I^e + \hat{\mathbf{v}} I^h, \quad \tilde{\mathbf{H}}_t = -\hat{\mathbf{u}} I^h + \hat{\mathbf{v}} I^e \quad (23)$$

On substituting this into (16), (17) and projecting the resulting equations on $\hat{\mathbf{u}}$ and $\hat{\mathbf{v}}$, we obtain two sets of transmission-line (TL) equations of the form

$$\begin{aligned} \frac{dV^\alpha}{dz} &= -jk_z^\alpha Z^\alpha I^\alpha + v^\alpha, \\ \frac{dI^\alpha}{dz} &= -jk_z^\alpha Y^\alpha V^\alpha + i^\alpha, \quad \alpha = (e, h) \end{aligned} \quad (24)$$

where

$$k_z^\alpha = \sqrt{k^2 - k_\rho^2 / v^\alpha} \quad (25)$$

$$Z^e = \frac{1}{Y^e} = \frac{k_z^e}{\omega\epsilon_0\epsilon}, \quad Z^h = \frac{1}{Y^h} = \frac{\omega\mu_0\mu}{k_z^h} \quad (26)$$

and where the source functions v^α and i^α are as given in Table 1. Hence, as anticipated by the notation introduced in (22), (23), the components of $\tilde{\mathbf{E}}_t$ and $\tilde{\mathbf{H}}_t$ in the spectral uv plane may be interpreted as voltages and currents⁸ on a transmission-line analog of the medium along the z axis, as illustrated in Fig. 4b. This analog comprises two transmission lines, with z -dependent propagation “constants” k_z^α and characteristic impedances Z^α , where $\alpha = (e, h)$. Since

⁸Note, however, that these “voltages” and “currents” have the units of V/m and A/m, respectively.

Table 1. Transmission-Line Sources in Terms of Field Sources

	$\alpha = e$ (TM)	$\alpha = h$ (TE)
v^x	$\frac{k_\rho}{\omega\epsilon_0\epsilon_z} \tilde{\mathbf{J}}_z - \tilde{\mathbf{M}}_v$	$\tilde{\mathbf{M}}_u$
i^x	$-\tilde{\mathbf{J}}_u$	$-\frac{k_\rho}{\omega\mu_0\mu_z} \tilde{\mathbf{M}}_z - \tilde{\mathbf{J}}_v$

the longitudinal field components may be found from the transverse components and the field sources by means of (18), (19), the original vector problem of Fig. 4a has in effect been reduced to the scalar TL problem of Fig. 4b. In fact, combining (22), (23) and (18), (19), we obtain the complete spectral domain fields as

$$\begin{aligned} \tilde{\mathbf{E}}(\mathbf{k}_\rho; z) = & \hat{\mathbf{u}}V^e(z) + \hat{\mathbf{v}}V^h(z) - \hat{\mathbf{z}} \frac{1}{j\omega\epsilon_0\epsilon_z(z)} \\ & \times [jk_\rho I^e(z) + \tilde{\mathbf{J}}_z(\mathbf{k}_\rho; z)] \end{aligned} \quad (27)$$

$$\begin{aligned} \tilde{\mathbf{H}}(\mathbf{k}_\rho; z) = & -\hat{\mathbf{u}}I^h(z) + \hat{\mathbf{v}}I^e(z) + \hat{\mathbf{z}} \frac{1}{j\omega\mu_0\mu_z(z)} \\ & \times [jk_\rho V^h(z) - \tilde{\mathbf{M}}_z(\mathbf{k}_\rho; z)] \end{aligned} \quad (28)$$

where $V^x(z)$ and $I^x(z)$ implicitly depend on k_ρ (but not on ξ). We observe that, outside the source region, (V^e, I^e) and (V^h, I^h) represent fields that are transverse magnetic (TM) and transverse electric (TE) to z , respectively. We also note from Table 1 that transverse x - or y -directed electric and magnetic currents, always excite both the TM and TE transmission lines, whereas longitudinal z -directed electric (magnetic) currents excite only the TM (TE) transmission line.

The preceding three-dimensional (3D) analysis can be specialized to the two-dimensional (2D) case, where there is a translational symmetry along one of the transverse axes—say, the y axis, and it may be assumed that the scalar components of all fields and sources have the form⁹

$$f(\mathbf{r}) = f_{2D}(x, \beta, z) e^{-j\beta y} \quad (29)$$

where β is a known or sought-after propagation constant [18–22 (Chap. 6 in Ref. 20)]. When (29) is substituted into (13), (14), one obtains

$$\mathcal{F}f(\mathbf{r}) = 2\pi\delta(k_y - \beta) \tilde{f}_{2D}(\mathbf{k}_\rho; z) \quad (30)$$

where

$$\tilde{f}_{2D}(\mathbf{k}_\rho; z) = \int_{-\infty}^{\infty} f_{2D}(x, k_y, z) e^{jk_x x} dx \quad (31)$$

⁹The term 2.5D is occasionally used in this context, with the 2D designation reserved for the $\beta=0$ case.

and

$$f_{2D}(x, k_y, z) = \frac{1}{2\pi} \int_{-\infty}^{\infty} \tilde{f}_{2D}(\mathbf{k}_\rho; z) e^{-jk_x x} dk_x \quad (32)$$

Hence, the transmission-line analog derived here is still applicable in 2D, with the understanding that the two-dimensional Fourier transform pair should be replaced by the one-dimensional transforms (31), (32), with $k_y = \beta$.

4. TRANSMISSION-LINE GREEN FUNCTIONS

To find the transmission-line voltages and currents appearing in (27), (28), it will be helpful to introduce transmission-line Green functions (TLGFs) as the voltages and currents excited by unit-strength impulsive sources. Hence, let $V_i(z|z')$ and $I_i(z|z')$ denote, respectively, the voltage and current at z , due to a 1-A shunt current source at z' , and let $V_v(z|z')$ and $I_v(z|z')$ denote, respectively, the voltage and current at z , due to a 1-V series voltage source at z' , as illustrated in Fig. 6.¹⁰ It then follows from (24) that the so-defined TLGFs satisfy the equations

$$\frac{dV_i}{dz} = -jk_z Z I_i, \quad \frac{dI_i}{dz} = -jk_z Y V_i + \delta(z - z') \quad (33)$$

$$\frac{dV_v}{dz} = -jk_z Z I_v + \delta(z - z'), \quad \frac{dI_v}{dz} = -jk_z Y V_v \quad (34)$$

In view of the linearity of the TL equations (24), we can use superposition¹¹ to express V and I at any point z as

$$V(z) = \langle V_i(z|z'), i(z') \rangle + \langle V_v(z|z'), v(z') \rangle \quad (35)$$

$$I(z) = \langle I_i(z|z'), i(z') \rangle + \langle I_v(z|z'), v(z') \rangle \quad (36)$$

The complete analogy with (6), (7) should be noted.

Let (v_a, i_a) and (v_b, i_b) be two separate TL source distributions, which give rise to (V_a, I_a) and (V_b, I_b) , respectively. Since both sets satisfy the TL equations (24) subject to the same boundary conditions, it can be shown that [4; p. 194; 24, p. 147]

$$\langle v_a, I_b \rangle - \langle i_a, V_b \rangle = \langle v_b, I_a \rangle - \langle i_b, V_a \rangle \quad (37)$$

which is the transmission-line counterpart of the reciprocity theorem (9). By substituting various combinations of point sources and their corresponding responses (35), (36) into the above, it is found that the TLGFs possess the re-

¹⁰Here and throughout this article, we omit the superscript α , whenever the equations apply to both the TM and TE transmission lines.

¹¹The principle of superposition for linear networks can be stated as follows. The response due to several independent voltage and current sources is equal to the sum of the responses due to each independent source acting alone, that is, with all other independent sources made inoperative. In the case of distributed sources, the sums become integrals [23, p. 63].

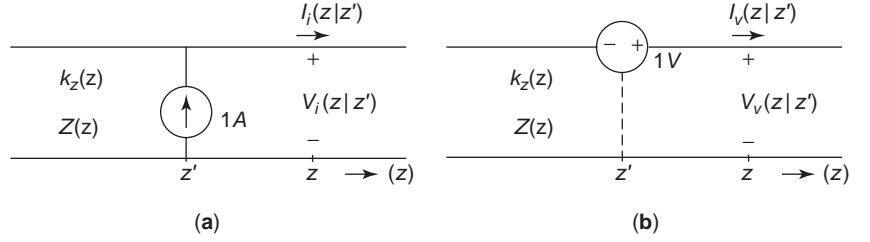


Figure 6. Network problems for determination of transmission-line Green functions: (a) current source excitation; (b) voltage source excitation.

reciprocity properties

$$\begin{aligned} V_i(z|z') &= V_i(z'|z), \quad I_v(z|z') = I_v(z'|z), \\ V_v(z|z') &= -I_i(z'|z) \end{aligned} \quad (38)$$

which are the transmission-line counterparts of (10)–(12).

The TL equations (33), (34) give rise to second-order differential equations of the Sturm–Liouville type [4, p. 278; 25, p. 53; 26, p. 291]. For example, equations (33) imply

$$\left[\frac{d}{dz} \mathcal{P}(z) \frac{d}{dz} - \mathcal{Q}(z) \right] V_i(z|z') = -\delta(z - z') \quad (39)$$

with

$$I_i(z|z') = -\mathcal{P} \frac{d}{dz} V_i(z|z') \quad (40)$$

where we have introduced the notation

$$\mathcal{P} = \frac{1}{jk_z Z}, \quad \mathcal{Q} = \frac{jk_z}{Z} \quad (41)$$

Assuming that the solution domain is restricted to $z_n \leq z \leq z_{n+1}$, to correspond to the n th layer in Fig. 1, we impose the boundary conditions

$$\left(\frac{V_i}{I_i} \right)_{z=z_n} = -\overleftarrow{Z}_n, \quad \left(\frac{V_i}{I_i} \right)_{z=z_{n+1}} = \overrightarrow{Z}_n \quad (42)$$

where \overleftarrow{Z}_n and \overrightarrow{Z}_n denote the “left-looking” and “right-looking” impedances at z_n and z_{n+1} , respectively. Let $\overleftarrow{V}(z)$ and $\overrightarrow{V}(z)$ be two homogeneous solutions of (39) that satisfy the boundary conditions at the left and at the right ends of the solution domain, respectively. Then, the solution of (39), subject to (42), can be found as

$$V_i(z|z') = \frac{\overleftarrow{V}(z_<) \overrightarrow{V}(z_>)}{-\mathcal{P} W(\overleftarrow{V}, \overrightarrow{V})} \quad (43)$$

where $z_< = \min(z, z')$, $z_> = \max(z, z')$, and where

$$W(\overleftarrow{V}, \overrightarrow{V}) = \overleftarrow{V} \frac{d\overrightarrow{V}}{dz} - \overrightarrow{V} \frac{d\overleftarrow{V}}{dz} \quad (44)$$

is the Wronskian determinant. It can be shown that the denominator in (43), which is referred to as the *conjugant*, is

independent of z . The solution of (34) follows by a dual procedure, in which voltages are replaced by currents, impedances by admittances, and vice versa.¹²

The simple and elegant result (43) clearly depends on the availability of the homogeneous solutions $\overleftarrow{V}(z)$ and $\overrightarrow{V}(z)$ in an analytical closed form. In Section 7, we derive such solutions for the most practically important case of piecewise homogeneous media.

5. SPECTRAL-DOMAIN DYADIC GREEN FUNCTIONS

On substituting (35), (36) into (27), (28) and referring to Table 1, one obtains, after some simple transformations, the spectral domain counterparts of (6), (7), specifically

$$\begin{aligned} \tilde{\underline{\underline{E}}}(\mathbf{k}_\rho; z) &= \langle \tilde{\underline{\underline{G}}}^{EJ}(\mathbf{k}_\rho; z|z'); \tilde{\underline{\underline{J}}}(\mathbf{k}_\rho; z') \rangle \\ &+ \langle \tilde{\underline{\underline{G}}}^{EM}(\mathbf{k}_\rho; z|z'); \tilde{\underline{\underline{M}}}(\mathbf{k}_\rho; z') \rangle \end{aligned} \quad (45)$$

$$\begin{aligned} \tilde{\underline{\underline{H}}}(\mathbf{k}_\rho; z) &= \langle \tilde{\underline{\underline{G}}}^{HJ}(\mathbf{k}_\rho; z|z'); \tilde{\underline{\underline{J}}}(\mathbf{k}_\rho; z') \rangle \\ &+ \langle \tilde{\underline{\underline{G}}}^{HM}(\mathbf{k}_\rho; z|z'); \tilde{\underline{\underline{M}}}(\mathbf{k}_\rho; z') \rangle \end{aligned} \quad (46)$$

with the spectral DGFs given as¹³

$$\begin{aligned} \tilde{\underline{\underline{G}}}^{EJ}(\mathbf{k}_\rho; z|z') &= -\hat{\mathbf{u}}\hat{\mathbf{u}}V_i^e - \hat{\mathbf{v}}\hat{\mathbf{v}}V_i^h + \hat{\mathbf{z}}\hat{\mathbf{u}} \frac{k_\rho}{\omega\epsilon_0\epsilon_z} I_i^e \\ &+ \hat{\mathbf{u}}\hat{\mathbf{z}} \frac{k_\rho}{\omega\epsilon_0\epsilon'_z} V_v^e + \hat{\mathbf{z}}\hat{\mathbf{z}} \frac{1}{j\omega\epsilon_0\epsilon'_z} \\ &\times \left[\frac{k_\rho^2}{j\omega\epsilon_0\epsilon_z} I_v^e - \delta(z - z') \right] \end{aligned} \quad (47)$$

$$\begin{aligned} \tilde{\underline{\underline{G}}}^{EM}(\mathbf{k}_\rho; z|z') &= -\hat{\mathbf{u}}\hat{\mathbf{v}}V_v^e + \hat{\mathbf{v}}\hat{\mathbf{u}}V_v^h + \hat{\mathbf{z}}\hat{\mathbf{v}} \frac{k_\rho}{\omega\epsilon_0\epsilon_z} I_v^e \\ &- \hat{\mathbf{v}}\hat{\mathbf{z}} \frac{k_\rho}{\omega\mu_0\mu'_z} V_i^h \end{aligned} \quad (48)$$

¹²Two equations of the same mathematical form are called *dual equations*, and quantities occupying the same position in dual equations are called *dual quantities*. When two equations are duals of each other, a systematic interchange of symbols changes the first equation into the second, and vice versa [27, p. 98].

¹³It is understood that the TLGFs in these equations depend on z and z' , such as $V_i^e = V_i^e(z|z')$, and also (implicitly) on k_ρ .

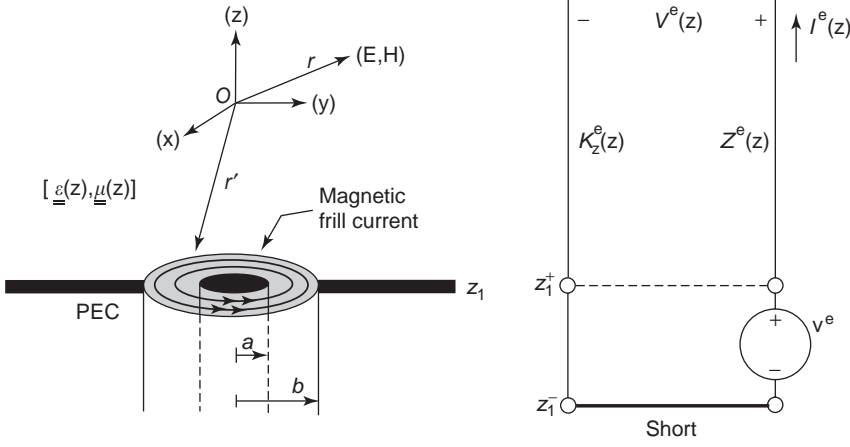


Figure 7. Coax-excited half-space medium: (a) computational model showing an equivalent magnetic surface current over a shorted-circuited annular aperture; (b) spectral-domain transmission-line equivalent circuit.

$$\begin{aligned} \underline{\tilde{\mathbf{G}}}^{HJ}(\mathbf{k}_\rho; z|z') &= \hat{\mathbf{u}}\hat{\mathbf{u}}I_i^h - \hat{\mathbf{v}}\hat{\mathbf{v}}I_i^e \\ &\quad - \hat{\mathbf{z}}\hat{\mathbf{v}}\frac{k_\rho}{\omega\mu_0\mu_z}V_i^h + \hat{\mathbf{v}}\hat{\mathbf{z}}\frac{k_\rho}{\omega\epsilon_0\epsilon'_z}I_v^e \end{aligned} \quad (49)$$

$$\begin{aligned} \underline{\tilde{\mathbf{G}}}^{HM}(\mathbf{k}_\rho; z|z') &= -\hat{\mathbf{u}}\hat{\mathbf{u}}I_v^h - \hat{\mathbf{v}}\hat{\mathbf{v}}I_v^e + \hat{\mathbf{z}}\hat{\mathbf{u}}\frac{k_\rho}{\omega\mu_0\mu_z}V_v^h \\ &\quad + \hat{\mathbf{u}}\hat{\mathbf{z}}\frac{k_\rho}{\omega\mu_0\mu'_z}I_i^h + \hat{\mathbf{z}}\hat{\mathbf{v}}\frac{1}{j\omega\mu_0\mu'_z} \\ &\quad \times \left[\frac{k_\rho^2}{j\omega\mu_0\mu_z}V_i^h - \delta(z-z') \right] \end{aligned} \quad (50)$$

where the primed and unprimed media parameters are evaluated at z' and z , respectively. It can readily be confirmed, using (38), that these DGFs possess the reciprocity properties

$$\underline{\tilde{\mathbf{G}}}^{EJ}(\mathbf{k}_\rho; z|z') = [\underline{\tilde{\mathbf{G}}}^{EJ}(-\mathbf{k}_\rho; z'|z)]^T \quad (51)$$

$$\underline{\tilde{\mathbf{G}}}^{HM}(\mathbf{k}_\rho; z|z') = [\underline{\tilde{\mathbf{G}}}^{HM}(-\mathbf{k}_\rho; z'|z)]^T \quad (52)$$

$$\underline{\tilde{\mathbf{G}}}^{EM}(\mathbf{k}_\rho; z|z') = -[\underline{\tilde{\mathbf{G}}}^{HJ}(-\mathbf{k}_\rho; z'|z)]^T \quad (53)$$

which are the counterparts of the spatial-domain relations (10)–(12).

The spectral-domain electric DGF (47) has been widely used in the analysis of planar microstrip antennas, resonators, and transmission lines by the spectral-domain approach (SDA) [16,28–33]. For planar circuits with infinitesimal metallization thickness, only the transverse part of $\underline{\tilde{\mathbf{G}}}^{EJ}$ is needed. This transverse dyadic, which has a

particularly simple form, can also be expressed as [34]

$$\begin{aligned} -\underline{\tilde{\mathbf{G}}}^{EJ}(\mathbf{k}_\rho; z|z') &= \underline{\mathbf{I}}_{\underline{\mathbf{t}}}V_i^h + \hat{\mathbf{u}}\hat{\mathbf{u}}(V_i^e - V_i^h) \\ &= \frac{1}{2}\underline{\mathbf{I}}_{\underline{\mathbf{t}}}(V_i^e + V_i^h) + \frac{1}{2}(2\hat{\mathbf{u}}\hat{\mathbf{u}} - \underline{\mathbf{I}}_{\underline{\mathbf{t}}})(V_i^e - V_i^h) \end{aligned} \quad (54)$$

where we have used the fact that $\underline{\mathbf{I}}_{\underline{\mathbf{t}}} = \hat{\mathbf{u}}\hat{\mathbf{u}} + \hat{\mathbf{v}}\hat{\mathbf{v}}$.

To demonstrate the application of the SDA, consider a half-space medium excited by a coaxial transmission line opening into a PEC flange at $z = z_1$, as illustrated in Fig. 7. The medium may be uniaxial, with z -dependent permittivity and permeability dyadics. It is desired to find the electric and magnetic fields in the half-space, assuming that the coax (coaxial TL) propagates the dominant TEM mode. This problem, which is relevant to coaxial feeds for microstrip antennas, PCB vias, and noninvasive testing, will also serve to introduce some results and notation needed in the subsequent development. We assume, without loss of generality, that the coax is concentric with the z axis. The field for $z > z_1$ can be found from the equivalent problem depicted in Fig. 7a, where the annular coax aperture has been short-circuited and covered by an equivalent magnetic surface current $\mathbf{M}_S = \mathbf{E}^a \times \hat{\mathbf{z}}$, where \mathbf{E}^a is the aperture electric field in the original problem. Although \mathbf{E}^a is not known, its distribution may be approximated by that existing in the cross section of an infinite coax, which results in the azimuthally oriented “frill current” [27, p. 112]

$$\mathbf{M}_S(\rho) = \hat{\boldsymbol{\phi}}\frac{K}{\rho}, \quad a < \rho < b, \quad z = z_1 \quad (55)$$

with $K = -V_c/\log(b/a)$, where V_c is the voltage at the mouth of the coax.¹⁴ Noting that the corresponding volume current density is $\mathbf{M}(\mathbf{r}) = \mathbf{M}_S(\rho)\delta(z - z_1)$, we may use

¹⁴We will assume that V_c is known, although this seldom is the case. In general, one must resort to numerical techniques to determine the aperture field [35].

(6) and (8) to express the electric field in the half-space as

$$\begin{aligned} \mathbf{E}(\mathbf{r}) &= \langle \underline{\mathbf{G}}^{EM}(\boldsymbol{\rho} - \boldsymbol{\rho}'; z|z_1); \mathbf{M}_S(\boldsymbol{\rho}') \rangle \\ &= \mathcal{F}^{-1} \{ \underline{\tilde{\mathbf{G}}}^{EM}(\mathbf{k}_\rho; z|z_1) \cdot \tilde{\mathbf{M}}_S(\mathbf{k}_\rho) \} \end{aligned} \quad (56)$$

where the second equality on the right side is the result of the well-known fact that a spatial-domain convolution of two functions corresponds to a product of their transforms in the spectral domain [36, p. 23]. Similarly, the magnetic field may be expressed as

$$\begin{aligned} \mathbf{H}(\mathbf{r}) &= \langle \underline{\mathbf{G}}^{HM}(\boldsymbol{\rho} - \boldsymbol{\rho}'; z|z_1); \mathbf{M}_S(\boldsymbol{\rho}') \rangle \\ &= \mathcal{F}^{-1} \{ \underline{\tilde{\mathbf{G}}}^{HM}(\mathbf{k}_\rho; z|z_1) \cdot \tilde{\mathbf{M}}_S(\mathbf{k}_\rho) \} \end{aligned} \quad (57)$$

To find the spectral-domain magnetic current density $\tilde{\mathbf{M}}_S$, we apply the Fourier transformation (13) to (55). The integration is facilitated by changing to polar coordinates in both domains, namely, $(x, y) \rightarrow (\rho, \varphi)$ and $(k_x, k_y) \rightarrow (k_\rho, \zeta)$, and invoking an integral representation of the Bessel function of order n

$$J_n(z) = \frac{(\pm j)^n}{2\pi} \int_{-\pi}^{\pi} e^{\mp j[z \cos(\varphi - \vartheta) + n(\varphi - \vartheta)]} d\varphi \quad (58)$$

where ϑ is an arbitrary angle [37, p. 106].¹⁵ From (58), we derive the formula

$$\frac{1}{2\pi} \int_{-\pi}^{\pi} \frac{\cos}{\sin} n\varphi e^{jk_\rho \rho \cos(\varphi - \zeta)} d\varphi = j^n J_n(k_\rho \rho) \frac{\cos}{\sin} n\zeta \quad (59)$$

and apply it to evaluate the φ integral in a closed form. The ρ integration is also evaluated in a closed form,¹⁶ with the final result

$$\tilde{\mathbf{M}}_S(\mathbf{k}_\rho) = \hat{\mathbf{v}} 2\pi j \frac{K}{k_\rho} \underbrace{[J_0(k_\rho a) - J_0(k_\rho b)]}_{\varpi(k_\rho)} \equiv \hat{\mathbf{v}} \tilde{\mathbf{M}}_S(k_\rho) \quad (60)$$

where $\hat{\mathbf{v}}$ is the unit vector defined in (21). Note that, as evident from Table 1, this source excites only the TM transmission line, as illustrated in Fig. 7b, where $v^e = -\tilde{\mathbf{M}}_S$. Finally, we substitute (60) together with (48) and (50) into (56), (57) and apply the inverse Fourier transformation (14) to obtain the desired electric and magnetic fields. The ζ integrals are evaluated in closed forms by means of the formula

$$\frac{1}{2\pi} \int_{-\pi}^{\pi} \frac{\cos}{\sin} n\zeta e^{-jk_\rho \rho \cos(\zeta - \varphi)} d\zeta = (-j)^n J_n(k_\rho \rho) \frac{\cos}{\sin} n\varphi \quad (61)$$

¹⁵This formula is also valid with n in the exponent of the integrand changed to $-n$, which can be confirmed by using the relationship $J_{-n}(z) = (-1)^n J_n(z)$ [38, p. 358]. Also, in view of the periodicity of the integrand, the limits of integration can be changed to any 2π range.

¹⁶This is done by invoking the formula $J_1(z) = -J_0'(z)$ [38, p. 361].

which can also be derived from (58). As a result, the non-zero field components are found as [8]

$$E_\rho(\mathbf{r}) = -2\pi K \mathcal{S}_1 \left\{ \frac{\varpi(k_\rho)}{k_\rho} V_v^e(z|z_1) \right\} \quad (62)$$

$$E_z(\mathbf{r}) = 2\pi K \frac{jn_1}{k_1 v_1^e} \mathcal{S}_0 \{ \varpi(k_\rho) I_v^e(z|z_1) \} \quad (63)$$

$$H_\varphi(\mathbf{r}) = -2\pi K \mathcal{S}_1 \left\{ \frac{\varpi(k_\rho)}{k_\rho} I_v^e(z|z_1) \right\} \quad (64)$$

with the notation

$$\begin{aligned} \mathcal{S}_n \{ \tilde{f}(k_\rho) \} &= \frac{1}{2\pi} \int_0^\infty \tilde{f}(k_\rho) J_n(k_\rho \rho) k_\rho dk_\rho \\ &= \frac{1}{4\pi} \int_{\infty e^{-j\pi}}^{\infty} \tilde{f}(k_\rho) H_n^{(2)}(k_\rho \rho) k_\rho dk_\rho \end{aligned} \quad (65)$$

where $H_n^{(2)}$ is the Hankel function of the second kind and order n .¹⁷ The integrals in (65) are recognized as Hankel (or Fourier-Bessel) transforms, but in the electromagnetics community they are generally known as *Sommerfeld integrals* [40,41]. The real-axis integration paths in (65) must be properly indented around the singularities of $\tilde{f}(k_\rho)$, as discussed in Section 8. Note that (62)–(64) can be used, in particular, when the upper half-space in Fig. 7 is a layered medium with piecewise constant parameters. The TLGFs for this case are derived in Section 7.

6. SPATIAL-DOMAIN DYADIC GREEN FUNCTIONS

The spatial-domain counterparts of (47)–(50) are obtained by the Fourier inversion

$$\underline{\mathbf{G}}^{PQ}(\boldsymbol{\rho}; z|z') = \mathcal{F}^{-1} \underline{\tilde{\mathbf{G}}}^{PQ}(\mathbf{k}_\rho; z|z') \quad (66)$$

which is performed by first projecting the unit vectors $(\hat{\mathbf{u}}, \hat{\mathbf{v}})$ on the xy coordinate system via (21) and then applying the transformation (14). Since all spectral integrands are of the form $\sin(n\zeta)\tilde{f}(k_\rho)$ or $\cos(n\zeta)\tilde{f}(k_\rho)$, with $n = 0, 1, \text{ or } 2$, the integration is facilitated by changing to polar coordinates in both domains and using the formula

$$\mathcal{F}^{-1} \left\{ \frac{\cos}{\sin} n\zeta \tilde{f}(k_\rho) \right\} = (-j)^n \frac{\cos}{\sin} n\varphi \mathcal{S}_n \{ \tilde{f}(k_\rho) \} \quad (67)$$

which follows from (61) and (65). We note that the second-order Hankel transforms in (67) can be expressed as

$$\mathcal{S}_2 \{ \tilde{f}(k_\rho) \} = \frac{2}{\rho} \mathcal{S}_1 \left\{ \frac{\tilde{f}(k_\rho)}{k_\rho} \right\} - \mathcal{S}_0 \{ \tilde{f}(k_\rho) \} \quad (68)$$

¹⁷The second integral form in [65] can be derived from the first by using the formulas $J_n(z) = \frac{1}{2}[H_n^{(1)}(z) + H_n^{(2)}(z)]$ and $H_n^{(1)}(ze^{j\pi}) = -e^{-jn\pi} H_n^{(2)}(z)$ [3, p. 453; 39, p. 231], under the assumption that the integrand functions $\tilde{f}(k_\rho)$ are even (odd) in k_ρ for even (odd) n .

Hence only the Hankel transforms of orders 0 and 1 are needed.¹⁸ Using (67), (68) in (66), we obtain the non-zero Cartesian components of the space-domain DGFs as

$$G_{xx}^{EJ}(\rho; z|z') = -\cos^2 \varphi \mathcal{S}_0\{V_i^e\} - \sin^2 \varphi \mathcal{S}_0\{V_i^h\} + \frac{\cos 2\varphi}{\rho} \mathcal{S}_1\left\{\frac{V_i^e - V_i^h}{k_\rho}\right\} \quad (69)$$

$$G_{xx}^{EJ}(\rho; z|z') = G_{yx}^{EJ}(\rho; z|z') = -\frac{\sin 2\varphi}{2} \mathcal{S}_0\{V_i^e - V_i^h\} + \frac{\sin 2\varphi}{\rho} \mathcal{S}_1\left\{\frac{V_i^e - V_i^h}{k_\rho}\right\} \quad (70)$$

$$G_{xz}^{EJ}(\rho; z|z') = \frac{\eta_0}{jk_0 \epsilon'_z} \cos \varphi \mathcal{S}_1\{k_\rho V_v^e\} \quad (71)$$

$$G_{yy}^{EJ}(\rho; z|z') = -\sin^2 \varphi \mathcal{S}_0\{V_i^e\} - \cos^2 \varphi \mathcal{S}_0\{V_i^h\} - \frac{\cos 2\varphi}{\rho} \mathcal{S}_1\left\{\frac{V_i^e - V_i^h}{k_\rho}\right\} \quad (72)$$

$$G_{yz}^{EJ}(\rho; z|z') = \frac{\eta_0}{jk_0 \epsilon'_z} \sin \varphi \mathcal{S}_1\{k_\rho V_v^e\} \quad (73)$$

$$G_{zx}^{EJ}(\rho; z|z') = \frac{\eta_0}{jk_0 \epsilon_z} \cos \varphi \mathcal{S}_1\{k_\rho I_i^e\} \quad (74)$$

$$G_{zy}^{EJ}(\rho; z|z') = \frac{\eta_0}{jk_0 \epsilon_z} \sin \varphi \mathcal{S}_1\{k_\rho I_i^e\} \quad (75)$$

$$G_{zz}^{EJ}(\rho; z|z') = -\frac{\eta_0^2}{k_0^2 \epsilon_z \epsilon'_z} \mathcal{S}_0\{k_\rho^2 I_v^e\} - \frac{\eta_0}{jk_0 \epsilon_z} \delta(\rho) \delta(z - z') \quad (76)$$

$$G_{xx}^{EM}(\rho; z|z') = -G_{yy}^{EM}(\rho; z|z') = \frac{\sin 2\varphi}{2} \mathcal{S}_0\{V_v^e - V_v^h\} - \frac{\sin 2\varphi}{\rho} \mathcal{S}_1\left\{\frac{V_v^e - V_v^h}{k_\rho}\right\} \quad (77)$$

$$G_{xy}^{EM}(\rho; z|z') = -\cos^2 \varphi \mathcal{S}_0\{V_v^e\} - \sin^2 \varphi \mathcal{S}_0\{V_v^h\} + \frac{\cos 2\varphi}{\rho} \mathcal{S}_1\left\{\frac{V_v^e - V_v^h}{k_\rho}\right\} \quad (78)$$

$$G_{xz}^{EM}(\rho; z|z') = \frac{1}{jk_0 \eta_0 \mu'_z} \sin \varphi \mathcal{S}_1\{k_\rho V_i^h\} \quad (79)$$

$$G_{yx}^{EM}(\rho; z|z') = \sin^2 \varphi \mathcal{S}_0\{V_v^e\} + \cos^2 \varphi \mathcal{S}_0\{V_v^h\} + \frac{\cos 2\varphi}{\rho} \mathcal{S}_1\left\{\frac{V_v^e - V_v^h}{k_\rho}\right\} \quad (80)$$

$$G_{yz}^{EM}(\rho; z|z') = -\frac{1}{jk_0 \eta_0 \mu'_z} \cos \varphi \mathcal{S}_1\{k_\rho V_i^h\} \quad (81)$$

$$G_{zx}^{EM}(\rho; z|z') = -\frac{\eta_0}{jk_0 \epsilon_z} \sin \varphi \mathcal{S}_1\{k_\rho I_v^e\} \quad (82)$$

$$G_{zy}^{EM}(\rho; z|z') = \frac{\eta_0}{jk_0 \epsilon_z} \cos \varphi \mathcal{S}_1\{k_\rho I_v^e\} \quad (83)$$

$$G_{xx}^{HJ}(\rho; z|z') = -G_{yy}^{HJ}(\rho; z|z') = -\frac{\sin 2\varphi}{2} \mathcal{S}_0\{I_i^h - I_i^e\} + \frac{\sin 2\varphi}{\rho} \mathcal{S}_1\left\{\frac{I_i^h - I_i^e}{k_\rho}\right\} \quad (84)$$

$$G_{xy}^{HJ}(\rho; z|z') = \cos^2 \varphi \mathcal{S}_0\{I_i^h\} + \sin^2 \varphi \mathcal{S}_0\{I_i^e\} - \frac{\cos 2\varphi}{\rho} \mathcal{S}_1\left\{\frac{I_i^h - I_i^e}{k_\rho}\right\} \quad (85)$$

$$G_{xz}^{HJ}(\rho; z|z') = -\frac{\eta_0}{jk_0 \epsilon'_z} \sin \varphi \mathcal{S}_1\{k_\rho I_v^e\} \quad (86)$$

$$G_{yx}^{HJ}(\rho; z|z') = -\sin^2 \varphi \mathcal{S}_0\{I_i^h\} - \cos^2 \varphi \mathcal{S}_0\{I_i^e\} - \frac{\cos 2\varphi}{\rho} \mathcal{S}_1\left\{\frac{I_i^h - I_i^e}{k_\rho}\right\} \quad (87)$$

$$G_{yz}^{HJ}(\rho; z|z') = \frac{\eta_0}{jk_0 \epsilon'_z} \cos \varphi \mathcal{S}_1\{k_\rho I_v^e\} \quad (88)$$

$$G_{zx}^{HJ}(\rho; z|z') = \frac{1}{jk_0 \eta_0 \mu_z} \sin \varphi \mathcal{S}_1\{k_\rho V_i^h\} \quad (89)$$

$$G_{zy}^{HJ}(\rho; z|z') = -\frac{1}{jk_0 \eta_0 \mu_z} \cos \varphi \mathcal{S}_1\{k_\rho V_i^h\} \quad (90)$$

$$G_{xx}^{HM}(\rho; z|z') = -\cos^2 \varphi \mathcal{S}_0\{I_v^h\} - \sin^2 \varphi \mathcal{S}_0\{I_v^e\} + \frac{\cos 2\varphi}{\rho} \mathcal{S}_1\left\{\frac{I_v^h - I_v^e}{k_\rho}\right\} \quad (91)$$

$$G_{xy}^{HM}(\rho; z|z') = G_{yx}^{HM}(\rho; z|z') = -\frac{\sin 2\varphi}{2} \mathcal{S}_0\{I_v^h - I_v^e\} + \frac{\sin 2\varphi}{\rho} \mathcal{S}_1\left\{\frac{I_v^h - I_v^e}{k_\rho}\right\} \quad (92)$$

$$G_{xz}^{HM}(\rho; z|z') = \frac{1}{jk_0 \eta_0 \mu'_z} \cos \varphi \mathcal{S}_1\{k_\rho I_i^h\} \quad (93)$$

$$G_{yx}^{HM}(\rho; z|z') = -\sin^2 \varphi \mathcal{S}_0\{I_v^h\} - \cos^2 \varphi \mathcal{S}_0\{I_v^e\} - \frac{\cos 2\varphi}{\rho} \mathcal{S}_1\left\{\frac{I_v^h - I_v^e}{k_\rho}\right\} \quad (94)$$

$$G_{yz}^{HM}(\rho; z|z') = \frac{1}{jk_0 \eta_0 \mu'_z} \sin \varphi \mathcal{S}_1\{k_\rho I_i^h\} \quad (95)$$

$$G_{zx}^{HM}(\rho; z|z') = \frac{1}{jk_0 \eta_0 \mu_z} \cos \varphi \mathcal{S}_1\{k_\rho V_i^h\} \quad (96)$$

¹⁸This follows from the recurrence relation $J_{n+1}(z) = (2n/z)J_n(z) - J_{n-1}(z)$ [38, p. 361].

$$G_{zy}^{HM}(\rho; z|z') = \frac{1}{jk_0\eta_0\mu_z} \sin \varphi \mathcal{S}_1\{k_\rho V_v^h\} \quad (97)$$

$$G_{zz}^{HM}(\rho; z|z') = -\frac{1}{k_0^2\eta_0^2\mu_z\mu'_z} \mathcal{S}_0\{k_\rho^2 V_i^h\} - \frac{1}{jk_0\eta_0\mu_z} \delta(\rho)\delta(z-z') \quad (98)$$

where $\eta_0 = \sqrt{\mu_0/\epsilon_0}$ denotes the intrinsic impedance of free space. Although these expressions are given for source points on the z axis, they are readily generalized by the substitutions $x \rightarrow (x-x')$, $y \rightarrow (y-y')$, and

$$\rho \rightarrow \varrho = \sqrt{(x-x')^2 + (y-y')^2}, \quad (99)$$

$$\varphi \rightarrow \phi = \arctan \frac{y-y'}{x-x'}$$

where the quadrant of the argument must be noted when the inverse tangent is evaluated.¹⁹ The new cylindrical coordinates (ϱ, ϕ) are illustrated in Fig. 8. It may be directly verified, using (38), that the resulting DGFs satisfy the reciprocity relations (10)–(12).²⁰

It will be instructive to briefly revisit the problem of Fig. 7 using the space-domain approach. In view of (55), the electric and magnetic fields in the half-space can be expressed as

$$\mathbf{E}(\mathbf{r}) = K \int_a^b d\rho' \int_{-\pi}^{\pi} d\varphi' \underline{\mathbf{G}}^{EM}(\rho - \rho'; z|z_1) \cdot \hat{\boldsymbol{\varphi}}' \quad (100)$$

$$\mathbf{H}(\mathbf{r}) = K \int_a^b d\rho' \int_{-\pi}^{\pi} d\varphi' \underline{\mathbf{G}}^{HM}(\rho - \rho'; z|z_1) \cdot \hat{\boldsymbol{\varphi}}' \quad (101)$$

where $\underline{\mathbf{G}}^{EM}$ and $\underline{\mathbf{G}}^{HM}$ are as given by (77)–(83) and (91)–(98), respectively. Note that the integrals above must be evaluated by numerical quadratures. These equations can provide an excellent check for the DGFs and the numerical procedures used to evaluate the Sommerfeld integrals, since the results must agree with those computed from the spectral-domain formulas (62)–(64) [43]. It is also possible to demonstrate analytically the equivalence between (100), (101) and (62)–(64); consider H_x , for example. From (101), we obtain

$$H_x(\mathbf{r}) = K \int_a^b d\rho' \int_{-\pi}^{\pi} d\varphi' [-\sin \varphi' G_{xx}^{HM}(\rho - \rho'; z|z_1) + \cos \varphi' G_{xy}^{HM}(\rho - \rho'; z|z_1)] \quad (102)$$

$$= 2\pi K \int_a^b d\rho' \int_{-\pi}^{\pi} d\varphi' \frac{1}{4\pi} [\sin \varphi' \mathcal{S}_0\{I_v^e + I_v^h\} - \sin(2\phi - \varphi') \mathcal{S}_2\{I_v^e - I_v^h\}]$$

¹⁹The intrinsic FORTRAN function ATAN2 does this automatically and returns a result in the range $(-\pi, \pi)$ [42, p. 178]. Note that under this transformation $\delta(\rho)\delta(z-z') \rightarrow \delta(\mathbf{r}-\mathbf{r}')$.

²⁰Note that $\phi \rightarrow \pi + \phi$ when the locations of the source and field points in Fig. 8 are swapped, whereas ϱ is unaffected.

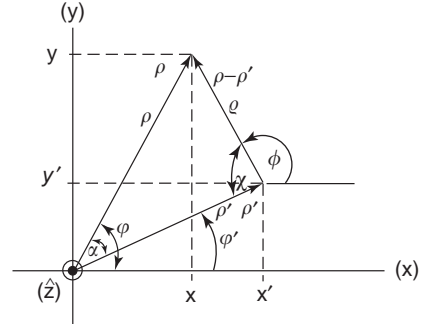


Figure 8. Cylindrical coordinates for off-axis source points.

where the Hankel transforms \mathcal{S}_0 and \mathcal{S}_2 are as given by (65) with ρ replaced by ϱ , and where we have omitted the arguments $(z|z_1)$ of the TLGFs for notational simplicity. Note that we have used (68) to simplify the second integral expression above. If we now change the order of the spatial and spectral integrals in the last equation, we obtain

$$H_x(\mathbf{r}) = 2\pi K \frac{1}{2\pi} \int_0^\infty dk_\rho k_\rho \int_a^b d\rho' \int_{-\pi}^{\pi} d\varphi' \times \frac{1}{4\pi} [\sin \varphi' J_0(k_\rho \varrho) \{I_v^e + I_v^h\} - \sin(2\phi - \varphi') J_2(k_\rho \varrho) \{I_v^e - I_v^h\}] \quad (103)$$

Next, we expand the Bessel functions in (103) using Graf's addition theorem [38, p. 363]

$$J_n(k_\rho \varrho) \begin{matrix} \cos \\ \sin \end{matrix} n\chi = \sum_{k=-\infty}^{\infty} J_k(k_\rho \rho) J_{n+k}(k_\rho \rho') \begin{matrix} \cos \\ \sin \end{matrix} k\alpha \quad (104)$$

where the angles $\chi = \pi - (\phi - \varphi')$ and $\alpha = (\phi - \varphi')$ are indicated in Fig. 8, which makes it possible to evaluate the spatial integrals in a closed form. As a result of the orthogonality of the trigonometric functions over the 2π range, many cancellations occur, leading to the remarkably simple final result

$$H_x(\mathbf{r}) = 2\pi K \sin \varphi \mathcal{S}_1 \left\{ \frac{\varpi(k_\rho)}{k_\rho} I_v^e(z|z_1) \right\} \quad (105)$$

where $\varpi(k_\rho)$ has been defined in (60). The other field components in (100), (101) can be transformed in a similar fashion, to arrive at (62)–(64).

The discussion above pertains to the general, 3D case. In 2D, where all field components have the form of (29), the space-domain DGFs can be obtained by applying the one-dimensional inverse transform (32) to (47)–(50), with k_y set to β and x replaced by $(x-x')$. Hence, the spectral integrals that arise in the 2D DGFs are ordinary Fourier transforms, rather than Sommerfeld integrals, with the

integrands expressed in terms of the TLGFs, exactly as in the 3D case [44].

We note that our Fourier representation of the DGFs is tantamount to a two-dimensional eigenfunction expansion in the transverse to z plane, with a closed-form solution in the z direction [45]. The appearance of the delta function terms in (76) and (98) is consistent with such “ z -propagating” eigenfunction representations [46–48].²¹ However, these terms do not represent the total source region singularity of the DGFs, since the remaining terms are still highly singular when $R = |\mathbf{r} - \mathbf{r}'| \rightarrow 0$ [50]. The level of these singularities is the same in layered media as in a homogeneous space (see the Appendix at the end of this article). In layered media, however, the DGFs are given in terms of the Sommerfeld integrals, and there is a direct relationship between the large- k_ρ divergence of the spectral integrands and the space-domain singularity, as discussed in the next section. It is found that in the source region $\underline{\mathbf{G}}^{EM}$ and $\underline{\mathbf{G}}^{HJ}$ behave as R^{-2} , while $\underline{\mathbf{G}}^{EJ}$ and $\underline{\mathbf{G}}^{HM}$ exhibit more severe R^{-3} singularities. Since such singularities are not generally integrable over a volume, special care has to be taken when the integrals (6), (7) are evaluated with $\mathbf{r} \in V$ [51]. The classical approach is to exclude from V an infinitesimal volume V_δ surrounding the field point [52–54], [12, p. 101]. The integral over $V - V_\delta$, which is referred to as the *principal value* (PV) integral, is then convergent, and the integral over V_δ gives rise to the so-called depolarization dyadic. Although both the PV integral and the depolarization dyadic depend on the shape of the exclusion volume, the sum of the two contributions is unique.²² The depolarization dyadic for several simple shapes, such as spherical, cubical, and cylindrical (with a needle shape and a disk as special cases), have been evaluated for both isotropic [54] and uniaxial [57] media.²³ An alternative approach is regularization, which uses the static form of the kernel to compensate for the singularity [59–62].

Still another way to “regularize” the integral representations with hypersingular DGF kernels is to convert them into the so-called mixed-potential forms, which express the fields in terms of the vector and scalar potentials [14,43,63–71]. Such potential representations, although not unique, have the advantage of being less singular (in space domain) and faster convergent (in spectral domain) than the field forms. The mixed-potential integral equations (MPIEs) have been frequently used in the analysis of antennas, printed-circuit boards, arbitrarily shaped scatterers, and other structures embedded in layered media.

²¹The occurrence of the Dirac deltas in $\underline{\mathbf{G}}^{EJ}$ and $\underline{\mathbf{G}}^{HM}$ indicates that these DGFs belong to the class of distributions (or generalized functions) [49, Chap. 1]. In the present context, a distribution may be defined as a function, which has meaning only when integrated against another, well-behaved function.

²²It should be mentioned here that in the special case of a uniform current and a cylindrical volume with the axis parallel to the direction of current flow, it is possible to evaluate the electric field inside the source region without invoking the concepts of exclusion volume or principal value [55,56].

²³It is interesting to note that the delta function terms in (76) and (98) give rise to depolarization dyadics corresponding to a disk-shaped exclusion volume perpendicular to the z axis [58].

Space limitations do not allow us to develop this important topic further here.

6.1. Comparison with Other Approaches

Before leaving this section, we wish to point out some salient features of the formulation presented here and to comment on other approaches. First, we note that the DGFs have been “scalarized”; that is, they are expressed in terms of the scalar Green functions of the transmission-line analog of the layered medium along the axis normal to the stratification [16,72–74]. The TLGFs are associated with the transverse field components, whose continuity at the media interfaces naturally translates into the continuity of the voltages and currents on the transmission-line network representation of the layered medium. As indicated in Fig. 1b, two transmission-line networks arise that represent the TM ($\alpha=e$) and TE ($\alpha=h$) partial fields. However, since the TM and TE networks have identical configurations and differ only in the propagation constants and characteristic impedances, it suffices to work out the solution for just one of them. The advantage of the TL representation is that it enhances the engineering insight and is amenable to the familiar network analysis techniques. By using these techniques, the TLGFs for any number of layers can easily be found, as discussed in the next section. Hence, the DGF expressions (69)–(98) are general, applicable to arbitrary source configurations and any number of layers. They are also in a convenient “ready to use” form, which cannot be further simplified—except, possibly, by invoking (68).²⁴

The transmission-line analogue employed here is based on the transverse field components and it treats the longitudinal components as dependent variables [4, p. 745]. However, it is also possible to scalarize the Maxwell equations in layered media by taking the longitudinal field components, (E_z, H_z) , as the independent variables (or “wave potentials”), from which the transverse components are derived [75–77]. A closely related approach is based on the longitudinal components of either the magnetic and electric vector potentials (A_z, F_z) , or the Hertz vectors (Π_x, Π_z) [29,78, p. 242; 79–82]. Although such representations achieve the TM-TE decomposition of the fields, they do not naturally lead to transmission-line equivalent circuits, because the chosen wave potentials are not continuous across the boundaries between dissimilar media. Perhaps to overcome this drawback, a formulation based on the longitudinal components of the electric and magnetic displacement vectors (D_z, B_z) has also been introduced [83].

Some authors have adopted Sommerfeld’s original approach [40,84,85], based on the horizontal and vertical components of the Hertz vector (Π_x, Π_z) ²⁵ [88–91]. However, the extension of this method, or its variant based on

²⁴However, using \mathcal{S}_2 to simplify equations does not necessarily lead to a more efficient formulation, because J_2 is usually computed from J_0 and J_1 .

²⁵It has been realized that Sommerfeld’s choice of Hertz potentials is nonunique, and that one could also use, for example, (Π_x, Π_y) [86,87](86), (87).

(A_x, A_z), to multilayered media is cumbersome, because the chosen wave potentials are coupled in the boundary conditions at the interfaces [55,92–96].

Another approach is based on the eigenfunction expansion of the DGFs in terms of vector wavefunctions [39, Chap. 11]. This method, although elegant and historically important, leads to representations that require much processing to render them tractable [89,97,98].

Still another formalism begins with a 3D Fourier transform representation of the DGF for a homogeneous medium [99, p. 38; 100–105]. The integration over the spectral variable associated with the z direction is then performed in closed form by the calculus of residues [12, p. 823]. This results in a 2D Fourier representation, which makes evident the TM and TE dyadic components and is suitable for application of the “scattering superposition method,” in which the spectral representation of the primary, whole-space DGF is augmented by homogeneous solutions, to account for the presence of the stratified medium. The augmented terms constitute upward- and downward-propagating waves, with coefficients that obey certain recurrence relations, which are determined by imposing the continuity of the transverse DGF components at the media interfaces. Finally, in the 3D case, the resulting two-dimensional spectral integrals are converted to Sommerfeld integrals.

In conclusion, the alternative techniques do not appear to offer any substantial advantages over the method espoused here.

7. TRANSMISSION-LINE ANALYSIS FOR PIECEWISE HOMOGENEOUS MEDIA

Although the theory presented thus far is applicable to media with parameters that have arbitrarily z dependence, only for a very few special media profiles can the transmission-line solution be found in an analytical closed form [106]. Therefore, we next focus attention on a multilayered medium with piecewise constant parameters, as illustrated in Fig. 1a, which is the most important and most frequently encountered case in practice. The transmission-line equivalent circuit now consists of a tandem connection of uniform transmission-line sections, where section n , with terminals at z_n and z_{n+1} , has propagation constant k_{zn}^z and characteristic impedance Z_n^z , as illustrated in Fig. 1b.

In this section, we first analyze the situation where there are no sources on the TL network, except possibly at infinity. This case is important in its own right, and it prepares the ground for the derivation of the TLGFs, which is presented next. We close with a brief discussion of the asymptotic behavior of the TLGFs.

7.1. Source-Free Case

The voltage and current on the n th TL section, which is assumed to be source-free, satisfy the homogeneous forms

of the transmission-line equations (24), which lead to

$$\begin{pmatrix} \frac{d^2}{dz^2} + k_{zn}^2 \\ I_n(z) \end{pmatrix} \begin{pmatrix} V_n(z) \\ I_n(z) \end{pmatrix} = 0, \quad I_n(z) = -\frac{1}{jk_{zn}Z_n} \frac{d}{dz} V_n(z) \quad (106)$$

Hence, choosing $e^{\pm jk_{zn}z}$ as the fundamental solutions, we may write²⁶

$$\begin{bmatrix} V_n(z) \\ Z_n I_n(z) \end{bmatrix} = \underbrace{V_n^+ e^{-jk_{zn}(z-z_n)}}_{V_n^+(z)} \pm \underbrace{V_n^- e^{jk_{zn}(z-z_n)}}_{V_n^-(z)} \quad (107)$$

where $V_n^+(z)$ and $V_n^-(z)$ represent the forward- and backward-propagating voltage waves, respectively, and where V_n^+ and V_n^- are as yet undetermined complex coefficients. The plus/minus signs between the forward and backward waves correspond, respectively, to the upper/lower terms on the left side of the equation. Note that, for later convenience, we use $(z - z_n)$, rather than just z , in the exponents. Thus, the phase reference point for the traveling waves has been arbitrarily selected at the left terminals of the TL section. An exception must be made if section 1 in Fig. 1b is of infinite extent; in this case, we move the phase reference to the right terminals—specifically we use z_2 in place of z_1 in (107).

We can also express (107) as

$$\begin{bmatrix} V_n(z) \\ Z_n I_n(z) \end{bmatrix} = V_n^+(z) [1 \pm \vec{\Gamma}_n(z)] \quad (108)$$

where

$$\vec{\Gamma}_n(z) = \frac{V_n^-(z)}{V_n^+(z)} \quad (109)$$

is the right-looking voltage reflection coefficient at z on the n th TL section. If we also define the right-looking impedance at z as

$$\vec{Z}_n(z) = \frac{V_n(z)}{I_n(z)} = Z_n \frac{1 + \vec{\Gamma}_n(z)}{1 - \vec{\Gamma}_n(z)} \quad (110)$$

where the second equality follows from (108), we obtain

$$\vec{\Gamma}_n(z) = \frac{\vec{Z}_n(z) - Z_n}{\vec{Z}_n(z) + Z_n} \quad (111)$$

Hence, the reflection coefficient at any location may be computed from the impedance, and vice versa. From (109)

²⁶The present choice of fundamental solutions leads to a traveling-wave representation of the voltages and currents. Another possible choice, $\sin(k_{zn}z)$ and $\cos(k_{zn}z)$, leads to a standing-wave representation [4, p. 203].

and (107), it follows that

$$\vec{\Gamma}_n(z_n) = \vec{\Gamma}_n e^{-j2\theta_n} \quad (112)$$

where

$$\theta_n = k_{zn} d_n, \quad d_n = z_{n+1} - z_n \quad (113)$$

and where $\vec{\Gamma}_n \equiv \vec{\Gamma}_n(z_{n+1})$. It should be noted that the terminal reflection coefficients shown above are evaluated on the inner sides of the TL section. This distinction is important, because unlike the impedances, the reflection coefficients are discontinuous across the TL terminals.²⁷ Using (110)–(112) and applying fact that $Z_n(z_{n+1}) \equiv Z_n = Z_{n+1}(z_{n+1})$, it is readily found that the right-looking reflection coefficients satisfy the recurrence relation

$$\vec{\Gamma}_n = \frac{\Gamma_{n+1,n} + \vec{\Gamma}_{n+1} e^{-j2\theta_{n+1}}}{1 + \Gamma_{n+1,n} \vec{\Gamma}_{n+1} e^{-j2\theta_{n+1}}} \quad (114)$$

where

$$\Gamma_{i,j} = \frac{Z_i - Z_j}{Z_i + Z_j} \quad (115)$$

Note that $\Gamma_{i,j}$ is analogous to the Fresnel reflection coefficient across an interface between two half-spaces filled with media i and j , looking from medium j [107, p. 62]. The recursion (114) is applied beginning with the rightmost TL section and it proceeds backward, toward the left end. If the N th layer is of infinite extent, as in Fig. 1, then it is reflectionless, and the starting value is $\vec{\Gamma}_N = 0$.

Using the translation formula [112] in (108), we can express the latter as

$$\begin{bmatrix} V_n(z) \\ Z_n I_n(z) \end{bmatrix} = V_n^+ e^{-jk_{zn}(z-z_n)} [1 \pm \vec{\Gamma}_n e^{-j2k_{zn}(z_{n+1}-z)}] \quad (116)$$

For simplicity, the terminal voltages will be denoted as $V_n \equiv V_n(z_n)$ and $V_{n+1} \equiv V_n(z_{n+1})$. Using the upper equation (116), we can eliminate the coefficient V_n^+ in favor of V_n , which results in

$$\begin{bmatrix} V_n(z) \\ Z_n I_n(z) \end{bmatrix} = \frac{V_n e^{-jk_{zn}(z-z_n)}}{1 + \vec{\Gamma}_n e^{-j2\theta_n}} [1 \pm \vec{\Gamma}_n e^{-j2k_{zn}(z_{n+1}-z)}] \quad (117)$$

Hence, the voltage and current at any location within a source-free TL section can be computed from the voltage at the left terminals. Evaluating the upper equation (117) at $z = z_{n+1}$, we find the right-looking voltage transmission

²⁷The continuity of the impedances is a consequence of the continuity of the voltages and currents when the sources are absent.

coefficient across the n th TL section as

$$\vec{\tau}_n \equiv \frac{V_{n+1}}{V_n} = \frac{(1 + \vec{\Gamma}_n) e^{-j\theta_n}}{1 + \vec{\Gamma}_n e^{-j2\theta_n}} \quad (118)$$

This formalism is useful if the excitation is to the left of the n th TL section. If the sources are to the right of the n th section, (107) is still applicable, except that V_n^- now plays the role of the ‘‘incident wave.’’ Hence, we define the left-looking reflection coefficient

$$\overleftarrow{\Gamma}_n(z) = \frac{V_n^+(z)}{V_n^-(z)} = \frac{\overleftarrow{Z}_n(z) - Z_n}{\overleftarrow{Z}_n(z) + Z_n} \quad (119)$$

and the left-looking impedance²⁸

$$\overleftarrow{\Gamma}_n(z) = -\frac{V_n(z)}{I_n(z)} = Z_n \frac{1 + \overleftarrow{\Gamma}_n(z)}{1 - \overleftarrow{\Gamma}_n(z)} \quad (120)$$

and from (119) and (107), we obtain

$$\overleftarrow{\Gamma}_n(z_{n+1}) = \overleftarrow{\Gamma}_n e^{-j2\theta_n} \quad (121)$$

where $\overleftarrow{\Gamma}_n \equiv \overleftarrow{\Gamma}_n(z_n)$. Applying (119)–(121) and the fact that $\overleftarrow{Z}_n(z_n) \equiv \overleftarrow{Z}_n = \overleftarrow{Z}_{n-1}(z_n)$, we readily derive the recurrence relation

$$\overleftarrow{\Gamma}_n = \frac{\Gamma_{n-1,n} + \overleftarrow{\Gamma}_{n-1} e^{-j2\theta_{n-1}}}{1 + \Gamma_{n-1,n} \overleftarrow{\Gamma}_{n-1} e^{-j2\theta_{n-1}}} \quad (122)$$

From this recursion, the left-looking reflection coefficients can be computed by the same procedure as that used for the right-looking coefficients, except now we begin in section 1 and progress forward, toward the right end of the TL network. The starting value, $\overleftarrow{\Gamma}_1$, is easily found. For example, if the first layer is backed by a plate with surface impedance Z_s , as illustrated in Fig. 1, then

$$\overleftarrow{\Gamma}_1 = \frac{Z_s - Z_1}{Z_s + Z_1} \quad (123)$$

which becomes -1 if the plate is PEC, and $+1$ if it is PMC. For a good, but not perfect, electrical conductor of conductivity σ , Z_s can be found as

$$Z_s = \frac{1+j}{\sigma\delta}, \quad \delta = \sqrt{\frac{2}{\omega\mu_0\sigma}} \quad (124)$$

where δ is the skin depth (not to be confused with the Dirac delta) [12, p. 201; [108]].

²⁸The minus sign arises because we maintain the positive- z direction as the reference direction for the current.

Using the translation formula [121] in (107), the latter can be expressed as

$$\begin{bmatrix} V_n(z) \\ -Z_n I_n(z) \end{bmatrix} = V_n^- e^{jk_{zn}(z-z_n)} [1 \pm \overleftarrow{\Gamma}_n e^{-j2k_{zn}(z-z_n)}] \quad (125)$$

where the coefficient V_n^- can be eliminated in favor of V_{n+1} , resulting in

$$\begin{bmatrix} V_n(z) \\ -Z_n I_n(z) \end{bmatrix} = \frac{V_{n+1} e^{-jk_{zn}(z_{n+1}-z)}}{1 + \overleftarrow{\Gamma}_n e^{-j2\theta_n}} [1 \pm \overleftarrow{\Gamma}_n e^{-j2k_{zn}(z-z_n)}] \quad (126)$$

Hence, the voltage and current at any point z within a source-free TL section can also be computed from the voltage at the right terminals. Finally, evaluating (126) at $z = z_n$, we find the left-looking voltage transmission coefficient for section n as

$$\overleftarrow{\tau}_n \equiv \frac{V_n}{V_{n+1}} = \frac{(1 + \overleftarrow{\Gamma}_n) e^{-j\theta_n}}{1 + \overleftarrow{\Gamma}_n e^{-j2\theta_n}} \quad (127)$$

To illustrate the application of this formalism, consider a TL network corresponding to an unshielded multilayer excited in the upper half-space (layer N). Let the incident field be represented by a voltage wave with the amplitude V_N^- . The resulting total voltage and current in the top layer are given by (125) with $n = N$, where $\overleftarrow{\Gamma}_N$ represents the overall reflection coefficient looking into the stack from the upper half-space, which can be computed from (122). Note that the voltage at the left terminals of section N is

$$V_N = (1 + \overleftarrow{\Gamma}_N) V_N^- \quad (128)$$

In layer 1 there is no reflection; hence

$$V_1(z) = V_1^- e^{jk_{z1}(z-z_2)} \quad (129)$$

and $V_2 = V_1^-$. The overall transmission coefficient of the stack can now be found as

$$\begin{aligned} \overleftarrow{T} &= \frac{V_1^-}{V_N^-} = (1 + \overleftarrow{\Gamma}_N) \frac{V_2}{V_N^-}, \\ \frac{V_2}{V_N^-} &= \frac{V_2}{V_3} \frac{V_3}{V_4} \cdots \frac{V_{N-1}}{V_N^-} = \prod_{n=2}^{N-1} \overleftarrow{\tau}_n \end{aligned} \quad (130)$$

where it is understood that the product is equal to one if the lower limit exceeds the upper.

As another interesting application, consider an arbitrary distribution of electric and magnetic currents radiating near a planar interface between a uniaxial medium (layer 1) and an isotropic medium (layer 2). The issue is whether it is possible to adjust the uniaxial medium parameters so that there is no reflection at the interface for any frequency and any configuration of the sources. Since the fields of arbitrary sources in layered media are expressible as Sommerfeld integrals whose integrands

comprise both TM and TE TLGFs, these requirements will be satisfied if the TM and TE Fresnel reflection coefficients given in (115) vanish for all values of k_ρ , that is, if $\Gamma_{1,2}^e = 0$ and $\Gamma_{1,2}^h = 0$, and thus $Z_1^e = Z_2^e$ and $Z_1^h = Z_2^h$. In view of (25), (26), these conditions imply

$$\frac{1}{\varepsilon_1} \sqrt{k_0^2 \varepsilon_1 \mu_1 - \frac{\varepsilon_1}{\varepsilon_2} k_\rho^2} = \frac{1}{\varepsilon_2} \sqrt{k_0^2 \varepsilon_2 \mu_2 - k_\rho^2} \quad (131)$$

and

$$\frac{1}{\mu_1} \sqrt{k_0^2 \varepsilon_1 \mu_1 - \frac{\mu_1}{\mu_2} k_\rho^2} = \frac{1}{\mu_2} \sqrt{k_0^2 \varepsilon_2 \mu_2 - k_\rho^2} \quad (132)$$

which will be simultaneously satisfied for all k_ρ if

$$\varepsilon_{z1} = \frac{\varepsilon_2^2}{\varepsilon_1}, \quad \mu_1 = \frac{\varepsilon_1 \mu_2}{\varepsilon_2}, \quad \mu_{z1} = \frac{\varepsilon_2 \mu_2}{\varepsilon_1} \quad (133)$$

where ε_1 may be selected arbitrarily. Hence, we may postulate a lossy medium with

$$\varepsilon_1 = \varepsilon_{r1} - j \frac{\sigma_1}{\omega \varepsilon_0} \quad (134)$$

where the dielectric constant ε_{r1} and conductivity σ_1 are arbitrary. It is interesting to note that, since ε_{z1} and μ_{z1} are inversely proportional to ε_1 , the resulting effective electric and magnetic conductivities along the optic axis are negative. Even though such media may be not realizable in practice, they have played an important role in the design of the so-called perfectly matched layers (PMLs) for reflectionless truncation of finite-difference and finite-element meshes [109–111]. Since such PMLs must be surrounded by impenetrable enclosures to be practical, let us consider the effect of terminating the perfectly absorbing medium characterized by (133), (134) with a PEC ground plane at a distance d_1 below the interface. The reflection coefficient looking into the uniaxial layer can be found using (122) with $n = 2$. Since in the present case $\Gamma_{1,2}^z = 0$ and $\overleftarrow{\Gamma}_1 = -1$, we obtain

$$\overleftarrow{\Gamma}_2^z = -e^{-j2k_{z1}d_1}, \quad k_{z1}^e = k_{z1}^h = \frac{\varepsilon_1}{\varepsilon_2} \sqrt{k_2^2 - k_\rho^2} \quad (135)$$

Using (134) here and making the substitutions $k_\rho = k_2 \sin \vartheta$, the reflectivity of this PML is found as²⁹

$$R^z(\theta) = e^{-4\eta_2 \sigma_1 d_1 \cos \vartheta} \quad (136)$$

where it is assumed that k_2 , η_2 (the intrinsic impedance of medium 2) and ϑ are real-valued. Here, ϑ can be interpreted as the angle of incidence, measured from the interface normal, of the continuous spectrum of plane waves representing the field radiated by the finite sources. We note that the reflectivity, which is the same for the TM and TE waves, can be made arbitrarily small by properly

²⁹Reflectivity is defined as the magnitude-squared reflection coefficient.

choosing the product $\sigma_1 d_1$. However, this PML works best for normal incidence and loses its effectiveness for waves incident at grazing angles ($\vartheta = 90^\circ$) and for evanescent waves (in which case ϑ is complex-valued [112, p. 231]).

For completeness, we also mention two alternative methods that have been extensively used in multilayer analysis [113–116]. The first is based on the relationship [3, p. 44; 12, p. 192]

$$\begin{bmatrix} V_n \\ I_n \end{bmatrix} = \begin{bmatrix} \cos \theta_n & jZ_n \sin \theta_n \\ \frac{j}{Z_n} \sin \theta_n & \cos \theta_n \end{bmatrix} \begin{bmatrix} V_{n+1} \\ I_{n+1} \end{bmatrix} \quad (137)$$

which can be derived from (107) by eliminating the traveling-wave coefficients V_n^\pm in favor of the terminal voltages and currents. The matrix in (137) is unimodular, that is, it has a unity determinant.³⁰ This property can be exploited in the analysis of periodic multilayers [117, p. 60], which have many important applications, such as gain-enhancing superstrates for microstrip antennas [118], or multilayer reflective coatings for EUV lithography [119]. The second method is based on the formula [12, p. 189; 120]

$$\begin{aligned} \begin{bmatrix} V_n^+ \\ V_n^- \end{bmatrix} &= \frac{1}{T_{n-1,n}} \begin{bmatrix} 1 & \Gamma_{n-1,n} \\ \Gamma_{n-1,n} & 1 \end{bmatrix} \begin{bmatrix} e^{-j\theta_{n-1}} & 0 \\ 0 & e^{+j\theta_{n-1}} \end{bmatrix} \\ &\times \begin{bmatrix} V_{n-1}^+ \\ V_{n-1}^- \end{bmatrix} \equiv Q_{n-1} \begin{bmatrix} V_{n-1}^+ \\ V_{n-1}^- \end{bmatrix} \end{aligned} \quad (138)$$

where $T_{i,j} = 1 + \Gamma_{i,j}$ is the Fresnel transmission coefficient from medium j to medium i . This equation can also be derived from (107), this time by eliminating the terminal voltages and currents in favor of the traveling-wave coefficients in adjacent layers. If layer 1 is of infinite extent, (138) is used with $\theta_1 = 0$.

Both matrix methods outlined above are useful in computation of the guided-wave poles of a multilayer, which correspond to the source-free solutions of the Maxwell equations, or waveguide modes. We will illustrate this for the second method, assuming an N -layer stack, as illustrated in Fig. 1. In this case, a repeated application of (138) leads to the relationship

$$\begin{aligned} \begin{bmatrix} V_N^+ \\ V_N^- \end{bmatrix} &= Q_{N-1} Q_{N-2} \cdots Q_1 \begin{bmatrix} V_1^+ \\ V_1^- \end{bmatrix} \\ &\equiv \begin{bmatrix} q_{11} & q_{12} \\ q_{21} & q_{22} \end{bmatrix} \begin{bmatrix} V_1^+ \\ V_1^- \end{bmatrix} \end{aligned} \quad (139)$$

which links the amplitudes of the forward- and backward-propagating voltage waves in the top and bottom layers. If layer 1 is shielded from below, the positive- and negative-propagating wave amplitudes can be expressed as $V_1^\pm = \frac{1}{2}(V_1 \pm Z_1 I_1)$, with the total voltage and current at

z_1 constrained by the impedance boundary condition $V_1 = -Z_0 I_1$. In layer N , assuming a stack open above, there should be no backward-propagating wave, thus $V_N^- = 0$. Using these constraints in (139), we obtain

$$\begin{bmatrix} 1 & (q_{11} \overleftarrow{\Gamma}_1 + q_{12}) \\ 0 & (q_{21} \overleftarrow{\Gamma}_1 + q_{22}) \end{bmatrix} \begin{bmatrix} V_N^+ \\ I_1 \end{bmatrix} = 0 \quad (140)$$

with $\overleftarrow{\Gamma}_1$ given by (123). Nontrivial solutions to this homogeneous system only exist for those values of k_ρ , which make the determinant vanish. This leads to the modal dispersion relation

$$q_{21} \overleftarrow{\Gamma}_1 + q_{22} = 0 \quad (141)$$

which also includes the cases of PEC backing ($\overleftarrow{\Gamma}_1 = -1$), PMC backing ($\overleftarrow{\Gamma}_1 = +1$), and no backing ($\overleftarrow{\Gamma}_1 = 0$). The zeros of (141) in the complex k_ρ plane determine the propagation constants of the guided-wave modes of the multilayer and are also the poles of the spectral integrands appearing in (69)–(98) [121,122]. A similar dispersion relation can be derived for a multilayer shielded from above.

The advantage of the matrix formulations is that they lead to analytic modal dispersion functions, which are amenable to the root finding methods based on Cauchy's theorem [123,124]. However, they are not well suited for use in the DGFs, because of the occurrence of growing exponentials when $k_\rho \rightarrow \infty$, which may cause numerical overflows in a computer implementation [6,125].

Finally, we mention that it is also possible to develop explicit recursive relationships between the coefficients of the forward- and backward-propagating waves in different layers, without using the matrix technique [13, p. 49; 126].

7.2. Source-Excited Case

Consider next a source-excited TL section n , as illustrated in Fig. 9, where $\overleftarrow{\Gamma}_n$ and $\overrightarrow{\Gamma}_n$ are the voltage reflection coefficients and Z_n and \overline{Z}_n are the total impedances, looking out of the left and right terminals, respectively. It will suffice to treat in detail only the current excitation case; the solution for the voltage source will follow by duality.

First, we note that the Sturm–Liouville theory of Section 4 can be directly applied to this problem. The homogeneous solutions satisfying the boundary conditions at the left and right terminals of TL section n have already been constructed in (125) and (116). Hence, we can choose

$$\overleftarrow{V}_n(z) = e^{jk_{zn}(z-z_n)} [1 + \overleftarrow{\Gamma}_n e^{-j2k_{zn}(z-z_n)}] \quad (142)$$

$$\overrightarrow{V}_n(z) = e^{-jk_{zn}(z-z_n)} [1 + \overrightarrow{\Gamma}_n e^{-j2k_{zn}(z_{n+1}-z)}] \quad (143)$$

The corresponding conjunct is readily found as

$$-\mathcal{P}W(\overleftarrow{V}_n, \overrightarrow{V}_n) = \frac{2}{Z_n} D_n \quad (144)$$

³⁰This matrix is sometimes referred to as the *ABCD matrix*.

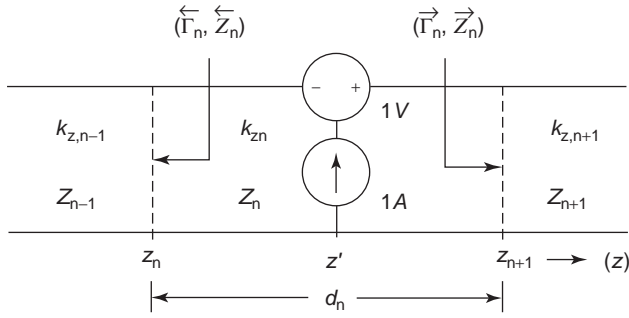


Figure 9. Voltage and current sources in a transmission-line section.

where we have introduced the notation

$$D_n = 1 - \overleftarrow{\Gamma}_n \overrightarrow{\Gamma}_n e^{-j2\theta_n} \quad (145)$$

Using these equations in (43), we finally obtain

$$V_i(z|z') = \frac{Z_n}{2D_n} \overleftarrow{V}_n(z_<) \overrightarrow{V}_n(z_>) \quad (146)$$

and $I_i(z|z')$ then follows from (40). However, this product form of solution can be cumbersome when used in the DGFs, where it may be necessary to combine terms arising from different TLGFs. Therefore, we derive below a more convenient TLGF form, which also offers more physical insight.

Assume at first that the TL section in Fig. 9 is either of infinite extent, or is matched at both ends, so that there are no reflections. Let this TL be driven by a unit-strength current generator at z' . Note that the voltage V_i must be continuous at the source location z' and must have the form of outgoing waves. Furthermore, the current source is in effect loaded by two impedances Z_n connected in parallel. Hence, the solution must have the form [4, p. 206]

$$V_i(z|z') = \frac{Z_n}{2} e^{-jk_{zn}|z-z'|}, \quad I_i(z|z') = \pm \frac{1}{2} e^{-jk_{zn}|z-z'|} \quad (147)$$

where the upper and lower signs correspond to $z > z'$ and $z < z'$, respectively. Next, to account for the presence of the terminations, as in Fig. 9, we augment the particular solution given above by a homogeneous solution, as follows

$$V_i(z|z') = \frac{Z_n}{2} (e^{-jk_{zn}|z-z'|} + A_n e^{-jk_{zn}z} + B_n e^{jk_{zn}z}) \quad (148)$$

$$I_i(z|z') = \frac{1}{2} (\pm e^{-jk_{zn}|z-z'|} + A_n e^{-jk_{zn}z} - B_n e^{jk_{zn}z}) \quad (149)$$

where the coefficients A_n and B_n can be found by enforcing the boundary conditions (42). This last step is straightforward, and we omit the details.³¹ Substituting the so-obtained coefficients A_n and B_n back into (148), (149) completes the solution procedure. The final result can be

³¹Note that we are in effect using the scattering superposition method at the transmission-line level.

expressed compactly as

$$V_i(z|z') = \frac{Z_n}{2} \left[e^{-jk_{zn}|z-z'|} + \frac{1}{D_n} \sum_{s=1}^4 R_n^{(s)} e^{-jk_{zn}\zeta_n^{(s)}} \right] \quad (150)$$

$$I_i(z|z') = \frac{1}{2} \left[\pm e^{-jk_{zn}|z-z'|} - \frac{1}{D_n} \sum_{s=1}^4 (-1)^s R_n^{(s)} e^{-jk_{zn}\zeta_n^{(s)}} \right] \quad (151)$$

where we have introduced the notation

$$R_n^{(1)} = \overleftarrow{\Gamma}_n, \quad \zeta_n^{(1)} = (z + z') - 2z_n, \quad (152)$$

$$R_n^{(2)} = \overrightarrow{\Gamma}_n, \quad \zeta_n^{(2)} = 2z_{n+1} - (z + z'), \quad (153)$$

$$R_n^{(3)} = \overleftarrow{\Gamma}_n \overrightarrow{\Gamma}_n, \quad \zeta_n^{(3)} = 2d_n + (z - z'), \quad (154)$$

$$R_n^{(4)} = \overleftarrow{\Gamma}_n \overrightarrow{\Gamma}_n, \quad \zeta_n^{(4)} = 2d_n - (z - z'), \quad (155)$$

Of course, Eqs. (146) and (150) are equivalent, and the former can be directly manipulated into the form of the latter.

The TLGF representation (150), (151) can be given an interesting ray (geometric optical) interpretation [127], as illustrated in Fig. 10. Hence, the first terms in the brackets represent the direct ray between the source and the field point (ray 0), whereas the second terms represent four categories of rays that undergo partial reflections at the upper and lower slab boundaries before reaching the observation point (rays 1 through 4). This ray interpretation is more evident if the inverse of the “resonant denominator” D_n is expanded as [127]

$$\frac{1}{D_n} = \sum_{k=0}^K \Omega^k + \frac{\Omega^{K+1}}{1 - \Omega}, \quad \Omega = \overleftarrow{\Gamma}_n \overrightarrow{\Gamma}_n e^{-j2\theta_n} \quad (156)$$

With finite K , this formula leads to a hybrid ray modal representation, whereas for $K \rightarrow \infty$, it gives a pure ray representation. However, the simple ray picture shown in Fig. 10 obtains for only a single layer, and it becomes unwieldy in a multilayer geometry [127].

The remaining TLGFs, I_v and V_v , are governed by equations (34), which are dual to equations (33) satisfied by V_i and I_i . Hence, the expressions for I_v and V_v can be obtained from those for V_i and I_i , respectively, by simply replacing the characteristic impedances by admittances, and

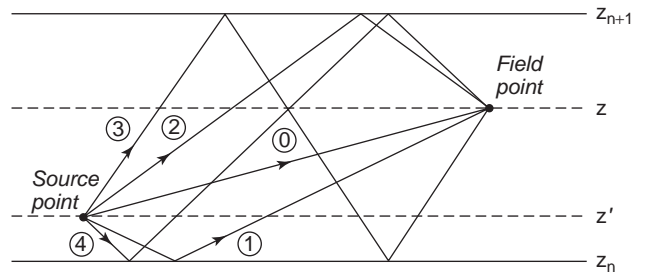


Figure 10. Ray interpretation of the TLGFs.

vice versa, which has also the effect of changing the signs of the reflection coefficients. We should mention here the important fact that all TLGFs can be derived from either V_i or I_v [4, p. 194]. For, suppose we have found V_i , as given by (150) above. Then, I_i follows from the first equation in (33), which in turn implies knowledge of V_v , in view of the last reciprocity relation in (38). Finally, V_v determines I_v via the first equation in (34). Thus, all the required information is contained in V_i ; an alternative statement applies to I_v . Because, as is evident from (18), (19), the E_z and H_z field components are specified by, respectively, the current on the TM transmission line and the voltage on the TE transmission line, it is convenient to use V_v^e and V_i^h as the basic TLGFs.³² As we show later in this section, I_v^e and V_i^h are also the least singular of all the TLGFs on conversion to the space domain.

Although the formulas given above assume observation points within the source TL section, they can easily be extended to arbitrary observation points outside section n , by using the results derived earlier for the source-free case. Hence, if z is within section $m < n$, we use the source section formulas to compute the voltage V_n at the left terminals of section n , and then invoke (126) with $n = m$ and

$$V_{m+1} = V_n \prod_{k=m+1}^{n-1} \overleftarrow{\tau}_k \quad (157)$$

Similarly, if z is within section $m > n$, we compute the voltage V_{n+1} at the right terminals of the source section, and then use (117) with $n = m$ and

$$V_m = V_{n+1} \prod_{k=n+1}^{m-1} \overrightarrow{\tau}_k \quad (158)$$

We note that it would suffice to implement only one of these cases and to handle the other case by using the reciprocity relations (38). However, if both cases are implemented, the reciprocity relations can provide a useful check of the formulation and the computer program.

The formulation adopted here easily specializes to the case where the source or observation layer is a half-space, and thus either the left- or right-looking reflection coefficient becomes zero; one simply omits the terms involving the vanishing reflection coefficients. Also, an important feature of this formulation is that all exponentials that occur are nongrowing as $k_\rho \rightarrow \infty$, which greatly reduces the danger of overflows in the computation of Sommerfeld integrals (see Section 8).

Finally, an important property of the TLGFs should be mentioned, which also has important consequences for the evaluation of the Sommerfeld integrals. Namely, the TLGFs are even functions of k_{zn} , if n corresponds to a finite-thickness layer. This can be directly confirmed by noting that (150), (151) are unaffected by the replacement $k_{zn} \rightarrow -k_{zn}$, which also causes the replacements $Z_n \rightarrow -Z_n$,

³²Some authors [45] prefer to express I_v^e in terms of the *current* reflection coefficients, which are just the negatives of the voltage reflection coefficients used here.

$\overleftarrow{\Gamma}_n \rightarrow 1/\overleftarrow{\Gamma}_n$, and $\overrightarrow{\Gamma}_n \rightarrow 1/\overrightarrow{\Gamma}_n$. Hence, the choice of the square-root branch in k_{zn} is arbitrary, which means that there are no branchpoints in the k_ρ plane associated with any of the finite layers [13, p. 112]. However, this observation applies only to the full TLGFs, including the direct-ray terms.

7.3. Asymptotic Behavior

It is important to understand the asymptotic, large- k_ρ behavior of the TLGFs, because it affects the convergence of the Sommerfeld integrals and determines the source-region singularity of the DGFs in the space domain.³³ This knowledge is needed, for example, in extrapolation methods [128], or to extract the quasistatic parts from the spectral kernels, both as a measure to accelerate the Sommerfeld integrals and to isolate the singular parts of the kernels [80, p. 36; 129]. As is evident from (150), (151), the TLGFs decay exponentially as $k_\rho \rightarrow \infty$, unless $z = z'$, which represents the worst-case situation. We therefore focus attention on the case where z lies within the source layer. The large- k_ρ quasistatic forms of V_i^z and I_i^z are readily found from (150) and (151) by expanding the inverse resonant denominator in the geometric series (156) and replacing the reflection coefficients by their asymptotic values. Each term of the series then represents a quasistatic image of the source in the lower or upper interface. Hence, keeping only the direct components and two dominant image terms, we find that, as $k_\rho \rightarrow \infty$

$$V_i^z \sim \frac{Z_n^z}{2} \left[e^{-jk_{zn}^z |z-z'|} + \chi_{n-1,n}^z e^{-jk_{zn}^z \zeta_n^{(1)}} + \chi_{n+1,n}^z e^{-jk_{zn}^z \zeta_n^{(2)}} \right] \quad (159)$$

$$I_i^z \sim \frac{1}{2} \left[\pm e^{-jk_{zn}^z |z-z'|} + \chi_{n-1,n}^z e^{-jk_{zn}^z \zeta_n^{(1)}} - \chi_{n+1,n}^z e^{-jk_{zn}^z \zeta_n^{(2)}} \right] \quad (160)$$

where we have used the asymptotic forms

$$\Gamma_{i,j}^e \sim \chi_{i,j}^e = -\frac{\kappa_i^e - \kappa_j^e}{\kappa_i^e + \kappa_j^e}, \quad \kappa_n^e = \sqrt{\epsilon_n \epsilon_{zn}} \quad (161)$$

$$\Gamma_{i,j}^h \sim \chi_{i,j}^h = \frac{\kappa_i^h - \kappa_j^h}{\kappa_i^h + \kappa_j^h}, \quad \kappa_n^h = \sqrt{\mu_n \mu_{zn}} \quad (162)$$

which follow from (115) on noting that the characteristic impedances (26) behave as

$$Z_n^e \sim \frac{k_\rho}{j\omega\epsilon_0\kappa_n^e}, \quad Z_n^h \sim \frac{j\omega\mu_0\kappa_n^h}{k_\rho} \quad (163)$$

The asymptotic behavior of I_v^z and V_v^z can be deduced from (159) and (160) by invoking duality, as explained earlier. We summarize these findings in Table 2, where we also indicate the small- R behavior of the corresponding

³³This follows from the final value theorem for Fourier transforms [12, p. 826]. It can be seen from [25] that the case $k_\rho \rightarrow \infty$ corresponds to $\omega \rightarrow 0$, that is, the static case. If the $k_\rho \rightarrow \infty$ limit is applied only to the reflection coefficients, the resulting expressions are referred to as the *quasistatic forms*.

Table 2. Worst-Case Asymptotic Behavior of Transmission-Line Green Functions and Corresponding Spatial-Domain Singularities

TL Green Function	Asymptotic Behavior	Space-Domain Singularity
$V_{i,v}^e, I_v^h$	$\mathcal{O}(k_\rho^{+1})$	$\mathcal{O}(R^{-3})$
$V_{v,i}^e, I_i^h, V_{v,i}^h, I_v^e$	$\mathcal{O}(k_\rho^0)$	$\mathcal{O}(R^{-2})$
$V_{i,v}^h, I_v^e$	$\mathcal{O}(k_\rho^{-1})$	$\mathcal{O}(R^{-1})$

Sommerfeld integrals.³⁴ By referring to this table, one can easily ascertain the asymptotic behavior of the spectral integrands, as well as the source region singularities of the DGF components (69)–(98). It should be noted that not only can singularities arise as a result of the direct ray [the first terms in brackets in (159), (160)]; one of the dominant images (the second and third terms) can also give rise to a singularity when z and z' are both on the same interface between adjacent layers.

8. SPECTRAL INTEGRALS AND THEIR COMPUTATION

Consider the formula [131, p. 455]

$$\mathcal{S}_0 \left\{ \frac{e^{-jk_z^z |z|}}{2jk_z^z} \right\} = v^\alpha \frac{e^{-jkr^\alpha}}{4\pi r^\alpha}, \quad r^\alpha = \sqrt{v^\alpha \rho^2 + z^2} \quad (164)$$

which is the Sommerfeld identity [40] extended to uniaxial media. From (164), another important identity can be derived [132, p. 164; 133, p. 428; 134, p. 264]:

$$\mathcal{S}_1 \left\{ \frac{e^{-jk_z^z |z|}}{2jk_z^z k_\rho} \right\} = \frac{e^{-jk|z|} - e^{-jkr^\alpha}}{4\pi jk\rho} \quad (165)$$

In the case of infinite, homogeneous media, these identities and their derivatives can be used to obtain closed-form expressions for the Sommerfeld integrals that arise in (69)–(98) [133, p. 376; 135; 136, p. 136]. We include the resulting whole-space DGFs in the Appendix. In layered media, however, such closed forms do not exist and one must resort to numerical quadrature.

The spectral integrands appearing in (69)–(98) are in general multivalued, as a result of the branchpoints introduced by the square-root definition of k_{zn}^z [137, p. 238]. However, as pointed out earlier, these integrands are even functions of the k_{zn}^z corresponding to finite layers,³⁵ and thus the only branchpoints that appear are those associated with the half-space media. If the multilayer is sandwiched between two isotropic half-spaces (which represent the substrate and cladding in optical applications), the branchpoints occur at $\pm k_1$ and $\pm k_N$, and the complex k_ρ plane consists of four overlying Riemann sheets (or two sheets, if the multilayer is shielded on one side, or if the media of the substrate and cladding are the same, i.e., $k_1 = k_N$), joined at the branchcuts emanating from the

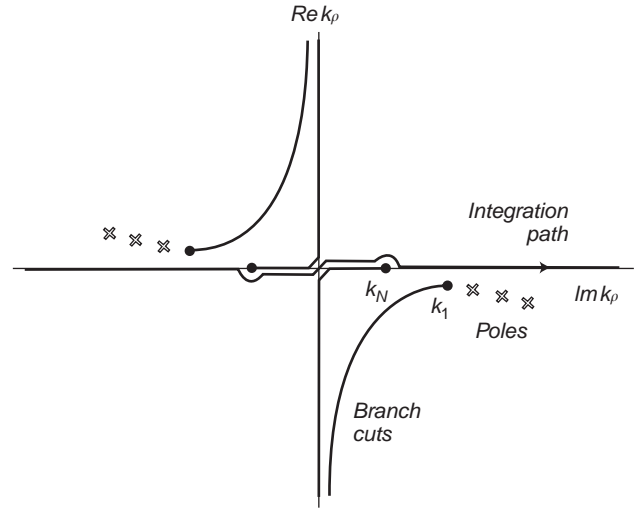


Figure 11. Integration path in the complex k_ρ plane.

branchpoints [13, p. 66; 85, p. 56; 137, p. 241]. Although the exact shape of these cuts is arbitrary, it is often convenient to specify them by the condition $\mathcal{I}m(k_{zn}^z) = 0$, which ensures that $\mathcal{I}m(k_{zn}^z)$ is of the same sign everywhere on a given sheet.³⁶ It is then customary to define the “proper” (also referred to as the “top” or “upper”) sheet as the one for which $-\pi < \arg\{k_{zn}^z\} \leq 0$. The spectral integrands also in general exhibit pole singularities in the complex k_ρ plane, contributed by the zeros of the resonant denominator and/or the reflection coefficients appearing in the TLGFs. For the layered medium geometry of Fig. 1, the poles can be found as the roots of the dispersion relation (141), as explained in the previous section. If the condition $-\pi < \arg\{k_{zN}^z\} \leq 0$ is imposed in the cladding, the roots of (141) are the proper poles, which are located on the top Riemann sheet and correspond to the bound modes of the structure. Otherwise, they are the “leaky-wave poles” located on the lower sheet [113].

The integration paths in the integrals (65) must be properly indented around the poles and branchpoints and must approach infinity on the proper Riemann sheet, to ensure that the fields are bounded as $z \rightarrow \pm \infty$ [105, 138]. An example path satisfying these requirements, referred to as the *Sommerfeld integration path* (SIP), is illustrated in Fig. 11, where only the right half of the path applies to the first integral form in (65). Note that the poles and branchpoints occur in pairs in the second and fourth quadrants of the k_ρ plane [4, p. 465].³⁷ In the limit of vanishing losses, all singular points move to the real axis. The Hankel function in the second integral in (65) introduces a logarithmic branchpoint [139] at the origin (not shown), and the path of integration must be indented around it into the

³⁶The so-defined branchcuts are referred to as the *Sommerfeld*, or *fundamental*, branchcuts.

³⁷Figure 11 corresponds to the situation where the media filling the lower and upper half-spaces are lossy and lossless, respectively. In the $e^{-i\omega t}$ convention, the singular points are complex conjugates of those shown here. Also, the SIP and the branchcuts are reflected in the real axis and $H_n^{(1)}$ replaces $H_n^{(2)}$ in [65] [4, p. 466].

³⁴The “big oh” symbol means “order of magnitude” [130, p. 9].

³⁵Provided that the whole-space terms are not extracted.

lower half of the k_ρ plane, which is emphasized in the notation by writing the lower integration limit as $\infty e^{-j\pi}$. If the SIP is used to compute the Sommerfeld integrals, the pole and branchpoint singularities that occur nearby must be avoided or, preferably, extracted and handled analytically [41,83, p. 161; 140–143]. Since the Bessel and Hankel functions are oscillatory on the real axis and the integrands are divergent, the integration is inefficient, unless extrapolation techniques (sequence accelerators) are employed. One proven and effective procedure is the “integration then summation” method [128,144–146]. In this approach, the Gauss–Kronrod or Patterson quadrature [147] is applied between consecutive zeros of the Bessel function and the resulting sequence of partial sums is accelerated by one of the extrapolation methods [148,149].

The integration may be more efficient if the SIP is deformed to another path, on which the integrand is rapidly convergent [41,88,150,151]. The contour deformation, which is based on Cauchy’s integral theorem [1, p. 294], is performed in a way, such that the conditions of Jordan’s lemma [12, p. 823; 139] are satisfied and no contribution results from any part of the path of integration at infinity. The residues of the poles “captured” by the deformation, as well as contributions from any branchcuts “swept” in this process, must be properly accounted for [152–155]. If the integration contour is restricted to the proper Riemann sheet, the pole contributions represent the guided-wave modes (or “discrete spectrum”) of the multilayer, and the branchcut integrals represent the radiation modes (“continuous spectrum”) [13, p. 333]. Near the surface of a layered medium, the latter assume the characteristics of “lateral waves” that propagate along the top and bottom interfaces [3, p. 484]. If the multilayer is shielded from below and above, the branchcuts are absent, but an infinite number of poles appear on the top (and, in this case, only) sheet. Hence, the spectrum is purely discrete, and the Sommerfeld integrals can be converted into series of pole residues [156].

One particularly attractive integration contour is the steepest-descent path (SDP), on which the integrand is most rapidly convergent [3, p. 462; 13, p. 107; 152,157]. However, this contour veers into a lower Riemann sheet, and thus there is a possibility of capturing some improper poles during the path deformation. The contribution from these leaky-wave poles, as well as any captured proper poles and branchcuts, must not be overlooked. In fact, the difficulty of tracking the location of these singularities vis-à-vis the SDP is a major obstacle in the practical implementation of the SDP integration. The SDP, which passes through the saddle point, also directly leads to the asymptotic techniques for the approximate evaluation of the integrals [4, Chap. 4; 13, p. 106]. These approximations are often performed in the complex angular spectrum plane, which is related to the k_ρ plane by $k_\rho = k_1 \sin w$ or $k_\rho = k_N \sin w$ [3, Sect. 15–7; 4, p. 541; 130, Sect. 1–7; 137, p. 241]. Either of these transformations “unfolds” one pair of branchcuts in the k_ρ plane and maps the associated two Riemann sheets onto a single sheet in the w plane. Another interesting transformation has been proposed, which unfolds all four sheets of the Riemann surface [158].

Other techniques that should be mentioned are the fast Hankel transform (FHT) method³⁸ [159,160] and the discrete complex image method (DCIM) [161–165]. In the FHT method the Sommerfeld integral is converted to a discrete convolution by a logarithmic transformation of the variables and the approximation of the transformed integrand [i.e., the $\tilde{f}(k_\rho)$ function in (65)] as a sum of sinc functions. This convolution has a form of a linear digital filter, which processes the “input function” [i.e., $\tilde{f}(k_\rho)$] to produce the “output function,” namely, the Sommerfeld integral. The coefficients of digital filters of various lengths, corresponding to Hankel transforms of orders 0 and 1, have been computed and are available in the literature [166,167]. The FHT method is effective only when there are no singularities near the real axis, as in the case of highly lossy media, or these singularities can be extracted and handled analytically. Also, the integrand envelope must be strictly decreasing as $k_\rho \rightarrow \infty$.

The basic idea of the DCIM is to approximate the spectral kernel on a suitable path in the complex k_ρ plane by a sum of complex exponentials, using an established system identification procedure [168], and then to use an identity, such as (164), to evaluate the Sommerfeld integrals in closed form.³⁹ The lateral range of applicability of DCIM is limited, unless the guided-wave poles are extracted from the integrands prior to the exponential fit. More recently, a related technique has been proposed, based on rational, rather than exponential, function fitting, which does not suffer from this limitation [169].

A remarkable property of both the FHT method and the DCIM is that no numerical integration is required and no evaluation of Bessel (or Hankel) functions is involved. As a result, these techniques are much faster than the most efficient numerical quadrature methods. However, they also share a significant drawback that they have no built-in convergence measures, and thus the accuracy of the result is usually difficult to ascertain.

Before any of the techniques discussed here is applied, a recommended and sometimes necessary practice is to improve the convergence of the Sommerfeld integrals by the subtraction of the large- k_ρ , quasi-static terms, which have closed-form space-domain counterparts [34,170]. The added benefit of this procedure is that it helps identify and isolate the singular parts of the space-domain Green functions. In the important special case where the source and observation points are on the same interface in a multilayer medium, the Sommerfeld integrals can be accelerated by the extraction of the half-space portion of the integrand, which makes the remainder exponentially convergent [171,172]. The extracted half-space part can be efficiently evaluated by SDP integration [152].

It should also be pointed out that the techniques described here are in practice usually applied to Sommerfeld integrals associated with electromagnetic potentials, rather than fields [41,129,173]. Since fields are related to potentials through differential operators, the potential forms

³⁸Also known as the “linear digital filter method.”

³⁹The layered media Green functions computed this way are often referred to, somewhat inappropriately, as “closed-form Green’s functions.”

are less singular (in spatial domain) and more rapidly convergent (in spectral domain), and thus more tractable, than the field forms. If repeated evaluation of Sommerfeld integrals is required, as is the case when integral equation techniques are used for objects in layered media, a viable alternative to the “on demand” computation is interpolation from a grid of precomputed and tabulated values [88,138,150,174]. The interpolation is in general over the three-dimensional (ρ, z, z') space. However, if the source and observation points are within the same layer, only two-dimensional interpolation is required, because, as is evident from (150), (151), the DGFs can always be split into parts that depend on either $(\rho, z - z')$ or $(\rho, z + z')$.

In the 2D case, the spectral integrals have the form of (32), where the integration can be limited to the positive real k_x axis, with the exponential function replaced by $-2j \sin(k_x x)$ or $2 \cos(k_x x)$, depending on whether the integrand \tilde{f}_{2D} is even or odd in k_x , respectively. Most of the techniques available for the Sommerfeld integrals can be adapted for this case. The singularities in the k_x plane are related to their k_ρ -plane counterparts by the mapping $k_x = \pm \sqrt{k_\rho^2 - \beta^2}$, where the propagation constant β may be complex-valued. Hence, the location of the poles and branchpoints changes with β , which may require a corresponding deformation of the integration path [18,175]. Finally, we note that the 2D counterpart of the Sommerfeld identity (164) is

$$\frac{1}{2\pi} \int_{-\infty}^{\infty} \frac{e^{-jk_z^2 |z|}}{2jk_z^2} e^{-jk_x x} dk_x = \frac{\sqrt{v^2}}{4j} H_0^{(2)}(\gamma^2 \sqrt{v^2 x^2 + z^2}) \quad (166)$$

where $\gamma^2 = \sqrt{k^2 - \beta^2}/v^2$, with $-\pi < \arg\{\gamma^2\} \leq 0$ [176; 177, p. 48].

9. FAR-ZONE RADIATION FIELDS

In some important applications, such as antenna engineering, the far-zone (radiation) fields due to arbitrary source distributions in layered media are of interest. In this section we demonstrate that these fields can be easily computed using the formalism developed in the previous sections.

Hence, let (\mathbf{J}, \mathbf{M}) be known currents occupying a volume V anywhere in a layered medium, which is not shielded from above, as illustrated in Fig. 1a. We assume, for simplicity, that the medium of the upper half-space is isotropic. Let z_0 be a point on the z axis, such that the layered medium and the volume V are confined to the region $z \leq z_0$, as illustrated in Fig. 12. Our goal is to derive leading-order asymptotic expressions for the fields radiated by (\mathbf{J}, \mathbf{M}) , valid when the field point is far from V in the half-space region $z > z_0$.

It should be clear from (47)–(50) and the TLGFs derived in Section 7 that, in the region $z > z_0$, the spectral DGFs may be expressed as

$$\begin{aligned} \tilde{\mathbf{G}}^{PQ}(\mathbf{k}_\rho; z|z') &= \tilde{\mathbf{G}}^{PQ}(\mathbf{k}_\rho; z_0|z') e^{-jk_{zN}(z-z_0)}, \\ k_{zN} &= \sqrt{k_N^2 - k_\rho^2} \end{aligned} \quad (167)$$

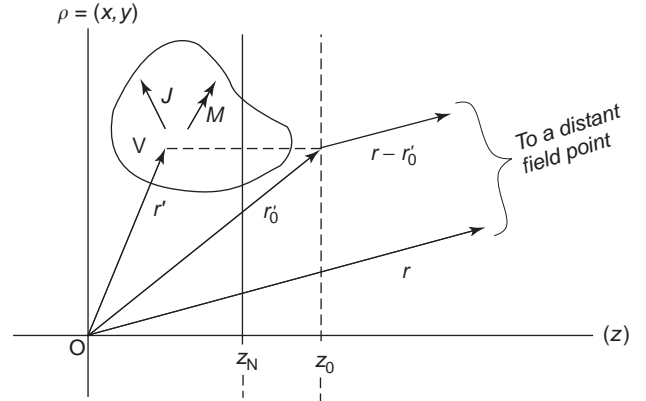


Figure 12. Geometry for the evaluation of the far-zone field.

In view of (8)–(66), the space-domain counterpart of (167) may be written as [178, Sect. 13]

$$\begin{aligned} \underline{\underline{\mathbf{G}}}^{PQ}(\mathbf{r}|\mathbf{r}') &= \frac{1}{(2\pi)^2} \int_{-\infty}^{\infty} \int_{-\infty}^{\infty} 2jk_{zN} \tilde{\mathbf{G}}^{PQ}(\mathbf{k}_\rho; z_0|z') \\ &\times e^{j\mathbf{k}_\rho \cdot \mathbf{r}'_0} \left\{ \frac{e^{-j\mathbf{k} \cdot \mathbf{r}}}{2jk_{zN}} \right\} dk_x dk_y \end{aligned} \quad (168)$$

where we have introduced the notation

$$\mathbf{k} = \mathbf{k}_\rho + \hat{\mathbf{z}}k_{zN}, \quad \mathbf{r}'_0 = \rho' + \hat{\mathbf{z}}z_0 \quad (169)$$

The integrand in (168) has been factorized into a slowly varying part and a part, enclosed in curly braces, that varies rapidly as $r = |\mathbf{r}| \rightarrow \infty$.⁴⁰ The integrals of the form (168) are amenable to the stationary phase method, or its equivalent, the steepest descent method [3, p. 594; 4, p. 386]. The stationary phase point is given by the conditions

$$\frac{\partial}{\partial k_x}(\mathbf{k} \cdot \mathbf{r}) = 0, \quad \frac{\partial}{\partial k_y}(\mathbf{k} \cdot \mathbf{r}) = 0 \quad (170)$$

which yield the solution

$$k_x^s = k_N \frac{x}{r}, \quad k_y^s = k_N \frac{y}{r}, \quad k_{zN}^s = k_N \frac{z}{r} \quad (171)$$

where the superscript “s” has been introduced to distinguish the stationary phase point values. This result has a clear physical interpretation; the stationary phase point corresponds to a plane wave with its propagation vector \mathbf{k} pointing to the far-zone field point [179]. Hence, we can write

$$\mathbf{k}_\rho^s = k_N \sin \vartheta (\hat{\mathbf{x}} \cos \phi + \hat{\mathbf{y}} \sin \phi), \quad k_{zN}^s = k_N \cos \vartheta \quad (172)$$

where the spherical angles (ϑ, ϕ) specify the observation direction. If we now replace the slowly varying part of the integrand in (168) by its value at the stationary phase point and perform the spectral integration in cylindrical

⁴⁰The reason for arbitrarily including the denominator $2jk_{zN}$ in the rapidly varying part will become evident in due course.

coordinates, we arrive at

$$\underline{\underline{\mathbf{G}}}^{PQ}(\mathbf{r}|\mathbf{r}') \sim 2jk_{zN}^s \underline{\underline{\mathbf{G}}}^{PQ}(\mathbf{k}_\rho^s; z_0|z') e^{i\mathbf{k}_\rho^s \cdot \mathbf{r}'_0} \mathcal{S}_0 \left\{ \frac{e^{-jk_{zN}z}}{2jk_{zN}} \right\}, \quad (173)$$

$$r \rightarrow \infty$$

where \mathcal{S}_0 is the zero-order Hankel transform defined in (65). Finally, we invoke the Sommerfeld identity (164), to obtain

$$\underline{\underline{\mathbf{G}}}^{PQ}(\mathbf{r}|\mathbf{r}') \sim -\frac{e^{-jk_N r}}{2\pi j r} e^{ik_{zN}^s z_0} k_{zN}^s \underline{\underline{\mathbf{G}}}^{PQ}(\mathbf{k}_\rho^s; z_0|z') e^{i\mathbf{k}_\rho^s \cdot \rho'}, \quad (174)$$

$$r \rightarrow \infty$$

The far-zone electric field can now be computed from (6), with the DGFs transformed according to (174). Note that at the stationary phase point $\hat{\mathbf{u}} = \hat{\rho}$ and $\hat{\mathbf{v}} = \hat{\phi}$, where the directions of the unit vectors $\hat{\rho}$ and $\hat{\phi} = \hat{\mathbf{z}} \times \hat{\rho}$ are fixed by the observation angle φ . Furthermore, since there are no reflected waves for $z > z_0$, the spectral-domain DGFs can be simplified by using the transmission line relationships (33),(34). As a result, we obtain the far-zone electric field components as [180,181]

$$E_{\vartheta,\varphi} \sim \frac{e^{-jk_N r}}{2\pi j r} e^{ik_{zN}^s z_0} k_N \left[\left\langle \mathbf{f}_{\vartheta,\varphi}^{EJ} e^{i\mathbf{k}_\rho^s \cdot \rho'}; \mathbf{J} \right\rangle + \eta_N \left\langle \mathbf{f}_{\vartheta,\varphi}^{EM} e^{i\mathbf{k}_\rho^s \cdot \rho'}; \mathbf{M} \right\rangle \right], \quad (175)$$

$$r \rightarrow \infty$$

where

$$\mathbf{f}_{\vartheta}^{EJ} = V_i^e(z_0|z') \hat{\rho} - \frac{\eta_0^2 \mu_N}{\epsilon_z'} \sin \vartheta \cos \vartheta I_v^e(z_0|z') \hat{\mathbf{z}} \quad (176)$$

$$\mathbf{f}_{\varphi}^{EJ} = \cos \vartheta V_i^h(z_0|z') \hat{\phi} \quad (177)$$

$$\mathbf{f}_{\vartheta}^{EM} = \cos \vartheta I_v^e(z_0|z') \hat{\phi} \quad (178)$$

$$\mathbf{f}_{\varphi}^{EM} = -I_v^h(z_0|z') \hat{\rho} + \frac{\epsilon_N}{\eta_0^2 \mu_z'} \sin \vartheta \cos \vartheta V_i^h(z_0|z') \hat{\mathbf{z}} \quad (179)$$

It is understood here that the TLGFs, which can be computed as explained in Section 7, are evaluated with $k_\rho = k_\rho^s = k_N \sin \vartheta$. Finally, the far-zone magnetic field components corresponding to (175) can be found as [27, p. 133]

$$H_\varphi = \frac{E_\vartheta}{\eta_N}, \quad H_\vartheta = -\frac{E_\varphi}{\eta_N} \quad (180)$$

The simple far-zone approximations derived here are not applicable when the observation point approaches the surface of the multilayer. In that case, there are singularities near the stationary phase point and a modified saddle-point technique must be used [3, p. 461; 12, p. 830].

10. PLANE-WAVE EXCITED FIELDS

In this section we show how the transmission-line formalism can be used to compute the electromagnetic field in any layer of a multilayer stack with piecewise constant parameters, due to a plane wave incident in the upper half-space (layer N). We assume, for simplicity, that the medium of the top layer is isotropic. The direction of arrival of the plane wave is specified by the angles (ϑ_i, φ_i) , and its polarization by the angle ψ_i , as illustrated in Fig. 13. Hence, the propagation vector of this wave can be expressed as $\mathbf{k}^i = \mathbf{k}_\rho^i + \hat{\mathbf{z}} k_{zN}$, where

$$\mathbf{k}_\rho^i = k_N \sin \vartheta_i (\hat{\mathbf{x}} \cos \varphi_i + \hat{\mathbf{y}} \sin \varphi_i), \quad k_{zN} = k_N \cos \vartheta_i \quad (181)$$

and the electric field as

$$\mathbf{E}^i = E_0 [(\hat{\rho}_i \cos \vartheta_i + \hat{\mathbf{z}} \sin \vartheta_i) \cos \psi_i + \hat{\phi}_i \sin \psi_i] \times e^{jk_{zN}(z-z_N)} e^{-j\mathbf{k}_\rho^i \cdot \rho} \quad (182)$$

where E_0 is the specified field amplitude and z_N is the phase reference point, selected to coincide with the upper interface of the multilayer. Note that the directions of the unit vectors $\hat{\rho}_i$ and $\hat{\phi}_i$ are fixed by the angle φ_i , which specifies the plane of incidence. Our goal is to find the total field $(\mathbf{E}_n, \mathbf{H}_n)$ established at any point of any layer n , as a result of the plane wave (182) incident in the upper half-space.

For the fields to match at the interfaces, the dependence of $(\mathbf{E}_n, \mathbf{H}_n)$ on the transverse coordinates must be the same in all layers and must match that of the incident plane wave (182). Furthermore, both the incident field and the total field must satisfy the source-free forms of (16)–(19), with $\mathbf{k}_\rho = \mathbf{k}_\rho^i$. Consequently, the transmission-line analog of the layered medium developed in Section 7 may be employed to find $(\mathbf{E}_n, \mathbf{H}_n)$. With (22) in mind,

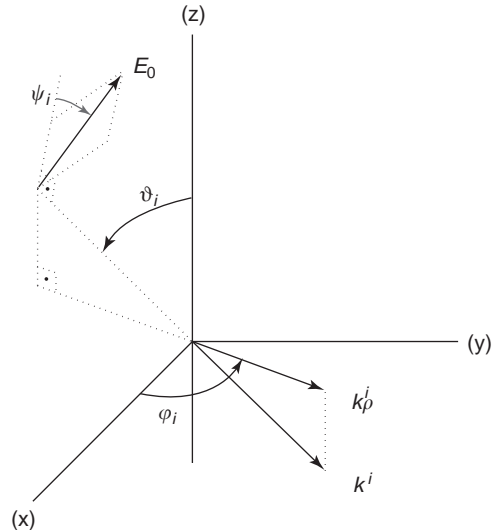


Figure 13. Geometry for the evaluation of the plane-wave incident field.

where now $(\tilde{\mathbf{u}}, \tilde{\mathbf{v}}) = (\hat{\rho}_i, \hat{\phi}_i)$, we express the transverse part of (182) as [180,181]

$$\mathbf{E}_i^e(\mathbf{r}) = [\hat{\rho}_i V_N^{e-}(z) + \hat{\phi}_i V_N^{h-}(z)] e^{-jk_\rho^i \cdot \rho} \quad (183)$$

where

$$\begin{aligned} V_N^{e-}(z) &= \underbrace{E_0 \cos \psi_i \cos \vartheta_i}_{V_N^{e-}} e^{jk_{zN}(z-z_N)}, \\ V_N^{h-}(z) &= \underbrace{E_0 \sin \psi_i}_{V_N^{h-}} e^{jk_{zN}(z-z_N)} \end{aligned} \quad (184)$$

We may interpret $V_N^{e-}(z)$ and $V_N^{h-}(z)$ are the leftward-propagating incident voltage waves exciting the TM and TE transmission line networks, respectively, in the TL section corresponding to the upper-half-space (layer N). In view of (27),(28), the total electric and magnetic fields in any layer n can be found as

$$\mathbf{E}_n(\mathbf{r}) = \left[\hat{\rho}_i V_n^e(z) + \hat{\phi}_i V_n^h(z) - \hat{\mathbf{z}} \frac{\eta_N^e \epsilon_N}{\epsilon_{zn}} \sin \vartheta_i I_n^e(z) \right] e^{-jk_\rho^i \cdot \rho} \quad (185)$$

$$\begin{aligned} \mathbf{H}_n(\mathbf{r}) &= \left[-\hat{\rho}_i I_n^h(z) + \hat{\phi}_i I_n^e(z) + \hat{\mathbf{z}} \frac{\mu_N}{\eta_N \mu_{zn}} \sin \vartheta_i V_n^h(z) \right] \\ &\times e^{-jk_\rho^i \cdot \rho} \end{aligned} \quad (186)$$

where $V_n^\alpha(z)$ and $I_n^\alpha(z)$, with $\alpha = (e, h)$, are the total voltage and current at a point z in layer n of the TL network. These voltages and currents can be found as explained in Section 7. Hence, in the upper layer they are given by (125), with $n = N$. In any other layer n , they can be found from (126), where

$$V_{n+1}^\alpha = V_N^{\alpha-} (1 + \overleftarrow{\Gamma}_N^\alpha) \prod_{k=n+1}^{N-1} \overleftarrow{\tau}_k^\alpha \quad (187)$$

with $V_N^{\alpha-}$ given in (184). Note that in deriving this equation, use has been made of (127) and (128). It is understood in the above that all transmission-line voltages and currents are evaluated with $k_\rho = k_\rho^i = k_N \sin \theta_i$.

With reference to Fig. 13, observe that the polarization of the incident plane wave is parallel for $\psi_i = 0$, and perpendicular for $\psi_i = \pi/2$. From (184) we see that the parallel- and perpendicularly polarized waves only excite the TM and TE transmission lines, respectively, and that both lines are excited by an arbitrarily polarized wave. In the case of normal incidence, the field is TEM and the plane of incidence, and thus also φ_i and ψ_i , are undefined. However, this situation may be treated as a limiting case of parallel or perpendicular polarization, as $\vartheta_i \rightarrow 0$.

11. SUMMARY AND CONCLUSION

A complete set of electric- and magnetic-type dyadic Green functions (DGFs) is derived for plane-stratified, multilay-

ered, uniaxial media, based on the transmission-line network analog along the axis normal to the stratification. The DGFs are expressed in terms of transmission-line Green functions (TLGFs), which are the voltages and currents on the transmission-line network excited by unit-strength voltage or current sources. A practical algorithm is given for the efficient computation of the TLGFs. Also, various state-of-the-art techniques for computation of the Sommerfeld integrals are reviewed. Finally, the transmission-line analog is applied to derive the far-zone fields and the plane-wave-excited fields in the layered medium. The unified formulation presented here is compact, convenient to implement, and computationally efficient. It also affords much insight into the layered medium Green functions, because the behavior of the transmission-line voltages and currents is well understood.

12. APPENDIX: WHOLE-SPACE DGFs

In this appendix we give closed forms of the whole-space, three-dimensional DGFs for a uniaxial medium with the parameters of layer n . These expressions have been obtained by retaining only the direct ray terms of the TLGFs (corresponding to ray 0 in Fig. 10) in (69)–(98) and using the identities (164),(165) and their derivatives to evaluate the resulting Sommerfeld integrals.⁴¹ Equivalent forms of these DGFs were derived previously [135] using a different approach.

First, to simplify the equations, we define

$$\Psi_n^\alpha = v_n^\alpha \frac{e^{-jk_n R_n^z}}{4\pi R_n^\alpha}, \quad D_n^\alpha = \frac{e^{-jk_n R_n^z}}{4\pi j k_n \varrho^2}, \quad (A.1)$$

$$R_n^\alpha = \sqrt{v_n^\alpha \varrho^2 + (z - z')^2}$$

$$S_n^\alpha = \frac{\varrho}{R_n^\alpha}, \quad C_n^\alpha = \frac{z - z'}{R_n^\alpha} \quad (A.2)$$

$$\Lambda_n^\alpha = \frac{j}{k_n R_n^\alpha} + \frac{1}{(k_n R_n^\alpha)^2}, \quad \Upsilon_n^\alpha = 1 - \frac{j}{k_n R_n^\alpha} \quad (A.3)$$

Using this notation, the whole-space terms of (69)–(76) can be written as

$$\begin{aligned} G_{xx}^{E,I}(\mathbf{r}|\mathbf{r}') &= -jk_n \eta_n \{ [(1 - \Lambda_n^e) + \cos^2 \phi v_n^e (S_n^e)^2 (3\Lambda_n^e - 1)] \Psi_n^e \\ &\quad - \sin^2 \phi (\Psi_n^e - \Psi_n^h) + \cos(2\phi) (D_n^e - D_n^h) \} \end{aligned} \quad (A.4)$$

⁴¹The delta function terms in [76] and [98] are canceled in this process; however, the z derivatives must be taken in the sense of distributions [182].

$$G_{xy}^{EJ}(\mathbf{r}|\mathbf{r}') = G_{yx}^{EJ}(\mathbf{r}|\mathbf{r}') = -jk_n\eta_n\{\sin\phi\cos\phi v_n^e(S_n^e)^2(3\Lambda_n^e - 1)\Psi_n^e + \sin\phi\cos\phi(\Psi_n^e - \Psi_n^h) + \sin(2\phi)(D_n^e - D_n^h)\} \quad (\text{A.5})$$

$$G_{yy}^{EJ}(\mathbf{r}|\mathbf{r}') = -jk_n\eta_n\{[(1 - \Lambda_n^e) + \sin^2\phi v_n^e(S_n^e)^2(3\Lambda_n^e - 1)]\Psi_n^e - \cos^2\phi(\Psi_n^e - \Psi_n^h) - \cos(2\phi)(D_n^e - D_n^h)\} \quad (\text{A.6})$$

$$G_{xz}^{EJ}(\mathbf{r}|\mathbf{r}') = G_{zx}^{EJ}(\mathbf{r}|\mathbf{r}') = -jk_n\eta_n\cos\phi S_n^e C_n^e \times (3\Lambda_n^e - 1)\Psi_n^e \quad (\text{A.7})$$

$$G_{yz}^{EJ}(\mathbf{r}|\mathbf{r}') = G_{zy}^{EJ}(\mathbf{r}|\mathbf{r}') = -jk_n\eta_n\sin\phi S_n^e C_n^e \times (3\Lambda_n^e - 1)\Psi_n^e \quad (\text{A.8})$$

$$G_{zz}^{EJ}(\mathbf{r}|\mathbf{r}') = -jk_n\eta_n[(1 - \Lambda_n^e) + (C_n^e)^2(3\Lambda_n^e - 1)]\frac{\Psi_n^e}{v_n^e} \quad (\text{A.9})$$

Similarly, the whole-space parts of (84)–(90) are found as

$$G_{xx}^{HJ}(\mathbf{r}|\mathbf{r}') = -G_{yy}^{HJ}(\mathbf{r}|\mathbf{r}') = jk_n[\sin\phi\cos\phi(C_n^e\Upsilon_n^e\Psi_n^e - C_n^h\Upsilon_n^h\Psi_n^h) + \sin(2\phi)(C_n^e D_n^e - C_n^h D_n^h)] \quad (\text{A.10})$$

$$G_{xy}^{HJ}(\mathbf{r}|\mathbf{r}') = jk_n[\sin^2\phi C_n^e\Upsilon_n^e\Psi_n^e + \cos^2\phi C_n^h\Upsilon_n^h\Psi_n^h - \cos(2\phi)(C_n^e D_n^e - C_n^h D_n^h)] \quad (\text{A.11})$$

$$G_{yx}^{HJ}(\mathbf{r}|\mathbf{r}') = -jk_n[\cos^2\phi C_n^e\Upsilon_n^e\Psi_n^e + \sin^2\phi C_n^h\Upsilon_n^h\Psi_n^h + \cos(2\phi)(C_n^e D_n^e - C_n^h D_n^h)] \quad (\text{A.12})$$

$$G_{xz}^{HJ}(\mathbf{r}|\mathbf{r}') = -jk_n\sin\phi S_n^e\Upsilon_n^e\Psi_n^e \quad (\text{A.13})$$

$$G_{zx}^{HJ}(\mathbf{r}|\mathbf{r}') = jk_n\sin\phi S_n^h\Upsilon_n^h\Psi_n^h \quad (\text{A.14})$$

$$G_{yz}^{HJ}(\mathbf{r}|\mathbf{r}') = jk_n\cos\phi S_n^e\Upsilon_n^e\Psi_n^e \quad (\text{A.15})$$

$$G_{zy}^{HJ}(\mathbf{r}|\mathbf{r}') = -jk_n\cos\phi S_n^h\Upsilon_n^h\Psi_n^h \quad (\text{A.16})$$

It is noted that the whole-space $\underline{\underline{G}}^{EJ}$ is symmetric. One also observes that considerable simplifications in both $\underline{\underline{G}}^{EJ}$ and $\underline{\underline{G}}^{HJ}$ occur for isotropic media, in which case $R_n^e = \bar{R}_n^h \equiv R$, $\Psi_n^e = \Psi_n^h$, $D_n^e = D_n^h$, $S_n^e = \rho/R \equiv \sin\Theta$ and $C_n^e = (z - z')/R \equiv \cos\Theta$. In particular, $\underline{\underline{G}}^{EJ}$ properly reduces to its isotropic form [2, p. 221] and $\underline{\underline{G}}^{HJ}$ becomes skew-symmetric (i.e., it is equal to the negative of its transpose, with zero diagonal).

In view of the duality between $\underline{\underline{G}}^{EJ}$ and $\underline{\underline{G}}^{HM}$, the whole-space components of the latter can be derived from by making the substitution of symbols $\varepsilon \rightarrow \mu$ and $\mu \rightarrow \varepsilon$, which also entails the superscript replacement $e \rightarrow h$ and $h \rightarrow e$. Finally, the components of the whole-space $\underline{\underline{G}}^{EM}$ can be obtained from (A.10)–(A.16) by using the recipro-

city relation (12), which in the present case (infinite, homogeneous medium) simplifies to $G_{ij}^{EM}(\mathbf{r}|\mathbf{r}') = G_{ji}^{HJ}(\mathbf{r}|\mathbf{r}')$, i.e., $\underline{\underline{G}}^{EM}$ is simply the transpose of $\underline{\underline{G}}^{HJ}$.

The above expressions make evident the source region singularities of the DGFs. Namely, $\underline{\underline{G}}^{EJ}$ and $\underline{\underline{G}}^{HM}$ behave as R^{-3} , and $\underline{\underline{G}}^{HJ}$ and $\underline{\underline{G}}^{EM}$ behave as R^{-2} , where R represents either R^e or R^h .

BIBLIOGRAPHY

1. J. A. Kong, *Electromagnetic Wave Theory*, 2nd ed., Wiley, New York, 1990.
2. J. Van Bladel, *Electromagnetic Fields*, Hemisphere, New York, 1985.
3. A. Ishimaru, *Electromagnetic Wave Propagation, Radiation, and Scattering*, Prentice-Hall, Englewood Cliffs, NJ, 1991.
4. L. B. Felsen and N. Marcuvitz, *Radiation and Scattering of Waves*, Prentice-Hall, Englewood Cliffs, NJ, 1973.
5. M. Paulus and O. J. F. Martin, Light propagation and scattering in stratified media: A Green's tensor approach, *J. Opt. Soc. Am. A* **18**:854–861 (April 2001).
6. M. Huang and L. C. Shen, Computation of induction logs in multiple-layer dipping formations, *IEEE Trans. Geosci. Remote Sens.* **27**:259–267 (May 1989).
7. C. H. Chan, Spectral Green's functions for a thin, circular, magnetic-current loop for microstrip via hole analysis, *Microwave Opt. Technol. Lett.* **2**:157–159 (May 1989).
8. D. Zheng and K. A. Michalski, Analysis of coaxially fed microstrip antennas of arbitrary shape with thick substrates, *J. Electromagn. Waves Appl.* **5**(12):1303–1327 (1991).
9. M. R. Abdul-Gaffoor, H. K. Smith, A. A. Kishk, and A. W. Glisson, Simple and efficient full-wave modeling of electromagnetic coupling in realistic RF multilayer PCB layouts, *IEEE Trans. Microwave Theory Tech.* **50**:1445–1457 (June 2002).
10. N. Kinayman, G. Dural, and M. I. Aksun, A numerically efficient technique for the analysis of slots in multilayer media, *IEEE Trans. Microwave Theory Tech.* **46**:430–432 (April 1998).
11. M. Javid and P. M. Brown, *Field Analysis and Electromagnetics*, McGraw-Hill, New York, 1963.
12. R. E. Collin, *Field Theory of Guided Waves*, 2nd ed., IEEE Press, New York, 1991.
13. W. C. Chew, *Waves and Fields in Inhomogeneous Media*, IEEE Press, New York, 1995.
14. K. A. Michalski and J. R. Mosig, Multilayered media Green's functions in integral equation formulations, *IEEE Trans. Antenn. Propag.* **45**:508–519 (March 1997) (invited review paper).
15. T. Itoh, Spectral-domain immittance approach for dispersion characteristics of generalized printed transmission lines, *IEEE Trans. Microwave Theory Tech.* **MTT-28**:733–736 (July 1980).
16. R. Kastner, E. Heyman, and A. Sabban, Spectral domain iterative analysis of single- and double-layered microstrip antennas using the conjugate gradient algorithm, *IEEE Trans. Antenn. Propag.* **36**:1204–1212 (Sept. 1988).
17. Y. T. Lo, S. M. Wright, and M. Davidovitz, Microstrip antennas, in K. Chang, ed., *Handbook of Microwave and Optical Components*, Wiley, New York, 1989, Vol. 1, Chap. 13.
18. K. A. Michalski and D. Zheng, Rigorous analysis of open microstrip lines of arbitrary cross section in bound and leaky

- regimes, *IEEE Trans. Microwave Theory Tech.* **37**:2005–2010 (Dec. 1989).
19. J. F. Kiang, S. M. Ali, and J. A. Kong, Integral equation solution to the guidance and leakage properties of coupled dielectric strip waveguides, *IEEE Trans. Microwave Theory Tech.* **38**:193–203 (Feb. 1990).
 20. N. Fáché, F. Olyslager, and D. De Zutter, *Electromagnetic and Circuit Modelling of Multiconductor Transmission Lines*, Clarendon Press, Oxford, 1993.
 21. M. Paulus and O. J. F. Martin, Green's tensor technique for scattering in two-dimensional stratified media, *Phys. Rev. E* **63**:066615 (2001).
 22. J. Bernal, F. Medina, and R. R. Boix, Full-wave analysis of nonplanar transmission lines on layered medium by means of MPIE and complex image theory, *IEEE Trans. Microwave Theory Tech.* **49**:177–185 (Jan. 2001).
 23. P. E. Mayes, *Electromagnetics for Engineers*, Dept. Electrical and Computer Eng., Univ. Illinois, Urbana, IL, 1965.
 24. W. L. Weeks, *Electromagnetic Theory for Engineering Applications*, Wiley, New York, 1964.
 25. D. G. Dudley, *Mathematical Foundations for Electromagnetic Theory*, IEEE Press, New York, 1994.
 26. G. W. Hanson and A. B. Yakovlev, *Operator Theory for Electromagnetics. An Introduction*, Springer-Verlag, New York, 2002.
 27. R. F. Harrington, *Time-Harmonic Electromagnetic Fields*, McGraw-Hill, New York, 1961.
 28. D. M. Pozar, Input impedance and mutual coupling of rectangular microstrip antennas, *IEEE Trans. Anten. Propag.* **AP-30**:1191–1196 (Nov. 1982).
 29. N. K. Das and D. M. Pozar, A generalized spectral-domain Green's function for multilayer dielectric substrates with application to multilayer transmission lines, *IEEE Trans. Microwave Theory Tech.* **MTT-35**:326–335 (March 1987).
 30. W. C. Chew and Q. Liu, Resonance frequency of a rectangular microstrip patch, *IEEE Trans. Anten. Propag.* **36**:1045–1056 (Aug. 1988).
 31. K. A. Michalski and D. Zheng, A spectral domain method for the analysis of the fundamental mode leakage effect in microstrip lines on uniaxial substrates, *Microwave Opt. Technol. Lett.* **4**:158–161 (March 1991).
 32. T.-S. Horng, W. E. McKinzie, and N. G. Alexopoulos, Full-wave spectral-domain analysis of compensation of microstrip discontinuities using triangular subdomain functions, *IEEE Trans. Microwave Theory Tech.* **40**:2137–2147 (Dec. 1992).
 33. T. Becks and I. Wolff, Analysis of 3-D metallization structures by a full-wave spectral domain technique, *IEEE Trans. Microwave Theory Tech.* **40**:2219–2227 (Dec. 1992).
 34. G. Plaza, F. Mesa, and F. Medina, Treatment of singularities and quasi-static terms in the EFIE analysis of planar structures, *IEEE Trans. Anten. Propag.* **50**:485–491 (April 2002).
 35. C. M. Butler, A. Q. Martin, and K. A. Michalski, Analysis of a cylindrical antenna in a circular aperture in a screen, *J. Electromagn. Waves Appl.* **8**(2):149–173 (1994).
 36. I. N. Sneddon, *Fourier Transforms*, McGraw-Hill, New York, 1951.
 37. G. Tyras, *Radiation and Propagation of Electromagnetic Waves*, Academic Press, New York, 1969.
 38. M. Abramowitz and I. A. Stegun, eds., *Handbook of Mathematical Functions*, Dover, New York, 1965.
 39. C. T. Tai, *Dyadic Green Functions in Electromagnetic Theory*, 2nd ed., IEEE Press, New York, 1994.
 40. A. Sommerfeld, Über die Ausbreitung der Wellen in der drahtlosen Telegraphie, *Ann. Phys.* **28**:665–736 (1909); **81**:1135–1153 (1926).
 41. M. Tsai, C. Chen, and N. G. Alexopoulos, Sommerfeld integrals in modeling interconnects and microstrip elements in multi-layered media, *Electromagnetics* **18**:267–288 (1998).
 42. M. Metcalf and J. Reid, *FORTTRAN 90/95 explained*, Oxford Univ. Press, Oxford, UK, 1996.
 43. P. Ylä-Oijala, M. Taskinen, and J. Sarvas, Multilayered media Green's functions for MPIE with general electric and magnetic sources by the Hertz potential approach, in J. A. Kong, ed., *Progress in Electromagnetics Research*, EMW Publ., Cambridge, MA; 2001, Vol. PIER 33, pp. 141–165.
 44. C.-I. G. Hsu, R. F. Harrington, K. A. Michalski, and D. Zheng, Analysis of a multiconductor transmission lines of arbitrary cross-section in multilayered uniaxial media, *IEEE Trans. Microwave Theory Tech.* **41**:70–78 (Jan. 1993).
 45. Y. Yamaguchi, H. Miyashita, and I. Chiba, A general method of construction for dyadic Green functions of plane-stratified media in uniform open or closed waveguides with separable cross sections, *Electron. Commun. Japan Pt. 1* **82**(1):31–42 (1999).
 46. C. Tai, Equivalent layers of surface charge, current sheet, and polarization in the eigenfunction expansion of Green's functions in electromagnetic theory, *IEEE Trans. Anten. Propag.* **AP-29**:733–739 (Sept. 1981).
 47. P. H. Pathak, On the eigenfunction expansion of electromagnetic dyadic Green's functions, *IEEE Trans. Anten. Propag.* **AP-31**:837–846 (Nov. 1983).
 48. K. A. Michalski, Missing boundary conditions of electromagnetics, *Electron. Lett.* **22**(17):921–922 (1986).
 49. J. Van Bladel, *Singular Electromagnetic Fields and Sources*, Clarendon Press, Oxford, 1991.
 50. W. A. Johnson, A. Q. Howard, and D. G. Dudley, On the irrotational component of the electric Green's dyadic, *Radio Sci.* **14**:961–967 (Nov.–Dec. 1979).
 51. W. S. Weiglhofer, Electromagnetic field in the source region: A review, *Electromagnetics* **19**:563–578 (1999).
 52. J. Van Bladel, Some remarks on Green's dyadic for infinite space, *IEEE Trans. Anten. Propag.* **AP-9**:563–566 (Nov. 1961).
 53. K. Chen, A simple physical picture of tensor Green's function in source region, *IEEE Proc.* **65**:1202–1204 (Aug. 1977).
 54. A. D. Yaghjian, Electric dyadic Green's functions in the source region, *IEEE Proc.* **68**:248–263 (Feb. 1980).
 55. P. Weidelt, Electromagnetic induction in three-dimensional structures, *J. Geophys.* **41**:85–109 (1975).
 56. R. C. Robertson, Computation of the electric field within a region of uniform current density, *Int. J. Electron.* **69**:707–716 (1990).
 57. W. S. Weiglhofer and A. Lakhtakia, New expressions for depolarization dyadics in uniaxial dielectric-magnetic media, *Int. J. Infrared Millim. Waves* **17**(8):1365–1376 (1996).
 58. W. C. Chew, Some observations on the spatial and eigenfunction representations of dyadic Green's functions, *IEEE Trans. Anten. Propag.* **37**:1322–1327 (Oct. 1989).
 59. J. G. Fikioris, Electromagnetic field inside a current-carrying region, *J. Math. Phys.* **6**:1617–1620 (Nov. 1965).
 60. S. W. Lee, J. Boersma, C. L. Law, and G. A. Deschamps, Singularity in Green's function and its numerical evaluation, *IEEE Trans. Anten. Propag.* **AP-28**:311–317 (May 1980).
 61. J. J. H. Wang, A unified and consistent view on the singularities of the dyadic Green's function in the source region, *IEEE Trans. Anten. Propag.* **AP-30**:463–468 (May 1982).

62. A. Lakhtakia and W. S. Weiglhofer, Time-harmonic electromagnetic field in a source region in a uniaxial dielectric-magnetic medium, *Int. J. Appl. Electromagn. Mech.* **8**:167–177 (1997).
63. K. A. Michalski, The mixed-potential electric field integral equation for objects in layered media, *Arch. Elek. Übertragung.* **39**:317–322 (Sept.–Oct. 1985).
64. K. A. Michalski and D. Zheng, Electromagnetic scattering and radiation by surfaces of arbitrary shape in layered media, Part I: Theory, *IEEE Trans. Anten. Propag.* **38**:335–344 (March 1990).
65. D. R. Wilton, Review of current status and trends in the use of integral equations in computational electromagnetics, *Electromagnetics* **12**:287–341 (July–Dec. 1992).
66. K. A. Michalski, Mixed-potential integral equation (MPIE) formulation for nonplanar microstrip structures of arbitrary shape in multilayered uniaxial media, *Int. J. Microwave Millim. Wave Comput. Aided Eng.* **3**(4):420–431 (1993) (invited article).
67. K. A. Michalski, Formulation of mixed-potential integral equations for arbitrarily shaped microstrip structures with uniaxial substrates, *J. Electromagn. Waves Appl.* **7**(7):899–917 (1993).
68. R. D. Cloux, G. P. J. F. M. Maas, and A. J. H. Wachtters, Quasi-static boundary element method for electromagnetic simulation of PCBs, *Philips J. Res.* **48**(1–2):117–144 (1994).
69. J. Sercu, N. Fiché, F. Libbrecht, and P. Lagasse, Mixed potential integral equation technique for hybrid microstrip-slotline multilayered circuits using a mixed rectangular-triangular mesh, *IEEE Trans. Microwave Theory Tech.* **43**:1162–1172 (May 1995).
70. R. Bunger and F. Arndt, Efficient MPIE approach for the analysis of three-dimensional microstrip structures in layered media, *IEEE Trans. Microwave Theory Tech.* **45**:1141–1153 (Aug. 1997).
71. M. Vrancken and G. A. E. Vandenbosch, Semantics of dyadic and mixed potential field representation for 3-D current distributions in planar stratified media, *IEEE Trans. Anten. Propag.* **51**:2778–2787 (Oct. 2003).
72. L. Vegni, R. Cicchetti, and P. Capece, Spectral dyadic Green's function formulation for planar integrated structures, *IEEE Trans. Anten. Propag.* **36**:1057–1065 (Aug. 1988).
73. P. Bernardi and R. Cicchetti, Dyadic Green's functions for conductor-backed layered structures excited by arbitrary tridimensional sources, *IEEE Trans. Microwave Theory Tech.* **42**:1474–1483 (Aug. 1994).
74. S.-G. Pan and I. Wolff, Scalarization of dyadic spectral Green's functions and network formalism for three-dimensional full-wave analysis of planar lines and antennas, *IEEE Trans. Microwave Theory Tech.* **42**:2118–2127 (Nov. 1994).
75. J. A. Kong, Antenna radiation in stratified media, in J. A. Kong, ed., *Research Topics in Electromagnetic Wave Theory*, Wiley, New York, 1981, pp. 211–234.
76. Y. S. Kwon and J. J. H. Wang, Computation of Hertzian dipole radiation in stratified uniaxial anisotropic media, *Radio Sci.* **21**:891–902 (Nov.–Dec. 1986).
77. W. C. Chew, J. S. Zhao, and T. J. Cui, The layered medium Green's function—a new look, *Microwave Opt. Technol. Lett.* **31**(4):252–255 (2001).
78. J. R. Wait, *Electromagnetic Wave Theory*, Harper & Row, New York, 1985.
79. P. E. Wannamaker, G. W. Hohmann, and W. A. SanFilipo, Electromagnetic modeling of three-dimensional bodies in layered earths using integral equations, *Geophysics* **49**:60–74 (Jan. 1984).
80. V. W. Hansen, *Numerical Solution of Antennas in Layered Media*, Research Studies Press, Taunton, UK, 1989.
81. S. Barkeshli and P. H. Pathak, On the dyadic Green's function for a planar multilayered dielectric/magnetic media, *IEEE Trans. Microwave Theory Tech.* **40**:128–142 (Jan. 1992).
82. S. Barkeshli, On the electromagnetic dyadic Green's functions for planar multi-layered anisotropic uniaxial material media, *Int. J. Infrared Millim. Waves* **13**(4):507–527 (1992).
83. A. K. Bhattacharyya, *Electromagnetic Fields in Multilayered Structures*, Artech House, Boston, 1994.
84. A. Sommerfeld, *Partial Differential Equations in Physics*, Academic Press, New York, 1949.
85. A. Baños, *Dipole Radiation in the Presence of a Conducting Half-Space*, Pergamon Press, New York, 1966.
86. A. Erteza and B. K. Park, Nonuniqueness of resolution of Hertz vector in presence of a boundary, and the horizontal dipole problem, *IEEE Trans. Anten. Propag.* **AP-17**:376–378 (May 1969).
87. K. A. Michalski, On the scalar potential of a point charge associated with a time-harmonic dipole in a layered medium, *IEEE Trans. Anten. Propag.* **AP-35**:1299–1301 (Nov. 1987).
88. G. J. Burke, E. K. Miller, J. N. Brittingham, D. L. Lager, R. J. Lytle, and J. T. Okada, Computer modeling of antennas near the ground, *Electromagnetics* **1**:29–49 (Jan.–March 1981).
89. R. R. Chance, A. Prock, and R. Silbey, Molecular fluorescence and energy transfer near interfaces, *Adv. Chem. Phys.* **37**:1–65 (1987).
90. M. A. Taubenblatt and T. K. Tran, Calculation of light scattering from particles and structures on a surface by the coupled-dipole method, *J. Opt. Soc. Am. A* **10**:912–919 (May 1993).
91. R. Schmehl, B. M. Nebeker, and E. D. Hirlleman, Discrete-dipole approximation for scattering by features on surfaces by means of a two-dimensional fast Fourier transform technique, *J. Opt. Soc. Am. A* **14**:3026–3036 (Nov. 1997).
92. J. R. Wait, Fields of a horizontal dipole over a stratified uniform half-space, *IEEE Trans. Anten. Propag.* **AP-14**:790–792 (Nov. 1966).
93. A. P. Raiche, An integral equation approach to three-dimensional modelling, *Geophys. J. Roy. Astrophys. Soc.* **36**:363–376 (1974).
94. C. H. Stoyer, Electromagnetic fields of dipoles in stratified media, *IEEE Trans. Anten. Propag.* **AP-25**:547–552 (July 1977).
95. J. S. Bagby and D. P. Nyquist, Dyadic Green's functions for integrated electronic and optical circuits waveguides, *IEEE Trans. Microwave Theory Tech.* **MTT-35**:206–210 (Feb. 1987).
96. Z. Xiong, Electromagnetic fields of electric dipoles embedded in a stratified anisotropic earth, *Geophysics* **54**:1643–1646 (Dec. 1989).
97. G. P. S. Cavalcante, D. A. Rogers, and A. J. Giarola, Analysis of electromagnetic wave propagation in multilayered media using dyadic Green's functions, *Radio Sci.* **17**:503–508 (May–June 1982).
98. D. H. S. Cheng, On the formulation of the dyadic Green's function in a layered medium, *Electromagnetics* **6**(2):171–182 (1986).
99. L. Tsang, J. A. Kong, and R. T. Shin, *Theory of Microwave Remote Sensing*, Wiley, New York, 1985.
100. L. Tsang, E. Njoku, and J. A. Kong, Microwave thermal emission from a stratified medium with nonuniform temperature distribution, *J. Appl. Phys.* **46**:5127–5133 (Dec. 1975).

101. S. M. Ali and S. F. Mahmoud, Electromagnetic fields of buried sources in stratified anisotropic media, *IEEE Trans. Anten. Propag.* **AP-27**:671–678 (Sept. 1979).
102. T. Sphicopoulos, V. Teodoridis, and F. E. Gardiol, Dyadic Green function for the electromagnetic field in multilayered isotropic media: An operator approach, *IEE Proc. H* **132**:329–334 (Aug. 1985).
103. J. E. Sipe, New Green-function formalism for surface optics, *J. Opt. Soc. Am. B* **4**:481–489 (April 1987).
104. E. W. Kolk, N. H. G. Baken, and H. Blok, Domain integral equation analysis of integrated optical channel and ridge waveguides in stratified media, *IEEE Trans. Microwave Theory Tech.* **38**:78–85 (Jan. 1990).
105. M. Paulus, P. Gay-Balmaz, and O. J. F. Martin, Accurate and efficient computation of the Green's tensor for stratified media, *Phys. Rev. E* **62**:5797–5807 (Oct. 2000).
106. L. Vegni, F. Bilotti, and A. Toscano, Microstrip disk antennas with inhomogeneous artificial dielectrics, *J. Electromagn. Waves Appl.* **14**:1203–1227 (2000).
107. P. Yeh, *Optical Waves in Layered Media*, Wiley, New York, 1988.
108. I. P. Theron and J. H. Cloete, On the surface impedance used to model the conductor losses of microstrip structures, *IEE Proc. Microwave Anten. Propag.* **142**:35–40 (Feb. 1995).
109. J. Berenger, Perfectly matched layer for the absorption of electromagnetic waves, *J. Comput. Phys.* **114**:185–200 (Oct. 1994).
110. Z. S. Sacks, D. M. Kingsland, R. Lee, and J. Lee, A perfectly matched anisotropic absorber for use as an absorbing boundary condition, *IEEE Trans. Anten. Propag.* **43**:1460–1463 (Dec. 1995).
111. S. D. Gedney and A. Taflove, Perfectly matched layer absorbing boundary conditions, in: A. Taflove and S. C. Hagness, eds., *Computational Electrodynamics: The Finite-Difference Time-Domain Method*, Artech House, Boston, 2000, pp. 285–348.
112. L. M. Brekhovskikh, *Waves in Layered Media*, 2nd ed., Academic Press, New York, 1980.
113. J. Chilwell and I. Hodgkinson, Thin-films field-transfer matrix theory of planar multilayer waveguides and reflection from prism-loaded waveguides, *J. Opt. Soc. Am. A* **1**:742–753 (July 1984).
114. L. M. Walpita, Solution for planar optical waveguide equations by selecting zero elements in a characteristic matrix, *J. Opt. Soc. Am. A* **2**:595–602 (April 1985).
115. Y. L. Chow, N. Hojjat, S. Safavi-Naeini, and R. Faraji-Dana, Spectral Green's functions for multilayer media in a convenient computational form, *IEE Proc. Microwave Anten. Propag.* **145**:85–91 (Feb. 1998).
116. L. Polerecky, J. Hamrle, and B. D. MacCraith, Theory of the radiation of dipoles placed within a multilayer system, *Appl. Opt.* **39**:3968–3977 (Aug. 2000).
117. M. Born and E. Wolf, *Principles of Optics. Electromagnetic Theory of Propagation, Interference and Diffraction of Light*, 7th ed., Cambridge Univ. Press, Cambridge, UK, 1999.
118. H. Y. Yang and N. G. Alexopoulos, Gain enhancement methods for printed circuit antennas through multiple superstrates, *IEEE Trans. Anten. Propag.* **AP-35**:860–863 (July 1987).
119. C. Montealm, B. T. Sullivan, H. Pépin, J. A. Dobrowolski, and M. Sutton, Extreme-ultraviolet Mo/Si multilayer mirrors deposited by radio-frequency-magnetron sputtering, *Appl. Opt.* **33**:2057–2068 (1994).
120. J. M. Vigoureux, Polynomial formulation of reflection and transmission by stratified planar structures, *J. Opt. Soc. Am. A* **8**:1697–1701 (Nov. 1991).
121. R. E. Smith, S. N. Houde-Walter, and G. W. Forbes, Mode determination for planar waveguides using the four-sheeted dispersion relation, *IEEE J. Quantum Electron.* **28**:1520–1526 (June 1992).
122. R. Rodriguez-Berral, F. Mesa, and F. Medina, Systematic and efficient root finder for computing the modal spectrum of planar layered waveguides, *Int. J. RF Microwave Comput. Aided Eng.* **14**:73–83 (Jan. 2004).
123. L. M. Delves and J. N. Lyness, A numerical method for locating the zeros of an analytic function, *Math. Comput.* **21**:543–560 (Oct. 1967).
124. T. Li, On locating all zeros of an analytic function within a bounded domain by a revised Delves/Lyness method, *SIAM J. Num. Anal.* **20**:865–871 (Aug. 1983).
125. N. Faché, J. Van Hesse, and D. De Zutter, Generalised space domain Green's dyadic for multilayered media with special application to microwave interconnections, *J. Electromagn. Waves Appl.* **3**(7):651–669 (1989).
126. W. C. Chew and S. Chen, Response of a point source embedded in a layered medium, *IEEE Anten. Wireless Propag. Lett.* **2**:254–258 (2003).
127. I. T. Lu, L. B. Felsen, and A. H. Kamel, Eigenreverberations, eigenmodes and hybrid combinations: A new approach to propagation in layered multiwave media, *Wave Motion* **6**:435–457 (May 1984).
128. K. A. Michalski, Extrapolation methods for Sommerfeld integral tails, *IEEE Trans. Anten. Propag.* **46**:1405–1418 (Oct. 1998) (invited review paper).
129. N. J. Champagne, J. T. Williams, and D. R. Wilton, Analysis of resistively loaded, printed spiral antennas, *Electromagnetics* **14**:363–395 (July–Dec. 1994).
130. R. Mittra and S. W. Lee, *Analytical Techniques in the Theory of Guided Waves*, Macmillan, New York, 1971.
131. E. Arbel and L. B. Felsen, Theory of radiation from sources in anisotropic media, Part 1: General sources in stratified media, in E. C. Jordan, ed., *Electromagnetic Theory and Antennas*, Part 1. Macmillan, New York, 1963, pp. 391–420.
132. P. C. Clemmow, *The Plane Wave Spectrum Representation of Electromagnetic Fields*, Pergamon Press, New York, 1966.
133. H. C. Chen, *Theory of Electromagnetic Fields. A Coordinate-Free Approach*, McGraw-Hill, New York, 1983.
134. J. R. Wait, *Geo-Electromagnetism*, Academic Press, New York, 1982.
135. W. S. Weiglhofer, Dyadic Green's functions for general uniaxial media, *IEE Proc. H* **137**:5–10 (Feb. 1990).
136. I. V. Lindell, *Methods for Electromagnetic Field Analysis*, Clarendon Press, Oxford, 1992.
137. A. Hessel, General characteristics of traveling-wave antennas, in R. E. Collin and F. J. Zucker, eds., *Antenna Theory—Part 2*, McGraw-Hill, New York, 1969, pp. 151–258.
138. P. Gay-Balmaz and J. R. Mosig, Three dimensional planar radiating structures in stratified media, *Int. J. Microwave Millim. Wave Comput. Aided Eng.* **7**:330–343 (Sept. 1997).
139. W. R. LePage, *Complex Variables and the Laplace Transform for Engineers*, Dover, New York, 1980.
140. N. K. Uzunoglu, N. G. Alexopoulos, and J. G. Fikioris, Radiation properties of microstrip dipoles, *IEEE Trans. Anten. Propag.* **AP-27**:853–858 (Nov. 1979).

141. J. R. Mosig and F. E. Gardiol, A dynamical radiation model for microstrip structures, in P. W. Hawkes, ed., *Advances in Electronics and Electron Physics*, Academic Press, New York, 1982, Vol. 59, pp. 139–237.
142. W. A. Johnson and D. G. Dudley, Real axis integration of Sommerfeld integrals: Source and observation points in air, *Radio Sci.* **18**:175–186 (March–April 1983).
143. V. Teodoridis, T. Spicopoulos, and F. Gardiol, The reflection from an open-ended rectangular waveguide terminated by a layered dielectric medium, *IEEE Trans. Microwave Theory Tech.* **MTT-33**:359–366 (May 1985).
144. A. D. Chave, Numerical integration of related Hankel transforms by quadrature and continued fraction expansion, *Geophysics* **48**:1671–1686 (Dec. 1983).
145. J. R. Mosig, Integral equation technique, in T. Itoh, ed., *Numerical Techniques for Microwave and Millimeter-Wave Passive Structures*, Wiley, New York, 1989, pp. 133–213.
146. S. K. Lucas and H. A. Stone, Evaluating infinite integrals involving Bessel functions of arbitrary order, *J. Comput. Appl. Math.* **64**:217–231 (1995).
147. G. Evans, *Practical Numerical Integration*, Wiley, New York, 1993.
148. H. H. Homeier, Scalar Levin-type sequence transformations, *J. Comput. Appl. Math.* **122**:81–147 (2000).
149. A. Sidi, *Practical Extrapolation Methods. Theory and Applications*, Cambridge Univ. Press, Cambridge, UK, 2003.
150. J. Chen, A. A. Kishk, and A. W. Glisson, A 3D interpolation method for the calculation of the Sommerfeld integrals to analyze dielectric resonators in a multilayered medium, *Electromagnetics* **20**(1):1–15 (2000).
151. J. R. Mosig and A. A. Melecón, Green's functions in lossy layered media: Integration along the imaginary axis and asymptotic behavior, *IEEE Trans. Anten. Propag.* **51**:3200–3208 (Dec. 2003).
152. K. A. Michalski, On the efficient evaluation of integrals arising in the Sommerfeld halfspace problem, in R. C. Hansen, ed., *Moment Methods in Antennas and Scatterers*, Artech House, Boston, 1990, pp. 325–331.
153. S. Barkeshli, P. H. Pathak, and M. Marin, An asymptotic closed-form microstrip surface Green's function for the efficient moment method analysis of mutual coupling in microstrip antennas, *IEEE Trans. Anten. Propag.* **38**:1374–1383 (Sept. 1990).
154. B. Popovski, A. Toscano, and L. Vegni, Radial and asymptotic closed form representation of the spatial microstrip dyadic Green's functions, *J. Electromagn. Waves Appl.* **9**:97–126 (1995).
155. T. J. Cui and W. C. Chew, Fast evaluation of Sommerfeld integrals for EM scattering and radiation by three-dimensional buried objects, *IEEE Trans. Geosci. Remote Sens.* **37**:887–900 (March 1999).
156. F. Olyslager and H. Derudder, Series representation of Green dyadics for layered media using PMLs, *IEEE Trans. Anten. Propag.* **51**:2319–2326 (Sept. 2003).
157. P. Cornille, Numerical saddle point method, *J. Math. Anal. Appl.* **38**:633–639 (1972).
158. R. E. Smith and S. N. Houde-Walter, The migration of bound and leaky solutions to the waveguide dispersion relation, *J. Lightwave Technol.* **11**:1760–1768 (Nov. 1993).
159. W. L. Anderson, Computation of Green's tensor integrals for three-dimensional electromagnetic problems using fast Hankel transforms, *Geophysics* **49**:1754–1759 (Oct. 1984).
160. R. Hsieh and J. Kuo, Fast full-wave analysis of planar microstrip circuit elements in stratified media, *IEEE Trans. Microwave Theory Tech.* **46**:1291–1297 (Sept. 1998).
161. D. G. Fang, J. J. Yang, and G. Y. Delisle, Discrete image theory for horizontal electric dipoles in a multilayered medium, *IEE Proc. H* **135**:297–303 (Oct. 1988).
162. K. A. Michalski and J. R. Mosig, Discrete complex image mixed-potential integral equation analysis of microstrip patch antennas with vertical probe feeds, *Electromagnetics* **15**:377–392 (July–Aug. 1995) (invited paper).
163. M. I. Aksun, A robust approach for the derivation of closed-form Green's functions, *IEEE Trans. Microwave Theory Tech.* **44**:651–658 (May 1996).
164. F. Ling and J. Jin, Discrete complex image method for Green's functions of general multilayer media, *IEEE Microwave Guided Wave Lett.* **10**:400–402 (Oct. 2000).
165. P. Ylä-Oijala and M. Taskinen, Efficient formulation of closed-form Green's functions for general electric and magnetic sources in multilayered media, *IEEE Trans. Anten. Propag.* **51**:2106–2115 (Aug. 2003).
166. N. B. Christensen, Optimized fast Hankel transform filters, *Geophys. Prosp.* **38**:545–558 (1990).
167. D. Guptasarma and B. Singh, New digital linear filters for Hankel J_0 and J_1 transforms, *Geophys. Prosp.* **45**:745–762 (1997).
168. T. K. Sarkar and O. Pereira, Using the matrix pencil method to estimate the parameters of a sum of complex exponentials, *IEEE Anten. Propag. Mag.* **37**:48–55 (Feb. 1995).
169. V. I. Okhmatovski and A. C. Cangellaris, Evaluation of layered media Green's functions via rational function fitting, *IEEE Microwave Wireless Compon. Lett.* **14**:22–24 (Jan. 2004).
170. L. Beyne and D. De Zutter, Green's function for layered lossy media with special application to microstrip antennas, *IEEE Trans. Microwave Theory Tech.* **36**:875–881 (May 1988).
171. J. L. Tsalamengas, TE-scattering by conducting strips right on the planar interface of a three-layered medium, *IEEE Trans. Anten. Propag.* **41**:1650–1658 (Dec. 1993).
172. L. Tsang, C. Huang, and C. H. Chan, Surface electric fields and impedance matrix elements of stratified media, *IEEE Trans. Anten. Propag.* **48**:1533–1543 (Oct. 2000).
173. K. A. Michalski and D. Zheng, Electromagnetic scattering and radiation by surfaces of arbitrary shape in layered media, Part II: Implementation and results for contiguous half-spaces, *IEEE Trans. Anten. Propag.* **38**:345–352 (March 1990).
174. F. Ling and J. Jin, Full-wave analysis of multilayer microstrip problems, in W. C. Chew, J. Jin, E. Michielssen, and J. Song, eds., *Fast and Efficient Algorithms in Computational Electromagnetics*, Artech House, Boston; 2001, pp. 729–780.
175. F. Mesa, C. Di Nallo, and D. R. Jackson, The theory of surface-wave and space-wave leaky-mode excitation on microstrip lines, *IEEE Trans. Microwave Theory Tech.* **47**:207–215 (Feb. 1999).
176. O. J. F. Martin and N. B. Piller, Electromagnetic scattering in polarizable backgrounds, *Phys. Rev. E* **58**:3909–3915 (Sept. 1998).
177. F. Olyslager, *Electromagnetic Waveguides and Transmission Lines*, Clarendon Press, Oxford, 1999.
178. S. W. Lee, Basics, in Y. T. Lo and S. W. Lee, eds., *Antenna Handbook: Theory, Applications, and Design*, Van Nostrand-Reinhold, New York, 1988, Chap. 1.
179. W. C. Chew, A quick way to approximate a Sommerfeld-Weyl-type integral, *IEEE Trans. Anten. Propag.* **36**:1654–1657 (Nov. 1988).

180. K. A. Michalski and C.-I. G. Hsu, RCS computation of coax-loaded microstrip patch antennas of arbitrary shape, *Electromagnetics* **14**(1):33–63 (1994).
181. M.-H. Ho, K. A. Michalski, and K. Chang, Waveguide excited microstrip patch antenna—theory and experiment, *IEEE Trans. Anten. Propag.* **42**:1114–1125 (Aug. 1994).
182. Y. Rahmat-Samii, On the question of computation of the dyadic Green's functions at source region in waveguides and cavities, *IEEE Trans. Microwave Theory Tech.* **MTT-23**:762–765 (Sept. 1975).

ELECTROMAGNETIC FIELD MEASUREMENT

MOTOHISA KANDA
National Institute of Standards
and Technology

To establish standards for conducting electromagnetic (EM) field measurements, measurements must be made (1) in anechoic chambers, (2) at open-area test sites, and (3) within guided-wave structures; and a means to transfer these measurements from one situation to another must be developed. The underlying principles of these measurement and transfer standards are (1) measurements and (2) theoretical modeling. Thus, a parameter or a set of parameters is measured, or a parameter is calculated by established physical and mathematical principles.

Various electromagnetic field sensors for measuring radiofrequency (RF) electric and magnetic fields are discussed below. For electric field measurements, electrically short dipole antennas with a high-input-impedance load, such as a field-effect transistor (FET) and a high-frequency diode detector, are discussed. Since the input impedance of an electrically short dipole antenna is predominantly a capacitive reactance, very broadband frequency responses can be achieved with a high-impedance capacitive load. However, because conventional dipole antennas support a standing-wave current distribution, the useful frequency range of these dipole antennas is usually limited by their natural resonant frequencies. In order to suppress these resonances, a resistively loaded dipole antenna has been developed. To obtain a standard antenna with increased sensitivity at a specific frequency, a half-wave tuned dipole antenna with a diode is used, to measure the induced open-circuit voltage. Also used was a tuned receiver with a half-wave tuned dipole antenna, to further improve antenna sensitivity.

For magnetic field measurements, this article discusses an electrically small, resistively loaded loop antenna to achieve a broadband response. Resistive loading is achieved either with the loading resistance at the loop terminal or by uniform resistive loading along the loop antenna. This short-circuit current loop configuration gives a very flat frequency response over a wide frequency range.

In the region near a transmitting antenna or a scatterer, the electric and magnetic field vectors are not necessarily (spatially) orthogonal or in phase. For time-harmonic fields, the endpoints of the field vectors trace out polarization ellipses, and the Poynting vectors lie on the surface of a cone with its endpoint on an ellipse. In these cases, the electric and magnetic fields may be measured separately, or, using the single-loop antenna element described in this article, they may be measured simultaneously.

Photonic sensors are also discussed; they provide the wide bandwidth and low dispersion necessary to maintain the fidelity of time-domain signals. Since they consist of electro-optic modulators and optical fibers, they are free from electromagnetic interference, and there is minimal perturbation of the field being measured.

Throughout the discussion, the interplay between measured quantities and predicted (modeled) quantities is emphasized. The ability of measurements and the restrictions imposed by rigorous theoretical analysis of given models are discussed for the frequencies from 10 kHz to 40 GHz and upward.

1. ELECTRIC FIELD SENSORS

1.1. An Electrically Short Dipole Antenna with a Capacitive Load

Most electric field sensors consist of dipole antennas. The induced open-circuit voltage V_{oc} at the dipole antenna terminal is given by

$$V_{oc} = E_{inc}L_{eff} \quad (1)$$

where E_{inc} is the normal incident electric field strength and L_{eff} is the effective length of the dipole antenna. For an electrically short dipole antenna whose physical length is much shorter than the wavelength, the effective length L_{eff} and driving point capacitance C_a are approximately [1]

$$L_{eff} = \frac{L(\Omega - 1)}{4(\Omega - 2 - \ln 4)} \quad (2)$$

and

$$C_a = \frac{4\pi\epsilon_0 L}{2(\Omega - 2 - \ln 4)} \quad (3)$$

where L is the physical length of the dipole antenna, ϵ_0 is the free-space permittivity, Ω is the antenna thickness factor $\Omega = 2 \ln(L/a)$, and a is the antenna radius.

For an electrically short dipole antenna with a capacitive load C , the transfer function is given by [1]

$$S(f) = \frac{V_o(f)}{E_{inc}(f)} = \frac{h\kappa/2}{1 + C/C_a} \quad (4)$$

where

$$C_a = \frac{4\pi h}{c\zeta_0(\Omega - 2 - \ln 4)} \quad (5)$$

$$\kappa = \frac{\Omega - 1}{\Omega - 2 + \ln 4} \quad (6)$$

and where

- a = antenna radius
- C = capacitance of load
- C_a = capacitance of antenna
- E_{inc} = incident electric field
- h = half of the physical length of the dipole antenna
- V_o = output voltage of the antenna
- ζ_0 = free-space impedance
- c = speed of light in free space
- Ω = antenna thickness factor, $\Omega = 2 \ln(2h/a)$

Since the input impedance of an electrically short dipole antenna is almost purely capacitive, it is possible to achieve a frequency-independent transfer function with a capacitive load, as indicated in Eq. (4). In practice, the load impedance is seldom purely capacitive, but also may have a resistive component. This resistive component will cause a 6-dB/octave rolloff at the low end of the frequency range.

1.2. An Electrically Short Dipole Antenna with a Diode

A common standard sensor used for EM field measurements is an electrically short dipole antenna with a diode load connected to a DC metering unit by an RF filter transmission line. The main advantage of including a diode is to make the frequency response of the sensor very flat, even at higher frequencies where an FET amplifier is not readily available. When used with a high-input-impedance detector, the sensor can serve as a portable and compact transfer standard.

Figure 1 represents a dipole antenna, which can be used to determine the signal from the transmission line for a given incident electric field [2]. This circuit is valid for the frequency range to be considered (DC and $f > 1$ MHz). In Fig. 1, the small antenna resistance has been neglected. The stray gap capacitance of the filter line from the antenna terminal connections has been included in the effective shunt capacitance C_d . The antenna capacitance is given by C_a .

When a first-order, nonlinear differential equation associated with the Thevenin's equivalent nonlinear circuit

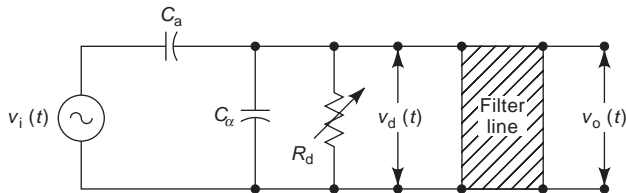


Figure 1. Thevenin's equivalent circuit of an electrically short dipole antenna with a shunt diode detector.

(shown in Fig. 1) is solved for the detected DC voltage V_o , for a small induced RF voltage V_i [2] we obtain

$$V_o = -\frac{\alpha}{4} \left(\frac{V_i}{1 + C_d/C_a} \right)^2 \quad (7)$$

where α ($\approx 38 \text{ V}^{-1}$) is derived from the diode characteristics, while for large V_i

$$V_o \cong -\frac{V_i}{1 + C_d/C_a} \quad (8)$$

Equation (7) indicates that for a small induced RF voltage V_i , the output DC voltage V_o is a square-law function of the induced voltage. On the other hand, Eq. (8) indicates that, for a large induced voltage V_i , the output DC voltage V_o is directly proportional to the induced voltage.

1.3. A Resistively Loaded Dipole Antenna with a Diode

A conventional dipole antenna essentially supports a standing-wave current distribution and is, therefore, highly frequency-sensitive. For the antenna to have a flat frequency response beyond any natural resonant frequency, a traveling-wave dipole antenna was realized by use of continuously tapered resistive loading [3,4]. If the internal impedance per unit length $Z^i(z)$ as a function of the axial coordinate z is expressed as

$$Z^i(z) = \frac{60\Psi}{h - |z|} \quad (9)$$

then the current distribution $I_z(z)$ along the linear antenna is that of a traveling wave

$$I_z(z) = \frac{V_i}{60\Psi(1 - j/kh)} \left[1 - \frac{|z|}{h} \right] e^{-jk|z|} \quad (10)$$

where $2h$ is the dipole antenna's total physical length, k is the wavenumber, V_i is the driving voltage, and Ψ is given by

$$\Psi = 2 \left[\sinh^{-1} \frac{h}{a} - C(2ka, 2kh) - jS(2ka, 2kh) \right] + \frac{j}{kh} (1 - e^{-j2kh}) \quad (11)$$

where a is the radius of the dipole and $C(x,y)$ and $S(x,y)$ are the generalized cosine and sine integrals. The main advantage of a resistively loaded dipole antenna with a diode is the very flat frequency response of the sensor system. A shortcoming of this sensor system is the relatively low sensitivity. To overcome this problem, a standard half-wave tuned dipole antenna should be used.

1.4. A Tuned Half-Wave Dipole Antenna

The magnitude of the electric field component at a given point in an electromagnetic field is determined from the open-circuit voltage V_{oc} induced in a standard half-wave

receiving dipole antenna as obtained from Eq. (1). The induced voltage is measured across the center gap of the dipole antenna, which is oriented parallel to the electric field vector of the incident field.

The RF voltage induced in the half-wave standard dipole antenna is rectified by a high-impedance Schottky barrier diode connected in shunt across the center gap of the antenna. The diode output is filtered by a balanced RC network, and this DC voltage is measured with a high-impedance DC voltmeter.

The effective length h_e of a thin dipole antenna near resonance and the required total length L for resonance are given by [1]

$$h_e = \frac{\lambda}{\pi} \tan\left(\frac{\pi h}{\lambda}\right) \quad (12)$$

and

$$L = \frac{\lambda}{2} \left[1 - \frac{0.2257}{\ln(\lambda/D) - 1} \right] \quad (13)$$

where D is the diameter of the standard dipole antenna.

To further increase the sensitivity of a standard antenna, a half-wave tuned dipole antenna with a narrowband receiver should be used. In this case, the transfer function $S(f)$ is given by

$$S(f) = \frac{V_L(f)}{E_{\text{inc}}(f)} = \frac{h_e Z_a}{Z_a + Z_r} \quad (14)$$

where V_L is the voltage across the receiver load, E_{inc} is the incident electric field, h_e is the effective length of the tuned dipole, Z_a is the antenna impedance, and Z_r is the receiver input impedance ($\sim 50 \Omega$). The input impedance of the antenna Z_a is complicated and is given in Ref. 1. When the cable losses are significant, they should be included in Z_a .

2. MAGNETIC FIELD SENSORS

2.1. An Electrically Small Loop Antenna with a Loading Resistance

A magnetic field sensor consists of an electrically small, balanced loop antenna. The voltage V_i induced in an electrically small loop antenna by an electromagnetic wave incident on the loop antenna is determined from Maxwell's equations and Stokes' theorem, and is given by [1]

$$V_i = \int E_i d\ell = j\omega\mu H_i NS \quad (15)$$

where E_i is the tangential electric field induced around the loop antenna, l is the circumference of the loop antenna, ω is the angular frequency of E_i , μ is the permeability of the loop antenna core, H_i is the component of the magnetic field normal to the plane of the loop antenna, N is the number of loop antenna turns, and S is the area of the loop antenna. The induced voltage V_i of an electrically small

loop antenna is proportional to frequency, the number of loop turns, and the area of the loop antenna.

To make the response of a loop antenna flat over the frequency range of interest, the Q of the antenna has to be reduced through a loading resistance. The resonance of a loop antenna is the result of the combined effect of the distributed capacitance of the loop antenna, the gap capacitance, and the capacitance of the amplifier along with the inductance of the loop antenna. The equivalent circuit for an electrically small loop antenna is shown in Fig. 2. Here V_i is the induced voltage, L is the loop inductance, C is the capacitance, R is the loading resistance, and V_o is the voltage across the loading resistance. Then the response of an electrically small loop antenna is given by [1]

$$\frac{V_o}{V_i} = \frac{-j\frac{1}{\delta}}{\frac{1}{Q} + j\left(\delta - \frac{1}{\delta}\right)} \quad (16)$$

where

$$Q = \frac{R}{X_0}, \quad X_0 = \omega_0 L = \frac{1}{\omega_0 C}, \quad \delta = \frac{\omega}{\omega_0}, \quad \omega_0 = \frac{1}{\sqrt{LC}} \quad (17)$$

The inductance L and the capacitance C of a loop antenna can be given by

$$L = \mu b \ln\left(\frac{b}{a}\right) \quad (18)$$

and

$$C = \frac{2\epsilon b}{\ln\left(\frac{b}{a}\right)} \quad (19)$$

where μ is the permeability of the medium, b is the loop antenna radius, and a is the radius of the loop wire.

The transfer function of $S(f)$ of an electrically small loop antenna can be obtained by combining Eqs. (15) and (16):

$$S(f) = \frac{V_o}{H_i} = \omega_0 \mu NS \frac{1}{\frac{1}{Q} + j\left(\delta - \frac{1}{\delta}\right)} \quad (20)$$

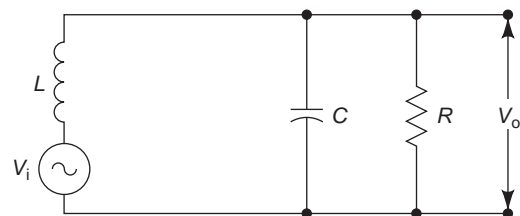


Figure 2. Thevenin's equivalent circuit of an electrically small loop antenna with a loading resistance.

The normalized transfer function $S_n(f)$ of a loop antenna with a loading resistor is given by

$$S_n(f) = \frac{1}{\frac{1}{Q} + j\left(\delta - \frac{1}{\delta}\right)} \tag{21}$$

as a function of the normalized frequency $\delta = \omega/\omega_0$ and is given in Fig. 3 for various $Q < 1$. Figure 3 shows that the upper frequency end ω_h of the 3-dB rolloff point is given by $\delta_h Q = 1$ and, similarly, the corresponding low frequency ω_l of the 3-dB rolloff point is given by $\delta_l/Q = 1$. Thus, from these conditions, we obtain

$$\delta_h \delta_l = \frac{\omega_h \omega_l}{\omega_0^2} = 1 \tag{22}$$

or

$$\omega_0 = \sqrt{\omega_h \omega_l} \tag{23}$$

The self-resonant frequency of a loop antenna is therefore the geometric mean of the highest and lowest cutoff frequencies.

3. AN ELECTROMAGNETIC FIELD SENSOR FOR SIMULTANEOUS ELECTRIC AND MAGNETIC FIELD MEASUREMENTS

The electric and magnetic field sensors discussed above measure either the electric or magnetic field only and, therefore, cannot measure complicated EM fields such as those with reactive near-field components and multipath reflections. For this reason, a single sensor capable of performing simultaneous electric and magnetic field measurements was developed [5,6]. In this case, a loop antenna is loaded at diametrically opposite points with equal impedances. Across one load, the magnetic loop response adds to the electric dipole response, whereas across the other load, the magnetic loop response subtracts from the electric dipole response. Thus, by taking the sum and difference of currents across loads at diametrically opposite points, the magnetic loop response and electric dipole response can be separated. Thus, the sum current gives a measure of the magnetic field, whereas the difference current gives a measure of the electric field.

To explain the basic characteristics of a doubly loaded loop antenna, the currents I_1 and I_2 at each load are given

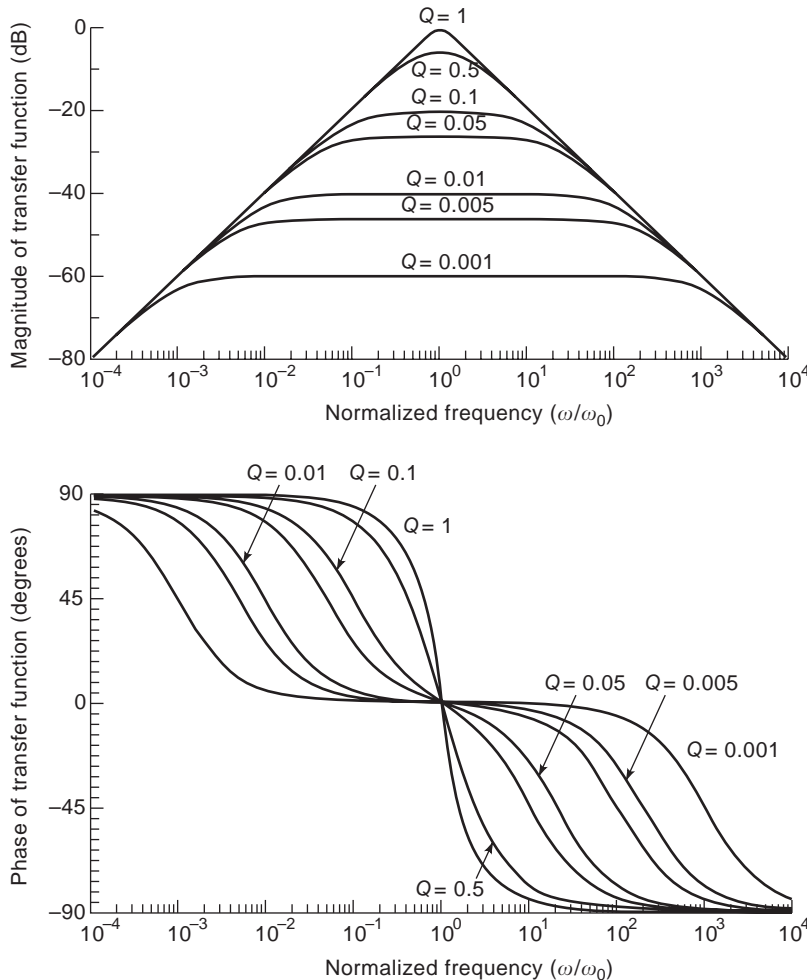


Figure 3. The normalized transfer function of a loop antenna as a function of normalized frequency for different values of Q .

by [5]

$$I_1 = 2\pi b E_{\text{inc}} \left(\frac{f_0 Y_0}{1 + 2Y_0 Z_L} + \frac{f_1 Y_1}{1 + 2Y_1 Z_L} \right) \quad (24)$$

and

$$I_2 = 2\pi b E_{\text{inc}} \left(\frac{f_0 Y_0}{1 + 2Y_0 Z_L} - \frac{f_1 Y_1}{1 + 2Y_1 Z_L} \right) \quad (25)$$

where b is the radius of the loop, E_{inc} is the incident electric field, Z_L is the load impedance, Y_0 is the admittance for the magnetic loop response, and Y_1 is the admittance for the electric dipole antenna response of a loop. In general, Y_0 is much larger than Y_1 . f_0 and f_1 are Fourier coefficients of the incident wave. For a loop antenna orientation of maximum electric and magnetic field response, $f_0 = j\beta b/2$ and $f_1 = \frac{1}{2}$. Taking the sum and difference of these currents yields [5]

$$I_\Sigma = \frac{1}{2} (I_1 + I_2) = 2\pi b E_{\text{inc}} \frac{f_0 Y_0}{1 + 2Y_0 Z_L} \quad (26)$$

and

$$I_\Delta = \frac{1}{2} (I_1 - I_2) = 2\pi b E_{\text{inc}} \frac{f_1 Y_1}{1 + 2Y_1 Z_L} \quad (27)$$

This indicates that the sum current can be used to measure the magnetic field and the difference current can be used to measure the electric field. In general, $2Y_0 Z_L > 1$ for the magnetic field loop antenna current. Therefore, when the antenna is oriented for maximum response, I_Σ can be approximated as

$$I_\Sigma \cong j \frac{E_{\text{inc}}}{2Z_L} \pi b^2 \beta \quad (28)$$

This indicates that the magnetic loop current is approximately proportional to the product of frequency and the area of the loop antenna, and is inversely proportional to the load impedance. Similarly, for the electric field dipole current, assuming that $2Y_1 Z_L \ll 1$, we have

$$I_\Delta \cong \pi b E_{\text{inc}} Y_1 \quad (29)$$

which is approximately proportional to the product of the circumference of the loop antenna and frequency, since Y_1 has a capacitive susceptance (positive) and increases with frequency. This device is intended to measure not only the polarization ellipses of the electric and magnetic field vectors in the near field region but also the time-dependent Poynting vector and thus describe the energy flow.

4. PHOTONIC ELECTROMAGNETIC FIELD SENSORS

Properly designed photonic EM field sensors provide the wide bandwidth and low dispersion necessary to maintain the fidelity of time-domain signals so that both amplitude and phase information can be retrieved [7]. They are free

from electromagnetic interference, and there is minimal perturbation of the field being measured.

A number of photonic passive sensors for EM field measurements have been reported in the literature [7]. These are systems in which the sensor head contains no active electronics or power supplies. Optical measurement systems of the typical photonic EM field sensors is shown schematically in Fig. 4. Light from a laser is launched into an optical fiber link and serves as an optical signal carrier. At the sensor head, the EM field induces a voltage across the modulator crystal and changes its index of refraction. The crystal index changes occur at the frequency of the impressed EM field and result in a modulation in the amplitude of the optical carrier. At the receiver end of the fiber the light is converted to an electrical signal by a photodiode and is suitably amplified for analysis with a spectrum analyzer, oscilloscope, or other signal processor. The electro-optic interaction is weak, and, except for very high fields, the gain of a small antenna is usually required to obtain adequate modulation.

For the measurement of a pulsed electric field, an antenna with a flat broadband response is most desirable. A resistively loaded dipole antenna gives a nonresonant frequency response and is, therefore, ideal for use in the time-domain measurement of electromagnetic fields [3,4]. Electro-optical modulators that are driven by antenna feeds are characterized as a function of the voltage applied to their electrodes. A convenient parameter for characterizing a modulator's performance is the voltage V_π that is needed across the electrode to drive a modulator between maximum and minimum optical power levels. In general, a modulator transfer function is nonlinear. However, in most cases of interest, the field-induced RF voltages on the modulator's electrodes are small compared to V_π , and a small-signal linear transfer function evaluated at the operating bias point is appropriate. The most desirable operating bias point is where the modulator's sensitivity and linear range are at maximum. The physical characteristics of four modulators used in photonic EM field sensors are given in Table 1.

4.1. Pockels Cell

Pockels cell modulators often are used in EM field sensors. The small signal transfer function takes the form given in Table 1, when the constant phase shift Φ_0 is set equal to $-\pi/2$ by introducing a quarter-wave retardation plate into the cell. This biases the modulator at its point of maximum sensitivity and linearity. The characteristic voltage of a bulk crystal modulator is limited by (1) the magnitude of the electro-optic coefficients for available materials, (2) the minimum dimensions of crystals that can be handled as discrete optical elements, and (3) the maximum crystal lengths acceptable for the highest desired operating frequency. For operation to 5 GHz, the lowest obtainable values for V_π are on the order of 100 V for LiNbO_3 . It is relatively easy to increase V_π and reduce the modulator's sensitivity in order to measure high fields. In one application of this technology for measuring fields from electromagnetic pulses, a crystal of $\text{Bi}_4\text{Ge}_3\text{O}_{12}$ (BGO), which has cubic symmetry and reduced temperature sensitivity,

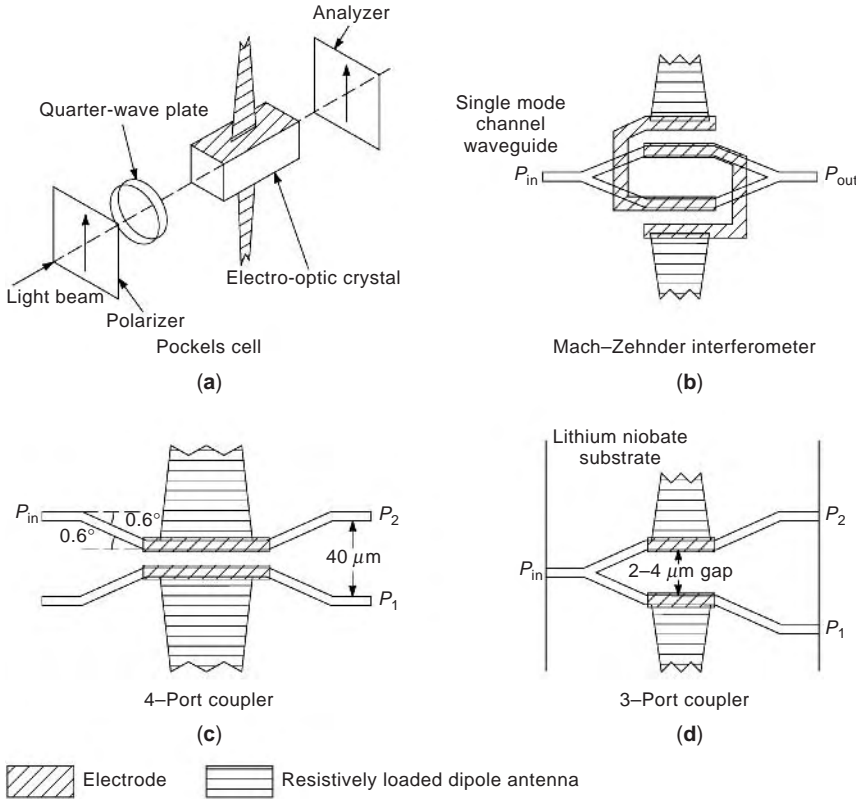


Figure 4. Measurement system of a photonic EM field sensor.

is used in a Pockels cell modulator and has a V_π of approximately 2100 V.

4.2. Mach-Zehnder Interferometer

Modulators based on Mach-Zehnder (MZ) interferometers and fabricated using optical guided wave (OGW) technologies have found widespread use in the fiberoptic communications industry. Their use as EM field sensors also has been investigated [7]. Photolithography is used to fabricate OGW modulators by defining the waveguide channels and then diffusing titanium into the surface of a LiNbO_3 crystal along these channels. The transfer function for an MZ interferometer is identical to that of the Pockels cell. The static phase shift Φ_0 is due to differences in the optical path length in the interferometer arms. Significantly, V_π for this device is typically two orders of magnitude smaller than that for a Pockels cell modulator of the same material and frequency response. The higher sensitivity is typical of most OGW modulators and arises from the higher fields created in the crystal with the closely spaced electrodes that are achievable using photo lithography. The principal problems to date with the MZ interferometer have been the difficulty in obtaining the correct value for Φ_0 during fabrication, and its temperature and wavelength dependence.

4.3. Directional Coupler

Directional couplers are also OGW devices that have been investigated for use as EM field sensors [7]. In the inter-

action region, the two waveguides lie close enough together that the evanescent field of the lightwave in one guide couples into the other guide. In such a coupled-mode system, the energy in one lightguide can be switched to the other guide by changing the relative propagation constants in the channels with the electro-optic effect. If the fabrication parameters are chosen correctly, the transfer function given in the literature [7] for the directional coupler can be written in the form given in Table 1.

5. ELECTROMAGNETIC FIELD STANDARDS

5.1. Transverse Electromagnetic Cell

Transverse electromagnetic (TEM) transmission-line cells are devices used for establishing standard EM fields in a

Table 1. Transfer Functions for Electro Optic Modulators

Modulator	General	Small Signal
Pockels cell	$\cos^2\left(\frac{\pi}{2}V_n + \frac{\phi_0}{2}\right)$	$\frac{\pi}{2V_\pi}$
Mach-Zehnder	$\cos^2\left(\frac{\pi}{2}V_n + \frac{\phi_0}{2}\right)$	$\frac{\pi}{2V_\pi}$
4-port coupler	$\frac{1}{1+3V_n^2} \sin^2\left(\frac{\pi}{2}\sqrt{1+3V_n^2}\right)$	$\approx \frac{1.6}{V_\pi}$
3-port coupler	$\frac{1}{2} - \frac{2V_n}{1+4V_n^2} \sin\left(\frac{\pi}{2\sqrt{2}}\sqrt{1+4V_n^2}\right)$	$\frac{2}{V_\pi} \sin \frac{\pi}{2\sqrt{2}} = \frac{1.79}{V_\pi}$

shielded environment [8]. Their application is becoming increasingly widespread because of their versatility, measurement accuracy, and ease of operation.

A TEM cell is essentially a 50-Ω triplate transmission line with the sides closed in, to prevent radiation of RF energy into the environment and to provide electrical isolation. A properly designed cell, terminated in its characteristic impedance, is capable of producing a calculable electric and magnetic field for calibrating an electrically small antenna or RF sensor. The cell consists of a section of rectangular coaxial transmission lines tapered at each end to adapt to standard coaxial connectors. The line and tapered transitions are designed to have a nominal characteristic impedance of 50 Ω along their length, to ensure minimum-voltage standing-wave ratio. A fairly uniform EM field is established between the plates inside the cell when RF energy is conducted in the line from a transmitter connected to the cell’s input port. A 50-Ω termination is connected to the cell’s output port. The expression for determining the electric field *E* in the cell is given by

$$E = \frac{V}{b} = \frac{\sqrt{PZ_0}}{b} \tag{30}$$

where *V* is the RMS voltage on the septum (center conductor), *b* is the separation distance between the septum and lower or upper walls, *P* is the net power flow to the cell, and *Z*₀ is the real part of the cell’s characteristic impedance $\cong 50 \Omega$.

A wave traveling through a cell has essentially the free-space impedance ($\cong 120\pi \Omega$), thus providing a close approximation to a far-field plane wave propagating in free space. The design of TEM cells can be based on an approximate equation for the characteristic impedance of a rectangular transmission line [8]

$$Z_0 \cong \frac{377}{4} \left\{ \left[\frac{p}{q} - \frac{2}{\pi} \ln \left(\sinh \frac{\pi g}{2q} \right) \right] - \frac{\Delta c}{\epsilon_0} \right\}^{-1} \tag{31}$$

where *p*, *q*, and *g* are as shown in Fig. 5 and $\Delta c/\epsilon_0$ is related to the fringing capacitance between the edges of the septum and the sidewalls. For large gaps ($g/p > 0.2$), this fringing term approaches zero [8].

The upper useful frequency for a cell is limited by distortion in the test field caused by multimoding and resonances that occur within the cell at frequencies above the

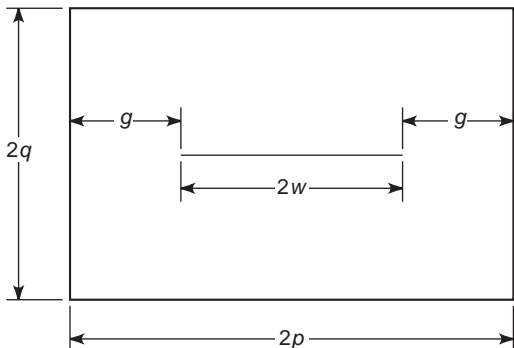


Figure 5. Cross-sectional view of a TEM cell.

cell’s multimode cutoff. Resonant frequencies associated with these modes can be found from the expression [8]

$$F_{\text{res}} = \sqrt{f_{mn}^2 + \left(\frac{cl}{2L} \right)^2} \tag{32}$$

where *f*_{*mn*} are the frequencies of the higher-order mode(s) excited inside the cell, *c* is the wave propagation velocity ($\cong 3.0 \times 10^8$ m/s), *L* is the resonant length of the cell in meters, and *l*, *m*, and *n* are integers corresponding to multiples of the resonant length and the particular waveguide mode. The influence of the first-order TE modes does not become significant until approaching their resonances. Since most cells are designed with the center plate (septum) centered symmetrically, the odd-order TE modes are not excited in an empty cell. The presence of a device placed in the cell will, however, excite these modes in varying degrees, depending on its size, shape, and placement.

5.2. Waveguide Chamber

For the frequency range of 300–1000 MHz, one can use a waveguide section with a rectangular cross section with a width-to-height (aspect) ratio of 2:1. The length of a guide “cell” must exceed two wavelengths over the specified frequency band, in order to create a fairly uniform field within the guide. Electromagnetic power is transmitted through the guide to a matched resistive load, and the maximum frequency is limited by the requirement that power propagates in the guide in the dominant TE₁₀ mode. In this well-known case, the direction of the electric field vector is across the narrow face of the guide.

Assuming good conductivity of the waveguide walls, an air dielectric, and sinusoidal excitation, the lowest cutoff frequency *f*_{co} is

$$f_{\text{co}} = \frac{c}{2a} \tag{33}$$

where *c* is the wave propagation velocity ($\cong 3.0 \times 10^8$ m/s) and *a* is the guide width.

The longest or cutoff wavelength is given by $\lambda_{\text{co}} = 2a$. The wavelength λ_{wg} inside the guide for these operating conditions is

$$\frac{1}{\lambda_{\text{wg}}} = \sqrt{\left(\frac{1}{\lambda_0} \right)^2 - \left(\frac{1}{\lambda_{\text{co}}} \right)^2} \tag{34}$$

where λ_0 is the free-space wavelength.

The transverse impedance *Z*_w of the wave traveling in the guide is

$$Z_w = \frac{-E_y}{H_z} = \zeta_0 \left(\frac{\lambda_{\text{wg}}}{\lambda_0} \right) = \frac{\zeta_0}{\sqrt{1 - (\lambda_0/2a)^2}} \tag{35}$$

where ζ_0 is the intrinsic impedance of free space ($\cong 120\pi$).

The direction of the electric field vector is across the narrow face of the guide, and its RMS magnitude at the

center of a rectangular waveguide is given by

$$E = \sqrt{\frac{2Z_w P_z}{ab}} \quad (36)$$

and, similarly, the RMS magnitude of the magnetic field in the guide center is given by

$$H = \sqrt{\frac{2P_z}{Z_w ab}} \quad (37)$$

where P_z is the total power flow in the guide and ab is the cross-sectional area of the waveguide ($= 0.5 a^2$).

5.3. Microwave Anechoic Chambers

Microwave anechoic chambers currently are used for a variety of indoor antenna measurements, electromagnetic field measurements, electromagnetic interference (EMI) measurements, and electromagnetic compatibility (EMC) measurements. The primary requirement is that a transmitting antenna at one location within a chamber or at a chamber wall generates a known field throughout a volume of the chamber, which has dimensions sufficient to perform EM field measurements. This volume is frequently called a *quiet zone*, and the level of reflected waves within it will determine the performance of the anechoic chamber.

Electromagnetic field measurements in an anechoic chamber usually are performed in the near-field region of a transmitting standard antenna. To establish the standard field, the radiated field intensity in the near-field region of the transmitting antenna is calculated. The antennas typically used for the anechoic chamber measurements consist of a series of open-ended waveguides at frequencies below 450 MHz, and a series of rectangular pyramidal horn antennas at frequencies above 450 MHz.

The electric field strength at a specific distance from the radiating antenna is calculated from measurements of the power delivered to the transmitting antenna and a knowledge of the gain of the antenna as a function of frequency and distance to the field point. The equation used to calculate the electric field E on the boresight axis of the transmitting antenna is

$$E = \frac{1}{d} \sqrt{\frac{\zeta_0 P_{\text{net}} G}{4\pi}} \approx \frac{\sqrt{30 P_{\text{net}} G}}{d} \quad (38)$$

where P_{net} is the net power delivered to the transmitting antenna, ζ_0 is the free-space impedance ($\approx 120\pi \Omega$), G is the near-field gain of the transmitting antenna at the given frequency and distance, and d is the distance from the center of the aperture of the transmitting antenna (horn or open-ended waveguide) to the on-axis field point.

The net power P_{net} delivered to the transmitting antenna is the difference between the incident P_{inc} and reflected P_{refl} powers as measured with a calibrated directional coupler (four ports) with calibrated power meters. In order for measurements to be accurate, an anechoic chamber must provide a truly free-space test

environment. The performance of a rectangular RF anechoic chamber can be determined by measuring the relative insertion loss versus separation distance between a source antenna and a receiving antenna.

Antenna insertion loss is the ratio of power received by a receiving antenna or probe to the power accepted by the transmitting antenna. If the anechoic chamber is a perfect free-space simulator, the relative insertion loss between two polarization-matched antennas will vary with distance according to the Friis transmission formula [9]

$$\frac{P_r}{P_t} = G_r G_t \left(\frac{\lambda}{4\pi d} \right)^2 \quad (39)$$

where P_t is the net power delivered to the transmitting antenna, P_r is the power received by the receiving antenna, G_t is the near-field gain of the transmitting antenna, G_r is the near-field gain of the receiving antenna, d is the separation distance between the two antennas, and λ is the wavelength. Experimental data can be compared with the calculated free-space transmission loss, using appropriate near-field transmitting antenna gains. The difference between the measured and calculated transmission loss is a measure of reflections from chamber surfaces.

5.4. Open-Area Test Sites

An open-area test site typically is used for the antenna calibration in the frequency range of 10 kHz–1000 MHz. A calibration consists of determining the antenna factor that permits a receiver (RF voltmeter) to be used with the calibrated antenna to conduct measurements of field strength.

At frequencies below about 50 MHz, loop antennas are calibrated in a quasi-static, near-zone, magnetic field produced by a balanced single-turn transmitting loop with a 10 cm radius. Above 25 MHz, dipole antennas are calibrated in a far-zone electric field, which is evaluated in terms of the open-circuit voltage induced in a self-resonant receiving dipole antenna. Between 30 kHz and 300 MHz, vertical monopole antennas and small probes are evaluated in an elliptically polarized electromagnetic field produced by a transmitting monopole antenna above a conducting ground screen.

Field strength can be evaluated using two independent techniques: (1) the standard field method and (2) the standard antenna method. For the standard field method, a transmitted field is calculated in terms of the type and dimensions of a transmitting antenna, its current distribution or net delivered power, the frequency of the transmitted signal, the distance from the transmitting antenna to the field point, and the effect of ground reflections (if present). For the standard antenna method, an unknown field is measured with a calculable receiving antenna. The voltage or current induced in a standard antenna by the component of field being evaluated is measured. The field strength is then calculated in terms of this induced voltage, the dimensions and form of the receiving antenna, and its orientation with respect to the field vector.

All the techniques described above for field strength standards are applicable only to steady-state RF fields with sinusoidal time variation. They are not intended for use with pulsed fields or other broadband applications.

5.5. Magnetic Field Strength Standards for Loop Antennas at 10 kHz–50 MHz (Standard Field Method)

The response of an electrically small receiving loop antenna is proportional to the average normal component of magnetic field strength incident on the antenna. A calculable quasi-static magnetic field can be produced to calibrate these antennas using a circular single-turn balanced transmitting loop. Up to 30 MHz, the current in a loop with a 10 cm radius is approximately constant in amplitude and phase around the loop. The receiving loop antenna being calibrated is positioned on the same axis as the transmitting loop at a distance of 1.5–3 m. The normal component of the magnetic field, averaged over the area of the receiving loop, is given by [10]

$$H = \frac{\beta I r_1}{r_2} \sum_{m=0}^{\infty} \frac{1}{(2m+1)!} \cdot \frac{1 \cdot 3 \cdots (2m+1)}{2 \cdot 4 \cdots (2m+2)} \left[\frac{\beta r_1 r_2}{R_0} \right]^{m+1} h_{2m+1}^{(2)}(\beta R_0) \tag{40}$$

where

- H = RMS value of magnetic field
- I = RMS current in transmitting loop
- r_1 = radius of transmitting loop
- r_2 = radius of receiving loop
- $R_0 = \sqrt{d^2 + r_1^2 + r_2^2}$
- d = axial distance between the two loops
- $\beta = 2\pi/\lambda_0$
- λ_0 = free-space wavelength
- $h_n^{(2)}$ = n th-order spherical Hankel function of second kind

The current in the transmitting loop antenna is measured with a vacuum thermocouple calibrated with direct current. The thermocouple is at the top of the loop winding.

While coaxial loop antennas normally are used for calibration purposes, the two-loop antennas also can be positioned in the same plane. Coplanar loop antennas are advantageous under certain conditions (e.g., with some ferrite core antennas in which the core length is large). In the coplanar loop antenna setup, the calibrating value of H would be half of that given by Eq. (41).

The calibration and subsequent measurement of magnetic field strength H often are expressed in terms of the electric field E that would exist if the measurement were made in free space, in which case $E/H \cong 120\pi \Omega$. When such a field strength meter is used to make measurements near the ground, the indicated value of the electric field is not necessarily valid. The same is true for measurements made in the near zone of a transmitting antenna. However, the value of the magnetic component H can still be measured correctly.

For calibrating loop antennas or magnetic field sensors at a higher field, it is possible to use the calculable magnetic field generated in a TEM cell, or a waveguide chamber, or at the center of a flat multiturn coil, or at the midpoint of a Helmholtz coil pair.

5.6. Electric Field Strength Standards for Dipole Antennas from 25 to 1000 MHz (Standard Antenna Method)

The magnitude of the electric field component at a given point in a locally generated field is determined from the open-circuit voltage V_{oc} induced in a standard (calculable) half-wave receiving dipole antenna. The induced voltage is measured across the center gap of the dipole antenna, which is oriented parallel to the electric field vector of the incident field. In using the standard antenna method, a plane-wave field can be generated by a suitable transmitting antenna, such as a log-periodic or half-wave dipole antenna. The magnitude of this incident field is measured with the standard dipole antenna by the relation

$$E_{inc} = \frac{V_{oc}}{L_{eff}} \tag{41}$$

where E_{inc} is the field strength of the locally generated field, V_{oc} is the open-circuit voltage induced in the standard dipole antenna, and L_{eff} is the effective length of the standard dipole antenna.

The RF voltage V_{oc} picked up by the $\lambda/2$ standard dipole is detected by a high-impedance Schottky barrier diode connected in shunt across the center gap of the antenna. The diode output is filtered by a balanced RC network, and this DC voltage is measured with a high-impedance DC voltmeter. The RF-to-DC-characteristic of the dipole antenna and its filter circuit is obtained experimentally. Assuming a cosinusoidal current distribution on an infinitesimally thin dipole, the effective length of a half-wave dipole antenna in free space is given by Eq. (12).

5.7. Electric Field Strength Standards for Vertical Monopole Antennas from 30 kHz to 300 MHz (Standard Field Method)

Several approaches were considered for generating a standard (calculable) field to calibrate vertically polarized antennas. The system chosen for this measurement consists of a thin cylindrical transmitting monopole antenna over a metallic ground plane. The field strength is calculated in terms of the magnitude and distribution of the monopole antenna current, and other factors such as (1) monopole height, (2) horizontal distance from the transmitting antenna to the field point, (3) vertical height of this point above the ground plane, and (4) electrical conductivity of the ground plane.

The height of the transmitting monopole antenna is adjustable, with a maximum height of about 3 m. The electrical height of this antenna is $\lambda/4$ (resonant) at 25 MHz, but only 0.0003λ at 30 kHz. At frequencies above 25 MHz, the antenna height is reduced to a $\lambda/4$ value. The base diameter of the monopole antenna is about 1 cm. The monopole antenna is excited through a coaxial cable from a transmitting room located beneath a concrete ground

slab that is covered by a conducting metal screen to form the electrical ground plane.

Equations (42), (43), and (44) give the magnitudes of the three field components E_z , E_ρ , and H_ϕ , respectively, of a transmitting $\lambda/4$ monopole antenna above a perfect ground plane of infinite extent:

$$E_z = 30I_0 \left(\frac{e^{-j\beta r_1}}{r_1} + \frac{e^{-j\beta r_2}}{r_2} \right) \quad (42)$$

$$E_\rho = \frac{30I_0}{r_0} \left[\left(\frac{e^{-j\beta r_1}}{r_1} \right) \left(z - \frac{\lambda}{4} \right) + \left(\frac{e^{-j\beta r_2}}{r_2} \right) \left(z + \frac{\lambda}{4} \right) \right] \quad (43)$$

$$H_\phi = \frac{I_0}{4\pi r_0} (e^{-j\beta r_1} + e^{-j\beta r_2}) \quad (44)$$

where

- E_z = vertical electric field component
- E_ρ = horizontal electric field component
- H_ϕ = magnetic field, encircling the monopole antenna
- I_0 = RMS base current of the monopole antenna
- $\beta = 2\pi/\lambda$ = the wavelength constant
- $r_1 = [d^2 + (z - l)^2]^{1/2}$
- $r_2 = [d^2 + (z + l)^2]^{1/2}$
- $r_0 = [d^2 + z^2]^{1/2}$
- l = monopole antenna length
- d = horizontal distance between the monopole antenna and the field point
- z = vertical distance from the ground plane to the field point

For frequencies near self-resonance, the monopole antenna base current is measured with an RF ammeter consisting of a thermoconverter that has been calibrated with known values of DC current. At lower frequencies, where the monopole antenna input impedance Z_{in} is a high-capacitance reactance, the base current is calculated from Ohm's law in terms of the base voltage measured with a high-input impedance voltmeter and the theoretical input impedance. At very low frequencies, Z_{in} may be calculated from the antenna capacitive reactance (11).

$$Z_{in} = \frac{1}{j\omega C_a} \quad (45)$$

where

$$C_a = \frac{5.56 \times 10^{-11} h}{\ln(h/a) - 1} \quad (46)$$

where C_a is the monopole antenna input capacitance (F), h is the monopole antenna height (m), and a is the monopole antenna radius (m).

The standard field equations are relatively simple for a ground plane with infinite extent and infinite conductivity. In addition, the current on a vertical monopole antenna with finite diameter departs from the sinusoidal current distribution of a filamentary monopole antenna. This does not seriously affect the calculated values of

current-related field components, such as the magnetic field or the far-zone electric field. However, the low-frequency near-zone quasi-static electric field components are more nearly charge-related and are given by the spatial derivative of the current distribution. Hence, there is greater uncertainty in calculating the electric field components at frequencies well below that of a $\lambda/4$ -resonant monopole antenna.

If a transmitting monopole antenna is electrically short—that is, if the height is less than $\lambda/4$ and the frequency is below resonance—the current distribution is triangular. The field equations are a little more complicated; only the vertical electric field is given below [11]:

$$E_z = \frac{-j30I_0}{\sin(\beta l)} \left[\frac{e^{-j\beta r_1}}{r_1} + \frac{e^{-j\beta r_2}}{r_2} - 2 \cos(\beta l) e^{-j\beta r_0} \right] \quad (47)$$

The EM field values in the half-space above a perfect ground are the same as those in each half-volume of a center-fed $\lambda/2$ dipole antenna in free space. The input impedance of a monopole antenna above perfect ground is half that of a dipole antenna in free space. The power required to generate a given field strength is half that required for a dipole antenna, but the radiated power goes into half the volume, so the field is the same. Measurements of Z_{in} with a commercial impedance meter are performed to check the theoretical values from 0.5 to 50 MHz. Measurements of the monopole antenna capacitance can be made at lower frequencies with a commercial Q meter.

6. FUTURE DIRECTIONS

Established techniques for EM field measurements will probably be extended to higher frequencies; however, such work would not involve fundamental changes in the instrumentation or measurement strategy. The measurement methods described earlier are suitable only for (1) measuring plane-wave sinusoidal fields of a given frequency and (2) calibrating the devices that measure such fields.

The challenge of the future resides in the development of standards for measurement of fields that are nonsinusoidal and/or nonplanar. The fundamental requirement for EM field sensors is that their outputs provide amplitude and phase information simultaneously over a broad spectrum for nonsinusoidal fields. For fields containing more than one frequency component, it is clear that such simultaneous measurement is necessary. Similarly, if phase information is preserved, then measurements of single-frequency nonplanar fields can be made in terms of true energy density or in terms of the Poynting vector.

The standard techniques of today rely on very high-resistance transmission lines to convey DC voltage and current to regions external to the field under measurement. Future standards of measurement employ optically sensed EM field sensors whose optical sensing signal paths will not perturb the EM field under measurement, but will also convey field amplitude and phase information to a region external to the field for measurement. Optically sensed sensors are being built today. However,

additional work is needed to transform these experimental devices into stable elements for standards applications. Also, standard fields need to be developed, in order to calibrate these probes of the future.

BIBLIOGRAPHY

1. M. Kanda, Standard probes for electromagnetic field measurement, *IEEE Trans. Anten. Propag.* **AP-41**:1349–1363 (1993).
2. M. Kanda, Analytical and numerical techniques for analyzing an electrically short dipole with a nonlinear load, *IEEE Trans. Anten. Propag.* **AP-28**:71–78 (1980).
3. M. Kanda, A relatively short cylindrical broadband antenna with tapered resistive loading for picosecond pulse measurements, *IEEE Trans. Anten. Propag.* **AP-26**:439–447 (1978).
4. M. Kanda and L. D. Driver, An isotropic electric-field probe with tapered resistive dipoles for broadband use, 100 kHz to 18 GHz, *IEEE Trans. Microwave Theory Tech.* **MTT-35**:124–130 (1987).
5. M. Kanda, An electromagnetic near-field sensor for simultaneous electric and magnetic field measurements, *IEEE Trans. Electromagn. Compat.* **EMC-26**:102–110 (1984).
6. L. D. Driver and M. Kanda, An optically linked electric and magnetic field sensor for Poynting vector measurements in the near fields of a radiating source, *IEEE Trans. Electromagn. Compat.* **30**:495–503 (1988).
7. M. Kanda and K. D. Masterson, Optically sensed EM-field probes for pulsed fields, *Proc. IEEE* **80**:209–215 (1992).
8. J. C. Tippet, *Model Characteristics of Rectangular Coaxial Transmission Line*, Ph.D. dissertation, Electrical Engineering Dept., Univ. Colorado, Boulder, 1978.
9. S. A. Schelkunoff and H. T. Friis, *Antennas, Theory and Practice*, Wiley, New York, 1952.
10. F. M. Greene, The near-zone magnetic field of a small circular-loop antenna, *J. Res. Nat. Bur. Stand. U.S. C. Eng. Instrum.* **71C**(4) (1967).
11. E. C. Jordan and K. G. Balmain, *Electromagnetic Waves and Radiating Systems*, Prentice-Hall, Englewood Cliffs, NJ, 1968.

ELECTROMAGNETIC INVERSE PROBLEMS

ANYONG QING
YEOW BENG GAN
National University of
Singapore
Singapore

1. INTRODUCTION

1.1. Definition of Electromagnetic Inverse Problems

Electromagnetic inverse problems, also known as *electromagnetic inverse scattering problems*, aim to recover information on some inaccessible region from the scattered electromagnetic fields measured in the exterior region [1]. This region (hereafter referred to as “scatterers”) could be homogeneous or inhomogeneous, of any dimension, with

or without electromagnetic scatterers embedded. The information of interest is the location, shape, size, electrical properties (penetrable or impenetrable), and electromagnetic constitutive parameters. Most of the electromagnetic inverse problems can be considered as “active,” where a known incident field is artificially applied to illuminate the inaccessible unknown scatterers to give rise to scattered fields, which is measured at some accessible area. There are some cases, however, such as passive remote sensing, in which the scattered electromagnetic fields from the unknown scatterers are not due to such artificially applied incident electromagnetic fields. Usually, the scattered electromagnetic fields are measured over limited domain of aspect angle, frequency, and polarization, and are contaminated by noise and measurement error.

Electromagnetic inverse scattering is concerned with how we can obtain a large part of information about the world surrounding us. An everyday example of electromagnetic inverse problems is human vision; from the measurements of scattered light that reaches our retinas, our brains construct a detailed three-dimensional map of the world around us. This is a highly automated process, and most of us do not stop to reflect on how difficult this problem is. In fact, a large part of the human brain is devoted to such activities.

It should be pointed out that this definition of electromagnetic inverse problems is made in a narrow sense. In fact, all synthetic problems in electromagnetics, for example, the design of microwave filters and the synthesis of antennas, and many others, can be regarded as electromagnetic inverse problems. However, we will stick to this narrow definition of the electromagnetic inverse problems, unless otherwise stated.

Electromagnetic inverse problems and electromagnetic scattering problems come in pairs. For a given electromagnetic scattering problem, a priori information on the size, shape, and material constituents of the scatterers and the incident electromagnetic fields is provided, and the scattered field is calculated for a specific area and frequency domain. The electromagnetic community has embraced scattering problems with a warmth that is not generally extended to inverse problems. In fact, our training on electromagnetics is dominated by direct problems (in the general sense), while inverse problems continue to be regarded as very new and challenging research topics.

Note that electromagnetic inverse problems belong to a much wider class of inverse problems and are closely related to inverse problems in acoustic and elastic waves. It is also known that some techniques used in one field are identical, at least in principle, to those used in other, completely different fields. These interdisciplinary applications of the inversion techniques are drawing increasing attention. Hence, although we focus on electromagnetic inverse problems here, other fields of inverse problems will be touched on slightly where necessary.

1.2. Some Mathematical Challenges in Electromagnetic Inverse Problems

Electromagnetic inverse scattering problems and the associated electromagnetic scattering problems are highly

additional work is needed to transform these experimental devices into stable elements for standards applications. Also, standard fields need to be developed, in order to calibrate these probes of the future.

BIBLIOGRAPHY

1. M. Kanda, Standard probes for electromagnetic field measurement, *IEEE Trans. Anten. Propag.* **AP-41**:1349–1363 (1993).
2. M. Kanda, Analytical and numerical techniques for analyzing an electrically short dipole with a nonlinear load, *IEEE Trans. Anten. Propag.* **AP-28**:71–78 (1980).
3. M. Kanda, A relatively short cylindrical broadband antenna with tapered resistive loading for picosecond pulse measurements, *IEEE Trans. Anten. Propag.* **AP-26**:439–447 (1978).
4. M. Kanda and L. D. Driver, An isotropic electric-field probe with tapered resistive dipoles for broadband use, 100 kHz to 18 GHz, *IEEE Trans. Microwave Theory Tech.* **MTT-35**:124–130 (1987).
5. M. Kanda, An electromagnetic near-field sensor for simultaneous electric and magnetic field measurements, *IEEE Trans. Electromagn. Compat.* **EMC-26**:102–110 (1984).
6. L. D. Driver and M. Kanda, An optically linked electric and magnetic field sensor for Poynting vector measurements in the near fields of a radiating source, *IEEE Trans. Electromagn. Compat.* **30**:495–503 (1988).
7. M. Kanda and K. D. Masterson, Optically sensed EM-field probes for pulsed fields, *Proc. IEEE* **80**:209–215 (1992).
8. J. C. Tippet, *Model Characteristics of Rectangular Coaxial Transmission Line*, Ph.D. dissertation, Electrical Engineering Dept., Univ. Colorado, Boulder, 1978.
9. S. A. Schelkunoff and H. T. Friis, *Antennas, Theory and Practice*, Wiley, New York, 1952.
10. F. M. Greene, The near-zone magnetic field of a small circular-loop antenna, *J. Res. Nat. Bur. Stand. U.S. C. Eng. Instrum.* **71C**(4) (1967).
11. E. C. Jordan and K. G. Balmain, *Electromagnetic Waves and Radiating Systems*, Prentice-Hall, Englewood Cliffs, NJ, 1968.

ELECTROMAGNETIC INVERSE PROBLEMS

ANYONG QING
YEOW BENG GAN
National University of
Singapore
Singapore

1. INTRODUCTION

1.1. Definition of Electromagnetic Inverse Problems

Electromagnetic inverse problems, also known as *electromagnetic inverse scattering problems*, aim to recover information on some inaccessible region from the scattered electromagnetic fields measured in the exterior region [1]. This region (hereafter referred to as “scatterers”) could be homogeneous or inhomogeneous, of any dimension, with

or without electromagnetic scatterers embedded. The information of interest is the location, shape, size, electrical properties (penetrable or impenetrable), and electromagnetic constitutive parameters. Most of the electromagnetic inverse problems can be considered as “active,” where a known incident field is artificially applied to illuminate the inaccessible unknown scatterers to give rise to scattered fields, which is measured at some accessible area. There are some cases, however, such as passive remote sensing, in which the scattered electromagnetic fields from the unknown scatterers are not due to such artificially applied incident electromagnetic fields. Usually, the scattered electromagnetic fields are measured over limited domain of aspect angle, frequency, and polarization, and are contaminated by noise and measurement error.

Electromagnetic inverse scattering is concerned with how we can obtain a large part of information about the world surrounding us. An everyday example of electromagnetic inverse problems is human vision; from the measurements of scattered light that reaches our retinas, our brains construct a detailed three-dimensional map of the world around us. This is a highly automated process, and most of us do not stop to reflect on how difficult this problem is. In fact, a large part of the human brain is devoted to such activities.

It should be pointed out that this definition of electromagnetic inverse problems is made in a narrow sense. In fact, all synthetic problems in electromagnetics, for example, the design of microwave filters and the synthesis of antennas, and many others, can be regarded as electromagnetic inverse problems. However, we will stick to this narrow definition of the electromagnetic inverse problems, unless otherwise stated.

Electromagnetic inverse problems and electromagnetic scattering problems come in pairs. For a given electromagnetic scattering problem, a priori information on the size, shape, and material constituents of the scatterers and the incident electromagnetic fields is provided, and the scattered field is calculated for a specific area and frequency domain. The electromagnetic community has embraced scattering problems with a warmth that is not generally extended to inverse problems. In fact, our training on electromagnetics is dominated by direct problems (in the general sense), while inverse problems continue to be regarded as very new and challenging research topics.

Note that electromagnetic inverse problems belong to a much wider class of inverse problems and are closely related to inverse problems in acoustic and elastic waves. It is also known that some techniques used in one field are identical, at least in principle, to those used in other, completely different fields. These interdisciplinary applications of the inversion techniques are drawing increasing attention. Hence, although we focus on electromagnetic inverse problems here, other fields of inverse problems will be touched on slightly where necessary.

1.2. Some Mathematical Challenges in Electromagnetic Inverse Problems

Electromagnetic inverse scattering problems and the associated electromagnetic scattering problems are highly

mathematical. This is an ideal area for applied mathematicians. Electromagnetic inverse problems provide a rich supply of challenging mathematical problems.

1.2.1. Electromagnetic Scattering. Studying an electromagnetic inverse problem always requires a solid knowledge of the corresponding direct scattering problem. Unfortunately, the study of electromagnetic scattering problems is very far from complete. For example, the current level of understanding on wave propagation in complex media and random media remains very poor.

1.2.2. Nonlinearity. The scattering problem is linear in the sense that for a known scatterer, the relationship between the incident field and scattered field is linear. However, for electromagnetic inverse problems, we are interested in the relationship between the scatterer and its action on the incident fields. This relationship is inherently nonlinear.

1.2.3. Ill-Posedness. According to Hadamard [2], a problem is well-posed if it has a unique solution that depends continuously on the given data. Problems that are not well-posed are known as ill-posed. In general, electromagnetic inverse problems are ill-posed. The ill-posedness of electromagnetic inverse problems comes from the incomplete and contaminated measurement data, and the existence of a nonradiating source.

For an ill-posed electromagnetic inverse problem, the following questions must be addressed:

Existence: Is there any solution?

Uniqueness: Is the solution unique?

Stability: Is the solution stable? In other words, do small perturbations of the measured scattered fields always result in small perturbation of the solution?

1.3. Applications of Electromagnetic Inverse Problems

Although the electromagnetic inverse problem is a relatively new area of applied mathematical research, it has been increasingly used in scientific, military, medical, industrial, agricultural, and many other civil areas. Since the mid-1980s we have witnessed an explosion in the applications of electromagnetic inverse problems.

1.3.1. Scientific Applications. Electromagnetic inverse problems have been enormously influential in the development of natural sciences, with great advances in science and technology made possible through their solutions. Electromagnetic inverse problems could lead to the establishment of physical laws via indirect observations. Their solutions provide us with a wealth of scientific information: the discovery of DNA structure through solving X-ray diffraction problems and the structure of the atom and its constituents from studies on the scattering phenomena when materials are bombarded with particles. Over the years, electromagnetic inverse problems have played an increasingly important role in many scientific areas, such

as archaeology, seismology, geophysics, optics, material science, and meteorology.

1.3.2. Military Applications. The area of electromagnetic inverse problems was strongly stimulated by the great success in military applications during World War II, which witnessed the invention of radar and sonar for detection and identification of both friendly and hostile objects. As the world is not devoid of violence and war, military demands on electromagnetic inverse problems continue to increase. As an example, for people living in countries under the threat of landmines left over from earlier wars, safe detection and removal of these landmines using electromagnetic waves is a lifesaving method. On the other hand, increasingly powerful radar, spy satellite networks, and missile defense systems are being built to defend against attacks from terrorists and hostile countries.

1.3.3. Medical Applications. So far, besides military applications, medical imaging is one of the most successful application areas of electromagnetic inverse problems. In fact, the X-ray radiography machine is used in almost every hospital to diagnosis tuberculosis and other anomalies in the human body. In 1972, G. N. Hounsfield introduced a new radiographic imaging procedure, X-ray computer-assisted tomography (CAT). A picture of the CAT apparatus in a hospital is shown in Fig. 1. It is replacing the conventional and obsolete X-ray radiography machines in many hospitals. More recently, even some CAT machines have been replaced by more advanced nuclear magnetic resonance imaging machines for more accurate diagnosis.

1.3.4. Industrial Applications. The electromagnetic inverse problems are of commercial value to the industries. Oil companies, for example, determine the location of oil through solving inverse scattering problems. A significant fraction of the computational workload is performed by the oil companies. In fact, much of the recent resurgence



Figure 1. CAT apparatus in a hospital.
(Source: <http://encyclopedia.thefreedictionary.com/Computer%20assisted%20tomography>.)

in the oil industry is due to improvements in mathematical algorithms that allow scientists to “see” through salt layers to detect the oil-bearing strata below.

Ground penetrating radar (GPR) is a highly commercialized solution for nondestructive evaluation (NDE) that produces a continuous cross-sectional profile or record of subsurface features, without drilling, probing, or digging. The GPR for a shallow survey is shown in Fig. 2. Ground penetrating radar profiles are used to evaluate the location and depth of buried objects such as pipes and cables, and to investigate the presence and continuity of natural subsurface conditions and features.

The commercial aviation industry has also benefited significantly from solving electromagnetic inverse problems. For example, it is now mandatory for passengers to receive security check, including metal detection, before boarding. Other industries taking advantage of electromagnetic inverse problems include nuclear energy, food, construction, and marine enterprises. For example, the nondestructive evaluation of steam generator tubes is a major issue in the nuclear industry.

1.3.5. Agricultural Applications. Electromagnetic inverse problems are also very important to agriculture. In China, a large amount of effort has been put into predicting the national crop harvest using remote sensing techniques and monitoring the coverage of plants within Chinese territory.

1.3.6. Other Civil Applications. Electromagnetic inverse problems are also applicable to many other civil areas. For example, the environment can be monitored using remote sensing techniques.

1.4. Some Outstanding Research Groups

Electromagnetic inverse problems have been one of the most challenging areas in electromagnetics. Many



Figure 2. Shallow ground-penetrating radar surveys. (Source: <http://www.geomodel.com/>)

research groups and researchers from both within and outside the electromagnetic community have devoted their efforts to study the fundamental theory of inverse problems, develop inversion algorithms for particular cases, produce real datasets to test the developed algorithms, develop prototypes for practical applications, and commercialize the developed prototypes. Because of the large number of researchers and groups involved in this area, it is not possible to list all of them. However, special tributes should be paid to the following researchers and organizations for their outstanding work in this field: Institut Fresnel (France), W. M. Boerner, R. E. Kleinman, K. J. Langenberg, Rome Laboratory (renamed as Air Force Research Laboratory in 1997), and A. N. Tikhonov.

Their well-established contributions to this field will be highlighted at the appropriate parts in this article.

1.5. Some Future Directions

The field of electromagnetic inverse problems is a relatively new area with apparent potential for applications. However, many problems remain to be solved. Besides the topics mentioned in this article, the following topics in electromagnetic inverse problems also require special attention.

1.5.1. Three-Dimensional Electromagnetic Inverse Problems. Researchers in the field of electromagnetic inverse problems typically simplify their work by concentrating on lower-dimensional problems. Electromagnetic inverse problems that have been extensively studied usually assume geometry of only one or two dimensions, with a half-space or layered medium. However, such an assumption is insufficient for many practical problems, leading to failure of the inversion algorithms to produce any meaningful results.

Increasing attention has been devoted to three-dimensional electromagnetic inverse problems. Researchers are attempting to extend well-established lower-dimensional inversion algorithms to three-dimensional cases, as well as to develop new inversion algorithms focusing on three-dimensional electromagnetic inverse problems.

1.5.2. Electromagnetic Inverse Problems of Complex Scatterers. Most of the existing inversion algorithms assume that the scatterers are simple, that is, isotropic and nondispersive. However, this assumption is not valid for many real scatterers, such as human brains and organs.

1.5.3. Electromagnetic Inverse Problems in Complex Media. Another important issue is the electromagnetic inverse problem of scatterers in complex media. Some examples of complex media are soil, foliage, sea ice, sea surface, and the human body.

2. AN OVERVIEW OF RESEARCHES ON ELECTROMAGNETIC INVERSE PROBLEMS

Because of the theoretical and practical significance of electromagnetic inverse problems, extensive studies have been performed on electromagnetic inverse problems.

These studies include fundamental theories of electromagnetic inverse problems, measurement of scattering data, development of inversion algorithms for specific electromagnetic inverse problems and testing them with synthetic and/or real measurement data, development of prototypes for practical applications, and commercialization of the developed prototypes. Numerous monographs, technical reports, and dissertations have been published. The number of journals specializing in inverse problems or with scope on inverse problems has increased significantly, with rapid growth in the number of special issues and papers on inverse problems. A large number of international conferences, workshops, and symposia (e.g., APS, MTTs, IGARSS, APMC, PIERS) on electromagnetic inverse problems have also been organized.

2.1. A Brief History

The study on electromagnetic inverse problems can be traced back to 1895 when X rays were discovered in the first body imaging tests conducted by Wilhelm Roentgen, the discoverer of X rays. The first major mathematical breakthrough took place in 1917 when the radon transform, the basic mathematical framework common to a large class of inverse problems, was proposed [3]; unfortunately, this work was not well appreciated in the application areas until the 1970s. The second stimulation to electromagnetic inverse problems occurred during World War II, when radar was invented by scientists and engineers to identify friendly and hostile aircraft. However, the field of electromagnetic inverse problems was not well recognized until A. N. Tikhonov established the fundamental theory of ill-posed problems in the mid-1960s [4]. In 1972, G. N. Hounsfield introduced CAT [5]. Since then, an extensive and intensive study on electromagnetic inverse problems and other related inverse problems has been carried out.

The first extensive survey covering many fields in which inverse problems were applied was presented in a NASA memorandum by Colin [6]. In 1981, the *IEEE Transactions on Antennas and Propagation* published a special issue on inverse methods in electromagnetics [7]. Subsequently, W. M. Boerner organized the NATO Advanced Research Workshop on Inverse Methods in Electromagnetic Imaging in 1983 [5]. Afterward, there was a burst in publication of research results scattered in many monographs [8], technical reports, dissertations, journals, and conference proceedings.

Nevertheless, the field of electromagnetic inverse problems remains one of the most challenging problems of applied electromagnetics. A review on the latest state of the art is presented in Ref. 1.

2.2. Mathematical Fundamentals of Electromagnetic Inverse Problems

Applied mathematicians such as D. Colton, R. Kress [8], and P. Monk studied the fundamental mathematical theories behind the electromagnetic inverse problems. Such studies strengthened our understanding of the electromagnetic inverse problems and gave confidence to developers of inversion algorithms. Apparently, these

fundamental mathematical theories are also directly applicable—or can be applied with minor modifications—to other fields of inverse problems.

2.2.1. Existence and Uniqueness. As mentioned before, in any realistic situation, the measured data are not exact. Hence, an exact solution to a real inverse problem seldom exists in its original solution space. However, existence can be forced by enlarging or reducing the solution space. Therefore, the common practice is to assume that an approximate solution does exist and is physically feasible. The existence of an inverse problem is rarely considered since it is of little theoretical and practical importance.

There are three famous uniqueness theorems in electromagnetic inverse problems [9]: Tikhonov's uniqueness theorem for a one-dimensional inverse problem, Weidelt's uniqueness theorem for a two-dimensional inverse problem with an electrical conductivity described by an analytic function, and Gusarov's uniqueness theorem for a two-dimensional inverse problem with a piecewise analytic function of electrical conductivity. Later, Colton, Kress [8], and P. Monk obtained the more general uniqueness theorems for electromagnetic inverse problems.

2.2.2. Stability and Regularization. We will now consider the issue of stability of inverse problems. This problem reflects the practical fact that although two sets of observation data may differ only in the noise level, the corresponding inversion results could be completely different. Negligence or improper remedy for the illness could have disastrous consequences. The common technique to restore stability of an inverse problem is to employ regularization methods, which are discussed in detail in the tutorial paper [10] as well as other topical review papers [11–14] and monographs [4,8,9,15].

Consider a general inverse problem

$$Au = f \quad (1)$$

where $A:u \in X \rightarrow f \in Y$ is an operator mapping space X into Y . The well-known Tikhonov regularization is designed to minimize the Tikhonov functional defined as

$$\|Au - f\|^2 + \gamma\|f\|^2 \quad (2)$$

2.3. Development of Inversion Algorithms

Development of inversion algorithms is always the key issue in the field of electromagnetic inverse problems. Extensive studies have been carried out on this subject, with many inversion algorithms developed.

As relevant literature are scattered over a large number of resources, a summary is given here for convenience for future study. However, the author makes no claim that this summary is exhaustive, since it is based only on the author's current knowledge.

As mentioned earlier, the field of inverse problems is interdisciplinary, as clearly demonstrated by the vast diversity of literature on electromagnetic inverse problems

and the background of researchers involved in the area. Some techniques used in one field are identical, at least in principle, to those used in completely different fields. Therefore, the inversion algorithm is considered here regardless of its origin, if it is applicable to electromagnetic inverse problems.

2.3.1. Linear Inversion Algorithms. The earliest attempts to solve the electromagnetic inverse problems simplified them by linearization through applying some approximations, such as the Born approximation, the Rytov approximation, and physical optics approximations (or Kirchhoff approximation). Generally speaking, such linear inversion algorithms are mathematically very elegant. For one-dimensional (1D) electromagnetic inverse problems, such linearization may lead to an analytical solution of the problem. Unfortunately, we seldom encounter 1D problems in practice. Moreover, the simplicity of the 1D case is rarely preserved in higher dimensions.

The most prominent inversion algorithms in this category include the layer-stripping algorithm, the method of characteristics, the Gelfand–Levitan–Marchenko integral equation method, the Born iterative method, and the linear diffraction tomography algorithm. K. J. Langenberg established his reputation in developing linear inversion algorithms. Readers are referred to Wirgin’s text [16] for detailed contributions by Langenberg to linear inversion algorithms.

2.3.2. Nonlinear Inversion Algorithms. As mentioned previously, nonlinearity is one of the distinct features of electromagnetic inverse problems. Developers of linear inversion algorithms usually ignore this basic feature of the inverse problems. In addition, the approximations made in linear inversion algorithms imposed too many restrictions, thereby limiting their applications.

The nonlinear inversion algorithms retain the nonlinearity of the electromagnetic inverse problems. Most of the nonlinear algorithms are mathematically more difficult and computationally more expensive, as nonlinear electromagnetic inverse problems are solved iteratively. On the other hand, such algorithms are usually more versatile and accurate, hence attracting more attention from practical applications.

In essence, electromagnetic inverse problems are optimization problems and can be solved by applying different optimization algorithms. Accordingly, nonlinear inversion algorithms can be further categorized in accordance with the optimization algorithms applied: the local inversion algorithms and the global inversion algorithm.

2.3.2.1. Local Inversion Algorithms. As the term implies, optimization algorithms involved in this category are local, or gradient-based. The prominent local algorithms include the distorted Born iterative method (or distorted wave Born iterative method, Newton–Kantorovitch algorithm), the conjugate-gradient method, the local shape function method, the modified gradient method, and the contrast source inversion method.

R. E. Kleinman and P. M. van den Berg proposed the modified gradient method and the contrast source inver-

sion method, which have been actively applied. The two algorithms have proved to be effective through experiment using two sets of real data to be discussed later in this article. Numerous papers have been published on their application in the field of electromagnetic inverse problems and other fields of inverse problems. For details of the two methods, please refer to their review paper [17].

2.3.2.2. Global Inversion Algorithms. The local algorithms rely critically on an initial solution to the electromagnetic inverse problem of interest. Under some strict hypotheses such as convexity, differentiability, and continuity of the object function, the solution can be obtained quickly from a good initial solution. Otherwise, the local algorithms will be trapped in local minima or may even diverge.

Global optimization algorithms have gained popularity in the optimization community for their simplicity, versatility and, most of all, strong ability in searching. The global optimization methods, including the genetic algorithms (GA), the evolution strategies, the Monte Carlo method, the neural network, the simulated annealing method, the memetic algorithm, and the particle swarm algorithm, are in general stochastic.

For developers of the inversion algorithm, interest in the global optimization algorithm has increased since the 1990s. Currently, S. Caorsi, C. C. Chiu, A. Massa, M. Pasatorino, and A. Qing are very active in this area.

2.3.2.3. Hybrid Inversion Algorithms. It is evident that local and global inversion algorithms are complementary to each other. It is therefore very logical to combine these two types of inversion algorithms in an attempt to obtain the global optimal solution within a shorter timeframe. The common practice of this approach is to use a preset threshold. Once the optimal objective function value obtained by the global inversion algorithm exceeds the threshold, the inversion is transferred to the local inversion algorithm. A smarter hybrid inversion algorithm combining the real-coded genetic algorithm (RGA) and the Newton–Kantorovitch algorithm (NKA) is presented in Ref. 18.

2.4. Verifications of Inversion Algorithms

Any developed inversion algorithm is subject to verification. Such verification includes tests on synthetic data (scattered field data obtained by numerical solution of the corresponding scattering problem from a known scatterer), tests on real data generated in controlled experiments, and practical testing in the real world, where possible.

2.4.1. Synthetic Test and Inverse Crime. It is acceptable and is almost a common practice to first verify an inversion algorithm on synthetic data. The inversion algorithm developer uses a synthetic test as a preliminary evaluation of the algorithm’s performance. The basic advantages of this test are that it is cost-effective and can be performed as and when required.

To ensure a reliable synthetic test of an inversion algorithm, inverse crime must be avoided. The inverse

crime, as defined by Colton and Kress [8], implies that the forward scattering solver used in generating the synthetic data is also used in the inversion algorithm, and/or the same discretization is used in both numerical procedures. Synthetic test committing inversion crime usually leads to surprisingly good results.

2.4.2. Test Using Controllable Experimental Data. As compared to the synthetic test, verifying an inversion algorithm based on laboratory-generated experimental data, especially the well-established data generated independently by other researchers, is more convincing. The algorithm developer can use such a test for an objective performance evaluation of the algorithm. It is also very beneficial for the developer to refine the algorithm on the basis of experience gained during such test.

The Ipswich dataset generated by Rome Laboratory in 1995 is well known in the community of electromagnetic inverse problems. Friendly contests among researchers based on this dataset have been conducted and presented in the *IEEE Antennas and Propagation Magazine* special sessions [19–22]. The tested algorithms include the Newton–Kantorovitch method, the modified gradient method, the conjugate-gradient method, the local shape function method, the backpropagation routine, the contrast source inversion method, and the variable metric method.

In 2001, Institut Fresnel provided a second set of real data for friendly contests among algorithm developers [23]. One interesting feature of this dataset comes from the wide frequency range. The tested inversion algorithms are the modified gradient method, the contrast source inversion method, the linear diffraction tomography algorithm, the real-coded genetic algorithm, the differential evolution strategy (DES), the distorted-wave Born iterative method, the linear spectral estimation technique, the iterative and distorted Born method, and some other inversion algorithms.

Of course, some other researchers from both within and outside the community of electromagnetic inverse problems have produced experimental data on their own. However, their works are more self-focused and their experimental setups are more specific to their own inversion algorithms.

2.5. Prototype Development and Commercialization

The ultimate objective in studying electromagnetic inverse problems is to apply the developed inversion algorithms and experimental setups in practical areas, and perhaps commercialization as well. Besides the successful commercialization of CAT and GPR, many researchers are building their own prototypes and testing them in different practical fields [1].

3. A STANDARD ELECTROMAGNETIC INVERSE PROBLEM

In this section, we consider a standard electromagnetic inverse problem, namely, the reconstruction of multiple perfectly conducting cylinders in free space.

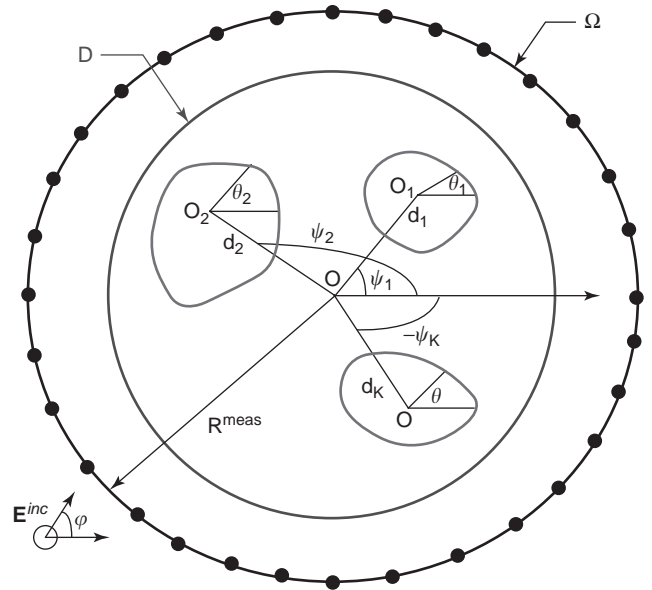


Figure 3. Geometry of the problem.

The geometry of the problem is depicted in Fig. 3, where O is the origin, Ω is a circle with radius R^{meas} in the measuring domain in which the scattered electric fields are measured, the black dots on Ω are receivers, and D is the imaging domain, which is usually chosen to be circular or rectangular; K perfectly conducting cylinders within D are the objects to be reconstructed, and O_i is the local origin of the i th cylinder, which can be any point within the cylinder contour C_i .

A transverse magnetic (TM) incident field is assumed (time factor of $e^{j\omega t}$ assumed and suppressed)

$$\mathbf{E}^{\text{inc}}(\mathbf{r}) = \hat{z} E_z^{\text{inc}} = \hat{z} \exp(-jk_0 \hat{\mathbf{k}} \cdot \mathbf{r}) \quad (3)$$

where $\omega = 2\pi f$ is the angular frequency, $\mathbf{r} = x\hat{x} + y\hat{y}$, $k_0 = \omega/c$ is the wavenumber in free space, c is the speed of light, $\hat{\mathbf{k}} = \cos \varphi \hat{x} + \sin \varphi \hat{y}$ is the incident wave unit vector, and φ is the incident angle; \hat{x} , \hat{y} , and \hat{z} are the unit vectors in the x , y , and z directions, respectively.

3.1. Problem Formulation

3.1.1. Direct Problem. Electric surface currents $\mathbf{J}_j(\mathbf{r}) = \hat{z} J_{zj}(\mathbf{r})$, $j = 1, K$ are induced on the surface of cylinders, and the scattered electric field $\mathbf{E}^{\text{scat}}(\mathbf{r}) = \hat{z} E_z^{\text{scat}}(\mathbf{r})$ is subsequently computed as follows

$$E_z^{\text{scat}}(\mathbf{r}) = \sum_{j=1}^K -\frac{\omega \mu_0}{4} \oint_{C_j} J_{zj}(\mathbf{r}') H_0^{(2)}(k_0 |\mathbf{r} - \mathbf{r}'|) d\mathbf{r}' \quad (4)$$

where μ_0 is the permeability of free space and $H_0^{(2)}(\cdot)$ is the Hankel function of the second kind of zeroth order.

On the surface of the cylinders, the tangential component of the total electric field vanishes:

$$[\mathbf{E}^{\text{scat}}(\mathbf{r}) + \mathbf{E}^{\text{inc}}(\mathbf{r})] \cdot \hat{\mathbf{z}} = 0 \quad \mathbf{r} \in \bigcup_{i=1}^K C_i \quad (5)$$

Therefore

$$\begin{aligned} E_z^{\text{inc}}(\mathbf{r}) &= \sum_{j=1}^K \frac{\omega \mu_0}{4} \oint_{C_j} J_{zj}(\mathbf{r}') H_0^{(2)} \\ &\cdot (k_0 |\mathbf{r} - \mathbf{r}'|) d\mathbf{r}', \quad \mathbf{r} \in \bigcup_{i=1}^K C_i \end{aligned} \quad (6)$$

The distribution of surface current is obtained after solving (6) by the point-matching method [24] with pulse basis function and the Dirac delta testing function.

3.1.2. Inverse Problem. The inverse problem is to locate the unknown cylinders and reconstruct the cylinder contours, given the scattered electric fields measured on Ω , $\mathbf{E}_{\text{meas}}^{\text{scat}}(\mathbf{r} \in \Omega)$. Usually, $\mathbf{E}_{\text{meas}}^{\text{scat}}$ is measured at a finite number of frequency points (N_f) and a finite number of incident angles for the incident plane waves (N_a) by a finite number of receivers (N_r). Accordingly, $\mathbf{E}_{\text{meas}}^{\text{scat}}$ becomes an ($N_f \times N_a \times N_r$)-dimensional vector. Equations (4) and (6) are the data and object (or state) equations of the present electromagnetic inverse problem.

Mathematically, the inverse problem described above is not well defined. The locations and contours of the cylinders must be represented by some mathematical quantities or functions. Usually, the location of a cylinder is represented by any point (center) $O_i(d_i, \psi_i)$ within its contour, while the contour is represented by a local shape function (LSF) $\rho_i = F_i(\theta_i)$ in its local polar coordinate system, where d_i and ψ_i are the polar radius and angle of O_i and ρ_i and θ_i are the local polar radius and angle of a point on the i th cylinder's contour, respectively.

The inverse problem is cast into an optimization problem by minimizing the object functional with respect to the local origins and local shape functions as follows

$$\begin{aligned} f\left(\bigcup_{i=1}^K [d_i, \psi_i, F_i]\right) &= \frac{\|\mathbf{E}_{\text{meas}}^{\text{scat}} - \mathbf{E}_{\text{simul}}^{\text{scat}}\|}{\|\mathbf{E}_{\text{meas}}^{\text{scat}}\|} \\ &+ \alpha \sum_{i=1}^K \sum_{j=1, j \neq i}^K \oint_{C_i} F_i(\theta_i) U \\ &\cdot [F_j(\theta_j) - \rho_{ij}(\theta_j)] d\theta_i \end{aligned} \quad (7)$$

where $\mathbf{E}_{\text{simul}}^{\text{scat}}$ is an ($N_f \times N_a \times N_r$)-dimensional vector constituting the scattered electric field simulated with the latest reconstruction results of cylinder locations O_i and local shape functions F_i and α is the intensity of penalty imposed on infeasible reconstruction results with inter-

secting cylinders as shown in Fig. 4:

$$\begin{aligned} \|\mathbf{E}_{\text{meas}}^{\text{scat}}\| &= \sqrt{\sum_{j=1}^{N_f \times N_a \times N_r} |(\mathbf{E}_{\text{meas}}^{\text{scat}})_j|^2} \\ \|\mathbf{E}_{\text{meas}}^{\text{scat}} - \mathbf{E}_{\text{simul}}^{\text{scat}}\| &= \sqrt{\sum_{j=1}^{N_f \times N_a \times N_r} |(\mathbf{E}_{\text{meas}}^{\text{scat}})_j - (\mathbf{E}_{\text{simul}}^{\text{scat}})_j|^2} \\ U(t) &= \begin{cases} 0, & t < 0 \\ 1, & t \geq 0 \end{cases} \end{aligned}$$

The first term of the objective functional (7) is the relative reconstruction error that gives a measurement on how close the reconstruction results approach the true profile, while the second term is an artificial penalty applied only in the case of intersecting cylinders.

3.1.3. Local Shape Functions

3.1.3.1. Trigonometric Local Shape Function. Most researchers approximate the LSF by a trigonometric series of order $N/2$:

$$\begin{aligned} F_i(\theta_i) \approx F_i^T(\theta_i) &= \sum_{n=0}^{N/2} A_{in} \cos(n\theta_i) \\ &+ \sum_{n=1}^{N/2} B_{in} \sin(n\theta_i) \end{aligned} \quad (8)$$

Under such an approximation, the objective functional (7) becomes the following objective function

$$f\left(\bigcup_{i=1}^K [d_i, \psi_i, F_i]\right) \approx f_T(\mathbf{x}_T) \quad (9)$$

where $\mathbf{x}_T = [\mathbf{x}_1 \ \cdots \ \mathbf{x}_K]$, $\mathbf{x}_i = [d_i \ \psi_i \ A_{i0} \ \cdots \ A_{iN-1} \ B_{i1} \ \cdots \ B_{iN-1}]$.

A basic requirement on a LSF is that it be nonnegative. However, it is hardly possible to guarantee the nonnegative definiteness of the trigonometric local shape function (TLSF) when it is applied in the global inversion algorithms. The unrealistic initial profile shown in Fig. 5 is the

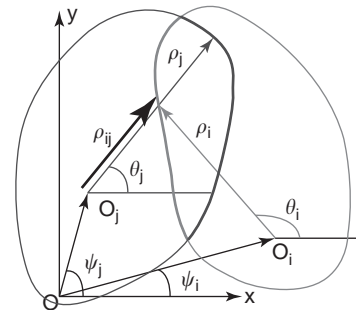


Figure 4. Intersecting cylinders.

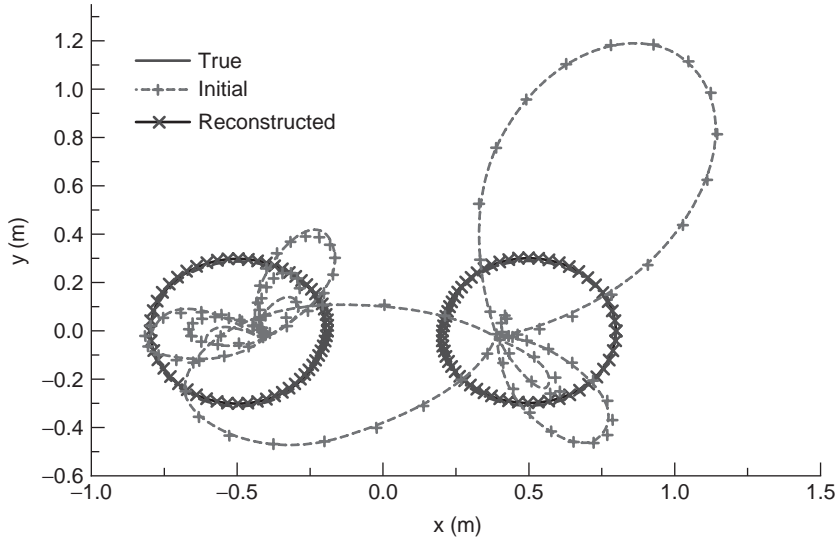


Figure 5. An unrealistic initial profile represented by trigonometric local shape functions. (This figure is available in full color at <http://www.mrw.interscience.wiley.com/erfme>.)

best profile in the initial population while reconstructing profile SP2, to be defined later in this article using RGA.

Some tricks can be used to guarantee the nonnegative definiteness of the TLSF, for example, by restricting the coefficient A_{i0} to be in a positive range with a big positive average value, and other coefficients in a much smaller range. However, for the present electromagnetic inverse problem, such tricks impose the unreasonable requirement of a priori knowledge of the cylinder's size.

3.1.3.2. Closed Cubic B-Spline Local Shape Function. The difficulty of the TLSF can be overcome by the closed cubic B-spline local shape function (BLSF) of N control points proposed by A. Qing [25]

$$F_i(\theta_i) \approx F_i^B(\theta_i) = R\left(\frac{N}{2\pi}\theta_i\right) \quad (10)$$

where

$$R(t') = \sum_{n=0}^{N-1} r_n(t' - n)$$

$$\begin{aligned} r_n(t) &= C_{\text{mod}(n-1,N)}Q_0(t) \\ &+ C_{\text{mod}(n,N)}Q_1(t) + C_{\text{mod}(n+1,N)}Q_2(t) \\ &+ C_{\text{mod}(n+2,N)}Q_3(t), \quad t \in [0, 1] \end{aligned}$$

$$Q_0(t) = \frac{1}{6}(1-t)^3$$

$$Q_1(t) = \frac{1}{2}t^3 - t^2 + \frac{2}{3}$$

$$Q_2(t) = -\frac{1}{2}t^3 + \frac{1}{2}t^2 + \frac{1}{2}t + \frac{1}{6}$$

$$Q_3(t) = \frac{1}{6}t^3$$

One promising feature of the BLSF is its boundedness, expressed mathematically as

$$\min_{0 \leq n \leq N-1} C_{\text{in}} \leq F_i^B(\theta_i) \leq \max_{0 \leq n \leq N-1} C_{\text{in}} \quad 0 \leq \theta_i \leq 2\pi \quad (11)$$

Therefore, the nonnegative definiteness of the BLSF can be guaranteed if all control points C_{in} are nonnegative. Such natural condition does not impose any artificial restrictions on the choice of the control points.

The corresponding objective function is

$$f\left(\bigcup_{i=1}^K [d_i, \psi_i, F_i]\right) \approx f_B(\mathbf{x}_B) \quad (12)$$

where $\mathbf{x}_B = [\mathbf{x}_1 \cdots \mathbf{x}_K]$, $\mathbf{x}_i = [d_i \ \psi_i \ C_{i0} \cdots C_{iN-1}]$

3.2. Applicable Inversion Algorithms

The present electromagnetic inverse problem has been solved using different inversion algorithms, including the linear diffraction tomography algorithm, the NKA, the GA, the DES, the differential evolution strategy with individuals in groups (GDES), and hybrid algorithms. Reconstruction using the linear diffraction tomography algorithm is conducted by K. J. Langenberg and his colleagues. Readers are referred to Ref. 23 for details, which will not be discussed here. In addition, since the hybrid algorithm is basically a combination of the NKA and one of the global inversion algorithms, it is also not included here. Interested readers are referred to Ref. 18 for more information.

3.2.1. Newton–Kantorovich Algorithm. The NKA, a generalization of the well-known Newton method, was proposed by Kantorovitch in 1948 and was applied to reconstruct the shape of a perfectly conducting cylinder in 1981 with a priori knowledge of the exact location of the cylinder [26]. The TLSF is used to approximate the cylinder contour. Although mathematically complicated, it is straightforward to generalize the formulation in Ref. 26 to reconstruct the locations and contours of multiple

perfectly conducting cylinders. The TLSF and the BLSF can be regarded as two special cases of a more general LSF in the form of expansion of basis functions.

The key idea in the NKA is to obtain the relationship between small variation in the measured scattered electric field, $\delta E_z^{\text{scat}}(\mathbf{r})$, and small variation in the cylinder's profile parameters $\delta \mathbf{x}$:

$$\delta E_z^{\text{scat}}(\mathbf{r}) = \mathbf{A} \cdot \delta \mathbf{x} \quad (13)$$

This equation is usually overdetermined and ill-posed. Different regularization measures can be applied to obtain an update of the cylinder's profile parameters $\delta \mathbf{x}$

$$\delta \mathbf{x} = \mathbf{A}^{-1} \cdot \delta E_z^{\text{scat}}(\mathbf{r}) \quad (14)$$

where \mathbf{A}^{-1} , the inverse of operator (matrix) \mathbf{A} , is in general obtained with regularization.

The cylinder's profile parameters are obtained iteratively as follows:

1. Select an initial solution \mathbf{X}^0 .
2. Solve the scattering problem for $\mathbf{E}_{\text{simul}}^{\text{scat},k}$ to obtain $\delta \mathbf{E}_z^{\text{scat},k} = \mathbf{E}_{\text{simul}}^{\text{scat},k} - \mathbf{E}_{\text{meas}}^{\text{scat}}$.
3. Update the cylinders' profile parameters $\mathbf{x}^{k+1} = \mathbf{x}^k + \delta \mathbf{x}^k = \mathbf{x}^k + \mathbf{A}_k^{-1} \cdot \delta E_z^{\text{scat},k}$.
4. Repeat steps 2 and 3 until the termination conditions are satisfied.

3.2.2. Genetic Algorithms. The concept of GA was first proposed by Holland [27]. It imitates the mechanism of natural selection and evolution, and aims to solve an optimization problem with object function $f(\mathbf{x})$ where \mathbf{x} is an N -dimensional vector of optimization parameters. Usually, the objective function $f(\mathbf{x})$ is scaled to a fitness function $\text{fit}(\mathbf{x})$.

Genes and chromosomes are the basic building blocks of GA. A gene can be the optimization parameter itself, or a code in a code string of the encoded optimization parameters. A chromosome is a concatenation of genes that takes the form

$$\text{Chromosome} = \underbrace{g_1^1 g_2^1 \cdots g_{L_1}^1}_{x_1} \underbrace{g_1^2 g_2^2 \cdots g_{L_2}^2}_{x_2} \cdots \underbrace{g_1^N g_2^N \cdots g_{L_N}^N}_{x_N} \quad (15)$$

where g_j^i is a gene and L_i is the length of the code string of the i th optimization parameter.

The GA operates on a population of N_{pop} individuals simultaneously. Each individual is related to a fitness value, an optimization parameter vector, and a chromosome. The GA starts with an initial population randomly generated within the search space. On completing the initialization, the population enters the main GA loop and performs a global optimization to search for the optimum solution of the problem. The GA loop continues until the termination conditions are fulfilled. A block diagram of the GA is shown in Fig. 6.

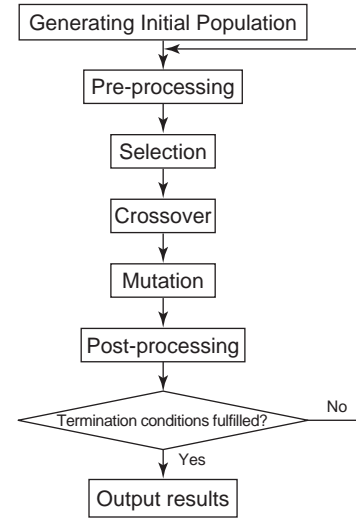


Figure 6. Block diagram of genetic algorithms.

In a GA loop, the three basic genetic operations—selection (or reproduction), crossover, and mutation—are executed sequentially. The selection operator selects good individuals on the basis of their fitness values and produces a temporary population, namely, the mating pool. This can be achieved by many different schemes, but the most common methods are the roulette wheel, ranking, and stochastic binary tournament selection. The selection operator is responsible for the convergence of GA. The crossover operator is the main search tool. It mates individuals in the mating pool by pairs and generates candidate offspring by crossing over the mated pairs with probability p_{cross} . Many crossover schemes, such as one-point crossover and continuous or random multipoint crossover, have been developed. After crossover, some of the genes in the candidate offspring are subjected to mutation with a probability p_{mut} . The mutation operator is included to prevent premature convergence by ensuring diversity in the population. There may be preprocessing operation(s) before selection and postprocessing operation(s) after mutation. However, these are not considered as basic genetic operations.

The promising advantages of GA are the robust global search ability, simplicity, and versatility, while the notorious disadvantage of GA is the long runtime.

The GA was appreciated by the electromagnetic community in 1990s and has gained popularity since then. Details of the genetic algorithms and its applications in electromagnetics are comprehensively summarized in the two tutorial papers [28,29] and a review paper [30].

3.2.2.1. Standard Genetic Algorithm. C. C. Chiu [31] applied the conventional standard (or simple) genetic algorithm (SGA, also known as binary genetic algorithm, BGA), to reconstruct the shape of a perfectly conducting cylinder in free space with an exact a priori knowledge of the cylinder location. Unfortunately, the results presented in this pioneering work are dubious.

The SGA encodes the optimization parameters into a string of binary codes. A gene in SGA is a binary code. The

correspondence between a chromosome and the optimization parameters is given by

$$x_i = x_i^{\min} + \frac{x_i^{\max} - x_i^{\min}}{2^{L_i} - 1} \sum_{j=1}^{L_i} g_j^i 2^{L_i - j} \quad i = 1, N \quad (16)$$

where $[x_i^{\min}, x_i^{\max}]$ is the search range for the i th optimization parameter, $g_j^i \in [0, 1]$.

3.2.2.2. Real-Coded Genetic Algorithm. The SGA does not operate directly on the optimization parameters but on a discretised representation of them. Discretization error will inevitably be introduced when encoding a real parameter. The encoding and decoding operations also make the algorithm more computationally expensive for problems with real optimization parameters. The RGA, a GA working directly on real optimization parameters, is more desirable.

In the RGA, a gene is the optimization parameter itself, and the chromosome of the i th individual in the n th population takes the form

$$\text{Chromosome}^{n,i} = \mathbf{x}^{n,i} = [x_1^{n,i} \quad x_2^{n,i} \quad \dots \quad x_N^{n,i}] \quad (17)$$

Consequently, the crossover and mutation operators used in the RGA are quite different from those in the SGA. Commonly used crossover schemes in RGA include one-point mixture, continuous or random multipoint mixture, and arithmetical one-point crossover. The mutation in RGA takes the form of random perturbation.

A. Qing has successfully applied the RGA to reconstruct the location and shape of multiple perfectly conducting cylinders [1,32,33]. It has also been verified by real data reconstruction [34].

3.2.3. Differential Evolution Strategy. It is evident that the genetic operators in the genetic algorithms could be destructive: (1) the selection operation discriminates those less-fit parents—hence, their chance to produce possibly better babies is deprived; and (2) for crossover and mutation operations, all parents are replaced by their baby children, even if their children are less fit.

The DES [35] is a very simple but very powerful global optimizer. Its apparent distinction from GA is in the order of execution of the genetic operations. In the DES, the three genetic operations are executed in the order of mutation, crossover, and selection (or mother-child competition). Each parent individual is given equal chance to have her child. Selection is conducted between the mother and her child for a survival chance. In this way, destructive genetic operations are avoided. The other key behind the success of the DES is a scheme for generating trial parameter vectors.

The DES was first applied to reconstruct the location and radius of buried circular conductors or tunnels [36]. It was later applied to the present standard electromagnetic inverse problem [37].

The block diagram of the DES is shown in Fig. 7. (Please refer to Refs. 35–37 for a detailed explanation.)

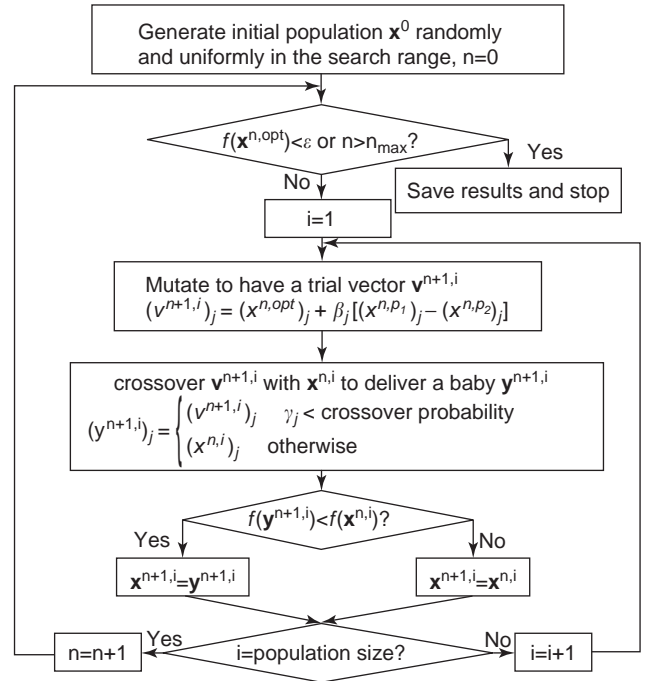


Figure 7. Block diagram of differential evolution strategy (ϵ —convergence threshold for minimization problem; β_j —random number uniformly distributed in $[0,1]$, γ_j —random number uniformly distributed in $[0,1]$; $1 \leq p_1 \neq p_2 \neq i \leq \text{population size}$).

3.2.4. Differential Evolution Strategy with Individuals in Groups. Although an inexact a priori knowledge of the number of cylinders in the imaging domain enables the execution of the NKA, the GA, and the DES, in terms of reconstruction time and quality of reconstruction results, an exact a priori knowledge of the number of cylinders in the imaging domain is crucial for these algorithms. Unfortunately, it is never easy to obtain such an exact a priori knowledge.

Such difficulty is overcome by the recently (in 2004) proposed GDES [38]. The number of cylinders is treated as an additional optimization parameter, to keep it flexible during the reconstruction. Therefore, no a priori knowledge on the number of cylinders is necessary. A crude guess on the maximum number of cylinders in the imaging domain is sufficient.

The key idea of the GDES is to organize the entire population into different groups according to the number of optimization parameters that they have; for instance, individuals in the same group have the same number of optimization parameters. This is possible since the maximum number of cylinders is limited and because individuals with the same number of cylinders have the same number of optimization parameters. The basic genetic operations of the DES (mutation, crossover, and mother-child competition) are performed within each group to determine the optimal profile in the group. An additional operator, the group competition, is introduced to adjust the group's size during evolution.

Since the number of cylinders of the reconstructed profile matches the exact number of cylinders of the true profile, the quality of the reconstruction results are therefore

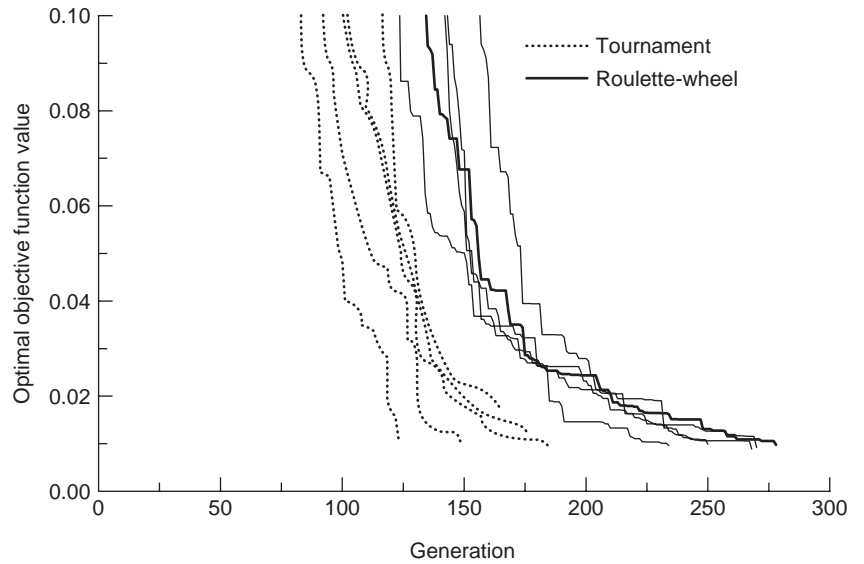


Figure 8. Optimization of function $f(\mathbf{x}) = \sum_{k=1}^{14} (x_k - k)^2$, $x_k \in [-500, 500]$ using RGA.

much better, while the reconstruction time required is correspondingly reduced.

3.3. Numerical Results

3.3.1. Optimization of a Mathematical Function

3.3.1.1. Function for Optimization. The mathematical function to be optimized is

$$f(\mathbf{x}) = \sum_{k=1}^K (x_k - k)^2 \tag{18}$$

The optimal solution is $f(x_k = k) = 0$.

3.3.1.2. Search Range. The optimization parameters are searched within the range $[-500, 500]$, unless otherwise specified.

3.3.1.3. Termination Conditions. The two termination conditions are

1. Normal termination: $\min_{1 \leq i \leq N_{pop}} f^n(\mathbf{x}^{n,i}) \leq \varepsilon = 0.01$
2. Abnormal termination: $n > N_{max} = 1000$

3.3.1.4. SGA versus RGA. Here, $K = 14$ is considered, with $N_{pop} = 256$, $p_{cross} = 1.0$, $p_{mut} = 0.1$ for RGA. The one-point arithmetic crossover scheme is chosen as the crossover operator. The converging curves of RGA are shown in Fig. 8, in which the applied selection schemes are also shown.

For the SGA, $N_{pop} = 256$, $p_{cross} = 0.8$, $p_{mut} = 0.04$ are used. No test is successful for SGA within the same search range, which is subsequently narrowed to $[-20, 20]$ for SGA. The corresponding curves are shown in Fig. 9. The

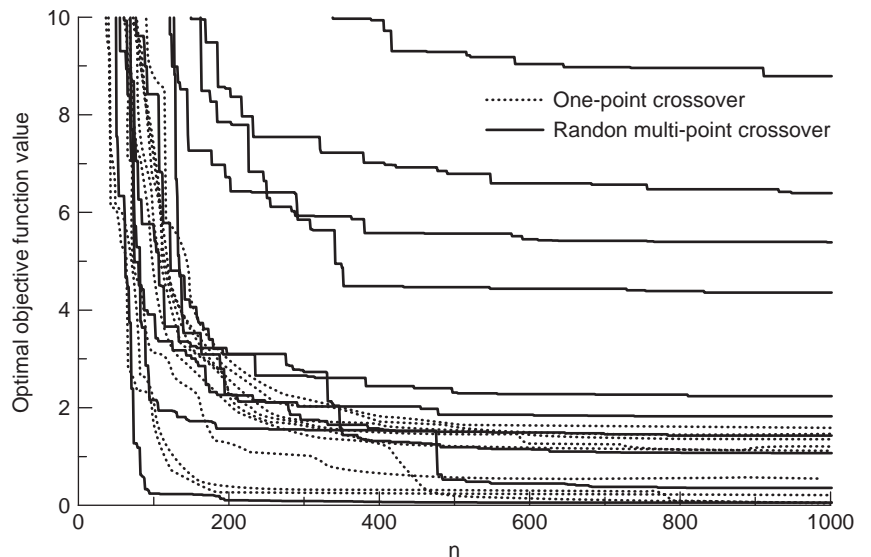


Figure 9. Optimization of function $f(\mathbf{x}) = \sum_{k=1}^{14} (x_k - k)^2$, $x_k \in [-20, 20]$ using SGA.

convergence is not satisfactory even with the narrowed search range.

This comparison clearly shows the advantages of RGA over SGA.

3.3.1.5. RGA versus DES. Here, $K=20$ is considered, with $N_{\text{pop}}=256$, $p_{\text{cross}}=1.0$, $p_{\text{mut}}=0.1$ for RGA and $N_{\text{pop}}=100$, $p_{\text{cross}}=0.9$, $\beta=0.7$ for DES. The convergence performances are shown in Fig. 10.

The DES converges to the true solution with fewer generations and a smaller population size. It is apparent that the DES outperforms the RGA.

3.3.2. Synthetic Reconstruction

3.3.2.1. Synthetic Profiles. The following profiles are reconstructed using one or more of the abovementioned inversion algorithms:

SP1—a single cylinder: $d=0$, $\psi=0$, $F(\theta)=0.3+0.05\sin 2\theta$

SP2—two parallel circular cylinders: $d_1=0.5$, $\psi_1=0$, $F_1(\theta_1)=0.3$; $d_2=0.5$, $\psi_2=\pi$, $F_2(\theta_2)=0.3$

SP3—a single cylinder: $d=0$, $\psi=0$, $F(\theta)=0.3+0.06\cos\theta+0.03\sin\theta+0.025\cos 2\theta$

SP4—two parallel circular cylinders: $d_1=0.8$, $\psi_1=0$, $F_1(\theta_1)=0.3$; $d_2=0.8$, $\psi_2=180^\circ$, $F_2(\theta_2)=0.3$

SP5—a single circular cylinder: $d=0$, $\psi=0$, $F(\theta)=0.3$

3.3.2.2. Settings of Parameters. The incident frequency is 300 MHz ($\lambda=1$ m). It illuminates the unknown objects from eight incident directions, $\varphi_i=i\pi/4$, $i=1-8$; 32 receivers are located uniformly on Ω , with $R^{\text{meas}}=10\lambda$.

For SGA, $N_{\text{pop}}=256$, $p_{\text{cross}}=0.8$, $p_{\text{mut}}=0.04$ are used. For the RGA, $N_{\text{pop}}=256$, $p_{\text{cross}}=1.0$, $p_{\text{mut}}=0.1$ are chosen, and for DES, $p_{\text{cross}}=0.9$, $\beta=0.7$. The population size is 5 times that of the number of optimization parameters for DES. Finally, for the GDES, $N_{\text{pop}}=300$, $p_{\text{cross}}=0.9$,

$\beta=0.7$ are used. The local origins of the cylinders are searched in a circle around the origin with a radius of 1λ .

BLSF is used to approximate the cylinder's contours. The number of control points of a BLSF is 6. The search range of control points is $[0, \lambda]$

Settings that differ from the above specification will be pointed out explicitly.

3.3.2.3. Generation of Synthetic Data. The measured scattering data are obtained from simulation through solving the direct problem with finer subdivision of the cylinder contours. The synthetic data are assumed to be noise free.

3.3.2.4. Search Ability and Robustness

3.3.2.4.1. NKA versus RGA. The NKA and the RGA are applied to reconstruct SP1 and SP2. For SP1, an inexact a priori knowledge of the cylinder's location, $d=0.1$, $\psi=\pi/4$, is assumed. The contour of SP1 is approximated by a TLSF of order 4. The search ranges for the coefficients of the TLSF are $[0,2]$ for A_0 and $[-0.5,0.5]$ for A_i and B_i , $i=1-4$. Similarly, the locations of cylinders are known in advance for SP2, with $d_1=0.4$, $\psi_1=0$, $d_2=0.4$, and $\psi_2=\pi$. The order of the TLSF for SP2 is 3. The search ranges are set to be similar. The initial guess for the NKA is generated using the four schemes described in Ref. 1.

SP1 and SP2 are reconstructed successfully by the RGA. However, most of the trials with NKA fail to reconstruct the profiles. On the other hand, the few successful trials consume significantly less time.

3.3.2.4.2. SGA versus RGA. SP3, the profile considered in Ref. 31, is reconstructed using SGA and RGA. To be consistent with Ref. 31, the cylinder location is assumed to be known exactly in advance. The contour is approximated by a TLSF of order 4. The search range of A_0 is $[0,2]$. For A_i and B_i , $i=1-4$, the search ranges of $[-0.5,0.5]$ and $[0,2]$ are tested. RGA successfully obtained the profile with the narrow search range, while SGA can obtain only a

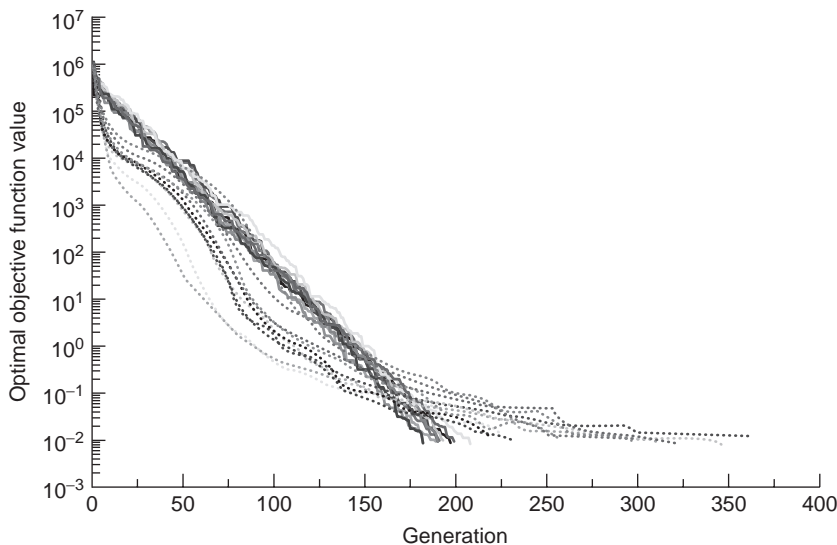


Figure 10. Optimization of function $f(\mathbf{x}) = \sum_{k=1}^{20} (x_k - k)^2$, $x_k \in [-500, 500]$ using DES (solid lines) and RGA (dotted lines). (This figure is available in full color at <http://www.mrw.interscience.wiley.com/erfme>.)

quasioptimal result ($\epsilon=0.03$) in affordable simulation time. The corresponding convergence performances are shown in Fig. 11. Both RGA and SGA failed to reconstruct the true profile with wide search range.

3.3.2.4.3. *RGA versus DES.* Profile SP4 is reconstructed using both RGA and DES. For the DES, $N_{pop} = 100$, $p_{cross} = 0.9$, $\beta = 0.7$ are used. A priori knowledge of the exact locations of the cylinders is assumed for RGA. The convergence performances are shown in Fig. 12.

3.3.2.5. *Effect of A Priori Knowledge of the Number of Cylinders.* A priori knowledge of the number of cylinders in the imaging domain is absolutely required for all algorithms considered, with the exception of the GDES. However, such a priori knowledge is rarely available. Here, its effect on the reconstruction will be studied.

SP4 and SP5 are the profiles of interest. The inversion algorithms studied are DES and GDES. The GDES requires a maximum number of cylinders in the imaging domain, which is set to be 3 here. This requirement does not impose too much inconvenience, since the maximum value is not necessarily exact and is usually restricted only by the available computational resources.

When reconstructing SP4 using DES, two cases of such a priori knowledge are considered. The first case is that the number (2) is exactly known. The other case is that the number is incorrectly assumed to be 3. The relationship between the optimal objective function value and generation is shown in Fig. 13. Apparently, the incorrect assumption on the number of cylinders significantly delays the reconstruction. However, the quality of the reconstruction result is not significantly affected.

It is worth noting that the difference in the reconstruction time for these two cases is more significant, since it takes much longer for the second case to complete one generation due to the larger population size and longer time required to evaluate an individual.

The GDES obtained the true profile within a much shorter time as shown in Fig. 14.

Similar results are observed for SP5 as shown in Fig. 15 and Fig. 16. However, in this case, the quality of the

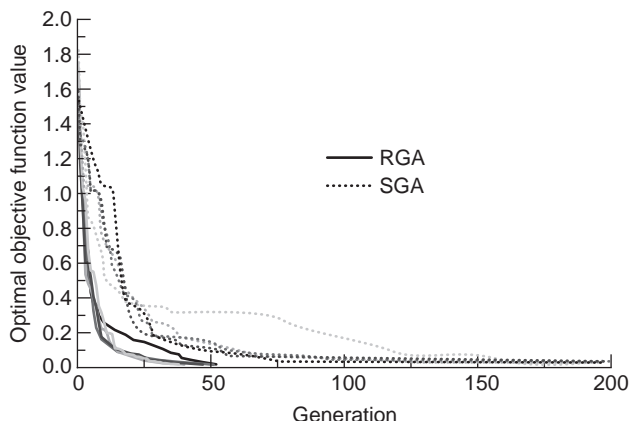


Figure 11. Reconstruction of profile SP3 using RGA (solid lines) and SGA (dotted lines). (This figure is available in full color at <http://www.mrw.interscience.wiley.com/erfme>.)

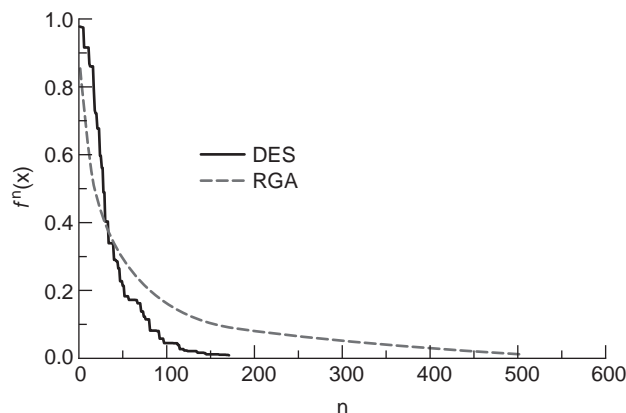


Figure 12. Reconstruction of profile SP4 using DES (black solid line) and RGA (red dashed line).

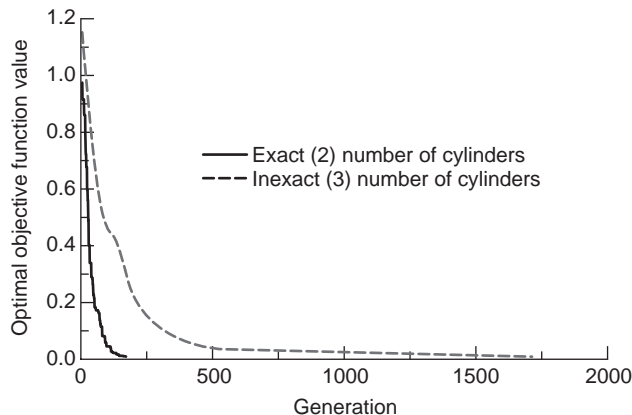


Figure 13. Reconstruction of profile SP4 using DES with exact (black solid line) and inexact (red dashed line) a priori knowledge of the number of cylinders.

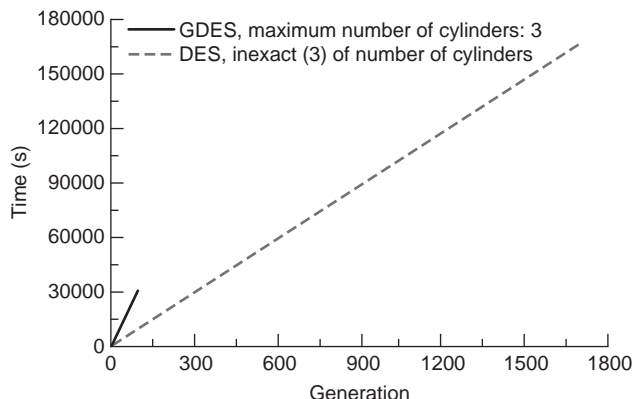


Figure 14. Reconstruction of profile SP4 using GDES (black solid line) and DES (red dashed line) with inexact a priori knowledge of the number of cylinders.

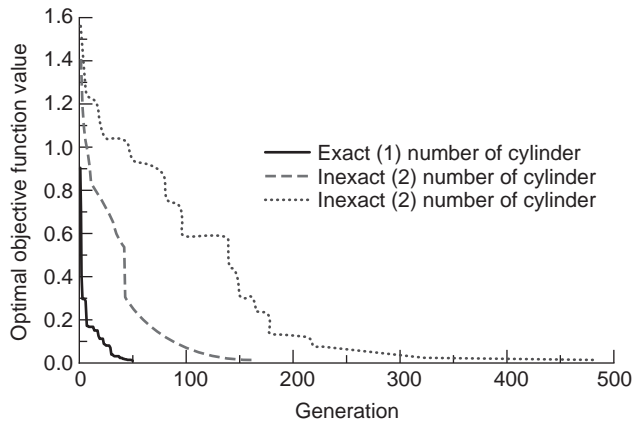


Figure 15. Reconstruction of profile SP5 using DES with exact (black solid line) and inexact a priori knowledge of the number of cylinders (red dashed line—2; blue dotted line—3).

reconstruction results using DES deteriorates with inexact assumption on the number of cylinders in the imaging domain, as shown in Fig. 17.

3.3.3. Reconstruction Using Fresnel Real Dataset

3.3.3.1. Experimental Setup. As mentioned earlier, the set of data was measured at Institut Fresnel, France [23]. The experimental setup is shown in Fig. 18. Please refer to Ref. 23 for more details.

3.3.3.2. Profiles Tested. The following two profiles are considered here:

RP1—centered 12.7×25.4 -mm rectangular cylinder (center position known before reconstruction)

RP2—decentered 12.7×25.4 -mm rectangular cylinder (center position unknown before reconstruction)

3.3.3.3. Measurement Noise. The data are very noisy, as shown in Table 1.

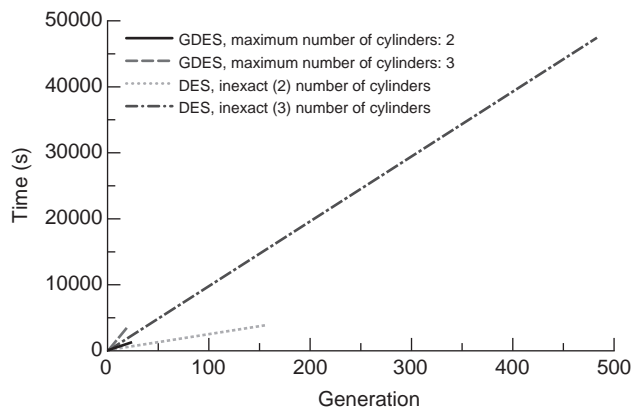
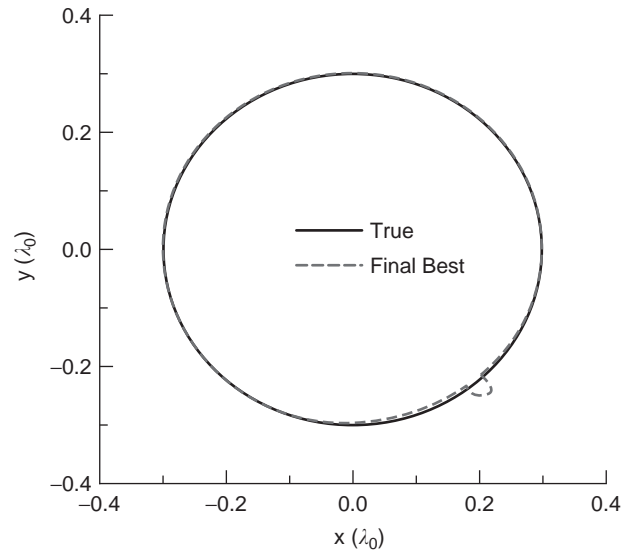
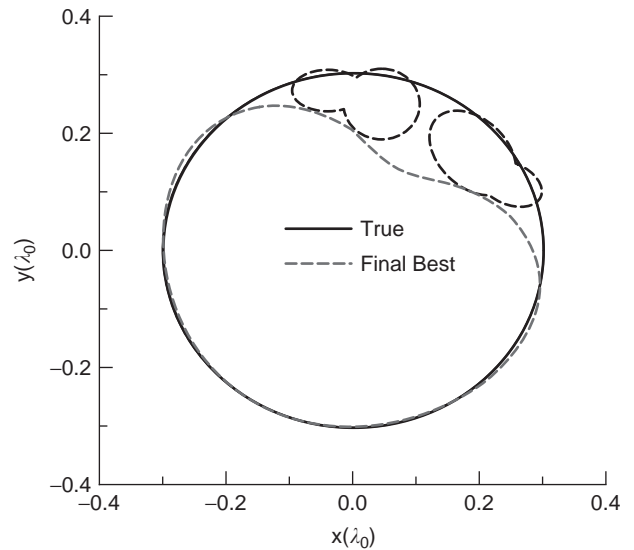


Figure 16. Reconstruction of profile SP5 using GDES (black solid line—2; red dashed line—3) and DES with inexact a priori knowledge of the number of cylinders (green dotted line—2, blue dashed-dotted line—3).



(a)



(b)

Figure 17. Reconstruction of profile SP5 using DES with inexact assumption of the number of cylinders: (a) assumed number of cylinders two; (b) assumed number of cylinders three.

3.3.3.4. Reconstruction Results. Both RGA and DES are applied to reconstruct the profiles.

The local origin is searched within a circle around the origin with radius 100 mm. Other parameters are identical as specified earlier. The reconstruction results are shown in Fig. 19 and 20. The cylinder is exactly located in all reconstructions. For RP1, excellent reconstruction results on the shape of RP1 are obtained at 8 and 16 GHz. The shape of RP1 at 4 and 12 GHz are a bit poorer but acceptable. The reconstructed shape of RP2 is good at 8, 10, 14, and 16 GHz, but a little bit poorer at 2, 4, 6, and 12 GHz. It is also observed that the reconstruction result of the centered case is in general better than those of the decentered case.

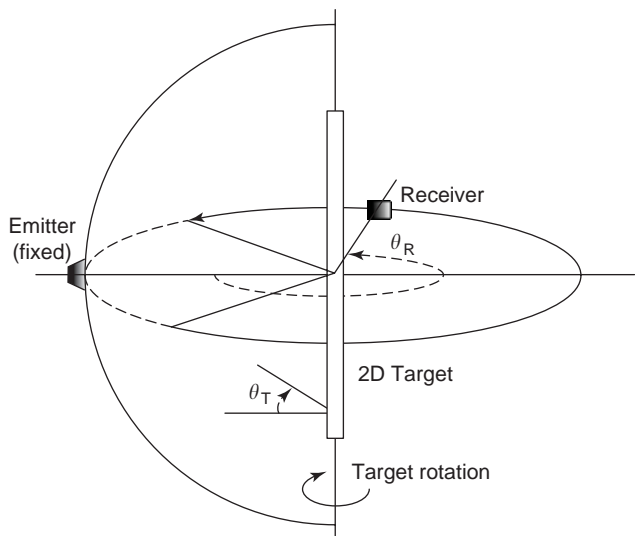


Figure 18. Fresnel experimental configuration.

It should be noted that the sample target, which is a rectangular cylinder, has four sharp corners. From the reconstruction results, it is noted that the cubic *B*-splines have difficulties in modeling these sharp corners.

Because of the strong noise in the experimental data, the reconstructed profile is quasioptimal. It is observed that the number of generations required to obtain the quasioptimal profile is comparable between the DES and the RGA. However, it is still reasonable to claim that the DES converges faster than the RGA, since the population size of the DES here (40) is much smaller than that of the RGA (256).

3.4. General Remarks

The abovementioned reconstructions and numerical experiences show that

1. The NKA is mathematically much more complicated. Its mathematical formulation is strongly related to the problem under consideration.
2. A good initial solution is very critical to the NKA. When such an initial solution is available, the NKA obtains the optimal solution very quickly.
3. In practice, the TLSF is applicable in the NKA since the NKA requires good a priori knowledge.
4. The BLSF applies equally well in all inversion algorithms considered.

Table 1. Measurement Error of RP1

Frequency (GHz)	Relative Error (%)
4	59.89
8	38.97
12	75.40
16	29.23

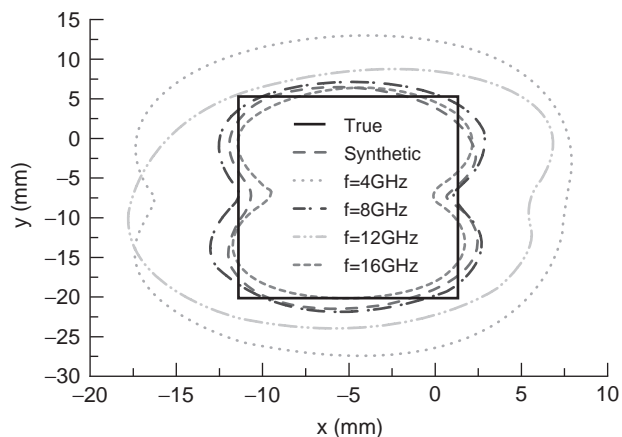
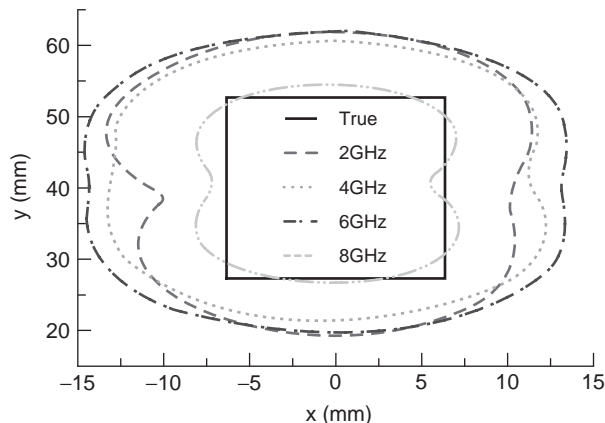
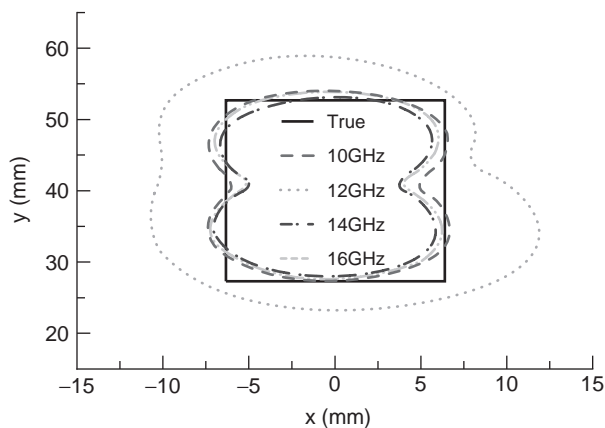


Figure 19. Reconstruction results of RP1. (This figure is available in full color at <http://www.mrw.interscience.wiley.com/erfme>.)

5. The SGA applies equally well to problems with any kinds of parameters (discrete, integer, real, or their mixture). However, its evolution mechanism needs to be improved.



(a)



(b)

Figure 20. Reconstruction results of RP2: (a) 2–8 GHz; (b) 10–16 GHz. (This figure is available in full color at <http://www.mrw.interscience.wiley.com/erfme>.)

6. For problems involving real parameters only, the DES outperforms the RGA and the RGA outperforms the SGA.
7. The GDES is the first choice, if the number of cylinders in the imaging domain is unknown.

More recently, large-scale numerical experiments on the DES have been carried out. It is confirmed that the performance of the DES is dependent on the choice of genetic parameters. It is also noted that the required number of objective function evaluations is proportional to the population size, while the success probability is inversely proportional to the population size. Therefore, a tradeoff between success probability and time must be made.

We have developed a novel global inversion algorithm: the dynamic differential evolution strategy. Preliminary results show that the required number of objective function evaluations is independent of the population size. Detailed and complete results will be reported soon, when the simulation is completed.

4. CONCLUSIONS

This article addresses the electromagnetic inverse problem, beginning with a definition of this problem, followed by detailed discussion of the mathematical challenges involved and the application areas. We then attempt to predict some future directions in electromagnetic inverse problems and present a survey of the research in electromagnetic inverse problems. This survey includes a brief history of electromagnetic inverse problems, an overview of practical application fields, and a brief summary of the fundamental theories involved in the electromagnetic inverse problems and the inversion algorithms developed. The survey also covers the well-known real dataset and the tested inversion algorithms. Subsequently, a standard electromagnetic inverse problem—the reconstruction of multiple perfectly conducting cylinders—is considered. The inversion algorithms applicable to the cases presented in this article have been discussed. Comparisons between different algorithms have been made. Remarks on the advantages and disadvantages of each algorithm are given. The most recent advancements in this area are also briefly discussed.

Acknowledgment

The authors would like to thank Ms. Cassie Craig and Prof. Kai Chang for their kind invitation to make this contribution.

BIBLIOGRAPHY

1. A. Qing, Electromagnetic inverse scattering of two-dimensional perfectly conducting objects by real-coded genetic algorithm, *IEEE Trans. Geosci. Remote Sens.* **39**(3):665–676 (March 2001).
2. J. Hadamard, *Lectures on the Cauchy Problem in Linear Partial Differential Equations*, Yale Univ. Press, New Haven, CT, 1923.
3. S. R. Deans, *The Radon Transform and Some of Its Applications*, Krieger, Malabar, FL, 1993.
4. A. N. Tikhonov and V. Y. Arsenin, *Solutions of Ill-Posed Problems*, Wiley, New York, 1977.
5. G. Schwierz, Review of tomographic imaging methods applied to medical imaging, in W. M. Boerner, et al., eds., *NATO Advanced Research Workshop on Inverse Methods in Electromagnetic Imaging*, Bad Windsheim, Franconia, FRG, Germany, Sept. 18–24, 1983, Reidel, Dordrecht, 1983.
6. L. Colin, *Proc. Workshop on Mathematics of Profile Inversion*, NASA Technical Memorandum x-62, 150, Ames Research Center, Moffett Field, CA, 1972.
7. W. M. Boerner, A. K. Jordan, and I. W. Kay, eds., Special issue on inverse methods in electromagnetics, *IEEE Trans. Anten. Propag.* **29**(2):185–417 (March 1981).
8. D. Colton and R. Kress, *Inverse Acoustic and Electromagnetic Scattering Theory*, 2nd ed., Springer, Berlin, 1998.
9. M. S. Zhdanov, *Geophysical Inverse Theory and Regularization Problems*, Elsevier, Amsterdam, 2002.
10. G. A. Deschamps and H. S. Cabayan, Antenna synthesis and solution of inverse problems by regularization methods, *IEEE Trans. Anten. Propag.* **20**(3):268–274 (1972).
11. M. Nashed, Operator-theoretic and computational approaches to ill-posed problems with applications to antenna theory, *IEEE Trans. Anten. Propag.* **29**(2):220–231 (1981).
12. C. de Mol, A critical survey of regularized inversion methods, in M. Bertero and E. R. Pike, eds., *NATO Advanced Research Workshop, on Inverse Problems in Scattering and Imaging*, Cape Cod, April 14–19, 1991, Adam Hilger, Bristol–Philadelphia–New York, 1992, pp. 345–370.
13. B. Hofmann, Regularization of nonlinear problems and the degree of ill-posedness, in G. Anger, R. Gorenflo, and H. Jockmann, eds., *Inverse Problems: Principles and Applications in Geophysics, Technology, and Medicine*, Wiley, New York, 1993, pp. 174–188.
14. F. Natterer, Regularization techniques in medical imaging, in M. A. Viergever and A. Todd-Pokropek, eds., *Mathematics and Computer Science in Medical Imaging*, Springer-Verlag, New York, 1988, pp. 127–141.
15. A. Asanov, *Regularization, Uniqueness and Existence of Solutions of Volterra Equations of the First Kind*, VSP, Utrecht, The Netherlands, 1998.
16. K. J. Langenberg, M. Brandfass, R. Hannemann, C. Hofmann, T. Kaczorowski, J. Kostka, R. Marklein, K. Mayer, and A. Pitsch, Inverse scattering with acoustic, electromagnetic, and elastic waves as applied in nondestructive evaluation, in A. Wirgin, ed., *Wavefield Inversion*, Springer, New York, 1999, pp. 59–118.
17. P. M. van den Berg and A. Abubakar, Contrast source inversion method: State of art, *Progress in Electromagnetics Research*, 2001, Vol. 34, Chap. 8, pp. 189–218.
18. A. Qing and C. K. Lee, A study on improving the convergence of the real-coded genetic algorithm for electromagnetic inverse scattering of multiple perfectly conducting cylinders, *IEICE Trans. Electron.* **E85-C**(7):1460–1471 (2002).
19. R. V. McGahan and R. E. Kleinman, eds., Image reconstruction using real data, special session, *IEEE Anten. Propag. Mag.* **38**(3):39–59 (June 1996).

20. R. V. McGahan and R. E. Kleinman, eds., Image reconstruction using real data, second annual special session, *IEEE Anten. Propag. Mag.* **39**(2):7–32 (April 1997).
21. R. V. McGahan and R. E. Kleinman, eds., Image reconstruction using real data, special session, *IEEE Anten. Propag. Mag.* **41**(1):34–51 (1999).
22. R. V. McGahan and R. E. Kleinman, eds., Image reconstruction using real data, special session, *IEEE Anten. Propag. Mag.* **41**(2):20–36 (1999).
23. K. Belkebir and M. Saillard, eds., Special issue on testing inversion algorithms against experimental data, *Inverse Problems* **17**(6):1565–1701 (Dec. 2001).
24. R. F. Harrington, *Field Computation by Moment Methods*, IEEE Press, New York, 1993.
25. A. Qing, Microwave imaging of parallel perfectly conducting cylinders with transverse electric scattering data, *J. Electromagn. Waves Appl.* **15**(5):665–685 (2001).
26. A. Roger, Newton-Kantorovitch algorithm applied to an electromagnetic inverse problem, *IEEE Trans. Anten. Propag.* **29**(2):232–238 (1981).
27. J. H. Holland, *Adaption in Natural and Artificial Systems*, Univ. Michigan Press, Ann Arbor, MI, 1975.
28. R. L. Haupt, An introduction to genetic algorithms for electromagnetics, *IEEE Anten. Propag. Mag.* **37**(2):8–15 (1995).
29. J. M. Johnson and V. Rahmat-Samii, Genetic algorithms in engineering electromagnetics, *IEEE Anten. Propag. Mag.* **39**(4):7–21 (1997).
30. D. S. Weile and E. Michielssen, Genetic algorithm optimization applied to electromagnetics: A review, *IEEE Trans. Anten. Propag.* **45**(3):343–353 (March 1997).
31. C. C. Chiu and P. T. Liu, Image reconstruction of a perfectly conducting cylinder by the genetic algorithm, *IEE Proc. Microwave Anten. Propag.* **143**(3):249–253 (1996).
32. A. Qing, C. K. Lee, and L. Jen, Microwave imaging of parallel perfectly conducting cylinders using real-coded genetic algorithm, *J. Electromagn. Waves Appl.* **13**(8):1121–1143 (Aug. 1999).
33. A. Qing and C. K. Lee, Microwave imaging of a perfectly conducting cylinder using real-coded genetic algorithm, *IEE Proc. Microwave Anten. Propag.* **146**(6):421–425 (Dec. 1999).
34. A. Qing, An experimental study on electromagnetic inverse scattering of a perfectly conducting cylinder by using real-coded genetic algorithm, *Microwave Opt. Technol. Lett.* **30**(5):315–320 (2001).
35. R. Storn and K. Price, *Differential Evolution—a Simple and Efficient Adaptive Scheme for Global Optimization over Continuous Spaces*, TR-95-012, International Computer Science Institute, March 1995 (<ftp://ftp.icsi.berkeley.edu/pub/tech-reports/1995/tr-95-012.pdf>).
36. K. A. Michalski, Electromagnetic imaging of circular-cylindrical conductors and tunnels using a differential evolution algorithm, *Microwave Opt. Technol. Lett.* **27**(5):330–334 (Dec. 2000).
37. A. Qing, Electromagnetic inverse scattering of multiple two-dimensional perfectly conducting objects by the differential evolution strategy, *IEEE Trans. Anten. Propag.* **51**(6):1251–1262 (June 2003).
38. A. Qing, Electromagnetic inverse scattering of multiple perfectly conducting cylinders by differential evolution strategy with individuals in groups (GDES), *IEEE Trans. Anten. Propag.* **52**(5):1223–1229 (May 2004).

ELECTROMAGNETIC MATERIALS

P. K. CHOUDHURY
Multimedia University
Cyberjaya, Selangor, Malaysia
O. N. SINGH
Banaras Hindu University
Varanasi, India

1. INTRODUCTION

Greek philosophers Plato and Socrates were aware of the polarities of lodestone, an iron ore, which could attract iron. Pierre de Marri-court used this property of lodestone to construct a compass to locate the North Pole. Gilbert (1540–1603) postulated that Earth is like a giant spherical magnet, and Kirchner (1601–1680) demonstrated that the magnetic poles of a magnet are of equal strength. Isaac Newton (1642–1727) made the first attempt to determine the law of force for a bar magnet, but the correct version (i.e., the inverse square law) was determined in 1750 by John Mitchell (1724–1793). In 1785 Charles de Coulomb (1736–1806) used the same inverse square law for determining the force between electric charges. Hans Christian Oersted (1777–1851) discovered in 1820 that a current-carrying wire could deflect a compass, and later on André Ampère (1775–1836) discovered that two current-carrying wires exert force on each other. Then Jean-Baptiste Biot (1774–1862) and Félix Savart (1791–1841) formulated their famous Biot–Savart law, which quantifies the force between the currents.

The inverse square law for magnetism was more or less established by the early nineteenth century. Benjamin Franklin (1706–1790) proposed an experiment to postulate the inverse square law for stationary electric charges, similar to the law of gravitation. In succeeding years considerable amount of work was carried on by Cavendish (in the early 1770s) and by Coulomb in 1785 to verify the inverse square law for electric charges. Karl Frederick Gauss (1777–1855) proposed the divergence theorem and presented the famous Gauss law of electrostatics, specifically, that the integral of the normal component of the electric flux over a closed surface is directly related to the net charge enclosed by that surface. In 1831 Michael Faraday (1791–1867) discovered that a time-varying magnetic field produces an electric field, and verified his law using the battery invented in 1800 by Alessandro Volta (1745–1827). In 1873, James Clerk Maxwell (1831–1879), a Scottish mathematician, published his famous treatise *Electricity and Magnetism*, which unified not only electricity and magnetism but also optics, and laid the foundation of electromagnetics through his four equations. Excellent descriptions of the groundwork of earlier researchers in connection with the foundation of electromagnetics are provided in Refs. 1–3.

On the application of electromagnetic (EM) fields, materials react in variety of ways. The applied electric field would influence both free and bound electrons, whereas the magnetic field would change the orientation of tiny

atomic moments. However, these responses are mostly linear (i.e., proportional to the applied field) over a specified range of the field. If the response to the field is independent of the orientation of material with respect to the direction of field; the material is isotropic. By applying time-varying EM fields to such linear, isotropic materials, their response would greatly depend on the frequency of the applied field. A few examples of such linear, isotropic materials are common dielectrics such as fused silica and glass, and common conductors such as copper and aluminum. Materials are classified as dielectric, conductor, and magnetic on the basis of their dominant response; for example, ferromagnetic materials are mostly highly conductive but are classified as magnetic materials because that property is most significant and useful. In practice, all materials have some response to magnetic fields but, except for ferromagnetic and ferrimagnetic, the response is usually small.

2. DIELECTRIC MATERIALS

Dielectric materials do not possess free electric charges and hence do not conduct electric current. The polar *dielectric materials* possess a dipole moment, but not the nonpolar ones. In an external electric field the molecules of dielectric materials are deformed and an induced electric moment appears. In some crystalline dielectric, spontaneous orientation of the dipole moments occurs even in the absence of electric field, and these substances are called *ferroelectric materials* (all fields are harmonic in time t).

For *lossy nonmagnetic dielectric materials*, permittivity can be represented as

$$\varepsilon = \varepsilon' - j\varepsilon'' \quad (1)$$

In this equation both ε' and ε'' are functions of frequency, and for solid, liquid, and gaseous states, the various physical phenomena contributing to ε' and ε'' essentially differ [4–6].

It can be shown that polarized atoms or molecules in a volume V present a *dipole moment density* defined as

$$\mathbf{P}_d = \lim_{\Delta v \rightarrow 0} \frac{\sum_i \mathbf{P}_i}{\Delta V}$$

Neglecting higher-order multipoles, this is identical to the so-called polarization, which exists in the relationship between \mathbf{D} and \mathbf{E} .

$$\mathbf{D} = \varepsilon_0 \mathbf{E} + \mathbf{P} = \varepsilon_0 (1 + \chi_e) \mathbf{E} \quad (2)$$

where χ_e is the dielectric susceptibility. Here we have assumed that the polarization is *linearly* dependent on the field \mathbf{E} . If N represents the number of *like* molecules per unit volume, the induced polarization will have the form

$$\mathbf{P} = \varepsilon_0 \chi_e \mathbf{E} = N \alpha \mathbf{E}_l = N \alpha \Omega \mathbf{E} \quad (3)$$

where α is the *molecular* polarizability, Ω is the ratio between local field \mathbf{E}_l acting on the molecule and the applied

field \mathbf{E} . It should be noted at this point that the local field \mathbf{E}_l differs from applied electric field owing to the effect of molecules in the surrounding region. The displacement vector \mathbf{D} is related to the applied electric field \mathbf{E} as

$$\mathbf{D} = \varepsilon \mathbf{E} = \varepsilon_0 \varepsilon_r \mathbf{E} \quad (4)$$

Using Eqs. (2) and (4), the *relative permittivity* ($\varepsilon_r = \varepsilon / \varepsilon_0$) can be written as

$$\varepsilon_r = 1 + \frac{N \alpha g}{\varepsilon_0} = 1 + \chi_e \quad (5)$$

If the surrounding molecules have a spherically symmetric behavior, the factor g can then be written as

$$\frac{\varepsilon_r - 1}{\varepsilon_r + 2} = \frac{N \alpha}{3 \varepsilon_0} \quad (6)$$

This relationship is called the *Mossotti–Clausius equation*. If the effects of frequency on the *molecular polarizability* α are included, this relationship is known to be *Debye equation*.

Basically the molecular polarizability α consists of electronic and ionic effects of molecules. The electronic effect arises from the shift of the electron cloud (in each atom) from its positive molecules, and the ionic part is due to the displacement of positive and negative ions from their neutral positions. However, if the individual molecules have permanent dipole moments, these also contribute to the molecular polarizability, and the applied electric field tends to align these permanent dipoles. Thus the total molecular polarizability can be written as

$$\alpha_T = \alpha_e + \alpha_i + \alpha_d \quad (7)$$

with α_e , α_i and α_d denote electronic, ionic, and permanent dipole contributions, respectively.

According to the classical model of electronic polarization, any displacement of the charge cloud from its central ion produces a restoring force, and its interaction with the inertia of the moving charge cloud produces a resonance. This phenomenon is the same as discussed for a spring–mass system in mechanics. Similarly, the displacement of one ion from another produces resonances in the *ionic polarizability*. The *electronic polarizability* α_e is given as

$$\alpha_e = \frac{(e^2/m)}{(\omega_0^2 - \omega^2) + j\omega\Gamma} \quad (8)$$

where Γ is a *damping constant* and ω_0 is related to the restoring force. This equation can be generalized to represent all electronic and ionic resonant responses as

$$\alpha_j = \frac{F_j}{(\omega_j^2 - \omega^2) + j\omega\Gamma_j} \quad (9)$$

where F_j measures the strength of the j th resonance; real and imaginary parts of the equation contribute to $\varepsilon'(\omega)$ and

$\epsilon''(\omega)$, respectively. According to *Debye model*, $\epsilon'(\omega)$ can take negative as well as positive values. The relationships between $\epsilon'(\omega)$ and $\epsilon''(\omega)$ are known as *Kramers-Kronig relations* [7], and are given by

$$\epsilon'(\omega) = \epsilon_0 + \frac{2}{\pi} P \int_0^\infty \frac{\omega' \epsilon''(\omega')}{(\omega^2 - \omega'^2)} d\omega' \quad (10)$$

$$\epsilon''(\omega) = -\frac{2\omega}{\pi} P \int_0^\infty \frac{[\epsilon'(\omega') - \epsilon_0]}{(\omega^2 - \omega'^2)} d\omega' \quad (11)$$

where P denotes that the principal value of the integral that should be considered.

At optical frequencies one uses the refractive index rather than permittivity, and this is also a complex quantity for materials with absorption. With $\mu = \mu_0$, the complex refractive index is given as

$$n_c(\omega) = n_r(\omega) - jn_i(\omega) = \left\{ \frac{\epsilon'(\omega) - j\epsilon''(\omega)}{\epsilon_0} \right\}^{1/2} \quad (12)$$

3. CONDUCTORS, SEMICONDUCTORS, AND SUPERCONDUCTORS

Ohm’s law is truly obeyed in the case of good conductors. Also, for such materials the displacement current is negligible as compared to the conduction current, and therefore, the current and the electric field are in phase. The *displacement current* becomes increasingly important at higher frequencies. For example, at microwave frequencies semiconductors may have comparable conduction as well as displacement currents.

Let n_e be the density of free electrons in a medium with a background of fixed positive ions having the same density; this model may be considered for a conductor, semiconductor, or an ionized gas (plasma) with different values of parameters. It can be shown that the components of the *complex permittivity* defined by Eq. (1) will have the forms

$$\epsilon' = \epsilon_1 - \frac{n_e e^2}{m(v^2 + \omega^2)} \quad (13)$$

$$\epsilon'' = \frac{n_e e^2 v}{\omega m(v^2 + \omega^2)} \quad (14)$$

where ϵ_1 represents the effect of bound electrons of the positive ion background, v is the collision frequency, and e and m , respectively, are the electronic charge and mass. It is to be noted that $(n_e e^2 / m v)$ is the low-frequency conductivity σ . In the case of materials with moderate to low conductivities such as semiconductors, for microwave and millimeter-wave frequencies where $\omega^2 \gg v^2$, the second term in Eq. (13) is negligible. Thus, the complex permittivity ultimately becomes

$$\epsilon = \epsilon_1 - j \frac{\sigma}{\omega} \quad (15)$$

On the other hand, in the case of ionized gas with very low density and negligible collision frequency, we can have $\epsilon_1 = \epsilon_0$ and $\epsilon'' = 0$, and therefore, the permittivity takes the form

$$\epsilon = \epsilon_0 \left[1 - \left(\frac{\omega_p}{\omega} \right)^2 \right] \quad (16)$$

where ω_p is called the *plasma frequency*, and is given as

$$\omega_p = \left(\frac{n_e e^2}{\epsilon_0 m} \right)^{1/2} \quad (17)$$

Thus, we observe from Eq. (16) that the permittivity is negative for all frequencies below the plasma frequency. Therefore, for $\omega < \omega_p$, the intrinsic wave impedance $\eta (= \sqrt{(\mu/\epsilon)})$ becomes imaginary. As such, when a wave with $\omega < \omega_p$ incidents from free space on a region of ionized gas, the wave is reflected. The ω - β diagram for TEM waves propagating in an ionized gas is shown in Fig. 1.

For perfect conductors, there is no electric field at any frequency, and also, there is then no time-varying magnetic field. A truly static magnetic field is unaffected by conductivity of any value. For a metallic electrode, the “perfect conductor” approximation ensures uniform potential over its surface. A perfect conductor can be approximated as a conductor in which the collision frequency approaches zero, and this was considered to be the correct model for a superconductor in the period between its discovery (in 1911) by H. K. Onnes and the experiment (in 1933) by W. Meissner and Ochsenfeld [8]. A collision conductor can be modeled as a dense plasma, and for frequencies below the plasma frequency, the fields inside the conductor can exist only near the interface where they are excited. For extremely pure metallic crystals, very low collision frequencies may occur at temperature near the absolute zero. The ideal collisionless conductor excludes

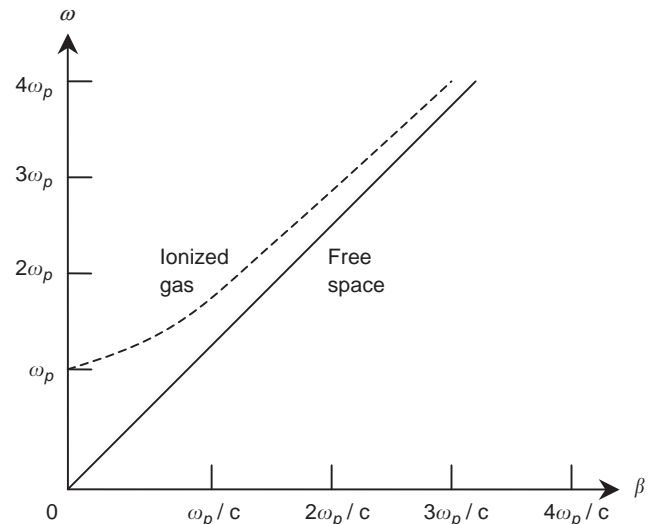


Figure 1. The ω - β diagram for a plane wave propagating through an ionized gas.

time-varying fields from the interior. However, the experiments conducted by Meissner and Ochenfeld on a superconductor showed that constant magnetic fields are also excluded from the interior. In 1935 London showed that this result could be obtained if

$$\nabla \times \mathbf{J} = -\Lambda \mathbf{B} \quad (18)$$

with $\Lambda = n_e e^2 / m$ at $T = 0$. Substituting (18) in Maxwell's curl \mathbf{H} equation, and neglecting the displacement current, one finally obtains

$$\nabla^2 \mathbf{B} - \mu \Lambda \mathbf{B} = 0 \quad (19)$$

This last equation can be applied for the fields inside the surface of a superconductor by considering a half-space of superconductor filling $z \geq 0$ (Fig. 2). If we assume that only the x component of \mathbf{B} exists with its variation along the z direction only, then Eq. (19) finally becomes

$$\frac{d^2 B_x}{dz^2} - \frac{B_x}{\lambda_L^2} = 0 \quad (20)$$

where $\lambda_L = (m / \mu n_e e^2)^{1/2}$ at $T = 0$; λ_L is called the *London penetration depth*. The solution of Eq. (20) will be of the form

$$B_x = B_{x0} e^{-z/\lambda_L} \quad (21)$$

Experimentally determined values of penetration depths typically lie in the range 50–200 nm.

The phenomenon of superconductivity requires that the material be held at temperatures near absolute zero. Superconductors are mostly metallic elements,

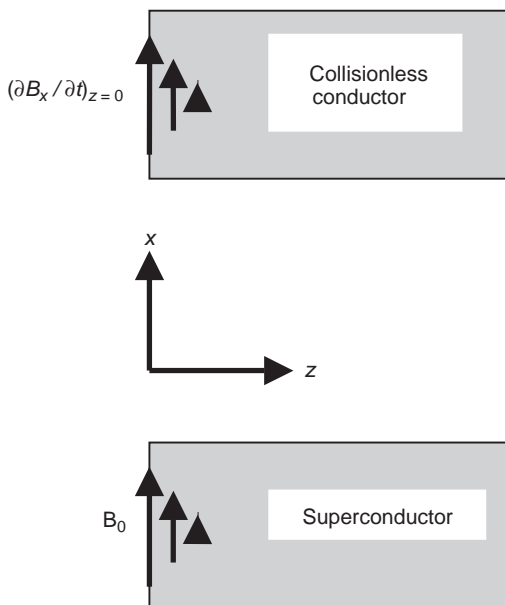


Figure 2. Fields at the surface of a half-space of collisionless conductor or superconductor.

compounds, or alloys that make transitions into the superconducting state at critical temperatures below ~ 23 K. Among the others, niobium has the highest critical temperature about 9.2 K. Compounds of niobium with higher critical temperatures are widely used in many applications. A new family of oxide-based superconductors was discovered in 1986, which have much higher *critical temperatures* about 125 K [9]. However, the oxide-based superconductors are highly anisotropic as compared with metallic superconductors.

Superconductive transmission lines are nearly nondispersive in nature. Losses occur in superconductors at nonzero frequencies and nonzero temperatures (unlike the case for the ideal collisionless conductor) because the conduction electrons are not in the superconducting state and the penetrating fields can cause them to have collisions, resulting in heat dissipation. For frequencies throughout the microwave range, these losses are much smaller than in normal metals such as copper.

4. ANISOTROPIC DIELECTRICS

For isotropic dielectric materials, the quantities permittivity and permeability are scalar, and may be nonlinear and frequency-dependent. In fact, every permittivity is frequency-dependent because of the Kramers–Kronig relations. However, in some frequency bands, it may be possible to ignore the frequency dependence. Materials that respond differently to fields with different orientations are termed *anisotropic*, and the property of anisotropy may be in the response to either the electric or magnetic field. The anisotropy in the electric field response is represented by a matrix permittivity, which is an array of nine scalar quantities that may be nonlinear and frequency-dependent. Similarly, the anisotropy in the magnetic field response is represented by a matrix permeability [10,11]. Materials that have both the permittivity and the permeability are anisotropic, and are rarely found.

For *anisotropic dielectrics*, the relationship between \mathbf{D} and \mathbf{E} [12–14] is given as

$$D_x = \varepsilon_{11} E_x + \varepsilon_{12} E_y + \varepsilon_{13} E_z \quad (22a)$$

$$D_y = \varepsilon_{21} E_x + \varepsilon_{22} E_y + \varepsilon_{23} E_z \quad (22b)$$

$$D_z = \varepsilon_{31} E_x + \varepsilon_{32} E_y + \varepsilon_{33} E_z \quad (22c)$$

which may be presented in matrix form as

$$\begin{bmatrix} D_x \\ D_y \\ D_z \end{bmatrix} = \begin{bmatrix} \varepsilon_{11} & \varepsilon_{12} & \varepsilon_{13} \\ \varepsilon_{21} & \varepsilon_{22} & \varepsilon_{23} \\ \varepsilon_{31} & \varepsilon_{32} & \varepsilon_{33} \end{bmatrix} \begin{bmatrix} E_x \\ E_y \\ E_z \end{bmatrix} \quad (23)$$

This equation can be written in a more compact form as

$$[\mathbf{D}] = [\boldsymbol{\varepsilon}][\mathbf{E}] \quad (24)$$

For physically real materials, the *permittivity matrix* is *Hermitian*, which is defined as

$$\epsilon_{ij} = \epsilon_{ji}^* \quad (25)$$

However, the permittivity is Hermitian only if a material is lossless (no physical material is lossless, by virtue of causality). For lossless crystals, Eq. (25) implies real and symmetric matrices, which can be diagonalized by a rotation of coordinates. Thus, Eqs. (22) reduce to the form

$$D_x = \epsilon_{11}E_x; \quad D_y = \epsilon_{22}E_y; \quad D_z = \epsilon_{33}E_z \quad (26)$$

where ϵ_{11} , ϵ_{22} , and ϵ_{33} are called as *principal permittivities*.

5. ELECTROOPTIC MATERIALS

Some certain materials show a change in permittivity on application of an electric field. If the change in permittivity is directly proportional to the applied electric field, this is known as *Pockels effect*. Certain noncentrosymmetric solids [13,15], such as lithium niobate and gallium arsenide, are examples of materials showing the Pockels effect. On the other hand, if the change in permittivity is directly proportional to the square of the applied electric field, this is known as *Kerr effect*. Some liquids such as carbon disulfide and nitrobenzene, and some centrosymmetric solids present the Kerr effect. Both the effects are, however, relatively small for practical values of externally applied electric field.

The electrooptic effect can be described by considering the change in permittivity element ϵ_{ij} on application of the electric field component E_k . However, the effect is defined in terms of the reciprocal matrix. Let us define the matrix

$$\left[\frac{1}{n^2} \right] = \left[\epsilon \right]^{-1} \quad (27)$$

Now, when the electric field is applied, the change in an element of this matrix is

$$\Delta \left(\frac{1}{n^2} \right)_{ij} = \sum_{k=1}^3 r_{ijk} E_k \quad (28)$$

where r is the distance from an arbitrary origin, where the subscripts i,j,k each range over the three spatial coordinates x,y,z , denoted by the integers 1,2,3, respectively. Since the matrices $[\epsilon]$, and hence $(1/n^2)$, are symmetric, one may implement contracted notations as $11 \rightarrow 1$, $22 \rightarrow 2$, $33 \rightarrow 3$, $23 = 32 \rightarrow 4$, $13 = 31 \rightarrow 5$, $12 = 21 \rightarrow 6$, so that Eq. (27) may be written in another form as

$$\Delta \left(\frac{1}{n^2} \right)_{ij} = \sum_{k=1}^3 r_{pk} E_k \quad (29)$$

Here the subscript k has values ranging from 1 to 3 and the subscript p ranges from 1 to 6. Table 1 shows the values of r_{pk} [as in Eq. (29)] for a few anisotropic crystals [15].

Table 1. Electrooptic Properties of a Few Materials

Materials	n_o ($\lambda_0 = 550$ nm)	N_e ($\lambda_0 = 550$ nm)	r_{pk} ($\times 10^{-12}$ mV $^{-1}$)
KDP	1.51	1.47	$r_{41} = 8.6$ $r_{63} = 10.6$
GaAs (10.6 μ m)	3.34		$r_{41} = 1.6$
LiNbO ₃	2.29	2.20	$r_{33} = 30.8$ $r_{13} = 8.6$ $r_{22} = 3.4$ $r_{42} = 28.0$
BaTiO ₃	2.437	2.365	$r_{33} = 23.0$ $r_{13} = 8.0$ $r_{42} = 820.0$

6. MAGNETIC MATERIALS

Under the influence of an external magnetic field the internal dipole moments align themselves. Also, a magnetic moment is induced in the magnetic material. As such, in the presence of a magnetic material, the resultant magnetic flux density will be different from its value in free space. The effect of magnetization can be studied by incorporating the equivalent volume current density, \mathbf{J}_m into the basic curl equation for the magnetic induction \mathbf{B} , given as

$$\nabla \times \mathbf{B} = \mu_0 \mathbf{J} \quad (30)$$

We thus have

$$\frac{1}{\mu_0} \nabla \times \mathbf{B} = \mathbf{J} + \mathbf{J}_m \quad (31)$$

where

$$\mathbf{J}_m = \nabla \times \mathbf{M} \quad (32)$$

It is assumed that an externally applied magnetic field causes the atomic circulating currents to align with it, thereby magnetizing the material. In Eq. (32) \mathbf{M} is the magnetization vector which measures the strength of magnetizing effect. From Eqs. (31) and (32), we finally get

$$\nabla \times \left(\frac{\mathbf{B}}{\mu_0} - \mathbf{M} \right) = \mathbf{J} \quad (33)$$

We now define the *magnetic field intensity* \mathbf{H} , which is a new fundamental field quantity, such that

$$\mathbf{H} = \frac{\mathbf{B}}{\mu_0} - \mathbf{M} \quad (34)$$

From Eqs. (33) and (34), we obtain the new equation

$$\nabla \times \mathbf{H} = \mathbf{J} \quad (35)$$

where \mathbf{J} is the volume density of free current. Equation (35) along with the equation $\nabla \cdot \mathbf{B} = 0$ (the divergence equation for the magnetic induction) form the two funda-

mental governing differential equations for magnetostatics [16–18]. Clearly, the factor permeability of the medium does not appear in both of these equations. For linear and isotropic materials the magnetization is directly proportional to the magnetic field intensity, and therefore

$$\mathbf{M} = \chi_m \mathbf{H} \quad (36)$$

where χ_m is a dimensionless quantity called the *magnetic susceptibility*. Using Eqs. (34) and (36), we obtain

$$\mathbf{B} = \mu_0(1 + \chi_m)\mathbf{H} = \mu_0\mu_r\mathbf{H} = \mu\mathbf{H} \quad (37)$$

or $\mathbf{H} = (1/\mu)\mathbf{B}$, where

$$\mu_r = 1 + \chi_m = \frac{\mu}{\mu_0} \quad (38)$$

μ_r is again a dimensionless quantity called as the *relative permeability* of the medium. The parameter $\mu = \mu_0\mu_r$ is said to be the *absolute permeability* (or the permeability) of the medium, and the unit of μ is henries per meter. Linear, isotropic, and homogeneous media have constant values of μ and χ_m . At this point, it is to be noted that the value of permeability for most materials is very close to that of free space, namely, μ_0 . For ferromagnetic materials such as Fe, Ni, and Co, the value of μ_r could be very large (e.g., 50–500 and $\geq 10^6$ for certain types of alloys). In fact, the value of permeability depends not only on the magnitude of magnetizing field \mathbf{H} but also on the previous history of the material.

6.1. Behavior of Magnetic Materials

The classification of magnetic materials can be roughly made according to their relative permeability μ_r . In general, magnetic materials are classified into three main groups; *diamagnetic* ($\mu_r \leq 1$; i.e., χ_m is a very small negative number), *paramagnetic* ($\mu_r \geq 1$; i.e., χ_m is a small positive number), and *ferromagnetic* ($\mu_r \gg 1$; i.e., χ_m is a large positive number) [19]. As such, the macroscopic magnetic property of a linear, isotropic medium can be described by defining the *magnetic susceptibility* χ_m . Generally, all materials have some response to magnetic fields. Except for ferromagnetic and *ferrimagnetic* (a special class of ferromagnetics) materials, the magnetic response is usually very weak. The magnetic response can either decrease or increase the flux density for a given magnetizing field \mathbf{H} . If \mathbf{B} is decreased, the material is said to be *diamagnetic*, and if it is increased, it is *paramagnetic*. However, a knowledge of quantum mechanics is essentially required in order to deal with the microscopic magnetic phenomena. A qualitative description of the behavior of various types of magnetic materials is given below, which is based on the classical atomic model.

The property of diamagnetism arises primarily from the orbital motion of electrons within an atom, and it is present in almost all materials. However, in most of the materials the effect of diamagnetism is too weak to be of any practical significance. In the absence of an externally applied magnetic field, the atoms of diamagnetic materials

have vanishing net magnetic moment (due to the orbital and spin motions of electrons). When an external magnetic field is applied to diamagnetic materials, it produces a force on the orbiting electrons, causing a perturbation in angular velocities, which results into a net magnetic moment. Now the induced magnetic moment always tends to oppose the externally applied field (according to *Lenz law*), and therefore, the magnetic flux density is ultimately reduced. The macroscopic effect of this process is analogous to that of a negative magnetization that can be described by a negative magnetic susceptibility χ_m . Thus, the diamagnetic response of atoms arises from the changes of electron orbits when an external magnetic field is applied. According to *Faraday's law*, an electric field can be produced by a changing magnetic field. That field induces currents which, in turn, produce a magnetic field that opposes the change. The response of electron orbits in an atom is of this kind. However, this kind of effect is generally extremely small. The effect produces fractional changes in μ from μ_0 by only 10^{-8} – 10^{-5} . The value of χ_m for most of the known diamagnetic materials (Bi, Cu, Pb, Hg, Ge, Au, silver, etc.) is of the order -10^{-5} . Diamagnetic materials do not exhibit permanent magnetism, and the induced magnetic moment disappears when the applied field is withdrawn.

On the other hand, in some materials the magnetic moments due to the orbiting and spinning electrons do not cancel each other completely, and therefore, the atoms and molecules possess a net magnetic moment. In such materials the diamagnetic response is usually obscured. When an external magnetic field is applied, tiny molecular magnetic moments tend to align in the direction of applied field, increasing the magnetic flux density. In addition, a very weak diamagnetic effect is also caused. The macroscopic effect of this process is equivalent to that of a positive magnetization that can be described by a positive magnetic susceptibility. Materials with this kind of behavior are said to be paramagnetic. Generally, such materials (Al, Mg, Ti, and W) have very small positive values of χ_m , of the order of 10^{-5} .

The property of paramagnetism primarily arises because of the magnetic dipole moments of spinning electrons. The externally applied field acts on molecular dipoles to align those, and the alignment forces are counteracted by the deranging effects of thermal agitation. The property of paramagnetism is temperature-dependent, unlike the case for diamagnetism (it is independent). Therefore, *paramagnetic effects* are stronger at lower temperatures because there is less thermal agitation.

If there are induced magnetic dipoles in the atoms or there is a nonzero average alignment of natural dipoles, in that case, the term *dipole density* can be defined as

$$\mathbf{M} = \lim_{\Delta v \rightarrow 0} \frac{\sum_i \mathbf{m}_{0i}}{\Delta V} \quad (39)$$

This is identical to the so-called magnetization that enters the relation between \mathbf{B} and \mathbf{H} as in Eq. (34). It can be shown that the magnitude of magnetization can be expressed in terms of molecular magnetic field \mathbf{H}_i acting on

the atomic dipoles and the absolute temperature T [20] as

$$M = Nm_0 \left(\coth \frac{m_0 \mu_0 H_i}{k_B T} - \frac{k_B T}{m_0 \mu_0 H_i} \right) \quad (40)$$

where k_B is Boltzmann’s constant, N is the number of dipoles per unit volume, and m_0 is the *natural dipole moment*. Equation (40) is derived considering the statistical distribution of the orientation of dipoles. In such materials, the direction of \mathbf{M} is the same as that of the molecular field \mathbf{H}_i ; that is, they are aligned parallel. If the external magnetic field \mathbf{H} is not too strong and the temperature is not too low, the terms in parentheses in Eq. (40) may be approximated by the first term only in its series expansion. In this case the magnetization is linearly related to the applied field:

$$\mathbf{M} = \chi_m \mathbf{H} \quad (41)$$

$$\chi_m \cong \frac{N \mu_0 m_0^2}{3k_B T} \quad (42)$$

At room temperature, the values of χ_m for a variety of materials are of the order of 10^{-5} .

6.2. Materials with Residual Magnetization

If the temperatures of paramagnetic substances are reduced below a certain value, which depends essentially on materials, the magnetization \mathbf{M} would be sufficient enough to produce the field necessary to hold the dipoles aligned even after the removal of the external field. The molecular field produced by the magnetization is given as [4]

$$\mathbf{H}_i = \kappa \mathbf{M} \quad \text{or} \quad \mathbf{M} = \frac{1}{\kappa} \mathbf{H}_i \quad (43)$$

where κ is the factor measuring the interaction of neighboring dipoles (it must be on the order of 1000). We see that there exists another relationship between \mathbf{H}_i and \mathbf{M} , as observed in Eq. (40). By equating the Eqs. (43) and (40), one may obtain the condition for *spontaneous magnetization*. The temperature below which a material exhibits spontaneous magnetization is called its *Curie temperature*.

For ferromagnetic materials, the effect of magnetization can be many orders of magnitude larger than that of paramagnetics. The effect of ferromagnetism can be explained on the basis of the model of magnetized domains, according to which ferromagnetic materials (e.g., Co, Ni, Fe) are composed of several tiny domains with their linear dimensions ranging from a few micrometers to ~ 1 mm. Each domain contains $\sim 10^{15}$ atoms, which are fully magnetized; that is, they contain aligned magnetic dipoles (even in the absence of an externally applied magnetic field) resulting from spinning electrons. In a molecular domain, strong coupling forces exist between the magnetic dipole moments (of the atoms). As a result, the different dipole moments are aligned parallel to each other. There exists a transition region between adjacent domains,

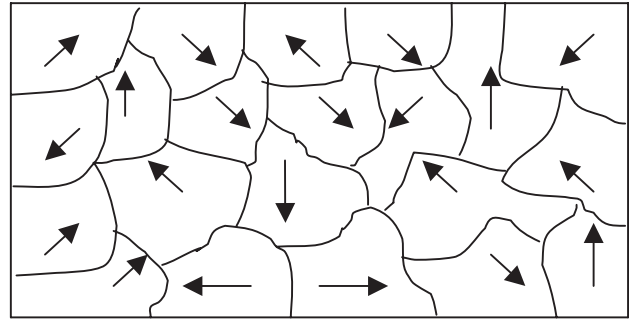


Figure 3. Domain structure of a polycrystalline ferromagnetic specimen.

which is about 100 atoms thick. This region is called the *domain wall* [21]. For ferromagnetic materials, when these are not magnetized, the magnetic moments of the adjacent domains have different directions (Fig. 3), and the random nature of orientations of these domains results in no net magnetization.

In ferromagnetic materials, under the influence of external magnetic field, the walls of domains having magnetic moments in the direction of applied field move in such a way that the volumes of those domains grow, resulting thereby an increase in magnetic flux density. When the applied field is weak (up to point P_1 in Fig. 4), the movements of domain walls are reversible. However, for stronger applied fields (i.e., after point P_1 is crossed), domain wall movements are no longer reversible. Also, domains rotate toward the direction of the externally applied field. If the applied strong field is reduced to zero at point P_2 , the B – H relationship will no longer follow the solid curve path P_2P_1O , but will decrease from P_2 to P'_2 instead, and the path followed will be along the broken lines as shown in Fig. 4. This phenomenon is called *hysteresis*, which is derived from a Greek word meaning “to

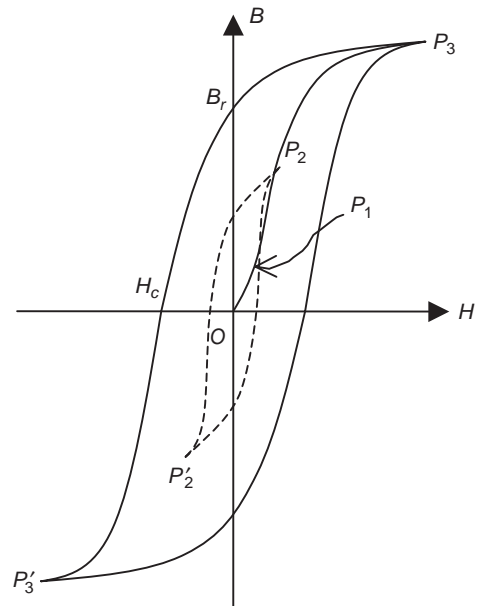


Figure 4. Hysteresis loop for ferromagnetic material.

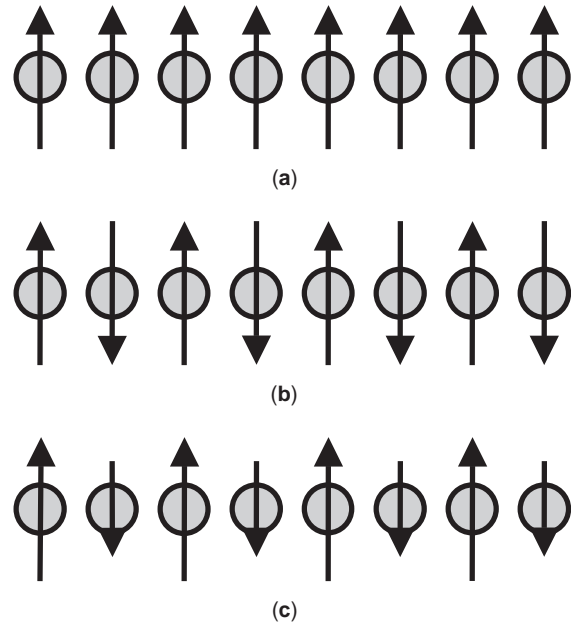
Table 2. Properties of a Few Hard Magnetic Materials

Materials	Composition (%)	Remanence B_r (T)	Coercive Force H_c (A/m)
Iron	Bonded powder	0.6	0.0765
Iron-cobalt	Bonded powder	1.08	0.0980
Alnico V	Ni 14%;Al 8%,Co 24%; Cu 3%,Fe 51%	1.27	0.0650
Ticonol II	Ni 15%;Al 7%;Co 34%; Cu 4%;Ti 5%;Fe 35%	1.18	0.1315

lag"; in this case we observe the lagging of magnetization behind the applied field. When the applied field strengthens (i.e., from point P_2 to P_3 in Fig. 4), domain rotation as well as domain wall motion will cause a complete alignment of the magnetic moments with the externally applied field. At this point, the ferromagnetic magnetic material is said to be saturated. The curve $OP_1P_2P_3$ (on the $B-H$ plane) is called the *normal magnetization curve*. If, after reaching point P_3 , the applied magnetic field is reduced to zero, the magnetic flux density does not fall to zero, but assumes the value at B_r , instead. This value of B is called as the residual flux density, and its unit is Webers per square meter (Wb/m^2). The value of B_r depends on the maximum intensity of the applied field. The property of the existence of a residual flux density in ferromagnetic materials is exploited in transforming them to permanent magnets.

In order to render the magnetic flux density of a ferromagnetic material zero, it is necessary to apply a magnetic field intensity H_c , called the *coercive force* (or the *coercive field intensity*), in the opposite direction. The unit of H_c is A/m, and its value also depends on the maximum value of the intensity of the applied field. It can be seen from the Fig. 4 that the relationship between B and H fields is nonlinear. Therefore, from the relationship $\mathbf{B} = \mu\mathbf{H}$, the permeability μ is not a constant, and it is a function of the magnitude of magnetizing field \mathbf{H} . The value of μ also depends on the history of magnetization of the material.

Some important applications of ferromagnetic materials include permanent magnets, signal recording tapes and disks, magnetic shielding, and cores for electromagnets, transformers, electric motors, and generators [21]. These materials can be roughly divided into two different categories called *hard* and *soft*; the designations refer to

**Figure 5.** Schematic atomic spin structures for (a) ferromagnetic, (b) antiferromagnetic, and (c) ferrimagnetic materials.

permanence of magnetization when the external applied field is removed, with hard materials retaining a strong magnetization. Ferromagnetic applications require that the material should acquire a large magnetization for a very small magnetic field. As such, these materials should have tall and narrow *hysteresis loops*. The properties of some technically important materials for permanent magnets are listed in Table 2 [22]. Generally, the coercive field intensity of hard ferromagnetic materials (such as Alnico alloys) would be about $\geq 10^5$ A/m, whereas that for soft ferromagnetic materials, it is usually around ≤ 50 A/m. The properties of some important soft materials are listed in Table 3 [22,23].

It may thus be inferred that ferromagnetism is the result of strong coupling effects between the magnetic dipole moments of atoms in a domain. The atomic spin structure of a ferromagnetic material is illustrated in Fig. 5a. If the temperature of a ferromagnetic material is raised to such a value that the thermal energy exceeds the coupling energy, the tiny magnetized domains lose their organized orientation, thus losing the property of magnetization. As

Table 3. Properties of a Few Soft Magnetic Materials

Materials	Composition (%)	Initial Permeability (μ_r) ₀	Maximum Permeability (μ_r) _{max}	Coercive Force ($\times 10^4$) (A/m)	Saturation Induction (T)
Iron	Commercial (Fe 99%)	2×10^2	6×10^3	0.9	2.16
Iron	Pure (Fe 99.9%)	2.5×10^4	3.5×10^5	0.01	2.16
Hypersil	Fe 97%;Si 3%	9×10^3	4×10^4	0.15	2.01
78 permalloy	Ni 78%;Fe 22%	4×10^3	10^5	0.05	1.05
Mumetal	Fe 18%;Ni 75%;Cu 5%;Cr 2%	2×10^4	10^5	0.05	0.75
Supermalloy	Fe 15%;Ni 79%;Mo 5%;Mn 0.5%	9×10^4	10^6	0.004	0.8
Cryoperm	Usable at cryogenic temp.	6.5×10^4			

such, a critical value of temperature can be defined, above which a ferromagnetic material behaves like a paramagnetic material; the critical temperature is known as the *Curie temperature*. For most of the ferromagnetic materials, the Curie temperature lies between a few hundred to a thousand degrees Celsius. For iron, the Curie temperature is about 770°C.

In the case of very small crystals, there are factors such as crystal shape, energetically preferred crystal directions, and the magnetic history of the sample that lead to nonzero net magnetization [24]. In the presence of an applied field the existence of domain walls in thin films is exploited for the so-called bubble memory devices for computer memories [25].

Some elements, such as chromium and manganese, also have strong coupling forces between the atomic dipole moments. However, their coupling forces produce antiparallel alignments of electron spins (Fig. 5b), and the spins alternate in direction from atom to atom, resulting in no net magnetic moment. Such materials are referred to as *antiferromagnetics*, and this property is also temperature-dependent. An antiferromagnetic material, on heating above its Curie temperature, exhibits random spin directions, and the materials ultimately become paramagnetic.

Another class of magnetic materials that exhibit behavior between ferromagnetism and antiferromagnetism are called as *ferrimagnetic materials*. Here quantum-mechanical effects cause the directions of magnetic moments in the ordered spin structure to alternate, and their magnitudes to be unequal. As a result, a nonzero magnetic moment exists for such materials (Fig. 5c). As such, in ferrimagnetic materials, the neighboring dipoles are aligned in an antiparallel arrangement, but different types of atoms are present and the dipoles do not cancel. As seen in Fig. 5c, because of the partial cancellation of magnetic moments, the maximum magnetic flux density for ferrimagnetic materials is much lower than that for ferromagnetics. Typically, its value is about 0.3 Wb/m², which is approximately one-tenth the value of that for ferromagnetic materials.

6.3. Ferrites

Ferrites are a subgroup of ferrimagnetic materials that have low loss and strong magnetic effects at microwave frequencies [26]. These materials have a particular type of solid crystal structure made up of oxygen, iron, and another element such as lithium, magnesium, or zinc. These mostly have the formula XO-Fe₂O₃, where X denotes a divalent metallic ion such as Fe, Co, Ni, Mn, Mg, Zn, or Cd. There are also some ceramiclike compounds with very low conductivity as well as magnetic garnets which are used as ferrites such as yttrium-iron-garnet (YIG; Y₃Fe₅O₁₂). Ferrites present relatively low losses at microwave frequencies. The dielectric constants of ferrites are relatively high, and the anisotropic behavior of permeability comes into existence when the material is subjected to a steady magnetic field [27].

In order to define the energy state of an atom, both the orbital and spin quantum numbers must be specified. As

mentioned above, the electron spin generates a strong magnetic moment. These magnetic moments are randomly oriented in paramagnetic substances. However, a strong coupling between spin magnetic moments of neighboring atoms exists in ferromagnetics, antiferromagnetics, and ferrites. This results in parallel or antiparallel alignment of spin magnetic moments. The model of a spinning electron is shown in Fig. 6. For a rotating body, the applied torque **T** is the rate of change of angular momentum **J**:

$$\frac{d\mathbf{J}}{dt} = \mathbf{T} \tag{44}$$

Since the magnetic moment **m** can be given as

$$\mathbf{m} = \gamma\mathbf{J} \tag{45}$$

γ being the gyromagnetic ratio, for a spinning electron, the magnetic moment **m** can be related to the applied torque. Now, the torque resulting from subjecting a magnetic moment **m** to a magnetic field **B_i** is

$$\mathbf{T} = \mathbf{m} \times \mathbf{B}_i \tag{46}$$

From Eq. (44), we would obtain

$$\frac{d\mathbf{m}}{dt} = \gamma \frac{d\mathbf{J}}{dt} = \gamma\mathbf{T} = \gamma(\mathbf{m} \times \mathbf{B}_i) \tag{47}$$

In a magnetic material, the magnetic field **B_i** acting on a molecule can be represented as

$$\mathbf{B}_i = \mu_0\mathbf{H} + \mathbf{M} \tag{48}$$

where μ_0 is the free-space permeability and **M** is the *magnetization vector*. The vector **M** may also be treated as magnetic dipole density, and can be given as $N_0\mathbf{m}$ with N_0 as the effective number density. The relationship between the intensity of magnetic field **H** and the external applied field **B** depends on the shape of the ferrite body. The matrices [**B**] and [**H**] are related as

$$[\mathbf{B}] = [\mu][\mathbf{H}] \tag{49}$$

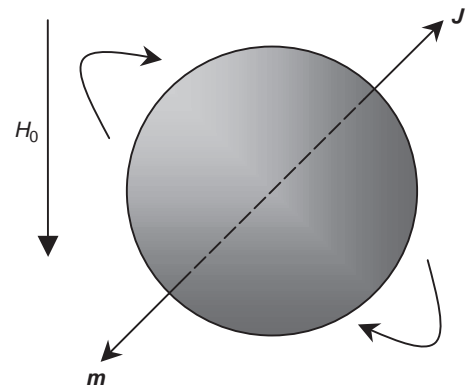


Figure 6. Model of a spinning electron in a magnetic field.

or

$$\begin{bmatrix} B_x \\ B_y \\ B_z \end{bmatrix} = \begin{bmatrix} \mu_{11} & \mu_{12} & 0 \\ \mu_{21} & \mu_{22} & 0 \\ 0 & 0 & \mu_0 \end{bmatrix} \begin{bmatrix} H_x \\ H_y \\ H_z \end{bmatrix} \quad (50)$$

Here the permeability components are

$$\mu_{11} = \mu_{22} = \mu_0 \left(1 + \frac{\omega_0 \omega_M}{\omega_0^2 - \omega^2} \right) \quad (51)$$

$$\mu_{12} = \mu_{21}^* = j \frac{\mu_0 \omega_0 \omega_M}{\omega_0^2 - \omega^2} \quad (52)$$

with

$$\omega_M = -\mu_0 \gamma M_0 \quad \text{and} \quad \omega_0 = -\mu_0 \gamma H_0 \quad (53)$$

where M_0 is the *saturation magnetization* and H_0 is the strength of the DC magnetic field. It is to be noted that the value of magnetic intensity \mathbf{H} is averaged over the space of many molecules within the material, and therefore, the magnetic field within the ferrite differs from the applied field.

It can be shown that linearly polarized waves cannot propagate through ferrites, and therefore, it is not a normal mode of propagation for the medium. In reality, circularly polarized waves are normal modes for ferrites; media having this property are called *gyrotropic media*. In ferrite media, the propagation constants for clockwise- and counterclockwise- polarized waves are different.

In 1845, Michael Faraday observed that when optical waves are allowed to propagate through a dielectric with an applied magnetic field, there occurs a rotation of plane of polarization of the optical wave, and the angle of rotation θ can be given as

$$\theta \propto H_0 l \quad (54)$$

where H_0 is the DC magnetic field strength and l is the interaction length. The rotation of the plane of polarization of optical waves is called *Faraday rotation*, and this effect is very strong in ferrites. Equation (54) can be rewritten as

$$\theta = V H_0 l \quad (55)$$

where the constant of proportionality V is known as the *Verdet constant*.

Faraday rotation is also observed even in ordinary dielectrics (e.g., silica), but the angle of rotation θ is relatively small, and the value of V is about 0.014 min/Oe · cm at the operating wavelength 600 nm. In silica, the angle of rotation decreases at longer wavelengths approximately as λ^{-2} .

There are waveguides and stripline devices that employ ferrites, and these devices have found enormous use in microwave applications. Waveguide devices operate on the *Faraday effect* principle. The operation of stripline devices is based on the asymmetry caused by an applied

steady magnetic field. In waveguide devices, according to the principle of Faraday rotation, for both the positive and the negative traveling waves (as shown in Fig. 7), the linearly polarized wave is oriented in the same direction relative to the direction of the DC magnetic field. The *gyrator* [28] is the simplest microwave device that uses the effect of Faraday rotation, and it produces a phase shift of 180° in one direction but no shift in the opposite direction.

The *absorption isolator* is another Faraday rotation device where the wave traveling to one side is appreciably attenuated (about 30 dB) and that traveling to the other side suffers only a little attenuation (say, ~0.5 dB). *Circulators* also exploit the principle of Faraday rotation, and these devices transmit a wave from one guide to the other. These devices employ ferrite rods, and can also be used as switches or modulators (by controlling the field that magnetizes the ferrite rod). The dimensional structure of ferrite rods used in Faraday rotation devices is designed so that the required rotation is easily achieved with reasonable magnetic fields, and the wave reflections are minimized with maximum power-handling capacity. These devices are useful only for low power.

The *stripline Y-junction circulator* is one among stripline devices, and it can be used as a switch or isolator. Such a device employs ferrite disks, and a DC magnetic field is applied perpendicular to the disks. Standing-mode patterns are formed in ferrite disks; a detailed description [29,30] of the operating principle is beyond the scope of this article.

7. BIANISOTROPIC MATERIALS

Since the mid-1990s, intensive research on new artificially engineered physical systems has been reported

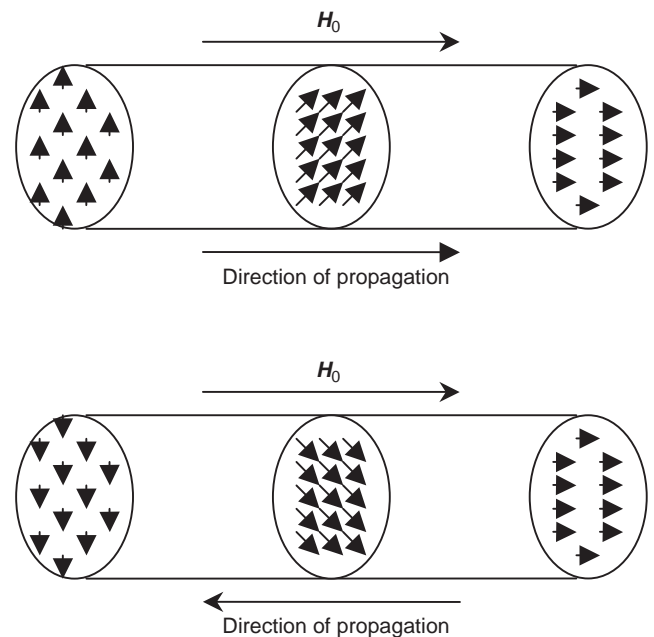


Figure 7. Rotation of waves in magnetized ferrite rods.

emphasizing the different aspects of nanostructure and mesoscopic physics as well as physics of microwave composite materials. A good example of an artificially engineered physical system would be a small ferrite disk with the magnetostatic wave oscillation spectrum. The magnetostatic wave oscillations in a small ferrite disk resonator are characterized by a discrete spectrum of energy levels. Reports have been made on the different mechanisms of excitation of magnetostatic wave oscillations in small ferrite specimens by external RF magnetic fields.

Since the mid-1990s, rapid advancements in materials science enabled the fabrication of complex materials in the form of thin films and particulate composites, thus rendering the term *bianisotropy* quite fashionable [31,32]. In bianisotropic materials the electromagnetic field vectors are coupled in a pattern more complex than that in the usual type of anisotropy. *Artificial bianisotropic materials*, because of their potential usefulness for a variety of applications, have attracted considerable attention of the R&D community devoted to research on the electromagnetics of bianisotropic materials [33]. Artificial, isotropic chiral materials have been made (although quite useless for RAM purposes). Artificial anisotropic materials with a wide variety of properties have also been made. Their properties are local when the long-wavelength approximation is valid. With the use of composites, a wide variety of novel response properties become achievable.

There are several bianisotropic materials that possess the property of chirality [34], specifically, optical activity or handedness. Also, many bianisotropic materials have the property of *nonreciprocity*, meaning that they exhibit direction-dependent responses. However, all materials with direction-dependent response properties are not non-reciprocal. Thus, bianisotropic materials have a wide variety of response properties owing to their complexity in structure, and have found many different applications in the areas of microwaves, electrical engineering, and optics. Sculptured thin films which present nanoengineered response properties, have been developed [35–40]. Many new composite materials with nonlinear optical applications are now emerging.

7.1. Linear Constitutive Equations

The reciprocity theorem due to Lorentz states that fields $\mathbf{E}_a, \mathbf{H}_a$ and $\mathbf{E}_b, \mathbf{H}_b$ from two different sources at the same frequency satisfy the condition

$$\nabla \cdot (\mathbf{E}_a \times \mathbf{H}_b - \mathbf{E}_b \times \mathbf{H}_a) = 0 \quad (56)$$

This theorem is easily verified for isotropic media by substituting Maxwell's equations in complex form. It can also be shown that this holds for an anisotropic medium provided the permittivity and permeability matrices are symmetric. The reciprocity theorem does not hold if the matrices are asymmetric.

The theory of reciprocal bianisotropic materials can be described on the basis of following equations [41]

$$\mathbf{D} = \bar{\bar{\epsilon}} \cdot \mathbf{E} + j\bar{\bar{\alpha}}^T \cdot \mathbf{H} \quad (57)$$

$$\mathbf{B} = \bar{\bar{\mu}} \cdot \mathbf{H} - j\bar{\bar{\alpha}}^T \cdot \mathbf{E} \quad (58)$$

where the electric and the magnetic fields are coupled. These equations are valid in both the time and the frequency domains, and are called *constitutive relations* as they contain information about the nature of the material under consideration. It is to be noted that the constitutive relations relate the matter-derived fields \mathbf{D} and \mathbf{H} to the basic fields \mathbf{E} and \mathbf{B} in any material medium. Both permittivity and permeability of a reciprocal material are symmetric.

In Eqs. (57) and (58), the tensor $\bar{\bar{\alpha}}$ measures the optical activity (or chirality) of the medium, the superscript "T" represents the transpose operation, and j stands for the imaginary part. The fundamental properties of the material tensors $\bar{\bar{\epsilon}}$ (the permittivity), $\bar{\bar{\mu}}$ (the permeability), and $\bar{\bar{\alpha}}$ have been determined [41–43]. Possible alternative constitutive relations have also appeared in the literature [44]. However, different constitutive equations are actually equivalent (after appropriate redefinition of the field vectors). Equations (57) and (58) provide the most rational and convenient way to describe the effects of chirality, especially in nonuniform media.

7.2. Electromagnetics of Bianisotropic Materials

Investigators have presented the study of spherical waves in chiral bianisotropic materials with the scalar dielectric permittivity and dyadic chirality parameter. The electromagnetic behavior of bianisotropic materials with uniaxial symmetry [45,46] have been discussed in the literature with the appropriate constitutive equations as [45]

$$\mathbf{D} = \bar{\bar{\epsilon}} \cdot \mathbf{E} + j(-\alpha \bar{\bar{I}}_t + \kappa \bar{\bar{J}}) \cdot \mathbf{H} \quad (59)$$

$$\mathbf{B} = \bar{\bar{\mu}} \cdot \mathbf{H} + j(\alpha \bar{\bar{I}}_t + \kappa \bar{\bar{J}}) \cdot \mathbf{E} \quad (60)$$

In these equations, the dielectric permittivity $\bar{\bar{\epsilon}}$ and the magnetic permeability $\bar{\bar{\mu}}$ are uniaxial diadics given as

$$\bar{\bar{\epsilon}} = \epsilon_t \bar{\bar{I}}_t + \epsilon_n \bar{z}_0 \bar{z}_0 \quad (61)$$

$$\bar{\bar{\mu}} = \mu_t \bar{\bar{I}}_t + \mu_n \bar{z}_0 \bar{z}_0 \quad (62)$$

where \bar{z}_0 represents the unit vector along the geometric axis and $\bar{\bar{I}}_t = \bar{x}_0 \bar{x}_0 + \bar{y}_0 \bar{y}_0$ is the transverse unit dyadic. Further, in Eqs. (59) and (60), $\bar{\bar{J}} (= \bar{z}_0 \times \bar{\bar{I}}_t = \bar{y}_0 \bar{x}_0 - \bar{x}_0 \bar{y}_0)$ is the 90° rotator in the transverse (x - y) plane, α is the chirality parameter as defined in Eqs. (57) and (58), and the parameter κ measures the coupling of orthogonal transverse electric and magnetic fields. Composite materials governed by the constitutive relations (59) and (60) can be fabricated by embedding small Ω -shaped metal elements in isotropic dielectric, together with chiral

elements. Such materials are useful in microwave applications.

Bianisotropic omega materials can be described by the constitutive relations [47]

$$\mathbf{D} = \bar{\bar{\epsilon}} \cdot \mathbf{E} + j\bar{\bar{\kappa}}_{em} \cdot \mathbf{H} \quad (63)$$

and

$$\mathbf{B} = \bar{\bar{\mu}} \cdot \mathbf{H} - j\bar{\bar{\kappa}}_{me} \cdot \mathbf{E} \quad (64)$$

In these equations, the dielectric permittivity $\bar{\bar{\epsilon}}$ and the magnetic permeability $\bar{\bar{\mu}}$ are diagonal dyadics given as

$$\bar{\bar{\epsilon}} = \epsilon_0(\epsilon_{xx}\bar{\mathbf{x}}_0\bar{\mathbf{x}}_0 + \epsilon_{yy}\bar{\mathbf{y}}_0\bar{\mathbf{y}}_0 + \epsilon_{zz}\bar{\mathbf{z}}_0\bar{\mathbf{z}}_0) \quad (65)$$

$$\bar{\bar{\mu}} = \mu_0(\mu_{xx}\bar{\mathbf{x}}_0\bar{\mathbf{x}}_0 + \mu_{yy}\bar{\mathbf{y}}_0\bar{\mathbf{y}}_0 + \mu_{zz}\bar{\mathbf{z}}_0\bar{\mathbf{z}}_0) \quad (66)$$

If the equivalent electric dipoles of molecules (or stems of the omega particles in composite materials) are all aligned with the z axis and the magnetic dipoles are in the y direction (the loops lie in the $(x-z)$ plane), then $\bar{\bar{\kappa}}_{em}$ and $\bar{\bar{\kappa}}_{me}$ can be given as

$$\bar{\bar{\kappa}}_{em} = \kappa\bar{\mathbf{z}}_0\bar{\mathbf{y}}_0 \quad (67)$$

$$\bar{\bar{\kappa}}_{me} = \kappa\bar{\mathbf{y}}_0\bar{\mathbf{z}}_0 \quad (68)$$

The combination of omega-shaped layers with biased ferrites provides good microwave applications. For optical applications, chiral bianisotropic materials can be manufactured as multilayered structures formed by anisotropic layers [48].

Apart from linear bianisotropic materials, there are *nonlinear* bianisotropic materials as well, the crystals of which combine the practical advantages of liquid crystals possessing spiral structures with those of nonlinear materials [49,50]. The property of chirality facilitates frequency-selective and polarization-sensitive reflection together with polarization rotation, whereas the nonlinearity makes the parametric interaction and frequency transformation effects possible.

8. MAGNETOSTRICTION

In the early 1840s James Prescott Joule observed that the magnetization of an iron sample induces a change in the length of the sample. Since then this phenomenon, known as the *Joule effect*, is often exploited in *magnetostrictive actuators*. The converse of this effect, in which the magnetization of the sample can be changed on application of stress, known as the *Villari effect*, and also at times referred to as the *magnetostrictive effect*, is usually exploited in magnetostrictive sensors. There also exists another pair – Wiedemann effect and its converse Matteucci effect, which correlate, respectively, twist in the sample to the generation of the helical magnetic field, and vice versa. Both of these effects are used in devices and torque sensors. The Joule, the Wiedemann, the Villari and the

Matteucci effects lead to two modes of operation of magnetostrictive transducers: transformation of magnetic energy into mechanical energy and of mechanical energy into magnetic energy. The former is exploited in actuators for generating motion or force, and also, in sensors for detecting the states of magnetic field; the latter is used in sensors to detect motion or force, passive damping devices, and devices for inducing change in the state of magnetic fields in materials.

Magnetoelasticity (or magnetostriction) is a phenomenon that describes the interaction between magnetism and elasticity in ferromagnetic materials. In magnetoelasticity, *Hooke's law* of elasticity is violated, since an additional expansion/contraction results from the reorientation of tiny magnetic domains. Thus in magnetostriction phenomenon strain is caused by the magnetic field. When an external stress is applied, the initially randomly oriented magnetic domains align themselves in the direction of the resultant strain, and produce an irreversible change in the dimension of the material. The total strain in the magnetic material is the sum of pure *elastic strain* and the strain produced by the displacement of domain walls. Although the elastic strain vanishes when the stress is removed, the *magnetostrictive strain* can be restored only by applying a compressive stress. Such a behavior of magnetic materials generates a hysteresis loop on the alternating stress–strain curve. The *saturation magnetostriction coefficient*, represented by λ_s , a dimensionless quantity, is defined as the ratio of the change of length to the original length, and is measured at the saturation flux density. If the magnetostriction is sufficiently large and the applied field is an alternating one (in the audible frequency range of 50–60 Hz), it creates noise (sound). It has been discovered that alloys of iron and rare-earth elements (Sm, Tb, Dy, Ho, Er, Tm, etc.) cause intense magnetostriction 100–1000 times greater than that generated by CoFeNi alloys (the conventional magnetostrictive materials). Thus, rare-earth alloys are designated as *supermagnetostrictive materials*. Magnetostrictive actuators, based on magnetostrictive effects, are driven by external magnetic fields.

In the beginning, the magnetostrictive materials were used in telephone receivers, hydrophones, magnetostrictive oscillators, torque meters, and scanning sonars, employing nickel and other magnetostrictive materials that exhibit bulk saturation strains up to 100 $\mu\text{m}/\text{m}$. Some of the current applications of magnetostrictive devices include ultrasonic cleaners, high-force linear motors, active vibration or noise control systems, medical and industrial ultrasonics, pumps, and sonars. Ultrasonic magnetostrictive transducers have been developed for chemical and material processing, surgical tools, and underwater sonars.

Applications of amorphous magnetoelastic materials for numerous tagging [51,52] and remote sensing applications are now prevalent [53,54]. In sensors, these materials exhibit sufficiently large magnetoelastic effect [55]; specifically, the material effectively converts magnetic energy into elastic energy and vice versa. Magnetoelastic sensors are magnetostrictive; therefore, they launch magnetic flux oscillations when they become mechanically

deformed. A magnetoelastic sensor, when coated uniformly with a layer of an elastic material, its characteristic resonant frequency changes owing to the loading of additional mass as well as the influence of elasticity in the coating [56]. Usually, in magnetoelastic sensors, the resonant frequency is observed by using a pickup coil [53]. For example, in case of a thin longitudinally vibrating bar, the frequency of magnetoelastic resonance coincides with the resonance of acoustic vibration, and therefore, the resonance (of the magnetoelastic sensor) can be described as the mechanical resonance of the vibrating bar.

Magnetic shape memory (MSM) alloys are also gaining importance as possible “smart” materials that can function as both actuators and sensors. The MSM effect is due to the magnetic field induced by the redistribution of twin variants in a martensitic phase, and it offers faster response compared to conventional temperature-driven shape memory alloys. In addition, the strains generated are much larger than in ordinary magnetostrictive materials [57].

8.1. Magnetoelastic Damping

Magnetoelastic (or magnetostrictive) materials are attractive materials for the purpose of damping and for the absorption of energy. Terfenol-D is an example of such a material, which, in a stress–strain cycle, will absorb up to 80% of the mechanical energy input to the system. However, pure Terfenol-D has low tensile strength, which limits its use in applications related to energy absorption. The damping mechanism in Terfenol-D arises from the *jumping* of the magnetization from one easy magnetic direction to another through the process of *magnetoelastic coupling*, which describes the relation between magnetic properties of ferromagnetic materials and the applied mechanical tension. The jumping requires a minimum amount of energy that corresponds to a critical value of the applied stress. When the material is returned to a lower level of stress, the magnetization may not return to the original state, and this indicates the absorption of energy. A simplified domain structure is illustrated in Fig. 8, which shows the “jump” from a vertical orientation under tension to a horizontal orientation under compression.

By incorporating Terfenol-D powder into a resin matrix, the composite may be loaded in tension in order to realize the damping properties. The mechanism of magnetoelastic damping is not related to the rate of loading, but it depends on the magnitude of loading. Thus, this type of mechanism is completely different from the typical damping mechanisms, which are highly rate-dependent. The aspect of magnetoelastic damping, along with the composite material approach, allows the possibility of nanoengineered hybrid dampers for certain applications similar to impedance matching in transducers.

As mentioned earlier, in magnetostrictive materials, vibrational energy is damped through the movement of magnetic domains. Consequently, the dissipation of vibrational energy generates heat. This effect is not diminished even at low temperatures, and therefore, magnetostrictive materials can be expected to be effective in damping vibrations at very low temperatures. In order to suppress

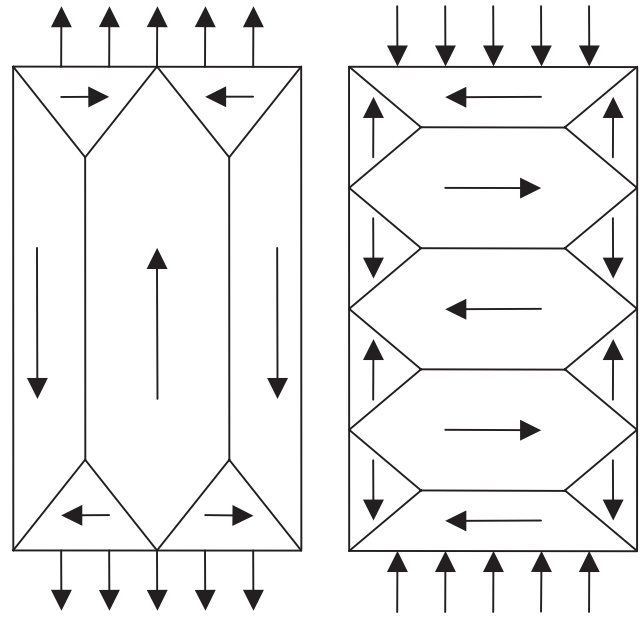


Figure 8. Domain structure of magnetoelastic material.

vibrations of large motors and transformers that operate at temperatures below 100 K, initially viscoelastic dampers were in use, which are based on the principle of *viscoelasticity*. Viscoelastic damping involves the movements of atoms and, at low temperatures, these movements become very small. Therefore, such viscoelastic dampers cannot work efficiently at low temperatures. As such, in order to operate at such low temperatures, for such applications, magnetoelastic dampers have also been proposed. This type of damper is usually made of magnetostrictive materials such Tb/Dy alloys [58,59]. At a temperature of ~ 77 K, a specimen of Tb/Dy alloy is found to dissipate about 30% of the vibrational energy per stress–strain cycle. It has been observed that the dissipation factor can be further enhanced by adding very small amounts of N, Ta, or some other elements to a Tb/Dy alloy, and also, by changing the processing conditions.

9. PIEZOELECTRICITY

Piezo is the Greek word for pressure. As such, *piezoelectricity* is also termed *pressure electricity*. The phenomenon of piezoelectricity was discovered in the 1880s by Pierre and Jacques Curie. They found that some crystalline materials, when compressed, produce a voltage proportional to the applied pressure, and that when an electric field is applied across the material, there occurs a corresponding change in shape. This characteristic is called *piezoelectricity*. Thus, piezoelectric materials are those that generate an electric charge when deformed mechanically. This is commonly referred to as the “generator effect.” Conversely, when an external electric field is applied to piezoelectric materials, they assume mechanical deformation or stress. This is commonly referred to as the “motor effect.”

Typical examples of the naturally occurring piezoelectric materials are quartz, tourmaline, human skin, and

human bone, although the latter two have very low coupling efficiencies. Some artificially produced piezoelectric crystals are Rochelle salt, lithium sulfate, and ammonium dihydrogen phosphate. Another class of materials possessing piezoelectric properties is polarized piezoelectric ceramic. They are typically referred to as *ferroelectric materials*. In contrast to the naturally occurring piezoelectric crystals, ferroelectric ceramics are polycrystalline in nature. The most commonly produced piezoelectric ceramics are barium titanate, lead titanate, lead metaniobate, and lead zirconate titanate (PZT). Although piezoelectricity is found in several types of natural materials, most modern devices use PZT. Piezoelectric ceramics respond rapidly to the changes in input voltage; noise due to the power supply is the only limiting factor in the positional resolution. Although high voltages are used to produce piezoelectric effect, the power consumption is low, and the energy consumption is minimal in maintaining a fixed position with a fixed load.

Production of all piezoelectric ceramic materials involves detailed processing, and the material properties may be altered by modifying the chemical composition and the manufacturing process. This essentially provides the designer with a means to tailor the material properties to the application. The processing involves different stages such as calcination, high firing, polling, and aging. To discuss the details of these processes is beyond the scope of the present article.

Piezoelectric ceramic materials possess electrical, mechanical, and electrochemical properties resulting from the chemical formulation and the manufacturing process. Typical electrical parameters are the dielectric constant and the dissipation. High dielectric constants of the materials are desirable as this property provides low impedance. Materials with low dissipations are required because they result in low electrical losses. Typical electromechanical parameters are the electromechanical coupling constant k and the piezoelectric constants g and d . High values of the electromechanical coupling result in a more efficient transfer of electrical energy to the mechanical energy. In fact, the constant k is a dimensionless number related to the ratio of the energy stored in the mechanical and electrical portion of the material. The constant d relates to mechanical strain and applied electrical field, and it is defined as the ratio of the strain to the field, with the unit meters per volt. The constant g relates the open-circuit voltage and mechanical stress, and it is defined as the ratio of the voltage to stress. The unit of g is voltmeters per newton. Typical mechanical parameters are the density and the elastic constants.

Depolarization of piezoelectric ceramics would result if these materials were exposed to excessive heat, electrical drive, or mechanical stress or any combination of these. The temperature at which piezoelectric ceramic is completely depoled is known as the *Curie point*. Piezoelectric ceramics also possess the properties of *pyroelectricity*, in which a change in ceramic temperature results in a change in mechanical dimensions, thereby producing stress within the ceramic and a corresponding electrical charge on the surface of electrodes.

An example of a piezoelectric device is ultrasonic probes (transducers) employed to create underwater Sonar. This area of exploitation of piezoelectric materials is quite mature, and nowadays ultrasonic probes work almost exclusively according to the piezoelectric effect. A series of powerful piezoelectric materials are now available to generate ultrasound in ultrasonic probes. These materials differ in their physical properties, and depending on the technical application and the required probe characteristics, an appropriate selection of the piezoelectric material can be made. Knowledge of the constructional details of the utilized piezoelectric materials, however, not only contributes toward a better technical understanding of the basic action of the probe but also helps us understand the behavior of the probe under certain operation conditions.

For the construction of ultrasonic probes, the diameter and the frequency of the piezoelectric element are the important parameters to be considered. However, it is essential to have a detailed knowledge of the physical and the acoustic properties of the piezoelectric material used; the relevant information will not only contribute to a better technical understanding of the basic working principle of probes but will also give an insight into the behavior of the probe under various operating conditions. Information about the piezoelectric materials will also be helpful in detecting the suitability of the type of probe under the given circumstances. As such, it would be worthwhile to introduce the different types of piezoelectric materials currently in use. We shall explain their strengths and weaknesses and to show how they can be exploited for various probe designs.

9.1. Piezoelectric Materials

In the early days of ultrasound technology, materials such as quartz, lithium sulfate, and barium titanate were used. However, such materials are rarely in use today; instead, new powerful piezoelectric materials are available, which have varieties of basic acoustic and electric characteristics. Table 4 lists the important physical characteristics of different piezoelectric materials used today to generate ultrasonic waves [60].

The acoustic impedances of *piezoceramic* materials are usually high and comparable to those of many metallic or ceramic solids. The coupling coefficient for radial (or transverse) vibrations indicates to what extent a piezoelectric element can convert energy into transverse modes, which are perpendicular to the thickness mode. Transverse modes should be suppressed as much as possible as they cause undesired signal distortions. These modes are developed at low frequencies, because they correspond to the lateral dimensions of the piezoelectric element. Lead titanate is the only piezoelectric material that has a negligibly small coupling coefficient k . The *electromechanical coupling coefficient* k_t is a measure of the fraction of electrical energy, which is converted into mechanical energy in the thickness mode. It determines the efficiency of generating ultrasonic waves in a particular vibrational mode utilized in probes. The values of k_t for piezoceramic materials are usually high. However, if ultrasonic waves prop-

Table 4. Characteristics of Piezoelectric Materials

Physical Properties	Lead Zirconate Titanate PZT-5	Lead Titanate PT	Lead Metaniobate PbNb ₂ O ₆	Polyvinylidene Fluoride PVDF (Copolymer)	1-3 Composite
Acoustic impedance Z ($10^6 \text{ kg m}^{-2} \text{ s}^{-1}$)	33.7	33	20.5	3.9	9
Resonant frequency f (MHz)	<25	<20	<30	160–10 (55–2)	<10
Coupling coefficient (thickness mode) k_t	0.45	0.51	0.30	0.2 (0.3)	0.6
Coupling coefficient (radial mode) k_p	0.58	<0.01	<0.1	0.12 (k_{31})	~0.1
Relative permittivity ϵ_r	1700	215	300	10	450
Maximum temperature ($^{\circ}\text{C}$)	365	350	570	80	100

agate into liquids or plastics, most of the acoustic energy generated by the piezoceramic element is reflected at the boundary between the piezoelectric material and the medium of propagation. Therefore, only a fraction of the acoustic energy is transferred into the medium of propagation. Such piezoceramics are used for up to a maximum of 30 MHz.

Piezoelectric plastics such as PVDF or related copolymers are better matched to the low acoustic impedance of liquids or plastics. In addition, they are mechanically flexible. It becomes possible to generate ultrasound at frequencies up to 160 MHz with very thin foils of PVDF. However, it becomes evident from the coupling coefficient k_t for the thickness mode that PVDF is less sensitive than ceramics.

The so-called 1–3 composite materials [61] appear more promising as they have high values of k_t and low values of k . Such composites perform better within the approximate temperature range of 100°C . Table 4 shows typical values for 1–3 piezocomposites. However, these values will vary in a wide range by varying the piezoceramic material as the design.

9.2. Applications of Piezoelectric Materials in Probes

Different properties of piezoelectric materials are very useful for the design of different types of probes. The most suitable material can be selected depending on the intended application of the probe. As we can see from Table 4, lead metaniobate has the lowest acoustic impedance of all the piezoceramics. This is better suited to design high-resolution shockwave probes (shockwaves have extremely short pulses). The relatively low impedance of lead metaniobates is also useful for the design of broadband angle probes and TR probes. Lead titanate has small values of k , and therefore, radial vibrational modes of this material are negligible. As such, lead titanate can be utilized to produce probes with especially small measurements. Lead zirconate titanate (PZT) is used where large measurements and high ultrasonic absorption are required. In such cases, it is important that the probe should generate ultrasound of higher intensity than usual, so that even echoes from the far end can still be detected. For receiver probes, it is better to use a bulk PZT element of appropriate thickness. This is because, at a given input pressure, the voltage across the

electrodes of a piezoelectric element is proportional to its thickness.

At high frequencies the use of piezoceramics is limited. Since the resonant frequency of piezoelectric disks vibrating in the thickness mode is inversely proportional to the thickness, piezoceramic disks become thinner than 0.1 mm above 20 MHz. Such piezoceramic disks are brittle and difficult to handle during the manufacturing process of the probe. However, at higher frequencies, thin foils of PVDF are easier to handle [62]. Because of their low acoustic impedance, an effective transfer of ultrasonic waves is possible only into water or plastic materials. Even at normal frequencies the high flexibility of PVDF and its low impedance, are useful for the design of special line-focused immersion probes. Such line-focused PVDF probes have been in use since 1990 in high-speed test systems for steel pipes. These are described in more detail in other publications [63,64].

Because of their relatively low acoustic impedance and high sensitivity, 1–3 composites are also suitable for generating ultrasound in liquids and plastics. However, the manufacturing of such probes is less complicated than the manufacturing process of the piezo element itself. 1–3 composites are also suitable for the manufacturing of line-focused immersion probes. However, PVDF foils are less expensive.

In conclusion, the currently available piezoelectric materials complement each other in their physical characteristics. PVDF is very flexible, and it is easy to handle and shape. Further, it exhibits good stability over time, and does not depolarize when subjected to very high alternating fields. But the coupling constant of PVDF is significantly lower than that of PZT. Shaping of PVDF can reduce the effective coupling of mechanical and electrical energies due to edge effects. In the design of ultrasonic probes, it is very important to use a material that has the best suitable characteristics. In addition, economy also plays a vital role for the user, as well as for the manufacturer. As a result, PZT has been considered as an economic piezoelectric material over the years.

Acknowledgment

The authors are immensely grateful to Prof. Akhlesh Lakhtakia of the Pennsylvania State University (USA) for reviewing and making constructive suggestions to improve the manuscript.

BIBLIOGRAPHY

1. R. S. Elliott, *Electromagnetics*, McGraw-Hill, New York, 1966.
2. P. F. Mottelay, *Biographical History of Electricity and Magnetism*, Ayer Publishers, Salem, NH, 1975.
3. E. T. Whittaker, *A History of the Theories of Aether and Electricity*, American Institute of Physics, New York, 1987.
4. C. Kittel, *Introduction to Solid State Physics*, 6th ed., Wiley, New York, 1986.
5. B. K. P. Scaife, *Principles of Dielectrics*, Oxford Univ. Press, Oxford, UK, 1989.
6. E. D. Palik, ed., *Handbook of Optical Constants of Solids II*, Academic Press, Boston, MA, 1991.
7. J. D. Jackson, *Classical Electrodynamics*, 2nd ed., Wiley, New York, 1975.
8. T. Van Duzer and C. W. Turner, *Principles of Superconductive Devices and Circuits*, Elsevier, New York, 1981.
9. V. Z. Kresin and A. Wolf, *Fundamentals of Superconductivity*, Plenum, New York, 1990.
10. J. A. Stratton, *Electromagnetic Theory*, McGraw-Hill, New York, 1941.
11. R. E. Collin, *Field Theory of Guided Waves*, 2nd ed., IEEE Press, Piscataway, NJ, 1991.
12. M. Born and E. Wolf, *Principles of Optics*, 6th ed., Pergamon Press, New York, 1980.
13. A. Yariv and P. Yeh, *Optical Waves in Crystals*, Wiley, New York, 1984.
14. H. A. Haus, *Waves and Fields in Optoelectronics*, Prentice-Hall, Englewood Cliffs, NJ, 1984.
15. A. Yariv, *Quantum Electronics*, 3rd ed., Wiley, New York, 1989.
16. M. Javid and P. M. Brown, *Field Analysis and Electromagnetics*, McGraw-Hill, New York, 1963.
17. P. Lorrian and D. Corson, *Electromagnetic Fields and Waves*, 2nd ed., Freeman, San Francisco, CA, 1970.
18. J. D. Kraus, *Electromagnetics*, 3rd ed., McGraw-Hill, New York, 1984.
19. D. T. Paris and F. K. Hurd, *Basic Electromagnetic Theory*, McGraw-Hill, New York, 1969.
20. J. R. Reitz and F. J. Milford, *Foundations of Electromagnetic Theory*, Addison-Wesley, Reading, MA, 1960.
21. J. E. Parton, S. J. T. Owen, and M. S. Raven, *Applied Electromagnetics*, 2nd ed., Macmillan, London, 1986.
22. A. H. Morrish, *The Physical Principles of Magnetism*, Krieger, Malabar, FL, 1982.
23. R. Boll, ed., *Soft Magnetic Materials*, Heyden, London/Philadelphia/Rheine, 1979.
24. R. Plonsey and R. E. Collin, *Principles and Applications of Electromagnetic Fields*, 2nd ed., McGraw-Hill, New York, 1982.
25. H. Jouve, *Magnetic Bubbles*, Academic Press, San Diego, CA, 1987.
26. A. Goldman, *Modern Ferrite Technology*, Van Nostrand-Reinhold, New York, 1990.
27. R. S. Elliott, *An Introduction to Guided Waves and Microwave Circuits*, Prentice-Hall, Englewood Cliffs, NJ, 1993.
28. C. L. Hogan, *Bell Syst. Tech. J.* **31**:1 (1952).
29. C. E. Fay and R. L. Comstock, *IEEE Trans. Microwave Theory Tech.* **MTT-13**:15 (1965).
30. E. F. Schloemann, *Proc. IEEE* **76**:188 (1988).
31. A. Lakhtakia, *Beltrami Fields in Chiral Media*, World Scientific, Singapore, 1994.
32. A. Priou, A. Sihvola, S. Tretyakov, and A. Vinogradov, eds., *Advances in Complex Electromagnetic Materials*, Kluwer, Dordrecht, The Netherlands, 1997.
33. O. N. Singh and A. Lakhtakia, eds., *Electromagnetic Fields in Unconventional Materials and Structures*, Wiley, New York, 2000.
34. W. S. Weiglhofer and A. Lakhtakia, Casuality and natural optical activity (chirality), *J. Opt. Soc. Am. A* **13**:385–386 (1996).
35. A. Lakhtakia, R. Messier, M. J. Brett, and K. Robbie, Sculptured thin films (STFs) for optical, chemical and biological applications, *Innovat. Mater. Res.* **1**:165–176 (1996).
36. A. Lakhtakia and R. Messier, Sculptured thin films—I. Concepts, *Mater. Res. Innovat.* **1**:145–148 (1997).
37. V. C. Venugopal and A. Lakhtakia, Dielectric sculptured nematic thin films for rugate-like filters, *Opt. Commun.* **149**:217–222 (1998).
38. R. Messier and A. Lakhtakia, Sculptured thin films—II. Experiments and applications, *Mater. Res. Innovat.* **2**:217–222 (1999).
39. A. Lakhtakia and M. McCall, Sculptured thin films as narrow-bandpass circular polarization filters, *Opt. Commun.* **168**:457–466 (1999).
40. V. C. Venugopal and A. Lakhtakia, Sculptured thin films: Conception, optical properties, and applications, in O. N. Singh and A. Lakhtakia, eds., *Electromagnetic Fields in Unconventional Materials and Structures*, Wiley, New York, 2000.
41. B. V. Bokut, A. N. Serdyukov, and F. I. Fedorov, On the form of constitutive equations in optically active crystals, *Optika i Spektroskopiya* **37**:288–293 (1974).
42. F. I. Fedorov, *Theory of Gyrotropy*, Nauka i Tekhnika (Science and Technology Publishers), Minsk, 1976.
43. B. V. Bokut and A. N. Serdyukov, On the theory of optical activity of non-uniform media. *Zh. Prikladnoi Spektroskopii* **20**:677–682 (1974).
44. L. D. Landau and E. M. Lifshitz, *Electrodynamics of Continuous Media*, 2nd ed., Pergamon Press, Oxford, 1984.
45. S. A. Tretyakov and A. A. Sochava, Eigenwaves in uniaxial chiral omega media, *Microwave Opt. Technol. Lett.* **6**:701–705 (1993).
46. S. A. Tretyakov and A. A. Sochava, Proposed composite material for non-reflecting shields and antenna radomes, *Electron. Lett.* **29**:1048–1049 (1993).
47. S. A. Tretyakov, Thin pseudochiral layers: Approximate boundary conditions and potential applications, *Microwave Opt. Technol. Lett.* **6**: 112–115 (1993).
48. I. V. Semchenko, Gyrotropic properties of superlattices in the long-wave approximation, *Kristallografiya* **35**:1047–1050 (1990).
49. N. I. Gheludiyev and A. D. Petrenko, Physical mechanisms of non-linear optical activity in crystals, *Kristallografiya* **29**:1045–1053 (1984).
50. I. N. Akhramenko, I. V. Semchenko, and A. N. Serdyukov, Selective interaction of electromagnetic waves in crystals with spiral-modulated non-stationary dielectric permittivity, *Optika i Spektroskopiya* **66**:618–622 (1989).
51. M. Wun-Fogle, H. T. Savage, L. T. Kabacoff, K. B. Hathaway, J. M. Merchant, and B. Beihoff, Magnetoelastic effects in amorphous wires and amorphous ribbons with nonmagnetic thin-film coatings, *J. Appl. Phys.* **64**:5405–5407 (1988).
52. T. H. O'Dell, Measurement of magnetomechanical coupling factor in amorphous ribbons, *Physica Status Solidi A* **74**: 565–572 (1982).

53. C. A. Grims, K. G. Ong, K. Loisel, P. G. Stoyanov, D. Kouzoudis, Y. Liu, C. Tong, and F. Tefiku, Magnetoelastic sensors for remote query environmental monitoring, *Smart. Mater. Struct.* **8**:639–645 (1999).
54. M. K. Jain, S. Schmidt, K. G. Ong, C. Mungle, and C. Grimes, Magnetoacoustic remote query temperature and humidity sensors, *Smart Mater. Struct.* **9**:502–510 (2000).
55. J. Gutiérrez, J. M. Barandiarán, and O. V. Nielsen, Magnetoelastic properties of some Fe-rich Fe-Co-Si-B metallic glasses, *Physica Status Solidi A* **111**:279 (1989).
56. S. Schmidt and C. Grimes, Elastic modulus measurement of thin films coated onto magnetoelastic ribbons, *IEEE Trans. Magn.* **37**:2731–2733 (2001).
57. J. Enkovaara, A. Ayuela, L. Nordstöm, and R. M. Nieminen, Structural, thermal, and magnetic properties of Ni₂MnGa, *J. Appl. Phys.* **91**:7798–7800 (2002).
58. J. Dooley, B. Fultz, J. Voccio, and R. Chave, Magnetoelastic vibration dampers, *NASA Tech. Briefs* **25**:56–57 (2001).
59. J. Dooley, R. Chave, B. Fultz, A. Clark, N. Good, and J. Graetz, Progress in magnetoelastic vibration dampers, *NASA Tech. Briefs* **25**:57 (2001).
60. M. Lach, M. Platte, and A. Ries, Piezoelectric materials for ultrasonic probes, *NDTnet* **1**(9):(1996).
61. L. Chofflet, M. Gauchet, and J. M. Tellier, Which piezoelectric material for which transducer? *Revue Annuelle LEP*:37–38 (1990).
62. R. G. Swartz and J. D. Plummer, On the generation of high-frequency acoustic energy with polyvinylidene Fluoride, *IEEE Trans. Sonics Ultrason.*, SU **27**, 295–303, 1980.
63. V. Deutsch, M. Platte, and P. Möller, Ultraschallprüfköpfe aus piezoelektrischen Hochpolymeren, *Materialprüfung* **32**: 333–337 (1990).
64. M. Platte and P. Möller, Automatisches Ultraschallprüfen von Blechen und Rohren, *Bänder Bleche Rohre* **34**:25–32 (1993).

ELECTROMAGNETIC MODELING

R. VAHLDIECK
 Swiss Federal Institute of
 Technology Zürich (ETHZ)
 Zürich, Switzerland
 WOLFGANG J.R. HOEFER
 University of Victoria
 Victoria, BC, Canada

Numerical modeling of electromagnetic (EM) fields or *computational electromagnetics* is a combination of numerical methods and field theory—a discipline in its own right and of growing importance in such diverse areas as microwave and RF (radiofrequency) engineering, antenna design, EM field scattering, semiconductor physics, bioelectromagnetics, and electromagnetic compatibility and interference (EMC/EMI).

The starting point for modeling electromagnetic fields is Maxwell's equations considering a set of known boundary/initial conditions. In addition, certain theorems and principles, such as superposition, equivalence, and duality can be utilized. Entirely analytical solutions to Maxwell's equations are possible only for a narrow range of problems

and most of them were solved a long time ago. Classical analytical methods are the methods of separation of variables, conformal mapping, series expansion, and integral methods (if the integrals have analytical solutions).

Today's complexity of relevant EM field problems prevent entirely analytical (closed-form) solutions to Maxwell's equations. Rather, numerical approaches are necessary that approximate the exact solution with any desired degree of accuracy. Does this eliminate the need for analytical methods? Certainly not! In fact, analytical preprocessing is part of all numerical methods, and if the analytical content is high, the method is often described as semianalytical.

In general, the electromagnetic field problem can be conveniently formulated as a partial-differential equation while that of the source problem as an integral equation (operator equation). The objective of numerical methods is to transform an exact operator equation into a solvable (discrete) matrix equation. To achieve this, virtually all numerical methods follow the same principal steps:

1. To express the unknown function of the operator equation by a sum of linear independent functions with unknown expansion coefficients. This is often called a trial function which approximates the real function if the number of terms in the sums goes to infinity.
2. The continuous solution domain is represented by a set of discretized subdomains consisting of a finite number of elements or nodes.
3. To determine the unknown expansion coefficients in the trial function, some form of error minimization is chosen. Employing either variational principles or the method of weighted residuals, the operator equation is transformed into a matrix equation that must be solved by appropriate techniques.

Depending on the kind of operator used, numerical methods are in general categorized into domain methods and boundary methods. More recently a new category has been added, that of hybrid methods.

Domain methods solve the electromagnetic field problem described by partial differential equations. Examples are the finite difference method and the finite element method. Both methods are based on differential equations and on discretization of the entire computational domain. *Boundary methods* solve the electromagnetic source problem described by integral equations, either volume integral equations or boundary integral equations. Examples are the boundary element method or the method of moments. The latter can also be used to solve differential equations. *Hybrid methods* are a combination of two or more different methods. A hybrid numerical approach can be a two-step procedure or an implicit hybrid algorithm. In the two-step procedure, one part of the problem is solved with one method, the results of which become the input parameters for the next method. In the implicit hybrid algorithm two or more modeling approaches are combined into one new algorithm to exploit only the advantageous features of each method. Hybrid methods are very useful

for problems that can either not be solved within the framework of a single technique or in cases where a combination of methods results in a computationally more efficient algorithm to model the electromagnetic field.

Since the late 1970s the importance of modeling electromagnetic fields has increased manifold. This refers not only to the analysis of arbitrary electromagnetic field problems but also to the CAD (computer-aided design) of circuits and components. With rising operating frequency and higher circuit density, quasistatic analysis methods are replaced by full-wave analysis methods to account for near-field effects or higher-order mode interaction. Simplifying assumptions about material properties have been replaced by realistic material descriptions taking dispersion and losses into account. With the steady increase in computer power, research in electromagnetic modeling is still advancing at a rapid pace, introducing new techniques, expanding the capability of existing methods or simply improving their computational efficiency and accuracy. Only some of the multitude of electromagnetic modeling techniques available today can be outlined here.

This article will focus only on some mainstream techniques, most of which employ either the method of weighted residuals or variational principles. We will begin with modeling techniques in the frequency domain, most importantly the method of moments (MoM). This section is followed by time-domain methods and here in particular the finite-difference time-domain method (FDTD) and the transmission-line matrix (TLM) method. Finally, a brief overview with respect to hybrid methods concludes this article. A comparison between the various modeling approaches as well as their advantages and disadvantages is added where appropriate.

For a more detailed representation of the various methods, the interested reader is referred to the books by Sadiku [1] or Zhou [2]. Another excellent source of information is the book edited by Itoh [3], which discusses the various methods in the context of passive microwave circuit modeling.

1. FREQUENCY-DOMAIN METHODS

Most electromagnetic modeling techniques operate in the frequency domain; that is, the time derivative d/dt is replaced by $j\omega t$. Therefore, all calculations are performed at a single frequency only. In cases where the electromagnetic field is of interest over a frequency band, repeated calculations are necessary. This is in contrast to time-domain methods. Here a single run of the algorithm, after a proper impulse excitation, followed by a Fourier transform of the impulse response, provides the information over a wide frequency range. Which method to use depends on the problem at hand.

1.1. The Method of Moments

The *method of moments* (MoM) is a general form of weighted residuals to solve integral, differential, and integrodifferential equations. The method itself does not provide any information about the derivation of the gov-

erning equation, thereby allowing its applicability to a wide range of physical phenomena.

The equations solved by MoM are normally an electric field integral equation (EFIE) or a magnetic field integral equation (MFIE) of the following form

$$\text{EFIE : } \mathbf{E} = f_e(\mathbf{J})$$

$$\text{MFIE : } \mathbf{H} = f_m(\mathbf{J})$$

whereby \mathbf{E} and \mathbf{H} are the incident field quantities and \mathbf{J} is the induced current density. The form of integral equation (EFIE or MFIE) depends on the problem. In most cases these integrals are formulated in the frequency domain, although the MoM can also be applied to solve problems in the time domain.

The MoM as a mathematical technique was first introduced by Mikhlin [4] and later popularized in the area of numerical electromagnetics by Harrington [5]. The mathematical formulation of the MoM is simple and general. Consider a linear operator L such that

$$L\mathbf{J} = \mathbf{g} \quad (1)$$

The function \mathbf{J} (e.g., current density) is the response of the system represented by the operator L to the excitation \mathbf{g} (magnetic or electric field). When L and \mathbf{g} are known, Eq. (1) represents an analysis problem from which \mathbf{J} is determined. A synthesis problem is one in which both \mathbf{J} and \mathbf{g} are known but L is to be determined.

The MoM solution of Eq. (1) takes advantage of the linearity of the operator L to expand \mathbf{J} in a series of the form

$$\mathbf{J} = \sum_m a_m \mathbf{J}_m \quad (2)$$

The a_m 's are unknown expansion coefficients and the \mathbf{J}_m 's are known functions in the domain of the operator L . The functions \mathbf{J}_m , which are assumed to form a complete set, are called *basis functions*. Substituting the expansion of \mathbf{J} in Eq. (1) and using the linearity of L , we get

$$L\mathbf{J} = L \sum_m a_m \mathbf{J}_m = \sum_m a_m L\mathbf{J}_m = \mathbf{g} \quad (3)$$

The original problem is now reduced to determining the expansion coefficients from this last equation. In the MoM, both sides of the equation are projected onto the range of the operator L . Let \mathbf{T}_m denote a complete set of functions in the range of L . The \mathbf{T}_m 's are referred to as testing or weighting functions. Taking the inner product of Eq. (3) against the testing functions, yields

$$\sum_m a_m \langle \mathbf{T}_n, L\mathbf{J}_m \rangle = \langle \mathbf{T}_n, \mathbf{g} \rangle \quad n = 1, 2, \dots \quad (4)$$

Here, a suitable inner product (a linear form) is assumed to be known. Usually, the inner product is taken as the

integral of the product of the arguments

$$\langle \mathbf{J}, \mathbf{g} \rangle = \int \mathbf{J} \mathbf{g} \quad (5)$$

Equation (4) can be rewritten in a more convenient matrix form

$$[A][a] = [U] \quad (6)$$

where

$$[A]_{mn} = \langle \mathbf{T}_m, \mathbf{L} \mathbf{J}_n \rangle \quad (7)$$

$$[U]_m = \langle \mathbf{T}_m, \mathbf{g} \rangle \quad (8)$$

If the matrix $[A]$ is not singular, its inverse $[A]^{-1}$ exists. The expansion coefficients a_m are then given by

$$[a] = [A]^{-1}[U] \quad (9)$$

Once the expansion coefficients are known, the solution is given by Eq. (2). The MoM is most commonly implemented in the form of Galerkin’s method in which the testing functions are equal to the basis functions, $\mathbf{T}_m = \mathbf{J}_m$.

In practice, the infinite expansion Eq. (2) is truncated at some upper value of m . The approximate solution, given by Eq. (9), is then straightforwardly computed using a computer. The efficiency of the technique depends heavily on having basis functions which approximate well the exact solution with only a few terms. Therefore, MoM techniques are not very effective in the analysis of complex geometries or inhomogeneous dielectrics. On the other hand, MoM techniques are particularly efficient for the analysis of antennas and electromagnetic scattering problems.

1.2. The Mode-Matching Technique

The mode-matching technique (MMT), or modal analysis method, can be viewed as a special case of the method of moments and is a frequently used analysis tool for scattering of electromagnetic waves at metal waveguide discontinuities. In this method, the fields immediately left and right from the discontinuity are expanded in a series of weighted eigenfunctions. From the matching condition or continuity condition of the fields tangential to the discontinuity plane the coefficients of the series expansions can be determined. Details of the method can be found in Refs. 6 and 7. The MMT has been successfully applied to eigenvalue as well as to scattering problems both in homogeneous waveguides as well as partially dielectric loaded waveguides. Numerous application examples for eigenvalue problems are given, for example, in Refs. 8 and 9 and for scattering problems in Refs. 10 and 11.

The basic problem to be solved in the MMT is to find the coefficients of the field expansion to minimize the least square error between the exact EM field and the approximating series of eigenfunctions. If we postulate $g(x)$ as the exact field in the aperture between two subregions, the approximation by a series of orthogonal eigenfunctions

$f_i(x)$ is written

$$g(x) \cong \sum_i^N a_i f_i(x), \quad x \in x_1, x_2 \quad (10)$$

where a_i denote the weighting (expansion) coefficients. Multiplying both sides of Eq. (10) with a set of weighting functions $w_j(x)$ and integrating over the domain of x results in

$$\int_{x_1}^{x_2} w_j(x) g(x) dx = \sum_i^N a_i \int_{x_1}^{x_2} w_{ji}(x) f_i(x) dx \quad (11)$$

We solve Eq. (11) such that its weighted residual is zero:

$$\int_{x_1}^{x_2} w_j(x) \left[g(x) - \sum_i^N a_i f_i(x) \right] dx = 0, \quad (12)$$

$$j = 1, 2, \dots, N$$

If the weighting function is a set of delta functions

$$w_j(x) = \delta(x - x_j)$$

Eq. (10) becomes Eq. (13) which is known as *point matching* Eq. (11):

$$g(x_j) \cong \sum_i^N a_i f_i(x_j), \quad j = 1, 2, \dots, N \quad (13)$$

This equation is solved for a_i . If the weighting functions are the eigenfunctions themselves, we use the least-square error to select the expansion coefficients such as to minimize the integrated squared error

$$0 = \frac{\partial}{\partial a_i} \int \left[g(x) - \sum_i^N a_i f_i(x) \right]^2 dx$$

By using the orthogonality of the eigenfunctions $f_i(x)$ we find the individual coefficients

$$\frac{\int_{x_1}^{x_2} f_i(x) g(x) dx}{\int_{x_1}^{x_2} f_i(x)^2 dx} = a_i \quad (14)$$

It should be noted that the integral in the denominator of Eq. (14) is a normalization constant while the integral in the numerator (the coupling integral) can in most cases be solved analytically, except in cases where the geometry of the regions left and right of a discontinuity is described by different coordinate systems.

The MMT becomes a powerful analysis tool in conjunction with the generalized scattering matrix (GSM) approach. The GSM relates all reflected wave amplitudes of fundamental and higher-order modes at discontinuities to the incident wave amplitudes. Wave amplitudes are in this context the power normalized expansion coefficients in Eq. (10).

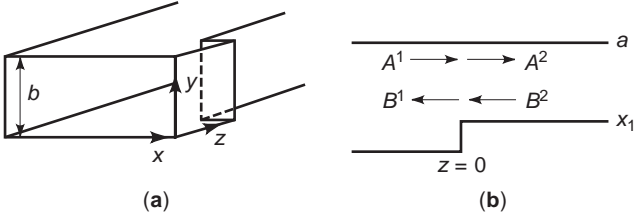


Figure 1. H -plane discontinuity in rectangular waveguide; (a) perspective view; (b) scattered wave amplitudes.

A simple example illustrates the MMT in conjunction with the GSM technique. A waveguide step discontinuity is shown in Fig. 1. We assume that in both waveguide sections only the fundamental TE_{10} mode can propagate.

The TE_{10} mode consists of three field components of which two, E_y and H_x , are tangential to the discontinuity plane at $z=0$ (Fig. 1b). In regions 1 and 2, the electric field component can be expressed as a series of eigenfunctions such as in Eq. (10). Applying the continuity condition at the discontinuity plane ($z=0$), $E_y^1 = E_y^2$, results in

$$\begin{aligned} & \sum_{m=1}^M T_m^1 \sin\left(\frac{m\pi}{a}x\right) (A_m^1 + B_m^1) \\ &= \sum_{n=1}^N T_n^2 \sin\left(\frac{n\pi}{a-x_1}(x-x_1)\right) (A_n^2 + B_n^2) \end{aligned} \quad (15)$$

The coefficients T in Eq. (15) ensure power normalization of the incident A and reflected B wave amplitudes for fundamental and higher-order modes. The products $T \cdot A$ or $T \cdot B$ are the expansion coefficients of Eq. (10). Multiplying both sides of Eq. (15) with $\sin(i\pi/a x)$ and integrating over the cross section $x=0-a$ yields

$$E_y : A_i^1 + B_i^1 = \frac{\sum_{n=1}^N T_n^2 \int_{x_1}^a \sin\left(\frac{n\pi}{a}x\right) \sin\left(\frac{i\pi}{a-x_1}(x-x_1)\right) dx}{\underbrace{\int_0^a \sin^2\left(\frac{i\pi}{a}x\right) dx}_{LE}} (A_n^2 + B_n^2) \quad (16)$$

The normal modes satisfy the orthogonality relation, and the integral in the denominator of Eq. (16) thus becomes

$$\int_0^a \sin^2\left(\frac{i\pi}{a}x\right) dx = \frac{a}{2} \quad (17)$$

A similar equation is obtained from the continuity condition of the H_x component

$$H_x : \frac{\sum_{m=1}^M T_m^2 Y_m \int_{x_1}^a \sin\left(\frac{m\pi}{a}x\right) \sin\left(\frac{i\pi}{a-x_1}(x-x_1)\right) dx}{\underbrace{\int_{x_1}^a \sin^2\left(\frac{i\pi}{a-x_1}x-x_1\right) dx}_{LH}} \quad (18)$$

$$A_i^1 - B_i^1 = A_m^2 - B_m^2$$

Both equations can be written in matrix notation:

$$\begin{aligned} E_y : & [A]^1 + [B]^1 = [L_E] \cdot ([A]^2 + [B]^2) \\ H_x : & [L_H] \cdot ([A]^1 - [B]^1) = [A]^2 - [B]^2 \end{aligned}$$

Rearranging these equations leads to the generalized scattering matrix of the waveguide discontinuity

$$\begin{bmatrix} [B]^1 \\ [A]^2 \end{bmatrix} = \begin{bmatrix} [S_{11}] & [S_{12}] \\ [S_{21}] & [S_{22}] \end{bmatrix} \begin{bmatrix} [A]^1 \\ [B]^2 \end{bmatrix} \quad (19)$$

A well-known problem in the MMT is the slow convergence rate and the relative convergence phenomenon. The latter can be alleviated to some degree by choosing the number of modes on both sides of the discontinuity in the same ratio as the waveguide dimensions left and right from the discontinuity. The MMT is also not well suited for problems in which the structure contains a mixed-coordinate system. Coupling integrals must then be solved numerically, which makes the algorithm slow and not very effective. In those cases the MMT can be combined with other techniques (hybrid methods discussed later) that are more appropriate for certain parts of the problem.

1.3. Coupled Integral Equation Technique

The problem of slow convergence in the MMT is due mainly to the fact that the eigenfunctions of the waveguides left and right from the discontinuity do not accommodate the boundary conditions of the fields in the discontinuity plane. This is not so in the coupled integral equation technique (CIET). A major advantage of the CIET is its ability to include a priori information, such as the edge conditions, at multiple discontinuities simultaneously. The salient features of the technique can be found in Refs. 12 and 13; here we only show how the edge condition at a single discontinuity is handled through the CIET. For this we refer again to the example of Fig. 1.

The tangential electric field within the discontinuity region (the gap region) is expanded in a series of basic functions that are chosen such that they include the edge condition of the electric field at $x=x_1$:

$$E_{\text{gap}}(x) = \sum_i^I c_i E_i(x) \begin{cases} E_{\text{gap}} = 0, & 0 \leq x \leq x_1 \\ E_{\text{gap}} \neq 0, & x_1 < x \leq a \end{cases} \quad (20)$$

A possible set of basic functions that satisfy the edge condition is the following:

$$E_i(x) = \frac{\sin\left[\frac{i\pi}{a-x_1}(x-x_1)\right]}{[(x-x_1)(2a-x_1-x)]^{1/3}}$$

Matching the tangential electric field of both regions (1 and 2) to the electric field in the discontinuity plane

E_{gap} yields

$$\begin{aligned} E_y^1(x) &= E_{\text{gap}}(x), & 0 \leq x \leq a \\ E_y^2(x) &= E_{\text{gap}}(x), & x_1 \leq x \leq a \end{aligned} \tag{21}$$

From Eq. (21), using Eq. (20), one obtains

$$\begin{aligned} B_i^1 &= -\delta_{i1} + \frac{2}{a} \int_{x_1}^a E_{\text{gap}}(x) \sin\left(\frac{i\pi}{a}x\right) dx \\ B_i^2 &= \frac{2}{a-x_1} \int_{x_1}^a E_{\text{gap}}(x) \sin\left(\frac{i\pi}{a-x_1}x-x_1\right) dx \end{aligned} \tag{22}$$

Utilizing the matching condition from the tangential magnetic field, $H_x^1 = H_x^2$, which is defined in the interval $x_1 \leq x \leq a$ and replacing the expansion coefficients therein by using Eq. (22), leads to the following integral equation

$$\begin{aligned} 2Y_1^1 \sin\left(\frac{\pi}{a}x\right) &= \sum_i Y_i^2 \frac{2}{a-x_1} \int_{x_1}^a E_{\text{gap}}(x) \sin\left(\frac{i\pi}{a-x_1}x'-x_1\right) \\ &\sin\left(\frac{i\pi}{a-x_1}x-x_1\right) dx' + \sum_n Y_n^1 \frac{2}{a} \int_{x_1}^a E_{\text{gap}}(x) \\ &\sin\left(\frac{n\pi}{a}x'\right) \sin\left(\frac{n\pi}{a}x\right) dx' \end{aligned} \tag{23}$$

The remaining step is to find the expansion coefficients c_i in Eq. (20). This is accomplished by substituting Eq. (20) in Eq. (23) and using the method of moments in the form of Galerkin’s method. The number of terms in Eq. (20), the value of I , is increased until convergence is achieved. Typically only a few terms are needed to accurately describe the discontinuity. Although the analytical content of the CIET is higher than for the MMT, the numerical efficiency is significantly better and no relative convergence problems are encountered.

1.4. The Spectral-Domain Method

The spectral-domain method (SDM) [14] utilizes the Fourier transformation to eliminate all but one space variable in the Helmholtz equation. The latter is then solved analytically for the remaining space variable. The SDM is a computationally very efficient analysis tool for microwave transmission lines. The method has found numerous applications, mainly in the analysis of electromagnetic fields in planar transmission line structures where the overall cross section can be divided into homogeneous dielectric subregions. Although the method was originally introduced for single conductor transmission lines with infinitely thin conductor [15], the SDM has been generalized [16,17] to include finite metallization thickness and multiple dielectric layers.

The method is best illustrated by considering the example of a microstrip line (Fig. 2). In regions with constant μ and ϵ the electromagnetic field, represented by a potential function $\phi^{e,h}$, satisfies the Helmholtz

equation

$$\left(\frac{\partial}{\partial x^2} + \frac{\partial}{\partial y^2} + \frac{\partial}{\partial z^2} + k^2\right)\phi^{e,h}(x,y,z) = 0$$

A two-dimensional Fourier transform on $\phi^{e,h}$ (e.g., on x and z)

$$\tilde{\phi}^{e,h}(\alpha,y,\beta) = \iint e^{-j(\alpha x + \beta z)} \phi^{e,h}(x,y,z) dx dz \tag{24}$$

transforms the Helmholtz equation into one that contains only one space variable

$$\frac{\partial^2 \tilde{\phi}^{e,h}}{\partial y^2} - (\alpha^2 + \beta^2 - k^2)\tilde{\phi}^{e,h} = 0 \tag{25}$$

A solution to this equation is known in the form of exponential functions or hyperbolic functions. In each homogeneous subregion, $\phi^{e,h}$ can thus be transformed from one boundary to the opposite. With respect to Fig. 2, this implies that the known boundary condition of the electromagnetic field at planes $y=0$ and $y=h$ can be transformed into plane $y=d$. The final step in the formulation of the SDM is then to satisfy the boundary condition of the tangential fields at the interface $y=d$, which are in the transformed domain

$$\tilde{E}_{z1} = \tilde{E}_{z2}; \tilde{E}_{x1} = \tilde{E}_{x2}; \tilde{H}_{x2} - \tilde{H}_{x1} = \tilde{J}_z; \tilde{H}_{z2} - \tilde{H}_{z1} = -\tilde{J}_x$$

\tilde{J}_x and \tilde{J}_z are the Fourier transforms of the unknown currents on the strip. From this, a matrix equation can be derived as follows

$$\begin{bmatrix} \tilde{E}_{z1} \\ \tilde{E}_{x1} \end{bmatrix} = \begin{bmatrix} \tilde{Z}_{zz} & \tilde{Z}_{zx} \\ \tilde{Z}_{xz} & \tilde{Z}_{xx} \end{bmatrix} \begin{bmatrix} \tilde{J}_z \\ \tilde{J}_x \end{bmatrix} \tag{26}$$

with $\tilde{J}_z = \sum_m^M c_m \tilde{J}_{zm}(\alpha)$ and $\tilde{J}_x = \sum_m^M d_m \tilde{J}_{xm}(\alpha)$.

Using Galerkin’s technique, \tilde{E}_x and \tilde{E}_z in Eq. (26) can be eliminated and a matrix equation for the expansion

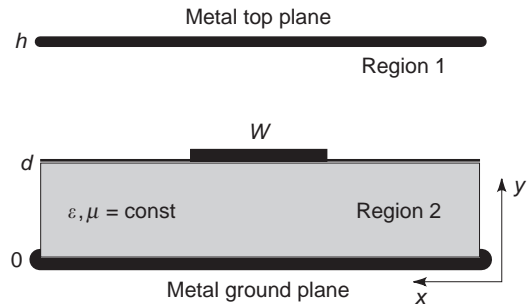


Figure 2. Cross section of a microstrip transmission line.

coefficients c_m and d_m is found

$$\underbrace{\begin{bmatrix} \int_{\gamma} \tilde{\mathbf{J}}_z \tilde{\mathbf{Z}}_{zz} \tilde{\mathbf{J}}_z \int_{\gamma} \tilde{\mathbf{J}}_z \tilde{\mathbf{Z}}_{zx} \tilde{\mathbf{J}}_x \\ \int_{\gamma} \tilde{\mathbf{J}}_x \tilde{\mathbf{Z}}_{xz} \tilde{\mathbf{J}}_z \int_{\gamma} \tilde{\mathbf{J}}_1 \tilde{\mathbf{Z}}_{xx} \tilde{\mathbf{J}}_x \end{bmatrix}}_{[A]} \begin{bmatrix} c \\ d \end{bmatrix} = 0 \quad (27)$$

The propagation constant β is contained in the matrix elements of $\tilde{\mathbf{Z}}$. The transformed currents on the strip are found from an educated guess of the current distribution on the strip in the space domain. To describe the current in the space domain as accurate as possible, basis functions must be employed that are zero outside the strip area and also model the singular behavior of the magnetic field components normal to the strip edge. Equation (27) can then be solved for β by finding the zeros of the determinant of $[A]$ (i.e., $\det[A] = 0$).

A disadvantage of the SDM is that the algorithm is developed for very specific transmission-line geometries. If the geometry changes, for example, substrate regions become inhomogeneous, or conductor contours do not fit into a rectangular coordinate system, the SDM algorithm must be reformulated. This applies also to the previous methods and can be avoided only if more general methods are utilized that are based on finite-element or finite-difference discretization of Maxwell's equations or the Helmholtz equation.

1.5. The Generalized Multipole Method

The generalized multipole technique (GMT) is also based on the weighted residual technique. It is a unique form of the method of moments in that the expansion functions are analytic solutions of the fields generated by sources a distance away from the surface where the boundary condition is being enforced. The GMT is a frequency domain method for calculating electromagnetic fields both in 2D and in 3D. The method is also known as the *multiple-multipole method* (MMT) [19]. In the GMT the field domain is separated into a number of subdomains D_i , each with linear and homogeneous material. In each D_i , a separate expansion of the electromagnetic field is given as

$$\begin{pmatrix} E \\ H \end{pmatrix} = \begin{pmatrix} E_0 \\ H_0 \end{pmatrix} + \sum_{l=1}^{\infty} a_l \begin{pmatrix} E_l \\ H_l \end{pmatrix} \quad (28)$$

In static cases, either the electric or magnetic field is replaced by a potential. E_0, H_0 in Eq. (28) is a given excitation. Any choice of the unknown coefficients a_l results in a correct solution of Maxwell's equation, since E_l and H_l is such a solution. Thus, all degrees of freedom in this solution, that is, the set a_l , may be used to satisfy the boundary conditions. The GMT is often referred to as a *semianalytical* method since the differential equations (i.e., Maxwell's equations) in each subdomain D_i are solved analytically (= exactly), while the boundary conditions on the boundaries ∂D_{ij} between subdomains D_i and D_j are solved numerically (= approximately). In order to accelerate convergence and to keep the number of unknowns as low as possible, the expansion in each subdomain D_i is

chosen such that it fits best to the particular shape of D_i and the particular excitation.

The boundary conditions are fulfilled numerically (approximately), using the extended point-matching technique. This is numerically equivalent to both a projection technique using Galerkin's choice of test functions and a least-squares error minimization. All the boundary conditions concerning fields may be taken into account. As a special case, surface impedance boundary conditions are also possible. Also in the GMT/MMT, a system of linear equations is developed which is solved for the best coefficients of the expansion functions. In order to save computer memory and to improve the numerical stability, matrix solvers like Givens plane rotation may be used.

The difference between the GMT and the MoM is that the latter normally employs expansion functions that are located on the boundary representing quantities such as charge or current. The fields are then determined by integrating these quantities over the entire surface. This integration is not necessary in the GMT since the expansion functions are already field solutions corresponding to multiple poles.

Dielectric and conducting boundaries are treated with the same efficiency in the GMT because the same expansion functions are used. Therefore, GMT models are quite general and do not suffer from the limitations of most MoM models. On the other hand, MoM models that employ functions optimized for a particular problem, are generally more efficient than GMT models.

An overview article about GMT was published by Ludwig [18]. Details of the GMT and application examples are given in the text by Hafner [19] and Leuchtman [20].

1.6. The Method of Lines

The method of lines (MoL) is also a semianalytical method that was developed by Russian mathematicians [21,22] to solve partial-differential equations. In this scheme a set of coupled differential equations is transformed into a set of ordinary differential equations which can be solved analytically. As such the MoL can also be classified as a hybrid method since it combines an analytical approach with the finite-difference method. For the microwave domain, Pregla and coworkers were the first to adopt this method, mainly for the analysis of planar microwave circuits. A very detailed description of the method is given by Pregla and Pascher in Ref. 23. The MoL provides, in comparison to the MMT or the SDM, more flexibility in the analysis of transmission-line geometries with almost arbitrary cross section. The only restriction is that at least one space direction must be amenable to an analytical solution, which is always true for planar transmission lines.

To illustrate the MoL, it is best to choose a two-dimensional problem, although three-dimensional problems can be solved as well. An example of a cross section suitable for an MoL analysis is again the microstrip line as shown in Fig. 2, only this time we consider also the finite metallization thickness. The objective is to find the effective permittivity ϵ_{eff} . Assuming a symmetric structure, the domain is bounded with a magnetic wall at the symmetry plane, and with electric walls elsewhere. The discretization

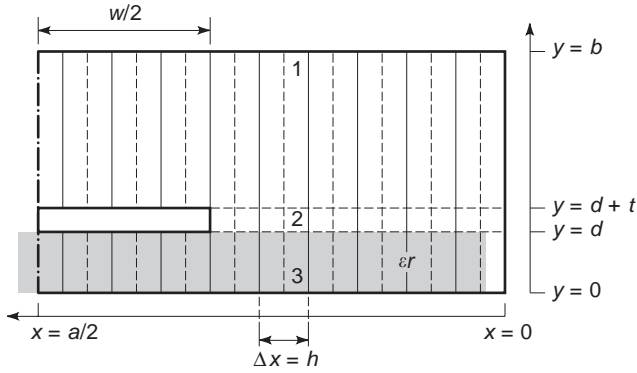


Figure 3. Discretization scheme of the method of lines for a microstrip transmission line with metallic enclosure of dimensions $a \times b$.

of the cross section by lines is shown in Fig. 3 with three homogeneous subdomains. In each subregion the wave equation is discretized in x direction with stepsize h , and analytical solutions are sought in y direction along the solid and dashed lines shown in the figure. To be more precise, analytical solutions for the electric field components are defined on the solid lines ($x = kh, k = 0, 1, 2, \dots$) in order to fulfill the Dirichlet boundary condition at $x = 0$ by setting $E_{\text{tangential}} = 0$. The magnetic field will be defined on the dashed lines ($x = kh + h/2, k = 0, 1, 2, \dots$), where the Neumann boundary condition at $x = 0$ can be fulfilled to a first order [$H_{\text{tangential}}(+h/2) = H_{\text{tangential}}(-h/2)$]. Similar considerations apply to the magnetic wall boundary at $x = a/2$, as well as to subdomain 2 besides the strip. The discretization in x direction is done by a finite difference scheme, and the second-order derivative at line i can be written as

$$\left. \frac{\partial^2 \phi}{\partial x^2} \right|_i \approx \frac{\phi^{i-1} - 2\phi^i + \phi^{i+1}}{h^2}$$

The coupled differential equations in each subregion are then found in matrix form as

$$\frac{\partial^2 \phi}{\partial y^2} - \frac{1}{h^2} [P] \phi + k_c^2 \phi = 0 \tag{29}$$

whereby the vector ϕ represents either the longitudinal electric (E_z) or magnetic (H_z) field component. The second-order difference operator $[P]$ couples the differential equations of three neighboring lines. Because matrix $[P]$ is symmetric, decoupling of the differential equations above is possible by an orthogonal transformation matrix $[T]$ ($[T]^{-1} = [T]^t$) such that

$$\bar{\phi} = [T]^t \phi$$

The eigenvectors of $[P]$ are the columns of $[T]$. The discretized wave equations in the transformed domain is

decoupled and written as

$$\frac{\partial^2 \bar{\phi}}{\partial y^2} + \left(k_c^2 - \left(\frac{\lambda_k}{h} \right)^2 \right) \bar{\phi} = 0 \tag{30}$$

where λ_k^2 are the eigenvalues of $[P]$. Equation (30) can now be solved analytically along each line by using trigonometric functions. In other words, the EM fields in the transformed domain can be transformed from one boundary of a subregion to the opposite. At the interfaces between subregions (i.e., at $y = d$ and at $y = d + t$, Fig. 3), the tangential fields are matched at the points where the lines cross the interface planes. Depending on the problem at hand, field matching is done either in the transformed domain or in the space domain. The latter requires full matrix inversions, which complicates the algorithm. Regarding the example of the microstrip line, field matching in the space domain becomes necessary due to the finite thickness of the strip (i.e., the number of lines to match is different from one subregion to another). The assumption of an infinitely thin strip would make possible a field matching in the transformed domain and, therefore, lower the computational cost of the algorithm by avoiding several matrix inversions. In any case, an eigenvalue problem must be solved for k_c . The size of the eigenvalue matrix corresponds to the minimum number of lines in one layer: the number of lines in region 2 besides the strip. The effective permittivity of the microstrip line is then found from the wavenumber k_c .

A significant advantage of the MoL over other space discretization methods such as the finite-difference method or the finite-element method is that a two-dimensional problem requires only a one-dimensional space discretization. This feature can lower the computational requirements significantly at the cost of a higher analytical content.

1.7. The Finite-Difference Method

The finite-difference method (FDM) is an approximate method to solve partial-differential equations. In contrast to the method of lines, the computational domain is discretized in all three space directions. The derivative operations, for example, for the space variable x , $\partial \phi / \partial x$ and $\partial^2 \phi / \partial x^2$ are approximated by $\Delta \phi(x) / \Delta x$ and $\Delta^2 \phi(x) / \Delta x^2$, and thus the partial-differential equation is reduced to a set of algebraic equations. In electromagnetics as in other areas of engineering, the FDM is one of the most important methods to solve a wide range of problems. These include linear and nonlinear problems, time- and frequency-domain problems, wave propagation in homogeneous and inhomogeneous media and in media with different boundary conditions. An early example on the application of the FDM to waveguide problems is given in Refs. 25 and 26. Detailed chapters on the FDM can be found in books by Sadiku and Zhou [1,2].

To illustrate the FDM, we choose a problem that can be described by the two-dimensional Laplace equation

$$\frac{\partial^2 \phi}{\partial x^2} + \frac{\partial^2 \phi}{\partial y^2} = 0 \quad (31)$$

Sampling the continuous electromagnetic field in the computational domain by a mesh of regular points separated by a constant distance h (Fig. 4), Eq. (31) is approximated by the difference quotients at the adjacent mesh points. Depending on the choice of the difference and the difference quotient, different methods can be used to derive the discretization formulations. Using a Taylor expansion, the potentials surrounding the center node o (Fig. 4) can be expressed as

$$\begin{aligned} \phi_{x-h} &= \phi_o - h \left(\frac{\partial \phi}{\partial x} \right)_o + \frac{h^2}{2!} \left(\frac{\partial^2 \phi}{\partial x^2} \right)_o \\ &\quad - \frac{h^3}{3!} \left(\frac{\partial^3 \phi}{\partial x^3} \right)_o + \varepsilon(h^4) \\ \phi_{x+h} &= \phi_o + h \left(\frac{\partial \phi}{\partial x} \right)_o + \frac{h^2}{2!} \left(\frac{\partial^2 \phi}{\partial x^2} \right)_o \\ &\quad + \frac{h^3}{3!} \left(\frac{\partial^3 \phi}{\partial x^3} \right)_o + \varepsilon(h^4) \\ \phi_{y-h} &= \phi_o - h \left(\frac{\partial \phi}{\partial y} \right)_o + \frac{h^2}{2!} \left(\frac{\partial^2 \phi}{\partial y^2} \right)_o \\ &\quad - \frac{h^3}{3!} \left(\frac{\partial^3 \phi}{\partial y^3} \right)_o + \varepsilon(h^4) \\ \phi_{y+h} &= \phi_o + h \left(\frac{\partial \phi}{\partial y} \right)_o + \frac{h^2}{2!} \left(\frac{\partial^2 \phi}{\partial y^2} \right)_o \\ &\quad + \frac{h^3}{3!} \left(\frac{\partial^3 \phi}{\partial y^3} \right)_o + \varepsilon(h^4) \end{aligned} \quad (32)$$

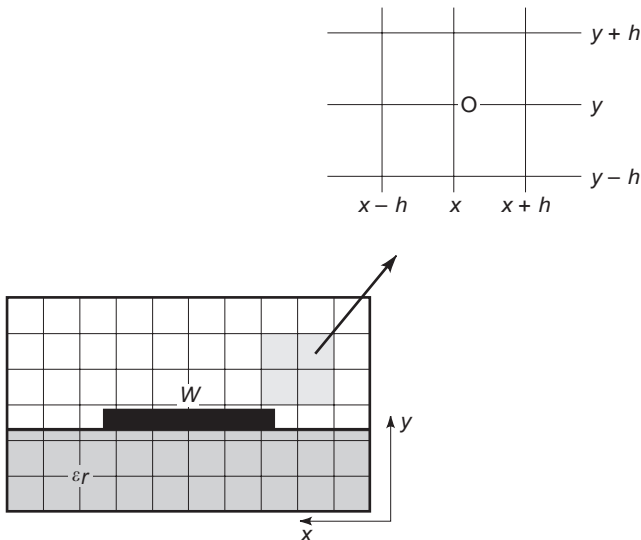


Figure 4. Finite-difference discretization of a microstrip transmission line.

where $\varepsilon(h^4)$ is the remaining error. Adding these equations and considering that the resulting term

$$h^2 \left(\frac{\partial^2 \phi}{\partial x^2} + \frac{\partial^2 \phi}{\partial y^2} \right)_o = 0$$

the approximation of ϕ_o at node center o becomes

$$\frac{1}{4} (\phi_{x+h} + \phi_{x-h} + \phi_{y+h} + \phi_{y-h}) = \phi_o$$

whereby it is assumed that $\varepsilon(h^4)$ is negligible. This equation shows that the value of ϕ_o is the average of the potentials at the four neighboring points. The above equation for the 2D problem is also said to be the five-point difference equation of the Laplacian problem. For a 3D problem the above equation expands to a seven-star node

$$\frac{1}{6} (\phi_{x+h} + \phi_{x-h} + \phi_{y+h} + \phi_{y-h} + \phi_{z+h} + \phi_{z-h}) = \phi_o$$

Repeating this procedure over the whole computational domain and considering the boundary conditions on ϕ , leads to the following matrix equation

$$[A]\mathbf{f} = \mathbf{X}$$

Since the individual grid points are connected only to their neighboring points, the coefficient matrix $[A]$ contains a large number of zero elements (banded sparse matrix) and only the diagonal and nearby elements are filled. \mathbf{f} is a vector of all potentials on the interior nodes and \mathbf{X} contains the information about the boundary conditions (or sources). Matrix $[A]$ can be solved by the Gauss elimination method but due to the sparsity of the matrix, iterative methods such as the over-relaxation iteration are more economical in terms of computer resources.

1.8. Finite-Element Method

Although the finite-element method (FEM) was used by mechanical and civil engineers for many years [27], its application to the electromagnetics area was not before 1967 by Winslow [28] and in 1970 by Silvester and co-workers [29]. Since then, the FEM has become a widely used numerical simulation tool for electromagnetic fields in structures with arbitrary boundary shape [30,31]. In contrast to the finite-difference method, the finite element method discretizes the computational domain with a number of small interconnected subregions, called *elements* (Fig. 5). The shape of these elements is typically rectangular or triangular. This explains why there are virtually no restrictions on the shape of the structures that can be analyzed with the FEM. This feature is its main advantage over other methods.

The FEM is based on the fact that the potential function ϕ^e (superscript “e” denotes *element*) within each element, can be approximated by an (often linear) interpolation function which is zero outside the element. Summation of ϕ^e over all elements N gives an approximate

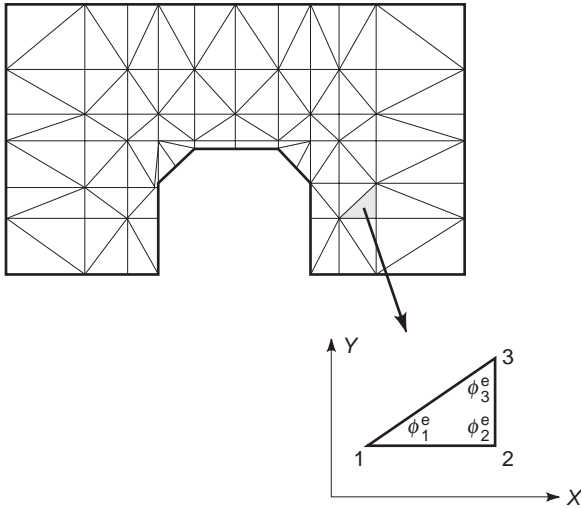


Figure 5. Finite-element discretization of a ridged waveguide.

solution for the total potential in the computational domain

$$\phi = \sum_p^N \phi^e(x,y) \tag{33}$$

The simplest form of approximation for ϕ^e within a triangular element (Fig. 5) is the following:

$$\phi^e = a + bx + cy \tag{34}$$

It is assumed that the field strength is uniform within a small element and that the potential varies linearly depending on the coordinates x and y . The unknown parameters a, b, c are found from the nodal parameters $\phi_p^e, x_p,$ and y_p ($p = 1, 2, 3$) as

$$\begin{bmatrix} a \\ b \\ c \end{bmatrix} = \begin{bmatrix} 1 & x_1 & y_1 \\ 1 & x_2 & y_2 \\ 1 & x_3 & y_3 \end{bmatrix}^{-1} \begin{bmatrix} \phi_1^e \\ \phi_2^e \\ \phi_3^e \end{bmatrix} \tag{35}$$

Substituting the functions obtained from Eq. (35) into Eq. (34) yields

$$\phi^e = \sum_p N_p^e \phi_p^e \tag{36}$$

N_p^e are the so-called shape functions. The potential ϕ^e within each element is thus a linear combination of the shape functions and the three nodal values of the triangle.

The next step in the FEM is to determine the potential at the corners of all elements. This is usually done by minimizing (or maximizing) a functional that is known to be stationary about the true solution (variational method). For a Laplacian problem, the equivalent functional for

each element is

$$I^e(\phi^e) = \int_{s^e} \frac{1}{2} \epsilon |\nabla \phi^e|^2 dx dy \tag{37}$$

The functional over all elements is then the sum over Eq. (37). From a physical point of view, I^e is the energy per unit length of the element e . Substituting the approximation for ϕ^e into Eq. (37) yields

$$I^e = \frac{1}{2} \sum_{p=1}^3 \sum_{k=1}^3 \epsilon \phi_p^e \underbrace{\left[\int_{s^e} \nabla N_p^e \cdot \nabla N_k^e dx dy \right]}_{C_{pk}} \phi_k^e \tag{38}$$

or in matrix form

$$I^e = \frac{1}{2} \epsilon [\phi^e]^T [C^e] [\phi^e] \tag{39}$$

$[C^e]$ is the element coefficient matrix (stiffness matrix in structural analysis). The matrix elements represent the coupling between the nodes. Summation of Eq. (39) over all the elements and applying the extremum condition of the functional

$$\frac{\partial I(\phi)}{\partial \phi_i} = 0$$

yields the system matrix equation

$$[C][\phi] = 0 \tag{40}$$

$[C]$ is a sparse, symmetric, and banded matrix of size $M \times M$ (M =total number of nodes). Equation (40) can be solved for the potentials of all nodes in the computational domain.

The FEM is one of the most flexible numerical modeling approaches which can be applied to nonlinear problems and also can be formulated in time and frequency domain. Although its formulation is more involved than the finite-difference method the advantage of the FEM is that it can be applied to almost arbitrarily shaped boundaries. Application to open boundaries is difficult except if the FEM is combined with other methods which are more suitable for open boundary problems.

1.9. The Boundary-Element Method

The boundary-element method (BEM) or boundary integral element method is similar to the finite-element method applied to the boundary only. As such the BEM is also known as a form of weighted residual technique that falls under the category of moment methods. The main advantage of the BEM over the FEM is that it reduces the dimension of the problem by one. For example, in a three-dimensional problem only the surface of the computational domain needs to be discretized and not the entire volume, which leads to a much smaller number of algebraic equations. For two-dimensional problems the boundary elements are taken as straight line segments,

whereas for three-dimensional problems triangular elements are taken. Disadvantages of the BEM are that the number of integrations required are great and that singularities must be considered. The calculation of the coefficient matrix may require more time than in the FEM.

A very detailed account of the BEM may be found in Ref. 2. In the BEM the quantity of interest ϕ anywhere within the computational domain is expressed in terms of a functional, except that this functional now depends only on the value of ϕ at the boundary and its normal derivative thereon. Again, for the Laplace equation in a source free volume Ω bounded by a surface Γ , for example, the potential ϕ_i inside the volume is given by the integral equation

$$\phi_i = \frac{1}{4\pi} \int_{\Gamma} \left[\frac{1}{r} \frac{\partial \phi}{\partial n} - \phi \frac{\partial}{\partial n} \left(\frac{1}{r} \right) \right] d\Gamma$$

In most of the relevant EM problems, the governing equation is not Laplacian and ϕ on the boundary is unknown. Then the boundary contour is discretized and ϕ for each boundary element is derived using the method of weighted residuals where the expansion and weighting functions are only defined within the boundary cell. The integral equation is thus transformed into a set of algebraic equations at the nodes of the boundary, and the value for ϕ and its derivatives are found simultaneously by solving a matrix equation [2].

2. TIME-DOMAIN METHODS

Time-domain methods are important if the time-domain response of an electromagnetic structure is required. Lately, time-domain methods have also gained momentum over frequency-domain methods since they deliver, depending on the excitation, all frequencies of interest with one computation run without the need for large matrix inversions. This feature is attractive if a wide band frequency response is required. One might also add that a variety of problems are more naturally formulated in the time domain than in the frequency domain. This is in particular the case for nonlinear problems.

Some of the frequency-domain methods discussed before can be formulated also in the time domain. This is a great advantage if one is already familiar with a particular method. Extending the formulation from one domain into the other without leaving the framework of one method not only minimizes the development effort but also expands the application range of that method. Among the many different techniques that can be formulated in both domains, the finite-difference time-domain (FDTD) method and the time-domain transmission-line matrix (TDTLM) method are the most prominent ones. While the finite-difference method in the frequency domain, the FDM or FDFDM, has been discussed in a previous section, the frequency-domain version of the TLM method, the FDTLM method [32], is not discussed here. However, as in the framework of the finite-difference methods the duality between frequency- and time-domain methods exists also in the framework of the TLM method.

In the FDTD and TDTLM methods of electromagnetic modeling the continuous field functions that satisfy Maxwell's equations are approximated by samples of these functions defined only at discrete points in space and time. In the most general sense, FDTD and TLM belong to the method-of-moments (MoM) family. In FDTD the electromagnetic field is approximated by a set of local pulse functions in space and time, while in TLM it is expressed as a superposition of impulse waves traveling forward and backward along the coordinate directions, their sum yielding the electric and their difference the magnetic field values, respectively. Thus, FDTD is formulated in terms of total electric and magnetic field samples in discretized space, whereas the TLM formulation employs elementary incident and reflected waves traveling on a mesh of transmission lines (scattering formulation).

While both methods can be derived rigorously from Maxwell's equations using MoM formalism [33], a more intuitive approach that is also historically authentic will be used to formulate the basic FDTD and TLM algorithms. Their properties and associated errors will be discussed, and some more recent variations will be mentioned.

2.1. Finite-Difference Time-Domain Method

The finite-difference time-domain (FDTD) scheme is obtained by replacing the partial derivatives (space *and* time) in Maxwell's curl equations by finite differences. The best approximation is obtained by central differencing (trapezoidal rule), resulting in an error that is proportional to the square of the space and time step (second-order accuracy).

The first FDTD formulation was proposed by Yee in 1966 [34] and subsequently applied and developed further by Taflov and Brodwin [35]. Yee simply replaced the partial derivatives in Maxwell's curl equations by central finite differences. Weiland [36] derived an equivalent discretization approach using finite integration of Maxwell's equations in 1977. Fig. 6 shows a unit FDTD cell (Yee cell) of a Cartesian space grid. Continuous space and time coordinates (x,y,z,t) are replaced by discrete coordinates $l \Delta x, m \Delta y, n \Delta z, k \Delta t$, where l,m,n,k are integers and

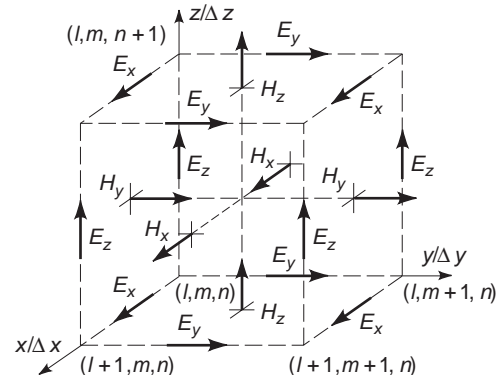


Figure 6. Topology of the elementary FDTD cell (Yee cell). Electric and magnetic field components are interleaved in space and time.

Δx , Δy , Δz , and Δt are the space/timesteps. Note that the three electric field components are defined along the edges of the cell, while the magnetic field components are normal to the cell faces. The staggering of the field components by one-half of the cell dimensions is due to the central-difference approximation of the differential operators. For the same reason, electric and magnetic field components are also staggered in time, the electric field components being defined at time points $k \Delta t$ and the magnetic field components at $(k + \frac{1}{2}) \Delta t$.

If we assume that $\Delta x = p \Delta l$; $\Delta x = q \Delta l$; $\Delta x = r \Delta l$, where Δl is the unit reference length, and the scaling coefficients p , q , and r are all smaller or equal to unity, then the finite difference equations for the electric and magnetic field components in each cell are given by

$$\begin{aligned} {}_{k+1}E_x(l + \frac{1}{2}, m, n) &= {}_kE_x(l + \frac{1}{2}, m, n) \\ &+ sx \{ [{}_{k+1/2}H_z(l + \frac{1}{2}, m + \frac{1}{2}, n) \\ &- {}_{k+1/2}H_z(l + \frac{1}{2}, m - \frac{1}{2}, n)]/q \\ &+ [{}_{k+1/2}H_y(l + \frac{1}{2}, m, n - \frac{1}{2}) \\ &- {}_{k+1/2}H_y(l + \frac{1}{2}, m, n + \frac{1}{2})]/r \} \end{aligned}$$

$$\begin{aligned} {}_{k+1}E_y(l, m + \frac{1}{2}, n) &= {}_kE_y(l, m + \frac{1}{2}, n) \\ &+ sy \{ [{}_{k+1/2}H_x(l, m + \frac{1}{2}, n + \frac{1}{2}) \\ &- {}_{k+1/2}H_x(l, m + \frac{1}{2}, n - \frac{1}{2})]/r \\ &+ [{}_{k+1/2}H_z(l - \frac{1}{2}, m, n + \frac{1}{2}, n) \\ &- {}_{k+1/2}H_z(l + \frac{1}{2}, m + \frac{1}{2}, n)]/p \} \end{aligned}$$

$$\begin{aligned} {}_{k+1}E_z(l, m, n + \frac{1}{2}) &= {}_kE_z(l, m, n + \frac{1}{2}) \\ &+ sz \{ [{}_{k+1/2}H_x(l, m - \frac{1}{2}, n + \frac{1}{2}) \\ &- {}_{k+1/2}H_x(l, m + \frac{1}{2}, n + \frac{1}{2})]/q \\ &+ [{}_{k+1/2}H_y(l + \frac{1}{2}, m, n + \frac{1}{2}) \\ &- {}_{k+1/2}H_y(l - \frac{1}{2}, m, n + \frac{1}{2})]/p \} \end{aligned}$$

$$\begin{aligned} {}_{k+1/2}H_x(l, m + \frac{1}{2}, n + \frac{1}{2}) &= {}_{k-1/2}H_x(l, m + \frac{1}{2}, n + \frac{1}{2}) \\ &+ sx' \{ [{}_kE_y(l, m + \frac{1}{2}, n + 1) \\ &- {}_kE_y(l, m + \frac{1}{2}, n)]/p \\ &+ [{}_kE_z(l, m, n + \frac{1}{2}) \\ &- {}_kE_z(l, m + 1, n + \frac{1}{2})]/q \} \end{aligned}$$

$$\begin{aligned} {}_{k+1/2}H_y(l + \frac{1}{2}, m, n + \frac{1}{2}) &= {}_{k-1/2}H_y(l + \frac{1}{2}, m, n + \frac{1}{2}) \\ &+ sy' \{ [{}_kE_x(l + \frac{1}{2}, m, n) \\ &- {}_kE_x(l + \frac{1}{2}, m, n + 1)]/r \\ &+ [{}_kE_z(l + 1, m, n + \frac{1}{2}) \\ &- {}_kE_z(l, m, n + \frac{1}{2})]/p \} \\ {}_{k+1/2}H_z(l + \frac{1}{2}, m + \frac{1}{2}, n) &= {}_{k-1/2}H_z(l + \frac{1}{2}, m + \frac{1}{2}, n) \\ &+ sz' \{ [{}_kE_x(l + \frac{1}{2}, m + 1, n) \\ &- {}_kE_x(l + \frac{1}{2}, m, n)]/q \\ &+ [{}_kE_y(l, m + \frac{1}{2}, n) \\ &- {}_kE_y(l + 1, m + \frac{1}{2}, n)]/r \} \end{aligned} \quad (41)$$

where

$$\begin{aligned} sx &= Z_0 c \Delta t / (\epsilon_{rx} \Delta l) \\ sy &= Z_0 c \Delta t / (\epsilon_{ry} \Delta l) \\ sz &= Z_0 c \Delta t / (\epsilon_{rz} \Delta l) \\ sx' &= c \Delta t / (\mu_{rx} Z_0 \Delta l) \\ sy' &= c \Delta t / (\mu_{ry} Z_0 \Delta l) \\ sz' &= c \Delta t / (\mu_{rz} Z_0 \Delta l) \end{aligned} \quad (42)$$

In these expressions, c and Z_0 are the velocity of light and the wave impedance in vacuo, and ϵ_{rx} , ϵ_{ry} , ϵ_{rz} and μ_{rx} , μ_{ry} , μ_{rz} are the diagonal elements of the relative permittivity and permeability tensors of the medium, respectively. This algorithm explicitly updates each field component in a leapfrog timestepping process. The change in each E -field component is computed from the four H -field components circulating around it, and vice versa.

2.1.1. Stability. The process is stable as long as the timestep is smaller than a maximum value known as the so-called Courant stability limit. For electrically and magnetically isotropic media characterized by ϵ_r and μ_r the stability criterion is

$$\Delta t \leq \frac{\Delta l \sqrt{\mu_r \epsilon_r}}{c \sqrt{\frac{1}{p^2} + \frac{1}{q^2} + \frac{1}{r^2}}} \quad (43)$$

Since in anisotropic media the wave velocity depends on the (generally unknown) polarization, it is prudent to enter the smallest of the three μ and ϵ values of the diagonal tensors into the stability condition. For free space discretized into cubic cells ($\mu_r = \epsilon_r = p = q = r = 1$), it

becomes

$$\Delta t \leq \frac{\Delta l}{c\sqrt{3}} \quad (44)$$

2.1.2. Initial and Boundary Conditions. At the start of a computation the initial values of all electric and/or magnetic field components in the computational domain are specified before the updating process can begin. By enforcing the field values in certain regions at each timestep, source functions with arbitrary time and space dependence can be modeled.

Boundary conditions must be enforced at each timestep as well. Electric and magnetic walls are modeled by extending the discretized space one cell beyond the boundary and imposing appropriate symmetry conditions on the field values on each side of the boundary. For example, the tangential electric field components must be identical on either side of a magnetic wall (ideal open circuit) and equal and opposite on either side of an electric wall (ideal short circuit). A dual condition applies to the tangential magnetic field components. Lossy resistive boundary conditions call for a fixed ratio between the tangential electric and magnetic field components at the boundary. More complex boundary conditions such as wide band absorbing walls or frequency dispersive boundaries call for special algorithms, such as one-way absorbing boundary conditions [37,38] or Berenger's perfectly matched layer [39]. A detailed discussion of absorbing boundary conditions in FDTD and TLM can be found in Ref. 40. Similar approaches are required for the modeling of complex materials and devices.

The books by Kunz and Luebbers [41] and Taflové [42] are excellent sources of information on all aspects of FDTD modeling and contain extensive bibliographies on the theory, implementation, and application of the FDTD method. Together with Yee's seminal paper [34] they are good starting points for exploring the extensive literature on FDTD theory and applications.

2.2. Transmission-Line Matrix Method

2.2.1. The Expanded Node. The transmission-line matrix (TLM) formulation of Maxwell's equations was first proposed in 1971 by Johns and Beurle [43]. In their seminal paper they describe a novel numerical technique for solving two-dimensional scattering problems. Inspired by earlier network simulation techniques [44], they employ a Cartesian mesh of shunt-connected two-wire transmission lines as a discretized 2D propagation medium. The nodes of this mesh act as scattering centers for short voltage impulses. Johns and Akhtarzad [45] extended the method to three space dimensions (the expanded node TLM model) in 1974, by creating an intricate 3D lattice of shunt- and series-connected transmission lines, as shown in Fig. 7. This model is, in many respects, similar to the Yee cell in Fig. 6 since it yields identical solutions for the six field components when the time step in the Yee algorithm is set to $\Delta t = \Delta l/(2c)$ (free space, cubic cell). However, in contrast to the strictly mathematical formulation of FDTD, the TLM model is a "hardwired" network

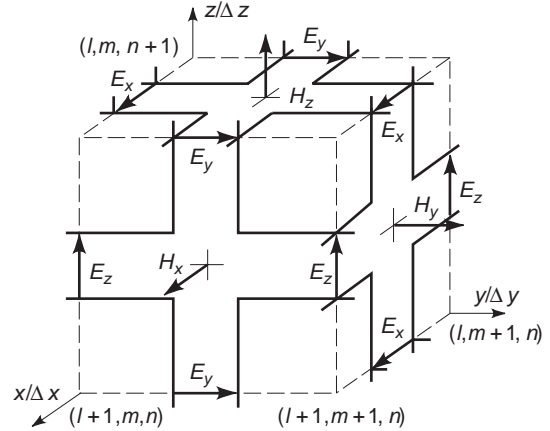


Figure 7. Topology of the expanded TLM node. Electric field components are modeled by the voltage across shunt connections, while magnetic field components are modeled by the loop current in series connections of transmission lines. The positions of the field components in space and time are identical to those in the Yee cell.

(albeit conceptual rather than material) to which all known techniques of circuit and transmission line analysis can be applied in both frequency and time domains.

2.2.2. The Symmetric Condensed Node. One of the shortcomings of these algorithms resides in the complicated topology of their unit cells and in the separate locations of electric and magnetic field components in space and time. This makes the modeling of complex boundary conditions and interfaces between materials more difficult and may introduce errors. To overcome these drawbacks, Johns [46,47] introduced the symmetrical condensed TLM node in 1986. This spawned the development of several new TLM formulations, from the hybrid and supercondensed nodes to the alternating and rotated alternating [48] TLM models. In the following, the basic formulation proposed by Johns will be outlined. However, the port numbering scheme proposed by Russer [48] will be used since it allows a simpler and more compact representation of the TLM algorithm than Johns' original numbering scheme.

2.2.3. The Symmetric Condensed Node TLM Algorithm. A unit cell of the symmetric condensed TLM model is shown in Fig. 8. It contains a hybrid junction of 12 transmission lines (the node) that is characterized by a 12×12 scattering matrix. The time-domain TLM algorithm is executed in two steps. First, 12 short voltage pulses are simultaneously injected into the node ports 1–12. The pulses are scattered and give rise to 12 reflected voltage pulses. Second, the reflected pulses are transferred to the neighboring nodes where they become incident pulses at the subsequent timestep, and the process is repeated. This series of events can be described in symbolic form as follows

$$[{}_k v^r] = S \cdot [{}_k v^i], \quad [{}_{k+1} v^i] = C \cdot [{}_k v^r] \quad (45)$$

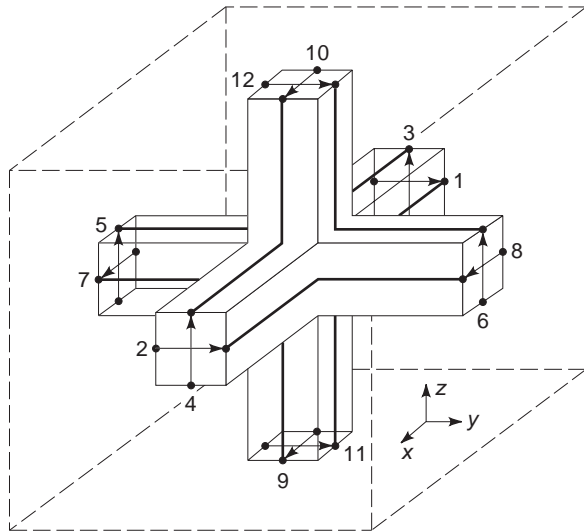


Figure 8. Topology of the symmetric condensed TLM node. All six electric and magnetic field components are defined in the center of the node, and tangential field components are defined in the cell boundaries as well.

where $[{}_k v^r]$ and $[{}_k v^i]$ are the vectors of reflected and incident pulses at the k th timestep, \mathbf{S} is the impulse scattering matrix of the node, and \mathbf{C} is a connection matrix describing the topology of the network. It governs the transfer of the reflected pulses to the connected ports of the neighboring cells and/or the reflection from boundaries. The subscripts k and $k + 1$ denote the discrete time points at which the pulses are scattered at the nodes.

For a homogeneous, lossless, and isotropic medium, all transmission lines of a cubic cell have the same characteristic impedance. The 12×12 scattering matrix \mathbf{S} is then

$$\mathbf{S} = \begin{bmatrix} 0 & \mathbf{S}_0 & \mathbf{S}_0^T \\ \mathbf{S}_0^T & 0 & \mathbf{S}_0 \\ \mathbf{S}_0 & \mathbf{S}_0^T & 0 \end{bmatrix} \quad (46)$$

where the submatrix \mathbf{S}_0 is given by

$$\mathbf{S}_0 = \begin{bmatrix} 0 & 0 & \frac{1}{2} & -\frac{1}{2} \\ 0 & 0 & -\frac{1}{2} & \frac{1}{2} \\ \frac{1}{2} & \frac{1}{2} & 0 & 0 \\ \frac{1}{2} & \frac{1}{2} & 0 & 0 \end{bmatrix} \quad (47)$$

Since the transit time Δt of the pulses is linked to the space step Δl by the pulse propagation velocity along the transmission lines, the TLM process is unconditionally stable. The time step is automatically set to $\Delta t = \Delta l / (2c)$.

2.2.4. Inhomogeneous Materials and Losses. Dielectric or magnetic materials can be modeled by loading the nodes

situated inside these materials with reactive shunt stubs of appropriate normalized characteristic admittance and a length $\Delta l / 2$ [46]. An open-circuited shunt stub will produce the effect of additional capacitance at the node, while a short-circuited series stub creates additional inductance. The resulting storage of reactive energy reduces the phase velocity and alters the intrinsic impedance in the structure. The interface conditions at the boundary between different materials are automatically fulfilled. Each cell can have a different set of stubs (three permittivity and three permeability stubs), thus allowing the modeling of inhomogeneous anisotropic materials with diagonal permittivity and permeability tensors. The six stubs add six more ports to the node, and as a result, the \mathbf{S} becomes an 18×18 matrix. Losses can be modeled by connecting so-called loss stubs to the nodes. The loss stubs are matched transmission line sections that extract a fraction of the energy scattered at the node at each time step. Since no pulses travel back into the nodes on these stubs, they only modify the elements of \mathbf{S} without increasing its size.

2.2.5. Initial and Boundary Conditions. At the start of a computation the initial values of all pulses incident on all field components are uniquely determined in the center of the nodes by a linear combination of these pulses at the moment of scattering (47). When the pulses transit from one cell to the next ($t / \Delta t = k + 1/2$) the tangential components of the fields are obtained in the cell boundaries as well. By enforcing the pulse values (and hence the corresponding electric and magnetic field values) in certain regions at each timestep, source functions with arbitrary time and space dependence can be modeled.

Boundary conditions can be imposed either in the center of the nodes or in the cell boundaries. In the latter case, boundaries are represented by means of impulse reflection coefficients. Electric walls reflect pulses with “ $a - 1$ ” reflection coefficient, while magnetic walls have “ $a + 1$ ” reflection coefficient. Lossy resistive boundaries have impulse reflection coefficients less than unity in magnitude. More complex boundary conditions such as wide-band absorbing walls or frequency dispersive boundaries are treated in the same way as FDTD boundaries with the difference that the boundary operators are applied to the incident pulses rather than to the field quantities at the boundaries. It is straightforward to implement nonrecursive and recursive convolution techniques for the modeling of frequency dispersive boundaries and for partitioning large computational domains using time-domain diakoptics [49]. Similar approaches are required for the modeling of complex materials and devices [50].

Johns’ seminal papers [43,45–47] are good starting points for exploring the world of TLM modeling, as are an introductory chapter on TLM by Hoefer [51] and a book by Christopoulos [52]. They contain many references and describe the implementation and applications of TLM in detail.

3. HYBRID METHODS

None of the previous methods is capable of solving all electromagnetic modeling problems. The methods are

either limited by the available computer memory and/or by computer runtime, or the numerical model can simply not be applied to the structure at hand. For example, the method of moments is not applicable to structures with inhomogeneous or nonlinear dielectrics. The finite difference method is difficult to implement when fine circuit details must be resolved within a structure of large dimensions. The discretization size chosen for the smallest circuit detail determines the total number of discretization cells and thus the total matrix size to be handled may become too large. This problem is even more pronounced for the time-domain version of the finite-difference method, the FDTD, since here also the time is discretized. Similarly, the finite-element method cannot efficiently model large radiation problems because of the large computational space that must be discretized.

In practice, many of these—and more—complicating factors are encountered. Not all appear in the same problem and at the same time, thus making it possible to choose one electromagnetic modeling approach over the other. But there is a significant number of problems (and others are emerging) that cannot be solved within the framework of any of the previous methods.

A solution to those problems is possible by combining two or more techniques. The task is to apply each method to the problem domain for which it is best suited. There are two possible approaches. A two or more step procedure is utilized in which one part of the problem is solved by one method and the results are used as input data to solve remaining parts of the problem with other techniques. That requires that boundary conditions are established that must be enforced at the interfaces between the different regions. This approach is called an explicit hybrid approach. An implicit hybrid approach is one in which the advantageous features of one technique are combined with those of another technique to form a new standalone algorithm.

Several successful implementations of hybrid methods have been reported in the literature. Although this research direction does not replace the effort to improve existing single methods, hybrid methods offer electromagnetic modeling of a whole new class of problems and may in particular be important in the area of CAD.

3.1. Combinations of Frequency-Domain Methods

3.1.1. GTD and MoM. The first combinations of electromagnetic modeling approaches appeared in the analysis of antenna problems and radar cross sections. The geometric theory of diffraction (GTD) and the method of moments were used to analyze antenna problems in Ref. 53. The GTD is an extension to geometric optics, which includes the effect of diffraction. This method is only accurate if the dimensions of the object being analyzed is large compared to the wavelength of the field. For that reason this method is also called a *high-frequency method*. In the combination of the GTD and the MoM, the latter is used to solve the region close to the antenna, while the GTD is used for the free space surrounding the antenna.

3.1.2. FEM and GSM Technique. A combination of the finite-element method (FEM) and the generalized scattering matrix (GSM) technique was utilized in the study of scattering from jet engines [54]. The FEM was applied to the complex part of the scatterer to generate the GSM at its boundary which can then be interfaced with high-frequency techniques for computation of the engine's scattered fields without reference to the geometry of the jet engine. One of the methods alone would not have been able to solve this complex problem.

3.1.3. FEM/FDM and MMT. For the analysis of micro-wave circuits the combination of the FEM and the mode-matching technique (MMT) has been proposed to study large cavities [55]. In Ref. 56 the FEM was applied to analyze waveguide discontinuities with arbitrary boundary shape. In Ref. 57 the FDM was employed instead of the FEM to analyze segments of waveguide structures that are not suitable for a MMT analysis, for example a circular stub in a rectangular waveguide. In all these papers the MMT was used to characterize the uniform sections of the waveguide while the FEM or FDM was employed to analyze rounded corners or discontinuity shapes that do not fit into the coordinate system of the MMT. The latter was then used to derive the scattering parameters of the overall circuit.

3.1.4. Method of Lines and SDM. For the 3D analysis of planar waveguide problems a combination of the method of lines and the spectral-domain method was introduced in Ref. 58. The purpose of this combination was to eliminate some of the problems associated with the 2D MoL and the 2D SDM. The problem in the latter was the difficulty to find 2D basis functions that converge easily, while for the 2D MoL a 2D discretization may not always be able to satisfy all boundary conditions simultaneously with effortable computer memory. The combination of the computationally very efficient 1D SDM in transverse direction of the propagating wave with the equally efficient 1D MoL in propagation direction eliminates these problems.

3.2. Combinations of Time- and Frequency-Domain Methods

3.2.1. Hybrid Finite-Difference–Time-Domain Method. The hybrid finite-difference–time-domain (HFDTD) method is a combination of frequency-domain and time-domain concepts. In its widest sense, the technique utilizes a standard FDTD mesh in the areas of structure inhomogeneity and expansion into a known set of modes in transversely homogeneous regions of the structure. This provides substantial savings both in terms of computer memory and CPU time as was first demonstrated in the eigenvalue analysis of planar transmission lines [60]. A conventional FDTD analysis of such a structure requires a 3D mesh, which, depending on the space resolution required, needs several thousand time iterations before a Fourier transform can provide the results for the propagation constant. By replacing the space discretization in propagation direction (z) by a simple phase shift (note that the field at location l_z is different from that at location $l_z + z$ by only a factor $e^{-j\beta z}$), results in a 2D FDTD mesh

[59]. Multiplying the field equations furthermore by a factor j such that

$$\begin{aligned} E_x, E_y, H_z &= j(E_x, E_y, H_z)e^{-j\beta z} \\ H_x, H_y, E_z &= (H_x, H_y, E_z)e^{-j\beta z} \end{aligned}$$

leads to discretized Maxwell's equations without complex quantities. This feature accelerates the computation considerably. Exciting the 2D mesh with a time domain impulse requires much less time iterations for the impulse to settle than in the case of a 3D mesh. A Fourier transform provides the frequency at which the assumed value of β is valid.

The same principle can be applied to the time domain TLM method, and also here significant savings in computer resources are possible if only the propagation constant and related quantities (characteristic impedance, losses) are of interest.

3.2.2. TD TLM and MMT. In the TD TLM analysis of complex cascaded discontinuity problems, diakoptics is used to subdivide the problem into simpler subsections that are then modeled individually. Interconnecting the individual solutions requires a node to node convolution at the interface. This approach tends to be computationally quite demanding since the number of convolutions increases with N^2 (N is the number of branches of interest). To reduce the computational effort, it was suggested in Ref. 61 that the uniform sections of the problem domain are modeled by modal functions treated in the time domain (time-domain Green function), while the discontinuity region is represented by the TD TLM method for which the incident fields are superpositions of those modes. The response of that subvolume to an excitation is obtained by convolution of the excitation with the time-domain Green function. This approach leads to a significant reduction of the computational resources as compared to the analysis with only the TD TLM. Furthermore, the complex discontinuity region is now represented by its generalized scattering matrix (GSM), which makes it easy to cascade discontinuities.

3.3. Combinations of Time-Domain Methods

3.3.1. FDTD and FEM. The FDTD method is well suited for applications in Cartesian coordinates. However, as soon as mixed coordinates are necessary to describe the problem contour, a staircase approximation must be utilized. For example, a round structure within a rectangular mesh layout can be described accurately only by a fine staircase approximation. This leads to a very fine mesh and consequently a small timestep to satisfy the stability condition. The computational effort to calculate such a structure with acceptable accuracy becomes prohibitive. An alternative solution is to model the arbitrary boundary with the finite-element method and incorporate this approach in the FDTD method which is applied elsewhere in the problem domain [62].

The list of methods that have been combined can be continued and new combinations appear every month in

the various periodicals. A good starting point to find out more about hybrid methods and the rationale behind their combinations is in Ref. 63.

4. SUMMARY

The tremendous increase of computer power since the late 1980s has inspired a new era in the field of electromagnetic modeling or computational electromagnetics. Numerical codes that ran only on supercomputers yesterday are running on workstation computers today. This development will not stop here, and the electromagnetic modeling problem that appears to be inaccessible by any of today's available codes (because the required computer resources are just too large) will be solvable with tomorrow's computers and the then available (unlimited?) computer memory.

Because of this rapid development in computer hardware, electromagnetic modeling has become commonplace in the world of electrical engineers. Many of the methods that we have briefly described are already implemented in commercial simulation tools used in practice to analyze a wide variety of problems and to design (CAD) a wide range of circuits and components that would not function otherwise.

We have divided the methods into frequency-domain, time-domain, and hybrid methods. They all have advantages and disadvantages depending on the problem range they are applied to. The aim of this article was not to provide extensive information on all of these methods but to introduce the reader to those numerical methods that have a broad enough application as well as to provide key references for further reading.

5. LITERATURE

The literature on electromagnetic field modeling is quite extensive, and only a few key references could be cited here. For more information on the subject the reader is referred to the books by R. Sorrentino [65] and E. Miller et al. [66], who have assembled a collection of reprints of key papers on the subject, and the book by E. Yamashita [64]. Furthermore, various journals and conferences are devoted to the topic of numerical modeling of electromagnetic fields.

BIBLIOGRAPHY

1. Sadiku, *Numerical Techniques in Electromagnetics*, CRC Press, Boca Raton, FL, 1992.
2. P. B. Zhou, *Numerical Analysis of Electromagnetic Fields*, Springer-Verlag, New York, 1993.
3. T. Itoh, *Numerical Techniques for Microwave and Millimeter-Wave Passive Structures*, Wiley, New York, 1989.
4. G. S. Mikhlin, *Variational Methods in Mathematical Physics*, Pergamon Press, New York, 1968.
5. R. F. Harrington, *Field Computation by Moment Methods*, Krieger, Malabar, FL, 1968.

6. A. Wexler, Solution of waveguide discontinuities by modal analysis, *IEEE Trans. Microwave Theory Tech.* **MTT-15**:508–517 (1967).
7. R. Mittra and W. W. Lee, *Analytical Techniques in the Theory of Guided Waves*, Macmillan, New York, 1971.
8. R. Vahldieck, Accurate hybrid mode analysis of various finline configurations including multilayered dielectrics, finite metallization thickness and substrate holding grooves, *IEEE Trans. Microwave Theory Tech.* **MTT-32**:1454–1460 (1984).
9. R. R. Mansour and R. McPhie, A unified hybrid-mode analysis for planar transmission lines with multilayer isotropic/anisotropic substrates, *IEEE Trans. Microwave Theory Tech.* **MTT-35**:1382–1391 (1987).
10. Y. C. Shih, The mode-matching method, in T. Itoh, ed., *Numerical Techniques for Passive Microwave and Millimeter-Wave Structures*, Wiley, New York, 1989, Chap. 9.
11. J. Bornemann and F. Arndt, Modal s-matrix design of optimum, stepped, ridged and finned waveguide transformers, *IEEE Trans. Microwave Theory Tech.* **MTT-35**:561–567 (1987).
12. S. Amari, J. Bornemann, and R. Vahldieck, Accurate analysis of scattering from multiple waveguide discontinuities using the coupled-integral equation technique, *J. Electromagn. Waves Appl.* **10**:1623–1644 (1996).
13. S. Amari, J. Bornemann, and R. Vahldieck, Accurate and fast analysis of waveguide filters by the coupled-integral equation technique, *IEEE Trans. Microwave Theory Tech.* **MTT-45**:1611–1618 (1997).
14. T. Itoh and R. Mittra, Spectral-domain approach for calculating the dispersion characteristics of microstrip lines, *IEEE Trans. Microwave Theory Tech.* **MTT-21**:496–499 (1973).
15. T. Uwaro and T. Itoh, Spectral domain approach, in T. Itoh, ed., *Numerical Techniques for Microwave and Millimeter-Wave Passive Structures*, Wiley, New York, 1989, Chap. 5.
16. T. Kitazawa, Metallization thickness effect of striplines with anisotropic media: quasi-static and hybrid mode analysis, *IEEE Trans. Microwave Theory Tech.* **MTT-37**:769–775 (1989).
17. T. Kitazawa and R. Mittra, Analysis of finline with finite metallization thickness, *IEEE Trans. Microwave Theory Tech.* **MTT-32**:1484–1487 (1984).
18. A. Ludwig, A new technique for numerical electromagnetics, *IEEE AP-S Newslett.* **31**:40–41 (Feb. 1989).
19. C. Hafner and L. Bomholt, *The 3D Electrodynamic Wave Simulator*, Wiley, New York, 1993.
20. P. Leuchtman, The multiple multipole program (MMP): theory, practical use and latest features, *ACES*, March 1995 (121 pp.; available from author at leuchtman@ifh.ee.ethz.ch).
21. O. A. Liskovets, The method of lines, *Diff. Uravneniya*, **1**:1662–1678 (1965) (review).
22. B. P. Demidowitsch et al., *Numerical Methods of Analysis*, VEB Wissenschaften, Berlin, 1968, Chap. 5 (in German).
23. R. Pregla and W. Pascher, The method of lines, in T. Itoh, ed., *Numerical Techniques for Microwave and Millimeter-Wave Passive Structures*, Wiley, New York, 1989, Chap. 6, pp. 381–446.
24. S. Xiao, R. Vahldieck, and J. Hesselbarth, Analysis of cylindrical transmission lines with the method of lines, *IEEE Trans. Microwave Theory Tech.* **MTT-44**:993–999 (1996).
25. G. Mur, Finite difference method for the solution of electromagnetic waveguide discontinuity problem, *IEEE Trans. Microwave Theory Tech.* **MTT-22**:54–57 (1974).
26. H. E. Green, The numerical solution of some important transmission-line problems, *IEEE Trans. Microwave Theory Tech.* **MIT-13**:676–692 (1965).
27. O. C. Zienkiewicz and Y. K. Cheung, *The Finite Element Method in Structural and Continuum Mechanics*, McGraw-Hill, London, 1967.
28. A. M. Winslow, Numerical solution of the quasilinear poisson's equation in a nonuniform triangular mesh, *J. Comput. Phys.* **2**:149–172 (1967).
29. P. P. Silvester and M. V. K. Chari, Finite element solution of saturable magnetic field problems, *IEEE Trans. Power Appar. Syst.* **PAS-89**:1642–1651 (1970).
30. P. Silvester, Finite element analysis of planar microwave networks, *IEEE Trans. Microwave Theory Tech.* **MTT-21**:104–108 (1973).
31. B. M. A. Rahman, A. Fernandez, and J. Davie, Review of finite element methods for microwave and optical waveguides, *Proc. IEEE* **79**(10):1442–1448 (1991).
32. H. Jin and R. Vahldieck, The frequency-domain transmission line matrix method—a new concept, *IEEE Trans. Microwave Theory Tech.* **MTT-40**:2207–2218 (1992).
33. M. Krumpholz, C. Huber, and P. Russer, A field theoretical comparison of FDTD and TLM, *IEEE Trans. Microwave Theory Tech.* **MTT-43**:1935–1959 (1995).
34. K. S. Yee, Numerical solutions of initial boundary value problems involving Maxwell's equations in isotropic media, *IEEE Trans. Anten. Propag.* **AP-14**:302–307 (1966).
35. A. Taflove and M. E. Brodwin, Numerical solution of steady-state electromagnetic scattering problems using the time-dependent Maxwell's equations, *IEEE Trans. Microwave Theory Tech.* **MTT-23**:623–630 (1975).
36. T. Weiland, A discretization method for the solution of Maxwell's equations for six-component fields, *Electron. Commun. AEU* **31**:116–124 (1977).
37. G. Mur, Absorbing boundary conditions for the finite-difference approximation of the time-domain electromagnetic field equations, *IEEE Trans. Electromagn. Compat.* **EMC-23**:377–382 (1981).
38. T. G. Moore et al., Theory and application of radiation boundary operators, *IEEE Trans. Anten. Propag.* **AP-36**:1797–1812 (1988).
39. J.-P. Berenger, A perfectly matched layer for the absorption of electromagnetic waves, *J. Comput. Phys.* **114**:185–200 (1994).
40. C. Eswarappa and W. J. R. Hofer, Absorbing boundary conditions for time-domain TLM and FDTD analysis of electromagnetic structures, *Electromagnetics* **16**(5):489–519 (1996).
41. K. S. Kunz and R. J. Luebbers, *Finite Difference Time Domain Method for Electromagnetics*, CRC Press, Boca Raton, FL, 1993.
42. A. Taflove, *Computational Electrodynamics, the Finite-Difference Time-Domain Method*, Artech House, Norwood, MA, 1995.
43. P. B. Johns and R. L. Beurle, Numerical solution of 2-dimensional scattering problems using a transmission-line matrix, *IEE Proc.* **118**:1203–1208 (1971).
44. G. Kron, Equivalent circuit of the field equations of Maxwell-I, *Proc. IEEE* **32**:289–299 (1944).
45. S. Akhtarzad and P. B. Johns, Solution of 6-component electromagnetic fields in three space dimensions and time by the T.L.M. method, *Electron. Lett.* **10**:535–537 (1974).

46. P. B. Johns, New symmetrical condensed node for three-dimensional solution of electromagnetic wave problems by TLM, *Electron. Lett.* **22**:162–164 (1986).
47. P. B. Johns, A symmetrical condensed node for the TLM method, *IEEE Trans. Microwave Theory Tech.* **MTT-35**:370–377 (1987).
48. P. Russer and B. Bader, The alternating transmission line matrix ATLM scheme, in *1995 IEEE MTT Int. Microwave Symp. Digest*, Orlando, FL, 1995, pp. 19–21.
49. W. J. R. Hoefer, The discrete time domain Green's function or Johns matrix—a new powerful concept in TLM, *Int. J. Num. Model.* **2**:215–225 (1989).
50. L. R. A. X. de Menezes and W. J. R. Hoefer, Modeling of general constitutive relationships in SCN TLM, *IEEE Trans. Microwave Theory Tech.* **MTT-44**:854–861 (1996).
51. W. J. R. Hoefer, The transmission line matrix, TLM method, in T. Itoh, ed., *Numerical Techniques for Passive Microwave and Millimeter-Wave Structures*, Wiley, New York, 1989, Chap. 8.
52. C. Christopoulos, *The Transmission-Line Modeling Method TLM*, IEEE Press, Piscataway, NJ, 1995.
53. G. A. Thiele and T. H. Newhouse, A hybrid technique for combining moments method and geometrical theory of diffraction, *IEEE Trans. Anten. Propag.* **23**:62 (1975).
54. D. C. Ross, J. L. Volakis, and H. T. Anastassiou, Hybrid finite element-modal analysis of jet engine inlet scattering, *IEEE Trans. Anten. Propag.* **43**:277–285 (1995).
55. M. S. Tharf and G. I. Costache, Finite element solutions of field distributions in large cavities, *Int. J. Num. Model. Electron. Networks, Device Fields* **7**(5):343–356 (1994).
56. R. Beyer and F. Arndt, Efficient modal analysis of waveguide filters including the orthogonal mode coupling elements by an MM/FE method, *IEEE Microwave Guided Wave Lett.* **5**(1):1–3 (1995).
57. M. Mogiardo and R. Sorrentino, Efficient and versatile analysis of microwave structures by combined mode matching and finite difference methods, *IEEE Microwave Guided Wave Lett.* **3**(8):241–243 (1993).
58. K. Wu, M. Yu, and R. Vahldieck, Rigorous analysis of 3D planar circuit discontinuities using the space-spectral domain approach, *IEEE Trans. Microwave Theory Tech.* **MTT-40**:1475–1483 (1992).
59. S. Xiao and R. Vahldieck, An efficient 2-D FDTD algorithm using real variables, *IEEE Microwave Guided Wave Lett.* **3**:127–129 (1993).
60. F. Alimenti et al., Efficient analysis of waveguide components by FDTD combined with time domain modal expansion, *IEEE Microwave Guided Wave Lett.* **5**:351–353 (1995).
61. M. Righi and W. J. R. Hoefer, Efficient 3D-SCN-TLM diakoptics for waveguide components, *IEEE Trans. Microwave Theory Tech.* **MTT-42**:2381–2385 (1994).
62. R. Wu and T. Itoh, Hybridizing FDTD analysis with unconditionally stable FEM for objects with curved boundary, *1995 IEEE MTT Int. Microwave Symp. Digest*, Orlando, FL, 1995, pp. 833–836.
63. Session on hybrid methods, *IEEE AP-S Int. Symp. Digest*, Newport Beach, CA, June 1995, pp. 1456–1483.
64. E. Yamashita, ed., *Analysis Methods for Electromagnetic Wave Problems*, Artech House, Norwood, MA, 1990.
65. R. Sorrentino, ed., *Numerical Methods for Passive Microwave and Millimeter Wave Structures*, IEEE Press, Piscataway, NJ, 1989.
66. E. Miller, L. Medgyesi-Mitschang, E. Newman, *Computational Electromagnetics*, IEEE Press, Piscataway, NJ, 1991.

ELECTROMAGNETIC SHIELDING

SALVATORE CELOZZI
 RODOLFO ARANEO
 University of Rome "La
 Sapienza"
 Rome, Italy

1. GENERAL ASPECTS

Electromagnetic shielding is an important constraint in the design of RF and microwave devices consisting in the mitigation of the emission levels of electromagnetic (EM) sources and/or in the protection of people or electrical and electronic apparatus and systems against possible effects due to external EM fields. Very often the need for electromagnetic shielding depends not only on functioning motivations but also on the compliance with standards fixing the limits of emission or immunity for various classes of apparatus and systems. Such a limitation or protection is generally obtained by means of a structure that is often, but not necessarily, metallic called a *shield*. Shield performance depends on its geometric and electrical parameters and on the characteristics of the unperturbed EM field (i.e., the EM field that would exist without any shielding structure, often referred to as *incident*). Various constructive peculiarities affect the performance of the overall shielding system. The most important factors in determining the performance of a shielding structure are the geometric configuration and the thickness of the shield and its materials, generally characterized by the values of conductivity σ , permeability μ , and permittivity ϵ . Also very important are the so-called discontinuities of the shield such as junctions, seams, gaps, and apertures, which are always present in practical configurations and considerably affect the performance in the radio frequency range.

The performance of a shield configuration is often expressed synthetically in terms of *shielding effectiveness* (SE), which is defined by the IEEE as the ratio of electric or magnetic field strength (modulus of the vector) at a point before (E^i or H^i) and after (E or H) the placement of the shield between a given external source and the observation point considered. In terms of Cartesian coordinates x_0, y_0, z_0 , the following expressions apply:

$$SE_E = \frac{E^i(x_0, y_0, z_0)}{E(x_0, y_0, z_0)} \quad (1a)$$

$$SE_H = \frac{H^i(x_0, y_0, z_0)}{H(x_0, y_0, z_0)} \quad (1b)$$

These two figures of merit are usually expressed in decibels, as

$$SE_{E(\text{dB})} = 20 \log_{10} \frac{E^i(x_0, y_0, z_0)}{E(x_0, y_0, z_0)} \quad (2a)$$

$$SE_{H(\text{dB})} = 20 \log_{10} \frac{H^i(x_0, y_0, z_0)}{H(x_0, y_0, z_0)} \quad (2b)$$

In case of sinusoidal sources the electric and the magnetic fields, expressed as root mean-square (RMS) values in the expressions above, do not account for polarization and are local quantities.

Also very important is the evaluation of SE performance in terms of EM power (incident) P^i and transmitted power P :

$$SE_{(dB)} = 10 \log_{10} \frac{P^i(x_0, y_0, z_0)}{P(x_0, y_0, z_0)} \quad (3)$$

Figure 1 shows the configuration leading to the evaluation of SE.

2. SHIELDING THEORY AND PREDICTION OF PERFORMANCE

Shielding theory, including analytical formulations, has been well developed in order to obtain guidance in practical problems and to firmly grasp the key factors on which the theory of electromagnetic shielding is based. The initial studies are due to Maxwell, although King presented perhaps the first work specifically oriented to the radio-frequency range [1]. For difficulty in handling real configurations by means of exact analytical expressions, approximate formulations have been developed and im-

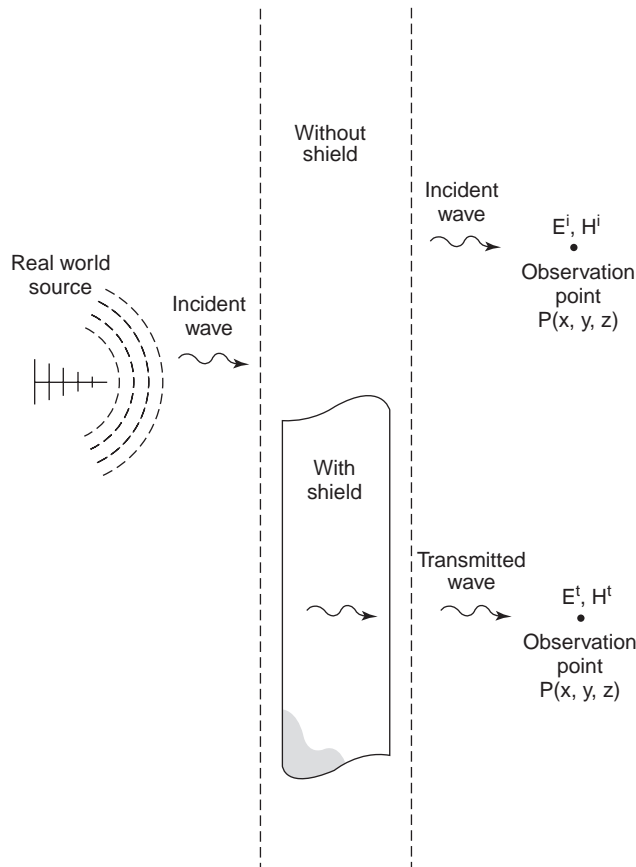


Figure 1. System configurations for the evaluation of the shielding effectiveness (SE).

proved over the years, while the analysis of the SE of closed structures, often referred to as *enclosures*, is generally performed, in either the frequency or the time domain, by using numerical techniques, and can require significant computational effort, depending on the geometric configuration, the characteristics of the shield material, and the source type; the latter aspect is the starting point of every shielding study.

Among the analytical methods used to solve shielding problems, the most relevant and successful are the direct solution of the Maxwell equations governing the system and the so-called transmission-line approach, proposed by Schelkunoff [2].

2.1. Direct Solution of Maxwell Equations

The direct solution of the equations governing the shielding problem is available only in a few simple configurations. However, some relevant cases with reasonable assumptions may be studied in this way. Moreover, such exact solutions may serve as reference for the validation of other methods and thus represent a fundamental tool in shielding analyses. The system configurations for which an analytical solution of the Maxwell equations has been found include those characterized by planar shields of infinite extent in the presence of straight or circular filamental wire current sources [3–6]. The ideal configuration of a planar shield of infinite extension and illuminated by a plane wave provides an exact solution, which is described in detail below.

2.2. Transmission-Line Approach

This method was initially introduced with reference to a plane wave impinging with a normal angle of incidence on an infinite planar shield and successively extended to accommodate other source and shield configurations. The method is based on the analogy existing between the equations governing voltage and current in a transmission line and those describing the electric and the magnetic field propagation inside a planar shield subjected to a plane wave, as shown in Fig. 2. Assuming a sinusoidal field source, the problem may be solved in the frequency domain, provided the shield material is linear. For a normal angle of incidence of a plane wave having only the y component of the electric field and the z component of the magnetic field, Maxwell curl equations governing the field propagation through the shield become

$$\frac{dE_y}{dx} = -j\omega\mu H_z \quad (4a)$$

$$\frac{dH_z}{dx} = -(\sigma + j\omega\epsilon)E_y \quad (4b)$$

It is readily recognized that this equation system describes the electric and magnetic field propagation as well as the voltage and current propagation in a transmission line, when expressing voltage and current instead of E_y and H_z , respectively, and substituting $j\omega\mu$ and $(\sigma + j\omega\epsilon)$ with the per unit length impedance and admittance of the line, respectively. The electric and magnetic

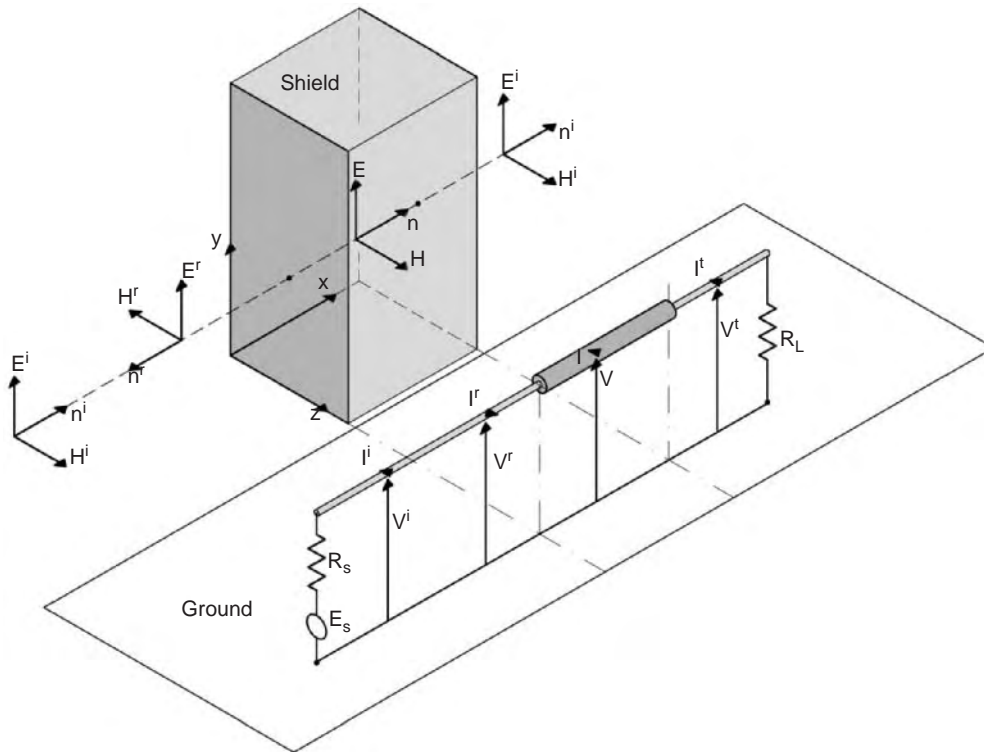


Figure 2. Shielding of a plane-wave electromagnetic field by means of a planar shield and analogy with the transmission-line configuration.

fields inside the shield material, $E_y(x)$ and $H_z(x)$, at the generic distance x from the first interface between air and shield, are expressed as functions of the corresponding quantities at $x = 0$

$$E_y(x) = E_y(0) \cosh(\gamma x) + \eta H_z(0) \sinh(\gamma x) \quad (5a)$$

$$H_z(x) = \frac{1}{\eta} E_y(0) \sinh(\gamma x) + H_z(0) \cosh(\gamma x) \quad (5b)$$

where η is the intrinsic impedance of the shield given by

$$\eta = \left(\frac{j\omega\mu}{\sigma + j\omega\epsilon} \right)^{1/2} \quad (6)$$

and γ is the propagation constant of the electromagnetic field inside the shield:

$$\gamma = [j\omega\mu(\sigma + j\omega\epsilon)]^{1/2} \quad (7)$$

The system is solved by applying the boundary conditions at the interfaces. Usually, such boundary conditions are applied considering the continuity of the tangential components of the electric and magnetic fields incident on the shield surfaces, which are also the only components propagating through the shield by virtue of the Poynting theorem. In the configuration considered, they are

expressed as

$$E_y^i + E_y^r = E_y^t \quad \text{at } x = 0 \quad (8a)$$

$$H_z^i - H_z^r = H_z^t \quad \text{at } x = 0 \quad (8b)$$

$$E_y^t = E_y^o \quad \text{at } x = d \quad (8c)$$

$$H_z^t = H_z^o \quad \text{at } x = d \quad (8d)$$

where superscripts i, r, t, and o respectively denote the incident, reflected, transmitted, and outgoing fields and $x = d$ is the abscissa of the second interface. The incident field is due to the source alone, the reflected field is due to the contribution of the induced currents on the shield surface, the transmitted field is the field propagating through the shield medium, and the outgoing field is the field that passes behind the shield.

2.2.1. Uniform Plane-Wave Field Source. A uniform plane wave is, by definition, a wave in which the electric and magnetic fields are perpendicular to each other, their direction of propagation does not vary in time, and their amplitude is constant in space and in time. This is, of course, an idealization because the EM field produced by real sources must decay in space, but if the observation point is very far from the real source, that is, if its distance is much greater than the wavelength of the electromagnetic field, the uniform plane-wave assumption is quite realistic. In a plane wave both incident and reflected electric and magnetic fields remain in a fixed ratio, which is

defined as the wave impedance Z_w of the EM field, and its value in vacuum is

$$Z_w = \frac{E_y^i}{H_z^i} = \frac{E_y^r}{H_z^r} = \frac{E_y^o}{H_z^o} = \sqrt{\frac{\mu_0}{\epsilon_0}} = 120 \pi \Omega \cong 377 \Omega \quad (9)$$

Equations (8b) and (8d), expressing the continuity of the tangential components of the magnetic field, are multiplied by Z_w , and the results are added to Eqs. (8a) and (8c), respectively, in order to find the relationships between the incident and the transmitted fields at the two shield interfaces:

$$2E_y^i = E_y^t + Z_w H_z^t \quad \text{at } x=0 \quad (10a)$$

$$0 = E_y^t - Z_w H_z^t \quad \text{at } x=d \quad (10b)$$

In this way the reflected fields, which are generally unknown and not always easy to evaluate, do not appear in the boundary conditions. It is evident that Eqs. (10) are formally identical to those valid for a real voltage source and a simple load impedance, allowing the use of the analogy with a transmission line also with respect to the boundary conditions, as shown in Fig. 2. In case of a uniform plane wave presenting an oblique angle of incidence on a shield surface, the problem may be solved considering that an arbitrarily oriented wave may be split up into various waves, each formed by the orthogonal electric and magnetic field components propagating along different directions [7]. The use of the superposition principle, provided the shield material is linear, allows one to easily accomplish all the possible physical situations. It is worthy noting that, with reference to the coordinate system shown in Fig. 2, the two waves constituted by (E_y, H_z) and $(E_z, -H_y)$ propagate toward the shield and must be accounted for in shielding analyses, as they are the other waves responsible for sliding in directions parallel to the shield. Thus, two wave impedances are considered to extend the previous formulation to the oblique incidence case:

$$Z_{w1} = \frac{E_y}{H_z} \quad (11a)$$

$$Z_{w2} = -\frac{E_z}{H_y} \quad (11b)$$

These two wave impedances are used to impose the boundary conditions in Eqs. (10) and allow the evaluation of the total electric and magnetic field components transmitted beyond the shield.

2.2.2. Near-Field Sources. In order to analyze the performance of shields against near-field sources, it is useful to introduce the elementary EM field sources known as the *electric* and the *magnetic dipoles*. Although these sources are ideal (i.e., do not exist in the real world), the EM field that they produce is easy to determine and very similar to that of some common real sources. The EM field produced by these sources depends strongly on the distance r from the observation point. In fact, the amplitude

of the electric field due to an electric dipole is expressed, in spherical coordinates as the sum of three terms depending on $1/r$, $1/r^2$, and $1/r^3$, respectively, whereas the magnetic field is a function of $1/r$ and $1/r^2$ only:

$$E_r^i(r, \omega) = \sqrt{\frac{\mu_0}{\epsilon_0}} \frac{I(\omega)L}{4\pi} 2 \cos(\theta) \left[\frac{1}{r^2} + \frac{1}{j\beta r^3} \right] e^{-j\beta r} \quad (12a)$$

$$E_\theta^i(r, \omega) = \sqrt{\frac{\mu_0}{\epsilon_0}} \frac{I(\omega)L}{4\pi} \sin(\theta) \left[\frac{j\beta}{r} + \frac{1}{r^2} + \frac{1}{j\beta r^3} \right] e^{-j\beta r} \quad (12b)$$

$$E_\phi^i(r, \omega) = 0 \quad (12c)$$

$$H_r^i(r, \omega) = 0 \quad (12d)$$

$$H_\theta^i(r, \omega) = 0 \quad (12e)$$

$$H_\phi^i(r, \omega) = \frac{I(\omega)L}{4\pi} \sin(\theta) \left[\frac{j\beta}{r} + \frac{1}{r^2} \right] e^{-j\beta r} \quad (12f)$$

where $I(\omega)$ is the current flowing in the elementary source of length L . Therefore, at points far from an electric dipole (far-field region), at a distance r from the EM source much greater than the wavelength λ , the term proportional to $1/r$ prevails in the expressions for both the electric and magnetic fields, so that their ratio, representing the wave impedance Z_w at a distance r , assumes the same value it assumes in case of a uniform plane wave: 377Ω . On the contrary, in the near-field region, where $(r/\lambda) \ll 1$, the terms proportional to $1/r^3$ and $1/r^2$ are the dominant ones in the electric and magnetic field expressions, respectively. Consequently, the wave impedance Z_w is a function of both the position and the frequency; its value is generally greater than 377Ω and, because of this characteristic, the electric dipole is termed a *high-impedance source*. Magnetic dipoles present characteristics that are dual with respect to electric ones. The amplitude of the radiated magnetic field is expressed as the sum of three terms depending on $1/r$, $1/r^2$, and $1/r^3$, respectively, whereas the electric field is a function of $1/r$ and $1/r^2$ only

$$E_r^i(r, \omega) = 0 \quad (13a)$$

$$E_\theta^i(r, \omega) = 0 \quad (13b)$$

$$E_\phi^i(r, \omega) = -\frac{j\omega\mu_0 I(\omega)A}{4\pi} \sin(\theta) \left[\frac{j\beta}{r} + \frac{1}{r^2} \right] e^{-j\beta r} \quad (13c)$$

$$H_r^i(r, \omega) = \frac{j\beta I(\omega)A}{4\pi} 2 \cos(\theta) \left[\frac{1}{r^2} + \frac{1}{j\beta r^3} \right] e^{-j\beta r} \quad (13d)$$

$$H_\theta^i(r, \omega) = \frac{j\beta I(\omega)A}{4\pi} \sin(\theta) \left[\frac{j\beta}{r} + \frac{1}{r^2} + \frac{1}{j\beta r^3} \right] e^{-j\beta r} \quad (13e)$$

$$H_\phi^i(r, \omega) = 0 \quad (13f)$$

where $I(\omega)$ is the current flowing in the loop with surface A . In the far-field region, the EM field is characterized by the free-space wave impedance. Conversely, in the near-field region, the terms proportional to $1/r^3$ and $1/r^2$ are

the dominant ones in the magnetic and electric fields, respectively, and the wave impedance Z_w is lower than 377 Ω . For this reason, the magnetic dipole represents a low impedance source.

In Fig. 3, the trends of the wave impedances of an electric dipole and a magnetic dipole are reported, as functions of the distance, normalized by λ , of the observation point from the source.

These considerations are of great importance in extending the transmission-line approach to solve near field source problems. It should be noted that generally the electric and the magnetic fields are not perpendicular to each other and the various components directed toward the shield, according to the Poynting theorem, may be accounted for separately, as described for the oblique incidence of uniform plane waves. According to the studies carried out for the oblique incidence of a plane wave on a planar shield, the wave impedances associated with the various directions may be defined and utilized to determine the field incident onto a prefixed shield surface. In fact, the boundary conditions may be imposed following the procedure described for the plane-wave source, provided the electric and the magnetic field are considered space- and frequency-dependent.

2.2.3. Shielding Effectiveness Evaluation. In case of uniform plane waves, the electromagnetic field amplitudes remain constant in space and the shielding effectiveness may be evaluated as the ratio between the incident field and the outgoing field. Moreover, SE_E and SE_H are numerically coincident. SE may be expressed in the following very compact form

$$SE = A + R + B \tag{14}$$

where the absorption loss A , reflection loss R , and multiple reflections coefficient B for a planar shield of thickness d

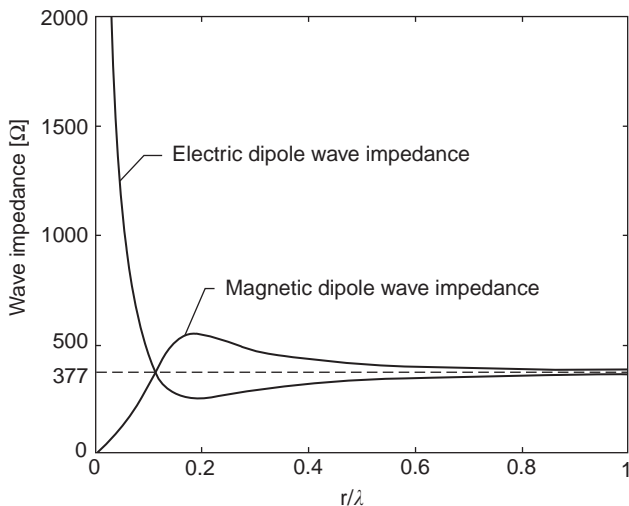


Figure 3. Trend of the wave impedances associated with electric and magnetic dipoles, as a function of the normalized distance from the of the sinusoidal elemental source.

are respectively given (in decibels) by

$$A_{dB} = 20 \log_{10} |e^{\gamma d}| \tag{15a}$$

$$R_{dB} = 20 \log_{10} |(Z_w + \eta)^2 (4Z_w \eta)^{-1}| \tag{15b}$$

$$B_{dB} = 20 \log_{10} \left| 1 - \frac{(Z_w - \eta)^2}{(Z_w + \eta)^2} e^{-2\gamma d} \right| \tag{15c}$$

The absorption loss coefficient A_{dB} is a function of the shield characteristics only; the reflection loss coefficient R_{dB} depends on the mismatch between the wave impedance and the intrinsic impedance of the shield. The multiple-reflection coefficient B_{dB} depends on both the physical characteristics of the shield material and the incident field. Coefficient A_{dB} can be expressed in the following simple form:

$$A_{dB} = 131.44 \sqrt{f \mu_r \sigma_r} d \tag{16}$$

where μ_r and σ_r denote respectively the relative magnetic permeability and the relative conductivity (with respect to the conductivity of copper $\sigma_{Cu} = 5.8 \cdot 10^7$ S/m) of the material.

Different approximate expressions hold for coefficient R for plane-wave sources, high-impedance sources, and low-impedance sources, respectively:

$$R_{dB} = 168.1 - 20 \log_{10} \sqrt{\frac{f \mu_r}{\sigma_r}} \tag{17a}$$

$$R_{dB} = 321.7 - 10 \log_{10} \left(\frac{\sigma_r}{f^3 \mu_r r^2} \right) \tag{17b}$$

$$R_{dB} = 20 \log_{10} \left(5.35 \sqrt{\frac{\sigma_r f}{\mu_r}} r + 0.0117 \sqrt{\frac{\mu_r}{\sigma_r f}} \frac{1}{r} + 0.5 \right) \tag{17c}$$

Figure 4 shows the absorption loss coefficient A_{dB} as function of the frequency for different thicknesses of a copper shield. Figure 5 shows the frequency dependence of coefficient R_{dB} of copper against typical low- or high-impedance fields, respectively, both located at a distance of 30.48 cm from the shield surface.

It should be noted that in (and sometimes below) the microwave band of the frequency spectrum, the SE is completely dominated by the discontinuities, since the conductive materials behave like perfect electric conductors, present at a skin depth that is much lower than the shield thickness.

The coefficient B_{dB} in the radiofrequency range is often negligible. In case of low-impedance sources, the reflection loss coefficient exhibits values increasing with the frequency, for copper and aluminum, while for ferromagnetic materials it initially decreases and then increases. For high-impedance sources, the reflection loss coefficient always decreases for all the materials. The values of R_{dB} are much lower in the low-impedance source case, confirming the difficulty in shielding magnetic fields in the low-frequency range. It should also be noted that the previous expressions are rigorously valid for a plane-

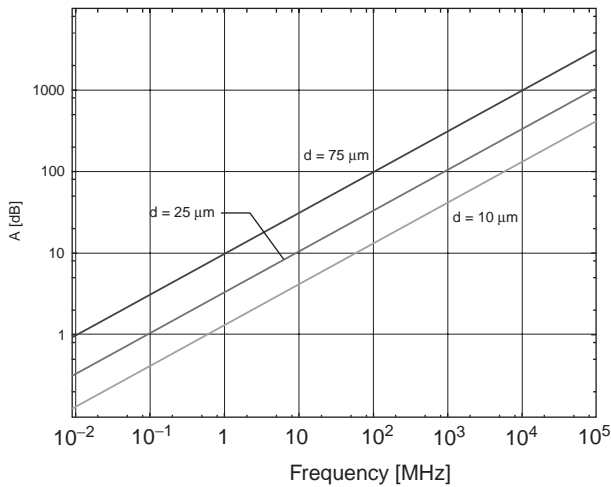


Figure 4. Frequency dependence of the absorption loss coefficient A_{dB} for different shield thicknesses. (This figure is available in full color at <http://www.mrw.interscience.wiley.com/erfme>.)

wave source impinging normally onto a shield that is conductive, infinite, and planar. When extending the transmission-line-approach to waves with an oblique angle of incidence, another hypothesis is necessary—the electromagnetic field propagation inside the shield must occur normally to the shield surface; this assumption is generally satisfied in consideration of the high values of conductivity, as stated by Snell’s law of refraction [8]

$$\gamma_0 \sin(\theta_i) = \gamma_s \sin(\theta_s) \tag{18}$$

where γ_0 and γ_s are respectively the propagation constant in air and in the shield medium and θ_i and θ_s are the directions of propagation of the electromagnetic field in the two media, respectively.

2.3. Ideal Enclosures without Apertures

Real enclosures may be analyzed only by means of numerical methods because of their complex shape; however,

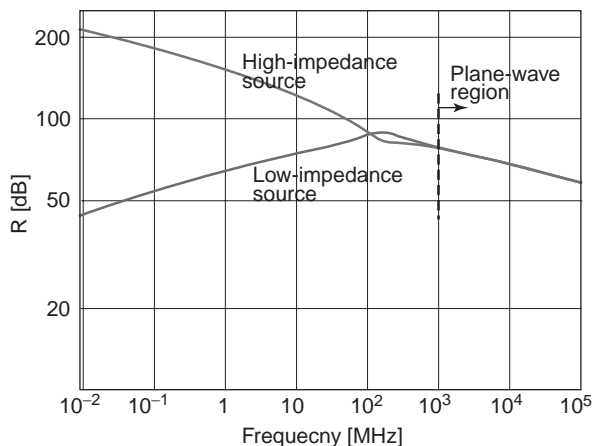


Figure 5. Frequency dependence of the reflection loss coefficient R_{dB} of copper against low-impedance and high-impedance sources. (This figure is available in full color at <http://www.mrw.interscience.wiley.com/erfme>.)

some formulations exist allowing an estimation of shielding performance under simplifying hypotheses and approximations concerning the absence of constructive defects and discontinuities in the structure and the shape of the shield configuration. The effect of the discontinuities such as junctions and apertures may be accounted for at a successive stage, as reported in the following. An analytical expression valid, for example, for the SE against a uniform magnetic field incident transversely onto a cylindrically shaped enclosure of infinite length is

$$SE = 20 \log_{10} \frac{1}{\cosh(\gamma \cdot d) + \left(\frac{r_0 \cdot \gamma}{2\mu_r} + \frac{\mu_r}{2r_0 \cdot \gamma} \right) \cosh(\gamma \cdot d)} \tag{19}$$

where r_0 is the radius of the cylindrical shield.

The SE of a spherically-shaped enclosure against an incident uniform magnetic field is given by the following expression, where r_0 represents the sphere radius:

$$SE = 20 \log_{10} \frac{1}{\cosh(\gamma \cdot d) + \frac{r_0 \cdot \gamma}{3\mu_r} \cosh(\gamma \cdot d)} \tag{20}$$

More complex shapes have been also analyzed, and several useful expressions are reported in [9,10].

2.4. Shielded Cables

Cables are critical components because they may connect apparatus sensitive to external radiofrequency EM fields, or they may radiate unintentionally, becoming sources of interference. With this twofold motivation, cables are often shielded in various ways and either compact or perforated braided shield may be effective in reducing EM susceptibility or interference [11,12]. Generally, a synthetic parameter termed *transfer impedance* is introduced to account for the penetration through the cable shield. The transfer impedance may be regarded as the per unit length voltage drop occurring on the external surface of the cable shield when the inner conductor is driven by a unit current or, by reciprocity, the effect on the inside of the shield due to a current on the external shield surface. Also of particular relevance are the status of ground connections at the ends of the cable, and the type of connectors, apart, of course, from the shield characteristics.

2.5. Numerical Methods for Shielding Analysis

The intrinsic limitations of analytical formulations have lead to a wide literature concerning studies of the application of various numerical methods to shielding problems, which would be an exhaustive, practically impossible report. However, examples of the application of the method of moments to shielding configurations may be found in Refs. 13 and 14, while the finite-difference time-domain method has been applied in Refs. 15 and 16, the boundary element method in Ref. 17, the transmission-line method in Ref. 18, and the finite-element method in Ref. 19.

3. OTHER FACTORS AFFECTING SHIELDING PERFORMANCE

The analytical methods described previously are based on the assumption that no discontinuities (e.g., apertures, holes, junctions, seams) are present in the shield; nevertheless, such a hypothesis is quite unrealistic because intentional apertures for various purposes and unintentional defects always exist and may considerably degrade the performance of real shields. Moreover, the presence of standing waves in closed enclosures may deteriorate the shielding performance even in absence of discontinuities.

No general theory is available to account for the discontinuities; however, some studies have been conducted to quantify the EM field transmitted through intentional apertures of some regular shapes. In fact, when the aperture is electrically small and the shield is perfectly conducting, its contribution to the EM field beyond the shield may be represented as that due to a combination of appropriate elementar electric and magnetic dipoles, located in the centre of the aperture with the shield removed [20]. Periodically perforated shields have been also studied to some extent [21]. Measured data and approximate formulations have been also presented to quantify the effect of various types of discontinuity in EM penetrable shields, and, in particular, in case of single or multiple apertures two approaches can be used to evaluate the overall effect of the aperture(s) in terms of EM leakage whose value must be subtracted from the SE value of the ideal shield [10], or to obtain a modified expression for the SE that individually accounts for various effects such as the number of openings per unit square, coupling between apertures, and reduced absorption loss terms [6].

3.1. Shielding Applications

Several practical rules and solutions are recommended for the design and evaluation of the SE performance of real shield configurations and may be found elsewhere [10]. It is worth mentioning that care must be taken to bond seams and joints according to their permanent or operational nature; permanent joints should be riveted or screwed, and SE performance is influenced by the spacing between the transverse components. Operational joints should be finished with the so-called gaskets, flexible and elastic conductive components capable of establishing a good electrical continuity between fixed and mobile parts of the shield enclosure. Various commercial gaskets are available, and their performance is generally good enough to limit efficiently the performance deterioration. Another situation requiring a special treatment is represented by windows for visualization; because of their aperture dimensions, their presence may considerably reduce the efficiency of an otherwise good structure. It is highly advisable to apply on the required aperture a conductive optical substrate or a shield realized by means of a thin wire mesh.

4. SHIELDING PERFORMANCE MEASUREMENT AND STANDARDS

The most common documents describing the test procedures recommended for assessment of the shielding characteristics of enclosures are:

- Military Standard 285: *Method of Attenuation Measurements for Enclosures, Electromagnetic Shielding, for Electronic Test Purposes.*
- National Security Agency (NSA) Specification 65-6: *General Specifications for RF Shielded Enclosures for Communications Equipment.*
- National Security Agency (NSA) Specification 73-2: *General Specifications for Foil RF Shielded Enclosures for Communications Equipment.*
- IEEE 299: *Standard Method of Measuring the Effectiveness of Electromagnetic Shielded Enclosures.*
- Several ASTM standards, including D4935-99, provide the procedures for measuring the SE of a planar material due to a plane-wave, far-field EM wave, in the frequency range from 30 MHz to 1.5 GHz.

All these documents describe antenna geometries and configurations and also delineate some measurement practices, classifying the source as a type of magnetic, electric, or plane wave. It is important to mention that the data obtained from any of the setups described above cannot be applied to source configurations different from those used in the experiments. Typical experimental setups are shown in Figs. 6–9. Thus, they have only reference value and other methods and experimental setups have been also proposed and applied [22,23].

5. FINAL REMARKS

Some controversial aspects concerning electromagnetic shielding have to be highlighted; the most important are represented by the definition itself of the figure of merit adopted for all the considerations and for design purposes.

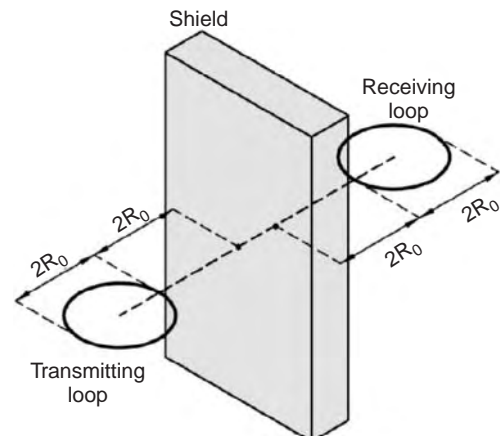


Figure 6. Experimental configuration for the measurement of magnetic field shielding effectiveness, according to IEEE 299 and MIL-STD 285.

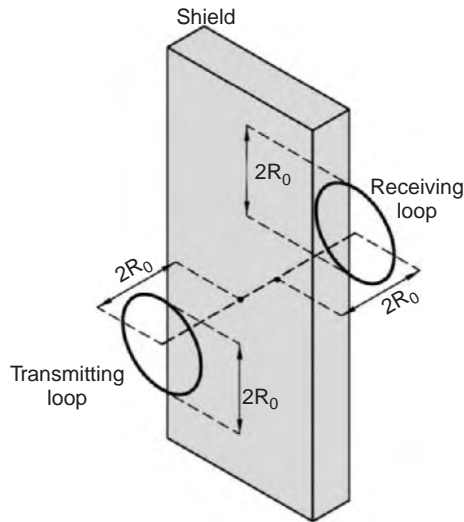


Figure 7. Experimental configuration for the evaluation of magnetic field shielding effectiveness, according to NSA 65-6.

In fact, the SE, as defined, is a local quantity, in the sense that it represents a field (or power) ratio at a specific point, giving no information on the situation over a finite surface or volume. For this reason, it is difficult to extrapolate a general evaluation of the real performance of the shield from such limited information. Moreover, the SE measurement may be cumbersome or even impossible in some real configurations because of either the shield dimensions (e.g., too small) or the coupling between the enclosure and the transmitting and receiving antennas. Other controversial aspects concern the validity of the transmission-line analogy, which must be assessed case by case, otherwise possibly leading to incorrect predictions.

6. CURRENT RESEARCH TOPICS

Various aspects of electromagnetic shielding are currently under investigation. One of the most challenging research

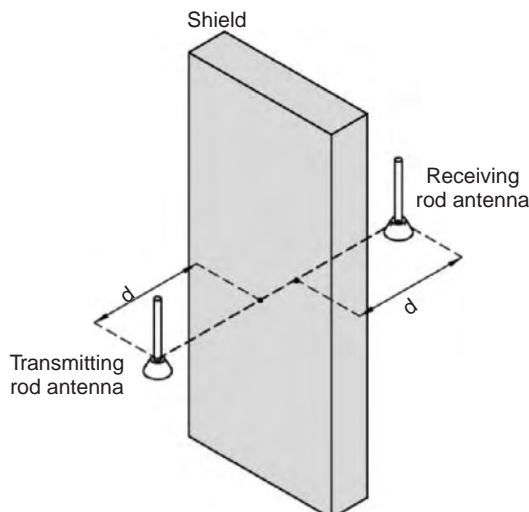


Figure 8. Typical NSA 65-6 setup for SE measurement in high-impedance source configuration.

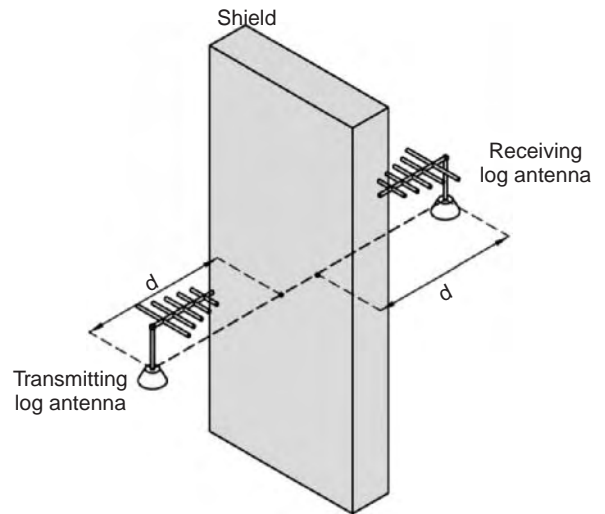


Figure 9. Typical NSA 65-6 setup for SE measurement in plane-wave source configuration.

topics is the design of real shielding structures. The need for significant but measurable quantities is of paramount importance in the shielding practice, making possible the experimental verification of predictions, the design of shielding structures, as well as the promulgation of standards; in this regard, the search for new figures of merit is still underway, especially for small enclosures. Of course, new, reliable, and simple ways to perform measurements for the characterization of both materials and shielding structures are always under investigation.

Another important field of research is the development of new synthetic materials providing good performance in specific applications.

In addition, active shielding, realized by means of additional sources capable of generating an electromagnetic field opposite that undesired and to be mitigated, is a research topic of great interest, inasmuch as in the design of optimal configurations.

Finally, since all the abovementioned research topics necessitate the formulation of work hypotheses and their successive experimental verification, numerical modelling and analysis methods must continuously deal with more complex materials and configurations, and thus their improvement in terms of accuracy and efficiency represents a fundamental research topic in electromagnetic shielding.

BIBLIOGRAPHY

1. L. V. King, Electromagnetic shielding at radio frequencies, *Phil. Mag.* **15**(Ser. 7):201–223 (Feb. 1933).
2. S. A. Schelkunoff, *Electromagnetic Waves*, Van Nostrand, New York, 1943.
3. J. A. Tegopoulos and E. E. Kriezis, *Eddy Currents in Linear Conducting Media*, Elsevier, Amsterdam, 1985.
4. J. R. Moser, Low-frequency low-impedance electromagnetic shielding, *IEEE Trans. Electromagn. Compat.* **30**(3):202–210 (1988).
5. R. Araneo and S. Celozzi, On the exact solution of the low-frequency coplanar loops shielding configuration, *IEE Proc. Sci. Meas. Technol.* **149**:37–44 (2002).

6. R. B. Schulz, V. C. Plantz, and D. R. Brush, Shielding theory and practice, *IEEE Trans. Electromagn. Compat.* **30**(3): 187–201 (1988).
7. R. A. Adler, L. J. Chu, and R. M. Fano, *Electromagnetic Energy Transmission and Radiation*, Wiley, New York, 1960.
8. C. A. Balanis, *Advanced Engineering Electromagnetics*, J Wiley, New York, 1989.
9. T. Rikitake, *Magnetic and Electromagnetic Shielding*, Terra Scientific Publishing, Tokyo, 1987.
10. D. R. J. White and M. Mardiguian, *Electromagnetic Shielding*, Vol. 3, EMF-EMI Control, Inc., Gainesville, FL, 1988.
11. A. Tsaliovich, *Cable Shielding for Electromagnetic Compatibility*, J Wiley, New York, 1995.
12. F. M. Tesche, M. V. Ianoz, and T. Karlsson, *EMC Analysis Methods and Computational Models*, J Wiley, New York, 1997.
13. H. Singer, H. D. Bruns, and G. Burger, State of the art in the method of moments, *Proc. IEEE 1996 Int. Symp. Electromagnetic Compatibility*, Santa Clara, CA, 1996, pp. 122–127.
14. G. Burger, H. D. Bruns, and H. Singer, Simulation of thin layers in the method of moments, *Proc. 11th Int. Zurich Symp.*, Zurich, Switzerland, 1995, pp. 339–344.
15. R. J. Luebbers, K. Kumagai, S. Adachi, and T. Uno, FDTD calculation of transient pulse propagation through a nonlinear magnetic sheet, *IEEE Trans. Electromagn. Compat.* **33**(1):90–94 (1993).
16. S. Celozzi and M. D'Amore, Magnetic field attenuation of nonlinear shields, *IEEE Trans. Electromagn. Compat.* **38**(3):318–326 (1996).
17. J. Shen and A. Kost, Hybrid FE-BE method for EMC problems in cable systems, *IEEE Trans. Magn.* **32**(3):1493–1496 (1996).
18. A. Mallik, D. P. Johns, and A. J. Wlodarczyk, TLM modelling of wires and slots, *Proc. 10th Int. Zurich Symp.*, Zurich, Switzerland, 1993, pp. 515–520.
19. S. Celozzi, FE-TD analysis of ferromagnetic shields against near field sources, *Proc. 12th EMC Zurich Symp. Electromagnetic Compatibility*, Feb. 18–20, 1997, Zurich, Switzerland, pp. 281–286.
20. F. De Meulenaere and J. van Bladel, Polarizability of some small apertures, *IEEE Trans. Anten. Propag.* **25**(2):198–205 (1977).
21. K. F. Casey, Electromagnetic shielding behavior of wire-mesh screens, *IEEE Trans. Electromagn. Compat.* **30**(3):298–306 (1988).
22. P. F. Wilson and M. T. Ma, Shielding effectiveness measurements with a dual TEM cell, *IEEE Trans. Electromagn. Compat.* **27**(3):137–142 (1985).
23. J. A. Catrysse and C. P. J. H. Borgmans, Measuring methods and measuring setups for the characterisation of shielding materials under different conditions, *Proc. Int. Symp. Electromagnetic Compatibility EMC '96 ROMA*, Rome, Italy, 1996, pp. 562–568.

FURTHER READING

- First Special Issue on Electromagnetic Shielding, *IEEE Trans. Electromagn. Compat.* **10**(1) (1968).
- Second Special Issue on Electromagnetic Shielding, *IEEE Trans. Electromagn. Compat.* **30**(3) (1988).
- L. H. Hemming, *Architectural Shielding*, IEEE Press, New York, 1992.

ELECTROMAGNETIC SUBSURFACE REMOTE SENSING

S. Y. CHEN
W. C. CHEW
University of Illinois at Urbana-
Champaign
Urbana, Illinois

Subsurface electromagnetic (EM) methods are applied to obtain underground information that is not available from surface observations. Since electrical parameters such as dielectric permittivity and conductivity of subsurface materials may vary dramatically, the response of electromagnetic waves can be used to map the underground structure. This technique is referred to as geological surveying. Another major application of subsurface EM methods is to detect and locate underground anomalies such as mineral deposits.

Subsurface EM methods include a variety of techniques depending on the application, surveying method, system, and interpretation procedure, and thus a “best” method simply does not exist. Even though each system has its own characteristics, they still share some common features. In general, each system has a transmitter, which can be either natural or artificial, to send out the electromagnetic energy that serves as an input signal. A receiver is needed to collect the response signal. The underground can be viewed as a system, which is characterized by the material parameters and underground geometry. The task of subsurface EM methods is to derive the underground information from the response signal.

The EM transmitter radiates the primary field into the subsurface, which consists of conductive earth material. This primary field will induce a current, which in turn radiates a secondary field. Either the secondary field or the total field will be detected by the receiver. After the data interpretation, one can obtain the underground information.

One of the most challenging parts of subsurface EM methods is interpretation of the data. Since the incident field interacts with the subsurface in a very complex manner, it is never easy to subtract the information from the receiver signal. Many definitions, such as apparent conductivity, are introduced to facilitate this procedure.

Data interpretation is also a critical factor in evaluating the effectiveness of the system. How good the system is always depends on how well the data can be explained. In the early development of subsurface EM systems, data interpretation largely depended on the personal experience of the operator, due to the complexity of the problem. Only with the aid of powerful computers and improvements in computational EM techniques is it possible to analyze such a complicated problem in a reasonable time. Computer-based interpretation and inversion methods are attracting more and more attention. Nevertheless, data interpretation is still “an artful balance of physical understanding, awareness of the geological constraints, and pure experience” [1].

In the following sections, we will use several typical applications to outline the basic principles of subsurface

EM methods. Physical insight is emphasized rather than rigorous mathematical analysis. Details of each method can be found in the references.

1. BOREHOLE EM METHODS

Borehole EM methods are an important part of well-logging methods. Since water is conductive and oil is an insulator, resistivity measurements are good indicators of oil presence. Water has an unusually high dielectric constant, and permittivity measurement is a good detector of moisture content.

Early borehole EM methods consist of mainly electrical measurements using very simple low-frequency electrodes like the short and the long normal. Then more sophisticated electrode tools were developed. Some of these tools are mounted on a mandrel, which performs measurements centered in a borehole. These tools are called mandrel tools. Alternatively, the sensors can be mounted on a pad, and the corresponding tool is called a pad tool.

One of the most successful borehole EM methods is induction logging. Since Doll published his first paper in 1949 (2), this technique has been used widely with confidence in the petroleum industry. Extensive research work has been done in this area. The systems in use now are so sophisticated that many modern electrical techniques are involved. Nevertheless, the principles still remain the same and can be understood by studying a simple case.

The induction logging technique, as proposed by Doll, makes use of several coils wound on an isolating mandrel, called a sonde. Some of the coils, referred to as transmitters, are powered with alternating current (AC). The transmitters radiate the field into the conductive formation and induce a secondary current, which is nearly proportional to the formation conductivity. The secondary current radiates a secondary field, which can be detected by the receiver coils. The receiver signal (voltage) is normalized with respect to the transmitter current and represented as an apparent conductivity, which serves as an indication of underground conductivity.

To obtain information from the apparent conductivity, we need to understand how apparent conductivity and true conductivity are related. According to Doll's theory, the relation in cylindrical coordinates is given by

$$\sigma_a = \int_{-\infty}^{+\infty} dz' \int_0^{+\infty} d\rho' g_D(\rho', z') \sigma(\rho', z') \quad (1)$$

where σ_a is the formation conductivity. The kernel $g_D(\rho, z)$ is the so-called Doll geometric factor, which weights the contribution of the conductivity from various regions in the vicinity of sonde.

We notice that $g_D(\rho, z)$ is not a function of the true conductivity and hence is only determined by the tool configuration. The interpretation of the data would be simple if Doll's theory were exact. Unfortunately, this is rarely the case. Further studies show that Eq. (1) is true only in some extreme cases. The significance of Doll's theory, however, is that it relates the apparent conductivity and formation conductivity, even though the theory is not exact. In the

early development of induction logging techniques, tool design and data interpretation were based on Doll's theory, and in most cases it gives reasonable answers.

To establish a firm understanding of induction logging theory, we need to perform a rigorous analysis by using Maxwell's equations as follows:

$$\nabla \times \mathbf{H} = -i\omega\epsilon\mathbf{E} + \mathbf{J}_s + \sigma\mathbf{E} \quad (2)$$

$$\nabla \times \mathbf{E} = i\omega\mu\mathbf{H} \quad (3)$$

$$\nabla \cdot \mathbf{H} = 0 \quad (4)$$

$$\nabla \cdot \mathbf{D} = \rho \quad (5)$$

where $\nabla \cdot \mathbf{J}_s = i\omega\rho$.

In the preceding equations, the time dependence $e^{-i\omega t}$ is assumed, and \mathbf{J}_s corresponds to the impressed current source. Parameters μ, ϵ, σ are the magnetic permeability, dielectric permittivity, and electric conductivity, respectively. To simplify the analysis, we assume that both the impressed source and geometry of the problem are axisymmetric; consequently, all the field components are independent of the azimuthal angle. Furthermore, it can be shown that there is no stored charge under the preceding assumption. The working frequency of induction logging is about 20 kHz, so the displacement current $-i\omega\epsilon\mathbf{E}$ is very small compared to the conduction current $\sigma\mathbf{E}$ and hence is neglected in the following discussion. After these simplifications, we have

$$\nabla \times \mathbf{H} - \sigma\mathbf{E} = \mathbf{J}_s \quad (6)$$

$$\nabla \times \mathbf{E} - i\omega\mu\mathbf{H} = 0 \quad (7)$$

$$\nabla \cdot \mathbf{H} = 0 \quad (8)$$

$$\nabla \cdot \mathbf{E} = 0 \quad (9)$$

where we assume $\nabla \cdot \mathbf{J}_s = i\omega\rho = 0$.

For convenience, the auxiliary vector potential is introduced. Since $\nabla \cdot \mathbf{H} = 0$ and $\nabla \cdot (\nabla \times) = 0$, it is possible to define $\mathbf{H} = \nabla \times \mathbf{A}$. To specify the field uniquely, we choose $\mathbf{E} = i\omega\mu\mathbf{A}$, which is true only when there is no charge accumulation. Substituting these expressions into Eq. (6), we have

$$\nabla \times \nabla \times \mathbf{A} - i\omega\mu\sigma\mathbf{A} = \mathbf{J}_s \quad (10)$$

By using the vector identity, we have

$$\nabla^2 \mathbf{A} + k^2 \mathbf{A} = -\mathbf{J}_s \quad (11)$$

where

$$k^2 = i\omega\mu\sigma \quad (12)$$

To demonstrate how the apparent conductivity and formation conductivity are related, we first write down the solution of Eq. (11) in a homogeneous medium as

follows [3,4]:

$$\mathbf{A}(\rho, z, \phi) = \frac{1}{4\pi} \int_V \frac{\mathbf{J}_s(\rho', z', \phi')}{\bar{r}_1} e^{ik\bar{r}_1} dV' \quad (13)$$

where

$$\bar{r}_1 = \{(z - z')^2 + \rho^2 + \rho'^2 - 2\rho\rho' \cos(\phi - \phi')\}^{1/2} \quad (14)$$

The volume integration is evaluated over regions containing the impressed current sources and the coordinate system used in Eq. (13), as shown in Fig. 1. Usually, a small current loop is used as an excitation, which implies that only A_ϕ exists. Hence, Eq. (13) can be furthermore simplified as

$$A_\phi(\rho, z) = \frac{1}{4\pi} \int_V \mathbf{J}_\phi(\rho', z') \cos(\phi - \phi') \frac{e^{ik\bar{r}_1}}{\bar{r}_1} dV' \quad (15)$$

When the radius of the current loop becomes infinitely small, it can be viewed as a magnetic dipole, and thus the preceding integration can be approximated as

$$A_\phi = \frac{m}{4\pi r_1^3} (1 - ikr_1) e^{ikr_1} \quad (16)$$

where $m = N_T I (\pi a^2)$ is the magnetic dipole moment and N_T is the number of turns wound on the mandrel. At the receiver point, the voltage induced on the receiver with N_R

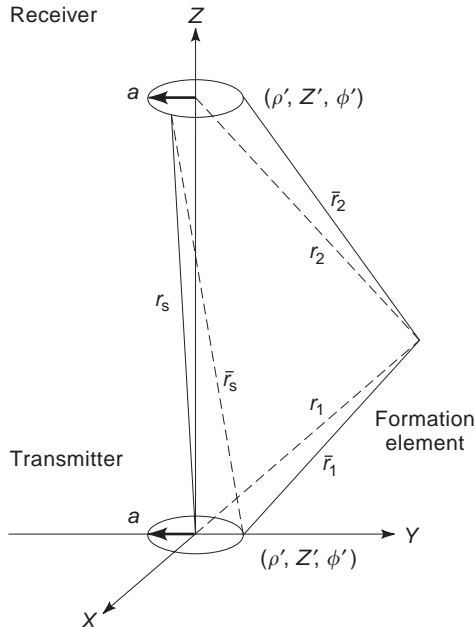


Figure 1. Induction logging tool transmitter and receiver coil pair used to explain the geometric factor theory. (Redrawn from Ref. 4.)

turns can be represented as

$$\begin{aligned} V &= 2\pi a N_R E_\phi \\ &= \frac{2N_T N_R (\pi a^2)^2 I}{4\pi} i\omega\mu (1 - ikL) \frac{e^{ikL}}{L^3} \end{aligned} \quad (17)$$

where

$$E_\phi = i\omega\mu A_\phi(a, L) \quad (18)$$

and L is the distance between the transmitter and the receiver. Since the voltage is a complex quantity, it can be separated into real and imaginary parts and expanded in powers of kL as follows [3]

$$V_R = -K\sigma \left(1 - \frac{2L}{3\delta} + \dots \right) \quad (19)$$

$$V_X = K\sigma \frac{\delta^2}{L^2} \left(1 - \frac{2L^2}{3\delta^3} + \dots \right) \quad (20)$$

where

$$K = \frac{(\omega\mu)^2 (\pi a^2)^2 N_T N_R I}{4\pi L} \quad (21)$$

and

$$\delta = \sqrt{\frac{2}{\omega\mu\sigma}} \quad (22)$$

The quantity K is known as the “tool constant” and is totally determined by the configuration of the tool, and σ is the so-called skin depth, which describes the attenuation of a conductor in terms of the field penetration distance. The quantity V_R is called the R signal. The apparent conductivity is defined as [3]

$$\sigma_a = -\frac{V_R}{K} \cong \sigma \left(1 - \frac{2L}{3\delta} \right) \quad (23)$$

In the preceding analysis, there are some important facts that need to be mentioned. In Eq. (19), we see that the apparent conductivity is a nonlinear function of the true conductivity, even in a homogeneous medium. The lower the working frequency or lower the true conductivity, the more linear it will be. The difference between true conductivity and apparent conductivity is defined as the skin effect signal:

$$\sigma_s = \sigma - \sigma_a \quad (24)$$

The leading term of the imaginary part V_X is not a function of true conductivity. In fact, it corresponds to the direct coupling field, which does not contain any formation information. What remains in V_X is the so-called X signal. Since the direct term is much larger than the residual part including V_R , it is difficult to separate the X signal. The

importance of the X signal is seen by comparing Eqs. (19) and (20), from which we find that the X signal is the first-order approximation of the nonlinear term in V_R , the R signal. This fact can be used to compensate for the skin effect.

So far we have introduced the concept of apparent conductivity by studying the homogeneous case. In practice, the formation conductivity distribution is far more complicated. The apparent conductivity and formation conductivity are related through a nonlinear convolution. As a proof we derive the solution in an integral form, instead of directly solving the differential equations. To this end, we first rewrite Eq. (11) as

$$\nabla^2 \mathbf{A} = -\mathbf{J}_s - \mathbf{J}_i \quad (25)$$

where $\mathbf{J}_i = -k^2 \mathbf{A}$ is the induced current. The solution of Eq. (25) can be written in the integral form as

$$\mathbf{A} = \frac{1}{4\pi} \int_V \frac{\mathbf{J}_s}{\bar{r}_s} dV' + \frac{1}{4\pi} \int_V \frac{\mathbf{J}_i}{\bar{r}_2} dV \quad (26)$$

The first integral is evaluated over the regions containing the impressed sources, and the second one is performed over the entire formation. Under the same assumption as we have made in the preceding analysis, the receiver voltage can be written as [4]

$$V = \frac{i2\pi a N_R \omega \mu}{4\pi} \int_V \frac{J_\phi}{\bar{r}_s} dV' - \frac{2\pi a N_R \omega^2 \mu^2}{4\pi} \int_V \frac{\sigma(\rho', z') A_\phi(\rho', z')}{\bar{r}_2} dV \quad (27)$$

The vector potential can also be separated into real and imaginary parts:

$$A_\phi = A_{\phi R} + iA_{\phi I} \quad (28)$$

Substituting Eq. (28) into Eq. (27) and separating out the real part of the receiver voltage, we have

$$V_R = \frac{-(\omega \mu)^2 (2\pi a N_R)}{4\pi} \int_{-\infty}^{\infty} dz' \int_0^{\infty} d\rho' \sigma(\rho', z') A_{\phi R} \int_0^{2\pi} \frac{\cos(\phi - \phi')}{\bar{r}_2} d\phi' \quad (29)$$

Applying the same procedure, we obtain the apparent conductivity as

$$\sigma_a = -\frac{V_R}{K} = \int_0^{\infty} d\rho' \int_{-\infty}^{\infty} dz' \sigma(\rho', z') g_P(\rho', z') \quad (30)$$

where

$$g_P = \frac{2\pi L \rho'}{(\pi a)^3 N_T I} A_{\phi R} \int_0^{2\pi} \frac{\cos(\phi - \phi')}{\bar{r}_2} d\phi' \quad (31)$$

The function g_P is the exact definition of the geometric factor. In comparison with Doll's geometric factor, g_P depends not only on the tool configuration but also on the formation conductivity, since the vector potential depends on the formation conductivity. The integral form solution does not provide any computational advantage, since the differential equation for the vector potential $A_{\phi, R}$ must still be solved. But it is now clear from Eq. (30) that the apparent conductivity is the result of a nonlinear convolution. Equation (30) also represents the starting point of inverse filtering techniques, which make use of both the R and X signals to reconstruct the formation conductivity.

Finding the vector potential A is still a challenge. Analytic solutions are available only for a few simple geometries. In most cases, we have to use numerical techniques such as the finite-element method (FEM), finite-difference method (FDM), numerical mode matching (NMM), or the volume integral equation method (VIEM). Interested readers may find Refs. 5 through 8 useful.

Previously, we mentioned that Doll's geometric factor theory is valid only under some extreme conditions. In fact, it can be derived from the exact geometric factor as a special case [4]. In a homogeneous medium, the vector potential $A_{\phi, R}$ can be calculated as

$$A_{\phi R} \cong \frac{(\pi a^2) N_T I \rho'}{4\pi r_1^3} \mathcal{R}e\{(1 - ikr_1)e^{ikr_1}\} \quad (32)$$

The integration with respect to ϕ' in Eq. (31) can also be performed for $\bar{r}_2 \gg a$. The final result is

$$\sigma_a = \int_{-\infty}^{\infty} \int_0^{\infty} \sigma_D(\rho', z') \mathcal{R}e\{(1 - ikr_1)e^{ikr_1}\} d\rho' dz' \quad (33)$$

where

$$g_D(\rho', z') = \frac{L \rho'^3}{2 r_1^3 r_2^3} \quad (34)$$

It is now clear that Doll's geometric factor and the exact geometric factor are the same when the medium is homogeneous and the wavenumber approaches zero.

So far we have discussed the basic theory of induction logging. We now use a simple example to show some practical concerns and briefly discuss the solutions. In Fig. 2, we show an apparent resistivity (the inverse of apparent conductivity) response of a commercial logging tool 6FF40 (trademark of the Schlumberger Company) in the Oklahoma benchmark. The black line is the formation resistivity, and the red line is the unprocessed data of 6FF40. We notice that the apparent resistivity data roughly indicate the variation of the true resistivity, but around 4850 ft the apparent resistivity R_a is much higher than the true resistivity R_t , which results from the "skin effect" [9]. From 4927 to 4955 ft, R_a is substantially lower than R_t ,

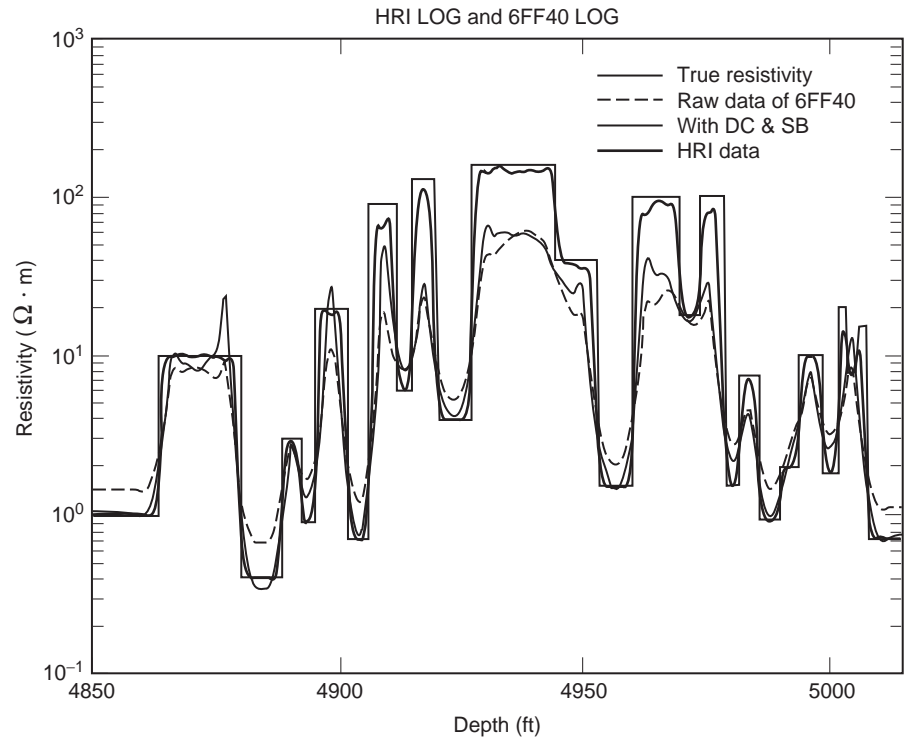


Figure 2. Apparent resistivity responses of a different tool in the Oklahoma benchmark. The improvement of resolution ability of the HR1 tool is significant.

which is caused by the so-called shoulder effect. The shoulder effect arises when two adjacent low-resistance layers generate strong signals, even though the tool is not in these two regions. Around 5000 ft, there are a number of thin layers, but the tool's response fails to indicate them. This failure results from the tool's limited resolution, which is represented in terms of the smallest thickness that can be identified by the tool.

The blue line is the processed 6FF40 data after skin effect boosting and a three-point deconvolution. Skin effect boosting is based on Eq. (19), which is solved iteratively for the true conductivity from the apparent conductivity. The three-point deconvolution is performed under the assumption that the convolution in Eq. (30) is almost linear [10]. These two methods do improve the final results to some degree, but they also cause spurious artifacts observed near 4880 ft, since the two effects are considered separately. The green curve is the response of the HRI (high-resolution induction) tool (trademark of Halliburton) [11]. A complex coil configuration is used to optimize the geometric factor. After the raw data are obtained, a nonlinear deconvolution based on the X signal is performed. The improvement in the final results is significant.

In 1991 Schlumberger Company released its AIT (array induction image tool), which uses eight induction coil arrays operating at different frequencies [12]. The deconvolutions are performed in both radial and vertical directions, and a quantitative two-dimensional image of formation resistivity is possible after a large number of measurements [13,14].

The aforementioned data processing techniques are based on the inverse deconvolution filter, which is computationally effective and easily run in real time on a logging

truck computer. An alternative approach is to use inverse scattering theory, which is becoming increasingly practical and promising with the development of high-speed computers [8,15].

Besides the induction method, there are other methods, such as electrode methods and propagation methods. Induction methods are suitable for the freshwater mud, oil-base mud, or air-filled boreholes, since the little or no conductivity in the borehole has a lesser effect on the measurement. If the mud is very conductive, it will generate a strong signal at the receiver and hence seriously degrade the tool's ability to make a deep reading. In such a case, electrode methods are preferable, since the conductive mud places the electrodes into better electrical contact with the formation. In the electrode methods, very low frequencies ($\ll 1000$ Hz) are used and Laplace's equation is solved instead of the Helmholtz equation. The typical tools are DLL (dual laterolog) and SFL (spherical focusing log), both from Schlumberger. The dual laterolog is intended for both deep and shallow measurements, while the SFL is for shallow measurements [16–19].

In addition, there are many tools mounted on pads to perform shallow measurements on the borehole wall. These may be just button electrodes mounted on a metallic pad. Due to their small size, they have high resolution but a shallow depth of investigation. Their high-resolution capability can be used to map out fine stratifications on the borehole wall. When four pads are equipped with these button electrodes, the resistivity logs they measure can be correlated to obtain the dip of a geologic bed. An example of this is the SHDT (stratigraphic high-resolution dip-meter tool), also from Schlumberger [20].

When an array of buttons are mounted on a pad, they can be used to generate a resistivity image of the borehole

wall for formation evaluation, such as dips, cracks, and stratigraphy. Such a tool is called a formation microscanner (FMS) and is available from Schlumberger [21].

For oil-based mud the SHDT does not work well, and microinduction sensors have been mounted on a pad to dipping bed evaluation. Such a tool is known as the OBMDT (oil-based mud dipmeter tool) and is manufactured by Schlumberger [22,23].

Sometimes information is needed relating not only to the conductivity but also to the dielectric permittivity. In such cases, the EPT (electromagnetic wave propagation tool), from Schlumberger can be used. The working frequency of EPT can be as high as hundreds of megahertz to 1 GHz. At such high frequencies, the real part of ϵ' is dominant, as follows:

$$\epsilon' = \epsilon + i \frac{\sigma}{\omega} \quad (35)$$

EPT measurements provide information about dielectric permittivity and hence can better distinguish fresh water from oil. Water has a much higher dielectric constant ($80\epsilon_0$) compared to oil ($2\epsilon_0$). Phase delays at two receivers are used to infer the wave phase velocity and hence the permittivity. Interested readers can find materials on these methods in Refs. 24 and 25.

Other techniques in electrical well logging include the use of borehole radar. In such a case, a pulse is sent to a transmitting antenna in the borehole, and the pulse echo from the formation is measured at the receiver. Borehole radar finds application in salt domes where the electromagnetic loss is low. In addition, the nuclear magnetic resonance (NMR) technique can be used to detect the percentage of free water in a rock formation. The NMR signal in a rock formation is proportional to the spin echos from free protons that abound in free water. An example of such a tool is the PNMT (pulsed nuclear magnetic resonance tool), from Schlumberger [26].

2. GROUND PENETRATING RADAR

Another outgrowth of subsurface EM methods is ground penetrating radar (GPR). Because of its numerous advantages, GPR has been widely used in geological surveying, civil engineering, artificial target detection, and some other areas.

The GPR design is largely application oriented. Even though various systems have different applications and considerations, their advantages can be summarized as follows: (1) because the frequency used in GPR is much higher than that used in the induction method, GPR has a higher resolution; (2) since the antennas do not need to touch the ground, rapid surveying can be achieved; (3) the data retrieved by some GPR systems can be interpreted in real time; and (4) GPR is potentially useful for organic contaminant detection and nondestructive detection [27–31].

On the other hand, GPR has some disadvantages, such as shallow investigation depth and site-specific applicability. The working frequency of GPR is much higher than

that used in the induction method. At such high frequencies, the soil is usually very lossy. Even though there is always a tradeoff between the investigation depth and resolution, a typical depth is no more than 10 m and highly dependent on soil type and moisture content.

The working principle of GPR is illustrated in Fig. 3a [28]. The transmitter T generates transient or continuous EM waves propagating in the underground. Whenever a change in the electrical properties of underground regions is encountered, the wave is reflected and refracted. The receiver R detects and records the reflected waves. From the recorded data, information pertaining to the depth, geometry, and material type can be obtained. As a simple example, we use Figs. 3b and 3c to illustrate how the data are recorded and interpreted. The underground contains one interface, one cavity, and one lens. At a single position, the receiver signals at different times are stacked along the time axis. After completing the measurement at one position, the procedure is iterated at all subsequent positions. The final results are presented in a two-dimensional map, which is called an echo sounder-type display. To locate objects or interfaces, we need to know the wave speed in the underground medium. The wavespeed in a medium of relative dielectric permittivity ϵ_r is

$$C_s = \frac{C_0}{\sqrt{\epsilon_r}} \quad (36)$$

where $C_0 = 3 \times 10^8$ m/s. Usually, the transmitter and the receiver are close enough, and thus the wave's path of propagation is considered to be vertical. The depth of the

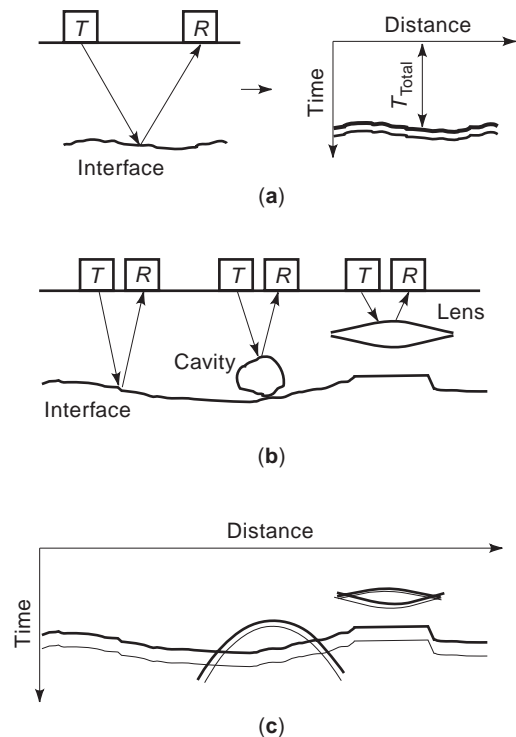


Figure 3. Working principle of the GPR. (Redrawn from Ref. 20.)

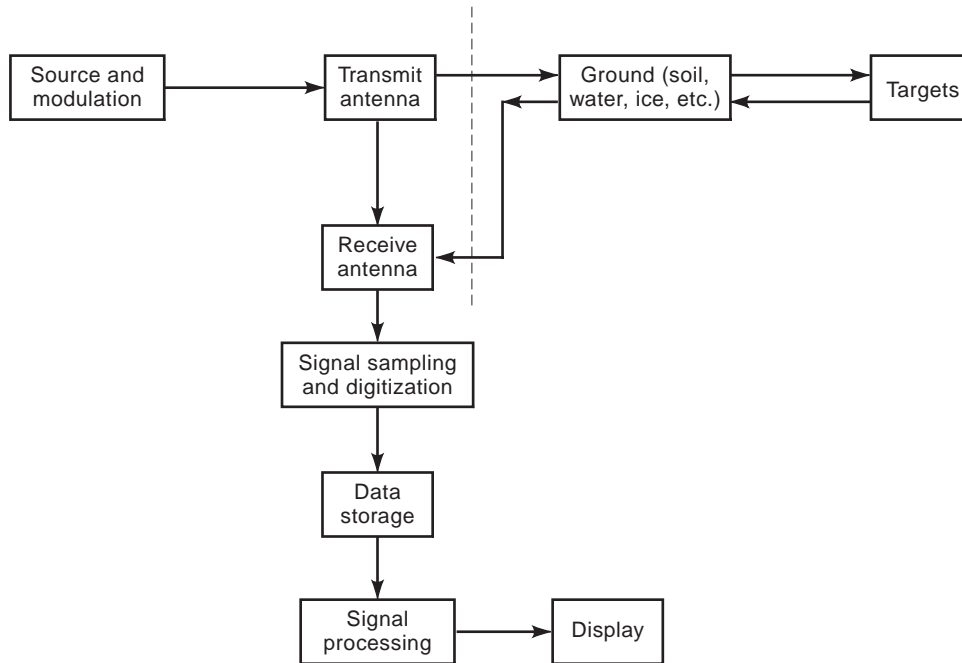


Figure 4. Block diagram showing operation of a typical baseband GPR system. (Redrawn from Ref. 19.)

interface is approximated as

$$D = 0.5 \times (C_s \times T_{\text{total}}) \quad (37)$$

where T_{total} is the total wave propagation time.

A practical GPR system is much more complicated, and a block diagram of a typical baseband GPR system is shown in Fig. 4. Generally, a successful system design should meet the following requirements [27]: (1) efficient coupling of the EM energy between antenna and ground, (2) adequate penetration with respect to the target depth, (3) sufficiently large return signal for detection, and (4) adequate bandwidth for the desired resolution and noise control.

The working frequency of typical GPR ranges from a few tens of megahertz to several gigahertz, depending on the application. The usual tradeoff holds—the wider the bandwidth, the higher the resolution but the shallower the penetration depth. A good choice is usually a tradeoff between resolution and depth. Soil properties are also critical in determining the penetration depth. It is observed experimentally that the attenuation of different soils can vary substantially. For example, dry desert and nonporous rocks have very low attenuation (about 1 dBm^{-1} at 1 GHz) while the attenuation of sea water can be as high as 300 dBm^{-1} at 1 GHz. Some typical applications and preferred operating frequencies are listed in Table 1 [27].

To meet the requirements of different applications, a variety of modulation schemes have been developed and can be classified in the following three categories: amplitude modulation (AM), frequency-modulated continuous wave (FMCW), and continuous wave (CW). We will briefly

discuss the advantages and limitations of each modulation scheme.

There are two types of AM transmission used in GPR. For investigation of low-conductivity medium, such as ice and fresh water, a pulse modulated carrier is preferred [32,33]. The carrier frequency can be chosen as low as tens of megahertz. Since the reflectors are well spaced, a relatively narrow transmission bandwidth is needed. The receiver signal is demodulated to extract the pulse envelope. For shallow and high-resolution applications, such as the detection of buried artifacts, a baseband pulse is preferred

Table 1. Desired Frequencies for Different Applications^a

Material	Typical Desired Penetration Depth ^b	Approximate Maximum Frequency at Which Operation May Be Usefully Performed
Cold pure fresh-water ice	10 km	10 MHz
Temperate pure ice	1 km	2 MHz
Saline ice	10 m	50 MHz
Fresh water	100 m	100 MHz
Sand (desert)	5 m	1 GHz
Sandy soil	3 m	1 GHz
Loam soil	3 m	500 MHz
Clay (dry)	2 m	100 MHz
Salt (dry)	1 km	250 MHz
Coal	20 m	500 MHz
Rocks	20 m	50 MHz
Walls	0.3 m	10 GHz

^aRedrawn from Ref. 19.

^bThe figures used under this heading are the depths at which radar probing gives useful information, taking into account the attenuation normally encountered and the nature of the reflectors of interest.

to avoid the problems caused by high soil attenuation, since most of the energy is in the low-frequency band. A pulsetrain with a duration of 1 to 2 ns, a peak amplitude of about 100 V, and a repetition rate of 100 kHz is applied to the broadband antenna. The received signal is downconverted by sampling circuits before being displayed. There are three primary advantages of the AM scheme: (1) it provides a real-time display without the need for subsequent signal processing, (2) the measurement time is short, and (3) it is implemented with small equipment but without synthesized sources and hence is cost-effective. But for the AM scheme, it is difficult to control the transmission spectrum, and the signal-to-noise ratio (SNR) is not as good as that of the FMCW method.

For the FMCW scheme, the frequency of the transmitted signal is continuously swept, and the receiver signal is mixed with a sample of transmitted signals. The Fourier transform of the received signal results in a time-domain pulse that represents the receiver signal if a time domain pulse were transmitted. The frequency sweep must be linear in time to minimize signal degradation, and a stable output is required to facilitate signal processing. The major advantage of the FMCW scheme is easier control of the signal spectrum; the filter technique can be applied to obtain better SNR. A shortcoming of the FMCW system is the use of a synthesized frequency source, which means that the system is expensive and bulky. Additional data processing is also needed before the display [34,35].

A continuous-wave scheme was used in the early development of GPR, but now it is mainly employed in synthetic aperture and subsurface holography techniques [36–38]. In these techniques, measurements are performed at a single or a few well-spaced frequencies over an aperture at the ground surface. The wave front extrapolation technique is applied to reconstruct the underground region, with the resolution depending on the size of the aperture. Narrowband transmission is used and hence high-speed data capture is avoided. The difficulty of the CW scheme comes from the requirement for accurate scanning of the two-dimensional aperture. The operation frequencies should be carefully chosen to minimize resolution degradation [27].

Antennas play an important role in the system performance. An ideal antenna should introduce the least distortion on the signal spectrum or else one for which the modification can be easily compensated. Unlike the antennas used in the atmospheric radar, the antennas used in GPR should be considered as loaded. The radiation pattern of the GPR antenna can be quite different due to the strong interaction between the antenna and ground. Separate antennas for transmission and reception are commonly used, because it is difficult to make a switch that is fast enough to protect the receiver signal from the direct coupling signal. The direct breakthrough signals will seriously reduce the SNR and hence degrade the system performance. Moreover, in a separate-antenna system, the orientation of antennas can be carefully chosen to reduce further the cross-coupling level.

Except for the CW scheme, other modulation types require wideband transmission, which greatly restricts the choice of antenna. Four types of antennas, including ele-

ment antennas, traveling-wave antennas, frequency-independent antennas, and aperture antennas, have been used in GPR designs. Element antennas, such as monopoles, cylindrical dipoles, and biconical dipoles, are easy to fabricate and hence widely used in GPR systems. Orthogonal arrangement is usually chosen to maintain a low level of cross-coupling. To overcome the limitation of narrow transmission bandwidth of thin dipole or monopole antennas, the distributed loading technique is used to expand the bandwidth at the expense of reduced efficiency [39–42].

Another commonly used antenna type is traveling-wave antennas, such as long-wire antennas, V-shaped antennas, and rhombic antennas. The traveling-wave antennas distinguish themselves from standing-wave antennas in the sense that the current pattern is a traveling wave rather than a standing wave. Standing-wave antennas, such as half-wave dipoles, are also referred to as *resonant antennas* and are narrowband, while traveling-wave antennas are broadband. The disadvantage of traveling-wave antennas is that half of the power is wasted at the matching resistor [43,44].

Frequency-independent antennas are often preferred in the impulse GPR system. It has been proved that if the antenna geometry is specified only by angles, its performance will be independent of frequency. In practice, we have to truncate the antenna, due to its limited outer size and inner feeding region, which determine the lower bound and upper bound of the frequency, respectively. In general, this type of antenna will introduce nonlinear phase distortion, which results in an extended pulse response in the time domain [27,45]. A phase correction procedure is needed if the antenna is used in a high-resolution GPR system.

A wire antenna is a one-dimensional antenna that has a small effective area and hence lower gain. For some GPR systems, higher gain or a more directive radiation pattern is sometimes required. Aperture antennas, such as horn antennas, are preferred because of their large effective area. A ridge design is used to improve the bandwidth and reduce the size. Ridged horns with gain better than 10 dBm over a range of 0.3–2 GHz and VSWR lower than 1.5 over a range of 0.2–1.8 GHz have been reported [46]. Since many aperture antennas are fed via waveguides, the phase distortion associated with the different modulation schemes needs to be considered.

Generally, antennas used in GPR systems require broad bandwidth and linear phase in the operating frequency range. Since the antennas work in close proximity to the ground surface, the interaction between them must be taken into account.

Signal processing is one of the most important parts in the GPR system. Some modulation schemes directly give the time-domain data while the signals of other schemes need to be demodulated before the information is available. Signal processing can be performed in the time domain, frequency domain, or space domain. A successful signal processing scheme usually consists of a combination of several kinds of processing techniques that are applied at different stages. Here, we outline some basic signal processing techniques involved in the GPR system.

The first commonly used method is noise reduction by time averaging. It is assumed that the noise is random, so that the noise can be reduced to $1/Nt$ by averaging N identical measurements spaced in time t . This technique only works for random noise but has no effect on the clutter.

Clutter reduction can be achieved by subtracting the mean. This technique is performed under the assumption that the statistics of the underground are independent of position. A number of measurements are performed at a set of locations over the same material type to obtain the mean, which can be considered as a measure of the system clutter.

The frequency filter technique is commonly used in the FMCW system. Signals that are not in the desired information bandwidth are rejected. Thus the SNR of the FMCW scheme is usually higher than that of the AM scheme.

In some very lossy soils, the return signal is highly attenuated, which makes interpretation of the data difficult. If the material attenuation information is available, the results can be improved by exponentially weighting the time traces to counter the decrease in signal level due to the loss. In practice, this is done by using a specially designed amplifier. Caution is needed when using this method, since the noise can also increase in such a system [27].

3. MAGNETOTELLURIC METHODS

The basic idea of the magnetotelluric (MT) method is to use natural electromagnetic fields to investigate the electrical conductivity structure of Earth. This method was first proposed by Tikhonov in 1950 [47]. In his paper, the author assumed that Earth's crust is a planar layer of finite conductivity lying on an ideally conducting substrate, such that a simple relation between the horizontal components of the E and H fields at the surface can be found [48]

$$i\mu_0\omega H_x \cong E_y\gamma \cosh(\gamma l) \tag{38}$$

where

$$\gamma = (i\sigma\mu_0\omega)^{(1/2)} \tag{39}$$

The author used the data observed at Tucson (Arizona) and Zui (former USSR) to compute the value of conductivity and thickness of the crust that best fit the first four harmonics. For Tucson, the conductivity and thickness were about 4.0×10^{-3} S/m and 1000 km, respectively. For Zui, the corresponding values are 3.0×10^{-1} S/m and 100 km.

The MT method distinguishes itself from other subsurface EM methods because very-low-frequency natural sources are used. The actual mechanisms of natural sources have been under discussion for a long time, but now it is well accepted that the sources of frequency above 1 Hz are thunderstorms while the sources below 1 Hz are due to the current system in the magnetosphere caused by solar activity. In comparison with other EM methods, the use of a natural source is a major advantage. The frequencies used

range from 0.001 Hz to 10^4 Hz, and thus investigation depth can be achieved from 50 to 100 m to several kilometers. Installation is much simpler and has less impact on the environment. The MT method has also proved very useful in some extreme areas where conventional seismic methods are expensive or ineffective. The main shortcomings of the MT method are limited resolution and difficulty in achieving a high SNR, especially in electrically noisy areas [49].

In MT measurements, the time-varying horizontal electrical and magnetic fields at the surface are recorded simultaneously. The data recorded in the time domain are first converted into frequency-domain data by using a fast Fourier transform (FFT). An apparent conductivity is then defined as a function of frequency. To interpret the data, theoretical apparent conductivity curves are generated by the model studies. The model whose apparent conductivity curve best matches the measurement data is taken as an approximate model of the subsurface.

Since it is more convenient and meaningful to represent the apparent conductivity in terms of skin depth, we first introduce the concept of skin depth by studying a simple case. The model we use is shown in Fig. 5, which consists of a homogeneous medium with conductivity σ and a uniform current sheet flowing along the x direction in the xy plane. If the density of current at the ground ($z = 0$) is represented as [50]

$$I_x = \cos \omega t, I_y = I_z = 0 \tag{40}$$

then the current density at depth z is

$$I_x = e^{-z\sqrt{2\omega\mu\sigma}/2} \cos(\omega t - z\sqrt{2\omega\mu\sigma}), I_y = I_z = 0 \tag{41}$$

When z increases, we notice that the amplitude of the current decreases exponentially with respect to z ; meanwhile the phase retardation progressively increases. To describe the amplitude attenuation, we introduce the skin depth p as [50]

$$p = \sqrt{\frac{2}{\omega\mu\sigma}} \tag{42}$$

where the current amplitude decreases to e^{-1} of the current at the surface. Since the unit in Eq. (42) is not

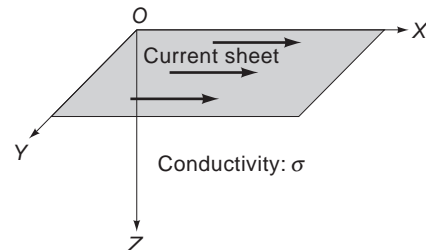


Figure 5. Current sheet flowing on Earth's surface, used to explain magnetotelluric method.

convenient, some prospectors like to use the following formula

$$p = \frac{1}{2\pi} \sqrt{10\rho T} \quad (43)$$

where T is the period in seconds, ρ is the resistivity in Ωm , and the unit for p is km. The skin depth indicates the depth the wave can penetrate the ground. For example, if the resistivity of the underground is 10 S/m and the period of the wave is 3 s, the skin depth is 2.76 km. Subsurface methods seldom have such a great penetration depth.

The data interpretation of the MT method is based on the model studies. Earth is modeled as a two- or three-layer medium. For a two-layer model as shown in Fig. 6, the general expression for the field can be written as [50] $0 \leq z \leq h$:

$$E_z = Ae^{a\sqrt{\sigma_1}z} + be^{-a\sqrt{\sigma_1}z} \quad (44a)$$

$$H_y = e^{i\pi/4} \sqrt{2\sigma_1 T} [-Ae^{a\sqrt{\sigma_1}z} + Be^{-a\sqrt{\sigma_1}z}] \quad (44b)$$

$h \leq z \leq \infty$:

$$E_x = e^{-a\sqrt{\sigma_2}z} \quad (45a)$$

$$H_x = e^{i\pi/4} \sqrt{2\sigma_2 T} e^{-a\sqrt{\sigma_2}z} \quad (45b)$$

where h is the thickness of the upper layer, and σ_1, σ_2 are the conductivities of the upper and lower layers, respectively. Matching the boundary conditions at $z = h$, we have

$$A = \frac{\sqrt{\sigma_1} - \sqrt{\sigma_2}}{2\sqrt{\sigma_1}} e^{-ah(\sqrt{\sigma_1} + \sqrt{\sigma_2})} \quad (46)$$

$$B = \frac{\sqrt{\sigma_1} + \sqrt{\sigma_2}}{2\sqrt{\sigma_1}} e^{ah(\sqrt{\sigma_1} - \sqrt{\sigma_2})} \quad (47)$$

Since we are interested in the ratio between the E and H field on the surface, Eq. (44) can be rewritten for $z = 0$ as

$$\frac{E_x}{H_y} = \frac{1}{\sqrt{2\sigma_1 T}} \frac{M}{N} e^{-i(\pi/4 + \phi + \psi)} \quad (48)$$

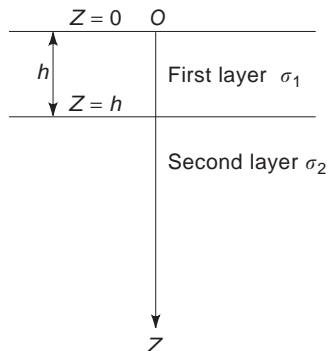


Figure 6. Two-layer model of Earth's crust, used to demonstrate the responses of the magnetotelluric method.

where M, N, ϕ , and ψ satisfy the following equations:

$$M \cos \phi = \left(\frac{1}{p_1} \cosh \frac{h}{p_1} + \frac{1}{p_2} \sinh \frac{h}{p_1} \right) \cos \frac{h}{p_1} \quad (49a)$$

$$M \sin \phi = \left(\frac{1}{p_1} \sinh \frac{h}{p_1} + \frac{1}{p_2} \cosh \frac{h}{p_1} \right) \sin \frac{h}{p_1} \quad (49b)$$

$$N \cos \psi = \left(\frac{1}{p_1} \sinh \frac{h}{p_1} + \frac{1}{p_2} \cosh \frac{h}{p_1} \right) \cos \frac{h}{p_1} \quad (49c)$$

$$N \sin \psi = \left(\frac{1}{p_1} \cosh \frac{h}{p_1} + \frac{1}{p_2} \sinh \frac{h}{p_1} \right) \sin \frac{h}{p_1} \quad (49d)$$

where p_1, p_2 are the skin depths of upper and lower layers, respectively.

For a multilayer medium, after applying the same procedure, we can obtain exactly the same relation between E_x and H_y as shown in Eq. (48) except that the expressions for M, N, ϕ , and ψ are much more complicated. Because of this similarity, we have

$$\left| \frac{E_x}{H_y} \right| = \frac{1}{\sqrt{2\sigma_a T}} = \frac{M}{N} \frac{1}{\sqrt{2\sigma_1 T}} \quad (50)$$

where σ_a is defined as the apparent conductivity. If the medium is homogeneous, the apparent conductivity is equal to the true conductivity. In a multilayer medium the apparent conductivity is an average effect of all layers.

To obtain a better understanding of the preceding formulas, we first study two two-layer models and their corresponding apparent conductivity curves, as shown in Fig. 7 (51). At very low frequencies, the wave can easily penetrate the upper layer, and thus its conductivity has little effect on the apparent conductivity. Consequently, the apparent resistivity approaches the true resistivity of the lower layer. As the frequency increases, less energy can penetrate the upper layer due to the skin effect, and thus the effect from the upper layer is dominant. As a result, the apparent resistivity is asymptotic to ρ_1 . Comparing the two curves, we note that both of them change smoothly, and for the same frequency, case A has lower

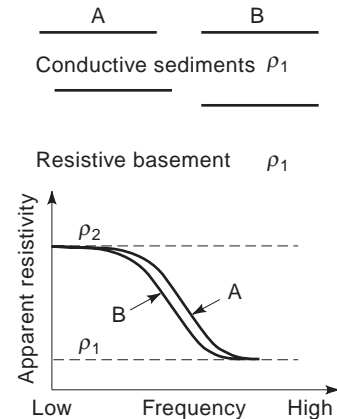


Figure 7. Diagrammatic two-layer apparent resistivity curves for the models shown. (Redrawn from Ref. 43.)

apparent resistivity than case B, since the conductive sediments of case B are thicker.

Our next example is a three-layer model as shown in Fig. 8 [51]. The center layer is more conductive than the two adjacent ones. As expected, the curve approaches ρ_1 and ρ_2 at each end. The existence of the center conductive bed is obvious from the curve, but the apparent resistivity never reaches the true resistivity of the center layer, since its effect is averaged by the effects from the other two layers.

So far we have only discussed the horizontally layered medium, which is a one-dimensional model. In practice, two-dimensional or even three-dimensional structures are often encountered. In a 2D case, the conductivity changes not only along the z direction but also along one of the horizontal directions. The other horizontal direction is called the “strike” direction. If the strike direction is not in the x or y direction, we obtain a general relation between the horizontal field components as [51]

$$E_x = Z_{xx}H_x + Z_{xy}H_y \tag{51a}$$

$$E_y = Z_{yx}H_x + Z_{yy}H_y \tag{51b}$$

Since $E_x, E_y, H_x,$ and H_y are generally out of phase, $Z_{i,j}$ are complex numbers. It can also be shown that $Z_{i,j}$ have the following properties:

$$Z_{xx} + Z_{yy} = 0 \tag{52}$$

$$Z_{xy} - Z_{yx} = \text{constant} \tag{53}$$

A simple vertical layer model and its corresponding curves are shown in Fig. 9 [51]. In Fig. 9b, the apparent resistivity with respect to $E_{||}$ changes slowly from ρ_1 to ρ_2 because of the continuity of H_{\perp} and $E_{||}$ across the interface. On the other hand, the apparent resistivity corresponding to E_{\perp} has an abrupt change across the contact, since the E_{\perp} is discontinuous at the interface. The relative amplitude of H_{\perp} varies significantly around the interface and approaches a constant at a large distance, as shown in

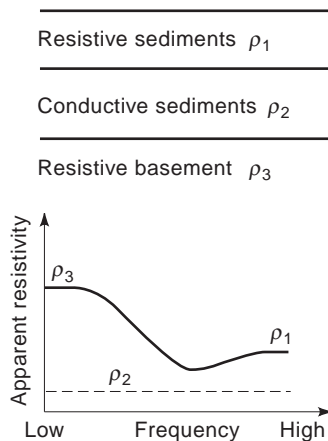


Figure 8. Diagrammatic three-layer apparent resistivity curve for the model shown. (Redrawn from Ref. 43.)

Fig. 9d. This is caused by the change in current density near the interface, as shown in Fig. 9f. We also observe that H_z appears near the interface, as shown in Fig. 9c. The reason is that the partial derivative of $E_{||}$ with respect to \perp direction is nonzero.

We have discussed the responses in some idealized models. For more complicated cases, their response curves can be obtained by forward modeling. Since the measurement data are in the time domain, we need to convert them into the frequency domain data by using a Fourier transform. In practice, five components are measured. There are four unknowns in Eqs. (51a) and (51b), but only two equations. This difficulty can be overcome by making use of the fact that $Z_{i,j}$ changes very slowly with frequency. In fact, $Z_{i,j}$ is computed as an average over a frequency band that contains several frequency sample points. A commonly used method is given in Ref. 52, according to which Eq. (51a) is rewritten as

$$\langle E_x A^* \rangle = Z_{xx} \langle H_x A^* \rangle + Z_{xy} \langle H_y A^* \rangle \tag{54}$$

and

$$\langle E_x B^* \rangle = Z_{xx} \langle H_x B^* \rangle + Z_{xy} \langle H_y B^* \rangle \tag{55}$$

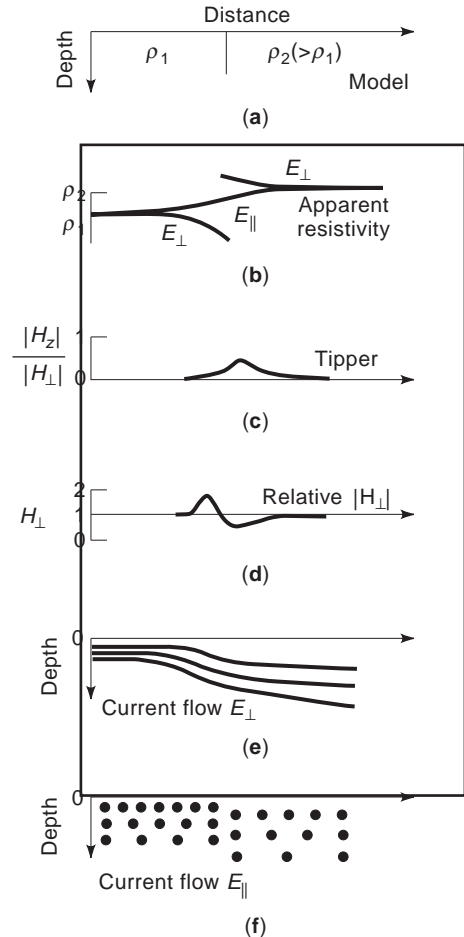


Figure 9. Diagrammatic response curves for a simple vertical contact at frequency f . (Redrawn from Ref. 43.)

where A^* and B^* are the complex conjugates of any two of the horizontal field components. The cross-powers are defined as

$$\langle AB^* \rangle_{(\omega_1)} = \frac{1}{\Delta\omega} \int_{\omega_1 - (\Delta\omega/2)}^{\omega_1 + (\Delta\omega/2)} AB^* d\omega \quad (56)$$

There are six possible combinations, and the pair (H_x, H_y) is preferred in most cases due to its greater degree of independence. Solving Eqs. (54) and (55), we have

$$Z_{xx} = \frac{\langle E_x A^* \rangle \langle H_y B^* \rangle - \langle E_x B^* \rangle \langle H_y A^* \rangle}{\langle H_x A^* \rangle \langle H_y B^* \rangle - \langle H_x B^* \rangle \langle H_y A^* \rangle} \quad (57a)$$

and

$$Z_{xy} = \frac{\langle E_x A^* \rangle \langle H_x B^* \rangle - \langle E_x B^* \rangle \langle H_x A^* \rangle}{\langle H_y A^* \rangle \langle H_x B^* \rangle - \langle H_y B^* \rangle \langle H_x A^* \rangle} \quad (57b)$$

Applying the same procedure to Eq. (51b), we have

$$Z_{yx} = \frac{\langle E_y A^* \rangle \langle H_y B^* \rangle - \langle E_y B^* \rangle \langle H_y A^* \rangle}{\langle H_x A^* \rangle \langle H_y B^* \rangle - \langle H_x B^* \rangle \langle H_y A^* \rangle} \quad (57c)$$

and

$$Z_{yy} = \frac{\langle E_y A^* \rangle \langle H_x B^* \rangle - \langle E_y B^* \rangle \langle H_x A^* \rangle}{\langle H_y A^* \rangle \langle H_x B^* \rangle - \langle H_y B^* \rangle \langle H_x A^* \rangle} \quad (57d)$$

After obtaining $Z_{i,j}$, they can be substituted into Eqs. (51a) and (51b) to solve for the other pair (E_x, E_y) , which is then used to check the measurement data. The difference is due either to noise or to measurement error. This procedure is usually used to verify the quality of the measured data.

4. AIRBORNE ELECTROMAGNETIC METHODS

Airborne EM methods (AEMs) are widely used in geologic surveys and prospecting for conductive ore bodies. These methods are suitable for large area surveys because of their speed and cost-effectiveness. They are also preferred in some areas where access is difficult, such as swamps or ice-covered areas. In contrast to ground EM methods, airborne EM methods are usually used to outline large-scale structures while ground EM methods are preferred for more detailed investigations [53].

The difference between airborne and ground EM systems results from the technical limitations inherent in the use of aircraft. The limited separation between transmitter and receiver determines the shallow investigation depth, usually from 25 to 75 m. Even though greater penetration depth can be achieved by placing the transmitter and receiver on different aircraft, the disadvantages are obvious.

The transmitters and receivers are usually 200–500 ft above the surface. Consequently, the amplitude ratio of the primary field to the secondary field becomes very small

and thus the resolution of airborne EM methods is not very high. The operating frequency is usually chosen from 300 to 4000 Hz. The lower limit is set by the transmission effectiveness, and the upper limit is set by the skin depth.

Based on different design principles and application requirements, many systems have been built and operated all over the world since the 1940s. Despite the tremendous diversity, most airborne EM systems can be classified in one of the following categories according to the quantities measured: phase component measuring systems, quadrature systems, rotating field systems, and transient response systems [54].

For a phase component measuring system, the in-phase and quadrature components are measured at a single frequency and recorded as parts per million (ppm) of the primary field. In the system design, vertical loop arrangements are preferred, since they are more sensitive to the steeply dipping conductor and less sensitive to the horizontally layered conductor [55]. Accurate maintenance of transmitter-receiver separation is essential and can be achieved by fixing the transmitter and receiver at the two wingtips. Once this requirement is satisfied, a sensitivity of a few ppm can be achieved [54]. A diagram of the phase component measuring system is shown in Fig. 10 [55]. A balancing network associated with the reference loop is used to buck the primary field at the receiver. The receiver signal is then fed to two phase-sensitive demodulators to obtain the in-phase and quadrature components. Lowpass filters are used to reject very-high-frequency signals that do not originate from the earth. The data are interpreted by matching the curves obtained from the modeling. Some response curves of typical structures are given in Ref. 56.

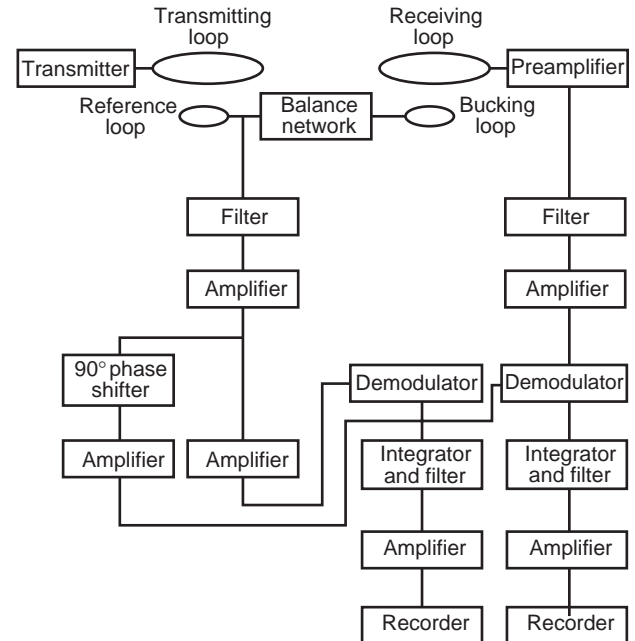


Figure 10. Block diagram showing operation of a typical phase component measuring system. (Redrawn from Ref. 43.)

The quadrature system employs a horizontal coil placed on the airplane as a transmitter and a vertical coil towed behind the plane as a receiver. The vertical coil is referred to as a “towed bird.” Since only the quadrature component is measured, the separation distance is less critical. To reduce the noise further, an auxiliary horizontal coil, powered with a current 90° out of phase with respect to the main transmitter current, is used to cancel the secondary field caused by the metal body of the aircraft. Since the response at a single frequency may have two interpretations, two frequencies are used to eliminate the ambiguity. The lower frequency is about 400 Hz, and the higher one is chosen from 2000 to 2500 Hz. The system responses in different environments can be obtained by model studies. Reference 57 gives a number of curves for thin sheets and shows the effects of variation in depth, dipping angle, and conductivity.

In an airborne system, it is hard to control the relative rotation of receiver and transmitter. The rotating field method is introduced to overcome this difficulty. Two transmitter coils are placed perpendicular to each other on the plane, and a similar arrangement is used for the receiver. The two transmitters are powered with current of the same frequency shifted 90° out of phase, so that the resultant field rotates about the axis, as shown in Fig. 11 [58]. The two receiver signals are phase-shifted by 90° with respect to each other, and then the in-phase and quadrature differences at the two receivers are amplified and recorded by two different channels. Over a barren area, the outputs are set to zero. When the system is within a conducting zone, anomalies in the conductivity are indicated by nonzero outputs in both the in-phase and quadrature channels. The noise introduced by the fluctuation of orientation can be reduced by this scheme, but it is relatively expensive and the data interpretation is complicated by the complex coil system [58].

The fundamental problem of airborne EM systems is the difficulty in detecting the relatively small secondary

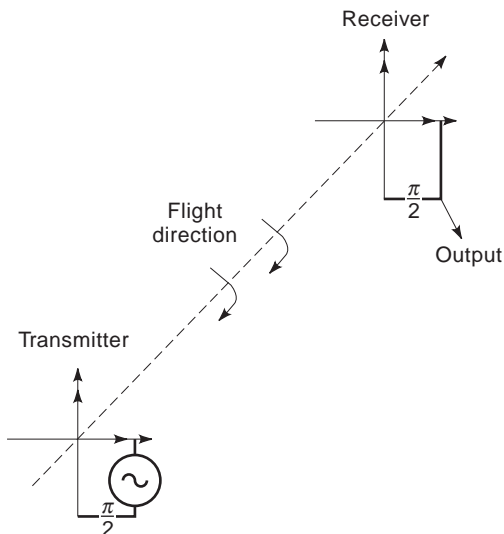


Figure 11. Working principle of the rotary field AEM system. (Redrawn from Ref. 50.)

field in the presence of a strong primary field. This difficulty can be alleviated by using the transient field method. A well-known system based on the transient field method is INPUT (induced pulsed transient) [59], which was designed by Barringer during the 1950s. In the INPUT system, a large horizontal transmitting coil is placed on the aircraft and a vertical receiving coil is towed in the bird with the axis aligned with the flight direction.

The working principle of INPUT is shown in Fig. 12 [60]. A half-sine wave with a duration of about 1.5 ms and quiet period of about 2.0 ms is generated as the primary field, as shown in Fig. 12a. If there are no conducting zones, the current in the receiver is induced only by the primary field, as shown in Fig. 12b. In the presence of conductive anomalies, the primary field will induce an eddy current. After the primary field is cut off, the eddy current decays exponentially. The duration of the eddy current is proportional to the conductivity anomalies, as shown in Fig. 12c. The higher the conductivity, the longer the duration time. The decay curve in the quiet period is sampled successively in time by six channels and then displayed on a strip, as shown in Fig. 13. As we can see,

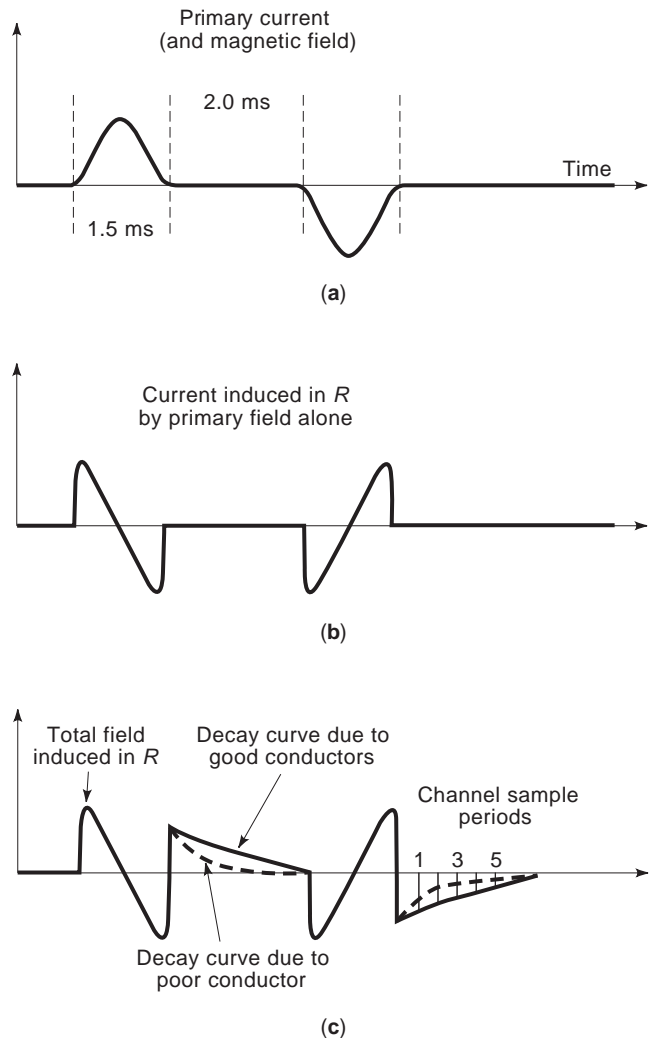


Figure 12. Working principle of the INPUT system. (Redrawn from Ref. 52.)

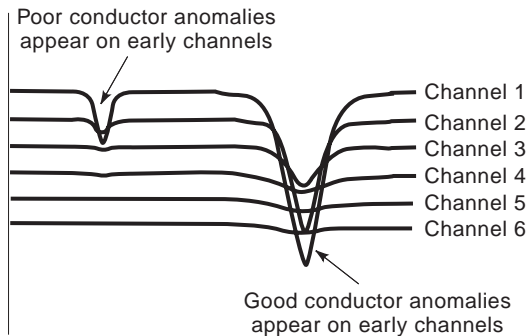


Figure 13. Responses of different anomalies appearing on different channels. (Redrawn from Ref. 52.)

the distortion caused by a good conductor appears in all the channels, while the distortion corresponding to a poor conductor only registers on the early channels.

Since the secondary field can be measured more accurately in the absence of the primary field, transient systems provide greater investigation depths, which may reach 100 m under favorable conditions. In addition, they can also provide a direct indication of the type of conductor encountered [58].

On the other hand, this system design gives rise to other problems inherent in the transient method. Since the eddy current in the quiet period becomes very small, a more intense source has to be used in order to obtain the same signal level as that in the continuous-wave method. The circuitry for the transient system is much more complicated, and it is more difficult to reject the noise due to the wideband property of the transient signal.

BIBLIOGRAPHY

- C. M. Swift, Jr., Fundamentals of the electromagnetic method, in M. N. Nabighian, ed., *Electromagnetic Methods in Applied Geophysics: Theory*, Society of Exploration Geophysicists, Tulsa, OK, 1988.
- H. G. Doll, Introduction to induction logging and application to logging of wells drilled with oil based mud, *J. Petroleum Technol.* 1:148–162 (1949).
- J. H. Moran and K. S. Kunz, Basic theory of induction logging and application to study of two-coil sondes, *Geophysics* 27(6):829–858 (1962).
- S. J. Thandani and H. E. Hall, Propagated geometric factors in induction logging, *Trans. SPWLA*, Vol. 2, Paper WW, 1981.
- B. Anderson, Induction sonde response in stratified medium, *The Log Analyst* XXIV(1):25–31.
- W. C. Chew, Response of a current loop antenna in an invaded borehole, *Geophysics* 49:81–91 (1984).
- J. R. Lovell, *Finite Element Method in Resistivity Logging*, Schlumberger Technology Corp., Ridgefield, CT, 1993.
- W. C. Chew and Q. H. Liu, Inversion of induction tool measurements using the distorted Born iterative method and CG-FFHT, *IEEE Trans. Geosci. Remote Sens.* 32(4):878–884 (1994).
- S. Gianzero and B. Anderson, A new look at skin effect, *The Log Analyst* 23(1):20–34 (1982).
- L. C. Shen, Effects of skin-effect correction and three-point deconvolution on induction logs, *The Log Analyst* (July–Aug.) 217 (1989).
- R. Strickland et al., New developments in the high resolution induction log, *Trans. SPWLA*, Vol. 2, Paper ZZ, 1991.
- T. D. Barber and R. A. Rosthal, Using a multiarray induction tool to achieve high resolution logs with minimum environmental effects, *Trans. SPE*, Paper SPE 22725, 1991.
- G. P. Grove and G. N. Minerbo, An adaptive borehole correction scheme for array induction tools, presented at the 32nd *Ann. SPWLA Symp.*, Midland, TX, 1991.
- Schlumberger Educational Services, *AIT Array Induction Image Tool*, 1992.
- R. Freedman and G. N. Minerbo, Maximum entropy inversion of induction log data, *Trans. SPE* 5:381–394, Paper SPE 19608, 1989.
- S. J. Grimaldi, P. Poupon, and P. Souhaite, The dual laterolog- R_{xo} tool, *Trans. SPE* 2:1–12, Paper SPE 4018, 1972.
- R. Chemali et al., The shoulder bed effect on the dual laterolog and its variation with the resistivity of the borehole fluid, *Trans. SPWLA*, Paper UU, 1983.
- Q. Liu, B. Anderson, and W. C. Chew, Modeling low frequency electrode-type resistivity tools in invaded thin beds, *IEEE Trans. Geosci. Remote Sens.* 32(3):494–498 (1994).
- B. Anderson and W. C. Chew, SFL interpretation using high speed synthetic computer generated logs, *Trans. SPWLA*, Paper K, 1985.
- Y. Chauvel, D. A. Seeburger, and C. O. Alfonso, Application of the SHDT stratigraphic high resolution dipmeter to the study of depositional environments, *Trans. SPWLA*, Paper G, 1984.
- A. R. Badr and M. R. Ayoub, Study of a complex carbonate reservoir using the Formation MicroScanner (FMS) tool, *Proc 6th Middle East Oil Show*, Bahrain, March, 1989, pp. 507–516.
- R. L. Kleinberg et al., Microinduction sensor for the oil-based mud dipmeter, *SPE Formation Evaluation*, Dec. 1988, Vol. 3, pp. 733–742.
- W. C. Chew and R. L. Kleinberg, Theory of microinduction measurements, *IEEE Trans. Geosci. Remote Sens.* 26:707–719 (1988).
- W. C. Chew and S. Gianzero, Theoretical investigation of the electromagnetic wave propagation tool, *IEEE Trans. Geosci. Remote Sens.* GE-19:1–7 (1981).
- W. C. Chew et al., An effective solution for the response of electrical well-logging tool in a complex environment, *IEEE Trans. Geosci. Remote Sens.* 29:303–313 (1991).
- D. D. Griffin, R. L. Kleinberg, and M. Fukuhara, Low-frequency NMR spectrometer measurement, *Sci. Technol.* 4:968–975 (1993).
- D. J. Daniels, D. J. Gunton, and H. F. Scott, Introduction to subsurface radar, *IEEE Proc.* 135:278–320 (1988).
- D. K. Butler, Elementary GPR overview, *Proc. Government Users Workshop on Ground Penetrating Radar Application and Equipment*, 1992, pp. 25–30.
- W. H. Weedon and W. C. Chew, Broadband microwave inverse scattering for nondestructive evaluation, *Proc. 20th Annual Review Progress Quantitative Nondestructive Evaluation*, Drunswick, ME, 1993.
- F. C. Chen and W. C. Chew, Time-domain ultra-wideband microwave imaging radar system, *Proc. IEEE Instrum. Meas. Technol. Conf.*, St. Paul, MN, 1998, pp. 648–650.
- F. C. Chen and W. C. Chew, Development and testing of the time-domain microwave nondestructive evaluation system,

- Review of Progress in Quantitative Evaluation*, Vol. 17, Plenum, New York, 1998, pp. 713–718.
32. M. Walford, Exploration of temperate glaciers, *Phys. Bull.* **36**:108–109 (1985).
 33. D. K. Hall, A review of the utility of remote sensing in Alaskan permafrost studies, *IEEE Trans. Geosci. Remote Sens.* **GE-20**:390–394 (1982).
 34. A. Z. Botros et al., Microwave detection of hidden objects in walls, *Electron. Lett.* **20**:379–380 (1984).
 35. P. Dennis and S. E. Gibbs, Solid-state linear FM/CW radar systems—their promise and their problems, *Proc. IEEE MTT Symp.*, 1974, pp. 340–342.
 36. A. P. Anderson and P. J. Richards, Microwave imaging of sub-surface cylindrical scatters from cross-polar backscatter, *Electron. Lett.* **13**:617–619 (1977).
 37. K. Lizuka et al., Hologram matrix radar, *Proc. IEEE*, **64**:1493–1504 (1976).
 38. N. Osumi and K. Ueno, Microwave holographic imaging method with improved resolution, *IEEE Trans. Anten. Propag.* **AP-32**: 1018–1026 (1984)
 39. M. C. Bailey, Broad-band half-wave dipole, *IEEE Trans. Anten. Propag.* **AP-32**:410–412 (1984).
 40. R. P. King, Antennas in material media near boundaries with application to communication and geophysical exploration, *IEEE Trans. Anten. Propag.* **AP-34**:483–496 (1986).
 41. M. Kanda, A relatively short cylindrical broadband antenna with tapered resistive loading for picosecond pulse measurements, *IEEE Trans. Anten. Propag.*, **AP-26**:439–447 (1978).
 42. C. A. Balanis, *Antenna Theory*, Wiley, New York, 1997, Chap. 9.
 43. P. Degauque and J. P. Thery, Electromagnetic subsurface radar using the transient radiated by a wire antenna, *IEEE Trans. Geosci. Remote Sens.* **GE-24**:805–812 (1986).
 44. C. A. Balanis, *Antenna Theory*, Wiley, New York, 1997, Chap. 10.
 45. C. A. Balanis, *Antenna Theory*, Wiley, New York, 1997, Chap. 11.
 46. J. L. Kerr, Short axial length broadband horns, *IEEE Trans. Anten. Propag.* **AP-21**:710–714 (1973).
 47. A. N. Tikhonov, Determination of the electrical characteristics of the deep strata of the earth's crust, *Proc. Acad. Sci. USSR* **83**(2):295–297 (1950).
 48. J. R. Wait, Theory of magneto-telluric field, *J. Res. Natl. Bur. Stand. D, Radio Propagation*, **66D**:509–541 (1962).
 49. K. Vozoff, The magnetotelluric method, in M. N. Nabighian, ed., *Electromagnetic Methods in Applied Geophysics: Application*, Society of Exploration Geophysicists, Tulsa, OK, 1988.
 50. L. Cagniard, Basic theory of the magneto-telluric method of geophysical prospecting, *Geophysics* **18**:605–635 (1952).
 51. K. Vozoff, The magnetotelluric method in the exploration of sedimentary basins, *Geophysics* **37**:98–141 (1972).
 52. T. Madden and P. Nelson, A defense of Cagniard's magneto-telluric method, *Geophysics Reprinted Series 5: Magnetotelluric Methods*, Society of Exploration Geophysicists, Tulsa, OK, 1985, pp. 89–102.
 53. G. J. Palacky and G. F. West, Airborne electromagnetic methods, in M. N. Nabighian, ed., *Electromagnetic Methods in Applied Geophysics: Theory*, Society of Exploration Geophysicists, Tulsa, OK, 1988.
 54. J. C. Gerkens, *Foundation of Exploration Geophysics*, Elsevier, New York, 1989.
 55. G. V. Keller and F. Frischknecht, *Electrical Methods in Geophysical Prospecting*, Pergamon, New York, 1966.
 56. D. Boyd and B. C. Roberts, Model experiments and survey results from a wing tip-mounted electromagnetic prospecting system, *Geophys. Proc.* **9**:411–420 (1961).
 57. N. R. Patterson, Experimental and field data for the dual frequency phase-shift method of airborne electromagnetic prospecting, *Geophysics* **26**:601–617 (1961).
 58. P. Kearey and M. Brooks, *An Introduction to Geophysical Exploration*, Blackwell Scientific, Boston, 1984.
 59. A. R. Barringer, The INPUT electrical pulse prospecting system, *Min. Cong. J.* **48**:49–52 (1962).
 60. A. E. Beck, *Physical Principles of Exploration Methods*, Macmillan, New York, 1981.

ELECTROMAGNETIC SURFACE WAVES

ZHIPENG WU
UMIST
Manchester, United Kingdom

1. INTRODUCTION

In electromagnetic waves, the term “surface wave” has been used to describe the nonradiating electromagnetic waves propagating along the interface between two media [1,2]. It has also been used to describe the electromagnetic waves propagating along the air-ground interface produced by an antenna on or near the ground surface [3–10]. Both types of surface wave will be introduced in this article, and the “surface wave” is broadly defined as the wave propagating along an interface separating two media, or an interface between air and a layered structure. The surface waves considered include

1. The Zenneck surface wave
2. Surface wave on a conductor-backed dielectric slab
3. Radial cylindrical surface wave on a flat surface
4. Axial cylindrical surface wave
5. Surface wave on a dielectric-coated conducting cylinder
6. Norton and trapped surface waves on flat ground interface
7. Surface-wave propagation over an inhomogeneous flat surface
8. Surface-wave propagation over a spherical ground

The governing equations and properties of these surface waves are presented in the following section.

2. SURFACE WAVES

2.1. Zenneck Wave

The Zenneck wave is a solution of Maxwell's equations obtained by Zenneck in 1907 [11]. It is a plane wave that

travels along an interface between two dielectric media. Consider the air–dielectric interface with the established rectangular coordinates shown in Fig. 1. The properties of the dielectric medium (medium 1) is characterized by conductivity σ_1 , permeability μ_0 , and permittivity ε_1 . The vertically polarised Zenneck wave is also a transverse magnetic (TM) plane wave with zero magnetic field in the propagation direction, z . The field components of the Zenneck wave above the surface ($x \geq 0$) in air (medium 2) with permeability μ_0 and permittivity ε_0 , are given by

$$\begin{aligned} H_{y2} &= Ae^{-u_2x}e^{-\gamma z} \\ E_{z2} &= -A \frac{u_2}{j\omega\varepsilon_0} e^{-u_2x}e^{-\gamma z} \\ E_{x2} &= A \frac{\gamma}{j\omega\varepsilon_0} e^{-u_2x}e^{-\gamma z} \end{aligned} \quad (1)$$

where A is a constant, and u_2 and γ are the propagation constants in x and z directions, respectively. The electromagnetic field components below the surface ($x < 0$) are

$$\begin{aligned} H_{y1} &= Ae^{u_1x}e^{-\gamma z} \\ E_{z1} &= A \frac{u_1}{\sigma_1 + j\omega\varepsilon_1} e^{u_1x}e^{-\gamma z} \\ E_{x1} &= A \frac{\gamma}{\sigma_1 + j\omega\varepsilon_1} e^{u_1x}e^{-\gamma z} \end{aligned} \quad (2)$$

where u_1 is the propagation constant along the x direction in the dielectric medium. The propagation constants satisfy the following equations

$$\begin{aligned} \gamma^2 + u_2^2 &= -\omega^2\mu_0\varepsilon_0 \\ \gamma^2 + u_1^2 &= j\omega\mu_0(\sigma_1 + j\omega\varepsilon_1) \\ \frac{u_1}{(\sigma_1 + j\omega\varepsilon_1)} &= -\frac{u_2}{j\omega\varepsilon_0} \end{aligned} \quad (3)$$

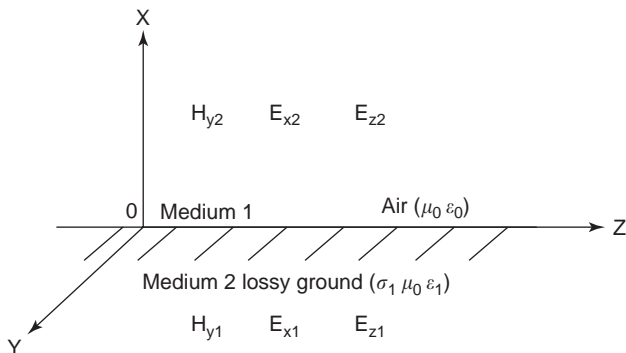


Figure 1. Zenneck wave on a planar surface separating two dielectric media.

where ω is the angular frequency of the electromagnetic wave. Solving these equations gives

$$\begin{aligned} u_1 = a_1 + jb_1 &= \frac{j\omega\mu_0(\sigma_1 + j\omega\varepsilon_1)}{\sqrt{j\omega\mu_0(\sigma_1 + j\omega\varepsilon_1) - \omega^2\mu_0\varepsilon_0}} \\ u_2 = a_2 - jb_2 &= \frac{\omega^2\mu_0\varepsilon_0}{\sqrt{j\omega\mu_0(\sigma_1 + j\omega\varepsilon_1) - \omega^2\mu_0\varepsilon_0}} \\ \gamma = \alpha + j\beta &= \sqrt{\frac{-j\omega\mu_0(\sigma_1 + j\omega\varepsilon_1)\omega^2\mu_0\varepsilon_0}{j\omega\mu_0(\sigma_1 + j\omega\varepsilon_1) - \omega^2\mu_0\varepsilon_0}} \end{aligned} \quad (4)$$

The Zenneck wave propagates along the surface and in the direction normal to the surface with two different propagation constants. The wave attenuates in both directions, particularly in the direction normal to the surface. For example, the attenuation constants a_2 , a_1 , and α of a surface wave at 300 MHz propagating over a dry ground of $\sigma_1 = 4$ and $\varepsilon_1 = 4\varepsilon_0$ are 0.167, 1.008, and 0.083 Np/m [nepers (napiers) per meter], respectively. The equal-amplitude contour of the H_y component above and below the dry ground surface with $A = 1$ is shown in Fig. 2 over the range $-5 \text{ m} < x < 5 \text{ m}$ and $0 < z < 20 \text{ m}$. The field attenuates more rapidly inside the ground. The surface wave above the surface has less attenuation. The phase velocity of the Zenneck wave is greater than the speed of light. Hence, the Zenneck surface wave is a fast wave.

On the surface, the ratio of the tangential electric field and magnetic field gives the surface impedance [1,2]:

$$Z_s = R_s + jX_s = \frac{E_{z2}(x=0)}{H_{y2}(x=0)} \quad (5)$$

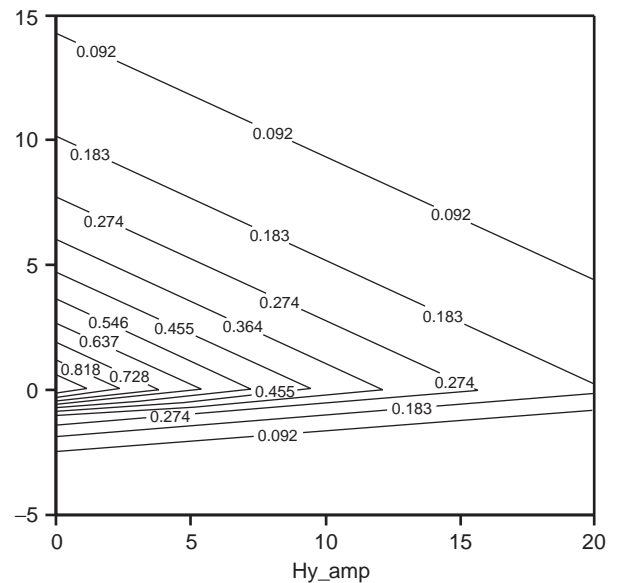


Figure 2. Contour plot of the $|H_y|$ component of the Zenneck wave above and below a dry ground of $\sigma_1 = 4$ and $\varepsilon_1 = 4\varepsilon_0$ with $A = 1$ in range $-5 \text{ m} < x < 5 \text{ m}$ and $0 < z < 20 \text{ m}$.

The surface impedance and u_2 are related by

$$Z_s = R_s + jX_s = -\frac{u_2}{j\omega\epsilon_0} = \frac{1}{\omega\epsilon_0} (b_2 + ja_2) \quad (6)$$

Hence, the attenuation constant of the surface wave along the x direction above the surface is determined by the surface reactance, and the phase constant by the surface resistance as

$$a_2 = \omega\epsilon_0 X_s; \quad b_2 = \omega\epsilon_0 R_s \quad (7)$$

In order to support a Zenneck surface wave, the dielectric medium has to be lossy so that $a_2 > 0$, which is a feature of a Zenneck wave.

2.2. Surface Wave on a Conductor-Backed Dielectric Slab

A conductor-backed dielectric slab structure, as shown in Fig. 3, is a typical example of multilayered structures. This structure is commonly used in microwave printed circuits. For simplicity, the conductor is treated as a “perfect” conductor, and the dielectric of thickness d is assumed to be lossless with a real permittivity ϵ_1 , or a relative dielectric constant ϵ_r . With these assumptions, a surface wave can propagate along the surface with

$$\gamma = j\beta; \quad u_1 = jk_x; \quad u_2 = h \quad (8)$$

For a TM surface wave, the solutions of the field components above the dielectric surface ($x \geq d$) are [12,13]

$$\begin{aligned} H_{y2} &= \frac{j\omega\epsilon_0}{h} A \sin(k_x d) e^{-h(x-d)} e^{-j\beta z} \\ E_{x2} &= -\frac{j\beta}{h} A \sin(k_x d) e^{-h(x-d)} e^{-j\beta z} \\ E_{z2} &= A \sin(k_x d) e^{-h(x-d)} e^{-j\beta z} \end{aligned} \quad (9)$$

where A is a constant, and the fields in the dielectric slab are

$$\begin{aligned} H_{y1} &= -\frac{j\omega\epsilon_1}{k_x} A \cos(k_x x) e^{-j\beta z} \\ E_{x1} &= -\frac{j\beta}{k_x} A \cos(k_x x) e^{-j\beta z} \\ E_{z1} &= A \sin(k_x x) e^{-j\beta z} \end{aligned} \quad (10)$$

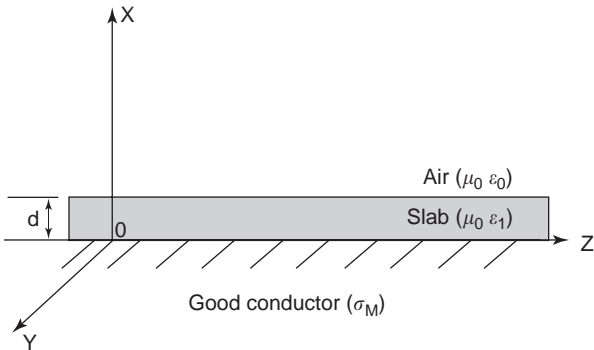


Figure 3. Surface wave on a conductor-backed dielectric slab.

The propagation constants satisfy the following equations

$$\begin{aligned} -h^2 + \beta^2 &= k_0^2 = \omega^2 \mu_0 \epsilon_0 \\ k_x^2 + \beta^2 &= \epsilon_r k_0^2 \end{aligned} \quad (11)$$

where k_0 is the wavenumber in air and k_x and h are related by the transcendental equation

$$k_x \tan(k_x d) = \epsilon_r h \quad (12)$$

with

$$k_x^2 + h^2 = (\epsilon_r - 1)k_0^2 \quad (13)$$

There exists a sequence of solutions of k_x and h , which give rise to a set of TM_n modes. The n th mode, where $n = 0, 1, 2, \dots$, has a cutoff frequency of

$$f_{c, TM_n} = \frac{nc}{2d\sqrt{\epsilon_r - 1}} \quad (14)$$

Similarly, for a transverse electric (TE) surface wave, the field components above the dielectric surface ($x \geq d$) are [12]

$$\begin{aligned} E_{y2} &= \frac{j\omega\mu_0}{h} A \cos(k_x d) e^{-h(x-d)} e^{-j\beta z} \\ H_{x2} &= -\frac{j\beta}{h} A \cos(k_x d) e^{-h(x-d)} e^{-j\beta z} \\ H_{z2} &= A \cos(k_x d) e^{-h(x-d)} e^{-j\beta z} \end{aligned} \quad (15)$$

where A is a constant, and the fields in the dielectric slab are

$$\begin{aligned} E_{y1} &= -\frac{j\omega\mu_0}{k_x} A \sin(k_x x) e^{-j\beta z} \\ H_{x1} &= \frac{j\beta}{k_x} A \sin(k_x x) e^{-j\beta z} \\ H_{z1} &= A \cos(k_x x) e^{-j\beta z} \end{aligned} \quad (16)$$

The propagation constants also satisfy Eq. (11), but k_x and h are related by the transcendental equation

$$k_x \cot(k_x d) = -h \quad (17)$$

with

$$k_x^2 + h^2 = (\epsilon_r - 1)k_0^2 \quad (18)$$

There exists, again, a sequence of solutions of k_x and h , which give rise to a set of TE_n modes. The n th mode, where $n = 1, 2, \dots$, has a cutoff frequency of

$$f_{c, TE_n} = \frac{(2n - 1)c}{4d\sqrt{\epsilon_r - 1}} \quad (19)$$

Hence, the surface wave may propagate above the dielectric slab in a sequence of $TM_0, TE_1, TM_1, TE_1, \dots$ modes if the frequency of the wave is greater than their cutoff frequencies. The phase velocities of these modes are less than the speed of light. Hence, the surface wave on a conductor-backed dielectric slab is a slow wave.

For example, a surface wave of 10 GHz on a microwave printed circuit board of $\epsilon_r = 4.4$ and $d = 0.6$ mm can propagate in TM_0 mode as the cutoff frequency of the next mode is 67.8 GHz. The k_x and h values of the mode are 385.6 rad/m and 20.6 Np/m, respectively. The surface wave attenuates slowly along the x axis at a rate of 0.0124 Np per slab thickness or 0.6 mm. The electromagnetic fields are not confined within the dielectric slab, as shown in Fig. 4 for the plot of the equal-amplitude contour of the H_y component with $A = 1000$ over the range $0 < x < 20d$ and $0 < z < 20d$. However, at 50 GHz, the fields are more confined within the dielectric slab with $k_x = 1783$ rad/m and $h = 740.5$ Np/m or 0.444 Np per slab thickness. The equal-amplitude contour plot of the H_y component with $A = 1000$ over the range $0 < x < 3d$ and $0 < z < 20d$ is shown in Fig. 5. The fields of the surface wave attenuate more rapidly as the frequency approaches the cutoff frequency of TE_1 mode.

2.3. Radial Cylindrical Surface Wave on a Flat Surface

The Zenneck wave in Section 2.1 is a plane surface wave on a flat surface with fields in $x, y,$ and z directions. A similar radial cylindrical surface wave can be set up on a flat surface with propagation and attenuation in r and x directions, as shown in Fig. 6. The electromagnetic fields

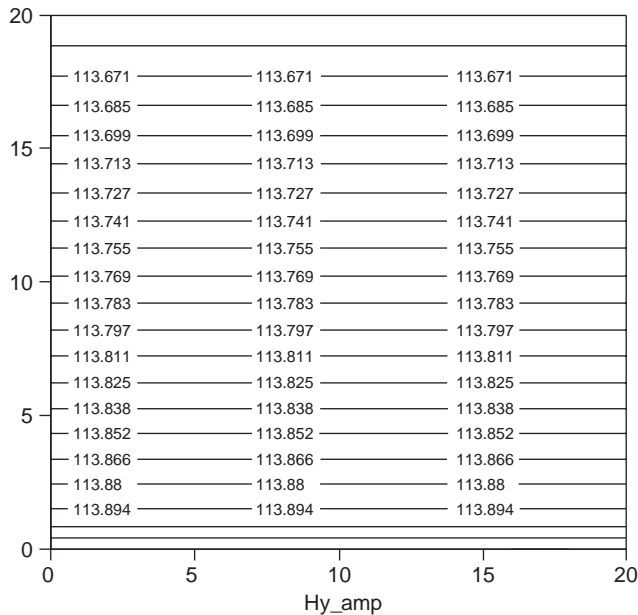


Figure 4. Contour plot of the $|H_y|$ component of the surface wave at 10 GHz above and inside the dielectric slab of $\epsilon_r = 4.4$ and $d = 0.6$ mm with $A = 1000$ in the range $0 < (x/d) < 20$ and $0 < (z/d) < 20$.

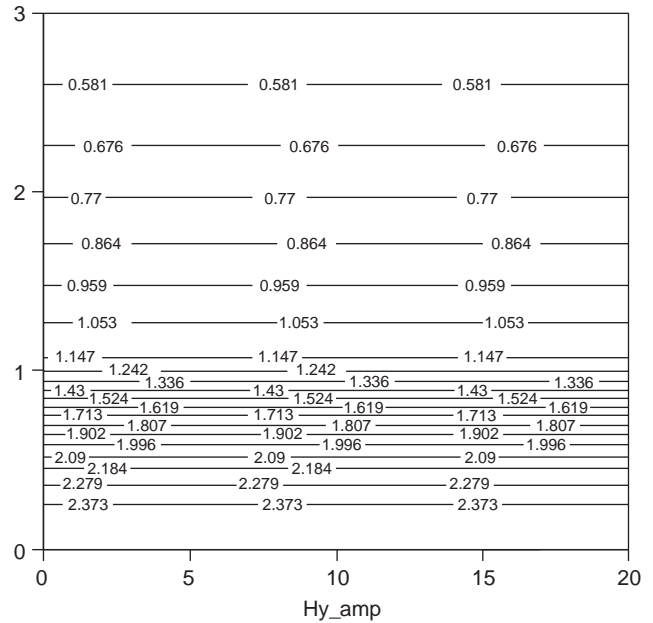


Figure 5. Contour plot of the $|H_y|$ component of the surface wave at 50 GHz above and inside the dielectric slab of $\epsilon_r = 4.4$ and $d = 0.6$ mm with $A = 1000$ in the range $0 < (x/d) < 3$ and $0 < (z/d) < 20$.

above the surface ($x \geq 0$) are [1]

$$\begin{aligned}
 H_{\phi 2} &= A e^{-u_2 x} H_1^{(2)}(-j\gamma r) \\
 E_{r 2} &= A \frac{u_2}{j\omega\epsilon_0} e^{-u_2 x} H_1^{(2)}(-j\gamma r) \\
 E_{x 2} &= A \frac{\gamma}{\omega\epsilon_0} e^{-u_2 x} H_0^{(2)}(-j\gamma r)
 \end{aligned} \tag{20}$$

where A is a constant, and $H_0^{(2)}$ and $H_1^{(2)}$ are the Hankel functions of the second kind and orders 0 and 1,

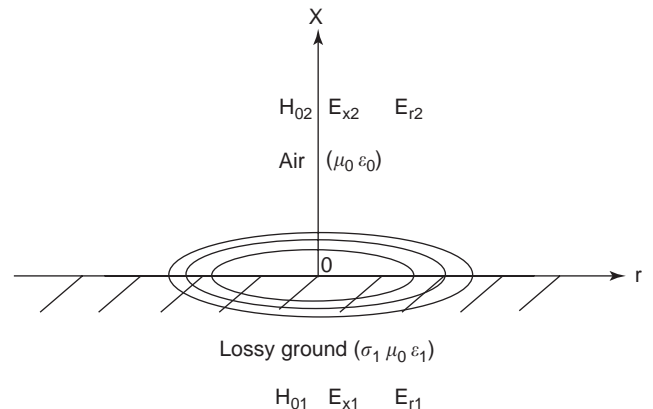


Figure 6. Planar surface with radial cylindrical surface wave.

respectively. The fields in the dielectric medium are

$$\begin{aligned} H_{\phi 1} &= Ae^{u_1 x} H_1^{(2)}(-j\gamma r) \\ E_{r1} &= -A \frac{u_1}{\sigma_1 + j\omega\epsilon_1} e^{u_1 x} H_1^{(2)}(-j\gamma r) \\ E_{x1} &= A \frac{j\gamma}{\sigma_1 + j\omega\epsilon_1} e^{u_1 x} H_0^{(2)}(-j\gamma r) \end{aligned} \tag{21}$$

where the propagation constants are determined in the same way as the Zenneck wave. For large r , we obtain

$$H_n^{(2)}(-j\gamma r) \Rightarrow \frac{e^{-\gamma r}}{\sqrt{r}} \tag{22}$$

Hence, the radial surface wave is a cylindrical wave with electric and magnetic fields proportional to $r^{-(1/2)}$ at large distances. The radial cylindrical surface wave is also a fast wave with phase velocity greater than the speed of light.

2.4. Axial Cylindrical Surface Wave

The axial cylindrical surface wave is also called the Sommerfeld–Goubau surface wave [1]. For a cylindrical dielectric structure, as shown in Fig. 7, with the radius a , conductivity σ_1 , permeability μ_0 and permittivity ϵ_1 , an axial surface wave may propagate along the air–dielectric interface in the z direction. The surface-wave fields of a TM wave outside the surface ($r \geq a$) are [1,7]

$$\begin{aligned} H_{\theta 2} &= A \frac{\omega\epsilon_0}{u_2} e^{-\gamma z} H_1^{(1)}(ju_2 r) \\ E_{z2} &= Ae^{-\gamma z} H_0^{(1)}(ju_2 r) \\ E_{r2} &= A \frac{\gamma}{ju_2} e^{-\gamma z} H_1^{(1)}(ju_2 r) \end{aligned} \tag{23}$$

where A is a constant and $H_0^{(1)}$ and $H_1^{(1)}$ are the Hankel functions of the first kind and orders 0 and 1, respectively.

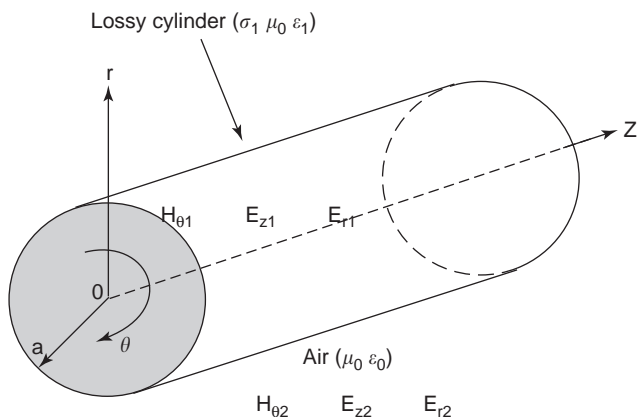


Figure 7. Cylindrical dielectric structure supporting axial cylindrical surface wave.

The fields in the dielectric cylinder are

$$\begin{aligned} H_{\theta 1} &= -A \frac{\sigma_1 + j\omega\epsilon_1}{ju_1} e^{-\gamma z} J_1(ju_1 r) \\ E_{z1} &= Ae^{-\gamma z} J_0(ju_1 r) \\ E_{r1} &= A \frac{\gamma}{ju_1} e^{-\gamma z} J_1(ju_1 r) \end{aligned} \tag{24}$$

where J_0 and J_1 are Bessel functions of the first kind, orders 0 and 1, respectively, and the propagation constants are determined in the same way as the Zenneck wave. The surface impedance of the axial cylindrical surface wave is

$$Z_s = \frac{u_2}{\omega\epsilon_0} \frac{H_0^{(1)}(ju_2 a)}{H_1^{(1)}(ju_2 a)} \tag{25}$$

For a large cylinder in which $u_2 a \gg 1$, the surface impedance can be approximated as

$$Z_s \approx \frac{u_2}{j\omega\epsilon_0} \tag{26}$$

which is the same as that of the Zenneck wave for a flat surface. Hence, for large cylinders, the axial cylindrical surface wave has propagation characteristics similar to those of the Zenneck wave on a flat surface. However, for small cylinders, the axial cylindrical surface wave may have characteristics different from those of the Zenneck wave [1].

2.5. Surface Wave on a Dielectric Coated Conducting Cylinder

Like the conductor-backed dielectric slab structure described in Section 2.2, a dielectric-coated conducting cylinder or wire as shown in Fig. 8 can support a surface wave [13]. The conductor of radius a is treated as a perfect conductor. The dielectric layer of thickness d is assumed to be lossless with a real permittivity ϵ_1 , or a relative dielectric constant ϵ_r . The propagation constants, γ in the

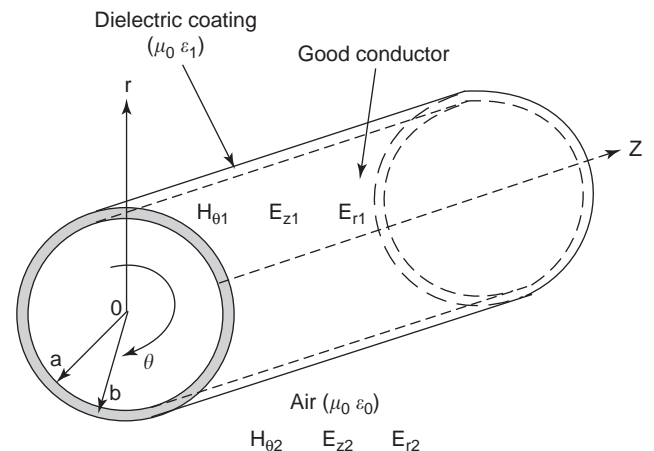


Figure 8. Dielectric-coated conducting cylinder.

z direction and u_1 and u_2 in the r direction in the dielectric layer and air medium, can be expressed as

$$\gamma = j\beta; \quad u_1 = jk_r; \quad u_2 = h \quad (27)$$

For a TM surface wave, the field components outside the dielectric surface [$r \geq (a + d)$] are

$$\begin{aligned} E_{z2} &= \frac{A}{K_0(hb)} \left[J_0(k_rb) - \frac{J_0(k_ra)}{Y_0(k_ra)} Y_0(k_rb) \right] K_0(hr) e^{-j\beta z} \\ E_{r2} &= \frac{j\beta A}{hK_0(hb)} \left[J_0(k_rb) - \frac{J_0(k_ra)}{Y_0(k_ra)} Y_0(k_rb) \right] K'_0(hr) e^{-j\beta z} \\ H_{\phi 2} &= \frac{k_0}{\beta Z_0} E_{r2} \end{aligned} \quad (28)$$

where A is a constant; $b = a + d$, Y_0 and Y_1 are the Bessel functions of the second kind, orders 0 and 1, respectively; and K_0 is the modified Bessel function of the second kind and order 0. The field components in the dielectric coating layer are

$$\begin{aligned} E_{z1} &= A \left[J_0(k_rr) - \frac{J_0(k_ra)}{Y_0(k_ra)} Y_0(k_rr) \right] e^{-j\beta z} \\ E_{r1} &= -\frac{j\beta}{k_r} A \left[J'_0(k_rr) - \frac{J_0(k_ra)}{Y_0(k_ra)} Y'_0(k_rr) \right] e^{-j\beta z} \\ H_{\phi 1} &= \frac{\varepsilon_r k_0}{\beta Z_0} E_{r1} \end{aligned} \quad (29)$$

where A is a constant, and

$$\begin{aligned} -h^2 + \beta^2 &= k_0^2 = \omega^2 \mu_0 \varepsilon_0 \\ k_r^2 + \beta^2 &= \varepsilon_r k_0^2 \end{aligned} \quad (30)$$

The parameters k_x and h are the solutions of the transcendental equation

$$\frac{K'_0(hb)}{K_0(hb)} = -\frac{\varepsilon_r h J'_0(k_rb) Y_0(k_ra) - Y'_0(k_rb) J_0(k_ra)}{k_r J_0(k_rb) Y_0(k_ra) - Y_0(k_rb) J_0(k_ra)} \quad (31)$$

with

$$k_r^2 + h^2 = (\varepsilon_r - 1) k_0^2 \quad (32)$$

There exists a sequence of solutions of k_x and h , corresponding to TM_n modes where $n = 0, 1, 2, \dots$. The cutoff frequency of the TM_0 mode is 0.

Similarly, for a TE surface wave, the field components outside the dielectric surface ($x \geq d$) are

$$\begin{aligned} H_{z2} &= \frac{A}{K_0(hb)} \left[J_0(k_rb) - \frac{J'_0(k_ra)}{Y'_0(k_ra)} Y_0(k_rb) \right] K_0(hr) e^{-j\beta z} \\ H_{r2} &= \frac{j\beta A}{hK_0(hb)} \left[J_0(k_rb) - \frac{J'_0(k_ra)}{Y'_0(k_ra)} Y_0(k_rb) \right] K'_0(hr) e^{-j\beta z} \\ E_{\phi 2} &= -\frac{k_0 Z_0}{\beta} H_{r2} \end{aligned} \quad (33)$$

and those inside the dielectric layer are

$$\begin{aligned} H_{z1} &= A \left[J_0(k_rr) - \frac{J'_0(k_ra)}{Y'_0(k_ra)} Y_0(k_rr) \right] e^{-j\beta z} \\ H_{r1} &= -\frac{j\beta}{k_r} A \left[J'_0(k_rr) - \frac{J'_0(k_ra)}{Y'_0(k_ra)} Y'_0(k_rr) \right] e^{-j\beta z} \\ E_{\phi 1} &= -\frac{\varepsilon_r k_0 Z_0}{\beta} H_{r1} \end{aligned} \quad (34)$$

The parameters k_x and h of the TE wave are the solutions of the following transcendental equation

$$\frac{K'_0(hb)}{K_0(hb)} = -\frac{\varepsilon_r h J'_0(k_rb) Y'_0(k_ra) - Y'_0(k_rb) J'_0(k_ra)}{k_r J_0(k_rb) Y'_0(k_ra) - Y_0(k_rb) J'_0(k_ra)} \quad (35)$$

There exists again a sequence of solutions of k_x and h , which give rise to a set of TE_n modes, such as that in a conductor-backed dielectric slab. As an approximation, the cutoff frequencies of the TE_n and TM_n modes can be estimated using the same formulas as those for the conductor-backed dielectric slabs.

For example, a surface wave of 50 GHz on a dielectric-coated cylinder with $d = 0.6$ mm, $\varepsilon_r = 4.4$, and $a = 10$ mm can propagate in TM_0 mode with $k_r = 1762$ rad/m and $h = 789.4$ Np/m or 0.473 Np per dielectric thickness. The equal-amplitude contour plot of the H_ϕ component with $A = 1000$ over the range $0 < r < 3d$ and $0 < z < 20d$ is shown in Fig. 9. The fields of the surface wave attenuate rapidly with the increase of radial distance r at this frequency. The plot is very similar to that for a conductor-backed dielectric slab shown in Fig. 5.

2.6. Norton and Trapped Surface Waves on Flat Ground Interface

When a short antenna radiates at a point above the ground surface of Earth, the general solution of electromagnetic fields in air consists of both "space wave" and "surface wave" [7–10]. The properties of the ground can be characterized either by conductivity σ_1 , permeability μ_0 , and permittivity ε_1 for a homogenous ground, or by the surface impedance Z_s , or the normalized surface impedance $\Lambda_s = Z_s/Z_0 = \text{constant } \Delta_0$, where $Z_0 = 120\pi$ for loaded ground, corrugated ground [2], and multilayered structures [7,9]. The surface impedance can be obtained by

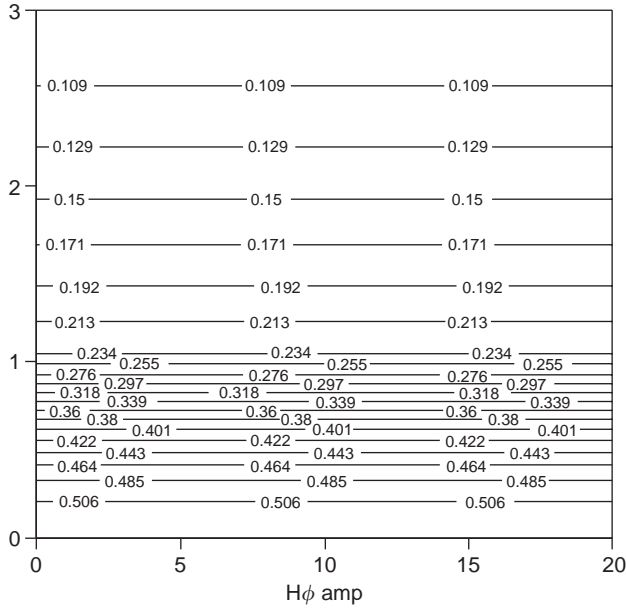


Figure 9. Contour plot of the $|H_\phi|$ component of the surface wave at 50 GHz above and inside the dielectric coating layer of $\epsilon_r = 4.4$ and $d = 0.6$ mm on a conducting cylinder of radius 10 mm with $A = 1000$ in the range $0 < (r/d) < 3$ and $0 < (z/d) < 20$.

considering a plane-wave incidence onto the ground surface.

The historical development of the solution to such a radiation problem has not been straightforward since the

Highly Capacitive	Capacitive	Inductive (Normal Ground)	Highly Inductive
$-\pi/2 \leq \arg(Z_s) < -\pi/4$	$-\pi/4 \leq \arg(Z_s) < 0$	$0 \leq \arg(Z_s) < \pi/4$	$\pi/4 \leq \arg(Z_s) \leq \pi/2$
$-3\pi/2 \leq \phi_w < -\pi$	$-\pi \leq \phi_w < -\pi/2$	$-\pi/2 \leq \phi_w < 0$	$0 \leq \phi_w \leq \pi/2$

work of Sommerfeld in 1909 [1,5,7,14–17]. But the subject is now well understood [10,17], and the electromagnetic wave propagation over the ground surface can be accurately predicted [18]. The “surface wave” in the solution dominates when the antenna is on or close to the ground surface. For simplicity, the short antenna is considered to be on the ground surface as shown in Fig. 10. In this case,

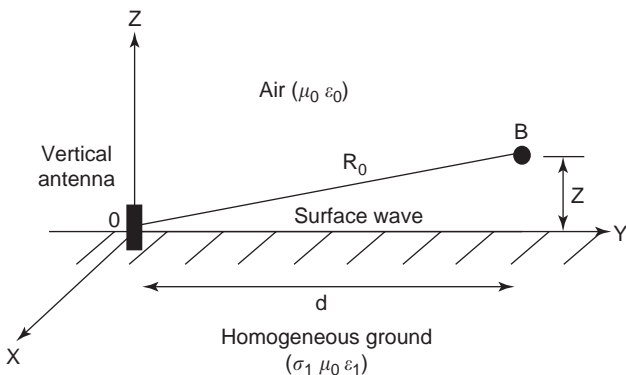


Figure 10. Short antenna radiation on a homogeneous flat ground surface.

the “space wave” component vanishes. The short antenna is further considered to be vertically orientated so that it produces a TM wave with a vertical electric field component [7–10]

$$E_z = A \frac{e^{-jk_0 R_0}}{R_0} F(w) \tag{36}$$

where A is a constant, k_0 is the wavenumber in free space, R_0 is the distance from the antenna to the receiving point B at height z , and $F(w)$ is the Sommerfeld attenuation function given by

$$F(w) = 1 - j(\pi w)^{1/2} e^{-w} \operatorname{erfc}(jw^{1/2}) \tag{37}$$

with the numerical distance

$$w = -\frac{jk_0 R_0}{2} \Delta_s^2 \left(1 + \frac{z}{\Delta_s R_0}\right)^2 = |w| e^{j\phi_w} \tag{38}$$

and the complementary error function,

$$\operatorname{erfc}(jw^{1/2}) = \frac{2}{\sqrt{\pi}} \int_{jw^{1/2}}^{\infty} e^{-u^2} du \tag{39}$$

The modulus of the numerical distance $|w|$ is proportional to the physical distance R_0 and $|Z_s|^2$. Its argument is related to the argument of Z_s as listed below for different types of ground [8]:

For the range $0 \leq \operatorname{Re}(w) \leq 2.4$ and $-1 \leq \operatorname{Im}(w) \leq 3$, the equal-amplitude contour plots of $F(w)$ in dB and $\arg(F(w))$ in degrees are shown in Fig. 11. Both $|F(w)|$ and $\arg(F(w))$ have smooth variations when $\phi_w < 0$. However, when $\phi_w < 0$, several dips appear in the vicinity of those w values that make $|F(w)|$ small or zero. The amplitudes of $|F(w)|$ in dB are again shown in Fig. 12 for $10^{-2} \leq |w| \leq 10^3$ and $-90^\circ \leq \phi_w \leq 80^\circ$. The variation of $|F(w)|$ is now examined in terms of series expansion for large values of $|w|$.

For $-2\pi \leq \phi_w \leq 0$, or highly capacitive, capacitive, and inductive ground surfaces, the Sommerfeld attenuation function for large $|w|$ can be expanded to

$$F(w) = -\frac{1}{2w} - \frac{1.3}{(2w)^2} - \frac{1.3 \cdot 5}{(2w)^3} - \frac{1.3 \cdot 5 \cdot 7}{(2w)^4} - \dots \tag{40}$$

$$= F_{\text{Norton}}(w)$$

The wave associated with the attenuation function given in this series $[F_{\text{Norton}}(w)]$ is referred to as the *Norton surface wave* [7–10]. The Norton surface wave or its field

components decay as the inverse square of the distance. However, for $0 \leq \phi_w \leq \pi/2$ or a highly inductive surface, $F(w)$ has a different expansion for large $|w|$

$$F(w) = F_{\text{trapped}}(w) + F_{\text{Norton}}(w) \tag{41}$$

where

$$F_{\text{trapped}}(w) = -2j(\pi w)^{1/2}e^{-w} \tag{42}$$

An additional term [$F_{\text{trapped}}(w)$] has appeared in the series. This term dominates at short distances, but it attenuates exponentially as the distance increases. $F_{\text{trapped}}(w)$ has a maximum modulus value at $|w| = 0.5 \cos(\phi_w)$. The wave associated with this additional term of attenuation function is referred to as the *trapped surface wave* [7–10]. The dips in Fig. 11 are therefore the result of interference between the trapped and Norton surface waves. Unlike the Norton surface wave, the trapped wave or its field components decay inversely with the product of the square root of the distance and the exponential of this distance. A highly inductive surface impedance can be obtained by loading a metal surface with a thin dielectric

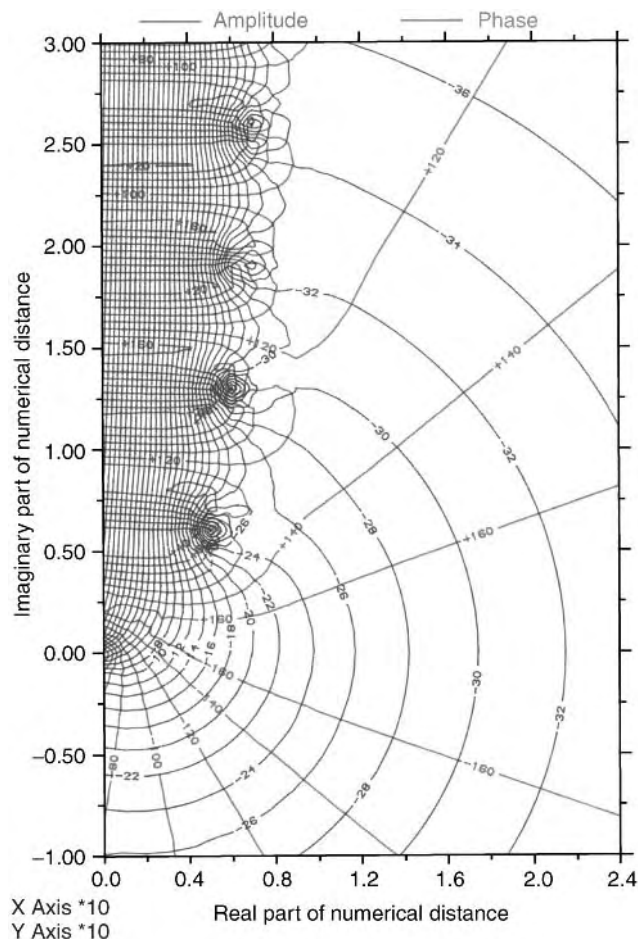


Figure 11. $|F(w)|$ and $\arg(F(w))$ contour plots for $0 \leq \text{Re}(w) \leq 2.4$ and $-1 \leq \text{Im}(w) \leq 3$. (This figure is available in full color at <http://www.mrw.interscience.wiley.com/erfme>.)

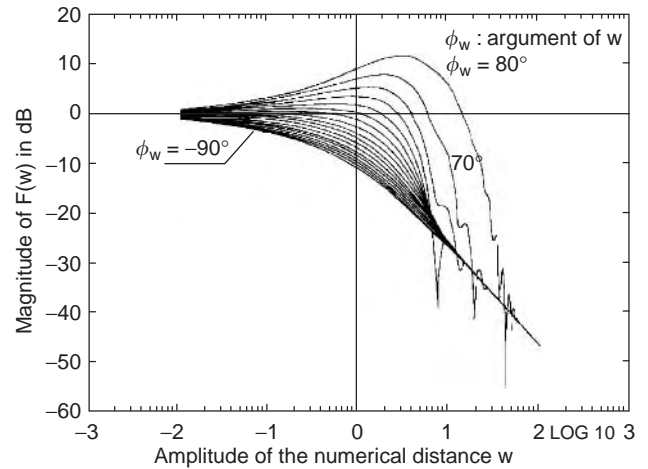


Figure 12. Amplitudes of $|F(w)|$ in dB for $10^{-2} \leq |w| \leq 10^3$ and $-90^\circ \leq \phi_w \leq 80^\circ$.

layer or by corrugating a metal surface [2]. Such surfaces can therefore support a trapped surface wave.

For a normal dry ground with $\sigma_1 = 0.01$ and $\epsilon_r = 4$, the predicted electric field E_z of the surface wave at 10 MHz on the ground surface with transmitted power of 1 kW and antenna gain $G_t = 1$ using the software package in described in Ref. 18 is shown in Fig. 13 over a horizontal distance of 1–60 km. The amplitude of the electric field attenuates monotonically against the distance for the homogeneous (inductive) ground. The surface wave is thus a Norton surface wave. For comparison, a prediction of the electric field E_z of the surface wave over a highly inductive ground with $\Delta_0 = 0.01 + j0.09$ at the same frequency with the same transmitted power and antenna gain is shown in Fig. 14. It can be seen that $|E_z|$ does not decrease monotonically, but varies against distance as a result of the interference of Norton and trapped surface waves. Comparison between Figs. 13 and 14 shows that the surface wave on the ground surface is much stronger when the surface impedance is highly inductive.

The surface wave on the ground surface has a height gain factor when the receiving point is considered to move from the ground surface to a height z . The height gain

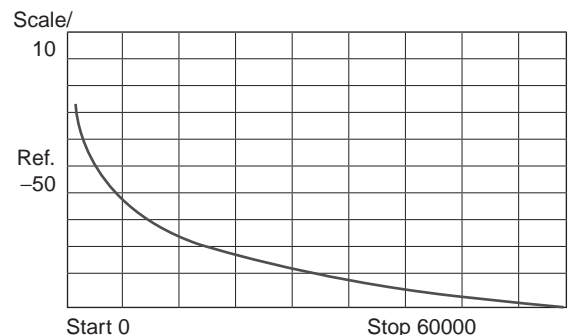


Figure 13. Prediction of surface-wave propagation at 10 MHz over a dry flat ground surface with $\sigma_1 = 0.01$ and $\epsilon_r = 4$: $|E_z|$ in dB versus horizontal distance.

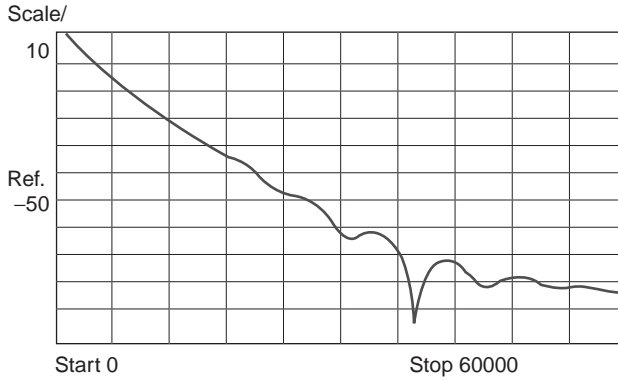


Figure 14. Prediction of surface-wave propagation at 10 MHz over a highly inductive ground surface with $\Delta_0 = 0.01 + j0.09$: $|E_z|$ in dB versus horizontal distance.

factor is given by

$$G = 1 + jk_0 \Delta_0 z \tag{43}$$

For a highly capacitive or capacitive ground, the electric field tends to increase when the receiving point is raised. On the other hand, for a normal homogeneous ground or a highly inductive ground, the electric field tends to decrease as the receiving height is increased.

2.7. Surface Wave Propagation over an Inhomogeneous Flat Surface

If the flat ground surface is inhomogeneous along the path of propagation as shown in Fig. 15, the normalised surface impedance Δ_s will not be a constant, but a function of position. For the TM wave considered in Section 2.6 with the antenna on the ground surface, the Sommerfeld attenuation function in Eq. (36) has to be replaced by an attenuation factor $F(d)$, where d is the distance to the antenna, which takes into account the effect of boundary discontinuities along the propagation path. The vertical electric field on the inhomogeneous ground surface then becomes [7,9,10]

$$E_z = A \frac{e^{-jk_0 R_0}}{R_0} F(d) \tag{44}$$

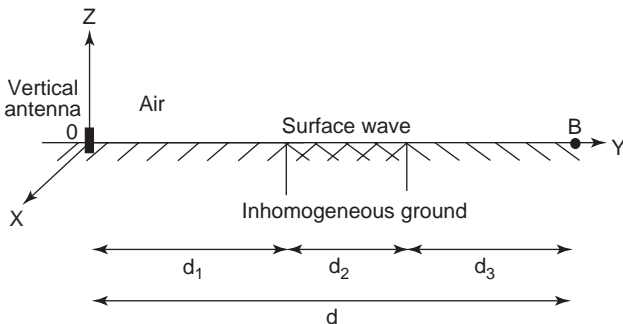


Figure 15. Short antenna radiation on an inhomogeneous flat ground surface.

The attenuation factor is given by the integral equation

$$F(d) = 1 - \left(\frac{jk_0 d}{2\pi} \right)^{1/2} \int_0^d \Delta_s(y) F(y) \frac{dy}{[y(d-y)]^{1/2}} \tag{45}$$

where y is the distance from a point on the propagation path to the antenna. The integral equation can be solved numerically [10]. $F(d)$ can also be expressed in other forms of the integral equation, or in closed forms for special cases [10]. The propagation of the surface wave along the inhomogeneous path can thus be predicted.

Figure 16 shows an example prediction of the surface-wave propagation along a land-sea-land-sea-land mixed path over a range of 30 km using the software package in described in Ref. 18. The surface wave has a frequency of 10 MHz. Each mixed-path section has a length of 6 km. The electrical properties of the land are $\sigma = 0.01$ and $\epsilon_r = 4$, and those of the sea are $\sigma = 4$ and $\epsilon_r = 80$. The well-known “sea gain” phenomenon in ground-wave propagation can be seen from the prediction.

2.8. Surface-Wave Propagation over a Spherical Ground

If the curvature of Earth’s surface is taken into consideration, the surface wave guided along the curvature of Earth as shown in Fig. 17 can also be modeled [7,10,19–26]. For the TM wave considered in Section 2.6 with the antenna and the receiving points both on the ground surface, the electric field normal to the surface of the spherical Earth model with radius a at angle θ away from the antenna at $\theta = 0$ can be expressed as

$$E_r(\theta) = A \frac{e^{-jk_0 a \theta}}{a \theta} F(\theta) \tag{46}$$

where $F(\theta)$ is the attenuation factor given by the residue series [7,10]

$$F(\theta) = e^{-j(\pi/4)} (\pi x_0)^{1/2} \sum_{s=1}^{\infty} \frac{e^{-jx_s \theta}}{t_s} \tag{47}$$

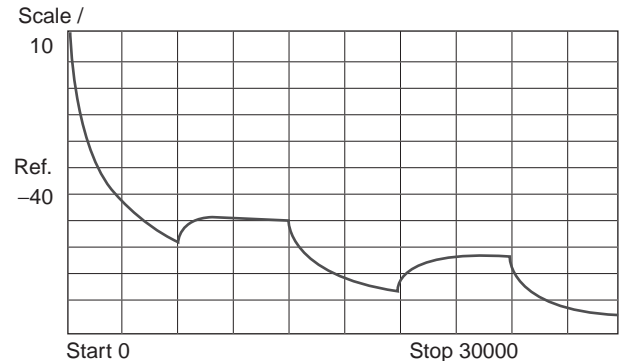


Figure 16. Prediction of surface-wave propagation at 10 MHz over a land-sea-land-sea-land mixed path: $|E_z|$ in dB versus horizontal distance.

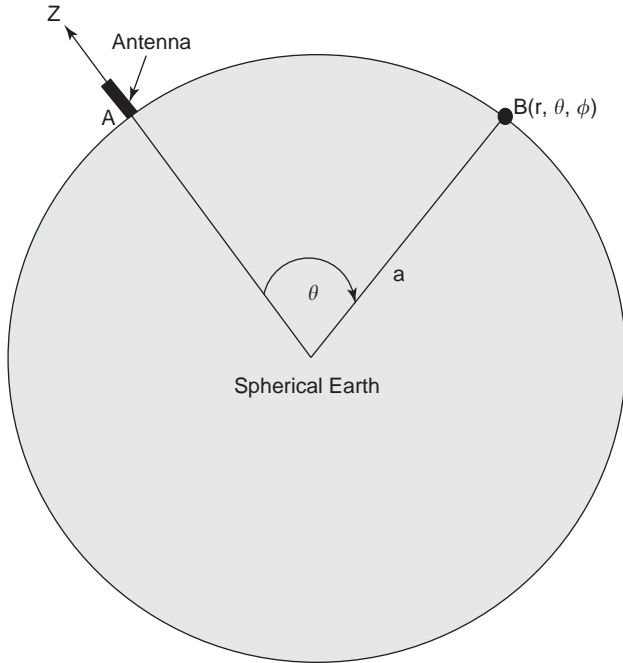


Figure 17. Short antenna radiation on a homogeneous spherical ground surface.

In the equation above, the electrical distance x_θ is defined as

$$x_\theta = \left(\frac{k_0 a}{2} \right)^{1/3} \theta \quad (48)$$

and t_s ($s = 1, 2, \dots$) are given by

$$t_s = |t_s| e^{-j\pi/3} \quad (49)$$

with

$$\begin{aligned} |t_1| &= 1.01879, & |t_2| &= 3.24820, & |t_3| &= 4.82010, \\ |t_4| &= 6.16331, & |t_5| &= 7.37218 \end{aligned} \quad (50)$$

and

$$|t_s| = [1.5(s - 0.75)\pi]^{2/3} \quad (51)$$

for $s > 5$. The correction due to the effect of Earth's curvature becomes necessary if the distance from the receiving point to the antenna is greater than $5 \times 10^3 (\lambda_0)^{1/3}$ or $10^4 (\lambda_0)^{1/3}$ meters [24].

Figure 18 shows an example prediction of the surface-wave propagation along the surface of a spherical Earth with $\sigma = 0.01$ and $\epsilon_r = 4$ at 10 MHz over a range of 1–500 km. The electric field normal to the surface attenuates at 26 dB per 100 km, as the surface wave is guided along the curvature of the spherical Earth, compared with 6 dB per 100 km for a flat Earth model shown in Figs. 18 and 19. Earth's curvature therefore causes the surface wave to attenuate more quickly as it propagates.

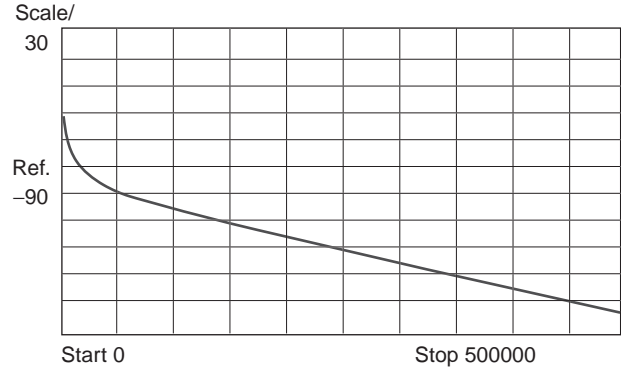


Figure 18. Prediction of surface-wave propagation at 10 MHz over a dry spherical ground surface with $\sigma_1 = 0.01$ and $\epsilon_r = 4$: $|E_z|$ in dB versus arc distance.

3. DISCUSSIONS

In this article, the “surface waves” guided along an interface between two media, or an interface between air and a multilayered structure in planar, cylindrical, and spherical geometries have been introduced. Several examples have been used to illustrate the propagation of surface waves in these geometric structures. In some cases, only TM surface waves are considered, but TE waves can be treated in a similar way. For propagation over a flat or spherical Earth, TE Norton surface waves tend to attenuate much more rapidly than do TM waves. Details of the formulation of both TM and TE waves over flat, spherical, homogeneous, and inhomogeneous ground can be found in Ref. 10, and the prediction of such propagation can be made using the software package described in Ref. 18.

The propagation of radio surface waves along Earth's surface can be utilized for long-distance wireless communications and remote sensing. On the other hand, the surface waves on microwave printed circuits and microstrip antenna systems should be avoided to minimize the electromagnetic coupling between circuit elements, or power loss in the systems. The understanding and control of surface waves are thus important in radio systems.

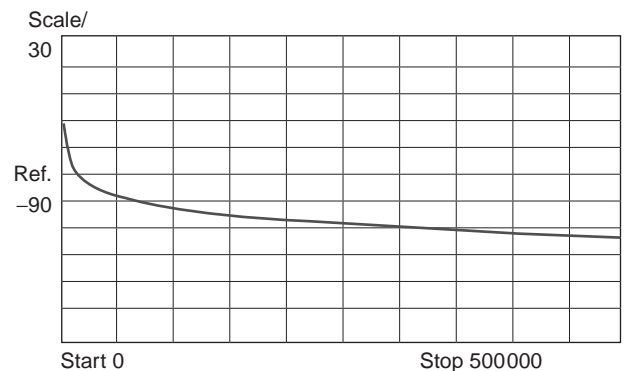


Figure 19. Prediction of surface-wave propagation at 10 MHz; the same path as Fig. 18, but without curvature correction.

BIBLIOGRAPHY

1. H. M. Barlow and A. L. Cullen, Surface waves, *Proc. IEE* **100**(Part III):329–341 (1953).
2. H. M. Barlow and J. Brown, *Radio Surface Waves*, Oxford Univ. Press, Oxford, 1962.
3. K. A. Norton, The physical reality of space and surface waves in the radiation field of radio antennas, *Proc. IRE* **25**: 1192–1202 (1937).
4. K. A. Norton, The propagation of radio waves over the surface of the earth and in the upper atmosphere, *Proc. IRE* **25**: 1203–1236 (1937).
5. W. H. Wise, The physical reality of Zenneck's surface wave, *Bell Syst. Tech. J.* **16**:35–44 (1937).
6. H. Bremmer, The surface-wave concept in connection with propagation trajectories associated with the Sommerfeld problem, *IRE Trans. Anten. Propag.* S175–S182 (1959).
7. J. R. Wait, Electromagnetic surface waves, in J. A. Saxton, ed., *Advances in Radio Research*, Academic Press, New York, 1964, Vol. 1, pp. 157–217.
8. R. J. King, Electromagnetic wave propagation over a constant impedance plane, *Radio Sci.* **4**:255–268 (1969).
9. R. J. King and J. R. Wait, Electromagnetic ground wave propagation theory and experiment, *Symp. Math.* **18**:107–208 (1976).
10. T. S. M. Maclean and Z. Wu, *Radiowave Propagation over Ground*, Chapman & Hall, London, 1993.
11. J. Zenneck, Über die Fortpflanzung ebener elektromagnetischer Wellen langs einer ebener Leiterfläche und ihre Beziehung zur drahtlosen Telegraphie, *Annal. Phys.* **23**:846–866 (1907).
12. D. M. Pozar, *Microwave Engineering*, Addison-Wesley, New York, 1990.
13. R. E. Collin, *Foundations for Microwave Engineering*, McGraw-Hill, New York, 1966.
14. A. Sommerfeld, *Partial Differential Equations in Physics*, Academic Press, New York, 1949.
15. A. Sommerfeld, Über die Ausbeutung der Wellen in der drahtlosen Telegraphie, *Annal. Phys.* **28**:655–736 (1909).
16. A. Sommerfeld, Über die Ausbeutung der Wellen in der drahtlosen Telegraphie, *Annal. Phys.* **81**:1135–1153 (1926).
17. A. Banos, *Dipole Radiation in the Presence of a Conducting Half-space*, Pergamon Press, Oxford, 1966.
18. Z. Wu and T. S. M. Maclean, *Radiowave Propagation over Ground Software*, Chapman & Hall, London, 1998.
19. G. N. Watson, The transmission of electric waves round the Earth, *Proc. Roy. Soc. Lond. A* **95**:546–563 (1919).
20. B. von der Pol and H. Bremmer, The diffraction of electromagnetic waves from an electrical point source round a finitely conducting sphere, *Phil. Mag. Ser. 7* **24**:141–176 (1937).
21. B. von der Pol and H. Bremmer, The diffraction of electromagnetic waves from an electrical point source round a finitely conducting sphere, *Phil. Mag. Ser. 7* **24**:825–864 (1937).
22. B. von der Pol and H. Bremmer, The diffraction of electromagnetic waves from an electrical point source round a finitely conducting sphere, *Phil. Mag. Ser. 7* **25**:817–834 (1938).
23. B. von der Pol and H. Bremmer, The diffraction of electromagnetic waves from an electrical point source round a finitely conducting sphere, *Phil. Mag. Ser. 7* **26**:261–275 (1939).
24. H. Bremmer, *Terrestrial Radio Waves*, Elsevier, New York, 1949.
25. J. R. Wait, Recent analytical investigations of electromagnetic ground wave propagation over inhomogeneous earth models, *Proc. IEEE* **62**:1061–1071 (1974).
26. V. A. Fock, *Electromagnetic Diffraction and Propagation Problems*, Pergamon Press, Oxford, 1965.

ELECTROMAGNETIC WAVE PROPAGATION

FERNANDO L. TEIXEIRA
The Ohio State University
Columbus, Ohio

FERNANDO J. S. MOREIRA
ODILON M. C. PEREIRA-
FILHO
Federal University of Minas
Gerais
Belo Horizonte, Brazil

1. INTRODUCTION

1.1. Historical Perspective

Electromagnetic waves play a major role in remote sensing and communication systems. The equations governing electromagnetic wave propagation were first established by J. C. Maxwell (1831–1879) in 1864. However, one should not overlook previous contributions of many scientists over the centuries, especially in optics. Speculations regarding the nature of light date since ancient Greece, when philosophers were already acquainted with the rectilinear propagation, reflection, and refraction of light [1]. The major contributions to the field, however, initiated during the Renaissance, on the foundations of the experimental method introduced by Galileo (1564–1642). Some examples are the law of refraction discovered by Snell (1580–1626) in 1621, the principle of least time established by Fermat (1601–1665) in 1657, the observation of light diffraction by Grimaldi (1618–1663) and Hooke (1635–1703) circa 1665, and Huygen's (1629–1695) envelope construction (leading to the principle named after him) in 1678 [1]. Such observations and experiments lead to the development of a wave theory to explain the nature of light as luminous sources vibrating in adjacent portions of an ethereal medium, an interpretation similar to that of acoustic waves. The wave theory of light was, however, later rejected by Newton (1642–1727), who proposed a corpuscular interpretation instead [1].

Many years passed until new experiments reinforced the wave theory of light. Among the leading scientists responsible for that is Fresnel (1788–1827), who developed the theory of light reflection and refraction in a more quantitative way and as well as a firmer mathematical basis for the interpretation of light as a transverse wave. Fresnel's work temporarily obscured the corpuscular theory of light, which regained strength only after Planck (1858–1947) and Einstein (1879–1955) started to unveil the quantum aspects of light in the beginning of the 1900s. The nineteenth century also witnessed the efforts of many

physicists to experimentally determine the speed of light, such as Michelson (1852–1931).

Apart from the developments in optics, many scientists dedicated efforts to establish the physical nature of magnetism and electricity. Among them, it is worth mentioning Coulomb (1736–1806), who demonstrated the inverse square law for electrical forces in 1785; Oersted (1777–1851), who was perhaps the first to observe experimentally the effect of electrical currents on the magnetic field in 1820; and Ampère (1775–1836), who formulated the circuit force law and postulated magnetism as an electrical phenomenon. The milestone experiment for the unification of magnetism and electricity, however, was carried out by Faraday (1791–1867), who discovered electromagnetic induction in 1831. The electromagnetic theory known at that time was put on analytical ground by Maxwell (1831–1879) in 1855/56. He further developed a model to explain electromagnetics as a mechanical phenomenon, which lead into the concept of displacement currents and the consequent generalization of Ampère’s law in 1861. The mechanical model was finally abandoned and Maxwell, in 1864, published his third paper on the subject, establishing the basis of the electromagnetic theory [2]. Besides postulating the displacement current, Maxwell was the first to predict the propagation of electromagnetic waves and to postulate light itself as an electromagnetic radiation. This provoked strong opposition from scientists at that time, as no evidence of such waves had been observed by experiments.

Maxwell did not survive to see his ideas been accepted by the majority of the scientists, which came just after the first experimental observation of electromagnetic wave propagation by Hertz, published in 1888. After that, the use of electromagnetic waves for practical purposes was just a matter of time, and in 1901 Marconi (1874–1937) achieved the first transmission of radio signals across the Atlantic. Today, electromagnetic waves permeate most of modern technologies.

In this article, we will briefly discuss some fundamental aspects of the electromagnetic wave propagation. Further details on this vast subject can be found in several books, such as Refs. 1 and 3–11.

1.2. The Electromagnetic Wave Spectrum

Electromagnetic waves can propagate at different frequencies. It is common to classify electromagnetic waves according to their frequency range as 3–30 Hz, ELF (extra-low-frequency or extremely-LF) waves; 30–300 Hz, SLF (super-low-frequency) waves; 300 Hz–3 kHz, ULF (ultra-low-frequency) waves; 3–30 kHz, VLF (very-low-frequency) waves; 30–300 kHz, LF (low-frequency or long) waves; 300 kHz–3 MHz, MF (medium-frequency or medium) waves, which include most AM radiowaves; 3–30 MHz, HF (high-frequency or short) waves, which include most of shortwave radio; 30–300 MHz, VHF waves, which include FM radio and TV signals; 300 MHz–3 GHz, UHF waves, which include TV signals, radar waves at L and S bands, and microwave oven radiation; 3–30 GHz, SHF (centimeter) waves, which include radars at C, X, Ku,

and K bands, satellite communication links, and aircraft landing systems; and 30–300 GHz, EHF (millimeter) waves, which include radars at Ka band.

Electromagnetic waves can also be classified by their wavelength. For an electromagnetic wave propagating in air or vacuum, the wavelength λ and frequency f are related by $\lambda = c/f$, where $c \approx 3 \times 10^8$ m/s is the speed of light in vacuum. Microwaves correspond to electromagnetic waves with λ around 1 cm–1 m (300 MHz–30 GHz). Millimeter and submillimeter waves have λ around 1 mm–1 cm (30–300 GHz) and just below it, respectively. Visible light is a form of electromagnetic wave with $\lambda = 0.38$ – $0.72 \mu\text{m}$. Wavelengths just below visible light correspond to ultraviolet waves, while wavelengths just above visible light correspond to near-infrared waves (0.72–1.3 μm) and thermal infrared waves (7–15 μm). At even smaller wavelengths (higher frequencies) one encounters X and gamma rays [10].

2. MAXWELL’S EQUATIONS AND THE WAVE EQUATION

The propagation of electromagnetic waves is governed by Maxwell’s equations, which in SI units and for macroscopic field quantities are

$$\begin{aligned} \nabla \times \mathcal{E} &= -\frac{\partial \mathcal{B}}{\partial t} & \nabla \cdot \mathcal{D} &= q \\ \nabla \times \mathcal{H} &= \mathcal{J} + \frac{\partial \mathcal{D}}{\partial t} & \nabla \cdot \mathcal{B} &= 0 \end{aligned} \quad (1)$$

These four equations are supplemented by *constitutive relations* that relate \mathcal{D} and \mathcal{B} to \mathcal{E} and \mathcal{H} . We shall assume propagation in *simple media*, with vacuum as a special case. The term *simple media* in this context denotes linear, homogeneous, and isotropic materials, which will be assumed lossless for the time being. The constitutive relations in this case are expressed as (see MAXWELL’S EQUATIONS article)

$$\mathcal{D} = \varepsilon \mathcal{E} \quad \text{and} \quad \mathcal{B} = \mu \mathcal{H} \quad (2)$$

where ε is the permittivity ($\varepsilon = \varepsilon_0 \approx 8.85418782 \times 10^{-12}$ F/m in vacuum) and μ is the permeability ($\mu = \mu_0 = 4\pi \times 10^{-7}$ H/m in vacuum), constant scalar numbers for simple media. The electric current \mathcal{J} and charge q densities can be interpreted as the sources of the electromagnetic field and are interrelated by the *continuity equation*:

$$\nabla \cdot \mathcal{J} = -\frac{\partial q}{\partial t} \quad (3)$$

which is implicit in (1) (see MAXWELL’S EQUATIONS article). From (1) one can also derive a law for the conservation of electromagnetic energy, the *Poynting theorem* (see MAXWELL’S EQUATIONS article). For our purposes, we just need to emphasize the *Poynting vector*, defined as

$$\mathcal{S} = \mathcal{E} \times \mathcal{H} \quad (4)$$

This vector gives the magnitude and direction of power flow density (watts per square meter).

We will discuss the relations between sources (\mathcal{J}) and fields (\mathcal{E} and \mathcal{H}) later. For now, we shall only investigate simple characteristics of the electromagnetic propagation. In regions of a simple media where no source is present (i.e., $\mathcal{J} = q = 0$) the (homogeneous) *wave equations* below can be derived from (1) (see MAXWELL'S EQUATIONS article):

$$\begin{aligned} \nabla^2 \mathcal{E} - \frac{1}{c^2} \frac{\partial^2 \mathcal{E}}{\partial t^2} &= 0 \\ \nabla^2 \mathcal{H} - \frac{1}{c^2} \frac{\partial^2 \mathcal{H}}{\partial t^2} &= 0 \end{aligned} \tag{5}$$

where $c = 1/\sqrt{\mu\epsilon}$ is the *speed of light* in the medium ($c = c_0 = 299,792,458$ m/s in vacuum, by definition). From (5) one can readily show that each Cartesian component of \mathcal{E} and \mathcal{H} also satisfies the following homogeneous (scalar) wave equation

$$\nabla^2 \psi - \frac{1}{c^2} \frac{\partial^2 \psi}{\partial t^2} = 0 \tag{6}$$

where ψ represents one of such components. This wave equation governs the behavior of ψ with respect to both position (x, y, z) and time (t). For simplicity, let us consider a one-dimensional problem (i.e., with no variation in x or y), such that (6) simplifies to

$$\frac{\partial^2 \psi}{\partial z^2} - \frac{1}{c^2} \frac{\partial \psi}{\partial t} = 0 \tag{7}$$

It can be easily verified that a solution to (7) is

$$\psi = f(z - ct) + g(z + ct) \tag{8}$$

where f and g are arbitrary real functions [12]. These are called *D'Alembert's solutions*, where $f(z - ct)$ represents an arbitrary waveform propagating in the positive z direction with speed equal to c , while $g(z + ct)$ represents another waveform with the same speed but propagating in the negative z direction.

Although (8) represents the solution of an idealized problem, it illustrates one fundamental property of the solutions of (6); namely, for unbounded simple media they represent a wave traveling with the speed of light. In real-life situations, obstacles (ground, vegetation, human-produced constructions, etc.) are present and impose additional constraints (*boundary conditions*) on the solutions of (6). In general, the presence of obstacles complicates the problem and simple analytical solutions can be found only for simple geometries.

2.1. Time-Harmonic Regime

Most RF and microwave applications deal with time-invariant linear media [6]. In this case, the use of a time-harmonic representation is often more convenient for dealing with electromagnetic wave phenomena. Assuming a $e^{j\omega t}$ time variation, where ω is the angular

frequency, Maxwell's equations (1) are rewritten as [6]

$$\begin{aligned} \nabla \times \mathbf{E} &= -j\omega \mathbf{B} & \nabla \cdot \mathbf{D} &= \rho \\ \nabla \times \mathbf{H} &= \mathbf{J} + j\omega \mathbf{D} & \nabla \cdot \mathbf{B} &= 0 \end{aligned} \tag{9}$$

where the functions (of space only) in (9) are now complex phasor representations of the corresponding quantities in (1), according to

$$\mathcal{E} = \text{Re}(\mathbf{E}e^{j\omega t}) \tag{10}$$

Here Re denotes the real part. A similar relation holds for the other fields (and sources). For simple media and from (2), the constitutive relations are then

$$\mathbf{D} = \epsilon \mathbf{E} \text{ and } \mathbf{B} = \mu \mathbf{H} \tag{11}$$

The wave equations (5) also assume a simpler representation [6]:

$$\begin{aligned} \nabla^2 \mathbf{E} + k^2 \mathbf{E} &= 0 \\ \nabla^2 \mathbf{H} + k^2 \mathbf{H} &= 0 \end{aligned} \tag{12}$$

known as the (homogeneous) *Helmholtz equations*, where $k = \omega\sqrt{\mu\epsilon}$ is the *wave number*.

It is useful to define *time-average* powers when dealing with time-harmonic fields. For instance, from (4) and the definition in (10) one can define the *complex Poynting vector*

$$\mathbf{S} = \frac{1}{2} \mathbf{E} \times \mathbf{H}^* \tag{13}$$

The real part of the complex Poynting vector is the time average of \mathcal{S} [4]. Equation (13) stresses an important characteristic of electromagnetic wave propagation. In-phase components of \mathbf{E} and \mathbf{H} contribute to $\text{Re}(\mathbf{S})$, representing the *power density* propagating in the direction of $\text{Re}(\mathbf{S})$ [6]. On the other hand, components of \mathbf{E} and \mathbf{H} in phase quadrature contribute to the imaginary part of \mathbf{S} , representing a (stationary) *reactive power density*.

In the time-harmonic regime, (7) becomes

$$\frac{d^2 \Psi}{dz^2} + k^2 \Psi = 0 \tag{14}$$

where Ψ is the complex representation of ψ according to (10). The solution of (14) is

$$\Psi = p_1 e^{j(kz + \phi_1)} + p_2 e^{-j(kz + \phi_2)} \tag{15}$$

Consequently, from (10) and observing that for simple media $k = \omega/c$, we obtain

$$\psi = p_1 \cos[k(z + ct) + \phi_1] + p_2 \cos[k(z - ct) + \phi_2] \tag{16}$$

which is a particular time-harmonic solution of (7) and (8) known as a *plane wave*.

3. PLANE, TEM, AND STATIONARY WAVES

The plane wave is the simplest solution of the homogeneous wave equation. Many important properties of electromagnetic wave propagation can be inferred from this fundamental solution. Moreover, an arbitrary electromagnetic wave in sourceless linear media can be decomposed in terms of plane waves ($e^{\pm jkz}$ in one dimension) in a manner similar to the decomposition of a time-domain signal in terms of its spectral components $e^{j\omega t}$ [13].

The complex representation of a plane wave in (15) specifies an amplitude (p) and phase ($kz + \phi$). Moreover, since Ψ represents a Cartesian component of \mathbf{E} or \mathbf{H} , it also indicates the orientation (i.e., the *polarization*) of the vector field.

The plane-wave solution of Ψ in three dimensions is written as $e^{-j(k_x x + k_y y + k_z z)}$, where $k_{x,y,z}/k$ can be understood as the cosine directors of the wavefront. By defining the *propagation vector* $\mathbf{k} = k_x \hat{\mathbf{x}} + k_y \hat{\mathbf{y}} + k_z \hat{\mathbf{z}}$ and putting the components of \mathbf{E} and \mathbf{H} back together, we arrive at a more general complex representation for plane waves [6]

$$\mathbf{E} = \mathbf{E}_0 e^{-j\mathbf{k} \cdot \mathbf{r}} \quad \text{and} \quad \mathbf{H} = \mathbf{H}_0 e^{-j\mathbf{k} \cdot \mathbf{r}} \quad (17)$$

where $\mathbf{r} = x\hat{\mathbf{x}} + y\hat{\mathbf{y}} + z\hat{\mathbf{z}}$ denotes the observation point, and amplitudes and phases of each component are incorporated in the constant complex vectors \mathbf{E}_0 and \mathbf{H}_0 (which also determine the wave polarization). Substituting (17) into (12), one obtains the *characteristic equation* or *dispersion relation* (for simple media):

$$k^2 = \omega^2 \mu \epsilon = k_x^2 + k_y^2 + k_z^2 \quad (18)$$

The plane-wave relations for \mathbf{E} and \mathbf{H} in simple media are obtained by substituting (11), (17), and (18) into (9) with no sources present

$$\begin{aligned} \mathbf{k} \times \mathbf{E} &= \omega \mu \mathbf{H} & \mathbf{k} \cdot \mathbf{E} &= 0 \\ \mathbf{k} \times \mathbf{H} &= -\omega \epsilon \mathbf{E} & \mathbf{k} \cdot \mathbf{H} &= 0 \end{aligned} \quad (19)$$

from which one observes that for sourceless simple media Ampère's and Faraday's laws are independent equations. Actually, this is also true for any wave solution in such media, which can be inferred from (9) and (11) [6].

Note that $k_{x,y,z}$ can be complex and still satisfy (18). Consequently, it is useful to regard \mathbf{k} as a complex vector

$$\mathbf{k} = \beta - j\alpha \quad (20)$$

where α and β are real vectors [6]. Since both α and β are real, they can be interpreted geometrically. Substituting (20) into (17), one verifies that the plane-wave spatial variation in complex notation is of the form $e^{-\alpha \cdot \mathbf{r}} e^{-j\beta \cdot \mathbf{r}}$, representing the variations of the amplitude (first term) and phase (second one) of the wave as it propagates through the medium. Consequently, the constant amplitude and phase surfaces are planes (hence the name plane waves), with α and β pointing to their normal directions, respectively. If such planes coincide (i.e., $\alpha \parallel \beta$), then the plane wave is denoted as a *uniform* plane wave. Other-

wise, it is denoted as *nonuniform*. Furthermore, $\hat{\boldsymbol{\beta}}$ (i.e., unit normal vector to the equiphase surface) denotes the *direction of propagation* of the plane wave.

For uniform plane waves, one can show from (18) and (20) that $\mathbf{k} = k\hat{\boldsymbol{\beta}}$, where $\hat{\boldsymbol{\beta}} = \hat{\mathbf{k}}$ is the direction of propagation. Now \mathbf{k} has a geometrically defined direction and one can inspect from (19) that Ampère's and Faraday's laws reduce to

$$\begin{aligned} \mathbf{H} &= \frac{k}{\omega \mu} \hat{\mathbf{k}} \times \mathbf{E} = \frac{1}{\eta} \hat{\mathbf{k}} \times \mathbf{E} \\ \mathbf{E} &= \frac{-k}{\omega \epsilon} \hat{\mathbf{k}} \times \mathbf{H} = -\eta \hat{\mathbf{k}} \times \mathbf{H} \end{aligned} \quad (21)$$

where $\eta = \sqrt{\mu/\epsilon}$ is the *intrinsic impedance* of the medium ($\eta = \eta_0 \approx 376.730313 \Omega$ in vacuum). So, a uniform plane wave has \mathbf{E} , \mathbf{H} , and $\hat{\mathbf{k}}$ mutually orthogonal to each other (which is not the case for nonuniform plane waves). Waves with such characteristics, that is, obeying the relations in (21), are called *transverse electromagnetic* (TEM) waves, the simplest example of which is the plane wave.

3.1. Wavelength and Phase Velocity

For simplicity, let us consider a uniform plane wave propagating in the $\hat{\mathbf{k}} = \hat{\mathbf{z}}$ direction. Consequently, $\mathbf{k} \cdot \mathbf{r} = kz$. Since $\hat{\mathbf{k}} \cdot \mathbf{E} = 0$, let us further consider $\mathbf{E} = E_0 e^{-jkz} \hat{\mathbf{x}}$ with $E_0 = p e^{j\phi}$. Consequently, from (21), $\mathbf{H} = (E_0/\eta) e^{-jkz} \hat{\mathbf{y}}$. Note that this is a one-dimensional problem; specifically, the components of \mathbf{E} and \mathbf{H} satisfy (14), with constant amplitude and phase planes perpendicular to $\hat{\mathbf{z}}$.

To obtain corresponding expressions in time domain, we apply the definition in (10):

$$\begin{aligned} \mathcal{E} &= p \cos(\omega t - kz + \phi) \hat{\mathbf{x}} \\ \mathcal{H} &= \frac{p}{\eta} \cos(\omega t - kz + \phi) \hat{\mathbf{y}} \end{aligned} \quad (22)$$

So, for a certain instant of time, the spatial variation of \mathcal{E} and \mathcal{H} is sinusoidal with a period equal to $\lambda = 2\pi/k$, the *wavelength* of the electromagnetic wave. Since $k = \omega/c$, then

$$\lambda = \frac{c}{f} \quad (23)$$

where f is the frequency. For such sinusoidal variation, $\omega/k = c$ is called the *phase velocity* (v_p) of the TEM wave.

3.2. Polarization

In the previous example we have assumed $\mathbf{E} \parallel \hat{\mathbf{x}}$, but any combination between x and y components also satisfies $\hat{\mathbf{k}} \cdot \mathbf{E} = 0$ for $\hat{\mathbf{k}} = \hat{\mathbf{z}}$. In this situation, such components are said to be *orthogonal* to each other and their phase and amplitude relationships describe the nature of the wave polarization. Wave polarization plays an important role in RF and microwave systems, as the interaction between fields and obstacles can strongly depend on it. In principle,

it is possible to transmit and receive orthogonal polarizations in a communication channel independently, thus doubling the capacity of the channel. In practice, *depolarization* effects (partial conversion of energy in one polarization to another) often occur. This effect can cause, for instance, cochannel interference in wireless communications. Orthogonal polarizations can also be used in closely spaced radiolinks to minimize cochannel interference.

According to (21), TEM wave polarization can be fully characterized by \mathbf{E} and $\hat{\mathbf{k}}$. So, let us assume $\mathbf{E} = (p_x e^{j\phi_x} \hat{\mathbf{x}} + p_y e^{j\phi_y} \hat{\mathbf{y}}) e^{-jkz}$. Then, from (10), we obtain

$$\mathcal{E} = p_x \cos(\omega t - kz + \phi_x) \hat{\mathbf{x}} + p_y \cos(\omega t - kz + \phi_y) \hat{\mathbf{y}} \quad (24)$$

If the x and y components are in phase (i.e., $\phi_x = \phi_y$), then (24) can be rewritten as

$$\mathcal{E} = (p_x \hat{\mathbf{x}} + p_y \hat{\mathbf{y}}) \cos(\omega t - kz + \phi_x) \quad (25)$$

and, for any position and time, \mathcal{E} is always parallel to the plane containing $\hat{\mathbf{z}} (= \hat{\mathbf{k}})$ and $p_x \hat{\mathbf{x}} + p_y \hat{\mathbf{y}}$. Then, the wave is said to have a *linear polarization*, as depicted in Fig. 1. Note that $\phi_x = \phi_y \pm \pi$ also provides a linear polarization. Now, let us assume that $p_x = p_y = p$ and $\phi_y - \phi_x = \pm \pi/2$. Then, from (24), we have

$$\mathcal{E} = p[\cos(\omega t - kz + \phi_x) \hat{\mathbf{x}} \mp \sin(\omega t - kz + \phi_x) \hat{\mathbf{y}}] \quad (26)$$

and the wave has a *circular polarization*, as the tip of \mathcal{E} describes a circular helix in space with an axis in the direction of $\hat{\mathbf{z}}$. This is depicted in Fig. 2. For $\hat{\mathbf{k}} = \hat{\mathbf{z}}$, $\phi_y - \phi_x = \pi/2$ ($= -\pi/2$) defines a *left (right)-hand circular polarization*. For any other combination between ϕ_x, ϕ_y and p_x, p_y , the wave polarization is *elliptical*. Finally, from the discussion conducted here it should be clear that any circular or elliptical polarization can be decomposed into two orthogonal linear polarizations with appropriate amplitude and phase relations. For pictorial depictions of the different wave polarizations, the reader is referred to, for instance, the text by Balanis [14].

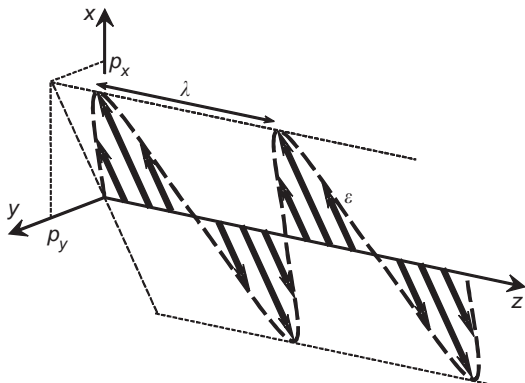


Figure 1. Snapshot of the electric field vector of a linearly polarized wave traveling in the z direction.

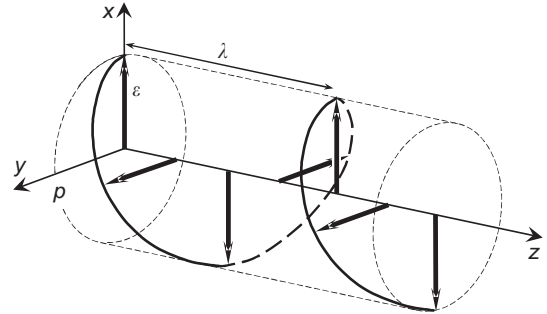


Figure 2. Snapshot of the electric field vector of a circularly polarized wave traveling in the z direction.

3.3. Complex Poynting Vector and Stationary Waves

We will now investigate in further detail the behavior of \mathbf{S} for uniform plane waves.

From (13) and (21) we can verify that for a TEM plane wave

$$\mathbf{S} = \frac{|\mathbf{E}|^2}{2\eta} \hat{\mathbf{k}} = \frac{\eta |\mathbf{H}|^2}{2} \hat{\mathbf{k}} \quad (27)$$

indicating that (in a lossless simple media) \mathbf{S} is real (i.e., a pure active power density) and, consequently, the direction of propagation of a uniform plane coincides with the direction of energy flux. For instance, in the examples of Sections 3.1 and 3.2, one immediately observes that $\text{Re}(\mathbf{S}) \parallel \hat{\mathbf{z}}$.

So, let us now extend the example of Section 3.1 to investigate the case of a *stationary wave*, which is described here as a superposition of two TEM plane waves propagating in opposite directions (i.e., $\hat{\mathbf{k}} = \pm \hat{\mathbf{z}}$)

$$\begin{aligned} \mathbf{E} &= (E_0^+ e^{-jkz} + E_0^- e^{jkz}) \hat{\mathbf{x}} \\ \mathbf{H} &= \frac{1}{\eta} (E_0^+ e^{-jkz} - E_0^- e^{jkz}) \hat{\mathbf{y}} \end{aligned} \quad (28)$$

where \mathbf{H} was directly obtained from (21), noting that each individual wave has its $\hat{\mathbf{k}}$ pointing in the opposite direction of the other. Substituting (28) into (13), we obtain

$$\mathbf{S} = \left[\frac{|E_0^+|^2}{2\eta} - \frac{|E_0^-|^2}{2\eta} + j \frac{|E_0^+| |E_0^-|}{\eta} \sin(2kz - \phi^+ + \phi^-) \right] \hat{\mathbf{z}} \quad (29)$$

where ϕ^\pm are the corresponding phases of E_0^\pm . So, (29) indicates that \mathbf{S} has real (corresponding to the net flux of power density) and imaginary (corresponding to the stationary reactive power density) parts. This is the case, for instance, of fields on a transmission line terminated by a load that does not match the line impedance. If $|E_0^+| = |E_0^-|$ the wave of (28) is *purely stationary* and there is no average power flux [i.e., $\text{Re}(\mathbf{S}) = \mathbf{0}$, that occurs when the line is terminated, for example, by a short circuit].

4. WAVES AND SOURCES

Until this point, we have focused on wave propagation through regions of simple media where no source is present. We shall now present relations describing fields produced by elementary electric current sources in simple media. The most common way to accomplish this objective is by obtaining the so-called *Green's functions*. For a systematic treatment, the reader is referred to Collin's text [7] (for guided-wave examples) and Silver's treatise [9] (for radiation examples with applications to antenna theory). The approach adopted here is more restricted and can be found in most of the Bibliography.

Observing from (1) that $\nabla \cdot \mathcal{B} = 0$, one can define the *magnetic vector potential* \mathcal{A} such that $\nabla \times \mathcal{A} = \mathcal{B}$. In simple media, and after applying the *Lorenz gauge condition* given by $c^2 \nabla \cdot \mathcal{A} = -\partial \Phi / \partial t$, where Φ is the *electric scalar potential*, it can be shown that \mathcal{A} satisfies a wave equation as follows [4]:

$$\nabla^2 \mathcal{A} - \frac{1}{c^2} \frac{\partial^2 \mathcal{A}}{\partial t^2} = -\mu \mathcal{J} \quad (30)$$

For time-harmonic fields, this equation can be represented in complex notation as

$$\nabla^2 \mathbf{A} + k^2 \mathbf{A} = -\mu \mathbf{J} \quad (31)$$

A solution of these equations can be written in a generic form as [4]

$$\mathbf{A} = \mu \iiint_V \mathbf{J}(\mathbf{r}') G(\mathbf{r}, \mathbf{r}') dv' \quad (32)$$

where V denotes the volumetric region encompassing \mathbf{J} ; \mathbf{r}' and \mathbf{r} denote source and observation points, respectively; and $G(\mathbf{r}, \mathbf{r}')$ is the *Green's function*. $G(\mathbf{r}, \mathbf{r}')$ can be interpreted physically as the field produced by a point source, namely, the solution of

$$\nabla^2 G + k^2 G = -\delta(\mathbf{r} - \mathbf{r}') \quad (33)$$

satisfying the appropriate boundary conditions [4]. For instance, for bounded sources in unbounded simple media (free space), it can be shown that

$$G(\mathbf{r}, \mathbf{r}') = \frac{e^{-jk|\mathbf{r}-\mathbf{r}'|}}{4\pi|\mathbf{r}-\mathbf{r}'|} \quad (34)$$

which is known as the *free-space Green's function*. Furthermore, the time-harmonic electromagnetic field can be written in terms of \mathbf{A} as [4]

$$\mathbf{H} = \frac{1}{\mu} \nabla \times \mathbf{A} \quad (35)$$

$$\mathbf{E} = -j\omega \left[\mathbf{A} + \frac{1}{k^2} \nabla(\nabla \cdot \mathbf{A}) \right]$$

Use of the Lorenz condition in the derivation of (30) has an important consequence—one does not need to explicitly consider the charge densities to obtain the field. That should come as no surprise, since charges are related to currents by the continuity equation (3). In the time-harmonic regime their effects become implicit in (35). In any event, it is important to mention that (in a classical sense) gauge conditions other than those due to Lorenz can be applied [4].

As a simple example, we consider a uniform time-harmonic electric current distribution over a small segment (wire) ℓ along the z axis, centered at the origin ($z=0$). The length ℓ is assumed very small, such that $\ell \ll \lambda$. The electric current flows along $\hat{\mathbf{z}}$, with a constant phasor I_0 for $|z| \leq \ell/2$ ($I_0=0$ for $|z| > \ell/2$). This source distribution is called *infinitesimal electric dipole*. If the dipole radiates in free space, then the resulting vector potential \mathbf{A} is given by (32) and (34). Since $\mathbf{r}' = z'\hat{\mathbf{z}}$ with $|z'| \leq \ell/2 \ll \lambda$, then $k|\mathbf{r} - \mathbf{r}'| \approx kr$ and, consequently, $G(\mathbf{r}, \mathbf{r}') \approx e^{-jkr}/(4\pi r)$. The integral in (32) can then be readily evaluated to give [9]

$$\mathbf{A} = \frac{\mu I_0 \ell e^{-jkr}}{4\pi r} \hat{\mathbf{z}} \quad (36)$$

where $I_0 \ell$ is the *electric dipole moment*. The expressions for the associated electric and magnetic fields are obtained by substituting (36) into (35). The result can be easily extended to arbitrary dipole's locations and orientations [9].

Note from (35) and (36) that the dipole radiation depends on the length ℓ multiplied by k , that is, on the ratio ℓ/λ (also called the *electrical length*). Any bounded source distribution in a simple medium can be written as a superposition of infinitesimal dipoles. As a result, the free-space radiation properties of any bounded source distribution depend on its electrical dimension, namely, its dimension relative to the wavelength. This is also the case for scattering by bounded obstacles immersed in simple media.

We note that the integral (32) is generally difficult to evaluate except for simple current distributions and simple Green's functions (such as the free-space Green's function described above).

4.1. Far-Field (Radiation) Region

In free space and for observation points located sufficiently far away from (bounded) sources, (34) and, consequently, (32) can be simplified by means of a Taylor expansion on $|\mathbf{r} - \mathbf{r}'|$ for small values of $|\mathbf{r}'|$ with respect to $|\mathbf{r}|$. By keeping just the first few terms on this expansion, one ends up with a simplified relation valid for the so-called radiation (or *far-field*) region [9]

$$\mathbf{A} \approx \frac{\mu}{4\pi r} e^{-jkr} \iiint_V \mathbf{J}(\mathbf{r}') e^{jk\hat{\mathbf{r}} \cdot \mathbf{r}'} dv' \quad (37)$$

where $r = |\mathbf{r}|$, in which case relations (35) simplify to

$$\begin{aligned} \mathbf{E} &\approx -j\omega[\mathbf{A} - (\mathbf{A} \cdot \hat{\mathbf{r}})\hat{\mathbf{r}}] \\ \mathbf{H} &\approx \frac{1}{\eta} \hat{\mathbf{r}} \times \mathbf{E} \end{aligned} \tag{38}$$

4.2. Spherical and Cylindrical TEM Wavefronts

A closer look at (37) and (38) reveals some interesting properties of the far-field radiation of bounded sources in simple media. The field dependence on the radial distance r is of the form e^{-jkr}/r . This indicates that the surfaces of constant phase are concentric spheres and that the field intensity decays with $1/r$. Also, the propagation direction (normal to the equiphase surface) is $\hat{\mathbf{r}}$. Furthermore, \mathbf{E} , \mathbf{H} , and $\hat{\mathbf{r}}$ are mutually orthogonal. This characterizes a *spherical TEM wave*, for which the basic TEM relations of Section 3 still hold, but now with $\hat{\mathbf{k}} = \hat{\mathbf{r}}$. For instance, a complex E -field notation of the form $\mathbf{E} = p(\theta, \phi)(\hat{\theta} \pm j\hat{\phi}) \exp(-jkr)/r$ characterizes a spherical TEM wave with a circular polarization, according to the basic definitions of Section 3.2. For such a wave, the complex Poynting vector is given by $\mathbf{S} = \hat{\mathbf{k}}|E|^2/(2\eta) = \hat{\mathbf{r}}|p(\theta, \phi)|^2/(\eta r^2)$, according to (27).

Such observations show that the average power density of a spherical TEM wave decays with $1/r^2$ in lossless simple media. This result is also expected from simple considerations about energy conservation. Since total radiated power in a lossless medium is conserved and the spherical area of the wavefront increases with r^2 , the power *density* of the spherical wavefront must decay with $1/r^2$. Furthermore, note that a spherical TEM wave behaves *locally* as a plane wave when $kr \gg 1$, so that, in free space, the field close to a receiver antenna located sufficiently far away from the transmitter antenna can be locally approximated as a plane wave.

Apart from plane and spherical waves, another simple kind of wavefront is the cylindrical one. It is useful to picture a cylindrical wave as the field produced by an infinitely long line current [6]. For observation points far away from the current axis, the corresponding wavefronts can be approximated as cylindrical surfaces with a cross-sectional area that increases linearly with distance (the cylindrical ρ -coordinate). Consequently, from considerations on energy conservation, the radiating field decays with $\rho^{-1/2}$ [6]. It can also be shown that such cylindrical wave is also a TEM field obeying those basic relations of Section 3, now with $\hat{\mathbf{k}} = \hat{\rho}$. Furthermore, for $k\rho \gg 1$ the cylindrical wavefront can also be *locally* approximated as a plane wave.

4.3. Ray Optics Limit

The discussion in the previous section leads toward the picture of TEM wavefronts propagating far away from the radiating sources, with directions of propagation normal to the corresponding equiphase surfaces. As stressed previously, distances and dimensions are to be considered large or small vis-à-vis the wavelength of operation. In the limit of $\lambda \rightarrow 0$ or, alternatively, $k \rightarrow \infty$, the electromagnetic

field is expected to behave locally as a TEM wave (i.e., far away from sources). This is often called the *geometric optics* (GO) limit, where diffraction effects are neglected and a number of simplifications of the nature of electromagnetic wave propagation can be made, such as those in (21) [15].

The GO principles are directly related to the classical treatment of light. The developments date from ancient Greece and are intrinsically related to those of Euclidean geometry [1]. Obviously, such studies were not based on Maxwell's equations, but, as expected, the GO principles can be derived from Maxwell's equations. The usual starting point for this derivation is to assume a monochromatic wave (i.e., a time-harmonic field) governed by (12) in complex notation. Adopting the notation of Section 2.1, we let Ψ be a Cartesian component of \mathbf{E} or \mathbf{H} (a function of position only). Consequently

$$\nabla^2 \Psi + k^2 \Psi = 0 \tag{39}$$

From the TEM waves discussed up to here, it can be assumed, as a first-order *ansatz*, that [1]

$$\Psi \approx p(\mathbf{r})e^{-jk_0\Phi(\mathbf{r})} \tag{40}$$

where p represents the (complex) amplitude variation, Φ represents the phase variation with position only, and k_0 is the wavenumber for vacuum. For other simple media one can define the *index of refraction*

$$n = \sqrt{(\mu\epsilon)/(\mu_0\epsilon_0)} \tag{41}$$

such that $k = nk_0$. In (40), n is accounted for by $\Phi(\mathbf{r})$. Furthermore, the wavefront is given by the surfaces of constant $\Phi(\mathbf{r})$ (equiphase surfaces). Consequently, the direction of propagation is $\hat{\mathbf{k}} = \nabla\Phi/|\nabla\Phi|$. The equation that establishes the optical path (trajectory) in terms of the wavefront properties is accomplished by substituting (40) into (39) and, in the $k_0 \rightarrow \infty$ limit, assuming that any variation of $p(\mathbf{r})$ with position is negligible with respect to that of $k_0\Phi(\mathbf{r})$. After some algebraic manipulations, one arrives at the so-called *eikonal equation* [1]:

$$|\nabla\Phi|^2 = n^2 \tag{42}$$

This equation can be used to derive Fermat's principle [1]

$$\Phi(\mathbf{r}_2) - \Phi(\mathbf{r}_1) = \int_{r_1}^{r_2} n \, d\ell = \int_{t(r_1)}^{t(r_2)} c \, dt \tag{43}$$

where $\Phi(\mathbf{r}_2) - \Phi(\mathbf{r}_1)$ is the optical arc length (along the optical path ℓ) between points \mathbf{r}_1 and \mathbf{r}_2 , as illustrated in Fig. 3. This principle states that light (or, more precisely, electromagnetic waves in the GO limit) follows the path corresponding to the shortest travel time [1]. For simple media, both n and c are constants, but (43) holds for inhomogeneous media as well. From (43) one can also derive the laws of reflection and refraction [1], or establish approximate trajectories of radiowave propagation through Earth's atmosphere [16].

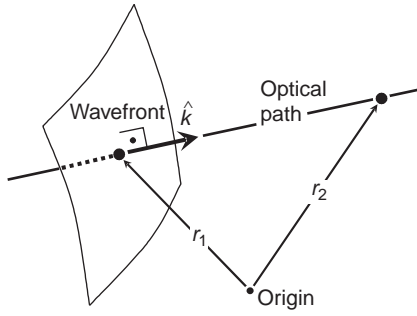


Figure 3. Wavefront and optical path in the geometric optics approximation.

GO principles are useful (although approximate) tools for the characterization of electromagnetic wave propagation not only at optical frequencies but also often at RF and microwave frequencies. For instance, such approximation can be used (possibly augmented by small corrections) for characterization of some radio channels at UHF or higher frequencies [17]. The range of validity of such approximation can depend on many factors, but it is fair to say that GO can be used as long as the characteristic lengths of the problem (obstacle feature sizes, mutual distances, etc.) are much larger than λ .

5. WAVES IN LOSSY AND DISPERSIVE MEDIA

So far, we have considered the propagation of electromagnetic waves in simple media without losses or dispersion. This assumption implies that the permittivity and permeability in the constitutive relations (2) and (11) are constant scalar parameters. In general, however, constitutive relations are not that simple. For example, ferroelectric and ferromagnetic materials are an example of *nonlinear media*, where the constitutive parameters at a point depend on the field strength at that point [4]. Even dielectrics can exhibit nonlinear effects under sufficiently large field strengths (e.g., breakdowns inside capacitors or transmission lines). On the other hand, crystals present a well-organized atomic structure, where the field response is highly dependent on wave polarization. Crystals are an example of *anisotropic* materials, where the permittivity (or permeability) has a tensorial nature [18]. The ionosphere is another example of anisotropic medium at radiofrequencies, although due to very different reasons [4].

Wave propagation on nonlinear or anisotropic media will not be considered here; The interested reader may consult Refs. 4 and 18 for further details. We shall continue to assume simple (linear, homogeneous, and isotropic) media, but now accounting for the presence of losses (lossy simple media).

In simple media and for a time-harmonic regime, losses in the medium cause a phase delay between the electric displacement (\mathcal{D}) and the electric field (\mathcal{E}), such that, in complex notation, we obtain

$$\mathbf{D} = \varepsilon(\omega)\mathbf{E} = [\varepsilon'(\omega) - j\varepsilon''(\omega)]\mathbf{E} \quad (44)$$

where ε' and $-\varepsilon''$ are the real and imaginary parts of the *complex permittivity* ε , respectively. The negative imaginary part of ε indicates the phase *delay* on \mathbf{D} . Here, we still assume that (11) applies for the magnetic relation, since for conductors and dielectrics $\mu \approx \mu_0$ at radiofrequencies, although, in general, a complex permeability of the form $\mu(\omega) = \mu'(\omega) - j\mu''(\omega)$ can also be defined [6].

For dielectrics, the ratio $\varepsilon''/\varepsilon'$ defines the *loss tangent*, where $\tan^{-1}(\varepsilon''/\varepsilon')$ is the phase difference between \mathbf{E} and \mathbf{D} due to the polarization inertia of the atomic structure (macroscopic interpretation). For conductors, net free charges are present and generate a *conduction current* \mathbf{J}_c whenever an external field is applied. For most conductors, \mathbf{J}_c is given by Ohm's law [4]

$$\mathbf{J}_c = \sigma\mathbf{E} \quad (45)$$

where σ is the material conductivity of the medium (approximately constant for frequencies below the infrared region). For conductive media, \mathbf{J}_c and the corresponding net charge density ρ_c can be subtracted from \mathbf{J} and ρ in (9), respectively, and Maxwell's equations in complex notation can be rearranged in the same form as in (9), but now with the permittivity replaced by the complex permittivity of (44), where ε' is the real permittivity and $\varepsilon'' = \sigma/\omega$ [6]. After that, \mathbf{J} and ρ in (9) correspond to the impressed (external) sources only, as \mathbf{J}_c and ρ_c are implicitly taken into account by the complex ε .

It is important to note that, once the complex permittivity in (44) is adopted, $k = \omega\sqrt{\mu\varepsilon}$ and $\eta = \sqrt{\mu/\varepsilon}$ are complex quantities as well. These quantities now depend on ω but are still spatially uniform (for homogeneous media). Therefore, all the results derived from Maxwell's equations (in complex notation) in previous sections still hold true, except for those where one had to deal with conjugate or absolute values (i.e., relations regarding average energy and power densities). For instance, (4) is still valid, since it is a general definition. However, for a TEM wave propagating in a lossy simple medium, (27) must account to the fact that η is now complex and hence generalizes to

$$\mathbf{S} = \frac{|\mathbf{E}|^2}{2\eta^*} \hat{\mathbf{k}} = \frac{\eta|\mathbf{H}|^2}{2} \hat{\mathbf{k}} \quad (46)$$

5.1. Wave Attenuation and Frequency Dispersion

One of the important consequences of losses is the attenuation of electromagnetic waves inside the medium. To illustrate this, we revisit the problem of Section 3.1, where a uniform plane wave propagates in the $\hat{\mathbf{z}}$ direction, but now in a lossy simple medium. From (20), and as the wave is considered uniform, then $\alpha\|\beta\|\hat{\mathbf{z}}$ and, consequently, $\mathbf{k} = k\hat{\mathbf{z}} = k\hat{\mathbf{k}}$, where k is a complex-valued quantity. So, if one defines

$$k = \beta - j\alpha \quad (47)$$

where α and β are nonnegative real quantities, then $\alpha = \alpha \hat{\mathbf{k}}$ and $\beta = \beta \hat{\mathbf{k}}$. Such definition is valid for any TEM wave propagating through a lossy simple medium in the direction $\hat{\mathbf{k}}$. The expressions for α and β are obtained from the definition $k = \omega \sqrt{\mu \epsilon}$ and (44):

$$\begin{cases} \alpha \\ \beta \end{cases} = \omega \sqrt{\frac{\mu \epsilon'}{2} \left(\sqrt{1 + \left(\frac{\epsilon''}{\epsilon'}\right)^2} \pm 1 \right)} \quad (48)$$

The plane-wave complex representation of Section 3.1 now becomes

$$\begin{aligned} \mathbf{E} &= E_0 e^{-\alpha z} e^{-j\beta z} \hat{\mathbf{x}} \\ \mathbf{H} &= \frac{E_0}{\eta} e^{-\alpha z} e^{-j\beta z} \hat{\mathbf{y}} \end{aligned} \quad (49)$$

Note that η is now complex. We observe from (49) that the *phase factor* β controls the phase variation with distance, whereas the *attenuation factor* α controls the amplitude attenuation as the wave propagates (i.e., as z increases). Despite the attenuation effect, the surfaces of constant amplitude and phase are still planes perpendicular to $\hat{\mathbf{z}}$, characterizing a uniform plane wave.

Note that the oscillatory behavior is controlled by $e^{-j\beta z}$, and this factor defines the wavelength and phase velocity, now represented as

$$\lambda = \frac{2\pi}{\beta} \quad \text{and} \quad v_p = \frac{\omega}{\beta} \quad (50)$$

To have a better picture of the wave behavior, we apply the definition in (10) to (49) in order to obtain \mathcal{E} in time domain. Assuming $E_0 = p e^{-j\phi}$, we obtain

$$\mathcal{E} = p e^{-\alpha z} \cos(\omega t - \beta z + \phi) \hat{\mathbf{x}} \quad (51)$$

So, the picture here is that of a sinusoidal function (with spatial period λ) multiplied by an envelope variation given by $|p e^{-\alpha z}|$. The field behavior is sketched in Fig. 4 for a fixed instant of time.

By extending the present analysis to the spherical wave solution of Section 4.1, one arrives at a field dependence with the radial distance r according to $e^{-\alpha r} e^{-j\beta r}/r$. The definitions in (50) still apply in this case. Besides the original (algebraic) amplitude attenuation caused by the spherical spreading factor $1/r$, the presence of losses produce an additional (exponential) attenuation factor $e^{-\alpha r}$.

Equation (48) indicates that both β and α have a non-linear variation with ω , due to $\epsilon'(\omega)$ and $\epsilon''(\omega)$. Consequently, one observes from (50) that v_p varies with ω , that is, different frequency components travel at different phase velocities. This causes the *dispersion* of an electromagnetic wave composed by several frequencies. In RF and microwave applications, electromagnetic waves often have a certain frequency bandwidth, and dispersion may cause waveform distortion as the wave propagates. In general, losses can significantly decrease the signal-to-noise ratio (SNR) over RF and microwave links, and need

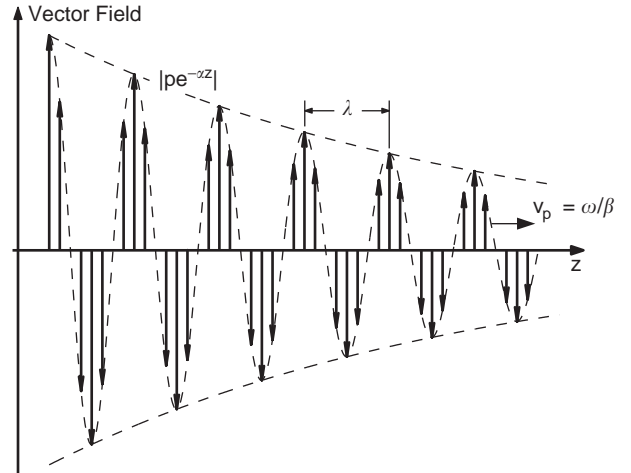


Figure 4. Uniform plane wave propagating in a lossy medium.

to be minimized and/or compensated (by using, e.g., repeaters through long-distance links).

5.2. Group Velocity

In a dispersive (simple) medium, the phase velocity v_p depends on ω . In this case, it becomes necessary to define the velocity of a wavepacket (i.e., a wave composed by different spectral components) for v_p is no longer adequate. To better understand this aspect, let us assume a wavepacket composed of two time-harmonic TEM components, propagating in a lossy simple medium in the $\hat{\mathbf{z}}$ direction and with the same linear polarization, such that

$$\begin{aligned} \mathcal{E} &= [p_1 e^{-\alpha_1 z} \cos(\omega_1 t - \beta_1 z + \phi_1) \\ &+ p_2 e^{-\alpha_2 z} \cos(\omega_2 t - \beta_2 z + \phi_2)] \hat{\mathbf{x}} \end{aligned} \quad (52)$$

For the sake of simplicity, we assume $p_1 = p_2 = p$, $\phi_1 = \phi_2 = 0$, and small losses, so that $\alpha_1 \approx \alpha_2 \approx 0$. Furthermore, we define $\omega_c = (\omega_1 + \omega_2)/2$, such that $\omega_{1,2} = \omega_c \mp \delta_\omega$, where $\delta_\omega = (\omega_2 - \omega_1)/2$. By so doing, (52) can be rewritten as

$$\mathcal{E} = 2p \cos \left[\omega_c t - (\beta_2 + \beta_1) \frac{z}{2} \right] \cos \left[\delta_\omega t - (\beta_2 - \beta_1) \frac{z}{2} \right] \hat{\mathbf{x}} \quad (53)$$

which corresponds to the envelope distribution depicted in Fig. 5. The first cosine (representing, e.g., a carrier with angular frequency ω_c) propagates with a velocity equal to $2\omega_c/(\beta_2 + \beta_1)$. In the limit $\delta_\omega \rightarrow 0$, $(\beta_2 + \beta_1)/2 \approx \beta_c$ (where β_c is the phase constant at ω_c) and, consequently, the carrier's velocity tends to the phase velocity at ω_c . The second cosine in (53) modulates the amplitude of the carrier (see Fig. 5) and propagates with a velocity equal to $\delta_\omega/\delta\beta$, where $\delta\beta = (\beta_2 - \beta_1)/2$ corresponds to the variation of β around ω_c . We then define the *group velocity*

$$v_g = \lim_{\delta_\omega \rightarrow 0} \frac{\delta_\omega}{\delta\beta} = \left(\frac{\partial\beta}{\partial\omega} \right)^{-1} \Bigg|_{\omega=\omega_c} \quad (54)$$

as the velocity of the wavepacket envelope, which can also be interpreted as the velocity of the signal (information)

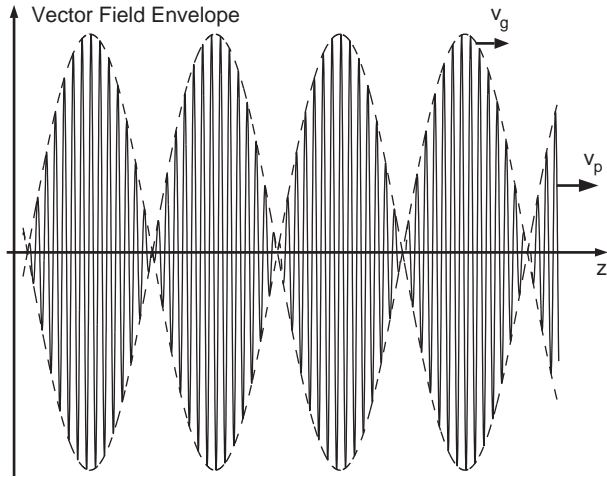


Figure 5. Group and phase velocities for a wave with two spectral components with distinct frequencies.

that modulates the carrier. A spectral analysis will demonstrate that (54) still holds for more arbitrary but bandlimited wavepackets propagating through a medium with little dispersion (i.e., with relatively small variations of β) [4]. As the wave energy is intrinsically related to the field strength (amplitude), for bandlimited signals v_g is also defined as the *velocity of energy flow* [4]. Obviously, $v_g = v_p = c$ for a TEM propagating through a lossless simple medium. More detailed discussions on wave velocities can be found in Refs. 4 and 5.

6. ELECTROMAGNETIC WAVE INTERACTION WITH OBSTACLES

6.1. Boundary Conditions

Boundary conditions are needed for the proper solution of Maxwell's equations at the interface between two dissimilar media (due to the discontinuity on their physical properties) or at discontinuous source distributions.

One boundary condition is associated with each one of (1) [6]. For a time-invariant interface between two regions 1 and 2, the four boundary conditions read as

$$\begin{aligned} \hat{\mathbf{n}} \times (\mathcal{E}_2 - \mathcal{E}_1) &= 0 & \hat{\mathbf{n}} \cdot (\mathcal{D}_2 - \mathcal{D}_1) &= q_s \\ \hat{\mathbf{n}} \times (\mathcal{H}_2 - \mathcal{H}_1) &= \mathcal{J}_s & \hat{\mathbf{n}} \cdot (\mathcal{B}_2 - \mathcal{B}_1) &= 0 \end{aligned} \quad (55)$$

where $\hat{\mathbf{n}}$ is the unit normal to the interface pointing toward region 2 and \mathcal{J}_s and q_s denote surface (or line) current and charge distributions over the interface, respectively. In (55), the field components are evaluated right next to each side of the interface, at region 1 or 2, respectively. In the time-harmonic regime, the complex representation of the boundary conditions have the same form as (55). If both regions represent simple media, then

(11), (44), and the complex representation of (55) gives

$$\begin{aligned} \hat{\mathbf{n}} \times (\mathbf{E}_2 - \mathbf{E}_1) &= 0 & \hat{\mathbf{n}} \cdot (\varepsilon_2 \mathbf{E}_2 - \varepsilon_1 \mathbf{E}_1) &= \rho_s \\ \hat{\mathbf{n}} \times (\mathbf{H}_2 - \mathbf{H}_1) &= \mathcal{J}_s & \hat{\mathbf{n}} \cdot (\mu_1 \mathbf{H}_2 - \mu_1 \mathbf{H}_1) &= 0 \end{aligned} \quad (56)$$

where μ_j and ε_j refer to region j ($j = 1, 2$).

In simple media and if no surface currents or charges are present at the interface, both (55) and (56) indicate that the tangential (to the interface) components of the electric and magnetic fields must be continuous across the interface, and these are the only boundary conditions that must be imposed for the proper wave solution, as at regions of a simple medium without sources only Faraday's and Ampère's laws are needed [6]. A particular case of interest is that at the interface of a perfect electric conductor, which will be discussed in Section 6.3.

6.2. Reflection and Refraction of Plane Waves

The plane-wave reflection and refraction at a planar interface is a canonical problem in electromagnetic wave theory and provides many useful insights into the behavior of waves in the presence of more general obstacles [19–22]. Consider a plane interface between two simple media (lossy or not), characterized by their (complex)

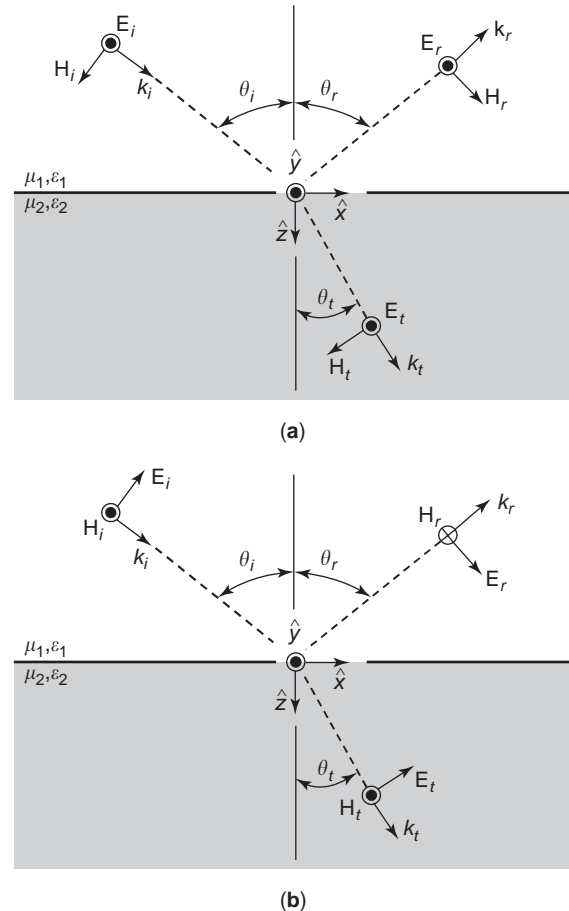


Figure 6. Plane-wave incidence on a plane interface: (a) perpendicular and (b) parallel polarizations.

permeabilities (μ_1 and μ_2) and permittivities (ε_1 and ε_2), as shown in Fig. 6. An incident plane wave (index i) impinges on the interface from medium 1, generating a reflected plane wave (index r), propagating back into medium 1, and a transmitted plane wave (index t) into medium 2. The exact reflected and transmitted energies of the corresponding waves depend on the media properties and on the direction of propagation and polarization of the incident wave.

Any arbitrary polarization can be decomposed into two linear and orthogonal ones in simple media (see Section 3.2). For the present analysis, the most commonly used are the perpendicular (no E -field component normal to the interface) and parallel (no H -field component normal to the interface) linear polarizations, as depicted in Figs. 6a and 6b, respectively. The formulas to be presented are valid for any incident plane wave, uniform or not. According to the discussion in Section 3, the geometric interpretation illustrated in Fig. 6 (i.e., with real-valued θ angles) is valid only for uniform waves. Depending on the case, some θ angles may come out complex, indicating that the corresponding plane wave is nonuniform. In any event, Fig. 6 is indeed useful for establishing the tangential (and normal) components of the fields at the interface, necessary for the application of the pertinent boundary conditions and, consequently, the solution of the problem. For uniform waves, Fig. 6 also provides a nice picture of the problem.

We will assume a time-harmonic regime (i.e., monochromatic waves) and use the complex phasor notation. According to (19), we can assume, without loss of generality, that the incident propagation vector (\mathbf{k}_i) has no component in the $\hat{\mathbf{y}}$ direction. The boundary conditions will further prove that the same occurs for the reflected (\mathbf{k}_r) and transmitted (\mathbf{k}_t) propagation vectors. With that we can define the xz plane in Fig. 6 as the *plane of incidence*. For uniform plane waves, that is in conformity with Fermat's principle; specifically, the trajectories are rectilinear (in simple media) and corresponding to the least travel time (see Section 4.3).

Starting with the perpendicular polarization and with the help of (17) and Fig. 6a, we define the electric fields of the plane waves as

$$\begin{aligned} \mathbf{E}_i &= E_0 e^{-j\mathbf{k}_i \cdot \mathbf{r}} \hat{\mathbf{y}} \\ \mathbf{E}_r &= \Gamma_{\perp} E_0 e^{-j\mathbf{k}_r \cdot \mathbf{r}} \hat{\mathbf{y}} \\ \mathbf{E}_t &= T_{\perp} E_0 e^{-j\mathbf{k}_t \cdot \mathbf{r}} \hat{\mathbf{y}} \end{aligned} \quad (57)$$

where Γ_{\perp} and T_{\perp} are Fresnel's reflection and transmission coefficients for the perpendicular polarization, respectively, relating the amplitude and phase of the corresponding field to those of the incident one. The propagation vectors are written as

$$\begin{aligned} \mathbf{k}_i &= k_1 (\sin \theta_i \hat{\mathbf{x}} + \cos \theta_i \hat{\mathbf{z}}) \\ \mathbf{k}_r &= k_1 (\sin \theta_r \hat{\mathbf{x}} - \cos \theta_r \hat{\mathbf{z}}) \\ \mathbf{k}_t &= k_2 (\sin \theta_t \hat{\mathbf{x}} + \cos \theta_t \hat{\mathbf{z}}) \end{aligned} \quad (58)$$

where $k_j = \omega \sqrt{\mu_j \varepsilon_j}$ (with $j=1,2$). Note that (58) is in agreement with (18). From (19), (57), and (58) one immediately obtains the H -field expressions, observing that $\eta = \eta_j = \sqrt{\mu_j / \varepsilon_j}$ with $j=1$ for the incident and reflected waves and $=2$ for the transmitted wave.

Enforcing the boundary conditions (i.e., the continuity of the tangential E - and H -field components) at the interface plane $z=0$, one comes up with *Snell's law*

$$k_1 \sin \theta_i = k_1 \sin \theta_r = k_2 \sin \theta_t \quad (59)$$

and also with

$$\begin{aligned} \Gamma_{\perp} &= \frac{\eta_2 \cos \theta_i - \eta_1 \cos \theta_t}{\eta_2 \cos \theta_i + \eta_1 \cos \theta_t} \\ T_{\perp} &= \frac{2\eta_2 \cos \theta_i}{\eta_2 \cos \theta_i + \eta_1 \cos \theta_t} \end{aligned} \quad (60)$$

Snell's law (59) comes from the matching of the phase variation of the fields at the interface. For a uniform incident wave (with a real-valued θ_i), (59) imposes that $\theta_r = \theta_i$ (i.e., the reflected wave is also uniform), which is the law of reflection known for centuries in optics and in conformity with Fermat's principle [1]. The Snell law for refraction is given by the second equality in (59), which can be rewritten with the help of (41)

$$n_1 \sin \theta_i = n_2 \sin \theta_t \quad (61)$$

where $n_{1,2}$ are the indices of refraction at regions 1 and 2, respectively. Equations (59) and (61) provide the value of θ_t with respect to θ_i and the physical properties of the medium. If one obtains a complex-valued θ_t , this indicates simply that the transmitted wave is nonuniform. That may happen even for a uniform incident wave if losses are present in one of the media (resulting in a complex index of refraction) or at *total reflection*.

The analysis of the parallel polarization follows along a line similar to that of its perpendicular counterpart and a comparison between Figs. 6a and 6b provides the necessary insights. After enforcement of the boundary conditions at the interface, one comes up with (59) and (61) once more (i.e., Snell's law is valid for any plane-wave polarization) and

$$\begin{aligned} \Gamma_{\parallel} &= \frac{\eta_2 \cos \theta_t - \eta_1 \cos \theta_i}{\eta_2 \cos \theta_t + \eta_1 \cos \theta_i} \\ T_{\parallel} &= \frac{2\eta_2 \cos \theta_i}{\eta_2 \cos \theta_t + \eta_1 \cos \theta_i} \end{aligned} \quad (62)$$

which are the Fresnel's reflection and transmission coefficients for the parallel polarization, respectively.

For simplicity, we shall assume next that both media are lossless simple dielectrics (i.e., $\mu_1 \approx \mu_2 \approx \mu_0$ and real-valued ε_1 and ε_2) and that the incident plane wave is uniform (θ_i is real). The incidence is defined *external* if $\varepsilon_2 > \varepsilon_1$ (e.g., the incidence of a radiowave on ground in a RF link). For real-valued θ_t , (61) provides that $\theta_t < \theta_i$ for

external incidences. Otherwise, the incidence is *internal* (e.g., a refraction from water into air).

The behavior of $|\Gamma|$ and $|T|$ with respect to θ_i is sketched in Figs. 7a and 7b for external and internal incidences, respectively. From the figures one observes two particular angles of incidence: the *Brewster* (or polarizing) angle θ_B , for which $|\Gamma_{\parallel}| = 0$, and the *critical* angle θ_C , such that, at internal incidence and for $\theta_i \geq \theta_C$, $|\Gamma| = 1$ and *total reflection* occurs. For lossless and simple media, the Brewster angle just occurs for the parallel polarization [1]. Its value can be determined from (61) and (62) by setting $\Gamma_{\parallel} = 0$:

$$\tan \theta_B = \frac{n_2}{n_1} \quad (63)$$

If losses are present, then Γ_{\parallel} is complex and $|\Gamma_{\parallel}| = 0$ is never met for any θ_i . Instead, $|\Gamma_{\parallel}|$ passes through a minimum, and that defines an *effective* Brewster angle. In any event, one can infer from Fig. 7 that $|\Gamma_{\parallel}| \leq |\Gamma_{\perp}|$

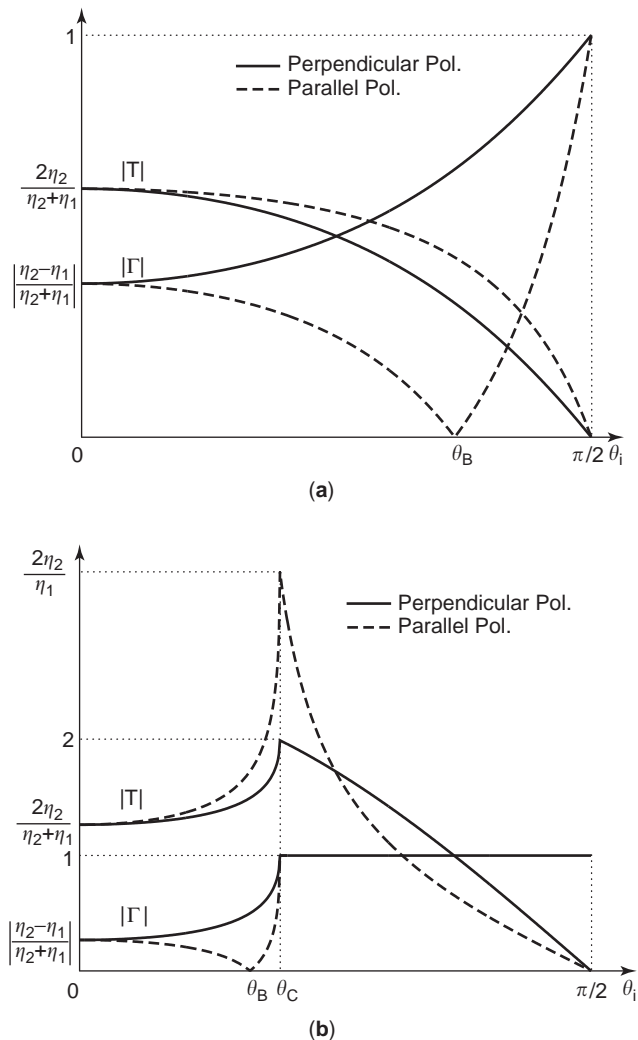


Figure 7. $|\Gamma|$ and $|T|$ as a function of θ_i : (a) external and (b) internal incidences.

for $0 < \theta_i < \pi/2$. For this reason, polarizing glasses are designed to block horizontally polarized light reflected by the ground. For this reason also, vertically polarized RF waves are preferred when attempting to obtain a uniform coverage of a urban cell in mobile communications at UHF (due to reflections from vertical buildings).

In lossless simple media, the critical angle θ_C occurs just at internal incidence. This is established from (61) and from the fact that $n_1 > n_2$ for internal incidence, yielding $\theta_t > \theta_i$ for $\theta_i \leq \theta_C$ with $\theta_t = \pi/2$ when $\theta_i = \theta_C$ by definition. Besides, θ_t becomes complex for $\theta_C < \theta_i \leq \pi/2$, indicating that the transmitted wave is nonuniform for incidence angles greater than θ_C . The primary consequence is $|\Gamma| = 1$ for $\theta_i \geq \theta_C$, as depicted in Fig. 7b.

To better understand the behavior of the transmitted wave at total reflection, let us recall the propagation vector \mathbf{k}_t of (58). For the present scenario and from (59) one will verify that the x component of \mathbf{k}_t is real-valued while its z component is purely imaginary, such that the transmitted wave propagates along the \hat{x} direction while its intensity dies off exponentially from the interface. So, the transmitted wave is strongly localized near the interface and propagates parallel to it, characterizing a *surface wave*. Also, if one obtains the \mathbf{E} - and \mathbf{H} -field components—with the help of (21) and (58)—and substitutes them into (13), it will be shown that the complex Poynting vector has a purely imaginary \hat{z} component and, consequently, there is no average flux of active (real) power through the interface (i.e., the incident power is totally reflected by the interface). In practical situations, losses will prevent such idealized conditions from occurring and a (small) amount of energy will eventually be transmitted through the interface [4]. The critical angle and the consequent total reflection helps in providing a nice picture of how light is guided throughout an optical fiber [23].

6.3. Waves on Good Electric Conductors

The equations of Section 6.2 can also be used to investigate the behavior of a plane wave incident on the surface of a good electric conductor. Let us assume that region 1 in Fig. 6 is a lossless simple medium (i.e., μ_1 and ϵ_1 are real-valued constants), while region 2 is a good conductor, in which case $\mu_2 \approx \mu_0$ and ϵ_2 is complex and according to (44). By definition, for good conductors $\sigma \gg \omega\epsilon$, such that $\epsilon_2 \approx -j\sigma/\omega$ for our purposes, where σ is the conductivity of region 2. Consequently, $k_2 \approx \sqrt{-j\mu_0\sigma/\omega}$ and $\eta_2 \approx \sqrt{j\omega\mu_0/\sigma}$.

Applying such definitions to (59), one should observe that $\theta_i = \theta_r$, as expected, and that $\theta_t \approx \pi/2$ as $\sigma \rightarrow \infty$. Besides, from (58) it is verified that $\mathbf{k}_t \approx k_2 \hat{z} \approx \sqrt{-j\mu_0\sigma/\omega} \hat{z}$. So, we come to the conclusion that the transmitted plane wave tends to behave as a uniform one inside the good conductor, propagating in the direction normal to the conductor's surface. The corresponding amplitude factor $\alpha_2 \approx \sqrt{(\mu_0\sigma)/(2\omega)}$ has a considerably large value, so that the field intensity dies off very rapidly away from the surface (tending to zero when $\sigma \rightarrow \infty$, as expected). Thus, a *skin depth* (δ) is defined as the propagation distance

needed for the field intensity to decay by e^{-1} , namely, $\delta = 1/\alpha_2 \approx \sqrt{(2\omega)/(\mu_0\sigma)}$.

As a consequence, \mathbf{E}_t is highly concentrated nearby and parallel to the surface. So, from (45) we end up concluding that there will be a volumetric conduction current highly concentrated nearby and flowing parallel to the conductor's surface. In the limit of a perfect electric conductor (i.e., $\sigma \rightarrow \infty$), such a current behaves as a surface one (\mathbf{J}_s), in which case (55) and (56) apply with null fields inside region 2 (note that $\hat{\mathbf{n}} = \hat{\mathbf{z}}$ in Fig. 6).

It is interesting to stress that the results presented here are valid for any angle of incidence θ_i and for any wave polarization. So, according to the discussion in the beginning of Section 3, the results are valid for any electromagnetic wave impinging on the surface of a good electric conductor.

The limiting case of a perfect electric conductor is not useful just for good conductors. As an example, let us assume an horizontally polarized radiowave propagating over ground and at *grazing incidence* (i.e., with $\theta_i \rightarrow \pi/2$, which is generally the case in a long-distance UHF radiolink). This corresponds to a perpendicular polarization and, according to (60), $\Gamma_{\perp} \rightarrow -1$. Note also from (60) that $\Gamma_{\perp} \rightarrow -1$ as well for incidences on a good electric conductor, as $|\eta_2| \rightarrow 0$ in this case. So, it is often used to approximate the ground as a perfect (or good) electric conductor to simplify the analysis [16]. For vertical polarization the approximation to be adopted also depends on other factors (such as the value of θ_B) [16].

6.4. Scattering and Diffraction

The scattering of an electromagnetic wave by an arbitrary obstacle is a difficult problem to solve using purely analytical techniques. Usually, numerical methods are employed. Among these, one can cite the method of moments [24], the finite-element method [25], and the finite-difference time-domain method [26].

However, if the incidence wave is locally TEM and if the obstacle is immersed in a simple medium and has a smooth surface, the concepts discussed in Sections 4.3 and 6.2 can be adopted (as approximations), to the extent that the obstacle's dimensions are large compared to the wavelength. Corrections to account for the curvatures of the incident wavefront (in case it is not a plane wave) and of the obstacle surface can be derived from GO principles and included in Γ of (60) and (62), according to the wave polarization [15,27]. The procedure is then conducted by *tracing rays* from the transmitter point to the receiver, such that any reflection on the obstacle must obey Fermat's principle, according to which the trajectories are rectilinear (in simple media) and $\theta_i = \theta_r$ with respect to the surface's normal. The difficulty of such technique generally appears in the determination of the *specular* points (where reflection occurs) over the surface of the obstacle.

If the obstacle presents curvature discontinuities (such as, e.g., at the edge of a wedge or at the border of a reflector antenna), then the propagation mechanisms associated with the incidence on such regions is classified as a *diffraction* (as the diffraction of a laser beam by a metallic slit). Asymptotic (in the sense of $k \rightarrow \infty$) techniques based

on the geometric theory of diffraction (GTD) can be applied to account for diffraction [27]. Such techniques are also based on ray tracing and can be accommodated together with GO principles to characterize the wave propagation through regions with several obstacles, such as a urban scenario in mobile communications [18].

7. GUIDED WAVES

Electromagnetic waves can propagate either in open space or through guiding structures such as transmission lines and waveguides. The choice of transmission lines depends on characteristics such as frequency of operation, bandwidth, power-handling capability, and losses. Some of the most usual transmission lines are two-wire lines, coaxial cables, rectangular and circular waveguides, microstrips, and striplines. These structures are discussed in more detail elsewhere in this encyclopedia in the article titled HIGH FREQUENCY TRANSMISSION LINES.

Some authors employ the *waveguide* denomination for guiding structures that allow propagation only of *transverse electric* (TE) and/or *transverse magnetic* (TM) waves, as described below, while the term *transmission lines* is used for guiding structures that allow propagation of TEM waves as well. Other authors use these terms interchangeably, as we will do here. We discuss TE and TM waves next.

7.1. TE and TM Waves

We will assume that the waves are guided in the z direction. TE and TM waves are a class of solutions of Maxwell's equations. As we are looking for propagating fields, their z dependence will be assumed on the form $e^{-jk_z z}$. In this case, the transverse components of the electric and magnetic fields can be written as [20]

$$\begin{aligned} \mathbf{E}_t &= \frac{1}{k^2 - k_z^2} [-j\omega\mu(\nabla_t H_z) \times \hat{\mathbf{z}} - jk_z \nabla_t E_z] \\ \mathbf{H}_t &= \frac{1}{k^2 - k_z^2} [j\omega\epsilon(\nabla_t E_z) \times \hat{\mathbf{z}} - jk_z \nabla_t H_z] \end{aligned} \quad (64)$$

where ∇_t stands for the transverse (to the z direction) portion of the ∇ operator. The electric field of the TE component is entirely transverse ($E_z = 0$), while the magnetic field has a longitudinal component ($H_z \neq 0$). From (64), the TE field is given by H_z and the corresponding transverse components \mathbf{E}_t and \mathbf{H}_t . On the other hand, the magnetic field of the TM component is entirely transverse ($H_z = 0$), while the electric field has a longitudinal component ($E_z \neq 0$). From (64) the TM field is given by the longitudinal electric field E_z and the corresponding transverse components.

TE and TM waves are supported by waveguides containing one or more perfect conductors and a homogeneous dielectric. In this case, each wave (or mode) satisfies the boundary conditions at the waveguide walls, and these waves are decoupled from each other. A useful example of such structure is the rectangular waveguide, formed by four metallic walls (perfect conductors), as shown in Fig. 8.

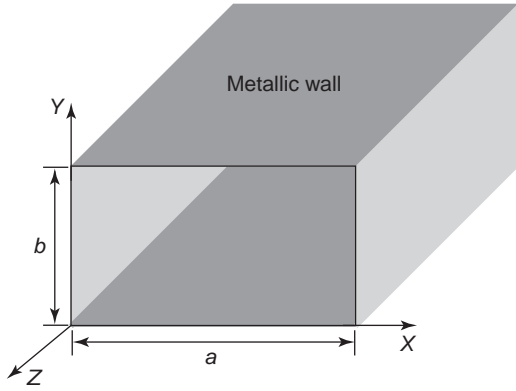


Figure 8. Rectangular waveguide geometry.

In general, a rectangular waveguide may be empty inside or *loaded*, that is, partially or completely filled with a dielectric. We will consider homogeneous (i.e., empty or completely filled with a uniform dielectric) rectangular waveguides next.

For TE modes (also known as *H modes*), the longitudinal component $H_z(x,y,z)$ is given by the solution of the scalar wave equation that satisfies the appropriate boundary conditions at the four metallic walls (in this case, $\partial H_z/\partial n = 0$)

$$H_z = H_0 \cos\left(\frac{m\pi x}{a}\right) \cos\left(\frac{n\pi y}{b}\right) e^{-jk_z z} \quad (65)$$

where $k_z = \sqrt{k^2 - (m\pi/a)^2 - (n\pi/b)^2}$, $m = 0, 1, 2, \dots$, $n = 0, 1, 2, \dots$ (but not $m = n = 0$). The transverse components of the electric and magnetic fields can be obtained directly from (64). These modes are denoted TE_{mn} , in reference to the indices m and n of (65). According to the frequency of operation, the TE_{mn} modes may propagate or not inside the waveguide. A propagating mode is characterized by a real k_z . The parameter k_z is real only if $k^2 > (m\pi/a)^2 + (n\pi/b)^2$. Otherwise, the mode is *evanescent* (exponentially decaying). The threshold frequency (where $k_z = 0$) is called *cutoff frequency* and is given by

$$f_{mn} = \frac{1}{2\sqrt{\mu\epsilon}} \sqrt{\left(\frac{m}{a}\right)^2 + \left(\frac{n}{b}\right)^2} \quad (66)$$

For TM modes (also known as *E modes*), the longitudinal component of the electric field is obtained from the solution of the scalar wave equation satisfying the boundary conditions at the four metallic walls (in this case, $E_z = 0$)

$$E_z = E_0 \sin\left(\frac{m\pi x}{a}\right) \sin\left(\frac{n\pi y}{b}\right) e^{-jk_z z} \quad (67)$$

where $m = 1, 2, \dots$, $n = 1, 2, \dots$, and k_z is the same as above. The transverse components of the fields are obtained by substituting (67) into (64). Again the TM_{mn} modes propagate only for frequencies above the cutoff frequency f_{mn} given by (66).

Assuming that $a > b$, the first mode that propagates (i.e., the one with smallest cutoff frequency) is the TE_{10} , which is called the *dominant* (or *fundamental*) mode. Usually, waveguides are designed to operate in a frequency range where only the dominant mode can propagate. This avoids intermodal dispersion [7] that results from the different phase velocities of two or more propagating modes. Note that if the waveguide is filled with a lossy dielectric, the modes are attenuated even above cutoff.

Mathematically, TE and TM modes are orthogonal to each other and form a complete set. This means that any field distribution inside the waveguide can be represented as a superposition of TE and TM modes [7]. However, when the finite conductivity of the metallic walls are considered, this orthogonality is no longer valid, and the modes become coupled. Also, when the dielectric is not homogeneous, the propagating modes become a combination of TE and TM fields, also called *hybrid modes* [7].

7.2. Surface and Leaky Waves

Surface waves were introduced in Section 6.2, under the condition of total internal reflection. This type of wave exhibits an exponential decay away from a guiding interface, while propagating in a direction parallel to it. Such a wave is also supported by dielectric waveguides, where no conductor is needed to guide the fields. A simple example of this kind of waveguide is the dielectric slab waveguide, formed by a dielectric layer (infinite in \hat{x} and \hat{z} directions), surrounded by air, as shown in Fig. 9. In the air, surface-wave modes are evanescent, and there is no average power flow from the dielectric to the air. TE and TM modes can be obtained for dielectric waveguide by following a procedure similar to the one described in Section 7.1 [6]. For TE and TM modes, there is also a possibility of even and odd modes. For example, even TM modes are given by [6]

$$E_z = \begin{cases} E_d \cos(\beta_y y) e^{-jk_z z} & \text{for } |y| \leq \frac{d}{2} \\ E_0 e^{-\alpha_y |y|} e^{-jk_z z} & \text{for } |y| \geq \frac{d}{2} \end{cases} \quad (68)$$

The associated transverse field components are obtained by substituting (68) into (64). The characteristic equations

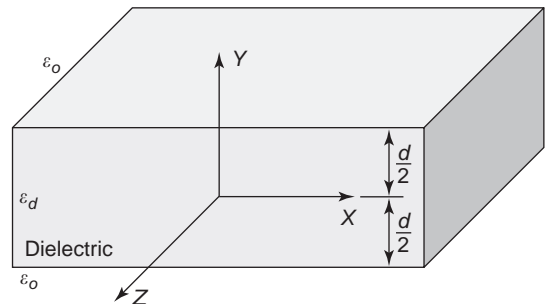


Figure 9. Dielectric slab waveguide.

in the dielectric and in air are given by $k_z^2 + \beta_y^2 = \omega^2 \mu_0 \epsilon_d$ and $k_z^2 - \alpha_y^2 = \omega^2 \mu_0 \epsilon_0$. The boundary conditions at the dielectric interfaces provides the relation between the amplitudes $[E_d \cos(\beta_y d/2) = E_0 e^{-\alpha_y d/2}]$ and require that [6]

$$\beta_y \cot \frac{\beta_y d}{2} = \frac{-\alpha_y \epsilon_d}{\epsilon_0} \quad (69)$$

which is the transcendental equation for k_z , and consequently β_y and α_y . Multiple solutions of this transcendental equation are often identified by a subscript n (TM_{*n*} mode).

These modes present surface waves properties when α_y is real and positive. The cutoff frequency of the TM_{*n*} mode is the lowest frequency for which it propagates with no attenuation [$\alpha_y = 0, \beta_y = \omega \sqrt{\mu_0(\epsilon_d - \epsilon_0)}$]. In this case, (69) results in

$$f_n = \frac{n}{2d \sqrt{\mu_0(\epsilon_d - \epsilon_0)}}, \text{ with } n = 1, 3, 5, \dots \quad (70)$$

For frequencies below the cutoff, the power is no longer confined within the dielectric, and part of it is radiated into air. As a consequence of this radiation loss, the modes propagate with attenuation, having complex $k_z = \beta_z - j\alpha_z$. This kind of wave is called a *leaky wave* [7]. A simple interpretation of these waves comes from the plane-wave expansion of a field within the dielectric. As mentioned earlier, any field can be written as a superposition of plane waves in a sourceless linear medium. From the dielectric interface problem, it is known that the plane waves with incidence angles above the critical angle will be totally reflected back to the dielectric, forming a surface wave. But those plane waves with incidence angles below the critical angle will be refracted into the air (radiation), forming a leaky wave. Odd TM modes and both even and odd TE modes can be obtained similarly, and present the same properties as described for even TM modes.

An important example of dielectric waveguide is the optical fiber [23], which is extensively used in long-distance and high-bandwidth communications. An optical fiber is formed by a dielectric rod, called *core*, and one or more surrounding cylindrical dielectric layers, called *claddings*. In the simplest format, only one cladding is used. Usually the refraction index of the core is slightly above that of the cladding, allowing the propagation of surface waves. When the refraction index of the core is constant, the configuration is known as a *stepped-index fiber*. Otherwise, it is known as a *graded-index fiber*. The modes that propagate in the fiber are, in general, hybrid (combination of TE and TM), and the dominant mode is called the *HE₁₁* mode, with no cutoff frequency [23].

8. COHERENT AND INCOHERENT WAVES

Electromagnetic waves can also be classified as coherent or incoherent [1]. Coherent waves have definite phase

fronts (for each wavelength), while incoherent waves do not. Coherent waves are produced by sources that emit energy through a collectively dependent process such as antennas. Most electromagnetic waves produced by synthetic devices at RF and microwave frequencies are coherent, as we have been considering here. Lasers are also an example of coherent wave sources.

On the other hand, incoherent waves result from the radiation of many collectively independent sources. In this case, the wavefront is not well defined and random phase fluctuations occur across space (spatial incoherence) and with varying wavelengths at random intervals (temporal incoherence). Incoherent sources include most natural sources of radiation such as the sun, light from fluorescent lamps and lightbulbs, and LEDs (light-emitting diodes). In general, electromagnetic waves exhibit some *partial* degree of coherence. As such, this classification corresponds to two ideal extremes. In reality, electromagnetic waves are at most highly incoherent (in one extreme) or mostly coherent (in the other extreme).

9. FURTHER REMARKS

In this article, we have focused mainly on classical aspects of electromagnetic wave propagation in simple media. For the vast majority of RF and microwave applications, this classical description is sufficient. However, the detailed interaction and propagation of electromagnetic waves in material media, including molecular and atomic effects, depends on quantum aspects that are not covered by a strictly classical description. The theory of electromagnetic interaction that takes into account the laws of quantum mechanics is called *quantum electrodynamics* (QED) [28,29]. The development of QED was the basis for the 1965 Nobel Prize in Physics, shared by Tomonaga (1906–1979), Schwinger (1918–1994), and Feynmann (1918–1988), who followed earlier developments by Dirac (1902–1984). When averaged at a macroscopic level, QED reduces to Maxwell's equations augmented by phenomenological equations that can be expressed in terms of macroscopic constitutive laws.

As a final side remark, it should also be noted here that Maxwell's equations in their classical form are invariant to Lorentz transformations [30] and already incorporate special relativity. Indeed, the need to preserve the form of Maxwell's equations in any nonaccelerated frames of reference (special relativity principle) was a major motivation to the development of special relativity theory by Einstein [31].

BIBLIOGRAPHY

1. M. Born and E. Wolf, *Principles of Optics*, 6th ed., Pergamon Press, Oxford, 1980.
2. J. C. Maxwell, *Electricity and Magnetism*, Academic Press, New York, 1935.
3. R. S. Elliott, *Electromagnetics: History, Theory, and Applications*, IEEE Press, Piscataway, NJ, 1993.

ELECTROMAGNETIC WAVE SCATTERING

RANDALL L. MUSSELMAN
USAF Academy
Colorado Springs, Colorado

1. TYPES OF ELECTROMAGNETIC SCATTERING

Fundamentally, there are three types of electromagnetic scattering mechanisms: reflection, refraction, and diffraction. These scattering mechanisms can radiate specularly or diffusely. *Specular scattering*, caused by electrically large flat objects, means that electromagnetic reradiation travels in parallel rays. *Diffuse scattering*, caused by irregular or electrically small objects, means that the electromagnetic reradiation spreads as it propagates away from the scattering object.

1.1. Specular Scattering

Of the three fundamental scattering mechanisms, the most familiar are specular reflection and refraction. If any corners or bends that exist at the boundary are very gradual compared to the wavelength of the incident field, then the boundary tends to cause *specular* scattering. Optical scattering is often assumed to be specular because most obstructing bodies that are smooth are electrically large compared to optical wavelengths. Specular scattering can be modeled with the specular law of reflection and Snell's law of refraction.

1.1.1. Reflection. A familiar example of specular reflection is the common reflection of a visible image in a mirror, since the dimensions of the mirror would be huge compared to the wavelength of visible light. Other examples are the radar return from a large flat target, cellular telephone multipath from a water tower, or a parabolic dish used to reflect microwave energy to the antenna at its focal point. The ratio of the reflected electric field E_r , to the incident electric field E_i , is called the *reflection coefficient*:

$$\Gamma = \frac{E_r}{E_i} \quad (1)$$

If the electric field in Fig. 1 is parallel to the plane of incidence containing all three propagation paths (i.e., incident, reflected, and transmitted paths), then it has *parallel polarization*. When the electric field is perpendicular to the plane of incidence (the x - z plane in Fig. 1), then it has *perpendicular polarization*. The reflection coefficients for parallel and perpendicular polarizations are

$$\Gamma_{\parallel} = \frac{\eta_2 \cos \theta_t - \eta_1 \cos \theta_i}{\eta_2 \cos \theta_t + \eta_1 \cos \theta_i} \quad (2a)$$

$$\Gamma_{\perp} = \frac{\eta_2 \cos \theta_i - \eta_1 \cos \theta_t}{\eta_2 \cos \theta_i + \eta_1 \cos \theta_t} \quad (2b)$$

4. J. D. Jackson, *Classical Electrodynamics*, 3rd ed., Wiley, New York, 1999.
5. J. A. Stratton, *Electromagnetic Theory*, McGraw-Hill, New York, 1941.
6. R. F. Harrington, *Time-Harmonic Electromagnetic Fields*, McGraw-Hill, New York, 1961.
7. R. E. Collin, *Field Theory of Guided Waves*, 2nd ed., IEEE Press, Piscataway, NJ, 1991.
8. L. B. Felsen and N. Marcuvitz, *Radiation and Scattering of Waves*, IEEE Press, Piscataway, NJ, 1994.
9. S. Silver, ed., *Microwave Antenna Theory and Design*, McGraw-Hill, New York, 1949.
10. J. A. Kong, *Electromagnetic Wave Theory*, EMW Publishing, Cambridge, MA, 2000.
11. W. Chew, *Waves and Fields in Inhomogeneous Media*, IEEE Press, Piscataway, NJ, 1995.
12. P. M. Morse and H. Feshbach, *Methods of Theoretical Physics*, Vol. 1, New York: McGraw-Hill Book Co., 1953.
13. P. C. Clemmow and J. Wait, *The Plane Wave Spectrum Representation of Electromagnetic Fields*, Oxford Univ. Press, 1996.
14. C. A. Balanis, *Antenna Theory Analysis and Design*, 2nd ed., Wiley, New York, 1997.
15. G. A. Deschamps, Ray techniques in electromagnetics, *Proc. IEEE* **60**(9):1022–1035 (Sept. 1972).
16. D. E. Kerr, ed., *Propagation of Short Radio Waves*, McGraw-Hill, New York, 1949.
17. J. D. Parsons, *The Mobile Radio Propagation Channel*, 2nd ed., Wiley, New York, 2000.
18. A. Yariv and P. Yeh, *Optical Waves in Crystals*, Wiley, New York, 1984.
19. C. A. Balanis, *Advanced Engineering Electromagnetics*, Wiley, New York, 1989.
20. D. K. Cheng, *Field and Wave Electromagnetics*, 2nd ed., Addison-Wesley, Reading, MA, 1992.
21. D. M. Pozar, *Microwave Engineering*, 2nd ed., Wiley, New York, 1998.
22. S. Ramo, J. R. Whinnery, and T. Van Duzer, *Field and Waves in Communication Electronics*, 2nd ed., Wiley, New York, 1984.
23. J. A. Buck, *Fundamentals of Optical Fibers*, Wiley, New York, 1995.
24. J. J.-H. Wang, *Generalized Moment Methods in Electromagnetics*, Wiley, New York, 1991.
25. J. Jin, *The Finite Element Method in Electromagnetics*, 2nd ed., Wiley, New York, 2002.
26. A. Taflove and S. C. Hagness, *Computational Electrodynamics: The Finite-Difference Time-Domain Method*, 2nd ed., Artech House, Boston, 2000.
27. D. A. McNamara, C. W. I. Pistorius, and J. A. G. Malherbe, *Introduction to the Uniform Geometrical Theory of Diffraction*, Artech House, Boston, 1990.
28. V. B. Berestetskii, E. M. Lifshitz, and L. P. Pitaevskii, *Quantum Electrodynamics*, 2nd ed., Pergamon Press, Oxford, 1982.
29. J. Schwinger, ed., *Selected Papers on Quantum Electrodynamics*, Dover, New York, 1958.
30. C. W. Misner, K. S. Thorne, and J. A. Wheeler, *Gravitation*, Freeman, San Francisco, 1973.
31. A. Einstein and L. Infeld, *Evolution of Physics*, Simon & Schuster, New York, 1966.

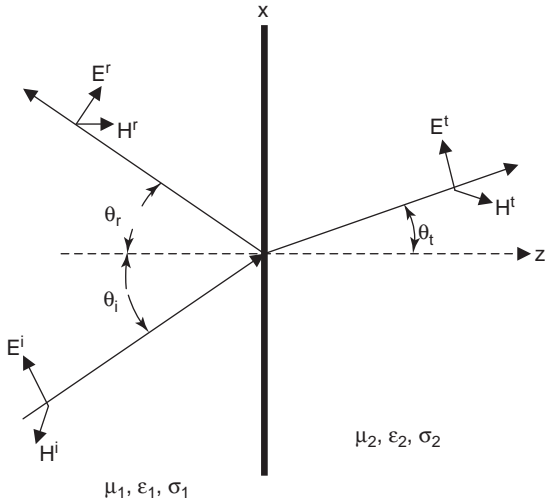


Figure 1. Illustration of Snell’s law. A plane-wave electromagnetic field obliquely incident onto a plane boundary, separating medium 1 ($\mu_1, \epsilon_1, \sigma_1$) from medium 2 ($\mu_2, \epsilon_2, \sigma_2$). A reflected field and a transmitted field scatter from this discontinuity in electrical constants.

where $\eta = (\mu/\epsilon)^{1/2}$ is the intrinsic impedance for each medium.

1.1.2. Refraction. The energy that is not reflected from the electrically large boundary is transmitted through the boundary. The ratio of the transmitted field strength to the incident field strength is called the *transmission coefficient*:

$$\tau = \frac{E_t}{E_i} \tag{3}$$

The transmission coefficients for parallel and perpendicular polarizations are

$$\tau_{||} = \frac{2\eta_2 \cos \theta_i}{\eta_2 \cos \theta_t + \eta_1 \cos \theta_i} \tag{4a}$$

$$\tau_{\perp} = \frac{2\eta_2 \cos \theta_i}{\eta_2 \cos \theta_i + \eta_1 \cos \theta_t} \tag{4b}$$

Equations (2) and (4) are known as *Fresnel’s equations*.

In the process of propagating from one electrical medium to the next, the speed of propagation changes. This change in speed causes a change in the propagation angle at the boundary, known as *refraction*. This phenomenon is commonly seen with visible light at the surface of a calm pool of water. The fact that an object extending from the air into the water appears bent is due to the increase in the propagation velocity of light as it leaves the water and enters the air. This phenomenon can be modeled with Snell’s law of refraction.

1.2. Diffuse Scattering

The laws for specular scattering are valid only for electrically large scattering bodies. If the object causing the elec-

tromagnetic scattering is small compared to the wavelength of the incident electromagnetic field, the induced currents would tend to radiate around the contour of the object, creating *diffuse* scattering. Unlike specular scattering, diffuse scattering results when the electromagnetic energy spreads outward as it radiates from the scattering object. The smaller the object, the more the energy will spread as it reradiates.

A simple example of diffuse scattering is an electromagnetic field incident on a very thin cylindrical conductor of length L along the z axis. At frequencies at or below the microwave region of the electromagnetic spectrum ($f \leq 20$ GHz), a thin copper wire will have an electrically small radius. A first approximation is to assume that the cylinder is a uniform line source [1], with a current distribution of

$$I(z) = \begin{cases} I_0 e^{j\beta_0 z} & -\frac{L}{2} < z < \frac{L}{2} \\ 0 & \text{elsewhere} \end{cases} \tag{5}$$

assuming that the source of the incident field is sufficiently far away that the induced current magnitude is approximately constant across the entire cross section and along the length of the wire. The phase angle $\beta_0 z$ along the length of the wire, is a result of the angle of incidence, where β_0 is the phase shift per unit length along the wire. The scattered or reradiated field from this wire is similar to the field radiated from a wire antenna and will radiate as

$$E = j\omega\mu \frac{e^{-j\beta r}}{4\pi r} \sin \theta \int_{-L/2}^{L/2} I_0 e^{j\beta_0 z} e^{j\beta z \cos \theta} dz \tag{6}$$

The radiation pattern of this scattered field is of the form $(\sin u)/u$, where $u = (\beta_0 + \beta \cos \theta)L/2$. The total field around the wire is the superposition, or vector sum at each point in space, of the scattered field and the original incident field that would have existed without the wire present. The scattered field added to the incident field creates a pattern with constructive reinforcement in some directions, and destructive cancellation in other directions. This is the function of the passive elements found on the Yagi-Uda antenna, common in television and other VHF and UHF communications.

In the Yagi-Uda antenna, only one set of elements is active. A half-wavelength dipole antenna usually makes up the active (or driven) element. The other elements are simply conductive cylinders or wires that reradiate some of the energy incident on them from the active element. Depending on the relative lengths of these passive elements, each of their re-radiated fields will add to the incident field of the active element, to create an overall pattern of power flow [2]. This focusing of energy is called *directivity* or *antenna gain*. Other forms of diffuse scattering by electrically small bodies are not so intentional.

1.3. Diffraction

Another form of scattering that cannot be accounted for by reflection or refraction is diffraction. For electrically large

scattering bodies, diffraction appears to occur at geometric discontinuities such as edges and corners. A first approximation is that currents induced only at these discontinuities reradiate electromagnetic energy. Diffraction is the scattering mechanism that accounts for radiation filling in the region that would have been completely blocked (shadowed) by an opaque obstruction.

Diffraction and reflection are important scattering mechanisms in communications. Whether in an urban or rural environment, a cellphone user will rarely have direct line of sight to the cell base station. Often, the communication link can be established only by energy reflecting off of a nearby building, or energy diffracted around a building or over a hill. Since these obstructions are typically electrically large, ray tracing techniques, which incorporate the laws for specular reflection and diffuse diffraction at edges, are often used to model the propagation characteristics of the communication channel.

2. THE LAWS OF SPECULAR REFLECTION AND REFRACTION

In many applications, an electromagnetic field can be assumed to be a plane wave. A plane wave is a convenient approximation amounting to the assumption that the electromagnetic field does not vary over the plane perpendicular to the direction of propagation. This approximation is similar to assuming that over small geographic areas, the planet Earth is flat. For wave propagation, this assumption is valid for a small observation area at a great distance from the source of a spherically propagating wave.

Figure 1 shows a plane-wave electromagnetic field incident on a boundary in the x - y plane. The generalized electric field will have components in the x , y , and z directions, that is

$$\mathbf{E} = (\hat{x}E_x + \hat{y}E_y + \hat{z}E_z)e^{-j\beta(\sin \theta_x + \cos \theta_z)} \quad (7)$$

where $\beta = \omega(\mu\epsilon)^{1/2}$ is the phase constant or wavenumber in units of radians per meter, μ is the permeability in henries per meter, and ϵ is the permittivity of the material in farads per meter. Imposing the tangential boundary condition for the electric field, the sum of the tangential components of the incident and reflected fields must equal that of the transmitted field [3–5]:

$$\begin{aligned} & (\hat{x}E_x^i + \hat{y}E_y^i)e^{-j\beta_1 \sin \theta_{1x}} + (\hat{x}E_x^r + \hat{y}E_y^r)e^{-j\beta_1 \sin \theta_{1x}} \\ & = (\hat{x}E_x^t + \hat{y}E_y^t)e^{-j\beta_2 \sin \theta_{2x}} \end{aligned} \quad (8)$$

This equality can be true for all x only when the exponents, or phases, are equal:

$$\beta_1 \sin \theta_{1x} = \beta_1 \sin \theta_{1r} = \beta_2 \sin \theta_{2x} \quad (9)$$

Equation (9) proves the well-known specular law for reflection, namely

$$\theta_i = \theta_r \quad (10)$$

which simply states that the angle of reflection equals the angle of incidence. Equation (9) also leads to Snell's law of refraction:

$$\frac{\sin \theta_i}{\sin \theta_t} = \left(\frac{\mu_2 \epsilon_2}{\mu_1 \epsilon_1} \right)^{1/2} \quad (11)$$

For most materials, the permeability is the same as that of free space, $\mu = \mu_0$. Assuming $\mu_1 = \mu_2$, Eq. (11) reduces to $n_1 \sin \theta_1 = n_2 \sin \theta_2$, where $n = (\epsilon_r)^{1/2}$ is the index of refraction and ϵ_r is the relative permittivity or dielectric constant.

3. ELECTROMAGNETIC THEOREMS

Few electromagnetic scattering problems lend themselves to the simple application of the laws of reflection and refraction. To develop more sophisticated analysis tools, a discussion of some basic electromagnetic theorems will be useful.

3.1. Uniqueness Theorem

Knowledge of the sources (currents) induced on the surface of a scattering body S enables unique solutions of the fields reradiated by those induced sources. Conversely, the known fields allow a unique calculation of the induced sources. The electric field \mathbf{E} and magnetic field \mathbf{H} are uniquely determined if [6,7]

1. $\hat{n} \times \vec{\mathbf{E}}$, the tangential component of \mathbf{E} , is specified on S .
2. $\hat{n} \times \vec{\mathbf{H}}$, the tangential component of \mathbf{H} , is specified on S .
3. $\hat{n} \times \vec{\mathbf{E}}$ is specified on part of S , and $\hat{n} \times \vec{\mathbf{H}}$ is specified on the remaining part of S .

3.2. Induction Theorem

In general, sources, such as conduction, displacement, and polarization currents, are induced at electrical discontinuities in the medium through which the incident field is propagating. Figure 2 shows a typical discontinuity represented by region 2. Region 2 represents a scattering body of material consisting of a permittivity ϵ , permeability μ , and conductivity σ , different from those of the surrounding region 1. Region 2 is bounded by a surface S . Assume that an electric field \mathbf{E}_1 and its associated magnetic field \mathbf{H}_1 , originate from a source current density \mathbf{J}_0 . This source could simply be the current oscillating in a transmitting antenna. These fields propagate undisturbed, through region 1, until they become incident upon the scattering body of region 2. As the fields cross the boundary between regions 1 and 2, they will be perturbed, that is, \mathbf{E}_2 and \mathbf{H}_2 in region 2 will generally not be equal to the fields \mathbf{E}_1 and \mathbf{H}_1 propagating in region 1. This abrupt change or discontinuity in electric and magnetic field strength results in currents that are induced at the discontinuity. In general, these currents will be

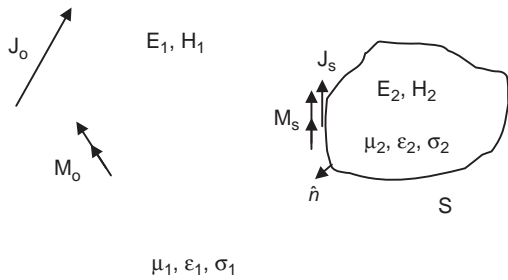


Figure 2. A scattering body. The incident field propagates from the source current, J_0 , through region 1. As this field strikes region 2, the currents J_s and M_s are induced at the surface S of the scattering body.

distributed through the volume of regions 1 and 2, depending on their electrical constants.

According to the induction theorem, whenever there is a discontinuity of the \mathbf{E} and \mathbf{H} fields crossing a boundary S between two media with different electrical constants, one can assume that induced currents at S cause the discontinuities in the fields. The induced current can be an electric current sheet [6–8]

$$\vec{J}_s = \hat{n} \times (\vec{H}^s - \vec{H}^i) = -\hat{n} \times \vec{H}^i \quad (12a)$$

or a fictitious, but mathematically useful, magnetic current sheet

$$\vec{M}_s = -\hat{n} \times (\vec{E}^s - \vec{E}^t) = \hat{n} \times \vec{E}^t \quad (12b)$$

The superscripts “i,” “s,” and “t,” pertain to the incident, outwardly scattered (reflected), and transmitted fields, respectively, and \hat{n} is the normal unit vector pointing out of the scattering body. If the scattering object is a perfect conductor, the transmitted fields vanish, leaving

$$\vec{J}_s = -\hat{n} \times \vec{H}^i = \hat{n} \times \vec{H}^s \quad (13a)$$

and

$$\vec{M}_s = \hat{n} \times \vec{E}^i = -\hat{n} \times \vec{E}^s \quad (13b)$$

The induction theorem alleviates the problem of knowing the exact distribution of current densities throughout the volume of the scattering body. The assumed currents exist only on the boundary S between the two media. Furthermore, the induced currents can be calculated directly from knowledge of the incident field that would have existed in the absence of any scattering object.

3.3. Equivalence Principle

If two different sources produce the same radiating field within a region, these sources are equivalent [8]. If both regions have the same electrical constants, only an inwardly scattered (transmitted) field exists. It follows from

Eq. (13) that the fields that are incident on the boundary S can be replaced by the equivalent current sheets

$$\vec{J}_s = \hat{n} \times \vec{H}^s = \hat{n} \times \vec{H}^i \quad (14a)$$

and

$$\vec{M}_s = -\hat{n} \times \vec{E}^s = -\hat{n} \times \vec{E}^i \quad (14b)$$

where in this case, \hat{n} is pointing in the direction of the transmitted or scattered wave. The equivalence theorem is useful for modeling radiation through apertures, such as a slot in a conductive plane or a horn antenna.

4. DIFFRACTION

Diffraction is the scattering mechanism that neither reflects off nor transmits through an obstruction. Even with opaque material allowing no transmission, diffraction accounts for radiation into the geometric shadow region. This scattering mechanism cannot be modeled with the specular laws of reflection and refraction, such as Snell’s law. To analyze diffraction exactly would require more knowledge about the induced current distribution around the scattering structure than would typically be feasible. Therefore approximations must be made to simplify the analysis. Two common approaches to analyzing diffraction are the use of geometrical optics and physical optics.

4.1. Geometrical Optics

Geometrical optics (GO) is a ray tracing technique that assumes that the electromagnetic energy travels in straight parallel lines or *rays* that are perpendicular to the wavefront. These rays travel from the point of reradiation to the observation point. While relatively easy to implement [9,10], GO is an approximation that relies on some important assumptions, primarily that the wavelength of the electromagnetic field must approach zero. Clearly, GO is an asymptotic technique valid only for sufficiently high frequencies, such that the wavelength is infinitesimal compared to the dimension of the obstruction. Since GO assumes infinite frequency, it ignores the wave nature of the electromagnetic scattering field, thus ignoring diffraction. The GO model creates an abrupt change in energy at the transition from the illuminated region to the shadow region. The abrupt change in field strength, without currents or charges to account for this discontinuity, violates boundary conditions. Therefore, GO provides only the crudest model, accounting only for reflection and refraction, but not for diffraction.

The geometrical theory of diffraction (GTD) extends GO to account for diffraction, by introducing a diffraction coefficient D , analogous to Γ for reflection and to τ for transmission [11–13]. The total electric field \mathbf{E}^T around the obstruction is

$$\mathbf{E}^T = \mathbf{E}^g + \mathbf{E}^d \quad (15)$$

where E^g is the electric field predicted by GO and is zero in the shadow region. The diffracted field for a plane wave of incidence is given by [14]

$$E^d(r) = DE_0(r)^{-1/2} e^{-j\beta r} \tag{16}$$

Figure 3 shows a plane wave incident on a perfectly absorbing half-screen. The diffraction coefficient can be quite involved even for this simple scattering structure. However, away from the shadow boundary [15]

$$E^d = -\frac{1}{2} E_0 \frac{(\lambda)^{1/2} r}{\pi x} e^{-j\beta r} \tag{17}$$

In the shadow ($-x$), the diffracted field given in Eq. (17) is the only field present. In the region of GO illumination ($+x$), the magnitude of the diffracted field of Eq. (17) subtracts from the incident field. Figure 4 illustrates the sum of the diffracted field and the GO incident field for (a) $z = 2\lambda$ and (b) $z = 20\lambda$. Clearly, there is a discontinuity at the transition between the GO illumination and shadow regions, around $x = 0$. This is an obvious limitation of the GTD, since there should be a smooth transition. One crude solution would be to simply draw a smooth curve connecting each side of the discontinuity through the point $x = 0, E = E_0/2$. A more sophisticated method is the uniform theory of diffraction (UTD), which is an extension of GTD that forces a smooth transition between the GO illumination and the shadow boundary [16].

Many common diffraction problems, such as hilltops and buildings, can be modeled with this half-screen or knife-edge approximation. However, the GTD still relies on several assumptions. The diffracted ray is assumed to depend entirely on the incident ray and the characteristics of the discontinuity itself, such as an edge of a scattering

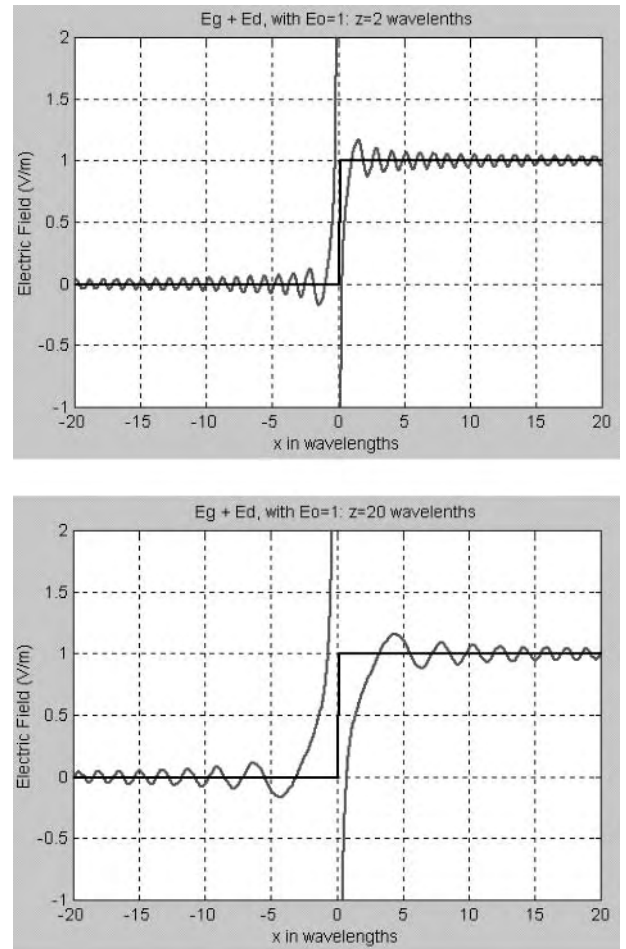


Figure 4. Simulation of half-screen diffraction by GTD. The solid straight line represents the GO incident field. The oscillating curve is the diffracted field, calculated by GTD, added to the GO field, at a distance behind the screen of (a) $z = 2$ wavelengths and (b) $z = 20$ wavelengths. (This figure is available in full color at <http://www.mrw.interscience.wiley.com/erfme>.)

structure [17]. The GTD is still a high-frequency asymptotic approximation because it assumes that the structure is electrically large and conductive [18]. Furthermore, GTD suffers from the unrealistic discontinuity problem at the GO illumination–shadow boundary.

4.2. Physical Optics

The edge diffraction problem of Fig. 3 can also be analyzed using the concept of physical optics (PO), which relies on Huygen’s principle. Huygen’s principle states that each point of a primary wavefront acts as a secondary point source. Each of these secondary sources radiates a spherical wave [14]. The primary difference between PO and GTD is that GTD assumes rays connect from the geometric discontinuity to the observation point, while PO assumes that secondary spherical waves radiate from the unobstructed primary wavefront. Figure 5 shows Huygen sources radiating into the GO shadow region behind the absorbing half-screen. The elemental electric field due to

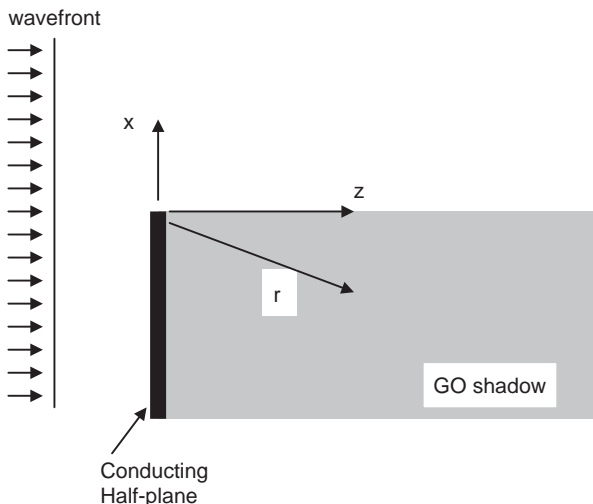


Figure 3. Half-screen diffraction using GTD. The currents induced at the edge, of the conducting half-screen, radiate into the GO shadow region.

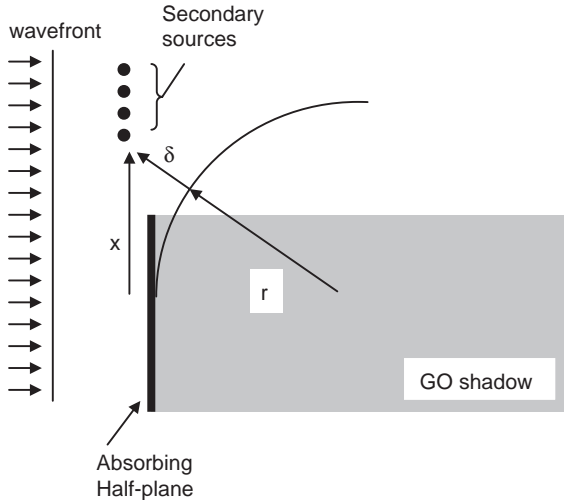


Figure 5. Half-screen diffraction using PO. The unblocked secondary sources radiate into the GO shadow region, accounting for diffraction.

each secondary point source is

$$dE = \frac{E_0}{r + \delta} e^{-j\beta(r+\delta)} \quad (18)$$

where E_0 is the electric field incident on the half plane, r is the distance from the observation point to the absorbing half plane, and δ is the additional distance to the secondary sources. From Fig. 5, we obtain

$$(r + \delta)^2 = r^2 + 2r\delta + \delta^2 = x^2 + r^2 \quad (19)$$

Clearly, the secondary sources closest to the half-screen will dominate the amplitude term in Eq. (18). Therefore, one could assume that $r > \delta$ in the amplitude term and $r^2 > \delta^2$ in the phase term of Eq. (18). Thus, Eq. (19) reduces to

$$\delta = \frac{x^2}{2r} \quad (20)$$

and Eq. (18) for the total electric field becomes

$$E = \frac{E_0}{r} e^{-j\beta r} \int_{x_0}^{\infty} e^{-j\beta(x^2/2r)} dx \quad (21)$$

where r is a constant of integration. Letting $u = (2/\lambda r)^{1/2}x$, and $u_0 = (2/\lambda r)^{1/2}x_0$, Eq. (21) becomes

$$E = \left(\frac{\lambda}{2r}\right)^{1/2} E_0 e^{-j\beta r} \int_{u_0}^{\infty} e^{-j(\pi u^2/2)} du \quad (22)$$

The limits of integration can be split into two terms:

$$E = \left(\frac{\lambda}{2r}\right)^{1/2} E_0 e^{-j\beta r} \left(\int_0^{\infty} e^{-j(\pi u^2/2)} du - \int_0^{u_0} e^{-j(\pi u^2/2)} du \right) \quad (23)$$

which has the form of Fresnel cosine and sine integrals. Equation (23) can be written as

$$E = \left(\frac{\lambda}{2r}\right)^{1/2} E_0 e^{-j\beta r} \left\{ \frac{1}{2} + j \frac{1}{2} - [C(u_0) + jS(u_0)] \right\} \quad (24a)$$

where $C(u_0)$ and $S(u_0)$ are the Fresnel sine and cosine integrals, respectively [19–21]. The solution to Eq. (24a) is similar to the GTD solution found in Fig. 3, with the exception that Eq. (24a) for PO does not suffer the discontinuity of Eq. (17) for GTD. In fact, Eq. (18a) has an analytic solution in the GO illumination–shadow transition region. The total electric field at $x_0 = 0$ is

$$E(x_0 = 0) = \left(\frac{\lambda}{2r}\right)^{1/2} E_0 e^{-j\beta r} \left(\frac{1}{2} + j \frac{1}{2} \right) \quad (24b)$$

and has a magnitude of $(E_0/2)(\lambda/r)^{1/2}$.

5. DIFFRACTION THROUGH AN APERTURE

The equivalence principle can be combined with PO to analyze scattering through an aperture. Let an electromagnetic plane wave be incident normal to the $a \times b$ aperture in a thin conducting screen of infinite extent, shown in Fig. 6. While this assumption of a screen with infinite extent may not be realistic, it can provide a good approximation for an aperture in an electrically large conductive plane. From the equivalence principle, the reradiated field appears to be generated by the current sheets described in Eq. (12). Starting from Maxwell's equations, the electric and magnetic fields radiated from the electric and magnetic current sources are

$$\begin{aligned} \vec{E} &= -j \frac{\omega\mu}{4\pi} \iint_{S'} \vec{J}' \frac{e^{-j\beta R}}{R} dx' dz' - \\ &\nabla \times \left(\frac{1}{4\pi} \iint_{S'} \vec{M}' \frac{e^{-j\beta R}}{R} dx' dz' \right) \end{aligned} \quad (25a)$$

and

$$\begin{aligned} \vec{H} &= -j \frac{\omega\epsilon}{4\pi} \iint_{S'} \vec{M}' \frac{e^{-j\beta R}}{R} dx' dz' + \\ &\nabla \times \left(\frac{1}{4\pi} \iint_{S'} \vec{J}' \frac{e^{-j\beta R}}{R} dx' dz' \right) \end{aligned} \quad (25b)$$

where the primed terms refer to the source, rather than the field. The equivalence principle allows the electric field in the aperture to be replaced by the magnetic current sheet \vec{M}_s over a continuous conducting screen [7]. The aperture is essentially short-circuited, which cancels \vec{J}_s .

From image theory, it appears as though an identical image of M_s lay on the opposite side of the screen. Since these two current sheets nearly coincide, the entire problem can be replaced with $2M_s$ at the aperture location, and no screen at all. Then Eq. (25b) becomes

$$\vec{H} = -j \frac{\omega\epsilon}{2\pi} \iint_{S'} M' \frac{e^{-j\beta R}}{R} dx' dz' \quad (26)$$

Rather than solving the integrodifferential equation (25a), Ampere's law can be used to obtain directly the scattered electric field in the source-free region:

$$\nabla \times \vec{H} = j\omega\epsilon \vec{E} \quad (27)$$

The distance R from each elemental source to the field point can be obtained from the law of cosines

$$R = [r^2 + (r')^2 - 2rr' \cos \psi]^{1/2} \quad (28)$$

where $r' \cos \psi = x' \sin \theta \cos \phi + y' \sin \theta \sin \phi$. Equation (26) would be difficult to integrate with a direct substitution of Eq. (28). However, if the scattered field is observed in the far-field Fraunhofer region, R and r will be virtually parallel. The far-field limit is usually taken to be

$$r \geq \frac{2D^2}{\lambda} \quad (29)$$

where D is the largest dimension of the aperture, in this case, the length of the diagonal [19]. The far-field assumption allows for the approximation $R \approx r - r' \cos \psi$ for the phase, and $R \approx r$ in the amplitude. Furthermore, in the far field, $E = \eta H$, where $\eta = (\mu/\epsilon)^{1/2}$ is the intrinsic impedance of the surrounding medium. This eliminates the need to solve Eq. (25a) or (27). Since in this case the incident plane wave is normal to the aperture, it will not vary over the aperture. Therefore, it can be brought out of the integral. Then the equation for the scattered magnetic field becomes

$$H = -j \frac{\omega\epsilon}{2\pi r} E_0 \int_{-a/2}^{a/2} \int_{-b/2}^{b/2} e^{-j\beta(x' \sin \theta \cos \phi + y' \sin \theta \sin \phi)} dx' dz' \quad (30)$$

While appearing messy, Eq. (30) is a straightforward integral. After integrating the two exponential terms, substituting the limits, and applying the identity

$$\sin \alpha = \frac{e^{j\alpha} - e^{-j\alpha}}{j2}$$

the scattered magnetic field in Eq. (30) becomes

$$H = j \frac{abe^{-j\beta r}}{\eta\lambda r} \left(\frac{\sin(X)}{X} \right) \left(\frac{\sin(Y)}{Y} \right) \quad (31a)$$

where

$$X = \frac{\beta a \sin \theta \cos \phi}{2} \quad (31b)$$

and

$$Y = \frac{\beta b \sin \theta \sin \phi}{2} \quad (31c)$$

Figure 7 is a plot of Eq. (31), with the amplitude normalized. The x dimension is $a = 6\lambda$, the y dimension is $b = 3\lambda$, and the observation screen is $z = 100\lambda$ from the aperture.

The normal angle of incidence was chosen for this problem to illustrate the concept, while keeping the mathematics simple. However, Eq. (31) can be extended to oblique incidence by modifying the current source M_s . Assuming that the source of the incident field is far from the aperture, the amplitude will not vary significantly across the aperture. However, the phase of each differential element of M_s will vary. The procedure is the same as for this analysis, except that some angle terms for the incident field will be added to X and Y in Eq. (25). The integration then follows in a similar manner [22].

6. BABINET'S PRINCIPLE

Scattering from a conductive plate can be modeled in a manner that virtually parallels the preceding solution to the aperture. In the case of scattering from a conductive plate, the current sources are obtained using the induction theorem. In fact, scattering through the aperture is the exact complement to the scattering off of the conductive plate that was essentially cut out of the conductive screen to create the aperture. If every electric parameter and every magnetic parameter were swapped, the solutions would be identical. Babinet's principle originally stated

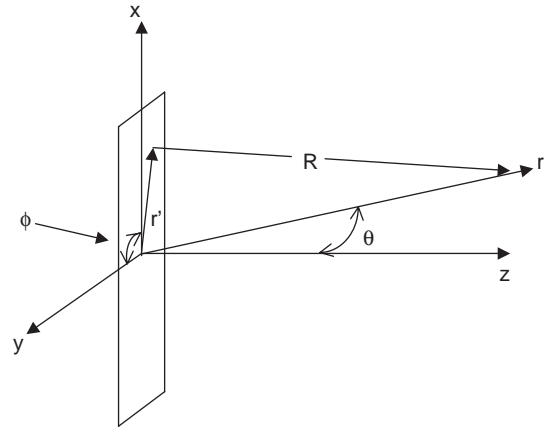


Figure 6. Coordinate system for the aperture diffraction problem. R is the vector pointing from the differential element $dx dy$ to the field point, and is the resultant vector sum of r and r' . The position vector from the origin to the secondary source in the aperture plane is $r' = [(x')^2 + (y')^2]^{1/2}$.

that the sum of the intensities from an obstruction and its complement (i.e., a similarly shaped aperture in the infinite screen) is equal to the intensity that would have existed if no obstruction existed at all

$$S_a + S_c = S_0 \tag{32}$$

While this relationship works for optics, it does not take into account polarization. To apply Babinet’s principle to vector fields, it must be modified to [23]

$$\frac{H^a}{H^i} + \frac{E^c}{E^i} = 1 \tag{33}$$

The first term in this equation is the ratio of the field diffracted by the aperture to the field with no screen present at all, and the second term is the ratio of the field produced by the complementary screen to the conjugate source. The *conjugate source* refers to the opposite field rotated by 90°. In vector form, Eq. (33) can be rewritten as

$$E^c = E^i - \eta H^a \tag{34}$$

which indicates that the electric field scattered from a conductive plate can be calculated from the field scattered from the aperture, by subtracting the latter from the incident field [22].

7. SPECIAL CASES OF ELECTROMAGNETIC WAVE SCATTERING

7.1. Rayleigh Scattering

If the scattering object is much smaller than a wavelength, its scattered energy varies inversely as the fourth power of the wavelength [1,24,25]. Therefore, for a given subwavelength object, higher frequencies will scatter more than will lower frequencies. This is the basis behind the concept of Rayleigh scattering for small scatterers. In fact, Rayleigh scattering answers the proverbial question: Why is the sky blue? Since the blue end of the visible spectrum has the shortest wavelength, blue light scatters more than does the rest of the visible spectrum from dust, water, and even air molecules. As the scattering objects become larger, they fall into the category called *Mie scattering*.

7.2. Radar Cross Section

Electromagnetic wave scattering is the basis by which radar signals are returned to the radar receiver from a target. Since the typical radar system employs a collocated transmit/receive antenna, the source and observation points are the same. This scenario is a specific case of electromagnetic wave scattering, known as *monostatic scattering*.

As the transmitted power P_T propagates through space, it spreads over an increasing surface area A , resulting in decreased power density $S_T = P_T/A$. If P_T spreads spherically as with a point source or isotropic radiator, then $A = 4\pi d^2$, where d is the distance from the transmitter. A target can intercept part of the transmitted power and scatter it in various directions. The radar cross section

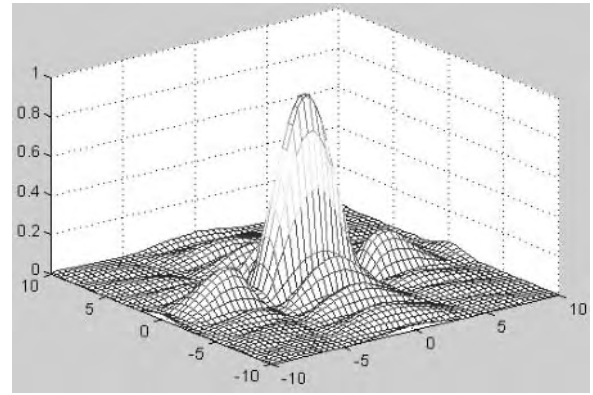


Figure 7. Normalized scattering pattern through the aperture. The dimensions of the aperture are 6×3 wavelengths; the observation screen is 100 wavelengths from the plane of the aperture. The scattering pattern is wider in the x direction, since the x dimension of the aperture is twice that of the y dimension. (This figure is available in full color at <http://www.mrw.interscience.wiley.com/erfme>.)

(RCS) is the effective area of the target that would return the monostatic power density back to the source, if this target scattered the power isotropically [1,26,27]. The amount of power returned to the source is

$$P_R = \frac{P_T G^2 \lambda^2 (\text{RCS})}{(4\pi)^3 d^4} \tag{35}$$

where G is the antenna gain and λ is the wavelength of the radar signal. The RCS is related to the physical cross-sectional area of the target but also depends on factors such as the frequency and polarization of the radar signal as well as the target’s shape, material, and orientation with respect to the transmitter.

Bistatic radar differs from monostatic radar in that the receiver and transmitter are not collocated. In the case of bistatic radar, we obtain

$$P_R = \frac{P_T G_T G_R \lambda^2 (\text{RCS})}{(4\pi)^3 d_1^2 d_2^2} \tag{36}$$

where G_T and G_R are the gains of the transmitting and receiving antennas, respectively, and d_1 and d_2 are the distances from the transmitter to the scatterer and the distance from the scatterer to the receiver, respectively. This can be a useful model for determining the power density and thus the electric field scattered off of an object when the transmitter power and antenna gain are known. [The product of transmitter power and antenna gain is known as *effective isotropic radiated power* (EIRP).] The scattered power density (in Watts per square meter) is

$$S \text{ (in } W/m^2) = \frac{P_T G_T (\text{RCS})}{(4\pi)^2 d_1^2 d_2^2} \tag{37}$$

and the RMS electric field (in volts per meter) is $E = (\eta S)^{1/2}$. If the EIRP is not known, Eq. (37) can be modified by substituting a measured power density S_0

measured at a distance d_0 from the original source. In terms of the measured power density, the scattered power density is

$$S \text{ (in } \text{W/m}^2\text{)} = S_0 \left(\frac{d_0}{d_1} \right)^2 \frac{\text{RCS}}{4\pi d_2^2} \quad (38)$$

8. SUMMARY

Since electromagnetic scattering perturbs the incident field, it can create interference, both constructive and destructive. The three main mechanisms of scattering are reflection, refraction, and diffraction. Reflection and refraction are the most common, and since these scattering mechanisms tend to be specular, they are easiest to analyze. Diffraction is much more difficult to analyze, and is typically not as dominant as the other two. Various approximations can lead to solutions of diffraction problems. The two main approximations covered were the GTD, which takes advantage of ray tracing, and PO, which relies on Huygen secondary sources. Slight modifications to the PO solution for the aperture problem can lead to solutions for backscattering, and forward scattering from a conductive plate. This simple structure can serve as a building block for more complicated structures, which can be modeled as composites of conductive plates.

BIBLIOGRAPHY

1. W. L. Stutzman, *Antenna Theory and Design*, 2nd ed., Wiley, New York, 1998.
2. J. D. Kraus, *Antennas*, 2nd ed., McGraw-Hill, New York, 1988.
3. C. R. Paul and S. A. Nasar, *Introduction to Electromagnetic Fields*, McGraw-Hill, New York, 1987.
4. C. T. A. Johnk, *Engineering Electromagnetic Fields and Waves*, Wiley, New York, 1988.
5. G. G. Skitek and S. V. Marshall, *Electromagnetic Concepts and Applications*, Prentice-Hall, Englewood Cliffs, NJ, 1982.
6. C. A. Balanis, *Advanced Engineering Electromagnetics*, Wiley, New York, 1989.
7. E. C. Jordan and K. G. Balmain, *Electromagnetic Waves and Radiating Systems*, Prentice-Hall, Englewood Cliffs, NJ, 1968.
8. R. F. Harrington, *Time-Harmonic Electromagnetic Fields*, McGraw-Hill, New York, 1961.
9. G. E. Corazza, V. Degli-Esposti, M. Frullone, and G. Riva, A characterization of indoor space and frequency diversity by ray-tracing modeling, *IEEE J. Select. Areas Commun.* **14**(3): 411–419 (April 1996).
10. M. Kimpe, V. Bohossian, and H. Leib, Ray tracing for indoor radio channel estimation, *Proc. IEEE, 2nd Int. Conf. Universal Personal Communication (ICUPC)*, Oct. 1993, pp. 64–68.
11. J. B. Keller, A geometrical theory of diffraction, in L. M. Graves, ed., *Calculus of Variations and its Applications*, *Proc. Symp. Applied Mathematics*, Vol III, McGraw-Hill, New York, 1958, pp. 27–52.
12. G. E. Athanasiadou, A. R. Nix, and J. P. McGeehan, Indoor 3D ray tracing predictions and their comparison with high resolution wideband measurements, *Proc. IEEE, 46th Vehicle Technology Conf.*, April 1996, Vol. 1, pp. 36–40.
13. O. Landron, M. J. Feuerstein, and T. S. Rappaport, A comparison of theoretical and empirical reflection coefficients for typical exterior wall surfaces in a mobile radio environment, *IEEE Trans. Anten. Propag.* **44**(3):341–351 (March 1996).
14. R. H. Clarke and J. Brown, *Diffraction Theory and Antennas*, Wiley, New York, 1980.
15. J. D. Kraus, *Electromagnetics*, 4th ed., McGraw-Hill, New York, 1992, pp. 622–627.
16. R. G. Kouyoumjian and P. H. Pathak, A uniform geometrical theory of diffraction for an edge in a perfectly conducting surface, *Proc. IEEE* **62**(11):1448–1461 (Nov. 1974).
17. J. B. Keller, Geometrical theory of diffraction, *J. Opt. Soc. Am.* **52**(2):116–130 (Feb. 1962).
18. J. B. Keller and A. Blank, Diffraction and reflection of pulses by wedges and corners, in *The Theory of Electromagnetic Waves*, Interscience Publishers, New York, 1951, pp. 139–158.
19. C. A. Balanis, *Antenna Theory, Analysis and Design*, Harper & Row, New York, 1982, pp. 92–94, 448.
20. E. Hecht, *Optics*, 2nd ed. Addison-Wesley, Reading, MA, 1987, p. 393.
21. M. Spiegel, *Advanced Mathematics for Engineers and Scientists*, Schaum's Outline Series, McGraw-Hill, New York, 1971.
22. R. L. Musselman, Analytic scattering model for indoor propagation, *Proc. IEEE Antennas & Propagation Society Int. Symp.*, 2001, Vol. 4, pp. 734–737.
23. H. G. Booker, Slot aerials and their relation to complementary wire aerials, *J. Inst. Electric. Eng. (Part IIIA)*: 620–626 (1946).
24. A. Ishimaru, *Wave Propagation and Scattering in Random Media*, Academic Press, San Diego, 1978.
25. H. C. van de Hulst, *Light Scattering by Small Particles*, Dover Publications, New York, 1981.
26. M. I. Skolnik, *Introduction to Radar Systems*, 2nd ed., McGraw-Hill, New York, 1980.
27. S. A. Hovanessian, *Radar System Design and Analysis*, Artech House, Norwood, MA, 1984.

ELECTROMAGNETIC WAVES IN IONOSPHERE

ROBERT D. HUNSUCKER
RP Consultants
Klamath Falls, Oregon

Although the emphasis of this encyclopedia is on the higher frequencies in the radio spectrum, the importance of the solar-terrestrial environment on radiowaves of all frequencies is of considerable importance to engineers designing radio systems for various services. An idealized representation of the solar-terrestrial environment is shown in Fig. 1.

It is interesting to note that EM waves over a very large spectral range interact with the terrestrial ionosphere and with radio receivers on Earth's surface or in space: (1) solar radiation, including the extreme ultraviolet (EUV):

measured at a distance d_0 from the original source. In terms of the measured power density, the scattered power density is

$$S \text{ (in } \text{W/m}^2\text{)} = S_0 \left(\frac{d_0}{d_1} \right)^2 \frac{\text{RCS}}{4\pi d_2^2} \quad (38)$$

8. SUMMARY

Since electromagnetic scattering perturbs the incident field, it can create interference, both constructive and destructive. The three main mechanisms of scattering are reflection, refraction, and diffraction. Reflection and refraction are the most common, and since these scattering mechanisms tend to be specular, they are easiest to analyze. Diffraction is much more difficult to analyze, and is typically not as dominant as the other two. Various approximations can lead to solutions of diffraction problems. The two main approximations covered were the GTD, which takes advantage of ray tracing, and PO, which relies on Huygen secondary sources. Slight modifications to the PO solution for the aperture problem can lead to solutions for backscattering, and forward scattering from a conductive plate. This simple structure can serve as a building block for more complicated structures, which can be modeled as composites of conductive plates.

BIBLIOGRAPHY

1. W. L. Stutzman, *Antenna Theory and Design*, 2nd ed., Wiley, New York, 1998.
2. J. D. Kraus, *Antennas*, 2nd ed., McGraw-Hill, New York, 1988.
3. C. R. Paul and S. A. Nasar, *Introduction to Electromagnetic Fields*, McGraw-Hill, New York, 1987.
4. C. T. A. Johnk, *Engineering Electromagnetic Fields and Waves*, Wiley, New York, 1988.
5. G. G. Skitek and S. V. Marshall, *Electromagnetic Concepts and Applications*, Prentice-Hall, Englewood Cliffs, NJ, 1982.
6. C. A. Balanis, *Advanced Engineering Electromagnetics*, Wiley, New York, 1989.
7. E. C. Jordan and K. G. Balmain, *Electromagnetic Waves and Radiating Systems*, Prentice-Hall, Englewood Cliffs, NJ, 1968.
8. R. F. Harrington, *Time-Harmonic Electromagnetic Fields*, McGraw-Hill, New York, 1961.
9. G. E. Corazza, V. Degli-Esposti, M. Frullone, and G. Riva, A characterization of indoor space and frequency diversity by ray-tracing modeling, *IEEE J. Select. Areas Commun.* **14**(3): 411–419 (April 1996).
10. M. Kimpe, V. Bohossian, and H. Leib, Ray tracing for indoor radio channel estimation, *Proc. IEEE, 2nd Int. Conf. Universal Personal Communication (ICUPC)*, Oct. 1993, pp. 64–68.
11. J. B. Keller, A geometrical theory of diffraction, in L. M. Graves, ed., *Calculus of Variations and its Applications*, *Proc. Symp. Applied Mathematics*, Vol III, McGraw-Hill, New York, 1958, pp. 27–52.
12. G. E. Athanasiadou, A. R. Nix, and J. P. McGeehan, Indoor 3D ray tracing predictions and their comparison with high resolution wideband measurements, *Proc. IEEE, 46th Vehicle Technology Conf.*, April 1996, Vol. 1, pp. 36–40.
13. O. Landron, M. J. Feuerstein, and T. S. Rappaport, A comparison of theoretical and empirical reflection coefficients for typical exterior wall surfaces in a mobile radio environment, *IEEE Trans. Anten. Propag.* **44**(3):341–351 (March 1996).
14. R. H. Clarke and J. Brown, *Diffraction Theory and Antennas*, Wiley, New York, 1980.
15. J. D. Kraus, *Electromagnetics*, 4th ed., McGraw-Hill, New York, 1992, pp. 622–627.
16. R. G. Kouyoumjian and P. H. Pathak, A uniform geometrical theory of diffraction for an edge in a perfectly conducting surface, *Proc. IEEE* **62**(11):1448–1461 (Nov. 1974).
17. J. B. Keller, Geometrical theory of diffraction, *J. Opt. Soc. Am.* **52**(2):116–130 (Feb. 1962).
18. J. B. Keller and A. Blank, Diffraction and reflection of pulses by wedges and corners, in *The Theory of Electromagnetic Waves*, Interscience Publishers, New York, 1951, pp. 139–158.
19. C. A. Balanis, *Antenna Theory, Analysis and Design*, Harper & Row, New York, 1982, pp. 92–94, 448.
20. E. Hecht, *Optics*, 2nd ed. Addison-Wesley, Reading, MA, 1987, p. 393.
21. M. Spiegel, *Advanced Mathematics for Engineers and Scientists*, Schaum's Outline Series, McGraw-Hill, New York, 1971.
22. R. L. Musselman, Analytic scattering model for indoor propagation, *Proc. IEEE Antennas & Propagation Society Int. Symp.*, 2001, Vol. 4, pp. 734–737.
23. H. G. Booker, Slot aerials and their relation to complementary wire aerials, *J. Inst. Electric. Eng. (Part IIIA)*: 620–626 (1946).
24. A. Ishimaru, *Wave Propagation and Scattering in Random Media*, Academic Press, San Diego, 1978.
25. H. C. van de Hulst, *Light Scattering by Small Particles*, Dover Publications, New York, 1981.
26. M. I. Skolnik, *Introduction to Radar Systems*, 2nd ed., McGraw-Hill, New York, 1980.
27. S. A. Hovanessian, *Radar System Design and Analysis*, Artech House, Norwood, MA, 1984.

ELECTROMAGNETIC WAVES IN IONOSPHERE

ROBERT D. HUNSUCKER
RP Consultants
Klamath Falls, Oregon

Although the emphasis of this encyclopedia is on the higher frequencies in the radio spectrum, the importance of the solar-terrestrial environment on radiowaves of all frequencies is of considerable importance to engineers designing radio systems for various services. An idealized representation of the solar-terrestrial environment is shown in Fig. 1.

It is interesting to note that EM waves over a very large spectral range interact with the terrestrial ionosphere and with radio receivers on Earth's surface or in space: (1) solar radiation, including the extreme ultraviolet (EUV):

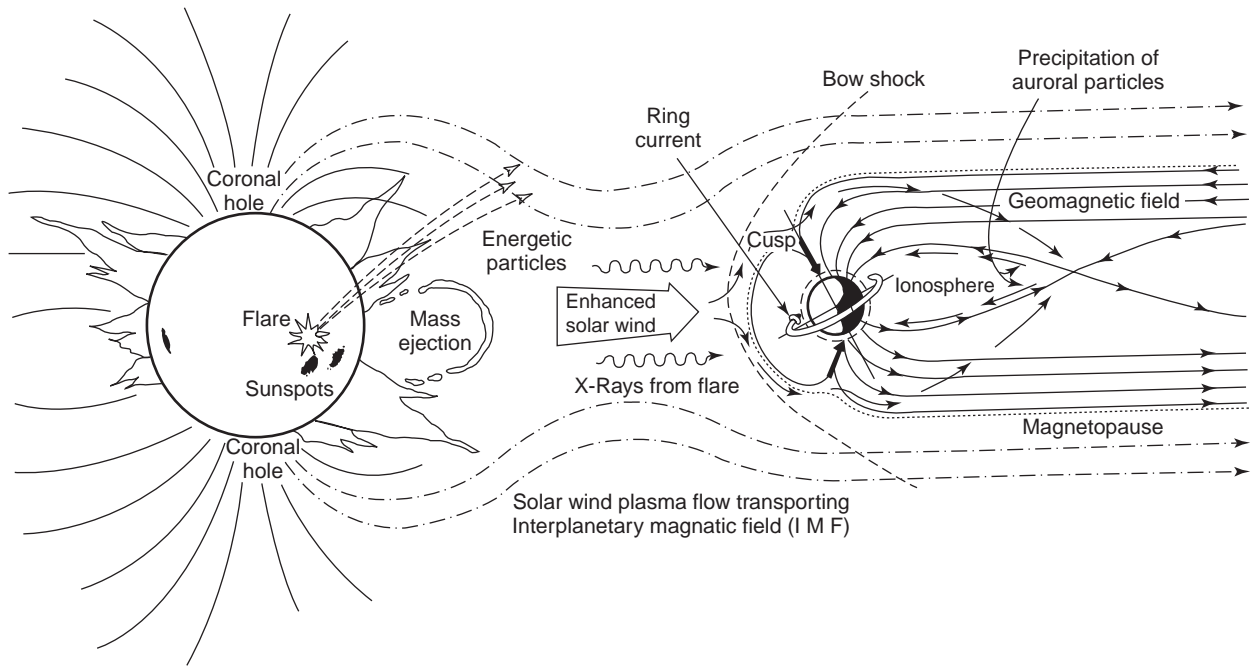


Figure 1. Idealized schematic representation of the solar-terrestrial environment.

102.7–111.8 nm), soft X rays, Lyman Alpha (121.5 nm); hard X rays (0.2–0.8 nm) and cosmic rays produce the ionospheric layers; (2) solar radio noise of frequencies ~20 MHz up to 1 GHz penetrates the terrestrial ionosphere and can degrade the signal-to-noise ratio (SNR) received on various radio services; (3) radio signals from ELF through low VHF (~10 Hz to ~35 MHz) propagate over long terrestrial paths by reflection and refraction by the ionosphere.

The main ionizing agents are listed in the preceding paragraph. At high geomagnetic latitudes, energetic electrons and protons also can produce areas of high ionization density. The terrestrial ionosphere is a roughly spherical shell of weakly ionized plasma that surrounds Earth. A plasma is a gas that has been ionized by radiation or by charged particles, so that it consists of free electrons, ions, and neutrals; it is sometimes referred to as the fourth state of matter [1], the characteristics of various plasmas are displayed in Fig. 2.

This spherical shell is stratified into distinct layers; the lowest region is the D layer, starting at about 50 km height; the E region, starting at about 100 km; the F1 layer (during the day) near 250 km; and the F2 layer at about 350 km. At high geomagnetic latitudes, solar energetic charged particles are also important ionizing agents. Figure 2 is a plot of log density versus log kinetic temperature showing the relative state of ionization of various plasmas, and Fig. 3 illustrates the various ionospheric layers and their ionizing agents.

1. THE RADIO SPECTRUM

A considerable portion of the radio spectrum (ELF through HF) is affected by our ionosphere, and the ITU

nomenclature for the frequency bands, along with the principal modes and uses, are shown in Table 1. The so-called wireless frequencies lie in the UHF and SHF bands.

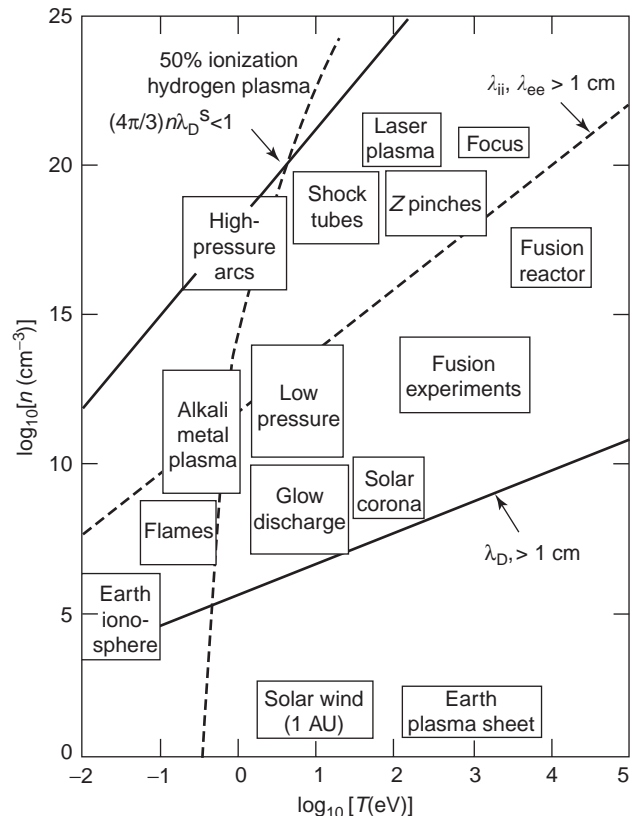


Figure 2. Logarithmic plot of approximate magnitudes of some typical laboratory and natural plasmas.

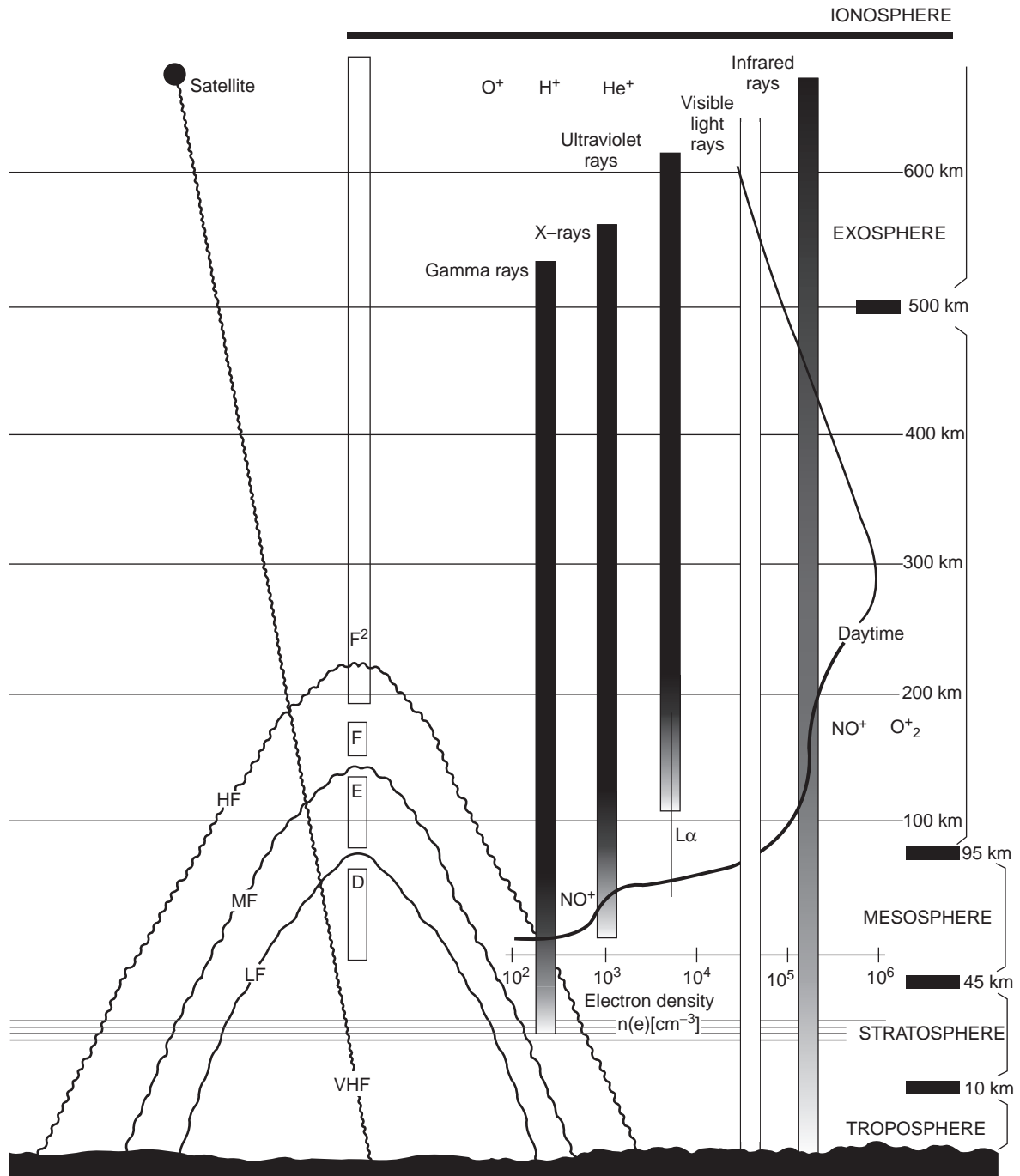


Figure 3. The ionospheric regions and their ionizing agents. (From Ref. 2.)

2. IONOSPHERIC INTERACTION WITH EM WAVES

The basic interaction mechanism between radio- (EM) waves and the ionosphere involves the oscillation of the electric component of the wave acting on free electrons, which are 1800 times less massive than the ionospheric neutrals or ions. The E wave induces motion of the electrons, and at the same time the ionosphere abstracts energy from the electrons, resulting in a bending of the radio wave and in some energy loss from the wave. Figure 4

illustrates the attenuation of radiowaves in the ionosphere as a function of frequency from 1 Hz to 30 MHz.

As may be seen in Fig. 4, there is a variation in radio-wave attenuation from day to night. The virtual height (the height at which radiowaves at vertical incidence are reflected) varies with time of day, with season of the year, and with geomagnetic activity. The most regular variation is the local time variation, as shown in Fig. 5.

There are many techniques used to investigate the characteristics of the ionosphere [2-4]. The propagation

Table 1. The Radio Spectrum as Defined by the International Telecommunications Union (ITU); Primary Modes of Propagation, and Effects of the Terrestrial Ionosphere

ITU Designation	Frequency Range	Principal Propagation Modes	Principal Uses
Extralow frequency (ELF)	30–300 Hz	Ground wave and Earth–ionosphere waveguide mode	Submarine communication
Very low frequency (VLF)	3–30 kHz	Same as above	Navigation, standard-frequency and -time dissemination
Low frequency (LF)	30–300 kHz	Same as above	Navigation LORAN-C ^a
Medium frequency (MF)	300–3000 kHz	Primarily ground wave, but sky wave ^b at night	AM broadcasting, maritime, aeronautical communication
High frequency (HF)	3–30 MHz	Primarily sky wave, some ground wave	Shortwave broadcasting, amateur, fixed services
Very high frequency (VHF)	30–300 MHz	Primarily LoS, ^c some sky wave at lower VHF	FM broadcasting, television, aeronautical communication
Ultrahigh frequency (UHF)	300–3000 MHz	Primarily LoS, some refraction and scattering by the ionosphere	Television, radar, navigation, ^d aeronautical communication
Superhigh frequency (SHF)	3–30 GHz	Same as above	Radar, space communication

^aThe LORAN-C system will probably be superseded by the GPS system.

^bSky wave denotes the Earth–ionosphere–Earth reflection mode.

^cLine of sight.

^dGlobal Positioning System satellite constellation.

of radio waves in the ionosphere is described in considerable detail in Ref. 5, and solar–terrestrial relations and their effects on radio propagation are covered in Ref. 6. Radiowave propagation at all frequencies depends to different degrees on the geographic and geomagnetic latitudinal region of the ionosphere. The most benign latitudinal region is the midlatitudes; the most disturbed regions are the auroral, equatorial, and polar regions, as described in detail in Ref. 4.

In the next section we describe qualitatively the salient propagation modes and ionospheric effects on radiowaves as a function of frequency. The section after provides a mathematical description and the physical principles of the interaction of radiowaves with the ionosphere. The final section will introduce the reader to the frontiers of ionospheric research at the start of the twenty-first century.

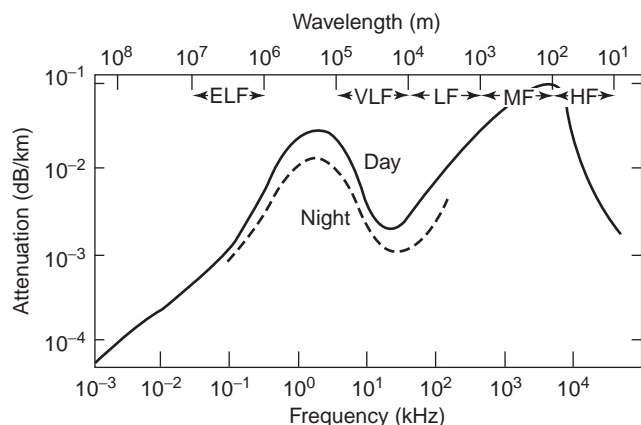


Figure 4. Night–day variation of attenuation on radio paths as a function of frequency from 1 Hz to 30 MHz. (Courtesy of D. Llanwyn Jones.)

3. EFFECTS ON SPECIFIC RADIO SERVICES

3.1. Extremely Low and Very Low Frequencies (ELF and VLF)

As indicated in Table 1, at the lowest frequencies (ELF–VLF) the basic propagation mode is a spherical waveguide mode, with the D and E regions of the ionosphere forming the upper boundary, and Earth’s surface the lower boundary. A simplified Earth–ionosphere waveguide geometry is shown in Fig. 6. A schematic diagram of the first two waveguide modes in an ideal earth-ionosphere mode is presented in Fig. 7.

In reality, the ELF–VLF waveguide mode is considerably more complicated because of its spherical nature and the electrical characteristics of the upper and lower boundaries. At ELF frequencies, the wavelength is of the same order of magnitude as the transverse dimensions of the waveguide, and the signal propagates deeply into both land and sea because of the skin-depth effect.

At global distances, the signal is very stable, but extremely long antennas and high transmitter powers are required and the signaling rate is extremely slow. One unique advantage of ELF is the ability of the signal to penetrate relatively deeply into seawater (at 100 Hz, the attenuation in seawater is 0.3 dB/m, which is $\approx \frac{1}{3}$ of the

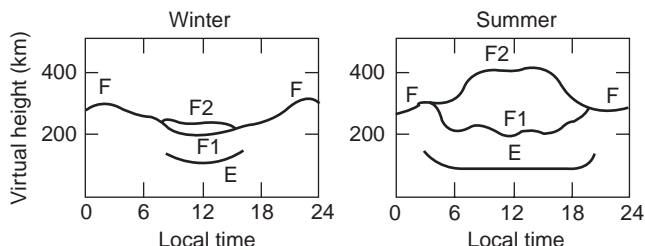


Figure 5. Average variation of ionospheric layer height as a function of season and local time. Note the large change in height of the F2 layer in summer.

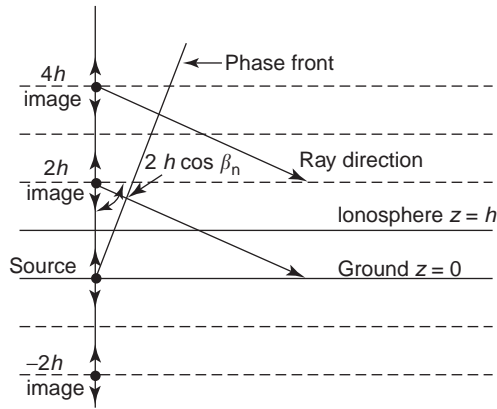


Figure 6. Simplified ray geometry for the first-order and second-order VLF-ELF modes. The two conducting planes are representative at the earth surface and the ionosphere.

attenuation in the Earth-ionosphere waveguide). The attenuation of ELF signals penetrating normal Earth is approximately $\frac{1}{10}$ th that in seawater, so ELF signals can also be used to probe or communicate into the solid Earth. There is also some evidence that high-latitude effects such as D-region irregularities can cause some phase anomalies in ELF and VLF transmissions [7-9].

VLF (3-30 kHz) transmissions also require large antennas and high-power transmitters, but are used more than ELF for time- and frequency-standard dissemination and navigational systems. VLF signals are also influenced by anomalies on Earth's surface [10] and in the high-latitude ionosphere [4].

3.2. Low Frequencies (LF)

Moving up in frequency to the LF band (30-300 kHz), the basic propagation mode below ≈ 100 kHz is by the ground

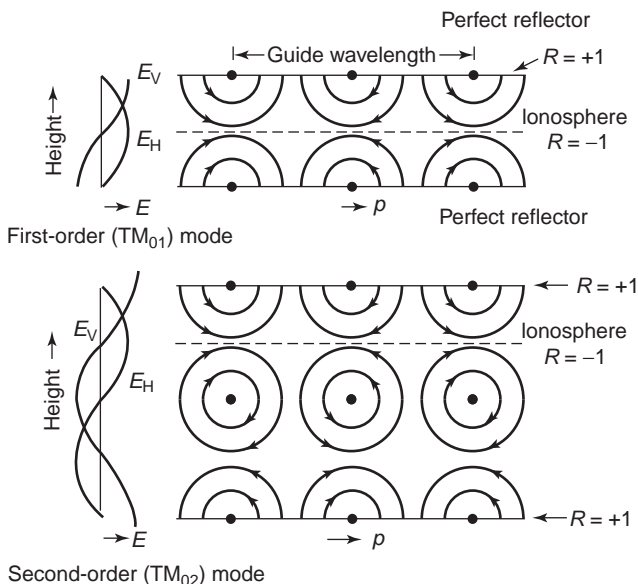


Figure 7. The E field for ideal Earth-ionosphere waveguide modes.

(surface) wave, which follows Earth's curvature, and above 100 kHz is the sky wave and the waveguide mode. The sky wave is, of course, influenced by the ionospheric diurnal, seasonal, and latitudinal variations.

3.3. Medium Frequencies (MF)

Propagation during the daytime in the MF (300-3000 kHz) band is by ground wave, and for frequencies above 500 kHz, at night by sky wave. At geomagnetic latitudes greater than 55° , the auroral ionosphere introduces some anomalous sky-wave propagation modes [10].

3.4. High Frequencies (HF)

The ionosphere has the most profound effect on signals in the HF (3-30 MHz) band, making the sky-wave mode the dominant means of propagation. The ground wave at HF is sometimes used in the frequency range of 3-6 MHz, especially over seawater, whose conductivity is much greater than that of ordinary land. At HF wavelengths relatively high efficiency, gain, and directivity can be achieved in the antenna systems, so directive communications and broadcasting are realizable. Above 6 MHz, the sky wave is dominant, so one must really understand ionospheric behavior and phenomenology in order to predict propagation. Since the ionosphere varies with time of day, season, solar activity, and sunspot cycle, predicting HF propagation over a specific path can be somewhat complicated. Propagation paths up to $\approx 10,000$ km are quite common for shortwave (SW) broadcasters, who use antennas with gains of up to 20 dBi (dBi is gain referenced to an isotropic source) and transmitter powers of 250 kW and higher. With much less reliability, amateur radio operators (hams) sometimes also achieve two-way communications over similar pathlengths using antenna gains of 3-12 dB and transmitter powers of 5-1000 W.

The ionosphere also behaves differently in the equatorial, midlatitude, auroral, and polar latitudinal regions. Fortunately, several fairly reliable and easy-to-use HF propagation prediction programs are now available to HF system planners for PCs (ASAPS, VOACAP, PropLab-Pro, etc.). The sources of these programs may be found in more recent books and articles [4,5,12,13] and in the amateur radio magazines (*QST*, *CQ*, *Worldradio*, etc.).

Unfortunately, none of the existing prediction programs gives very reliable results at equatorial and high latitudes. They are based on climatological data, so they are not intended for forecasting. A following section describes the mathematical essentials of ionospheric propagation in considerable detail.

3.5. Very High Frequencies (VHF)

Propagation in the VHF band (30-300 MHz) is primarily by line of sight (LoS) to the optical horizon, so if the antenna patterns direct most of the RF power in the horizontal plane, there are essentially no ionospheric effects. For Earth-space propagation paths, however, the ionosphere can affect the signal adversely by refraction, diffraction, scattering, or reflection. These effects can be

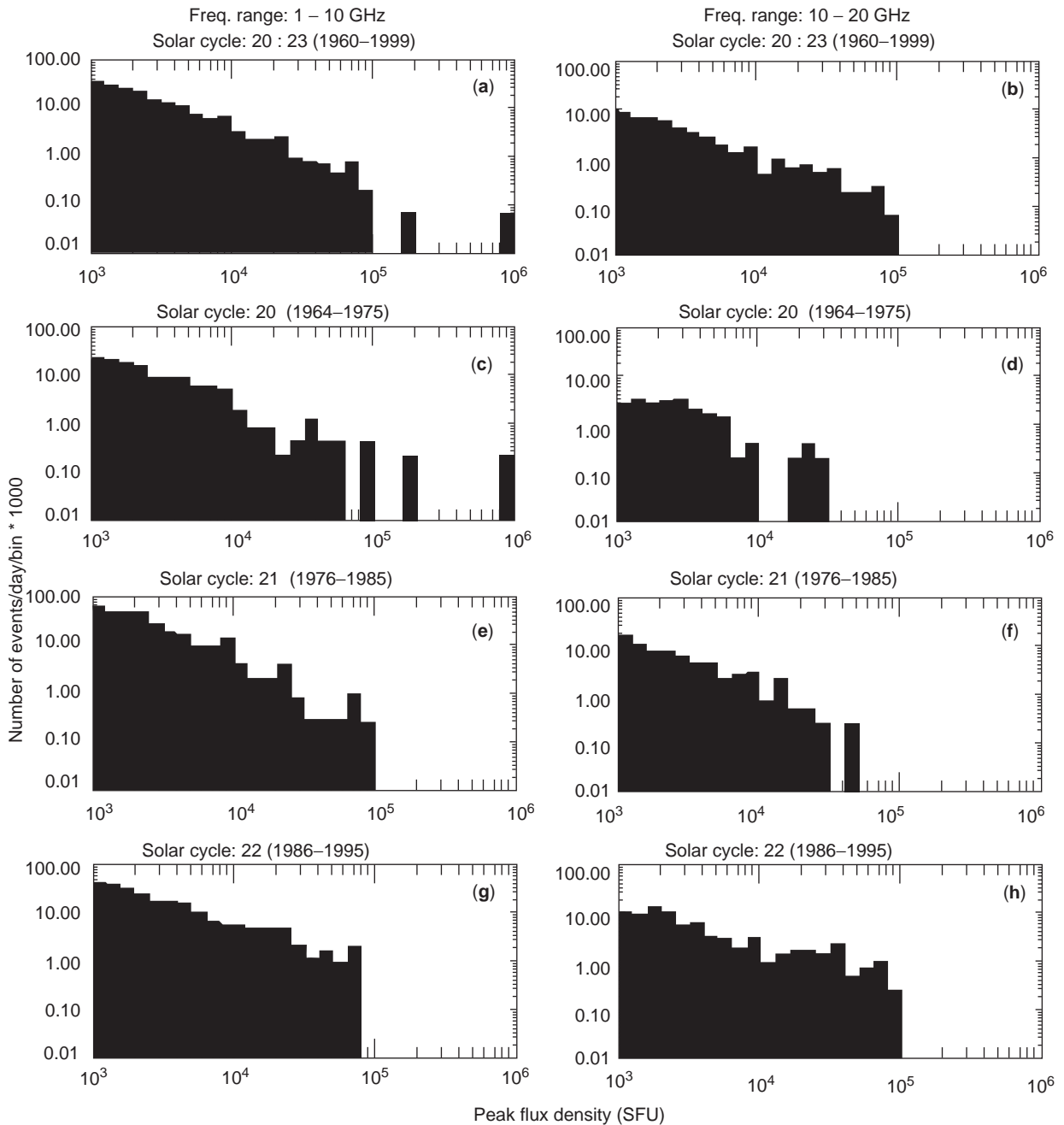


Figure 8. Number of events per day with amplitudes $> 10^3$ SFU (a,b) for 40 years, (c,d) for cycle 20, (e,f) for cycle 21, and (g,h) for cycle 22. The frequency ranges are 1–10 GHz (excluding 10 GHz) shown in the left panels and 10–20 GHz (excluding 20 GHz) in the right panels. Here, the number of events per day per bin is multiplied by 1000.

especially important when the path traverses the equatorial, auroral, and polar ionosphere. The amplitude, phase, and polarization of the signal may change measurably. These effects will be quantified in the following section.

3.6. Ultra High Frequencies (UHF)

At UHF and above, propagation is primarily LoS, and because of the higher frequencies ($f \geq 300$ MHz), these

signals are less affected by the ionosphere than lower frequencies. On Earth–space paths that traverse the equatorial and/or high-latitude ionosphere, however, the signal quality can be significantly degraded at certain times. At “wireless” frequencies ($f \approx 800$ MHz–20 GHz) solar radio bursts can sometime seriously degrade certain wireless systems. Figure 8 shows the variation of peak flux density of solar radio noise with frequency and time, and Fig. 9 shows the total number of events per day as a

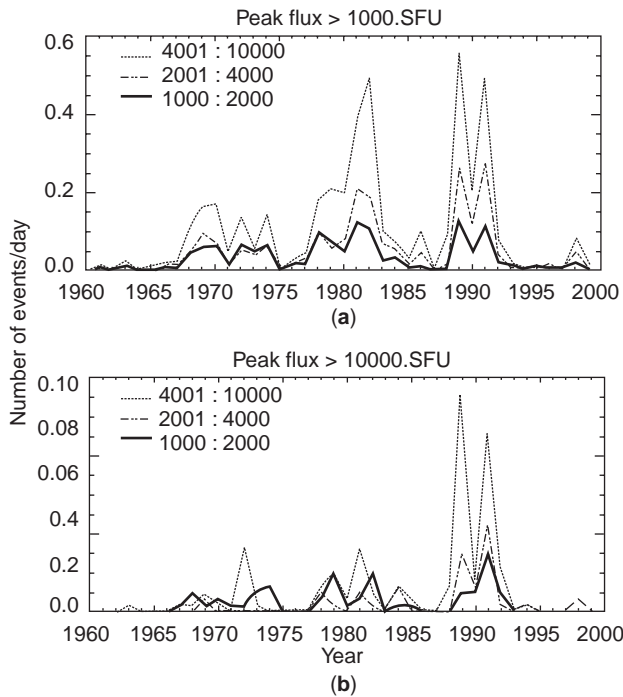


Figure 9. Total number of events/day as a function of time in years (a) for peak flux > 10³ SFU and (b) for peak flux > 10⁴ SFU. The frequency ranges are 1–2, 2–4, and 4–10 GHz.

function of time in years for two different solar flux levels [14].

In a 2002 paper [15], the ionospheric effects on satellite land–mobile services tabulated the estimated maximum ionospheric effects on these services as shown in Table 2. The complete report may be seen at <http://www.utexas.edu/mopro/>.

To summarize, the radio services most affected by the ionosphere lie in the frequency range of 1–150 MHz [fixed communication services, AM (amplitude modulation) and SW (shortwave) broadcasting, amateur radio]. To a lesser degree, services in the 20 kHz–300-MHz region (mainly some of the navigation services) also suffer some ionospheric perturbation effects.

There is a plethora of radio instrumentation currently deployed globally that operates routinely or on a campaign

basis to measure characteristics of the terrestrial ionosphere. It is beyond the scope of this article to describe these techniques, but they have been described in considerable detail in the literature [2–4].

4. PHYSICAL PRINCIPLES AND MATHEMATICAL DESCRIPTION OF ELECTROMAGNETIC INTERACTION WITH THE IONOSPHERE

Because of the complexity of the terrestrial ionosphere (a weakly ionized plasma with a superimposed magnetic field in which electric currents flow), we must utilize the magnetoionic theory to quantify the ionosphere physical parameters. The most successful formulation of the appropriate magnetoionic theory was derived by Appleton and others in the mid-1920s [15–18]. We can obtain some first-order properties of the ionosphere by ignoring the magnetic field [19,20]. A simple dispersion equation for electromagnetic (EM) waves in the ionosphere is

$$\mu = \sqrt{1 - \frac{Ne^2}{\pi mf^2}} \tag{1}$$

where

- μ = refractive index of the ionosphere (real part of complex refractive index n)
- N = electron number density of the ionosphere (electrons/cm³ or electrons/m³)
- e = electronic charge = 1.6×10^{-19} C
- m = mass of the electron = 9.1×10^{-31} kg
- f = frequency of the radiowave in the ionosphere (Hz)

For reflection at vertical incidence, $\mu = 1$ and

$$\begin{aligned} N &= \frac{\pi mf^2}{e^2} \\ &= 1.24 \times 10^4 f^2 \text{ (electrons/cm}^3 \text{ and } f \text{ in MHz)} \\ &= 1.24 \times 10^{10} f^2 \text{ (electrons/cm}^3 \text{ and } f \text{ in MHz)} \end{aligned} \tag{2}$$

Table 2. Estimated Maximum Ionospheric Effects (Elevation Angle of 30°, One-Way Traversal)

Effect	Frequency Dependence	0.1 GHz	0.25 GHz	0.5 GHz	1 GHz	3 GHz	10 GHz
Faraday rotation	f^{-2}	30 rot. ^a	4.8 rot.	1.2 rot.	108°	12°	1.1°
Time (group) delay	f^{-2}	25 μs	4 μs	1 μs	0.25 μs	0.028 μs	0.0025 μs
Refraction	f^{-2}	<1°	<0.16°	<2.4'	<0.6'	<4"	<0.36"
Change in direction of arrival	f^{-2}	20'	3.2'	48"	12"	1.33"	0.12"
Absorption (auroral and/or polar cap)	f^{-2}	5 dB	0.8 dB	0.2 dB	0.05 dB	0.006 dB	0.0005 dB
Absorption (mid-latitude)	f^{-2}	<1 dB	<0.16 dB	<0.04 dB	<0.01 dB	<0.001 dB	<0.0001 dB
Dispersion	f^{-3}	400 ps/kHz	26 ps/kHz	3.2 ps/kHz	0.4 ps/kHz	45 ts/kHz	0.4 ts/kHz

^aRotations.

Note: Extrapolated from 1-GHz values given by the former CCIR Study Group 6 in Table VII of Report 263, and based on a total electron content (TEC) of 10¹⁸ electrons/m², which is a high value of TEC encountered at low latitudes in daytime with high solar activity. A similar chart may be found in Recommendation ITU-R P.618-6 of Study Group III.

Another useful quantity is the plasma frequency,

$$\begin{aligned}
 F_n &= \sqrt{\frac{Ne^2}{\pi m}} \\
 &= 9\sqrt{N} \quad (f \text{ in kHz and } N \text{ in electrons/cm}^3) \\
 &= 9 \times 10^{-3}\sqrt{N} \quad (f \text{ in MHz and } N \text{ in electrons/cm}^3)
 \end{aligned}
 \tag{3}$$

4.1. The Virtual Height Concept

If we consider an RF pulse traveling vertically upward into the ionosphere at the speed of light, $v = c$, it will be reflected at the virtual height, h' . The time required for the pulse to be reflected from an ionospheric layer and return to Earth is

$$t = \frac{2}{c} \int_0^h \frac{dz}{\mu} \tag{4}$$

then the virtual height can be found from $h(f) = \frac{1}{2} ct$, or

$$h'(f) = \int_0^h \frac{dz}{\sqrt{1 - f_n^2/f^2}} \tag{5}$$

Since the pulse always travels more slowly in the layer than in free space, the virtual height of a layer is always greater than the true height. The true height and virtual height are related by the integral equation

$$h'(f) = \int_0^{Z_{\max}} \frac{dz}{\mu(f, z)} \tag{6}$$

where z is the true height, Z_{\max} is the maximum height reached by the frequency f , and n is the refractive index at Z_{\max} for the frequency f . A good discussion of the relation between true height and virtual height is given in Ref. 20.

4.2. Vertical and Oblique Propagation

Before considering the behavior of a radio signal in a magnetoionic medium, we will state three theorems that relate oblique and vertical incidence propagation as depicted in Fig. 10. The first is the secant law, which relates the vertical-incidence frequency f_v reflected at B to the oblique-incidence frequency f_{ob} reflected at the same true height. A typical derivation of this relation is given in Ref. 5, and it is usually written as

$$f_{ob} = f_v \sec \varphi_0 \tag{7}$$

The secant law, then, relates the two frequencies f_v and f_{ob} reflected from the same true height (the distance BD in Fig. 10).

In order to determine $\sec \varphi$ and f_{ob} values from vertical-incidence soundings (which measure the virtual height h'), we need two more theorems. Breit and Tuve's theorem states that the time taken to traverse the actual curved path $TABCR$ in Fig. 10 at the group velocity v_g equals the

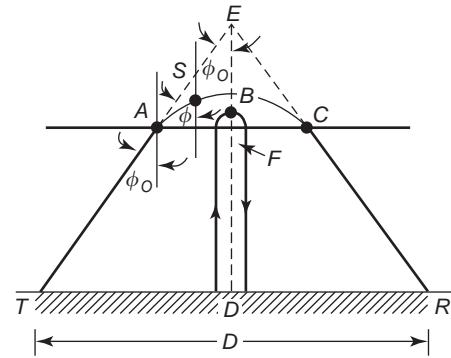


Figure 10. Plane geometry describing vertical and oblique ionospheric propagation.

time necessary to travel over the straight-line path TER at the free-space velocity c . Referring to the geometry shown in Fig. 10, we can write the expression

$$\begin{aligned}
 T &= \frac{1}{c} \int_{TER} \frac{dx}{\sin \varphi_0} \\
 &= \frac{D}{c} \sin \varphi_0 \\
 &= \frac{TE + ER}{c}
 \end{aligned}
 \tag{8}$$

Martyn's theorem may be written concisely as

$$h' = h'_v \tag{9}$$

Smith [21] devised a set of logarithmic transmission curves, parametric in range, for the curved earth and ionosphere. They are shown in Fig. 11 and are sufficiently accurate for the distances shown.

4.3. Radio Propagation in a Magnetized Plasma

Before proceeding with a discussion of the Appleton (magnetoionic) equations, we need to define two quantities contained explicitly in the equations. The first is ν , the number of collisions per second (collision frequency) between electrons and heavier particles (ions and neutrals). Another quantity, the gyro-magnetic frequency or gyrofrequency, is the natural frequency (Hz) of gyration of an ion or electron in a magnetic field of strength B_0 (Wb/m²) and is given by

$$f_H = \frac{|e|\hbar}{2\pi m} B_0 \approx 2.80 \times 10^{10} B_0 \tag{10}$$

and the angular gyrofrequency is given by

$$\omega_H = \frac{|e|\hbar}{m} B_0 \approx 1.76 \times 10^{11} B_0 \tag{11}$$

Since electrons are much less massive than ions, the electron gyrofrequency affects the propagation of HF waves in the ionosphere more than the ion gyrofrequencies. For example, since $B \approx 0.5 \times 10^{-4}$ Wb/m², the electron gyrofrequency is ≈ 1.40 MHz, which falls at the upper end of the medium waveband.

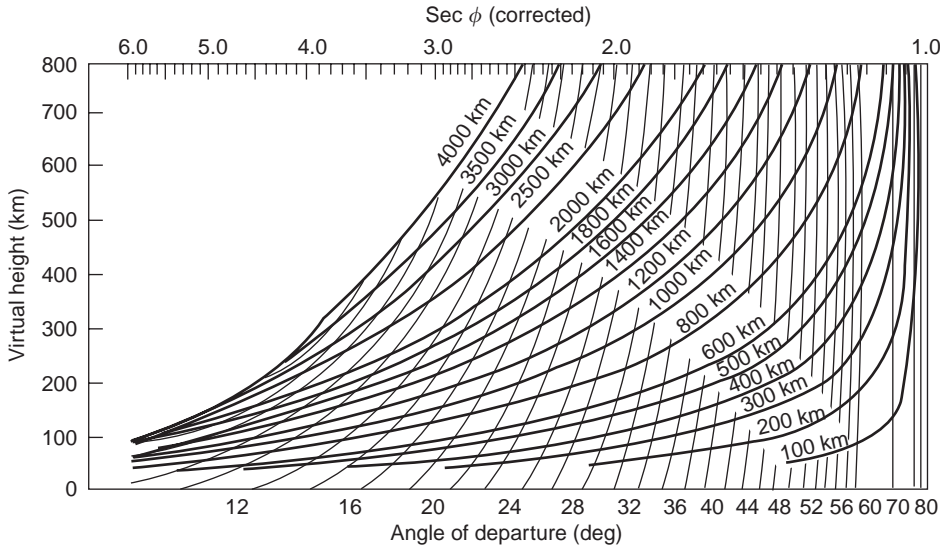


Figure 11. Logarithmic transmission curves for curved Earth and ionosphere, parametric in distance between transmitter and receiver.

4.4. The Dispersion Relation

Using the recommended URSI (International Union at Radio Science) notation, the magnetoionic dispersion equation for a radiowave in a homogeneous, partially absorbing ionized gas on which a constant magnetic field is impressed is given by

$$n^2 = 1 - \frac{X}{(1-jZ) - \left[\frac{Y_T^2}{2(1-X-jZ)} \right]} \pm \left[\frac{Y_T^4}{4(1-X-jZ)^2} + Y_L^2 \right]^{1/2} \quad (12)$$

where

n = complex refractive index $= (\mu - jX)$
 ω = angular frequency of the exploring wave (rad/s)
 ω_N = angular plasma frequency
 ω_H = angular gyrofrequency $= B_o |e| / m$ (rad/s)
 ω_L = longitudinal angular gyrofrequency $= (B_o |e| / m) \cos \theta$
 ω_T = transverse angular gyrofrequency $= (B_o |e| / m) \sin \theta$
 $X = \omega_N^2 / \omega^2$
 $Y = \omega_H / \omega$
 $Y_L = \omega_L / \omega$
 $Y_T = \omega_T / \omega$
 $Z = \nu / \omega$
 θ = angle between the wave-normal and the magnetic field inclination

4.5. The Polarization Relation

We begin by defining the polarization ratio R as

$$R = \frac{-H_y}{H_x} = \frac{E_x}{E_y} \quad (13)$$

Then we can write the double-valued polarization equation as

$$R = -\frac{j}{Y_L} \left[\frac{1}{2} \frac{Y_T^2}{(1-X-jZ)} \mp \left(\frac{1}{4} \frac{Y_T^2}{(1-X-jZ)^2} + Y_L^2 \right)^{1/2} \right] \quad (14)$$

In the upper F region of the ionosphere where the electron-ion collision frequency is very low, we may simplify the dispersion and polarization equations by dropping the Z term (since $\nu \approx 0$). Equations (12) and (14) then become (for no absorption)

$$n^2 = 1 - \frac{2X(1-X)}{2(1-X) - Y_T^2 \pm [Y_T^4 + 4Y_L^2(1-X)^2]^{1/2}} \quad (15)$$

and

$$R = -\frac{H_y}{H_x} = -\frac{j}{Y_L} \left(1 + \frac{X}{n^2 - 1} \right) \quad (16)$$

If we further simplify Eq. (12) by dropping the Y terms (no magnetic field), then we obtain $n^2 = 1 - X$, which is equivalent to Eq. (1).

According to magnetoionic theory, a plane-polarized EM wave traveling in a medium like the terrestrial ionosphere will be split into two characteristic waves. The wave that most closely approximates the behavior of a signal propagating in this medium without an imposed magnetic field, is called the *ordinary wave*, and the other is called the *extraordinary wave*. These terms are taken from the nomenclature for double refraction in optics, although the magnetoionic phenomena are more complicated than the optical ones. The ordinary wave is represented by the upper sign in the polarization Eq. (14), except when the wavenormal is exactly along the direction of the magnetic field. Anomalous absorption

occurs for the extraordinary wave when its frequency equals the electron gyrofrequency ($f_H = |B|e/me \approx 0.8\text{--}1.6$ MHz). These frequencies lie in the medium-frequency (MF) band; consequently the absorption of the extraordinary wave [$A \approx (f - f_H)^2$] is large and the polarization of the transmitted wave is important in the determination of the fraction of the incident power that goes into the extraordinary wave. This is especially true near the magnetic dip equator, where the magnetic field is nearly horizontal.

In addition to anomalous absorption effects near the electron gyrofrequency, the wave may also experience significant lateral deviation. This is illustrated for vertical and oblique propagation in Sections 11.2.2–11.2.4 of Ref. 4.

If Eq. (16) is recast as a function of ω and we define $f(\theta) = \frac{1}{2}(\sin^2 \theta)/\cos \theta$ and $\omega_c = (B_0 |e|/m) f(\theta)$, then it will be seen to describe an ellipse. The quantities $f(\theta)$ and ω_c play an important part in the description of the polarization behavior of waves in magnetoionic theory. The magnitude of ω_c is independent of frequency, but varies with the angle between the wavenormal and the magnetic field θ , whereas the sign of ω_c depends on the sign of the charge e and the direction of the magnetic field. For longitudinal propagation $\omega_c = 0$, and for transverse propagation $\omega_c \rightarrow \infty$. In the case where $X=1$, the quantity ω_c primarily determines the polarization of the wave. A very complete discussion of R as a function of X and of the variation of the polarization ellipse is given in Ref. 22.

A more complete understanding of the behavior of EM waves in the terrestrial ionosphere may be obtained by employing two approximations. The quasilonitudinal (QL) approximation applies when the wave is propagating nearly parallel to the geomagnetic field, and the quasitransverse (QT) approximation applies when the wave propagates in a direction nearly normal to the geomagnetic field. References 22 and 23 contain extended discussions of the QL and QT approximations:

$$\text{QT: } Y_T^4 \gg 4(1-X)^2 Y_L^2$$

$$\text{QL: } Y_T^4 \ll 4(1-X)^2 Y_L^2$$

4.6. Absorption of Radiowaves in the Ionosphere

The refractive index n is modified when one introduces collisions between the electrons and heavy particles, and the wave then experiences absorption, which physically is due to the conversion of ordered momentum into random motion of the particles after collision. For each collision, some energy is transferred from the EM wave to the neutral molecules and appears as thermal energy. We will follow the standard treatment of absorption of radio waves in the ionosphere presented by Davies [23] and Budden [24].

For the propagation of an EM wave in an unmagnetized plasma, we can define the absorption index (or coefficient) as

$$K = \frac{\omega}{c} X \quad (17)$$

where X is the imaginary part of the refractive index n . For a magnetized plasma without collisions, we can write

$$K = \frac{e^2}{2\varepsilon_0 m c \mu} \cdot \frac{N\nu}{\omega^2 + \nu^2} \quad (18)$$

On this basis, we can conveniently divide absorption into two limiting types, commonly called *nondeviative* and *deviative absorptions*. Nondeviative absorption occurs in regions where the product $N\nu$ is large and $\mu \approx 1$, and is characterized by the absorption of HF waves in the D region. Deviative absorption, on the other hand, occurs near the top of the ray trajectory or anywhere else on the ray path where significant bending takes place (for small $N\nu$ and $\mu < 1$).

When the refractive index ≈ 1 , there is essentially no bending of the ray and we can write

$$K \approx 4.6 \times 10^{-2} \frac{N\nu}{\mu(\omega^2 + \nu^2)} \text{ dB/km} \quad (19)$$

We can further simplify Eq. (19) for the VHF case, since $\omega^2 \gg \nu^2$, as

$$K = 1.15 \times 10^{-3} \frac{N\nu}{f^2} \text{ dB/km} \quad (20)$$

In the MF and HF bands, Eq. (19) may be written as

$$K = 4.6 \times 10^{-2} \frac{N}{\nu} \text{ dB/km} \quad (21)$$

Unlike nondeviative absorption, deviative absorption occurs when the wave experiences significant group retardation and consequently spends a relatively long time in the absorbing layer and there is considerable curvature of the ray path. The general expression for the absorption index in a deviating region of a nonmagnetic plasma is

$$K = \frac{\nu}{2c\mu} (1 - \mu^2 - X^2) \quad (22)$$

In the ionosphere, Eq. (22) reduces to

$$K = \frac{\nu}{2c} \mu' \quad (23)$$

where μ' is the group refractive index. For large values of μ' , we can write the preceding equation as

$$K = \frac{\nu}{2c} \frac{X}{\sqrt{1-X}} \quad (24)$$

We should remember that the concepts of deviative and nondeviative absorption are limiting cases, and that as a wave approaches the reflecting level, ray theory breaks down, so we must employ full wave theory to obtain a complete description of the behavior of the wave. Extended discussions of application of the QL and QT approximations to ionospheric absorption may be found in Refs. 5 and 23.

4.7. Scattering of Radiowaves in the Ionosphere

The principles of scattering of radiowaves in general are discussed in the articles on electromagnetic wave scattering in this encyclopedia. One can qualitatively describe ionospheric scattering as either strong or weak in terms of the received signal strength of the scattered signal at the receiving radar antenna. An example of the former is VHF–UHF backscatter echoes received from electron density gradients in the auroral E region, and an example of the latter is incoherent backscatter received by a VHF–UHF radar from the undisturbed E or F layer.

Another way of classifying scattered echoes is in terms of their backscatter cross section (using a pulsed radar system) and their temporal stability. A coherent echo exhibits a statistical correlation of the amplitude and phase from one pulse to another and emanates from quasideterministic gradients in electron density, which have correlation times usually greater than 1 ms, corresponding to a spectral width of the radar echo of less than 1000 Hz (sometimes less than 100 Hz). It also has a backscatter cross section 10^4 – 10^9 times greater than that from an incoherent echo. Other important considerations in the case of coherent backscatter are the relation between the scattering irregularity size relative to the backscatter sounder free-space wavelength, the mean fractional deviation in electron density of the scatterer, and the aspect angle between the radar line of sight and the major axis of the irregularity. On the other hand, an incoherent echo arises from random thermal fluctuations in the ionosphere, which have typical correlation times of $\approx 20 \mu\text{s}$, corresponding to a radar echo spectral width of $\approx 50 \text{ kHz}$.

The physical principles governing coherent and incoherent scattering from the ionosphere are covered in Refs. 2, 5, and 6, while plasma wave theory is covered in detail in Ref. 5, and extended descriptions of techniques for studying the ionosphere using coherent- and incoherent-scattering sounders are given in Refs. 2,3,5, and 6.

Because of charged particle precipitation of solar origin, ionospheric electric currents and fields, and plasma dynamics, there exists a wide spectrum of scale sizes of ionospheric irregularities, as shown in Fig. 12. Irregularities are most prevalent at auroral, polar, and equatorial latitudes, although they also exist at midlatitudes [23]. The global morphology of ionospheric irregularities is covered in Refs. 4–6.

4.8. Ionospheric Scintillation

Ionospheric scintillations are fluctuations of amplitude, phase, and angle of arrival of a VHF–UHF signal passing through irregularities located mainly in the F region. Ionospheric scintillations can have deleterious effects on satellite-based communication and navigation systems. Either extragalactic sources (such as radio stars) or satellite beacon transmitters may be used as the signal sources for Earth-observed studies of ionospheric scintillations, and both geostationary and orbiting satellite beacons have been used. There is a voluminous body of literature since

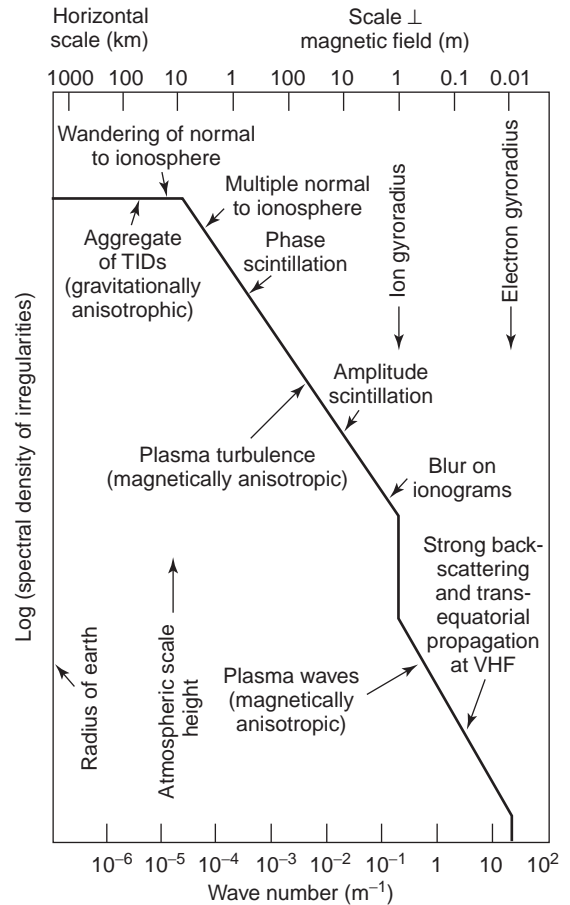


Figure 12. Composite spectrum of ionospheric irregularities as a function of wavenumber over a large spatial scale. (Courtesy of H. G. Booker.)

1970 describing the theory, technique, and results of ionospheric scintillation measurements [2–6].

4.9. Faraday Rotation

One physical principle that makes possible the determination of ionospheric columnar electron content is Faraday rotation. This effect (for optics) was discovered by Michael Faraday in 1845, when he subjected a block of glass to a strong magnetic field. He observed that a plane-polarized monochromatic beam of light passing through the glass in a direction parallel to the imposed magnetic field has its plane of polarization rotated. The amount of rotation is given by the expression

$$\Omega = KHI \quad (25)$$

where Ω is the angle of rotation, K is a constant associated with each substance, l is the pathlength of light through the substance (m), and H is the magnetic field intensity (A/m).

The Faraday rotation of the electric vector of a radio-wave (see Ref. 45) propagating from a satellite radio beacon in a direction parallel to Earth's magnetic field (as seen by an observer looking up, in the Northern Hemisphere) is counterclockwise, as shown in Fig. 13.

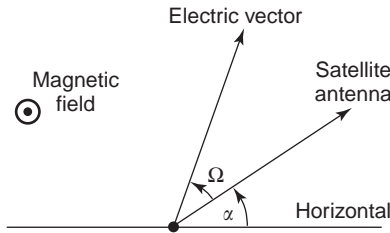


Figure 13. Simplified plane geometry of satellite–Earth propagation path in the Northern Hemisphere to explain Faraday rotation effects.

Ignoring refraction, the Faraday rotation of the electric vector is given by

$$\Omega = \frac{\pi f}{2c} \int_R^S X \sqrt{\frac{Y_T^4 + 4(1 - X)^2 Y_L^2}{(1 - X)(1 - Y_L^2 - Y_T^2)}} ds \quad (26)$$

where

Ω = Faraday rotation (rad/s)

f = wave frequency (Hz)

$c = 2.998 \times 10^8$ m/s

$X = kN/f^2$

$k = 80.61$

N = electron density (electrons/m³)

and Y_L, Y_T are as previously defined.

The integration is between the receiver R , and the satellite S . For VHF frequencies the QL approximation holds and we can express Eq. (26) as

$$\Omega = \frac{\pi K}{c f^2} \int_R^S f_L N ds \quad (27)$$

where $N ds$ is the ionospheric electron content. Evaluating the constants yields the relation

$$\Omega \approx 8.447 \times 10^{-7} f^{-2} \int_R^S f_L N ds \text{ rad} \quad (28)$$

where $f_L = 2.80 \times 10^{10} B_L$, the electron gyrofrequency corresponding to the longitudinal component of the geomagnetic field along the ray path. Details of the application of Faraday rotation theory and other techniques to deduce ionospheric columnar electron content may be found in Refs. 2, 5, and 6.

4.10. Whistlers

Whistlers are bursts of EM radiation at VLF that are initiated by lightning discharges and then travel through the ionosphere and magnetosphere in ducts approximately parallel to geomagnetic lines of force. When translated into sound waves, whistlers are distinguished by tones of decreasing (or sometimes increasing) frequency, and they may easily be detected by connecting a suitable antenna to the input of a very sensitive audio amplifier. In fact, whistlers were first observed in the last years of the nineteenth

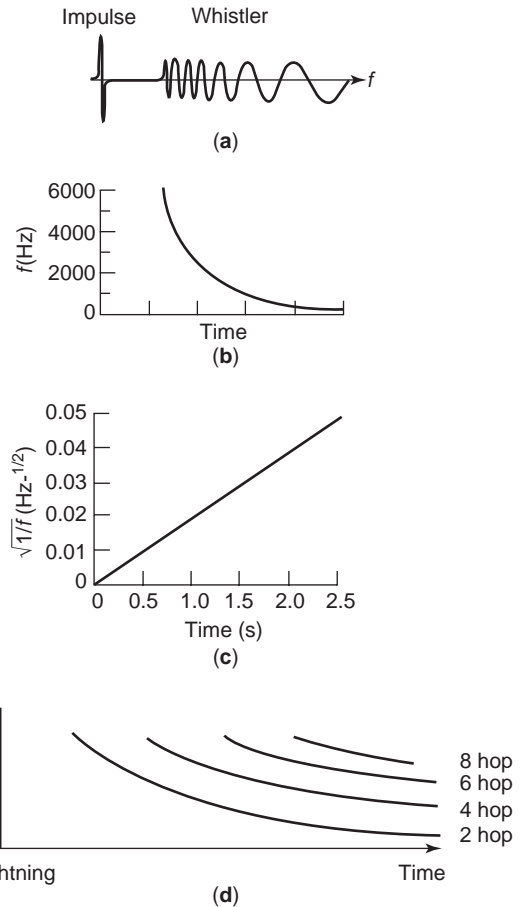


Figure 14. Sketch of basic manifestations of a whistler and its initiating disturbance: (a) the frequency spectrum; (b) frequency–time curve of a typical whistler; (c) curve of $\sqrt{1/f}$ with time. Initiating disturbance and multiple hops when the source and receiver are at the same end of a magnetic line of force. (After Helliwell [26].)

century, and were also heard on the primitive field telephone systems used in World War I. They have been studied intermittently since 1898, basically as a diagnostic probe of the ionosphere and magnetosphere [2,26]. A graphical representation of whistler behavior is shown in Fig. 14, and the somewhat rarer nose whistler behavior is illustrated in Fig. 15.

The dispersion relation for whistlers is

$$T = \frac{1}{2c} \int_S \frac{(f_N f_L ds)}{f^{1/2} (f_L - f)^{3/2}} = \frac{D}{f^{1/2}} \quad (29)$$

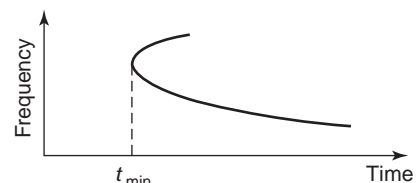


Figure 15. Idealized sketch of the frequency–time characteristics of a nose whistler. (After Davies [5].)

where D is dispersion $= (1/2c) \int_s (f_N/f_L^{1/2}) ds$, f_N is plasma frequency, and f_L is a longitudinal component of the plasma frequency. This is the time T for a signal burst to go from one hemisphere to its conjugate point in the opposite hemisphere.

Other natural VLF emissions (called “dawn chorus,” “risers,” “hiss,” etc.) that are thought to originate in the ionosphere can also be heard on whistler detection equipment. Since the 1960s, high-power VLF transmitters have been used to generate whistlers to study properties of the magnetosphere [27–29].

5. FRONTIERS OF IONOSPHERIC RESEARCH

The use of radiowaves to explore the terrestrial ionosphere began with the pioneering efforts of Appleton and of Breit and Tuve in 1926, when they independently used different techniques to detect the ionospheric layers. Their work was founded on Marconi’s demonstration of transatlantic radio transmission and on the hypotheses of Kennelly and Heaviside, who independently in 1922 postulated that there must be radio-reflecting layers in the upper atmosphere to explain certain experimental results. The foregoing discoveries rested on the bedrock of the experimental and theoretical work of Heinrich Hertz (1893) and James Clerk Maxwell (1873), respectively.

There seems to have been several crests in the history of ionospheric research: (1) in the 1920s, following World War I; (2), starting shortly after the end of World War II; and (3) perhaps starting in the mid-1970s with the advent of digital techniques, and (4) more recently with the advent of the National Space Weather Program (see Ref. 30 or <http://www.geo.nsf.gov/atm/>).

While much of the ionospheric research up until about 1960 was in support of HF communications, the advent of satellite communications changed the emphasis to ionospheric research concerning the effects of the ionosphere on transionospheric propagation and research relating the ionosphere to the magnetosphere. Most current ionospheric research is related to the interrelationship and coupling between regions over the entire height region of the terrestrial atmosphere from the troposphere to the magnetosphere and through interplanetary space to the sun.

There are several areas of ionospheric research that currently seem to be producing exciting new results, and these areas will probably continue to be emphasized in the twenty-first century. These areas include (not necessarily in order of importance) satellite sensors, ionospheric mod-

ification by using high-power HF transmissions, ionospheric imaging, coherent radars operating from HF through VHF, and incoherent scatter radars [2–5]. Most of these techniques are employed at high geomagnetic latitudes as part of the Space Weather Program [31], but some are also deployed in equatorial regions. We will briefly describe the essentials of each of these areas of current ionospheric research emphasis.

5.1. Satellite Sensors

The total number of currently operational solar-terrestrial environment satellite probes is too numerous to list in this article, but examples of representative satellite sensors may be found at <http://www.nasa.gov>, and <http://www.esa.int>. These satellites probe the solar physical properties, the solar wind, the interplanetary magnetic field, and the terrestrial magnetosphere and ionosphere and provide realtime data to aid in forecasting and describing solar-terrestrial conditions.

5.2. Ionospheric Modification

In the late 1960s the availability of military surplus equipment such as very-high-voltage and -current power supplies and HF vacuum tubes capable of many kilowatts of RF output, together with advances in antenna array theory and practice, induced experimenters to design systems to heat or otherwise modify the ionosphere. As a result of experiments performed in the early 1970s at the Platteville, Colorado HF high-power heating facility [32], some 10 new ionospheric modification facilities were established and have produced significant information on ionospheric physics. (see Chapter 14 of Ref. 5). The various modification facilities are listed in Table 3. Other ionospheric modification facilities are located in Russia and Ukraine at Kharkov, Moscow, Zimenki, and Monchegorsk. More information on the HAARP and other heaters may be obtained on the Internet at <http://www.haarp.alaska.edu>.

5.3. Ionospheric Imaging by Radio

For over three decades now (as of 2003), ionospheric scientists have investigated using radio methods to image the ionosphere. Rogers [33] was probably the first to suggest using the wavefront reconstruction method for this purpose. Many attempts have been made to produce holographic images of the ionosphere, but it has not proved to be a very successful technique—probably because of the difficulty in uniformly illuminating a sufficiently large

Table 3. Ionospheric Modification Facilities (1970–1978)

Facility	First Used	Latitude	Longitude	Geomagnetic Latitude	Transmit Power	Frequency Range (MHz)	Antenna Gain (dB)
Platteville, CO	1970	40.2°N	104.7°W	49°	1.6 MW	2.7–25	18
Arecibo, PR	1980	18°N	67°W	32°	800 kW	3–15	25
SURA, Russia	1980	56.1°N	46.1°E	71°	750 kW	4.5–9	26
Tromsø, Norway	1980	69.6°N	19.2°E	67°	1.5 MW	2.5–8	28
HIPAS, Alaska	1977	64.9°N	146.8°W	65°	800 kW	2.8, 4.5	17
HAARP ^a Alaska	1997	62.4°N	145.2°W	62°	3.6 MW ^a	2.8–10	30 ^a

^aHAARP is currently under construction. Values given are for the completed facility.

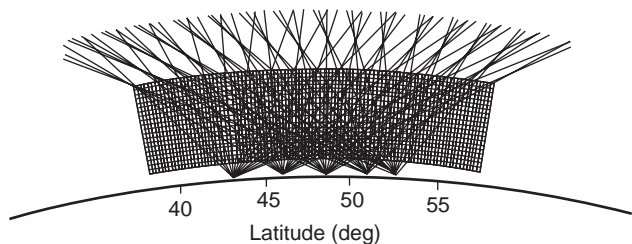


Figure 16. Basic satellite–Earth geometry for computer ionospheric tomography, illustrating the multiple ray paths on which the total electron content is measured.

horizontal slab of the ionosphere, not using a sufficient number of receivers, and the inability to achieve precise enough measurements of amplitude and phase of the reflected wave.

On the other hand, another technique (borrowed from medical technology), computerized ionospheric tomography (CIT), has produced quite significant results in imaging the regular (and some irregular) features of the ionosphere. Basically, this technique utilizes radio beacons on satellites in near-polar orbits and a latitudinal chain on the Earth subsatellite path of carefully calibrated TEC receivers, to make many measurements of total electron content (TEC). The basic geometry is illustrated in Fig. 16.

Currently, VHF–UHF beacons on the TRANSIT, GLONASS, and GPS satellites are the most used as signal sources to measure TEC to use in CIT ionosphere reconstructions. One must also use some a priori informa-

tion (ionospheric models) and ionosonde data in the algorithms in order to achieve realistic results. Some recent results are summarized in Refs. 34–39 and on the Internet at <http://www.nwra-az.com/iitc>, and at <http://sideshow.jpl.nasa.gov:80/gpsiono>.

Another ionospheric imaging technique is the IRIS system (imaging riometer–ionospheric studies) [46], which uses an antenna array of up to 64 elements to provide images of enhanced auroral absorption structure in the D region.

5.4. Coherent Radars

As described in the Section 4.7, HF–UHF coherent backscatter from ionospheric irregularities can provide very useful information on the morphology and physics of a wide range of irregularity scale sizes. At this time there are about 20 of these backscatter sounders deployed, operating on frequencies from 8 to 200 MHz, distributed mainly in the high-latitude and equatorial regions. These radars are sited so that the main antenna lobe is directed to intercept irregularities at near-normal incidence at E- and F-region heights.

The HF coherent radars are mainly grouped into a large network, which covers approximately half of the northern polar cap ionosphere—the SuperDARN network [40], which is shown on the map in Fig. 17. Much information has been gained on the F-region plasma convection patterns in the polar cap, atmospheric gravity waves, and other ionospheric phenomena related to ionosphere magnetosphere interaction; see Refs. 40–43 or <http://sd-www>.

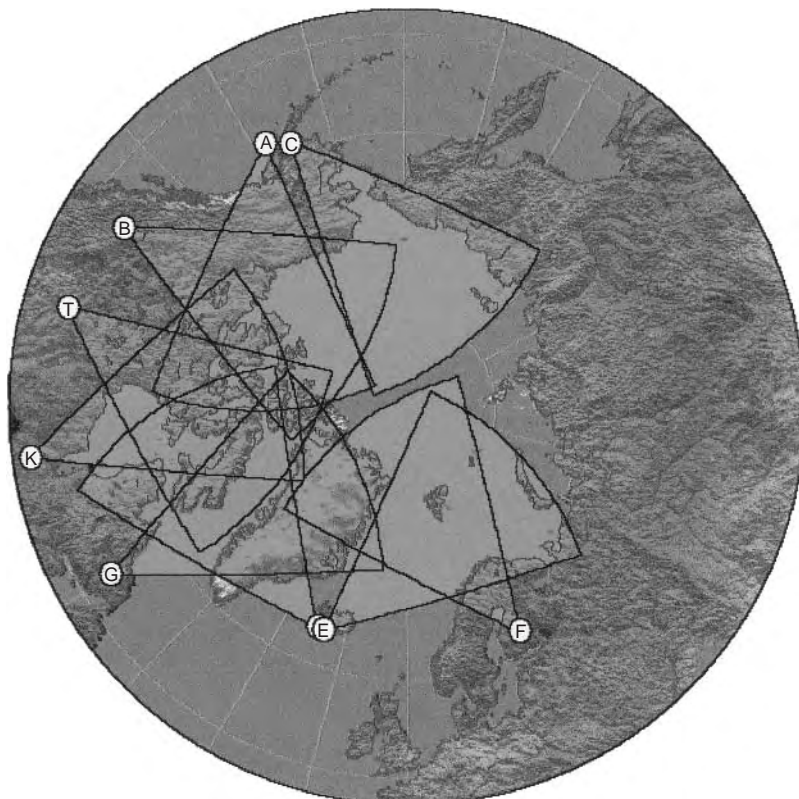


Figure 17. Map of Northern Hemisphere showing coverage of SuperDARN high-frequency radars.

jhuapl.edu/RADAR. The VHF–UHF coherent radars are documented in Refs. 2–5, and a useful Internet sources is to be found at http://www.dan.sp-agency.ca/www/canopus_home.html.

5.5. Incoherent Scatter Radars

One of the most powerful Earth-based radio methods for studying the ionosphere is the incoherent scatter radar (ISR) technique, which has been in use since the early 1960s. ISRs can reveal the electron density, electron and ion temperature, plasma velocity, and other ionospheric parameters, even during very disturbed conditions [2–5]. At the present time there are some seven ISRs in operation, located from the north polar cap to the magnetic equator and spread longitudinally from Scandinavia to Japan. The newest ISR is located at Svalbard, Norway [44]. Data from ISRs are essential in studying the relation between the magnetosphere, ionosphere, and middle atmosphere at high and equatorial latitudes [47,48].

5.6. Large-Scale Ionospheric Data Assimilation

At this time there is a staggering amount of solar terrestrial and ionospheric data available from many diverse sources—especially from the “Space Weather” sensors, and there are several sophisticated ionospheric computer models [49].

BIBLIOGRAPHY

- H. Alfvén, *Cosmic Plasma*, D. Reidel, Dordrecht, Holland, 1981.
- R. D. Hunsucker, *Radio Techniques for Probing the Terrestrial Ionosphere*, Springer-Verlag, Heidelberg, 1991.
- R. D. Hunsucker, A review of ionospheric radio techniques: Present status and recent innovations, in W. R. Stone, ed., *Review of Radio Science 1990–1992*, Oxford Univ. Press, Oxford, 1993, Chapter 22.
- R. D. Hunsucker and J. K. Hargreaves, *The High-Latitude Ionosphere and Its Effects on Radio Propagation*, Cambridge Univ. Press, Cambridge, UK, 2003.
- K. Davies, *Ionospheric Radio*, Peter Peregrinus, London, 1990.
- J. K. Hargreaves, *The Solar-Terrestrial Environment*, Cambridge Univ. Press, Cambridge, UK, 1992.
- J. R. Wait, *Electromagnetic Waves in Stratified Media*, Pergamon Press, Oxford, 1970.
- J. R. Wait, EM Scattering from a vertical column of ionization in the earth-ionosphere waveguide, *IEEE Trans. Anten. Propag.* **39**:1051–1054 (1991).
- A. D. Watt, *VLF Radio Engineering*, Pergamon press, Oxford, 1967.
- R. D. Hunsucker and B. S. Delana, *High-Latitude Field-Strength Measurements of Standard Broadcast Band Sky-wave Transmissions Monitored at Fairbanks, Alaska*, Final Report on FCC Contract FCC-0375, Geophysical Institute/Univ. Alaska, 1988.
- J. M. Goodman, *HF Communications—Science and Technology*, Van Nostrand Reinhold, New York, 1992.
- E. E. Johnson et al., *Advanced High-Frequency Radio Communications*, Artech House, Boston, 1997.
- R. D. Hunsucker, Auroral and polar-cap ionospheric effects on radio propagation, *IEEE Trans. Anten. Propag.* **40**:818–828 (1992).
- B. Bala, L. J. Lanzerotti, D. E. Gary, and D. J. Thomson, Noise in wireless systems produced by solar radio bursts., DOI 10.1029/2001RS002481; *Radio Sci.* **37**(2) (March–April 2002).
- K. Davies and E. K. Smith, Ionospheric effects on satellite land mobile systems, *IEEE Anten. Propag. Mag.* **44**(6) (Dec. 2002).
- E. V. Appleton, Geophysical influence on the transmission of wireless waves, *Proc. Phys. Soc. Lond.* **37**(2):16D–22D (1925).
- H. W. Nichols and J. C. Schelling, The propagation of electric waves over the earth, *Bell Syst. Tech. J.* **4**:215 (1925).
- C. S. Gillmor and W. Altar, Edward Appleton and the magnetoionic theory, *Proc. Am. Philos. Soc.* **126**(5):395–440 (1982).
- W. H. Eccles, *Proc. Roy. Soc. Lond. A, Math. Phys. Sci.* **87**:79 1912.
- J. M. Kelso, *Radio Ray Propagation in the Ionosphere*, McGraw-Hill, New York, 1964.
- N. Smith, The relation of radio sky-wave transmission to ionospheric measurements, *Proc. IRE* **27**:332–347 (1939).
- J. A. Ratcliffe, *The Magnetoionic Theory and Its Applications to the Ionosphere: A Monograph*, Cambridge Univ. Press, London, 1959.
- K. Davies, *Ionospheric Radio Waves*, Blaisdell, Waltham, MA, 1969.
- K. G. Budden, *The Propagation of Radio Waves. The Theory of Radio Waves of Low Power in the Ionosphere and Magnetosphere*, Cambridge Univ. Press, Cambridge, UK, 1985.
- R. D. Hunsucker, Characteristic signatures of the midlatitude ionosphere observed with a narrow-beam HF backscatter sounder, *Radio Sci.* **6**:535–548 (1971).
- R. A. Helliwell, *Whistlers and Related Ionospheric Phenomena*, Stanford Univ. Press, Stanford, CA, 1956.
- D. Park and D. Carpenter, Very low frequency radio waves in the magnetosphere, in L. J. Lanzerotti and C. G. Parrs, eds., *Upper Atmosphere Research in Antarctica*, Res. Ser. Vol. 29, Monograph 72, American Geophysical Union, Washington, DC, 1978.
- D. L. Carpenter, Remote sensing of the magnetospheric plasma by means of whistler mode signals, *Rev. Geophys.* **26**:535–549 (1988).
- R. A. Helliwell, *VLF Whistler Mode Experiments*, Cambridge Univ. Press, Cambridge, MA, in press.
- J. W. Wright, Jr., ed., *National Space Weather Program—Strategic Plan*, FCM-P30-1995, 1995, OFCMSSR; 8455 Coleville Road, Suite 1500; Silver Spring, MD 20910.
- The National Space Weather Program—The Implementation Plan, FCM-P31-1997, Jan. 1997.
- W. F. Utlaut, ed., Special issue: Ionospheric modification by high power transmitters, *Radio Sci.* **9**:881–1089 (1974).
- G. L. Rogers, A new method of analyzing ionospheric movement records, *Nature* **177**:613–614 (1956).
- B. D. Wilson, Subdaily northern hemisphere ionospheric maps using an extensive network of GPS receivers, *Radio Sci.* **30**(3):639–648 (1995).
- H. Na, J. Shen, and H. Lee, A Fourier domain technique for ionospheric tomography, *Radio Sci.* **30**(3):747–754 (1995).

36. A. J. Mannucci et al., GPS and the ionosphere, in W. Ross Stone, ed., *Reviews of Radio Science, 1996–1999*, Oxford Univ. Press, 1999, Chapter 25.
37. L. Kersley et al., Imaging of electron density troughs by tomographic techniques, *Radio Sci.* **32**(4):1607–1621 (1997).
38. R. Leitinger, Ionospheric tomography, in W. Ross Stone, ed., *Reviews of Radio Science 1996–1999*, Oxford Univ. Press, 1999, Chapter 24.
39. C. Coker, R. Hunsucker, and G. Lott, Detection of auroral activity using GPS satellites, *Geophys. Res. Lett.* **22**(23):3259–3262 (1995).
40. R. A. Greenwald et al., DARN/Superdarn: A global view of the dynamics of high-latitude convection, *Space Sci. Rev.* **71**:761–796 (1995).
41. A. S. Rodger, Recent scientific advances in geospace research using coherent and incoherent scatter radars, in W. Ross Stone, ed., *Review of Radio Science 1996–1999*, Oxford Univ. Press, 1999, Chapter 23.
42. W. A. Bristow and R. A. Greenwald, On the spectrum of thermospheric gravity waves observed by the SuperDARN network, *J. Geophys. Res.* **102**(A6):11,585–11,595 (1997).
43. A. V. Kustov et al., Dayside ionospheric plasma convection, electric fields and field-aligned currents derived from the SuperDARN radar observations and predicted by the IZEMEM model, *J. Geophys. Res.* **102**(A11):24,057–24,067 (1997).
44. G. Wannberg et al., The EISCAT Svalbard radar: A case study in modern incoherent scatter radar system design, *Radio Sci.* **32**(6):2283–2307 (1997).
45. W. A. S. Murray and J. K. Hargreaves, Lunar radio echoes and the Faraday effect in the ionosphere, *Nature* **173**:944 (1954).
46. J. K. Hargreaves, D. L. Detrick, and T. J. Rosenberg, Space-time structure of auroral radio absorption events observed with Imaging-Riometer of South Pole, *Radio Sci.* **26**:925–930 (1991).
47. J. V. Evans, Ionospheric movement measured by ISR: A review, *J. Atmos. Terrest. Phys.* **34**:175 (1972).
48. C. LaHoz, ed., Special issue: Selected papers from the 6th Int. EISCAT Workshop, *J. Atmos. Terrest. Phys.* **58**:1–507 (1996).
49. R. Schunk et al., Global assimilation of ionospheric measurements (GAIM), *Radio Sci.* (in press).

ELECTROMAGNETICS, TIME-DOMAIN

NATHAN A. BUSHYAGER
 MANOS M. TENTZERIS
 Georgia Institute of Technology
 Atlanta, Georgia

1. INTRODUCTION

1.1. Electromagnetics Overview

The modeling, design, and optimization of RF/microwave structures is a very challenging and time-consuming task because of the difficulties in predicting the high-frequency effects (multimoding, loss mechanisms, parasitics) for specific devices and their interaction with other devices in close proximity. Even if a single component is well char-

acterized in isolation, effects such as surface waves and parasitics lead to signal corruption and degraded performance when the element is placed in a circuit with other components. The study of electromagnetic interaction is key to properly understanding the operation of any RF or microwave device. In these devices, it is often better to think in terms of electromagnetic fields rather than voltages and currents, as is usually done in lower-frequency circuits. The characterization of low-frequency circuits by voltage and current is possible because Maxwell's equations, which govern electromagnetic interaction, can be approximated with circuit equations when a structure is significantly smaller than the maximum wavelength supported by the device. As the wavelength approaches and becomes comparable to the size of the device being studied, as in RF devices (and, as another example, in low-frequency power transmission lines), these approximations are no longer valid. When electromagnetic interactions are not evaluated in these devices, performance degradation often results. For example, when digital circuitry and RF components are used in close proximity, digital switching noise can corrupt RF signals, rendering the device useless. Proper consideration of electromagnetics in this case can account for this interaction and lead to the creation of a successful design.

To analyze these components and their interaction mechanisms, it is often necessary to use electromagnetic simulation software. There are a number of commercial simulation packages, and significant research is ongoing to find new methods and to solve new classes of problems such as MEMS (microelectromechanical systems), periodic structures, and metamaterials. These tools allow the characterization of RF and microwave devices before the fabrication stage, which can save considerable time and money in the design process. In addition, they can be used to optimize devices, allowing hundreds or thousands of configurations to be tested. Because of the complexities of modern microwave structures, it would be impossible to design many modern RF devices and modules without the use of electromagnetic simulators.

Electromagnetics is the study of the fields created from the motion of charge. If these charges are stationary, a static, or unchanging, electric field results. If these charges are moving with constant velocity, a static magnetic field results. If these charges accelerate (change speed or direction with time), then the result is a coupled electromagnetic field. This is because a changing electric field creates a magnetic field, and a changing magnetic field creates an electric field. The result is a propagating electromagnetic wave. The equations that govern electromagnetic phenomena are called *Maxwell's equations*.

Because of the difficulty of applying the necessary boundary conditions on arbitrary structures, Maxwell's equations cannot be solved analytically for most cases of interest to the RF or microwave designer. Beyond special cases no analytic expressions can be found that relate the fields in the structure to a specific source condition. Instead, the equations that represent electromagnetic interaction must be discretized (expressed as simple arithmetic equations) so that they can be solved numerically. Although it is possible to solve these equations by hand, the

number required to accurately characterize a typical RF device is usually in the millions or billions, necessitating the use of computers. As these methods use computers to perform mathematical operations on numbers, they are referred to as *computational* or *numerical electromagnetic methods*. Numerical methods are a branch of mathematics in their own right, and are used in all of science and engineering, from quantum mechanics to meteorology. These techniques are chosen and applied largely according to the type of differential equation modeled. In electromagnetics, they are often split into two categories: time-domain and frequency-domain methods.

Maxwell's equations are usually expressed in terms of either time or frequency. The time form of the equations shows the propagation of electromagnetic fields as they could be observed by recording the time variation of the electromagnetic fields at any point in space. Another method of representing electromagnetic phenomena is by considering the response to a harmonic (single sinusoidal frequency) or "monochromatic" source. Maxwell's equations can be transformed to give frequency-domain solutions in this case. The choice of the domain of the simulator depends on whether the response of the device has to be modeled over a wide or narrow frequency band and whether the field variation changes significantly for different bands (multimode propagation). Results in either domain can be transformed to the other, but computational requirements vary.

In the world of electromagnetics, there are distinct advantages to both time- and frequency-domain simulations. Each frequency-domain simulation is valid for only a single frequency. If the response of the device over a band is desired, then several frequency points over the band must be simulated. Time domain simulations, on the other hand, can be transformed to give results over a wide frequency band. A drawback of time-domain techniques is that it is more difficult to apply the effects of materials that have characteristics that change with frequency, such as dispersive media. These materials are common in RF circuits, and thus complicated methods must be used to allow their accurate modeling in the time domain. Likewise, it is difficult to extract transient data from a frequency-domain simulation.

The two major computational criteria for the selection of a specific numerical simulator are speed and accuracy. These are not independent parameters, all simulators can be made more accurate at the expense of speed. It is not possible to choose a simulator that is the best for all situations. Many comparisons have been made between simulators [1,2], and depending on the problem type, certain techniques are often preferred.

The purpose of this article is to give an overview of the most widely used time-domain simulation techniques. In addition, specific advantages and weaknesses of each method are highlighted, along with some references that can provide more details about each method. With the information presented here, the reader should be able to understand how the different simulation techniques can be applied to specific problems and how the features of that problem place restrictions on the simulation techniques. The article begins with a quick overview of elec-

tromagnetics and then uses this information to explain the simulation methods.

2. THEORY

2.1. Maxwell's Equations

The differential form of Maxwell's equations in the time domain can be expressed as

$$\nabla \times \mathbf{E}(t) = -\frac{\partial \mathbf{B}(t)}{\partial t} \quad (1)$$

$$\nabla \times \mathbf{H}(t) = \frac{\partial \mathbf{D}(t)}{\partial t} + \mathbf{J}(t) \quad (2)$$

$$\nabla \cdot \mathbf{D}(t) = \rho(t) \quad (3)$$

$$\nabla \cdot \mathbf{B}(t) = 0 \quad (4)$$

where \mathbf{E} is the electric field (V/m), \mathbf{H} is the magnetic field (A/m), \mathbf{D} is the electric flux density (C/m²), \mathbf{B} is the magnetic flux density (Wb/m²), ρ is charge density (C/m³), and \mathbf{J} is the electric current density (A/m²). These equations relate the electric and magnetic fields at points in space. Likewise, these equations can be expressed in integral form that relates the fields over contours and areas. In isotropic, nondispersive linear media the constitutive equations are

$$\mathbf{D}(\mathbf{r}) = \varepsilon(\mathbf{r})\mathbf{E}(\mathbf{r}) \quad (5)$$

$$\mathbf{B}(\mathbf{r}) = \mu(\mathbf{r})\mathbf{H}(\mathbf{r}) \quad (6)$$

where \mathbf{r} is the position vector. In general, the relationship between the fields and their flux density is dependent on the media parameters in tensor form and is a convolution due to frequency dependence.

An alternative frequency-domain representation of Maxwell's equations that is often presented in the literature makes use of the phasor form of the fields, assuming a harmonic time dependence ($e^{j\omega t}$). While equations (3) and (4) remain the same (with the exception that t is transformed to ω), the time derivatives in (1) and (2) disappear, giving

$$\nabla \times \tilde{\mathbf{E}}(\omega) = -j\omega \tilde{\mathbf{B}}(\omega) \quad (7)$$

$$\nabla \times \tilde{\mathbf{H}}(\omega) = j\omega \tilde{\mathbf{D}}(\omega) + \tilde{\mathbf{J}}(\omega) \quad (8)$$

This representation is often used to derive frequency-domain methods. The form of the equations given in (1)–(4) is usually used as the starting point for the derivation of time-domain computational methods. However, derivations have been given for several techniques using the integral form of Maxwell's equations as well as the differential form.

Maxwell's equations, with the appropriate constitutive equations and boundary conditions at media interfaces, can be used to solve for the electric and magnetic fields due to any source fields, charges, and currents in any

given structure. For a general material interface, the boundary conditions are

$$\hat{\mathbf{n}} \cdot (\mathbf{D}_2 - \mathbf{D}_1) = \rho_s \quad (9)$$

$$\hat{\mathbf{n}} \cdot \mathbf{B}_2 = \hat{\mathbf{n}} \cdot \mathbf{B}_1 \quad (10)$$

$$\hat{\mathbf{n}} \cdot \mathbf{E}_2 = \hat{\mathbf{n}} \cdot \mathbf{E}_1 \quad (11)$$

$$\hat{\mathbf{n}} \times (\mathbf{H}_2 - \mathbf{H}_1) = \mathbf{J}_s \quad (12)$$

where ρ_s and \mathbf{J}_s are the charge and electric current densities on the interface and $\hat{\mathbf{n}}$ is the normal unit vector to the interface. In the more specific case of a dielectric interface, no charge or surface currents exist. As such, (9)–(12) simply state that the normal components of the electric and magnetic fluxes are constant across the boundary, while the tangential electric and magnetic fields are constant across the boundary. Likewise, on a perfect electrical conductor (PEC) interface the tangential electric field and normal magnetic flux are zero, while the normal electric flux and tangential magnetic field are equal to the charge and current densities, respectively, on the PEC. While (1)–(12) can be used to create a system of equations that can be solved for the fields in any problem, in most cases the resulting partial differential equations have no closed-form solution, requiring the use of numerical methods.

The first simulation technique presented is the finite-difference time-domain (FDTD) [3] technique. It is one of the oldest and most widely used electromagnetic simulation techniques. Many methods, such as finite-volume time-domain (FVTD) [4], finite-element time-domain (FETD) [5], and multiresolution time-domain (MRTD) [6] techniques, which are also presented in this article, have advantages over the FDTD technique at the expense of added complexity. Also presented in this article is the transmission-line matrix (TLM) [7] technique. Mathematically it can be shown to be similar to FDTD while possessing unique advantages. Another interesting feature of TLM is that it is directly based on a physical model of wave propagation, instead of a mathematical discretization of Maxwell's equations. The purpose of this article is to give a basic overview of the operation of these techniques, a summary of the limitations of each, and an overview of how they can be used to determine useful device characteristics such as S parameters and radiation patterns.

3. TIME-DOMAIN NUMERICAL TECHNIQUES

3.1. FDTD

The finite-difference time-domain (FDTD) technique was originally proposed by K. S. Yee in his seminal 1966 paper [3]. The defining factor of the Yee FDTD scheme is the arrangement of the FDTD gridpoints that became known as the ‘‘Yee cell.’’ This scheme is sometimes referred to as the ‘‘Yee leapfrog scheme,’’ for the manner in which the electric and magnetic gridpoints are interleaved in both space and time, as shown in Fig. 1 for three-dimensional grids. In this field arrangement, the electric field Cartesian components are located half a cell width apart along their axis

from each gridpoint. Similarly, the magnetic field components are located half a cell width in both directions normal to their axis from each gridpoint. This arrangement places the electric field components along the edges of the cells and the magnetic fields in the faces. The importance of this arrangement becomes clear when the FDTD update scheme is examined.

The FDTD update scheme can be derived by applying central differences to Maxwell's curl equations [8]. Specifically, Faraday's and Ampere's laws, (1) and (2), in differential form are used. The Yee cell field arrangement is convenient in this case because it defines the fields at discrete points, and the differential form of Maxwell's equations relates the fields at a point instead of an area or loop.

Equations (1) and (2) are vector equations, which can be easily split into three scalar equations. For example, (2) can be written as

$$\frac{\partial E_x}{\partial t} = \frac{1}{\varepsilon} \left[\frac{\partial H_z}{\partial y} - \frac{\partial H_y}{\partial z} - J_x \right] \quad (13)$$

$$\frac{\partial E_y}{\partial t} = \frac{1}{\varepsilon} \left[\frac{\partial H_x}{\partial z} - \frac{\partial H_z}{\partial x} - J_y \right] \quad (14)$$

$$\frac{\partial E_z}{\partial t} = \frac{1}{\varepsilon} \left[\frac{\partial H_y}{\partial x} - \frac{\partial H_x}{\partial y} - J_z \right] \quad (15)$$

if the constitutive relationship for linear, isotropic, non-dispersive media, (5), is used. Central differences can then be applied to discretize the time and space derivatives of these equations. A central-difference discretization of a first derivative

$$\frac{\partial F}{\partial x} = \frac{F_{x+\Delta x/2} - F_{x-\Delta x/2}}{\Delta x} \quad (16)$$

approximates the derivative of a function F at the point x by using the ratio of the difference of two surrounding points, $F_{x+\Delta x/2}$ and $F_{x-\Delta x/2}$, and the distance between those points, Δx .

Observing the field configurations in Fig. 1 it is clear that each E -field component is surrounded by the H -field components that appear in its scalar equation, and vice versa. Furthermore, they are separated from each H component by half a cell in the direction of differentiation of the H component. The time offset between the E and H components can similarly be set to $\Delta t/2$. If (13) is expanded in finite differences, ignoring the current terms (loss and source currents), we obtain

$$\begin{aligned} & \frac{E_{x;ij,k}^{t+\Delta t} - E_{x;ij,k}^t}{\Delta t} \\ &= \frac{1}{\varepsilon} \left[\frac{H_{z;ij+\Delta y/2,k}^{t+\Delta t/2} - H_{z;ij-\Delta y/2,k}^{t+\Delta t/2}}{\Delta y} \right. \\ & \quad \left. - \frac{H_{y;ij,k+\Delta z/2}^{t+\Delta t/2} - H_{y;ij,k-\Delta z/2}^{t+\Delta t/2}}{\Delta z} \right] \end{aligned} \quad (17)$$

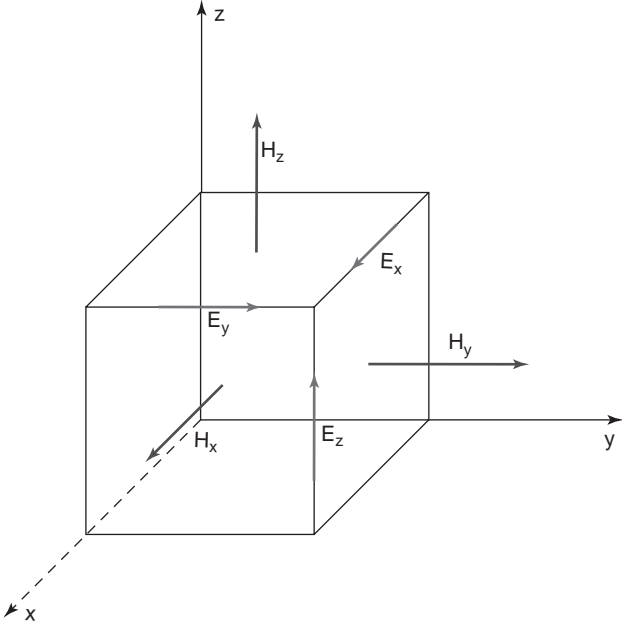


Figure 1. Yee cell in three dimensions.

where i, j, k specify coordinates in a grid of Yee cells ($x, y, z = i\Delta x, j\Delta y, k\Delta z$).

In (17) the value of the E_x component at time $t + 1$ is given in terms of prior values of the surrounding H -field components and the prior value of the E_x field at the same point. Solving for $E_{x;i,j,k}^{t+\Delta t}$

$$E_{x;i,j,k}^{t+\Delta t} = E_{x;i,j,k}^t + \frac{\Delta t}{\varepsilon} \left[\frac{H_{z;i,j+\Delta y/2,k}^{t+\Delta t/2} - H_{z;i,j-\Delta y/2,k}^{t+\Delta t/2}}{\Delta y} - \frac{H_{y;i,j,k+\Delta z/2}^{t+\Delta t/2} - H_{y;i,j,k-\Delta z/2}^{t+\Delta t/2}}{\Delta z} \right] \quad (18)$$

gives a discrete update equation for E_x that requires only the surrounding fields at the previous timestep. Similar equations can be found for the other E - and H -field components, and a time-marching scheme results. If the current terms are not neglected a scheme that includes source currents and Ohmic losses results. It is important to reinforce that the E and H fields are not evaluated at the same time instant; they are separated by half timestep.

The derivation of the FDTD update equations presented do not provide a method for choosing the temporal and spatial steps. It has been shown [8] that the spatial step required for accurate results with an acceptable numerical dispersion performance is related to the spectrum of the excitation waveform and is at maximum one-tenth of the smallest wavelength in the excited waveform. For this reason, the input waveform must be bandlimited. Gaussian pulses, the derivative of Gaussian pulses, and other easily parameterized waveforms are popular choices. Using these functions it is possible to simulate the fre-

quency band of interest without generating nonphysical results.

In the FDTD update equations, such as (18), the value of ε and μ are specified by gridpoint. PEC structures are represented by setting electric field components tangential to PEC structures to zero. In order to accurately simulate a structure, several gridpoints must be used across each feature. Most RF structures have features that are significantly smaller than the wavelength at their frequency of operation, and thus the spatial step is constrained by the structure.

The timestep used in FDTD must be specified as a function of the spatial step [8]. In order for the scheme to be stable

$$\Delta t = \frac{1}{\sqrt{\frac{1}{\mu\varepsilon} \left(\frac{1}{\Delta x^2} + \frac{1}{\Delta y^2} + \frac{1}{\Delta z^2} \right)}} \quad (19)$$

is the maximum value of Δt [known as the Courant-Friedrichs-Levy (CFL) Limit] that can be used in the simulation. One other important rule of thumb for the application of FDTD is that Δx , Δy , and Δz should differ by a factor of ≤ 10 .

Because of the discrete nature of the FDTD grid, the numerical propagation velocity of a wavefront becomes frequency-dependent, an effect that is called *numerical dispersion*. This places a limitation on cell size (usually it must be smaller than $\frac{1}{10}$ th of the wavelength) and the timestep. Often fine grids are required because of the features of the modeled structure, leading to a large number of gridpoints and a small timestep. One modification to the FDTD technique that has been created to address this limitation is the ADI (alternating-direction-implicit) FDTD [9] technique. In this technique the timestep is no longer fixed by stability requirements and can be made larger than the CFL limit, although the fact that ADI is an implicit technique complicates its application. Still the size of the timestep affects the numerical accuracy of ADI simulations.

3.2. Transmission-Line Matrix

The transmission-line matrix (TLM) method is a powerful technique that is unique because of its historical basis and its derivation from Huygens' principle. Before modern computers were available to simulate wave propagation problems, methods were developed that utilized the relationship between electromagnetic propagation and voltages and currents in lumped-element networks [10,11]. As modern computers were made available that could represent these circuits, it became possible to translate these physical simulators to computer models. In this way, the TLM method is a digital representation of an analog simulator. Both of the models are based on a discretization of Huygens' principle.

The TLM method was first suggested by Johns and Beurel [7]. Huygens' principle states that a propagating wavefront consists of an infinite number of radiating sources, and the sum of the radiation from these sources

forms the new wavefront. This principle is rarely presented mathematically, but can be used as the basis of a numerical method that describes radiation through a discrete grid. A two-dimensional discretization of the TLM method is presented here; a number of references provide a 3D representation as well as a broader overview of the method [12,13].

In order to discretize Huygens' principle in two dimensions, a Cartesian grid is chosen such that the distance between elements, Δl corresponds to the distance that the electromagnetic wave will propagate in one timestep Δt ; therefore

$$\Delta t = \Delta l / c \tag{20}$$

A pulse incident on a node in this grid must be equally radiated in all four directions. The grid and pulse radiation on a node are demonstrated in Fig. 2. From this it can be seen that this matrix of nodes acts like a network of transmission-line elements. If these pulses are thought of as voltages in the transmission-line matrix, then the following equation represents the radiated pulses on the lines surrounding a node at timestep $n + 1$ based on the incident pulses at timestep n [14].

$$\begin{pmatrix} V_1 \\ V_2 \\ V_3 \\ V_4 \end{pmatrix}_{n+1}^r = \begin{pmatrix} -1 & 1 & 1 & 1 \\ 1 & -1 & 1 & 1 \\ 1 & 1 & -1 & 1 \\ 1 & 1 & 1 & -1 \end{pmatrix}_n \begin{pmatrix} V_1 \\ V_2 \\ V_3 \\ V_4 \end{pmatrix}_n^i \tag{21}$$

As the radiated pulses become the incident pulses on the neighboring nodes, the incident pulses for the next time-

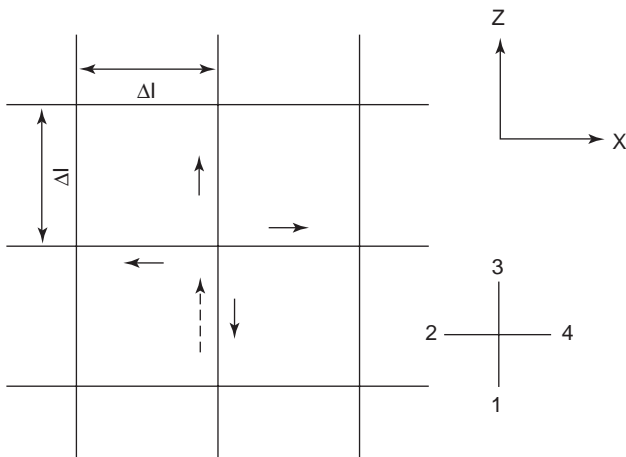


Figure 2. Mesh demonstrating incident (dashed) pulse and radiated pulses (solid).

step are computed as

$$\begin{aligned} k_{+1}V_1^i(x,z) &= k_{+1}V_3^i(x,z-1) \\ k_{+1}V_2^i(x,z) &= k_{+1}V_4^i(x-1,z) \\ k_{+1}V_3^i(x,z) &= k_{+1}V_1^i(x,z+1) \\ k_{+1}V_4^i(x,z) &= k_{+1}V_2^i(x+1,z) \end{aligned} \tag{22}$$

if the distance between the gridpoints is normalized. These equations can be used to in a timestepping fashion by setting an initial condition on the TLM grid and then using (21) and (22) to update the values on each node in the grid.

The grid presented in Fig. 2 and the update equations given in (21) and (22) demonstrate the propagation of any wave. The derivation of the TLM technique will be presented for the two-dimensional TE simulations, utilizing the E_y , H_x , and H_z fields. It was already stated that this network of grids acts like an electrical network of interconnected transmission lines, so it is natural to develop a transmission-line network in which the field values can be determined from the currents and voltages in the network. This unit cell is presented in Fig. 3. The equations that represent signal propagation on these transmission lines are very similar to Maxwell's equations. In fact, there is a simple relationship [14]

$$\begin{aligned} E_y &\equiv V_y \\ H_z &\equiv I_x \\ H_x &\equiv -I_z \\ \mu &\equiv L \\ \epsilon &\equiv 2C \end{aligned} \tag{23}$$

that equates the electromagnetic fields to voltages and currents in the network.

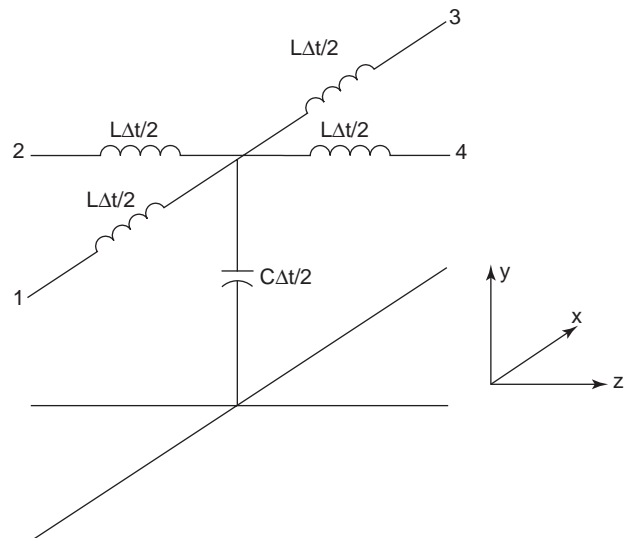


Figure 3. Lumped-element unit cell for TLM [12].

In order to apply the algorithm to a physical problem, it is important to understand the conditions under which it can be used. The line matrix does not represent a continuous space, but rather a tightly spaced periodic structure. As such, electromagnetic waves cannot propagate in any direction, as they can in nature, but only along the lines of the grid. By reducing the spacing between the gridpoints, the space can be made to closely represent natural propagation. However, because of the nature of the discrete grid, the speed of wave propagation through the grid will not match the speed through a physical medium. Furthermore, this difference between physical and numerical propagation speeds is a function of both frequency and propagation direction, and is thus referred to as *grid dispersion*. For diagonal propagation, the grid experiences no dispersion. The maximum dispersion occurs in the axial direction and the velocities are related as [12]

$$\frac{v_n}{c} = \frac{\omega}{\beta_n c} = \frac{\beta}{\beta_n} = \frac{\pi \Delta l / \lambda}{\arcsin(\sqrt{2} \sin(\pi \Delta l / \lambda))} \quad (24)$$

The TLM grid propagation velocity is naturally $c/2^{1/2}$ for square cells in the diagonal direction [12] (as the grid represents a medium with a permittivity twice that of free space); but for a Δl that is a quarter a-wavelength, the network velocity is $c/2$ in the axial direction. Therefore, for an accurate simulation, a grid size much smaller than $\lambda/4$ must be chosen. In practice, however, the grid size is often constrained by the structure being simulated, resulting in grids significantly smaller than this limit.

A major advantage of the TLM method is that it simulates actual electromagnetic wave propagation; no approximations are applied to the wave equations. This makes it more computationally intensive than other methods (although on the same order as others presented here), an aspect that becomes apparent in the requirement that is placed on the grid size. However, the advantage of this method is that it can be used to simulate almost any structure. The model that has been presented thus far only allows free-space propagation, but can be easily extended to simulate structures such as perfect electrical conductors (PEC), perfect magnetic conductors (PMC), dielectric interfaces, and lossy metals.

By modifying the unit cell presented in Fig. 3, the effects mentioned above can be modeled. All of these techniques have been presented in the literature [12]. PEC interfaces can be modeled with short circuits; PMC interfaces, with an open circuit. In a similar way, the reflection from a lossy boundary can simply be represented by setting the reflected field to be equal to the incident field multiplied by a loss parameter ρ (which is, of course, less than 1). Homogeneous materials other than free space can be modeled by simply setting the values of μ and ϵ to match the desired materials. Of course, it is also possible to model inhomogeneous and dispersive materials, but their treatment is beyond the scope of this article.

3.3. Conformal Mesh Techniques

The FDTD and TLM techniques that have been presented are the two most widely used time-domain simulation

techniques. Both techniques have proved to model an extremely wide variety of cases from radar cross sections of aircraft to circuits in broadband communications devices. Nevertheless, there are many structures that cannot conform to a Cartesian grid. When these structures, such as circular metal and dielectric elements, are encountered, they are typically treated in FDTD and TLM by staircasing a fine grid around the nonconformal shape. When staircased finely enough, it is often possible to accurately simulate the structure. However, this can lead to extremely fine grids and thus excessive execution time. Furthermore, some structures cannot be accurately modeled with a staircase configuration [15]. To more accurately represent these structures, methods have been developed that use conformal, nonorthogonal meshes with fewer cells, although the update of each cell is more computationally intensive. As an added benefit, a number of codes produce unstructured meshes that are compatible with these methods. As all of these methods are quite complex, complete derivations will not be presented here. However, the major points and differences of three of the most popular methods, the generalized Yee scheme [16,17] and the finite-volume time-domain (FVTD) [4] and finite-element time-domain (FETD) [5] techniques will be briefly presented.

The Yee FDTD technique presented earlier in this article has been actively researched since the early 1970s. As such, a number of methods have been developed that allow FDTD to be used to model structures that do not conform to the fixed Cartesian grid. One of the simplest of these methods is the variable-grid technique [18]. A similar method has been presented for the TLM technique [19]. This grid is very easy to use with any existing code, as the orthogonality between the grid directions is maintained. By simply varying the Δx , Δy , and Δz values as a function of position along their respective axes, a much wider variety of structures can be modeled. In addition, the grid can be dense in the area of fine features while remaining relatively sparse in large homogeneous areas. Figure 4a depicts a two-dimensional variable grid. In this grid the two coordinate directions are independently varied, thus allowing a much finer grid to be used in a localized region.

Another simple extension to FDTD is subgridding [20]. In these methods, the resolution is increased in a subset of the grid, as shown in Fig. 4b. This allows fine features to be locally matched while adding no additional computational demands away from the finely detailed region. The difficulty of applying this method comes from the interface between the subgridded region and the surrounding mesh. At these interfaces, cells intersect where there are no gridpoints. In these regions the fields must be interpolated to obtain values where gridpoints do not exist, introducing nonphysical dispersion and numerical velocity mismatch. The subgridding method allows the fine grid to be applied in a more local fashion than variable gridding. However, as with the variable grid method, the timestep is constrained by the smallest cell; whereas the simulation uses fewer gridpoints (and is thus faster), it requires the same number of timesteps as a grid made entirely of the smallest cell.

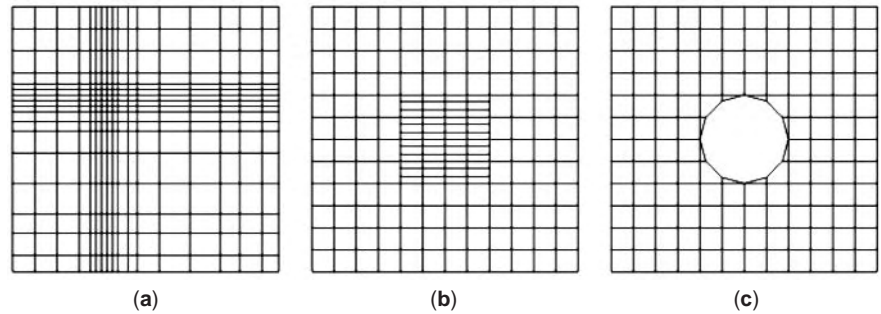


Figure 4. Alternate gridding methods for Yee FDTD: (a) variable gridding; (b) subgridding; (c) locally conformal mesh.

A final extension that will be mentioned here is a method of local conformal modeling where individual cells are modified such that an interface that intersects a cell is modeled while the surrounding cells are treated as normal FDTD cells [21]. An example of this grid is presented in Fig. 4c, where a circle is inscribed into the Cartesian grid. Cells that are intersected by the circle approximate the curve with a diagonal edge. These methods can allow the modeling of curved elements with significantly fewer cells than staircasing, and they converge more accurately to the actual shape as the cell size is reduced. For more complex structures a grid that is conformal everywhere, such as in Fig. 5, is appropriate. This method can be viewed as a local, limited version of the generalized Yee scheme.

The generalized Yee scheme [16,17] is so named because it extends the use of the Yee cell, which is based on a Cartesian grid, into a scheme where the space is filled with interlocking polyhedra, the faces and edges on which the field values are constant. As the polyhedra that represent the electric fields intersect at the centroids of the magnetic field polyhedra, the resulting field orientation is similar to the conventional Yee scheme. However, in the generalized scheme the points do not have to be regularly spaced, and the edges that connect them are not orthogonal. Furthermore, all the polyhedra do not have the same shape. Removing the structure of the grid adds significant

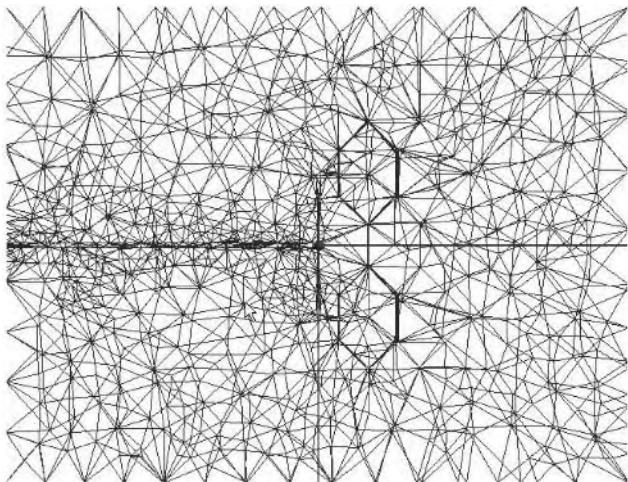


Figure 5. Conformal mesh using triangular elements, created with HFSS (high-frequency structure simulation) [22].

complexity to the method. However, there are several benefits to using the technique: (1) as in traditional FDTD, the electric and magnetic fields are offset, allowing a second-order representation while remaining explicit; (2) complex shapes can be modeled with fewer cells than conventional FDTD because the need for staircasing has been eliminated; and (3) the update of each field point is still dependent only on the nearest neighbors, allowing the technique to be efficiently parallelized.

Another technique that uses a conformal mesh is the finite-volume time-domain (FVTD) method [4]. While it uses a similar grid as the generalized Yee scheme, it has a very different derivation and characteristics. The FVTD method is derived using the integral form of Maxwell's equations on contours made in the grid and collocates all the fields in both time and space (as opposed to the leapfrog arrangement of the Yee scheme). One difference between this method and FDTD is that it is not dispersive, but rather dissipative [4].

The final conformal method that will be reviewed here is the finite-element time-domain (FETD) technique [5]. Finite-element schemes are very different from the techniques presented thus far because the fields are represented on elements on which a field distribution is assumed and coefficients representing the magnitude of the fields on these elements are determined. Like the FVTD and generalized Yee scheme, the FETD method can use a conformal mesh and thus represent complex structures with larger cells than can the FDTD method. The FETD method can be complicated in a full 3D scheme, but, as it is an important and widely used time-domain method, a brief derivation is presented here.

3.4. Finite-Element Time Domain

A multitude of algorithms apply finite-element techniques to time-domain electromagnetic modeling. The technique presented here is the point-matched time-domain finite-element method [5], which was developed in the mid-1980s. It is one of the earliest finite-element methods in the time domain, and is representative of the techniques used in finite-element time-domain (FETD) modeling.

FETD shares many similarities to FDTD. As in FDTD, Maxwell's equations in differential form, Eqs. (1)–(4) are used as a starting point. However, instead of discretizing the equations using finite differences, the electric and magnetic fields in the equations are replaced with a sum

of coefficients multiplied by basis functions chosen by the user. The electric and magnetic fields are expressed as

$$\mathbf{E}(\mathbf{r}, t) = \sum_{i=1}^M \varphi_i(\mathbf{r}) \mathbf{E}_i(t) \quad (25)$$

$$\mathbf{H}(\mathbf{r}, t) = \sum_{j=1}^N \psi_j(\mathbf{r}) \mathbf{H}_j(t) \quad (26)$$

where M and N are the number of nodes (\mathbf{r}_i and \mathbf{r}_j , respectively) used to represent the fields over the simulated space. These nodes are not necessarily collocated. It is important to note that, unlike in the finite-difference technique, all components of each field are collocated at their respective gridpoints. The characteristics of the resulting simulator are dependent on the basis functions, φ and ψ , chosen.

The basis functions are restricted such that

$$\varphi_i(\mathbf{r}) = \begin{cases} 1 & \mathbf{r} = \mathbf{r}_i \\ 0 & \text{all other nodes} \end{cases} \quad (27)$$

$$\psi_j(\mathbf{r}) = \begin{cases} 1 & \mathbf{r} = \mathbf{r}_j \\ 0 & \text{all other nodes} \end{cases} \quad (28)$$

The domain of each basis function ends at the neighboring grid locations. The effect of the functions is to interpolate the fields over the cell. The electric and magnetic gridpoints are offset, in much the same way as in the FDTD method, so that the locations of the magnetic gridpoints are in the center of the electric field cells. With this arrangement, update equations very similar to the FDTD update equations can be developed. The basis functions for the electric or magnetic gridpoints located at the points \mathbf{r}_i and \mathbf{r}_j , respectively, will only overlap the neighboring gridpoints of the corresponding magnetic or electric field. If each element has K nodes, and (25) and (26) are inserted into (1) and (2) (ignoring the current term), the following results

$$\frac{\partial \mathbf{H}_j(t)}{\partial t} = -\frac{1}{\mu(\mathbf{r}_j)} \sum_{l=1}^K \nabla \varphi_l(\mathbf{r}_j) \times \mathbf{E}_l(t) \quad (29)$$

$$\frac{\partial \mathbf{E}_i(t)}{\partial t} = \frac{1}{\mu(\mathbf{r}_i)} \sum_{l=1}^K \nabla \psi_l(\mathbf{r}_i) \times \mathbf{H}_l(t) \quad (30)$$

where the points denoted by the index l correspond to the points where the basis functions overlap.

The coefficients $\mathbf{E}_i(t)$ and $\mathbf{H}_j(t)$ in (25) and (26) are discrete functions of time. They can be used to determine the magnitude of the electric and magnetic fields at integer multiples of the timestep Δt . The size of the timestep required for a stable simulation is limited by the grid, but its calculation will not be covered here. In (29) and (30) the time derivative is not discretized. If central differences are

used, we obtain

$$\mathbf{H}_j^{n+(1/2)} = \mathbf{H}_j^{n-(1/2)} - \frac{1}{\mu(\mathbf{r}_j)} \sum_{l=1}^K \nabla \varphi_l(\mathbf{r}_j) \times \mathbf{E}_l(t) \quad (31)$$

$$\mathbf{E}_i^{n+1} = \mathbf{E}_i^{n+1} + \frac{1}{\mu(\mathbf{r}_i)} \sum_{l=1}^K \nabla \psi_l(\mathbf{r}_i) \times \mathbf{H}_l(t) \quad (32)$$

where n is the timestep index. As in the finite-difference technique, the \mathbf{E} and \mathbf{H} fields are interleaved in time, and an explicit time-marching scheme results. The only step remaining to determine the time-marching scheme is to calculate the derivatives in (31) and (32), which is an easy task once the basis functions have been chosen.

While the scheme presented seems relatively straightforward, several details involved in implementing the method can be quite daunting. First, the grid used in this method, unlike that in FDTD and TLM, does not have to be rectangular. Each element can be shaped differently. This is an advantage of the method, but the grid generation can be challenging. A common method is to use a rectangular mesh everywhere except at material boundaries. This significantly simplifies grid generation. There are several existing codes and algorithms that can be used for mesh generation. The creation of an effective meshing algorithm can be at least as complicated as the FETD technique itself. Similar grids are used for finite-element discretizations in a variety of applications, such as mechanics, aerodynamics, and frequency-domain electromagnetics.

The second difficulty that must be mentioned is the intricacy of representing boundary conditions in the finite-element method. A system of equations that can be used to solve for the fields on the boundary of a PEC are

$$\hat{\mathbf{n}} \times \mathbf{E}^1 = -\hat{\mathbf{n}} \times \mathbf{E}^2 \quad (33)$$

$$\nabla_0 \cdot (\hat{\mathbf{n}} \times \mathbf{H}_{\text{total}}) = -\epsilon \hat{\mathbf{n}} \cdot \frac{\partial \mathbf{E}_{\text{total}}}{\partial t} \quad (34)$$

where ∇_0 is the surface divergence (derivatives are taken only along the surface). In the finite-difference time-domain method, only (33) is used. This is because the components of the electric field are offset in space, and only the tangential fields ever contact a PEC surface. Thus, instead of simply zeroing components, such as in the FDTD method, a system of equations must be solved at each timestep. Similar considerations must be taken when implementing dielectric boundaries.

3.5. Multiresolution Time Domain

The multiresolution time-domain (MRTD) technique [6] was originally introduced by M. Krumpholz and L. P. B. Katehi in 1996. The MRTD method is derived through the application of wavelets to the space discretization of Maxwell's equations (multiresolution analysis). Time differentiation is modeled using central differences as in FDTD. One of the advantages of using MRTD is that the resolution of the discretization can be altered as a function of

time and space. This timespace-adaptive grid can result in a significant reduction in operations per timestep and significantly quicker simulations. Another advantage of the MRTD method is that, depending on the wavelet basis functions used, the numerical dispersion relationship can allow the use of significantly fewer basis functions per wavelength than required in the FDTD method [23]. The adaptive nature of wavelets and their ability to efficiently represent complex waveforms has led to their use in several frequency- and time-domain techniques.

Many wavelet bases are commonly used in electromagnetics, each with distinct advantages and challenges in its implementation. Several of these techniques allow not only adaptive resolution but also the use of fewer points per wavelength and are comparable to high-order FDTD techniques. For simplicity, a 2D derivation of MRTD using the relatively simple Haar wavelets is presented here. This set of basis functions has the same dispersion properties as FDTD, and thus requires the same number of basis functions per wavelength [24]. The Haar basis functions are chosen over other wavelet basis functions for several reasons: (1) they are based on pulses and thus are simpler to apply than other basis functions and (2) when the basis functions are summed to determine the field values, they form regions of constant field value. Therefore, when set to zero, they form a finite region of zero field value. This enables efficient modeling of PECs. The main advantage of Haar MRTD over FDTD is the timespace adaptive gridding capability. The Haar scaling function and mother wavelet are presented in Fig. 6.

The Haar scaling function is a simple pulse function in space. If the MRTD update derivation is followed using only the Haar scaling functions, the FDTD scheme results [25]. All wavelets used in the Haar MRTD scheme are based on the mother wavelet. With each increase in resolution level, the number of wavelets is doubled, the domain of each is halved, and the magnitude is increased so that the norm (integral of the function multiplied by itself over

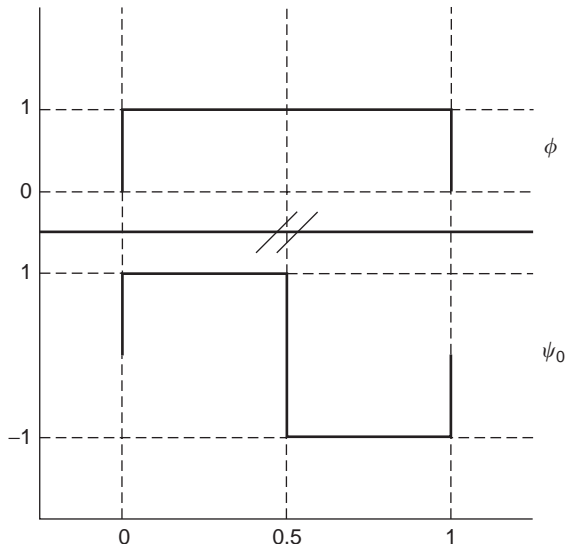


Figure 6. Haar basis scaling function ϕ and mother wavelet ψ_0 .

its entire domain) of each function is 1. The wavelet basis functions for resolution 1 and 2 are presented in Fig. 7.

MRTD update equations can be determined by expanding Maxwell's curl equations in terms of wavelets and scaling coefficients in space and pulses in time and then applying the method of moments. Maxwell's curl equations, in the 2D TE_z mode, are given by

$$\frac{\partial E_x}{\partial t} = \frac{1}{\varepsilon} \frac{\partial H_z}{\partial y} \quad (35)$$

$$\frac{\partial E_y}{\partial t} = -\frac{1}{\varepsilon} \frac{\partial H_z}{\partial x} \quad (36)$$

$$\frac{\partial H_z}{\partial t} = \frac{1}{\mu} \left[\frac{\partial E_x}{\partial y} - \frac{\partial E_y}{\partial x} \right] \quad (37)$$

E_x can be expanded as

$$E_x(x) = \sum_{n,i,j} h_{n\Delta t} \left[\begin{aligned} & n E_{ij}^{x,\phi\phi} \phi_i(x) \phi_j(y) + \sum_{r=0}^{r_{\max}} \sum_{p=0}^{2^r-1} n E_{ij,r,p}^{x,\phi\psi} \psi_{i,p}^r(x) \phi_j(y) \\ & + \sum_{r=0}^{r_{\max}} \sum_{p=0}^{2^r-1} n E_{ij,r,p}^{x,\psi\psi} \phi_i(x) \psi_{j,p}^r(y) \\ & + \sum_{r=0}^{r_{\max}} \sum_{p=0}^{2^r-1} \sum_{s=0}^{2^s-1} n E_{ij,r,p,s,q}^{x,\psi\psi} \psi_{i,p}^r(x) \psi_{j,q}^s(y) \end{aligned} \right] \quad (38)$$

following the notation in Ref. 6. In this case $\phi_i(x) = \phi(x/\Delta x - i)$ and $\psi_{i,p}^r(x) = 2^{r/2} \psi_0(2^{r/2}(x/\Delta x - i) - p)$, and $h(t)$ is a simple pulse of duration Δt . The maximum level of wavelet resolution is r_{\max} . The four groups of terms in the equations above represent the product of the x - and y -oriented wavelet expansions. The terms are the x -scaling/ y -scaling, x -wavelet/ y -scaling, x -scaling/ y -wavelet, and x -wavelet/ y -wavelet terms, respectively. In each cell, represented by (i,j) in 2D, there is a set of $2^{D(r_{\max}+1)}$ coefficients, where D is the dimension of the simulator [$2^{2(r_{\max}+1)}$ in the 2D case]. It has been noted [24,25] that an offset of $1/2^{r_{\max}+2}$ between the E and H cells in space leads to a true doubling of resolution for each increase in r_{\max} , and dispersion performance equivalent to an FDTD grid that has cell spacings of the MRTD equivalent gridpoints. For this scheme, there are $2^{2(r_{\max}+1)}$ equivalent gridpoints per cell, distributed evenly in the cell. These gridpoints exist at each independent field value that can be determined by summing all of the basis functions in a cell. It should be noted that there are as many of these points as there are basis functions.

The MRTD update equations can be determined by inserting the scaling/wavelet function expansions of the fields into Maxwell's equations and applying the method of moments. The method of moments is applied by multiplying both sides of the equation by user chosen testing functions and then taking an integral over their domain. In MRTD, Galerkin's method is normally used, where the testing functions are the same as the basis functions. For

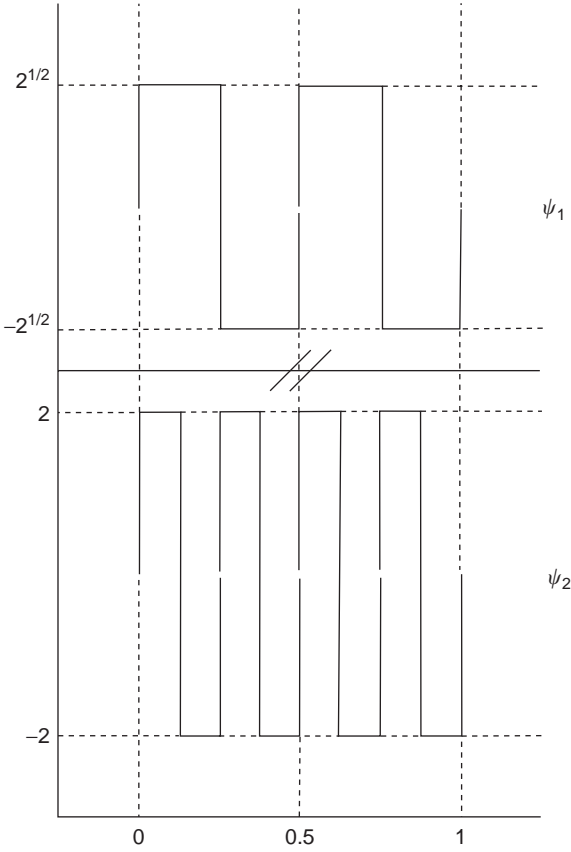


Figure 7. Haar wavelets for resolution levels 1 and 2.

example, time localization (limiting the time coefficients required for an update to the current and previous time step) is achieved by multiplying both sides of the equation by the time pulse, positioned at the point of the fields in the space derivative of the equation. As in FDTD, the coefficients for the field values are interleaved in time, using (38), the electric field coefficients are calculated at times $n\Delta t$, and in a similar expansion the magnetic fields are calculated at times $(n + \frac{1}{2})\Delta t$. The method of moments can be applied to discretize time as

$$\int h_{[n+(1/2)\Delta t]} \frac{\partial \mathbf{E}_x}{\partial t} \partial t = \int h_{[n+(1/2)\Delta t]} \frac{1}{\epsilon} \frac{\partial H_z}{\partial y} \partial t \quad (39)$$

where $h_{[n+(1/2)\Delta t]}$ represents a pulse of duration Δt centered at time $(n + \frac{1}{2})\Delta t$. The integral

$$\int h_{[n+(1/2)\Delta t]} h_{[m\Delta t]} \partial t \quad (40)$$

which appears on the left hand side of (39), evaluates to 1 when $n = m$ and $n = m - 1$ and 0 elsewhere. Thus, the only electric field components that are needed to update the coefficients are the current and previous timesteps. On the right hand side of (39), the integral

$$\int h_{[n+(1/2)\Delta t]} h_{[m+(1/2)\Delta t]} \partial t \quad (41)$$

is nonzero only when $n = m$. Thus, the magnetic field components are only required at one location in time. A similar procedure can be applied for each of the wavelet and scaling coefficients, so that each the update of each wavelet/scaling coefficient is in terms of its previous value and the values of the wavelet/scaling values of the surrounding fields.

Using a vector notation similar to [25], the following results are derived

$$\mathbf{n} \mathbf{E}_{ij}^x = \mathbf{n}_{-1} \mathbf{E}_{ij}^x + \frac{\Delta t}{\epsilon \Delta y} \mathbf{U}_{\mathbf{E}_x} \begin{bmatrix} \mathbf{n}_{-1} \mathbf{H}_{ij}^z \\ \mathbf{n}_{-1} \mathbf{H}_{i,j-1}^z \end{bmatrix} \quad (42)$$

$$\mathbf{n} \mathbf{E}_{ij}^y = \mathbf{n}_{-1} \mathbf{E}_{ij}^y - \frac{\Delta t}{\epsilon \Delta x} \mathbf{U}_{\mathbf{E}_y} \begin{bmatrix} \mathbf{n}_{-1} \mathbf{H}_{ij}^z \\ \mathbf{n}_{-1} \mathbf{H}_{i-1,j}^z \end{bmatrix} \quad (43)$$

$$\mathbf{n} \mathbf{H}_{ij}^z = \mathbf{n}_{-1} \mathbf{H}_{ij}^z + \frac{\Delta t}{\mu} \left(\frac{1}{\Delta y} \mathbf{U}_{\mathbf{H}_{E_x}} \begin{bmatrix} \mathbf{n}_{-1} \mathbf{E}_{ij}^x \\ \mathbf{n}_{-1} \mathbf{E}_{i,j+1}^x \end{bmatrix} - \frac{1}{\Delta x} \mathbf{U}_{\mathbf{H}_{E_y}} \begin{bmatrix} \mathbf{n}_{-1} \mathbf{E}_{ij}^y \\ \mathbf{n}_{-1} \mathbf{E}_{i+1,j}^y \end{bmatrix} \right) \quad (44)$$

This vector representation appears very similar to its FDTD analogue. To give an example of the vectors in (42)–(44), if the maximum resolution $r_{\max} = 0$, then

$$\mathbf{n} \mathbf{E}_{ij}^x = \begin{bmatrix} \mathbf{n} \mathbf{E}_{ij}^{x,\phi\phi} \\ \mathbf{n} \mathbf{E}_{ij}^{x,\psi\phi} \\ \mathbf{n} \mathbf{E}_{ij}^{x,\phi\psi} \\ \mathbf{n} \mathbf{E}_{ij}^{x,\psi\psi} \end{bmatrix} \quad (45)$$

The U matrices represent the results of the inner products from the method of moments. For the $r_{\max} = 0$ case, we obtain

$$\mathbf{U}_{\mathbf{H}_{E_y}}(r_{\max} = 0) = \begin{bmatrix} -1 & -1 & 0 & 0 & 1 & 1 & 0 & 0 \\ 1 & -3 & 0 & 0 & -1 & -1 & 0 & 0 \\ 0 & 0 & -1 & -1 & 0 & 0 & 1 & 1 \\ 0 & 0 & 1 & -3 & 0 & 0 & -1 & -1 \end{bmatrix} \quad (46)$$

The MRTD method has a timestep requirement similar to that of FDTD:

$$\Delta t = \frac{1}{c \sqrt{\left(\frac{2^{r_{\max}+1}}{\Delta x}\right)^2 + \left(\frac{2^{r_{\max}+1}}{\Delta y}\right)^2}} \quad (47)$$

In the case of Haar wavelets, the resolution r_{\max} is equivalent to having $2^{r_{\max}+1}$ FDTD gridpoints per cell.

As an alternative to the Haar techniques presented here, other wavelet bases are commonly used with the

MRTD technique. Two of the most popular are the Battle-Lemarie [6] and CDF wavelets [26]. These techniques have the advantage of requiring the use of fewer basis functions per wavelength than FDTD or Haar MRTD. One disadvantage of these techniques is that it is difficult to apply hard boundary conditions, such as PECs and PMCs using these basis functions. Extending these techniques to allow the modeling of more structures is currently a busy research area.

3.6. Parallelization

One common method of decreasing the execution time of these computationally intensive codes is parallelization. Code parallelization allows programmers to rewrite code to distribute the problem over the several processors in a multiprocessor system. This is becoming especially popular with the advent of low-cost computer clusters. These clusters, sometimes referred to as *Beowulf clusters* (as named by their developers at NASA) or workstation clusters, allow the combination of several off-the-shelf computers into a networked supercomputer. These computers are significantly cheaper than traditional supercomputers, and several rank among the fastest in the world. While the slower interconnects between the computers can limit their application, most time-domain methods are ideal for workstation cluster parallelization.

Most of the time-domain methods presented here are explicit, meaning that the fields are updated directly from other field values and no matrices are inverted. Furthermore, they are nearest-neighbor techniques; the field update at any given point depends only on the fields at the neighboring points. Therefore, these techniques can be parallelized by dividing the computational space into subgrids. The only data that needs to be exchanged between the processes are the data on the edges of the subgrids. As these data are two-dimensional, and the data to be updated are three-dimensional, the computation time grows on the order of the number of gridpoints faster than the time taken to pass data between grids. As the problem size increases, the communication time becomes less of a hindrance, resulting in excellent performance on workstation clusters.

4. IMPORTANT FEATURES OF TIME-DOMAIN SIMULATION TECHNIQUES

4.1. Performing Simulations and Analyzing Output

All the simulators that have been presented in this article are full-wave simulators. They are so named because they simulate Maxwell's equations without approximations, and thus give the electric and magnetic fields over the entire simulation domain as they evolve in time. For most applications, the quantities of interest from simulation are not the values of the fields, but rather macroscopic parameters of the devices being simulated (such as S parameters, input impedance, and bandwidth). In addition, while the methods that have been presented here allow for the simulation of field propagation through various media, no mention has been made of how to terminate the com-

putational space, or introduce a source condition. This section contains information about how to use the information obtained from these simulators.

It is important to remember when using these tools that they simulate actual physical phenomena. As such, when an excitation is introduced, it should closely match the source condition in the physical circuit. This may include introducing a gap voltage in a dipole antenna or a current on a wire in a waveguide probe feed. In many ways not only the circuit but also the measurement environment are simulated. A network analyzer, for example, excites a field on a feedline and then analyzes the output of the device. In simulation, fields can be probed in response to an excitation. By doing this in as close a fashion to actual measurement as possible, useful information can be obtained. Of course, simulated fields can be injected and measured at any point in space, even where it would be physically impossible in practice. Used wisely, this allows for results that are independent of many common sources of measurement error.

An example structure that can be used to explain many of these concepts is presented in Fig. 8. The presented structure is a microstrip coupled-line filter. The physical structure being simulated consists of metal lines printed on a dielectric substrate. This is a two-port structure, with ports 1 (input) and 2 (output) labeled in the figure. If this structure were to be fabricated and measured, connectors would have to be added at the ports to allow connection to the network analyzer. These could be either coaxial or coplanar waveguide depending on the measurement equipment. In either case, the input and output lines would be made long enough to prevent coupling between the measurement ports and the structure. In the case of

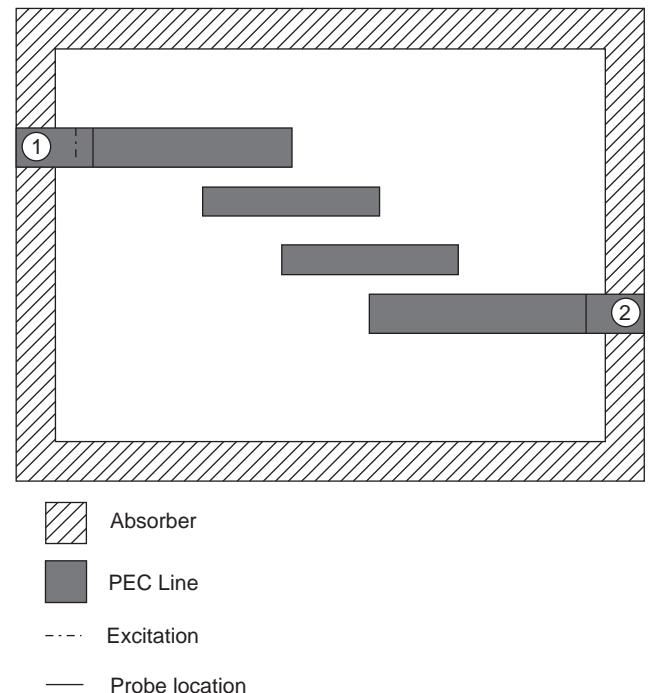


Figure 8. Example simulation structure showing location of absorbers, excitations, and probes.

simulation, these connectors are not required. Instead, a microstrip excitation is impressed on the grid. To prevent reflections of the impressed signal from the input and output ports, an absorber is placed around the structure. This numerical absorber is analogous to the absorbing materials used in antenna measurement systems. The voltage under the microstrip is then measured at the input and output ports. By simulating the structure over the entire frequency band of interest and transforming the probed voltages to the frequency domain, S parameters and other important parameters such as input impedance and bandwidth can be determined. Field plots, showing the field distribution in a 2D cross section of the grid, in both the time and frequency domains, can also be used to optimize structures by highlighting areas that cause unwanted crosstalk, radiation, loss, and maximum coupling.

4.2. Source Conditions

When exciting a structure it is necessary to consider both the spatial distribution of the excitation (how much of the grid is covered and which mode is excited) and the frequency content of the source signal. As most methods are numerically dispersive, there is a grid-dependent maximum frequency that can be accurately simulated. For the simulation of RF and wireless circuits, it is usually desirable to provide an excitation over a small portion of the grid to represent a physical incident source condition. The frequency content of the pulse is chosen to cover the frequencies of operation of the device. For many structures, such as rectangular and circular waveguides, there are closed-form expressions for the modes that can propagate. These expressions give relative field magnitudes as a function of space that are dependent on the structure. To excite these structures, the mode shape must be discretized, and then the field values can be set to match the mode shape. Due to discretization error, it is often difficult to excite just the modes of interest, and mode decomposition must be performed when the output is analyzed. For other structures, such as microstrip lines, no exact closed-form expressions exist. In this case, the mode shape is approximated [8]. As the signal propagates through the circuit, it will automatically assume the proper mode shape. It is also possible to build a library of these nonanalytic excitations by simulating lines and storing the mode shapes created on the line by a simpler excitation.

To restrict the excitation to a specific frequency band, its waveform must be shaped in time. The frequency content of the input signal can then be determined by Fourier-transforming the time-shaping function. As the simulation time must be finite, the actual frequency response of any time waveform is infinite. As such, pulse shapes that have quickly decreasing magnitude as frequency is increased are necessary. In order to accurately control the frequency content of the pulse, expressions with well-defined Fourier transforms are often chosen. Commonly chosen waveforms are Gaussian pulses, Gaussian derivative pulses, sinusoidal pulses, and modulated Gaussians (Gaussians multiplied by sinusoids). It is important to remark that while sinusoidal pulses will give the response to a single frequency, this is not a very efficient use of time-

domain methods. One of the chief advantages of time-domain methods is that they simulate a broad band in comparable time to a single frequency in a frequency domain code. For this reason it is usually best to use a broadband excitation.

Alternatives to these excitations are plane-wave sources. For many applications, such as illuminating targets for radar cross section evaluation or modeling bulk material properties [e.g., electronic bandgap (EBG) and metamaterials], the response to a plane-wave illumination is desired. In FDTD it is often useful to use a total-field/scattered-field formulation [27]. In this formulation the computational domain is divided into total-field region that is surrounded by a scattered-field region. A connecting surface is developed that effectively removes the incident field from the scattered region. An alternate method is a pure scattered-field formulation [28], in which the incident wave is not impressed on the grid, but rather the response of the surface of the scatterer is applied, and thus the scattered field is generated. As the scatterer responses must be calculated analytically, this can be a difficult method to apply, however, there is no error due to the incident field propagating through the numerical grid.

4.3. Numerical Absorbers

For all of the presented methods, the fields at any one point in time and space are dependent on the fields at previous timesteps and neighboring spatial points. The computational domain, however, must be finite. In order to update the field points, the fields on the boundaries must be known. Two conditions on which the fields are always known are perfect electrical conductors (PECs) and perfect magnetic conductors (PMCs). On these surfaces the tangential electric or magnetic fields, respectively, are zero. In techniques with staggered grids, such as FDTD and TLM, these conditions can be applied by simply zeroing the appropriate field values. In collocated grid techniques, such as FVTD and FETD, these conditions must be applied using all the field values. For either type of simulator, these boundaries will cause total reflection of an incident signal. If the response of a structure is to be known to an incident signal, then the reflection from the boundaries will combine with the response of the structure, and the results will be useless. To use these hard boundary conditions, the computational space must be sufficiently large for the time response of the device to end before reflections interfere. This can easily result in impractically large grids. Therefore, another technique, an *absorbing* (sometimes called *radiating*) *boundary condition* (ABC), must be applied. The goal of these techniques is to absorb incoming waves with a minimum of numerical reflection.

There are several techniques for applying absorbing boundary conditions (ABCs), most of which can be applied to the methods presented here. A number of these methods, usually referred to by the surnames of their developers, such as Bayliss-Turkel [29], Mur [30], and Ramahi [31], can often reduce reflections by 50–80 dB. Another technique, which has become the standard for numerical absorbers, is the perfectly matched layer (PML). Introduced

by Berenger in 1994 [32], the PML is manifested in a simulator as a physical material with very specific properties. It offers excellent performance over a wide frequency band and range of incident angles. It has been shown to be equivalent to a similar method, the uniaxial perfectly matched layer (UPML) [33]. The UPML is the numerical representation of a uniaxial anisotropic medium with both electric and magnetic permittivity tensors, that offers numerical reflection coefficient lower than -100 db for most RF open structures.

4.4. S Parameters

The output of a time-domain simulator is the values of the electric and magnetic fields at all points in space over the time period simulated. To calculate useful characteristics of the device being simulated, these responses must be transformed into meaningful parameters. The S parameters are frequency-domain characteristics that provide the response at a port of a structure due to an incident signal. As such, in time-domain simulators, the input and output voltages/currents on a structure can be recorded, converted to the frequency domain, and postprocessed to give S parameters. The structure in Fig. 8 can be used as an example for determining S parameters.

The nature of the input and output signal depends on the type of device being simulated. For a quasi-TEM structure, such as the microstrip of Fig. 8, the voltage from ground to signal line and the current in the signal line can be used to determine S parameters. The voltage can be determined by summing the electrical fields normal to the line from the ground to the signal line, numerically integrating

$$V = - \int_a^b \mathbf{E} \cdot d\mathbf{s} \quad (48)$$

Likewise, the current on the line can be determined using

$$I = \oint \mathbf{H} \cdot d\mathbf{l} \quad (49)$$

which is numerically equivalent to summing the magnetic fields tangential to a contour surrounding the conductor.

These parameters are then transformed to the frequency domain using either a fast or discrete Fourier transform. In order for the Fourier transform to be accurate, the simulation must run until the fields at the measurement points go to zero (or a very small value relative to their peaks, usually less than 0.1%). Once the frequency domain voltages/currents are determined, they can be processed to determine the S parameters. The general formula for an S parameter is to divide the output signal at port m by the incident signal on port n :

$$S_{mn}(\omega) = \frac{V_{m,\text{out}}(\omega)}{V_{n,\text{in}}(\omega)} \left(\frac{Z_n(\omega)}{Z_m(\omega)} \right)^{1/2} \quad (50)$$

The expression in (50) is valid for the general case where the impedance of the input and output ports are not equal.

It should be noted that this is not always the ratio of the total signal at the input and output probes.

The fields recorded during the simulation are the total fields. For example, the input probe of Fig. 8 will record the incident field from the excitation as well as the reflection from the filter. For the computation of S_{21} , however, voltage used in (50) must be only the incident. In this case the incident voltage can be determined by performing a separate simulation with an identical probe on an identical transmission line (without the filter). To compute S_{11} , the output field can be computed by subtracting the incident from the total field.

One other parameter that can be easily calculated using voltage and current probes is the characteristic impedance of a transmission line. For a signal traveling through a transmission line, the characteristic impedance can be determined as the ratio of the voltage to the current on the line. It is important to note that to measure these values, only one signal should propagate on the line, with no reflections. For most simulators, exciting a transmission line terminated with PML on both ends will suffice. For a simulator that has electric and magnetic field collocated in time and space, the impedance formula is

$$\tilde{Z}(\omega) = \frac{\tilde{V}(\omega)}{\tilde{I}(\omega)} \quad (51)$$

while, for other simulators, the offset must be accounted for. In FDTD, for example, the half-space-cell offset can be accounted for by using the geometric average of two current probes that surround a voltage probe, and an exponential multiplier can be used to compensate for the half-timestep offset. For FDTD, the impedance formula is [34]

$$\tilde{Z}_0(x) = \frac{\tilde{V}(x)e^{-j\omega(\Delta t/2)}}{\sqrt{\tilde{I}(x + \frac{1}{2})\tilde{I}(x - \frac{1}{2})}} \quad (52)$$

This discussion has focused on microstrip structures; however, it can easily be extended to more general lines. For any given structure, it is necessary to determine what output voltage can be used to characterize the device. For a coplanar waveguide, for example, the energy is also carried between the signal and ground lines; however, they are in the same plane and thus the recorded voltage is tangential to the lines. Similarly, stripline, slotline, and coaxial structures can be characterized by determining the voltage between the appropriate conductors. Finally, using the S parameters, other important parameters such as input impedance, insertion loss, and bandwidth can be directly calculated.

4.5. Near-Field/Far-Field Transformation

Antennas are often simulated with time-domain simulators. The techniques presented in the previous section can be used to calculate antenna parameters such as input impedance and bandwidth, but they do not give the polarization, directivity, gain, and many other antenna parameters. To analyze the antenna in terms of these

parameters, it is necessary to know the far-field radiation pattern of the antenna. The far field is often tens of wavelengths away from the antenna structure, and an enormous grid is required for accurate simulation. Fortunately, there is another method that can be used to determine the far-field radiation pattern, the near-to-far-field (NFF) transform.

The far-field radiation pattern is calculated by first reducing the radiation problem to one set of electric and magnetic equivalent sources on a closed surface surrounding the radiating structure. The problem of an antenna radiating into free space is demonstrated in Fig. 9, in which the entire antenna and feeding structure are surrounded by free space. This space is terminated with an absorbing boundary condition, such as PML. A transformation surface is placed in between the antenna and the absorber. This surface has no effect on the simulation; it is used only to record fields.

The surface equivalence theorem [35] states that the problem in Fig. 9 can be represented by electric and magnetic current sources placed on the NFF transformation surface. Using these current sources, the fields outside the surface are the same as those produced by the radiator, and the radiation at any point outside the contour can be determined mathematically. The first step in performing the NFF transformation is to determine the equivalent currents on the transformation surface.

If the electric and magnetic fields on the surface are known, the sources can be calculated as

$$\tilde{\mathbf{J}}_s = \mathbf{n} \times \tilde{\mathbf{H}} \quad (53)$$

$$\tilde{\mathbf{M}}_s = -\mathbf{n} \times \tilde{\mathbf{E}} \quad (54)$$

where \mathbf{n} is the unit vector normal to the transformation surface. Of course, the antenna pattern has meaning only as a function of frequency, and thus the fields on the transformation surface must be transformed to the frequency domain. To Fourier-transform the fields, the field

values at all timesteps are required. As the surface completely surrounds the antenna, and thus consists of a very large number of points, the Fourier transform is performed during simulation to avoid the burden of storing the field values for all points on the surface at all timesteps. Once the currents are known, they can be used to solve for the far (or near)-field radiation pattern. The equation that gives the radiation at any point in space due to these sources can be simplified to give results for only the far field. For these simplifications, the distance from any point on the radiating surface to an observation point is assumed to be the same, except for the phase terms. This is possible because the source is very far from the observation point.

Using these approximations, the electric field in the far field is [35]

$$\tilde{\mathbf{E}}_r \approx 0 \quad (55)$$

$$\tilde{\mathbf{E}}_\theta \approx -\frac{jke^{-jkr}}{4\pi r} (\tilde{\mathbf{L}}_\theta + \eta_0 \tilde{\mathbf{N}}_\theta) \quad (56)$$

$$\tilde{\mathbf{E}}_\phi \approx -\frac{jke^{-jkr}}{4\pi r} (\tilde{\mathbf{L}}_\phi - \eta_0 \tilde{\mathbf{N}}_\phi) \quad (57)$$

where

$$\tilde{\mathbf{N}} = \int_S \int \tilde{\mathbf{J}}_s e^{jkr' \cos \psi} dS \quad (58)$$

$$\tilde{\mathbf{L}} = \int_S \int \tilde{\mathbf{M}}_s e^{jkr' \cos \psi} dS \quad (59)$$

where r' is the distance between the origin and the source point on the contour and ψ is the angle between the vector to the surface and the vector to the observation point.

This procedure yields the far electric and magnetic fields at any position on a sphere surrounding the antenna. By normalizing these fields, one can plot the radiation pattern. The total radiated power can be found by calculating the Poynting vector and integrating over the surface. Using the total radiated power and the field values, directivity and gain can be determined. This technique demonstrates that while the electromagnetic simulation techniques discussed here are powerful tools, analyzing the output can also be a difficult, time-consuming task.

5. SUMMARY

An overview of the purpose and application of time-domain electromagnetic simulation methods has been presented. These methods serve as powerful tools for RF designers if used correctly. The reader should take from this section not a complete understanding of time-domain computational methods, but rather an appreciation of how they can be applied and, hopefully, where mistakes can be avoided in simulation. Often the choice of simulator depends on software already at hand, and this article should help the reader gain confidence in determining how different packages can be applied. In addition, this article

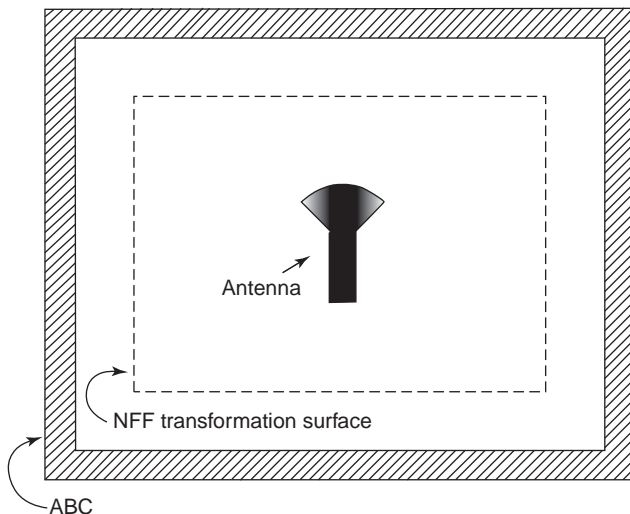


Figure 9. Diagram demonstrating setup of antenna simulation.

provides a strong background that can be used as a starting point for further research in time-domain electromagnetic methods. Through the discussion not only of the techniques but also how to analyze the results, the usefulness of time-domain simulation techniques has been demonstrated. Almost any problem can be simulated using these techniques, and understanding their operation is the first step in using them properly.

BIBLIOGRAPHY

1. M. Schuh and A. Woo, Code scaling, *IEEE Anten. Propag. Mag.* **37**(4):82–86 (Aug. 1995).
2. S. D. Gedney, A comparison of the performance of finite difference time-domain, finite element time-domain, and discrete surface integral equation methods on high performance parallel computers, *Proc. IEEE Antennas and Propagation Symp.*, June 1994, Vol. 1, pp. 384–387.
3. K. S. Yee, Numerical solution of initial boundary value problems involving Maxwell's equations in isotropic media, *IEEE Trans. Anten. Propag.* **AP-14**:302–307 (March 1966).
4. V. Shankar, A. Mohammadian, and R. W. Ziolkowski, A three-dimensional modified finite volume technique for Maxwell's equations, *Electromagnetics* **10**:147–161 (1990).
5. A. C. Cangellaris, C. Lin, and K. Mei, Point-matched time domain finite element methods for electromagnetic radiation and scattering, *IEEE Trans. Anten. Propag.* **35**(10):1160–1173 (Oct. 1987).
6. M. Krumpholz and L. P. B. Katehi, New time domain schemes based on multiresolution analysis, *IEEE Trans. Microwave Theory Tech.* **44**:555–561 (April 1996).
7. P. B. Johns and R. L. Beurle, Numerical solution of 2-dimensional scattering problems using a transmission-line matrix, *Proc. Inst. Electrical Eng.* **118**(9):1203–1208 (Sept. 1971).
8. A. Taflove and S. C. Hagness, Introduction to Maxwell's equations and the Yee algorithm, in A. Taflove, ed., *Computational Electrodynamics: The Finite Difference Time Domain Method*, Artech House, Norwood, MA, 1995, Chap. 3.
9. F. Zheng, Z. Chen, and J. Zhang, Towards the development of a three-dimensional unconditionally stable finite-difference time-domain method, *IEEE Trans. Microwave Theory Tech.* **48**(9):1550–1558 (Sept. 2000).
10. J. R. Whinnery and S. Ramo, A new approach to the solution of high-frequency field problems, *Proc. IRE* **32**:284–288 (May 1944).
11. J. R. Whinnery, C. Concordia, W. Ridgway, and G. Kron, Network analyzer studies of electromagnetic cavity resonators, *Proc. IRE* **32**:360–367 (June 1944).
12. W. J. R. Hoefer, The transmission line matrix (TLM) method, in T. Itoh, ed., *Numerical Techniques for Microwave and Millimeter-Wave Passive Structures*, Wiley, New York, 1989, Chap. 8.
13. C. Christopoulos, *The Transmission-Line Modeling Method: TLM*, Oxford Univ. Press, Oxford, UK, 1995.
14. P. B. Johns, The solution of inhomogeneous waveguide problems using a transmission-line matrix, *IEEE Trans. Microwave Theory Tech.* **MIT-22**:209–215 (March 1974).
15. A. C. Cangellaris and D. B. Wright, Analysis of the numerical error caused by the stair-stepped approximation of a conducting boundary in FDTD simulations of electromagnetic phenomena, *IEEE Trans. Anten. Propag.* **39**(10):1518–1525 (Oct. 1991).
16. N. Madsen, *Divergence Preserving Discrete Surface Integral Methods for Maxwell's Equations Using Nonorthogonal Unstructured Grids*, Technical Report UCRL-JC-109787, Lawrence Livermore Natl. Lab., Berkeley, CA, Feb. 1992.
17. S. Gedney, F. Lansing, and D. Rascoe, A generalized Yee-algorithm for the analysis of MMIC devices, *IEEE Trans. Microwave Theory Tech.* **44**:1393–1499 (Aug. 1996).
18. P. Monk and E. Suli, Error estimates for Yee's method on non-uniform grids, *IEEE Trans. Magn.* **30**(5):3200–3203 (Sept. 1994).
19. D. A. Al-Mukhtar and J. E. Sitch, Transmission-line matrix method with irregularly graded space, *IEE Proc. H: Microwaves, Opt. Anten.* **128**:299–305 (Dec. 1981).
20. J. Ritter and F. Arndt, Fast subgrid FD-TD matrix pencil technique for the rigorous analysis of resonant 3D microwave structures, *Proc. IEEE Microwave Symp.*, June 1998, Vol. 3, pp. 1271–1274.
21. S. Dey and R. Mittra, A locally conformal finite-difference time-domain algorithm for modeling three-dimensional perfectly conducting objects, *IEEE Microwave Guided Wave Lett.* **7**:273–275 (Sept. 1997).
22. HFSS, Ansoft Corporation, Pittsburgh, PA.
23. E. M. Tentzeris, R. L. Robertson, J. F. Harvey, and L. P. B. Katehi, Stability and dispersion analysis of Battle-Lemarie-based MRTD schemes, *IEEE Trans. Microwave Theory Tech.* **47**(7):1004–1013 (July 1999).
24. C. Sarris and L. P. B. Katehi, Fundamental gridding-related dispersion effects in multiresolution time-domain schemes, *IEEE Trans. Microwave Theory Tech.* **49**(12):2248–2257 (Dec. 2001).
25. T. Dogaru and L. Carin, Application of Haar-wavelet-based multiresolution time-domain schemes to electromagnetic scattering problems, *IEEE Trans. Anten. Propag.* **50**(6):774–784 (June 2002).
26. T. Dogaru and L. Carin, Efficient time-domain electromagnetic analysis using CDF biorthogonal wavelet expansion, *Proc. IEEE Int. Microwave Symp.*, May 2001, Vol. 3, pp. 2019–2022.
27. K. R. Umashankar and A. Taflove, A novel method to analyze electromagnetic scattering of complex objects, *IEEE Trans. Electromagn. Compat.* **24**:397–405 (1982).
28. R. Holland, Threde: A field free EMP coupling and scattering code, *IEEE Trans. Nucl. Sci.* **24**:2416–2421 (1977).
29. A. Bayliss and E. Turkel, Radiation boundary conditions for wave-like equations, *Commun. Pure Appl. Math.* **23**:707–725 (1980).
30. G. Mur, Absorbing boundary conditions for the finite-difference approximation of the time-domain electromagnetic field equations, *IEEE Trans. Electromagn. Compat.* **23**:377–382 (1981).
31. O. M. Ramahi, The complementary operators method in FDTD simulations, *IEEE Anten. Propag. Mag.* **39**(6):33–45 (Dec. 1997).
32. J. P. Berenger, A perfectly matched layer for the absorption of electromagnetic waves, *J. Comput. Phys.* **114**:185–200 (1994).
33. S. Gedney, *An Anisotropic Perfectly Matched Layer Absorbing Media for the Truncation of FDTD Lattices*, Technical Report EMG-95-006, Univ. Kentucky, Lexington, KY, May 1997.
34. J. Fang and D. Xeu, Numerical errors in the computation of impedances by FDTD method and ways to eliminate them, *IEEE Microwave Guided Wave Lett.* **5**(1):6–8 (Jan. 1995).
35. A. Taflove and S. C. Hagness, Near-to-far-field transformation, in A. Taflove, ed., *Computational Electrodynamics: The Finite Difference Time Domain Method*, Artech House, Norwood, MA, 1995.

ELECTRONIC WARFARE

ANTHONY E. SPEZIO
 ALAN N. DUCKWORTH
 FRANCIS J. KLEMM
 STANLEY A. MOROZ
 JAMES M. TALLEY
 Naval Research Laboratory

Electronic warfare (EW) is the systems discipline that exploits an adversary's use of the electromagnetic spectrum to overcome threats that use communications, navigation, and radar systems. It is an important tool in pursuing military objectives and advancing national policy and sovereignty. EW provides the means to counter, in all battle phases, hostile actions that use the electromagnetic spectrum—from the beginning, when enemy forces are mobilized for an attack, through to the final engagement. EW exploits the electromagnetic spectrum through electromagnetic sensing, analysis, and countermeasures to establish operational advantage in a hostile encounter.

The use of electronic warfare accelerated rapidly during World War II, and it has been used in most military conflicts since. The aircraft used by Nazi Germany to bomb the fog-shrouded British Isles were guided by radio beacons from the European mainland. By using false guidance signals, the British were able to redirect the German bombing attacks from densely populated urban areas to less populated rural areas. In this same conflict, U.S. bombers used chaff (packets of tinfoil cut into thin strips) jettisoned from the attacking U.S. aircraft to reflect anti-aircraft radar signals, thereby reducing the effectiveness of the German anti-aircraft batteries and bomber force attrition. In the Pacific theater of operations during World War II, U.S. Navy submariners detected and determined

the bearing and location of Japanese ship radio transmissions for weapons targeting. In the Korean conflict, detection and location of North Korean anti-aircraft radar signals provided targeting data for subsequent air strikes. In Vietnam, the exploitation of anti-aircraft and missile radars was refined with the use of U.S. Air Force Wild Weasel weapons—suppression aircraft that used sensors to detect and locate the weapons-associated threat signals to provide targeting information for ordnance delivery. Electronic warfare applications are described extensively in military accounts of the past half century.

Military operations use EW as one means to gather tactical intelligence from noncooperative forces and to counter their electromagnetic, radio-, and radar-controlled weapons. Land, sea, and air forces use the electromagnetic spectrum for command and control, weapons targeting, and weapons control. Figure 1 shows multiple land, sea, and air platforms in a typical tactical environment. Also indicated are links for sensing, communications, and navigation in support of the military mission.

Electronic warfare provides use of the electromagnetic (EM) spectrum by the host force and denial or limitation of its use by an adversary. Realization of this goal occurs when host force systems use the EM spectrum while adversary systems are denied its use. Countermeasures (CM) to threat systems that use the EM spectrum can be selectively applied on a time- and/or frequency-multiplexed basis so that host force use of the EM spectrum is uninhibited.

Electronic warfare includes the *operational* functions of electronic support (ES), electronic self-protection (EP), and electronic attack (EA). ES provides surveillance and warning information for EW system use. CM to threat systems, including jamming, false-target generation, and decoying, are performed for EP (protection of the host platform against an electronically controlled threat). EA performs these same CM functions to protect a battle force

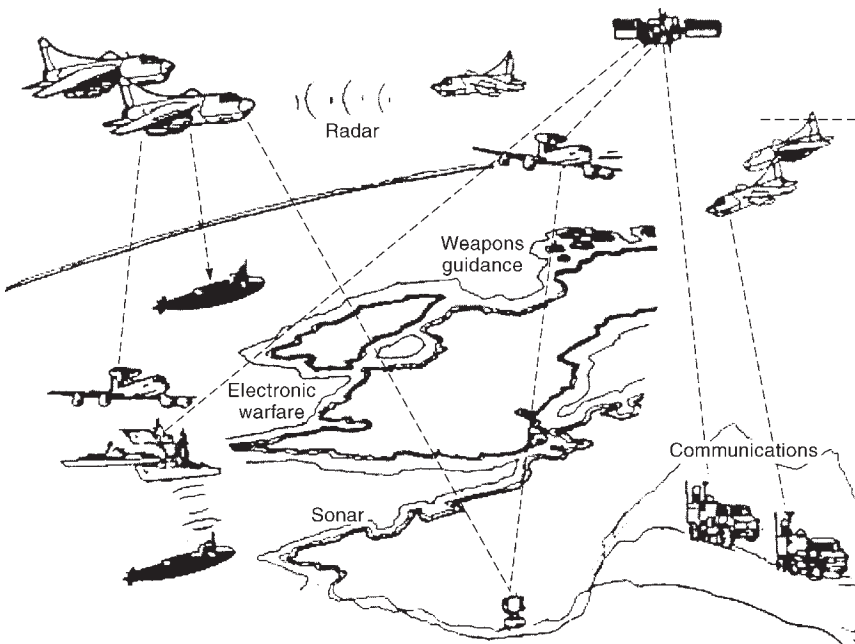


Figure 1. Tactical operational concept indicating systems that use the EM spectrum.

composed of several platforms or battle units. The ES, EA, and EP functions are interrelated because EA and EP can be queued using ES information, and EA and EP can use some of the same sensing and CM equipment for distinct operational objectives.

This article includes a description of the EW timeline and the various phases of conflict. Also provided is a summary description of the signal environment in which EW systems operate. Those interested in more detailed descriptions of the EM communications, radar, and navigation technology against whose signals EW systems operate are referred to the appropriate sections of this encyclopedia. A discussion of EW functional areas ES, EP, and EA provides a functional framework for supporting EW technologies.

1. ELECTRONIC WARFARE TIMELINE

Electronic warfare is used in a layered operational interaction with electronically controlled threat systems. The electronic warfare system provides its own force with data for self-protection and threat weapons suppression. Figure 2 graphically illustrates the EW functional timeline.

Electronic support provides operational intelligence relating to electronically controlled threat systems and communications systems in the battle group or theater environment. Electronic threat-warning information derives from ES surveillance data, recognizing that hostile force deployments or weapons-related transmissions constitute a threat. Air defense combines electronic and radar surveillance with tactics and countermeasures to control the air battle. EA and active EP, using countertargeting (CTAR) jamming, false target generation, and/or decoying, attempt to deny target acquisition by adversary sensors. CTAR endeavors to deny weapon's sensors use of the spectrum, and decoys dispersed into the environment provide preferred target signatures to the threat weapon's sensor.

The EW battle timeline provides the general context in which the discipline of EW is used in the tactical environ-

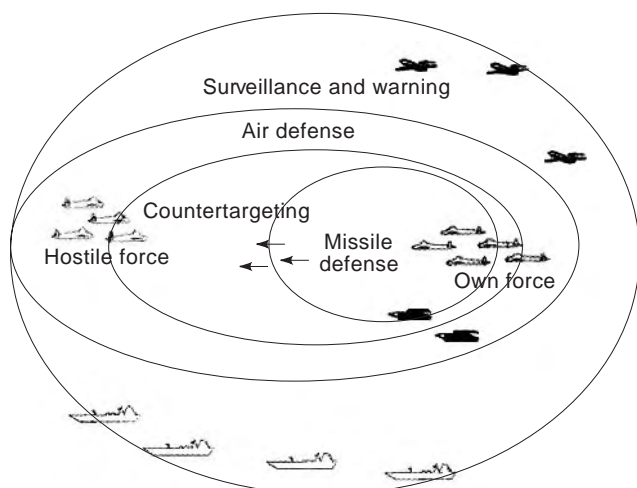


Figure 2. Electronic warfare battle situation showing various phases of the engagement timeline.

ment. The EW timeline stage in a specific engagement depends on the deployment of forces and the perceived imminence of hostile engagement. Note that the technologies used in the various stages of the engagement are dynamic, and EW systems and weapon systems technologies evolve to overcome susceptibilities. The boundaries and definitions of EW timeline stages are redefined with each new advance in weapon and EW technology.

1.1. Electronic Support

Electronic support provides operational intelligence that is related to radiated signals in the battle group or theater environment. Surveillance includes monitoring of both combatants and commercial transports. Control of contraband and critical materials is an EW surveillance mission that provides critical intelligence data to the area commander. Surveillance of noncooperative combatant forces provides deployment intelligence in the area of observation. Early threat-warning information extracted from surveillance data occurs by recognizing hostile force weapons-related transmissions.

Within the lethal range of hostile force weapons, battle space surveillance updates are required rapidly. Deployment and operational modes of hostile forces are monitored closely to determine imminence of hostile activity. In some environments, potentially hostile forces remain within weapons' lethal range and a high level of vigilance is necessary to maintain security.

1.2. Air Defense

Air defense is used to maintain control of the battle group airspace and defend against threat aircraft and missiles. Battle group surveillance, implemented by the combination of EW, infrared/electrooptic (IR/EO), and radar sensors, provides environmental data required for air defense. Electronic combat techniques and weapons are used to counter an airborne threat.

Air defense is an extensive, complex, electronic combat interaction between hostile forces. EW assets are a key tool of the battle force commander and of the individual elements within the command. These assets provide information for developing tactical intelligence in all phases of the engagement. The outcome of the air battle is by no means established by the quantity of EW assets possessed by each of the opposing forces, but depends greatly on how the EW assets are used in conjunction with other sensor systems, weapons, and air defense tactics.

Aircraft ships and/or battlefield installations participate in air defense. Own force aircraft operating at altitude can engage a threat force at long line-of-sight ranges. Aircraft, together with ship and battlefield installations, provide coordinated air defense as the hostile force approaches own force locations. The EW objective in the early air defense or outer air battle is to prevent threat force detection and location of own force. Electronic combat actions that prevent or delay own force detection provide a distinct advantage by allowing additional time to develop tactics to counter the threat force. In addition, the threat force battle timeline and interplatform coordination are perturbed. Fragmentation or dissolution of the hostile

force attack can occur if own force electronic combat is effective in the outer battle.

As the hostile force overcomes the outer battle electronic attack and approaches the own force within weapons range, air defense assumes the role of denying targeting information to the hostile sensors. The EW objective at this stage of the engagement is to prevent hostile force weapons launch by denying targeting data to their sensors. Electronic combat surveillance, warning, and countermeasure assets are used for countertargeting. Surveillance sensors assess hostile force deployment and provide information about the adversarial tactics being used. Warning sensors indicate the status of threat sensors as they attempt to acquire targeting data for weapons systems handoff. Countermeasure assets, including jamming, spoofing, and decoying, continue to provide a virtual environment to threat platform sensors to prevent own force target acquisition by the hostile force.

The terminal phases of an air defense engagement are characterized by heightened activity. The combatants, both hostile and own force, are confined to a smaller portion of the battle space. Weapons and decoys in flight add to the physical and EM signal density. Electronically, both own force and hostile forces struggle to exploit the EM environment to achieve their respective operational objectives. Countermeasures jamming and spoofing are used with full appreciation that coordinated jamming produces degradation of hostile force sensors, but that weapons with home-on-jam (HoJ) capability can exploit this action to the destructive detriment of the radiating platform.

1.3. Countertargeting

Countertargeting (CTAR) is a subset of radar electronic countermeasures (ECM) used in electronic attack. CTAR provides specially modulated radiofrequency (RF) signal transmissions to counter hostile force longrange surveillance or targeting radar. The transmission modulation can be amplitude-modulated (AM) or frequency-modulated (FM) noise, or combinations of these, and they can be pulsed or continuous-wave. CTAR transmission is used both to disrupt and interfere with the threat radar operation, thereby preventing it from correctly locating and identifying own force target(s).

Countertargeting success criteria includes mission completion prior to threat force interdiction or weapon launch. Realistically, the results of a CTAR electronic attack against a hostile force are probabilistic, in that some opposing forces at some time during the battle timeline succeed in launching missiles. CTAR can delay and reduce the coordination of hostile missile firings and, consequently, reduce the number of missiles fired and the attrition of personnel, ships, and aircraft.

1.4. Terminal Defense

Terminal defense against electronically controlled missiles and guns is the final phase of the EW battle timeline. Weapons are launched in the terminal phase of hostile force engagement, and EP and EA capability is brought to bear on the weapons and their electromagnetic (EM) guidance and control signals. Onboard jamming and

false-target radiation that is effectively used for counter-targeting is less effective for terminal defense. Jamming or false-target radiation makes the target platform vulnerable to missiles with home-on-jam capability. Home on jam is an electronic counter-countermeasure that exploits the target countermeasure's radiation to steer the missile to the target. Consequently, offboard countermeasures, or decoys, are used to lure the missile away from the high-value target.

2. THE ELECTRONIC WARFARE ENVIRONMENT

2.1. Threat Systems

Electronic warfare interacts with an adversary's EM systems for signal exploitation and potentially for electronic attack. Threat systems of EW interest include radar, communications, and weapons control. Some of the threat systems exploited by EW are briefly described in the following.

2.1.1. Radar. Radar uses radiofrequency transmissions ranging from high frequency (HF) to millimeter waves (from 30 MHz to 40 GHz) in pulsed and continuous-wave (CW) modes to illuminate targets and collect reflected echoes. Radar-transmission-reflected echoes are used to measure target characteristics and determine target location. Military forces use radar for both offensive and defensive weapon systems. Radar functions include target detection and identification, target acquisition, target tracking, and navigation. Weapons systems using radar may be land-based, airborne, shipboard, or in space. A typical radar system contains a transmitter that produces a high-powered RF signal, tunable over a band of frequencies; an antenna system that radiates energy and collects reflected echoes; a receiver that detects signal return; and signal processing electronics that extract target measurements, such as range, bearing, and speed. Target location information is provided to a weapon system to control and direct the weapon onto the target.

Land-based radars function as ground-controlled intercept (GCI) systems, surface-to-air missile (SAM), anti-aircraft artillery (AAA) batteries, and space tracking systems. GCI is used to direct interceptor aircraft against attacking aircraft and to coordinate the air battle. SAM sites use early warning/surveillance radar, target acquisition radar, target tracking (TT) radar and/or illuminators for missile guidance, beam-riding systems. AAA radars have operating frequencies and data rates similar to those of SAM tracking radars and usually receive targeting information from SAM surveillance and target acquisition (TA) facilities. Advanced SAM systems handle ballistic missile defense with higher data rates against high-speed targets. Airborne intercept and control (IC) radars provide early warning and information for the command and control of forces operating in the tactical environment. Space surveillance and tracking radars usually use large, fixed, phased arrays operating in the HF (3–30 MHz) to 1 GHz frequency range. Table 1 gives parameters of typical radars categorized by radar function. The reader is referred

Table 1. Parameter Ranges Associated with Radar Functions

Radar Parameter	Radar Function					
	GCI	IC	Surveillance	TA	TT, AA	Space Surveillance
Frequency range	30 MHz–3.0 GHz	3.0–10.0 GHz	30 MHz–3.0 GHz	3.0–8.0 GHz	6.0–10.0 GHz	30 MHz–1.0 GHz
PRF range	100–500 pps	1000–3000 pps	100–500 pps	1000–2000 pps	2000–4000 pps	—

to radar and electromagnetic wave propagation articles within this encyclopedia.

Radar advancements can be expected in the areas of phased-array antennas, complex modulations on the radar pulse, improved signal processing to extract enhanced data from the radar return, and frequency diversity to cover the less used regions of the spectrum. Advanced designs from the U.S., European, and Russian inventories can be expected because of operational needs for enhanced sensor performance and the availability of affordable technologies to provide additional capability.

2.1.2. Communications. Communications systems provide information exchange for command and control to coordinate between surveillance sites and between combat units. Communications networks range from basic field radio networks to long-distance, wide-area systems and point-to-point, high-data-rate installations. Communications systems cover the spectrum from very low frequency (5 Hz) to the frequencies of visible light, and they can be either free-space transmissions or confined to a transmission line. Free-space transmission links may be line of sight or cover longer distances by reflecting from the ionosphere, atmospheric layers, or troposcatter, or by relaying via satellite.

Command and control communication links, using HF direct microwave and satellite relay, disseminate voice and digital data transmissions to land forces, air forces, and ships. Land combat units use ultrahigh frequency (UHF) (300 MHz–3 GHz), very high frequency (VHF) (30–300 MHz), landlines, and cellular phones over shorter distances mainly for voice transmissions. Surveillance activities and weapons sites may exchange data via voice or digital data link over a transmission path appropriate for the link span. Such links are used to transmit surveillance radar reports to an operations center or directly to a SAM battery. Communication link data rates depend on link bandwidth, modulation technique, and signal-to-noise ratio. Individual transmission link throughput rates are in the range of hundreds of megabytes per second. Computer technology has enabled increased communication link capacity for handling and processing data. The high data rates attainable permit transmission from airborne observers and between precision weapons and launch platforms.

Communications in hostile environments are transmitted via protected cable between fixed sites, thus providing protection from physical damage, security from intercept, and immunity from jamming. Mobile communications require free-space transmissions that are susceptible to intercept and jamming. Communications counter-countermeasures, complex modulation, encryption, and spatial radiation constraints are used to miti-

gate the effects of EA. The use of modulation techniques increases privacy, reduces interference, improves reception, and reduces the probability of detection. Spread-spectrum communication systems that use four categories of signal modulation [direct sequence-modulated, frequency hopping, intrapulse FM (chirp), and time hopping] provide some level of signal protection from detection, demodulation, and interference. However, this is at the expense of increased bandwidth.

2.1.3. Passive Weapons Sensors. Electrooptical and infrared (EO/IR) systems sense spectral energy that is radiated by an object or reflected from an object from a source such as the sun, moon, or stars. The electrooptical spectral regions are categorized according to atmospheric propagative characteristics or spectral transmittance. The EO/IR spectrum used for passive weapons sensors spans the 0.2–15 μm wavelength range.

Electrooptical/infrared guidance provides angle target tracking information only. EO/IR weapons system guidance sensors fall into three classes: nonimaging, pseudoimaging, and imaging. Generally, countermeasure techniques exhibit preferential effectiveness against guidance approach. Some countermeasures techniques may be effective against pseudoimaging sensors and less effective against nonimaging and imaging sensors. Other countermeasures techniques may be preferentially effective against nonimaging and imaging sensors. Figure 3 illustrates the most common seeker design approaches. These approaches are quadrant, spin scan, conical scan (conscan), transverse-line scan, and rosette scan. In the quadrant approach, an intentionally defocused spot images on a four-element square array. Tracking is achieved by balancing the signal on all four detectors. In spin scan, a spinning reticle provides phase and amplitude information with respect to a fixed reference. With conscan, the target image is nutated by using a scanning mirror or optical wedge imaged onto a fixed reticule or pattern of detectors. The nutated target image generates a modulated frequency proportional to the angular and radial offset from the center. In the transverse-line scan approach, a rotating or reciprocating mirror at a depressed elevation angle generates a scanline transverse to the missile axis, and the forward motion of the missile creates the orthogonal axis of the search pattern. With the rosette scan, a petal pattern is scanned over a small instantaneous field of view (IFoV) by two counterrotating optical elements.

Rosette-scan tracking is accomplished by balancing the signal output from all petals with the target present in the central apex of the rosette. The small IFoV of the transverse-line scan and rosette scan provide high spatial resolution and the ability to resolve multiple sources

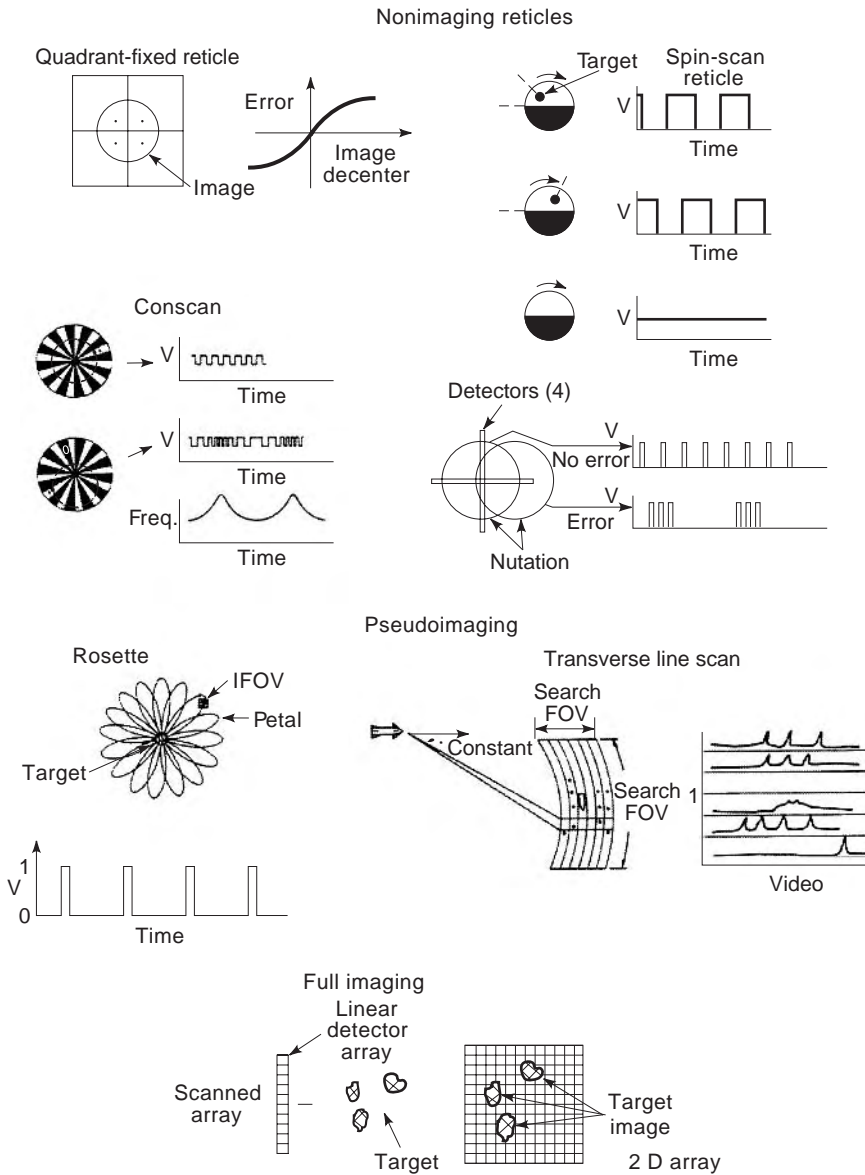


Figure 3. Common IR/EO sensor types including nonimaging reticules, line scanning detectors, and area array imagers.

within the scanned field of view. Focal plane arrays, scanning-linear arrays, or two-dimensional arrays of detectors in the image plane provide high-resolution “pictures” of the target space. Many image-processing algorithms are available to classify targets and establish track points. Figure 3 illustrates the basic features of common seekers.

Passive electro-optic sensors are desirable targeting and weapons guidance systems because they radiate no energy to warn the target of an impending attack. These sensor systems are vulnerable to decoys, with thermal signatures similar to true targets and to high-intensity sources that can saturate the electro-optic sensor detector or cause physical damage.

3. ELECTRONIC WARFARE FUNCTIONAL AREAS

Threat systems use the EM spectrum extensively. This section discusses functional aspects of EW. The

relationships that govern their systems’ application are described in the following section. These functional areas are electronic support (ES), electronic protection (EP), and electronic attack (EA). Electronic attack uses countertargeting (CTAR), jamming, false-target generation, and decoys to defeat the threat sensors. Electronic protection uses electronic support and electronic attack for own-platform self-protection.

3.1. Electronic Support

Electronic support provides surveillance and warning information to the EW system. ES is a passive, nonradiating, EW system function that provides a fast, accurate assessment of the EM radiating environment. ES is the aspect of EW that involves techniques to search for, intercept, locate, record, and analyze radiated energy for exploitation in support of military operations. Electronic support provides EW information for use in EA and EP

and in tactical planning. ES directly provides threat identification/detection and early warning. It also provides data for electronic countermeasures (ECM), electronic counter-countermeasures (ECCM), threat avoidance, target acquisition, and homing.

Electronic support provides timely EM environment information for the EW system. The spatial and spectral environment over which ES operates may span a hemispherical spatial segment and a spectrum of tens of gigahertz. In tactical EW systems, signals in the environment are analyzed and reports of environment activity are provided on the order of a second after threat signal reception.

3.2. Electronic Attack

As an EW function, EA provides an overt active response capability against enemy combat systems with the intent of degrading, deceiving, neutralizing, or otherwise rendering them ineffective or inoperative. EA responds to threat systems to protect multiple platform or battle group units. EA includes measures and countermeasures directed against electronic and electrooptical systems by using the electromagnetic spectrum (radio, microwave, infrared, visual, and ultraviolet frequencies). EA technical functions include radio and radar signal jamming, false target generation, and the use of decoys for threat system confusion and distraction.

Electronic attack is reactive to environment threats. To function effectively, therefore, the EA system requires threat information from the environment, including threat classification, bearing and, if possible, range. These functions are performed by the ES system or by other surveillance systems such as radar or infrared search and track (IRST). Effective EA response selection requires knowledge of the threat class and operating mode. Threat signal data are derived from measuring signal parameters (frequency, scan type, scan rates, pulse repetition frequency, or continuous-wave radiation characteristics). Absence of radiation may indicate that the threat uses a passive RF or an electrooptical sensor. The detected threat electronic parameters are compared to an extensive emitter database. The EW database, derived from intelligence sources, is used to identify the threat and correlate the threat and operating mode with effective EA techniques. Operational threat exploitation is often impeded by intelligence gaps and/or threat use of parameters reserved for wartime.

3.2.1. Nondestructive Electronic Attack. Nondestructive EA produces electromagnetic signals at a predetermined radio, infrared, visual, or ultraviolet frequency with characteristics that temporarily interfere with the threat's receiving system, that is, power level, frequency, and polarization. EA degrades or overcomes threat system operation by overpowering the target signal at the threat sensor. "Dazzling" is laser or high-power lamp EO/IR jamming. Dazzling saturates the detectors or focal plane arrays of electrooptical (infrared, visual, ultraviolet) guided missiles and target tracking systems. Deceptive EA presents a confusing signal to the threat sensor that degrades

its performance to the point where it is no longer effective. Power levels used for deception are less than those required for jamming because deception does not require threat sensor saturation.

3.2.2. Destructive Electronic Attack. Destructive EA physically damages or destroys the threat electronic system. Specially designed missiles such as the HARM (high-speed antiradiation missile) missile, shown being released from an A-6 aircraft in Fig. 4, are equipped with radar-homing seekers that attack the threat radar antenna and nearby electronic equipment within the blast radius of the missile warhead. More recently, similar seekers have been fitted to loitering remotely piloted vehicles for a similar purpose. Advances in high-power microwave and laser technology have made directed energy more practical. At very high power levels, microwave energy destroys the components in a missile seeker or threat radar, rendering them inoperative. High-power lasers also physically damage both RF and electrooptical threat systems.

3.3. Electronic Protection

Electronic protection provides EW protection for the host platform. Key environment surveillance and threat-warning information is provided by the ES system function (as it is for EA). EP responds to threats in the environment with information for evasive action and with the countermeasure responses described previously. EP is primarily directed against the terminal threat targeted on the host platform, and preferred EP techniques use decoys that are less susceptible to the home-on-jam weapon mode.

4. ELECTRONIC WARFARE TECHNICAL AREAS

Technical areas that support the ES, EA, and EP functional EW systems areas are discussed in this section. All aspects of EW are addressed by modeling and simulation because this is the most practical means for functional



Figure 4. HARM missile (shown after separation from an EA-6B aircraft) is an EW weapon for physically destroying the source of hostile radiation.

evaluation. System architectural analyses address the formulation of efficient EW system configurations to provide the operational functions required within the constraints of available equipment, techniques, and technology. Technical areas that address ES primarily are signal detection, measurement, and processing issues that deal with environment surveillance and warning. Technical areas associated with EA and EP include CTAR jamming and false-target generation, EO/IR CM, and decoys. Also included in these technical area discussions are technology challenges to EW technologies for future capability.

4.1. Modeling and Simulation for Electronic Warfare

Electronic warfare uses modeling and simulation extensively in three areas of investigation: research into new hardware, threat domination/exploitation, and tactics development. The effectiveness of an EW architecture or equipment suite is assessed by using a computer model and parametric studies run against the model. Estimates of a threat system's capabilities are incorporated into the model as environment sources because acquiring foreign hardware and measuring its performance is difficult. Environment signal models stimulate the EW system model. The EA effectiveness modeled against the threat is measured, and tactics are developed to further reduce threat system efficiency.

Modeling and simulation (M&S) combine detailed antiship missile models with ship models, antiair missile models with aircraft models, electromagnetic propagation models, and chaff RF decoy models. (Chaff RF decoys are described later.) Chaff effectiveness evaluation considers the spatial relationship between the missile seeker and the ship while accounting for radar clutter and multipath returns. Signals at the missile are processed through the seeker receiver and missile guidance and tracking logic. A chaff cloud(s) injected into the simulation provides a false radar target signal at the missile seeker. By varying the amount of chaff and/or the chaff round spatial relationship with respect to both the defended ship and the threat missile, chaff effectiveness and tactics can be evaluated. However, the accuracy of the M&S results depends on the accuracy of the models used. An accurate missile sensor and control model is necessary to determine the effects of the complex signal returns from the target ship and the chaff on the missile controls and resultant flight path. In a simulated engagement, detailed missile functions are required to provide an accurate assessment of chaff effectiveness. These functions include monopulse antenna processing, range and angle tracking, missile guidance, and aerodynamics. Multiple threat seeker modes, such as acquisition, reacquisition, track, home-on-jam (HoJ), and simulated coherent combinations of signal segments are also required in the model.

Target ship, aircraft, and chaff radar cross section (RCS) must be accurately modeled. Typically, a multireflector target simulation is used to represent the RCS signature. Ideally, a model of thousands of scatterers would provide greater accuracy. However, careful selection of several hundred scatterers is adequate.

The accuracy of the missile and target interaction depends on the propagative environment model including multipath. Typically, a ray-tracing algorithm models the propagation of RF energy. Useful models rely on a stochastic representation of clutter as a function of wind-speed, grazing angle, frequency, polarization, and ducting. Modeling of an ocean environment can be extended to include reflection from wave segments. Models are verified by using measured field test data.

4.1.1. Electronic Warfare System Architectures. The EW system architecture ties system functional elements into an efficient configuration optimized to the operational mission. Figure 5 shows a typical EW system architecture. The system performs signal acquisition and parameter measurement, direction finding, countermeasure generation, and decoy deployment. The system central processing unit (CPU) provides sensor and countermeasure coordination and EW system interface with other onboard systems.

Fusing the measurements of EW sensors and processors is a complex technological challenge. This information includes radar, communications, EO/IR, direction finding, and signal analysis. Data fusion within the EW system requires algorithmic development and significant enhancement in computational throughput. The EW system includes antenna(s), receiver(s), and processor(s) elements that provide data on signals in the environment. System sensors detect and measure threat signal characteristics. Multiple sensor subsystems measure the characteristics of the signal. For example, a signal acquisition detects the presence of a signal and measures the envelope characteristics (frequency, time of arrival, and signal duration). Another sensor that may include multiple antennas and receivers provides signal bearing-angle data. Separate subsystem sensors measure intrapulse signal modulation and/or received polarization.

A countermeasures receiver may use an independent electromagnetic environment interface. The countermeasures receiver accepts signals from the environment and provides them to the techniques generator. Target signals designated by CPU algorithms are selected for countermeasure generation as are the countermeasure modulation

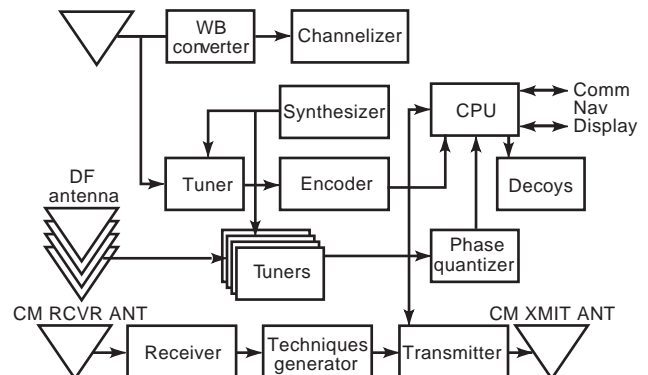


Figure 5. Electronic warfare system architecture indicating system functional elements required to provide ES, EA, and EP functions to the host platform and operational battle group.

techniques to be applied. The resulting jamming signals are amplified to the desired power levels and radiated into the environment.

Decoys are part of the EW system architecture. This subsystem is controlled by the CPU based on sensor inputs. Decoys provide the important function of separating the countermeasure signal source from the host platform. In this operational mode, decoys provide alternative highly visible targets to divert a weapon from its intended target. Also required are the means, such as the coordination of jamming with the use of decoys, to neutralize the HoJ weapons threat.

4.2. Surveillance and Warning

Electronic support surveillance and warning perform the functions of noncooperative intercept and exploitation of radiated energy in the EM environment. Surveillance and warning detection relationships are those associated with communications systems. Additional signal detection constraints result because the signal’s spatial location and its characteristics may not be known. Signal unknowns require tradeoffs of detection sensitivity and environment search. Once detected and measured, environment signals require sophisticated signal processing for signal sorting, formation, and characterization before they can be correlated with signal intelligence libraries for classification. Some fundamental tradeoff relationships for detection and warning are discussed below.

4.2.1. Threat Signal Detection. Threat signal detection occurs as the electronic support system is illuminated above the system sensitivity level with signals that satisfy the single-pulse detection criteria. Detection is performed as the ES system scans the environment. Detection metrics include incident radiation sensitivity, detection probability, false detection probability, corruption probability, simultaneous detection, and throughput rate.

Aircraft are often used to carry electronic warfare battlefield surveillance equipment. The operating altitude of surveillance aircraft provides a long line-of-sight range to the horizon. The range to the electromagnetic horizon accounting for nominal atmospheric refractions is given by

$$R = \left[\left(\frac{3}{2} \right) h \right]^{1/2} \tag{1}$$

where h is the aircraft sensor altitude in feet and R is the observer-to-horizon range in statute miles.

The time required to survey the environment depends on the surveillance alert status, system sensitivity, instantaneous observation segment, and rate of environment search. The number of instantaneous environment segments in frequency and bearing establish the number of environment dwell periods required for an environment scan. The larger the environment segments, the more rapidly the system performs the scan. The dwell at given environment segment is scheduled to span the signal event

period. Time to intercept is modeled by

$$T_I = \frac{(T_D N M)}{P_T} \tag{2}$$

where T_I is the time required to survey the environment, T_D is the EW support system dwell period, N is the number of frequency segments in the environment, M is the number of spatial segments in the environment, and P_T is the probability that the signal occurs above the sensitivity level.

In Eq. (2), spatial environment segmentation, spectral environment segmentation, and detection probability combine multiplicatively to define the time required to survey the environment. Wide instantaneous bandwidths and a large instantaneous field of view reduce environment survey time unless equipment choices reduce system sensitivity and the corresponding probability of signal detection. Equations (3) and (4) describe receiver sensitivity and aperture gain functional relationships:

$$S = (NF)(SNR)(kTB) \tag{3}$$

where S is receiver sensitivity, NF is receiver noise factor, SNR is the required sensitivity for detection and false alarm criteria, k is Boltzmann’s constant, T is temperature in degrees kelvin, and B is bandwidth in hertz

$$G = 2K\pi/\theta \tag{4}$$

where G is antenna gain, K is antenna efficiency (less than unity), and θ is antenna beamwidth in steradians.

A tradeoff between sensitivity and time to intercept is implied in Eqs. (3) and (4). By using multichannel processing, the tradeoff can be resolved in either domain. A wideband channelizer provides instantaneous spectral coverage equal to the span of the channelizer frequency coverage, and receiver sensitivity is established by the bandwidth of an individual channel. Multichannel spatial processing provides the instantaneous spatial coverage of the sum of the channels being processed. System antenna gain is based on channel beamwidth.

Detection sensitivity requires consideration of the desired detection range. Equation (5) defines the electronic support detection range in terms of the threat signal parameters and the electronic support antenna, receiver, and processor system parameters:

$$R_{MAX} = \left[\frac{P_t G_t G_r \lambda^2}{(4\pi)^3 \left(\frac{S}{N} \right)_{MIN} kTB_n L} \right]^{1/2} \tag{5}$$

where R_{MAX} is the maximum detection range, P_t is the threat signal transmit power, G_t is the threat signal antenna gain, G_r is the antenna gain of the electronic support subsystem, λ is the wavelength of the threat signal transmission, $(S/N)_{MIN}$ is the minimum signal-to-noise ratio required by the electronic support subsystem for detection, k is Boltzmann’s constant, T is absolute temperature, B_n is the effective noise bandwidth of the electronic support

receiver, and L represents the combined feed losses of the threat transmitter and the electronic support receiver.

The probabilistic characteristic of signal detection is illustrated by considering the intercept of a threat at a signal level considerably above the receiver threshold level. Detection probability arises primarily from the independent probabilities that the ES system observes the environment in the spatial and spectral location of the threat emitter and that the threat emitter illuminates the receiver with the required power for detection.

Also of importance is the probability of signal detection once the ES system is steered to the signal spatial and spectral location. Then detection probability P_D is based on the signal characteristics, that is, the probability that the threat signal illuminates the EW system during the observation period. The time required to perform a detection T_I is derived from the scan interval T_S and is given by $T_I = T_S/P_D$.

False reports from the electronic support receiver are highly undesirable. Limited computational resources are needed to process each pulse received in an attempt to form an association with other pulse reports. The rate of false reports is established by the proximity of the detector threshold level to the noise level. Figure 6 shows the relationship between the single-event probability of detection, the probability of false signal report generation, and the signal-to-noise ratio. This figure shows that both the probability of detection and the probability of false generation are strong functions of the signal-to-noise ratio.

The probability of pulse interference P_{OL} depends on the duration T_D of the signal and the rate R at which signals are expected. A reduction in P_{OL} results from adding parallel measurement channels. The functional relationship approximating P_{OL} is

$$P_{OL} = \frac{(T_D R)^N}{N!} \left(1 + \sum_{N=1}^N \left(\frac{T_D R}{N} \right) \right) \quad (6)$$

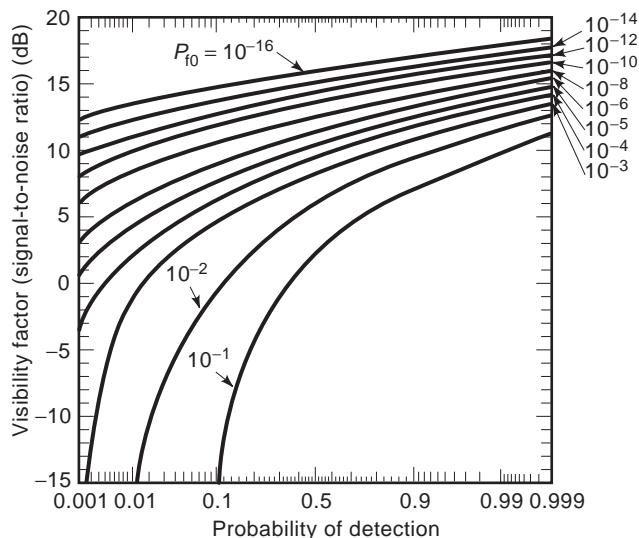


Figure 6. Detection probability and false detection probability for various signal-to-noise ratio conditions.

where T_D is the event duration, R is the event repetition rate, N is the number of parallel measurement functions provided, and P_{OL} is less than 0.9.

4.2.2. Electronic Support Signal Processing. The ES signal processor derives signal information from the multitude of environment event measurements. Signal processing is the focal point of the ES subsystem where operationally relevant sense is made of large data inputs. ES processing includes sorting event data and correlating sorted event data with emitter libraries to establish the class or family of signals to which the emitter belongs. Beyond sorting, intensive processing is applied to identify intercepted emitters specifically and to locate them precisely within the battle space.

Sorting, a key electronic support signal processing function, correlates event descriptors from the same emitter. Correlation is performed on the basis of both instantaneous and temporal signal parameters. Instantaneous parameter sorts are less computationally demanding than temporal deinter-leaving.

The initial signal sorting is histogramming based on instantaneous signal parameters. The signal parameters used for histogram-based sorting are those available from a single event or pulse measurement. They include external signal parameters, such as signal frequency, start time, duration, power level, and angle of arrival. Other instantaneous parameters used are measurements of signal modulation. Signals measurements with like parameters are binned together, and it is postulated that each bin contains event descriptor data from the same emitter.

After sorting, event descriptors are placed in individual emitter-associated groups. The monopulse and interpulse characteristics of the event group measurements are quantified into a signal descriptor. The signal descriptors are classified into an emitter class by correlation with a library database.

In some instances, high-resolution signal measurements identify specific emitters. As might be expected, identification parameter sets and the processing required to establish them are significantly in excess of that required for classification. Here, as in the case of classification, detailed signal descriptors are correlated with a library to define a specific emitter.

The spatial distribution of threat signals in the environment is operationally important. Determining the threat signal bearing angle with respect to own platform is a key step toward establishing threat signal position information. Conventional techniques used for direction-finding measurements include the use of differential amplitude processing of squinted antennas (antennas aimed in different directions), differential phase measurements from a phased-array antenna, and differential time of arrival measurements from spatially separated receivers.

Both hostile and benign operational scenarios require information about the location of both noncooperative fixed and mobile emitter installations. Electronic warfare target location exploits direction-finding data and navigational data to provide a signal location solution. Single or multiple platforms are used to generate location data.

The accuracy of target location depends on the precision of the direction-finding data and the navigation measurement and on the length of the baseline between measurements and the range to the target. Figure 7 shows target location geometry. The major error location axis A is modeled by

$$A = R\varphi \csc\left(\frac{\psi}{2}\right) \quad (7)$$

where R is the range from observer to the target emitter, φ is the direction-finding measurement error, and ψ is the angle subtended by the maximum difference in observation bearings with respect to the target, which provides location measurement error for the condition $\psi < \pi/2$. The range R from the observer to the target is given by

$$R = L \frac{\sin(\pi - \theta - \gamma)}{\sin \theta} \quad (8)$$

where L is the separation between observations, θ is the angle between the baseline and the opposite bearing angle, and γ is the angle between the baseline and the adjacent bearing angle.

4.2.3. Electronic Support Digital Signal Processing Technology. Electronic warfare system processing, both dedicated and programmable, assimilates environment data from the receivers and wideband processors. It uses these data to sort, classify, and identify the sources of emissions to represent the environment relevantly. The digital signal processor provides the means for applying an array of algorithms to both predetection and detection signal data to extract threat information for EW system use. Digital signal processing metrics include high-rate signal throughput processing in a compact module.

Digital signal processing is the heart of the ES function. It provides the flexibility of applying an extensive array of algorithms to system data. Critical digital signal processing technology challenges include processing throughput and developing efficient processing algorithms. Although signal data can be refined by applying sequential algorithms, the ES response is time-critical; it

must provide the most accurate assessment of available data within the required response time. Great potential exists for advancing digital signal processing technology, but optimum ES performance can be expected from judicious allocation of processing tasks between wideband processors and the digital signal processor.

An example of digital signal processing technology is L-MISPE (little monopulse information signal processing element), a special-purpose signal processor designed to operate with high-quality superheterodyne RF receiver systems. L-MISPE provides extremely accurate pulse analysis and parameter extraction for signal classification and specific emitter identification (SEI). It is contained in a single rack-mounted enclosure.

4.2.4. Surveillance and Warning Technology. Surveillance and warning are the sensor and environment processing functions for the EW system. Speed and accuracy of measurements and processing functions are the primary metrics for ES. Accurate throughput is important in providing sufficient time for effective threat response to the EA or platform commander. In addition, precision threat assessment provided to the EA subsystem facilitates optimum technique selection and conservation of EA power resource for engaging multiple threats. The ES performance challenge is further constrained by space limitations aboard platforms, particularly aircraft. Receiver technology performs environment sensing for the EW application.

4.2.5. Receiver Technology. Electronic support throughput and physical displacement metrics are addressed in developing wideband, small-size monolithic microwave integrated circuit (MMIC) technology. MMIC monolithic integrated analog processing at multigigahertz operating frequencies provides a capability suited to ES receiver applications. Advantages sought in the exploitation of this technology base include economies of size, weight, power, and cost. Increased receiver dynamic range for continuous environment intercept during active countermeasures transmission remains a receiver technology challenge. The MMIC receiver shown in Fig. 8 is an example of this technology.

4.2.6. Wideband Processing. Wideband receivers provide high probability of signal intercept. Wide spectral segment processing is necessary to increase signal detection sensitivity and to provide copulse reception of multiple simultaneous signals and rejection of interference signals. Requirements for wide instantaneous bandwidth, rapid throughput, and small modules are wideband processing metrics.

Acoustooptic channelization technology is being developed for wideband processing as a compact, economical means for performing high-resolution environment segmentation. Wide-band signal frequency demultiplexing is performed using Bragg regime acoustooptic diffraction and electronic signal detection and encoding. Functions performed by these acoustooptic processors include channelized correlation, convolution, and spectral processing.

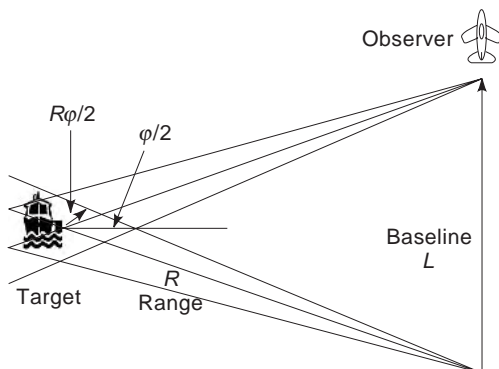


Figure 7. Emitter location geometry supporting Eq. (7), with observer track and signal measurement angles indicated.

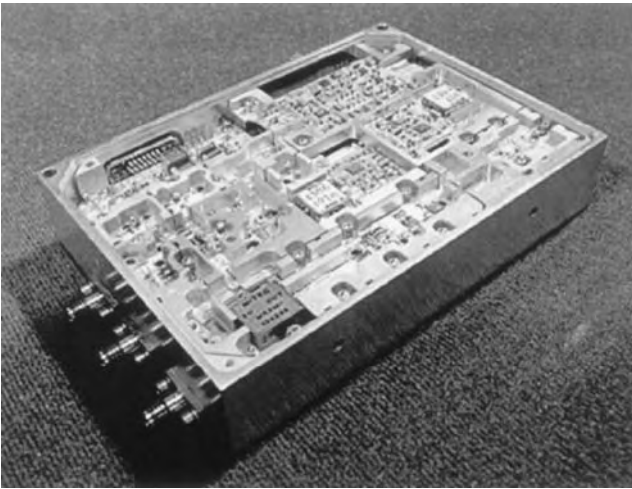


Figure 8. The MMIC receiver, a combination of monolithic microwave, analog, and digital circuits, performs signal selection and conversion to a convenient intermediate frequency.

Acoustooptic channelizers are based on Bragg diffraction of light (Fig. 9). The Bragg cell serves as the optical deflection or optical modulator element within the processor. The Bragg cell is an optically transparent medium, such as a crystal, that is driven at the applied RF frequency by using a piezoelectric RF-to-acoustic transducer. The Bragg cell transduces the RF signal into acoustic waves that are collimated into the Bragg cell crystal. The propagating acoustic wave creates sequential regions of crystal compression and extension that correspond to the period of the acoustic wave. The acoustically induced diffraction grating in the Bragg cell interacts with a coherent optical source to perform RF input frequency demultiplexing. The deflected lightbeams output from the Bragg cell are focused onto a detector array where light is detected to indicate energy in segments of the applied RF spectrum.

4.2.7. Wideband Interconnections. Electronic warfare sensors require broad access to the electromagnetic

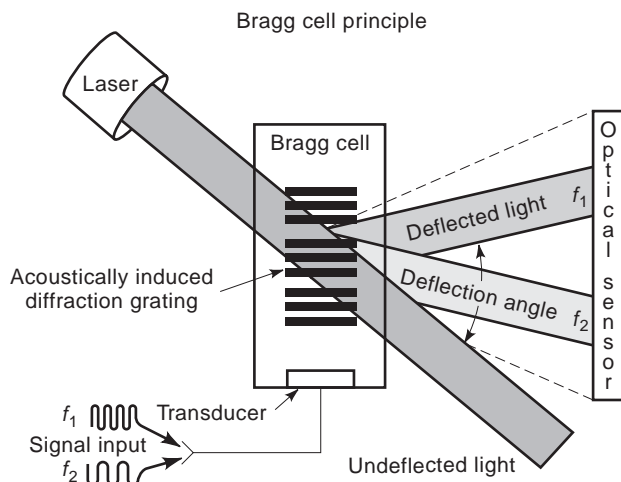


Figure 9. The acoustooptic Bragg regime signal transform processing principle used for signal frequency analysis, sensitivity enhancement, and direction-finding functions.

environment to provide quick response to hostile electromagnetic activity. For convenience and efficiency, central stowage of signal processing functional elements is important. To assure signal visibility, environment apertures, antennas, and EO/IR sensors must occupy locations on the periphery of the aircraft, ship, or land vehicle. Wideband interconnects transmit electromagnetic environment data from the EW system apertures to processing subsystems.

With the current RF bandwidth of the electronic warfare environment expanding through tens of gigahertz, just finding a medium that supports that level of frequency coverage is a challenge. At light frequencies, however, a 100-GHz spectrum spans less than a third of 1% of light frequency. In addition, low-loss-transmission optical fibers provide a nearly lossless means to transfer wide spectra across a platform. Indeed, wideband interconnect technology is developing the use of fiberoptics.

Usable optical fiber bandwidth is limited by dispersion. Conventional fiber exhibits dispersion of 20 ps/km/nm of bandwidth. A typical signal operating within a 10MHz bandwidth would exhibit dispersion of less than 0.1°. Clearly, bandwidth limitations are elsewhere in the link.

Detectors have also been developed to provide bandwidths on the order of tens of gigahertz. High RF operating frequency detection is performed by using small-geometry detectors that exhibit maximum power limitations. Limitation in maximum power levels applied to the detector restricts the output signal intensity range. More recent developments in distributed detector elements are extending detector power-handling capabilities.

Dynamic range is a significant fiber optic link metric because the EW sensor system must process low-power signals on the horizon in an environment with high-power local transmissions. Modulator and detector attenuation reductions are technological issues being addressed to enhance the dynamic range performance of fiber optic links.

4.3. Countertargeting

Countertargeting (CTAR) is the technical area that provides the means for protecting the host platform or force from weapons targeting by a hostile force. CTAR functions include obscuration, false-target generation, and confusion. Associated techniques include jamming and onboard and offboard false-target generation.

Countertargeting operates against radars that feature a target, locating or surveillance mode, as shown in the functional sequence of Fig. 10. Airborne surveillance radar is generally used against ship and ground forces because the aircraft altitude provides extended surface target detection range. Conversely, when defending against aircraft with CTAR, the radar could be ground-based. Some radars are designed with the sole purpose of surveillance, whereas others are multimode and can track targets. By using imaging processing, modern surveillance radars that include synthetic aperture, inverse synthetic aperture, high range resolution, and moving target indication processing can accurately determine target location and identify the type of target.

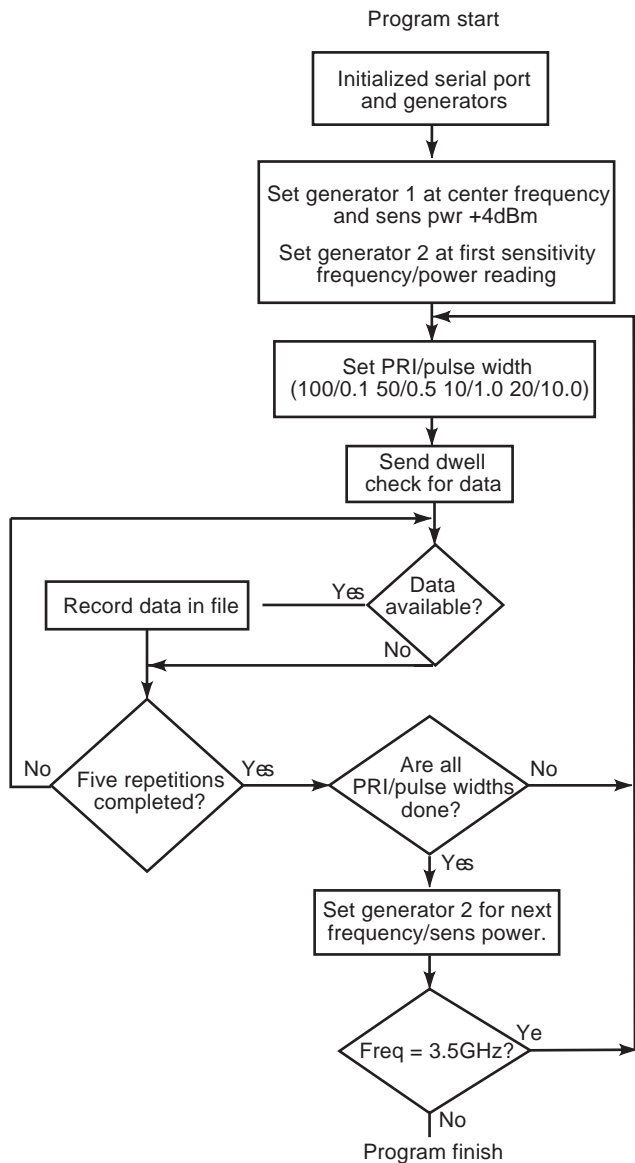


Figure 10. CTAR functional diagram showing sequence used in engaging a surveillance or targeting radar signal.

4.3.1. Countertargeting Techniques. Figure 10 shows the CTAR functional sequence. CTAR EA techniques are categorized as environment obscuration and jamming and false-target signal generation. CTAR provides either confusing or ambiguous data to adversary surveillance and targeting radar displays to confuse the human operators who interpret these presentations. Radar displays include plan position indicators (PPIs), A or B scopes, or combinations of these. Obscuration screens targets over selected portions of the display with a jamming signal power above that of the target signal in environment segments spanning both range and azimuth (see radar articles for descriptions of radar displays). The amplitude of the obscuration CTAR signal exceeds that of any target-reflected signal in the screened sector.

Experienced operators can recognize obscuration and radar jamming and initiate procedures to mitigate its



Figure 11. EA-6B aircraft equipped with the AN/ALQ-99 EA system for airborne CTAR.

effects. The false-target CTAR technique, however, is a more subtle form of EA that is less apparent to the operator. Here, the CTAR signal creates false indications on the radar display that appear as real targets to the operator. When the display is cluttered with false targets, radar operator time is consumed sorting through them. Selecting a false target for missile engagement dissipates an expensive weapon.

CTAR EA systems can be used to protect an entire military force. CTAR force protection systems are generally large and use human operators for system control. An example is the AN/ALQ-99 system installed on the EA-6B (Fig. 11), and EF-111 EW aircraft. Some EA systems, such as the AN/SLQ-32 installed on surface ships (Fig. 12), are for self-protection and support EA functions.

The EA system selects a specific technique from a large EA technique library. Selection is based on knowledge of the threat location, class, electronic parameters, and operating mode. The EA system, using an embedded receiver subsystem, rapidly adapts to threat signal operating mode changes. The threat changes operating mode as either a

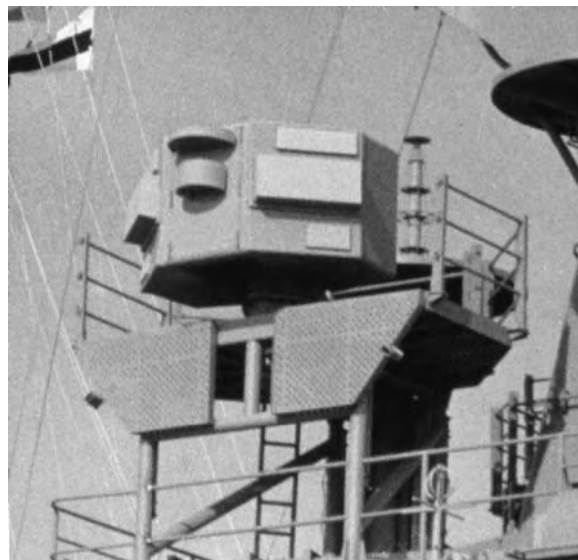


Figure 12. Shipboard installation of the AN/SLQ-32 EW equipment used for CTAR.

counter-countermeasures technique to circumvent EA or as part of the hostile targeting and homing sequence. Adaptive EA provides rapid changes in techniques as the threat sequences through operating modes.

Both jamming and deception CTAR techniques may be used. RF jamming techniques are either “barrage” or “spot.” Barrage jamming covers a wider frequency band at lower power density levels and is used to jam either several radars at once or spread-spectrum systems where the precise frequency of the threat is uncertain. Spot jamming concentrates the entire jamming power within the bandwidth of a single threat radar receiver with correspondingly better results. In both cases, a radial jamming strobe will appear on the threat radar PPI scope, as shown in Fig. 13. If the ratio of jamming signal power to the reflected radar signal power (J/S) is insufficient, the real target will “burn through” the jamming signal and become visible within the jamming strobe. For greater jamming effectiveness, it is desirable to have sufficiently large J/S to prevent burn through in the mainbeam and the principal sidelobes (see jam-to-signal calculations later).

Deception techniques are more varied and are generally threat-specific. Many deception techniques are directed against threat-tracking radars or missile-seeker radars. These techniques attack the threat radar target-tracking loops in range, angle, or Doppler. Deception techniques are often used in combinations and can be sequenced as the threat modes vary, or they can sequence according to a programmed pattern. False-target deception techniques are generated to emulate true target returns. The threat-radar operator, in response to deception, may conclude that all detected targets are genuine and simply select false targets for weapons engagement, or, if deception is suspected, time and computational resources must be used to identify the true target prior to engagement. In automated weapons systems, the EA subsystem may create so many false targets that the radar computer becomes overloaded. Because Doppler radar and missile seekers process large numbers of ambiguous radar returns to fix the true target, they are particularly vulnerable to coherent false-target techniques. An effective CTAR approach combines jamming and deception. Jamming creates a radial strobe that obscures the true target, whereas the deceptive CTAR provides false targets that project through the jamming strobe.

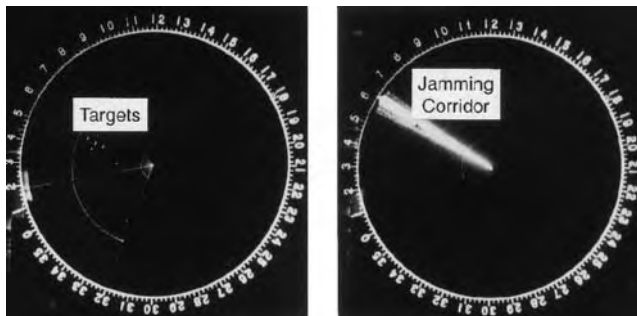


Figure 13. PPI radar scope without and with jamming, showing the effects of CTAR jamming on the threat radar display.

4.3.2. Countertargeting Effectiveness. Countertargeting effectiveness is assessed by comparing threat system performance in benign and CM environments. The ability of the threat system to detect, acquire, and target true targets, including parameters, such as target acquisition time and weapon release range, is assessed by evaluating threat performance against live targets on test ranges. Evaluating missile-seeker countermeasure effectiveness presents a more difficult problem. Computer simulations model the missile flyout from an actual or surrogate threat system against a live target. A measure of CTAR effectiveness (MoE) is the ratio of the number of missiles that approach their target outside of the missile lethal range to those missiles that approach the target within lethal range. Software simulates multiunit engagements. U.S. Navy ship EA is evaluated by flying test aircraft carrying captive instrumented seekers against the ships and recording the threat system performance.

A statistical technique to assess CTAR effectiveness compares the number of missiles required to defeat an EA-equipped aircraft versus the number required to defeat a non-EA-equipped aircraft. Similar statistics assess the number of antiradiation missiles fired versus the number of radar systems defeated. Additional effectiveness information can also be gleaned from intelligence sources.

4.3.2.1. Obscuration Burnthrough. A measure of CTAR obscuration effectiveness is the range at which the radar displays the target in the presence of jamming. This is called the *burnthrough* range. At this range, the radar is sufficiently close to the target that the processed target-reflected radar power exceeds the jamming signal display masking. The real target becomes visible superimposed on the jamming signal. Burnthrough is modeled in Eq. (9) by using the radar range equation and free-space propagation. The radar range equation provides the signal power S that is received at the radar after being transmitted to and reflected from the target. The free-space signal propagation equation models the jammer power J that is received at the radar from the jammer. The quotient of jammer to signal power constitutes a figure of merit known as the jam-to-signal (J/S) ratio. This ratio is unique for each radar and depends on radar processing gain and on the display format and screen phosphor. Operator proficiency also plays a significant role. Rearranging the terms of this equation to solve for range yields the burnthrough equation

$$R_b = \sqrt{\frac{J}{S} \left(\frac{P_R \sigma B_J}{P_J 4\pi B_R} \right)} \quad (9)$$

where R_b is the burn through range, J/S is the ratio of jammer-to-signal power required to jam the victim radar, P_R is the effective radiated power of the radar, P_J is the effective radiated power of the jammer, σ is the radar cross section of the target, B_J is the jamming signal bandwidth, and B_R is the processing bandwidth of the radar receiver. This equation models the case with the jammer located on the radar target platform.

4.3.2.2. Jammer-to-Signal-Power Relationships. The J/S power ratio at the threat radar is a concept central to predicting EA effectiveness. To degrade the threat radar, an interfering jammer power J of sufficient strength is required to overcome the target-reflected signal at the radar S . For effective EM noise jamming, the J/S required is 0–6 dB minimum, depending on the noise modulations used and the detailed characteristics of the threat. The minimum J/S ratio required for effective CTAR deception techniques varies from 0 dB for false targets, to 0–6 dB for range deception, to 10–25 dB for angle-tracking deception, and to 20–40 dB for monopulse deception. Equations (10)–(12) are based on two typical EA tactical situations. *Self-protection* CTAR [Eq. (10)] addresses the case with the target in the threat radar mainbeam. *Support* CTAR [Eq. (11)] addresses the case of the target in the threat main radar beam but with the EA jamming emanating from a separate platform and radiating into an arbitrary bearing of the threat radar antenna pattern. In both cases, the radar is assumed monostatic (i.e., the radar receiver and transmitter are collocated):

J/S for self-protection EP CTAR:

$$J/S = \frac{4\pi P_j G_j B_r R^2}{P_r G_r \sigma g^2 B_j} \tag{10}$$

where P_j is jammer power output; G_j is gain of jammer antenna in direction of radar; B_r is radar receiver noise band-width; R is radar-to-jammer range; P_r is radar power output; G_r is gain of radar antenna in target direction; σ is target radar cross section; g^2 is propagation one-way power gain (square of the ratio of field strength to free-space field strength due to direct and reflected ray combination), $0 < g^2 < 4$ (interferometer lobing); and B_j is the jammer noise bandwidth.

J/S for support EA:

$$J/S = \frac{4\pi P_j G_{jr} G_{rj} B_r R_t^4 g_j^2}{P_r G_r^2 \sigma B_j R_j^2 g_t^4} \tag{11}$$

where G_{jr} is the gain of the jammer antenna in the direction of the radar, G_{rj} is the gain of the radar antenna in the direction of the jammer, R_t is the radar-to-target range, g_j is the jammer-to-radar propagation factor, R_j is the radar-to-jammer range, and g_t is the radar-to-target propagation factor. The remaining terms are as defined previously.

Effect of target radar cross-sectional reduction:

$$S = \frac{P_r G_r \sigma \lambda^2 g^4}{(4\pi)^3 R^4} \tag{12}$$

where λ is the wavelength of the radar operating frequency. All the remaining terms are as defined previously.

Equation (12) defines the signal at the receiver of a mono-static radar. Note that the power received at the radar is directly proportional to the target radar cross section σ and inversely proportional to the fourth power of the range R (R is the separation between the target and radar). Therefore, as the radar cross section is reduced, the

signal at the radar is correspondingly reduced. If the cross section is sufficiently reduced, the target becomes indistinguishable from the radar noise and background clutter. Low observable platforms, such as the B-2 and F-117 aircraft, provide sufficiently low radar cross section to make radar detection difficult. The implication of radar cross-sectional reduction technology to CTAR is twofold: first, with sufficiently low radar cross section, EP may not be necessary, and secondly, if the cross section merely lowers the signal power at the radar, then a lower power, low-cost CTAR transmitter becomes sufficient to provide the J/S necessary to achieve the desired level of survivability.

4.3.3. Countermeasure Technology. Countermeasure technology addresses the evolving threat in addition to the need for economic force protection. Significant advances in radar, communications, EO/IR weapons' sensors, and weapons control present heightened challenges to maintaining effective EA capability.

4.3.3.1. Radar Countermeasures Technology. Countertargeting equipment for use against advanced synthetic aperture radar (SAR) or inverse synthetic aperture (ISAR) surveillance and targeting radar requires wide instantaneous bandwidths and high processing speeds. Furthermore, because these radars use coherent processing, CTAR effectiveness consequently requires coherent radar signal storage and reproduction to enhance effectiveness. Digital RF memory (DRFM) technology is being developed to convert the analog radar RF signals into a digital format for convenient storage. As required, the radar signal is retrieved from storage and converted to RF for use in countermeasure waveform generation. Technology limitations and costs constrain currently available DRFM designs, each optimized for a specific application.

Radiofrequency-tapped delay lines provide precise timing between portions of the CTAR waveform. Analog RF-tapped delay lines use surface acoustic wave (SAW) and acoustic charge transport technology. Research is underway to create digital tapped delay lines. Noise modulation is commonly applied to CTAR signals, and high-quality tunable noise sources are required. The output EA stage is the transmitter/antenna combination that generates and radiates the CTAR signal. Antennas for EA applications, once considered a dedicated asset, are currently envisioned as multifunction phased-array antennas with elements fed by solid-state amplifiers.

Radio-frequency isolation between the countermeasures transmitter and the receiver is a common problem of countermeasures-equipped platforms. The countermeasure signal appears at the receiver antenna. When the transmitter and receiver are insufficiently isolated, the countermeasure signal interferes with lower level threat signal reception from the environment. Interference demands careful attention to antenna design, isolation, and platform siting.

4.3.3.2. Radar Countermeasure Signal Source Technology. Electronic attack transmitters require signal sources that can be rapidly switched in azimuth, elevation, frequency, and polarization to generate multiple high-power beams

with low sidelobes over large multioctave bandwidths. CTAR requirements for economical compact transmitters are challenged by the lack of appropriate low-cost EM power sources. Furthermore, few commercial applications exist for wideband EM power source technology. Research and development in this area is limited primarily to EA applications. Original EW power sources, tunable magnetrons, and cross-field amplifiers provided only narrow operating bandwidths. Traveling-wave tubes (TWTs) evolved to fill the need for wide, instantaneous bandwidth. Over time, TWT bandwidths grew from a single-octave 2–4 GHz band to multiple octaves at frequencies beyond 40 GHz. However, TWTs are expensive and unreliable. Although new mini-TWTs and microwave power modules have become available, their basic design remains vacuum-envelope-based. MMIC technology is steadily advancing, and it now provides solid-state chips with multioctave signal generation capability, wide instantaneous bandwidth, and signal power levels approaching 5 W. With MMIC technology, solid-state active aperture arrays become achievable, and such arrays for EA applications are now being developed. Although MMIC active aperture array signal source promises good performance and reliability, the system remains expensive.

4.4. Passive Electrooptic/Infrared Electronic Warfare

Electronic warfare in a passive EO/IR target acquisition and weapons sensors environment applies to a growing threat capability. The open-ocean blue-water scenario requires EO/IR EA and EP ship protection, typically 200 nautical miles or more from shore, against massive and coordinated attack. EO/IR EA applications have more recently focused on littoral scenarios involving amphibious operations in support of peacekeeping operations for regional conflicts, providing humanitarian assistance in politically and militarily unstable regions; evacuating

civilians from regions of conflict, and ensuring safe passage of commerce through disputed littoral waters and choke points.

The traditional EO/IR threat, the long-range antiship missile, has been intensified in the littoral areas by a large variety of air-to-surface, air-to-air, and surface-to-air EO/IR missile weapons. These missiles can inflict severe damage to the smaller craft used for littoral warfare.

Electrooptic system target detection range depends on detector sensitivity and resolution. A target image is defined by contrast with the background. Sensitivity determines whether the contrast is discernible. Resolution depends on the spatial environment angle illuminating the detector, which is a function of detector surface area and focusing optics. The distance at which target features are resolvable determines the maximum operating range of the system.

The target signature detectability is determined not by the absolute temperature of the object but rather by the contrast between the target and background within a given spectral band. Environment backgrounds range from the cold, uniform background of space to thermally cluttered land areas. Solar interaction with the target and background reflection and heating further degrade the background contrast with the target. Typical target contrasts range from about 1 kW/sr (kilowatt per steradian) in the 2–3 μm atmospheric window for an aircraft engine to tens of kilowatts per steradian for ships in the 8–12 μm window. Target aspect, especially the location of hotspots, greatly influences the signature.

4.4.1. Electrooptic/Infrared Countermeasures. Electrooptic/infrared countermeasures are constrained by specular atmospheric propagative characteristics, as is the threat (Fig. 14). The contrast of the target to the background within the weapon sensor’s specular passband, the type of seeker spatial localization processing, and

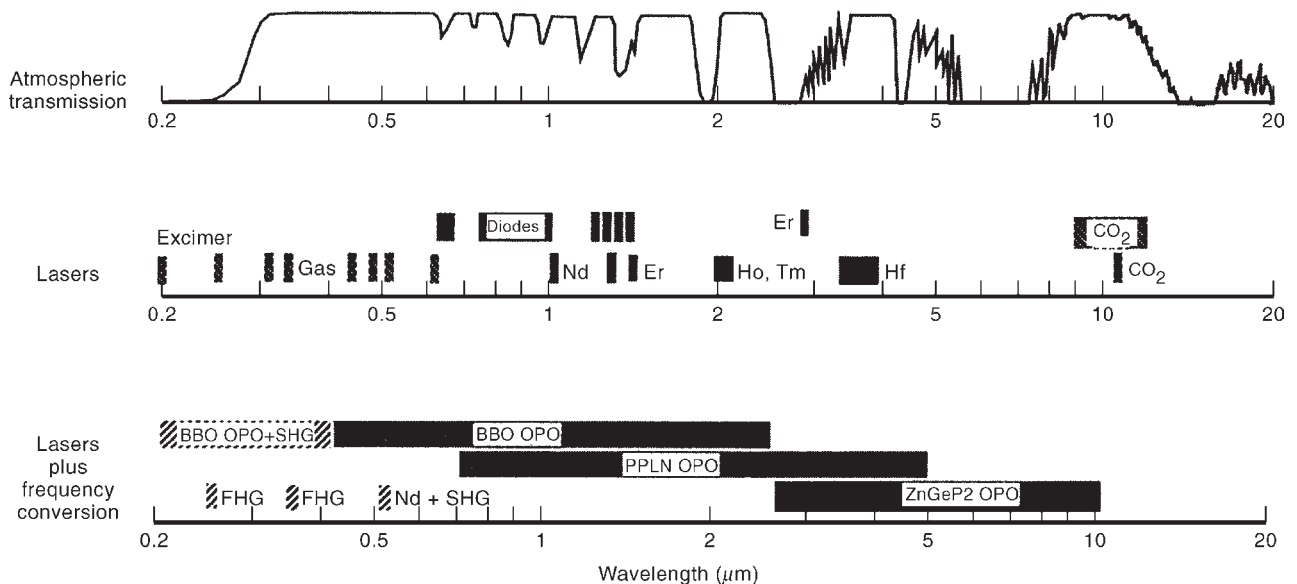


Figure 14. EO/IR atmospheric transmission spectral segments and laser and laser harmonics countermeasures source spectral regions.

available practical radiation sources are also prime considerations.

The missile flyout and CM sequence of events occurs in several seconds. As part of an integrated electronic warfare suite, the EO/IR EA system is designed to engage a large number of missiles launched in a coordinated attack. Figure 15 shows a typical timeline of the CM response to an attack by a subsonic antiship missile. The time line indicates the interaction of EO/IR EA with other ship defense systems.

To preclude detection by a threat EO/IR sensor, target signature can be reduced through a combination of convective, conductive, and radiative mechanisms. Exterior surfaces of ship stacks are cooled by convective air flow between the engine exhaust ports and the outer stacks. Engine plume and exhaust gases from all types of engines can be cooled by dilution with air. Radiation from hotspots can be reduced by spectral emissivity modifications or by obscuring the hot areas from view. On new platforms, low-observability design criteria have led to low-signature aircraft and ships.

Onboard aircraft CM sources initially generated false-target location and/or guidance degradation through weapon automatic gain control (AGC) manipulation. This technique remains highly effective against many threats. The onboard jammer sources can be chemically fueled IR sources or electrically powered incandescent and metal vapor lamps. As the wavelength passbands of anti-air and antiship seekers gradually migrate to longer wavelengths, out to the 8–14 μm window, noncoherent sources will no longer be practical.

Basic spin scan and conical scan (conscan) “hotspot” seekers are vulnerable to flare decoys. Almost universally, these flares are composed of magnesium and polytetrafluoroethylene and are designed with a radiant intensity several times that of the target. In the distraction mode, the decoy is an excellent target; in the seduc-

tion mode, the weapon’s seeker control signal is biased by the decoy or transferred to it. Because pseudoimaging seekers exhibit spatial and temporal processing capabilities, simple flares are relatively ineffective, and simple flares perform even more poorly against imaging sensors. Newer decoys overcome advanced seeker-discriminating processing with improved spectral characteristics that more closely match the target platform spectral emissions. Improved decoy spatial distribution in the form of clouds and multiple hotspots, temporal risetimes, and persistence match target signature increase rates and lifetimes, thus preventing time–history discrimination. Kinematics model realistic target movement.

The small beam divergence of lasers can result in high-radiance, low-power sources that provide the *J/S* power ratios needed for effective EA. Two laser sources, primary lasers and nonlinearly shifted lasers, are available for CM applications. Lasers shifted by nonlinear conversion include harmonic generation and tunable optical parametric oscillators (OPOs). Primary lasers do not produce spectral lines in all the potential threat passbands of interest and are susceptible to notch-filter counter-countermeasure techniques. Although harmonic generating EA techniques provide additional wavelengths, they are also subject to counter-CM. Promising sources for IR/EO CM are tunable OPOs pumped by diode-pumped, solid-state lasers. Two nonlinear materials currently demonstrating the highest potential are periodically poled lithium niobate (PPLN) and zinc germanium phosphide (ZnGeP₂). Figure 14 shows the primary lasers of interest and the wavelength coverage possible with PPLN and ZnGeP₂ OPOs.

Although noncoherent sources provide wide angular protection, high-resolution detection is necessary to point and track the threat system and effectively use laser power. Timely threat detection and warning ES is essential to the success of all nonpreemptive EA.

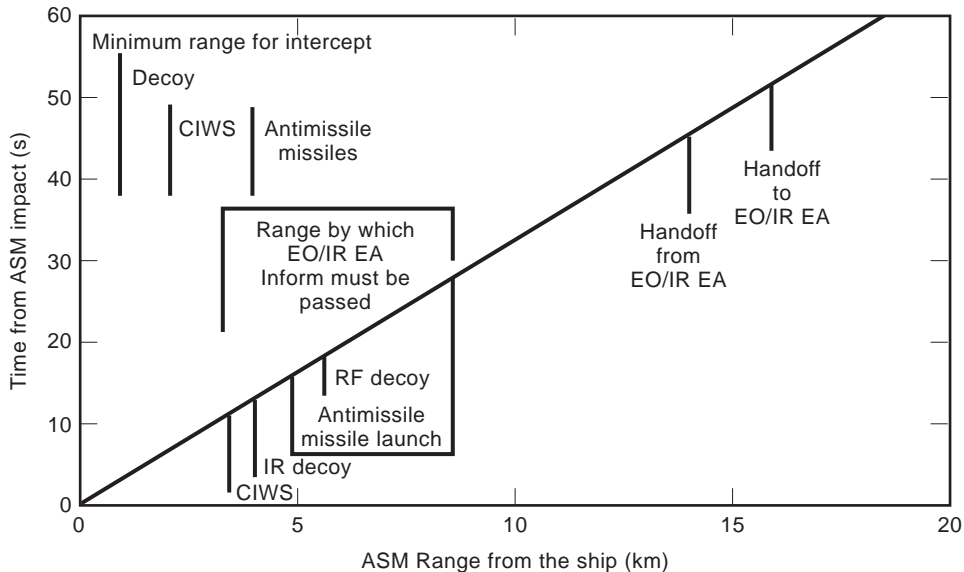


Figure 15. Missile attack timeline showing launch, acquisition, and homing phases of the missile as well as the CM attack on missile sensors and control circuits.

4.4.2. Electrooptic/Infrared Countermeasure Technology.

Key EO/IR EA technologies required to counter threat performance improvements include higher throughput data processing using more capable algorithms, laser beamsteering, and decoy launcher design. Needed processing improvements include faster signal processing, more efficient image processing, and false alarm reduction. High-performance, high-speed beamsteering, preferably nonmechanical, is required to reduce response time in multiple threat environments. Improved decoy launchers to position decoys quickly and accurately within the scenario are also needed. Low observability technologies are being developed to decrease or mask the IR/EO signatures of targets. Target signature reduction increases the effectiveness of conventional countermeasure responses by reducing the jamming power required to counter the missile system effectively. Low observability enables application of new technologies to IR/EO countermeasures by reducing the size, weight, and power requirements of decoy and laser CM sources. For example, diode laser and diode-pumped nonlinear optical sources can be integrated with unmanned aerial vehicles to produce new classes of CM devices and tactics. Large-area spectrally selective sources and obscurants provide advanced capability against spatially and spectrally discriminating threats. Primary laser and laser-pumped nonlinear sources are important evolving technologies. Launchers and vehicles that provide rapid and precise CM placement with realistic kinematic performance are areas of increasing importance.

4.5. Decoy Countermeasures

Decoys are EW devices, usually expendable, deployed from the platforms to be protected. Decoys generate a jamming response to the threat or false targets. In either case, the decoy lures the threat away from the intended target toward the decoy. A jamming decoy generates a cover signal that masks the target signal. Thereby the threat sensor signal fidelity is degraded, making detection and tracking of the intended target more difficult. A jamming signal may also activate the antijam home-on-jam mode of the weapon system. As false targets, the decoys generate credible target signatures to provide weapon system seduction or distraction. Decoys create confusion that causes weapons to attack false targets.

Decoys may be either passive or active. A passive decoy generates a countermeasure response without the direct, active amplification of the threat signal. Principal examples of passive decoys are chaff and corner reflectors in the RF spectrum and flares in the EO/IR spectrum.

4.5.1. Decoy Operational Employment. Decoys provide EA capability across the entire EW battle timeline. Decoys are used primarily for EP missile defense and self-protection missile defense but also for countersurveillance and countertargeting applications.

Jamming is used in conjunction with decoys to obscure the target signal at the threat radar during decoy deployment. As decoys are deployed, jamming ceases and the threat radar acquires the decoy as a target or transfers radar tracking from the target to the decoy. Threat radar

acquisition of the decoy as a target is probable because decoys present prominent signatures.

Decoys used for missile defense perform either seduction, distraction, or preferential acquisition functions. A single-decoy type may perform multiple functions, depending on deployment geometry with respect to the launch aircraft or ship and the stage of electronic combat.

Decoys are used in a seduction role as a terminal defense countermeasure against missile weapons systems. A seduction decoy transfers the lock of the missile guidance radar or EO/IR sensor from the defending platform onto itself. The decoy that generates a false-target signature is initially placed in the same threat tracking gate, missile sensor range, and/or angle segment as the defending target and is subsequently separated from the launching platform. The decoy signature captures the missile guidance sensor, and the target lock is transferred from the ship or aircraft to the decoy. Typically, the decoy is separated in both range and angle from the defending target to assure target-to-missile physical separation greater than the missile warhead's blast range. The seduction decoy missile interaction is typically initiated within 10 s of deployment. Distraction decoys are deployed prior to missile-seeker acquisition and provide multiple false targets from which the seeker may select. Deployed distraction decoys provide a confusing environment to the missile seeker, causing it to attack a decoy rather than the intended target.

The ALE-129 chaff decoy (Fig. 16) is representative of RF seduction decoys for aircraft defense. The NATO Sea Gnat MK-214 cartridge shown fired from a shipboard launcher in Fig. 17 provides surface defense against radar-guided weapons. Figure 18 shows a TORCH decoy deployed at sea for IR defense.

Distraction decoys are observed for extended periods in the engagement scenario. Consequently, the distraction decoy must generate a credible signature that is sufficient to preclude short-term and extended missile decoy discrimination.

The AN/SLQ-49 inflatable corner reflector (Fig. 19) and the rocket-launched NATO Sea Gnat MK-216 chaff cartridge (Fig. 20) are representative of distraction decoys for surface ship defense. The TALD decoy (Fig. 21) is an example of a distraction decoy used for aircraft defense.



Figure 16. ALE-129 RF chaff round with the bundle of reflector elements partially deployed from the canister.

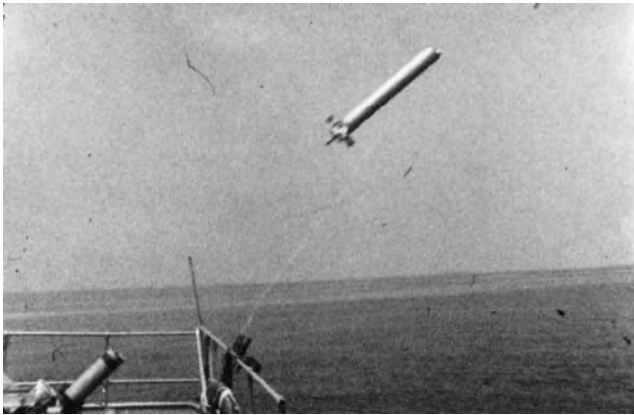


Figure 17. NATO Sea Gnat MK-214 seduction RF decoy deployed from a shipboard rocket launcher.

Frequently, persistent seduction decoys perform a distraction function after separating sufficiently from the defended platform. This “residual distraction” further minimizes the number of distraction decoys required in an engagement.

An EA preferential acquisition decoy provides a signature to the missile seeker such that during acquisition the missile seeker senses the real target only in combination with the decoy signature. In the endgame, the decoy signature in the missile field of view biases the aim point of the missile tracker away from the intended target.

The preferential acquisition concept requires decoys positioned close to the defending platform. Decoys can be towed behind the target aircraft or tethered to the defending ship. The AN/ALE-50 (Fig. 22) is a towed decoy used for air defense preferential acquisition, and the EAGER decoy (Fig. 23) is being developed for ship defense preferential acquisition.

4.5.2. Chaff Decoys. A chaff decoy is composed of multiple—tens of thousands to millions—of electrically conductive dipole filament elements deployed in the air to reflect and scatter radar signal radiation and create a false-target radar response. Figure 24 shows a typical deployed chaff decoy. The chaff decoy frequency response is determined by the length of the dipole elements, and the chaff radar cross-sectional (RCS) magnitude results from the number of dipoles deployed. Figure 25 shows a radar



Figure 18. TORCH EO/IR decoy deployed at sea.

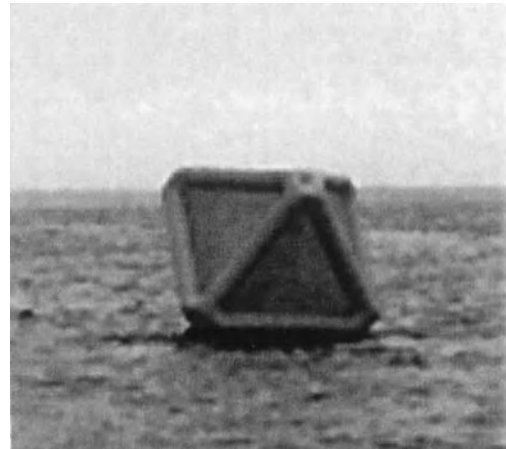


Figure 19. AN/SLQ-49 inflatable corner reflector decoy deployed at sea.

PPI display of an environment containing numerous chaff clouds.

The RCS of a chaff cloud is tuned for a given frequency (with the dipole length one-half the wavelength of the incident radar signal), and its RCS can be approximated by

$$\text{RCS}(\text{m}^2) = \frac{0.018c^2N}{f^2} \quad (13)$$

where c is the speed of light (3×10^8 m/s), f is the frequency in hertz, and N is the number of dipoles in the cloud.

4.5.3. Corner Reflector Decoys. Corner reflectors are conductive geometric structures that are typically shaped in the form of a perpendicular triangular corner. The shape maximizes the reflection of incident radar signals and provides a large apparent target signature. Figure 26 shows a multifaceted triangular corner reflector that provides wide angular coverage.

The apparent RCS normal to a triangular corner reflector is given by

$$\text{RCS}(\text{m}^2) = \frac{4\pi L^4 f^2}{3c^2} \quad (14)$$



Figure 20. NATO Sea Gnat MK-216 distraction decoy deployed from a rocket launcher.



Figure 21. TALD decoy distraction decoy.

where L is the length from the outside corner to the apex of the reflector, f is the frequency in hertz, and c is the speed of light (3×10^8 m/s). The 3 dB beamwidth of this type of corner reflector is 40° .

4.5.4. Flare Decoys. Flares are typically incendiary devices that produce EO/IR radiation to generate a false target. Figure 27 is an IR image of a magnesium–Teflon flare deployed from an aircraft.

4.5.5. Active Decoys. An active decoy uses direct threat signal amplification to generate the countermeasure response. In the case of RF systems, it is generally an RF amplifier (transistor or tube). In the EO/IR spectrum, a laser or flash tube amplifies the threat signal. Jammer and repeater decoys are active decoys.

Repeater decoys receive, amplify, and retransmit the received signal to generate a false target. Multiple signals may be retransmitted to generate multiple target returns. Modulation techniques (amplitude and frequency) may also be applied to the signal before retransmission to enhance effectiveness. The apparent radar cross section of an active RF decoy is given by

$$RCS(m^2) = \frac{(P_d G_d 4\pi R^2)}{P_r G_r} \quad (15)$$



Figure 22. AN/ALE-50 towed decoy deployed from a tactical aircraft in flight.



Figure 23. EAGER shipboard-tethered decoy in field trials.

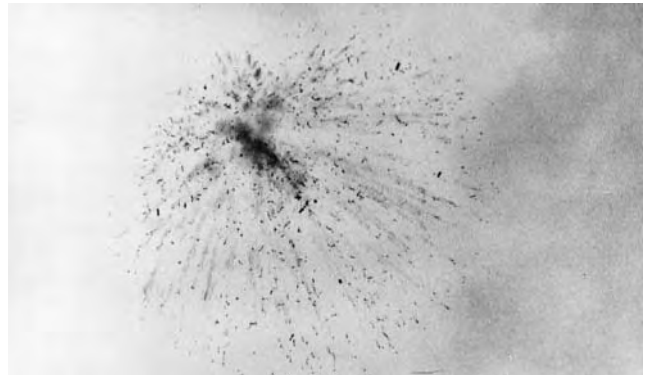


Figure 24. Deployed chaff round shown as a burst of reflector elements against a sky background.

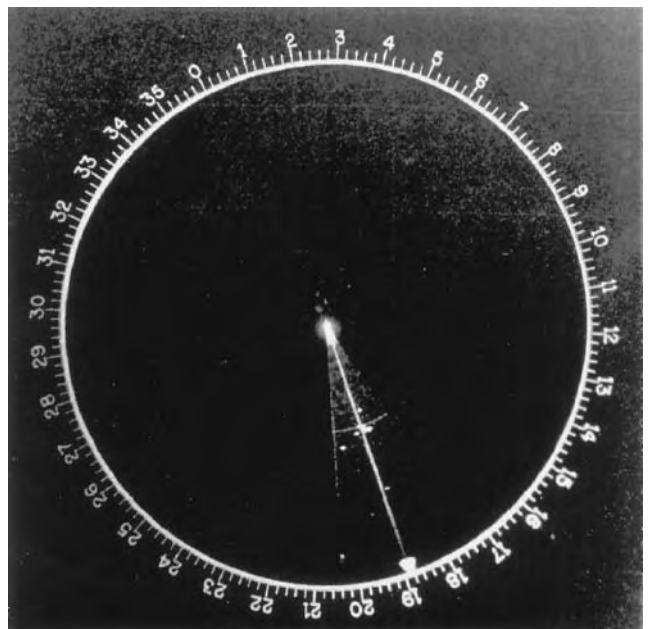


Figure 25. Radar PPI display showing target reflections from multiple chaff decoys.



Figure 26. Multifaceted corner reflector deployed on a ship bow to provide a high cross-sectional reflection at several frequencies.

where $P_d G_d$ is the effective radiated power (ERP) of the decoy, R is the range between the decoy and the radar in meters, and $P_r G_r$ is the effective radiated power (ERP) of the radar.

For a decoy operating with linear gain, that is, a decoy whose transmission signal power is directly proportional to the input signal level (up to the signal compression level), the RCS relationship simplifies to the relationship given by

$$\text{RCS}(\text{m}^2) = \frac{(G_t c^2)}{4\pi f^2} \quad (16)$$

where G_t is the combined electronic and antenna gains (receive and transmit) of the decoy, c is the speed of light (3×10^8 m/s), and f is the frequency in hertz.

4.5.6. Decoy Effectiveness. A distraction decoy is deployed at an extended range from the defending platform and provides an alternate target for seeker lockon. Distraction decoys require deployment before seeker lockon to engage the radar in its acquisition process. Usually more than one distraction decoy is used to defend a platform. An estimate of the effectiveness of the distraction decoy is given by

$$P_s = 1 - \frac{1}{N+1} \quad (17)$$



Figure 27. Flare IR decoy deployed from a tactical aircraft in flight.

where P_s is the probability that the missile will be distracted to the decoy and N is the number of distraction decoys deployed.

Equation (17) assumes that all of the distraction decoys exhibit viable target signatures and are equally likely to be acquired by the missile sensor. The number of decoys deployed can be reduced with the same probability of success with knowledge of the seeker acquisition logic, for example, a near-to-far/right-to-left acquisition search.

Seduction decoy effectiveness is primarily determined by the intensity of the decoy signature compared with the target being defended. However, the radar track bias, for example, leading-edge tracker and discrimination algorithms, can significantly impact decoy effectiveness. In some cases, the radar track bias can be exploited to increase decoy seduction effectiveness.

4.5.7. Decoy Countermeasure Technology. Diverse technologies are required to support decoy launch and station-keeping and countermeasure generation. Because most decoys are single-event, short-term items, cost plays a major role in selecting and developing technology for decoy use. Furthermore, because the defending platform must generally deploy a number of decoys throughout an engagement, decoy size and weight criteria also are critical. Attendant decoy platform technologies include aerodynamics, aircraft/projectile design, propulsion systems, avionics, and mechanical structures. Decoy payload technologies that will have significant importance in future systems include broad-bandwidth microwave and millimeter-wave components (e.g., antennas and amplifiers).

Microwave and millimeter-wave output power sources are required with high power, efficiency, and duty cycle to support the projected threat environments. The future RF threat environment is expected to be densely populated with long-pulse radar. Higher decoy radiated power at higher duty cycles will be needed to prevent decoy saturation as the number of simultaneous threat signals in the environment increases.

Ultra-high-speed countermeasure frequency set on circuitry is necessary to queue jammer frequency rapidly. Signals with rapid frequency hopping and frequency chirping require rapid activation for effective countermeasures. Spatially large and efficient spectrally matched IR materials and radiating structures are needed to counter multispectral, imaging IR seekers. Safe, nontoxic, highly opaque, broad-spectrum IR and electrooptical obscuration materials are required to mask targets and confuse image processing seekers. Efficient, primary power sources capable of high peak power and dense energy storage are needed to provide the increasing demand for electrical power used in decoy systems.

FURTHER READING

J. S. Accetta and D. L. Shumaker, eds., *The Infrared and Electro Optical Systems Handbook*; D. H. Pollock, ed., Vol. 7, *Countermeasure Systems*, Infrared Information Analysis Center, Ann Arbor, MI; SPIE Optical Engineering Press, Washington DC, 1993.

- B. Blake, *Jane's Radar and Ele+9ctronic Warfare Systems*, Jane's Information Group, Surrey, UK, 1993.
- J. A. Boyd et al., *Electronic Countermeasures*, Peninsula Publishing, Los Altos, CA, 1978.
- E. J. Chrzanowski, *Active Radar Electronic Countermeasures*, Artech House, Norwood, MA, 1990.
- N. C. Currie, *Techniques of Radar Reflectivity Measurement*, Artech House, Dedham, MA, 1984.
- R. D. Hudson, Jr., *Infrared Systems Engineering*, Wiley-Interscience, New York, 1969.
- W. L. McPherson, *Reference Data for Radio Engineers*, Howard W. Sams, Indianapolis, 1977.
- R. J. Schlesinger, *Principles of Electronic Warfare*, Peninsula Publishing, Los Altos, CA, 1961.
- M. I. Skolnik, *Radar Handbook*, McGraw-Hill, New York, 1970.
- L. B. Van Brunt, *Applied ECM*, Vol. 1, EW Engineering, Dunn Loring, VA, 1978.
- W. Z. Wolfe and G. J. Zississ, eds., *The Infrared Handbook*, rev. ed., Environmental Res. Inst. Michigan, Ann Arbor, MI, 1985.

ELLIPTIC FILTERS

KENNETH V. NOREN
University of Idaho
Moscow, Idaho

JERRY MICHAEL GRIMM
JMG Consulting
Irving, Texas

1. INTRODUCTION

Real electrical signals are usually composed of an infinite number of components of various frequencies. Each single component occurs at a single frequency has a distinct magnitude and phase. An *electrical filter* will be defined as an electrical network that processes electrical signals on the basis of the individual frequencies of the signals composing that signal. The signal processing can affect both the magnitude and phase of each component. For example, the output signal of an antenna may represent an electrical signal that requires processing by a receiver. The signal may have a fairly wide spectrum, is composed of signals at a wide range of frequencies, but it is often desired that the receiver process a small range of these frequencies, or channel, where important information is contained. One solution is to use a bandpass filter in one of the stages following the antenna. The filter would process the signal so that the range or band of frequencies containing the desired information would pass through to the output, and the signals outside the range would be rejected. From here, signal processing of the desired information may take place. Although this example is greatly simplified in comparison to what actually happens in a receiver, it nonetheless illustrates the general idea of filtering.

Over time, several "standard" types of filters, or signal-processing schemes for filters, have evolved. These are

lowpass, highpass, bandpass, band-reject, and all-pass filters. Lowpass filters strive to allow frequencies below a specific "passband frequency" to pass, while rejecting those frequencies above the passband frequency. Highpass filters strive to allow frequencies above a specific passband frequency to pass, while rejecting those frequencies below the passband frequency. Bandpass filters allow a range or band of frequencies to pass, while rejecting frequencies outside of that band. Band-reject filters reject a band of frequencies, allowing frequencies outside that band to pass. The main objective of these four types of filter is to process the magnitude of the signal as a function of frequency in a particular way. The all-pass filter lets all signals pass through, but selects a band of frequencies for phase angle processing, while not affecting the magnitudes. Time delay of the input to the output is an important consideration for all-pass filters. The overall choice of filter type depends on the application.

Filter design can be broken down into two broad stages. The first stage is the selection of a transfer function possessing the mathematical properties of filtering that will meet a set of specifications that are determined from the particular application. A *transfer function* is a mathematical description that describes the relationship between the input signal and the output signal of a network. We will use it in the sense that for a given input signal, we will have a specific output signal that is determined by the transfer function. Since filters process electrical signals according to the frequency content, the transfer function for a filter is a function of $s = j\omega = j2\pi f$, where ω is the frequency in rad/s (radians per second) and f is the frequency in hertz.

The second stage of filter synthesis is the realization of a circuit that possesses the same transfer function as the mathematical function selected to do the filtering. In general, the circuit may be an analog, digital, or a mixed analog-digital circuit depending on the application. However, to date, most filters used at RF and microwave frequencies are of the analog type.

2. THE APPROXIMATION PROBLEM

When filtering, engineers usually desire ideal filters. For example, when deciding to use a lowpass filter, the engineer typically desires that all frequencies above a specified passband or cutoff frequency be rejected by the filter. An ideal lowpass transfer function magnitude with a passband frequency, $\omega_p = 1$ rad/s, is shown in Fig. 1, and the ideal lowpass transfer function phase characteristics are shown in Fig. 2. For the magnitude-frequency plot, all frequencies below ω_p are passed, with a gain of 1 V/V, and all frequencies above ω_p are rejected. It is a "brick wall" function. It is intuitively obvious that this is an ideal magnitude characteristic for a lowpass filter. The ideal phase characteristics are not so intuitive. The important feature of the ideal phase characteristics are not the values of the phase, but that the phase response is linear. A transfer function that has linear phase characteristics means that a signal composed of two different frequencies applied at the same instant of time at the input of the filter will

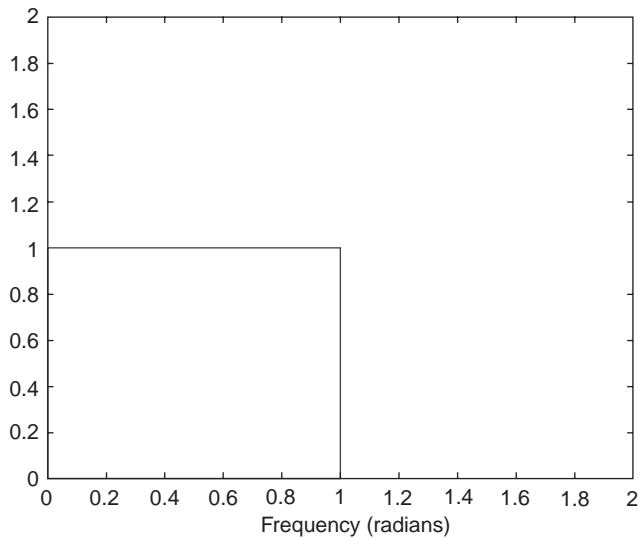


Figure 1. Magnitude–frequency plot of the ideal lowpass filter transfer function, showing that all frequencies of a signal below 1 rad/s are passed while those above 1 rad/s are rejected.

arrive, after processing, at the output of the filter at the same time. If the two input signals add together to create a distinct waveform in the time domain, it may be important that they reconstruct together at the output to maintain the “shape” of the input signal. Sometimes this is important, and sometimes it is not. A deviation from the linear phase response results in phase distortion.

The characteristics depicted in Figs. 1 and 2 are for a *normalized* filter; that is, they have passband frequencies ω_p equal to 1 rad/s and the magnitude–frequency characteristics have a maximum gain of 0 dB, or 1 V/V, in the passband. It is conventional to begin a lowpass filter design with a normalized filter. This allows for a common starting point for all lowpass filters, for example, and is also a convenient way of comparing the characteristics of different types of lowpass filter functions with each other. Moreover, numerous tables exist that provide the

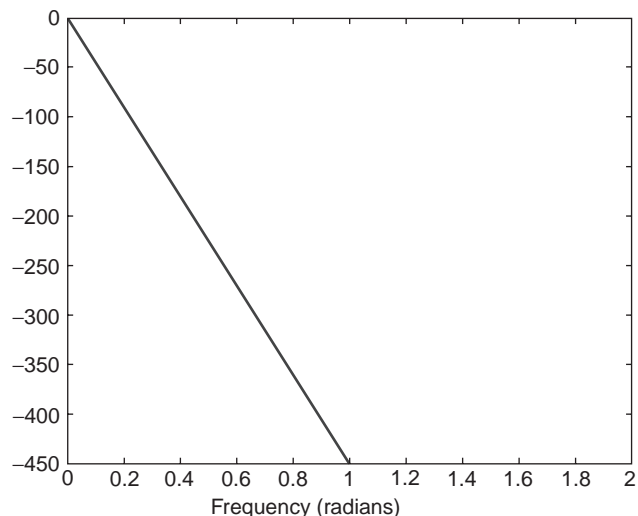


Figure 2. The ideal lowpass filter transfer function phase characteristics, which may be summarized as a linear phase response.

coefficients or poles and zeros of filter transfer functions. These tables provide information for normalized filters. Since there is an infinite number of possibilities for passband frequencies, and similar parameters, it would be impractical, if not impossible, to generate tables for all possible cases. Thus, the tables deal only with the normalized case. It is trivial to scale a filter for a desired passband frequency from the normalized frequency of 1 rad/s while retaining all other characteristics of the filter.

The first step in filter design is to find a transfer function having magnitude characteristics similar to those of the magnitude–frequency plot depicted in Fig. 1. Unless a transfer function has an infinite number of terms, it is impossible to devise a transfer function with these characteristics. Although an engineer may desire an ideal response, he/she must live with a nonideal response. Hence, from this simple example arises the *approximation problem*. In other words, may we find a transfer function whose magnitude response comes close enough to the ideal characteristics of Fig. 1 to meet or slightly exceed the filter specifications for a particular application. In general, the higher the order of the filter, the closer the transfer function will approach the ideal case. However, the higher the order of a filter, the more complex the design and the more components that are needed to realize the transfer function. Thus, the concept of tradeoffs and compromises arises. In general, a set of filter specifications must be determined before selecting the transfer function. The specifications may be viewed as to how far the actual filter application may deviate from the ideal case. The ideal filter response provides a metric with which to compare practical transfer functions.

Since it is impossible to come up with an ideal transfer function that is practically realizable, several terms have been defined and have been accepted as conventions that allow the description of the deviation of a practical filter function from the ideal filter function. These terms are depicted in Fig. 3 and may be referred to as filter specifications. The specifications are: the passband, the stopband, the passband ripple (PBR), the stopband ripple (SBR), and the stopband attenuation A . PBR, SBR, and A are usually specified in decibels. There are three distinct regions. The passband is located from 0 rad/s to ω_p rad/s. The second region is the stopband region located from ω_s to infinity. Finally, there is the transition region, composed of the range between ω_p and ω_s . Figure 3 should be interpreted as follows: Signals at or below ω_p will have a gain of at least of G dB and at the most H dB, and signals above ω_s will be attenuated by at least A dB or have a maximum gain of SBR dB. Note that $(G - H)$ dB = PBR in decibels. Filter types other than lowpass filters have similar specifications and the reader is encouraged to investigate these [1,2].

Previous research in network theory has resulted in several classic mathematical approximations to the ideal filter magnitude function. Each of these was designed to optimize a property of the filter function. The lowpass filter approximations are usually of the form

$$|H(j\omega)|^2 = \frac{1}{1 + \varepsilon^2 P^2(\omega)} \quad (1)$$

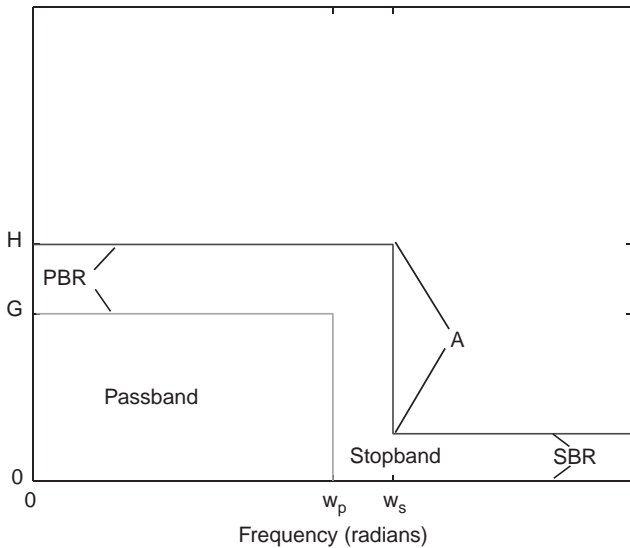


Figure 3. Filter specifications. PBR, SBR, A, passband, and stopband are ways of characterizing an actual filter function’s magnitude versus frequency response to that of an ideal response. For an ideal filter function, PBR = SBR = 0 V/V and ω_s and ω_p are equal.

When $P(\omega)$ is replaced with different types of functions, different approximations to the ideal lowpass filter response arise. The standard approximations to the ideal lowpass magnitude response are the Butterworth approximation, the Chebyshev approximation, the inverse Chebyshev approximation, and the elliptic approximation. Each of these has strong points and weak points. A fifth classic approximation worth mentioning is the Bessel function. This approximation will not be discussed because it strives to approximate the ideal phase response. This article focuses on the elliptic approximation.

3. THE ELLIPTIC APPROXIMATION

Before beginning a mathematical discussion on the elliptic approximation, it is useful to examine a plot of an elliptic filter function. A plot of the magnitude versus frequency of a fifth-order lowpass elliptic filter transfer function is depicted in Fig. 4. The frequency range of the passband is $\omega \leq \omega_p$. The frequency range of the stopband is $\omega \geq \omega_s$. The passband and stopband may be characterized as *equiripple*; that is, the amplitude oscillates between a maximum and minimum throughout each band. If the order of the filter function is even, there are $n/2$ peaks in the passband and $n/2$ minimums or zeros in the stopband. If the order of the filter is odd, there are $(n - 1)/2$ peaks, plus one at $\omega = 0$ in the passband. Also for the odd-order case, there are $(n - 1)/2$ minimums or zeros, plus one at $\omega = \infty$, in the stopband.

In discussing the properties of the elliptic filter, it is beneficial to compare its characteristics with those of the other classic filter types. The magnitude responses for normalized fifth order low pass Butterworth, Chebyshev, and elliptic filter magnitude functions are compared in Fig. 5 and the phases are compared in Fig. 6. Table 1 summarizes the comparisons and the main attributes of

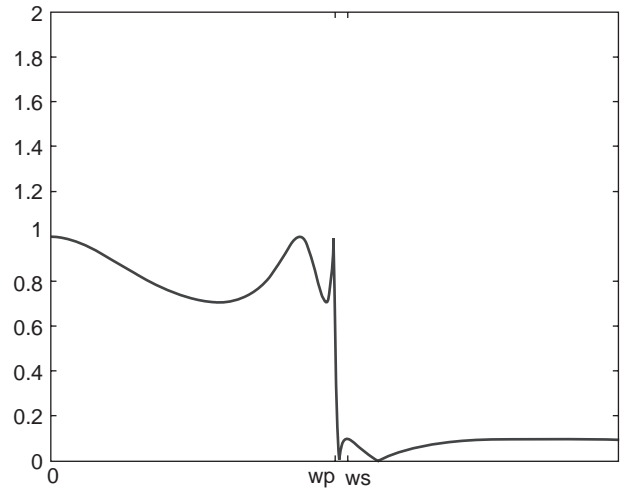


Figure 4. The magnitude characteristics of a fifth-order elliptic filter showing an equiripple passband and stopband, and a zero at $\omega = \infty$.

the elliptic filter may be stated. For a given filter order, the elliptic filter provides the sharpest cutoff characteristics, and thus out of all three filter types, it best approximates the ideal lowpass magnitude function in terms of a sharp transition region. This is very important if filtering is required for frequencies close to each other, if it is desired to pass one of these frequencies and reject the other. The compromise in using the elliptic filter is its very poor phase characteristics.

The theory underlying the mathematics of the elliptic filter is complicated, and beyond the scope of this article. Interested readers may consult Refs. 2 and 3. A summary of the mathematics is discussed in this article. The derivation assumes that $\omega_p = 1$ rad/s and that $\omega_s^{norm} = \omega_s/\omega_p$. This results in *normalized* passband and stopband

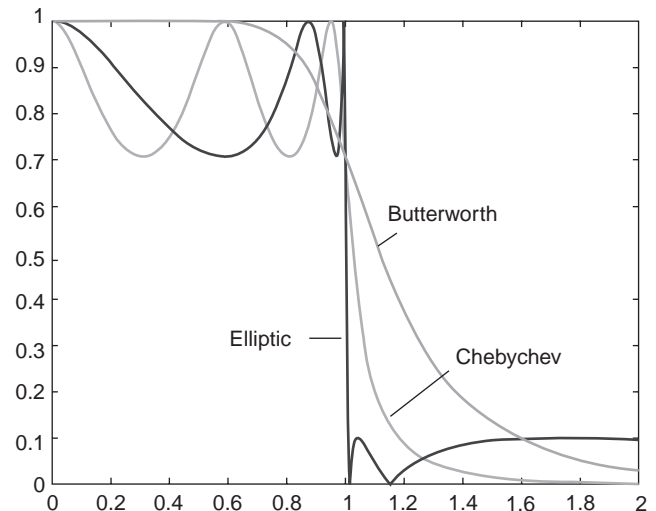


Figure 5. Amplitude comparison. The fifth-order elliptic function magnitude characteristics show a much sharper transition for the passband to the stopband than do the Butterworth and Chebyshev function characteristics. (This figure is available in full color at <http://www.mrw.interscience.wiley.com/erfme>.)

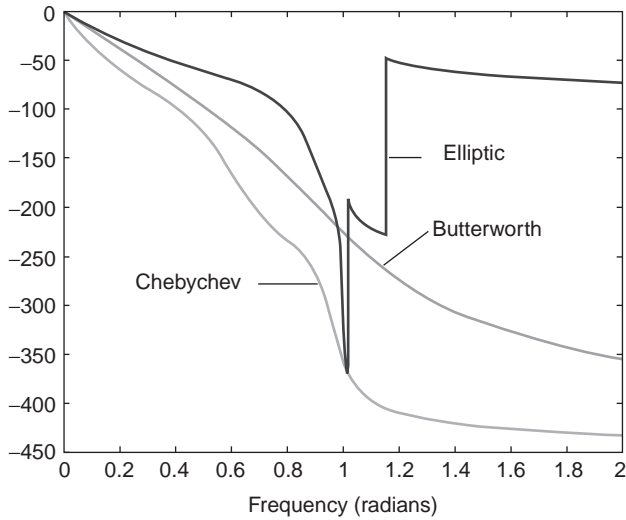


Figure 6. Phase comparison. The fifth-order elliptic function phase characteristics deviate much farther from the desired ideal linear phase characteristics than do the Butterworth and Chebyshev function characteristics. (This figure is available in full color at <http://www.mrw.interscience.wiley.com/erfme>.)

frequencies. The normalized stopband frequency ω_s^{norm} is determined by divided the ω_s by ω_p . In a latter stage in the design process, the circuit is then *denormalized*, so the passband and stopband frequencies are those specified by the application.

The general form of the elliptic filter magnitude squared transfer function is given by Eq. (1). For the low-pass elliptic filter function, $P(j\omega)$ is replaced with $R_n(j\omega)$. $R_n(j\omega)$ has two different forms, one for an even-order function and one for an odd-order function. $R_n(j\omega)$ will be described for a normalized lowpass filter. For the even-order case

$$R_n(\omega) = M \prod_{i=1}^{n/2} \frac{\omega^2 - (\omega_s^{norm}/\omega_i)^2}{\omega^2 - \omega_i^2} \tag{2}$$

and for the odd-order case

$$R_n(\omega) = N\omega \prod_{i=1}^{(n-1)/2} \frac{\omega^2 - (\omega_s^{norm}/\omega_i)^2}{\omega^2 - \omega_i^2} \tag{3}$$

where M and N are normalization constants and are chosen so that $R_n(1) = 1$. The ω_i are calculated for the even- or

Table 1. Filter Comparisons

Filter Type	Transition Region	Linear Phase Properties
Butterworth	Poor	Good
Chebyshev	Good	Poor
Elliptic	Best	Very poor

odd-order case. For the former case, we have

$$\omega_i = \frac{\omega_s^{norm}}{sn \left[\frac{(2i-1)K \left(\frac{1}{\omega_s^{norm}} \right)}{n} \right]} \tag{4}$$

and for the latter case

$$\omega_i = \frac{\omega_s^{norm}}{sn \left[\frac{2iK \left(\frac{1}{\omega_s^{norm}} \right)}{n} \right]} \tag{5}$$

where sn is the Jacobian elliptic sine function and $K(k)$ is the complete elliptic integral of the first kind, and is defined as

$$K(k) = \int_0^{\pi/2} (1 - k^2 \sin^2 x)^{-1/2} dx \tag{6}$$

The order of the filter function may be determined by rounding up n to the nearest integer in the expression

$$n = \frac{K \left(\frac{1}{\omega_s^{norm}} \right) K' \left(\frac{1}{L} \right)}{K' \left(\frac{1}{\omega_s^{norm}} \right) K \left(\frac{1}{L} \right)} \tag{7}$$

where L is defined as

$$L = \sqrt{\frac{10^{0.1PBR} - 1}{10^{0.1A} - 1}} \tag{8}$$

and PBR and A are in decibels. Finally

$$K'(k) = K\sqrt{1 - k^2} \tag{9}$$

When $R_n(\omega)$ is found, the substitution $s = \omega/j$ is made, and $R_n(\omega/j)$ may be inserted into Eq. (1). The poles of $H(s)H(s^*) = |H(j\omega)|^2$ are then found. This is a standard synthesis technique [4]. The left half-plane poles and half of the zeros are selected and combined to give the final form of the elliptic filter transfer function. For n even, we obtain

$$H(s) = H \frac{\prod_{i=1}^{n/2} (s^2 + \omega_i^2)}{a_0 + a_1s + \dots + a_{n-1}s^{n-1} + a_ns^n} \tag{10}$$

For the case of n odd, we obtain

$$H(s) = H \frac{\prod_{i=1}^{(n-1)/2} (s^2 + \omega_i^2)}{a_0 + a_1s + \dots + a_{n-1}s^{n-1} + a_ns^n} \tag{11}$$

Note that the even-order transfer function given by Eq. (10) has n poles and zeros and thus no zeros at infinity while the odd-order transfer function of Eq. (11) has n poles and $n - 1$ zeros and thus has a single zero at infinity. It may be convenient to express the denominator in the form of coefficients or in terms of products of poles and zeros, depending on the type and method of realization.

Because of the complexity of the calculations required to find the transfer function, the usual method of finding $H(s)$ is usually either with a computer program, or using one of the numerous tables that have been generated and published [2,5]. Today's simulators allow the filter designer to readily vary zeros to modify the elliptic filter function to take on more specialized tasks.

4. FREQUENCY AND IMPEDANCE SCALING

Frequently, a normalized design is the first step in filter realization. A frequency-normalized filter is designed for a passband frequency of 1 rad/s. A typical normalized realization has component values on the order of ohms, farads, and henries. The design is then frequency-scaled so that the normalized response is *shifted* into place; that is, the passband and stopband frequencies are transformed from normalized values to the design values. The procedure is performed by finding the scaling constant ω_p and replacing s with s/ω_p in the circuit. This results in new values for the capacitances and inductances, while the values for resistances remain unchanged. In certain circumstances it may be desirable to frequency-scale the normalized transfer function first and then do the circuit synthesis.

Frequency scaling usually results in values for capacitors and inductors that are close to practical, but still not practical. Moreover, the impedances of the resistors remain unchanged. The next step in denormalizing a normalized realization is to impedance-scale. Impedance scaling amounts to multiplying each impedance by a specified constant. The constant is picked so that after scaling, the components have reasonable values. If all impedances

are scaled by the same factor, the voltage transfer function of the circuit remains the same. With good selection of the constant, practical values may be achieved.

5. ELLIPTIC FILTERS

5.1. Highpass Filters

In the preceding sections we discussed the properties and applications of lowpass elliptic filters; there is little difference when discussing those of the highpass elliptic filter.

The first step in highpass filter design is to normalize the highpass parameters to the parameters that describe the normalized lowpass filter. The parameters that describe the highpass are identical to those of the lowpass filter. One difference is that $\omega_s < \omega_p$. In general, a lowpass filter transfer function may be transformed into a highpass transfer function by a s -to- $1/s$ transform. This simply means that wherever s appears in the transfer function, $1/s$ is substituted.

Once the normalized lowpass elliptic transfer function has been determined and a normalized circuit has been synthesized, a lowpass-to-highpass transform is applied. This means that everywhere in the circuit, s is replaced with $1/s$. This results in capacitors becoming inductors, and inductors becoming capacitors. If, in an active RC circuit, for example, inductors are not desired, the circuit may be magnitude-scaled by $1/s$. This results in the inductors becoming resistors and the resistors becoming capacitors.

Alternatively, if a normalized lowpass elliptic function has been determined, it is possible to apply the s -to- $1/s$ transform on the transfer function, resulting in a normalized highpass elliptic transfer function. It is now possible to synthesis a circuit from directly from this transfer function.

5.2. Bandpass Filters

Bandpass filters may be classified as wideband or narrowband. A wideband bandpass filter allows a wide range of

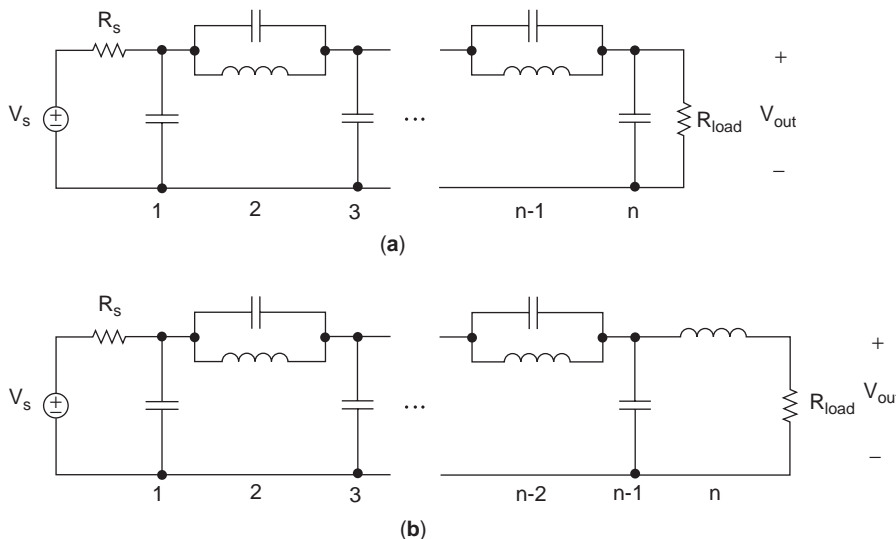


Figure 7. Typical n th-order lowpass passive elliptic filters are realized with inductors and capacitors, and include the source and load resistances in the overall design. The circuit in (a) is for the odd-order case and has n capacitors and $(n - 1)/2$ inductors. The circuit in (b) is for the even-order case and has $(n - 1)$ capacitors and $n/2$ inductors. Both have a total of n stages, and n is the order of the filter transfer function.

frequencies to pass with equal magnitude scaling, ideally. A narrowband filter seeks to allow only one frequency or a very small band of frequencies to pass. One definition of narrowband versus wideband filters is given in Ref. 1. This particular definition states that if the ratio of the upper cutoff frequency to the lower cutoff frequency is greater than 1 octave, the filter is considered a wideband filter.

Synthesis of wideband bandpass filters may be performed by a cascade of a highpass filter and a lowpass filter where the cutoff frequency of the lowpass filter is greater than that of the highpass filter. The lower bound of the definition of wideband results in a separation of the highpass and lowpass filters such that there is minimal interaction between the filters. If the ratio of the lowpass cutoff frequency to the highpass cutoff frequency is smaller than 1 octave, the cutoff frequencies are too close together and the filters interact and must be treated as a single filter.

Narrowband filters require alternative synthesis techniques, such as a transformation. Like the highpass filter functions, bandpass filter functions may be synthesized from lowpass filter functions. This is done by performing the transformation

$$s \rightarrow \frac{\omega_0}{\text{BW}} \left(\frac{s}{\omega_0} + \frac{\omega_0}{s} \right) \quad (12)$$

on a normalized lowpass filter function, where ω_0 is the center frequency and BW is the bandwidth of the filter. Equation (12) should be interpreted as s is replaced by the expression on the right. The effect of performing this operation on the lowpass circuit is that inductors are replaced by a series combination of an inductor and a capacitor and capacitors are replaced by a parallel combination of a capacitor and an inductor. This transform may also be used in the design of wideband bandpass filters.

5.3. Band-Reject Filters

Like bandpass filters, band-reject filters may also be classified as wideband or narrowband. A wideband band-reject filter seeks to block a wide range of frequencies while allowing frequencies outside that band to pass with ideally equal magnitude scaling. A narrowband band-reject filter seeks to block only one frequency or a very small band of frequencies. In much the same way that it defines narrowband versus wideband bandpass filters, Ref. 1 defines narrowband versus wideband band-reject filters. The definition is identical to that for the bandpass filter.

Synthesis of wideband band-reject filters may be performed by a cascade of a highpass filter and a lowpass filter where the cutoff frequency of the highpass filter is greater than that of the lowpass filter. The lower bound of the definition of wideband results in a separation of the highpass and lowpass filters such that there is minimal interaction between the filters. If the ratio of the cutoff frequency of the highpass filter to that of the lowpass filter is less than 1 octave, the cutoff frequencies are too close together and the filters interact and must be treated as a single filter.

Narrowband filters require alternative synthesis techniques, such as a transformation. Band-reject filters may also be synthesized from normalized lowpass filter functions by performing a transform of

$$s \rightarrow \frac{\frac{\text{BW}}{\omega_0}}{\left(\frac{s}{\omega_0} + \frac{\omega_0}{s} \right)} \quad (13)$$

on a normalized low-pass filter, where ω_0 is the center frequency and BW is the bandwidth of the filter. The affect of performing this operation on the lowpass circuit is that inductors are replaced by a parallel combination of an inductor and capacitor and capacitors are replaced by a series combination of a capacitor and an inductor. This transform may also be used in the design of wideband bandpass filters.

5.4. Realizations of Elliptic Filters

There are an infinite number of possible synthesis algorithms that may be used. In this section we describe one.

The first step in elliptic filter design is to find a transfer function that will meet a set of specifications that have been determined from the application. The design usually begins with specifying the passband frequency ω_p , PBR, ω_s , and A . If filter tables are to be used, the frequencies of the filter specifications must first be normalized. This is achieved by dividing ω_s and ω_p by ω_p . Other normalizations are possible. This results in a normalized passband frequency of 1 rad/s, and a normalized stopband frequency of ω_s/ω_p rad/s. If a highpass filter is desired, the specifications must be transformed further, by inverting ω_p to $1/\omega_p$. Once the desired transfer function is determined, a method of realization is selected. Presently, most RF and microwave realizations of elliptic filters are analog circuits. Moreover, the greater majority of the analog realizations are passive, although active realizations are achievable at the lower end of the RF frequency spectrum.

5.4.1. Passive Realizations. One may ask if the passive realizations may utilize only discrete elements. There is considerable ongoing research in realizing passive filters in integrated circuit (IC) technologies, and there are published research results of such filters, although this is not yet commonplace. A principal problem with passive LC realizations in an IC technology are low quality factors (Q_s) of the inductors presently available in standard IC technologies. The lower the inductor Q , the more losses in the inductor, and the more difficult it becomes to design high-performance filters. At the time of this writing, there is considerable interest in fabricating high- Q on-chip or on-package inductors in integrated circuit (IC) technologies. If progress in these inductor-technologies continues at today's present rate, it is not inconceivable that passive synthesis could become commonplace in integrated filter design.

Passive realizations utilize capacitors, inductors, and resistors. The source and load resistances are considered part of the realization. Systematic procedures exist for the synthesis of passive filters to realize elliptic transfer

functions. Moreover, normalized passive filters are available as part of table lookup approaches [5]. An example of odd and even passive filter topologies is depicted in Fig. 7.

Even-order passive realizations synthesized from Eq. (10) will have negative elements because they do not have at least a zero at infinity. This problem can be solved by shifting the highest-frequency zero to infinity. The resulting elliptic filter function will have a double zero at infinity, and the passive filter realization will now have positive elements but unequal terminating resistances. This even-order elliptic transfer function is known as *case B*, while the original even-order transfer function given by Eq. (10) is called *case A*. Equal terminating resistances can be obtained by shifting the first maximum to the origin. The resulting even-order elliptic transfer function is known as *case C* [2,5]. The new filter functions will be of the forms given by Eq. (14) for case B and Eq. (15) for case C:

$$H_B(s) = H \frac{\prod_{i=2}^{n/2} (s^2 + \omega_{B,i}^2)}{b_0 + b_1s + \cdots + b_{n-1}s^{n-1} + b_n s^n} \quad (14)$$

$$H_C(s) = H \frac{\prod_{i=2}^{n/2} (s^2 + \omega_{C,i}^2)}{c_0 + c_1s + \cdots + c_{n-1}s^{n-1} + c_n s^n} \quad (15)$$

The magnitude response in for the case B and C filter functions are now slightly modified from the original type A.

5.4.2. Active Realizations. Active realizations of elliptic filters for high-frequency applications tend to be limited to a few types. These types include Gm-C, synthetic-inductor-based, and negative-resistance-based. Gm-C filters utilize transconductors and capacitors to realize elliptic filter functions. Synthetic-inductor-based filters utilize transconductors and capacitors to synthesize an impedance that is inductive. These are often classified as Gm-C filters as well. Negative resistance based utilize active elements to synthesize an impedance that looks like a negative resistor. The “negative resistor” used to cancel out the resistance of an inductor, thereby providing the inductor with a higher “effective Q .” All include realizations in both IC and discrete technologies. However, because of limited bandwidth of active components, the upper end of the frequency range tends to be around 200–400 MHz for practical applications, although there have been reports in the literature demonstrating research results at greater frequency, particularly in monolithic microwave integrated circuit (MMIC) technologies. But the majority of elliptic filters are passive in nature, fabricated using discrete techniques. Pushing active filter synthesis, and in particular higher-order filters such as elliptic filters, into the high MHz and even low GHz ranges appears to be a rich research area.

5.5. Microwave Filters

Elliptic filters are common for microwave filters; typical applications occur after the final power amplifier or before the first low-noise amplifier in a system where insertion losses have direct impact on system performance. Typical

applications include transmit–receive duplexers, multi-band combiners, interference rejection, spurious emission control, and channelized power combining.

The circuits depicted in Fig. 7 are often used as the starting point for a passive elliptic filter regardless of the technology being used to realize the circuit. However, the zeros of elliptic filters are frequently modified from the ideal values to provide design freedoms that can sharpen rejection (at the cost of phase linearity), or can better phase response (at the cost of rejection). The result is a *quasielliptic* filter. In conjunction with appropriate technology and physical layout, elliptic microwave filters realize high performance in compact geometries.

At microwave frequencies, lumped inductors and capacitors are physically large when compared to the wavelengths of the application and seldom perform well (especially inductors) because of parasitic effects. Moreover, the lumped elements must be considered as distributed elements. Microwave filters use stages that consist of distributed elements (e.g., microstrip lines or resonant cavities) and transitions between elements (e.g., coupling slots or impedance steps) that appear inductive or capacitive. Performance depends on the electrical size of elements. There are many ways to realize microwave filters. Choosing the technology to use depends on a variety of factors, some obvious, some subtle, but all with impact on realizing the needed performance.

5.5.1. Tradeoffs. A primary consideration is the placement of the filter used in the system. Filters integrated with MMICs require planar layouts such as with microstrip or coplanar waveguide (CPW). Filters integrated on RF circuit boards may be stripline, surface acoustic wave (SAW), ceramic, or helical, depending on the frequency and space available. If the filter is a separate unit, handles high power, or interfaces with an antenna system, waveguides and coupled cavities are the best choices. Bandpass and band-reject filters are easily realized using resonant elements; lowpass and highpass filters use propagating elements.

Frequency also plays a role in technology selection. Waveguides and waveguide cavities are natural choices above 5 GHz. Waveguides become too large for the wireless bands from 400 MHz to 2.5 GHz; here, combine cavity filters and coaxial line filters are useful, as are planar filters. Helical and SAW filters are useful in the lower-MHz RF bands.

Another consideration is the natural tradeoff that occurs between insertion loss versus quality factor of the components. Each stage in a multistage microwave filter loses power to the finite conductivities of metal and losses in dielectrics (even lumped inductors and capacitors possess parasitic resistances that absorb power). In general, filters composed of a larger number of stages with identical Q values will have higher insertion loss; using higher- Q stages can reduce insertion loss. The Q factor of a filter stage can be increased by increasing unit volume, silver-plating the RF path, or loading with low-loss ceramics. Superconducting filters have extremely high Q values. Dielectric material allows filter size to be physically reduced and Q factors to generally improve; both effects can reduce

insertion loss. Using multimode stages, where one physical element supports multiple electrical stages, also can reduce insertion loss.

There are less obvious considerations to choosing a technology as well. Power handling may be critical, which tends toward using waveguides and cavities and places limits on how small gaps may be. Microwave elements have dispersive propagation effects and support multiple modes; these in turn lead to bandwidth limits and higher-frequency spurious responses in which the stopband begins to resemble the passband. Coupling and tuning methods also have bandwidth limits. Manufacturability is also important; it is possible for unwanted coupling mechanisms to occur and change the filter response, or for production tolerances to change passbands. Last but not least, cost plays a role, especially for commercial applications.

5.5.2. Elliptic Filter Design Concerns Unique to Microwave Frequencies. Microwave filters start with elliptic prototype filters, designed as mentioned previously. The challenge is mapping lumped inductors and capacitors into the correct distributed equivalents for the microwave technology chosen. Fundamental to all microwave filters realization is inclusion of transmission-line effects. A very useful property that follows from this is the ability to invert impedances to more easily realize certain filter topologies; impedance inverters convert impedances to admittances (for e.g., convert a series inductor into a shunt capacitor). A common way of realizing an inverter is to employ the quarter-wave transformer; for cavity filters, an impedance inverter is realized as a shunt inductance in cascade between equal-length negative line lengths. Admittance inverters convert admittances into impedances; they realize as quarter-wave transformers or as series capacitance in cascade between equal-length negative line lengths. The negative line lengths serve to reduce the lengths of the loads on either side, usually resulting in more compact designs. The most limiting transmission-line effect is that the effective L and C values change as frequency deviates from the design center and the response changes.

Transmission lines can be implemented into prototype filters converting lumped impedances, for example, $Z_1 = j\omega L$, to their transmission-line form of $Z_1 = j\Omega L$ using Richard's transformation, $\Omega = \tan \beta 1$. For a lowpass prototype, the passband frequency ω_c of unity results in an electrical length of 45° (or $\lambda/8$). Inductors become a short-circuited stub with characteristic impedance (Z_0) of L ; capacitors become open-circuited stubs with $Z_0 = 1/C$. However, the stub impedance is not the same as the lumped element for frequencies away from passband, and the filter response differs.

The physical elements used in microwave filters have mode structures with cutoff frequencies determined by their geometries; at frequencies below cutoff, the mode rejects energy. As frequencies increase, more modes "turn on" and again, spurious responses can occur. Cutoff frequencies can be changed by small perturbations to the geometries; this allows filter tuning by elements such as screws. Square and circular geometries support degenerate modes that can be coupled to each other; this easily

supports multimode filters but can add limitations to exploiting the design freedom of elliptic zeros.

Discontinuities in transmission lines and cavities have responses that behave inductive or capacitive, depending on whether primarily magnetic or electric energy is being stored at the discontinuity. Microwave resonators have equivalent circuits that look like lumped LC resonators. Intercavity couplings via slots or probes also appear inductive or capacitive, depending on how the modes couple between cavities. All these discontinuities have effects on the electrical lengths of filter sections and adjustments must be made. Slots in cavity walls seem inductive; exploiting this idea and reducing cavity electrical length on either side of the slot will implement an impedance inverter like that mentioned previously. Marcuvitz [7] provides in-depth discussions on finding equivalent circuits for all types of discontinuities, perturbations, and couplings. Another good reference overall for traditional microwave filter synthesis is Matthaei et al. [8].

Today, numerical simulation tools are employed to determine the actual broadband equivalent circuits and their impact on the basic mode behavior of waveguides and cavities. Their use has improved the ability to design filters, reduced design cycle time, and provided insight into building filters. Using these tools effectively still requires an understanding of the underlying basic principles.

6. TECHNOLOGY OVERVIEW

Stripline-type filters are planar in design. This makes them appropriate for use with MMICs and for use on RF and microwave board layouts. While the microstrip filter is most common, filtering structures using coplanar waveguide (CPW), slotguide, and suspended stripline are used as well. These filters generally are small because of the shorter wavelengths of the planar substrates. They also are low- Q filters (200–300), due to etch thickness and substrate losses. Planar filters have limited power-handling capability as well. For microstrip filters, shunt open stubs are commonly used, since short-circuiting elements in microstrips involves extra fabrication steps. Alternating high-impedance/low-impedance stages and coupled-line segments help realize lowpass or highpass filters; microstrip resonators and coupled-line filters allow for realization of bandpass and band-reject filters. Coupled-line filters are generally edge-coupled for microstrip; coupled lines gain an extra design dimension when considering suspended stripline filters, with both vertical and planar separation contributing to the performance. Planar filters also take up board or die space.

Ceramic filters also find use on RF boards and for small devices from 800 MHz and up; a typical application is for duplexers in mobile phones and wireless LAN cards. Ceramic, high-dielectric materials dramatically reduce the physical size of a filter. They have low Q (200–400) and low power handling primarily because of their small size.

Helical filters are used on RF and IF boards. Helical filters use wound wire coils as bandpass resonators; this allows medium- Q performance in compact packaging in the 75–800 MHz range.

Surface acoustic wave (SAW) filters are typically used more at IF frequencies (50–400 MHz). These filters use piezoelectric materials that support acoustic-type leaky waves; typical wavelengths are 10^{-5} those of light. This means that filter dimensions can also be much smaller; SAW filters also achieve brick-wall-type responses. SAW filters have low- Q (50–100) and low power-handling capabilities; more recent developments are pushing SAW performance up into the 1–2 GHz range.

Waveguide filters have high- Q (typically 10,000) and high power-handling capabilities. They are common above 2 GHz, or in low-frequency, high-power applications. Waveguide types used include circular, rectangular, square, ridged, and corrugated, depending on the application. Walls are placed approximately $\lambda/4$ apart to generate resonant cavities within the waveguide, the resonant modes are endwall-coupled to each other. Waveguide filters are large in size and can be quite heavy. As frequencies increase above 50 GHz, mechanical tolerances become extremely critical in the production process.

Coaxial resonator filters (also called *comblines filters* or *TEM filters*) are common from 400 MHz to 6 GHz. They consist of sidewall-coupled cavities whose resonance is controlled by an inductive resonator and a capacitive airgap. They can be realized as interdigital filters, with $\lambda/4$ resonator lengths and airgaps between top and bottom walls. More commonly, they are realized as combline filters where all resonators are on the same wall. This allows for ease of manufacture. The resonator length can be less than $\lambda/4$; this allows freedom to control when cavity harmonic frequencies occur. These are medium- Q (3000–6000) and medium-power devices. Combline resonators may be dielectrically loaded to increase cavity Q (typically 15,000 or higher). The resonators can also be of dielectric material; this increases Q (typically above 10,000) and adds the ability to generate multiple modes.

The highest- Q resonators exist in superconducting filters. These filters use either thin-film or bulk high- T_c (critical temperature) materials, and operate at 77 K. The thin-film resonators are used in planar circuits; bulk materials show up in cavity resonators. Because of the zero resistance of the superconductor, almost no power is lost per stage (some loss occurs because cavity walls are still metal and substrates are still lossy). Consequently, true brick-wall filters, comprising 30, 40, or more stages, are practical with small insertion loss. Superconducting filters require external cooling support to maintain 77 K temperatures; consequently, as a system they are more complicated than other choices. Superconducting filters have found use in situations with severe interference; here, the performance they provide outweighs the added complexity of the system.

The advent of MEMS technology is having an impact on microwave filters as well. MEMS techniques allow realization of lumped inductors with reasonable Q values at microwave frequencies. MEMS switches also have potential to work with tunable filters and switched filterbanks. MEMS processes are generally compatible with IC production and stand to improve stripline filtering. For standalone MEMS parts, packaging is a concern—it is usually packaging that provides most of the parasitics that ruin the performance of lumped elements at microwave frequencies.

7. SUMMARY

Elliptic filters are a class of filters used to shape the magnitude of an electric signal. They may be used in applications for any of the standard magnitude processing filters. In comparisons to other available filters, they provide the sharpest transition from the passband to the stopband for a given order. The magnitude response is equiripple in the passband and the stopband. The drawback of elliptic filters is very poor phase characteristics in comparison to other filter types. Furthermore, evaluation of elliptic filter parameters is considerably more difficult than other filter approximation functions, due to the use of elliptic sine functions and elliptic integrals.

BIBLIOGRAPHY

1. A. B. Williams, *Electronic Filter Design Handbook*, McGraw-Hill, New York, 1981.
2. L. P. Huelsman and P. E. Allen, *Introduction to the Theory and Design of Active Filters*, McGraw-Hill, New York, 1980.
3. R. W. Daniels, *Approximation Methods for Electronic Filter Design*, McGraw-Hill, New York, 1974.
4. A. Budak, *Passive and Active Network Analysis and Synthesis* (reissue), Waveland Press, Prospect Heights, IL, 1991.
5. A. I. Zverev, *Handbook of Filter Synthesis*, Wiley, New York, 1967.
6. E. P. Cunningham, *Digital Filtering: An Introduction*, Houghton-Mifflin, Boston, 1992.
7. N. Marcuvitz, *Waveguide Handbook*, IEE Electromagnetic Wave Series 21, IEE Publishing, 1986.
8. G. Matthaei, L. Young, and E. M. Jones, *Microwave Filters, Impedance Matching Circuits and Coupling Structures*, Artech House, Norwood, MA, 1980.

FURTHER READING

- C. S. Lindquist, *Active Network Design with Signal Filtering Applications*, Long Beach, CA: Steward & Sons, 1977.
- W.-K. Chen, ed., *The Circuits and Filters Handbook*, CRC Press, Boca Raton, FL, and IEEE Press, New York, 1995.

ENHANCEMENTS OF THE FINITE DIFFERENCE TIME DOMAIN METHOD

RAJ MITTRA
WENHUA YU
YINCHAO CHEN
Pennsylvania State University
University Park, Pennsylvania

1. INTRODUCTION

The fundamentals of the conventional finite-difference time-domain (FDTD) algorithm on a Cartesian grid have been adequately covered by the article FINITE-DIFFERENCE TIME-DOMAIN ANALYSIS, and it has been demonstrated that the algorithm can be used to simulate a wide variety of electromagnetic problems because of its flexibility and

versatility. In this article we discuss some variations and extensions of the method that have been designated to enhance the performance of the algorithm. The first of these deals with the problems of handling conductors or dielectrics with curved surfaces and edges by using a “conformal” FDTD scheme, which mitigates the errors introduced by the staircasing employed in the conventional FDTD. The second, referred to in the literature as the “multiresolution time-domain (MRTD) method,” has been introduced for the purpose of reducing the requirements of both the CPU time and memory.

The conformal FDTD technique has had a long history with many contributors [1–6]. It is beyond the scope of this article to discuss the various proposed approaches in detail. Instead we briefly describe one conformal FDTD technique [7–12], which not only circumvents the need for complex mesh generation but also does not suffer from late-time instability problems that plague many of the proposed schemes.

The method we detail below handles both the PEC and dielectric objects of arbitrary shape, and does not require a significant modification of the Cartesian-type FDTD; hence, it preserves the computational efficiency of the conventional FDTD technique—which is desirable.

2. CONFORMAL FINITE-DIFFERENCE TIME-DOMAIN TECHNIQUE

In order to describe the conformal approach, we first present below two typical difference equations derived from the time-dependent Maxwell’s curl equations (for details, see FINITE-DIFFERENCE TIME-DOMAIN ANALYSIS). As we have seen in the above chapter, the electric fields are located along the edges of cells, while the magnetic fields are positioned at the centers of these cells. Maxwell’s difference equations in this scheme are written as

$$H_x^{n+(1/2)}(i,j,k) = H_x^{n-(1/2)}(i,j,k) + \frac{\Delta t}{\mu_x(i,j,k)} \left(\frac{E_y^n(i,j,k+1) - E_y^n(i,j,k)}{\Delta z(k)} - \frac{E_z^n(i,j+1,k) - E_z^n(i,j,k)}{\Delta y(j)} \right) \quad (1)$$

$$E_y^{n+1}(i,j,k) = \frac{\varepsilon_y(i,j,k) - 0.5 \cdot \Delta t \cdot \sigma_y(i,j,k)}{\varepsilon_y(i,j,k) + 0.5 \cdot \Delta t \cdot \sigma_y(i,j,k)} E_y^n(i,j,k) + \frac{\Delta t}{\varepsilon_y(i,j,k) + 0.5 \cdot \Delta t \cdot \sigma_y(i,j,k)} \times \left(\frac{H_x^{n+(1/2)}(i,j,k+1) - H_x^{n+(1/2)}(i,j,k)}{\Delta z(k)} - \frac{H_z^{n+(1/2)}(i+1,j,k) - H_z^{n+(1/2)}(i,j,k)}{\Delta x(i)} \right) \quad (2)$$

where the superscripts represent the time index and the arguments correspond to spatial sampling locations. The equations for the other field components can also be written similarly. As pointed out by Taflov in FINITE-DIFFERENCE TIME-DOMAIN ANALYSIS, to avoid numerical instabilities, the time increment Δt must satisfy the Courant condition

$$\Delta t \leq \frac{1}{c \sqrt{\left(\frac{1}{\Delta x}\right)^2 + \left(\frac{1}{\Delta y}\right)^2 + \left(\frac{1}{\Delta z}\right)^2}} \quad (3)$$

where $\Delta x, \Delta y, \Delta z$ are the lattice dimensions of the cells.

2.1. Conformal FDTD Technique for a Perfect Electric Conductor (PEC)

If the equations above are used for conductors with curved surfaces and/or edges (see Figs. 1 and 2), the staircasing version of the conventional FDTD may introduce significant errors, unless a very fine discretization is employed at a considerable cost of CPU time and memory. It has been shown [7–9] that this difficulty can be overcome by employing a modification of the conventional FDTD update equations, called the *conformal FDTD* algorithm. A key step in this approach is to assume that both the electric and magnetic fields inside the distorted cell are located at the same positions as those in the conventional FDTD scheme, and that Faraday’s law is applied over the entire FDTD cell, rather than only in the distorted part—thus implying that the contour path follows the edges of the FDTD in its entirety. Since parts of the contour path are located inside the PEC region, we discard their contributions and write the $\oint \vec{E} \cdot d\vec{l}$ contour integral as

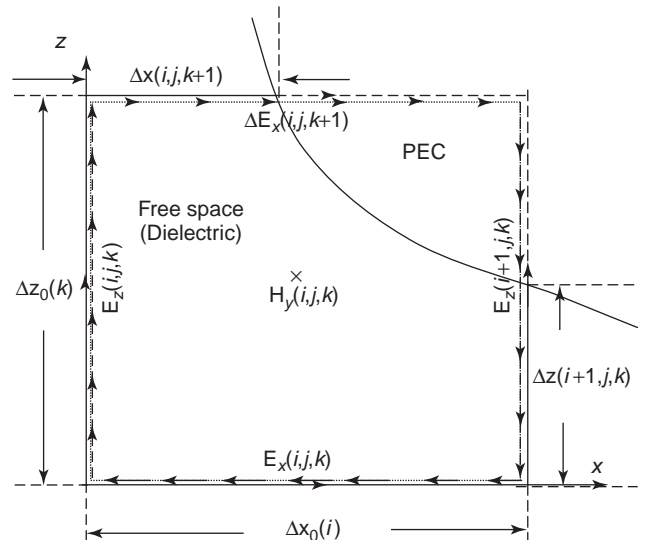


Figure 1. Intersection between the FDTD mesh and a PEC surface in the x - z plane.

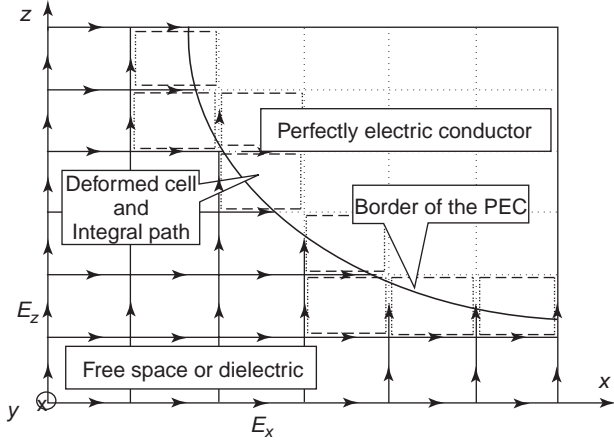


Figure 2. Contour path of the conformal FDTD in a deformed cell.

follows:

$$\oint \vec{E} \cdot d\vec{l} = \begin{bmatrix} \int_{\Delta x_0(i)} E_x(i,j,k) \cdot dx + \int_{\Delta z_0(k)} E_z(i,j,k) \cdot dz \\ + \int_{\Delta x(i,j,k+1)} E_x(i,j,k+1) \cdot dx \\ + \int_{\Delta z(i+1,j,k)} E_z(i+1,j,k) \cdot dz \end{bmatrix} \quad (4)$$

The definitions of the variables used in this equation are shown in Fig. 1. We note that the E -field representation remains unchanged from that in the conventional FDTD scheme. However, the magnetic fields inside the partially filled cells are updated slightly differently to account for the deformation of the cell, as shown below:

$$H_y^{n+(1/2)}(i,j,k) = \begin{bmatrix} \frac{\Delta z(i,j,k)E_z^n(i,j,k) - \Delta z(i-1,j,k)E_z^n(i-1,j,k)}{\Delta x_0(i) \times \Delta z_0(k)} \\ + \frac{\Delta x(i,j,k-1)E_x^n(i,j,k-1) - \Delta x(i,j,k)E_x^n(i,j,k)}{\Delta x_0(i) \times \Delta z_0(k)} \end{bmatrix} \quad (5)$$

Equations (4) and (5) enable us to handle PEC objects whose geometries do not conform to the Cartesian coordinates.

2.2. Conformal FDTD Technique for Dielectric Objects

For the partially filled cells, the conformal technique for dielectric objects utilizes a modified version of the concept

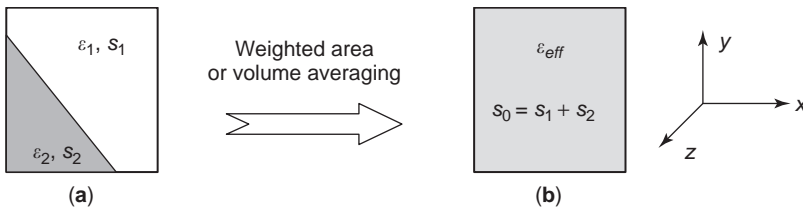


Figure 3. Conformal dielectric techniques: (a) original problem; (b) after averaging.

of effective dielectric constant (see Figs. 3 and 4). Rather than using a weighted volume average to define the effective dielectric constant, the conformal dielectric algorithm [12] utilizes a weighted-line average concept instead. The calculation of the weighted-line average dielectric constant is carried out on the bold lines in Fig. 5a. The effective dielectric constants $\epsilon_x^{\text{eff}}(i,j,k)$ and $\epsilon_y^{\text{eff}}(i,j,k)$ are defined below:

$$\epsilon_x^{\text{eff}}(i,j,k) = \frac{\Delta x_2(i,j,k)}{\Delta x} \epsilon_2 + \frac{\Delta x - \Delta x_2(i,j,k)}{\Delta x} \epsilon_1 \quad (6)$$

$$\epsilon_y^{\text{eff}}(i,j,k) = \frac{\Delta y_2(i,j,k)}{\Delta y} \epsilon_2 + \frac{\Delta y - \Delta y_2(i,j,k)}{\Delta y} \epsilon_1 \quad (7)$$

We note from the Figs. 5b and 5c that $E_x(i,j+1,k)$ and $E_y(i+1,j,k)$ do not penetrate the dielectric; hence, the dielectric constant ϵ_1 is used in place of the effective dielectric constant in the conformal dielectric FDTD update equations for the electric and magnetic fields. Typical update equations take the form

$$E_x^{n+1}(i,j,k) = E_x^n(i,j,k) + \frac{\Delta t}{\epsilon_x^{\text{eff}}(i,j,k)\Delta y} \times [H_z^{n+(1/2)}(i,j+1,k) - H_z^{n+(1/2)}(i,j,k)] \quad (8)$$

$$- \frac{\Delta t}{\epsilon_x^{\text{eff}}(i,j,k)\Delta z} \times [H_y^{n+(1/2)}(i,j,k+1) - H_y^{n+(1/2)}(i,j,k)]$$

$$E_x^{n+1}(i,j+1,k) = E_x^n(i,j+1,k) + \frac{\Delta t}{\epsilon_1(i,j+1,k)\Delta y} \times [H_z^{n+(1/2)}(i,j+2,k) - H_z^{n+(1/2)}(i,j+1,k)] - \frac{\Delta t}{\epsilon_1(i,j+1,k)\Delta z} \times [H_y^{n+(1/2)}(i,j+1,k+1) - H_y^{n+(1/2)}(i,j+1,k)] \quad (9)$$

where Δy and Δz are the mesh dimensions along the y and z directions, respectively. Note that the effective dielectric constant is used in (8) because the edge on which $E_x(i,j,k)$ lies does penetrate the dielectric. Furthermore, the update equation in (9) has a form that is identical to that used in the conventional FDTD formula, because $E_x(i,j+1,k)$ is located entirely within a single dielectric region, whose

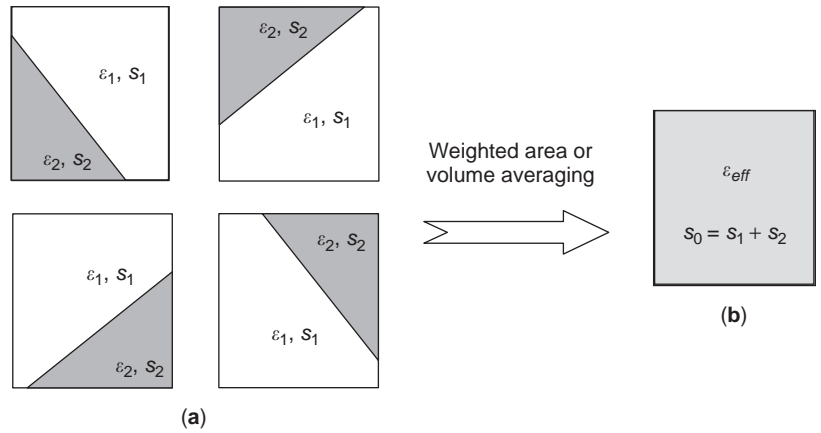


Figure 4. Illustrative examples showing that different material distributions lead to the same effective dielectric constant: (a) original problem; (b) after averaging.

permittivity is ϵ_1 . Similar update equations can also be written for other electric field components.

3. ILLUSTRATIVE EXAMPLES

We now present some examples to illustrate the application of the conformal FDTD method. We use a Gaussian pulse modulated by a sine function for the excitation, and a six-layer unsplit PML [13] to truncate the FDTD domain on the open boundary. On the basis of the Courant condition, the timestep is chosen to be:

$$\Delta t = \frac{0.995}{c \sqrt{\left(\frac{1}{\Delta x}\right)^2 + \left(\frac{1}{\Delta y}\right)^2 + \left(\frac{1}{\Delta z}\right)^2}} \quad (10)$$

which is very close to that dictated by the Courant condition for the undistorted cell.

3.1. Cylindrical Cavity

For the first example, we consider the problem of computing the resonant frequencies of the dominant TE and TM modes of a cylindrical cavity of circular cross section. The results for the resonant frequencies are shown in Table 1, together with the dimensions of the cavities, with R and H representing the radius and height of the cylindrical cavities, respectively. The spatial discretization is chosen to be 0.005 m for each of the four cases studied. We observe good agreement between the conformal FDTD results and those obtained analytically. Furthermore, the CFDTD algorithm, described herein, has been found to be totally stable.

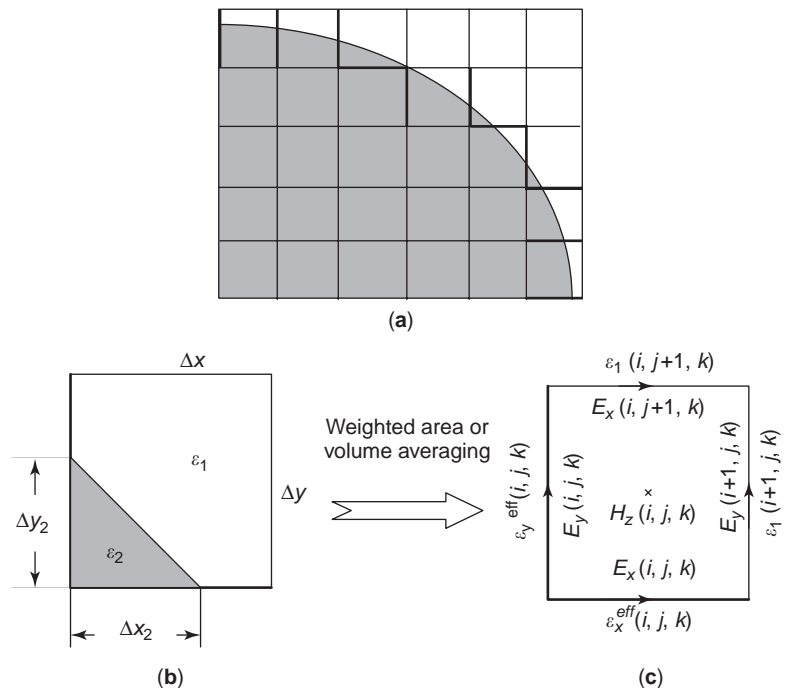


Figure 5. Linear weighted dielectric constant averaging procedure used in the present conformal dielectric FDTD scheme: (a) Intersection between FDTD mesh and curved dielectric surface; (b) original problem; (c) equivalent problem.

Table 1. Comparison of Resonant Frequencies of a Circularly Cylindrical Cavity Derived Using Analytical and CFDTD Techniques

Modes	Methods	Geometry I	Geometry II	Geometry III	Geometry IV
		$R \times H = (0.1 \times 0.1 \text{ m})$	$R \times H = (0.1 \times 0.08 \text{ m})$	$R \times H = (0.1 \times 0.06 \text{ m})$	$R \times H = (0.06 \times 0.06 \text{ m})$
TE ₁₁₁	CFDTD	1.734	2.062	2.639	3.133
	Analytical	1.738	2.071	2.650	3.148
	Difference	0.23	0.43	0.42	0.48
TM ₀₁₁	CFDTD	1.88	2.194	2.742	2.872
	Analytical	1.889	2.199	2.751	2.897
	Difference (%)	0.48	0.23	0.33	0.86

3.2. Radial Stub

For the next example of the CFDTD simulation, we consider a radial stub whose geometry is shown in Fig. 6. The dimensions of the computational domain are $8.12 \times 8.12 \times 0.889 \text{ mm}^3$, and the domain is discretized into $40 \times 40 \times 7$ cells. In order for the edges of the microstrip lines to coincide with those of the FDTD grid, we choose a nonuniform mesh whose dimensions are $\Delta x(i) = 0.20175 \text{ mm}$, $i = 1, 2, 3, 4$; $\Delta x(i) = 0.203357 \text{ mm}$, $i = 5, \dots, 18$; $\Delta x(i) = 0.203 \text{ mm}$, $i = 19, 20, 21$; $\Delta x(i) = 0.20333 \text{ mm}$, $i = 26, \dots, 36$; and $\Delta x(i) = 0.20175 \text{ mm}$, $i = 37, 38, 39, 40$. A uniform mesh is used in the z direction with a cell dimension of $\Delta z(k) = 0.127 \text{ mm}$. A voltage source between the ground plane and the left microstrip line is placed at a distance of 5 cells away from the domain boundary ($y = 0$), while the observation point is located at a distance of 10 cells away from the boundary ($y = y_{\max}$) in the y direction. The 3 dB cutoff frequency of the excitation source is 25 GHz, and the timestep is $\Delta t = 0.3146 \text{ ps}$. The scattering parameter S_{21} versus frequency is shown in Fig. 7. Good agreement with the experimental data reported in Ref. 14 is observed.

3.3. Microstrip Patch Antenna of Circular Shape

Next, we compute the scattering parameter of a microstrip patch antenna of circular shape, as shown in Fig. 8. The dimensions of the computational domain are $0.11 \times 0.088 \times 0.00795 \text{ m}^3$ and are subdivided into $55 \times 44 \times 10$ cells. The cell dimensions are chosen to be 0.002, 0.002, and 0.000795 m, in the x , y , and z directions, respectively. The simulation was run with a timestep of $\Delta t = 2.29847 \text{ ps}$, and no stability problems were encountered. The reflection plot of the circular patch antenna as a function of frequency is shown in Fig. 9. The results reported in Ref. 2 via the application of the symmetric and asymmetric

planar generalized Yee (PGY) approaches, with a timestep of 0.725 ps [2], and those obtained using the MoM (method of moments) [15] are also plotted in the same figure for comparison. The CFDTD results are seen to compare quite favorably with those obtained via the MoM.

3.4. Dielectric-Loaded Cavity

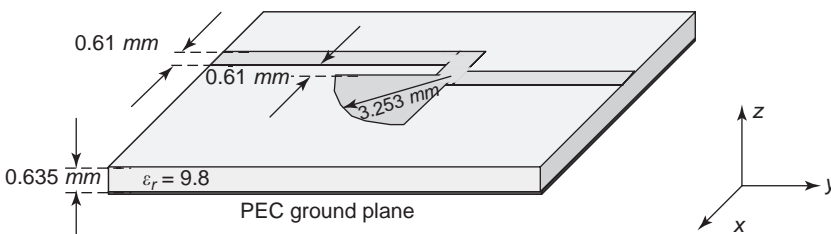
Finally, we turn to an example pertaining to a curved dielectric structure, namely, rectangular cavity loaded with a cylindrical dielectric rod (see Fig. 10) [16].

The relative dielectric constant of the rod is 38, while it is 1 for the pedestal below. The computational domain is discretized in to $48 \times 44 \times 47$ cells, and the Δx and Δy are chosen to be 0.519112 mm inside, and 0.549275 and 0.563033 mm outside the dielectric rod. Also Δz is 0.537307, 0.5537, and 0.53658 mm below, inside, and above the dielectric resonator, respectively. For the other structures listed in Table 2, the discretizations are chosen in a similar manner.

The simulation results, shown in Table 1, demonstrate that the results agree well with both the mode-matching values and the measured data, thus validating the accuracy of the CFDTD algorithm, even for these narrowband structures.

4. SUMMARY OF CFDTD

In this section, we have described a conformal FDTD approach, designated for both PEC and dielectric objects without the use of staircasing and the need for complex mesh generation techniques. We have shown, by comparison with analytical and experimental results, that the CFDTD algorithm is both accurate and computationally efficient. For further information, the reader may refer to Refs. 17 and 18.


Figure 6. Microstrip line with a radial stub.

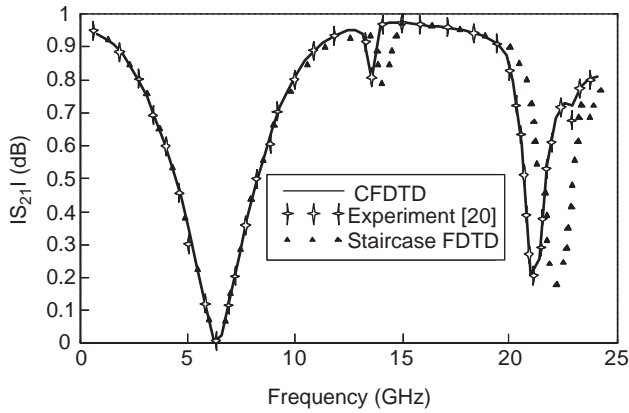


Figure 7. Transmission coefficient of the microstrip line with a radial stub comparison of CFDTD and experimental results.

5. INTRODUCTION TO MRTD

The multiresolution time-domain (MRTD) scheme for solving electromagnetic field problems, introduced by Krumpholz and Katehi [19,20], is based on expansions of unknown fields in terms of scaling or wavelet functions. It has been shown that the use of the MRTD improves the computational capacity and efficiency over those of the conventional finite-difference time-domain (FDTD) method [19–23].

The MRTD approach, described in this section, retains the philosophy of the leapfrog algorithm employed in the conventional FDTD, and places the MRTD scheme in the context of the FDTD, although it differs considerably in detail, as we will see below.

To illustrate the application of MRTD, we analyze a two-layer, dielectric-loaded cavity, and develop a systematic formulation for constructing the constitutive relations; then update equations in the MRTD transform domain by utilizing only the field quantities defined in the real structures. We introduce the concepts of the multiple-image technique (MIT) and present a criterion for determining the number of images needed along each side of the structure that is based on the localization properties of the scaling basis functions.

In this section, we also present a two-dimensional (2D) version of the MRTD, in conjunction with the unsplit anisotropic perfectly matched layer (APML), for the analysis of printed transmission lines. We apply the MIT

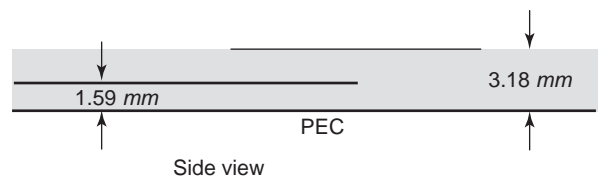
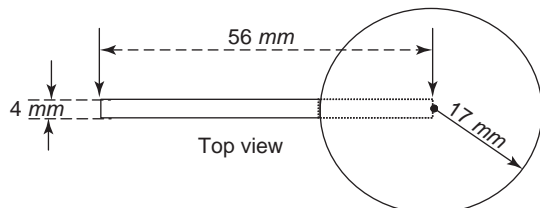


Figure 8. Microstrip-coupled circular patch antenna. The microstrip line is located on a 1.59-mm substrate ($\epsilon_r = 2.62$) backed by a ground plane, and the patch antenna is printed on the same dielectric at a height of 1.59 mm, above the microstrip line.

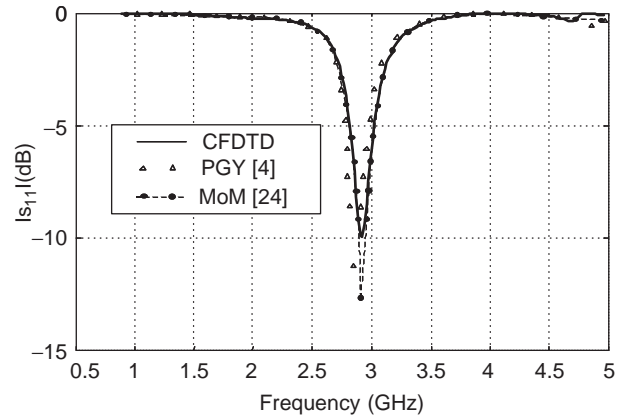


Figure 9. Comparison of reflection loss of the microstrip-coupled circular patch antenna computed by using the CFDTD, the MoM, and the PGY techniques.

APML concept for the analysis of microwave structures with inhomogeneous materials, including different dielectrics and conductors with infinite conductivity. Such imaging is needed to handle the boundaries in the MRTD formulation.

6. MIT MRTD METHOD FOR PEC-SHIELDED STRUCTURES

6.1. MRTD Update Equations

By using the generalized differential matrix operators (GDMOs) [24], the two curl relations of the Maxwell’s equations can be expressed as

$$\begin{bmatrix} 0 & -\partial_z & \partial_y \\ \partial_z & 0 & -\partial_x \\ -\partial_y & \partial_x & 0 \end{bmatrix} \begin{bmatrix} H_x \\ H_y \\ H_z \end{bmatrix} = \frac{\partial}{\partial t} \begin{bmatrix} D_x \\ D_y \\ D_z \end{bmatrix} \quad (11)$$

$$\begin{bmatrix} 0 & -\partial_z & \partial_y \\ \partial_z & 0 & -\partial_x \\ -\partial_y & \partial_x & 0 \end{bmatrix} \begin{bmatrix} E_x \\ E_y \\ E_z \end{bmatrix} = -\mu_0 \frac{\partial}{\partial t} \begin{bmatrix} H_x \\ H_y \\ H_z \end{bmatrix} \quad (12)$$

where, for generality, we assume that the relative permittivity is a biaxial tensor. Then the associated constitutive

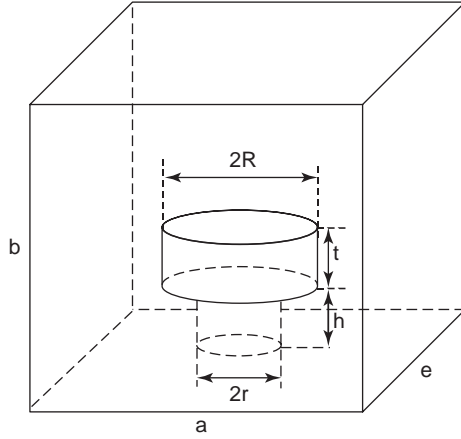


Figure 10. Dielectric resonator comprising a cylindrical rod in a rectangular cavity. The pedestal below is assumed to be free space in this work.

relation in the space domain becomes

$$\begin{bmatrix} D_x \\ D_y \\ D_z \end{bmatrix} = \epsilon_0 \begin{bmatrix} \epsilon_{xx}(\vec{r}) & 0 & 0 \\ 0 & \epsilon_{yy}(\vec{r}) & 0 \\ 0 & 0 & \epsilon_{zz}(\vec{r}) \end{bmatrix} \begin{bmatrix} E_x \\ E_y \\ E_z \end{bmatrix} \quad (13)$$

In the MRTD domain, the local relationship between the \mathbf{D} and \mathbf{E} fields shown above is no longer valid; hence, we must work simultaneously with both the \mathbf{D} and \mathbf{E} fields.

As a first step in the MRTD formulation, we begin by representing all the field quantities in terms of the scaling function in space and pulse function in time as follows

$$\begin{aligned} D_x(\vec{r}, t) &= \sum_{i,j,k,n=-\infty}^{\infty} \phi_x D_{i+(1/2),j,k}^n \phi_{i+(1/2)}(x) \phi_j(y) \phi_k(z) h_n(t) \end{aligned} \quad (14)$$

$$\begin{aligned} H_x(\vec{r}, t) &= \sum_{i,j,k,n=-\infty}^{\infty} \phi_x H_{i+(1/2),k+(1/2)}^n \phi_i(x) \phi_{j+(1/2)}(y) \\ &\times \phi_{k+(1/2)}(z) h_{n+(1/2)}(t) \end{aligned} \quad (15)$$

where $\phi(x)$ denotes the cubic spline *Battle-Lemarie* scaling function [25,26] and $h_n(t)$ is a rectangular pulse function. Substitution of these field expansions into the Maxwell equations, followed by the application of the Galerkin method [27], leads us to the following set of update equations

$$\begin{aligned} \phi_x D_{i+(1/2),j,k}^{n+1} &= \phi_x D_{i+(1/2),j,k}^n + \sum_{\nu} a(\nu) \\ &\times \left[\phi_z H_{i+(1/2),j+\nu+(1/2),k}^{n+(1/2)} \frac{\Delta t}{\Delta y} \right. \\ &\left. - \phi_y H_{i+(1/2),j,k+\nu+(1/2)}^{n+(1/2)} \frac{\Delta t}{\Delta z} \right] \end{aligned} \quad (16)$$

$$\begin{aligned} \phi_x H_{i,j+(1/2),k+(1/2)}^{n+(1/2)} &= \phi_x H_{i,j+(1/2),k+(1/2)}^{n-(1/2)} + \frac{1}{\mu_0} \sum_{\nu} a(\nu) \\ &\times \left[\phi_y E_{i,j+(1/2),k+\nu+1}^n \frac{\Delta t}{\Delta z} \right. \\ &\left. - \phi_z E_{i,j+\nu+1,k+(1/2)}^n \frac{\Delta t}{\Delta y} \right] \end{aligned} \quad (17)$$

where the quantities being updated are the expansion coefficients in the field expansions, and their corresponding superscripts and subscripts represent the discretized time and space positions, respectively. The coefficient $a(\nu)$, appearing in (16) and (17), may be derived by utilizing a nonorthogonal relationship [19,22]. Although the summation index ν in (16) and (17) spans from positive to negative infinity, it is usually sufficient to truncate it at 9, by taking advantage of the localized nature of the *Battle-Lemarie* scaling function.

6.2. MIT for Derivation of the Constitutive Relationship

The constitutive relationship in the transform domain of the MRTD is considerably more involved than its counterpart in the spatial domain presented in (13). This is because the MRTD-transformed \mathbf{D} field at a particular point is determined not only by the \mathbf{E} field at the same location but also by the distribution of the \mathbf{E} field in its neighborhood. To solve for the constitutive relation in the MRTD domain, we once again represent the \mathbf{E} fields as expansions in terms of the same basis functions as (14), and substitute the above expansion into (13). Next, an application of the Galerkin's method leads us to the constitutive relationships in the MRTD domain that

Table 2. Comparison of Different Methods for a Dielectric Rod in a Rectangular Cavity^a

Size (in.)	t	Resonant Frequencies (GHz)			
		Present	Kaneda's [11]	Mode Matching [17]	Measured [17]
0.654	0.218	4.388	4.40	4.3880	4.382
0.689	0.230	4.163	4.17	4.1605	4.153
0.757	0.253	3.725	3.78	3.721	3.777

^a $a = 1.0$ in., $b = 1.0$ in., $e = 0.92$ in., $h = 0.275$ in., $r = 0$ in.; $\epsilon_r = 38$.

read

$$\phi_x D_{i+(1/2),j,k}^n = \epsilon_0 \sum_{i',j',k'=-\infty}^{+\infty} (\epsilon_{xx})_{ii',jj',kk'} \phi_x E_{i'+(1/2),j',k'}^n \quad (18)$$

where

$$\begin{aligned} (\epsilon_{xx})_{ii',jj',kk'} &= \int_{-\infty}^{+\infty} \int_{-\infty}^{+\infty} \int_{-\infty}^{+\infty} \phi_{i+(1/2)}(x) \phi_j(y) \phi_k(z) \epsilon_{xx}(\vec{r}) \\ &\quad \times \phi_{i'+(1/2)}(x) \phi_{j'}(y) \phi_{k'}(z) \frac{dx dy dz}{\Delta x \Delta y \Delta z} \\ &= \delta_{i,i'} \delta_{j,j'} \delta_{k,k'} + \sum_{p=1}^P [\epsilon_{xx}(p) - 1] \zeta_{ii',jj',kk'}(p) \end{aligned} \quad (19a)$$

$$\begin{aligned} \zeta_{ii',jj',kk'} &= \alpha_{i,i'}(p) \beta_{j,j'}(p) \gamma_{k,k'}(p) \\ &= \int_{x_1(p)}^{x_2(p)} \phi_{i+(1/2)}(x) \phi_{i'+(1/2)}(x) \frac{dx}{\Delta x} \\ &\quad \times \int_{y_1(p)}^{y_2(p)} \phi_j(y) \phi_{j'}(y) \frac{dy}{\Delta y} \int_{z_1(p)}^{z_2(p)} \phi_k(z) \phi_{k'}(z) \frac{dz}{\Delta z} \end{aligned} \quad (19b)$$

where we assume that all dielectric objects are rectangular and P is the total number of dielectric objects.

We now present an example of deriving the constitutive relationship for a two-layer, dielectric-loaded cavity shown in Fig. 11. By expressing

$$\begin{aligned} \epsilon_{xx} &= \epsilon_{xx}(y) \\ &= \begin{cases} \epsilon_r(p), & y_1(p) \leq y \leq y_2(p) \\ 1, & \text{otherwise} \end{cases} \quad (p = 1, 2) \end{aligned} \quad (20)$$

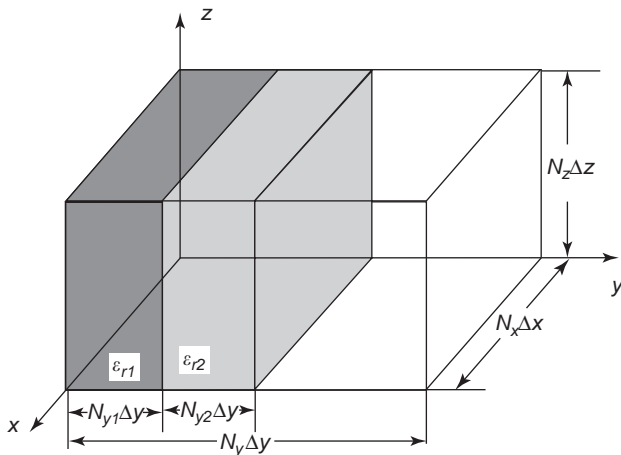


Figure 11. Geometry of a two-layer, dielectric-loaded cavity.

we can write the x component of the constitutive relation in the MRTD domain

$$\phi_x D_{i+(1/2),j,k}^n = \epsilon_0 \sum_{j'=j-M}^{j+M} (\epsilon_{xx})_{jj'} \phi_x E_{i+(1/2),j',k}^n \quad (21)$$

with

$$\begin{aligned} (\epsilon_{xx})_{jj'} &= \delta_{j,j'} + \sum_{p=1}^P [\epsilon_r(p) - 1] \\ &\quad \times \int_{y_1(p)}^{y_2(p)} \phi_j(y) \phi_{j'}(y) \frac{dy}{\Delta y} \end{aligned} \quad (22)$$

where M is the number of the sampled E fields in the MRTD domain. It is usually set equal to a number slightly greater than 9, by taking advantage of the localization of the scaling function.

It is very important to note that the summations in (21) cover not only the original computation domain but also the entire image regions, as shown in Fig. 12. In fact, for a PEC-shielded structure, all the field quantities in the image regions can be expressed in terms of the ones inside the original cavity structure. Toward this end, we employ the principle that the tangential components of the image E fields (parallel to the PEC mirror wall) or the normal components of the image H fields (normal to the PEC mirror wall) are always odd symmetric about the original fields, whereas the normal components of the image E fields and the tangential components of the image H fields are even symmetric. Using these above guidelines we can express all the image field quantities in terms of the fields in the original region, and this leads to a degeneration of the summation index in (21) to N_y , the grid number along the y direction, defined only inside the original cavity structure. Consequently,

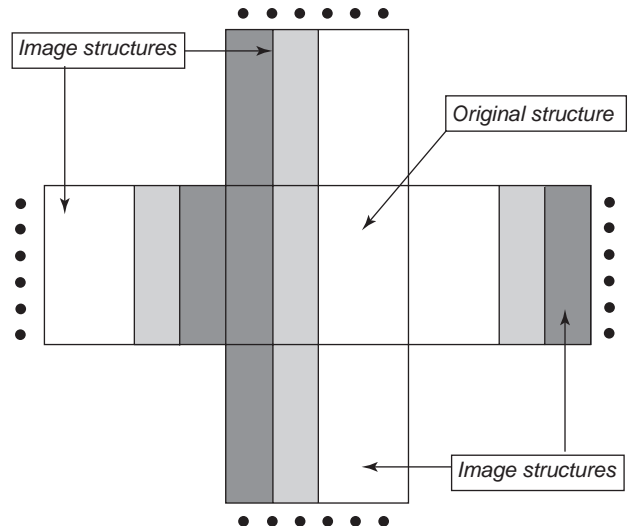


Figure 12. Original structure and multiple images in the y - z plane.

(21) can be simplified to read

$$\phi_x D_{i+(1/2),j,k}^n = \varepsilon_0 \sum_{j'=0}^{N_y} (\hat{\varepsilon}_{xx})_{jj'} \phi_x E_{i+(1/2),j',k}^n \quad (23)$$

where we define the equivalent permittivity matrix in the MRTD domain as follows

$$\begin{aligned} \sum_{j'=0}^{N_y} (\hat{\varepsilon}_{xx})_{jj} &= \sum_{j'=0}^{N_y} (\varepsilon_{xx})_{jj'} - \sum_{j'=-1}^{-N_y} (\varepsilon_{xx})_{jj'} \\ &\quad - \sum_{j'=N_y+1}^{2N_y} (\varepsilon_{xx})_{jj'} - \dots \\ &\quad + (-1)^m \sum_{j'=(m-1)N_y-1}^{j-M} (\varepsilon_{xx})_{jj'} \\ &\quad + (-1)^m \sum_{j'=mN_y+1}^{j+M} (\varepsilon_{xx})_{jj'} \end{aligned} \quad (24a)$$

or in a matrix form as

$$\begin{aligned} [\hat{\varepsilon}_{xx}] &= [\varepsilon_{xx}]_{\text{orig}} - [\varepsilon_{xx}]_{\text{Im}g(-1)} - [\varepsilon_{xx}]_{\text{Im}g(-1)} \\ &\quad - \dots + (-1)^m [\varepsilon_{xx}]_{\text{Im}g(-m)} + (-1)^m [\varepsilon_{xx}]_{\text{Im}g(+m)} \end{aligned} \quad (24b)$$

where the m is the number of images. The first term in (24b) corresponds to the original structure, and the rest are associated with the images.

Next, we present a criterion for determining the number of image m along the y direction (positive or negative). The criterion is derived from knowledge of the effective range of the basis functions at the PEC boundary locations

$$m = \begin{cases} \text{INT} \left[\frac{M}{N_y} \right] + 1, & \text{if } \frac{M}{N_y} \text{ is not an integer} \\ \frac{M}{N_y}, & \text{if } \frac{M}{N_y} \text{ is an integer} \end{cases} \quad (25)$$

where INT is the integer-converting function that truncates all the decimal parts of a number. For example, if $M = 10, N_y = 5$, then $m = \text{INT}(2.5) + 1 = 3$, this implies that we need three images in both sides of the $+y$ and $-y$ directions.

We will now illustrate the procedure for deriving the equivalent permittivity matrix in the MRTD domain. We consider a cavity with the discretization grid number $N_y = 6$ in the y direction. To simplify the notation, we omit the subscript x , and write $(\varepsilon_{xx})_{jj}$ simply as ε_{jj} . In this

example we choose $M = 9$ and $m = 2$. We then have

$$\begin{aligned} &\begin{bmatrix} \phi_x D_{i+(1/2),0,k}^n \\ \phi_x D_{i+(1/2),1,k}^n \\ \phi_x D_{i+(1/2),2,k}^n \\ \phi_x D_{i+(1/2),3,k}^n \\ \phi_x D_{i+(1/2),4,k}^n \\ \phi_x D_{i+(1/2),5,k}^n \\ \phi_x D_{i+(1/2),6,k}^n \end{bmatrix} = \varepsilon_0 \begin{bmatrix} \hat{\varepsilon}_{0,0} & \hat{\varepsilon}_{0,1} & \hat{\varepsilon}_{0,2} & \hat{\varepsilon}_{0,3} & \hat{\varepsilon}_{0,4} & \hat{\varepsilon}_{0,5} & \hat{\varepsilon}_{0,6} \\ \hat{\varepsilon}_{1,0} & \hat{\varepsilon}_{1,1} & \hat{\varepsilon}_{1,2} & \hat{\varepsilon}_{1,3} & \hat{\varepsilon}_{1,4} & \hat{\varepsilon}_{1,5} & \hat{\varepsilon}_{1,6} \\ \hat{\varepsilon}_{2,0} & \hat{\varepsilon}_{2,1} & \hat{\varepsilon}_{2,2} & \hat{\varepsilon}_{2,3} & \hat{\varepsilon}_{2,4} & \hat{\varepsilon}_{2,5} & \hat{\varepsilon}_{2,6} \\ \hat{\varepsilon}_{3,0} & \hat{\varepsilon}_{3,1} & \hat{\varepsilon}_{3,2} & \hat{\varepsilon}_{3,3} & \hat{\varepsilon}_{3,4} & \hat{\varepsilon}_{3,5} & \hat{\varepsilon}_{3,6} \\ \hat{\varepsilon}_{4,0} & \hat{\varepsilon}_{4,1} & \hat{\varepsilon}_{4,2} & \hat{\varepsilon}_{4,3} & \hat{\varepsilon}_{4,4} & \hat{\varepsilon}_{4,5} & \hat{\varepsilon}_{4,6} \\ \hat{\varepsilon}_{5,0} & \hat{\varepsilon}_{5,1} & \hat{\varepsilon}_{5,2} & \hat{\varepsilon}_{5,3} & \hat{\varepsilon}_{5,4} & \hat{\varepsilon}_{5,5} & \hat{\varepsilon}_{5,6} \\ \hat{\varepsilon}_{6,0} & \hat{\varepsilon}_{6,1} & \hat{\varepsilon}_{6,2} & \hat{\varepsilon}_{6,3} & \hat{\varepsilon}_{6,4} & \hat{\varepsilon}_{6,5} & \hat{\varepsilon}_{6,6} \end{bmatrix} \\ &\quad \times \begin{bmatrix} \phi_x E_{i+(1/2),0,k}^n \\ \phi_x E_{i+(1/2),1,k}^n \\ \phi_x E_{i+(1/2),2,k}^n \\ \phi_x E_{i+(1/2),3,k}^n \\ \phi_x E_{i+(1/2),4,k}^n \\ \phi_x E_{i+(1/2),5,k}^n \\ \phi_x E_{i+(1/2),6,k}^n \end{bmatrix} \end{aligned} \quad (26)$$

with

$$[\varepsilon_{xx}]_{\text{orig}} = \begin{bmatrix} \varepsilon_{0,0} & \varepsilon_{0,1} & \varepsilon_{0,2} & \varepsilon_{0,3} & \varepsilon_{0,4} & \varepsilon_{0,5} & \varepsilon_{0,6} \\ \varepsilon_{1,0} & \varepsilon_{1,1} & \varepsilon_{1,2} & \varepsilon_{1,3} & \varepsilon_{1,4} & \varepsilon_{1,5} & \varepsilon_{1,6} \\ \varepsilon_{2,0} & \varepsilon_{2,1} & \varepsilon_{2,2} & \varepsilon_{2,3} & \varepsilon_{2,4} & \varepsilon_{2,5} & \varepsilon_{2,6} \\ \varepsilon_{3,0} & \varepsilon_{3,1} & \varepsilon_{3,2} & \varepsilon_{3,3} & \varepsilon_{3,4} & \varepsilon_{3,5} & \varepsilon_{3,6} \\ \varepsilon_{4,0} & \varepsilon_{4,1} & \varepsilon_{4,2} & \varepsilon_{4,3} & \varepsilon_{4,4} & \varepsilon_{4,5} & \varepsilon_{4,6} \\ \varepsilon_{5,0} & \varepsilon_{5,1} & \varepsilon_{5,2} & \varepsilon_{5,3} & \varepsilon_{5,4} & \varepsilon_{5,5} & \varepsilon_{5,6} \\ \varepsilon_{6,0} & \varepsilon_{6,1} & \varepsilon_{6,2} & \varepsilon_{6,3} & \varepsilon_{6,4} & \varepsilon_{6,5} & \varepsilon_{6,6} \end{bmatrix} \quad (27a)$$

$$[\varepsilon_{xx}]_{\text{Im}g(-1)} = \begin{bmatrix} 0 & \varepsilon_{0,-1} & \varepsilon_{0,-2} & \varepsilon_{0,-3} & \varepsilon_{0,-4} & \varepsilon_{0,-5} & \varepsilon_{0,-6} \\ 0 & \varepsilon_{1,-1} & \varepsilon_{1,-2} & \varepsilon_{1,-3} & \varepsilon_{1,-4} & \varepsilon_{1,-5} & \varepsilon_{1,-6} \\ 0 & \varepsilon_{2,-1} & \varepsilon_{2,-2} & \varepsilon_{2,-3} & \varepsilon_{2,-4} & \varepsilon_{2,-5} & \varepsilon_{2,-6} \\ 0 & \varepsilon_{3,-1} & \varepsilon_{3,-2} & \varepsilon_{3,-3} & \varepsilon_{3,-4} & \varepsilon_{3,-5} & \varepsilon_{3,-6} \\ 0 & \varepsilon_{4,-1} & \varepsilon_{4,-2} & \varepsilon_{4,-3} & \varepsilon_{4,-4} & \varepsilon_{4,-5} & 0 \\ 0 & \varepsilon_{5,-1} & \varepsilon_{5,-2} & \varepsilon_{5,-3} & \varepsilon_{5,-4} & 0 & 0 \\ 0 & \varepsilon_{6,-1} & \varepsilon_{6,-2} & \varepsilon_{6,-3} & 0 & 0 & 0 \end{bmatrix} \quad (27b)$$

$$[\hat{\epsilon}_{xx}]_{\text{Im}g(+1)} = \begin{bmatrix} 0 & 0 & 0 & \epsilon_{0,9} & \epsilon_{0,8} & \epsilon_{0,7} & 0 \\ 0 & 0 & \epsilon_{1,10} & \epsilon_{1,9} & \epsilon_{1,8} & \epsilon_{1,7} & 0 \\ 0 & \epsilon_{2,11} & \epsilon_{2,10} & \epsilon_{2,9} & \epsilon_{2,8} & \epsilon_{2,7} & 0 \\ \epsilon_{3,12} & \epsilon_{3,11} & \epsilon_{3,10} & \epsilon_{3,9} & \epsilon_{3,8} & \epsilon_{3,7} & 0 \\ \epsilon_{4,12} & \epsilon_{4,11} & \epsilon_{4,10} & \epsilon_{4,9} & \epsilon_{4,8} & \epsilon_{4,7} & 0 \\ \epsilon_{5,12} & \epsilon_{5,11} & \epsilon_{5,10} & \epsilon_{5,9} & \epsilon_{5,8} & \epsilon_{5,7} & 0 \\ \epsilon_{6,12} & \epsilon_{6,11} & \epsilon_{6,10} & \epsilon_{6,9} & \epsilon_{6,8} & \epsilon_{6,7} & 0 \end{bmatrix} \quad (27c)$$

$$[\hat{\epsilon}_{xx}]_{\text{Im}g(-2)} = \begin{bmatrix} 0 & 0 & 0 & \epsilon_{0,-9} & \epsilon_{0,-8} & \epsilon_{0,-7} & 0 \\ 0 & 0 & 0 & 0 & \epsilon_{1,-8} & \epsilon_{1,-7} & 0 \\ 0 & 0 & 0 & 0 & 0 & \epsilon_{2,-7} & 0 \\ 0 & 0 & 0 & 0 & 0 & 0 & 0 \\ 0 & 0 & 0 & 0 & 0 & 0 & 0 \\ 0 & 0 & 0 & 0 & 0 & 0 & 0 \\ 0 & 0 & 0 & 0 & 0 & 0 & 0 \end{bmatrix} \quad (27d)$$

$$[\hat{\epsilon}_{xx}]_{\text{Im}g(+2)} = \begin{bmatrix} 0 & 0 & 0 & 0 & 0 & 0 & 0 \\ 0 & 0 & 0 & 0 & 0 & 0 & 0 \\ 0 & 0 & 0 & 0 & 0 & 0 & 0 \\ 0 & 0 & 0 & 0 & 0 & 0 & 0 \\ 0 & \epsilon_{4,13} & 0 & 0 & 0 & 0 & 0 \\ 0 & \epsilon_{5,13} & \epsilon_{5,14} & 0 & 0 & 0 & 0 \\ 0 & \epsilon_{6,13} & \epsilon_{6,14} & \epsilon_{6,15} & 0 & 0 & 0 \end{bmatrix} \quad (27e)$$

where (27a) is associated with the original structure, whereas (27b)–(27e) are contributed by the image regions. As seen from the above, these latter contributions to the equivalent permittivity matrix decrease dramatically with the increase in the number of image regions. Since the elements of the equivalent permittivity matrix depend only on the basis functions and the material properties of the structure, both the $[\hat{\epsilon}_{xx}]$ and its inverse $[\hat{\epsilon}_{xx}]^{-1}$ can be computed in advance and saved in the MRTD Maxwell solver for the update equations. Consequently, the E field can be updated as follows

$$\phi_x E_{i+(1/2),j,k}^n = \frac{1}{\epsilon_0} \sum_{j'=0}^{N_y} ([\hat{\epsilon}_{xx}]^{-1})_{j,j'} \phi_x D_{i+(1/2),j',k}^n \quad (28)$$

where, apparently, we need to compute the product of only two small matrices, whose dimensions are typically 6 or less in this work, to update the E fields at each timestep.

6.3. MIT in Update Equations

Although, in principle, (16) and (17) can be employed to update the fields, they are numerically inefficient and somewhat impractical for coding and computation, because the summations in these update expressions include both the original and image regions. In this section, we truncate the summations in these update equations by

excluding some of the image field quantities. This is accomplished by carrying out the following two steps: (1) expressing all the field quantities in terms of those defined in the original structure by the MIT technique described in the previous section and, (2) maintaining the values and positions of the coefficients $a(v)$ unchanged for all of the terms, but expressing them only by using the grid indices inside the structure. Following this procedure, we can rewrite the update equations for the x components using the MIT as follows

$$\begin{aligned} & \phi_x D_{i+(1/2),j,k}^n \\ &= \phi_x D_{i+(1/2),j,k}^n + \left\{ \sum_{v=0}^{N_y-1} a(v-j)_{\phi_z} H_{i+(1/2),v+(1/2),k}^{n+(1/2)} \right. \\ &+ \left[\sum_{\text{Im}g=\text{even}} \left(\sum_{v=0}^{N_y-1} a(-\text{Im}g-2) \cdot N_y - v - j - 1 \right) \right. \\ &+ \left. \left. \sum_{v=0}^{N_y-1} a(\text{Im}g \cdot N_y + v - j) \right) \phi_z H_{i+(1/2),v+(1/2),k}^{n+(1/2)} \right] \\ &+ \left[\sum_{\text{Im}g=\text{odd}} \left(\sum_{v=0}^{N_y-1} a(-\text{Im}g \cdot N_y - v - j - 1) \right) \right. \\ &+ \left. \sum_{m=0}^{N_y-1} a(\text{Im}g \cdot N_y + v - j) \right] \\ &\times \left. \phi_z H_{i+(1/2),N_y-v-1+(1/2),k}^{n+(1/2)} \right\} \frac{\Delta t}{\Delta y} \\ &+ \left\{ \sum_{v=0}^{N_z-1} a(v-k)_{\phi_y} H_{i+(1/2),j,v+(1/2)}^{n+(1/2)} \right. \\ &+ \left[\sum_{\text{Im}g=\text{even}} \left(\sum_{v=0}^{N_z-1} a(-\text{Im}g-2) \cdot N_z - v - k - 1 \right) \right. \\ &+ \left. \sum_{v=0}^{N_z-1} a(\text{Im}g \cdot N_z + v - k) \right] \\ &\times \left. \phi_y H_{i+(1/2),j,v+(1/2)}^{n+(1/2)} \right] \\ &+ \left[\sum_{\text{Im}g=\text{odd}} \left(\sum_{v=0}^{N_z-1} a(-\text{Im}g \cdot N_z - v - k - 1) \right) \right. \\ &+ \left. \sum_{v=0}^{N_z-1} a(\text{Im}g \cdot N_z + v - k) \right] \\ &\times \left. \phi_y H_{i+(1/2),j,N_z-v-1+(1/2)}^{n+(1/2)} \right\} \frac{\Delta t}{\Delta z} \end{aligned} \quad (29a)$$

$$\begin{aligned}
 & H_{ij+(1/2),k+(1/2)}^{n+(1/2)} \\
 &= \phi_x H_{ij+(1/2),k+(1/2)}^{n-(1/2)} + \frac{1}{\mu_0} \left\{ \sum_{v=0}^{N_z} \alpha(v-k-1) \phi_y E_{ij+(1/2),v}^n \right. \\
 &+ \left[\sum_{\text{Im}g=\text{even}} \left(-\sum_{v=0}^{N_z-1} \alpha(-\text{Im}g-2) \cdot N_z - v - k - 2 \right) \right. \\
 &+ \left. \left. \sum_{m=0}^{N_z-1} \alpha(\text{Im}g \cdot N_z + v - k) \right) \phi_y E_{ij+(1/2),v+1}^n \right] \\
 &+ \left[\sum_{\text{Im}g=\text{odd}} \left(\sum_{v=0}^{N_z-1} \alpha(-\text{Im}g \cdot N_z - v - k - 2) \right) \right. \\
 &- \left. \sum_{v=0}^{N_z-1} \alpha(\text{Im}g \cdot N_z + v - k) \right) \\
 &\times \phi_z E_{ij+(1/2),N_z-v-1}^{n+(1/2)} \left. \right\} \frac{\Delta t}{\Delta z} \\
 &- \frac{1}{\mu_0} \left\{ \sum_{v=0}^{N_y} \alpha(v-j-1) \phi_z E_{i,v,k+(1/2)}^n \right. \\
 &+ \left[\sum_{\text{Im}g=\text{even}} \left(-\sum_{v=0}^{N_y-1} \alpha(-\text{Im}g-2) \cdot N_y - v - j - 2 \right) \right. \\
 &+ \left. \sum_{v=0}^{N_y-1} \alpha(\text{Im}g \cdot N_y + v - j) \right) \\
 &\times \phi_z E_{i,v+1,k+(1/2)}^n \left. \right] \\
 &+ \left[\sum_{\text{Im}g=\text{odd}} \left(\sum_{v=0}^{N_y-1} \alpha(-\text{Im}g \cdot N_y - v - j - 2) \right) \right. \\
 &- \left. \sum_{v=0}^{N_y-1} \alpha(\text{Im}g \cdot N_y + v - j) \right) \\
 &\times \phi_z E_{i,N_y-v-1,k+(1/2)}^n \left. \right\} \frac{\Delta t}{\Delta y} \quad (29b)
 \end{aligned}$$

where N_y and N_z are the numbers of cells along the y and z directions inside the structure, respectively, and the summation indexes, “odd” (1,3, ...) and “even” (2,4, ...), denote the contributions to the updated field quantities from the specified odd or even image regions, respectively.

Before closing this section, it would be worthwhile to point out that although the (29a) and (29b) are quite lengthy, they are actually quite efficient in terms of coding and computation. Because all the field quantities usually have small dimensions, the coefficients $\alpha(v)$ can be

computed in advance and saved in the MRTD solver for later use.

7. 2D MRTD ANALYSIS FOR PRINTED TRANSMISSION LINES

7.1. Field Construction

Following the procedure described in Refs. 28 and 29, we develop a two-dimensional (2D) MRTD analysis by deriving a set of governing equations for the problem at hand, specifically, a lossless guided-wave structure shown in Fig. 13. We begin by expanding the field quantities as

$$\begin{aligned}
 & \left\{ \begin{array}{l} E_x(x,y,z,t), E_y(x,y,z,t), E_z(x,y,z,t) \\ H_x(x,y,z,t), H_y(x,y,z,t), H_z(x,y,z,t) \end{array} \right\}^t \\
 &= \left\{ \begin{array}{l} jE_x(x,y,t), jE_y(x,y,t), E_z(x,y,t) \\ H_x(x,y,t), H_y(x,y,t), jH_z(x,y,t) \end{array} \right\}^t e^{-j\beta z} \quad (30)
 \end{aligned}$$

where β is the propagation constant for the structure. Next, we use the GDMOs to obtain the following governing equations from the Maxwell's curl equations

$$\begin{aligned}
 & \begin{bmatrix} 0 & j\beta & \partial_y \\ -j\beta & 0 & -\partial_x \\ -\partial_y & \partial_x & 0 \end{bmatrix} \begin{bmatrix} H_x \\ H_y \\ 0 \end{bmatrix} \\
 &= \left(\varepsilon_0 \frac{\partial}{\partial t} \begin{bmatrix} \varepsilon_{xx} & 0 & 0 \\ 0 & \varepsilon_{yy} & 0 \\ 0 & 0 & \varepsilon_{zz} \end{bmatrix} + \begin{bmatrix} \sigma_x^e & 0 & 0 \\ 0 & \sigma_y^e & 0 \\ 0 & 0 & \sigma_z^e \end{bmatrix} \right) \begin{bmatrix} jE_x \\ jE_y \\ E_z \end{bmatrix} \quad (31a)
 \end{aligned}$$

$$\begin{aligned}
 & \begin{bmatrix} 0 & j\beta & \partial_y \\ -j\beta & 0 & -\partial_x \\ -\partial_y & \partial_x & 0 \end{bmatrix} \begin{bmatrix} jE_x \\ jE_y \\ E_z \end{bmatrix} \\
 &= \left(-\mu_0 \frac{\partial}{\partial t} \begin{bmatrix} \mu_{xx} & 0 & 0 \\ 0 & \mu_{yy} & 0 \\ 0 & 0 & \mu_{zz} \end{bmatrix} + \begin{bmatrix} \sigma_x^m & 0 & 0 \\ 0 & \sigma_y^m & 0 \\ 0 & 0 & \sigma_z^m \end{bmatrix} \right) \\
 &\times \begin{bmatrix} H_x \\ H_y \\ jH_z \end{bmatrix} \quad (31b)
 \end{aligned}$$

In practice, we set $\sigma_x^m = 0$. Note that a printed planar transmission line is usually inhomogeneous in the vertical

direction, but homogenous in the horizontal direction, which leads to $\varepsilon_{\alpha\alpha} = \varepsilon_{\alpha\alpha}(y)$, ($\alpha = x, y, z$).

7.2. 2D MRTD Algorithm

Next, we represent all the field quantities by using scaling functions in space and pulse functions in time. For instance, for the x component of the fields we write

$$E_x(x, y, t) = \sum_{n, i, j = -\infty}^{+\infty} \phi_x E_{i+(1/2)j}^n \phi_{i+(1/2)}(x) \phi_j(y) h_n(t) \quad (32)$$

$$H_x(x, y, t) = \sum_{n, i, j = -\infty}^{+\infty} \phi_x H_{i+(1/2)j}^{n+(1/2)} \phi_i(x) \phi_{j+(1/2)}(y) h_{n+(1/2)}(t) \quad (33)$$

Substitution of the field expansions into Maxwell's equations, followed by application of Galerkin's method, leads us to obtain a set of field update equations. For instance, the x components of the update equations are given by

$$\begin{aligned} \phi_x H_{i+(1/2)j}^{n+(1/2)} &= \phi_x H_{i+(1/2)j}^{n-(1/2)} + \frac{\Delta t}{\mu_0 \mu_x} \\ &\times \left[\beta_{\phi_y} E_{i+(1/2)j}^n - \sum_v a(v) \phi_z E_{i+(1/2)j+v+1}^n \frac{1}{\Delta y} \right] \end{aligned} \quad (34)$$

$$\begin{aligned} &\sum_{i', j' = -\infty}^{+\infty} (\sigma_x^e)_{i'i', j'j'} \frac{\Delta t}{2} \left(\phi_x E_{i'+(1/2)j'}^{n+1} + \phi_x E_{i'+(1/2)j'}^n \right) \\ &+ \varepsilon_0 \sum_{j' = -\infty}^{+\infty} (\varepsilon_{xx})_{j'j'} \left(\phi_x E_{i+(1/2)j'}^{n+1} - \phi_x E_{i+(1/2)j'}^n \right) \\ &= \Delta t \left[\beta_{\phi_y} H_{i+(1/2)j}^{n+(1/2)} + \sum_m a(m) \phi_z H_{i+(1/2)j+m+1}^{n+(1/2)} \frac{1}{\Delta y} \right] \end{aligned} \quad (35)$$

where the coefficient $a(v)$ is as given in Ref. 19. Assuming that the conducting strip is infinitely thin, we can express its conductivity as

$$\sigma_x^e = \begin{cases} \sigma, & i_1 \Delta x \leq x \leq i_2 \Delta x, \left(j_0 \Delta y - \frac{\tau}{2} \right) < y < \left(j_0 \Delta y + \frac{\tau}{2} \right) \\ 0, & \text{otherwise} \end{cases} \quad (\Delta = x, y) \quad (36)$$

Thus, we can express $(\varepsilon_{xx})_{j'j'}$ and $(\sigma_x^e)_{i'i', j'j'}$ as

$$(\varepsilon_{xx})_{j'j'} = \int_{-\infty}^{+\infty} \phi_j(y) \varepsilon_{xx}(y) \phi_{j'}(y) \frac{dy}{\Delta y} \quad (37a)$$

$$\begin{aligned} (\sigma_x^e)_{i'i', j'j'} &= \int_{-\infty}^{+\infty} \int_{-\infty}^{+\infty} \phi_{i+(1/2)}(x) \phi_j(y) \sigma \phi_{i'+(1/2)} \\ &\times (x) \phi_{j'}(y) \frac{dx dy}{\Delta x \Delta y} \end{aligned} \quad (37b)$$

By including the image contributions and using the first-order approximation, we can derive

$$(\sigma_x^e)_{i'i', j'j'} = \sigma_{i,i'} \delta_{i,i'} \zeta_{j,j'} \delta_{j,j'} (\delta_{j,j_0} + \delta_{j,-j_0} + \delta_{j,2j_0} + \dots) \quad (38)$$

where $\delta_{i'i'}$ is the Kronecker symbol, which is 1 for $i = i'$, otherwise 0. Then, we further rewrite the discretized time-domain equation as

$$\begin{aligned} &(\phi_x E_{i+(1/2)j}^{n+1} + \phi_x E_{i+(1/2)j}^n) \frac{\sigma^e (\delta_{j,j_0} + \delta_{j,-j_0} + \delta_{j,2j_0} + \dots) \Delta t}{2} \\ &+ \varepsilon_0 \sum_{j' = -\infty}^{+\infty} (\varepsilon_{xx})_{j'j'} (\phi_x E_{i+(1/2)j'}^{n+1} - \phi_x E_{i+(1/2)j'}^n) \\ &= \Delta t \left[\beta_{\phi_y} H_{i+(1/2)j}^{n+(1/2)} + \sum_v a(v) \phi_z H_{i+(1/2)j+v+1}^{n+(1/2)} \frac{1}{\Delta y} \right] \end{aligned} \quad (39)$$

The summation index v in (39) includes not only the regions in the interior of the original structure but also the image regions. Two types of boundary are frequently used for truncating the grids: the absorbing boundary condition for open structures and the perfect electric conductor (PEC) for shielded ones. Usually, the PEC boundary is handled by using the MIT described earlier. Figure 13 shows the original structures: shielded and open microstrip lines, as well as their images.

$$\begin{aligned} &(\phi_x E_{i+(1/2)j}^{n+1} + \phi_x E_{i+(1/2)j}^n) \frac{\sigma^e \delta_{j,j_0} \Delta t}{2} \\ &+ \varepsilon_0 \sum_{j' = 0}^{N_y} (\hat{\varepsilon}_{xx})_{j'j'} (\phi_x E_{i+(1/2)j'}^{n+1} - \phi_x E_{i+(1/2)j'}^n) \\ &= \Delta t \left[\beta_{\phi_y} H_{i+(1/2)j}^{n+(1/2)} + \sum_v a(v) \phi_z H_{i+(1/2)j+v+1}^{n+(1/2)} \frac{1}{\Delta y} \right] \end{aligned} \quad (40)$$

By taking an inverse of (30), we can obtain the update equation for the x component of the E field as

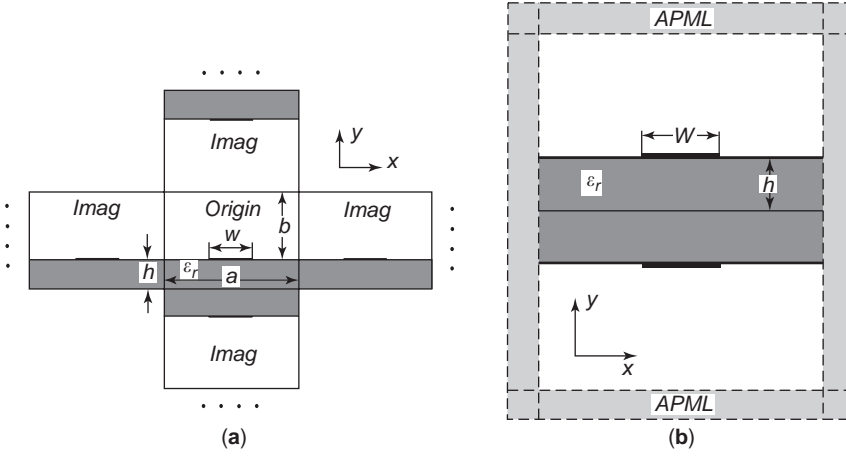


Figure 13. Cross section of printed transmission lines and their images: (a) shielded microstrip line; (b) open microstrip line.

follows

$$\begin{aligned} \phi_x \mathbf{E}_{i+(1/2),j}^{n+1} &= \sum_{j'=0}^{N_y} ([A])_{j,j'} \phi_x \mathbf{E}_{i+(1/2),j'}^n \\ &+ \frac{1}{\varepsilon_0} \sum_{j'=0}^{N_y} ([B])_{j,j'} \left[\beta_{\phi_y} \mathbf{H}_{i+(1/2),j'}^{n+(1/2)} \Delta t \right. \\ &\left. + \sum_m a(m)_{\phi_z} \mathbf{H}_{i+(1/2),j'+m+1}^{n+(1/2)} \frac{\Delta t}{\Delta y} \right] \end{aligned} \quad (41)$$

with

$$[A] = \left[[\hat{\varepsilon}_{xx}]_{j,j'} + [I] \frac{\sigma^e \delta_{j,j_0} \Delta t}{2\varepsilon_0} \right]^{-1} \cdot \left[[\hat{\varepsilon}_{xx}]_{j,j'} - [I] \frac{\sigma^e \delta_{j,j_0} \Delta t}{2\varepsilon_0} \right] \quad (42a)$$

$$[B] = \left[[\hat{\varepsilon}_{xx}]_{j,j'} + [I] \frac{\sigma^e \delta_{j,j_0} \Delta t}{2\varepsilon_0} \right]^{-1} \quad (42b)$$

For a shielded structure, we need to employ the MIT for constructing the $[\hat{\varepsilon}_{xx}]$ matrix. Since the matrix $[A]$ and $[B]$ depend only on the basis functions and the material properties of the structure, they can be computed in advance and saved in the MRTD Maxwell solver for the update equations.

7.3. Application of APML

In this section we address the problem of mesh truncation for open structures. We find that the 2D version of the lossy, uniaxial, anisotropic PML (APML) [30] medium is well suited for this purpose. Since the APML is applied only in the x and y directions, the frequency-domain Maxwell curl equation in the APML medium can be

written as

$$\begin{bmatrix} j \frac{\partial H_z}{\partial y} + j \beta H_y \\ -j \beta H_x - j \frac{\partial H_z}{\partial x} \\ \frac{\partial H_y}{\partial x} - \frac{\partial H_x}{\partial y} \end{bmatrix} \quad (43a)$$

$$= j \omega \varepsilon_0 \begin{bmatrix} \frac{\varepsilon_{xx} s_y}{s_x} & 0 & 0 \\ 0 & \frac{\varepsilon_{yy} s_x}{s_y} & 0 \\ 0 & 0 & \varepsilon_{zz} s_x s_y \end{bmatrix} \begin{bmatrix} j E_x \\ j E_y \\ E_z \end{bmatrix}$$

$$\begin{bmatrix} \frac{\partial E_z}{\partial y} + \beta E_y \\ \beta E_x - \frac{\partial E_z}{\partial x} \\ j \frac{\partial E_y}{\partial x} - j \frac{\partial E_x}{\partial y} \end{bmatrix} \quad (43b)$$

$$= -j \omega \mu_0 \begin{bmatrix} \frac{\mu_{xx} s_y}{s_x} & 0 & 0 \\ 0 & \frac{\mu_{yy} s_x}{s_y} & 0 \\ 0 & 0 & \mu_{zz} s_x s_y \end{bmatrix} \begin{bmatrix} H_x \\ H_y \\ j H_z \end{bmatrix}$$

with

$$s_\alpha = \begin{cases} 1 + \frac{\sigma_\alpha}{j \omega \varepsilon_0}, & \text{for absorption in } \alpha \text{ direction} \\ 1, & \text{elsewhere} \end{cases} \quad (\alpha = x, y) \quad (44)$$

Depending on combination of the values of s_x and s_y , the equations above are applicable to all of the APML regions, which include two side edges, the top wall, as well as the two corners. By expanding these equations for the case of the corners, we immediately obtain the x components of the governing equations given below:

$$\frac{\partial H_z}{\partial y} - \frac{\partial H_y}{\partial z} = j\omega D_x + \frac{\sigma_y}{\varepsilon_0} D_x \quad (45)$$

$$\frac{\partial E_z}{\partial y} - \frac{\partial E_y}{\partial z} = -j\omega B_x - \frac{\sigma_y}{\varepsilon_0} B_x \quad (46)$$

We use a two-step update approach to timestepping fields inside APML regions. Following the MRTD discretization procedure, described previously, we obtain the desired E -field update equations:

$$\begin{aligned} \phi_x D_{i+(1/2)j}^{n+1} &= \frac{1 - \frac{\sigma_y \Delta t}{2\varepsilon_0}}{1 + \frac{\sigma_y \Delta t}{2\varepsilon_0}} \phi_x D_{i+(1/2)j}^n + \frac{1}{1 + \frac{\sigma_y \Delta t}{2\varepsilon_0}} \\ &\times \left(\beta_{\phi_y} H_{i+(1/2)j}^{n+1} \Delta t \right. \\ &\left. + \sum_m a(m)_{\phi_z} H_{i+(1/2)j+m+1}^{n+1} \frac{\Delta t}{\Delta y} \right) \end{aligned} \quad (47)$$

$$\begin{aligned} \phi_x E_{i+(1/2)j}^{n+1} &= \phi_x E_{i+(1/2)j}^n + \frac{1}{\varepsilon_0} \sum_{j'} ([\varepsilon_x]^{-1})_{jj'} \\ &\times \left[\left(1 + \frac{\sigma_x \Delta t}{2\varepsilon_0} \right) \phi_x D_{i+(1/2)j'}^{n+1} \right. \\ &\left. - \left(1 - \frac{\sigma_x \Delta t}{2\varepsilon_0} \right) \phi_x D_{i+(1/2)j'}^n \right] \end{aligned} \quad (48)$$

We can employ the same procedure to obtain the remaining E and H -field update equations.

In applying the MRTD method, we chose the time step Δt to satisfy the stability and limit condition [19] in all simulations. Starting from the convergence condition of the update equations of D fields given above, it can be shown that, to obtain good absorption, the APML parameters may be chosen as

$$\sigma_\alpha = \sigma_{\max} \left| \frac{\alpha - \alpha_0}{N_p \Delta \alpha} \right|^p = \gamma \frac{\varepsilon_0}{\Delta t} \left| \frac{i - i_0}{N_p} \right|^p, \quad (\alpha = x, y) \quad (49)$$

where α_0 is the starting position in the α direction, d is the thickness of the APML, and N_p is the number of cells within the APML region. In principle, it can be shown that this relationship is consistent with the standard form, which can be derived from a plane wave, normally incident on a PML region. We found that we can minimize the reflection error, and have good absorption, if we choose $p = 2$ and $\gamma = 0.8-1.6$.

7.4. Computation of the Propagation Characteristics

Typically, for the printed transmission lines, the two parameters of interest are the effective dielectric constant ε_{eff} , and the characteristic impedance Z_0 , which can, in general, be derived from the MRTD calculated field quantities. For example, the time-domain voltage V defined as an integral from the PEC ground to the stripline can be calculated as follows

$$\begin{aligned} V &= - \int_0^h E_y(x_0, y, t_0) dy \\ &= - \sum_{l=0}^{N_s} \int_{l\Delta y}^{(l+1)\Delta y} E_y(x_0, y, t_0) dy \\ &= - \sum_{l=0}^{N_s} \int_{l\Delta y}^{(l+1)\Delta y} \left[\iint E_y(x, y, t) \delta(x - x_0) \delta(t - t_0) dx dt \right] dy \\ &= - \sum_{l=0}^{N_s} \left[\sum_{i,j=-\infty}^{\infty} \phi_y E_{i,j-l+(1/2)}^n \phi_i(x_0) b(j) \Delta y \right] \end{aligned} \quad (50)$$

where N_s is the number of the cells from the bottom ground to the PEC strip and the indices i and j of the summation span the original microstrip line and its image regions. The integral coefficient $b(j)$ forms a localized distribution with even symmetric $b(j) = b(-j)$ listed in Table 3. We can apply a similar procedure to solve for all required field quantities.

7.5. BHW Function Truncation and Modulation

To eliminate the Gibb phenomenon that results from an abrupt truncation of the time-domain response, the Blackman-Harris (BH) window function is used to truncate and modulate the time domain [29]. We write

$$\begin{aligned} [E_\kappa^W(t_n), H_\kappa^W(t_n)] &= [E_\kappa(t_n), H_\kappa(t_n)] \\ W_{\text{BH}}(t_n) \quad (\kappa = x, y, z) \end{aligned} \quad (51)$$

where $[E_\kappa(t_n), H_\kappa(t_n)]$ represent the original time-domain electromagnetic fields defined in the MRTD algorithm, and $[E_\kappa^W(t_n), H_\kappa^W(t_n)]$ are the windowed versions. Since the frequency-domain response is the convolution of the frequency-domain signature and its window function, the

Table 3. Integral Coefficient $b(j)$

j	$b(j)$
0	0.9143952
1	0.0385998
2	0.0095740
3	-0.0086579
4	0.0050629
5	-0.0027034
6	0.0014053
7	-0.0007203
8	0.0000695

choice of the window function can significantly affect the accuracy of the propagation characteristics. Extremely low sidelobe levels (-92 dB) of the BH window ensures the accuracy of the extracted frequency domain signals, whereas the use of the conventional rectangular window function, which has a much higher sidelobe level (-13 dB), can seriously corrupt the frequency signatures, especially for a resonant structure.

8. NUMERICAL RESULTS

8.1. MIT MRTD Application

We have applied the MRTD scheme in conjunction with the MIT to analyze a number of dielectric-loaded cavities, *viz.*, an empty cavity, two partially filled (25% and 50%) cavities containing a single dielectric medium, and two different two-layer, dielectric-filled cavities. The dimensions of the cavity were set to be $1 \times 2 \times 1.5$ m³, in the $x, y,$ and z directions, respectively, in all these cases.

We begin with an empty cavity that is discretized with $2 \times 4 \times 3$ cells. The frequency spectrum of E_x sampled at the gridpoint [1,3,1] is displayed in Fig. 14, and the extracted resonant frequencies for the dominant and higher-order modes are summarized in Table 4, along with the discretization parameters. It is evident that the results obtained with the MRTD scheme show good agreement with both the analytical results and those derived using the FDTD. However, the MRTD scheme demands only 0.8% of the computational resources needed in the conventional FDTD technique. In addition, we have investigated the required CPU time for conventional MRTD and the MIT MRTD schemes. For a total timestep of $N_t = 10^4$, it was found that the CPU time for the conventional MRTD was about 19.27 s, whereas of the MIT MRTD required about 27.08 s on a 500-MHz Alpha digital workstation. Obviously, this increase in the CPU time is

Table 4. Resonant Frequencies (in MHz) for an Empty Cavity^a

Analytic	FDTD [20] ($10 \times 20 \times 15$)	S-MRTD [20] ($2 \times 4 \times 3$)	This Method ($2 \times 4 \times 3$)	Percentage Difference (%)
125.00	124.85	125.10	124.95	-0.040
180.27	179.75	180.50	180.39	0.067
213.60	212.40	214.60	214.30	0.328
246.22	244.50	248.70	248.55	0.946
250.00	248.70	251.00	250.75	0.300
301.04	298.95	303.90	303.65	0.580
336.34	334.35	339.20	338.91	0.764

^a $V = 1 \times 2 \times 1.5$ m³; $\Delta x = \Delta y = \Delta z = \frac{1}{2}$ m.

due to the use of additional images in the process of implementing the MIT MRTD technique. Specially, we use five images along the positive and negative x directions, and three in the remaining directions. By comparison, the conventional MRTD uses only a single image irrespective of the direction. We also note that the introduction of the MIT in the MRTD scheme enhances the accuracy of the results.

The MRTD analysis of the half- and quarter-filled dielectric cavities, with $\epsilon_{r1} = \epsilon_{r2} = 64$ and $\epsilon_{r1} = 64, \epsilon_{r2} = 1$, respectively, also yields excellent results, as is evident from Figs. 15 and 16 and Tables 5 and 6. Once again, the MRTD scheme is found to be highly efficient when compared to the conventional FDTD method, since it requires only 0.8% and 1.2% of the CPU memory for the two cases described above. In general, the accuracy of the MRTD technique is again improved when it is combined with the multiple-image technique.

Next, we consider a two-layer, dielectric-filled cavity, using only $2 \times 6 \times 3$ cells to discretize the computational domain. We investigate the following two cases: (1) $\epsilon_{r1} = 64, \epsilon_{r2} = 8$ and (2) $\epsilon_{r1} = 8, \epsilon_{r2} = 64$, with $N_{y1} = N_{y2} = 1.5$ cells. The structure dimensions still remain

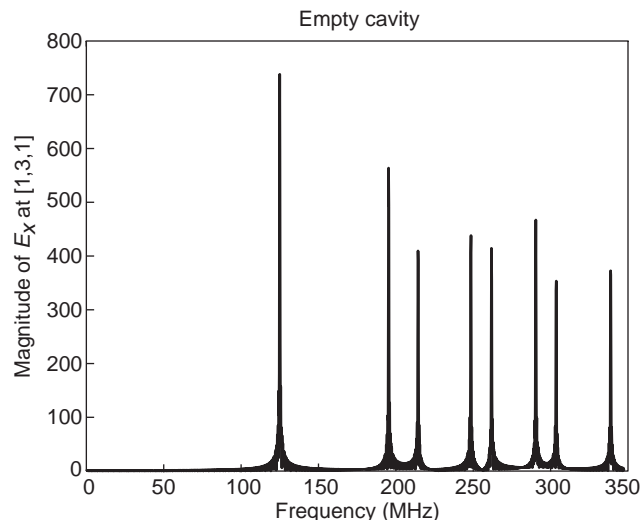


Figure 14. Frequency spectrum of E_x at the location [1,3,1] for an empty cavity.

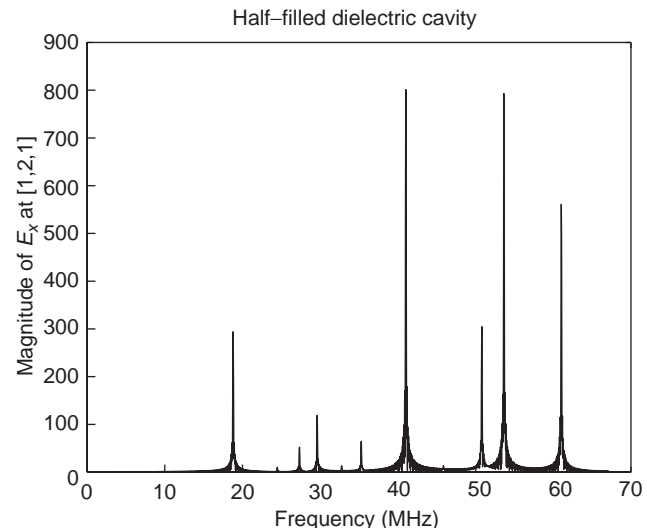


Figure 15. Frequency spectrum of E_x at the location [1,2,1] for a dielectric cavity with 50% filling.

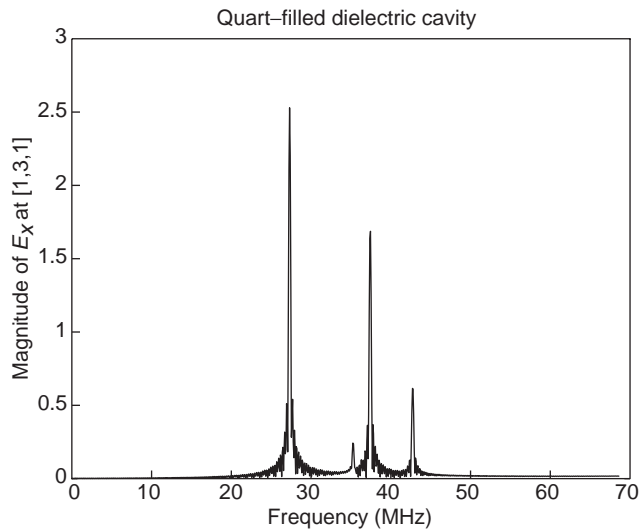


Figure 16. Frequency spectrum of E_x at [1,3,1] for a dielectric cavity with 25% filling.

$V = 1 \times 2 \times 1.5 \text{ m}^3$. We also analyze the same problem using the traditional FDTD mesh with a discretization of $\Delta x = \Delta y = 2.5 \text{ cm}$ and $\Delta z = 3 \text{ cm}$, specifically, $40 \times 40 \times 50$ cells. As seen from Figs. 17 and 18 and from Table 7, the two sets of computed results agree very well with each other and the percentage differences are 0.038% and 0.343%, for cases 1 and 2, respectively. However, the MIT MRTD scheme uses only 0.045% of the computational resources relative to the conventional FDTD algorithm.

8.2. Application of 2D MRTD

We consider a shielded microstrip line shown in Fig. 13a, whose trace is assumed very thin and perfectly conducting. Figure 19 shows that the propagation characteristics derived from an application of the present 2D MRTD scheme agree quite well with those derived from the spectral-domain approach (SDA) [31].

Next, we study the propagation characteristics of a shielded microstrip line, shown in Fig. 13a, whose dimensions and substrate material are given in the caption of Fig. 20. We observe, from Fig. 20, that the MRTD-computed results are in good agreement with those published in the literature, derived by using the FDTD [29]. For this case, the distance from the air-dielectric interface of the

Table 5. Resonant Frequencies (in MHz) for a Partially Filled Dielectric Cavity with 50% Filling^a

Analytic	FDTD [20] ($10 \times 20 \times 15$)	S-MRTD [20] ($2 \times 4 \times 3$)	This Method ($2 \times 4 \times 3$)	Percentage Difference (%)
18.627	18.615	18.715	18.692	0.349
27.172	27.140	27.350	27.313	0.519
29.375	29.215	29.580	29.526	0.514
35.069	34.970	35.280	35.247	0.507

^a $\epsilon_{r1} = \epsilon_{r2} = 64; N_{y1} = N_{y2} = 1.5; V = 1 \times 2 \times 1.5 \text{ m}^3; \Delta x = \Delta y = \Delta z = \frac{1}{2} \text{ m}$.

Table 6. Resonant Frequencies (in MHz) for a Partially Filled Dielectric Cavity with 25% Filling^a

Analytic	FDTD [21] ($10 \times 20 \times 15$)	S-MRTD [21] ($2 \times 6 \times 3$)	This Method ($2 \times 6 \times 3$)	Percentage Difference (%)
27.290	27.250	27.370	27.313	0.084
37.136	37.000	37.370	37.323	0.503
42.343	42.200	42.420	42.602	0.611

^a $\epsilon_{r1} = 64, \epsilon_{r2} = 1; N_{y1} = N_{y2} = 1.5; V = 1 \times 2 \times 1.5 \text{ m}^3; \Delta x = \Delta z = \frac{1}{2} \text{ m}; \Delta y = \frac{1}{3} \text{ m}$.

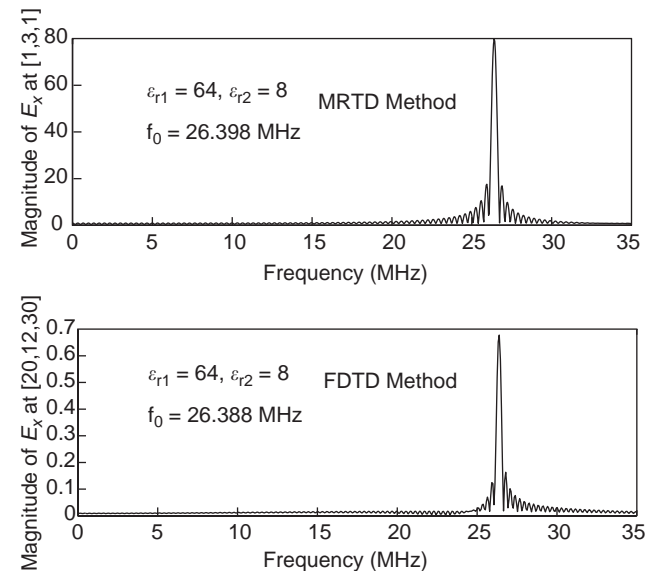


Figure 17. Frequency spectrum of E_x of a two-layer, dielectric-loaded cavity.

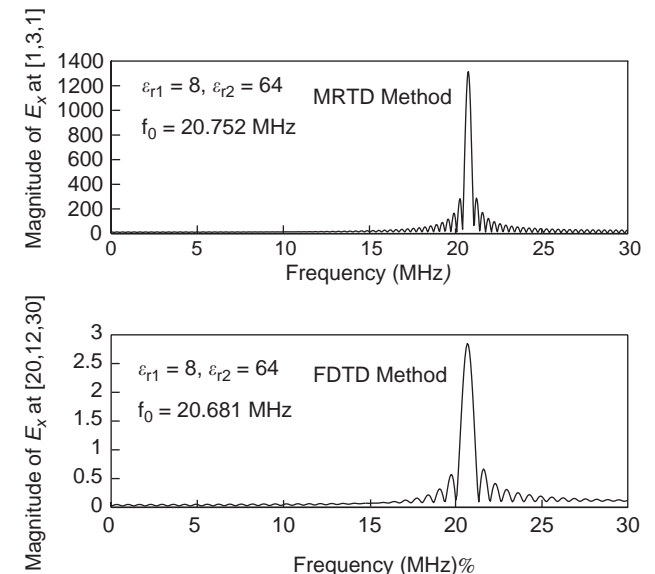


Figure 18. Frequency spectrum of E_x for a two-layer, dielectric-loaded cavity.

Table 7. Resonant Frequencies (in MHz) for a Two-Layer, Dielectric-Filled Cavity^a

Case	10.1 FDTD (40 × 40 × 50)	This Method (2 × 6 × 3)	Percentage Difference (%)
1	26.388	26.398	0.038
2	20.681	20.752	0.343

^a $N_{y1} = N_{y2} = 1.5$; $V = 1 \times 2 \times 1.5 \text{ m}^3$; $\Delta x = \Delta z = \frac{1}{2} \text{ m}$; $\Delta y = \frac{1}{3} \text{ m}$.

structure to the inner surface of the APML is seven cells. The corresponding discretization parameters employed in the FDTD and the MRTD methods are summarized in Table 8, and a comparison of the total number of cells needed in the MRTD and FDTD technique is presented in Table 8, and the relative advantage of the former is evident from the table.

Finally, we investigate an open microstrip line, whose geometry is specified in Fig. 13b. Once again, from Fig. 21 we observe good agreement between the computed results and those derived by using the FDTD [29,32], as well as the empirical approach [33,34]. The corresponding discretization parameters employed in the FDTD and MRTD methods are summarized Table 9. We note that the memory required in the 2D MRTD method is only about 6.25% or 7.64% of the 2D FDTD scheme for the same shielded and open microstrip lines, respectively. We further notice that, to ensure computational accuracy, we must employ at least two cells along the width of the narrow PEC strip.

9. SUMMARY OF MRTD

In this section we have presented an adjustable multiple-image technique, which can be incorporated in the multi-resolution time-domain (MRTD) scheme for the boundary truncation of PEC-shielded. We have also developed a 2D version of the MRTD, and have applied it in conjunction with an APML mesh truncation technique, for the analysis of both shielded and open microstrip lines. We have developed a systematic technique for constructing the multiple images, extracting the constitutive relations,

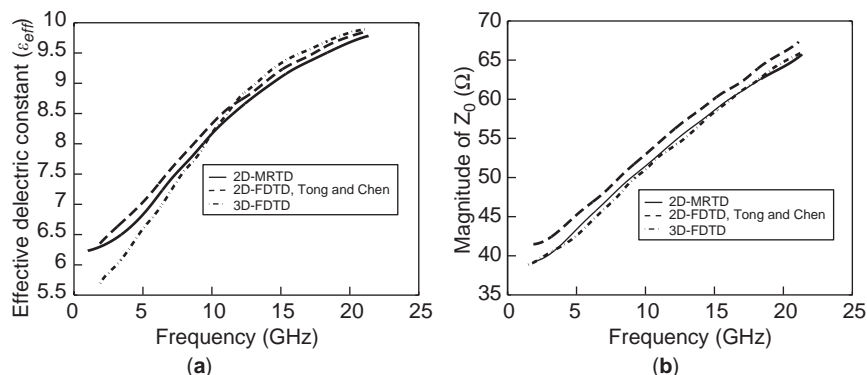


Figure 20. Frequency dependence of propagation characteristics of a shielded microstrip line with $w = h = 1.5 \text{ mm}$, $a = 6.5 \text{ mm}$, $b = 3.5 \text{ mm}$; $\epsilon_{xx} = \epsilon_{zz} = 9.4$, $\epsilon_{yy} = 11.6$: (a) ϵ_{eff} ; (b) magnitude of Z_0 in ohms. (Tong and Chan [29].)

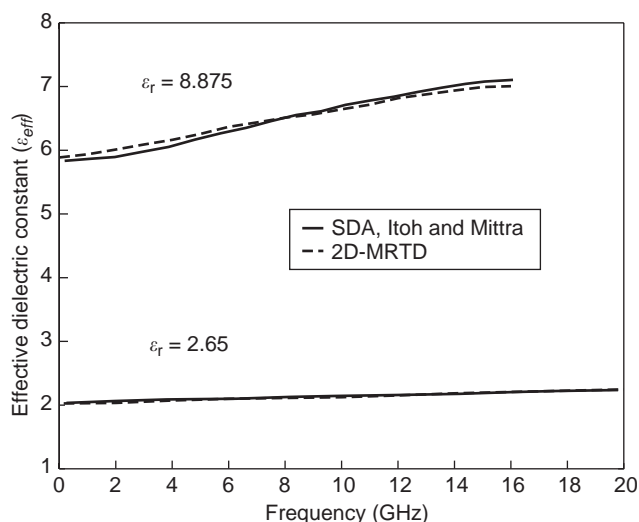


Figure 19. Effective dielectric constant ϵ_{eff} versus frequency of a shielded microstrip line with $w = h = 1.27 \text{ mm}$ and $a = b = 12.7 \text{ mm}$. (SDA, Itoh and Mittra [31].)

Table 8. Discretization Dimensions of a Shielded Microstrip Line^a

Method	Δx (mm)	Δy (mm)	N_x	N_y
2D MRTD	0.5	0.5	13	7
2D FDTD	0.125	0.125	52	28
3D FDTD	0.125	0.125	52	28

^a $\epsilon_{xx} = \epsilon_{zz} = 9.4$, $\epsilon_{yy} = 11.6$.

Table 9. Discretization Dimensions of an Open Microstrip Line^a

Method	Δx (mm)	Δy (mm)	N_x	N_y
2D MRTD	0.05	0.0333	21	12
2D FDTD	0.0125	0.0125	110	30
3D FDTD	0.0125	0.0125	55	30

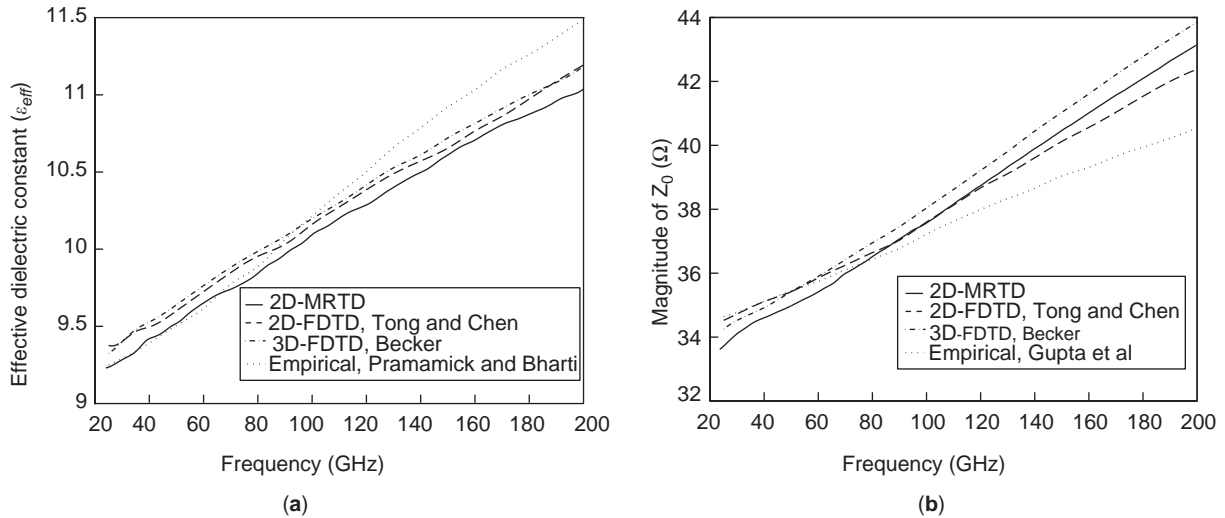


Figure 21. Frequency dependence of propagation characteristics of an open microstrip line with $w/h = 1.5$ mm, $h = 0.10$ mm; $\epsilon_r = 13.0$; (a) ϵ_{eff} ; (b) magnitude of Z_0 in ohms. (Tong and Chan [29], Becker [32], Gupta, Grag, and Chadha [34].)

deriving the update equations, and determining the number of images in the transform domain of the MRTD. The propagation characteristics computed via the MRTD have been shown to be in good agreement with those obtained by using other numerical techniques. The computational resources needed in the MRTD scheme are only a small fraction of those of the FDTD algorithm, albeit the computational complexity is higher in the MRTD. Although we have presented only a few representative examples of the application of the MRTD, its scope is wider, as is evident from a variety of problem to which it has been applied.

10. CONCLUSION

In this article we have briefly discussed two techniques for enhancing the FDTD algorithm: the conformal method and the MRTD algorithm. Space does not permit us to include two other approaches that are also quite important: the pseudospectral time-domain (PSTD) method and the multiscale analysis for dealing with geometries requiring a fine discretization in a subregion of the computational domain. We have simply chosen, as a compromise, to include some selected set of references on these two topics. The references on the multiscale analysis have been limited to those related to the FDTD/ADI algorithm and do not include a vast array of literature dealing with the problem of subgridding in FDTD.

BIBLIOGRAPHY

1. A. R. Bretones, R. Mittra, and R. G. Martin, A hybrid technique combining the method of moments in the time domain and FDTD, *IEEE Microwave Guided Wave Lett.* **8**(8):281–283 (Aug. 1998).
2. S. Gedney, F. Lansing, and D. Rescoe, A full wave analysis of passive monolithic integrated circuit devices using a generalized Yee algorithm, *IEEE Trans. Microwave Theory Tech.* **44**:1393–1400 (1996).
3. M. Fusco, FDTD algorithm in curvilinear coordinates, *IEEE Trans. Anten. Propag.* **38**(1):76–89 (Jan. 1990).
4. T. G. Jurgens, A. Taflove, K. Umashankar, and T. G. Moore, Finite-difference time-domain modeling of curved surfaces, *IEEE Trans. Anten. Propag.* **AP-40**(4):357–366 (April 1992).
5. S. Dey and R. Mittra, A locally conformal finite difference time domain (FDTD) algorithm for modeling three-dimensional perfectly conducting objects, *IEEE Microwave Guided Wave Lett.* **7**(9):273–275 (Sept. 1997).
6. K. S. Yee and J. S. Chen, The finite-difference time-domain (FDTD) and the finite-volume time-domain (FVTD) methods in solving Maxwell's equations, *IEEE Trans. Anten. Propag.* **AP-45**(3):355–363 (March 1997).
7. W. Yu, R. Mittra, D. Arakaki, and D. H. Werner, A conformal finite difference time domain (CFDTD) algorithm for modeling perfectly conducting objects, *16th Annual Review of Progress in Applied Computational Electromagnetics*, Monterey, CA, 2000.
8. W. Yu and R. Mittra, Accurate modeling of planar microwave circuit using conformal FDTD algorithm, *IEE Electron. Lett.* **36**(4) (2000).
9. W. Yu, and R. Mittra, A conformal FDTD software package for modeling of antennas and microstrip circuit components, *IEEE Anten. Propag. Mag.* **42**(5):28–39 (10 Oct. 2000).
10. N. Kaneda, B. Houshmand, and T. Itoh, FDTD analysis of dielectric resonators with curved surfaces, *IEEE Trans. Microwave Theory Tech.* **45**(9):1645–1649 (Sept. 1997).
11. S. Dey and R. Mittra, A conformal finite-difference time-domain technique for modeling cylindrical dielectric resonators, *IEEE Trans. Microwave Theory Tech.* **47**(9):1737–1739 (Sept. 1999).
12. W. Yu and R. Mittra, A conformal finite difference time domain technique for modeling curved dielectric surfaces, *IEEE Microwave Guided Wave Lett.* **11**(1):25–27 (Jan. 2001).

13. S. D. Gedney, An anisotropic PML absorbing media for FDTD solution of fields in lossy dispersive media, *Electromagnetic* **16**:399–415 (1996).
14. I. Wolff, Applications of finite-difference time-domain technique to planar microwave circuit design, in T. Itoh, ed., *Time-Domain Methods for Microwave Structures*, IEEE Press, 1998.
15. IE3D, Zeland Software, 39120 Argonaut Way, Suite 499, Fremont, CA 94538.
16. X.-P. Liang and K. A. Zakim, Modeling of cylindrical dielectric resonators in rectangular waveguides and cavity, *IEEE Trans. Microwave Theory Tech.* **41**(12):2174–2181 (Dec. 1993).
17. W. Yu and R. Mittra, *CFDTD: Conformal Finite-Difference Time-Domain Maxwell's Equations Solver: Software and User's Guide*, Artech House, Norwood, MA, 2003.
18. W. Yu and R. Mittra, A conformal FDTD software package for modeling of antennas and microstrip circuit components, *IEEE Anten. Propag. Mag.* **42**(5):28–39 (Oct. 2000).
19. M. Krumpholz and L. P. B. Katehi, MRTD: New time domain schemes based on multiresolution analysis, *IEEE Trans. Microwave Theory Tech.* **44**:555–571 (April 1996).
20. R. Robertson, E. Tentzeris, M. Krumpholz, and L. P. B. Katehi, MRTD analysis of dielectric cavity structures, *IEEE MTT-S Digest*, 1996, pp. 1861–1864.
21. E. Tentzeris, M. Krumpholz, and L. P. B. Katehi, Application of MRTD to printed transmission lines, *IEEE MTT-S Digest*, 1996, pp. 573–576.
22. Q. Cao and Y. Chen, MRTD analysis of a transient electromagnetic pulse propagating through a dielectric layer, *Int. J. Electron.* **86**:459–474 (April 1999).
23. R. L. Roberson, E. M. Tentzeris, M. Krumpholz, and L. P. B. Katehi, Modeling of dielectric cavity structures using multi-resolution time domain analysis, *Int. J. Num. Model. Electron. Networks Devices Fields* **11**:55–68 (April 1998).
24. Y. Chen, K. Sun, B. Berker, and R. Mittra, Unfield matrix presentation of Maxwell's and wave equations using generalized different differential matrix operators, *IEEE Trans. Educ.* **41**:61–69 (Feb. 1998).
25. G. Battle, A block spin construction of ondelettes, *Commun. Math. Phys.* **67**:601–615 (1987).
26. P. G. Lemarie, Ondelettes a localization exponentielle, *J. Math. Pure Appl.* **67**:277–236 (1988).
27. R. F. Harrington, *Field Computation by Moment Methods*, Krieger, Malabar, FL, 1982.
28. S. Xiao and R. Vahldieck, An efficient 2-D FDTD algorithm using real variables, *IEEE Microwave Guided Wave Lett.* **3**:127–129 (May 1993).
29. M. Tong and Y. Chen, Analysis of propagation characteristics and field images for printed transmission lines printed on anisotropic substrates using a 2D-FDTD method, *IEEE Trans. Microwave Theory Tech.* **MTT-46**:1507–1510 (Oct. 1998).
30. S. D. Gedney, An anisotropic perfectly matched layered-absorbing medium for the truncation of FDTD lattices, *IEEE Trans. Anten. Propag.* **44**:1630–1939 (1996).
31. T. Itoh and R. Mittra, A technique for computing dispersion characteristics of shielded microstrip line, *IEEE Trans. Microwave Theory Tech.* **MTT-22**:896–898 (Oct. 1974).
32. W. D. Becker, *The Application of Time-Domain Electromagnetic Field Solvers to Computer Package Analysis and Design*, Ph.D. dissertation, Dept. Electrical and Computer Engineering, Univ. Illinois at Urbana–Champaign, 1993.
33. P. Pramanick and P. Bharti, An accurate description of dispersion in microstrip, *Microwave J.* 89–96 (Dec. 1981).
34. K. C. Gupta, R. Grag, and R. Chadha, *Computer-aided Design of Microwave Circuits*, Artech House, Dedham, MA, 1981.

REFERENCES ON PSTD

- Q. H. Liu, A spectral-domain method with perfectly matched layers for time-domain solutions of Maxwell's equations, paper presented at 1996 URSI Meeting, Baltimore, MD, July 1996.
- Q. H. Liu, The PSTD algorithm: A time-domain method requiring only two cells per wavelength, *Microwave Opt. Technol. Lett.* **15**(3):158–165 (1997).
- Q. H. Liu, Large-scale simulations of electromagnetic and acoustic measurements using the pseudospectral time-domain (PSTD) algorithm, *IEEE Trans. Geosci. Remote Sens.* **37**(2):917–926 (1999).
- Q. H. Liu, PML and PSTD algorithm for arbitrary lossy anisotropic media, *IEEE Microwave Guided Wave Lett.* **9**(2):48–50 (1999).
- Q. H. Liu and G. X. Fan, A frequency-dependent PSTD algorithm for general dispersive media, *IEEE Microwave Guided Wave Lett.* **9**(2):51–53 (1999).
- Q. H. Liu and G. X. Fan, Simulations of GPR in dispersive media using the PSTD algorithm, *IEEE Trans. Geosci. Remote Sens.* **37**(5):2317–2324 (1999).
- Q. H. Liu and J. Q. He, An efficient PSTD algorithm for cylindrical coordinates, *IEEE Trans. Anten. Propag.* **49**(9):1349–1351 (2001).
- Q. H. Liu, X. M. Millard, B. Tian, and Z. Q. Zhang, Applications of nonuniform fast transform algorithms in numerical solutions of differential and integral equations, *IEEE Trans. Geosci. Remote Sens.* **38**(4):1551–1560 (2000).
- H. O. Kreiss and J. Olinger, Comparison of accurate methods for the integration of hyperbolic equations, *Tellus* **24**:199–215 (1972).
- S. A. Orszag, Comparison of pseudospectral and spectral approximation, *Stud. Appl. Math.* **51**:253–259 (1972).
- D. Gottlieb and S. A. Orszag, *Numerical Analysis of Spectral Methods*, SIAM, Philadelphia, 1997.
- C. Canuto, M. Y. Hussani, A. Quarteroni, and T. Zang, *Spectral Methods in Fluid Dynamics*, Springer-Verlag, New York, 1988.
- B. Fornberg, On a Fourier method for the integration of hyperbolic equations, *SIAM J. Num. Anal.* **12**:509–528 (1975).
- B. Fornberg, *A Practical Guide to Pseudospectral Methods*, Cambridge Univ. Press, New York, 1996.
- B. Yang, D. Gottlieb, and J. S. Hesthaven, Spectral simulation of electromagnetic wave scattering, *J. Comput. Phys.* **134**(2): 216–230 (1997).
- J. S. Hesthaven, Spectral collocation time-domain modeling of diffractive optical elements, *J. Comput. Phys.* **155**(2):287–306 (1999).
- B. Yang and J. S. Hesthaven, A pseudospectral method for time-domain computation of electromagnetic scattering by bodies of revolution, *IEEE Trans. Anten. Propag.* **47**(1): 132–141 (1999).
- B. Yang and J. S. Hesthaven, Multidomain pseudospectral computation of Maxwell's equations in 3-D general curvilinear coordinates, *Appl. Num. Math.* **33**(1–4):281–289 (2000).

- B. Tian and Q. H. Liu, Nonuniform fast cosine transform and Chebyshev PSTD algorithm, *Progr. Electromagn. Res.* **28**:259–279 (2000).
- G. X. Fan, Q. H. Liu, and S. A. Hutchinson, FDTD and PSTD simulations for plasma applications, *IEEE Trans. Plasma Sci.* **29**(2):341–348 (2001).
- G. X. Fan, Q. H. Liu, and J. S. Hesthaven, Multidomain pseudospectral time-domain method for simulation of scattering from buried objects, *IEEE Trans. Geosci. Remote Sens.* **40**(6):1366–1373 (2002).
- G. X. Fan and Q. H. Liu, Pseudospectral time-domain algorithm applied to electromagnetic scattering from electrically large objects, *Microwave Opt. Technol. Lett.* **29**(2):123–125 (2001).
- G. Zhao and Q. H. Liu, The 2.5-D multidomain pseudospectral time-domain algorithm, *IEEE Trans. Anten. Propag.* **51**(3):619–627 (2003).
- G. Zhao, Y. Q. Zeng, and Q. H. Liu, The 3-D multidomain pseudospectral time-domain method for wideband simulation, *IEEE Microwave Wireless Compon. Lett.* **13**(5):184–186 (2003).
- J. S. Hesthaven, Spectral penalty methods, *Appl. Num. Math.* **33**(1–4):23–41 (2000).
- D. Funaro and D. Gottlieb, A new method of imposing boundary conditions in pseudospectral approximations of hyperbolic equations, *Math. Comput.* **51**(184):599–613 (1988).

REFERENCES ON MULTISCALE ANALYSIS

- M. W. Chevalier, R. J. Luebbers, and V. P. Cable, FDTD local grid with material traverse, *IEEE Trans. Anten. Propag.* **45**:411–421 (March 1997).
- M. Okoniewski, E. Okoniewska, and M. A. Stuchly, Three dimensional subgridding algorithm for FDTD, *IEEE Trans. Anten. Propag.* **45**:422–429 (March 1997).
- M. Feliziani and F. Maradei, Mixed finite-difference/Whitney-elements time domain (FD/WE-TD) method, *IEEE Trans. Magn.* **34**:3222–3227 (March 1998).
- B. Z. Wang, Y. Wang, W. Yu, and R. Mittra, A hybrid 2D ADI-FDTD subgridding scheme for modeling on-chip interconnects, *IEEE Trans. Adv. Pack.* **24**:528–533 (Sept. 2001).
- Z. Chen and J. Zhang, An unconditionally stable 3-D ADI-MRTD method free of the CFL stability condition, *IEEE Microwave Wireless Compon. Lett.* **11**:349–351 (Aug. 2001).
- O. Podebrand, M. Clemens, and T. Weiland, New flexible subgridding scheme for the finite integration technique, *IEEE Trans. Magn.* **39**:1662–1665 (May 2003).
- M. Marrone, R. Mittra, and W. Yu, A novel approach to deriving a stable hybridized FDTD algorithm using the cell method, *Proc. IEEE AP-S URSI*, Columbus, OH, June 22–27, 2003.
- M. Marrone and R. Mittra, A theoretical study of the stability criteria for hybridized FDTD algorithms for multiscale analysis, *IEEE Anten. Propag. Mag.* (in press).

FABRY–PEROT RESONATORS

RONAN SAULEAU
University of Rennes
Rennes, France

1. THE PLANE-PARALLEL FABRY–PEROT INTERFEROMETER

1.1. Historical Background and Generalities

Two French physicists (Alfred Perot and Charles Fabry) developed the classical Fabry–Perot interferometer (FPI) or *etalon* at the beginning of the twentieth century. This novel form of interference device was based on multiple reflections of waves between two closely spaced and highly reflecting mirrors (the original thinly silvered *plane* glass mirrors were adjusted to be as flat and parallel to each other as possible). Alternative but conceptually equivalent elements are (1) the “solid” etalon made from some low-loss materials (e.g., fused quartz or sapphire) or (2) the Fabry-Perot (FP) cavity whose reflectors are partially transparent metal mirrors (e.g., perforated plates) or multilayer dielectric coatings (e.g., Bragg mirrors). The modal analysis of resonators with *spherical* mirrors is beyond the scope of this article. Nevertheless, all the abovementioned topologies are widely used at microwave frequencies; their choice depends on the envisaged applications, as described in Section 3.

The general concepts and theoretical analysis of these resonant optical cavities were published by George Airy about the middle of the nineteenth century. As we will see, plane-parallel FPIs have sharp resonances or transmission passbands at discrete frequencies. They thus behave as *narrowband frequency filters*. Their main characteristics (standing-wave resonance conditions, resonant frequencies, fringe contrast, free spectral range, half-power bandwidth, Q factor, reflectivity finesse) can be found in any general textbook dealing with optical resonators e.g., [1,2]. However, for consistency, these parameters are voluntarily derived in Section 1.2 using a *ray* approach. Although approximate, this analytical treatment reveals itself very fruitful for the analysis of FP-based devices operating at *microwave* and *millimeter-wave* frequencies (Section 2).

In their original form, FPIs used only flat reflecting surfaces, and the spacing between the mirrors was usually smaller than, or at most on the same scale as, the transverse diameters of the mirrors. Moreover, the FP interferometers were usually illuminated with a converging or diverging beam having a spread of angular directions, which resulted in “Fabry–Perot rings” transmitted through the interferometer in given discrete angular directions. Thus FPIs are also *spatial filters*. In particular, we will show in Section 3 that the high directivity of FP-based resonator antennas originates from this property.

Since its invention, the FPI has continued to evolve and find many new fields of applications, ranging, for instance, from astronomy, astrophysics, atomic spectroscopy, optics,

and similar applications to metrology, optical bistability, infrared, sensors, and plasma physics. A detailed and well-documented description of the FPI is given by Vaughan [3] at optical wavelengths. Here we concentrate only on radio-frequency and microwave implementations of FP resonators, such as quasioptical frequency filters, highly directive antennas, open resonators, or power combiners (Section 3).

1.2. Ray Analysis

The simplest way to define the basic properties of plane-parallel FPI is to use an infinite plane-wave model, with the plane waves assumed to be arriving at either normal or oblique incidence. The standard formulas developed here describe the transmission properties of FP etalons as a function of (1) the operating frequency and (2) the mirror spacing and reflectivity (the oblique incidence case is introduced in Section 3.1). The Gaussian beam optics [2] or full-wave methods (Section 2.1.3) should be applied to account for (1) the transverse width or shape of the two mirrors, (2) the transverse field variations, or (3) the complex geometry of reflectors.

The geometry of a plane-parallel FPI, depicted in Fig. 1, consists of two semitransparent plane mirrors, M_1 and M_2 , separated by a lossy medium of thickness D and refractive index n ($n = \epsilon_r^{1/2}$). As the mirrors are not confined by an aperture, diffraction is negligible and beam propagation inside the FPI can be described using geometric optics. Losses generated by scattering and absorption are incorporated in our model using the absorption coefficient α . A monochromatic plane wave illuminates the FPI under an incident angle θ . Its amplitude and angular frequency are labeled E_i and $\omega = 2\pi f$, respectively ($f = c_0/\lambda_0$ is the operating frequency; c_0 and λ_0 are the speed of light and wavelength in vacuum). The incident light is partially reflected and partially transmitted by the input mirror M_1 . The transmitted field travels to the output mirror M_2 , where it is again partially reflected and transmitted. The many reflected components add to produce a total field traveling in each direction. Consequently *multiple-beam interference*

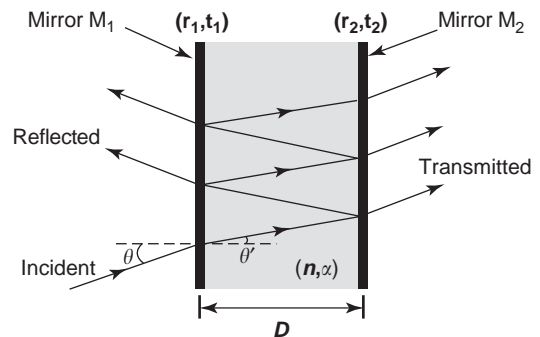


Figure 1. Schematic diagram of a plane-parallel Fabry–Perot interferometer (FPI) illuminated by a slightly off-axis incident plane wave. The two partially reflective mirrors M_i are characterized by their reflection and transmission coefficients r_i and t_i ($i = 1, 2$).

occurs. Two important points should be kept in mind: (1) the reflection and transmission coefficients at the interfaces are not the same for rays traveling in different directions; and (2) at optical wavelengths, highly reflecting mirrors of modern FPI are coated with multi-layer dielectric thin films, whereas they often consist of metallic grids (Section 2) from microwave to submillimeter wavelengths. Hence their reflection and transmission coefficients are in general complex quantities (Section 2.1.4), unlike the case of simple dielectric slabs for which the phase shift is either 0° or 180° depending on the dielectric contrast 1:n.

For convenience, we now assume that the mirrors are located in free space (n = 1). {r₁, t₁} and {r₂, t₂} denote the (frequency-dependent) reflection and transmission coefficients of M₁ and M₂, respectively. With these notations, the reflected and transmitted fields, E_r and E_t, at normal incidence (θ = 0) are given by

$$E_r = E_i \{ r_1 + r_2 t_1^2 \exp(-j2\varphi) \exp(-\alpha 2D) + r_1 r_2^2 t_1^2 \exp(-j4\varphi) \exp(-\alpha 4D) + \dots \} \tag{1}$$

$$E_t = E_i \{ t_1 t_2 \exp(-j\varphi) \exp(-\alpha D) + t_1 t_2 r_1 r_2 \exp(-j3\varphi) \exp(-\alpha 3D) + t_1 t_2 (r_1 r_2)^2 \exp(-j5\varphi) \exp(-\alpha 5D) + \dots \} \tag{2}$$

where φ = (2π/λ₀)D represents the phase change due to the optical path through the device.

Since the magnitude of the factor exp(-j2φ) exp(-α2D) is less than unity, both summations (1) and (2) are convergent geometric progressions

$$\frac{E_r}{E_i} = \left\{ r_1 + \frac{t_1^2 r_2 \exp(-j2\varphi) \exp(-2\alpha D)}{1 - r_1 r_2 \exp(-j2\varphi) \exp(-2\alpha D)} \right\} \tag{3}$$

$$\frac{E_t}{E_i} = \left\{ \frac{t_1 t_2 \exp(-j\varphi) \exp(-\alpha D)}{1 - r_1 r_2 \exp(-j2\varphi) \exp(-2\alpha D)} \right\} \tag{4}$$

The total power transmitted by the interferometer T_{FPI} is written

$$T_{FPI} = \left[\frac{E_t}{E_i} \right] \left[\frac{E_t}{E_i} \right]^* = \frac{T_1 T_2 \exp(-2\alpha D)}{1 - 2(R_1 R_2)^{1/2} \cos(2\varphi - \rho_1 - \rho_2) \exp(-2\alpha D) + R_1 R_2 \exp(-4\alpha D)} \tag{5}$$

where t_i = T_i^{1/2} exp(jτ_i) and r_i = R_i^{1/2} exp(jρ_i), i = 1, 2. T_i and R_i are known as the power transmittance and reflectance of mirrors M_i, respectively.

Neglecting all absorption processes (α = 0, T_i = 1 - R_i, i = 1, 2), we obtain

$$T_{FPI} = \frac{(1 - R_1)(1 - R_2)}{1 - 2(R_1 R_2)^{1/2} \cos(2\varphi - \rho_1 - \rho_2) + R_1 R_2} \tag{6}$$

Using the identity

$$1 - \cos \Psi = 2 \sin^2 \left(\frac{\Psi}{2} \right) \tag{7}$$

T_{FPI} can now be written

$$T_{FPI} = \frac{(1 - R_1)(1 - R_2)}{(1 - (R_1 R_2)^{1/2})^2 + 4(R_1 R_2)^{1/2} \sin^2 \left(\frac{2\varphi - \rho_1 - \rho_2}{2} \right)} \tag{8}$$

Equation (8) is known as the *Airy formula*.

Similarly, the power reflectance R_{FPI} of the FPI can be computed by multiplying the reflection coefficient E_r/E_i (3) by its complex conjugate. If absorption losses are negligible, we get

$$R_{FPI} = \frac{R_1 - 2(R_1 R_2)^{1/2} \cos(2\varphi - \rho_1 - \rho_2) + R_2}{1 - 2(R_1 R_2)^{1/2} \cos(2\varphi - \rho_1 - \rho_2) + R_1 R_2} \tag{9}$$

As our discussion has assumed for simplicity that any coating or gap absorption may be neglected (A_{FPI} = 0), it is left as an exercise to show that Eqs. (8) and (9) must add to unity

$$R_{FPI} + T_{FPI} = 1 \tag{10}$$

since energy must be conserved (A_{FPI} + R_{FPI} + T_{FPI} = 1).

Let us return to the interferometer transmission and assume that the reflectivities R₁ and R₂ are frequency-independent. In that case, inspection of relation (8) shows that a maximum of transmission occurs whenever the sine term becomes zero. This happens for

$$\frac{\Phi}{2} = \frac{2\varphi - \rho_1 - \rho_2}{2} = q\pi \tag{11}$$

where q = 0, 1, 2, ... is an integer referred to as the *longitudinal* (or *axial*) *mode number*.

Equation (11) corresponds exactly to the familiar *standing-wave condition* of multiple interference filters for which the total transmitted field is maximum whenever the round-trip phase shift Φ is an integer multiple of 2π [to account for the incidence angle and the dielectric constant of the substrate, D should be replaced by D(n² - sin² θ)^{1/2} in the definition of φ].

From (11) we deduce the expression of the *resonant frequency* $f_{\text{res},q}$ of the q th interference mode

$$f_{\text{res},q} = \frac{c_0}{2D} \left(q + \frac{\rho_1 + \rho_2}{2\pi} \right) \quad (12)$$

For full metal reflectors: $\rho_1 = \rho_2 = \pi$ and $f_{\text{res},q} = f_{\text{res},q,\text{metal}} = (q+1)(c_0/2D)$. As is well known, this corresponds to a gap spacing equal to an integer number of half-wavelengths at resonance [$D = (q+1)(\lambda_0/2)$]. At microwave frequencies, frequency-selective surfaces (FSSs) [4] are often employed as semitransparent mirrors (Section 2). Therefore, compared to the ideal case, two main differences appear:

- $\rho_1 < \pi$ and $\rho_2 < \pi \Rightarrow f_{\text{res},q} < f_{\text{res},q,\text{metal}}$.
- The frequency response of the mirrors is dispersive and $f_{\text{res},q}$ has to be computed numerically by solving the following equation

$$f_{\text{res},q} = \frac{c_0}{2D} \left(q + \frac{\rho_1(f_{\text{res},q}) + \rho_2(f_{\text{res},q})}{2\pi} \right) \quad (13)$$

This relation assumes that the frequency variations of ρ_1 and ρ_2 are known and the mutual coupling between mirrors is negligible (this hypothesis is false for thin FP resonators with capacitive mirrors; see Section 2.1.5).

At resonance, according to Eqs. (8) and (11), the maximum value $T_{\text{FP,max}}$ of T_{FP} is given by

$$T_{\text{FP,max}} = \frac{(1 - R_1)(1 - R_2)}{(1 - (R_1 R_2)^{1/2})^2} \quad (14)$$

whereas a minimum appears in the transmission curve if the sine term in (8) is unity

$$T_{\text{FP,min}} = \frac{(1 - R_1)(1 - R_2)}{(1 + (R_1 R_2)^{1/2})^2} \quad (15)$$

The q th *antiresonance frequency* $f_{\text{antires},q}$ is deduced from

$$\frac{\Phi}{2} = \frac{2\varphi - \rho_1 - \rho_2}{2} = (2q+1)\frac{\pi}{2} \quad (16)$$

and is equal to

$$f_{\text{antires},q} = \frac{c_0}{2D} \left(q + \frac{1}{2} + \frac{\rho_1 + \rho_2}{2\pi} \right) \quad (17)$$

The ratio of maximum to minimum transmission at normal incidence is called the *fringe contrast*

$$\frac{T_{\text{FP,max}}}{T_{\text{FP,min}}} = \frac{(1 + (R_1 R_2)^{1/2})^2}{(1 - (R_1 R_2)^{1/2})^2} \quad (18)$$

When mirrors are identical and lossless ($r_i = r$, $t_i = t$, $R_i = R$, $T_i = T = 1 - R$ for $i = 1, 2$), the maximum and minimum lev-

els of transmission become

$$T_{\text{FP,max}} = 1, \forall R \quad (19)$$

$$T_{\text{FP,min}} = \frac{(1 - R)^2}{(1 + R)^2} \quad (20)$$

Equation (19) implies that all the light impinging on the interferometer is transmitted and none is reflected; the FPI is matched and is analogous to a transmission line terminated by its characteristic impedance. Moreover, as the power transmittance of M_2 is $(1 - R)$, the intensity of the incident field on M_2 (inside the cavity) must be $[1/(1 - R)]|E_i|^2$. For instance, if $R = 99\%$, the incident intensity on M_2 must be 100 times larger than the intensity used to excite the cavity. Although the running-wave intensities on the inside of the resonator can be much larger than those on the outside, we have not violated conservation of energy. Rather, the intensity enhancement is a manifestation of the energy storage capabilities of a cavity with highly reflecting mirrors. As demonstrated in Section 3.2, the high directivity of FP-based antennas and their small bandwidth originate from this startling fact. Finally, we can account for the effect of the dielectric substrate in Eqs. (12), (13), and (17) if we substitute nD for D .

The variations of T_{FP} are represented in Fig. 2 as a function of frequency (or single-pass phase change φ) for symmetric lossless fused-quartz cavities ($\epsilon_r = 3.80$, $D = 3$ mm). These curves confirm that the fringe sharpness and contrast increase with R , while maintaining the transmission peak at unity. For asymmetric resonators (i.e., $R_1 \neq R_2$), $T_{\text{FP,max}} < 1$ (even for an ideal FPI). This issue and the influence of dielectric and conductor losses will be discussed in Section 2.2.2.

According to Eq. (12), the frequency interval Δf_{res} between two successive resonances (known as the *free spectral range*) is given by (21) or (22) (for grid or full metal

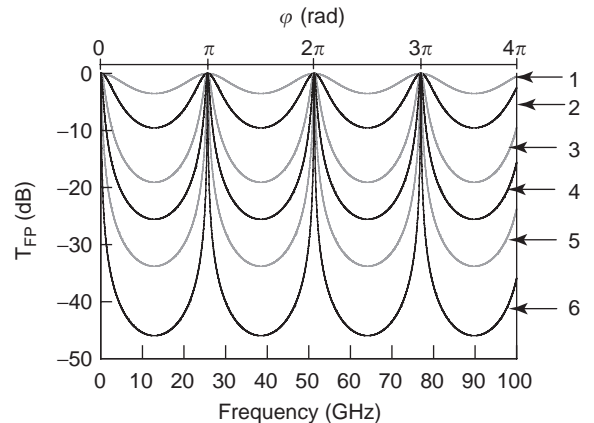


Figure 2. Influence of the reflectivity R of the mirrors on the transmittance T_{FP} [Eq. (8)] of a lossless FPI ($D = 3$ mm, $n = 1.95$, $\rho_1 = \rho_2 = \pi$, $\alpha = 0$). R varies between 20 and 99%. Curves (1) $R = 20\%$; (2) $R = 50\%$; (3) $R = 80\%$; (4) $R = 90\%$; (5) $R = 96\%$; (6) $R = 99\%$. (This figure is available in full color at <http://www.mrw.interscience.wiley.com/erfme>.)

mirrors, respectively)

$$\Delta f_{\text{res}} = \frac{c_0}{2D} \left(\frac{\rho_1 + \rho_2}{2\pi} \right) \quad (21)$$

$$\Delta f_{\text{res,metal}} = \frac{c_0}{2D} \quad (22)$$

The *half-power bandwidth* $\Delta f_{1/2}$ quantifies the sharpness of the transmission peaks ($\Delta f_{1/2}$ is referred to as the *resolution* at optical frequencies). Defining f_q^+ as the higher frequency at which the transmission has dropped to half its maximum value around the q th resonance, we have

$$\Delta f_{1/2} = 2(f_q^+ - f_{\text{res},q}) \quad (23)$$

f_q^+ is deduced from Eqs. (8) and (14)

$$\sin\left(\frac{2\varphi_q^+ - \rho_1 - \rho_2}{2}\right) = \frac{1 - (R_1 R_2)^{1/2}}{2(R_1 R_2)^{1/4}} \quad (24)$$

with $\varphi_q^+ = (2\pi D/c_0)f_q^+$. Substituting for f_q^+ from Eq. (23) and assuming that the angular variable $(\pi D/c_0)\Delta f_{1/2}$ is very small (which is true for narrow resonances), we obtain

$$\Delta f_{1/2} = \frac{c_0}{\pi D} \frac{1 - (R_1 R_2)^{1/2}}{2(R_1 R_2)^{1/4}} \quad (25)$$

This relation shows that the -3 dB bandwidth of a FPI whose mirrors are *nondispersive* depends only on the mirror reflectivities. Inspection of Eqs. (12) and (25) suggests that it seems possible to design a FPI with a prescribed resonant frequency and resolution. This will be discussed in Section 2.3 for the case of dispersive mirrors.

The frequency selectivity of the resonator is usually characterized by the *Q factor* of the q th longitudinal mode

$$Q_q = \frac{f_{\text{res},q}}{\Delta f_{1/2}} = \frac{(R_1 R_2)^{1/4}}{1 - (R_1 R_2)^{1/2}} \left[q\pi + \frac{\rho_1 + \rho_2}{2} \right] \quad (26)$$

$$Q_{q,\text{metal}} = \frac{f_{\text{res},q,\text{metal}}}{\Delta f_{1/2}} = \frac{\pi D}{\lambda_0/2} \frac{(R_1 R_2)^{1/4}}{1 - (R_1 R_2)^{1/2}} \quad (27)$$

Figure 3 represents the variations of Q for the first three resonances. At microwave frequencies, typical values of Q vary between 10 and 500 for antenna applications and can easily exceed 10^5 for highly resonant structures such as open resonators (Section 3.3). Unfortunately, at optical wavelengths, the Q values are astronomical, primarily because of the smallness of λ_0 (if $D = 1$ m, $n = 1$, $R_1 = R_2 = 99\%$, and $\lambda_0 = 0.6 \mu\text{m}$, then $Q_0 = 3.3 \times 10^8$). To avoid such large numbers and yet provide a measure of the frequency-filtering properties of the cavity, we may introduce a figure of merit known as the *reflectivity finesse* F_R and

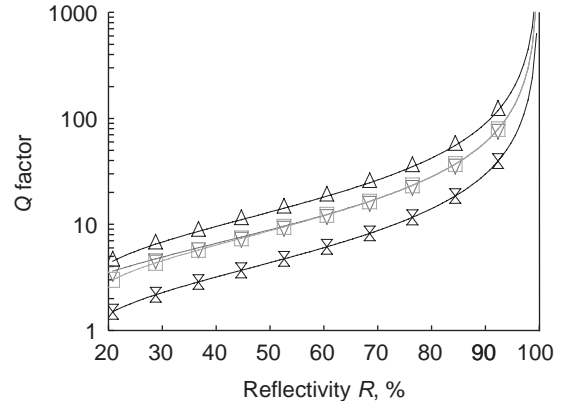


Figure 3. Variation of the Q factor of the q th longitudinal mode of a lossless FPI ($D = 3$ mm, $n = 1.95$, $\rho_1 = \rho_2 = \pi$, $\alpha = 0$) as a function of R . Q values are computed from Eq. (8). They are also compared to Eq. (26) for $q = 1$. Key: \times , $q = 0$ [Eq. (8)]; \square , $q = 1$ [Eq. (8)]; \triangle , $q = 2$ [Eq. (8)]; ∇ , $q = 1$ [Eq. (26)]. (This figure is available in full color at <http://www.mrw.interscience.wiley.com/erfme>.)

defined as

$$F_R = \frac{\Delta f_{\text{res}}}{\Delta f_{1/2}} = \frac{\rho_1 + \rho_2}{2\pi} \frac{\pi(R_1 R_2)^{1/4}}{1 - (R_1 R_2)^{1/2}} \quad (28)$$

For the numbers used above, this yields a more reasonable value ($F_R = 312$). The finesse is a dimensionless quantity depending only on the mirror reflectivities and gives the width of the resonance as a fraction of the spacing between the resonances for an ideal monochromatic source. As it is independent of the free spectral range, this is a measure of the resolving power of the FPI.

2. GEOMETRY, METHODS OF ANALYSIS, PERFORMANCE, AND DESIGN OF MICROWAVE FABRY-PEROT CAVITIES

In the previous section, the basic properties of *optical* FP resonators have been established using a ray model. In particular, it has been shown that the reflection and transmission coefficients of the mirrors play a crucial role in the frequency response of a FPI. For this reason the first part of this section deals exclusively with the analysis and the performance of *periodic* metal grid mirrors that are often used at *microwave* frequencies. Although we do not voluntarily delve deep into the details, this introduction appears essential for a coherent presentation of the characteristics and design rules of *plane-parallel* FP cavities (Sections 2.2 and 2.3). Finally, we investigate briefly the performance of multilayer semitransparent structures (Section 2.4) and compare them to stacked dielectric slabs (Section 2.5). Applications involving all these devices are discussed in Section 3, where we also summarize the properties of *convex* resonators.

2.1. Geometry, Modeling, and Characteristics of Metallic Reflecting Mirrors

For most applications, it is often desirable to obtain a high value of Q in an order as low as possible ($1 - R \ll 1$) and low

absorption losses ($A \ll 1-R$). These requirements cannot be fulfilled simultaneously by thin homogeneous metal layers in the far-infrared and at microwave and (sub) millimeter-wave frequencies. In that frequency range, two kinds of mirrors are mainly used: (1) partially reflective metal grids [or frequency-selective surfaces (FSSs)] and (2) multilayer dielectric mirrors (or Bragg mirrors). The latter are briefly described in Section 2.5.

FSSs have an extremely broad range of applications (e.g., laser technologies, quasioptical components diplexers, interference filters, polarizers, etc., FPIs, dichroic reflectors and subreflectors, high-gain antennas), and a very abundant literature is available on that subject¹ [4].

For the sake of coherence and concision, and for the purpose of this discussion, only the basic principles of FSS operation are reviewed. After a preliminary introduction about the modeling of infinite periodic structures (Section 2.1.1), we will start with devices that can be treated as simple transmission-line elements operating in the long-wavelength regime and can be analyzed using the transmission-line matrix techniques (Section 2.1.2). In particular, this includes one-dimensional (1D) and two-dimensional (2D) inductive and capacitive metal grids. Alternative global electromagnetic approaches are also discussed in Section 2.1.3. The frequency response of such mirrors is finally presented in Sections 2.1.4 and 2.1.5.

2.1.1. Preliminaries. Let us consider a 2D planar periodic infinite array illuminated by a linearly polarized homogeneous plane wave of incident wavevector \vec{k}^i (Fig. 4). The spatial periods are labeled d_x and d_y in x and y directions, respectively. By analogy with Fourier decomposition of periodic signals, it can be demonstrated that the electric field \vec{E}_s scattered by the array is an infinite sum of Floquet space harmonics [5]

$$\vec{E}_s(\vec{r}) = \sum_{n=-\infty}^{+\infty} \sum_{m=-\infty}^{+\infty} \vec{E}_{s, nm} e^{-j\vec{k}_{nm} \cdot \vec{r}} \quad (29)$$

The wavevector \vec{k}_{nm} of each harmonic can be decomposed in transverse (to z direction) and longitudinal components

$$\vec{k}_{nm} = \vec{k}_{t, nm} + k_{z, nm} \cdot \vec{e}_z$$

With

$$\vec{k}_{t, nm} = k_{x, n} \cdot \vec{e}_x + k_{y, nm} \cdot \vec{e}_y$$

$$k_{x, n} = k_x^i + \frac{2\pi n}{d_x} = -k \sin(\theta) \cos(\varphi) + \frac{2\pi n}{d_x}$$

$$k_{y, nm} = k_y^i + \frac{2\pi m}{d_y} = -k \sin(\theta) \sin(\varphi) + \frac{2\pi m}{d_y}$$

¹For further information, refer also to the articles entitled FREQUENCY-SELECTIVE SURFACES AND PERIODIC STRUCTURES published in that Encyclopedia.

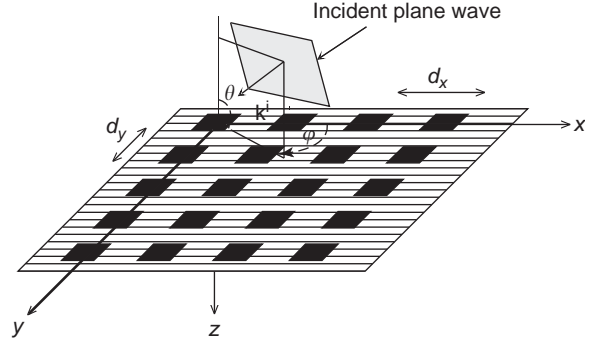


Figure 4. Incident plane wave illuminating a 2D planar periodic array.

And with

$$k_{z, nm} = \sqrt{k^2 - k_{x, n}^2 - k_{y, nm}^2}, \quad \text{if } k^2 > k_{x, n}^2 + k_{y, nm}^2 = k_{t, nm}^2$$

or

$$k_{z, nm} = -j\sqrt{-k^2 + k_{x, n}^2 + k_{y, nm}^2}, \quad \text{if } k^2 < k_{x, n}^2 + k_{y, nm}^2$$

respectively.

The effective direction of propagation (\vec{k}_{nm}) of each mode depends on (1) the order (n, m) of the mode under consideration, (2) the geometry of the unit periodic cell, and (3) the frequency, polarization, and directions (θ, φ) of the incident plane wave.

If $k_{t, nm}^2 > k^2$, then $k_{z, nm}$ is a pure imaginary number; the scattered field is evanescent along (Oz) and is propagating along the plane of the periodic array ($\theta_{nm} = 90^\circ$). It interacts with the metallic patterns and contributes to the *inductive* or *capacitive* behavior of the screen. On the contrary, if $k_{z, nm}$ is real, the wave is propagating outside the structure, and grating lobes may appear, depending on the operating frequency and angles of incidence.

According to Eq. (29), each component of \vec{E}_s can be written as

$$X(\vec{r}) = e^{-j\vec{k}^i \cdot \vec{r}_T} \sum_{n=-\infty}^{+\infty} \sum_{m=-\infty}^{+\infty} X_{nm} e^{-j(n\vec{k}_1 + m\vec{k}_2) \cdot \vec{r}_T} e^{-jk_{z, nm} z} \quad (30)$$

where $\vec{r}_T = x\vec{e}_x + y\vec{e}_y$, $\vec{r} = x\vec{e}_x + y\vec{e}_y + z\vec{e}_z$, $\vec{k}_1 = -(2\pi/A)\vec{e}_z \times \vec{d}_y$, $\vec{k}_2 = (2\pi/A)\vec{e}_z \times \vec{d}_x$; $A = d_x d_y$ is the area of the unit periodic cell. The factor

$$e^{-j\vec{k}^i \cdot \vec{r}_T} = e^{-j[k \sin(\theta) \cos(\varphi)x + k \sin(\theta) \sin(\varphi)y]} \quad (31)$$

is referred to as the *Floquet phase factor*.

To conclude: (1) the field distributions from one periodic cell to another are identical, except to a phase factor; and (2) the computation of the scattering matrix of the infinite array requires to model only *one single unit cell*.

2.1.2. Transmission-Line Matrix Approach. The transmission-line (TL) matrix method is a very convenient

one for the analysis or design of multilayer systems including layers of different dielectric permittivities and planar geometries. It has been described in details elsewhere [e.g., 6]. We present only the fundamental concepts: (1) *ABCD* matrix, (2) modeling of dielectric slabs, and (3) modeling of periodic metallic mirrors.

2.1.2.1. ABCD matrix. We assume that only a single mode is propagating. The various elements of the system affect only the complex amplitude of the reflected and transmitted waves. Let us consider a linear two-port device. The input and output currents and voltages, defined in Fig. 5a, are related by the following matrix equation

$$\begin{bmatrix} V_1 \\ I_1 \end{bmatrix} = \begin{bmatrix} A & B \\ C & D \end{bmatrix} \begin{bmatrix} V_2 \\ I_2 \end{bmatrix} \quad (32)$$

The elements of the matrix are called the *ABCD parameters*, and the matrix itself is referred to as the *transmission-line matrix* or *ABCD matrix*.

When considering N cascading elements (Fig. 5b), the convention for the currents and voltages is such that the output current and voltage for a given element are equal to the input current and voltage for the following element. As a result, the *ABCD* matrix of the whole system is simply the product of the individual matrices

$$\begin{bmatrix} V_{in,1} \\ I_{in,1} \end{bmatrix} = \begin{bmatrix} A_1 & B_1 \\ C_1 & D_1 \end{bmatrix} \begin{bmatrix} A_2 & B_2 \\ C_2 & D_2 \end{bmatrix} \begin{bmatrix} A_3 & B_3 \\ C_3 & D_3 \end{bmatrix} \begin{bmatrix} V_{out,3} \\ I_{out,3} \end{bmatrix} \quad (33)$$

The scattering matrix [S] of the two-port junction is easily deduced from the *ABCD* coefficients [6]

$$S_{11} = \frac{A + B/Z_c - CZ_c - D}{A + B/Z_c + CZ_c + D} \quad (34)$$

$$S_{12} = \frac{2(AD - BC)}{A + B/Z_c + CZ_c + D} \quad (35)$$

$$S_{21} = \frac{2}{A + B/Z_c + CZ_c + D} \quad (36)$$

$$S_{22} = \frac{-A + B/Z_c - CZ_c + D}{A + B/Z_c + CZ_c + D} \quad (37)$$

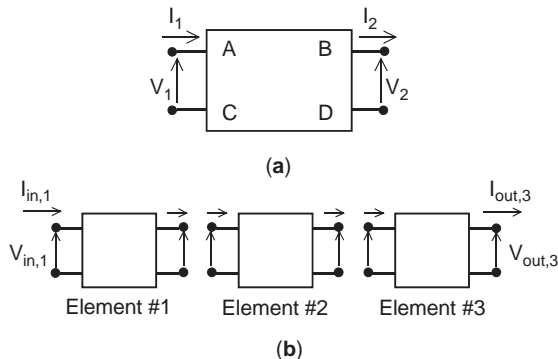


Figure 5. (a) Definition of the *ABCD* parameters of a linear two-port device modeled by the transmission-line matrix approach; (b) cascading transmission-line elements ($N=3$).

where Z_c is the normalization characteristic impedance. Note that the *ABCD* matrix has the following properties: (1) for reciprocal elements, $AD-BC=1$ ($S_{12}=S_{21}$); (2) $A=D$ for symmetric devices.

2.1.2.2. Modeling of Dielectric Slabs. The TL matrix of a dielectric slab of thickness D and refractive index $n = \epsilon_r^{1/2}$ ($\epsilon_r = \epsilon' - j\epsilon''$) is

$$\begin{bmatrix} \cosh \gamma D & Z \sinh \gamma D \\ \frac{1}{Z} \sinh \gamma D & \cosh \gamma D \end{bmatrix} \quad (38)$$

where γ is the propagation constant in the dielectric material; the wave impedance Z differs for the parallel ($||$) and perpendicular (\perp) polarizations

$$\gamma = j \left(\frac{2\pi n}{\lambda_0} \right) \cos \theta \quad (39)$$

$$Z_{||} = \frac{Z_0(\epsilon' - \sin^2 \theta_i)^{1/2}}{\epsilon'} \quad (40)$$

$$Z_{\perp} = \frac{Z_0}{(\epsilon' - \sin^2 \theta_i)^{1/2}} \quad (41)$$

Here, θ_i and θ are the angles of incidence of the plane wave illuminating the slab and the propagation angle relative to normal incidence in this material, respectively. Both angles are related by Snell's law. For low-loss materials, $n \approx (\epsilon')^{1/2} [1 - j(\tan \delta/2)]$, and for lossless materials, Eq. (38) becomes

$$\begin{bmatrix} \cos \beta D & jZ \sin \beta D \\ \frac{j}{Z} \sin \beta D & \cos \beta D \end{bmatrix} \quad (42)$$

$\beta = (2\pi/\lambda_0)(\epsilon' - \sin^2 \theta_i)^{1/2}$ is the imaginary part of γ .

Other TL matrices are given in the literature [e.g. 6,7].

2.1.2.3. Modeling of Periodic Metallic Mirrors. The extremely extensive literature on metallic periodic structures includes many elaborate analytical treatments as well as numerical methods (Section 2.1.3). We restrict ourselves to the simplest cases, referring the reader to specific publications for detailed information [4,5,8-10]. Figure 6a represents typical geometries of 1D and 2D metallic grids (of thickness t and conductivity σ) commonly used in microwave applications involving FP cavities. 1D grids are also called ("strip") gratings; and 2D grids, "meshes". These grids are located at the interface between two semiinfinite dielectric materials $(\epsilon_{r,i}, \tan \delta_i)_{i=1,2}$ and are assumed illuminated by a normally incident ($\theta_i=0$) linearly polarized plane wave \mathbf{E}_i (Fig. 6b). As suggested in the preliminaries, they are typically classified into two categories (*inductive* or *capacitive*) depending on their geometry and the orientation of \mathbf{E}_i . This terminology is

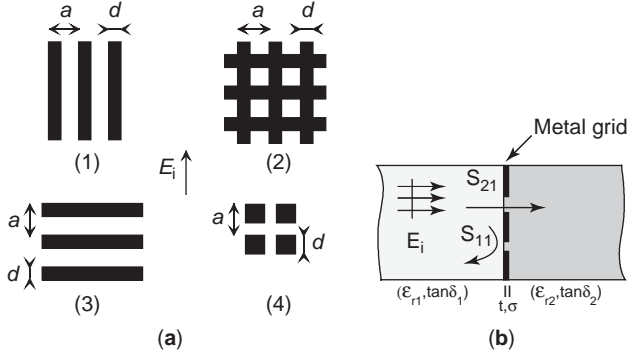


Figure 6. (a) Traditional geometries of metallic periodic grids employed as reflecting mirrors of FP cavities. The grid is illuminated by an incident electric field \mathbf{E}_i . The general terminology qualifying these grids is the following: (1) 1D inductive; (2) 2D inductive; (3) 1D capacitive; (4) 2D capacitive. (b) Metallic grid located at the interface between two semiinfinite dielectric media $(\epsilon_{r,i}, \tan \delta_i)_{i=1,2}$.

justified later on. Their spatial period is labeled a ; d denotes the width of the metallic patterns.

At long wavelengths regime ($a \ll \lambda_0$), only the fundamental mode $(n,m) = (0,0)$ is propagating. The other modes are evanescent (Section 2.1.1) and decay exponentially away from the grid. Consequently such structures reflect and transmit in zero order only in specular directions (no grating lobes appear in the visible region [4,5]). They can be modeled by an impedance Z shunting a transmission line (Fig. 6b) whose $ABCD$ matrix is given by Eq. (43)

$$\begin{bmatrix} 1 & 0 \\ Y & 1 \end{bmatrix} \quad (43)$$

$$Z = \frac{1}{Y} = R_\sigma + jX \quad (44)$$

The real part R_σ accounts for conductor losses inside finite conductivity grids. Ulrich [11] found a good agreement with experience if $(R_\sigma/Z_0) = (a/d)[\pi f(\epsilon_0/\sigma)]^{1/2}$, where f is the operating frequency and $Z_0 = (\mu_0/\epsilon_0)^{1/2}$ is the wave impedance in free space.

The reactance X depends on λ_0 and grid parameters (a,d) . Surveying literature on that subject is well beyond the scope of this article and would require much more space; a well-documented description of equivalent circuits is given elsewhere [e.g., 12, Chap. 9]. Their range of validity is also discussed in Refs. 13 and 14. Here we present only general principles for the purpose of discussion.

Historically, Marcuvitz [8] was probably one of the first authors to propose explicit expressions of Z for inductive (Fig. 6a, grid 1) and capacitive (Fig. 6a, grid 3) strip gratings illuminated by a TM/TE incident plane wave. The reactance of a freestanding ($\epsilon_{r,1} = \epsilon_{r,2} = 1$) zero-thickness inductive grid ($X = X_i$, $Z = Z_i$) has the following form [8]

$$\frac{X_i}{Z_{fs}} = \omega \ln \frac{1}{\sin\left(\frac{\pi d}{2a}\right)} \quad (45)$$

where $\omega = (a/\lambda_0)$ is the normalized frequency and Z_{fs} is the characteristic transmission-line impedance. Z_{fs} is given by Eqs. (40) and (41) for TM and TE polarizations, respectively. At normal incidence ($Z_{fs} = Z_0$), a more accurate expression is available [8]

$$\begin{aligned} \frac{X_i}{Z_0} = \omega \left\{ \ln\left(\frac{1}{\sin(\beta)}\right) \right. \\ \left. + \frac{Q_2 \cos^4(\beta)}{1 + Q_2 \sin^4(\beta)} + \frac{1}{16} \omega^2 (1 - 3 \sin^2(\beta))^2 \cos^4(\beta) \right\} \end{aligned} \quad (46)$$

with $\beta = (\pi d/2a)$ and $Q_2 = (1 - \omega^2)^{-1/2} - 1$. Equation (46) is deduced from an integral formulation in which only the first two diffraction modes are taken into account.

According to Eqs. (34), (36), (43), and (44), the reflection and transmission coefficients of zero-thickness grids are equal to

$$r = S_{11} = \frac{-1}{1 + 2\frac{Z}{Z_{fs}}} \quad (47)$$

$$t = 1 + r = S_{21} = \frac{1}{1 + \frac{2Z}{Z_{fs}}} \quad (48)$$

The power reflectivity $R = |r|^2$ and the phase $\arg(r)$ of the reflection coefficient are represented as a function of ω in Figs. 7a and 7b for a strip grating modeled by Eq. (46). As expected, for a given frequency, R and $\arg(r)$ are decreasing functions of the filling factor d/a . Similarly, they decrease with ω for given values of a and d/a . Keeping in mind these evolutions is important to understand and interpret the influence of the grid geometry on the frequency response of FP cavities (Section 2.2.2).

It is advisable to mention that the equivalent circuits of grids should be applied cautiously [14]. As an illustration, Figs. 8a and 8b quantify the range of validity and the accuracy of Marcuvitz model (46) in the nondiffraction region for a wide range of grid geometries ($a = 1$ mm, $5\% < d/a < 75\%$). For that purpose, two indicators are defined

$$\Delta R = R - R_{\text{FDTD}} \quad (49)$$

$$\Delta \arg(r) = \arg(r) - \arg(r)_{\text{FDTD}} \quad (50)$$

R and R_{FDTD} [resp. $\arg(r)$ and $\arg(r)_{\text{FDTD}}$] are the reflectivities (resp. the phases of r) computed with the TL method and the finite-difference time-domain (FDTD) technique (Section 2.1.4).

Ulrich [11] later developed equivalent models for freestanding 2D grids; at long wavelengths, inductive meshes (Fig. 6a, grid 2) reflect most of the incident power. Their frequency response is thus very similar to that of inductive strip gratings. Nevertheless they present a resonance around $\lambda_0 \approx a$, where they are totally transparent. This single-pole highpass behavior can be represented by an oscillatory equivalent circuit (L,C) whose reactance X_i has

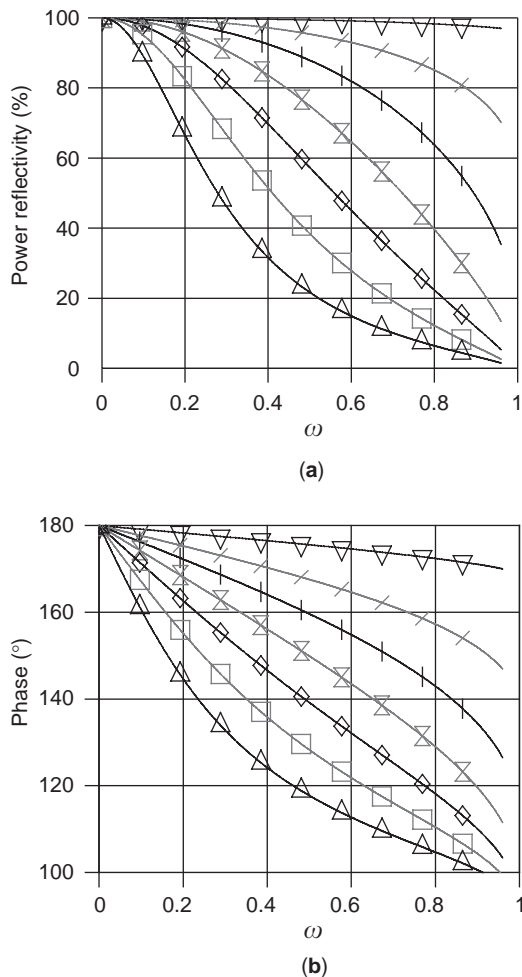


Figure 7. Reflection properties of freestanding 1D inductive strip gratings ($a = 1$ mm) illuminated by a normally incident plane wave. Their geometry is represented in Fig. 6a, grid 1. The grid is assumed lossless ($\sigma = \infty$, $R_s = 0$) and infinitely thin ($t \ll \lambda_0$). Its equivalent reactance is given by Eq. (46). (a) Power reflectivity R ; (b) phase of the reflection coefficient $\arg(r)$. Key: \triangle , $d/a = 11.07\%$; \square , $d/a = 20.7\%$; \diamond , $d/a = 30.7\%$; \times , $d/a = 40.7\%$; $+$, $d/a = 50.7\%$; --- , $d/a = 60.7\%$; ∇ , $d/a = 75.7\%$. (This figure is available in full color at <http://www.mrw.interscience.wiley.com/erfme>.)

the following expression

$$X_i = -\omega_0 \ln \left\{ \frac{1}{\sin\left(\frac{\pi d}{2a}\right)} \right\} \left(\frac{\omega}{\omega_0} - \frac{\omega_0}{\omega} \right)^{-1} \quad (51)$$

$$\omega_0 = 1 - 0.27 \frac{d}{2a} \quad (52)$$

where ω_0 defines the position of the resonance (52) and was obtained by fitting experimental data and calculation [11]. More accurate expressions for X_i and ω_0 have been proposed [14] over a very wide frequency band.

The interested reader will find more details about (1) other equivalent models and (2) the influence of (a) the

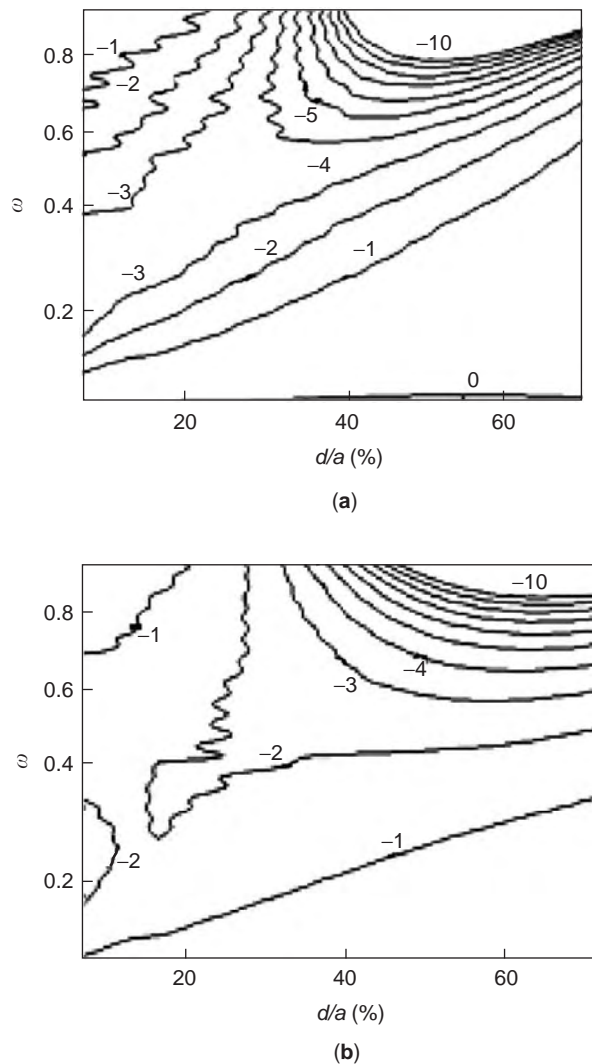


Figure 8. Validity and accuracy of the equivalent circuit [Eq. (46)] proposed by Marcuvitz [8]. ΔR (a) and $\Delta \arg(r)$ (b) are defined by Eqs. (49) and (50), respectively. The equiamplitude contours show that Marcuvitz formulation is accurate ($|\Delta R| < 3\%$ and $|\Delta \arg(r)| < 2^\circ$) in the nondiffraction region ($\omega < 1$) for $d/a < 35\%$, and for any d/a if $\omega < 0.6$. (From Ref. 14; copyright Kluwer Academic/Plenum Publishers, reproduced by permission).

oblique incidence illumination, (b) the dielectric substrates supporting the mirrors, or (c) the finite conductivity and thickness of the grids in the literature [8–10,13–22]. A very interesting discussion about periodic grids is also provided in the bibliographic notes [12, pp. 307–312].

2.1.3. Electromagnetic Modeling. Many modeling approaches have been developed to predict the scattering properties of multilayer periodic structures. They could be applied for the analysis of complex FP cavities coupled to real feeds. The following references might be consulted for further information.

Analytical treatments, including the homogenization technique and the averaged boundary conditions, are explained in detail in Refs. 9, 10, and 23. Generally

sophisticated numerical methods can also be implemented, such as (1) the equivalent multimode network method [24,25]; (2) the modal expansion method in which the diffracted and aperture fields are decomposed in space harmonics and waveguide modes, respectively [16,19,26]; (3) the spectral domain approach [27]; (4) the generalized scattering matrix theory [27,28]; (5) the finite-element method [29,30]; (6) the boundary element method [31]; or (7) the finite-difference techniques applied either in the time domain (FDTD) [32] or in the frequency domain (FDFD) [33].

2.1.4. Frequency Response of 2D Inductive Metal Meshes. The complex reflection coefficient of freestanding perfectly conducting meshes ($\epsilon_{r,i}=1$, $\tan \delta_i=0$, $i=1,2$; $a=1$ mm; $\sigma=\infty$, $t=0$) is represented in Figs. 9a and 9b for a normally incident plane wave and for various filling factors d/a [34]. These curves confirm the highpass filter behavior of inductive meshes. The reflectivity and phase increase with d/a but decrease with the normalized frequency ω . Comparison with the frequency response of 1D grids (Fig. 7) provides evidence of the resonance of 2D grids appearing for $0.9 < \omega < 1$, as suggested by Eq. (52).

2.1.5. Complementary and capacitive grids. Impact on FP resonators. The grids discussed so far correspond to the commonly used geometry of semitransparent mirrors of microwave FP cavities. They are oriented parallel to the direction of the incident electric field in order to obtain a high reflectivity (for $a \ll \lambda_0$), and thus high- Q resonators.

According to the Babinet principle, if we interchange the perfectly conducting and empty parts of infinitely thin ($t=0$) grids and rotate by 90° the polarization direction of the incident plane wave, then the reflection and transmission coefficients of the original and *complementary* grids, labeled $\{r,t\}$ and $\{r_c,t_c\}$, respectively are related as follows [11]

$$\begin{aligned} t + t_c &= 1 \\ t_c &= -r \\ r_c &= -t \end{aligned} \quad (53)$$

The shunt impedance Z_c of the complementary grid is deduced from Eqs. (47), (48), and (53)

$$\frac{Z_c}{Z_{fs}} = \frac{Z_{fs}}{4Z_i} \quad (54)$$

As Z_c is inversely proportional to frequency, these structures are called *capacitive grids*. Their reflection coefficient, computed with the FDTD technique, is represented in Figs. 10a and 10b for various values of d/a . As expected, their reflectivity naturally increases with frequency (dual behavior of inductive grids).

Transmission line models of capacitive grids have been also proposed by several authors [8, pp. 218–219, 280–284] [11,15,18–20,102]. Their accuracy and range of validity have been defined recently [103] over the whole visible region ($\lambda_0 > a$) by comparison with the FDTD results given in Figs. 10a and 10b (the methodology implemented is

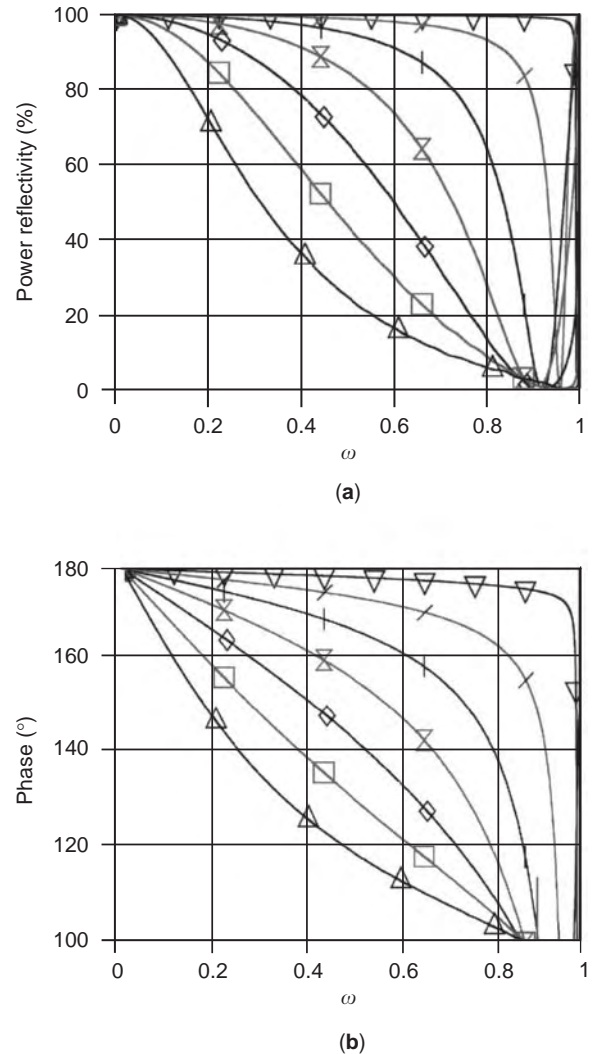


Figure 9. Theoretical frequency response of perfectly conducting 2D inductive meshes computed with the FDTD method: (a) power reflectivity R ; (b) phase of the reflection coefficient $\arg(r)$. The geometry of the mesh is represented in Fig. 6a, grid 2. Key: \triangle , $d/a=11.07\%$; \square , $d/a=20.7\%$; \diamond , $d/a=30.7\%$; \times , $d/a=40.7\%$; $+$, $d/a=50.7\%$; $-$, $d/a=60.7\%$; ∇ , $d/a=72.7\%$. (From Ref. 34; copyright Kluwer Academic/Plenum Publishers, reproduced by permission.) (This figure is available in full color at <http://www.mrw.interscience.wiley.com/erfme>.)

similar to the one associated with Eqs. (49) and (50)). By analogy with inductive meshes [14], very accurate and ultra-wideband explicit formulations are also introduced in [103] for the wave reactances.

To obtain a high- Q cavity, both capacitive grids should be highly reflecting [Eq. (26)]. This implies

- $\omega > 0.85$ and $d/a \approx 1$ (Fig. 10a).
- $-160^\circ < \arg(r) < -180^\circ$ (Fig. 10b).
- The first resonant frequency is defined for $q=1$ [Eq. (12)].

Consequently the gap D is very thin [35], and such cavities are at least 10 times more *compact* than resonators with inductive grids. This peculiar property is interesting for

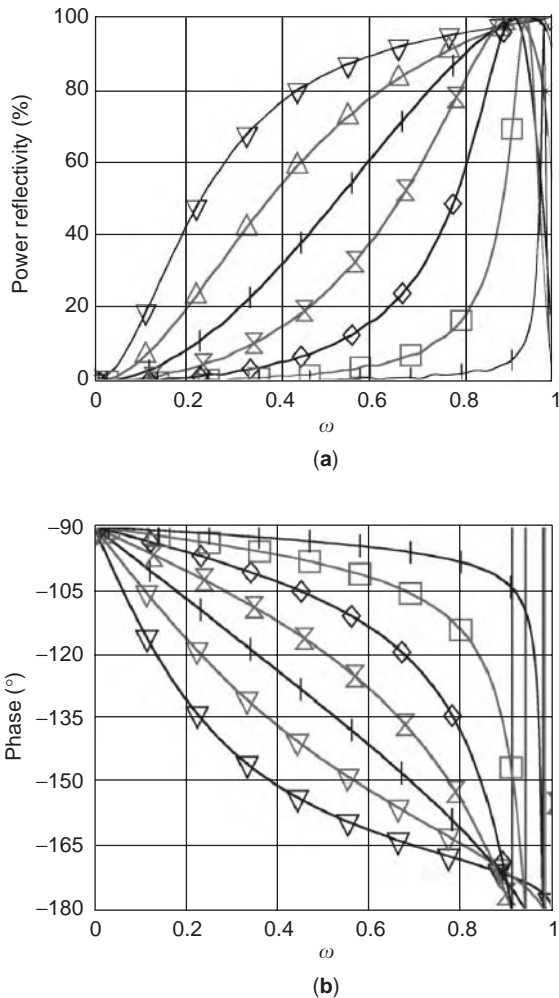


Figure 10. Theoretical frequency response of perfectly conducting 2D capacitive meshes computed with the FDTD method: (a) power reflectivity R ; (b) phase of the reflection coefficient $\arg(r)$. The geometry of the mesh is represented in Fig. 6a, grid 4. Key: --- , $d/a = 30.7\%$; \square , $d/a = 40.7\%$; \diamond , $d/a = 50.7\%$; \times , $d/a = 60.7\%$; --- , $d/a = 70.7\%$; \triangle , $d/a = 80.7\%$; ∇ , $d/a = 90.7\%$. (This figure is available in full color at <http://www.mrw.interscience.wiley.com/erfme>.)

the design of liquid crystal tunable frequency filters (Section 3.1).

2.2. Performance of Microwave FP Resonators

2.2.1. Modeling. The modeling techniques discussed in Sections 2.1.2. and 2.1.3 can be directly applied to study FP resonators of infinite size in extent. As an example, Figs. 11 and 12 represent the equivalent circuit and the FDTD computational domain of a FP cavity analyzed with the TL matrix method and with the FDTD technique [36], respectively. In Fig. 11, the mirrors are identical and modeled by a shunt impedance $Z_m = 1/Y_m$. They are fabricated on both faces of a dielectric slab ($\epsilon_r, \tan \delta$) of thickness D , as depicted in Fig. 1. The transmission coefficient S_{21} of the cavity excited under normal incidence is deduced from

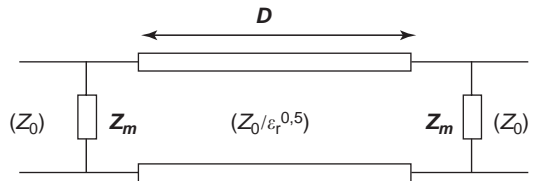


Figure 11. Transmission-line model of a symmetric FP cavity. The semitransparent mirrors are modeled by an impedance Z_m shunting a transmission line whose characteristic impedance and propagation constant depend on the thickness D of the substrate and its electrical properties ($\epsilon_r, \tan \delta$) [13].

Eqs. (33), (36), (38) and (43)

S_{21}

$$= \frac{2}{2(1+Z_0 Y_m) \cosh(\gamma D) + \left(\frac{2Z_0 Y_m}{n} + \frac{1}{n} + n + \frac{(Z_0 Y_m)^2}{n} \right) \sinh(\gamma D)} \quad (55)$$

where $n = \epsilon_r^{1/2}$ is the refractive index of the substrate.

2.2.2. Frequency Response and Parametric Study. The FDTD frequency response of a FP resonator is given in Fig. 13 for the first five transmission peaks ($q = 0, \dots, 4$). Comparison with the transmission coefficient of an ideal FPI [Eq. (8)] demonstrates that

- The theoretical FDTD resonant frequencies are systematically lower than those predicted by Eq. (8); besides, this discrepancy increases with frequency. These particularities are due to the phase of an

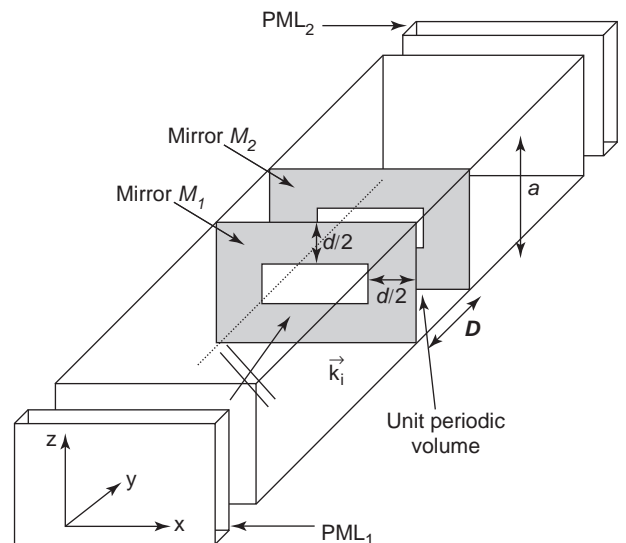


Figure 12. FDTD computational domain for the modeling of plane-parallel FP cavities. Periodic boundary conditions (PBC) are applied in the transverse directions, and perfectly matched layers (PML) are oriented in the direction of propagation (y axis) of the incident plane wave.

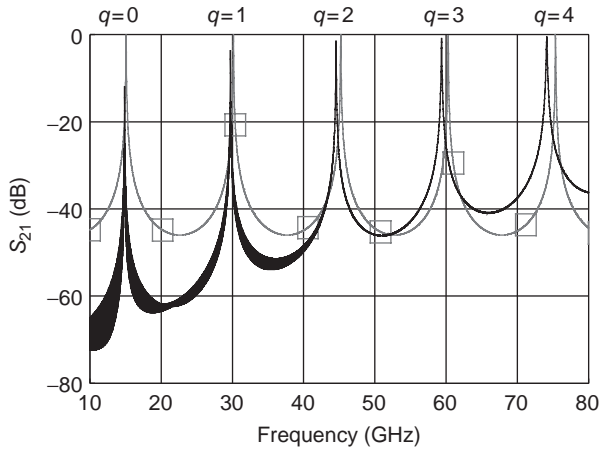


Figure 13. Comparison between the frequency responses of an ideal FPI (Section 1.2) and a FP cavity ($\epsilon_r = 3.80$, $\tan \delta = 10^{-4}$, $D = 5.106$ mm) whose inductive mesh mirrors are identical ($a = 1100$ μm , $d/a = 50\%$, $\sigma = \infty$, $t = 0$). Key: \square , Ideal FPI; $-$, FP cavity with mesh mirrors (FDTD). (This figure is available in full color at <http://www.mrw.interscience.wiley.com/erfme>.)

inductive grid, which is always smaller than 180° and decreases with frequency (Fig. 9b).

- The fringe contrast decreases with the interference order q , while it remains constant for an ideal FPI. This comes from the frequency variation of the mirror reflectivity (Fig. 9a).

This example demonstrates unambiguously that the *dispersive* characteristics of the reflectors must be taken into account to accurately predict the scattering parameters of a FP cavity with grid mirrors.

Let us now consider the influence of the mesh parameters (a, d) on the frequency response [resonant frequency f_{res} , -3 dB bandwidth (BW) and insertion losses (IL)] of fused-quartz half-wavelength cavities ($\epsilon_r = 3.80$, $D \approx \lambda_0/2\epsilon_r^{1/2}$). This material is ideal as a dielectric holder because of its low loss ($\tan \delta < 5 \times 10^{-4}$ at 60 GHz) and good temperature stability, particularly for the design of open resonators (Section 3.3) and oscillators (Section 3.4) with semitransparent mirrors. The samples studied here (Fig. 14) have been fabricated using a precise liftoff process (± 2 μm) of sputtered-copper film ($t = 1.2$ μm , $\sigma_{\text{Cu}} = 5.8 \times 10^7$ S/m) with a thin chromium adhesion layer ($t = 0.1$ μm , $\sigma_{\text{Cr}} = 7.5 \times 10^6$ S/m). Two cases are considered [37]: symmetric ($R_1 = R_2 = R$) and asymmetric ($R_1 \neq R_2$) resonators.

2.2.2.1. Symmetric Resonators. Figures 15a and 15b show the theoretical and experimental variations of f_{res} and BW as a function of (a, d) for two sets of cavities ($D = 1.263 \pm 0.003$ mm): the mirrors of set 1 have a constant spatial period ($a = 0.6$ mm) and a variable filling factor d/a ($17.7\% < d/a < 46.2\%$); for set 2, $d/a = 50\%$ and a varies between 0.5 and 2.1 mm with a constant step equal to 0.2 mm; a scale indicating the value of the mirror reflectivity R of each sample is also inserted in Fig. 15a. The transmission coefficients S_{21} have been computed with the FDTD and TL methods (Section 2.2.1). They were measured in far field under normal incidence between two V-band standard horn

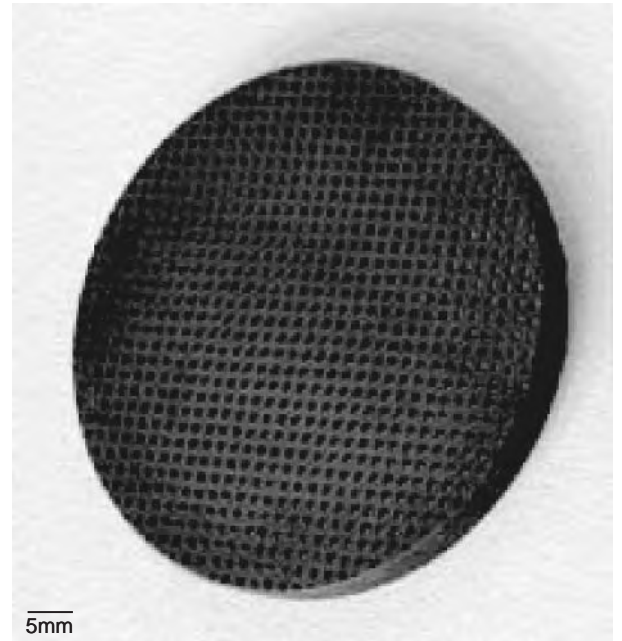


Figure 14. Fused-quartz FP resonator operating in the 60-GHz band. The highly reflecting mirrors are 2D sputtered-copper meshes ($\epsilon_r = 3.80$, $D = 5.105$ mm \pm 0.003 mm, diameter = 50 mm, $a = 1500$ $\mu\text{m} \pm 3$ μm , $d/a = 50\%$). (This figure is available in full color at <http://www.mrw.interscience.wiley.com/erfme>.)

antennas. As expected [relations (12) and (25)], f_{res} (BW) increases (resp. decreases) with R . The theoretical resonant frequencies computed with the FDTD and TL [19] methods are in very good agreement; this is due to the range of validity of the equivalent reactance of the mesh (Ref. 14 and Section 2.1.2, above). Moreover, the discrepancy between the values of f_{res} measured and computed by FDTD is lower than 600 MHz (Fig. 15a). The larger deviation observed for the bandwidth (Fig. 15b) comes from the diffraction losses (substrates of finite diameter) that are not taken into account in the modeling. These losses can be reduced significantly using focusing planoconvex cavities (Section 3.2, below and Ref. 36, Table 4). Finally, Fig. 15c shows that the insertion losses (IL) due to the finite conductivity of the meshes increase exponentially with R . Comparison with the IL due only to the dielectric loss ($\sigma = \infty$, $\tan \delta = 10^{-4}$) demonstrates that metal losses contribute, for the most part, to the IL of millimeter-wave FP cavities. In particular, this explains the moderate radiation efficiencies of FP-based Gaussian beam antennas (Section 3.2.1).

2.2.2.2. Asymmetric Resonators. Relations (12) and (25) suggest that f_{res} and BW of asymmetric devices can be adjusted by a convenient choice of the complex reflection coefficient of each mirror, but at the price of a slight increase of their transmission loss [$R_1 \neq R_2$, relation (14)]. FDTD simulations are used to determine accurately the variations of f_{res} , BW, and IL with the width d_2 of the metal strips of M_2 . The grid parameters of M_1 remain unchanged ($a_1 = 1.3$ mm, $d_1/a_1 = 50.7\%$). Figure 16a represents the theoretical transmission coefficients of several cavities ($D = 1.259$ mm, $\sigma_{\text{Cu}} = 5.8 \times 10^7$ S/m, $t = 1.2$ μm) for which

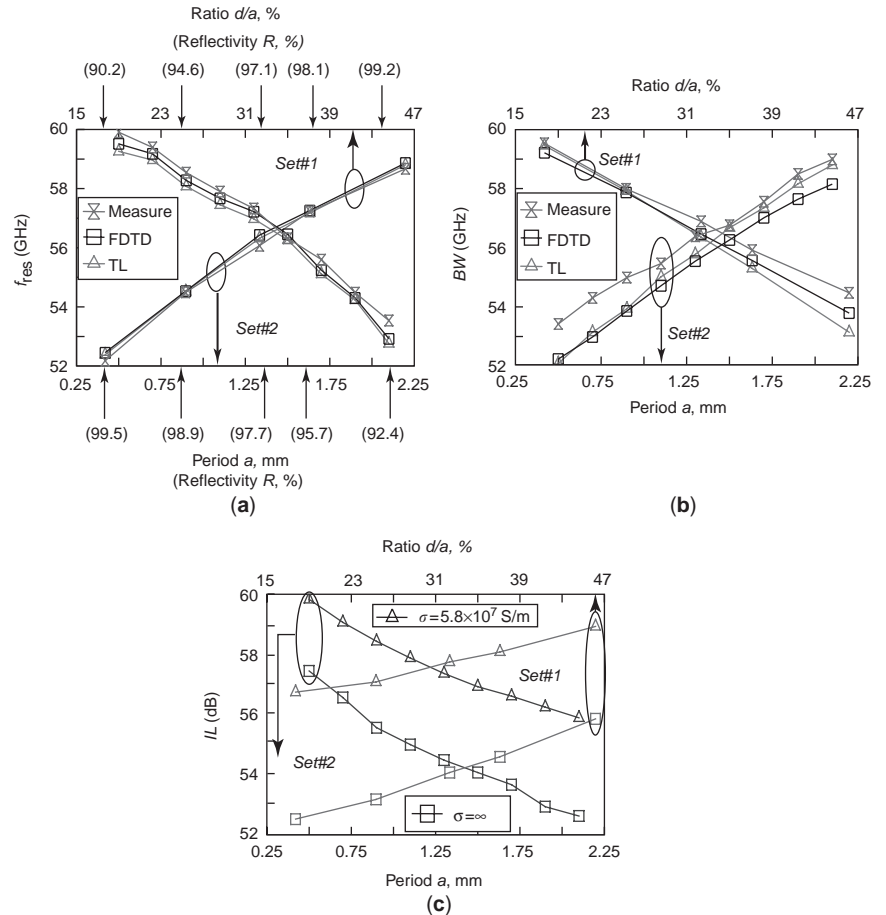


Figure 15. Variations of (a) the resonant frequency f_{res} ; (b) the half-power bandwidth BW, and (c) the insertion losses IL, as a function of the mesh parameters of symmetric resonators. Metal meshes are perfectly conducting ($\sigma = \infty$) or in copper ($\sigma = \sigma_{Cu}$). (From Ref. 37; copyright John Wiley & Sons, Inc., reproduced by permission.) (This figure is available in full color at <http://www.mrw.interscience.wiley.com/erfme>.)

$32.7\% < d_2/a_2 < 74.7\%$ ($a_2 = a_1 = 1.3$ mm, $87.10\% < R_2 < 99.95\%$), and Fig. 16b shows the resulting change in f_{res} , BW, and IL as a function of R_2 . As expected, IL is minimum ($IL_{min} = 1.3$ dB) for $R_2 = R_1 = 97.8\%$ ($d_2/a_2 = d_1/a_1 = 50.7\%$) and increases very rapidly for $R_2 > R_1$. Besides, we notice that f_{res} can be tuned between 55.4 and 57.6 GHz if we tolerate an increase in IL of 1 dB above IL_{min} . Controlling the complex reflection coefficient of a mirror then constitutes a possible solution for the design of tunable FP devices using active grids or MEMS (micro-electromechanical system) technologies (Section 3.1).

2.3. Design of Microwave FP Resonators

In the previous section, we have quantified the influence of the mirror properties on the performance of FP cavities. However, from a design perspective, the *inverse* problem should be solved.

For that purpose, *approximate* or *purely numerical* synthesis methods can be implemented. In the first case, the simplest way to describe the frequency response of the device is to use the theory of multilayer structures in which each individual layer is described by its own scattering matrix (Section 2.1.2 above). This approach is typically applied to design FP cavities operating at a given frequency; it basically consists in graphically solving

Eq. (13) [38]. From the resonance condition (11), we have

$$\frac{\rho_1 + \rho_2}{2} = k_0 D - q\pi, \quad \text{with} \quad k_0 = \frac{2\pi}{\lambda_0} \quad (56)$$

When plotted as a function of frequency, the right-hand side of this equation is a set of straight lines, representing the ray pathlength with a slope depending on D (and eventually on θ_i and ϵ_r). These are referred to as *phase lines*. The left-hand side is the average reflection phase of both mirrors. Equation (56) is satisfied when the phase lines intersect this curve (Fig. 17a); transmission peaks appear then in the frequency response of the structure. These plots are useful guides to systematically adjust the resonant frequency of cascaded layers, by appropriate adjustment of the dielectric spacer parameters and $[\rho_1(f) + \rho_2(f)]/2$.

Nevertheless, this technique does not account for mutual coupling and evanescent waves, and fails when the mirror spacing is smaller than half the spatial period of each grid [9] [which is dramatically the case for resonators with capacitive strip gratings (Section 3.1)]. Moreover, the choice of grid geometries is necessarily limited because their frequency characteristics must be known a priori [Eq. (56)]. These are the reasons why global electromagnetic

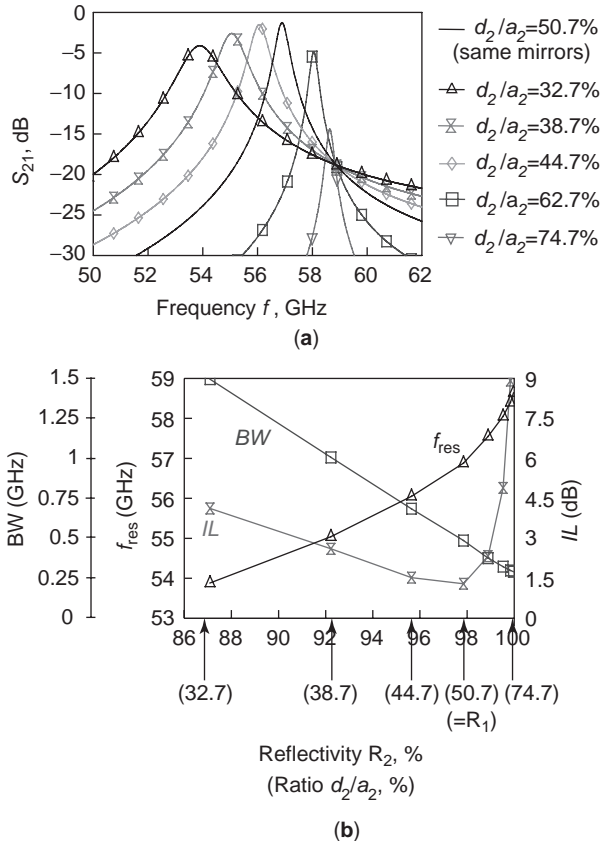


Figure 16. (a) Influence of the reflectivity R_2 of mirror M_2 on the transmission coefficient S_{21} of asymmetric resonators ($a_1 = 1.3$ mm, $d_1/a_1 = 50.7\%$); (b) variations of the resonant frequency f_{res} , the half-power bandwidth BW , and the insertion losses IL , as a function of R_2 ($a_1 = 1.3$ mm, $d_1/a_1 = 50.7\%$). (From Ref. 37; copyright John Wiley & Sons, Inc., reproduced by permission.) (This figure is available in full color at <http://www.mrw.interscience.wiley.com/erfme>.)

analysis tools combined with optimization procedures, such as simulated annealing or genetic algorithms [39], may be required for accurate and innovative designs. A simplified example of FDTD-based methodology is schematized in Fig. 17b, in which a very wide range of grid geometries is explored [37]. In this work, it has been shown in particular that an infinite number of 2D metal meshes can be used to design a symmetric resonator with prescribed values of f_{res} and BW . However, all the solutions are not equivalent in terms of insertion losses.

2.4. Multilayer FP Resonators

Multilayer FP cavities are of particular interest for the design of interference filters (Section 3.1) or frequency beam scanning antennas (Section 3.2.2). Their frequency response can be computed using the $ABCD$ formalism (Section 2.1.2) or full-wave methods (Section 2.1.3). To minimize the number of degrees of freedom and for the purpose of discussion, we assume that the device comprises N identical 2D meshes separated by air slabs ($\epsilon_r = 1$) of thickness D (Fig. 18a). Each mesh is characterized by its complex reflection and transmission coefficients $\{r_1, t_1\}$.

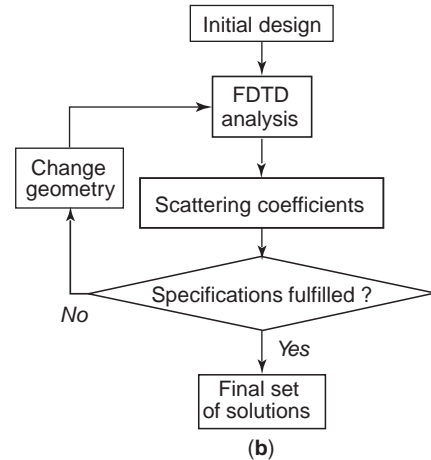
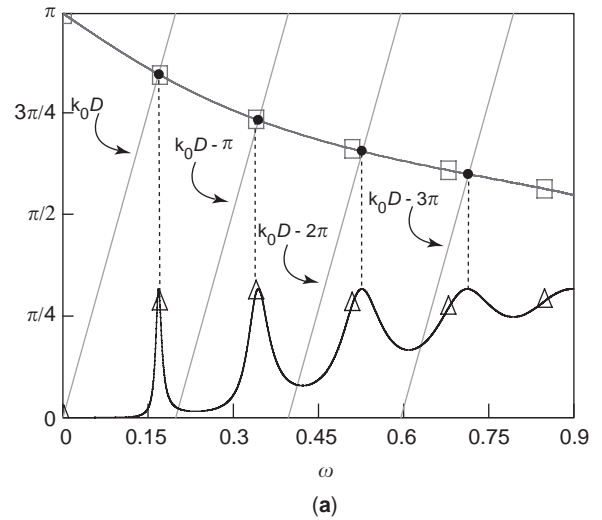


Figure 17. (a) Graphical procedure for the approximate design of FP cavities whose mirrors are dispersive. The resonant frequencies are given by the intersection points of the phase lines ($k_0 D - q\pi$) with the average reflection phase of both mirrors (\square). These points (\bullet) are in very good agreement with the transmission peaks of the FDTD frequency response of the cavity (\triangle) ($a = 1$ mm, $d/a = 11.4\%$, $D = 2.52$ mm, $\epsilon_r = 1$). (b) FDTD-based synthesis algorithm. (From Ref. 37; copyright John Wiley & Sons, Inc., reproduced by permission.) (This figure is available in full color at <http://www.mrw.interscience.wiley.com/erfme>.)

Under normal incidence, it can be easily shown that the scattering parameters $\{r_N, t_N\}$ of the whole structure are given by the following recursive relations

$$t_N = \frac{t_{N-1} t_1 \exp(-jk_0 D)}{1 - r_{N-1} r_1 \exp(-j2k_0 D)} \quad (57)$$

$$r_N = r_{N-1} + \frac{t_{N-1}^2 r_1 \exp(-j2(N-1)k_0 D)}{1 - r_{N-1} r_1 \exp(-j2k_0 D)} \quad (58)$$

In the forbidden band, the minimum level of transmission is equal to

$$|t_N|_{\min} = \frac{2\{(1 - |r_1|)/(1 + |r_1|)\}^{N/2}}{1 + \{(1 - |r_1|)/(1 + |r_1|)\}^{N/2}} \quad (59)$$

Typical transmission coefficients are represented in Fig. 18b for $N \leq 3$. In each transmission band (1) the number of propagation peaks equals $N-1$ and (2) the intersection points between $|t_1|$ and $|t_{N-1}|$ correspond to the case $|t_N|=1$. Further details can be found in general textbooks dealing with infinite periodic structures and electromagnetic bandgap (EBG) materials.

2.5. Dielectric FP Resonators

Highly directive FP-based antennas (Section 3.2.1) may be obtained from resonators comprising N stacked identical freestanding dielectric slabs (Fig. 18c) behaving as Bragg mirrors ($D_s = \lambda_0/4\epsilon_r^{1/2}$, $D_a = \lambda_0/4$). Their transmission coefficient is represented in Fig. 18d for alumina slabs ($N \leq 3$). As expected, the forbidden band is all the deeper as the number of layers and the dielectric contrast (1: ϵ_r) increase. High-performance reflecting mirrors based on this concept are very popular at optical wavelengths. Comparison between Figs. 18b and 18d reveals the dual behavior of multilayer metallic and dielectric mirrors (the positions of the forbidden bands and passbands are inverted). Metal meshes usually lead to lower profile structures and are compatible with the integration of active circuits. Nevertheless, as frequency increases, ohmic losses of partially reflective mirrors may significantly reduce the Q factor of the resonator (Section 2.2.2) and justify the use of Bragg mirrors, especially for high-gain antennas (Section 3.2.1).

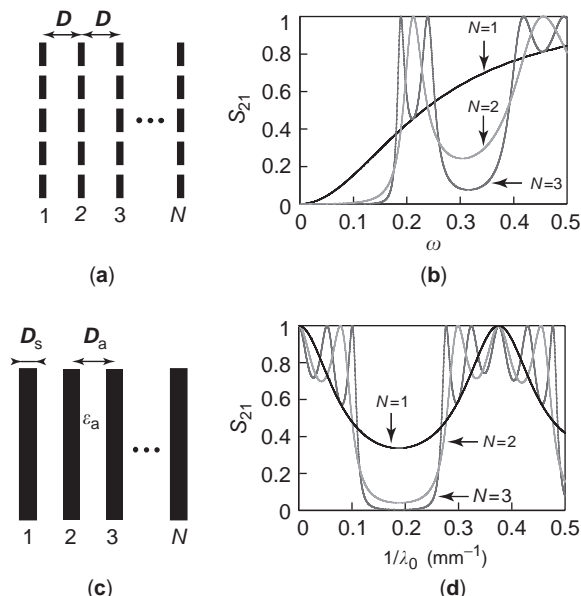


Figure 18. (a) Generalized FP resonator comprising N identical freestanding partially reflective mirrors; (b) theoretical transmission coefficients for $N \leq 3$ (inductive mesh, [Fig. 6a, grid 2], $a = 1$ mm, $d/a = 5.40\%$, $D = 1.8$ mm, $\epsilon_r = 1$); (c) generalized FP resonator comprising N cascaded identical dielectric slabs (D_s, ϵ_r) separated by air gaps (D_a, ϵ_a); (d) theoretical transmission coefficients of a Bragg mirror for $N \leq 3$. The alumina and air sections have a quarter-wave electrical thickness at 56.8 GHz ($D_s = 0.42$ mm, $D_a = 1.32$ mm, $\epsilon_r = 9.87$, $\epsilon_a = 1$). (This figure is available in full color at <http://www.mrw.interscience.wiley.com/erfme>.)

3. APPLICATIONS OF FABRY-PEROT CAVITIES AT MICROWAVE FREQUENCIES

FP cavities are employed in many microwave applications, such as quasioptical circuits and systems [filters, diplexers (Section 3.1), oscillators and power combiners (Section 3.4)], directive, multibeam, and beam scanning antennas (Section 3.2), or dielectric measurement systems (Section 3.3). A series of three review articles [40–42] reviews the concepts of FP resonators and describes some possible applications from microwave to infrared wavelengths (open resonators for characterization of gases, or liquid, solid, anisotropic and magnetic materials; laser output couplers; plasma diagnostics, etc.).

3.1. Frequency Filters and Diplexers

FP resonators are widely used not only as bandpass frequency filters [11,13,18,19,36–38], but also as diplexers [43,44]. The simple plane-parallel devices described in Section 2 suffer from two disadvantages:

1. It seems impossible to design filters with both broad bandwidth and high attenuation in the stopband, since these parameters are not independent [Eqs. (15) and (25)]. However alternative ways have been proposed in the literature, [e.g., 45–47]; these filters are constructed either from more than two grids (Section 2.4), or from capacitive grid arrays (Section 2.1.5) deposited on a dielectric substrate. Note that any interference filter may be discussed in terms of only two effective interfaces (Section 2.1.2), which may themselves consist of many interfaces (Sections 2.4 and 2.5) [48].
2. The second drawback is the transmission level at higher orders. Here again, the use of capacitive reflectors might solve this problem [11] because the bandwidth of capacitive FP filters decreases with frequency (Section 2.1.5); higher modes no longer lie at harmonics of the fundamental mode.

The rapid variation of bandwidth [roughly as f^3 according to Eqs. (25), (45), and (47)] limits performance when scanning over a wide range of frequencies. One solution might to use a hybrid FP, with one inductive mesh and one capacitive mesh [11]. This kind of configuration has also been investigated by Lockyer et al. [49] for the design of low-profile filters (Fig. 19a) presenting two narrow highly stable passbands separated by a distinct null (Fig. 19b).

Reflecting mirrors may also be built from photonic crystals [50]. In that case, they consist of multilayer metallodielectric 1D, 2D or 3D periodic structures (see Sections 2.4 and 2.5 for the 1D and 2D cases). Conceptually, the gap between the (composite) mirrors can be interpreted as the creation of a defect inside the periodicity of the electromagnetic crystal. An example of devices is schematized in Fig. 19c, where each mirror is constructed from a square lattice of lossy dielectric rods [51].

McCleary et al. [52] has reported improved filter performance by slot coupling to higher-order Gaussian beam modes [53] in concave resonators; these results include

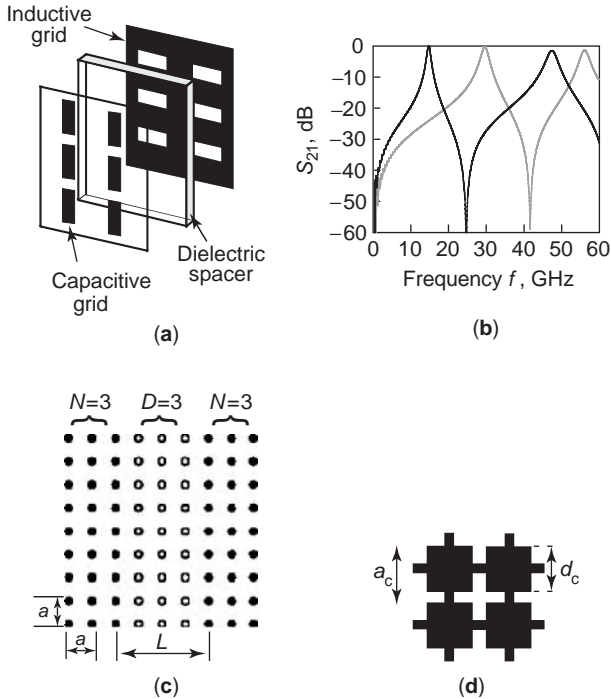


Figure 19. (a) FP filter constructed from complementary frequency-selective surfaces (CP FSS) [49]; (b) theoretical transmission coefficient of CP FSS FP filters for two different lengths of dipoles; (c) top view of a FP resonator operating in the 4–8-GHz band. The mirrors, of adjustable reflectivity and thickness, are built from square lattice ($a = 2.08$ cm) 2D photonic crystals constituting N layers of lossy dielectric rods of radius 3.175 mm ($11 < \epsilon_r < 13$, $\tan \delta \approx 0.004$). They are separated by an airgap of varying thickness L (from Ref. 51; copyright 2003 IEEE, reproduced by permission); (d) mirror geometry of tunable nematic liquid crystal FP filters operating at 27 GHz [$a_c = 5$ mm, $d_c/a_c = 98.75\%$, $D = 110$ μm ($\approx \lambda_0/100$)] [54].

mechanically tunable (20%) X-band filters with insertion losses less than 1 dB and unloaded Q values ranging from 1000 to 7000. Electronically tunable filters can also be built from liquid crystal (LC) materials [54–56], Barium strontium titanate (BSTO) ferroelectric films [57], or active grids [58]. Note that an efficient low-voltage driving (< 10 V) of microwave LC-FPI requires ultrathin substrates ($D \ll \lambda/2$) [35] to ensure covering of the whole anisotropic spectrum of nematic crystals [54]. As suggested in Section 2.1.5, this can be achieved using interconnected capacitive grids serving simultaneously as reflecting mirrors and driving electrodes (Fig. 19d). Tunable filters based on MEMS technologies have been reported at optical wavelengths [59], but not yet at microwave frequencies due to the large-scale technological challenges.

3.2. Fabry-Perot-Based Antennas

3.2.1. Highly Directive Antennas

3.2.1.1. Spatial Filtering. Partially reflective surfaces (PRSs) have been studied [60–62] for the design of spatial filters. To demonstrate the focusing ability of PRS, let us

consider an ideal isotropic electromagnetic source S located on a perfect electromagnetic screen, inside a FP cavity of thickness D (Fig. 20a). The reflection coefficient of the output mirror is labeled $r = R^{1/2} \exp(j\rho)$. The sum of all outgoing waves yields the following expression for the far-field power pattern [61]

$$P(\theta) = \frac{1 - R(\theta)}{1 + R(\theta) - 2(R(\theta))^{1/2} \cos\left(\rho(\theta) - \pi - \frac{4\pi D}{\lambda_0} \cos(\theta)\right)} \quad (60)$$

The variations of $|P(\theta)|$ are represented in Fig. 20b as a function of θ and $R_0 = R(\theta = 0^\circ)$ at resonance

$$f_{r,q} = \frac{c_0}{4D} \left(2q - 1 + \frac{\rho(0)}{\pi} \right) \quad (61)$$

with $q \leq 0$ (or 1) for capacitive (or inductive) grids. Figure 20b shows that

- $|P(\theta)|$ decreases with θ for a given value of R_0 .
- The maximum directivity of the antenna (for $\theta = 0^\circ$) increases with the broadside reflectivity R_0 .

This simple model also enables us to establish an analytical relation between *frequency* and *angular* selectivities. For highly reflecting mirrors ($R \approx 1$), simple algebra shows that the half-power beamwidth $\theta_{3 \text{ dB}}$ is minimum for the fundamental mode ($q = 0$) and is written at resonance [63] as follows

$$\theta_{3 \text{ dB}} \approx 2 \arccos \left(1 - \frac{1}{2Q_0} \right) \approx \frac{2}{Q_0^{1/2}} \quad (62)$$

As a consequence, highly directive FP-based antennas are necessarily narrowband. For real applications, the exact value of $\theta_{3 \text{ dB}}$ can be obtained from the dispersion diagram of Bloch modes [64].

3.2.1.2. Radiating Structures and Applications. PRS and FP resonators are specific electromagnetic bandgap (EBG) materials [50,65]. With the exception of antennas based on ultrarefractive metamaterials [66], most of them can be considered as photonic crystals operating in a defect mode [67] (e.g., Fig. 19c).

In that context, a very wide variety of geometries of primary feeds and focusing devices has been proposed. To excite the structure, we can use waveguide apertures [61,62,68], horn antennas [60,68], dipole and monopole antennas [63,69], or printed patches and arrays fed by a coaxial probe, a microstrip transmission line, or coupling slots [70–73]. As a first approximation, for PRS mirrors, the thickness D of the cavity is chosen to maximize the broadside directivity (Fig. 20b) at the operating frequency. Nevertheless, we should keep in mind that when the cavity is excited by a real primary source, a slight difference ($< 1\%$) appears between the frequency maximizing the antenna directivity and the quasioptical resonant frequency of the FP cavity alone.

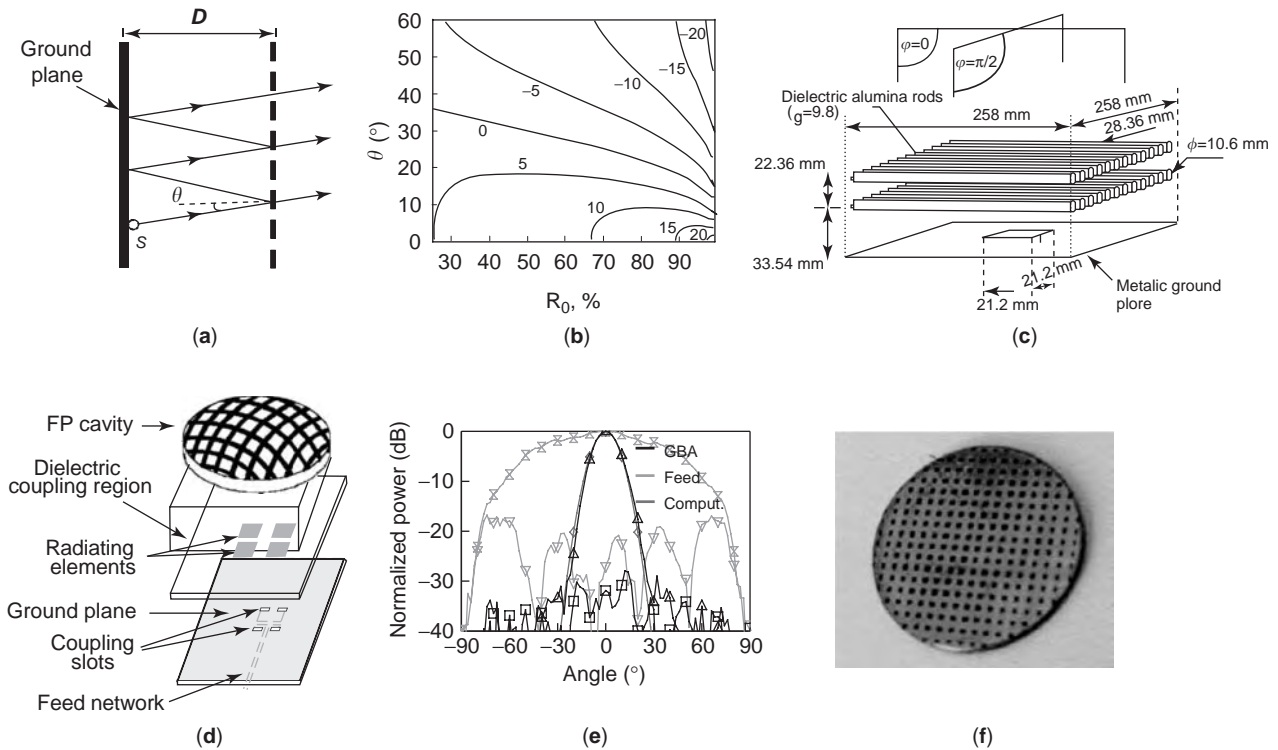


Figure 20. (a) Multiple reflections between a ground plane and a semi-transparent sheet; (b) variation of the antenna directivity (equimagnitude contours in dB) as a function of the broadside reflectivity R_0 of the output mirror and elevation angle θ (inductive grid, $q = 1$, $D = 2.5$ mm); (c) directive antenna using a Bragg mirror (4.75 GHz), where each reflecting surface of the superstrate is built from one layer of alumina rods (from Ref. 73; copyright 2003 IEEE, reproduced by permission); (d) general architecture of multilayer Gaussian beam antennas (GBAs): a planoconvex FP cavity with periodic mirrors is fed by a printed primary radiator through a dielectric coupling region. (from Ref. 72; copyright John Wiley & Sons, Inc., reproduced by permission); (e) measured and computed radiation patterns of a GBA in H plane at 56.6 GHz [the primary source is a patch antenna printed on a 150 μm -fused-quartz substrate; the mirrors of the quartz ($\epsilon_r = 3.80$) FP resonator are inductive metal meshes ($a = 600 \mu\text{m}$, $d/a = 46\%$; see grid 2 in Fig. 6a); the thickness and the radius of curvature of the cavity equal 1.310 mm and 2595 mm, respectively]; (f) FP resonator with nonuniform mesh operating in V band.

The focusing elements can be classified in three main categories:

- A single PRS [61,62,74,75] (in that case, we may consider that the source is located *in the middle* of a FP cavity defined by the actual PRS and its electrical image with respect to the ground plane (Fig. 20a)).
- Two cascaded PRS arranged in a plane-parallel [70,76,77] or planoconvex [68,71,72] configuration—by analogy with open resonators (Section 3.3), the planoconvex structure generates a symmetric Gaussian beam and minimizes the sidelobe level.
- Reflecting mirrors constructed from multilayer 1D, 2D or 3D dielectric [63,69,73,78] (e.g., alumina plates or rods) or metallic (e.g., crossed wires, strip gratings) [70] EBG materials, as emphasized in Sections 2.4, 2.5 and 3.1.

This antenna technology usually leads to low-profile high-gain (≤ 32 dB today) radiating structures. Despite

their narrow bandwidth ($< 0.5\%$ for 30 dB gain), they might be competitive for (1) applications requiring medium-gain antennas (< 25 dB), (2) fixed wireless access [e.g., local multipoint distribution services (LMDS)] and satellite reception [76], (3) high-data-rate indoor 60-GHz WLANs [68,77], or (4) interleaved feeds of focal array-fed reflector (FAFR) antennas that simultaneously need an efficient illumination of the reflector and a low rollover between the beams [79].

Two examples of directive antennas based on the FP concept are represented in Figs. 20c and 20d. In both cases, the distance separating the printed source from the input mirror of the superstrate is near $\lambda/2$; this opens a defect mode inside the forbidden band of the periodic structure [72, Fig. 4; 73, Fig. 10]. The input impedance of the antenna and its radiation performance (gain, efficiency, co- and cross-polarization levels) have been investigated as a function of the Q factor of the FP cavity, the topology of the feed, and the mutual coupling between the feed and the resonator [71,72,80]. Figure 20e compares the radiation patterns of the primary source alone and the

FP-based antenna. It clearly demonstrates the focusing effect induced by the cavity, thereby confirming the ability of a FPI to spread the electromagnetic energy over its whole surface (i.e., to increase significantly the directivity of an elementary feed). Design rules have been proposed [71,78] for Gaussian beam antennas and EBG resonator antennas, respectively. Finally, let us mention the possibility to further reduce the total height of the antenna by a factor two by virtue of employing a planar artificial magnetic conductor (AMC) [65,104] as a ground plane [105].

The PRS that we have considered until now were *periodic*; when the FP approach applies, their geometry is determined according the antenna specifications [directivity, Eqs. (26) and (62); bandwidth, Eq. (25); resonant frequency, Eq. (13)]. Several authors have proposed *nonuniform* PRS (1) to shape the beam radiated by horn antennas [106] and printed antennas [77] (Fig. 20f), or (2) to increase the radiation purity and bandwidth usually altered by phase aberrations of the aperture electric field around sharp resonance [75].

3.2.2. Frequency Beam Scanning Antennas and Multi-beam Antennas. Frequency beam scanning antennas rely simultaneously on the angular (Section 3.2.1) and frequency (Section 1.2) selectivities of FP cavities. According to Eq. (60), the radiated power is maximum in the direction $\theta_s = \arccos(f_{r,q}/f)$ where f is the operating frequency and $f_{r,q}$ is given by Eq. (61). Frequency beam scanning is thus possible if $f_{r,q}$. To minimize the variation of the maximum directivity during scanning, periodic arrays insensitive to oblique incidence are of particular interest.

On the other hand, we have seen in Section 2.4 that multiple propagation peaks appear in each passband if the FP resonator comprises more than two PRSs (e.g., Fig. 18b). Therefore several beams can be radiated by the antenna, depending on the operating frequency, that is, the cavity mode chosen. These multilayer FP cavities may be excited by linear [81] or printed [82] antennas.

Adjusting the radiation characteristics by frequency tuning may prove constraining for many applications. An alternative solution consists in combining astutely and simultaneously two *independent* modes of reconfiguration; the first one uses agile materials as substrates (e.g., liquid crystals or ferroelectric thin films), and the second one controls the reflection/transmission properties of capacitive grids by integrating varactor diodes or MEMS switches in the PRS [82].

3.3. Open Resonators and Concave Mirrors

Accurate knowledge of the complex permittivity of dielectric materials² is crucial for the design of microwave circuits and antennas. The most widely used techniques in the microwave region are cavity resonators; free-space, open-ended coaxial probes; and wideband transmission lines based on one- or two-port measurements. Although

²For further information, refer also to the article entitled “DIELECTRIC MEASUREMENTS” in this encyclopedia.

narrowband, the open-resonator (OR) technique has established itself as a powerful and precise tool for measuring the permittivity of *low-loss* dielectric materials [40,41,83,84]. A very extensive literature is available on that subject since interest in OR was generated in the 1960s by the invention of the laser and the need for resonators with large volume and low loss.

In its most general form, an OR comprises two axially aligned spherical mirrors of radii of curvature R_1 and R_2 and separated by a distance D (Fig. 21a). The sample S is located in the middle of the structure. Compared to the plane-parallel FPI, the use of (at least) one *concave* mirror has the advantage to focus the field into a smaller volume and thus remove diffraction and alignment problems provided the mirrors are of sufficiently large aperture [85,86]. An additional advantage is gained if one (or both) of the mirrors is (are) *spherical*; in the paraxial approximation, the orthogonal modes are the well-known *Gaussian beam* modes, as in laser and maser cavities. In that case, no sophisticated numerical methods [31,87,88] is required for an accurate analysis of the OR:

- Kogelnik and Li [89] provided a very clear scalar analysis of these modes and determined a criterion ensuring stability for the beam resonances: $0 \leq (1 - D/R_1)(1 - D/R_2) \leq 1$. Three particular configurations, located at the limit between the stable and unstable regions, appear from the stability diagram: the symmetric confocal resonator ($R_1 = R_2 = D$), the plane-parallel resonator ($R_1 = R_2 = \infty$) discussed in Section 1.2, and the concentric resonator ($R_1 = R_2 = D/2$) for which the centers of the two mirrors coincide.
- Rigorous vector theory has been proposed later by Yu and Cullen [90].

Detailed treatments about optics of Gaussian beams and resonant cavities can be found in textbooks [e.g., 2, Chaps. 4 and 5; 53]. We just state that the resonant modes are quasi- TEM_{plq} (or TEM_{mnq}) modes, where q denotes the longitudinal mode number (Section 1.2) and pl (or mn) describes the transverse variations of the electromagnetic fields in terms of Laguerre–Gaussian beams in cylindrical coordinates (or Hermite–Gaussian beams in Cartesian coordinates). The resonant frequency of the

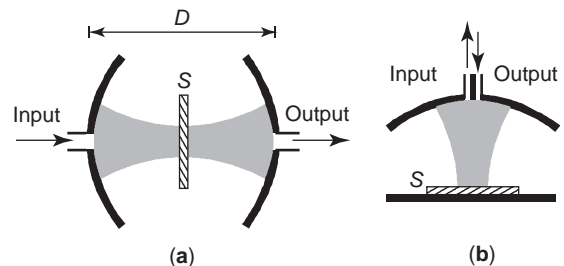


Figure 21. (a) FP open resonator for dielectric measurement—the sample of dielectric material S is located in the middle of the device and the shaded area symbolizes the transverse extent of the Gaussian beam mode; (b) hemispherical open resonator.

TEM_{plq} mode is given by [89]

$$f_{\text{res},plq} = \frac{c_0}{2D} \left(q + 1 + \frac{2p+l+q}{\pi} \arccos \left\{ \left(1 - \frac{D}{R_1} \right) \left(1 - \frac{D}{R_2} \right) \right\}^{1/2} \right) \quad (63)$$

This equation is consistent with relation (12), that provides the q th resonant frequency of an ideal plane-parallel FPI with full metal mirrors ($\rho_1 = \rho_2 = \pi$).

The resonator technique relies on perturbation of the electric field distribution by a sample of the material into the resonant structure. The resulting shift of resonant frequency and change in Q factor are analyzed to determine the material properties. The relevant theory is described in a number a review articles, (e.g., see Refs. 84 and 90). There are two basic procedures. In the first, the resonant frequency is measured with and without the sample under test, in a FP cavity of fixed length [91,92]. In the second, the frequency is fixed and the length of the resonator is adjusted to establish resonance with and without the sample [83,92]. Accurate measurements are facilitated by using a high Q for the resonator (up to 2×10^5 in Ref. 93; 6×10^5 in Ref. 94). Experimental errors depend on a number of factors, but the fractional uncertainties obtained in determining the index of refraction have been on the order of 10^{-4} . Loss-tangent measurements are considerably less precise, with fractional uncertainties in the range 0.01–0.1. Among the various OR geometries already employed, configurations with one plane mirror (Fig. 21b), namely, the hemispherical ($D \approx R$) and semiconfocal ($D \approx R/2$) resonators, are convenient because (1) they are unconditionally stable, (2) the boundaries of flat materials conform closely to the phase fronts of the field distribution in the resonator, and (3) they enable the characterization of liquid specimen. Small samples can also be studied with hemispherical structures because the beam radius is very small at the plane mirror.

Coupling energy in and out of the device must perturb as little as possible the configuration of the resonant Gaussian beam modes. A commonly employed method utilizes small apertures in the reflectors to couple energy from waveguides. This approach may significantly increase the insertion losses since small holes radiate energy into a large solid angle. An alternative solution consists in coupling to a quasioptical beam using partially reflecting surfaces, such as grid mirrors [93], as discussed in Section 2.

3.4. Oscillators and Quasioptical Power Combiners

There is a strong need for high-power, solid-state sources at microwave and millimeter wavelengths. At microwave frequencies, waveguide or cavity combiners have been successful; but at higher frequencies, problems appear in terms of loss, combining efficiency, power output, and dimensional tolerances. Spatial or quasioptical techniques³ could provide a possible solution since they are able to integrate many active devices, minimize signal distribution

³For further information, refer to the article entitled SPATIAL AND QUASI-OPTICAL POWER COMBINING in this encyclopedia.

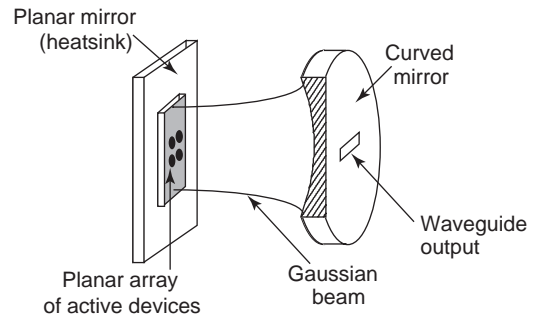


Figure 22. Quasioptical power combiner using a semiconfocal open resonator.

and combining losses, and maintain desired amplitude and phase relationships.

An enhanced RF efficiency is achieved with quasioptical power combiners by coupling a planar array of active devices to a propagating Gaussian beam in free space (and vice versa). Compared to circuit-combining structures, these systems have low losses because (1) energy is distributed or combined in free space and ohmic losses are minimized and (2) the use of beams with large beam waist size enables to integrate a lot of devices in a *single* stage of combining (causing them to operate in parallel). Most of the losses are associated with coupling efficiency from active devices to the beam, and with the coupling to a power collection port.

This concept was suggested in the 1980s [95,96]. The classic paper published by Mink [96] is generally credited with providing the impetus for the increased research activity that followed. In that work, Mink analyzed theoretically a power combiner based on an array of negative resistance devices located inside a semiconfocal open resonator (Fig. 22).

Practical considerations include (1) the choice of solid-state components themselves (Gunn diodes [97,98], HEMT transistors [99,100], operating from X band to V band), (2) coupling of the individual devices to the cavity (for instance using grooved mirrors [97–99] and (3) coupling to the outside of the cavity via waveguides [97–99] or partially reflecting surfaces fabricated on quartz substrates [100]. A more complete summary of this technique is given by York and Popovic [101].

BIBLIOGRAPHY

1. M. Born and E. Wolf, *Principles of Optics (Electromagnetic Theory of Propagation, Interference and Diffraction of Light)*, 5th ed., Pergamon Press, New York, 1975.
2. J. Hawkes and I. Latimer, *Lasers. Theory and Practice*, Prentice-Hall, Englewood Cliffs, NJ, 1995.
3. J. M. Vaughan, *The Fabry-Perot Interferometers, History, Theory, Practice and Applications*, Adam Hilger, Bristol, UK, 1989.
4. B. A. Munk, *Frequency Selective Surfaces. Theory and Design*, Wiley, New York, 2000.
5. R. E. Collin, *Field Theory of Guided Waves*, McGraw-Hill, New York, 1960.

6. D. M. Pozar, *Microwave Engineering*, Wiley, New York, 1997.
7. K. C. Gupta, R. Garg, and R. Chadha, *Computer-Aided Design of Microwave Circuits*, Artech House, MA, Dedham, 1982.
8. N. Marcuvitz, *Waveguide Handbook*, McGraw-Hill, New York, 1951.
9. S. Tretyakov, *Analytical Modeling in Applied Electromagnetics*, Artech House, Dedham, MA, 2003.
10. T. B. A. Senior and J. L. Volakis, *Approximate Boundary Conditions in Electromagnetics*, IEE Electromagnetic Wave Series Vol. 41, IEE, London, 1995.
11. R. Ulrich, Far infrared properties of metallic mesh and its complementary structure, *Infrared Phys.* **7**:37–55 (1967).
12. P. F. Goldsmith, *Quasi-optical Systems. Gaussian Beam, Quasi-optical Propagation and Applications*, IEEE Press, New York, 1998.
13. R. Sauleau, Ph. Coquet, J.-P. Daniel, T. Matsui, and N. Hirose, Study of Fabry-Perot cavities with metal mesh mirrors using equivalent circuit models. Comparison with experimental results in the 60 GHz band, *Int. J. Infrared Millimeter Waves* **19**(12):1693–1710 (Dec. 1998).
14. R. Sauleau, Ph. Coquet, and J.-P. Daniel, Validity and accuracy of equivalent circuit models of passive inductive meshes. Definition of a novel model for 2D grids, *Int. J. Infrared Millimeter Waves* **23**(3):475–498 (March 2002).
15. W. Wang and Y. Guo, Analysis of metal grating polarizers for quasi-optical power combining applications, *Int. J. Infrared Millimeter Waves* **16**(1):123–133 (1995).
16. M. S. Durschlag and T. A. De Temple, Far IR optical properties of freestanding and dielectric backed metal meshes, *Appl. Opt.* **20**(7):1245–1253 (April 1981).
17. R. C. Compton and D. B. Rutledge, Approximation techniques for planar periodic structures, *IEEE Trans. Microwave Theory Techn.* **33**(10):1083–1088 (Oct. 1985).
18. S. W. Lee, G. Zarrillo, and C. L. Law, Simple formulas for transmission through periodic metal grids or plates, *IEEE Trans. Anten. Propag.* **30**(5):904–909 (Sept. 1982).
19. C. C. Chen, Transmission of microwave through perforated flat plates of finite thickness, *IEEE Trans. Microwave Theory Techn.* **21**(1):1–6 (Jan. 1973).
20. L. B. Whitbourn and R. C. Compton, Equivalent circuit formulas for metal grid reflectors at a dielectric boundary, *Appl. Opt.* **24**(2):217–220 (Jan. 1985).
21. R. C. Compton, L. B. Whitbourn, and R. C. McPhedran, Strip gratings at a dielectric interface and application of Babinet's principle, *Appl. Opt.* **23**(18):3236–3242 (Sept. 1984).
22. C. K. Lee, R. J. Langley, and C. Eng, Equivalent-circuit models for frequency selective surfaces at oblique angles of incidence, *IEE Proc. Microwaves Anten. Propag.* **132**(6):395–399 (Oct. 1985).
23. R. R. De Lyser, *Homogenization Analysis of Electromagnetic Strip Grating Antennas*, Ph.D. thesis, Univ. Colorado, Boulder, 1991.
24. M. Guglielmi and A. A. Oliner, Multimode network description of a planar periodic metal-strip grating at a dielectric interface—Part I: Rigorous network formulations, *IEEE Trans. Anten. Propag.* **37**(3):534–541 (March 1989).
25. M. Guglielmi and A. A. Oliner, Multimode network description of a planar periodic metal-strip grating at a dielectric interface—Part II: Small-aperture and small-obstacle solutions, *IEEE Trans. Anten. Propag.* **37**(3):542–551 (March 1989).
26. R. C. McPhedran and D. Maystre, On the theory and application of inductive grids, *Appl. Phys.* **14**:1–20 (1977).
27. R. Mittra, C. H. Chan, and T. Cwick, Techniques for analyzing frequency selective surfaces—a review, *Proc. IEEE* **76**(12):1593–1615 (Dec. 1988).
28. R. C. Hall, R. Mittra, and K. M. Mitzner, Analysis of multilayered periodic structures using generalized scattering matrix theory, *IEEE Trans. Anten. Propag.* **36**(4):511–517 (April 1988).
29. D. S. Filipovic, J. L. Volakis, and L. S. Andersen, Efficient modeling and analysis of infinite periodic antenna arrays by tetrahedral finite elements, *IEEE Int. Symp. Anten. Propag.* **4**:2504–2507 (1999).
30. D. T. McGrath and V. P. Pyati, Phased array antenna analysis with hybrid finite element method, *IEEE Trans. Anten. Propag.* **42**(12):1625–1630 (Dec. 1994).
31. H. Cam, S. Toutain, Ph. Gelin, and G. Landrac, Study of a Fabry-Perot cavity in the microwave frequency range by the boundary element method, *IEEE Trans. Microwave Theory Techn.* **40**(2):298–304 (Feb. 1992).
32. A. Taflove, *Advances in Computational Electrodynamics: The Finite-Difference Time-Domain Method*, Artech House, Dedham, MA, 1998.
33. W. Sun, K. Liu, and C. A. Balanis, Analysis of singly and doubly periodic absorbers by frequency-domain finite-difference method, *IEEE Trans. Anten. Propag.* **44**(6):798–805 (June 1996).
34. R. Sauleau, D. Thouroude, Ph. Coquet, and J.-P. Daniel, Theoretical reflection coefficient of metal grid reflectors at a dielectric boundary, *Int. J. Infrared Millimeter Waves* **20**(2):325–340 (Feb. 1999).
35. Y. N. Kazantsev, V. P. Mal'tsev, and A. D. Shatrov, Plane wave transmission through a pair of capacitive gratings, *IEE Proc. Microwaves Anten. Propag.* **147**(6):455–462 (Dec. 2000).
36. R. Sauleau, Ph. Coquet, D. Thouroude, J.-P. Daniel, H. Yuzawa, N. Hirose, and T. Matsui, FDTD analysis and experiment of Fabry-Perot cavities at 60 GHz, *IEICE Trans. Electron.* **E82-C**(7):1139–1147 (July 1999).
37. R. Sauleau, G. Le Ray, and Ph. Coquet, Parametric study and synthesis of 60-GHz Fabry-Perot resonators, *Microwave Opt. Technol. Lett.* **34**(4):247–252 (Aug. 2002).
38. A. C. de Lima and E. A. Parker, Fabry-Perot approach to the design of double layer FSS, *IEE Proc. Microwaves Anten. Propag.* **143**(2):157–162 (April 1996).
39. Y. Rahmat-Samii and E. Michielens, *Electromagnetic Optimization by Genetic Algorithms*, Wiley, New York, 1999.
40. G. W. Chantry, The use of Fabry-Perot interferometers, etalons and resonators at infrared and longer wavelengths—an overview, *J. Phys. E: Sci. Instrum.* **15**:3–8 (Jan. 1982).
41. R. N. Clarke and C. B. Rosenberg, Fabry-Perot and open resonators at microwave and millimeter wave frequencies, 2–300 GHz, *J. Phys. E: Sci. Instrum.* **15**:9–24 (Jan. 1982).
42. E. A. M. Baker and B. Walker, Fabry-Perot interferometers for use at submillimeter wavelengths, *J. Phys. E: Sci. Instrum.* **15**:25–32 (Jan. 1982).
43. J. A. Arnaud, A. A. M. Saleh, and J. T. Ruscio, Walk-off effects in Fabry-Perot diplexers, *IEEE Trans. Microwave Theory Techn.* **22**(5):486–493 (May 1974).
44. H. P. Pickett and A. E. T. Chiou, Folded Fabry-Perot quasi-optical ring resonator diplexer: Theory and experiment, *IEEE Trans. Microwave Theory Techn.* **31**(5):373–380 (May 1983).
45. T. Timusk and P. L. Richards, Near millimeter wave bandpass filters, *Appl. Opt.* **20**(8):1355–1360 (April 1981).
46. G. D. Holah, Far-infrared and submillimeter-wavelengths filters, in K. J. Button, ed., *Infrared and Millimeter Waves*, Academic Press, San Diego, 1982, Vol. 6, Chap. 6, pp. 345–409.

47. M. M. Pradhan, Multigrad interference filters for the far infrared region, *Infrared Phys.* **11**:241–245 (Dec. 1971).
48. S. D. Smith, Design of multilayer filters by considering two effective interfaces, *J. Opt. Soc. Am.* **48**(1):43–50, 1958.
49. D. S. Lockyer, J. C. Vardaxoglou, and R. A. Simpkin, Complementary frequency selective surfaces, *IEE Proc. Microwaves Anten. Propag.* **147**(6):501–507 (Dec. 2000).
50. J. D. Joannopoulos, R. D. Meade, and J. N. Win, *Photonic Crystals: Molding the Flow of Light*, Princeton Univ. Press, Princeton, NJ, 1995.
51. M. M. Beaky, J. B. Burk, H. O. Everitt, M. A. Haider, and S. Venakides, Two-dimensional photonic crystal Fabry–Perot resonators with lossy dielectrics, *IEEE Trans. Microwave Theory Tech.* **47**(11):2085–2091 (Nov. 1999).
52. J. McCleary, M. Li, and K. Chang, Slot-fed higher order mode Fabry–Perot filters, *IEEE Trans. Microwave Theory Tech.* **41**(10):1703–1709 (Oct. 1993).
53. A. E. Siegman, *Lasers*, University Science Books, Chaps. 16, 17, 1986.
54. R. Sauleau, N. Tentillier, B. Spingart, and Ph. Coquet, Résonateurs de Perot–Fabry accordables en fréquence par cristal liquide, *Treizièmes Journées Nationales Micro-ondes*, Lille, France, Paper 1B6, May 21–23, 2003.
55. M. Tanaka and S. Sato, Electrically controlled millimetre-wave transmission properties of stacked liquid crystal cells with metal substrates, *Jpn. J. Appl. Phys.* **40**:4131–4135 (2001).
56. K. C. Lin and W. C. Chuang, Polarization independent and electronically tunable Fabry–Perot etalons with cross-orthogonal liquid-crystals layers, *Microwave Opt. Technol. Lett.* **36**(6):475–477 (Sept. 2003).
57. E. A. Parker and S. B. Savia, Active frequency selective surfaces with ferroelectric substrates, *IEE Proc. Microwaves Anten. Propag.* **148**(2):103–108 (April 2001).
58. L. B. Sjögren, Active beam control arrays, in T. K. Wu, ed., *Frequency Selective Surfaces and Grid Arrays*, Wiley, New York, 2000, Chap. 7, pp. 211–247.
59. J. D. Patterson, *Micro-mechanical Voltage Tunable Fabry–Perot Filters Formed in (111) Silicon*, NASA Technical Paper 3702, Sept. 1997.
60. A. Ortusi and J.-C. Simon, *Hertzian Optics*, U.S. Patent 2,763,860 (Sept. 18, 1956).
61. G. Von Trentini, Partially reflecting sheet arrays, *IRE Trans. Anten. Propag.* **4**(10):666–671 (Oct. 1956).
62. A. P. Feresidis and J. C. Vardaxoglou, High gain planar antenna using optimised partially reflective surfaces, *IEE Proc. Microwaves Anten. Propag.* **148**(6):345–350 (Dec. 2001).
63. T. Akalin, J. Danglot, O. Vanbésien, and D. Lippens, A highly directive dipole antenna embedded in a Fabry–Perot type cavity, *IEEE Microwave Wireless Components Lett.* **12**(2):48–50 (Feb. 2002).
64. S. Enoch, G. Tayeb, and D. Maystre, Dispersion diagrams of Bloch modes applied to the design of directive sources, in J. A. Kong, ed., *Progress in Electromagnetic Research Series*, PIER 41, special issue on electromagnetic applications of PBG materials and structures, 2003.
65. Mini-special issue on electromagnetic crystal structures, design, synthesis and applications, *IEEE Trans. Microwave Theory Tech.* **47**(11): (Nov. 1999).
66. B. Gralak, G. Tayeb, and S. Enoch, Anomalous refractive properties of photonic crystals, *J. Opt. Soc. Am. A* **17**:1012–1020 (2000).
67. D. R. Smith, S. Schultz, S. L. McCall, and P. M. Platzmann, Defect studies in a two-dimensional periodic photonic lattice, *J. Modern Opt.* **41**(2):395–404 (1994).
68. R. Sauleau, Ph. Coquet, D. Thouroude, J.-P. Daniel, and T. Matsui, Radiation characteristics and performance of millimeter wave horn fed Gaussian beam antennas, *IEEE Trans. Anten. Propag.* **51**(3):378–387 (March 2003).
69. E. Ozbay, B. Temelkuran, and M. Bayindir, Microwave applications of photonic crystals, in J. A. Kong, ed., *Progress in Electromagnetic Research Series*, PIER 41, special issue on electromagnetic applications of PBG materials and structures, 2003.
70. S. Enoch, N. Guérin, G. Tayeb, and P. Vincent, Study of photonic crystal based directive antennas, *Proc. 24th ESTEC Antenna Workshop on Innovative Periodic Antennas: Photonic Bandgap, Fractal and Frequency Selective Structures*, Estec, Noordwijk, The Netherlands, June 2001, pp. 11–16.
71. R. Sauleau, Ph. Coquet, and T. Matsui, Low-profile directive quasi-planar antennas based on millimeter wave Fabry–Perot cavities, *IEE Proc. Microwaves Anten. Propag.* **150**(4):274–278 (Aug. 2003).
72. R. Sauleau, Ph. Coquet, and T. Matsui, Near-field coupling between a printed antenna and a Fabry–Perot resonator: Experimental study of the radiation properties at millimeter wave frequencies, *Microwave Opt. Technol. Lett.* **38**(6):438–443 (Sept. 2003).
73. M. Thèvenot, C. Cheype, A. Reinex, and B. Jecko, Directive photonic bandgap antennas, *IEEE Trans. Microwave Theory Tech.* **47**(11):2115–2122 (Nov. 1999).
74. S. Chandran and C. Vardaxoglou, Performance of two single-layer frequency selective surface as spatial filters, *Microwave Opt. Technol. Lett.* **6**(6):339–342 (May 1993).
75. F. Croq and H. Legay, *Radiating Structure*, U.S. Patent 6,061,027 (May 5, 2000).
76. J. Shaker and M. Cuhaci, A double-layer FSS structure to suppress far side-lobes of an antenna, *Microwave Opt. Technol. Lett.* **39**(5):428–432 (Dec. 2003).
77. R. Sauleau, Ph. Coquet, T. Matsui, and J.-P. Daniel, A new concept of focusing antennas using plane-parallel Fabry–Perot cavities with non-uniform mirrors, *IEEE Trans. Anten. Propag.* **51**(11):3171–3175 (Nov. 2003).
78. C. Cheype, C. Serier, M. Thèvenot, Th. Monédière, A. Reinex, and B. Jecko, An electromagnetic bandgap resonator antenna, *IEEE Trans. Anten. Propag.* **50**(9):1285–1290 (Sept. 2002).
79. R. Chantalat, P. Dumon, B. Jecko, M. Thèvenot, and Th. Monédière, Interlaced feeds design for a multibeam reflector antenna using a 1-D dielectric PBG resonator, *Proc. IEEE Int. Symp. Antennas and Propagation*, June 22–27, 2003, Vol. 4, pp. 867–870.
80. R. Sauleau and Ph. Coquet, Input impedance of electromagnetic bandgap resonator antennas, *Microwave Opt. Technol. Lett.* (in press).
81. H. Boutayeb, K. Mahdjoubi, and A.-C. Tarot, Frequency beam scanning and gain enhancement properties of PBG antennas, *Proc. IEEE Int. Symp. Antennas and Propagation, URSI Digest*, June, 22–27, 2003, p. 526.
82. R. Sauleau, *Antenne à Cavité Résonante Reconfigurable*, Fr. Patent 309,415 (July, 30, 2003).
83. M. N. Afsar and H. Ding, A novel open-resonator system for precise measurement of permittivity and loss-tangent, *IEEE Trans. Instrum. Meas.* **50**(2):402–405 (April 2001).

84. A. L. Cullen, Millimeter-wave open-resonator techniques, in K. J. Button, ed., *Infrared and Millimeter-wave*, Academic Press, San Diego, 1983, Vol. 10, Chap. 4, pp. 233–281.
85. A. G. Fox and T. Li, Resonant modes in a maser interferometer, *Bell Syst. Tech. J.* **40**:453–488 (March 1961).
86. G. D. Boyd and J. P. Gordon, Confocal multimode resonator for millimeter through optical wavelength masers, *Bell Syst. Tech. J.* **40**:489–508 (March 1961).
87. M. Rewienski and M. Mrozowski, Iterative application of boundary conditions in the parallel implementation of the FDFD method, *IEEE Microwave Guided Wave Lett.* **10**(9):362–364 (Sept. 2000).
88. T. E. Harrington, J. Wosik, and S. A. Long, Open resonators mode patterns for characterization of anisotropic dielectric substrates for HTS thin films, *IEEE Trans. Appl. Superconduct.* **7**(6):1861–1864 (June 1997).
89. H. Kogelnik and T. Li, Laser beams and resonators, *Proc. IEEE* **54**(10):1312–1329 (1966).
90. P. K. Yu and A. L. Cullen, Measurement of permittivity by means of an open resonator, *Proc. Roy. Soc. Lond. A* **380**:49–71 (1982).
91. B. Komiya, M. Kiyokawa, and T. Matsui, Open resonator for precision dielectric measurements in the 100 GHz band, *IEEE Trans. Microwave Theory Tech.* **39**(10):1792–1796 (Oct. 1991).
92. M. N. Afsar, X. Li, and H. Chi, An automated 60 GHz open-resonator system for precision dielectric measurement, *IEEE Trans. Microwave Theory Tech.* **38**(12):1845–1853 (Dec. 1990).
93. T. Matsui, K. Araki, and M. Kiyokawa, Gaussian beam open resonator with highly reflective circular coupling regions, *IEEE Trans. Microwave Theory Tech.* **41**(10):1710–1714 (Oct. 1993).
94. A. F. Krupnov, V. N. Markov, G. Y. Golubyatnikov, I. I. Leonov, Y. N. Konoplev, and V. V. Parshin, Ultra-low absorption measurement in dielectrics in millimeter- and submillimeter-wave range, *IEEE Trans. Microwave Theory Tech.* **47**(3):284–289 (March 1999).
95. L. Wandering and V. Nalbandian, Millimeter-wave power combiner using quasi-optical techniques, *IEEE Trans. Microwave Theory Tech.* **31**(2):189–193 (Feb. 1983).
96. J. W. Mink, Quasi-optical power combining of solid-state millimeter-wave sources, *IEEE Trans. Microwave Theory Tech.* **34**(2):273–279 (Feb. 1986).
97. H. Kondo, M. Hieda, M. Nakayama, T. Tanaka, K. Osakabe, and K. Mizuno, Millimeter and submillimeter wave quasi-optical oscillator with multi-elements, *IEEE Trans. Microwave Theory Tech.* **40**(5):857–862 (May 1992).
98. M. Sanagi and S. Nogi, Power combining by a Fabry–Perot resonator with active devices mounted on both the mirrors, *IEICE Trans. Electron.* **E84-C**(10):1575–1580 (Oct. 2001).
99. J. Bae, S. Sugawara, F. Takei, K. Kikuyama, T. Fujii, and K. Mizuno, Design of a quasi-optical oscillator using a grooved mirror with a HEMT array, *IEICE Trans. Electron.* **E81-C**(6):857–861 (June 1998).
100. M. Kiyokawa and T. Matsui, A new quasi-optical oscillator with Gaussian output beam, *IEEE Microwave Guided Wave Lett.* **4**(5): 129–131 (May 1994).
101. R. A. York and Z. B. Popovic, *Active and Quasi-optical Arrays for Solid-State Power Combining*, Wiley, New York, 1997.
102. R. C. Compton, L. B. Whitbourn and R. C. McPhedran, Simple formulae for the transmittance of strip gratings, *Int. J. Infrared Millimeter Waves* **4**(6):901–912 (Nov. 1983). See also erratum, *Int. J. Infrared Millimeter Waves* **7**(11):1823 (Dec. 1986).
103. R. Sauleau and N. Falola, Ultra-wideband wave reactance of capacitive grids, submitted to *Microwave Opt. Technol. Lett.* (April 2004).
104. Mini-special issue on metamaterials, *IEEE trans. Anten. Propag.* **51**(10):(Oct. 2003).
105. S. Wang, A. P. Feresidis, G. Goussetis and J. C. Vardaxoglou, Low-profile resonant cavity antenna with artificial magnetic conductor ground plane, *Elec. Letters* **40**(7):405–406 (April 2004).
106. R. Sauleau, Ph. Coquet, D. Thouroude and J.-P. Daniel, Beam focusing using 60-GHz Fabry-Perot resonators with uniform and non-uniform metal grids, *Elec. Letters* **39**(4):341–342 (Feb. 2003).

FAST FOURIER TRANSFORMS AND NUFFT

QING HUO LIU
Duke University
Durham, North Carolina

1. INTRODUCTION

The Fourier transform has been an essential analytical tool for many fields. The discretized version of the Fourier transform, the discrete Fourier transform (DFT), on the other hand, is an important numerical tool for ubiquitous applications in every branch of science and engineering. The fast Fourier transform (FFT) algorithm, as an efficient way of calculating DFT, has become an indispensable part of modern numerical computation since the pioneering work of Cooley and Tukey [18], although some related earlier FFT concepts can be dated back to Gauss in 1805 [32] and Danielson and Lanczos in 1942 [21].

The FFT algorithms have found widespread applications in engineering and sciences. In this article we will discuss only its application in numerical solution of Maxwell's equations. Within this important area, the FFT has been widely applied in solving both time-domain and frequency-domain partial-differential equations and integral equations.

Over the decades since the invention of the FFT algorithms, there has been increasing demand for nonuniform discrete Fourier transform (NUFFT), where data are sampled at nonuniform points in either the spectral or physical domain, or both. Although the need for such nonuniform discrete Fourier transform has been recognized for a long time, fast transform algorithms were developed as recently as the mid-1990s. This article includes the latest developments in these nonuniform fast Fourier transform (NUFFT) algorithms [5,24,52,65].

This article is organized as follows. In Section 2, we will introduce the Fourier transform and its properties. In Section 3, the discrete Fourier transform (DFT) will be given in detail, followed by the fast Fourier transform (FFT) algorithms in Section 4. Applications of the FFT algorithms will be briefly summarized in Section 5. Finally, the nonuniform fast Fourier transform (NUFFT) will be discussed in Section 6.

2. FOURIER TRANSFORMS

2.1. One-Dimensional Fourier Transform

Given a complex function $s(x)$ in terms of a real variable x , its Fourier transform is defined by

$$S(k) = \frac{1}{\sqrt{2\pi}} \int_{-\infty}^{\infty} s(x)e^{-jkx} dx \equiv \mathcal{F}[s(x)] \tag{1}$$

where x may be a time or space coordinate, k is the corresponding angular frequency or wavenumber (spatial frequency), and $S(k)$ is in general a complex function. The inverse Fourier transform can be defined as

$$\frac{1}{2}[s(x+0) + s(x-0)] = \frac{1}{\sqrt{2\pi}} \int_{-\infty}^{\infty} S(k)e^{jkx} dk \tag{2}$$

The inverse Fourier transform involves the average of left and right limits of function $s(x)$ because the function may be discontinuous. In the special case where the function is continuous, the left-hand side of (2) simply reduces to $s(x)$:

$$s(x) = \frac{1}{\sqrt{2\pi}} \int_{-\infty}^{\infty} S(k)e^{jkx} dk \tag{3}$$

In what follows, unless otherwise stated, we will assume that function $s(x)$ is continuous; the transform of discontinuous functions will be discussed in Section 6. Thus, Eqs. (1) and (2) form a Fourier transform pair. Note in this article that a factor of $1/\sqrt{2\pi}$ is used for both the forward and inverse Fourier transforms (and similarly a factor of $1/\sqrt{N}$ for the forward and inverse discrete Fourier transform) to make them symmetric; other choices of such factors are possible but will not be described in detail here.

If $s(x)$, $s_1(x)$, and $s_2(x)$ have the corresponding Fourier transforms $S(k)$, $S_1(k)$, and $S_2(k)$, respectively, the Fourier transform has the following basic properties:

- *Linearity*—for any complex constants c_1 and c_2 , the Fourier transform of function $s(x) = c_1s_1(x) + c_2s_2(x)$ is

$$S(k) = \mathcal{F}[c_1s_1(x) + c_2s_2(x)] = c_1S_1(k) + c_2S_2(k) \tag{4}$$

where \mathcal{F} denotes the Fourier transform.

- *Symmetry*—the Fourier transform of $S(x)$ is

$$s(-k) = \mathcal{F}[S(x)] \tag{5}$$

- *Spatial (temporal) scaling*—for any nonzero real constant a , we have

$$\frac{1}{|a|} S\left(\frac{k}{a}\right) = \mathcal{F}[s(ax)] \tag{6}$$

- *Spectral (frequency) scaling*—for any nonzero real constant a , we have

$$S(ak) = \mathcal{F}\left[\frac{1}{|a|} s\left(\frac{x}{a}\right)\right] \tag{7}$$

- *Spatial (temporal) shifting*—if the spatial function is shifted by a constant value x_0 , the Fourier transform of the shifted function is

$$e^{-jkx_0} S(k) = \mathcal{F}[s(x - x_0)] \tag{8}$$

- *Spectral (frequency) shifting*—a constant shift k_0 in the spectral function corresponds to the Fourier transform of the modulated function $s(x)e^{jk_0x}$:

$$S(k - k_0) = \mathcal{F}[s(x)e^{jk_0x}] \tag{9}$$

- *Alternative inverse Fourier transform*—the inverse Fourier transform can be written in two ways:

$$s(x) = \mathcal{F}^{-1}[S(k)] = \{\mathcal{F}[S^*(k)]\}^* \tag{10}$$

- *Even function*—for an even function $s_e(x) = s_e(-x)$, the Fourier transform

$$S_e(k) = S_e(-k) \tag{11}$$

is also an even function.

- *Odd function*—for an odd function $s_o(x) = -s_o(-x)$, its Fourier transform

$$S_o(k) = -S_o(-k) \tag{12}$$

is also an odd function.

- *Convolution theorem*—the Fourier transform of the convolution between $s_1(x)$ and $s_2(x)$ is the product of $S_1(k)$ and $S_2(k)$,

$$\begin{aligned} \sqrt{2\pi} S_1(k) S_2(k) &= \mathcal{F}[s_1(x) * s_2(x)] \\ &= \mathcal{F}\left[\int_{-\infty}^{\infty} s_1(\tau) s_2(x - \tau) d\tau\right] \end{aligned} \tag{13}$$

where $*$ denotes the convolution.

- *Correlation theorem*—the Fourier transform of the correlation between $s_1(x)$ and $s_2(x)$ is the product of $S_1(-k)$ and $S_2(k)$

$$\begin{aligned} \sqrt{2\pi} S_1(-k) S_2(k) &= \mathcal{F}[s_1(x) \otimes s_2(x)] \\ &= \mathcal{F}\left[\int_{-\infty}^{\infty} s_1(\tau) s_2(x + \tau) d\tau\right] \end{aligned} \tag{14}$$

where \otimes denotes the correlation.

These Fourier transform properties are important in applications. Corresponding properties are found in discrete Fourier transform (see Section 3).

2.2. Multidimensional Fourier Transform

Multidimensional Fourier transform is a straightforward extension of one-dimensional Fourier transform. Given an M -dimensional function $s(\mathbf{r})$, where $\mathbf{r} = (x_1, x_2, \dots, x_M)$ is the position vector, its Fourier transform in terms of the M -dimensional spectral vector $\mathbf{k} = (k_1, k_2, \dots, k_M)$ is defined as

$$S(\mathbf{k}) = (2\pi)^{-M/2} \int_{-\infty}^{\infty} s(\mathbf{r}) e^{-j\mathbf{k} \cdot \mathbf{r}} d\mathbf{r} \quad (15)$$

and its inverse is defined as

$$s(\mathbf{r}) = (2\pi)^{-M/2} \int_{-\infty}^{\infty} S(\mathbf{k}) e^{j\mathbf{k} \cdot \mathbf{r}} d\mathbf{k} \quad (16)$$

where $s(\mathbf{r}) = [s(\mathbf{r} - 0) + s(\mathbf{r} + 0)]/2$ is understood for discontinuous functions. The properties of the multidimensional Fourier transform can be summarized easily as given in Table 1.

3. DISCRETE FOURIER TRANSFORM

Although many functions have closed-form Fourier transforms, for applications in signal processing and numerical analysis, many more functions have no closed-form Fourier transforms. Thus, numerical computation of Fourier transform is necessary for most applications. As the computer can deal only with discrete numbers, one has to convert the continuous Fourier transform into a discrete Fourier transform. Below we first define the discrete Fourier transform pairs, and then make the connection between the continuous and discrete Fourier transforms. The development here follows closely the book by Brigham [9].

3.1. Definition of 1-D DFT

Consider a 1-D periodic, discrete array $\{h(n)\}$ having a period of N , i.e., $h(n+rN) = h(n)$ for any integer r . The 1-D forward discrete Fourier transform of $\{h_n\}$ is defined as

$$H(m) = \frac{1}{\sqrt{N}} \sum_{n=0}^{N-1} h(n) e^{-j2\pi mn/N}, \quad m = 0, 1, \dots, N-1 \quad (17)$$

Table 1. Properties of Fourier Transform

Property	Inverse FT	Forward FT
Linearity	$c_1 s_1(\mathbf{r}) + c_2 s_2(\mathbf{r})$	$c_1 S_1(\mathbf{k}) + c_2 S_2(\mathbf{k})$
Symmetry	$S(\mathbf{r})$	$s(-\mathbf{k})$
Spatial shifting	$s(\mathbf{r} - \mathbf{r}_0)$	$S(\mathbf{k}) e^{-j\mathbf{k} \cdot \mathbf{r}_0}$
Spectral shifting	$s(\mathbf{r}) e^{j\mathbf{k}_0 \cdot \mathbf{r}}$	$S(\mathbf{k} - \mathbf{k}_0)$
Conjugation	$S^*(\mathbf{r})$	$s^*(\mathbf{k})$
Even function	$s_e(\mathbf{r})$	$S_e(\mathbf{k})$
Odd function	$s_o(\mathbf{r})$	$S_o(\mathbf{k})$
Convolution	$s_1(\mathbf{r}) * s_2(\mathbf{r})$	$(2\pi)^{M/2} S_1(\mathbf{k}) S_2(\mathbf{k})$
Correlation	$s_1(\mathbf{r}) \otimes s_2(\mathbf{r})$	$(2\pi)^{M/2} S_1(-\mathbf{k}) S_2(\mathbf{k})$
Parseval's theorem	$\int_{-\infty}^{\infty} s(\mathbf{r}) ^2 d\mathbf{r}$	$\int_{-\infty}^{\infty} S(\mathbf{k}) ^2 d\mathbf{k}$

Due to the periodic nature of $\exp(-j2\pi mn/N)$, it is easy to show that the DFT array $\{H(m)\}$ is also periodic with a period N , namely, $H(m+rN) = H(m)$, where r is any integer.

The inverse DFT can be shown to be given by

$$h(n) = \frac{1}{\sqrt{N}} \sum_{m=0}^{N-1} H(m) e^{j2\pi mn/N}, \quad n = 0, 1, \dots, N-1 \quad (18)$$

3.2. Properties of DFT

The properties of the DFT are analogous to those of the continuous Fourier transform, as summarized in Table 2.

Of particular importance are the convolution and correlation theorems. Cyclic convolution between $h_1(n)$ and $h_2(n)$ is defined as

$$h(n) = \sum_{p=0}^{N-1} h_1(p) h_2(n-p) \quad (19)$$

while their correlation is defined as

$$g(n) = \sum_{p=0}^{N-1} h_1(p) h_2(n+p) \quad (20)$$

It is important to note that all the arrays involved, $h_1(n)$, $h_2(n)$, $h(n)$, and $g(n)$, are periodic arrays with period N . The cyclic convolution and correlation theorems in Table 2 are based on this important property. The DFT is a simple way to perform these cyclic convolution and correlation. Later we will discuss how to use the DFT to perform linear convolution and correlation when the arrays are non-periodic.

3.3. Relationship between FT and DFT

Discrete Fourier transform can be considered as a tool entirely independent of continuous Fourier transform. However, the application of the DFT is primarily in the approximation of continuous Fourier transform. Therefore, we must establish the connection between the DFT and continuous FT. As will be seen below, the question of this approximation is entirely dependent on the function

Table 2. Properties of DFT

Property	Inverse DFT	Forward DFT
Linearity	$c_1 h_1(n) + c_2 h_2(n)$	$c_1 H_1(m) + c_2 H_2(m)$
Symmetry	$H(n)$	$h(-m)$
Time shifting	$h(n-p)$	$H(m) e^{-j2\pi mp/N}$
Frequency shifting	$h(n) e^{j2\pi np/N}$	$H(m-p)$
Conjugation	$H^*(n)$	$h^*(m)$
Even array	$h_e(n)$	$H_e(m)$
Odd array	$h_o(n)$	$H_o(m)$
Convolution	$h_1(n) * h_2(n)$	$\sqrt{N} H_1(m) H_2(m)$
Correlation	$h_1(n) \otimes h_2(n)$	$\sqrt{N} H_1(m) H_2(N-m)$
Parseval's theorem	$\sum_{n=0}^{N-1} h(n) ^2$	$\sum_{m=0}^{N-1} H(m) ^2$

and its sampling. For a bandlimited function, the DFT can be designed to completely capture the information of the underlying function without any error, while for other functions the DFT will provide an approximate representation of the functions.

3.3.1. General Complex Waveforms. Consider a general complex-valued function $s(x)$ having an infinite support; thus, the function is nonzero even at $x \rightarrow \pm \infty$. In order to convert the Fourier transform into a discrete Fourier transform, the following steps are taken:

1. This function $s(x)$ is first truncated to the function

$$\tilde{s}(x) = s(x)[U(x - x_{\min}) - U(x - x_{\max})] \quad (21)$$

with a finite support $x \in [x_{\min}, x_{\max}]$, where $U(x)$ is the Heaviside step function.

2. The truncated function is then made periodic by repeating this function with a period equal to $T = x_{\max} - x_{\min}$. Mathematically, this is equivalent to convolving $\tilde{s}(x)$ with a delta function train:

$$\delta_1(x) = \sum_{k=-\infty}^{\infty} \delta(x - kT) \quad (22)$$

The resulting periodic function of this convolution is given by

$$s_T(x) = \tilde{s}(x) * \delta_1(x) = \sum_{k=-\infty}^{\infty} \tilde{s}(x - kT) \quad (23)$$

3. Now, since $s_T(x)$ is a periodic function, one can find its Fourier series

$$s_T(x) = \sum_{m=-\infty}^{\infty} S_m e^{j2\pi mx/T} \quad (24)$$

where the Fourier coefficients $\{S_m\}$ are given by

$$S_m = \frac{1}{T} \int_{x_{\min}}^{x_{\max}} s(x) e^{-jmk_0 x} dx \quad (25)$$

where $k_0 = 2\pi/T$, and we have made use of the fact that $s_T(x) = s(x)$ within the period.

4. Using the trapezoidal rule (or other integration rules) to approximate the integral in step 3 in terms of the function values at some sampling points, we have

$$S_m = \frac{1}{N} \sum_{n=0}^{N-1} s\left(x_0 + \frac{nT}{N}\right) e^{-jmk_0 x_0} e^{-j2\pi mn/N} \quad (26)$$

where $x_0 = x_{\min} + T/2N$ is the first sampling point.

5. Finally, we truncate the Fourier series to N terms by keeping $m = -N/2, \dots, N/2 - 1$.

Therefore, the inverse Fourier series in (24) becomes

$$s_T(x) = \sum_{m=-N/2}^{N/2-1} S_m e^{j2\pi mx/T} \quad (27)$$

In particular, at the sample points, we have

$$s\left(x_0 + \frac{nT}{N}\right) = \sum_{m=-N/2}^{N/2-1} S_m e^{j2\pi mx_0/T} e^{j2\pi mn/N} \quad (28)$$

In general, these steps give rise to approximation errors; the only exception is the bandlimited function. The approximation errors associated with these steps are the spatial truncation error (step 1), aliasing error (integration error) due to inadequate sampling density (step 4), and spectral truncation error (step 5). From these steps, it is obvious that the relationship between the continuous Fourier transform and DFT is

$$h(n) \approx \frac{1}{\sqrt{N}} s\left(x_0 + \frac{nT}{N}\right), \quad H(m) \approx S_m e^{j(2\pi mx_0/T)} \quad (29)$$

These are only approximate because of the errors introduced in the above steps. Note that in the preceding equations, we intentionally express the forward and inverse DFT to contain a factor of $1/\sqrt{N}$ to make the forward and inverse transforms symmetric; it is not a necessary, but a convenient, choice of the multiplication factor.

3.3.2. Bandlimited Nonperiodic Functions. The *bandwidth* of a function is defined as the frequency band $k_{\min} \leq k \leq k_{\max}$ beyond which the spectrum is zero. In the preceding equations for a general complex function, we note that the bandwidth of the function is usually infinite; its spectrum is nonzero even when the frequency approaches $\pm \infty$. However, there is one special class of functions that are bandlimited; that is, their spectra are zero beyond a finite frequency. Such bandlimited functions have some special properties, as given by the Nyquist sampling theorem.

3.3.2.1. Nyquist Sampling Theorem. If function $s(x)$ is bandlimited, that is, if

$$S(k) = 0, \quad \text{for } |k| > k_{\max} \quad (30)$$

then under the condition that $\Delta x \leq \pi/k_{\max}$, the function can be uniquely determined by the sample points at $x = n\Delta x$ ($n = -\infty, \dots, \infty$)

$$s(x) = \sum_{n=-\infty}^{\infty} s(n\Delta x) \text{sinc}\left[\pi\left(\frac{x}{\Delta x} - n\right)\right] \quad (31)$$

where the sinc function is defined as

$$\text{sinc}(x) = \frac{\sin x}{x} \quad (32)$$

However, bandlimited functions have infinite support. In other words, the truncation in Eq. (21) (step 1) will cause errors.

3.3.3. Bandlimited Periodic Functions. It is only for bandlimited periodic functions that an exact relationship between FT and DFT can be established. For a bandlimited function $s_T(x)$, by definition its spectrum is nonzero only within $|k| \leq k_{\max}$, where k_{\max} is a finite real number, representing the maximum angular frequency where the spectrum is nonzero. If the period of the function is T , we can sample the function at an increment

$$\Delta x = \frac{T}{N} \quad (33)$$

Since this function is already periodic, the truncation in Eqs. (21) (step 1) and (23) (step 2) are no longer necessary. We can directly perform the Fourier series in Eq. (23).

Furthermore, in the spectral truncation step, that is, the last step in Eq. (28), if

$$\Delta x = \frac{T}{N} \leq \frac{\pi}{k_{\max}} \quad (34)$$

then according to Nyquist sampling theorem there is no spectral truncation error. Therefore, under this Nyquist sampling rate (34), the equations in (29) are exact. Moreover, the reconstruction formula for $s(x)$ in Eq. (31) reduces to

$$s(x) = \sum_{n=0}^{N-1} s(n\Delta x) \text{sinc} \left[\pi \left(\frac{x}{\Delta x} - n \right) \right] \quad (35)$$

In Eqs. (34) and (35), we consider that the truncation interval is exactly equal to the period T . Note that if this truncation is integer number of periods, the conclusion given above still applies, namely, that there is no approximation error between the continuous Fourier transform and DFT, and the original function can be reconstructed perfectly using discrete Fourier transform. However, if the truncation interval is not equal to an integer number of periods, a discontinuity is present at the two end truncation points because the function is no longer continuous (i.e., it has nonsmooth function value or derivatives) at the truncation point when the function is made periodic. Such discontinuities make Eq. (26) (step 4) inexact because the trapezoidal rule is approximate for this discontinuous function. In other words, a result of this truncation is that the function is no longer bandlimited. This effect is called ‘‘leakage.’’

4. FAST FOURIER TRANSFORM

Now that we have established the relationship between FT and DFT, we can use DFT to calculate the exact FT for bandlimited periodic functions, or approximate FT for other more general functions. Our objective is to calculate

efficiently the sum in (17), rewritten here for convenience:

$$H(m) = \frac{1}{\sqrt{N}} \sum_{n=0}^{N-1} h(n) e^{-j2\pi mn/N}, \quad m = 0, 1, \dots, N-1 \quad (36)$$

However, we note that the straightforward summation in (36) requires N^2 complex multiplications and $N(N-1)$ complex additions. Our goal is to evaluate equation (36) more efficiently than the direct summation so that these numbers of arithmetic operations will be reduced to $O(N \log N)$.

There are many variations of FFT algorithms. In this section, we will discuss only the Cooley–Tukey FFT algorithm for arbitrary factors. Then we will discuss the applications of FFT in fast convolution and correlation, and in fast methods in computational electromagnetics.

4.1. The Cooley–Tukey FFT Algorithm without Twiddle Factors

First, following Brigham [9] we summarize the derivation of Cooley–Tukey FFT algorithm for arbitrary factors as extended by Bergland [3]. We assume the number of points N can be factored as

$$N = \prod_{i=1}^I r_i \quad (37)$$

where r_i ($i = 1, \dots, I$) are positive integers.

To present the FFT algorithm, it is more convenient to express indices m and n in (36) in a variable radix representation

$$m = m_{I-1}(r_1 r_2 \cdots r_{I-1}) + m_{I-2}(r_1 r_2 \cdots r_{I-2}) + \cdots + m_1 r_1 + m_0 \quad (38)$$

$$= \sum_{k=0}^{I-1} m_k \prod_{l=0}^k r_l$$

$$n = n_{I-1}(r_2 r_3 \cdots r_I) + n_{I-2}(r_3 r_4 \cdots r_I) + \cdots + n_1 r_I + n_0 = \sum_{p=0}^{I-1} n_p \prod_{q=I-p+1}^{I+1} r_q \quad (39)$$

where $r_0 = r_{I+1} = 1$ and

$$m_i = 0, 1, 2, \dots, r_{i+1} - 1, \quad 0 \leq i \leq I-1$$

$$n_i = 0, 1, 2, \dots, r_{I-i} - 1, \quad 0 \leq i \leq I-1$$

Then (36) can be rewritten as

$$H(m_{I-1}, m_{I-2}, \dots, m_1, m_0) = \frac{1}{\sqrt{N}} \sum_{n_0=0}^{r_1-1} \sum_{n_1=0}^{r_2-1} \cdots \sum_{n_{I-1}=0}^{r_I-1} h(n_{I-1}, n_{I-2}, \dots, n_0) W_N^{mn} \quad (40)$$

where $W_N = \exp(-j2\pi/N)$. This may seem to make the new DFT summation even more complicated than the original equation (36), but we will see that this factorization actually saves some arithmetic operations. We will carry out this factorization in several stages allowed by the radix factorization:

Stage 1. Noting that $W_N^{\prod_{i=1}^I r_i} = W_N^N = 1$, we can rewrite the first terms of $W_N^{mn} = W_N^{m[n_{I-1} \prod_{i=1}^I r_i + \dots + n_0]}$ as

$$W_N^{mn_{I-1} \prod_{i=2}^I r_i} = W_N^{m_0 n_{I-1} \prod_{i=2}^I r_i} \tag{41}$$

Therefore

$$H(m_{I-1}, m_{I-2}, \dots, m_1, m_0) = \sum_{n_0=0}^{r_I-1} \sum_{n_1=0}^{r_{I-1}-1} \dots \left[\sum_{n_{I-1}=0}^{r_1-1} x_0(n_{I-1}, n_{I-2}, \dots, n_0) \cdot W_N^{m_0 n_{I-1} \prod_{i=2}^I r_i} \right] \cdot W_N^{m[n_{I-2} (\prod_{i=3}^I r_i) + \dots + n_0]} \tag{42}$$

where $x_0 = h/\sqrt{N}$. We define the item inside the square brackets as x_1 :

$$x_1(m_0, n_{I-2}, \dots, n_0) = \sum_{n_{I-1}=0}^{r_1-1} x_0(n_{I-1}, n_{I-2}, \dots, n_0) W_N^{m_0 n_{I-1} \prod_{i=2}^I r_i} \tag{43}$$

Note that this stage for calculating (43) requires Nr_1 operations (one complex multiplication and one complex addition), without considering the symmetries of the complex exponential. Then, equation (42) can then be written as

$$H(m_{I-1}, m_{I-2}, \dots, m_1, m_0) = \sum_{n_0=0}^{r_I-1} \sum_{n_1=0}^{r_{I-1}-1} \dots \sum_{n_{I-2}=0}^{r_2-1} x_1(m_0, n_{I-2}, \dots, n_0) \times W_N^{m[n_{I-2} (\prod_{i=3}^I r_i) + \dots + n_0]} \tag{44}$$

Stage 2. Similar to equation (41), we can now show that

$$W_N^{mn_{I-2} \prod_{i=3}^I r_i} = W_N^{(m_1 r_1 + m_0) n_{I-2} \prod_{i=3}^I r_i} \tag{45}$$

Hence, by defining

$$x_2(m_0, m_1, n_{I-3}, \dots, n_0) = \sum_{n_{I-2}=0}^{r_2-1} x_1(m_0, n_{I-2}, \dots, n_0) W_N^{(m_1 r_1 + m_0) n_{I-2} \prod_{i=3}^I r_i} \tag{46}$$

we can rewrite (44) as

$$H(m_{I-1}, m_{I-2}, \dots, m_1, m_0) = \sum_{n_0=0}^{r_I-1} \sum_{n_1=0}^{r_{I-1}-1} \dots \sum_{n_{I-3}=0}^{r_3-1} x_2(m_0, m_1, n_{I-3}, \dots, n_0) \times W_N^{m[n_{I-3} (\prod_{i=4}^I r_i) + \dots + n_0]} \tag{47}$$

This stage requires Nr_2 arithmetic operations without considering the symmetries of the complex exponential.

Stage p. In the same manner, if we continue reducing (47), we will obtain a set of recursive equations of the form

$$x_p(m_0, m_1, \dots, m_{p-1}, n_{I-p-1}, \dots, n_0) = \sum_{n_{I-p}=0}^{r_p-1} x_{p-1}(m_0, m_1, \dots, m_{p-2}, n_{I-p}, \dots, n_0) \tag{48}$$

$$\cdot W_N^{[m_{p-1}(r_1 r_2 \dots r_{p-1}) + \dots + m_1 r_1 + m_0] n_{I-p} \prod_{i=p+1}^I r_i},$$

$$p = 1, 2, \dots, I$$

where we have defined $(r_{p+1} \dots r_I) = 1$ for $p > I - 1$ and $n_{-1} = 0$. This stage requires Nr_p arithmetic operations without considering the symmetries of the complex exponential.

The Complete FFT Algorithm. The final results are given by

$$H(m_{I-1}, m_{I-2}, \dots, m_1, m_0) = x_I(m_0, \dots, m_{I-1}) \tag{49}$$

from which the total number of multiplications is

$$M = N \sum_{p=1}^I r_p$$

In the special case where the radix representation is constant, $r_1 = r_2 = \dots = r_I = r$, $I = \log_r N$, we have the total number of multiplications $M = Nr \log_r N$, without considering the symmetries of the complex exponential. Thus, the FFT algorithm requires only $O(N \log N)$ operations.

4.2. The Cooley–Tukey FFT Algorithm with “Twiddle” Factors

As discussed above, in the Cooley–Tukey FFT algorithm without “twiddle” factors, the p th stage calculation in (48) requiring Nr_p operations. However, recognizing that one factor in (48) can be rewritten as

$$W_N^{m_{p-1}(r_1 r_2 \cdots r_{p-1})n_{I-p}} \prod_{i=p+1}^I r_i = W_N^{m_{p-1}n_{I-p}N/r_p} = W_{r_p}^{m_{p-1}n_{I-p}} \quad (50)$$

we can rewrite the p th stage equation (48) as

$$\begin{aligned} & x_p(m_0, m_1, \dots, m_{p-1}, n_{I-p-1}, \dots, n_0) \\ &= \left[\sum_{n_{I-p}=0}^{r_p-1} x_{p-1}(m_0, m_1, \dots, m_{p-2}, n_{I-p}, \dots, n_0) W_{r_p}^{m_{p-1}n_{I-p}} \right] \\ & \cdot W_N^t = [DFT_{r_p}\{x_{p-1}\}] \cdot W_N^t \end{aligned} \quad (51)$$

where

$$t = [m_{p-1}(r_1 r_2 \cdots r_{p-2}) + \cdots + m_1 r_1 + m_0]n_{I-p} \prod_{i=p+1}^I r_i$$

It is obvious that the summation inside the brackets in Eq. (51) is an r_p -point DFT (denoted by $DFT_{r_p}\{x_{p-1}\}$); the factor W_N^t outside the bracket is called the twiddling factor. Thus, the p th stage in the FFT algorithm can be computed by the r_p -point DFT followed by the twiddling operation (i.e., by the referencing operation of W_N^t).

Because of the symmetries in $W_{r_p}^{m_{p-1}n_{I-p}} \equiv W_{r_p}^d$, it is important to recognize that this r_p -point DFT can be computed very efficiently, with much fewer operations than r_p^2 . For example, if $r_p = 2$ (i.e., a base 2 transform), the W_2^d factor takes only ± 1 , and there is no need for multiplications; the total number of complex multiplications is

$$M_2 = \frac{1}{4}[2 \log_2 N - 4]N + 1$$

If $r_p = 4$ (i.e., a base 4 transform), there is no need for multiplications in the DFT since the W_2^d factor takes only ± 1 and $\pm j$; the total number of complex multiplications is

$$M_4 = \frac{1}{4}[1.5 \log_2 N - 4]N + 1$$

If $r_p = 8$ (i.e., a base 8 transform), there are only four real multiplications in the DFT since the W_2^d factor takes only ± 1 , $\pm j$, $\pm e^{j\pi/4}$; and $\pm e^{j3\pi/4}$; the total number of complex multiplications is

$$M_8 = \frac{1}{4}[1.333 \log_2 N - 4]N + 1$$

For more details, the reader is referred to Ref. 9.

5. APPLICATIONS OF FFT IN ELECTROMAGNETICS

The FFT algorithm is one of the most important developments in numerical analysis. Its applications are ubiquitous. Here we will only summarize its applications in fast computational methods for electromagnetics, including the pseudospectral time-domain (PSTD) methods and the integral equation methods.

5.1. Fast Derivatives and the Pseudospectral Time-Domain (PSTD) Methods

The finite-difference time-domain (FDTD) method has become a standard technique to solve transient electromagnetic problems by solving time-domain Maxwell equations [82]. However, the major difficulty with the FDTD method is the required high sampling density (≥ 20 cells per wavelength) because of its low-order accuracy. It is known that the accuracy of the FDTD method is second-order in a homogeneous medium, but only first order in a discontinuous medium.

In order to improve the FDTD method, many researchers have proposed various techniques. One class of such techniques is pseudospectral time-domain methods, which use trigonometric functions or Chebyshev polynomials to approximate spatial derivatives [27,36,49–51,79–81,86,87]. These PSTD methods have been developed for unbounded and bounded media, and have been shown to greatly outperform the FDTD methods, especially for large-scale problems.

The key to the PSTD methods lies in the fast and accurate spatial derivatives by using either the FFT or the Chebyshev polynomials. Consider a 1D function $u(x, t)$. In the regular FDTD method, the spatial (and temporal) derivatives are approximated by the central finite-difference scheme, which has a second-order accuracy. In contrast, in the PSTD methods, the spatial derivatives are approximated by either trigonometric functions or by Chebyshev polynomials.

5.1.1. The Fourier PSTD Method. In the Fourier PSTD method, we consider a spatially periodic function $u(x, t)$ in x ($0 \leq x \leq L$), where L is the period. If $\Delta x = L/N$ is used as the cell size and $x_n = n\Delta x$, $n = 0, 1, \dots, N-1$, the approximation of the spatial derivative can be in general written as

$$\frac{\partial u(x, t)}{\partial x} \approx \mathcal{D}_x\{u(x, t)\} \quad (52)$$

where the derivative operator is given by

$$\mathcal{D}_x f(x) = \mathcal{F}_x^{-1}\{jk_x \mathcal{F}_x[f(x)]\} \quad (53)$$

where \mathcal{F} and \mathcal{F}^{-1} denote the forward and inverse Fourier transforms that are achieved by an FFT algorithm with the number of operations $O(N \log N)$. Such an approximation in (53) has a spectral accuracy; that is, the error

decreases exponentially as N increases, given that $u(x, t)$ is analytic.

In contrast to the FDTD method, which uses a staggered grid, the Fourier PSTD method uses a centered grid where all field components are located at the cell centers. In addition to its simplicity, this centered grid provides an important advantage over the FDTD algorithm since the material properties are not altered by the presence of the staggered grid. Furthermore, the centered grid is more advantageous for anisotropic media [51], and removes the singularity problem for EM waves in cylindrical coordinates [55].

Since the Fourier PSTD method assumes periodicity in the wave fields, in order to apply this method to unbounded media, the perfectly matched layer (PML) absorbing boundary condition should be used at the computational edge to remove the so-called wraparound effect caused by the periodicity [49].

5.1.1.1. Time Integration. The temporal grid, however, is staggered since the central differencing is used for time-stepping. Therefore, the time integration is exactly the same as in the regular Yee scheme. The dispersion analysis and stability condition of the FDTD and Fourier PSTD algorithm has been formulated for a homogeneous, lossless medium [49,50]. The Courant-Friedrichs-Lewy (CFL) stability conditions can be written compactly as

$$\frac{c\Delta t}{\Delta x} \leq \frac{1}{\alpha\sqrt{D}} \quad (54)$$

for a problem of dimensionality D , where $\alpha = 1$ for FDTD, and $\alpha = \pi/2 \approx 1.5708$ for PSTD [51]. Higher-order time-integration methods such as the fourth-order Runge-Kutta method can be used to further improve the time integration accuracy.

The Fourier PSTD method is easy to implement and requires only two points per minimum wavelength, but the medium under study needs to be homogeneous or smoothly varying to ensure the exponential accuracy.

The Fourier PSTD method, originally proposed in Refs. 49 and 50, has been applied to the simulation of many engineering problems [31,41–44,56,74]. This method provides spectral accuracy when the medium is very smooth. However, its major limitation is that it is not applicable to problems with perfect conductors; theoretically, it has the spectral accuracy only for smoothly varying inhomogeneous media, although numerical examples show that it is much more efficient and accurate than the FDTD method. One way to deal with strongly inhomogeneous media is to use a nonuniform grid to account for the material variation, by using the nonuniform fast Fourier transform (NUFFT) [56] or the nonuniform grid mapping [43]; a hybrid of PSTD and FDTD techniques has also been suggested [42,44]. However, all these remedies still cannot remove the staircasing error associated with the Kröner product grid (i.e., the mesh is parallel to coordinate directions). An alternative method for perfect conductors and discontinuous inhomogeneous media is the multidomain Chebyshev PSTD method discussed below.

5.1.2. The Multidomain Chebyshev PSTD Method. The Fourier PSTD method discussed above is applied for both periodic problems (such as the frequency-selective surfaces and photonic crystals), and for unbounded media with the PML absorbing boundary condition. For bounded media, on the other hand, one can develop a single-domain Chebyshev PSTD method [74]. However, the single-domain Chebyshev PSTD method, similar to the Fourier PSTD method, has spectral accuracy only for smoothly varying media.

In order to apply the PSTD method to perfect conductors and discontinuous media with spectral accuracy, it is necessary to develop a multidomain PSTD method [36,79,80]. Examples of multidomain Chebyshev PSTD method have been shown for perfect conductors and for discontinuous inhomogeneous lossy media, including the applications in GPR (ground penetrating radar) sensing [27], waveguides [86], and scattering problems [87]. It has demonstrated the great flexibility of dealing with complex objects, with a slightly increased computational burden because it requires π cells per minimum wavelength.

In order to develop a multidomain Chebyshev PSTD method, the problem domain is divided into hexahedron subdomains naturally conformal to the geometry. In general, each subdomain has curved boundaries in the (x, y, z) coordinates, but can be mapped into a cube in the curvilinear coordinates (ξ, η, ζ) with $\xi, \eta, \zeta \in [-1, 1]$. In each direction ξ, η, ζ , the spatial derivative can be found by using Chebyshev polynomials. For example, in the ξ direction, for $\xi \in [-1, 1]$, the region can be discretized by $N + 1$ Gauss-Chebyshev-Lobatto points (or simply called the Chebyshev points) defined at

$$\xi_i = -\cos\frac{i\pi}{N}, \quad i = 0, 1, \dots, N \quad (55)$$

Then function $u(\xi, t)$ can be represented as

$$u(\xi, t) = \sum_{n=0}^N a_n(t) T_n(\xi) \quad (56)$$

where $T_n(\xi) = \cos[n \cos^{-1}(\xi)]$ is the n th-order Chebyshev polynomial. Equivalently

$$u(\xi, t) = \sum_{i=0}^N u(\xi_i, t) \phi_i(\xi) \quad (57)$$

where

$$\phi_i(\xi) = \frac{(1 - \xi^2) T'_N(\xi) (-1)^{i+1+N}}{c_i N^2 (\xi - \xi_i)} \quad (58)$$

and $c_i = 1 + \delta_{i,0} + \delta_{i,N}$. With the interpolation in (56), the spatial derivative of $u(\xi, t)$ with respect to ξ is approximated as

$$\frac{\partial u(\xi_i, t)}{\partial \xi} = \sum_{k=0}^N D_{ik}^{(\xi)} u(\xi_k, t) \quad (59)$$

where the differential matrix elements are given by

$$D_{ik} = \phi'_k(\xi_i) \quad (60)$$

and the explicit expressions can be found in Refs. 10 and 87.

Alternatively, using (56), one can obtain the derivative of $u(\xi, t)$ as

$$\frac{\partial u(\xi, t)}{\partial \xi} = \sum_{n=0}^N b_n(t) T_n(\xi) \quad (61)$$

where the coefficients $\{b_n\}$ can be derived through the recursion relations of the Chebyshev polynomials

$$\begin{cases} b_N = 0 \\ b_{N-1} = 2Na_N \\ b_{N-2} = 2(N-1)a_{N-1} \\ b_{i-1} = b_{i+1} + 2ia_i, \quad i = N-2, N-3, \dots, 2 \\ b_0 = a_1 + b_2/2 \end{cases} \quad (62)$$

Obviously, the choice of the gridpoints in (55) makes (56) a cosine transform; thus, the coefficients $\{a_n\}$ in (56) can be found from $\{u(\xi_i)\}$ by using the fast cosine transform (FCT) algorithm, which can be derived from the FFT algorithm. The derivative coefficients $\{b_n\}$ are then obtained by the recursion relation (62); then the derivative can be obtained by the fast cosine transform using equation (61). In general, if $N > 16$, it is more efficient to obtain the derivative by using the CFT than the direct matrix-vector multiplication [10].

Once the spatial derivatives have been found accurately, the fields inside each subdomain can be updated by a time integration method such as the fourth-order Runge–Kutta method. Then, the fields between adjacent subdomains must be reconciled by a patching procedure so that the boundary conditions between subdomains are satisfied. For details of the multidomain PSTD method, the reader is referred to Refs. 27, 36, 79, and 86–88 and a review paper [59].

5.2. Fast Convolution, Correlation, and k -Space Methods for Integral Equations

In addition to the PSTD methods discussed above, the FFT algorithm is an essential ingredient in modern computational methods for electromagnetics, in the areas of fast forward and inverse problems involving integral equations.

The use of the FFT to accelerate the solution of integral equations dates back to the k -space method proposed by Bojarski in the early 1980s [6]. In general, to solve an integral equation in electromagnetics with the conventional method of moments (MoM) [35], one uses some basis functions to express the unknown field (or unknown current density); after tested by some weighting functions, the integral equation can be converted into N algebraic equations with N discrete unknowns. Solving this problem involves the inversion of the $N \times N$ matrix, which can be a prohibitive task as the memory requirement is $O(N^2)$, and the CPU time is $O(N^3)$ (if a direct method is used for the matrix inversion) or $O(KN^2)$ (if an iterative method is used, where K denotes the number of iterations).

The original k -space method [6] was proposed for objects in a homogeneous background medium. In this case, the k -space method utilizes the fact that the scattered field from an object can be written as a convolution integral between the background Green function and the induced current in the scatterer. Therefore, after discretization with a uniform grid, the operation of the Green's function onto the induced current (called "Green's operation") can be carried out by using the FFT with only $O(N \log N)$, rather than $O(N^2)$ arithmetic operations in the MoM. The integral equation has to be solved iteratively; within each iteration Green's operation and its adjoint operation are accelerated by the FFT, thus resulting in an algorithm requiring only $O(KN \log N)$ CPU time, where K is the number of iterations required. Furthermore, the memory requirement has been greatly reduced from $O(N^2)$ in MoM to $O(N)$ in the k -space method as the MoM matrix is no longer needed. The idea of the k -space method was later improved by the CG-FFT (conjugate-gradient fast Fourier transform) methods. Early works include Refs. 8, 12, 39, 68, 69 and 75; 3D CG-FFT-type methods include Refs. 37, 73, 77, 83, 84, and 90; see Ref. 13 for more complete references. In the CG-FFT method, the conjugate-gradient method is used as the iterative method to improve the convergence of the original k -space method. The k -space and the CG-FFT methods can be applied to a wide variety of integral equations, including volume integral equations and surface integral equations with planar geometries. They are not applicable to surface equations with arbitrary geometries where the shift invariance of Green's function no longer holds along the scatterer surface.

Traditionally, the k -space and CG-FFT methods have been applied to objects in a homogeneous background. The CG-FFT method has been further improved by the biconjugate-gradient (BCG-FFT) method [37, 83] and stabilized biconjugate-gradient (BCGS-FFT) method [77]. Since all these iterative methods solve the integral equation using the FFT, we categorize them as the general k -space method for integral equations.

The k -space method has also been applied to planar conductor structures in a multilayered medium where the scatterer is parallel to the layer interfaces. In this case, the shift-invariance of the Green function again ensures that the FFT can be used to accelerate the convolution integral along the parallel planar directions [13, 46, 66, 89]. More recently, the k -space method has been applied to acoustic scattering in a layered medium [76], electromagnetic scattering in a half-space [19, 20], and a multilayered medium [63, 64, 78], by penetrable inhomogeneous objects. The major difference between the multilayered background medium and the homogeneous background medium is that the Green function is no longer shift-invariant in the direction perpendicular to the layer interfaces; thus, the Green operation is no longer a convolution integral. However, it has been shown that if the objects are located within one single layer in the multilayered medium, one can split the Green's operation into a convolution integral and a correlation integral, making the FFT algorithm still applicable to accelerate the Green's operation [19, 20, 63, 64, 76, 78].

To illustrate these important applications of the FFT in computational electromagnetics, we summarize the latest development in the solution of electromagnetic scattering by penetrable objects embedded in a multilayered medium [63,64,78]. As shown in Fig. 1, if an inhomogeneous dielectric object of arbitrary shape is completely embedded in the i th layer, the scattered magnetic vector potential in the m th layer, then $A^{mi}(\mathbf{r})$, due to the induced current source \mathbf{J} inside the inhomogeneous object embedded in the i th layer, is given by

$$\begin{aligned} \mathbf{A}^{mi}(\mathbf{r}) &= \mu_m \int_V \mathbf{G}^{mi}(\mathbf{r}, \mathbf{r}') \cdot \mathbf{J}(\mathbf{r}') d\mathbf{r}' \\ &= j\omega\mu_m \int_V \mathbf{G}^{mi}(\mathbf{r}, \mathbf{r}') \cdot \chi(\mathbf{r}') \mathbf{D}(\mathbf{r}') d\mathbf{r}' \end{aligned} \quad (63)$$

where \mathbf{G}^{mi} is the dyadic Green function for the magnetic vector potential, V is the volume of the scattering object, $\chi(\mathbf{r}) = [\tilde{\epsilon}(\mathbf{r}) - \tilde{\epsilon}_i]/\tilde{\epsilon}_i$ is the contrast function, $\tilde{\epsilon}(\mathbf{r}) = \epsilon(\mathbf{r}) + \sigma(\mathbf{r})/j\omega$, $\mathbf{D}(\mathbf{r}) = \tilde{\epsilon}(\mathbf{r})\mathbf{E}(\mathbf{r})$ is the unknown electric flux density inside the object, and $\tilde{\epsilon}_i$ is the complex permittivity of the i th layer. We can form the integral equation for the unknown electric flux density inside the object as

$$\mathcal{L}[\mathbf{D}_i(\mathbf{r})] = \mathbf{E}_i^{\text{inc}}(\mathbf{r}), \quad \mathbf{r} \in V \quad (64)$$

where \mathcal{L} is a linear operator defined as

$$\mathcal{L}[\cdot] = \left[\frac{\cdot}{\tilde{\epsilon}} - (k_i^2 + \nabla\nabla \cdot) \right] \frac{1}{\tilde{\epsilon}_i} \int_V \mathbf{G}^{ii}(\mathbf{r}, \mathbf{r}') \cdot \chi[\cdot] d\mathbf{r}', \quad \mathbf{r} \in V \quad (65)$$

and $k_i = \omega\sqrt{\tilde{\epsilon}_i\mu_i}$ is the wavenumber of the i th layer. Solving Eq. (64), the electric flux density $\mathbf{D}_i(\mathbf{r})$ is obtained for $\mathbf{r} \in V$. The relationship $\mathbf{J} = j\omega\chi\mathbf{D}$ can be used to calculate the induced current inside the scattering object, and thus the electric field at any location.

The volume EFIE (electric field integral equation) has been formulated with the electric flux density as the unknown because the continuity of the normal component of electric flux density can be easily enforced by choosing the rooftop basis functions for \mathbf{D} . On the other hand, if the electric/magnetic fields are chosen as the unknown, implementation of the boundary conditions is not trivial. Furthermore, the ‘‘weak form’’ discretization process proposed in Ref. 90 for the scattering of objects in a homoge-

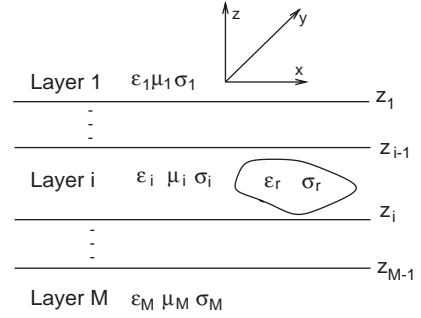


Figure 1. Typical configuration of an inhomogeneous object in a planar layered medium.

neous background can be extended to layered media to reduce the singularity of the problem. To make use of the FFT to accelerate the solution, the integral equation in (64) is usually solved iteratively by Krylov subspace methods such as the conjugate-gradient, biconjugate-gradient, or stabilized biconjugate-gradient methods, as summarized in Table 3.

When solving the integral equation in (64) iteratively, we need to calculate the interactions of the dyadic Green function $\mathbf{G}^{ii}(\mathbf{r}, \mathbf{r}')$ with the induced current density $\mathbf{J} = j\omega\chi\mathbf{D}$ for every testing function within the object. If the object is discretized into N unknowns, the straightforward computation of these interactions requires $O(N^2)$ arithmetic operations. In free space, this computation can be accelerated by using the fast Fourier transform (FFT) algorithm because the Green function there is shift-invariant.

As a result of the inhomogeneity along the z direction, however, the dyadic Green function for a layered medium is no longer shift-invariant; thus the integral kernel of the volume EFIE (64) is not convolutional. For example, in the spectral domain, we obtain

$$\begin{aligned} \tilde{\mathbf{G}}_{xx}^{ii}(k_\rho, z, z') &= \frac{1}{2jk_{z,i}} \left[e^{-jk_{z,i}|z-z'|} \right. \\ &+ \frac{1}{D_i^{\text{TE}}} \{ \bar{R}_i^{\text{TE}} e^{-jk_{z,i}[(z+z')-2z_i]} + \bar{R}_{i-1}^{\text{TE}} e^{-jk_{z,i}[2z_{i-1}-(z+z')] } \\ &\left. + 2\bar{R}_i^{\text{TE}} \bar{R}_{i-1}^{\text{TE}} e^{-j2\psi_i} \cos k_{z,i}(z-z') \} \right] \end{aligned} \quad (66)$$

Table 3. Three Krylov Subspace Methods

CG Method	BCG Method	BCGSTAB Method
$\mathbf{r}_0 = \mathbf{E}^{\text{inc}} - \mathcal{L}\mathbf{D}_0$ $\mathbf{p}_0 = \mathbf{r}_0$	$\mathbf{r}_0 = \mathbf{p}_0 = \mathbf{E}^{\text{inc}} - \mathcal{L}\mathbf{D}_0$ $\tilde{\mathbf{r}}_0 = \tilde{\mathbf{p}}_0 = \mathbf{r}_0^*$	$\mathbf{r}_0 = \mathbf{E}^{\text{inc}} - \mathcal{L}\mathbf{D}_0$ Choose $\tilde{\mathbf{r}}_0$ so that $(\tilde{\mathbf{r}}_0, \mathbf{r}_0) \neq 0$ $\rho_0 = \alpha = \omega_0 = 1$, $\mathbf{v}_0 = \mathbf{p}_0 = 0$
$\alpha_k = \frac{\langle \mathbf{r}_{k-1}, \mathbf{r}_{k-1} \rangle}{\langle \mathbf{p}_k, \mathbf{p}_k \rangle}$	$\alpha_k = \frac{\langle \mathbf{r}_k, \tilde{\mathbf{r}}_k \rangle}{\langle \mathcal{L}\mathbf{p}_k, \tilde{\mathbf{p}}_k \rangle}$	$\rho_k = \langle \tilde{\mathbf{r}}_0, \mathbf{r}_{k+1} \rangle$
$\beta_k = -\frac{\langle \mathbf{r}_k, \tilde{\mathbf{r}}_k \rangle}{\langle \mathbf{r}_{k-1}, \tilde{\mathbf{r}}_{k-1} \rangle}$	$\beta_k = \frac{\langle \mathbf{r}_{k+1}, \tilde{\mathbf{r}}_{k+1} \rangle}{\langle \mathbf{r}_k, \tilde{\mathbf{r}}_k \rangle}$	$\beta = \alpha\rho_k/(\omega_{k-1}\rho_{k-1})$
$\mathbf{D}_{k+1} = \mathbf{D}_k + \alpha_k \mathbf{p}_k$	$\mathbf{D}_{k+1} = \mathbf{D}_k + \alpha_k \mathbf{p}_k$	$\mathbf{p}_k = \mathbf{r}_{k-1} + \beta(\mathbf{p}_{k-1} - \omega_{k-1}\mathbf{v}_{k-1})$
$\mathbf{r}_{k+1} = \mathbf{r}_k - \alpha_k \mathcal{L}\mathbf{p}_k$	$\mathbf{r}_{k+1} = \mathbf{r}_k - \alpha_k \mathcal{L}\mathbf{p}_k$	$\mathbf{v}_k = \mathcal{L}\mathbf{p}_k$, $\alpha = \rho_k/(\tilde{\mathbf{r}}_0, \mathbf{v}_k)$
$\mathbf{p}_{k+1} = \mathbf{r}_{k+1} + \beta_k \mathbf{p}_k$	$\tilde{\mathbf{r}}_{k+1} = \tilde{\mathbf{r}}_k - \alpha_k^* \mathcal{L}^* \tilde{\mathbf{p}}_k$	$\mathbf{s} = \mathbf{r}_{k-1} - \alpha \mathbf{v}_k$, $\mathbf{t} = \mathcal{L}\mathbf{s}$
	$\mathbf{p}_{k+1} = \mathbf{r}_{k+1} + \beta_k \mathbf{p}_k$	$\omega_k = \langle \mathbf{t}, \mathbf{s} \rangle / \langle \mathbf{t}, \mathbf{t} \rangle$
	$\tilde{\mathbf{p}}_{k+1} = \tilde{\mathbf{r}}_{k+1} + \beta_k^* \tilde{\mathbf{p}}_k$	$\mathbf{D}_k = \mathbf{D}_{k-1} + \alpha \mathbf{p}_k + \omega_k \mathbf{s}$
		$\mathbf{r}_k = \mathbf{s} - \omega_k \mathbf{t}$

where \vec{R}_i^{TE} and $\vec{R}_{i-1}^{\text{TE}}$ define some global reflection coefficients, $\psi_i = k_{z,i}(z_{i-1} - z_i)$, and $D_i^{\text{TE}} = 1 - \vec{R}_i^{\text{TE}} \vec{R}_{i-1}^{\text{TE}} e^{-j2\psi_i}$ [60–62]. Obviously, this Green function is not shift-invariant in the z direction, even though it is still shift-invariant in the x and y directions. Consequently, unlike the scattering problem in free space, the integral in (65) is no longer convolutional; thus, the convolutional theorem cannot be used directly to arrive at the FFT acceleration in the CG-FFT, BCG-FFT, and BCGS-FFT methods as in the case of a homogeneous background.

Fortunately, we are able to develop a splitting technique to rewrite the dyadic Green function into two terms, one is shift-invariant in all directions, the other is shift-invariant in the x and y directions, but as a function of $z + z'$ in the z direction ([19,20,63,64,76,78]). More specifically, as indicated in (66), the dyadic Green's function in a layered medium can be written as the summation of two terms:

$$\mathbf{G}^{ii}(\mathbf{r}, \mathbf{r}') = \mathbf{G}_1^{ii}(|\bar{\rho} - \bar{\rho}'|, z - z') + \mathbf{G}_2^{ii}(|\bar{\rho} - \bar{\rho}'|, z + z') \quad (67)$$

As a result, in Eq. (65), the interaction between $\mathbf{G}_1^{ii}(\mathbf{r}, \mathbf{r}')$ and $\chi(\mathbf{r}')\mathbf{D}(\mathbf{r}')$ is a convolution in all (x, y, z) directions, and that between $\mathbf{G}_2^{ii}(\mathbf{r}, \mathbf{r}')$ and $\chi(\mathbf{r}')\mathbf{D}(\mathbf{r}')$ is a convolution in x and y directions, but a correlation in z direction. In other words, the integral kernel in the EFIE is convolutional in the x and y directions and convolutional or correlational in the z direction after the splitting. Consequently, the FFT can be applied to these two operations separately through the convolution and correlation theorems, reducing CPU time of the ‘‘Green’s operation’’ from $O(N^2)$ to $O(N \log N)$.

5.2.1. Linear convolution and correlation. In order to make use of the FFT algorithm to achieve discrete convolution and correlation for non-periodic, finite functions $\{h_1(n)\}$ of length N_1 and $\{h_2(n)\}$ of length N_2 , one needs to pad zeros to these arrays and assume that the new arrays are periodic. These new arrays must have a length at least equal to $N = N_1 + N_2 - 1$ to avoid the overlap in the resulting circular convolution and correlation. Furthermore, the convolution and correlation integrals in the volume integral equations actually involve discrete convolution and correlation of a non-periodic array $h(n)$ of finite duration M with a non-periodic function $g(n)$, namely the Green’s function, of infinite support but truncated to length N . In this case, since both functions must be made periodic of length N , to avoid the end effect one must choose the total number $N \geq 2M - 1$ to obtain the correct result for the M points within the scatterer.

5.2.2. Fast Multipole Method. The FFT algorithm is also an important component in the fast multipole method (FMM) [17,70] that has significantly reduced the computational complexity of the numerical solution of integral equations, especially surface integral equations. For more details of this FMM algorithm, the reader is referred to Ref. 16.

5.3. Fast Inverse Scattering Methods

Electromagnetic waves have widespread applications in areas such as medical diagnosis, geophysical exploration,

nondestructive evaluation, and other areas of imaging. In such applications, one needs to solve the inverse problem, that is, to infer the characteristics of the target from the observed electromagnetic fields. The inverse scattering problems can be classified into two types: (1) approximate, linear inverse problems and (2) nonlinear inverse scattering methods. The FFT plays an important role in both types of electromagnetic inverse scattering problems.

Electromagnetic inverse problems are inherently nonlinear because of the multiple scattering within different parts of the scatterer. However, in the low-frequency regime, one can approximately neglect the multiple scattering; such an approximation is known as the *Born approximation* [7]. Similarly, in the high-frequency regime, one can use Rytov approximation or Kirchhoff approximation to make the inverse problem linear. Such linear inverse methods include the low-frequency diffraction tomography [22], high-frequency synthetic aperture radar (SAR) processing [72], and the related migration processing. For example, in a SAR processing scheme, the principal idea is to synthesize the effect of a large-aperture radar whose physical construction is infeasible. In three-dimensional SAR, the antennas move along a 2D trajectory in the 3D space. Denote the location of the antenna as $(0, u, v)$, where (u, v) are the azimuthal and elevation coordinates of the radar, and the wideband signal emitted by the antenna as $p(t)$. We may assume for simplicity an omnidirectional radar radiation pattern. Then, the SAR signal [72] can be expressed as

$$s(t, u, v) = \sum_n f_n p \left(t - 2\sqrt{x_n^2 + (y_n - u)^2 + (z_n - v)^2} / c \right) \quad (68)$$

where c is the velocity of light (or sound) and f_n is the normalized reflectivity of the n th point scatterer. Taking the Fourier transform of (68) in (t, u, v) yields the reconstruction equation for the unknown reflectivity

$$f(x, y, z) = \frac{\mathcal{F}_{k_x, k_y, k_z}^{-1} S(\omega, k_u, k_v)}{P(\omega)} \quad (69)$$

where \mathcal{F}^{-1} denotes the inverse Fourier transform and $[k_x, k_y, k_z]$ are governed by the SAR (SAS) spatial frequency mapping

$$\begin{aligned} k_x(\omega, k_u, k_v) &= \sqrt{4\omega^2/c^2 - k_u^2 - k_v^2}, \\ k_y(\omega, k_u, k_v) &= k_u, \quad k_z(\omega, k_u, k_v) = k_v \end{aligned} \quad (70)$$

The image of the object can thus be found by using the FFT algorithm from (69).

To address the high-contrast problems where the electrical properties of the object are very different from the background, nonlinear inverse scattering methods in 2D [11,14,15,38] and 3D [1,2,85] have been developed. For more recent developments in this area, the reader is referred to the references cited in Refs. 45 and 85.

6. NONUNIFORM FAST FOURIER TRANSFORM (NUFFT)

As illustrated above, the FFT has been enjoying widespread applications in numerical analysis and other areas of applied mathematics since the work of Cooley and Tukey [18] in the 1960s. However, the requirement for using FFT algorithms is that the input data must be equally sampled. In many practical situations, however, the input data are not equally spaced either by error or by design, and hence the regular FFT does not apply. To overcome this limitation Dutt and Rokhlin [24] studied the problem of FFT for nonuniform (unequally spaced) data. Later, the fast FFT for nonuniform data has been termed (*nonuniform fast Fourier transform*) (NUFFT) [52,65].

6.1. Nonuniform Discrete Fourier Transforms (NUDFTs)

The nonuniform discrete Fourier transform (NUDFT) is an extension of the regular (uniform) DFT. This extension has widespread applications because many measurements, ranging from synthetic aperture radar (SAR), ground penetrating radar (GPR), to biomedical imaging using magnetic resonance imaging (MRI) and X-ray computerized tomography (CT), are sampled nonuniformly in a given space. First, we define the temporal sampling point locations $\{t_n, n = 0, \dots, N - 1\} \in [0, N)$, and frequency sampling point locations $\{\omega_m, m = 0, \dots, N - 1\} \in [0, N)$, where periodicity is implied with a period of N in both domains. There are three basic types of NUDFT as given below. The complex sequence and its spectrum are defined as $h = \{h(t_0), \dots, h(t_{N-1})\}$ and $H = \{H(\omega_0), \dots, H(\omega_{N-1})\}$, respectively:

1. *NUDFT-1*. Nonuniform temporal sampling points $\{t_n\} \in [0, N)$, but uniform frequency sampling points $\omega_m = 0, \dots, N - 1$. This NUDFT is termed NUDFT-1 here and is defined as the sum

$$H(m) = \frac{1}{\sqrt{N}} \sum_{n=0}^{N-1} h(t_n) e^{-j t_n m (2\pi/N)}, \quad (71)$$

$$m = 0, \dots, N - 1$$

2. *NUDFT-2*. Uniform temporal sampling points $t_n = 0, \dots, N - 1$, but nonuniform frequency sampling points $\{\omega_m\} \in [0, N)$. This NUDFT is termed *NUDFT-2* here and is defined as the sum

$$G(\omega_m) = \frac{1}{\sqrt{N}} \sum_{n=0}^{N-1} g(n) e^{-j \omega_m n (2\pi/N)}, \quad (72)$$

$$m = 0, \dots, N - 1$$

3. *NUDFT-3*. Nonuniform temporal sampling points $t_n \in [0, N)$, and nonuniform frequency sampling points $\omega_m \in [0, N)$. This NUDFT is termed *NUDFT-3*

here and is defined as the sum

$$F(\omega_m) = \frac{1}{\sqrt{N}} \sum_{n=0}^{N-1} f(t_n) e^{-j \omega_m t_n (2\pi/N)}, \quad (73)$$

$$m = 0, \dots, N - 1$$

The corresponding fast algorithms for these sums are designated NUFFT-1, NUFFT-2, and NUFFT-3, respectively.

As shown in Ref. 24, once the solution to NUFFT-1 is found, NUFFT-2 and NUFFT-3 algorithms follow analogously. Therefore, here we will only discuss the NUFFT-1 algorithm for the fast solution of (71). Furthermore, the nonuniform inverse transforms corresponding to (18) can be defined similarly, and the algorithms are analogous to (71)–(73).

Now let's focus on the NUDFT-1 given by (71). The properties of the NUDFT-1 are largely analogous to those of the regular DFT, as summarized in Table 4.

6.2. The Forward NUFFT Algorithm

The aim of the NUFFT is to find a fast way to evaluate the sums in (71)–(73). Note that the direct summation in these equations requires $O(N^2)$ operations, much more than the FFT algorithm that requires only $O(N \log N)$ operations. The NUFFT algorithms developed by various groups [5,24,29,52,65] can provide approximate solutions to the NUDFT summations with $O(N \log N)$ operations. We will describe the algorithms reported in Refs. 52, 57, and 65 below.

We now consider the NUDFT-1 defined in (71). Instead of interpolating the input data $\{h(t_n)\}$, we will interpolate the exponential function $\exp(-j2\pi t m/N)$ for each $t = t_n$ ($n = 0, \dots, N - 1$). In applications, we only need to consider a discrete sequence

$$f(m) = s_m e^{-j2\pi t m/N}, \quad m \in \{0, \dots, N - 1\} \quad (74)$$

where t is real, $0 \leq s_m \leq 1$ for $m = 0, \dots, N - 1$ are called the “scaling factors,” and are chosen to minimize the error, and q an even positive integer. Denoting $w = e^{-j(2\pi t/N)}$, we will now interpolate $f(m)$ using the exponential function at $q + 1$ points on a unit circle

$$s_m w^{mvt} = \sum_{k=-q/2}^{q/2} x_k(t) w^{m(vt+k)}, \quad m = 0, \dots, N - 1 \quad (75)$$

Table 4. Properties of NUDFT-1

Property	Inverse NUDFT-1	Forward NUDFT-1
Linearity	$c_1 h_1(t_n) + c_2 h_2(t_n)$	$c_1 H_1(m) + c_2 H_2(m)$
Symmetry	None	None
Timeshifting	$h(t_n - T_0)$	$H(m) e^{-j2\pi m T_0/N}$
Frequency shifting	$h(t_n) e^{j2\pi t_n p/N}$	$H(m - p)$
Time reversal	$h(-t_n)$	$H(-m)$
Conjugation	$h^*(t_n)$	$H^*(-m)$
Even array	$h_e(t_n)$	$H_e(m)$
Odd array	$h_o(t_n)$	$H_o(m)$

where $[a]$ denotes the integer nearest to a , and $x_{-q/2}(t), \dots, x_{q/2}(t)$ are some unknown interpolation coefficients to be determined.

The unknown interpolation coefficients $x(t) = [x_{-q/2}(t), \dots, x_{q/2}(t)]^T$ can be determined by the least-squares method. Remarkably, this solution can be written almost analytically as

$$x(t) = F^{-1}y(t) \quad (76)$$

where for $i, k = 0, \dots, q$ we have

$$F_{ik}(v, N, q) = \begin{cases} N & i = k \\ \frac{w^{(i-k)N/2} - w^{(k-i)N/2}}{1 - w^{(k-i)}}, & i \neq k \end{cases} \quad (77)$$

$$y_k(t) = \sum_{m=0}^{N-1} s_m w^{(vt) + q/2 - km} \quad (78)$$

Observe that while $y(t)$ depends on t , matrix $F(v, N, q)$ is completely independent of t and is uniquely determined by v, N , and q . This remarkable property of this interpolation is important because it reduces the number of operations required by the NUFFT algorithms. The matrix $F(v, N, q)$ is called the *regular Fourier matrix*; it is a $(q+1) \times (q+1)$ Hermitian matrix, $F(v, N, q)^\dagger = F(v, N, q)$. These formulas make sense for any $q \in \mathcal{N}$, and therefore $F(v, N, q)$ can be defined for any $v, N, q \in \mathcal{N}$.

In the equations above, the coefficients $0 < s_m \leq 1$, for $m = 0, \dots, N-1$, called the *scaling factors*, are chosen to minimize the errors. Two scaling factors have been investigated:

- *Cosine scaling factors* $s_m = \cos(\pi m/vN)$ for $m = 0, \dots, N-1$.
- *Gaussian scaling factors* $s_m = e^{-b(2\pi m/vN)^2}$ for $m = 0, \dots, N-1$.

For the cosine scaling factors $s_m = \cos(\pi j/vN)$ for $j = 0, \dots, N-1$, it turns out that $y_k(t)$ can be written in a closed form by

$$y_k(t) = j \sum_{\gamma=-1,1} \frac{\sin\left[\frac{\pi}{2v}(2k - \gamma - q - 2\{vt\})\right]}{1 - e^{j(\pi/vN)(2\{vt\} + q - 2k + \gamma)}} \quad (79)$$

Unfortunately, for the Gaussian scaling factor, we are unable to find a closed-form expression for $y_k(t)$.

The NUFFT-1 algorithm consists of following steps:

1. Compute $y_k(t_n)$ by (79) for $k = 0, \dots, q$ and $n = 0, \dots, N-1$. The complexity is $O(Nq)$.
2. Compute $P_{\text{in}} = \sum_{k=0}^q [F^{-1}]_{ik} y_k(t_n)$, where the inverse regular Fourier matrix F^{-1} is precomputed. The complexity is $O(Nq^2)$.
3. Find the inverse of the scaling factor s_m^{-1} . For the cosine scaling factors $s_m^{-1} = \sec(\pi m/vN)$ for $m = 0, \dots, N-1$. The complexity is $O(N)$.

4. Calculate Fourier coefficients

$$\tau_l = \sum_{i, n, [vt_n] + i = l} h(t_n) \cdot P_{\text{in}}$$

The complexity is $O(Nq)$.

5. Use uniform FFT to evaluate

$$T_m = \sum_{l=-vN/2}^{vN/2-1} \tau_l \cdot e^{-j2\pi ml/vN}$$

The complexity is $O(vN \log N)$.

6. With a complexity of $O(N)$, scale the values to arrive at the approximated nonuniform FFT:

$$\tilde{H}(m) = T_m \cdot s_m^{-1}$$

The total complexity is $O(N \cdot q^2 + vN \log N)$, noting that $q \sim \log(1/\epsilon)$ where ϵ is the precision, and $v^2 \ll N$ (usually $v = 2$).

6.3. The Inverse NUFFT Algorithm

The inverse NUFFT algorithm is to find $h(t_n)$ from known $H(m)$ in Eq. (71). We first rewrite the NUFFT-1 in (71) and NUFFT-2 in (72) as

$$H(m) = \frac{1}{\sqrt{N}} \sum_{n=0}^{N-1} h(n) e^{-jt_n m 2\pi/N} \quad (80)$$

$$\equiv \sum_{n=0}^N A_{mn} h(t_n), \quad A_{mn} = \frac{1}{\sqrt{N}} e^{-jt_n m 2\pi/N}$$

$$G(\omega_m) = \frac{1}{\sqrt{N}} \sum_{n=0}^{N-1} g(n) e^{-jn\omega_m 2\pi/N} \quad (81)$$

$$\equiv \sum_{n=0}^{N-1} B_{mn} g(n), \quad B_{mn} = \frac{1}{\sqrt{N}} e^{-jn\omega_m 2\pi/N}$$

These forward NUFFT summations can be evaluated by NUFFT-1 and NUFFT-2 algorithms with $O(vN \log N)$ arithmetic operations (v is the oversampling rate).

For the regular, uniformly sampled data where both $\{t_k\}$ and $\{\omega_j\}$ are uniform, the inverse FFT (IFFT) can share the same algorithm as the FFT simply because $A^{-1} = A^\dagger$ and $B^{-1} = B^\dagger$ in these special cases (the superscript \dagger denotes the complex conjugate and transpose of a matrix). Unfortunately, this is no longer true for matrices A and B for nonuniformly sampled data. Hence, the inverse NUFFT can no longer share the same algorithm as the forward NUFFT. Obviously, the direct inversion of (80) and (81) to obtain $h(n)$ and $g(n)$ is prohibitively expensive as it requires $O(N^3)$ arithmetic operations. In Refs. 24 and 52, the inverse NUFFT algorithms have been developed.

We first rewrite (80) using a matrix notation $H = Ah$. From elementary matrix identities we observe that

$A^{-1} = A^\dagger(AA^\dagger)^{-1}$. Therefore the inverse DFT solution of (80) is

$$h = A^\dagger f, \quad f = (AA^\dagger)^{-1}H \quad (82)$$

The advantage of rewriting the solution in the form of (82) is clear because matrix AA^\dagger is a Toeplitz matrix. That is, $(AA^\dagger)_{kl} = a_{k-l}$, where

$$a_k = \frac{1}{\sqrt{N}} \sum_{n=0}^{N-1} e^{-jt_n 2\pi k/N}, \quad k = -N+1, \dots, N-1 \quad (83)$$

Observe that there are only N independent elements in the array a since $a_{-k} = (a_k)^*$. Furthermore, these N elements in (83) can be obtained by the NUFFT-1 algorithm

$$a_k = \frac{1}{\sqrt{N}} \sum_{n=0}^{N-1} e^{-jt_n 2\pi k/N}, \quad k = 0, \dots, N-1 \quad (84)$$

with $O(vN \log N)$ arithmetic operations.

Since AA^\dagger is a Toeplitz matrix, the vector f in (82) can be obtained efficiently using the conjugate-gradient FFT (CG-FFT) method [24]. In the CG-FFT method, the solution of f in (82) is obtained iteratively. Each iteration involves operations such as $y = (AA^\dagger)x$, which can be written as a discrete convolution

$$y_n = \sum_l a_{n-l} \cdot x_l = \{\text{FFT}^{-1}[\text{FFT}(a)\text{FFT}(x_p)]\}_j \quad (85)$$

and has been calculated by the regular FFT algorithm through the convolution theorem. Note that in (85), the size of the FFT's is $2N$, and x_p is the array x padded with N zeros. After f is solved by the above CG-FFT method, we can obtain h from (82) by

$$h(t_n) = \sum_{m=0}^{N-1} A_{mn}^* f_m = \frac{1}{\sqrt{N}} \left[\sum_{m=0}^{N-1} f_m^* e^{-jmt_n 2\pi/N} \right]^* \quad (86)$$

which can be achieved by the NUFFT-2 algorithm.

In summary, the procedures for the inverse NUFFT-1 algorithm for Eq. (80) is

1. *Preprocessing*—use the NUFFT-1 to obtain array $\{a_j\}$ through Eq. (84), and use the FFT algorithm to find $[\text{FFT}(a)]$.
2. *Inversion*—use the CG-FFT method for the solution f in (82).
3. *Transposition*—apply the NUFFT-2 to the transposed problem in Eq. (86).

In these steps, since NUFFT-1 and NUFFT-2 require $O(vN \log N)$ arithmetic operations, the most expensive step is the CG-FFT solution. It requires $O(KN \log N)$ arithmetic operations, where the number of iterations K in the CG method is proportional to the condition number of AA^\dagger . In most applications K is rather small as the points $\{t_m\}$ are fairly uniformly spaced. A similar algorithm has been developed for the inverse NUFFT of equation (81).

6.4. FFT for Discontinuous Functions—the DFFT Algorithm

The NUFFT algorithms presented above have been developed for nonuniform discrete Fourier transform. However, in practice, we often need to consider the continuous functions. In many applications in antennas, scattering, and computational electromagnetics, as well as in signal and image processing and other areas of computational science and engineering, one often needs to compute the Fourier transform of discontinuous functions. For example, in the well-known conjugate-gradient fast Fourier transform (CG-FFT)-type methods for integral equations (see Ref. 13 and references cited therein), one needs to find the Fourier transform of the unknown fields; in discontinuous media, some components of these unknown fields are discontinuous functions across the interfaces between different materials. In the conventional CG-FFT methods, discrete Fourier transforms (DFT) of these discontinuous functions are calculated through FFT algorithms. However, it is known that the conventional DFT cannot give accurate results for discontinuous function. This approach has a poor accuracy of $O(N^{-1})$, where N is the number of sample points. This large error is a result of the trapezoidal rule for the Fourier integration; in comparison, if the function is smooth and periodic, the DFT has exponential accuracy. A highly accurate fast Fourier transform algorithm for discontinuous functions, called the *discontinuous fast Fourier transform* (DFFT) algorithm, was proposed by Fan and Liu [25,28], based on the previous work for piecewise constant functions [71].

An accurate and efficient FFT algorithm for discontinuous data include two basic steps:

1. A highly accurate quadrature for improving the accuracy of integration
2. The standard FFT for efficiently evaluating the discretized summation of the integration

To combine these two steps, we need to resort to an interpolation procedure. Since the FFT algorithm requires uniformly sampled points while the function to be transformed has discontinuities at potentially nonuniform points, the interpolation procedure should interpolate such nonuniform data points to the uniform FFT data points. Unfortunately, many existing interpolation algorithms are either not directly applicable or cannot be utilized in this problem. Previously, two algorithms for discontinuous data were found in the literature [5,71]. Sorets proposed a fast Fourier transform algorithm for piecewise constant functions via the Gaussian quadrature and Lagrange interpolation, together with an application of the standard FFT [71], but the algorithm cannot be directly applied to piecewise smooth functions. The FFT of functions with similar singularities has also been treated by Beylkin [5] using piecewise polynomial splines, although numerical results are yet to be given for piecewise smooth functions.

The DFFT reported by Fan and Liu [26,28] considers the Fourier transform of a periodic piecewise smooth

function $f(x)$ defined in a period $T = 1$

$$\hat{f}(n) = \int_0^1 f(x) e^{-j2\pi nx} dx \quad -\frac{N}{2} < n \leq \frac{N}{2} - 1 \quad (87)$$

where n is an integer. We divide the integration interval $[0,1]$ into L subdivisions within which $f(x)$ is a smooth function. Step discontinuities are allowed at the boundaries of these subdivisions. In subdivision l ($l = 1, \dots, L$), there are at most p^l uniformly or nonuniformly sampling points, where p^l is referred to as the order of interpolation as shown later. Then (87) can be written as

$$\hat{f}(n) = \sum_{l=1}^L \int_{x_{l-1}}^{x_l} f(x) e^{-j2\pi nx} dx \quad (88)$$

where $\{x_l\}$ ($l = 1, \dots, L$) are the endpoints of the subdivisions. Using the change of variables

$$x = a^l + b^l t = \frac{x_l + x_{l-1}}{2} + \frac{x_l - x_{l-1}}{2} t \quad (89)$$

and the Gaussian Legendre quadrature

$$\int_{-1}^1 f(t) dt \cong \sum_{k=1}^q f(t_k) \omega_k \quad (90)$$

where t_k and ω_k ($k = 1, \dots, q$) are the Gaussian-Legendre nodes and weights, respectively, we obtain

$$\hat{f}(n) \cong \sum_{l=1}^L b^l \sum_{k=1}^q \omega_k^l f(t_k^l) e^{-j2\pi n t_k^l} \quad (91)$$

In this expression, the values of both function $f(x)$ and the exponential function $\exp(-j2\pi nx)$ at the nonuniform distributed points $\{t_k^l\}$ can be obtained via the Lagrange interpolation

$$g(x) = \sum_{m=1}^p g(x_m) \delta_m(x) \quad (92)$$

where

$$\delta_m(x) = \prod_{\substack{n=1 \\ n \neq m}}^p \frac{x - x_n}{x_m - x_n} \quad (93)$$

Here we perform this interpolation separately for $f(x)$ with order $p = p_1$ and $\exp(-j2\pi nx)$ with order $p = p_2$. Note that p_1 and p_2 can vary for different subdivisions; thus, they take p_1^l and p_2^l , respectively. (However, to simplify the presentation, we take the same p value in the following discussion.)

Note that we use this double-interpolation scheme because these two functions to be interpolated have different properties. The former, $f(x)$, is a piecewise function, while the latter, $\exp(-j2\pi nx)$, is a periodic analytic function but highly oscillating when n becomes large. Therefore we normally interpolate the two functions with different sets

of sampling points and orders of interpolation. For the exponential function, we use a uniform grid in order to apply the uniform FFT for the discrete summation; furthermore, we always place the interpolated points at the center of the interpolation region to obtain the highest accuracy for a p th-order Lagrange interpolation. With this double interpolation, (90) becomes

$$\hat{f}(n) = \sum_{l=1}^L b^l \sum_{k=1}^q \omega_k^l \left(\sum_{m_1=1}^{p_1} f(t_{m_1}^l) \delta_{m_1}(t_k^l) \right) \left(\sum_{m=1}^{p_2} e^{-j2\pi n t_m^l} \delta_m(t_k^l) \right) \quad (94)$$

Transforming the local coordinate into a global coordinate and changing the order of summation, we finally obtain

$$\hat{f}(n) = \sum_{i=1}^{vN} g_i e^{-j2\pi n x_i} \quad (95)$$

where

$$g_i = \sum_{l=1}^L \sum_{k=1}^q F_{lk} \sum_{m=1}^{p_2} \delta_m(t_k^l) |_{x(t_m^l)=x_i}, \quad (96)$$

$$F_{lk} = b^l \omega_k^l \sum_{m_1=1}^{p_1} f(t_{m_1}^l) \delta_{m_1}(t_k^l)$$

and v is the oversampling factor. Note that F_{lk} can be calculated independently and stored in a temporary vector of size $N \approx L \times q$, and all g_i values can be obtained by performing only once the triple summations over l, k, m , only for the terms with $x(t_m^l) = x_i$. Hence the calculation of g_i is very efficient with $O(vNp_2)$ complexity. Finally, (95) can be efficiently evaluated via a standard uniform FFT algorithm since $\{x_i\}$ are now on a uniform grid in $[0,1]$.

Furthermore, note that taking $L = 1$, the above formulas are directly reduced to the FFT algorithm for nonuniformly sampled continuous functions. In such a nonuniform fast Fourier transform (NUFFT) algorithm, however, it is desirable to further subdivide the domain (i.e., to increase L) when N is large, since this can reduce the computational cost in the Lagrange interpolation, resulting a more effective NUFFT algorithm for continuous functions. Such an NUFFT algorithm by itself is very useful in many engineering applications.

It is worth pointing out that compared with a single interpolation procedure, the double-interpolation procedure described above has several advantages:

- Double interpolation can ensure that the interpolation points for the exponential function are always located at the center of the interpolation region, leading to the highest accuracy for a given Lagrange interpolation order. In contrast, if a single interpolation were applied to the product of these two functions, the resulting function would not have the periodicity.

As a result, the locations of the interpolated points would not be always located at the center of the interpolation region, especially for those points near a function discontinuity point. Therefore, the accuracy of the interpolation for the product, and thus the accuracy of the FT, would be significantly reduced, especially when n becomes large.

- Since the Lagrange interpolation allows for nonuniform sampling, the algorithm described above can be applied to both uniform and nonuniform sampled data with the same number of arithmetic operations. Hence, it provides an FFT algorithm for nonuniformly sampled data. In contrast, a single interpolation allows only uniformly sampled data in order to use uniform FFT to evaluate the summation.
- Double interpolation allows for a lower-order interpolation, that is, a lower sample density, for $f(x)$ if it is a slowly varying function within each subdivision.
- Double interpolation allows other efficient algorithms, such as the fast multipole method (FMM) [23], to be incorporated readily into the interpolation procedure.

Implementation of the algorithm includes the following steps:

Step 1. Initialization of $\delta_{m_1}(t_k^l)$ and $\delta_m(t_k^l)$. This preprocessing step is needed only once and has a complexity of $O(Np^2)$, taking $q = p = \max(p_1, p_2)$.

Step 2. Calculation of F_{lk} and g_i in (96). The complexities are $O(vNp_1)$ and $O(vNp_2)$, respectively.

Step 3. Calculation of $\hat{f}(n)$ in (95) by a standard FFT. The complexity is $O(vN \log N)$.

The total complexity is $O(vNp + vN \log N)$ for steps 2 and 3. The preprocessing step needs to be done only once, and its computation time is negligible for repeated applications.

The DFFT algorithm has been utilized in several applications in computational electromagnetics, including the CG-FFT method [26] and the precorrected FFT solution [33].

7. CONCLUSIONS

The fast Fourier transform algorithm is a fundamental numerical computation tool in electrical engineering. It reduces the number of arithmetic operations in the discrete Fourier transform from $O(N^2)$ to $O(N \log N)$. More recent efforts have extended the FFT algorithm to nonuniform sampled data (NUFFT), and to discontinuous functions (DFFT). These algorithms have played and are continuing to play a central role in many modern applications in electromagnetics.

Acknowledgment

The author acknowledges the financial support by the National Science Foundations under Grants IIS-0086075, CCR-009814, and CCR-0219528, and by DARPA under Grant DAAD19-02-1-0252.

BIBLIOGRAPHY

1. A. Abubakar and P. M. van den Berg, A conjugate gradient contrast source technique for 3D profile inversion, *IEICE Trans. Electron.* **E83C**(12):1864–1874 (2000).
2. A. Abubakar, P. M. van den Berg, and S. Y. Semenov, Two- and three-dimensional algorithms for microwave imaging and inverse scattering, *Prog. Electromagn. Res.* **37**:57–79 (2002).
3. G. D. Bergland, The fast Fourier transform recursive equations for arbitrary length records, *Math. Comput.* **21**:236–238 (April 1967).
4. J. P. Berenger, A perfectly matched layer for the absorption of electromagnetic waves, *J. Comput. Phys.* **114**(2):185–200 (1994).
5. G. Beylkin, On the fast fourier transform of functions with singularities, *Appl. Comput. Harm. Anal.* **2**:363–382 (1995).
6. N. N. Bojarski, The k -space formulation of the scattering problem in the time domain, *J. Acoust. Soc. Am.* **72**:570–584 (1982).
7. M. Born and E. Wolf, *Principles of Optics*, Pergamon Press, New York, 1980.
8. D. T. Borup and O. P. Gandhi, Calculation of high-resolution SAR distributions in biological bodies using the FFT algorithm and conjugate-gradient method, *IEEE Trans. Microwave Theory Tech.* **33**(5):417–419 (1985).
9. E. O. Brigham, *The Fast Fourier Transform*, Prentice-Hall, Englewood Cliffs, NJ, 1974.
10. C. Canuto, M. Y. Hussani, A. Quarteroni, and T. Zang, *Spectral Methods in Fluid Dynamics*. Springer-Verlag, New York, 1988.
11. S. Caorsi, G. L. Gragnani, and M. Pastorino, A multiview microwave imaging system for two-dimensional penetrable objects, *IEEE Trans. Microwave Theory Tech.* **39**:845–851 (1991).
12. M. F. Catedra, J. G. Cuevas, and L. Nuno, A scheme to analyze conducting plates of resonance size using the conjugate-gradient method and fast Fourier transform, *IEEE Trans. Anten. Propag.* **36**:1744–1752 (1988).
13. M. F. Catedra, R. P. Torres, J. Basterrechea, and E. Gago, *The CG-FFT Method: Application of Signal Processing Techniques to Electromagnetics*, Artech House, Norwood, MA, 1995.
14. W. C. Chew, *Waves and Fields in Inhomogeneous Media*, Van Nostrand Reinhold, New York, 1990.
15. W. C. Chew and Y. M. Wang, Reconstruction of two-dimensional permittivity distribution using the distorted Born iteration method, *IEEE Trans. Med. Imag.* **9**:218–225 (1990).
16. W. C. Chew, J. M. Jin, E. Michielssen, and J. M. Song, eds., *Fast and Efficient Algorithms in Computational Electromagnetics*, Artech House, Boston-London, 2001.
17. R. Coifman, V. Rokhlin, and S. Wandzura, The fast multipole method for the wave equation: A pedestrian prescription, *IEEE Anten. Propag. Mag.* **35**:7–12 (1993).
18. J. W. Cooley and J. W. Tukey, Algorithm for the machine computation of complex fourier series, *Math. Comput.* **19**:297–301 (1965).

19. T. J. Cui and W. C. Chew, Fast algorithm for electromagnetic scattering by Buried 3-D Dielectric objects of large size, *IEEE Trans. Geosci. Remote Sens.* **37**:2597–2608 (1999).
20. T. J. Cui, W. C. Chew, A. A. Aydinler, and Y. H. H. Zhang, Fast-forward solvers for the low-frequency detection of buried dielectric objects, *IEEE Trans. Geosci. Remote Sens.* **41**(9):2026–2036 (Sept. 2003).
21. G. Danielson and C. Lanczos, Some improvements in practical Fourier analysis and their application to x-ray scattering from liquids, *J. Franklin Inst.* **233**:365–380, 435–452 (1942).
22. A. J. Devaney, A filtered backpropagation algorithm for diffraction tomography, *Ultrasound. Imag.* **4**:336–350 (1982).
23. A. Dutt, M. Gu, and V. Rokhlin, Fast algorithms for polynomial interpolation, integration, and differentiation, *SIAM J. Num. Anal.* **33**:1689–1711 (1996).
24. A. Dutt and V. Rokhlin, Fast fourier transforms for nonequipped data, *SIAM J. Sci. Comput.* **14**:1368–1393 (1993).
25. G.-X. Fan and Q. H. Liu, Fast fourier transform of functions with jump discontinuities, *Intl. IEEE/AP-S Symposium Digest*, Salt Lake City, UT, 2000, pp. 148–151.
26. G.-X. Fan and Q. H. Liu, The CGFFT method with a discontinuous fft algorithm, *Microwave Opt. Technol. Lett.* **29**(1):47–49 (2001).
27. G. X. Fan, Q. H. Liu, and J. S. Hesthaven, Multi-domain pseudospectral time-domain method for simulation of scattering from buried objects in lossy media, *IEEE Trans. Geosci. Remote Sens.* **40**(6):1366–1373 (June 2002).
28. G.-X. Fan and Q. H. Liu, Fast fourier transform for discontinuous functions, *IEEE Trans. Anten. Propag.* **52**(2):461–465 (Feb. 2004).
29. J. A. Fessler and B. P. Sutton, Nonuniform fast fourier transforms using min-max interpolation, *IEEE Trans. Signal Process.* **51**(2):560–574 (Feb. 2003).
30. B. Fornberg, *A Practical Guide to Pseudospectral Methods*, Cambridge Univ. Press, New York, 1996.
31. X. Gao, M. S. Mirotznik, S. Y. Shi, and D. W. Prather, Applying a mapped pseudospectral time-domain method in simulating diffractive optical elements, *J. Opt. Soc. Am. A* **21**(5):777–785 (2004).
32. C. Gauss, *Theoria Interpolationis Methodo Nova Tractata*, Carl Friedrich Gauss Werke, Vol. 3, Kiniglichen Gesellschaft der Wissenschaften, Göttingen, 1866.
33. S. Gedney, A. Zhu, T. W. Hua, and P. Petre, High-order pre-corrected fft solution for electromagnetic scattering, *Proc. Int. IEEE/AP-S Symp.*, San Antonio, TX, 2002, Vol. 3, pp. 566–569.
34. D. Gottlieb and S. A. Orszag, *Numerical Analysis of Spectral Methods*, SIAM, Philadelphia, 1977.
35. R. F. Harrington, *Field Computation by Moment Methods*, Macmillan, New York, 1968.
36. J. S. Hesthaven, P. G. Dinesen, and J. P. Lynov, Spectral collocation time-domain modeling of diffractive optical elements, *J. Comput. Phys.* **155**:287–306 (1999).
37. H. Gan and W. C. Chew, A discrete BCG-FFT algorithm for solving 3D inhomogeneous scatterer problems, *J. Electromagn. Waves Appl.* **9**:1339–1357 (1995).
38. N. Joachimowicz, C. Pichot, and J. P. Hugonin, Inverse scattering: An iterative numerical method for electromagnetic imaging, *IEEE Trans. Anten. Propag.* **39**:1742–1752 (Dec. 1991).
39. R. Kastner and R. Mittra, Iterative analysis of finite-size planar frequency selective surfaces with rectangular patches or perforations, *IEEE Trans. Anten. Propag.* **35**:372–377 (1987).
40. H. O. Kreiss and J. Olinger, Comparison of accurate methods for the integration of hyperbolic equations, *Tellus* **24**:199–215 (1972).
41. T. W. Lee and S. C. Hagness, A PSTD method with fourth-order time-stepping for the analysis of nonlinear optical structures, *IEEE Antennas and Propagation Society Int. Symp. Digest*, 2002, Vol. 3, pp. 232–235.
42. W. K. Leung and C. H. Chan, Combining the FDTD and PSTD methods, *Microwave Opt. Technol. Lett.* **23**(4):249–254 (1999).
43. W. K. Leung and Y. Chen, Transformed-space nonuniform pseudospectral time-domain algorithm, *Microwave Opt. Technol. Lett.* **28**(6):391–396 (2001).
44. Q. Li, Y. Chen, and C. K. Li, Hybrid PSTD-FDTD technique for scattering analysis, *Microwave Opt. Technol. Lett.* **34**(1):19–24 (2002).
45. F. Li, Q. H. Liu, and L.-P. Song, Three-dimensional reconstruction of objects buried in layered media using Born and distorted Born iterative methods, *IEEE Geosci. Remote Sens. Lett.* **1**(2):107–111 (2004).
46. F. Ling, C. F. Wang, and J. M. Jin, An efficient algorithm for analyzing large-scale microstrip structures using adaptive integral method combined with discrete complex-image method, *IEEE Trans. Microwave Theory Tech.* **48**(5):832–939 (May 2000).
47. Q. L. Li and Y. C. Chen, Applications of the PSTD for scattering analysis, *IEEE Trans. Anten. Propag.* **50**(9):1317–1319 (2002).
48. Q. H. Liu, A spectral-domain method with perfectly matched layers for time-domain solutions of Maxwell's equations, paper presented at 1996 URSI Meeting, Baltimore, MD, July 1996.
49. Q. H. Liu, The PSTD algorithm: A time-domain method requiring only two cells per wavelength, *Microwave Opt. Technol. Lett.* **15**(3):158–165 (1997).
50. Q. H. Liu, Large-scale simulations of electromagnetic and acoustic measurements using the pseudospectral time-domain (PSTD) algorithm, *IEEE Trans. Geosci. Remote Sens.* **37**(2):917–926 (1999).
51. Q. H. Liu, PML and PSTD algorithm for arbitrary lossy anisotropic media, *IEEE Microwave Guided Wave Lett.* **9**(2):48–50 (1999).
52. Q. H. Liu and N. Nguyen, An accurate algorithm for nonuniform fast Fourier transforms (NUFFT), *IEEE Microwave Guided Wave Lett.* **8**(1):18–20 (1998).
53. Q. H. Liu and G.-X. Fan, A frequency-dependent PSTD algorithm for general dispersive media, *IEEE Microwave Guided Wave Lett.* **9**(2):51–53 (1999).
54. Q. H. Liu and G.-X. Fan, Simulations of GPR in dispersive media using the PSTD algorithm, *IEEE Trans. Geosci. Remote Sens.* **37**(5):2317–2324 (1999).
55. Q. H. Liu and J. Q. He, An efficient PSTD algorithm for cylindrical coordinates, *IEEE Trans. Anten. Propag.* **49**(9):1349–1351 (2001).
56. Q. H. Liu, X. M. Millard, B. Tian, and Z. Q. Zhang, Applications of nonuniform fast transform algorithms in numerical solutions of differential and integral equations, *IEEE Trans. Geosci. Remote Sens.* **38**:1551–1560 (2000).
57. Q. H. Liu and X. Y. Tang, An iterative algorithm for nonuniform inverse fast fourier transform (NU-IFFT), *Electron. Lett.* **34**(20):1913–1914 (1998).
58. Q. H. Liu and Z. Q. Zhang, A nonuniform fast hankel transform (nuffht) algorithm, *Appl. Opt.* **38**(32):6705–6708 (1999).

59. Q. H. Liu and G. Zhao, Review of PSTD Methods for transient electromagnetics, *Int. J. Num. Model. Electron. Networks Devices Fields* **22**(17):299–323 (2004).
60. K. A. Michalski and D. Zheng, Electromagnetic scattering and radiation by surface of arbitrary shape in layered media, Part I: Theory, *IEEE Trans. Anten. Propag.* **38**(3):335–344 (March 1990).
61. K. A. Michalski and D. Zheng, Electromagnetic scattering and radiation by surface of arbitrary shape in layered media, Part II: Implementation and results for contiguous half-space, *IEEE Trans. Anten. Propag.* **38**(3):344–352 (March 1990).
62. K. A. Michalski and J. R. Mosig, Multilayered media Green's functions in integral equation formulations, *IEEE Trans. Anten. Propag.* **45**(3):508–519 (March 1997).
63. X. Millard and Q. H. Liu, A fast volume integral equation solver for electromagnetic scattering from large inhomogeneous objects in planarly layered media, *IEEE Trans. Anten. Propag.* **51**(9):2393–2401 (2003).
64. X. Millard and Q. H. Liu, Simulations of near-surface detection of objects in layered media by the BCGS-FFT method, *IEEE Trans. Geosci. Remote Sens.* **42**(2):327–334 (2004).
65. N. Nguyen and Q. H. Liu, The regular fourier matrices and nonuniform fast fourier transforms, *SIAM J. Sci. Comput.* **21**(1):283–293 (1999).
66. V. I. Okhmatovski, J. D. Morsey, and A. C. Cangellaris, Enhancement of the numerical stability of the adaptive integral method at low frequencies through a loop-charge formulation of the method-of-moments approximation, *IEEE Trans. Microwave Theory Tech.* **52**(3):962–970 (2004).
67. S. A. Orszag, Comparison of pseudospectral and spectral approximation, *Stud. Appl. Math.* **51**:253–259 (1972).
68. T. J. Peters and J. L. Volakis, Application of a conjugate gradient FFT method to scattering from thin planar material plates, *IEEE Trans. Anten. Propag.* **36**:518–526 (1988).
69. T. K. Sarkar, E. Arvas, and S. M. Rao, Application of fast Fourier transform and the conjugate gradient method for efficient solution of electromagnetic scattering from both electrically large and small conducting bodies, *Electromagnetics* **5**:99–122 (1985).
70. J. M. Song and W. C. Chew, Multilevel fast-multipole algorithm for solving combined field integral equations of electromagnetic scattering, *Microwave Opt. Technol. Lett.* **10**:15–19 (1995).
71. E. Sorets, Fast fourier transforms of piecewise constant function, *J. Comput. Phys.* **116**:369–379 (1995).
72. M. Soumekh, *Synthetic Aperture Radar Signal Processing with Matlab Algorithms*, Wiley, New York, 1999.
73. C. C. Su, The three-dimensional algorithm of solving the electric field integral equation using face-centered node points, conjugate gradient method, and FFT, *IEEE Trans. Microwave Theory Tech.* **41**:510–515 (1993).
74. B. Tian and Q. H. Liu, Nonuniform fast cosine transform and Chebyshev PSTD algorithm, *Prog. Electromagn. Res. PIER* **28**:259–279 (2000); abstract in *J. Electromagnet. Waves Appl.* **14**(6):797–798 (2000).
75. L. Tsang, C. H. Chan, K. Pak, and H. Sangani, Monte Carlo simulations of large-scale problems of random rough surface scattering and applications to grazing incidence with the BMIA/canonical grid method, *IEEE Trans. Anten. Propag.* **43**:851–859 (1995).
76. J. W. Wiskin, D. T. Borup, and S. A. Johnson, Inverse scattering from arbitrary two-dimensional objects in stratified environments via a Green's operator, *J. Acoust. Soc. Am.* **102**(2):853–864 (1997).
77. X. M. Xu, Q. H. Liu, and Z. Q. Zhang, The stabilized biconjugate gradient fast Fourier transform method for electromagnetic scattering, *J. Appl. Comput. Electromagn. Soc.* **17**(1):97–103 (2002).
78. X. M. Xu and Q. H. Liu, The BCGS-FFT method for electromagnetic scattering from inhomogeneous objects in a planarly layered medium, *IEEE Anten. Wireless Propag. Lett.* **1**:77–80 (2002).
79. B. Yang, D. Gottlieb, and J. S. Hesthaven, Spectral simulation of electromagnetic wave scattering, *J. Comput. Phys.* **134**:216–230 (1997).
80. B. Yang and J. S. Hesthaven, A pseudospectral method for time-domain computation of electromagnetic scattering by bodies of revolution, *IEEE Trans. Anten. Propag.* **47**:132–141 (1999).
81. B. Yang and J. S. Hesthaven, Multidomain pseudospectral computation of Maxwell's equations in 3-D general curvilinear coordinates, *Appl. Num. Math.* **33**:281–289 (2000).
82. K. S. Yee, Numerical solution of initial boundary value problems involving Maxwell's equations in isotropic media, *IEEE Trans. Anten. Propag.* **14**(5):302–307 (1966).
83. Z. Q. Zhang and Q. H. Liu, Three-dimensional weak-form conjugate- and biconjugate-gradient FFT methods for volume integral equations, *Microwave Opt. Technol. Lett.* **29**(5):350–356 (2001).
84. Z. Q. Zhang, Q. H. Liu, and X. M. Xu, RCS computation of large inhomogeneous objects using a fast integral equation solver, *IEEE Trans. Anten. Propag.* **51**(3):613–618 (March 2003).
85. Z. Q. Zhang and Q. H. Liu, 3-D nonlinear image reconstruction for microwave biomedical imaging, *IEEE Trans. Biomed. Eng.* **51**(3):544–548 (2004).
86. G. Zhao and Q. H. Liu, The 2.5-D multidomain pseudospectral time-domain algorithm, *IEEE Trans. Anten. Propag.* **51**(3):619–627 (March 2003).
87. G. Zhao, Y. Q. Zeng, and Q. H. Liu, The 3-D multidomain pseudospectral time-domain method for wideband simulation, *IEEE Microwave Wireless Compon. Lett.* **13**(5):184–186 (2003).
88. G. Zhao and Q. H. Liu, The 3-D multidomain pseudospectral time-domain method for inhomogeneous conductive media, *IEEE Trans. Anten. Propag.* **52**(3):742–749 (March 2004).
89. Y. A. Zhunag, K. L. Wu, C. Wu, and J. Litva, A combined full-wave CG-FFT method for rigorous analysis of large microstrip antenna arrays, *IEEE Trans. Anten. Propag.* **44**(1):102–109 (Jan. 1996).
90. P. Zwamborn and P. M. van den Berg, The three-dimensional weak form of the conjugate gradient FFT method for solving scattering problems, *IEEE Trans. Microwave Theory Tech.* **9**(40):1757–1766 (1992).

FEEDBACK AMPLIFIERS

THOMAS F. SCHUBERT Jr.
University of San Diego
San Diego, California

Feedback is the process of combining a portion of the output of a system with the system input to achieve modified performance characteristics. Found in a multitude of engineering applications, the process has become the foun-

dition several disciplines such as feedback control systems, feedback receivers, feedback oscillators, and feedback amplifiers. It has become particularly pervasive in amplifier design since the advent of transistors that can provide high gain cheaply, but cannot provide stable gain.

Negative feedback was originally applied by Harold S. Black in 1927 at Bell Labs to valve (vacuum tube) amplifiers to reduce distortion. In 1957 Black's work was described by Mervin Kelly, president of Bell Labs, as one of the two inventions of broadest scope and significance in electronics and communications is the first half of the century. Negative feedback is the process of mixing an inverted portion of the output of a system with the input to alter system performance characteristics. The process of negative feedback has become especially important in linear amplifier design and is characterized by several significant *benefits*:

- The gain of the amplifier is stabilized against variation in the characteristic parameters of the active devices due to voltage or current supply changes, temperature changes, or device degradation with age. Similarly, amplifier gain is stabilized within a group of amplifiers that have active devices with somewhat different characteristic parameters.
- Nonlinear signal distortion is reduced.
- The frequency range over which there is constant linear amplification (the midband region) is increased.
- The input and output impedance of the amplifier can be selectively increased or decreased.

It is a rare occurrence when benefits come without a price. In the case of negative feedback, the listed above benefits are accompanied by two primary *drawbacks*:

- The gain of the circuit is reduced. In order to regain the losses due to feedback, additional amplification stages often must be included in the system design. Complexity, size, weight, and cost may be added to the final amplifier design.
- There is a possibility for oscillation to occur. Should oscillation occur, the basic gain properties of the amplifier are destroyed.

This article considers the benefits of negative feedback on amplifier design. Basic definitions are followed by a general discussion of the properties of a feedback system. Amplifiers are divided into four categories of feedback topology, and the specific properties of each topological type are stated. While the emphasis of discussions must focus on circuit analysis techniques, a clear understanding of feedback in general, and effects of circuit topology in particular, is a necessity for good feedback amplifier design.

1. BASIC FEEDBACK CONCEPTS

Electronic amplifiers are fundamentally characterized by four properties:

- The gain of the amplifier. *Gain* is defined as the ratio of the output signal to the input signal. Each signal may be either a voltage signal or current signal.
- The range of frequencies over which the gain is essentially constant. This range of frequencies is identified as the midband region. It is bounded by the frequencies at which the output power is halved: the high and low 3-dB frequencies.
- The midband input impedance. Defined as the ratio of input voltage to input current.
- The midband output impedance. Defined as the Thévenin impedance seen at the amplifier output terminals.

The application of feedback to an amplifier alters each of these fundamental properties.

The basic topology of a feedback amplifier is shown in Fig. 1. An input signal X_i enters a summing (or *mixing*) junction, symbolized by a circular symbol. At the summing junction, the feedback signal X_f is subtracted from the input signal and the resultant signal X_δ is passed on to a linear amplifier, shown as a triangular symbol, of gain A . The output of the linear amplifier X_o forms the output of the feedback system. The rectangular symbol indicates a feedback network that samples the output signal, scales it by a feedback factor f and passes it forward to the input of the system. Each signal can take the form of either a voltage or a current, and ideally travels only in the direction of the indicated arrows. Subtraction of the two inputs at the summing junction is the key factor in negative feedback systems.

Feedback systems can be mathematically modeled with a set of simple relationships. The output X_o of the amplifier is related to the input signal X_δ by a linear amplification factor (gain) A , often called the *forward* or *open-loop gain*:

$$X_o = A(X_\delta) \quad (1)$$

Since the quantities X_o and X_δ can be either voltage or current signals, the forward gain A can be a voltage gain, a current gain, a transconductance, or a transresistance. *Voltage gain* is the ratio of output voltage to input voltage. Similarly, *current gain* relates output and input currents. *Transresistance* is the ratio of output voltage to input current and *transconductance* is the ratio of output current to input voltage. The feedback signal X_f (a fraction of the output signal X_o) is then subtracted from the input signal

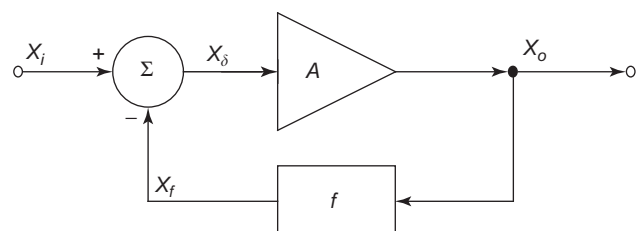


Figure 1. Basic negative feedback topology.

X_i to form the difference signal X_δ

$$X_\delta = (X_i - X_f) = (X_i - fX_o) \quad (2)$$

where f is the *feedback ratio* defining the relationship between X_f and X_o :

$$X_f = fX_o \quad (3)$$

As is the case with the amplifier gain, the feedback ratio f is either a ratio of voltages, a ratio of currents, a transconductance, or a transresistance. The product fA , called the *loop gain*, must be a positive, dimensionless quantity in order to have stable negative feedback. Thus it is necessary, for negative feedback, that the mathematical sign of f be the same as that of A within the midband region. The input–output relationship for the overall feedback system can be derived from Eqs. (1) and (2):

$$X_o = \frac{A}{1+fA} X_i = A_f X_i \quad (4)$$

The overall gain of the system including the effects of feedback is then written as

$$A_f = \frac{X_o}{X_i} = \frac{A}{1+fA} \quad (5)$$

The overall feedback amplifier gain A_f has the same dimensions as the forward gain A . Equation (5) has special significance in the study of feedback systems and is typically identified as the *basic feedback equation*. The denominator of the basic feedback equation is identified as the *return difference D* but is also commonly referred to as “the amount of feedback”:

$$D = 1 + fA \quad (6)$$

The return difference, for negative-feedback systems, has magnitude larger than unity (in the midband frequency region) and is often specified in decibels:

$$D_{\text{dB}} = 20 \log_{10} |1 + fA| \quad (7)$$

The return difference quantifies the reduction in gain due to the addition of feedback to the system. It also plays a significant role in quantifying changes in frequency bandwidth and input and output impedance. Specifically, the high and low 3-dB frequencies are increased and decreased, respectively, by approximately a factor of D , and the input and output impedance are increased or decreased by a factor of D depending on the sampling and mixing circuit topologies.

Derivation of the basic feedback equation is based on two basic assumptions:

- The reverse transmission through the amplifier is negligible (a signal at the output produces essentially no signal at the input) compared to the reverse transmission through the feedback network.

- The forward transmission (left to right in Fig. 1) through the feedback network is negligible compared to the forward transmission through the amplifier.

In most feedback amplifiers, the amplifier is an active device with significant forward gain and near-zero reverse gain: the feedback network is almost always a passive network. Thus, in the forward direction, the large active gain will exceed the passive attenuation significantly. Similarly, in the reverse direction, the gain of the feedback network, albeit typically small, is significantly greater than the near-zero reverse gain of the amplifier. In almost every electronic application, the above-stated requirements for the use of the basic feedback equation are easily met by the typical feedback amplifier.

2. ANALYSIS OF FEEDBACK AMPLIFIER PROPERTIES

The analysis and design of electronic amplifiers is typically a multistep process. Complete, analytic characterization of an amplifier is a complex process whose results are in a form that often masks the individual amplifier properties. Amplifier designers therefore investigate the amplifier gain, frequency response, and impedance properties separately, carefully balancing system requirements to converge on a successful design. In addition to simplifying the process, separate investigation of the amplifier properties often leads to greater insight into design improvement. When a successful design is apparent, final fine tuning is accomplished with the aid of a computerized circuit simulator [i.e., System Program with Integrated Circuit Emphasis (SPICE)] and a prototype.

Essentially all of the drawbacks and benefits of feedback systems can be investigated on a simple level by looking at the properties of the basic feedback equation [Eq. (5)]. Gain stabilization, the reduction in nonlinear signal distortion, the increase in the frequency range over which there is linear amplification, the reduction in gain, and the possibility of oscillation all can be investigated on a simple level. The change in the input and output impedances cannot be investigated at this level: it is necessary to specify the nature (voltage or current) of the input and output quantities and the circuit topology in order to investigate these impedance changes.

2.1. Amplifier Gain

In Section 1, it was shown that feedback reduces amplifier gain by a factor of the return difference D . While reduction of gain can be a significant drawback, the ancillary gains are significant. Primary among those benefits is the stabilization of the amplifier gain against variation in the characteristic parameters of the active devices. It is well known that the forward gain A of an electronic amplifier is highly dependent on the parameters of the active devices contained within that amplifier. These parameters are typically dependent on temperature, bias conditions, and manufacturing tolerances. In order to maintain consistent amplifier performance it is desirable to design amplifiers that are reasonably insensitive to the variation of the device parameters.

The relationship between the differential change in gain due to device parameter variation with and without feedback is obtained by differentiating Eq. (5):

$$dA_f = \frac{1}{(1+fA)^2} dA \quad (8)$$

Stable negative-feedback amplifiers require that the return difference have magnitude greater than unity:

$$1 \quad (9)$$

Thus the absolute variation in gain is reduced by a factor of the return ratio squared. Another measure of the change in gain variation can be found by regrouping terms:

$$\left| \frac{dA_f}{A_f} \right| = \left| \frac{1}{(1+fA)} \right| \left| \frac{dA}{A} \right| \quad (10)$$

The factors in this equation more realistically describe the benefits: Equation (10) demonstrates the change in the percentage of gain variation about the nominal value. It can be seen that the percentage variation of the overall amplifier gain A_f is reduced by a factor of the return ratio when compared to the percentage variation of the gain A of the forward amplifier.

For example, if a feedback amplifier is constructed with an amplifier that is subject to a 3% variation in gain as its fundamental forward-gain element and it is desired that the feedback amplifier have no more than 0.1% variation in its overall gain due to the variation in this element. The necessary return difference to achieve this design goal can be obtained as follows:

Equation (10) is the significant relationship in determining the gain variation:

$$\left| \frac{dA_f}{A_f} \right| = \left| \frac{1}{(1+fA)} \right| \left| \frac{dA}{A} \right|$$

The significant properties are

$$0.001 \geq \left| \frac{1}{(1+fA)} \right| 0.03 \Rightarrow D = 1 + Af \geq 30$$

The minimum necessary return ratio is 30, more often identified as its decibel equivalent, $D_{dB} = 20 \log_{10} D \geq 29.54$ dB

Equation (10) is extremely useful for small changes in amplification due to parameter variation but is inaccurate for large changes. If the change in amplification is large, the mathematical process must involve differences rather than differentials:

$$\Delta A_f = A_{2f} - A_{1f} = \frac{A_2}{1+fA_2} - \frac{A_1}{1+fA_1} \quad (11)$$

In order to put this into the same format as Eq. (10), it is necessary to divide both sides of the equation by A_{1f}

$$\left| \frac{\Delta A_f}{A_{1f}} \right| = \left| \frac{A_2}{1+fA_2} \left(\frac{1+fA_1}{A_1} \right) - 1 \right| = \left| \frac{(A_2 - A_1)}{1+fA_2} \left(\frac{1}{A_1} \right) \right| \quad (12)$$

or

$$\left| \frac{\Delta A_f}{A_{1f}} \right| = \left| \frac{1}{1+fA_2} \right| \left| \frac{\Delta A}{A_1} \right| = \left| \frac{1}{1+f(A_1 + \Delta A)} \right| \left| \frac{\Delta A}{A_1} \right| \quad (13)$$

The results are similarly a reduction in gain sensitivity by a factor of the form of the return difference.

The differential change in feedback amplifier gain due to variation in the feedback ratio f can be obtained by differentiating Eq. (5) with respect to the feedback ratio. Appropriate mathematical manipulation leads to the desired results:

$$\frac{dA_f}{A_f} = \frac{-fA}{1+f} \frac{df}{Af} \Rightarrow \left| \frac{dA_f}{A_f} \right| = \frac{fA}{1+fA} \left| \frac{df}{f} \right| \quad (14)$$

It is easily seen that the percentage variation of the overall amplifier gain A_f is of approximately the same magnitude (actually it is slightly lesser) as the percentage variation of the feedback ratio f . Since electronic feedback amplifiers typically employ a feedback network constructed entirely with passive elements (usually resistors), variation in the feedback ratio can be kept relatively small through the utilization of precision elements in the feedback network. In good amplifier designs, the variation of amplifier gain due to variability in the feedback network is usually of lesser significance than that due to variability of the basic forward amplifier gain.

2.2. Nonlinear Signal Distortion

Stabilization of gain with parameter variation suggests that amplifier gain will be stabilized with respect to other gain-changing effects. One such effect is nonlinear distortion. Nonlinear distortion is a variation of the gain with respect to input signal amplitude. A simple example of non-linear distortion is demonstrated in Fig. 2. Here the transfer characteristic of a simple amplifier is approximated by two regions, each of which is characterized by

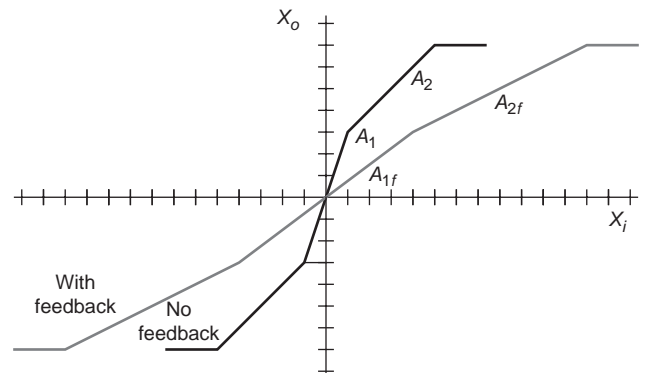


Figure 2. The effect on feedback on an amplifier transfer characteristic.

different amplification, A_1 and A_2 . To this transfer characteristic, a small amount of feedback is applied so that $fA_1 = 1$, and the resultant feedback transfer characteristic is shown. As can be easily seen, the overall feedback transfer characteristic also consists of two regions with overall amplification A_{1f} and A_{2f} . In this demonstration, the amplification ratios are:

$$\frac{A_1}{A_2} = 3, \quad \frac{A_{1f}}{A_{2f}} = 1.5$$

Feedback has significantly improved the linearity of the system and consequently has reduced the nonlinear distortion. Larger amounts of feedback (increasing the feedback ratio f) will continue to improve the linearity. For this example, increasing the feedback ratio by a factor of 5 will result in a ratio of overall gain in the two regions of 1.067 (as compared to 1.5, above). It should be noted that the saturation level of an amplifier is not significantly altered by the introduction of negative feedback. Since the incremental gain in saturation is essentially zero, the incremental feedback difference is also zero. No significant change to the input occurs and the output remains saturated.

Another viewpoint on gain stabilization comes from a limiting form of the basic feedback equation:

$$A_f = \frac{A}{1+fA} = \frac{1}{f} \left(1 - \frac{1}{1+fA} \right) \approx \frac{1}{f} \quad (15)$$

For large return difference ($D = 1 + Af$) the overall gain with feedback is dominated by the feedback ratio f and is therefore virtually independent of the forward gain A and any variations in A .

2.3. Frequency Response

Typical linear amplifiers have a range of frequencies over which the gain is essentially constant: this frequency range is called the *midband*. As frequencies increase, the performance parameters of an amplifier degrade. Similarly, coupling and bypass capacitors internal to the amplifier, when present, will degrade low-frequency performance. Using feedback to broaden the frequency range over which gain is relatively constant can be considered a special case of the stabilization of gain due to variation in amplifier performance characteristics. Feedback reduces the effects of these frequency-dependent degradations and thereby increases the frequency band over which the amplifier has stable gain.

A more exact description of the increase in the width of the midband region can be obtained through a frequency-domain analysis. It is common practice to use the frequencies at which the output power is reduced by 50% (the high and low 3-dB frequencies) as descriptors of the limits of the midband region. Discussion focuses on the change in these 3-dB frequencies.

It can be shown that the basic forward amplifier gain A is described as the midband gain A_0 , divided by a polynomial in frequency (written as s or $j\omega$)

$$A(s) = \frac{A_0}{P(s)} \quad (16)$$

The locations of the first few poles of $A(s)$ (or the zeroes of $P(s)$) closest to the midband region are the dominant predictors of amplifier frequency response; specifically, their location controls the 3-dB frequencies.

The application of feedback to an amplifier alters the gain expression through the basic feedback equation so that the total gain A_f is described by:

$$A_f(s) = \frac{\frac{A_0}{P(s)}}{1 + f \frac{A_0}{P(s)}} = \frac{A_0}{P(s) + fA_0} \quad (17)$$

Application of feedback to the basic forward amplifier has the effect of vertically shifting the denominator polynomial by a constant, fA_0 (see Fig. 3). This shift upward causes movement in the zeros of the denominator, thereby changing the location of the poles of the frequency response. Any movement of the poles nearest the region of constant gain (the midband region) equates into a change in the width of the midband region. Observation of the consequences of the result in graphical format is a great aid to understanding pole migration.

For example, when the high-frequency response is described by a single pole p_1 , Eq. (17) takes the following form:

$$\begin{aligned} A_f(s) &= \frac{A_0}{P(s) + fA_0} = \frac{A_0}{\left(1 + \frac{s}{p_{H1}} \right) + fA_0} \\ &= \frac{1}{1 + fA_0} \frac{A_0}{\left(1 + \frac{s}{p_{H1}(1 + fA_0)} \right)} \end{aligned} \quad (18)$$

It can easily be seen that the gain has been reduced by a factor of the return difference D and the pole frequency has been increased by the same factor. Similarly, if the low-frequency response is described by a single pole p_{L1} , the pole frequency will be reduced (i.e., divided by) by a factor of D . Since, in single-pole systems, the 3-dB frequency coincides with the pole frequencies, the high and low 3-dB frequencies, ω_H and ω_L , are shifted by a factor of the return ratio:

$$\omega_{Hf} = (1 + fA_0)\omega_H = D\omega_H \quad \text{or} \quad \omega_{Lf} = \frac{\omega_L}{1 + fA_0} = \frac{\omega_L}{D} \quad (19)$$

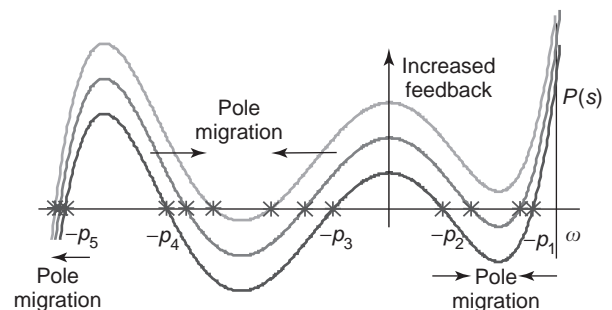


Figure 3. Pole migration due to feedback.

As the number of poles increases, description of the bandwidth increase with the application of feedback increases in complexity. When the high or low frequency response can be described by two poles, the damping coefficient due to the application of feedback is function ratio of the initial pole locations k and the return difference. The damping coefficient can be calculated to be

$$\zeta = \frac{1+k}{2\sqrt{k(1+fA_0)}} = \frac{1+k}{2\sqrt{kD}} \quad (20)$$

where k is defined as the ratio of the larger pole to the smaller pole at high or low frequencies:

$$k_H = \frac{\omega_{2H}}{\omega_{1H}} \quad \text{or} \quad k_L = \frac{\omega_{1L}}{\omega_{2L}} \quad (21)$$

This simple expression for the damping coefficient is a particularly important result in that it can tell the circuit designer the flatness of the frequency response in relation to the amount of feedback applied; a flat frequency response requires overdamped pole pairs ($\zeta \geq 0.707$).

Once the damping coefficient is determined, the exact expression for the high or low 3-dB frequency shift with the application of feedback takes a form similar to the single-pole case with an additional factor

$$\omega_{Hf} = K(\zeta_H, k_H) \cdot D \cdot \omega_{1H} \quad \text{or} \quad \omega_{Lf} = \frac{\omega_{1L}}{K(\zeta_L, k_L) \cdot D} \quad (22)$$

where k is the ratio of the initial pole spacing ($k \geq 1$), ζ is the pole pair damping coefficient, ω_{1H} and ω_{1L} are the poles closest to the midband, and the factor, $K(\zeta, k)$, is given by

$$K(\zeta, k) = \frac{2k\zeta}{k+1} \sqrt{1 - 2\zeta^2 + \sqrt{(1 - 2\zeta^2)^2 + 1}} \quad (23)$$

This relationship is shown in Fig. 4 for a variety of initial pole spacing ratios k . In most amplifier applications, $0.9 < K(\zeta, k) < \sqrt{2}$; some designers use a $K(\zeta, k) \approx 1$ as a first-order approximation.

For amplifiers where the frequency response must be described by more than two poles, description of the fre-

quency shift is even more complicated. Fortunately, amplifiers with a high or low frequency response that is described by more than two poles are reasonably modeled by considering them to be two-pole systems [13]: Eq. (22) adequately approximates the change in bandwidth for these higher-order systems.

For example, if an amplifier has a midband gain $A_0 = 1000$ and has frequency response described by one low-frequency pole, $f_L = 10$ kHz and two high-frequency poles, $f_{H1} = 1$ MHz and $f_{H2} = 10$ MHz and feedback is applied so that the midband gain is reduced to $A_{of} = 140$. The new low and high 3-dB frequencies can be determined as follows:

The return difference is the ratio of the two gains:

$$D = \frac{A_0}{A_{of}} = \frac{1000}{140} = 7.14286$$

The low-frequency response is described by a single pole; thus the low 3-dB frequency is changed by a factor of D :

$$f_{Lf} = \frac{f_L}{D} = \frac{10 \text{ kHz}}{7.14286} = 1.4 \text{ kHz}$$

The high-frequency response is described by two poles with ratio k :

$$k = \frac{\omega_{2H}}{\omega_{1H}} = \frac{f_{2H}}{f_{1H}} = \frac{10 \text{ MHz}}{1 \text{ MHz}} = 10$$

The damping coefficient for the two poles are found to be

$$\zeta_H = \frac{1+k}{2\sqrt{k(1+fA_0)}} = \frac{1+10}{2\sqrt{10(7.14286)}} = 0.6508$$

Note that the high poles of the feedback amplifier are slightly underdamped and that there will be a small “bump” (≈ 0.1 dB for this case) in the frequency response as a result. The high 3-dB frequency f_{Hf} is then found from

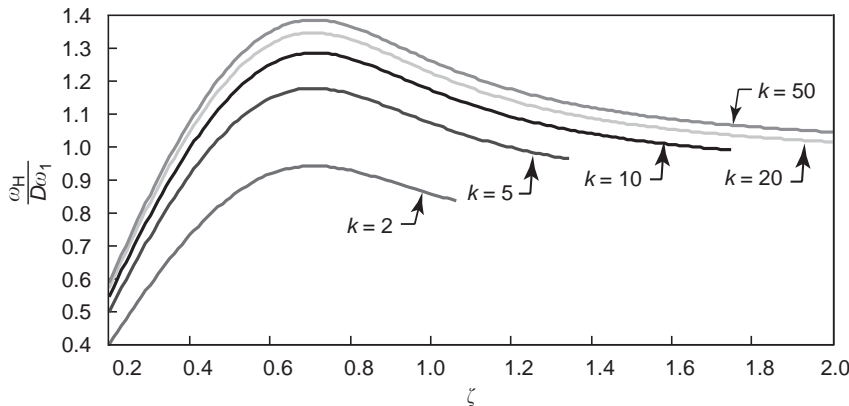


Figure 4. High 3-dB frequency as a function of ζ and nonfeedback pole spacing.

$K(\zeta_H, k)$, D , and f_1 :

$$f_{Hf} = K(\zeta_H, k)Df_1 = (1.277)(7.14286)(1 \text{ MHz}) = 9.12 \text{ MHz}$$

The resultant frequency response plots are shown in Fig. 5.

2.4. Input and Output Impedance

The input and output impedance of a feedback amplifier can be selectively increased or decreased through the application of feedback. As has been seen in the previous sections, general discussions provide great insight into many of the properties of feedback systems. In order to consider the design of electronic feedback amplifiers, it is necessary, however, to specify the details of the feedback sampling and mixing processes and the circuits necessary to accomplish these operations. The sampling and mixing processes have a profound effect on the input impedance, the output impedance, and the definition of the forward gain quantity that undergoes *quantified* change due to the application of feedback. This section will characterize the various idealized feedback configurations: the following section looks at practical feedback configurations.

The mixing and the sampling process for a feedback amplifier utilize either voltages or currents. Voltage mixing (subtraction) implies a series connection of voltages at the input of the amplifier; current mixing implies a shunt connection. Voltage sampling implies a shunt connection of the sampling probes across the output voltage; current sampling implies a series connection so that the output current flows into the sampling network. Either type of mixing can be combined with either type of sampling. Thus, a feedback amplifier may have one of four possible combinations of the mixing and sampling processes. These

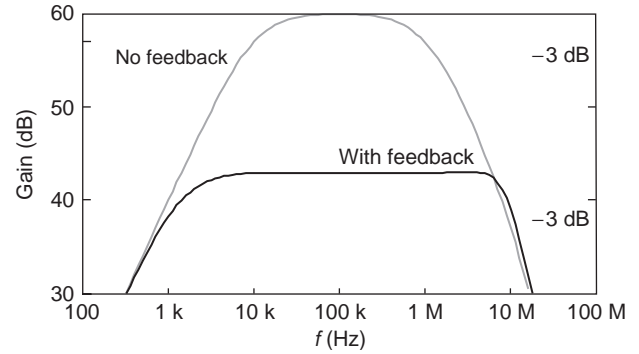


Figure 5. An example of the effect of feedback on frequency response.

four combinations are commonly identified by a hyphenated term: mixing topology–sampling topology. The four types are

- *Shunt–shunt feedback* (current mixing and voltage sampling)
- *Shunt–series feedback* (current mixing and current sampling)
- *Series–shunt feedback* (voltage mixing and voltage sampling)
- *Series–series feedback* (voltage mixing and current sampling).

These four basic feedback amplifier topologies are shown schematically in Fig. 6. A source and a load resistance have been attached to model complete operation. In each diagram the input, feedback, and output quantities are shown properly as voltages or currents. Forward gain A must be defined as the ratio of the output sampled quantity divided by the input quantity that undergoes mixing.

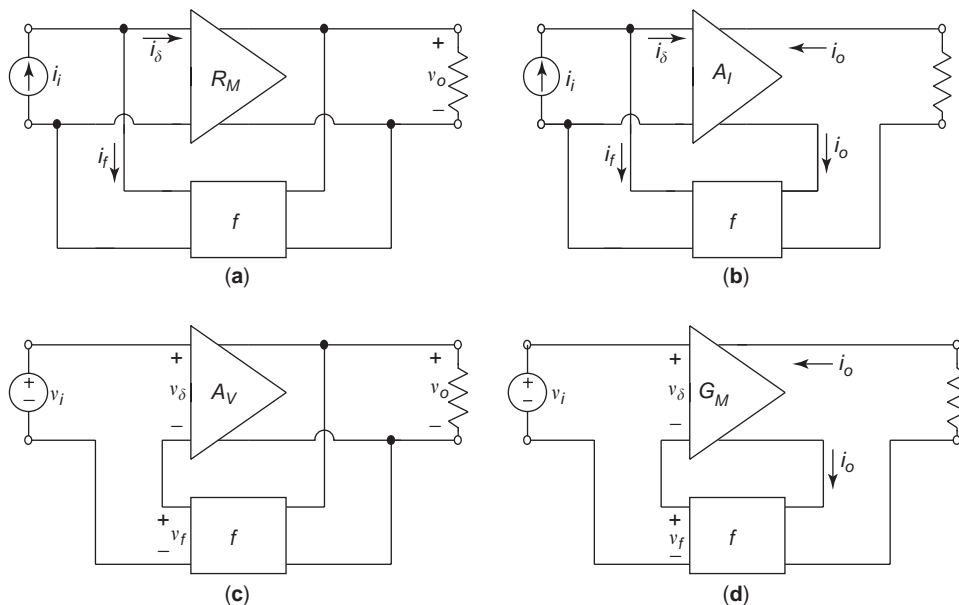


Figure 6. Feedback amplifier topologies: (a) shunt–shunt feedback; (b) shunt–series feedback; (c) series–shunt feedback; (d) series–series feedback.

Table 1. Feedback Amplifier Topology Parameters

Parameter	Shunt–Shunt	Shunt–Series	Series–Shunt	Series–Series
Input quantity X_i	Current i_s	Current i_s	Voltage v_s	Voltage v_s
Output quantity X_o	Voltage v_o	Current i_o	Voltage v_o	Current i_o
Forward gain A	Transresistance R_M	Current gain A_I	Voltage gain A_V	Transconductance G_M
Feedback ratio f	i_f/v_o	i_f/i_o	v_f/v_o	v_f/i_o

As such, it is a transresistance, current gain, voltage gain, or transconductance. The feedback network, as described by the feedback ratio (f), must sample the output quantity and present a quantity to the mixer that is of the same type (current or voltage) as the input quantity. As such it is a transconductance, current gain, voltage gain, or transresistance. Table 1 lists the appropriate quantities mixed at the input, the output sampled quantity, the forward gain, and the feedback ratio for each of the four feedback amplifier topologies. It is important to remember that the product fA must be dimensionless and, in the midband region of operation, positive.

In the previous section, all benefits of feedback were discussed *except* the modification of input–output impedance. The specific definitions of the four feedback amplifier topologies allow for that discussion to begin here. The *mixing process alters the input impedance* of a negative-feedback amplifier. Heuristically, one can see that subtraction of a feedback quantity at the mixing junction increases the input quantity necessary for similar performance. Thus, subtracting current (shunt mixing) requires an increase in overall input current and decreases the input impedance. Similarly, subtracting voltage (series mixing) requires an increase in overall input voltage and increases input impedance.

Although it can be easily shown that in each case, the change in resistance is proportional to the return difference D , it is important to note that the measurement point of the input and output resistance changes with each circuit topology. Two amplifier types are shown as examples: a *shunt–shunt* feedback amplifier (Fig. 7) and a *series–series* feedback amplifier (Fig. 8). Similarly, the return difference D is calculated using different gain and feedback parameters for each topology. The changes due to feedback on each feedback amplifier topology are summarized in Table 2.

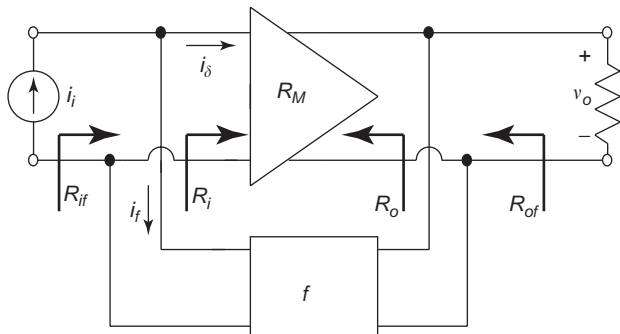


Figure 7. Input–output resistance for shunt–shunt feedback.

3. PRACTICAL FEEDBACK CONFIGURATIONS

Previous discussions of feedback and feedback configurations have been limited to idealized systems and amplifiers. The four idealized feedback schematic diagrams of Fig. 6 identify the forward-gain amplifier and the feedback network as two-port networks with a very specific property—each is a device with one-way gain. Realistic electronic feedback amplifiers can only approximate that idealized behavior. In addition, in practical feedback amplifiers there is always some interaction between the forward-gain amplifier and the feedback network. This interaction most often takes the form of input and output resistive loading of the forward-gain amplifier. The division of the practical feedback amplifier into its forward-gain amplifier and feedback network is also not always obvious. These apparent obstacles to using idealized feedback analysis can be resolved through the use of two-port network relationships in the derivation of practical feedback amplifier properties. Once amplifier gain and impedance relationships have been derived, the utility of the two-port representations becomes minimal and is typically discarded.

3.1. Identification of the Feedback Topology

Feedback topology is determined through careful observation of the interconnection of the feedback network and forward-gain amplifier. Shunt mixing occurs at the input terminal of the amplifier. Thus, *shunt mixing* is identified by a connection of feedback network and the forward-gain amplifier at the input terminal of first active device within the amplifier, in one of the following locations:

- At the base of a bipolar junction transistor (BJT) for a common-emitter or common-collector first stage

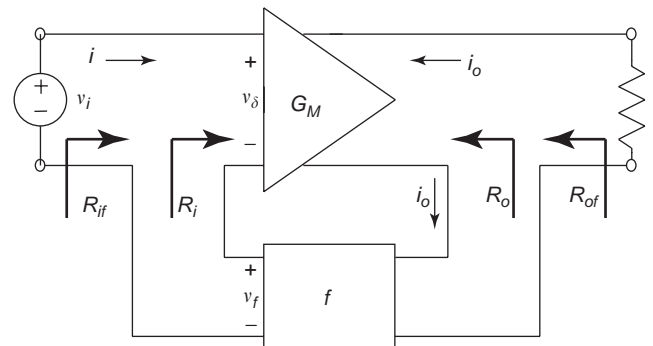


Figure 8. Input–output resistance for series–series feedback.

Table 2. Feedback Amplifier Analysis

Characteristic	Topology			
	Shunt–Shunt	Shunt–Series	Series–Shunt	Series–Series
Input X_i	Current i_s	Current i_s	Voltage v_s	Voltage v_s
Output X_o	Voltage v_o	Current i_o	Voltage v_o	Current i_o
Signal source	Norton	Norton	Thévenin	Thévenin
Input circuit ^a	Include shunting resistances; set $v_o = 0$	Include shunting resistances; set $i_o = 0$	Exclude all shunt resistances; set $v_o = 0$	Exclude all shunt resistances; set $i_o = 0$
Output circuit ^a	Include shunting resistances; set $v_i = 0$	Exclude all shunt resistances; set $v_i = 0$	Include shunting resistances; set $i_i = 0$	Exclude all shunt resistances; set $i_i = 0$
Feedback ratio f	i_f/v_o	i_f/i_o	v_f/v_o	v_f/i_o
Forward gain A	Transresistance R_M	Current gain A_I	Voltage gain A_V	Transconductance G_M
Input resistance ^b	$R_{if} = \frac{R_i}{1 + f R_M}$	$R_{if} = \frac{R_i}{1 + f A_I}$	$R_{if} = R_i(1 + f A_V)$	$R_{if} = R_i(1 + f G_M)$
Output resistance ^b	$R_{of} = \frac{R_o}{1 + f R_M}$	$R_{of} = R_o(1 + f A_I)$	$R_{of} = \frac{R_o}{1 + f A_V}$	$R_{of} = R_o(1 + f G_M)$

^aInput–output circuit: These procedures give the basic forward amplifier without feedback but including the effects of loading due to the feedback network.
^bResistance: The resistance modified at *shunted* ports will include all shunting resistances that were included in the basic forward amplifier. The resistance modified at *series* ports will include only the resistances included in the basic forward amplifier. The true amplifier input–output impedance must be modified to reflect the point of measurement desired.

- At the emitter of a BJT for a common-base first stage
- At the gate of a field-effect transistor (FET) for a common-source or common-drain first stage
- At the source of a FET for a common-gate first stage

Series mixing occurs in a loop that contains the input terminal of the forward-gain amplifier and the controlling port of the first active device. The controlling port of a BJT in the forward-active region is the base–emitter junction; a FET in the saturation region is controlled by the voltage across the gate–source input port. *Series mixing* is characterized by a circuit element or network that is *both* connected to the output *and* in series with the input voltage and the input port of the first active device.

Identification of the sampling is derived from direct observation of the connection of the output of the basic forward amplifier and the feedback network. *Shunt sampling* is typically characterized by a direct connection of the feedback network to the output node; *series sampling* implies a series connection of the amplifier output, the feedback network, and the load. Two tests performed at the feedback amplifier output can aid in the determination of sampling topology:

- If the feedback quantity vanishes for a short-circuit load, the output voltage must be the sampled quantity. Thus zero feedback for a short-circuit load implies *shunt sampling*.
- If the feedback quantity vanishes for an open-circuit load, the output current must be the sampled quan-

ity. Thus zero feedback for an open-circuit load implies *series sampling*.

After the topological type has been identified, each amplifier must be transformed into a form that allows for the use of the idealized feedback formulations. This transformation includes modeling the amplifier and the feedback network with a particular two-port representation that facilitates combination of elements. Once the transformations are accomplished, the amplifier performance parameters are easily obtained using the methods previously outlined. The particular operations necessary to transform each of the four feedback amplifier topological types require separate discussion. Only the shunt–shunt topology is discussed in detail; the other three topologies use similar techniques that lead to the results shown in Fig. 11 and described in Table 2.

3.1.1. Shunt–Shunt Feedback: A Detailed Derivation.

Figure 9 is a small-signal model representation of a typical shunt–shunt feedback amplifier. In this representation, the forward-gain amplifier and the feedback network have been replaced by their equivalent *y*-parameter two-port network representations so that parallel parameters can be easily combined. A resistive load has been applied to the output port; and, since shunt–shunt feedback amplifiers are transresistance amplifiers, a Norton equivalent source has been shown as the input. It should also be noted that

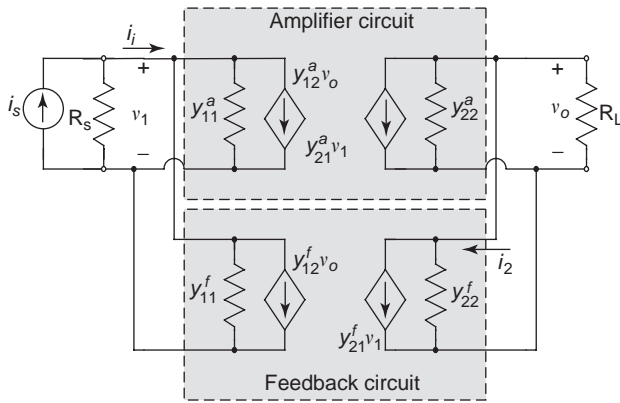


Figure 9. Two-port realization of a shunt–shunt feedback amplifier.

the forward-gain parameter of each two-port y_{21} is the transadmittance.

The basic feedback equation for a transresistance amplifier takes the form

$$R_{Mf} = \frac{R_M}{1 + R_{Mf}} \quad (24)$$

The application of the basic feedback equation to this circuit in its current form is not immediately clear. It is necessary to transform the feedback amplifier circuit into a form that allows for easy application of the basic feedback equation, [Eq. (24)]. Such a transformation must meet the previously stated feedback requirements:

- The forward-gain amplifier is to be a forward transmission system only—its reverse transmission must be negligible.
- The feedback network is to be a reverse transmission system that presents a feedback current, dependent on the output voltage, to the amplifier input port.

While a mathematically rigorous derivation of the transformation is possible, greater insight to the process comes with a heuristic approach.

The two-port y -parameter representation, in conjunction with the shunt–shunt connection, is used to describe the two main elements of this feedback amplifier so that all the input port elements of both two-port networks are in parallel. Similarly, all output port elements are in parallel. It is well known that circuit elements in parallel may be rearranged and, as long as they remain in parallel, the circuit continues to function in an identical fashion. Hence, it is possible, *for analysis purposes only*, to *conceptually* move elements from one section of the circuit into another (from the feedback circuit to the amplifier circuit or the reverse). The necessary conceptual changes made for the transformation are

- The source resistance, the load resistance, and all input and output admittances, y_{11} and y_{22} , are placed in the modified amplifier circuit. While inclusion of the source and load resistance in the amplifier seems, at first, counterproductive, it is necessary, however, to

include these resistances so that the use of the feedback properties produces correct results for input and output resistance (after appropriate transformations).

- All forward transadmittances y_{21} (represented by current sources dependent on the input voltage v_1) are placed in the modified amplifier circuit.
- All reverse transadmittances y_{12} (represented by current sources dependent on the output voltage v_o) are placed in the modified feedback circuit.

The dependent current source can be easily combined:

$$y_{12}^t = y_{12}^a + y_{12}^f \quad (25)$$

$$y_{21}^t = y_{21}^a + y_{21}^f \quad (26)$$

In virtually every practical feedback amplifier the reverse transadmittance of the forward-gain amplifier is much smaller than that of the feedback network ($y_{12}^a \ll y_{12}^f$) and the forward transadmittance of the feedback network is much smaller than that of the forward-gain amplifier ($y_{21}^f \ll y_{21}^a$). Thus, approximate simplifications of the amplifier representation can be made:

$$y_{12}^t = y_{12}^a + y_{12}^f \approx y_{12}^f \quad (27)$$

$$y_{21}^t = y_{21}^f + y_{21}^a \approx y_{21}^a \quad (28)$$

The shunt–shunt feedback amplifier circuit of Fig. 9 is, with these changes and approximations, thereby transformed into the circuit shown in Fig. 10.

This transformed circuit is composed of two simple elements:

- The original amplifier with its input shunted by the source resistance and the feedback network short-circuit input admittance y_{11}^f and its output shunted by the load resistance and the feedback network short-circuit output admittance y_{22}^f .
- A feedback network composed solely of the feedback network reverse transadmittance y_{12}^f .

It is also important to note that the input resistance R_{if} of this circuit includes the source resistance R_s ; as such, *it is*

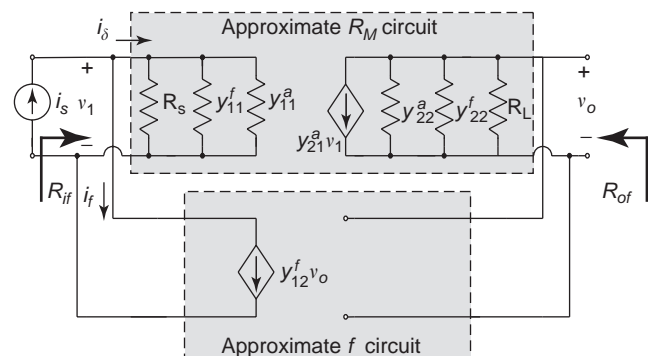


Figure 10. Redistributed shunt–shunt realization.

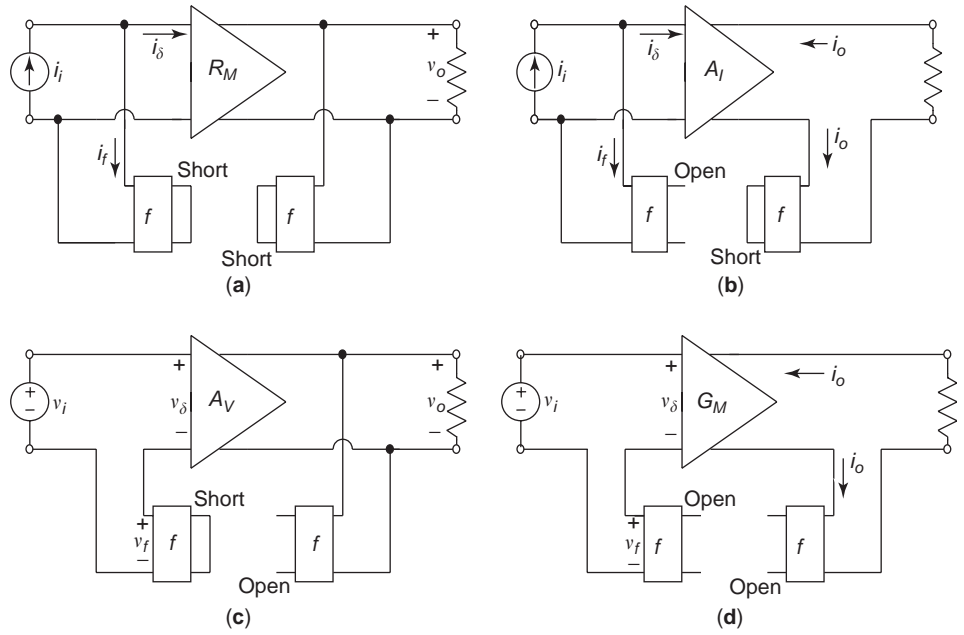


Figure 11. Feedback network loading of a basic forward amplifier: (a) shunt–shunt feedback; (b) shunt–series feedback; (c) series–shunt feedback; (d) series–series feedback.

not the same as the input resistance of the true amplifier R_{in} . The input resistance of the true amplifier can be obtained as

$$R_{in} = \left(\frac{1}{R_{if}} - \frac{1}{R_s} \right)^{-1} \quad (29)$$

Similarly, the output resistance R_{of} of this circuit includes the load resistance R_L ; similar operations may be necessary to obtain the true output resistance of the amplifier.

The y parameters of the feedback network can be obtained

$$y_{11}^f = \left. \frac{i_f}{v_1} \right|_{v_o=0}, \quad y_{22}^f = \left. \frac{i_2}{v_o} \right|_{v_1=0}, \quad y_{12}^f = \left. \frac{i_f}{v_o} \right|_{v_1=0} \quad (30)$$

where i_2 is the current entering the output port of the feedback network (see Fig. 8). With the determination of these two-port parameters, the circuit has been transformed into a form that is compatible with all previous discussions. The forward-gain parameter (in this case, G_M) of the loaded basic amplifier must be calculated, while the feedback ratio has been determined from the two-port analysis of the feedback network:

$$f = y_{12}^f \quad (31)$$

In the case of totally resistive feedback networks, the shunting resistances can be found in a simple fashion:

- $r_{in} = (y_{11}^f)^{-1}$ is found by setting the output voltage to zero value $v_o = 0$ and determining the resistance from the input port of the feedback network to ground.

- $r_{out} = (y_{22}^f)^{-1}$ is found by setting the input voltage to zero value $v_i = 0$ and determining the resistance from the output port of the feedback network to ground.

The feedback ratio f is simply the ratio of the feedback current i_f to the output voltage when the input port of the feedback network v_i is set to zero value. All idealized feedback methods can be applied to this transformed amplifier, and all previously derived feedback results are valid.

The other three feedback amplifier topologies can be similarly analyzed using various two-port parameters for analysis:

- Shunt–series: g parameters
- Series–shunt: h parameters
- Series–series: z parameters

Such analysis leads to a characterization of the loading of the basic forward amplifier as is described in Fig. 11. As is the case with the shunt–shunt topology, individual elements within the feedback network may appear more than one in the loaded basic forward-amplifier equivalent circuit. Table 2 summarizes the analysis of feedback amplifier properties:

4. STABILITY IN FEEDBACK AMPLIFIERS

Under certain conditions, feedback amplifiers have the possibility of being unstable. This instability stems from the frequency-dependent nature of the forward gain of the basic amplifier, A and the feedback factor f . The frequency dependence is exhibited in the changes in magnitude and phase of the product fA as a function of frequency.

Instability can be visualized by studying the basic feedback equation as a function of frequency:

$$A_f(j\omega) = \frac{A(j\omega)}{1 + f(j\omega)A(j\omega)} \quad (32)$$

It is important that an amplifier be designed so that stability is present at all frequencies, not only those in the midband region. If the product $-f(j\omega)A(j\omega)$ approaches unity at any frequency, the denominator of Eq. (32) approaches zero value; the total gain of the amplifier approaches infinity. This condition represents an output that is truncated only by power supply limitations regardless of input magnitude and is an unstable condition that is intolerable in amplifiers. In order to avoid this instability, it is necessary to avoid a simultaneous approach of $|f(j\omega)A(j\omega)| = 1$ and $\angle f(j\omega)A(j\omega) = \pm 180^\circ$. Since each pole can provide a phase shift ranging from 0° and -90° only, the second condition is possible only for amplifiers that have high or low frequency responses described by three or more poles. Simultaneously satisfying both conditions can be avoided if the magnitude of fA is always less than unity when the phase angle of fA is $\pm 180^\circ$. Designers of feedback amplifiers typically verify that this is the case through the use of amplifier frequency response plots.

4.1. Gain Margin and Phase Margin

A frequency response plot of the loop gain fA for a typical amplifier is shown in Fig. 12. The frequency at which $|f(j\omega)A(j\omega)| = 1$ is identified as ω_m , and the frequency at which $\angle f(j\omega)A(j\omega) = -180^\circ$ is identified as ω_p . Since $\omega_m \neq \omega_p$, it is apparent that this is a stable amplifier; that is, the two instability conditions are not simultaneously met. It is, however, important to ensure that the two conditions are not met simultaneously with a margin of safety. The *margin of safety* is defined by the gain margin and the phase margin of the feedback amplifier.

Gain margin is defined as the difference in the loop gain magnitude (in decibels) between 0 dB (unity gain) and the loop gain magnitude at frequency ω_p :

$$\text{Gain margin} = -20 \log |f(j\omega_p)A(j\omega_p)| \quad (33)$$

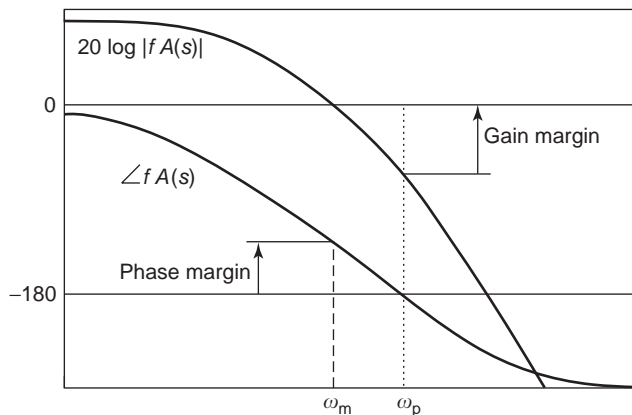


Figure 12. Gain margin and phase margin.

Phase margin is the difference between the loop gain phase angle at frequency ω_m and -180° :

$$\text{Phase margin} = \angle f(j\omega_m)A(j\omega_m) + 180^\circ \quad (34)$$

Each safety margin is shown in Fig. 12. It is common to specify the design of feedback amplifiers with gain and phase margins greater than 10 dB and 50° , respectively. These margins ensure stable amplifier operation over component parameter variation, temperature change, and other variations found in typical amplifiers.

4.2. Compensation Networks

Two fundamental techniques are available for ensuring amplifier stability:

- Reducing the midband loop gain fA of the amplifier
- Adding a compensation network to the amplifier to shape the loop gain frequency response so that the phase and gain margins are positive and in an acceptable range

Careful design is required in each of these cases to ensure stable amplifier operation over typical performance conditions.

In many cases, decreasing the loop gain to achieve stability is not an acceptable design possibility. Additionally, as is often the case in operational amplifier circuits, the feedback quantity f may be determined by the user rather than the amplifier designer and can range widely. In such cases, compensation networks are added within the feedback loop of the amplifier to increase the gain and phase margins. Such compensation networks add poles or a combination of poles and zeros to the loop gain characteristic. The most commonly used compensation techniques are

- Dominant pole compensation
- Lag-lead (pole-zero) compensation
- Lead compensation

Each technique modifies the gain and phase profiles of the basic forward amplifier through pole and zero manipulation.

In dominant-pole compensation, the amplifier is modified by adding a dominant pole that is much smaller in magnitude than all other poles in the amplifier gain function; typically it is chosen so that the gain reaches 0 dB at the frequency of the next pole (the first pole of the uncompensated amplifier). Consequently, the modified loop gain falls below 0 dB before the nondominant poles shift the total phase shift near 180° and the circuit is inherently stable. Dominant-pole compensation will typically result in a phase margin of approximately 45° .

The location of the new compensation pole can be determined by modeling the loop gain response with a single pole and setting its value to 0 dB at the first pole of the uncompensated amplifier:

$$20 \log |fA_0| - 20 \log \left| 1 + \frac{j\omega_c}{\omega_{p1}} \right| = 0 \text{ dB} \quad (35)$$

Solving Eq. (35) for the compensation pole frequency ω_c , results in

$$\omega_c \approx \frac{\omega_{p1}}{fA_0} \tag{36}$$

If the design goals of the feedback amplifier includes a range of feedback ratios, the frequency of the compensation pole is determined by the maximum value of the feedback ratio; that is, ω_c is chosen to be the smallest value predicted by Eq. (36).

An example of dominant-pole compensation is shown in Fig. 13 in the frequency domain. For clarity, the gain plots are represented by straight-line Bode approximations, while the exact phase plots are retained. The example amplifier is described by a midband gain of 60 dB with poles at 1, 5, and 50 MHz; the feedback ratio is $f=0.1$.

The possibility of feedback amplifier instability is focused at the frequency where $|fA|=1$ or equivalently where $|A|_{dB} = -20 \log(f)$. For this particular three-pole example, instability may occur at $\omega_m \approx 21$ MHz. Here the phase margin is very small and negative ($\approx -7^\circ$). After compensation, the focus is again centered where the gain plot (now compensated) intersects the negated feedback ratio plot. Addition of the compensation pole ω_c shifts this intersection to the frequency of the first uncompensated pole ω_{p1} . For this example, the compensation pole is placed at 10 kHz and yields a phase margin of $\approx 43^\circ$ and a gain margin of ≈ 14 dB.

Dominant-pole compensation reduces the open-loop bandwidth drastically. In this example the 3-dB frequency was lowered by two decades to 10 kHz. Still, it is common in many circuits with inherently large gain; internally compensated operational amplifiers often utilize dominant-pole compensation.

Lead-lag (or pole-zero) compensation is similar to dominant-pole compensation with one major exception. In addition to a dominant pole, a higher-frequency zero is added. This zero is used to cancel the first pole of the uncompensated amplifier. The added dominant pole can then be chosen so that the gain reaches 0 dB at the frequency of the next pole (the second pole of the uncompensated amplifier). Lead-lag compensation has a distinct bandwidth advantage over dominant-pole compensation.

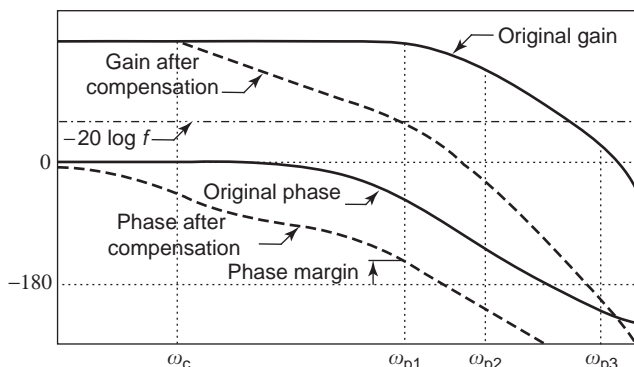


Figure 13. Bode diagram for a dominant-pole-compensated amplifier.

The location of the new compensation pole can be determined in a method similar to the method utilized under dominant-pole compensation with the exception that the loop gain (without the first original pole) is to reach 0 dB at the second pole of the uncompensated amplifier. Solving Eq. (35) for the compensation pole frequency ω_c results in

$$\omega_c \approx \frac{\omega_{p2}}{fA_0} \tag{37}$$

As with dominant-pole compensation, design goals including a range of feedback ratios lead to the determination of frequency of the compensation pole by the maximum value of the feedback ratio; that is, ω_c is chosen to be the smallest value predicted by Eq. (37).

The uncompensated amplifier described previously, is compensated with a lag-lead pole-zero pair, and the frequency domain results are displayed in Fig. 14. The possibility of feedback amplifier instability is again focused at the intersection of the gain and the negated feedback ratio plots. After compensation, the focus is centered where the gain plot (now compensated) intersects the negated feedback ratio plot. The addition of the compensation pole ω_c and a zero at the first uncompensated pole ω_{p1} shifts this intersection to the frequency of the second uncompensated pole ω_{p2} . The previously identified amplifier parameters lead to a compensation pole at 50 kHz (also the 3-dB frequency), a positive phase margin of $\approx 48^\circ$, and a gain margin of ≈ 20 dB.

Lead compensation can lead to the largest bandwidth of the three most common compensation networks. Here, as in lead-lag compensation, a pole and a zero are added. The zero is used to cancel the *second* pole of the uncompensated amplifier, and the added pole is positioned at a frequency higher than the zero. The objective is to reduce the phase shift of the uncompensated amplifier at the frequency where the loop gain reaches 0 dB (ω_m). It can be extremely effective in feedback amplifiers where there are two or three dominant poles in the uncompensated amplifier.

The uncompensated amplifier described above is compensated with a lead pole-zero pair, and the frequency-domain results are displayed in Fig. 15. After compensation, the focus is again centered where the gain plot (now compensated) intersects the negated feedback ratio plot.

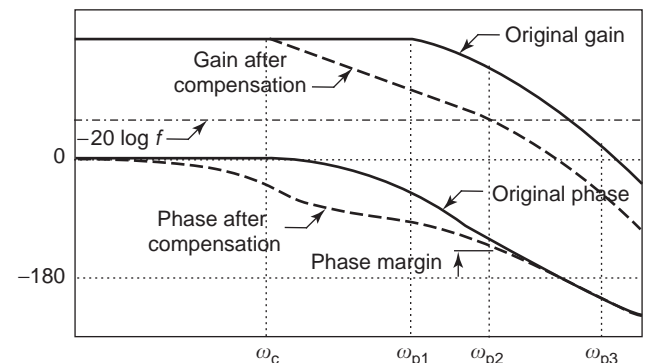


Figure 14. Bode diagram for a lag-lead-compensated amplifier.

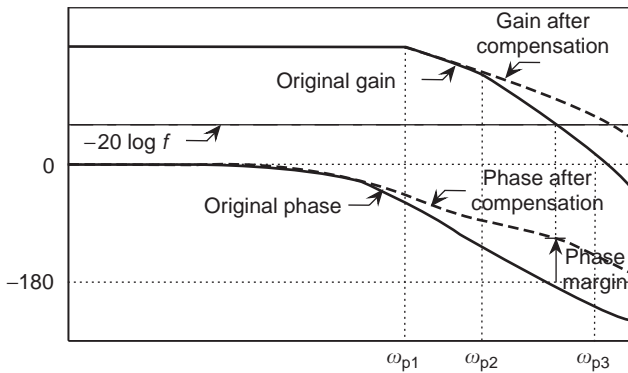


Figure 15. Bode diagram for a lead-compensated amplifier.

The addition of a zero at the second uncompensated pole ω_{p2} and a high-frequency compensation pole ω_c , shifts this intersection to a frequency beyond the second uncompensated pole ω_{p2} . For this example, the high-frequency pole was chosen at 500 MHz. This design choice leads to a positive phase margin of $\approx 35^\circ$ and a gain margin of ≈ 15 dB. Note that with lead compensation there is no significant reduction in the frequency response of the feedback amplifier; the 3 dB frequency for this example is 999.6 kHz (0.04% reduction).

A passive component circuit implementation of each of the three compensation techniques is schematically shown in Fig. 16. For the circuit of Fig. 16a, the compensation network component values are chosen so that

$$(R_p + R_o)C_p = \frac{fA_0}{\omega_{p1}} \quad (38)$$

where A_0 , R_o , and ω_{p1} are the midband gain, the output resistance, and the first pole frequency, of the basic forward amplifier, respectively. For the circuit of Fig. 16b, the compensation network component values are chosen so that

$$R_b C_c = \frac{1}{\omega_{p1}} \quad (39)$$

and

$$(R_a + R_b + R_o)C_c = \frac{fA_0}{\omega_{p2}} \quad (40)$$

For the circuit of Fig. 16c, the compensation network component values are chosen so that

$$R_a C_c = \frac{1}{\omega_{p2}} \quad (41)$$

$$(R_a // R_b)C_c \ll \frac{1}{\omega_{p1}} \quad (42)$$

While the placement of a compensation network at the output of the basic forward amplifier is an effective technique for feedback topologies with shunt sampling, other

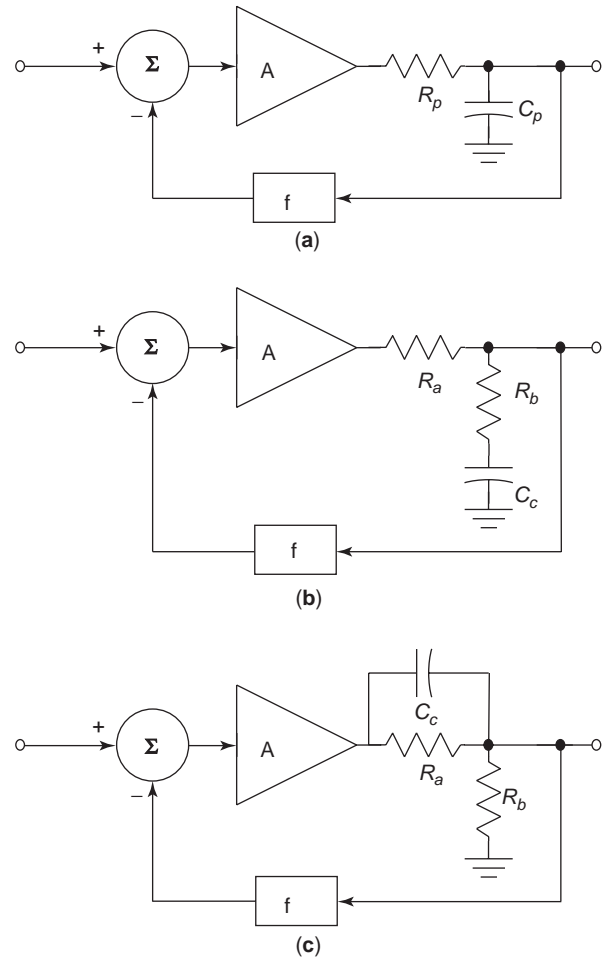


Figure 16. Compensation networks: (a) dominant-pole compensation; (b) lag-lead (pole-zero) compensation; (c) lead compensation.

placement may be necessary. In particular, connections at the output of a feedback amplifier with series sampling are *not within the feedback loop* and are therefore invalid. In such cases, alternate placement of the compensation is necessary; one common placement intersperses the compensation network between individual gain stages of the amplifier. Similarly, it is possible to compensate a feedback amplifier within the feedback network rather than the basic forward amplifier. Unfortunately, analysis of compensation within the feedback network is often extremely complex because of the loading of the basic forward amplifier by feedback network components.

BIBLIOGRAPHY

1. F. C. Fitchen, *Transistor Circuit Analysis and Design*, Van Nostrand, Princeton, NJ, 1966.
2. M. S. Ghauri, *Electronic Devices and Circuits: Discrete and Integrated*, Holt Rinehart and Winston, New York, 1985.
3. P. R. Gray, P. J. Hurst, S. H. Lewis, and R. G. Meyer, *Analysis and Design of Analog Integrated Circuits*, 4th ed., J Wiley, New York, 2001.

4. D. H. Horrocks, *Feedback Circuits and Op. Amps*, Chapman & Hall, London, 1990.
5. P. J. Hurst, A comparison of two approaches to feedback circuit analysis, *IEEE Trans. Ed.* **35**(3) (1992).
6. J. Millman, *Microelectronics, Digital and Analog Circuits and Systems*, McGraw-Hill, New York, 1979.
7. J. Millman and C. C. Halkias, *Integrated Electronics: Analog and Digital Circuits and Systems*, McGraw-Hill, New York, 1972.
8. J. W. Nilsson and S. A. Riedel, *Electric Circuits*, 6th ed., Prentice-Hall, New York, 1999.
9. S. Rosenstark, *Feedback Amplifier Principles*, Macmillan, New York, 1986.
10. A. S. Sedra and K. C. Smith, *Microelectronic Circuits*, 4th ed., Oxford Univ. Press, New York, 1998.
11. D. L. Schilling and C. Belove, *Electronic Circuits*, 3rd ed., McGraw-Hill, New York, 1989.
12. T. F. Schubert, Jr. and E. M. Kim, *Active and Non-Linear Electronics*, J Wiley, New York, 1996.
13. T. F. Schubert, Jr., A heuristic approach to the development of frequency response characteristics in the design of feedback amplifiers, *Proc. 1996 Frontiers in Education Conf.*
14. T. F. Schubert, Jr., Feedback amplifiers, in J. G. Webster, ed., *Wiley Encyclopedia of Electrical and Electronics Engineering*, Vol. 7, J Wiley, New York, 1999, pp. 336–339.
15. R. Spencer and M. Ghausi, *Introduction to Electronic Circuit Design*, Prentice Hall, New York, 2003.

FEEDBACK OSCILLATORS

JIANYI ZHOU
WEI HONG
Southeast University
Nanjing, China

1. INTRODUCTION

An oscillator is a type of circuit that converts DC power to AC signals automatically without external excitation, and has been widely used as a key component in various electronic products, such as communication systems, measurement instruments, and computers. In communication systems, oscillators are ubiquitous, generating carrier signals in both the transmitter and the receiver [1–3]. In many digital systems, oscillators provide the clock for CPUs, A/D converters, D/A converters, frequency synthesizers, and other devices.

Most oscillators are sinusoidal, generating a steady-state sinusoidal signal; some oscillators generate other types of waveform such as square and triangular waves. The sinusoidal oscillators are the basic type of oscillator because many other kinds of waveform can be obtained with the sinusoidal oscillator and waveshaping circuits.

There are two fundamental concerns in a sinusoidal oscillator—one is the purity of the output sinusoidal signal, and the other is the frequency stability. Actually, all oscillators are not perfect, and the output signal is always the superposition of the desired sinusoidal signal and

many undesired harmonics and noise. The power contained in the harmonics should be small relative to the desired fundamental signal. The noise accompanying the output signal of an oscillator will be the factor that limits system performance in many communication systems. There are two kinds of noise: amplitude noise and phase noise. Because amplitude fluctuations are usually greatly attenuated in many systems, the phase noise generally dominates [4,5]. The output signal frequency of an oscillator varies inevitably with the parameters of components in the oscillator because of the temperature variation. In many applications, especially in communication systems and electronic clocks, the frequency drift is required to be as small as possible [6].

In general, either the positive feedback or the negative resistance in a circuit can generate oscillation. Therefore, from the physical mechanism of oscillation, there are two kinds of oscillators: feedback oscillators and negative-resistance oscillators.

2. PRINCIPLE OF FEEDBACK OSCILLATORS

The basic method of generating sinusoidal oscillation electronically is to insert a positive-feedback circuit in an amplifier. The basic topology for a feedback oscillator, shown in Fig. 1, consists of three fundamental parts: the amplifier or active device, the feedback circuit, and the output load [1–3].

In Fig. 1, the feedback loop is broken at “×” for analysis. The input voltage of the amplifier is V_i , and the output voltage of the amplifier is

$$V_o(j\omega) = A(j\omega)V_i(j\omega) \tag{1}$$

where $A(j\omega)$ is the transfer function or gain of the amplifier, ω denotes the angular frequency, and $j = \sqrt{-1}$ is an imaginary unit.

The output voltage of the feedback circuit is

$$V_f(j\omega) = \beta(j\omega)V_o(j\omega) = A(j\omega)\beta(j\omega)V_i(j\omega) \tag{2}$$

and the loop gain is defined as

$$T(j\omega) = \frac{V_f(j\omega)}{V_i(j\omega)} = A(j\omega)\beta(j\omega) \tag{3}$$

For the closed loop, the closed-loop gain is defined as

$$G_{CL}(j\omega) = \frac{A(j\omega)}{1 - A(j\omega)\beta(j\omega)} \tag{4}$$

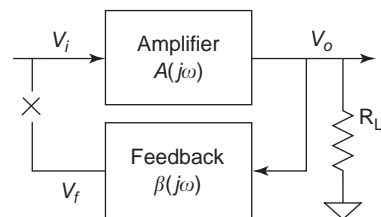


Figure 1. Block diagram of a feedback oscillator.

Because there is no input signal for an oscillator (i.e., $V_i = 0$) to maintain a nonzero output voltage, the denominator of the closed-loop gain (4) should be equal to zero. This is the Barkhausen criterion [1–3,7,8]

$$T(j\omega_0) = A(j\omega_0)\beta(j\omega_0) = T(\omega_0)e^{j\varphi_T(\omega_0)} = 1 \quad (5)$$

where ω_0 is the oscillation frequency.

Note that the Barkhausen criterion really implies two conditions for oscillation:

1. The magnitude of the loop gain must be 1, which termed the *magnitude-balanced condition*.
2. The phase of the loop gain must be 0 (or an integral multiple of 2π), which is termed the *phase-balanced condition*.

The Barkhausen criterion requires the magnitude of the loop gain $T(\omega_0)$ to be exactly 1 at the oscillation frequency. If $T(\omega_0) < 1$, the oscillation will be decaying. On the other hand, if $T(\omega_0) > 1$, the oscillation amplitude will continue to increase until it is limited by the nonlinearity of the active devices in the amplifier. In fact, this nonlinearity is an essential feature of practical oscillators.

Suppose that the oscillator satisfies the Barkhausen criterion when $V_i = V_{iA}$ other than $V_i = 0$, i.e., the magnitude of the loop gain $T(\omega_0)$ equates to 1. As the circuit characteristics drift, $T(\omega_0)$ may be either smaller or larger than 1. For the former case, the oscillation will decay to stop; for the latter case it increases until limited by the nonlinearity of the amplifier. Therefore, in order to initially establish an oscillation, $T(\omega_0)$ must be larger than 1. The phase-balanced condition and the startup condition for a feedback oscillator are as follows [1,7,8]:

$$T(\omega_0)|_{t=t_0} > 1 \quad (6a)$$

$$\varphi_T(\omega_0)|_{t=t_0} = 2n\pi \quad (n = 0, 1, 2, \dots) \quad (6b)$$

Moreover, in order to maintain a steady oscillation, nearby V_{iA} , $T(\omega_0)$ must decrease when V_i increases; in other words, the derivative of $T(\omega_0)$ at $V_i = V_{iA}$ must be negative. This yields the magnitude stability condition of the feedback oscillator as [7,8]

$$\left. \frac{\partial T(\omega_0)}{\partial V_i} \right|_{V_i = V_{iA}} < 0 \quad (7)$$

Note that, although an oscillator satisfies the magnitude stability condition, its amplitude of the output voltage may fluctuate with the change of its environment. To suppress such amplitude fluctuations, besides minimizing the environment fluctuations and decreasing the sensitivity of devices in the oscillator, one important point is to increase the slope of $T(\omega_0)$ at the balanced point, that is, to increase the absolute value of

$$\left. \frac{\partial T(\omega_0)}{\partial V_i} \right|_{V_i = V_{iA}}$$

Hence, a small drift of V_i will cause a large change of $T(\omega_0)$. Because of the negative slope of $T(\omega_0)$, the drift of V_i is countered and a new balanced condition will be established very close to V_{iA} .

Suppose that the oscillator satisfies the phase-balanced condition when $\omega = \omega_0$, that is, $\varphi_T(\omega_0) = 0$. As the circuit characteristics drift, $\varphi_T(\omega_0)$ may be either larger or smaller than 0. In the former case, the phase of the feedback voltage leads the phase of the original input voltage of the amplifier. In the latter case, the phase of the feedback voltage lags behind the phase of the original input voltage of the amplifier. It is known that the frequency is the derivative of the phase. If $\varphi_T(\omega_0) > 0$, the phase of the feedback voltage leads continuously, so the corresponding frequency will be higher than the original oscillation frequency. However, if $\varphi_T(\omega_0) < 0$, the phase of the feedback voltage lags behind continuously, and the corresponding frequency will be lower than the original oscillation frequency.

In fact, $\varphi_T(\omega)$ varies with the frequency. If $\varphi_T(\omega)$ decreases with an increase of ω [i.e., if $\varphi_T(\omega)$ and ω are inversely proportional], and if the oscillation frequency is higher than the original oscillation frequency, then $\varphi_T(\omega)$ decreases; therefore, the frequency increase will be prevented. However, if the oscillation frequency is lower, $\varphi_T(\omega)$ increases, and thus the frequency decrease will be prevented. Thus, a new balanced condition will be established very close to the original frequency. On the other hand, if $\varphi_T(\omega)$ increases with an increase of ω , the drift of the oscillation frequency is accelerated and cannot satisfy the phase-balanced condition.

Hence, in order to maintain a steady oscillation, nearby ω_0 , $\varphi_T(\omega)$ must decrease with the increase of ω ; thus, the derivative of $\varphi_T(\omega)$ at $\omega = \omega_0$ must be negative. This is the phase stability condition of the feedback oscillator [7,8]:

$$\left. \frac{\partial \varphi_T(\omega)}{\partial \omega} \right|_{\omega = \omega_0} < 0 \quad (8)$$

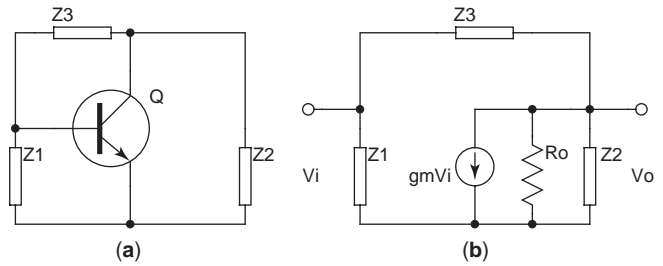
Note that although an oscillator satisfies the phase stability condition, the frequency of its output voltage may fluctuate with the change in its environment. To suppress such frequency fluctuations, besides to minimizing the environment fluctuations and decreasing the sensitivity of devices in the oscillator, one important point is to increase the slope of $\varphi_T(\omega)$ at the balanced point, that is, to increase the absolute value of

$$\left. \frac{\partial \varphi_T(\omega)}{\partial \omega} \right|_{\omega = \omega_0}$$

Hence, a small drift of ω will cause a large change of $\varphi_T(\omega)$. Because of the negative slope of $\varphi_T(\omega)$, the drift of ω is countered and a new balanced condition will be established very close to ω_0 [1–3,6–8].

In a practical feedback oscillator, the amplifier is an active device such as an operational amplifier, a field-effect transistor (FET), a bipolar junction transistor (BJT), or a logical gate. The feedback system is generally a passive resonant network. Any network can be used as

Figure 2. Schematic of π -type network feedback oscillator: (a) π -type network feedback oscillator; (b) simplified equivalent circuit.



the feedback network as long as the Barkhausen criterion is satisfied.

Practical feedback oscillators can be realized with different active devices and feedback network.

3. LC OSCILLATORS

LC oscillators are widely used in modern communication systems as the local oscillator for the upconverters and downconverters. LC oscillators use passive inductors and capacitors as the feedback network. Usually, the LC oscillators use a transistor or differential pairs as the active device. Many LC oscillator circuits use a π -type impedance network as the feedback network [1–3,5–9]. The circuit schematic is shown in Fig. 2.

The forward gain is

$$A = -\frac{g_m R_0 Z_L}{Z_L + R_0} \quad (9)$$

where

$$Z_L = \frac{Z_2(Z_1 + Z_3)}{Z_1 + Z_2 + Z_3} \quad (10)$$

The feedback factor is

$$\beta = \frac{Z_1}{Z_1 + Z_3} \quad (11)$$

Therefore, the loop gain is

$$T = A\beta = \frac{-g_m R_0 Z_1 Z_2}{Z_1 Z_2 + Z_2 Z_3 + R_0(Z_1 + Z_2 + Z_3)} \quad (12)$$

Suppose that the impedances are purely reactive (either inductive or capacitive), specifically, $Z_i = jX_i$ ($i = 1,2,3$); we then have

$$T = \frac{g_m R_0 X_1 X_2}{-X_2(X_1 + X_3) + jR_0(X_1 + X_2 + X_3)} \quad (13)$$

According to the Barkhausen criterion, the phase of the loop gain should be equal to zero; thus we have

$$X_1 + X_2 + X_3 = 0 \quad (14)$$

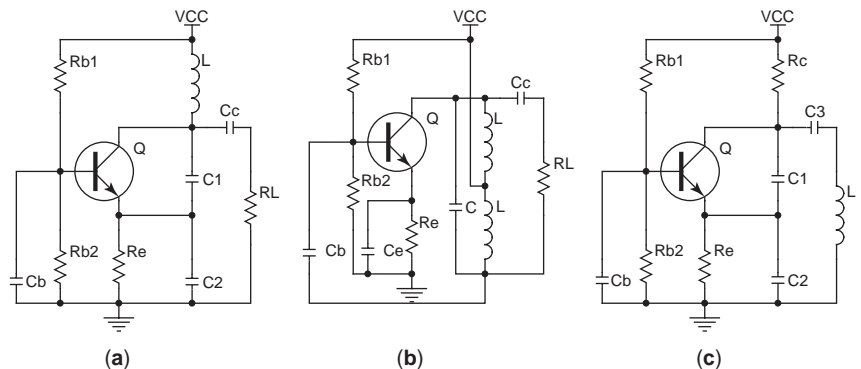
$$T = \frac{g_m R_0 X_1}{X_2} \quad (15)$$

According to the Barkhausen criterion, the magnitude of the loop gain should be equal to 1. Therefore, X_1 and X_2 must have the same sign; specifically, they must have the same kind of reactance, either inductive or capacitive. It follows from (14) that $X_3 = -(X_1 + X_2)$ must possess the other type of reactance. If X_1 and X_2 are capacitors and X_3 is an inductor, the circuit is called a *Colpitts oscillator*; if X_1 and X_2 are inductors and X_3 is a capacitor, the circuit is called a *Hartley oscillator*. Other combinations are also used. For example, if X_1 and X_2 are capacitors and X_3 is a series combination of an inductor and a capacitor, the circuit is called a *Clapp oscillator*. Figure 3 shows the schematic of these typical oscillators.

4. FREQUENCY STABILITY

Frequency stability is one of the most important performance factors for an oscillator. The feedback oscillator involves an active amplifier with a passive resonant

Figure 3. Schematics of typical LC oscillators: (a) Colpitts oscillator; (b) Hartley oscillator; (c) Clapp oscillator.



feedback network. The oscillation frequency ω_0 is determined mainly by the resonant of the feedback network. For an LC oscillator, suppose that the drift of the inductor and capacitor is ΔL and ΔC , respectively. The offset of the resonant frequency is [7]

$$\Delta\omega \approx -\frac{1}{2}\omega_0\left(\frac{\Delta L}{L} + \frac{\Delta C}{C}\right) \quad (16)$$

Hence, one means to improve the frequency stability is to reduce the drift of the inductor and capacitor in the resonant network.

Besides the parameter drift, the effective quality factor Q_e is also very important for frequency stability.

As we discussed before, increasing the absolute value of

$$\left.\frac{\partial\omega_T(\omega)}{\partial\omega}\right|_{\omega=\omega_0}$$

will also enhance the frequency stability. Thus, we may define the frequency stability factor as [7]

$$\text{SF} = \omega_0 \left.\frac{\partial\omega_T(\omega)}{\partial\omega}\right|_{\omega=\omega_0} \quad (17)$$

For a parallel RLC circuit, the impedance is

$$\mathbf{Z}(j\omega) = \frac{j\omega\frac{1}{C}}{\omega_0^2 - \omega^2 + j\frac{\omega_0\omega}{Q_e}} \quad (18)$$

where $\omega_0 = 1/\sqrt{LC}$ and $Q_e = R\sqrt{C/L}$.

The phase angle of the impedance as a function of frequency is

$$\varphi(\omega) = \frac{1}{2}\pi - \arctan\frac{\frac{\omega_0\omega}{Q_e}}{\omega_0^2 - \omega^2} \quad (19)$$

and its derivative with respect to ω is

$$\frac{\partial\varphi}{\partial\omega} = -\frac{Q_e\omega_0(\omega_0^2 + \omega^2)}{(\omega_0\omega)^2 + Q_e^2(\omega_0^2 - \omega^2)} \quad (20)$$

At the resonant frequency, this yields

$$\left.\frac{\partial\varphi}{\partial\omega}\right|_{\omega=\omega_0} = -\frac{2Q_e}{\omega_0} \quad (21)$$

and then the frequency stability factor

$$\text{SF} = -2Q_e \quad (22)$$

This result implies that the higher the Q value of the resonant circuit, the higher the frequency stability of the oscillator. Hence, another way to improve the frequency stability is to increase the effective quality factor of the resonant circuit [6–8].

5. PHASE NOISE

Phase noise is another important performance factor of an oscillator. Phase noise is usually characterized in terms of the signal sideband noise spectral density [4,5,10–16], namely, the decibels below the carrier per hertz (dBc/Hz), and is defined as

$$L_{\text{total}}(\Delta\omega) = 10 \cdot \log\left[\frac{P_{\text{sideband}}(\omega_0 + \Delta\omega, 1\text{ Hz})}{P_{\text{carrier}}}\right] \quad (23)$$

where $P_{\text{sideband}}(\omega_0 + \Delta\omega, 1\text{ Hz})$ represents the signal sideband power within a measurement bandwidth of 1 Hz at the frequency with offset $\Delta\omega$ from the carrier.

The most used approach to calculate the phase noise of an oscillator is the extended Leeson–Cutler phase noise model expressed as [4,5]

$$L(\Delta\omega) = 10 \log\left\{\frac{2FkT}{P_{\text{sig}}} \cdot \left[1 + \left(\frac{\omega_0}{2Q_e\Delta\omega}\right)^2\right] \cdot \left(1 + \frac{\omega_c}{|\Delta\omega|}\right)\right\} \quad (24)$$

where F denotes the noise figure of the active device, k is Boltzmann's constant, T is the absolute temperature, P_{sig} is the average power dissipated in the resistive part of the tank, ω_0 is the oscillation frequency, Q_e is the effective quality factor of the tank with all the loadings, $\Delta\omega$ is the offset from the carrier, and ω_c is the flicker frequency of the active device. A typical plot of the phase noise is shown in Fig. 4.

6. OTHER KINDS OF FEEDBACK OSCILLATORS

6.1. Microwave Oscillators

The LC oscillators described above are usually used in the low-frequency band. As the frequency increases to the microwave band and even millimeter-wave band, the lumped components are no longer suitable for resonance. Distributed components, such as transmission lines and cavities, should be adopted. Another important consideration is the treatment of the active devices in microwave band. The junction capacitance, parasitic capacitances, and inductances of microwave active devices should be taken into account. Generally, the S parameters are often employed to characterize the behavior of a microwave active device;

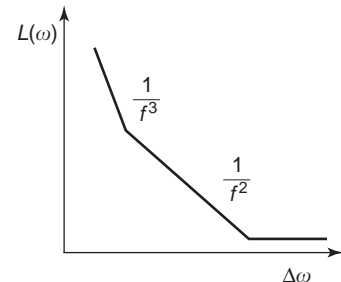


Figure 4. Typical plot of the phase noise of an oscillator versus offset from the carrier.

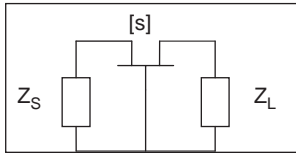


Figure 5. Design of microwave oscillators based on *S* parameters.

thus the design of microwave oscillators based on *S* parameters is widely adopted.

The oscillation condition of the circuit shown in Fig. 5 is given by [2,3]

$$\begin{aligned}
 K &< 1 \\
 S'_{11}\Gamma_1 &= 1 \\
 S'_{22}\Gamma_2 &= 1
 \end{aligned}
 \tag{25}$$

where

$$\begin{aligned}
 K &= \frac{1 - |S_{11}|^2 - |S_{22}|^2 + |S_{11}S_{22} - S_{12}S_{21}|^2}{2|S_{12}S_{21}|} \\
 S'_{11} &= S_{11} + \frac{S_{12}S_{21}\Gamma_2}{1 - S_{22}\Gamma_2} \\
 S'_{22} &= S_{22} + \frac{S_{12}S_{21}\Gamma_1}{1 - S_{11}\Gamma_1} \\
 \Gamma_1 &= \frac{Z_S - Z_0}{Z_S + Z_0} \\
 \Gamma_2 &= \frac{Z_L - Z_0}{Z_L + Z_0}
 \end{aligned}$$

In many cases, the *S* parameters of a microwave transistor do not satisfy the oscillation condition; some type of external feedback network is needed. The usual method is to add a segment of transmission line between the grid of the FET or the base of the BJT and the ground as a serial feedback network to aid the oscillation. A typical microwave oscillator with microstrip is shown in Fig. 6, where TL means microstrip transmission line [2]. TL2 acts as the

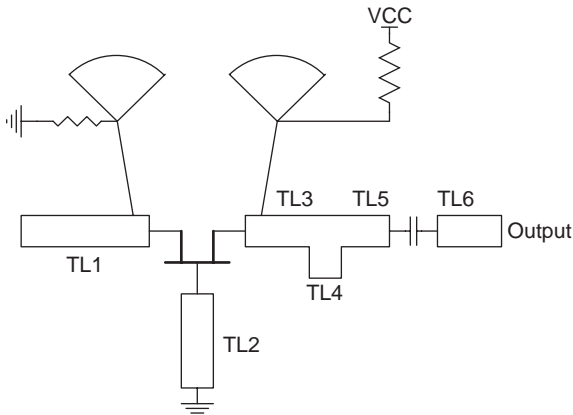


Figure 6. An FET microwave oscillator with microstrip as distributed feedback network.

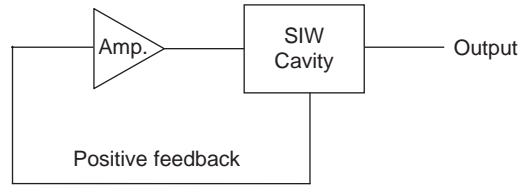


Figure 7. An SIW feedback oscillator.

serial feedback network. Usually, the length of TL2 dominates the oscillation frequency.

A so-called substrate integrated waveguide (SIW) cavity [43] has been used as the feedback resonant network, followed by development of a feedback microwave oscillator [44]. Figure 7 is a flowchart of the SIW feedback oscillator (for further details, please see Ref. 44).

The oscillator operates at 12.02 GHz. Good phase noise and harmonic level have been obtained.

6.2. Crystal and Dielectric Oscillators

As component characteristics change with age, temperature, signal level, and other parameters, the oscillation frequency will drift. The main cause of frequency drift is the drift of circuit parameters and the *Q* factor. The crystals used in oscillators are usually quartz, and the quartz crystal has extremely high *Q* and mechanical stability. A crystal oscillator is often used in extremely high stability oscillators. Figure 8 shows two typical crystal oscillators [17–19].

Besides the quartz crystals, other kinds of materials, such as SAW devices [20,21], Sapphire [22–25], and dielectric resonators [26–33] are often used for high-performance oscillators. In the microwave band, the dielectric resonator oscillator (DRO) has become one of the most widely used oscillators. A typical microwave DRO is shown in Fig. 9 [33].

6.3. RC Oscillators

RC oscillators using *RC* feedback network are useful oscillators in low-frequency bands [6–8]. The Wien bridge oscillator is the most widely used *RC* oscillator that adopts a balanced bridge as the feedback network, as shown in Fig. 10.

The oscillation frequency is determined by *R* and *C* as

$$f_0 = \frac{1}{2\pi RC}
 \tag{26}$$

The oscillation will be sustained if

$$\frac{R_2}{R_1} = 2
 \tag{27}$$

6.4. Ring Oscillators

Ring oscillators are commonly used in integrated circuits [34–38]. They consist simply of *n* inverters in a ring, where *n* is odd. A simple schematic of the ring oscillator is shown in Fig. 11.

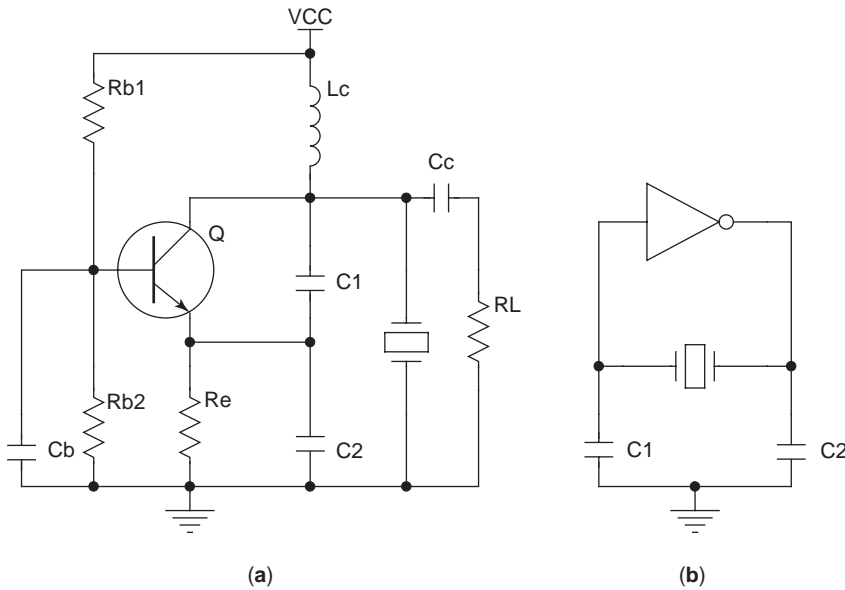


Figure 8. Two typical crystal oscillators: (a) Pierce crystal oscillator; (b) crystal oscillator with a NOT gate.

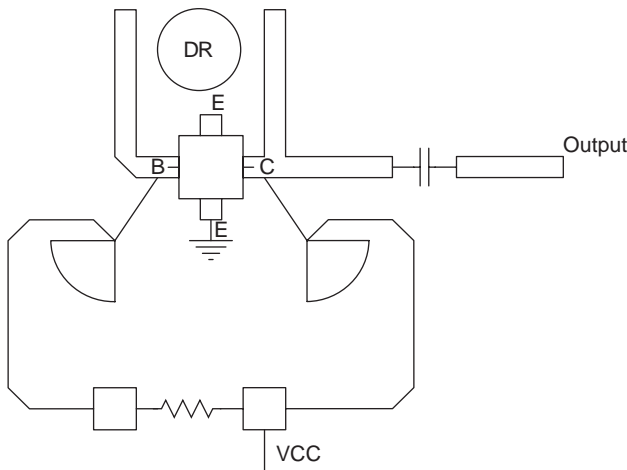


Figure 9. Microwave dielectric resonator oscillator (DRO).

For a simple analysis of the ring oscillator, it is assumed that each inverter can be characterized by a propagation time delay T_{pd} . The oscillation period is then simply twice the total propagation time delay:

$$f_0 = \frac{1}{2n \cdot T_{pd}} \quad (28)$$

6.5. Comparison of Different Oscillator Types

Table 1 compares the different types of feedback oscillators described above.

7. VOLTAGE-CONTROLLED OSCILLATORS

Many applications require oscillators to be electrically tunable. For example, in the superheterodyne receiver, the local oscillator should be tuned over an appropriate

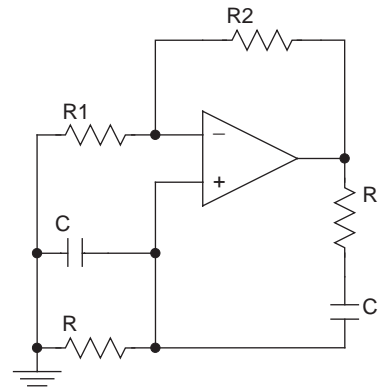


Figure 10. Wien bridge oscillator.



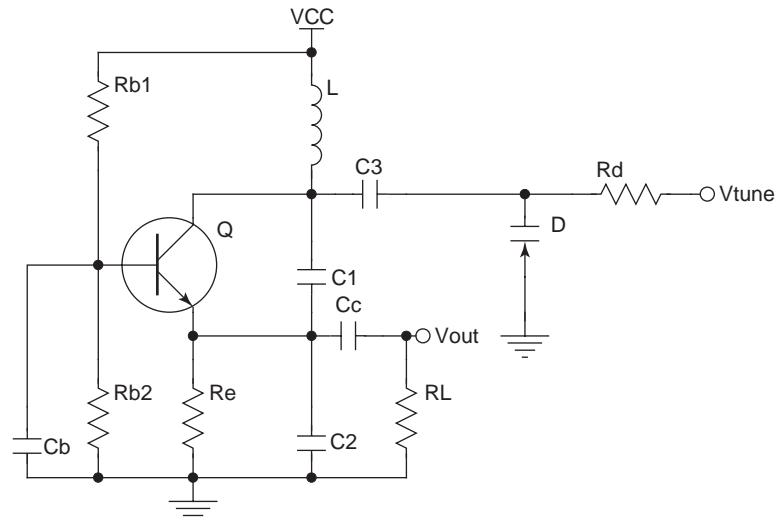
Figure 11. Ring oscillator.

frequency range so that the mixer will convert the incoming RF signal with different frequency down to the IF signal with the same intermediate frequency. In many applications, such as direct FM or in phase-locked loops, the tuning of the oscillator should be automatic. One way to achieve this purpose is using a voltage-controlled oscillator (VCO) [1–3,6–8,39–42]. A device that can be used in a VCO is the varactor diode. Any diode is a p-n junction, and thus has a junction capacitance. A varactor diode is designed so that the junction capacitance can be controlled by the reverse bias voltage across the junction

$$C(V) = C_0 \left(1 - \frac{V}{V_d}\right)^{(1/2)} \quad (29)$$

Table 1. Comparison of Feedback Oscillators

Type	Operation Frequency	Stability	Phase Noise	Cost	Tuning
LC	Low frequency–UHF	Moderate	Moderate	Low	Easy
Microwave	Microwave band	Moderate	Moderate	Moderate	Hard
Crystal	Low frequency–VHF	Good	Very low	Moderate	Moderate
Dielectric	Microwave band	Good	Low	High	Very hard
RC	Low-frequency band	Poor	Poor	Low	Easy
Ring	Low frequency–UHF	Poor	Poor	Low	Hard

**Figure 12.** Typical schematic of a voltage-controlled oscillator.

where V is the reverse bias, C_0 is a constant, and V_d is the diffusion barrier voltage of the junction [1–3,6–8].

A typical schematic of the voltage-controlled oscillator is shown in Fig. 12.

8. CONCLUSION

The principles and typical practical circuits of feedback oscillators are reviewed. Three important conditions and two kinds of main specifications required in an oscillator are summarized. Typical practical oscillators, such as the LC oscillators, RC oscillators, crystal oscillators, microwave oscillators, and voltage-controlled oscillators, are illustrated. These circuits are widely used in communication systems and other electronic equipment.

BIBLIOGRAPHY

1. K. K. Clarke and D. T. Hess, *Communication Circuits: Analysis and Design*, Addison-Wesley, Reading, MA, 1971.
2. R. Ludwig and P. Bretchko, *RF Circuit Design: Theory and Applications*, Prentice-Hall, 2000.
3. R. E. Collin, *Foundations for Microwave Engineering*, 2nd ed., McGraw-Hill, 1992.
4. D. B. Leeson, A simple model of feedback oscillator noise spectrum, *Proc. IEEE* **54**:329–330 (Feb. 1966).
5. T. H. Lee and A. Hajimiri, Oscillator phase noise: A tutorial, *IEEE J. Solid-State Circ.* **35**:326–336 (March 2000).
6. A. S. Sedra and K. C. Smith, *Micro-electronic Circuits*, 4th ed., Oxford Univ. Press, 1998.
7. X. Jiakui and X. Yuqing, *Electronic Circuits*, 3rd ed., High Education Press, Beijing, 1988.
8. J. R. Smith, *Modern Communication Circuits*, 2nd ed., McGraw-Hill, 1998.
9. G. M. Maggio, O. De Feo, and M. P. Kennedy, Nonlinear analysis of the Colpitts oscillator and applications to design, *IEEE Trans. Circ. Syst. I* **46**(9):1118–1130 (Sept. 1999).
10. A. N. Riddle and R. J. Trew, A novel GaAs FET oscillator with low phase noise, *1985 IEEE MTT-S Int. Microwave Symp. Digest 85.1*, 1985, pp. 257–260.
11. C. P. Lusher and W. N. Hardt, Effects of gain compression, bias conditions, and temperature on the flicker phase noise of an 8.5 GHz GaAs MESFET amplifier (short papers), *IEEE Trans. Microwave Theory Tech.* **37**:643–646 (March 1989).
12. G. K. Montress, T. E. Parker, and M. J. Loboda, Residual phase noise measurements of VHF, UHF, and microwave components, *IEEE Trans. Ultrason., Ferroelectr. Freq. Control* **48**(5):664–679 (Sept. 1994).
13. V. Gungerich, J. Deuring, W. Anzill, and P. Russer, Phase noise reduction of microwave oscillators by optimization of the dynamic behaviour, *1994 IEEE MTT-S Int. Microwave Symp. Digest*, 1994, Vol. 2, pp. 953–936.
14. V. Gungerich, F. Zinkler, W. Anzill, and P. Russer, Noise calculations, and experimental results of varactor tunable oscillators with significantly reduced phase noise, *IEEE Trans. Microwave Theory Tech.* **43**:278–285 (Feb. 1995).
15. M. N. Tutt, D. Pavlidis, A. Khatibzadeh, and B. Bayraktaroglu, The role of baseband noise and its upconversion

- in HBT oscillator phase noise, *IEEE Trans. Microwave Theory Tech.* **43**:1461–1471 (July 1995).
16. X. Zhang, D. Sturzebecher, and A. S. Daryoush, Comparison of the phase noise performance of HEMT and HBT based oscillators, *1995 IEEE MTT-S Int. Microwave Symp. Digest*, 1995, Vol. 2, pp. 697–700.
 17. M. E. Frerking, *Crystal Oscillator Design and Temperature Compensations*, Van Nostrand Reinhold, New York, 1978.
 18. D. V. Bogomolov and E. A. Silaev, Nonlinear dependencies and phase noise in precision crystal oscillator, *Proc. 2000 IEEE/EIA Int. Frequency Control Symp. and Exhibition*, 2000, pp. 549–552.
 19. Y. Shmaliy, S. Nedorezov, and R. Besson, Statistical model of an anharmonic sensor of precision crystal oscillator, *Proc. 2001 IEEE Int. Frequency Control Symp. and PDA Exhibition*, 2001, pp. 758–766.
 20. D. P. Klemmer, K.-M. Shih, and E. E. Clark, III, Phase noise characterization of SAW oscillators based on a Newton minimization procedure, *IEEE Trans. Microwave Theory Tech.* **39**:883–889 (May 1991).
 21. G. K. Montress, T. E. Parker, and D. Andres, Review of SAW oscillator performance, *Proc. 1994 IEEE Ultrasonics Symp.*, 1994, Vol. 1, pp. 43–54.
 22. M. E. Tobar, A. J. Giles, S. Edwards, and J. Searls, High-Q TE stabilized sapphire microwave resonators for low noise applications, *Proc. 1993 IEEE Int. Frequency Control Symp.*, 1993, pp. 749–756.
 23. M. E. Tobar, E. N. Ivanov, R. A. Woode, and J. H. Searls, Low noise microwave oscillators based on high-Q temperature stabilized sapphire resonators, *Proc. 1994 IEEE Int. Frequency Control Symp.*, 1994, pp. 433–440.
 24. C. Wong, W. F. Miccioli, D. M. Insanna, and C. A. Drubin, An extremely low noise, phase lockable, sapphire loaded cavity based microwave oscillator, *1999 IEEE MTT-S Int. Microwave Symp. Digest*, 1999, Vol. 1, pp. 91–94.
 25. O. Llopis, G. Gibiel, Y. Kersale, M. Regis, M. Chaubet, and V. Giordano, Ultra low phase noise sapphire-SiGe HBT oscillator, *IEEE Microwave Wireless Compon. Lett.* **12**:157–159 (May 2002).
 26. S. J. Ha, Y. D. Lee, Y. H. Kim, J. J. Choi, and U. S. Hong, Dielectric resonator oscillator with balanced low noise amplifier, *IEE Electron. Lett.* **38**(24):1542–1544 (Nov. 2002).
 27. J. K. Plourde and C.-L. Ren, Application of dielectric resonators in microwave components, *IEEE Trans. Microwave Theory Tech.* **29**:754–770 (Aug. 1981).
 28. K. K. Agarwal, Dielectric resonator oscillators using GaAs/(Ga, Al) As heterojunction bipolar transistors, *1986 IEEE MTT-S Int. Microwave Symp. Digest*, 1986, Vol. 1, pp. 95–98.
 29. M. J. Loboda, T. E. Parker, and G. K. Montress, Frequency stability of L-band, two-port dielectric resonator oscillators, *1987 IEEE MTT-S Int. Microwave Symp. Digest*, 1987, Vol. 2, pp. 859–862.
 30. J. Caldinhas Vaz, J. L. Caceres, J. Freire Costa, and J. Perez, Design and performance of dielectric resonator oscillators with series feedback, *Proc. 1989 Electrotechnical Conf.* 1989, pp. 339–342.
 31. R. Jones and V. Estrick, Low phase noise dielectric resonator oscillator, *Proc. 44th Annual Symp. Frequency Control*, 1990, pp. 549–554.
 32. S. Qi, K. Wu, and Z. Ou, Hybrid integrated HEMT oscillator with a multiple-ring nonradiative dielectric (NRD) resonator feedback circuit, *IEEE Trans. Microwave Theory Tech.* **46**:1552–1558 (Oct. 1998).
 33. J. K. Plourde and C.-L. Ren, Application of dielectric resonators in microwave components, *IEEE Trans. Microwave Theory Tech.* **29**:754–770 (Aug. 1981).
 34. T. H. Lee, *The Design of CMOS Radio-Frequency Integrated Circuits*, Cambridge Univ. Press, 1998.
 35. D.-Y. Jeong, S.-H. Chai, W.-C. Song, and G.-H. Cho, CMOS current-controlled oscillators using multiple-feed-back-loop ring architectures, *1997 IEEE Int. Solid-State Circuits Conf. Digest Tech. Papers*, 1997, pp. 386–387, 491.
 36. H. Kato, A dynamic formulation of ring oscillator as solitary-wave propagator, *IEEE Trans. Circ. Syst. I Fund. Theory Appl.* **45**:98–101 (Jan. 1998).
 37. S. L. J. Gierkink, A. van der Wel, G. Hoogzaad, E. A. M. Klumperink, and A. J. M. van Tuijl, Reduction of the 1/f noise induced phase noise in a CMOS ring oscillator by increasing the amplitude of oscillation, *Proc. 1998 IEEE Int. Symp. Circuits and Systems*, 1998, Vol. 1, pp. 185–188.
 38. L. Sun, T. Kwasniewski, and K. Iniewski, A quadrature output voltage controlled ring oscillator based on three-stage sub-feedback loops, *Proc. 1999 IEEE Int. Symp. Circuits and Systems*, 1999, Vol. 2, pp. 176–179.
 39. A. Gruhle, A. Schuppen, U. Konig, U. Erben, and H. Schumacher, Monolithic 26 GHz and 40 GHz VCOs with SiGe heterojunction bipolar transistor, *Proc. 1995 Int. Electron Devices Meeting*, 1995, pp. 725–728.
 40. H.-C. Chang and R. A. York, Enhanced MESFET/VCO injection-locking bandwidth using low frequency feedback techniques, *1996 IEEE MTT-S Int. Microwave Symp. Digest*, 1996, Vol. 3, pp. 1515–1518.
 41. H. J. Siweris, H. Tischer, T. Grave, and W. Kellner, A monolithic W-band HEMT VCO with feedback topology, *1999 IEEE MTT-S Int. Microwave Symp. Digest*, 1999, Vol. 1, pp. 17–20.
 42. H. J. Siweris, H. Tischer, and E. Rohrer, Monolithic 38 GHz coplanar feedback VCOs fabricated by a production PHEMT technology, *2001 IEEE MTT-S Microwave Symp. Digest*, 2001, Vol. 3, pp. 1555–1558.
 43. Y.-T. Lee, J.-S. Lim, D. A. Park, and S. Nam, A novel phase noise reduction technique in oscillators using defected ground structure, *IEEE Microwave Wireless Compon. Lett.* **12**:39–41 (Feb. 2002).
 44. Y. Cassivi and K. Wu, Low cost microwave oscillator using substrate integrated waveguide cavity, *IEEE Microwave Wireless Compon. Lett.* **13**(2):48–50 (Feb. 2003).

FEEDFORWARD AMPLIFIERS

P. GARDNER
The University of Birmingham
Edgbaston, Birmingham
United Kingdom

1. INTRODUCTION

Highly linear transmitters are required in modern RF and microwave radiocommunication systems, to facilitate the transmission of multiple carriers and/or nonconstant envelope, bandwidth efficient modulated signals, while minimizing the intermodulation and spectral spreading distortion caused by nonlinearity, particularly in the

power amplifier. Approaches to this problem may be divided broadly into

- Amplifier linearization techniques, whereby the RF/microwave transmitter is linearized as a separate component
- Linear transmitter architectures, in which the modulation and amplification processes are merged, with feedback or other control applied to the whole transmitter, usually by demodulating a sample of the output, and comparing with the modulation input

The three main techniques for linearization of the amplifier itself are feedforward linearization, RF predistortion, and feedback linearization.

Feedforward, the subject of this article, uses two analog signal loops. The first extracts the distortion occurring in the amplifier, and the second subtracts distortion from the output signal. One of the main attractions of this technique is that the correcting signal is derived from the nonlinear amplifier itself; the correction circuit does not need to be programmed with a nonlinear model of the amplifier. High levels of distortion cancellation (≥ 30 dB) can be achieved, and broad bandwidths are possible, at the expense of very precise phase and amplitude matching in the two loops.

In RF predistortion, a circuit module at the amplifier input is designed to have a nonlinear characteristic opposite to that of the main amplifier. For example, if the main amplifier has a gain that compresses as the input level increases, the predistorter is designed to have a compensating gain expansion. Similarly, the variation of phase with signal level in the predistorter is designed to compensate the phase change with signal level in the amplifier. An alternative view of the operation of a predistorter is that it generates intermodulation distortion components with an amplitude and phase such that, after amplification in the main amplifier, they cancel out the corresponding components generated within the amplifier itself. Predistortion linearisers provide an excellent method for achieving modest levels of distortion reduction (~ 10 dB), without the additional circuit complexity of feedforward systems.

Amplifier linearization using negative RF feedback relies on the fact that the transfer function of a closed-loop system is dominated by the feedback path, so long as the open-loop gain is high compared to the closed-loop gain. Thus, if the feedback path is linear, the closed-loop gain and phase remain linear. The main difficulty of this technique at RF and microwave frequencies is that the feedback path necessarily has a significant electrical length, compared to a guided wavelength, so the linearization works only over a narrow bandwidth, and instabilities are likely to occur at other frequencies. Negative feedback is therefore not widely used as a linearization technique in the RF–microwave range.

Linear transmitter architectures include a number of configurations, such as polar loop, Cartesian loop, and adaptive digital predistortion. These techniques can provide extremely high levels of linearity, usually measured in terms of low adjacent-channel power levels. However, because much of the associated processing is done digitally at baseband or IF, the achievable percentage bandwidth

is relatively low. Since the modulation scheme is effectively programmed into the transmitter architecture, such linearization techniques could be regarded as less adaptable than a standalone amplifier lineariser. Continual improvements in DSP (digital signal processing) hardware, however, will make linear architectures increasingly attractive options in system design.

2. BASIC PRINCIPLE OF FEEDFORWARD OPERATION

The invention of feedforward linearization can be traced back to a patent by Black [1]. After long neglect, the idea was revived for microwave applications by Seidel [2]. The basic principle of the feedforward amplifier is illustrated in Fig. 1. At the input to the main amplifier, coupler 1 samples the undistorted input signal. A sample of the signal at the output of the main amplifier is also taken using coupler 2. If the main amplifier were perfectly linear, this would be simply an amplified version of the input sample. In reality, nonlinear distortions in the amplifier cause the output sample to be an amplified version of the input signal along with an additional error signal. The error signal includes the intermodulation components generated in the main amplifier. The function of the feedforward system is first to isolate the error signal and then to remove it from the amplifier output, leaving an undistorted, linearly amplified signal.

This is achieved by first linearly adjusting the levels of the two samples and combining them in antiphase (i.e., subtracting them) using coupler 3, to cancel out the wanted signal and leave only the error signal. The coupling ratios in couplers 1, 2, and 3, and the phase shifts, delays, and attenuations in the first loop, are adjusted to achieve this cancellation. The error signal is then adjusted in phase and amplified by the auxiliary amplifier to a suitable amplitude level, so that when recombined, using coupler 4, with the output from the main amplifier, the error signal is canceled completely from the final output. To illustrate this operation, Fig. 1 includes spectrum diagrams showing the operation of a feedforward linearised amplifier with a two-tone input signal.

In principle, therefore, feedforward is a way to achieve perfect linear amplification without distortion. To assess its applicability in a practical transmitter system, several key performance parameters must be assessed, including

- Efficiency
- Bandwidth
- Degree of distortion suppression required
- Size and complexity

These parameters and the factors that influence them are outlined in this section and in more detail in Section 3.

2.1. Efficiency

Three main and interacting factors limit the overall efficiency of a feedforward amplifier:

1. The auxiliary amplifier consumes a significant level of DC power without adding to the level of the

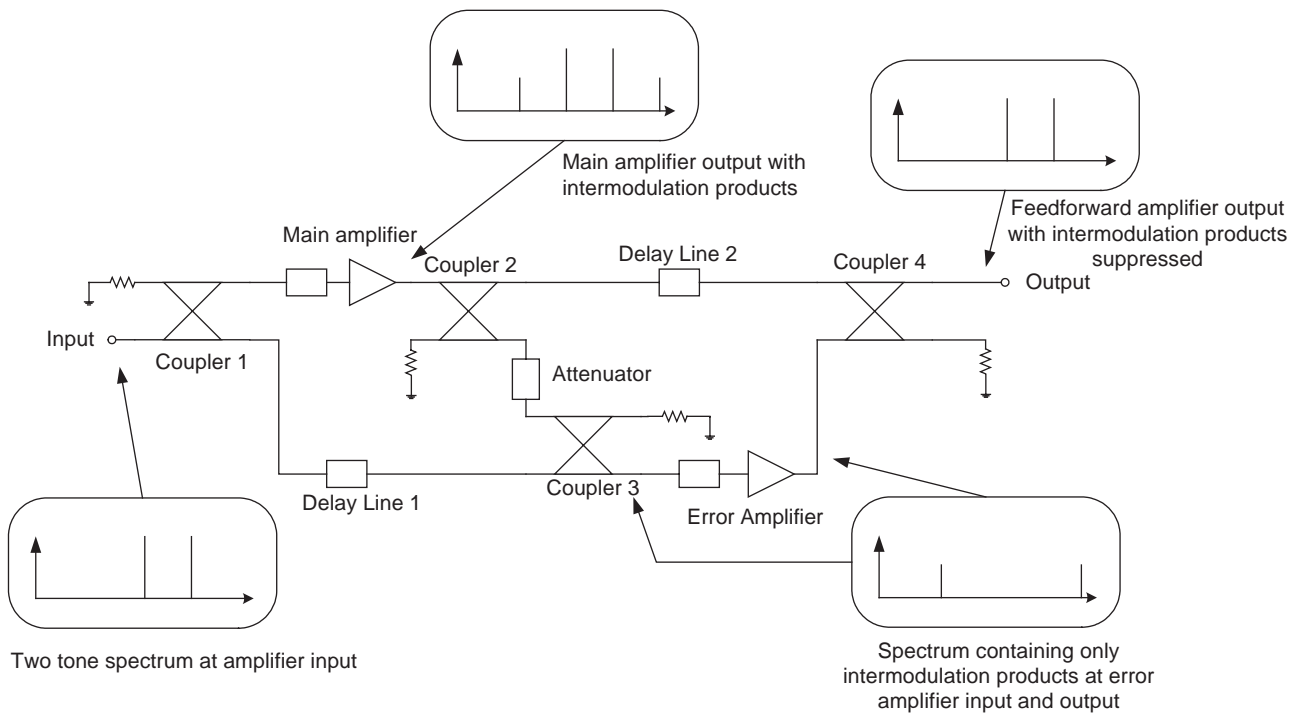


Figure 1. Basic configuration for a feedforward amplifier, including indicative spectra for the case of a two-tone input.

wanted output signal. If the first loop of the feedforward system is correctly balanced, the auxiliary amplifier only has to amplify the distortion. However, it has to amplify it linearly, and to a level somewhat higher than the distortion in the main branch of the system, because of the coupling ratio of coupler 4. For example, if the main amplifier produces intermodulation products 20 dB below the output carriers, and the output coupler has a 13 dB coupling ratio, the error signal at the output of the auxiliary amplifier must be 13 dB above the level of the main amplifier intermodulation products, or in other words, only 7 dB below the level of the wanted signal in the main branch. For perfect operation, the auxiliary amplifier must not introduce any significant level of further distortion. A class A amplifier, backed off well below saturation, is therefore normally used. In the example above, therefore, the auxiliary amplifier would need to have a DC power rating of the same order of magnitude as that of the main amplifier. Thus, to a crude approximation, the cancellation of distortion is achieved at the expense of doubling the DC power consumption or halving the efficiency.

2. The output coupler (coupler 4 in Fig. 1) degrades the overall efficiency because of its inherent ohmic and dielectric losses, and also because it couples a portion of the wanted output power into the matched termination on its fourth port. Clearly there is a tradeoff here between loose coupling in coupler 4 (say, > 20 dB), to limit the wastage of main amplifier power, and tight coupling (say, < 10 dB) to limit the

demands on the auxiliary amplifier. The ideal level of coupling, for maximum overall efficiency, therefore depends on the level of distortion occurring in the main amplifier that needs to be canceled.

3. The efficiency of the main amplifier strongly influences the overall efficiency. To limit the demands on the auxiliary amplifier, it is desirable not to operate the main amplifier too close to saturation; however, this reduces its efficiency.

The net result of these three factors influencing efficiency is that the overall efficiency of a typical feedforward amplifier is at best about 10%. However, to achieve comparable levels of intermodulation suppression without feedforward, by simply using a higher power linear amplifier and backing off its output power, could reduce the efficiency by several further orders of magnitude. Thus feedforward amplifiers can be a good choice where linear amplification is required with reasonable efficiency.

2.2. Bandwidth and the Degree of Distortion Suppression

In feedforward amplifiers, the main and auxiliary signals both propagate in the same forward direction through the system. This is in contrast to the situation in feedback amplifiers, where, self-evidently, the feedback signal propagates in the reverse direction. This leads to two advantages of feedforward systems as compared to feedback systems: (1) because there is no closed loop (assuming ideal coupler directivity), we do not have the danger inherent in feedback systems where the feedback becomes positive

at certain frequencies, leading to oscillation problems; and (2) by ensuring that the propagation delays are equal on both sides of each loop of the feedforward system, we can maintain signal cancellation in the first loop and suppression cancellation in the second, over a broad frequency range.

In practice, the accuracy of the two cancellation processes depends on the bandwidth over which the designer attempts to achieve them. Near-perfect cancellation, leading to extremely low intermodulation levels, is possible in a very narrowband design. In more realistic scenarios, there is a tradeoff between the bandwidth and the degree of suppression achievable. This is made more difficult by the fact that the delays through the active and passive components of the system are not frequency-independent.

The practical tradeoff between bandwidth and suppression level depends on the complexity of the balancing and adaptation circuits used; there is no exact rule to relate the parameters. However, the following examples give an idea of what is achievable. A feedforward amplifier operating over greater than an octave bandwidth was reported by Steel et al. [3], with an implied suppression of 14 dB. A feedforward bandwidth of the order of 8% was reported by Konstantinou et al. [4], with intermodulation product suppression of around 20 dB. A review article by Raab et al. [5] quotes 25–30 dB as the practical upper limit for manufactured equipment.

2.3. Size and Complexity

The addition of an auxiliary amplifier and the associated couplers, attenuators, and phase shift networks clearly adds to the overall size and complexity of the amplifier subsystem. Achieving a sufficiently accurate balance over the full bandwidth requires fine adjustment of phase and amplitude. Fine tuning in production can be achieved by means of mechanically trimmed variable attenuators and phase shifters, or by electronically controlled components such as vector modulators. Where electronic adjustment is incorporated, it is possible to introduce electronic control to compensate for drift with time and temperature. Feed-

forward amplifiers reported to date have been hybrid systems, too complex to allow monolithic integration, given the need for fine adjustment. Mechanical and thermal issues and the establishment of tuning procedures are crucial in the design of a complete feedforward amplifier for a production environment. In many circumstances, it is also necessary to devise control and adaptation algorithms to maintain optimum performance, compensating for parameter drifts that occur with aging, temperature, or variations in signal-level statistics.

3. DETAILED DESIGN CONSIDERATIONS

In this section, design equations for the basic feedforward system are established, using a revised and expanded version of the analysis given by Potheary [6], leading to phase and amplitude margins for accurate cancellation. Further feedforward amplifier parameters, such as the overall input and output match, noise figure, and efficiency are also analyzed.

3.1. Basic Signal Flow Analysis

In the generic form of the feedforward amplifier shown in Fig. 2, the lowercase symbols indicate the following complex voltage transfer coefficients:

- c_1 through c_4 are coupling coefficients of the couplers.
- a_1 through a_4 are coupler losses, that is, the transfer coefficients from the input port to the direct output port of each coupler.
- i_1 through i_4 are the isolation coefficients of the four couplers, that is, the transfer coefficients from the input to the nominally isolated port.
- l_1 and l_3 are the transfer coefficients of the two delay lines.
- l_2 is the attenuation of the attenuator mounted between couplers 2 and 3.
- g_m and g_e are the complex gains of the main and error amplifier, respectively.

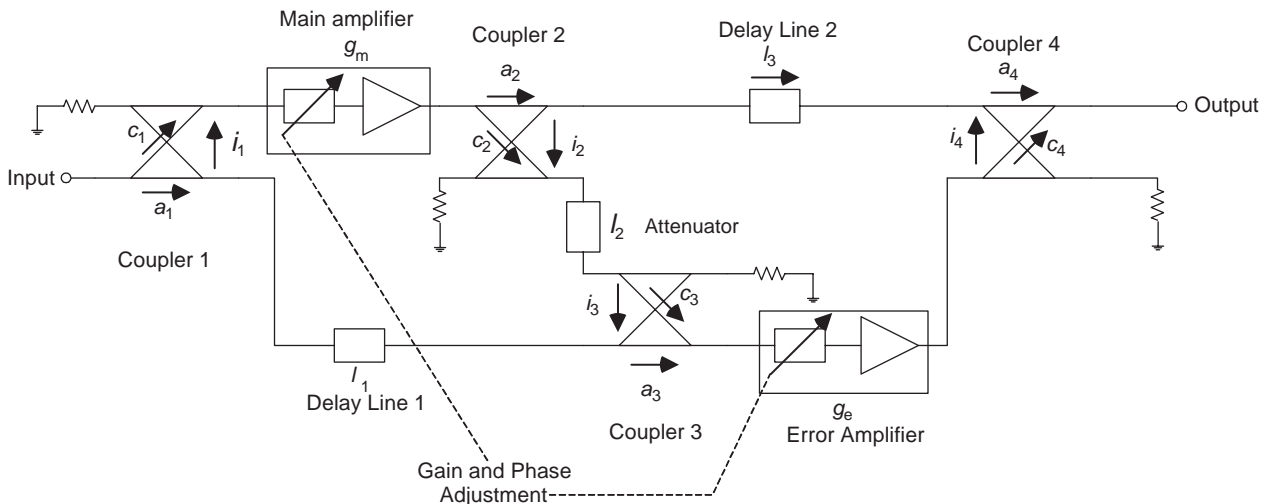


Figure 2. Feedforward amplifier annotated for signal flow analysis.

Note that although the transfer coefficients are indicated using arrows showing the main signal flow direction, the passive components are all reciprocal, and at some points in the analysis it is necessary to use the same transfer coefficients for a signal in the opposite direction. The same symbols in uppercase are used later to indicate the corresponding quantities expressed in decibels.

It is assumed that both amplifiers have adjustable gain and phase to facilitate balancing of the loops. In practice, this adjustability would be built into the early amplifier stages, rather than the output stages and so would be achieved without significantly affecting the output power ratings or DC power consumption.

It is also assumed that the individual passive components are well matched to the system impedance (typically $50\ \Omega$), so that the complications of multiple reflections can be ignored.

The input voltage wave amplitude is V_{in} . The distortion and noise in the main amplifier are represented by the addition of a voltage V_d to the amplified input. Thus the total output of the main amplifier, at the input to coupler 2, is given by

$$V_{out_main} = g_m c_1 V_{in} + V_d$$

The resulting voltage at the input to the error amplifier is given by

$$\begin{aligned} V_{in_error} &= (g_m c_1 V_{in} + V_d) c_2 l_2 c_3 + a_1 l_1 a_3 V_{in} \\ &= (g_m c_1 c_2 l_2 c_3 + a_1 l_1 a_3) V_{in} + c_2 l_2 c_3 V_d \end{aligned} \quad (1)$$

The condition for balancing the first loop is that the input to the error amplifier should depend only on the distortion voltage V_d . The condition is therefore found by setting the coefficient of V_{in} in (1) to zero:

$$g_m c_1 c_2 l_2 c_3 + a_1 l_1 a_3 = 0 \quad (2)$$

The output from coupler 4 (i.e., the output of the whole feedforward amplifier) is given by

$$\begin{aligned} V_{out} &= V_{out_main} a_2 l_3 a_4 + g_e c_4 V_{in_error} \\ &= a_2 l_3 a_4 (g_m c_1 V_{in} + V_d) \\ &\quad + g_e c_4 ((g_m c_1 c_2 l_2 c_3 + a_1 l_1 a_3) V_{in} + c_2 l_2 c_3 V_d) \end{aligned}$$

If the first loop matching condition (2) is met, then this reduces to

$$V_{out} = a_2 l_3 a_4 g_m c_1 V_{in} + (g_e c_4 c_2 l_2 c_3 + a_2 l_3 a_4) V_d \quad (3)$$

Balancing of the second loop is achieved when the coefficient of V_d in this equation is zero, that is, when

$$g_e c_4 c_2 l_2 c_3 + a_2 l_3 a_4 = 0 \quad (4)$$

Then, substituting (4) into (3), we can express the gain of the whole feedforward amplifier as

$$g_{ff} = \frac{V_{out}}{V_{in}} = g_m c_1 a_2 l_3 a_4 \quad (5)$$

If we represent the transfer coefficients in decibels instead of in complex amplitude format, using the corresponding upper case symbols, then

$$G_{ff} = G_m + C_1 + A_2 + L_3 + A_4 \quad (6)$$

As expected, the overall gain is the gain of the main amplifier reduced by the losses of the passive components in the main signal path.

3.2. First-Loop Balance

Balancing the first loop is necessary to minimize the load on the error amplifier. Any distortion resulting from overloading the error amplifier with residual carrier power adds to the overall distortion of the feedforward amplifier—there is no mechanism to cancel it out. The amplified residual carrier signal reaching coupler 4 through the error amplifier would also alter the overall gain of the feedforward amplifier. This could be an increase or a decrease depending on the phase of the residual signal. The balance conditions for the first loop need to be achieved over a frequency range that encompasses the input signal spectrum.

3.3. Second-Loop Balance

Balancing the second loop is necessary to ensure deep cancellation of distortion. The bandwidth over which balance must be achieved is normally greater than that required for the first loop because distortion products (e.g., intermodulation products) are likely to fall outside the range of the wanted signal.

3.4. Phase and Amplitude Matching Limits

Considering further the balance condition for the second loop, we can rewrite (4) as

$$1 - x = 0, \quad \text{where } x = \frac{-c_2 l_2 c_3 g_e c_4}{a_2 l_3 a_4} \quad (7)$$

where x is a complex number, equal to unity for perfect balance and equal to zero if the second-loop correction is not applied. The squared magnitude of the distortion suppression ratio is thus $|s|^2 = |1 - x|^2$.

Analyzing this in terms of the magnitude and phase imbalance, we obtain

$$\begin{aligned} |s|^2 &= |1 - x|^2 = |1 - |x| \cos \theta - j|x| \sin \theta|^2 \\ &= (1 - |x| \cos \theta)^2 + |x|^2 \sin^2 \theta \\ &= 1 - 2|x| \cos \theta + |x|^2 \end{aligned} \quad (8)$$

where θ is the phase imbalance and $20 \log_{10} |x|$ is the amplitude imbalance in decibels.

Figure 3 shows plots of the loop suppression in decibels versus phase imbalance, for varying levels of amplitude imbalance. It shows that there is some limited scope for trading off phase error against amplitude error, but for high levels of suppression, very good phase and amplitude accuracy are both required. For example, 30 dB suppression can be achieved if the phase balance is better than 1.2° and the amplitude balance is better than 0.2 dB. To illustrate the fine adjustment required, in physical layout terms this 1.2° phase balance corresponds to a pathlength balance between the two sides of the loop of better than $1/f\sqrt{\epsilon_{\text{eff}}}$ mm, where f is the frequency in gigahertz and ϵ_{eff} is the effective dielectric constant of the circuit medium.

3.5. Noise Figure

The noise figure of a feedforward amplifier is dominated by the error amplifier path. If the loops are properly balanced, the noise generated in the main amplifier (being uncorrelated with the input signal) is canceled at the output of the fourth coupler, in just the same way as the distortion. Thus, with reference to Fig. 2, the total noise figure f_{total} is given by

$$f_{\text{total}} = \frac{f_e}{|a_1 l_1 a_3|^2}$$

where f_e is the noise figure of the error amplifier. Alternatively, expressing all quantities in decibels, we obtain

$$F_{\text{total}} = F_e - A_1 - L_1 - A_3 \tag{9}$$

Since A_1 , L_1 , and A_3 are all negative, the total noise figure is clearly somewhat higher than that of the error amplifier. L_1 may be regarded as a parasitic loss and should be fairly small (of the order of a few tenths of a decibel). A_3 can also be made small in most cases because other degrees of freedom are available to balance the loops. So the main design choice affecting the noise figure is the input coupler loss A_1 . In a feedforward amplifier design in which the noise figure must be kept to a minimum, it is therefore necessary to direct most of the input power toward the linear branch of the first loop by making a_1 close to unity (i.e., A_1 close to 0 dB). Consequently, as power is conserved

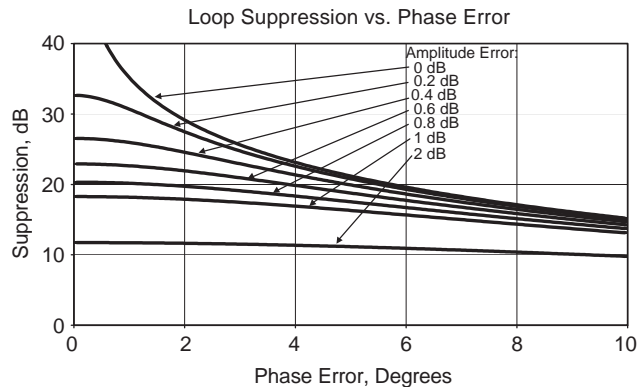


Figure 3. Loop suppression versus phase error.

in the input coupler, c_1 is small, and the gain of the main amplifier must be increased to compensate for this input attenuation. This is rarely a problem because small-signal gain is relatively cheap in terms of components and DC power.

3.6. Return Losses

The input and output return losses of the feedforward amplifier are affected by the multiple signal paths.

3.6.1. Input Return Loss. Considering first the input port, with reference to Fig. 2, the reflected voltage wave is made up of the vector combination of reflections from couplers 1 and 3, the two amplifiers, and the first delay line. There is also a potentially significant contribution from the main amplifier output, fed back to the input via coupler 2 and the isolated path through coupler 3. It is assumed that the reverse isolations (output to input) through the amplifiers and the isolation factors of the couplers are sufficiently high to eliminate any significant contributions to the input return loss from all other possible signal paths.

Assuming further that the individual passive components have negligible reflection coefficients, we can write the input reflection coefficient as follows:

$$\begin{aligned} \Gamma_{\text{in}} &= c_1^2 \Gamma_{\text{in_main}} + a_1^2 l_1^2 a_3^2 \Gamma_{\text{in_error}} \\ &\quad + c_1 g_m c_2 l_2 c_3 \Gamma_{\text{in_error}} a_3 l_1 a_1 \\ &\quad + c_1 g_m c_2 l_2 i_3 l_1 a_1 \\ &= c_1^2 \Gamma_{\text{in_main}} \\ &\quad + a_1 l_1 a_3 (a_1 l_1 a_3 + c_1 g_m c_2 l_2 c_3) \Gamma_{\text{in_error}} \\ &\quad + c_1 g_m c_2 l_2 i_3 l_1 a_1 \end{aligned} \tag{10}$$

If the first-loop balance condition (2) is met, the coefficient of $\Gamma_{\text{in_error}}$ in (10) is zero, and the equation can be simplified to

$$\Gamma_{\text{in}} = c_1^2 \Gamma_{\text{in_main}} - \frac{a_1^2 l_1^2 a_3 i_3}{c_3} \tag{11}$$

The first contribution will be small if the input coupling ratio is made low, as also required for a low-noise figure (see Section 3.5). The second contribution in (11) can be minimized by designing coupler 3 to have a high directivity factor, $d_3 = c_3/i_3$.

3.6.2. Output Return Loss. Considering now a signal injected into the output port of the feedforward amplifier, and making corresponding assumptions again about the reverse isolation factors of the amplifiers and the reflection coefficients of the passive components, we can arrive at the following equation for the output reflection

coefficient:

$$\begin{aligned}
 \Gamma_{\text{out}} &= c_4^2 \Gamma_{\text{out_error}} + a_4^2 l_3^2 a_2^2 \Gamma_{\text{out_main}} \\
 &\quad + a_4 l_3 a_2 \Gamma_{\text{out_main}} c_2 l_2 c_3 g_e c_4 \\
 &\quad + a_4 l_3 i_2 l_2 c_3 g_3 a_4 \\
 &= c_4^2 \Gamma_{\text{out_error}} \\
 &\quad + a_4 l_3 a_2 (a_4 l_3 a_2 + c_2 l_2 c_3 g_e c_4) \Gamma_{\text{out_main}} \\
 &\quad + a_4 l_3 i_2 l_2 c_3 g_3 a_4
 \end{aligned} \tag{12}$$

If the second-loop balancing condition (4) is met, the coefficient of $\Gamma_{\text{out_main}}$ is zero. This is a result of the fact that the second loop fulfills its function of canceling any output signals not originating from the input. The signal reflected by the output of the main amplifier is canceled just as noise and distortion are. Thus Eq. (12) can be rearranged to give

$$\Gamma_{\text{out}} = c_4^2 \Gamma_{\text{out_error}} + \frac{a_4^2 l_3^2 a_2 i_2}{c_2} \tag{13}$$

c_4 is typically small, to avoid wasting main amplifier power (but not so small as to overstretch the error amplifier), so the second term, involving the directivity of coupler 2, namely, $d_2 = c_2/i_2$, could be the dominating contribution to the output return loss.

3.7. Stability

Although feedforward is generally regarded as an inherently stable amplifier configuration, it does contain closed signal loops that need to be analyzed carefully to check for possible instabilities. As in the case of the input and output return losses, a key consideration here is again the directivity of the couplers.

Considering the first loop first, we can express a loop gain factor g_1 as

$$g_1 = i_1 g_m c_2 l_2 i_3 l_1 \tag{14}$$

If the first loop balance condition (2) is met, this can be written as:

$$g_1 = -\frac{a_1 l_1^2 a_3}{d_1 d_3} \tag{15}$$

Since $|d| \gg 1$ for a well-designed directional coupler, and since all the parameters in the numerator have magnitudes less than unity, Eq. (15) suggests that stability is unlikely to be a problem, since $|g_1| < 1$. However, care must be taken if the bandwidth of the main amplifier is significantly broader than the bandwidths of the couplers, since their isolation may degrade out of band, leading to an unstable condition where Eq. (14) gives $|g_1| > 1$, at some frequency outside the intended frequency range of the feedforward amplifier.

Similarly, considering the second loop, we can express a loop gain factor g_2 as follows:

$$g_2 = g_e i_4 l_3 i_2 l_2 c_3 \tag{16}$$

Applying the second-loop balance condition (4) allows this to be rewritten as

$$g_2 = -\frac{a_2 l_3^2 a_4}{d_2 d_4} \tag{17}$$

As in the case of the first loop, good directivity in the couplers ensures stability over the intended operating range, but if the error amplifier has a bandwidth broader than those of the couplers or than the intended operating frequency range of the feedforward amplifier, it is advisable to check that (16) does not lead to $|g_2| > 1$ at any frequency.

3.8. Efficiency

The overall efficiency of a feedforward amplifier (not including power consumption by power conditioning, control circuits and cooling systems) is a function of the efficiencies of both the main and error amplifiers, as well as the losses in the output circuit.

If the output power of the main amplifier is P_M , then the output from the feedforward amplifier is $P_{\text{OUT}} = |a_2|^2 |l_3|^2 |a_4|^2 P_M$. If the efficiencies of the main and error amplifiers are N_M and N_E , then the total DC power consumption is $P_{\text{DC_TOTAL}} = P_M/N_M + P_E/N_E$, where P_E is the power output of the error amplifier.

Thus the overall efficiency can be written as follows:

$$\begin{aligned}
 N_{\text{TOTAL}} &= \frac{P_{\text{OUT}}}{P_{\text{DC_TOTAL}}} \\
 &= \frac{|a_2|^2 |l_3|^2 |a_4|^2 P_M}{P_M/N_M + P_E/N_E} \\
 &= \frac{|a_2|^2 |l_3|^2 |a_4|^2 N_M}{1 + P_E N_M / P_M N_E}
 \end{aligned} \tag{18}$$

This shows that in the limiting case where the power demands on the error amplifier are very small compared to those on the main amplifier, the overall efficiency approaches that of the main amplifier, but reduced by the losses of the output couplers and delay lines. In the more typical situation where the powers are comparable, the overall efficiency is reduced by the presence of the error amplifier. Typically, the error amplifier is likely to have an efficiency lower than that of the main amplifier because it needs to be highly linear to avoid generating additional uncompensated distortion, and it may also have been designed with an emphasis on noise figure rather than efficiency.

Figure 4 shows a set of curves indicating the efficiency reduction factor, $1/(1 + P_E N_M / P_M N_E)$, as a function of P_E/P_M for typical values of N_E and N_M . They show, as expected, that the efficiency is halved if $P_E = P_M$ and $N_E = N_M$.

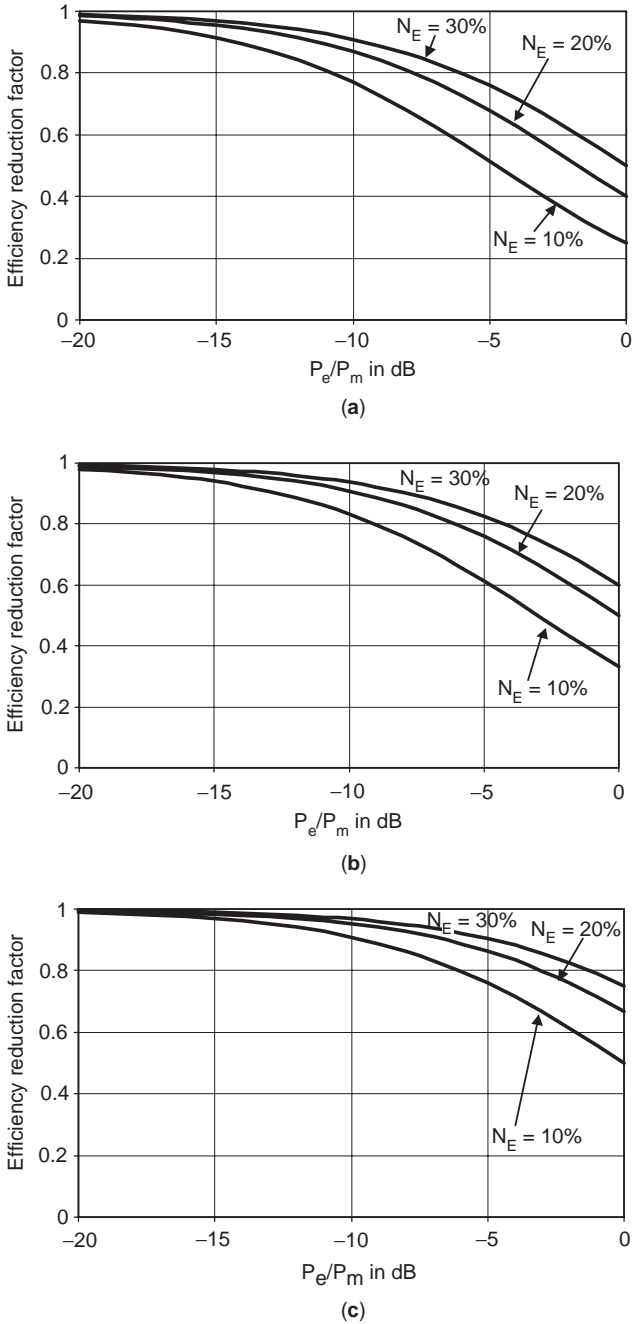


Figure 4. Feedforward efficiency reduction with $N_M = 30\%$ (a), 20% (b), and 10% (c).

3.9. Bandwidth

As discussed earlier, the main limitation on the bandwidth of a feedforward amplifier is usually the frequency range over which the rigorous phase and amplitude matching conditions can be met.

Considering Figs. 2 and 3 again, the problem becomes one of meeting amplitude and phase matching limits required for the desired degree of suppression over the full bandwidth. The two paths from the main amplifier output to the feedforward output have transfer functions t_a and t_b , where $t_a = a_2 l_3 a_4$ and $t_b = c_2 l_2 c_3 g_e c_4$.

Typically, the main path characterized by t_a has a relatively small variation of amplitude with frequency and a phase that varies linearly with frequency, consistent with a constant delay. Some amplitude variation and deviation from constant delay may occur if the couplers are working near the edge of their frequency ranges. The phase of transfer function t_a can thus be expected to vary with frequency as follows:

$$\text{Arg}(t_a) = \phi_a - \tau_d(\omega - \omega_0) \tag{19}$$

where τ_d is the time delay at center frequency ω_0 .

The path through the error amplifier, characterized by transfer function t_b , is likely to have more complex amplitude and phase variations with frequency. The phase variation is typically characterized by a polynomial, of the form

$$\text{Arg}(t_b) = \phi_b - \tau_g(\omega - \omega_0) + p(\omega - \omega_0)^2 + R(\omega) \tag{20}$$

where τ_g is the group delay at center frequency ω_0 , p is a parabolic phase coefficient, arising mainly from the band-pass response of the error amplifier, and $R(\omega)$ is a residual phase ripple function, caused by higher-order transfer function terms and multiple reflections within the error amplifier and associated components.

The second-loop balance equation requires that

$$\text{Arg}(t_a) - \text{Arg}(t_b) = \pm \pi$$

From (19) and (20), it is clear that this can be satisfied by making $\phi_a - \phi_b = \pm \pi$ and $\tau_d = \tau_g$, as long as the amplifier bandwidth is large enough to render the influence of the parabolic and ripple components negligible. Thus, to achieve broadband feedforward cancellation, it is necessary to have at least 2 degrees of freedom in the adjustable parameters of the second loop, so that both the phase offset and the delay can be equalized. It may be necessary to arrange for cancellation of quadratic and higher terms also, necessitating the inclusion of carefully designed all-pass filter networks. However, if only narrowband operation is required, it is sufficient to have just one adjustable phase parameter in each loop. Similar considerations apply to achieving amplitude balance.

In a more realistic design scenario, it is likely that a CAD model rather than an analytical equation would be used to characterize the amplifier and the associated passive components. A procedure such as that reported by Konstantinou et al. [7] can then be used. First, the loop 1 balance is optimized by injecting a small signal into the input of coupler 1 and adjusting the variable elements to achieve minimum power at the input to the error amplifier, over the required range of frequency and input power. The reference path is then broken by removing the delay line and replacing it with two matched and isolated terminations. The carrier signal should then appear at the input to the error amplifier. If the second loop is correctly adjusted, this will cancel the carrier signal at the output of coupler 4. Thus the second loop can be optimized by adjusting the variable elements for minimum output from

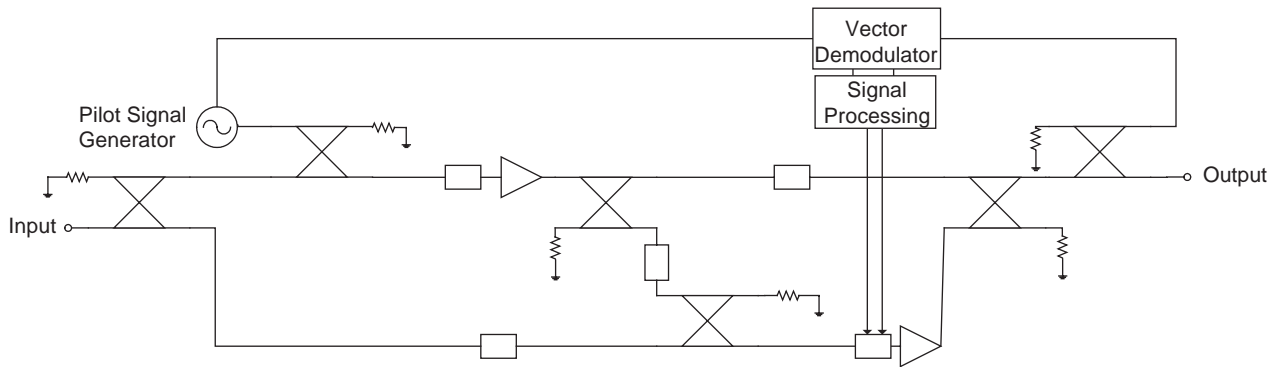


Figure 5. Feedforward amplifier with pilot signal injection for loop 2 control.

coupler 4, while the input signal varies over the full frequency range. Then, after loop 1 is reestablished, a nonlinear measurement or simulation, such as a two-tone test, can be performed to ensure that adequate cancellation occurs.

An alternative to the technique of opening the first loop while optimizing the second would be to inject a pilot signal at the input to the main amplifier, as illustrated in Fig. 5 [6]. The first loop is optimized by ensuring that the ratio of the input signal to the pilot signal at the input to the error amplifier is minimized. The second loop is optimized by ensuring that the level of the pilot signal seen at the feedforward amplifier output is minimized. This concept forms one basis for automatic control of a feedforward loop, to compensate for changes in the amplifier performance with temperature, aging, and varying signal statistics.

4. ADVANCED TECHNIQUES AND CHALLENGES

This section briefly reviews some advanced techniques in recent and current (as of 2004) research on feedforward linearisation.

4.1. Dual-Loop Feedforward

Since a complete feedforward amplifier is itself an amplifier in its own right, it is possible to incorporate the whole thing, recursively, inside an outer feedforward loop, as

shown in Fig. 6. The outer loop can be used to compensate for the residual distortion left by the inner loop and for any distortion introduced by the first error amplifier, leading to even lower distortion levels but increasing the tuning complexity even further.

4.2. Nonlinear Phase Equalizers for Improved Broadband Suppression

Hau et al. [8] demonstrated that by the use of nonlinear phase equalizers formed from allpass networks, the IM3 cancellation of a feedforward amplifier operating over the full 1.7–1.9-GHz band could be improved from 15 to 21 dB.

4.3. Feedforward Adaptation and Control

Cavers [9] established a theoretical basis for the adaptation of a feedforward system, showing that different considerations apply in the two loops. In the first loop (the signal cancellation loop) adaptation can be achieved by monitoring the error signal (at the input to the error amplifier). One possible method is to seek minimum power in this signal, but the favored method seeks zero correlation between the error signal and the input modulation, leading to a gradient-based adaptation algorithm that does not require pilot signals or other deliberate periodic perturbations to ensure that the optimum setting is maintained. Adaptation times of the order of 1–10 ms can be achieved in this way. In the second loop (the error correction loop) the high level of the wanted signal

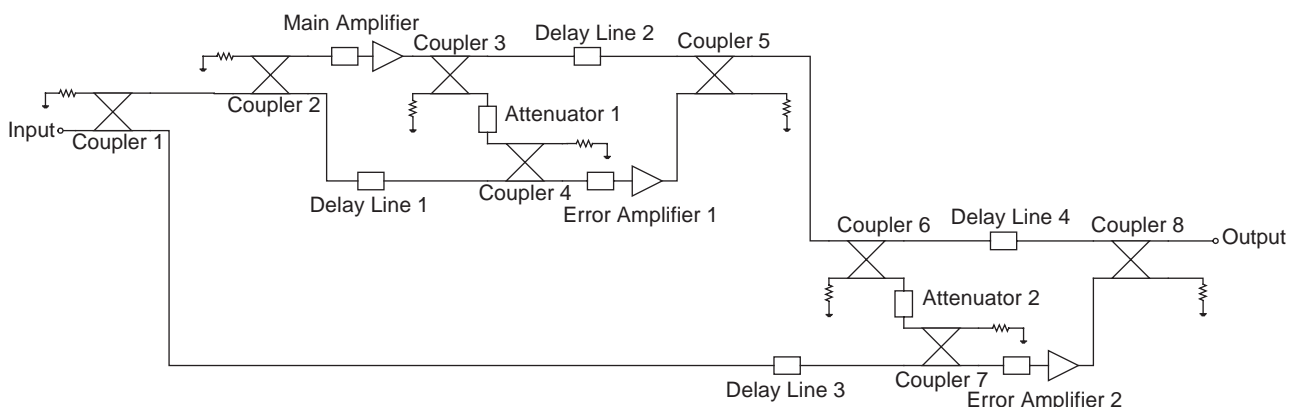


Figure 6. A dual-loop feedforward amplifier.

relative to the error necessitates much longer integration times, leading to much slower adaptation. This problem can be overcome, and the accuracy improved, by using a carrier suppression filter before performing the gradient calculation.

Chen et al. [10] proposed an alternative fast adaptive algorithm to track the linearizer control parameters, separating the rapidly varying but known factors (i.e., the signal statistics) from the slowly varying environmental factors affecting the power amplifier model, resulting in swift and accurate convergence.

Echeverría et al. [11] demonstrated that very high levels of intermodulation suppression, over 60 dB, could be achieved by tuning the control loops manually for individual 10 MHz subbands, over a total bandwidth of 19 MHz (2.01–2.205 GHz).

4.4. Hybrid Feedforward Amplifiers

It is possible to combine feedforward linearization with other linearization methods for improved overall results. For example, Horiguchi et al. [12] demonstrated a high-power 2.12 GHz feedforward power amplifier in which the overall operating efficiency was improved by 1% by the addition of a simple predistortion linearizer to the input of the main amplifier.

Another more radical hybrid feedforward amplifier concept has been proposed by Randall et al. [13], in which part of the first loop is replaced by a DSP implementation. The main and reference signals are both generated by DSP before upconversion to the carrier frequency. The second loop would operate conventionally. The advantage of DSP implementation is that phase and amplitude equalization of both the main and reference signals can be carried out and adapted as required in DSP software, rather than in RF analog components, allowing more accurate cancellation.

4.5. MMIC Integration

Integrating the whole feedforward amplifier onto a single MMIC is an attractive proposition from the point of view of miniaturization and repeatability at higher microwave frequencies or even millimeter-wave frequencies. Achieving such integration is, however, a major research challenge, because of the difficulty of creating the necessary high-isolation couplers, low-loss delay lines, and phase shifters on a MMIC, along with high linearity, high efficiency, and accurately modeled amplifiers. Parkinson and Paul [14] have carried out initial studies of the possibility of using a distributed amplifier structure as an active coupler within a MMIC feedforward amplifier, as a starting point for full MMIC integration.

BIBLIOGRAPHY

1. H. S. Black, *Translating System*, U.S. Patent 1,686,792 (1928).
2. H. Seidel, A microwave feedforward experiment, *Bell Syst. Tech. J.* **50**:2879–2916 (1971).
3. V. Steel, D. Scott, and S. Ludvik, A 6–18 GHz high dynamic range MMIC amplifier using a feedforward technique, *IEEE MTT-S Microwave Symp. Digest*, 1990, Vol. 2, pp. 911–914.
4. K. Konstantinou and D. K. Paul, Analysis and design of broadband, high efficiency feedforward amplifiers, *IEEE MTT-S Microwave Symp. Digest*, 1996, Vol. 2, pp. 867–870.
5. F. H. Raab, P. Asbeck, S. Cripps, P. B. Kenington, Z. B. Popovic, N. Pothecary, J. Sevic, and N. O. Sokal, Power amplifiers and transmitters for RF and microwave, *IEEE Trans. Microwave Theory Tech.* **MTT-50**(3):814–826 (2002).
6. N. Pothecary, *Feedforward Linear Power Amplifiers*, Artech House, Norwood, MA, 1999.
7. K. Konstantinou, P. Gardner, and D. K. Paul, Optimisation method for feedforward linearisation of power amplifiers, *Electron. Lett.* **29**(18):1633–1635 (1993).
8. Y. K. Hau, V. Postoyalko, and J. R. Richardson, Design and characterization of a microwave feed-forward amplifier with improved wide-band distortion cancellation, *IEEE Microwave Theory Tech.* **MTT-49**(1):200–203 (2001).
9. J. K. Cavers, Adaptation behavior of a feedforward amplifier linearizer, *IEEE Trans. Veh. Technol.* **44**(1):31–40 (1995).
10. J. Chen, H. Tsai, and Y. Chen, Fast adaptive wide-band power amplifier feed-forward linearizer, *IEEE Vehicular Technology Conf.*, 1998, pp. 2167–2171.
11. A. Echeverría, L. Fan, S. Kanamaluru, and K. Chang, Frequency tunable feedforward amplifier for PCS applications, *Microwave Opt. Technol. Lett.* **23**(4):218–221 (1999).
12. K. Horiguchi, M. Nakayama, Y. Sakai, K. Totani, H. Senda, Y. Ikeda, and O. Ishida, A high efficiency feedforward amplifier with a series diode linearizer for cellular base stations, *IEEE MTT-S Microwave Symp. Digest*, 2001, pp. 797–800.
13. R. G. Randall, J. G. McRory, and R. H. Johnston, Broadband DSP based feedforward amplifier lineariser, *Electron. Lett.* **38**(23):1470–1471 (2002).
14. G. Parkinson and D. K. Paul, Non-reciprocal couplers using distributed amplifier topology, *Microwave Opt. Technol. Lett.* **38**(5):366–368 (2003).

FERRITE CIRCULATORS

E. K. N. YUNG
D. X. WANG
City University of Hong Kong
Kowloon, Hong Kong, P.R. China
R. S. CHEN
Nanjing University of Science
and Technology
Nanjing, P.R. China

1. INTRODUCTION

The circulator is one of the elementary building blocks in radiofrequency and microwave circuits. It is used extensively in making basic devices for communications and radar systems. The latter are often used in broadband and high-power rating systems at microwave and millimeter-wave frequencies. It is, however, seldom found in consumer products because some of its functions can be performed

relative to the error necessitates much longer integration times, leading to much slower adaptation. This problem can be overcome, and the accuracy improved, by using a carrier suppression filter before performing the gradient calculation.

Chen et al. [10] proposed an alternative fast adaptive algorithm to track the linearizer control parameters, separating the rapidly varying but known factors (i.e., the signal statistics) from the slowly varying environmental factors affecting the power amplifier model, resulting in swift and accurate convergence.

Echeverría et al. [11] demonstrated that very high levels of intermodulation suppression, over 60 dB, could be achieved by tuning the control loops manually for individual 10 MHz subbands, over a total bandwidth of 19 MHz (2.01–2.205 GHz).

4.4. Hybrid Feedforward Amplifiers

It is possible to combine feedforward linearization with other linearization methods for improved overall results. For example, Horiguchi et al. [12] demonstrated a high-power 2.12 GHz feedforward power amplifier in which the overall operating efficiency was improved by 1% by the addition of a simple predistortion linearizer to the input of the main amplifier.

Another more radical hybrid feedforward amplifier concept has been proposed by Randall et al. [13], in which part of the first loop is replaced by a DSP implementation. The main and reference signals are both generated by DSP before upconversion to the carrier frequency. The second loop would operate conventionally. The advantage of DSP implementation is that phase and amplitude equalization of both the main and reference signals can be carried out and adapted as required in DSP software, rather than in RF analog components, allowing more accurate cancellation.

4.5. MMIC Integration

Integrating the whole feedforward amplifier onto a single MMIC is an attractive proposition from the point of view of miniaturization and repeatability at higher microwave frequencies or even millimeter-wave frequencies. Achieving such integration is, however, a major research challenge, because of the difficulty of creating the necessary high-isolation couplers, low-loss delay lines, and phase shifters on a MMIC, along with high linearity, high efficiency, and accurately modeled amplifiers. Parkinson and Paul [14] have carried out initial studies of the possibility of using a distributed amplifier structure as an active coupler within a MMIC feedforward amplifier, as a starting point for full MMIC integration.

BIBLIOGRAPHY

1. H. S. Black, *Translating System*, U.S. Patent 1,686,792 (1928).
2. H. Seidel, A microwave feedforward experiment, *Bell Syst. Tech. J.* **50**:2879–2916 (1971).
3. V. Steel, D. Scott, and S. Ludvik, A 6–18 GHz high dynamic range MMIC amplifier using a feedforward technique, *IEEE MTT-S Microwave Symp. Digest*, 1990, Vol. 2, pp. 911–914.
4. K. Konstantinou and D. K. Paul, Analysis and design of broadband, high efficiency feedforward amplifiers, *IEEE MTT-S Microwave Symp. Digest*, 1996, Vol. 2, pp. 867–870.
5. F. H. Raab, P. Asbeck, S. Cripps, P. B. Kenington, Z. B. Popovic, N. Pothecary, J. Sevic, and N. O. Sokal, Power amplifiers and transmitters for RF and microwave, *IEEE Trans. Microwave Theory Tech.* **MTT-50**(3):814–826 (2002).
6. N. Pothecary, *Feedforward Linear Power Amplifiers*, Artech House, Norwood, MA, 1999.
7. K. Konstantinou, P. Gardner, and D. K. Paul, Optimisation method for feedforward linearisation of power amplifiers, *Electron. Lett.* **29**(18):1633–1635 (1993).
8. Y. K. Hau, V. Postoyalko, and J. R. Richardson, Design and characterization of a microwave feed-forward amplifier with improved wide-band distortion cancellation, *IEEE Microwave Theory Tech.* **MTT-49**(1):200–203 (2001).
9. J. K. Cavers, Adaptation behavior of a feedforward amplifier linearizer, *IEEE Trans. Veh. Technol.* **44**(1):31–40 (1995).
10. J. Chen, H. Tsai, and Y. Chen, Fast adaptive wide-band power amplifier feed-forward linearizer, *IEEE Vehicular Technology Conf.*, 1998, pp. 2167–2171.
11. A. Echeverría, L. Fan, S. Kanamaluru, and K. Chang, Frequency tunable feedforward amplifier for PCS applications, *Microwave Opt. Technol. Lett.* **23**(4):218–221 (1999).
12. K. Horiguchi, M. Nakayama, Y. Sakai, K. Totani, H. Senda, Y. Ikeda, and O. Ishida, A high efficiency feedforward amplifier with a series diode linearizer for cellular base stations, *IEEE MTT-S Microwave Symp. Digest*, 2001, pp. 797–800.
13. R. G. Randall, J. G. McRory, and R. H. Johnston, Broadband DSP based feedforward amplifier lineariser, *Electron. Lett.* **38**(23):1470–1471 (2002).
14. G. Parkinson and D. K. Paul, Non-reciprocal couplers using distributed amplifier topology, *Microwave Opt. Technol. Lett.* **38**(5):366–368 (2003).

FERRITE CIRCULATORS

E. K. N. YUNG
D. X. WANG
City University of Hong Kong
Kowloon, Hong Kong, P.R. China
R. S. CHEN
Nanjing University of Science
and Technology
Nanjing, P.R. China

1. INTRODUCTION

The circulator is one of the elementary building blocks in radiofrequency and microwave circuits. It is used extensively in making basic devices for communications and radar systems. The latter are often used in broadband and high-power rating systems at microwave and millimeter-wave frequencies. It is, however, seldom found in consumer products because some of its functions can be performed

by simpler and cheaper alternatives. However, interest in circulators has been revitalized with the emergence of mobile communications. As an increasing number of users are accustomed to the freedom provided by cellular phones, communication without the constraint of an attached wire is considered as natural as breathing air. In addressing the ever-increasing public demands, numerous wireless systems have been launched and more are coming. The most notable ones are wireless local area network, wireless local subscriber loops, and other high-bit-rate yet low-error-rate systems of data transmission. For these systems, the overlooked circulator enjoys a competitive edge as most active switches could not deliver the needed power rating and bandwidth at a reasonable price, especially those in the ultra-high-frequency band and beyond.

For engineering students, the circulator is perhaps the first multiport device covered in their foundation course on microwave engineering, and it might be the first nonreciprocal passive device encountered [1,2]. The importance of this three-port device in communication systems can be explained by its functionality. Simply put, waves entering one of the identical ports of a circulator, say, port 1, are totally transmitted to one of the output ports, port 2, with none to the remaining one, port 3. Similarly, those inputted to port 2 are passed on to port 3 without loss while port 1 is isolated. The cycle is completed as signals entering port 3 are outputted to port 1 only. Schematically, a circulator is shown in Fig. 1.

The scattering matrix of the clockwise circulator shown in Fig. 1 is

$$[S]_{\text{clockwise}} = \begin{bmatrix} 0 & 0 & 1 \\ 1 & 0 & 0 \\ 0 & 1 & 0 \end{bmatrix} \quad (1)$$

Depending on the physical layout of a circuit and one's point of view, a circulator can also be counter-clockwise

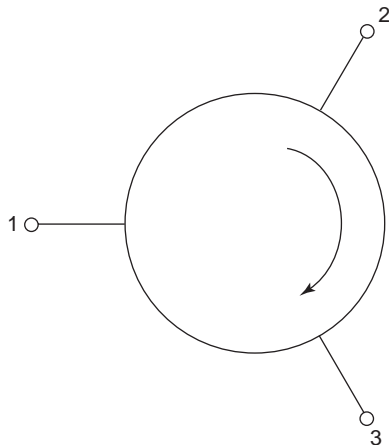


Figure 1. A schematic sketch of a circulator.

and the relevant scattering matrix is

$$[S]_{\text{counterclockwise}} = \begin{bmatrix} 0 & 1 & 0 \\ 0 & 0 & 1 \\ 1 & 0 & 0 \end{bmatrix} \quad (2)$$

Extension of a three-port circulator to an m -port one is possible, but it is skipped here because it introduces no new concepts, yet the algebra involved is so tedious that the logic flow of this introductory article could be derailed. Note that, the scattering matrices given in (1) and (2) are valid for lossless three-port circulators with perfectly matched inputs and outputs. Modifications of the theories and practices presented in this article to low-loss m -port ones with less than perfect matched input and output ports have been conducted in many pioneering studies [3,4]. Again, they are omitted here, and interested readers are referred to a comprehensive book [5].

The passive traffic control in circulators is facilitated by an anisotropic element. Isotropy or anisotropy is an intrinsic characteristic of all matters that finds its origin in their molecular structures and atomic dipole moments of electric or magnetic nature [6]. In general, these dipole moments are randomly oriented in the absence of an external excitation; therefore the material on the whole has a negligibly small net dipole moment. The scenario could change abruptly with the introduction of an applied static electric field as the electric dipole moments align themselves with the impressed force and a net electric dipole moment results. Similarly, a spontaneous magnetic dipole moment is obtained by a biasing magnetic field. The dipole alignment is dependent on the strength of the excitation until all dipoles are almost perfectly oriented. The alignment, in fact, depends on the molecular structure of the material, the ambient temperature, the initial settings, and other physical conditions. In general, the relationship between the dipole alignment and the applied field is nonlinear, and for some materials, it is anisotropic.

The principles of circulator operation, basic theories of anisotropy, wave propagation in anisotropic materials, and circulator applications will be briefly presented in Sections 2–4, followed by a general description of selected circulators in Section 5. The most popular ones, especially waveguide junction circulators, will be analyzed in depth in Section 6. A few concluding remarks will be presented in Section 7.

2. ANISOTROPY AND ANISOTROPIC MATERIALS

In theory, both electrical and magnetic materials can be used to produce anisotropic effects in a circulator. Magnetic anisotropy is, however, still used in practically all circulators over a half-century since its invention. Hence, the discussion in this section focuses on magnetic anisotropy. Nevertheless, the potential of using electrically anisotropic materials in circulators in the future cannot be dismissed. One of the major candidates for this is the uniaxial chiral material especially made for microwave frequencies. Although significant progress has been observed

in this area in recent years, the technologies at our disposal at this moment are far from satisfactory. Thus it has been decided not to further investigate the use of electrically anisotropic materials in circulators until more mature technologies are available.

As this is only an introductory article on circulators, we will not attempt to cover all circulators available on the market. For similar reasons, only theories of anisotropy directly relevant to the selected circulators discussed here will be presented.

2.1. Spinning Electron in Free Space

The angular momentum of an electron in an atom or an ion arises from two factors: its orbital motion around the atomic nucleus and its spin. Based on quantum mechanics, the total angular momentum of an electron in free space is given by

$$s = \frac{1}{g} \frac{h}{2\pi} \quad (3)$$

where $h = 6.626 \times 10^{-34}$ J/s is Planck's constant and g is Lande's factor. If the angular momentum of an electron is due solely to its orbital motion, then $g = 1$. At the other extreme, a $g = 2$ factor is used to signify a spin-only momentum. For most materials of interest in microwave systems, it can be shown that g ranges from 1.98 to 2.01; therefore $g = 2$ is a good approximation. Based on Bohr's model, the magnetic dipole moment of an electron is

$$m = \frac{e}{m_0} \frac{h}{4\pi} = 9.27 \times 10^{-24} \text{ A/m}^2 \quad (4)$$

where $e = 1.6 \times 10^{-19}$ C is the charge of an electron and $m_0 = 9.1 \times 10^{-31}$ kg is its mass.

Comparing (3) and (4), it is found that the ratio of the magnetic dipole moment of a spinning electron to its angular momentum is a constant, the so-called called gyro-magnetic ratio:

$$\gamma = \frac{m}{s} = \frac{e}{m_0} = 1.759 \times 10^{11} \text{ C/kg} \quad (5)$$

According to Hund's rule, electrons in a shell would spread out over the available states with spins in the same direction until the shell is half-filled, and all subsequent additions would have spins in the opposite direction. Thus, the magnetic dipole moment of an atom with a fully filled outermost shell such as found in the inert gases is zero. At the other extreme, the maximum dipole moment is obtained in a half-filled shell, and in the 10-state d shell it is 5.

Returning to the familiar Newtonian mechanics, the magnetostatic torque acting on the dipole moment due to an impressed static magnetic field \mathbf{H}_{DC} is

$$\mathbf{T} = \mu_0 \mathbf{m} \times \mathbf{H}_{DC} \quad (6)$$

As electrons are negatively charged, its angular momentum is opposite to its dipole moment:

$$\mathbf{m} = -\gamma \mathbf{s} \quad (7)$$

Since torque is equal to the rate of change of angular momentum, one arrives at

$$\frac{d\mathbf{s}}{dt} = \mathbf{T} = -\mu_0 \gamma \mathbf{s} \times \mathbf{H}_{DC} \quad (8)$$

The equation of motion for a spinning electron is obtained by substituting (7) into (8)

$$\frac{d\mathbf{m}}{dt} = -\mu_0 \gamma \mathbf{m} \times \mathbf{H}_{DC} \quad (9)$$

Without loss of generality, the study can be furthered with a \hat{z} -biased \mathbf{H}_{DC} . Thus, the components of the vector equation above are

$$\frac{dm_x}{dt} = -\mu_0 \gamma m_y H_{DC} \quad (10)$$

$$\frac{dm_y}{dt} = \mu_0 \gamma m_x H_{DC} \quad (11)$$

$$\frac{dm_z}{dt} = 0 \quad (12)$$

Differentiating (10) and (11) once more, two harmonic equations are derived

$$\frac{d^2 m_x}{dt^2} + \omega_0^2 m_x = 0 \quad (13)$$

$$\frac{d^2 m_y}{dt^2} + \omega_0^2 m_y = 0 \quad (14)$$

where ω_0 is the Larmor frequency of precession, given by

$$\omega_0 = \mu_0 \gamma H_{DC} \quad (15)$$

A solution to both (13) and (14) is

$$m_x = A \cos \omega_0 t \quad (16)$$

$$m_y = A \sin \omega_0 t \quad (17)$$

It is observed from (4) that the magnitude of \mathbf{m} is fixed; therefore one gets

$$m^2 = \left(\frac{\gamma h}{4\pi} \right)^2 = m_x^2 + m_y^2 + m_z^2 = A^2 + m_z^2 \quad (18)$$

In short, \mathbf{m} would precess around the \hat{z} axis with an angle θ :

$$\sin \theta = \frac{A}{m} \quad (19)$$

Moreover, the projection of \mathbf{m} on the x - y plane would trace a circular path with an angular frequency ω_0 as depicted in Fig. 2. For a standalone atom in free space, \mathbf{m} could precess indefinitely. However, for an atom in a crystal, the electron would experience numerous gravitational and

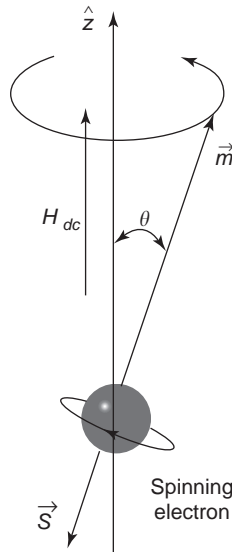


Figure 2. Angular momentum and magnetic dipole moment of a spinning electron.

electromagnetic forces. Altogether, these interactions would constitute a damping force that causes \mathbf{m} to spiral inward, and in due course, \mathbf{m} would align with the biasing field.

Even after the dipole alignment is completed, the magnetic flux density due to magnetization for most materials is very weak, compared with the biasing magnetic field. Hence, the relative permeability in paramagnetic materials is slightly greater than 1, while that of diamagnetic materials is marginally less than unity.

Here, it is worthwhile to comment on the units used in this article. Traditionally, studies of magnetism are conducted in CGS units with the magnetic field strength expressed in oersteds and the magnetization in gauss. The units are chosen such that the magnetic flux density B and the magnetic field strength H in free space would have equal numeric values. On the other hand, in line most engineering texts, formulas presented in this article will be derived in MKS units. Hence, utmost care must be taken in using some properties of magnetic materials quoted in CGS units. For easy reference, some of the most frequently used unit conversions are tabulated in Table 1.

2.1.1. Ferromagnetic and Ferrimagnetic Materials. In general, magnetization effects are very weak even for atoms with a half-filled outermost shell such as chromium and manganese. A different mechanism is needed to enhance the magnetization. It is found in some substances, called *ferromagnetic materials*. From a microscopic point

of view, ferrous metals are composed of tiny domains of linear dimensions of a few micrometers. It is proved in quantum mechanics that strong coupling forces exist between atoms in each domain such that all atomic dipole moments are kept in parallel even when there is no external field. As the dipole moments of these domains are randomly oriented, a demagnetized ferromagnetic material shows no magnetization effect, from a macroscopic perspective. Analogous to the ionic dipole moments in paramagnetic and diamagnetic materials, the magnetic dipole of every domain in ferrous metals reacts to an impressed field, except that the responses are much stronger. Consequently, the permeability of ferromagnetic materials is notably higher than its paramagnetic and diamagnetic counterparts, a factor of many orders. Again, the magnetization depends on the field strength until saturation. Probably as a result of some form of domain deformation during the magnetization processes, certain domain rotations are not reversible after the external bias is removed, and a residue magnetic effect results. This remanent magnetization plays a key role in subsequent magnetizations and contributes to the infamous hysteresis loop.

Significant magnetization can also be observed in the so-called antiferromagnetic materials. Even though the dipole moments in the latter class of materials align with the applied field equally fervently, their directions are either in line with or opposite to that of the excitation, and the end result is a complete cancellation of magnetization effects.

Another class of substances, termed *ferrimagnetic materials*, exhibits a behavior intermediate between ferromagnetism and antiferromagnetism. The pattern of dipole alignment in these materials is similar to that of antiferromagnetic ones except the number of magnetic dipoles in opposite polarities is different and their magnitudes are not equal. Hence, a partial cancellation of dipole moments is observed. As expected, magnetization of ferrimagnetic materials is considerably lower than that of ferrous metals. The maximum magnetic flux density in ferrimagnetic materials is seldom greater than 0.3 Wb/m^2 , approximately one-tenth that of ferromagnetic ones. However, a magnetization of this magnitude is significantly higher than that of nonmagnetic matters; therefore they are often used in picking up spurious waves in electromagnetic compatibility and electromagnetic interference control.

Ferrimagnetic materials can be found in nature in a variety of forms such as lodestones. They were first mentioned in history more than 4500 years ago when natural magnets played a decisive role in a major battle in China as a component in compasses. A nonnatural ferrimagnetic material was first produced by Hilpert in 1909 [7], and practical ones were developed shortly after

Table 1. Conversion between CGS and MKS Units

	Symbol	MKS Units	CGS Units
Magnetic flux	ψ	1 weber	10^8 maxwell
Magnetic flux density	B	1 tesla = 1 weber/meter ²	10^4 gauss
Magnetic field intensity	H	1 ampere-turn/meter	$4\pi \times 10^{-3}$ oersted
Magnetization	M	1 weber/meter ²	$2500/\pi$ gauss

World War II [8]. Synthetic ferrimagnetic materials are usually polycrystalline. For some applications, large crystals can be made, but they are seldom used as they are very expensive.

Humanmade (synthetic) ferrimagnetic materials are now called *ferrites* for easy reference. Over the years, numerous ferrites have been synthesized for assorted applications at different frequencies. Based on their crystal structures, these ferrites can be grouped into three categories, namely, spinels, garnets, and hexagonal ferrites.

Mineral spinels have a molecular formula of $(\text{MgAl}_2\text{O}_4)_8$. Over the years, many synthetic spinels have been developed and they share a structure similar to that of $(\text{MFe}_2\text{O}_3)_8$, where “M” represents divalent metal, including cobalt, aluminum, cadmium, copper, lithium, iron, magnesium, manganese, nickel, titanium, zinc, and their combinations. As metallic ions are smaller than oxygen ions, the crystal structure of spinels depends solely on the arrangement of oxygen ions, the face-centered cubic lattice [10] as shown in Fig. 3. Also shown in Fig. 3 are the sites where metallic ions can be found. It can be shown that a metallic ion in site A has four oxygen neighbors and thus is called *tetrahedral site*; site B is termed *octahedral* because it has six adjacent oxygen ions. In a unit crystal of 56 ions, there are only 8 tetrahedral and 16 octahedral metallic ions; therefore not all sites in the crystal lattices of 32 oxygen ions are filled. It is also found that the magnetic moments in tetrahedral and octahedral sites cancel one another; the remaining 8 octahedral ones give the ferrite crystal its net magnetic moment [11].

Common garnet or andradite has a molecular structure of $\text{Ca}_3\text{Fe}_2\text{Si}_3\text{O}_{12}$. The frequently used yttrium iron garnet (YIG) is obtained by replacing calcium by yttrium and silicone by iron. The net magnetic moment can be adjusted by substituting some iron ions by aluminum ones (YAG), or yttrium by a rare earth such as gadolinium, holmium, or dysprosium. For synthetic garnets, a unit crystal of 40 ions has a molecular formula of $(\text{Fe}_2\text{O}_3)_5 (\text{M}_2\text{O}_3)_3$; where “M” stands for rare earth. There exist three types of sites in the crystal structure for housing the metallic ions and all sites are filled.

Ferrites can be mass-produced as if they were ceramics, except the demands on purity of raw materials, uniformity in grain sizes, correctness in mix proportion, homogeneity of the suspension, precision in casting, timing and temperature control in firing, and other manufacturing pro-

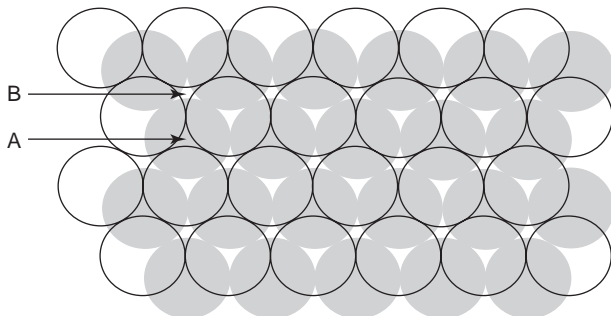


Figure 3. Tetrahedral (A) and octahedral (B) sites in the crystal structure of oxygen ions.

cesses are very stringent and the error margin is very slim. The raw materials include oxides, carbonates, nitrates, oxalates, and some metallic compounds. As the facilities used in making ferrites are very expensive and the exact procedures are usually company secrets, few laboratories can make them from scratch. It is, however, recommended that research centers be equipped with diamond wheels and other apparatuses for cutting and grinding raw ferrites into the desired shapes because the physical dimensions of ferrites have direct consequences on the performance of circulators, as are the smoothness and the cleanliness of their surfaces.

As ferrites are ceramiclike compounds, they are very hard, brittle, and low in thermal conductivity. Unlike ferromagnetic materials, ferrites have low electrical conductivities; thus, they are frequently used in electrical and electronic devices for a variety of purposes. However, the feature that makes ferrites indispensable in microwave circuit designs is anisotropy, not low conductivity. Of course, an in-depth study of anisotropy is beyond the scope of this article, but a brief outline of its origin is deemed appropriate for a better understanding the nature of wave circulations in magnetized ferrites.

2.1.2. Magnetization of Ferrites. The configuration of interest is a ferrite crystal under an internal magnetic field \mathbf{H}_{int} . The excitation exterior to a ferrite specimen is different from \mathbf{H}_{int} , and it will be treated later. For a sample with N unbalanced electron spins per unit volume, the total magnetization is

$$\mathbf{M}_{\text{DC}} = N\mathbf{m} \quad (20)$$

Similar to (9), the equation of motion is

$$\frac{d\mathbf{M}_{\text{DC}}}{dt} = -\mu_0\gamma\mathbf{M}_{\text{DC}} \times \mathbf{H}_{\text{int}} \quad (21)$$

As the damping force inside a ferrite crystal is much stronger than that acting on a standalone atom in free space, the magnetic dipole moments will align with the magnetic excitation readily. With an increase in \mathbf{H}_{int} , an increasing number of magnetic dipoles line up with the biasing field, and eventually the alignment process is completed and the magnetization is saturated as depicted in Fig. 4. The saturation magnetization \mathbf{M}_s is a physical property of ferrite, and typically it ranges within $4\pi M_s = 300\text{--}5000$ G. Unless mentioned otherwise, ferrites operate in the state of saturation magnetization because they are very lossy at lower levels of magnetization. Hence, the equation of motion in (21) could be rewritten as

$$\frac{d\mathbf{M}_s}{dt} = -\mu_0\gamma\mathbf{M}_s \times \mathbf{H}_{\text{int}} \quad (22)$$

Regardless of whether the magnetization is saturated, ferrite will be permanently magnetized after the magnetization process. The crystal structure of having dipole moments of opposite polarities in an alternating fashion may constitute a cementing force that keeps the alignment intact after the external bias is removed. In some

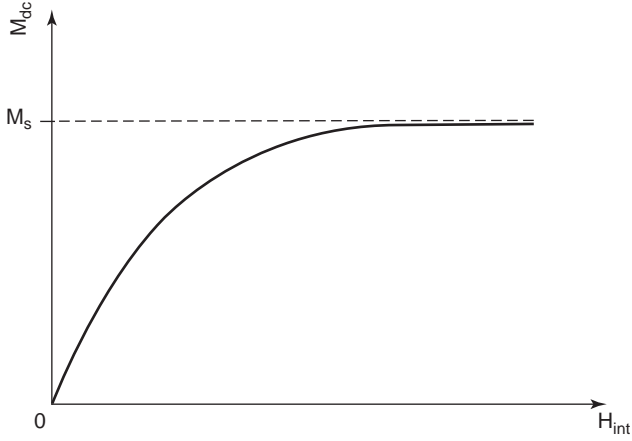


Figure 4. Magnetization of ferrites versus magnetic field intensity.

circulators, a premagnetized ferrite is adequate and external magnetization is not needed [32].

It is well known that atoms can pick up thermal energy from the surrounding environment and vibrate accordingly. Sometimes, the atomic vibration in ferrites could make the dipole alignment very difficult even at room temperature. As a rule of thumb, an increase in ambient temperature is accompanied by a decrease in saturation magnetization. At a sufficiently high temperature, called the Curie temperature T_c , the vibrational energy could overwhelm the electromagnetic energy, and the process of dipole alignment would break down as illustrated in Fig. 5.

3. WAVE PROPAGATION IN FERRITE

Our attention now turns to wave propagations in magnetized ferrites. Without loss of generality, a ferrite specimen is magnetized in the \hat{z} direction and is illuminated by an incident plane wave of arbitrary orientation and of amplitude H_{RF} . The total magnetic field and magnetization are

$$\mathbf{H} = \mathbf{H}_{int} + \mathbf{H}_{RF} = H_x \hat{x} + H_y \hat{y} + (H_{int} + H_z) \hat{z} \quad (23)$$

$$\mathbf{M} = \mathbf{M}_s + \mathbf{M}_{RF} = M_x \hat{x} + M_y \hat{y} + (M_s + M_z) \hat{z} \quad (24)$$

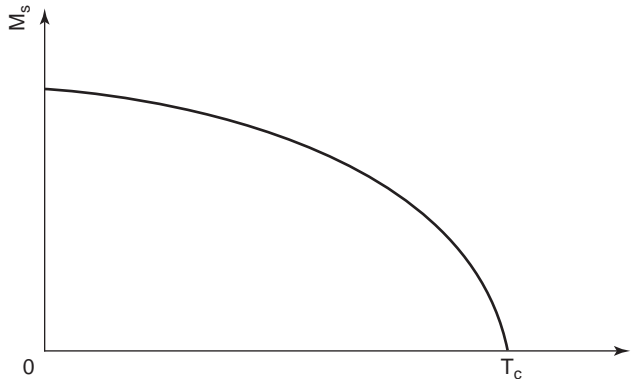


Figure 5. Magnetization of ferrites versus ambient temperature.

The corresponding equation of motion is

$$\begin{aligned} \frac{d\mathbf{M}}{dt} &= \frac{d\mathbf{M}_s}{dt} + \frac{d\mathbf{M}_{RF}}{dt} \\ &= \frac{d\mathbf{M}_{RF}}{dt} = -\mu_0 \gamma \mathbf{M} \times \mathbf{H}. \end{aligned} \quad (25)$$

In its components, the equation of motion is

$$\begin{aligned} \frac{dM_x}{dt} &= +\mu_0 \gamma M_y (H_{int} + H_z) \\ &\quad - \mu_0 \gamma H_y (M_s + M_z) \end{aligned} \quad (26)$$

$$\begin{aligned} \frac{dM_y}{dt} &= \mu_0 \gamma M_x (H_{int} + H_z) \\ &\quad - \mu_0 \gamma H_x (M_s + M_z) \end{aligned} \quad (27)$$

$$\frac{dM_z}{dt} = -\mu_0 \gamma M_x H_y + \mu_0 \gamma M_y H_x \quad (28)$$

Since $H_{RF} \ll H_{int}$, $M_x H_y$ and similar products can be ignored in accordance with the small signal approximations. As a result, the preceding equations can be simplified to

$$\begin{aligned} \frac{dM_x}{dt} &= -\mu_0 \gamma M_y H_{int} + \mu_0 \gamma M_s H_y \\ &= -\omega_0 M_y + \omega_m H_y \end{aligned} \quad (29)$$

$$\begin{aligned} \frac{dM_y}{dt} &= \mu_0 \gamma M_x H_{int} - \mu_0 \gamma M_s H_x \\ &= \omega_0 M_x - \omega_m H_x \end{aligned} \quad (30)$$

$$\frac{dM_z}{dt} = 0 \quad (31)$$

where ω_0 is the Larmor frequency of precession, and

$$\omega_m = \mu_0 \gamma M_s \quad (32)$$

Comparing (15) and (32), ω_m can be expressed as

$$\omega_m = \omega_0 \frac{M_s}{H_{int}} \quad (33)$$

Differentiating (29) and (30) once more, one gets

$$\frac{d^2 M_x}{dt^2} = -\omega_0^2 M_x + \omega_0 \omega_m H_x + \omega_m \frac{dH_y}{dt} \quad (34)$$

$$\frac{d^2 M_y}{dt^2} = -\omega_0^2 M_y + \omega_0 \omega_m H_y - \omega_m \frac{dH_x}{dt} \quad (35)$$

In a time-harmonic analysis, these equations can be simplified to

$$(\omega_0^2 - \omega^2) M_x = \omega_0 \omega_m H_x + j \omega \omega_m H_y \quad (36)$$

$$(\omega_0^2 - \omega^2) M_y = -j \omega \omega_m H_x + \omega_0 \omega_m H_y \quad (37)$$

Note that both M_x and M_y are dependent on H_x as well as H_y . In other words, a tensor is needed to characterize the relationship between magnetization \mathbf{M} and its driving force, the magnetic field intensity \mathbf{H} ; that is

$$\mathbf{M} = \bar{\bar{\chi}} \mathbf{H} = \begin{bmatrix} \chi_{xx} & \chi_{xy} & 0 \\ \chi_{yx} & \chi_{yy} & 0 \\ 0 & 0 & 0 \end{bmatrix} \mathbf{H} \quad (38)$$

The nonzero components of the susceptibility tensor $\bar{\bar{\chi}}$ are

$$\chi_{xx} = \chi_{yy} = \frac{\omega_0 \omega_m}{\omega_0^2 - \omega^2} \quad (39)$$

$$\chi_{xy} = -\chi_{yx} = \frac{j\omega \omega_m}{\omega_0^2 - \omega^2} \quad (40)$$

Consequently, the magnetic flux density \mathbf{B} must be modified to

$$\mathbf{B} = \mu_0(\mathbf{H} + \mathbf{M}) = \bar{\bar{\mu}} \mathbf{H}. \quad (41)$$

The z -bias Polder permeability tensor $\bar{\bar{\mu}}$ is given by [13]

$$\bar{\bar{\mu}} = \mu_0(\bar{\bar{I}} + \bar{\bar{\chi}}) = \begin{bmatrix} \mu & j\kappa & 0 \\ -j\kappa & \mu & 0 \\ 0 & 0 & \mu_0 \end{bmatrix} \quad (42)$$

where $\bar{\bar{I}}$ is an identity tensor.

The components of the permeability tensor are

$$\mu = \mu_0(1 + \chi_{xx}) = \mu_0 \left(1 + \frac{\omega \omega_m}{\omega_0^2 - \omega_m^2} \right) \quad (43)$$

$$\kappa = -j\mu_0 \chi_{xy} = \mu_0 \frac{\omega_0 \omega_m}{\omega_0^2 - \omega_m^2} \quad (44)$$

It is observed that an \hat{x} -directed or \hat{y} -directed \mathbf{H} would give rise to both \hat{x} and \hat{y} components of \mathbf{B} with a quadratic phase shift between them. A material having this type of properties is called *gyrotropic*.

If the biasing magnetic field is \hat{x} -directed, the corresponding gyrotropic permeability tensor is

$$\bar{\bar{\mu}} = \begin{bmatrix} \mu_0 & 0 & 0 \\ 0 & \mu & j\kappa \\ 0 & -j\kappa & \mu \end{bmatrix} \quad (45)$$

3.1. Forced Precession

If the incoming wave in the preceding section is a right-handed circularly polarized plane wave propagating in the z direction, $H_x = -jH_y = H_0^+$, the relevant magnetization can be determined by (36) and (37):

$$M_x = \frac{\omega_m H_0^+}{\omega_0^2 - \omega^2} (\omega_0 + \omega) = \frac{\omega_m H_0^+}{\omega_0 - \omega} \quad (46)$$

$$M_y = \frac{-j\omega_m H_0^+}{\omega_0^2 - \omega^2} (\omega + \omega_0) = \frac{-j\omega_m H_0^+}{\omega_0 - \omega} = -jM_x \quad (47)$$

Hence, the magnetization vector is also circularly polarized and rotates in the same direction with an angular velocity ω . It then follows that the magnetic flux density is circulating synchronously with the driving force and the effective permeability is given by

$$\mu_0^+ = \mu_0 \left(1 + \frac{\omega_m}{\omega_0 - \omega} \right) \quad (48)$$

It is interesting to compare the angle of precession of the magnetic field intensity θ_H and that of the magnetization vector θ_M^+ :

$$\tan \theta_H = \frac{H_0^+}{H_{\text{int}} + H_z} \cong \frac{H_0^+}{H_{\text{int}}} \quad (49)$$

$$\begin{aligned} \tan \theta_M^+ &= \frac{M_x}{M_s + M_z} \cong \frac{\omega_m}{\omega_0 - \omega} \frac{H_0^+}{M_s} \\ &= \frac{\omega_0}{\omega_0 - \omega} \frac{H_0^+}{H_{\text{int}}} \end{aligned} \quad (50)$$

By invoking (32), we can rewrite (50) as

$$\tan \theta_M^+ = \frac{\omega_0}{\omega_0 - \omega} \frac{H_0^+}{H_{\text{int}}} \quad (51)$$

Hence, as long as $\omega < 2\omega_0$, then $\theta_M^+ > \theta_H$ as shown in Fig. 6. Since $H_0^+ \ll H_{\text{int}}$, the angle of precession is usually very small except when $\omega = \omega_0$, the Larmor frequency. As indicated in (29) and (30), the magnetization could be infinitely large at $\omega = \omega_0$; therefore ω_0 is also known as *ferrimagnetic resonance*. We will revisit ferrimagnetic resonance later because circulators usually operate in its vicinity.

If the driving force is a \hat{z} -directed left-handed circularly polarized wave, the magnetization and the magnetic flux

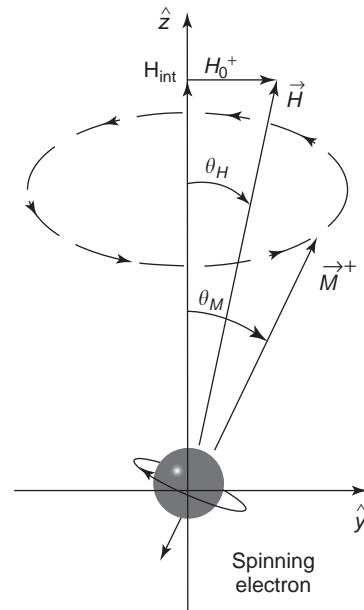


Figure 6. Force precession with $\theta_M^+ > \theta_H$.

density are also similarly polarized, and the corresponding effective permeability and angles of precession are

$$\mu_0^- = \mu_0 \left(1 + \frac{\omega_m}{\omega_0 + \omega} \right) \quad (52)$$

$$\tan \theta_M^- = \frac{\omega_0}{\omega_0 + \omega} \frac{H_0^-}{H_{\text{int}}^-} \quad (53)$$

Here, $\theta_M^- < \theta_H$ and the magnetic dipole moment rotates in a direction opposite to its free precession as indicated in Fig. 7. In short, the external excitation sets up a preferential pattern of precession and leads to nonreciprocal characteristics in wave propagation.

3.2. Damping

As mentioned previously, circulators are usually magnetized such that they operate in the vicinity of ferrimagnetic resonance. Based on (47), both M_x and M_y could be infinitely large with $\theta_M = 90^\circ$. To stabilize the magnetization vector at resonance, a damping term must be added into the equation of motion in (25). Landau and Lifshitz (as cited by Helszajn [12]) have shown that the damping force pulling the magnetization vector toward the driving force \mathbf{H}_{int} is

$$\mathbf{F}_{\text{damping}} \propto \mathbf{M} \times \frac{d\mathbf{M}}{dt} \quad (54)$$

The damping force acting on the precession is illustrated in Fig. 8. The equation of motion with the damping force

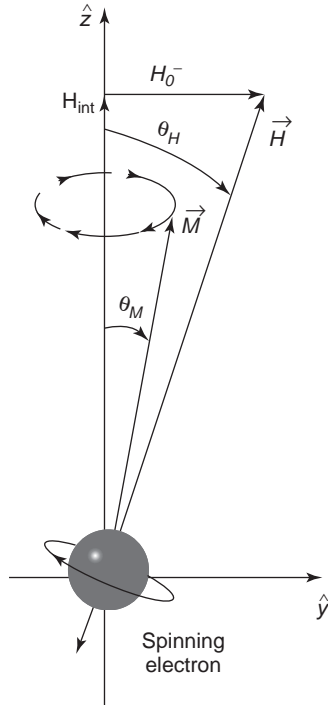


Figure 7. Forced precession with $\theta_M^- < \theta_H$.

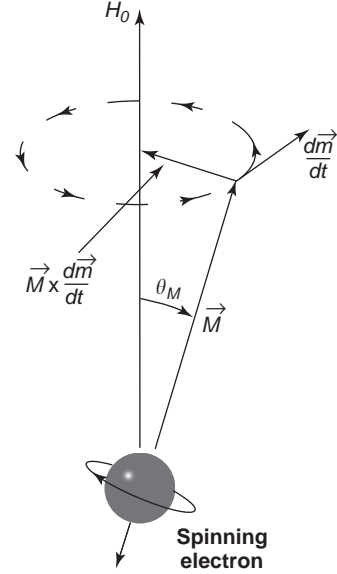


Figure 8. Effect of damping force on the precession.

included is

$$\frac{d\mathbf{M}}{dt} = -\mu_0 \gamma \mathbf{M} \times \mathbf{H} - \frac{\alpha \mu_0}{|\mathbf{M}|} \mathbf{M} \times \frac{d\mathbf{M}}{dt} \quad (55)$$

where α is a dimensionless constant.

Using small argument approximations and following procedures presented in deriving (39) and (40), the components in the susceptibility tensor can be derived as

$$\chi_{xx} = \chi_{yy} = \frac{\omega_m(\omega_0 + j\alpha\omega)}{(\omega_0 + j\alpha\omega)^2 - \omega^2} \quad (56)$$

$$\chi_{xy} = -\chi_{yx} = \frac{j\omega\omega_m}{(\omega_0 + j\alpha\omega)^2 - \omega^2} \quad (57)$$

It appears that the susceptibility with damping factors can be obtained by replacing ω_0 in the loss-free formulas with $\omega_0 + j\alpha\omega$. Watch out, the conventional way in deriving damping effects is to replace ω by $\omega + j\alpha\omega$! Usually, the susceptibility tensor is expressed in its real and imaginary parts; that is

$$\chi_{xx} = \chi'_{xx} + j\chi''_{xx} \quad (58)$$

$$\chi_{xy} = \chi'_{xy} + j\chi''_{xy} \quad (59)$$

where

$$\chi'_{xx} = \frac{\omega_0\omega_m(\omega_0^2 - \omega^2) + \alpha^2\omega_0\omega_m\omega^2}{[\omega_0^2 - \omega^2(1 + \alpha^2)]^2 + 4\alpha^2\omega_0^2\omega^2} \quad (60)$$

$$\chi''_{xx} = \frac{\alpha\omega_m\omega[\omega_0^2 + \omega^2(1 + \alpha^2)]^2}{[\omega_0^2 - \omega^2(1 + \alpha^2)]^2 + 4\alpha^2\omega_0^2\omega^2} \quad (61)$$

$$\chi'_{xy} = \frac{-\omega_m\omega[\omega_0^2 - \omega^2(1 + \alpha^2)]^2}{[\omega_0^2 - \omega^2(1 + \alpha^2)]^2 + 4\alpha^2\omega_0^2\omega^2} \quad (62)$$

$$\chi''_{xy} = \frac{2\alpha\omega_0\omega_m\omega^2}{[\omega_0^2 - \omega^2(1 + \alpha^2)]^2 + 4\alpha^2\omega_0^2\omega^2} \quad (63)$$

Note that all components reach a common peak at

$$\omega_{0,\max} = \omega\sqrt{1 + \alpha^2} \approx \omega\left(1 + \frac{\alpha^2}{2}\right) \quad (64)$$

Since ω_0 is given in terms of the impressed driving force H_{int} , the magnetic field needed to attain a ferrimagnetic resonance at a given frequency is

$$H_{\text{fr}} = \frac{\omega_{0,\max}}{\mu_0\gamma} \approx \frac{\omega}{\mu_0\gamma}\left(1 + \frac{\alpha^2}{2}\right) \quad (65)$$

The susceptibility component of particular interest is χ''_{xx} , whose maximum is

$$\chi''_{xx,\max} = \frac{\omega_m}{2\alpha\omega} \quad (66)$$

Variation of χ''_{xx} with the impressed magnetic field is sketched in Fig. 9, which shows the so-called linewidth of ferrites. Linewidth is the parameter provided by ferrite manufacturers to describe magnetic losses at resonance. It is defined as the difference between the magnetic fields where χ''_{xx} is one-half of $\chi''_{xx,\max}$ for a given frequency.

Assuming that χ''_{xx} is changing quadratically near resonance, the linewidth can be derived as

$$\Delta H \approx \frac{2\alpha\omega}{\mu_0\gamma} \quad (67)$$

In general, circulators are operated in the region either above resonance $H_{\text{int}} > H_{\text{fr}}$ or below resonance $H_{\text{int}} < H_{\text{fr}}$ as indicated in Fig. 9.

3.3. Demagnetization

As mentioned previously, the biasing field exterior to a ferrite sample is different from the interior one. This relationship is dependent on the shape of the specimen as well as the orientation of the external excitation. For example, if the impressed field \mathbf{B}_{ext} is normal to the surface of a ferrite slab or infinite extent, the continuity of the

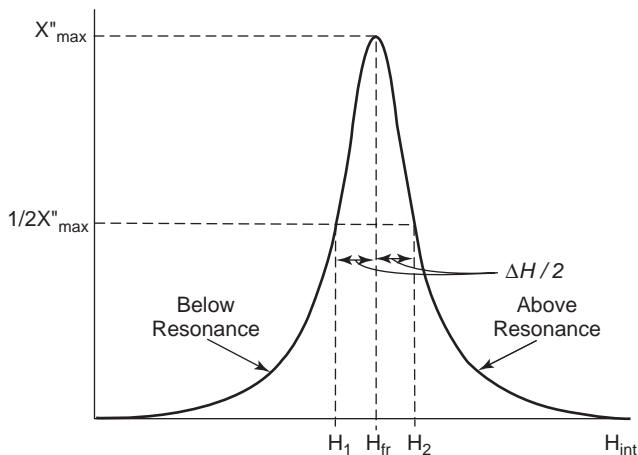


Figure 9. Variation of χ''_{xx} with H_{int} .

normal component of magnetic flux density dictates that

$$B_{\text{ext}} = \mu_0 H_{\text{ext}} = \mu_0 (H_{\text{int}} + M_s) \quad (68)$$

Hence

$$H_{\text{int}} = H_{\text{ext}} - M_s \quad (69)$$

However, if the applied field is parallel to the slab's surface, the continuity of the tangential magnetic field intensity demands that

$$H_{\text{ext}} = H_{\text{int}} \quad (70)$$

In general, the magnetic field intensity in ferrite can be determined in terms of a demagnetization factor ζ :

$$H_{\text{int}} = H_{\text{ext}} - \zeta M_s \quad (71)$$

The argument is valid for all directions; therefore there are three ζ values, one for each coordinate. Moreover, the demagnetization factors are dependent on the shape of the ferrite sample as well as the direction of the external field, relative to the specimen. It can be proved that the sum of three demagnetization factors in Cartesian coordinates is equal to 1:

$$\zeta_x + \zeta_y + \zeta_z = 1 \quad (72)$$

For a circular ferrite disk of negligible thickness, the demagnetization factors can be determined as if it were a slab such as that just mentioned, that is, $\zeta_z = 1$ and $\zeta_x = \zeta_y = 0$. On the other hand, if a ferrite post of infinite length is magnetized axially, the demagnetization factor in the z direction is zero, and the ζ values on the x - y plane can be determined by twofold symmetry; therefore $\zeta_x = \zeta_y = \frac{1}{2}$. Similarly, on the basis of threefold symmetry, the demagnetization factors for a sphere excited in any coordinate are $\zeta_x = \zeta_y = \zeta_z = \frac{1}{3}$.

3.4. Propagation Transverse to Magnetization

In the study of forced precessions, a plane wave propagates in the direction of the static magnetic excitation. Preferential treatment of some waves and ferrimagnetic resonance are established. However, wave propagations in most circulators are transverse to the biasing magnetic field. To illustrate the latter phenomenon, the simplest configuration is used. It is a rectangular ferrite slab of infinite width and depth but of negligible thickness. For consistency with the notations used in waveguides and microstrip lines, the external magnetic field is \hat{x} -directed and the permeability tensor given in (45) is applicable.

The ferrite slab is illuminated by an incident plane wave propagating in the \hat{z} direction:

$$\mathbf{E} = (\hat{x}E_x + \hat{y}E_y)e^{-j\beta_0 z} \quad (73)$$

$$\mathbf{H} = (\hat{x}H_x + \hat{y}H_y)e^{-j\beta_0 z} \quad (74)$$

In a gyrotropic medium, the Maxwell equations are

$$\nabla \times \mathbf{E} = -j\omega\bar{\mu}\mathbf{H} \quad (75)$$

$$\nabla \times \mathbf{H} = j\omega\epsilon\mathbf{E} \quad (76)$$

$$\nabla \cdot \mathbf{D} = 0 \quad (77)$$

$$\nabla \cdot \mathbf{B} = 0 \quad (78)$$

It is found that (75) can be satisfied with a nonzero E_z or a nonzero H_z , but not both. Hence, a more general form for waves in ferrite is selected:

$$\mathbf{E} = (\hat{x}E_x + \hat{y}E_y + \hat{z}E_z)e^{-j\beta z} \quad (79)$$

$$\mathbf{H} = (\hat{x}H_x + \hat{y}H_y + \hat{z}H_z)e^{-j\beta z} \quad (80)$$

According to this postulation, $\partial/\partial z = -j\beta$; by symmetry, $\partial/\partial y = 0$; and by the negligible thin approximation, $\partial/\partial x = 0$. Thus, the constituents of the curl equations in (58) can be reduced to

$$j\beta E_y = -j\omega\mu_0 H_x \quad (81)$$

$$-j\beta E_x = -j\omega(\mu H_y + j\kappa H_z) \quad (82)$$

$$0 = -j\omega(-j\kappa H_y + \mu H_z) \quad (83)$$

Similarly, the curl equation in (76) can be simplified to

$$j\beta H_y = j\omega\epsilon E_x \quad (84)$$

$$-j\beta H_x = j\omega\epsilon E_y \quad (85)$$

$$0 = j\omega\epsilon E_z \quad (86)$$

Based on (86), E_z is zero; therefore H_z must be nonzero. Moreover, from both (84) and (85), the intrinsic impedance of the medium is found:

$$\eta = \frac{E_x}{H_y} = -\frac{E_y}{H_x} = \frac{\beta}{\omega\epsilon} \quad (87)$$

Substituting (87) into (81), the propagation constant is derived:

$$\beta^2 = \omega^2\mu_0\epsilon \quad (88)$$

It is also observed in (83) that H_z can be evaluated in terms of H_y :

$$H_z = \frac{j\kappa}{\mu} H_y \quad (89)$$

This formula can be used to eliminate H_z from (82):

$$\begin{aligned} \beta E_x &= \omega \left(\mu + j\kappa \frac{j\kappa}{\mu} \right) H_y \\ &= \frac{\omega}{\mu} (\mu^2 - \kappa^2) H_y \end{aligned} \quad (90)$$

Combining (87) and (90), another solution for the propagation constant is obtained

$$\beta_e^2 = \frac{\omega^2\epsilon}{\mu} (\mu^2 - \kappa^2) = \omega^2\mu_e\epsilon \quad (91)$$

where β is denoted by β_e to distinguish it from the other solution given in, and μ_e is an effective permeability of the medium, given by

$$\mu_e = \frac{\mu^2 - \kappa^2}{\mu} \quad (92)$$

If the electric field of the incident wave is \hat{y} -directed, the continuity of the tangential electric field intensity at the air-ferrite interface implies that $E_x = 0$; so that H_y is also zero, and by (89) H_z also vanishes. Hence, the only solution for β is (88) and the wave is called ‘‘ordinary,’’ which means that wave propagation in ferrite is not affected by the magnetization. However, if the electric vector is \hat{x} -directed, the only viable β is that given in (91). With a nonzero H_y , H_z is also nonzero, and the resultant wave is called ‘‘extraordinary.’’ Thus, wave propagation in ferrite is polarization-dependent. On the other hand, if the incident field has both \hat{x} and \hat{y} components, it is treated as a combination of two linearly independent entities, and each propagates independently with a different phase velocity. As a result, two images are created, the so-called birefringence effect. It is also noticed that κ is frequency-dependent; therefore the effective permeability for a given H_{int} and M_s could become negative if the frequency is high enough, and an incident wave will be totally reflected from ferrite. This scenario can be viewed from a different angle in which the frequency is fixed and evanescent effects can be obtained by changing the external magnetic field intensity.

3.5. Wave Circulation around a Ferrite Cylinder of Infinite Length

The configuration of interest in this subsection is a ferrite cylinder of radius a and of infinite length. It is placed on the \hat{z} axis and magnetized axially; therefore the permeability tensor given in (42) is appropriate. Wave propagation in ferrite can be determined by treating the cylinder as a dielectric resonator. It is assumed that the cylindrical surface would behave as if it were a magnetic wall; that is, $E_\phi = 0$ at $\rho = a$. So are the surfaces on top of and at the bottom of the cylinder; therefore $E_\rho = 0$ for $z = \pm \infty$. Since the cylinder is infinitely long, $\partial/\partial z = 0$; consequently $E_z = 0$ everywhere. Using standard coordinate transformations, the nonzero components of the magnetic flux density can

be determined by (41):

$$\begin{aligned} B_\rho &= B_x \cos \varphi + B_y \sin \varphi \\ &= (\mu H_x + j\kappa H_y) \cos \varphi \\ &\quad + (-j\kappa H_x + \mu H_y) \sin \varphi \\ &= \mu H_\rho + j\kappa H_\varphi \end{aligned} \tag{93}$$

$$\begin{aligned} B_\varphi &= -B_x \sin \varphi + B_y \cos \varphi \\ &= -(\mu H_x + j\kappa H_y) \sin \varphi \\ &\quad + (-j\kappa H_x + \mu H_y) \cos \varphi \\ &= -j\kappa H_\rho + \mu H_\varphi \end{aligned} \tag{94}$$

The components of the curl equation in (75) in cylindrical coordinates can be expressed as

$$\frac{1}{\rho} \frac{\partial E_z}{\partial \varphi} = -j\omega(\mu H_\rho + j\kappa H_\varphi) \tag{95}$$

$$= -j\omega\mu H_\rho + \omega\kappa H_\varphi$$

$$-\frac{\partial E_z}{\partial \rho} = -j\omega(-j\kappa H_\rho + \mu H_\varphi) \tag{96}$$

$$= -\omega\kappa H_\rho - j\omega\mu H_\varphi$$

Hence, the magnetic field components can be written in terms of E_z :

$$H_\rho = \frac{1}{\omega\mu_e} \left(-\frac{\kappa}{\mu} \frac{\partial E_z}{\partial \rho} + \frac{j}{\rho} \frac{\partial E_z}{\partial \varphi} \right) \tag{97}$$

$$H_\varphi = \frac{j}{\omega\mu_e} \left(-\frac{\partial E_z}{\partial \rho} + \frac{j}{\rho} \frac{\kappa}{\mu} \frac{\partial E_z}{\partial \varphi} \right) \tag{98}$$

Similarly, the curl equation in (59) can be reduced to a scalar one:

$$\frac{1}{\rho} \left(\frac{\partial(\rho H_\varphi)}{\partial \rho} - \frac{\partial H_\rho}{\partial \varphi} \right) = j\omega\epsilon E_z \tag{99}$$

Substituting (97) and (98) into (99), a wave equation of E_z is obtained:

$$\frac{\partial^2 E_z}{\partial \rho^2} + \frac{1}{\rho} \frac{\partial E_z}{\partial \rho} + \frac{1}{\rho^2} \frac{\partial^2 E_z}{\partial \varphi^2} + \beta_e^2 E_z = 0 \tag{100}$$

This wave equation is the characteristic equation for finding the admissible a . It is identical to that of a cylindrical dielectric waveguide whose solutions are

$$E_{z,n} = (A_n^+ e^{jn\varphi} + A_n^- e^{-jn\varphi}) J_n(\beta_e \rho), \quad n = 1, 2, \dots \tag{101}$$

where J_n is a Bessel function of the first kind of the n th order. The magnetic field of interest is H_φ , which can be

found by substituting (101) into (98):

$$\begin{aligned} H_\varphi &= \frac{-j}{\eta_e} \left\{ A_n^+ e^{jn\varphi} \left[J'_n(\beta_e \rho) + \frac{n}{\beta_e \rho} \frac{\kappa}{\mu} J_n(\beta_e \rho) \right] \right. \\ &\quad \left. + A_n^- e^{-jn\varphi} \left[J'_n(\beta_e \rho) - \frac{n}{\beta_e \rho} \frac{\kappa}{\mu} J_n(\beta_e \rho) \right] \right\} \end{aligned} \tag{102}$$

The resonance can be obtained by enforcing that $H_\varphi = 0$ at $\rho = a$:

$$J'_n(\beta_e a) \pm \frac{n}{\beta_e a} \frac{\kappa}{\mu} J_n(\beta_e a) = 0; \quad n = 1, 2, \dots \tag{103}$$

Note that there are two possible roots for each n , associated with waves circulating in the clockwise direction $e^{jn\varphi}$ and the other in the counterclockwise direction, $e^{-jn\varphi}$. In most cases, the $n = 1$ mode is the dominant one, and the corresponding solution of (103) is 1.84. Hence, β_e is derived as

$$\beta_e a = 1.84 \tag{104}$$

The waves circulating in opposite directions could be made in phase at one of the output ports and out of phase at the remaining port. Assume that port 1 at $\varphi = 0$ is the input, the electric field at $\rho = a$ can be obtained by (101) for $n = 1$:

$$E_{z,1} = E_0 = (A_1^+ + A_1^-) J_1(\beta_e a) \tag{105}$$

At the isolated port at $\varphi = -120^\circ$, the electric field intensity is

$$E_{z,1} = (A_1^+ e^{-j120^\circ} + A_1^- e^{j120^\circ}) J_1(\beta_e a) \tag{106}$$

If the output at the isolated port is made zero, the unknown constants can be determined by solving the simultaneous equations in (105) and (106):

$$A_1^+ = \frac{1+j/\sqrt{3}}{2J_1(\beta_n a)} E_0 \tag{107}$$

$$A_1^- = \frac{1-j/\sqrt{3}}{2J_1(\beta_n a)} E_0 \tag{108}$$

It is interesting to find that the electric field at the output port at $\varphi = 120^\circ$ is

$$E_{z,1} = (A_1^+ e^{j120^\circ} + A_1^- e^{-j120^\circ}) J_1(\beta_e a) = -E_0 \tag{109}$$

By substituting (107) and (108) into (102), the tangential magnetic field at every port of the circulator can be determined in terms of E_0 . After a lengthy yet straightforward algebraic manipulation, the results are

$$H_\varphi(\rho = a) = \begin{cases} E_0/\eta_e, & \varphi = 0^\circ \\ E_0/\eta_e, & \varphi = 120^\circ \\ 0, & \varphi = 240^\circ \end{cases} \tag{110}$$

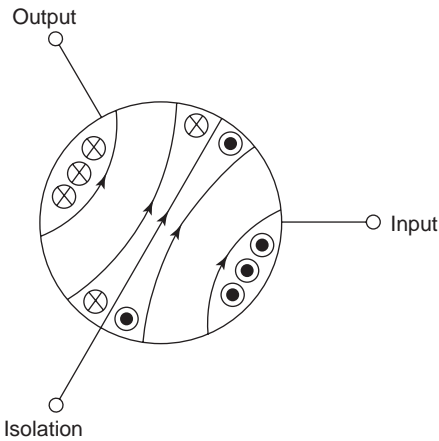


Figure 10. Standing-wave pattern in a magnetized ferrite cylinder.

where η_e is the effective impedance of ferrite, given by

$$\eta_e = \sqrt{\frac{\mu_e}{\epsilon}} \tag{111}$$

Sketched in Fig. 10 is the standing-wave pattern in a magnetized ferrite cylinder. It is clearly shown that energy inputted to port 1 is outputted to port 2 with none to port 3.

For comparison, the field pattern in a cylindrical dielectric resonator is shown in Fig. 11, where the signals at ports 2 and 3 are equal in both amplitude and phase.

3.6. Typical Ferrites Used in Circulators

In circulator designs, the selection of an appropriate ferrite element is of paramount importance. On one hand, it must satisfy the electromechanical requirements on size, weight, power handling, and temperature range. On the other hand, it must meet the stipulated performance electronically, including center frequency, bandwidth, insertion loss, and linearity.

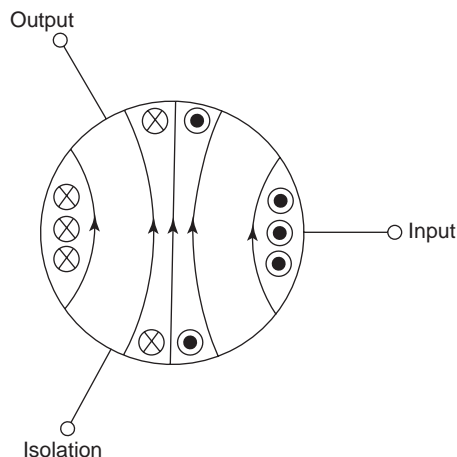


Figure 11. Standing-wave pattern in a demagnetized ferrite cylinder.

Table 2. Major Characteristics of Spinel

Composition	$4\pi M_s$ (G)	T_c ($^{\circ}$ C)	ΔH (Oe)
MgAl	650	100	115
	1700	225	120
	2420	310	180
MgMn	1130	175	180
	1900	280	350
	2800	300	300
MgMnAl	750	90	120
	1300	140	135
	1750	225	225
MgMnZn	2500	275	520
	3000	240	190
	NiAl	1000	400
NiZn	2500	570	490
	4000	500	270
LiTi	5000	375	160
	1000	330	300
	2000	490	400
	2900	600	550

Besides the physical dimensions and shape of a ferrite specimen, the characteristics of the material could make a major difference in the performance of a circulator. The most important ferrite parameters are saturation magnetization ($4\pi M_s$), Curie temperature (T_c), and linewidth (ΔH). For reference, the characteristics of some spinels and garnets are listed in Tables 2 and 3.

For example, the magnetic field needed to establish ferrimagnetic resonance at $f = 4$ GHz is

$$H_{fr} \approx \frac{\omega}{\mu_0 \gamma} = 1.137 \times 10^5 \text{ A/m} = 1429 \text{ Oe}$$

For a specimen of zinc–nickel spinel with $4\pi M_s = 5000$ G, the Cuire temperature is 375° C, and the damping factor is

$$\alpha \approx \frac{\mu_0 \gamma}{2c\omega} \Delta H = \frac{1}{2H_{RF}} \Delta H = 0.17 \text{ Np/m}$$

Table 3. Major Characteristics of Garnets

Composition	$4\pi M_s$ (G)	T_c ($^{\circ}$ C)	ΔH (Oe)
Y	1800	280	45
Yal	250	100	40
	550	160	40
	1000	210	40
	1600	265	40
	210	110	65
YgdAl	550	185	65
	800	260	75
	1400	265	50
	500	225	95
YGdAlDy	800	245	70
	1200	260	60
	1600	280	75
YgdAlHo	550	180	100
	700	240	90
	800	240	110
CaVIn	600	200	25
	1200	220	10
	1850	240	15

If the circulator is designed to operate in the abovementioned resonance region, the external magnetic field required must be greater than

$$H_{\text{ext}} = H_{\text{int}} + M_s > H_{\text{RF}} + M_s = 1827 \text{ Oe}$$

4. APPLICATIONS

4.1. Isolator

The principal application of circulators is load isolation, a low transmission loss in one direction, and a relatively high attenuation in the reverse path. At microwave frequencies, generators are vulnerable to frequency shifting due to load variations; therefore isolation is needed to protect them from waves reflected from the less than perfectly matched loads. Reasonable isolation can be implemented by inserting a circulator between the source and its load as depicted in Fig. 12.

For better protection, the isolation can be obtained by a series of circulators. However, if amplifiers are used, additional isolations as shown in Fig. 13 are recommended because amplifiers are seldom unconditionally stable for all loads.

Shown in Fig. 14 is a circulator inserted between a receiving antenna and a low-noise amplifier. In satellite receiving antennas, isolation is needed to prevent waves leaking from the low-noise amplifier from interfering with the weak signals picked up by the antenna.

Good isolation between the source and the load can be obtained by using a one-port negative-resistance amplifier as illustrated in Fig. 15. It is noted that many IMPATT (impact ionization avalanche transit time) and BARITT (barrier-injected transit time) diodes exhibit a negative input impedance of Z_d . The output signal is that reflected from the diode as a result of impedance mismatch, and the gain of the amplifier is equal to

$$\rho^2 = \left(\frac{Z_d - Z_0}{Z_d + Z_0} \right)^2 = \left(\frac{Z_0 + |Z_d|}{Z_0 - |Z_d|} \right)^2 \tag{112}$$

where Z_0 is the characteristic impedance of the transmission line.

In fact, greater isolation can be obtained by inserting an additional circulator in the isolator in Fig. 15 as shown in Fig. 16.

4.2. Duplexer

A duplexer is a device that allows an antenna to serve as a transmitter as well as a receiver. Many duplexers made of hybrids junctions, solid-state switches, and others are available on the market, but simple ferrite duplexers are preferred because they allow a single antenna to carry out both functions simultaneously. The outgoing waves are coupled to the transmitting antenna through a circulator, and signals picked up by the antenna are fed to the receiving amplifier via a circulator such as that shown in Fig. 17.

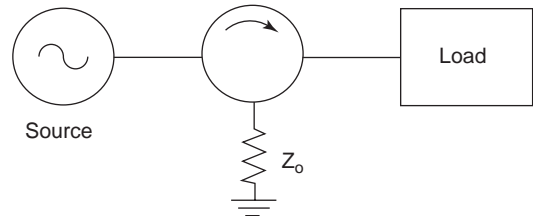


Figure 12. Isolation between the source and its load.

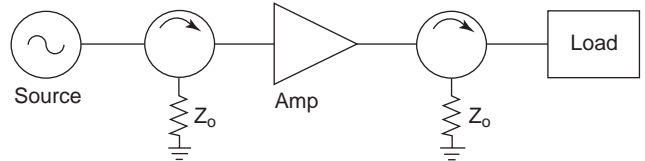


Figure 13. Isolation between the source, the amplifiers, and the load.

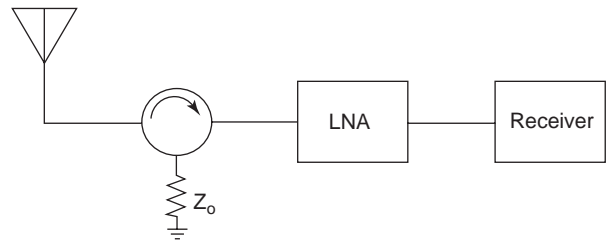


Figure 14. Isolation between a receiving antenna and a low noise amplifier.

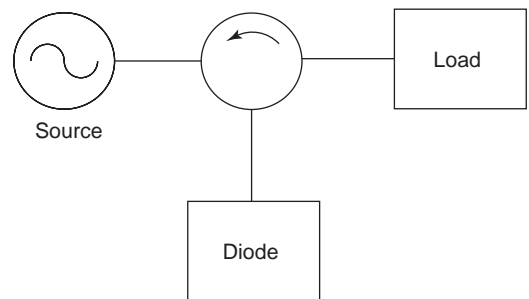


Figure 15. A negative-resistance isolator.

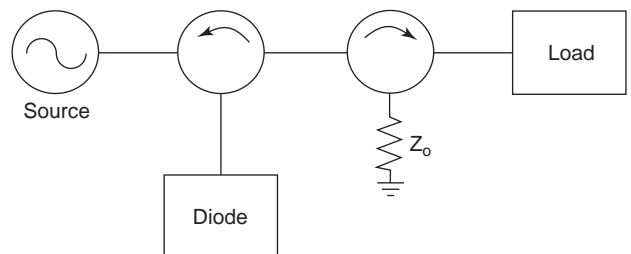


Figure 16. An enhanced negative-resistance isolator.

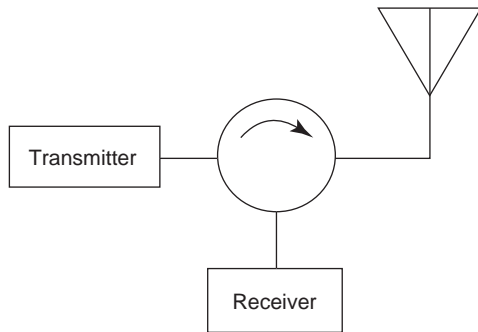


Figure 17. A ferrite duplexer.

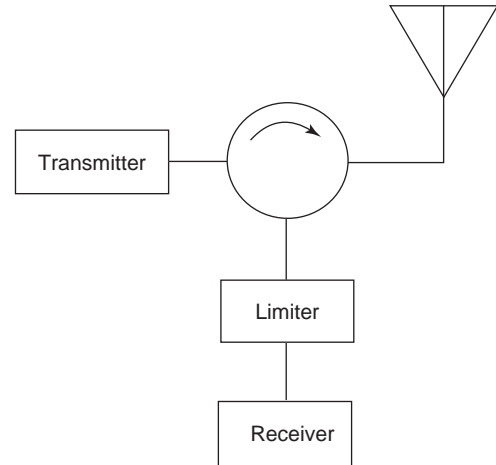


Figure 18. A ferrite duplexer with a limiter.

For a poorly matched antenna, part of the outgoing signal is reflected by the antenna and is directed by the circulator to the amplifier with the incoming signal. In order to enhance the transmitter-receiver isolation and to prevent damage to the amplifier, a limiter is usually added at the output port of the circulator as shown in Fig. 18.

4.3. Reciprocal Ferrite Switch

As wave circulation in a circulator is dependent on the polarity of its excitation, the direction of circulation can be reversed by reversing the biasing magnetic field. It is also noted that ferrite retains its magnetization even after the external driving force is removed and waves can circulate in the same course until the permanent magnetization effect wears off. If the magnetic field is generated electromagnetically by a current coil, magnetization can be reversed by a large current pulse in an appropriate direction. On the basis of this idea, a reciprocal ferrite switch has been designed and is sketched in Fig. 19.

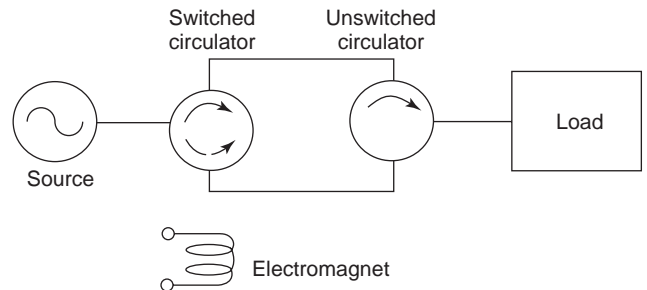


Figure 19. A reciprocal ferrite switch.

4.4. Multiplexing

A multiplexer is a device that carries many channels of signals in a given bandwidth. The simplest one is the diplexer in Fig. 20. Signals output from the lowpass filter are directed by the circulator to the highpass filter, where they are rejected. The reflected waves are then forwarded to the common channel with the output of the highpass filter via the same circulator.

In general, multiplexers can be built by simply interconnecting the filters together, but utmost care must be taken to reduce interactions among various filters. Multiplexers with circulators, on the other hand, can accommodate almost any filter because the circulator serves as an isolator as well as an integrator. Naturally, this concept can be extended to design a three-channel multiplexer as sketched in Fig. 21. As circulators have insertion losses, this configuration is not recommended for building a multiplexer of many channels.

5. TYPES OF CIRCULATORS

Of all the available circulators, the junction circulator is by far the dominant one. Over the years, many types of junction circulators of different power ratings have been developed for use at a wide range of frequencies, from VHF

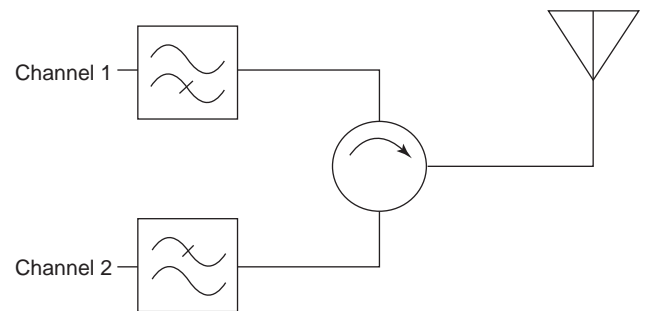


Figure 20. A diplexer.

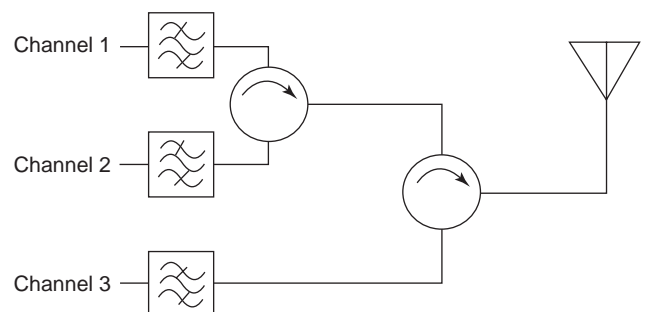


Figure 21. A three-channel multiplexer.

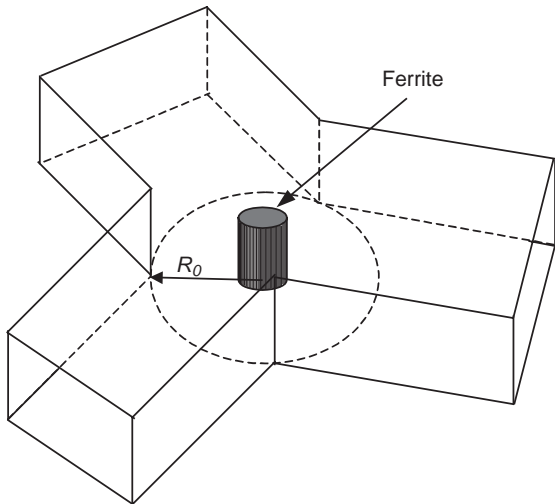


Figure 22. A Y-junction waveguide circulator.

to millimeter waves. Depending on the transmission medium, circulators can be sorted into categories of waveguides, microstrip lines, striplines, and coaxial lines. Common to all junction circulators, the magnetization is transverse to the direction of wave propagation.

For comparison, waves propagate in the direction of magnetization in differential phase shift circulators and Faraday rotation circulators. Hence, the principle of operation is drastically different from that of junction circulators. These four-port circulators are skipped in this article simply because they are seldom used in modern systems.

5.1. Waveguide Y-Junction Circulators

At microwave and millimeter-wave frequencies, the only feasible circulator is a waveguide junction circulator, constituting a Y junction of three *H*-plane rectangular waveguides as shown in Fig. 22 [13,14]. A ferrite cylinder spanning the height of the waveguide is mounted normal to the floor of the waveguide junction. It is placed at the center of the Y junction for symmetry. Moreover, a metal plate with three symmetric spikes pointing toward the ports of entry is added between the ferrite specimen and the waveguide floor for better impedance matching as shown in Fig. 23. Also shown in the same figure is the glue that serves as an insulating layer separating the ferrite post and the impedance-matching plate. The ferrite post is magnetized axially by a permanent magnet or an electromagnet outside the waveguide.

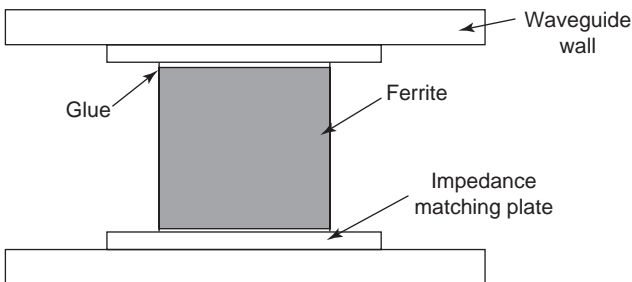


Figure 23. Side view of a ferrite post in a waveguide Y junction.

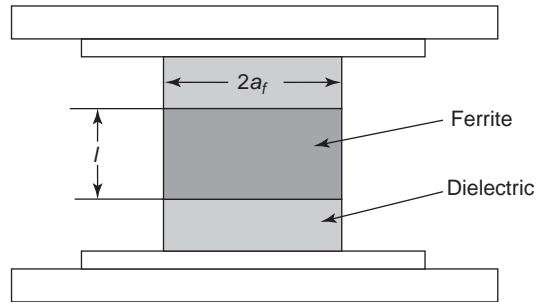


Figure 24. Side view of a partial ferrite post in a waveguide Y junction.

Even though the connecting waveguides are operating in TE_{10} modes, higher-order modes, including the evanescent ones, exist in the junction. Note that the ferrite cylinder itself is a dielectric resonator whose resonant frequency is dependent on its length ℓ and its radius a_f . To bring about wave circulations in the waveguide junction, a_f is obtained by solving the characteristic equation given in (103). However, the result obtained from (104) is adequate for most cases:

$$a_f = \frac{1.84}{\beta_e} = \frac{1.84\lambda}{2\pi\sqrt{\mu_e\epsilon}} \tag{113}$$

The leverage in adjusting ℓ does provide us a mechanism to generate higher-order modes [33] such as HE_{11} for improving the performance of the circulator, including impedance matching, bandwidth, quality factor, and insertion loss [15]. To this end, a partial-height ferrite cylinder on an elevated floor as shown in Fig. 24 is developed. For stronger mechanical support, the space above and below the shortened post is filled by two dielectric cylinders of similar shape. Moreover, it is observed that the electric field tangential to the central plane of the waveguide is either maximum or zero due to symmetry. If the post is cut into two halves, a zero tangential field is obtained. Hence, an additional option is gained by cutting the ferrite post into two with one remaining on the floor and the other attached to the ceiling as shown in Fig. 25.

Ferrite posts of circular and triangular cross sections are the popular choices, but hexagonal and other shapes can also be used. Since disks can be made by slicing a cylinder and their principles of operation are identical, it is

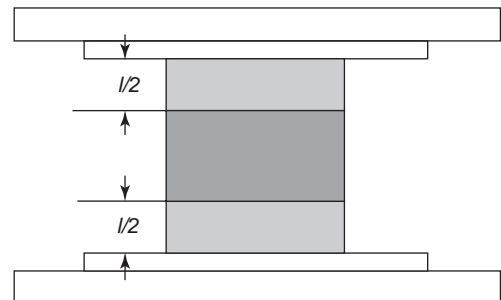


Figure 25. Side view of a divided partial ferrite post in a waveguide Y junction.

considered as a cylinder. It has been shown that circulator with a triangular ferrite cylinder might have a marginally lower insertion loss [16], but its overall performance is comparable to that of a circular one. However, in cases where the tolerance on physical dimensions is very slim, the circular post prevails because grinding and polishing the superhard and brittle ferrite cylinder to a cross section of a perfect circle is much easier than making one with a faultless equilateral triangle. The situation is especially critical for millimeter-wave circulators because the diameter of the relevant ferrite posts is less than a millimeter. Along this line of thought, a new design is proposed in which the cylinder is replaced by a sphere as shown in Fig. 26. Spheres are chosen because they can be mass-produced with the highest precision as if they were ball bearings produced by the time-honored technologies [17]. In fact, the major gain in this maneuver is ease in implementation. As the base of a ferrite cylinder is very small, mounting it normally on a flat surface is easier said than done; therefore erecting one properly on the floor of an equally minuscule Y-junction circulator is very tricky. This agony is totally resolved in the present design because a sphere is always normal to the floor. The performance of this circulator is at least on par with the traditional one. Rigorous analysis and experimental studies of waveguide circulators with ferrite spheres will be examined in later sections.

5.2. Stripline Y-Junction Circulators

At ultrahigh frequencies, stripline circulators are more popular because waveguides are seldom used in this frequency range [18]. The junction where three striplines meet is a conducting disk of radius a_c . Anisotropic effects are provided by two ferrite disks of radius a_f above and below the center conductor. For better performance, $a_f \geq a_c$, and both of them are much larger than the width of the stripline w . Preferably, the ferrite disks are thin enough such that the sandwich can be squeezed between the upper and lower conducting plates of the original striplines as shown in Fig. 27. The junction circulator is magnetized externally such that the magnetic vector is normal to the surface of the ferrite disks. The ferrite disks and the center conductor may be in any shape as long as the threefold symmetry is retained.

The striplines carry TEM modes only; therefore wave propagations are transverse to the magnetization vector. As $w \ll a_c$, the tangential magnetic field is constant over the widths of the striplines and is zero on the circumfer-

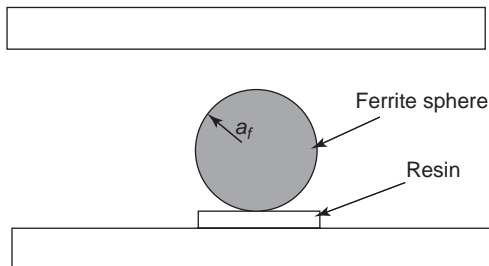


Figure 26. Side view of a ferrite sphere in a waveguide Y junction.

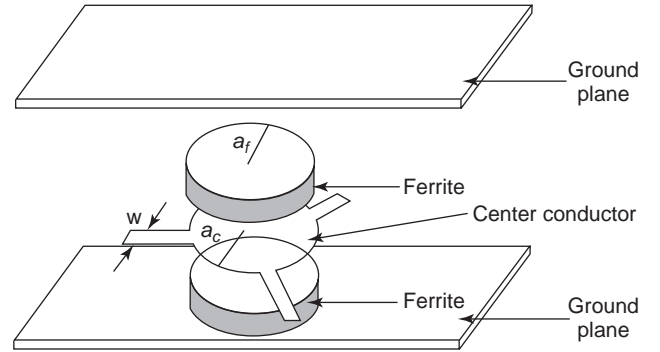


Figure 27. A stripline junction circulator.

ence of the center conductor. Since $a_f \approx a_c$, the magnetic field strength on the peripheral of the ferrite disk is obtained by enforcing the continuity of tangential magnetic fields, a constant at the input ports and zero elsewhere. The normal electric field in ferrite E_z satisfies the Helmholtz equation given in (100), and the magnetic fields are expressed in terms of E_z as given in (97) and (98).

The required wave equation is derived by expressing E_z as

$$E_z(\varphi) = \int_{-\pi}^{\pi} G(\varphi; \varphi') H_\varphi(\varphi') d\varphi' \quad (114)$$

where $G(\varphi; \varphi')$ is the Green function [18], given by

$$G(\varphi; \varphi') = -j \frac{\eta_e}{2\pi} \frac{J_0(\beta_e a_f)}{J_0(\beta_e a_f)} + \frac{\eta_e}{\pi} \sum_{n=1}^{\infty} \frac{\frac{\kappa n J_n(\beta_e a_f)}{\mu \beta_e a_f} \sin n(\varphi - \varphi') - j J_n'(\beta_e a_f) \cos n(\varphi - \varphi')}{[J_n'(\beta_e a_f)]^2 - \left[\frac{\kappa n J_n(\beta_e a_f)}{\mu \beta_e a_f} \right]^2} J_n(\beta_e a_f) \quad (115)$$

Except for simple configurations, the wave equation in a Y-junction stripline circulator stated in (103), (114), and (115) cannot be solved analytically in a closed form. However, the electric and magnetic fields can be accurately and efficiently determined by numerical means. In terms of the field quantities, other characteristics of the junction circulator such as input impedance, reflection coefficient, transfer function, isolation, bandwidth, quality factor, and insertion loss can be derived.

However, for most applications, the radius of the ferrite disks required for resonance can be obtained by (113) and the field pattern in ferrite is similar to that sketched in Fig. 10. Moreover, stripline junction circulators are usually biased far above resonance in the UHF region: $H_{\text{int}} \gg H_{\text{fr}}$. It then follows that μ and κ can be approximated by

$$\mu_e \approx \mu = 1 + \frac{4\pi M_s}{H_{\text{int}}} \quad (116)$$

$$\kappa = \frac{4\pi M_s H_{\text{fr}}}{H_{\text{int}}^2} \quad (117)$$

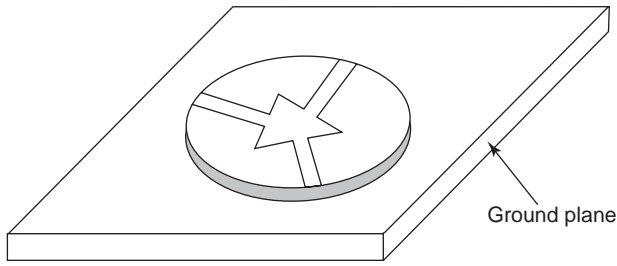


Figure 28. A junction circulator with microstrip lines on a substrate of ferrite disk.

It is also recommended that the minimum radius required be

$$a_f > \frac{4w}{3} \tag{118}$$

5.3. Microstrip-Line Y-Junction Circulators

One reason why circulators are seldom used today is the lack of effective circulators for microstrip lines, the most popular media of wave transmission at UHF and microwave bands. Traditionally, a microstrip-line junction circulator is made by laying three metallic strips on a ferrite disk as shown in Fig. 28. For better impedance matching, the center conductor may assume any three-way symmetric shape such as the equilateral triangle shown in Fig. 28. Unlike its stripline counterpart, a microstrip-line junction circulator has only one ferrite disk on a large ground plane. For the microstrip line on a substrate of ferrite, its characteristic impedance is quite different from that on a dielectric substrate. Hence, an additional impedance matching is needed at every port of entry.

In order to improve impedance matching and to reduce cost, a simpler version is developed. Instead of putting the microstrip lines and the center conductor on a ferrite disk, they are printed on a dielectric substrate as illustrated in Fig. 29. Wave circulation is made possible by covering the junction with a ferrite disk of radius a_f . Similar to a waveguide Y-junction circulator, the disk can be replaced by a hemispherical one. The major advantage gained in this maneuver is flexibility because the frequency of a given circulator can easily be altered by replacing its ferrite by a different material or by changing its physical shape or dimension. Unfortunately, the performances of the aforementioned circulators are not very satisfactory and further improvements are needed.

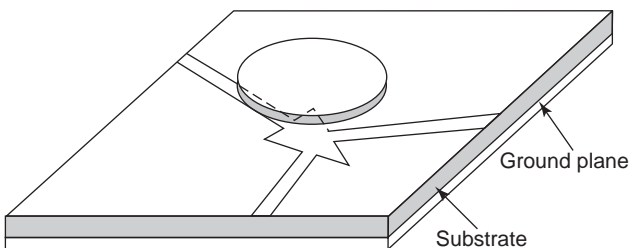


Figure 29. A microstrip-line junction circulator with a ferrite disk on top.

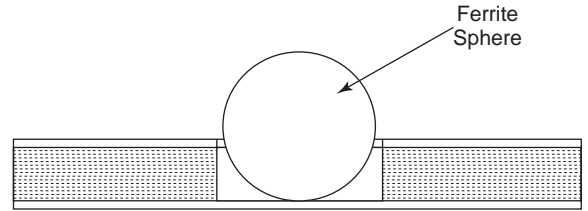


Figure 30. A microstrip-line junction circulator with a ferrite sphere.

One improvement proposed is a microstrip-line circulator with a ferrite sphere as shown in Fig. 30 [19]. Even though a better performance is observed, it remains inferior to those waveguide and stripline circulators. With the increasing popularity of microstrip lines and other coplanar waveguides, development in this direction is desperately needed.

5.4. Lumped-Element Circulators

Common to all junction circulators, as mentioned previously, the size of the ferrite specimen is proportional to wavelength. This means that the circulator could become prohibitively large in HF and VHF regions. To this end, a simple circulator is designed by winding three coils around a ferrite disk as shown in Fig. 31 [20]. The coils in these lumped-element circulars are oriented 120° from one another, so are the magnetic fields created by these coils. Two ferrite disks of 10–15 mm in diameter and 1–2 mm thick are packed inside a grounded metal box. The so-called coil in each port in fact consists of two one-turn coils in parallel; one returns through the bottom of the shielding box and the other via its top, as illustrated in Fig. 32. In order to distribute the magnetic field more evenly in ferrite, the current is divided into multiple filaments as shown in Fig. 33. The magnetic field is parallel to the surface of the ferrite disk. The magnetization vector is normal to the magnetic fields due to the coils and the ferrite disk is usually biased above resonance.

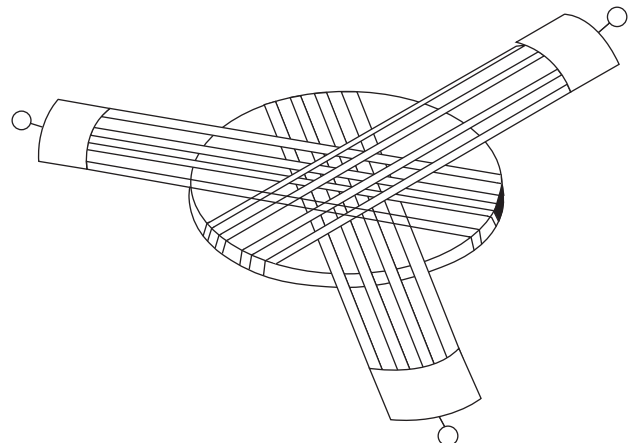


Figure 31. A lumped constant circulator.

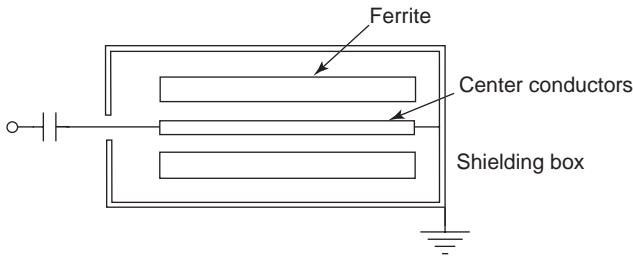


Figure 32. Side view of a lumped constant circulator.

Applying the concept of a balanced three-phase power circuit, the neutral or return line can be obliterated, provided the three branches are 120° out of phase from one another. The combined length of each coil is much shorter than a wavelength, so it is essentially an inductor. To restore resonance at the junction, each branch is shunted to ground via a capacitor, and the resultant star circuit is depicted in Fig. 34a. Alternatively, a series capacitor C_s can be added in series with the coil as shown in Fig. 34b. It can be shown that the waves rotating in opposite directions in ferrite can be characterized by two inductances, namely

$$L_+ = L_0(\mu + \kappa) \tag{119}$$

$$L_- = L_0(\mu - \kappa) \tag{120}$$

where L_0 is the inductance of each phase with the ferrite disk removed. For an ideal circulation, these inductances are given by

$$L_+ + L_- = \frac{2}{\omega^2 C_s} \tag{121}$$

$$L_+ - L_- = 1.156 \frac{Z_0}{\omega} \tag{122}$$

The gyrotropic parameters can be determined on the basis of (119)–(122):

$$\mu = \frac{1}{\omega^2 L_0 C_s} \tag{123}$$

$$\kappa = \frac{Z_0}{1.73 \omega L_0} \tag{124}$$

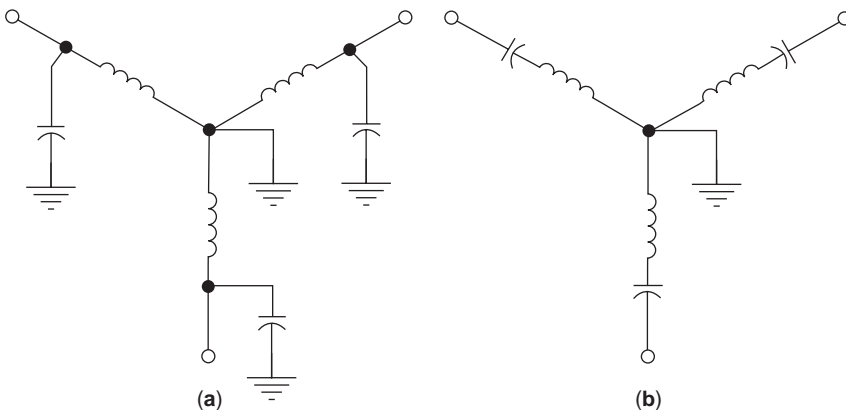


Figure 34. Equivalent circuit of the lumped constant circulator: (a) shunt; (b) series.

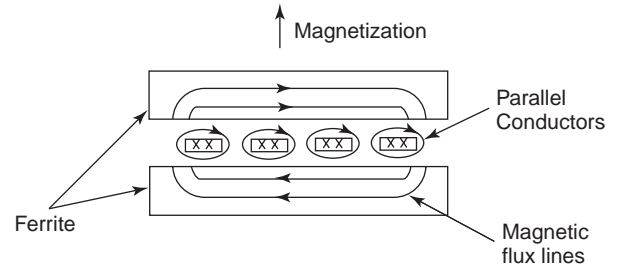


Figure 33. Magnetic field lines in ferrite and around the current coil.

6. IN-DEPTH ANALYSIS OF SOME SELECTED CIRCULATORS

The formulas presented in Section 4 are derived for circulators with clear-cut geometries, and they are based on many approximations, including the over simplified ones. It is obvious that these simple formulas are not accurate enough for computer-aided designs of miniature circulators at microwave and millimeter-wave frequencies. In-depth analyses of circulators, on the other hand, do exist, but the number is limited because the topic itself is commonly considered as old-fashioned, compared with mobile communications, networking, nanotechnology, and other trendy ones. Even if one exists, it is customarily developed for waveguide circulators. Nonetheless, it is worthwhile to present some of the techniques in detail in this section because they can be modified to treat other types of circulators. Most important of all, the rationale behind the development of these techniques and the insights gained during the process are invaluable in the design of innovative circulators in the future.

All in all, four techniques for analyzing typical circulators will be covered. Note that the emphasis is not placed on the techniques themselves, but on how the technique is applied to solve the problem and the characteristics of the circulators. Through the examples, readers may pick up the skill for identifying an appropriate method for analyzing their circulators.

6.1. Finite-Difference Method

The configuration of interest is an H -plane waveguide Y-junction circulator with a full-length ferrite post as sketched in Fig. 22. Consistent with the assumption that the only mode propagating in the waveguide in the dominant TE_{10} mode, all field quantities in the circulator are independent of z , a direction normal to its floor. Hence, the problem is reduced to a two-dimensional one. It can be shown that the transverse components of the electromagnetic wave in ferrite can be determined in terms of E_z and H_z . In the cylindrical coordinate system, the characteristic equations in ferrite are

$$\frac{\partial^2 E_z}{\partial \rho^2} + \frac{1}{\rho} \frac{\partial E_z}{\partial \rho} + \frac{1}{\rho^2} \frac{\partial^2 E_z}{\partial \phi^2} + \beta_e^2 E_z = 0 \tag{125}$$

$$\frac{\partial^2 H_z}{\partial \rho^2} + \frac{1}{\rho} \frac{\partial H_z}{\partial \rho} + \frac{1}{\rho^2} \frac{\partial^2 H_z}{\partial \phi^2} + \beta^2 H_z = 0 \tag{126}$$

where β and β_e are as given in (88) and (91), respectively. Equations similar to (125) and (126) can be used to determine both E_z and H_z exterior to the ferrite post in the junction, provided β_e in (125) is replaced by β .

The major difficulty in solving the characteristic equations is to resolve the conflict due to the rectangular waveguides and the cylindrical junction. The simplest yet sufficiently in-depth method for solving this boundary problem is the finite-difference method proposed by Yung and his researchers [21]. In order to keep the boundary of a waveguide Y junction cylindrical in shape, a truncation boundary as illustrated in Fig. 35 is introduced. With evanescent modes ignored, the field values at the truncation boundary can be expressed in terms of the TE_{10} modes at the input and output ports; therefore all boundary values are defined. It is readily recognized that discretization of (125) requires the field values at five nodes. A unique solution is obtained by enforcing that the tangential electric and magnetic fields are continuous on the surface of the ferrite post.

The finite-difference method is applied to analyze a waveguide Y circulator with a G1002 ferrite post ($\epsilon_r = 15.4$, $4\pi M_s = 1000$ G, $\Delta H = 20$ Oe, and $a_f = 3$ mm). The width of the waveguide is 22.86 mm and the internal

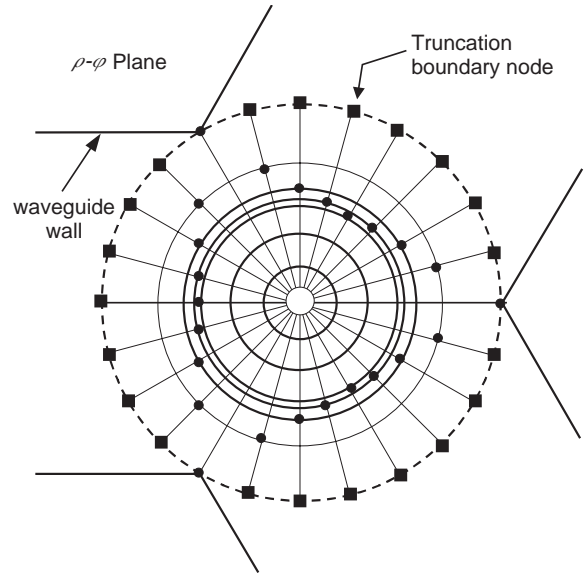


Figure 35. The truncation boundary and the nodal pattern in the waveguide junction.

magnetic field is $H = 200$ Oe. The reflection coefficient, the insertion loss, and the isolation are plotted in Figs. 36 and 37, and 38, respectively. Also shown in these figures are the experimental data published in Ref. 22. Excellent agreement between the analytical results and measurements is seen. It is also observed from the plots that the finite loss of ferrite has negligible effects on the general performance of a circulator except when the frequency is close to ferrimagnetic resonance.

6.2. Finite-Difference Time-Domain Method

Other than full-height ferrite posts, the field quantities in the waveguide junction are usually dependent on z , even though the dominance of TE_{10} remains valid in the input and output waveguides. For a three-dimensional case, the finite difference method just mentioned is no longer adequate, but the finite-difference time-domain (FDTD) method is. Yee's discretization scheme [23] is chosen because it does not require the time-consuming matrix inversion and convergence is assured. In terms of Yee's mesh, the FDTD

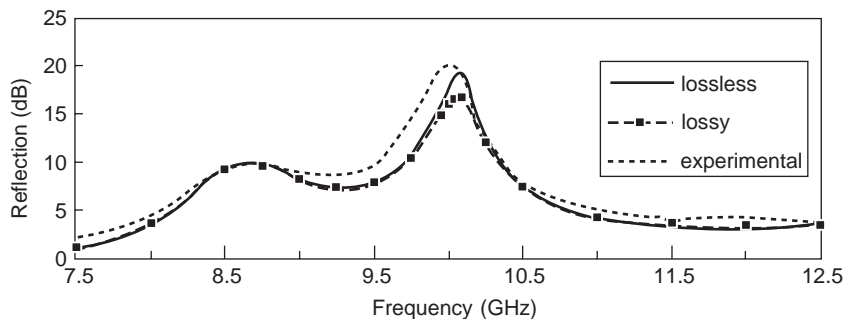


Figure 36. Variation of the reflection coefficient at the input port with frequency.

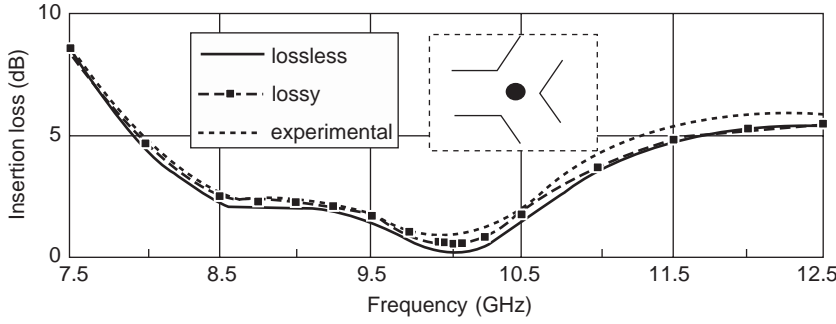


Figure 37. Variation of the insertion loss at the output port with frequency.

approximations of six field components in (75) through (78) are

$$\begin{aligned}
 & H_x^{n+1/2} \left(i, j + \frac{1}{2}, k + \frac{1}{2} \right) \\
 &= H_x^{n-1/2} \left(i, j + \frac{1}{2}, k + \frac{1}{2} \right) \\
 &+ \frac{\mu_{22}}{\mu_0^2(\mu^2 - pa^2)} \text{tat} \left\{ \frac{1}{\text{taz}} \left[E_y^n \left(i, j + \frac{1}{2}, k + 1 \right) \right. \right. \\
 &\quad \left. \left. - E_y^n \left(i, j + \frac{1}{2}, k \right) \right] \right. \\
 &\quad \left. - \frac{1}{\text{tay}} \left[E_z^n \left(i, j + 1, k + \frac{1}{2} \right) - E_z^n \left(i, j, k + \frac{1}{2} \right) \right] \right\} \\
 &- \frac{\mu_{12}}{\mu_0^2(\mu^2 - pa^2)} \text{tat} \left\{ \frac{1}{\text{tax}} \left[E_z^n \left(i + \frac{1}{2}, j + \frac{1}{2}, k + \frac{1}{2} \right) \right. \right. \\
 &\quad \left. \left. - E_z^n \left(i - \frac{1}{2}, j + \frac{1}{2}, k + \frac{1}{2} \right) \right] \right. \\
 &\quad \left. - \frac{1}{\text{taz}} \left[E_z^n \left(i, j + \frac{1}{2}, k + 1 \right) - E_z^n \left(i, j + \frac{1}{2}, k \right) \right] \right\}
 \end{aligned} \tag{127}$$

$$\begin{aligned}
 & H_y^{n+1/2} \left(i + \frac{1}{2}, j, k + \frac{1}{2} \right) \\
 &= H_y^{n-1/2} \left(i + \frac{1}{2}, j, k + \frac{1}{2} \right) \\
 &+ \frac{\mu_{11}}{\mu_0^2(\mu^2 - pa^2)} \text{tat} \left\{ \frac{1}{\text{tax}} \left[E_z^n \left(i + 1, j, k + \frac{1}{2} \right) \right. \right. \\
 &\quad \left. \left. - E_z^n \left(i, j, k + \frac{1}{2} \right) \right] \right. \\
 &\quad \left. - \frac{1}{\text{taz}} \left[E_x^n \left(i + \frac{1}{2}, j, k + 1 \right) - E_x^n \left(i + \frac{1}{2}, j, k \right) \right] \right\} \\
 &- \frac{\mu_{21}}{\mu_0^2(\mu^2 - pa^2)} \text{tat} \left\{ \frac{1}{\text{taz}} \left[E_y^n \left(i + \frac{1}{2}, j, k + 1 \right) \right. \right. \\
 &\quad \left. \left. - E_y^n \left(i + \frac{1}{2}, j, k \right) \right] \right. \\
 &\quad \left. - \frac{1}{\text{tay}} \left[E_z^n \left(i + \frac{1}{2}, j + \frac{1}{2}, k + \frac{1}{2} \right) \right. \right. \\
 &\quad \left. \left. - E_z^n \left(i + \frac{1}{2}, j - \frac{1}{2}, k + \frac{1}{2} \right) \right] \right\}
 \end{aligned} \tag{128}$$

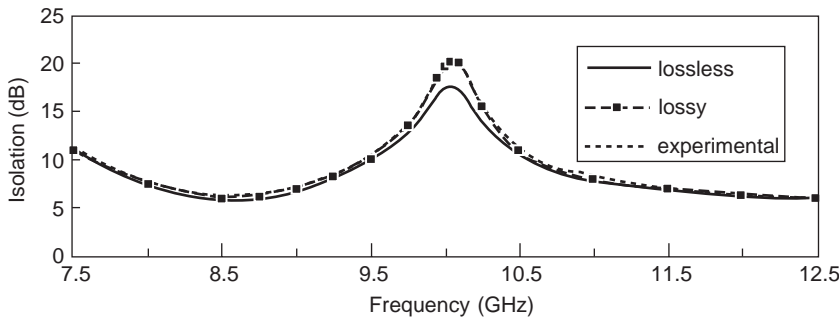


Figure 38. Variation of the isolation at the third port with frequency.

$$\begin{aligned}
 & H_z^{n+1/2} \left(i + \frac{1}{2}, j + \frac{1}{2}, k \right) \\
 & = H_z^{n-1/2} \left(i + \frac{1}{2}, j + \frac{1}{2}, k \right) \\
 & + \frac{tat}{\mu_0} \left\{ \frac{1}{tay} \left[E_x^n \left(i + \frac{1}{2}, j + 1, k \right) \right. \right. \\
 & - E_x^n \left(i + \frac{1}{2}, j, k \right) \\
 & - \frac{1}{tax} \left[E_y^n \left(i + 1, j + \frac{1}{2}, k \right) \right. \\
 & \left. \left. - E_y^n \left(i, j + \frac{1}{2}, k \right) \right] \right\} \tag{129}
 \end{aligned}$$

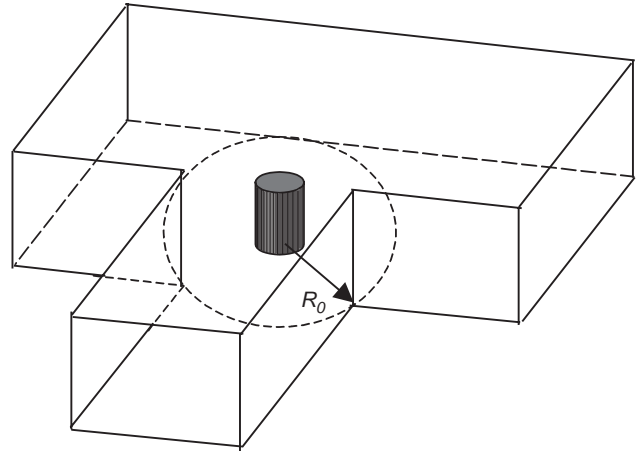


Figure 39. A waveguide T-junction circulator.

$$\begin{aligned}
 E_x^{n+1} \left(i + \frac{1}{2}, j, k \right) & = E_x^n \left(i + \frac{1}{2}, j, k \right) \\
 & + \frac{tat}{\epsilonpsilon_r} \left\{ \frac{1}{tay} \left[H_z^{n+1/2} \left(i + \frac{1}{2}, j + \frac{1}{2}, k \right) \right. \right. \\
 & \left. \left. - H_z^{n+1/2} \left(i + \frac{1}{2}, j - \frac{1}{2}, k \right) \right] \right. \\
 & - \frac{1}{tax} \left[H_y^{n+1/2} \left(i + \frac{1}{2}, j, k + \frac{1}{2} \right) \right. \\
 & \left. \left. - H_y^{n+1/2} \left(i + \frac{1}{2}, j, k - \frac{1}{2} \right) \right] \right\} \tag{130}
 \end{aligned}$$

$$\begin{aligned}
 E_y^{n+1} \left(i, j + \frac{1}{2}, k \right) & = E_y^n \left(i, j + \frac{1}{2}, k \right) \\
 & + \frac{tat}{\epsilonpsilon_r} \left\{ \frac{1}{tax} \left[H_x^{n+1/2} \left(i, j + \frac{1}{2}, k + \frac{1}{2} \right) \right. \right. \\
 & \left. \left. - H_x^{n+1/2} \left(i, j + \frac{1}{2}, k - \frac{1}{2} \right) \right] \right. \\
 & - \frac{1}{tay} \left[H_z^{n+1/2} \left(i + \frac{1}{2}, j + \frac{1}{2}, k \right) \right. \\
 & \left. \left. - H_z^{n+1/2} \left(i - \frac{1}{2}, j + \frac{1}{2}, k \right) \right] \right\} \tag{131}
 \end{aligned}$$

$$\begin{aligned}
 E_z^{n+1} \left(i, j, k + \frac{1}{2} \right) & = E_z^n \left(i, j, k + \frac{1}{2} \right) \\
 & + \frac{tat}{\epsilonpsilon_r} \left\{ \left[H_y^{n+1/2} \left(i + \frac{1}{2}, j, k + \frac{1}{2} \right) \right. \right. \\
 & \left. \left. - H_y^{n+1/2} \left(i - \frac{1}{2}, j, k + \frac{1}{2} \right) \right] \right. \\
 & - \frac{1}{tax} \left[H_x^{n+1/2} \left(i, j + \frac{1}{2}, k + \frac{1}{2} \right) \right. \\
 & \left. \left. - H_x^{n+1/2} \left(i, j - \frac{1}{2}, k + \frac{1}{2} \right) \right] \right\} \tag{132}
 \end{aligned}$$

where Δx , Δy and Δz are the widths of the Yee cell, and $\mu_{11} = \mu_{22} = \mu_{xx}$ and $\mu_{12} = \mu_{21} = \mu_{xy}$ are as given in (56) and (57), respectively.

As the FDTD approximations above are expressed in Cartesian coordinates, the algebra involved in solving a waveguide Y-junction circulator will be very tedious and the resultant time of computation prohibitively long. To better depict the nature of the FDTD scheme, it is applied to solve a waveguide T-junction waveguide as shown in Fig. 39. Although a partial-height ferrite post is shown, the FDTD scheme is, in fact, applicable for any body of arbitrary shape, including a sphere. Moreover, it is noted that some values in (127)–(132) are not available directly from Yee’s scheme, but fortunately, they can be generated by a linear interpolation of the neighboring fields. Details are not given here; interested readers are referred to the paper by Schneider and Hudson [24].

The waveguide T-junction circulator under investigation consists of three X-band waveguides of dimensions 22.86×10.16 mm, and the radius of its full-height ferrite post is $a_f = 3.5$ mm. Variations of the reflection coefficient at the input, the insertion loss at the output, and the isolation at the isolated port are respectively plotted in Figs. 40 and 41, and 42 as a function of frequency. It is readily seen that excellent agreement with the results published in Ref. 25 is observed.

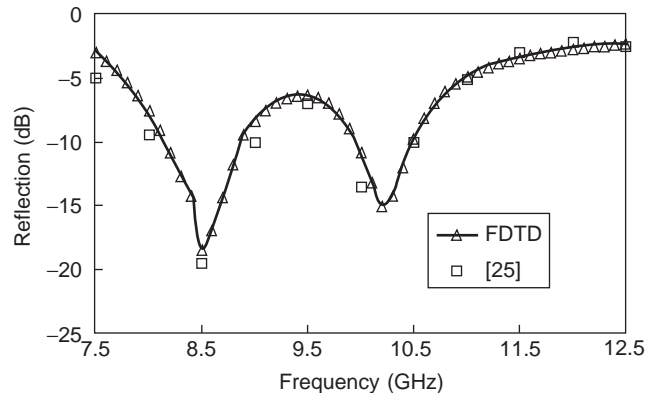


Figure 40. Variation of the reflection coefficient at the input port with frequency.

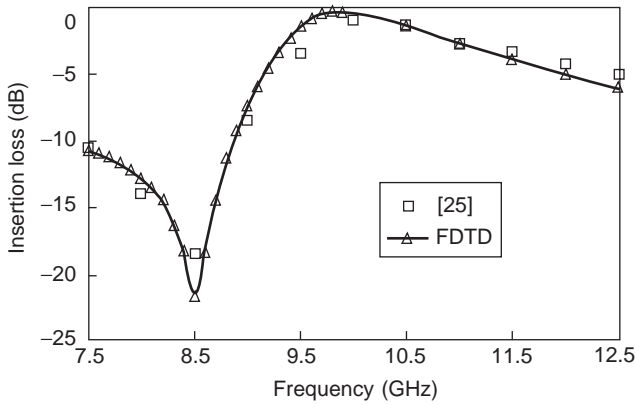


Figure 41. Variation of insertion loss at the output port with frequency.

To better depict the characteristics of wave circulation, the power density in the ferrite post is plotted in Fig. 43 as a function of φ at $f = 10.3$ GHz for three different ρ values. The input and output power densities in a closed path at a given ρ are always conserved as ferrite is assumed to be lossless and no power is dissipated in the waveguide junction area. It is also observed that the power entering the input port at $\varphi = 90^\circ$ is transmitted to the output port at $\varphi = 270^\circ$.

For comparison, the variations of power densities outside the ferrite post are plotted in Fig. 44, where R_0 is the radius of the largest circle inside the T junction. The nature of power transfer to the output port is clearly demonstrated.

Although we have absolute faith in the accuracy of our results computed in the numerical analysis, it is always nice to know that they compare well with those obtained in experimental studies. In fact, readings in measurement are vulnerable to numerous errors and constraints, including purity of the materials, uniformity of the mixture, tolerance of the physical cuttings, stability of the frequency generation, imperfect matching of the interconnects, loss due to spurious radiations, and precision of the measuring instrument. There is no reason to believe that

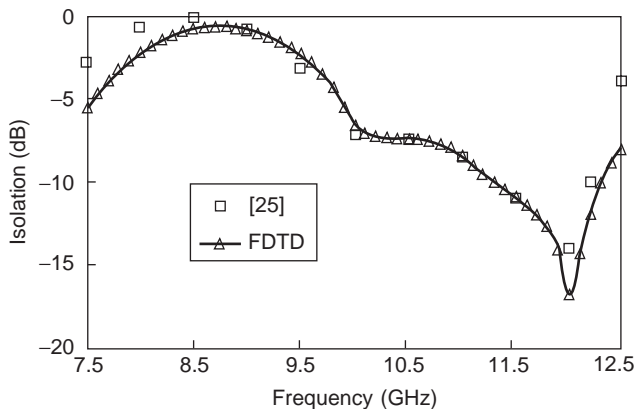


Figure 42. Variation of the isolation at the other output port with frequency.

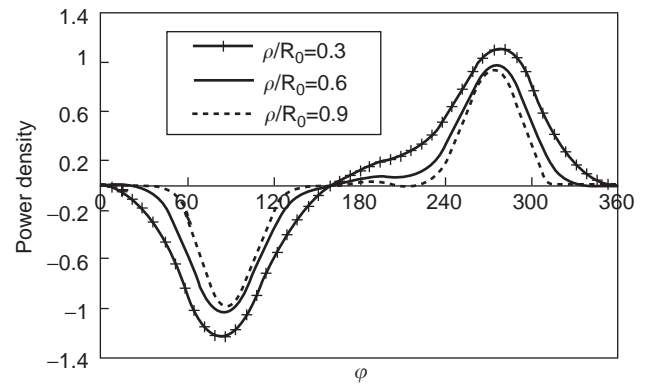


Figure 43. Variation of the power density inside the ferrite post with φ .

measurements are more reliable than computational data. However, most engineers and researchers will feel more comfortable whenever they see a reasonably good agreement between the analytical and the experimental results. In this connection, the FDTD study is repeated for a waveguide circulator with a NiZn ferrite sphere ($a_f = 1.0$ mm, $\epsilon_r = 2.25$, $4\pi M_s = 5000$ G, $H_{ext} = 1700$ Oe, and $\Delta H = 120$ Oe). The numerically obtained reflection coefficients, insertion losses, and isolations are plotted against the experimental data in Fig. 45. Given the complexity of the configuration and the gyrotropic nature of the problem, the agreements between the analytical results and the measurement are more than acceptable.

6.3. Finite-Element Method

The finite-element method (FEM) is known for its capability to model complex structures. Since it requires only information about the geometry of the device to be analyzed, the method can be developed into a general-purpose software package, for example, Ansoft HFSS. With the use of edge-based vector elements, the FEM can handle discontinuity interfaces between different materials without invoking spurious solutions. When combined with the

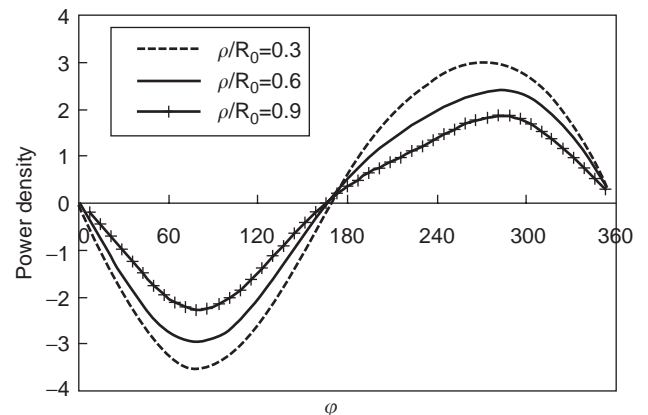


Figure 44. Variation of the power density outside the ferrite post with φ .

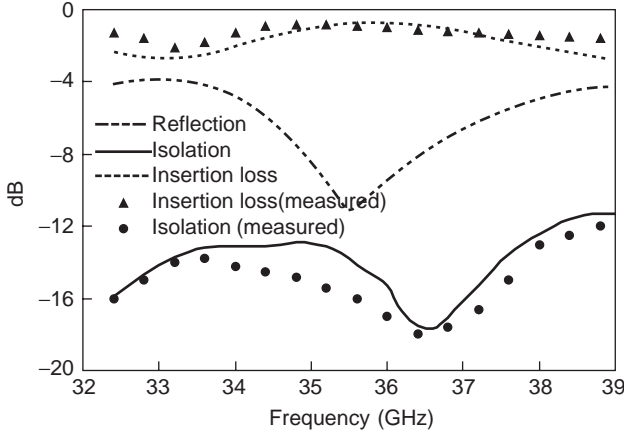


Figure 45. Comparison of reflection coefficients, insertion losses, and isolations for a waveguide T-junction circulator with a ferrite sphere with measurements.

asymptotic waveform evaluation (AWE) and complex frequency-hopping (CFH) techniques, the FEM can generate frequency responses over a wide band very efficiently. Although the low-order FEM suffers from the problem of numerical dispersion, which tends to accumulate as the wave propagates, this problem has been largely overcome with the development of higher-order finite elements [28]. The major remaining difficulty is the relatively long computing time and the associated memory requirements for the resulting finite-element system. More recently, the preconditioned iterative solutions [29] and numerical de-embedding techniques [30] have been developed to accelerate solutions and reduce memory.

Consider a microwave ferrite device with multiple ports, inside the ferrite device, where the field satisfies the vector partial differential equation

$$\nabla \times \{[\mu_r]^{-1} \cdot (\nabla \times \mathbf{E})\} - k_0^2 \epsilon_r \cdot \mathbf{E} = 0 \quad (133)$$

The boundary condition on the surface of port i can be derived as

$$\hat{\mathbf{n}}_i \times \nabla \times \mathbf{E} + P_i(\mathbf{E}) = U_i^{\text{inc}} \quad (134)$$

where $\hat{\mathbf{n}}_i$ denotes the outward unit vector normal to the surface S_i , the cross section of port i , and

$$P_i(\mathbf{E}) = \sum_m \frac{k_0^2}{jk_m} e_{e,m}^{\text{TM}} \iint_{S_i} e_{e,m}^{\text{TM}} \cdot \mathbf{E} ds - \sum_n jk_n e_n^{\text{TE}} \iint_{S_i} e_{e,n}^{\text{TE}} \cdot \mathbf{E} ds \quad (135)$$

$$U_i^{\text{inc}} = \hat{\mathbf{n}}_i \times \nabla \times \mathbf{E}_i^{\text{inc}} + \sum_m \frac{k_0^2}{jk_m} e_{e,m}^{\text{TM}} \iint_{S_i} e_{e,m}^{\text{TM}} \cdot \mathbf{E}_i^{\text{inc}} ds - \sum_n jk_n e_n^{\text{TE}} \iint_{S_i} e_{e,n}^{\text{TE}} \cdot \mathbf{E}_i^{\text{inc}} ds \quad (136)$$

In the above, $e_{t,m}^{\text{TM}}$ denotes the transverse part of the electric field of the m th transverse magnetic (TM) mode, and $e_{t,n}^{\text{TE}}$ denotes the transverse part of the electric field of the n th transverse magnetic (TE) mode. E_i^{inc} denotes the incident fields at port i . In accordance with the general variational theory, the functional for the boundary value problem defined above given by

$$F(\mathbf{E}, \mathbf{E}_a) = \frac{1}{2} \iiint_V \{(\nabla \times \mathbf{E}_a) \cdot (\nabla \times \mathbf{E}) - \epsilon_r k_0^2 \mathbf{E}_a \cdot \mathbf{E}\} dV - \frac{1}{2} \sum_{i=1}^N \iint_{S_i} [\mathbf{E}_a \cdot P_i(\mathbf{E}) - \mathbf{E}_a \cdot U_i^{\text{inc}}] ds \quad (137)$$

where N denotes the total number of ports and \mathbf{E}_a denotes the solution to a properly defined adjoint problem. The FEM discretization of (137) using vector basis functions yields the resulting matrix equation:

$$[A][E] = \{b\} \quad (138)$$

The solution of (138) can be done using an iterative solver such as conjugate-gradient method (CGM) and generalized minimum residuals method (GMRES), and preconditioned techniques can be used to improve the condition number of the FEM system and accelerate the convergence rate of iterative solvers. As a result, this will yield the electric fields everywhere, including those over the ports from which the S parameters can be determined. A three-port circulator loaded with a full-height ferrite post is simulated with the FEM algorithm given above. The circulation characteristics are shown in Fig. 46 and are compared with the experimental data of Ref. 31. Another example considers an 8-mm waveband H -plane Y-junction waveguide circulator with a partial-height ferrite post [30]. The computed and experimental results are given in Fig. 47 and show good agreement.

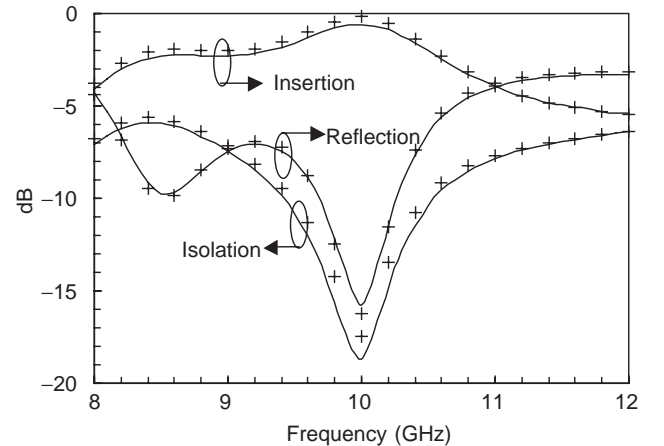


Figure 46. Performance of the H -plane Y-junction circulator with a full-height TT1-109 circular ferrite post (— values computed from this theory; + + + values given by Ref. 31).

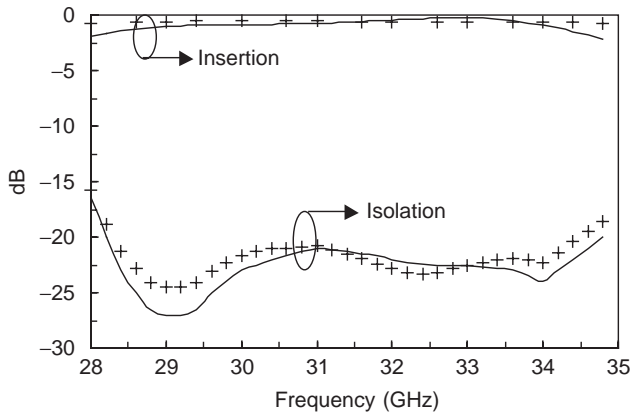


Figure 47. Performance of the H -plane Y-junction circulator with a partial-height circular ferrite post (—values computed from this theory; + + + experimental results given by Ref. 30).

6.4. Mode-Matching Method

Discrete-domain techniques such as the finite-difference and finite-element methods are slowly convergent, even for those with simple configurations. Straight application of the aforementioned FDTD scheme to analyze a waveguide Y-junction circulator with a ferrite specimen of arbitrary shape is possible but is used only as a last resort. The culprit is its complex boundary condition, which involves rectangular walls in the feeding waveguides, cylindrical truncation border of the waveguide junction, and the spherical surface of the ferrite sphere. It is further complicated by the anisotropic nature of ferrite. As illustrated earlier in this section, the computation time can be significantly reduced if a three-dimensional problem can be approximated by a two-dimensional one. Of course, this is not a realistic assumption for most circulators, but sometimes this scenario can be created in a piecewise sense by partitioning the configuration of interest appropriately. For example, the partial-height ferrite post shown in Figs. 23 and 24 can be divided horizontally into three parts such that each part contains a cylindrical resonator of uniform content. In contrast to the previous example, the field quantities in a resonator of finite height is not independent of z , yet the subsequent computation can be significantly cut by assuming that its dependence takes up the $e^{j\beta_z z}$ form. As a result, the relevant characteristic equation is similar to that of a two-dimensional case given in (100) with β_e replaced by β_n , given by

$$\beta_n = \sqrt{\beta_e^2 - \beta_z^2} \quad (139)$$

The electric and magnetic fields in these resonators are obtained by summing up all possible solutions or modes of the characteristics equation. Finally, the overall solution is deduced by stipulating that the tangential electric and magnetic fields be continuous at both ends of the cylindrical resonators in the adjacent parts.

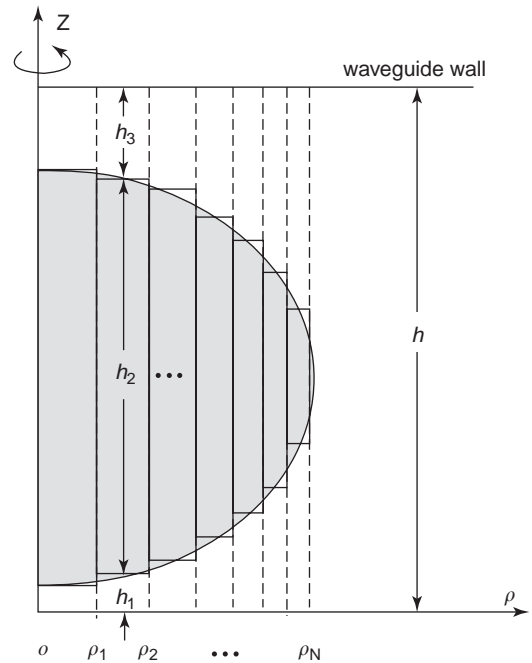


Figure 48. Segmentation of a half circle into a cascade of waveguide tubes with annulus bases.

The mode-matching scheme can be extended to cover a ferrite body of revolution such as a sphere. For illustration, if the circle shown in Fig. 48 is segmented vertically into parallel parts, a cascade of tubes is formed by revolving the partitioned circle around the z axis. Note that each tube consists of three components of heights h_1 , h_2 , and h_3 . Success of the present scheme relies on our ability to find the field quantities in a waveguide tube of uniform content analytically. Again, details are skipped and readers are referred to another source [27] for an in-depth analysis of a waveguide tube of an annular base. The final solution is obtained by requiring that the tangential electric and magnetic fields be continuous on the cylindrical surfaces as well as the annular bases of the waveguide tubes.

Although the mathematical derivation is very time-consuming and the equations obtained are very lengthy, the required computation time is very short. Characteristics of a waveguide Y-junction circulator with a ferrite sphere can easily be determined. Results similar to those given in Figs. 49–51 can be computed in a personal computer in milliseconds, and excellent agreement between the analytical with experimental results is observed. Due to the computational efficiency, we can afford to find the general field pattern inside a waveguide junction circulator. Shown in Fig. 49 are the strength and direction of the electric field vector in a magnetized ferrite sphere. The field pattern in the waveguide junction exterior to the magnetized ferrite sphere is shown in Fig. 50. In both figures, the nature of wave circulation is clearly demonstrated. For comparison, the symmetric field pattern in the waveguide with a demagnetized ferrite sphere is sketched in Fig. 51.

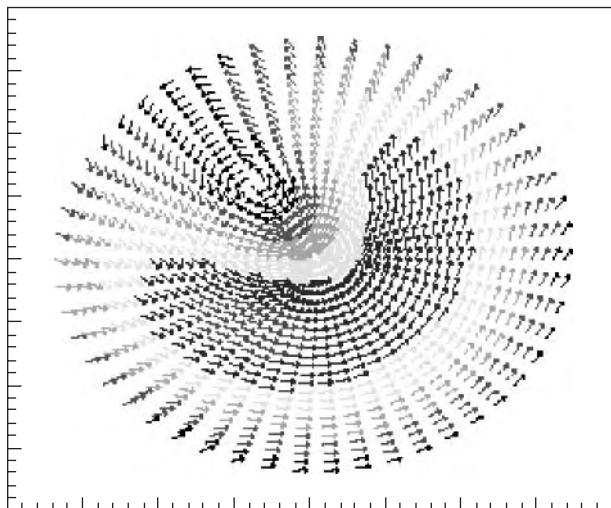


Figure 49. Strength and direction of the electric vector inside a magnetized ferrite sphere. (This figure is available in full color at <http://www.mrw.interscience.wiley.com/erfme>.)

7. CONCLUDING REMARKS

Study of circulators is a multidisciplinary one that covers material science, ferrimagnetism, wave propagation, and circuit design; therefore, it finds a special position in many engineering curricula. Design of circulators marks a sharp deviation from the current trend in problem solving as engineers are inclined to solve their assignments by brute force, such as using a faster computer, a better database, a larger memory, and a wider bandwidth at a higher frequency. Here, an engineer's ingenuity can be fully shown as significant improvement can be obtained by using different material, changing the size and shape of ferrite, fine-tuning its location, and other insignificant altera-

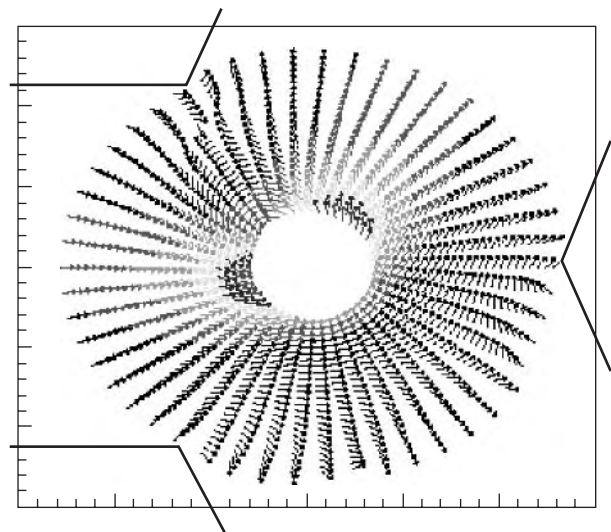


Figure 50. Strength and direction of the electric vector in a waveguide Y junction with a magnetized ferrite sphere. (This figure is available in full color at <http://www.mrw.interscience.wiley.com/erfme>.)

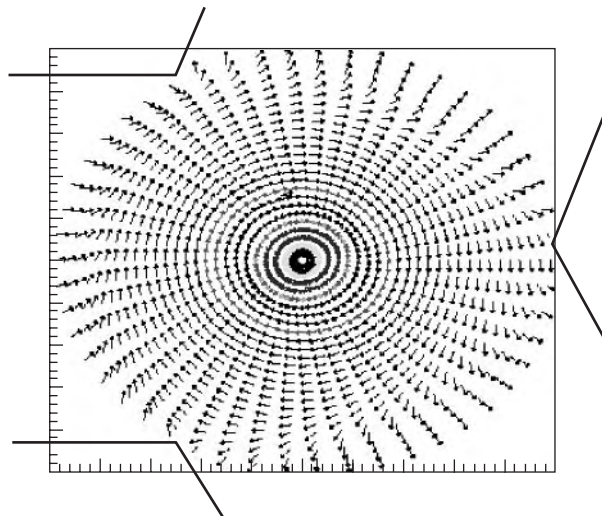


Figure 51. Strength and direction of the electric vector in a waveguide Y junction with a demagnetized ferrite sphere. (This figure is available in full color at <http://www.mrw.interscience.wiley.com/erfme>.)

tions. Circulators may be replaced in the future, but the underlying principles will prevail forever as it is an excellent manifestation of our ability in harnessing the nature for our benefit.

BIBLIOGRAPHY

1. D. M. Pozar, *Microwave Engineering*, Addison-Wesley, Reading, MA, 1990.
2. R. E. Collin, *Field Theory of Guided Waves*, 2nd ed., IEEE Press, New York, 1991.
3. H. Bosma, Performance of lossy H-plane Y-circulators, *IEEE Trans. Magn.*, **Mag-2**:273-277 (1966).
4. J. B. Davis, An analysis of the m-port symmetrical H-plane waveguide junction with central ferrite post, *IEEE Trans. Microwave Theory Tech.* 596-604 (Nov. 1962).
5. J. Helszajn, *Microwave Junction Circulators: Theory and Practice*, Wiley, New York, 1998.
6. D. K. Linkhart, *Microwave Circulator Design*, Artech House, Norwood, MA, 1989.
7. R. A. Waldon, *Ferrites: An Introduction for Microwave Engineers*, Van Nostrand, London, 1962.
8. F. Keffer, *The Magnetic Properties of Materials*, Freeman, San Francisco, 1967.
9. P. J. B. Clarricoats, *Microwave Ferrites*, Wiley, New York, 1961.
10. R. B. Leighton, *Principles of Modern Physics*, McGraw-Hill, New York, 1959.
11. R. F. Soohoo, *Microwave Magnetics*, Harper & Row, New York, 1970.
12. J. Helszajn, *Ferrite Phase Shifters and Control Devices*, McGraw-Hill, New York, 1989.
13. B. A. Auld, The synthesis of symmetrical waveguide circulators, *IRE Trans. Microwave Theory Tech.* 238-246 (April 1959).
14. C. E. Fay and R. L. Comstock, Operation of the ferrite junction circulator, *IEEE Trans. Microwave Theory Tech.* 1527 (Jan. 1965).

15. J. Helszajn, Design data for radial waveguide circulators using partial height ferrite resonators, *IEEE Trans. Microwave Theory Tech.* **MTT-23**(3):288–298 (March 1975).
16. J. Helszajn, Planar triangular resonators with magnetic walls, *IEEE Trans. Microwave Theory Tech.* **MTT-26**(2):95–100 (Feb. 1978).
17. E. K. N. Yung, D. G. Zhang, and Roger S. K. Wong, Novel waveguide Y-junction circular with a ferrite sphere for millimeter waves, *IEEE Trans. Microwave Theory Tech.* **44**(3):454–457 (March 1996).
18. H. Bosma, On stripline Y-circulators at UHF, *IEEE Trans. Microwave Theory Tech.* 61–71 (Jan. 1964).
19. E. K. N. Yung, W. B. Dou, D. G. Zhang, and R. S. Chen, Microstrip circulator made of a magnetized ferrite sphere, *Microwave Opt. Technol. Lett.* **28**(2):130–131 (Jan. 20, 2001).
20. Y. Konishi, Lumped element Y circulator, *IEEE Trans. Microwave Theory Tech.* **MTT-13**(6):852–864 (Nov. 1965).
21. E. K. N. Yung, H. Y. Ding, R. S. Chen, and Z. M. Xie, Finite difference analysis of H-plane waveguide Y-junction circulators, *Microwave Opt. Technol. Lett.* **20**(6):414–422 (March 20 1999).
22. J. B. Castillo Jr. and L. E. Davis, Computer-aided design of three-port waveguide junction circulator, *IEEE Trans. Microwave Theory Tech.* **MTT-18**:25–34 (1970).
23. K. L. Kunz and R. Luebbers, *Finite-Difference Time Domain in Electromagnetics*, CRC Press, Boca Raton, FL, 1993.
24. J. Schneider and S. Hudson. The finite-difference time-domain method applied to anisotropic material, *IEEE Trans. Anten. Propag.* **41**(7):994–999 (July 1993).
25. R. S. Chen. E. K. N. Yung, Z. M. Xie, and Y. Wang, FDTD analysis of EM wave circulating a magnetized ferrite body in free space, *Int. J. Infrared Millimeter Wave* **19**(2):329–341 (Feb. 1998).
26. S. A. Ivanov, Applications of the planar model to the analysis and design of the Y-junction stripline circulator, *IEEE Trans. Microwave Theory Tech.* **43**(6):1253–1263 (June 1995).
27. E. K. N. Yung, R. S. Chen, K. Wu, and D. X. Wang, Analysis and development of millimeter wave waveguide junction circulator with a ferrite sphere, *IEEE Trans. Microwave Theory Tech.* **46**(11):1721–1734 (Nov. 1998).
28. J. Liu, J. M. Jin, Edward K. N. Yung, and R. S. Chen, A fast, higher order three-dimensional finite-element analysis of microwave waveguide devices, *Microwave Opt. Technol. Lett.* **32**(5):342–352 (March 5, 2002).
29. R. S. Chen, E. K. N. Yung, C. H. Chan, D. X. Wang, and D. G. Fang, Application of the SSOR preconditioned CG algorithm to the vector FEM for 3-D full-wave analysis of electromagnetic-field boundary-value problems, *IEEE Trans. Microwave Theory Tech.* **50**(4):1165–1172 (April 2002).
30. R. S. Chen. D. X. Wang, and Edward K. N. Yung, Analysis of ferrite waveguide devices by use of the edge FEM combined with SOC technique. *Int. J. Electron.* **89**(10):771–790 (2002).
31. El-Shandwily, et al., General field theory treatment of H-plane waveguide junction circulators, *IEEE Trans. Microwave Theory Tech.* **21**(6):392–403 (June 1973).
32. N. Zeina, H. How, and C. Vittoria, Self-biasing circulators operating at Ka-band utilizing M-type hexagonal ferrites, *IEEE Trans. Magn.* **28**(5):3219–3221 (Sept. 1992).
33. M. A. Tsankov, S. I. Ganchev, and L. G. Milenova, Higher-order mode waveguide circulators for millimeter wavelengths, *IEEE Trans. Magn.* **28**(5):3228–3230 (Sept. 1992).

FERRITE ISOLATORS

B. BAYARD
 B. SAUVIAC
 D. VINCENT
 Jean Monnet University
 St. Etienne, France

1. ISOLATORS AND THEIR APPLICATIONS

The transmission of a radiofrequency or microwave signal (above 1 GHz) along a line differs with that of a low-frequency signal essentially in the fact that one of the dimensions of the line is greater than the wavelength. This means that at a given time the instant value of the signal varies along this dimension. Furthermore, the signal may propagate along the line according to the opposite directions (forward and backward propagations).

The behavior of the wave is characterized by the mapping of the electric and magnetic fields. This mapping depends on the geometry of the line as well as the conductivity, the dielectric, and the magnetic constant of the materials used in the structure. The *characteristic impedance* is calculated from the mapping of the electric field and the magnetic field; its value is often set at 50 Ω for practical use.

If several kinds of lines are used to transmit a signal from a source to a load, the electromagnetic field map will be different along each line. As a result, the signal will be perturbed at each connection. The impedance mismatch between two lines causes a *return loss*, that is, a reflection of a part of the signal toward the source and a weaker wave transmitted to the load. Since this reflection is undesirable and may be disruptive or even destructive, it has to be eliminated by the use of an *isolator*.

Isolators are two-port circuits that allow the microwave energy to propagate along a direction and stop it along the opposite one (Fig. 1a). The flow is restricted to one direction; hence any reflected energy at the load is trapped or dissipated. Because the behavior of the isolator differs for direct and reverse propagations, it is referred to as a *non-reciprocal device*.

Operating frequencies above 10 GHz are currently the higher limit for a correct functioning of active isolators or circulators, not only because of the limited bandwidth of semiconductors but also because of noise generation and power dissipation. On the other hand, microwave ferrite material can be regarded as a mature technology, and their interesting anisotropic properties have been widely exploited for passive nonreciprocal applications [1,2].

1.1. Applications

Isolators are intensively used in microwave communication systems. Their applications include the decoupling between a generator and its load, the decoupling of several amplifiers, and the combining of two or more transmitters.

1.1.1. Decoupling between Generator and Load. Generators are usually affected by any power coming back to

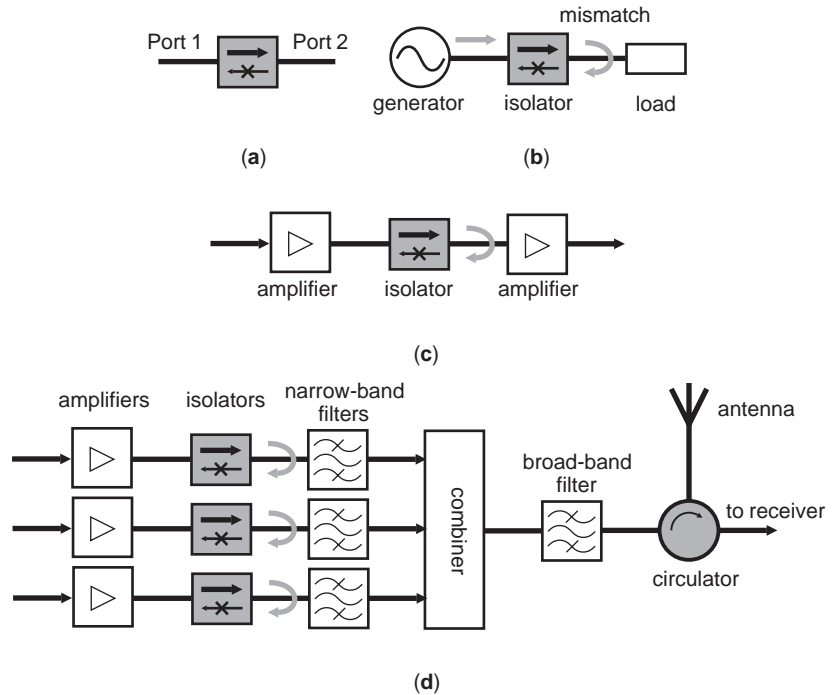


Figure 1. Some applications of isolators: (a) circuit symbol; (b) decoupling of generator and load; (c) decoupling of amplifiers; (d) combination of transmitters.

them, which may result in nonlinear effects such as frequency shift and instability. To overcome these problems, an isolator is used to eliminate the coupling between the generator and the load as shown in Fig. 1b, where the isolator attenuates only the backward wave and protects the generator.

1.1.2. Decoupling of Amplifier Stages. In applications where amplifiers are connected in series, they can affect each other in relation to their input impedance. The influence increases if their working frequency band is narrow because their input impedance varies sharply. If different amplifier stages are decoupled by isolators as shown in Fig. 1c, they can be tuned and adjusted without affecting the others, and if one stage is unbalanced, the others will not be overloaded.

1.1.3. Combination of Several Transmitters. A typical emitter stage of a mobile phone base station includes several transmitters working at different frequencies (Fig. 1d). The signal of each transmitter passes through an isolator, which has a low insertion loss, and a filter centered on the transmitter’s frequency. It travels then to the combiner. This lets the signal of each transmitter travel to the antenna without disturbing the others.

1.2. Characteristics

A perfect isolator should transmit all the energy from port 1 to port 2, cut all the backward energy from port 2 to port 1, and provide no reflection at port 1 and at port 2 (Fig. 2a).

The corresponding *S* parameters can be expressed in the following matrix:

$$\begin{pmatrix} S_{11} & S_{12} \\ S_{21} & S_{22} \end{pmatrix} = \begin{pmatrix} 0 & 0 \\ 1 & 0 \end{pmatrix} \tag{1}$$

Actual isolators response is not so ideal (Fig. 2b), and their specification must take into account several fundamental parameters such as insertion loss, isolation, and standing-wave ratio, as well as frequency bandwidth, intermodulation, and thermal and power considerations.

1.2.1. Insertion Loss. It corresponds to the neutrality of the component in the forward direction and its magnitude must be close to the unity. When a signal is applied to port 1, the insertion loss (IL) will be the ratio of the input power (port 1) to the output power (port 2). Typical values, expressed in decibels (dB), are between 0.1 and 1 dB and are calculated by the following expression:

$$IL \text{ (dB)} = 20 \log_{10} \left| \frac{a_1}{b_2} \right| = -20 \log_{10} |S_{21}| \geq 0 \tag{2}$$

1.2.2. Isolation. This corresponds to the ability of cutting the backward wave. Its magnitude must reach high values. When a signal is applied to port 2, the isolation (IS) will be the ratio of the input power (port 2) to the output power (port 1). Typical values, expressed in dB, are between 20 and 30 dB and are calculated by the following

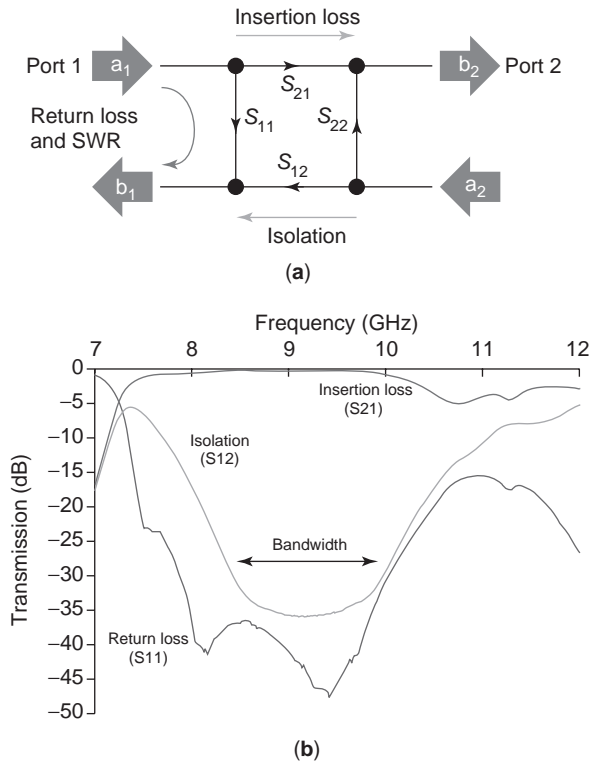


Figure 2. Characteristics of an isolator: (a) S parameters; (b) actual frequency response.

expression:

$$IS \text{ (dB)} = 20 \log_{10} \left| \frac{a_2}{b_1} \right| = -20 \log_{10} |S_{12}| \gg 0 \quad (3)$$

1.2.3. SWR. The standing-wave ratio (SWR) specifies how the input signal will be reflected back toward the source. It depends directly on the magnitude of return loss (R) at port 1, that is, the ratio of the incident power to the reflected power. The SWR is always greater than one and typical values are between 1.05 and 1.2, to maintain a good impedance matching:

$$|R| = \left| \frac{b_1}{a_1} \right| = |S_{11}| \simeq 0 \quad (4)$$

$$SWR = \frac{1 + |R|}{1 - |R|} \gtrsim 1 \quad (5)$$

1.2.4. Bandwidth. The operating bandwidth can be expressed as the difference between the high and low working frequencies divided by the center frequency multiplied by 100 (percentage bandwidth). Various bandwidth values are available according to the technology of the isolator, but 10% is often presented.

1.2.5. Intermodulation. When nonlinear elements such as ferrite materials are used, harmonics ($2f_1$, $3f_1$, etc.) appear but can be easily eliminated thanks to their high frequency value. However, in the case of several but close frequencies (f_1 and f_2), intermodulation rays appear

($2f_1 - f_2$ and $2f_2 - f_1$) and their influence is qualified by a third-order intermodulation product defined as the ratio of the intermodulation magnitude to the fundamental magnitude.

1.2.6. Temperature Range. The operating temperature range of an isolator is limited by the materials used in the device, especially by ferrites. Magnetic materials indeed exhibit nonlinear behaviors and frequency shift due to temperature variation and become nonmagnetic above their Curie temperature. Operating temperatures from -20 to $+70^\circ\text{C}$ are common.

1.2.7. Power Dissipation. For low-power isolators, exceeding the power limit causes nonlinearity effects in the ferrite material and provides a frequency shift and an increase in the insertion loss. For high-power isolators, average power induces an increase of temperature and cooling of the device is sometimes needed. The peak power should cause breakdown or arcing, which generally results in permanent degradation of performance. Power depends on the technology and can be limited from a few watts (planar drop-in isolators) to several hundred watts (waveguide isolators). Acceptable average power decreases with the working frequency. Peak power can reach several kilowatts.

2. DEVICES

The first experimental microwave ferrite device was demonstrated in 1949. The development of this type of device was strongly linked to ferrite materials preparation and to the knowledge of spin interaction in ferrimagnetic materials [3–5].

The behavior of microwave ferrite devices is based on the gyromagnetic property of ferrimagnetic materials. Several effects can be exploited to provide nonreciprocal propagation of the signal, such as *Faraday rotation*, *ferrimagnetic resonance*, and *field displacement*.

Many microwave components such as circulators, isolators, phase shifters, or gyromagnetic filters are using ferrite materials and are always essential because there is no alternative semiconductor-based device that satisfies similar requirements.

Furthermore, microwave technologies are moving to higher frequencies, up to 100 GHz, where high-resistivity materials are needed so that ferrites remain the first choice and semiconductor materials are currently not competitive.

2.1. Waveguide Isolators

The microwave applications of ferrites had their foundations in the Faraday effects, and the first devices were circular waveguide Faraday rotators. Then, rectangular waveguide components were developed using resonance absorption or field displacement [6].

2.1.1. Faraday Rotation Isolator. The linear polarization of a wave rotates if it propagates in a longitudinally magnetized ferrite. This phenomenon, called *Faraday*

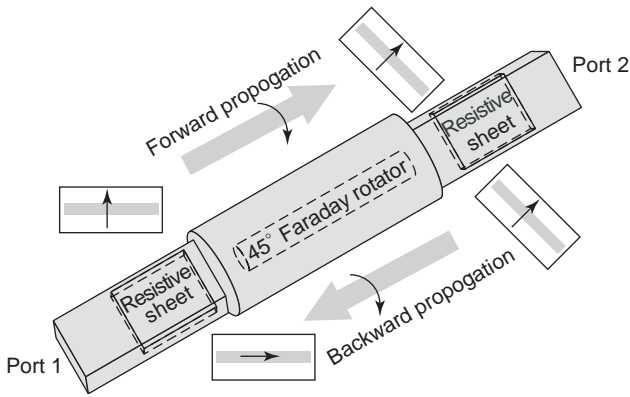


Figure 3. Waveguide Faraday rotation isolator.

rotation, is nonreciprocal so that the polarization always rotates in the same direction whatever the propagation direction. The Faraday rotation can be used in an isolator if waves are absorbed or not, according to the rotation of their polarization. The device is made from a circular waveguide containing a 45° rotator between two 45° shifted rectangular waveguides. Absorbing sheets are placed in rectangular-to-round waveguide transitions (Fig. 3).

The polarization of the electric field of a wave entering port 1 is parallel to the smallest side of the rectangular waveguide so that it is normal to the first resistive sheet and is not affected by it. The polarization is rotated 45° clockwise by the rotator and becomes normal to the second resistive sheet. The wave can therefore emerge without attenuation.

In the reverse direction, a wave entering port 2 is rotated 45° in the same direction (clockwise) so that the electric polarization is parallel to the port 1 resistive sheet. The wave is then absorbed and cannot propagate.

The average power that can be absorbed is limited by resistive sheets. On the other hand, insertion loss and isolation are improved if the magnitude of circular polarizations is not affected by the rotator so that no perpendicular polarization appears before resistive sheets.

2.1.2. Resonance Isolator. A circularly polarized wave that penetrates into a magnetized ferrite may be absorbed or not, according to its rotation direction. The effect is maximum at the gyromagnetic resonance frequency of the ferrite. This phenomenon can be used in a rectangular waveguide where the polarization is circular at two different positions (Fig. 4). If a ferrite is placed at one of these

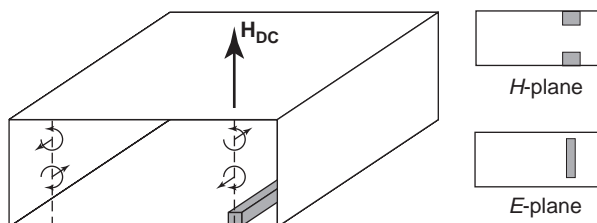


Figure 4. Waveguide resonance isolator.

positions, the nonreciprocal absorption of the microwave energy is used to make an isolator [7]. A transverse DC field is required to magnetize the ferrite.

The optimum position of the ferrite is chosen for a circular polarization of the internal microwave magnetic field. This position may however differ from that of the empty guide because of the ferrite presence. Several ferrite shapes can be used (*E*-plane or *H*-plane resonance isolator), but *H*-plane ferrite geometry, consisting of two thin flat ferrite rods, shows better performance. It has the particular advantage of setting the ferrite rods against the waveguide with a maximum contact area so that the material can be cooled through the metal waveguide.

2.1.3. Field Displacement Isolator. In a partially ferrite-filled waveguide, the microwave energy may be rejected from the material according to its direction of propagation. As a result, the microwave electric field vanishes near the ferrite for direct propagation direction and is maximum for the reverse direction (Fig. 5).

If a resistive sheet is placed against the ferrite slab where the difference of energy is maximum, it will have little effect on the direct propagation, but there will be strong absorption in the backward propagation.

As for resonance isolator, a transverse DC magnetic field is applied to the ferrite, but a lower intensity is required. This kind of isolator gives low insertion loss about 0.1 dB. It is well suited for low-power operations because the resistive sheet cannot be cooled as it is not in contact with the waveguide.

2.2. Planar Isolators

The development of planar circuits, fabricated by conventional printed-circuit techniques, has liberated the microwave designer from high costs and many constraints encountered with waveguides and coaxial lines [8,9]. Ferrite devices were rapidly developed for stripline and microstrip circuits such as *edge-guided-mode* isolators or *Y-junction* circulators.

2.2.1. Coplanar Resonance Isolator. The coplanar waveguide is a surface strip transmission line and consists of a central conductor strip separated from ground planes by two slots on a dielectric substrate [10]. At high frequencies, the propagation in this structure is no longer TEM (transverse electromagnetic) because a longitudinal

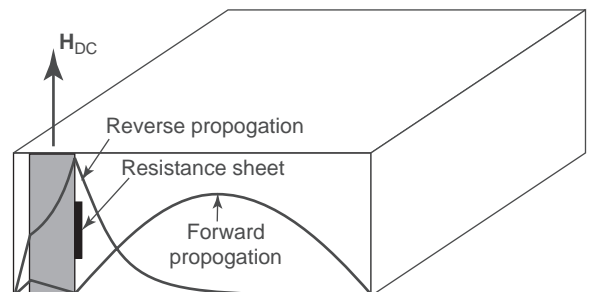


Figure 5. Waveguide field displacement isolator.

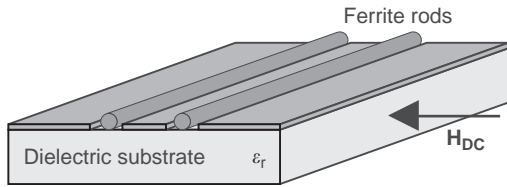


Figure 6. Coplanar resonance isolator.

component of the microwave magnetic field appears. Thus the resulting elliptically polarized magnetic field in the slot can be used for nonreciprocal operations if it interacts with a ferrite material. A resonant isolator can be fabricated by attaching ferrite rods at the air–dielectric interface between the conductors (Fig. 6). A horizontal magnetic polarization is applied to the ferrite, perpendicular to the microwave elliptic polarization plane.

This device will show better performances if the microwave polarization is circular. High insertion loss and moderate isolation values are the consequences of an ellipticity different from unity. However, since the dominant propagation mode is TEM, the microwave polarization will never be circular but the ellipticity could be improved under one of these conditions: a higher permittivity substrate, wider strip and slots dimensions, or a higher working frequency [11].

2.2.2. Stripline Resonance Isolator. TEM transmission lines are not suitable for nonreciprocal devices because there is no longitudinal component of the microwave magnetic field. However, the line may be antisymmetrically loaded with a dielectric material so that a longitudinal field appears according to Maxwell’s equations and boundary conditions [6]. Ferrite rods are placed near the air–dielectric interface, where the longitudinal field is higher. A longitudinal magnetic field is required to obtain an elliptic polarization such as that in the device described above as it will interact with the magnetic rods to provide nonreciprocal attenuation of the signal. Figure 7 shows ferrite isolators based on a coaxial line and a stripline. They are both half-filled with a dielectric material and contain vertically magnetized ferrite rods. The nonreciprocal effect is maximum at the ferrite resonance as in the case of the coplanar isolator.

2.2.3. Coupled Microstrip Line Isolator. The coupling between two microstrip lines on a ferrite substrate is nonreciprocal if the gyrotropic material is magnetized [12]. The nonreciprocal effect is a differential phase shift between S_{12} and S_{21} that can be used to create an isolator.

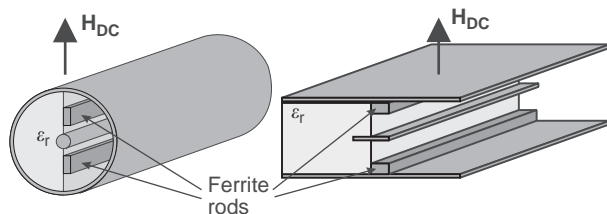


Figure 7. Coaxial and stripline resonance isolator. (From [10]; © 1969 IEEE, reproduced with permission.)

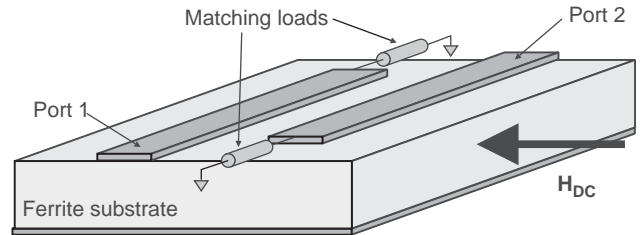


Figure 8. Coupled microstrip-line isolator.

The coupling length is adjusted so that the direct signal at one port is coupled to the other line and the reverse one is not delivered to the first line. External matching loads are placed at the end of each line to absorb reflected power (Fig. 8).

2.2.4. Microstrip Edge-Guided-Mode Isolator. A microstrip or a stripline using a ferrite substrate, with a magnetization normal to the ground plane, with a wide strip conductor, shows an exponential field variation of the dominant mode along the device width (Fig. 9). This field displacement effect is nonreciprocal as it is reversed for each direction of wave propagation and for opposite magnetic polarizations [13]. The energy is concentrated near opposite edges of the component and may be dissipated in the reverse propagation direction by placing an absorbing film on one edge of the strip.

The field displacement is caused by the gyromagnetic properties of the ferrite, which is magnetized below the resonance in the low-loss region. The device therefore shows better performance with a low field bias. On the other hand, the use of a strip much wider than the substrate thickness produces a low characteristic impedance so that suitable impedance transformers are required for approximate matching to 50-Ω-impedance lines.

Because the presence of the absorber should provide insertion loss, several improvements were proposed. The absorbing film can be replaced by a short circuit of one edge of the strip with the ground plane. The addition of an iron plate near the short circuit provides a strong interaction with the magnetic field that improves the nonreciprocal effect [14].

2.2.5. Sawtooth Edge-Mode Isolator. Other authors suggested printing the wide strip with a slots on its edge without absorber [15]. The direct wave is not affected by the slot discontinuity, while the reverse one is reflected by this effective open circuit and dissipates in the ferrite substrate. This device is strictly planar and requires no absorber.

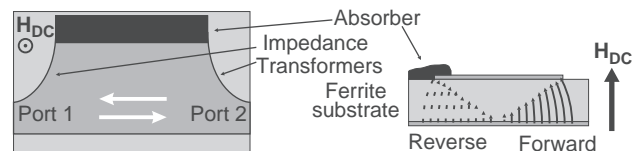


Figure 9. Microstrip edge-guided-mode isolator. (From [13]; © 1971 IEEE, reproduced with permission.)

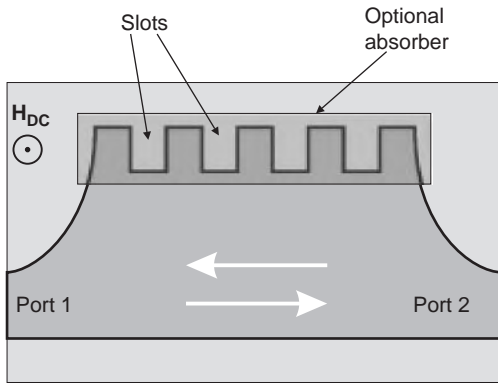


Figure 10. Sawtooth edge-mode isolator. (From [16]; © 2001 IEEE, reproduced with permission.)

To improve the bandwidth, a multislot (sawtooth) configuration is used and a lossy material covers only the sawtooth to reduce insertion loss (Fig. 10). The behavior of the device can be tuned by varying the size of those slots; isolation is increased with a large sawtooth design, while low insertion loss is obtained with a small sawtooth design [16].

2.2.6. Slotline Field Displacement Isolator. It is also possible to obtain a nonreciprocal field displacement in a ferrite-loaded slotline (Fig. 11). If a horizontal static magnetic field is applied, the energy travels along each side of the ferrite according to the propagation direction [17]. Thus the presence of an absorbing material at the bottom of the ferrite provides the isolation. An alumina substrate may be placed between the ferrite and the lines to reduce the insertion losses of the device. The main drawback of such a structure is the transition between the slotline and a coaxial line (or other lines) at each port of the device that provides mismatch losses. The same kind of device can be built using a finline structure [18].

2.2.7. Circulator-Based Isolator. One of the most popular planar isolators proposed by manufacturers for low-power applications is based on a three-port circulator by adding a matching termination to one port. A usual form consists of a stripline symmetric Y junction with a circular center conductor surrounded with two ferrite disks (Fig. 12). The circular junction behaves like a resonant cavity with two contrarotating modes resulting in a standing wave. If a static magnetic field is applied perpendicularly to the disks, the resonant frequencies of the two modes are different. The pattern of the standing wave



Figure 11. Slotline field displacement isolator. (From [17]; © 1975 IEEE, reproduced with permission.)

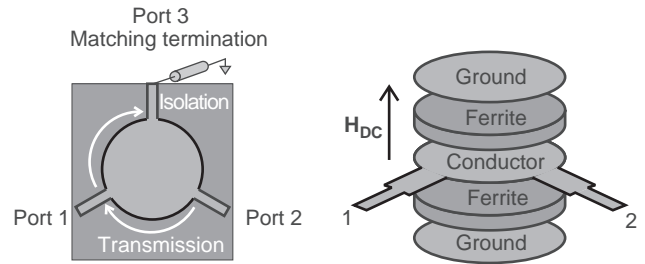


Figure 12. Circulator-based isolator. (From [24]; © 1965 IEEE, reproduced with permission.)

is therefore rotated so that the third port is isolated while the others are coupled [19].

The easy fabrication and the good performance of the Y-junction circulator make this miniature nonreciprocal device one of the most widely used, as a circulator as well as an isolator.

3. NONRECIPROCAL EFFECTS

The functioning of passive microwave isolators is based on ferromagnetic resonance properties of ferrite materials. Magnetized ferrites are indeed anisotropic and characterized by an antisymmetric permeability tensor, which is necessary to obtain nonreciprocal effects such as isolation. Most passive magnetic devices need a saturated state of the ferrite or at least a magnetic polarization that is performed by permanent magnets or magnetic coils.

3.1. Ferromagnetic Resonance

To understand the origin of the anisotropy, the interaction between magnetic moments of the ferrite and a magnetic field needs to be studied.

3.1.1. Magnetic Units. The current ferrite literature still uses cgs units (centimeter, gram, second) for historical reasons. Therefore, conversions between this system and SI units (meter, kilogram, second, ampere) frequently have to be performed.

In the SI system, the following relations correspond to the response of a material (M and B) immersed in an applied field (H)

$$\chi \mathbf{H} = \mathbf{M} = \frac{d\mathbf{m}}{dV} \tag{6}$$

$$\mathbf{B} = \mu_0(\mathbf{H} + \mathbf{M}) = \mu_0\mathbf{H}(1 + \chi) = \mu_0\mu_r\mathbf{H} \tag{7}$$

The ratio of the magnetization to the applied field is the susceptibility (6), and the ratio of the induction to the field is the permeability (7). The susceptibility vanishes and the relative permeability equals one for nonmagnetic materials. In the case of anisotropic materials, induction, magnetization, and applied field are not parallel and the susceptibility as well as the permeability become tensorial.

In the cgs system, vacuum permeability is set at the unity and (7) must be written as follows

$$\mathbf{B} = \mathbf{H} + 4\pi\mathbf{M} \quad (8)$$

and the conversion between cgs and SI units are [20]

$$1 \text{ A/m} = 4\pi 10^{-3} \text{ Oe magnetic field } (H) \quad (9)$$

$$1 \text{ A/m} = 10^{-3} \text{ emu/cm}^3 \text{ magnetization } (M) \quad (10)$$

$$1 \text{ T} = 10^4 \text{ G induction } (B) \quad (11)$$

3.1.2. Static Magnetic Field. When a static magnetic field (\mathbf{H}_0) is applied to a magnetic material, its magnetic moments (\mathbf{m}) and the corresponding magnetization (\mathbf{M}) for a given volume precess around the field axis with an angular velocity proportional to the magnitude of the field (Fig. 13a). This phenomenon, called *Larmor's precession*, is governed by the following relations, which give the gyromagnetic equation of motion, the angular velocity, and the gyromagnetic ratio, respectively:

$$\frac{d\mathbf{m}}{dt} = -\gamma\mu_0(\mathbf{m} \times \mathbf{H}_0) \quad (12)$$

$$\omega_0 = \gamma\mu_0 H_0 \quad (13)$$

$$\gamma = 176 \cdot 10^9 \text{ rad s}^{-1} \text{ T}^{-1} (\Leftrightarrow 28 \text{ GHz/T}) \quad (14)$$

3.1.3. Microwave Field. If, in addition, the material is submitted to a microwave field (\mathbf{h}) perpendicular to the static one, the magnetic moments tend to precess around a total field that oscillates (Fig. 13b). When the angular velocity of the moments reaches the frequency of microwave oscillations, the microwave energy is transmitted to the material and absorbed.

3.1.4. Polder's Model. After taking into account the microwave field, the spectral expression of the equation of motion leads to a relative permeability tensor:

$$\bar{\mu}_r = \begin{pmatrix} \mu_r & 0 & +jk \\ 0 & 1 & 0 \\ -jk & 0 & \mu_r \end{pmatrix} \quad (15)$$

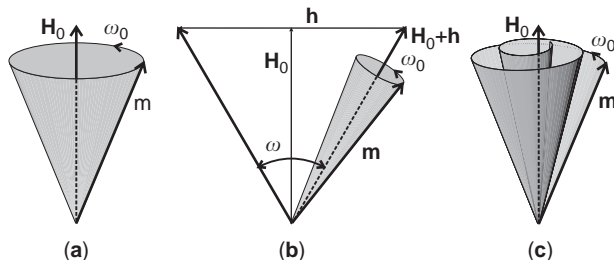


Figure 13. Precession of ferrite moments under an applied field: (a) static applied field; (b) static and microwave applied fields; (c) with losses.

This tensor is used for a y -axis applied field (xy , yx , yz , and zy elements vanish) and for a saturated material (yy element is equal to 1). The presence of the imaginary number j corresponds to the rotation of the moments; that is, there is a 90° phase difference between m_x and m_z .

The elements of the permeability tensor depend on the frequency

$$\mu_r = 1 + \frac{\omega_0 \omega_M}{\omega_0^2 - \omega^2} \quad (16)$$

$$\kappa = \frac{\omega \omega_M}{\omega_0^2 - \omega^2} \quad (17)$$

$$\omega_M = \gamma\mu_0 M_S \quad (18)$$

and they both depend on the magnitude of the applied field (13) and on the saturation magnetization of the material (18).

3.1.5. Damping Factor. If losses are taken into account, the angle between \mathbf{m} and \mathbf{H}_0 will decrease until these elements are aligned (Fig. 13c). Tensor elements become complex quantities, and a damping parameter is introduced in (16) and (17):

$$\mu_r = \mu_r' - j\mu_r'' = 1 + \frac{(\omega_0 + j\alpha\omega)\omega_M}{(\omega_0 + j\alpha\omega)^2 - \omega^2} \quad (19)$$

$$\kappa = \kappa' - j\kappa'' = \frac{\omega \omega_M}{(\omega_0 + j\alpha\omega)^2 - \omega^2} \quad (20)$$

The real and imaginary parts of the elements of the permeability tensor are shown in Fig. 14 for a 180 mT saturation magnetization and 0.1 damping factor. Figure 14a shows a frequency sweep with a fixed applied field, which is currently the most common representation, thanks to vector analyzer measurements facilities. For historical reasons, Fig. 14b is the most widely known representation because it was previously easier to work with a single-frequency microwave source and to vary the applied field by adjusting a continuous current.

According to Fig. 14b, the resonance losses are characterized by the width of the imaginary part, which increases for lossy materials. The width at midheight of the curve is called *linewidth* and is frequently used by manufacturers (often expressed in oersteds). It depends on the damping factor and on the working frequency:

$$\gamma\mu_0 \Delta H = 2\alpha\omega \quad (21)$$

Figure 14b also shows three different zones according to the magnitude of the applied field. The expressions *below*, *above*, or *at resonance* refer to a field sweep and not to a frequency sweep. The confusion could be reinforced if the static field were expressed as a frequency as in (13).

Polder's model is defined for saturated material so that the magnetization of the ferrite reaches the saturation magnetization. Under particular operation conditions such as low bias fields, several magnetic domains with different magnetization magnitudes and orientations are

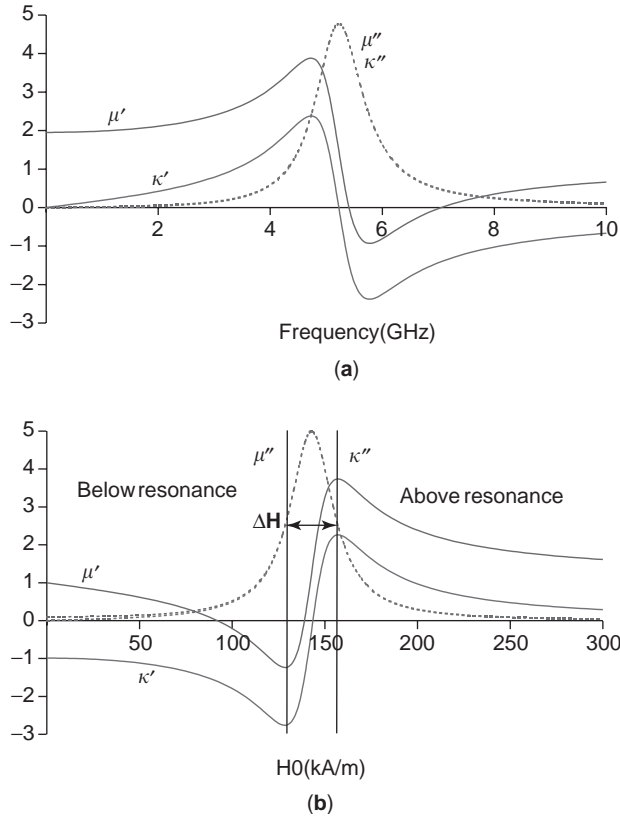


Figure 14. Ferromagnetic resonance; real and imaginary parts of the elements of the permeability tensor: (a) frequency sweep and 150 kA/m applied field; (b) field magnitude sweep and 5 GHz frequency.

present. Therefore new models must be used to take into account the resulting effects on the gyromagnetic phenomenon [21].

3.1.6. Demagnetizing Factors. All the previous definitions concern materials influenced by an internal magnetic field, that is, the actual field experienced by the spin dipoles. In an infinite medium, the internal field equals the applied field, but in the case of a finite medium, there is a discontinuity of the magnetic field at the boundary between materials with different permeability values. Determining the field inside an arbitrarily shaped sample is not always possible, but the problem is tractable for an approximate ellipsoidal shape. Thus, the internal field can be expressed from the applied field as follows

$$\mathbf{H}_i = \mathbf{H}_0 - \bar{\mathbf{N}}\mathbf{M} \tag{22}$$

$$\bar{\mathbf{N}} = \begin{pmatrix} N_x & 0 & 0 \\ 0 & N_y & 0 \\ 0 & 0 & N_z \end{pmatrix} \tag{23}$$

where the demagnetizing factors, N_x , N_y , and N_z , depend on the shape of the sample. The sum of these terms are equal to one. Each term equals $\frac{1}{3}$ in the case of a sphere;

the term tends to zero if the corresponding size increases and to one if it becomes thinner. Several approximations have been calculated and are helpful in estimating internal fields for arbitrary shapes [22].

Since the demagnetizing factors concern static and microwave fields, the tensor elements are dramatically changed and the resonant frequency is given by Kittel's equation for a z -direction applied field:

$$\omega_r = \gamma\mu_0 \sqrt{[H_0 + (N_x - N_z)M][H_0 + (N_y - N_z)M]} \tag{24}$$

3.2. Nonreciprocal Wave Propagation

Because waveguide or planar configurations are difficult to solve, nonreciprocal effects in ferrites can be more elementarily understood by considering the microwave propagation in infinite media. Maxwell's equations can be combined to include the permeability tensor and, considering a propagation along the z axis, it gives

$$\nabla \times \nabla \times \mathbf{H} - \omega^2 \epsilon_0 \mu_0 \epsilon_r \bar{\mu}_r \mathbf{H} = 0 \tag{25}$$

$$\mathbf{H} = \mathbf{h} \exp(j\omega t) \exp(-\gamma z) \tag{26}$$

where

$$\gamma = \alpha + j\beta = j \frac{\omega}{c} \sqrt{\epsilon_e \mu_e} \tag{27}$$

is the propagation coefficient that represents both the attenuation and the phase delay of the signal. In an infinite medium, they depend on the effective permittivity and permeability of the material.

According to the direction of the static magnetic field, which fills the permeability tensor (15) in different ways, several phenomena on the effective permeability and on the propagation occur.

3.2.1. Longitudinal Field. If a static magnetic field is applied parallel to the propagation direction (z axis), then (25) leads to an eigenproblem where the eigenvalues are

$$\mu_+ = \mu_r + \kappa \tag{28}$$

$$\mu_- = \mu_r - \kappa \tag{29}$$

These associated eigenvectors are respectively a right-hand circular polarized magnetic field for (28) and a left-hand polarization for (29). This means that the microwave must be decomposed according to these two polarizations and each part propagates with the corresponding effective permeability.

The effective permeability values, obtained from Fig. 14b, are plotted versus the applied field in Fig. 15a. In an infinite medium, the propagation coefficients of the corresponding plane wave are given by

$$\gamma_{\pm} = j \frac{\omega}{c} \sqrt{\epsilon_r \mu_{\pm}} = j \frac{\omega}{c} \sqrt{\epsilon_r (\mu_r \pm \kappa)} \tag{30}$$

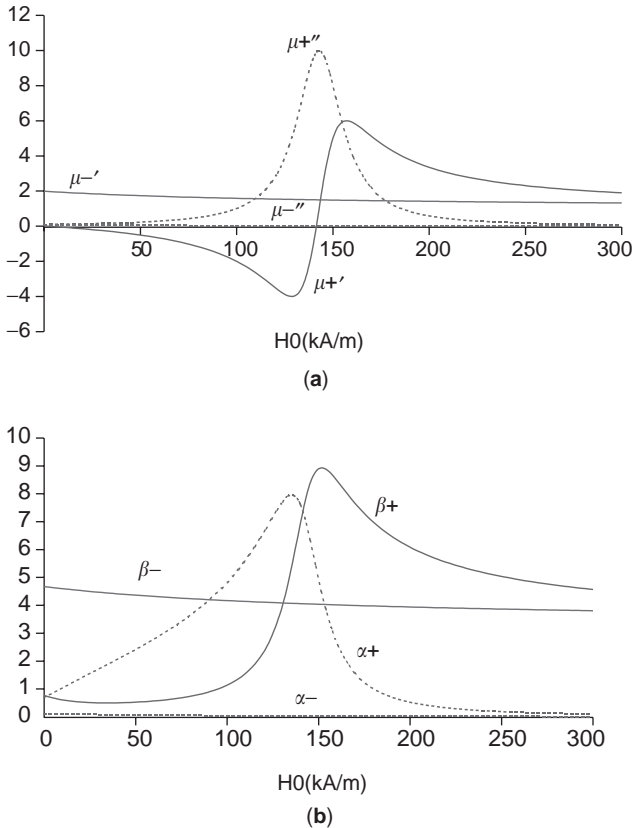


Figure 15. Microwave propagation parallel to the applied field: (a) effective permeability values; (b) nonreciprocal propagation coefficients.

and are plotted in Fig. 15b. Since real parts and imaginary parts are all different, nonreciprocal effects can be obtained not only for absorption but also for phase.

3.2.2. Transverse Field. If the permeability tensor is filled according to a perpendicular field (x or y axis), propagation will occur with two effective permeability values

$$\mu_{+} = \frac{\mu_r^2 - \kappa^2}{\mu_r} \quad (31)$$

$$\mu_{-} = 1 \quad (32)$$

The eigen vectors are now linear polarizations. Permeability values and propagation coefficients are plotted in Fig. 16. Nonreciprocal effects are also possible.

Although the explanations above are defined for plane waves (without longitudinal field components), they can be generalized for cases of propagation in waveguides or planar lines where longitudinal fields (non-TEM modes) appear.

3.2.3. Faraday Rotation. Figure 15b shows different values of the phase delay. If a linearly polarized incident microwave field is decomposed in both right-hand and left-hand circular polarizations, each part will be differently phase-shifted for a given distance (Fig. 17). Then the combination of the two emerging circular polarizations (with

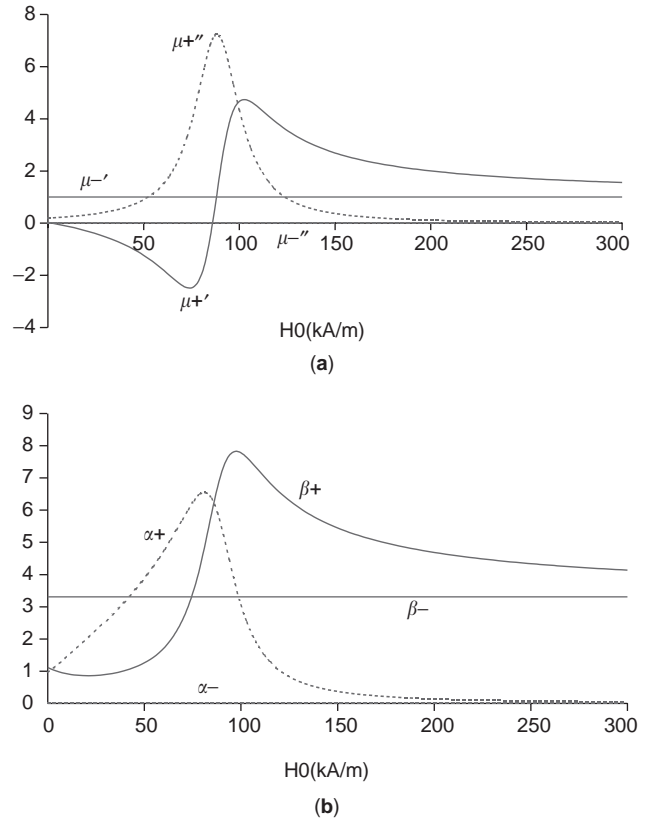


Figure 16. Microwave propagation perpendicular to the applied field: (a) effective permeability values; (b) nonreciprocal propagation coefficients.

the same magnitude) gives a linear polarization with a rotation equal to the half phase difference:

$$\theta = \frac{\Delta\phi}{2} = \frac{\beta_{-} - \beta_{+}}{2} L \quad (33)$$

The rotation is nonreciprocal. The polarizations of backward and forward waves rotate in opposite directions (respectively to the left or to the right) according to their own coordinate system because the applied field is inverted. As a result, rotations are in the same direction according to the ferrite axes.

Faraday rotation should be performed for low field values where losses are weak to ensure that the circular magnitudes are not attenuated and the emerging

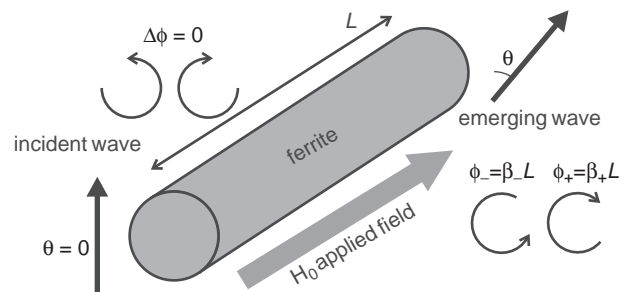


Figure 17. Faraday rotation of a linearly polarized wave.

polarization remains linear. The nonreciprocal rotation effect, similar to the behavior of Faraday rotation in optical media, was the first phenomenon exploited in microwave ferrite devices and is widely used to build circulators or isolators as shown in Fig. 3.

3.2.4. Resonance Absorption. Figures 15b and 16b both show nonreciprocal absorption according to the polarization of the wave. Losses are added in (28) and vanish in (29), where the imaginary part of the effective permeability is nearly zero regardless of the applied field. The maximum nonreciprocal attenuation occurs at the resonance where phases are equal.

In the first configuration, a left-hand circular polarization is absorbed while a right-hand polarization can propagate. If the polarization of the incident wave is elliptic, the attenuation depends on whether the magnitude of the right-hand circular polarization is maximum or not (Fig. 18).

In the second configuration, a linearly polarized microwave magnetic field parallel to the static field does not interact with the ferrite and the wave propagates in the same way as in a dielectric material. On the other hand, a polarization perpendicular to the applied field is strongly absorbed.

The resonance absorption is widely used in devices where a longitudinal magnetic field exists. If longitudinal and transverse fields are 90° phase-shifted, then they form an elliptic polarization that can interact with the rotation of the moments in a ferrite. The material must be magnetized perpendicular to the plane where the microwave polarization and the magnetic moments rotate. If longitudinal and transverse magnitudes are equal, the polarization becomes circular and effects are maximum. This configuration is used in rectangular waveguide resonance isolators (Fig. 4) and in coplanar and stripline isolators (Figs. 6 and 7).

3.2.5. Transverse Field Displacement. The negative value of the effective permeability, in Figs. 15b and 16b, implies that the microwave field is rejected from the material, while the other permeability allows the wave to penetrate. If a waveguide is partially filled with a ferrite material and if the case of a negative permeability occurs, the energy therefore propagates in the empty region. This phenomenon is a form of field displacement and is used in the rectangular waveguide isolator described in Fig. 5.

Another configuration where field displacement can be observed is the case of two wide strips separated by a ferrite substrate. In this type of structure, only TE modes are considered because TM modes cannot exist between parallel strips when the spacing is less than a half-wavelength [13].

The field components can be expressed as follows

$$E_x, H_y, H_z = A_{x,y,z} \exp(-\alpha_y y) \exp(-j\beta_z z) \tag{34}$$

where the propagation coefficients depend on the elements of the permeability tensor:

$$\beta_z = \omega \sqrt{\mu_0 \epsilon_0 \epsilon_r \mu_r} \tag{35}$$

$$\alpha_y = \omega \frac{\kappa}{\mu_r} \sqrt{\mu_0 \epsilon_0 \epsilon_r \mu_r} \tag{36}$$

The corresponding wave can therefore propagate along the z axis (purely imaginary coefficient in the propagation direction) while it is attenuated along the y axis (purely real coefficient along the width), so that the field magnitudes decrease exponentially along the width. This is the edge-guided mode (Fig. 19). The phenomenon is more efficient if the material is magnetized below the resonance with a weak internal field to avoid losses, just enough for the saturation.

If the applied field is inverted, the sign of the attenuation is changed and the exponential decay is inverted.

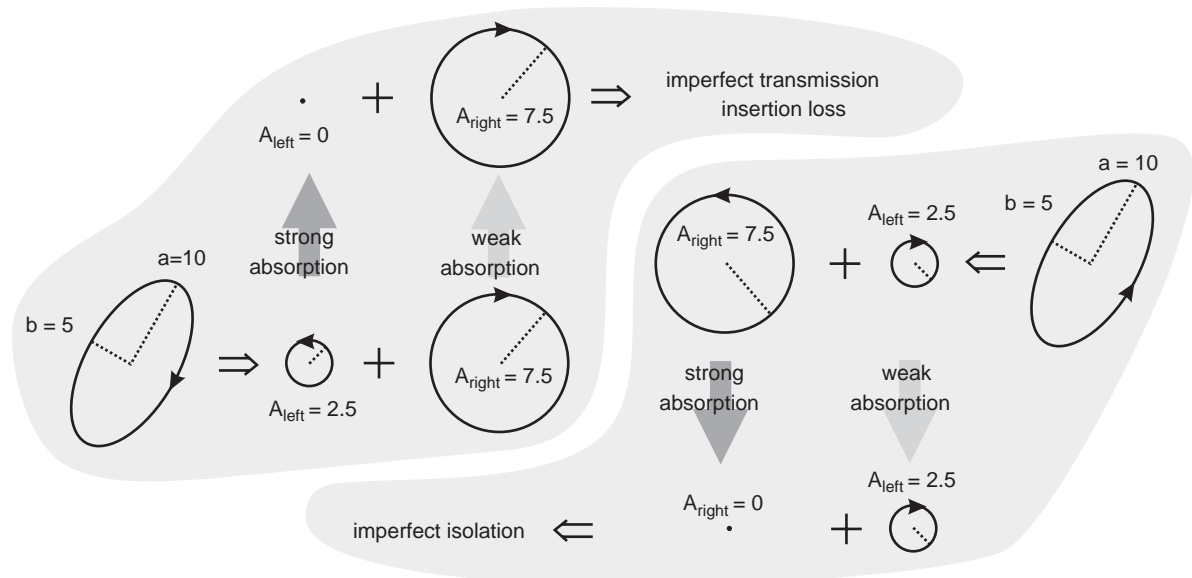


Figure 18. Resonance absorption of left-hand and right-hand polarizations.

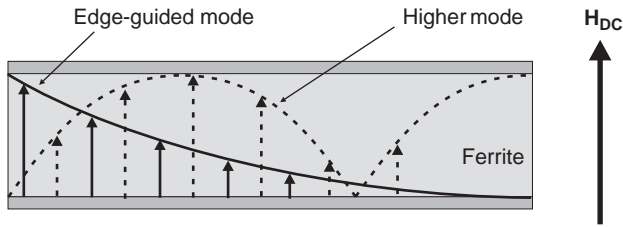


Figure 19. Field displacement and edge-guided mode. (From [13]; © 1971 IEEE, reproduced with permission.)

The same changes occur for a reverse propagation. The field displacement is therefore nonreciprocal and can be used to build a stripline or a microstrip isolator by adding an absorber on one edge as shown in Fig. 9. For high frequencies, other modes of propagation with a sinusoidal pattern can exist. As a result, the field displacement, corresponding to the edge-guided mode, is frequency-limited.

3.2.6. Ferrite Junction Circulation. A ferrite disk placed between two conducting planes is a geometry of planar junction circulator. Electric fields are supposedly mainly perpendicular to the conductors and the boundary conditions lead to two different configurations of electromagnetic waves: right-handed and left-handed rotating waves. A standing-wave pattern is established where fields intensities are equal and oppositely directed on either side of the conductor (Fig. 20).

For an isotropic substrate (or unmagnetized ferrite), the corresponding effective indices where the rotating waves propagate are equal. The standing wave intensity is maximum at the input port (port 1), and vanishes at 90° from the input port. As a consequence, a small amount of energy is coupled to ports 2 and 3.

For a gyrotropic substrate (magnetized ferrite), the two rotating modes are oppositely phase-shifted so that a rotation of the electromagnetic pattern occurs. If the rotation reaches 30°, port 2 is then coupled (transmission) and port 3 is isolated [23].

In this case, the effective permeability is given by

$$\mu_e = \frac{\mu_r^2 - \kappa^2}{\mu_r} \tag{37}$$

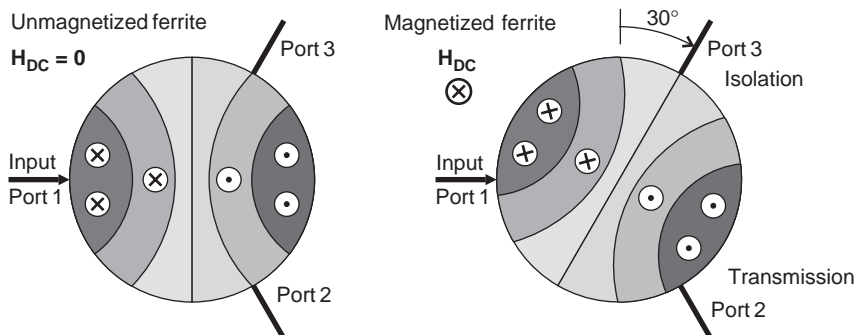


Figure 20. Ferrite junction circulation. (From [24]; © 1965 IEEE, reproduced with permission.)

and the solutions of the electromagnetic equations give magnetic microwave fields [24] proportional to

$$A_+ = J_{n-1}(kr) - \frac{J_n(kr)}{kr} \left(1 + \frac{\kappa}{\mu}\right) \tag{38}$$

$$A_- = J_{n-1}(kr) - \frac{J_n(kr)}{kr} \left(1 - \frac{\kappa}{\mu}\right) \tag{39}$$

where J_n are n th-order Bessel functions, and where

$$k^2 = \omega^2 \epsilon_0 \mu_0 \epsilon_r \mu_e \tag{40}$$

is the wavenumber associated with the effective permeability and r is the distance to the center of the ferrite disk. The first modes ($n = 1$) show two opposite areas of maximum energy as in Fig. 20. The positive and negative rotating modes are strongly linked to the ratio of the terms of the ferrite permeability tensor and differ in sign.

Magnetic fields vanish at the boundaries (magnetic wall if r equals the radius). Magnitudes (38) and (39) are then equal to zero, and their solutions lead to the radius of the ferrite disk for given working frequency and permeability tensor.

The input impedance of each port can be adjusted with the thickness of the disk, and the width of the access strip and can be improved by an impedance transformer.

The best performance is obtained above the resonance (according to the applied field, that is, at low frequencies), but the circulator can also operate below resonance [25]. The rotation is then inverted because the sign of the ratio is changed.

One of the most popular structure is the stripline Y-junction circulator with two ferrite disks (Fig. 12).

3.3. Ferrite Materials

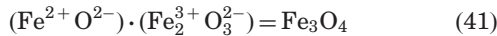
Microwave ferrites are high-resistivity ferrimagnetic materials used at frequencies above 0.1 GHz. They are ferrimagnetic oxides made of oxygen anions around metal (such as iron) divalent or trivalent cations [26]. The possibility of mixing the composition to adjust their behavior is one very attractive property of ferrites. If a divalent iron cation is replaced by any divalent composition, it gives a mixed ferrite with sometimes completely different properties. In addition, the substitution of a trivalent iron cation

gives a substituted ferrite whose behavior can be thinly adjusted.

3.3.1. Properties. Although ferrites usually show weaker performance than do magnetic metals, they are highly resistive, so that an electromagnetic wave can penetrate and interact with the material. Their resistivity can indeed vary between 10 and $10^8 \Omega \cdot \text{cm}$, a value that must be compared to the $10^{-4} \Omega \cdot \text{cm}$ resistivity of ferromagnetic metals. The relative dielectric permittivity of ferrites is almost constant at microwave frequencies and close to 15. Dielectric losses result mainly from the existence of both trivalent and divalent iron cations. There is an excess of electrons that may jump from one iron cation to another and therefore cause some conduction and losses.

A fundamental property such as permeability has to be considered because it governs the interaction between the wave and the material. Low coercivity is a condition for low losses. High Curie temperature and low magnetostriction constant are the main factors in improving the stability of ferrites. High saturation magnetization implies high gyromagnetic anisotropy but also intense magnetic field to saturate the material.

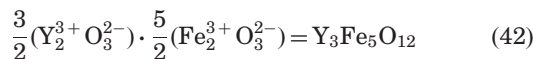
3.3.2. Spinel. Historically, spinel ferrites were the first type of ferrite used in microwave devices, in the 3–30 GHz range. The typical composition of a spinel ferrite is as follows:



Nickel mixed ferrite has a Curie temperature of about 570°C and is therefore rather stable. Its saturation magnetization is about 320 mT. Because it contains Ni ion, which is a relaxing ion, the spinel ferrite is a lossy material reserved for power applications. Lower magnetizations (down to 140 mT) are obtained by aluminium substitution for iron, while partial substitution of zinc for nickel increases the saturation magnetization (480 mT) at a lower temperature (400°C).

Lithium ferrite has a magnetization of about 360 mT with a high Curie temperature near 645°C . The lack of divalent iron ions results in a narrow linewidth that renders this ferrite suitable for low power levels with low losses. Magnetization can be decreased (down to 230 mT) by Ti substitution and increased by Zn substitution (500 mT).

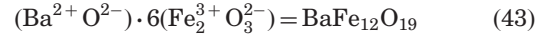
3.3.3. Garnets. Yttrium iron Garnet (YIG) is a very-narrow-linewidth material (near 3 kA/m, compared to 15–35 kA/m of spinels) that remains the best microwave material in the 1–10-GHz band. It can easily be saturated thanks to its weak saturation magnetization (175 mT). As the Curie temperature of YIG is 286°C , the stability with temperature is low. The chemical formula is



Aluminum substitution of iron ions decreases the magnetization as well as the Curie temperature, while Gd substitution of Y ions reduces the magnetization without

changing this temperature, which results in a better stability. Narrow linewidth as low as 0.8 kA/m can be obtained with In or Zn substitutions (associated with Ca ions).

3.3.4. Hexaferrites. These materials have a hexagonal structure with a c axis of symmetry. Their crystalline structure is essentially uniaxial of the M-type with the following formula



for barium (BaM) or strontium (SrM) hexaferrites. They have a high saturation magnetization (480 mT) and a Curie temperature as high as 700°C .

They also have a high magnetocrystalline anisotropy, which results in an anisotropy field H_a (mainly near 1500 kA/m and up to 2700 kA/m) that can be added to the internal field to reach resonance frequencies higher than (24)

$$\omega_r = \gamma\mu_0 \sqrt{[H_0 + H_a + (N_x - N_z)M][H_0 + H_a + (N_y - N_z)M]} \quad (44)$$

They are also characterized by a squared hysteresis loop with high remanence that allows a self-polarization of the material.

4. CURRENT DEVELOPMENTS

The manufacturing of ferrite materials is difficult, especially for small dimensions. These constraints do not make this kind of components easy to integrate or to miniaturize. Several ways of improving the performance and compactness of ferrite devices are proposed [27,28].

In order to reduce the size of the devices, some authors propose using hard magnetic materials with high remanence so that no external field is needed. Hexagonal ferrites such as SrM (315 mT saturation magnetization and 1500 kA/m anisotropy field) were successfully used in a 33-GHz rectangular waveguide circulator [29]. A 30-GHz self-biased microstrip circulator using a 130- μm -thick SrM substrate were realized [30]. Another interesting property of this material is its high crystalline anisotropy, which can be added to the internal field so that the resonance occurs at higher frequencies, above 10 GHz and up to 90 GHz.

In the case of thin ferrite plates, ohmic losses caused by metal resistivity may become the main contribution to total loss. To overcome this effect, the integration of superconductive materials in ferrite microwave devices has been investigated and its feasibility has been demonstrated in the case of a 10-GHz ring network circulator made of niobium or YBaCuO superconductors cooled to 77 and 4 K [31]. The same criteria are considered for the choice of ferrite material at either cryogenic temperature or at room temperature with, however, higher saturation magnetization values.

The main issue of current research is the integration of ferrite devices with semiconductor technologies. Several attempts at depositing ferrite films on silicon substrates were performed using pulsed laser deposition, evaporation, or sputtering [32]. Since the deposited film is amorphous and nonmagnetic, a thermal process is needed to recover ferrimagnetic properties. High temperature values above 600°C are required, either during the deposition process or during a postdeposition annealing, in order to crystallize the material.

It may be possible to use a semiconductor to make a millimeter-wave isolator or circulator instead of a ferrite because its permittivity becomes tensorial if a static magnetic field is applied. This phenomenon is the dual of permeability tensor of ferrites. A 60-GHz circulator was demonstrated experimentally using an n-type indium antimonide (InSb) disk at an operating temperature of 77 K [33].

Isolator structures can also be used as a microwave measurement technique for determination of the complex permeability tensor components of magnetized materials. A microstrip measurement cell based on Fig. 19 was realized and provided measurements up to 6 GHz [34]. The central zone between the strip and lower ground plane is filled with the ferrite, and two different dielectric materials are placed on each side to provide a nonreciprocal effect necessary to extract all the tensor components.

BIBLIOGRAPHY

1. K. Chang, ed., *Handbook of Microwave and Optical Components*, Vol. 1, Wiley, New York, 1989.
2. J. D. Adam, E. L. Davis, G. F. Dionne, E. F. Schloemann, and S. N. Stitzer, Ferrite devices and materials, *IEEE Trans. Microwave Theory Tech.* **50**(3):721–737 (March 2002).
3. K. J. Button, Microwave ferrite devices: The first ten years, *IEEE Trans. Microwave Theory Tech.* **32**(9):1088–1096 (Sept. 1984).
4. R. H. Knerr, An annotated bibliography of microwave circulators and isolators: 1968–1975, *IEEE Trans. Microwave Theory Tech.* **23**(10):818–825 (Oct. 1975).
5. G. P. Rodrigue, A generation of microwave ferrite devices, *Proc. IEEE* **76**(2):121–137 (Feb. 1988).
6. B. Lax and K. J. Button, *Microwave Ferrites and Ferromagnetics*, McGraw-Hill, New York, 1962.
7. F. E. Gardiol, Anisotropic slabs in rectangular waveguides, *IEEE Trans. Microwave Theory Tech.* **8**(18):461–467 (1970).
8. K. C. Gupta, R. Garg, I. J. Bahl, and P. Bhartia, *Microstrip Lines and Slotlines*, 2nd ed., Artech House, Boston, 1996.
9. R. M. Barrett, Microwave printed circuits—the early years, *IEEE Trans. Microwave Theory Tech.* **32**(9):983–990 (Sept. 1984).
10. C. P. Wen, Coplanar waveguide: A surface strip transmission line suitable for non-reciprocal gyromagnetic device application, *IEEE Trans. Microwave Theory Tech.* **17**(2):1087–1090 (Dec. 1969).
11. B. Bayard, D. Vincent, C. R. Simovski, and G. Noyel, Electromagnetic study of a ferrite coplanar isolator suitable for integration, *IEEE Trans. Microwave Theory Tech.* **51**(7):1809–1814 (July 2003).
12. Y. C. Moon, J. R. Lee, S. W. Yun, and I. S. Chang, A broadband planar isolator using coupled microstrip lines on a magnetized gyrotropic substrate, *Microwave J.* **44**(11):90–103 (Nov. 2001).
13. M. E. Hines, Reciprocal and nonreciprocal modes of propagation in ferrite stripline and microstrip devices, *IEEE Trans. Microwave Theory Tech.* **19**(5):442–451 (May 1971).
14. T. Nuguchi, New edge-guided mode isolator using ferromagnetic resonance absorption, *IEEE Trans. Microwave Theory Tech.* **25**(2):100–106 (Feb. 1977).
15. R. C. Kane and T. Wong, An edge-guided mode microstrip isolator with transverse slot discontinuity, *IEEE MTT-S Digest*, 1990, pp. 1007–1010.
16. A. H. Aly and E. B. El-Sharawy, Performance and modeling of saw tooth edge mode isolators, *IEEE MTT-S Digest*, 2001, pp. 475–477.
17. L. Courtois and M. de Vecchis, A new class of nonreciprocal components using slotlines, *IEEE Trans. Microwave Theory Tech.* **23**:511–516 (June 1975).
18. A. Beyer and K. Solbach, A new fin-line isolator for integrated millimeter-wave circuits, *IEEE Trans. Microwave Theory Tech.* **29**(12):1344–1348 (Dec. 1981).
19. D. K. Linkhart, *Microwave Circulator Design*, Artech House, 1989.
20. J. D. Huba, *NRL Plasma Formulary*, rev. ed., Naval Research Laboratory, Washington, DC, 2002.
21. Ph. Gelin and K. Berthou-Pichavant, New consistent model for ferrite permeability tensor with arbitrary magnetization state, *IEEE Trans. Microwave Theory Tech.* **45**(8):1185–1192 (Aug. 1997).
22. M. Sato and Y. Ishii, Simple and approximate expressions of demagnetizing factors of uniformly magnetized rectangular rod and cylinder, *J. Appl. Phys.* **66**(2):983–985 (July 1989).
23. H. Bosma, On the principle of stripline circulation, *Proc. IEE* **109**:137–146 (Jan. 1962).
24. C. E. Fay and R. L. Comstock, Operation of the ferrite junction circulator, *IEEE Trans. Microwave Theory Tech.* **13**:15–27 (Jan. 1965).
25. E. Schloemann and R. E. Blight, Broad-band stripline circulators based on yig and li-ferrite single crystals, *IEEE Trans. Microwave Theory Tech.* **34**(12):1394–1400 (Dec. 1986).
26. J. Nicolas, *Ferromagnetic Materials*, North-Holland, Amsterdam, 1980, Vol. 2, Chap. 4, pp. 243–296.
27. E. Schloemann, Advances in ferrite microwave materials and devices, *J. Magn. Magn. Mater.* **209**:15–20 (2000).
28. M. Pardavi-Horvath, Microwave applications of soft ferrites, *J. Magn. Magn. Mater.* **215–216**:171–183 (2000).
29. M. A. Tsankov and L. G. Milenova, Design of self-biased hexaferrite waveguide circulators, *J. Appl. Phys.* **73**(10):7018–7020 (May 1993).
30. S. A. Oliver, P. Shi, W. Hu, H. How, S. W. McKnight, N. E. McGruer, P. M. Zavracky, and C. Vittoria, Integrated self-biased hexaferrite microstrip circulators for millimeter-wavelength applications, *IEEE Trans. Microwave Theory Tech.* **49**(2):385–387 (Feb. 2001).
31. G. F. Dionne, D. E. Oates, D. H. Temme, and J. A. Weiss, Ferrite-superconductor devices for advanced microwave applications, *IEEE Trans. Microwave Theory Tech.* **44**(7):1361–1368 (July 1996).
32. B. Bayard, J. P. Chatelon, M. Le Berre, H. Joisten, J. J. Rousseau, and D. Barbier, The effects of deposition and annealing conditions on crystallographic properties of sputtered barium ferrite thick films, *Sensors Actuators A* **99**:207–212 (2002).

33. Z. M. Ng, L. E. Davis, and R. Sloan, Coplanar waveguide gyroelectric circulator, *Int. J. RF Microwave Comput. Aided Eng.* **12**(4):367–374 (July 2002).
34. P. Quéffelec, S. Mallécol, and M. Le Floch, Automatic measurement of complex tensorial permeability of magnetized materials in a wide microwave frequency range, *IEEE Trans. Microwave Theory Tech.* **50**(9):2128–2134 (Sept. 2002).

FERRITE-LOADED WAVEGUIDES

RICARDO MARQUÉS
University of Seville
Seville, Spain

Ferrites and their technological applications have been known for a long time. *Magnetite*, the first known magnetic material, is actually a ferrous ferrite. In 1269 Peter Peregrinus gave a detailed description of a compass made with a floating *magnetite* needle, probably a Chinese invention. The Spanish word for the compass, *brújula*, which literally means “small witch,” clearly shows former navigators’ amazement with the mysterious magnetic properties of the lodestone. The first experimental ferrite device in microwave technology was demonstrated in 1949 [1]. Since then, applications of artificial ferrite materials in microwave technology have grown rapidly and have become a mature technology, which has been discussed in many classical textbooks [2–10]. A good historical survey of the beginnings of the microwave ferrite technology can be found in Button [1]. A complete bibliography containing the most relevant contributions in this field during the years that followed can be found in Refs. 11 and 12. Finally, an authorized survey of the most recent advances in microwave ferrite technology in Europe, the United States, and Japan is found in Refs. 13, 14, and 15, respectively.

This article describes the main physical effects due to the propagation and guidance of electromagnetic waves in ferrite-loaded waveguides useful in microwave technology. The linear approach, in which the high-frequency magnetic susceptibility of the ferrite is a function of the internal static magnetic field, will be considered valid. This approach includes the analysis of exchange free electromagnetic waves, as well as magnetostatic waves and other approximations, but not the analysis of spin waves and nonlinear effects, magnetoelastic waves, and other complex interactions.

The choice of units in the analysis of microwave applications of ferrites presents some particularities. SI (International System) units are preferred for most of the electronic and electrical engineers. Nevertheless, cgs (centimeter–gram–second) units are used mainly by researchers in the area of the constitutive electromagnetic properties of ferrites. The usage in this text is a compromise between both alternatives. Since in the linear theory the equations for the static biasing magnetic field are decoupled from the radiofrequency field equations, we will use cgs units in the derivation of the internal magneto-static field, as well as in the expression of the magnetic

permeability in terms of the static bias field \mathbf{H}_0 , measured in oersteds, and the saturation magnetization $4\pi\mathbf{M}_0$, with \mathbf{M}_0 measured in gauss (1 Oe = 4πG). For the electromagnetic RF equations we will use SI units.

1. FUNDAMENTALS OF ELECTRODYNAMICS OF FERRITE MATERIALS

As long as the linear approach remains valid, the problem of finding the radiofrequency electromagnetic field inside a magnetized ferrite can be divided into three steps. First we must find the internal static field \mathbf{H}_0 as a function of the external applied static field \mathbf{H}_{ext} . Then we must obtain the RF magnetic permeability tensor that will be a function of the internal static field. Finally, we must solve the Maxwell equations for the RF field with the appropriate boundary conditions. Note that, in the linear approach, the equations for the static field \mathbf{H}_0 remains independent from the equations for the RF field. The coupling between these two fields occurs only by means of the dependence of the RF magnetic permeability tensor on the static magnetic field.

1.1. The Static Field

As a general statement, the internal static field \mathbf{H}_0 is the solution of the static equations inside the ferrite with the appropriate constitutive relations and boundary conditions. In the simplest case of a saturated isotropic ferrite, the static constitutive relations reduces to $\mathbf{B}_0 = \mathbf{H}_0 + 4\pi\mathbf{M}_s$ (remember that we will use cgs units in this part of the analysis), where \mathbf{M}_s is the magnetization of the ferrite at saturation, which, in isotropic ferrites, will be parallel to both \mathbf{B}_0 and \mathbf{H}_0 . In many cases, the ferrite is placed in a known external static and uniform field \mathbf{H}_{ext} provided by a magnet. In this case the internal static field is the sum of the external field and a demagnetization field H_d created by the ferrite internal magnetization. For ellipsoidal ferrite samples, rods and plates this problem is a classical one and is solved analytically, expressing the demagnetization field as the dot product of the saturation magnetization by a known demagnetization tensor, which depends on the shape and the orientation of the ferrite sample. In particular, for ferrite plates and rods placed in an external magnetic field parallel to the rod axis or the plane of the plate, it is easy to show that $\mathbf{H}_0 = \mathbf{H}_{\text{ext}}$. For ferrite plates placed in an external magnetic field perpendicular to the plate, it is $H_0 = H_{\text{ext}} - 4\pi M_s$.

1.2. The RF Magnetic Permeability Tensor

In this section we will state the more usual RF constitutive relationships for magnetized ferrites. First we will consider the simplest case of an intrinsically isotropic ferrite. In this context *intrinsic isotropy* means that the internal static magnetic field is the only source of anisotropy (induced anisotropy). Thus, after magnetization, the ferrite becomes an uniaxial medium with an RF permeability tensor given by (the z axis is chosen as the direction of

internal magnetization)

$$[\mu] = \mu_0 \begin{pmatrix} [\mu]_t & 0 \\ 0 & \mu_z \end{pmatrix} = \mu_0 \begin{pmatrix} \mu & j\kappa & 0 \\ -j\kappa & \mu & 0 \\ 0 & 0 & \mu_z \end{pmatrix} \quad (1)$$

where μ and κ are in general complex quantities that depend on the internal magnetic field and ferrite magnetization. This particular form of both $[\mu]$ and $[\mu]_t$ ensures the invariance of the permeability tensor after rotations around the z axis, which is the unique symmetry requirement. Notice that, if $\kappa \neq 0$, the tensor is not symmetric. Thus, a magnetized ferrite is a nonreciprocal medium. For lossless ferrites the permeability tensor must be Hermitian, and therefore μ , κ , and μ_z are real numbers.

The theory leading to appropriate expressions for μ , κ , and μ_z , valid for intrinsically isotropic saturated ferrites was first developed by Polder in 1949 from an analysis of the precession of molecular magnetic dipoles in the static internal field. The derivation of such expressions may be found in many textbooks [2–7]. The final expressions are given here for completeness

$$\mu = 1 + \frac{\omega_M \omega_H}{\omega_H^2 - \omega^2} \quad (2)$$

$$\kappa = \frac{\omega \omega_M}{\omega_H^2 - \omega^2} \quad (3)$$

and $\mu_z = 1$, where ω_H is the resonance frequency given by

$$\omega_H = \gamma H_0 \quad (4)$$

and

$$\omega_M = 4\pi\gamma M_s \quad (5)$$

(γ is the gyromagnetic ratio $\gamma = ge/2m_e c$, where g is the Lande factor; $-e$ and m_e , are the electron charge and mass, respectively; and c the speed of light. In most ferrites the magnetization is due to the electron spin alone; therefore $g = 2$ and $\gamma = 1.76 \times 10^7$ rad/s.Oe).

There is also a wide class of useful microwave devices that use ferrites at the remanent magnetization. These are termed *latch* ferrite devices and use ferrite materials with a square hysteresis loop, so that the remanence magnetization M_r is very close to the saturation magnetization. At remanence $H_0 = 0$ and (2) and (3) simplify to $\mu = 1$ and $\kappa = -4\pi M_r / \omega$. Nevertheless, the use of these expressions is subject to some restrictions related to the magnetic losses that may appear at low values of \mathbf{H}_0 [6].

The lossless ferrite is an approximation. Actually, there are many mechanism of losses in ferrites. Some of them, such as the ohmic conductivity, can be introduced in the RF constitutive relationships adding an imaginary part to the dielectric permittivity. Moreover, they are magnetic losses as a consequence of the damping of the magnetic oscillations described by the Polder tensor. The presence of the resonance frequency ω_0 in that tensor clearly suggest the presence of losses in real ferrites, with a maximum at

this frequency. Magnetic losses may be included in the Polder tensor after the transformation [10]

$$\omega_H \rightarrow \omega_H + j\alpha\omega \quad (6)$$

where α is a new parameter that accounts for the losses. The α parameter is often substituted by the *resonance linewidth* ΔH , which is the width of the resonance curves for the real part of κ and $\mu - 1$ plotted against H_0 . The resonance linewidth is related to α by $\Delta H = 2\alpha\omega_H/\gamma$. The magnitude of magnetic losses varies widely in ferrites used for microwave applications. The resonance linewidth ranges from about 0.1 Oe for single YIG crystals to several hundreds for polycrystalline ferrite materials. In the first case we can obtain meaningful results neglecting magnetic losses, but this approximation may lead to significant misleadings in other cases.

Until now we have considered only ferrites with intrinsic isotropy. This assumption is not realistic in all cases because ferrites are crystalline materials with complex internal structure. Magnetocrystalline intrinsic anisotropy usually induces in the crystal easy and hard directions of magnetization (i.e., directions on which the ferrite can—or cannot—be magnetized to saturation by a small applied magnetic field). The modifications of the Polder tensor induced by the magnetocrystalline anisotropy are complex and will not be analyzed here. The reader interested in this topic is referred to any of the textbooks that develop such expressions [e.g., 8].

The most important magnetocrystalline effect occurs in uniaxial hexagonal ferrites. In these crystals, the resonance is pushed to a extremely high frequency, even when the applied static field is small. Thus, hexagonal ferrites found most of its practical applications at millimeter wave frequencies.

1.3. The Radiofrequency Field

The RF field in a ferrite, characterized by the tensor permeability (1), is obtained by solving the Maxwell equations with the appropriate boundary conditions. Assuming a time-harmonic dependence of the kind $\exp j\omega t$, as well as the vanishing of current sources, these equations will read

$$\nabla \times \mathbf{E} = -j\omega[\mu] \cdot \mathbf{H} \quad (7)$$

$$\nabla \times \mathbf{H} = j\omega\epsilon\mathbf{E} \quad (8)$$

where the dielectric permittivity ϵ will be in general a complex quantity, in order to incorporate dielectric and ohmic losses.

1.3.1. Uniform Plane Waves with Longitudinal Magnetization. Although the aim of this article is to analyze the propagation along waveguides, the analysis of the propagation in an unbounded ferrite medium will provide a useful introduction to some relevant aspects of the propagation in waveguides. We will first suppose a uniform plane wave with a spacetime dependence of the kind $\exp j(-kz + \omega t)$ (this factor will be suppressed in the following

text) and an internal static magnetic field directed along the z axis: $\mathbf{H}_0 = H_0 \mathbf{a}_z$.

The analysis of (7) and (8) with these restrictions leads to two TEM-wave solutions with right-handed circular polarization (RCP) and left-handed circular polarization (LCP) referred to the static field \mathbf{H}_0 orientation. These two waves have different phase constants given by

$$k^\pm = \omega \sqrt{\epsilon \mu_{\text{eff}}^\pm} \tag{9}$$

where the plus sign stands for the RCP polarization and the minus sign, for the LCP polarization and μ_{eff} is an effective magnetic permeability given by the two eigenvalues of $[\mu]$:

$$\mu_{\text{eff}}^\pm = \mu_0 (\mu \pm \kappa) \tag{10}$$

Note that the hand of polarization has been referred to the internal static magnetic field orientation, regardless of the direction of propagation. Therefore, if one of these waves is fully reflected (e.g., by a perfect conducting plate perpendicular to propagation), the hand of the circular polarization, as well as the effective magnetic permeability, will remain unchanged, giving rise to a stationary wave.

The values of k^\pm for an isotropic lossless ferrite with RCP and LCP polarizations are shown in Fig. 1 for a ferrite magnetized under the usual technological condition of $H_0 < 4\pi M_0$. A forbidden frequency range for RCP waves, in which k^+ becomes imaginary, is given by

$$\omega_H < \omega < \omega_H + \omega_M \tag{11}$$

If magnetic losses are considered, the transformation (6) must be introduced in the expressions for μ_{eff}^\pm . This leads to two complex propagation constants, that of the RCP wave having a typical resonant behavior with high resonance losses (see Fig. 1).

The most important effect related to plane-wave propagation in a longitudinally magnetized ferrite is the non-

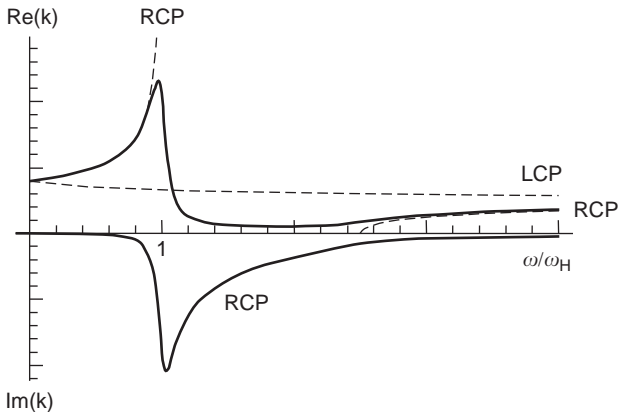


Figure 1. Normalized complex propagation constant for the RCP wave (10) in a lossy ferrite with $\omega_M = 1.5 \omega_H$ and $\gamma \Delta H = 0.1 \omega_H$ (solid lines). The normalized phase constants for the two RCP and LCP waves in a lossless ferrite with $\omega_M = 1.5 \omega_H$ and $\gamma \Delta H = 0$ are also shown (dashed lines).

reciprocal Faraday rotation of the plane of polarization of a linearly polarized wave. A linearly polarized wave is not a solution of (7) and (8), but it can be obtained by adding two contrarotating RCP and LCP waves of equal amplitude. Since the phase constants of these two waves are not equal, the result is a rotation of the plane of polarization of the linearly polarized wave. The rotation angle after the wave has advanced a length Δz is given by

$$\theta = \frac{1}{2} (k^- - k^+) \Delta z \tag{12}$$

When a linearly polarized wave is reflected backward, the hand of rotation of the polarization plane remains unchanged. Thus, the planes of polarization of the incident and the reflected waves will be different at a given distance from the plane of reflection. Therefore, the Faraday rotation in ferrites is nonreciprocal. If losses are considered, both the RCP and the LCP waves in which the linearly polarized wave splits have different attenuation constants. This leads to an unequal change in the amplitudes of the RCP and LCP waves, which causes Faraday ellipticity of the original linearly polarized wave. Detailed treatments of Faraday rotation and ellipticity may be found in the literature cited in the introduction [1–15].

1.3.2. Transverse Magnetization. We will now suppose an uniform plane wave with a spacetime dependence of the kind $\exp j(-kx + \omega t)$ (this factor will be suppressed in the following text) and an internal static magnetic field directed along the z axis: $\mathbf{H}_0 = H_0 \mathbf{a}_z$. The solution to (7) and (8) with these restrictions leads two independent uniform plane waves with the \mathbf{E} field linearly polarized. One of them is a TEM wave with the magnetic field parallel to \mathbf{H}_0 . Thus, there is no interaction between the RF field and the electronic spins, and the effective magnetic permeability is $\mu_{\text{eff}} = \mu_0 \mu_z$. This solution is called the ordinary wave, with phase constant $k^2 = \omega \sqrt{\epsilon \mu_0 \mu_z}$. There is also an extraordinary wave, whose propagation constant is still given by (9), but with μ_{eff} given by

$$\mu_{\text{eff}} = \mu_0 \frac{\mu^2 - \kappa^2}{\mu} \tag{13}$$

The extraordinary wave is a TE wave with the electric field polarized parallel to \mathbf{H}_0 and the magnetic field elliptically polarized in the plane perpendicular to \mathbf{H}_0 . The values of the propagation constants of the extraordinary waves for the lossless and the lossy ferrites of Fig. 1 are shown in Fig. 2. For the lossless extraordinary wave there is a frequency-forbidden range, in which k becomes imaginary, defined by

$$\sqrt{\omega_H(\omega_H + \omega_M)} < \omega < \omega_H + \omega_M \tag{14}$$

The presence of an ordinary wave and an extraordinary wave with orthogonal polarization, recalls the birefringence of uniaxial crystals. This birefringence can be used

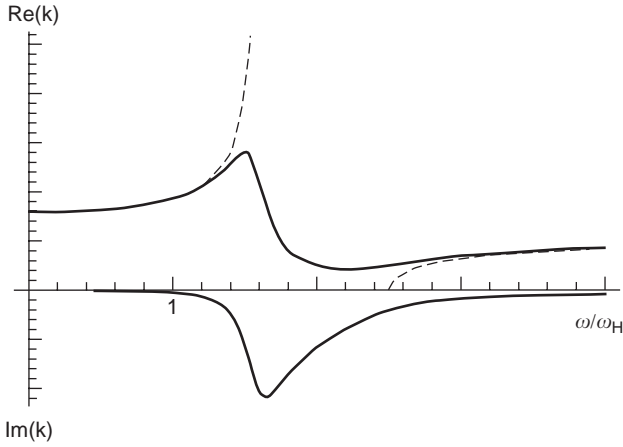


Figure 2. Normalized phase and complex propagation constants for the extraordinary waves in the infinite lossless (dashed lines) and lossy (solid lines) ferrites of Fig. 1 with transverse magnetization.

in the design of microwave devices such as half- and quarter-wave plates and polarizers.

1.3.3. Magnetization at Any Angle. In this case, the phase constant can still be written as in (9), with an effective magnetic permeability that depends on the angle θ_k between the static magnetization and the wave phase velocity. The final expression for this effective permeability is [10]

$$\mu_{\text{eff}}(\theta_k) = \mu_0 \frac{2 + \left(\frac{\mu_t}{\mu_z} - 1\right) \sin^2 \theta_k \pm \sqrt{\left(\frac{\mu_t}{\mu_z} - 1\right)^2 \sin^4 \theta_k + 4 \frac{\kappa^2}{\mu^2} \cos^2 \theta_k}}{2 \left(\frac{\sin^2 \theta_k}{\mu_z} + \frac{\cos^2 \theta_k}{\mu} \right)} \quad (15)$$

with $\mu_t = (\mu^2 - \kappa^2)/\mu$. For a fixed frequency, a plot of k , θ_k in polar coordinates, with $k = \omega \sqrt{\epsilon \mu_{\text{eff}}}$, gives the phase constants corresponding to the two solutions of (15). These curves can also be interpreted as isofrequency curves of the dispersion equation $\omega = \omega(k, \theta_k)$ in the k , θ_k plane. Thus, the group velocity $\mathbf{v}_g = \nabla_k \omega$ will be perpendicular to these curves at each angle θ_k . For an arbitrary θ_k , the direction of the optical ray will not be parallel to the direction of propagation of the wavefronts.

1.3.4. Nonreciprocity. One of the basic theorems of electromagnetism is the Lorentz reciprocity theorem. It applies to any linear and causal medium whose constitutive relationships can be described by symmetric frequency-dependent dielectric permittivity and/or magnetic susceptibility tensors. As was already mentioned, since the tensor magnetic susceptibility (1) is not symmetric, this is not the case for ferrites. In fact, many of the practical applications of ferrites in microwave technology, such as circulators or isolators, arise from this nonreciprocal

behavior. However, it is still possible to reformulate the reciprocity theorem in a form that is applicable to ferrite media. Following Harrington [16] and McIsaac [17], we will start from the Onsager relation, which states that any tensor macroscopic susceptibility of a causal and linear medium must be equal to the medium's transpose after reversal in time of all the physical relevant quantities. For an externally magnetized ferrite, taking into account that the static bias field changes of sign after reversal in time, we conclude that the tensor magnetic susceptibility of a ferrite (1) must equal its transpose after the change of sign of the static biasing field. From this conclusion, we can directly state the reciprocity theorem for ferrite media

$$\iint (\mathbf{E} \times \mathbf{H}' - \mathbf{E}' \times \mathbf{H}) \cdot d\mathbf{S} = \iiint (\mathbf{E}' \cdot \mathbf{J} - \mathbf{E} \times \mathbf{J}') dV \quad (16)$$

where the physical quantities must be reinterpreted as follows: \mathbf{E} , \mathbf{H} and \mathbf{E}' , \mathbf{H}' are two independent electromagnetic field configurations produced by source current densities \mathbf{J} and \mathbf{J}' respectively, at frequency ω in the same ferrite medium, except that the medium in which the prime quantities are defined has a reverse static magnetization: $\mathbf{H}'_0 = -\mathbf{H}_0$. The surface integrals on the left side of (16) are over any surface containing the source current densities included in the volume integral on the right side. This generalized reciprocity theorem is useful in the analysis of mode orthogonality in ferrite-loaded waveguides, as well as in the analysis of ferrite-loaded waveguide junctions.

2. MICROWAVE PROPAGATION IN FERRITE-LOADED WAVEGUIDES

In the preceding section microwave propagation in unbounded ferrite media was analyzed. Many of the studied effects, such as Faraday rotation and nonreciprocity, also appear when the RF field propagates along waveguides. Moreover, the microwave propagation along ferrite-loaded waveguides presents new useful effects, such as unidirectionality and field displacement, complex and backward modes, slow magnetostatic waves, and circulation.

In the following paragraphs we will choose the z axis as the waveguide axis, and a spacetime dependence of the kind $\exp j(\omega t - kz)$ will be supposed. The mode phase constant k will be in general a complex number $k = \beta - j\alpha$. Both β and α will be chosen real without loss of generality, and the factor $\exp j(\omega t - kz)$ will be suppressed.

2.1. Unidirectional and Bidirectional Modes

A mode with phase constant k that does not have a symmetric pair with the opposite phase constant $-k$ is called *unidirectional*. All lossless and reciprocal waveguides are bidirectional. This is not the case for ferrite loaded waveguides, because ferrites are nonreciprocal media that are not invariant after time reversal. The presence of unidirectional modes of propagation in ferrite-loaded waveguides is useful in many microwave devices, such as isolators and nonreciprocal phase shifters. However, many ferrite-loaded waveguides, which remain invariant

after some symmetry transformations, are bidirectional; specifically, unidirectional modes cannot propagate along these waveguides. McIsaac [18] and, more recently, Dmitriyev [19] have investigated these symmetries. McIsaac [18] concludes that bidirectionality is ensured if the waveguide remains the same after one or more of the following transformations:

- Reflection in a plane perpendicular to z axis
- Rotation by 180° about an axis perpendicular to the z axis
- Inversion at any point

In performing these transformations, the pseudovectorial nature of the static bias field \mathbf{H}_0 has to be taken into account (i.e., \mathbf{H}_0 remains the same after spatial inversion and after reflection in a perpendicular plane, but changes sign after a reflection in a parallel plane). In particular, any ferrite-loaded waveguide with longitudinal magnetization must be bidirectional, because this waveguide remains unchanged after reflection in a plane perpendicular to the z axis.

Bidirectionality does not imply that all the characteristics of the modes remain unchanged when the direction of propagation is reversed. For instance, the energy distribution and/or the polarization of a pair of bidirectional modes having the same but opposite phase constants may be different. Moreover, although all modes in bidirectional ferrite-loaded waveguides must be bidirectional, not all the modes in nonbidirectional ferrite-loaded waveguides are unidirectional; some of them, having the appropriate polarization, may be bidirectional.

2.2. Complex and Backward Modes

Complex modes in inhomogeneously filled lossless waveguides were first reported by Tai in 1960 and Carri coats in 1965 [20]. Complex modes in lossless isotropic waveguides are characterized by a complex propagation constant $k = \pm\beta \pm j\alpha$ and appear in groups of four solutions, in which all the possible combination of signs are allowed. Carri coats also shown that, for a single complex mode, power flows in opposite directions along the different media filling the waveguide, giving a zero net power flux. Therefore, complex modes in lossless waveguides are reactive modes. Complex modes have proved to be a very important part of the spectra of ferrite-loaded waveguides [20] (in fact, they were first reported for ferrite-loaded waveguides by Tai). In particular, all the unidirectional and reactive modes in ferrite-loaded waveguides must be complex [21,22].

Complex modes are closely related to *backward modes* (i.e., modes with negative group velocity). In fact, a pair of complex modes in lossless waveguides usually changes to a pair of propagating *forward* and *backward* modes when frequency varies [20]. Backward modes in the spectra of ferrite loaded waveguides, mainly in the *magnetostatic wave* region, has been widely analyzed (see, e.g., Ref. 8).

2.3. Mode Orthogonality

Mode orthogonality in ferrite-loaded waveguides was analyzed in Ref. 23. Applying the generalized reciprocity

theorem (16) to two modes $bfe_m, \mathbf{h}_m(x, y) \exp j(\omega t - k_m z)$ and $bfe'_n, \mathbf{h}'_n(x, y) \exp j(\omega t - k'_n z)$ of the actual waveguide and the *complementary* waveguide (the *complementary waveguide* is defined as the original one with the static magnetic field reversed), the following relation is obtained

$$(k'_n + k_m) \iint (\mathbf{e}'_n \times \mathbf{h}_m - \mathbf{e}_m \times \mathbf{h}'_n) \cdot \mathbf{u}_z dx dy = 0 \quad (17)$$

where the integral is over the cross section of the waveguide. This equation may be considered as a general orthogonality relation since the integral must be zero unless $k_m = k'_n$. This relation simplifies for most practical situations in which the static magnetic field is either parallel or perpendicular to the waveguide axis. The explicit orthogonality relationships for these particular but important magnetizations can be found in Ref. 23.

2.4. Field Displacement Effects

It was pointed out earlier that electromagnetic wave propagation in ferrites at an arbitrary angle with respect to the magnetizing field usually implies that the optical rays (and the power flux) are not parallel to the phase velocity. However, in a nonradiating waveguide, both power flux and wave propagation are forced to be parallel to the waveguide axis. Thus, this effect cannot be present in nonradiating waveguides. Instead, this tendency of power to flow in a direction different from the wave propagation may cause strongly unsymmetric accumulations of electromagnetic energy across the waveguide section. This nonreciprocal field displacement effect is used in the design of microwave isolators and phase shifters.

2.5. The Magnetostatic Approximation

Near the resonances $\mu_{\text{eff}} \rightarrow \infty$ and the effect of the Maxwell displacement current may be neglected with regard to the Faraday induction effects. This leads to the magnetostatic approximation. Taking into account that $\nabla \cdot \mathbf{B} = 0$, a magnetostatic potential $\mathbf{H} = -\nabla\psi$ is defined, which must satisfy

$$\nabla \cdot ([\mu] \cdot \nabla\psi) = 0 \quad (18)$$

(in ferrite-loaded waveguides, the nabla operator is replaced by $\nabla \rightarrow \nabla_t - jk\mathbf{u}_z$). The solutions to (18), with the appropriate boundary conditions, are the magnetostatic modes of the waveguide. Magnetostatic waves in ferrite-loaded waveguides, have been analyzed extensively [8]. The main applications of magnetostatic waves in microwave technology arise from its small wavelength. This result in broad applications in miniature controllable devices, such as delay lines, filters, power limiters, and signal-to-noise enhancers [24].

2.6. Basic Properties of Ferrite-Loaded Waveguide Junctions

A waveguide junction is characterized by its scattering matrix S_{ij} . It is a well-known fact that if the materials filling the junction are reciprocal, the scattering matrix must be symmetric. If the junction is nonreciprocal, this

statement must be modified as a consequence of the reformulation of the reciprocity theorem (16). This modification leads to the following relations between the scattering matrix elements of a ferrite-loaded junction and its complementary (i.e., the junction with the biasing static magnetic field reversed):

$$S_{ij}(\omega, \mathbf{H}_0) = S_{ji}(\omega, -\mathbf{H}_0) \quad (19)$$

If the junction is also lossless, the scattering matrix must be unitary ($S_{ij}S_{kj}^* = \delta_{ik}$, where the rule of summation over all the repeated subindex has been used). Other symmetries of the scattering matrix may be deduced from the spatial symmetries of the junction (including the bias field) [19].

The use of the scattering matrix symmetry properties is useful in the design of many microwave devices, such as isolators, phase shifters, and circulators. The *Y circulator* is perhaps the most useful and best known nonreciprocal junction. An *Y circulator* is a symmetric three-port junction with some specific properties. A symmetric three-port junction must have $S_{1,1} = S_{2,2} = S_{3,3}$, $S_{1,2} = S_{2,3} = S_{3,1}$, and $S_{2,1} = S_{1,3} = S_{3,2}$. These relations are fulfilled by any junction having a rotation symmetry axis of third order and magnetized along this axis. The circuit theory of three- and *N*-port circulators may be found in Ref. 6 and other textbooks. It can be shown that if a lossless, nonreciprocal, and symmetric three-port waveguide junction is matched (i.e., $S_{1,1} = 0$), it is also an ideal *Y circulator* [i.e., $S_{1,2} = 1$ or 0 and $S_{1,3} = 0$ or 1]. If the magnetization of a nonreciprocal three-port *Y circulator* is reversed, the direction of circulation is also reversed, as a consequence of (19).

3. FERRITE-LOADED WAVEGUIDES FOR PRACTICAL APPLICATIONS

In this section we will describe the most widely used ferrite-loaded waveguides. There are many classical textbooks and papers [2,3,5–7], and more recent ones [9,25] that describe these waveguides, as well as the most useful microwave devices that may be designed using them. The reader may use these and other texts to broaden the information contained in this section.

3.1. Circular Waveguides with Longitudinal Magnetization

It is well known from the theory of hollow waveguides that the fundamental mode of the empty circular waveguide is the $TE_{1,1}$ mode, which is a double degenerate mode with two perpendicular polarizations in the waveguide cross section. This mode has a field distribution that is almost TEM in the vicinity of the waveguide axis. Thus, if a ferrite rod with longitudinal magnetization is placed at the center of the waveguide (see Fig. 3), the two orthogonal and degenerate $TE_{1,1}$ fundamental modes will interact as a consequence of the Faraday rotation effect, giving rise to two nondegenerate circularly polarized RCP and LCP modes (with the hand of polarization defined with respect to the static bias field orientation). These modes can be approximated by the same RCP and LCP modes of a cir-

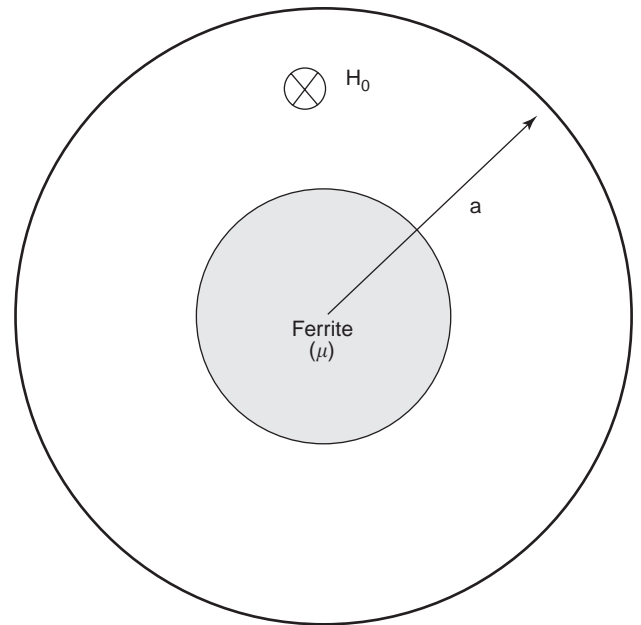


Figure 3. Cylindrical waveguide with an inner centered ferrite rod of longitudinal magnetization.

cular waveguide with an inner isotropic rod with a scalar magnetic susceptibility given by (10). In the same way, if a linearly polarized wave with linear polarization enters the ferrite-loaded waveguide, this wave will experience a Faraday rotation by an angle given approximately by (12), where k^+ and k^- are now the phase constants of the RCP and LCP ferrite-loaded waveguide modes.

The phase constants, as well as the mode fields of the two nondegenerate RCP and LCP ferrite-loaded waveguide modes, were obtained analytically by Waldron in 1958. Analytical solutions, not only for the cylindrical waveguide with a ferrite rod but also for many other related structures, such as cylindrical waveguides loaded with ferrite and dielectric tubes, may also be found in the literature [4]. Modes in this kind of ferrite-loaded waveguide are not TE nor TM, but become TE and TM at cutoff [4], these modes are termed *HE* and *EH* depending on whether the magnetic H_z or the electric E_z field dominates. At cutoff, *HE* modes become TE and *EH* modes become TM.

Ferrite-loaded circular waveguides with longitudinal magnetization are extensively used in Faraday rotation devices, based on the aforementioned rotation of the polarization plane of a linearly polarized wave. The most known Faraday rotation device is the four-port circulator, described in many textbooks. Faraday rotation may be also used in the design of magnetically tuned variable attenuators, isolators and phase shifters (see, e.g., Ref. 9 and references cited therein). In the early years of microwave ferrite technology, much effort was devoted to develop Faraday rotation circulators and other microwave devices with cylindrical geometry. In the following years, however, the *Y*-junction circulators, as well as phase shifters and attenuators in rectangular and/or planar technology, were found to be smaller, simpler, and more appropriate for

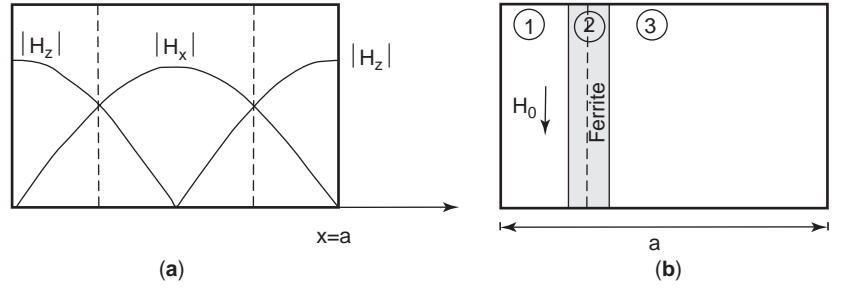


Figure 4. (a) Plot of the intensities of the magnetic field components $|H_x|$ and $|H_z|$ of the fundamental $TE_{1,0}$ mode in a rectangular hollow waveguide (frequency 9 GHz, $a = 23$ mm; dashed lines—planes of circular polarization); (b) rectangular waveguide loaded with a transversely magnetized ferrite slab at a plane of circular polarization of the RF magnetic field.

most applications; the research effort then began to focus on these devices.

3.2. E-Plane Transversely Magnetized Ferrite-Loaded Rectangular Waveguides

Figure 4a shows the variation of the magnetic field components H_x and H_z of the fundamental $TE_{1,0}$ mode in a hollow rectangular waveguide. The magnetic field is circularly polarized around the y axis where $|H_z| = |H_x|$. This condition occurs at two symmetric positions, at a distance d of the rectangular sidewalls, given by

$$d = \frac{a}{\pi} \cot^{-1} \left(\sqrt{\frac{4a^2}{\lambda_0^2} - 1} \right) \quad (20)$$

If an E -plane ferrite slab biased with a static magnetic field directed along the y axis is placed at a distance d of one of the lateral sidewalls (see Fig. 4b), the wave propagating in the positive (negative) direction along the z axis is right (left)-handed-polarized with respect to the static bias field. Thus we can expect that the forward (backward) wave will see the effective magnetic permeability of the slab $\mu_{\text{eff}}^+(\mu_{\text{eff}}^-)$, given by (10). Therefore, wave propagation will be unidirectional, with different phase constants for opposite directions of propagation. Moreover, since the dependence of μ_{eff}^+ with \mathbf{H}_0 is much stronger than those of μ_{eff}^- , the forward wave will be much more affected by variations in the intensity of \mathbf{H}_0 than the backward one. If the bias field is chosen in a region in which μ_{eff}^+ is positive and presents a strong dependence on the bias field intensity, the waveguide may be used as a nonreciprocal phase shifter. If the bias field is chosen at the resonance condition ($\omega_H = \omega$), the forward wave will see a resonant magnetic permeability and will experience strong attenuation due to the resonance losses. Then, the waveguide may be used as a resonance isolator. If the bias field is chosen at the antiresonance condition $\omega_H = \omega - \omega_M$, the forward wave will see a perfect diamagnet with $\mu_{\text{eff}}^+ = 0$, which imposes perfect diamagnetic boundary conditions at both slab sides and, therefore, zero tangential electric RF field at these boundaries. If an absorber is located at the inner boundary of the slab, it is expected that the forward wave will not be attenuated whereas the backward wave will be strongly attenuated. This waveguide may thus be used as a field displacement isolator.

The wave propagation characteristics along this waveguide may also be found analytically. The first published

results on this subject are due to of Kales (1953). Gardiol [26] gave a general method for computing the propagation characteristics of rectangular waveguides filled with an arbitrary number of anisotropic slabs, including ferrite slabs, making use of the transverse transmission matrix method. Referred to the geometry of Fig. 4b, the transverse transmission matrix of the i region $[\mathbf{T}_i]$ is defined as the matrix relating the tangential fields, E_y and H_z , at both sides of the i th region of the waveguide. In a notation that becomes apparent, we can write

$$\begin{aligned} \begin{pmatrix} E_y \\ H_z \end{pmatrix}_{x=a} &= [\mathbf{T}_3] \cdot [\mathbf{T}_2] \cdot [\mathbf{T}_1] \cdot \begin{pmatrix} E_y \\ H_z \end{pmatrix}_{x=0} \\ &= \begin{pmatrix} t_{1,1} & t_{1,2} \\ t_{2,1} & t_{2,2} \end{pmatrix} \cdot \begin{pmatrix} E_y \\ H_z \end{pmatrix}_{x=0} \end{aligned} \quad (21)$$

Since the lateral sidewalls are assumed to be perfect conducting walls, the tangential electric field must vanish at these boundaries. This implies that $t_{1,2} = 0$, which may be considered an implicit equation for the phase constant. This method may be applied to rectangular waveguides with any number of E -plane transversely magnetized ferrite slabs and/or lossy dielectric slabs, thus providing a general method for the analysis of isolators and phase shifters.

The nonreciprocal isolation and phase variation effects of the E -plane ferrite-loaded waveguide of Fig. 4b may be increased by placing a symmetric ferrite slab with reverse magnetization at the remaining plane of circular polarization of the $TE_{1,0}$ mode. Since at this plane the circular polarization of the $TE_{1,0}$ wave has opposite handedness, the effect of the new ferrite slab adds to the effect of the former one. A variation of this two-slab ferrite-loaded waveguide is the latch ferrite toroid in rectangular waveguide (Fig. 5a) proposed by Treuhaft (1958) [9] for phase-shifting applications. The main advantage of this configuration is that the permanent magnet is substituted by a ferrite toroid magnetized at remanence by an electric current pulse, driven by a single wire at the center of the waveguide (this wire is perpendicular to the RF electric field and has a negligible effect on microwave propagation). This structure is also suitable for rapid switching between the two opposite nonreciprocal states of the waveguide. In the analysis of this structure, the upper and lower branches of the ferrite toroid, which do not have substantial effect on phase change, may be neglected

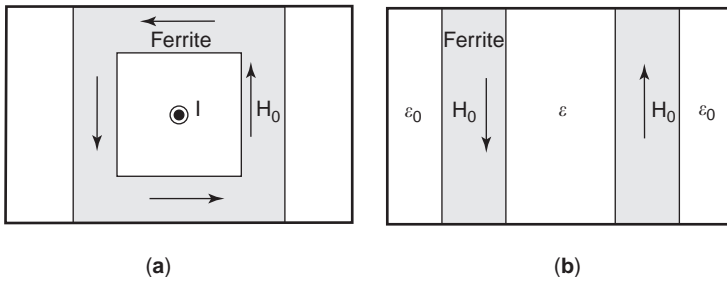


Figure 5. (a) Rectangular waveguide loaded with a latch ferrite toroid; (b) rectangular waveguide loaded with two oppositely magnetized ferrite slabs at the planes of circular polarization of the RF magnetic field.

leading thus to the simpler structure of Fig. 5b. Gardiol [27] gives expressions that transform the geometry of Fig. 5a into the geometry of Fig. 5b with a gain in accuracy. An alternative for reducing the unwanted effects of the upper and lower branches of the ferrite toroid is to replace this into a rectangular grooved waveguide, as proposed in Ref. 28. If nonreciprocity is not desired, a reciprocal phase shifter may still be obtained magnetizing both slabs of Fig. 5b with parallel and equal static magnetic fields. This structure is symmetric after inversion at a point in the waveguide axis and, therefore, is bidirectional.

3.3. Other Useful Cylindrical and Rectangular Ferrite-Loaded Waveguides

Although the circular and rectangular geometries seem to be the natural geometries for longitudinal and transverse magnetization, respectively, there are also some useful devices that use transversely magnetized circular waveguides and longitudinally magnetized rectangular waveguides. Field displacement effects similar to those reported earlier for rectangular waveguides may be achieved in cylindrical waveguides loaded with latch ferrite tubes magnetized in the azimuthal direction. The dual-mode ferrite phase shifters include latch and transversely magnetized circular waveguide sections [29]. A widely used ferrite-loaded rectangular waveguide with longitudinal magnetization is the Reggia–Spencer phase shifter [30], which consists of a ferrite rod with longitudinal magnetization placed at the center of a rectangular waveguide. If the dimensions of the hollow waveguide allows for the propagation of only the first $TE_{1,0}$ mode, Faraday rotation cannot take place. Instead, a strong variation of the wave phase constant with the applied static magnetic field occurs. Like all waveguides having longitudinal magnetization, the Reggia–Spencer phase shifter is bidirectional; thus the phase change is reciprocal.

4. FERRITE-LOADED MICROSTRIPS, SLOTLINES, AND FINLINES

After the mid-1960s, when planar microwave integrated circuits became a viable technology, ferrite-loaded microstrips and slotlines began to be investigated as an alternative to traditional ferrite-loaded waveguides for the design of reciprocal and nonreciprocal phase shifters [31], isolators [32], and other useful devices, which have been summarized in some classical review papers [25] and textbooks [9]. Later, when finlines emerged as a useful

alternative for planar technology in millimeter-wave circuits, ferrite-loaded finlines [33,34] also began to be investigated.

4.1. The Ferrite-Loaded Parallel-Plate Waveguide

Before considering more complicated structures, it will be useful to analyze the simpler parallel-plate waveguide loaded with ferrite slabs (Fig. 6). It has been shown [25] that for magnetization parallel to propagation, these waveguides supports a quasi-TEM mode and that the ferrite layers may be characterized by an effective permeability given by (13). For magnetization perpendicular to both the direction of propagation and the plane of the waveguide, the ferrite layers may be again characterized by the scalar effective permeability (13), but the field is no longer TEM because of the birefringence effects. Finally, for magnetization perpendicular to propagation and parallel to the waveguide plane, there is almost no interaction between the static magnetic field and the RF field and the ferrite layers are characterized by the scalar permeability μ_z . Near the forbidden frequency range, the analysis becomes more involved, due to the apparition of magnetostatic modes. Magnetostatic modes in parallel-plate ferrite-loaded waveguides have been extensively analyzed (see, e.g., Ref. 8 and references cited therein).

4.2. Ferrite-Loaded Microstrip Lines

Microstrip line (see Fig. 7a) is the most widely used waveguide in planar technology. Although exact methods of analysis are now available, considerable insight into the physical behavior of ferrite-loaded microstrip lines may be obtained from the well-known parallel-plate microstrip

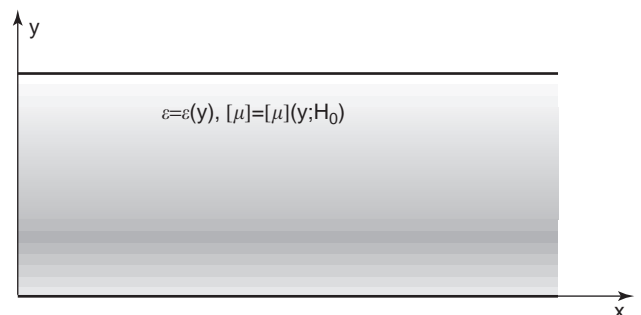


Figure 6. Parallel-plate waveguide filled by a multilayer medium including one or more ferrite slabs [$\epsilon(y)$ and $[\mu](y)$ are piecewise constant functions of y].

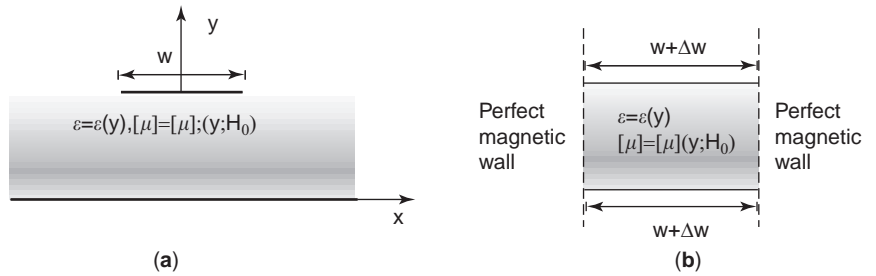


Figure 7. (a) Microstrip line on a multilayer ferrite-loaded substrate [as in Fig. 6, $\varepsilon(y)$ and $[\mu](y)$ are piecewise constant functions of y]; (b) parallel-plate waveguide model for the microstrip line of (a).

model (see Fig. 7b). In this model, the microstrip line is substituted by a section of parallel-plate waveguide between two magnetic walls. This section is slightly wider than the microstrip, in order to incorporate the effects of the fringing fields. Nevertheless, if, at the operating frequency, magnetostatic modes could be excited in the housing surface waveguide at both sides of the microstrip (see Fig. 7a), they could actually be excited by the microstrip, which would then become a magnetostatic wave transducer [8,24].

4.2.1. Microstrip with Longitudinal Magnetization. Using the model of Fig. 7b and the results reported earlier, the qualitative behavior of these kinds of microstrips may be investigated by means of the analysis of a section of parallel-plate waveguide loaded with one or more slabs of effective magnetic permeability given by (13), bounded by two perfect magnetic walls. This model provides a quasi-TEM and bidirectional fundamental mode with a phase constant that is a function of the biasing magnetic field. The same qualitative results are provided by more accurate quasi-TEM analyses of the actual microstrip line, using either the effective permeability (13) [25], the tensor magnetic permeability (1) [35,36], or by a full-wave analysis, discussed later in this article. The main application of microstrip lines with longitudinal magnetization is in phase shifting by meanderlines, a design that minimize the size of the device [31]. The phase variation with the applied magnetic field may be increased if strongly coupled quarter-wave meanderline sections are used. These structures provides strong nonreciprocal phase shifting [31] were nonreciprocity is due to the coupling effects.

4.2.2. Transversely Magnetized Microstrip Lines. We will consider the two orthogonal magnetizations, perpendicular and parallel to the ground plane. For the second one there is no expected interaction between the static bias field and the RF field in the parallel plate waveguide model of Fig. 7b because of the RF magnetic field parallel to the static bias field. In fact, only a slightly nonreciprocal phase shift may be observed, due to the fringing field near the microstrip edges.

Of much more interest is the microstrip line with magnetization perpendicular to the ground plane. Considering anew the parallel plate model of Fig. 7b, the ferrite slab can be characterized by a layer of effective magnetic permeability (13). However it must be realized that, for this magnetization, the RF field is not quasi-TEM, due to the

birefringence effects in the ferrite layer. Hines [32] showed that in a semiinfinite ferrite-filled parallel-plate waveguide, with a perpendicular magnetic wall at its end, and magnetized along the direction perpendicular to the ground planes, there is a TEM mode propagating along the waveguide and attenuating in the direction perpendicular to the magnetic wall. The phase constant of this mode is given by $\mathbf{k} = k_0(j\sqrt{\varepsilon_r}\mu\mathbf{a}_z - (\kappa/\mu)\sqrt{\varepsilon_r}\mu\mathbf{a}_x)$ [note that $\mathbf{k} \cdot \mathbf{k} = k_0^2\varepsilon_r(\mu_{\text{eff}}/\mu_0)$; that is, \mathbf{k} is the same as for a nonuniform plane wave in a slab of effective permeability μ_{eff}]. Hines also showed that this mode is unidirectional. The TEM mode described by Hines fulfills all the requirements imposed by the lateral magnetic walls of Fig. 7b for sufficiently wide strips. Moreover, since the mode in the semiinfinite parallel-plate waveguide was unidirectional, the microstrip mode will present a strong field displacement from one to another strip edge when the direction of propagation is reversed.

Although the analysis above has focused on ferrite-filled parallel-plate waveguides, the same qualitative results also apply to multilayered ferrite-loaded parallel-plate waveguides and microstrips. Hines modes are usually termed *edge modes* in microstrips because the RF field is concentrated mainly in the vicinity of a microstrip edge. Edge modes in microstrip are useful in the design of wideband edge-mode isolators and nonreciprocal edge-mode phase shifters [32,38,39], which use the same principle as do field displacement isolators and phase shifters. Analysis of such structures is usually performed using approximate models. More recently, spectral-domain analysis has been successfully applied to analyze edge-mode isolators without approximations [40].

4.3. Ferrite-Loaded Slotlines and Finlines

Slotlines (Fig. 8a) and coplanar waveguides are an useful alternative to microstrip in the design of microwave integrated circuits. In millimeter-wave technology, finlines in rectangular waveguides (Fig. 8b) also represent a good alternative for integration without radiation losses. By adding ferrite layers to these waveguides, many of the effects described for ferrite-loaded microstrips may be achieved. Since the RF magnetic field in slotlines and finlines is concentrated mainly in the slot and directed perpendicular to the air interface, it is expected that the strongest effects for transversely magnetized slotlines and finlines will occur for magnetization parallel to the fins. These structures have been extensively analyzed for the design of field displacement isolators and phase shifters [25]. A

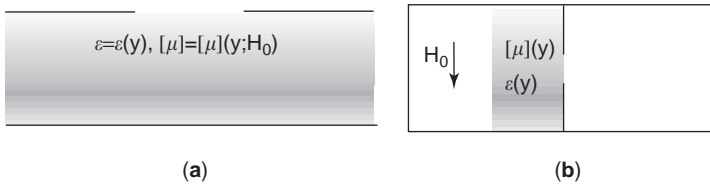


Figure 8. (a) Slotline on a multilayer ferrite-loaded substrate; (b) finline with a multilayer ferrite-loaded substrate. As in Figs. 6 and 7, $\epsilon(y)$ and $\mu(y)$ are piecewise constant functions of y .

millimeter-wave field displacement finline isolator has been proposed [33]. Transversely magnetized slotlines and finlines for nonreciprocal phase-shifting applications have also been analyzed [37,42–44]. Applications of finlines with longitudinal magnetization have been also investigated [34].

4.4. Methods of Analysis of Ferrite-Loaded Quasiplanar Layered Structures

With a few exceptions, quasi-TEM analysis usually provide sufficiently accurate results for the analysis of conventional microstrip and coplanar or slotlines. However, this analysis is seldom suitable for these structures when they are ferrite-loaded. In fact, quasi-TEM modes are by definition bidirectional, and therefore the quasi-TEM analysis cannot account for many of the most relevant physical effects in ferrite-loaded transmission lines. Quasi-TEM analysis in its standard form is restricted to longitudinally magnetized lines [35,36]. More recently, however, some attempts have been made in order to generalize this analysis to transversely magnetized structures [41]. Nevertheless, in general, planar and quasiplanar ferrite-loaded transmission lines require full-wave analysis.

With respect to numerical techniques, spectral-domain analysis (SDA) is by far the most widely used technique for the analysis of ferrite-loaded strip and/or slot structures [35–37,40,43–45]. The basic fundamentals of SDA may be found in many textbooks, such as that of Mirshekar-Syahkal [46]. SDA is specially well suited for the analysis of microstrips and/or slot- and finlines on planar single- or multilayer substrates, because of the translational symmetry of these substrates. Since the SDA applied to microstrip or microslot structures is adequately described in Ref. 46 and other textbooks, we only briefly describe here the main specific characteristics of the SDA when it is applied to ferrite-loaded microstrip and/or microslot waveguides. The main difficulty in the application of the SDA to ferrite-loaded microstrip or microslot on infinite planar substrates is in the determination of the spectral-domain Greens function dyad $\bar{\mathbf{G}}(k_x, k_z)$, which relates a surface current source $\mathbf{J}_s = \mathbf{J}_{s,0} \exp -jk_x x \exp -jk_z z$ in the plane of the structure, with the RF tangential electric field $\mathbf{E}_t = \mathbf{E}_{t,0} \exp -jk_x x \exp -jk_z z$ ($\mathbf{E}_t = (E_x, E_z)^t$) over the same or other parallel plane:

$$\mathbf{J}_0 = \bar{\mathbf{G}}(k_x, k_z) \cdot \mathbf{E}_{t,0} \quad (22)$$

General methods for the computation of the spectral Green dyad in multilayered ferrite-loaded substrates (in fact, in general layered bianisotropic substrates) have

been reported [47,48]. The *Fourier-transformed matrix method* reported in Ref. 47 is, in fact, an application of the transverse transmission matrix procedure described earlier to the determination of the spectral Green dyad (22) in general bianisotropic media with arbitrary surface current sheets. The equivalent boundary method, described in Ref. 48, proposes a procedure for computing the spectral Green dyad of an n -layered medium starting from $4n$ (in the worst case) single-layer Green dyads defined for each layer of the structure with appropriate boundary conditions. This results in a recurrence algorithm that is found to have a high numerical stability [45,48].

The SDA may also be applied to boxed stripline and finline structures. In this case the integral Fourier transform of the field and currents must be substituted by a Fourier series transform in an equivalent periodic structure. For magnetized ferrite-layered media in rectangular metallic boxes, this imposes an important restriction—strictly speaking, the SDA can be applied only to substrates with static magnetization perpendicular to the lateral sidewalls. In any other case, due to the properties of the magnetic field after spatial reflection, it is not possible to find an equivalent periodic structure with translational symmetry suitable for the application of the series Fourier transform. Therefore, the application of the SDA to boxed structures magnetized in any direction different from the aforementioned one, must be considered only as an approximation.

The SDA, as described previously, applies only to structures with strips or fins of negligible thickness. Structures with nonnegligible fin or strip thickness may be analyzed using a mode-matching technique in the transverse direction, which also implies an SDA [49]. A similar method may be applied to boxed structures with asymmetric rectangular piecewise boxes [50]. Finally, the SDA also applies to structures having fully or partly lossy strips or fins, provided these lossy strips or fins can be described by a suitable surface impedance, defined over the strip or the fin region [40].

BIBLIOGRAPHY

1. K. J. Button, *Microwave ferrite devices: The first ten years*, *IEEE Trans. Microwave Theory Tech.* **32**:1088–1096 (1984).
2. A. G. Gurevich, *ferrites at Microwave Frequencies*, English transl. Heywood, 1963.
3. P. J. B. Carricoats, *Microwave ferrites*, Chapman & Hall, 1961.
4. R. A. Waldron, *ferrites*, Van Nostrand, 1961.

5. B. Lax and K. J. Button, *Microwave ferrites and Ferrimagnetics*, McGraw-Hill, 1962.
6. J. Helszajn, *Principles of Microwave ferrite Engineering*, Wiley, 1969.
7. C. E. Fay and W. Von Aulock, *Linear ferrite Devices*, Academic Press, 1969.
8. M. S. Sodha and N. C. Shrivastava, *Microwave Propagation in Ferrimagnetics*, Plenum Press, 1981.
9. A. J. Baden Fuller, *ferrites at Microwave Frequencies*, Peter Peregrinus, 1987.
10. A. G. Gurevich and G. A. Melkov, *Magnetization Oscillations and Waves*, CRC Press, 1996.
11. L. E. Whicker and D. E. Bolle, Annotated literature survey of microwave ferrite control components and materials for 1968–1974, *IEEE Trans. Microwave Theory Tech.* **23**:908–919 (1975).
12. R. H. Knerr, An annotated bibliography of microwave circulators and isolators: 1968–1975, *IEEE Trans. Microwave Theory Tech.* **23**:818–825 (1975).
13. L. E. Davis, Status of microwave ferrite technology in Europe, 1993 *IEEE Microwave Theory Tech. Symp. Digest*, 1993, pp. 199–202.
14. D. C. Webb, Status of ferrite technology in the United States, 1993 *IEEE Microwave Theory Tech. Symp. Digest*, 1993, pp. 203–206.
15. Y. Murakami, Microwave ferrite technology in Japan: Current status and future expectations, 1993 *IEEE Microwave Theory Tech. Symp. Digest*, 1993, pp. 207–210.
16. R. F. Harrington and A. T. Villeneuve, Reciprocity relationships for gyrotropic media, *IRE Trans. Microwave Theory Tech.* **6**:308–310 (1958).
17. P. R. McIsaac, A general reciprocity theorem, *IEEE Trans. Microwave Theory Tech.* **27**:340–342 (1979).
18. P. R. McIsaac, Bidirectionality in gyrotropic waveguides, *IEEE Trans. Microwave Theory Tech.* **24**:223–226 (1976).
19. V. A. Dmitriyev, Symmetry of microwave devices with gyrotropic media—complete solution and applications, *IEEE Trans. Microwave Theory Tech.* **45**:394–401 (1997).
20. M. Mrozowski, *Guided Electromagnetic Waves. Properties and Analysis*, Wiley, 1997.
21. R. Marqués, F. Mesa, and M. Horno, On the complex nature of higher order modes in lossless nonreciprocal transversely magnetized waveguides, *IEEE Microwave Guided Wave Lett.* **2**:278–280 (1992).
22. R. Marqués, F. Mesa, and M. Horno, Nonreciprocal and reciprocal complex and backward waves in parallel plate waveguides with a ferrite slab arbitrarily magnetized, *IEEE Trans. Microwave Theory Tech.* **41**:1409–1418 (1993).
23. P. R. McIsaac, Mode orthogonality in reciprocal and nonreciprocal waveguides, *IEEE Trans. Microwave Theory Tech.* **39**:1808–1816 (1991).
24. P. Kabos and V. S. Stalmachov, *Magnetostatic Waves and Their Applications*, Chapman & Hall, 1994.
25. F. J. Rosenbaum, Integrated ferrimagnetic devices, in L. Young and H. Sobol, eds., *Advances in Microwaves*, Academic Press, 1974, Vol. 8, pp. 203–294.
26. F. E. Gardiol, Anisotropic slabs in rectangular waveguides, *IEEE Trans. Microwave Theory Tech.* **18**:461–467 (1970).
27. F. E. Gardiol, Computer analysis of latching phase shifters in rectangular waveguide, *IEEE Trans. Microwave Theory Tech.* **21**:57–61 (1973).
28. A. Mizobuchi and H. Kurebayashi, Nonreciprocal remanence ferrite phase shifters using grooved waveguide, *IEEE Trans. Microwave Theory Tech.* **26**:1012–1016 (1978).
29. W. E. Hord, C. R. Boyd, and D. Diaz, A new type fast switching dual mode ferrite phase shifter, *IEEE Trans. Microwave Theory Tech.* **35**:1219–1225 (1987).
30. F. Reggia and E. G. Spencer, A new technique in ferrite phase shifting for beam scanning of microwave antennas, *Proc. IRE* **45**:1517–1570 (1957).
31. G. T. Roome and H. A. Hair, Thin ferrite devices for microwave integrated circuits, *IEEE Trans. Microwave Theory Tech.* **16**:411–420 (1968).
32. M. E. Hines, Reciprocal and non-reciprocal modes of propagation in ferrite stripline and microstrip devices, *IEEE Trans. Microwave Theory Tech.* **19**:442–451 (1971).
33. A. Beyer and K. Solbach, A new fin-line ferrite isolator for integrated millimeter-wave circuits, *IEEE Trans. Microwave Theory Tech.* **29**:1344–1348 (1981).
34. L. E. Davis and D. B. Sillars, Millimetric nonreciprocal coupled-slot finline components, *IEEE Trans. Microwave Theory Tech.* **34**:804–808 (1986); see also comments and reply in E. Jemsen and C. Schieblich, *IEEE Trans. Microwave Theory Tech.* **35**:470–471 (1987).
35. T. Kitazawa, Variational method for planar transmission lines with anisotropic magnetic media, *IEEE Trans. Microwave Theory Tech.* **37**:1749–1754 (1989).
36. M. Horno, F. Mesa, F. Medina, and R. Marqués, Quasi-TEM analysis of multilayered, multi-conductor coplanar structures with dielectric and magnetic anisotropy including substrate losses, *IEEE Trans. Microwave Theory Tech.* **38**:1059–1068 (1990).
37. E. B. El-Sharawy and R. W. Jackson, Full wave analysis of infinitely long magnetic surface wave transducer, *IEEE Trans. Microwave Theory Tech.* **38**:730–737 (1990).
38. S. H. Talisa and D. M. Bolle, On the modeling of the edge-guided mode stripline isolators, *IEEE Trans. Microwave Theory Tech.* **27**:584–591 (1979).
39. D. M. Bolle and S. H. Talisa, The edge-guided mode nonreciprocal phase shifter, *IEEE Trans. Microwave Theory Tech.* **27**:878–882 (1979).
40. T. M. F. Elshafey, J. T. Aberle, and E. B. El-Sharawy, Full wave analysis of edge-guided mode microstrip isolator, *IEEE Trans. Microwave Theory Tech.* **44**:2661–2668 (1996).
41. R. Marqués, F. Mesa, and F. Medina, Theory of magnetoelectric multiconductor transmission lines with application to chiral and gyrotropic lines, *Microwave Opt. Technol. Lett.* **38**:3–9 (2003).
42. G. Böck, New multilayered slot-line structures with high nonreciprocity, *Electron. Lett.* **19**:966–968 (1983).
43. E. B. El-Sharawy and R. W. Jackson, Coplanar waveguide and slot-line on magnetic substrates: Analysis and experiment, *IEEE Trans. Microwave Theory Tech.* **36**:1071–1078 (1988).
44. E. B. El-Sharawy and C. J. Koza, Dual-ferrite slot line for broadband, high-nonreciprocity phase shifters, *IEEE Trans. Microwave Theory Tech.* **39**:2204–2210 (1991).
45. F. Mesa, R. Marqués, and M. Horno, An efficient numerical spectral domain method to analyze a large class of nonreciprocal planar transmission lines, *IEEE Trans. Microwave Theory Tech.* **40**:1630–1641 (1992).
46. D. Mirshekar-Syahkal, *Spectral Domain Method for Microwave Integrated Circuits*, Wiley, 1990.

47. C. M. Krowne, Fourier transform matrix method of finding propagation characteristics of complex anisotropic layered media, *IEEE Trans. Microwave Theory Tech.* **32**:1617–1625 (1984).
48. F. Mesa, R. Marqués, and M. Horno, A general algorithm for computing the bidimensional spectral Green's dyad in multilayered complex bianisotropic media: The equivalent boundary method, *IEEE Trans. Microwave Theory Tech.* **39**:1640–1649 (1991).
49. T. Kitazawa, Analysis of shielded striplines and finlines with finite metallization thickness containing magnetized ferrites, *IEEE Trans. Microwave Theory Tech.* **39**:70–74 (1991).
50. Z. Fan and R. Pennock, Analysis of asymmetrical multilayer ferrite-loaded finlines by the extended spectral domain approach, *IEEE Trans. Microwave Theory Tech.* **44**:497–504 (1996).

FERRITE PHASE SHIFTERS

WILLIAM E. HORD
 Microwave Applications Group
 Santa Maria, CA

Phase shifters are used extensively in the microwave and millimeter-wave region primarily as array elements in phased-array antennas. The first application of ferrite phase shifters in antenna arrays was during the decade of the 1960s. Since then growth has been dramatic with military applications being the motivating force. The air defense systems of the former Soviet Union are designed and built around ferrite phase shifting devices as are several of the ground-based, naval, and airborne systems of the United States. The article describes the evolution of ferrite phase shifters that have made the transition from the research laboratory to the production floor. Wherever possible, the author has identified the systems that use a specific type device.

Ferrite phase shifters are two-port devices operating in the microwave and millimeter-frequency range between 1.4 and 100 GHz. A variable insertion phase between input port and output port is accomplished by varying the bias magnetic field of the ferrite material. The insertion phase of a phase shifter is the phase delay experienced by a radiofrequency (RF) signal propagating between port 1 and port 2 and is the angle of S_{21} , the transmission coefficient from port 1 to port 2. If the angle of S_{21} equals the angle of S_{12} , the transmission coefficient from port 2 to port 1, the phase shifter is *reciprocal*, while if these two angles are not equal the device is *nonreciprocal*. The phase shifter consists of (1) a microwave circuit containing magnetized ferrite whose purpose is to provide a variable insertion phase to the RF signal and (2) an electrical circuit containing electronic components whose purpose is to vary the magnetic bias of the ferrite and control the amount of variable insertion phase. Because the state-of-the-art of electronic control circuits changes rapidly depending on device availability, the focus of the following discussion will be on the microwave portion of the ferrite

phase shifter and the electronic control techniques will be limited to basic principles.

The use of magnetized ferrite to provide the variable phase shift was recognized as early as 1953 [1]. Phase shifter applications were stimulated by the discovery of the reciprocal, ferrite phase shifter in 1957 [2] and the latching ferrite phase shifter in 1958 [3]. During the 1960s, major efforts were undertaken on phase shifter development, and the toroid phase shifter [4] and dual-mode phase shifter [5] evolved into their present configurations during this decade. The rotary-field phase shifter was reported in the early 1970s [6].

Although they find application in many areas, the major use of ferrite phase shifters are as phase shifting elements in electronic scanning antennas where the data rate is high enough to preclude the use of a mechanical scanning antenna or where the aperture must be shared by several functions requiring the antenna have an agile beam shape. Antennas used for systems tracking large numbers of targets such as the AWACS (airborne warning and control system) require data rates not attainable with mechanical scanning antennas. A ground-based air defense system such as the Patriot must track a particular target while continuing to search for other threats necessitating an electronic scanning system. Ferrite phase shifters are also used as feed elements for reflector antennas where the pattern of the reflector may be changed by changing the feed pattern providing different coverages. Electronic control is desirable since the system may be located in space and the reliability of mechanical switches is not adequate. Other antenna feeds use four phase shifters to provide a variable phase to each quadrant of the antenna resulting in a conical scanning beam for the antenna. A third use is as the variable element in microwave circuits used for high-power switches and variable-power dividers and combiners. Because of the low insertion loss and excellent phase accuracy attainable with ferrite phase shifters, high-power electronic switches with insertion loss as low as 0.5 dB and with isolations approaching –40 dB may be realized. A circuit providing variable phase shift in each leg of a bridge circuit has been used to combine the azimuth and elevation difference signals from a monopulse antenna and by properly phasing the signals compensate electronically for aircraft roll. Finally, ferrite phase shifters have been used as Doppler simulators, frequency translators, and so on.

1. FERRITE MATERIALS AND PROPERTIES

A material is called *magnetic* if it exhibits a magnetic moment in the absence of an applied magnetic field. The magnetic moment is due to the presence in the material of at least two different electronic spin systems. If these spin systems are equal and parallel, the material is ferromagnetic; if the spin systems are equal and antiparallel, the material is antiferromagnetic; and if the spin systems are unequal and antiparallel, the material is ferrimagnetic and is generically referred to as *ferrite*. Ferrite materials are ionic crystals with no free electrons, resulting in high resistivity and making them potentially useful for

application in the microwave and millimeter frequency ranges. Two types of ferrites both with cubic crystalline structure but one (spinel) having structure similar to spinel and the other (garnets) having the garnet structure have been used for phase shifter fabrication. A sample of ferrite material of a size required for microwave components usually does not exhibit a net magnetic moment in the absence of an external bias field. The material is composed of magnetic domains; each of these exhibits a net magnetic moment but is randomly aligned, resulting in zero net magnetic moment when summed over the sample. Application of an external magnetic bias field rotates the domains that align with the bias field and produce a net magnetization. When all domains in a sample are aligned, the material is saturated and the magnetization is called the *saturation magnetization* $4\pi M_s$. A virgin sample of material exhibits a magnetization curve similar to that of iron.

When the magnetizing current is removed, some magnetic flux may remain in the sample, and a current in the opposite direction must be applied to reduce this flux to zero. This phenomenon is called *hysteresis*. A ferrite material formed in a closed loop exhibits a hysteresis loop similar to that shown in Fig. 1, where the squareness of the loop is a function of the chemical composition of the material. The magnetic field intensity required to reduce the magnetic flux density to zero is called the *coercive force* H_c , while that magnetic flux density remaining after the magnetic field intensity has been reduced to zero is called the *remanent flux density* B_r . Magnetic material properties are sensitive to temperature; and above a certain temperature, called the *Curie temperature*, the magnetic properties vanish.

Ferrite phase shifters require values of saturation magnetization ranging from approximately 200 to 5500 G (gauss) (the maximum attainable value with commercially available materials). By substituting aluminum ions for

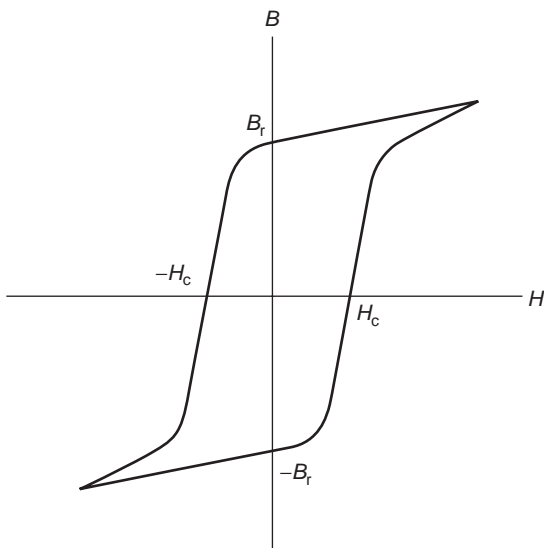


Figure 1. Ferrite hysteresis loop for a square-loop material defining the remanent magnetization B_r and the coercive force H_c .

ferric ions in YIG, the saturation magnetization may be reduced from 1780 gauss (the value for pure YIG) to about 175 G. For the lithium spinel family the substitution of titanium ions for ferric ions is used, and both aluminum and zinc separately or in combination have been used to vary the saturation magnetization for the magnesium–manganese ferrite family and the nickel ferrite family. In general, when substitution is made the Curie temperature is lowered from that of the unadulterated material. Doping with rare-earth ions may be used to increase peak power capacity, although the insertion loss may increase slightly.

Phase shifters providing variable values of insertion phase operate with the ferrite partially magnetized. The ferrite exhibits a tensor permeability whose on-diagonal elements μ vary slightly as a function of the applied magnetization. The off-diagonal elements of the tensor $\pm j\kappa$ are equal but of opposite sign, leading to the nonreciprocal behavior of ferrite devices. These off-diagonal elements are in phase quadrature with the on-diagonal elements and are proportional to the ratio of applied magnetization to saturation magnetization. If the RF energy is circularly polarized, the effective permeability of the ferrite medium is equal to $(\mu + \kappa)$ for one sense of circular polarization and $(\mu - \kappa)$ for the other sense of circular polarization, both of which are dependent on the applied magnetization through the off-diagonal element of the permeability tensor. The permittivity of the ferrite is scalar with a dielectric constant in the range 10–18. The dielectric loss tangent of ferrite is about 0.0002 for garnets, 0.0003 for magnesium spinels, 0.0005 for lithium spinels, and 0.001 for nickel spinels.

Phase shifter characteristics determined by the microwave circuit are the mode of operation, either reciprocal or nonreciprocal; operating frequency; instantaneous and tunable bandwidth; polarization of the input and the output signals; peak and average RF power; insertion loss and modulation of the insertion loss; and return loss. Parameters determined by the microwave circuit and the electrical control circuit are phase quantization, phase accuracy, switching time, switching rate, and control power. Physical parameters of the phase shifter include size; weight; cooling requirements; input interfaces for RF signal, data, and control power; and output interfaces for RF signal and built-in test. The phase shifter must conform with environmental requirements such as operating and storage temperature range, operating and transportation shock, operating and transportation vibration, and operating and storage humidity. Finally, requirements generally exist for the reliability, interchangeability, and maintainability of the phase shifter.

2. TYPES OF FERRITE PHASE SHIFTERS

Many ferrite phase shifters are described in the literature, but only three types have been produced in quantity and deployed in the field in various antenna systems. The one characteristic shared by these three different devices is an insertion loss less than 1 dB. System and antenna designers are unwilling to use devices with higher loss because of

reduction in antenna gain and cooling problems associated with dissipation of the transmitter power in the antenna.

The J-STARS airborne surveillance system, the Patriot mobile, ground-based air defense system, and the Aegis naval air defense system use variations of the nonreciprocal toroidal phase shifter. This device operates in a nonreciprocal mode, requiring that the phase shifter be switched immediately after the transmitter pulse to provide the proper phase shift for propagation in the receive direction. The phase shifter is switched again just prior to the next transmitter pulse, resulting in a switching rate twice the pulse repetition rate of the radar. Switching time is a few microseconds depending on operating frequency. This type of phase shifter may be designed to have extremely wide operating bandwidth approaching 2 octaves in some cases.

The second type of phase shifter, also nonreciprocal, consists of a longitudinally magnetized ferrite rod located on the axis of either square or circular waveguide. Several of the ground-based, mobile air defense systems of the Confederation of Independent States use these phase shifters in antennas, radiating one sense of circular polarization and receiving the orthogonal sense of circular polarization—the “single bounce” return. An adaptation of the phase shifter that provides reciprocal phase shift is referred to as the “dual mode” device and has been successfully employed in several antenna designs most notably the multimode offensive radar systems of the B-1B. Switching times for these phase shifters are in the tens of microseconds depending on the frequency of operation. Operating bandwidth is more modest than the toroid phase shifter, typically being 10–15%, although 40% bandwidth has been achieved for experimental devices.

The phase shifters described above provide a variable insertion phase by varying the magnitude of the bias magnetic field, resulting in a variation in the equivalent inductance of the waveguide and yielding a variable propagation delay through the device. The final phase shifter described in this section does not use this phenomenon but rather makes use of the variation in the direction of the bias magnetic field to effect change in insertion phase with no change in the propagation delay. Because of the similarity of the phase shifter to the rotary-vane [7] mechanical phase shifter, it has been called the *rotary-field phase shifter*. The rotary-vane device uses a dielectric vane to realize a half-wave plate that can be rotated about the axis of a circular waveguide housing. A circularly polarized RF signal receives phase shift when passing through the half-wave plate equal to twice the mechanical angle of rotation of the half-wave plate. Substitution of a transversely magnetized ferrite rod for the dielectric half-wave plate results in an electrically variable version of this phase shifter. This phase shifter has been employed in a single-axis scanning configuration for the antenna for the AWACS surveillance aircraft and for several single-axis scanning, ground-based, mobile air defense systems. The switching time for the device is of the order of hundreds of microseconds, and the operating bandwidth is about the same as that of the dual-mode phase shifter.

2.1. Toroidal Phase Shifters

The toroidal phase shifter consists of one or more ferrite toroids inserted into a rectangular waveguide as shown in Fig. 2. The cross section shown in Fig. 3a is the original version of the toroidal phase shifter reported by Truehaft and Silber (3) in 1958. The toroid is fabricated from a material with a square hysteresis loop. Current flowing in the switching wire induces a magnetic flux in the toroid that remains after the current is removed. The phase shifter is said to be “latched”; operation in this mode is desirable since control energy is required only when the phase shifter is set to a new state. The magnetic field intensity of the TE_{10} mode in a rectangular waveguide is circularly polarized in a longitudinal plane parallel to the narrow wall of the waveguide and located a distance from the waveguide centerline, which makes the longitudinal magnetic field intensity equal in magnitude to the transverse magnetic field intensity. The opposite sense of circular polarization exists in the longitudinal plane located the same distance on the other side of the waveguide centerline. If a sample of magnetized ferrite is placed in the region of circular polarization, a strong interaction between the RF and the ferrite will occur, provided the direction of the bias field is interchanged on either side of the waveguide centerline.

The geometry shown in Fig. 3b makes more efficient use of the ferrite toroid and provides more total phase shift than the geometry of Fig. 3a at a minimal increase in insertion loss by loading the “window” in the toroid with a dielectric. The dielectric loading effect of the ferrite toroid and dielectric used to load the toroid window distorts the behavior of the fields of the waveguide mode so that the region of circular polarization no longer lies in the same plane as that of the air-filled waveguide. Computer-aided analysis programs have been evolved [8,9] to predict the performance of the phase shifter as a function of toroid placement and dielectric loading. A disadvantage of the geometries shown in Figs. 3a and 3b is the excitation of the TEM mode, which is easily established by the switching wire coupling to the rectangular waveguide. Two toroids separated by a dielectric slab spacer as shown in

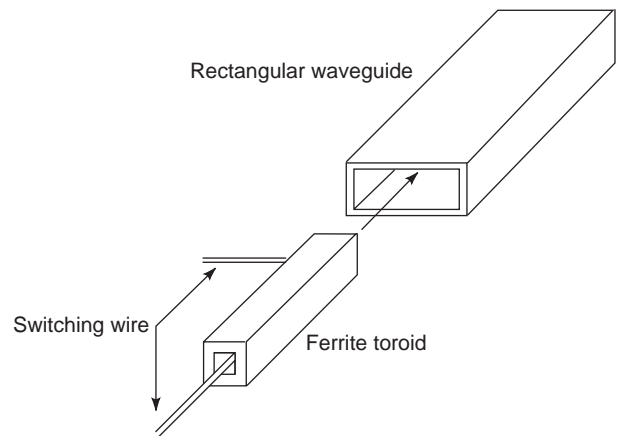


Figure 2. Prototypical toroidal phase shifter. First described in the 1950s, this device was the first latching, ferrite phase shifter. By pulsing the switching wire the flux may be latched to either $+B_r$ or $-B_r$. Sustaining drive current is not required.

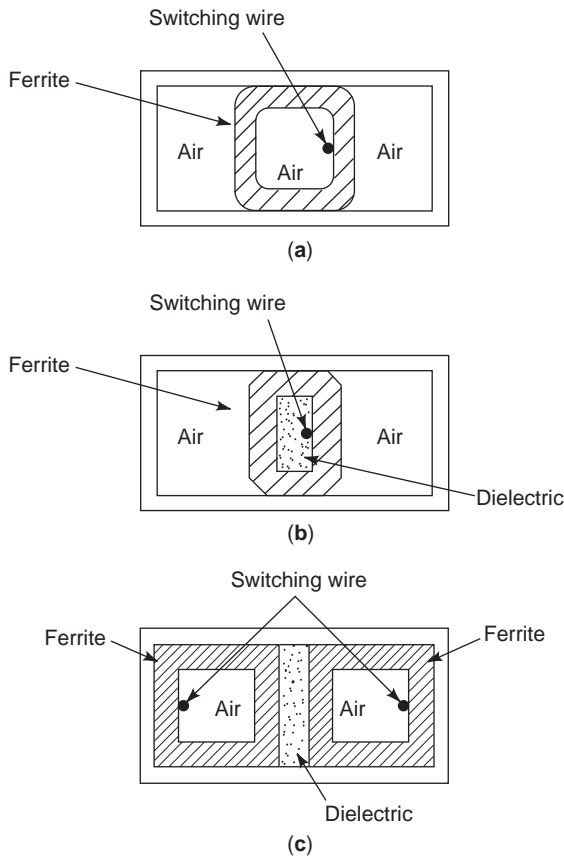


Figure 3. Evolution of the toroidal phase shifter into the twin-toroid device. The window inside the toroid is loaded with high dielectric material in order to improve the phase shifter RF performance in (b) while in (c) another toroid is added that greatly decouples the switching wires from the RF field.

Fig. 3c reduce this coupling by concentrating the RF energy in the region adjacent to the dielectric slab and locating the switching wires in regions of very low RF energy. This geometry is referred to as the *dual-toroid* and has come to be the preferred realization for this class device.

The ferrite–dielectric composite is housed in a rectangular waveguide that typically has a cross section smaller than that of the connecting waveguide because of the dielectric loading. Quarter-wave transformers are used to match into and out of the ferrite–dielectric composite. These transformers increase the length of the device but do not contribute significantly to the insertion loss. When the connecting transmission line is a TEM-type line such as microstrip, a high dielectric constant (≈ 100) material may be used as the dielectric spacer to reduce the cross-sectional dimensions of the phase shifter and lower the characteristic impedance level to around $50\ \Omega$. This has the added benefit of reducing the length of the device because of the increase in electrical length caused by the dielectric loading. The ferrite toroids are bonded to the high-dielectric-constant rib, and the composite is coated with a conducting material to form the waveguide. Connection to the TEM line may be made with a short length of wire

with a chip capacitor located at the point of connection of the wire to the phase shifter in order to resonate the inductance of the wire loop.

In order to establish a reference condition for the phase shifter the toroid is *reset*; that is, a voltage pulse of magnitude and duration sufficient to saturate the toroidal core is applied to the control wire. The current in the control wire remains roughly constant until the core saturates, at which time the current increases sharply. Sensing the current and removing the drive voltage when a predetermined current has been attained allows the core to relax to the remanent flux and establishes a stable reference point. The magnitude of the voltage pulse is not critical for the reset operation. The *set* operation establishes a flux level in the core corresponding to a given value of phase shift. Faraday’s law states that the change of flux is equal to the time integral of the applied voltage; a variable flux level may be set by using a variable amplitude voltage pulse for a fixed time duration or a fixed amplitude voltage pulse for a variable time duration. If either the voltage or the pulse-width varies substantially from that used to calibrate the phase shifter, the error in setting the flux may be excessive and resorting to more complicated methods such as integration of the voltage pulse may be necessary. Typical switching waveforms are shown in Fig. 4.

During switching, the toroidal core presents a resistive load to the source. Application of a voltage pulse to the control wire results in a current pulse whose amplitude is determined by Ampere’s law, $NI = \int H dl$. The magnetic field intensity is constant and equal to the coercive force, the number of turns is unity, and the integral of dl is equal to the mean length around the ferrite toroid. Thus $I = H_c l$. The flux change from one remanent state to the other remanent state is $2B_r A$, where B_r is the remanent flux density and A is the cross-sectional area of the toroid normal to the direction of flux. For a constant voltage V applied to the core for a time T , $VT = 2B_r A$, yielding a switching time $T = 2B_r A/V$. This is the maximum value of the time to establish the reset condition; the total switching time would

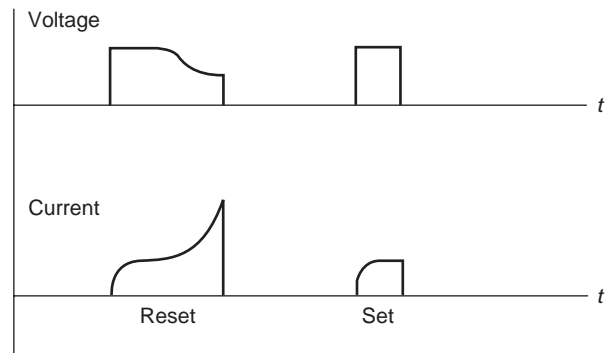


Figure 4. Switching waveforms of the latching phase shifter when driven from a constant voltage source. The voltage remains approximately constant during switching until the ferrite saturates. Saturation of the core to obtain a stable reset state is exhibited by the abrupt rise in the current in the reset waveform. The area under the voltage waveform for the set pulse determines the amount of flux switched into the ferrite core and hence the amount of phase shift.

be at least twice this value. Increasing the applied voltage reduces the switching time and increases the dynamic core resistance, which is given by $R = 2B_r A / (TH_c l)$.

2.2. Dual-Mode Phase Shifters

Latching operation of the ferrite rod phase shifter is realized by filling the waveguide completely with ferrite and providing a magnetic return path for the bias flux through the use of external ferrite yokes as shown in Fig. 5. The control power is furnished by a coil that is wound around the waveguide. Again the insertion phase of the device is dependent on the value of magnetic flux existing in the ferrite rod, and variable phase is realized by changing this value. The RF energy propagating through the ferrite rod must be circularly polarized, which may require the input polarization be converted from linear polarization to circular polarization. Each sense of circular polarization receives a different value of insertion phase when propagated through the device, and these values are interchanged when either the direction of propagation or the direction of magnetization is reversed. However, if an antenna uses these phase shifters and receives the “single bounce” return, transmitting right-hand circular and receiving left-hand circular or vice versa, switching between transmit and receive is not required.

Adaptation of the ferrite rod phase shifter to the reciprocal dual-mode phase shifter is illustrated schematically in Fig. 6, and the physical realization of the phase shifter is shown in Fig. 7. Nonreciprocal circular polarizers (NCPs) located on either end of the ferrite rod function as the circulators shown in the schematic diagram converting linearly polarized RF energy into circularly polarized RF energy and vice versa. The NCP physically consists of a section of the ferrite rod that is transversely magnetized with a four-pole bias field by a permanent magnet located exterior to the microwave circuit. This four-pole bias field provides a differential phase shift of 90° to cross-polarized signals. If the input to the NCP is

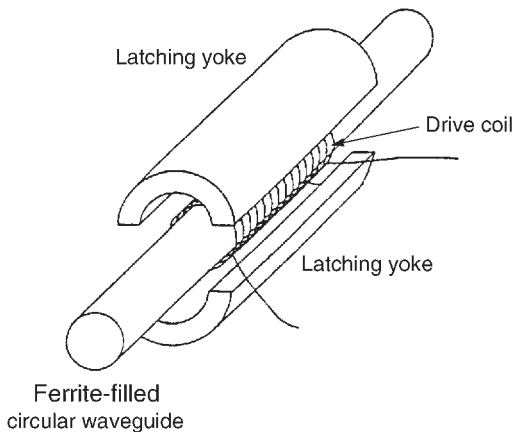


Figure 5. The Faraday rotation phase shifter. The ferrite-filled circular waveguide provides the signal path for the RF energy. Longitudinal magnetization is obtained using a drive coil wrapped around the ferrite rod. Latching operation is realized using latching yokes for a return path for the bias magnetic flux.

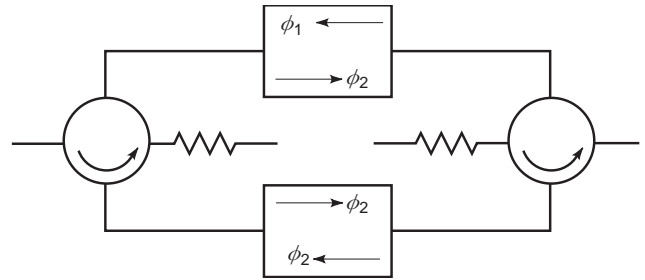


Figure 6. A reciprocal phase shifter realized using four nonreciprocal components. The two circulators and two nonreciprocal phase shifters provide port-to-port reciprocal behavior.

linearly polarized at an angle of 45° with respect to the axis of the NCP, the output will be circularly polarized with the sense of circular polarization depending on the orientation of the input linear polarization. For a circularly polarized input signal, the output of the NCP will be linearly polarized with orientation depending on the sense of the circularly polarized input signal. The NCP on the left side of the device in Fig. 7 converts input linear polarization into right-hand circular polarization in the ferrite rod section when RF energy is propagated from left to right. This circularly polarized energy receives a variable value of insertion phase dependent on the magnitude of the remanent bias flux density in the ferrite rod. The circular polarization is then restored to linear polarization by the NCP on the right side of the figure. For propagation from right to left, the RF energy in the ferrite rod is converted to left-hand circular polarization by the NCP on the right side of the figure, resulting in the signal receiving the same value of variable insertion phase irrespective of the direction of propagation through the device. The signal is restored to linear polarization by the NCP located on the left side of the device.

The electronic control of the dual-mode device is similar to that used for the toroid, but two major exceptions exist.

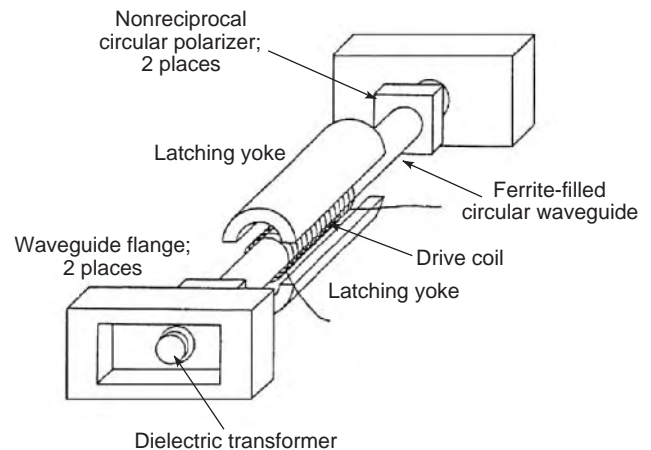


Figure 7. Physical realization of the dual-mode reciprocal phase shifter. This compact realization of the schematic shown in Fig. 6 has proved to be compatible with the packaging requirements for electronic scanned phased array antennas with wide-scan-angle requirements.

The drive coil is almost always a multiturn coil, which results in the apparent resistance and inductance of the ferrite core being increased by the square of the number of turns of the drive coil. Second, the waveguide walls do not enclose the magnetic circuit in its entirety. The magnetic flux cuts through the waveguide walls as it passes from the ferrite rod and is returned through the external yokes, resulting in an induced voltage in the waveguide walls whenever the flux is changed. Since the waveguide walls are made of low-resistivity material, a low-resistance path allows eddy currents to flow in the waveguide walls and produces the phenomenon called *shorted-turn damping*. This effect may be modeled by including a parallel resistance due to this damping in the equivalent-circuit of the phase shifter.

2.3. Rotary-Field Phase Shifters

The geometry of the rotary-field phase shifter is shown in Fig. 8. A composite ferrite–dielectric rod is metallized with a thin metallic coating to form the microwave portion of the circuit. This is inserted into a laminated steel yoke that provides the variable magnetic bias field. The rod–yoke assembly is housed in a two-piece metallic housing that interfaces to standard rectangular waveguide. Two interlaced windings wound on the multislot yoke generate the four-pole bias field. Dielectric quarter-wave plates on either end of the ferrite rod convert linearly polarized RF energy to circularly polarized energy, and vice versa, for propagation through the ferrite half-wave section. The linearly polarized RF input signal is converted to circularly polarized energy by means of the dielectric quarter-wave plate. This circularly polarized energy passes through the ferrite half-wave plate and receives a variable phase shift dependent on the orientation of the ferrite half-wave plate. At the output of the ferrite half-wave plate the sense of circular polarization is reversed, allowing the output dielectric quarter-wave plate to

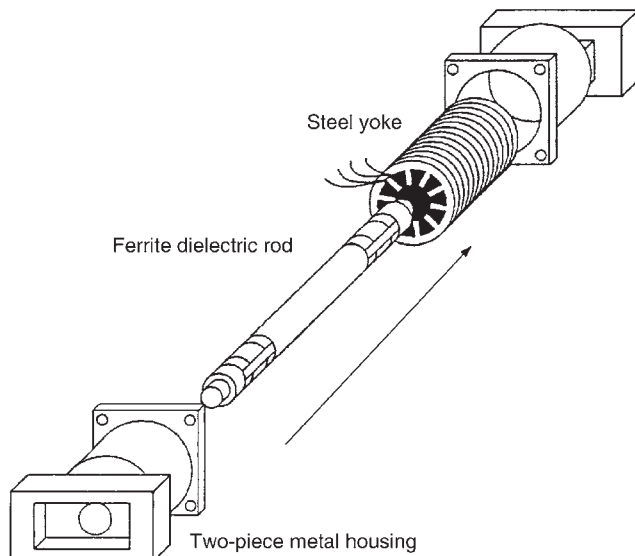


Figure 8. The rotary-field phase shifter. This device provides excellent phase accuracy and is capable of relatively high values of RF power.

reconstitute the same sense of linear polarization as the input polarization. The phase shift through the device is the same for either direction of propagation so that it is referred to as a *reciprocal device*. In the strictest sense it is nonreciprocal since a fixed 180° phase shift exists between signals propagating through it in opposite directions.

Latching operation of the rotary-field device was reported in 1995 [10] and units presently deployed operate with continuous holding current, resulting in a substantial DC power supply for array applications. This has limited the device to single-axis electronic scanning antenna applications such as the surveillance antenna for the AWACS aircraft. Typically the electronic control for these devices are two parallel drivers to control the two independent windings on the yoke, with the control current on one winding set proportional to the cosine of the desired phase angle and the control current on the remaining winding set proportional to the sine of the desired phase angle.

3. PHASE SHIFTER CHARACTERISTICS

Most phase shifter designs are custom designs having been developed for specific purposes and programs. Specific operating parameters will not be provided, but rather general electrical and physical characteristics will be discussed. Finally, typical numbers are provided for the reliability of the devices.

3.1. Electrical Characteristics

Electrical characteristics of importance are the operating mode (reciprocal/nonreciprocal), the operating frequency, the instantaneous bandwidth, the tunable bandwidth, the input polarization, the output polarization, the peak and average RF power, the insertion loss and the insertion loss modulation, the return loss, the quantization of the phase shift, the phase accuracy, the switching time, the switching rate, and the control power. Although it would seem that reciprocal operation would be preferred over nonreciprocal operation, there are many more nonreciprocal phase shifters deployed than reciprocal ones. The interaction of ferrite with RF energy is nonreciprocal and historically the earlier successful phase shifters were the nonreciprocal toroidal types. The choice of operating mode is generally dictated by system requirements; and in several cases such as communication satellites, nonreciprocal operation is not a handicap.

The operating frequency is another choice of the system designer with phase shifters having been developed from 1.4 to 94 GHz. The *instantaneous bandwidth* refers to the frequency band over which the phase shift remains within specified tolerances, while the *tunable bandwidth* refers to the frequency band over which the phase shifter may be adjusted to bring the phase shift within the specified tolerance. The nonreciprocal toroidal phase shifter has been designed to yield two octaves of instantaneous bandwidth, while the dual-mode phase shifter and the rotary-field phase shifter yield instantaneous bandwidths in the 2–4% range with tunable bandwidth of the order of 15%.

The input and output polarization depends on the application for which the phase shifter is intended and may be either linear or circular or switchable between the various linear and circular polarizations. The nonreciprocal toroidal phase shifter operates in a linearly polarized waveguide mode so that the input and output polarizations are linearly polarized. The dual-mode phase shifter may use circularly polarized input–output polarization operating in the non-reciprocal mode or linearly polarized input–output polarizations when operating in the reciprocal mode. This phase shifter lends itself well to incorporating polarization switching so that various output polarizations are available even when the phase shifter is excited with a linearly polarized input. The rotary-field phase shifter usually uses linearly polarized input and output signals, although this is not required.

The peak RF power capacity of a ferrite phase shifter is determined by the choice of ferrite used to realize the phase shifter. If the RF magnetic field intensity exceeds a threshold value, excitation of spin waves results and the RF insertion loss increases substantially. Doping of garnet material with rare-earth ions may be used to increase the threshold value, but at the expense of increased low power insertion loss. The average RF power capacity of a phase shifter is determined by the mechanical design and may be increased only by improving the heat flow path away from the ferrite.

The insertion loss of the phase shifter, as mentioned previously, should be below 1 dB in order to merit consideration from antenna designers. Of the phase shifters discussed, the rotary-field device has the lowest loss with values as low as 0.3 dB obtained in production quantities for a device operating in the 5 GHz frequency range. The toroidal phase shifter and the dual-mode phase shifters have insertion loss in the range from 0.6 to 1.0 dB. The variation of the insertion loss as a function of the insertion phase of the device is greatest for the reciprocal devices, generally of the order 0.2–0.4 dB, while the toroidal device has loss modulation less than 0.1 dB.

The return loss of the ferrite phase shifters depends on the RF input and output connections, and values cited will be for linearly polarized input–output configurations. The toroidal phase shifter generally has a maximum value of return loss of -20 dB, while the reciprocal phase shifters have maximum values of return loss of the order of -14 to -17 dB.

Ferrite phase shifters are generally designed to provide 360° of electrical phase shift. Early ferrite phase shifters were realized using discrete lengths of ferrite to provide quantization of the phase shift in steps of 180° , 90° , 45° , and 22.5° . This method results in a simple electronic driver design but a complicated microwave structure. Modern ferrite phase shifters are realized using a continuous piece of ferrite in order to minimize the cost of the microwave structure, resulting in a continuous range of phase shift. Quantization is provided by the electronic driver. Since the driver commands are distributed over the total range of phase shift, which is often greater than 360° , the final quantization is 1 bit less than that provided by the electronic driver; that is, an 8-bit driver command results in 7-bit phase shift quantization. Quantization levels greater

than this are found in the control electronics of variable power dividers/combiners but rarely are used in other phase shifter applications.

The *phase accuracy* of the phase shifter refers to the precision with which the insertion phase of the device may be set. For the toroid phase shifter, this parameter is a function of the stability of the reset state, the operating frequency, and the operating temperature, and accuracies of the order of 2–3° RMS error can be achieved. Improvements in accuracy can be achieved at the expense of added calibration. For the dual-mode phase shifter the alignment of the nonreciprocal polarizer magnets is another source of phase error, and accuracies of the order of 3–4° RMS error are common with this device. The rotary-field phase shifter may be set very accurately since the insertion phase is proportional to the ratio of the two currents that control the rotation angle of the magnetic bias field. Typical phase accuracies for this device are in the range 1–1.5° RMS and are not particularly sensitive to frequency and/or temperature.

The switching time of the phase shifter is the time required to establish a new insertion phase state and includes the times for resetting and setting the toroid and dual-mode phase shifter. The switching time is a function of the operating frequency since the size of the phase shifter is dependent on the frequency. Typical switching times for a toroid phase shifter range from about 20 μ s at 2 GHz operating frequency to about 5 μ s at 20 GHz. Typical switching times for a dual-mode phase shifter range from about 200 μ s at 5 GHz to about 50 μ s at 20 GHz. The nonlatching rotary-field phase shifter requires switching times ranging from 200 μ s at 3 GHz to about 100 μ s at 10 GHz but requires a high-voltage boost circuit in order to attain these speeds. The switching rate of the phase shifter is generally determined by system requirements, where the control power is directly proportional to the switching rate.

3.2. Physical Characteristics

Important physical characteristics of the phase shifter are the size, the weight, the cooling requirements, and the physical location of the input and output interfaces. The size is dictated by the operating frequency, average power requirements, and type of phase shifter. In general the toroid phase shifter has the smallest cross section, and the rotary-field phase shifter has the largest cross section with the dual-mode somewhere between the two. The weight of the phase shifter is proportional to size; the toroid phase shifter is generally the lightest weight unit, the rotary field the heaviest, and the dual-mode in between the two. The RF interfaces are the input and output RF ports, which may be coaxial cable, microstrip transmission line, rectangular waveguide, radiating elements into free space, or any combination of these. Electrical interfaces consist of the input data and any output data, such as built-in-test, control, power, and ground.

The electrical and mechanical design must be such that the phase shifter meets the specified values over operating temperatures ranging from -40 to $+95^\circ\text{C}$. In many cases a reduced temperature range for full performance with

degraded performance over the temperature extremes is allowed. Nonoperating temperatures normally range from -55 to $+125^{\circ}\text{C}$. Operating shock and vibration requirements are determined by the mechanical design of the system and the phase shifter mounting.

The reliability of the phase shifter as measured by the mean time before failure (MTBF) is an important consideration. The microwave portion of the phase shifter has high reliability since it is composed of a ferrite core and associated windings. The overall reliability is generally determined by the electronic driver with values of roughly 200,000 h for the latching phase shifters and values of 50,000 h for the nonlatching phase shifters because of the requirement for continuous drive current.

4. FUTURE DEVELOPMENTS

Two developments in waveguide devices offer promise. The first is an attempt to provide a reciprocal phase shifter using the toroid phase shifter in a geometry similar to that of the dual-mode device but using microstrip circulators. The difficulty with this approach is that the microstrip circulator is realized naturally as a three-port device and the schematic diagram of Fig. 6 requires a four-port circulator to adequately isolate the input and output ports. Work continues in this development. The second development in the waveguide area is the latching rotary-field phase shifter, which has been reported in the literature [6] but has not been deployed in the field. Data taken on experimental units are very encouraging.

There is a continuing effort to develop a ferrite phase shifter in a planar geometry suitable for integration with microstrip transmission line. The literature contains many references to these devices, but the insertion loss continues to be a drawback to deployment. The textbook cited in the Further Reading section contains several examples of planar phase shifters as well as many references.

BIBLIOGRAPHY

1. N. G. Sakiotis and H. N. Chait, Ferrites at microwaves, *Proc. IRE* **41**:87–93 (1953).
2. F. Reggia and E. G. Spencer, A new technique in ferrite phase shifting for beam scanning of microwave antennas, *Proc. IRE* **45**:1510–1517 (1957).
3. M. A. Treuhaft and L. M. Silber, Use of microwave ferrite toroids to eliminate external magnets and reduce switching power, *Proc. IRE* **46**:1538 (1958).
4. W. J. Ince and E. Stern, Non-reciprocal remanence phase shifters in rectangular waveguide, *IEEE Trans. Microwave Theory Tech.* **15**:87–95 (1967).
5. C. R. Boyd, Jr., A dual-mode latching reciprocal ferrite phase shifter, *IEEE Trans. Microwave Theory Tech.* **18**:1119–1124 (1970).
6. C. R. Boyd, Jr. and G. Klein, A precision analog duplexing phase shifter, *IEEE Int. Microwave Symp. Digest* 248–250 (1972).
7. A. G. Fox, An adjustable waveguide phase changer, *Proc. IRE* **35**:1489–1498 (1947).

8. E. Schloemann, Theoretical analysis of twin-slab phase shifters in rectangular waveguide, *IEEE Trans. Microwave Theory Tech.* **14**:15–23 (1966).
9. J. L. Allen, D. R. Taft, and F. K. Hurd, Computer-aided design of ferrite devices using intrinsic material parameters, *J. Appl. Phys.* **38**:1407–1408 (1967).
10. C. R. Boyd, Jr., A latching ferrite rotary-field phase shifter, *IEEE Int. Microwave Symp. Digest* 103–106 (1995).

FURTHER READING

- S. K. Koul and B. Bhat, *Microwave and Millimeter Wave Phase Shifters*, Vol. I: *Dielectric and Ferrite Phase Shifters*, Artech House, Norwood, MA, 1991.

FERROELECTRIC MATERIALS

R. K. PANDEY
The University of Alabama
Tuscaloosa, Alabama

1. INTRODUCTION

Before discussing the fundamentals of ferroelectric materials and their applications, it is important to acquire some background on how any material, especially insulators such as ferroelectrics, behave under the equilibrium conditions given by forces such as electrical, mechanical, and thermal. Each of these forces gives rise to certain properties depending on the basic physical nature of the material. For example, an electric field (E) causes displacement (D) [or polarization (P)], stress (T_{ij}) causes strain (S_{ij}), and entropy (S) is caused by temperature (T). These effects are not isolated from each other. In fact, when the system is in equilibrium, they interact with each other and give rise to additional properties. It is helpful to understand the relationship between these effects in order to appreciate the nature and properties of electronic and other materials.

In 1925 Heckmann [1] proposed an equilibrium diagram between electrical field, temperature, and stress, which was later modified by Nye [2] in 1957. A simplified version of this diagram is given in Fig. 1. It is assumed that the system is in equilibrium and the properties can be described with reference to changes that are thermodynamically reversible. Interaction between stress (T_{ij}) and displacement (D) causes direct piezoelectric effect whereas the converse piezoelectric effect is caused by the strain (S_{ij}) and electric field (E). The relationship between displacement and temperature is called the *pyroelectric effect*. The piezoelectric and pyroelectric effects are inherently important for discussing ferroelectricity.

The interactions between the three principal agents (E , T_{ij} , and T) within themselves and between the secondary agents such as displacement (D), strain (S_{ij}), and entropy (S) are responsible for materials to acquire certain properties. Many of them are identified in Fig. 1. However, for our purpose we need to consider only two more effects:

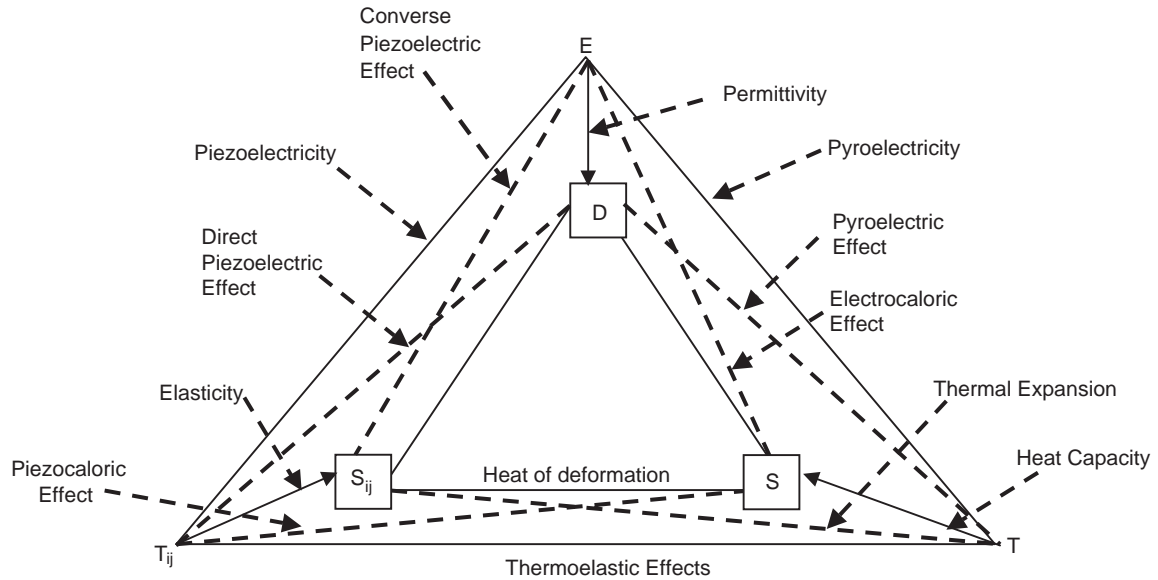


Figure 1. Modified equilibrium diagram between electric field (E), temperature (T), and stress (T_{ij}) and their associated effects.

(1) the thermal expansion effect, which is caused by the interaction between strain (S_{ij}) and temperature (T); and (2) the heat of deformation, which originates from the interaction between the strain (S_{ij}) and entropy (S). Both these, especially the thermal expansion coefficient, is a very important parameter for the selection of a suitable substrate for the growth of piezoelectric or ferroelectric films to produce integrated structured devices for many novel applications.

The three parameters—entropy, displacement, and strain—undergo small changes corresponding to the small changes experienced by the agent's temperature, electric field, and stress, respectively. Mathematically they can be represented by the following three simple relationships

$$ds = \frac{C_v}{T} dT \quad (1)$$

where c_v is the specific heat per unit volume and it is assumed that the system is in equilibrium and fully reversible; and

$$dD_i = \kappa_{ij} dE_j \quad (2)$$

where κ_{ij} is the permittivity tensor and

$$dS_{ij} = s_{ijkl} dT_{kl} \quad (3)$$

where s_{ijkl} is the elastic compliance.

In discussing ferroelectric materials and associated topics, we will make use of these concepts in gaining a good insight into the field of ferroelectricity.

The phenomenon now universally known as *ferroelectricity* got its name more because of its phenomenological similarity with ferromagnetism than because of the underlying physics describing these two phenomena found in materials. The name is deceptive in some sense. Ferro-

electricity, as the word implies, leads us to assume that it has something to do with iron (*ferum* in Latin). In reality it has hardly anything to do with this magnetic metal. In fact only a handful of materials having iron (or other prominent members of the ferromagnetic family such as nickel and cobalt) have been reported to exhibit ferroelectricity. However, they are certainly not members of the mainstream ferroelectrics and are rarely researched actively. Some examples are cadmium iron niobate, $\text{Cd}_2\text{FeNbO}_6$, some members of the barium fluoride group [e.g., barium iron fluoride (BaFeF_4), barium cobalt fluoride (BaCoF_4), and barium nickel fluoride (BaNiF_4)], and antimony sulfide-iodide-type compounds such as iron sulfide (FeS) [3,4]. Apart from the naturally found mineral FeS , another mineral termed *ilmenite* (FeTiO_3), containing copper has also been reported to be ferroelectric with a Curie point of approximately 580 K [5]. No other group has made such a claim. This author's research group [6] has searched extensively for ferroelectricity in laboratory-processed doped ilmenite without any success.

Almost all well-known ferroelectric materials are man-made (synthetic), in contrast to leading ferromagnetic materials, which are found abundantly in nature. Classic examples are iron, cobalt, and nickel and their alloys. So far as ferroelectricity is concerned only FeS and FeTiO_3 are naturally found in which the possibility of ferroelectricity might exist. Further research is warranted to establish the fact.

Ferromagnetism was already a well-established field of science and technology long before the birth of so-called ferroelectricity. In 1921 Valasek [7] discovered the hysteresis effect between polarization and electric field in potassium sodium tartarate tetrahydrate ($\text{KNaC}_4\text{H}_4\text{O}_6 \cdot 6\text{H}_2\text{O}$), which is commonly known as *Rochelle salt* after its discoverer who lived in France in the seventeenth century. Since its discovery over 80 years ago, the field of ferroelectricity has established itself as an important branch of

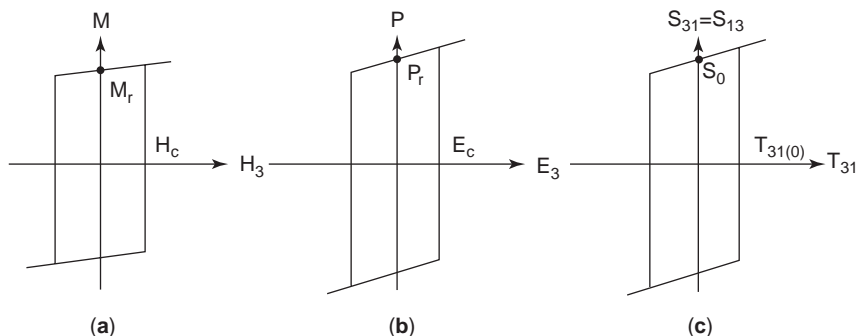


Figure 2. Idealized hysteresis loops of typical (a) ferromagnet, (b) ferroelectric, and (c) ferroelastic materials [4].

physics and engineering. During this span of time, hundreds of new ferroelectric materials have been discovered leading to the emergence of novel technologies that exploit various properties commonly found in ferroelectrics. The range of applications of this class of materials is vast, encompassing the spectrum from classical to ultramodern applications. On one hand, because of their high dielectric constant, ruggedness, and the reliability with which the materials can be processed reproducibly in very large volumes, ferroelectrics are the materials of choice for the fabrication of capacitors varying in size from miniature, used in microelectronics, to large, used in power circuits. On the other extreme, they find applications in such modern technologies as electrooptics, nonvolatile memory, uncooled focal plane arrays, microelectromechanical system (MEMS), and wireless communication.

The physical mechanisms involved in these two fields are entirely different and have practically nothing to do with each other. While ferromagnetism is anchored in the quantum-mechanical properties of an electron, especially its spin, ferroelectricity is macroscopic in nature, originating from the long-range interactions of the electric dipoles and the noncentrosymmetry of the unit cell of the crystal.

The phenomenological similarity between these two mechanisms goes beyond the existence of a hysteresis loop. Like ferromagnetism, ferroelectricity also shows the existence of the Curie point, at which it ceases to be ferroelectric and enters the nonpolar phase called the *paraelectric state*, analogous to paramagnetism. Furthermore, as there are antiferromagnetic materials, there are also antiferroelectric materials. Both ferromagnetic and ferroelectric materials have domains, and their structures help in describing terms such as *paramagnetism* and *paraelectric* as well as *antiferromagnetism* and *antiferroelectricity*. Piezoelectricity and pyroelectricity are inherently present in all ferroelectric materials and are strongly coupled with each other. In other words, all ferroelectrics are piezoelectric as well as pyroelectric, whereas not all piezoelectrics are ferroelectrics; nor are all pyroelectrics also ferroelectrics. The simultaneous presence of piezoelectricity and pyroelectricity in a ferroelectric material makes it truly a multifunctional material and therefore very attractive for the emerging fields of applications where multifunctionality is the most desired property of a material. Ferromagnetic and ferroelectric materials are not the only ones that display hysteresis loops. There is another class of material in which a hys-

teresis loop exists between the stress and the strain; these are called ferroelastic materials. Grouped together, ferromagnetic, ferroelectric, and ferroelastic are called “ferroic” materials.

According to the IEEE standard definitions [8], ferroelectrics, ferroelastics, and ferromagnetics define the class of *primary ferroics*. It is entirely possible to switch the direction of spontaneous magnetization, spontaneous polarization, or spontaneous strain by applying magnetic or electric fields or stresses, respectively. Figure 2 shows the idealized examples of the three types of hysteresis loops for typical (a) ferromagnet, (b) ferroelectric, and (c) ferroelastic materials [8].

2. FERROELECTRICITY AND ASSOCIATED PHENOMENA

2.1. Background Information

Ferroelectric materials are important members of the ferroic group. Compared to magnetism, they represent a relatively new field and yet have significantly impacted the development of electronic technology. As described in the preceding section, ferroelectric materials are truly multifunctional in nature because at least two other important phenomena, namely, piezoelectricity and pyroelectricity, coexist with them. Even a casual inspection of Fig. 1 makes it obvious that cause and effect between the electric field (E), temperature (T), and mechanical stress (T_{ij}) respectively play a dominant role in inducing dielectric, electric, and thermal properties in any material. Ferroelectricity is a typical example of such a manifestation. Because of the interplay between these forces, special effects take place, giving rise to distortion of the unit cell of a crystal structure and rendering it noncentrosymmetric. Table 1 and Fig. 3 will help in understanding the background of crystal symmetry, structure, and other classifications.

As shown in Table 1, the seven crystal systems are divided into three groups based on their optical classification. “Isotropic” means that the refractive index of the cubic crystal remains unchanged irrespective of whether it is measured in the a , b , or c direction of the crystal; thus, cubic crystal has no birefringence. The terms *tetragonal*, *hexagonal*, and *trigonal* are lumped together as *uniaxial*, meaning that they have one value of birefringence because they can have two different values of refractive index when measured along the different crystallographic

Table 1. Crystal System and Symmetry

Crystal System	Optical Classification	Characteristic Symmetry	Order of Symmetry
Cubic	Isotropic (also called <i>anaxial</i>)	Four 3-fold axes	Highest ↑ Lowest
Tetragonal	Uniaxial	One 4-fold axis	
Hexagonal	Uniaxial	One 6-fold axis	
Trigonal (also called <i>rhomboidal</i>)	Uniaxial	One 3-fold axis	
Orthorhombic	Biaxial	Three mutually perpendicular 2-fold axes; no axes of higher order	
Monoclinic	Biaxial	One 2-fold axis	
Triclinic	Biaxial	A center of symmetry or no symmetry at all	

directions *a*, *b*, or *c*. Similarly, because of three possible values of refractive index, the biaxial crystals can have maximum of two values of birefringence. Such a classification is very important for determining the electrooptic properties of ferroelectrics and other electrooptic crystals. The third column in Table 1 gives the number of characteristic symmetry for each crystal system. As we can imagine, the order of symmetry is the highest in the cubic system and the lowest in triclinic. Progressively from the lowest to the highest order, it goes from triclinic to cubic system as indicated by the arrow in the last (rightmost) column.

It is a well-established fact of crystal physics that out of the seven fundamental crystal systems one can generate 14 fundamental three-dimensional (3D) configurations called the *unit cells*. It was the French physicist Auguste Bravais in 1850 who first demonstrated that, according to the periodic arrangements of atoms found in a crystal, there could be only 14 possible arrangements of atoms in space. These are the famous 14 Bravais lattices, which are also known as *fundamental unit cells*. They can be in four types: primitive (P), body-centered (I), face-centered (F) and base-centered (C). For example, a cubic crystal can exist as simple cubic, or body-centered, or face-centered. Only in the orthorhombic structure are all four classes of unit cells found. Out of

the possible 14 Bravais lattices, 32 point groups originate. These are possible combinations of macroscopic symmetry elements, and once again, on the basis of the atomic periodicity of crystal, there can be only 32 point groups.

In Fig. 3 we show how these 32 point groups can be subdivided into groups of centrosymmetric and noncentrosymmetric unit cells. Out of these 32 classes, 11 are centrosymmetric and 21 noncentrosymmetric. These 21 are theoretically capable of exhibiting either ferroelectricity, piezoelectricity, or pyroelectricity, or a combination thereof. In reality only 20 of these 21 noncentrosymmetric crystals do show these properties. One of them has other symmetry elements, making this a special class of point groups.

Noncentrosymmetry of the unit cell of a crystal is a necessary condition for the existence of ferroelectricity, piezoelectricity and pyroelectricity. Figures 4a and 4b show a simple representation of a centrosymmetric crystal before and after being subjected to a mechanical force [9]. Obviously, in the presence of an external force, the interplanar distance becomes smaller in the direction of the applied force. But the crystal still retains its center of symmetry. From Figs. 5a and 5b we also see that the crystal retains its noncentrosymmetry before and after application of an external force while experiencing, as in the

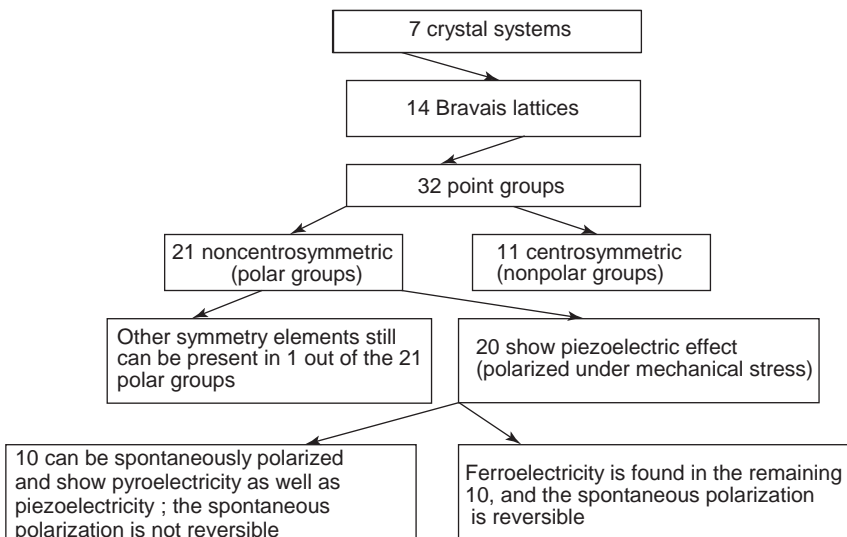


Figure 3. Point groups and their subgroups.

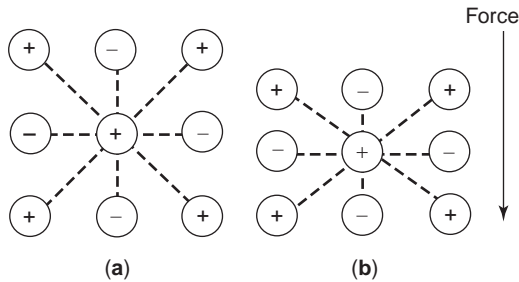


Figure 4. Schematic representation of a unit cell with center of symmetry (a) before and (b) after application of a mechanical force [9].

previous case, contraction in the interplanar distance along the direction of the force [9].

2.2. Parameters, Symbols, and Units

As are many other fields of science, ferroelectricity is also described by inconsistent symbols spread over decades of literature. This causes confusion, which might lead to misinterpretation of phenomena and the applications originating from their properties. To avoid such confusion, we follow here the definitions and symbols recommended by the Committee of the Institute of Electrical and Electronics Engineers, Inc. (IEEE). This group was charged with developing standard definitions of terms used in ferroelectricity and associated polar phenomena of piezoelectricity as well as pyroelectricity [8]. Important parameters, their symbols and units are reproduced in Table 2.

2.3. Ferroelectricity

We have already discussed some of the general features of ferroelectricity in order to grasp an understanding of its differences with ferromagnetism. A *ferroelectric* material is defined as a class of material in which the spontaneous polarization exists even when no electric field is applied to it. It is capable of existing in two equivalent states that are totally reversible, making ferroelectrics suited for many applications.

There is another class of materials known as *electrets*, which are often confused with *ferroelectricity*. These are also dielectric materials in which quasipermanent real charges can reside on the surface. They can also be found in the bulk of the material, or as frozen-in aligned dipoles in the bulk. Electrets behave in the same way as a battery

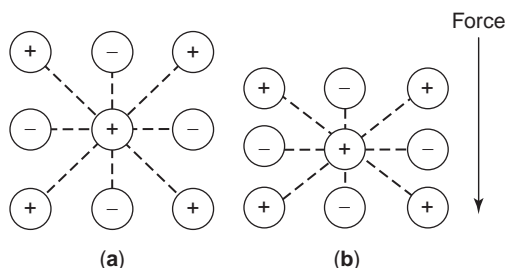


Figure 5. Schematic representation of a unit cell with no center of symmetry (a) before and (b) after application of a mechanical force [9].

Table 2. Physical Properties and Their Symbols and Units

Terms	Symbol	Units (SI Units)
Curie constant	C	K (Kelvin)
Capacitance	C_x, C_p, C_i	F (Farad)
Elastic stiffness constant	c_{ijkl}, c_{pq}	N/m ² (newtons/meter ²)
Electric displacement (vector)	D_i	C/m ² (coulombs/meter ²)
Piezoelectric charge (or strain) coefficient	d_{ijk}, d_{ij}	C/N (or m/V)
Electric field (vector)	E_i	V/m (volts/meter)
Coercive field (or coercivity)	E_c	V/m
Piezoelectric stress coefficient	e_{ijk}, e_{ij}	C/m ²
Pyroelectric current	i_p	A (ampere)
Dielectric polarization (vector)	P_i	C/m ²
Remanent polarization	P_r	C/m ²
Spontaneous polarization	P_s	C/m ²
Maximum polarization	P_{max}	C/m ²
Pyroelectric coefficient	p_i	C/m ² · K
Strain (second-rank tensor)	S_{ij}	Dimensionless
Elastic compliance constant	s_{ijkl}, s_{pq}	Dimensionless
Curie point	T_c	K or °C
Stress (second-rank tensor)	T_{ij}	N/m ²
Permittivity of free space	ϵ_0	F/m
Permittivity (second-rank tensor)	ϵ_{ij}	F/m
Relative dielectric constant	K_{ij}	Dimensionless

Source: Ref. [8].

or an electrical counterpart of a permanent magnet. However, they are not ferroelectrics. Ferroelectric materials are distinctly different from electrets in two respects: (1) its polarization is spontaneous, which is retained even at zero electric field; and (2) this polarization is controlled by the crystal's symmetry.

From Fig. 3 we find that the ferroelectric effect can be present in the 10 noncentrosymmetric polar groups in which the spontaneous polarization is reversible. Absence of the center of symmetry is the essential condition for the existence of not only ferroelectricity but also of piezoelectricity and pyroelectricity. As we will see later, a piezoelectric material assumes its polarization when subjected to a mechanical stress. Here the polarization is not spontaneous. It disappears when the mechanical force is removed. However, pyroelectrics are also spontaneously polarized in the same way as ferroelectrics but are not switchable. This is an important distinction between these two closely related phenomena. Ferroelectrics are also distinguished from pyroelectrics in one additional important way—only in ferroelectrics does the spontaneous polarization disappear at a well-defined temperature, called the *Curie point*. There is no concept of the Curie point in either piezoelectric materials, pyroelectric materials, or electrets. This characteristic temperature enables ferroelectrics to exist in two distinct phases: the polar (i.e., ferroelectric) phase and the nonpolar (the paraelectric) phase. Furthermore, ferroelectrics are well known to be materials showing very high dielectric constant, sometimes in excess of 50,000. The uniqueness of ferroelectric materials reflects itself in many ways, which make them

extremely attractive for diverse applications. We will discuss some of these later in this article. To sum up, the characteristic features of a ferroelectric material are (1) switchable spontaneous polarization, (2) high dielectric constant, (3) the Curie point that clearly defines the transition between the polar and nonpolar states, (4) hysteresis loop between polarization and electric field, and (5) crystal structures that lack center of symmetry.

The relationship between barium titanate (BaTiO_3) and ferroelectricity is similar to that between silicon and a semiconductor. It is the most prominent member of the family of ferroelectricity and well established in technology. It is isostructural with the mineral calcium titanate (CaTiO_3) and synthesizes in *perovskite* structure, commonly represented by the formula ABO_3 . The typical structure of BaTiO_3 in its ferroelectric phase (below the Curie point of 120°C) is shown in Fig. 6.

Here the Ba^{2+} ions occupy the eight corners of the unit cell, which is based on close-packed face-centered cubic crystal, the Ti^{4+} ions are located in the body-centered position, and the O^{2-} ions are at the face-centered positions. The barium ions are coordinated with 12 oxygen ions and the Ti ions in the octahedral interstices. At and above the Curie point, the unit cell of BaTiO_3 undergoes a phase transition from nonpolar to polar state. That is, it is no more ferroelectric above the transition point. The presence of the Curie point is an important characteristic of all ferroelectrics. Obviously, this is a material constant and can vary for different materials.

The majority of the well-known ferroelectric materials synthesize in perovskite structure. Some examples of technologically important ferroelectric materials with this structure are K niobate, K tantalate niobate (KTN), Pb titanate, and Pb zirconate-titanate (PZT). It is interesting to note that besides ferroelectrics, many other electronic materials of great scientific and technological importance can also crystallize in this structure. This was realized in the late 1980s, when high-temperature superconductivity was discovered. Leading examples were prominent members of the high-temperature superconductor family, namely, 123 YBCO (YBaCu oxide) and the colossal magnetoresistive materials of the type LaCaCu oxide and LaSrCu oxide. These discoveries have made the perovskite group of materials a subject of intensive research in attempts to discover some novel phenomenon.

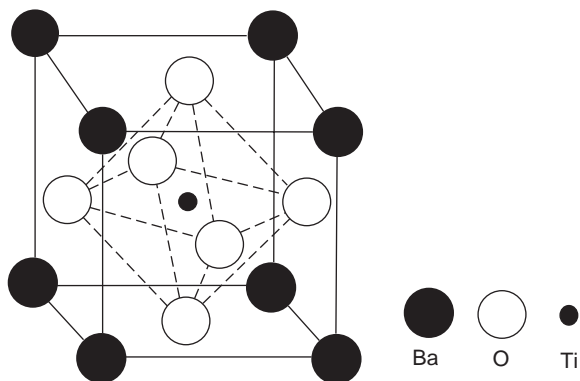


Figure 6. Perovskite structure of BaTiO_3 below T_c .

Another prominent ferroelectric group is found in the tungsten bronze structure shown in Fig. 7. They are represented by the generic formula of AB_2O_6 . Leading members of the family are Pb (meta)niobate (PbNb_2O_6), Pb (meta)tantalate (PbTa_2O_6), PbK niobate (PKN) having the formula ($\text{Pb}_2\text{KNb}_5\text{O}_{15}$), and BaSr niobate (SBN) with the formula of $\text{Ba}_2\text{Sr}_3\text{Nb}_{10}\text{O}_{30}$ [4]. PKN has been identified to have the largest piezoelectric coupling coefficient and was researched heavily in the mid-1980s. However, it was almost impossible to grow good crystals without producing multiple cracks. With the advancement of film technology and integration with silicon, PKN may once again receive renewed attention. Among all the electrooptic materials, SBN crystals show the most interesting properties and was the choice material for the fabrication of delay lines.

Ferroelectric crystals, like their magnetic counterparts, consist of a large number of *domains* in which the polarization is oriented in one unique direction. The neighboring domains are separated from each other by *domain walls*. All the polarization vectors point in one single direction and are parallel to each other, resulting in the maximum value of the spontaneous polarization for the bulk of the material. This picture is attainable under two conditions: (1) close to the absolute zero temperature and (2) when subjected to a strong external electric field. Between absolute zero and the Curie point the domain structure goes from fully ordered state (maximum polarization) to fully disordered state (zero polarization). Figure 8 shows schematically the parallel and antiparallel configurations of ferroelectric domains. Even at room

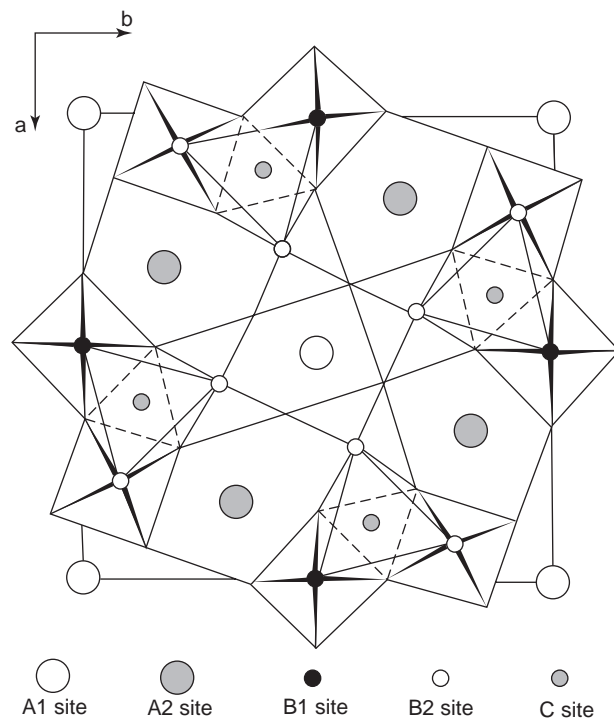


Figure 7. The framework of the tungsten bronze structure looking down the tetragonal c axis. The interstitial sites labeled A1, A2, and C can accommodate A-type cations. The B-type cations occupy the octahedron centers labeled B1 and B2 [10].

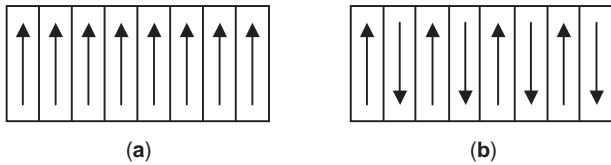


Figure 8. Schematic of domain configurations of a ferroelectric crystal: (a) parallel orientation ($P_s = \text{maximum}$) and (b) antiparallel ($P_s = \text{zero}$) orientation.

temperature the energy associated with lattice vibration is sufficient to destroy the ordered structure and cause the domains to orient randomly, resulting in zero polarization in the absence of an external field.

The hysteresis loop of ferroelectrics is obtained by using the simple circuit originally given by Sawyer and Tower [11] in 1930 and later modified by Sinha [12]. The switching time between the two states of remanent polarization is determined by the method proposed in 1966 by Fatuzo and Fatuzo [13]. A typical hysteresis loop of a ferroelectric material is shown in Fig. 9.

The material at room temperature has randomly oriented domains, as discussed earlier, and therefore zero value of the polarization. Initially when the field is applied and its magnitude is small, the P -versus- E curve is linear because the field induces the polarization here. This corresponds to the linear portion of the curve OA in Fig. 9 when the applied field is very small. Once its magnitude increases, an increasing number of domains orient in its direction. Eventually the polarization enters the nonlinear region and continues to increase with the field until it reaches its maximum value $+P_m$ in the first quadrant labeled I. This path is followed as shown by the dashed

curve OA and called the “virgin curve.” After this the effect of increasing field is negligible. At point $+P_m$ all the domains are fully oriented in one unique direction as shown by the upward-pointing arrows. The interpolation of the uppermost curve in quadrant I cuts the polarization axis at zero field at point P_s ; P_s is termed the *spontaneous polarization*. Strictly speaking, this definition is not exactly correct because theoretically the value of the spontaneous polarization is defined as the polarization at absolute zero. However, the value derived from the hysteresis curve is the value of the spontaneous polarization for all practical purposes. In quadrant I, when the field is reduced from its maximum value at P_m , it does not retrace its original path. Instead, it shows hysteric effect and meets the polarization axis at $+P_r$. This is the value of the polarization remaining from its original value of P_m at zero field; it is called the *remanent polarization*. Usually the ratio of P_r to P_m is less than 1. Ferroelectric materials with this ratio close to 1 are of great importance to memory applications. On further reduction of the field, in quadrant II, we see that the polarization disappears at point $-E_c$; E_c is called the *coercivity* or *coercive field*. In the second quadrant this is the field that is needed to bring the remanent polarization to zero. Here the hysteresis curve has completed its half-cycle. Further reduction of the field, in the third quadrant (III) brings us to $-P_m$. Thus, here the spontaneous polarization has switched by 180° as indicated by the downward arrows representing the orientation of the domains at this point. Once this point is reached, there is no sense in increasing the field in the negative direction any further. The field direction now is reversed and the P -versus- E curve cuts the polarization axis at $-P_r$. From the symmetry of the curve we observe that once again it is the remanent polarization.

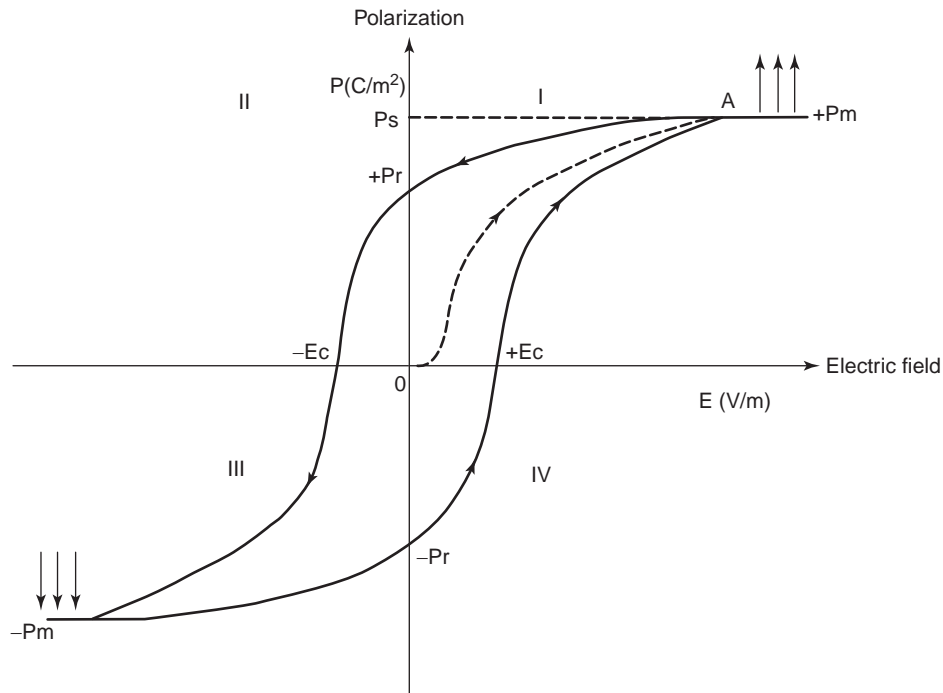


Figure 9. Polarization (P) versus electric field (E) hysteresis loop of a ferroelectric material.

The presence of two equivalent states of P_r lends ferroelectrics bistable state similar to that found in ferromagnetism. This particular property is of great technical significance and is the basis of nonvolatile ferroelectric memory. This property is also exploited for many other applications where memory effects are important. In the fourth quadrant (IV) the increasing field brings us back to the coercive field, $+E_c$. Further increase of the electric field allows the polarization to traverse the first quadrant nonlinearly. It eventually reaches the $+P_m$ point. This completes the full cycle of the loop.

No matter how many times the loops are generated, they retrace their original paths. This reproducibility is needed for designing devices based on the nonlinear property of ferroelectrics. The shape of the loop is dependent on the frequency of the AC electric field applied. It is also strongly dependent on temperature. At and very close to the Curie temperature of the ferroelectric material, the nonlinearity ceases to exist because of the disappearance of the spontaneous polarization. For all practical purposes it reduces to a straight line. The temperature at which the hysteresis loop collapses is also a measure of the Curie point. However, it gives only the approximate value. The exact value is to be determined by careful measurement of the spontaneous polarization as a function of temperature. The temperature dependence of the spontaneous polarization is shown in Figs. 10 and 11 [8].

From Figs. 10 and 11 it becomes clear that at the Curie point the material goes through a phase transition from a polar to a nonpolar state. Phase transition can be of two kinds: first-order, in which the change is discontinuous; and the second-order, in which the change is continuous. For many ferroelectrics the first-order transition occurs when it goes through a change in crystal structure such as from tetragonal to cubic. Such is the case for BaTiO₃, PZT, and KTN. Also, we observe that the Curie point is the dividing line between the polar and nonpolar states. Below this temperature ferroelectricity and therefore the nonlinear behavior dominates whereas above it the material is linear, as is any other dielectric. The polar and nonpolar

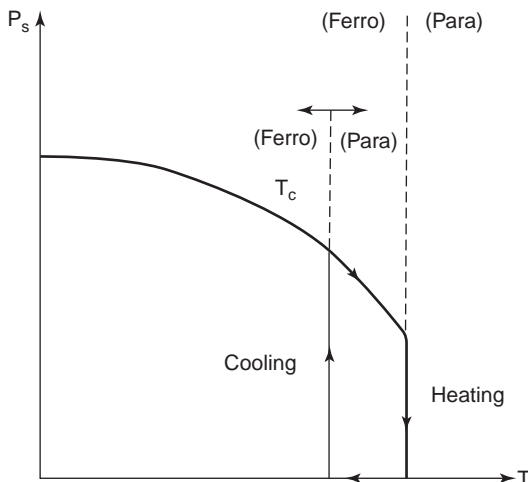


Figure 10. Spontaneous polarization versus temperature for first-order phase transition [8].

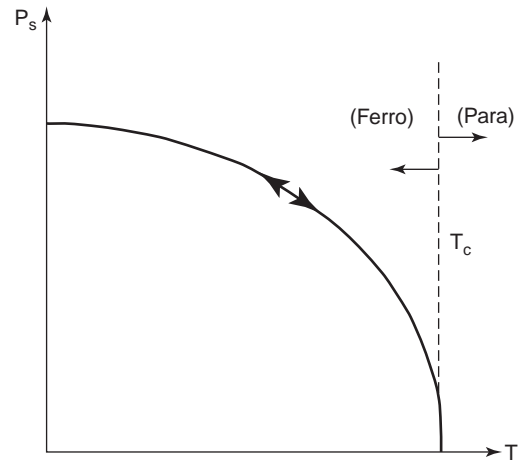


Figure 11. Spontaneous polarization versus temperature for second-order phase transition [8].

phases in a ferroelectric are totally reversible, and this can be explained on the basis of domain theory; specifically, above the Curie point the domain orientations are random, and as the temperature is lowered below the Curie point, the spontaneous polarization in these domains begins to renucleate and the number of these domains continues to increase as the temperature is lowered. At absolute zero they attain the highest order, allowing the spontaneous polarization to reach its maximum possible value.

The nature of the phase transition is also reflected in the temperature dependence of the relative dielectric constant (K) as shown in Fig. 12. In each case, the value of K goes to infinity at the Curie point. Ideally above the Curie point K^{-1} increases linearly with increase in temperature. This is predicted by the Curie-Weiss law

$$K = \frac{C}{T - T_c} \tag{4}$$

In Fig. 12(a), θ is the asymptotic Curie point at which K reaches its maximum value and in almost all cases it is close to the value of the Curie point determined by other

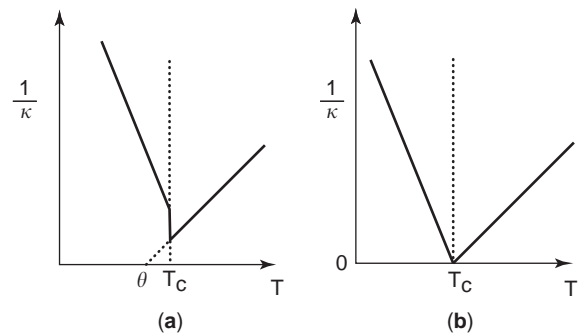


Figure 12. Temperature dependence of inverse of relative dielectric constant of a ferroelectric material undergoing phase transformations at the Curie point of the (a) first order and (b) second order [8].

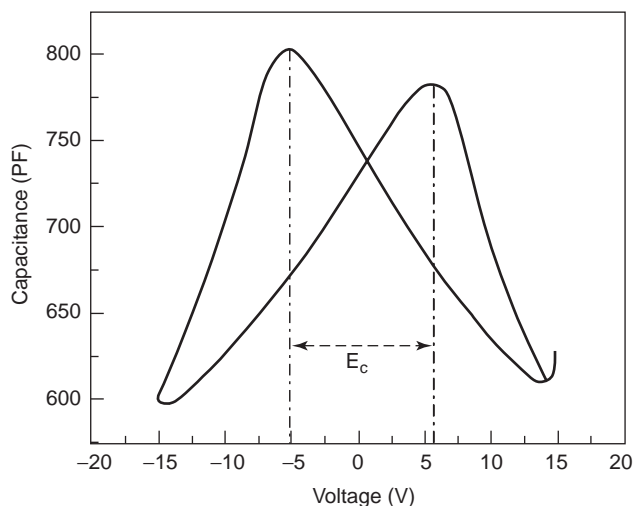


Figure 13. Capacitance versus bias voltage plot of PNZT solgel film [14].

experiments. It should also be emphasized that not all ferroelectrics follow the Curie–Weiss law strictly.

The capacitance–voltage plot, shown in Fig. 13, is also a good indication of the materials quality of a ferroelectric. Here too we observe that the nature of the curve is hysteric with respect to the decreasing and increasing bias voltage. The width of the peak of the curves, as shown by dashed lines, is a measure of the coercive force. Selected

examples of ferroelectric materials and their properties are presented in Table 3.

2.4. Piezoelectricity

Like many other terms of science, this, too, is derived from a Greek word meaning “to press.” As we have seen in Fig. 1, the relationship between the mechanical stress (T_{ij}) and the electric field (E) gives rise to piezoelectricity. Also, we find from this figure that there are two types of piezoelectric effects: direct and converse. Direct piezoelectric effect occurs because of the interaction between the mechanical stress (T_{ij}) and the displacement (D). Similarly the interaction between the electric field (E) and the strain (S_{ij}) gives rise to the converse effect. Both these piezoelectric effects have significant importance in technology.

If a stress is applied to a piezoelectric crystal, it develops an electric moment per unit volume (or charge per unit area). The magnitude of polarization is proportional to the stress applied. This is called *direct piezoelectric effect*.

Mathematically this is represented by the following equation

$$P = dT \quad (5)$$

where d is the piezoelectric coefficient, P the polarization, and T the stress; or, more precisely as

$$\Delta P_i = d_{ijk} \Delta T_{jk} \quad (6)$$

Table 3. Selected Ferroelectric Materials and Their Properties

Name (Abbreviation)	Chemical Formula	Curie Temperature (°C)	Spontaneous Polarization P ($\mu\text{C}/\text{m}^{-2}$) at (°C)	Crystal Structure	
				$>T_C$	$<T_C$
Barium titanate	BaTiO ₃	120	26.0 (23)	Cubic	Tetragonal
Lead titanate	PbTiO ₃	490	50.0 (23)	Cubic	Tetragonal
Potassium niobate	KNbO ₃	435	30.0 (250)	Cubic	Tetragonal
Potassium dihydrogen phosphate (KDP)	KH ₂ PO ₄	−150	4.8 (−177)	Tetragonal	Orthorhombic
Triglycine sulfate (TGS)	(NH ₂ CH ₂ COOH) ₃ H ₂ SO ₄	49	2.8 (20)	Monoclinic (centrosymmetric)	Monoclinic (noncentrosymmetric)
Potassium sodium tartrate tetrahydrate (Rochelle salt)	KNaC ₄ H ₄ O ₆ · 4H ₂ O	24	0.25 (5)	Orthorhombic (centrosymmetric)	Monoclinic (noncentrosymmetric)
Lead zirconium titanate (PZT) [21]	Pb(Zr,Ti)O ₃	200–480	Composition-dependent	Cubic	Rhombohedral or Tetragonal (depends on composition)
Lead niobium zirconium titanate (film), PNZT ^a	See below	400	58 (20)	Cubic	Tetragonal
Antimony sulfiodide (crystal)	SbSI	22	25.0 (5)	Orthorhombic (centrosymmetric)	Orthorhombic (noncentrosymmetric)
Antimony sulfiodide ^b	SbSI	19	0.03 (19)	Orthorhombic (centrosymmetric)	Orthorhombic (noncentrosymmetric)
Potassium tantalate niobate ^c (KTN)	See below	−108 to +19	Composition-dependent	Cubic (centrosymmetric)	Tetragonal (noncentrosymmetric)

^aPb_{1.1}Nb_{0.04}Zr_{0.2}Ti_{0.8}O₃ [17,18].

^bPLD-grown film [19].

^cKTN of various compositions, KTa_(1-x)Nb_xO₃, [20].

Source: Ref. 15.

The converse piezoelectric effect takes place on the application of an electric field to a piezoelectric material that induces the shape to deform (or, change) slightly. This is also a linear effect and can be represented by the following simple relationship

$$\Delta S_{jk} = d_{ijk} \Delta E_i \quad (7)$$

where S is the strain and E the electric field.

We have seen earlier that the elastic coefficient, the piezoelectric coefficient, and the dielectric constant are tensors and there can be as many as 45 independent coefficients. For example, the elastic constant can have 21 values; the dielectric constant, 6; and the piezoelectric coefficient, 18. But in practice one need not worry about all these different coefficients. One would usually apply the electric field, for example, in only one direction and measure the mechanical response in some other direction. For all practical purposes, the following two simple equations will suffice to describe piezoelectricity [9]

$$T = cS - dE \quad (8)$$

$$D = \varepsilon E + dS \quad (9)$$

where ε is the dielectric constant. The validity of these equations is given by the following arguments.

If $d = 0$, that is there is no piezoelectric effects present in the material, then we have $T = cS$, which is simply the famous Hooke's law; and $D = \varepsilon E$, which is the most familiar equation of electromagnetism. Alternatively, by setting $E = 0$ in Eqs. (8) and (9) $T = cS$, we once again get the famous Hooke's law and $D = dS$. The latter relation indicates that even in the absence of an electric field in a piezoelectric crystal a finite amount of polarization can develop on the application of strain. Similarly, an electric field can induce strain in a piezoelectric crystal even when there is no mechanical stress applied.

In short, because of the piezoelectric properties, a crystal develops strain when subjected to an electric field. Alternatively, polarization develops under mechanical stress. What follows from these arguments is that piezoelectric materials are ideally suited for applications related to electromechanical transducers. They are the materials of choice for many MEMS devices. Some examples of leading piezoelectric materials are shown in Table 4.

Table 4. Representative Piezoelectric Materials

Material	Type	Piezoelectric Constant $C/N \times 10^{-9}$	Relative Permittivity
Quartz, SiO ₂	Crystal	$d_{33} = 2.33$	4.0–4.5
Polyvinylidene fluoride (PVDF)	Polymer	$d_{31} = 23, d_{33} = 1.59$	12
Barium titanate (BaTiO ₃)	Ceramic crystal	$d_{31} = 78$ $d_{33} = 190$	1700 4100
Lead zirconate (PZ)	Ceramic	$d_{31} = 110, d_{33} = 370$	1200–3000
Zinc oxide (ZnO)	Ceramic	$d_{33} = 246$	1400
Nb-doped PZT ^a (PNZT)	Textured film	$d_{31} = 54$	2200

^aFor further details, see Refs. 16 and 18.
Source: Ref. 15.

2.5. Pyroelectricity Effect

We have already encountered the term *pyroelectricity* in Figs. 1 and 3. The origin of this effect lies in the following two facts: (1) interaction between the displacement and temperature and (2) noncentrosymmetry of the unit cell. Thus, pyroelectricity is caused when a crystal having a noncentrosymmetric unit cell and spontaneous polarization undergoes a temperature change. The change in temperature can induce a change in surface charge, which in turn can cause a change in electrical polarization of the material. The end result is the emergence of a thermal current, which can be detected, in an external circuit.

From electromagnetic theory we know that when an electric field is applied to a polar material, the resultant displacement is given by the following simple equation

$$\begin{aligned} D &= \varepsilon_0 E + P_{\text{net}} \\ &= \varepsilon_0 E + (P_s + P_{\text{ind}}) \end{aligned} \quad (10)$$

where D is the displacement, E the electric field, ε_0 the permittivity of vacuum, and P_{net} the net polarization.

Since the total polarization consists of both spontaneous component (P_s) and induced part (P_{ind}), we rewrite Eq. (10) considering that $P_s \gg P_{\text{ind}}$ as follows

$$D \approx \varepsilon E + P_s \quad (11)$$

where ε is the dielectric constant of the material. Differentiating this equation with respect to dT , we get

$$\frac{dD}{dT} \approx \frac{dP_s}{dT} + E \frac{d\varepsilon}{dT} \quad (12)$$

assuming that the E remains constant. We obtain

$$p_{\text{eqv}} \approx p_i + E \frac{d\varepsilon}{dT} \quad (13)$$

where p_{eqv} represents the equivalent pyroelectric coefficient and p_i , the true pyroelectric coefficient.

It is obvious from Eq. (13) that the true pyroelectric coefficient p_i can be evaluated by differentiating the P_s -temperature curves as shown in Figs. 10 and 11. It is also obvious from Eq. (12) that the change in temperature will induce change in the polarization vector. Therefore,

the pyroelectric coefficient can now be defined as

$$\Delta P_i = p_i \Delta T \quad (14)$$

where $i = 1, 2, 3, \dots$

The basic definition of the true pyroelectric coefficient is given by Eq. (14), whereas Eq. (13) gives the actual pyroelectric coefficient measured. The contribution from the second term representing the temperature coefficient of the dielectric constant ($d\epsilon/dT$) cannot be neglected if the pyroelectric measurements are done on a ferroelectric material for which, as we know, the temperature coefficient of the dielectric constant can assume large values.

We have already seen that the large values of the dielectric constant are also one of the most important features of a ferroelectric material and reaches its maximum value at the Curie point. This would mean that the equivalent pyroelectric coefficient (p_{eqv}) would be large for a ferroelectric with the Curie point near room temperature. This is an important consideration while designing a pyroelectric detector. Another important consideration in the device design is the contribution made by the piezoelectric coupling on the performance of the detector. Most of the practical pyroelectrics are also piezoelectrics. Therefore they will experience strain because of the thermal expansion leading to the development of surface charges.

The thermal current (I_p) that can be generated by heating uniformly a pyroelectric material is given by

$$i_p = \frac{dQ}{dt} = A \frac{dP_s}{dT} \cdot \frac{dT}{dt} \quad (15)$$

or

$$i_p = A p_i \frac{dT}{dt} \quad (16)$$

where A is the area of the electrode and p_i the pyroelectric coefficient. Here it is important to note that the heating of the sample must take place at a uniform rate. The current is generally determined when the experiment is conducted in a dynamic mode. Alternatively, the pyroelectric coefficient can be evaluated directly by measuring the charge (using an electrometer) that is generated at different temperatures. The following equation can be used for this

purpose:

$$p_i = \frac{Q_2 - Q_1}{A(T_2 - T_1)} \quad (17)$$

Some examples of technologically important pyroelectric materials are given in Table 5. These materials are used mostly for infrared imaging.

2.6. Pyrooptic Effect

A lesser known property called the *pyrooptic effect* of dielectric materials can also be potentially exploited for detection of infrared. The temperature dependence of the refractive index gives rise to this parameter. It is defined as

$$\theta_p = \left(\frac{d\eta}{dT} \right) \quad (18)$$

where θ_p is the pyrooptic coefficient and η the refractive index.

Performance of a pyrooptic detector will be significantly superior to pyroelectric or photon detector because no metallic contacts to pixel elements are needed to operate this device. Because it is an optical system, it allows for non-contact readout. This leads to an ideal thermal detecting structure as it eliminates a major source of signal-to-noise ratio in the system. In addition, for a pyrooptic detector, the sample thickness need not be greater than the optimum thickness required for supporting the optical waves on reflection. Thus, the pixel volume (or, mass) can be very small.

The concept of a pyrooptic detector was proposed in the early 1990s [24,25]. The device can be built on a single-crystal base or on films of a pyrooptic material. The film can be freestanding or supported on a transparent substrate having poor thermal conductivity.

Leading pyrooptic materials with their pyrooptic coefficients are presented in Table 6. As we can see from this table, once again ferroelectrics appear to be the material for the pyrooptic technology.

It is to be noted that in spite of many attractive features and simplicity, no practical device has become commercially available that is based on this effect. However, with the phenomenal progress made since the mid-1990s in processing of materials, especially films, and in producing

Table 5. Representative Pyroelectric Materials

Materials	Type	Pyroelectric Coefficient/ p_i ($\mu\text{C} \cdot \text{m}^{-2} \text{K}^{-1}$) at $^\circ\text{C}$
Triglycine sulfate (TGS)	Single crystal	280 (35)
Deuterated TGS	Single crystal	550 (40)
Lithium tantalite (LiTaO_3)	Single crystal	230 (25)
SBT, $(\text{SrBa})\text{Nb}_2\text{O}_6$	Single crystal	550 (23)
Modified lead zirconate (PZ)	Ceramic	400 (23)
PVDF	Polymer film	27 (25)
BST ($\text{Ba}_{0.65}\text{Sr}_{0.35}$) TiO_3 (bias field = 0.6 V/ μm)	Ceramic	7000 (20)
PST, $\text{Pb}(\text{Sc}_{0.5}\text{Ta}_{0.5})\text{O}_3$ (bias field = 10 V/ μm)	Sputtered film	850 (20)
Antimony sulfiodide, SbSI^a	Film, laser ablated on Pt/Si	12.4 (19.2)
PNZT, Nb-doped PZT ^b	Film, solgel grown on Pt/Si	1080 (23)

^aThick film grown on Pt/Si substrate by PLD [22].

^bSolgel film on Pt/Si of $\text{Pb}(\text{Nb}_{0.02}\text{Zr}_{0.2}\text{Ti}_{0.8})_3$ [14].

Source: Ref. 23.

Table 6. Examples of Some Pyrooptic Materials

Materials	Formula	Temperature Range (°C)	Pyrooptic Coefficient θ_p ($\times 10^{-4} \text{K}^{-1}$)
Antimony sulfoiodide	SbSI	0–15	75
Bismuth vanadate	BiVO ₄	20–100	2.8
Molybdenum disulfide	MoS ₂	–100 to +18	1.63
Lead titanate	PbTiO ₃	–60 to +40	1.5
Barium titanate	BaTiO ₃	29–120	3.1
Triglycine sulfate	TGS	40–300	5.0

Source: Ref. 24.

integrated structures with silicon [26], it is reasonable to assume that the pyrooptic effect might attain its rightful importance in the infra-red technology.

2.7. Antiferroelectricity

Once again we have copied this term from the vocabulary of magnetism. In antiferromagnets electronic spins are in antiparallel configuration. Similarly, the dipoles are antiparallel to each other in an antiferroelectric material. In these crystals the polarization is distributed throughout in the bulk of the material in an antiparallel arrangement such that the net polarization is zero. Figure 8b may be considered to schematically represent such a system. Note that this is a highly ordered configuration and must not be confused with the randomness of the dipoles caused by lattice vibrations. According to the classic work by Jona and Shirane [21], an antiferroelectric material is to be defined as an antipolar crystal whose free energy is comparable to that of a polar crystal. In an antipolar crystal the dipole interactions are such that they cause the antiparallel domains to dominate. Obviously these materials do not exhibit hysteresis loops between the polarization and the electric field. But a large anomaly is experimentally detectable when the structure changes from a completely unpolarized state to the antiferroelectric state at the transition point. Antiferroelectricity is a fundamental part of ferroelectricity and plays an important role in understanding the physics behind dielectric materials. Lead zirconate (PbZrO₃) is one of the most famous examples of antiferroelectricity. It shows a large anomaly in the temperature dependence of the dielectric constant at about 250°C and no dielectric loop at all [21]. This is a very important constituent of PLZT, PNZT, PZT, and other compounds that have enormous technical importance.

2.8. Multiferroic Magnetolectrics

No discussion of ferroelectricity can be complete without considering multiferroic materials. These are the materials in which ferroelectricity and ferromagnetism can co-exist in the same phase. They are also known by different terms, such as *magnetolectrics* and *ferromagnetolectrics*.

Ferromagnetism and ferroelectricity have been extensively researched and used in developing many applications and technologies. They both remain to a great extent independent fields of science with little or no overlap. However, the scientific and technological importance has long been realized for materials showing both ferromagnetism and ferroelectricity in the same phase and prefer-

ably above room temperature. Unfortunately such materials are not found in nature and have until relatively recently frustrated the efforts to produce them with a high degree of reproducibility in laboratories. This scarcity might be anchored in the fact that the transition metal *d* electrons, which are essential for the origin of ferromagnetism, tend to reduce the lattice distortion that causes ferroelectricity [27]. This results in a weak coupling between the spontaneous magnetization and spontaneous polarization. Because of the advancement in film technology and successful fabrication of integrated structures and superlattices, the search for new multiferroic materials has become very active. This covers a broad spectrum of materials ranging from composites to epitaxial films. It has been reported that magnetoelectric effects can be introduced in the thin film consisting of nanometric level of CoFe₂O₄ [cobalt ferrite (CFO)], which is a ferromagnetic material, and ferroelectric lead titanate (PbTiO₃) [28]. Bismuth manganate (BiMnO₃) is another material in which magnetoelectricity has been predicted [29]. The experimental search for this effect in BiMnO₃ was presented at a workshop conducted under the sponsorship of the US Office of Naval Research [30].

Of special importance are the two new discoveries. The presence of ferroelectricity in magnetic bismuth ferrite (BiFeO₃) has been conclusively shown by Palkar et al. [31]. They grew pure phase of bismuth ferrite on platinized silicon substrates by the pulsed-laser ablation method (PLD) under multiple partial pressures of oxygen. They report the existence of saturated ferroelectric loop for their samples, and the typical anomalous behavior of the temperature dependence of dielectric constant, which is the signature of a ferroelectric material. This anomaly occurs at the antiferromagnetic transition temperature (T_N) of $\sim 380^\circ\text{C}$. The ferroelectric transition occurs at $\sim 810^\circ\text{C}$. This is a remarkable result and is certain to contribute to the field of multiferroic materials and their applications.

Another equally important discovery has been reported by Hur et al. [32]. Electric polarization reversal and memory effects were induced by external magnetic field ranging from 0 to 2 T (tesla) in terbium manganate (TbMn₂O₃) multiferroic material. This is the first time anyone has been able to demonstrate strong coupling between magnetic and ferroelectric states. Besides polarization reversal induced by a magnetic field, the investigators were also successful in attaining memory effects under the combined influence of magnetic and electric fields. Like the previous work, this outstanding discovery is certain to impact the science and information technology.

3. MATERIALS PROCESSING

The ferroelectric materials are processed in three principal ways: ceramic processing, film deposition, and single-crystal growth. Each of these methods has its merits and demerits. Their selection depends primarily on the factors such as cost, volume of materials needed, and intended use. In the next few paragraphs we will briefly survey the three processing techniques applicable to ferroelectric materials.

3.1. Ceramic Processing

For large-scale production and applications this is the most widely preferred processing technique applied to produce dielectric materials including ferroelectrics. It is a relatively simple technique, is moderately expensive, and gives high returns on investment. Additionally, it lends itself easily to implementation of modifications and parameter adjustments for producing materials with predictable properties in large volumes. On a smaller scale, it provides an excellent research tool for designing and discovering new dielectric materials.

This consists of seven major steps as shown in Fig. 14. The first and foremost step is to begin with highest possible purity grades of raw materials in proper weight or mole

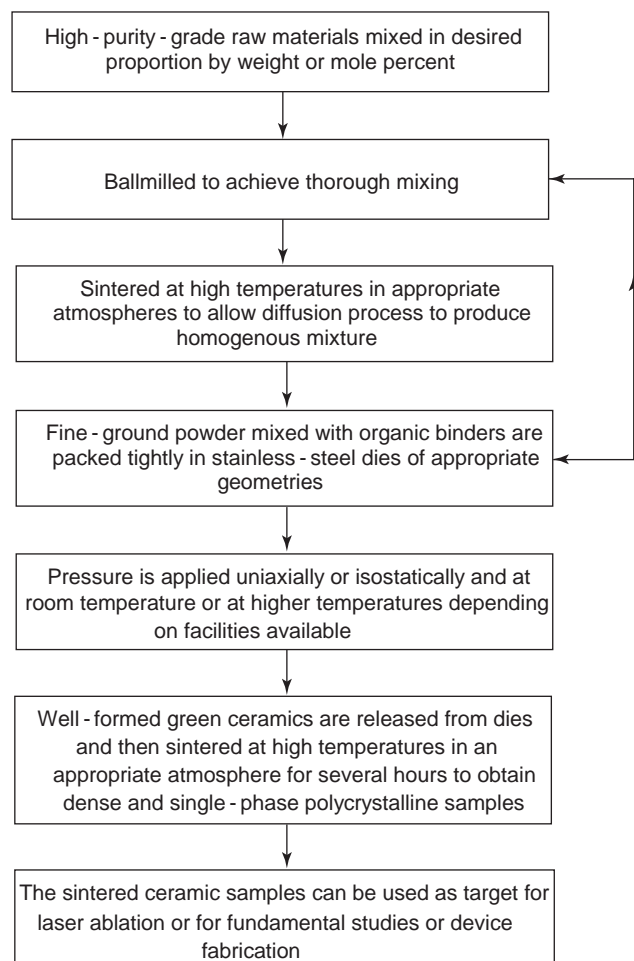


Figure 14. Flow diagram for ceramic pressing.

ratio. Then they should be mixed thoroughly such as by ballmilling to break down the particle size and obtain a homogeneous mixture. The subsequent steps of heat treatment and forming desired shapes and sizes follow this step. Then the most critical step is undertaken. The compaction takes place by applying uniformly high pressures to the dies containing the desired shapes and forms. Hydrostatic pressing at elevated temperatures is the most desirable approach to obtain a high-density and high-quality material. However, if such a system is not available, cold hydrostatic pressing, or simply cold or hot isostatic pressing are available alternatives. Once the pressing is done, the green ceramic needs to be sintered at high temperatures, which are mostly 90% of the melting temperature of the materials, for hours in a specialized atmosphere. Air annealing is usually sufficient. However, depending on the chemistry of the material, it is necessary to do annealing in reducing, oxidizing, or neutral atmospheres. The logic behind sintering at high temperatures for extended time periods is to allow the diffusion process to produce single-phase, homogenous materials with large grains (crystallites) and with practically no voids. Each heat treatment aids in attaining this goal. It is important that the steps shown in boxes (second, third, and fourth seen from the top) in Fig. 14 should be repeated at least 3 times before high-pressure operation takes place. This laborious and time-consuming processing method ensures the quality of the material to be produced. Once the ceramic samples become available, they are ready for use either for scientific experiments or for product development.

3.2. Film Deposition

Because of their multifunctional nature, ferroelectrics lend themselves to a large number of applications and development of novel devices for which high-quality epitaxial or textured films are required. They are grown by a variety of techniques; the most common ones are sputtering, electron-beam evaporation, solgel, metallorganic deposition (MOD), physical vapor transport (PVT), and pulsed-laser deposition (PLD). As in the case of ceramic processing, the choice of the method for film growth depends on many factors; again, the foremost are the cost and quality of films needed. As can be expected, each of these methods has its merits and limitations. The literature is full of excellent books and publications dealing with each of these techniques. Unfortunately, we are not in a position to cover any of these methods in depth in this article. However, we are giving here some basic information related to the methods mostly used by the ferroelectric community for the benefit of the reader.

For large-scale production, sputtering and solgel are the leading methods used on industrial scale. Having similarity with solgel MOD is also widely used but it is not as effective a method as solgel. The PVT method is used only when other methods are not applicable such as if the material has high vapor pressure. These are mostly iodides, fluorides, sulfides, and similar compounds. The PVT method is capable of producing high-quality textured or even single crystalline films on a variety of substrates. However, it has its own limitations and is not easily modifiable

for large-scale applications. Figure 15 shows a simple experimental arrangement developed by us [22] for the growth of antimony sulphoiodide (SbSI) films for pyroelectric and pyrooptic research [26]. High-quality textured or even single-crystal films could be grown of this high vapor pressure material by the PVT method.

The PLD method is versatile and has been used for the growth of a large number of oxides including ferroelectrics, high-temperature superconductors, and colossal magneto-resistant (CMR) materials. Since its discovery in late 1980s when it was first introduced very successfully for the growth of high-temperature superconductor, especially 123 YBCO, PLD has become the choice method for research on oxide growth. It is a versatile method and can be easily adopted to implement necessary changes in growth parameters. Its greatest strength lies in the fact that it retains the chemical homogeneity of the film with respect to its source (called “targets” in the language of PLD) and can produce polycrystalline, textured, or single-crystalline films; integrated structures; and superlattices. It is also used for the growth of complex device configurations. An excellent treatment is given of PLD technology in Ref. 33.

3.3. Single-Crystal Growth

Single-crystal growth has been the most fascinating and challenging area of materials processing. Ceramics, films, integrated structures, and superlattices can meet many scientific and technical needs, yet there are still some very specialized needs for high-quality bulk single crystals. Substrates for epitaxial growth of films are exclusively bulk single crystals. This has been a very well-established field for more than a century. Its biggest impact in technology came with the invention of transistors in the late 1950s when it was realized that device-quality single crystals of silicon were needed for superior performance and reproducibility of the transistors. The crystal growth method, which is today widely known as the “Czochralski technique,” lived up to this enormous technical challenge. It is the most widely used method for crystal growth. Other growth methods are high-temperature solution growth (HTSG), aqueous solution growth (ASG), Bridg-

man growth, top-seeded solution growth (TSSG), and temperature-gradient transport growth (TGTG), to name only a few. The literature is full of crystal growth methods applicable to a variety of materials. Obviously it is not within the scope of this article to survey the literature for the crystal growth of even ferroelectric materials. Interested readers are referred to some excellent work such as given in Refs. 34–36.

Here we plan to limit ourselves to a very introductory presentation of this subject. The selection of an appropriate growth method depends on all the factors outlined in the previous two sections. But the most important criterion is to determine whether a material melts congruently or incongruently. When, for example, the melt and the solid of a material have the same chemical composition, then the material’s melting point is congruent. Otherwise, it is incongruent. Very few ferroelectrics melt congruently. As a result, the famous Czochralski technique cannot be employed for the growth of these materials. This is unfortunate in the sense that other methods are not as versatile as the Czochralski technique in producing large single crystals in a reasonable amount of time. The most successful methods for the growth of ferroelectric crystals have been HTSG, TGTG, TSSG, and ASG. The Czochralski technique has been widely used for the congruently melting members of the family of barium strontium titanate (BST), strontium barium niobate, and lithium niobate (LiNbO_3). All these are highly attractive materials for electrooptic applications and fabrication of optical waveguides. Lithium niobate, an excellent ferroelectric and piezoelectric material, is also widely used as substrates for building integrated structures.

The famous pyroelectric material, TGS, is grown by AGS method. This is an excellent material for IR imaging. But its hygroscopic nature is a drawback. A large number of ferroelectric crystals have been grown by the HTSG method, which is also known as the “flux growth method.” Here a suitable solvent is used for dissolving the raw materials (called “charge” in the vocabulary of crystal growth) at high temperatures and then cooled very slowly (usually $1\text{--}2^\circ/\text{h}$) over many weeks. Relatively large (a few millimeters to a few centimeters) crystals grow that are harvested by dissolving the frozen flux in a suitable solvent. Barium titanate (BaTiO_3) has been grown in device quality by the TSSG method.

A variation of this method is TGTG. This is a very innovative technique and has been applied for the growth of some otherwise difficult-to-grow ferroelectrics with a minimum of compositional gradient within the bulk of the sample. Potassium tantalate niobate (KTN), (Fig. 16), which has excellent electrooptic, ferroelectric, and pyrooptic properties, has been grown as a large single crystal by this method [20].

4. APPLICATIONS

In the preceding sections we have established the multifunctional nature of ferroelectrics. Ferroelectrics, as we have already seen, are high dielectric constant materials, which also possess reversible spontaneous polarization

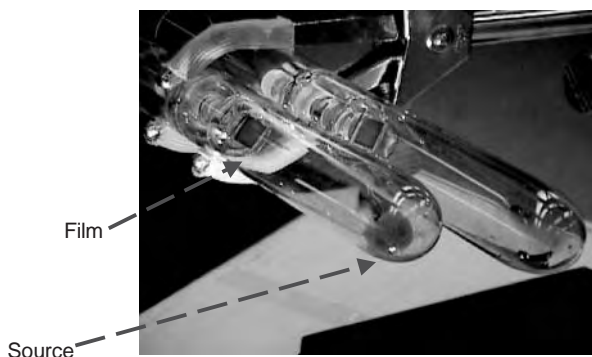


Figure 15. SbSI films grown by physical vapor transport method.

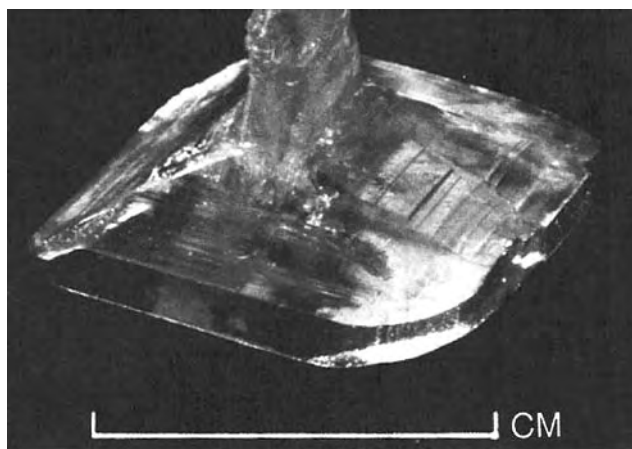


Figure 16. Potassium tantalate niobate (KTN) single crystals [20]; the length scale shown here corresponds to 1 cm.

and piezoelectric coupling as well as pyroelectricity simultaneously. These properties are the driving forces behind the importance of ferroelectrics in a wide range of technologies. In fact, they play a very vital role in the advancement of technologies ranging from classical to ultramodern. Classically, ferroelectrics are ceramics. Owing to their unique electrical properties they are also important members of the family of *electroceramics*.

It is not within the scope of this article to discuss in depth even the most important applications based on the multifunctional nature of ferroelectric materials. Interested readers will find the two publications [15,37] useful in understanding of applications based on ferroelectrics and associated phenomena and their impact on technology, especially electronic, electrooptic, communication, and information technology.

By carefully evaluating the multiple properties and phenomena associated with these classes of polar materials, we can get an idea of the enormity of its importance to technology and its potential for the development of novel devices. We can summarize them as follows:

- Because ferroelectrics are piezoelectric as well as pyroelectric, they are also multifunctional.

- Piezoelectricity can exist alone in some polar materials, or it can be accompanied by pyroelectricity, or in some other materials all three effects—ferroelectricity, piezoelectricity, and pyroelectricity—can coexist.
- All pyroelectrics are piezoelectrics but not necessarily ferroelectrics as well.
- The discovery of existence of both ferroelectricity and ferromagnetism in the same phase (previously referred to as *multiferroic* or *magnetoelectric*) opens avenues for world-class research in materials science, physics, and microelectronics.
- Because piezoelectricity is an excellent class of electro-optic materials, its impact on the optical industry is conspicuous.

In the beginning of this article we briefly examined the equilibrium diagram (Fig. 1) between three forces, electric field (E), temperature (T), and mechanical stress (T_{ij}), and their respective consequences; namely, displacement (D), entropy (S), and stress (S_{ij}). These six agents couple together in noncentrosymmetric crystals to produce the multifunctional phenomenon of ferroelectricity. Figure 17 presents some of these interactions and their consequences.

We have already seen that the domains in ferroelectrics even at room temperature can be randomly oriented. Therefore, the materials need to be *poled* before they can be utilized for device fabrication and integration. Poling is a relatively simple operation. First, metallic electrodes are deposited by thermal evaporation or sputtering or by other means on the surfaces of the samples so that an electric field can be applied to them. Then they are subjected to a DC electric field, which is much greater than the sample's coercivity, while slowly raising the temperature to a point above the Curie point of the material, where it is held for some time to ensure that the entire material is in equilibrium in its paraelectric state. Subsequently, the temperature is slowly lowered to room temperature in the presence of the field. The process involves the nucleation of domains as soon as the temperature is lowered slightly below the Curie point. Once the domains form they orient themselves in the

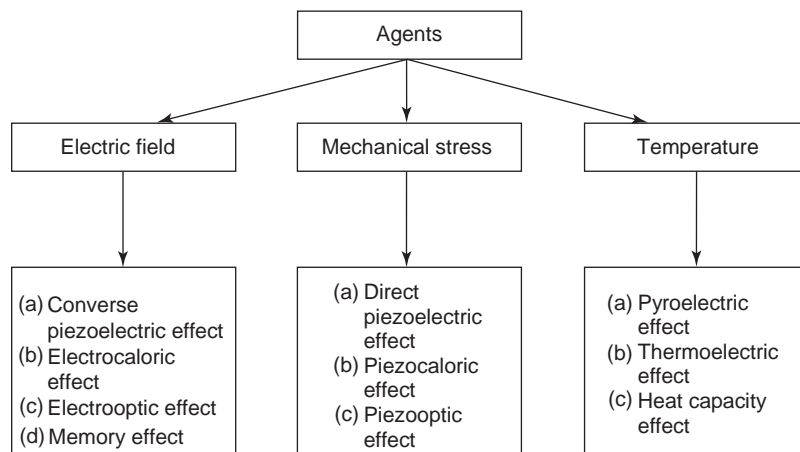


Figure 17. Agents and effects responsible for ferroelectric applications [15].

direction of the field that is present in the sample. Their number keeps on increasing, as the sample is finally reaches room temperature. Now all the domains in the material are should be fully aligned and will remain so even after the field is removed. At this stage, the *poling* has been completed and the field is removed. The sample will retain its poled status as long as it is not reheated above the Curie point. In that event, one will have to re-pole the specimen.

On one end of the application spectrum, ferroelectrics are the dominant material for design and fabrication of ceramics. They are produced in large volumes and have the largest share of capacitor market throughout the world. Because of their unusually high dielectric constant, a large quantity of electrical energy can be stored in a relatively small volume and capacitor size. Therefore, ferroelectric-based capacitors can be made in large to miniaturized shapes and fulfill vital functions in electronics and integrated circuits.

On the other end of the spectrum, ferroelectrics are conspicuously present in an array of modern applications covering as varied fields as MEMS technology, radiofrequency and microwave communication, information technology, electrooptics, optical communications, infrared imaging, uncooled focal plane arrays, and nonvolatile memory, to name just a few applications and technologies to which ferroelectric materials have contributed.

Ferroelectrics dominate the scene of actuators and transducers because of their piezoelectric properties. Among all commercially available piezoelectric materials, Pb zirconate titanate (PZT) plays a very prominent role. Table 4 lists other piezoelectric materials. PZT is the most widely used piezoelectric material and has established itself as a leading transducer material in microelectromechanical (MEMS) technology.

When it comes to infrared imaging applications, ferroelectric materials once again lead the pack of materials suitable for fabrication of detectors that can operate above room temperature. These are the so-called uncooled focal plane arrays. Around 1990 Texas Instruments in Dallas, Texas championed ferroelectric-based *uncooled* focal plane arrays. The original material used was highly dense ceramic of barium strontium titanate (BST) having a transition temperature of around room temperature. In this type of device, the unique pyroelectric properties of ferroelectrics are exploited. In Table 5 we list the leading pyroelectric materials.

Memory devices based on ferroelectric materials are nonvolatile, meaning that the data stored are retained in the memory even when the power fails or is switched off. This is comparable to the well-established magnetic memories. Another class of widely used memory is DRAM (or dynamic random access memory), which consists of volatile memories. These memories are based on silicon integrated circuit technology, in which the stored data are lost once the electrical power of the device is switched off. In spite of this serious drawback and inconvenience, DRAMs are widely used because of their high integration capability. Nonvolatility of a ferroelectric memory is the result of the stable bipolar states of its hysteresis loop

discussed previously in this article. Constant improvements are being made in the design and integration of FeRAMs.

Ferroelectrics are also an established group of materials for microwave communications. Barium strontium titanate (BST) appears to be the leading material for such applications. The literature is full of reports on how BST can be used in developing integrated structured devices to meet various requirements of the microwave communication. Ferroelectrics are attractive materials for microwave devices because (1) they have low microwave losses in the paraelectric phase, (2) dielectric permittivity is DC-field-dependent, (3) tunability is high, and (4) extremely high values of permittivity make it possible to miniaturize the devices. The ferroelectric integrated structures (with silicon and superconductors) are attractive for many microwave applications:

- Varactors and varactor-based devices such as mixers and harmonic generators
- Tunable resonators, filters, and antennas
- Miniature tunable delay lines and phase shifters
- High-density capacitors and small-size low-impedance transmission lines
- Thin-film “bulk acoustic wave” resonators and filters
- Surface acoustic wave (SAW devices) filters, convolvers, converters, and similar devices
- MEMS switches for actuation and transduction.

A good survey of applications of ferroelectric materials in microwave communications is covered by Patel et al. [38]. Interested readers will benefit greatly from consulting this resource. Integrated structured devices using ferroelectric materials as one of the components are becoming increasingly important for development of new microwave [39] and other applications [40–46].

The following books and other publications are recommended for serious readers who would like to gain an insight in the field of ferroelectricity and related phenomena.

BIBLIOGRAPHY

1. G. Heckmann, *Ergebnisse der exacten Naturwissenschaften* 4:140 (1925).
2. J. F. Nye, *Physical Properties of Crystals*, Oxford Science Publications, 1986.
3. M. E. Lines and A. M. Glass, *Principles and Applications of Ferroelectrics and Related Material*, Clarendon Press, 1977.
4. E. C. Subbarao, *Ferroelectrics* 5:267 (1973).
5. R. P. Viswanath and A. T. Seshadri, *Solid State Commun.* 92:831 (1993).
6. R. K. Pandey, P. Padmini, and P. Kale, unpublished results, Laboratory for Electronic Materials and Device Technology (www.emdtech.eng.ua.edu), Univ. Alabama, Tuscaloosa, AL.
7. J. Valasek, *Phys. Rev.* 17:475 (1921).
8. Draft 16 of a Working Document for a Proposed Standard to be entitled *IEEE Standard Definitions of Terms Associated with Ferroelectric and Related Materials*; see *IEEE*

- Trans. Ultrason., Ferroelectrics Freq. Control* **50**:1613 (2003).
9. L. Solymar and D. Walsh, *Electrical Properties of Materials*, 6th ed., Oxford Science Publications, 1999.
 10. P. B. Jamieson, S. C. Abrahams, and J. L. Bernstein, *J. Chem. Phys.* **48**:5048 (1968).
 11. C. B. Sawyer and C. H. Tower, *Phys. Rev.* **35**(3):269 (1930).
 12. J. K. Sinha, *J. Sci. Instrum.* **42**:696 (1965).
 13. E. Fatuzo and W. J. Merz, *Ferroelectricity*, North-Holland, Amsterdam, 1966.
 14. H. Han, X. Song, J. Zhong, P. Padmini, S. Kotru, and R. K. Pandey, *Appl. Phys. Lett.* (Nov. 2004).
 15. K. C. Kao, *Dielectric Phenomena in Solids*, Elsevier Academic Press, 2004.
 16. G. T. A. Kovacs, *Micromachined Transducers Sourcebook*, McGraw-Hill, 1988.
 17. C. Nistorica, J. Zhang, P. Padmini, S. Kotru, and R. K. Pandey, *Integr. Ferroelectrics* **62** (2004).
 18. C. Nistorica, *Integrated PNZT Film Structures for MEMS Gyroscope*, dissertation, Univ. Alabama, Tuscaloosa, AL, 2003.
 19. S. Kotru, W. Liu, and R. K. Pandey, *Proc. 12th IEEE Int. Symp. Applications of Ferroelectrics (ISAF 2000)*, 2001.
 20. K. W. Goeking, R. K. Pandey, P. J. Squattrito, A. Clearfield, and H. R. Beratan, *Ferroelectrics* **92**:89 (1989).
 21. F. Jona and G. Shirane, *Ferroelectric Crystals*, Dover Publications, 1993 (originally published in 1962).
 22. S. Kotru and R. K. Pandey, unpublished result, Laboratory for Electronic Materials and Device Technology (www.emd-tech.eng.ua.edu), Univ. Alabama, Tuscaloosa, AL.
 23. A. J. Moulson and J. M. Herbert, *Electroceramics*, 2nd ed., Wiley, 2003.
 24. J.-F. Li, D. Viehland, A. S. Bhalla, and L. E. Cross, *J. Appl. Phys.* **71**(5):2106 (1992).
 25. L. E. Cross, A. S. Bhalla, F. Ainger, and D. Demjanovic, *Pyro-Optic Detector and Imager*, US Patent 4,994,672 (1991).
 26. R. K. Pandey, S. Kotru, X. Song and D. Donnelly, *Bulletin of the American Physical Society*, paper P. 21.6, presented at March 2003 Meeting of American Physical Society, Montreal, Canada, 2004.
 27. N. Spaldin, *Why Are So Few Magnetic Ferroelectrics?* graduate seminar abstract, Univ. California, Santa Barbara, 2003.
 28. I. Takeushi, K.-S. Chang, M. Murakami, M. Aronova, C. I. Lin, and J. Hattrick-Simpers, *Bulletin of the American Physical Society*, paper P. 21.3, presented at March 2003 Meeting of American Physical Society, Montreal, Canada, 2004.
 29. N. A. Hill and K. M. Rabe, *Phys. Rev. B* **59**:8759 (1999).
 30. D. Schlom, V. Gopalan, X. Pan, A. K. Cheetham, and R. Ramesh, ONR Workshop on Frontiers of Epitaxial Engineering, Moab, UT, 2004.
 31. V. R. Palkar and R. Pinto, *PRAMANA-J. Phys.* (Indian Academy of Sciences) **58**(5):1003 (2002).
 32. H. Hur, S. Park, P. A. Sharma, J. S. Ahn, S. Guha, and S.-W. Cheng, *Nature* **2572** (2004).
 33. D. B. Chrisey and G. K. Hubler, *Pulsed Laser Deposition of Thin Films*, Wiley, 1994.
 34. D. Elwell and H. J. Scheel, *Crystal Growth from High-Temperature Solutions*, Academic Press, 1975.
 35. J. J. Gilman, ed., *The Art and Science of Growing Crystals*, Wiley, 1963.
 36. B. R. Pamplin, ed., *Crystal Growth*, 2nd ed., Pergamon Press, 1980.
 37. K. Uchino, *Ferroelectric Devices*, Marcel Dekker, 2000.
 38. D. M. Patel, J. M. Pond, and J. B. I. Rao, Microwave ferroelectric devices, in J. G. Webster, ed., *Wiley Encyclopedia of Electrical and Electronics Engineering*, Vol. 13, Wiley, New York, 1999, p. 109.
 39. S. Hontsu, H. Nishikawa, H. Nakai, J. Ishii, M. Nakamori, A. Fujimaki, Y. Noguchi, H. Tabata, and T. Kawai, *Superconduct. Sci. Technol.* **12**:836 (1999).
 40. Y. Watanabe, *Appl. Phys. Lett.* **66**:1770 (1995).
 41. S. Mathews, R. Ramesh, T. Venkatesan, and J. Benedetto, *Science* **276**:238 (1997).
 42. W. Wu, K. H. Wong, C. L. Mak, C. L. Choy, and Y. H. Zhang, *J. Appl. Phys.* **88**:2068 (2000).
 43. A. M. Grishin, S. I. Khartsev, and P. Johnsson, *Appl. Phys. Lett.* **74**:1015 (1999).
 44. T. Wu, S. B. Ogale, J. E. Garrison, B. Nagaraj, A. Biswas, Z. Chen, R. L. Greene, R. Ramesh, T. Venkatesan, and A. J. Millis, *Phys. Rev. Lett.* **86**:5998 (2001).
 45. S. R. Surthi, S. Kotru, and R. K. Pandey, *Integr. Ferroelectrics* **48**:263 (2002).
 46. S. Surthi, *Integration of Colossal Magnetoresistive Materials with Ferroelectrics*, dissertation, Univ. Alabama, Tuscaloosa, AL, 2001.

FURTHER READING

- F. Jona and G. Shirane, *Ferroelectric Crystals*, Dover Publications, 1993 (a classic piece of literature on ferroelectricity).
- J. F. Nye, *Physical Properties of Crystals*, Oxford, Univ. Press, 1985 (a fundamental work essential for all students of ceramics and dielectrics).
- J. C. Burfoot and G. W. Taylor, *Polar Dielectrics and Their Applications*, Univ. California Press, 1979 (a good introductory book on polar materials).
- M. E. Lines and A. M. Glass, *Principles and Applications of Ferroelectrics and Related Materials*, Clarendon Press, 1977 (this book deals comprehensively with physics of ferroelectricity and its applications; intended for advanced study and research in the field).
- K. C. Kao, *Dielectric Phenomena in Solids*, Elsevier, 2004 (an excellent treatment of dielectric materials, including ferroelectrics and associated phenomena; a must-read book for students at the senior undergraduate and graduate levels).
- J. Moulson and J. M. Herbert, *Electroceramics*, 2nd ed., Wiley, 2003 (offers an in-depth treatment of electroceramics).
- K. Uchino, *Ferroelectric Devices*, Marcel Dekker, 2000 (an introductory book of its kind on device aspects of ferroelectricity and related materials).
- IEEE Standard Definitions of Terms Associated with Ferroelectric and Related Materials*, Draft 16, reprinted in *IEEE Trans. Ultrason. Ferroelectrics Freq. Control* **50**:1613 (2003) (this standard should be consulted for basic definitions and terms in the field of ferroelectricity and related materials; it is an essential work to consult for ferroelectric research).

FILTER SYNTHESIS

ERNST LUEDER
University of Stuttgart

1. AN OVERVIEW OF CLASSICAL FILTERS

Electrical filters are, as a rule, lossless two-ports embedded in resistances R_1 and R_2 , as shown in Fig. 1. A lossless two-port may contain only inductors, capacitors, and ideal transformers. The filters allow a band of the input frequencies to pass with only a small attenuation while all remaining frequencies are to a large extent suppressed. The transfer function

$$\frac{V_2(p)}{V_0(p)} = F^*(p) \tag{1}$$

also called the *transfer voltage ratio* or the *insertion voltage gain*, is a function of the complex frequency p , where $p=j\omega$ stands for the natural and measurable angular frequencies ω . For brevity ω will from now on be called simply the *frequency*. From $F^*(j\omega) = A(\omega)e^{j\varphi(\omega)}$ are derived the magnitude $A(\omega) = |F^*(j\omega)|$ and the phase $\varphi(\omega) = \arg F^*(j\omega)$ with the group delay $\tau(\omega) = -d\varphi(\omega)/d\omega$. The attenuation function is $a(\omega) = -20 \log |F^*(j\omega)|$ in dB (decibels) or, more seldom, $\ln |F^*(j\omega)|$ in Np (nepers). The relation is $1 \text{ Np} = 8.686 \text{ dB}$.

The synthesis of filters follows a well-established pattern. First the properties of a transfer function $F^*(p)$ of a two-port with given types of components have to be established. This guarantees the existence of a solution with realizable positive values of the components as long as the desired transfer function exhibits the above mentioned properties. The most common types of components for classical filters are lossless inductors and capacitors, as well as ideal transformers for the two-port and resistances R_1 and R_2 as internal resistance of the source and as the terminating load. This case is treated in this article. Other types of components are switches such as FETs, capacitors, and operational amplifiers in so-called switched capacitor filters or delays, adders and multipliers in digital filters or resistors, capacitors and operational amplifiers in RC-active filters, or electromechanical transducers and a set of electrodes in surface acoustic wave (SAW) filters, which are treated in the last section.

The next step in filter synthesis is the approximation of given specifications for a particular filter by functions meeting the requirements of $F^*(p)$. The last step is the

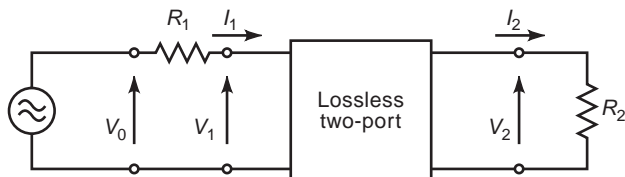


Figure 1. Lossless two-port embedded in resistances R_1 and R_2 .

calculation of the values of the components by mathematical means from the functions approximating the specifications. This step also provides the topology of the two-port. For approximations it is mathematically easier to handle the square of the magnitude $|F^*(j\omega)|^2$. For a lossless two-port in Fig. 1 $F^*(p)$ has the following properties [1,2]:

1. $F^*(p)$ is a rational function in p , real-valued for real-valued p ; as a consequence, the coefficients in $F^*(p)$ are real-valued if the numerator and the denominator of $F^*(p)$ do not contain a common complex factor.
2. Stability requires the poles of $F^*(p)$ to lie in $\text{Re } p < 0$ and the degree of the numerator not to exceed the degree of the denominator. The denominator is hence a Hurwitz polynomial.
3. The numerator is either an even or an odd polynomial in p if common factors in the numerator and the denominator are not canceled.
4. The maximum power available at the output reveals the upper bound (Feldtkeller condition):

$$|F^*(j\omega)| \leq \frac{1}{2} \sqrt{\frac{R_2}{R_1}} = \frac{1}{q} \tag{2}$$

A given $F^*(p)$ meeting these requirements is always realizable by a lossless two-port embedded in R_1 and R_2 . $|F^*(j\omega)|^2$ can also be expressed by the reflection coefficient introduced by S. Darlington [3]

$$S_{11}(j\omega) = \frac{R_1 - Z_1(j\omega)}{R_1 + Z_1(j\omega)} \tag{3}$$

as

$$|F^*(j\omega)|^2 = \frac{R_2}{4R_1} (1 - |S_{11}(j\omega)|^2) \tag{4}$$

where $Z_1(j\omega)$ represents the input impedance of the two-port loaded by R_2 . S_{11} is an element of the scattering matrix. Instead of transfer functions the inverse of the transfer function V_0/V_2 or $V_0/2V_2$ is also applied. These functions are also called the *insertion voltage loss*. In this article

$$\frac{V_0(p)}{V_2(p)} = K^*(p) \tag{5}$$

will be used.

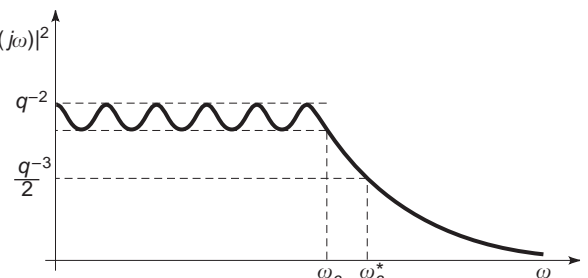


Figure 2. Lowpass filter with cutoff frequency ω_c , 3 dB cutoff frequency ω_c^* , and the equiripple between q^{-2} and $q^{-2} - a^2$.

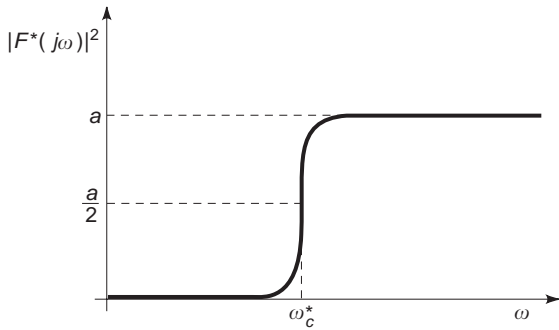


Figure 3. Highpass filter.

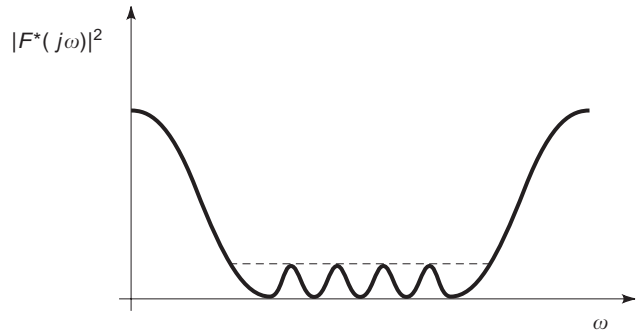


Figure 5. Bandstop filter.

The insertion loss [4]

$$20 \log \frac{R_2}{R_1 + R_2} \left| \frac{V_0(j\omega)}{V_2(j\omega)} \right| = 10 \log \frac{P_0}{P_2} \quad (6)$$

is based on the ratio between the power $P_0 = |V_0(j\omega)|^2 R_2 / (R_1 + R_2)^2$ dissipated in R_2 without the two-port inserted in between the source V_0 with R_1 and the load R_2 and the power $P_2 = |V_2(j\omega)|^2 / R_2$ dissipated in R_2 in the presence of the two-port.

Figures 2–5 depict examples for $|F^*(j\omega)|^2$ of characteristic filters, such as a lowpass, a highpass, a bandpass, and a bandstop. The beginning and the end of the passband are defined by a cutoff frequency ω_c or ω_c^* . For the lowpass in Fig. 2, ω_c^* is chosen as the frequency, where $|F^*(j\omega)|^2$ has decreased to half of the value at $\omega = 0$ (3 dB frequency).

Another choice is a specific frequency ω_c . For example, in Fig. 2 $|F^*(j\omega)|^2$ leaves the band of equiripple behavior, later also called *Chebyshev behavior*.

A typical example for a lowpass circuit is shown in Fig. 6. The zeros of $F^*(p)$ that generate a zero output voltage are visible in the circuit diagram. The series-parallel resonator exhibits an infinite impedance at the resonant frequency ω_1 , preventing signals from reaching the output. The same is true for the shunt-series resonator exhibiting a zero impedance at the resonant frequency ω_2 . Finally, a zero output is observed at $\omega = \infty$ because the shunt capacitors have a zero impedance and the series inductor exhibits an infinite impedance. Nonideal resonators represent a resistor R at the resonant frequency. The larger the quality factor Q of a resonator is, the better the

transmission zero is realized. For series resonators $Q = Z/R$, whereas for parallel resonators $Q = R/Z$ with $Z = \sqrt{L/C}$. L stands for the value of the inductor and C for the value of the capacitor. $|F^*(j\omega)| = \text{const}$ means a lack of amplitude distortion; together with an arbitrary phase $\varphi(\omega)$ it defines an allpass, the transfer function of which is

$$F^*(p) = k \frac{r(-p)}{r(p)}$$

where $r(p)$ is a Hurwitz polynomial in p and k a constant. $F^*(p)$ with a linear phase $\varphi(\omega) = -\omega t_0$ reflecting in a constant group delay t_0 and with an arbitrary magnitude belongs to a two-port without phase distortion. $F^*(p)$ with a constant nonzero magnitude in $|\omega| \in [0, \omega_c]$, zero magnitude otherwise, and a linear phase $-\omega t_0$ is called an “ideal” lowpass, which works as a delay line with delay t_0 for frequencies in the passband.

A filter cascaded by an amplitude equalizer exhibits an overall transfer function with an approximately constant magnitude, whereas a phase equalizer in cascade provides a linear phase of the overall two-port [4]. The phase equalizer is an allpass.

If all reactances in a two-port are discharged at time $t = 0$, then $F^*(p)$ is the Laplace transform of the impulse response $h(t)$ with

$$h(t) = \frac{1}{2\pi j} \int_{\sigma-j\infty}^{\sigma+j\infty} F^*(p) e^{pt} dp$$

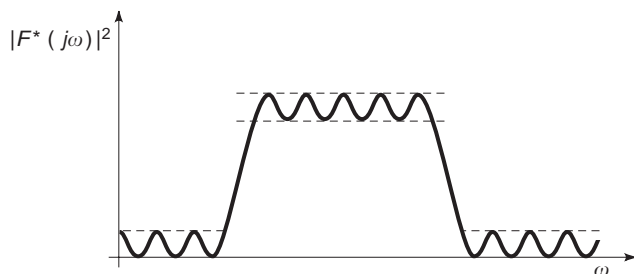


Figure 4. Bandpass filter.

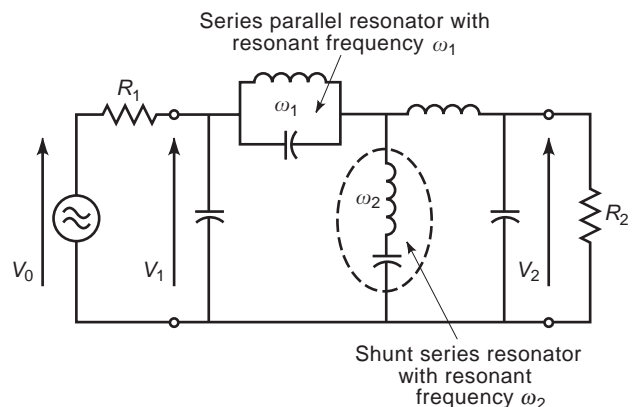


Figure 6. Example of a lowpass circuit.

where $F^*(p)$ is an analytical function in $\text{Re } p \geq \sigma_0 \leq \sigma$. The step response is

$$a(t) = \int_{0-}^t h(\tau) d\tau$$

Some lowpasses with specific characteristics are discussed together with amplitude and phase equalizers in the following subsections.

Guidelines will be presented on how to determine from filter tables the component values of a filter meeting given specifications. This should enable a system engineer to achieve a quick filter design by selecting the appropriate type of filter and by then finding the component values in a table.

1.1. Butterworth Lowpasses

The Butterworth lowpass [9] in Fig. 7 exhibits a maximum flat magnitude $|F^*(j\omega)|$ at $\omega = 0$ —that is, $d^v |F^*(j\omega)| / d\omega^v = 0$ for $v = 1, 2, \dots, n$, where n is the degree of $F^*(p)$. The decay of the magnitude is moderately steep in the transition region and approaches $n \times 20$ dB per frequency decade for large values of ω . $K^*(p) = 1/F^*(p)$ is a polynomial.

We investigate the step response $a(t)$ for various lowpasses, including the Butterworth lowpass. To compare $a(t)$ for those lowpasses, we normalize all of them with the frequency ω_c , where $|F^*(j\omega_c)| = 0.9 \times F^*(0)$ holds. For lowpasses with equiripple behavior, ω_c also stands for the end of the equiripple band. The normalized time is $\tau = \omega_c t$. Figure 8 shows $a(\tau)/a(\infty)$ for a Butterworth lowpass with $F^*(p)$ of seventh degree [10]. There is an overshoot of 15.4% over the value $a(\infty)$, the largest of the lowpasses compared, but followed by rapidly decreasing oscillations around the value $a(\infty)$. Values for the overshoot in % and for the risetime in τ from 10% to 90% of $a(\infty)$ are listed in Table 1 for Butterworth lowpasses with $F^*(p)$ of degree 1–7. For a Butterworth lowpass with $F^*(p)$ of 7th degree the risetime is $t = 2.51\omega_c^{-1}$, the 2nd smallest rise time of all lowpasses in Table 5.

1.2. Thomson Lowpasses

Thomson lowpasses [11] are given by $K^*(p) = 1/F^*(p)$ representing a modified Bessel polynomial. They are therefore often also called *Bessel lowpasses*. $F^*(p)$ exhibits a maximum flat group delay t_0 at $\omega = 0$. The decay of the

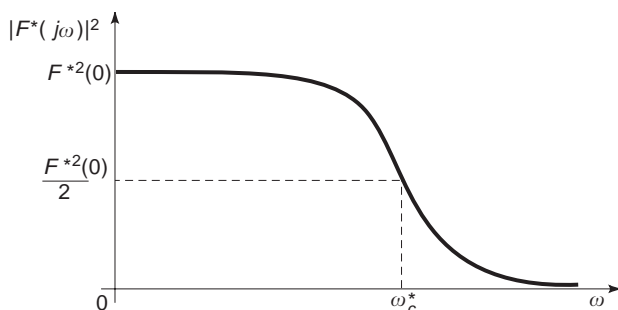


Figure 7. A Butterworth lowpass, maximally flat at $\omega = 0$.

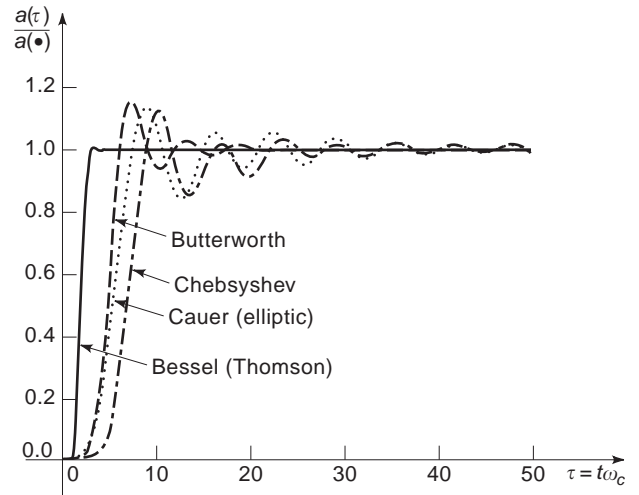


Figure 8. Step responses $a(\tau)/a(\infty)$ of various filters with transfer functions $F^*(p)$ of seventh degree. The common characteristics of the filters are provided in the caption and footnote of Table 1.

magnitude is moderately steep in the transition region and for a large ω is again $n \times 20$ dB/decade, where n is the degree of $F^*(p)$. The step response $a(\tau)/a(\infty)$ for the Thomson lowpass with $n = 7$ is plotted in Fig. 8 [10]. It is a remarkably good approximation of an undistorted delayed step. The overshoot is only 0.49% over $a(\infty)$. Oscillations around $a(\infty)$ are only marginal. Table 2 contains values for overshoot and risetime of $a(\tau)$ for $n = 1-7$ [10]. According to Table 5, the risetime for $n = 7$ is $t = 1.22\omega_c^{-1}$, the smallest value of all lowpasses listed in that table.

1.3. Chebyshev Lowpasses

Chebyshev lowpasses (Fig. 2) possess a magnitude oscillating between two constant boundaries in the passband, where each extremum touches the boundaries. This is called an *equiripple*, or a *Chebyshev behavior* in the passband. $K^*(p) = 1/F^*(p)$ is a polynomial. The larger the ripple a^2 (Fig. 2), the steeper is the decay of $|F^*(j\omega)|^2$ in the transition region from the passband into the stopband. From all polynomials this decay is steepest. However, independent of a^2 the decay at large ω s is again $n \times 20$ dB/decade. The step response $a(\tau)/a(\infty)$ for $n = 7$ in Fig. 8 [10]

Table 1. Overshoot and Risetime of Butterworth Lowpasses with $F^*(p)$ of Degree $n = 1-7^a$

n	Overshoot (%)	Risetime, 10–90% (τ)
1	0	1.06
2	4.32	1.50
3	8.15	1.80
4	10.83	2.03
5	12.78	2.22
6	14.25	2.38
7	15.41	2.51

^aNormalizing frequency ω_c is given by $|F^*(j\omega_c)| = 0.9 \times F^*(0)$ leading to the normalized time $\tau = \omega_c t$.

Table 2. Overshoot and Risetime of Thomson Lowpasses with $F^*(p)$ of Degree $n = 1-7^a$

n	Overshoot (%)	Risetime, 10–90% (τ)
1	0	1.06
2	0.43	1.21
3	0.75	1.25
4	0.84	1.25
5	0.77	1.24
6	0.64	1.23
7	0.49	1.22

^aNormalization as in Table 1.

exhibits the third largest overshoot over $a(\infty)$; however, the oscillations around $a(\infty)$ decay rather rapidly. According to Table 5 the value for the overshoot is 12.7%, whereas the rise time is $t = 3.4\omega_c^{-1}$, the second largest value in Table 5. Overshoot and risetime of $a(\tau)$ for $n = 1-7$ are listed in Table 3 [10].

1.4. Cauer Filters as Lowpasses

Elliptic filters or Cauer filters [12] (Fig. 9) are lowpasses exhibiting an equiripple behavior in both the passband and the stopband. They are based on elliptic integrals, which is why they are also called “elliptic filters.” $K^*(p) = 1/F^*(p)$ is a rational function in p . The step response of the Cauer lowpasses for $n = 7$ in Fig. 8 exhibits the second largest overshoot and only slowly decaying oscillations around $a(\infty)$ [10]. Overshoot and risetime for $n = 1-7$ are listed in Table 4 [10]. In addition to the properties of the normalization mentioned previously for Butterworth lowpasses, the minimum stopband attenuation of the Cauer filters is chosen to be 60 dB.

Table 5 shows a comparison of overshoot and risetime of the step response for four filter types with $F^*(p)$ of degree 7.

Further filters such as bandpasses, highpasses, bandstops, or filters with several passbands are obtained by a frequency transformation applied to the lowpass, where the frequency characteristics are preserved.

1.5. Design of Filters Using Filter Tables

Three characteristic lowpasses are tabulated to be chosen from for a given task: the Butterworth, the Chebyshev, and the Cauer lowpass, the features of which have been

Table 3. Overshoot and Risetime of Chebyshev Lowpasses with $F^*(p)$ of Degree $n = 1-7^a$

n	Overshoot (%)	Risetime, 10–90% (τ)
1	0	1.06
2	14.0	1.59
3	6.82	2.36
4	21.2	2.45
5	10.7	2.98
6	24.25	2.95
7	12.68	3.40

^aNormalization as in Table 1.

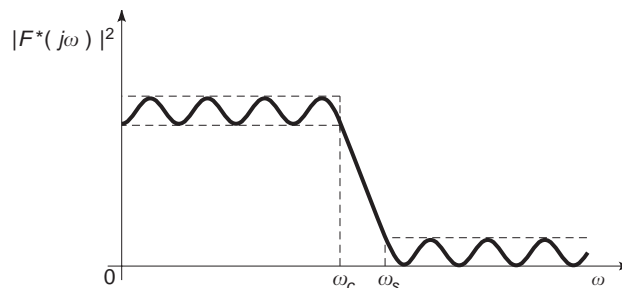


Figure 9. A Cauer lowpass (elliptic filter) with equiripple in passband and stopband; ω_s is end of transition region.

discussed above. The Bessel lowpass is, as a rule, not contained in tables as it deals mainly with properties in the time domain.

After the selection of the appropriate type of lowpass the designer turns to the pertinent filter tables. As a rule only solutions for the special case $R_1 = R_2$ are tabulated. If this is not acceptable because an additional amplifier may be required, one has to go through the general design procedure as described in the next paragraph. The general procedure is also mandatory if different types of specifications are given, such as steps in the attenuation in the stopband or the suppression of specific pilot frequencies.

As shown in Fig. 12, the filter requirements are given by four values for the attenuation $a(\Omega) = -20 \log |F^*(j\Omega)|$ in dB, where

$$\Omega = \frac{\omega}{\omega_c} \tag{7a}$$

is the normalized frequency. Those four values in dB are A_0 the minimum attenuation in the passband, A_{\max} the maximum attenuation in the passband, A_{\min} the minimum attenuation in the stopband, and the frequency Ω_s defining the end of the transition region with $a(\Omega_s) = A_{\min}$. For $R_1 = R_2$ we obtain $A_0 = 0$ as a special case. This reduces the number of specifications to three.

First the reflection coefficient $\rho = \sqrt{1 - 10^{-0.1A_{\max}}}$ has to be calculated. A table with $A_{\min} + 10 \log(\rho^{-2} - 1)$ as ordinate and Ω_s as abscissa reveals the required degree n for a given $\Omega_s(\rho)$, A_{\min} , and filter type. Then one turns to tables for the chosen type of lowpass, the degree n , and the value ρ , which provide the normalized values of the components.

Table 4. Overshoot and Risetime of Cauer Lowpasses with $F^*(p)$ of Degree $n = 1-7^a$

n	Overshoot (%)	Risetime, 10–90% (τ)
1	0	1.06
2	14.0	1.59
3	7.10	2.38
4	22.2	2.57
5	12.2	3.23
6	25.9	3.31
7	13.72	3.81

^aNormalization as in Table 1; in addition, minimum attenuation in stopband 60 dB.

Table 5. Comparison of Overshoot and Risetime of Step Response for Four Lowpasses with $F^*(p)$ of Degree 7^a

Lowpass Type	Overshoot (%)	Risetime, 10–90% (τ)
Thomson	0.49	1.22
Butterworth	15.4	2.51
Chebyshev	12.7	3.40
Cauer	13.7	3.81

^aNormalization as in Table 1.

The normalized values ℓ and c of the reactances provided by the tables are with a normalizing resistor R_1

$$\frac{\omega L}{R_1} = \frac{\omega}{\omega_c} \frac{\omega_c L}{R_1} = \Omega \times \ell \quad (7b)$$

and

$$\omega C R_1 = \frac{\omega}{\omega_c} \omega_c C R_1 = \Omega \times c \quad (7c)$$

where

$$\ell = \frac{\omega_c L}{R_1} \quad (8a)$$

and

$$c = \omega_c C R_1 \quad (8b)$$

ℓ and c are values without dimension.

For the inductors, the denormalized values are

$$L = \frac{R_1}{\omega_c} \cdot \ell$$

and for the capacitors

$$C = \frac{1}{\omega_c R_1} \cdot c$$

This concludes the design with the help of a table.

1.6. Equalization of Amplitude and Phase

In systems the need can arise to change the amplitude, that is, the attenuation $a(\omega)$, most often to render it constant in a given range of frequencies. A simple solution is to replace the resistance R_2 at the output by a two-port with input resistance $R = R_2$, but a frequency-dependent inverse transfer function $K_B^*(p)$ and the associated attenuation $a(\omega) = 10 \log |K_B^*(j\omega)|^2$. $K_B^*(p)$ is multiplied with the inverse transfer function of the given two-port, whereas $a(\omega)$ is added to its attenuation. Such an amplitude equalizer is shown in Fig. 38 with the design equation in the figure caption. If several of those equalizers have to be cascaded it is easily done by replacing the loading resistance $R = R_2$ of the first equalizer by the next equalizer and so on. Table 9 shows $a(\omega)$ for various equalizer two-ports. The shapes of $a(\omega)$ are chosen such that they add to the attenuation to be equalized at the frequencies where this is needed. The equalizers, however, also change the phase of the entire two-port, which is tolerable for all filters where phase is not important, such as in audio systems.

The correction of the phase or the group delay of a given two-port is done by cascading phase equalizers at the output of the given two-port. They are allpasses as depicted in Fig. 40. The phase equalizers exhibit an input resistance $R = R_2$ if terminated by R_2 , thus replacing the load R_2 of the given two-port. The design equations are given in the caption of Fig. 40. The equalizers further offer a unit magnitude that is an attenuation $a(\omega) = 0$ and a group delay as shown in Figs. 39a and 39b. By cascading two-ports, the transfer functions are multiplied and hence the phases in the exponent of the exponential functions are added. This also applies to the group delay. The attenuation of the given two-port remains unchanged due to $a(\omega) = 0$ of the allpasses. Figures 39a and 39b reveal how the allpasses must be chosen to add to the group delay at those frequencies where an increase is needed. Most often the group delay has to become constant by a phase equalization.

So far we have dealt with two-ports. There are also m - n -ports with n input ports and m output ports. They can realize filterbanks.

2. THE SYNTHESIS OF FILTERS

To obtain general results for lowpasses independent of the values of the cutoff frequencies ω_c , we introduce a normalized frequency $\Omega = \omega/\omega_c$ pertaining to the s plane with the imaginary axis $s = j\Omega$. This translates $K^*(p)$ in Eq. (5) in which $p = j\omega$ as follows:

$$\frac{V_0}{V_2} = K^*(j\omega) = K^*\left(j \frac{\omega}{\omega_c} \omega_c\right) = K^*(j\Omega\omega_c) = K(j\Omega)$$

and hence

$$\frac{V_0}{V_2} = K^*(p) = K(s)$$

The synthesis follows the steps as listed and explained here:

1. The given tolerance scheme for $|K(j\Omega)|^2 = P(\Omega)$ is approximated by a realizable

$$|K(j\Omega)|^2 \geq q^2 = 4 \frac{R_1}{R_2} \quad (9)$$

with q in Eq. (2).

2. From $|K(j\Omega)|^2$ the function $K(s)$, the characteristic function $f(s)$; and the elements of the chain matrix $A(s)$ are determined.
3. $A(s)$ is realized by a lossless two-port by a pole removal process.

2.1. Calculations for the Individual Steps

The approximation and calculation may be performed by a general approach based on a least square procedure. However, as a rule, special functions with suitable properties are chosen to solve the approximation problem. These

functions will be discussed. Finally, a general approximation procedure based on a conformal mapping will be outlined.

2.1.1. The Chebyshev Approximation and the Calculation of $K(s)$. The square $|K(j\Omega)|^2$ of the magnitude of the function $K(j\Omega)$ according to the Chebyshev approximation is plotted in Fig. 11. In the passband $|K(j\Omega)|^2$ completely exhausts the tolerance stripe; that is, each extremum of $|K(j\Omega)|^2$ touches the limit of the tolerance band from the inside. In the stopband $|K(j\Omega)|^2$ tends to infinity. As these filter characteristics are most widely used, more detailed information on the Chebyshev approximation must be given. The differential equation for a Chebyshev polynomial $y(x)$ is

$$m^2(1 - y^2) = \left(\frac{dy}{dx}\right)^2 (1 - x^2) \tag{10a}$$

or

$$m^2(y^2 - 1) = \left(\frac{dy}{dx}\right)^2 (x^2 - 1) \tag{10b}$$

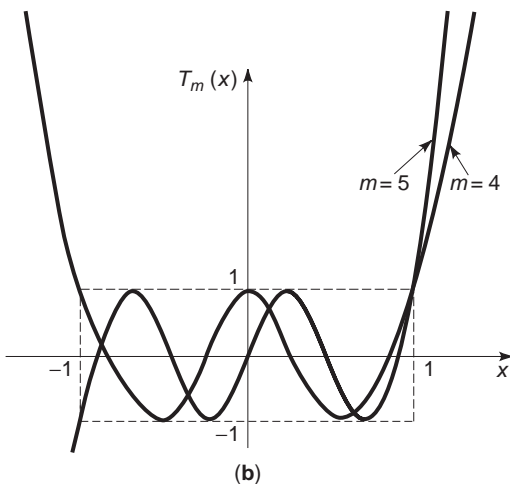
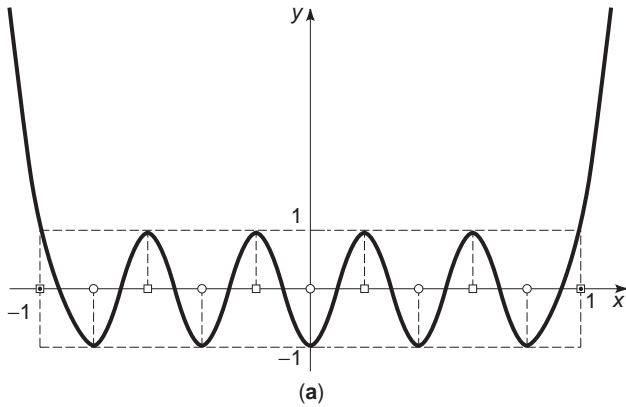


Figure 10. (a) A Chebyshev polynomial $y(x)$. (b) The Chebyshev polynomial of fourth and fifth degree m .

where m is a constant. The differential equation equates the zeros in Fig. 10a of $y + 1$ \circ and $y - 1$ \square with the zeros of y^2 and $x - 1$ \bullet as well as $x + 1$ \bullet . The statement

$$x = \cos \vartheta \quad \text{and} \quad y = \cos \eta$$

provides the solution

$$y = \cos(m\vartheta + c) \quad \text{with} \quad \vartheta = \arccos x \text{ for } |x| \leq 1$$

whereas the statement

$$x = \cosh \vartheta \quad \text{and} \quad y = \cosh \eta$$

yields the solution

$$y = \cosh(m\vartheta + c) \quad \text{with} \quad \vartheta = \operatorname{arcosh} x \text{ for } |x| \geq 1$$

where c is the integration constant. For $c = 0$ we obtain

$$T_m(x) = y = \cos m\vartheta \tag{11a}$$

and

$$\vartheta = \arccos x \quad \text{for } |x| \leq 1 \tag{11b}$$

and

$$T_m(x) = y = \cosh m\vartheta \tag{12a}$$

and

$$\vartheta = \operatorname{arcosh} x \quad \text{for } |x| \geq 1 \tag{12b}$$

The known trigonometric equality

$$\begin{aligned} \cos(m + 1)\vartheta &= \cos m\vartheta \cos \vartheta - \sin m\vartheta \sin \vartheta \\ &= \cos m\vartheta \cos \vartheta - \frac{1}{2}(\cos(m - 1)\vartheta \\ &\quad - \cos(m + 1)\vartheta) \end{aligned}$$

yields

$$\cos(m + 1)\vartheta = 2 \cos m\vartheta \cos \vartheta - \cos(m - 1)\vartheta$$

or the recursion for $T_{m+1}(x)$:

$$T_{m+1}(x) = 2T_m(x) \times x - T_{m-1}(x) \tag{13}$$

The starting solutions for $m = 0$ and $m = 1$ are provided by Eqs. (11a) and (11b) as $T_0(x) = 1$ and $T_1(x) = x$. Some polynomials $T_m(x)$ for $m = 2, 3, \dots, 11$ obtained from Eq. (13) are listed in Table 6 and plotted for $m = 4$ and $m = 5$ in Fig. 10b. Even m provide even and odd m odd polynomials $T_m(x)$. The coefficient at the leading term x^m is 2^{m-1} .

We first construct the function $V_0/V_2 = K(s)$ from a given $|K(j\Omega)|^2$. $|K(j\Omega)|^2 = P(\Omega)$ in Fig. 11 is expressed by

$$|K(j\Omega)|^2 = \varepsilon^2 T_m^2(\Omega) + q^2 = p(\Omega) \tag{14}$$

Table 6. Chebyshev Polynomials of Degree $n = 2-11$

$T_2(x) = 2x^2 - 1$
$T_3(x) = 4x^3 - 3x$
$T_4(x) = 8x^4 - 8x^2 + 1$
$T_5(x) = 16x^5 - 20x^3 + 5x$
$T_6(x) = 32x^6 - 48x^4 + 18x^2 - 1$
$T_7(x) = 64x^7 - 112x^5 + 56x^3 - 7x$
$T_8(x) = 128x^8 - 256x^6 + 160x^4 - 32x^2 + 1$
$T_9(x) = 256x^9 - 576x^7 + 432x^5 - 120x^3 + 9x$
$T_{10}(x) = 512x^{10} - 1280x^8 + 1120x^6 - 400x^4 + 50x^2 - 1$
$T_{11}(x) = 1024x^{11} - 2816x^9 + 2816x^7 - 1232x^5 + 220x^3 - 11x$

For $\Omega \gg 1$ we obtain with the coefficient 2^{m-1} of the leading term

$$|K(j\Omega)|^2 \approx \varepsilon^2 2^{2(m-1)} \Omega^{2m} \quad (15)$$

and

$$\begin{aligned} a(\omega) &= 10 \log |K(j\Omega)|^2 \\ &\approx 20[m \log \Omega + (m-1) \log 2 + \log \varepsilon] \end{aligned} \quad (16)$$

This reveals that for a small ripple $\varepsilon < 1$, $\log \varepsilon < 0$ decreases the rise of the attenuation for large Ω and for a large ripple $\varepsilon > 1$, $\log \varepsilon > 0$ increases the rise of the attenuation for large Ω . The increase of $a(\Omega)$ for a decade 10Ω is $\Delta a(\Omega) = 20 m$; that is, 20 dB per decade and per degree m of $T_m(\Omega)$. The attenuation $a(\omega)$ belonging to Fig. 11 is depicted in Fig. 12 with minimum (respectively maximum) attenuation A_0 (respectively, A_{\max}) in the passband and the minimum attenuation A_{\min} in the stopband. The upper limit of the transition region is Ω_s . Chebyshev filters represent the rare case in which all characteristic values q , ε , and m in Eq. (14) can be determined from the given values A_0 , A_{\max} ,

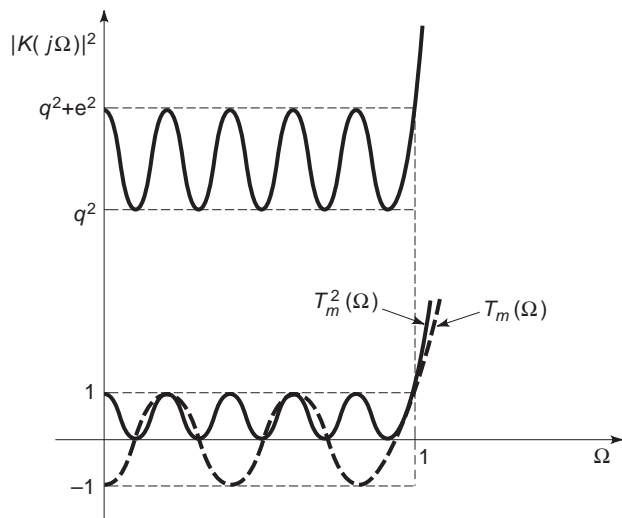


Figure 11. The square of the magnitude $|K(j\Omega)|^2$ of a Chebyshev lowpass with $|K(j\Omega)|^2 = \varepsilon^2 T_m^2(\Omega) + q^2$.

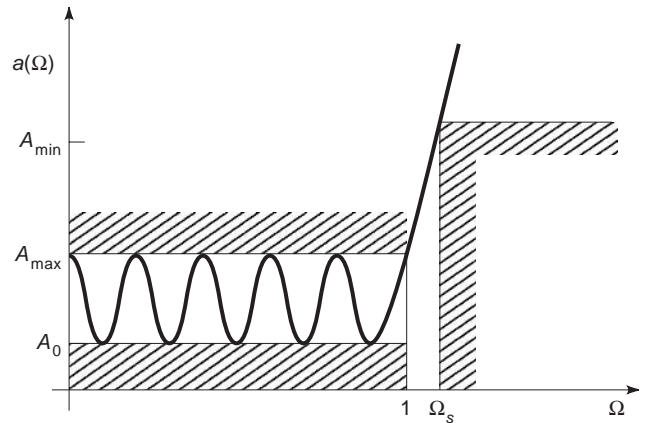


Figure 12. The tolerance scheme in decibels for a Chebyshev lowpass.

and A_{\min} at Ω_s by the equations

$$10 \log q^2 = A_0 \quad (17)$$

and hence

$$q^2 = 10^{A_0/10}$$

$$10 \log(q^2 + \varepsilon^2) = A_{\max} \quad (18)$$

and hence

$$\varepsilon^2 = 10^{A_{\max}/10} - 10^{A_0/10}$$

and

$$a(\Omega_s) = 10 \log(q^2 + \varepsilon^2 \cosh^2 m \times \operatorname{arcosh} \Omega_s) = A_{\min}$$

and hence

$$m = \frac{1}{\operatorname{arcosh} \Omega_s} \operatorname{arcosh} \frac{\sqrt{10^{A_{\min}/10} - 10^{A_0/10}}}{\sqrt{10^{A_{\max}/10} - 10^{A_0/10}}} \quad (19)$$

In Eq. (19) the expression for $T_m(\Omega)$ for $|\Omega| \geq 1$ was used.

The general synthesis procedure outlined next was established by W. Bader [1;16a,b]. It is explained with Chebyshev lowpasses as an example.

From the known $|K(j\Omega)|^2$ we have to calculate the rational function $K(s)$. We consider

$$|K(j\Omega)|^2 = P(\Omega) = P\left(\frac{s}{j}\right) = Q(s) \quad (20)$$

for $s = j\Omega$ and extend s into the entire complex plane. On the other hand, as $K(s)$ is real for real s , we obtain

$$|K(j\Omega)|^2 = K(j\Omega)\overline{K(j\Omega)} = K(j\Omega)K(-j\Omega) = K(s)K(-s) \quad (21)$$

for $s = j\Omega$, which is also extended into the s plane. Equations (20) and (21) hence provide

$$K(s)K(-s) = Q(s) \quad (22a)$$

Obviously, $Q(s)$ is even in s , and real for real s . Hence the zeros occur at $s = s_i$ and $s = -s_i$ as well as at $s = \bar{s}_i$ and $s = -\bar{s}_i$, as plotted in Fig. 13. For $q = 0$, zeros on $s = j\Omega$ are feasible and have an even multiplicity. The zeros in $\text{Re } s < 0$ and half the multiplicity of the zeros on $s = j\Omega$ are assigned to $K(s)$, thus forming a stable or at least quasi-stable $K(s)$ if the zeros on $s = j\Omega$ are single. We perform these operations on $|K(j\Omega)|^2$ in Eq. (14) starting from $P(\Omega)$ and $Q(s)$ in Eqs. (20) and (22b), which yields

$$Q(s) = q^2 + \varepsilon^2 T_m^2\left(\frac{s}{j}\right) = 0 \tag{22b}$$

or

$$T_m^2\left(\frac{s}{j}\right) = -\left(\frac{q}{\varepsilon}\right)^2 \tag{23}$$

As the zeros are complex, we form

$$\begin{aligned} T_m\left(\frac{s}{j}\right) &= \cos m\vartheta \\ &= \cos m(\vartheta_1 + j\vartheta_2) \text{ and } \frac{s}{j} = \cos \vartheta \end{aligned} \tag{24}$$

from which follows

$$\begin{aligned} T_m\left(\frac{s}{j}\right) &= \cos m\vartheta_1 \cosh m\vartheta_2 \\ &\quad - j \sin m\vartheta_1 \sinh m\vartheta_2 = \pm j\left(\frac{q}{\varepsilon}\right) \end{aligned} \tag{25}$$

The solutions are

$$\begin{aligned} \cos m\vartheta_1 \cosh m\vartheta_2 &= 0 \\ \sin m\vartheta_1 \sinh m\vartheta_2 &= \mp \frac{q}{\varepsilon} \end{aligned}$$

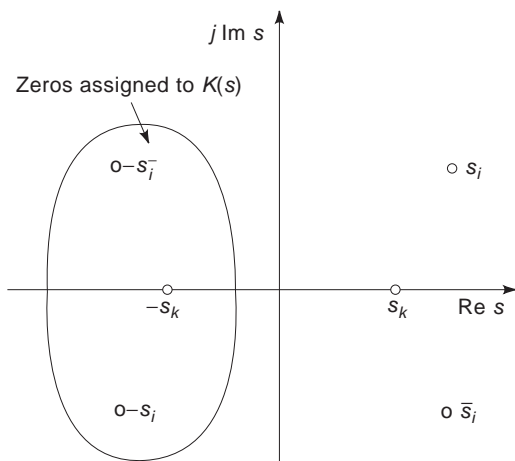


Figure 13. Zeros of $Q(s) = K(s)K(-s)$ in Eq. (22a).

or

$$\vartheta_1 = \frac{2v + 1}{m} \frac{\pi}{2} \quad v = 0, 1, 2, \dots, 2m - 1 \tag{26a}$$

and

$$\vartheta_2 = \frac{1}{m} \text{arsinh} \frac{q}{\varepsilon} \tag{26b}$$

The location of the zeros is, with Eq. (24), $s = j \cos \vartheta = j \cos(\vartheta_1 + j\vartheta_2)$ or

$$s = \sin \vartheta_1 \sinh \vartheta_2 + j \cos \vartheta_1 \cosh \vartheta_2 = \beta + j\gamma \tag{26c}$$

This finally provides

$$\frac{\beta^2}{\sinh^2 \vartheta_2} + \frac{\gamma^2}{\cosh^2 \vartheta_2} = \sin^2 \vartheta_1 + \cos^2 \vartheta_1 = 1 \tag{27}$$

The zeros obviously lie on an ellipse, as shown for $m = 3$ in Fig. 14. Finally

$$K(s) = \pm \varepsilon 2^{m-1} \prod_{i=1}^m (s - s_i) \tag{28a}$$

or

$$F(s) = \frac{\pm 1}{\varepsilon 2^{m-1} \prod_{i=1}^m (s - s_i)} \tag{28b}$$

represents the solution for the desired $K(s)$ and $F(s)$ with the m zeros of Eq. (22b) and the coefficient of the leading

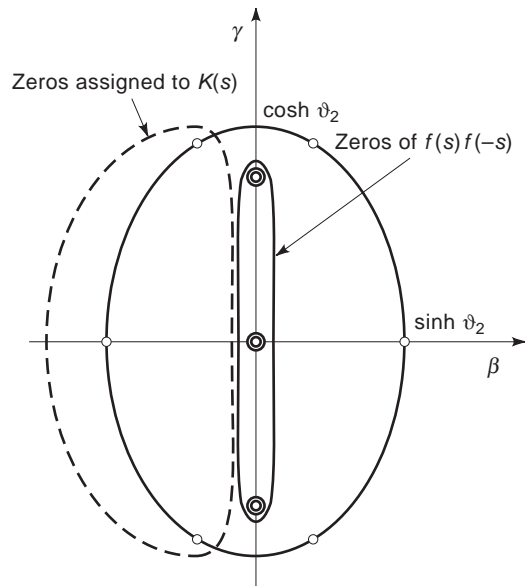


Figure 14. Zeros of $K(s)K(-s)$ and $f(s)f(-s)$ for Chebyshev filters with $m = 3$.

term stemming from the Chebyshev polynomial in Eqs. (14) and (15).

2.1.2. Determination of the Chain Matrix A and of $f(s)$. The chain matrix of the lossless two-port in Fig. 1 is

$$A = \begin{pmatrix} A_{11} & A_{12} \\ A_{21} & A_{22} \end{pmatrix} \quad (29)$$

with

$$\begin{pmatrix} V_1 \\ I_1 \end{pmatrix} = A \begin{pmatrix} V_2 \\ I_2 \end{pmatrix} \quad (30)$$

Necessary and sufficient conditions for a realizable LC chain matrix are as follows [17]:

1. The four elements of A are rational in s and real for real s . A_{11} and A_{22} are even, and A_{12} , A_{21} are odd functions of s .
2. $\det A = 1$.
3. At least three ratios of horizontally or vertically adjoining elements are LC driving point impedances. For $A_{12} \equiv 0$ or $A_{21} \equiv 0$ or $A_{12}, A_{21} \equiv 0$, the elements A_{11} and A_{22} are constants reciprocal to each other.

$K(s)$ can be expressed as

$$K(s) = \frac{V_0}{V_2} = \left(A_{11} + \frac{A_{12}}{R_2} + \left(\frac{q}{2}\right)^2 (R_2 A_{21} + A_{22}) \right) \quad (31)$$

$$\text{with } q = 2\sqrt{\frac{R_1}{R_2}}$$

The term q is explained in Eq. (2). With an unknown ‘‘characteristic’’ function $f(s)$, we obtain

$$A_{11} + \frac{A_{12}}{R_2} = \frac{1}{2}(K(s) + f(s)) \quad (32a)$$

and

$$\left(\frac{q}{2}\right)^2 (A_{22} + R_2 A_{21}) = \frac{1}{2}(K(s) - f(s)) \quad (32b)$$

According to condition 1, A_{11} —respectively, $(q/2)^2 A_{22}$ —are the even parts of $\frac{1}{2}(K(s) + f(s))$ —respectively, $\frac{1}{2}(K(s) - f(s))$. A_{12}/R_2 —respectively, $(q/2)^2 R_2 A_{21}$ —are the odd parts

of $\frac{1}{2}(K(s) + f(s))$ —respectively, $\frac{1}{2}(K(s) - f(s))$. This provides

$$A_{11} = \frac{1}{4}(K(s) + f(s) + K(-s) + f(-s)) \quad (33a)$$

$$\frac{A_{12}}{R_2} = \frac{1}{4}(K(s) + f(s) - K(-s) - f(-s)) \quad (33b)$$

$$\left(\frac{q}{2}\right)^2 A_{22} = \frac{1}{4}(K(s) - f(s) + K(-s) - f(-s)) \quad (33c)$$

$$\left(\frac{q}{2}\right)^2 R_2 A_{21} = \frac{1}{4}(K(s) - f(-s) - K(-s) + f(-s)) \quad (33d)$$

From $\det A = 1$, we drive

$$A_{11} \left(\frac{q}{2}\right)^2 A_{22} - \frac{A_{12}}{R_2} \left(\frac{q}{2}\right)^2 R_2 A_{21} = \left(\frac{q}{2}\right)^2$$

or, with Eqs. (33a)–(33d)

$$K(s)K(-s) - q^2 = f(s)f(-s), \quad \text{with } q = 2\sqrt{R_1/R_2} \quad (34)$$

As $K(s)$ and q^2 are known, $f(s)$ can be determined by the same consideration as applied for finding $K(s)$. The product $f(s)f(-s)$ is even; its zeros are assigned in complex conjugate pairs, if complex, to $f(s)$ and the location with the opposite sign to $f(-s)$. The constraint of stability, mandatory for $K(s)$, does not apply for $f(s)$ as $f(s)$ is no insertion voltage loss.

For Chebyshev filters, from Eqs. (22a), (22b) and (34), we obtain

$$f(s)f(-s) = \varepsilon^2 T_m^2\left(\frac{s}{j}\right) = 0 \quad (35)$$

The zeros can be derived from Eqs. (23), (26a), and (26b) for $q/\varepsilon = 0$, yielding

$$\vartheta_1 = \frac{2\nu + 1}{m} \frac{\pi}{2} \quad (36a)$$

and

$$\vartheta_2 = 0 \quad (36b)$$

with the zeros in Eq. (26c) as

$$s_k = j \cos \vartheta_1 = j \cos \frac{2\nu + 1}{m} \frac{\pi}{2} \quad (37a)$$

$$\nu = 0, 1, \dots, 2m - 1 \text{ and hence } k = 1, 2, \dots, 2m$$

These zeros on the imaginary axis are double as demonstrated in Fig. 14 for $m = 3$.

Finally, from Eq. (35) we obtain

$$f(s) = \pm \varepsilon 2^{m-1} \prod_{k=1}^m (s - s_k)$$

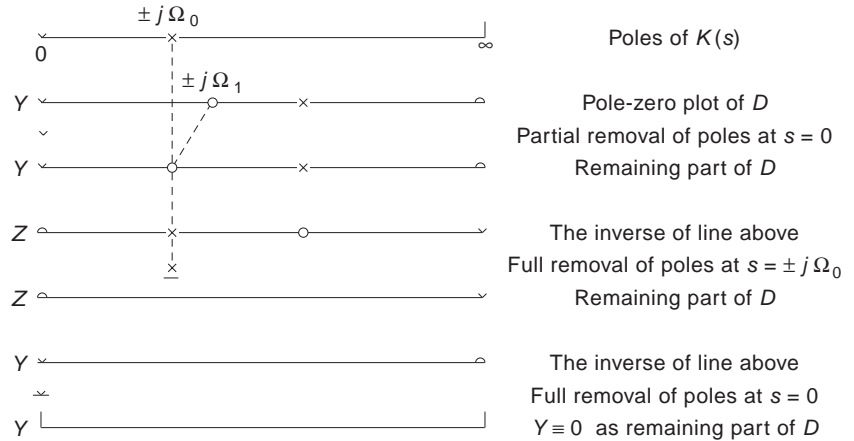


Figure 15. Pole-zero plot of D with admittances Y and impedances Z during partial \surd and full \times removal of poles.

where s_k are half the zeros in Eq. (35) and where a single zero is taken from each location.

Now the elements A_{ik} of the chain matrix can be calculated using Eqs. (33a)–(33d). There are four possibilities to calculate A depending on the selection of the signs for $K(s)$ and $f(s)$.

2.1.3. Development of an LC Two-Port. Starting with a chain matrix A with known elements A_{ik} , the steps leading to an LC two-port embedded in the resistances R_1 and R_2 in Fig. 1 will be given and explained. The basic concept is the development of an LC reactance function into an LC circuit in such a way that the poles of $K(s)$ are realized. The poles of $K(s)$ in Eq. (31) are the zeros of the denominator and the $n - m$ poles at $s = \infty$ that occur if the degree n of the numerator exceeds the degree m of the denominator, manifested by $n - m > 0$. For an all-pole filter, $K(s)$ is a polynomial where all poles lie at $s = \infty$. The Chebyshev filter is an example of an all-pole filter as well as the Butterworth filter or the Thomson filter, which are treated later.

The development of A into an LC two-port starts with the selection of an element A_{ikL} with the largest degree in s . If there is more than one such element, any one may be chosen, yielding different solutions with the same inverse transfer function $K(s)$. Then we form the ratio $D = A_{ikL} / A_{ikN}$ or the inverse $D = A_{ikN} / A_{ikL}$, where A_{ikN} is the element horizontally or vertically next to A_{ikL} . The ratios are LC two-terminal functions. There are four possibilities to form them depending on the selection of the neighbor to A_{ikL} . Together with the four possible chain matrices, we are at this point already faced with at least 16 possible LC one-ports, with every one ensuring an equivalent solution.

The ratios may represent either an input or an output driving point impedance function with a short circuit or an open circuit at the receiving end. The short circuit or the open circuit is later replaced either by the load R_2 or the input voltage V_0 with the resistance R_1 depending on the physical meaning of the two-terminal function.

The development of the LC driving point impedance function is based on a modified continued fraction expansion [16a,b] with partial pole removals [18–20] al-

lowed only at poles of $K(s)$ and preferably at those poles of $K(s)$ at $s = \infty$ or $s = 0$. The process is explained by the pole-zero plot in Fig. 15. The headline shows the poles of $K(s)$ to be realized. A full circle \circ or cross mark \times stands for the two zeros or the two poles at $s = \pm j\Omega$ and for the associated degree 2 in s , whereas a half-circle \cap or a half-cross mark \surd stands for the degree 1 in s . We assume that Y in the second line is the admittance D we have chosen from the chain matrix. The partial fraction to the pole at $s = 0$ is a_0/s . We remove part of this pole by subtracting a_1/s with $a_1 < a_0$. It can be shown (16a,b) that by doing this, all zeros beside the one at $s = \infty$ move toward the pole partially removed. a_1 is chosen such that the zero at $s = j\Omega_1$ moves to $s = j\Omega_0$. a_1/s is realized by the first inductor in Fig. 16. A proof that there is always a $0 < a_1 < a_0$ able to generate the desired zero is missing. Now the admittance Y is inverted, and the pole of the impedance Z at $s = j\Omega_0$ is fully removed (\times) and realized by the series-parallel resonator in Fig. 16. The two-port will exhibit a transmission zero at $s = j\Omega_0$ because the infinite impedance of the series-parallel resonator prevents energy from being delivered into the resistor R_2 , which hence exhibits a zero voltage at frequency Ω_0 . The same is true for a shunt zero impedance. It is even true for a series infinite impedance or a shunt zero impedance, which are generated by a partial pole removal, because these impedances block the energy transfer to

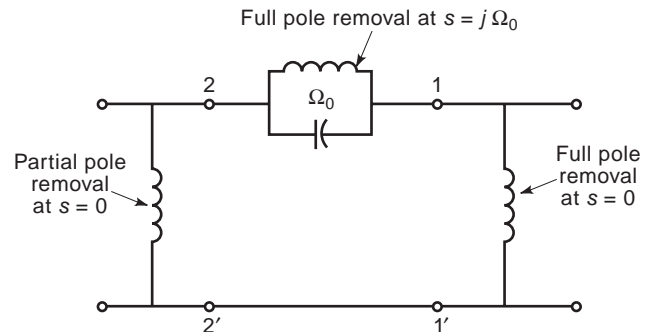


Figure 16. LC two-port generated by the development in Fig. 15.

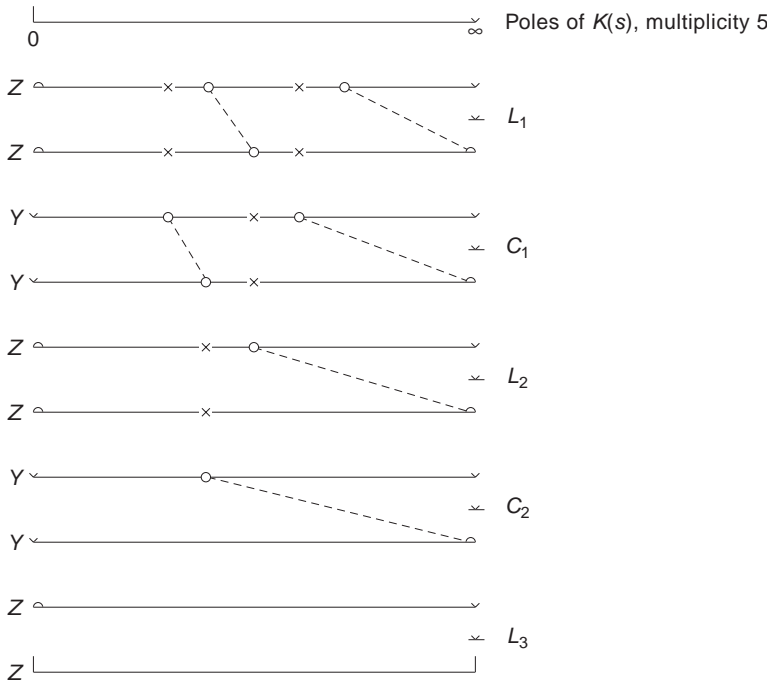


Figure 17. Always in full pole removal \surd if $K(s)$ is a polynomial in s ; Y =admittances, Z =impedances.

the output resistance R_2 . This imposes the constraint that a partial pole removal is allowed only at poles of $K(s)$.

The partial removal of a pole does not lower the degree of the driving point function. As a consequence, the two-port generated does not exhibit the minimum number of components. To minimize the number of components, partial pole removal preferably should take place at $s = 0$ or $s = \infty$, where it is associated with only one reactance.

So far, the procedure for rational functions D has been described. The function $K(s)$ of Chebyshev filters in Eq. (28a) is a polynomial where all poles lie at $s = \infty$. The development of the LC two-port is a special case plotted in Figs. 17 and 18 [16c]. We start with an impedance, the pole of which at $s = \infty$ is fully removed, realizing a pole of $K(s)$ at $s = \infty$ by the inductor L_1 in Fig. 18. The full pole removal in the admittance of the next step provides the shunt capacitor C_1 realizing another pole at $s = \infty$. The process continues in Figs. 17 and 18 [16c] until all poles are realized by three inductors and two capacitors. Since only full pole removals were used for the Chebyshev filter, the circuit generated exhibits the minimum number of components.

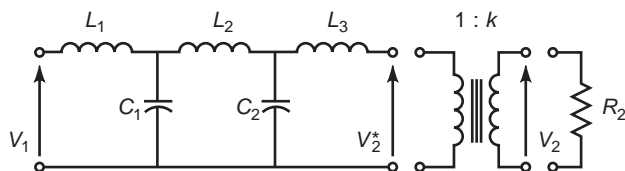


Figure 18. An LC two-port if $K(s)$ is a polynomial.

So far, from the given matrix A in Eq. (29), the matrix A^* in Eq. (37b)

$$A^* = \begin{pmatrix} kA_{11} & A_{12}^* \\ kA_{21} & A_{22}^* \end{pmatrix} \quad (37b)$$

is realized if we assume that the driving point function D was selected as $D = A_{11}/A_{21}$. In D a common constant factor k may have been canceled. The physical meaning of A_{11} is $A_{11} = V_1/V_2$ for $I_2 = 0$ and of $A_{11}^* = kA_{11} = V_1/V_2^*$ for $I_2^* = 0$, where V_2^* (respectively, I_2^*) are the output voltage (respectively, current) in Fig. 19 at the LC two-port A^* so far realized. The terms are evaluated at an arbitrarily chosen frequency, where $s_0 = 0$ or $s_0 = \infty$ are especially easy to handle. The result is $k = A_{11}^*(s_0)/A_{11}(s_0)$. The correction for $k \neq 1$ is achieved by an ideal transformer in Fig. 19 with matrix T in cascade with A^* providing

$$A^*T = \begin{pmatrix} kA_{11} & A_{12}^* \\ kA_{21} & A_{22}^* \end{pmatrix} \begin{pmatrix} \frac{1}{k} & 0 \\ 0 & k \end{pmatrix} = \begin{pmatrix} A_{11} & kA_{12}^* \\ A_{21} & kA_{22}^* \end{pmatrix} \quad (37c)$$

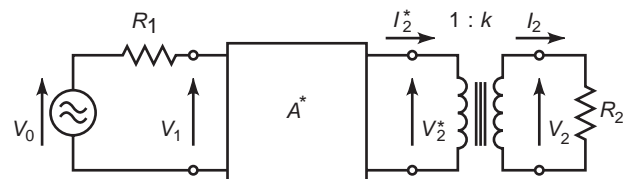


Figure 19. The intermediate steps A^* , the ideal transformer, and the embedding in R_1 and R_2 during the synthesis of two-ports.

We claim that with this last step the given matrix A is realized. For proof we consider for the matrices A and A^*T the equations

$$\det A = A_{11}A_{22} - A_{12}A_{21} = 1$$

and

$$\det A^*T = A_{11}kA_{22}^* - kA_{12}^*A_{21} = 1$$

The poles of $K(s)$ are given by the denominators of the elements A_{ik} according to Eq. (31). They are already realized by the synthesis procedure and are equal in A and A^* . Therefore, we now concentrate on the numerators of A_{ik} . We assume that A_{11} has the highest degree in s . At the n zeros of A_{11} we obtain $A_{12} = -1/A_{21}$ and $kA_{12}^* = -1/A_{21}$. This means that the numerators of A_{12} and kA_{12}^* of degree $< n$ are identical at n points; hence they are identical for all s . The same applies to A_{22} and kA_{22}^* . Therefore, $A^*T = A$, as desired.

Some remarks about the procedure for synthesizing an LC two-port are necessary:

1. As mentioned previously, a proof has not yet been found that partial pole removal with positive value of the components is always feasible. However, so far there has always been a realizable two-port among all the alternatives for equivalent solutions.
2. If in each element in A the common factors are canceled, then it can be proved that horizontally or vertically adjoining elements exhibit no common zeros. However, for some developments it is necessary to represent all elements with one single common denominator. Then common zeros of adjoining elements may occur. They are also zeros of $K(s)$ and are realized by a partial fraction expansion. The pertinent circuits are added in series of an open-circuit reactance function and in the shunt of a short-circuit reactance function D . This brief remark may suffice.
3. The alternative solutions can differ in the number of inductors and capacitors. Hence a search for a circuit with the minimum number of inductors is worthwhile because capacitors are, as a rule, less costly.
4. Developments with capacitors connected to a common terminal, such as ground, are advantageous since parasitic capacitances can be included in these capacitors.
5. Tuning of the transmission zeros can be carried out by adjusting one element, preferably the capacitor, in the series or parallel resonators.
6. The procedure can be used to generate specific one-ports such as the equivalent circuit for a quartz oscillator in Fig. 20.

The general procedure for the synthesis of an LC filter embedded in R_1 and R_2 from a given $|K(j\omega)|^2$ was pre-

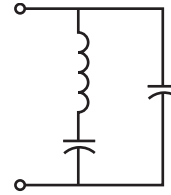


Figure 20. Equivalent circuit of a quartz oscillator.

sented with Chebyshev filters as an example. The procedure will be applied to all further filters discussed in this article.

2.1.4. Further Filters Derived from Chebyshev Polynomials. In the previous section a lowpass was derived from the squared Chebyshev polynomials $T_m^2(\Omega)$, $\Omega = \omega/\omega_c$. Further filters are generated from $1/T_m^2(\Omega)$, $T_m^2(1/\Omega)$, and $1/T_m^2(1/\Omega)$. These functions are depicted in Figs. 21a–21c. In the Figs. 22a–22c the pertaining filters and their $K(s)$ are shown. It can be seen that a highpass with Chebyshev behavior in the stopband (Fig. 22a), a highpass with Chebyshev behavior in the passband (Fig. 22b), and a lowpass with Chebyshev behavior in the stopband (Fig. 22c) can be generated.

2.1.5. The Butterworth Approximation [9]. Contrary to the Chebyshev approximation, the normalizing frequency usually chosen for the Butterworth filters is ω_c^* , the 3 dB frequency, yielding $\Omega = \omega/\omega_c^*$. We again work with the function $K(j\Omega)$ instead of $F(j\Omega) = K(j\Omega)^{-1}$.

The function

$$|K(j\Omega)|^2 = A_0(1 + \Omega^{2n}) = p(\Omega) \geq q^2 = 4R_1/R_2 \quad (38)$$

exhibits $d^v P(\Omega)/d\Omega^v = 0$ for $\Omega = 0$ and $v = 1, 2, \dots, 2n - 1$ and is hence maximally flat at $\Omega = 0$.

The inequality in Eq. (38) is met for $A_0 \geq q^2$. $|K(j\Omega)|$ and $|F(j\Omega)| = |K(j\Omega)|^{-1}$ are plotted in Fig. 23. The 3 dB cutoff frequency is reached at $\Omega = 1$. For large $\Omega \gg 1$, we obtain $|K(j\Omega)| \approx \sqrt{A_0}\Omega^n$ and the attenuation $\alpha(\Omega) = 20 \log |K(j\Omega)| \approx 20n \log \Omega + 20 \log \sqrt{A_0}$, from which an increase in attenuation $\Delta\alpha$ for one frequency decade of $\Delta\alpha = n \cdot 20$ dB/decade can be seen.

According to Eq. (38), we obtain

$$Q(s) = P\left(\frac{s}{j}\right) = A_0(1 + (-1)^n s^{2n}) = K(s)K(-s) \quad (39)$$

The zeros of $Q(s)$ are given by $s^{2n} = (-1)^{n-1} = e^{j\pi(n-1+2k)}$ for $k = 0, 1, 2, \dots, 2n - 1$. This yields the zeros

$$S_k = e^{j(\pi/2n)(n-1+2k)} \quad (40)$$

Obviously, the zeros lie on the unit circle of the complex s plane. If they are complex, they have to be complex conjugate, as $Q(s)$ possesses only real coefficients. For $n = 4$ the zeros are plotted in Fig. 24. The zeros in $\text{Re } s < 0$ are assigned to $K(s)$, yielding a stable two-port. For $n = 4$ we

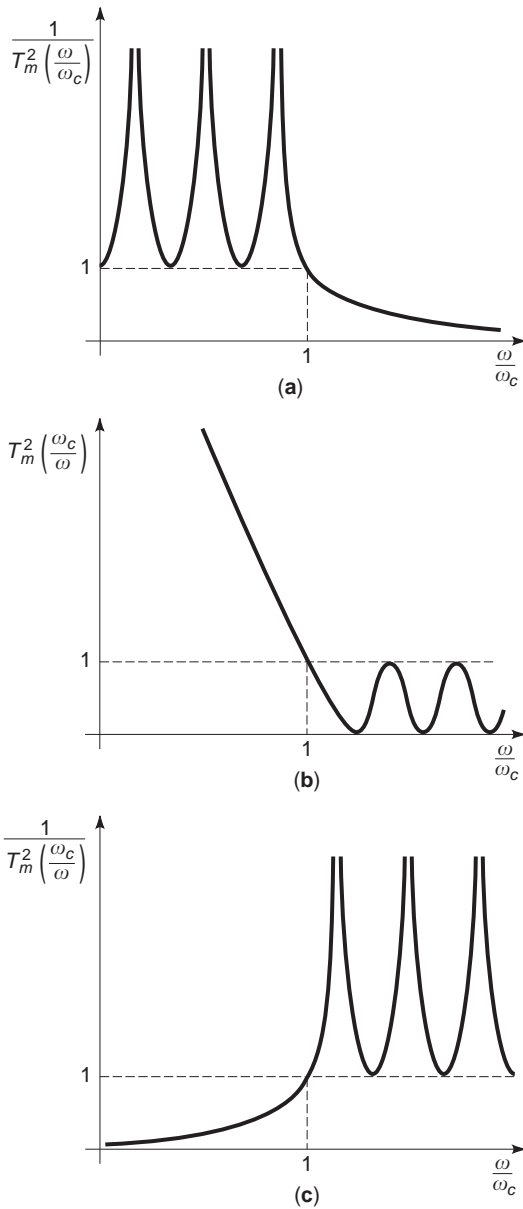


Figure 21. (a) The polynomial $T_m^2(\omega/\omega_c)$. (b) The polynomial $T_m^2(\omega_c/\omega)$. (c) The polynomial $T_m^2(\omega_c/\omega)$.

obtain

$$K(s) = \pm \sqrt{A_0}(s - e^{j5\pi/8})(s - e^{-j5\pi/8})(s - e^{j7\pi/8})(s - e^{-j7\pi/8})$$

or

$$K(s) = \pm \sqrt{A_0}(s^4 + 2.163s^3 + 3.414s^2 + 2.613s + 1)$$

Table 7 lists $K(s)/\sqrt{A_0}$ for Butterworth filters with degree $n = 1-4$.

The characteristic polynomial is determined due to Eq. (34) by

$$K(s)K(-s) - q^2 = f(s)f(-s) \tag{41}$$

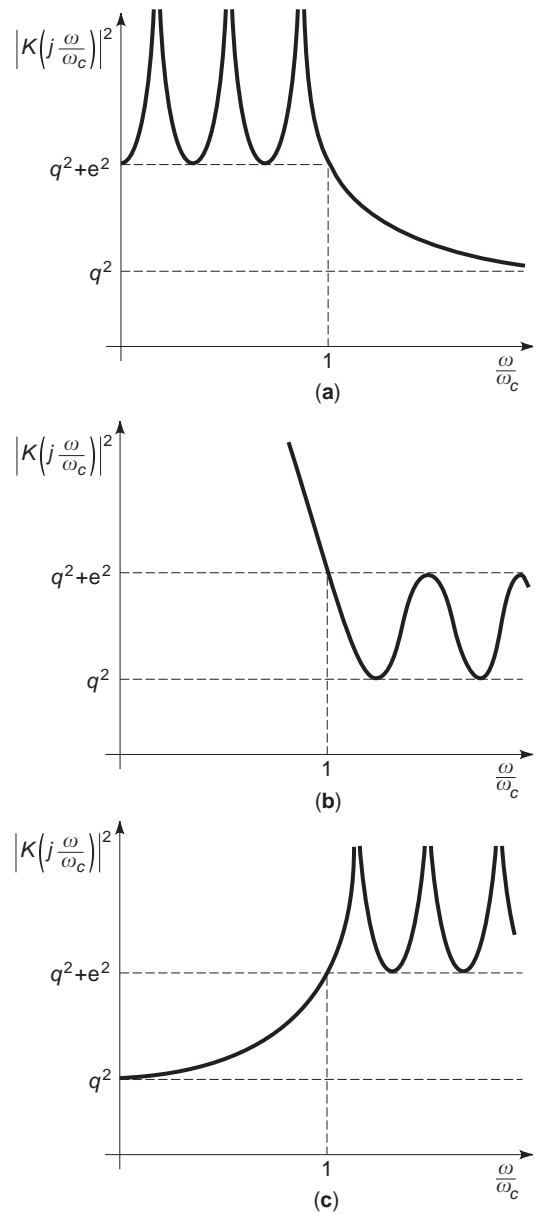


Figure 22. (a) The highpass with $|K(j(\omega/\omega_c))|^2 = q^2 + \epsilon^2 T_m^2(\omega/\omega_c)$ and Chebyshev behavior in the stopband; (b) the highpass with $|K(j(\omega/\omega_c))|^2 = q^2 + \epsilon^2 T_m^2(\omega_c/\omega)$ and Chebyshev behavior in the passband; (c) the lowpass with $|K(j(\omega/\omega_c))|^2 = q^2 + \epsilon^2 T_m^2(\omega_c/\omega)$ and Chebyshev behavior in the stopband.

or

$$A_0(1 + (-1)^n s^{2n}) - q^2 = f(s)f(-s) \tag{42}$$

The zeros are given by

$$s^{2n} = (-1)^{n-1} \left(1 - \frac{q^2}{A_0}\right)$$

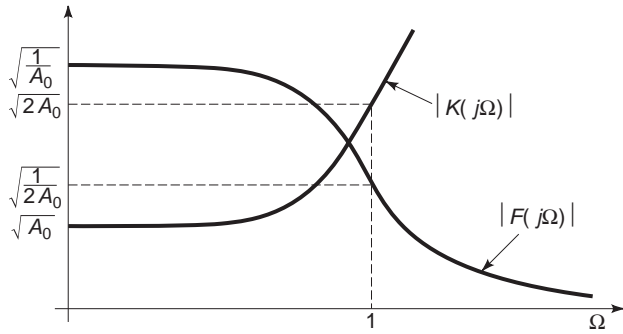


Figure 23. The magnitude $|F(j\Omega)|$ of the transfer function and the magnitude $|K(j\Omega)|$ of the inverse transfer function for Butterworth filters.

or

$$s_r = \left(1 - \frac{q^2}{A_0}\right)^{1/2n} e^{j(\pi/2n)(n-1+2k)} \quad (43)$$

where $k=0, 1, \dots, 2n-1$ and hence $r=1, 2, \dots, 2n$.

The $2n$ zeros lie on a circle in the s plane with radius

$$r_0 = \left(1 - \frac{q^2}{A_0}\right)^{1/2n}$$

and are complex conjugate or real. Any complex conjugate pair and any real zero can be assigned to $f(s)$, while the negative locations of these zeros belong to $f(-s)$. This yields

$$f(s) = \pm \sqrt{A_0} \prod_{r=1}^n (s - s_r)$$

With $K(s)$ and $f(s)$ now known, the elements of the chain matrix are calculated by Eqs. (33a)–(33d), followed by the development of the matrix into a two-port with the procedure outlined previously. As an example, the solution for the chain matrix A and for the pertaining two-port is now

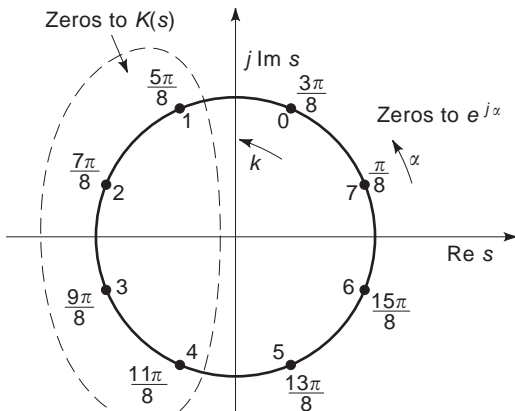


Figure 24. The zeros of $Q(s)=K(s)K(-s)$ in Eq. (39) of Butterworth filters for $n=4$.

Table 7. Polynomials $K(s)$ for Butterworth Filters

n	$K(s)/\sqrt{A_0}$
1	$s + 1$
2	$s^2 + \sqrt{2}s + 1$
3	$s^3 + 2s^2 + 2s + 1$
4	$s^4 + 2.613s^3 + 3.414s^2 + 2.613s + 1$

listed for $n=3, A_0=1$, and $R_1=R_2$:

$$A_{11} = 2s^2 + 1; \quad A_{12} = R_2(2s^3 + 2s)$$

$$A_{21} = \frac{2s}{R_2}; \quad A_{22} = 2s^2 + 1$$

As all elements are polynomials in s , the pertaining two-port in Fig. 25 was found by full pole removals and therefore exhibits the minimum number of components.

The solution, based on the normalized frequency $\Omega = \omega/\omega_c^*$, provides the normalized values for the components l_1, l_2 , and c in Fig. 25, where the denormalized values L_1, L_2 , and C are also listed.

2.1.6. The Thomson or Bessel Approximation [11]. A filter with a linear phase $\psi(\omega) = \omega t_0$ provides an ideal delay by t_0 and exhibits the function

$$K\left(j \frac{\omega}{\omega_0}\right) = ae^{j(\omega/\omega_0)\omega_0 t_0}$$

With $\omega_0 t_0 = 1$ and $\Omega = \omega/\omega_0$ we obtain for $s = j\Omega$ extended into the s plane

$$K(s) = ae^s \quad (44)$$

This normalization with ω_0 is different from the one used previously for the comparison of $a(t)$. It is commonly used and emphasizes the delay $t_0 = 1/\omega_0$ as the most important property of Bessel filters.

The group delay $d\psi/d\omega = t_0$ is a constant. We have to approximate the filter with constant group delay by a realizable function $K(s)$. A Taylor series for e^s is no more Hurwitz from the fifth-order term on. A realizable solution is provided by setting $K(s) = ae^s = a(\cosh s + \sinh s)$, where

$$\cosh s = 1 + \frac{s^2}{2!} + \frac{s^4}{4!} + \dots \quad (45a)$$

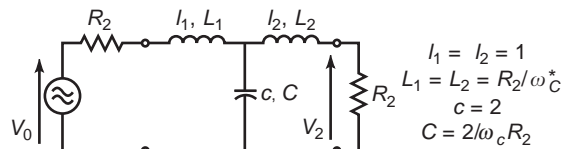


Figure 25. The Butterworth filter for $n=3, A_0=1$, and $R_1=R_2$.

is an even function and

$$\sinh s = s + \frac{s^3}{3!} + \frac{s^5}{5!} + \dots \tag{45b}$$

is an odd function in s .

A theorem states that if the ratio of the even part of a polynomial over the odd part is an LC driving point function and if the even and odd parts are coprime, then the sum of the even and odd parts is Hurwitz. To check the property of an LC driving point impedance function, we develop the continued fraction based on Eqs. (45a) and (45b):

$$\frac{\cosh s}{\sinh s} = \frac{1}{s} + \frac{1}{\frac{3}{s} + \frac{1}{\frac{5}{s} + \frac{1}{\frac{7}{s} + \dots + \frac{1}{\frac{2N-1}{s} + \dots}}}} = \frac{m(s)}{n(s)} \tag{46}$$

Since all terms in the infinite continued fraction expansion are positive, $h(s) = m(s) + n(s)$ calculated from Eq. (46) truncated at $(2N - 1)/s$ is Hurwitz. For $2N - 1 = 7$, we obtain from Eq. (46)

$$\begin{aligned} \frac{m(s)}{n(s)} &= \frac{s^4 + 45s^2 + 105}{10s^3 + 105s} \quad \text{and} \quad K(s) = aC[m(s) + n(s)] \\ &= aC(s^4 + 10s^3 + 45s^2 + 105s + 105) \end{aligned}$$

The factor C is needed to render $K(0) = a$, as required by Eq. (44). In the example $C = \frac{1}{105}$, $m(s) + n(s)$ can be expressed by modified Bessel polynomials

$$B_\nu(s) = s^\nu B_\nu^*\left(\frac{1}{s}\right) = m(s) + n(s) \tag{47a}$$

with

$$B_\nu^*\left(\frac{1}{s}\right) = \sum_{k=0}^{\nu} \frac{(v+k)!}{(v-k)!k!(2s)^k} \tag{47b}$$

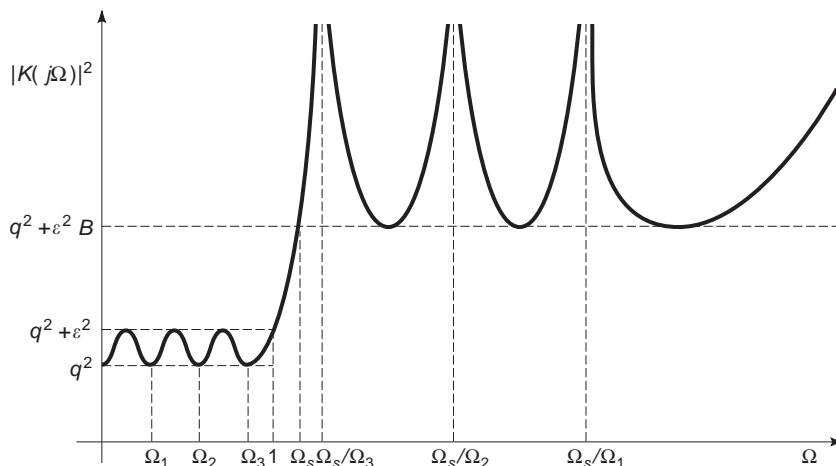


Figure 26. The characteristic $|K(j\Omega)|^2$ of a Cauer filter for n odd in Eq. (49).

Table 8. A List of Modified Bessel Polynomials $B_\nu(s)$ and Their Factored Form for $\nu \leq 5$

$B_0(s) = 1$
$B_1(s) = s + 1$
$B_2(s) = s^2 + 3s + 3$
$B_3(s) = s^3 + 6s^2 + 15s + 15 = (s + 2.322)(s^2 + 3.678s + 6.460)$
$B_4(s) = s^4 + 10s^3 + 45s^2 + 105s + 105 = (s^2 + 5.792s + 9.140) \times (s^2 + 4.208s + 11.488)$
$B_5(s) = s^5 + 15s^4 + 105s^3 + 420s^2 + 945s + 945 = (s + 3.647)(s^2 + 6.704s + 14.272)(s^2 + 4.679s + 18.156)$

A recursion formula is given by

$$B_\nu(s) = (2\nu - 1)B_{\nu-1}(s) + s^2$$

$B_{\nu-2}(s)$. With Eqs. (47a) and (47b), we finally obtain

$$K(s) = aB_\nu(0)^{-1}B_\nu(s) \tag{48}$$

Table 8 lists the Bessel polynomials up to $\nu = 5$ [4].

The constant a is chosen such that the constraint for $|K(j\Omega)|$ is met. The characteristic function is determined by $K(s)K(-s) - q^2 = f(s)f(-s)$. The LC two-port is then calculated by the procedure given previously, applied for polynomials.

2.1.7. Cauer Filters [4,12,21]. These filters exhibit Chebyshev behavior in the passband and in the stopband, as depicted in Fig. 26. They are based on elliptic functions as derived by Cauer and are therefore also called *elliptic filters*. The theory of elliptic filters is very involved. A simpler approach based on the results is given here.

The filter function in Fig. 26 is represented by

$$|K(j\Omega)|^2 = q^2 + \varepsilon^2 F_n^2(\Omega) \tag{49}$$

with

$$F_n(\Omega) = \begin{cases} k \prod_{v=1}^{n/2} \frac{\Omega^2 - \Omega_v^2}{\Omega^2 - (\Omega_s/\Omega_v)^2} & n \text{ even} \end{cases} \quad (50)$$

$$F_n(\Omega) = \begin{cases} k\Omega \prod_{v=1}^{(n-1)/2} \frac{\Omega^2 - \Omega_v^2}{\Omega^2 - (\Omega_s/\Omega_v)^2} & n \text{ odd} \end{cases} \quad (51)$$

The equiripple behavior of $F_n^2(\Omega)$ in $\Omega \in [0, 1]$ in Fig. 27 is guaranteed by the choice of Ω_v according to

$$\Omega_v = \begin{cases} \text{sn} \left(\frac{E \left(\frac{1}{\Omega_s} \right) (2v - 1)}{n} \right) & n \text{ even}, v = 1, 2, \dots, \frac{n}{2} \end{cases} \quad (52a)$$

$$\Omega_v = \begin{cases} \text{sn} \left(\frac{E \left(\frac{1}{\Omega_s} \right) 2v}{n} \right) & n \text{ odd}, v = 1, 2, \dots, \frac{n-1}{2} \end{cases} \quad (52b)$$

where

$$E \left(\frac{1}{\Omega_s} \right) = \int_0^{\pi/2} \frac{d\phi}{\left(1 - \frac{1}{\Omega_s^2} \sin^2 \phi \right)^{1/2}} \quad (53a)$$

is the complete elliptic integral of the first kind and the Jacobi elliptic function $\text{sn}(u) = \sin \phi$ is calculated from the inverse $\phi(u)$ of the incomplete elliptic integral of the first kind

$$u = \int_0^\phi \frac{d\phi}{\left(1 - \frac{1}{\Omega_s^2} \sin^2 \phi \right)^{1/2}} \quad (53b)$$

followed by forming $\sin \phi = \text{sn}(u)$. Ω_s is chosen as $\Omega_s > 1$; Eqs. (52a) and (52b) yield $0 < \Omega_v < 1$, $v = 1, 2, \dots, n/2$, or $(n - 1)/2$. Obviously, the zeros of $F_n^2(\Omega)$ lie in $|\Omega| < 1$ and the poles in $|\Omega| > \Omega_s$. k in Eqs. (50) and (51) is chosen such that $F_n^2(\Omega)$ in Fig. 27 oscillates between 0 and 1 in $\Omega \in [0, 1]$.

Finally, the minimum value B of $F_n^2(\Omega)$ in the stopband in Fig. 27 is given by

$$B = \begin{cases} k \prod_{v=1}^{n/2} \frac{\Omega_s^2 - \Omega_v^2}{\Omega_s^2 - (\Omega_s/\Omega_v)^2} & n \text{ even} \end{cases} \quad (54a)$$

$$B = \begin{cases} k\Omega_s \prod_{v=1}^{(n-1)/2} \frac{\Omega_s^2 - \Omega_v^2}{\Omega_s^2 - (\Omega_s/\Omega_v)^2} & n \text{ odd} \end{cases} \quad (54b)$$

if the degree n of $F_n(\Omega)$ is chosen as

$$n \geq \frac{E(1/\Omega_s)E(\sqrt{1-1/B})}{E(\sqrt{1/B})E(\sqrt{1-(1/\Omega_s)^2})} \quad (55)$$

If the minimum value for n is not an integer, then the next-larger integer has to be chosen. In this case the realized B in Eqs. (54a) and (54b) is larger than the desired B in Eq. (55).

From Eq. (49) and Fig. 27, we derive

$$|K(j1)|^2 = q^2 + \varepsilon^2$$

and

$$|K(j\Omega_s)^2| = q^2 + \varepsilon^2 B$$

For the filter design the desired R_1 and R_2 yield

$$q = 2\sqrt{\frac{R_1}{R_2}},$$

the desired ripple in the passband provides ε , and the minimum $q^2 + \varepsilon^2 B$ of $|K(j\Omega)|^2$ in the stopband yields B in Eqs. (54a) and (54b).

2.1.8. Approximation of $|K(j\Omega)|^2$ by Conformal Mapping [4]. Lowpasses with Chebyshev behavior in the passband and arbitrary characteristics in the stopband can be designed by a conformal mapping. This includes also the case of Chebyshev behavior in the passband and the stopband as a special case.

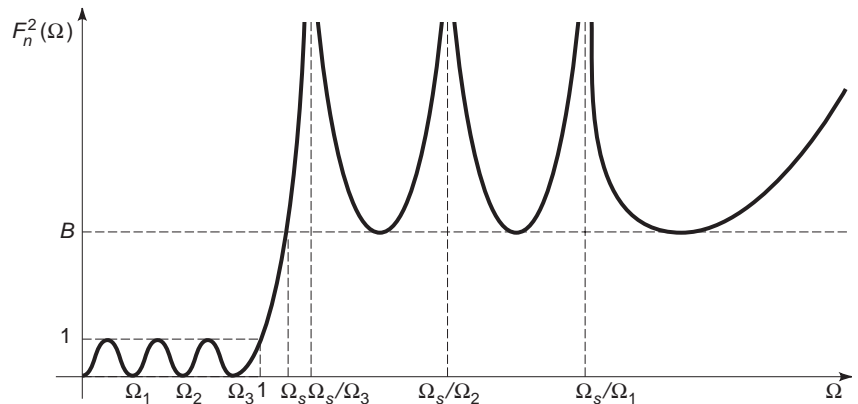


Figure 27. $F_n^2(\Omega)$ for a Cauer filter in Fig. 26 and in Eqs. (50) and (51).

The procedure is based on the fact that the Hurwitz polynomial

$$h(s) = m(s) + n(s) \tag{56}$$

where $m(s)$ is even and $n(s)$ is odd, provides the reactance function $m(s)/n(s)$. It can be further shown that the driving point impedance function

$$w(s) = \frac{m/n}{1 + \frac{m}{n}} = \frac{m(s)}{m(s) + n(s)} \tag{57}$$

has the property

$$|w(j\Omega)|^2 = \frac{m^2(j\Omega)}{m^2(j\Omega) - n^2(j\Omega)} \in [0, 1] \tag{58}$$

for $\Omega \in [-\infty, \infty]$. This provides the Chebyshev behavior. We investigate

$$f(z^2) = \frac{m^2(z)}{m^2(z) - n^2(z)} \quad \text{with } z = u + jv \tag{59}$$

and the transformation

$$z^2 = 1 + \frac{1}{s^2} \tag{60}$$

providing

$$f(z^2) = f\left(1 + \frac{1}{s^2}\right) = g(s^2) = \frac{m^2\left(\sqrt{1 + \frac{1}{s^2}}\right)}{m^2\left(\sqrt{1 + \frac{1}{s^2}}\right) - n^2\left(\sqrt{1 + \frac{1}{s^2}}\right)} \tag{61}$$

The properties of the transformation in Eq. (60) are investigated in Figs. 28a–28e, where the passband $s = j\Omega$ with $|\Omega| \leq 1$, denoted by dashed lines, and the stopband with $|\Omega| \geq 1$, denoted by solid lines, are step by step mapped into the z plane. The steps from s plane to the z plane in Fig. 28 are $w_1 = s^2$, $w_2 = 1/w_1$, $w_3 = w_2 + 1$, $z = +\sqrt{w_3}$. The result is the following mapping:

$$\Omega \in [-1, 1] \text{ into } v \in [-\infty, \infty] \tag{62a}$$

$$|\Omega| \geq 1 \text{ into } u \in [0, 1] \tag{62b}$$

The complex conjugate pair of poles \times in $|\Omega| \geq 1$ results in a double pole in $u \in [0, 1]$. The consequences of this mapping for $f(z^2) = g(s^2)$ in Eqs. (59) and (61) are as follows. For $z = jv$, $v \in [-\infty, \infty]$, and the pertaining $\Omega \in [-1, 1]$

$$f(-v^2) = g(-\Omega^2) = \frac{m^2(jv)}{m^2(jv) - n^2(jv)} \in [0, 1] \tag{63a}$$

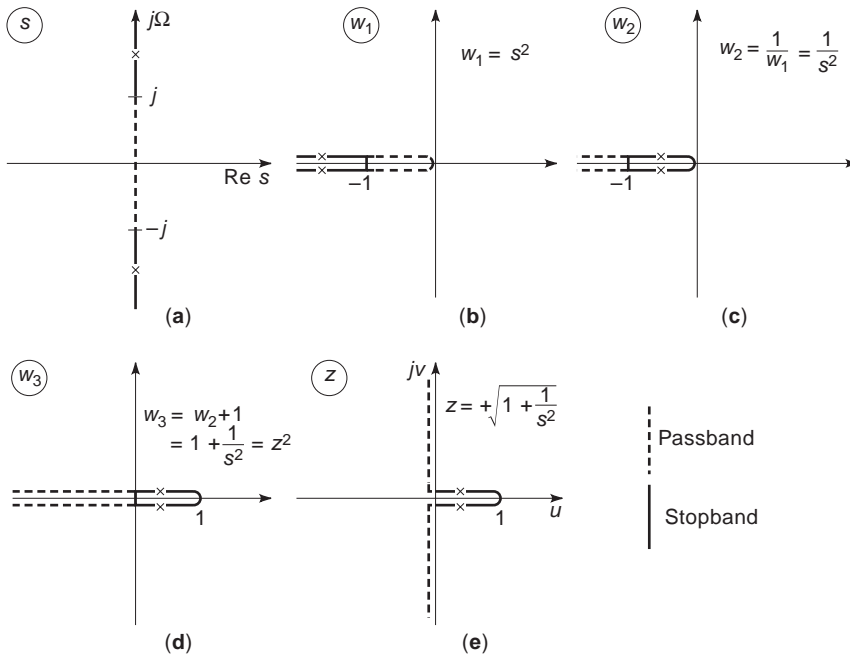


Figure 28. The steps in the conformal mapping $z = +\sqrt{1 + 1/s^2}$ for $s = j\Omega$.

for $z = u, u \in [0, 1]$ and the pertaining $|\Omega| \geq 1$ with the constraint $|m(u)| \geq |n(u)|$ and hence

$$0 \leq \frac{n^2(u)}{m^2(u)} \leq 1$$

$$f(u^2) = g(-\Omega^2) = \frac{m^2(u)}{m^2(u) - n^2(u)}$$

$$= \frac{1}{1 - \frac{n^2(u)}{m^2(u)}} \geq 1 \tag{63b}$$

With these results

$$g(-\Omega^2) = \frac{m^2(\sqrt{1+1/s^2})}{m^2(\sqrt{1+1/s^2}) - n^2(\sqrt{1+1/s^2})} \text{ for } s = j\Omega$$

assumes the shape in Fig. 29. The function $g(-\Omega^2)$ oscillates between 0 and 1 in the passband as long as $m(s)$ is even and $n(s)$ is odd and $h(s) = m(s) + n(s)$ is Hurwitz. The selection of $m(s)$ and $n(s)$ is the freedom for the design of filters.

For the filter, as in all previous cases, we obtain

$$|K(j\Omega)|^2 = q^2 + \varepsilon^2 g(-\Omega^2) \tag{64}$$

with

$$\varepsilon^2 g(s^2) = \varepsilon^2 \frac{m^2(\sqrt{1+1/s^2})}{m^2(\sqrt{1+1/s^2}) - n^2(\sqrt{1+1/s^2})} \tag{65}$$

or

$$\varepsilon^2 g(s^2) = \frac{\varepsilon^2}{2} \left[1 + \frac{1}{2} \frac{m+n}{m-n} + \frac{1}{2} \frac{m-n}{m+n} \right] \tag{66}$$

The dominant term in the stopband, especially around the poles, is

$$|K(j\Omega)|^2 \approx \frac{\varepsilon^2}{4} \frac{m(z) + n(z)}{m(z) - n(z)} \tag{67}$$

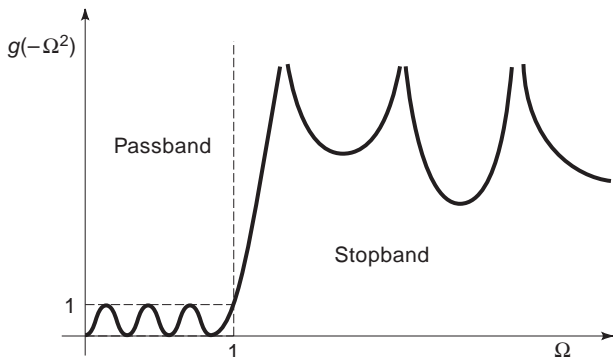


Figure 29. The function $g(-\Omega^2)$ of Eq. (63a) in the passband and the stopband.

with $z \in [0, 1]$ and $|\Omega| \geq 1$ in the stopband. The term with the denominator $m(z) + n(z) = h(z)$ in Eq. (66) exhibits no poles in the stopband as $h(z)$ is Hurwitz. Hence the term with the denominator $m(z) - n(z)$ provides the poles. Now we determine m and n from the requirements in the stopband. With the pole locations $z_i \in [0, 1]$ in Eq. (67), which are found later, we obtain

$$m(z) - n(z) = (-z + 1)^\varphi \prod_{i=1}^r (-z + z_i)^2 \tag{68}$$

and by exchanging z with $-z$

$$m(z) + n(z) = (z + 1)^\varphi \prod_{i=1}^r (z + z_i)^2 \tag{69}$$

The term $z = z_i$ in Eq. (68) represents the double pole in $z \in [0, 1]$, while $z = 1$ stands for the pole of multiplicity φ at $\Omega = \infty$. The even part in Eq. (69) provides $m(z)$, whereas the odd part yields $n(z)$. Hence

$$f(z^2) = g(s^2) = \frac{m^2(z)}{m^2(z) - n^2(z)} \tag{70}$$

and $|K(j\Omega)|^2$ in Eq. (67) valid in the stopband are known. The attenuation pertaining to Eqs. (67)–(69) is

$$\alpha(\Omega) = 10 \log |K(j\Omega)|^2$$

$$= 20 \log \varepsilon - 10 \log 4 + \sum_{i=1}^r 10 \log \left(\frac{z + z_i}{-z + z_i} \right)^2$$

$$+ \varphi 10 \log \frac{(z + 1)}{(-z + 1)}$$

The substitution

$$\gamma = \ln z \quad \text{and} \quad \gamma_i = \ln z_i$$

yields

$$r_i = 10 \log \left(\frac{z + z_i}{-z + z_i} \right)^2 = 10 \log \left(\frac{e^{\gamma_i} + e^\gamma}{e^{\gamma_i} - e^\gamma} \right)^2 \tag{71}$$

$$= 10 \log \left(\frac{e^{\gamma_i - \gamma} + 1}{e^{\gamma_i - \gamma} - 1} \right)^2 = 20 \log \coth \left| \frac{\gamma_i - \gamma}{2} \right|$$

For $z_i = 1$ we obtain

$$r_\infty = 10 \log \left(\frac{z + 1}{-z + 1} \right)^\varphi = 10\varphi \log \coth \frac{|\gamma|}{2} \tag{72}$$

The terms r_i and r_∞ can be considered a template in Fig. 30 that can be shifted to all pole locations $\gamma = \gamma_i$ and $\gamma = 0$.

Any given tolerance scheme in the stopband can be met by a sum of the templates in Eqs. (71) and (72). The number of those templates is minimized by shifting them to appropriate locations γ_i . This numerical search procedure

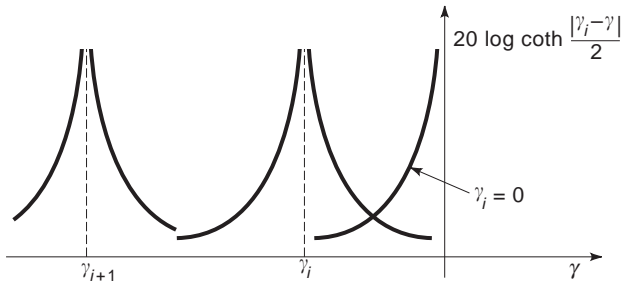


Figure 30. The templates $20 \log \coth |\gamma_i - \gamma|/2$ for the approximation of the given characteristics in the stopband.

is performed either by a computer program or by trials consisting of shifting and adding templates. The result consists of pole locations z_i , their number r , and the multiplicity φ of the poles at $z = 1$.

As all considerations for the conformal mapping have now been discussed, we are ready to list the sequence of the synthesis steps:

1. The given R_1, R_2 and the ripple in the passband yield q and ε .
2. Determine poles z_i .
 - a. If only discrete pilot frequencies

$$z_i = \sqrt{1 - \frac{1}{\Omega_i^2}}$$

have to be suppressed, then these z_i provide Eq. (68).

- b. If a tolerance scheme in the stopband has to be met, templates provide the pole locations z_i together with r and φ in Eq. (68).
3. Form

$$m(z) - n(z) = (-z + 1)^\varphi \prod_{i=1}^r (-z + z_i)^2$$

$$m(z) + n(z) = (z + 1)^\varphi \prod_{i=1}^r (z + z_i)^2$$

and

$$f(z^2) = g(s^2) = \frac{m^2(\sqrt{1+1/s^2})}{m^2(\sqrt{1+1/s^2}) - n^2(\sqrt{1+1/s^2})}$$

4. Form

$$|K(j\Omega)|^2 = q^2 + \varepsilon^2 g(-\Omega^2) = P(\Omega) = P\left(\frac{s}{j}\right) = Q(s)$$

and

$$K(s)K(-s) = Q(s)$$

The zeros and poles of $Q(s)$ provide a stable $K(s)$.

- 5.

$$\begin{aligned} f(s)f(-s) &= Q(s) - q^2 \\ &= \varepsilon^2 \frac{m^2(\sqrt{1+1/s^2})}{m^2(\sqrt{1+1/s^2}) - n^2(\sqrt{1+1/s^2})} \end{aligned}$$

The zeros and poles of $Q(s) - q^2$ determine $f(s)$.

6. With $K(s)$ and $f(s)$, calculate the elements A_{ik} of the chain matrix and synthesize the LC two-ports embedded in R_1 and R_2 .

2.1.9. Transformation of Lowpasses into Other Filters [19].

The synthesis procedures presented were all geared to lowpasses. The standard approach to generate other filter types is a transformation of the lowpass with frequency variable s and $s = j\Omega$ into a new filter with frequency w and $w = j\lambda$. The general transformation is

$$s = f(w) \quad (73)$$

where $f(w)$ is a reactance function. This will also allow transformation of the reactances Ls and Cs into realizable reactances in the w domain.

2.1.9.1. Lowpass Bandpass Transformation. The transformation

$$s = \frac{a}{w} + bw \quad (74)$$

with $a, b > 0$ maps $s = j\Omega$ into $w = j\lambda$ according to

$$\Omega = -\frac{a}{\lambda} + b\lambda \quad (75)$$

as depicted in Fig. 31. The passband of the lowpass with $\Omega \in [-1, 1]$ is translated into the passband with $\lambda \in [\lambda_1, \lambda_2]$ of the bandpass, as indicated by bold lines in Fig. 31. The cutoff frequencies are

$$\lambda_1 = -\frac{1}{2b} + \sqrt{\frac{1}{4b^2} + \frac{a}{b}} \quad (76)$$

$$\lambda_2 = \frac{1}{2b} + \sqrt{\frac{1}{4b^2} + \frac{a}{b}} \quad (77)$$

The center frequency as an image of $\Omega = 0$ is

$$\lambda_0 = \sqrt{\frac{a}{b}} \quad (78)$$

with $\lambda_0^2 = \lambda_1 \lambda_2$ representing the geometric mean of λ_1 and λ_2 . The reactances Ls and Cs translate into the series and parallel resonators in Fig. 32. Due to $f(w)$ in Eq. (73) of second degree, a doubling of the reactances is observed. A transformation $f(w)$ of higher degree provides more than one passband, as outlined by the transformation of sixth

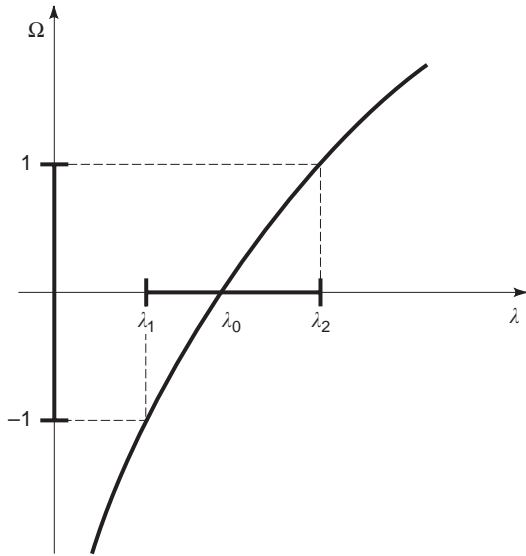


Figure 31. The lowpass bandpass transformation.

degree

$$s = aw + \frac{b}{w} + \frac{cw}{w^2 + \lambda_c^2} + \frac{dw}{w^2 + \lambda_d^2} \quad (79)$$

with $a, b, c, d, \lambda_c^2, \lambda_d^2 > 0$.

The mapping of $s = j\Omega$ into $w = j\lambda$ is shown in Fig. 33, where three passbands are generated. The number of reactances has increased by a factor of 6 due to $f(w)$ of sixth degree.

2.1.9.2. The Lowpass Bandstop Transformation. For the transformation

$$s = \frac{1}{\frac{a}{w} + bw} \quad \text{with } a, b > 0 \quad (80)$$

the function $\Omega = f(\lambda)$ is shown in Fig. 34 with a stopband for $\lambda \in [\lambda_1, \lambda_2]$ with λ_1, λ_2 , and λ_0 , as in Eqs. (76)–(78). The doubling of the reactances is demonstrated in Fig. 35.

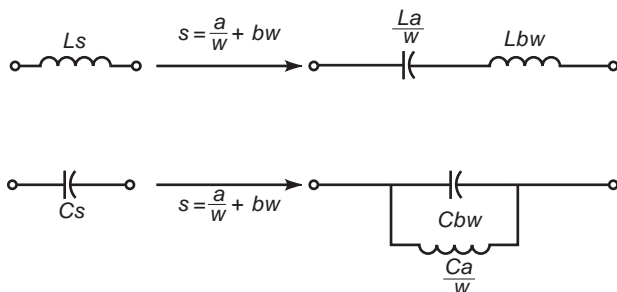


Figure 32. Transformation of reactances for bandpasses.

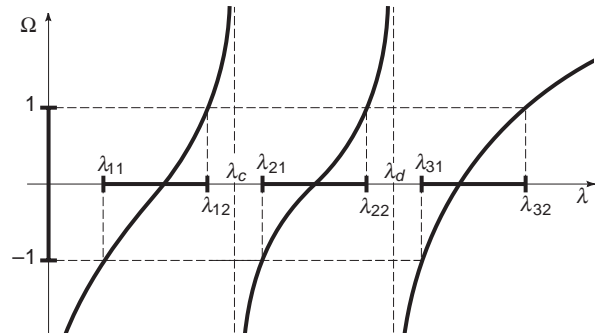


Figure 33. Transformation of a lowpass into a bandpass with multiple passbands.

2.1.9.3. The Lowpass–Highpass Transformation. The transformation

$$s = \frac{a}{w} \quad (81)$$

$a > 0$ yields

$$\Omega = -\frac{a}{\lambda} \quad (82)$$

which is drawn in Fig. 36.

The cutoff frequency of the highpass is

$$\lambda_1 = a \quad (83)$$

According to Fig. 37, inductors and capacitors are interchanged.

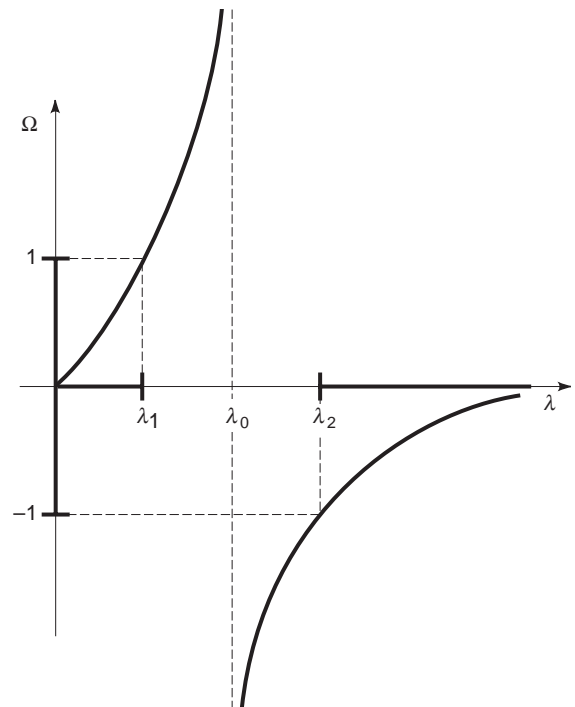


Figure 34. Lowpass bandstop transformation with $\lambda_0 = \sqrt{a/b}$.

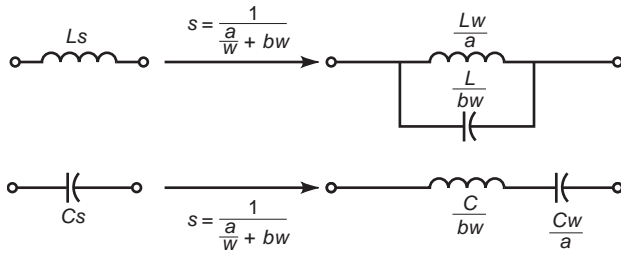


Figure 35. Transformation of reactances for bandstops.

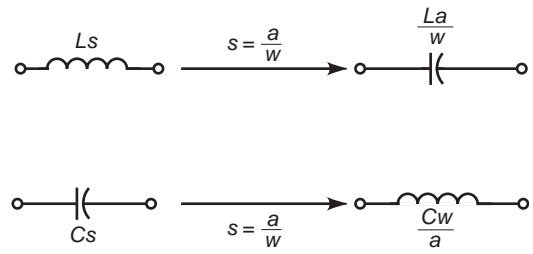


Figure 37. Transformation of reactances for highpasses.

2.1.10. Amplitude and Phase Equalizers. Amplitude equalizers generate two-ports with a constant magnitude of the insertion voltage loss function $K(s)$ at least in a limited frequency range. An often encountered solution to this problem is cascading the unequalized two-port with the bridged-T network in Fig. 38. If the impedances Z_1 and Z_2 are chosen according to

$$Z_1 Z_2 = R^2 \tag{84}$$

and if the network is terminated by the resistor R , then the input impedance is also R . This implies that the bridged T terminated by R can replace the load $R_2 = R$ of the original two-port without interaction. The inverse transfer function of the bridged T loaded by R is

$$K_B^*(p) = 1 + \frac{Z_1(p)}{R} \tag{85}$$

For

$$Z_1/R = \frac{1}{G + jY(\omega)}$$

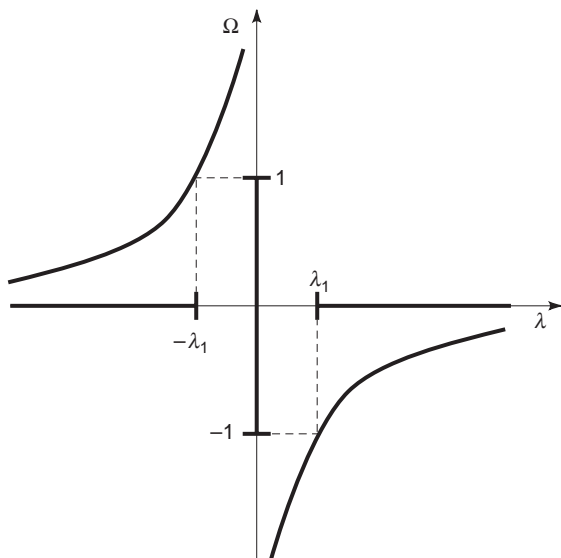


Figure 36. Lowpass-highpass transformation.

we obtain

$$|K_B^*(j\omega)|^2 = \frac{(1 + G)^2 + Y^2(\omega)}{G^2 + Y^2(\omega)}$$

and

$$a(\omega) = 10 \log \frac{(1 + G)^2 + Y^2(\omega)}{G^2 + Y^2(\omega)} \tag{86}$$

The term $a(\omega)$ is the attenuation added to the attenuation of the original two-port in order to equalize the magnitude.

Table 9 lists $a(\omega)$ for various impedances Z_1 and $Z_2 = R^2/Z_1$ [4].

Phase equalizers have the tasks to provide a linear phase or a constant delay for the equalized two-port. They are commonly allpasses. The inverse transfer function of a first-order and of a second-order allpass are

$$K_1^*(p) = \frac{p + \omega_0}{-p + \omega_0} \tag{87}$$

and

$$K_2^*(p) = \frac{p^2 + \frac{2\omega_0}{b}p + \omega_0^2}{p^2 - \frac{2\omega_0}{b}p + \omega_0^2} \tag{88}$$

with the phase $\psi(\omega)$ and the group delay $\tau(\omega)$ as

$$\psi_1(\omega) = \arg K_1(j\omega) = 2 \arctan \frac{\omega}{\omega_0}$$

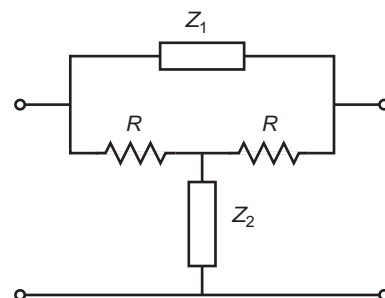





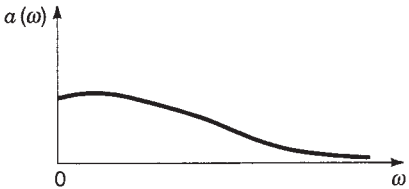


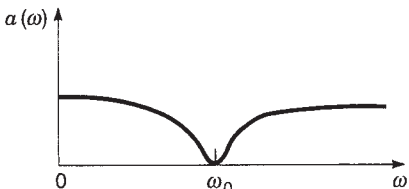
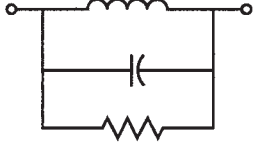

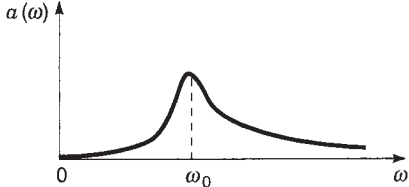


Figure 38. Bridged-T network with $Z_1 Z_2 = R^2$ for amplitude equalization.

Table 9. A List of Impedances Z_1 and Z_2 and the Pertinent $a(\omega)$ for Amplitude Equalization

Z_1	Z_2	Shape of $a(\omega)$ in Eq. (86)
		
		
		
		

and

$$\psi_2(\omega) = \arg K_2(j\omega) = 2 \operatorname{arccot} \frac{b}{2} \left(\frac{\omega_0}{\omega} - \frac{\omega}{\omega_0} \right)$$

$$\tau_1(\omega) = \frac{d \arg K_1(j\omega)}{d\omega} = \frac{\frac{2}{\omega_0}}{1 + \left(\frac{\omega}{\omega_0} \right)^2} \quad (89)$$

$$\tau_2(\omega) = \frac{d \arg K_2(j\omega)}{d\omega} = \frac{b}{\omega_0} \frac{1 + \left(\frac{\omega_0}{\omega} \right)^2}{1 + \left(\frac{b^2}{4} \right) \left(\frac{\omega}{\omega_0} - \frac{\omega_0}{\omega} \right)^2} \quad (90)$$

The group delays $\tau_1(\omega)$ and $\tau_2(\omega)$ are depicted in Figs. 39a and 39b. For $\tau_2(\omega)$ the maximum is approaching $\omega = \omega_0$ depending on increasing values of b . These bell-like curves are added to the nonconstant group delay of the given two-port and thus straighten it out. Several different frequencies ω_0 may be needed for this end. The network in Fig. 40 represents a second-order allpass if it is terminated by R and if the element values are as listed in the figure caption. With the element values given in the figure caption, it exhibits constant input and output impedances and can therefore be cascaded without interaction with the unequaled two-port.

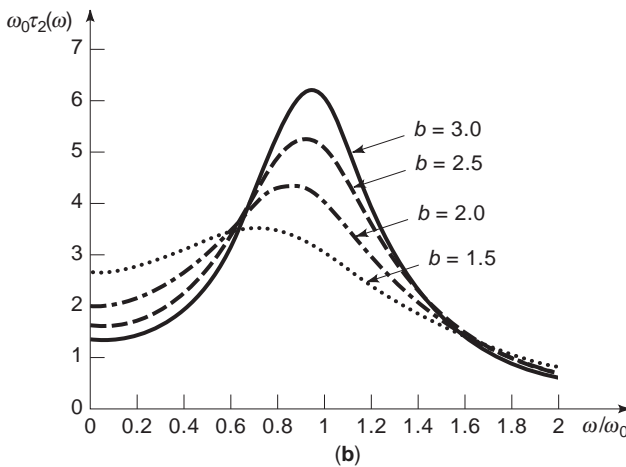
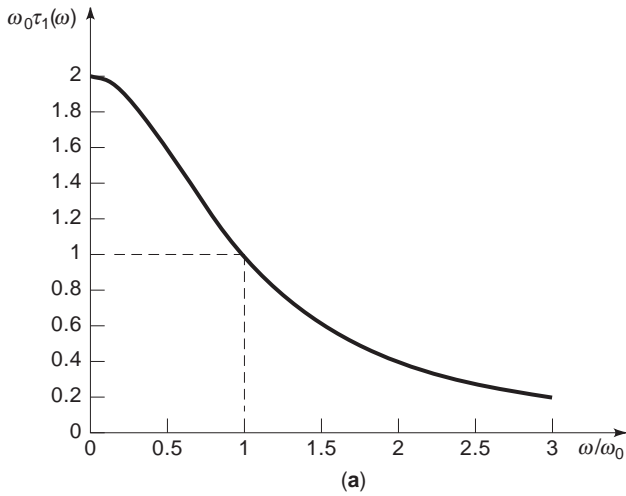


Figure 39. (a) The group delay of a first-order allpass in Eq. (87). (b) The group delay of a second-order allpass in Eq. (88).

3. SURFACE ACOUSTIC WAVE FILTERS

Filters for high frequencies in the megahertz or gigahertz range are difficult to realize as the calculation of a three-

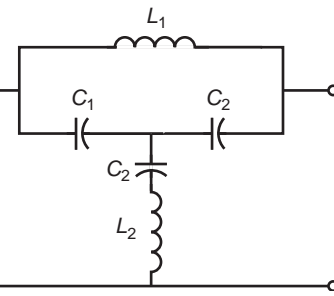
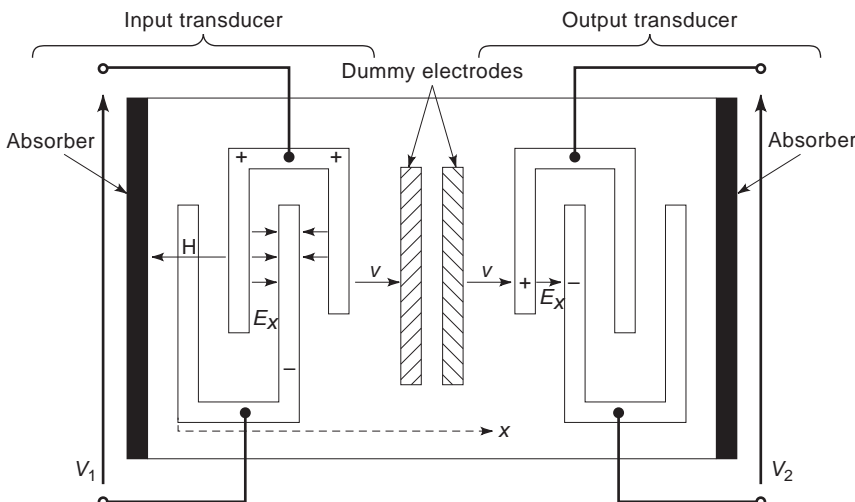


Figure 40. Bridged-T network realizing a second-order allpass with constant input and output impedances R for the element values $L_1 = 2 \frac{R^2 C_1 C_2}{2C_1 + C_2}$, $L_2 = \frac{1}{2} R^2 C_1$ and for a termination by R .

dimensional electromagnetic field is required. To achieve this, one has to resort to numerical methods, which, as a rule, are inaccurate and hence necessitate complicated tuning of the filters. Filters based on surface acoustic waves (SAWs) are somewhat easier to design and build. They are economically one of the most important extensions of classical filters and have reached operating frequencies of more than 10 GHz.

The surface of a piezoelectric substrate such as monocrystalline barium titanate or tantalate carries input and output transducers as shown in Fig. 41. They translate the electric field E stemming from the input voltage V_1 through the piezoelectric effect into a mechanical wave that travels with speed v mainly in the surface of the substrate to the output transducer. Waves traveling backward or through the bulk of the substrate disappear in an absorbing layer in Figs. 41 and 42. The inverse piezo effect changes the mechanical wave in the output transducer back to a charge separation, resulting in the output voltage V_2 .

In its simplest form, the fingers and the gaps of the transducers exhibit all the same width as depicted at the top of Fig. 43. In a more complicated but also more versatile case, they are all unequal, as shown also in Fig. 43. The latter layout provides more degrees of freedom for the filter design. The electrical field in the gaps as response to

Figure 41. Top view on surface acoustic wave filter (SAW filter).

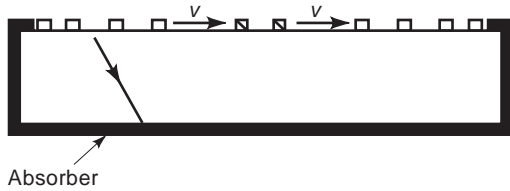


Figure 42. Cross section of SAW filter.

Dirac impulses at the input reaches infinite values in the borders of the fingers, as depicted in Fig. 43. This shape is approximated also by Dirac impulses, as drawn in the last plot in Fig. 43. This so-called δ approximation renders the calculation of the transfer function $F(p)$ rather easy. Each location of a δ impulse is the origin of a mechanical δ im-

pulse traveling with the speed v to the output transducer. Figure 44 shows the distances from the pair of fingers μ in the input transducer to the pair of fingers ν in the output transducer; in Fig. 44 x_0 is the distance between the last fingers of the input transducer and the first fingers of the output transducer. A most important parameter is the overlap h_μ (respectively, g_ν) of a pair of fingers in the transducers. They determine the width of the wave leaving the input and being received by the output. Due to diffraction, the width expands while the wave travels through the substrate. This effect is limited by the dummy electrodes in Fig. 41. They form a surface with equal potential from where the wave again starts with a given width.

The two δ impulses in the edges of the finger pair μ in the input transducer in Fig. 44 reach the center of the gap of the finger pair ν in the output transducer after the

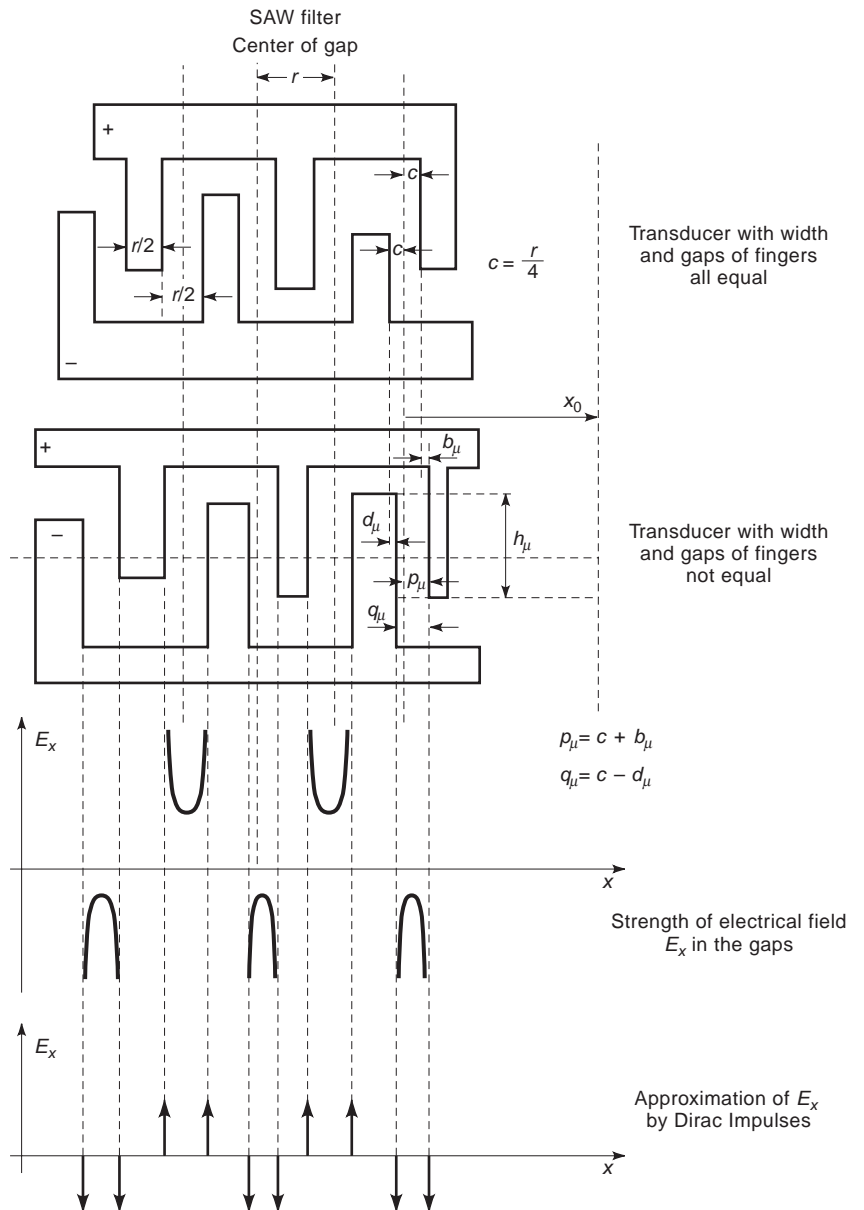


Figure 43. Top view of fingers and electrical field in the gaps.

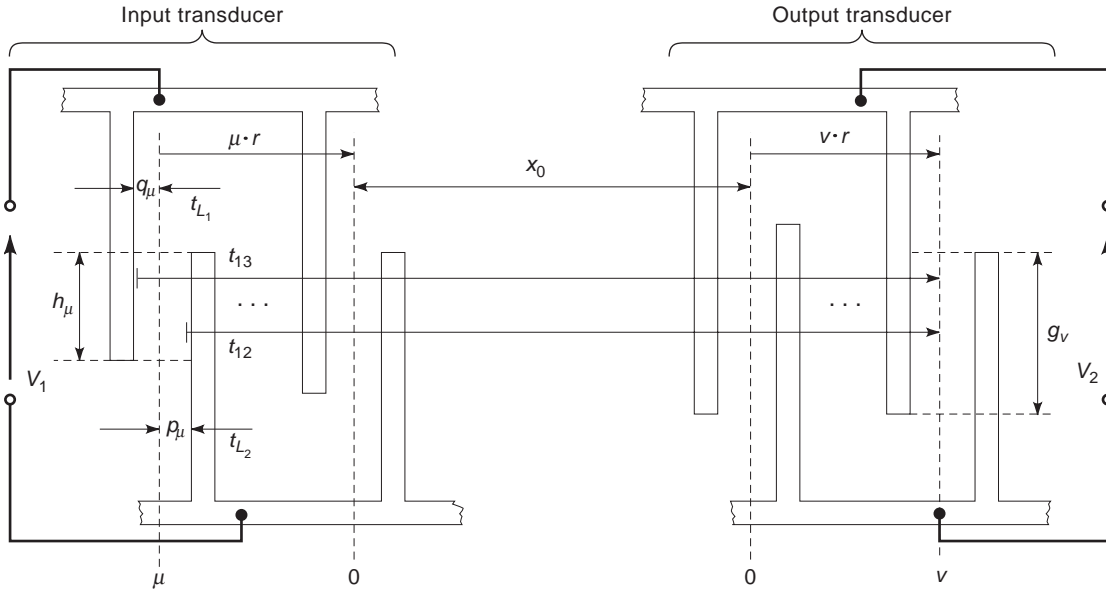


Figure 44. Top view of input and output transducer with unequal widths and gaps of fingers.

delays

$$t_{L_1} = \frac{x_0 + (v + \mu)r + q_\mu}{v} \quad (91)$$

and

$$t_{L_2} = \frac{x_0 + (v + \mu)r - p_\mu}{v} \quad (92)$$

with

$$p_\mu = c + b_\mu \quad (93a)$$

and

$$q_\mu = c - d_\mu \quad (93b)$$

generating the voltage

$$e_{\mu v}(t) = k(\delta(t - t_{L_1}) + \delta(t - t_{L_2})) \quad (94a)$$

with

$$k = \frac{k_0}{p_\mu + q_\mu} (-1)^v (-1)^\mu \min(h_\mu, g_v) \quad (94b)$$

The factor k describes the strength (area) of the impulse, which is inversely proportional to the width of the gap $1/(p_\mu + q_\mu)$ of the finger pair μ , proportional to the $\min(h_\mu, g_v)$ because the minimum of either the width h_μ of the transmitted wave or the width g_v of the overlap of the receiving finger pair determines the received wave, and, finally, proportional to the alternating sign of E in the gaps represented by $(-1)^v (-1)^\mu$; k_0 is a factor of proportionality representing the transducer constant. As a syn-

thesis with $\min(h_v, g_\mu)$ is hard to achieve, we put

$$\min(h_v, g_\mu) = h_\mu \quad (95)$$

meaning $g_v > h_\mu$ for all v and μ ; thus the output transducer receives the full energy transmitted by the input transducer.

The full impulse response $h(t)$ of the SAW filter is given by adding over all N transmitting finger pairs and over all M receiving pairs, which provides, with Eqs. (91)–(95)

$$h(t) = \sum_{\mu=0}^{N-1} \sum_{v=0}^{M-1} \frac{k_0 (-1)^{v+\mu} h_\mu}{2c + b_\mu - d_\mu} \left(\delta \left(t - \frac{x_0 + (v + \mu)r + c - d_\mu}{v} \right) + \delta \left(t - \frac{x_0 + (v + \mu)r - c - b_\mu}{v} \right) \right) \quad (96)$$

A Laplace transform of Eq. (96) yields the transfer function

$$F^*(j\omega) = k_0 e^{j\omega x_0/v} \sum_{\mu=0}^{N-1} \sum_{v=0}^{M-1} (-1)^{v+\mu} \frac{h_\mu}{2c + b_\mu - d_\mu} e^{-j\omega(v+\mu)r/v} \times \left[e^{-j\omega c/v} e^{j\omega d_\mu/v} + e^{j\omega c/v} e^{j\omega b_\mu/v} \right] \quad (97)$$

This general result is, for practical applications, usually simplified by setting $b_\mu = 0$ and $d_\mu = 0$ for all μ , which means that all fingers have the same width $r/2$, which is

also the width of all gaps. This reduces $F^*(j\omega)$ in Eq. (97) to

$$F^*(j\omega) = \frac{k_0}{c} \cos \frac{c\omega}{v} e^{-j\frac{\omega x_0}{v}} \sum_{\mu=0}^{N-1} (-1)^\mu h_\mu e^{-j\omega \mu r/v} \tag{98}$$

$$\times \sum_{v=0}^{M-1} (-1)^v e^{-j\omega vr/v}$$

In Eq. (98) the term $e^{-j\omega x_0/v}$ stands for the delay x_0/v of the wave between the two transducers; the sum over v is the essentially unwanted contribution of the output transducer, whereas the \cos term stems from the two δ impulses per finger pair. The desired frequency characteristic has to be realized with the individual overlaps h_μ of the input transducer. We set

$$(-1)^\mu h_\mu = h'_\mu \tag{99a}$$

and

$$z = e^{j\omega r/v} \tag{99b}$$

and obtain from Eq. (98)

$$\frac{F^*(j\omega)}{\frac{k_0}{c} \cos \frac{c\omega}{v} e^{-j\omega x_0/v} \sum_{v=0}^{M-1} (-1)^v e^{-j\omega vr/v}} = \sum_{\mu=0}^{N-1} h'_\mu z^{-\mu} \tag{100}$$

$F^*(j\omega)$ is the desired transfer function to be synthesized; the denominator on the left-hand side of Eq. (100) is the unavoidable contribution of the transducers. The ratio of both terms on the left has to be approximated by the right-hand term. This term is the same as the transfer function of digital filters with finite impulse response (FIR filters). Therefore, the synthesis procedures known from FIR filters can be applied [21,22]. Even though SAW filters are continuous time systems, the approximation by δ impulses

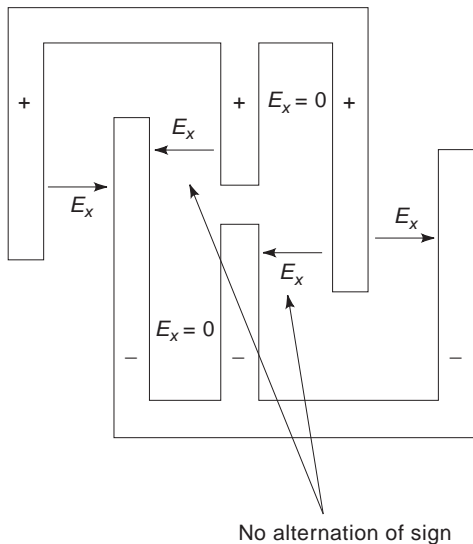


Figure 45. Top view of layout of fingers without alternating signs of electric field.

renders them similar to time discrete systems, where r/v in Eq. (99b) plays the role of the sampling time.

We cannot expect the approximation to provide h'_μ with alternating signs. Hence the layout of the fingers must be modified according to Fig. 45, where the alternation of signs is interrupted.

The pitch r in Fig. 46 is chosen such that the output signal is maximum at the center frequency of the passband. This is achieved by a constructive interference of the wave traveling the distance $2r$ in time $2r/v$ and the sin wave with frequency ω_0 imposed by the voltage V_1 exhibiting the period $2\pi/\omega_0$. This yields

$$\frac{2r}{v} = \frac{2\pi}{\omega_0}$$

or

$$r = \frac{v\pi}{\omega_0} = \frac{v}{2f_0} \tag{101}$$

Due to the approximations made, the design of SAW filters as a rule requires a corrective redesign based on the measured deviations from the desired characteristics. Further damaging parasitic effects are the triple transit signals, which are reflected by the fingers at the output transducer and then again reflected back to the output by the input transducer.

Economically important applications of the SAW technology are filters for the intermediate frequency in TV sets and filters for mobile communications.

The bandpass for TV sets possesses a center frequency of 38 MHz; the SAW substrate exhibits $v = 1000$ m/s. This yields, according to Eq. (101), a width of the fingers that equals the gaps of $r/2 = 13 \mu\text{m}$. A shortcoming of SAW filters is the relatively large insertion loss in the passband of around 8 dB, stemming mainly from the loss in the sub-

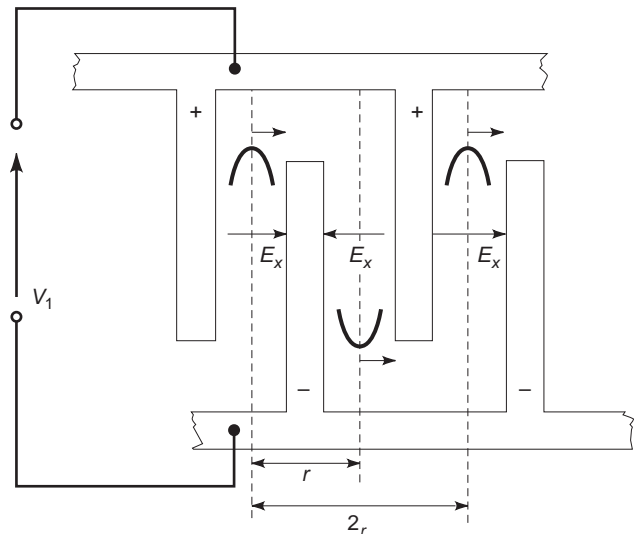


Figure 46. Construction of superposition of traveling wave and wave fed in by V_1 .

strate material. The loss can be decreased to around 5 dB by employing a second output transducer in Fig. 47, which catches the so far unused backward-traveling wave. However, the placement of the two output transducers both in the distance x_0 has to be accurate in order to maintain the same phase of the waves added in the output transducers.

4. AREAS FOR FUTURE STUDY

Classical filter synthesis is a well-established area for which the first contributions were published more than 70 years ago. Most of the important problems were indeed solved in the meantime. Some remaining unresolved problems will be outlined in this section. There has been increased focus on those problems in recent years because the classical filters serve as models for filter implementations in new technologies, such as digital filters, RC active filters, and switched-capacitors filters.

The following problems need to be resolved:

1. A proof that the synthesis of lossless two-ports with partial and full pole removal is always possible with realizable reactances is still missing. It is a difficult task, as many unsuccessful attempts may testify. However, a proof would certainly offer a deeper insight into one of the most important synthesis procedures. A helpful hint for further investigations would be the fact that negative impedances are also tolerable for partial pole removal, as they can represent the negative component, and inductor or a capacitor, in the equivalent circuit for a transformer with tight couplings.
2. Guidelines on how to find lossless two-ports with a minimum number of the more expensive inductors would be of economic interest. The guidelines could make use of the large number of equivalent solutions.

3. A procedure is needed to control the various possibilities for synthesizing a lossless two-port such that the component values lie in a desired range. This could help in using the components of an advantageous price-performance category and in implementing parasitic components of a given value.

For filters in new miniaturized technologies, the solution to the problem could provide component values that are feasible in the new technology, such as multipliers with values in the raster 2^v , v integer, in digital signal processing or capacitors in the pF range for CMOS technology while still maintaining a closed-loop gain around 1 of the operational amplifiers. The same goal may be reached by a linear transformation into an equivalent two-port either for the time continuous classical filters [12,23] or for digital filters [24].

4. A method is needed to generate equivalent reactance circuits for nonelectric components, such as coupled quartz oscillators, or for other mechanical oscillators during the synthesis procedure for lossless two-ports.
5. In the approximation method based on a conformal mapping, the approximation of arbitrary but realizable requirements in the stopband by a minimum number of $\coth |(\gamma_i - \gamma)/2|$ functions should be achieved by an analytical solution and not by a search procedure, guaranteeing that the minimum number of \coth functions is always reached. This design method would be one of the most powerful.
6. There is a need for synthesis of RLC two-ports that also include lossy two-ports with a complex impedance as a load and as internal impedance of the voltage source. This becomes more important the higher the operating frequencies are, which imply complex impedance loads. The synthesis of either lossy two-ports with resistive loads or of lossless two-ports

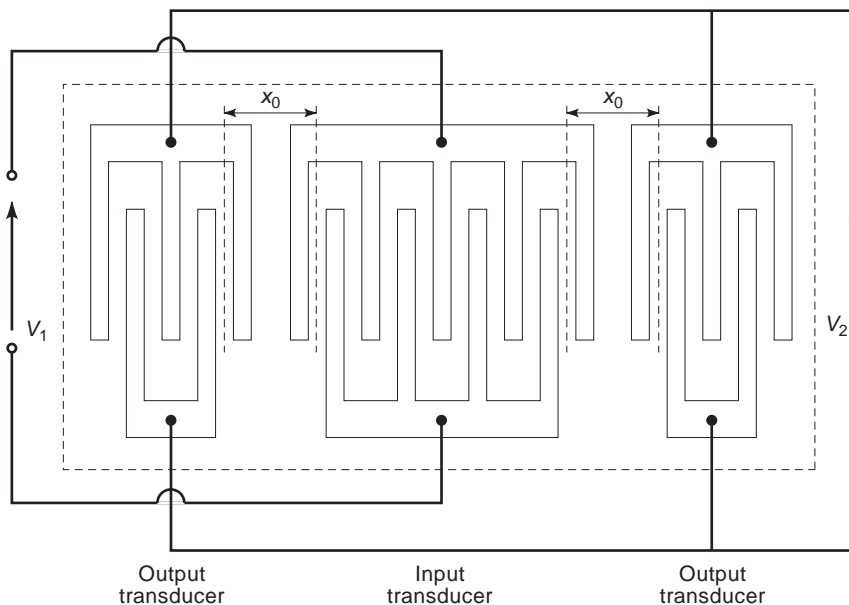


Figure 47. SAW filter with two parallel-connected output transducers in two identical distances x_0 from the input transducer.

with complex impedance loads [25] has been solved. Still unknown is the synthesis of two-ports combining the two properties.

7. There is a need for synthesis of SAW filters based on a more accurate but still easy-to-handle simulation of the device, which should eliminate the need for a corrective redesign.
8. A straightforward synthesis of SAW filters with the large number of geometric parameters in Eq. (69) will save fingers and hence chip area. The synthesis should also compensate for parasitic effects, such as the triple transit signal.
9. Materials science ought to synthesize piezoelectric substrates with a diminished attenuation of the SAW in order to decrease the insertion loss of filters.

Acknowledgments

The author acknowledges the valuable discussions with and the proofreading by his coworkers Markus Gaida, Joachim Selinger, Axel Wenzler, Markus Wintermantel, and Christof Zeile.

BIBLIOGRAPHY

1. W. Bader, Elektrische Netzwerke mit vorgeschriebenem Einschwingvorgang, *VDE-Fachberichte* **13**:289–295 (1949).
2. E. Lueder, *Die Verwirklichung der Kettenmatrix des allgemeinen passiven Vierpols durch eine Schaltung mit der geringsten Zahl von Teilen*, Habilitationsschrift, Univ. Stuttgart, 1966.
3. S. Darlington, Synthesis of reactance four-poles which produce prescribed insertion loss characteristics, *J. Math. Phys.* **18**:257–353 (1939).
4. R. W. Daniels, *Approximation Methods for Electronic Filter Design*, McGraw-Hill, New York, 1974.
5. M. S. Ghauri, *Principles and Design of Linear Active Circuits*, McGraw-Hill, New York, 1965.
6. D. O. Pederson and E. S. Kuh, *Principles of Circuit Synthesis*, McGraw-Hill, New York, 1959.
7. L. Weinberg, *Network Analysis and Synthesis*, International Student Edition, McGraw-Hill, New York, 1962.
8. S. K. Mitra, *Analysis and Synthesis of Linear Active Networks*, Wiley, New York, 1969.
9. S. Butterworth, On the theory of filter amplifiers, *Wireless Eng.* **13**:536–541 (1930).
10. A. Wenzler and M. Wintermantel, private communication, Inst. Network and Systems Theory, Univ. Stuttgart, 1997.
11. W. E. Thomson, Delay networks having maximally flat frequency characteristics, *Proc. IEEE (Part 3)* **96**:487–490 (1949).
12. W. Cauer, *Synthesis of Linear Communication Networks*, 2nd ed., transl. from the German by G. E. Knausenberger, McGraw-Hill, New York, 1958.
13. R. Saal and W. Entenmann, *Handbuch zum Filterentwurf [Handbook of Filter Design]*, 2nd ed., Hüthig, Heidelberg, 1988.
14. E. Christian and E. Eisenmann, *Filter Design Tables and Graphs*, Wiley, New York, 1966.
15. R. Saal, *Der Entwurf von Filtern mit Hilfe des Kataloges normierte Tiefpässe*, Allg. Electricitäts-Ges. AEG-Telefunken, Backnang, 1968.
16. (a) W. Bader, Kopplungsfreie Kettenschaltungen, *Telegraphen-Fernsprech-Funk-und-Fernseh-Technik* **31**:177–189 (1942); (b) W. Bader, Kettenschaltungen mit vorgeschriebener Kettenmatrix, *Telegraphen-Fernsprech-Funk-und-Fernseh-Technik* **32**:119–125, 144–147 (1943); (c) W. Bader, Polynomvierpole vorgeschriebener Frequenzabhängigkeit, *Archiv für Elektrotechnik* **34**:181–209 (1940).
17. H. Piloty, Über die Realisierbarkeitssätze der Kettenmatrix von Reaktanzvierpolen, *Telegraphen-Fernsprech-Funk-und-Fernseh-Technik* **30**:217–223 (Aug. 1941).
18. R. M. Foster, A reactance theorem, *Bell Syst. Tech. J.* **3**:259–267 (1924).
19. E. Guillemin and S. A. Ernst, *Synthesis of Passive Networks: Theory and Methods Appropriate to the Realization and Approximation Problems*, Wiley, New York, 1957.
20. M. E. Van Valkenburg, *Analog Filter Design*, Holt, Rinehart & Winston, New York, 1982.
21. B. Gold and C. M. Rader, *Digital Processing of Signals*, McGraw-Hill, New York, 1969.
22. S. K. Mitra and J. F. Kaiser, *Handbook for Digital Signal Processing*, Wiley, New York, 1993.
23. E. Lueder, *Äquivalente Schaltungen und Topologie der Schaltungen geringsten Aufwandes*, Ph.D. thesis, Univ. Stuttgart, June 1962.
24. E. Lueder and K. Haug, Calculations of all equivalent and canonic 2nd order digital filter structures, *Proc. IEEE Int. Conf. Acoustics, Speech Signal Processing*, Tulsa, April 10–12, 1978, pp. 51–54.
25. W. Bader, Die Synthese des linearen passiven Vierpols bei beliebigen komplexwertigen Quellen-und-Abschlusswiderständen, *Nachrichtentechnische Zeitschrift* 549–555 (Nov. 1964).

FURTHER READING

- L. O. Chua, C. A. Desoer, and E. S. Kuh, *Linear and Non-Linear Circuits*, McGraw-Hill, New York, 1997.

FILTER THEORY

ADNAN GÖRÜR
Niğde University
Niğde, Turkey

1. INTRODUCTION

Filters are commonly used to transmit a particular thing and stop everything else. For instance, a car's oil filter passes the oil and rejects the dirt particles, or a pool filter passes the water and stops substances such as dirt, leaves, and twigs. Similarly, the electrical filters also transmit the desired signal or band of signals required for an electrical system and reject spurious signals or harmonics. Electrical filters have been employed in practical applications for more than eight decades, and are currently used in all frequency ranges to provide as nearly perfect transmission as possible for signals falling within desired passband

frequency ranges, together with rejection of those signals and noise outside the desired frequency bands. RF and microwave systems often require means of suppressing unwanted signals and/or separating signals having different frequencies in the microwave region. Naturally, these functions also are performed by electrical filters. RF/microwave filter technology stimulates many microwave applications, such as equalizers, impedance-matching networks, transformers, shaping networks, power dividers, attenuators, and directional couplers. In addition, they are fundamental components in a variety of RF/microwave systems, such as cellular radiocommunications, satellite communications, military applications, and radar.

A paper published in 1937 by Mason and Sykes [1] became a starting point of studies on microwave filters. Much of the foundation of modern filter theory and practice took place during the World War II years and the years immediately following. In particular, the invention of the radar as well as the war itself led to important developments in the area of filter technology. Both theoretical filter design methods and technology employed to realize them have shown a continuous development since World War II. Satellite communications that began in the 1960s stimulated filter transfer functions and network synthesis as well as rapid advances in waveguide and dielectric resonator filters. Later, cellular communications led to further developments in filter technologies such as the dielectric resonator, coaxial resonator, and ceramic and surface acoustic-wave filters, due to the necessity of low-loss high-power-handling selective filters with reduced size and at low cost. Much of developments in microwave filters in historical perspective were surveyed in 1984 by Levy and Cohn [2]. A survey of the significant techniques employed in the design of microwave filters after the first survey published in 1984 is also presented [3]. Additional details on numerous advances in microwave filter technology in the context of their applications may be found in the paper by Hunter et al. [4].

Electrical filters may be classified into several main categories in terms of their general response types: lowpass, bandpass, highpass, and bandstop. Their frequency responses are illustrated in Fig. 1. Lowpass filters transmit all frequencies between zero frequency and some upper frequency limit (cutoff frequency ω_c), while they attenuate all frequencies above the cutoff frequency. In contrast to lowpass filters, highpass filters pass all frequencies above a lower cutoff frequency and attenuate all frequencies below cutoff value. Bandpass filters transmit all frequencies in a specific frequency band (ω_1 to ω_2 , where ω_1 is lower cutoff frequency and ω_2 is upper cutoff frequency as shown in Figs. 1c and 1d, respectively) and reject all frequencies below and above that band. Finally, bandstop filters are complementary to bandpass filters, and reject all frequencies in a frequency band (ω_1 to ω_2) and pass all frequencies outside the band.

The ideal electrical filters are devices that provide perfect transmission for all frequencies in one or more passband regions and infinite attenuation in one or more stopband regions. Since such ideal filters cannot be realized in the practical sense, the aim of filter design is to ap-

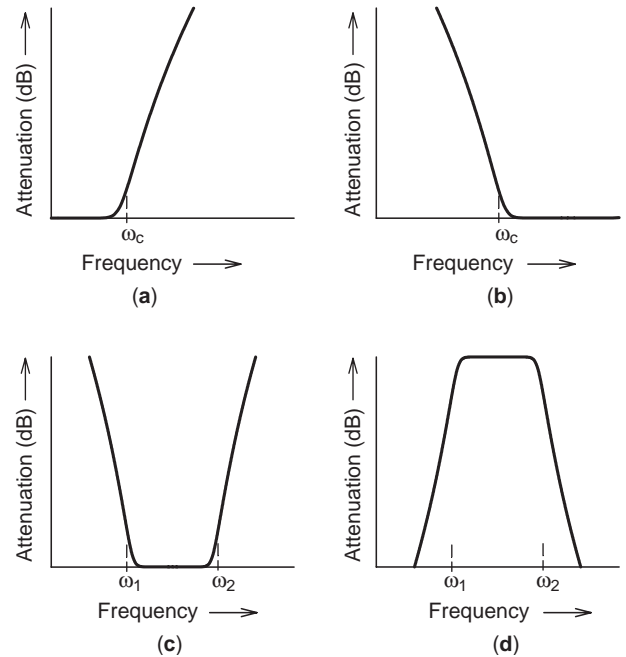


Figure 1. General response types of electrical filters: (a) lowpass; (b) highpass; (c) bandpass; (d) bandstop.

proximate the ideal characteristics within an acceptable tolerance. The electrical filters may also be classified according to their response functions, such as maximally flat or Butterworth, equally ripple or Chebyshev, elliptic function, generalized Chebyshev or pseudoelliptic, and maximally flat time delay or linear phase. These filter responses can be distinguished from each other by examining the locations of the poles and the zeros of their transfer functions. Briefly, the zeros of a transfer function are termed *transmission zeros* (or *attenuation poles*), and its poles, *transmission poles*. Of the filter responses, all the transmission zeros of the Butterworth or maximally flat transfer function are at infinity, and the poles of this function are located on a unit circle in the left-half complex plane. A Butterworth filter that has maximally flat characteristic within the passband is therefore an all-pole filter.

Like the Butterworth response, all the transmission zeros of the Chebyshev transfer function are also at infinity, but the poles of a Chebyshev filter are distributed on an ellipse in the left-half complex plane, where the major and minor axes of the ellipse are the imaginary and real axes of the complex plane. The filter having such a characteristic is often called as an *all-pole Chebyshev filter*, or simply a *Chebyshev filter*. The selectivity (or stopband slope) of a Chebyshev filter is steeper than that of a Butterworth filter of the same degree (the degree or order of a filter is equal to the number of elements used in filter design).

When frequency selectivity or stopband slope and passband loss are considered to be the significant filtering parameters, then Butterworth and Chebyshev filters are not optimum. Therefore, the filters can also be designed such that the transfer function has equal ripples in both passband and stopband. In this particular case, since the transfer function is result in expressions containing elliptic functions, a filter of this type is often called an *elliptic*

function filter or a *Cauer parameter filter* [5,6], or simply an *elliptic filter*. Elliptic filters have the maximum number of poles located at finite frequencies. In comparison to the Chebyshev filter, they show better passband performance and a steeper stopband slope.

On the other hand, if one or more transmission zeros are located at finite frequencies within the stopband of a Chebyshev filter, such a filter is then described as a *generalized Chebyshev* or *pseudoelliptic filter* [7,8]. The use of the generalized Chebyshev filter makes possible filter implementations with the minimum impedance variation, which is considerable for a printed circuit implementation, because when realizing the elliptic function filter, the impedance variation in the filter increases and leads to problems for printed circuit implementation. This filter approach offers high selectivity as the elliptic function filter.

Low loss in the passband and sharp stopband slope at the band edges are typical requirements for RF/microwave filter design. In some applications, however, the other significant characteristic also is behavior of the transmission phase over the passband [9]. For instance, modern microwave communication systems require, especially in satellite communications, filters passing the desired signal with a minimum distortion. In order to prevent the distortion, both the insertion loss and group delay of the filter must be constant within the passband. The group delay remains constant when the transmission phase varies linearly with frequency. Therefore, such a filter is frequently called a *maximally flat time-delay filter*. In addition, although maximally flat time-delay filters generally have a poor selectivity, they have a rather flat group delay within the passband. Since the group delay becomes flat over a wider frequency region as the filter degree n is increased, high-degree maximally flat time-delay filters are often used for obtaining a flat group delay over a large passband. Since the polynomials encountered in the transfer function providing such a filter characteristic are associated with Bessel functions, and as the maximally flat phase approximation was firstly derived by Thomson [10], these filters are also known *Bessel* or *Thomson filters*. The maximal time-delay filters have poles placed on an ellipselike path outside a unit circle in the complex plane, and like Butterworth and Chebyshev filters, they are also all-pole filters.

It is well known that microwave filters can be realized with only lumped elements such as inductors, capacitors, and resistors or only distributed elements such as waveguide sections, coaxial lines, microstrip lines, and strip-lines, or mixed lumped/distributed elements, arranged in a particular configuration. Although lumped-element filters can be utilized up to about Ku band, lumped realizations of the microwave filters with high- Q inductors and capacitors are seldom convenient because the operation wavelength is comparable with the physical size of circuit elements. Consequently, at microwave frequencies, this difficulty in realization of lumped-element filters requires the use of various distributed elements where the size of the elements is comparable with the wavelength. However, the study of lumped-element filters is very important for comprehension of the design of distributed microwave filters based on lumped-element theory. More details on

the role of lumped-element filters in microwave realizations and design may be found in Ref. 3.

The design of microwave filters using two-port lumped-element lowpass prototype networks has been a conventional method because the methods for lumped-element electrical filter design are well established. For this reason, the lowpass prototype filter design is usually a starting point for the design of microwave filters. In such a case, it is not important which media (e.g., transmission line, waveguide, or other media) in which the filter is practically realized. There are two filter theories for design of the lowpass prototype filter: the image parameter theory and the insertion loss theory [11]. The oldest method of filter design is based on the image parameter theory. In the design of lumped-element filters, however, the insertion loss theory is generally preferable because the use of the image parameter theory presents the desired cutoff frequencies and attenuation characteristics, but avoids the specification of a frequency response over the comprehensive operating frequency range. In addition, although this method is relatively simple, it is not an exact procedure and is based on a good deal of cut-and-try procedures for obtaining an adequate overall frequency characteristic. Unlike the image parameter method, the insertion loss theory can produce any possible transfer function and offers a filter design with a completely specified frequency response. Therefore, only insertion loss theory will be discussed here.

In the following paragraphs, the basic concepts and theories for design of general RF/microwave filters are defined. Filter transfer functions, two-port lumped-element lowpass prototype filters, and filter transformations are discussed. Richards' transformation, Kuroda's transformations (or identities), impedance, and admittance inverters are also investigated, which are required for transforming lumped elements to transmission-line sections, for physically separating filter elements and to change impractical elements into more realizable elements in a filter network.

2. BASIC CONCEPTS

2.1. Transfer Function

The transfer function of a linear and time-invariant network as illustrated in Fig. 2 may be expressed in form of a rational function as

$$S_{21}(s) = \frac{N(s)}{D(s)} \quad (1)$$

where $N(s)$ and $D(s)$ are polynomials in a complex frequency variable s . The s plane ($\sigma + j\Omega$) is a particularly convenient representation of a two-port network response as a function of the neper frequency σ and radian frequency Ω , which turns out to be very useful for modern network synthesis. When the network is a lossless passive network, then the neper frequency becomes $\sigma = 0$, and hence $s = j\Omega$. In this case, the transfer function of a lossless two-port network is also expressed as

$$|S_{21}(j\Omega)|^2 = \frac{1}{1 + \epsilon^2 F_n^2(\Omega)} \quad (2)$$

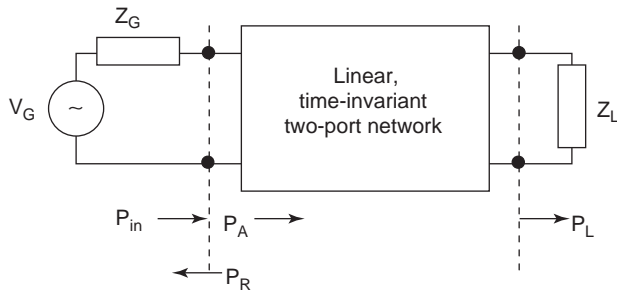


Figure 2. General form of a linear and time-invariant two-port network, where $P_L = P_A$ if the network is lossless, and $P_L = P_{in}$ if the network is lossless and there are no reflections.

where Ω is a frequency variable, ϵ is a ripple constant, and $F_n(\Omega)$ is a filtering function. Thus, to obtain the desired response, the rational transfer function given by (1) can be realized using (2).

The rational transfer function described in (1) is defined on the s -complex plane. The s values that make $S_{21}(s) = 0$ are the zeros of the rational transfer function, and the s values that constitute $S_{21}(s) = \infty$ are the singularities (usually the poles) of the rational transfer function. Briefly, the roots of polynomial $N(s)$ give the zeros of the transfer function $S_{21}(s)$, while the roots of polynomial $D(s)$ give the poles of the transfer function $S_{21}(s)$. These poles and zeros are often called *transmission poles* and *transmission zeros*, respectively, and they can be illustrated on the s -complex plane [12,13]. The poles become the natural frequencies of the filter when its frequency response is represented by the transfer function $S_{21}(s)$. The denominator $D(s)$ is a Hurwitz polynomial [12]. Hurwitz requires that all roots (zeros) of $D(s)$ occur only in the left-half plane, or on the imaginary axis of the s plane. Therefore, for the filter to be a stable and causal network, the transfer function described by (1) must satisfy the following constraints:

- It must be a rational function of complex frequency variable s with a real coefficient.
- The natural frequencies (or poles) of the filter must lie in the left-half complex plane, or on the imaginary axis $j\Omega$.
- The degree of the numerator $N(s)$ must be equal to or less than that of the denominator $D(s)$.

Unlike the denominator $D(s)$, the roots of numerator $N(s)$ may place anywhere on the s -complex plane, and they are defined as *finite-frequency transmission zeros* of the filter.

2.2. Insertion Loss

The transmitted power through a two-port network is characterized as insertion loss. The insertion loss, L_A (measured in decibels), of a two-port network at a particular frequency is defined as

$$L_A(\Omega) = 10 \log \frac{P_{in}}{P_L} = 10 \log \frac{1}{|S_{21}(j\Omega)|^2} \text{ dB} \quad (3)$$

where P_{in} is the power delivered (incident power) to the load when connected directly to the source and P_L is the power delivered to the same load after insertion of the two-port network, as shown in Fig. 2. A typical insertion loss response for a lowpass filter with an equal-ripple passband and stopband is shown in Fig. 3, where Ω_c , Ω_s , and Ω_z are the cutoff frequency, the frequency of the stopband edge, and the frequencies of the transmission zeros, respectively. Insertion loss becomes infinite at transmission zeros (or attenuation poles), while it is zero at reflection zeros (or transmission poles). All transmission zeros must be located in stopband(s) to achieve maximum signal attenuation in these frequency bands. Each transmission zero at infinite frequency increases one the degree of filter while the transmission zeros at finite frequencies appends double degrees.

2.3. Return Loss

The return loss L_R (measured in decibels) characterizes the reflected power and is defined as the ratio of the input to reflected power. Since $|S_{11}|^2 + |S_{21}|^2 = 1$ for a lossless, passive two-port network, the return loss response of the filter is given by

$$\begin{aligned} L_R(\Omega) &= 10 \log \left(\frac{P_{in}}{P_R} \right) = 10 \log \frac{1}{|S_{11}(j\Omega)|^2} \\ &= 10 \log \frac{1}{1 - |S_{21}(j\Omega)|^2} \text{ dB} \end{aligned} \quad (4)$$

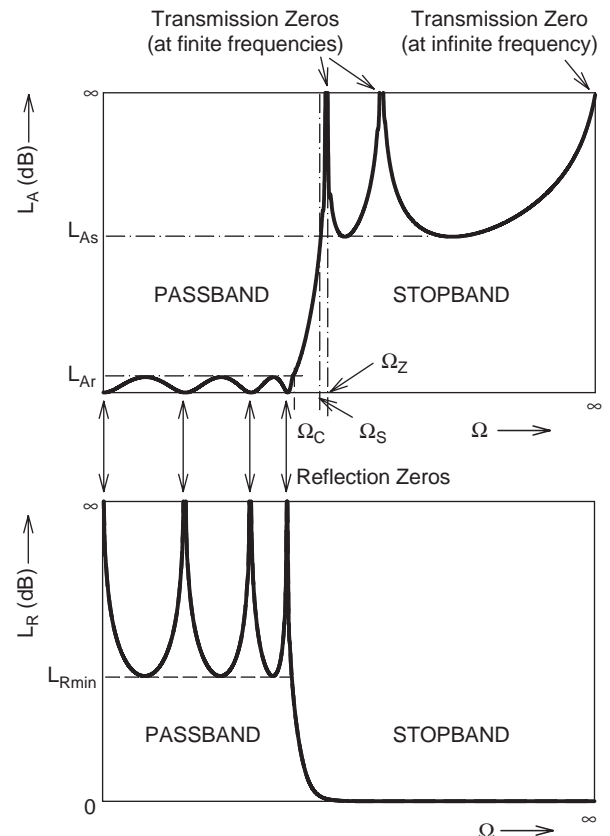


Figure 3. Insertion loss and return loss of a lowpass filter with an equal-ripple passband and stopband.

where P_R is the reflected power, as shown in Fig. 2, and $|S_{11}|^2$ is power reflection coefficient. A typical return loss response for a lowpass filter is shown in Fig. 3. Return loss is infinite at reflection zeros but it becomes zero at transmission zeros. In other words, reflected power is an infinite number of decibels (∞ dB) smaller than the incident power at reflection zeros, whereas it is equal to incident power at transmission zeros. It should be known that the return loss becomes infinite at frequencies where insertion loss is zero, and the return loss has minimum value at frequencies where passband ripple has maximum value. All reflection zeros must be located in passband to enable transfer of power to output with minimal reflection. The total number of reflection zeros is equal to the total number of transmission zeros. The degree or order of a filter is also equal to the total number of transmission zeros or reflection zeros.

2.4. Phase Delay

In phase delay, the output signal in relation to the input signal is delayed while a signal is transmitted through a frequency-selective network such as a filter. The phase delay t_p (in seconds) is one of two parameters that play a role in characterizing filter performance related to this delay, and is defined by

$$t_p = \frac{\arg(L_A)}{\Omega} = \frac{\phi_{21}(\Omega)}{\Omega} \tag{5}$$

where ϕ_{21} (in radians) is the phase of the transfer function of the filter and Ω is measured in radians per second. In other words, phase delay is the ratio of the total phase shift (usually expressed in radians) of a sinusoidal signal during transmission through a transducer to the frequency (usually expressed in radians per second) of the signal.

2.5. Group Delay

The second type of signal delay is the group delay described as the negative of the slope of insertion phase. Group delay is defined as

$$t_d = - \frac{d\phi_{21}(\Omega)}{d\Omega} \tag{6}$$

The group delay determines the time required for a signal to pass through a circuit and represents the true signal delay.

3. FILTER CHARACTERISTICS

3.1. The Butterworth (or Maximally Flat) Characteristic

The ideal filter response can be approximated in a number of different ways. A common approximation is the Butterworth or maximally flat response, and its transfer function (or power loss ratio) is commonly described as

$$|S_{21}(j\Omega)|^2 = \frac{1}{1 + \varepsilon^2(\Omega/\Omega_c)^{2n}} \tag{7}$$

where Ω_c is the cutoff frequency or the edge of the passband and n is the degree or the order of filter, which is also

the number of reactive elements required in the lowpass prototype filter. In (7), ε defines the insertion loss at the cutoff frequency $\Omega_c = 1$ and is commonly set equal to 1. Hence, the filter has an insertion loss of $L_{Ar} = 3.01$ dB at the cutoff frequency $\Omega_c = 1$. For $\Omega > \Omega_c$, the insertion loss increases indefinitely with frequency at a rate dependent on the exponent $2n$, as shown in Fig. 4.

3.2. The Chebyshev (or Equal-Ripple) Characteristic

The transfer function that describes this type of filter response is given by

$$|S_{21}(j\Omega)|^2 = \frac{1}{1 + \varepsilon^2 T_n^2(\Omega/\Omega_c)} \tag{8}$$

where $T_n(\Omega/\Omega_c)$ is a Chebyshev polynomial of the first kind of order n and is defined by

$$T_n(\Omega/\Omega_c) = \begin{cases} \cos(n \cos^{-1}(\Omega/\Omega_c)) & |(\Omega/\Omega_c)| \leq 1 \\ \cosh(n \cosh^{-1}(\Omega/\Omega_c)) & |(\Omega/\Omega_c)| \geq 1 \end{cases} \tag{9}$$

Insertion loss responses for Fifth- and Seventh-degree Chebyshev filters are illustrated in Fig. 5. If the passband response is allowed to have ripples between a minimum value and a maximum value and the maximally flat stopband response, then the filter realized using (8) will have a cutoff (or stopband slope) sharper than that of a corresponding Butterworth filter, because the Chebyshev polynomial $T_n(\Omega/\Omega_c)$ oscillates between ∓ 1 for $|\Omega/\Omega_c| \leq 1$, while it increases monotonically for $|\Omega/\Omega_c| \geq 1$. This means that the transfer function oscillates between 1 and $1/(1 + \varepsilon^2)$ in the passband and equals $(1 + \varepsilon^2)$ at cutoff frequency, and increases monotonically for $|\Omega/\Omega_c| \geq 1$. Thus, the ripple constant ε that defines the magnitude of the ripple in the passband is given by

$$\varepsilon = (10^{0.1L_{Ar}} - 1)^{1/2} \tag{10}$$

where the insertion loss L_{Ar} at cutoff frequency is measured in decibels.

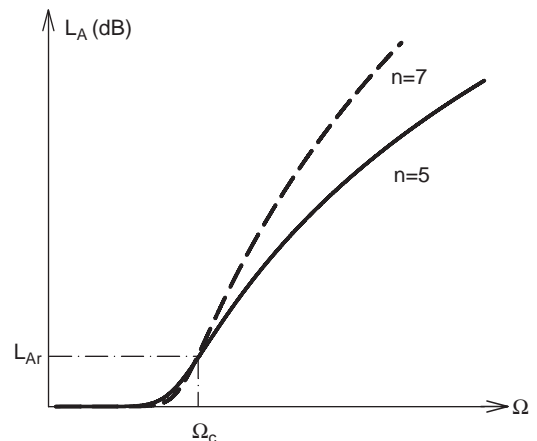


Figure 4. Butterworth (or maximally flat) filter characteristic of degrees 5 and 7.

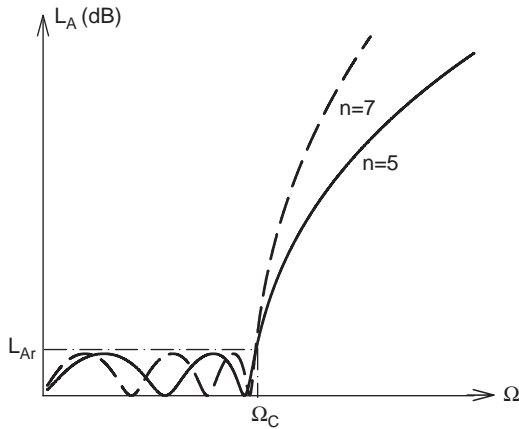


Figure 5. Chebyshev (or equal-ripple) filter characteristic of degrees 5 and 7.

3.3. The Elliptic Function Characteristic

The filter characteristic that can offer an equal-ripple response in both the passband and stopband is known as an *elliptic function response*. The transfer function for elliptic function filter is given by

$$|S_{21}(j\Omega)|^2 = \frac{1}{1 + \varepsilon^2 F_n^2(\Omega/\Omega_c)} \quad (11)$$

where the ripple constant ε is defined by

$$\varepsilon = (10^{0.1L_R} - 1)^{-1/2} \quad (12)$$

and L_R is the minimum return loss level in the passband and is given by

$$L_R = -20 \log |S_{11}| \text{ dB} \quad (13)$$

In (11), the filtering function F_n is an elliptic rational function and can be expressed in terms of its zeros and poles [5,14,15]

$$F_n(\Omega) = \begin{cases} F_0 \frac{\prod_{i=1}^{n/2} (\Omega^2 - \Omega_{z,i}^2)}{\prod_{i=1}^{n/2} (\Omega^2 - \Omega_{p,i}^2)} & \text{for } n \text{ even} \\ F_0 \frac{\Omega \prod_{i=1}^{(n-1)/2} (\Omega^2 - \Omega_{z,i}^2)}{\prod_{i=1}^{(n-1)/2} (\Omega^2 - \Omega_{p,i}^2)} & \text{for } n \text{ odd} \end{cases} \quad (14)$$

where $\Omega_{z,i}$ are the zeros of the elliptic rational function, $\Omega_{p,i}$ are the poles of the elliptic rational function, $\Omega_s > 1$ is frequency at which minimum stopband insertion loss L_{As} (in decibels) occurs, and the scaling constant F_0 that ensures $F_n(1) = 1$, which is described as

$$F_0 = \begin{cases} \frac{\prod_{i=1}^{n/2} (1 - \Omega_{p,i}^2)}{\prod_{i=1}^{n/2} (1 - \Omega_{z,i}^2)} & \text{for } n \text{ even} \\ \frac{\prod_{i=1}^{(n-1)/2} (1 - \Omega_{p,i}^2)}{\prod_{i=1}^{(n-1)/2} (1 - \Omega_{z,i}^2)} & \text{for } n \text{ odd} \end{cases} \quad (15)$$

It should be noted that the poles $\Omega_{p,i}$ are inversely proportional to the zeros $\Omega_{z,i}$ of the elliptic rational func-

tion $F_n(\Omega)$ and the relationship between them is described as

$$\Omega_{p,i} = \frac{\Omega_s}{\Omega_{z,i}} \quad (16)$$

A typical insertion loss response for an elliptic function filter is illustrated in Fig. 6. The elliptic filter provides a much steeper stopband slope for a given degree, and relatively small insertion losses as compared to Butterworth and Chebyshev filters.

3.4. The Generalized Chebyshev (or Pseudoelliptic) Characteristic

Generalized Chebyshev response or pseudoelliptic response is one of the responses used frequently for microwave filters. The responses of these types between the Chebyshev and elliptic function filter characteristics have a pair of transmission zeros at finite frequencies. The transfer function that describes this type of response is given by

$$|S_{21}(j\Omega)|^2 = \frac{1}{1 + \varepsilon^2 F_n^2(\Omega/\Omega_c)} \quad (17)$$

where the ripple constant ε is as given by (12) and the filtering function $F_n(\Omega)$ for the odd-degree generalized Chebyshev characteristic with three transmission zeros at infinity and the remainder at a finite frequency is given as [7]

$$F_n(\Omega) = \cosh \left\{ (n-3) \cosh^{-1} \left[\Omega \left(\frac{\Omega_z^2 - 1}{\Omega_z^2 - \Omega^2} \right)^{1/2} \right] + 3 \cosh^{-1}(\Omega) \right\} \quad (18)$$

where n is the degree of the filter and an odd number. It should be noted that $\Omega = \pm \Omega_z$ ($\Omega > 1$) are the frequency locations of a pair of transmission zeros, and when $\Omega_z \rightarrow \infty$, the filtering function $F_n(\Omega)$ converts to the ordinary Chebyshev filter function. A typical insertion loss response for a generalized Chebyshev filter is illustrated in Fig. 7, where Ω_c , Ω_s , Ω_z , and Ω_m , are the cutoff frequency, the frequency at which minimum stopband insertion loss L_{As} (in decibels) occurs (or the frequency of the stopband

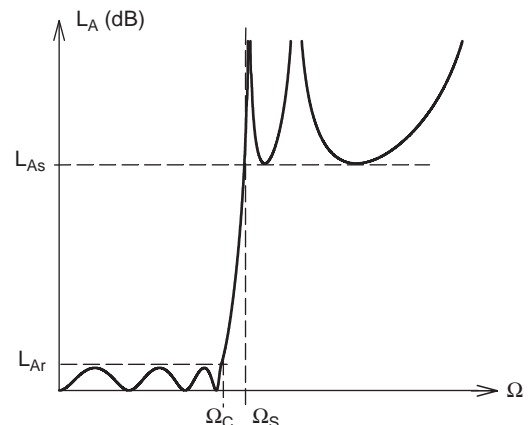


Figure 6. A typical elliptic function filter characteristic.

edge), the frequency of the transmission zero, and the frequency of the minimum insertion loss in the stopband, respectively.

3.5. The Maximally Flat Time-Delay Characteristic

Modern microwave communication systems require, especially in satellite and mobile communications, filters passing the desired signal with a minimum amount of distortion. This problem can be solved successfully when both the insertion loss and the group delay of the filter remains constant within the passband. The group delay will be constant if the transmission phase varies linearly with frequency. Thus, filters of this type are often called *maximally flat time-delay filters*.

For a maximally flat time-delay lowpass prototype filter with the cutoff frequency of $\Omega_c = 1$, the insertion loss is given as [16]

$$L_A(\Omega) = \frac{10\Omega^2}{(2n - 1) \ln 10} \text{ dB} \quad (19)$$

For $n \geq 3$, the 3 dB bandwidth is approximately given by

$$\Omega_{3\text{dB}} \approx \sqrt{(2n - 1) \ln 2} \quad (20)$$

As can be seen from this expression, the 3 dB bandwidth of a maximally flat time-delay filter is a function of the filter degree n only, and it widens as the degree is increased. In addition, the insertion loss responses of the maximally flat time-delay, Butterworth, and Chebyshev lowpass filters, which have identical topologies, are compared in Fig. 8. As can be seen, the insertion loss of the maximally flat time delay gradually increases outside the passband and its stopband rejection is not as good as those of the other two filters.

4. FILTER DESIGN USING THE INSERTION LOSS THEORY

This procedure of the filter design starts with deciding on filter specifications such as frequency range, bandwidth,

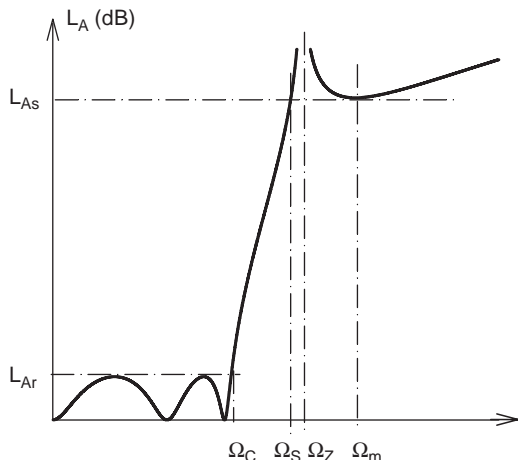


Figure 7. A typical generalized Chebyshev (or pseudoelliptic) filter characteristic.

insertion loss, stopband attenuation and frequencies, input and output impedances, VSWR (voltage standing-wave ratio), group delay, and phase linearity. This process is followed by synthesis of a suitable filter network. In this step, the lowpass prototype filter having desired filter characteristics such as Butterworth, Chebyshev, elliptic, pseudoelliptic, or maximally flat time-delay is designed. We shall investigate design of lowpass prototype filters using LC elements here, but the prototype networks can also be designed employing ideal impedance or admittance inverters that will be discussed later on. It should be mentioned that all filters that can be designed with impedance or admittance inverters are also designable employing LC prototype networks. In this article, therefore, only lowpass prototype filters utilizing LC elements will be discussed. For additional information on filter design using prototypes with inverters, the reader is referred to Refs. 13 and 16. The lowpass prototype filter is then transformed to the required type (lowpass, highpass, bandpass, or bandstop) filter with the specified center and/or edge frequencies. Finally, the filter network is realized in terms of lumped- and/or distributed-circuit elements. This filter design procedure is schematically illustrated in Fig. 9.

The design of microwave filters is based principally on transforming the lumped-element lowpass prototype filter network having desired filter characteristics into a physically realizable filter. Lowpass prototype filters are two-port lumped-element networks with an angular cutoff frequency of 1 rad/s and operating in a $1-\Omega$ system that have been synthesized to elicit a desired filter response. The elements of such a prototype filter are composed of inductors and capacitors of the ladder networks as illustrated in Fig. 10. The networks depict the two possible implementations of the lowpass prototype filter topologies providing the same power transfer function. Lowpass filters have characteristics such that they transmit all frequencies between zero frequency and some upper frequency limit (cutoff frequency ω_c) and attenuate all frequencies above the cutoff frequency. These prototype networks are all-pole networks with all their transmission zeros at infinity.

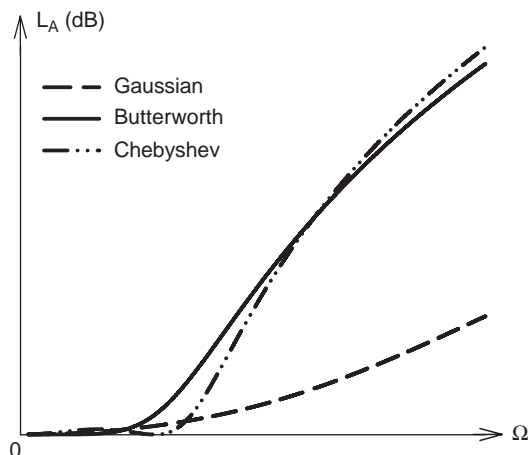


Figure 8. Comparison of characteristics of maximally flat time-delay filter, Butterworth filters, and Chebyshev lowpass filters.

In this section, only the equations and tables needed to determine the basic values of some lowpass prototype filters will be presented. It should be mentioned that the filter synthesis procedures will not be discussed here. (See the article titled FILTER SYNTHESIS.)

4.1. Butterworth (or Maximally Flat) Lowpass Prototype Filters

For Butterworth or maximally flat low-pass prototype filters with an insertion loss of 3.01 dB and at the cutoff frequency of $\Omega_c = 1$, the transfer function is given as

$$|S_{21}(j\Omega)|^2 = \frac{1}{1 + \Omega^{2n}} \quad (21)$$

The element values of such a prototype filter can be calculated using

$$g_0 = 1.0 :$$

$$g_k = 2 \sin\left(\frac{(2k-1)\pi}{2n}\right) \text{ for } k = 1, 2, 3, \dots, n \quad (22)$$

$$g_{n+1} = 1.0$$

The Butterworth filters considered here are always symmetric in network structure, namely, $g_0 = g_{n+1}$, $g_1 = g_n$, $g_2 = g_{n-1}$, and so on. For a normalized lowpass design where the source impedance and the cutoff frequency are 1Ω and $\Omega_c = 1$, respectively, the element values for the ladder-type circuits of Fig. 10 can be tabulated [16]. These circuits may be considered as the dual of each other, and either will offer the same response. For convenience, their element values g_n are given in Table 1 for filter degree n values up to 10, $\Omega_c = 1$ and $L = 3.01$ dB at cutoff frequency Ω_c .

On the other hand, a designer often needs to be able to select the number of elements in filter or the degree of filter to achieve a specified attenuation at the some frequency in the stopband. In such a case, the degree of a Butterworth lowpass prototype filter may be determined as

$$n \geq \frac{\log(10^{0.1L_{As}} - 1)}{2 \log \Omega_s} \quad (23)$$

where L_{As} is the minimum stopband attenuation at a frequency $\Omega = \Omega_s$ in the stopband. For example, if $L_{As} = 35$ dB and $\Omega_s = 1.9$, then $n \geq 6.278$, that is, a Butterworth prototype of degree 7 ($n = 7$) should be selected.

4.2. Chebyshev (or Equal-Ripple) Lowpass Prototype Filters

For a Chebyshev or equal-ripple lowpass prototype filter with a cutoff frequency of $\Omega_c = 1$, the transfer function is

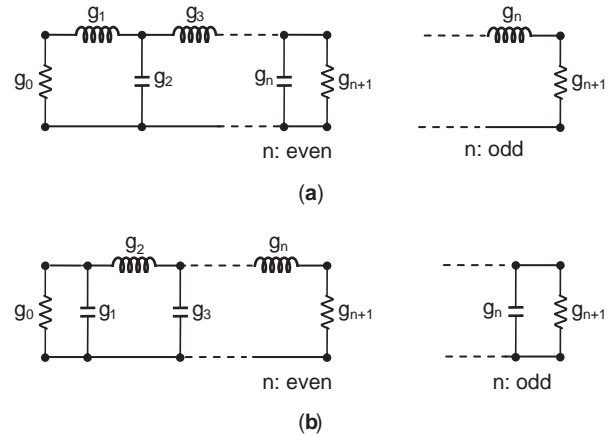


Figure 10. Lumped-element lowpass prototype networks for all-pole filters including Butterworth, Chebyshev, and maximally flat time-delay responses with (a) a ladder network structure and (b) its dual.

given as

$$|S_{21}(j\Omega)|^2 = \frac{1}{1 + \varepsilon^2 T_n^2(\Omega)} \quad (24)$$

The element values of the prototype filters shown in Fig. 10 may be computed using the formulas

$$g_0 = 1.0 \quad (25a)$$

$$g_1 = \frac{2a_1}{\gamma} \quad (25b)$$

$$g_k = \frac{4a_{k-1}a_k}{b_{k-1}g_{k-1}} \text{ for } k = 2, 3, \dots, n \quad (25c)$$

$$g_{n+1} = \begin{cases} 1.0 & \text{for } n \text{ odd} \\ \coth^2(\beta/4) & \text{for } n \text{ even} \end{cases} \quad (25d)$$

with

$$a_k = \sin\left(\frac{(2k-1)\pi}{2n}\right) \text{ for } k = 1, 2, 3, \dots, n \quad (26a)$$

$$b_k = \gamma^2 + \sin^2\left(\frac{k\pi}{n}\right) \text{ for } k = 1, 2, 3, \dots, n \quad (26b)$$

$$\gamma = \sinh\left(\frac{\beta}{2n}\right) \quad (26c)$$

$$\beta = \ln\left[\coth\left(\frac{L_{Ar}}{17.37}\right)\right] \quad (26d)$$

where L_{Ar} is the passband ripple in decibels. Some element values for Chebyshev lowpass prototype filters with a normalized source impedance 1Ω and cutoff frequency $\Omega_c = 1$ for various L_{Ar} and $n = 1-10$ are listed in Table 2 [16].

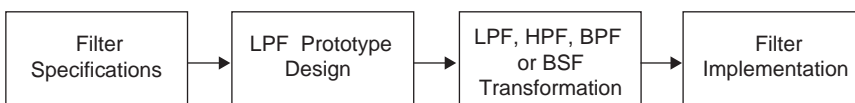


Figure 9. Filter design procedure.

Table 1. Element Values for Butterworth or Maximally Flat Response Prototype Filter ($g_0 = 1.0, \Omega_c = 1, L_{Ar} = 3.01$ dB at Ω_c)

n	g_1	g_2	g_3	g_4	g_5	g_6	g_7	g_8	g_9	g_{10}	g_{11}
1	2.0000	1.0									
2	1.4142	1.4142	1.0								
3	1.0000	2.0000	1.0000	1.0							
4	0.7654	1.8478	1.8478	0.7654	1.0						
5	0.6180	1.6180	2.0000	1.6180	0.6180	1.0					
6	0.5176	1.4142	1.9318	1.9318	1.4142	0.5176	1.0				
7	0.4450	1.2470	1.8019	2.0000	1.8019	1.2470	0.4450	1.0			
8	0.3902	1.1111	1.6629	1.9616	1.9616	1.6629	1.1111	0.3902	1.0		
9	0.3473	1.0000	1.5321	1.8794	2.0000	1.8794	1.5321	1.0000	0.3473	1.0	
10	0.3129	0.9080	1.4142	1.7820	1.9754	1.9754	1.7820	1.4142	0.9080	0.3129	1.0

The degree of a Chebyshev lowpass prototype filter may be determined by

$$n \geq \frac{\cosh^{-1} \left(\frac{10^{0.1L_{As}} - 1}{10^{0.1L_{Ar}} - 1} \right)^{1/2}}{\cosh^{-1} \Omega_s} \tag{27}$$

where L_{Ar} is the passband ripple and L_{As} is the minimum stopband attenuation at $\Omega = \Omega_s$. Again, when the filter specifications stipulate $L_{As} = 35$ dB, $L_{Ar} = 0.1$ dB, and $\Omega_s = 1.9$, then $n \geq 5.252$, that is, a Chebyshev prototype of degree 6 ($n = 6$) should be selected to meet this specification.

Since this example is the same as the example given above for the Butterworth prototype, the Chebyshev design has a better frequency characteristic than the Butterworth design, and at microwave frequencies, the Former design is preferred over the latter design.

Moreover, for given minimum return loss L_R or maximum voltage standing-wave ratio (VSWR) in the passband, the corresponding passband ripple L_{Ar} may be calculated as

$$L_{Ar} = -10 \log(1 - 10^{0.1L_R}) \text{ dB} \tag{28}$$

Table 2. Element Values for Chebyshev Prototype Filters ($g_0 = 1.0, \Omega_c = 1$)

n	g_1	g_2	g_3	g_4	g_5	g_6	g_7	g_8	g_9	g_{10}	g_{11}
<i>0.01 dB Ripple</i>											
1	0.0960	1.0									
2	0.4488	0.4077	1.1007								
3	0.6291	0.9702	0.6291	1.0							
4	0.7128	1.2003	1.3212	0.6476	1.1007						
5	0.7563	1.3049	1.5773	1.3049	0.7563	1.0					
6	0.7813	1.3600	1.6896	1.5350	1.4970	0.7098	1.1007				
7	0.7969	1.3924	1.7481	1.6331	1.7481	1.3924	0.7969	1.0			
8	0.8072	1.4130	1.7824	1.6833	1.8529	1.6193	1.5554	0.7333	1.1007		
9	0.8144	1.4270	1.8043	1.7125	1.9057	1.7125	1.8043	1.4270	0.8144	1.0	
10	0.8196	1.4369	1.8192	1.7311	1.9362	1.7590	1.9055	1.6527	1.5817	0.7446	1.1007
<i>0.1 dB Ripple</i>											
1	0.3052	1.0									
2	0.8430	0.6220	1.3554								
3	1.0315	1.1474	1.0315	1.0							
4	1.1088	1.3061	1.7703	0.8180	1.3554						
5	1.1468	1.3712	1.9750	1.3712	1.1468	1.0					
6	1.1681	1.4039	2.0562	1.5170	1.9029	0.8618	1.3554				
7	1.1811	1.4228	2.0966	1.5733	2.0966	1.4228	1.1811	1.0			
8	1.1897	1.4346	2.1199	1.6010	2.1699	1.5640	1.9444	0.8778	1.3554		
9	1.1956	1.4425	2.1345	1.6167	2.2053	1.6167	2.1345	1.4425	1.1956	1.0	
10	1.1999	1.4481	2.1444	1.6265	2.2253	1.6418	2.2046	1.5821	1.9628	0.8853	1.3554
<i>0.5 dB Ripple</i>											
1	0.6986	1.0									
2	1.4029	0.7071	1.9841								
3	1.5963	1.0967	1.5963	1.0							
4	1.6703	1.1926	2.3661	0.8419	1.9841						
5	1.7058	1.2296	2.5408	1.2296	1.7058	1.0					
6	1.7254	1.2479	2.6064	1.3137	2.4758	0.8696	1.9841				
7	1.7372	1.2583	2.6381	1.3444	2.6381	1.2583	1.7372	1.0			
8	1.7451	1.2647	2.6564	1.3590	2.6964	1.3389	2.5093	0.8796	1.9841		
9	1.7504	1.2690	2.6678	1.3673	2.7239	1.3673	2.6678	1.2690	1.7504	1.0	
10	1.7543	1.2721	2.6754	1.3725	2.7392	1.3806	2.7231	1.3485	2.5239	0.8842	1.9841

or

$$L_{Ar} = -10 \log \left[1 - \left(\frac{VSWR - 1}{VSWR + 1} \right)^2 \right] \text{ dB} \quad (29)$$

where $L_R < 0$ (in decibels) is the minimum return loss given by (13), and VSWR is

$$VSWR = \frac{1 + |S_{11}|}{1 - |S_{11}|} \quad (30)$$

4.3. Elliptic Function Lowpass Prototype Filters

If frequency selectivity and passband loss are considered to be the significant filtering features, the elliptic function filters exhibiting equal-ripple response in both passband and stopband are optimum filters. Lumped-element lowpass elliptic function prototype filters are shown in Fig. 11. For the lowpass prototype filter shown in Fig. 11a, the transmission zeros (or attenuation poles) at finite frequencies in the stopband are produced by the parallel-resonant circuits in the series branches since this resonant circuit is open-circuited at resonance, while the transmission zeros (or attenuation poles) at finite frequencies for the prototype network in Fig. 11b are produced by the series-resonant circuits in the shunt branches since this resonant circuit is short-circuited at resonance.

Unlike the simple method of computing element values for the Butterworth and Chebyshev lowpass prototype filters described above, there are no simple methods for computing element values of the elliptic lowpass prototype filter, but the low-pass prototype element values derived by synthesis [17] have been published for a wide range of passband and, stopband ripple values, and a number of branches. However, the element values for some useful cases are presented in Table 3 [13] for a passband ripple $L_{Ar} = 0.1$ dB, a cutoff $\Omega_c = 1$, various minimum stopband insertion loss L_{As} , and frequency Ω_s at which minimum stopband insertion loss L_{As} occurs. More extensive tables for element values of elliptic filters were offered by Saal and Ulbrich [6].

For an elliptic function lowpass prototype filter with a cutoff frequency of $\Omega_c = 1$, the transfer function is given as

$$|S_{21}(j\Omega)|^2 = \frac{1}{1 + \varepsilon^2 F_n^2(\Omega)} \quad (31)$$

where the filtering function is as given by Eqs. (14) and (15).

The degree equation for an elliptic lowpass prototype filter may be written as

$$n \geq \frac{K(k_s) K(k'_0)}{K(k'_s) K(k_0)} \quad (32)$$

where $K(k)$ is the complete elliptic integral of the first kind, given by

$$\frac{K(k)}{K(k')} = \begin{cases} \frac{1}{\pi} \ln \left(2 \frac{1+k^{1/2}}{1-k^{1/2}} \right) & 0.707 \leq k \leq 1.0 \\ \frac{1}{\pi} \ln \left(2 \frac{1+(k')^{1/2}}{1-(k')^{1/2}} \right)^{-1} & 0 \leq k \leq 0.707 \end{cases} \quad (33)$$

The arguments of the complete elliptic integral of the first kind k_s, k'_s, k_0, k'_0 , are described as

$$k_s = \frac{1}{\Omega_s}, \quad k'_s = (1 - k_s^2)^{1/2} \quad (34)$$

$$k_0 = \varepsilon(10^{0.1L_{As}} - 1)^{-1/2}, \quad k'_0 = (1 - k_0^2)^{1/2} \quad (35)$$

where L_{As} is the minimum stopband attenuation at $\Omega = \Omega_s$. If $L_{As} = 35$ dB and $\Omega_s = 1.9$, then $n \geq 3.957$, namely, an elliptic function prototype network of degree 4 ($n = 4$), should be selected to meet this specification.

4.4. Generalized Chebyshev (or Pseudoelliptic) Lowpass Prototype Filters

The generalized Chebyshev filters have finite-frequency transmission zeros at a single frequency (just outside the edge of the passband) rather than being distributed freely throughout the stopband. When attempting to realize the elliptic function lowpass prototype filter, the impedance variation in the filters becomes large, and this impedance variation leads to problems for printed circuit implementation such as microstrip. The generalized Chebyshev fil-

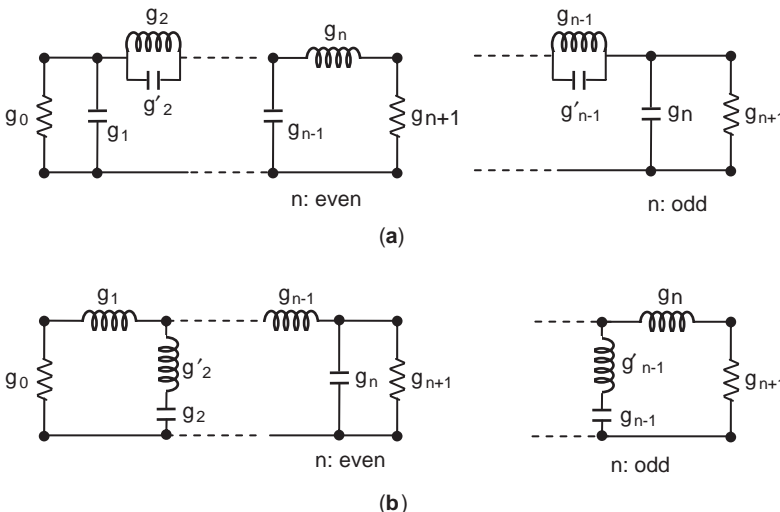


Figure 11. Lumped-element lowpass prototype filters for elliptic function response with (a) series-parallel-resonant branches and (b) its dual with shunt series-resonant branches.

Table 3. Element Values for Lumped-Element Elliptic Function Lowpass Prototype Filters ($g_0 = g_{n+1} = 1, \Omega_c = 1, L_{Ar} = 0.1$ dB)

n	Ω_s	L_{As} (dB)	g_1	g_2	g'_2	g_3	g_4	g'_4	g_5	g_6	g'_6	g_7
3	1.4493	13.5698	0.7427	0.7096	0.5412	0.7427						
	1.6949	18.8571	0.8333	0.8439	0.3252	0.8333						
	2.0000	24.0012	0.8949	0.9375	0.2070	0.8949						
	2.5000	30.5161	0.9471	1.0173	0.1205	0.9471						
4	1.2000	12.0856	0.3714	0.5664	1.0929	1.1194	0.9244					
	1.2425	14.1259	0.4282	0.6437	0.8902	1.1445	0.9289					
	1.2977	16.5343	0.4877	0.7284	0.7155	1.1728	0.9322					
	1.3962	20.3012	0.5675	0.8467	0.5261	1.2138	0.9345					
	1.5000	23.7378	0.6282	0.9401	0.4073	1.2471	0.9352					
	1.7090	29.5343	0.7094	1.0688	0.2730	1.2943	0.9348					
	2.0000	36.0438	0.7755	1.1765	0.1796	1.3347	0.9352					
5	1.0500	13.8785	0.7081	0.7663	0.7357	1.1276	0.2014	4.3812	0.0499			
	1.1000	20.0291	0.8130	0.9242	0.4934	1.2245	0.3719	2.1350	0.2913			
	1.1494	24.5451	0.8726	1.0084	0.3845	1.3097	0.4991	1.4450	0.4302			
	1.2000	28.3031	0.9144	1.0652	0.3163	1.3820	0.6013	1.0933	0.5297			
	1.2500	31.4911	0.9448	1.1060	0.2694	1.4415	0.6829	0.8827	0.6040			
	1.2987	34.2484	0.9681	1.1366	0.2352	1.4904	0.7489	0.7426	0.6615			
	1.4085	39.5947	1.0058	1.1862	0.1816	1.5771	0.8638	0.5436	0.7578			
	1.6129	47.5698	1.0481	1.2416	0.1244	1.6843	1.0031	0.3540	0.8692			
	1.8182	54.0215	1.0730	1.2741	0.0919	1.7522	1.0903	0.2550	0.9367			
	2.0000	58.9117	1.0876	1.2932	0.0732	1.7939	1.1433	0.2004	0.9772			
6	1.0500	18.6757	0.4418	0.7165	0.9091	0.8314	0.3627	2.4468	0.8046	0.9986		
	1.1000	26.2370	0.5763	0.8880	0.6128	0.9730	0.5906	1.3567	0.9431	1.0138		
	1.1580	32.4132	0.6549	1.0036	0.4597	1.0923	0.7731	0.9284	1.0406	1.0214		
	1.2503	39.9773	0.7422	1.1189	0.3313	1.2276	0.9746	0.6260	1.1413	1.0273		
	1.3024	43.4113	0.7751	1.1631	0.2870	1.2832	1.0565	0.5315	1.1809	1.0293		
	1.3955	48.9251	0.8289	1.2243	0.2294	1.3634	1.1739	0.4148	1.2366	1.0316		
	1.5962	58.4199	0.8821	1.3085	0.1565	1.4792	1.3421	0.2757	1.3148	1.0342		
	1.7032	62.7525	0.9115	1.3383	0.1321	1.5216	1.4036	0.2310	1.3429	1.0350		
	1.7927	66.0190	0.9258	1.3583	0.1162	1.5505	1.4453	0.2022	1.3619	1.0355		
	1.8915	69.3063	0.9316	1.3765	0.1019	1.5771	1.4837	0.1767	1.3794	1.0358		
7	1.0500	30.5062	0.9194	1.0766	0.3422	1.0962	0.4052	2.2085	0.8434	0.5034	2.2085	0.4110
	1.1000	39.3517	0.9882	1.1673	0.2437	1.2774	0.5972	1.3568	1.0403	0.6788	1.3568	0.5828
	1.1494	45.6916	1.0252	1.2157	0.1940	1.5811	0.9939	0.5816	1.2382	0.5243	0.5816	0.4369
	1.2500	55.4327	1.0683	1.2724	0.1382	1.7059	1.1340	0.4093	1.4104	0.7127	0.4093	0.6164
	1.2987	59.2932	1.0818	1.2902	0.1211	1.7478	1.1805	0.3578	1.4738	0.7804	0.3578	0.6759
	1.4085	66.7795	1.1034	1.3189	0.0940	1.8177	1.2583	0.2770	1.5856	0.8983	0.2770	0.7755
	1.5000	72.1183	1.1159	1.3355	0.0786	1.7569	1.1517	0.3716	1.6383	1.1250	0.3716	0.9559
	1.6129	77.9449	1.1272	1.3506	0.0647	1.8985	1.3485	0.1903	1.7235	1.0417	0.1903	0.8913
	1.6949	81.7567	1.1336	1.3590	0.0570	1.9206	1.3734	0.1675	1.7628	1.0823	0.1675	0.9231
	1.8182	86.9778	1.1411	1.3690	0.0479	1.9472	1.4033	0.1408	1.8107	1.1316	0.1408	0.9616

ter has the advantage of leading to a more suitable range of impedance levels in the filters. Lumped-element lowpass prototype filter networks are shown in Fig. 12. For the prototype filter networks of degrees 5, 7, 9, and 11, the element values for $RL \geq 20$ dB and $RL \geq 26$ dB when $g_0 = 1, \Omega_c = 1$ and $L_{As} \geq 40$ dB are presented in Table 4 [7]. The table also contains the values of Ω_z and Ω_s .

Moreover, apart from the LC prototype networks shown in Fig. 12, a generalized Chebyshev prototype filter using inverters is introduced in Refs. 13 and 18 for any filter degree. However, since we have considered only the LC prototype filter networks, such a network will not be discussed here. For information on the design and characteristics of generalized Chebyshev prototype filters

employing inverters, the reader is referred to Chapt. 10 of Ref. 13 and to Ref. 18.

4.5. Maximally Flat Time-Delay Lowpass Prototype Filters

Lowpass prototype filters for all-pole filters with a ladder network structure as illustrated in Fig. 10 can serve as maximally flat time-delay lowpass prototype filters because these are also all-pole filters. The lowpass prototype element values for filters of this type are often derived by network synthesis. However, for convenience, some element values are provided in Table 5 [11,16]. It should be noted that the first-degree maximally flat time-delay low-

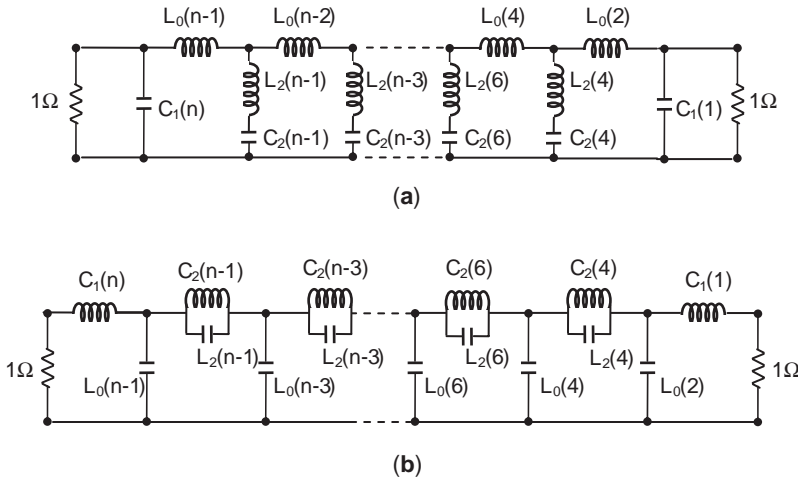


Figure 12. Lumped-element lowpass prototype filters for generalized Chebyshev response with (a) with shunt series-resonant branches and (b) its dual with series-parallel-resonant branches.

pass prototype filter is identical to the first-degree Butterworth lowpass prototype filter.

5. IMPEDANCE AND FREQUENCY SCALING

Lowpass prototype filters are not practical for most applications because they have cutoff frequencies of 1 rad/s and 1 Ω source and load terminations. Therefore, to obtain a practical filter response such as lowpass, highpass, bandpass, and bandstop, these prototypes can be scaled in terms of impedance and frequency.

As mentioned above, the source and load terminations of the prototype network are 1 Ω, except for Chebyshev filters with even n , which have load impedance different from 1 Ω. Therefore, the prototype filter reactances can be considered as normalized by the source impedance Z_0 . The $g_0 = 1$ normalization can be removed by multiplying the impedances of the prototype network by the source impedance Z_0 . Thus, if the component values of the prototype design are represented by g_n , and Z_{PL} , then the new filter

component element values can be obtained as

$$L = Z_0 g_n \quad (\text{for series inductors}) \quad (36)$$

$$C = \frac{g_n}{Z_0} \quad (\text{for shunt capacitors}) \quad (37)$$

$$Z_s = Z_0 \quad (38)$$

$$Z_L = Z_0 Z_{PL} \quad (39)$$

The impedance scaling process has no effect on the filter response.

5.1. Frequency Scaling for Lowpass Filters

To transform the cutoff frequency of a lowpass prototype filter from $\Omega_c = 1$ to ω_c , we can choose a frequency transformation as

$$\Omega = \frac{\omega}{\omega_c} \quad (40)$$

Table 4. Element Values for Generalized Chebyshev Prototype Filters ($g_0 = 1.0$, $\Omega_c = 1$, $L_{As} \geq 40$ dB)

	$RL \geq 20$ dB				$RL \geq 26$ dB			
	Element Number n				Element Number n			
	11	9	7	5	11	9	7	5
Ω_z	1.08873	1.14922	1.29516	1.78780	1.11580	1.19397	1.38122	2.01033
Ω_s	1.03927	1.08480	1.21229	1.69345	1.05564	1.11696	1.28362	1.90012
$L_2(10)$	1.395820				1.360350			
$L_0(10)$	0.840267				0.804735			
$C_2(8)$	0.805350	0.8135680				0.837434	0.799104	
$L_2(8)$	1.047550	0.9306790			0.959128	0.877829		
$L_0(8)$	0.661279	0.9474160			0.755266	0.928279		
$C_2(6)$	0.805350	0.9814700	1.100060		0.837434	1.000880	1.063870	
$L_2(6)$	1.047550	0.7714660	0.541922		0.959128	0.700860	0.492702	
$L_0(6)$	0.672323	0.8009000	1.080270		0.774110	0.898068	1.067530	
$C_2(4)$	0.604410	0.8135680	1.100060	1.374990	0.590439	0.799104	1.063870	1.257590
$L_2(4)$	1.395820	0.9300679	0.541922	0.227543	1.360350	0.877829	0.492702	0.196755
$L_0(4)$	0.661279	0.8009000	0.984147	1.206800	0.755266	0.898068	1.066170	1.170448
$L_0(2)$	0.840267	0.9474160	1.080270	1.206800	0.804735	0.928279	1.067530	1.170480
$C_1(1), C_1(n)$	1.044280	1.0396900	1.026470	0.985022	0.846644	0.840714	0.824706	0.778435

Table 5. Element Values for Maximally Flat Time-Delay Prototype Filters ($g_0 = 1.0, \Omega_c = 1$)

n	g_1	g_2	g_3	g_4	g_5	g_6	g_7	g_8	g_9	g_{10}	g_{11}
1	2.0000	1.0000									
2	1.5774	0.4226	1.0000								
3	1.2550	0.5528		1.0000							
4	1.0598	0.5116	0.3181	0.1104	1.0000						
5	0.9303	0.4577	0.3312	0.2090	0.0718	1.0000					
6	0.8377	0.4116	0.3158	0.2364	0.1480	0.0505	1.0000				
7	0.7677	0.3744	0.2944	0.2378	0.1778	0.1104	0.0375	1.0000			
8	0.7125	0.3446	0.2735	0.2297	0.1867	0.1387	0.0855	0.0289	1.0000		
9	0.6678	0.3203	0.2547	0.2184	0.1859	0.1506	0.1111	0.0682	0.0230	1.0000	
10	0.6305	0.3002	0.2384	0.2066	0.1808	0.1539	0.1240	0.0911	0.0557	0.0187	1.0000

where the angular frequency ω_c is the new cutoff frequency and cutoff occurs when the operation frequency ω is equal to the cutoff frequency ω_c . If we use the frequency transformation given by (40) together with the impedance scaling expressions in (36)–(39), the new component values are obtained as

$$L_n = \frac{Z_0 g_n}{\omega_c} \quad (\text{for series inductors}) \quad (41)$$

$$C_n = \frac{g_n}{Z_0 \omega_c} \quad (\text{for shunt capacitors}) \quad (42)$$

5.1.1. Lowpass-to-Highpass Transformation. To transform a lowpass filter response into a highpass filter response, the frequency transformation is given by

$$\Omega = -\frac{\omega_c}{\omega} \quad (43)$$

If this transformation is applied to the elements of a lowpass prototype network, then, as a result of the negative sign, the inductors and capacitors of the prototype network convert to a capacitors and inductors in the highpass filter, respectively. With impedance transformation, the new element values are obtained as

$$C_n = \frac{1}{Z_0 \omega_c g_n} \quad (\text{for series capacitors}) \quad (44)$$

$$L_n = \frac{Z_0}{\omega_c g_n} \quad (\text{for shunt inductors}) \quad (45)$$

5.1.2. Lowpass-to-Bandpass Transformation. If the angular frequencies ω_1 and ω_2 indicate the edges of the passband, then a practical bandpass response may be found using a frequency transformation as

$$\Omega = \frac{1}{\text{FBW}} \left(\frac{\omega}{\omega_0} - \frac{\omega_0}{\omega} \right) \quad (46)$$

where the fractional bandwidth of the passband FBW and the center frequency ω_0 are, respectively

$$\text{FBW} = \frac{\omega_2 - \omega_1}{\omega_0} \quad (47)$$

$$\omega_0 = \sqrt{\omega_1 \omega_2} \quad (48)$$

The practical bandpass filter elements can be obtained by applying the frequency transformation given in (46) to the lowpass prototype filter elements. In this case, a series inductive element g_n in the prototype network is transformed to a series-connected series-resonant circuit in a practical bandpass filter, while a shunt capacitive element g_n in the prototype network is transformed to a shunt-connected parallel-resonant circuit. Thus, the new elements for the series-connected series-resonant circuit in the bandpass filter and the shunt-connected parallel-resonant circuit in the bandpass filter are, respectively

$$L_{sn} = \frac{Z_0 g_n}{\omega_0 \text{FBW}} \quad (\text{for series inductor in lowpass prototype})$$

$$C_{sn} = \frac{\text{FBW}}{\omega_0 Z_0 g_n} \quad (49)$$

and

$$C_{pn} = \frac{g_n}{Z_0 \omega_0 \text{FBW}} \quad (\text{for shunt capacitor in lowpass prototype})$$

$$L_{pn} = \frac{Z_0 \text{FBW}}{\omega_0 g_n} \quad (50)$$

Since both series- and parallel-resonant circuits have a resonant frequency of ω_0 , the resonant frequency ω_0 is $\omega_0^2 = 1/L_{sn}C_{sn}$ and $\omega_0^2 = 1/L_{pn}C_{pn}$.

5.1.3. Lowpass-to-Bandstop Transformation. A practical bandstop response may be found using a frequency transformation as

$$\Omega = \frac{\text{FBW}}{(\omega_0/\omega - \omega/\omega_0)} \quad (51)$$

where FBW and ω_0 are as given in (47) and (48), respectively. It should be noted that this transformation is opposite to the bandpass transformation described above. In the case of (51), the series inductors of the lowpass prototype filter are, respectively, transformed to series-connected

parallel-resonant circuits using

$$L_{pn} = \frac{g_n Z_0 \text{FBW}}{\omega_0}$$

(for series inductor in lowpass prototype)

$$C_{pn} = \frac{1}{Z_0 g_n \omega_0 \text{FBW}} \tag{52}$$

and shunt capacitors to shunt-connected series-resonant circuits using

$$L_{sn} = \frac{Z_0}{g_n \omega_0 \text{FBW}}$$

(for shunt capacitor in lowpass prototype)

$$C_{sn} = \frac{g_n \text{FBW}}{\omega_0 Z_0} \tag{53}$$

Again, since both series- and parallel-resonant circuits have a resonant frequency of ω_0 , the resonant frequency ω_0 is $\omega_0^2 = 1/L_{sn}C_{sn}$ and $\omega_0^2 = 1/L_{pn}C_{pn}$. All the transformations from lowpass prototype filters to other types of filters are summarized in Table 6.

6. FILTER REALIZATION

Distributed filters, including combline, interdigital, hair-pin-line, parallel-coupled-line, stepped-impedance, loop, and patch filters can be realized in a variety of media such as waveguide, coaxial lines, dielectric resonators, microstrip, stripline, and suspended substrate depending on the desired application. The transformation of lumped elements to transmission-line sections can be realized in

terms of Richards' transformation [19], while Kuroda's transformations or identities [20,21] can be employed to physically separate filter elements, to convert series elements into parallel elements or vice versa, and to change impractical elements into more realizable elements in a filter network. In addition, to convert a filter network composed of both series elements and parallel elements into one that contains either only series-resonant elements or only parallel-resonant elements, impedance or admittance inverters are especially useful, particularly for bandpass or bandstop having narrow (<10%) bandwidths.

6.1. Richards' Transformation

Richards' frequency transformation is defined as

$$S = j\Omega = j \tan \beta\ell = j \tan \frac{\omega\ell}{v_p} = j \tan \frac{\pi\omega}{2\omega_0} \tag{54}$$

where Ω is the distributed frequency variable, β is the phase constant, ℓ is transmission-line length, ω is the usual angular frequency, v_p is the phase velocity independent of frequency, and ω_0 is the angular frequency at which the lengths of all transmission lines are a quarter-wavelength long (or $\beta\ell = \pi/2$). This transformation maps the ω plane to the Ω plane. As the frequency ω changes from 0 to ω_0 , the new variable Ω changes from 0 to ∞ . Therefore, by applying Richards' transformation of (54), the entire frequency response of a lumped-element prototype is reproduced over a finite portion of the frequency band. Responses of a typical lumped-element filter and a corresponding transmission-line filter are illustrated in Fig. 13. Note that the response of a transmission-line filter repeats with a period of $2\omega_0$, which is due to repeated increments of $\lambda/2$ in the electrical length of the transmission-line sections. Under Richards' transformation, there is a

Table 6. Transformation Relations

Lowpass Prototype	Lowpass Filter	Highpass Filter	Bandpass Filter	Bandstop Filter
	 $L_n = Z_0 g_n / \omega_c$	 $C_n = 1 / Z_0 \omega_c g_n$	 $L_{sn} = Z_0 g_n / \omega_0 \text{FBW}$ $C_{sn} = \text{FBW} / \omega_0 Z_0 g_n$	 $L_{pn} = g_n Z_0 \text{FBW} / \omega_0$ $C_{pn} = 1 / Z_0 g_n \omega_0 \text{FBW}$ $\omega_0^2 = 1 / L_{pn} C_{pn}$
	 $C_n = g_n / Z_0 \omega_c$	 $L_n = Z_0 / \omega_c g_n$	 $C_{pn} = g_n / Z_0 \omega_0 \text{FBW}$ $L_{pn} = Z_0 < \text{FBW} / \omega_0 g_n$	 $L_{sn} = Z_0 / g_n \omega_0 \text{FBW}$ $C_{sn} = g_n \text{FBW} / \omega_0 Z_0$ $\omega_0^2 = 1 / L_{sn} C_{sn}$
$\text{FBW} = \frac{\omega_2 - \omega_1}{\omega_0}, \quad \omega_0 = \sqrt{\omega_1 \omega_2}$				

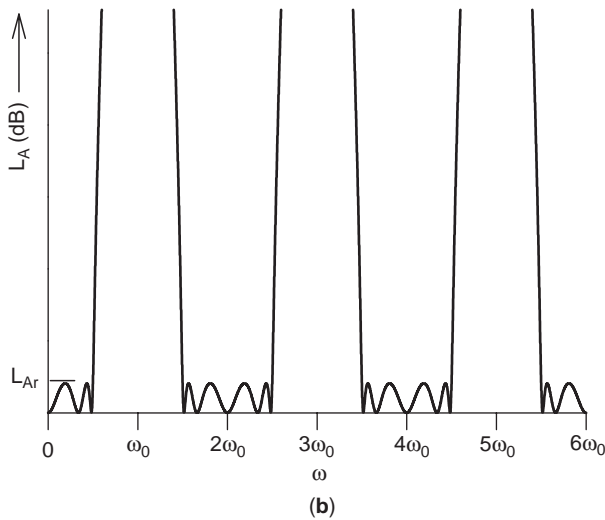
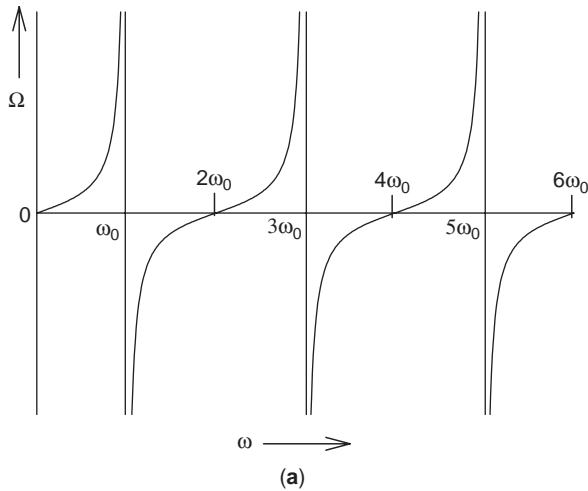


Figure 13. (a) Richards' transformation (b) Chebyshev lowpass filter characteristic using the Richards transformation.

relation between the lumped elements and the quarter-wave lines. The input impedance of short-circuited transmission line is

$$Z = jZ_0 \tan \beta \ell = jZ_0 \tan \left(\frac{\pi \omega}{2\omega_0} \right) = j\Omega Z_0 \quad (55)$$

where Z_0 is the characteristic impedance of the line and the length ℓ is $\lambda/4$ at ω_0 . Similarly, the input admittance of an open-circuited line is

$$Y = jY_0 \tan \left(\frac{\pi \omega}{2\omega_0} \right) = j\Omega Y_0 \quad (56)$$

where $Y_0 = 1/Z_0$ is the characteristic admittance of the line. According to Eqs. (55) and (56), since the impedance of a lumped inductor and the admittance of a lumped capacitor are, respectively, $j\omega L$ and $j\omega C$, a lumped inductor corresponds to a short-circuited line of $\lambda/4$ at ω_0 with an input impedance $Z = j\Omega Z_0$, while a lumped capacitor corresponds to an open-circuited line of $\lambda/4$ at ω_0 with an input admittance $Y = j\Omega Y_0$. These equivalences are illustrated in Fig. 14. In addition, note that the lumped resis-

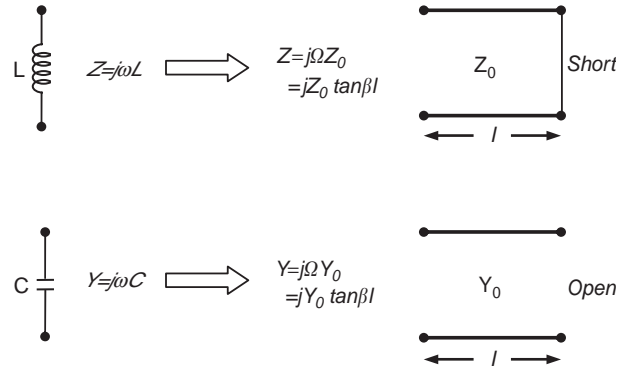


Figure 14. Correspondence between short-circuited and open-circuited transmission-line sections and lumped elements.

tors are unaffected by Richards' transformation because they are independent of frequency. As a result, Richards' transformation can be utilized for realizing transmission-line filters consisting of commensurate (equal electrical length) transmission-line sections.

6.2. Kuroda's Transformations (or Identities)

Since the realization of series-connected stubs in transmission-line filters leads to complexity, certain network equivalences without compromising filter performance may be desirable to realize filter networks. Such network equivalences are known as *Kuroda's transformations* or *identities* [20,21]. Kuroda's transformations have properties such as effecting physical separation between stubs, mapping series stubs into parallel stubs or vice versa, and changing impractical elements into more realizable elements in a filter network. Four network equivalences known as *Kuroda's transformations of the first and second kinds* are illustrated in Fig. 15, where the commensurate line sections having the same electrical length $\theta = \beta \ell$ are assumed for each identity. Kuroda's transformations, as well as the unit element, were also discussed in Ref. 22. The unit element labeled "UE" in Fig. 15 is simply a lossless transmission-line section with characteristic impedance Z_0 , and its length is a quarter-wavelength at frequency ω_0 . Levy [21] has generalized the Kuroda transformations to include any two-port network and unit element.

6.3. Impedance and Admittance Inverters

At microwave frequencies, it is desirable to convert a filter network composed of both series- and parallel-resonant elements into one that contains only one type of these elements. This can be achieved by using impedance and admittance inverters. Impedance inverters are also known as *K inverters* and admittance inverters, as *J inverters*. Ideal *K* and *J* inverters are defined in Fig. 16, where *K* (*J*) is real and is the characteristic impedance (admittance) of the inverter. These inverters have a phase shift of $\pm 90^\circ$ [16,23].

Briefly, lowpass filters can be implemented by employing only one sort of reactance, while bandpass filters can be implemented by employing series (parallel) *LC* series

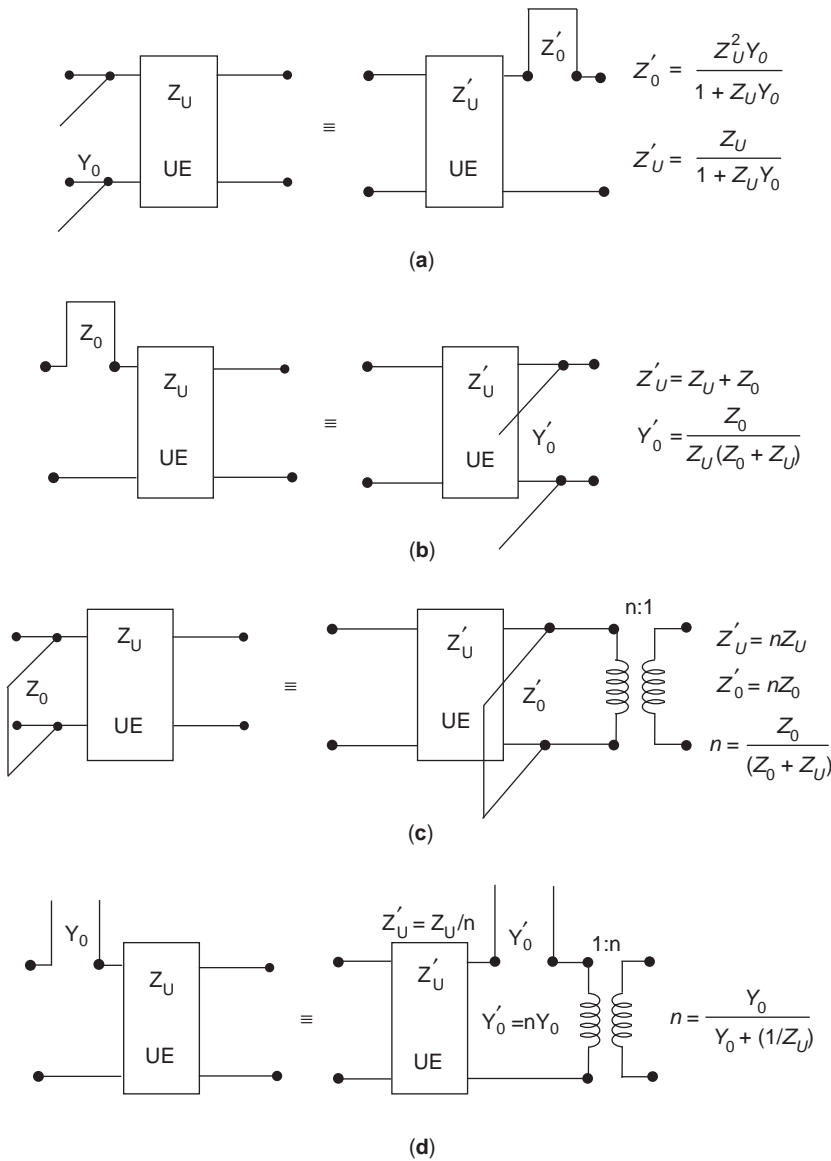


Figure 15. (a,b) Kuroda's transformations of the first kind; (c,d) Kuroda's transformations of the second kind.

(shunt) resonant circuits separated by impedance (admittance) inverters. Thus, the lowpass prototype filters in Fig. 10 can be transformed into the filter networks with the impedance and admittance inverters shown in Fig. 17. In this case, both the prototype filters and the filters with inverters will have the same frequency responses, provid-

ed the inverter parameters K and J are computed by the equations given in Fig. 17.

On the other hand, by applying suitable element transformations, the impedance and admittance inverters can also be utilized to convert the lowpass filters shown in Fig. 17 into two bandpass filter or into other types of filters commonly employed because impedance and admittance inverters are frequency-invariable. Two bandpass filters with the impedance and admittance inverters are illustrated in Fig. 18. The expressions for element transformation as well as for impedance and admittance of the inverters are also given in the figures. It should be noted that the source impedances are assumed to be the same for the networks in Figs. 17 and 18, and again, since no impedance transformation is required, the impedance Z_0 in (49) and (50) is assumed to be 1.0. Figure 18a illustrates a bandpass filter composed of only series resonators, while the filter in Fig. 18b includes only shunt parallel resonators.

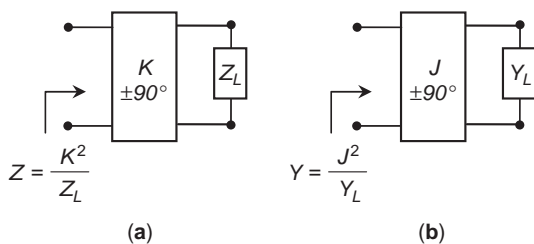


Figure 16. Definition of (a) impedance (K) and (b) admittance (J) inverters.

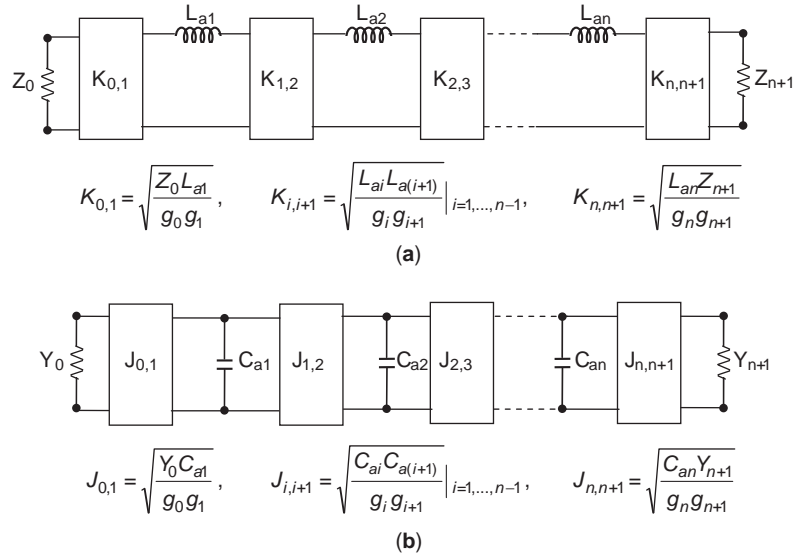


Figure 17. Lowpass prototype filter with (a) impedance inverters and (b) admittance inverters.

As mentioned previously, difficulties in realization of lumped-element microwave filters require the use of distributed elements such as waveguide sections, coaxial lines, microstrip lines, striplines, and dielectric resonators. Consequently, it is generally desirable to employ distributed-element resonators instead of lumped-element ones to realize microwave filters. Under ideal circumstances, the reactances or susceptances of lumped and distributed resonators should be equal to each other, but they approximate each other only near resonance. So, for narrowband distributed filters, the distributed resonator reactance (susceptance) and the reactance (susceptance) slope are determined by equating to those of their corresponding

lumped resonator at resonant frequency, and it is convenient to introduce their reactance and susceptance slope parameters. The reactance slope parameter for any resonator having zero reactance at resonant frequency ω_0 (such a resonator exhibits series resonance properties) is given by

$$x = \frac{\omega_0}{2} \frac{dX}{d\omega} \Big|_{\omega=\omega_0} \quad \Omega \tag{57}$$

where X is the reactance of the distributed resonator. For a lumped series LC resonator, this expression reduces to $x = \omega_0 L = 1/\omega_0 C$. The susceptance slope parameter for any resonator having zero susceptance at resonant frequency ω_0 (such a resonator exhibits shunt resonance properties)

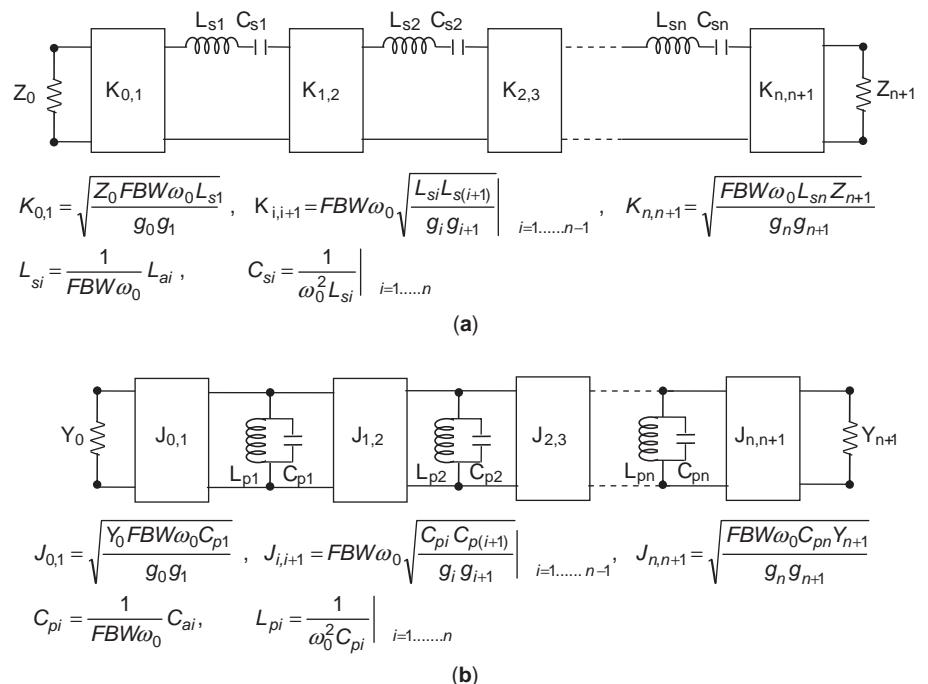


Figure 18. Bandpass filters with (a) impedance inverters and (b) admittance inverters.

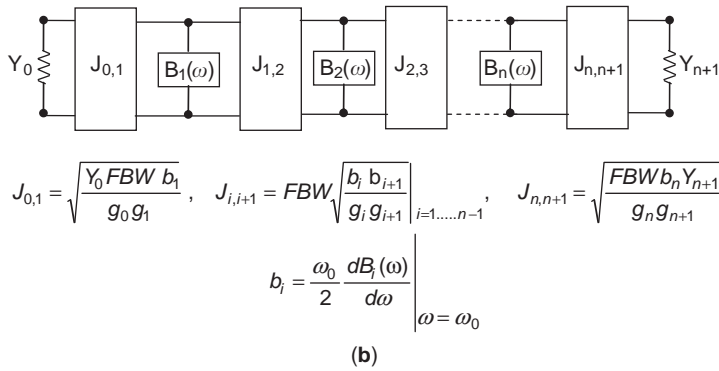
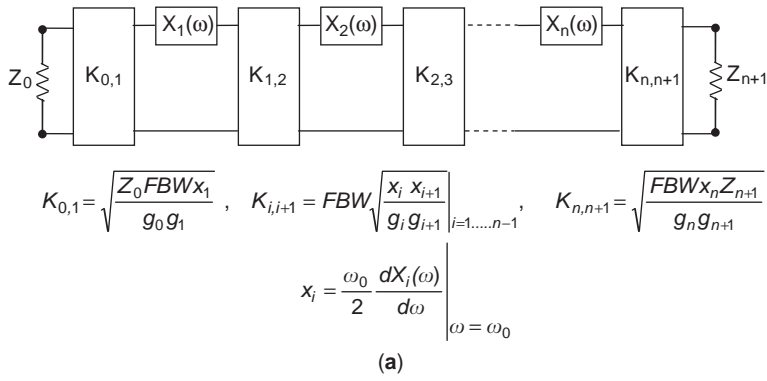


Figure 19. Generalized bandpass filters including distributed resonators with (a) impedance inverters and (b) admittance inverters.

Table 7. Practical Impedance and Admittance Inverters

Lumped-Element Inverters	Lumped- and Distributed-Element Inverters			
	<i>Impedance Inverters</i>			
<p style="text-align: center;">$K = \omega L$</p>	<p style="text-align: center;">$K = 1/\omega C$</p>	<p style="text-align: center;">$\phi < 0$ for $X > 0$ $K = Z_0 \tan \phi/2 ,$</p>	<p style="text-align: center;">$\phi > 0$ for $X < 0$ $\phi = -\tan^{-1}(2X/Z_0)$</p>	
	$\left \frac{X}{Z_0} \right = \frac{K/Z_0}{1 - (K/Z_0)^2}$			
	<i>Admittance Inverters</i>			
<p style="text-align: center;">$J = 1/\omega L$</p>	<p style="text-align: center;">$J = \omega C$</p>	<p style="text-align: center;">$\phi > 0$ for $B < 0$ $J = Y_0 \tan \phi/2 ,$</p>	<p style="text-align: center;">$\phi < 0$ for $B > 0$ $\phi = -\tan^{-1}(2B/Y_0)$</p>	
	$\left \frac{B}{Y_0} \right = \frac{J/Y_0}{1 - (J/Y_0)^2}$			

is defined by

$$b = \frac{\omega_0}{2} \left. \frac{dB}{d\omega} \right|_{\omega=\omega_0} \Omega^{-1} \quad (58)$$

where B is the susceptance of the distributed resonator. For a lumped shunt LC resonator, this expression reduces to $b = \omega_0 C = 1/\omega_0 L$ (see article titled RESONATORS).

To transform the filters including lumped resonance elements with K and J inverters in Fig. 18 into the filters including distributed resonance elements with K and J inverters in Fig. 19, we can add $\omega_0 L_{si} = x_i$ and $\omega_0 C_{pi} = b_i$ to the expressions indicated in Fig. 18. As a result, generalized bandpass filters composed of distributed resonators with impedance inverters and admittance inverters are derived as shown in Fig. 19.

Essentially, an ideal quarter-wave impedance transformer can be used as an impedance inverter. Besides a quarter-wave transformer, there are various other circuits that have properties of K and J inverters. Such types of practical K and J inverters are summarized in Table 7. More details on impedance and admittance inverters and their applications may be found in the literature [13,16,21].

7. CONCLUSION

As mentioned previously, distributed filter topics including lowpass, bandpass, highpass, and bandstop constructed in a variety of media, such as waveguide, coaxial line, microstrip, stripline, and dielectric resonators, are generally based on lumped-element filters. Many filter designs commence with a lumped-element lowpass prototype filter. Therefore, the objective of this study was to present the basic topics of filter theory for newcomers to the area and to point out how a filter may be designed. Various filter characteristics generally used, such as Butterworth, Chebyshev, elliptic, pseudoelliptic, and maximally flat time delay, were discussed. Insertion loss theory only for lowpass prototype filter design was investigated because of its superior to image parameter theory. Although the image parameter theory is the oldest method of filter design, it has hardly ever been used.

Note that the subject here is not to discuss the microwave filter technologies, such as waveguide, coaxial, combline, interdigital, parallel-coupled, hairpin, patch and ring, ceramic resonator, dielectric resonator, suspended substrate stripline, and superconducting filters from an applications perspective or a historical perspective. However, the topics of microwave filters are extensively investigated in the classic book of Matthaei et al. [16]. This book, even in its first edition, has been a milestone in the history of microwave filters. Although it has become a classic for microwave filters, it was published in 1980 and somewhat dated. The book by Hong and Lancaster [13] may be considered as an alternative of this classic. It provides a comprehensive treatment of RF and microwave filters based on microwave structures and also discusses advanced microwave filters. The

1984 survey by Levy and Cohn [2] and the 2002 surveys by Levy et al. [3] and Hunter et al. [4] may also be considered as good reference sources for newcomers to the field.

BIBLIOGRAPHY

1. W. P. Mason and R. A. Sykes, The use of coaxial and balanced transmission lines in filters and wide band transformers for high radio frequencies, *Bell Syst. Tech. J.* **16**: 275–302 (1937).
2. R. Levy and S. B. Cohn, A history of microwave filter research, design, and development, *IEEE Trans. Microwave Theory Tech.* **MTT-32**(9):1055–1067 (1984).
3. R. Levy, R. V. Snyder, and G. Matthaei, Design of microwave filters, *IEEE Trans. Microwave Theory Tech.* **MTT-50**(3): 783–793 (2002).
4. I. C. Hunter, L. Billonet, B. Jarry, and P. Guillon, Microwave filters—applications and technology, *IEEE Trans. Microwave Theory Tech.* **MTT-50**(3):794–805 (2002).
5. A. E. Williams, A four-cavity elliptic waveguide filter, *IEEE Trans. Microwave Theory Tech.* **MTT-18**(12):1109–1114 (1970).
6. R. Saal and E. Ulbrich, On the design of filters by synthesis, *IRE Trans. Circ. Theory* **CT-5**:284–327 (1958).
7. S. A. Aloseyab, A novel class of generalized Chebyshev low-pass prototype for suspended substrate stripline filters, *IEEE Trans. Microwave Theory Tech.* **MTT-30**(9):1341–1347 (1982).
8. C. I. Mobbs and J. D. Rhodes, A generalized Chebyshev suspended substrate stripline bandpass filter, *IEEE Trans. Microwave Theory Tech.* **MTT-31**(5):397–402 (1983).
9. K. T. Jokela, Narrow-band stripline or microstrip filters with transmission zeros at real and imaginary frequencies, *IEEE Trans. Microwave Theory Tech.* **MTT-28**(6):542–547 (1980).
10. W. E. Thomson, Delay network having maximally flat frequency characteristics, *Proc. IEE* **96**:487–490 (1949).
11. D. M. Pozar, *Microwave Engineering*, Wiley, New York; 1998.
12. M. W. Medley, *Microwave and RF Circuits: Analysis, Synthesis and Design*, Artech House, Norwood, MA; 1993.
13. J.-S. Hong, and M. J. Lancaster, *Microstrip Filters for RF/Microwave Applications*, Wiley, New York; 2001.
14. J. D. Rhodes, Waveguide bandstop elliptic function filters, *IEEE Trans. Microwave Theory Tech.* **MTT-20**(11):715–718 (1972).
15. A. E. Atia and A. E. Williams, Narrow-bandpass waveguide filters, *IEEE Trans. Microwave Theory Tech.* **MTT-20**(4): 258–265 (1972).
16. G. Matthaei, L. Young, and E. M. T. Jones, *Microwave Filters, Impedance Matching Networks, and Coupling Structures*, Artech House, Norwood, MA; 1980.
17. J. D. Rhodes, *Theory of Electrical Filters*, Wiley, New York; 1976.
18. R. Levy, Filters with single transmission zeros at real and imaginary frequencies, *IEEE Trans. Microwave Theory Tech.* **MTT-24**(4):172–181 (1976).
19. P. I. Richards, Resistor transmission-line circuits, *Proc. IRE* **36**:217–220 (1948).

20. H. Ozaki and J. Ishii, Synthesis of a class of stripline filters, *IRE Trans. Circ. Theory* **CT-5**:105–109 (1958).
21. R. Levy, A general equivalent circuit transformation for distributed networks, *IEEE Trans. Circ. Theory* **CT-12**:457–458 (1965).
22. R. J. Wenzel, Exact design of TEM microwave networks using quarter-wave lines, *IEEE Trans. Microwave Theory Tech.* **MTT-12**(1):94–111 (1964).
23. R. E. Collin, *Foundations for Microwave Engineering*, McGraw-Hill, New York; 1992.

FINITE-DIFFERENCE TIME-DOMAIN ANALYSIS

ALLEN TAFLOVE
Northwestern University
Evanston, Illinois
SUSAN C. HAGNESS
University of Wisconsin-
Madison
Madison, Wisconsin

Prior to 1990, numerical modeling of electromagnetic engineering systems was implemented primarily using solution techniques for the sinusoidal steady-state (frequency-domain) Maxwell's equations. Principal computational approaches included high-frequency asymptotic methods and integral equation techniques. However, while asymptotic analyses are well suited for modeling the scattering properties of electrically large complex shapes, such methods have difficulty treating nonmetallic material composition and volumetric complexity of a structure. Conversely, while integral equation methods can deal with material and structural complexity, their need to construct and solve systems of linear equations limits the electrical size of possible models, especially those requiring detailed treatment of geometric details within a volume, as opposed to just the surface shape.

While significant progress has been made in solving the large systems of equations generated by frequency-domain integral equations, the capabilities of even the latest such technologies are exhausted by many volumetrically complex structures of engineering interest. This also holds for frequency-domain finite-element techniques. Further, incorporation of material and device nonlinearities into frequency-domain solutions of Maxwell's equations poses difficult problems as engineers seek to design active electromagnetic, electronic, and/or quantum-optical systems such as high-speed digital circuits, microwave and millimeter-wave amplifiers, and lasers.

Realization of the limitations of frequency-domain solutions of Maxwell's equations led to exploration of alternative approaches aimed at direct time-domain solutions of Maxwell's differential (curl) equations on spatial grids or lattices. The finite-difference time-domain (FDTD) method introduced by Yee in 1966 [1] was the first technique in this class. FDTD has remained the subject of continuous active development and expanding application areas [2] with numerous available software packages (e.g., see the list of WWW links to such softwares provided in

Ref. 3). Two related numerical approaches for solving Maxwell's equations, the finite integration technique (FIT) introduced by Weiland [4,5] and the transmission-line matrix (TLM) technique introduced by Johns [6,7], have also been studied for many years and are also the basis of commercial software packages. FIT and TLM techniques will not be discussed in this article, which focuses on the foundation and illustrative applications of the FDTD method.

There are six primary reasons for the expansion of interest in FDTD and related grid-based time-domain numerical solution techniques for Maxwell's equations:

1. *FDTD uses no linear algebra.* Being a fully explicit computation, FDTD avoids the difficulties with linear algebra that limit the size of frequency-domain integral equation and finite-element electromagnetics models to generally fewer than 10^7 field unknowns. FDTD models with as many as 10^9 field unknowns have been run. There is *no intrinsic upper bound* to this number.
2. *FDTD is accurate and robust.* The sources of error in FDTD calculations are well understood and can be bounded to permit accurate models for a very large variety of electromagnetic wave interaction problems.
3. *FDTD treats impulsive behavior naturally.* FDTD directly calculates the impulse response of an electromagnetic system. For a linear system, a single FDTD simulation can provide both the ultrawideband temporal response and (via discrete Fourier transformation) the sinusoidal steady-state response at any frequency within the excitation spectrum. For a nonlinear system, FDTD avoids the need to perform harmonic balance calculations that are required when using frequency-domain analyses.
4. *FDTD is systematic and simple to implement.* With FDTD, specifying a new structure to be modeled is reduced to a problem of mesh generation rather than the potentially complex reformulation of an integral equation. For example, FDTD requires no calculation of structure-dependent Green functions.
5. *Computer memory capacities are increasing rapidly.* While this trend positively influences all numerical techniques, it is of particular advantage to FDTD methods which are founded on discretizing space over a volume, and therefore inherently require a large random access memory.
6. *Computer visualization capabilities are increasing rapidly.* While this trend positively influences all numerical techniques, it is of particular advantage to FDTD methods that generate time-marched arrays of field quantities suitable for use in color videos to illustrate the field dynamics.

An indication of the expanding level of interest in FDTD Maxwell's equations solvers is the hundreds of papers currently published in this area worldwide each year, as opposed to fewer than 10 as recently as 1985 [8]. This expansion continues as engineers and scientists in

nontraditional electromagnetics-related areas such as digital systems and integrated optics become aware of the power of such direct solution techniques for Maxwell's equations.

1. CHARACTERISTICS OF FDTD TECHNIQUES

FDTD and related space-grid time-domain techniques are direct solution methods for Maxwell's curl equations. These methods employ no potentials. Rather, they are based on volumetric sampling of the unknown electric and magnetic fields within and surrounding the structure of interest, and over a period of time. The sampling in space is at subwavelength resolution set by the user to properly sample the highest near-field spatial frequencies thought to be important in the physics of the problem. Typically, 10–20 samples per wavelength are needed. The sampling in time is selected to ensure numerical stability of the algorithm.

Overall, FDTD and related techniques are marching-in-time procedures that simulate the continuous actual electromagnetic waves in a finite spatial region by sampled-data numerical analogs propagating in a computer data space. Timestepping continues as the numerical wave analogs propagate in the space lattice to causally connect the physics of the modeled region. For simulations where the modeled region must extend to infinity, absorbing boundary conditions are employed at the outer lattice truncation planes, which ideally permit all outgoing wave analogs to exit the region with negligible reflection. Phenomena such as induction of surface currents, scattering and multiple scattering, aperture penetration, and cavity excitation are modeled timestep by timestep by the action of the numerical analog to the curl equations. Self-consistency of these modeled phenomena is generally assured if their spatial and temporal variations are well resolved by the spacetime sampling process. In fact, the goal is to provide a self-consistent model of the mutual coupling of all the electrically small-volume cells constituting the structure and its near field, even if the structure spans tens of wavelengths in three dimensions and there are hundreds of millions of space cells.

Timestepping is continued until the desired late-time pulse response is observed at the field points of interest. Prolonged “ringing” of the computed field waveforms due to a high Q factor or large electrical size of the structure being modeled requires a combination of extending the computational window in time and extrapolation of the windowed data before Fourier transformation.

2. CLASSES OF FDTD SPACE LATTICES

Current FDTD and related space-grid time-domain algorithms are fully explicit solvers employing highly vectorizable and parallel schemes for time-marching the six components of the electric and magnetic field vectors at each of the space cells. The explicit nature of the solvers is usually maintained by employing a leapfrog timestepping scheme. Current methods differ primarily in how the space lattice is set up. In fact, gridding methods can be

categorized according to the degree of structure or regularity in the mesh cells:

1. *Almost Completely Structured.* In this case, the space lattice is organized so that its unit cells are congruent wherever possible. The most basic example of such a mesh is the pioneering work of Yee [1], who employed a uniform Cartesian grid having rectangular cells. Staircasing was used to approximate the surface of structural features not parallel to the grid coordinate axes. Later work showed that it is possible to modify the size and shape of the space cells located immediately adjacent to a structural feature to conformally fit its surface [9,10]. This is accurate and computationally efficient for large structures because the number of modified cells is proportional to the surface area of the structure. Thus, the number of modified cells becomes progressively smaller relative to the number of regular cells filling the structure volume as its size increases. As a result, the computer resources needed to implement a fully conformal model approximate those required for a staircased model. However, a key disadvantage of this technique is that special mesh generation software must be constructed.

2. *Surface-Fitted.* In this case, the space lattice is globally distorted to fit the shape of the structure of interest. The lattice can be divided into multiple zones to accommodate a set of distinct surface features [11]. The major advantage of this approach is that well-developed mesh generation software of this type is available. The major disadvantage is that, relative to the Yee algorithm, there is substantial added computer burden due to (a) memory allocations for the position and stretching factors of each cell and (b) extra computer operations to implement Maxwell's equations at each cell and to enforce field continuity at the interfaces of adjacent cells. Another disadvantage is the possible presence of numerical dissipation in the timestepping algorithm used for such meshes. This can limit the range of electrical size of the structure being modeled due to numerical wave attenuation artifacts.

3. *Completely Unstructured.* In this case, the space containing the structure of interest is completely filled with a collection of lattice cells of varying sizes and shapes, but conforming to the structure surface [12]. As for the case of surface-fitted lattices, mesh generation software is available and capable of modeling complicated three-dimensional shapes possibly having volumetric inhomogeneities. A key disadvantage of this approach is its potential for numerical inaccuracy and instability due to the unwanted generation of highly skewed space cells at random points within the lattice. A second disadvantage is the difficulty in mapping the unstructured mesh computations onto the architecture of either parallel vector computers or massively parallel machines. The structure-specific irregularity of the mesh mandates a robust preprocessing algorithm that optimally assigns specific mesh cells to specific processors.

At present, the best choice of computational algorithm and mesh remains unclear. In the near future, we expect

continued progress in this area as various groups develop their favored approaches and perform validations.

3. SOURCES OF ERROR

FDTD techniques have four primary sources of numerical error. Each error source represents a type of behavior of the numerical waves within the FDTD grid that differs from that of the desired physical electromagnetic waves being modeled. The error sources are as follows:

1. *Imperfect Absorbing Boundary Conditions.* For open-region simulations wherein the FDTD lattice would ideally extend throughout all of space, outgoing numerical waves are spuriously reflected back toward the lattice interior at the outermost grid boundaries.
2. *Wave Propagation Speed Errors.* Numerical waves in the FDTD space lattice have propagation speeds that differ from that of light, as they are a function of the lattice resolution and the propagation direction. The resulting positional and/or phase errors of the numerical waves are cumulative and can be significant for lattices that extend over many wavelengths of the numerical modes.
3. *Spurious Numerical Wave Reflections.* A space lattice region with position-dependent resolution and/or unit cell shape causes numerical waves to propagate with position-dependent speeds within its interior. This generates spurious internal wave reflections even if the lattice region has otherwise uniform electrical properties.
4. *Inaccurate Rendering of Surface Shapes.* The shape and/or size of the space lattice cells may not permit fully conformal modeling of the surface of the wave interaction structure being modeled.

Error source 1 has been practically eliminated for many problems due to the development of highly effective absorbing boundary conditions such as Berenger's perfectly matched layer [13]; the anisotropic perfectly matched layer [14,15], and the complementary operator method [16]. Error sources 2 and 3 are being attacked by a new generation of low-dispersion algorithms including the wavelet-based multiresolution time-domain technique [17] and the pseudospectral time-domain technique [18]. Finally, error source 4 is being attacked by a new generation of conformal-surface FDTD algorithms [10].

4. SCALING TO VERY LARGE PROBLEM SIZES

Using FDTD, we can model electromagnetic wave interaction problems requiring the solution of considerably more than one-billion field vector unknowns. At this level of complexity, it is possible to develop high-resolution, volumetric, three-dimensional models of complete physical and engineering systems, including the following:

- The entire Earth-ionosphere cavity for extremely low-frequency wave propagation
- Entire aircraft and missiles illuminated by radar at 1 GHz and above
- Entire multilayer circuit boards and multichip modules for digital signal propagation, crosstalk, and radiation
- Entire microwave and millimeter-wave amplifiers, including the active and passive circuit components and packaging
- Entire integrated optical structures, including lasers, waveguides, couplers, and resonators

A key goal for such large models is to achieve algorithm/computer architecture scaling such that for N field unknowns to be solved on M processors, we approach an order(N/M) scaling of the required computational resources.

We now consider the factors involved in determining the computational burden for the class of FDTD and related space-grid time-domain solvers.

1. *Number of Volumetric Grid Cells N .* The six-vector electromagnetic field components located at each lattice cell must be updated at every timestep. This yields by itself an order(N) scaling.
2. *Number of Timesteps n_{\max} .* A self-consistent solution in the time domain mandates that the numerical wave analogs propagate over timescales sufficient to causally connect each portion of the structure of interest. Therefore, n_{\max} must increase as the maximum electrical size of the structure. In three dimensions, it can be argued that n_{\max} is a fractional power function of N such as $N^{1/3}$. Further, n_{\max} must be adequate to step through "ring-up" and "ringdown" times of energy storage features such as cavities. These features vary from problem to problem and cannot be ascribed a dependence relative to N .
3. *Cumulative Propagation Errors.* Additional computational burdens may arise because of the need for either progressive mesh refinement or progressively higher-accuracy algorithms to bound cumulative positional or phase errors for propagating numerical modes in progressively enlarged meshes. Any need for progressive mesh refinement would feed back to factor 1.

For most free-space problems, factors 2 and 3 are weaker functions of the size of the modeled structure than factor 1. This is because geometric features at increasing electrical distances from each other become decoupled as a result of radiative losses by the electromagnetic waves propagating between these features. Further, it can be shown that replacing second-order accurate algorithms by higher-order versions sufficiently reduces numerical dispersion error to avoid the need for progressive mesh refinement for object sizes up to the order of 100 wavelengths. Overall, a computational burden of order($N \cdot n_{\max}$) = order($N^{4/3}$) is estimated for very large FDTD and related models.

5. THE BASIS OF FDTD: MAXWELL'S TIME-DEPENDENT CURL EQUATIONS

Using MKS units, the time-dependent Maxwell's curl equations in three dimensions are given in differential equation form for general materials by

$$\frac{\partial \mathbf{B}}{\partial t} = -\nabla \times \mathbf{E} - \mathbf{M} \quad (1)$$

$$\frac{\partial \mathbf{D}}{\partial t} = \nabla \times \mathbf{H} - \mathbf{J} \quad (2)$$

where

- \mathbf{E} = electric field intensity (V/m)
- \mathbf{D} = electric flux density (C/m²)
- \mathbf{H} = magnetic field intensity (A/m)
- \mathbf{B} = magnetic flux density (Wb/m²)
- \mathbf{J} = electric current density (A/m²)
- \mathbf{M} = equivalent magnetic current density (V/m²)

are the space- and time-dependent vectors that constitute the electromagnetic field and its associated current densities.

The constitutive relations between the field vector pairs (\mathbf{B}, \mathbf{H}) and (\mathbf{D}, \mathbf{E}) which describe the macroscopic interaction of the electromagnetic field with materials are given in a general form by

$$\mathbf{H} = f(\mathbf{B}) \quad (3a)$$

$$\mathbf{E} = g(\mathbf{D}) \quad (3b)$$

where f and g can be scalar, polynomial, matrix, time-derivative, time-integral, or time-convolution operators. Appropriate selection of f and g provides the description of material anisotropies, frequency dispersions, and nonlinearities. For the simplest case of an isotropic, nondispersive, linear material, f and g are multiplicative scalars and (3a) and (3b) reduce to

$$\mathbf{H} = \frac{\mathbf{B}}{\mu} \quad (4a)$$

$$\mathbf{E} = \frac{\mathbf{D}}{\varepsilon} \quad (4b)$$

where μ and ε are, respectively, the material's magnetic permeability (in henries per meter) and electric permittivity (in farads per meter).

When expressed in a desired global or local spatial coordinate system, Eqs. (1)–(3) directly form the basis of the FDTD numerical algorithm for modeling electromagnetic wave phenomena. For example, implementation of (1) and (2) in Cartesian coordinates yields the following system of six coupled differential equations for the vector components of the fields:

$$\frac{\partial B_x}{\partial t} = \frac{\partial E_y}{\partial z} - \frac{\partial E_z}{\partial y} - M_x \quad (5a)$$

$$\frac{\partial B_y}{\partial t} = \frac{\partial E_z}{\partial x} - \frac{\partial E_x}{\partial z} - M_y \quad (5b)$$

$$\frac{\partial B_z}{\partial t} = \frac{\partial E_x}{\partial y} - \frac{\partial E_y}{\partial x} - M_z \quad (5c)$$

$$\frac{\partial D_x}{\partial t} = \frac{\partial H_z}{\partial y} - \frac{\partial H_y}{\partial z} - J_x \quad (6a)$$

$$\frac{\partial D_y}{\partial t} = \frac{\partial H_x}{\partial z} - \frac{\partial H_z}{\partial x} - J_y \quad (6b)$$

$$\frac{\partial D_z}{\partial t} = \frac{\partial H_y}{\partial x} - \frac{\partial H_x}{\partial y} - J_z \quad (6c)$$

In this example, we would (1) numerically approximate the spatial partial derivatives of (5) and (6) with finite-differences implemented in a Cartesian coordinate system, (2) numerically integrate the resulting system of spatial difference equations with respect to time by a finite-difference approximation of the time partial derivatives, and (3) concurrently numerically implement the constitutive relations of (3) to relate the Cartesian components of the field-vector pairs (\mathbf{B}, \mathbf{H}) and (\mathbf{D}, \mathbf{E}) appearing separately in (5) and (6). This yields a means to evolve each vector component of the electromagnetic field in space and time in a manner that mimics nature.

We note that the FDTD method involves only finite-difference approximations of Maxwell's curl equations, and not Gauss' laws for the electric and magnetic fields. This is because FDTD space grids *implicitly* enforce Gauss' laws by properly (1) positioning the E - and H -field vector components about each unit cell of the grid and (2) defining the finite-difference approximations of the space partial derivatives. Yee's space grid and timestepping method [1], which is the foundation of the FDTD method in Cartesian coordinates, satisfies these criteria [2].

6. YEE'S SPACE GRID AND TIMESTEPPING METHOD

Yee [1] originated a system of finite-difference approximations of the time-dependent Maxwell's curl equations of (5) and (6). Consider first his *central-difference* approximations of the spatial partial derivatives comprising the curl operators. Referring to Fig. 1, this is based on centering the Cartesian components of \mathbf{E} and \mathbf{H} about rectangular unit cells of size Δx , Δy , and Δz so that every \mathbf{E} component is surrounded by four "looping" \mathbf{H} components and every \mathbf{H} component is surrounded by four "looping" \mathbf{E} components. Then, for example, the value of $\partial H_z / \partial y$ observed at the E_x component located at the centerpoint of the front-face of the unit cell, $[i\Delta x, (j+0.5)\Delta y, (k+0.5)\Delta z]$, is calculated at the timepoint $(n+0.5)\Delta t$ as

$$\begin{aligned} & \frac{\partial H_z}{\partial y} [i\Delta x, (j+0.5)\Delta y, (k+0.5)\Delta z, (n+0.5)\Delta t] \\ &= \frac{H_z|_{i,j+1,k+0.5}^{n+0.5} - H_z|_{i,j,k+0.5}^{n+0.5}}{\Delta y} + O[(\Delta y)^2] \end{aligned} \quad (7)$$

where Δt is the timestep and i, j, k , and n are integers. This calculation is *second-order accurate* in Δy . For example, halving Δy reduces the error in the numerical

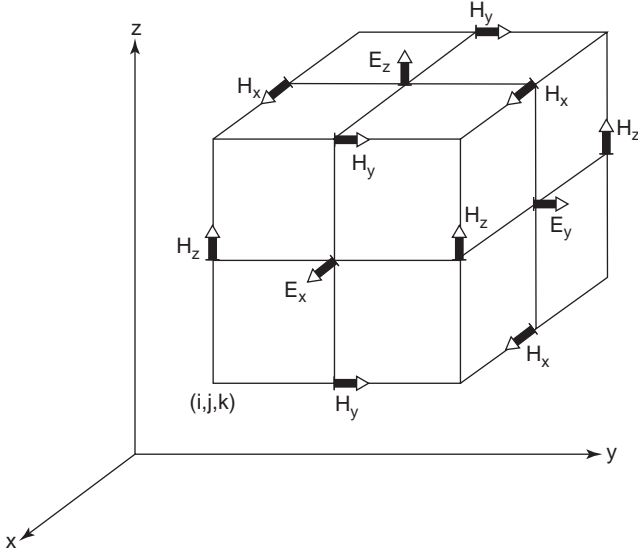


Figure 1. Position of the electric and magnetic field vector components about a cubic unit cell of the Yee space lattice [1].

approximation of $\partial H_z/\partial y$ by 4:1. Central-difference approximations analogous to (7) can be written for all the spatial partial derivatives of the Cartesian components of \mathbf{E} and \mathbf{H} in (5) and (6).

Consider next Yee's central-difference approximations of the temporal partial derivatives in (5) and (6). The following is a sample calculation of a field component time derivative, $\partial D_x/\partial t$ as observed at grid location $[i\Delta x, (j+0.5)\Delta y, (k+0.5)\Delta z]$ and at timepoint $(n+0.5)\Delta t$:

$$\begin{aligned} \frac{\partial D_x}{\partial t} [i\Delta x, (j+0.5)\Delta y, (k+0.5)\Delta z, (n+0.5)\Delta t] \\ = \frac{D_x|_{i,j+0.5,k+0.5}^{n+1} - D_x|_{i,j+0.5,k+0.5}^n}{\Delta t} + O[(\Delta t)^2] \end{aligned} \quad (8)$$

Referring to Fig. 2, this approach to time-differentiation permits a fully explicit, second-order accurate, *leapfrog* (alternating) calculation of the field vector pairs (\mathbf{B}, \mathbf{H}) and (\mathbf{D}, \mathbf{E}) in time. Specifically, this permits the set $\{\mathbf{B}\}$ of all magnetic flux density vector components in the space grid to be calculated at a particular timepoint by having (5) operate on the existing set $\{\mathbf{E}\}$ of electric field intensity vector components. Then, (3a) operates on the newly obtained $\{\mathbf{B}\}$ to yield the updated set $\{\mathbf{H}\}$ of all magnetic field intensity vector components. Next, the set $\{\mathbf{D}\}$ of all electric flux density vector components can be calculated by having (6) operate on the updated $\{\mathbf{H}\}$. Then, (3b) operates on the newly obtained $\{\mathbf{D}\}$ to yield the updated set $\{\mathbf{E}\}$. The computational cycle now begins again with the updating of $\{\mathbf{B}\}$ based on the newly calculated $\{\mathbf{E}\}$. This process continues until timestepping is concluded. A key point to note is that the numerical time evolution of the electromagnetic fields with this approach requires no usage of simultaneous equations and matrix inversion.

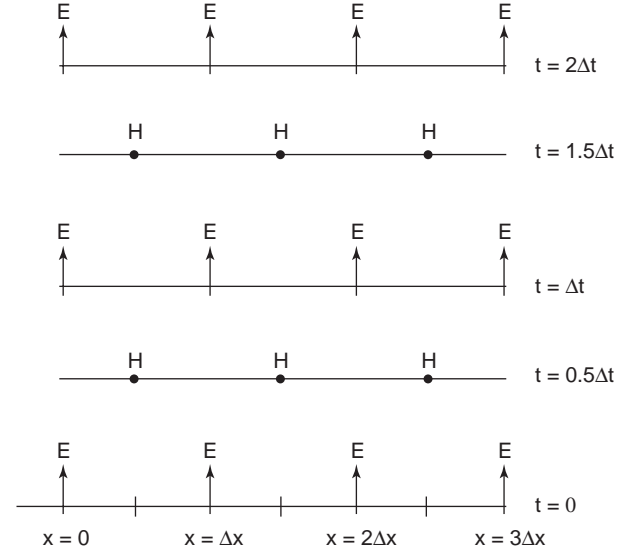


Figure 2. Spacetime chart of the Yee algorithm for a one-dimensional wave propagation example showing the use of central differences for the space derivatives and leapfrog for the time derivatives [2]. Initial conditions for both electric and magnetic fields are zero everywhere in the grid.

7. APPLICATION TO MAXWELL'S EQUATIONS IN CARTESIAN COORDINATES

On applying the abovementioned ideas and notation, and referring to Figs. 1 and 2, we proceed as follows:

1. We implement the following FDTD approximation of Maxwell's curl equation (5) to obtain $\{\mathbf{B}^{n+0.5}\}$ from $\{\mathbf{E}^n\}$:

$$\begin{aligned} B_x|_{i-0.5,j+1,k+1}^{n+0.5} &= B_x|_{i-0.5,j+1,k+1}^{n-0.5} + \Delta t \\ &\times \left(\frac{E_y|_{i-0.5,j+1,k+1.5}^n - E_y|_{i-0.5,j+1,k+0.5}^n}{\Delta z} \right. \\ &- \frac{E_z|_{i-0.5,j+1.5,k+1}^n - E_z|_{i-0.5,j+0.5,k+1}^n}{\Delta y} \\ &\left. - M_x|_{i-0.5,j+1,k+1}^n \right) \end{aligned} \quad (9a)$$

$$\begin{aligned} B_y|_{i,j+0.5,k+1}^{n+0.5} &= B_y|_{i,j+0.5,k+1}^{n-0.5} + \Delta t \\ &\times \left(\frac{E_z|_{i+0.5,j+0.5,k+1}^n - E_z|_{i-0.5,j+0.5,k+1}^n}{\Delta x} \right. \\ &- \frac{E_x|_{i,j+0.5,k+1.5}^n - E_x|_{i,j+0.5,k+0.5}^n}{\Delta z} \\ &\left. - M_y|_{i,j+0.5,k+1}^n \right) \end{aligned} \quad (9b)$$

$$\begin{aligned}
 B_z|_{i,j+1,k+0.5}^{n+0.5} &= B_z|_{i,j+1,k+0.5}^{n-0.5} + \Delta t \\
 &\times \left(\frac{E_x|_{i,j+1.5,k+0.5}^n - E_x|_{i,j+0.5,k+0.5}^n}{\Delta y} \right. \\
 &\left. - \frac{E_y|_{i+0.5,j+1,k+0.5}^n - E_y|_{i-1/2,j+1,k+0.5}^n}{\Delta x} \right. \\
 &\left. - M_z|_{i,j+1,k+0.5}^n \right)
 \end{aligned} \tag{9c}$$

2. We implement constitutive relation (3a) to obtain $\{\mathbf{H}^{n+0.5}\}$ from $\{\mathbf{B}^{n+0.5}\}$ (and possibly earlier values):

$$\begin{aligned}
 H_x|^{n+0.5} &= f_{H_x}(\mathbf{B}^{n+0.5}, \mathbf{B}^{n-0.5}, \mathbf{B}^{n-1.5}, \dots; \\
 &H_x|^{n-0.5}, H_x|^{n-1.5}, H_x|^{n-2.5}, \dots)
 \end{aligned} \tag{10a}$$

$$\begin{aligned}
 H_y|^{n+0.5} &= f_{H_y}(\mathbf{B}^{n+0.5}, \mathbf{B}^{n-0.5}, \mathbf{B}^{n-1.5}, \dots; \\
 &H_y|^{n-0.5}, H_y|^{n-1.5}, H_y|^{n-2.5}, \dots)
 \end{aligned} \tag{10b}$$

$$\begin{aligned}
 H_z|^{n+0.5} &= f_{H_z}(\mathbf{B}^{n+0.5}, \mathbf{B}^{n-0.5}, \mathbf{B}^{n-1.5}, \dots; \\
 &H_z|^{n-0.5}, H_z|^{n-1.5}, H_z|^{n-2.5}, \dots)
 \end{aligned} \tag{10c}$$

3. We implement the following FDTD numerical approximation of Maxwell's curl equation (6) to obtain $\{\mathbf{D}^{n+1}\}$ from $\{\mathbf{H}^{n+0.5}\}$:

$$\begin{aligned}
 D_x|_{i,j+1,k+0.5}^{n+1} &= D_x|_{i,j+0.5,k+0.5}^n + \Delta t \\
 &\times \left(\frac{H_z|_{i,j+1,k+0.5}^{n+0.5} - H_z|_{i,j,k+0.5}^{n+0.5}}{\Delta y} \right. \\
 &\left. - \frac{H_y|_{i,j+0.5,k+1}^{n+0.5} - H_y|_{i,j+0.5,k}^{n+0.5}}{\Delta z} \right. \\
 &\left. - J_x|_{i,j+0.5,k+0.5}^{n+0.5} \right)
 \end{aligned} \tag{11a}$$

$$\begin{aligned}
 D_y|_{i-0.5,j+1,k+0.5}^{n+1} &= D_y|_{i-0.5,j+1,k+0.5}^n + \Delta t \\
 &\times \left(\frac{H_x|_{i-0.5,j+1,k+1}^{n+0.5} - H_x|_{i-0.5,j+1,k}^{n+0.5}}{\Delta z} \right. \\
 &\left. - \frac{H_z|_{i,j+1,k+0.5}^{n+0.5} - H_z|_{i-1,j+1,k+0.5}^{n+0.5}}{\Delta x} \right. \\
 &\left. - J_y|_{i-0.5,j+1,k+0.5}^{n+0.5} \right)
 \end{aligned} \tag{11b}$$

$$\begin{aligned}
 D_z|_{i-0.5,j+0.5,k+1}^{n+1} &= D_z|_{i-0.5,j+0.5,k+1}^n + \Delta t \\
 &\times \left(\frac{H_y|_{i,j+0.5,k+1}^{n+0.5} - H_y|_{i-1,j+0.5,k+1}^{n+0.5}}{\Delta x} \right. \\
 &\left. - \frac{H_x|_{i-0.5,j+1,k+1}^{n+0.5} - H_x|_{i-0.5,j,k+1}^{n+0.5}}{\Delta y} \right. \\
 &\left. - J_z|_{i-0.5,j+0.5,k+1}^{n+0.5} \right)
 \end{aligned} \tag{11c}$$

4. Finally, we implement constitutive relation (3b) to obtain $\{\mathbf{E}^{n+1}\}$ from $\{\mathbf{D}^{n+1}\}$ (and possibly earlier values):

$$E_x|^{n+1} = g_{E_x}(\mathbf{D}^{n+1}, \mathbf{D}^n, \mathbf{D}^{n-1}, \dots; \tag{12a}$$

$$E_x|^{n-1}, E_x|^{n-2}, \dots)$$

$$E_y|^{n+1} = g_{E_y}(\mathbf{D}^{n+1}, \mathbf{D}^n, \mathbf{D}^{n-1}, \dots; \tag{12b}$$

$$E_y|^{n-1}, E_y|^{n-2}, \dots)$$

$$E_z|^{n+1} = g_{E_z}(\mathbf{D}^{n+1}, \mathbf{D}^n, \mathbf{D}^{n-1}, \dots; \tag{12c}$$

$$E_z|^{n-1}, E_z|^{n-2}, \dots)$$

The computational cycle now repeats with implementation of (9).

With the system of (9)–(12), the new value of an electromagnetic field vector component at any space lattice point depends only on previously calculated values of field vector components in the lattice and known electric and magnetic current sources. Therefore, at any given time-step, the computation of a field vector can proceed either one point at a time, or, if p parallel processors are employed concurrently, p points at a time.

We note that constitutive relations (10) and (12) are stated here in a very general form. In fact, for modeling dispersive and nonlinear materials, a significant literature exists that describes specific means to implement (10) and (12). There are three primary techniques: recursive convolution [19], auxiliary differential equations [20], and z transforms [21]. Currently, multiple Debye and Lorentzian dielectric dispersions can be efficiently modeled by any of these approaches. For nonlinear dispersive materials, this has led to the ability to use FDTD to model the propagation and interaction of temporal and spatial optical solitons [22].

8. NUMERICAL DISPERSION

The FDTD algorithm for Maxwell's curl equations reviewed above causes nonphysical dispersion of the simulated waves in a free-space computational lattice; that is, the phase velocity of numerical wave modes can differ from c by an amount varying with the wavelength, direction of propagation in the grid, and grid discretization. This artifact causes propagating numerical waves to accumulate delay or phase errors that can lead to

nonphysical results such as broadening and ringing of pulsed waveforms, imprecise cancellation of multiple scattered waves, anisotropy, and pseudorefraction. Numerical dispersion is a factor that must be accounted to understand the operation of FDTD algorithms and their accuracy limits, especially for electrically large structures.

Following the procedure discussed in Ref. 2, arbitrary numerical waves propagating in the FDTD space lattice can be considered as being fundamentally consisting of a sum of plane, monochromatic, and sinusoidal traveling waves ("Fourier modes"). For example, a general Fourier mode of free-space wavelength λ_0 for the E_z component in a Cartesian space lattice is given by $E_z|_{I,J,K}^n = E_{z0} \exp[j(\omega_F n \Delta t - k_{F_x} I \Delta x - k_{F_y} J \Delta y - k_{F_z} K \Delta z)]$, where (I, J, K) is the observation point in the space lattice; k_{F_x} , k_{F_y} , and k_{F_z} are the components of the Fourier mode wavevector \mathbf{k}_F ; and ω_F is the angular frequency of the Fourier mode. Substituting this and similar expressions for the other electromagnetic field components into the system of (9)–(12) yields, after simplification, the following relation between ω_F and \mathbf{k}_F for the linear, lossless, isotropic, nondispersive material case:

$$\left[\frac{1}{c\Delta t} \sin\left(\frac{\omega_F \Delta t}{2}\right) \right]^2 = \left[\frac{1}{\Delta x} \sin\left(\frac{k_{F_x} \Delta x}{2}\right) \right]^2 + \left[\frac{1}{\Delta y} \sin\left(\frac{k_{F_y} \Delta y}{2}\right) \right]^2 + \left[\frac{1}{\Delta z} \sin\left(\frac{k_{F_z} \Delta z}{2}\right) \right]^2 \quad (13)$$

where $c = (\mu\epsilon)^{-1/2}$ is the speed of light in the material being modeled. Equation (13) is the *numerical dispersion relation* of the Yee algorithm for the three-dimensional case. In contrast to (13), the dispersion relation for a physical electromagnetic plane wave propagating in three dimensions in a homogeneous lossless medium is simply $(\omega/c)^2 = (k_x)^2 + (k_y)^2 + (k_z)^2$.

We consider the important special case of a cubic cell space lattice having $\Delta x = \Delta y = \Delta z = \Delta$, and assume a real-valued $\omega_F = \omega$ (indicating a numerically stable algorithm, as discussed later). Then, defining the *Courant stability factor* $S = c\Delta t/\Delta$ and the *spatial sampling density* $N_\lambda = \lambda_0/\Delta$, we can solve (13) analytically for \mathbf{k}_F and the corresponding Fourier mode phase velocity $v_F = \omega/\mathbf{k}_F$ for a few special cases of wave propagation direction in the lattice, for example:

Propagation parallel to the x -, y -, or z -coordinate axes of the space lattice

$$v_F = \frac{\pi}{N_\lambda \sin^{-1}\left[\frac{1}{S} \sin\left(\frac{\pi S}{N_\lambda}\right)\right]} c \quad (14a)$$

Propagation along a 45° diagonal within any $(x-y)$, $(x-z)$, or $(y-z)$ plane of the space lattice

$$v_F = \frac{\pi}{2^{1/2} N_\lambda \sin^{-1}\left[\frac{1}{2^{1/2} S} \sin\left(\frac{\pi S}{N_\lambda}\right)\right]} c \quad (14b)$$

As an example, assume a space lattice having $S = 0.5$ and $N_\lambda = 20$. Then (14a) and (14b) provide unequal v_F values of

0.996892 c and 0.998968 c , respectively. The implication is that a sinusoidal numerical wave propagating obliquely within any $(x-y)$, $(x-z)$, or $(y-z)$ plane of this lattice has a speed that is $0.998968/0.996892 = 1.00208$ times that of a wave propagating along the x , y , or z axis of the same lattice. This represents a velocity anisotropy of about 0.2% between oblique and along-axis numerical wave propagation. Reference 2 demonstrated that this theoretical anisotropy of the numerical phase velocity appears in actual FDTD simulations.

It would be very useful to derive closed-form expressions for v_F analogous to (14a) and (14b) for any wave-propagation direction within the space lattice. However, for this general case, the underlying dispersion relation (13) is a transcendental equation. Reference 2 provides a means to calculate sample values of v_F by applying Newton's method to solve (13) for k_F . Figure 3 graphs results obtained using this procedure that illustrate the variation of v_F with propagation direction ϕ within any $(x-y)$, $(x-z)$, or $(y-z)$ plane of the space lattice. Here, for the Courant factor fixed at $S = 0.5$, three different grid sampling densities N_λ are examined: $N_\lambda = 5$ points per λ_0 , $N_\lambda = 10$, and $N_\lambda = 20$. We see that $v_F < c$ and is a function of both ϕ and N_λ . It is clear that v_F is maximum for waves propagating obliquely within the plane ($\phi = 45^\circ$), and is minimum for waves propagating along either major axis ($\phi = 0^\circ, 90^\circ$).

It is useful to quantify the algorithmic dispersive error performance by defining two normalized error measures: (1) the physical phase velocity error Δv_p , and (2) the phase velocity anisotropy error Δv_a . These are given by

$$\Delta v_p = \frac{\min[v_F(\phi)] - c}{c} \times 100\% \quad (15a)$$

$$\Delta v_a = \frac{\max[v_F(\phi)] - \min[v_F(\phi)]}{\min[v_F(\phi)]} \times 100\% \quad (15b)$$

The first velocity error measure, Δv_p , provides an upper bound on the phase error that numerical modes suffer

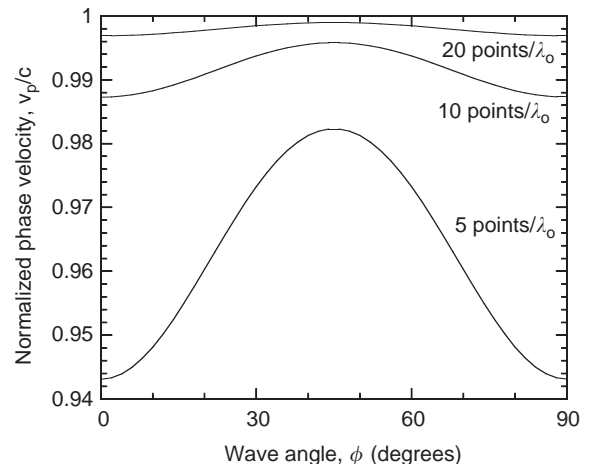


Figure 3. Variation of the numerical phase velocity with wave propagation angle in a 2D FDTD grid for three sampling densities of the square unit cells [2]; $S = c\Delta t/\Delta = 0.5$ for all cases.

relative to physical modes propagating at c . For example, from (14a) and (15a), $\Delta v_p = -0.31\%$ for $N_\lambda = 20$. This means that a sinusoidal numerical wave traveling parallel to the x -, y -, or z -coordinate axes of this space lattice over a $10\lambda_0$ distance (200 cells) develops a lagging phase error of 11° . We note further that Δv_p is a function of N_λ . Since the mesh cell size Δ is fixed, for an impulsive wave propagation problem there exists a spread of effective N_λ values for the Fourier spectral components constituting the pulse. This causes a spread of Δv_p over the pulse spectrum, which in turn yields a temporal dispersion of the pulse evidenced in the spreading and distortion of its waveform as it propagates. Figure 4 plots the variation of Δv_p versus N_λ within any x - y , x - z , or y - z plane of the space lattice for on-axis and oblique wave propagation for a sample Courant factor $S = 0.5$. Here, we see that a mesh resolution $N_\lambda > 20$ is required for any particular Fourier component to limit its physical velocity error to less than 0.3%.

The second velocity error measure, Δv_a , provides an upper bound on the wavefront distortion. For example, a circular cylindrical wave would suffer progressive distortion of its wavefront since the portions propagating along the grid diagonals would travel slightly faster than the portions traveling along the major grid axes. For example, from (14a), (14b), and (15b), $\Delta v_a = 0.208\%$ for $N_\lambda = 20$. The wavefront distortion due to this anisotropy would total about 2.1 cells for each 1000 cells of propagation distance.

Liu [23] has shown that, for $N_\lambda > 10$, Δv_a is virtually independent of the timestep size and can be approximated by the following simple expression:

$$\Delta v_a \cong \frac{\pi^2}{12(N_\lambda)^2} \times 100\% \quad (16)$$

For example, (16) yields $\Delta v_a \cong 0.206\%$ for $N_\lambda = 20$. This is very close to the 0.208% value previously obtained using the complete dispersion relation.

We note that errors due to inaccurate numerical wave velocities are cumulative, increasing linearly with the wave propagation distance. These errors represent a

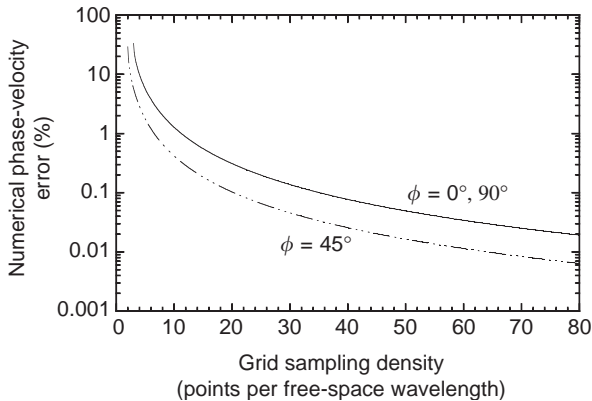


Figure 4. Percent physical phase velocity error relative to the free-space speed of light as a function of the mesh sampling density for on-axis and oblique wave propagation [2]; $S = 0.5$ is assumed.

fundamental limitation of all grid-based time-domain Maxwell equation algorithms, and can be troublesome when modeling electrically large structures. A positive aspect is that both Δv_p and Δv_a decrease as the square of the sampling density N_λ . Therefore, finer meshing is one way to control the dispersion error.

There are ongoing active investigations of means to reduce the dispersion error of FDTD algorithms with the goal of allowing electrically very large structures to be modeled in a computationally efficient manner [17,18]. Specifically, with emerging pseudospectral time-domain algorithms [18], Δv_a can be reduced to very low levels approaching zero. In this case, residual errors involve primarily the dispersion of Δv_p with N_λ , which can be optimized by the proper choice of Δt . However, the new approaches presently have limitations regarding their ability to model material discontinuities, and require more research.

9. NUMERICAL STABILITY

We have seen that the choice of Δ and Δt can affect the propagation characteristics of numerical waves in the FDTD space lattice, and therefore the numerical error. In addition, Δt must be bounded to ensure numerical stability. This can be seen from the following discussion, which summarizes the primary results on this topic reported in Ref. 2. We solve dispersion relation (13) for a potentially complex-valued numerical angular frequency ω_F , obtaining:

$$\omega_F = \frac{2}{\Delta t} \sin^{-1}(\xi) \quad (17a)$$

where

$$\xi = c\Delta t \left[\frac{1}{(\Delta x)^2} \sin^2\left(\frac{k_{F_x}\Delta x}{2}\right) + \frac{1}{(\Delta y)^2} \sin^2\left(\frac{k_{F_y}\Delta y}{2}\right) + \frac{1}{(\Delta z)^2} \sin^2\left(\frac{k_{F_z}\Delta z}{2}\right) \right]^{1/2} \quad (17b)$$

and k_{F_x} , k_{F_y} , and k_{F_z} are assumed to be real numbers. With a general field component V propagating in the space lattice as $V_{I,J,K}^n = V \exp[j(\omega_F n \Delta t - k_{F_x} I \Delta x - k_{F_y} J \Delta y - k_{F_z} K \Delta z)]$, we see that V grows exponentially with time (i.e., is numerically unstable) if $\text{Im}(\omega_F) < 0$. From (17), it can be shown that this condition is avoided if

$$\Delta t \leq \frac{1}{c \left[\frac{1}{(\Delta x)^2} + \frac{1}{(\Delta y)^2} + \frac{1}{(\Delta z)^2} \right]^{1/2}} \quad (18)$$

For a cubic cell space lattice with $\Delta x = \Delta y = \Delta z = \Delta$, (18) reduces to

$$\Delta t \leq \frac{\Delta/c}{3^{1/2}} \quad (19a)$$

which is equivalent to the following upper bound on the Courant stability factor $S = c\Delta t/\Delta$:

$$S_{3D} \leq 3^{-1/2} \quad (19b)$$

If S exceeds S_{3D} uniformly at all points within the space lattice, Ref. 2 shows that the following multiplicative growth factor occurs each timestep for the computed field components:

$$q_{3D} = \left\{ 3^{1/2}S + (3S^2 - 1)^{1/2} \right\}^2 \quad \text{for } S > 3^{-1/2} \quad (20)$$

For example, if S exceeds S_{3D} by only 0.05% (i.e., $S = 1.0005 \times 3^{-1/2}$), then (20) indicates a growth factor of 1.0653 every timestep. This is equivalent to field growth by 1.8822 every 10 timesteps, 558.7 every 100 timesteps, and 2.96×10^{27} every 1000 timesteps.

Similarly, Ref. 2 shows for a two-dimensional, square cell Yee grid the stability requirement

$$S_{2D} \leq 2^{-1/2} \quad (21a)$$

and the multiplicative growth factor per timestep

$$q_{2D} = \left\{ 2^{1/2}S + (2S^2 - 1)^{1/2} \right\}^2 \quad \text{for } S > 2^{-1/2} \quad (21b)$$

if the stability limit is exceeded. For a one-dimensional Yee grid, [2] shows the stability requirement

$$S_{1D} \leq 1 \quad (22a)$$

and the multiplicative growth factor per timestep

$$q_{1D} = \left\{ S + (S^2 - 1)^{1/2} \right\}^2 \quad \text{for } S > 1 \quad (22b)$$

if the stability limit is exceeded.

We note that numerical instability can arise if the Courant stability condition is violated at only a *single* point in a space lattice. In this case, a rapidly oscillating and growing noise component due to numerical instability originates at this point, rather than everywhere within the lattice. Despite this localization of the source of the instability, the numerical noise grows exponentially with timestep number n , ultimately filling and corrupting the entire grid.

There are ongoing active investigations of means to surmount the numerical stability constraints of standard FDTD methods based on Yee leapfrog timestepping. Techniques being considered fall into two primary categories: (1) unconditionally stable alternating-direction-implicit (ADI) formulations [24,25] wherein explicit Yee timestepping is replaced by a sequence of implicit field updates along linear cuts through the space grid and (2) novel "one-step" matrix exponential techniques, which, in principle, can eliminate timestepping altogether [26,27]. Thus far, the ADI approaches proposed in Refs. 24 and 25 have the limitation of progressively reduced accuracy as their

timestep is increased well beyond the normal FDTD stability limit [28]. Further, the one-step approaches proposed by De Raedt et al. [26,27] have not yet been able to incorporate absorbing outer grid boundaries, which are essential for the modeling of open-region electromagnetic wave interaction problems (see the following section). Advances in both ADI and one-step techniques for FDTD can be expected soon since the potential reward of greatly reduced computer running time per model is so attractive.

10. INTRODUCTION TO ABSORBING BOUNDARY CONDITIONS

Many electromagnetic wave interaction problems are defined on "open" regions where the spatial domain is partially or completely unbounded. Since no computer can store an unlimited dataset, FDTD space lattices for such problems must somehow be truncated without introducing error due to spurious reflection of outward-propagating numerical waves. Grid truncation conditions of this type are popularly called *absorbing boundary conditions* (ABCs) because of their requirement to absorb outward-propagating numerical modes with negligible reflection.

ABCs cannot be directly obtained from the Yee algorithm since it requires field data on both sides of an observation point, and hence cannot be implemented at the outermost planes of a space lattice. Although backward finite differences could be used, these are generally of lower accuracy for a given spatial resolution and have not been used in any major FDTD software.

Research in this area since 1970 has resulted in two principal categories of computationally efficient ABCs for FDTD simulations:

1. *Analytical*. Boundary conditions are imposed on the electromagnetic field and its spatial and temporal derivatives at the outermost planes of the space lattice [2]. Small numerical wave reflection coefficients in the order of 10^{-2} to 10^{-3} can be attained.
2. *Perfectly Matched Layer (PML)*. Specially formulated wave absorbing media are located within the space lattice adjacent to its outer planes, by analogy with the treatment of the walls of an anechoic chamber [13–15]. Extremely small numerical wave reflection coefficients in the order of 10^{-5} – 10^{-6} can be attained.

PML ABCs have proved to be significantly more effective than analytical ABCs, and are used in virtually all current commercial FDTD software. There are two primary categories of PML ABCs: (1) Berenger's split-field formulation [13] and (2) the anisotropic formulation [14,15]. These are now reviewed, following the more detailed discussion in Ref. 2.

11. BERENGER'S SPLIT-FIELD PML ABC

Consider implementing an ABC by using an impedance-matched electromagnetic wave absorbing layer adjacent to the outer planes of the FDTD space lattice. Ideally, the

absorbing medium is only a few lattice cells thick, reflectionless to all impinging waves over their full frequency spectrum, highly absorbing, and effective in the near field of a source or a scatterer. An early attempt at implementing such an absorbing material boundary condition was reported [29] utilizing a conventional lossy, dispersionless, absorbing medium. The difficulty with this tactic is that such an absorbing layer is matched only to normally incident plane waves.

Berenger [13] provided the seminal insight that a non-physical PML ABC can be implemented at the outer boundary of an FDTD grid to effectively absorb outgoing waves virtually regardless of their frequency, angle of incidence, and polarization, assuming that the interior medium is lossless, isotropic, and nondispersive. The key is to exploit additional degrees of freedom arising from a novel split-field formulation of Maxwell's equations. Here, each field vector component is split into two orthogonal components. For example, in Cartesian coordinates in three dimensions we have [30]

$$H_x = H_{xy} + H_{xz}; \quad H_y = H_{yx} + H_{yz}; \quad (23)$$

$$H_z = H_{zx} + H_{zy}$$

$$E_x = E_{xy} + E_{xz}; \quad E_y = E_{yx} + E_{yz}; \quad (24)$$

$$E_z = E_{zx} + E_{zy}$$

The 12 resulting field components are expressed as satisfying the following set of coupled partial-differential equations that are modifications of Maxwell's equations in source-free space:

$$\left(\mu \frac{\partial}{\partial t} + \sigma_y^*\right) H_{xy} = -\frac{\partial}{\partial y} (E_{zx} + E_{zy}) \quad (25a)$$

$$\left(\mu \frac{\partial}{\partial t} + \sigma_z^*\right) H_{xz} = \frac{\partial}{\partial z} (E_{yx} + E_{yz}) \quad (25b)$$

$$\left(\mu \frac{\partial}{\partial t} + \sigma_x^*\right) H_{yx} = \frac{\partial}{\partial x} (E_{zx} + E_{zy}) \quad (25c)$$

$$\left(\mu \frac{\partial}{\partial t} + \sigma_z^*\right) H_{yz} = -\frac{\partial}{\partial z} (E_{xy} + E_{xz}) \quad (25d)$$

$$\left(\mu \frac{\partial}{\partial t} + \sigma_x^*\right) H_{zx} = -\frac{\partial}{\partial x} (E_{yx} + E_{yz}) \quad (25e)$$

$$\left(\mu \frac{\partial}{\partial t} + \sigma_y^*\right) H_{zy} = \frac{\partial}{\partial y} (E_{xy} + E_{xz}) \quad (25f)$$

$$\left(\varepsilon \frac{\partial}{\partial t} + \sigma_y\right) E_{xy} = \frac{\partial}{\partial y} (H_{zx} + H_{zy}) \quad (26a)$$

$$\left(\varepsilon \frac{\partial}{\partial t} + \sigma_z\right) E_{xz} = -\frac{\partial}{\partial z} (H_{yx} + H_{yz}) \quad (26b)$$

$$\left(\varepsilon \frac{\partial}{\partial t} + \sigma_x\right) E_{yx} = -\frac{\partial}{\partial x} (H_{zx} + H_{zy}) \quad (26c)$$

$$\left(\varepsilon \frac{\partial}{\partial t} + \sigma_z\right) E_{yz} = \frac{\partial}{\partial z} (H_{xy} + H_{xz}) \quad (26d)$$

$$\left(\varepsilon \frac{\partial}{\partial t} + \sigma_x\right) E_{zx} = \frac{\partial}{\partial x} (H_{yx} + H_{yz}) \quad (26e)$$

$$\left(\varepsilon \frac{\partial}{\partial t} + \sigma_y\right) E_{zy} = -\frac{\partial}{\partial y} (H_{xy} + H_{xz}) \quad (26f)$$

Here, σ_x , σ_y , and σ_z denote electric conductivities, and σ_x^* , σ_y^* , and σ_z^* denote magnetic losses.

Equations (25) and (26) represent a generalization of the electrodynamics of physical media. In the normal case, if $\sigma_x = \sigma_y = \sigma_z = \sigma$ and $\sigma_x^* = \sigma_y^* = \sigma_z^* = \sigma^*$, then (25) and (26) describe a physically realizable isotropic medium having a combination of electric and magnetic losses. Additional possibilities present themselves, however. For example, if $\sigma_x \neq 0$ and $\sigma_x^* \neq 0$ but $\sigma_y = \sigma_y^* = 0$ and $\sigma_z = \sigma_z^* = 0$, then (25) and (26) describe a nonphysical medium that can attenuate waves propagating along the $\pm x$ directions but not along the $\pm y$ or $\pm z$ directions.

It is the latter situation that permits the PML ABC to be established. Continuing with the example above, assume that the interior of the FDTD space lattice is filled with a homogeneous, lossless, isotropic medium characterized by the electrical properties (ε_1, μ_1) . Berenger showed that, to effectively absorb waves propagating out of the lattice in the $\pm x$ directions, it is sufficient to locate adjacent to the x_{\min} and x_{\max} lattice outer boundaries layers of material that have the same (ε_1, μ_1) as the lattice interior and are subject to (25) and (26) with the constraint that σ_x and σ_x^* satisfy the "perfect" matching condition

$$\frac{\sigma_x}{\varepsilon_1} = \frac{\sigma_x^*}{\mu_1} \quad (27a)$$

At the interface between the lattice interior and the PML, this yields theoretically zero wave reflection for incident angles $-90^\circ < \phi < 90^\circ$ relative to the $\pm x$ axis regardless of the wave frequency. Within the PML, the transmitted wave propagates with the same speed and direction as the impinging wave while simultaneously undergoing exponential decay along the $\pm x$ axis. Choosing the PML thickness appropriately permits negligible overall wave reflection from the lattice terminations at x_{\min} and x_{\max} , which are usually assumed to be perfect electric conductors (PECs) having tangential electric field components set to zero for all timesteps.

In a similar manner, PML absorbers can be established adjacent to the other lattice outer-boundary planes. Adjacent to y_{\min} and y_{\max} , the PMLs again have the same (ε_1, μ_1) as the lattice interior, but here are subject to (25) and (26) with $(\sigma_x = \sigma_x^* = 0, \sigma_z = \sigma_z^* = 0)$ and $(\sigma_y \neq 0, \sigma_y^* \neq 0)$ satisfying

$$\frac{\sigma_y}{\varepsilon_1} = \frac{\sigma_y^*}{\mu_1} \quad (27b)$$

Adjacent to z_{\min} and z_{\max} , the PMLs again have the same (ε_1, μ_1) as the lattice interior, but here are subject to (25)

and (26) with $(\sigma_x = \sigma_x^* = 0, \sigma_y = \sigma_y^* = 0)$ and $(\sigma_z \neq 0, \sigma_z^* \neq 0)$ satisfying

$$\frac{\sigma_z}{\epsilon_1} = \frac{\sigma_z^*}{\mu_1} \quad (27c)$$

Figure 5 illustrates the structure of a two-dimensional FDTD grid employing the Berenger PML ABC in this manner. Note that the electric and magnetic losses defined in any overlapping PMLs in the grid corners are continued into the overlap regions.

12. ANISOTROPIC PML (APML) ABC

The split-field PML introduced by Berenger is a hypothetical, nonphysical medium based on a mathematical model. Because of the coordinate dependence of the loss terms, if such a physical medium exists, it must be anisotropic. Indeed, a physical model based on an anisotropic, perfectly matched medium can be formulated. This was first discussed by Sacks et al. [14]. For a single interface, the anisotropic medium is uniaxial and is composed of both electric and magnetic constitutive tensors. This anisotropic PML, or APML, performs as well as Berenger's PML while avoiding its nonphysical field splitting. Further, as summarized in Ref. 2, the APML has capabilities exceeding those of Berenger's PML by providing additional degrees of freedom which permit it to attenuate evanescent waves and terminate conductive and dispersive materials.

We first summarize the analytical formulation of the APML. Following Ref. 2, this can be most easily done in the phasor (sinusoidal steady-state) domain, where we can write Maxwell's curl equations in a three-dimensional APML medium as

$$\nabla \times \mathbf{H} = j\omega\epsilon\mathbf{E}; \quad \nabla \times \mathbf{E} = -j\omega\mu\mathbf{H} \quad (28)$$

Here, the field vectors are complex-valued phasors, and s is the tensor defined by

$$s = \begin{bmatrix} s_x^{-1} & 0 & 0 \\ 0 & s_x & 0 \\ 0 & 0 & s_x \end{bmatrix} \begin{bmatrix} s_y & 0 & 0 \\ 0 & s_y^{-1} & 0 \\ 0 & 0 & s_y \end{bmatrix} \begin{bmatrix} s_z & 0 & 0 \\ 0 & s_z & 0 \\ 0 & 0 & s_z^{-1} \end{bmatrix} \quad (29)$$

$$= \begin{bmatrix} s_y s_z s_x^{-1} & 0 & 0 \\ 0 & s_x s_z s_y^{-1} & 0 \\ 0 & 0 & s_x s_y s_z^{-1} \end{bmatrix}$$

Allowing for a nonunity real part κ , the multiplicative components of the diagonal elements of s are given by

$$s_x = \kappa_x + \frac{\sigma_x}{j\omega\epsilon}; \quad s_y = \kappa_y + \frac{\sigma_y}{j\omega\epsilon}; \quad (30)$$

$$s_z = \kappa_z + \frac{\sigma_z}{j\omega\epsilon}$$

If desired, the APML medium can be specialized to apply throughout the entire FDTD space lattice. The following lists all of the possible special cases.

Lossless, Isotropic Interior Zone. s is the identity tensor realized by setting $s_x = s_y = s_z = 1$ in (29). This requires $\sigma_x = \sigma_y = \sigma_z = 0$ and $\kappa_x = \kappa_y = \kappa_z = 1$ in (30).

APML Absorbers at x_{\min} and x_{\max} Lattice Outer-Boundary Planes. We set $s_y = s_z = 1$ in (29). This requires $\sigma_y = \sigma_z = 0$ and $\kappa_y = \kappa_z = 1$ in (30).

APML Absorbers at y_{\min} and y_{\max} Lattice Outer-Boundary Planes. We set $s_x = s_z = 1$ in (29). This requires $\sigma_x = \sigma_z = 0$ and $\kappa_x = \kappa_z = 1$ in (30).

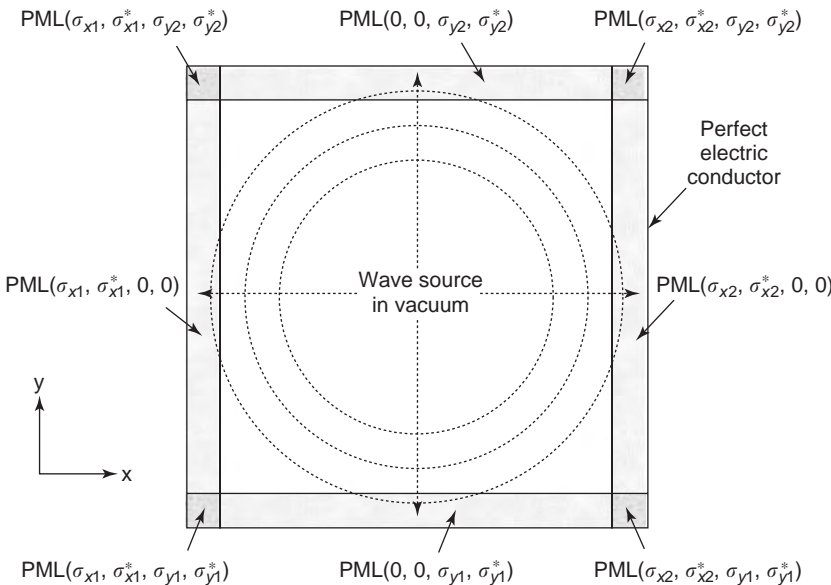


Figure 5. Structure of a two-dimensional FDTD grid employing the Berenger PML absorbing boundary condition [13].

APML Absorbers at z_{\min} and z_{\max} Lattice Outer-Boundary Planes. We set $s_x = s_y = 1$ in (29). This requires $\sigma_x = \sigma_y = 0$ and $\kappa_x = \kappa_y = 1$ in (30).

Overlapping APML Absorbers at x_{\min} , x_{\max} and y_{\min} , y_{\max} Dihedral Corners. We set $s_z = 1$ in (29). This requires $\sigma_z = 0$ and $\kappa_z = 1$ in (30).

Overlapping APML Absorbers at x_{\min} , x_{\max} and z_{\min} , z_{\max} Dihedral Corners. We set $s_y = 1$ in (29). This requires $\sigma_y = 0$ and $\kappa_y = 1$ in (30).

Overlapping APML Absorbers at y_{\min} , y_{\max} and z_{\min} , z_{\max} Dihedral Corners. We set $s_x = 1$ in (29). This requires $\sigma_x = 0$ and $\kappa_x = 1$ in (30).

Overlapping APML Absorbers at all Trihedral Corners. We use the complete general tensor in (29).

We next summarize the efficient implementation of the APML in a Cartesian FDTD formulation. Following the derivation discussed in detail in Ref. 2, explicit timestepping of the components of \mathbf{E} in the APML requires two steps in sequence: (1) updating the values of the components of an auxiliary-defined field variable \mathbf{D} and (2) using these new \mathbf{D} components to obtain updated values of the \mathbf{E} components. For example, the D_x update is given by

$$D_x|_{i+1/2,j,k}^{n+1} = \left(\frac{2\varepsilon\kappa_y - \sigma_y\Delta t}{2\varepsilon\kappa_y + \sigma_y\Delta t} \right) D_x|_{i+1/2,j,k}^n + \left(\frac{2\varepsilon\Delta t}{2\varepsilon\kappa_y + \sigma_y\Delta t} \right) \times \left(\frac{H_z|_{i+1/2,j+1/2,k}^{n+1/2} - H_z|_{i+1/2,j-1/2,k}^{n+1/2}}{\Delta y} - \frac{H_y|_{i+1/2,j,k+1/2}^{n+1/2} - H_y|_{i+1/2,j,k-1/2}^{n+1/2}}{\Delta z} \right) \quad (31a)$$

The subsequent E_x update is given by

$$E_x|_{i+1/2,j,k}^{n+1} = \left(\frac{2\varepsilon\kappa_z - \sigma_z\Delta t}{2\varepsilon\kappa_z + \sigma_z\Delta t} \right) E_x|_{i+1/2,j,k}^n + \left[\frac{1}{(2\varepsilon\kappa_z + \sigma_z\Delta t)\varepsilon} \right] \times \left[(2\varepsilon\kappa_x + \sigma_x\Delta t)D_x|_{i+1/2,j,k}^{n+1} - (2\varepsilon\kappa_x - \sigma_x\Delta t)D_x|_{i+1/2,j,k}^n \right] \quad (31b)$$

A similar two-step procedure is required to implement an explicit timestepping of the components of \mathbf{H} in the APML: (1) updating the values of the components of an auxiliary-defined field variable \mathbf{B} and (2) using these new \mathbf{B} components to obtain updated values of the \mathbf{H} components. For example, the B_x update is given by

$$B_x|_{i,j+1/2,k+1/2}^{n+3/2} = \left(\frac{2\varepsilon\kappa_y - \sigma_y\Delta t}{2\varepsilon\kappa_y + \sigma_y\Delta t} \right) B_x|_{i,j+1/2,k+1/2}^{n+1/2} - \left(\frac{2\varepsilon\Delta t}{2\varepsilon\kappa_y + \sigma_y\Delta t} \right) \times \left(\frac{E_z|_{i,j+1,k+1/2}^{n+1} - E_z|_{i,j,k+1/2}^{n+1}}{\Delta y} - \frac{E_y|_{i,j+1/2,k+1}^{n+1} - E_y|_{i,j+1/2,k}^{n+1}}{\Delta z} \right) \quad (32a)$$

The subsequent H_x update is given by

$$H_x|_{i,j+1/2,k+1/2}^{n+3/2} = \left(\frac{2\varepsilon\kappa_z - \sigma_z\Delta t}{2\varepsilon\kappa_z + \sigma_z\Delta t} \right) H_x|_{i,j+1/2,k+1/2}^{n+1/2} + \left[\frac{1}{(2\varepsilon\kappa_z + \sigma_z\Delta t)\mu} \right] \left[(2\varepsilon\kappa_x + \sigma_x\Delta t)B_x|_{i,j+1/2,k+1/2}^{n+3/2} - (2\varepsilon\kappa_x - \sigma_x\Delta t)B_x|_{i,j+1/2,k+1/2}^{n+1/2} \right] \quad (32b)$$

Nehrbass et al. [31] showed that such an algorithm is numerically stable within the Courant limit. Further, Abarbanel and Gottlieb [32] showed that the resulting discrete fields satisfy Gauss' law, and the APML is well posed. Finally, Ref. 2 discussed how the APML formulation in both the frequency and the time domains can be extended to terminate material regions in the FDTD space grid that are either electrically lossy or have frequency-dispersive dielectric parameters.

13. PML PERFORMANCE

Consider a PML of thickness T used to terminate the FDTD space lattice, which is assumed to have PEC outermost planes. There are two primary contributors to nonphysical wave reflections generated by this ABC configuration: (1) the PEC wall backing the PML and (2) the interface between the interior lattice medium and the PML.

Minimizing wave reflection due to the PEC backing wall calls for the greatest possible PML thickness and/or electrical loss. However, blindly increasing the PML loss can actually lead to degraded overall performance due to increased wave reflections at the interior PML interface. The latter represent a numerical artifact arising from the finite spatial sampling inherent in the FDTD algorithm. To reduce this artifact, Berenger [13] proposed that PML losses gradually increase with depth d within the PML along the w direction normal to the PML interface. Subsequently, several such profiles have been investigated. One of the most successful uses a simple polynomial variation of the PML loss:

$$\sigma_w(d) = \left(\frac{d}{T} \right)^m \sigma_{w,\max} \quad (33a)$$

$$\kappa_w(d) = 1 + (\kappa_{w,\max} - 1) \cdot \left(\frac{d}{T} \right)^m \quad (33b)$$

This increases the value of the PML σ_w from zero at $d = 0$ (the interior surface of the PML) to $\sigma_{w,\max}$ at $d = T$ (the PEC outer boundary of the space lattice). Similarly, for the APML, κ_x increases from one at $d = 0$ to $\kappa_{w,\max}$ at $d = T$.

For a fixed PML thickness T , the polynomial grading of (33a) provides two adjustable parameters: polynomial order m and $\sigma_{w,\max}$. Through extensive numerical experimentation [2], $3 \leq m \leq 4$ has been found to be nearly optimal for many FDTD simulations. Furthermore, for many applications, an optimal value of $\sigma_{w,\max}$ for

10-cell-thick PML is estimated to be [2]

$$\sigma_{w,\max} \approx \frac{0.8(m+1)}{\eta\Delta} \quad (34)$$

where η is the wave impedance of the PML medium. For detailed discussions and examples of PML performance over a wide range of possible loss profiles, see Ref. 2.

14. WAVE SOURCES

In this section, we consider means to introduce into the FDTD space lattice electromagnetic wave excitations appropriate for modeling engineering problems. Six numerical wave sources are reviewed: (1) \mathbf{E} and \mathbf{H} hard sources, (2) \mathbf{J} and \mathbf{M} current sources, (3) total-field/scattered-field lattice zoning, (4) the all-scattered-field formulation, (5) waveguide sources, and (6) interface with linear and nonlinear electronic circuits.

14.1. \mathbf{E} and \mathbf{H} Hard Sources

\mathbf{E} and \mathbf{H} hard sources are set up simply by assigning desired time functions to specific components of \mathbf{E} and/or \mathbf{H} in the FDTD space lattice. The time functions are independent of anything else in the model. Hard sources radiate numerical waves having time waveforms corresponding to the source functions.

While hard sources are very easy to implement, they cause spurious, nonphysical reflections of any numerical waves propagating in their vicinity. This is because hard sources effectively enforce nonphysical field boundary conditions. One way to time-limit the reflective nature of an impulsive hard source is simply to replace it with a normal free-space Yee field update after its pulse time waveform has decayed essentially to zero. However, this is not appropriate for source waveforms such as continuous sinusoids that have extended durations.

In FDTD models where hard sources can be used, analysis has shown that such sources do not behave as pointwise emitters of numerical waves. In fact, hard sources have a finite effective radius of approximately 0.2 lattice cell [33].

14.2. \mathbf{J} and \mathbf{M} Current Sources

\mathbf{J} and \mathbf{M} current sources are set up simply by assigning desired time functions to specific components of \mathbf{J} and/or \mathbf{M} in the FDTD space lattice. Similar to \mathbf{E} and \mathbf{H} hard sources, \mathbf{J} and \mathbf{M} current sources radiate numerical waves having time waveforms corresponding to the source functions. However, unlike hard sources, \mathbf{J} and \mathbf{M} current sources cause *no* nonphysical reflections of numerical waves propagating in their vicinity. This is because such current sources behave in an additive manner relative to the ambient electromagnetic field and set no field boundary conditions whatsoever.

A key nuance is that \mathbf{J} and \mathbf{M} current sources can deposit charge and generate charge-associated fields in three-dimensional FDTD space lattices. These fields, which are required to satisfy the continuity equation,

can persist indefinitely and hence remain in the computational domain even after all of the radiated fields have exited [34].

14.3. Total-Field/Scattered-Field Lattice Zoning

Total-field/scattered-field (TF/SF) lattice zoning permits implementation of a numerical plane-wave source in the FDTD space lattice. Such a wave source is characterized by

- Arbitrary wave propagation direction, polarization, time waveform, and duration
- Constant field amplitude along planes perpendicular to the direction of propagation
- Invisibility relative to any other numerical waves in the space lattice

The TF/SF formulation is based on the linearity of Maxwell's equations. It assumes that the physical (measurable) total electric and magnetic fields $\mathbf{E}_{\text{total}}$ and $\mathbf{H}_{\text{total}}$ can be decomposed as

$$\mathbf{E}_{\text{total}} = \mathbf{E}_{\text{inc}} + \mathbf{E}_{\text{scat}} \quad (35a)$$

$$\mathbf{H}_{\text{total}} = \mathbf{H}_{\text{inc}} + \mathbf{H}_{\text{scat}} \quad (35b)$$

Here \mathbf{E}_{inc} and \mathbf{H}_{inc} are the values of the incident-wave fields, assumed to be known at all points of the space lattice at all timesteps. These are the fields that would exist in vacuum, that is, if there were no materials of any sort in the modeling space. \mathbf{E}_{scat} and \mathbf{H}_{scat} are the values of the scattered-wave fields, which are initially unknown. These result from the interaction of the incident wave with any materials in the space lattice.

We note that the finite-difference operations of the Yee algorithm can be applied with equal validity to the incident field, the scattered field, and the total field. As shown in Fig. 6, this property permits zoning of the Yee space lattice into two distinct regions:

- *Region 1*—the inner zone of the space lattice. Here, total fields are assumed to be stored in the computer memory and operated on by the Yee algorithm. The interacting structure of interest is embedded within this region.
- *Region 2*—the outer zone of the space lattice surrounding region 1. Here, scattered fields are assumed to be stored in the computer memory and operated on by the Yee algorithm. There is no incident wave in region 2. The outer lattice planes bounding region 2 truncate the computation space and serve to implement an absorbing boundary condition, as discussed in the previous section.

Regions 1 and 2 are separated by the TF/SF interface, a virtual surface connecting the fields in each region that generates the incident numerical plane wave. The algorithms that implement the TF/SF interface for one-, two-, and three-dimensional FDTD space lattices are discussed in detail in Ref. 2.

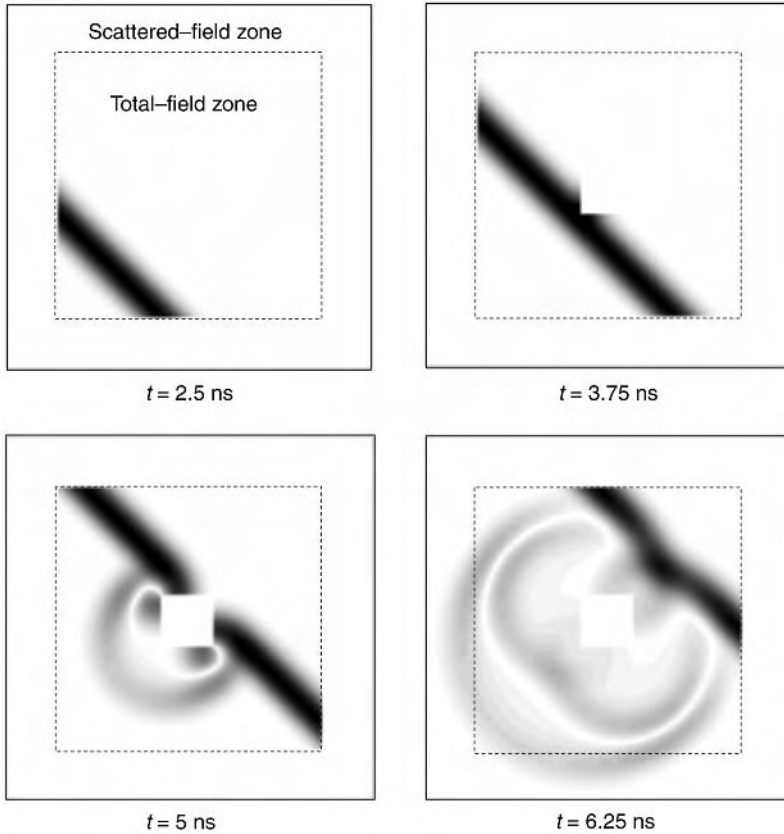


Figure 7. Action of total-field/scattered-field grid zoning for a plane wave propagating obliquely within a transverse electric grid impinging on a square perfectly conducting cylinder [2]. The H_z field is visualized in four successive snapshots as the wave propagates through the total-field zone.

technique. Incident fields can be calculated *exactly* using an analytical expression, rather than via numerical propagation through the FDTD space lattice. This eliminates phase/delay errors in the incident wave excitation caused by numerical dispersion, an increasingly important consideration as the electrical size of the modeled structure increases.

Holland et al. [36] reported the initial application of the all-scattered-field formulation of FDTD to lossy dielectric structures showing that Maxwell's equations could be written for isotropic nondispersive dielectrics as

$$\mu \frac{\partial \mathbf{H}_{\text{scat}}}{\partial t} + \sigma^* \mathbf{H}_{\text{scat}} = -\nabla \times \mathbf{E}_{\text{scat}} - \sigma^* \mathbf{H}_{\text{inc}} - (\mu - \mu_0) \frac{\partial \mathbf{H}_{\text{inc}}}{\partial t} \quad (37)$$

$$\varepsilon \frac{\partial \mathbf{E}_{\text{scat}}}{\partial t} + \sigma \mathbf{E}_{\text{scat}} = \nabla \times \mathbf{H}_{\text{scat}} - \sigma \mathbf{E}_{\text{inc}} - (\varepsilon - \varepsilon_0) \frac{\partial \mathbf{E}_{\text{inc}}}{\partial t} \quad (38)$$

Equations (37) and (38) can be numerically implemented in the conventional manner using Yee differences. The additional computational burden is that the incident fields and/or their time derivatives must be calculated at all lattice locations where $\sigma^* \neq 0$, $\sigma \neq 0$, $\mu \neq \mu_0$, or $\varepsilon \neq \varepsilon_0$.

14.5. Waveguide Sources

FDTD models of waveguides can be excited in ways analogous to those discussed above for the free-space case [2]. In certain cases, the transverse field distribution of the desired propagating waveguide mode is known analytically, allowing the numerical wave that is launched to immediately represent the desired mode without generating undesired propagating modes or below-cutoff reactive fields. In other cases, the transverse distribution of the desired mode is initially unknown or can be only approximated. There are two options in this situation:

- *Implement an approximation of the true mode.* An example is the excitation of a collinear array of \mathbf{E} or \mathbf{J} components in the FDTD space lattice to simulate a probe extending from a waveguide wall and dead ending in air at a point halfway to the opposing wall. Depending on the frequency content of the excitation, this can generate a spectrum of numerical waves including the desired mode, undesired high-order modes, and nonpropagating (cutoff) reactive fields. A substantial buffer length of waveguide may be required in the model to permit any reactive fields to decay.
- *Use "bootstrapping."* This involves running a preliminary FDTD model of the waveguide that is designed to propagate only the desired fundamental mode and is sufficiently long to decay undesired reactive fields.

The complete normalized transverse field distribution at the far end of this preliminary model is stored in a data file and is subsequently used in all production runs as a compact \mathbf{E} hard source or \mathbf{J} current source. (In the case of a dielectric waveguide, this includes the significant transverse fields located both internal and external to the waveguide.) Effectively, the preliminary FDTD run is used to solve for the correct transverse modal field distribution.

14.6. Interface with Linear and Nonlinear Electronic Circuits

An emerging sixth type of wave source involves interfacing a passive FDTD space lattice with a time-domain numerical model of an active linear or nonlinear electronic device or circuit. Here, potential excitation sources include discrete transistors and logic gates, and even complete circuits composed of many such discrete devices. Hybrid FDTD/electronic circuit models are increasingly useful in constructing self-consistent simulations of high-speed circuits embedded within electromagnetic wave transmission and radiation systems. A summary of techniques in this area is provided in Ref. 2.

15. NEAR-FAR-FIELD TRANSFORMATION

The provision of a scattered-field region in the FDTD space lattice via either total-field/scattered-field lattice zoning or an all-scattered-field lattice (as described in the previous section) permits a systematic *near-far-field transformation*. In other words, there is *no* need to extend the FDTD space lattice to the far field to obtain far-field data.

The near-far-field transformation is based on the surface equivalence theorem [37], illustrated in Fig. 8. This theorem permits electromagnetic fields in an exterior region to be rigorously calculated from equivalent non-physical currents properly defined over an arbitrary virtual surface S that completely encloses the original antenna or scatterer, even if S is located in the near field.

Figure 8a depicts schematically the most general case dealing with an arbitrary three-dimensional structure. Following the notation of Balanis [37], we assume that a field $(\mathbf{E}_1, \mathbf{H}_1)$ filling all of space is generated by the action of the physical electric and magnetic currents \mathbf{J}_1 and \mathbf{M}_1 associated with the antenna or scatterer of interest. In Fig. 8b, we assume that \mathbf{J}_1 and \mathbf{M}_1 are removed, and that there now exists a new field (\mathbf{E}, \mathbf{H}) inside virtual surface S

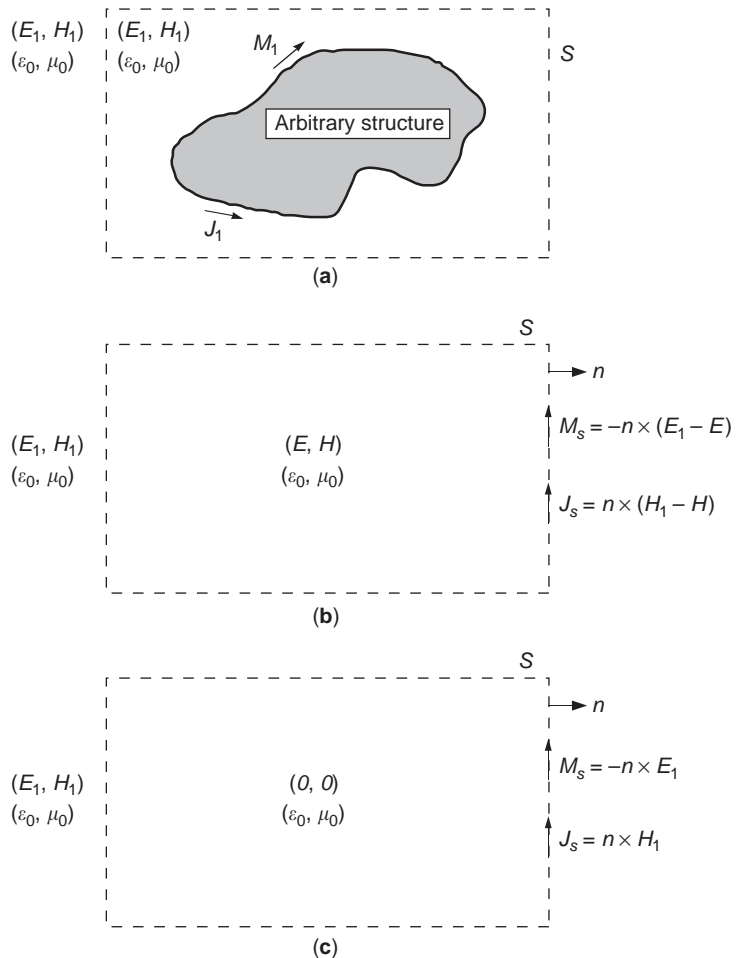


Figure 8. Definition of electromagnetic fields and equivalent electric and magnetic virtual currents for the surface equivalence theorem: (a) original interaction geometry; (b) intermediate equivalent problem; (c) final equivalent problem [37].

that completely encloses the structure. However, we wish to observe the original field $(\mathbf{E}_1, \mathbf{H}_1)$ outside S . For this desired situation to satisfy the required electromagnetic field boundary conditions on the tangential \mathbf{E} - and \mathbf{H} -field components at S , there must exist the following virtual electric and magnetic currents flowing tangentially along S :

$$\mathbf{J}_S = \mathbf{n} \times (\mathbf{H}_1 - \mathbf{H}) \quad (39a)$$

$$\mathbf{M}_S = -\mathbf{n} \times (\mathbf{E}_1 - \mathbf{E}) \quad (39b)$$

where \mathbf{n} is the unit outward normal vector to S . The virtual electric and magnetic currents of (39) radiate into free space everywhere (inside and outside S), and generate the original field $(\mathbf{E}_1, \mathbf{H}_1)$ in the unbounded free-space region outside S . Since the fields within S can be anything (and we are not concerned with this region anyway with regard to developing far-field information), it is useful to assume that $\mathbf{E} = 0$ and $\mathbf{H} = 0$ inside S . Then, the equivalent problem of Fig. 8b reduces to Fig. 8c, with equivalent current densities equal to

$$\mathbf{J}_S = \mathbf{n} \times (\mathbf{H}_1 - \mathbf{H})|_{\mathbf{H}=0} = \mathbf{n} \times \mathbf{H}_1 \quad (40a)$$

$$\mathbf{M}_S = -\mathbf{n} \times (\mathbf{E}_1 - \mathbf{E})|_{\mathbf{E}=0} = -\mathbf{n} \times \mathbf{E}_1 \quad (40b)$$

Using the surface equivalence theorem, a phasor-domain near-far-field transformation can be efficiently implemented for Cartesian FDTD models of arbitrary three-dimensional structures. Here, S is a six-sided rectangular “box” that completely encloses the structure of interest in the scattered-field zone of the FDTD space lattice. Along each face of S , distributions of the equivalent phasor electric current \mathbf{J}_S and phasor magnetic current \mathbf{M}_S are calculated from (40) using discrete Fourier transformations (DFTs) that are applied to the FDTD-computed tangential \mathbf{H} and \mathbf{E} fields, respectively, “on the fly” during timestepping. Then, as introduced in Ref. 38 and discussed in detail in Ref. 2, these equivalent currents are integrated with a free-space Green’s function weighting to obtain the desired normalized far-field patterns of the scattered or radiated power.

In this manner, a single FDTD run that models the impulsive plane-wave illumination of a scattering object provides sufficient data to calculate the complete far-field bistatic radar cross-sectional pattern of the object at *multiple* sinusoidal frequencies for the incidence and polarization angles of the illuminating wave used in the modeling run. Similarly, a single FDTD run that models the impulsive excitation of an antenna provides sufficient data to calculate the complete far-field radiation pattern of the antenna at multiple sinusoidal frequencies.

An alternative time-domain near-far-field transformation is discussed by Luebbers et al. [39]. While FDTD timestepping proceeds in a particular modeling run, this transformation allows calculation of the evolving time waveforms of the scattered or radiated \mathbf{E} and \mathbf{H} fields at selected angular locations in the far field. Phasor-domain

results can be obtained in a subsequent postprocessing step via Fourier transformation of the calculated time waveforms.

16. EXAMPLES OF FDTD MODELING APPLICATIONS

Current examples of FDTD modeling applications span much of the electromagnetic spectrum. A worldwide FDTD developer/user community is involved in numerical simulation of electrodynamic phenomena ranging from extremely low-frequency (ELF) propagation about the entire Earth to the lasing behavior of aggregates of micrometer-scale particles exhibiting four-level quantum system characteristics. Such applications of FDTD vividly illustrate the principle that “Maxwell’s equations work from DC to light.” This section provides examples of current and emerging FDTD applications that literally span this range.

16.1. Global ELF Propagation within the Earth-Ionosphere Waveguide

Global propagation of extremely low-frequency (ELF: 3 Hz–3 kHz) and very low-frequency (VLF: 3 kHz–30 kHz) electromagnetic waves within the Earth-ionosphere waveguide has been the subject of recurring theoretical and experimental interest for decades. ELF/VLF propagation phenomena form the physics basis of submarine communications and remote-sensing investigations of lightning and sprites, global temperature change, subsurface structures, and potential earthquake precursors.

Most theoretical techniques for modeling ELF/VLF propagation are based on frequency-domain waveguide-mode theory. However, these techniques cannot account for arbitrary horizontal as well as vertical geometric and electrical inhomogeneities of the ionosphere, continents, and oceans. Recently, a full-vector, three-dimensional, spherical coordinate FDTD model has been used to calculate impulsive ELF propagation within the entire Earth-ionosphere waveguide. All features of the lithosphere and ionosphere located within ± 100 km of sea level are modeled with a resolution of approximately $40 \times 40 \times 5$ km [40]. Periodic boundary conditions are used in conjunction with a variable-cell grid that wraps around the complete Earth sphere. The model is verified by numerical studies of frequency-dependent propagation attenuation with distance, antipodal propagation, and the Schumann resonance. Figure 9 visualizes the results of one such model, which illustrates the propagation about Earth of an ELF electromagnetic pulse generated by a vertical lightning stroke off the coast of South America.

16.2. High-Speed Electronics

High-speed electronic circuits have been traditionally grouped into two classes: analog microwave circuits and digital logic circuits.

1. Microwave circuits typically process bandpass signals at frequencies above 3 GHz. Common circuit features include microstrip transmission lines,

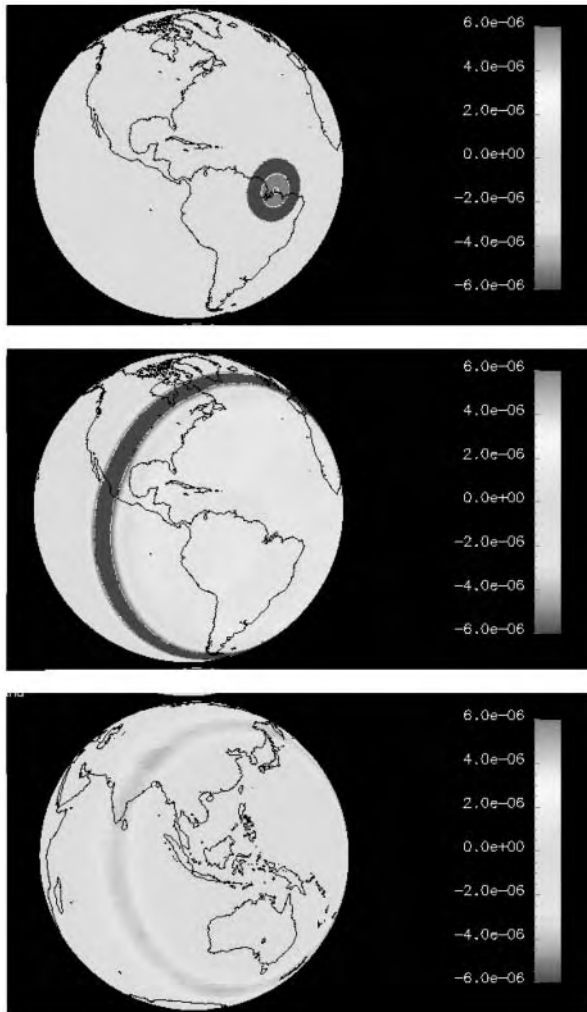


Figure 9. Snapshot visualizations of the FDTD-computed global propagation of an ELF electromagnetic pulse generated by a lightning strike off the coast of South America [40]. All features of the lithosphere and atmosphere located within ± 100 km of sea level are modeled in three dimensions with a resolution of approximately $40 \times 40 \times 5$ km. (This figure is available in full color at <http://www.mrw.interscience.wiley.com/erfme>.)

directional couplers, circulators, filters, matching networks, and individual transistors. Circuit operation is fundamentally based on electromagnetic wave phenomena.

2. Digital circuits typically process lowpass pulses requiring a DC return. Typical circuits include multiple planes of metal traces for signal transmission, power supply, and ground return. Via pins provide electrical connections between the planes. Circuit operation is nominally not based on electromagnetic wave effects.

However, the distinction between the design of these two classes is blurred. The rise of everyday computer clock speeds above 3 GHz implies digital signal bandwidths above 10 GHz, well into the microwave range. Electromagnetic wave effects that, until now, were in the domain of the microwave engineer are becoming a limiting factor in

digital circuit operation. For example, hard-won experience has shown that high-speed digital signals can spuriously

- Distort as they propagate along the metal circuit paths
- Couple (create crosstalk) from one circuit path to another
- Radiate and create interference to other circuits and systems

An example of electromagnetic field effects in a digital circuit is shown in Fig. 10, which illustrates the results of FDTD modeling of an ultra-high-speed logic pulse entering a microchip embedded within a conventional dual in-line package [41]. The fields associated with the logic pulse are not confined to the metal circuit paths and, in fact, smear out and couple to all adjacent circuit paths. We note that FDTD modeling permits incorporation of (1) a very high level of detail of the geometry and materials of the chip packaging and (2) the nonlinear active circuit components within the chip that terminate the metal

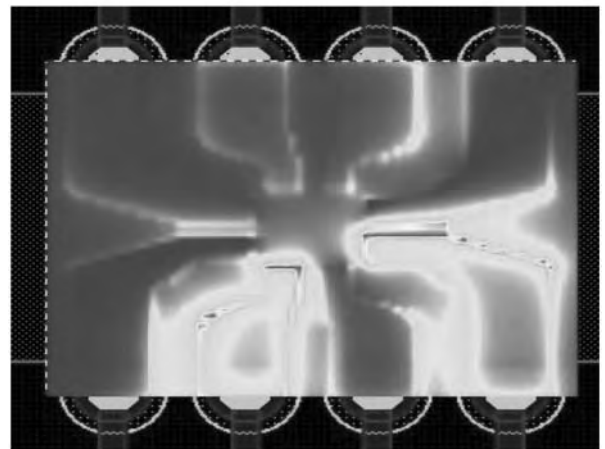
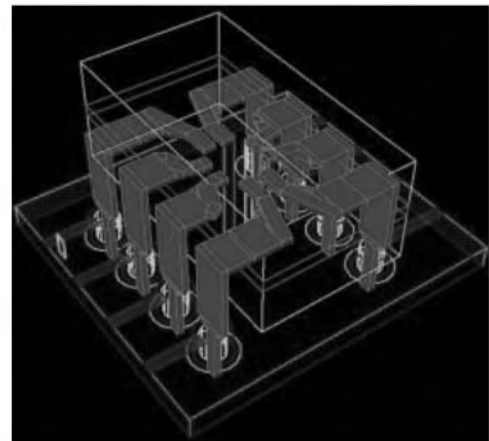


Figure 10. Snapshot visualization of the FDTD-computed coupling and crosstalk of a high-speed logic pulse entering and leaving a microchip embedded within a conventional dual in-line integrated circuit package [41]. The fields associated with the logic pulse are not confined to the metal circuit paths and, in fact, smear out and couple to all adjacent circuit paths. (This figure is available in full color at <http://www.mrw.interscience.wiley.com/erfme>.)

connections. These attributes provide the engineer with robust modeling capabilities to accurately assess the crosstalk problem and test potential remedies involving redesign of the microchip packaging.

16.3. Microwave Penetration and Coupling

FDTD computational electromagnetics has played an important role in helping to assess and mitigate the effects of electromagnetic wave coupling into sensitive electrical and electronic equipment. The primary sources of such waves include lightning, nuclear electromagnetic pulses (NEMPs), and high-power microwaves (HPMs).

NEMP can burn out electrical and electronic equipment on Earth's surface located many hundreds of miles away from the detonation of a nuclear bomb above Earth's atmosphere. Equipment failures on this geographic scale could leave a nation largely defenseless against subsequent attack. HPM can neutralize electronics in the manner as NEMP, but can be applied on a more selective basis for either tactical or strategic applications. For both NEMP and HPM, FDTD modeling has been used to understand the complex electromagnetic wave penetration and coupling mechanisms into potential targets, and means to mitigate these mechanisms. FDTD is particularly useful for these purposes since it can model extremely complicated three-dimensional structures in a straightforward manner. As an example, Fig. 11 illustrates the results of applying FDTD modeling to calculate the penetration of a pulsed 10-GHz microwave beam into a missile radome containing a horn antenna [42].

16.4. Ultrawideband Microwave Imaging for Early-Stage Breast Cancer Detection

Several researchers have conducted theoretical investigations of the use of ultrawideband microwave pulses for early-stage breast cancer detection. In principle, this technique could detect much smaller tumors over larger regions of the breast than is currently possible using X-ray mammography, and further avoid exposing the patient to potentially hazardous ionizing radiation. In this proposed technique, an array of small antennas would be placed on the surface of the breast to emit and then receive a short electromagnetic pulse lasting less than 100 ps. Signal processing techniques would then be applied to the received pulses at each antenna element to form the breast image.

In work to date, FDTD modeling has provided crucial simulated test data and allowed optimization of the imaging algorithms. As shown in Fig. 12, these simulations indicate promise for imaging small, deeply embedded malignant breast tumors in the presence of the background clutter due to the complicated surrounding normal tissues [43]. In this figure, the simulated 2-mm-diameter tumor has a volume that is about one order of magnitude smaller than that needed for reasonably reliable detection by X-ray mammography.

16.5. Photonic Integrated Circuits

Microcavity ring and disk resonators are proposed components for filtering, routing, switching, modulation, and

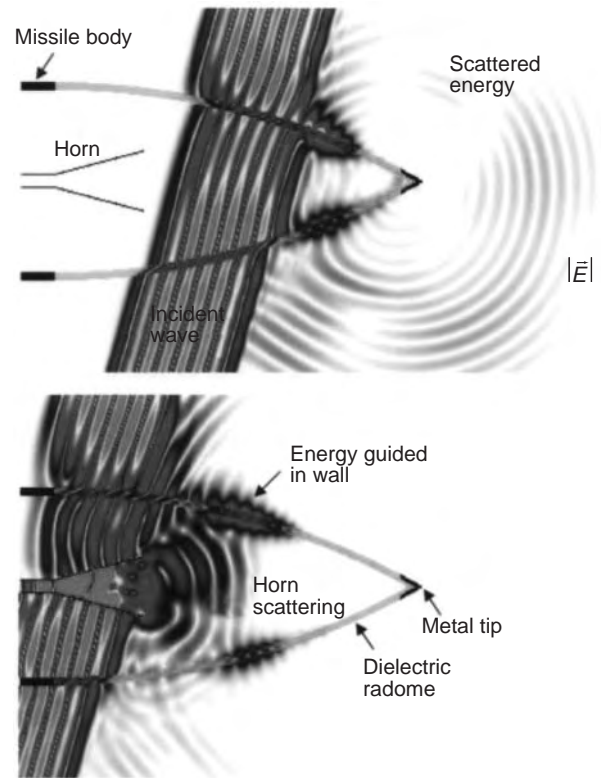


Figure 11. Snapshot visualizations of the FDTD-computed penetration of a short microwave pulse into a missile radome containing a horn antenna [42]. The impinging plane wave propagates from right to left at the speed of light and is obliquely incident at 15° from boresight. Complicated electromagnetic wave interactions visible within the radome structure require FDTD Maxwell's equations solutions to permit effective design. (This figure is available in full color at <http://www.mrw.interscience.wiley.com/erfme>.)

multiplexing/demultiplexing tasks in ultra-high-speed photonic integrated circuits. Figure 13 is a scanning electron microscope image of a prototype photonic circuit consisting of 5.0- μm -diameter aluminum gallium arsenide (AlGaAs) microcavity disk resonators coupled to 0.3- μm -wide optical waveguides across airgaps spanning 0.1–0.3 μm [44].

FDTD solutions of Maxwell's equations permit calculation of the optical coupling, transmission, and resonance behavior of the microoptical structures in Fig. 13. This permits effective engineering design. For example, Fig. 14 shows visualizations of the FDTD-calculated sinusoidal steady-state optical electric field distributions for a typical microdisk in Fig. 13 [45]. In the upper left panel, the optical excitation is at a nonresonant frequency, 193.4 THz (an optical wavelength λ of 1.55 μm). Here, 99.98% of the rightward-directed power in the incident signal remains in the lower waveguide. In the upper right panel, the excitation is at the resonant frequency of the first-order radial whispering-gallery mode of the microdisk, 189.2 THz ($\lambda = 1.585 \mu\text{m}$). Here, there is a large field enhancement within the microdisk, and 99.79% of the incident power switches to the upper waveguide in the reverse (leftward) direction. This yields the action of a passive, wavelength-selective switch.

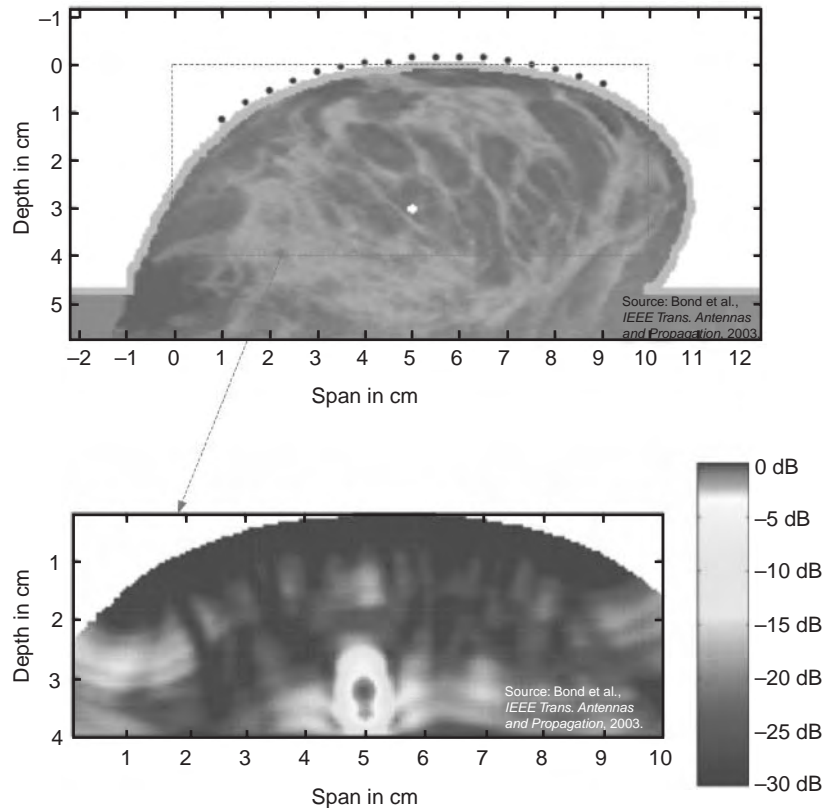


Figure 12. Top: 2D FDTD breast model derived from magnetic resonance imaging containing a 2-mm-diameter malignant lesion at a depth of 3.1 cm. The black dots along the surface of the breast represent positions from which an antenna transmits low-power ultrawideband pulses into the breast. Bottom: Image showing the backscattered energy as a function of location in the breast. The image was reconstructed from FDTD-computed backscattered waveforms using a spacetime beamforming approach. Note that the tumor signature is almost 100 times stronger than the backscattering clutter generated by the surrounding heterogeneous normal tissue [43]. (This figure is available in full color at <http://www.mrw.interscience.wiley.com/erfme>.)

The lower left and right panels of Fig. 14 are visualizations at, respectively, the resonant frequencies of the second- and third-order whispering-gallery modes, 191.3 THz ($\lambda = 1.567 \mu\text{m}$) and 187.8 THz ($\lambda = 1.596 \mu\text{m}$). A goal of current design efforts is to suppress higher-order modes to allow the use of microdisks as passive wave-

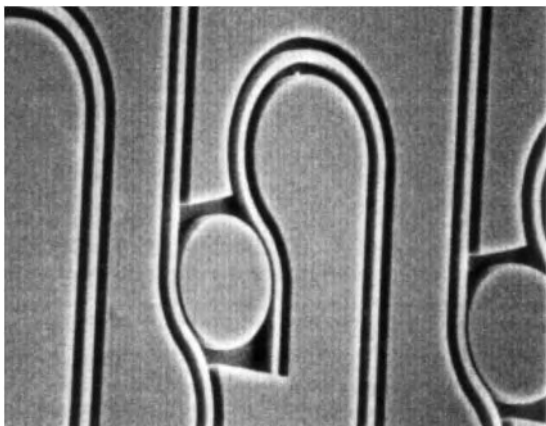


Figure 13. Scanning electron microscope image of a prototype photonic integrated circuit [44]. The photonic circuit is composed of 5.0- μm -diameter aluminum gallium arsenide (AlGaAs) microcavity disk resonators coupled to 0.3- μm -wide AlGaAs optical waveguides across airgaps spanning as little as 0.1 μm .

length-division multiplexing devices having low crosstalk across a wide spectrum, or as active single-mode laser sources.

16.6. Applications in Microcavity Laser Design

FDTD solutions of Maxwell's equations are being used to design the world's smallest microcavity laser sources for use in ultra-high-speed photonic integrated circuits. These sources are based on the physics of photonic crystals, which are artificial structures having a periodic variation of the refractive index. Photonic crystals have a frequency stopband over which there is no transmission of electromagnetic waves. However, a defect introduced into the periodic structure creates a resonant mode at a frequency that lies inside the bandgap. This defect behaves as a microcavity resonator to trap light.

Figure 15 (top) illustrates how light is contained inside a laser microcavity in a photonic crystal structure [46]. First, a half-wavelength thick high-refractive-index slab (consisting of indium gallium arsenic phosphide) is used to trap light in the vertical direction by total internal reflection. Then, light is localized in plane by the action of a two-dimensional photonic crystal consisting of a hexagonal array of submicrometer-radius airholes etched into the slab. In the simplest structure, a single airhole is removed from the photonic crystal,

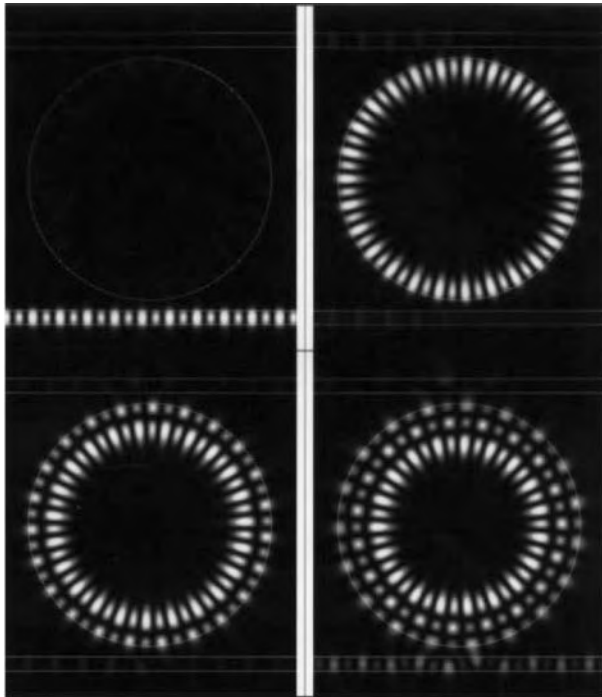


Figure 14. Visualizations of the FDTD-computed sinusoidal steady-state optical electric field distributions in a 5.0- μm -diameter AlGaAs microdisk resonator coupled to straight 0.3- μm -wide AlGaAs optical waveguides for single-frequency excitations propagating to the right in the lower waveguide [45]. Upper left: off-resonance signal. Upper right: on-resonance signal, first-order radial mode. Lower left: second-order radial-mode resonance. Lower right: third-order radial-mode resonance. (This figure is available in full color at <http://www.mrw.interscience.wiley.com/erfme>.)

thereby forming a resonant microcavity which traps light energy.

Figure 15 (bottom) visualizes along a planar cut through the middle of the slab the magnitude of the optical electric field calculated from a three-dimensional FDTD solution of Maxwell's equations. Nearly all of the laser power is emitted vertically. Experimental realization of this microcavity laser design indicates a lasing wavelength within 0.3% of the FDTD-predicted value. Ongoing research involves optimizing this and similar laser cavities by performing FDTD simulations to reduce the required pump power and facilitate room-temperature operation.

16.7. Incorporation of Quantum Effects

The final modeling example illustrates one of the most interesting current frontiers in FDTD theory and applications that may lead to significant advances in overall electrical engineering technology. This frontier involves the self-consistent modeling of a system of nanometer-scale sources (originating from quantum phenomena) interacting with each other and with external material geometries via electromagnetic wave energy transport over micrometer-distance scales.

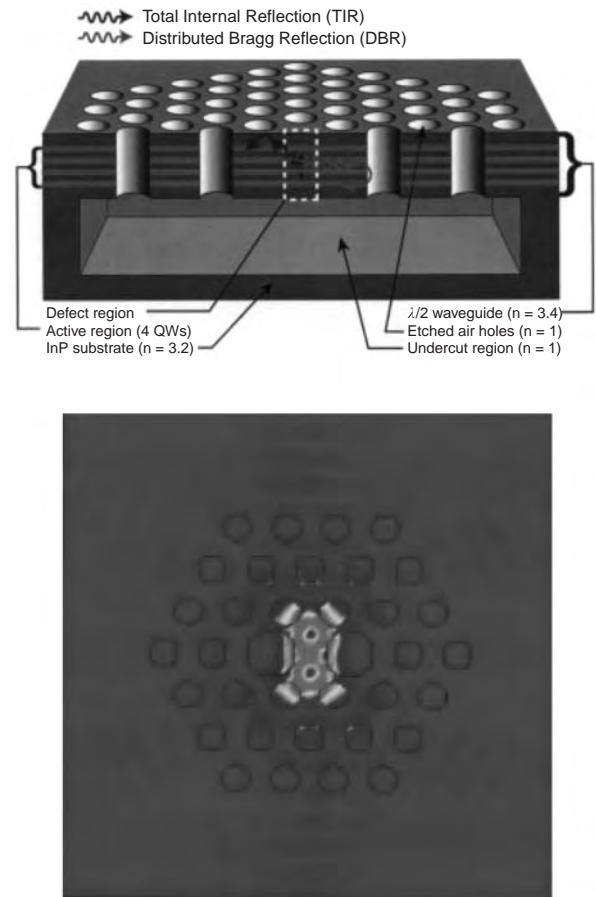


Figure 15. Photonic crystal microcavity laser [46]. Top: geometry. Bottom: visualization of the FDTD-computed optical electric field along a horizontal planar cut through the middle of the laser geometry. (This figure is available in full color at <http://www.mrw.interscience.wiley.com/erfme>.)

Figure 16 shows a specific problem where this type of modeling is being pursued: the exploration of the physics of lasing in random clusters of zinc oxide (ZnO_2) nanoparticles [47]. Here, quantized electron energy states in ZnO_2 are described by a four-level two-electron model consisting of a system of six simultaneous time-domain differential equations for the electron population densities and resulting induced polarizations. This system is coupled to a conventional two-dimensional FDTD Maxwell equation solver. Quantum phenomena such as the excitation of electrons to higher energy states, population inversion, and photon emission/stimulated emission are modeled concurrently with the classical phenomena of multiple scattering of optical electromagnetic waves within the particle cluster leading to light localization and potential lasing action.

As computing capabilities advance, the extension of such a multiphysics quantum/classical electrodynamics model to three dimensions will enable the development of robust and comprehensive engineering design tools for active photonic and quantum nanostructures. Nanostructures of these types may become the basis of much of mid-21st century communications and computing technologies in our society.

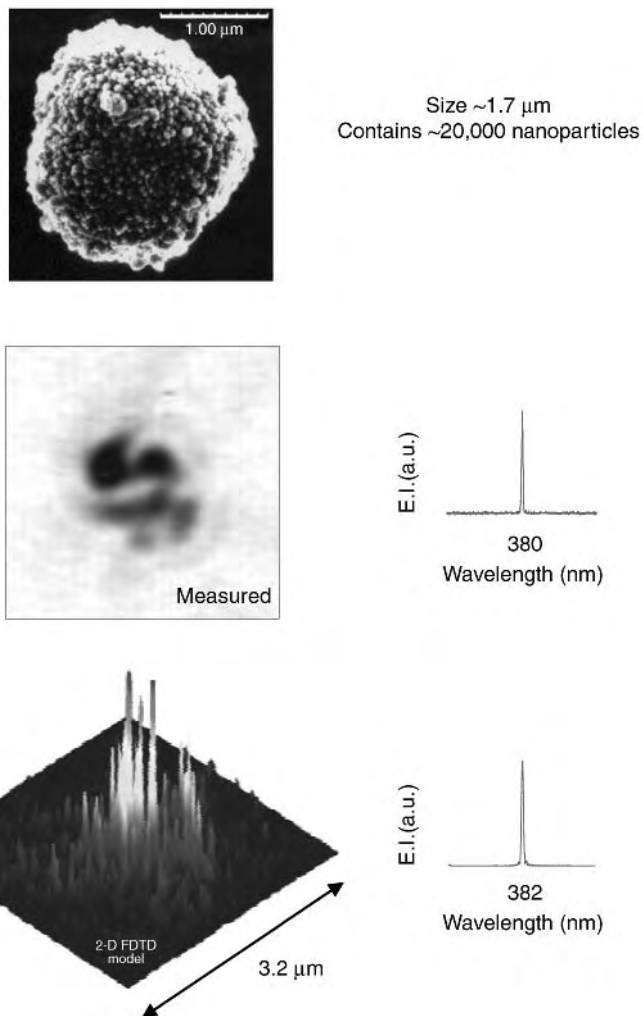


Figure 16. FDTD model of lasing in a random clump of zinc oxide (ZnO_2) nanoparticles. Population inversion and stimulated emission can be modeled using a four-energy-level, two-electron quantum model for ZnO_2 [47]. (This figure is available in full color at <http://www.mrw.interscience.wiley.com/erfme>.)

BIBLIOGRAPHY

1. K. S. Yee, Numerical solution of initial boundary value problems involving Maxwell's equations in isotropic media, *IEEE Trans. Anten. Propag.* **14**:302–307 (1966).
2. A. Taflove and S. C. Hagness, *Computational Electrodynamics: The Finite-Difference Time-Domain Method*, 2nd ed., Artech House, Norwood, MA, 2000.
3. (Online) <http://www.ece.northwestern.edu/ecefaculty/Allen1.html>.
4. T. Weiland, A discretization method for the solution of Maxwell's equations for six-component fields, *Electron. Commun.* **31**:116–120 (1977).
5. T. Weiland, Time domain electromagnetic field computation with finite difference methods, *Int. J. Num. Model.* **9**:295–319 (1996).
6. P. B. Johns and R. L. Beurle, Numerical solution of two-dimensional scattering problems using a transmission-line matrix, *Proc. Inst. Electric. Eng.* **118**:1203–1208 (1971).
7. W. J. R. Hoefer, The transmission line matrix (TLM) method, in T. Itoh ed., *Numerical Techniques for Microwave and Millimeter Wave Passive Structures*, Wiley, New York, 1989.
8. K. L. Shlager and J. B. Schneider, A survey of the finite-difference time-domain literature, in A. Taflove, ed., *Advances in Computational Electrodynamics: The Finite-Difference Time-Domain Method*, Artech House, Norwood, MA, 1998.
9. T. G. Jurgens, A. Taflove, K. R. Umashankar, and T. G. Moore, Finite-difference time-domain modeling of curved surfaces, *IEEE Trans. Anten. Propag.* **40**:357–366 (1992).
10. S. Dey and R. Mittra, A locally conformal finite-difference time-domain algorithm for modeling three-dimensional perfectly conducting objects, *IEEE Microwave Guided Wave Lett.* **7**:273–275 (1997).
11. V. Shankar, A. H. Mohammadian, and W. F. Hall, A time-domain finite-volume treatment for the Maxwell equations, *Electromagnetics* **10**:127–145, (1990).
12. N. K. Madsen and R. W. Ziolkowski, A three-dimensional modified finite volume technique for Maxwell's equations, *Electromagnetics* **10**:147–161 (1990).
13. J. P. Berenger, A perfectly matched layer for the absorption of electromagnetic waves, *J. Comput. Phys.* **114**:185–200 (1994).
14. Z. S. Sacks, D. M. Kingsland, R. Lee, and J. F. Lee, A perfectly matched anisotropic absorber for use as an absorbing boundary condition, *IEEE Trans. Anten. Propag.* **43**:1460–1463 (1995).

15. S. D. Gedney, An anisotropic perfectly matched layer absorbing medium for the truncation of FDTD lattices, *IEEE Trans. Anten. Propag.* **44**:1630–1639 (1996).
16. O. M. Ramahi, The concurrent complementary operators method for FDTD mesh truncation, *IEEE Trans. Anten. Propag.* **46**:1475–1482 (1998).
17. M. Krumpholz and L. P. B. Katehi, MRTD: New time-domain schemes based on multiresolution analysis, *IEEE Trans. Microwave Theory Tech.* **44**:555–572 (1996).
18. Q. H. Liu, The pseudospectral time-domain (PSTD) method: A new algorithm for solutions of Maxwell's equations, *Proc. IEEE Antennas & Propagation Society Int. Symp.*, 1997, Vol. 1, pp. 122–125.
19. D. F. Kelley and R. J. Luebbers, Piecewise linear recursive convolution for dispersive media using FDTD, *IEEE Trans. Anten. Propag.* **44**:792–797 (1996).
20. R. M. Joseph, S. C. Hagness, and A. Taflove, Direct time integration of Maxwell's equations in linear dispersive media with absorption for scattering and propagation of femtosecond electromagnetic pulses, *Opt. Lett.* **16**: 1412–1414 (1991).
21. D. M. Sullivan, Z transform theory and the FDTD method, *IEEE Trans. Anten. Propag.* **44**:28–34 (1996).
22. R. M. Joseph and A. Taflove, FDTD Maxwell's equations models for nonlinear electrodynamics and optics, *IEEE Trans. Anten. Propag.* **45**:364–374 (1997).
23. Y. Liu, Fourier analysis of numerical algorithms for the Maxwell's equations, *J. Comput. Phys.* **124**:396–416 (1996).
24. T. Namiki, A new FDTD algorithm based on alternating-direction implicit method, *IEEE Trans. Microwave Theory Tech.* **47**:2003–2007 (1999).
25. F. Zheng, Z. Chen, and J. Zhang, Toward the development of a three-dimensional unconditionally stable finite-difference time-domain method, *IEEE Trans. Microwave Theory Tech.* **48**:1550–1558 (2000).
26. H. A. De Raedt, K. F. L. Michielsen, J. S. Kole, and M. T. Fige, One-step algorithm to solve the time-dependent Maxwell equations, *Phys. Rev. E* **67**:056706 (2003).
27. H. A. De Raedt, K. F. L. Michielsen, J. S. Kole, and M. T. Fige, Solving the Maxwell equations by the Chebyshev method: A one-step finite-difference time-domain algorithm, *IEEE Trans. Anten. Propag.* **51**:3150–3155 (2003).
28. S. Gonzalez Garcia, T. W. Lee, and S. C. Hagness, On the accuracy of the ADI-FDTD method, *IEEE Anten. Wireless Propag. Lett.* **1**:31–34 (2002).
29. R. Holland and J. Williams, Total-field versus scattered-field finite-difference, *IEEE Trans. Nucl. Sci.* **30**:4583–4587 (1983).
30. D. S. Katz, E. T. Thiele, and A. Taflove, Validation and extension to three-dimensions of the Berenger PML absorbing boundary condition for FDTD meshes, *IEEE Microwave Guided Wave Lett.* **4**:268–270 (1994).
31. J. W. Nehrbass, J. F. Lee, and R. Lee, Stability analysis for perfectly matched layered absorbers, *Electromagnetics* **16**:385–389 (1996).
32. S. Abarbanel and D. Gottlieb, A mathematical analysis of the PML method, *J. Comput. Phys.* **134**:357–363 (1997).
33. G. Waldschmidt and A. Taflove, The determination of the effective radius of a filamentary source in the FDTD mesh, *IEEE Microwave Guided Wave Lett.* **10**:217–219 (2000).
34. C. L. Wagner and J. B. Schneider, Divergent fields, charge, and capacitance in FDTD simulations, *IEEE Trans. Microwave Theory Tech.* **46**: 2131–2136 (1998).
35. R. Holland, Threde: A free-field EMP coupling and scattering code, *IEEE Trans. Nucl. Sci.* **24**:2416–2421 (1977).
36. R. Holland, L. Simpson, and K. S. Kunz, Finite-difference analysis of EMP coupling to lossy dielectric structures, *IEEE Trans. Electromagn. Compat.* **22**:203–209 (1980).
37. C. A. Balanis, *Advanced Engineering Electromagnetics*, Wiley, New York, 1989.
38. K. R. Umashankar and A. Taflove, A novel method to analyze electromagnetic scattering of complex objects, *IEEE Trans. Electromagn. Compat.* **24**:397–405 (1982).
39. R. J. Luebbers, K. S. Kunz, M. Schneider, and F. Hunsberger, A finite-difference time-domain near zone to far zone transformation, *IEEE Trans. Anten. Propag.* **39**:429–433 (1991).
40. J. J. Simpson and A. Taflove, Three-dimensional FDTD modeling of impulsive ELF propagation about the Earth-sphere, *IEEE Trans. Anten. Propag.* **52**:443–451 (2004); also (online) <http://www.ece.northwestern.edu/ecefaculty/taflove/3Dmovietext.gif>
41. Modeling example provided by M. J. Piket-May, University of Colorado—Boulder, Boulder, CO.
42. Modeling example provided by J. G. Maloney, Georgia Tech Research Institute, Atlanta, GA.
43. E. J. Bond, X. Li, S. C. Hagness, and B. D. Van Veen, Microwave imaging via space-time beamforming for early detection of breast cancer, *IEEE Trans. Anten. Propag.* **51**:1690–1705 (2003).
44. Graphic provided by S.-T. Ho, Northwestern University, Evanston, IL.
45. S. C. Hagness, D. Rafizadeh, S. T. Ho, and A. Taflove, FDTD microcavity simulations: Design and experimental realization of waveguide-coupled single-mode ring and whispering-gallery-mode disk resonators, *J. Lightwave Technol.* **15**:2154–2165 (1997).
46. O. Painter, R. K. Lee, A. Scherer, A. Yariv, J. D. O'Brien, P. D. Dapkus, and I. Kim, Two-dimensional photonic band-gap defect mode laser, *Science* **284**:1819–1821 (1999).
47. S.-H. Chang, *FDTD Modeling of Light Propagation and Correlations in Active Random Media*, Ph.D. dissertation, Northwestern Univ., Evanston, IL, 2004.

FINITE ELEMENT ANALYSIS

JIAN-MING JIN
MATTHYS M. BOTHA
University of Illinois at
Urbana—Champaign
Urbana, Illinois

1. INTRODUCTION

The finite-element method is a numerical procedure used to obtain approximate solutions to boundary value problems of mathematical physics. The method was first proposed by Courant in 1943 to solve variational problems in potential theory [1]. Thereafter, the method was developed and applied extensively to problems of structural analysis and increasingly to problems in other fields. Today, the finite-element method is recognized as a general, preeminent method applicable to a wide variety of engineering and mathematical problems, including those in RF and microwave engineering.

15. S. D. Gedney, An anisotropic perfectly matched layer absorbing medium for the truncation of FDTD lattices, *IEEE Trans. Anten. Propag.* **44**:1630–1639 (1996).
16. O. M. Ramahi, The concurrent complementary operators method for FDTD mesh truncation, *IEEE Trans. Anten. Propag.* **46**:1475–1482 (1998).
17. M. Krumpholz and L. P. B. Katehi, MRTD: New time-domain schemes based on multiresolution analysis, *IEEE Trans. Microwave Theory Tech.* **44**:555–572 (1996).
18. Q. H. Liu, The pseudospectral time-domain (PSTD) method: A new algorithm for solutions of Maxwell's equations, *Proc. IEEE Antennas & Propagation Society Int. Symp.*, 1997, Vol. 1, pp. 122–125.
19. D. F. Kelley and R. J. Luebbers, Piecewise linear recursive convolution for dispersive media using FDTD, *IEEE Trans. Anten. Propag.* **44**:792–797 (1996).
20. R. M. Joseph, S. C. Hagness, and A. Taflove, Direct time integration of Maxwell's equations in linear dispersive media with absorption for scattering and propagation of femtosecond electromagnetic pulses, *Opt. Lett.* **16**: 1412–1414 (1991).
21. D. M. Sullivan, Z transform theory and the FDTD method, *IEEE Trans. Anten. Propag.* **44**:28–34 (1996).
22. R. M. Joseph and A. Taflove, FDTD Maxwell's equations models for nonlinear electrodynamics and optics, *IEEE Trans. Anten. Propag.* **45**:364–374 (1997).
23. Y. Liu, Fourier analysis of numerical algorithms for the Maxwell's equations, *J. Comput. Phys.* **124**:396–416 (1996).
24. T. Namiki, A new FDTD algorithm based on alternating-direction implicit method, *IEEE Trans. Microwave Theory Tech.* **47**:2003–2007 (1999).
25. F. Zheng, Z. Chen, and J. Zhang, Toward the development of a three-dimensional unconditionally stable finite-difference time-domain method, *IEEE Trans. Microwave Theory Tech.* **48**:1550–1558 (2000).
26. H. A. De Raedt, K. F. L. Michielsen, J. S. Kole, and M. T. Fige, One-step algorithm to solve the time-dependent Maxwell equations, *Phys. Rev. E* **67**:056706 (2003).
27. H. A. De Raedt, K. F. L. Michielsen, J. S. Kole, and M. T. Fige, Solving the Maxwell equations by the Chebyshev method: A one-step finite-difference time-domain algorithm, *IEEE Trans. Anten. Propag.* **51**:3150–3155 (2003).
28. S. Gonzalez Garcia, T. W. Lee, and S. C. Hagness, On the accuracy of the ADI-FDTD method, *IEEE Anten. Wireless Propag. Lett.* **1**:31–34 (2002).
29. R. Holland and J. Williams, Total-field versus scattered-field finite-difference, *IEEE Trans. Nucl. Sci.* **30**:4583–4587 (1983).
30. D. S. Katz, E. T. Thiele, and A. Taflove, Validation and extension to three-dimensions of the Berenger PML absorbing boundary condition for FDTD meshes, *IEEE Microwave Guided Wave Lett.* **4**:268–270 (1994).
31. J. W. Nehrass, J. F. Lee, and R. Lee, Stability analysis for perfectly matched layered absorbers, *Electromagnetics* **16**:385–389 (1996).
32. S. Abarbanel and D. Gottlieb, A mathematical analysis of the PML method, *J. Comput. Phys.* **134**:357–363 (1997).
33. G. Waldschmidt and A. Taflove, The determination of the effective radius of a filamentary source in the FDTD mesh, *IEEE Microwave Guided Wave Lett.* **10**:217–219 (2000).
34. C. L. Wagner and J. B. Schneider, Divergent fields, charge, and capacitance in FDTD simulations, *IEEE Trans. Microwave Theory Tech.* **46**: 2131–2136 (1998).
35. R. Holland, Threde: A free-field EMP coupling and scattering code, *IEEE Trans. Nucl. Sci.* **24**:2416–2421 (1977).
36. R. Holland, L. Simpson, and K. S. Kunz, Finite-difference analysis of EMP coupling to lossy dielectric structures, *IEEE Trans. Electromagn. Compat.* **22**:203–209 (1980).
37. C. A. Balanis, *Advanced Engineering Electromagnetics*, Wiley, New York, 1989.
38. K. R. Umashankar and A. Taflove, A novel method to analyze electromagnetic scattering of complex objects, *IEEE Trans. Electromagn. Compat.* **24**:397–405 (1982).
39. R. J. Luebbers, K. S. Kunz, M. Schneider, and F. Hunsberger, A finite-difference time-domain near zone to far zone transformation, *IEEE Trans. Anten. Propag.* **39**:429–433 (1991).
40. J. J. Simpson and A. Taflove, Three-dimensional FDTD modeling of impulsive ELF propagation about the Earth-sphere, *IEEE Trans. Anten. Propag.* **52**:443–451 (2004); also (online) <http://www.ece.northwestern.edu/ecefaculty/taflove/3Dmovietext.gif>
41. Modeling example provided by M. J. Piket-May, University of Colorado—Boulder, Boulder, CO.
42. Modeling example provided by J. G. Maloney, Georgia Tech Research Institute, Atlanta, GA.
43. E. J. Bond, X. Li, S. C. Hagness, and B. D. Van Veen, Microwave imaging via space-time beamforming for early detection of breast cancer, *IEEE Trans. Anten. Propag.* **51**:1690–1705 (2003).
44. Graphic provided by S.-T. Ho, Northwestern University, Evanston, IL.
45. S. C. Hagness, D. Rafizadeh, S. T. Ho, and A. Taflove, FDTD microcavity simulations: Design and experimental realization of waveguide-coupled single-mode ring and whispering-gallery-mode disk resonators, *J. Lightwave Technol.* **15**:2154–2165 (1997).
46. O. Painter, R. K. Lee, A. Scherer, A. Yariv, J. D. O'Brien, P. D. Dapkus, and I. Kim, Two-dimensional photonic band-gap defect mode laser, *Science* **284**:1819–1821 (1999).
47. S.-H. Chang, *FDTD Modeling of Light Propagation and Correlations in Active Random Media*, Ph.D. dissertation, Northwestern Univ., Evanston, IL, 2004.

FINITE ELEMENT ANALYSIS

JIAN-MING JIN
MATTHYS M. BOTHA
University of Illinois at
Urbana—Champaign
Urbana, Illinois

1. INTRODUCTION

The finite-element method is a numerical procedure used to obtain approximate solutions to boundary value problems of mathematical physics. The method was first proposed by Courant in 1943 to solve variational problems in potential theory [1]. Thereafter, the method was developed and applied extensively to problems of structural analysis and increasingly to problems in other fields. Today, the finite-element method is recognized as a general, preeminent method applicable to a wide variety of engineering and mathematical problems, including those in RF and microwave engineering.

The first application of the finite-element method to microwave engineering and electromagnetics appeared in 1969, when Silvester employed it to analyze wave propagation in a hollow waveguide [2]. The importance of the method was quickly recognized, and successful applications were achieved for the analysis of electrostatic, magnetostatic, and dielectric-loaded waveguide problems. In 1974, Mei developed a technique that combined the finite-element method with eigenfunction expansion to deal with open-region electromagnetic problems such as antenna and scattering analysis [3]. In 1982, Marin developed an alternative method to deal with open-region scattering problems, which combined the finite-element method and a boundary integral equation [4].

An important breakthrough in the finite-element analysis of vector field problems occurred in the 1980s with the development of edge-based vector elements [5–7]. These new elements accurately model the nature of the electric and magnetic fields and eliminate much of the problems associated with traditional node-based scalar elements. Since the development of the vector elements, the finite-element method has become a very powerful numerical technique in computational electromagnetics. Today, the method is used as a major design tool for RF and microwave devices. Its basic principle and a variety of applications have been described in many books, such as those by Silvester and Ferrari [8], Jin [9], and Volakis et al. [10].

2. FINITE-ELEMENT ANALYSIS OF SCALAR POTENTIAL PROBLEMS

To illustrate the basic principle of the finite-element method, consider the problem of calculating the static electric potential ϕ due to electric charge density ρ distributed in domain Ω . The domain can be either two- or three-dimensional and is filled with a medium having a permittivity ϵ . On the basis of electromagnetic theory, the problem is to solve the following Poisson equation

$$-\nabla \cdot (\epsilon \nabla \phi) = \rho \quad \text{on } \Omega \tag{1}$$

subject to given boundary conditions. Typical boundary conditions include the Dirichlet type, which specifies the value of the potential on the boundary, and the Neumann type, which prescribes the normal derivative of the potential. To illustrate the treatment of both boundary conditions, the following boundary conditions are assumed for this example

$$\phi = \phi_D \quad \text{on } \Gamma_D \tag{2}$$

$$\hat{n} \cdot (\epsilon \nabla \phi) = \kappa_N \quad \text{on } \Gamma_N \tag{3}$$

where ϕ_D denotes the specified value of the potential on the Dirichlet boundary Γ_D and κ_N denotes the prescribed value for the normal derivative of the potential on the Neumann boundary Γ_N . The entire boundary of domain Ω consists of Γ_D and Γ_N and is denoted by Γ .

The boundary value problem expressed by Eqs. (1)–(3) is usually too complex to allow a closed-form solution. This

is particularly true when Ω has an irregular shape and the medium, characterized by ϵ , is inhomogeneous. In this case, a numerical solution is the only alternative. Among numerical methods, the finite-element method is very powerful because of its ability to deal with arbitrary shapes and inhomogeneous media. The basic principle of the finite-element method is to divide the entire domain into many small subdomains, called *finite-elements*, and then seek an approximate solution in each of the subdomains. The commonly used subdomains are triangular elements in two dimensions and tetrahedral elements in three dimensions (Fig. 1) because of their flexibility in modeling complex shapes, although other elements can also be used for special problems.

Once the domain Ω is divided into small elements, the potential in each element can be approximated as a simple function, such as linear, quadratic, and cubic functions. This approximation can be obtained by interpolating the potential values at a set of discrete points on the element. For example, the potential in a triangular element (Fig. 2) can be approximated as

$$\phi^e(x, y) = N_1^e(x, y)\phi_1^e + N_2^e(x, y)\phi_2^e + N_3^e(x, y)\phi_3^e \tag{4}$$

where ϕ_1^e , ϕ_2^e and ϕ_3^e denote the values of the potential at nodes 1, 2, and 3, respectively, and $N_1^e(x, y)$, $N_2^e(x, y)$, and $N_3^e(x, y)$ are the corresponding interpolation functions. These interpolation functions are completely determined by the coordinates of the three nodes. The interpolation functions, also known as *basis functions* or *expansion functions*, determine the order of the elements. An important requirement for the interpolation functions is that they guarantee the continuity of the interpolated potential.

When the potential in each element is interpolated using its values at discrete points, the potential in the entire

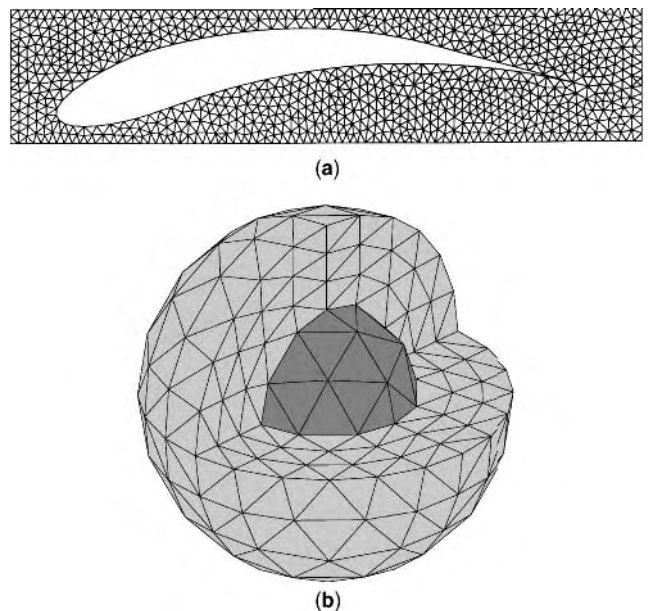


Figure 1. Finite-element mesh with (a) triangular and (b) tetrahedral elements.

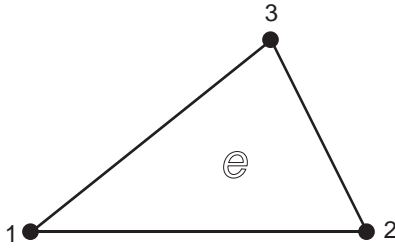


Figure 2. Linear triangular element.

domain can be expressed as

$$\phi = \sum_{i=1}^N N_i \phi_i + \sum_{i=1}^{N_D} N_i^D \phi_i^D \quad (5)$$

where N denotes the total number of nodes, at which the potential is unknown, and N_D denotes the number of nodes on Γ_D , where the potential is as given by (2). Furthermore, ϕ_i denotes the value of the potential at node i and N_i is the corresponding interpolation or basis function (the superscript “D” denotes the quantities on Γ_D). This interpolation function consists of the corresponding interpolation functions in all the elements that are directly connected to the associated node. Figure 3 shows the linear interpolation function in a two-dimensional triangular mesh.

Expression (5) can now be substituted into (1) to determine the unknown potentials ϕ_i , using the method of weighted residuals. It should be noted that the method of weighted residuals is only one of the methods for the finite-element formulation. Another commonly used method is the so-called variational method, which starts from the variational representation of the boundary value problem defined in (1)–(3). The method of weighted residuals is used here for its simplicity. In this method, a suitable testing or weighting function w is applied to (1) and the resulting equation is integrated over the problem domain, yielding

$$-\int_{\Omega} [\nabla \cdot (\varepsilon \nabla \phi)] w \, dV = \int_{\Omega} \rho w \, dV \quad (6)$$

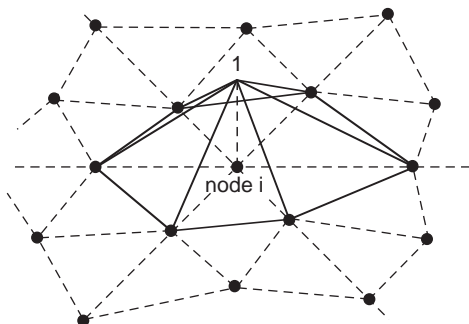


Figure 3. Basis function N_i for linear triangular elements. (After Jin [9], ©2002 Wiley.)

Using the well-known vector identity $\nabla \cdot (w \varepsilon \nabla \phi) = [\nabla \cdot (\varepsilon \nabla \phi)] w + \varepsilon \nabla \phi \cdot \nabla w$ and Gauss theorem

$$\int_{\Omega} \nabla \cdot f \, d\Omega = \oint_{\Gamma} \hat{n} \cdot f \, d\Gamma \quad (7)$$

(6) can be written as

$$\int_{\Omega} \varepsilon \nabla \phi \cdot \nabla w \, d\Omega = \int_{\Omega} \rho w \, d\Omega + \oint_{\Gamma} (\hat{n} \cdot \varepsilon \nabla \phi) w \, d\Gamma \quad (8)$$

where one of the del operators is now transferred from ϕ to w . Substituting (3) into (8), one obtains

$$\begin{aligned} & \int_{\Omega} \varepsilon \nabla \phi \cdot \nabla w \, d\Omega \\ &= \int_{\Omega} \rho w \, d\Omega + \int_{\Gamma_D} [\hat{n} \cdot (\varepsilon \nabla \phi)] w \, d\Gamma + \int_{\Gamma_N} \kappa_N w \, d\Gamma \end{aligned} \quad (9)$$

This equation is called the weak-form representation of the boundary value problem defined by (1)–(3). The corresponding solution is called the weak-form solution, which satisfies (1) in the weighted average sense.

Next, a suitable weighting function needs to be chosen for w . A popular choice is

$$w = N_i \quad i = 1, 2, \dots, N \quad (10)$$

where N_i is the interpolation function associated with unknown ϕ_i . The resulting formulation is known as Galerkin’s formulation. Doing so, one obtains

$$\begin{aligned} \sum_{j=1}^N \phi_j \int_{\Omega} \varepsilon \nabla N_i \cdot \nabla N_j \, d\Omega &= \int_{\Omega} \rho N_i \, d\Omega + \int_{\Gamma_N} \kappa_N N_i \, d\Gamma \\ &\quad - \sum_{j=1}^{N_D} \phi_j^D \int_{\Omega} \varepsilon \nabla N_i \cdot \nabla N_j^D \, d\Omega \end{aligned} \quad (11)$$

and it is noted that the integral over Γ_D in (9) disappears here since N_i vanishes on Γ_D . Equation (11) can be written more compactly as

$$\sum_{j=1}^N K_{ij} \phi_j = b_i \quad i = 1, 2, \dots, N \quad (12)$$

where

$$K_{ij} = \int_{\Omega} \varepsilon \nabla N_i \cdot \nabla N_j \, d\Omega \quad (13)$$

$$\begin{aligned} b_i &= \int_{\Omega} \rho N_i \, d\Omega + \int_{\Gamma_N} \kappa_N N_i \, d\Gamma \\ &\quad - \sum_{j=1}^{N_D} \phi_j^D \int_{\Omega} \varepsilon \nabla N_i \cdot \nabla N_j^D \, d\Omega \end{aligned} \quad (14)$$

Equation (12) represents a set of linear equations, which can also be written in matrix form as

$$[K]\{\phi\} = \{b\} \tag{15}$$

where $[K]$ is an $N \times N$ square and symmetric matrix, $\{\phi\}$ is an $N \times 1$ column vector containing the unknown potential values at all the nodes except those on Γ_D , and $\{b\}$ is the $N \times 1$ known vector contributed by the known charge density and the Dirichlet and Neumann boundary conditions. The matrix equation (15) can be solved using one of the many standard matrix solvers, and its solution yields the potential values at all the nodes. The potential elsewhere can then be obtained by interpolation in (5).

A very important property of the finite-element method is that its matrix $[K]$ is extremely sparse. This becomes obvious from (13), which is nonzero only when N_i and N_j overlap with each other. Since N_i is nonzero only within the elements directly connected to node i , it overlaps with N_j only when nodes i and j belong to the same element. Hence, in each row of matrix $[K]$, there are only a few nonzero elements no matter how large the dimension of the matrix is. Therefore, the memory required to store $[K]$ is proportional to $\mathcal{O}(N)$, and the solution can also be made very efficient by using special solvers that exploit the property of sparsity. Such solvers are often referred to as *sparse solvers*. As a result, the finite-element method is very suitable for large-scale applications, where one has to deal with a very large number of unknowns.

In the actual implementation of the finite-element method described above, it might prove difficult to find the explicit expressions of N_i and N_j to evaluate K_{ij} , since a node may be connected to a different number of elements, each having a different shape. To alleviate this difficulty, (13) is rewritten as

$$K_{ij} = \sum_{e=1}^M \int_{\Omega_e} \epsilon \nabla N_i \cdot \nabla N_j \, d\Omega \tag{16}$$

where Ω_e denotes the domain of element e and M denotes the total number of elements in Ω . Using (16), one can process elements one by one and calculate its contribution to $[K]$. This process, called *assembly*, is described in detail in Ref. 9 using a specific example.

3. FINITE-ELEMENT ANALYSIS OF VECTOR FIELD PROBLEMS

The finite-element method described in Section 2 can be extended to deal with problems involving vector fields. For this, consider the problem of calculating the electric field intensity \mathbf{E} due to electric current density \mathbf{J} in a domain Ω characterized by relative permittivity ϵ_r and relative permeability μ_r . Maxwell's equations for this case can be converted into the vector Helmholtz equation

$$\nabla \times \left(\frac{1}{\mu_r} \nabla \times \mathbf{E} \right) - k_0^2 \epsilon_r \mathbf{E} = -jk_0 Z_0 \mathbf{J} \quad \text{on } \Omega \tag{17}$$

where k_0 denotes the free-space wavenumber and Z_0 denotes the free-space intrinsic impedance. Typical boundary conditions for the electric field include the homogeneous Dirichlet condition on a perfectly conducting surface and the mixed boundary condition on an impedance surface. To illustrate the treatment of these two conditions, the following are assumed for this example

$$\hat{n} \times \mathbf{E} = 0 \quad \text{on } \Gamma_D \tag{18}$$

$$\hat{n} \times \left(\frac{1}{\mu_r} \nabla \times \mathbf{E} \right) + \frac{jk_0}{\eta} \hat{n} \times (\hat{n} \times \mathbf{E}) = \mathbf{K}_N \quad \text{on } \Gamma_N \tag{19}$$

where η denotes the normalized surface impedance on Γ_N and \mathbf{K}_N is a known function introduced to make (19) more general.

Similar to the scalar problem discussed in Section 2, instead of solving the boundary value problem (17)–(19) directly, one can seek its weak-form solution by multiplying (17) by an appropriate weighting function \mathbf{W} and integrating over the problem domain, which yields

$$\begin{aligned} & \int_{\Omega} \mathbf{W} \cdot \left[\nabla \times \left(\frac{1}{\mu_r} \nabla \times \mathbf{E} \right) - k_0^2 \epsilon_r \mathbf{E} \right] d\Omega \\ & = -jk_0 Z_0 \int_{\Omega} \mathbf{W} \cdot \mathbf{J} \, d\Omega \end{aligned} \tag{20}$$

By invoking the vector identity

$$\begin{aligned} \mathbf{W} \cdot \left[\nabla \times \left(\frac{1}{\mu_r} \nabla \times \mathbf{E} \right) \right] & = -\nabla \cdot \left[\mathbf{W} \times \left(\frac{1}{\mu_r} \nabla \times \mathbf{E} \right) \right] \\ & \quad + \frac{1}{\mu_r} (\nabla \times \mathbf{W}) \cdot (\nabla \times \mathbf{E}) \end{aligned} \tag{21}$$

and Gauss theorem (7), one obtains

$$\begin{aligned} & \int_{\Omega} \left[\frac{1}{\mu_r} (\nabla \times \mathbf{W}) \cdot (\nabla \times \mathbf{E}) - k_0^2 \epsilon_r \mathbf{E} \cdot \mathbf{W} \right] d\Omega \\ & = \int_{\Gamma_D} \frac{1}{\mu_r} (\nabla \times \mathbf{W}) \cdot (\hat{n} \times \mathbf{E}) \, d\Gamma \\ & \quad - \int_{\Gamma_N} \left[\frac{jk_0}{\eta} (\hat{n} \times \mathbf{W}) \cdot (\hat{n} \times \mathbf{E}) + \mathbf{K}_N \cdot \mathbf{W} \right] d\Gamma \\ & \quad - jk_0 Z_0 \int_{\Omega} \mathbf{J} \cdot \mathbf{W} \, d\Omega \end{aligned} \tag{22}$$

after the boundary condition (19) is applied.

To find a numerical solution of (22) using the finite-element method, the entire domain Ω is first divided into small elements. Within each small element, \mathbf{E} can be interpolated using a set of discrete values. One approach is to assign \mathbf{E} at a few points on the element and then interpolate \mathbf{E} elsewhere using a set of scalar interpolation functions. This approach turns out to be very problematic because of the difficulty in applying correct boundary conditions to the interpolated field \mathbf{E} . A better approach is to assign the tangential component of \mathbf{E} at each edge of the

element and then interpolate \mathbf{E} elsewhere using a set of vector basis functions. For example, the field in a triangular element can be interpolated as

$$\mathbf{E}^e(x, y) = \mathbf{N}_1^e(x, y)E_1^e + \mathbf{N}_2^e(x, y)E_2^e + \mathbf{N}_3^e(x, y)E_3^e \quad (23)$$

where $E_1^e, E_2^e,$ and E_3^e denote the tangential component of \mathbf{E} at edges 1, 2, and 3, respectively, and $\mathbf{N}_1^e(x, y), \mathbf{N}_2^e(x, y),$ and $\mathbf{N}_3^e(x, y)$ are the corresponding interpolation or basis functions. Different from those in (4), these functions are vector functions and the corresponding element is called the *vector element* or *edge element*, in contrast to the previous scalar element or nodal element. Figure 4 shows the vector basis functions for a triangular element. Clearly, such basis functions ensure the tangential continuity of the interpolated field while allowing the normal component to be discontinuous. Hence, they accurately model the nature of the vector field \mathbf{E} .

When the field \mathbf{E} is interpolated in each element using its tangential values at the edges of the element, the field \mathbf{E} in the entire domain Ω can be expressed as

$$\mathbf{E} = \sum_{i=1}^{N_e} \mathbf{N}_i E_i \quad (24)$$

where N_e denotes the total number of edges excluding those on Γ_D , E_i denotes the tangential component of \mathbf{E} at the i th edge, and \mathbf{N}_i is the corresponding basis function. Obviously, for an edge inside Ω , \mathbf{N}_i spans over two neighboring elements that share the common edge, and for an edge on Γ_N , \mathbf{N}_i spans over only one element. Figure 5 shows \mathbf{N}_i for an interior edge.

By substituting (24) into (22) and using the same \mathbf{N}_i as the weighting function \mathbf{W} , one obtains

$$\sum_{j=1}^{N_e} K_{ij} E_j = b_i \quad i = 1, 2, \dots, N_e \quad (25)$$

where

$$K_{ij} = \int_{\Omega} \left[\frac{1}{\mu_r} (\nabla \times \mathbf{N}_i) \cdot (\nabla \times \mathbf{N}_j) - k_0^2 \epsilon_r \mathbf{N}_i \cdot \mathbf{N}_j \right] d\Omega \quad (26)$$

$$+ jk_0 \int_{\Gamma_N} \left[\frac{1}{\eta} (\hat{\mathbf{n}} \mathbf{N}_i) \cdot (\hat{\mathbf{n}} \times \mathbf{N}_j) \right] d\Gamma$$

$$b_i = -jk_0 Z_0 \int_{\Omega} \mathbf{J} \cdot \mathbf{N}_i d\Omega - \int_{\Gamma_N} \mathbf{K}_N \cdot \mathbf{N}_i d\Gamma \quad (27)$$

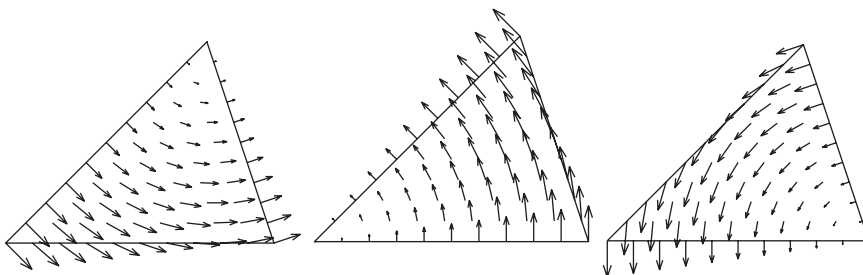


Figure 4. Vector basis functions \mathbf{N}_i^e for a linear triangular element. (After Jin [9], © 2002 Wiley.)

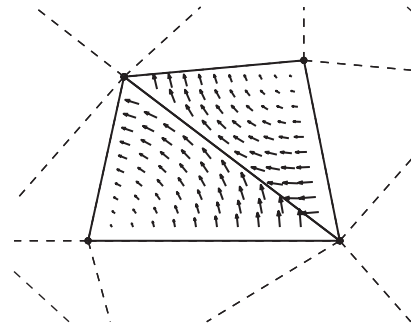


Figure 5. Vector basis function \mathbf{N}_i for linear triangular elements.

Note that the integral over Γ_D in (22) disappears here since $\hat{\mathbf{n}} \times \mathbf{N}_i = 0$ on Γ_D . Equation (25) can be written compactly as

$$[K]\{E\} = \{b\} \quad (28)$$

which can be solved for $\{E\}$. Similar to the scalar case, $[K]$ is a sparse and symmetric matrix, which can be solved efficiently using a sparse solver. Once $\{E\}$ is obtained, the field everywhere in Ω can be calculated using (24).

4. COMPUTATIONAL ASPECTS

When solving a problem using the finite-element method, one first sets up the mesh, then fills the matrix equation based on the mesh together with the boundary conditions, and finally solves the resulting system of linear equations. The computational issues of mesh generation and matrix solvers are discussed in this section.

4.1. Mesh Generation

The finite-element method assumes the availability of a mesh on the structure under consideration. However, obtaining this mesh is not trivial. Finite-element meshes can be split into two main categories: structured and unstructured meshes. Structured meshes have the property that all elements have the same number of neighbors, while unstructured meshes have no such constraint. When using rectangular or brick elements, structured meshes usually result, while unstructured meshes most often consist of triangles or tetrahedrons. Unstructured meshing with

triangles and tetrahedrons is much more general, since any polygonal/polyhedral domain may be represented by such a mesh.

The quality of an unstructured mesh is determined by the shape regularity of its elements, which is defined on an elemental basis as the ratio between the radius of the largest inscribed circle/sphere and the maximum dimension of the element. Among the most widely used approaches to unstructured meshing are "Octree," "Delaunay," and "Advancing front." The first approach breaks the structure into blocks until a desired resolution is obtained, and then the blocks are meshed. The second approach actually refers to a criterion for ensuring shape regularity when creating a mesh from a given set of nodes. The third approach relies on an already meshed boundary, to which elements are progressively added toward the interior.

As various requirements are placed on the meshing algorithm, such as continuity between different regions and variations in element size, the process becomes increasingly complicated. See [11,12] and the references therein for further discussions on mesh generation.

4.2. Matrix Solvers

An efficient solution of the finite-element matrix equation is very important, since in the course of solving a problem with finite-elements most computer resources (memory and time) are usually expended on this step. The important issues are matrix storage schemes, matrix solvers (direct or iterative), and matrix preconditioners (in the iterative case).

The matrices produced by the finite-element method are sparse with only a very small percentage of nonzero elements. By storing only the nonzero entries, the matrix storage requirement is reduced from $\mathcal{O}(N^2)$ to $\mathcal{O}(N)$. Popular approaches to sparse storage are compressed row and compressed column storage.

The choice of matrix solver can have a significant impact on computational efficiency, so it is important to choose a solver that best suits the properties of the matrix. There are two types of matrix solvers. The first type is direct solvers based on Gaussian elimination or *LU* decomposition. These solvers are commonly used for full matrices, but are also applicable to sparse matrices stored in a band format, or even a fully sparse format in the case of the frontal and multifrontal methods [13,14]. The alternative to direct solvers are iterative solvers, where very little extra memory is required, since they are based on calculating successive matrix-vector products according to an iterative algorithm to converge to the solution [15]. The main drawback of such algorithms is that they might require a prohibitive amount of iterations to converge, depending mainly on the locations of the eigenvalues of the matrix; if the eigenvalues are all located close to unity, convergence is usually rapid. This problem is addressed by using a preconditioner to move the eigenvalues closer to unity and thereby reduce the iteration count. Construction of a preconditioner can be based on physical insight into the problem or on the structure of the original matrix.

4.3. Fast Frequency Sweep

Many RF and microwave engineering applications require computation of frequency responses over a broad band rather than at one or a few isolated frequencies. Such calculations can be very time-consuming when a traditional frequency-domain numerical method is used because a set of algebraic equations must be solved repeatedly at many frequencies. The number of calculations is proportional to the electrical size of the problem and can be large for most applications. Therefore, there is a need to find approximate solution techniques that can efficiently simulate a frequency response over a broad band. This can be accomplished by the method of asymptotic waveform evaluation [16]. In this method, the unknown solution vector, the right-hand vector, and the system matrix are first expanded into Taylor series at a chosen frequency. The expansion coefficients of the solution vector are then determined by moment matching. The Taylor series of the solution vector is then converted into a Padé rational function to broaden the radius of convergence. With this approach, one obtains a solution that is accurate at frequencies near the point of expansion. The accuracy of the solution decreases when the frequency moves away from the point of expansion. In many practical applications, one is often required to find the solution over a specified frequency band, where one point of expansion may not be sufficient, and multiple points of expansion become necessary. These points can be selected automatically using a simple binary search algorithm [9].

5. APPLICATIONS OF THE FINITE-ELEMENT METHOD

The finite-element method has been widely applied to the analysis of problems in RF and microwave engineering. A few typical applications are discussed here to illustrate the treatment of various problems commonly encountered in the finite-element analysis.

5.1. Cavity Analysis

Typical cavity analysis involves finding the resonant frequencies and modal distributions of a given cavity. Mathematically, it translates to solving the homogeneous vector Helmholtz equation

$$\nabla \times \left(\frac{1}{\mu_r} \nabla \times \mathbf{E} \right) - k_0^2 \epsilon_r \mathbf{E} = 0 \quad \text{on } \Omega \quad (29)$$

for a set of discrete values of k_0^2 that yield nontrivial solutions for \mathbf{E} . Application of the finite-element analysis described in Section 3 to (29) yields a generalized eigenvalue problem

$$[A]\{E\} = k_0^2[B]\{E\} \quad (30)$$

where

$$A_{ij} = \int_{\Omega} \frac{1}{\mu_r} (\nabla \times \mathbf{N}_i) \cdot (\nabla \times \mathbf{N}_j) d\Omega \quad (31)$$

$$B_{ij} = \int_{\Omega} \epsilon_r \mathbf{N}_i \cdot \mathbf{N}_j d\Omega \quad (32)$$

The eigenvalues solved for in (30) yield the resonant frequencies of the cavity modes, and the corresponding eigenvectors $\{E\}$ provide the modal distributions.

5.2. Waveguide Analysis

Typical waveguide analysis involves finding the propagation constants and field distributions of the propagation modes in an infinitely long waveguide. Since the waveguide is assumed to be uniform in its longitudinal direction, say, the z direction, it is sufficient to consider (29) over the cross section of the waveguide.

For all the propagating modes, the electric field can be written as

$$\mathbf{E}(x, y, z) = \left[\frac{1}{\beta} \mathbf{e}_t(x, y) + j\hat{z}e_z(x, y) \right] e^{-j\beta z} \quad (33)$$

where β represents the propagation constant, \mathbf{e}_t represents the transverse component, and e_z represents the longitudinal component. The coefficients of \mathbf{e}_t and e_z are introduced to cast the final result in a more desirable form [17]. By introducing the weighting function

$$\mathbf{W}(x, y, z) = \left[\frac{1}{\beta} \mathbf{w}_t(x, y) - j\hat{z}w_z(x, y) \right] e^{j\beta z} \quad (34)$$

the weak form of (29) can be found as

$$\int_{\Omega} \left\{ \frac{1}{\mu_r} (\nabla_t \times \mathbf{e}_t) \cdot (\nabla_t \times \mathbf{w}_t) - k_0^2 \epsilon_r \mathbf{e}_t \cdot \mathbf{w}_t + \beta^2 \left[\frac{1}{\mu_r} (\nabla_t e_z + \mathbf{e}_t) \cdot (\nabla_t w_z + \mathbf{w}_t) - k_0^2 \epsilon_r e_z w_z \right] \right\} d\Omega = 0 \quad (35)$$

where ∇_t denotes the transverse del operator.

When edge elements are used for \mathbf{e}_t and nodal elements are employed for e_z , (35) can be converted into a generalized eigenvalue problem

$$\begin{bmatrix} A_{tt} & 0 \\ 0 & 0 \end{bmatrix} \begin{Bmatrix} e_t \\ e_z \end{Bmatrix} = -\beta^2 \begin{bmatrix} B_{tt} & B_{tz} \\ B_{zt} & B_{zz} \end{bmatrix} \begin{Bmatrix} e_t \\ e_z \end{Bmatrix} \quad (36)$$

in which

$$A_{ttij} = \int_{\Omega} \left[\frac{1}{\mu_r} (\nabla_t \times \mathbf{N}_i) \cdot (\nabla_t \times \mathbf{N}_j) - k_0^2 \epsilon_r \mathbf{N}_i \cdot \mathbf{N}_j \right] d\Omega \quad (37)$$

$$B_{ttij} = \int_{\Omega} \frac{1}{\mu_r} \mathbf{N}_i \cdot \mathbf{N}_j d\Omega \quad (38)$$

$$B_{tzij} = \int_{\Omega} \frac{1}{\mu_r} \mathbf{N}_i \cdot \nabla_t N_j d\Omega \quad (39)$$

$$B_{ztij} = \int_{\Omega} \frac{1}{\mu_r} \nabla_t N_i \cdot \mathbf{N}_j d\Omega \quad (40)$$

$$B_{zzij} = \int_{\Omega} \left[\frac{1}{\mu_r} \nabla_t N_i \cdot \nabla_t N_j - k_0^2 \epsilon_r N_i N_j \right] d\Omega \quad (41)$$

where the indices of \mathbf{N}_i and \mathbf{N}_j run from 1 to N_e and those of N_i and N_j run from 1 to N .

From (36), one can solve for a set of eigenvalues β^2 and the corresponding eigenvectors $\{e_t, e_z\}^T$ for a given value of k_0 . These eigenvalues and eigenvectors give the propagation constant and field distribution of each waveguide mode. Figure 6 shows the dispersion curves for an insulated image guide, calculated using the method described here.

5.3. Microwave Device Analysis

A microwave device has typically one or more ports, and it is usually characterized by its s parameters. To perform the finite-element analysis of a microwave device, it is necessary to terminate each port to limit the volume of analysis. A boundary condition is then required at each port to uniquely define the boundary value problem.

To derive such a boundary condition, one needs to know the propagation constants and field distributions of the waveguide modes. For most waveguides such as rectangular, circular, and coaxial waveguides, the propagation constants and modal fields can be obtained analytically. For other waveguides such as partially filled waveguides and microstrip lines, they can be calculated using the finite-element method described in Section 5.2. Once the waveguide modes are known, the total electric field

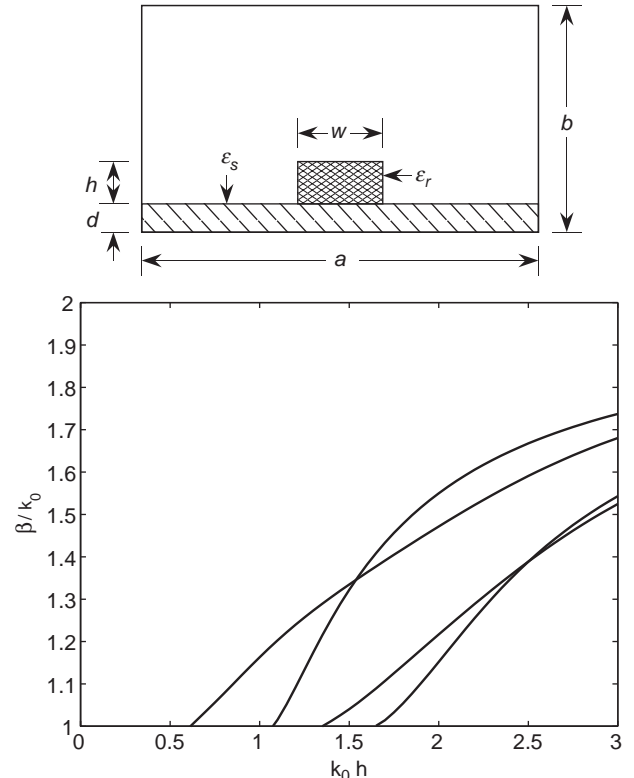


Figure 6. Dispersion characteristics of an insulated image guide ($w/h = 2.25$, $d/h = 0.5$, $a/h = 13.5$, $b/h = 8.0$, $\epsilon_r = 3.8$, and $\epsilon_s = 1.5$). (After Jin [9], ©2002 Wiley.)

at a port can be written as

$$\mathbf{E}(x, y, z) = \mathbf{E}^{\text{inc}}(x, y, z) + \sum_{n=1}^{\infty} a_n \left[\frac{1}{\beta_n} \mathbf{e}_{tn}(x, y) + j\hat{z}e_{zn}(x, y) \right] e^{-j\beta_n z} \quad (42)$$

where n denotes the mode number, (x, y, z) are the local coordinates (where z denotes the axis of the waveguide), and \mathbf{E}^{inc} represents the incident field at the port. Using the orthonormality property of the modes, one finds

$$a_n = \beta_n e^{j\beta_n z_0} \int_{\Gamma_A} \mathbf{e}_{tn}(x, y) \cdot [\mathbf{E} - \mathbf{E}^{\text{inc}}]_{z=z_0} d\Gamma \quad (43)$$

where Γ_A denotes the aperture of the port and z_0 denotes its position. From (42), it can be shown that

$$\hat{n} \times \left(\frac{1}{\mu_r} \nabla \times \mathbf{E} \right) + P(\mathbf{E}) = \mathbf{U}^{\text{inc}} \quad \text{at } z = z_0 \quad (44)$$

where

$$P(\mathbf{E}) = -\frac{j}{\mu_r} \sum_{n=1}^{\infty} \beta_n (\mathbf{e}_{tn} + \nabla_t e_{zn}) \int_{\Gamma_A} \mathbf{e}_{tn} \cdot \mathbf{E} d\Gamma \quad (45)$$

$$\mathbf{U}^{\text{inc}} = \hat{n} \times \left(\frac{1}{\mu_r} \nabla \times \mathbf{E}^{\text{inc}} \right) + P(\mathbf{E}^{\text{inc}}) \quad (46)$$

Equation (44) can be considered as a generalized mixed boundary condition and can be treated in a manner similar to that for (19).

Once the field inside the device and at its ports has been obtained, the s parameters can be calculated in a straightforward manner. Figure 7 shows the transmission coefficient $|S_{12}|$ for a cylindrical cavity resonator. The input and output ports are WR75 waveguides, coupled to the internal resonator through two rectangular slots.

5.4. Antenna Analysis

Most antennas are used to radiate electromagnetic waves into an open space. An antenna is typically characterized by its radiation pattern and input impedance. For multiple antennas such as an antenna array, the mutual coupling is also important. The main difficulty in the finite-element analysis of antennas is how to deal with the surrounding open space. A common approach is to introduce an artificial surface to truncate the infinite solution domain into a finite one. A boundary condition is then required at this surface for a unique solution of the electromagnetic fields. This boundary condition should be transparent to the radiated field; that is, it should permit the radiated field to pass through without any reflection. Unfortunately, there is no simple boundary condition that meets this requirement. Over the years, a variety of approximate boundary conditions, also called *absorbing boundary conditions*, have been developed to approximately satisfy this requirement. The simplest absorbing boundary condition is the well-known Sommerfeld radiation boundary condition, which states that if the truncation surface is sufficiently

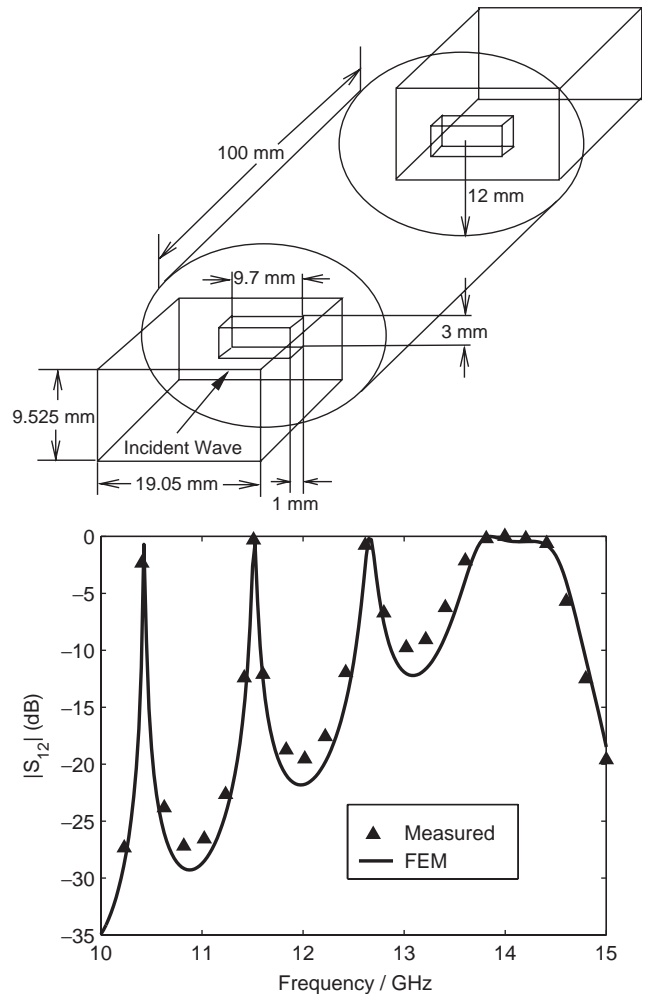


Figure 7. Transmission coefficient S_{12} of a cylindrical cavity resonator. (After Liu et al. [18], ©2002 Wiley.)

far away from the radiation source, the radiated field satisfies

$$\hat{n} \times \left(\frac{1}{\mu_r} \nabla \times \mathbf{E} \right) + jk_0 \hat{n} \times (\hat{n} \times \mathbf{E}) \approx 0 \quad (47)$$

This equation is simply the homogeneous version of the mixed condition (19), the treatment of which is discussed in Section 3.

Another issue in the finite-element analysis of antennas is the modeling of the antenna feeds. If the antenna feeds can be modeled approximately as electric current sources, they can be treated as \mathbf{J} in (17). If a more accurate modeling is desired, they can be modeled as waveguide ports, the treatment of which is described in Section 5.3.

It must be noted again that (47) is approximate; hence, the analysis result is also approximate. Although the accuracy can be improved by placing the truncation surface farther away from the antenna, one then has to deal with a very large computational domain, which makes the analysis inefficient. A better alternative is to use an exact boundary integral equation as a boundary condition at the truncation surface. This allows the truncation surface to

be placed as close to the antenna as possible. This approach is briefly described in Section 6.3.

Figure 8 shows the input impedance of a microstrip patch antenna, which consists of a 5.0×3.4 -cm rectangular patch residing on a substrate having thickness $t = 0.08779$ cm, relative permittivity $\epsilon_r = 2.17$, and a loss tangent of 0.0015. The antenna is excited by a current probe applied at $(x_f = 1.22, y_f = 0.85)$ cm and has a $50\text{-}\Omega$ resistor placed at $(x_L = -2.2, y_f = -1.5)$ cm, assuming that the patch is centered at the origin.

5.5. Scattering Analysis

The finite-element analysis of electromagnetic wave scattering by an object is similar to the analysis of antennas. An artificial surface is first introduced to enclose the entire object and to truncate the infinite solution domain to a finite one. An absorbing boundary condition is then

employed to permit the scattered field to leave the truncation surface without significant reflection. If the Sommerfeld radiation condition is used as the absorbing boundary condition, it can be written as

$$\hat{n} \times \left(\frac{1}{\mu_r} \nabla \times \mathbf{E}^{\text{sc}} \right) + jk_0 \hat{n} \times (\hat{n} \times \mathbf{E}^{\text{sc}}) \approx 0 \quad (48)$$

where \mathbf{E}^{sc} denotes the scattered field, which is the difference between the total and the incident fields ($\mathbf{E}^{\text{sc}} = \mathbf{E} - \mathbf{E}^{\text{inc}}$).

Since the absorbing boundary condition applies only to the scattered field, the formulation for scattering analysis is slightly different from that for the antenna analysis formulation. There are two approaches to formulating the scattering problem. One approach uses the total field that satisfies (29). The absorbing boundary condition (48) is then written in terms of the total field as

$$\hat{n} \times \left(\frac{1}{\mu_r} \nabla \times \mathbf{E} \right) + jk_0 \hat{n} \times (\hat{n} \times \mathbf{E}) = \mathbf{U}^{\text{inc}} \quad (49)$$

where

$$\mathbf{U}^{\text{inc}} = \hat{n} \times \left(\frac{1}{\mu_r} \nabla \times \mathbf{E}^{\text{inc}} \right) + jk_0 \hat{n} \times (\hat{n} \times \mathbf{E}^{\text{inc}}) \quad (50)$$

Another approach is to work on the scattered field using (48) directly. In this case, (29) can be written for the scattered field as

$$\nabla \times \left(\frac{1}{\mu_r} \nabla \times \mathbf{E}^{\text{sc}} \right) - jk_0 \epsilon_r \mathbf{E}^{\text{sc}} = \mathbf{F}^{\text{inc}} \quad (51)$$

where

$$\mathbf{F}^{\text{inc}} = \nabla \times \left(\frac{1}{\mu_r} \nabla \times \mathbf{E}^{\text{inc}} \right) - jk_0 \epsilon_r \mathbf{E}^{\text{inc}} \quad (52)$$

and the boundary conditions on conducting surfaces become

$$\hat{n} \times \mathbf{E}^{\text{sc}} = -\hat{n} \times \mathbf{E}^{\text{inc}} \quad (53)$$

Both approaches are mathematically equivalent. They differ in the numerical implementation, specifically, in the implementation of the excitation. In the first approach, the excitation is introduced as a boundary source on the truncation surface; in the second approach, it is introduced on the conducting surface and over the object. Numerical experiments show that the second approach is slightly more accurate since the wave travels a shorter distance in the finite-element mesh, resulting in a smaller dispersion error.

Figure 9 shows the VV-polarized monostatic radar cross section of a metallic double ogive at 9 GHz, which is formed by joining two different half-ogives. The top piece has a half-length of 12.7 cm, a maximum radius of 2.54 cm, and a half-angle of 22.62° at the tip, and the bottom has a half-length of 6.35 cm, a maximum radius of

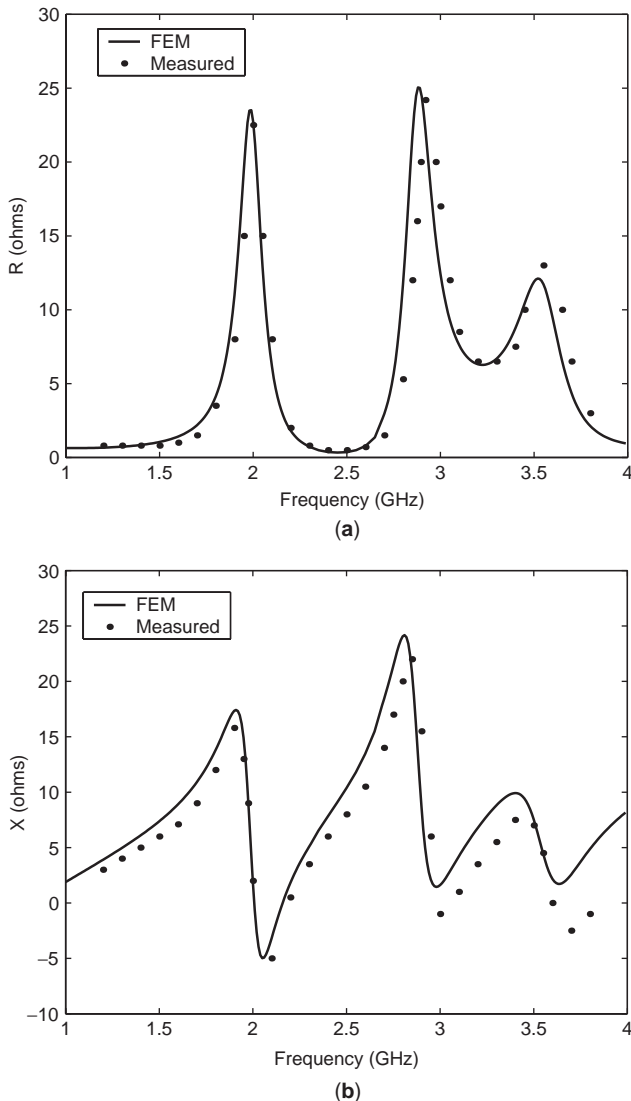


Figure 8. Input impedance of a loaded microstrip patch antenna: (a) resistance; (b) reactance. (After Jin and Volakis [19], ©1991 IEEE.)

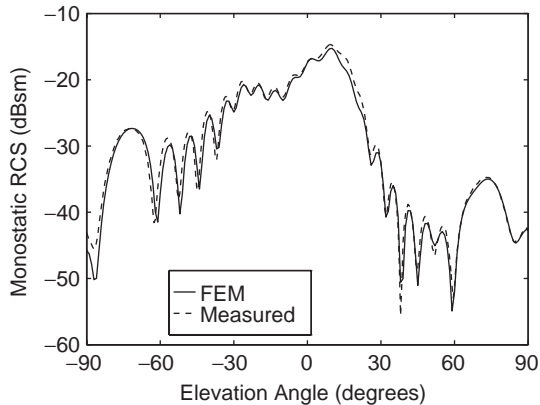


Figure 9. VV-polarized radar cross section of a metallic double ogive at 9 GHz. (After Greenwood and Jin [20], ©1999 IEEE.)

2.54 cm, and a half-angle of 46.4° at the tip. The calculated results are compared with measured data.

6. ADVANCED FINITE-ELEMENT ANALYSIS

There are many advanced methods that build on and complement the basic finite-element method framework as illustrated in Sections 2 and 3. A few of the most prominent of these methods are discussed here.

6.1. Higher-Order Elements

Most finite-element methods use basis functions that vary linearly within every element (see Figs. 3 and 5). However, it is also possible, and often very advantageous, to consider basis functions of higher polynomial orders. Such basis functions are defined for scalar nodal elements in Refs. 8 and 9 and for vector elements in Refs. 21 and 22.

Higher-order basis functions can be categorized into two classes: interpolatory and hierarchical. *Interpolatory* basis functions relate to a set of elemental points, such that every basis function is of the same order, and is equal to unity at one point and zero at all others. On the other hand, hierarchical basis functions are formed by adding new higher-order basis functions to the lower-order ones; thus the elemental solution is expanded in terms of basis functions of differing polynomial orders. Both approaches have the same accuracy, but one may be favored over the other, depending on the application. Interpolatory basis functions generally lead to better conditioned matrices, while hierarchical basis functions permit the use of different elemental orders in a single finite-element solution.

Since higher-order basis functions interpolate the solution field much more accurately, the finite-element method may be expected to yield much more accurate results, as the elemental order is increased. Specifically, for smooth functions it can be shown that if p is the order of the basis functions, h denotes the elemental size divided by the order of the element, and λ denotes the excitation wavelength, the interpolation error is of the order $\mathcal{O}((h/\lambda)^{p+1})$. Therefore, in the case of smooth solutions, the finite-element solution error may be reduced accord-

ingly by using higher-order basis functions. If the true solution to the finite-element analysis contains a singularity, this interpolation error estimate does not hold anymore and it becomes more advantageous to use smaller elements of low polynomial order around the singularity.

When the finite-element method is applied to the Helmholtz equations (scalar as well as vector cases), the simulated wave propagates at a speed slightly different from the exact value. Consequently, there is a numerical error in the phase of the numerical solution, which is called *dispersion error*. Analysis based on the finite-element discretization of plane wave propagation in a uniform medium shows that the dispersion error per wavelength is proportional to $\mathcal{O}((h/\lambda)^{2p})$. From this result follows the very important conclusion that phase errors may be decreased exponentially by increasing the order of the elements. Therefore, higher-order elements are especially suitable for simulating large-scale wave propagation problems.

6.2. Curvilinear Elements

In the same way that elemental basis functions can be defined to arbitrary polynomial order, the geometric representation of the elements can also be defined to arbitrary polynomial order. The elements shown in Figs. 3 and 5 are of linear geometric order since all edges and faces are straight and flat, and can thus be described by linear functions of position. Such elements are termed *rectilinear*. Elements of higher geometric polynomial order may be defined by modeling elemental edges and faces with higher-order polynomial functions of position. For example, one may require the edge of a triangular element to pass through two of its vertex nodes together with an additional node that may not lie on the straight line connecting the vertices. In this case, a second-order geometric representation would suffice. Such elemental representations are very useful when modeling curved boundaries and are termed *curvilinear*. When the order of geometric representation is the same as the order of basis functions, the element is called *isoparametric*. Otherwise, it is called either *subparametric* (when the order of geometric modeling is lower) or *superparametric* (when the order of geometric modeling is higher).

6.3. Finite-Element/Boundary Integral Method

As mentioned in Section 5.4, instead of using an absorbing boundary condition to approximate an infinite exterior volume to the finite-element domain, one may use a boundary integral equation as a boundary condition such that the infinite exterior region is modeled exactly through the Green function [9]. This approach, called the *finite-element/boundary integral method*, allows complete freedom in choosing the truncation surface enclosing the region of interest.

For example, consider the case of solving (17) on a truncated mesh with infinite exterior free space. The truncation surface, denoted by S , is closed, and given the electric and magnetic fields on such a surface, one can calculate the electric and magnetic fields to its exterior using the electric and magnetic field integral equations,

which are defined as follows

$$\mathbf{E} = \mathbf{E}^{\text{inc}} - Z_0 \mathcal{L}(S, \mathbf{J}_S) + \mathcal{K}(S, \mathbf{E} \times \hat{\mathbf{n}}) \quad (54)$$

$$Z_0 \mathbf{H} = Z_0 \mathbf{H}^{\text{inc}} - Z_0 \mathcal{K}(S, \mathbf{J}_S) - \mathcal{L}(S, \mathbf{E} \times \hat{\mathbf{n}}) \quad (55)$$

where \mathbf{E}^{inc} and \mathbf{H}^{inc} represent the exterior incident fields and

$$\mathcal{L}(S, \mathbf{v}) = jk_0 \oint_S \left[\mathbf{v}(\mathbf{r}') G_0(\mathbf{r}, \mathbf{r}') + \frac{1}{k_0^2} \nabla' \cdot \mathbf{v}(\mathbf{r}') \nabla G_0(\mathbf{r}, \mathbf{r}') \right] dS' \quad (56)$$

$$\mathcal{K}(S, \mathbf{v}) = \oint_S \mathbf{v}(\mathbf{r}') \times \nabla G_0(\mathbf{r}, \mathbf{r}') dS' \quad (57)$$

in which $G_0(\mathbf{r}, \mathbf{r}')$ denotes the scalar, free-space Green function [9,23] and $\mathbf{J}_S = \hat{\mathbf{n}} \times \mathbf{H}$ on S . For the finite-element region one may then use the simple boundary condition

$$\hat{\mathbf{n}} \times \left(\frac{1}{\mu_r} \nabla \times \mathbf{E} \right) = -jk_0 Z_0 \mathbf{J}_S \quad \text{on } S \quad (58)$$

and solve it together with a numerical system obtained by applying Galerkin's method to either (54) or (55) (or linear combinations of these), in terms of both \mathbf{E} and \mathbf{J}_S . This approach has been widely used, with various modifications to improve robustness and efficiency [9,24].

The finite-element/boundary integral method generally leads to sparse matrices with fully populated subblocks, corresponding to the unknowns associated with the exterior boundary. This aspect implies increased computational resource requirements, but on the other hand, the method enables one to reduce the computational domain's size to a minimum. More importantly, the method is accurate and reliable since its formulation involves no approximation other than numerical discretization.

6.4. Time-Domain Finite-Element Method

The finite-element method for electromagnetic fields may be formulated in the time domain, rather than the frequency domain, so that transient responses may be calculated directly. This is especially useful when data over a wide frequency band are required or when nonlinear devices are considered. In the time domain, the vector wave equation (17) takes the following form:

$$\nabla \times \left(\frac{1}{\mu} \nabla \times \mathbf{E} \right) + \varepsilon \frac{\partial^2 \mathbf{E}}{\partial t^2} + \sigma \frac{\partial \mathbf{E}}{\partial t} = - \frac{\partial \mathbf{J}}{\partial t} \quad \text{on } \Omega \quad (59)$$

In order to solve (59) with the finite-element method, both spatial and temporal discretization is required. The spatial discretization follows the procedure described in Section 3 by using vector elements to represent the fields, which yields the following system in terms of the time variable:

$$[T] \frac{d^2 \{E\}}{dt^2} + [R] \frac{d \{E\}}{dt} + [S] \{E\} + \{f\} = \{0\} \quad (60)$$

This equation represents a set of second-order ordinary differential equations in terms of the time-dependent

spatial unknowns $\{E\}$. This equation is solved numerically by first dividing the time axis into discrete intervals of length Δt . Next, the time derivatives are approximated such that $\{E\}$ can be calculated at successive timesteps, $t = n\Delta t$, $n = 1, 2, 3, \dots$. For this purpose, various timestepping schemes are available, such as central differencing and the Newmark β method [9,25]. The Newmark β method, when applied to (60), takes the following form:

$$\begin{aligned} & \left\{ \frac{1}{(\Delta t)^2} [T] + \frac{1}{2\Delta t} [R] + \beta [S] \right\} \{E\}^{n+1} \\ & = \left\{ \frac{2}{(\Delta t)^2} [T] - (1 - 2\beta) [S] \right\} \{E\}^n \\ & - \left\{ \frac{1}{(\Delta t)^2} [T] - \frac{1}{2\Delta t} [R] + \beta [S] \right\} \{E\}^{n-1} \\ & - [\beta \{f\}^{n+1} + (1 - 2\beta) \{f\}^n + \beta \{f\}^{n-1}] \end{aligned} \quad (61)$$

This method has a very important characteristic that when the parameter β is set to $\beta \geq 0.25$, it becomes unconditionally stable, which means that it can be used with a timestep independent of spatial discretization size. Usually the stability of a timestepping scheme is tied to the minimum size of the spatial discretization, given a fixed Δt .

When considering open-region problems, the time-domain equivalents of the absorbing boundary condition and the finite-element/boundary integral method can be employed [9].

6.5. Adaptive Finite-Element Method

Associated with any finite-element solution is an error due to the approximate representation of the solution on the mesh. Quantifying this error is an important extension to the finite-element method, since it opens up the possibility of adaptive finite-element analysis, which can enhance the efficiency of the finite-element method significantly.

The goal of an adaptive finite-element analysis is to optimize the mesh size (designated by h) and element orders (designated by p) with which a given accuracy can be obtained with the minimum number of unknowns. This is accomplished in the following way. Choose an initial discretization and solve the problem. On the basis of the solution, estimate the error distribution and the global solution error, as measured in a relevant quantity such as energy, impedance or scattering cross section. On the basis of the error distribution, refine the solution representation selectively with respect to h and/or p . Resolve the problem using the new discretization and repeat the process. Iterate in this way until the global error measure drops below a required level.

The core component of this process is the error estimation, which is termed a *posteriori error estimation*, since an existing solution is required. Many different approaches to a posteriori error estimation exist [26,27]. Usually the error estimator is derived mathematically, based on the finite-element formulation at hand and the output quantity of interest, but sometimes one can construct it on

the basis of physical insight alone. For example, for vector field problems one can use the residues of (17) and (19) to estimate the error over each element. The field continuity condition across each element edge or face can also be incorporated into the error estimation.

7. CONCLUSION

This article has described the basic principle, the numerical formulation, and some applications of the finite-element method for analysis of electromagnetic problems in RF and microwave engineering. It also has discussed briefly some computational aspects and advanced topics associated with the method. The finite-element method is a powerful analysis and design tool because it can model very complex geometries and can deal with a variety of media, including inhomogeneous and anisotropic cases. Moreover, the method yields a very sparse matrix that can be generated, stored, and solved efficiently.

The finite-element method in RF and microwave engineering, and electromagnetics in general, has undergone several important developments. For example, the development of vector elements enabled the correct modeling of the electric and magnetic vector fields for the first time. The development of higher-order versions of the vector elements permitted accurate and efficient modeling of large-scale field problems, especially wave propagation problems, because of the reduced interpolation and dispersion errors. The development of absorbing boundary conditions and perfectly matched layers [28,29] allowed fast, approximate analysis of wave radiation, scattering, and propagation problems. The development of the hybrid finite-element/boundary integral method provided a more reliable and robust approach to deal with these problems. It also created a mechanism to incorporate fast integral solvers into the finite-element simulations, such as FFT-based methods and the fast multipole method [30]. The hybridization with asymptotic methods [31] made it possible to analyze electrically very large scatterers with small and complex features. The development of adaptive methods [32] further enhanced the efficiency of the finite-element method and provided an error-controllable solution. The development of the time-domain finite-element method [33] enabled numerical modeling of nonlinear devices and materials and made efficient broadband simulation possible.

The material covered in this article represents only a fraction of the theory and application of the finite-element method in electromagnetics. With its continuous advancement and the rapid development of computer technology, RF and microwave devices will in future be designed routinely on computers in the same way as is done today with electronic circuit designs.

BIBLIOGRAPHY

1. R. L. Courant, Variational methods for the solution of problems of equilibrium and vibration, *Bull. Am. Math. Soc.* **49**: 1–23 (1943).
2. P. Silvester, Finite-element solution of homogeneous waveguide problems, *Alta Freq.* **38**:313–317 (May 1969).
3. K. K. Mei, Unimoment method of solving antenna and scattering problems, *IEEE Trans. Anten. Propag.* **22**:760–766 (Nov. 1974).
4. S. P. Marin, Computing scattering amplitudes for arbitrary cylinders under incident plane waves, *IEEE Trans. Anten. Propag.* **30**:1045–1049 (Nov. 1982).
5. J. C. Nédélec, Mixed finite elements in R^3 , *Numerische Mathematik* **35**:315–341 (1980).
6. A. Bossavit and J. C. Verite, A mixed FEM-BIEM method to solve 3-D eddy current problems, *IEEE Trans. Magn.* **18**:431–435 (March 1982).
7. M. L. Barton and Z. J. Cendes, New vector finite elements for three-dimensional magnetic field computation, *J. Appl. Phys.* **61**:3919–3921 (April 1987).
8. P. P. Silvester and R. L. Ferrari, *Finite Elements for Electrical Engineers*, 3rd ed., Cambridge Univ. Press, Cambridge; UK, 1996.
9. J.-M. Jin, *The Finite Element Method in Electromagnetics*, 2nd ed., John Wiley, New York; 2002.
10. J. Volakis, A. Chatterjee, and L. Kempel, *Finite Element Method for Electromagnetics: Antennas, Microwave Circuits and Scattering Applications*, Oxford Univ. Press, Oxford and IEEE Press, New York, 1998.
11. J. -F. Lee and R. Dyczij-Edlinger, Automatic mesh generation using a modified Delaunay tessellation, *IEEE Anten. Propag. Mag.* **39**:34–45 (Feb. 1997).
12. D. N. Shenton and Z. J. Cendes, Three-dimensional finite element mesh generation using Delaunay tessellation, *IEEE Trans. Magn.* **21**:2535–2538 (Nov. 1985).
13. B. M. Irons, A frontal method solution program for finite element analysis, *Int. J. Numer. Meth. Eng.* **2**:5–32 (1970).
14. J. W. H. Liu, The multifrontal method for sparse matrix solution: Theory and practice, *SIAM Rev.* **34**:82–109 (March 1992).
15. R. Barrett, M. Berry, T. F. Chan, J. Demmel, J. Donato, J. Dongarra, V. Eijkhout, R. Pozo, C. Romine, and H. V. der Vorst, *Templates for the Solution of Linear Systems: Building Blocks for Iterative Methods*, 2nd ed., SIAM, Philadelphia, 1994.
16. L. T. Pillage and R. A. Rohrer, Asymptotic waveform evaluation for timing analysis, *IEEE Trans. Comput.-Aided Design* **9**:352–366 (April 1990).
17. J. -F. Lee, D. -K. Sun, and Z. J. Cendes, Full-wave analysis of dielectric waveguides using tangential vector finite-elements, *IEEE Trans. Microwave Theory Tech.* **39**:1262–1271 (Aug. 1991).
18. J. Liu, J. -M. Jin, E. K. N. Yung, and R. S. Chen, A fast three-dimensional higher-order finite-element analysis of microwave waveguide devices, *Microwave Opt. Technol. Lett.* **32**:344–352 (March 2002).
19. J. -M. Jin and J. L. Volakis, A hybrid finite-element method for scattering and radiation by microstrip patch antennas and arrays residing in a cavity, *IEEE Trans. Anten. Propag.* **39**:1598–1604 (Nov. 1991).
20. A. D. Greenwood and J. M. Jin, A novel efficient algorithm for scattering from a complex BOR using vector FEM and cylindrical PML, *IEEE Trans. Anten. Propag.* **47**:620–629 (April 1999).
21. R. D. Graglia, D. R. Wilton, and A. F. Peterson, Higher order interpolatory vector bases for computational electromagnetics, *IEEE Trans. Anten. Propag.* **45**:329–342 (March 1997).

22. J. P. Webb, Hierarchical vector basis functions of arbitrary order for triangular and tetrahedral finite elements, *IEEE Trans. Anten. Propag.* **47**:1244–1253 (Aug. 1999).
23. C. T. Tai, *Dyadic Green Functions in Electromagnetic Theory*, 2nd ed., IEEE Press, New York, 1994.
24. X.-Q. Sheng, J.-M. Jin, J. Song, C.-C. Lu, and W. C. Chew, On the formulation of hybrid finite-element and boundary-integral methods for 3-D scattering, *IEEE Trans. Anten. Propag.* **46**:303–311 (March 1998).
25. N. M. Newmark, A method of computation for structural dynamics, *J. Eng. Mech. Div. Proc. Am. Soc. Civil Eng.* **85**:67–94 (July 1959).
26. M. Ainsworth and J. T. Oden, A posteriori error estimation in finite-element analysis, *Comput. Meth. Appl. Mech. Eng.* **142**:1–88 (1997).
27. J. T. Oden, L. Demkowicz, W. Rachowicz, and T. A. Westermann, Toward a universal h - p adaptive finite-element strategy, Part 2. A posteriori error estimation, *Comput. Meth. Appl. Mech. Eng.* **77**:113–180 (1989).
28. J. Berenger, A perfectly matched layer for the absorption of electromagnetic waves, *J. Comput. Phys.* **144**:185–200 (Oct. 1994).
29. D. Jiao, J.-M. Jin, E. Michielssen, and D. Riley, Time-domain finite-element simulation of three-dimensional scattering and radiation problems using perfectly matched layers, *IEEE Trans. Anten. Propag.* **51**:296–305 (Feb. 2003).
30. R. Coifman, V. Rohklin, and S. Wandzura, The fast multipole method for the wave equation: A pedestrian prescription, *IEEE Anten. Propag. Mag.* **35**:7–12 (June 1993).
31. J. M. Jin, S. Ni, and S. W. Lee, Hybridization of SBR and FEM for scattering by large bodies with cracks and cavities, *IEEE Trans. Anten. Propag.* **43**:1130–1139 (Oct. 1995).
32. M. Salazar-Palma, T. K. Sarkar, L.-E. García-Castillo, T. Roy, and A. Djordjević, *Iterative and Self-Adaptive Finite-Elements in Electromagnetic Modeling*, Artech House, Boston, 1998.
33. J.-F. Lee, R. Lee, and A. C. Cangellaris, Time-domain finite-element methods, *IEEE Trans. Anten. Propag.* **45**:430–442 (March 1997).

FINLINE COMPONENTS

WOLFGANG S. MENZEL
University of Ulm
Ulm, Germany

1. INTRODUCTION

The finline has been intensively investigated since 1970 as a planar transmission-line medium for millimeter-wave components. The electromagnetic wave is guided by slots in a metallization printed on a thin dielectric substrate. All passive circuit functions are realized by these slotline structures, partly in combination with other types of planar transmission lines, such as microstrips or coplanar lines printed on the same substrate. These circuits are correctly known as E -plane circuits, but the terms *finline* and E -plane circuits are often used interchangeably. Semiconductor devices, preferably beam-lead devices, can eas-

ily be soldered, glued, or bonded across the slot. The complete transmission line is held and shielded by a metal housing that most often has the (inner) dimension of the respective metal waveguide (Fig. 1). The transition from metal waveguide to finline can be achieved by tapering the finline slot to the waveguide height as shown in Fig. 1. Therefore, finline components can easily be combined with waveguide circuits. Because the circuit functions are determined by the planar structure, the tolerance requirements for this housing are considerably relaxed; thus this housing may be fabricated by low-cost methods such as metal casting or even plastic injection molding and electroplating.

Because of the relatively large transmission-line cross section, finline losses typically are lower than for microstrip or coplanar lines, but higher than those for metal waveguide. Typical finline types, cross sections, and propagation properties are described in detail in Ref. 1.

2. PASSIVE FINLINE COMPONENTS

2.1. Filters

Finline filters, especially band-pass and low-pass filters are based on transmission-line structures [2]. Bandpass filters typically are realized using either side-coupled (Fig. 2a) or end-coupled (Fig. 2b) resonators. To reduce losses, end-coupled filters may degenerate to pure E -plane waveguide filters as shown in Fig. 2c. In this case, the “slot width” is equal to the waveguide height, and no taper to waveguide is necessary; even the dielectric substrate material may be omitted, resulting in simple metal insert filters. For better stopband attenuation, bilateral finline or several side-by-side metal inserts may be used. These arrangements strongly suppress higher-order mode coupling and therefore improve the stopband behavior. Detailed descriptions of these kinds of filters, together with duplexers, are presented by Shih et al. [3] and Dittloff and Arndt [4].

Lowpass filters typically are based on low- and high-impedance line sections (Fig. 2d) or stub structures (Fig. 2e). High impedances are easily realized with wide slots. For uniplanar finline, the lowest impedance value is determined by the minimum slot width that can be technologically realized; for bilateral or antipodal finline, overlapping of the metallization may further reduce the characteristic impedance of the respective line segment. The discontinuities involved have to be included in the design procedure, especially for large steps in impedance.

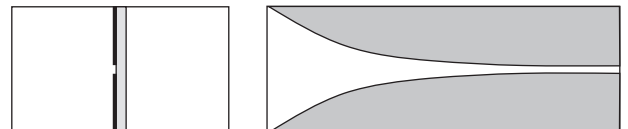


Figure 1. Cross section of a (unilateral) finline and metallization pattern for a transition from waveguide to finline.

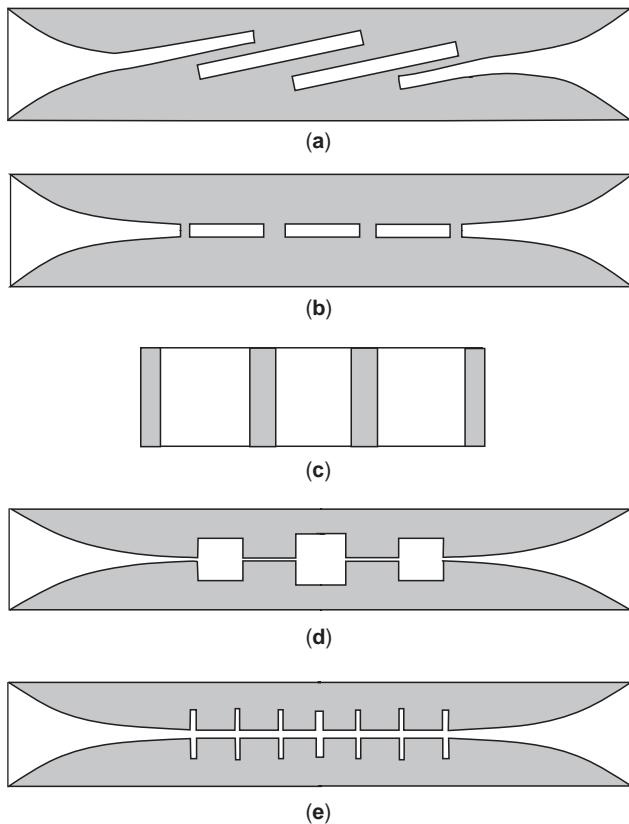


Figure 2. Typical metallization patterns of different finline filters: (a) side-coupled bandpass filter; (b) end-coupled bandpass filter; (c) end-coupled bandpass filter (the slot width has been increased to the waveguide height, losses are lower, and no taper to waveguide is required); (d) high-low impedance lowpass filter; (e) stub-type lowpass filter.

2.2. Directional Couplers

The design of a directional coupler in conjunction with finline was first reported by Meier [8] based on printed metal probes between two adjacent metal waveguides, placed in between two thin substrate layers in the E plane. Finline couplers, however, are designed mostly on the basis of coupled slots. Such a coupled transmission-line structure supports two modes; one is similar to the normal finline mode with the electric fields in the same direction, and the other one is a coplanar-type mode with zero cutoff frequency. The coupler design shown in Fig. 3a relies on a quarter-wave section of coupled lines. The fundamental principles of operation are comparable to those of respective couplers in the microstrip or microstrip/slot-line technique. The center strip may alternatively be replaced by a bond wire, or the metallization section containing the strip may be placed on the backside of the substrate (antipodal finline), thus achieving an increased design flexibility. Another coupler principle is based solely on the different phase velocity of the two modes on the coupled transmission line (Fig. 3b). Feeding a wave to one of the ports, an increasing part of the electromagnetic field couples from one slot to the other with increasing propagation distance; that is, the amount of coupling depends on the length of the coupled-line section.

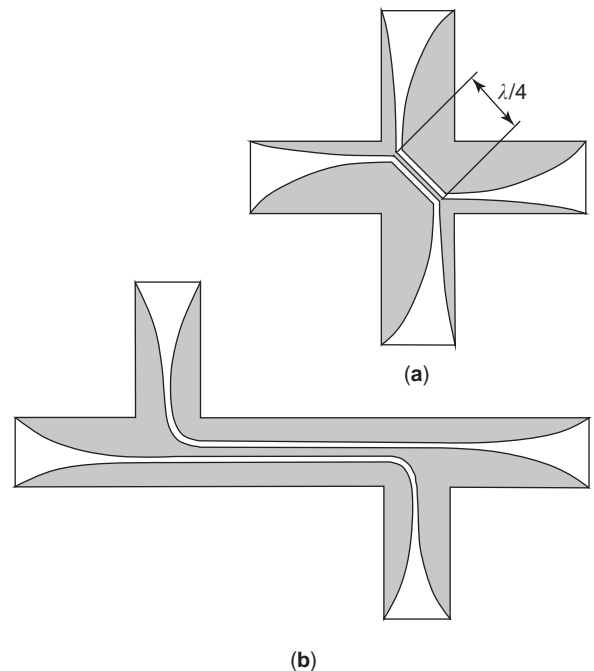


Figure 3. Metallization patterns of two different finline couplers.

This length will be several wavelengths, but in the millimeter-wave range, this problem is reduced because of the short wavelength. In contrast to the coupler design shown in Fig. 3a, a smooth transition from the feedline to the coupled-line section with minimum reflections is mandatory. Furthermore, the coupling of the transition region contributes to the coupler performance. With both types of couplers, broadband performance over a complete waveguide band is achieved [5–7].

2.3. Nonreciprocal Components

Some effort has been made to develop circulators and isolators in finline or by a compatible E -plane technique. A ferrite sphere or a small cylinder is placed in the center of a finline Y junction to realize circulators [9,10]. For a field displacement type of isolator, an additional layer of ferrite substrate together with an absorbing sheet is added to the finline on a standard substrate [11]; optimization is done by full-wave calculations of the composite structure. Both approaches, however, lead to rather complex and therefore mechanically sensitive structures, so these are rarely used in practical applications.

A more successful approach is the realization of waveguide-type circulators in a metal waveguide, Y junction in the E plane [12]. A ferrite disk is placed into the junction. The diameter of the disk is equal to the inner diameter of the waveguide Y junction. The center frequency is determined by the height of the disk. A permanent magnet is placed into a hole in the waveguide mount close to the ferrite disk. This type of circulator, therefore, is fabricated easily, and is integrated into the E -plane split block together with single or integrated finline components, as

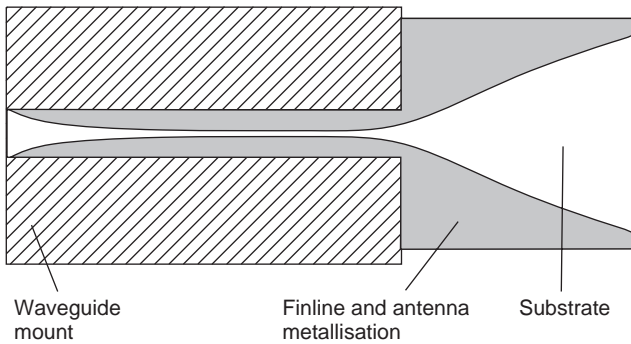


Figure 4. Waveguide mount and metallization pattern of a finline antenna. The planar substrate with the finline metallization protrudes out of the waveguide mount and acts as a slotline-type antenna.

shown later. Circulators of this type are even built up to the 140 GHz frequency range.

2.4. Finline Antennas

Extending the finline substrate out of the waveguide mount allows the realization of slotline or “Vivaldi”-type endfire antennas (Fig. 4). Beamform, sidelobe level, and bandwidth can be determined, to some extent, by the form of the tapered metallization structure and by a proper choice of the substrate thickness and its dielectric constant. Beamwidth, however, remains relatively wide associated with low gain. Applications of finline antennas are found in the integration of several antennas as an antenna array or as a feed cluster to form multiple beams in conjunction with lens or reflector antennas [13].

3. DIODE-BASED FINLINE COMPONENTS

Schottky diodes, pin diodes, and varactor diodes have been fabricated as beam-lead devices for many years and are ideally suited for integration into finline circuits. Because of their low parasitic capacitances and inductances, high-performance components with wide bandwidth can be built.

3.1. Detectors

For a finline detector, a low-barrier Schottky diode is placed across the finline slot. One of the finline metallizations has to be isolated from the metal mount by a thin dielectric sheet (10–20 μm). Alternatively, an oxidized aluminum mount is used. For broadband operation, some absorber material is placed behind the diode. Figure 5 is a

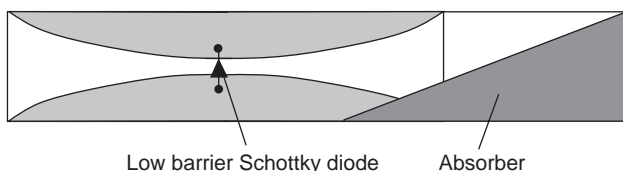


Figure 5. Basic setup of a finline detector. One of the finline metallizations is DC-isolated from the waveguide mount to allow extraction of the rectified output signal.

sketch of the detector layout. Detectors of this type are capable of zero-bias operation over one or two waveguide bands with sensitivities of several hundred millivolts (mV/mW) per milliwatt, and are even designed for frequencies up to 200 GHz and above [7,14].

3.2. pin Diode Attenuators and Switches

In the same way as with the detector, one or more beam-lead pin diodes can easily be placed across a finline slot. With bias applied to the pin diodes, these exhibit a low series resistance together with some parasitic inductance. Thus they basically short-circuit the finline slot. Without or with reverse bias, pin diodes load the finline slot only with their fairly low capacitance. Basically, two types of attenuator or switch have been developed. The first one uses diodes in the shunt configuration shown in Fig. 6a. Placing two or more diodes approximately a quarter-wavelength apart results in some compensation of the diode capacitance in the ON state of the switch, that is, without biasing the diodes or with reverse bias. Attenuators (the attenuation is controlled by the amount of diode bias) or switches of this type typically have an insertion loss of 0.5 dB in the Ka band (26–40 GHz) up to 1.5 dB in the W

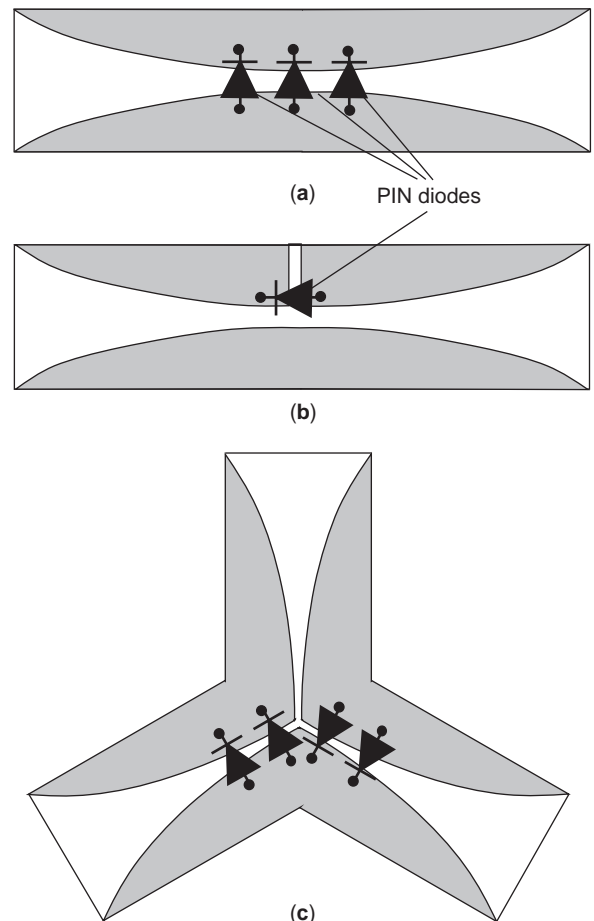


Figure 6. Metallization patterns of finline shunt-type (a) and series-type (b) attenuator or switch, and single-pole double-throw (SPDT) switch with shunt diode configuration (c).

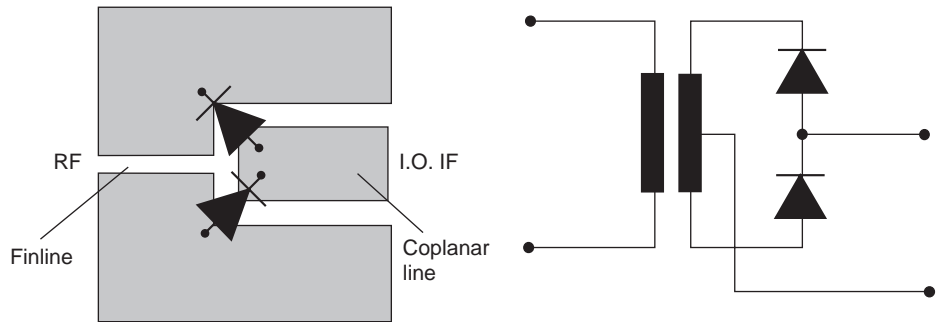


Figure 7. Basic principle of a balanced finline mixer and its equivalent circuit. The combination of finline and coplanar line forms an inherently broadband 180° hybrid junction.

band (75–110 GHz) over a nearly complete waveguide band. Maximum attenuation amounts to 15 dB per diode. For attenuation values higher than ~ 50 dB, parasitic power leakage along the DC isolation between the metallization pattern on the substrate and the waveguide mount is a concern, and absorbing isolating foils must be used to prevent this problem. For attenuators operating over even two waveguide bands, the finline can be placed in a ridged waveguide mount.

The second type of pin diode switch is based on a series configuration of the diode (Fig. 6b). A diode is placed across a lateral slot in the metallization. This slot is short-circuited for RF signals by the wall of the waveguide mount. Together with the diode capacitance, this stub forms a parallel resonator in the OFF position of the attenuator, whereas the stub is short-circuited in the ON position. Accordingly, this attenuator has a more narrow-band performance, but with increased attenuation for a single diode. Furthermore, it presents some advantages with respect to DC isolation from other components in integrated finline circuits. In the case of a single diode, the metallization at one side of the stub has to be DC-isolated from the waveguide mount. With two cascaded structures of this type, only the metallization between the stubs needs to be DC isolated (see also Section 5).

Two or three switches as described above, preferably those with the diodes in a shunt configuration, can also be arranged for single-pole double-throw (SPDT) or single-pole triple-throw (SPTT) switches, as shown in Fig. 6c. This results in performance similar to the single switches except for slightly increased losses due to the additional transmission line(s) loading. Further details and numerous results are described by Callsen et al. [15].

3.3. Finline Mixers

Although single-ended mixers are easily realized placing a beam-lead Schottky diode across the finline slot [8], much more effort has been put into the design of a balanced mixer based on a combination of finline and coplanar line as shown in Fig. 7. This structure gives an ideal combination for forming an inherently broadband, 180° , hybrid junction. The Schottky diodes are placed across the junction, in series with respect to the finline and antiparallel with respect to the coplanar line. The RF signal is fed to the diodes via the finline and the local oscillator (LO) signal via the coplanar line. Then the intermediate frequency

(IF) is also extracted from the coplanar line. Therefore, some diplexing circuit must be added to the coplanar line. This single balanced mixer design has inherent high mutual isolation between RF and LO ports (and RF and IF ports, respectively), but in practice this is limited by asymmetries in the circuit structure or the diodes.

Many mixers based on this configuration have been developed. Basic differences were found mainly in the LO/IF feeding arrangement. Some mixers use a transition from finline to coplanar line via an antipodal finline, as sketched in Fig. 8, possibly together with an end-coupled band-pass filter for the LO signal and a microstrip lowpass filter for the IF. A typical Ka-band finline filter of this type was presented by Ball and Bui [16] and is shown in the photograph in Fig. 9. Another design [7,17] uses a transition from finline to coplanar line based on magnetic coupling, as shown in Fig. 10. Very broadband performance and operating frequencies up to 150 GHz are reported [18] with this type of mixer. A photograph of a 140–150 GHz mixer is shown in Fig. 11.

Because sufficient LO power in the millimeter-wave frequency range is sometimes difficult or too expensive to generate, efforts have been undertaken to design subharmonically pumped mixers. For mixing with even harmonics of the LO frequency, two diodes are used in an antiparallel configuration. For odd harmonics, a circuit and diode configuration as used for the balanced mixer and shown in Fig. 7 can be employed. Together with suitable filter configurations (Fig. 12), mixers with a LO frequency at about half the RF frequency [19,20] and at much lower frequencies, for example, $f_{LO} \approx f_{RF}/8$ [21], have been realized.

Until the late 1990s, a major problem in the design of finline mixers was determination of the actual nonlinear

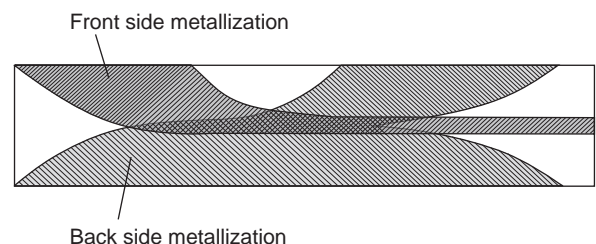


Figure 8. Layout of a transition from finline to coplanar line via an antipodal finline and a microstrip line.

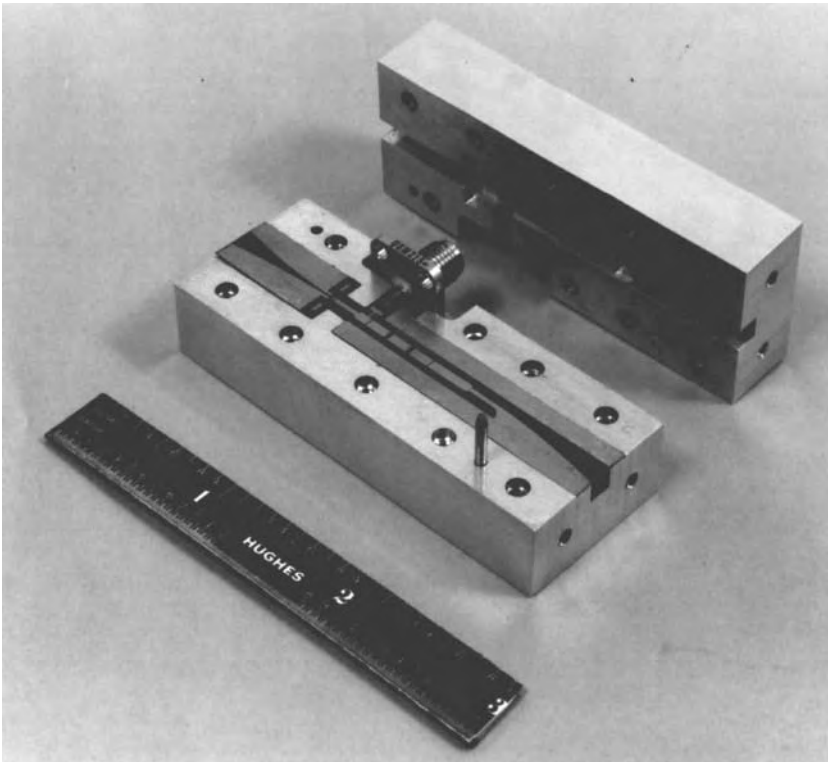


Figure 9. Photograph of a Ka-band balanced finline mixer [16] (courtesy of Academic Press).

diode impedances for signal, LO, and IF frequency. The problem is even more challenging as the diodes are placed in a major discontinuity (Fig. 7) where parasitic capacitances and inductances affect the impedances seen by input and output transmission lines. This problem now has been solved applying a full-wave finite difference in time-domain (FDTD) field solver, including lumped nonlinear elements such as the mixer diodes [22]. The mixer diodes are represented by a suitable equivalent circuit (valid up to the respective frequency of operation) and embedded into the FDTD computation. In the millimeter-wave range,

the actual size of the beam-lead diodes can be accounted for by distributing the equivalent circuit over several cells of the FDTD grid. The nonlinear response of the diodes to the LO power is calculated by a harmonic excitation of the diodes, including the actual power level. Following this, a

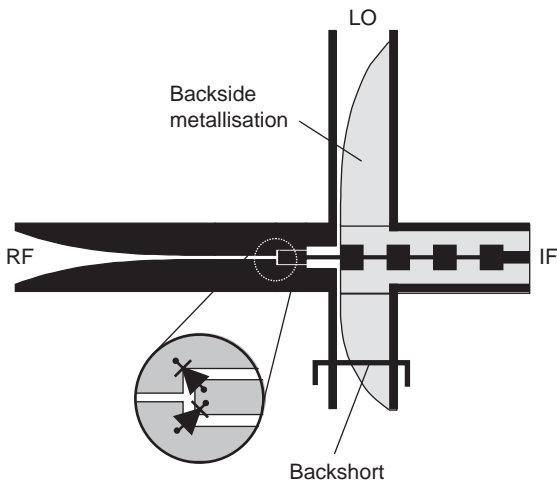


Figure 10. Basic layout of a balanced finline mixer with probe-type transition to coplanar line [18].

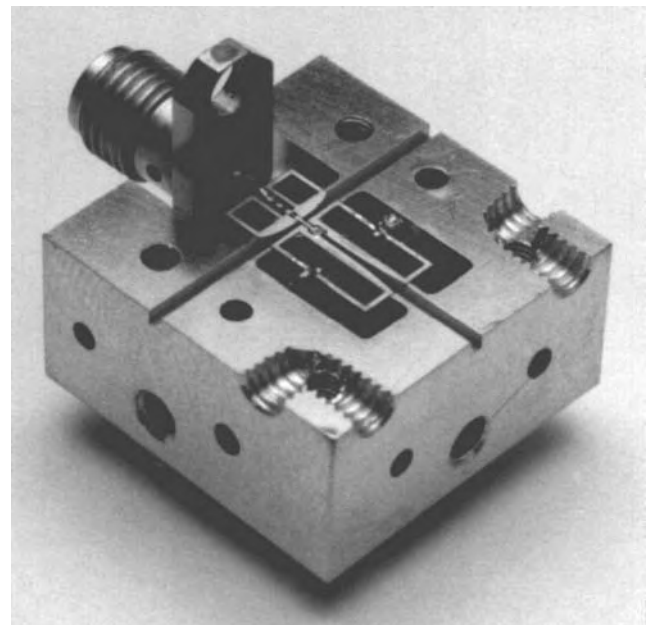


Figure 11. Photograph of a 140-GHz finline mixer [18]. The waveguide mount is opened, and the quartz substrate with the mixer circuitry can be clearly seen.

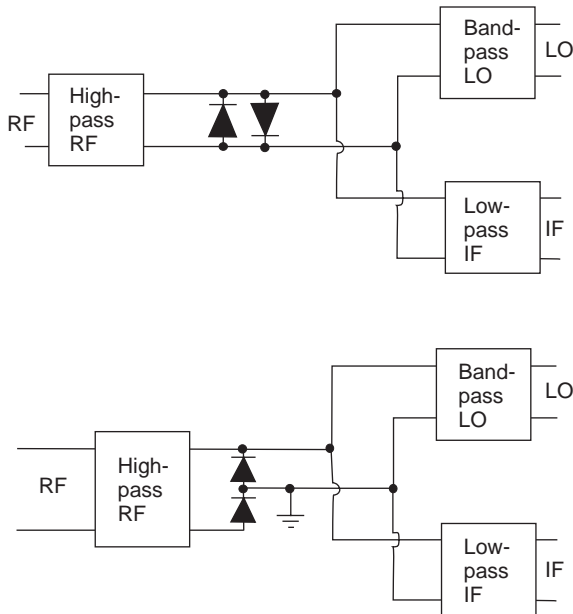


Figure 12. Basic block diagrams of harmonic mixers. For even harmonic mixing products, an antiparallel diode configuration is used; for odd mixing products, a parallel/antiparallel diode arrangement is preferred.

small-signal, modulated Gaussian pulse is fed to the signal port of the mixer (with the LO signal still present). From the reflected signals, the return loss at the respective ports is computed, and the conversion loss is extracted from the input signal and the IF output signal. On the basis of these calculations, a matching and an optimization of (harmonic) mixers are possible. An example of a harmonic mixer with the LO frequency at about one-third of the signal frequency is shown in Fig. 13. A conversion loss of down to 15 dB for a 60-GHz third-harmonic mixer is achieved using low-cost silicon Schottky diodes (Fig. 14).

3.4. Phase Shifters

Finline phase shifters are based on two different principles. The first one uses a 3-dB coupler described earlier in this article together with pin diode switches to modify the two output port loads [6]. The other principle uses a

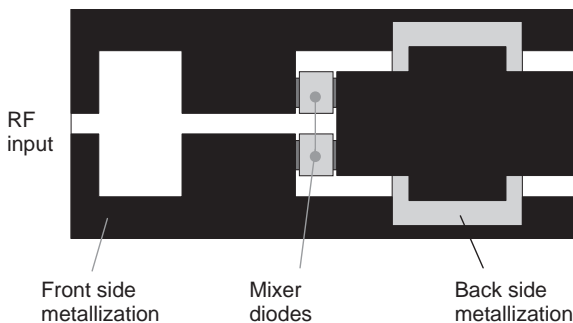


Figure 13. Layout of the key section of a third-harmonic 60-GHz mixer that has been optimized using a FDTD calculation. The steps in widths of slot and strips as well as the backside metallization under the LO/IF line provide the impedance matching for the different ports.

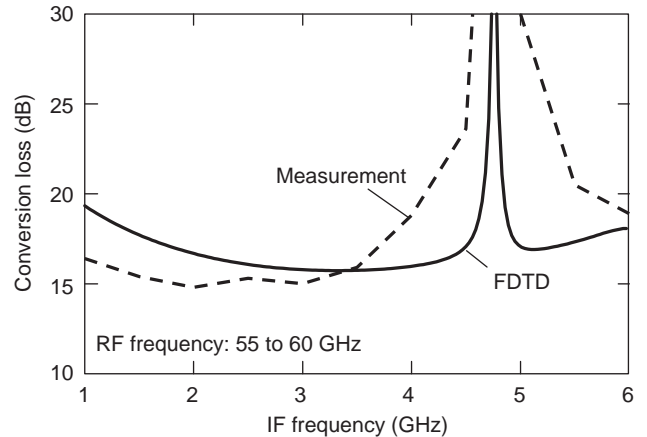


Figure 14. Conversion loss of the third-harmonic 60-GHz mixer. As a result of the full-wave calculation, even resonances can be predicted and shifted to uncritical frequencies.

configuration very similar to that of the balanced mixer (see Figs. 7 and 10 and (Refs. 23 and 24)). For the phase shifter, either pin or Schottky diodes are alternatively switched to the ON or OFF state via a bias applied to the coplanar line. With an appropriate matching of the circuitry, signal transmission between the finline port (RF port in the mixer case) and the coplanar port (LO port of the mixer) undergoes a phase differences of 180° depending on the sign of the control voltage, that is, depending on which diode is in the ON (biased) state.

4. FINLINE OSCILLATORS AND AMPLIFIERS

A number of efforts have been made to realize oscillators by the integrated finline technique. A basic problem is always heat removal from the active elements. Therefore, Gunn elements are usually used screwed directly into the broadside of the waveguide mount. Then the diode cap is soldered directly to one side of the finline metallization, which contains the necessary resonance and matching circuits (Fig. 15). Final tuning is typically done with a backshort in the metal waveguide behind the diode. A more detailed review of finline oscillators is given by Hofer [25]. Although some oscillators are used in integrated finline front ends (see next section), they have not proved suitable for high-volume and low-cost applications.

Some authors published designs of “finline” amplifiers [25,26]. Their arrangements, however, basically are microstrip FET amplifiers with transitions to finline, and

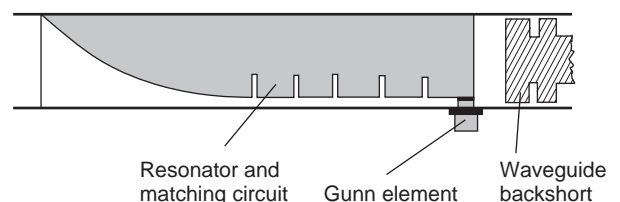


Figure 15. Basic setup of a finline Gunn oscillator. The Gunn element is screwed directly into the waveguide mount; resonance and matching structures are integrated into the planar structure.

they use the waveguide mount as some kind of package. Furthermore, because finline does not lend itself easily to a monolithic integration, amplifier design in finline was not pursued further.

5. INTEGRATED FINLINE COMPONENTS AND FRONT ENDS

The major advantages of planar components are exploited by integrating several components to “supercomponents” or complete front ends. With respect to finline, this can be done in two different ways. Because finline circuits consist of planar circuits and waveguide mounts, a first step is to integrate several finline circuits in a single waveguide mount, although each circuit still has its own transition(s) to waveguide. This concept allows optimizing and testing all finline circuits separately and combining them with waveguide circuits like oscillators, waveguide filters, or circulators realized in a waveguide mount split in the E plane. The complete waveguide mount can be fabricated using computer-controlled milling or, for high-production quantities, using plastic injection molding and electroplating. Some disadvantages of this arrangement are increased losses due to the repeated tapers from waveguide to finline and possibly some problems with interaction of components over greater distances causing an increased ripple in transmission and return loss behavior. Integrated front ends of this type have been realized for communication equipment in the Ka band [27], for military surveillance receivers [28], and for radar front ends for military seeker heads [29] or automotive radars for intelligent cruise control [30]. For example, Barnes et al. [27], describe a transmitter front end for a 29-GHz communication system that includes an E -plane waveguide circulator, two couplers, a pin diode biphase modulator, and a pin diode attenuator. The power is generated by an external Gunn oscillator. An E -plane, metal insert, bandpass filter is added to this unit with an additional waveguide mount.

An even higher degree of integration is achieved by integrating several components on a single substrate with direct finline interconnects, that is, without transitions from finline to waveguide and back to finline. This technique results much smaller components with reduced losses. Furthermore, the single components are placed close together, thus avoiding strong phase variations from mutual interactions as a function of frequency. On the other hand, the single components in such a supercomponent can no longer be tested separately.

A number of integrated front ends of this type have been realized by the author and his group, starting with the integration of balanced mixer and pin diode attenuators acting as sensitivity time control (STC) for radar applications [31] or as Dicke switch for a radiometer [32].

Figure 16 shows the opened waveguide mount with a quartz substrate containing a 94-GHz mixer and a SPDT switch. Two diodes in each of the two input arms of the circuit are mounted with opposite polarities. Thus only a single control input for the Dicke switch is necessary. Efforts were also made to integrate Gunn oscillators as shown previously (Fig. 15). In Ref. 32, the integration of

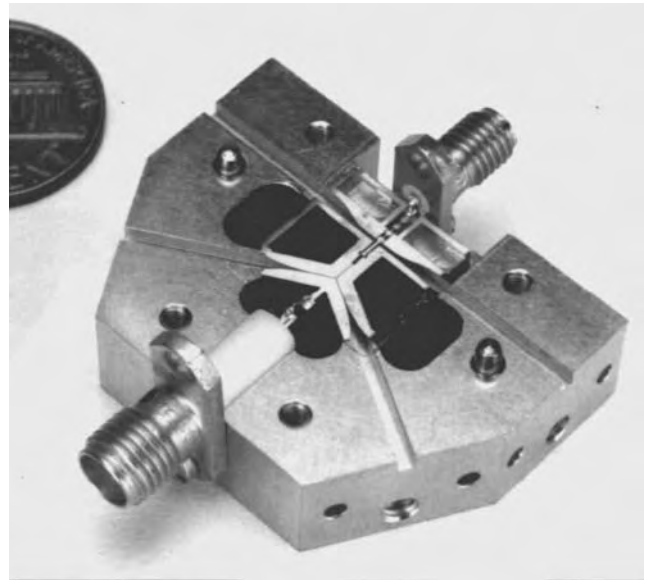


Figure 16. Photograph of a 94-GHz integrated finline circuit including a balanced mixer and a pin diode SPDT. The waveguide split block is opened to observe the quartz substrate with the planar circuit.

a mixer with a two-diode series type of pin diode attenuator (Fig. 6b) and a Gunn oscillator as LO is demonstrated (see photograph of Fig. 17). In this example, the series type of pin diode attenuator is used favorably for bias isolation; only the finline metallization between the two stubs loaded with the diodes must be DC-isolated.

Even the integration of a Ka-band pulse radar sensor on a single substrate including pulse oscillator and LO, an SPDT switch as a transmit/receive switch, a series type pin diode STC, and a balanced mixer were demonstrated [31].

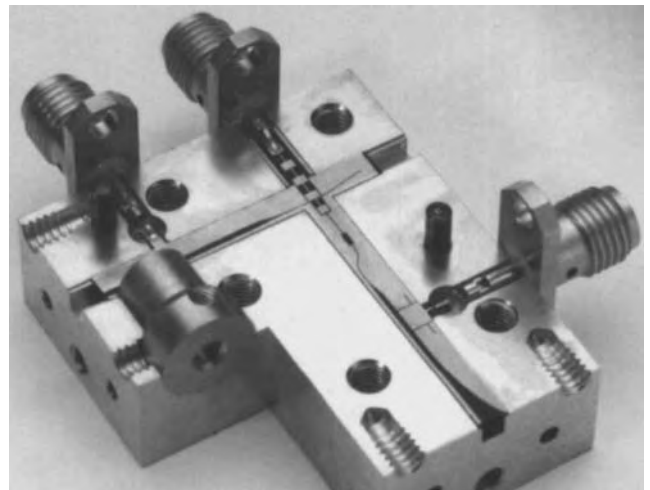


Figure 17. Photograph of a 60-GHz integrated finline receiver consisting of a Gunn oscillator as LO, a balanced mixer, and a series-type pin diode attenuator. The Gunn element is screwed into a copper heatsink in the waveguide mount; the series pin diode attenuator allows a DC isolation with respect to the other components.

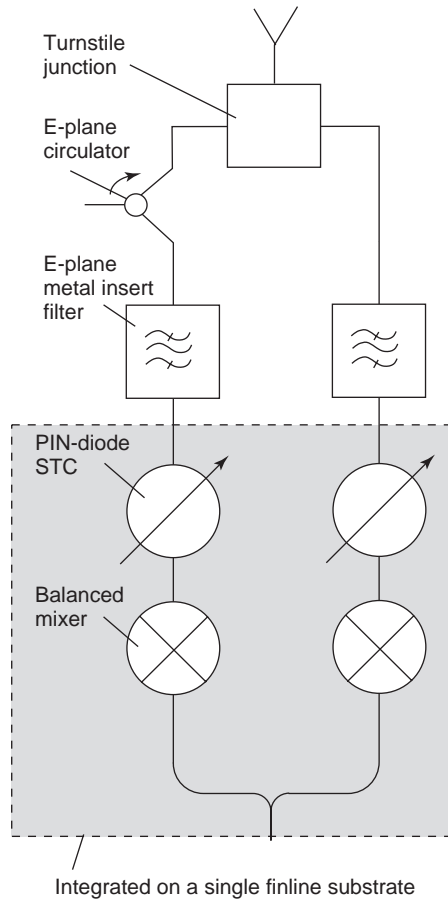


Figure 18. Block diagram of an integrated dual-channel 94-GHz radar receiver front end. All components (except for the turnstile junction) are combined in a single *E*-plane split-block mount. Balanced mixers, pin diode STCs, and the LO power divider are integrated on a single substrate.

For a 94-GHz dual-polarization radar, an integrated receiver front end was realized using both an integrated finline circuit (2 mixers, 2 pin diode STCs, and a power

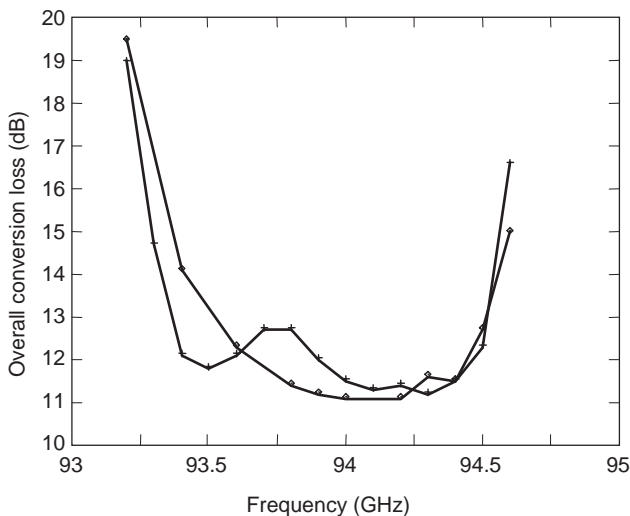


Figure 19. Overall conversion loss of the two channels of the 94-GHz radar receiver (see Fig. 18).

divider on a single substrate) and waveguide components (*E*-plane circulator, *E*-plane metal insert filters, and a turnstile coupler) [33]. Figure 18 shows a block diagram of the front end. Figure 19 shows the two receiver conversion loss curves. They include conversion loss of the mixers and the insertion losses of pin diode attenuators, the *E*-plane filters, and the *E*-plane circulator. The overall system noise figure amounts to 12 dB.

BIBLIOGRAPHY

1. W. J. R. Hofer, FINLINES (this encyclopedia).
2. R. Vahldieck, Quasi-planar filters for millimeter-wave applications, *IEEE Trans. Microwave Theory Tech.* **MTT-37**:324-334 (1989).
3. Y. C. Shih, T. Itoh, and L. Q. Bui, Computer-aided design of millimeter-wave *E*-plane filters, *IEEE Trans. Microwave Theory Tech.* **MTT-31**:135-141 (1983).
4. J. Dittloff and F. Arndt, Rigorous field theory design of millimeter-wave *E*-plane integrated circuit multiplexers, *IEEE Trans. Microwave Theory Tech.* **MTT-37**:340-350 (1989).
5. H. Callsen and L.-P. Schmidt, Quasiplanar 3-dB hybrid for mm-wave integrated circuits, *Electron. Lett.* **18**:161-163 (1982).
6. E. Kpodzo, K. Schuenemann, and G. Begemann, A quadri-phase fin-line modulator, *IEEE Trans. Microwave Theory Tech.* **MTT-28**:747-752 (1980).
7. B. Adelseck, H. Callsen, H. H. Meinel, W. Menzel, and K. Solbach, A survey of planar integrated mm-wave components, *Radio Electron. Eng.* **52**:46-50 (1982).
8. P. J. Meier, Millimeter integrated circuits suspended in the *E*-plane of rectangular waveguide, *IEEE Trans. Microwave Theory Tech.* **MTT-26**:726-733 (1978).
9. A. Beyer and I. Wolff, A fin line ferrite isolator and circulator for the R-band, *Proc. 11th European Microwave Conf.*, Amsterdam, The Netherlands, 1981, pp. 321-326.
10. M. Braas and C. Schieblich, *E*-type circulator for fin lines, *Electron. Lett.* **17**:701-702 (1981).
11. A. Beyer and K. Solbach, Fin line ferrite isolator for integrated millimeterwave circuits, *Proc. IEEE Int. Microwave Symp. MTT-S*, 1981, pp. 296-298.
12. K. Solbach, *E*-plane circulators aid millimeter-wave design, *Microwaves RF.* **73**-79 (Dec. 1983).
13. K. S. Yngvesson, T. L. Korzeniowski, Y.-S. Kim, E. L. Kollberg, and J. F. Johansson, The tapered slot antenna—a new integrated element for millimeter-wave applications, *IEEE Trans. Microwave Theory Tech.* **MTT-37**:365-374 (1989).
14. H. H. Meinel and H. Callsen, Fin-line detectors for frequencies up to 260 GHz, *Proc 7th Conf. Infrared and Millimeter-Waves*, Marseilles, France, 1983, Book of Abstracts, p. 34.
15. H. Callsen, H. H. Meinel, and W. J. P. Hofer, p-i-n diode control devices in *E*-plane techniques, *IEEE Trans. Microwave Theory Tech.* **MTT-37**:307-316 (1989).
16. D. W. Ball and L. Q. Bui, Wideband mm-wave mixers for EW applications, *Microwave J.* **25**:65-76 (June 1982).
17. W. Menzel, Integrated fin-line components for communication, radar, and radiometer applications, in K. J. Button ed., *Infrared and Millimeter Waves*, Vol. 13, *Millimeter Components and Techniques*, Part. IV, Academic Press, 1985, pp. 77-121.

18. W. Menzel, A 140 GHz balanced mixer for finline integrated circuits, *Proc. 13th European Microwave Conf.*, Nürnberg, Germany, 1983, pp. 179–182.
19. P. J. Meier, Wideband subharmonically pumped W-band mixer in single ridge finline, *Proc. IEEE Int. Microwave Symp.*, 1982, pp. 201–203.
20. U. Guettig, K. M. Strohm, and F. Schaeffler, D-band subharmonic mixer with silicon planar doped barrier diodes, *IEEE Trans. Microwave Theory Tech.* **MTT-39**:366–368 (1991).
21. L.-P. Schmidt and W. Menzel, Planar integrated harmonic mixers for use up to 150 GHz, *Proc. German Conference on Microwaves and Optoelectronics (MIOP)*, Sindelfingen, Germany, May 1987, Vol. I, p. 4A–4.
22. W. Thiel and W. Menzel, Full-wave design and optimization of mm-wave diode-based circuits in finline technique, *IEEE Trans. Microwave Theory Tech.* **MTT-47**:2460–2466 (1999).
23. W. Thorpe and J. D. Gilliland, 29 GHz *E*-plane biphas modulator, *Electron. Lett.* **19**:107–109 (1983).
24. B. Adelseck and B. Rembold, A 180° phase modulator in finline technique (in German), *Wiss. Berichte AEG-Telefunken*, **54**(4/5):238–240 (1981).
25. W. J. R. Hoefer, Oscillators and amplifiers in integrated *E*-phase techniques, *IEEE Trans. Microwave Theory Tech.* **MTT-37**:351–364 (1989).
26. J. Ruxton and W. J. R. Hoefer, A quasi-planar FET amplifier in integrated finline and microstrip techniques, *IEEE Trans. Microwave Theory Tech.* **MTT-37**:429–432 (1989).
27. B. C. Barnes, R. N. Bates, and I. M. Clarke, An integrated *E*-plane mm-wave 29 GHz transceiver, *Proc. 14th European Microwave Conf.*, Liège, Belgium, 1984, pp. 537–542.
28. B. H. Newton, A. F. Dodds, D. M. Nugent, and D. H. Body, A sensitive K-band receiver for ESM application, *Milit. Microwave Conf.* (Brighton, UK) (June 1986).
29. M. B. Williams and I. M. Clarke, Radar transceiver for smart-munition applications, *Microwave System News & Communication Technologies*, **48** (Dec. 1987).
30. A. G. Stove, Automotive radar at 80–90 GHz, *Proc. IEEE Int. Microwave Symp. MTT-S*, 1992, pp. 613–616.
31. W. Menzel, H. Callsen, K. Solbach, and H. Meinel, Integrated Ka-band radar increases target recognition, *Defense Electron.* 95–99 (Oct. 1982).
32. W. Menzel and H. Callsen, Integrated fin-line components and subsystems at 60 and 94 GHz, *IEEE Trans. Microwave Theory Tech.* **MTT-31**:142–146 (1983).
33. W. Menzel, H. Callsen, and K. Solbach, A integrated receiver frontend for a 94 GHz dual polarization radar, *Proc. 13th European Microwave Conf.*, 1983, Nürnberg, Germany, pp. 142–147.

FINLINES

WOLFGANG J. R. HOEFER
 University of Victoria
 Victoria, British Columbia
 Canada
 RUEDIGER VAHLDIECK
 Institut für Feldtheorie und
 Höchstfrequenztechnik

Finlines are guiding structures for electromagnetic waves that consist of one or several metallic fins suspended in

the *E* plane of a waveguide enclosure. They are the basic transmission media for the so-called integrated *E*-plane circuit technology. The fins can either be suspended freely (metallic *E*-plane lines) or supported by dielectric substrates of low permittivity. The general term “finline” usually applies to the latter type, and there exist many variations that are classified according to the manner in which the metallization is placed on the substrate, and how the planar structure is mounted in the enclosure.

Finlines are applied predominantly in the frequency range between 10 and 100 GHz; but some applications at frequencies up to 170 GHz have been realized. Having losses of typically 0.1 dB per wavelength, finlines are not suitable for long-distance transmission. However, they excel as a circuit medium for millimeter-wave components and systems due to their low manufacturing cost, wide single-mode bandwidth, compatibility with discrete active and passive devices, and suitability for integration with other hybrid circuit techniques as well as with standard rectangular waveguides. Manufacturing costs are moderate for two reasons: (1) the planar insert can be fabricated using printed-circuit batch processing; (2) since the circuit characteristics are dominated by the topology of the printed insert, dimensional tolerances for the waveguide enclosure can be greatly relaxed (typically by a factor of 5 compared with standard waveguide). The enclosure also prevents radiation losses, reduces susceptibility to outside interference, and may act as a heatsink for active devices. Unfortunately, there is a price to pay for the technological advantages of finlines; their analysis and design are difficult because of the metallic edges that lead to field singularities, the presence of two or more different dielectrics in the structure giving rise to hybrid modes of propagation, and to structural complications necessary for mounting the substrate and for biasing of devices.

1. A BRIEF HISTORY

Since the early 1940s it has been known that one or two metallic ridges in the *E* plane of a rectangular waveguide increased its single-mode bandwidth and lowered its characteristic impedance. In particular, Cohn [1] pointed out the potential of this feature for realizing impedance transformers, tapers, filters, slow-wave structures, and broadband matched loads by simply changing the ridge depth; Hopfer [2] published extensive and accurate data for the cutoff frequencies, characteristic impedances and power-handling capability of ridged waveguides. While the ridge waveguide is not truly quasiplanar, its early theoretical treatment and the manner in which circuit functions were realized have laid the groundwork for the design and realization of finline circuits. In 1955, Robertson [3] built the first truly planar finline component. It was a circular-to-rectangular waveguide coupler fitted with a pair of thin metal fins. Robertson recognized that this technique was suitable for very broadband hybrids, directional and polarization-sensitive couplers. Sixteen years later, Konishi and Hoshino [4] reported a 100-GHz converter featuring a planar metallic circuit in a waveguide. However, the major development in the evolution of *E*-plane technology was

Meier's invention of the "integrated finline" in 1972 [5–7], for which he received the Microwave Application Award of the IEEE-MTT society in 1984. By supporting the planar conducting fins with a thin, low-permittivity substrate, Meier extended thin-film fabrication techniques to E -plane circuitry and gained additional advantages such as DC isolation of the fins for bias purposes, intermediate-frequency (IF) and modulation connections, and mechanical support for discrete devices mounted in parallel or in series with the fins.

Meier's invention spurred intense international research activities and product development. First commercial finline products were announced in the late 1970s. They included mixers, broadband switches, attenuators, detectors, and complete integrated radar front ends for frequencies up to 140 GHz [8–12].

2. CLASSIFICATION OF FINLINES

Finline structures can be viewed as derivatives of the four generic structures shown in Fig. 1. In fact, they share some of their characteristics and can be reduced to any of them. A finline is thus created either by placing a slotline into the E plane of a rectangular waveguide, by partially loading a ridge waveguide with dielectric, or by partially metallizing the dielectric in a slab-loaded waveguide. Four basic types of finlines may result; their simplified cross sections are shown in Figs. 2a–2d. Insulated, unilateral, bilateral, and antipodal finlines can be distinguished by the way in which their fins are arranged on the substrate. Further variations of each type are obtained by moving the substrate or the slot away from the symmetric position, or by adding further planar inserts, strips, or slots. For example, Figs. 2e and 2f show cross sections of asymmetric finlines.

3. CONSTRUCTION OF FINLINES

A finline consists of printed metallic fins on a substrate (the planar insert) and a metallic housing that holds the insert and confines the electromagnetic fields. Both soft and hard substrate materials may be used. Fiberglass-reinforced Teflon (RT Duroid, $\epsilon_r = 2.2$) is the most widely

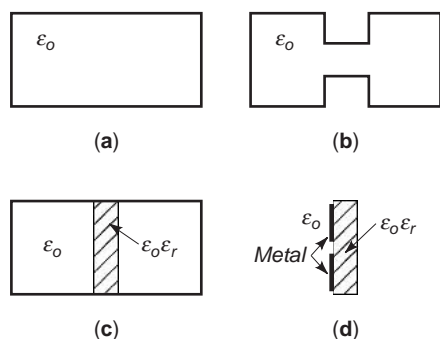


Figure 1. The four generic waveguides from which finlines can be derived: (a) rectangular waveguide; (b) double-ridged waveguide; (c) slab-loaded waveguide; (d) slotline.

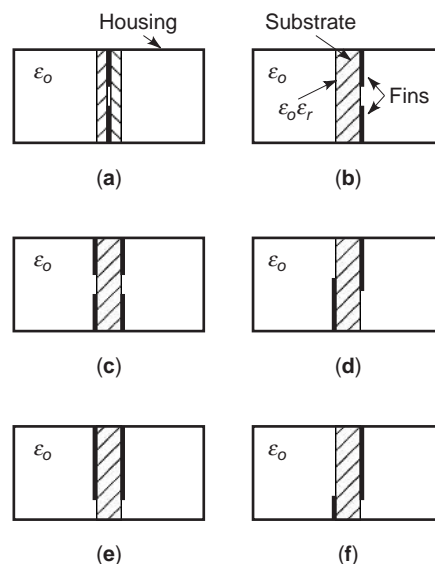


Figure 2. The four basic finline types and some of their variants: (a) insulated finline; (b) unilateral finline; (c) bilateral finline; (d) antipodal finline; (e) asymmetric bilateral finline; (f) asymmetric antipodal finline.

used soft substrate material. It is easily processed and cut, costs little, and has low dielectric permittivity and losses. It is employed mostly at lower millimetric frequencies; a thickness of 0.01 in. (0.254 mm) is suitable for components up to 40 GHz, and 0.005 in. (0.127 mm) is used for frequencies up to 90 GHz. Finline components and circuits of highest quality and for frequencies beyond 90 GHz call for quartz substrates ($\epsilon_r = 3.75$) which are more expensive, fragile, and difficult to process, but provide better mechanical support for delicate semiconductor devices. The housing is usually machined from brass or aluminum in the form of a split block. Metallized Plexiglas has also been used with mixed results because of adhesion problems. Three housing configurations (Fig. 3) can be found in practice.

The first type has been proposed by Meier [6]. Two Π -shaped metal pieces clamp the planar insert (Fig. 3a) held in place by nylon screws. Since the substrate extends beyond the confines of the inner waveguide channel, this configuration is partially open. To minimize RF leakage, the clamping region is made $\lambda_d/4$ wide, where λ_d is the wavelength in the dielectric substrate at midband frequency. Furthermore, to suppress the excitation of TEM-type modes in the slot region, longitudinal current flow must be impeded by serrating the substrate metallization in the slot region [42]. On the other hand, since one of the fins can be isolated from the housing with a dielectric insert, bias is easily supplied to embedded semiconductor devices.

The second type has been proposed by Adelseck et al. [8]. Here, the two halves of the split block touch each other, thus completely shielding the finline (Fig. 3b). A shallow groove is machined into one of the blocks to accommodate the substrate. However, stringent mechanical tolerances (typically $\pm 10\mu\text{m}$) must be maintained

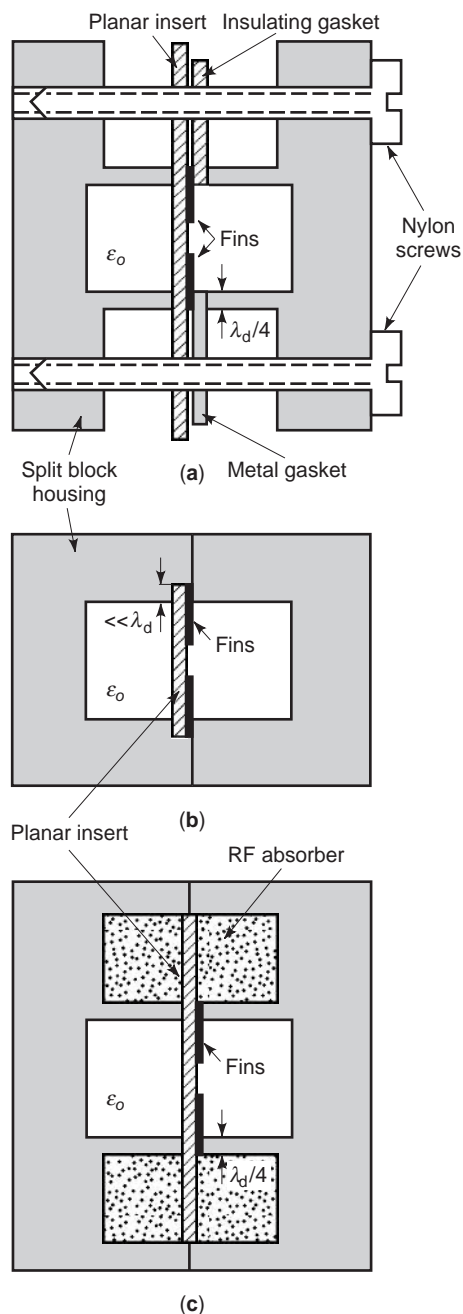


Figure 3. Three types of finline construction: (a) finline mount proposed by Meier; (b) finline mount proposed by Adelseck et al. (c) combination of (a) and (b) for hard substrates and high frequencies. (After Meier [6], copyright © 1974 IEEE, reprinted with permission.)

here. If the groove is too wide, poor contact between the fins and the housing can introduce considerable attenuation. If the groove is too narrow, hard substrates may break, and soft substrates may be compressed and pushed out into the waveguide channel, causing bending and possibly rupture of delicate leads of devices. Bias can be fed locally to the clamping region through the metal block, and fins can be insulated from the housing by inserting a thin Mylar sheet into the groove.

The third type combines the features of both approaches (Fig. 3c). It is suitable for quartz substrates at high frequencies (90 GHz and above), where machining tolerances become prohibitive because of the small size of the groove. As in type 1, the walls of the waveguide channel are made $\lambda_d/4$ wide to form a choke, but the substrate protrudes on either side into a secondary channel that contains RF absorbing material. In this way the finline is sealed. Fins can be biased by inserting a thin insulating sheet between fins and housing, and by contacting the fins through a feed connection.

All three techniques have been used successfully in the realization of finline components. Acceleration tests have shown that components of types 2 and 3 with hard substrates can survive up to 30,000 *g* for 2 ms, while components with soft substrates withstand 2000 *g* for 0.5 ms or shocks of up to 4000 *g* [9].

4. BASIC ELECTROMAGNETIC PROPERTIES OF FINLINES

The most important properties are the propagation constant and the characteristic impedance associated with the dominant mode of propagation. These depend on the geometry of the cross section, the substrate permittivity, and the frequency of operation. Furthermore, the single-mode bandwidth is proportional to the separation between the cutoff frequencies of the dominant and the first higher-order mode. If finline discontinuities are to be analyzed using mode matching in the longitudinal direction, a significant number of higher-order modes must be characterized as well. While the generic topologies in Fig. 2 yield the characteristics of real finlines quite accurately at lower frequencies, the influence of the geometric details shown in Fig. 3, such as the substrate mounting grooves and the finite thickness of the metal fins, must be included in the analysis and design of practical components, particularly at higher frequencies where the size of these features is not negligible vis-à-vis the dimensions of the waveguide channel and the substrate thickness.

Similar to regular waveguides, finlines are dispersive; that is, their guided wavelength λ_g changes nonlinearly with frequency. In waveguides without partial dielectric filling, the guided wavelength λ_g (or propagation constant β) at any frequency above cutoff can be calculated from the knowledge of the cutoff wavelength λ_c with the well-known formula

$$\lambda_g = \frac{\omega}{\beta} = \frac{\lambda}{\sqrt{1 - (\lambda/\lambda_c)^2}} \quad (1)$$

However, as soon as the waveguide is partially filled with a dielectric material, this formula no longer applies. With increasing frequency, more of the wave energy tends to concentrate inside the material with the higher permittivity, slowing down the propagation velocity. This effect is not included in Eq. (1). To accurately determine the guided wavelength in a finline at any frequency above cutoff, the field problem must be solved separately for each frequency.

As in all waveguides carrying non-TEM waves, voltage and characteristic impedance are not uniquely defined. While the voltage is usually obtained by integrating the electric field in the slot along the shortest path on the substrate surface, impedance definitions vary with the application, and the most appropriate definition must be established on a case-by-case basis. Meinel and Rembold [10] found that the voltage-current definition $Z_{v,i} = (\text{voltage across the slot})/(\text{current in the fins})$ was most appropriate for predicting the interaction of finlines with discrete devices, while Knorr and Shayda [14] reported best results with the ridged waveguide definition and Willing and Spielmann [15] preferred the voltage-power definition $Z_{v,p} = (\text{voltage across the slot})/(2 \times \text{average power transmitted})$.

There exist a variety of techniques for the computation of finline parameters, ranging from approximate analytical expressions to sophisticated numerical procedures. They will be outlined briefly in the following. For detailed information the reader is invited to consult to the appropriate references given in the bibliography.

4.1. Approximate Methods of Finline Analysis

Since most finlines are made with low-permittivity substrates such as RT Duroid ($\epsilon_r = 2.2$) or quartz ($\epsilon_r = 3.75$) that occupies only a small fraction of the waveguide cross section, their dispersion characteristics can be approximated by the behavior of commensurate waveguides that are filled uniformly with a fictitious frequency-independent dielectric of permittivity $\epsilon_0 \epsilon_{re}$ (Fig. 4). (The permittivity of this fictitious dielectric ϵ_{re} is called the equivalent dielectric constant to distinguish it from the so-called effective dielectric constant $\epsilon_{eff} = (\lambda/\lambda_g)^2$ of a finline.) The uniformly filled ridge waveguide obeys a rather simple dispersion formula for the guided wavelength λ_g and the characteristic impedance Z_0 :

$$\lambda_g = \frac{\lambda}{\sqrt{\epsilon_{re} - (\lambda/\lambda_c)^2}}; \quad Z_0 = \frac{Z_\infty}{\sqrt{\epsilon_{re} - (\lambda/\lambda_c)^2}} \quad (2)$$

According to Meier [6], these expressions agree with measurements within $\pm 2\%$ when λ_c and Z_∞ are the cutoff wavelength and characteristic impedance at infinite frequency of an air-filled ridge waveguide of identical dimensions (available from Cohn’s [1] or Hopfer’s [2] paper, or from other published data), and ϵ_{re} has been determined by measuring the guided wavelength of a test structure at a single frequency in mid-band [6].

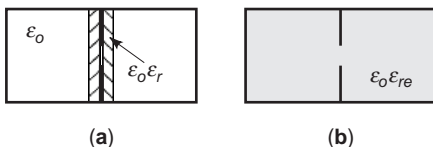


Figure 4. Insulated finline and its equivalent ridged waveguide with identical cross section and uniform dielectric filling of permittivity $\epsilon_0 \epsilon_{re}$.

More accurate results can be obtained by the transverse resonance approach that has previously been applied by Cohn [16] and other researchers to analyze ridge waveguides, slab-loaded waveguides, and slotlines. In the simplest formulation, the dominant mode in the finline is considered to be a TE mode in the transverse direction that resonates between the two sidewalls of the enclosure. In transverse direction, the finline thus appears as a chain of piecewise homogeneous waveguide sections of width $\lambda_g/2$ (λ_g is the wavelength in longitudinal direction of the finline and corresponds to the cutoff wavelength of the transverse waveguide sections). The fins form a capacitive transverse discontinuity. The characteristic admittances and propagation constants of the subsections are those of homogeneous waveguides. The corresponding equivalent circuit is shown in Fig. 5; its transverse resonance condition is obtained by setting the total admittance in the plane of the fins equal to zero

$$\frac{B}{Y_a} - \cot \beta_a h - \frac{Y_d}{Y_a} \cot \beta_d \left\{ d + \frac{1}{\beta_d} \tan^{-1} \left[\frac{Y_d}{Y_a} \tan \beta_a (a - d - h) \right] \right\} = 0 \quad (3)$$

where

$$\beta_a = \frac{2\pi}{\lambda} \sqrt{1 - (\lambda/\lambda_g)^2},$$

$$\beta_d = \frac{2\pi}{\lambda} \sqrt{\epsilon_r - (\lambda/\lambda_g)^2} \quad \text{and} \quad \frac{Y_d}{Y_a} = \frac{\beta_d}{\beta_a}$$

By fixing the guided wavelength λ_g and solving Eq. (3) for λ , one obtains the frequencies at which the dominant and higher-order modes propagate down the finline with that wavelength λ_g . The accuracy of the solution depends essentially on the accuracy of the capacitive susceptance B , and the various transverse resonance approaches reported in the literature differ in the way in which this susceptance is determined. They range from quasistatic approximations to variational expressions and mode-matching solutions [17–20]. The group of approximate methods also comprises the empirical closed-form equations that are essentially formulas fitted to more accurate numerical results [21,22]. Their advantage resides in their simplicity and their suitability for synthesis, but they are limited to certain combinations of parameters and have lost some of their attractiveness due to the proliferation of high-performance computers that yield more rigorous numerical solutions almost instantly.

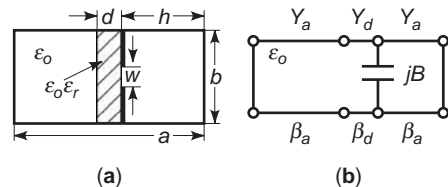


Figure 5. (a) Unilateral finline; (b) and its equivalent transverse network.

4.2. Rigorous Methods of Finline Analysis

Rigorous methods yield field solutions by solving Maxwell's equations subject to the boundary conditions imposed by the finline geometry. Several are based on the method of moments, from the first formulation in the space domain by Hofmann [23] to the spectral domain approaches described by Itoh [24], Knorr and Shayda [14], and Schmidt and Itoh [25]. A mode-matching solution was proposed by Beyer and Wolff [61], and a modified mode-matching approach was presented by Vahldieck and Bornemann [26,27]. A singular integral equation formulation was proposed by Omar and Schuenemann [28].

In all these approaches the fields in the dielectric and air-filled subregions of the finline are expressed in terms of rectangular waveguide TE and TM modes resonating in transverse direction, also called *longitudinal section electric* (LSE) and *longitudinal section magnetic* (LSM) modes. In fact, each of these modes must satisfy a condition similar to Eq. (3). The modal coefficients are determined such that their superposition satisfies all boundary and interface conditions, in particular, the edge condition at the metal fins where most of the energy in the structure is concentrated. Approaches differ in the way in which the relationship between slot field and fin current distributions is formulated. In the space domain formulation, this relationship takes the form of integral equations. Their kernels are the Green functions of the housing and substrate without the metal fins. These integral equations are then solved with the method of moments and Galerkin's procedure (identical basis and testing functions are used).

By performing a spatial Fourier transformation of all fields and currents with respect to the coordinates parallel to the substrate plane, one can transform the integral equations into a set of algebraic equations. The resulting spectral-domain formulation leads to a very efficient algorithm for the dominant and first higher-order finline eigensolutions and eigenvectors, especially when the slot fields or fin currents are developed into physically realistic basis functions that individually satisfy all the boundary and edge conditions in the plane of the fins. In fact, only a single constant basis function for the slot field is sufficient to determine the dominant wavenumber within 2–3%. However, the spectral-domain method is restricted to idealized finline geometries (no mounting grooves, zero metallization thickness). It is also less suitable than the singular integral formulation for determining eigensolutions of high order because the set of required basis functions for the slot field or fin current grows quickly in size and complexity.

The general mode matching approach that enforces conservation of tangential field components or complex power across all boundaries between subregions can take these realistic features into account more readily, as can the well-known family of space discrete solution methods, such as the finite-difference, finite-element, and TLM methods of analysis, in both their frequency and time-domain formulations, or the method of lines. A detailed description of these methods with extensive bibliographies can be found in Refs. 29 and 30. However, the salient features of the most frequently employed rigorous methods of

finline analysis, namely, the spectral-domain and the mode-matching methods, will be summarized in the following, together with some typical results.

4.2.1. Spectral-Domain Analysis of Finline. In the spectral-domain formulation the Fourier transform of the Green functions $\tilde{\mathbf{G}}_{ij}$ in the finline (expressed in terms of LSE and LSM modes) relates the transforms of the electric field in the slot with those of the current density on the fins via the equation

$$\begin{bmatrix} \tilde{\mathbf{G}}_{11}(\alpha_n, \beta, k_0) & \tilde{\mathbf{G}}_{12}(\alpha_n, \beta, k_0) \\ \tilde{\mathbf{G}}_{21}(\alpha_n, \beta, k_0) & \tilde{\mathbf{G}}_{22}(\alpha_n, \beta, k_0) \end{bmatrix} \begin{bmatrix} \tilde{\mathbf{E}}_x(\alpha_n) \\ \tilde{\mathbf{E}}_z(\alpha_n) \end{bmatrix} = \begin{bmatrix} \tilde{\mathbf{J}}_x(\alpha_n) \\ \tilde{\mathbf{J}}_z(\alpha_n) \end{bmatrix} \quad (4)$$

$$\tilde{\mathbf{G}}_{11} = -(\alpha_n^2 Z_{\text{LSE}} + \beta_n^2 Z_{\text{LSM}})/(\alpha_n^2 + \beta_n^2)$$

$$\tilde{\mathbf{G}}_{12} = \tilde{\mathbf{G}}_{21} = -\alpha_n \beta_n (Z_{\text{LSE}} - Z_{\text{LSM}})/(\alpha_n^2 + \beta_n^2)$$

$$\tilde{\mathbf{G}}_{22} = -(\alpha_n^2 Z_{\text{LSE}} + \beta_n^2 Z_{\text{LSM}})/(\alpha_n^2 + \beta_n^2)$$

where Z_{LSE} and Z_{LSM} are the impedances seen from the nodes of the current source, looking into the respective equivalent circuits of Fig. 6b and 6c. α_n is the Fourier variable, $\beta = 2\pi/\lambda_g$ is the propagation constant in the axial direction, and k_0 is the free-space wavenumber; $\tilde{\mathbf{E}}_x$, $\tilde{\mathbf{E}}_z$, $\tilde{\mathbf{J}}_x$, and $\tilde{\mathbf{J}}_z$ are the electric fields in the slot and the current densities on the fins, respectively. This relationship is most readily formulated using Itoh's [24] immittance approach. Figure 6 shows the cross section of a unilateral finline, together with the equivalent transverse modal circuits for the immittance formulation of the Green functions. The slot fields and fin currents are expressed in terms of known basis functions with unknown coefficients. Applying Galerkin's procedure and Parseval's theorem results in a set of algebraic equations. The roots of the characteristic equation yield the eigenvalues of the finline.

The method is particularly efficient when basis functions are selected that satisfy already the edge condition at the fins. Thus, only a few basis functions are necessary to accurately describe the field in the slot or the current density on the fins. Once the coefficients of the basis

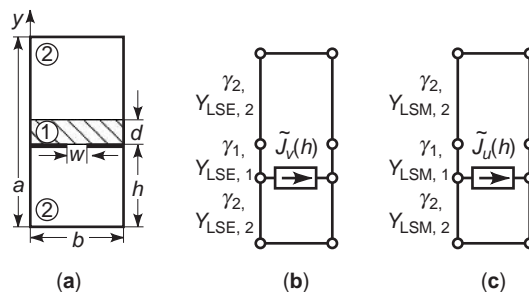


Figure 6. Cross section of a unilateral finline (a) and its equivalent transverse modal circuits for LSE (b) and LSM (c) modes.

functions are determined, the field functions inside the structure can be derived, and quantities such as slot voltage, fin current and characteristic impedances can be determined by appropriate integration over the field functions. Figure 7 shows the effective dielectric constant and voltage–power impedance of the unilateral finline in Fig. 6, computed with a single constant basis function for E_x in the slot. The enclosure is a standard WR-28 rectangular waveguide.

As mentioned earlier, geometric details such as the substrate mounting grooves and finite metallization thickness must be accounted for in practical realizations, particularly at higher frequencies. These can easily be included in the mode-matching analysis. Representative finline characteristics obtained with this approach will be presented in the following as well.

Two typical finline structures with realistic geometric details are presented in Fig. 8. Depending on the application, structures that support quasi-TEM modes (Fig. 8a) or configurations with pure slotline layout (Fig. 8b) are utilized. The principal difference between the two types is that in the first the dominant mode of propagation is the quasi-TEM mode without a lower cutoff frequency, while in the slotline structure the dominant mode is limited by a cutoff frequency that is determined mainly by the width of the slot(s).

Both types of finlines carry hybrid modes due to the presence of the dielectric substrate that supports the fins. Hybrid modes are neither TE nor TM but a combination of both, denoted as either HE or EH modes with all six field components present; HE modes are those with a predominant H_z field component, while EH modes exhibit a stronger E_z field component. Only at cutoff are these modes purely of type TE or TM. These modes often carry the same indices as TE and TM modes, such as HE_{nm} or EH_{nm} , indicating that the latter two originate from the corresponding TE or TM modes at cutoff. At frequencies

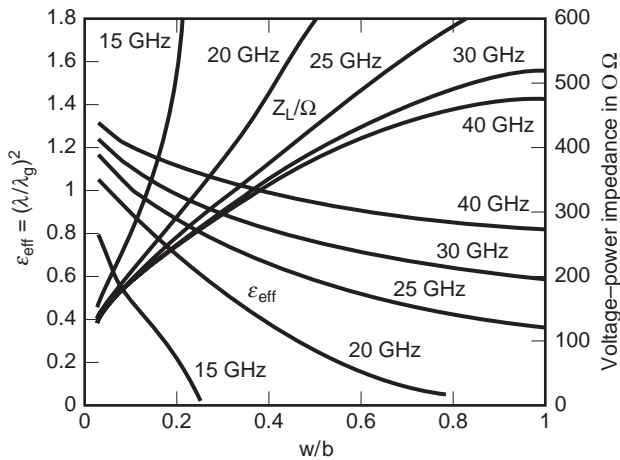


Figure 7. Effective dielectric constant and voltage–power impedance of the unilateral finline shown in Fig. 6, computed with the spectral–domain method using a single constant basis function for the slot field E_x . The dimensions are: $a = 7.112$ mm; $b = 3.556$ mm; $h = 3.429$ mm; $d = 0.254$ mm; $\epsilon_r = 2.2$.

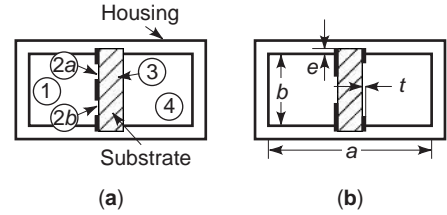


Figure 8. Two basic finline structures with finite metallization and substrate mounting grooves (t = finite metallization thickness, e = depth of mounting grooves, a = waveguide width, b = waveguide height): (a) edge-coupled unilateral finline; (b) asymmetric bilateral finline.

above cutoff, the field configuration of the individual hybrid modes can differ significantly from the TE and TM modes. Therefore, hybrid modes are equally often numbered according to the sequence at which they occur, such as HE_n and EH_m .

In the mode-matching approach, the finite metallization thickness and substrate mounting grooves are taken into account from the outset. It yields a somewhat longer guided wavelength than spectral domain analysis since a higher percentage of the electric field travels in air within the slot region. The hybrid modes are derived from the z components of the magnetic and electric vector potentials $\vec{\phi}_h$ and $\vec{\theta}_e$, respectively

$$\begin{aligned} \vec{E} &= \nabla \times \vec{\phi}_{hz} + \frac{1}{j\omega\epsilon} \nabla \times \nabla \times \vec{\theta}_{ez} \\ \vec{H} &= \nabla \times \vec{\theta}_{ez} - \frac{1}{j\omega\epsilon} \nabla \times \nabla \times \vec{\phi}_{hz} \end{aligned} \quad (5)$$

where

$$\begin{aligned} \phi_{hz} &= \sum_n Q_n^h(x) f_n(y) e^{-j\beta_n z} \\ \theta_{ez} &= \sum_n P_n^e(x) g_n(y) e^{-j\beta_n z} \end{aligned} \quad (6)$$

Q , P , f and g denote transverse eigenfunctions defined in each subregion of the finline cross section (i.e., regions 1, 2a, 2b, 3, 4 in Fig. 8a). The electric and magnetic fields tangential to the interfaces between the subregions are proportional to the vector potentials and their derivatives

$$E_y \propto \frac{dQ^h}{dx} = P^h, E_z \propto P^e, H_z \propto Q^h, H_y \propto \frac{dP^e}{dx} = Q^e \quad (7)$$

Matching the tangential field components at each interface and utilizing the orthogonality of modes leads to one coupling matrix (C_μ for $\mu = 1, 2a, 2b, 3, 4$) per interface. The coupling matrices can be linked successively by transferring the electric and magnetic fields from one boundary of a subregion to the opposite one. These transfer matrices (T_μ for $\mu = 1, 2a, 2b, 3, 4$) are the generalized (fundamental and higher-order modes) transmission-line equations in

each subregion. The resulting matrix equation yields

$$\begin{bmatrix} P^h = 0 \\ P^e = 0 \\ Q^h \\ Q^e \end{bmatrix}_{x=0} = \underbrace{\prod_{n=1}^{n=3} T^n C^n T^d}_G \begin{bmatrix} P^h = 0 \\ P^e = 0 \\ Q^h \\ Q^e \end{bmatrix}_{x=a} \quad (8)$$

From the resonance condition in Eq. (8) the characteristic equation G_{12} is obtained. Solving for $\det(G_{12})=0$ yields the propagation constant β or guided wavelength λ_g . Typical dispersion characteristics obtained in this way for the first six eigenmodes in a unilateral finline are shown in Fig. 9. The modes that are not excited by an incident TE_{10} mode are dashed. The first important higher-order mode is thus HE_3 ; the single-mode bandwidth of the dominant mode is situated between the cutoff frequencies of HE_1 and HE_3 (frequencies at which the curves intersect the frequency axis). Note that these dispersion curves change with both the groove depth e and the metallization thickness t as shown in the following.

4.2.2. Effect of Mounting Grooves. Mounting grooves are required to hold the substrate in the waveguide housing. A detailed analysis of the effect of the groove depth on the modes is given in Refs. 26 and 31. It was found that for unilateral finlines the cutoff frequencies of higher-order modes react very sensitively to the groove depth (e in Fig. 8), which for one-fifth of the waveguide height reduces the cutoff frequency of higher-order modes to such an extent that the finline is useless for most practical purposes. This is due to modes that originate from the TE_{20} (HE_3) and TE_{01} (HE_2) modes of the empty waveguide. Both modes appear to be coupled, are highly concentrated between the metallization within the substrate, and are thus very sensitive to changes in the groove depth. This effect is particularly pronounced in Fig. 10. The asymmetric bilateral finline carries an additional metallic strip inside the

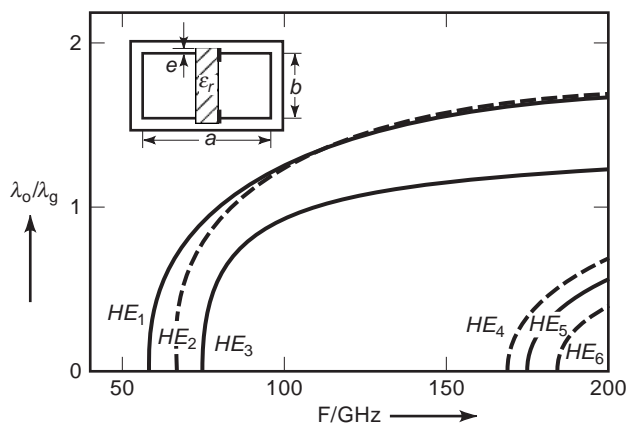


Figure 9. Dispersion characteristics of the first six hybrid eigenmodes in a unilateral finline. The dashed curves indicate modes that are not excited by the incident TE_{10} mode. The dimensions are $a = 1.65$ mm; $b = a/2$, $e = 0.5$ mm; $t = 5$ μ m, $\epsilon_r = 3.75$. (After Vahldieck [26], copyright © 1984 IEEE, reprinted with permission.)

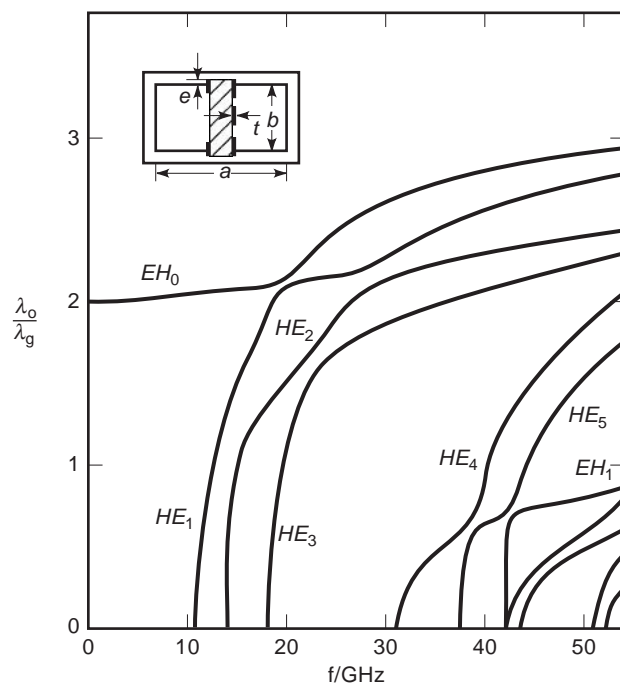


Figure 10. Dispersion characteristics of an asymmetric bilateral finline with an additional metallic strip in the gap on the right-hand side of the substrate. The modes appear to be strongly coupled and are very sensitive to changes in the groove depth. The dimensions are $a = 7.112$ mm; $b = 3.556$ mm; $e = 0.7$ mm; $t = 71$ μ m, $\epsilon_r = 10$. (After Vahldieck and Bornemann [27], copyright © 1985 IEEE, reprinted with permission.)

gap on the right-hand side of the substrate. For centered fin-lines this interaction between modes is greatly reduced since some of them will not be excited. This is not the case for unilateral finlines. However, since the metallization is only on one side of the substrate, the problem is not as pronounced.

4.2.3. Effect of Finite Metallization Thickness. The effect of finite metallization on the propagation constant and the characteristic impedance has been investigated by several researchers [26,31–33,62]. A typical behavior of the dominant mode in a unilateral finline with three different values of metallization thickness is shown in Fig. 11. The effect of mounting grooves is not included here. The characteristic impedance is reduced throughout the operating bandwidth when the metallization becomes thicker. This is consistent with the behavior of the ridge waveguide [1,2], where the capacitive loading of the waveguide increases when the ridge becomes wider. However, the propagation constant is not affected in the same way at lower and at higher frequencies. While the cutoff frequency is reduced by thicker metallization for the same reason as the characteristic impedance, the effect is reversed at higher frequencies; because of the wider airgap between thicker fins, more of the field energy travels in the airgap and less is concentrated in the dielectric, leading to a higher phase velocity. As a result, there is a crossover of the dispersion curves at midband. In conclusion, the effect

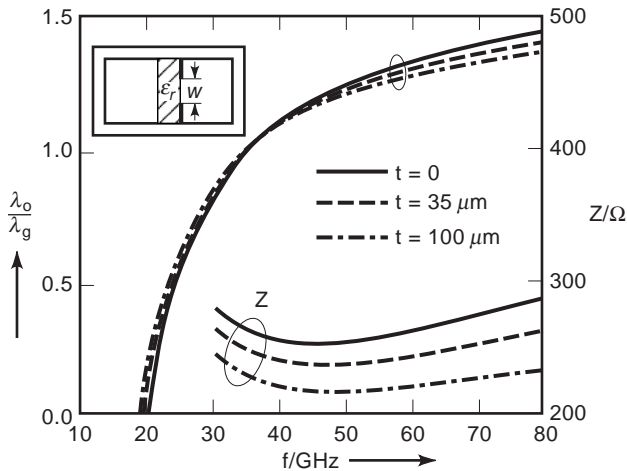


Figure 11. Effect of metallization thickness on the dispersion characteristics and the characteristic impedance of a unilateral finline. The dimensions are $a = 4.776$ mm; $b = 2.388$ mm; $d = 0.127$ mm; $w = 0.2b$; $\epsilon_r = 3.8$. (After Kitazawa and Mittra [32], copyright © 1984 IEEE, reprinted with permission.)

of finite metallization on the propagation constant is minimal around the center of the operating bandwidth.

5. FINLINE DISCONTINUITIES

Discontinuities in the finline geometry form the building blocks of finline circuits. Given the many degrees of freedom in the design of finlines, the possibilities are endless, and it would be impossible to give a complete treatment of this subject. Nevertheless, one can identify some generic types of finline discontinuities and provide some basic characteristics. Some of the most important are inductive strips, step changes in gap width, notches, dents, and series stubs. The shapes of typical discontinuities are shown in Fig. 12, together with their equivalent lumped-element networks. Note that, in contrast to similar waveguide discontinuities, the circuit elements are determined solely by the metallization pattern of the planar insert, while the geometry of the enclosure remains unchanged. This results in a considerable reduction in the manufacturing cost, as the discontinuities are realized using printed-circuit techniques rather than machining.

The effect of discontinuities on the guided wave in the finline can be represented either by generalized scattering parameters (S parameters) or by equivalent lumped networks. These are not determined solely by the local changes of the dominant waveguiding parameters, but include the effects of mode conversion, energy storage, and possibly multimode interactions between neighboring discontinuities. Within the single-mode propagation range, dominant-mode S parameters are sufficient to describe the behavior of discontinuities, provided that they have been determined at reference planes beyond the reach of evanescent higher-order modes.

The theoretical characterization of finline discontinuities is a challenge for the same reasons as the computation of finline characteristics. Inhomogeneous dielectric

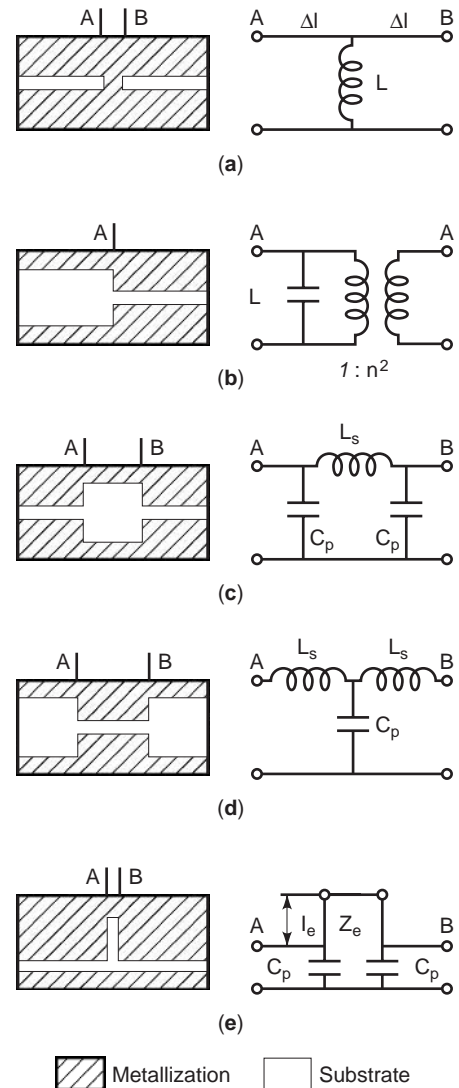


Figure 12. Profile of some important finline discontinuities and their equivalent lumped-element circuits: (a) inductive strip; (b) impedance step (step change in gap width); (c) inductive notch; (d) capacitive strip; (e) series stub. Note that the distance between planes A and B is short compared to the wavelength.

filling and edge singularities call for special approaches, ranging from experimental [6,34–36] over variational [37] and spectral domain techniques [35,38,39] to mode matching in longitudinal [40–42] as well as transversal [43] directions.

5.1. Inductive Strips

Inductive strips are important elements of bandpass filters. Meier [6] has determined the equivalent shunt inductance of strips from insertion loss measurements and from the resonant frequency of a one-section filter. Pic and Hoefler [34] have characterized strips and impedance steps by measuring the shift they caused in the resonant frequencies of an oversized cavity. The resulting empirical formulas for the strip inductance were confirmed by spectral-domain evaluations performed by Koster and Jansen

[39]. Further methodologies for the characterization of inductive strips and related discontinuities can be found in papers by Knorr and Deal [35], Zhang and Itoh [38], Saad and Schuenemann [44], and Omar and Schuenemann [45]. To achieve maximum Q factors in bandpass filters formed by inductive strips, the gap width of the resonant sections is usually maximized to the full height b of the enclosure. Such full-height strips and their interactions have been analyzed extensively with mode-matching techniques by Arndt et al. [46] and Shih et al. [47], leading to highly accurate CAD programs for E -plane bandpass filters.

5.2. Single and Interacting Impedance Steps

These discontinuities are formed by sudden changes in the gap width and come in many shapes and forms (Figs. 12b–12d). They serve as impedance transformers, tuning and matching elements, mounting platforms for semiconductor devices, or constitutive elements of filters. Besides empirical characterization [34], most systematic analytical approaches employ the representation of fields near the discontinuities by eigenmodes of either the adjacent uniform finline subsections (mode matching in longitudinal direction) or of transverse homogeneous waveguide subsections. As mentioned earlier, the former approach requires the determination of the eigensolutions of the finline subsections. It has been pointed out by Omar and Schuenemann [45] that the spectrum of finline modes can contain pairs of complex eigensolutions, and that their omission in the modal decomposition of the fields at the discontinuity can lead to significant errors. Various analyses and properties of impedance steps have also been described by El Hennawy and Schuenemann [40,41], Heilard et al. [42], Sorrentino and Itoh [43], and Beyer [48].

5.3. Narrow Series Slots

The series slot (Fig. 12e) is a popular tuning element in the design of oscillators and lowpass filters. It can be represented by a series-connected transmission line of effective length l_e and two stray capacitances that account for the field energy stored in the stray field at the junction. The effective length includes the stray effect at the end of the slot. Burton and Hooper [49] have characterized such slots experimentally and have given closed-form expressions for the elements of the equivalent circuit in Fig. 2e. These expressions are valid over an entire waveguide band and are independent of the dimensions of the enclosure. This indicates that narrow slots in the finline metallization behave essentially like slotline elements [16].

6. TRANSITIONS TO OTHER TRANSMISSION MEDIA

Most practical finline circuits include one or several types of transitions, either between different types of finlines or between finlines and other transmission media such as rectangular waveguides, coaxial line, or microstrip. Of particular importance and interest is the transition between finline and the commensurate rectangular waveguide due to the need to interface finline circuits with

measurement systems and conventional components. Transitions between different finline types and also between finlines and other planar circuits are needed to combine them and to take advantage of their respective properties in an integrated design. The topologies and properties of such transitions will be summarized in the following.

6.1. Transitions Between Finline and Waveguide

Transitions between finline and the commensurate rectangular waveguide are realized by varying in some way the slot between the full height of the waveguide and the final slot width. The bandwidth and the VSWR of the transition depend entirely on the profile of the fin contour and the length of the transition. The geometrically simplest transition is a linear taper extending over at least three guided wavelengths, as used by Cohen and Meier [13]. More sophisticated designs that are shorter than a wavelength employ single or double exponential profiles, cosine profiles, parabolic and circular profiles, as well as other profiles derived by nonuniform transmission-line theory [50–53]. Figure 13 shows some typical taper profiles employed for the realization of finline-to-waveguide transitions.

The problem of taper optimization amounts to realizing the lowest possible insertion loss over a given frequency band with a taper of minimum length. A rigorous treatment of the tapered transition leads to a nonlinear differ-

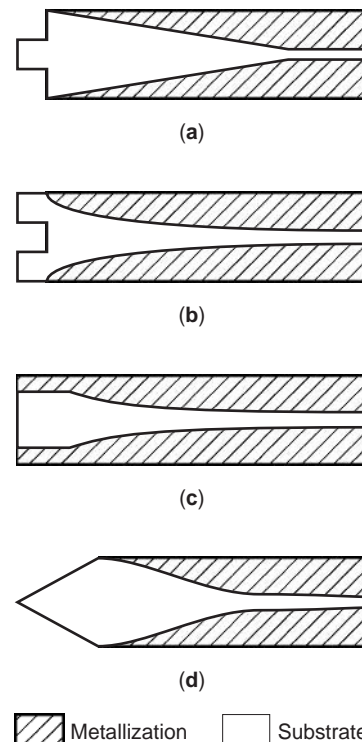


Figure 13. Profile of typical finline tapers and matching elements for the reduction of reflections from the dielectric slab interface: (a) linear taper with quarter-wave substrate protrusion; (b) exponential taper with quarter-wave substrate notch; (c) exponential taper with printer quarter-wave section; (d) double circular profile taper with triangular substrate protrusion.

ential equation of the Riccati type that must be solved numerically. Approximate solutions can be found, however, yielding the so-called Dolph–Chebyshev taper [51]. This taper has impedance discontinuities at its extremities that introduce parasitic reactances. However, since it is impossible to uniquely define the local characteristic impedance of a tapered finline, one might as well select a profile that approximates the “optimal” contour. Indeed, most researchers who have measured the characteristics of such tapers agree that the profile is not very critical, especially when the taper is about a wavelength long or more.

Detailed formulas and instructions for the synthesis of finline tapers have been reported by Hinken [50], Schieblich et al. [51], Beyer and Wolff [52], and Pramanick and Bhartia [53]. A transition comprising a short finline taper with a circular contour and matching capacitive discontinuities has been proposed by de Ronde [54], who claims that its performance is similar to that of an optimized taper, but its length does not exceed $\frac{3}{8}$ ths of λ_{\max} . Typical finline tapers have a return loss better than 20 dB over a standard waveguide band.

One feature that cannot be neglected in most applications is the discontinuity introduced by the finline substrate itself.

When the slotwidth is equal to the waveguide height, the finline becomes a dielectric slab-loaded waveguide. The reflection due to the substrate alone deteriorates the return loss of a subsequent taper typically by 5 dB. Cohen and Meier [13] reduced these spurious reflections by cutting a quarter-wave notch into the dielectric substrate with dimensions determined experimentally. Verver and Hoefer [55] later developed a closed-formed expression for the design of such notches and their dual, dielectric protrusions. Drawings by Piotrowski and Wojtasiak [56] and Beyer et al. [36] show transitions with triangular protrusions of the substrate, but no design information is given. For hard substrates that are difficult to cut (quartz), a printed transformer structure consisting of one or even two quarterwave sections in front of the taper is more appropriate [57]. Figure 13 shows how such matching elements can be incorporated in the design of a finline taper.

6.2. Transitions between Finline and Other Planar Media

Many transitions between various types of finlines [58] as well as between finlines and other planar media such as microstrip, coplanar waveguide, and suspended and inverted microstrip have been developed. A good survey of such transitions can be found in by Bhat and Koul [11]. The topologies are rather difficult to analyze and thus have been optimized empirically. Care must be taken not to excite unwanted modes and to avoid resonances that can considerably affect the transfer function of such transitions [59].

7. CONCLUSION

The principal advantages of finline technology at millimetric frequencies are wide single-mode bandwidth, moderate insertion loss, freedom from radiation and

interference, suitability for batch processing and low-cost production in both small and large quantities, potential for circuit integration, and compatibility with waveguide instrumentation. When properly constructed, finline components are rugged and reliable, withstanding considerable thermal and mechanical stress. Practically all imaginable circuit functions have been realized thanks to the many advances in the field-theoretic modeling of quasiplanar circuits. While early design efforts relied mostly on approximate and empirical characterization of finlines, rigorous formulations of the field problem and their numerical implementations have made it possible to design, optimize, and fabricate finline components entirely by computer.

The major drawback of the finline is its limited compatibility with transistors. On the other hand, active and passive diodes are easily embedded into a finline; oscillators, frequency converters, switches, phase shifters and attenuators with excellent performance have thus been realized. Entire integrated millimeter-wave radar front ends for frequencies up to 140 GHz have been built by the finline technique, demonstrating the potential and versatility of this technology that favorably combines the high electrical quality of the waveguide with the advantages of planar circuitry. When paired with the available computer-based design tools, finline stands out as an important and versatile technology in the arsenal of the modern microwave and millimeter-wave engineer.

8. LITERATURE

The literature on finlines is quite extensive; only a small number of key references could be cited here. The reader in search for more detailed information is referred to the comprehensive survey papers by Solbach [9] and Meier [60]. Bhartia and Pramanick [12] have assembled a collection of reprints of key papers on *E*-plane integrated circuits. Finally, in their book on the analysis, design, and applications of finlines, Bhat and Koul [11] have gathered and organized a wealth of design information, methods, and references on the subject. Further details on numerical techniques for the analysis of microwave circuits and electromagnetic wave problems can be found in two volumes edited by Itoh [29] and Yamashita [30].

BIBLIOGRAPHY

1. S. B. Cohn, Properties of ridge waveguide, *Proc. IRE* **35**:783–788 (1947).
2. S. Hopfer, The design of ridge waveguides, *IRE Trans. Microwave Theory Tech.* **MTT-3**:20–29 (1955).
3. S. D. Robertson, The ultra-bandwidth finline coupler, *Proc. IRE* **43**:739–788 (1955).
4. Y. Konishi and N. Hoshino, 100-GHz-band low-noise mixer, *Inst. Electron. Commun. Eng. Jpn.* **MMW-71** (July 1971).
5. P. J. Meier, Two new integrated-circuit media with special advantages at millimeter wavelengths, *1972 IEEE MTT Int. Microwave Symp. Digest*, Arlington Heights, IL, 1972, pp. 221–223.

6. P. J. Meier, Integrated finline millimeter components, *IEEE Trans. Microwave Theory Tech.* **MTT-22**:1209–1216 (1974).
7. P. J. Meier, *Microwave Transmission Line*, U.S. Patent 3,825,863 (1974).
8. B. Adelseck et al., A survey of planar integrated mm-wave components, *Radio Electron. Eng.* **45**:46–50 (1982).
9. K. Solbach, The status of printed millimeter-wave E-plane circuits, *IEEE Trans. Microwave Theory Tech.* **MTT-31**:107–121 (1983).
10. H. Meinel and B. Rembold, New millimeter-wave fin-line attenuators and switches, 1979 *IEEE MTT-S Int. Microwave Symp. Digest*, Orlando, FL, 1979, pp. 249–252.
11. B. Bhat and S. K. Koul, *Analysis, Design and Applications of Fin Lines*, Artech House, Norwood, MA, 1987.
12. P. Pramanick and P. Bhartia, *E-Plane Integrated Circuits*, Artech House, Norwood, MA, 1987.
13. L. D. Cohen and P. J. Meier, Advances in E-plane printed millimeter-wave circuits, *IEEE MTT-S Int. Microwave Symp. Digest*, 1978, pp. 27–29.
14. J. Knorr and P. Shayda, Millimeter-wave fin-line characteristics, *IEEE Trans. Microwave Theory Tech.* **MTT-28**:737–743 (1983).
15. H. A. Willing and B. E. Spielman, Experimental assessment of bilateral finline impedance for device matching, 1981 *IEEE MTT-S Int. Microwave Symp. Digest*, Los Angeles, CA, 1981, pp. 105–107.
16. S. B. Cohn, Slot-line on a dielectric substrate, *IEEE Trans. Microwave Theory Tech.* **MTT-17**:768–778 (1969).
17. A. M. K. Saad and G. Begemann, Electrical performance of fin-lines of various configurations, *IEE Proc. Microwaves Opt. Acoust. H* **1**:81–88 (1977).
18. W. J. R. Hofer, Finline design made easy, 1978 *IEEE MTT Int. Microwave Symp. Digest*, Ottawa, ON, 1978, p. 471.
19. R. N. Simons, Analysis of millimetre-wave integrated, fin line. *IEE Proc. Microwaves Opt. Acoust. H* **130**:166–169 (1983).
20. J. K. Piotrowski, Accurate and simple formulas for dispersion in finlines, 1984 *IEEE MTT Int. Microwave Symp. Digest*, San Francisco, CA, 1984, pp. 333–336.
21. A. K. Sharma and W. J. R. Hofer, Empirical expressions for finline design, *IEEE Trans. Microwave Theory Tech.* **MTT-31**:350–356 (1983).
22. P. Pramanick and P. Bhartia, Computer-aided design models for millimeter-wave finlines and suspended substrate microstrip lines, *IEEE Trans. Microwave Theory Tech.* **MTT-35**:1429–1435 (1985).
23. H. Hofmann, Dispersion of planar waveguides for millimeter-wave applications, *Arch. Elek. Übertragung* **31**:40–44 (1977).
24. T. Itoh, Spectral domain immittance approach for dispersion characteristics of generalized printed transmission lines, *IEEE Trans. Microwave Theory Tech.* **MTT-28**:733–736 (1980).
25. L.-P. Schmidt and T. Itoh, Spectral domain analysis of dominant and higher order modes in fin-lines, *IEEE Trans. Microwave Theory Tech.* **MTT-28**:981–985 (1980).
26. R. Vahldieck, Accurate hybrid mode analysis of various fin-line configurations including multilayered dielectrics, finite metallization thickness and substrate holding grooves, *IEEE Trans. Microwave Theory Tech.* **MTT-32**:1454–1460 (1984).
27. R. Vahldieck and J. Bornemann, A modified mode-matching technique and its application to a class of quasi-planar transmission lines, *IEEE Trans. Microwave Theory Tech.* **MTT-33**:916–926 (1985).
28. A. Omar and K. Schuenemann, Formulation of the singular integral equation technique for planar transmission lines, *IEEE Trans. Microwave Theory Tech.* **MTT-33**:1313–1321 (1985).
29. T. Itoh, *Numerical Techniques for Microwave and Millimeter-Wave Passive Structures*, Wiley, New York, 1989.
30. E. Yamashita, *Analysis Methods for Electromagnetic Wave Problems*, Artech House, Norwood, MA, 1990.
31. R. Vahldieck and W. J. R. Hofer, The influence of metallization thickness and mounting grooves on the characteristics of fin lines, *IEEE MTT Int. Microwave Symp. Digest*, St. Louis, MO, 1985, pp. 143–144.
32. T. Kitazawa and R. Mittra, Analysis of finline with finite metallization thickness *IEEE Trans. Microwave Theory Tech.* **MTT-32**:1484–1487 (1984).
33. J. K. Piotrowski, Efficient analysis of finline with finite metallization thickness, *IEEE MTT-S Int. Microwave Symp. Digest*, 1986, pp. 213–216.
34. E. Pic and W. J. R. Hofer, Experimental characterization of fin line discontinuities using resonant techniques, *IEEE MTT Int. Microwave Symp. Digest*, Los Angeles, CA, 1981.
35. J. B. Knorr and J. C. Deal, Scattering coefficients of an inductive strip in a fin-line: theory and experiment, *IEEE Trans. Microwave Theory Tech.* **MTT-33**:1011–1017 (1985).
36. A. Beyer, D. Köther, and I. Wolff, A combined theoretical and experimental characterization of discontinuities in unilateral finlines, *IEEE MTT Int. Microwave Symp. Digest*, Baltimore, 1986, pp. 127–130.
37. K. J. Webb and R. Mittra, A variational solution of the finline discontinuity problem, 15th *Eur. Microwave Conf. Digest*, 1985, pp. 311–316.
38. Q. Zhang and T. Itoh, Spectral domain analysis of scattering from E-plane circuit elements, *IEEE Trans. Microwave Theory Tech.* **MTT-35**:138–150 (1987).
39. N. H. L. Koster and R. H. Jansen, Some new results on the equivalent circuit parameters of the inductive strip discontinuity in unilateral fin-lines, *Arch. Elek. Übertragung* **35**:497–499 (1981).
40. H. El Hennawy and K. Schuenemann, Analysis of fin-line discontinuities, *IEE Proc.* **129**:342–350 (1982).
41. H. El Hennawy and K. Schuenemann, Impedance transformation in fin lines, 9th *Eur. Microwave Conf. Digest*, 1979, pp. 448–452.
42. M. Helard et al., Solution of fin-line discontinuities through the identification of its first four higher order modes, *IEEE MTT Int. Microwave Symp. Digest*, 1983, pp. 387–389.
43. R. Sorrentino and T. Itoh, Transverse resonance analysis of finline discontinuities, *IEEE MTT-S Int. Microwave Symp. Digest*, 1984, pp. 414–415.
44. A. M. K. Saad and K. Schuenemann, A rectangular waveguide equivalent for bilateral and unilateral finlines, *Arch. Elek. Übertragung* **35**:287–292 (1981).
45. A. S. Omar and K. Schuenemann, Transmission-matrix representation of fin-line discontinuities, *IEEE MTT-S Int. Microwave Symp. Digest*, 1984, pp. 339–341.
46. F. Arndt et al., Theory and design of low-insertion loss fin-line filters, *IEEE Trans. Microwave Theory Tech.* **MTT-30**:155–163 (1982).
47. Y. C. Shih, T. Itoh, and L. Q. Bui, Computer-aided design of millimeter-wave e-plane filters, *IEEE Trans. Microwave Theory Tech.* **MTT-31**:135–142 (1983).
48. A. Beyer, Calculation of discontinuities in grounded fin lines taking into account the metallization thickness and the

- influence of the mount-slits, *12th Eur. Microwave Conf. Digest*, 1982, pp. 681–686.
49. M. Burton and W. J. R. Hofer, An improved model for short- and open-circuited series stubs in fin lines, *IEEE MTT-S Int. Microwave Symp. Digest*, 1984, pp. 330–332.
 50. J. H. Hinken, Simplified analysis and synthesis of finline tapers, *Arch. Elek. Übertragung* **37**:375–380 (1983).
 51. C. Schieblich, J. K. Piotrowski, and J. H. Hinken, Synthesis of optimum finline tapers using dispersion formulas for arbitrary slot widths and locations, *IEEE Trans. Microwave Theory Tech.* **MTT-32**:1638–1645 (1984).
 52. A. Beyer and I. Wolff, Finline taper design made easy, *IEEE MTT-S Int. Microwave Symp. Digest*, 1985, pp. 493–496.
 53. P. Pramanick and P. Bhartia, Analysis and synthesis of tapered finlines, *Microwave RF* **26**:111–114 (1987).
 54. F. C. de Ronde, Miniaturization in E-plane technology, *15th Eur. Microwave Conf. Digest*, 1985, pp. 329–333.
 55. C. J. Verver and W. J. R. Hofer, Quarter wave transformers for matching transitions between waveguides and fin lines, *IEEE MTT-S Int. Microwave Symp. Digest*, 1984, pp. 417–421.
 56. J. K. Piotrowski and W. Wojtasiak, A waveguide-to-microstrip transition, *16th European Microwave Conf. Digest*, 1986, pp. 505–510.
 57. W. J. R. Hofer and C. J. Verver, Optimal waveguide to E-plane circuit transitions with binomial and Chebyshev transformers, *15th Eur. Microwave Conf. Digest*, 1985, pp. 305–310.
 58. H. El Hennawy and K. Schuenemann, Hybrid finline matching structures, *IEEE Trans. Microwave Theory Tech.* **MTT-30**:2132–2138 (1982).
 59. K. Solbach, H. Callsen, and W. Menzel, Spurious resonances in asymmetrical finline junctions, *IEEE Trans. Microwave Theory Tech.* **MTT-29**:1193–1195 (1981).
 60. P. J. Meier, Integrated finline, the second decade, *Microwave J.* **28**(12):30–48 (1985).
 61. A. Beyer and I. Wolff, A solution of the earthed fin line with finite metallization thickness, *1980 IEEE MTT-S Int. Microwave Symp. Digest*, Washington DC, pp. 258–260.
 62. A. Beyer, Analysis of the characteristics of an earthed fin line, *IEEE Trans. Microwave Theory Tech.* **MTT-29**:676–680 (1981).

FRACTAL-SHAPED ANTENNAS: A REVIEW

JAUME ANGUERA
 CARLES PUENTE
 CARMEN BORJA
 JORDI SOLER
 Fractus S.A.
 Barcelona, Spain

1. INTRODUCTION

Among the different telecommunications systems, mobile communication systems have experimented the fastest relative growth. A wireless system requires an antenna to radiate and receive electromagnetic waves. The antenna is therefore an essential component. Antenna performance is usually very sensitive to the antenna's geometric

form and size-wavelength ratio. This has two important consequences:

1. Once the antenna has been designed to operate at a particular wavelength, it will rarely be useful at other wavelengths. Since telecommunication systems operate at separate frequency bands to avoid mutual interference, one usually must account for an individual antenna for every single system.
2. Given a particular service band, the antenna cannot be made arbitrarily small owing to the same constraint.

In this sense, the present article deals with the investigation of antennas presenting small properties and multifunctionality features. The aim is to describe fractal techniques and their applications to design miniature, multifrequency, and high-directivity antennas. Fractal techniques have been chosen as their geometric properties are useful in designing miniature, multifrequency, and high-directivity antennas.

An overview of fractal-shaped antennas summarizes most of the work carried out since the early 1990s.

2. FRACTAL GEOMETRY

Since the early days of mathematics and Euclidian geometry, objects have been classified as one-, two-, or three-dimensional (1D, 2D, or 3D). The full stop we use to separate sentences in a written paper is 1D (i.e., point/line); the paper we use to write on can be considered approximately 2D (i.e., a plane/an area); while the ballpen we use to write these words is a 3D object (i.e., a cube/volume). However, we are surrounded by other objects (clouds, cost lines, arm trees, etc.) that are best described not by using Euclidian geometry but by using fractal geometry [1].

Among the several properties that characterize fractals, two are of interest in terms of antenna design: self-similarity/self-affinity and space-filling/fractal dimension properties. We will briefly define these properties and in the next section we will relate such geometric properties to the antenna field.

Some fractals are *self-similar*, which roughly implies that there are copies of the whole structure within the structure at different scales. For example, the futuristic tree of Fig. 1 can be understood in a loose sense to be self-similar; if we cut one branch, we will see that it is a reduced simplified copy of the whole structure. If such a scale factor is different for several directions, the structure is no longer self-similar but self-affine.

A characteristic feature of fractals is their space-filling property. To characterize such space-filling properties, the concept of fractal dimension is used. There are several definitions of fractal dimension. What really matters here is that a fractal object can have a fractional dimension or a larger dimension than its topological one [2], as it is the case of the Hilbert curve used to obtain a small monopole antenna presented in the next section.

Finally, two more definitions are presented here: mass fractals and boundary fractals. *Mass fractals* implies that

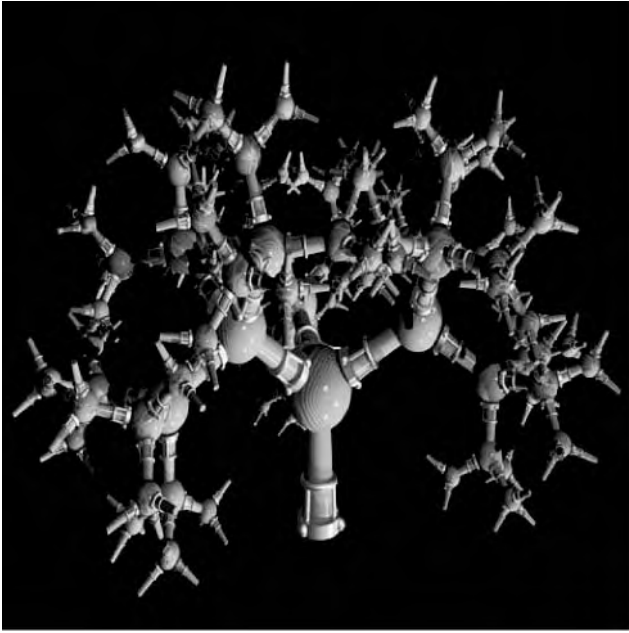


Figure 1. Futuristic vision of a tree. Every arm can be considered a scaled-down copy of the whole tree. (This figure is available in full color at <http://www.mrw.interscience.wiley.com/erfme>.)

the internal structure is fractal, as in the Sierpinski gasket presented next. *Boundary fractals* implies that the perimeter is fractal-like, as in the Koch island patch presented in the next section.

3. FRACTAL-SHAPED ANTENNAS

3.1. The Concept

Having seen the geometric properties of fractal geometry, it is interesting to explain what benefits are derived when such geometry is applied to the antenna field.

Fractals are abstract objects that cannot be physically implemented. Nevertheless, some related geometries can be used to approach an ideal fractal that are useful in constructing antennas. Usually, these geometries are called *prefractals* or *truncated fractals*. In other cases, other geometries such as multitriangular or multilevel configurations [3,4] can be used to build antennas that might approach fractal shapes and extract some of the advantages that can theoretically be obtained from the mathematical abstractions. In general, the term *fractal antenna technology* is used to describe those antenna engineering techniques that are based on such mathematical concepts that enable one to obtain a new generation of antennas with some features that were often thought impossible in the mid-1980s.

After all the work carried out thus far, one can summarize the benefits of fractal technology in the following way:

- *Self-Similarity.* This property is useful in designing multifrequency antennas, as, for instance, in the examples based on the Sierpinski gasket [5–10]. Another interesting application of the self-similar property

has been applied in designing multiband arrays [11,12].

- *Fractal Dimension.* It is useful to design electrically small antennas, such as the Hilbert and Koch monopoles, fractal loops, and microstrip antennas [13–17].
- *Mass Fractals and Boundary Fractals.* These fractals are useful in obtaining high-directivity elements [18–20] and undersampled arrays [21–23]. They have also been useful for designing low-sidelobe arrays [8,11,24,25].

The next section explores fractal techniques used to obtain multifrequency antennas and arrays; miniature, high-directivity antennas; and undersampled and low-sidelobe arrays.

3.2. Applications of the Self-Similar Property: Multifrequency Antennas and Arrays

3.2.1. Multifrequency Antenna Elements. The first reported multifrequency fractal-shaped antenna was designed by C. Puente at the Universitat Politècnica de Catalunya (UPC) in the early 1990s and was named the *Sierpinski monopole* (Fig. 2) [5,7,26]. This monopole is a five-iteration Sierpinski gasket that features five operating bands (as many bands as fractal iterations) spaced logperiodically by a factor of 2 (the same scale factor used to generate the fractal). At the five operating bands, this antenna presents a good level of return loss (around –10 dB) (Fig. 3) and similar radiation patterns across the bands (Fig. 4).

The antenna depicted in Fig. 2 was extensively studied [26] and first patented in May 1995 [27].

Besides the experimental work, numerical computation using the finite-difference time-domain (FDTD) and method-of moments (MoM) codes were also used to fully understand the antenna behavior. Perhaps the most interesting analysis is that related to the current distribution on the conductor surface. Figure 5 shows the electrical current distribution at each of the five operating bands, where it can be observed that the current is concentrated in several regions called *active regions*. At the lowest operating frequency, the active region is extended

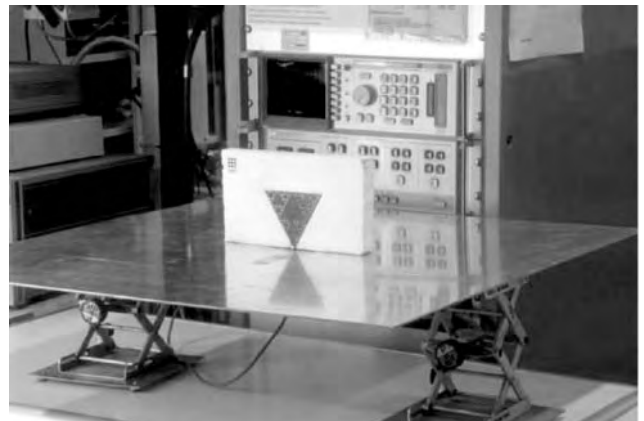
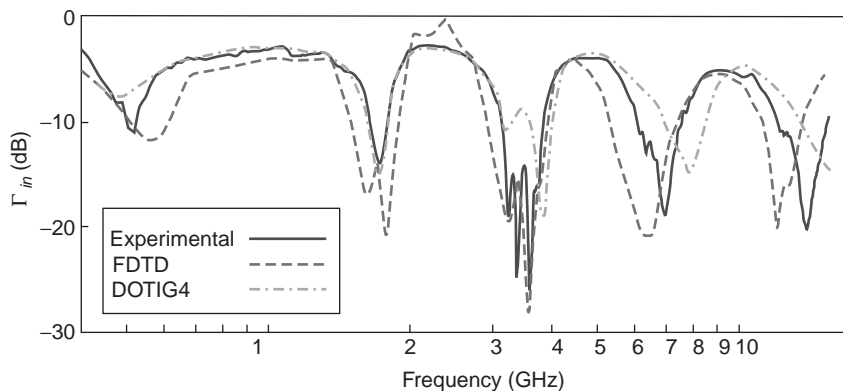


Figure 2. The Sierpinski monopole on a square ground plane.

Figure 3. Measured and computed return loss for the Sierpinski monopole of Fig. 2. Numerical simulations agree fairly well with measurements. The antenna is matched at -10 dB return loss at five bands, as many as the iterations (five). (This figure is available in full color at <http://www.mrw.interscience.wiley.com/erfme>.)



throughout the whole structure; on the other hand, for the highest operating frequency, the active region is concentrated in the smallest iteration number near the feed-point.

Figure 6 shows an iterative method that has been used to predict the return loss of the Sierpinski monopole and Sierpinski patch antennas. Such a method as well as the segmentation method is interesting because it enables parametric analysis to be performed in a very short time and allows us to understand what occurs if the scale factor is changed. The S matrix is the S parameter of interconnected transmission lines, where one can factor in the radiation loss mechanism by considering transmission

line with losses. The present method as well as the segmentation method have been used to predict input parameters of the Sierpinski monopole as well as other fractal-shaped antennas [28–31].

Another analytical method called the *multiperiodic traveling-wave “vee” model* has also been used to predict the radiation patterns as depicted in Fig. 7 [26]. Such a model is able to predict the radiation pattern of a Sierpinski monopole if the current along the edge is known.

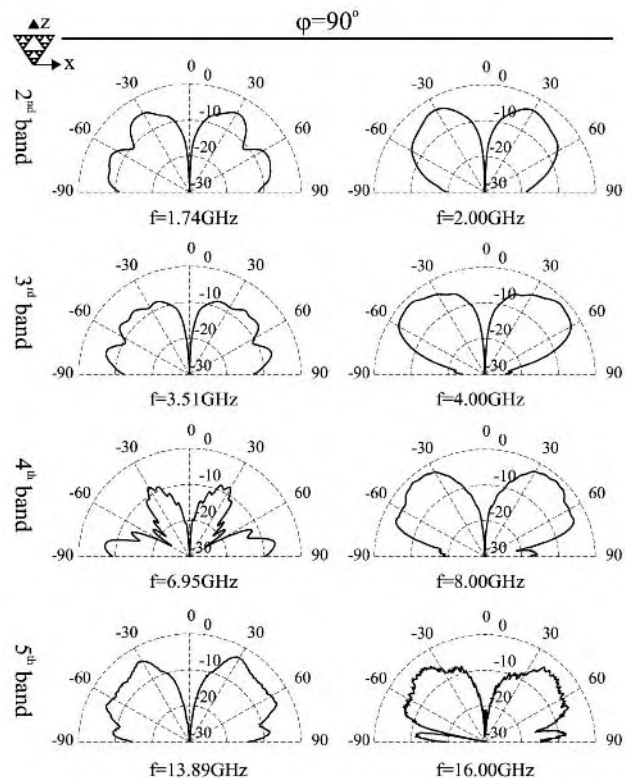


Figure 4. Measured radiation cuts at the four upper bands for $\phi = 90^\circ$ plane for the Sierpinski monopole of Fig. 2.

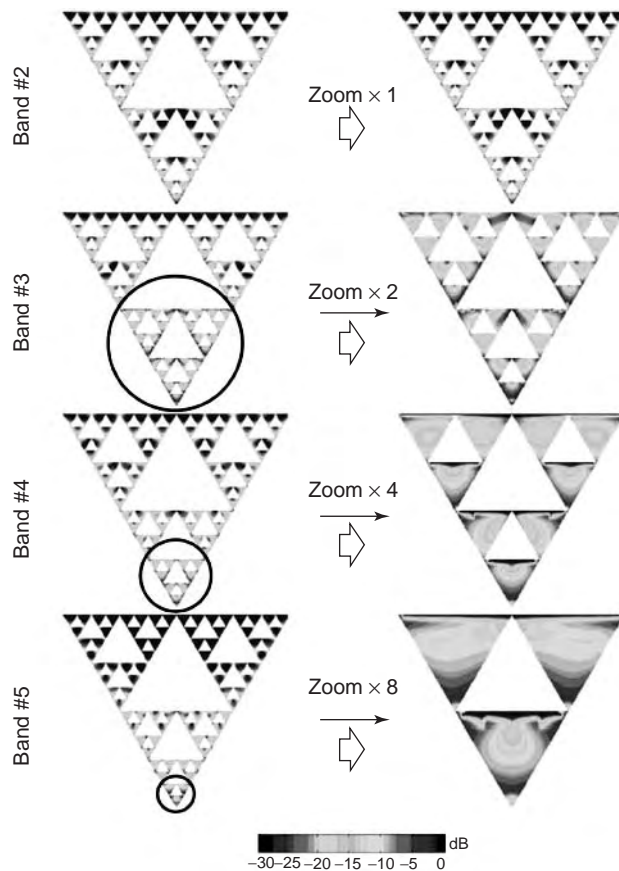


Figure 5. FDTD electrical current simulations on the conductor surfaces. An active region is observed (circled in the left column). (This figure is available in full color at <http://www.mrw.interscience.wiley.com/erfme>.)

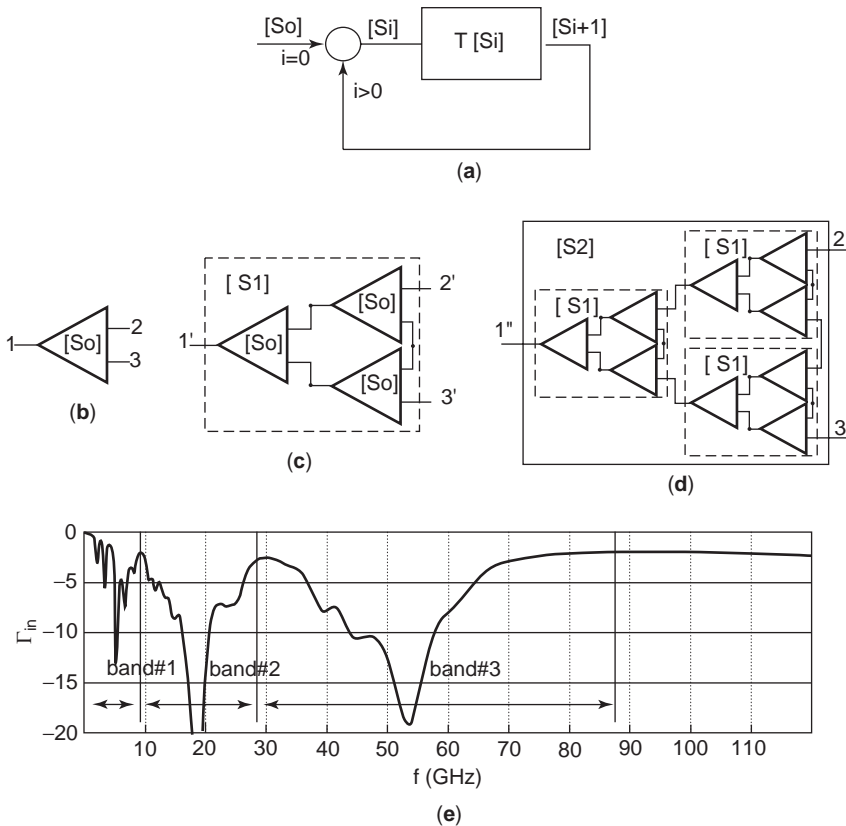


Figure 6. (a) Iterative method to calculate the input impedances of fractal-shaped antennas; (b–d) cascading the S parameters—in this case, the model is useful for predicting the evolution of the operating bands with the number of iterations; (e) result for a three-fractal-iterated Sierpinski antenna.

The model has been extended not only to better understand the physical radiation of the classic Sierpinski monopole [32,33] but also to obtain the radiation pattern of Mod-P Sierpinski monopoles [34,35].

For a fractal-shaped antenna operating at the highest frequency, the antenna is electrically very large. If the MoM is used for example, this requires a small discretization elements resulting in a large number of unknowns (N). If N is large enough, the matrix impedance Z of MoM does not fit in the computer memory (N^2) and moreover, large computation time is needed (time is proportional to N^3). Therefore, advanced numerical methods and other strategies are required to correctly model fractal-shaped antennas such as the multilevel matrix decomposition algorithm (MLMDA) and multilevel fast multipole method (MLFMM). MLFMM is very efficient for 3D problems, while MLMDA is very efficient for planar antennas, as is the case with microstrip patches or dipoles. Other methods such as adaptive meshes can be used (Fig. 8). For example, one can use a fine mesh for the active zone related to the highest frequency, while coarse meshes can be used to the lowest frequencies [36].

Genetic algorithms have also been used to optimize the fractal antenna geometry [37,38], as is the case of a dual-band dipole antenna having a SWR (standing-wave ratio) below 2 at 1.225 and 1.575 GHz and small monopole antennas [39].

For the numerical experiments, we have shown that an active zone is associated with the fractal Sierpinski

monopole antennas (Fig. 5). One can observe the same effect using experimental procedures [40]. Figure 9 photographically illustrates the temperature elevation on the antenna surface. A magnetron operating at 2.45 GHz was used. In order to observe the active region, several Sierpinski prototypes printed in fiberglass have been built. The losses on the fiberglass allow one to acquire thermic images. The antennas have been scaled to obtain the active region at 2.45 GHz.

Following those results, one can conclude that at each operating frequency, only some part of the structure is responsible for radiation. As these parts present approximately the same electrical height and shape, the antenna radiates similar at each band (Fig. 4).

After the successful result described above, research on the Sierpinski monopole continued and variation of the flare angle and geometric perturbation based on self-affine transformations were explored to study how one could control the input impedance and frequency allocation [41–44]. Those experiments were really interesting because they clarified the design of practical monopole antennas for base station systems such as GSM 900, GSM 1800, and UMTS [45–47]. Another interesting modification when changing the flare angle is to obtain a dual-band antenna with bidirectional pattern [48].

The Sierpinski gasket was also used to design a dipole antenna (Fig. 10), and it was used by Romeu and Rahmat-Samii [49–51] to implement a frequency-selective surface

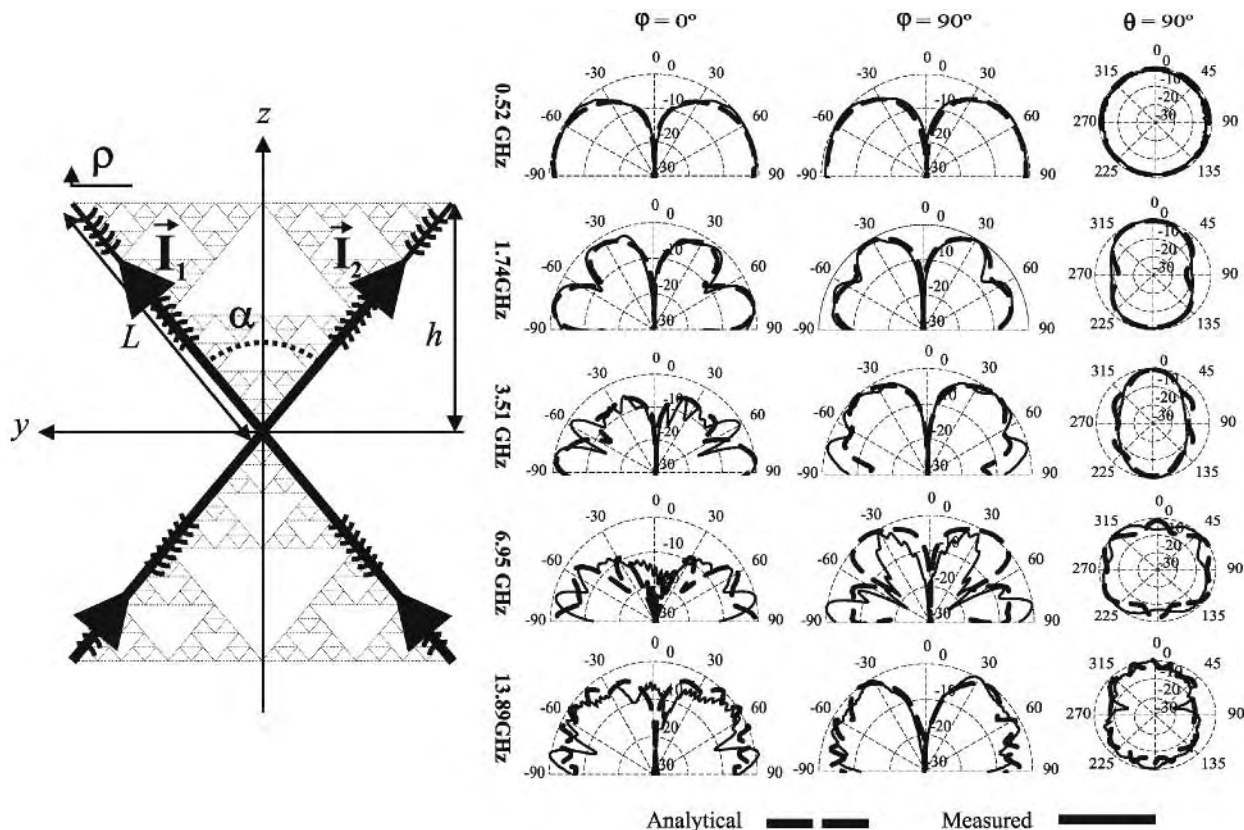


Figure 7. Multiperiodic traveling-wave V (“vee”) model is useful for predicting the radiation patterns of fractal-shaped antennas such as the Sierpinski monopole.

(FSS) operating at two bands. Other fractal shapes have also been studied to create FSS [52,53].

Novel geometries based on the Sierpinski triangle are investigated in Soler’s thesis [54] to control the num-

ber of bands and also to control the frequency separation (Fig. 11). These antennas are based on Pascal’s triangle [34,35]. By using the Mod-P Sierpinski structures, the frequency separation between bands can be larger than that obtained for the classic Sierpinski gasket [55].

In addition, fractal-related antenna structures can be top-loaded as shown in Fig. 12 in order to control the spacing between bands and the input resonances at each resonance [56,57].

In general, depending on the feeding scheme used for the antenna, the ground plane becomes a useful contributor in the radiating process [58]. The fractal geometry has been also used not only to shape the antenna but also to design ground planes inspired on the Sierpinski fractal shape [59] (Fig. 13).

It has been shown that by means of Sierpinski fractal and other related shapes, it is possible to obtain several matched bands with a similar radiation pattern [60–62]. To improve the radiation pattern, a 3D arrangement has been proposed [63] and is shown in Fig. 14.

The Sierpinski gasket was reexplored as a microstrip patch as well [64,65]. In Borja’s thesis [66,67], an in-depth study is devoted to analysis of the Sierpinski patch in order to obtain several bands with broadside radiation patterns. For the patch version, it is more difficult to obtain a multifrequency behavior, although several proposals have been already made [66,68]. Figure 15 shows a particular

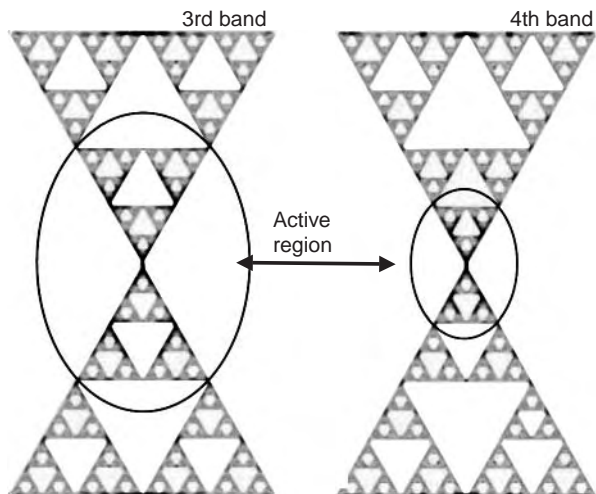


Figure 8. A fractal-shaped antenna becomes and electrically large structure at the highest operating bands. Advanced methods are required to model these complex structures. Adaptive meshing can be used to mesh properly the active regions.

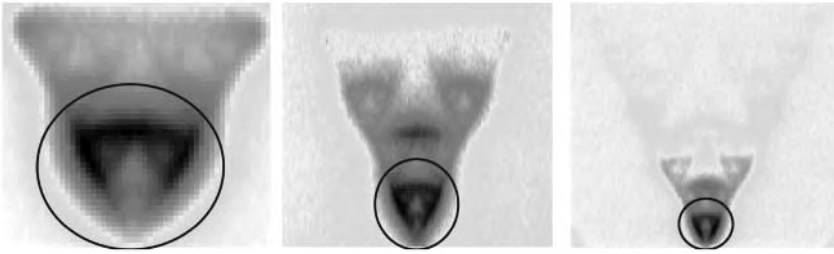


Figure 9. Temperature elevation on the antenna surface measured in operating bands 2–4 using an infrared camera. (This figure is available in full color at <http://www.mrw.interscience.wiley.com/erfme>.)

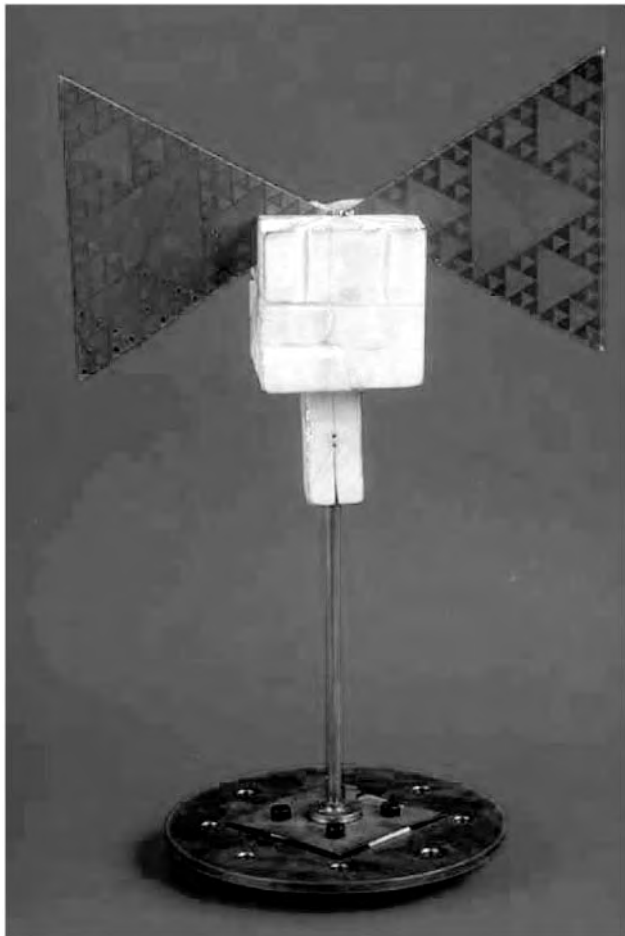


Figure 10. The Sierpinski gasket was also used to design a dipole antenna.

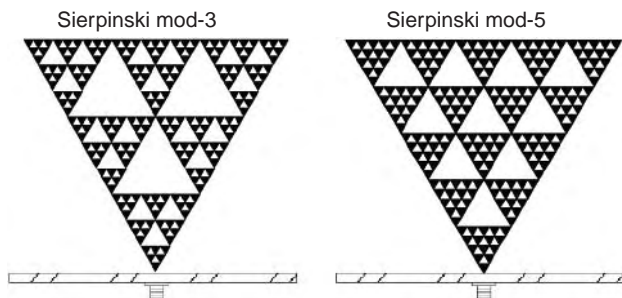


Figure 11. The Sierpinski monopole mod-3 and mod-5.

solution where some junctions are broken in order to eliminate undesired higher modes that degrade the radiation patterns.

By modifying the scale factor and fractal geometry, a dual-band dual-polarized microstrip antenna was designed to operate at GSM 900 and 1800 [69]. Moreover, such an element was the basic radiating element of a prototype for a dual-band dual-polarized array for mobile communications (Fig. 16). The feeding scheme is based on an etched capacitor designed to cancel the inductance effect of the coaxial probe [70].

In this sense, research continues with the aim to go a further step: investigate multifrequency microstrip antennas using fractal-based geometries (Fig. 17), while introducing a broadband behavior at each frequency band employing bandwidth enhancement techniques [6,71].

The current distributions of the multistacked antenna are calculated at the central operating frequencies as shown in Fig. 18. It is important to observe that when the antenna is excited at $f = 1.612$ GHz, the bottom parasitic patch remains nonexcited; that is, it seems to be transparent to the stated frequency, and only the top parasitic patch is operating. By contrast, when the antenna is excited at $f = 2.697$ GHz, the bottom patch is excited while the top patch is almost totally disconnected. Therefore, for the first operating frequency, the top parasitic patch is responsible for enhancing the bandwidth of the active patch while the bottom parasitic patch is responsible for broadening the second band. The measured prototype shows a $BW = 4.7\%$ and $BW = 6.8\%$ ($SWR = 2$) for the first and second operating bands, respectively, with similar radiation patterns for the entire bandwidth and similar for both bands, confirming the dual-broadband performance.

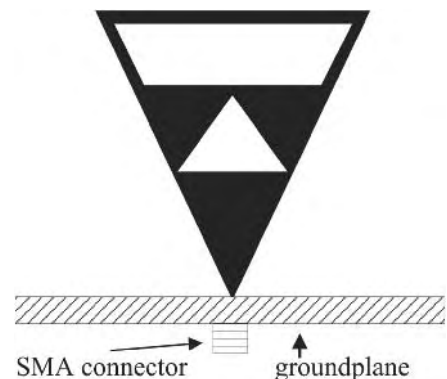


Figure 12. A top-loaded modified Sierpinski monopole.

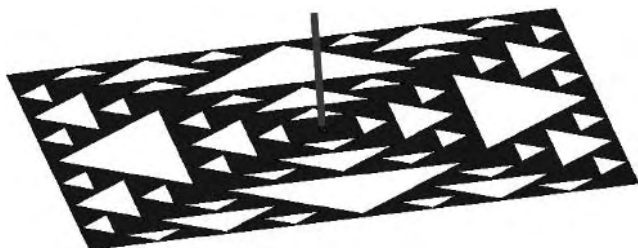


Figure 13. Straight monopole above a fractal-shaped ground plane derived from four mod-2 Sierpinski gaskets.



Figure 16. A dual-band microstrip array for GSM 900 and 1800 using a modified version of the Sierpinski geometry [3,4].



Figure 14. 3D antenna solution used to tailor the antenna patterns at different frequency bands. The antenna is built with two planar structures based on the Sierpinski fractal.

3.2.2. Antenna Arrays. The self-similar property of some fractals has been useful in designing multiband arrays [11,72]. This can be achieved if the array factor is a self-similar curve such as, for example, the Koch curve (Fig. 19). In Fig. 19, an array factor following the self-similar curve is shown. If the progressive phase $\beta = kd$, the same shape is obtained at $f, f/3, f/9$ and so on. Although the same radiation pattern is maintained at several frequencies, the radiation parameters such as gain, radiation resistance, and efficiency are not maintained because the pattern magnitude is reduced when the frequency increases.

Other functions as the Weierstrass function can be used as well to synthesize fractal arrays with self-similar properties [73].

Werner takes advantage profit of the self-similar property of fractal-based arrays to develop fast algorithms for calculating the impedance matrix of such arrays [74]. The self-similar property is also useful for developing rapid beamforming algorithms [75,76].

Having reviewed some of the work on multifrequency antennas and arrays using fractals, in the next section we

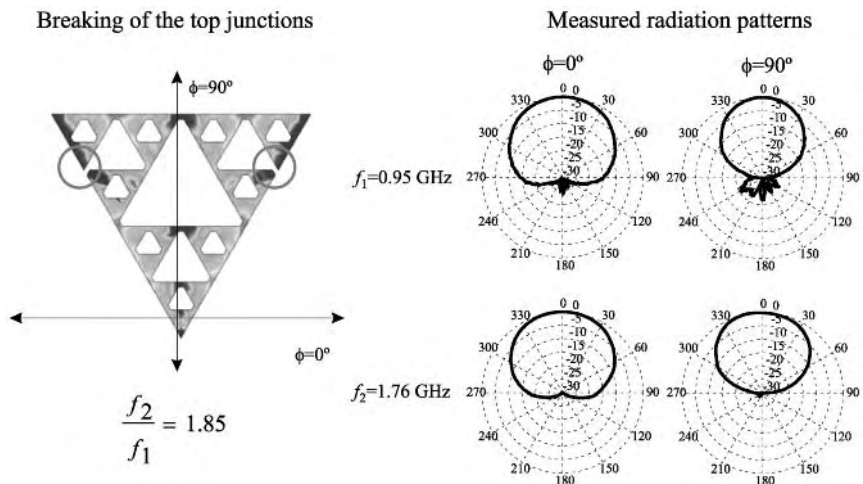


Figure 15. The Sierpinski patch with the top junction broken in order to obtain a dual-band antenna with broadside radiation patterns.

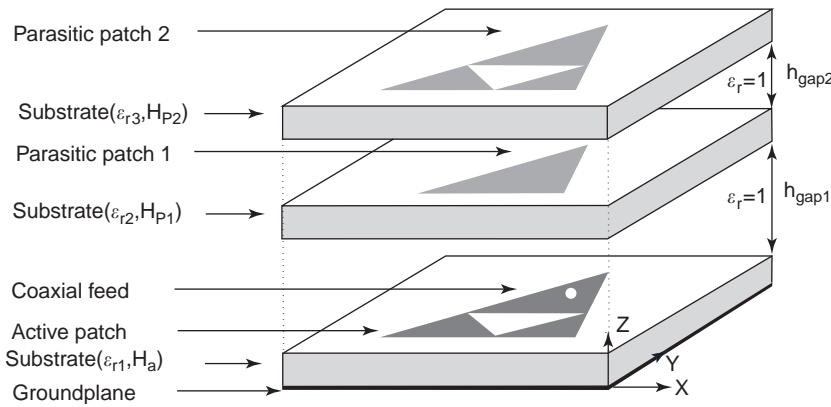


Figure 17. A multistacked microstrip patch antenna based on the modified Sierpinski fractal.

present some of the research related to electrically small antennas.

3.3. Applications of the Fractal Dimension Property: Electrically Small Antennas

Antenna size is a critical parameter because antenna behavior depends on antenna dimensions in terms of wavelength (λ). In many applications, space is a constraint factor; therefore an antenna cannot be comparable to the wavelength but smaller (i.e., a small antenna). An antenna is said to be small when its larger dimension is less than twice the radius of the radian sphere; its radius is $\lambda/2\pi$. Wheeler and Chu were the first who investigated the fundamental limitations of such antennas [77–79]. The goal of this section is to present the miniature features of the Hilbert monopole [14,80,81] and compare it with the Koch monopole studied previously [13,26,27]. Some new advancements are also presented. It should be pointed out that at the limit, the Koch and Hilbert curves feature fractal dimensions of 1.23 and 2, respectively.

Figure 20 shows a $\lambda/4$ monopole and the first five iterations of the Hilbert monopole where the total height for all antennas is $h = 7$ cm. The antennas are etched on a 1-mm FR4 substrate acting merely as an antenna support. The copper used is 0.4 mm wide. As the total length of the Hilbert monopole increases as iteration increases, the resonant frequency will decrease. Thus, the antenna becomes electrically smaller as the iteration number increases.

For the fifth iteration, the length is 65 times h . One might think that the resonant frequency for a fifth-iteration Hilbert monopole would be 65 times less than the resonant frequency of a linear monopole with height h , which will be an extraordinary frequency reduction. Obviously, this is not true since coupling between turns provides a shorter path for currents flowing from one tip to the other. However, even with the coupling effect, the resonant frequency reduction or compression factor (CF), which is defined as the ratio between the resonant frequency for the vertical monopole and the Hilbert resonant frequency, can achieve values up to 10, taking into account the negligible effect of the dielectric support. Large CF are interesting for designing miniature antennas where space is a constraint factor such as, for instance, integrated low-frequency antennas in automotive applications [82].

Finally, a new concept called *compression efficiency* (CE) is introduced. CE is defined as the ratio between the first resonant frequency of the equivalent vertical linear monopole with a height equal to the total length of a Hilbert (Koch) monopole and the first resonant frequency of the Hilbert (Koch) antenna. CE is an important parameter for comparing different space-filling geometries to determine which structure can decrease the resonant frequency with less wirelength.

Figure 21 shows CE as a function of the fractal iteration, showing that CE decreases as the iteration number increases. In the same figure, the CE for the Koch monopole is shown [14]. It is clearly seen that the CE decreases more rapidly for the Koch monopole. For example, for the same height (h) of the vertical monopole, the Hilbert 1 and the Koch 5 monopoles have approximately the same length; however, CE is 70% for the Hilbert monopole and only 40% for the Koch monopole, indicating that the Hilbert monopole (with a larger fractal dimension) achieves a larger frequency reduction with the same wirelength.

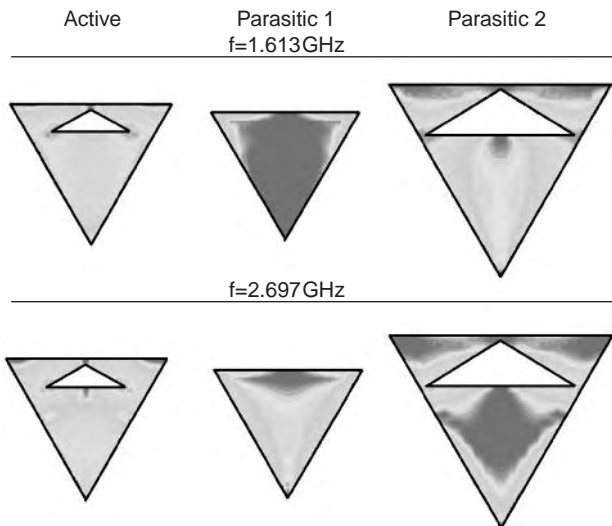


Figure 18. Simulated current distribution. It can be observed that only one parasitic patch contributes significantly to radiation depending on the operating frequency. (This figure is available in full color at <http://www.mrw.interscience.wiley.com/erfme>.)

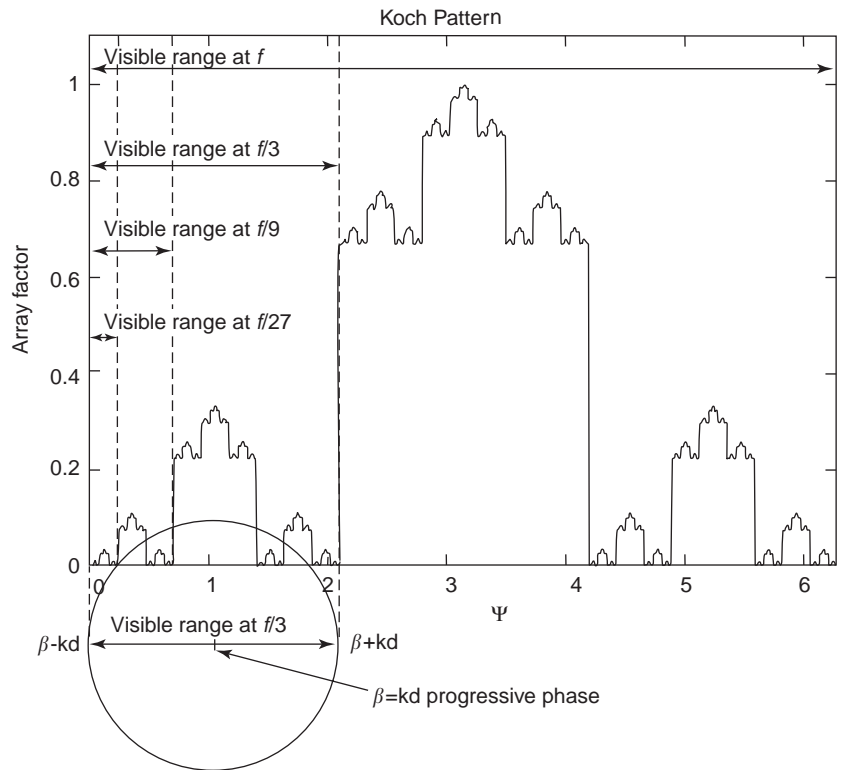


Figure 19. The Koch array factor. The curve retains its similarity at six different scales. By adding a progressive phase $\beta = kd$, the visible range is always centered at a secondary lobe that has the same shape as the total pattern. The frequency change by a factor $\frac{1}{3}$ reduces the visible range around this similar subpattern [11].

Analytical models have been proposed by Vinoy et al. to predict the resonant frequency of the Hilbert-based antenna [83]. Modifications of the feeding point have been investigated in order to match the antenna [84]. Methods for fast calculation of the input impedance of a Koch fractal dipole have also been proposed [85].

The Hilbert curve have also been useful in designing small microstrip patch antennas. In Ref. 86, a microstrip patch is loaded with a transmission line to reduce the resonant frequency of the fundamental mode of the unloaded patch [82]. The Hilbert curve has also been used to construct metamaterials, in particular to design artificial magnetic conductors as proposed by McVay, Engheta, and Hoorfar [87].

The classic miniature technique of short-circuited monopoles has been combined with fractal technology, as is the case of a shorted monopole inspired in the Sierpinski fractal in Song’s thesis [88,89].

Another advantage of miniature antennas is that they tend to reduce mutual coupling in an antenna array as studied in Gianvittorio’s thesis [90]. By reducing the mutual coupling, the scan-blindness effect can be reduced to shift the blind angle toward larger angles near the horizon [16,17,91].

In order to overcome the problem of miniature microstrip antennas, that is, small bandwidth and radiation efficiency, parasitic techniques have been combined with fractal techniques to obtain miniature and wideband antennas with improved efficiency [68,92,93]. Figure 22 shows a modified Sierpinski-based microstrip antenna consisting of an active patch and a parasitic patch. Using such a geometry, the resonant frequency of the antenna is 1.26 GHz while it is 2 GHz for the filled version. By adding the parasitic patch, the bandwidth with respect to the single active element is increased by a factor of 15, resulting in a bandwidth of $BW = 2.7\%$ at $SWR = 2$; the radiation efficiency for this antenna is 84% [68]. Similar approaches of stacking elements can be found in Ref. 94.

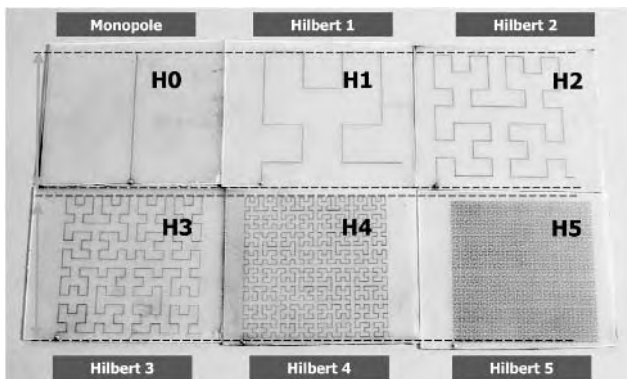


Figure 20. (a) Vertical monopole; (b) Hilbert 1; (c) Hilbert 2; (d) Hilbert 3; (e) Hilbert 4; (f) Hilbert 5. The antennas are etched on a FR4 substrate acting as a support.

3.4. Application of Mass and Boundary Fractals: High-Directivity Antennas and Undersampled and Low-Sidelobe Arrays

3.4.1. High-Directivity Antennas. Another interesting feature of fractal-based microstrip antennas is the existence of localized modes called *fractons* and *fractinos*

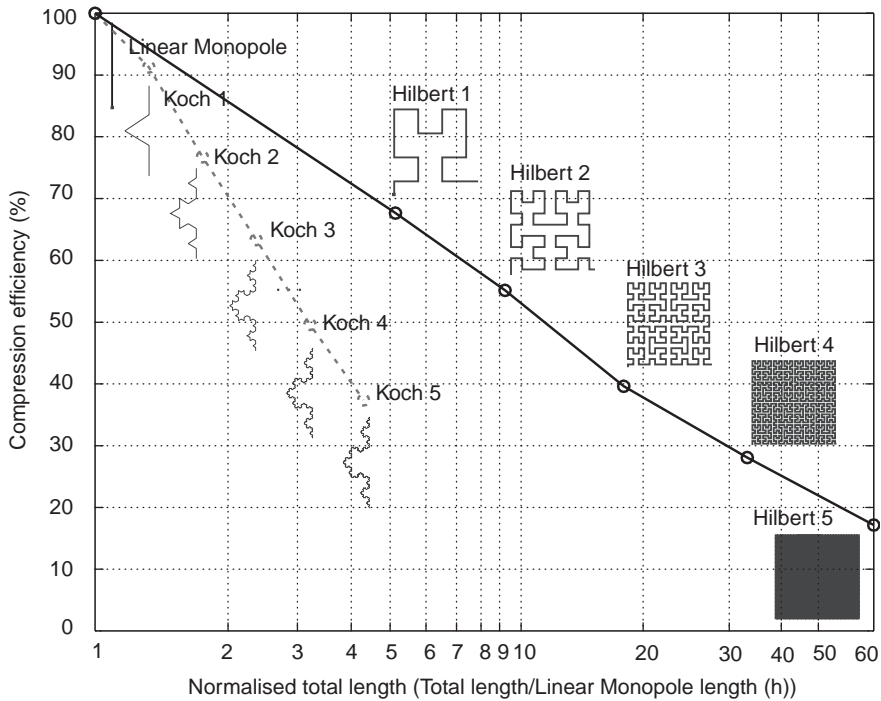


Figure 21. Compression efficiency for the Hilbert and Koch monopoles.

depending on whether the structure is based on mass fractals or boundary fractals [66,68,95–98]. Figure 23 shows a Koch-island patch where the current distribution for the fundamental mode and fractino mode are shown [18,99]. It is worth noting that for the fractino mode there are zones of high current density (localized mode). Moreover, such zones are coherent; that is, they radiate in

phase, and thus the radiation pattern is broadside. This feature is rarely obtained with classical Euclidian geometries such as squares, circles, and triangles. Other geometries presenting localized modes have been investigated [66,68].

The fracton-mode behavior of the Sierpinski bowtie patch has been investigated [100]. The fracton-mode properties are studied as a function of the iteration number.

Besides fracton and fractino modes, microstrip antennas supporting several fracton modes have also been studied. Figure 24 shows an example of the Sierpinski bowtie fractal-based antenna, which supports as many fracton modes as iterations [101–103]. It is interesting to note that the directivity of the fracton mode increases with the mode order.

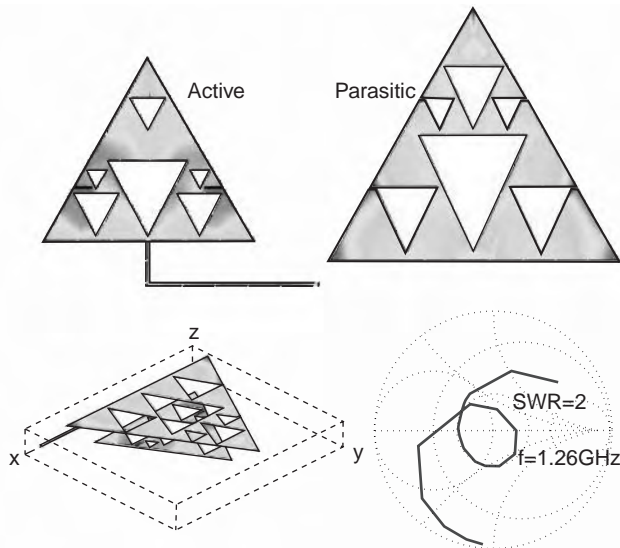


Figure 22. A miniature microstrip antenna inspired in the Sierpinski fractal. Current distributions on the patch surfaces are shown. The parasitic patch enhances the bandwidth when the input impedance loop is correctly centered at the center of the Smith chart.

3.4.2. Undersampled Arrays. Operating in such a fracton or fractino mode, one can obtain a larger directivity than that for a fundamental mode. In this sense, Anguera [68] has investigated structures supporting fracton modes for microstrip arrays (Fig. 25); this type of array is called an *undersampled array* [22,23,104,105]. Such a novel method presents an advantage over conventional designs in that one can obtain in the same electrical area of a conventional array using Euclidian-based elements, with the same directivity but using fewer elements. Other advantages are that the feeding network complexity decreases and there is more available space to integrate other microwaves devices such as, for example, amplifiers, filters, and matching networks. This reduces the antenna cost, volume and weight, which can be an enormous advantage for satellite antenna applications [21,106].

Figure 26 shows the radiation pattern in the upper space for the Euclidian and fractal arrays of Fig. 25. Both

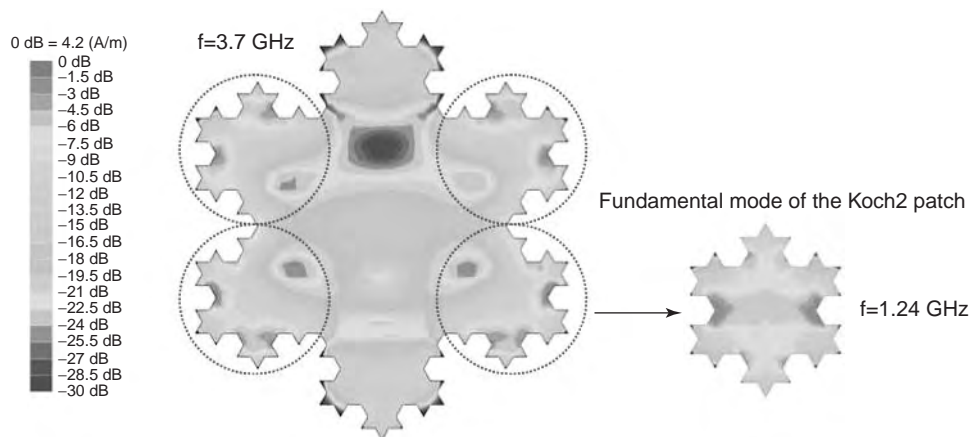


Figure 23. Current distribution for the fundamental and localized modes of a Koch microstrip patch. The localized mode presents high current density on the boundary with coherent radiation; a broadside radiation pattern with a directivity larger than that of the fundamental mode can be obtained. (This figure is available in full color at <http://www.mrw.interscience.wiley.com/erfme>.)

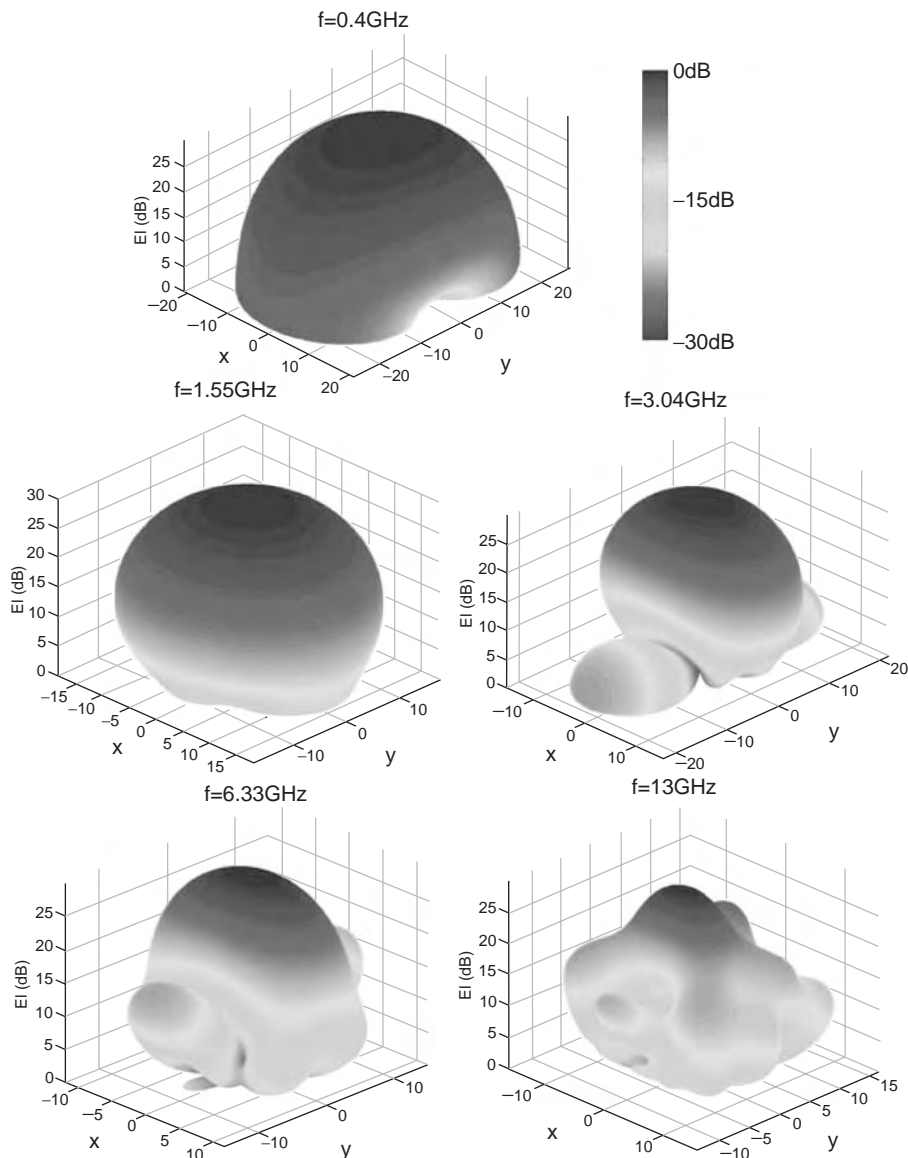


Figure 24. 3D-simulated radiation patterns for the Sierpinski bowtie 4: the fundamental and four fracton modes are shown. (This figure is available in full color at <http://www.mrw.interscience.wiley.com/erfme>.)

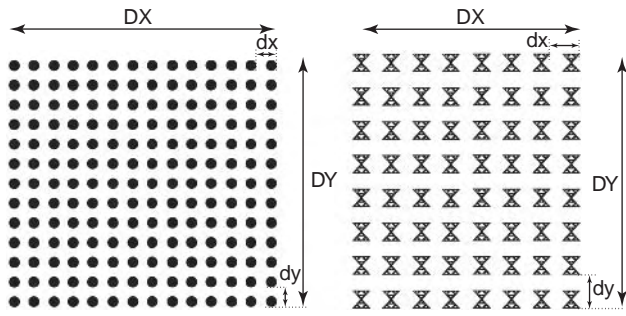


Figure 25. The classical microstrip array with circular patches and the novel scheme with fractal-shaped microstrip antennas.

arrays present the same electrical area; however, for the fractal array operating in a fracton mode, the number of elements is 2.8 times less (14×13 for the Euclidian and only 8×8 for the fractal one).

3.4.3. Low-Sidelobe Arrays. The fractal spatial arrangement of array elements have been useful for designing low-sidelobe arrays with equally weighted current elements, which is advantageous current element for practical purposes because the feeding network is easier than those used when different current amplitudes are required in order to reduce sidelobes.

Kim and Jaggard first proposed a nonuniform random fractal spacing for improving the sidelobe level of random arrays in 1986 [24]. The Cantor array has also been

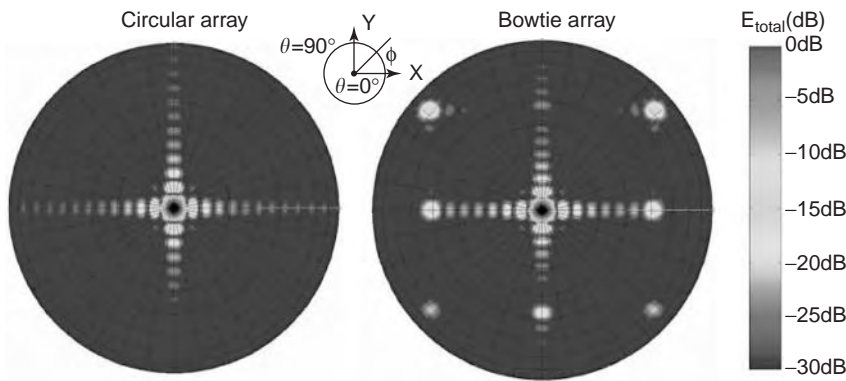


Figure 26. Normalized simulated radiation patterns for the arrays shown in Fig. 25. (This figure is available in full color at <http://www.mrw.interscience.wiley.com/erfme>.)

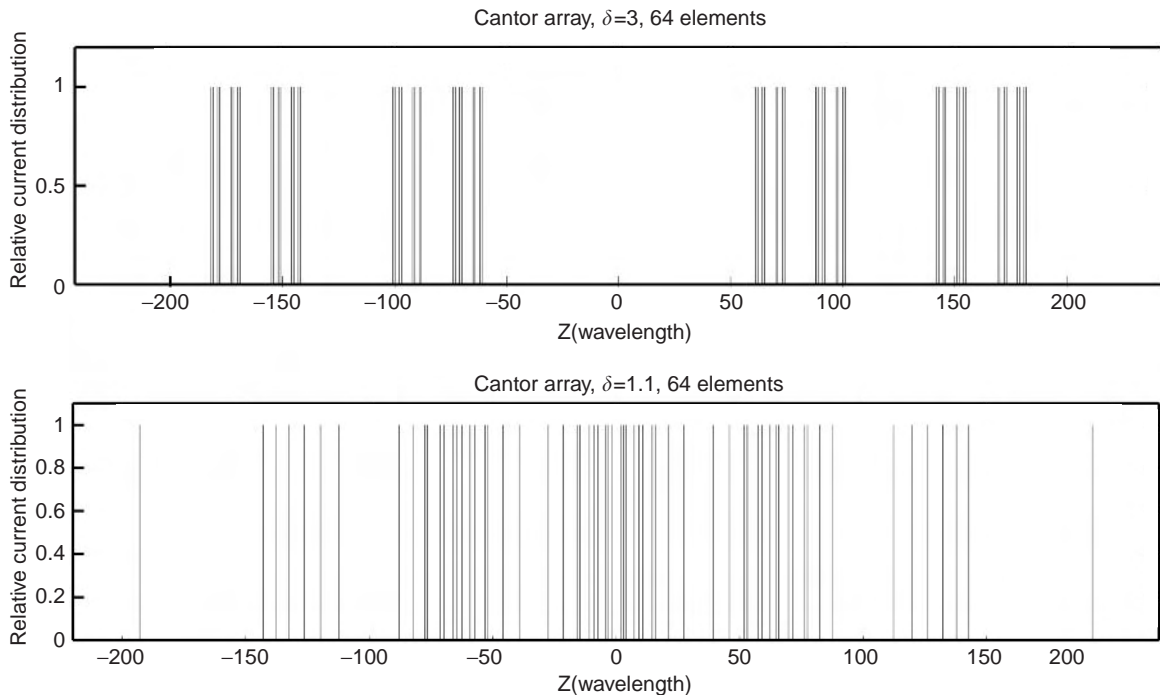


Figure 27. Cantor array constructed with 64 array elements from a 2^δ generator and a logperiod $\delta = 3$ (top) and $\delta = 1.1$ (bottom).

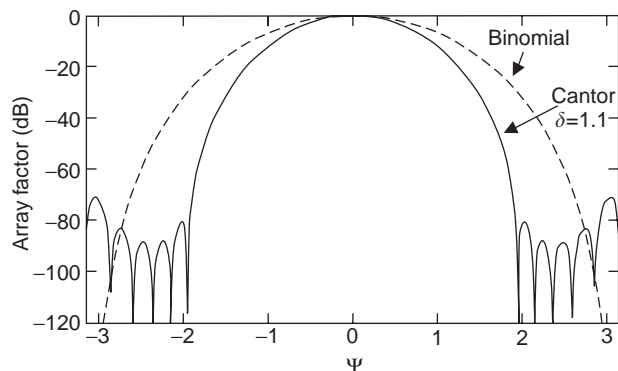


Figure 28. Array pattern of a binomial distribution and a Cantor distribution with a logperiod of $\delta=1.1$, both having the same number of array elements: 64.

analyzed [11,107,108]. Mathematically, the generalized Cantor distribution can be obtained by convoluting two delta function as

$$c(z) = \prod_{n=-\infty}^{\infty} \{f(z \cdot \delta^n)\} \quad (1)$$

where $f(z)$ is a 2δ function and δ is the scaling factor.

Figure 27 shows two cantor arrays formed by 64 array elements and scale factors of $\delta=3$ and $\delta=1.1$, respectively. For the Cantor array having a logperiod of $\delta=1.1$, the corresponding pattern looks very similar to a binomial distribution: sidelobe level below -65 dB (Fig. 28). The main advantage is that although the sidelobe level is close to the binomial distribution, the current excitation is uniform with drastically simplifies the feeding network.

An array with a low sidelobe level has been investigated by small position offsets of fractal elements [109].

4. CONCLUSIONS

Research and applications of fractal-shaped antennas is increasing [110,111]. So far, we can divide the applications into six main groups:

1. *Multifrequency Antennas, FSS, and Arrays.* The early work was dedicated to the Sierpinski dipole. Nowadays, fractal technology is also being applied to the design of multifrequency microstrip patches. Moreover, multifrequency FSS and arrays can be designed using the fractal technology.
2. *Electrically Small Antennas.* Koch and Hilbert curves have been used so far and are inspiring many researchers to search for new space-filling curves to optimize antenna performance.
3. *High-Directivity Elements.* Fractal-based antennas supports fracton and fractino modes. As we have shown, these modes present a broadside radiation pattern with a directivity larger than the fundamental mode.
4. *Low Sidelobe Array.* Using fractal arrangements, arrays with very low sidelobes can be achieved

with a uniform excitation. This is an advantage compared with nonuniform excitations, which required a complex feeding network.

5. *Undersampled Arrays.* With this novel application, microstrip arrays use a fewer elements than in the classic approach using Euclidian radiators. This reduction of the number of elements potentially reduces the feeding network complexity and might become a very interesting application for satellite antennas, where space, cost, and volume are constrain factors.
6. *Fast Computational Methods.* Taking advantage of the fractal geometry, rapid algorithms to calculate antenna parameters and beamforming are being developed.

Acknowledgment

This work has been financed by FRACTUS, S.A.

The authors would like to thank M. Navarro, J. Romeu, A. Cardama, J. M. Rius, F. Moyano, and the Electromagnetics and Photonics Engineering Group of the Universitat Politècnica de Catalunya and J. M. González for the thermograms of the Sierpinski gasket.

BIBLIOGRAPHY

1. B. B. Mandelbrot, *The Fractal Geometry of Nature*, Freeman, 1983.
2. H. O. Peitgen, H. Jürgens, and D. Saupe, *Chaos and Fractals*, New Frontiers of Science Series, Springer-Verlag, 1990.
3. C. Puente, C. Borja, J. Anguera, and J. Soler, *Multilevel Antennae*, Patent WO0122528.
4. C. Puente, C. Borja, M. Navarro, and J. Anguera, *Multi-triangular Antennas for Cellular Telephony GSM and DCS*, Patent App. WO9957784.
5. C. Puente, J. Romeu, R. Pous, and A. Cardama, On the behavior of the sierpinski multiband antenna, *IEEE Trans. Anten. Propag.*, **46**(4):517–524 (April 1998).
6. J. Anguera, E. Martínez, C. Puente, C. Borja, and J. Soler, Broadband dual-frequency microstrip patch antenna with modified sierpinski fractal geometry, *IEEE Trans. Anten. Propag.*, **52**(1):66–73 (2004).
7. C. Puente, J. Romeu, R. Pous, and X. García, Fractal multiband antenna based on the sierpinski gasket, *IEE Electron. Lett.*, **32**(1):1–2 (Jan. 1996).
8. D. L. Jaggard and A. D. Jaggard, Cantor ring arrays, *Micro-wave Opt. Technol. Lett.*, **19**:121–125 (1998).
9. N. Cohen, Are fractals naturally frequency invariant/independent? *15th Annual Review of Progress in Applied Computational Electromagnetics, Naval Postgraduate School, Monterey, CA, March 1999, Vol. I, pp. 101–106.*
10. N. Cohen, Fractal and shaped dipoles, *Commun. Quart.* 25–36 (spring 1996).
11. C. Puente and R. Pous, Fractal design of multiband and low side-lobe arrays, *IEEE Trans. Anten. Propag.*, **44**(5):730–739 (May 1996).
12. D. H. Werner, R. L. Haupt, and P. L. Werner, Fractal antenna engineering: The theory and design of fractal antenna arrays, *Anten. Propag. Mag.*, **41**(5):37–58 (Oct. 1999).

13. C. Puente, J. Romeu, R. Pous, J. Ramis, and H. Hijazo, Small but long koch fractal monopole, *IEE Electron. Lett.*, **34**(1): 9–10 (Jan. 1998).
14. J. Anguera, E. Martínez, C. Puente, and E. Rozan, The fractal hilbert monopole: A two-dimensional wire, *Microwave Opt. Technol. Lett.*, **36**(2):102–104 (Jan. 2003).
15. N. Cohen and R. G. Hohlfield, Fractal loops and the small loop approximation, *Commun. Quart.* 77–81 (winter 1996).
16. J. P. Gianvittorio and Y. Rahmat-Samii, Fractal element antennas: A compilation of configurations with novel characteristics, *IEEE Int. Symp. Antennas and Propagation Digest*, Salt Lake City, July 2002, Vol. 3, pp. 1688–1691.
17. J. P. Gianvittorio and Y. Rahmat-Samii, Fractal patch antennas: Miniaturizing resonant patches, *IEEE Antennas and Propagation Society Int. Symp. URSI Digest*, Boston, July 2001, p. 298.
18. C. Borja, G. Font, S. Blanch, and J. Romeu, High directivity fractal boundary microstrip patch antenna, *IEE Electron. Lett.*, **36**(9):778–779 (2000).
19. J. Anguera, C. Puente, C. Borja, R. Montero, and J. Soler, Small and high directivity bowtie patch antenna based on the sierpinski fractal, *Microwave Opt. Technol. Lett.*, **31**(3): 239–241 (Nov. 2001).
20. J. Romeu, A. Aguasca, S. Blanch, and J. Girona, Observation of localized modes in the koch waveguide, *Proc. IEEE Antennas and Propagation Society Int. Symp.*, Boston, July 2001, Vol. 3, pp. 644–647.
21. J. Anguera, G. Montesinos, C. Puente, C. Borja, and J. Soler, High-directivity microstrip array using high-directivity fractal-based elements, *Proc. 25th European Space Agency (ESA) Antenna Workshop on Satellite Antenna Technology*, Sept. 2002 ESTEC, Noordwijk, The Netherlands, 2002.
22. J. Anguera, G. Montesinos, C. Puente, C. Borja, and J. Soler, An under-sampled high directivity microstrip patch array with a reduced number of radiating elements inspired on the sierpinski fractal, *Microwave Opt. Technol. Lett.*, **37**(2):100–103 (April 2003).
23. J. Anguera, C. Puente, and C. Borja, *Undersampled Microstrip Array Using Multilevel and Space-Filling Shaped Elements*, Patent PCT/EP02/07835.
24. Y. Kim and D. L. Jaggard, The fractal random array, *Proc. IEEE*, **74**(9):1278–1280 (Sept. 1986).
25. D. L. Jaggard and A. D. Jaggard, Cantor ring arrays, *IEEE Int. Symp. Antennas and Propagation Digest*, Atlanta, June 1998, Vol. 2, pp. 866–869.
26. C. Puente, *Fractal Antennas*, Ph.D. dissertation, Dept. Signal Theory and Communications, Univ. Politècnica de Catalunya, 1997.
27. C. Puente, R. Pous, J. Romeu, and X. García, *Fractal and Multifractal Antennas*, Patent ES 9501019.
28. C. Borja, C. Puente, and A. Medina, Modelo sencillo para el estudio de los parámetros de entrada de una antena fractal de sierpinski (Simple model to study input impedance of the Sierpinski fractal antenna), *Proc. XII Symp. Natl. URSI*, Bilbao, 1997, pp. 363–371.
29. C. Puente, C. Borja, M. Navarro, and J. Romeu, An iterative model for fractal antennas: Application to the sierpinski gas- ket antenna, *IEEE Trans. Anten. Propag.*, **48**(5):713–719 (May 2000).
30. C. Borja, C. Puente, and A. Medina, Iterative network model to predict the behaviour of a sierpinski fractal networks, *IEE Electron. Lett.*, **34**(15):1443–1445 (July 1998).
31. C. Borja and C. Puente, Iterative network model to predict the performance of sierpinski fractal antennas and networks, *Proc. IEEE Antennas and Propagation Society Int. Symp.*, Orlando, FL, July 1999, pp. 652–655.
32. J. Soler, C. Puente, and J. Anguera, Extended multiperiodic traveling wave model for the accurate analysis of the radiation performance of the sierpinski fractal-like multiband antenna, *Microwave Opt. Technol. Lett.*, **36**(1):67–70 (Jan. 2003).
33. J. Soler, C. Puente, and J. Anguera, Results on a new extended analytic model to understand the radiation performance of mod-p sierpinski fractal multiband antennas, *Proc. IEEE Antennas and Propagation Society Int. Symp.*, Columbus, OH, June 2003.
34. J. Soler, J. Romeu, and C. Puente, Mod-p sierpinski fractal multiband antenna, *Proc. AP2000 Millenium Conf. Antennas and Propagation*, Davos, Switzerland, 2002.
35. J. Soler, D. García, C. Puente, and J. Anguera, Novel combined mod-p structures: A complete set of multiband antennas inspired on fractal geometries, *Proc. IEEE Antennas and Propagation Society Int. Symp.*, Columbus, OH, June 2003.
36. J. Parrón, J. M. Rius, and J. Romeu, Numerical analysis of highly iterated fractal antennas, *Proc. IEEE Antennas and Propagation Society Int. Symp.*, San Antonio, TX, 2002.
37. D. H. Werner, P. L. Werner, and K. H. Church, Genetically engineered multiband fractal antennas, *IEE Electron. Lett.*, **37**(19):1150–1151 (Sept. 2001).
38. D. H. Werner, P. L. Werner, J. W. Culver, S. D. Eason, and R. Libonati, Load sensitivity analysis for genetically engineered miniature multiband fractal dipole antennas, *Proc. IEEE Antennas and Propagation Society Int. Symp.*, June 2002, Vol. 4, pp. 86–89.
39. M. F. Pantoja, F. G. Ruiz, A. R. Bretones, R. G. Martín, S. G. García, J. M. G. Arbesú, J. Romeu, J. M. Rius, D. H. Werner, and P. L. Werner, On the design of small antennas using GA, *Proc. 27th ESA Antenna Technology Workshop on Innovative Periodic Antennas*, March 9–11, 2004.
40. J. M. González, M. Navarro, C. Puente, J. Romeu, and A. Aguasca, Active zone self-similarity of fractal-sierpinski antenna verified using infra-red thermograms, *IEE Electron. Lett.*, **35**(17):1393–1394 (Aug. 1999).
41. C. Puente, M. Navarro, J. Romeu, and R. Pous, Variations on the fractal sierpinski antenna flare angle, *Proc. IEEE Antennas and Propagation Society Int. Symp.*, Atlanta, June 1998.
42. M. Navarro, C. Puente, R. Bartolomé, A. Medina, J. Romeu, and R. Pous, Modificación de la antena de sierpinski para el ajuste de las bandas operativas (Modification of the Sierpinski antenna to allocate operating bands), *Proc. XII Symp. Natl. URSI*, Bilbao, 1997, pp. 363–371.
43. C. T. P. Song, P. S. Hall, H. Ghafouri-Shiraz, and D. Wake, Sierpinski monopole antenna with controlled band spacing and input impedance, *IEE Electron. Lett.*, **35**(13):1036–1037 (June 1999).
44. C. T. P. Song, P. S. Hall, and H. Ghafouri-Shiraz, Perturbed sierpinski multi-band fractal antenna with improved feeding technique. *IEEE Trans. Anten. Propag.*, **51**(5):1011–1017 (2003).
45. C. Puente, J. Romeu, and A. Cardama, *Fractal-Shaped Antennas*, Frontiers in Electromagnetics Series, D. H. Werner and R. Mittra, eds., IEEE Press, 2000.
46. Fractus, Fractal antennas: New generation of antennas for compact and versatile telecommunication services. A practical application to mobile GSM 900 and 1800 networks, *Microwave J.* (Jan. 2000).

47. C. Puente, J. Anguera, C. Borja, and J. Soler, Fractal-shaped antennas and their application to GSM 900/1800, *J. Inst. Br. Telecommun. Eng.* 2 (July–Sept. 2001).
48. J. Soler, C. Puente, and A. Puerto, A dual-band bidirectional multilevel monopole antenna, *Microwave Opt. Technol. Lett.*, **34**(6):445–448 (Sept. 2002).
49. J. Romeu and Y. Rahmat-Samii, Fractal fss: A novel dual-band frequency selective surface, *IEEE Trans. Anten. Propag.*, **48**(7):1097–1105 (July 2000).
50. J. Romeu and Y. Rahmat-Samii, A fractal based fss with dual band characteristics, *Proc. IEEE Antennas and Propagation Society Int. Symp.*, Orlando, FL, July 1999, Vol. 3, pp. 1734–1737.
51. J. Romeu and Y. Rahmat-Samii, Dual band fss with fractal elements, *IEE Electron. Lett.*, **35**(9):702–703 (April 1999).
52. D. H. Werner and D. Lee, Design of dual-polarized multiband frequency selective surfaces using fractal elements, *IEE Electron. Lett.*, **36**(6):487–488 (March 2000).
53. E. S. Siah, B. L. Ooi, P. S. Kooi, and X. D. Xhou, Experimental investigation of several novel fractal antennas—variants of the sierpinski gasket and introducing fractal fss screens, *Proc. Asia Pacific Microwave Conf.*, 1999, Vol. I, pp. 1710–1713.
54. J. Soler, *Novel Techniques for Small and Multifrequency Antennas*, Ph.D. dissertation, Dept. Signal Theory and Communications, Univ. Politècnica de Catalunya, in progress.
55. J. Romeu and J. Soler, Generalized sierpinski fractal multiband antenna, *IEEE Trans. Anten. Propag.*, **49**(8):1237–1239 (Aug. 2001).
56. J. Soler and J. Romeu, Dual-band sierpinski fractal monopole antenna, *Proc. IEEE Antennas and Propagation Society Int. Symp.*, Salt Lake City, July 2000.
57. J. Soler and C. Puente, *Loaded Antenna*, Patent PCT/EP01/11914.
58. R. Quintero and C. Puente, *Multilevel and Space-Filling Groundplanes for Miniature and Multiband Antennas*, Patent Appl. PCT/EP01/10589.
59. J. Soler, C. Puente, and J. Anguera, Multifrequency properties of monopole antennas using multilevel ground planes inspired on the sierpinski fractal shape, *Proc. IEEE Antennas and Propagation Society Int. Symp.*, Columbus, OH, June 2003.
60. S. R. Best, Operating band comparison of the perturbed sierpinski and modified parany gasket antennas, *IEEE Anten. Wireless Propag. Lett.*, **1**:35–38 (2002).
61. S. R. Best, On the radiation pattern characteristics of the sierpinski and modified parany gasket antennas, *IEEE Anten. Wireless Propag. Lett.*, **1**:39–42 (2002).
62. C. T. P. Song, P. S. Hall, and H. Ghafouri-Shiraz, Multiband quasi-fractal multiple ring monopole antenna, *IEEE Trans. Anten. Propag.*, **51**(4):722–729 (2003).
63. J. Soler, C. Puente, and J. Anguera, Solutions to tailor the radiation patterns of 2d and 3d multiband antennas based on the sierpinski fractal, *Proc. IEEE Antennas and Propagation Society Int. Symp.*, Columbus, OH, June 2003.
64. C. Borja, C. Puente, J. Romeu, and J. Anguera, Fractal multiband patch antenna, *Proc. Millennium Conf. Antennas and Propagation AP2000*, Davos, Switzerland, April 2000.
65. C. Borja, C. Puente, J. Anguera, J. Romeu, and R. Pous, Estudio experimental del parche de sierpinski (Experimental study of the Sierpinski patch antenna), *Proc. XII Symp. Natl. URSI*, Santiago de Compostela, 1999.
66. C. Borja, *Fractal Microstrip Patch Antennas with Fractal Perimeter and Self-Affine Properties*, Ph.D. dissertation, Dept. Signal Theory and Communications, Univ. Politècnica de Catalunya, 2001.
67. C. Borja and J. Romeu, Multiband sierpinski fractal patch antenna, *Proc. IEEE Antennas and Propagation Society Int. Symp.* Salt Lake City, July 2000, pp. 1708–1711.
68. J. Anguera, *Fractal and Broadband Techniques on Miniature, Multifrequency, and High-Directivity Microstrip Patch Antennas*, Ph.D. dissertation, Dept. Signal Theory and Communications, Univ. Politècnica de Catalunya, 2003.
69. C. Borja, C. Puente, and J. Anguera, *Dual-Band Dual-Polarized Antenna Array*, Patent PCT/EP01/04288.
70. J. Anguera, C. Puente, C. Borja, G. Font, and J. Soler, A systematic method to design single-patch broadband microstrip patch antennas, *Microwave Opt. Technol. Lett.*, **31**(3):185–188 (Nov. 2001).
71. J. Anguera, C. Puente, and C. Borja, A procedure to design stacked microstrip patch antenna based on a simple network model, *Microwave Opt. Technol. Lett.*, **30**(3):149–151 (Aug. 2001).
72. S. E. El-Khami, M. A. Aboul-Dahab, and M. I. Elkashlan, A simplified koch multiband fractal array using windowing and quantization techniques, *Proc. IEEE Antennas and Propagation Society Int. Symp.* Salt Lake City, July 2000, Vol. 3, pp. 1716–1719.
73. X. Liang, W. Zhensen, and W. Wenbing, On the synthesis of fractal patterns from the concentric-ring array, *IEE Electron. Lett.*, **32**:1940–1941 (Oct. 1996).
74. D. Baldacci and D. H. Werner, An efficient recursive procedure for calculating the driving point impedance of linear and planer fractal arrays, *Proc. IEEE Antennas and Propagation Society Int. Symp.* Boston, July 2001, Vol. 3, pp. 620–623.
75. D. H. Werner and P. L. Werner, A general class of self-scalable and self-similar arrays, *Proc. IEEE Antennas and Propagation Society Int. Symp.*, Orlando, FL, July 1999, Vol. 4, pp. 2882–2885.
76. R. L. Haupt and D. H. Werner, Fast array factor calculations for fractal arrays, *Proc. 13th Annual Review of Progress in Applied Computational Electromagnetics (ACES)*, Naval Postgraduate School, Monterey, CA, March 1997, Vol. I, pp. 291–296.
77. H. A. Wheeler, Fundamental limitations on small antennas, *Proc. IRE* 1479–1488 (Dec. 1947).
78. L. J. Chu, Physical limitations of omnidirectional antennas, *J. Appl. Phys.*, **19**:1163–1175 (Dec. 1948).
79. H. A. Wheeler, The radiansphere around a small antenna, *Proc. IRE* 1325–1331 (Aug. 1959).
80. J. Anguera, C. Puente, and J. Soler, Miniature monopole antenna based on the fractal hilbert curve, *Proc. IEEE Antennas and Propagation Society Int. Symp.*, San Antonio, TX, June 2002.
81. J. Anguera, E. Martínez, C. Puente, and J. Soler, El monopolo de hilbert: una curva fractal de dos dimensiones (The Hilbert monopole: A two dimensional fractal curve), *Proc. 17th Natl. Symp. Scientific International Union of Radio*, Alcalá de Henares, Spain, Sept. 2002.
82. C. Puente, E. Rozan, and J. Anguera, Space-filling miniature antennas, Patent WO0154225.
83. K. J. Vinoy, K. A. Jose, V. K. Varadan, and V. V. Varadan, Resonant frequency of hilbert curve fractal antennas, *Proc. IEEE Antennas and Propagation Society Int. Symp.*, Boston, July 2001, Vol. 3, pp. 648–651.

84. J. Zhu, A. Hoorfar, and N. Engheta, Feed-point effects in hilbert-curve antennas, *IEEE Antennas and Propagation Society Int. Symp. URSI Digest*, San Antonio, TX, June 2002, p. 373.
85. P. Thang and P. Wahid, Scaling property of the koch fractal dipole, *Proc. IEEE Antennas and Propagation Society Int. Symp.*, Boston, July 2001, Vol. 3, pp. 150–153.
86. D. Gala, J. Soler, C. Puente, C. Borja, and J. Anguera, Miniature microstrip patch antenna loaded with a space-filling transmission line based on the fractal hilbert curve, *Microwave Opt. Technol. Lett.*, **38**(4):311–312 (Aug. 2003).
87. J. McVay, N. Engheta, and A. Hoorfar, High-impedance metamaterial surfaces using hilbert-curve inclusions, *IEEE Microwave Wireless Compon. Lett.*, **14**(3):130–132 (March 2004).
88. C. T. P. Song, *Novel Antenna Design for Future Mobile Systems*, Ph.D. dissertation, School Electronic and Electrical Engineering, Univ. Birmingham, UK, 2001.
89. C. T. P. Song, P. S. Hall, H. Ghafouri, and I. Henning. Shorted fractal sierpinski monopole antenna, *Proc. IEEE Antennas and Propagation Society Int. Symp.*, Boston, July 2001, Vol. 3, pp. 138–141.
90. J. P. Gianvittorio, *Fractals, MEMS, and FSS Electromagnetic Devices: Miniaturization and Multiple Resonances*, Ph.D. dissertation, Univ. California, Los Angeles, 2003.
91. J. P. Gianvittorio and Y. Rahmat-Samii, Fractal antennas: A novel antenna miniaturization technique, and applications, *IEEE Anten. Propag. Mag.*, **44**(1):20–36 (Feb. 2002).
92. J. Anguera, C. Puente, C. Borja, and J. Romeu, Miniature wideband stacked microstrip patch antenna based on the sierpinski fractal geometry, *Proc. IEEE Antennas and Propagation Society Int. Symp.*, Salt Lake City, July 2000.
93. J. Anguera, C. Puente, and C. Borja, *Miniature Broadband Ring-like Microstrip Patch Antenna*, Patent Appl. PCT/EP01/01287.
94. G. J. Walker and J. R. James, Fractal volume antennas, *IEE Electron. Lett.*, **34**(16):1536–1537 (Aug. 1998).
95. B. Sapoval, Th. Gobron, and A. Margolina, Vibrations of fractal drums, *J. Am. Phys. Soc.*, **67**(21):2974–2977 (Nov. 1991).
96. B. Sapoval and Th. Gobron, Vibrations of strongly irregular or fractal resonators, *J. Am. Phys. Soc.*, **47**(5):3013–3024 (May 1993).
97. C. Borja and J. Romeu, Fracton vibration modes in the sierpinski microstrip patch antenna, *Proc. IEEE Antennas and Propagation Society Int. Symp.*, Boston, July 2001.
98. J. Anguera, C. Puente, and C. Borja, *Broadside High-Directivity Microstrip Patch Antennas*, Patent NPCT/EP03/00757.
99. C. Borja and J. Romeu, On the behaviour of the koch island fractal boundary microstrip patch antenna, *IEEE Trans. Anten. Propag.*, **51**(6):1281–1291 (June 2003).
100. J. Anguera, C. Puente, C. Borja, and R. Montero, Bowtie microstrip patch antenna based on the sierpinski fractal, *Proc. IEEE Antennas and Propagation Society Int. Symp.*, Boston, July 2001, Vol. 3, pp. 162–165.
101. J. Anguera, C. Puente, C. Borja, and R. Montero, Antena microstrip miniatura y de alta directividad basada en el fractal de sierpinski (Miniature and high-directivity microstrip antenna based on the Sierpinski fractal), *Proc. 16th Natl. Symp. Scientific Int. Union of Radio*, Madrid, Spain, Sept. 2001.
102. G. Montesinos, J. Anguera, C. Puente, and C. Borja, The sierpinski fractal bowtie patch: A multifracton-mode antenna, *Proc. IEEE Antennas and Propagation Society Int. Symp.*, San Antonio, TX, June 2002.
103. J. Anguera, G. Montesinos, C. Puente, C. Borja, and J. Soler, Modos multifracción en la antena microstrip bowtie fractal de sierpinski (Multifracton nodes in a microstrip antenna based on the bowtie Sierpinski fractal), *Proc. 17th Natl. Symp. Scientific Int. Union of Radio*, Alcalá de Henares, Spain, Sept. 2002.
104. J. Anguera, G. Montesinos, C. Puente, C. Borja, and J. Soler, A microstrip array operating in a fracton mode, *Proc. IEEE Antennas and Propagation Society Int. Symp.*, Columbus, OH, June 2003.
105. J. Anguera, G. Montesinos, C. Puente, C. Borja, and J. Soler, Agrupación submuestreada operando en modo fractón utilizando antenas microstrip inspiradas en el fractal de sierpinski (Undersampled array operating in a fracton mode using microstrip antennas inspired in the Sierpinski fractal), *Proc. 18th Natl. Symp. Scientific Int. Union of Radio*, La Coruña, Spain, Sept. 2003.
106. J. Anguera, C. Puente, C. Borja, and J. Soler, Scanning properties in an under-sampled microstrip array using sierpinski fractal-inspired elements, *Proc. 27th European Space Agency (ESA) Antenna Workshop on Innovative Periodic Antennas*, Santiago de Compostela, Spain, March 2003.
107. D. L. Jaggard, On fractal electrodynamics, in D. L. Jaggards and H. N. Kritikos, eds., *Recent Advances in Electromagnetics Theory*, Springer-Verlag, New York, 1990, pp. 183–224.
108. X. Sun and D. L. Jaggard, Wave interactions with generalized cantor bar fractal multilayers, *J. Appl. Phys.*, **70**(5):2500–2507 (Sept. 1991).
109. N. Cohen and R. G. Hofhied, Array sidelobe reduction by small position offsets of fractal elements, *16th Annual Review of Progress in Applied Computational Electromagnetics*, Naval Postgraduate School, Monterey, CA, March 2000, Vol. 2, pp. 822–828.
110. D. H. Werner and S. Ganguly, An overview of fractal antenna engineering research, *IEEE Anten. Propag. Mag.*, **45**(1):38–57 (Feb. 2003).
111. D. L. Jaggard, Fractal electrodynamics: From super antennas to superlattices, in J. L. Vehel, E. Lutton, and C. Tricot, eds., *Fractals in Engineering Series*, Springer-Verlag, New York, 1997, pp. 204–221.

FREQUENCY CONVERTERS AND MIXERS

ILTCHO ANGELOV
 ERIK L. KOLLBERG
 HERBERT ZIRATH
 Chalmers University of
 Technology
 Göteborg, Sweden

An essential part of most microwave receivers is the frequency converter, a device that converts the frequency of an incoming signal to another frequency. The output frequency may be *downconverted*, *upconverted*, *multiplied*, or *divided*. Important and common is the *mixer*, which downconverts a high-frequency input signal f_s to a much lower and more manageable signal f_{IF} , preserving information concerning the amplitude, frequency, and phase of the input signal. The devices used are nonlinear (i.e., the relationship between current and voltage is not

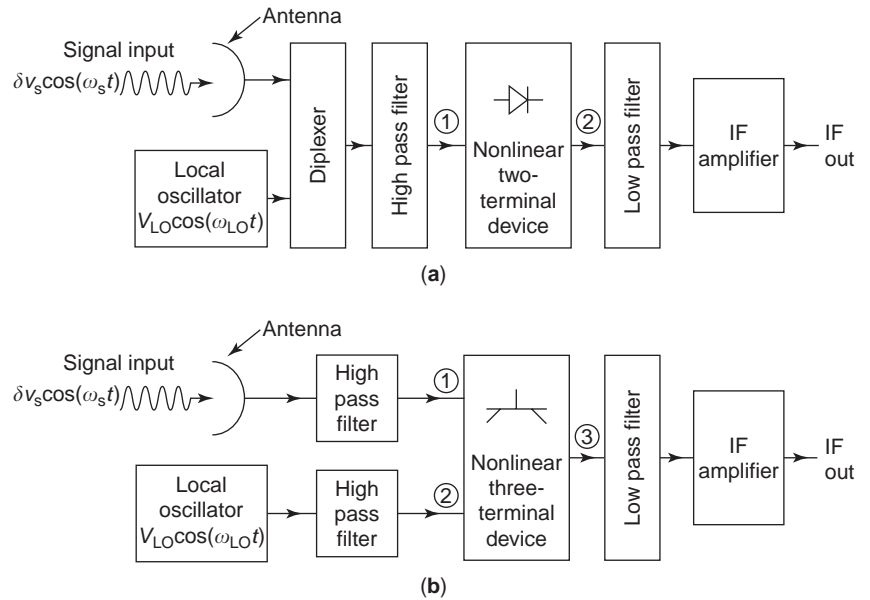


Figure 1. Typical mixer block diagram showing layouts for a two-terminal device (diode) (a) and a three-terminal device (transistor) (b). At the input there is a highpass filter that will prevent any low-frequency IF power from escaping to the mixer input (left). The lowpass filter will stop any input signal or LO power from going to the IF circuit (right).

linear). The devices may have either two terminals (diodes) or three terminals (transistors).

Mixers are important for very high frequencies, where amplifiers are not available and direct amplitude or phase detection is difficult. A mixer can be used to downconvert, say, a terahertz frequency signal to a microwave frequency one, where electronic methods are readily available for amplification and any kind of demodulation. In fact, in almost any radio set or mobile telephone receiver or base station, there are several mixers and other types of frequency converters.

Both two-terminal devices (diodes) and three-terminal devices (transistors) are used in mixers. The frequency conversion is accomplished by using the *nonlinear* properties of the device. Virtually all semiconductor devices, such as diodes and transistors, show nonlinear properties in certain bias ranges. Common devices for microwave mixer applications are the Schottky diode, the field-effect transistor (FET), and the bipolar transistor. There are many other devices available as well, for example, the superconducting tunneling device (SIS) and the superconducting hot-electron device for low-noise (high-sensitivity) millimeter- and sub-millimeter-wave receivers. For infrared wavelengths, metal-insulator-metal (MIM) devices and, for optical frequencies, photoconducting devices have been used. Note that ordinary resistors, capacitances, and inductances are linear components.

Figure 1 gives an example of how mixers are used in a receiving system. The antenna is connected directly to the

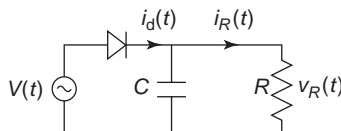


Figure 2. A rectifying diode circuit. If the capacitance C and the resistance R are large enough, $v_R(t)$ will follow the envelope of $v(t)$ (see Fig. 3).

mixer. For example, in a TV satellite receiver, an amplifier is placed just after the antenna to increase the signal amplitude. In reality there are many other systems (e.g., radar, radio, measurement systems) where mixers are used to frequency downconvert the input signal.

To give a simple illustration of how a diode mixer may work, consider the detector circuit shown in Fig. 2 using an ideal diode (zero resistance in the forward direction and infinite resistance in the backward direction). If a sinusoidal voltage $V(t) = V_{LO} \cos(2\pi f_{LO} t)$ is applied, it will be “rectified” (detected) by the diode. The voltage over the resistance $v_R(t)$ will be a constant DC voltage proportional to V_{LO} . Next, add a *small* signal voltage $\delta v_s \cos(2\pi f_s t)$, that is, $V(t) = V_{LO} \cos(2\pi f_{LO} t) + \delta v_s \cos(2\pi f_s t)$. Assuming that $\delta v_s / V_{LO} \ll 1$, the resulting voltage $V(t)$ will become amplitude-modulated, as shown in Fig. 2. The detected voltage $v_R(t)$ over the load resistance R will be proportional to the envelope $V_R(t)$ (assuming $\tau = RC \ll 1/\omega_{IF}$) (see Fig. 3),

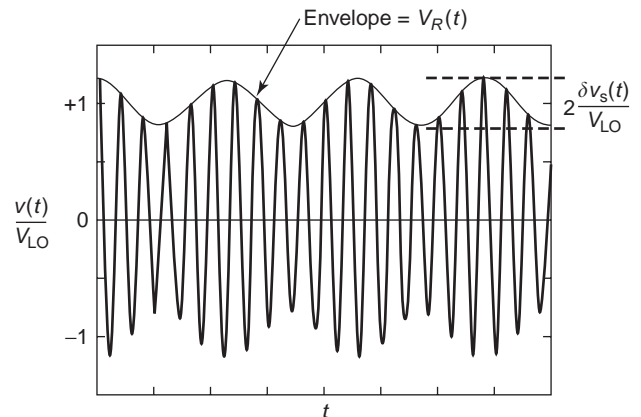


Figure 3. An example with a drive voltage $v(t)/V_{LO} = \cos(\omega_{LO} t) + (\delta v_s / V_{LO}) \cos(\omega_s t)$, where $\delta v_s / V_{LO} = 0.2$ and $\omega_{LO} / \omega_s = 1.18$. The IF is $0.18 \omega_{LO}$.

that is

$$v_R(t) = V_{\text{LO}} \left(1 + \frac{\delta v_s}{V_{\text{LO}}} \cos(2\pi f_{\text{IF}} t) \right) \quad (1)$$

where $f_{\text{IF}} = |f_{\text{LO}} - f_s|$ is the intermediate frequency (IF). The DC part of Eq. (1) is the “detected local oscillator (LO),” and the alternating part is identical to the IF voltage and, in this example, is equal in amplitude to the input signal. This IF signal is fed into an amplifier as described in Fig. 1.

Note that in the simplified example above we have not correctly accounted for a number of parameters, such as the impedances of the LO and signal sources. This means that the IF voltage will not become equal to δv_s . A more detailed description of a more correct calculation is given in the Section 3. For details concerning microwave mixers, see Refs. 1 and 2.

1. GENERAL PROPERTIES OF TWO-TERMINAL NONLINEAR DEVICES

Below we describe some general results obtained when a two-terminal device such as the Schottky diode is excited with a sinusoidal signal. The impedance of the Schottky diode is voltage-dependent. The speed of this device is indeed high. It shows a nonlinear behavior up to several terahertz.

1.1. Frequency Multiplication

Consider a nonlinear diode device exposed to LO (or pump) power yielding a large voltage swing $V(t) = V_{\text{LO}} \cos(\omega_{\text{LO}} t)$ over the diode. (Note: Below we use $\omega = 2\pi f$.) Since the relation between current and voltage is not linear (i.e., $I \neq \text{const.} \times V$), the resulting current will *not* have a sinusoidal shape like that of the input voltage. However, the current in this case is still a *periodic* function versus time with the same periodicity, $\tau = 2\pi/\omega_{\text{LO}}$, as the LO frequency and can consequently be expressed as a Fourier series with harmonics of the LO, $n\omega_{\text{LO}}$:

$$I(t) = \sum_{n=0}^{\infty} i_n \cos(n\omega_{\text{LO}} t + \varphi_n) \quad (2)$$

The component i_0 is the DC component. To obtain power at a particular harmonic, for example, the third harmonic, it

is required that the current component at $3\omega_{\text{LO}}$ pass through a resistance R_3 delivering a power of $\frac{1}{2}i_3^2 R_3$. To avoid any power being delivered at other harmonics, it is necessary to ensure that the device is reactively terminated at these harmonics.

In reality, the impedance of most nonlinear devices is complex with both the *real* and the *imaginary* parts voltage (or current)-dependent. For a more detailed theory, see Section 3.2.

1.2. Frequency Conversion

If two signal voltages at ω_{LO} and ω_s are simultaneously interacting with the nonlinear diode impedance, the resulting current can be expressed in a more complex Fourier series:

$$I(t) = \sum_{m=-\infty}^{+\infty} \sum_{n=-\infty}^{+\infty} i_{m,n} \cos((m\omega_{\text{LO}} + n\omega_s)t + \varphi_{m,n}) \quad (3)$$

In the case when both the signal voltage and the local oscillator voltage are large, a large number of frequency conversion products are obtained. Obviously it is possible to generate power at any frequency $m\omega_{\text{LO}} \pm n\omega_s$. If for $m = n = 1$ the required output frequency is higher than the signal frequency, one has *frequency upconversion*, and if the output frequency is lower than the signal frequency, one has *frequency downconversion*.

1.3. Linear Mixing

As already mentioned, a mixer receiver usually handles “small signals.” We have a small signal case if the amplitude of the signal at ω_s is much smaller than the LO amplitude at ω_{LO} . In this case only harmonics of ω_{LO} are important, and we are left with

$$I(t) \approx \sum_{m=-\infty}^{+\infty} i_m \cos[(m\omega_{\text{LO}} + \omega_s)t + \varphi_m] \quad (4)$$

In most mixer applications, we are interested in the “intermediate frequency,” $\omega_{\text{IF}} = |\omega_{\text{LO}} - \omega_s|$. An IF load resistance in the circuit will allow power at the IF frequency to be extracted (compare with Fig. 2). Equation (4) suggests that power may go not only to the IF but also to *harmonic sidebands*, as illustrated in Fig. 4. The only way to prevent this power loss is to make sure that the

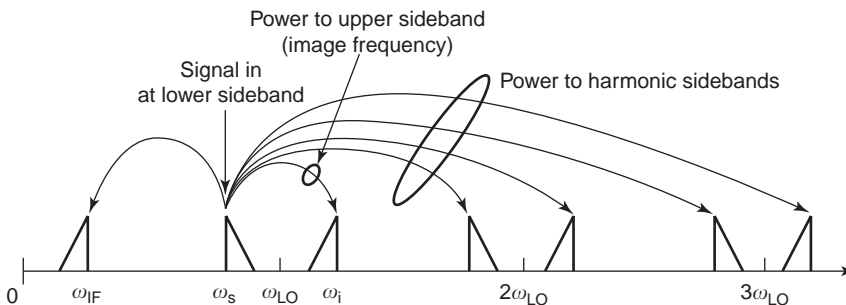


Figure 4. Power flow in a lower sideband mixer. The input signal power is distributed not only to the IF but also to the harmonic sidebands.

harmonic sideband current components are facing impedances that are purely reactive.

Note that an IF signal (Fig. 4) will be created if either $\omega_{su} = \omega_{LO} + \omega_{IF}$ or $\omega_{sl} = \omega_{LO} - \omega_{IF}$. The former frequency ω_{su} is the upper sideband, and the latter ω_{sl} the lower sideband. For a *lower sideband mixer* the upper sideband is denoted the *image frequency*, and vice versa for an *upper sideband mixer*. For a lower or upper sideband case, some signal power may go to the image frequency. In an *image-reject mixer* a filter prevents the image frequency from entering the mixer. In the *image-enhanced mixer*, the image terminal is terminated reactively so that the conversion loss is reduced.

At high signal powers, there may be confusion because the mixer may produce output signals in the IF band (see Section 1.5 below) for

$$|m\omega_{LO} - n\omega_s| = \omega_{IF} \tag{5}$$

1.4. Harmonic Mixer

In a harmonic and small-signal linear mixer one has $\omega_{IF} = |n\omega_{LO} - \omega_s|$. A spectrum analyzer always uses a harmonic mixer to analyze the signal, and the harmonic number n can be very high (> 10). The power flow in a harmonic mixer is shown in Fig. 5.

1.5. Intermodulation

All mixer products created by two or more signals are called *intermodulation* (IM) products. Most IM products are unwanted.

For example, if two signals at slightly different frequencies ω_{s1} and ω_{s2} and with a power of the same order of magnitude as the LO are interacting with the nonlinear device, the current will contain frequency products as shown in the following equation:

$$I(t) = \sum_{m=-\infty}^{+\infty} \sum_{n=-\infty}^{\infty} \sum_{k=-\infty}^{\infty} i_{m,n} \cos[(m\omega_{LO} + n\omega_{s1} + k\omega_{s2})t + \varphi_{m,n,k}] \tag{6}$$

All signals at frequencies fulfilling the requirement

$$\omega_{s1} \approx |m\omega_{LO} + n\omega_{s2} \pm \omega_{IF}| - \infty < m, n < \infty \tag{7}$$

may create IM products in the IF band. Indeed, intermodulation must be considered a potentially serious problem in all applications where strong signals may occur.

2. SYSTEMS ASPECTS

In a system, the following properties are important: (1) conversion loss, (2) noise properties, and (3) intermodulation properties.

2.1. Conversion Loss

An important property of a mixer is the conversion loss L , defined as

$$L = \frac{P_s}{P_{IF}} = \frac{\text{signal power available at the input}}{\text{IF power delivered to the IF load}} \tag{8}$$

In most practical mixers the conversion loss is larger than one. However, it is possible to obtain gain owing to parametric amplification caused by a nonlinear capacitance. In certain configurations using transistors (see Ref. 1 or 4) conversion gain can be obtained. Superconducting mixers, however, due to quantum phenomena, can show stable conversion gain.

There are several loss mechanisms causing the conversion loss:

1. Losses due to absorption in the nonlinear device
2. Losses due to power lost to harmonic sidebands
3. Losses due to reflection at the input port
4. Losses due to reflection at the IF output port

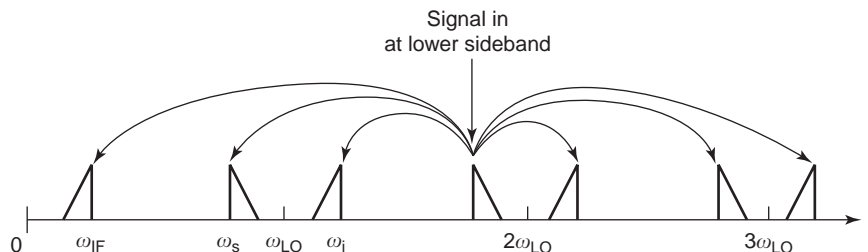
See also Section 3.

2.2. Mixer Receiver Noise

The important noise measure in practical applications is always the total receiver noise temperature. The contributions approximately in order of importance are (1) mixer device noise, (2) the IF amplifier noise, (3) thermal noise from the mixer circuit, and (4) LO noise. There are two different noise measures usually cited in the literature: the *single sideband* (SSB) noise temperature and the *double sideband* (DSB) noise temperature.

When calculating the noise temperature of a mixer, it is advisable to always start adding up all noise contributions at the IF amplifier input (see Fig. 6). The temperature

Figure 5. Power flow in a second-harmonic lower sideband mixer.



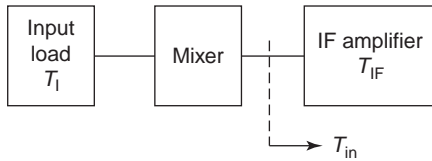


Figure 6. Receiver configuration for calculating the receiver noise. For the calculation it is wise to determine the noise temperature at the input of the IF amplifier T_{in} .

then becomes

$$T_{in} = \frac{T_1}{L_s} + \frac{T_1}{L_i} + \sum_{n=2}^{\infty} \left(\frac{T_1}{L_{n+}} + \frac{T_1}{L_{n-}} \right) + T_{M\ out} + T_{IF} \quad (9)$$

where L_s , L_i , L_{n+} , and L_{n-} are the conversion losses at the signal, image, and upper harmonic sidebands and lower harmonic sidebands, respectively. T_1 is the noise temperature of the input resistance, $T_{M\ out}$ is the noise from the mixer diode entering the IF amplifier. As the next step, identify the signal to noise ratio:

$$\frac{P_s}{P_{in}} = \frac{P_s/L_s}{kT_{in}\Delta f} = \frac{P_s}{kT_{syst}\Delta f} \quad (10)$$

where T_{syst} is by definition the system noise temperature for a *single-sideband* receiver. It is assumed that the useful and interesting signal enters only one sideband. Hence

$$T_{syst,SSB} = T_{in}L_s = T_1 \left[1 + \frac{L_s}{L_i} + \sum_{n=2}^{\infty} \left(\frac{L_s}{L_{n+}} + \frac{L_s}{L_{n-}} \right) \right] + T_{MXR,SSB} + L_s T_{IF} \quad (11)$$

where we have defined the equivalent noise temperature of the mixer itself, $T_{MXR,SSB} = T_{M\ out} L_s$.

For the double-sideband case, one assumes a useful signal to enter both the upper and the lower sidebands. Hence the signal-to-noise ratio for this case should be defined as

$$\frac{P_s}{P_n} = \frac{P_s(1/L_s + 1/L_i)}{kT_{in}\Delta f} = \frac{P_s}{kT_{syst}\Delta f} \quad (12)$$

that is,

$$T_{syst,DSB} = \frac{T_{in}}{1/L_s + 1/L_i} = T_1 \left[1 + \frac{L_s L_i}{L_s + L_i} \sum_{n=2}^{\infty} \left(\frac{1}{L_{n+}} + \frac{1}{L_{n-}} \right) \right] + T_{MXR,DSB} + \frac{L_s L_i}{L_s + L_i} T_{IF} \quad (13)$$

where the double sideband noise temperature of the mixer itself is defined as

$$T_{MXR,DSB} = T_{M\ out} \frac{L_s L_i}{L_s + L_i} \quad (14)$$

Note that if $L_s = L_i$, both the single-sideband mixer and system noise temperatures are twice as large as for the double-sideband case. The LO noise (if important) can be taken into account by adding a certain amount at the input port. Also note that the noise entering the mixer at the harmonic sidebands may considerably influence the total receiver performance.

3. SCHOTTKY DIODE MIXERS

The Schottky diode mixer is the most common type of mixer for frequencies from megahertz to terahertz.

3.1. Schottky Diode for Mixer Applications

A schematic diagram of a common design of millimeter-wave Schottky barrier diode is shown in Fig. 7. Note that the radiofrequency (RF) current is flowing from the diode contact at the surface of the diode chip to the back contact. Hence the RF series resistance is slightly larger for RF than for DC. The current-voltage (I - V) characteristic of the junction itself can be calculated from

$$i_d = I_0 \left[\exp\left(\frac{qV_j}{\eta kT}\right) - 1 \right] \quad (15)$$

where I_0 is the saturation current, V_j the junction voltage, q the charge of the electron, k Boltzmann's constant, T the physical temperature, and η the ideality factor, which for good diodes at room temperature is between, say, 1.03 and 1.10.

The small-signal RF junction properties of a Schottky diode can be modeled as a nonlinear resistance r_j in parallel with a nonlinear capacitance C_j

$$r(i_d) = \frac{\partial V_j}{\partial i_d} = \frac{k\eta T}{qi_d} \quad C(V_j) = \frac{C_0}{\sqrt{1 - \frac{V_j}{V_b}}} \quad (16)$$

where C_0 is the zero bias capacitance and V_b is the built-in voltage of the diode. For more details, see Ref. 3.

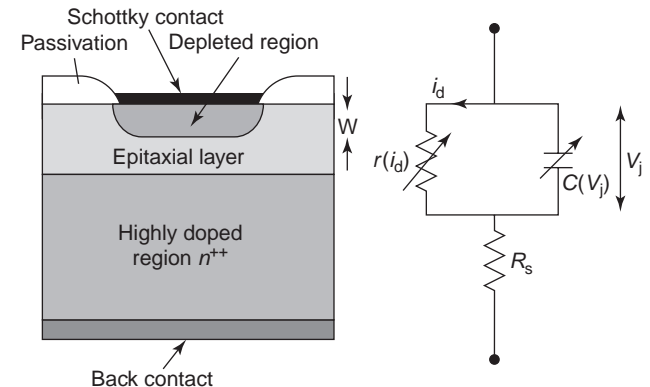


Figure 7. Simple design of a GaAs Schottky barrier diode and the corresponding equivalent circuit. The higher the frequency, the smaller the diodes required.

A common measure of the high-frequency properties is the cutoff frequency, which is defined for the diode at zero bias,

$$f_c = \frac{1}{2\pi R_s C_0} \quad (17)$$

where R_s is measured using the DC I - V characteristic. For good mixer performance this cutoff frequency must be much larger than the signal frequency. The series resistance uses up signal power and should for obvious reasons be made as small as possible. For the conversion efficiency the nonlinear capacitance is of much less importance than the nonlinear resistance. The diode is typically designed as a thin n-doped active layer of 1000 Å (Mott diode), which leaves one with a diode with reduced capacitance variation and a minimum series resistance.

GaAs is preferred for millimeter-wave diodes. The main reason is that the high mobility of GaAs yields a low series resistance and consequently a high cutoff frequency. Another advantage (to silicon) is that carriers do not freeze out when the diode is cooled to cryogenic temperatures in order to improve the mixer noise properties [see Eq. (7)].

The noise performance and the conversion efficiency are the prime properties of the diode for use in mixer applications. Noise properties are discussed next.

3.1.1. Shot Noise. The shot noise is due to fluctuations in the electron particle current between cathode and anode of the diode [3]. The root-mean-square (RMS) fluctuations in the current are $\delta i^2 = 2eI\Delta f$, where Δf is a small frequency interval. The noise power of the Schottky diode can then be calculated as

$$P_n = \frac{\delta i^2}{4 \frac{\partial I_d}{\partial V_j}} = \frac{1}{2} k\eta T \Delta f \quad (18)$$

Identifying this equation with the ordinary Johnson noise expression, $P_n = kT \Delta f$, it is seen that the equivalent noise temperature of the Schottky diode is

$$T_{sh} = \frac{1}{2} \eta T \quad (19)$$

Note that the noise temperature decreases linearly with decreasing physical temperature. However, the charge transport at room temperature over the Schottky barrier is due to thermionic emission and decreases when the temperature is lowered. Hence for temperatures on the order of 50–100 K and below, temperature-independent tunneling becomes the dominant process for electrons passing the barrier, and the equivalent temperature ηT of Eq. (6) becomes

$$T_{\text{tunnel}} = \frac{qh}{k} \sqrt{\frac{N_d}{4\epsilon m^*}} \quad (20)$$

where N_d is the doping concentration in the epitaxial layer, ϵ the dielectric constant of the semiconductor, and

m^* the effective mass of the electron. In practice, T_{tunnel} is 50 K for $N_d = 3 \times 10^{16}$. This doping concentration is recommended for mixers operated at 15 or 20 K, a typical temperature for commercial cryogenic cooling machines.

3.1.2. 1/f Noise. There is excess noise at low frequencies (of the order 100 kHz and lower for a good diode), which is related to surface phenomena at the metal–semiconductor interface. This noise is normally not important in mixers for millimeter–wave receivers. However, it is an important limiting factor for certain radar and communications systems.

3.1.3. Thermal Noise. The series resistance is essentially an ordinary resistor and consequently causes ordinary thermal (Johnson) noise. The main noise contribution of this type comes from the substrate (corresponding resistance R_{sub}) and is denoted as T_{sub} .

3.1.4. Hot-Electron Noise and Intervalley Scattering Noise. Since the diode area is very small in order to render the capacitance reasonably small, a high current density is required to make $r_j R_s$. This means that electrons may obtain energies larger than the energy related to their thermal movement and *hot-electron noise* is obtained. The increase in energy also means that electrons can be transferred from the main Γ valley in the E - k diagram (for details, see Ref. 3) to the upper L valley, causing fluctuations in the electron velocity and *intervalley scattering noise* is obtained. The hot electron and intervalley scattering noises occur essentially in the undepleted part of the epilayer (resistance R_{epi}) and are denoted as T_{epi} .

3.2. Large-Signal Analysis by Harmonic Balance

When the nonlinear device is pumped by the LO, harmonic currents are created [4–6]. The equivalent circuit of a Schottky diode mixer is shown in Fig. 8. Note that the series resistance is assumed to be linear and will be included in the embedding circuit.

The current $I_e(t)$ contains harmonics of the LO pump frequency, $k\omega_{\text{LO}}$. For a Schottky diode, this current consists of two parts: one that is associated with the nonlinear resistance $i_d(t)$, and one with the parallel nonlinear capacitance $i_c(t)$. We have [using the complex notation; of Eq. (2)]

$$I_e(t) = i_c(t) + i_d(t) = \sum_{k=-\infty}^{k=\infty} I_{ek} e^{jk\omega_{\text{LO}}t} \quad I_{ek} = I_{e-k}^* \quad (21)$$

This current $I_e(t)$ flows through the embedding circuit, creating voltages at harmonic frequencies at $k\omega_{\text{LP}}$:

$$V_j(t) = \sum_{k=-\infty}^{k=\infty} V_k e^{jk\omega_{\text{LO}}t} \quad V_k = V_{-k}^* \quad (22)$$

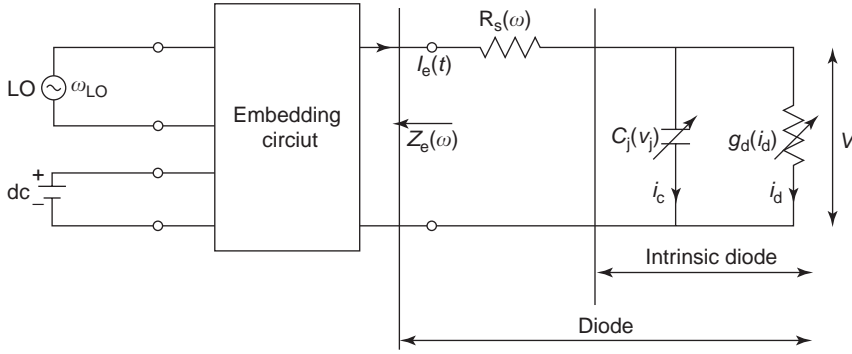


Figure 8. Equivalent circuit of a mixer. For the intrinsic diode, C_j and g_d are nonlinear and are characterized in the time domain, while the diode series resistance R_s and the embedding impedance Z_e are linear and can be described in the frequency domain.

The boundary conditions set by the *embedding circuit* require that

$$V_k = -I_{ek}[Z_{ek}(k\omega_{LO}) + R_s(k\omega_{LO})] \quad (23)$$

$$k = \pm 2, \pm 3, \dots, \pm\infty$$

$$V_{\pm 1} = V_{LO} - I_{e\pm 1}[Z_{e\pm 1}(\pm\omega_{LO}) + R_s(\pm\omega_{LO})] \quad (24)$$

$$V_0 = V_{DC} - I_{e0}[Z_e(0) + R_s(0)] \quad (25)$$

where V_{LO} and V_{DC} are the LO and DC bias voltages, respectively. The frequency dependence of R_s is due to the skin effect. If $V_j(t)$ is known, $i_d(t)$ and $i_c(t)$ (see Fig. 8) can be calculated from Eqs. (15) and (16). We now have a nonlinear problem to solve in order to determine I_{ek} and V_{ek} . Several iteration type methods have been suggested. See Refs. 4 and 5 for more details.

Having determined the components I_k and V_k , we have $V_j(t)$ and $I_e(t)$, and we can determine $i_d(t)$, $i_c(t)$, $g_d(t)$, and $C_j(t)$:

$$g_d(t) = \sum_{k=-\infty}^{k=\infty} G_k e^{jk\omega_{LO}t} \quad G_k = G_{-k}^* \quad (26)$$

$$C_j(t) = \sum_{k=-\infty}^{k=\infty} C_k e^{jk\omega_{LO}t} \quad C_k = C_{-k}^* \quad (27)$$

These equations together with the embedding impedance $Z_e(\omega)$ allow us to determine the small signal properties of the mixer.

3.3. Small-Signal Analyses

The relation between the small-signal current and voltage vectors $\delta\mathbf{I}$ and $\delta\mathbf{V}$ can be expressed in a more general form as

$$\delta\mathbf{I} = \mathbf{Y} \delta\mathbf{V} \quad (28)$$

where

$$Y_{mn} = G_{m-n} + j(\omega_0 + m\omega_{LO})C_{m-n} \quad (29)$$

where for convenience we use ω_0 for ω_{IF} . It is convenient to form an augmented \mathbf{Y} matrix, \mathbf{Y}' , as indicated in Fig. 9. This augmented network contains the whole mixer, including diode and embedding network, but does not contain signal sources associated with these terminations. Since we define the signal sources as current sources, the augmented network in this case is open-circuited. For the augmented network

$$\delta\mathbf{I}' = \mathbf{Y}' \delta\mathbf{V} \quad (30)$$

and

$$\mathbf{Y}' = \mathbf{Y} + \text{diag} \left[\frac{1}{Z_{em} + R_{sm}} \right] \quad (31)$$

Inverting Eq. (23) yields

$$\delta\mathbf{V} = \mathbf{Z}' \delta\mathbf{I}' \quad (32)$$

where

$$\mathbf{Z}' = \frac{1}{\mathbf{Y}'} \equiv \begin{bmatrix} \vdots & \vdots & \vdots & \vdots \\ \dots & Z'_{11} & Z'_{10} & Z'_{1-1} & \dots \\ \dots & Z'_{01} & Z'_{00} & Z'_{0-1} & \dots \\ \dots & Z'_{-11} & Z'_{-10} & Z'_{-1-1} & \dots \\ \vdots & \vdots & \vdots & \vdots & \vdots \end{bmatrix} \quad (33)$$

3.4. Mixer Port Impedances

The port impedance Z_{mm} , defined in Fig. 9, can be determined if the corresponding embedding impedance is open-circuited, that is

$$Z_m = Z'_{mm, \infty} \quad (34)$$

where the subscript ∞ means that Z'_{mm} is evaluated for $Z_{em} = \infty$. The IF output impedance becomes

$$Z_{\text{out}} = Z_0 + R_{s0} = Z'_{00, \infty} + R_{s0} \quad (35)$$

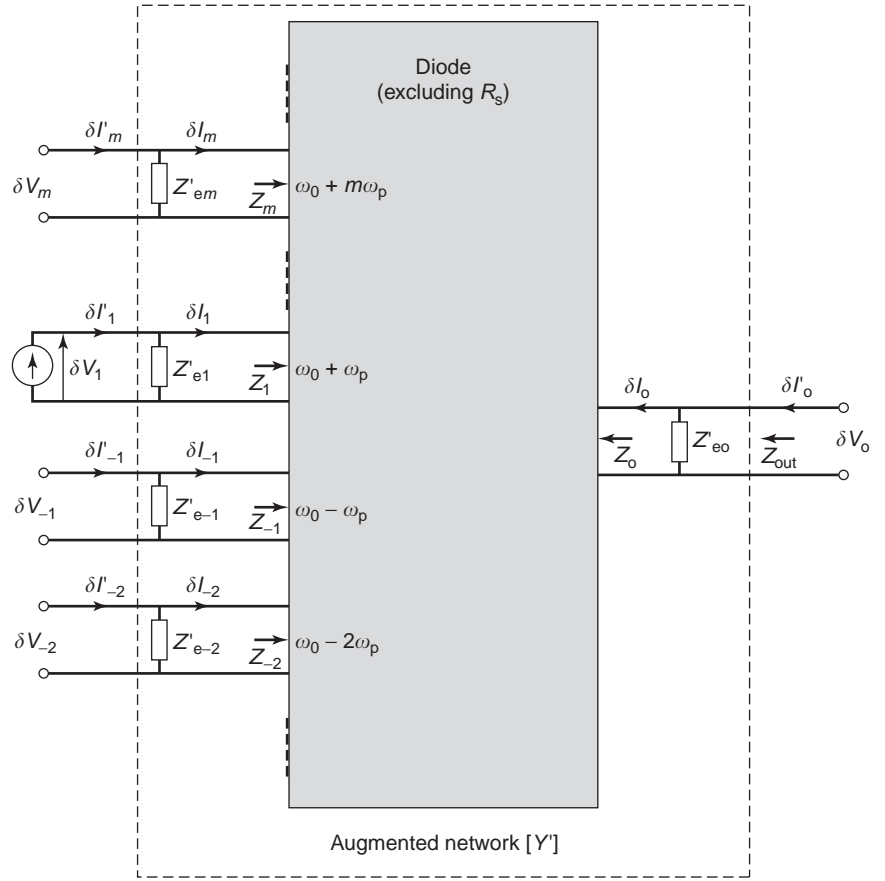


Figure 9. The *small-signal* representation of the mixer as a multifrequency linear multi-port network. Note that R_s is included in $Z' = Z_{ek} + R_s$. In a more exact model, R_s is frequency- and bias-dependent. In this text we use R_{s1} for the series resistance at the input frequency (fundamental mixer) and R_{s0} for the series resistance at the IF. Index 0 indicates parameters at the IF; ω_0 is the IF.

3.5. Conversion Loss

The conversion loss of a mixer is defined as [cf. Eq. (8)]

$$L = \frac{\text{power available from source } Z_{e1}}{\text{power delivered to load } Z_{e0}} \quad (36)$$

yielding the conversion loss

$$L = \frac{1}{4|Z'_{01}|^2} \frac{|Z_{e0} + R_{s0}|^2}{\text{Re}[Z_{e0}]} \frac{|Z_{e1} + R_{s1}|^2}{\text{Re}[Z_{e1}]} \quad (37)$$

where Z_{ek} is defined in Fig. 9 (see figure caption) and Z'_{01} is the 01 diagonal element of Eq. (33). A more general expression for the conversion loss from any sideband j to any other sideband i is

$$L_{ij} = \frac{1}{4|Z'_{ij}|^2} \frac{|Z_{ei} + R_{si}|^2}{\text{Re}[Z_{ei}]} \frac{|Z_{ej} + R_{sj}|^2}{\text{Re}[Z_{ej}]} \quad (38)$$

3.6. Equivalent-Noise Temperature of the Mixer

The equivalent input noise temperature of the mixer T_M is defined as the temperature that the real part of the Z_{e1}

(lower sideband) must have in order to generate the same noise voltage as the diode itself generates during mixer operation. It is

$$T_M = \frac{\langle \delta V_{N0}^2 \rangle}{4k\Delta f} \frac{|Z_{e1} + R_{s1}|^2}{|Z'_{01}|^2 \text{Re}[Z_{e1}]} \quad (39)$$

where $\langle \delta V_{N0}^2 \rangle$ is

$$\langle \delta V_{N0}^2 \rangle = Z'_0 \langle \delta \mathbf{I}'_s \delta \mathbf{I}'_s \dagger \rangle Z_0 \dagger + Z'_0 \langle \delta \mathbf{I}'_T \delta \mathbf{I}'_T \dagger \rangle Z_0 \dagger \quad (40)$$

where

$$\begin{aligned} \langle \delta \mathbf{I}'_{Tm} \delta \mathbf{I}'_{Tm} \dagger \rangle &= \frac{4kT_{eq} R_{sm} \Delta f}{|Z_{em} + R_{sm}|^2} \quad m \neq 0 \\ &= \frac{4kT_{eq} R_{sm} \Delta f}{|Z_0|^2} \quad m = 0 \end{aligned} \quad (41)$$

and

$$\langle \delta \mathbf{I}'_{sm} \delta \mathbf{I}'_{sn} \dagger \rangle = 2eI_{m-n} \Delta f \quad (42)$$

I_{m-n} is the current component at the harmonic $(m-n)$ and Z_0 is the zero row of the matrix Z' , Eq. (33). Z_{e1} is defined in Fig. 9.

The noise temperature as defined in Eq. (42) is the *single-sideband noise temperature* for the lower sideband.

Knowing the diode parameters, we can analyze the Schottky mixer with a high degree of accuracy using commercial software.

4. DIODE MIXER TOPOLOGIES AND MIXER DESIGN

One may consider a number of different approaches in designing mixers. Symmetry properties are one way of defining basic types of mixers:

1. The single-ended mixer with one diode and a common input port for the signal and the LO
2. The single-balanced mixer with two diodes and separate ports for signal and LO
3. The double-balanced mixer with four diodes and separate ports for signal and LO
4. The double-double-balanced mixer with eight diodes and separate ports for signal and LO

For millimeter- and submillimeter-wave applications, types 1 and 2 have been implemented experimentally and are described in the literature, while all four types are common in microwave frequency applications.

The performance of either mixer type depends on the *impedances* seen at the signal, at the IF, and at the harmonic sidebands. The LO should experience a reasonably good match in order to reduce the LO power requirement. In practice, the impedances at the harmonics of the LO and at the harmonic sidebands are very difficult to control. The exception is the impedance at the image frequency, which can often be controlled. The importance is illustrated by referring to properties of a typical broadband mixer (when $L_s = L_i$) used in a single-sideband application. In such a mixer a considerable amount of the signal power ($\approx 25\%$) may end up at the image frequency.

It is also obvious that the *noise* entering the mixer at the image port will be converted with the same efficiency as the signal at the signal port, adding to the system noise.

4.1. Single-Ended Mixer

A single-ended mixer has one input port, used for both the signal and the LO. Hence it is necessary to incorporate a circuit in front of the mixer itself for injecting the LO. This circuit should not significantly attenuate the signal. For example, using a 10-dB directional coupler will attenuate the signal $\sim 10\%$ and add noise (see Fig. 10). A common way of introducing the LO in microwave- and millimeter-wave mixers is to use a narrow band diplexer, for example, a filter structure in the input waveguide or a quasioptical interferometer in the signal path in front of the mixer (e.g., see Ref. 10).

4.2. Single-Balanced Mixers

In single-balanced mixers, the signal and the LO enter the mixer through different ports, isolated from each other. Either 90° or 180° hybrids or baluns are used (Fig. 11a)

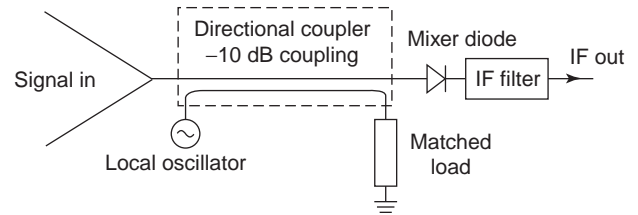


Figure 10. Example for a single-ended mixer configuration. Note that the directional coupler used for injecting the LO couples only 10% of the LO power to the mixer diode, and that the coupler consequently attenuates the signal by a factor of 0.9.

(see Ref. 1 for details). Figure 11b shows a low-frequency equivalent circuit of a single-balanced mixer. The paths of the signal current i_s and the LO current i_{LO} indicate that they add in one diode and subtract in the other. This causes an imbalance in A, which will slowly cycle at a frequency equal to the IF. Hence the IF power can be subtracted between A and ground. Note that if the LO is noisy, this will not cause any output noise at the IF port.

The use of two diodes rather than one means that the mixer can handle twice as much power for the same intermodulation as for the single-ended mixer. In summary, for the single-balanced mixer:

- The signal, LO, and IF ports are isolated from each other.
- The LO noise cancels at the IF port.
- The power handling is superior to the single ended mixer.

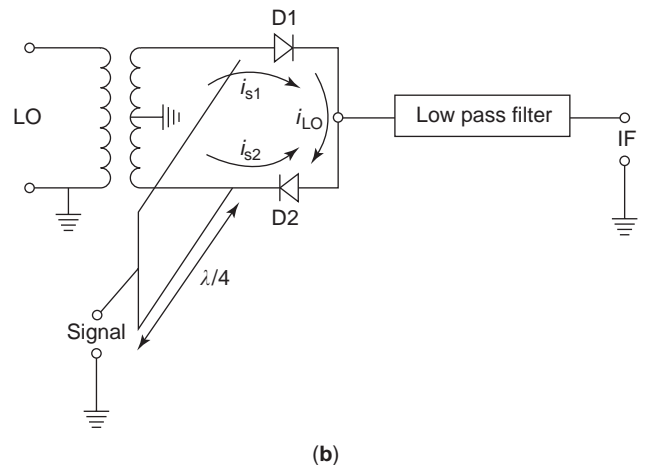
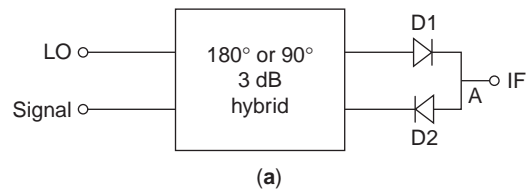


Figure 11. Basic design of the single-balanced mixer (a) and equivalent circuit of the 180° hybrid mixer, (b).

4.3. Double-Balanced Mixers

Essentially, a double-balanced mixer is constructed from two single-balanced mixers, coupled in parallel and 180° out of phase. The diodes can be arranged in either a star or ring configuration (see Fig. 12). The ring can be arranged very compactly as a monolithic circuit.

If the diodes are perfectly identical, the symmetry ensures perfect isolation between the signal and the LO ports. The topology also yields cancellation at the IF port of the even harmonics of both the signal and the LO frequencies. This also means that intermodulation is reduced as compared to the mixers mentioned above. Hence the advantages of the double-balanced mixer are:

- Excellent isolation between the signal, LO, and IF ports
- LO noise cancellation at the IF port
- Superior power handling compared to the double balanced mixer
- Superior intermodulation properties compared to the double balanced mixer

4.4. Double-Double-Balanced Mixers

Double-double-balanced mixers are constructed using two double-balanced mixers. Eight diodes are used, leading to further power-handling capacity and still better intermodulation properties.

4.5. Image Rejection and Image Enhancement

The system properties of a single-sideband mixer receiver can be improved by introducing a proper circuit at the image frequency. It is of particular importance to reactively terminate the image frequency so that no signal power is lost at the image frequency and no noise (or any other unwanted signal) at the image frequency can be converted to the IF frequency. Furthermore, if the reactance at the image frequency is chosen properly, the “signal will be reflected back into the mixer,” such that the conversion is *enhanced* and/or the noise properties are improved. A stopband filter can be added in the input transmission line to prevent one sideband from reaching the diode. The distance to the diode is chosen to optimize the mixer conversion loss. The conversion loss becomes

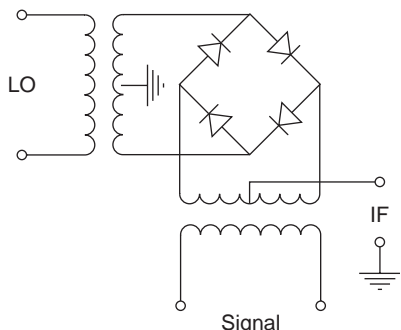


Figure 12. A double-balanced mixer configuration: the ring mixer.

several decibels lower than the typical 5 dB for a common broadband microwave mixer.

A most elegant method to realize a single sideband mixer is shown in Fig. 13. By using two balanced mixers and two 90° hybrids, it is possible to arrange that the upper sideband and the lower sideband exit the mixer at different ports (see Ref. 1 or 4 for details).

5. HARMONIC MIXERS

In a harmonic mixer a harmonic of the LO frequency, $n\omega_{LO}$, is used for mixing; that is, the IF is obtained as

$$\omega_{IF} = |n\omega_{LO} - \omega_s| \tag{43}$$

Harmonic mixers are practical when it is difficult to realize LO power at a frequency near the signal frequency. They are particularly useful at millimeter and submillimeter waves.

Large harmonic numbers n are often used when maximum sensitivity is not required. For example, in spectrum analyzers large harmonic numbers may be used.

5.1. Two-Diode Subharmonically Pumped Mixers

If two diodes are used in an antiparallel configuration (see Fig. 14), the small-signal conductance will vary with twice the LO frequency. Hence the mixer will convert signals located near $2f_{LO}$, and no conversion will occur near f_{LO} . The advantage of the two-diode over the single-diode subharmonically pumped mixers is that no conversion can occur at the fundamental frequency. Moreover, the LO noise will contribute less, since the frequency difference between the signal and the LO is of the order f_{LO} . Another advantage is inherent self-protection against large peak reverse voltage burnout.

6. PARAMETRIC FREQUENCY CONVERSION

In a parametric frequency converter, a nonlinear reactance, such as a backward-biased Schottky diode, is used. Common parametric components are frequency downconverters, frequency upconverters, and frequency

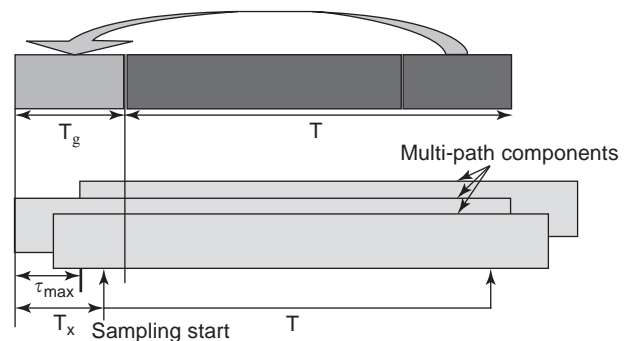


Figure 13. A single-sideband mixer using two balanced mixers and two 90° hybrids. Note that at one output port the upper sideband appears, while at the other output port the lower sideband appears.

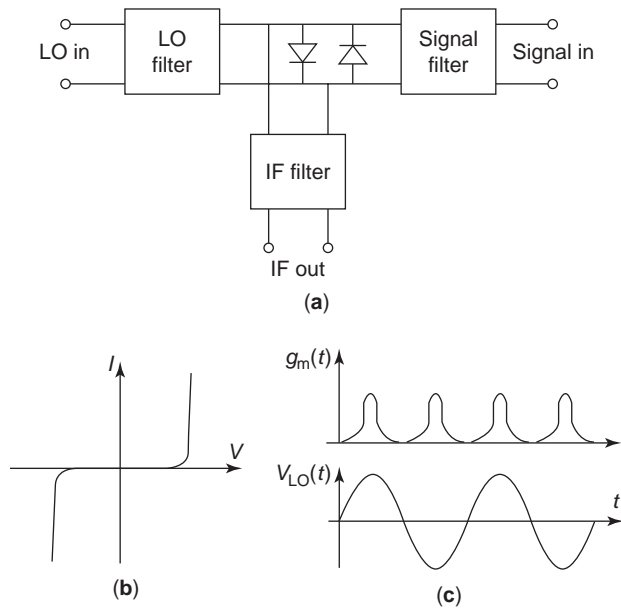


Figure 14. Subharmonically pumped mixer using antiparallel diodes, showing (a) the mixer circuit, (b) the DC I - V characteristic, and (c) the resulting waveforms for the LO voltage and the time-dependent small signal conductance.

multipliers. In a frequency downconverter, a strong pump signal f_{LO} and signal f_s (strong or weak depending on application) are applied to the device. The output frequency is

$$f_{out} = |f_{LO} - f_s| \text{ frequency downconversion} \quad (44)$$

For a frequency upconversion, we have

$$f_{out} = |f_{LO} + f_s| \text{ frequency upconversion} \quad (45)$$

The signal frequency in this case may be much lower than the LO (or pump) frequency; that is, the output frequency is not far from the LO frequency.

Note that if the device has no resistive parasitics, no power is lost in the device itself, and 100% efficiency is theoretically possible. However, power may go to harmonics or harmonic sidebands and there are always some parasitic resistances present, for example, the series resistance in a Schottky diode.

If we select a large ratio f_{LO}/f_s , the frequency upconverter may have high gain. This is possible since, by appropriate choice of the circuit parameters, parametric amplification is achieved [7]. In the case of gain, one has negative resistance in the circuit and one may face stability problems. However, it is very difficult to make a broadband parametric upconverter, since proper impedances have to be realized at f_s , f_{LO} , and f_{out} . Parametric converters are used much less today than a few decades ago. The reason is that the quality of mixer diodes and FETs has improved significantly and it is much easier to make diode (or FET) mixers very broadband. This is the reason why resistive mixers are preferred in most applications. Note that FET mixers can be designed for a conversion gain greater than one.

A classical reference concerning varactor circuits is the book by Penfield and Rafuse [7]. A parametric downconverter, like the Schottky mixer, can be analyzed using commercial software.

7. NEGATIVE-RESISTANCE DIODE MIXERS

In the current-voltage (I - V) characteristic of, say, the Esaki tunnel diode or the resonant tunneling diode, there is a region that has a differential negative resistance. This means that the mixer can have conversion gain. Tunnel diode mixers have been built and tested. However, a large junction capacitance made the frequency range quite limited, which, together with poor power handling, stability problems, and less favorable noise properties, means that these mixers have very little practical use today.

8. SELF-OSCILLATING MIXERS

The negative resistance devices can as well promote an oscillation. Hence it is possible to design circuits where the LO is delivered by the same device that is performing the mixing. Besides the devices mentioned already, Gunn diodes have also been used in self-oscillating mixers. The sensitivity of such mixers is limited. The advantage may be in applications where the best performance is less important and the lowest price is required, as, for instance, in low-priced Doppler radar applications.

9. BOLOMETER MIXERS

Bolometer mixers have been constructed since the 1950s. Since the electromagnetic absorption in bolometer devices can be essentially frequency-independent, it should be possible to do mixing to several terahertz. In this type of mixer, one is using the fact that when two signals at slightly different frequencies are superimposed the resulting signal can be described as a signal that is amplitude-modulated with the difference frequency. The first useful bolometer mixer was based on InSb devices cooled to temperatures of a few kelvins. When the device absorbs the modulated signal, the electron temperature becomes modulated, leading to a modulation in the device resistance. The theory is described in more detail in Section 10.2 and by Arams et al. [8].

However, the thermal time constant for the InSb device is long, allowing a maximum IF of only about 2 MHz. A more recent bolometer mixer is based on a two-dimensional electron gas in HEMT materials allowing an IF to about 1 GHz [9]. However, the most successful hot-electron bolometer mixer so far is the superconducting hot-electron bolometer mixer.

10. MIXERS BASED ON SUPERCONDUCTING DEVICES

Room-temperature mixers for frequencies from about 100 GHz to a few terahertz THz frequencies use only Schottky diodes. However, if sensitivity is an issue (e.g., as in radioastronomy), there is a better alternative in

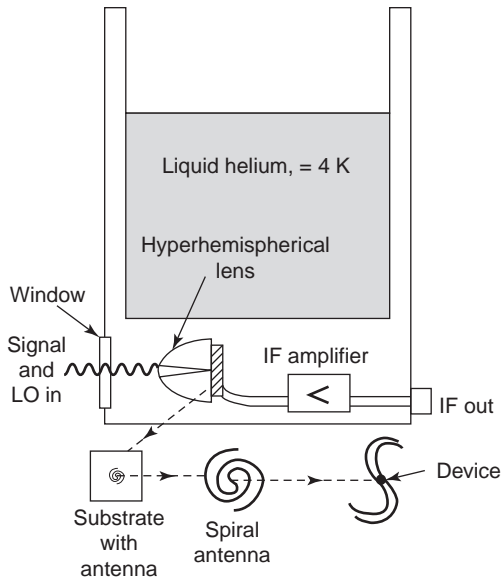


Figure 15. Schematic description of typical Dewar setup for a sub-millimeter-wave SIS or HEB mixer. The LO and the signal are entering together through the Dewar window. The radiation is focused on the antenna using a hyperhemispherical lens, downconverted to the IF in the nonlinear device, and finally amplified by the IF amplifier. In this figure the antenna is illustrated as a spiral antenna. There are many other possible planar antenna structures available (see Ref. 9 for details).

mixers based on superconducting devices cooled to a few kelvins. Low-noise superconductor–insulator–superconductor (SIS) mixers have excellent performance up to about 1 THz [10]. Superconductor hot-electron bolometer (HEB) mixers are the best alternative for frequencies above 1 THz.

Figure 15 shows a schematic of a receiver (except for the input quasi-optics) based on superconducting devices.

10.1. The SIS Mixer

The SIS mixer is also called the “quasiparticle mixer.” Because of the extremely strong nonlinearity in the I - V characteristic of the SIS device, quantum effects are important. Indeed, for certain choices of embedding impedance network, this can result in a conversion gain (see Ref. 11 for details).

In a superconductor and at a temperature below the superconducting transition temperature, electrons form

pairs, called *Cooper pairs*. When they do so, the energy of the electrons near the Fermi energy is lowered by a certain amount Δ . Hence, to break up a Cooper pair, an energy of 2Δ is required. This can be described in terms of a bandgap with the energy 2Δ , as shown in Fig. 16.

In the SIS mixer, a tunneling phenomenon is used. In the device, two superconducting films are separated by a thin (~ 20 -Å) layer of insulator. Under bias, Cooper pairs on one side of the insulator break up into two electrons (quasiparticles) that individually tunnel through the insulator and recombine on the other side of the insulator. This is illustrated in Fig. 16. It is interesting to note that the density of states near the band edges becomes “infinite.” This is one important reason why there is such a sharp increase in the current when the device is biased to a voltage $V = 2\Delta/e$ (e is the charge of the electron). The I - V characteristic is shown in Fig. 17. Note that the voltage scale is in millivolts, and that 1 meV corresponds to 240 GHz. The steps in the I - V curve correspond to DC bias voltages, where exactly $eV = 2\Delta - hf$ ($V \approx 1.35$ mV). Since the I - V characteristic is strongly nonlinear within a fraction of a millivolt, the mixer is operating in the quantum regime. See also Fig. 18, where the I - V character of an SIS device is compared with a Schottky diode. The Schottky diode obviously is not very nonlinear within a voltage interval of 1 mV and is therefore operating fully as a classical mixer for frequencies up to several terahertz. It should also be mentioned that the required LO power is very low, on the order nanowatts. This is of great importance for sub-millimeter-wave mixers, where substantial LO power is difficult to obtain.

The best SIS devices are realized in so-called Nb trilayer technology [11]. The device structure is Nb/Al₂O₃/Nb, where the ~ 20 -Å-thick Al₂O₃ serves as the insulator in the SIS device. For frequencies above ~ 700 GHz, one is trying to develop devices based on NbN, which has a higher bandgap (≈ 1.2 THz) than does Nb. So far these attempts have not been very successful.

The basic noise in the SIS mixer is shot noise. Comparing the I - V characteristics of the SIS device and Schottky diode and using the classical theory described in Section 3, one can see that the mixer noise and the conversion loss are essentially lower for the SIS mixer. However, the theory must include quantum effects (see Ref. 11 for more details). This leads to a conversion gain that is possibly larger than one, a fact that has been demonstrated in practice.

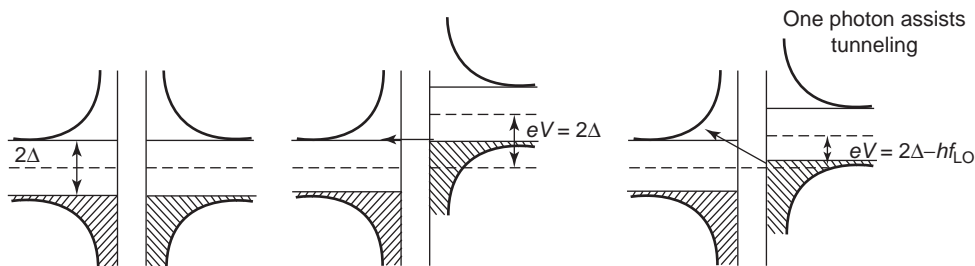


Figure 16. The SIS device under bias: (a) no bias; (b) for a voltage bias $V > 2\Delta/e$ electrons will tunnel from right to the left; (c) tunneling is assisted by a photon with energy hf_{LO} for the bias voltage $V = (\Delta - hf_{LO})/e$.

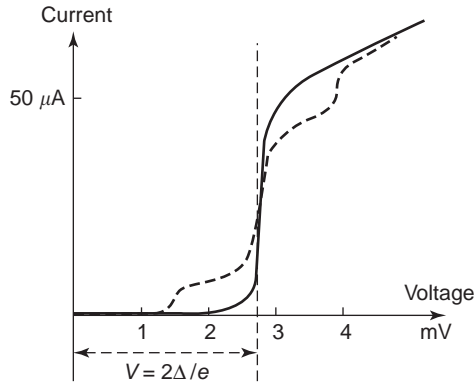


Figure 17. Typical I - V characteristic of a SIS element. The thin line indicates the shape of the pumped I - V characteristic, where $f_{LO} \hbar \approx 1.4$ meV ($f_{LO} = 325$ GHz), while the thick line is for the unpumped device.

10.2. Hot-Electron Bolometer Mixer

A bolometer consists of an absorber that is heated by radiation and a temperature-dependent resistance as a “thermometer.” The bolometer has a thermal time constant τ_0 limiting the maximum detectable modulation frequency of the absorbed power. This means that the maximum feasible IF is $f_{IF} = 1/(2\pi\tau_0)$. When the LO and signal are added together, the instantaneous power variation is described by $[V_{LO} \cos(\omega_{LO}t) + v_s \cos(\omega_s t)]^2 (1/R_{RF})$ (see Fig. 3). If the bolometer can respond to ω_{IF} but not to $(\omega_{LO} + \omega_s)$, $2\omega_{LO}$, and $2\omega_s$, the bolometer temperature and the resistance will be approximately proportional to $P_{LO} + P_s + 2\sqrt{P_{LO}P_s} \cos(\omega_{IF}t)$. Note that the “slow” response of the bolometer device means that there are no harmonics of the LO created and no signal power is transformed to the image frequency, as is the case for both the SIS and Schottky mixers.

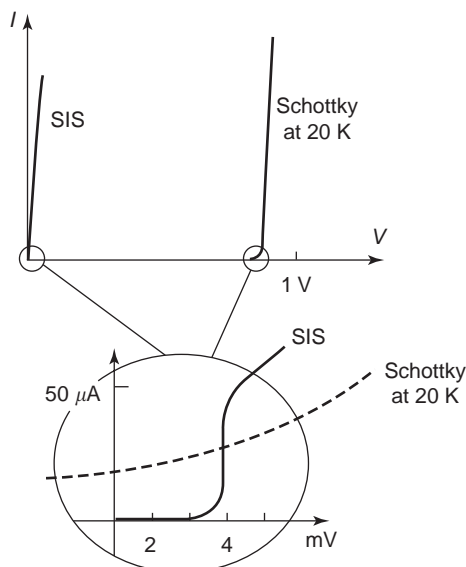


Figure 18. Comparing the I - V characteristic of a SIS element with that of a Schottky diode. Note the enormous difference in nonlinearity.

A superconducting hot-electron bolometer (HEB) consists of one or several superconducting thin-film strips in parallel, deposited on a substrate, for example, silicon, single-crystalline quartz, or sapphire. The strips are cooled to the superconducting state and then heated by DC and microwave power to temperatures near the superconducting to normal transition temperature, where the superconductor will gradually become normal (Fig. 19).

The maximum IF is determined by the electron temperature relaxation time τ_0 , that is, $f_{IF} < 1/(2\pi\tau_0)$, and a major issue is to find ways of making the time constant τ_0 short enough. Figure 20 indicates how cooling occurs in the so-called phonon-cooled and the diffusion-cooled bolometer, respectively [10,12].

When operating the mixer, the device is absorbing LO power (P_{LO}) and signal power (P_s) as well as power from the DC bias supply ($P_{DC} = V_0 I_0$). When the power increases, obviously the electron temperature increases and the resistance of the device increases as $\Delta R = (dR_0/dP)\Delta P = C_0 \Delta P$. Figure 21 shows a simple equivalent circuit of the mixer, where the device is biased by a constant DC current. Consequently, the modulation at the IF of the resistance will cause an IF voltage to appear across the device, causing an IF current through the IF load resistance R_L . The IF current ΔI is superimposed on the DC bias current through the mixer device $R_0(P)$ and will cause a “modulation” of the DC power $\Delta P_{DC} \cos(\omega_{IF}t)$. The total power dissipated in the device is then

$$\begin{aligned}
 P(t) &= P_0 + \Delta P(t) \\
 &= P_{DC} + \Delta P_{DC} \cos(\omega_{IF}t) + P_{LO} \\
 &\quad + P_s + 2\sqrt{P_{LO}P_s} \cos(\omega_{IF}t)
 \end{aligned}
 \tag{46}$$

Assuming that DC and RF power affect the resistance by the same amount, the IF modulation of the device resistance becomes $C_0 \Delta P(t)$. There is a resulting bias point of the device $V = V_0$ and $I = I_0$. Defining the device DC resistance R_0 as the time average of $R_0(P)$, that is, $R_0 =$

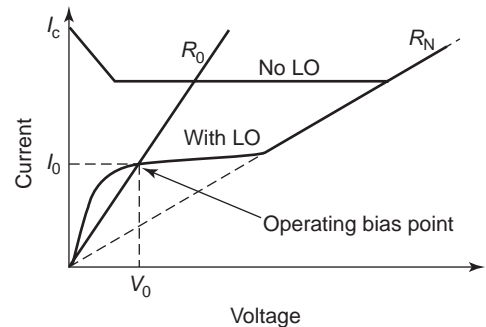


Figure 19. Current-voltage (I - V) characteristic of a HEB with and without a LO. At the operating point, $V_0/I_0 = R_0$. For large bias voltage the whole strip is normally conducting ($R = R_N$). I_c is the critical current, the maximum current in the completely superconducting state.

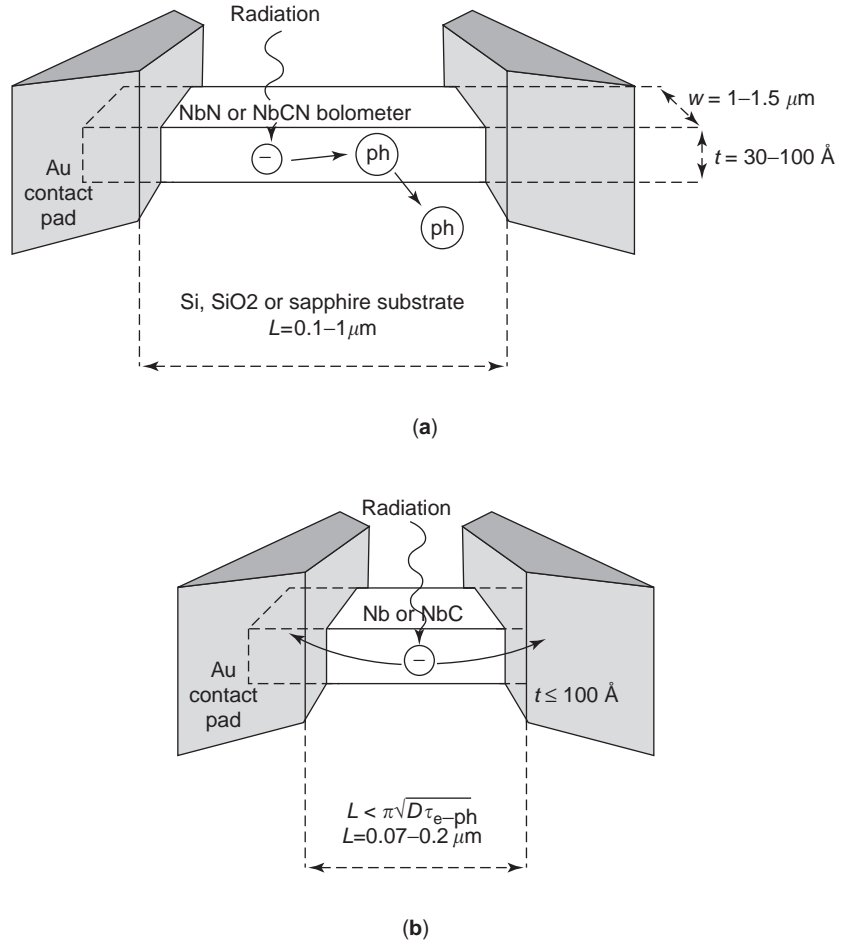


Figure 20. Two types of bolometer devices: (a) phonon-cooled; (b) diffusion-cooled.

V_0/I_0 , one obtains (8) the conversion gain

$$G = \frac{P_{IF}}{P_s} = 2C_0^2 \frac{P_{LO}P_{DC}}{(R_L + R_0)^2} \cdot \frac{R_L}{R_0} \left(1 - C_0 \frac{P_{DC}}{R_0} \cdot \frac{R_L - R_0}{R_L + R_0} \right)^{-2} \quad (47)$$

where $C_0 = dR_0/dP$; R_L is the IF load resistance and P_{IF} , P_s , P_{LO} , and P_{DC} are the IF, signal, LO, and DC power, respectively, dissipated in the device.

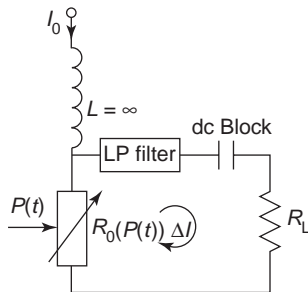


Figure 21. Equivalent circuit of bolometer with load.

The commonly assumed fundamental limit of -6 dB gain for hot-electron mixers is not valid if a negative differential resistance of the unpumped $I-V$ curve is available (see Ref. 13 for details). The load resistance for maximum gain is equal to the differential resistance of the $I-V$ curve at the bias point of the pumped mixer.

10.3. Experimental Results

In experiments on phonon-cooled NbN HEB mixers, noise temperatures of about 400 K (DSB) have been obtained at 600 GHz, and 1000 K (DSB) at 900 GHz. At 2.5 THz a noise temperature of about 1400 K has been obtained. The conversion loss is typically 10 dB, including losses from the optics in front of the mixer.

The noise of these mixers is caused by thermal fluctuations in the bolometer device (causing resistance fluctuations) and by Nyquist noise. For diffusion-cooled mixers a noise temperature of 650 K DSB at 533 GHz was measured by Skalare et al. [14]. These experiments indicate that an IF bandwidth of at least 3 GHz is achievable. Later experiments show that it should be possible to obtain at least 50% higher IF bandwidths in practical mixers. A crucial number is the maximum IF bandwidth. For a phonon-cooled HEB mixer, a 3.7 GHz IF bandwidth

(−3 dB reduction in conversion gain) has been measured and diffusion-cooled between 2 and 6 GHz. While this bandwidth is defined for a *conversion loss* increase of 3 dB, the bandwidth defined for when the *noise temperature* has increased by 3 dB is about 1.5 times larger (~5.5 GHz for the phonon-cooled one).

The LO power needed is less than 100 nW, which is much lower than that needed for Schottky diode mixers.

BIBLIOGRAPHY

1. S. A. Maas, *The RF and Microwave Circuit Design Cookbook*, Artech House, Norwood, MA, 1998.
2. E. L. Kollberg, Mixers and detectors, in K. Chang, ed., *Handbook of Microwave and Optical Components*, Wiley, New York, 1990.
3. K. S. Yngvesson, *Microwave Semiconductor Devices*, Kluwer, Norwell, MA, 1991.
4. S. A. Maas, *Microwave Mixers*, 2nd ed., Artech House, Norwood, MA, 1993.
5. S. A. Maas, *Nonlinear Microwave Circuits*, IEEE Press, Piscataway, NJ, 1997.
6. D. N. Held, Conversion loss and noise of microwave and millimeter-wave mixers, Part 1—Theory, and Part 2—Experiment, *IEEE Trans. Microwave Theory Tech.* **26**:49–61 (1978).
7. P. Penfield and R. P. Rafuse, *Varactor Applications*, MIT Press, Cambridge, MA, 1962.
8. F. Arams et al., Millimeter mixing and detection in bulk InSb, *Proc. IEEE* **54**:308–318 (1966).
9. J.-X. Yang et al., Wide-bandwidth electron bolometric mixers: A 2DEG prototype and potential for low-noise THz receivers, *IEEE Trans. Microwave Theory Tech.* **41**:581–589 (1993).
10. R. Blundell and C. E. Tong, Submillimeter receivers for radio astronomy, *Proc. IEEE* **80**:1702–1720 (1992).
11. M. J. Wengler, Submillimeter-wave detection with superconducting tunnel diodes, *Proc. IEEE* **80**:1810–1826 (1992).
12. J. E. Carlstrom and J. Zmuidzinas, Millimeter and submillimeter techniques, in W. R. Stone, ed., *Reviews of Radio Science 1993–1995*, Oxford Univ. Press, London, 1996.
13. H. Ekström et al., Conversion gain and noise of niobium superconducting hot-electron-mixers, *IEEE Trans. Microwave Theory Tech.* **43**:938–947 (1995).
14. A. Skalare et al., A heterodyne receiver at 533 GHz using a diffusion cooled superconducting hot electron mixer, *IEEE Trans. Appl. Superconduct.* **5**:2236–2240 (1995).

FREQUENCY-DIVISION MULTIPLEXERS

RICHARD V. SNYDER
RS Microwave
Butler, New Jersey

1. INTRODUCTION

Frequency multiplexers are networks used to distribute an input spectrum, either through separation into spectral subcomponents or by combination of subcomponents. In the first case, a given input spectrum is separated by fre-

quency-sensitive elements into discrete (but possibly contiguous) segments. In the second case, a multiplicity of discrete (but possibly contiguous) input segments are similarly combined into a composite output spectrum. In most situations, it is required to maintain desirable passband characteristics, such as match to source and load impedances, amplitude flatness, low ripple, and minimum group delay distortion, for all ports of the multiplexer. Certainly the separate spectral portions have to be isolated by maintaining specified stopband slopes for each portion. Because of interactions between the separate portions, these requirements are very difficult to realize. However, there are many techniques that have been developed for frequency multiplexing. Coordination of direct synthesis and mathematical optimization provides the tools necessary to solve the problem.

2. STATEMENT OF THE PROBLEM

It is required to separate a contiguous spectrum into specified portions. In most cases, it is necessary to avoid reflections from the ports associated with the specified portions in order to preserve the total energy contained in the initial contiguous spectrum. The associated problem is combination of specified spectral segments into a contiguous output spectrum, again with the low port reflection criterion pertaining to the combining scheme. These closely related problems are shown in a two-port configuration in Fig. 1. Note that simply minimizing port reflections is normally inadequate, because the intention of the multiplexing schemes is availability of total spectral energy at the respective ports, rather than internal dissipation as an alternative to external reflection. However, examples of important exceptions to this condition will be presented in later sections.

Consideration of Fig. 1 reveals a deceptively simple configuration for the three-port multiplexer, known as a “diplexer.” It consists of two selective filters and an interconnection network. The idealized response is shown in Fig. 2. It is required to determine the criteria for the selective filters and the interconnection network. The filters can employ almost any of the available design approaches, including lumped element, crystal, dielectric resonators, evanescent mode, waveguide, cavity, and SAW. The interconnection network must be physically compatible with the chosen filter approach, but can also consist of a very wide variety of transmission lines, lumped

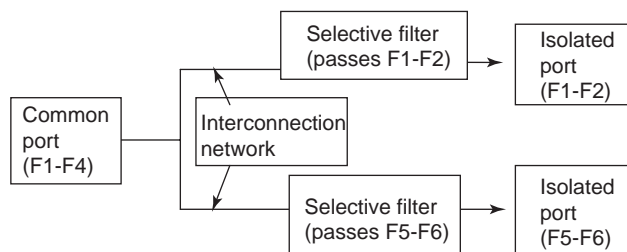


Figure 1. Three-port multiplexer (a “diplexer”). The common port can be an input or an output, while the isolated ports are, respectively, outputs or inputs.

(−3 dB reduction in conversion gain) has been measured and diffusion-cooled between 2 and 6 GHz. While this bandwidth is defined for a *conversion loss* increase of 3 dB, the bandwidth defined for when the *noise temperature* has increased by 3 dB is about 1.5 times larger (~5.5 GHz for the phonon-cooled one).

The LO power needed is less than 100 nW, which is much lower than that needed for Schottky diode mixers.

BIBLIOGRAPHY

1. S. A. Maas, *The RF and Microwave Circuit Design Cookbook*, Artech House, Norwood, MA, 1998.
2. E. L. Kollberg, Mixers and detectors, in K. Chang, ed., *Handbook of Microwave and Optical Components*, Wiley, New York, 1990.
3. K. S. Yngvesson, *Microwave Semiconductor Devices*, Kluwer, Norwell, MA, 1991.
4. S. A. Maas, *Microwave Mixers*, 2nd ed., Artech House, Norwood, MA, 1993.
5. S. A. Maas, *Nonlinear Microwave Circuits*, IEEE Press, Piscataway, NJ, 1997.
6. D. N. Held, Conversion loss and noise of microwave and millimeter-wave mixers, Part 1—Theory, and Part 2—Experiment, *IEEE Trans. Microwave Theory Tech.* **26**:49–61 (1978).
7. P. Penfield and R. P. Rafuse, *Varactor Applications*, MIT Press, Cambridge, MA, 1962.
8. F. Arams et al., Millimeter mixing and detection in bulk InSb, *Proc. IEEE* **54**:308–318 (1966).
9. J.-X. Yang et al., Wide-bandwidth electron bolometric mixers: A 2DEG prototype and potential for low-noise THz receivers, *IEEE Trans. Microwave Theory Tech.* **41**:581–589 (1993).
10. R. Blundell and C. E. Tong, Submillimeter receivers for radio astronomy, *Proc. IEEE* **80**:1702–1720 (1992).
11. M. J. Wengler, Submillimeter-wave detection with superconducting tunnel diodes, *Proc. IEEE* **80**:1810–1826 (1992).
12. J. E. Carlstrom and J. Zmuidzinas, Millimeter and submillimeter techniques, in W. R. Stone, ed., *Reviews of Radio Science 1993–1995*, Oxford Univ. Press, London, 1996.
13. H. Ekström et al., Conversion gain and noise of niobium superconducting hot-electron-mixers, *IEEE Trans. Microwave Theory Tech.* **43**:938–947 (1995).
14. A. Skalare et al., A heterodyne receiver at 533 GHz using a diffusion cooled superconducting hot electron mixer, *IEEE Trans. Appl. Superconduct.* **5**:2236–2240 (1995).

FREQUENCY-DIVISION MULTIPLEXERS

RICHARD V. SNYDER
RS Microwave
Butler, New Jersey

1. INTRODUCTION

Frequency multiplexers are networks used to distribute an input spectrum, either through separation into spectral subcomponents or by combination of subcomponents. In the first case, a given input spectrum is separated by fre-

quency-sensitive elements into discrete (but possibly contiguous) segments. In the second case, a multiplicity of discrete (but possibly contiguous) input segments are similarly combined into a composite output spectrum. In most situations, it is required to maintain desirable passband characteristics, such as match to source and load impedances, amplitude flatness, low ripple, and minimum group delay distortion, for all ports of the multiplexer. Certainly the separate spectral portions have to be isolated by maintaining specified stopband slopes for each portion. Because of interactions between the separate portions, these requirements are very difficult to realize. However, there are many techniques that have been developed for frequency multiplexing. Coordination of direct synthesis and mathematical optimization provides the tools necessary to solve the problem.

2. STATEMENT OF THE PROBLEM

It is required to separate a contiguous spectrum into specified portions. In most cases, it is necessary to avoid reflections from the ports associated with the specified portions in order to preserve the total energy contained in the initial contiguous spectrum. The associated problem is combination of specified spectral segments into a contiguous output spectrum, again with the low port reflection criterion pertaining to the combining scheme. These closely related problems are shown in a two-port configuration in Fig. 1. Note that simply minimizing port reflections is normally inadequate, because the intention of the multiplexing schemes is availability of total spectral energy at the respective ports, rather than internal dissipation as an alternative to external reflection. However, examples of important exceptions to this condition will be presented in later sections.

Consideration of Fig. 1 reveals a deceptively simple configuration for the three-port multiplexer, known as a “diplexer.” It consists of two selective filters and an interconnection network. The idealized response is shown in Fig. 2. It is required to determine the criteria for the selective filters and the interconnection network. The filters can employ almost any of the available design approaches, including lumped element, crystal, dielectric resonators, evanescent mode, waveguide, cavity, and SAW. The interconnection network must be physically compatible with the chosen filter approach, but can also consist of a very wide variety of transmission lines, lumped

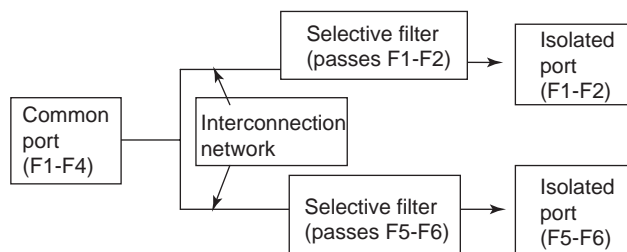


Figure 1. Three-port multiplexer (a “diplexer”). The common port can be an input or an output, while the isolated ports are, respectively, outputs or inputs.

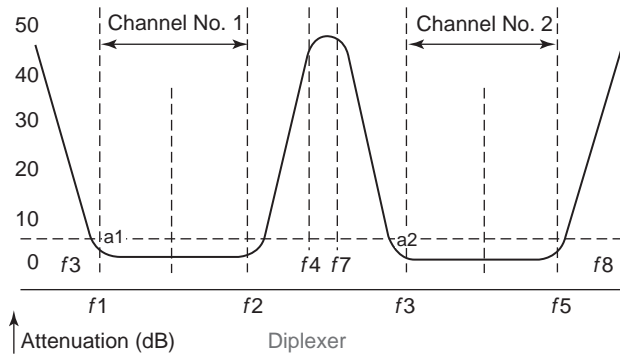


Figure 2. Diplexer, showing “crossover” region (the frequencies between f2 and f5).

elements, phase shifters, and other components. Interconnection of the various filters and combining networks is an artform, but requires awareness of the parasitic lengths that must be included between the selective filters and necessary reactive elements. These parasitic lengths can cause serious response problems, but the effects can be evaluated during the simulation cycle preceding finalization of any design. A summary of many currently used

multiplexing techniques is presented in Table 1. It is not the purpose of this article to discuss filter implementations, but a summary chart of available approaches will be provided at the conclusion of this article (Fig. 18), following the detailed description and examples of multiplexing.

To maintain match at the common port, the following must be satisfied:

$$Y_{in} = [Y_{ch1}] + [Y_{ch2}] = Y_0 \tag{1}$$

where

- Y_{in} = common port input admittance
- Y_{ch1} = input admittance of the F1–F2 selective filter
- Y_{ch2} = input admittance of the F5–F6 selective filter
- Y_0 = nominal circuit characteristic impedance (e.g., 0.02 mho)

All admittances are generally complex quantities. Satisfaction of this requirement can be accomplished if each of the channel-selective filters is designed so as to present a complementary admittance at the common junction, or if the interconnection network provides the appropriate admittance transformation from the filter to the common junction. If the admittance presented at the common

Table 1. Multiplexer Design Methods

Type	Typical Application	Restrictions or cautions	Comments
Circulator-coupled channel dropping	High-power communication	All circulators must cover the full system bandwidth	Almost plug-and-play (filters can be removed and replaced without retuning), but stopband level limited to intrinsic circulator isolation (see Fig. 6)
Common-connection susceptible cancellation	Electronic warfare: electronic intelligence gathering and radar warning receivers	Difficult and expensive to produce because of element sensitivity and common-junction design; composite performance is quite sensitive to all elements in the structure	Compact, efficient use of available filter topologies (see Figs. 7 and 8)
Directly synthesized singly terminated filters with common-junction connection	Wideband communication and electronic warfare	Composite performance is sensitive to all elements in structure, but less so than in the susceptible cancellation approach	Filters can be essentially designed individually, but filter order is higher than required for doubly terminated designs (see example in Fig. 16)
Separable manifold and filters (channel dropping)	Electronic warfare: electronic intelligence gathering and radar warning receivers	Manifold and filters are separable, designed essentially as independent networks, relatively easy to produce; element sensitivity is acceptable for production	Not as compact as the common-junction approach (see Figs. 9–12 and then Figs. 16 and 17 for special configurations)
Double-diplexing (or double <i>n</i> th-order multiplexing, in general)	Provides multiple passbands for communication applications	Useful when nonmonotonic stopband or guardband between channels is allowed	Limited stopband between filter channels (see Figs. 13–15)
Power-divider-coupled “frequency thinner”	Electronic warfare: electronic intelligence gathering and radar warning receivers	Crossover region not required to display 3 dB dip at common frequency between channels	Flat loss of at least 3 dB (see text and Fig. 4)
Hybrid methods including power dividers and switches	In all systems in which simultaneity of information at all ports is not of primary consideration, i.e., when significant processing of channel information occurs	If it takes longer to process information than to simply acquire information, this approach offers compact designs and ease of production	DC power usually required (see Fig. 5)

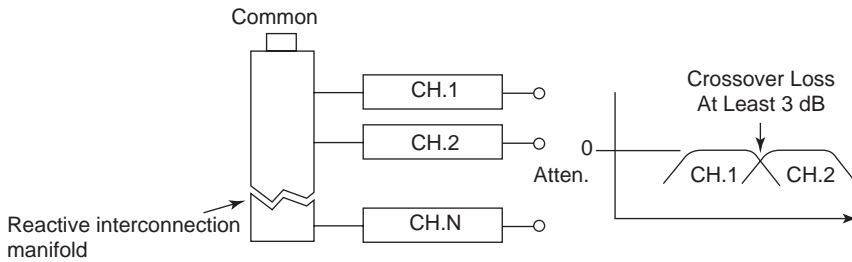


Figure 3. *N*-way reactively connected multiplexer.

junction by one filter is the complex conjugate of that presented by the other filter, Eq. (1) can be satisfied. The imaginary parts of the filter input admittances thus cancel. What is additionally required to ensure compliance with 1.1 is the inclusion of a real transformer, transforming the parallel combination of two real admittances back to Y_0 . These two conditions are summarized in the following equation:

$$\begin{aligned} \text{Re}[Y_{ch1}] + \text{Re}[Y_{ch2}] &= Y_0 = 1 \\ \text{Im}[Y_{ch1}] + \text{Im}[Y_{ch2}] &= 0 \end{aligned} \tag{2}$$

In general, it is not possible to accomplish the requirements of this equation both above and below the passband for each of the two filters, but it is usually sufficient to accomplish the susceptive cancellation in the region closest to the common, or “crossover” region. This region is illustrated in Fig. 2 (between f_2 and f_5 , but of most concern between f_4 and f_7).

An alternative method is presentation of an effective open circuit by each filter to the opposite filter, over a significant part of the frequency range of the opposite filter. To clarify, filter F1–F2 must essentially be open-circuited over the frequency range F5–F6. Filter F5–F6 must essentially be open-circuited over the frequency range F1–F2. Although this is not illustrated, the application of this approach is obvious and will be further clarified in examples to be presented later in this article.

Figure 3 illustrates the *N*-channel extension of the two-channel multiplexer. A three-channel version is known as a *triplexer*; a four-channel version, a *quadruplexer*; a five-channel version, a *quintaplexer*; a six-channel version, a *sextaplexer*, and almost no one is bold enough to attempt higher-order versions but if designed, the Latin-based nomenclature scheme is traditionally extended. Conservation of energy dictates that at the actual frequency common to adjacent channels (the “crossover” frequency), minimum insertion loss is 3 dB because the available energy would be equally shared between the two adjacent channels. The loss might be much higher than 3 dB because the selective filters might be designed with channels more widely separated in frequency than illustrated in Fig. 3. Such separation is known as a “guardband.” If the adjacent passbands of each channel “cross over” at a level of about -3 dB, the device is called a “contiguous” multiplexer. With a guardband (i.e., crossover at levels greater than 3 dB), the device is known as “noncontiguous.”

The -3 dB crossover loss creates a dip at the crossover point, as illustrated in Fig. 3. Although the 3 dB minimum loss cannot be avoided, it is possible to eliminate or drastically reduce the dip with a scheme such as is illustrated in Fig. 4.

The scheme illustrated in Fig. 4 has been termed a “frequency thinner,” and the use of the input isolated power divider allows for common port energy to be distributed equally between the two channels, with non-common-mode reflected energy terminated internally (in the resistor). The circuit thus provides the response with a flat crossover characteristic, as illustrated, at a cost of 3 dB minimum circuit insertion loss (plus the loss associated with each channel filter). The approach can be extended to higher numbers of channels, but if three channels are chosen, for example, the input power divider is three-way, and the minimum insertion loss is thus 4.8 dB. A four channel design would employ a four-way power divider (or an array of two way dividers) with a minimum loss of 6 dB. Although the loss seems high, in many applications in which this scheme is utilized, the loss can be overcome with gain and thus is not a significant problem.

3. FREQUENCY MULTIPLEXING SCHEMES

Let us now explore some of the available techniques (what’s covered and what’s not) for implementing frequency-domain multiplexers. Because many design approaches are considered proprietary by designers and their organizations, this will probably not be a comprehensive coverage, but it will be as comprehensive as the author can provide. Approaches have typically been developed in response to system requirements. Although more than one of the design methodologies can frequently be applied to specific system requirements, some are more appropriate than others. A summary is presented in Table 1. Note that the scope of this article does not include much discussion of time-division multiplexing schemes incorporating switches, but it should be recognized that combinations

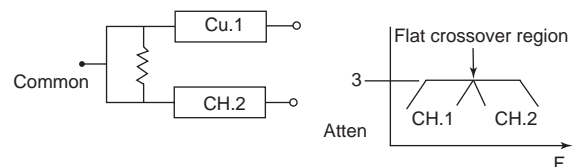


Figure 4. Power divider combined diplexer.

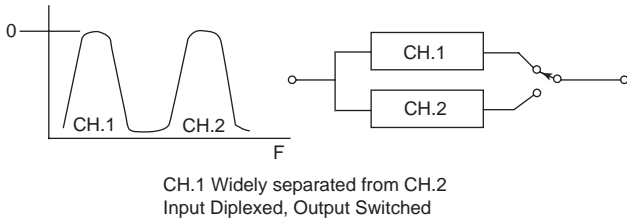


Figure 5. Use of time-division multiplexing with switching.

of frequency- and time-domain multiplexing are quite common and efficient. This is indicated in Table 1, with a typical schematic illustrated in Fig. 5.

3.1. Circulator-Coupled Channel Dropping

The first technique to be discussed is illustrated in Fig. 6. Nonreciprocal gyrating devices (“circulators” in the microwave domain but other gyrators such as active filters at lower frequencies) are used to provide unidirectional flow of signal energy while simultaneously achieving port impedance match. This approach can realize isolated passbands and stopbands, good port match conditions, but without a guarantee of stopband levels greater than the intrinsic isolation of the circulators.

Some notes on the circulator-coupled channel dropping method are as follows:

- Relatively lossy due to addition of all circulator losses
- Very flexible (simply replace one filter with another, no retuning)
- Stopband level between channels limited by intrinsic circulator isolation

3.2. Common-Junction Susceptance Annulling Approach

When filters are connected to a common junction as shown in Fig. 7a, one resonator may be “shared” in common, between the filters. Figure 7 illustrates a connection of three combline or perhaps evanescent-mode filters in such a parallel combination. The filters could, however, consist of dielectric resonators, lumped resonators, SAW, superconducting, printed or other form of resonator array, and the same problem would be encountered: the need to satisfy Eq. (2). Note that each filter starts with a shunt tank equivalent circuit, and thus tends toward a short circuit to ground at frequencies outside of the passband. The input susceptance becomes very negative below the passband

Figure 6. Circulator-coupled channel dropping scheme.

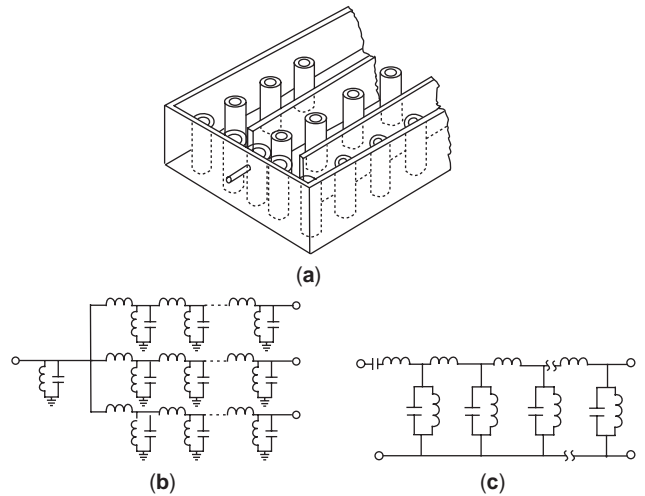
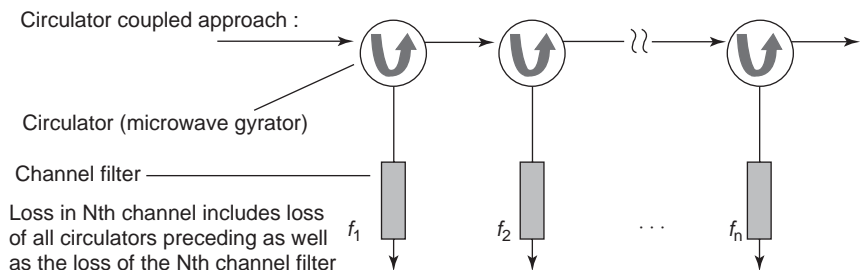
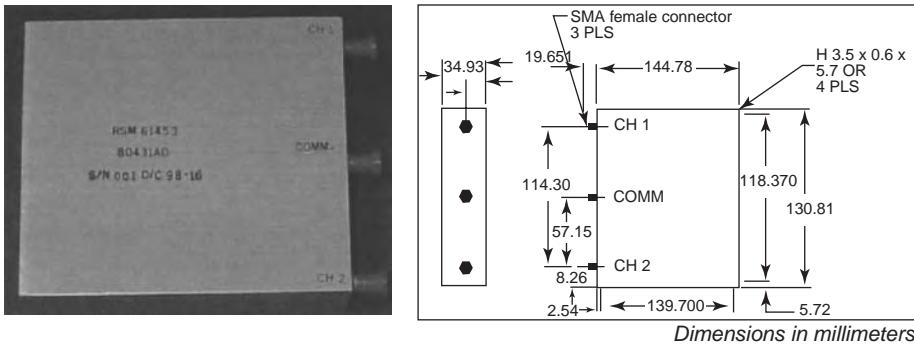


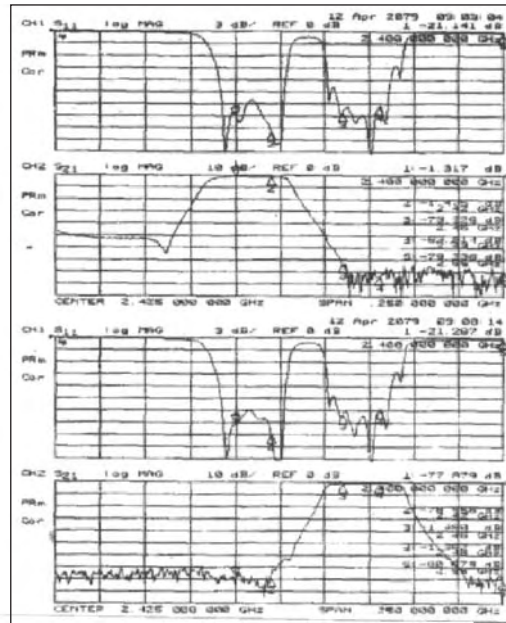
Figure 7. (a) Typical triplexer (three filters connected to common junction); (b) schematic showing common resonator (i.e., shared resonator; can be used for susceptance annulling); (c) schematic showing modification to allow common connection (series-resonant input connection used to assist common connection).

(inductive) and very positive (capacitive) above the passband. This results in very poor input VSWR for the circuit shown in Fig. 7a. If an additional resonator is added, as shown in Fig. 7b, the net susceptance is reduced outside the passband areas. This additional resonator has a resonant frequency well below the operating passband of the bandpass filters. The situation can be further improved if the constituent filters are modified as shown in Fig. 7c, to include a series-resonant input circuit. Without including simulation details, it is sufficient to say that the modification physically takes the form of a high-impedance (large-value) inductor and a small capacitor, inserted between each filter and the additional redundant susceptance annulling resonator, in turn connected to the common junction. The resonator and series circuit result in broadband satisfaction of Eq. (1), for a wide variety of constituent filters. The filters can also be synthesized from singly terminated prototypes, further improving the input VSWR, but at the cost of additional elements in each filter because such prototypes are not as efficient in providing selectivity as doubly terminated prototype designs. Today, it is also possible to implement a variety of cross-coupling schemes between the multiplexer filters, further reducing the problem. An example of such a diplexer is shown in Fig. 8. It is beyond the scope of this article to present



P/N 80431AD Diplexer

TEST DATA



RS Microwave Company, Inc.
 22 Park Place
 P.O. Box 273
 Butler, NJ 07405 USA
 4/14/98

PHONE: 973-492-1207 FAX: 973-492-2471
 INTERNET: www.rsmicro.com
 EMAIL: queries@rsmicro.com

"We Duplicate what We Simulate."™

Figure 8. Susceptance annulling diplexer using cross-coupled filters to implement finite transmission zeros.

details of the many and varied implementations of this technique, but the Bibliography will provide additional references and examples.

The P/N 80431AD (Fig. 8, top) is a true diplexer. The channel responses are quasielliptic, using crossover coupling to implement real frequency transmission zeros for close-in rejection while still achieving maximum passband width. Specifications are as follows:

- Minimum passband channel 1: 2400–2420 MHz
- Minimum passband channel 2: 2460–2480 MHz
- Maximum loss over either passband as above: 1.5 dB
- Maximum common port return loss over either passband: –16 dB
- Maximum output port return loss over either passband: –14 dB

- Minimum interchannel isolation, common port terminated in 50Ω: 70 dB
- Normal impedance: 50 Ω
- Input power: ≥2 W
- Operating temperature: From –20 to +60°C
- Relative humidity: ≤95%

3.3. Separable Multiplexing

Construction of multiplexers frequently involves many contiguous channels, each with great selectivity. The problem of combining filters of this type at a common junction can be readily approached by separating the filters from the multiplexing network. Slope complementary arrays of lowpass and highpass filters can be used to implement a multiplexing (“combining”) network compatible with sep-

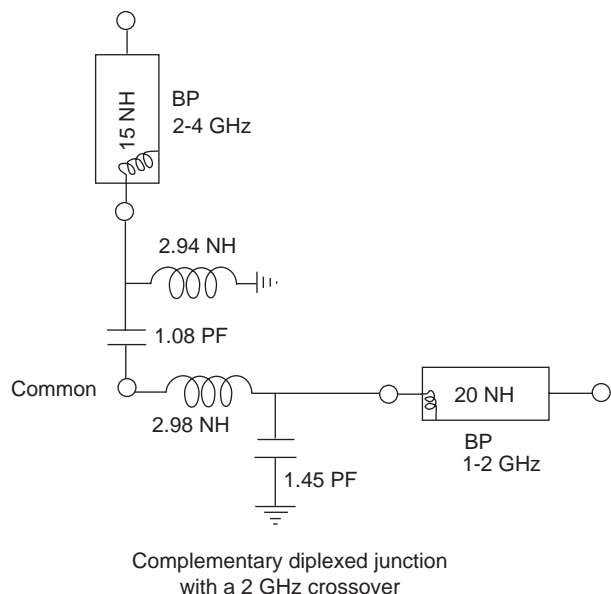


Figure 9. Schematic of second-order complementary low/high-pass combining network (with attached bandpass filters).

arately synthesized and tuned bandpass filters. The bandpass filters are used to provide the required selectivity. The combining network is required only to provide a limited isolation value outside a specified crossover region. Two–five-element lowpass and highpass networks can provide the required isolation. For example, a pair of two-element low/highpass filters will provide 10 dB isolation at a distance (in frequency) of 30% from the crossover of the two. Five-element filters can provide crossover regions with a width of about 5% of the crossover frequency. Isolation of 10 dB is sufficient to provide passband VSWR levels of 1.7–1 over the full range of frequencies covered by the bandpass filters connected to the combining network. The use of these combining networks permits implementation of the bandpass filters as separate networks, with a simple representation of the bandpass filter as a shunt inductor or series capacitor used during modeling and

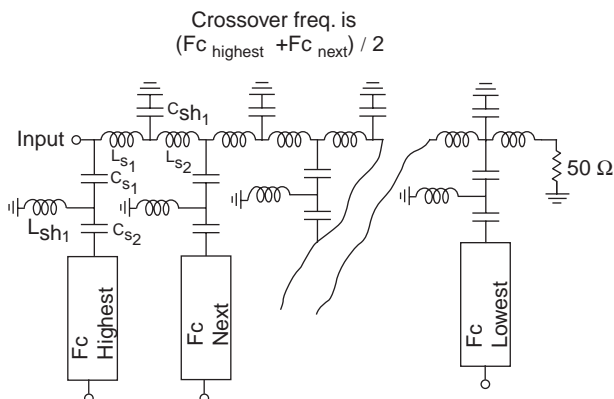


Figure 10. Third-order complementary combining network with bandpass filters; sequential cross over frequencies and channel drop-off.

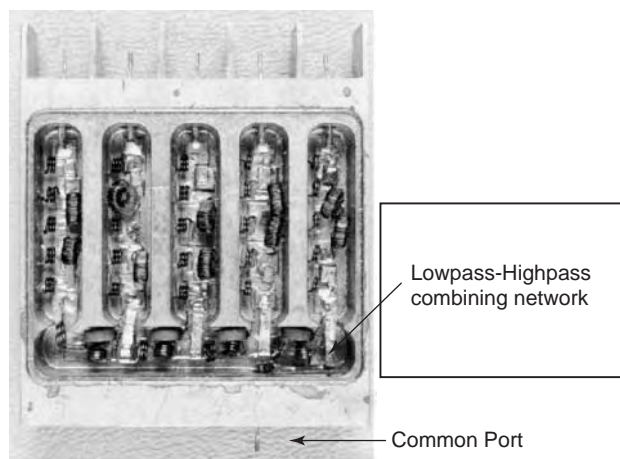


Figure 11. Quintaplexer using third-order complementary combining network (as depicted schematically in Fig. 10).

tuning of the combining network. A schematic of an example two-element combining network, with crossover frequency of 2 GHz, is shown in Fig. 9; a third-order, *N*-way extension is shown in Fig. 10. Simulation of measurement of the response for this network will show satisfaction of Eq. (1), with matched 50-Ω ports, and at least 10 dB isolation at 1400 and 2600 MHz, or 30 % away from the crossover. This enables immediate connection of almost tuning-free bandpass filters with center frequencies below 1400 or above 2600 MHz. As stated, higher-order combining networks can be used to accommodate bandpass filters with spacing closer to the crossover frequency. An example of a quintaplexer (five-way multiplexer) using third-order complementary combining networks in a channel dropping scheme is pictured in Fig. 11, with typical data for a sixth-degree (sextaplexer) version of the same device shown in Fig. 12.

3.4. Double *N*-Plexing

Filters can be multiplexed by parallel combination at both ends. For example, if two bandpass filters are multiplexed at both input and output, a network results that provides one input and one output, with two passbands, essentially attenuating everything else. Such assemblies are useful in systems such as GPS, which have two or more operating frequencies, with the requirement for isolation between the operating channels and adjacent, cluttered regions of the spectrum. Typically, common-junction multiplexing is employed for this application, but in principle, any of the described combinatorial methods can be used. An example of such an application (double diplexer for combining the L1 and L2 GPS channels) is shown in Fig. 13 (schematic and response). An actual example is shown in Fig. 14. Note the limited stopband between the two bandpass channels as shown in the data. An example illustrating double triplexing is shown in Fig. 15a, with data in Fig. 15b.

Some notes regarding double *N*-plexing are as follows:

- Stopband between filter channels limited by filter order and spacing of channels

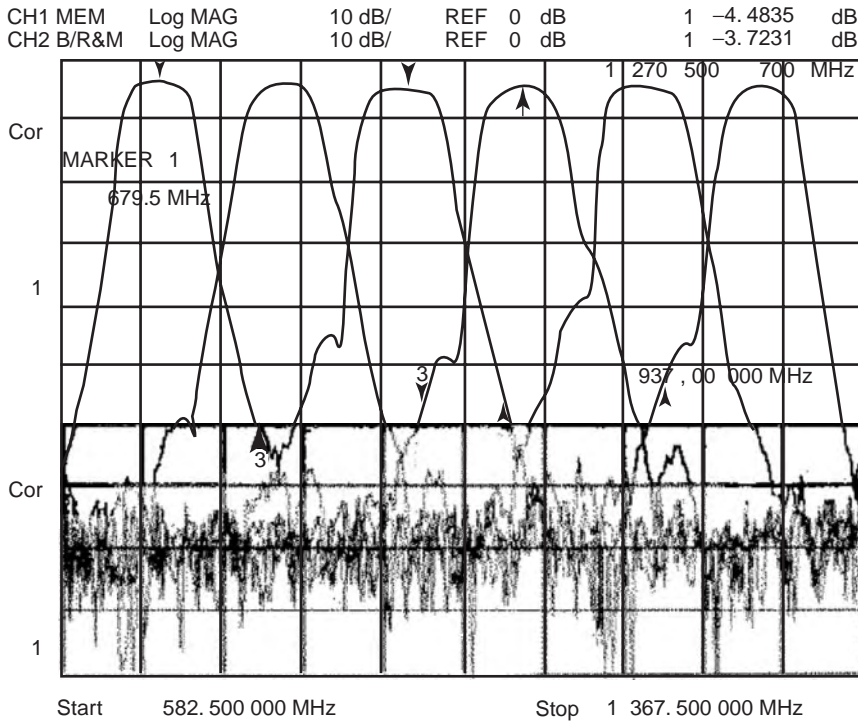


Figure 12. Data on six-channel (sex-taplexer) version of quintaplexer pictured in Fig. 11.

- Diplexing methods include nulling, complementary lowpass and highpass
- Very efficient way to meet limited stopband and difficult passbands

P/N 63491A-1 (Fig. 14, top) is a double diplexer, for GPS application. The filter passes only the GPS L1 and L2 channels, rejecting everything else, to at least 10 GHz. An evanescent mode structure, the 63491A-1 is truly GPS “state of the art.” Specifications are as follows:

The fully military-standard, highly ruggedized assembly shown in Fig. 15a is a GPS triple-channel dual triplexer. There are three evanescent-mode bandpass filters connected together at input and output. The bandpass filters tune the L1, L2, and L5 GPS channels. Two of the bandpass filters are provided with internal cross-coupling so as to achieve sharp rejection near their passbands, and thus display at least 20 dB isolation to the adjacent GPS channel. The assembly thus provides passbands for the L1, L2 and L5 GPS frequencies, rejecting all other

Channel L1		Channel L2	
Minimum - 3 dBc passband:	1550.4–1600.4 MHz	Minimum - 3 dBc passband:	1202.6–1252.6 MHz
Maximum loss at 1575.4 ± 10 MHz:	2 dB	Maximum loss at 1227.6 ± 10 MHz:	2 dB
Phase linearity at 1575.4 ± 10 MHz:	6° maximum	Phase linearity at 1227.6 ± 10 MHz:	6° maximum
Maximum passband VSWR:	1.5:1 (50 Ω)	Maximum passband VSWR:	1.5:1 (50 Ω)
Minimum - 60 dB rejection:	1775.4 MHz	Minimum - 60 dB rejection:	1047.6 MHz
Minimum - 40 dB rejection:	1455.4 MHz	Minimum - 40 dB rejection:	1347.6 MHz
Operating power level:	≥ 0.25 W	Operating power level:	≥ 0.25 W

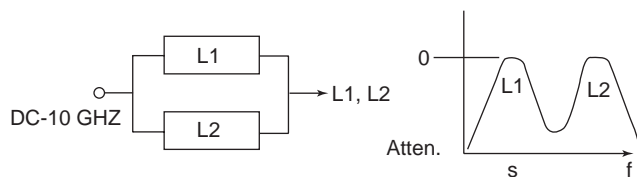


Figure 13. Double-diplexed two channel filter for GPS.

frequencies in accordance with the specifications tabulated below:

- Midband attenuation at 1227.6 and 1575.42 MHz: 1.5 dB maximum (1.0 dB typical)
- Midband attenuation at 1176.45 MHz: 1.9 dB maximum (1.7 dB typical)



P/N 63491A-1 Double diplexer

Maximum group delay difference at L1 and L2 center frequencies: 5 ns

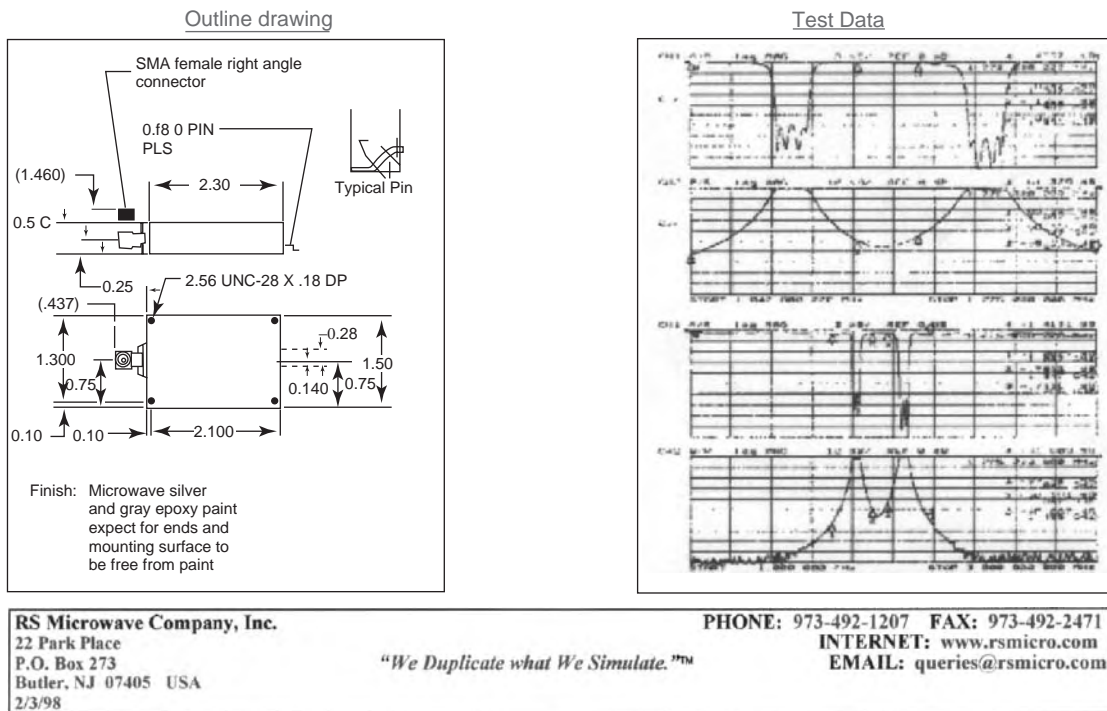


Figure 14. GPS double diplexer. (This figure is available in full color at <http://www.mrw.interscience.wiley.com/erfme>.)

- 3 dBc bandwidth centered at 1176.45 MHz: ≥ 20.46 MHz
- 1 dBc bandwidth centered at 1227.6 and 1575.42 MHz: ≥ 20.46 MHz
- Maximum VSWR at center frequencies: 1:5-1 (50 Ω)
- Minimum - 20 dBc stopbands: 200-1159.5 MHz
1192.5-1207.5 MHz
1250-1500 MHz
1600-8000 MHz
- Power handling: ≥ 10 W peak, 1 W average
- Size
- Connectors: type N(f)
- Operating environment: JTIDS/MIDS military standard shock, vibration

4. OTHER SPECIAL CONFIGURATIONS

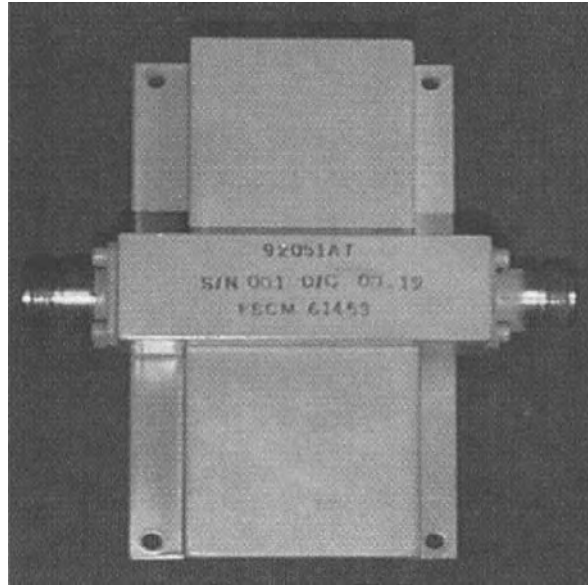
Some other configuration examples are shown in Fig. 16 (waveguide channel dropping multiplexer for communica-

tion application) and Fig. 17 (low/highpass elliptic complementary filters for ECM application).

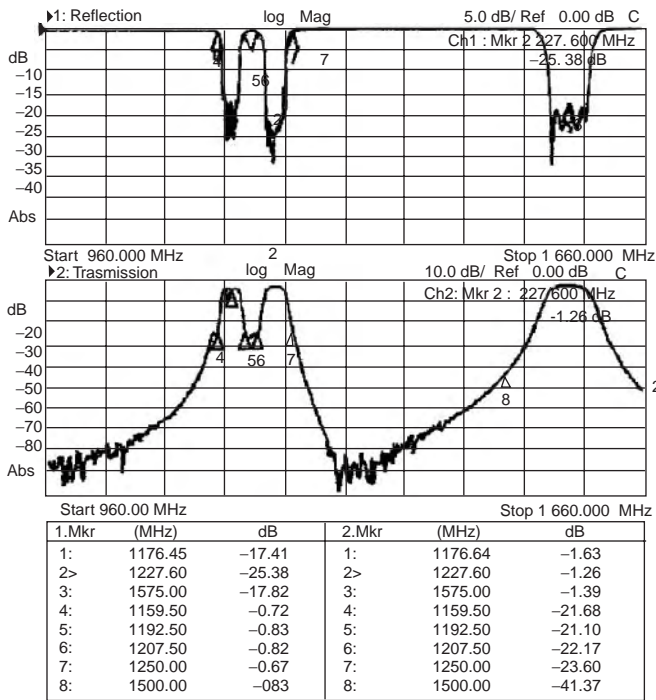
5. CONCLUSIONS

The art and science of combining properly designed selective filters to achieve spectrum separation or combining ("multiplexing") is complex, although the requirements for proper combination are easily summarized in a single pair of equations. The intention of this article has been to provide a summary of several available methods for such multiplexing and examples of their use. What has been presented is certainly not all-inclusive, and is based primarily on the experience of this author. Practitioners have tended to treat the subject secretly, with solutions kept as proprietary. With the advent of modern CAD and the ready access to circuit simulation software, the various possible techniques are found to be quite amenable to analysis. Network synthesis now becomes dominant, in the competitive world in which most practitioners function, and the emphasis is on selection of the filter topology and

P/N 92051 AT

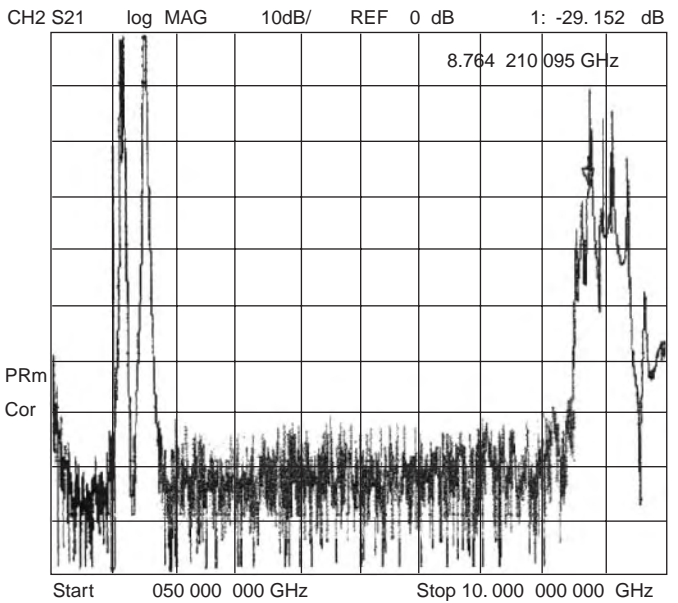


(a)



(b)

Figure 15. GPS dual (double) triplexer (for channels L1, L2, and L5); (b) data for this triplexer. (This figure is available in full color at <http://www.mrw.interscience.wiley.com/erfme>.)



technology to be employed with cleverly conceived inter-connection schemes. Truly synthesized combinations of lumped, evanescent, and distributed elements, into both filters and connection elements, awaits progress in multivariable synthesis. Real-life combinations of these elements are quite possible and common today, using analysis and optimization. However, much “black art” is still to be found in the multiplexer arena, leaving an

opening for new ideas and concepts and certainly, more participants.

Figure 18 presents a partial summary of filter techniques available for use in multiplexer applications. Many variations are possible, including superconductive implementations, “mixing” techniques (such as combinations of lumped and distributed elements), and nonadjacent element coupled designs. Because of the ever-changing



Figure 16. Waveguide channel dropping multiplexer for communication application. The bandpass channel filters are dual-mode and are connected to the common manifold, isolated using band-stop filters between each bandpass channel.

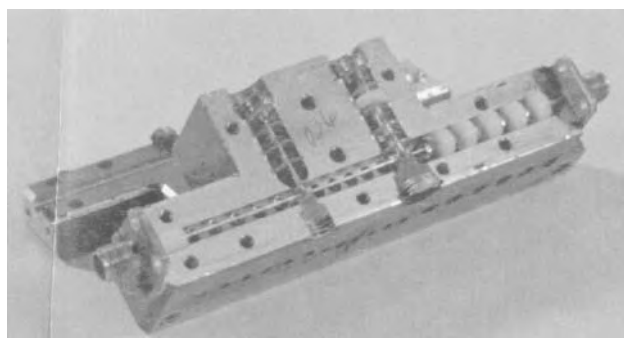


Figure 17. Low/highpass lumped filters arranged in a complementary set providing wideband channels for ECM application.

Lumped Wave guide Coaxial TEM	Dielectric resonator Stripline, Microstrip, CSS, CPW, Finline	Active, SAW, Crystal Helical and stripline, etc	Quasi-optical Evanescent
-------------------------------------	--	--	---------------------------------

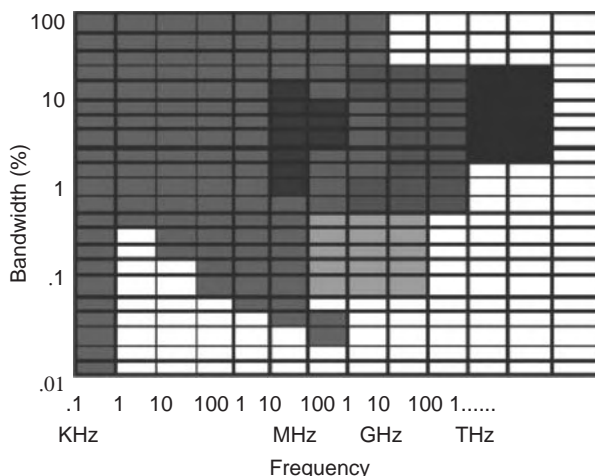


Figure 18. Filter technologies available for use in multiplexers. (This is certainly an incomplete list but can be used as a filter selection guide.) (This figure is available in full color at <http://www.mrw.interscience.wiley.com/erfme>.)

developments in the filter field, the list is unlikely to ever be complete, but the chart provides an overview applicable in 2004.

More than one technology applies to some of the frequency ranges shown in Fig. 18. New cross-coupling techniques are extending the applicability of many types. Active filters achieve responses similar to those of passive filters but with noise or stability problems.

BIBLIOGRAPHY

1. S. B. Cohn, Direct-coupled resonator filters, *Proc. IRE* **45**:187–196 (Feb. 1957).
2. B. M. Schiffman and G. L. Matthaei, Exact design of band-stop microwave filters. *IEEE Trans. Microwave Theory Tech.* **MTT-12**:6–15 (Jan. 1964).
3. H. J. Orchard and G. C. Temes, Filter design using transformed variables, *IEEE Trans. Circ. Theory* **CT-15**:385–408 (Dec. 1968).
4. R. J. Wenzel, Application of exact synthesis methods to multichannel filter design, *IEEE Trans. Microwave Theory Tech.* **MTT-13**:5–15 (Jan. 1965).

5. R. J. Wenzel, Printed circuit complementary filters for narrow band multiplexers, *IEEE Trans. Microwave Theory Tech.* 147–157 (March 1968).
6. S. B. Cohn, Microwave filters containing high-Q dielectric resonators, *IEEE Trans. Microwave Theory Tech.* **MTT-16**:218–227 (April 1968).
7. R. J. Wenzel, Synthesis of combline and capacitively-loaded interdigital bandpass filters of arbitrary bandwidth, *IEEE Trans. Microwave Theory Tech.* **MTT-19**:678–686 (Aug. 1971).
8. P. LaTourette, Combline filter multiplexers, *Microwave J.* (1977).
9. G. L. Matthaei, L. Young, and E. M. T. Jones, *Microwave Filters, Impedance-Matching Networks and Coupling Structures*, McGraw-Hill, New York, 1964.
10. R. J. Wenzel, Exact theory of interdigital bandpass filters and related coupled structures, *IEEE Trans. Microwave Theory Tech.* **MTT-13**:559–575 (Sept. 1965).
11. W. A. Edson and J. Wakabayashi, Input manifolds for microwave channelizing filters, *IEEE Trans. Microwave Theory Tech.* **MTT-18**:270–276 (May 1970).
12. R. Levy and J. D. Rhodes, A combline elliptic filter, *IEEE Trans. Microwave Theory Tech.* **MTT-19**:26–29 (Jan. 1971).

13. J. D. Rhodes, Microwave filters, *IEEE Circ. Syst. Mag.* **2-8** (Aug. 1975).
14. J. K. Plourde and C.-L. Ren, Application of dielectric resonators in microwave components, *IEEE Trans. Microwave Theory Tech.* **MTT-29**:754-770 (Aug. 1981).
15. S. J. Fiedziuszko, Dual-mode dielectric resonator loaded cavity filters, *IEEE Trans. Microwave Theory Tech.* **MTT-30**:1311-1316 (Sept. 1982).
16. R. Levy and S. B. Cohn, A history of microwave filter research, design and development, *IEEE Trans. Microwave Theory Tech.* **MTT-32**:1055-1067 (Sept. 1984).
17. R. Levy, Direct synthesis of cascaded-quadruplet (CQ) filters, *IEEE Trans. Microwave Theory Tech.* **43**:2940-2945 (Dec. 1995); correction, **MTT-45**:1517 (May 1995).
18. R. Hershtig, R. Levy, and K. A. Zaki, Synthesis and design of cascaded trisection (CT) dielectric resonator filters, *1997 European Microwave Conf. Digest*, Jerusalem, Israel, Sept. 1997, 784-791.
19. G. L. Matthaei, N. O. Fenzi, R. Forse, and S. Rohlfing, Hairpin-comb filters for HTS and other narrow-band applications, *IEEE Trans. Microwave Theory Tech.* **45**:1226-1231 (Aug. 1997).
20. J. A. Curtis and S. J. Fiedziuszko, Miniature dual mode microstrip filters, *IEEE MTT-S Int. Microwave Symp. Digest*, June 1991, (Vol. II, pp. 443-446).
21. R. V. Snyder, Inverted Resonator evanescent mode filters, *Proc. IEEE MTT-S Symp.*, 1996
22. R. V. Snyder, Present and future filter design philosophy: Paradigm shift in progress, *Proc. European Microwave Conf. Workshop on Filters*, Paris, Sept. 2000.
23. R. V. Snyder, R. Levy, and G. Matthaei, Design of microwave filters, *IEEE Trans. Microwave Theory Tech.* **50** (special issue): 783-793 (March 2002).
24. R. V. Snyder, E. Niver, S. Shin, and K. Um, Suspended resonators for filters using high dielectric constant feedlines, *IEEE Trans. Microwave Theory Tech.* **50**:2890-2895 (Dec. 2002).

FREQUENCY-DOMAIN CIRCUIT ANALYSIS

MARIO BIEY
 IVAN A. MAIO
 Politecnico di Torino

When a designer is examining the behavior of an electrical circuit, the first thing to do, as in the case of any other physical system, is to write down a suitable set of equations describing the existing links between the involved physical variables, which are, in this case, voltages and currents. Generally, these equations arise from Kirchhoff's voltage and current laws and from the branch relations that describe circuit components.

If there are *dynamic* components (i.e., described by branch relations where time derivatives of voltages and/or currents are present), then the circuit is governed by a system of mixed algebraic and integrodifferential equations. The solution of such a system may be carried out using time as the independent variable and evaluating the wanted voltages and/or currents by numerical or analytical integration techniques. In this case the analysis is said to be performed in the *time domain*.

A completely different approach may be followed for linear time-invariant circuits. By using suitable transformations—that is, Laplace transform or Fourier transform—the original integrodifferential equations, which are linear with constant coefficients, are reduced to algebraic equations, where the original time functions are substituted by complex-valued functions of a complex variable $s = \sigma + j\omega$ in the case of Laplace transform, or simply $j\omega$ in the case of Fourier transform. Then the system of linear algebraic equations is solved for the new transformed functions. Finally, an inverse transformation recovers the requested voltages or currents as functions of time. When following this procedure, the analysis is said to be performed in the frequency domain or, alternatively, in the s domain when an explicit reference to the Laplace transform is preferred.

The frequency-domain approach offers several advantages over the direct solution of time-domain circuit equations:

1. The solution is reduced to algebra and is greatly simplified by the extensive use of tables.
2. The conditions of energy storage elements within the circuit at the time when the input signal is applied (i.e., the initial conditions) become part of circuit equations and hence are automatically accounted for.
3. There is no need to evaluate initial conditions at $t = 0+$, as in the case of time-domain analysis, when a jump discontinuity occurs at $t = 0$. Only their values immediately before the beginning of the transient (i.e., at $t = 0-$) are required.
4. The sinusoidal steady-state behavior of a linear circuit may be easily analyzed by resorting to network functions defined in terms of Laplace transforms.
5. Frequency-domain analysis provides a deeper insight in the behavior of linear circuits. For example, it is possible to effectively compute sensitivities, to give stability conditions, to establish necessary and sufficient conditions for the realization of one-port and multiport networks, and so on.
6. Many design techniques are based on a description of the circuit behavior in the frequency domain, via network functions. The knowledge of these functions is of paramount importance in designing feedback amplifier, one-ports, multiports, active and passive filters, equalizers, oscillators, and so on.
7. Frequency-domain formulation allows an effective description of transmission lines, which would otherwise require partial differential equation in the time domain.
8. Frequency-domain formulation allows model simplification techniques not possible in the time domain.

1. FREQUENCY-DOMAIN CIRCUIT EQUATIONS

This section introduces the one-sided Laplace transform and a number of its properties, relevant to circuit analysis.

A complete discussion of this topic may be found in Refs. 1 and 2. Successively, we will illustrate the use of Laplace transform to write and solve frequency-domain circuit equations.

1.1. The One-Sided Laplace Transform

Given a function of time $f(t)$ defined for all $t \geq 0$, its one-sided Laplace transform is defined as

$$F(s) = \mathcal{L}[f(t)] = \int_{0-}^{\infty} f(t)e^{-st} dt \tag{1}$$

where $s = \sigma + j\omega$ is a complex variable, called the *complex frequency*. Note that in Eq. (1) the lower limit of integration equals $0-$, to include functions that have a discontinuity or an impulse at $t = 0$.

Equation (1) establishes a correspondence between the time function $f(t)$ defined for all $t \geq 0$ and its Laplace transform $F(s)$. This fact ensures that the solution coming from the frequency-domain approach is identical to the one obtainable by operating in the time domain.

The integral that defines the Laplace transformation exists under mild conditions on the function $f(t)$, generally met for the signals used in engineering. A sufficient condition is that $f(t)$ is exponentially bounded—that is, $|f(t)| \leq Me^{ct}$ —for some constant $M > 0$ and some constant c , for all $t > 0$ (or only for t greater than some t_0).

The greatest lower bound σ_+ of the values of σ for which the Laplace integral (1) exists is called *abscissa of convergence*. It can be shown that the Laplace integral defines an analytic function within the half-plane of convergence $\sigma > \sigma_+$.

Extensive tables of transform pairs have been built (see Refs. 3 and 4) by using the definition given in Eq. (1). Examples of Laplace transforms of elementary functions are reported in Table 1. Some of the main properties of one-sided Laplace transform, relevant in circuit analysis, are shown in Table 2. For proofs and a complete collection of these properties, see Refs. 1 and 2.

The inverse transform, which gives $f(t)$ from its Laplace transform $F(s)$, is denoted by $\mathcal{L}^{-1}[F(s)]$ and is

expressed by

$$\begin{aligned} f(t) &= 0, \quad t < 0 \\ f(t) &= \mathcal{L}^{-1}[F(s)] \\ &= \frac{1}{2\pi j} \int_{\sigma_1 - j\infty}^{\sigma_1 + j\infty} F(s)e^{st} ds, \quad t > 0, \quad \sigma_1 > \sigma_+ \end{aligned} \tag{2}$$

In many practical situations, the inverse transform may be simply obtained by resorting to a partial-fraction expansion of the original function. Then, the inverse transforms of the elementary fractions are found by inspection, resorting to tables of Laplace transforms.

1.2. Tableau Equations

We start by considering the time-domain tableau equations for a linear time-invariant circuit [5,6]. The (node) tableau equations are

$$\mathbf{A}\mathbf{i} = 0 \tag{3}$$

$$\mathbf{v} - \mathbf{A}^T \mathbf{e} = 0 \tag{4}$$

$$(\mathbf{M}_0 \mathbf{D} + \mathbf{M}_1) \mathbf{v} + (\mathbf{N}_0 \mathbf{D} + \mathbf{N}_1) \mathbf{i} = \mathbf{u}_s(t) \tag{5}$$

where \mathbf{i} is the vector of branch currents, \mathbf{v} is the vector of branch voltages, and \mathbf{e} is the vector of node voltages with respect to a datum node. Equations (3) and (4) are the matrix formulation of Kirchhoff's current and voltage laws: \mathbf{A} is the $(n - 1) \times b$ reduced incidence matrix, n being the number of nodes and b the number of branches; the superscript T denotes transposition. The branch equations are given (in matrix form) by Eq. (5): $\mathbf{M}_0, \mathbf{M}_1, \mathbf{N}_0, \mathbf{N}_1$ are $b \times b$ matrices with real constant elements; \mathbf{D} is the differentiation operator d/dt and $\mathbf{u}_s(t)$ is the vector of independent sources.

The application of Laplace transform to both sides of Eqs. (3)–(5), taking into account the properties shown in Table 2, gives the (node) tableau equations in the fre-

Table 1. Elementary One-Sided Laplace Transform Pairs

Time Function $f(t)$	Type	Laplace Transform $F(s) = \mathcal{L}[f(t)]$
$\delta(t)$	Impulse function	1
$u(t)$	Unit step function	$\frac{1}{s}$
t	Ramp	$\frac{1}{s^2}$
e^{-at}	Exponential	$\frac{1}{s+a}$
$e^{-at} \sin \omega_0 t$	Damped sine	$\frac{\omega_0}{(s+a)^2 + \omega_0^2}$
$e^{-at} \cos \omega_0 t$	Damped cosine	$\frac{s+a}{(s+a)^2 + \omega_0^2}$

Table 2. Main Properties of One-Sided Laplace Transform

Property	Transform Pair
Linearity	$\mathcal{L}[a_1 f_1(t) + a_2 f_2(t)] = a_1 F_1(s) + a_2 F_2(s)$
Time differentiation	$\mathcal{L}\left[\frac{df}{dt}\right] = sF(s) - f(0^-)$
Time integration	$\mathcal{L}\left[\int_{0-}^t f(\tau) d\tau\right] = \frac{1}{s} F(s)$
Time shift	$\mathcal{L}[f(t - t_0)u(t - t_0)] = e^{-t_0 s} F(s), \quad t_0 > 0$
Frequency shift	$\mathcal{L}[e^{s_0 t} f(t)] = F(s - s_0)$
Initial-value theorem	$f(0^+) = \lim_{t \rightarrow 0^+} f(t) = \lim_{s \rightarrow \infty} sF(s)$
Final-value theorem	$\lim_{t \rightarrow \infty} f(t) = \lim_{s \rightarrow 0} sF(s), \quad sF(s)$ regular on the $j\omega$ axis and in right half-plane

Table 3. Branch Equations in the Frequency Domain

Component	Parameter(s)	Time Domain	Frequency Domain ^a
Resistor	R	$v(t) = Ri(t)$	$V(s) = RI(s)$
Capacitor	C	$i(t) = C \frac{dv}{dt}$	$I(s) = sCV(s) - CV_0$ or $V(s) = \frac{1}{sC}I(s) + \frac{V_0}{s}$
Inductor	L	$v(t) = L \frac{di}{dt}$	$V(s) = sLI(s) - LI_0$ or $I(s) = \frac{1}{sL}V(s) + \frac{I_0}{s}$
Coupled inductors	M, L_1, L_2	$v_1(t) = L_1 \frac{di_1}{dt} + M \frac{di_2}{dt}$ $v_2(t) = M \frac{di_1}{dt} + L_2 \frac{di_2}{dt}$	$V_1(s) = sL_1I_1(s) + sMI_2(s) - L_1I_{10} - MI_{20}$ $V_2(s) = sMI_1(s) + sL_2I_2(s) - MI_{10} - L_2I_{20}$

^aNote that V_0, I_0, I_{10} and I_{20} are initial values computed at $t = 0^-$.

quency domain

$$\mathbf{A}\mathbf{I}(s) = 0 \tag{6}$$

$$\mathbf{V}(s) - \mathbf{A}^T\mathbf{E}(s) = 0 \tag{7}$$

$$(\mathbf{M}_0s + \mathbf{M}_1)\mathbf{V}(s) + (\mathbf{N}_0s + \mathbf{N}_1)\mathbf{I}(s) = \mathbf{U}_s(s) + \mathbf{U}_0 \tag{8}$$

where $\mathbf{I}(s)$, $\mathbf{V}(s)$, and $\mathbf{E}(s)$, are vectors of transformed branch currents, branch voltages, and node-to-datum voltages, respectively. $\mathbf{U}_s(s)$ is the vector of transformed independent sources and $\mathbf{U}_0 = \mathbf{M}_0\mathbf{v}(0) + \mathbf{N}_0\mathbf{i}(0)$ is the vector of initial conditions. In matrix form we have

$$\mathbf{T}(s)\mathbf{W}(s) \equiv \begin{bmatrix} \mathbf{0} & \mathbf{0} & \mathbf{A} \\ -\mathbf{A}^T & \mathbf{1} & \mathbf{0} \\ \mathbf{0} & \mathbf{M}_0s + \mathbf{M}_1 & \mathbf{N}_0s + \mathbf{N}_1 \end{bmatrix} \begin{bmatrix} \mathbf{E}(s) \\ \mathbf{V}(s) \\ \mathbf{I}(s) \end{bmatrix} \tag{9}$$

$$= \begin{bmatrix} \mathbf{0} \\ \mathbf{0} \\ \mathbf{U}_s(s) + \mathbf{U}_0 \end{bmatrix}$$

where matrix \mathbf{T} is constituted by elements that are either real constants or real polynomials of degree 1 and \mathbf{W} is the vector of output variables.

Other forms of the tableau equations are possible if reference is made to fundamental cutsets or fundamental loops of the connected digraph associated to the considered circuit. These forms of the tableau equations are not considered here, and the interested reader is referred to Ref. 6, pp. 715–717.

As a concluding remark, let us consider tableau equations (6)–(8) in more detail. Equations (6) and (7) may be obtained from Eqs. (3) and (4) by a simple substitution of time functions with their Laplace transforms: They may be viewed as Kirchhoff’s current and voltage laws in the frequency domain. Equation (8) contains the frequency-domain branch equations. They are listed in the fourth column of Table 3, for the components shown in Fig. 1a,

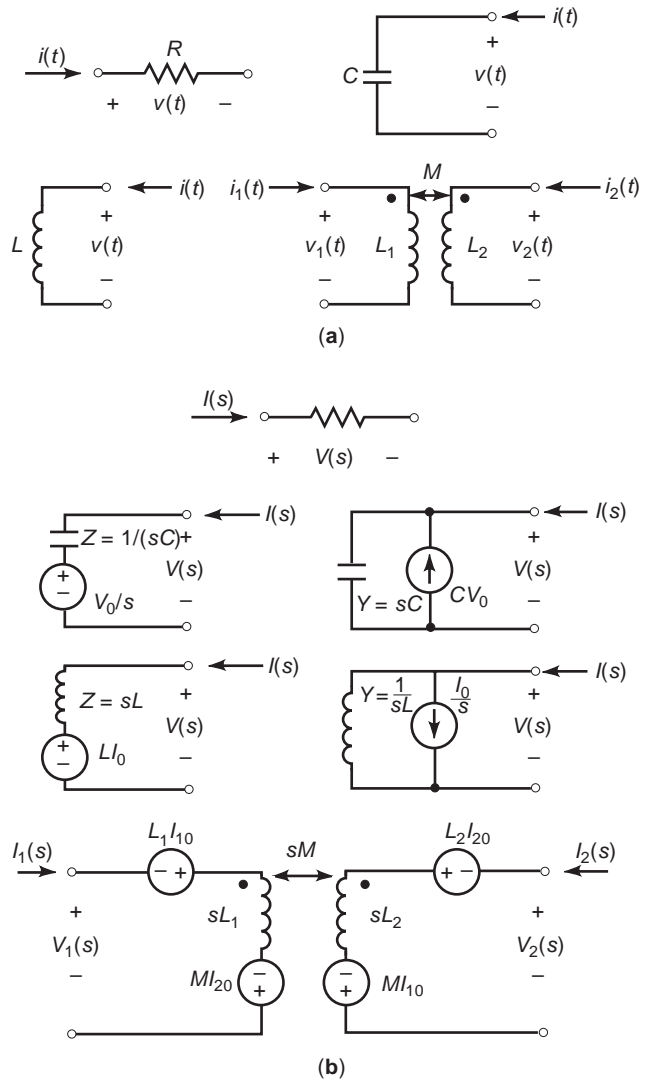


Figure 1. (a) Symbols and associated reference directions for voltages and currents of resistors, capacitors, inductors and coupled inductors; (b) frequency-domain equivalent circuits of resistors, capacitors, inductors, and coupled inductors. For capacitors and inductors both the series and the parallel frequency-domain equivalent circuits are shown. Initial values are denoted by $V_0 = v(0^-)$, $I_0 = i(0^-)$, $I_{10} = i_1(0^-)$ and $I_{20} = i_2(0^-)$.

Table 4. Impedance $Z(s)$ and Admittance $Y(s)$ of Resistors, Capacitors, and Inductors

Component	Parameter	$Z(s)$	$Y(s)$
Resistor	R	R	$G = 1/R$
Capacitor	C	$\frac{1}{sC}$	sC
Inductor	L	sL	$\frac{1}{sL}$

while in the third column the corresponding time-domain equations are shown for comparison.

1.2.1. Impedance and Admittance. Consider a two-terminal element, with zero initial conditions. Let us choose *associated reference directions* for input current and terminal voltage, (e.g., see Fig. 1a) and denote their transforms by $I(s)$ and $V(s)$, respectively. The ratio

$$Z(s) = \frac{V(s)}{I(s)} \tag{10}$$

is called the *impedance* of the two-terminal element. The reciprocal of the impedance

$$Y(s) = \frac{1}{Z(s)} = \frac{I(s)}{V(s)} \tag{11}$$

is referred to as the *admittance* of the two-terminal element. In the frequency domain, impedance and admittance play the same role as resistance and conductance in Ohm's laws, respectively. Table 4 gives impedances and admittances of resistors, capacitors, and inductors.

1.2.2. Writing Circuit Equations by Inspection. Taking into account Eqs. (10) and (11), one can easily verify that the circuits shown in Fig. 1b are governed by the algebraic frequency-domain equations reported in the fourth column of Table 3. These circuits are called the *equivalent circuits* in the frequency domain for resistors, capacitors, inductors, and coupled inductors.

As a consequence, the frequency-domain equations of any circuit may be written directly, avoiding the preliminary step of writing time-domain equations. In fact, it is sufficient to apply the same analysis methods used for resistive circuits (see Ref. 6, Chap. 5; and Ref. 7, Chap. 4) to a frequency-domain equivalent circuit, hereafter called the *transformed circuit*, obtained by replacing each element with its impedance or admittance and adding the appropriate sources to take into account initial conditions.

Furthermore, for this transformed circuit all general theorems, valid for linear time-invariant resistive circuits, (superposition, Thevenin's, Norton's, Tellegen's, etc.), still hold.

Example 1. The results presented above are used to write tableau equations for the very simple circuit of Fig. 2a. The transformed circuit is shown in Fig. 2b, where $v_3(0^-) = V_0$ and $i_4(0^-) = I_0$ are initial values of capacitor voltage and inductor current, respectively. The frequency-domain tableau equations, written in matrix form and partitioned according to Eq. (9), are

$$\begin{bmatrix}
 0 & 0 & \vdots & 0 & 0 & 0 & 0 & \vdots & -1 & 1 & 1 & 0 \\
 0 & 0 & \vdots & 0 & 0 & 0 & 0 & \vdots & 0 & 0 & -1 & 1 \\
 \dots & \dots & \dots & \dots & \dots & \dots & \dots & \dots & \dots & \dots & \dots & \dots \\
 1 & 0 & \vdots & 1 & 0 & 0 & 0 & \vdots & 0 & 0 & 0 & 0 \\
 -1 & 0 & \vdots & 0 & 1 & 0 & 0 & \vdots & 0 & 0 & 0 & 0 \\
 -1 & 1 & \vdots & 0 & 0 & 1 & 0 & \vdots & 0 & 0 & 0 & 0 \\
 0 & -1 & \vdots & 0 & 0 & 0 & 1 & \vdots & 0 & 0 & 0 & 0 \\
 \dots & \dots & \dots & \dots & \dots & \dots & \dots & \dots & \dots & \dots & \dots & \dots \\
 0 & 0 & \vdots & 0 & 0 & 0 & 0 & \vdots & 1 & 0 & 0 & 0 \\
 0 & 0 & \vdots & 0 & 1 & 0 & 0 & \vdots & 0 & -R_2 & 0 & 0 \\
 0 & 0 & \vdots & 0 & 0 & -sC_3 & 0 & \vdots & 0 & 0 & 1 & 0 \\
 0 & 0 & \vdots & 0 & 0 & 0 & 1 & \vdots & 0 & 0 & 0 & -sL_4
 \end{bmatrix}
 \begin{bmatrix}
 E_1 \\
 E_2 \\
 \dots \\
 V_1 \\
 V_2 \\
 V_3 \\
 V_4 \\
 \dots \\
 I_1 \\
 I_2 \\
 I_3 \\
 I_4
 \end{bmatrix}
 =
 \begin{bmatrix}
 0 \\
 0 \\
 \dots \\
 0 \\
 0 \\
 0 \\
 0 \\
 \dots \\
 I_{g1} \\
 0 \\
 -C_3V_0 \\
 -L_4I_0
 \end{bmatrix} \tag{12}$$

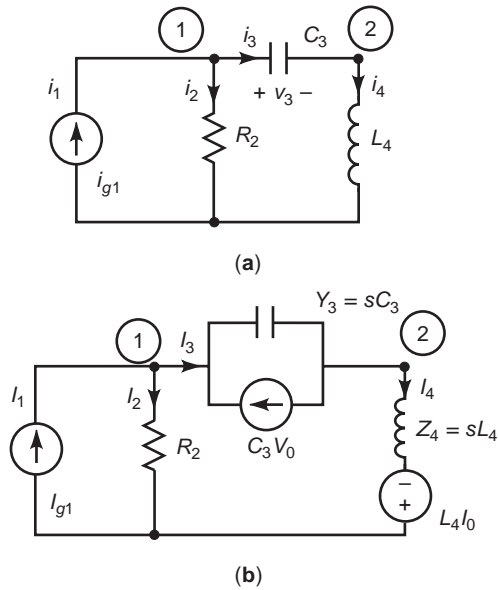


Figure 2. (a) A simple RLC circuit; at $t = 0^-$ the capacitor has an initial voltage $v_3(0^-) = V_0$ and inductor has an initial current $i_4(0^-) = I_0$ (associated reference directions are assumed); (b) the frequency-domain transformed circuit.

1.3. Loop Equations

The set of loop equations may be written directly in the frequency domain by substituting each circuit element with the appropriate series equivalent circuit of Fig. 1b and then applying the standard technique used for resistive circuits. Note that for nonzero initial conditions, supplemental voltage sources of the form LI_0 and/or V_0/s are added to the original circuit.

The final set of loop equations has the form

$$\mathbf{Z}_1(s)\mathbf{I}_1(s) = \mathbf{V}_s(s) + \mathbf{V}_0(s) \tag{13}$$

where $\mathbf{Z}_1(s)$ is called the *loop impedance matrix*, $\mathbf{V}_s(s)$ is the vector of independent voltage sources, and $\mathbf{V}_0(s)$ is the voltage vector due to initial conditions.

The restriction imposed in loop analysis is that all elements must be current-controlled. If this is not the case, one may resort to circuit transformations or to the modified loop analysis (8).

Loop equations may be written by inspection. If the circuit is formed only by resistors, capacitors, and inductors, the rules are particularly simple. The matrix \mathbf{Z}_l is symmetric, the k th diagonal element z_{kk} is the sum of all impedances in loop k , and any off-diagonal element z_{jk} is the sum of all impedances common to loops j and k if the reference directions for the two loops are the same, the negative of the sum otherwise.

Finally, for a circuit with a planar graph, meshes may be used instead of fundamental loops. In this case, mesh equations are obtained in terms of fictitious circulating currents, generally referred to as “mesh currents”.

Example 2. Consider the (planar) circuit of Fig. 3a. The initial values of voltages across capacitors C_p and C are

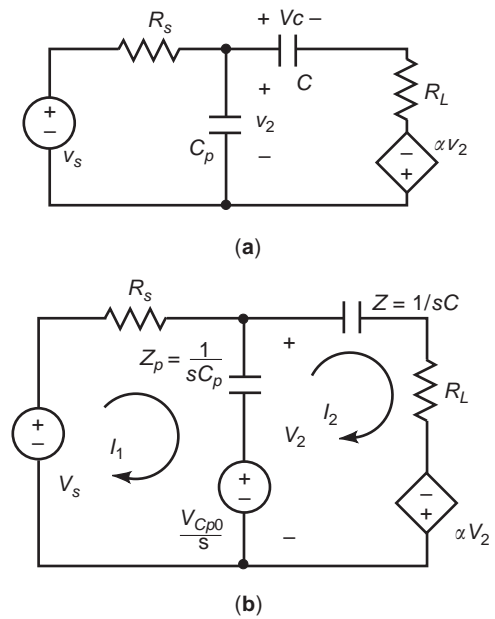


Figure 3. (a) Loop (mesh) analysis—at $t = 0^-$ capacitors C_p and C have initial voltages $v_2(0^-) = V_{C_p,0}$ and $v_c(0^-) = 0$ V, respectively; (b) the frequency-domain transformed circuit.

$v_2(0^-) = V_{C_p,0}$ and $v_c(0^-) = 0$ V, respectively. In this case, meshes can be chosen as fundamental loops. Assuming for the mesh currents I_1 and I_2 the reference directions shown in the transformed circuit of Fig. 3b, we write the following frequency-domain mesh equations:

$$\begin{bmatrix} 1/(sC_p) + R_s & -1/(sC_p) \\ -(1 + \alpha)/(sC_p) & R_L + 1/(sC) + (1 + \alpha)/(sC_p) \end{bmatrix} \begin{bmatrix} I_1 \\ I_2 \end{bmatrix} = \begin{bmatrix} V_s(s) \\ 0 \end{bmatrix} + \begin{bmatrix} -V_0/s \\ (1 + \alpha)V_0/s \end{bmatrix} \tag{14}$$

1.4. Node Equations

Node equations may be written directly in the frequency domain by substituting each circuit element with the appropriate parallel equivalent circuit of Fig. 1b and then applying the standard technique used for resistive circuits. Note that for nonzero initial conditions, supplemental current sources of the form I_0/s and/or CV_0 are added to the original circuit.

The final form of node equations is

$$\mathbf{Y}_n(s)\mathbf{E}(s) = \mathbf{I}_s(s) + \mathbf{I}_0(s) \tag{15}$$

where $\mathbf{Y}_n(s)$ is called the *node admittance matrix*, $\mathbf{I}_s(s)$ is the vector of independent current sources, and $\mathbf{I}_0(s)$ is the current vector due to initial conditions.

Node equations may be written by inspection. If the circuit is formed only by resistors, capacitors, and inductors, the rules are particularly simple: The matrix \mathbf{Y}_n is symmetric, the k th diagonal element y_{kk} is the sum of all admittances connected to node k , and any off-diagonal

The frequency-domain transformed circuit is shown in Fig. 5b, where V_{20} and V_{30} are initial values of capacitor voltages v_2 and v_3 , respectively. The modified nodal equations are

$$\begin{bmatrix} G_{11} & -G_{11} & 0 & 0 \\ -G_{11} & G_{11} + G_{12} + s(C_2 + C_3) & -sC_3 & -sC_2 \\ 0 & -sC_3 & G_4 + sC_3 & -G_4 \\ 0 & -sC_2 & -G_4 & G_4 + G_6 + sC_2 \\ 0 & 0 & 0 & -G_6 \\ 1 & 0 & 0 & 0 \\ 0 & 0 & -1 & 0 \end{bmatrix} \begin{bmatrix} E_1 \\ E_2 \\ E_3 \\ E_4 \\ E_5 \\ I_1 \\ I_2 \end{bmatrix} = \begin{bmatrix} 0 \\ 0 \\ 0 \\ 0 \\ 0 \\ V_i(s) \\ 0 \end{bmatrix} + \begin{bmatrix} 0 \\ C_3 V_{30} - C_2 V_{20} \\ -C_3 V_{30} \\ C_2 V_{20} \\ 0 \\ 0 \\ 0 \end{bmatrix} \quad (18)$$

1.6. State Equations

State equations are best suited for time-domain analysis, even if sometimes it may be useful to solve these equations in the frequency domain. Also in this case, all known methods used to write time-domain state equations (inspection, equivalent sources, or network graph theory; see Ref. 11, Chapter 6) may be applied to the transformed circuit obtained by substituting inductors and capacitors with the series and parallel circuits of Fig. 1(b), respectively. In spite of that, state equations are generally written first in the time domain and then transformed to the frequency domain, where they take the following form:

$$s\mathbf{X}(s) = \mathbf{A}\mathbf{X}(s) + \mathbf{B}\mathbf{U}(s) + \mathbf{X}_0 \quad (19)$$

In this equation, $\mathbf{X}(s)$, \mathbf{X}_0 , and $\mathbf{U}(s)$ are the vectors of transformed state variables, of initial conditions, and of transformed independent sources, respectively. \mathbf{A} and \mathbf{B} are matrices of appropriate dimensions (note that \mathbf{A} is not the incidence matrix).

Equation (19) may be rearranged to yield

$$[s\mathbf{1} - \mathbf{A}]\mathbf{X}(s) = \mathbf{B}\mathbf{U}(s) + \mathbf{X}_0 \quad (20)$$

where $\mathbf{1}$ is the identity matrix.

1.7. Natural Frequencies

Let us consider a (linear time-invariant) circuit described by its tableau equations [Eq. (9)]. This system of linear algebraic equations admits a unique solution if and only if matrix $\mathbf{T}(s)$ is invertible; that is, $\det[\mathbf{T}(s)]$ is not identically zero. Furthermore, since all elements of $\mathbf{T}(s)$ are polynomials of degree either 0 or 1 in s , $\det[\mathbf{T}(s)]$ is a polynomial in s too, with real coefficients, called the *characteristic polynomial* of the circuit. The roots λ_i , of

$$\det[\mathbf{T}(s)] = 0 \quad (21)$$

are called the *natural frequencies* of the circuit. They are either real or occur in complex-conjugate pairs.

Note that when working in the time domain, $\mathbf{T}(s)$ becomes $\mathbf{T}(D)$, where D is the differentiation operator d/dt , and hence the definition of natural frequencies presented above coincides with that given in the time domain [12, Chap. 12].

If all independent sources are set to zero (i.e., considering the circuit in the zero-input state), then, applying Kramer's rule, a generic output variable $W_k(s)$ is given by

$$W_k(s) = \frac{\sum_{i=1}^b \Delta_{ik} U_{i0}}{\det[\mathbf{T}(s)]} \quad (22)$$

where Δ_{ik} is the cofactor of the element $(b + n - 1 + i)$, k of $\mathbf{T}(s)$ and U_{i0} denotes the i th source due to initial conditions.

Expanding the right-hand side of Eq. (22) in partial fractions and then taking the inverse Laplace transform of both sides, it turns out that, in general, any zero-input response is a linear combination of exponentials $e^{\lambda_i t}$ (or polynomials in t times $e^{\lambda_i t}$), called *modes*, where each λ_i is a natural frequency of the circuit. For some particular response, some modes may be absent.

If all the natural frequencies of the circuit have a negative real part, then the zero-input response, for any initial state, goes to zero exponentially with increasing time. In this case, the circuit is referred to as *strictly* (or *exponentially*) stable.

Natural frequencies are an intrinsic feature of the circuit: They depend only on the circuit and not on the method used to analyze it. In fact, it can be shown that the nonzero natural frequencies of any linear time-invariant circuit are identical to the nonzero roots of the determinantal polynomial of the matrix of any system of equations describing the circuit, when framed as a set of linear algebraic equations of the form $\mathbf{R}(s)\mathbf{W}(s) = \mathbf{F}(s)$ [13, Chap. 14]. The total number of natural frequencies is not greater than the number of energy-storing elements present in the circuit and it defines the order of complexity of the circuit [14, Chap. 8]. Zero natural frequencies are of

limited physical significance, and in some cases their number may be determined by inspection [12, Chap. 11].

In the case of tableau analysis and MNA, the determinantal polynomials of matrices $\mathbf{T}(s)$ and $\mathbf{P}(s)$ differ from each other only for a multiplicative constant, and hence they give the same set of natural frequencies, including those at $s = 0$ (if any), with the same multiplicities [6, Sect. 10.4.2].

In the case of state equations, let us consider them in the form given by Eq. (20). The natural frequencies are the roots of the determinantal polynomial

$$\det[s\mathbf{1} - \mathbf{A}] = 0 \quad (23)$$

and hence they coincide with the eigenvalues of matrix \mathbf{A} . As in the case of tableau analysis and MNA, Eq. (23) supplies all natural frequencies, including zero natural frequencies, with their own multiplicities.

2. NETWORK FUNCTIONS

Given a linear time-invariant network in the zero state—that is, with zero initial voltages across all capacitors and zero initial current through all inductors—a *network function* $H(s)$ is defined as the ratio of the Laplace transform $W(s)$ of an *output variable* $w(t)$ to the Laplace transform $Q(s)$ of an *input variable* $q(t)$:

$$H(s) = W(s)/Q(s) \quad (24)$$

If the input is an unit impulse, then $Q(s) = 1$ and hence $H(s)$ turns out to be the Laplace transform of the impulse response of the circuit.

If input and output variables are defined at the same terminal pair, the network function is either an impedance or an admittance, as defined in Eqs. (10) and (11), respectively. If input and output are measured at two different terminal pairs, the network function is referred to as a *transfer function*. A transfer function may have the dimension of impedance or admittance or be dimensionless.

In the case of multiple-input multiple-output circuits, a matrix transfer function $\mathbf{H}(s)$ may be defined, whose k, i element is the ratio of the Laplace transform of the k th output variable to the Laplace transform of the i th input variable, when all others input variables are set to zero.

Network functions may be efficiently obtained by resorting to network symbolic analysis programs. In general, these programs are also able to perform mixed numerical-symbolic analysis [15,16] and to evaluate sensitivities [17, Chap. 10; 18, Chap. 8].

2.1. Fundamental Properties

Consider, for simplicity, a single-input single-output circuit. Any network function may be determined starting from any set of circuit equations described in the previous section. Referring again to tableau equations [Eq. (9)] and

using Kramer's rule, we have

$$H_{ki}(s) = \frac{W_k(s)}{Q_i(s)} = \frac{\Delta_{ik}}{\det[\mathbf{T}(s)]} \quad (25)$$

where $W_k(s)$ denotes the k th output variable and Δ_{ik} is the cofactor of the element i, k of $\mathbf{T}(s)$, where i is the position of the independent source $Q_i(s)$ into the right-hand side vector of Eq. (9).

From Eq. (25), it follows that any network function of a linear circuit is a real rational function of s —that is, the ratio of two polynomials with real coefficients. Its finite poles are natural frequencies of the circuit, according to Eq. (21); due to a possible pole-zero cancellation, some natural frequencies may not appear as poles of the network function [6, p. 612].

The transform $W_k(s)$ of the output variable is given by

$$W_k(s) = H_{ki}(s)Q_i(s) = \frac{\Delta_{ik}}{\det[\mathbf{T}(s)]}Q_i(s) \quad (26)$$

Transient response is computed by finding a partial-fraction expansion of the right-hand side of Eq. (26) and then taking the inverse Laplace transform of each term of the expansion. If the network function has no poles inside the right half-plane and if its $j\omega$ -axis poles (if any) are simple, then the (zero-state) impulse response of the circuit remains bounded and the network function is said to be *stable*. If there are no poles on the $j\omega$ axis, then the impulse response decays with time, and moreover, any (zero-state) response remains bounded for any bounded input. In this case the network function is said to be *strictly stable* [e.g., 19, Chap. 9].

When the network functions are impedances or admittances of *RCLM* networks—that is, networks composed of a finite number of resistors, capacitors, inductors, and coupled inductors—they must be positive real functions; other constraints are added for two-element-kind (i.e., *RC*, *RL*, and *LC*) networks (20).

2.2. The Sinusoidal Steady State

The large use of network functions in circuit analysis is only partially due to their utility in evaluating complicated transients. One of the reasons for their acknowledged importance is related to their capability to describe the sinusoidal steady state of stable networks according to the following theorem, usually referred to as the *fundamental theorem of sinusoidal steady state* [19, Sect. 9.4; 6, Sect. 10.5].

Theorem 1. Consider any linear time-invariant circuit, driven by sinusoidal independent sources, all at the same frequency ω . If the circuit is strictly stable (i.e., all the natural frequencies have negative real part), then, for any set of initial conditions, all voltages and currents tend, as time goes to infinity, to a unique sinusoidal steady-state at the same frequency ω .

In the case of a single-input single-output circuit described by Eq. (24), magnitude W_m and phase ϕ_w of

the output waveform are given by [6, Sect. 10.5]

$$W_m = |H(j\omega)|Q_m \quad (27)$$

$$\phi_w = \arg[H(j\omega)] + \phi_q \quad (28)$$

where Q_m and ϕ_q are magnitude and phase of the input signal, respectively.

In terms of phasors [6, Chap. 9] we have

$$\hat{W} = H_\omega \hat{Q} \quad (29)$$

where $\hat{W} = |\hat{W}|e^{j\phi_w}$ and $\hat{Q} = |\hat{Q}|e^{j\phi_q}$ are the phasors of output and input waveforms, respectively, and H_ω is the transfer function defined in terms of the sinusoidal steady state. A comparison of Eq. (29) with Eqs. (27) and (28) shows that any phasor transfer function, defined in the sinusoidal steady state, may be obtained simply by setting $s = j\omega$ in the corresponding transfer function $H(s)$ defined in terms of Laplace transforms.

$H(j\omega)$ is a complex valued function of ω and may be written as

$$H(j\omega) = \mathcal{R}(\omega) + j\mathcal{I}(\omega) = |H(j\omega)|e^{j\phi_h(\omega)} \quad (30)$$

The parts of $H(j\omega)$ —that is, real part $\mathcal{R}(\omega)$, imaginary part $\mathcal{I}(\omega)$, magnitude $|H(j\omega)|$ (or gain $20 \log |H(j\omega)|$), and phase $\phi_h(\omega)$ —are the quantities involved in the steady-state response to sinusoidal excitations. Generally speaking, the overall information contained in any pair of these parts [i.e., magnitude (or gain) and phase, or real and imaginary parts], when considered as a function of frequency $f = \omega/(2\pi)$, is referred to as *frequency response* of the circuit.

It is easily verified that real part $\mathcal{R}(\omega)$ and magnitude-squared function $|H(j\omega)|^2$ are even functions of ω , whereas imaginary part $\mathcal{I}(\omega)$ and $\tan \phi_h(\omega)$ are odd functions of ω .

Transfer functions play an important role in engineering, since they can be easily and accurately measured, resorting to stable sinusoidal oscillators and to precise measurement equipments—for example, to network analyzers. On the other hand, they are the starting point for designing networks with a prescribed frequency behavior, as in the case of electrical filters and equalizers.

When poles and zeros of network functions are known, gain and phase versus frequency curves can be easily plotted, resorting to the so-called Bode plots [21, Sect. 8.2]. On the contrary, if curves of magnitude or phase, or real or imaginary parts, versus frequency are given, methods have been developed to build realizable network functions [20].

It is important to remember that real and imaginary parts of any stable network function are related to each other and, hence, constraints on them cannot be assigned arbitrarily. In fact, for a network function with no poles in the right half-plane and on the $j\omega$ axis (infinity included),

they satisfy the following equations [e.g., 18, Chap. 7]

$$\mathcal{R}(\omega) = \mathcal{R}(\infty) + \frac{1}{\pi} \int_{-\infty}^{+\infty} \frac{\mathcal{I}(x)}{\omega - x} dx \quad (31)$$

$$\mathcal{I}(\omega) = -\frac{1}{\pi} \int_{-\infty}^{+\infty} \frac{\mathcal{R}(x)}{\omega - x} dx \quad (32)$$

where $\mathcal{R}(\infty)$ is the value of the network function at infinity. Equations (31) and (32) state that if the imaginary part is specified over all frequencies, then the real part is determined to within an additive constant and that, if the real part is specified, then the imaginary part is completely determined. Similar results hold also for gain and phase of a network function, provided that it has no zeros in the right half-plane—that is, it is a minimum-phase function [18].

3. TWO-SIDED LAPLACE AND FOURIER TRANSFORMS IN CIRCUIT ANALYSIS

In addition to the one-sided Laplace transform, other frequency representations of time functions are possible and yield circuit equations closely related to the ones introduced in the previous sections. In this section, we discuss the use of two of such representations, the two-sided Laplace transform and the Fourier transform. The two-sided Laplace transform has a marginal role in circuit applications; however, it is considered here because it completes the theoretical framework of frequency-domain analysis. The Fourier transform, instead, adds significant possibilities to the frequency-domain analysis of circuits and, therefore, is discussed for both its theoretical and practical importance. In the following, we briefly review the definition and the properties of the two transforms, along with the frequency-domain circuit equations which arise when such transforms are used.

3.1. Two-Sided Laplace Transform

The two-sided Laplace transform of the function $f(t)$ is

$$\overline{F}(s) = \int_{-\infty}^{+\infty} f(t)e^{-st} dt \quad (33)$$

where $s = \sigma + j\omega$ and lowercase and overlined uppercase letters are used for transform pairs [22].

The following decomposition is useful to compute the two-sided Laplace transform

$$\begin{aligned} \overline{F}(s) &= F_-(s) + F(s) \\ F_-(s) &= \int_{-\infty}^{0-} f(t)e^{-st} dt = \int_{0+}^{+\infty} f(-t)e^{st} dt \end{aligned} \quad (34)$$

where $F(s)$ is the one-sided Laplace transform of $f(t)$ and $F_-(s)$ is the one-sided Laplace transform of $f(-t)$ computed for $t \in [0+, \infty]$ and argument $-s$. The two-sided Laplace transform exists for any s such that both $F_-(s)$ and $F(s)$ exist. If $F_-(s)$ has abscissa of convergence

σ_- (i.e., it exists for $\sigma < \sigma_-$), $F(s)$ has abscissa of convergence σ_+ (i.e., it exists for $\sigma > \sigma_+$), and $\sigma_+ < \sigma_-$, then $\bar{F}(s)$ exists and is an analytic function of s in the strip of convergence $\sigma_+ < \sigma < \sigma_-$. When $\sigma_+ = \sigma_-$, $\bar{F}(s)$ can exist as a distribution, whereas when $\sigma_+ > \sigma_-$, $\bar{F}(s)$ does not exist.

The inversion of the two-sided Laplace transform can be obtained by the line integral

$$f(t) = \frac{1}{2\pi j} \int_{\sigma_0 - j\infty}^{\sigma_0 + j\infty} \bar{F}(s)e^{st} ds \tag{35}$$

where the integration line is in the strip of convergence, or by $F_-(s)$ and $F(s)$ decomposition and tables of one-sided Laplace transform pairs. In the latter case, $F_-(s)$ and $F(s)$ are identified by their poles, since the poles of $F_-(s)$ are on the right of σ_- and those of $F(s)$ are on the left of σ_+ .

3.2. Fourier Transform

The Fourier transform of the function $f(t)$ is

$$\mathcal{F}(\omega) = \int_{-\infty}^{+\infty} f(t)e^{-j\omega t} dt \tag{36}$$

where lowercase and script uppercase letters are used for transform pairs [23]. The inverse transformation is

$$f(t) = \frac{1}{2\pi} \int_{-\infty}^{+\infty} \mathcal{F}(\omega)e^{j\omega t} d\omega \tag{37}$$

The term ‘‘spectrum of $f(t)$ ’’ is also used to indicate $\mathcal{F}(\omega)$, or, less often, the magnitude of $\mathcal{F}(\omega)$.

A sufficient condition for the existence of $\mathcal{F}(\omega)$ requires that $f(t)$ has bounded variations (i.e., finite variations for finite time increments) and is absolutely integrable. For time functions with nonvanishing asymptotic values, the Fourier transform may exist as a distribution [23].

3.3. Properties of Two-Sided Laplace Transform and Fourier Transform

Table 5 summarizes two-sided Laplace transform and Fourier transform pairs of common use, with emphasis

Table 5. Elementary Two-Sided Laplace Transform and Fourier Transform Pairs

$w(t)$	$\bar{W}(s)$, s.c. ^a	$\mathcal{W}(\omega)$
1	$2\pi\delta(s)$, $\sigma = 0$	$2\pi\delta(\omega)$
t	$-2\pi\delta'(s)$, $\sigma = 0$	$-2\pi\delta'(\omega)$
t^2	$2\pi\delta''(s)$, $\sigma = 0$	$2\pi\delta''(\omega)$
$\delta(t)$	1, $-\infty < \sigma < \infty$	1
$\exp(s_0 t)$	$2\pi\delta(s - s_0)$, $\sigma = \sigma_0$	$2\pi\delta(\omega + js_0)$
$\cos(\omega_0 t)$	$\pi[\delta(s - j\omega_0) + \delta(s + j\omega_0)]$, $\sigma = 0$	$\pi[\delta(\omega - \omega_0) + \delta(\omega + \omega_0)]$
$\text{sign}(t)$	$2/s$, $\sigma = 0$	$2/j\omega$
$\sum_{n=-\infty}^{\infty} \delta(t - nT)$		$\omega_T \sum_{n=-\infty}^{\infty} \delta(\omega - n\omega_T)$

^aNote that s.c. indicates the strip of convergence of $\bar{W}(s)$; $\delta'(\cdot)$ and $\delta''(\cdot)$ are the first and second derivative of the delta function, respectively; $s_0 = \sigma_0 + j\omega_0$ is a complex constant; and $\omega_T = 2\pi/T$.

on two-sided time functions, as algebraic, rational and harmonic signals [22,23]. Table 6 lists the main properties of the two transformation methods.

Most properties of Table 6 are identical to the corresponding properties of Table 2 for the one-sided Laplace transform, or follow from these by simply replacing s with $j\omega$. A major difference in the properties of the two-sided Laplace transform and of the Fourier transform concerns the derivation formula, where the $f(0-)$ term is dropped. Owing to the latter point, these transforms are not suited for the inclusion of the initial conditions in the solution of circuit equations.

Other properties, involving the parts $\mathcal{F}(\omega)$, are stated for network functions in Section 2.2.

3.4. Relations between Transforms

The different transforms of a waveform can be obtained one from the other via direct relations. Such relations ease the shift between frequency representations, allowing one to exploit their specific properties.

The two Laplace transforms coincide for one-sided functions ($f(t) = 0$ for $t < 0$).

The Fourier transform $\mathcal{F}(\omega)$ exists when $\bar{F}(s)$ exists on the $j\omega$ axis and is given by $\mathcal{F}(\omega) = \bar{F}(j\omega)$ [see Eqs. (33) and (36)]. Graphically, each part of $\mathcal{F}(\omega)$ is the profile of the

Table 6. Main Properties of Two-Sided Laplace Transform and Fourier Transform^a

Property	$w(t)$	$\bar{W}(s)$	$\mathcal{W}(\omega)$
Linearity	$a_1 f_1(t) + a_2 f_2(t)$	$a_1 \bar{F}_1(s) + a_2 \bar{F}_2(s)$	$a_1 \mathcal{F}_1(\omega) + a_2 \mathcal{F}_2(\omega)$
Time differentiation	$\frac{df(t)}{dt}$	$s\bar{F}(s)$	$j\omega\mathcal{F}(\omega)$
Time integration	$\int_{-\infty}^t f(t') dt'$	$\frac{1}{s}\bar{F}(s)$	$\frac{1}{j\omega}\mathcal{F}(\omega) + \pi\mathcal{F}(0)\delta(\omega)$
Time shift	$f(t - t_0)$	$\bar{F}(s)\exp(-st_0)$	$\mathcal{F}(\omega)\exp(-\omega t_0)$
Frequency shift	$f(t)\exp(s_0 t)$	$\bar{F}(s - s_0)$	$\mathcal{F}(\omega + js_0)$
Convolution	$f(t) * g(t)$	$\bar{F}(s)\bar{G}(s)$	$\mathcal{F}(\omega)\mathcal{G}(\omega)$
Moment theorem	$\int_{-\infty}^{\infty} t^n f(t) dt$	$(-1)^n \frac{d^n \bar{F}(s)}{ds^n}$	$j^n \frac{d^n \mathcal{F}(\omega)}{d\omega^n}$

^aNote that * and s_0 indicate convolution and a complex constant, respectively.

corresponding part of $\bar{F}(s)$ along the $j\omega$ axis. If the $j\omega$ axis does not belong to the strip of convergence of $\bar{F}(s)$, $\mathcal{F}(\omega)$ does not exist, whereas if the $j\omega$ axis is a boundary of the strip, $\mathcal{F}(\omega)$ exists as a distribution [e.g., 23, Sect. 9.2].

Finally, $\bar{F}(s)$ can be interpreted as the Fourier transform of the function $f(t)\exp(-\sigma t)$, which is $\mathcal{F}(\omega + \sigma/j) = \mathcal{F}(s/j)$ (see Table 6, frequency shift) for every σ where $f(t)\exp(-\sigma t)$ is Fourier-transformable.

3.5. Circuit Equations and Network Functions

Frequency-domain circuit equations based on the two-sided Laplace transform and on the Fourier transform arise by applying such transformations to the time-domain circuit equations. The equations obtained in this way differ from those based on the one-sided Laplace transform only in the branch relations of dynamic elements. The transformation of linear time-invariant dynamic branch relations via two-sided Laplace transform and Fourier transform replaces the time-derivative operator with s and $j\omega$, respectively, and adds no initial contribution.

For the two-sided Laplace transform, furthermore, the time-integral operator is simply replaced by $1/s$, and, hence, the equivalent circuits of basic elements follow from those of Fig. 1b by simply dropping the initial condition sources. Accordingly, the one-sided Laplace equations written in Section 1 become two-sided Laplace equations by setting initial conditions to zero and representing variables by two-sided Laplace transform [i.e., $F(s) \rightarrow \bar{F}(s)$].

For the Fourier transform, instead, some additional care is required. In order to avoid frequency-domain equations containing $\delta(\omega)$ terms, it is expedient to avoid the Fourier transformation of time-domain equations involving the time-integral operator (e.g., see row 3 of Table 6). Every one-sided Laplace equation written in Section 1 that does not contain the factor $1/s$ can be turned into an equation based on the Fourier transform by replacing s with $j\omega$, setting initial conditions to zero and representing variables by a Fourier transform. As an example, the tableau equations in the Fourier domain are

$$\mathbf{T}(j\omega) \begin{bmatrix} \mathcal{E}(\omega) \\ \mathcal{V}(\omega) \\ \mathcal{I}(\omega) \end{bmatrix} = \begin{bmatrix} \mathbf{0} \\ \mathbf{0} \\ \mathcal{U}_s(\omega) \end{bmatrix} \quad (38)$$

Similarly, in Section 2 we define network functions in terms of two-sided Laplace and Fourier transforms by

$$\bar{H}(s) = \frac{\bar{W}(s)}{\bar{Q}(s)}, \quad \mathcal{H}(\omega) = \frac{\mathcal{W}(\omega)}{\mathcal{Q}(\omega)} \quad (39)$$

The network functions H , \bar{H} , and \mathcal{H} are the different transforms of the same impulse response $h(t)$. Since $h(t)$ is supposed to be causal (i.e., one-sided) function, $\bar{H}(s) = H(s)$ and, provided $H(s)$ is strictly stable (i.e., the $j\omega$ axis belongs to its strip of convergence), $\mathcal{H}(\omega) = \bar{H}(j\omega) = H(j\omega)$ (see Section 3.4). The latter relation also highlights that $\mathcal{H}(\omega)$ yields the steady-state response to a harmonic input

signal (see Section 2.2). In the following, network functions are indicated only by $H(s)$ and $H(j\omega)$.

3.6. Additional Fourier Transform Properties

Additional properties of the Fourier transform relevant to circuit analysis are briefly reviewed.

3.6.1. Physical Meaning of the Fourier Representation. The Fourier representation describes signals in terms of harmonic components and the behavior of linear time-invariant systems in terms of transformation of harmonic components. This interpretation arises from Eqs. (37) and (39)

$$\begin{aligned} w(t) &= \frac{1}{2\pi} \int_{-\infty}^{+\infty} \mathcal{W}(\omega) e^{j\omega t} d\omega \\ &= \frac{1}{2\pi} \int_{-\infty}^{+\infty} H(j\omega) \mathcal{Q}(\omega) e^{j\omega t} d\omega \end{aligned} \quad (40)$$

where $q(t)$ and $w(t)$ are the input and output signals of a circuit with network function $H(s)$, respectively, and \mathcal{W} and \mathcal{Q} are their Fourier transforms. In the above equation, $[1/2\pi \mathcal{W}(\omega) d\omega] e^{j\omega t}$ are the complex harmonic signals composing $w(t)$, each of which comes from the corresponding component of the input signal $[1/2\pi \mathcal{Q}(\omega) d\omega] e^{j\omega t}$ modified by $H(j\omega)$. Such an equation formalizes the operation of linear frequency selective circuits and is the basis for the physical interpretation of frequency responses.

3.6.2. Energy and Power Spectra. The Fourier transform allows also a frequency representation of the energy content of signals [24]. The energy of $q(t)$ can be expressed by the sum of the energies of its harmonic components

$$\mathcal{E} \stackrel{\text{def}}{=} \int_{-\infty}^{+\infty} q(t) q^*(t) dt = \frac{1}{2\pi} \int_{-\infty}^{+\infty} \mathcal{Q}(\omega) \mathcal{Q}^*(\omega) d\omega \quad (41)$$

where $*$ denotes complex conjugation. This equation stems from the orthogonality of harmonic components and is known as the Parseval's formula for finite-energy signals. This relation leads to the definition of the energy spectrum $G_q(\omega) \stackrel{\text{def}}{=} \mathcal{Q}(\omega) \mathcal{Q}^*(\omega) / 2\pi$ [i.e., the energy density of $q(t)$ within $[\omega, \omega + d\omega]$] and of the autocorrelation function $R_q(\tau)$ as the inverse Fourier transform of $G_q(\omega)$.

The autocorrelation and energy spectrum concepts can be extended to signals with finite average power and to stationary stochastic processes, thereby providing a frequency representation also for these important class of signals [24]. In this case, the energy spectrum is renamed power spectrum and the frequency-domain analysis results extend to these signals by the transfer relation

$$G_w(\omega) = |\bar{H}(j\omega)|^2 G_q(\omega) \quad (42)$$

where $G_q(\omega)$ and $G_w(\omega)$ are the power spectra of the input and output related by the network function $H(j\omega)$, respectively.

4. APPLICATIONS OF FREQUENCY-DOMAIN ANALYSIS

The procedure for the frequency-domain analysis of circuits is almost independent of the transformation method used. This latter decides only which waveforms can be represented, how they are represented, and which elements of the circuit behavior are highlighted. Apparently, Laplace transform seems able to handle a more general class of functions and, therefore, seems preferable. This point, however, is controversial [e.g., 23] and the transformation method, instead, should be chosen according to applications.

Roughly speaking, network functions in the s domain offer zero-pole portraits of the circuit behavior and provide the most reliable information on system dynamics and stability. Furthermore, the one-sided Laplace transform takes into account the initial conditions of energy-storing elements and is the preferred transformation method for the frequency-domain solution of transient problems.

When network functions are computed on the $j\omega$ axis (i.e., the Fourier representation is used), they offer a frequency-by-frequency portrait of the circuit behavior, describing how the harmonic components of the input signals are changed. This is useful both in obtaining and in specifying the circuit frequency responses, helps the physical interpretation of frequency-domain results, and allows the frequency characterization of circuits by measurements. For its properties, the Fourier approach is common in problems involving steady-state analysis, signal propagation, and stochastic signals.

In this section we show examples of frequency-domain circuit analysis, which illustrate typical applications and remark the features of the different transformation methods.

4.1. Transient and Frequency Responses

In order to illustrate the evaluation of transient and frequency responses, we consider the circuit of Fig. 4a. For such a circuit, we compute the zero-state response of voltage $v_0(t)$ across resistor R_L to a rectangular input pulse of duration T and height E_0 ; that is, $v_s(t) = E_0[u(t) - u(t - T)]$. Besides, we also compute the frequency response of v_0 to the input v_s . The components have the following (normalized) values: $R_s = R_L = 1 \Omega$, $C_1 = C_2 = 1 \text{ F}$, $L = 2 \text{ H}$, $E_0 = 2 \text{ V}$, and $T = 1 \text{ s}$.

To solve this problem, we first compute the voltage transfer function $H(s) = V_0(s)/V_s(s)$, by using Eq. (16) and setting to zero the sources related to initial conditions

$$H(s) = \frac{V_0(s)}{V_s(s)} = \frac{\Delta_{12}}{\Delta} = \frac{0.5}{s^3 + 2s^2 + 2s + 1} \quad (43)$$

where Δ is the determinant of the node admittance matrix Y_n and Δ_{12} is the cofactor of element 1,2 of Y_n .

From Tables 1 and 2, the Laplace transform of the input waveform turns out to be $V_s(s) = E_0(1 - e^{-Ts})/s = 2(1 - e^{-s})/s$. As a consequence, the transform of output

voltage is

$$V_0(s) = H(s)V_s(s) = \frac{1}{s(s^3 + 2s^2 + 2s + 1)}(1 - e^{-s}) \quad (44)$$

By expanding in partial fractions, we obtain

$$V_0(s) = \left[\frac{1}{s} - \frac{1}{s + 1} - \frac{1}{(s + 0.5)^2 + (\sqrt{3}/2)^2} \right] (1 - e^{-s}) \quad (45)$$

Taking the inverse Laplace transform of each term of the above equation and resorting again to Tables 1 and 2, we have

$$v_0(t) = \left[1 - e^{-t} - \frac{2}{\sqrt{3}} e^{-0.5t} \sin \frac{\sqrt{3}}{2} t \right] u(t) - \left[1 - e^{-t+1} - \frac{2}{\sqrt{3}} e^{-0.5t+0.5} \sin \left(\frac{\sqrt{3}}{2} (t - 1) \right) \right] \times u(t - 1) \quad (46)$$

where v_0 is expressed in volts and t in seconds.

To obtain the frequency response, we set $s = j\omega$ in Eq. (43):

$$H(j\omega) = \frac{0.5}{(1 - 2\omega^2) + j\omega(2 - \omega^2)} \quad (47)$$

The parts of $H(j\omega)$ are easily computed from the above equation. Figure 6 shows the curves of gain $g_H = 20 \log |H(j\omega)|$ and phase $\phi_H = \arg[H(j\omega)]$ for $0 \leq \omega \leq 4 \text{ rad/s}$.

4.2. Asymptotic Responses of Circuits

The response of (strictly) stable circuits can be intuitively divided into a *transient part* and an *asymptotic part* (see Ref. 25 for a complete discussion). The two parts can be visualized and computed by a partial-fraction expansion of the circuit response. Fractions from the poles of the circuit

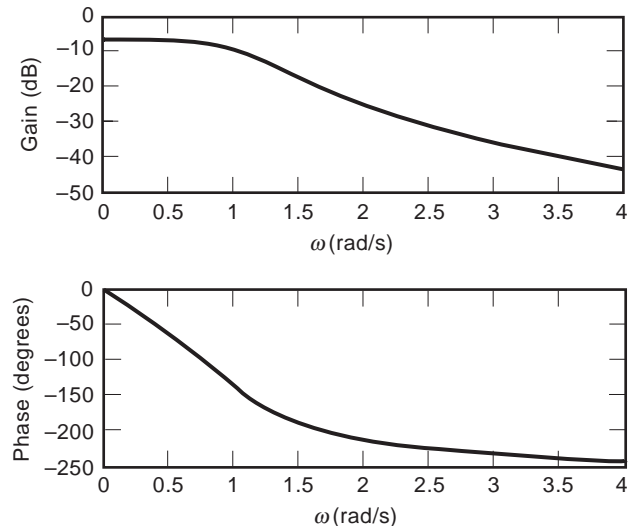


Figure 6. Frequency response for the circuit of Fig. 4.

transfer function $H(s)$ represent decreasing time functions and form the transient part, whereas the other terms form the asymptotic part. The asymptotic part can also be computed directly by the two-sided Laplace transform [e.g., 26, Chap. 9].

The evaluation of the asymptotic part is particularly important for periodic input signals. In this case, the asymptotic response is usually named *steady-state response*. Here, we illustrate two typical approaches to the evaluation of such a response. For this, we write a periodic input signal of period T as

$$q(t) = \sum_{n=-\infty}^{\infty} q_T(t - nT) = q_T(t) * \sum_{n=-\infty}^{\infty} \delta(t - nT) \quad (48)$$

where $q_T(t)$ is the *cycle function*, which coincides with $q(t)$ in $[0, T]$ and is null elsewhere, and $*$ denotes convolution.

5. ONE-SIDED APPROACH

The steady-state response $w_a(t)$ is a periodic function of period T . The one-sided approach consists in applying the periodic input from $t=0$ and leads to the cycle function $w_{aT}(t)$ of $w_a(t)$.

With this approach, the transform $W(s)$ of the complete response $w(t)$ is given by

$$W(s) = H(s)Q(s) = H(s) \frac{Q_T(s)}{1 - e^{-sT}} = W_t(s) + W_a(s) \quad (49)$$

where W_t and $W_a = W_{aT}(s)/(1 - e^{-sT})$ collect the poles of $H(s)$ and $1/(1 - \exp(-sT))$, respectively ($Q_T(s)$ is analytic everywhere but at infinity). In Eq. (49), $W_t(s)$ can be explicitly computed from the partial fraction terms of $W(s)$ involving the poles of $H(s)$. Once $W_t(s)$ is computed, $W_{aT}(s)$ is obtained as

$$W_{aT}(s) = H(s)Q_T(s) - W_t(s)(1 - e^{-sT}) \quad (50)$$

The interested reader is referred to Ref. 27 for a detailed discussion and illustrative examples.

6. FOURIER APPROACH

In this approach $w_a(t)$ is obtained as a Fourier series via $H(j\omega)$ and the Fourier transform of the periodic input.

The Fourier transform of the periodic input is a *line spectrum* composed of equispaced ideal pulses [see Eq. (48) and Table 5] and $\mathcal{W}_a(\omega)$ is composed of the same input lines modified by $H(j\omega)$

$$\begin{aligned} \mathcal{Q}(\omega) &= \mathcal{Q}_T(\omega) \sum_{n=-\infty}^{\infty} \omega_T \delta(\omega - n\omega_T), \quad \omega_T = 2\pi/T \\ \mathcal{W}_a(\omega) &= H(j\omega) \mathcal{Q}(\omega) \\ &= H(j\omega) \mathcal{Q}_T(\omega) \sum_{n=-\infty}^{\infty} \omega_T \delta(\omega - n\omega_T) \end{aligned} \quad (51)$$

from which the Fourier series of $w_a(t)$ follows

$$w_a(t) = \sum_{n=-\infty}^{\infty} \frac{1}{T} H(jn\omega_T) \mathcal{Q}(jn\omega_T) e^{jn\omega_T t} \quad (52)$$

Although the computation of $w_a(t)$ via its Fourier series is simple, it is practically useful only when the number of significant harmonic component is small. On the other hand, this representation can be exploited also for the asymptotic responses of weakly nonlinear circuits driven by periodic sources. For such an analysis, each nonlinear circuit element is characterized by generalized network functions describing how the element combines its input spectral lines into output ones [28].

6.1. Noise Sources

In this section we illustrate the frequency-domain analysis of circuits containing stochastic sources characterized by their power spectra [24, Chap. 10].

We consider the very simple example of Fig. 7a. Noise sources $e_1(t)$ and $e_2(t)$ model the thermal noise generated by the two resistors. A typical problem in noisy two-port elements is the evaluation of the source terms of their chain matrix constitutive relations—that is, the equivalent sources v_{01} and i_{01} shown in Fig. 7b.

In order to obtain the equivalent sources for this example, we replace $e_1(t)$ and $e_2(t)$ with deterministic signals with spectra $\mathcal{E}_1(\omega)$ and $\mathcal{E}_2(\omega)$ and generate the transformed circuit of the problem. $\mathcal{V}_{01}(\omega)$ and $\mathcal{I}_{01}(\omega)$ be computed as the voltage and current at port 1, ensuring null voltage and current at port 2. This analysis yields the

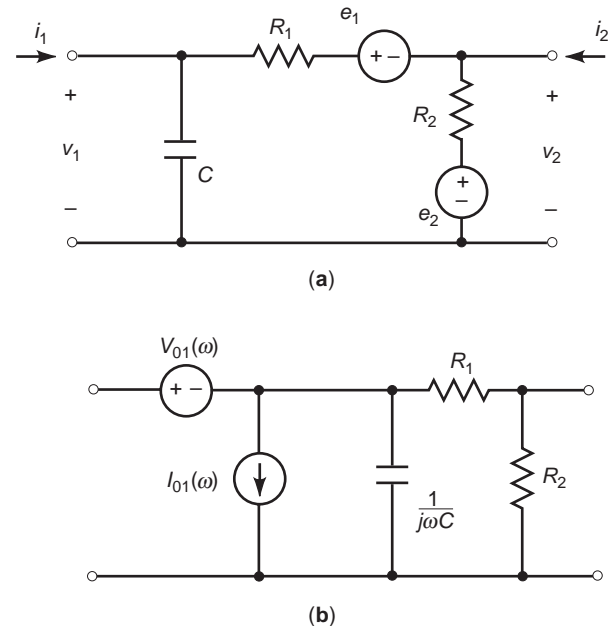


Figure 7. Evaluation of equivalent noise sources for a two-port element with noisy resistors: (a) original problem; (b) transformed circuit with equivalent sources $\mathcal{V}_{01}(\omega)$ and $\mathcal{I}_{01}(\omega)$.

following transfer relations:

$$\begin{aligned}\mathcal{V}_{01}(\omega) &= \mathcal{E}_1(\omega) + (R_1/R_2)\mathcal{E}_2(\omega) \\ \mathcal{I}_{01}(\omega) &= j\omega C\mathcal{E}_1(\omega) + [j\omega C(R_1/R_2) - 1/R_2]\mathcal{E}_2(\omega)\end{aligned}\quad (53)$$

When noise sources are described by their power spectra $G_{e1}(\omega)$ and $G_{e2}(\omega)$, the power spectra of the equivalent sources are obtained by using the statistical independence of e_1 and e_2 , so that Eq. (42) yields

$$\begin{aligned}G_{v01}(\omega) &= G_{e1}(\omega) + (R_1/R_2)^2 G_{e2}(\omega) \\ G_{i01}(\omega) &= (\omega C)^2 G_{e1}(\omega) + [(\omega C(R_1/R_2))^2 + 1/R_2^2] G_{e2}(\omega)\end{aligned}\quad (54)$$

6.2. Frequency-Domain Analysis of Large Circuits

The evaluation of network functions and of frequency responses amounts to the symbolic or numerical solution of frequency-domain equations. For large networks, with hundreds or thousands of dynamic elements, both tasks can be prohibitively expensive. In these cases, approximate frequency solutions are sought, which reproduce the exact solution in a limited frequency range. The approximate solutions are defined by a reduced number of poles, which approximate some of the poles of the exact solution.

The most used approach to generate reduced order approximations of network functions relies on Padé approximants [29]. A rational approximation $\hat{H}(s)$ of order p to $H(s)$

$$\hat{H}(s) = \sum_{j=1}^p \frac{\hat{k}_j}{s - \hat{s}_j} \quad (55)$$

can be sought by expanding the Maclaurin series of $\hat{H}(s)$ and $H(s)$, up to order $n = 2p - 1$:

$$\sum_{n=0}^{2p-1} s^n \left[-\sum_{j=1}^p \frac{\hat{k}_j}{\hat{s}_j^{n+1}} \right] = \sum_{n=0}^{2p-1} s^n \left[\frac{H^{(n)}(0)}{n!} \right] \quad (56)$$

This equation requires

$$-\sum_{j=1}^p \frac{\hat{k}_j}{\hat{s}_j^{n+1}} = \frac{H^{(n)}(0)}{n!}, \quad n = 0, 1, \dots, 2p - 1 \quad (57)$$

which yield the unknown parameters \hat{k}_j and \hat{s}_j as functions of the coefficients $H^{(n)}(0) = [d^n H(s)/ds^n]_{s=0}$. Such coefficients are shortly named moments of $H(s)$ (see Table 6), and are much easier to compute than $H(s)$ itself. In this basic version, $\hat{H}(s)$ approximates $H(s)$ for small s values (i.e., in the low-frequency range), however, different series expansion and coefficient identities have been devised to cope with different frequency ranges (the interested reader may refer to Ref. 30 for a detailed discussion).

The moments of network functions can be easily obtained by MNA. It is expedient to compute simultaneously the moments of all network functions relating a source $q(t)$ with the unknowns of the MNA equations. Such network functions are the responses of the transformed circuit when q is the only active source and $Q(s) = 1$. They can be collected in a vector $\mathbf{H}(s)$, which is the solution of $(s\mathbf{P}_1 + \mathbf{P}_0)\mathbf{H}(s) = \mathbf{E}$, where $(s\mathbf{P}_1 + \mathbf{P}_0)$ is the MNA matrix (\mathbf{P}_0 and \mathbf{P}_1 being constant matrices) and \mathbf{E} is the source vector, containing only the source $Q(s) = 1$. When $\mathbf{H}(s)$ is represented by its moments, the following equations arise [30]:

$$(s\mathbf{P}_1 + \mathbf{P}_0)(\mathbf{H}(0) + s\mathbf{H}^{(1)}(0) + (s^2/2)\mathbf{H}^{(2)}(0) + \dots) = \mathbf{E} \quad (58)$$

$$\mathbf{P}_0\mathbf{H}(0) = \mathbf{E} \quad (59)$$

$$\mathbf{P}_0\mathbf{H}^{(n)}(0) = -\mathbf{P}_1\mathbf{H}^{(n-1)}(0), \quad n > 0$$

From these equations, the zeroth-order moments $\mathbf{H}(0)$ are obtained as $\mathbf{H}(0) = \mathbf{P}_0^{-1}\mathbf{E}$ (which requires one matrix inversion), and the higher-order moments are obtained as $\mathbf{H}^{(n)}(0) = -\mathbf{P}_0^{-1}\mathbf{P}_1\mathbf{H}^{(n-1)}(0)$ (which requires one matrix multiplication for every vector of moments). This procedure is nearly equivalent to a DC solution of the network.

6.3. Transmission-Line Frequency-Domain Analysis

Transmission lines (TLs) are important circuit elements, because of their many applications (e.g., the modeling of electrically long interconnects). As linear time-invariant elements, TLs are effectively treated by the frequency-domain approach. Both one-sided Laplace transform (transient problems) and Fourier transform (steady-state problems and physical interpretation) are used for TL analysis.

The Fourier transform of voltages and currents along a two-conductor uniform TL supporting a quasi-TEM field are related by the telegrapher equations [31]:

$$\frac{d\mathcal{V}(\omega, z)}{dz} = -\tilde{\mathbf{Z}}(j\omega)\mathcal{I}(\omega, z) \quad (60)$$

$$\frac{d\mathcal{I}(\omega, z)}{dz} = -\tilde{\mathbf{Y}}(j\omega)\mathcal{V}(\omega, z)$$

In these equations, z is the longitudinal coordinate (see Fig. 8), and $\tilde{\mathbf{Z}}(j\omega)$ and $\tilde{\mathbf{Y}}(j\omega)$ are the TL per unit length impedance and admittance, respectively [31].

The solution of Eqs. (60) is

$$\mathcal{V}(\omega, z) = \mathcal{V}^+(\omega)e^{-Kz} + \mathcal{V}^-(\omega)e^{Kz} \quad (61)$$

$$\mathcal{I}(\omega, z) = (\mathcal{V}^+(\omega)e^{-Kz} + \mathcal{V}^-(\omega)e^{Kz})Y(j\omega)$$

where $\mathcal{V}^+(\omega)$ and $\mathcal{V}^-(\omega)$ are arbitrary functions and K and Y are the TL complex propagation constant and

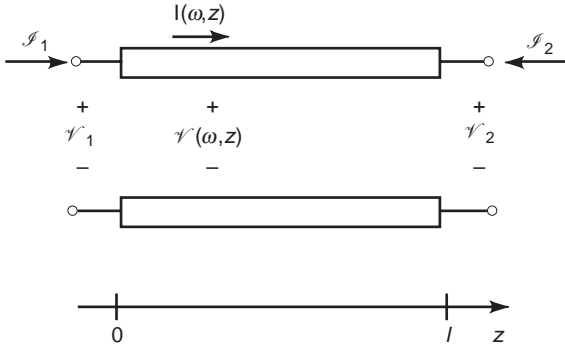


Figure 8. A two-conductor transmission line and the quantities relevant to its analysis.

characteristic admittance, respectively:

$$K(j\omega) = \alpha(\omega) + j\beta(\omega) = \sqrt{\tilde{\mathbf{Z}}(j\omega)\tilde{\mathbf{Y}}(j\omega)} \quad (62)$$

$$Y(j\omega) = \sqrt{\tilde{\mathbf{Y}}(j\omega)/\tilde{\mathbf{Z}}(j\omega)}$$

The waveform described by $\mathcal{V}^+(\omega) \exp(-Kz)$ has harmonic components $\mathcal{V}^+(\omega) \exp[-\alpha(\omega)z - j\beta(\omega)z + j\omega t] d\omega/2\pi$. Each of such components is a harmonic function $\mathcal{V}^+(\omega) \exp(j\omega t)$ traveling toward increasing z with phase velocity $v_\phi = \omega/\beta(\omega)$ and attenuating according to $\exp(-\alpha(\omega)z)$. It describes a transverse electromagnetic field concentrated on the line cross section and propagating along $+z$ as a plane wave.

The frequency-domain analysis of a circuit containing the TL can be carried out by relating voltages and currents at the line ends through the TL solution [Eq. (61)]. The relations are (see Fig. 8)

$$\begin{aligned} \mathcal{V}_1(\omega) &= \mathcal{V}^+ + \mathcal{V}^- \\ \mathcal{V}_2(\omega) &= \mathcal{V}^+ \exp(-\Theta) + \mathcal{V}^- \exp(+\Theta) \\ \mathcal{I}_1(\omega) &= Y(\mathcal{V}^+ - \mathcal{V}^-) \\ \mathcal{I}_2(\omega) &= -Y\mathcal{V}^+ \exp(-\Theta) + Y\mathcal{V}^- \exp(+\Theta) \end{aligned} \quad (63)$$

with $\Theta = K(j\omega)\ell$, where ℓ is the linelength. The arbitrary functions $\mathcal{V}^+(\omega)$ and $\mathcal{V}^-(\omega)$ are determined by the preceding relations and the constitutive relations of the circuit connected at the TL ends. Alternatively, the TL can be characterized as a two-port circuit by a set of network parameters. The network parameters can be obtained by expressing two of the TL end variables as a function of the other two through Eqs. (63). As an example, the chain matrix of the TL is obtained by computing $\mathcal{V}^+(\omega)$ and $\mathcal{V}^-(\omega)$ via the second and fourth lines of Eqs. (63) and by using the first and third lines of Eqs. (63) to obtain $\mathcal{V}_1(\omega)$ and $\mathcal{I}_1(\omega)$. The chain relations

are

$$\mathcal{V}_1(\omega) = \cosh(\Theta)\mathcal{V}_2(\omega) + [\sinh(\Theta)/Y][-\mathcal{I}_2(\omega)] \quad (64)$$

$$\mathcal{I}_1(\omega) = Y \sinh(\Theta)\mathcal{V}_2(\omega) + \cosh(\Theta)[-\mathcal{I}_2(\omega)] \quad (65)$$

Chain parameters can be interpreted as transfer functions in the s domain by replacing $j\omega$ with s in $\Theta = K(j\omega)\ell$ and $Y(j\omega)$. The network functions of distributed circuits, however, are not rational functions of s , because they have infinitely many poles. For small $\Theta(s)$ values (i.e., electrically short lines), the lumped parameter formulation can be recovered by approximating the TL transfer functions with rational functions.

Multiconductor TLs can be treated similarly, by replacing scalar relations for voltages and currents along the line with vector relations for voltages and currents on the different conductors [31]. The formulation becomes considerably complicated, yet it maintains the same properties of the two-conductor case.

BIBLIOGRAPHY

1. G. Doetsch, *Introduction to the Theory and Application of the Laplace Transformation*, Springer-Verlag, Berlin, 1974.
2. M. R. Spiegel, *Theory and Problems of Laplace Transforms*, McGraw-Hill, New York, 1965.
3. G. Doetsch, *Tabellen zur Laplace-Transformation*, Springer-Verlag, Berlin, 1947.
4. F. Oberhettinger and L. Badii, *Tables of Laplace Transforms*, Springer-Verlag, Berlin, 1973.
5. G. D. Hatchel, R. K. Brayton, and F. G. Gustavson, The sparse tableau approach to network analysis and design, *IEEE Trans. Circ. Theory* **CT-18**:101–113 (1971).
6. L. O. Chua, C. A. Desoer, and E. S. Kuh, *Linear and Nonlinear Circuits*, McGraw-Hill, New York, 1987.
7. R. A. DeCarlo and P.-M. Lin, *Linear Circuit Analysis*, Prentice-Hall, Englewood Cliffs, NJ, 1995.
8. A. M. Rushdi, Development of modified nodal analysis into a pedagogical tool, *IEEE Trans. Educ.* **E-28**:17–25 (1985).
9. J. Vlach and K. Singhal, *Computer Methods for Circuit Analysis and Design*, Van Nostrand-Reinhold, New York, 1983.
10. C. W. Ho, A. E. Ruehli, and P. A. Brennan, The modified nodal approach to network analysis, *IEEE Trans. Circ. Syst.* **CAS-22**:504–509 (1975).
11. B. C. Kuo, *Linear Networks and Systems*, McGraw-Hill, New York, 1967.
12. W.-K. Chen, *Linear Networks and Systems: Algorithms and Computer-Aided Implementations*, 2nd ed., World Scientific, Singapore, 1990.
13. C. A. Desoer and E. S. Kuh, *Basic Circuit Theory*, McGraw-Hill, New York, 1969.
14. L. O. Chua and P.-M. Lin, *Computer-Aided Analysis of Electronic Circuits*, Prentice-Hall, Englewood Cliffs, NJ, 1975.
15. G. Gielen, H. Walscharts, and W. Sansen, Isaac: A symbolic simulator for analog integrated circuits, *IEEE J. Solid-State Circ.* **SC-24**:1587–1597 (1989).

16. Anonymous, *Sspice-Symbolic SPICE-Circuit Analyzer and Approximator, Version 1.0*. Michigan State Univ., 1991.
17. G. C. Temes and J. W. LaPatra, *Circuit Synthesis and Design*, McGraw-Hill, New York, 1977.
18. N. Balabanian and T. Bickart, *Linear Network Theory, Matrix*, Chesterland, OH, 1981.
19. L. A. Zadeh and C. A. Desoer, *Linear System Theory*, McGraw-Hill, New York, 1963.
20. L. Weinberg, *Network Analysis and Synthesis*, McGraw-Hill, New York, 1962.
21. F. F. Kuo, *Networks Analysis and Synthesis*, Wiley, New York, 1962.
22. B. V. der Pol and H. Bremmer, *Operational Calculus Based on the Two Sided Laplace Transform*, Cambridge Univ. Press, New York, 1950.
23. A. Papoulis, *The Fourier Integral and its Applications*, McGraw-Hill, New York, 1987.
24. A. Papoulis, *Probability, Random Variables, and Stochastic Process*, McGraw-Hill, New York, 1965.
25. P. Dorato, A. M. Lepschy, and U. Viaro, Some comments on steady-state and asymptotic responses, *IEEE Trans. Educ.* **37**:264–268 (1994).
26. G. V. Lago and L. M. Benningfield, *Circuit and System Theory*, Wiley, New York, 1979.
27. S. Seshu and N. Balabanian, *Linear Network Analysis*, Wiley, New York, 1959.
28. D. D. Weiner and J. F. Spina, *Sinusoidal Analysis and Modeling of Weakly Nonlinear Circuits*, Van Nostrand-Reinhold, New York, 1980.
29. E. Chiprout and M. S. Nakhla, *Asymptotic Waveform Evaluation*, Kluwer Academic Publishers, Norwell, MA, 1994.
30. G. A. Baker, *Essentials of Padé Approximants*, Academic Press, New York, 1975.
31. C. R. Paul, *Analysis of Multiconductor Transmission Lines*, Wiley-Interscience, New York, 1994.

FREQUENCY-INDEPENDENT ANTENNAS

DEJAN S. FILIPOVIC
University of Colorado
Boulder, Colorado

THOMAS P. CENCICH
Lockheed Martin
Denver, Colorado

MICHAEL W. NURNBERGER

1. INTRODUCTION

Frequency-independent (FI) antennas are characterized by virtually invariant impedance and pattern performance over wide bandwidths or over multiple logarithmically periodic bands. A true FI antenna must have an infinitely large aperture (no low-frequency limit) and an infinitely fine and small central/feeding region

(no high-frequency limit). Its geometry must be described by angles, and no single structural characteristic should depend on length. To eliminate contaminating radiation from various regions on the FI structure, the nonradiated (often referred to as *residual*) currents must decay to zero after passing an appropriate active region and before entering the next radiating region. The most desirable way to attenuate excited currents on an FI antenna is through radiation, but complete radiation from a single active region (constructive radiation) is not possible. Ideal FI antennas must use a frequency-independent feed to realize their full bandwidth.

Certainly, no practically realizable antenna can fulfill these requirements, and thus a more lenient definition of a FI antenna (from the beginning of the text) is generally accepted. After half of century of development, consistent impedance and pattern characteristics over 100:1 bandwidths can be achieved today with a single antenna. Even in the early days (mid-1950s), the bandwidth of the first FI antennas was larger than the bandwidth of the supporting electronics, so once the range of 20:1 was demonstrated, antenna researchers attempted to gain a theoretical understanding of FI antenna performance. The list of individuals and respective electromagnetics groups with significant contributions in FI research is rather large, but a special place belongs to the early work of Prof. Victor H. Rumsey and his colleagues and their students at the Antenna Laboratories at the University of Illinois at Urbana and Champaign (UIUC) and at the University of California at Berkeley (UCB). In addition to the FI concept, quite a few pioneering antenna designs, including spirals, log-periodic antennas, and FI arrays, to mention only a few, emerged from these two laboratories.

In this article, Rumsey's theory of FI antennas [1,2] is reviewed and some historical highlights of the most important contributions in this area are outlined. A mathematical derivation for a general FI structure is provided, and some special cases are considered both theoretically and practically. The underlying theory of operation for several FI antenna types, including equiangular spirals, sinuous antennas, and log-periodic slot arrays, is also described.

2. HISTORICAL OVERVIEW

Professor Victor Rumsey first proposed the FI concept in the mid-1950s. He initiated the research while he was with the Ohio State University, but the major contributions to the definition and analytical treatment of FI antennas came during his stay with UIUC, where he and other researchers, such as Raymond DuHamel and Dwight Isbell (log-periodic antenna concept, etc.), John Dyson (experimental work on spiral antennas, etc.), Paul Mayes (multiarm spirals, backward-traveling waves in periodic structures, etc.), Georges Deschamps (theoretical concepts on impedance, etc.), and their students were instrumental in both theoretical and experimental verification of this revolutionary concept in

antenna theory. The list of individuals and their inventions is extensive, and since a comprehensive overview of historical developments can be found in Ref. 3, here we outline only a few contributions available in the open literature (it is important to note that the work of many researchers was shielded from the public eye for decades; thus some concepts might have been proposed earlier than the cited publications):

- 1943: Schelkunoff [4] developed a transmission-line model of a biconical antenna—the first antenna specified by angles. However, the currents do not decay faster than the far field of the antenna and the truncation principle is not satisfied. Thus, while the bicone is not an FI antenna, it was nevertheless instrumental in future developments.
- 1957: Rumsey [1] derived an analytical formulation of FI principles; specifically, a mathematical derivation of the generic angle-specified geometries.
- 1957: DuHamel and Isbell [5] proposed an analytical formulation of log-periodic principles: mathematical derivation of log-periodic geometry, planar sheet design, and experimental verification of log-periodic FI performance over 10:1 bandwidth.
- 1958: DuHamel and Ore [6], while designing wire log-periodic antennas, noticed that the current is concentrated at the edges of a planar sheet; thus they removed metal in between and obtained a lightweight structure. Their work included some circularly polarized designs, as well as unidirectional folded structure (origin of this concept is traced to D. Isbell's work published in a UIUC report).
- 1959: Deschamps [7], investigated the modal impedances of multiarm self-complementary structures, extending the concept suggested by Mushiake in 1949 (published in Japanese) to multiarm structures and derived the formula for arm impedances.
- 1959: Dyson [8,9] experimentally verified the FI performance of the spiral antenna and designed planar and conical slot spirals operating over bandwidths in excess of 10:1 and infinite (Dyson) balun feed with practically unrestricted bandwidth (for other contributions in spiral antennas, see article SPIRAL ANTENNAS).
- 1961: Carrel [10] established design guidelines for the log-periodic dipole antenna, with transposed feeder design.
- 1961: Berry and Ore [11] designed a log-periodic $\lambda/4$ monopole array over a finite-size ground plane, with reactive feeder design.
- 1961: Mayes et al. [12] investigated the excitation of backward-traveling waves on log-periodic structure.
- 1961: Cheo et al. [13] proposed an analytical treatment of the orthogonal radiation modes on an infinitely large spiral antenna with an infinite number of arms.
- 1965: Mei et al. [14] proposed the concept of highly directive FI array topology.
- 1968: Yeh and Mei [15] developed a method-of-moment characterization of spirals.
- 1968: Ingerson and Mayes [16] used an impedance-modulated feedline to prevent occurrence of bandstop behavior and also proposed a novel log-periodic cavity backing concept to support efficient flush mounting.
- 1987: DuHamel [17] designed the sinuous antenna: an omnipolarized, planar, single aperture, log-periodic antenna.

3. BASIC THEORETICAL PRINCIPLES

For the design and realization of FI antennas, the following principles play an important role and thus must be understood:

- Geometry/performance scaling
- Angular description of the geometry
- Termination of residual nonradiated currents
- Self-complementary geometry

The FI idea started with the notion that for a nondispersive medium, the current distribution on an antenna as a function of frequency remains fixed only if the dimensions of both the antenna and the operating wavelength are changed by the same fraction; that is, only if the electrical dimensions of the antenna remain invariant to changes in operating frequency. From another perspective, in order to maintain a constant (unaltered) current distribution on an antenna as a function of frequency, the antenna structure must scale with wavelength. Then, since the current distribution does not change with normalized frequency, neither will the impedance at the antenna terminals or the fields radiated from the antenna, and the antenna performance will be invariant with frequency. This concept can be extended to include an inhomogeneous structure (any combination of metals, dielectrics) provided all dimensions of the structure are scaled in proportion to the wavelength (inversely to frequency).

Rumsey [1] recognized that to obtain a continuous scaling of antenna performance with frequency, that is, with virtually unchanged characteristics, an antenna should have no lineal dependence. More specifically, if the antenna geometry is specified only by angles, then the frequency scaling, which for antennas with lineal structural form is manifested by the scaling of resonances, will correspond to rotation and translation of the basic structure. On the basis of this observation, and with some minor restrictions, he was able to derive a mathematical formula for a frequency independent radiator in both planar and nonplanar forms (see next section).

Ultimately, while yielding an infinitely broadband antenna, any structure defined purely by angles must also both be infinitely large and have infinitely fine center details. Therefore, in order to be practically useful, the antenna structure must be of finite size and should satisfy the truncation principle; that is, the currents on the

antenna must decay to zero after they radiate from the lowest-order active region. Any residual currents must be prevented from radiating from the higher-order active regions, as this ultimately will contaminate the far-field pattern of the antenna. If the currents indeed reduce to zero after passing this dominant active region, the antenna aperture can be terminated at a finite distance and the reflection from structural ends will be nonexistent. Another way of saying this is that the radiation pattern of the finite, truncated structure must approach a limiting form—generally, the pattern of the infinite structure—as the frequency is increased.

The truncation principle establishes the lower frequency limit of the FI behavior of the antenna. As the frequency decreases, a point will be reached when the currents on the antenna begin to encounter its end before decaying to zero. Below this frequency the antenna will still radiate, but its current distribution will be disturbed by the above-mentioned encounter. As a consequence, antenna gain, pattern, and input impedance will be inconsistent with frequency. A lossy termination is often integrated with the end of the radiator to mitigate end effects as well as to extend the low-frequency performance of the antenna (provided that lower efficiency is acceptable). The upper frequency limit of an FI antenna is based on the finesse, detail, and precision with which the balun and feed region can be fabricated.

Self-complementary geometry is not a necessary condition for FI performance, but certainly is one that helps to obtain consistent broadband behavior. Applied only to planar structures, this principle states that if the interchange between metallic and nonmetallic (or slot) parts on a planar antenna embedded in a homogeneous medium leaves the geometry unchanged except for a rotation equal to half of the angular periodicity, then the respective impedances of two complementary antennas are related by

$$Z_{\text{metal}}Z_{\text{slot}} = \left(\frac{\eta}{2}\right)^2 \quad (1)$$

where η is the plane-wave impedance for the homogeneous medium (for an antenna in air $\eta = 120\pi \Omega$, and the impedance is $Z_{\text{metal}} = Z_{\text{slot}} = 188.5 \Omega$). As noted by Mushiake in 1949, formula [1] is based on Booker's extension of Babinet's principle (see any antenna textbook, e.g., Ref. 18) can be utilized for designing antennas with broadband impedance matching. Several examples of planar self-complementary structures are shown in Fig. 1.

Finally, FI performance can also be claimed if minimal variation in the measurable parameters of the antenna—typically its gain, pattern, and input impedance—occurs within a certain frequency range and is repeated for several consecutive (logarithmic) periods. In the ideal case, an infinite number of these periods would exist, and the resulting infinitely large and detailed structure would have unlimited bandwidth. The connection between these two seemingly different approaches is mathematically supported through the logarithmic dependence of the structural features of a planar projection of a 3D truly FI antenna structure, known as a *conical screw*, as shown in the next section. This principle is a rule more for eval-

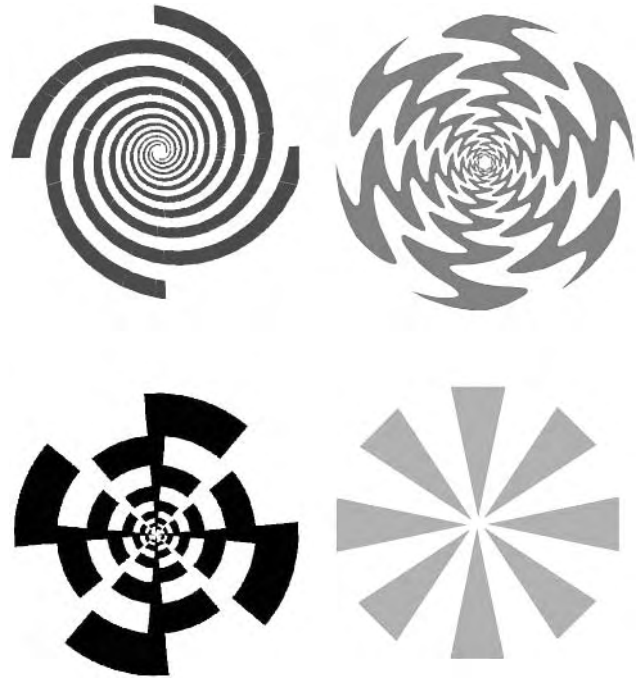


Figure 1. Several examples of self-complementary planar structures.

uation rather than the design, and implies that a properly designed FI antenna should have identical performance at frequencies related by the (logarithmic) periodicity of the antenna with as little variation as possible in the performance within each period.

A generic log-periodic structure is depicted in Fig. 2. The geometric ratio, or growth rate, is denoted by τ and is the ratio of frequencies between which “small” variations in antenna performance occur. The growth rate is also equal to the ratio of the lower (smaller) and the next-higher (larger) repeatable structural dimension, $\tau = f_n / f_{n+1} = r_{n+1} / r_n$. Achievement of a pattern null (zeroing) in the plane of the antenna is needed for reasons of truncation. If the zeroing of the pattern is not produced in the truncated direction, the currents will also exist to infinity and the end effect will be pronounced. As discussed earlier, this would violate the truncation principle and antenna would cease to produce FI behavior.

4. MATHEMATICAL DERIVATION OF FREQUENCY INDEPENDENCE

The analytical treatment of a generic FI structure given in this section follows the original derivation by Rumsey [1], with generalizations provided by Elliott [19] and certain specifics for log-periodic structures given by DuHamel and Isbell [5]. Thorough theoretical background can be found in Ref. 2. Assume the following:

- An antenna is fed through infinitesimally close ports symmetrically displaced around the origin of the spherical coordinate system.

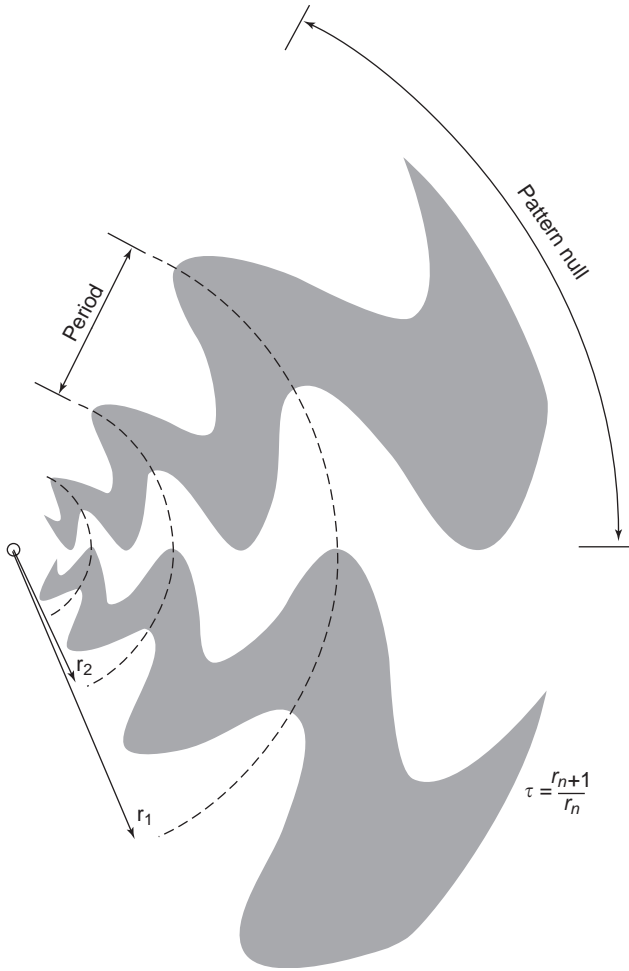


Figure 2. Schematic of a planar log-periodic geometry.

- An axis of symmetry coincides with the z axis.
- The antenna extends to infinity.
- The antenna arms are made of a perfect electrical conductor.
- The antenna is embedded in a homogeneous, isotropic, unbounded medium.
- The outline of the arms of the antenna can be described using the generic formula $R = R(\phi, \theta)$, where R, ϕ, θ are spherical coordinates and $R(\phi, \theta)$ denotes a mathematical dependence of the radial distance from the origin to any point on the antenna structure.

If we want to have the same performance of the original structure at K times lower frequency (K times larger wavelength), we must preserve the electrical dimensions of the original. In other words, every defining dimension or point of the antenna must be multiplied with K , and the new antenna can now be described by

$$R' = KR(\phi, \theta) \quad (2)$$

Examples of original and scaled geometry with the scale factor $K=2$ are shown in Fig. 3. The solid circle in the

middle denotes the infinite precision of the feeding region (remember that the geometry has infinite extension). As shown in the figure, the scaling discussed above produced merely the rotation of the geometry by the angle ϕ' around the fixed antenna terminals, and can be expressed as follows:

$$R' = KR(\phi, \theta) = R(\phi + \phi', \theta) \quad (3)$$

This equation, along with the discussion leading to its derivation, clearly shows that the two antennas will have the same performance at two frequencies related by the scale factor K , except for the associated azimuth rotation ϕ' . Additionally, the scaling factor K and associated azimuth rotation ϕ' are mutually dependent and invariant with any other parameter of the antenna. As a result, we can take partial derivatives of both sides of (3) with respect to ϕ and ϕ' and obtain Eqs. (4) and (5), respectively:

$$\begin{aligned} K \frac{\partial R(\phi, \theta)}{\partial \phi} &= \frac{\partial R(\phi + \phi')}{\partial \phi} \\ &= \frac{\partial R(\phi + \phi')}{\partial(\phi + \phi')} \frac{\partial(\phi + \phi')}{\partial \phi} \\ &= \frac{\partial R(\phi + \phi')}{\partial(\phi + \phi')} \end{aligned} \quad (4)$$

$$\begin{aligned} R(\phi, \theta) \frac{dK}{d\phi'} &= \frac{\partial R(\phi + \phi')}{\partial \phi'} \\ &= \frac{\partial R(\phi + \phi')}{\partial(\phi + \phi')} \frac{\partial(\phi + \phi')}{\partial \phi'} \\ &= \frac{\partial R(\phi + \phi')}{\partial(\phi + \phi')} \end{aligned} \quad (5)$$

Since the right-hand sides of (4) and (5) are the same, we can write

$$\frac{1}{R(\phi, \theta)} \partial R(\phi, \theta) = \left(\frac{1}{K} \frac{dK}{d\phi'} \right) \partial \phi = a \partial \phi \quad (6)$$

where $a = K^{-1} dK/d\phi'$ does not depend on any spherical coordinate (it is a constant). The solution of (6) is

$$R = R(\phi, \theta) = f(\theta) \exp(a\phi) \quad (7)$$

where $f(\theta)$ is an arbitrary function describing the dependence of the antenna structure on elevation angle θ . A generic antenna whose shape can be described using Eq. (7) will be frequency-independent. For the example shown in Fig. 3, the infinitely large structures represented by solid and dotted lines follow the same growth rate a and dependence on elevation angle $f(\theta) = \text{const}$. When the scaling factor is $K=2$, the original equiangular spiral (solid line) “rotates” in azimuth by $\phi' = \log 2/a$ to conform to the dotted spiral structure. Thus, the antenna scaling is equivalent to a rotation and the performance at any two frequencies f_1 and Kf_1 must be the same except for the rotation ϕ' in azimuth.

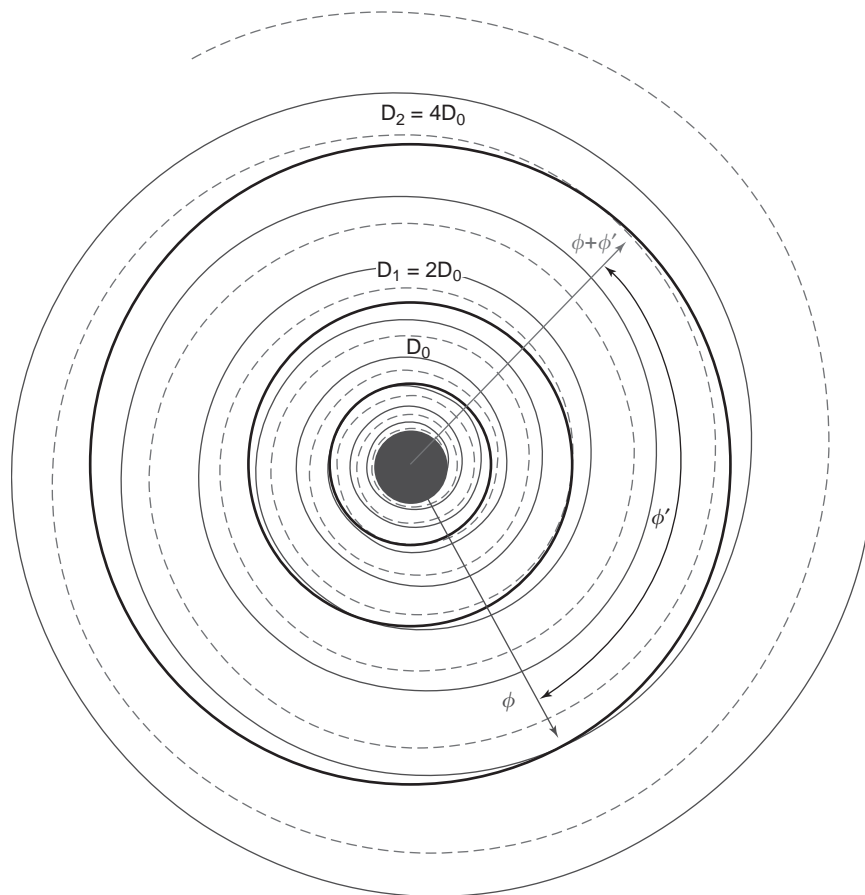


Figure 3. Notion of scaling through rotation of an infinite FI geometry. (This figure is available in full color at <http://www.mrw.interscience.wiley.com/erfme>.)

Special cases derived from Eq. (7) are [19]

- *Planar equiangular spiral*, for which $f(\theta) = A\delta(\pi/2 - \theta)$, where A is constant and $\delta(\pi/2 - \theta)$ is the Dirac delta function describing the planar nature of this structure. The governing equation which defines the planar equiangular spiral is then

$$R = A \exp(a\phi) \tag{8}$$

- *Conical equiangular spiral*, obtained if $f(\theta) = A\delta(\beta - \theta)$, where β is the apex angle of the cone and the spiral is projected to its surface. Note that the planar equiangular spiral is a special case of the conical spiral when $\beta = \pi/2$.
- *Conical screw*, obtained when an equiangular spiral is projected to the volume between two cones with the same axis and orientation but different apex angles. Multiple screws can be arranged within periodic azimuth angles ϕ .
- *Log-periodic planar sheet*, obtained using a $\phi = \text{const}$ cut through a conical screw with axis on the θ axis. A drawing of the first log-periodic antenna [5], whose 3D equivalent is a biconical screw, is shown in Fig. 4. A log-periodic structure can also be obtained by utilizing a projection between two spaces, $z(x,y)$ and

$w(\rho,\phi)$, connected using transformation $z = \ln(w)$. For example, the projections of the constant and variable growth planar sinusoidal antennas produce sinu-

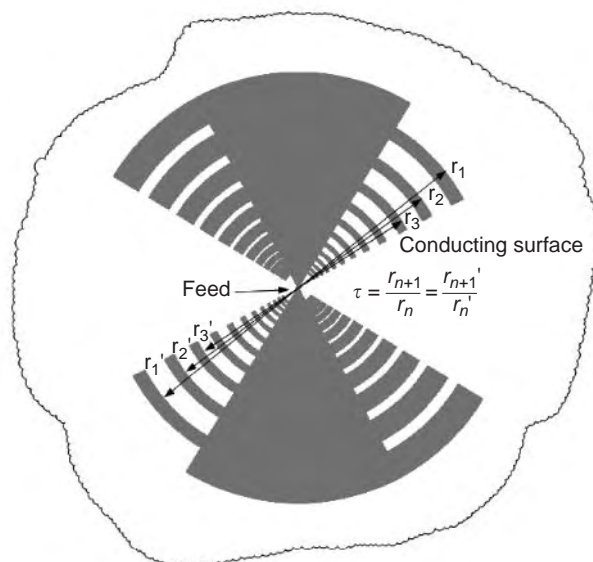


Figure 4. Drawing of the first planar sheet log-periodic antenna.

soidal lines with constant and varying periods, as will be shown in the next section.

5. TYPICAL FI ANTENNAS

5.1. Equiangular Spiral

The equiangular spiral (also known as a *logarithmic spiral*, or *log-spiral*) is a planar embodiment of an FI antenna, with a structure described by Eq. (8). For a constant growth rate a , an angle (α) subtended between the radius vector of an arbitrary point on the edge of the spiral arm and tangent to the arm through the same point is constant throughout the spiral structure. This angle and spiral growth rate are related as $a = 1/\tan \alpha$. Equiangular spirals are discussed in more detail in the SPIRAL ANTENNAS article, so only a few features unique to the FI performance of this antenna will be discussed here. More specifically, the spectral content of the higher-order modes excited on and supported by the spiral, including their radiated power densities (and associated gains) relative to that of a dominant mode, can be utilized for determining the high end of FI performance. Typically, this frequency is determined by the size and finesse of the feeding region, but if the attenuation of the traveling wave through the active region is insufficient, strong undulations in the antenna radiation pattern can occur [20,21], thus reducing the highest frequency of operation.

Figure 5 shows the relative gains of the higher-order modes M3 and M5 (compared to the gain of mode M1) excited on two (2A)-, four (4A)-, and eight (8A)-arm free-standing 5-cm-diameter equiangular wire spirals. The first higher-order mode on an 8A spiral, M9, is also shown. Two sets of antennas, shown in Fig. 6, are used for this demonstration: equiangular spirals with the same growth rate in Fig. 6a and spirals with equidistant arm-to-arm spacing measured at the same radii in Fig. 6b. Note that the 2A spiral is the base geometry. These results are obtained by applying modal decomposition to the radiated fields computed using a method-of-moments code (NEC). Although the gains of the dominant mode (M1) are virtually the same for all antennas, the higher-order mode gains are significantly different for the three antennas and the bandwidth with respect to the uncontaminated M1 radiation differs as well. As can be seen, the higher-order modes M3 and M5 for the 2A spiral are well above computational noise and could be seen in the patterns. The first higher-order mode for the 4A spiral, M5, turns on later (at higher frequency) than does the M3 of a 2A spiral, and its relative gain is higher than the gain of M5-2A (i.e., mode 5 for the two-arm spiral). Note that in the 2A case, modes M1 and M3 have already radiated from the 1 and 3 wavelengths rings; thus lower residual energy remains on the arms, giving rise to the reduced M5 efficiency. The first higher-order mode for the 8A spiral is M9, which turns on at much higher frequency than do the corresponding first higher-order modes for A2 and A4 spirals. Modes M3 and M5 of the 8A spiral are very inefficient, and the gains of M3-4A and M3-8A are too low to be seen in the figure. A cross-modal discrimination of 30–40 dB provides little, if any, visible effects in the radiation pattern, so, clearly an

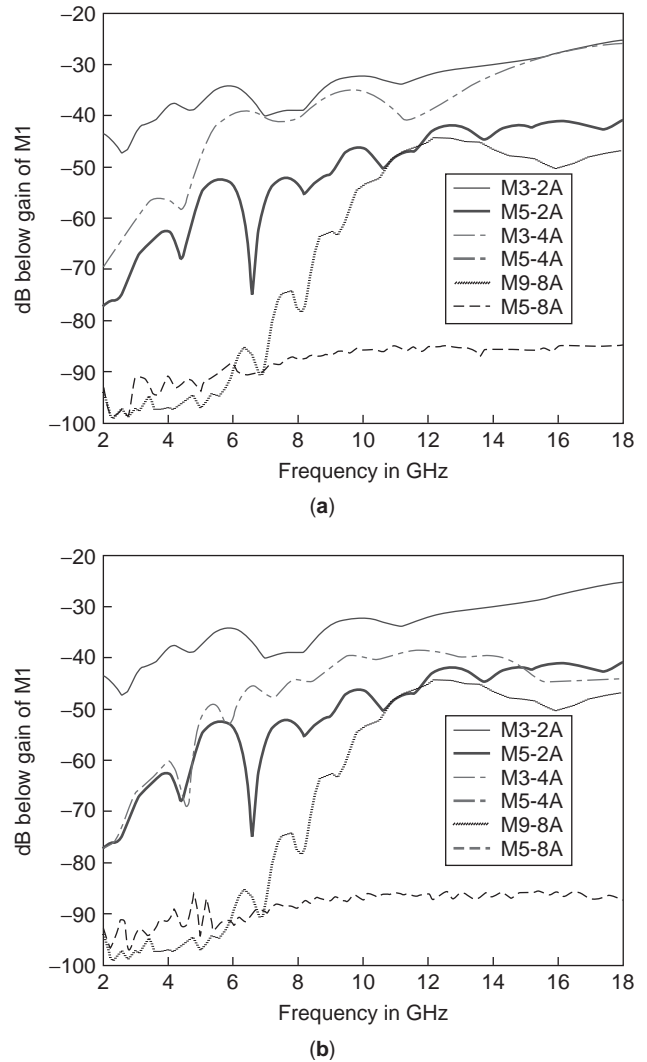


Figure 5. Modal decomposition of two-, four-, and eight-arm self-complementary equiangular spirals with same growth rate (a) and equal separation between arms measured at the same radii (b). (This figure is available in full color at <http://www.mrw.interscience.wiley.com/erfme>.)

eight-arm spiral has the largest FI bandwidth. The radiation from the higher-order mode regions contributes to the attenuated traveling wave in the outer region of the antenna, and care must be exercised when the truncation principle is applied. Also, note that the smaller growth rate [case (a)] for the 4A spiral amounts to more radiation in the M1 active region and thus lower gain in the higher-order mode M5.

Excellent discussions of planar and conical equiangular spirals, including some practical aspects of feeding, and multiarm designs, as well as FI-related differences with Archimedean spirals, can be found in the literature [8,9,21–23].

5.2. Log-periodic Antennas

DuHamel and Isbell [5] defined the log-periodic antenna as a structure whose electrical properties vary periodically

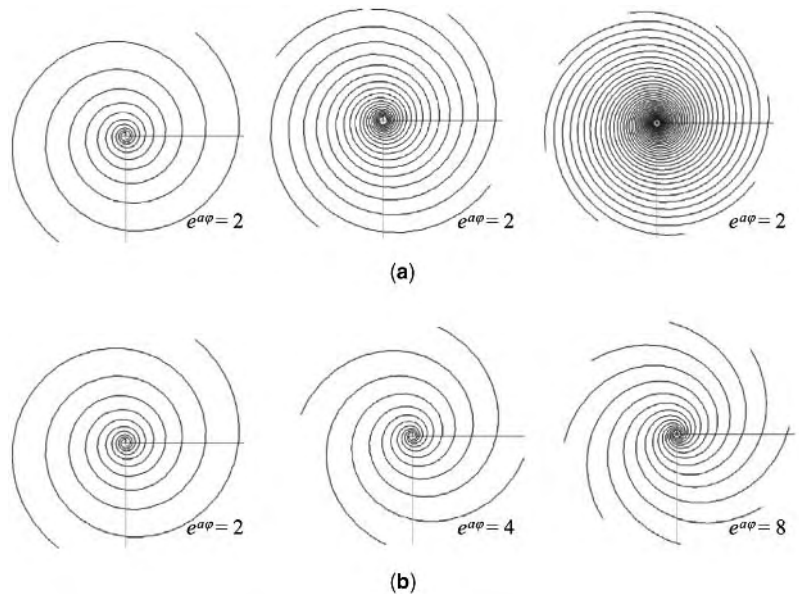


Figure 6. Two-, four-, and eight-arm spirals with the same growth rate (a) and equal separation between arms measured at the same radii (b). (This figure is available in full color at <http://www.mrw.interscience.wiley.com/erfme>.)

with the logarithm of frequency. If an antenna is realized such that within each period its performance changes within bandwidth-defined conditions (e.g., the real part of the input impedance = $70 \pm 20 \Omega$, or the gain = 5 ± 1 dBi), then multidecade operation can be achieved. As stated earlier, a log-periodic structure can be obtained by taking an appropriate 2D cut of a 3D FI antenna known as a *conical screw*. The first log-periodic designs (the very first one is shown in Fig. 4) were obtained that way. The list of contributions and different designs embracing the same principles is very long [3,24], so only a few will be reviewed here. A more in-depth discussion of log-periodic antennas can be found in Ref. 20.

5.2.1. Log-periodic Tooth Structure. Experimental verification of a decade-bandwidth log-periodic FI design was first demonstrated in 1957 [5]. The planar freestanding element, shown in Fig. 4, is a linearly polarized bidirectional radiator. Very efficient attenuation through the active region composed of several teeth in the neighborhood of a half-wavelength-long pair results in little (if any) observable end effect. The teeth can be of circular or straight/trapezoidal shape with respective antennas showing little difference in performance. For bidirectional operation, the feedline is planar and is realized using a coaxial cable (coax) soldered to the metal portion between the teeth (equivalent to the Dyson balun [8]). The coax transitions to the slot in the geometric center of antenna aperture. When unidirectional operation of a planar structure backed by a cavity is sought, a vertical balun feed is typically utilized (it also serves as an impedance transformer). The typical impedance at the balanced ports of an antenna with self-complementary geometry is $\sim 160 \Omega$. This is slightly lower than the theoretical value of 188.5Ω because of the nonzero metallization thickness, finite features of the feed region, dielectric support (if used), and so on. Lowering the impedance by increasing the

capacitance, namely, the metal-to-slot ratio (deviation from the self-complementary structure), have proved to be very challenging since impedance and pattern variations within both the period and the bandwidth are typically significant.

Efficient unidirectional operation can be achieved by folding the planar arms, that is, by reducing the angle between the axes of the arms (in planar configuration this angle is 180°). Folding eliminates the need for lossless reflective (bandlimited) and/or lossy absorptive (broadband) cavities and typically yields a 2–2.5 dB increase in forward gain when compared to the freestanding (or absorptive cavity-backed) antenna. To reduce the antenna weight and windload, the solid metallic arms can be replaced by a thin metallic wire or strip that outlines the previously solid structure [6]. Changes in impedance and pattern are minimal since the current is concentrated along the edges of the original geometry. By utilizing a simple $\pm 90^\circ$ hybrid or other more complicated beamformers, multipolarized operation can be obtained when two pairs of arms are placed in mutually orthogonal planes with their teeth interleaved. The first publications by the inventors of log-periodic antennas, conveying their enduring conclusions and vision, are not only a testament of the excellence coming from the UIUC but also a cornerstone and guideline for the future research and application of frequency-independent principles.

5.2.2. Log-periodic Dipole Arrays. The log-periodic dipole array antenna was the first FI antenna that immediately after being conceived truly made a huge impact on both commercial and military applications throughout the world. Although Carrel's studies have provided theoretical and experimental foundation of log-periodic dipole antennas [10], the concept was first proposed by Isbell [25], who made the following modifications to the structure he previously conceived with DuHamel (see Fig. 4):

- Arms of the tooth structure are folded and their axes are made parallel. This corresponds to the limiting case of the angle $\psi \sim 0^\circ$.
- The width of the teeth $r_n - r'_n$ is kept constant throughout the antenna structure.
- Planar circular teeth are replaced by straight wires with uniform cross section.
- The apex angle of an embedded cone (in the basic conical screw geometry, which, as discussed earlier, is the foundation for the planar sheet) approaches 0° in the limit. In other words, the supporting booms are straight rods typically with rectangular cross section.

As a result of these modifications, a log-periodic wire dipole antenna emerged, most frequently used worldwide as a receiving antenna for terrestrial VHF/UHF radio and television. As such, its structure, theory of operation, design guidelines, and performance are well documented in classical antenna textbooks and practitioner handbooks, and will not be discussed further in this article. Comprehensive discussion of the performance of this antenna can be found in a classic paper by Carrel [10].

5.2.3. Log-periodic Folded Slot Antenna. Figure 7 shows a 16-element log-periodic folded slot antenna with basic parameters and equations describing its structure depicted in the same drawing. The shading represents slots etched in a (typically) copper metallization of a thin low-dielectric constant, low-loss substrate. Between the folded slots are “phasing slots” needed to provide the proper phase delay necessary for endfire radiation. As with other log-periodic antennas, $\tau = L_{i+1}/L_i$ is the growth rate, which determines the period of logarithmic repetition in electrical performance. The parameter $\sigma = d_i/(2L_i)$ is the relative electrical distance between the active (half-wavelength) dipole and its neighbor, while 2α represents the angular opening of the structure. As seen from the figure, to uniquely specify the antenna geometry, we need to define the growth rate τ and either of the remaining two parameters. log-periodic folded slot antennas designed for the same frequency range but with three different growth rates and numbers of arms are shown in Fig. 8. The pa-

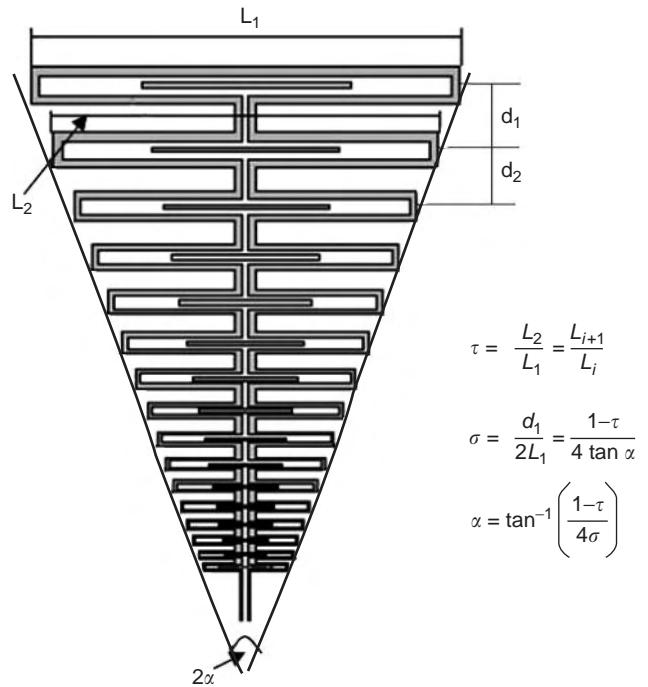


Figure 7. log-periodic folded slot antenna with corrective phasing slots and equations that fully describe its structure.

rameters for these antennas are determined for performance over a 4:1 range, so that the number of arms is $N = 9, 12, 17$ for $\tau = 0.8, 0.85, 0.9$, respectively. As stated earlier, the presence of the phasing slot is critical for endfire performance of this antenna. If the phasing slot is not used, the growth rate has to be very high (close to 1) in order to reduce (but ultimately not prevent) the gain dropouts and other anomalies in the radiation pattern. Maximum gain for two different lengths of the phasing slot is computed and compared with the case without it (see Fig. 9). Three-dimensional radiation patterns for the cases with and without the phasing slot are shown in Fig. 10. As seen, the narrowband gain dropouts, as well as deteriorated front-back ratio, multilobes, and other characteristics, are present when the phasing slot is not used. With the

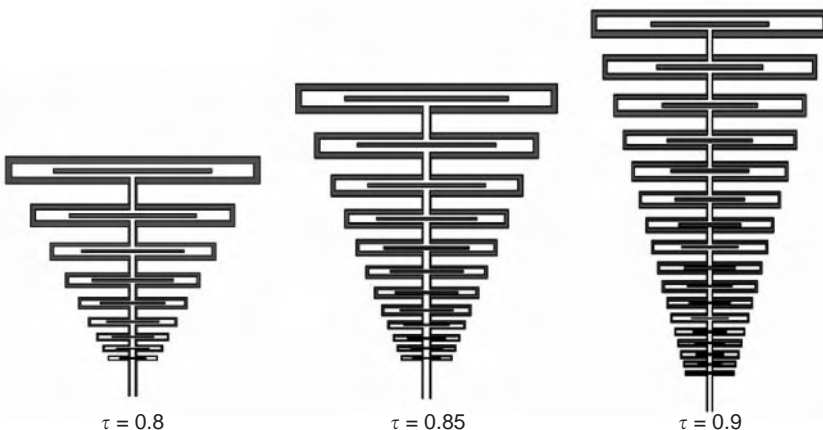


Figure 8. log-periodic folded slot antenna with different growth rates denoted in the figure.

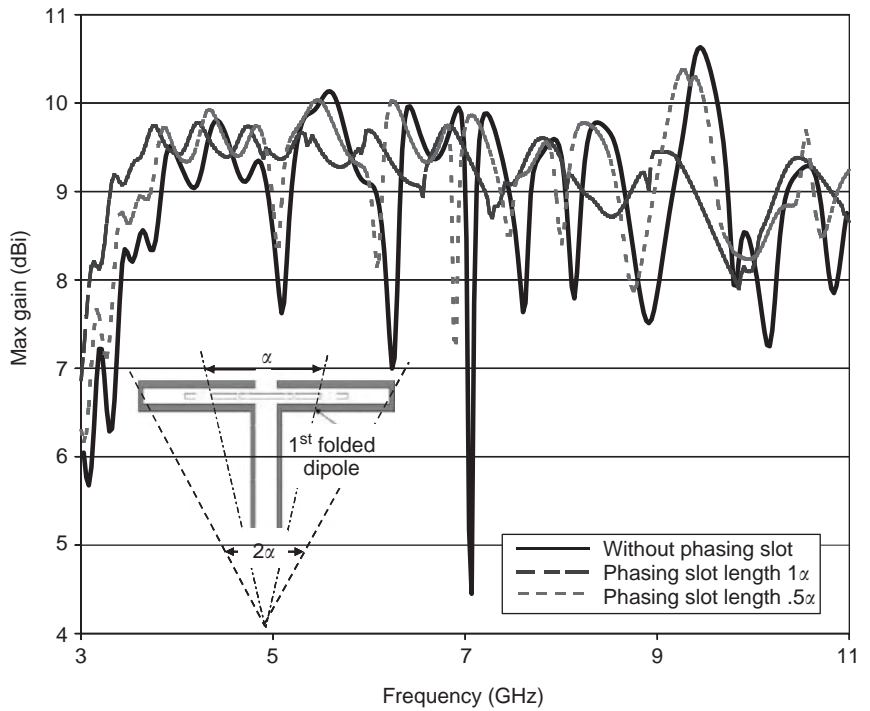


Figure 9. Maximum gain for different lengths of the phasing slot.

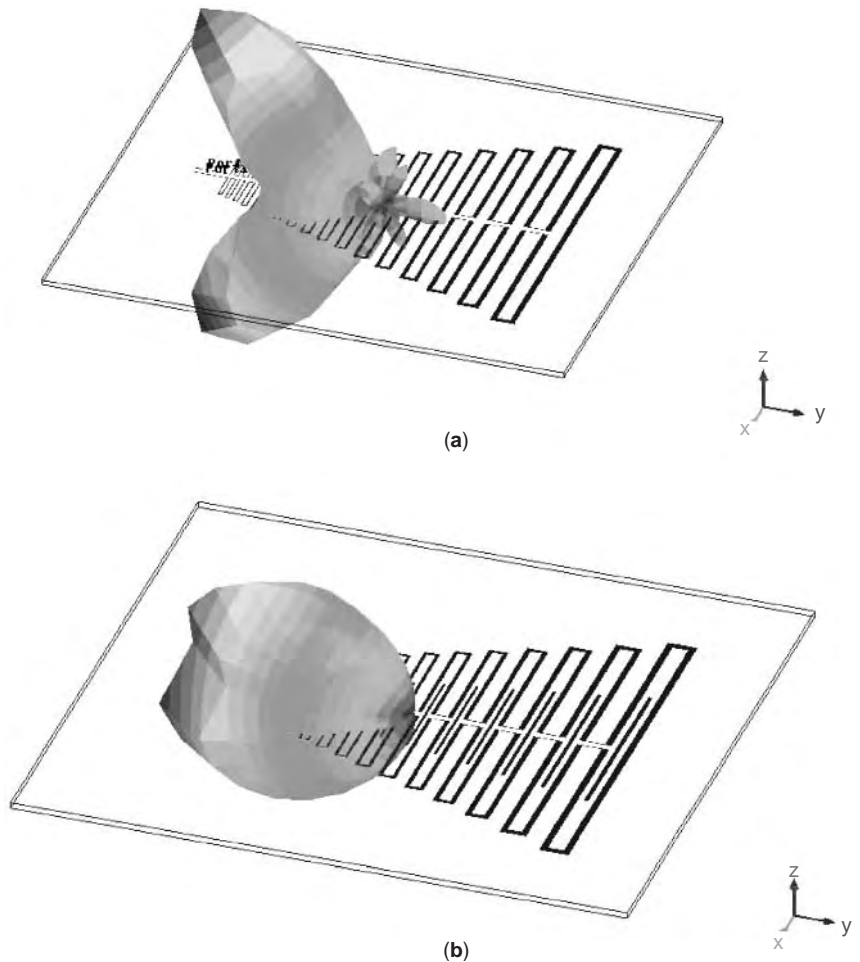


Figure 10. 3D radiation pattern of log-periodic folded slot antennas without (a) and with (b) phasing slots. (This figure is available in full color at <http://www.mrw.interscience.wiley.com/erfme>.)

phasing slot, the near- and far-field characteristics of the antenna improve vastly. The simulations have shown that the slot lengths around α produce the best antenna performance.

5.2.4. Sinuous Antenna. The traditional sinuous antenna is a broadband, log-periodic structure with $N \geq 4$ arms composed of arcs and bends, and whose low- and high-frequency operation limits are determined by the outer and inner diameter of the antenna, respectively. As shown in Fig. 11, the sinuous configuration is fully depicted by the angles α —angular span of defining sinuous curve—and δ —rotation angle needed to outline the sinuous arms—as well as the log-periodic growth rate— τ . If any of these three defining parameters is varied from cell to cell, a quasi log-periodic sinuous structure is obtained. Layouts of the constant-growth-rate (log-periodic) and variable-growth-rate (quasi log-periodic) four-arm sinuous antennas are shown in Fig. 12. Also depicted are their projections in the z plane, which clearly indicate not only the (quasi)log-periodic behavior of the essential sinuous curves but also the self-complementary feature of these planar shapes. Detailed description of a sinuous structure with various modifications, as well as its operation principles, practical aspects such as feeding, parameters, and modeforming, can be found in Ref. 17.

Most sinuous antenna research has been devoted to the planar four-arm printed/wire geometries. Since a free-standing antenna radiates bidirectionally, an absorptive

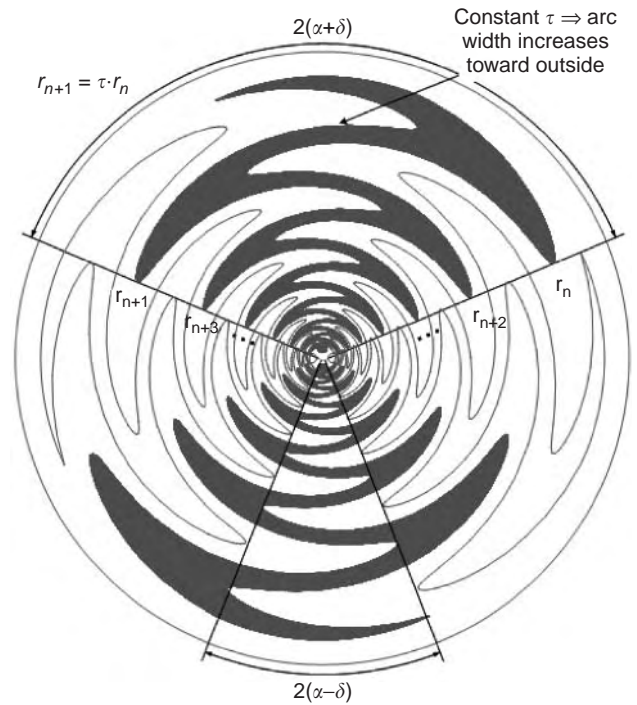


Figure 11. Sinuous antenna geometry and relevant parameters.

cavity or conical projection of the sinuous structure (as with spirals) are required for unidirectional operation. Although lossy cavity backing reduces the antenna efficiency, it is the preferred approach for conformal and

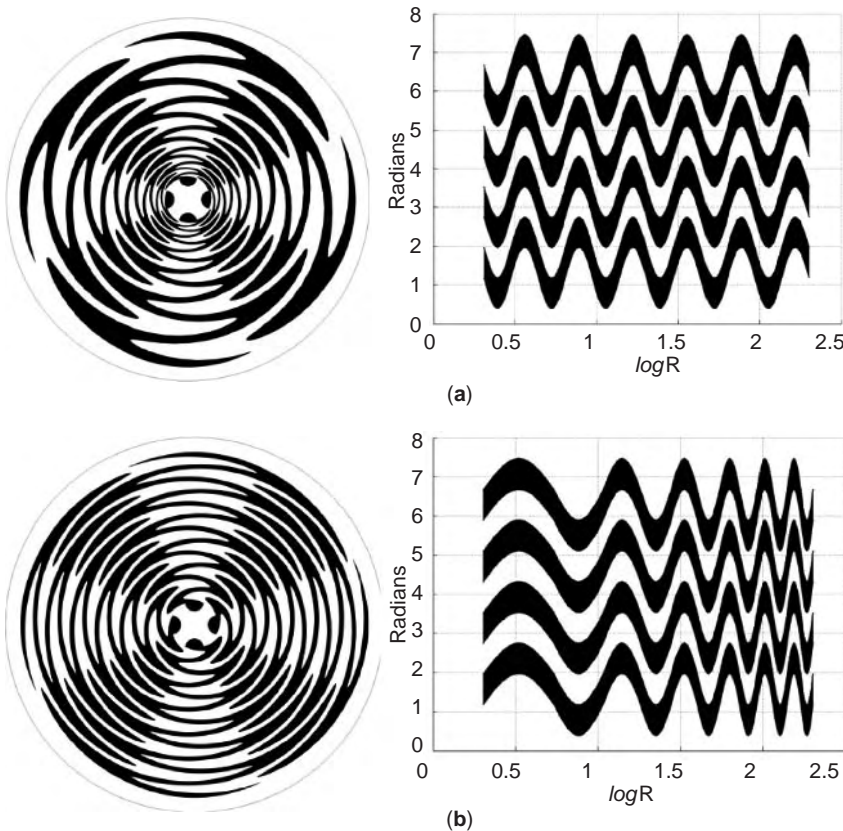


Figure 12. A layout of the constant-growth sinuous and its transform (a) and variable-growth sinuous and its transform (b).

flush-mounted applications. Reflective metal backing (empty cavity or cavity with vertical wall absorber liners) causes strong coupling into the sinuous feeds and severe mismatch as well as contaminated far-field radiation patterns [gain dropouts, increased axial ratio, and WoW (Wobble on Wave)]. Several sinuous antennas including an interferometer configuration manufactured by L-3 Communication Randtron Antenna Systems, are shown in Fig. 13.

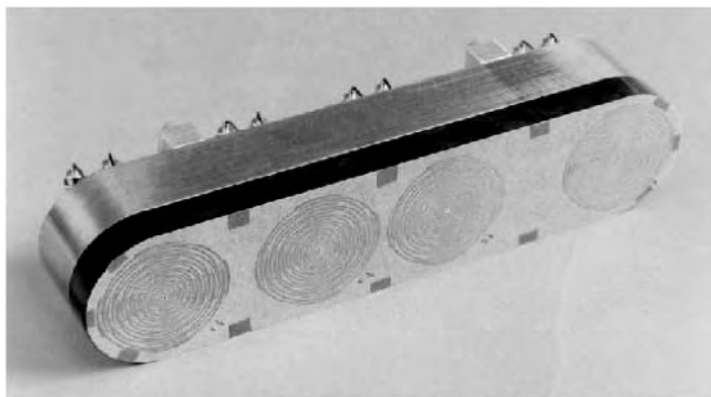
A special case of a sinuous antenna is the folded spiral, constructed as a spiral that is “folded” back on itself. The angular arm expansion of the folded spiral is the same as that of a sinuous antenna, and the main difference is in the shape or curvature of the arm bends. More specifically, the bends of a sinuous structure are rounded as opposed to the sharp tips of a folded spiral. The performance of the two antennas is virtually the same, and often the folded spirals are referred to as “sinuous” antennas. Thus any reference to one can be equally applied to the other antenna. Looking at a single arm composed of several cells of arcs and bends, we can see that the folded spiral is a combination of both clockwise (CW) and counterclockwise (CCW) wound spiral segments. Thus, the band theory used for describing spiral operation can be utilized for understanding the performance of sinuous antennas. A tightly coupled sinuous antenna, where arms have significant interlacing ($\tau > 0.8$), has approximately the same frequency limits as a spiral; that is, the sinuous antenna should be N wavelengths in circumference to support efficient mode N radiation. In practice, for a given low-frequency limit, the circumference of the sinuous antenna should be increased by a certain value (typically $\lambda/2$) to account for the finite width of the radiation region. Excitation of the sinuous antenna, when operated in a single circularly polar-

ized mode, is also identical to the feeding of a spiral antenna. One exception to the similarity is that the sinuous is dual-polarized and has additional capabilities, and unfortunately additional restrictions. Because of the alternating CW and CCW wrapping senses in each arm and inability of the aperture to perform polarization filtering, the sinuous antenna with N arms can support $(N - 1)/2$ broadband modes. Although the overall number of modes on an N -arm sinuous antenna is one-half the number of modes on a comparable N -arm spiral, their radiation patterns are very similar. Only mode 1 has a broadside radiating component, and all other modes have a null on boresight, with each higher-order mode peaking further from the null. Note that each mode on a sinuous antenna can be obtained in either left- or right-handed circular polarization (RCP, LCP). If we need M modes of operation with the same polarization, an $N = (2M + 1)$ -arm sinuous antenna is needed. These modes will be excited if equal amplitudes and phase progressions of $-360^\circ nm/N$ are provided at the arm feeds (taken in the CW direction). Here, n is the arm number ($n = 1, 2, \dots, N$), m is the mode number ($m = 1, 2, \dots, \lfloor (N - 1)/2 \rfloor$), and N is the total number of arms. If the highest-order mode that can be supported by an arbitrary N -arm sinuous antenna is m ($m > 0$), the following modes can coexist: $-m, -m + 1, \dots, -1, 1, \dots, m - 1, m$, with positive modes denoting the RCP and negative modes LCP, respectively. Therefore, at least $N = 5$ arms are needed to obtain dual-mode operation, which is important for monopulse direction finding.

To further understand the relation between the number of sinuous arms and the modal spectrum supported by its structure, we will examine in more detail an arbitrary ($N = 4$)-arm sinuous geometry. A corresponding four-arm CCW wound spiral antenna will support broadband RCP



(a)



(b)

Figure 13. Photographs of several sinuous antennas (a) and a high-pressure interferometer (b). (Courtesy of L-3 Communications Randtron Antenna Systems.)

modes M1 $\{0^\circ, 90^\circ, 180^\circ, 270^\circ\}$, M2 $\{0^\circ, 180^\circ, 360^\circ, 540^\circ\} \equiv \{0^\circ, 180^\circ, 0^\circ, 180^\circ\}$, and M3 $\{0^\circ, 270^\circ, 540^\circ, 810^\circ\} \equiv \{0^\circ, -90^\circ, 180^\circ, 90^\circ\}$ with the phase progression (in CW sense) denoted in brackets $\{ \}$. A four-arm sinuous antenna has spiral segments capable of radiating both senses of circular polarization; thus when the mode 2 phase progression is provided at the arm ports $\{0^\circ, -180^\circ, -360^\circ, -540^\circ\} \equiv \{0^\circ, 180^\circ, 0^\circ, 180^\circ\}$, the aperture cannot differentiate between it and the mode -2 phase progression $\{0^\circ, 180^\circ, 360^\circ, 540^\circ\} \equiv \{0^\circ, 180^\circ, 0^\circ, 180^\circ\}$, so the radiating region radiates the mixture of modes 2 and -2 . The mode 3 phase progression is $\{0^\circ, -270^\circ, -540^\circ, -810^\circ\}$, and the RCP four-arm spiral supports its efficient and broadband radiation (provided the circumference is larger than three wavelengths). If the same phase progression is provided to the sinuous antenna, we notice that it is equal to the progression of $\{0^\circ, 90^\circ, 180^\circ, 270^\circ\}$, which is identical to that of mode -1 . This mode will be excited first (it radiates from the area the traveling wave encounters before arriving at the mode 3 radiating region) and little energy will be left for mode 3. Thus, as stated above, for dual-mode operation a sinuous antenna must have at least five arms, with unique and unambiguous phase progressions for mode 2 $\{0^\circ, -144^\circ, 72^\circ, -72^\circ, 144^\circ\}$ and mode -2 $\{0^\circ, 144^\circ, -72^\circ, 72^\circ, -144^\circ\}$. Six or eight arms are generally used because of beamformer limitations. An eight-arm sinuous antenna has the additional benefit of supporting a third mode, or modes ± 3 . Radiation patterns for the three modes radiated from an eight-arm sinuous antenna are shown in Fig. 14. As seen, the previously discussed characteristics of modes 2 and 3 as well as a very good cross-polarization at beam peak angles are obtained with this structure.

With good-quality sinuous designs, currents decay rapidly past the radiation region and the radiated power of higher-order modes ($m+N, m+2N, \dots$ and $m-N, m-2N, \dots$) is low. Thus, the azimuth pattern symmetry is usually excellent. As with equiangular spirals, the modal decomposition of the radiated far-field pattern can show the level of modal isolation for each sinuous mode. For example, the radiation pattern of mode 1 of an eight-arm sinuous antenna (see Fig. 15a) is decomposed into the higher-order (contaminating) modes, and the cross-modal difference (with respect to the dominant mode 1) of the most significant modes is shown in Fig. 15b. As can be seen, the cross-modal difference is better than 30 dB for both higher-order modes supported by this antenna (modes -7 and 9), while mode 5 is (virtually) not excited. Since radiation from the dominant mode region is very efficient, end terminations are rarely needed, as opposed to spirals where some form of lossy arm termination is normally used. Also, for similarly sized and designed feed regions, the high-frequency radiation of a sinuous antenna is usually superior to that of a spiral.

The nominal modal impedance of a freestanding, self-complementary, N -arm printed sinuous antenna can be computed using the Deschamps formula [7]

$$Z_m = \frac{\eta_0/4}{\sin\left(\frac{|m|\cdot\pi}{N}\right)} \quad (9)$$

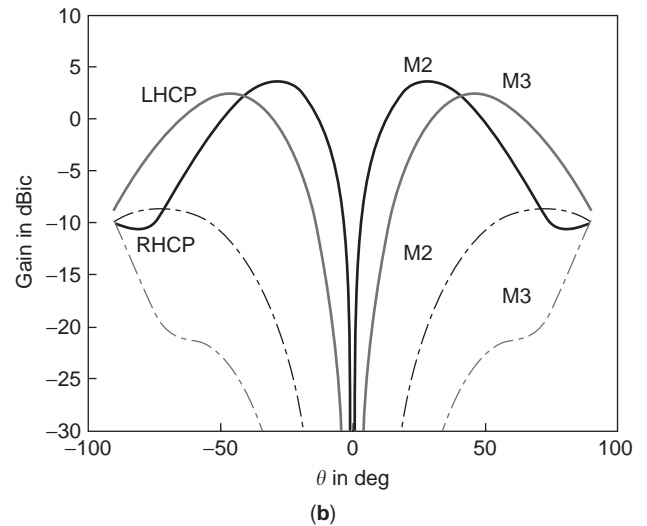
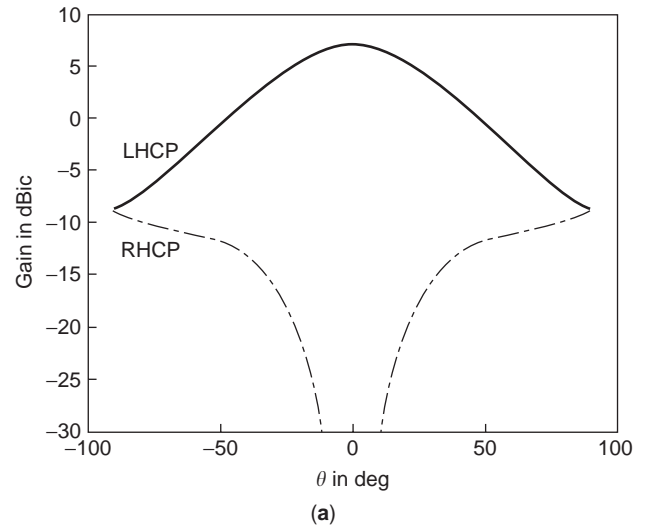


Figure 14. Radiation patterns for the M1 (a), M2, and M3 (b) of an eight-arm sinuous antenna. (This figure is available in full color at <http://www.mrw.interscience.wiley.com/erfme>.)

where $\eta_0 = 120\pi\Omega$ is the free-space impedance and m is the sinuous mode. Impedance variations from these nominal values can be significant, typically exceeding 2:1 for the mode ± 1 operation. Higher-order modes usually have smaller impedance variations, but these deviations are still larger than their spiral counterparts. If necessary, a spiral can be used in the sinuous interior as a tapered matching section.

Most commercial sinuous antennas are four-arm structures, and are designed to operate over different bands. The most common realization is a 5-cm-diameter 2–18-GHz antenna operating in a dual-circular mode 1, or dual-linear mode. The dual circularly polarized sinuous has already been discussed. A linearly polarized version has properties similar to those of a planar log-periodic antenna. As with good log-periodic design having a typical growth rate of $\tau > 0.8$, there are several arc sections in the active region. Opposite arms are fed antiphase $(0, 180^\circ)$, and the two orthogonal arm pairs of a four-arm sinuous

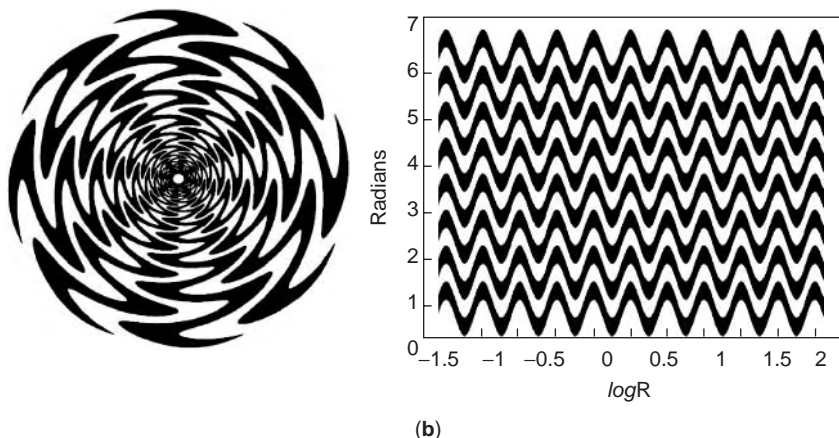
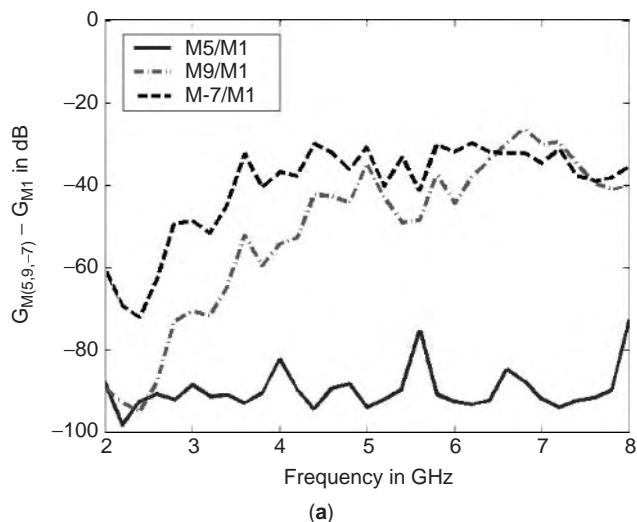


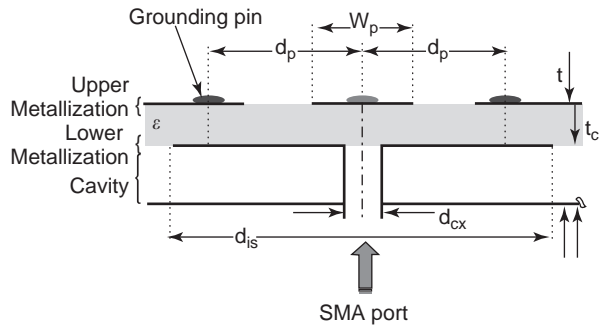
Figure 15. Higher-order mode gains relative to the gain of M1 (a) for an eight-arm sinuous antenna (b). (This figure is available in full color at <http://www.mrw.interscience.wiley.com/erfme>.)

antenna form two linearly polarized radiators. A small shift in the polarization vector with changing frequency is present as a consequence of the oscillating sinuous form of the structure. The polarization swings back and forth about the arms' central axis. When operating in circular polarization (with addition of a 90° QJ;hybrid), this polarization oscillation or wobble does not degrade the polarization purity since all arms have identical rotations.

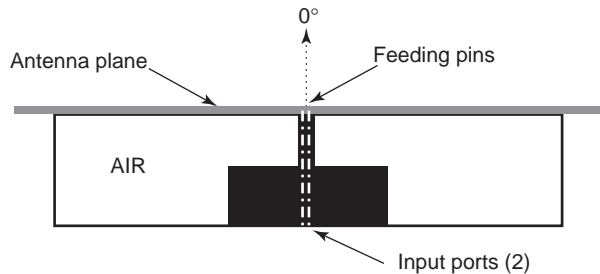
When the arms of a sinuous antenna are fed with ambiguous phasing, very interesting performance is obtained. For instance, two unconventional four- and two-arm sinuous designs [26,27] are shown in Fig. 16. Also given are drawings of their lossless reflective cavity backings used to enhance the quality of circularly polarized radiation. The four-arm slot sinuous antenna, shown in Fig. 16a, is fed using a nonradiating coplanar waveguide mode with resulting phase progression of {0°, 180°, 0°, 180°}. This phase progression is equivalent to the second mode excitation of a related four-arm spiral antenna and, as discussed above, is ambiguous for a broadband operation of a sinuous structure. Since the CW and CCW segments of the sinuous antenna allow it to support

both polarizations, a mixture of modes 2 and -2 is excited and unique multiband multipolarized performance is obtained. The polarization signature of this antenna, shown in Fig. 17a, illustrates that the bands of LCP and RCP are alternating, with the periodicity related to the growth rate of the structure (in this case it was variable growth rate). Since a simple, single-port feed is used for the excitation of this modal mixture, an efficient, small, flush-mounted antenna with simultaneous RCP and LCP operation is obtained without the need for a complex hybrid network. The same principle is applied to a two-arm folded spiral, shown in Fig. 16b, for which the balanced excitation of {0, 180°} cannot distinguish between the two polarization senses, and broadband operation is not possible. However, a multiband, multipolarized performance with maximum gain at broadside is demonstrated. The associated polarization signature depicted in Fig. 17b clearly shows the alternating handedness of the polarization over a relatively large bandwidth.

To summarize, the sinuous antenna is a very broadband radiator and can be classified as an FI antenna. It has many characteristics similar to those of a spiral,



(a)



(b)

Figure 16. Photographs of unconventional four-arm (a) and two-arm (b) sinuous antennas with sketched lossless cavity backing. (This figure is available in full color at <http://www.mrw.interscience.wiley.com/erfme>.)

which is also an FI antenna, but has the additional capability of broadband dual polarization. It should be noted that another spiral antenna, the modulated-armwidth (MAW) spiral, is also capable of dual-polarized FI operation and is discussed in the *SPIRAL ANTENNAS* article.

5.3. Cavity Backing

The projections of a planar spiral [9,22] or sinuous [17] FI structure onto a cone as well as folding a planar sheet antenna [6] produce efficient unidirectional radiation. However, for mounting an antenna in a flush or conformal manner, this approach is typically inadequate and some form of cavity backing is necessary. An absorbing (lossy) cavity must be used for sinuous antennas,

and is preferred as well for the multioctave bandwidth operation of spiral antennas. Of course, reduced radiation efficiency is the price to be paid, but consistent pattern and smooth impedance curves are usually more important.

Ingerson and Mayes [16] suggested a log-periodic cavity arrangement for backing an array of log-periodic slot antennas; specifically, they applied the same principles used for the design of a radiator to the design of its backing. As a result, a log-periodic array of rectangular lossless cavities with slanted metallic bottoms was developed as an embodiment of the log-periodic approach for the design of flush-mounted antenna backing. The growth rates of the slots and the cavities were the same, and a modulated impedance feeder was introduced to provide not only proper phasing for the endfire radiation but also to

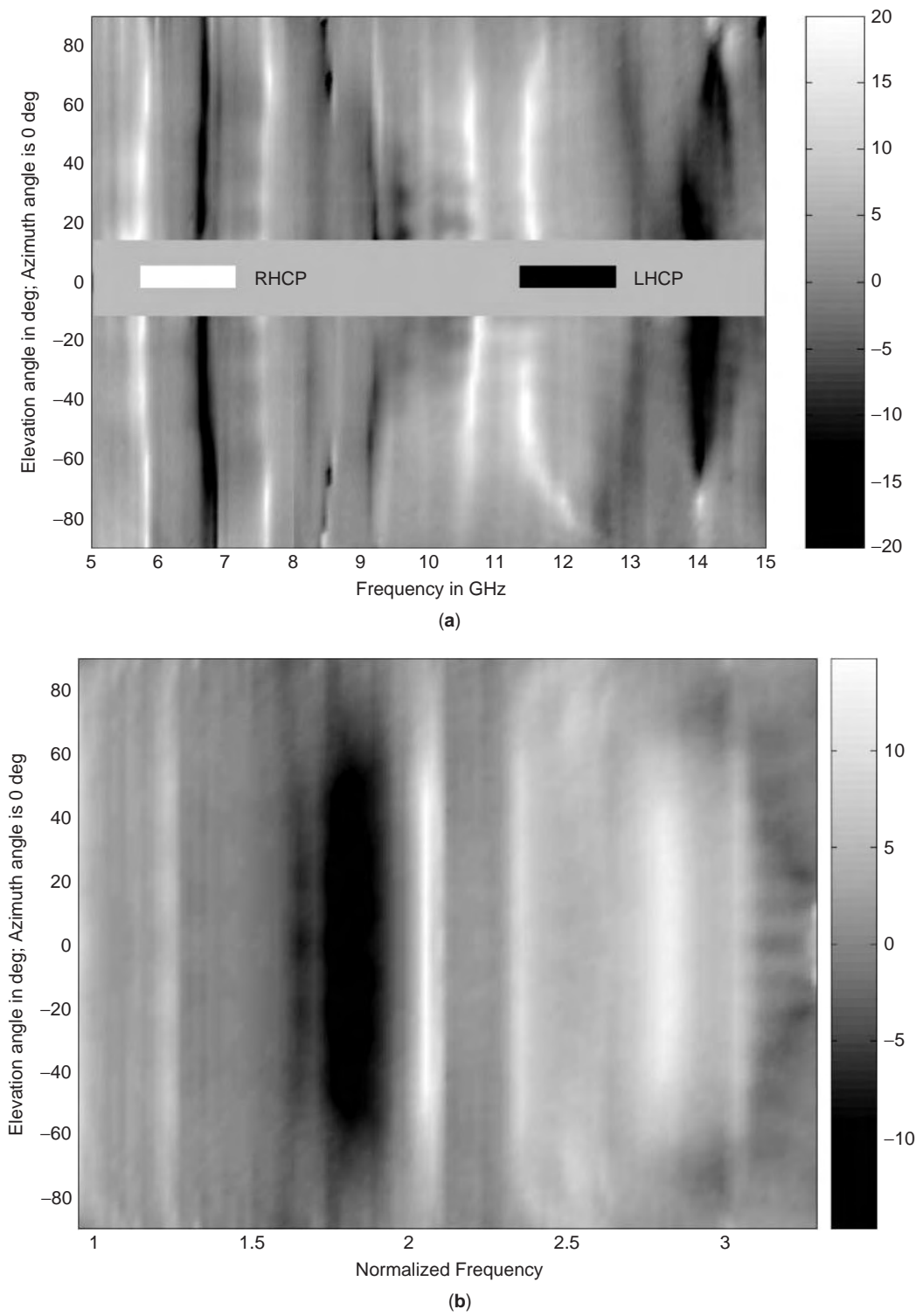


Figure 17. Polarization signature of unconventional four-arm (a) and two-arm (b) sinuous antennas.

eliminate the stopbands. Consistent radiation patterns and well-behaved VSWR performance were obtained.

An interesting approach for the design of a broadband cavity backing was explored by Nurnberger [28]. After investigating the excitation of various cavity modes, their effects on the radiation pattern of a slot spiral, and various

loading techniques for mitigating these, Nurnberger suggested that the same theoretical guidelines for achieving FI performance should be applied to the cavity backing. More specifically, the cavity must be entirely defined by angles, the currents should decay outside the “hot” active region, and periodicity in performance has to be attained.

The evolution of the FI cavity idea is depicted in Fig. 18, while the photograph of the developed conical cavity is shown in Fig. 19. Although the prototype from Fig. 19 does not obey all the abovementioned principles (similar to the bicone antenna, the conical inset does not satisfy the truncation principle for currents), the addition of radial and vertical absorber liners significantly reduced the negative effects of the enclosing cavity wall. Overall antenna gain was 2–2.5 dB higher than the gain of typical wire spiral antennas backed by a regular lossy cavity, while the radiation pattern and VSWR demonstrated very consistent behavior across an 8:1 bandwidth.

6. SUMMARY

The operation of frequency-independent antennas, including the underlying theory and mathematical foundation,

are reviewed in this article. Several FI antennas, including equiangular spirals, log-periodic planar sheets, and dipole and folded slot arrays, as well as sinuous antennas, are described and their performance is utilized for a practical demonstration of FI principles. Although FI antennas have been researched for a half-century, there are plenty of challenges still to be investigated. Some are classical/fundamental issues such as miniaturization versus bandwidth, the associated efficiency tradeoff (more efficiency since FI bandwidth can be well controlled), and broadband arraying, to mention just a few. More recent developments in artificial materials and the possibility of realizing antennas on substrates with any values of dielectric and magnetic constants are also of interest. Further investigation and developments of FI cavities, terminations, and feeds, as well as unconventional designs of basic radiating elements, will also play important role.

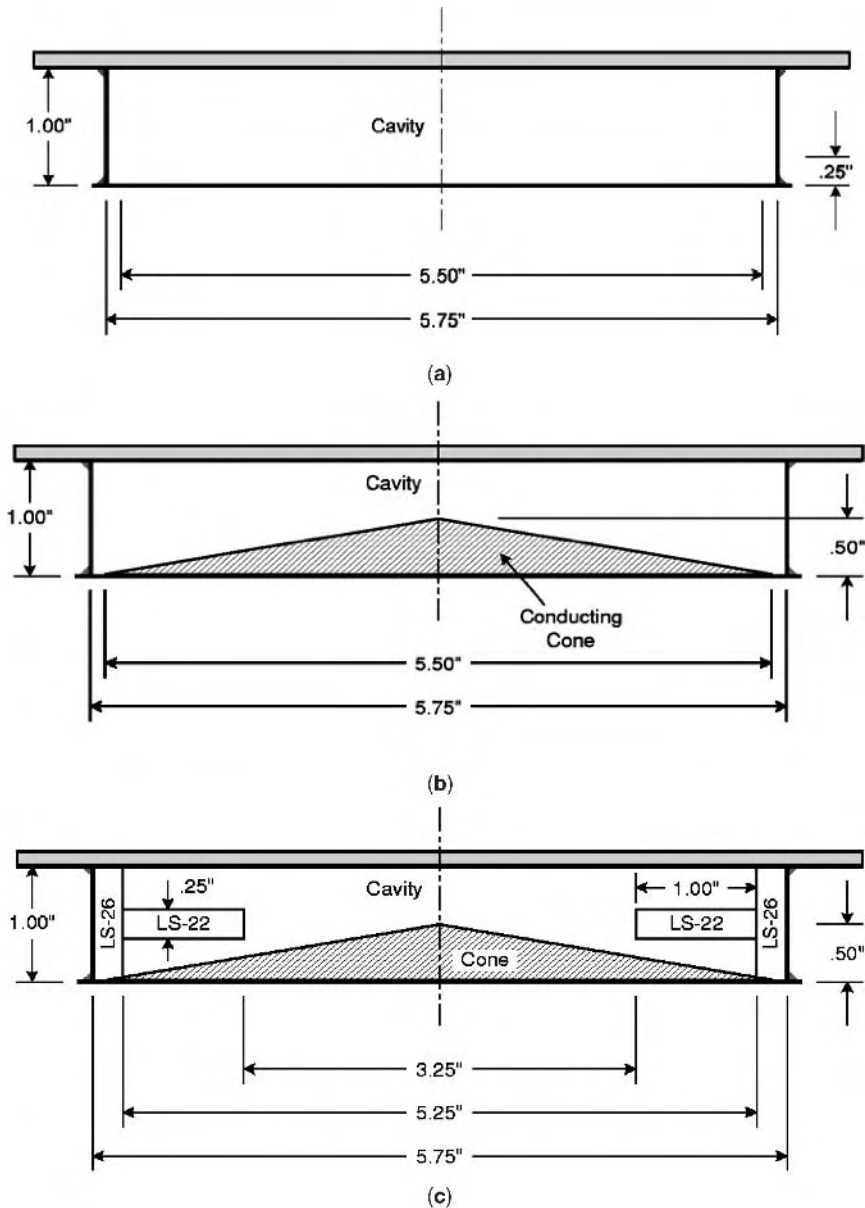


Figure 18. Evolution of an FI cavity concept: lossless flat cavity (a), lossless conical cavity (b), and realized cavity (c) with dimensions for a 5.75-in. spiral aperture.



Figure 19. Photograph of a realized conical cavity with vertical and radial absorber liners.

Acknowledgement

The authors would like to thank Mr. M. Buck and D. Del Rio for their assistance in preparing this manuscript.

BIBLIOGRAPHY

- V. H. Rumsey, Frequency independent antennas, *IRE Int. Convention Rec.* **5**:114–118 (1957).
- V. H. Rumsey, *Frequency-Independent Antennas*, Academic Press, New York–London, 1966.
- P. E. Mayes, Frequency-independent antennas: Birth and growth of an idea, *IEEE Anten. Propag. Soc. Newsl.* 4–8 (1982).
- S. A. Schelkunoff, *Electromagnetic Waves*, Van Nostrand, New York, 1943.
- R. H. DuHamel and D. E. Isbell, Broadband logarithmically periodic antenna structures, *IRE Int. Convention Rec.* **5**: 119–128 (1957).
- R. H. DuHamel and F. R. Ore, Logarithmically periodic antenna designs, *IRE Int. Convention Rec.* **6**:139–151 (1958).
- G. A. Deschamps, Impedance properties of complementary multiterminal planar structures, *IRE Trans. Anten. Propag.* **AP-7**:371–378 (1959).
- J. D. Dyson, The equiangular spiral antenna, *IRE Trans. Anten. Propag.* **AP-7**:181–187 (1959).
- J. D. Dyson, The unidirectional equiangular spiral antenna, *IRE Trans. Anten. Propag.* **AP-7**:329–334 (1959).
- R. L. Carrel, The design of log-periodic dipole antennas, *IRE Int. Convention Rec.* **9**:61–75 (1961).
- D. Berry and F. Ore, Log periodic monopole array, *IRE Int. Convention Rec.* **9**:76–85 (1969).
- P. E. Mayes, G. A. Deschamps, and W. T. Patton, Backward wave radiation from periodic structures and application to the design of frequency independent antennas, *Proc. IRE* **49**: 962–963 (1961).
- B. R.-S. Cheo, V. H. Rumsey, and W. J. Welch, A solution to the frequency-independent antenna problem, *IRE Trans. Anten. Propag.* **AP-9**:527–534 (1961).
- K. K. Mei, M. W. Moberg, V. H. Rumsey, and Y. S. Yeh, Directive frequency independent arrays, *IEEE Trans. Anten. Propag.* **AP-13**:807–809 (1965).
- Y. Yeh and K. Mei, Theory of conical equiangular spiral antennas: Part II—Current distributions and input impedance, *IEEE Trans. Anten. Propag.* **AP-16**:14–21 (1968).
- P. G. Ingerson and P. E. Mayes, Log-periodic antennas with modulated impedance feeders, *IEEE Trans. Anten. Propag.* **AP-16**:633–642 (1968).
- R. H. DuHamel, *Dual Polarized Sinuous Antennas*, U.S. Patent 4,658,262 (1987).
- C. A. Balanis, *Antenna Theory: Analysis and Design*, Wiley, New York, 1997.
- D. S. Elliott, A view of frequency independent antennas, *Microwave J.* 61–68 (1962).
- R. H. DuHamel and J. P. Scherer, Frequency-independent antennas, in *Antenna Engineering Handbook*, 3rd ed., Mc Graw-Hill, New York, 1993, Chap. 14.
- R. G. Corzine and J. A. Mosko, *Four-Arm Spiral Antennas*, Artech House, Norwood, MA, 1990.
- J. D. Dyson and P. E. Mayes, New circularly-polarized frequency independent antennas with conical beam or omnidirectional pattern, *IRE Trans. Anten. Propag.* **AP-8**:334–342 (1960).
- P. E. Mayes and J. D. Dyson, A note on the difference between equiangular and Archimedes spiral antennas, *IRE Trans. Microwave Theory Tech.* 203–204 (1961).
- P. E. Mayes, Frequency-independent antennas and broad-band derivatives of thereof, *Proc. IEEE* **80**:103–112 (1992).
- D. E. Isbell, Log-periodic dipole arrays, *IRE Trans. Anten. Propag.* **AP-8**:260–267 (1960).
- M. C. Buck and D. S. Filipovic, Split-beam mode four-arm slot sinuous antenna, *IEEE Anten. Wireless Propag. Lett.* **3**:83–86 (2004).
- M. C. Buck, J. Burford, and D. S. Filipovic, Multiband two-arm slot sinuous antenna, *Proc. IEEE APS/URSI*, 2004.
- M. W. Nurnberger, *The Broadband, Shallow, Reflecting Cavity-Backed Slot Spiral Antenna*, Ph.D. thesis, Univ. Michigan, Ann Arbor, 2002.

FREQUENCY MODULATION

L. B. FERTIG
J. H. MCCLELLAN
Georgia Institute of Technology

Frequency-modulated waveforms are commonly utilized for information transmission in radiocommunications, as well as for environmental sensing in radar, sonar, and bioengineering. In many of these situations, the desired information is extracted from the received signal by monitoring one or more dominant frequencies in the signal and examining their variation as a function of time. The process by which a local approximation to a signal's frequency is obtained is known as *instantaneous frequency estimation* (IFE).

In this article, concepts relating to instantaneous frequency, along with algorithms for its computation, are reviewed. First, several means by which instantaneous frequency is commonly defined are discussed, and the relationships between instantaneous frequency and time-frequency distributions are explored. Next, several measures of performance commonly used to evaluate instantaneous frequency algorithms, such as the Cramer-Rao lower bound, are examined. Finally, a number of algorithms that have been suggested for IFE are summarized. Despite the relative maturity of frequency modulation in the field of radiocommunications, the field of IFE is a growing one, and one in which research is still quite active.

1. INSTANTANEOUS FREQUENCY ESTIMATION: BACKGROUND AND DEFINITIONS

The instantaneous frequency of a signal can be defined in several different ways. Two of the most popular definitions relate the instantaneous frequency to time-frequency distributions and to the analytic signal. Either of these definitions can satisfy intuition in certain situations, but yield puzzling results in others. Nevertheless, useful estimates of the instantaneous frequency can usually be obtained for narrowband signals, and to a lesser degree for certain wideband signals. In this section, relationships between instantaneous frequency, time-frequency distributions, and the analytic signal are discussed.

1.1. Time-Frequency Distributions

The concept of frequency has long played a major role in the analysis of signals. Through the Fourier transform, a signal may be decomposed into a continuum of complex exponentials. In fact, the basis functions of the Fourier transform are pure tones of *infinite* time extent. However, when the spectral composition of a signal varies as a function of time, the Fourier transform no longer provides a simple spectral description of the signal. Instead, a *time-frequency distribution* yields more insight into the signal's behavior. The most common example of time-frequency analysis—the printed musical score—has existed for

hundreds of years. With a musical score, it is possible to denote the tones that are present in an arrangement at discrete intervals in time. In the following paragraphs, a short discussion of the key developments in time-frequency analysis that have been obtained since 1949 is provided. Among the topics explored are Gabor's time-frequency distribution, the short-time Fourier transform, perfect reconstruction filterbanks, the wavelet transform, and Cohen's class of time-frequency distributions. The relationship between instantaneous frequency and time-frequency distributions is then discussed.

The development of the first algorithm for time-frequency analysis of an arbitrary signal is generally credited to Gabor [1]. His work was motivated by a desire to define the information content of signals. He considered the time-frequency representation of a signal as a "diagram of information," where areas in the two-dimensional representation were proportional to the amount of data that they could convey. Gabor suggested that the time and frequency characteristics of a signal $x(t)$ be simultaneously observed with the expansion

$$x(t) = \sum_{m=-\infty}^{\infty} \sum_{n=-\infty}^{\infty} g_{mn} \psi_{mn}(t)$$

where $\psi_{mn}(t)$ is expressed in terms of an elementary signal $\psi(t)$ with

$$\psi_{mn}(t) = \psi(t - mT) \exp(jn\Omega t)$$

The time and frequency lattice intervals are defined by T and Ω , respectively. Gabor also proposed that the signal with minimum area on the time-frequency plane be used to generate the basis functions for his time-frequency decomposition. Furthermore, he demonstrated that the signal with minimum area, as defined by the product of the signal's root-mean-square (RMS) width in time and frequency, was given by the Gaussian-modulated sinusoid. The concept that the time and frequency widths of a signal cannot be made arbitrarily small simultaneously is a well-known property of Fourier analysis called the *uncertainty principle* (a term that originated in the physics community). These ideas form the cornerstones of time-frequency analysis.

The growing interest in time-frequency analysis accelerated in the 1970s due to research regarding the short-time Fourier transform (STFT) [2,3]. These efforts were motivated by a desire to analyze the time-varying spectral content of speech signals. The STFT is created by inserting a window function $h(n)$ into the computation of the Fourier transform, as expressed by

$$X(n, \omega) = \sum_{m=-\infty}^{\infty} x(m) h(n - m) \exp(-j\omega m)$$

The discrete index n varies from $-\infty$ to $+\infty$, while the continuous parameter ω varies from 0 to 2π . For a fixed analysis time n , the window function selects a portion of the original signal for spectral analysis, thereby allowing nonstationary behavior to be observed in a manner

impossible with the traditional Fourier transform. At each time instant, the signal segment selected for analysis is formed by the product of the timeshifted window function with the original signal. It is recognized that the result of this operation in the frequency domain is the convolution of the spectral representation of the two functions. Thus, the shape of the window function is fundamental to the STFT results. The rectangular window yields the minimum mainlobe spectral width (and therefore the best frequency resolution) at the cost of large sidelobes (the peak of the largest sidelobe has a magnitude only 13 dB less than the peak of the mainlobe). Other window functions, such as the Hamming window, generate lower sidelobes, at the price of a wider mainlobe. The length of the window function also affects the results produced by the STFT. The longer the timelength of the window, the greater the frequency resolution of the time–frequency representation, but the poorer the time resolution.

A second interpretation of the STFT is obtained by examining the structure of the discrete short-time Fourier transform (DSTFT), which is written as

$$X(n, k) = \sum_{m=-\infty}^{\infty} x(m)h(n - m) \exp\left(\frac{-j2\pi km}{N}\right)$$

The discrete index n varies from $-\infty$ to $+\infty$, while the discrete index k varies from 0 to $N - 1$. For a fixed frequency index k , it is seen that the signal of interest is modulated by $\exp(-j2\pi km/N)$ and then convolved with the window function (which typically has a lowpass frequency response). The series combination of the modulator and the window function results in a bandpass filter. The DSTFT can therefore be thought of as being generated by passing a signal through a set of bandpass filters. Furthermore, if the discrete signal is processed with an ideal bandpass filter with a passband equal to π/N , then the output of the filter can be *decimated* by a factor of N (all signal samples are discarded except those corresponding to indices of $N, 2N, 3N$, etc.) with no loss of information. The incorporation of this philosophy with the bandpass filter view of the STFT yields the analysis portion of the *filterbank* structure shown in Fig. 1. The rationale for decimating the output of each of the bandpass filters is to reduce the storage requirements of the filterbank. In a similar fashion, a signal approximately equal to the input

signal can be produced with the synthesis structure also shown in Fig. 1. Note that the synthesis network contains *interpolators* (which insert N zeros between each input sample) and window functions known as *synthesis filters*. In general, the synthesis filters are similar, but not identical, to the analysis filters. In a typical data compression application of a filterbank, the outputs of the analysis section are encoded, transmitted over a channel, and then reconstructed with the synthesis section. Equality between the input and output of the filterbank subject to a finite delay, called *perfect reconstruction*, is achieved only for specific combinations of analysis filters and synthesis filters.

It is evident that filterbanks are a natural extension of the STFT. As is the case for the STFT, filterbanks may be utilized for instantaneous frequency estimation. Properly implemented, they permit a compact representation of the time–frequency properties of a signal with no loss of information. The characteristics of analysis and synthesis filters that eliminate aliasing, along with the requirements for perfect reconstruction, are thus of interest.

In an actual implementation of a filterbank, the digital analysis filters are of finite length, and thus they cannot form an ideal bandpass filter with unity gain in the passband and zero gain in the stopband. Therefore, some degree of aliasing will occur when the output of each of the analysis filters is decimated as in Fig. 1. If the analysis filters are not correctly designed, the aliased signals propagate through the filterbank and severely limit the quality of the filterbank’s output. Croisier et al. [4] examined this problem for the two-channel filterbank shown in Fig. 2, and they derived conditions on the analysis and synthesis filters such that these aliased terms are completely canceled. Filters designed with this approach are called *quadrature mirror filters*, since the analysis filters of a two-channel network are mirrors of one another about $\pi/2$. It is important to note that while the output of a filterbank employing quadrature mirror filters does not contain aliased terms, other magnitude and phase distortions typically exist.

The necessary and sufficient conditions for the design of a perfect reconstruction filter bank were derived by Smith and Barnwell [5]. They also proposed an algorithm to construct analysis and synthesis filters that satisfied these conditions, using well-known filter design techniques [6]. Although they termed these filters *conjugate quadrature*

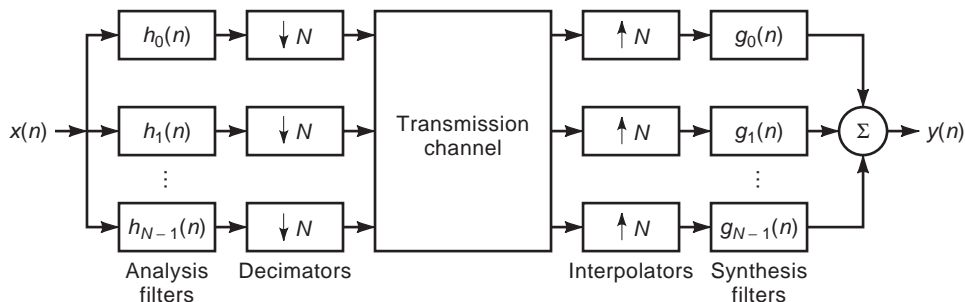


Figure 1. Structure for N -channel filterbank. This tool is frequently employed for time–frequency analysis.

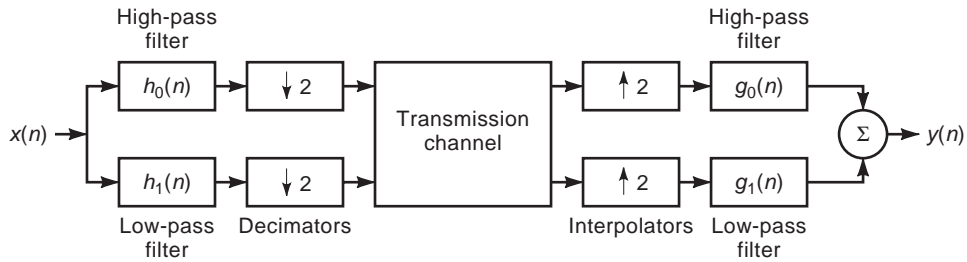


Figure 2. Structure for two-channel filterbank. This simple configuration can be used to construct more complicated structures.

filters, many researchers consider them to be a class of quadrature mirror filters. The power of Smith and Barnwell’s algorithm is demonstrated by the fact that it is applicable to the two-channel structure shown in Fig. 2, the N -channel structure shown in Fig. 1, and the tree-structured analysis section shown in Fig. 3, as well as to filterbanks employing nonuniform decimation and interpolation rates. Additional results regarding the implementation of perfect reconstruction filterbanks are included in Refs. 7 and 8.

A topic closely related to time–frequency analysis is *timescale* analysis, which is provided by the *wavelet transform*. Because of the similarity of the discrete wavelet transform with perfect reconstruction filterbanks, as well as the immense number of applications of the wavelet transform that have been investigated since 1989, a brief discussion of its development is included in the following.

In the late 1970s, the French geophysical engineer Morlet derived an alternative to the STFT for time–frequency analysis. The seismic signals of interest to Morlet contained high-frequency components with shorter time-spans than did the low-frequency components. With the STFT, it was impossible to simultaneously obtain good time resolution for the high-frequency components and good frequency resolution for the low-frequency

components. Morlet recognized that his goal could be obtained by decomposing the seismic signals not with *translated* and *modulated* versions of an elementary signal (as was done in Gabor’s work and the STFT), but with the *translated* and *scaled* versions of an elementary signal. This concept yielded basis functions that contained a constant number of cycles. Morlet chose to call his functions “wavelets of constant shape” [9]. Although the term “wavelet” had been used in the seismic field for a number of years before Morlet’s work, it had been used to denote seismic pulses, not a time–frequency tool.

Morlet later collaborated with Grossman to place the wavelet transform on a firm mathematical foundation [10]. They defined the continuous wavelet transform as

$$W_x(\tau, a) = \frac{1}{\sqrt{|a|}} \int_{-\infty}^{\infty} x(t) m^* \left(\frac{t - \tau}{a} \right) dt$$

where a is a scale factor and the “mother wavelet” $m(t)$ serves as a window function. The inverse wavelet transform is given by

$$x(t) = c \int_{-\infty}^{\infty} \int_{-\infty}^{\infty} \frac{1}{a^2} W_x(\tau, a) m \left(\frac{t - \tau}{a} \right) da d\tau$$

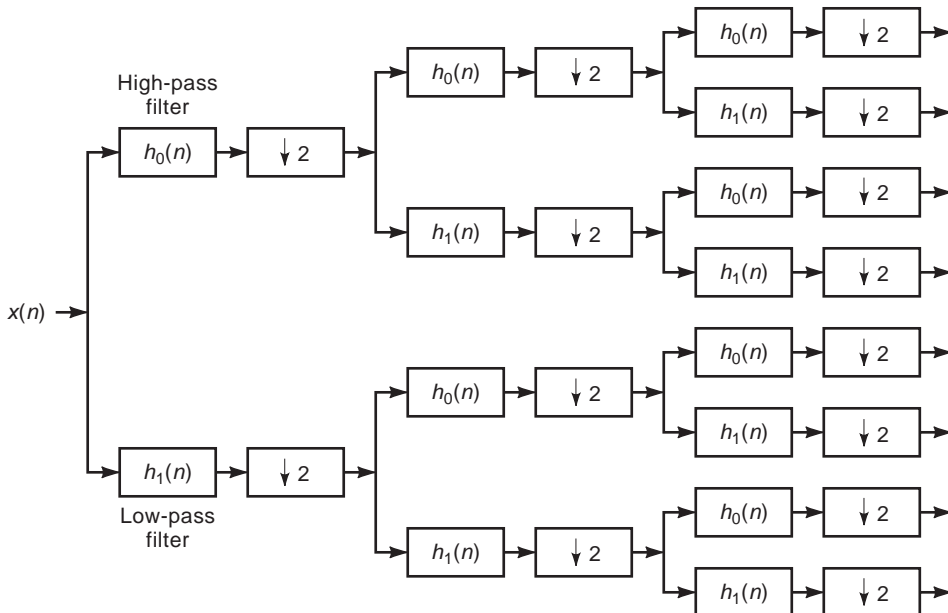


Figure 3. Analysis portion of tree-structured filterbank formed by the sequential application of two-channel filterbanks.

Morlet and Grossman used a nonorthogonal basis for the transform consisting of functions very similar to Gabor’s Gaussian-modulated sinusoids. An orthogonal basis was developed in 1985 by Meyer.

Structures for the discrete wavelet transform and its inverse were developed by Daubechies [11]. The form of the forward structure is shown in Fig. 4 and is seen to be very similar to a pruned version of the tree-structured filterbank shown in Fig. 3. At each level of the discrete wavelet transform, the input signal is passed through a lowpass filter and a highpass filter. The outputs of the filters are decimated by a factor of 2, and the decimated lowpass filter output is again passed to a lowpass/highpass filter pair. Daubechies derived conditions for the filters such that the structure yields perfect reconstruction, and she used these conditions to generate a set of viable filters frequently referred to as “Daubechies wavelets.” Of special interest to Daubechies was the relatively long impulse response of the filter produced by a series of short filters alternated with decimators. She termed the combined impulse response of the lowpass filters alternated with decimators the *scaling function* and the impulse response of the lowpass filters alternated with decimators and followed by a highpass filter, the *wavelet function*. She showed that as the number of levels in the transform grows large, the scaling function and the wavelet function converge to smooth waveforms, provided that the component filters have sufficient “regularity.” In digital signal processing terms, the regularity of a filter corresponds to the number of zeros at $z = -1$ ($\omega = \pi$) in the filter transfer function. Soon after Daubechies’ work was published, Mallat extended her results to two dimensions and applied them to image processing [12]. It has since been recognized that Daubechies’ conditions for perfect reconstruction are identical to those published by Smith and Barnwell. It has also been recognized that the structure corresponding to the discrete wavelet transform is equivalent to an octave-channel filterbank, a form of which had been investigated earlier for speech coding [3]. Nevertheless, the attention focused on filterbanks and time–frequency analysis due to the introduction of the wavelet transform has resulted in an explosion of new developments in these fields that has continued today.

In addition to the time–frequency distributions described above, many others have been developed since the late 1940s. A significant number of continuous time–frequency distributions can be characterized by what is

known as *Cohen’s class* of distributions [13], which is defined by

$$C_x(t, \omega) = \frac{1}{4\pi^2} \iiint x^*(u - \frac{1}{2}\tau)x(u + \frac{1}{2}\tau)\phi(\theta, \tau) \exp(-j\theta t - j\tau\omega + j\theta u) du d\tau d\theta$$

where $\phi(\theta, \tau)$ is a two-dimensional function known as the “kernel” and $x(t)$ is the signal under consideration. A particular member in Cohen’s class is identified by its kernel. For example, the *spectrogram*, which is defined as the magnitude squared of the STFT, is a recognized member of Cohen’s class of distributions, with a kernel given by

$$\phi(\theta, \tau) = \int h^*(u - \frac{1}{2}\tau)\exp(-j\theta u)h(u + \frac{1}{2}\tau) du$$

where $h(t)$ is the window function defined previously. A discrete form of Cohen’s class of time–frequency distributions is examined in Ref. 14.

With respect to a time–frequency distribution, there are two possible means of defining the instantaneous frequency of a signal at a point in time. The instantaneous frequency may be associated with either (1) the peak value of the signal’s distribution at that time or (2) the average of the frequencies present in the signal at that time. These approaches are appealing because they permit the introduction of the *instantaneous bandwidth* concept in a natural manner as the spectral spread of energy in the time–frequency plane about the instantaneous frequency. In the following section, it is shown that the instantaneous frequency estimate derived from certain time–frequency distributions is equivalent to the corresponding quantity derived from the analytic signal.

A major benefit obtained by employing a time–frequency distribution for instantaneous frequency estimation is the capability of the distribution to aid in determination of whether the signal under examination is monocomponent or multicomponent. Monocomponent signals are those that can be shown to possess energy in a contiguous portion of the time–frequency plane. At any point in time, this type of signal exhibits a narrowband characteristic. An example of this type of signal is a sinusoid with a continuous time-varying frequency. Conversely, multicomponent signals are those that can be shown to possess energy in multiple, well-isolated frequency bands at the same instant in time. Speech frequently displays this behavior. It

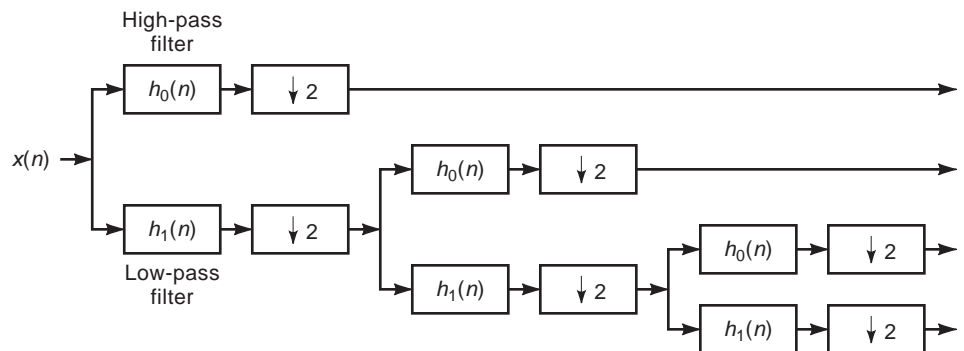


Figure 4. Structure for discrete wavelet transform. Note the similarity of this configuration to the structure shown in Fig. 3.

is noted that the preceding definition of monocomponent excludes signals such as an impulse, which could also be argued to be monocomponent because of its ridgeline time–frequency distribution. Obviously, the identification of a signal as monocomponent or multicomponent is not precise [15], but it is important, as the instantaneous frequency of a multicomponent signal may have no physical meaning [16].

A significant disadvantage of employing time–frequency distributions for IFE is that the construction of the distribution is a computationally complex procedure, even when filterbank structures are utilized. Fortunately, there is an alternative approach for IFE. In many situations, a reasonable estimate of the instantaneous frequency of a signal can instead be obtained from computationally simple operations on its analytic signal. Background for this philosophy is given in the following section. A summary of algorithms that have been suggested for implementation of this approach are provided in Section 3.

1.2. Analytic Signals

In this section, the relationships between the instantaneous frequency of a signal and its analytic signal are examined. First, a brief review of the analytic signal is provided. The definition of the instantaneous frequency in terms of the analytic signal is then discussed. Practical issues regarding the computation of the analytic signal are also presented. Finally, the situations for which the estimate of instantaneous frequency obtained via the analytic signal agrees with the estimate obtained from certain time–frequency distributions are examined.

Interestingly, as was the case with time–frequency analysis, the original work done in the area of analytic signals was conducted by Gabor [1]. He defined the complex analytic signal $z(t)$ corresponding to a real signal $x(t)$ to be the sum of the signal with a second signal generated via the Hilbert transform

$$\begin{aligned} z(t) &= x(t) + j\mathbf{H}\{x(t)\} \\ &= x(t) + jy(t) \end{aligned}$$

The continuous Hilbert transform is defined as

$$\mathbf{H}\{x(t)\} = \text{PV} \frac{1}{\pi} \int_{-\infty}^{\infty} \frac{x(\tau)}{t - \tau} d\tau$$

where PV indicates the Cauchy principal value of the integral. The signal $z(t)$ is similar to $x(t)$, in that for positive frequencies, $Z(f) = 2X(f)$. However, the spectrum of $z(t)$ contains no energy at negative frequencies. Indeed, one technique for deriving the analytic signal of a real signal is to compute its Fourier transform, ignore the spectral components corresponding to negative frequencies, apply the appropriate scaling factor, and then compute the inverse Fourier transform of the modified signal. Gabor developed the analytic signal concept to aid in derivation of the signal with minimum time–frequency extent. However, the most extensive application of analytic signals has been in the communications field.

The importance of the analytic signal to the definition of instantaneous frequency can be seen by considering a simple example. Suppose that a continuous real signal $x(t)$ is given by

$$x(t) = a(t) \cos(\phi(t))$$

where $a(t)$ represents a time-varying amplitude and $\phi(t)$ represents a time-varying phase. Since the “frequency” of a sinusoid is defined as the derivative of its phase, the instantaneous frequency of a signal $x(t)$ could be computed with the derivative of $\phi(t)$. This definition appears to agree with intuition. However, when the magnitude of $a(t)$ is bounded by b , the signal $x(t)$ can also be expressed as

$$x(t) = b \cos(\tilde{\phi}(t))$$

where $\tilde{\phi}(t) \neq \phi(t)$. Therefore, the postulated definition does not yield a unique instantaneous frequency for the signal $x(t)$. By defining the instantaneous frequency of $x(t)$ to be the derivative of the phase of the corresponding unique analytic signal $z(t)$, this ambiguity can be eliminated [17]. Since the analytic signal is complex, it can always be expressed uniquely as

$$z(t) = m(t) \exp(j\theta(t))$$

The instantaneous frequency can thus be uniquely defined as $d\theta(t)/dt$. However, it is not claimed that this definition provides satisfactory results in every scenario.

In practice, discrete sequences $x(n)$ corresponding to samples of the continuous signal $x(t)$ at time instants $t = nT$ are available, and it is desired to form the discrete analytic signal $z(n)$ where

$$z(n) = x(n) + jy(n)$$

The analytic signal $z(n)$ can be obtained in a number of ways, each with its own advantages and disadvantages. The sequence $y(n)$ can be generated by the brute-force approach of zeroing the spectral components of $x(n)$ corresponding to negative frequencies. This technique works well for finite datasets, but can be difficult to implement in real-time applications. The sequence $y(n)$ can also be generated by processing the sequence $x(n)$ with a digital filter designed to approximate the Hilbert transform [6]. However, the group delay introduced to $y(n)$ by the digital filter must also be introduced to $x(n)$, which can be difficult for noninteger delays. A third approach is to compute the complex sequence $z(n)$ directly, by processing the sequence $x(n)$ with a complex filter constructed by modulating a real lowpass filter by a complex exponential [18].

It is interesting to note the relationship between (1) the instantaneous frequency estimate obtained from a time–frequency distribution and (2) the instantaneous frequency estimate obtained from the derivative of the analytic signal’s phase. For continuous signals, it can be shown that the first moment of a time–frequency distribution of Cohen’s class is equivalent to the derivative of the analytic

signal's phase if the kernel $\phi(\theta, \tau)$ is selected such that

$$\left. \frac{\partial \phi(\theta, \tau)}{\partial \tau} \right|_{\tau=0} = 0$$

Furthermore, for signals with quadratic phase functions, the peak of the time–frequency distribution known as the *Wigner–Ville distribution* corresponds to the instantaneous frequency [19]. Results for the discrete signal case have appeared in Refs. 14 and 20.

2. MEASURES OF PERFORMANCE FOR INSTANTANEOUS FREQUENCY ESTIMATION ALGORITHMS

To evaluate various IFE algorithms, there must be a means of comparing the performance and implementation of a specific algorithm to an alternate approach. In this section, the measures of performance typically used to compare IFE algorithms to one another are discussed. The measures of performance that are considered include both statistical and computational issues. At the conclusion of this section, these criteria are demonstrated by utilizing them to evaluate the performance of the classical periodogram approach to estimating the frequency of a sinusoid embedded in white Gaussian noise.

Since the problem of interest concerns the estimation of an unknown quantity in the presence of noise, it is useful to introduce several statistical concepts from estimation theory. Typically, it is desired to estimate the value of an unknown parameter θ from N noisy measurements of a quantity related to θ . An estimator is considered *unbiased* when the expected value of the estimate $\hat{\theta}$ equals the true value of the parameter:

$$E\{\hat{\theta}\} = \theta$$

If this condition does not hold, the estimator is termed *biased*. An estimator is considered *consistent* if it yields an estimate that asymptotically converges in probability to the true value. For a consistent estimator, we obtain

$$\lim_{N \rightarrow \infty} \Pr\{|\hat{\theta} - \theta| > \varepsilon\} = 0$$

where \Pr denotes probability and ε is an arbitrary small positive number. Both of these characteristics are generally thought to be desirable but, depending on the problem of interest, may or may not be required.

The benchmark by which the variance of a particular unbiased estimator can be evaluated is given by the Cramer–Rao lower bound (CRLB). As its name implies, the CRLB provides a lower bound on the variance of any linear or nonlinear unbiased estimator. Thus, given the variance of a particular unbiased estimator, the CRLB may be used to determine if other unbiased estimators might exist that exhibit smaller variance. Although other bounds on estimator variance exist, it is generally agreed that the CRLB is the easiest to compute, and hence finds extensive use [21]. The CRLB for the scalar parameter θ is expressed

in terms of the measurement vector \mathbf{x} with

$$\text{var}(\hat{\theta}) \geq \frac{1}{-E\left\{\frac{\partial^2 \ln p(\mathbf{x}; \theta)}{\partial \theta^2}\right\}}$$

where $p(\mathbf{x}; \theta)$ is the probability density function (pdf) of \mathbf{x} given the parameter θ [22]. The expectation is taken with respect to $p(\mathbf{x}; \theta)$, which results in a function of θ . When the pdf is considered to be a function of the unknown parameter θ (with a fixed measurement vector \mathbf{x}), it is called the “likelihood function.”

Although the CRLB may be computed for a specific estimation problem, there is no guarantee that an unbiased estimator exists that will equal the bound for all values of the unknown parameter. If such an estimator does exist, it is said to be *efficient*. An estimator is considered *asymptotically efficient* if its variance converges to the CRLB as the number of observations becomes large. *Maximum-likelihood* (ML) estimators are known to be asymptotically efficient, and they can be constructed by computing the value of θ that maximizes the likelihood function. The performance of ML algorithms for large data records, along with the existence of an analytical approach to their derivation, makes ML algorithms very appealing. In practice, these algorithms can be computationally complex, such that other approaches may be preferred.

At high signal-to-noise ratio (SNR), the variance of ML estimators is typically very close to the CRLB. As the SNR is decreased, the CRLB and the estimator variance increase at the same rate. For nonlinear estimators, this behavior continues until a *threshold* is reached. Below this value of SNR, the variance of the estimator increases at a much faster rate than does the CRLB. In a plot of the variance as a function of SNR, a knee will be seen at the threshold. Thus, the estimator threshold is frequently used as a metric to compare several estimators that have similar high-SNR characteristics. For maximum-likelihood estimators, the threshold typically decreases as the size of the data window increases.

In addition to the factors described above, various algorithms for the estimation of a particular parameter may also be compared to one another with respect to computational considerations. Computational issues include the algorithm's complexity as measured by the number of arithmetic operations (such as multiplications or arctan function calls) required for its implementation, the storage requirements of the algorithm, and the data window size required for satisfactory performance.

As a demonstration of the concepts described in this section, the classical approach to the estimation of the frequency of a single complex sinusoid with unknown amplitude and phase in the presence of white Gaussian noise is considered. The CRLB for the frequency estimate is given by

$$\text{CRLB} = \frac{12}{T^2 N(N^2 - 1)} \left(\frac{\sigma^2}{A^2} \right)$$

where A is the amplitude of the complex sinusoid, σ^2 is the power of the complex white Gaussian noise, T is the

sampling period, N is the number of available data samples, and A^2/σ^2 is the SNR. To derive a ML estimator for this problem, the likelihood function L is computed in terms of the unknown frequency, amplitude, and phase. It has been shown that the likelihood function is given by

$$L(\omega, A, \theta) = 2A \operatorname{Re}[\exp(-j\theta) \exp(-j\omega t_0) X(\omega)]$$

where θ is the unknown phase, t_0 is the time corresponding to the first data sample, and $X(\omega)$ represents the discrete-time Fourier transform of the data sequence $x(nT)$ [23]. The ML estimate of the sinusoid's frequency is the maximum of $L(\omega, A, \theta)$ with respect to ω over all values of A and θ , and it can be shown to correspond to the frequency that maximizes the periodogram $|X(\omega)|^2$. To implement this approach, it has been suggested that a coarse frequency estimate be obtained from the peak magnitude of the discrete Fourier transform (DFT) and that a more accurate result be obtained via an interpolation algorithm. The performance of the overall algorithm is significantly improved if the length of the original data sequence is increased by a factor of 2 or 4 by zero padding, before the coarse DFT is computed. An accurate means of implementing the interpolation procedure with only three DFT points is presented in Ref. 24.

The ML algorithm for estimating the frequency of a single sinusoid in noise is conceptually simple but computationally intensive. This is especially the case when the algorithm must be implemented under a real-time schedule in order to track a time-varying frequency. In the following section, additional approaches to the implementation problem are examined.

3. ALGORITHMS FOR INSTANTANEOUS FREQUENCY ESTIMATION

In this section, a selection of algorithms that have been suggested for IFE are summarized. This selection is not all-inclusive, and it is in fact concentrated in two areas. The first set of algorithms employ *weighted phase averaging* techniques, and the second set of algorithms are designed to function with extremely short data windows in high-SNR environments. Both sets of algorithms are designed for monocomponent signals. References to other approaches for estimating the instantaneous frequency of monocomponent signals, along with approaches for multicomponent signals, are provided.

3.1. Algorithms Employing Weighted Phase Averaging

One way to represent a constant-amplitude, complex signal with time-varying frequency is to model the signal as a complex exponential with polynomial phase. From the Weierstass theorem, it is known that all continuous phase functions can be approximated to any desired accuracy by a polynomial. The polynomial phase model is thus very general, in addition to being easily analyzed. When P coefficients are considered in the polynomial, the signal

model is expressed by

$$z(n) = A \exp\left(j \sum_{p=0}^P c_p n^p\right) + \varepsilon(n)$$

where A is the constant signal amplitude, n is the sampling index, c_p is the polynomial coefficient, and $\varepsilon(n)$ is complex zero-mean white Gaussian noise. In the following discussion, algorithms that employ weighted phase averaging to estimate the coefficients of the polynomial phase model are examined. Before examining algorithms capable of estimating all P coefficients, less complex approaches corresponding to linear and quadratic phase models are summarized. The less sophisticated approaches are of interest because of their relatively undemanding computational requirements. In fact, it has been suggested that time-varying frequencies be tracked with sliding-window implementations of these simpler algorithms.

A sinusoid with constant frequency can be represented by the polynomial phase model with a constant plus linear phase term. As discussed in the previous section, the ML estimate of the frequency of a single sinusoid embedded in white Gaussian noise is given by the peak of the periodogram. Unfortunately, the construction of the periodogram is computationally intensive, and other less complex approaches are desired. One such approach was suggested by Tretter [25]. He considered the input data sequence to be modeled by

$$z(n) = A \exp(j(\theta + \omega n)) + \varepsilon(n)$$

where θ is a constant phase and ω is the signal's angular frequency. The angular frequency is assumed to be bounded by $-\pi < \omega \leq \pi$. The noise power is given by σ^2 , and the SNR is thus expressed as

$$\operatorname{SNR} = \frac{A^2}{\sigma^2}$$

Tretter showed that for $\operatorname{SNR} \gg 1$, the data sequence can be approximated as

$$\begin{aligned} z(n) &\approx A \exp(j(\theta + \omega n + v(n))) \\ &\approx A \exp(j\phi(n)) \end{aligned}$$

where $v(n)$ is a real Gaussian white noise sequence with variance equal to $1/(2\operatorname{SNR})$. The impact of this approximation is that all the information required to estimate the frequency ω is contained in the signal phase $\phi(n)$. Tretter suggested that the phase be estimated by unwrapping the sequence obtained from computing the arctan of $z(n)$. The frequency is then estimated via least-squares of linear regression. For high SNR, this estimation scheme achieves the CRLB.

An alternate viewpoint to this problem was provided by Kay [26]. He suggested that phase differences, rather than the phases themselves, be employed. The phase difference $\Delta(n)$ can be written as

$$\begin{aligned} \Delta(n) &= \phi(n+1) - \phi(n) \\ &= \omega + v(n+1) - v(n) \end{aligned}$$

The frequency estimation problem can then be expressed as the estimation of the mean of a colored Gaussian noise process. Kay showed that the ML frequency estimate for this problem is given by

$$\hat{\omega}_K = \sum_{n=0}^{N-2} \omega(n) \Delta(n)$$

where the total number of data samples available for processing is denoted by N , and $w(n)$ represents a parabolic weighting function given by

$$\omega(n) = \frac{1.5N}{N^2 - 1} \left[1 - \left(\frac{n - (0.5N - 1)}{0.5N} \right)^2 \right]$$

Kay noted that if a uniform weighting is applied, the phase differences are merely averaged, and the variance of the estimate is increased by a factor equal to $N/6$ at high SNR. It was later shown that Kay's algorithm can be derived from Tretter's algorithm using "summation by parts" [27].

As is typical with nonlinear estimation methods, the variance of Kay's algorithm departs from the CRLB when the SNR is reduced below a threshold value. Kim noted that the threshold of Kay's algorithm occurs when the SNR drops below a value for which the phase noise approximation is valid. He suggested that the SNR of the signal be increased before the phase of the data samples is computed, by averaging K adjacent data samples. In this manner, the threshold is decreased at the cost of a small loss in estimation performance and a decreased estimation range [28]. For example, for datalengths greater than 24 and $K=4$, Kim determined that his algorithm departs from the CRLB at high SNR by less than 0.2 dB. The threshold is reduced by a factor of $20 \log(K)$ dB, and the estimation range is reduced by a factor of K .

In the frequency estimation work conducted by Rife and Boorstyn [23], it was noted that the angular frequency estimate of their algorithm (described in the previous section of this article) was biased whenever the angular frequency was close to zero or the sampling frequency. Similarly, the variance of Kay's estimator also significantly degrades when the angular frequency is close to these values. A means of overcoming this problem was proposed by Lovell and Williamson [29]. They noted that the performance degradation is avoided if the weighting function is applied to the phase differences in a circular, rather than linear, fashion. For example, to compute the mean of a group of phases, they suggested that the phases first be expressed as unit magnitude phasors and that the argument of the sum of phasors then be computed. By incorporating these concepts into Kay's estimators, the sensitivity of the estimator variance with respect to angular frequency was significantly reduced.

The second coefficient relating to frequency in a polynomial phase model corresponds to frequency rate. Including this parameter μ , the signal model is written as

$$z(n) = A \exp(j(\theta + \omega n + \frac{1}{2} \mu n^2)) + \varepsilon(n)$$

The frequency rate is assumed to be bounded by $-\pi < \mu \leq \pi$. This type of modulation is termed *linear frequency mod-*

ulation (LFM), and the corresponding signal is termed a *chirp* signal. Despite its simple form, this signal is utilized in many fields and is thus of significant interest.

A procedure to jointly estimate θ , ω , and μ for a chirp signal was suggested by Djuric and Kay [30]. In this approach, the additive complex noise is modeled as real phase noise, as was the case in Refs. 25 and 26. However, a different technique is utilized to estimate the unambiguous phase sequence. First, two phase difference operations are implemented on the original data sequence, and the phases of the resulting data samples are computed with the arctan function. The sequence $d(n)$ is thus generated, where

$$d(n) = \mu + \Delta^2 \omega(n)$$

and $\Delta^2 \omega(n)$ denotes a colored-noise sequence. An estimate $\hat{\phi}(n)$ of the unambiguous phase sequence $\phi(n)$ corresponding to the original data sequence is then obtained by twice integrating $d(n)$. The estimates of θ , ω , and μ are then jointly obtained from $\hat{\phi}(n)$. If only the frequency rate is desired, μ may be estimated directly from $d(n)$ in a similar fashion as ω was estimated in Ref. 26.

One shortcoming of the algorithm suggested by Djuric and Kay is its performance for large values of μ . When the magnitude of this parameter is close to its upper bound, errors occur in the phase unwrapping algorithm, and the performance of the estimator degrades. To overcome this effect, they suggested that a third phase difference operation be employed. However, this approach increases the probability of an outlier occurring due to differentiation of the phase noise, thereby degrading the unwrapping process and hence the estimation performance. An alternative solution to this problem was proposed by Slocumb and Kitchen [31]. In their work, an iterative procedure is suggested in which the phase unwrapping and parameter estimation is conducted concurrently. A recursive least-squares (RLS) algorithm [32] is employed to improve the phase unwrapping process, thereby removing the sensitivity of the threshold to the value of μ . For large values of μ , the threshold corresponding to Slocumb and Kitchen's approach is as much as 12 dB lower than the threshold of Djuric and Kay's algorithm.

The approaches presented above for chirp signals can be extended to estimate an arbitrary number of coefficients of the polynomial phase model. To prevent aliasing in a critically sampled signal, the polynomial coefficients must be bounded by

$$|c_p| < \frac{\pi}{p!}$$

For the algorithm presented in Ref. 30, increasing the number of parameters to be estimated also increases the threshold of the algorithm.

3.2. Algorithms Employing Short Data Windows

In certain situations, it is reasonable to assume a very high SNR, even as high as 40 dB. It is then possible to obtain estimates of the instantaneous frequency of a monocomponent signal with only a few data samples. In this section, two computationally efficient algorithms are described that obtain accurate estimates of the

instantaneous frequency with only four or five data samples. This feature is very desirable, because the instantaneous frequency estimate is thus highly localized in time.

Teager's energy operator was originally proposed as a means of quantifying the "energy" present in a harmonic oscillation [33]. It has since been utilized to derive algorithms for instantaneous frequency estimation that are highly time-localized. The discrete form of this operator is given by

$$\Psi[x(n)] = x^2(n) - x(n+1)x(n-1)$$

where it is assumed that the sampling period is unity. Utilizing this operator, three different algorithms have been derived to estimate the instantaneous frequency and amplitude of a monocomponent AM-FM signal [34]. The three algorithms are denoted DESA-1a, DESA-1, and DESA-2, and the associated instantaneous frequency estimation algorithms are expressed as

$$\begin{aligned}\omega_{1a}(n) &= \arccos\left(1 - \frac{\Psi[x(n)] - x(n-1)}{2\Psi[x(n)]}\right) \\ \omega_1(n) &= \arccos\left(1 - \frac{\Psi[x(n)] - x(n-1) + \Psi[x(n+1)] - x(n)}{4\Psi[x(n)]}\right) \\ \omega_2(n) &= \frac{1}{2} \arccos\left(1 - \frac{\Psi[x(n+1)] - x(n-1)}{2\Psi[x(n)]}\right)\end{aligned}$$

The first algorithm requires four data points for its operation, and the remaining two algorithms require five data points. All three algorithms may be implemented with only a few multiplications per timestep.

A second means of constructing highly time-localized instantaneous frequency estimators is by symbolically expressing the roots of the predictor filter corresponding to a sinusoidal signal model in terms of the input data samples [35]. Two forms of linear prediction have been examined for this application: the covariance method and the modified covariance method. For the modified covariance method, two estimators were derived in Ref. 35. The first estimator requires four data samples for its operation, and the second requires five data samples. The estimators are expressed in terms of the input data samples via

$$\begin{aligned}\omega_{MC4}(n) \\ = \arccos\left(\frac{x(n-2)x(n-1) + 2x(n-1)x(n) + x(n)x(n+1)}{2(x^2(n-1) + x^2(n))}\right)\end{aligned}$$

and

$$\begin{aligned}\omega_{MC5}(n) \\ = \arccos\left(\frac{x(n-2)x(n-1) + 2x(n-1)x(n) + 2x(n)x(n+1) + x(n+1)x(n+2)}{2(x^2(n-1) + x^2(n) + x^2(n+1))}\right)\end{aligned}$$

Utilizing the covariance method, a single estimator was derived that required five data samples for its operation:

$$\omega_{C5}(n) = \arccos\left(\frac{x(n-1)x(n) - x(n-2)x(n+1)}{x^2(n) - x(n-1)x(n+1) + x^2(n-1)}\right)$$

These algorithms have been shown to require fewer computational operations per timestep than the DESAs. The linear predictive algorithms also yield smaller mean and RMS errors than the DESAs when simulated with signals having various amounts of amplitude and frequency modulation. The performance of linear predictive techniques with respect to the CRLB was investigated in Ref. 36.

3.3. Other Algorithms

The algorithms for IFE that were summarized in this section were concentrated in two general areas. Many other approaches for estimating the instantaneous frequency of monocomponent signals exist, such as the extended Kalman filter [37], the cross-power spectrum [38], and the discrete polynomial transform [39]. Still other techniques are described in Ref. 19. For multicomponent signals, proposed approaches include adaptive notch filters [40], recursive least squares [41], cross-coupled digital phase-locked loops [42], and the periodic algebraic separation energy demodulation algorithm [43]. Additional techniques are discussed in Ref. 43.

4. CONCLUSION

In this article, the connection between instantaneous frequency and time-frequency analysis were explored. Definitions for instantaneous frequency with respect to time-frequency distributions and to the analytic signal were provided. Measures of performance for estimators of instantaneous frequency were illustrated, such as the Cramer-Rao lower bound. Finally, a selection of algorithms that have been recently proposed for instantaneous frequency estimation were summarized.

Acknowledgments

L. B. Fertig's research was supported by a GTRC Ph. D. fellowship.

J. H. McClellan's research was supported by the Joint Services Electronics Program under contract DAAH-04-96-1-0161.

BIBLIOGRAPHY

1. D. Gabor, Theory of communication, *Proc. IEE* **93**:429-457 (1946).
2. J. B. Allen and L. R. Rabiner, A unified approach to short-time Fourier analysis and synthesis, *Proc. IEEE* **65**:1558-1564 (1977).
3. L. R. Rabiner and R. W. Schafer, *Digital Signal Processing of Speech Signals*, Prentice-Hall, Englewood Cliffs, NJ, 1978.

4. A. Croisier, D. Esteban, and C. Galand, Perfect channel splitting by use of interpolation decimation tree decomposition techniques, *Int. Conf. Information Science Systems*, 1976, pp. 443–446.
5. M. J. T. Smith and T. P. Barnwell, A procedure for designing exact reconstruction filter banks for tree structured subband coders, *Proc. ICASSP 27.1.1–27.1.4* (1984).
6. A. V. Oppenheim and R. W. Schaffer, *Discrete-Time Signal Processing*, Prentice-Hall, Englewood Cliffs, NJ, 1989.
7. P. P. Vaidyanathan, *Multirate Systems and Filter Banks*, Prentice-Hall, Englewood Cliffs, NJ, 1993.
8. M. Vetterli and J. Kovacevic, *Wavelets and Subband Coding*, Prentice-Hall, Upper Saddle River, NJ, 1995.
9. J. Morlet et al., Wave propagation and sampling theory, Part 1: Complex signal and scattering in multilayered media, *Geophysics* **47**(2):203–221 (1982).
10. A. Grossman and J. Morlet, Decomposition of Hardy functions into square integrable wavelets of constant shape, *SIAM J. Math. Anal.* **15**(4):723–736 (1984).
11. I. Daubechies, Orthonormal bases of compactly supported wavelets, *Commun. Pure Appl. Math.* **41**:909–996 (1988).
12. S. Mallat, Multifrequency channel decompositions of images and wavelet models, *IEEE Trans. Acoust. Speech Signal Process.* **37**:2091–2110 (1989).
13. L. Cohen, *Time–Frequency Analysis*, Prentice-Hall, Upper Saddle River, NJ, 1995.
14. P. J. Kootsookos, B. C. Lovell, and B. Boashash, A unified approach to the STFT, TFD's and instantaneous frequency, *IEEE Trans. Signal Process.* **40**:1971–1982 (1992).
15. L. Cohen, What is a multicomponent signal? *Proc. ICASSP* **5**:113–116 (1992).
16. P. J. Loughlin and B. Tacer, Comments on the interpretation of instantaneous frequency, *IEEE Signal Process. Lett.* **4**(5):123–125 (1997).
17. B. Picinbono, On instantaneous amplitude and phase of signals, *IEEE Trans. Signal Process.* **45**:552–560 (1997).
18. A. Reilly, G. Frazer, and B. Boashash, Analytic signal generation—tips and traps, *IEEE Trans. Signal Process.* **42**:3241–3245 (1994).
19. B. Boashash, Estimating and interpreting the instantaneous frequency of a signal, Part I and II, *Proc. IEEE* **80**:519–568 (1992).
20. M. Sun and R. J. Sclabassi, Discrete-time instantaneous frequency and its computation, *IEEE Trans. Signal Process.* **41**:1867–1880 (1993).
21. S. M. Kay, *Fundamentals of Statistical Signal Processing*, Prentice-Hall, Englewood Cliffs, NJ, 1993.
22. H. L. Van Trees, *Detection, Estimation, and Modulation Theory*, Part I, Wiley, New York, 1968.
23. D. C. Rife and R. R. Boorstyn, Single-tone parameter estimation from discrete-time observations, *IEEE Trans. Inform. Theory* **20**:591–598 (1974).
24. B. G. Quinn, Estimating frequency by interpolation using Fourier coefficients, *IEEE Trans. Signal Process.* **42**:1264–1268 (1994).
25. S. A. Tretter, Estimating the frequency of a noisy sinusoid by linear regression, *IEEE Trans. Inform. Theory* **31**:832–835 (1985).
26. S. M. Kay, A fast and accurate single frequency estimator, *IEEE Trans. Acoust. Speech Signal Process.* **37**:1987–1990 (1989).
27. S. W. Lang and B. R. Musicus, Frequency estimation from phase differences, *Proc. ICASSP* **4**:2140–2144 (1989).
28. D. Kim, M. J. Narasimha, and D. C. Cox, An improved single frequency estimator, *IEEE Signal Process. Lett.* **3**(7):212–214 (1996).
29. B. C. Lovell and R. C. Williamson, The statistical performance of some instantaneous frequency estimators, *IEEE Trans. Signal Process.* **40**:1708–1723 (1992).
30. P. M. Djuric and S. M. Kay, Parameter estimation of chirp signals, *IEEE Trans. Acoust. Speech Signal Process.* **38**:2118–2126 (1990).
31. B. J. Slocumb and J. Kitchen, A polynomial phase parameter estimation phase unwrapping algorithm, *Proc. ICASSP* **4**:1867–1880 (1994).
32. S. Haykin, *Adaptive Filter Theory*, Prentice-Hall, Englewood Cliffs, NJ, 1991.
33. J. F. Kaiser, On a simple algorithm to calculate the “energy” of a signal, *Proc. ICASPP* **1**:381–384 (1990).
34. P. Maragos, J. F. Kaiser, and T. F. Quatieri, On separating amplitude from frequency modulations using energy operators, *Proc. ICASSP* **2**:1–4 (1992).
35. L. B. Fertig and J. H. McClellan, Instantaneous frequency estimation using linear prediction with comparisons to the DESA's, *IEEE Signal Process. Lett.* **3**(2):54–56 (1996).
36. S. W. Lang and J. H. McClellan, Frequency estimation with maximum entropy spectral estimators, *IEEE Trans. Acoust. Speech Signal Process.* **28**:716–724 (1980).
37. K. Nishiyama, A nonlinear filter for estimating a sinusoidal signal and its parameters in white noise: On the case of a single sinusoid, *IEEE Trans. Signal Process.* **45**:970–981 (1997).
38. S. Umesh and D. Nelson, Computationally efficient estimation of sinusoidal frequency at low SNR, *Proc. ICASSP* **5**:2797–2800 (1996).
39. S. Peleg and B. Friedlander, Signal estimation using the discrete polynomial transform, *Proc. ICASSP* **4**:424–427 (1993).
40. G. Li, A stable and efficient adaptive notch filter for direct frequency estimation, *IEEE Trans. Signal Process.* **45**:2001–2009 (1997).
41. P. Tichavsky and P. Handel, Efficient tracking of multiple sinusoids with slowly varying parameters, *Proc. ICASSP* **3**:368–371 (1993).
42. J. N. Bradley and R. L. Kirilin, Phase-locked loop cancellation of interfering tones, *IEEE Trans. Signal Process.* **41**:391–395 (1993).
43. B. Santhanam, *Multicomponent AM–FM energy demodulation with applications to Signal Processing and Communications*, Ph.D. dissertation, Georgia Inst. Technology, Atlanta, GA, 1997.

FREQUENCY SELECTIVE SURFACES

TE-KAO WU
Northrop-Grumman
Redondo Beach, California

1. INTRODUCTION

A frequency-selective surface (FSS) is a structure consisting most typically of two-dimensional periodic elements, as depicted in Fig. 1, which exhibits frequency filtering

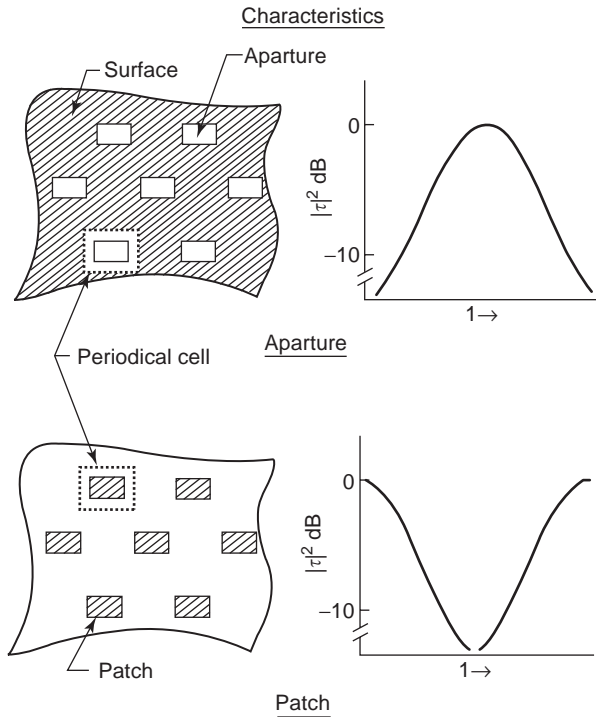


Figure 1. Typical frequency filtering characteristics of aperture and patch element FSS.

properties similar to those of frequency filters in traditional radiofrequency (RF) circuits. Here the periodic array of slots (or apertures) in a perfect conducting sheet act as a *bandpass* filter, namely, *passing* waves at the resonant frequency of the slots but rejecting them at higher and lower frequencies. On the contrary, the array of conducting patches act as a *bandstop* filter, namely, *rejecting* waves at the patches resonant frequency but passing them at higher and lower frequencies. In the case of freestanding and thin grids without dielectrics, the filtering performances of the patch element FSS and aperture FSS are exactly complementary to each other. Because of this filtering property, there are two major applications of FSS. One is in reflector antenna systems, where FSS reflectors are used to separate feeds of different bands. The other

application is to use FSS as antenna radomes for better control of the transmitted and reflected electromagnetic waves [1–3].

FSS may also be categorized as thick- or thin-screen FSS, depending on the thickness of the element. The term *thin-screen FSS* usually refers to a screen with printed-circuit-type elements, specifically, patch or aperture elements with thickness less than 0.001 wavelength of the screen’s resonant frequency. In general, the thin-screen FSS is light in weight, low-volume, and inexpensive, capable of being fabricated with conventional printed-circuit technology. On the other hand, a thick-screen FSS, used mostly for bandpass applications (aperture type), is a periodic array of elements with electrically large thickness. It is heavy, and the fabrication requires precise and expensive machining of a thick metal block. Waveguide stacks [4,5] have been a popular thick-screen FSS. The advantage of thick-screen FSS is that the transmission and reflection frequency ratio (f_t/f_r) or the band separation can be reduced to as low as 1.15 (= 14.0/12.2 GHz), which is required for the advanced multifrequency communication satellite antennas [5]. When filled with a dielectric such as paraffin wax, the waveguide’s cutoff frequency is reduced. This results in a smaller waveguide size; hence a closely packed array is achieved without any grating lobe occurring in the operation bands. It has also been found that increasing the angle of incidence increases the cross-polarization level and also causes ellipticity in circularly polarized waves. One way to overcome this is to make the holes slightly oval, instead of circular, as indicated in Ref. 6.

There are a variety of FSS element shapes (Fig. 2 illustrates some of the most common shapes), including square patch, dipole, circular patch, cross-dipole, Jerusalem cross, square loop, ring (or circular loop), square aperture, etc. The resonant frequency of a freestanding dipole array has the worst stability with incident angle variations. The reason for this can be explained as follows. When a vertically polarized incoming wave hits a half-wave vertical dipole, the dipole will resonate no matter what the incident angle is. However, if the incident direction is oblique to the broadside of the dipole, the dipole will not resonate effectively, depending on the incident angles. This is because the projected length of the dipole in the

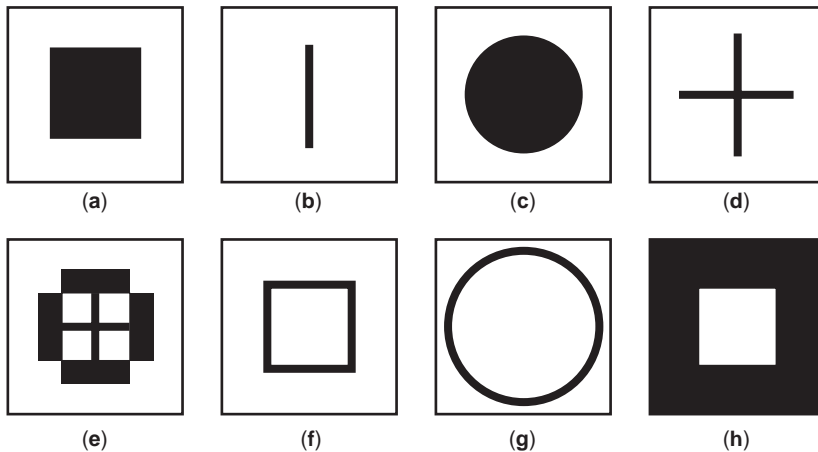


Figure 2. Some typical FSS element shapes.

incident direction is now less than a half-wavelength. This is why the resonant frequency of the dipole or the crossed-dipole element FSS shifts drastically, when the incoming waves have large incident angles.

For the square-loop and the circular-loop (ring) elements shown in Fig. 2, resonance occurs when the length of each half-loop is a multiple of one half-wavelength. In other words, each half-loop is acting as a dipole element. The length of the whole loop needs, therefore, to be a multiple of one full wavelength. To avoid a null in the scattered pattern, the length of the loop must be one wavelength instead of a multiple wavelength. This is because a one wavelength-long dipole will have a null in its broadside, a 1.5-wavelength long dipole will form two nulls in the off-broadside directions, and so on. Similarly, a multiwavelength loop is expected to have the undesirable nulls formed in its scattered pattern. To summarize, the mean circumference of a printed circular ring element for the FSS application must be one wavelength long. For a ring element printed on a dielectric substrate, the electrical length of the circumference must be one effective wavelength, and the physical circumference will therefore be less than one free-space wavelength; this requirement is the result of the dielectric loading effect.

2. FSS ANALYSIS TECHNIQUES AND TOOLS

Numerous methods have been employed in analyzing FSS. One of the simplest methods is the equivalent-circuit model [7,8]. In this analysis the various strip segments that form a freestanding patch element in a periodic array are modeled as inductive and capacitive components on a transmission line. The reflection and transmission coefficients of the FSS screen are found from the solution of this circuit. Since this approach uses the quasistatic approximation for the calculation of the circuit components, it is accurate only up to the resonant frequency of the screen. In addition, it will not model the dielectric loading effects accurately. Another method used successfully is the mutual impedance method [3]. This method uses antenna array theory and requires some knowledge of the mutual impedance between apertures.

The modal (or integral equation) method [1–3] has been the most successful in predicting the performance of the periodic structure, particularly in its ability to handle arbitrary incidence angles. The method involves first derivation of the integral equation by matching the Floquet modes in space and the aperture or current modes on the periodic surface. The integral equation may be formulated using the spatial or the spectral domain approach [1]. With the spectral domain approach the complicated integral equation is reduced to a simple algebraic multiplication of simple functions (trigonometric functions and integrals involve with them). Next, the method of moments or conjugate gradient technique is employed to solve the integral equation.

For a solution of the integral equation, the infinite number of equations with an infinite number of unknowns must be truncated to a finite number of equations with the same number of unknowns. This must be done in accor-

dance with the relative convergence criteria as indicated by Lee [9]. Another successful FSS analysis is the finite-difference time-domain (FDTD) approach [10].

Many analytical tools are available for analyzing and designing FSS [2,3]. Among them, the most popular one is the PMM (Periodic Moment Method) code [11], which implements the versatile method of moments to the solutions of arbitrarily shaped FSS elements. Ansoft Corporation also provides commercially available Designer (which integrates the PMM code with other system design codes) and HFSS (high-frequency structure simulator) tools [12].

3. DIELECTRIC LOADING EFFECTS

Dielectrics are often used for stabilizing the drift of FSS resonant frequency with the steering of incident angle or for structural support. A number of dielectric loading effects have been published in the literature [1–3,13]. Figure 3 shows that the resonant frequencies decrease

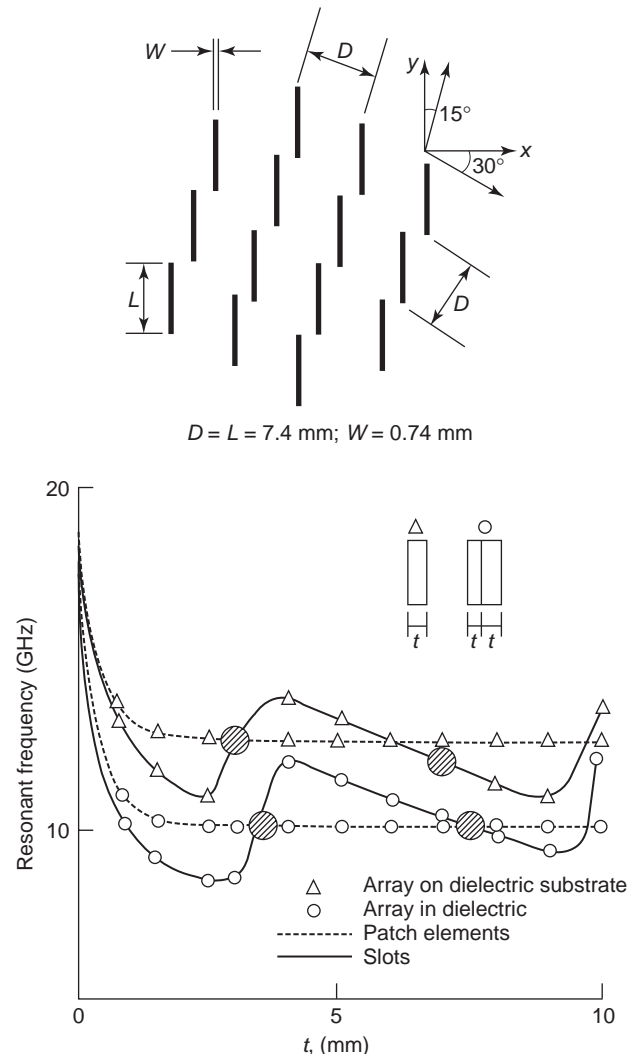


Figure 3. Variation of resonant frequency with the dielectric thickness for normal incidence.

as the dielectric thickness increases [13]. Note that two basic dielectric configurations are shown: (1) the grids are bonded on one side and (2) the grids are embedded centrally in the dielectrics. For a normally incident thin grid (with a 0.02-mm-thick dielectric with dielectric constant or $DK = 3$) the resonant frequency is at 20 GHz. As can be seen, the resonant frequency of the *patch* array embedded in the dielectrics (with $DK = 4$) approaches 10 GHz ($= 20/\text{square root of } DK = 4$) as the dielectric thickness is increased beyond 5 mm. The passband frequency of the *slot* (aperture element) array in the dielectrics also tends to this value, but it exhibits an oscillatory behavior about 10 GHz. For a patch or slot array bonded on one side of the dielectric (with $DK = 4$), the resonant frequency approaches 12.5 GHz (or $20/\text{square root of } DK = 2.5$, which is the average of 4 and 1).

The dielectric loading effect of a slot array is also dependent on the incident angle and the wave polarizations. For TE incidence, the resonance decreases as the dielectric thickness increases (similar to the case of normal incidence). For TM incidence, a significant reduction in the dielectric loading effect is noticed as the Brewster angle (63°) is approached. At this angle the air/dielectric interface does not reflect incident waves, and the resonant frequency behaves similarly to that of the patch array (i.e., it remain constant at 10 GHz). In fact, the angular stability of the slot arrays is lost for dielectric thickness greater than 1 mm. However, if the dielectric is a multiple quarter-wavelength thick (i.e., $t = 4$ and 7.5 mm) the resonant frequency becomes 10 GHz as shown by the hatched circles in Fig. 3.

Note that there is a mismatch loss for a slot array with dielectric on one side, unless it is a multiple half-wavelength thick. For example, the mismatch loss is 2 dB at normal incidence with a $DK = 4$ dielectric substrate. However, with an equal thickness of dielectric on both sides of the grid, the reflections at the two air/dielectric interfaces are tuned out at the resonant frequency; consequently there is no passband mismatch loss whatever the dielectric thickness.

One of the most important applications of dielectric loading is the multiband FSS design. For a multiband FSS application, the highest frequency generally determines the element spacing or lattice size. For the triband FSS [14] illustrated in Fig. 4, the element spacing is 0.39 free-space wavelengths at Ku band (13.8 GHz). This element spacing is too small to accommodate the circumference of the ring element, which has to be one electrical wavelength long at X band for reflection to occur. One method to achieve both criteria of one electrical wavelength circumference at X band and less than half free-space wavelength spacing at Ku band is to reduce the ring's physical size by the dielectric loading effect. Calculation shows that a triangular lattice can be used with a material of relative dielectric constant of 8.0. However, such material is not commercially available. Hence a material with a relative dielectric constant of 3.5 (Kevlar epoxy) and thickness of 0.064 cm is used as the substrate on both sides of the ring elements. In this design, the square lattice is adequate to avoid grating lobes. Although this Kevlar epoxy material

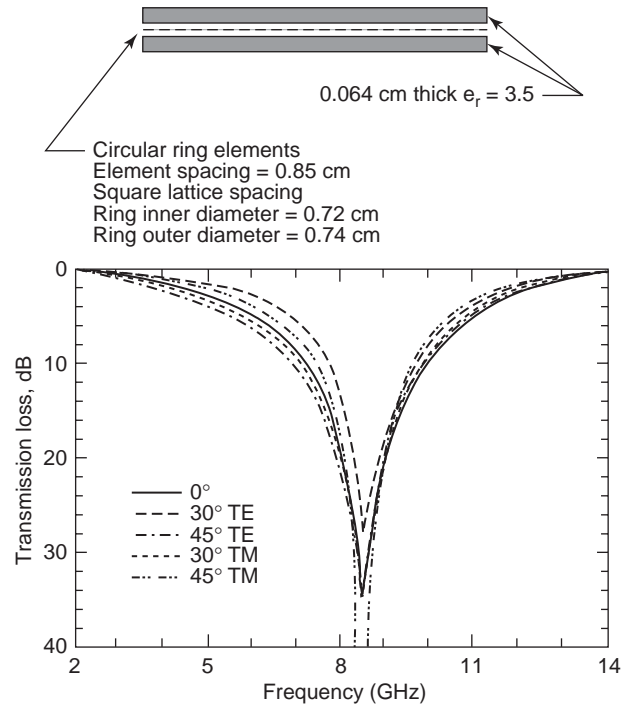


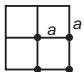
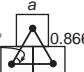
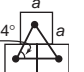
Figure 4. Transmission performance of a ring element FSS with dielectrics on both sides.

has a relatively higher loss tangent, it does not introduce significant insertion loss for the FSS. This is true because the RF energy travels only perpendicularly through the very thin substrate instead of parallel along the substrate, as in the case of a microstrip or stripline transmission line. Therefore, for the FSS application, the high-dielectric-constant substrate should be kept thin enough to prevent the generation of surface waves, especially at large incident angles. It should be noted that the surface wave (or Wood's anomaly; see Section 5) of an FSS grid embedded in dielectrics will not be eliminated, but only pushed higher in frequency, if the dielectric is thin. Furthermore, the occurrence of grating lobes is dependent on the physical size of the lattice and *not* the presence of the dielectrics [15].

4. GRATING LOBE PHENOMENON

Grating or Bragg lobes are undesired secondary mainbeams occurring at angles with higher-order constructive interference when the lattice size becomes electrically large. Since the periodic array elements behave similarly to the conventional array, the largest lattice size to avoid grating lobes should obey the same rule that governs a conventional array antenna. A general rule to avoid grating lobes is that the lattice size should be less than one wavelength for the normal incident case (0° incident angle). For large incident angles, the spacing should be kept below half free-space wavelength. Table 1 lists three different lattice types, such as square, triangular, and the brick lattices. It also shows the

Table 1. FSS Lattice Types and Grating Lobe Criteria

Lattice Type	Maximum Spacing	$\theta_0 = 0^\circ$	$\theta_0 = 45^\circ$
 Square spacing	$\frac{a}{\lambda_0} < \frac{1}{1 + \sin \theta_0}$	$\frac{a}{\lambda_0} < 1$	$\frac{a}{\lambda_0} < 0.59$
 Triangular spacing	$\frac{a}{\lambda_0} < \frac{1.15}{1 + \sin \theta_0}$	$\frac{a}{\lambda_0} < 1.15$	$\frac{a}{\lambda_0} < 0.67$
 Brick spacing	$\frac{a}{\lambda_0} < \frac{1.12}{1 + \sin \theta_0}$	$\frac{a}{\lambda_0} < 1.12$	$\frac{a}{\lambda_0} < 0.65$

Source: Ref. 2.

maximum lattice size to avoid grating lobes. As can be seen, the square lattice has the most closely packed elements, while the triangular lattice has the largest element spacing. The spacing requirements given in this table prevent the peak of the grating lobe from entering real space. To avoid wasted energy, not even the shoulder region of the grating lobe should enter real space; therefore, the lattice size should be approximately two-thirds or less of that given in Table 1.

5. WOOD'S ANOMALY PHENOMENON

Wood's anomalies were first observed in the diffraction spectrum of optical gratings in 1902 [2]. They exhibit themselves as rapid variations in the intensity of the various diffracted spectral orders in certain narrow frequency bands, which could not be explained by the grating theory at that time. These anomalies usually occur at frequencies near or higher than the resonant frequency of any periodic structure. Thus they have significant impacts on the design of periodic structures used in solar filters and FSS radomes [15]. Figure 5 shows the manifestation of these anomalies as the nulls in the transmission characteristics of a slot array. It also shows that the frequency of Wood's anomaly or the transmission null is decreased with an increase in the dielectric thickness. Further, for a slot array in free space, the Wood's anomaly will occur just below the frequency at which the grating lobe starts to propagate in real space, which for normal incidence on a rectangular grid array will first occur when the lattice size is one wavelength. It has been shown that these nulls are associated with a surface wave propagating along the surface of the array [15].

6. APPLICATIONS

FSS has a myriad of commercial and military applications. A good commercial application is the screen door of a microwave oven in a typical kitchen. It is a screen consisting

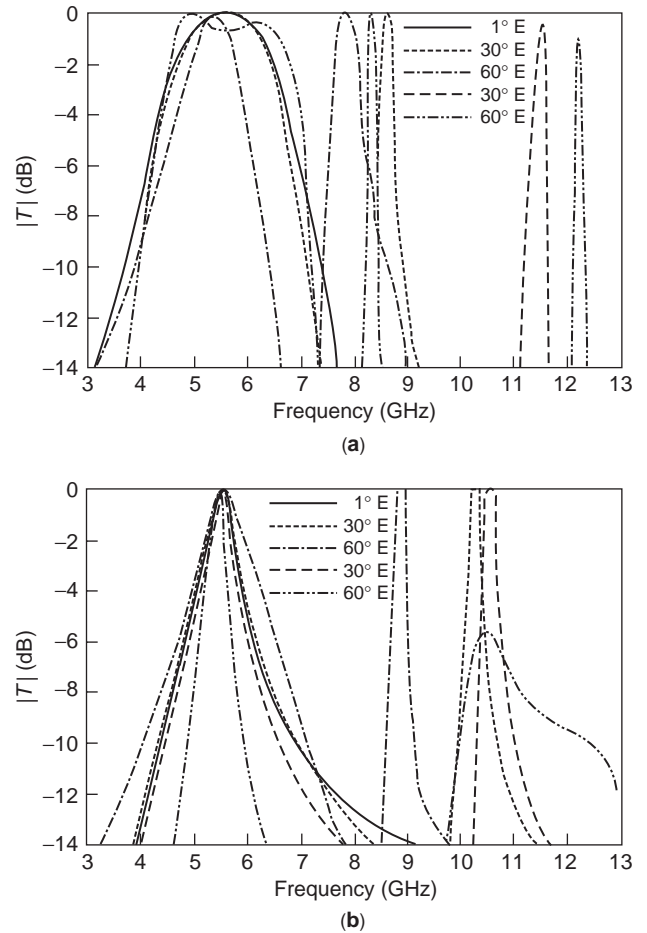


Figure 5. Transmission performance of a thin-slot FSS (square lattice, period = 1.78 cm, slot length = 1.32 cm, width = 0.128 cm) with dielectrics $DK = 4$, thickness = 0.7 and 0.35 cm for cases (a) and (b), respectively, on both sides.

of a periodic array of metallic holes designed for reflecting microwave energies at 2.45 GHz while passing through the light, allowing the user to see the food being cooked inside the oven.

In a dual-reflector antenna system, an FSS can be employed for the subreflector. Different frequency feeds are optimized independently and placed at the real and virtual foci of the subreflector. Hence, only a single main reflector is required for multifrequency operation. For example, the FSS on the high-gain antenna (HGA) of the Voyager spacecraft, as illustrated in Fig. 6, was designed to diplex S and X bands [2]. In that application the S-band feed is placed at the prime focus of the main reflector, and the X-band feed is placed at the Cassegrain focal point. Note that only one main reflector is required for this two-band operation. Thus, tremendous reductions in mass, volume and, most importantly, the cost of the antenna system are achieved with this two-band FSS subreflector. For a multiband and multifunction reflector antenna, a four-band (or S-, X-, Ku-, and Ka-band) double square-loop FSS, as shown in Fig. 7, was developed for the Cassini HGA [2].

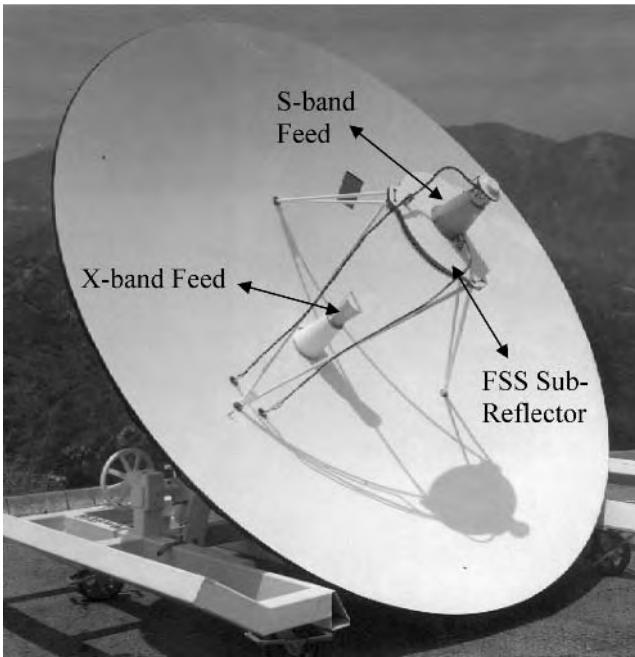


Figure 6. Voyager HGA with a two-frequency (S/X-band) subreflector.

FSS radomes [3] with aperture-type element can be tuned to provide bandpass characteristics and to reduce the radar cross section (RCS) of the antenna system enclosed inside a surface or airborne vehicle. In other words, at the operating (in-band) frequency of the antenna, the signal will pass through the radome with minimum insertion loss, while at the out-of-band frequencies, the signal will be reflected

exactly as from a conducting surface or the metallic outer skin of the vehicle. Usually the radome can be designed to blend with the outer curvature and skin of the vehicle to minimize backscattering or to achieve low RCS.

Another useful FSS application is the circuit analog absorber consisting of resistive cross-dipole array backed by a ground plane, which provides absorbing capability superior to that of the Salisbury and Jaumann absorbers [3]. Here the lossy dipole element exhibits circuit-type characteristics, namely, a capacitance and inductance in series as well as a series resistance. Circuit analog absorbers with more than 25 dB attenuation over a 10–1 bandwidth has been achieved by cascading several cross-dipole sheets.

A thick rectangular or circular aperture element FSS has been designed for collecting solar energy [16]. This type FSS is a bandpass screen; specifically, it is essentially transparent in the frequency band where the solar cells are most efficient, but is reflecting at frequencies outside this band. In the far-infrared region, passive quasioptical grids are used as beamsplitters and mirrors [17] for improving the pumping efficiency in molecular lasers. Typically, a laser cavity mirror is a rectangular mesh grid designed to totally reflect at the wavelength of the energy used to pump the cavity while partially transmit (0–40%) at the lasing wavelength. Since no energy used in the laser pumping is lost at the mirror, the efficiency of the system is optimized. Another interesting quasioptical application is the use of a sunshield as a thermal control cover of spacecraft antennas. The sunshield consists of a square lattice array of vacuum-deposited aluminum square patches on a thin Kapton film. This grid not only provides for sunlight blockage but also allows for RF signal transmission.

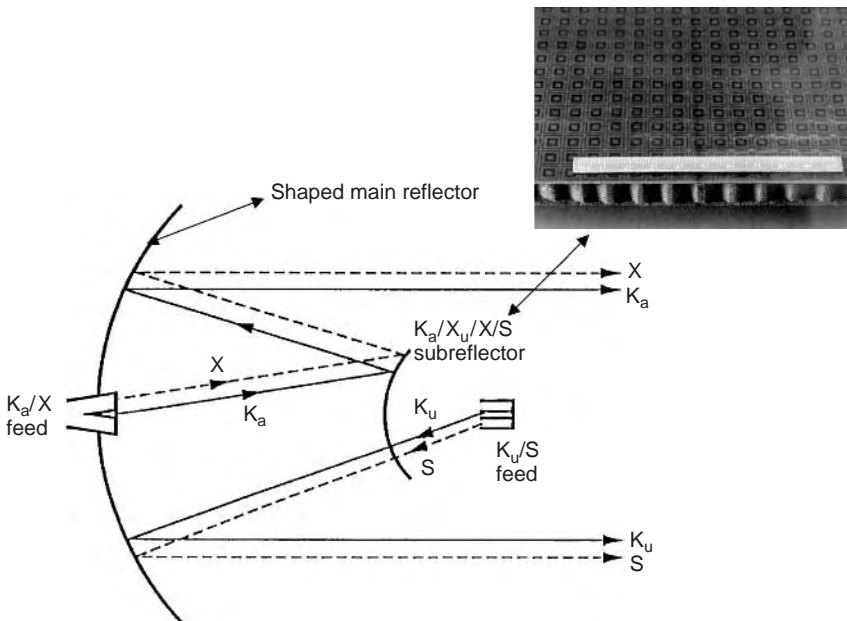


Figure 7. Cassini HGA with a four-band double square-loop FSS subreflector.

BIBLIOGRAPHY

1. R. Mittra, C. Chan, and T. Cwik, Techniques for analyzing frequency selective surfaces—a review, *IEEE Proc.* **76**(23):1593–1615 (Dec. 1988).
2. T. K. Wu, ed., *Frequency Selective Surface and Grid Array*, Wiley, New York, 1995.
3. B. A. Munk, *Frequency Selective Surface—Theory and Design*, Wiley, New York, 2000.
4. C. C. Chen, Transmission of microwave through perforated flat plates of finite thickness, *IEEE Trans.* **MTT-21**(1):1–6 (Jan. 1973).
5. J. J. Fratamico et al., A wide-scan quasi-optical frequency diplexer, *IEEE Trans.* **MTT-30**(1):(Jan. 1982).
6. P. D. Potter, *Improved Dichroic Reflector Design for the 64-m Antenna S- and X-Band Feed Systems*, JPL Technical Report 32-1526, Feb. 1974.
7. Anderson, I., On the theory of self-resonant grids, *BSTJ (Bell Systems Technical Journal)*, **54**(10): 1725–31, Dec. 1975.
8. R. J. Lagley and A. J. Drinkwater, Improved empirical model for the Jerusalem cross, *IEE Proc. H* **129**(1):1–6 (Feb. 1982).
9. S. W. Lee, Scattering by dielectric-loaded screen, *IEEE Trans.* **AP-19**(5):656 (Sept. 1971).
10. J. A. Roden et al., Time domain analysis of periodic structures at oblique incidence: orthogonal and non-orthogonal FDTD implementations, *IEEE Trans.* **MTT-46**:420–427 (April 1998).
11. L. W. Henderson, *Introduction to PMM*, OSU/ESL Technical Report 715582-5, Feb. 1986.
12. R. Remski, B. Gray, and L. Ma, Frequency selective surfaces design, paper presented at Ansoft Empowering Profitability Workshop, Sept. 16, 2002.
13. P. Callaghan, E. Parker, and R. Langley, Influence of supporting dielectric layers on the transmission properties of frequency selective surfaces, *IEE Proc. H.* **138**(5):448–454 (Oct. 1991).
14. J. Huang, T. K. Wu, and S. W. Lee, Tri-band FSS with circular ring elements, *IEEE Trans.* **TAP-42**(2):166–175 (Feb. 1994).
15. R. J. Luebbers and B. A. Munk, Some effects of dielectric loading on periodic slot arrays, *IEEE Trans.* **AP-26**(4): 536–542 (July 1978).
16. R. C. McPhedran and D. Maystre, On the theory and solar application of inductive grids, *Appl. Phys.* **14**:1–20 (Sept. 1977).
17. T. K. Wu, Quasi-optical grids with thin rectangular patch/aperture elements, *Int. J. Infrared Millimeter Waves* **14**(5):1017–1033 (May 1993).

FREQUENCY STABILITY

DAVID A. HOWE
 National Institute of Standards
 and Technology (NIST)
 Boulder, Colorado

1. THE SINE WAVE AND STABILITY

A sine-wave signal generator produces a voltage that changes in time in a sinusoidal manner as shown in Fig. 1. The signal is an *oscillating signal* because the

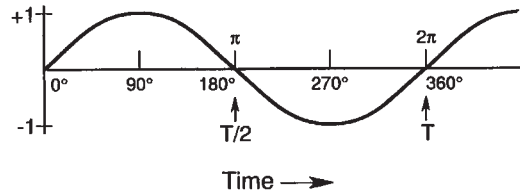


Figure 1. A repeating sine function is the basis of an oscillating signal.

sine wave repeats itself. A cycle (2π radians of phase) of the oscillation is produced in one period T .

It is convenient for us to express angles in radian units rather than in units of degrees, and positive zero crossings of the voltage will occur every 2π radians. The *frequency* ν is the number of cycles in one second (Hz), which is the reciprocal of period (seconds per cycle). The expression describing the voltage V produced by a sine-wave signal generator is given by

$$V(t) = V_0[1 + a(t)] \sin[\Phi(t)]$$

where V_0 is the peak voltage amplitude, $a(t)$ is amplitude noise, and $\Phi(t)$ is the total accumulated phase. Equivalent expressions are

$$V(t) = V_0[1 + a(t)] \sin\left(2\pi \frac{t}{T}\right)$$

and

$$V(t) = V_0[1 + a(t)] \sin(2\pi\nu t)$$

For the following discussion, we will assume the amplitude noise $a(t)$ is zero. Consider Fig. 2. Let's assume that the maximum value of V equals 1, hence $V_0 = 1$. We say that the voltage $V(t)$ is normalized to unity.

If we are given the frequency of the sine wave, then no matter how big or small Δt may be, we can determine ΔV . Let us look at this from another point of view. Suppose that we can measure ΔV and Δt . From this, there is a sine wave at a unique minimum frequency corresponding to the given ΔV and Δt . For infinitesimally small Δt , this frequency is called the *instantaneous frequency* at this t . The smaller the interval Δt , the better the approximation of

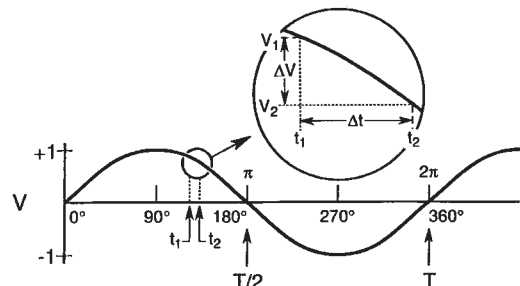


Figure 2. For a given phase, ΔV vs. Δt of the sine-wave signal corresponds to a unique minimum frequency called the instantaneous frequency if Δt is diminishingly small.

instantaneous frequency at t . In practice, because of finite bandwidths, we cannot measure the instantaneous frequency.

When we speak of oscillators and the signals they produce, we recognize that an oscillator has some nominal frequency at which it operates. The “frequency stability” of an oscillator is a term used to characterize how small the frequency fluctuations of the oscillator signal are. We usually refer to frequency stability when comparing one oscillator with another. As we shall see later, we can define particular aspects of an oscillator’s output, then draw conclusions about its relative frequency stability. People often speak of “frequency stability” when they actually mean “frequency instability.” Frequency stability is the degree to which an oscillating signal produces the same value of frequency for any interval Δt throughout a specified period of time. An internationally recommended definition of “frequency instability” is: “The spontaneous and/or environmentally caused frequency change within a given time interval.”¹

Let’s examine the two waveforms shown in Fig. 3. Frequency stability depends on the amount of time involved in its measurement. Of the two oscillating signals, it is evident that “2” is more stable than “1” from time t_1 to t_3 assuming that the horizontal scales are linear in time. From time t_1 to time t_2 , there may be some question as to which of the two signals is more stable, but it’s clear that from time t_2 to time t_3 , signal “1” is at a frequency different from that in interval t_1 to t_2 .

If we want an oscillator to produce a particular frequency ν_0 , then we’re correct in stating that if the oscillator signal frequency deviates from ν_0 over any interval, this is a result of something that is undesirable. In the design of an oscillator, it is important to consider the sources of mechanisms that degrade the oscillator’s frequency stability. These undesirable mechanisms cause random (noise) or systematic processes to exist on top of the sine-wave signal of the oscillator. To account for the noise components at the output of a sine-wave signal generator, we can express the output as

$$V(t) = V_0[1 + a(t)] \sin[2\pi\nu_0 t + \phi(t)] \quad (1)$$

where

V_0 = nominal peak voltage amplitude
 $a(t)$ = deviation of amplitude from nominal (i.e., $\delta V/V_0$)
 ν_0 = nominal fundamental frequency
 $\phi(t)$ = deviation of phase from nominal

Ideally a and ϕ should equal zero for all time. However, in the real world there are no perfect oscillators. To determine the extent of the noise components a and ϕ , we turn our attention to measurement techniques.

¹The present IEEE standard for the measure of frequency stability is the one-sided spectral density $S_y(f)$ in the frequency domain or the two-sample or Allan variance $\sigma_y(\tau)$ in the time domain. These are explained later.

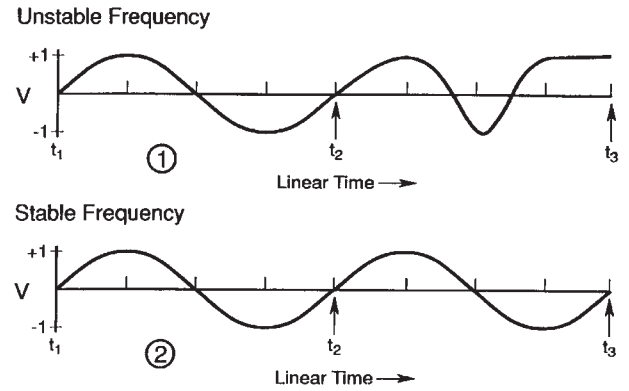


Figure 3. Top (1): Instantaneous frequency is inconsistent and less stable from t_2 to t_3 . Bottom (2): Instantaneous frequency is consistent and more stable throughout.

The typical precision oscillator, of course, has a presumably stable sinusoidal voltage output with a frequency ν and a period of oscillation T (which is the reciprocal of the frequency: $\nu = 1/T$). One goal is to measure the frequency and/or the frequency stability of the sinusoid. Instability is actually what is measured, but with little confusion it is usually called “stability” in the literature. Naturally, fluctuations in frequency correspond to fluctuations in the period. Almost all frequency measurements, with very few exceptions, are measurements not of frequency but of the phase or of the period fluctuations in an oscillator, even though the frequency may be the readout. As an example, most frequency counters sense the zero (or near-zero) crossing of the sinusoidal voltage, which is the point at which the voltage is the most sensitive to phase fluctuations.

We must also realize that any frequency measurement involves two oscillators. In some instances, one oscillator is in the counter. It is impossible to purely measure only one oscillator. In some instances one oscillator may sufficiently outperform the other, and the fluctuations measured may be considered essentially those of the latter. However, in general because frequency measurements are always dual, it is useful to define

$$y(t) = \frac{\nu_1 - \nu_0}{\nu_0} \quad (2)$$

as the fractional frequency difference or offset of oscillator one ν_1 with respect to a reference oscillator ν_0 divided by the nominal frequency ν_0 . Conceptually, we can also think of Eq. (2) as the free-running frequency of an individual oscillator ν_1 , differentiated with respect to its own nominal value ν_0 . Now, $y(t)$ is a dimensionless quantity and useful in describing oscillator and clock performance; that is, the time fluctuation or difference $x(t)$ of an oscillator over a period of time t is given simply by

$$x(t) = \int_0^t y(t') dt' = \frac{\phi(t)}{2\pi\nu_0} \quad (3)$$

We see that the time deviations and the phase deviations are related by a constant, $1/2\pi\nu_0$. Since it is impossible to

measure instantaneous frequency, any frequency or fractional frequency measurement always involves some sample time, Δt or τ —some time window through which the oscillators are observed; whether it’s a picosecond, a second, or a day, there must always be some sample time. So, when determining a fractional frequency $y(t)$, what is in fact happening is that the time difference is being measured starting at, say, some time t and again at a later time, $t + \tau$. The difference between these two time differences, divided by τ , gives the average fractional frequency over that period τ :

$$\bar{y}(t) = \frac{x(t + \tau) - x(t)}{\tau} \tag{4}$$

Tau (τ) may be called the sample time or averaging time; it may be determined, for example, by the gate time of an electronic counter.

What happens in many cases is that we sample a number of cycles of an oscillation during the preset gate time of a counter; after the gate time has elapsed, the counter latches the value of the accumulated count of cycles so that it can be read out, printed, or stored in some other way. Then there is a delay time for such processing of the data before the counter arms or initializes and resumes on the next cycle of the oscillation. During the delay time (or process time), information is lost. This is called “dead-time”, and in some instances it becomes a problem. Unfortunately for data processing in typical oscillators the effects of deadtime often hurt most when it is the hardest to avoid. In other words, for times that are short compared to a second, when it is very difficult to avoid deadtime, this is usually where deadtime can make a significant difference in the data analysis. Typically, for many oscillators, if the sample time is long compared to a second, the deadtime makes little difference in the data analysis, unless it is excessive [1]. New equipment or techniques are now available that contribute zero or negligible deadtime [2].

In reality, of course, the sinusoidal output of an oscillator is not pure; it contains noise (frequency) fluctuations as well. We will describe three different methods of measuring the frequency fluctuations in precision oscillators other than measuring the frequency directly with a frequency counter, listed as a fourth method. The direct frequency counter technique is often very limiting because the number of resolvable digits on the counter are often inadequate for precision oscillators, and counter input noise masks oscillator noise for short sample times. In all the methods one also needs to properly match the impedances of different connected electronic instruments, use short connecting cable lengths, and use high-quality, stable connectors.

1.1. Common Methods of Measuring Frequency Stability

1.1.1. Beat-Frequency Method. The first technique is called a heterodyne frequency-measuring method or beat-frequency method. The signals from two independent oscillators are fed into the two ports of a double balanced mixer, as illustrated in Fig. 4. The device labeled “Amp” is an amplifier.

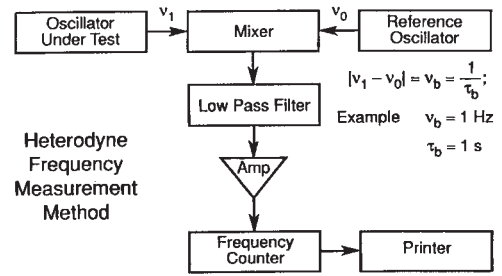


Figure 4. Measurement of the frequency difference (“beat note”) between oscillators can increase measurement precision. State-of-the-art oscillators can readily be measured by this method.

The difference frequency, or the beat frequency v_b , is obtained as the output of a lowpass filter (to suppress carrier frequency harmonics) that follows the mixer. This beat frequency is then amplified and fed to a frequency counter and printer or other recording device. The fractional frequency is obtained by dividing v_b by the nominal carrier frequency v_0 . This system has excellent precision; one can measure essentially all state-of-the-art oscillators.

1.1.2. Dual-Mixer Time-Difference (DMTD) System. This technique uses two heterodyne measurements operating simultaneously. The time difference of the zero crossings of each beat frequency is measured and yields an excellent precision, 10^{-13} seconds. A block diagram is shown in Fig. 5. It should be mentioned that if time or time fluctuations can be measured directly, an advantage is obtained over just measuring frequency. The reason is that we can readily calculate the frequency from the time, only if there is no deadtime. In the past, frequency was not inferred from the time (for sample times of the order of several

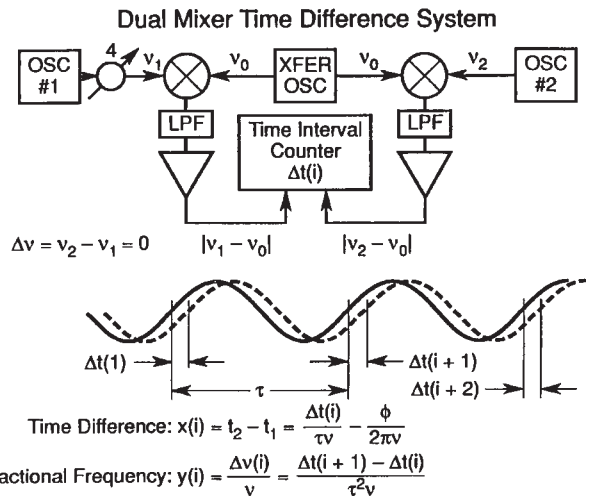


Figure 5. Measurement of the time difference between two beat notes from two oscillators with a common transfer oscillation can further increase measurement precision. Instability of transfer oscillator cancels to first order.

seconds and less) because the time difference between a pair of oscillators operating as clocks could not be measured with sufficient precision. However, now the precision of DMTD opens the door to measuring time fluctuations as well as frequency fluctuations for sample times as short as a few milliseconds, all without deadtime.

In Fig. 5, oscillator 1 could be considered to be under test and oscillator 2 could be considered to be the reference oscillator. Their outputs go to the ports of a pair of double-balanced mixers. Another oscillator with separate symmetric buffered outputs is fed to the other two ports of the pair of double-balanced mixers. This common oscillator's frequency is offset by a desired amount from those of the other two oscillators. Then two different beat frequencies are produced by the two mixers as shown. These two beat frequencies will be out of phase by an amount proportional to the time difference between oscillators 1 and 2—excluding the differential phase shift that may be inserted (component “4” is a phase shifter). Further, the beat frequencies differ in frequency by an amount equal to the frequency difference between oscillators 1 and 2.

This measurement technique is very useful where oscillators 1 and 2 outputs are at very nearly the same frequency. This is typical for atomic standards (cesium, rubidium, and hydrogen frequency standards).

Illustrated at the bottom of Fig. 5 is what might represent the beat frequencies from the two mixers. A phase shifter may be inserted as component “4” to adjust the phase so that the two beat rates are nominally in phase; this adjustment sets up the nice condition that the noise of the common oscillator tends to cancel (for certain types of noise) when the time difference is determined. After these beat signals are amplified, the start port of a time interval counter is triggered with the positive zero crossing of the other beat. Taking the time difference between the zero crossings of these beat frequencies, we measure the time difference between zero crossings of oscillators 1 and 2, but with a precision that has been amplified by the ratio of the carrier frequency to the beat frequency (over that normally achievable with this same time interval counter). The time difference $x(i)$ for the i th measurement between oscillators 1 and 2 is given by

$$x(i) = \frac{\Delta t(i)}{\tau_b \nu_0} - \frac{\phi}{2\pi \nu_0} \frac{k}{\nu_0} \quad (5)$$

where $\Delta t(i)$ is the i th time difference as read on the counter, τ_b is the beat period, ν_0 is the nominal carrier frequency, ϕ is the phase delay in radians added to the signal of oscillator 1, and k is an integer number of cycles of ν_0 to be determined in order to remove the cycle ambiguity. It is important to know k only if the absolute time difference is desired; for measurements of frequency and of time fluctuations, k may be assumed zero unless we go through a cycle during a data run. The fractional frequency $y(i, \tau)$ between oscillators 1 and 2 can be derived in the normal

way from the time fluctuations:

$$y_{1,2}(i, \tau) = \begin{cases} \frac{\nu_1(i, \tau) - \nu_2(i, \tau)}{\nu_0} \\ \frac{x(i+1) - x(i)}{\tau} \\ \frac{\Delta t(i+1) - \Delta t(i)}{\tau_b^2 \nu_0} \end{cases} \quad (6)$$

In Eqs (5) and (6), it is assumed that the transfer (or common) oscillator is set at a frequency lower than those of oscillators 1 and 2, and that the voltage zero crossing of the beat frequency $\nu_1 - \nu_c$ starts—and that $\nu_2 - \nu_c$ stops—the time interval counter. The fractional frequency difference may be averaged over any integer multiple of τ_b

$$y_{1,2}(i, m\tau_b) = \frac{x(i+m) - x(i)}{m\tau_b} \quad (7)$$

where m is any positive integer. If needed, τ_b can be made to be very small by having very high beat frequencies. The transfer (or common) oscillator may be replaced with a low phase noise frequency synthesizer, which derives its basic reference frequency from oscillator 2. In this setup the nominal beat frequencies are given simply by the amount by which the output frequency of the synthesizer is offset from ν_2 . Sample times as short as a few milliseconds with subpicosecond (< 1 ps) resolution are obtained. Note that logging the data at such a rate usually requires special equipment. The National Institute of Standards and Technology (NIST) timescale measurement system is based on the DMTD.

1.1.3. Loose Phase-Locked Loop Method. This type of method is illustrated in Fig. 6. The signal from an oscillator under test is fed into one port of a mixer. The signal from a reference oscillator is fed into the other port of this mixer. The signals are in quadrature; that is, they are 90° out of phase, so that the average voltage out of the new mixer is nominally zero, and the instantaneous voltage fluctuations correspond to phase fluctuations rather than to amplitude fluctuations between the two signals. The mixer is a key element in the system. The advent of the Schottky barrier diode was a significant breakthrough in

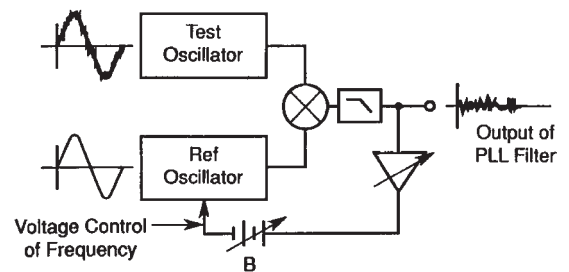


Figure 6. Direct measurement of the phase difference between two oscillators yields excellent precision. The technique requires electronic frequency control of a clean reference oscillator to maintain a loose phase lock, hence a zero beat.

making low-noise precision stability measurements. The output of this mixer is fed through a lowpass filter and then amplified in a feedback loop, causing the voltage-controlled oscillator (reference) to be phase-locked to the test oscillator. The response time of the loop is adjusted such that a very loose phase-lock (long-time-constant) condition exists.

The response (or attack) time is the time it takes the servo system to make 70% of its ultimate correction after being slightly disturbed. The response time is equal to $1/\pi w_h$, where w_h is the servo bandwidth. If the response time of the loop is about a second, then the voltage fluctuations will be proportional to the phase fluctuations for sample times shorter than one second. Depending on the coefficient of the tuning capacitor and the quality of the oscillators involved, the amplification used may vary significantly, but may typically range from 40 to 80 dB via a good low-noise amplifier. In turn this signal can be fed to a spectrum analyzer to measure the Fourier components of the phase fluctuations. It is of particular use for sample times shorter than one second (for Fourier frequencies greater than 1 Hz) in analyzing the characteristics of an oscillator. It is particularly useful if one has discrete sidebands such as 60 Hz, or detailed structure in the spectrum.

One may also take the output voltage from the above-mentioned amplifier and feed it to an analog-to-digital (A/D) converter. This digital output becomes an extremely sensitive measure of the short-term time or phase fluctuations between the two oscillators. Resolutions of the order of a picosecond (ps) are easily achievable.

1.1.4. Time-Difference Method Using a Counter. The last measurement method we will illustrate is very commonly used, but typically does not have the measurement precision that is more readily available in the first three methods illustrated above. This method, called the *time-difference method*, is shown in Fig. 7. Because of the wide bandwidth needed to measure fast-risetime pulses, this method is limited in signal-to-noise ratio. However, some commercially available counters allow us to do sig-

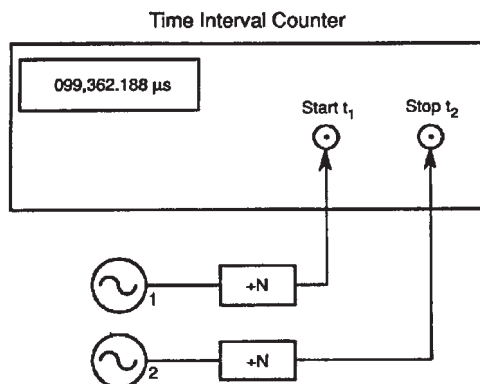


Figure 7. Measurement of the time difference between two oscillators, usually after division by N to obtain 1 pulse-per-second, yields only moderate measurement performance compared to previous methods. The technique is dependent on several properties of the counter and its trigger circuits.

nal averaging or precision risetime comparisons (precision of time-difference measurements in the range of 10 ns–10 ps are now available). Such a method yields a direct measurement of $x(t)$ without any translation, conversion, or multiplication factors. However, even if adequate measurement resolution is available, caution should be exercised in using this technique because it is not uncommon to have significant instabilities in the frequency dividers shown in Fig. 7—of the order of 100 ps. The technique is therefore suitable for long, not short, averaging times.

A trick to bypass divider problems is to feed the oscillator signals directly into the time interval counter and observe the zero-voltage crossing. The divided signal can be used to resolve cycle ambiguity of the carrier; otherwise the carrier phase at zero volts may be used as the time reference. The slope of the signal at zero volts is $2\pi V_0/\tau_1$, where $\tau_1 = 1/\nu_1$ (period of oscillation). For $V_0 = 1$ V and a 5-MHz signal, this slope is 3 mV/ns, which is a good sensitivity. (*Caution:* A correct impedance match of less than 1.5 VSWR is critical for this setup to be stable.)

2. CHARACTERIZATION

Given a set of data for the fractional frequency or time fluctuations between a pair of oscillators, it is useful to characterize these fluctuations with reasonable and tractable models of performance. In so doing for many kinds of oscillators, it is useful to consider the fluctuations as random (may be predicted only statistically) or nonrandom (i.e., systematic—environmentally induced or that have a causal effect that can be determined and in many cases be predicted).

2.1. Nonrandom Fluctuations

Nonrandom fluctuations are usually the main cause of departure from “true” time or “true” frequency in the long term.

If, for example, we have values of the frequency over a period of time, and a frequency offset from nominal is observed, one may calculate directly that the phase error will accumulate as a ramp. If, on the other hand, the frequency values drift linearly, then the time fluctuations will behave quadratically. In almost all oscillators, these “systematics,” as they are sometimes called, are the primary cause of time and/or frequency departure. A useful approach for determining the value of the frequency offset is to calculate the simple mean of the set, or for determining the value of the frequency drift by calculating a linear least-squares fit to the frequency. A least-squares quadratic fit to the phase or to the time deviations is rarely as efficient an estimator of the frequency drift for most oscillators. Precision frequency standards are affected by their environment. These environmental perturbations often cause long-term departures of frequency and time, which in a data run can look like drift, but are not.

2.2. Random Fluctuations

After the systematic or nonrandom effects of a dataset have been calculated or estimated, they may be subtracted

from the data, leaving the residual random fluctuations. They can usually be best characterized statistically using $\sigma_y(\tau)$, the Allan deviation, for short τ (values) and “Theo1” for long τ , the agreed-on standards (IEEE) in the time domain, to be explained in the next section. It is often the case for precision oscillators that these random fluctuations may be effectively modeled with power-law spectral densities. This topic and measurements of spectrum are discussed later. We have

$$S_y(f) = h_x f^\alpha \tag{8}$$

where $S_y(f)$ is the one-sided spectral density of the fractional frequency fluctuations, f is the Fourier frequency at which the density is taken, h_x is the coefficient indicating the level of that type of noise, and α is a number modeling the most appropriate type of power law for the data. If we observe from a $\log \sigma_y^2(\tau)/\log \tau$ diagram a particular slope (call it μ) over certain regions of sample time, τ , this slope has a correspondence to a power-law spectral density or a set of the same with some amplitude coefficient h_x . In particular, $\mu = -(\alpha + 1)$ for $-3 < \alpha < 1$ and $\mu \cong -2$ for $\alpha \geq 1$. Further, a correspondence exists between h_x and the coefficient for $\sigma_y(\tau)$ [1]. The transformations for some of the more common power-law spectral densities have been tabulated, making it quite easy to transform the frequency stability modeled in the time domain over to the frequency domain and vice versa. Examples of some power-law spectra and other types of noise that have been simulated by computer are shown in Fig. 8. The root Allan variance (an RMS or deviation called “Adev”) and Theo1-deviation are constructed to extract frequency instability and not measurement system noise. Synchronization and measurement system noise is phase or time instability characterized by other statistics such as time deviation (TDEV) and maximum time interval error (MTIE) [3].

Once the noise characteristics have been determined, one is often able to deduce whether the oscillators are performing properly, and whether they are meeting either the design specifications or the manufacturer’s specifications. For example, a cesium beam frequency standard or a rubidium gas cell frequency standard, when working

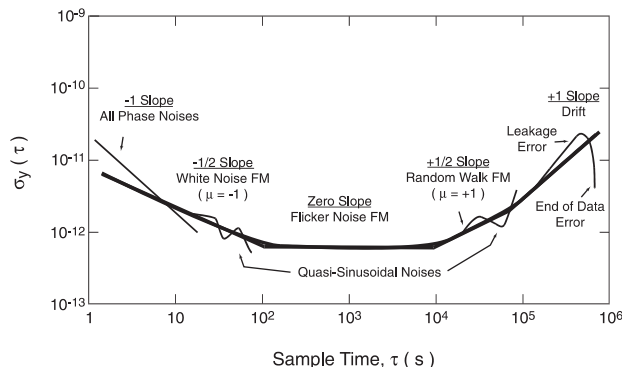


Figure 8. “Adev” (root Allan variance estimate) showing power-law noise as straight lines in addition to other errors. Our goal is to properly interpret this kind of plot of frequency stability.

properly, should exhibit white frequency noise (slope of $-\frac{1}{2}$) for values of τ of the order of a few seconds to several thousand seconds.

3. ANALYSIS OF TIME DOMAIN DATA

Suppose now that we are given the time or frequency fluctuations between a pair of precision oscillators measured, for example, by one of the techniques outlined in Section 1, and a stability analysis is desired. Let this comparison be depicted by Fig. 9. The minimum sample time is determined by the measurement system. If the time difference or time fluctuations are available, then the frequency or the fractional frequency fluctuations may be calculated from one period of sampling to the next. Suppose further there are M values of the fractional frequency y_i . Now there are many ways to analyze these data. Historically, people have typically used the standard deviation equation shown in Fig. 9, $\sigma_{\text{std.dev.}}(\tau)$, where y_i is the average fractional frequency over the dataset, and is subtracted from each value of y_i before squaring, summing, and dividing by the number of values minus one ($M - 1$), and taking the square root to get the standard deviation. We have studied what happens to the standard deviation when the dataset may be characterized by power-law spectra that are more dispersive than classical white-noise frequency fluctuations. In other words, if the fluctuations are characterized by flicker noise or any other non-white-noise frequency deviations, what happens to the standard deviation for that dataset? We can show that the standard deviation is a function of the number of data points in the set (discussed next), and it is also a function of the dead-time and of the measurement system bandwidth. For example, using flicker-noise frequency modulation as a model, as the number of data points increases, the standard deviation increases monotonically without limit. Some statistical measures have been developed that do not depend on the datalength and that are readily usable for characterizing the random fluctuations in precision oscillators. The IEEE has adopted a standard measure

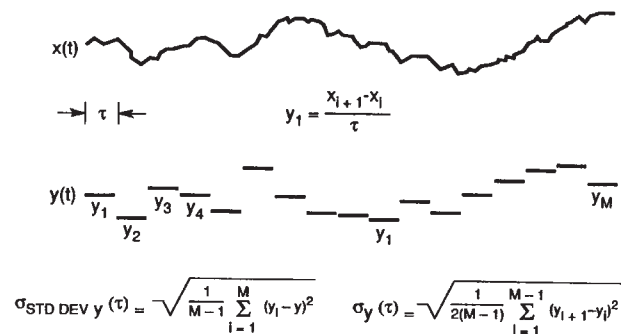


Figure 9. A simulated plot of the time fluctuations $x(t)$ between a pair of oscillators and of the corresponding fractional frequencies calculated from the time fluctuations each averaged over a sample time τ . At the bottom are the equations for the standard deviation (left) and for the time-domain measure of frequency stability as recommended by the IEEE (right).

known as the “Allan variance” taken from the set of useful variances developed, and an experimental estimation of the square root of the Allan variance is shown as the bottom right equation in Fig. 9 [2,4]. This equation is very easy to implement experimentally, as we need to simply add up the squares of the differences between adjacent values of y_i , divide by the number of them and by 2, and take the square root. We then have the quantity that the IEEE subcommittee has recommended for specification of stability in the time domain, denoted by $\sigma_y(\tau)$

$$\sigma_y(\tau) = \left\langle \frac{1}{2} (\bar{y}(t+\tau) - \bar{y}(t))^2 \right\rangle^{1/2} \tag{9}$$

where the brackets “ $\langle \rangle$ ” denote infinite time average. In practice this is easily estimated from a finite dataset as follows:

$$\sigma_y(\tau) = \left[\frac{1}{2(M-1)} \sum_{i=1}^{M-1} (y_{i+1} - y_i)^2 \right]^{1/2} \tag{10}$$

where the y_i are the discrete frequency averages as illustrated in Fig. 9.

We would like to know how $\sigma_y(\tau)$ varies with the sample time τ . A simple and very useful trick that we can use if there is no deadtime is to average the values for y_1 and y_2 and call that a new y_1 averaged over 2τ ; similarly average the values for y_3 and y_4 and call that a new y_2 averaged over 2τ , and so on, and finally apply the same equation as before to get $\sigma_y(2\tau)$. One can repeat this process for other desired integer multiples m of τ , and from the same dataset generate values for $\sigma_y(m\tau)$ as a function of $m\tau$, from which one may be able to infer a model for the process that is characteristic of this pair of oscillators. If we have deadtime in the measurements, adjacent pairs cannot be averaged in an unambiguous way to simply increase the sample time. We have to retake the data for each new sample time—often a very time-consuming task. This is another instance where deadtime can be a problem.

The classical variance (standard deviation squared) is the wrong statistic for measurements of frequency stability, because in most cases it depends on the number of data samples. Fig. 10 plots the ratio of the standard deviation squared for N samples to the standard deviation squared for two samples, $\langle \sigma^2(2, \tau) \rangle$, which is the same as the Allan variance, $\sigma_y^2(\tau)$. We can see the dependence of this standard deviation on the number of samples for various kinds of power-law spectral densities commonly encountered as reasonable models for many important precision oscillators. Note that $\sigma_y^2(\tau)$ has the same value as the classical variance for the classical noise case (white-noise FM). Figure 10 shows that with the increasing length of data the standard deviation of the common classical variance is not well behaved.

We may combine Eqs. (4) and (9) to obtain an equation for $\sigma_y(\tau)$ in terms of the time-difference or time-deviation measurements:

$$\sigma_y(\tau) = \left\langle \frac{1}{2\tau^2} (-x(t+2\tau) + 2x(t+\tau) - x(t))^2 \right\rangle^{1/2} \tag{11}$$

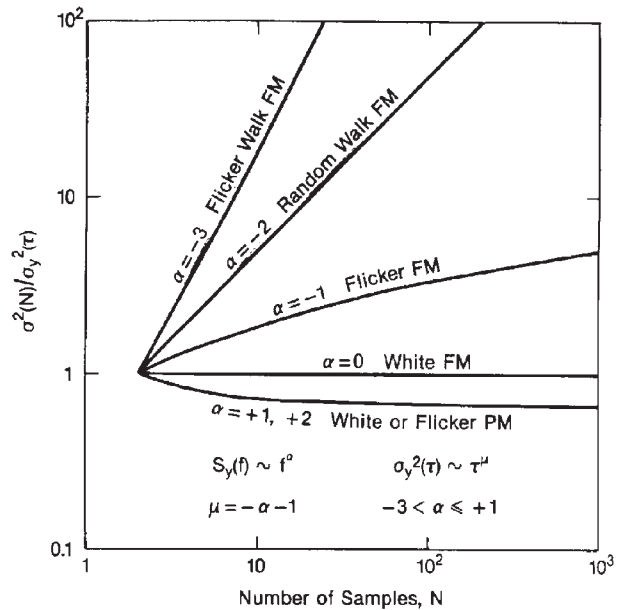


Figure 10. The ratio of the time average of the standard deviation squared for N samples over the time average of a two-sample standard deviation squared as a function of the number of samples N . The ratio is plotted for various power-law spectral densities that commonly occur in precision oscillators. This figure illustrates one reason why the standard deviation is not a suitable measure of frequency stability [4].

which for N discrete time readings, also called N_x , may be estimated as

$$\sigma_y(\tau) \cong \left[\frac{1}{2(N-2)\tau^2} \sum_{i=1}^{N-2} (-x_{i+2} + 2x_{i+1} - x_i)^2 \right]^{1/2} \tag{12}$$

where the i integer denotes the number of the reading in the set of N and the nominal spacing between readings is τ . If there is no deadtime in the data and the original data were taken with a sample time τ_0 , a set of x_i values can be obtained by integrating the y_i values:

$$x_{i+1} = x_i + \tau_0 \sum_{j=1}^i y_j \tag{13}$$

Once we have the x_i values, we can pick τ in Eq (13) to be any integer multiple m of τ_0 , specifically $\tau = m\tau_0$:

$$\sigma_y(m\tau_0) \cong \left[\frac{1}{2(N-2m)m^2\tau_0^2} \sum_{i=1}^{N-2m} (-x_{i+2m} + 2x_{i+m} - x_i)^2 \right]^{1/2} \tag{14}$$

Equation (14), called the “max-overlap estimator,” is regarded as the best estimator of $\sigma_y(m\tau_0)$.

Example 1. Find the two-sample (Allan) variance, $\sigma_y^2(\tau)$, of the following sequence of fractional frequency fluctuation

values y_k , each value averaged over one second:

$$\begin{aligned} y_1 &= 4.36 \times 10^{-5} & y_5 &= 4.47 \times 10^{-5} \\ y_2 &= 4.61 \times 10^{-5} & y_6 &= 3.96 \times 10^{-5} \\ y_3 &= 3.19 \times 10^{-5} & y_7 &= 4.10 \times 10^{-5} \\ y_4 &= 4.21 \times 10^{-5} & y_8 &= 3.08 \times 10^{-5} \end{aligned}$$

(assume no deadtime in measurement of averages).

Since each average of the fractional frequency fluctuation values is for one second, then the first variance calculation will be at $\tau=1$ s. We are given $M=8$ (eight values); therefore, the number of pairs in sequence is $M-1=7$. We have

Data Values y_k ($\times 10^{-5}$)	First Differences ($y_{k+1} - y_k$) ($\times 10^{-5}$)	First Difference Squared ($y_{k+1} - y_k$) ² ($\times 10^{-10}$)
4.36	—	—
4.61	0.25	0.06
3.19	-1.42	2.02
4.21	1.02	1.04
4.47	0.26	0.07
3.96	-0.51	0.26
4.10	0.14	0.02
3.08	-1.02	1.04
		Sum = 4.51

$$\sum_{k=1}^{M-1} (y_{k+1} - y_k)^2 = 4.51 \times 10^{-10}$$

Therefore the Allan variance is

$$\sigma_y^2(1 \text{ s}) = \frac{4.51 \times 10^{-10}}{2(7)} = 3.2 \times 10^{-11}$$

and the Allan deviation is

$$\sigma_y(1 \text{ s}) = [\sigma_y^2(1 \text{ s})]^{1/2} = [3.2 \times 10^{-11}]^{1/2} = 5.6 \times 10^{-6}$$

Using the same data, we can calculate the Allan variance for $\tau=2$ s by averaging pairs of adjacent values and using these new averages as data values for the same procedure as above. For three second averages ($\tau=3$ s), take adjacent threesomes and find their averages and proceed in a similar manner. More data must be acquired for use of longer averaging times.

The confidence of the estimate on $\sigma_y(\tau)$ improves nominally as the square root of the number of data values used. In this example $M=8$, and the confidence can be expressed as being no better than $1/\sqrt{8} \times 100\% = 35\%$. This is a one-sigma (1σ) uncertainty (68% confidence interval) in the estimate for the $\tau=1$ s average. We can dramatically improve confidence using a combination of signal processing, as discussed next.

For the particularly difficult measurement problem of determining the frequency stability of frequency

standards and oscillators for long averaging times, we can use the special-purpose statistic, the estimator of a theoretical variance 1 (“Theo1”), given in native form by [5]

$$\begin{aligned} \widehat{\text{Theo1}}(m, \tau_0, N_x) &= \frac{1}{0.75(N_x - m)(m\tau_0)^2} \\ &\times \sum_{i=1}^{N_x - m} \sum_{\delta=0}^{(m/2) - 1} \frac{1}{\left(\frac{m}{2} - \delta\right)} [(x_{i-x_i-\delta+\frac{m}{2}}) + (x_{i+m-x_i+\delta+\frac{m}{2}})]^2 \end{aligned} \tag{15}$$

for m even, $10 \leq m \leq N_x - 1$, and $\tau = 0.75 m \tau_0$. It has statistical properties like those of the Allan variance, with the significant enhancement that it can evaluate frequency stability at longer averaging times than by using the Allan definition. We can remove bias relative to “Avar” by a composite statistic given by

$$\begin{aligned} \text{TheoH}(m, \tau_0, N_x) &= \begin{cases} \text{Avar}(m, \tau_0, N_x) & \text{for } 1 \leq m < \frac{k}{\tau_0} \\ \text{TheoBR}(m, \tau_0, N_x) & \text{for } \frac{k}{0.75\tau_0} \leq m \leq N_x - 1, m \text{ even} \end{cases} \end{aligned} \tag{16}$$

where k is the largest $\tau \leq T/10$ where $\text{Avar}(m, \tau_0, N_x)$ has sufficient confidence. In this equation TheoBR is defined

$$\begin{aligned} \text{TheoBR}(m, \tau_0, N_x) &= \left[\frac{1}{n+1} \sum_{i=0}^n \frac{\text{Avar}(m = 9 + 3i, \tau_0, N_x)}{\widehat{\text{Theo1}}(m = 12 + 4i, \tau_0, N_x)} \right] \widehat{\text{Theo1}}(m, \tau_0, N_x), \end{aligned} \tag{17}$$

where

$$n = \left\lfloor \frac{0.1N_x}{3} - 3 \right\rfloor$$

(where $\lfloor \cdot \rfloor$ means the integer part). Equation (16) computes a function that is Avar in short term and Theo1 in long term.

4. SPECTRUM ANALYSIS

Another method of characterizing the noise in a signal source is by means of spectrum analysis [6–8]. To understand this approach, let’s examine the waveform shown in Fig. 11.

Here we have a sine wave that for short instances is perturbed by noise. Some workers loosely refer to these types of noises as “glitches.” The waveform has a nominal frequency over one cycle that we’ll call ν_0 ($\nu_0 = 1/T_0$). At times, noise causes the instantaneous frequency to differ markedly from the nominal frequency. If a pure sine-wave signal of frequency ν_0 is subtracted from this waveform,

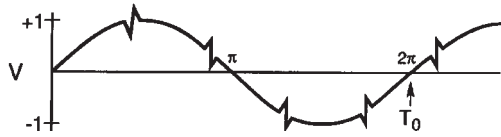


Figure 11. Sine wave that is perturbed by periodic glitches.

the remainder is the sum of the noise components. These components are of various frequencies and the sum of their amplitudes is nearly zero except for the intervals during each glitch, when their amplitudes momentarily reinforce each other. This is shown graphically in Fig. 12.

We can construct a graph plotting RMS power against frequency for a given signal into a given load. This kind of plot is called the *power spectrum*. For the waveform of Fig. 11, the power spectrum will have a high value at ν_0 and lower values for the signals produced by the glitches. Closer analysis reveals that there is a recognizable, somewhat constant, repetition rate associated with the glitches.

In fact, we can deduce that there is a significant amount of power in another signal whose period is the period of the glitches as shown in Fig. 12. Let's call the frequency of the glitches ν_s . Since this is the case, we will observe a noticeable amount of power in the spectrum at ν_s with an amplitude that is related to the characteristics of the glitches. The power spectrum shown in Fig. 13 has this feature. A predominant ν_s component has been depicted, but other harmonics also exist.

Some noise will cause the instantaneous frequency to "jitter" around ν_0 , with a distribution that is higher and lower than ν_0 . We thus usually find a "pedestal" associated with ν_0 as shown in Fig. 14.

The process of breaking a signal down into all of its various components of frequency is called *Fourier expansion*. In other words, the addition of all the frequency components, called *Fourier frequency components*, produces the original signal. The value of a Fourier frequency is the difference between the frequency component and the fundamental frequency. The power spectrum can be normalized to unity such that the total area under the curve equals one. The power spectrum normalized in this way is the *power spectral density*.

The power spectrum of $V(t)$, often called the *RF spectrum*, is very useful in many applications. Unfortunately, if we are given the RF spectrum, it is impossible to determine whether the power at different Fourier frequencies is a result of amplitude fluctuations " $a(t)$ " or phase fluctua-

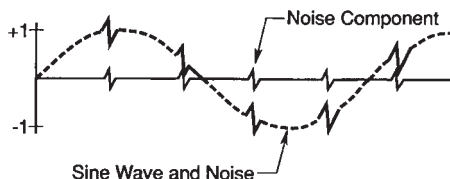


Figure 12. Periodic glitches are undesirable and can be separated from the desired sine wave and characterized in the frequency domain.

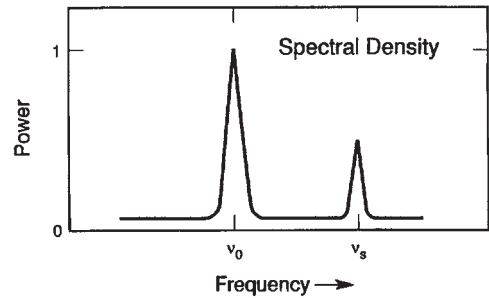


Figure 13. A plot of power (into a load) vs. frequency is a *power spectrum*.

tions " $\phi(t)$." The RF spectrum can be separated into two independent spectra, one of which is the *spectral density* of $\phi(t)$.

For the purpose here, the phase fluctuation components are the ones of interest. The spectral density of phase fluctuations is denoted by $S_\phi(f)$, where f is Fourier frequency. For the frequently encountered case where the AM power spectral density is negligibly small and the total modulation of the phase fluctuations is small (mean-square value is much less than 1 rad^2), the RF spectrum has approximately the same shape as the phase spectral density.

However, a main difference in the representation is that the RF spectrum includes the fundamental signal (carrier), and the phase spectral density does not. Another major difference is that the RF spectrum is a *power* spectral density and is measured in units of watts/hertz. The phase spectral density involves no "power" measurement of the electrical signal. The units are radians²/hertz. It is tempting to think of $S_\phi(f)$ as a "power" spectral density because in practice it is measured by passing $V(t)$ through a phase detector and measuring the detector's output power spectrum. The measurement technique makes use of the relation that for small deviations ($\delta\phi \leq 1$ radian)

$$S_\phi(f) = \left[\frac{V_{\text{RMS}}(f)}{V_s(f)} \right]^2 \tag{18}$$

where $V_{\text{RMS}}(f)$ is the root-mean-square noise voltage in a 1 Hz bandwidth (i.e., per $\sqrt{\text{Hz}}$) at a Fourier frequency f , and $V_s(f)$ is the sensitivity (volts per radian) at the phase quadrature output of a phase detector that is comparing the two oscillators. In the next section, we will look at a scheme for directly measuring $S_\phi(f)$ by determining $V_s(f)$.

SPECTRAL DENSITY

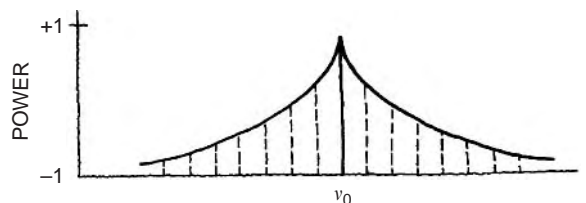


Figure 14. The power spectrum of an oscillator includes its "noise pedestal."

One question we might ask is “How do frequency changes relate to phase fluctuations?” After all, it’s the frequency stability of an oscillator that is a major consideration in many applications. The frequency is equal to a rate of change in the phase of a sine wave. This tells us that fluctuations in an oscillator’s output frequency are related to phase fluctuations since we must change the rate of $\phi(t)$ to accomplish a shift in $\nu(t)$, the frequency at time t . A rate of change of total $\phi_T(t)$ is denoted by $\dot{\phi}_T(t)$. We then have

$$2\pi\nu(t) = \dot{\phi}_T(t) \quad (19)$$

The dot denotes the mathematical operation of *differentiation* on the function ϕ_T with respect to its independent variable t .² From Eqs. (19) and (1) we get

$$2\pi\nu(t) = \dot{\phi}_T(t) = 2\pi\nu_0 + \dot{\phi}(t)$$

Rearranging, we have

$$2\pi\nu(t) - 2\pi\nu_0 = \dot{\phi}(t)$$

or

$$\nu(t) - \nu_0 = \frac{\dot{\phi}(t)}{2\pi} \quad (20)$$

The quantity $\nu(t) - \nu_0$ can be more conveniently denoted as $\delta\nu(t)$, a change in frequency at time t . Equation (20) tells us that if we differentiate the phase fluctuations $\phi(t)$ and divide by 2π , we will have calculated the frequency fluctuation $\delta\nu(t)$. Rather than specifying a frequency fluctuation in terms of shift in frequency, it is useful to denote $\delta\nu(t)$ with respect to the nominal frequency ν_0 . The quantity $\delta\nu(t)/\nu_0$ is called the *fractional frequency fluctuation*³ at time t and is signified by the variable $y(t)$. We then have

$$y(t) = \frac{\delta\nu(t)}{\nu_0} = \frac{\dot{\phi}(t)}{2\pi\nu_0} \quad (21)$$

The fractional frequency fluctuation $y(t)$ is a dimensionless quantity. When talking about frequency stability, its appropriateness becomes clearer if we consider the following example. Suppose that in two oscillators $\delta\nu(t)$ is consistently equal to +1 Hz and we have sampled this value for many times t . Are the two oscillators equal in their ability to produce their desired output frequencies? Not if one oscillator is operating at 10 Hz and the other at 10 MHz. In one case, the average value of the fractional frequency fluctuation is 1 in 10, and in the second is 1 in 10,000,000 or 1×10^{-7} . The 10 MHz oscillator is then more accurate. If frequencies are multiplied or divided using ideal electronics, the fractional stability is not changed.

In the frequency domain, we can measure the spectrum of frequency fluctuations $y(t)$. The spectral density of fre-

quency fluctuations is denoted by $S_y(f)$ and is obtained by passing the signal from an oscillator through an ideal FM detector and performing spectral analysis on the resultant output voltage. $S_y(f)$ has dimensions of (fractional frequency)²/Hz or Hz^{-1} . Differentiation of $\phi(t)$ corresponds to multiplication by f/ν_0 in terms of spectral densities. With further calculation, one can deduce that

$$S_y(f) = \left(\frac{f}{\nu_0}\right)^2 S_\phi(f) \quad (22)$$

We will address primarily $S_\phi(f)$, that is, the spectral density of phase fluctuations. For the purpose of noise measurements, $S_\phi(f)$ can be measured with a straightforward, easily duplicated equipment setup. Whether one measures phase or frequency spectral densities is of minor importance since they bear a direct relationship. It is important, however, to make the distinction and to use Eq. (22) when necessary.

4.1. The Loose Phase-Locked Loop

In Section 1.1.3 we described a method of measuring phase fluctuations between two phase-locked oscillators. Now we will review a common procedure for measuring $S_\phi(f)$.

Suppose that we have a noisy oscillator. We wish to measure the oscillator’s phase fluctuations relative to nominal phase. One can do this by phase-locking another oscillator (called the *reference oscillator*) to the test oscillator, and mixing the two oscillator signals 90° out of phase (phase quadrature). This is shown schematically in Fig. 15. The two oscillators are at the same frequency in the long term, as guaranteed by the phase-locked loop (PLL). A lowpass filter (to filter the RF sum component) is used after the mixer since the difference (baseband) signal is the one of interest. By holding the two signals at a relative phase difference of 90°, short-term phase fluctuations between the test and reference oscillators will appear as voltage fluctuations from the mixer.

With a PLL, if we can make the servo time constant very long, then the PLL bandwidth as a filter will be small. This may be done by lowering the gain A_v of the loop amplifier. We want to translate the phase modulation

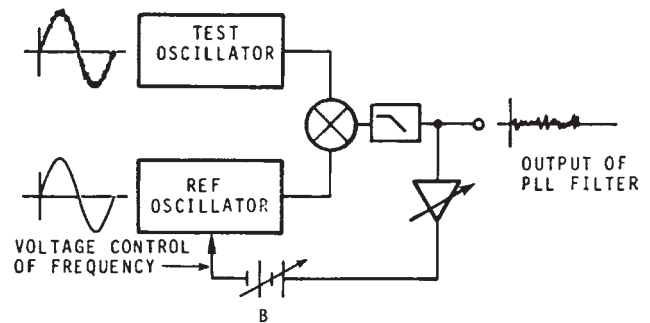


Figure 15. The *phase noise* of a test oscillator is usually measured by a loose phase-locked loop. The test and reference oscillators will naturally lock so that their signals have a phase difference of 90 deg. and the PLL output voltage fluctuations correspond to phase fluctuations between the oscillators.

²As an analogy, the same operation relates the velocity of an object to its acceleration.

³Some international recommendations replace “fractional” by “normalized.”

spectrum to baseband spectrum so that it is easily measured on a low-frequency spectrum analyzer. With a PLL filter, we must keep in mind that the reference oscillator should be as good as or better than the test oscillator. This is because the output of the PLL represents the noise from both oscillators, and if not properly chosen, the reference can have noise masking the noise from the test oscillator. Often, the reference and test oscillators are of the same type and have, therefore, approximately the same noise levels. We can acquire a meaningful measurement by noting that the noise we measure is from two oscillators. Many times a good approximation is to assume that the measured noise power is twice that associated with either single oscillator. $S_{\phi}(f)$ is general notation depicting spectral density on a reciprocal hertz (Hz^{-1}) basis. The output from PLL filter necessarily yields noise from two oscillators.

The output of the PLL filter at Fourier frequencies above the loop bandwidth is a voltage representing phase fluctuations between reference and test oscillator. It is necessary to make the time constant of the loop long compared to the inverse of the lowest Fourier frequency that we wish to measure, that is, $\tau_c > [1/2\pi f(\text{lowest})]$. This means that if we want to measure $S_{\phi}(f)$ down to 1 Hz, the loop time constant must be greater than $1/2\pi$ seconds. We can measure the time constant by perturbing the loop (momentarily disconnecting the battery is convenient) and noting the time it takes for the control voltage to reach 70% of its final value. The signal from the mixer can then be inserted into a spectrum analyzer. A preamplifier may be necessary in the signal path into the spectrum analyzer.

The analyzer determines the mean-square voltage that passes through the analyzer's bandwidth centered around a prechosen Fourier frequency f . It is desirable to normalize results to a 1 Hz bandwidth. Assuming white phase noise (white PM), this can be done by dividing the mean-square voltage by the analyzer bandwidth in hertz. We may have to approximate for other noise processes. [The phase noise sideband levels will usually be indicated in RMS volts per root hertz ($\text{V}/\sqrt{\text{Hz}}$) on most analyzers.]

4.2. Equipment for Frequency-Domain Stability Measurements

4.2.1. Low-Noise Mixer. This should be a high quality, double-balanced type as shown in Fig. 16 but single-ended types may be used. The oscillators should have well-buffered outputs to be able to isolate the coupling between the two input RF ports of the mixer. Results that are too good

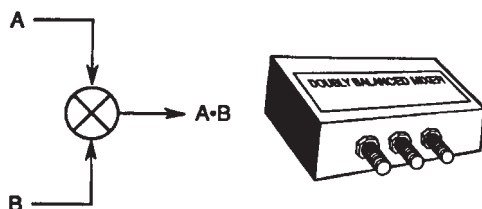


Figure 16. A low noise mixer is a key component for precise phase-noise measurements.

may be obtained if the two oscillators couple tightly via signal injection through the input ports. We want the PLL to control locking. One should read the specifications in order to prevent exceeding the maximum allowable input power to the mixer. However, it is best to operate near the maximum for best signal-to-noise ratio out of the IF port of the mixer, and, in some cases, it is possible to drive the mixer into saturation without burning out the device.

4.2.2. Low-Noise DC Amplifier. The amount of gain A_v needed in the loop amplifier will depend on the amplitude of the mixer output and the degree of varactor control in the reference oscillator. We may need only a small amount of gain to acquire lock. On the other hand, it may be necessary to add as much as 80 dB of gain. Good low-noise DC amplifiers are available from a number of sources, and with cascading stages of amplification, each contributing noise, it will be the noise of the first stage that will add most significantly to the noise being measured. Amplifiers with very low equivalent input noise performance are available from many manufacturers. The response of the amplifier should be flat from DC to the highest Fourier frequency one wishes to measure. The loop time constant is inversely related to the gain A_v , and A_v is best determined experimentally by sweeping the system with known modulation applied at the output of one oscillator [9].

4.2.3. Voltage-Controlled Reference Quartz Oscillator. This oscillator should be a good one with specifications available on its frequency-domain stability. The reference must be no worse than the test oscillator in the frequency domain. The varactor control should be sufficient to maintain phase lock of the reference. In general, test oscillators of moderate quality may have varactor control of as much as 1×10^{-6} fractional frequency change per volt. Some provision should be available on the reference oscillator for tuning the mean frequency over a frequency range that will enable phase lock. Many factors enter into the choice of the reference oscillator, and often it is convenient to simply use two test oscillators phase-locked together. In this way, we can assume that the noise out of the PLL filter is no worse than 3 dB greater than the noise from each oscillator. If it is uncertain whether both oscillators contribute approximately equal noise, then we should perform measurements on three oscillators, taking two at a time. The noisier-than-average oscillator will reveal itself.

4.2.4. Spectrum Analyzer. The signal analyzer should typically be capable of measuring the noise in RMS volts in a narrow bandwidth from near 1 Hz to the highest Fourier frequency of interest. This may be 50 kHz for carrier frequencies of 10 MHz or lower and several megahertz for microwave carrier frequencies. For voltage measuring analyzers, it is typical to use units of "volts per $\sqrt{\text{Hz}}$ ". The spectrum analyzer and any associated input amplifier will exhibit high-frequency rolloff. The Fourier frequency at which the voltage has dropped by 3 dB is the measurement system bandwidth f_h , or $\omega_h = 2\pi f_h$. This can be measured directly with a variable signal generator.

A frequency-domain measurement setup is shown schematically in Fig. 17. The component values for the lowpass filter out of the mixer are suitable for oscillators operating at around 5 MHz.

The active gain element (A_v) of the loop is a DC amplifier, hopefully with flat frequency response, or, if not, a known frequency response. One may replace this element by an integrator to achieve high gain near DC and hence, maintain better lock of the reference oscillator in long term. Otherwise long-term drift between the reference and test oscillators might require manual re-adjustment of the frequency of either oscillator [1,6].

Rather than measure the spectral density of phase fluctuations between two oscillators, it is possible to measure the phase fluctuations introduced by a device such as an active filter or amplifier. Only a slight modification of the existing PLL filter equipment setup is needed. The required scheme is shown in Fig. 18.

Figure 18 is a *differential phase noise measurement* setup. The output of the reference oscillator is split so that part of the signal passes through the device under test. We want the two signals going to the mixer to be 90° out of phase; thus, phase fluctuations between the two input ports cause voltage fluctuations at the output. The voltage fluctuations then can be measured at various Fourier frequencies on a spectrum analyzer.

To estimate the noise inherent in the test setup, one can in principle bypass the device under test and compensate for any change in amplitude and phase at the mixer. In order to measure inherent test equipment noise, the PLL filter technique must be converted to a differential phase noise technique. It is good practice to measure the system noise before proceeding to measurement of device noise.

4.3. Procedure and Example

For all of these setups, at the input to the spectrum analyzer, the voltage varies as the phase fluctuations in short term. The conversion to spectral density is

$$S_\phi(f) = \left(\frac{V_{RMS}(f)}{V_s(f)} \right)^2,$$

$$\text{and } \mathcal{L}(f) = \frac{1}{2} S_\phi(f)$$

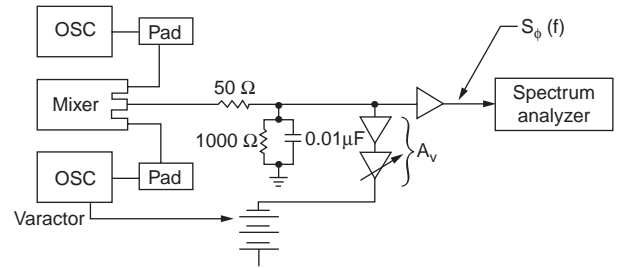


Figure 17. Typical hookup for a phase-noise measurement using a loose PLL.

where V_s is the phase sensitivity of the mixer in volts per radian at offset frequency f . Using the setup described previously, V_s can be measured by disconnecting the feedback loop to the varactor of the reference oscillator. The peak voltage swing is equal to V_s in units of V/rad (volts per radian) if the resultant beat note is a sine wave at frequency f . This may not be the case for state-of-the-art $S_\phi(f)$ measurements, where one must drive the mixer very hard to achieve low mixer noise levels. Hence the output will not be a sine wave, and the V/rad sensitivity must be estimated by the slew rate (through zero volts) of the resultant square wave from the mixer/amplifier.

The value for the measured $S_\phi(f)$ in decibels is given by

$$S_\phi(f) = 20 \log \frac{V_{RMS}(f)}{V_s \text{ full-scale } \phi - \text{detector voltage at } f}$$

Example 2. Given a PLL with two oscillators such that at the mixer output: $V_s = 1 \text{ V/rad}$ with a beat frequency $f = 45 \text{ Hz}$, $V_{RMS}(45 \text{ Hz}) = 100 \text{ nV}$ per root hertz. Solve for $S_\phi(45 \text{ Hz})$:

$$S_\phi(45 \text{ Hz}) = \left(\frac{100 \text{ nV/Hz}^{-1/2}}{1 \text{ V/rad}} \right)^2 = \left(\frac{10^{-7}}{1} \right)^2 \text{ rad}^2/\text{Hz}$$

$$= 10^{-14} \frac{\text{rad}^2}{\text{Hz}}$$

$$\mathcal{L}(45 \text{ Hz}) = 5 \times 10^{-15} \frac{\text{rad}^2}{\text{Hz}}$$

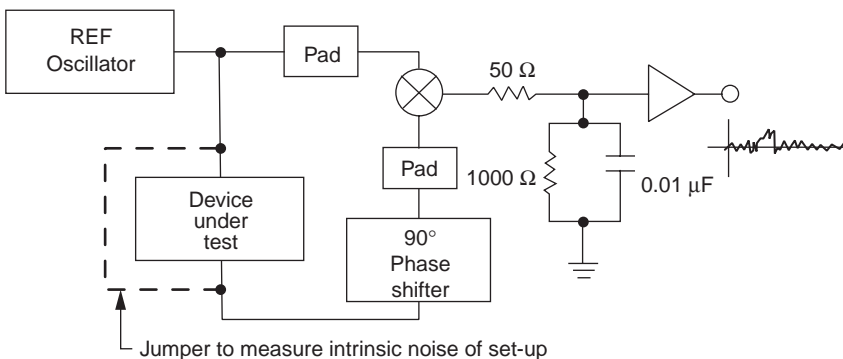


Figure 18. A differential measurement and measurement of the noise floor (by replacing the device under test with a through-cable) requires a 90 deg. phase shift at one of the mixer inputs.

In decibels

$$S_{\phi}(45 \text{ Hz}) = 20 \log \frac{100 \text{ nV}}{1 \text{ V}} = 20 \log \frac{10^{-7}}{10^0}$$

$$= 20(-7) = -140 \text{ dB at } 45 \text{ Hz,}$$

$$\mathcal{L}(45 \text{ Hz}) = -143 \text{ dB at } 45 \text{ Hz}$$

In the example, note that the mean frequency of the oscillators in the PLL was not essential to computing $S_{\phi}(f)$. However, in the application of $S_{\phi}(f)$, the mean frequency ν_0 is necessary information. Along with $S_{\phi}(f)$, one should always refer to ν_0 . In the example above, where $\nu_0 = 5 \text{ MHz}$, we have

$$S_{\phi}(45 \text{ Hz}) = 10^{-14} \frac{\text{rad}^2}{\text{Hz}}, \nu_0 = 5 \text{ MHz}$$

From Eq. (22), $S_y(f)$ can be computed as

$$S_y(45 \text{ Hz}) = \left(\frac{45}{5 \times 10^6} \right)^2 10^{-14} \frac{\text{rad}^2}{\text{Hz}}$$

$$= 5.1 \times 10^{-25} \text{ Hz}^{-1}, \nu_0 = 5 \text{ MHz.}$$

5. POWER-LAW NOISE PROCESSES

Power-law noise processes are models of precision oscillator noise that produce a particular *slope* on a spectral density plot. We often classify these noise processes into one of five categories. For plots of $S_{\phi}(f)$, they are

1. Random-walk FM (random walk of frequency), S_{ϕ} plot goes down as $1/f^4$.
2. Flicker FM (flicker of frequency), S_{ϕ} plot goes down as $1/f^3$.
3. White FM (white of frequency), S_{ϕ} plot goes down as $1/f^2$.
4. Flicker PM (flicker of phase), S_{ϕ} plot goes down as $1/f$.
5. White PM (white of phase), S_{ϕ} plot is flat.

Power-law noise processes are characterized by their functional dependence on Fourier frequency. Equation (22) relates $S_{\phi}(f)$ to $S_y(f)$, the spectral density of frequency fluctuations.

The spectral density plot of a typical oscillator’s output is usually a combination of different power-law noise processes. It is very useful and meaningful to categorize the noise processes. The first job in evaluating a spectral density plot is to determine which type of noise exists for a particular range of Fourier frequencies. It is possible to have all five noise processes generated from a single oscillator, but in general only two or three noise processes are dominant. Figure 19 is a graph of $S_{\phi}(f)$ showing the five noise processes on a log–log scale. Figure 20 shows the

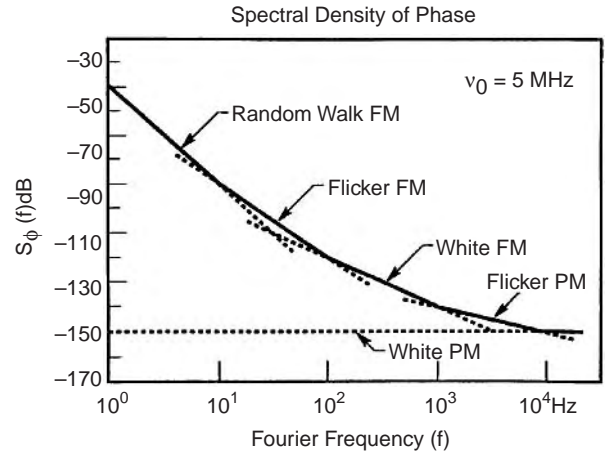


Figure 19. Power-law noise is indicated by a particular slope in the phase-noise measurement.

spectral density of phase fluctuations for a typical 5-MHz quartz oscillator.

6. CAUSES OF NOISE TYPES IN A SIGNAL SOURCE

6.1. Power-Law Noise Processes

Section 5 pointed out the five commonly used power-law models of noise. With respect to $S_{\phi}(f)$, one can estimate a straight-line slope (on a log–log scale) that corresponds to a particular noise type. This is shown in Fig. 19.

We can make the following general remarks about power-law noise processes:

1. Random-walk FM ($1/f^4$) noise is difficult to measure since it is usually very close to the carrier. “Random-walk FM” usually relates to the oscillator’s physical environment. If random walk FM is a predominant feature of the spectral density plot, then mechanical shock, vibration, temperature, or other environmental effects may be causing “random” shifts in the carrier frequency.
2. Flicker FM ($1/f^3$) is a noise whose physical cause is seldom fully understood but may typically be related

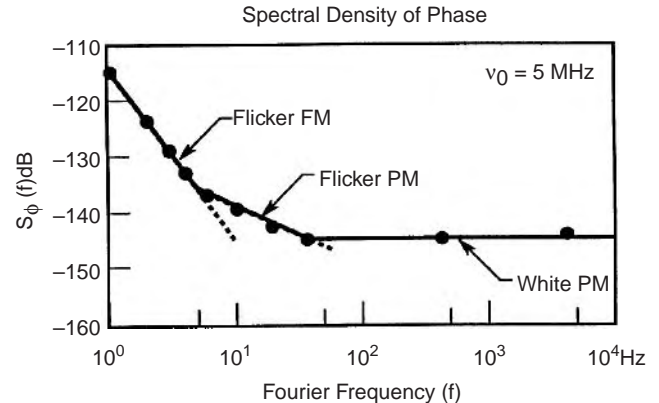


Figure 20. Different power-law noises have different causes in an oscillator’s output signal.

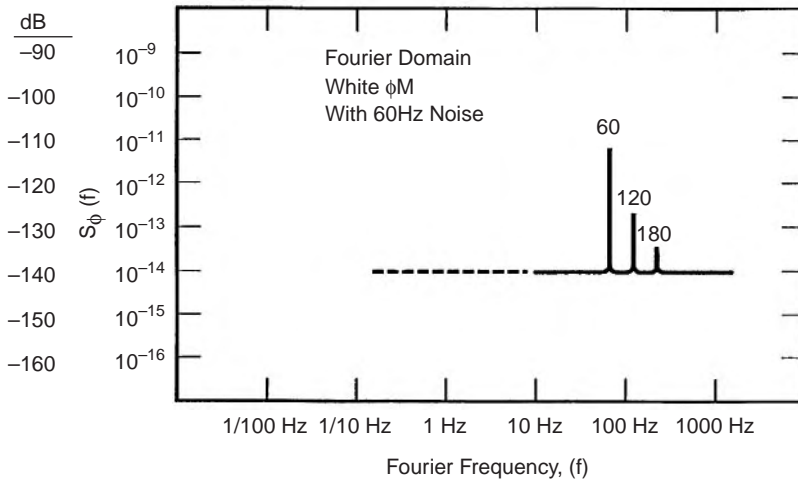


Figure 21. 60 Hz and harmonics are easily distinguished in a phase-noise measurement.

to the physical resonance mechanism of an active oscillator, or the design or choice of parts used for the electronics, or environmental properties. Flicker FM is common in high-quality oscillators, but may be masked by white FM ($1/f^2$) or flicker PM ($1/f$) in lower-quality oscillators.

3. White FM ($1/f^2$) noise is a common type found in passive-resonator frequency standards. These contain a slave oscillator, often quartz crystal, which is locked to a resonance feature of another device that behaves much like a high- Q filter. Cesium and rubidium standards have white FM noise characteristics.
4. Flicker PM ($1/f$) noise may relate to a physical resonance mechanism in an oscillator, but it usually is added by noisy electronics. This type of noise is common even in oscillators of the highest quality because in order to bring the signal amplitude up to a usable level, amplifiers are used after the signal source. Flicker PM noise may be introduced in these stages. It may also be introduced in a frequency multiplier. Flicker PM can be reduced with good low-noise amplifier design (i.e., using RF negative feedback) and hand-selecting transistors and other electronic components.
5. White PM (f^0) noise is broadband phase noise and has little to do with the resonance mechanism. It is probably produced by phenomena similar to that of flicker PM ($1/f$) noise. Stages of amplification are usually responsible for white PM noise. This noise can be kept at a very low value with good amplifier design, hand-selected components, the addition of narrowband filtering at the output, or, if feasible, increasing the power of the primary frequency source.

6.2. Other Types of Noise

A commonly encountered type of noise from a signal source or measurement apparatus is the presence of

60-Hz AC line noise. Shown in Fig. 21 is a constant white PM noise source with 60-, 120- and 180-Hz components added. This kind of noise is usually caused by AC power getting into the measurement system or the source under test. In the plot of $S_\phi(f)$, we observe discrete line spectra. Although $S_\phi(f)$ is a measure of spectral density, we can interpret the line spectra with no loss of generality, although one seldom refers to spectral densities when characterizing discrete lines. Figure 22 is the time-domain representation of the same white phase modulation level with 60-Hz noise. Note that the amplitude of $\sigma_y(\tau)$ varies up and down depending on sampling time. This is because in the time domain the sensitivity to a periodic wave varies directly as the sampling interval. This effect (which is an aliasing effect) can be used as a tool for filtering out a periodic wave imposed on a signal source. By sampling in the time domain at integer periods, we can be virtually insensitive to the periodic (discrete line) term, which is a useful strategy for removing the effect of the periodic wave.

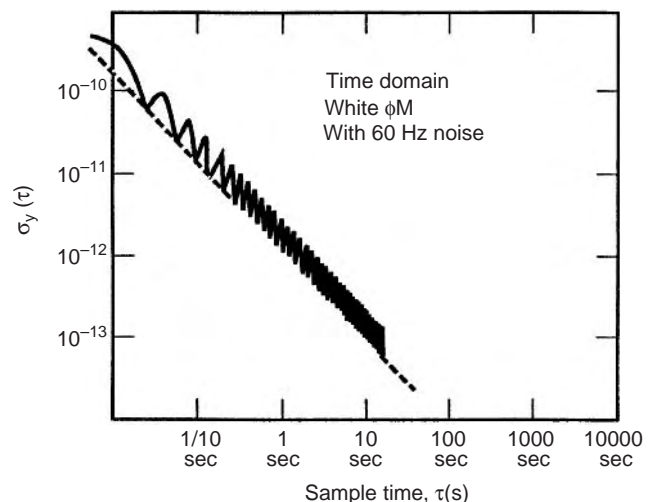


Figure 22. It is not easy to interpret an Allan deviation plot when 60 Hz noise is present on an oscillating signal.

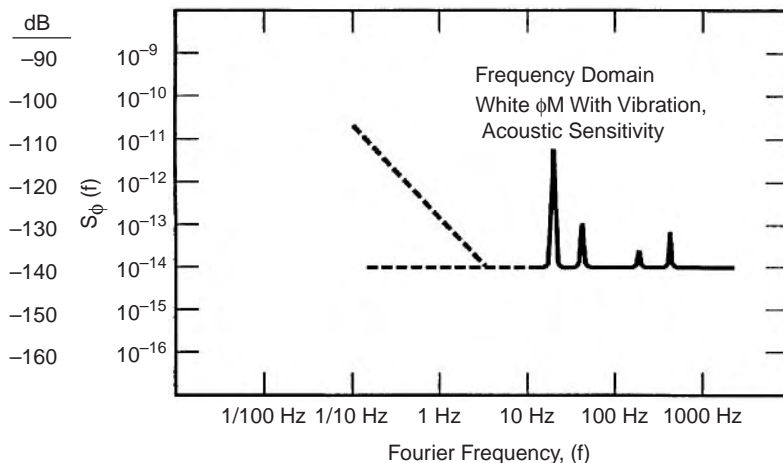


Figure 23. An oscillator under vibration causes sideband modulation that is apparent in a phase-noise measurement.

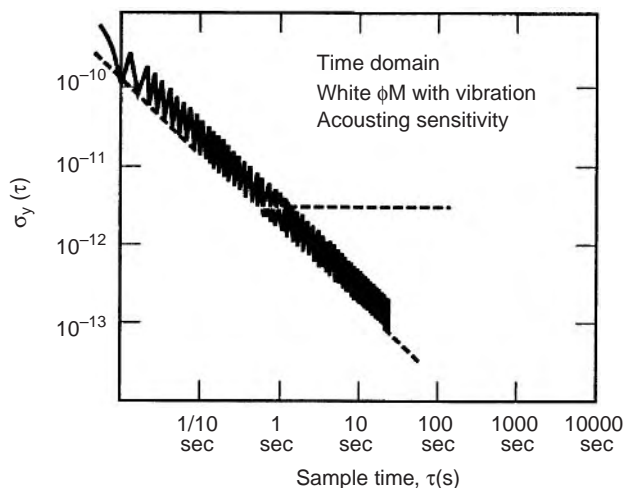


Figure 24. The Allan deviation of an oscillator under vibration causes a general increase in the level of frequency instability.

For example, diurnal variations in data due to day-to-day temperature, pressure, and other environmental effects can be eliminated by sampling the data once per day. This approach is useful for data with only one periodic term.

Figure 23 shows the kind of plot one might see of $S_{\phi}(f)$ with vibration and acoustic sensitivity in the signal source with the device under vibration. Figure 24 shows the translation of this effect to the time domain. Also noted in Fig. 23 is a (typical) flicker FM behavior in the low-frequency region. In the translation to time domain (Fig. 24), the flicker FM behavior masks the white PM (with the superimposed vibration characteristic) for long averaging times.

BIBLIOGRAPHY

1. D. B. Sullivan, D. W. Allan, D. A. Howe, and F. L. Walls, eds., *Characterization of Clocks and Oscillators*, NIST Technical Note 1337, 1990.

2. J. A. Barnes, A. R. Chi, L. S. Cutler, D. J. Healey, D. B. Leeson, T. E. McGunigal, J. A. Mullen, Jr., W. L. Smith, R. L. Sydnor, R. F. C. Vessot, and G. M. R. Winkler, *Characterization of Frequency Stability*, NBS Technical Note 394, 1970; *Proc. IEEE Trans. Instrum. Meas.* **IM-20**:105 (1971).
3. C. Audoin and B. Guinot, *The Measurement of Time: Time, Frequency and the Atomic Clock*, Cambridge Univ. Press, 2001.
4. D. W. Allan, Statistics of atomic frequency standards, *Proc. IEEE* **54**:221 (1966).
5. D. A. Howe and T. F. Pepler, Very long-term frequency stability: Estimation using a special-purpose statistic, *Proc. 2003 Joint Meeting IEEE Int. Frequency Control Symp. and EFTF Conf.*, 2003.
6. D. A. Howe, NIST Technical Note 679, *Frequency Domain Stability Measurements: A Tutorial Introduction*, 1976.
7. J. Rutman, Characterization of phase and frequency instabilities in precision frequency sources: fifteen years of progress, *Proc. IEEE* **66**(9):1048–1075 (1978).
8. IEEE Std 1139-1999, *Standard Definitions of Physical Quantities for Fundamental Frequency and Time Metrology—Random Instabilities*, IEEE-SA Standards Board, J. R. Vig, chairperson (1999).
9. F. L. Walls, Secondary standard for PM and AM noise at 5, 10, and 100 MHz, *Proc. IEEE Trans. Instrum. Meas.* **IM-42**:136–143 (1993).

FREQUENCY STANDARDS, CHARACTERIZATION

EVA S. FERRE-PIKAL
 University of Wyoming
 Laramie, Wyoming
 FRED L. WALLS
 Total Frequency
 Boulder, Colorado

In this article we describe the characterization of frequency standards following the general definitions accepted by the IEEE, the International Telecommunication Union—Radiocommunications (ITU-R), and International Radio

Consultative Committee (CCIR) [1–3]. In using the term “frequency standard”, we imply that changes in the frequency $\Delta\nu$ of the device are small compared to its nominal frequency ν_0 and that therefore the frequency would be about the same if we were to remeasure it. This permits us to treat the variations in fractional frequency $\Delta\nu/\nu_0$ as small compared to 1, and this greatly simplifies the mathematics of the characterization. We describe what is meant by accuracy and frequency stability of a frequency standard. The variations in frequency (which define the frequency stability) can be classified into two basic types: random and systematic. To characterize the random variations in frequency, the systematic effects must be removed from the data. Special statistical techniques other than the standard variance must then be used to quantify the random variations in frequency because some of the noise processes are not stationary. By this we mean that the mean of the frequency noise changes slowly with time. As part of the statistical treatment, we describe how to determine the confidence intervals for the estimates of the various types of random frequency noise.

1. ACCURACY

Frequency standards generate a periodic voltage signal, whose ideal frequency is defined as a specific number of oscillations per second. The second is the agreed unit of time, based on the energy difference between two energy levels of the unperturbed cesium atom [4], and it is this definition that allows the specification of accuracy of a frequency standard. Generally there will be offsets or biases in the actual frequency of a standard when compared to the ideal or defined value (according to the definition of the second) due to systematic and random effects [5–7]. The *accuracy* of a frequency standard, more recently described as an uncertainty, is a measure of the confidence relative to a physical model of the standard and the evaluation process. To evaluate the accuracy of a frequency standard, all the known sources of frequency offsets are listed, and the offset or bias due to each source and its uncertainty are carefully measured or computed. The uncertainty is a proper summation of the estimates of various systematic offsets and random noise [8]. For example, a frequency standard with an output frequency of 10 MHz and an uncertainty of 10^{-8} has a frequency error of $\leq \pm 0.1$ Hz.

2. STABILITY

Figure 1 shows the output voltage signal of an ideal *frequency standard* as a function of time. The maximum value V_0 is the nominal amplitude of the signal. The time required for the signal to repeat itself is the period T of the signal. The nominal frequency ν_0 of the signal is the reciprocal of the period, $1/T$. This voltage signal can be represented mathematically by a sine function

$$v(t) = V_0 \sin \theta = V_0 \sin(2\pi\nu_0 t) \tag{1}$$

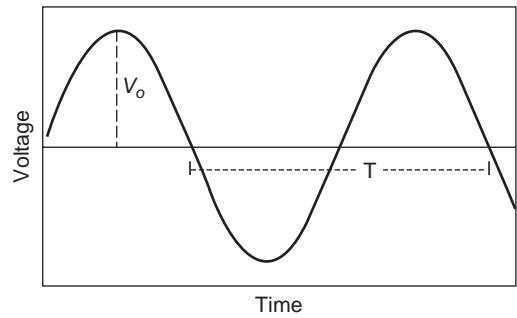


Figure 1. Ideal output voltage of a frequency standard.

where the argument $\theta = 2\pi\nu_0 t$ of the sine function is the nominal phase of the signal. The time derivative of the phase θ is $2\pi\nu_0$ and is called the *nominal angular frequency* ω_0 . In the frequency domain, this ideal signal is represented by a delta function located at the frequency of oscillation. Since this signal is ideal, there are no known sources that cause frequency shifts, and thus its frequency is *totally accurate* and its uncertainty is 0. Furthermore, its frequency, phase, and amplitude are constant; therefore the signal is also stable in frequency, phase, and amplitude.

In real situations, the output signal of an oscillator (source) or frequency standard has noise. Such a *noisy signal* is illustrated in Fig. 2. In this example we have depicted a case where the noise power is much less than the signal power. Frequency instability is the result of fluctuations in the period of the signal. Amplitude instability is the result of fluctuations in the peak values of the voltage. Phase instability is the result of fluctuations in the zero crossings. Since the period (and thus the frequency) of the signal is related to its phase, frequency instability and phase instability are directly related.

Figure 3 shows the *power spectrum of a noisy signal* (power as a function of frequency) as measured by a spectrum analyzer. Although the maximum power occurs at the frequency of oscillation, other peaks are observed at frequencies of $2\nu_0, 3\nu_0, \dots, n\nu_0$, where n is a positive integer. These frequencies are called *harmonics* of the fundamental frequency ν_0 ; $2\nu_0$ is the second harmonic, $3\nu_0$ is the third harmonic, and so on. The power at these harmonic frequencies will depend on the design of the source. The spectrum around the fundamental frequency displays power sidebands at frequencies above the carrier (upper

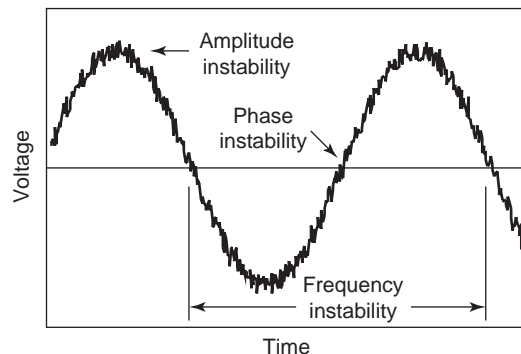


Figure 2. Output voltage of a noisy signal.

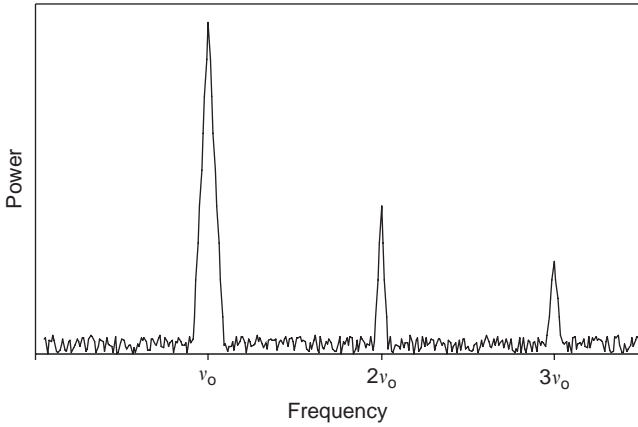


Figure 3. Power spectrum of a noisy signal.

sideband) and at frequencies below the carrier (lower sideband). These power sidebands are the result of phase fluctuations and amplitude fluctuations in the signal. While the power spectrum gives an idea of the total noise of a signal, it does not give information about the relative magnitude of its phase instabilities and amplitude instabilities. Furthermore, at frequencies close to v_0 it is difficult to separate the noise power from the power of the fundamental frequency. Therefore, special measurement techniques are needed to measure phase instabilities and amplitude instabilities in sources.

A noisy signal can be mathematically represented by

$$v(t) = [V_0 + \varepsilon(t)] \sin[2\pi v_0 t + \phi(t)] \quad (2)$$

where $\varepsilon(t)$ represents amplitude fluctuations (amplitude deviation from the nominal amplitude V_0) and $\phi(t)$ represents phase fluctuations (phase deviation from the nominal phase $2\pi v_0 t$) [1]. The instantaneous frequency of this signal is defined as

$$v(t) = \frac{1}{2\pi} \frac{d}{dt}(\text{phase}) = v_0 + \frac{1}{2\pi} \frac{d}{dt} \phi(t) \quad (3)$$

Frequency fluctuations refer to the deviation $v(t) - v_0$ of the instantaneous frequency from the nominal frequency. Fractional frequency fluctuations, denoted as $y(t)$, refer to frequency fluctuations normalized to v_0 :

$$y(t) = \frac{v(t) - v_0}{v_0} = \frac{1}{2\pi v_0} \frac{d}{dt} \phi(t) \quad (4)$$

Equation (4) indicates that there is a direct relation between phase fluctuations and fractional frequency fluctuations. Therefore, if a signal exhibits a certain amount of phase fluctuation, it also exhibits frequency fluctuation given by Eq. (4). The time deviation $x(t)$ of a signal is the integral of $y(t)$ from 0 to t . Thus one can write

$$y(t) = \frac{d}{dt} x(t) \quad (5)$$

The frequency stability of a frequency standard is affected by random-noise processes and by systematic, deterministic changes. Systematic effects often dominate the frequency stability in nonlaboratory environments. The sensitivity of the standard to temperature, humidity, atmospheric pressure, magnetic field, and radiation may play a role [9–11]. Generally, frequency (and thus phase) stability is divided into three regions: short-term, medium-term, and long-term stability. (Although the term *frequency stability* is used throughout most of the literature, the term actually refers to instabilities in the frequency.)

Short-term frequency stability refers to the random, nonsystematic fluctuations that are related to the signal-to-noise ratio (SNR) of the device. In quartz crystal resonators this refers to the region dominated by white phase noise, where the time between observed frequencies (sample time) is less than a second. In atomic frequency standards the short-term stability also includes white frequency noise and extends to sampling times of several minutes.

Medium-term frequency stability refers to the region where flicker noise dominates. The sampling time characteristic of this region is a function of the type of frequency standard. Short-term and medium-term frequency stability can be characterized in either the frequency domain or the time domain, after known systematic effects have been removed. Frequency-domain characterization and measurements are generally used when the sample time of interest is less than a second. For sampling times longer than a second, time-domain measurements are used to characterize frequency stability.

Long-term frequency stability includes random-walk frequency-noise processes in addition to systematic, deterministic changes in frequency observed when the sampling time is long. The long-term, systematic frequency change is called *frequency drift* [2,12]. Drift includes frequency changes due to changes in the components of the source in addition to those due to external parameters such as temperature, humidity, pressure, magnetic field, and radiation [9–11]. Frequency *aging*, on the other hand, refers to the long-term systematic frequency change due to changes in the components of the source, independent of parameters external to the source [2,12].

2.1. Frequency-Domain Characterization

Phase fluctuations in the frequency domain, or *phase modulation (PM) noise*, are characterized by the power spectral density (PSD) of the phase fluctuations, given by [13]

$$S_\phi(f) = \mathcal{F}[\mathcal{R}_\phi(\tau)] = \int_{-\infty}^{\infty} \mathcal{R}_\phi(\tau) e^{-j\omega\tau} d\tau \quad (6)$$

where $\mathcal{F}[\]$ is the Fourier transformation and $\mathcal{R}_\phi(\tau)$ is the autocorrelation function of the phase fluctuations given by

$$\mathcal{R}_\phi(\tau) = \langle \phi(\tau)\phi(t - \tau) \rangle \quad (7)$$

A more practical definition of PSD [$\phi(t)$] is

$$S_\phi(f) = \text{PSD}[\phi(t)] = [\phi(f)]^2 \frac{1}{\text{BW}} \quad (8)$$

where $[\phi(f)]^2$ is the mean-squared phase deviation at an offset frequency f from the frequency ν_0 (called the “carrier” in this context), and BW is the bandwidth of the measurement system [1,13–15]. The offset frequency f is also called the *Fourier frequency*. The units for $S_\phi(f)$ are rad^2/Hz . Equation (8) is defined for $0 < f < \infty$; nevertheless, it includes fluctuations from the upper and lower sidebands and thus is a double-sideband measure.

The PM noise measure recommended by the IEEE [1,14,15] is $\mathcal{L}(f)$, defined as

$$\mathcal{L}(f) \equiv \frac{S_\phi(f)}{2} \quad (9)$$

At Fourier frequencies far from the carrier frequency, where the integrated PM noise from ∞ to f (the Fourier frequency) is less than 0.1 rad^2 , $\mathcal{L}(f)$ is equal to the single-sideband phase noise. The units for $\mathcal{L}(f)$ are decibels below the carrier in a 1-Hz bandwidth (dBc/Hz).

Frequency fluctuations in the frequency domain, or *frequency modulation (FM) noise*, are characterized by the power spectral density of the fractional frequency fluctuations, given by

$$S_y(f) = \text{PSD}[y(t)] = [y(f)]^2 \frac{1}{\text{BW}} \quad (10)$$

where $y(f)^2$ represents the mean-squared fractional frequency deviation at an offset (Fourier) frequency f from the carrier [1,13–15]. $S_y(f)$ is defined for Fourier frequencies $0 < f < \infty$, and its units are inverse hertz.

The conversion between $S_y(f)$ and $S_\phi(f)$ can be obtained from Eq. (4). Applying the Fourier transformation to both sides of Eq. (4), squaring, and dividing by the measurement bandwidth results in

$$S_y(f) = \left(\frac{1}{2\pi\nu_0} \right)^2 (2\pi f)^2 S_\phi(f) = \left(\frac{f}{\nu_0} \right)^2 S_\phi(f) \quad (11)$$

Amplitude fluctuations in the frequency domain, or *amplitude modulation (AM) noise*, are characterized by the power spectral density of the fractional amplitude fluctuations, given by

$$S_a(f) = \text{PSD} \left[\frac{\varepsilon(t)}{V_0} \right] = \left[\frac{\varepsilon(f)}{V_0} \right]^2 \frac{1}{\text{BW}} \quad (12)$$

where $\varepsilon(f)^2$ represents the mean squared amplitude deviation at an offset frequency f from the carrier [1]. $S_a(f)$ is defined for Fourier frequencies $0 < f < \infty$, and its units are inverse hertz.

In free-running sources, the FM noise is usually modeled by the sum of five different power laws or noise types as

$$S_y(f) = \sum_{\alpha=-2}^2 h_\alpha f^\alpha = h_{-2}f^{-2} + h_{-1}f^{-1} + h_0f^0 + h_1f^1 + h_2f^2 \quad (13)$$

where $h_{-2}f^{-2}$ represents random-walk frequency noise, $h_{-1}f^{-1}$ represents flicker frequency noise, h_0f^0 represents white frequency noise, h_1f^1 represents flicker phase noise, and h_2f^2 represents white phase noise. Similarly, the PM noise can be modeled by

$$S_\phi(f) = \sum_{\beta=-4}^0 k_\beta f^\beta = k_{-4}f^{-4} + k_{-3}f^{-3} + k_{-2}f^{-2} + k_{-1}f^{-1} + k_0f^0 \quad (14)$$

where $k_{-4}f^{-4}$ represents the random-walk frequency noise, $k_{-3}f^{-3}$ represents flicker frequency noise, $k_{-2}f^{-2}$ represents white frequency noise, $k_{-1}f^{-1}$ represents flicker phase noise, and k_0f^0 represents white phase noise. Notice that $S_\phi(f)$ and $S_y(f)$ have different slopes for a specific type of noise, as implied by Eq. (11). Equation (11) can be used to obtain the conversion between the $S_\phi(f)$ and $S_y(f)$ coefficients, yielding

$$k_\beta = \nu_0^2 h_\alpha \quad \text{for } \beta = \alpha - 2 \quad (15)$$

Figure 4 shows the common noise types characteristic of the PM noise and the FM noise of a source [1,14–17]. Usually a source exhibits two or three of the noise types shown in the plots [17].

The AM noise of a source can typically be modeled by the sum of three different power laws of noise types:

$$S_a(f) = \sum_{\alpha=-2}^0 h_\alpha f^\alpha = h_{-2}f^{-2} + h_{-1}f^{-1} + h_0f^0 \quad (16)$$

where $h_{-2}f^{-2}$ represents random-walk amplitude noise, $h_{-1}f^{-1}$ represents flicker noise, and h_0f^0 represents white amplitude noise [18]. Figure 5 shows the common noise types characteristic of the AM noise of a source.

Upper and lower PM sidebands are always equal and 100% correlated. Likewise, the upper and lower AM sidebands are always equal and 100% correlated. This is true even when the RF spectrum is not symmetric about the carrier [19]. The phase between AM and PM noise varies randomly with time for broadband additive noise [19].

2.2. Time-Domain Characterization

In the time domain, the *fractional frequency stability* of a signal is usually characterized by the Allan variance, a type of two-sample frequency variance given by [1,13–15]

$$\sigma_y^2(\tau) = \frac{1}{2} \langle (\bar{y}_{i+1} - \bar{y}_i) \rangle \quad (17)$$

where \bar{y}_i is the average fractional frequency of interval i given by

$$\bar{y}_i = \frac{1}{\tau} \int_{t_i}^{t_i + \tau} y(t) dt = \frac{1}{\tau} [x(t_i + \tau) - x(t_i)] = \frac{1}{\tau} (x_{i+1} - x_i) \quad (18)$$

In practical situations only a finite number of fractional frequency samples are available, and the Allan variance is

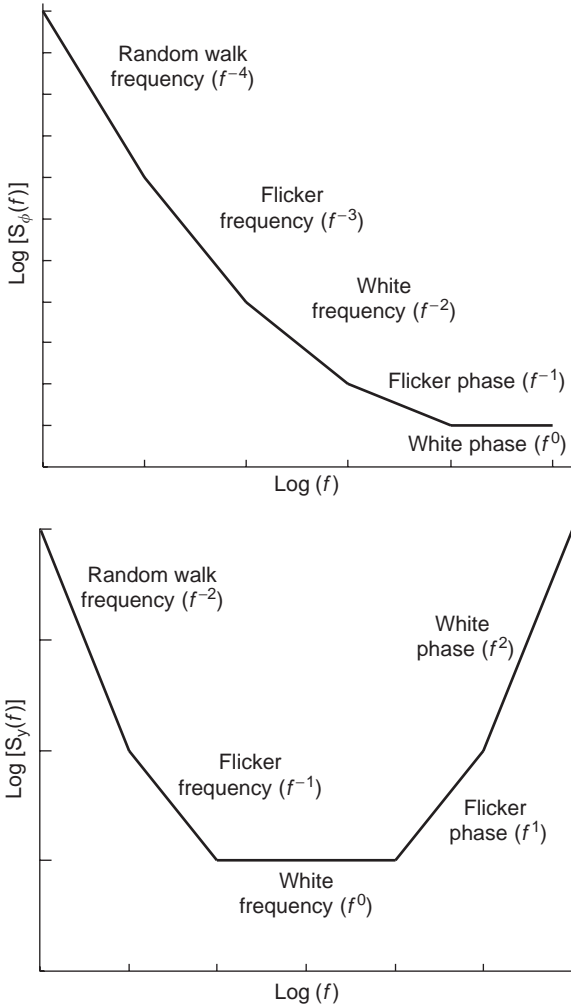


Figure 4. PM and FM noise characteristics of a source.

approximated by

$$\sigma_y^2(\tau) \approx \frac{1}{2(M-1)} \sum_{i=1}^{M-1} (\bar{y}_{i+1} - \bar{y}_i)^2 \quad (19)$$

where $M = N - 1$ is the number of frequency samples (N is the number of time samples) [1,14,15]. The Allan variance

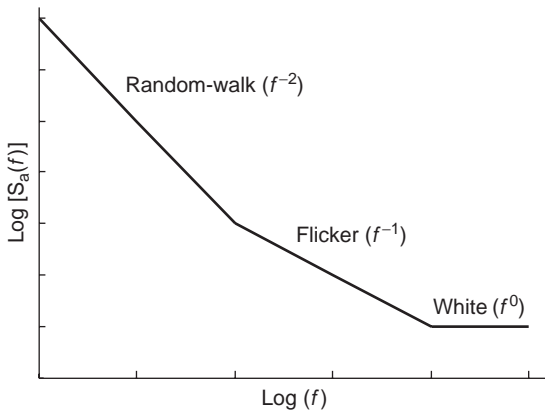


Figure 5. AM noise characteristics of a source.

can also be expressed in terms of time samples using $\bar{y}_i = (x_{i+1} - x_i)/\tau$:

$$\sigma_y^2(\tau) \approx \frac{1}{2(N-2)\tau^2} \sum_{i=1}^{N-2} (x_{i+2} - 2x_{i+1} + x_i)^2 \quad (20)$$

The square root of the Allan variance is called the *Allan deviation*, $\sigma_y(\tau)$.

When time samples are taken every τ_0 seconds, the Allan variance can be computed for several sampling times $\tau = n\tau_0$ where $n > 0$. For $n > 1$, overlapped samples can be used to compute σ_y^2 as shown in Fig. 6, providing better confidence intervals [1,20]. An expression for the fully overlapped Allan variance can be derived using Fig. 6 and Eq. (19). For $\tau = n\tau_0$, Eq. (19) becomes

$$\sigma_y^2(\tau) \approx \frac{1}{2(M-2n)} \sum_{i=1}^{M-2n} (\bar{y}_{i+n} - \bar{y}_i)^2 \quad (21)$$

which can also be expressed in terms of time-domain data by substituting \bar{y}_i for $(x_{i+n} - x_i)/n\tau_0$:

$$\sigma_y^2(\tau) \approx \frac{1}{2(N-2n)\tau^2} \sum_{i=1}^{N-2n} (x_{i+2n} - 2x_{i+n} + x_i)^2 \quad (22)$$

Figure 7a shows a log-log plot of the Allan variance as a function of the sampling time τ for a source that exhibits all five common noise types. The slopes of the white PM noise and the flicker PM noise are the same; therefore, these two noise types cannot be separated using this plot. The Allan variance can often be modeled by the sum of four different power laws

$$\sigma_y^2(\tau) = \sum_{\mu=-2}^1 p_\mu \tau^\mu = p_{-2}\tau^{-2} + p_{-1}\tau^{-1} + p_0\tau^0 + p_1\tau^1 \quad (23)$$

where $p_{-2}\tau^{-2}$ represents white phase and flicker phase noise, $p_{-1}\tau^{-1}$ represents white frequency noise, $p_0\tau^0$ represents flicker frequency noise, and $p_1\tau^1$ represents random-walk frequency noise.

When the dominant noise type in the short term is flicker PM or white PM, the modified Allan variance can be used to improve the estimate of the underlying frequency stability of the sources [1,14,21]. Here a new series $\{\bar{x}_i\}$ is created by averaging n adjacent phase (time) measurements of duration τ_0 . The average fractional frequencies are computed from the $\{\bar{x}_i\}$, as illustrated in Fig. 8. For

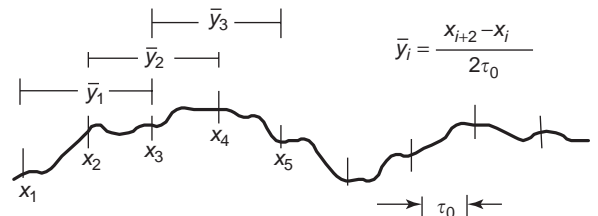


Figure 6. Computation of $\{\bar{y}_i\}$ for the overlapped Allan variance and $n = 2$.

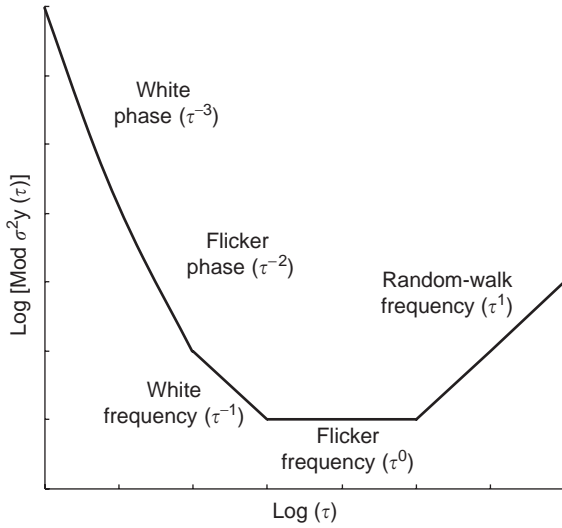
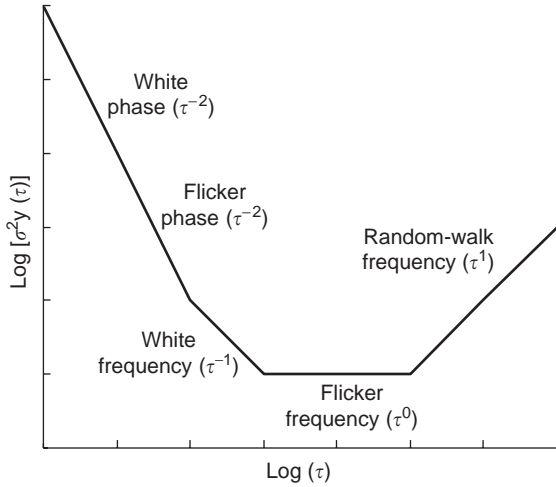


Figure 7. $\sigma_y^2(\tau)$ and $\text{Mod } \sigma_y^2(\tau)$ for the five noise types.

N time samples and $\tau = n\tau_0$, the resulting modified Allan variance is

$$\text{Mod } \sigma_y^2(\tau) \approx \frac{1}{2(N-3n+1)} \sum_{i=1}^{N-3n+1} (\bar{y}'_{i+n} - \bar{y}'_i)^2 \quad (24)$$

Equation (24) can also be expressed in terms of the initial time-domain data $\{x_k\}$:

$$\text{Mod } \sigma_y^2(\tau) \approx \frac{1}{2\tau^2 n^2 (N-3n+1)} \times \sum_{j=1}^{N-3n+1} \left[\sum_{i=j}^{n+j-1} (x_{i+2n} - 2x_{i+n} + x_i) \right]^2 \quad (25)$$

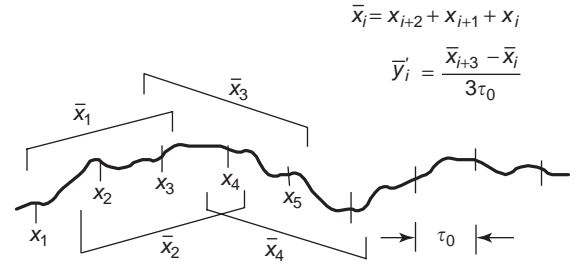


Figure 8. Computation of $\{\bar{x}_i\}$ and $\{\bar{y}'_i\}$ for the modified Allan variance and $n=3$.

where

$$\bar{y}'_i = \frac{\bar{x}_{i+n} - \bar{x}_i}{\tau} \quad (26)$$

$$\bar{x}_i = \frac{\sum_{k=0}^{n-1} x_{i+k}}{n} \quad (27)$$

Here \bar{x}_i is the phase (time) averaged over n adjacent measurements of duration τ_0 . Thus $\text{Mod } \sigma_y(\tau)$ is proportional to the second difference of the phase averaged over a time $n\tau_0$. Viewed from the frequency domain, $\text{Mod } \sigma_y(\tau)$ is proportional to the first difference of the frequency averaged over n adjacent samples. The square root of the modified Allan variance is called the *modified Allan deviation* $\text{Mod } \sigma_y(\tau)$.

Figure 9 shows the ratio $R(n) = [\text{Mod } \sigma_y^2(\tau)] / \sigma_y^2(\tau)$ as a function of n for all five types of noise processes [15]. For random-walk FM, flicker FM, and white FM the ratio is constant for $n \geq 5$. Therefore, $\text{Mod } \sigma_y^2(\tau)$ and $\sigma_y^2(\tau)$ have the same slope for these noise types. For white PM noise ($\alpha=2$), the slope is $-1/n$; therefore, the slope of $\text{Mod } \sigma_y^2(\tau)$ is equal to the slope of $\sigma_y^2(\tau)$ divided by τ . Finally, for flicker PM noise the ratio asymptotically reaches $3.37/(1.04 + 3 \ln \omega_h \tau)$. In this case and for $n > 10$, the slope of $\text{Mod } \sigma_y^2(\tau)$ is approximately τ^{-1} . Figure 9 also shows that $\text{Mod } \sigma_y^2(\tau)$ is considerably smaller than $\sigma_y^2(\tau)$ for white PM and flicker PM noise. Not only does $\text{Mod } \sigma_y^2(\tau)$ provide a different slope for white PM noise and flicker PM noise, allowing the separation of the two noise processes (see Fig. 7b); it can also speed the stability measurements. If a system is limited by white and flicker PM noise at short average times, using $\text{Mod } \sigma_y^2(\tau)$ reduces the measurement time required to observe white FM, flicker FM, and random-walk FM at longer averaging times, in comparison with that required when using $\sigma_y^2(\tau)$ [15].

At long averaging times when the ratio $N\tau_0/(2n\tau_0)$ is close to 1, the Allan variance has a bias related to its insensitivity to odd noise processes in the phase (time) fluctuations (odd with respect to the midpoint). In these situations an extension of the Allan variance that removes this bias can be used to characterize the frequency stability of a source. This variance, $\sigma_{y,\text{TOTAL}}^2(\tau)$, is obtained by extending the $\{x_i\}$ in both directions and then computing the Allan variance from the new $\{x'_i\}$ sequence [22–24]. Figure 10 illustrates this extension of $\{x_i\}$: on the left side the extension is the inverted mirror image of $\{x_i\}$ with

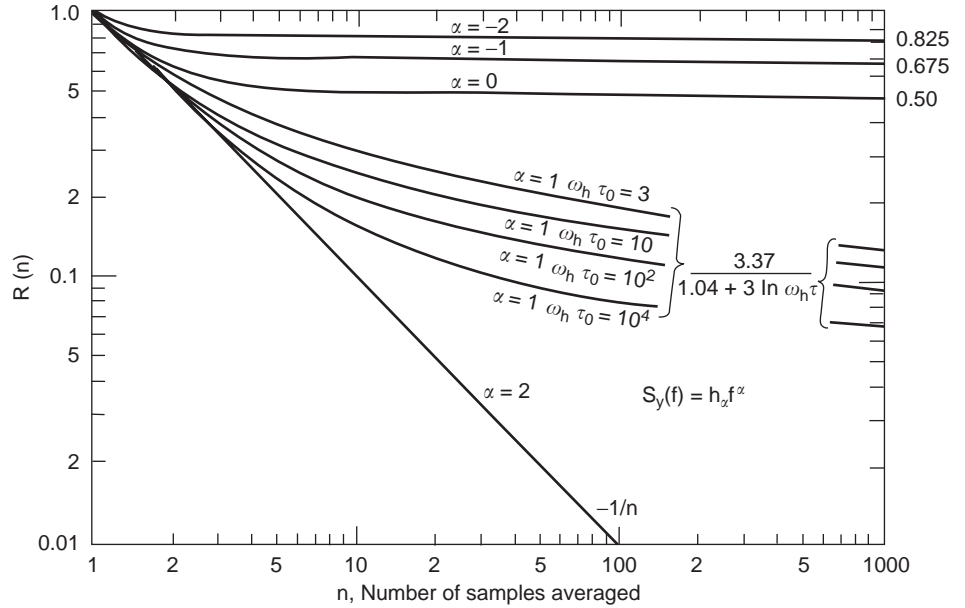


Figure 9. Ratio of the modified Allan variance to the Allan variance, $R(n) = [\text{Mod } \sigma_y^2(\tau)] / \sigma_y^2(\tau)$, as a function of n [15]; $\tau = n\tau_0$.

respect to x_N . How far this extension depends on the maximum value of n_m of n . For N time data points, n_m is the integer part of $(N - 1)/2$. The far-left data point is $x'_{2-n_m} = 2x_1 - x_{n_m}$; the far-right data point is $x'_{N+n_m-1} = 2x_N - x_{N-n_m+1}$. Thus $\sigma_{y,\text{TOTAL}}^2(\tau)$ is given by

$$\hat{\sigma}_{y,\text{TOTAL}}^2(\tau) = \frac{1}{2(N-2)} \sum_{i=2}^{N-1} (\bar{y}'_i - \bar{y}'_{i-n})^2 \quad (28)$$

Equation (28) can be expressed in terms of $\{x'_i\}$ using $\bar{y}'_i = (x'_{i+n} - x'_i) / \tau$ as

$$\hat{\sigma}_{y,\text{TOTAL}}^2(\tau) = \frac{1}{2\tau^2(N-2)} \sum_{i=2}^{N-1} (x'_{i-n} - 2x'_i + x'_{i+n})^2 \quad (29)$$

For a detailed description of $\sigma_{y,\text{TOTAL}}^2(\tau)$, see Refs. 22–24.

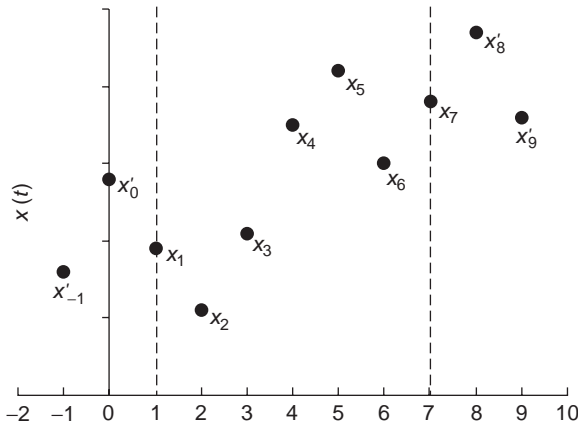


Figure 10. Extension of $\{x_i\}$ for $\sigma_y^2(\tau)$.

3. CONVERSION BETWEEN TIME-DOMAIN MEASURES AND FREQUENCY-DOMAIN MEASURES

Frequency-domain data $S_\phi(f)$ can be converted to time-domain data $\sigma_y^2(\tau)$ using the relation [1,25]

$$\sigma_y^2(\tau) = \frac{2}{(\pi\nu_0\tau)^2} \int_0^{f_h} S_\phi(f) \sin^4(\pi f\tau) df \quad (30)$$

Equation (30) is derived by expressing both $S_\phi(f)$ and $\sigma_y^2(\tau)$ in terms of the autocorrelation function $\mathcal{R}_\phi(\tau)$ of the random process $\phi(t)$ and then combining the two expressions to cancel $\mathcal{R}_\phi(\tau)$ [13]. Similarly

$$\sigma_y^2(\tau) = \frac{2}{(\pi\tau)^2} \int_0^{f_h} S_y(f) \frac{\sin^4(\pi f\tau)}{f^2} df \quad (31)$$

Expressions for $\text{Mod } \sigma_y^2(\tau)$ (15,24), obtained using a similar procedure are

$$\text{Mod } \sigma_y^2(\tau) = \frac{2}{n^4(\pi\nu_0\tau_0)^2} \int_0^{f_h} \frac{S_\phi(f) \sin^6(\pi\tau f)}{\sin^2(\pi\tau_0 f)} df \quad (32)$$

$$\text{Mod } \sigma_y^2(\tau) = \frac{2}{n^4(\pi\tau_0)^2} \int_0^{f_h} \frac{S_y(f) \sin^6(\pi\tau f)}{f^2 \sin^2(\pi\tau_0 f)} df \quad (33)$$

The inclusion of f_h as the upper limit of the integral assumes that the term inside the integral is multiplied or “filtered” by an infinitely sharp lowpass filter with cutoff frequency f_h . Table 1 shows the results of Eqs. (31) and (33) for the five types of noise for $2\pi f_h \tau \gg 1$ [1,14–16,25]. The results will depend on the type of filter assumed. While an infinitely sharp filter was assumed in Eqs. (30)–(33), actual measurement systems have different filter responses.

Table 1. Conversion Factors for $\sigma_y^2(\tau)$ and Mod $\sigma_y^2(\tau)$ [1,14–16,25]

Noise Type	$S_y(f)$	$\sigma_y^2(\tau)$	Mod $\sigma_y^2(\tau)$
Random-walk frequency	$h_{-2}f^{-2}$	$(2\pi^2\tau/3)h_{-2}$	$5.42h_{-2}\tau$
Flicker frequency	$h_{-1}f^{-1}$	$(2\ln 2)h_{-1}$	$0.936h_{-1}$
White frequency	h_0f^{08}	$h_0/2\tau$	$h_0/4\tau$
Flicker phase	h_1f^1	$\frac{1.038 + 3 \ln(\omega_h\tau)}{4\pi^2}h_1\frac{1}{\tau^2}$	$\frac{3.37}{4\pi^2}h_1\frac{1}{\tau^2}$
White phase	h_2f^2	$\frac{3f_h}{4\pi^2}h_2\frac{1}{\tau^2}$	$\frac{3f_h}{4\pi^2}h_2\frac{1}{n\tau^2}$

Expressions have also been derived for a single-pole filter [15,26,27]. These expressions, along with those in Table 1, constitute the boundaries for $\sigma_y^2(\tau)$ and Mod $\sigma_y^2(\tau)$, given a specific PSD of phase fluctuations [15]. For this reason it is important to specify the filter frequency response, including the high cutoff frequency, when specifying the Allan and modified Allan variances of a source.

Generally, conversion from $\sigma_y^2(\tau)$ or Mod $\sigma_y^2(\tau)$ to the frequency domain is not possible, unless specific information about the noise characteristics is known. Greenhall demonstrated that several different spectral densities of random processes can have the same Allan variance [28]. However, in the case where the spectral density follows the noise model in Eqs. (13) and (14), a one-to-one correspondence between $S_\phi(f)$ and $\sigma_y^2(\tau)$ and Mod $\sigma_y^2(\tau)$ is found, except that for white PM and flicker PM noise $\sigma_y^2(\tau)$ exhibits the same slope, corresponding to τ^{-2} . Often, uniqueness fails more generally. Some sources have internal phase-locked loops, and their noise spectra deviates from the model in Eqs. (13) and (14), [29]; others exhibit 60-Hz and other peaks that will affect $\sigma_y^2(\tau)$ [16,30]. Generally, multivariate analysis should be used to obtain frequency-domain coefficients for each type of noise from time-domain data [31].

4. CONFIDENCE INTERVALS FOR $\sigma_y^2(\tau)$ AND MOD $\sigma_y^2(\tau)$

The Allan variance is defined as the first difference of average fractional frequencies, averaged over an infinite time. Since only a finite number M of frequency samples can be taken, we can only estimate the Allan variance and deviation, and the confidence of this estimate depends on the number of samples.

A simple method to obtain confidence intervals is to use the chi-squared distribution function. The Allan variance has a chi-squared distribution function given by

$$\chi^2 = \text{df} \frac{\hat{\sigma}_y^2(\tau)}{\sigma_y^2(\tau)} \quad (34)$$

where df is the number of degrees of freedom [16]. The Allan variance is the sum of the squares of the first differences of adjacent fractional frequency values. If all the

first-difference values were independent, then the number of degrees of freedom would be equal to the number of first-difference values. This is not the case, and thus other procedures have been used to compute the number of degrees of freedom for $\sigma_y^2(\tau)$ [16]. Table 2 shows analytical (empirical) equations that approximate the number of degrees of freedom for the fully overlapped Allan variance [16]. The equation depends on the noise type. For nonoverlapped estimates, n in Table 2 is equal to 1, N refers to the equivalent number of time samples for $\tau = n\tau_0$ given by $\text{Int}((N-1)/n) + 1$, and $\text{Int}(\)$ refers to the integer part.

Usually a $(p \times 100)\%$ confidence interval is computed, where p is the probability that the true Allan variance or Allan deviation is within the computed confidence interval. The $(p \times 100)\%$ confidence interval for the overlapped Allan variance is given by

$$\chi^2\left(\frac{1-p}{2}\right) < \text{df} \frac{\hat{\sigma}_y^2(\tau)}{\sigma_y^2(\tau)} < \chi^2\left(p + \frac{1-p}{2}\right) \quad (35)$$

$$\frac{\text{df}}{\chi^2\left(p + \frac{1-p}{2}\right)} \hat{\sigma}_y^2(\tau) < \sigma_y^2(\tau) < \frac{\text{df}}{\chi^2\left(\frac{1-p}{2}\right)} \hat{\sigma}_y^2(\tau) \quad (36)$$

where the chi-squared value $\chi^2(C)$ for $(p \times 100)\%$ confidence can be obtained from chi-squared distribution tables or from several computer programs. The $(p \times 100)\%$ confidence interval for the Allan deviation is

$$\sqrt{\frac{\text{df}}{\chi^2\left(p + \frac{1-p}{2}\right)}} \hat{\sigma}_y(\tau) < \sigma_y(\tau) < \sqrt{\frac{\text{df}}{\chi^2\left(\frac{1-p}{2}\right)}} \hat{\sigma}_y(\tau) \quad (37)$$

The chi-squared distribution can also be used to find the confidence intervals for Mod $\sigma_y^2(\tau)$.

Table 2. Empirical Equations for the Number of Degrees of Freedom When Computing Confidence Intervals for the Overlapped Allan Variance [16]

Noise Type	α	Degrees of Freedom df
White phase	-2	$\frac{(N+1)(N-2n)}{2(N-n)}$
Flicker phase	-1	$\exp\left[\ln\left(\frac{N-1}{2n}\right) \ln\left(\frac{(2n+1)(N-1)}{4}\right)\right]^{1/2}$
White frequency	0	$\left(\frac{3(N-1)}{2n} - \frac{2(N-2)}{N}\right) \frac{4n^2}{4n^2+5}$
Flicker frequency	+1	$\frac{2(N-2)^2}{2.3N-4.9}$ for $n=1$ $\frac{5N^2}{4n(N+3n)}$ for $n \geq 2$
Random-walk frequency	+2	$\frac{N-2}{n} \frac{(N-1)^2 - 3n(N-1) + 4n^2}{(N-3)^2}$

Table 3. Confidence Intervals for the Nonoverlapped and Fully Overlapped $\sigma_y(\tau)$ [16] and for the Fully Overlapped Mod $\sigma_y(\tau)$ [32–34]^a

n	Noise Type	Confidence Interval (%)					
		Nonoverlapped $\sigma_y(\tau)$		Fullyoverlapped $\sigma_y(\tau)$		Fully overlapped Mod $\sigma_y(\tau)$	
		–	+	–	+	–	+
2	White PM	4.1	4.8	2.9	3.2	3.1	3.4
8		7.7	10.1	2.9	3.2	5.2	6.1
32		13.6	23.1	3.0	3.4	9.7	14
2	Flicker PM	3.7	4.3	2.9	3.1	3.0	3.3
8		7.1	9.0	3.6	4.0	5.7	6.8
32		12.7	20.7	5.2	6.1	11	16
2	White FM	3.6	4.0	2.8	3.0	3.0	3.2
8		6.8	8.6	4.8	5.6	5.8	7.0
32		12.5	20.1	8.8	12	11	16
2	Flicker FM	3.2	3.5	2.6	3.0	2.9	3.2
8		6.1	7.4	5.1	6.0	5.8	7.1
32		11.1	16.8	9.9	14	11	16
2	Random-walk FM	3.0	3.3	3.0	3.3	3.2	3.5
8		5.7	6.8	5.7	7.0	6.4	8.0
32		10.4	15.2	11	16	12	19

^aConfidence intervals for the nonoverlapped $\sigma_y(\tau)$ were obtained using the df in Table 2 [16]. The degrees of freedom used for the fully overlapped $\sigma_y(\tau)$ were computed using numerical methods and are approximately equal to those obtained using Table 2 [16,20]. Confidence intervals for the fully overlapped Mod $\sigma_y(\tau)$ were obtained from Ref. 34 ; $N = 1025$.

Walter [32] and Greenhall [33] have derived expressions for the number of degrees of freedom of Mod $\sigma_y^2(\tau)$ using different procedures. These expressions are complicated and will not be presented here. The two methods yield similar results (33). Table 3 shows the confidence intervals for $\sigma_y(\tau)$ with no overlap and full overlap (16), (19), and for Mod $\sigma_y(\tau)$ [32–34] for the five noise types. In general, the confidence intervals for the fully overlapped $\sigma_y(\tau)$ are smaller than those for the non-overlapped $\sigma_y(\tau)$. For random-walk FM noise, the confidence intervals for the nonoverlapped and the fully overlapped $\sigma_y(\tau)$ are approximately the same, although Table 3 shows a small degradation when using fully overlapped estimates. This degradation is due to the approximations used in the analytical expressions. Table 3 also shows that the confidence intervals for the fully overlapped Allan deviation are smaller than the ones for the fully overlapped modified Allan deviation. Nevertheless, the modified deviation is generally smaller than the Allan deviation, and thus the absolute confidence intervals for the two are similar.

BIBLIOGRAPHY

1. E. S. Ferre-Pikal et al., Draft Revision of IEEE Std 1139-1988: Standard definitions of physical quantities for fundamental frequency and time metrology—random instabilities, *Proc. 1997 IEEE Int. Freq. Control Symp.*, 1997, pp. 338–357.
2. R. L. Sydner and D. W. Allan, eds., *Handbook Selection and Use of Precise Frequency and Time Systems*, International Telecommunication Union, Geneva, Switzerland, 1997.
3. International Radio Consultative Committee (CCIR), Report 580, *Characterization of Frequency and Phase Noise*, 1986, pp. 142–150.
4. H. Hellwig, *Frequency Standards and Clocks: A Tutorial Introduction*, Technical Note 616, U.S. National Bureau of Standards, Washington, DC, 1977.
5. J. R. Vig and F. L. Walls, Fundamental limits on the frequency stabilities of crystal oscillators, *IEEE Trans. Ultrason. Ferroelectr. Freq. Control* **42**:576–589 (1995).
6. *IEEE Guide for Measurements of Environmental Sensitivities of Standard Frequency Generators*, IEEE Std. 1193, IEEE Press, Piscataway, NJ, 1994.
7. W. D. Lee et al., The accuracy evaluation of NIST-7, *IEEE Trans. Instrum. Meas.* **44**:120–124 (1995). (An example of evaluating the uncertainties of an atomic frequency standard.)
8. B. N. Taylor and C. E. Kuyatt, *Guidelines for Evaluating and Expressing the Uncertainty of NIST Measurement Results*, Technical Note 1297, National Institute of Standards and Technology, Washington, DC, 1994.
9. F. L. Walls, The influence of pressure and humidity on the medium and long-term frequency stability of quartz oscillators, *Proc. 42nd Annual Symp. Frequency Control*, 1988, Baltimore, MD, pp. 279–283.
10. J. J. Gagnepain, Sensitivity of quartz oscillators to the environment: Characterization methods and pitfalls, *IEEE Trans. Ultrason. Ferroelectr. Freq. Control* **37**:354 (1990).
11. F. L. Walls and J. J. Gagnepain, Environmental sensitivities of quartz oscillators, *IEEE Trans. Ultrason. Ferroelectr. Freq. Control* **39**:241–249 (1992).
12. J. R. Vig and T. R. Meeker, The aging of bulk acoustic wave resonators, filters and oscillators, *Proc. 45th Annual Symp. Frequency Control*, Los Angeles, CA, 1991, pp. 77–101.

13. J. A. Barnes et al., Characterization of frequency stability, *IEEE Trans. Instrum. Meas.* **IM-20**:105–120 (1971).
14. D. W. Allan et al., Standard Terminology for fundamental frequency and time metrology, *Proc. 42nd Annual Symp. Frequency Control*, Baltimore, MD, 1988, pp. 419–425.
15. D. B. Sullivan et al., *Characterization of Clocks and Oscillators*, Technical Note 1337, National Institute of Standards and Technology, 1990.
16. D. A. Howe, D. W. Allan, and J. A. Barnes, Properties of signal sources and measurement methods, *Proc. 35th Annual Symp. Frequency Control*, 1981, pp. A1–A47; also in Ref. 4.
17. T. E. Parker, Characteristics and sources of phase noise in stable oscillators, *Proc. 41st Annual Symp. Frequency Control*, Philadelphia, PA, 1987, pp. 99–110.
18. L. M. Nelson, C. W. Nelson, and F. L. Walls, Relationship of AM noise to PM noise in selected RF oscillators *IEEE Trans. Ultrason. Ferroelectr. Freq. Control*, **41**:680–684 (1994).
19. F. L. Walls, Correlation between upper and lower noise sidebands, *Proc. 1998 IEEE Int. Frequency Control Symp.*, Pasadena, CA, 1998, pp. 199–203.
20. S. R. Stein, Frequency and time—their measurement and characterization, in E. A. Gerber and A. Ballato, eds., *Precision Frequency Control*, Academic Press, New York, 1985, Vol. 2, Chapter 12.
21. D. W. Allan and J. A. Barnes, Modified Allan variance with increased oscillator characterization ability, *Proc. 35th Annual Symp. Frequency Control*, Philadelphia, PA, 1981, pp. 470–474.
22. D. A. Howe, An extension of the Allan variance with increased confidence at long-term, *Proc. 1995 IEEE Int. Frequency Control Symp.*, San Francisco, CA, 1995, pp. 321–329.
23. D. A. Howe, Methods of improving the estimation of long-term frequency variance, *Proc. European Frequency and Time Forum*, Swiss Foundation for Research in Microtechnology, Neuchatel, Switzerland, 1997, pp. 91–99.
24. D. A. Howe and C. A. Greenhall, Total variance: A progress report on a new frequency stability characterization, *Proc. 29th Annual Precise Time Time Interval PTTI Systems Applications Meeting*, Long Beach, CA, 1997, pp. 39–48.
25. F. L. Walls et al., Time-domain frequency stability calculated from the frequency domain: An update, *Proc. 4th European Frequency and Time Forum*, Swiss Foundation for Research in Microtechnology, Neuchatel, Switzerland, 1990, pp. 197–204.
26. P. Lesage and C. Audoin, Characterization and measurement of time and frequency stability, *Radio Sci.* **14**(4):521–539 (1979).
27. P. Lesage and T. Ayi, Characterization of frequency stability: Analysis of the modified Allan variance and properties of its estimate, *IEEE Trans. Instrum. Meas.* **IM-33**:332–336 (1984).
28. C. A. Greenhall, Does the Allan variance determine the spectrum? *Proc. 1997 Int. IEEE Frequency Control Symp.*, Orlando, FL, 1997, pp. 358–365.
29. F. L. Walls and S. R. Stein, *Servo Techniques in Oscillators and Measurement Systems*, Technical Note 692, U.S. National Bureau of Standards, Washington, DC, 1976, pp. 1–20.
30. J. Rutman and F. L. Walls, Characterization of frequency stability in precision frequency sources, *Proc. IEEE* **79**:952–960 (1991).
31. F. Vernotte et al., Oscillator noise analysis: multivariate measurement, *IEEE Trans. Instrum. Meas.* **IM-42**:342–350 (1993).
32. T. Walter, Characterizing frequency stability: A continuous power-law model with discrete sampling, *IEEE Trans. Instrum. Meas.* **IM-43**:69–79 (Feb. 1994).
33. C. A. Greenhall, Estimating the modified Allan variance, *Proc. 1995 IEEE Int. Frequency Control Symp.*, San Francisco, CA, 1995, pp. 346–353.
34. M. A. Weiss et al., Confidence on the modified Allan variance, *Proc. 9th European Frequency Time Forum*, Besancon, France, 1995, pp. 153–165.

FREQUENCY SYNTHESIZERS

BAR-GIORA GOLDBERG
Sciteq Electronics, Inc.

Frequency synthesis is the engineering discipline dealing with generation of a single or of multiple tones, all derived from a common timebase, always a crystal oscillator.

Traditionally, frequency synthesis (FS) generated a single tone with variable frequency or amplitude. There are new applications, especially for testing and simulation, that require multitone generation and even arbitrary wave generation, which relate to digital frequency synthesis. Since the late 1970s, FS has evolved from mainly analog to a mix of analog, radiofrequency (RF), digital, and digital signal processing (DSP) technologies.

There are three major FS techniques:

1. *Phase-Locked Loop*. Also known as *indirect synthesis*, this is the most popular FS technique, based on a feedback mechanism that enables simplicity and economics via digital division and analog processing.
2. *Direct Analog*. An analog technique using multiplication, division, and mix filtering, this offers excellent signal quality and speed.
3. *Direct Digital*. This DSP method generates and manipulates the signal in the numbers (digital) domain and eventually converts to its analog form via a digital-to-analog converter.

Frequency synthesis is a mature technology yet is evolving rapidly. The traditional analog designs are supplemented with ever-increasing digital and DSP methods and technologies. These allow a high level of integration, lower power, manufacturing uniformity (and thus yield uniformity), and low cost. Although a novel technology in 1979, FS and especially the phase-locked loop (PLL) are very popular, accessible, and economical. Traditionally, FS started to enter the field of electronics as quite bulky and expensive instruments, using multiple crystals and complex analog processing functions such as mixing, filtering, and division. Better architectures and simpler designs have replaced these. Accelerating integrated circuit (IC) technology and high-level integration silicon now offer complete synthesizers, especially PLL and direct digital synthesizers (DDSs) on a single chip and sometimes more than one on a single die (Tables 1 and 2).

Table 1. Integrated Circuits Used in Phase-Locked Loops

Fujitsu Semiconductors: MB15xx
National Semiconductors: 23xx
Philips: SA7025, SA8025, UMA1014
Motorola: MC145xxx
Plessey: SP55xx, SP56xx, SP88xx
Texas Instruments: TRF2020, 2050, 2052

In the engineering realm, all signals generated are *amplified and filtered noise*. There are no deterministic signals in nature. The cardinal issue for FS is therefore how clean these signals are and how close they come to a theoretical $\sin(\omega t)$. Such a theoretical signal will have all of its energy in a single spectral line. In reality, signal spectra have a noise distribution caused by amplitude modulation (AM) noise and phase perturbation, also known in FS as *phase noise*. Phase noise can be described by its spectral properties, usually its noise distribution designated in dBc/Hz, or its time equivalent, also known as “jitter”. Spectral distribution $L(fm)$ details the exact spectral shape of the signal’s noise and is defined by the single-sideband energy level of the signal at a specific offset from the carrier relative to the signal’s total energy. This detailed technique has become the de facto method used to describe and characterize phase noise (see Fig. 1).

For example, a 1000-MHz signal with a spectral noise characteristic of -70 dBc/Hz (dB is used almost exclusively because of the large ratios involved) at an offset of 1 kHz from the carrier means that at 1 kHz from the carrier (either 1000.001 or 999.999 MHz), the single-sideband noise power contained in 1 Hz bandwidth is 10^{-7} compared with the signal’s total power. The function $L(fm)$ that defines the noise distribution spectrum is always measured in decibels of the noise level. Note that the noise is part of the signal and that the integral energy under the $L(fm)$ curve is the signal total power (Fig. 1).

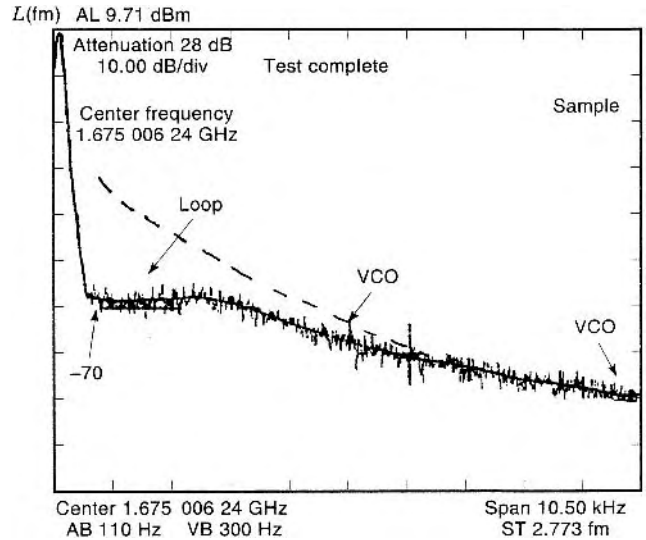
1. SYNTHESIZER PARAMETERS

1.1. Stepsize

This is also known as *resolution*, and it measures the smallest frequency increment the synthesizer can generate. As an example, an FS used in a North American cellular phone (AMPS—American Mobile Phone Service—standard), or time-division multiple access (TDMA), has 30 kHz resolution. In frequency modulation (FM) broadcasting radio, the step is usually 100 kHz.

Table 2. Integrated Circuits Used in Direct Digital Synthesis

Stanford Telecom: STEL-11xx and STEL-21xx
Analog Devices: AD7008, AD9830/9831, AD9720/9721
Sciteq Communications: SEI-432, SEI-631, DCP-1

**Figure 1.** Phase noise of a typical synthesizer.

1.2. Phase Noise

This parameter was already mentioned before. The issue of signal integrity, or otherwise the issue of the signal’s “cleanliness,” is the major challenge for FS designers. Long-term noise deals mainly with the accuracy, drift, and aging of the crystal, and short-term noise deals with rapid phase fluctuations.

1.3. Spurious Responses

These define the level of the discrete interferences, noise sources that are periodic and therefore exhibit spectral lines rather than a spectrum. These noise sources emerge from radiation—for example, line spurious responses at 60 Hz (US)—or from its multiples that always exist in the air and power supplies, as well as from other radiated energy that exists because of the enormous wireless traffic that is emerging and growing. Other sources are mixing products in the radio or synthesizer, nonlinearities, and ground currents.

1.4. Switching Speed

This defines the amount of time it takes the synthesizer to hop from a frequency F_1 to another F_2 . This parameter is usually measured in two ways: by checking when the new frequency settles to within a frequency tolerance (say, within 5 kHz), or (a more strict requirement) by checking the time it takes to settle to within a phase tolerance, in most cases to within 0.1 rad. The phase settling requirement can be as much as 3–5 times longer than the frequency settling.

1.5. Phase Transient

This defines the way the signal’s phase behaves in transition from frequency F_1 to frequency F_2 . There are three main ways to switch:

1. It might be a random parameter, so the phase is unknown after switching.

2. The phase can switch continuously, meaning that when switching from F_1 to F_2 , there will be no disturbance in the phase. Such switching requirements are necessary when generating linear FM signals or minimum shift keying (MSK) modulation, or other phase modulation waveforms.
3. In the case of phase memory, if switched from F_1 to F_2 and then back to F_1 , the signal's phase will be as if the switching did not occur. This is useful in coherent detection radars and frequency-hop communications.

1.6. Frequency Range

This defines the frequency band the FS covers.

1.7. Other Parameters

Other parameters are not unique to FS; these include output impedance, power flatness, size, power consumption, and the environment.

The main tools used in FS are as follows: multiplication by comb generation, addition and subtraction by mix and filtering, and division (digital) and feedback for PLL. Another cardinal principle in FS is as follows—multiplication by N corrupts phase noise and spurious by N^2 or $20 \log(N)$ dB; division improves by the same ratio.

2. SYNTHESIS TECHNIQUES

2.1. Direct Analog Synthesis

This method, the first to be used in FS, derives the signals directly from the reference—as compared to PLL, which it does indirectly. Direct analog uses building blocks such as comb generators, mix and filter, and dividers as the main tools. Many direct analog synthesizers use similar repeating blocks for resolution. These blocks usually generate a 10 MHz band in the ultra-high-frequency (UHF) range, in 1 MHz steps, and after division (mostly by 10) they are used as an input to the next similar stage. Every stage divides by 10, thereby increasing the resolution arbitrarily by as many stages as the designer chooses to use. Most direct analog synthesizers are instruments and traditionally use binary-coded decimal (BCD) for control. This is losing importance because a computer controls all modern applications.

Signals are therefore very clean because they are derived directly from the crystal; however, complexity is high and resolution comes at a high price. Direct analog synthesizers also achieve fast switching speed, limited mainly by filters propagation delay. Speed ranges from <1 to $50 \mu\text{s}$. Because there are no mechanisms to clean the signals at high offset frequencies from the carrier, their noise floor—where the phase noise levels—is comparatively (to PLL) high.

Direct analog synthesizers are available from DC to 26 GHz, are usually quite bulky and expensive, exhibit excellent phase noise and switching speed, and find applications in communications, radar, imaging, magnetic

resonance imaging, simulators, and automatic test equipment (ATE).

2.2. Direct Digital Synthesis (DDS)

DDS is a DSP technology based on the sampling theorem. The principle of its operation is based on storing the digital values of sine-wave amplitude in memory, then flushing these samples out by addressing the memory with an indexer. The indexer is always a digital accumulator, allowing the phase ramp (memory address) to change its slope to any value (compared with a counter that can index the RAM or ROM memory only by increments of 1).

As a consequence, the accumulator output can be interpreted as a signal phase, ωt (actually ωnT , where T is clock time, since it is sample data), with a variable slope given by the accumulator control. For example, if a 32 bit binary accumulator, which performs the function

$$S_n = S_{n-1} + W \quad (S_n \text{ is the output of sample } n, W \text{ is the input}) \tag{1}$$

is addressed with $W=0$, the output will not change, signifying direct current (dc) signal. However, if $W=1$, the accumulator will take 2^{32} clock ticks to come back to its original state. So a complete cycle of the phase from $\phi=0$ (accumulator is 0) to 2π (accumulator is full) takes 2^{32} ticks. Generally, a DDS output frequency is given by

$$F_o = F_{ck} W / \text{ACM} \tag{2}$$

where F_{ck} is the clock frequency, W is the input control, ACM is the accumulator size, and $W < \text{ACM}/2$.

For $\text{ACM} = 2^{32}$, $F_{ck} = 20 \text{ MHz}$, and $W = 1$, output frequency is given by $0.00465 \dots \text{ Hz}$, which is also the synthesizer resolution, its smallest step.

The read-only memory (ROM) output is connected to a digital-to-analog converter (DAC), which generates the analog signal smoothed by the output filter (see Fig. 2). According to the sampling theorem, the maximum output frequency is $F_{ck}/2$, also known as Nyquist frequency.

The various waveforms and modulation points are shown. Because the accumulator output is the signal phase, phase modulation can be applied; amplitude modulation can be applied at the output of the ROM, the amplitude point.

DDS is thus a numbers technology, related to frequency only by the clock. The artifacts caused by sampling generate many (mirror) frequencies as shown in the sampling theorem; these are usually referred to as aliasing frequencies.

DDS offers simplicity, economy, integration, and very fast switching speed. The digital nature of the technology offers design flexibility and simplicity, low-cost manufacturing, and very high density (small die).

As sampled data, DDS suffers the common problems of quantization. The level of accuracy determines the dynamic range of the design, in most cases 10–12 bits. The most significant weakness of DDS are limited bandwidth (clock frequencies are in the vicinity of 400 MHz

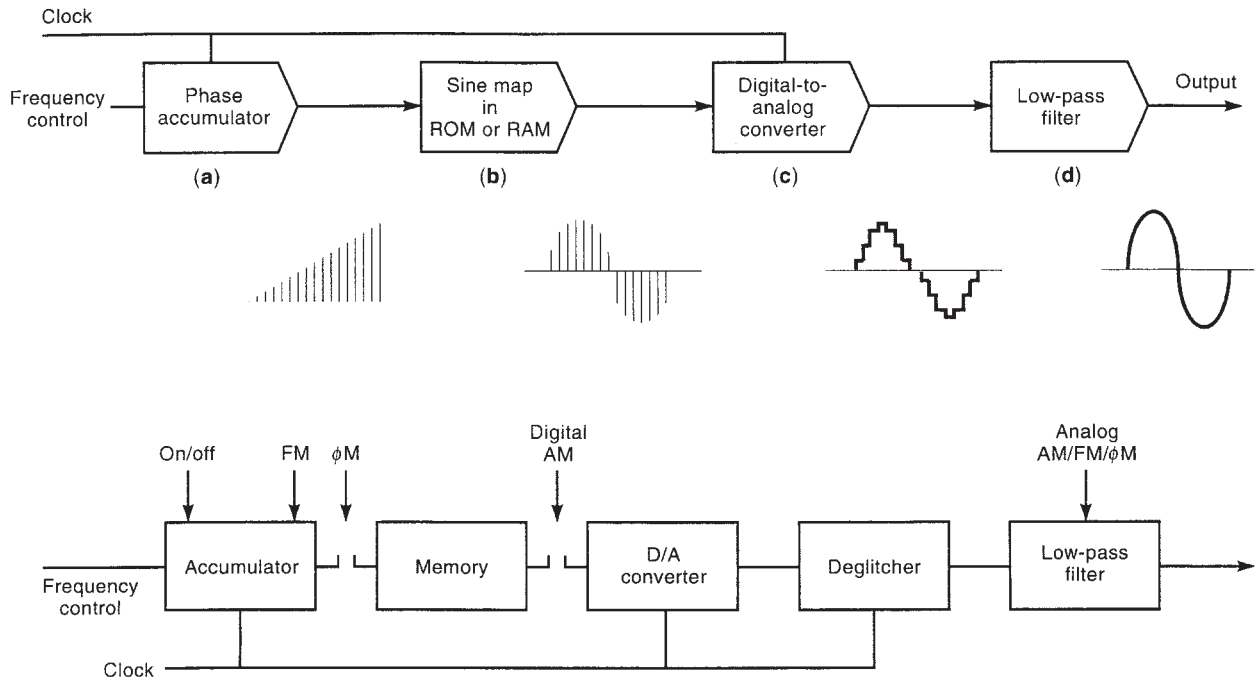


Figure 2. Direct digital synthesizer block diagram and functionality.

for CMOS devices and 1500 MHz for GaAs) and spurious response. Spurious responses are generally limited to $-6D$, where D is the number of bits used in the DAC. Thus a 10-bit DDS (using a 10 bit DAC) usually be limited to -60 dBC spurious responses. These spurious responses are either periodicities generated in the quantization process or intermodulation products generated by the DAC, the only analog part. As a rule of thumb, spurious performance deteriorates with increased output frequency or otherwise with decrease in samples per cycle. Arbitrary waveform generators (AWGs) are a superset of DDS. These enable the memory to be loaded with arbitrary wave samples, and then they sequentially flush the wave samples out. AWGs found use in simulation and testing.

2.3. Phase-Locked Loop

PLL is the technology of choice for generating radiofrequencies and microwave frequencies for radio applications. PLL, also known as *indirect synthesis*, is a negative-feedback loop structure that locks the phase of the output signal after division to the reference. Synthesis is simple because the variable counter (divider) N allows the generation of many frequencies F_o

$$F_o = NF_r \quad (F_o = \text{output frequency,} \\ F_r = \text{reference}) \quad (3)$$

by changing the division ratio N . Changing N is made easy by the use of dual modulus devices, capable of dividing by two (and sometimes more) ratios. For example, 64/65 or 128/129 are very common.

PLL chips are available in a great variety, in low power and at very low cost, and include all the functionality necessary with the exception of an external crystal, voltage-controlled oscillator (VCO) and loop filter (mainly resistors and capacitors). Convenience, economy, simplicity, and ease of use made PLL a household name used in television, radio, consumer electronics, cellular phones, and sat-com terminals, practically in almost any conceivable electronics radio (see Fig. 3).

When locked, PLL can be assumed to be a linear system, and classical feedback theory can be applied for analysis. The most common PLL structure is of second order, and there are two poles in the transfer function denominator: one from the VCO, with a Laplace domain transfer function given by K_v/s (K_v is the VCO constant, phase is the integral of frequency) and one from the loop filter having a memory device (capacitor). The loop transfer function is given by

$$\phi_o/\phi_i(s) = \frac{2\xi\omega_n s + \omega_n^2}{s^2 + 2\xi\omega_n s + \omega_n^2} \quad (4)$$

ω_n is the natural frequency and ξ is the damping, both borrowed from classical control theory. ω_n and ξ are given by (for the active loop structure shown in Fig. 4)

$$\omega_n = (K/T_1 N)^{0.5} \quad \text{and} \quad \xi = \omega_n T_2/2 \quad (5)$$

$T_1 = R_1 C$, $T_2 = R_2 C$, $K = K_v K_p/N$, K_v (Hz/V), and K_p (V/radian) are VCO and phase detector constants.

Overall performance is controlled by noise sources from phase detector, divider, and other active components within the loop bandwidth and by the VCO outside. Within the

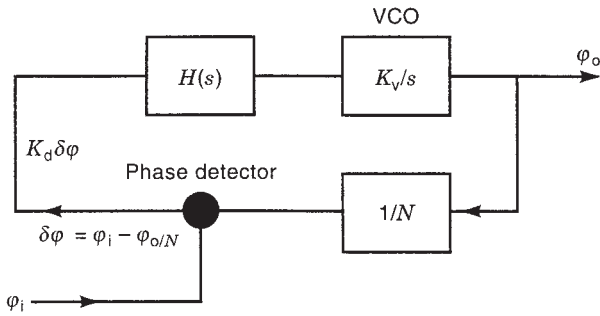


Figure 3. Phase lock loop block diagram.

loop bandwidth, VCO noise is suppressed by the loop. PLL noise sources within the loop are multiplied by $20 \log(N)$, which can be very significant when N is large. Typical phase detector noise is in the -150 dBc/Hz range for well-designed circuits. An advanced PLL technology known as fractional- n allows lowering N and generating step size smaller than F_r (hence fractional), thereby gaining phase noise performance. The fractional principle requires dynamic changes in division ratio N , thereby causing spurious signals, which are compensated by either extra filtering, analog feed forward correction (open loop), or digital waveshaping techniques.

FURTHER READING

R. E. Best, *Phase Lock Loops: Theory, Design and Applications*, McGraw-Hill, New York, 1984.
 F. M. Gardner, *Phaselock Techniques*, Wiley, New York, 1980.
 B.-G. Goldberg, *Digital Techniques in Frequency Synthesis*, McGraw-Hill, New York, 1996.
 V. Manassewitsch, *Frequency Synthesizers: Theory and Design*, Wiley, New York, 1983.

B. Miller and B. Conley, A multiple modulator fractional divider, *IEEE Trans. Instrum. Meas.* **40**:578–583 (1991).
 U. L. Rohde, *Digital PLL Frequency Synthesizers: Theory and Design*, Prentice-Hall, Englewood Cliffs, NJ, 1983.
 R. C. Stirling, *Microwave Frequency Synthesis*, Prentice-Hall, Englewood Cliffs, NJ, 1987.
 J. Tierney, C.M. Radar, and B. Gold, A digital frequency synthesizer, *IEEE Trans. Audio Electroacoust.* **AU-19**:48–57 (1971).

FRIIS FREE-SPACE TRANSMISSION FORMULA

CURT A. LEVIS
 The Ohio State University
 Columbus, Ohio

1. STATEMENT OF THE FORMULA

For a free-space transmission path, the power P_r available at the receiving antenna terminals is related to the power input P_t at the transmitting antenna terminals by the ratio

$$\frac{P_r}{P_t} = \frac{A_t A_r}{\lambda^2 R^2} \tag{1}$$

In this expression A_r denotes the effective area of the receiving antenna in the direction of the transmitter, A_t is the effective area of the transmitting antenna in the direction of the receiver, λ is the wavelength, and R is the distance separating the transmitting and receiving antennas, all measured in compatible units (e.g., both powers in watts, both areas in square meters, λ and R in meters). An alternative form is

$$\frac{P_r}{P_t} = \frac{G_t G_r \lambda^2}{(4\pi)^2 R^2} \tag{2}$$

where G_t and G_r denote, respectively, the gain of the transmitting antenna in the direction of the receiver and the gain of the receiving antenna in the direction of the transmitter, and λ and R must be given in the same units. For convenience, a decibel formulation is sometimes used. Such formulations are obtained from Eq. (2) by setting $\lambda = c/f$, where c is the free-space velocity of light and f the frequency, converting quantities to the desired units (e.g., R from meters to kilometers), taking the common logarithm of both sides of the resulting equation, and multiplying by 10. Algebraic and arithmetic manipulation then yield expressions such as

$$P_{r,\text{dBW}} = P_{t,\text{dBW}} + G_{t,\text{dB}} + G_{r,\text{dB}} - 20 \log_{10} R_{\text{km}} - 20 \log_{10} f_{\text{MHz}} - 32.4 \tag{3}$$

In this example of the decibel (dB) form of the formula, the power at the transmitting antenna terminals, and the power available at the receiving antenna terminals are expressed in dBW (i.e., the power relative to one watt expressed in decibels), the distance is given in kilometers, and the frequency is given in megahertz. Other units might have been used. The value of the constant (here -32.4)

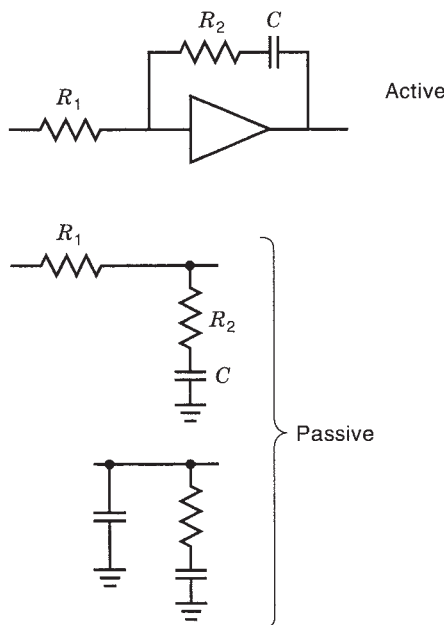


Figure 4. Second-order loop circuits.

depends on the units used. In the decibel form of the formula, the antenna gains are always specified in decibels.

2. ASSUMPTIONS

2.1. Free Space

The term “free space” implies that environmental effects, such as the effects of the ground and of the atmosphere, are negligible. This is sometimes a very good approximation. For example, in the case of a transmission from the Earth surface to a satellite appearing not too near the horizon in the frequency range 500 MHz–10 GHz, the antenna will usually be sufficiently directive to prevent substantial power from impinging on the ground. Also, in this frequency range atmospheric effects are small. Thus the Friis formulation is directly applicable. In other situations the free-space equation may be the starting formulation to which corrections for other effects (e.g., atmospheric attenuation, attenuation due to refraction by the ground) can be added. In fact, attenuation over a path is often specified as the attenuation relative to that for the same system in free space; the latter would be calculated by the Friis transmission formula [1].

2.2. Far Field

The antennas must be in the far field (Fraunhofer region) with respect to one another. This means that the distance must be sufficient so that the transmitted field at the receiving antenna is a spherical wave that may be approximated as a plane wave over the receiving antenna aperture. A frequently used criterion is that the longest and shortest paths between the two antenna apertures should not differ by more than $\frac{1}{16}$ wavelength.

2.3. Polarization

In this formulation it has been assumed that the polarization of the wave at the receiving antenna is optimal for that antenna; otherwise a polarization mismatch factor (in the decibel formula, a polarization mismatch term) must be included.

3. DERIVATION

Equations (1) and (2) can be derived easily from basic physical principles. For a lossless, isotropic transmitting

antenna the power applied to the input terminals would be spread uniformly over a sphere at radius R , giving a flux density

$$S_i = \frac{P_t}{4\pi R^2} \quad (4)$$

For an actual antenna, by the definition of antenna gain, the field in the receiver direction is obtained by

$$S = S_i G_t = \frac{P_t G_t}{4\pi R^2} \quad (5)$$

By definition of the effective area, the power available at the receiving antenna terminals for optimum polarization is given by

$$P_r = S A_r = \frac{P_t G_t A_r}{4\pi R^2} \quad (6)$$

Use of the relationship between gain and effective area

$$G = \frac{4\pi A}{\lambda^2} \quad (7)$$

then leads to either Equation (1) or (2).

4. HISTORICAL NOTE

The formulas (1) and (2) are named after Harald Trap Friis, who published Eq. (1) in 1946 while a research engineer at Bell Telephone Laboratories, Inc. [2] Mr. Friis later became Director of Research in High Frequency and Electronics at Bell Telephone Laboratories and was honored with numerous medals and awards for his technical work and his leadership.

BIBLIOGRAPHY

1. C. A. Levis, Friis free-space transmission formula, in J. G. Webster, ed., *Wiley Encyclopedia of Electrical and Electronics Engineering*, Wiley, New York, 1999. (The present article is adapted from that article.)
2. H. T. Friis, A note on a simple transmission formula, *Proc. IRE* (subsequently *Proc. IEEE*) **34**:254–256 (1946).

FURTHER READING

An interesting summary of derivations of the Friis formula from various perspectives can be found in D. C. Hogg, Fun with the Friis free-space transmission formula, *IEEE Anten. Propag. Mag.* **35**(4):33–35 (1993).

GALERKIN METHOD (RAYLEIGH–RITZ METHOD)

DANIEL S. WEILE
 RAYMOND A. WILDMAN
 GREESHMA PISHARODY
 ANURAAG MOHAN
 University of Delaware
 Newark, Delaware

1. INTRODUCTION

Galerkin’s method and the Rayleigh–Ritz method are perhaps the primary techniques used in the computational solution of boundary value problems and eigenvalue problems involving linear ordinary and partial-differential equations. Galerkin’s method is also used for the discretization of integral equations. In modern computational electromagnetics (CEM), these methods form the basis for the now ubiquitous method of moments (MoM) and finite-element method (FEM) [1–6]. While the Rayleigh–Ritz and Galerkin methods are in principle very different, they often lead to the same set of discretized equations, are closely related, and are often discussed as if they were identical.

Both methods assume that the unknown function in the problem at hand can be well approximated by a series of *basis* or *coordinate* functions with unknown coefficients, and both methods create a system of equations to solve for these unknown coefficients. Because both methods use basis functions, we will generically refer to Galerkin’s method and the Rayleigh–Ritz method collectively as *basis function approaches*.

In the Rayleigh–Ritz approach, the original problem is reformulated as a *variational problem*. More specifically, a *functional* (i.e., a function that maps functions to real numbers) is created that has a stationary point (most often a minimum) at the solution of the differential equation. The basis function series is then substituted into this functional, transforming the functional into a simple function of the unknown coefficients. Minimizing this function with respect to the unknown coefficients gives rise to a set of linear algebraic equations to be solved for the unknowns.

In the Galerkin approach, the basis function series is substituted directly into the equation at hand. This equation is then projected onto each of the basis functions in turn (in a manner to be explained in more detail below), again giving rise to a set of linear algebraic equations to be solved for the unknown coefficients.

Before discussing Galerkin’s method and the Rayleigh–Ritz method in more detail, we note that these methods are not the only methods used for the discretization of differential and integral equations. Alternative methods are used quite often in the CEM community, and a brief discussion of these approaches serves to define the Galer-

kin and Rayleigh–Ritz methods by contrast. In the differential equations realm, the primary competitors to basis function approaches are finite-difference methods [7–9]. Instead of approximating the unknown function as a series of basis functions, finite-difference methods seek to find the value of the unknown function on a (usually very regular) grid of points. The derivatives in the differential equations are then approximated by finite differences, leading to a set of linear algebraic equations to be solved for the values of the unknown function at the grid points.

The primary competitor to basis function approaches in the field of integral equations is the Nyström method [10,11]. In the Nyström method, the integral in the integral equation is approximated using a numerical quadrature rule, and the resulting equation is enforced at the quadrature points. This leads to a set of linear algebraic equations for the value of the unknown function at the quadrature points. Note that the primary difference between these techniques and the basis function approaches discussed here is that the former methods do not use basis functions at all, but instead seek to find the value of the unknown function at a set of points. Thus, the nomenclature “basis function approaches” serves to distinguish the methods described here from these other *point-based approaches*. [Actually, even the point-based approaches may be interpreted as basis function approaches with the proper choice of basis and testing functions. Nonetheless, as discussed above, the motivation for the point-based methods is completely different from that of the basis function approaches. Most importantly, their governing equations can be (and usually are) derived without reference to basis function approaches at all.]

In the remainder of this article we discuss the two basis function approaches in detail. Section 2 relates a brief history of the two basis function approaches. Section 3 discusses the Rayleigh–Ritz method and provides examples of its application. The same is done for the Galerkin approach in Section 4. Finally, Section 5 briefly discusses the MoM and FEM, and gives a few examples of their applications.

2. A BRIEF HISTORY OF BASIS FUNCTION APPROACHES

The history of basis function approaches begins with the prolific third Lord Rayleigh (John William Strutt). Rayleigh was one of the most accomplished physicists of the late nineteenth and early twentieth centuries; his accomplishments include the first correct explanation of the blueness of the sky, and the discovery of the inert gas argon for which he received the Nobel prize in 1904 [12]. (Indeed, Rayleigh was so famous even in his own time that he succeeded no less a physicist than James Clerk Maxwell to become the second Cavendish professor of experimental physics at Cambridge University [12].) In his book *The Theory of Sound* [13], Rayleigh describes a method for the approximate determination of the lowest frequency of vibration of an acoustical system. To verify the method, he

first applies it to the problem of determining the lowest frequency of vibration of a stretched string. His argument and conclusions are presented here in a modernized notation.

Consider a string length l with a constant mass density ρ and tension τ . The string is supposed to exist along the line segment $-l/2 \leq x \leq l/2$, and its height at position x and time t will be denoted by $y(x,t)$. Now, a natural mode of the string occurs when $y(x,t)$ is nonzero in the absence of an external driving force. Since the natural modes of lossless linear systems are always sinusoidal, the displacement of the string may be taken to be

$$y(x,t) = v(x) \cos \omega t \tag{1}$$

The total kinetic energy of the string can be expressed as

$$T(t) = \frac{1}{2} \int_{-l/2}^{l/2} \rho \left(\frac{\partial y}{\partial t} \right)^2 dx = \omega^2 \sin^2 \omega t [\tilde{T}(v)] \tag{2}$$

where

$$\tilde{T}(f) = \frac{1}{2} \int_{-l/2}^{l/2} \rho [v(x)]^2 dx \tag{3}$$

Similarly, the total potential energy of the string may be written as

$$V(t) = \frac{1}{2} \int_{-l/2}^{l/2} \tau \left(\frac{\partial y}{\partial x} \right)^2 dx = \cos^2 \omega t [\tilde{V}(v)] \tag{4}$$

where

$$\tilde{V}(f) = \frac{1}{2} \int_{-l/2}^{l/2} \tau [v'(x)]^2 dx \tag{5}$$

and the prime denotes differentiation.

The requirement that the energy of the system remain constant implies that

$$\frac{d}{dt} [T(t) + V(t)] = 0 \tag{6}$$

So long as $\omega \neq 0$ (which indicates a trivial solution anyway), the value of ω corresponding to a given $v(x)$ that solves the appropriate wave equation is given by

$$\omega^2 = \frac{\tilde{V}(v)}{\tilde{T}(v)} \tag{7}$$

In the paragraph preceding his derivation of this result (which was slightly different than that presented here), Rayleigh made a heuristic argument for discrete problems that demonstrates that the minimum positive value of ω delivered by this expression (over all admissible functions v) is in fact the minimum frequency of free vibration of the system. He then suggested that formulas of the form of Eq. (7) might be useful for computing the minimum free vibration frequency of systems. Specifically, if a function

$v(x)$ is a good approximation to the true solution, in error by a linear quantity Δv , then the approximation of ω^2 will be in error only by a quantity of order $(\Delta v)^2$. Moreover, if a set of functions $\tilde{u}_n(x)$ is substituted into Eq. (7), the best estimate of ω^2 is necessarily the smallest.

For the problem given above, the true solution is found when

$$v(x) = u(x) = \cos\left(\frac{\pi x}{l}\right) \tag{8}$$

for which

$$\omega^2 = \frac{\pi^2 \tau}{\rho l^2} \tag{9}$$

(We will always use the variable v to indicate arbitrary functions, and the variable u to indicate true solutions. Trial solutions are indicated by \tilde{u}_n , where the subscript indicates some parameter defining the trial.) Rayleigh suggested testing the method with the set of functions

$$\tilde{u}_n(x) = 1 - \left(\frac{2|x|}{l}\right)^n \tag{10}$$

for $n \geq 1$, for which

$$\tilde{T}(\tilde{u}_n) = \frac{\rho l n^2}{(n+1)(2n+1)} \tag{11}$$

and

$$\tilde{V}(\tilde{u}_n) = \frac{2\tau n^2}{(2n-1)l} \tag{12}$$

These expressions lead to an approximation of the form

$$\omega_n^2 = \frac{2(n+1)(2n+1)}{2n-1} \frac{\tau}{\rho l^2} = \lambda_n^2 \frac{\tau}{\rho l^2} \tag{13}$$

From this expression, $\lambda_1 = \sqrt{12}$, off from the true value of π by a little more than 10%. Similarly, $\lambda_2 = \sqrt{10}$, a value in error by 0.65%. The best possible value of n is the one that minimizes Eq. (13); this value is $n_{\text{opt}} = \frac{1}{2}(1 + \sqrt{6}) \approx 1.72474$. Using this value in Eq. (13) gives rise to the value $\lambda_{n_{\text{opt}}} = 3.1463$ and a scant error of 0.149%.

Throughout the rest of *The Theory of Sound*, Rayleigh continues to apply this method to problems that cannot be solved analytically, especially problems involving inhomogeneous material parameters. While Rayleigh’s method as presented above has been superceded by the Ritz (i.e., Rayleigh–Ritz) method described below, Rayleigh quotients similar to Eq. (7) are still used today in numerical linear algebra in the eigenvalue computation technique known as *Rayleigh quotient iteration* [14].

Rayleigh’s method was generalized by the Swiss physicist Walther Ritz shortly before he died of tuberculosis in 1909 [15]. Specifically, Ritz proposed a method for the solution of physical problems expressed variationally;

that is, as the minimization of some functional. Suppose that a given physical problem involves the minimization of a functional $F(v)$, where v is an arbitrary admissible function. (Both eigenvalue problems and boundary value problems can be expressed in this way.) Ritz suggested that the solution u be approximated as a series of the form

$$u \approx \tilde{u}_N = \sum_{i=1}^N x_i u_i \tag{14}$$

where the x_i are unknown coefficients and the u_i are what Ritz called “coordinate functions” [16,17]. (In modern parlance, these would be deemed *basis functions*.) These basis functions are known functions that can well approximate the unknown function u . (Notationally, they are differentiated from the true solution by the existence of the subscript.) Substituting Eq. (14) into the functional yields a function of the x_i :

$$G(x_1, \dots, x_N) = F\left(\sum_{i=1}^N x_i u_i\right) \tag{15}$$

The difficult problem of minimizing the functional is now reduced to the simpler problem of minimizing G . Thus, the original problem can be approximately be solved by enforcing the equations

$$\frac{\partial G}{\partial x_i} = 0 \tag{16}$$

for $i = 1, \dots, N$. Ritz also showed that under certain conditions, if the basis function set u_i is complete as $N \rightarrow \infty$, then the solutions obtained will converge to the true solution [18]. (In addition, he asserted that it not possible, in general, to say the same about the convergence of the derivatives.) Ritz applied his method to find the deflection of a fixed plate under a normal load, to solve Dirichlet’s problem for the Laplace equation, to the computation of the natural oscillation frequencies of a string, and to many other more complex problems [16,17].

After Ritz, the story continues in Russia in 1913 where a naval architect named Ivan Grigorievich Bubnov was reviewing a paper on the stability of plates and beams written by Stephen Prokofyevich Timoshenko. Timoshenko was applying the Ritz method to the problem, and Bubnov noted that the same results could be achieved without resorting to variational expressions [18]. Specifically, Bubnov noted that the same equations generated by the Ritz method could be more easily derived by simply substituting the approximation of Eq. (14) into the original differential equation, and then multiplying the result by each basis function in turn and integrating over the domain. Bubnov apparently believed, however, that the basis functions needed to be orthogonal for the procedure to be applicable. Nonetheless, because of this contribution, the Galerkin method described below is often called the *Bubnov–Galerkin method*, especially in the Russian literature.

In 1915, Boris Grigorievich Galerkin published a paper entitled “Rods and plates. Series occurring in various

questions concerning the elastic equilibrium of rods and plates,” in which he introduced the method that now bears his name [19]. Formally identical to the method suggested by Bubnov, Galerkin’s method drops the condition that the basis functions be orthogonal. Furthermore, Galerkin makes no mention of the Rayleigh–Ritz method, quite possibly cementing his name in history.

Both the Rayleigh–Ritz method and the Galerkin method are used today in the numerical solution of partial-differential equations, and the Galerkin method is used in the solution of integral equations as well. Specifically, the Ritz method is used as the basis of the variational FEM with very little change. Many authors trace the development of the FEM to a 1943 paper by Richard Courant [15], who suggests that the Ritz method be used together with piecewise linear basis functions situated on a triangular mesh. Modern variationally based FEM algorithms differ little from this suggestion, and indeed the variational FEM can be accurately characterized as the Ritz method applied to finite basis functions.

Modern MoM and Galerkin-based FEM algorithms also differ little from Galerkin’s original outline. Some approaches derive the set of equations to be solved by multiplying the equation with a set of functions other than the original basis functions; this *weighted-residual method* is a straightforward generalization of the original Galerkin idea. (The functions iteratively multiplied by the equation before integration are called *weighting* or *testing functions*. Indeed, many MoM papers refer to the use of the basis functions for testing as Galerkin testing. This serves to differentiate Galerkin’s specific choice from the more general approach discussed in Section 4.)

Since the history of basis function methods begins with Rayleigh and Ritz, our discussion of the methods begins with the method that today bears their names.

3. THE RAYLEIGH–RITZ METHOD

In this section, the Rayleigh–Ritz method is described in detail. Because variational approaches are not familiar to many readers, Section 3.1 describes the calculus of variations. Section 3.2 then discusses variational principles important in mathematical physics. The Rayleigh–Ritz method is finally described and applied to boundary value problems in Section 3.3. Finally, Section 3.4 describes the application of the Rayleigh–Ritz method to eigenvalue problems.

3.1. The Calculus of Variations

As mentioned in Section 2, a functional is a mapping from some space of functions to some field (usually complex or real numbers). In the context of the Rayleigh–Ritz method, the stationary point of such a functional corresponds to the solution of some differential equation under study. Thus, before proceeding to describe the Rayleigh–Ritz method in more detail, a bit of the variational calculus will be reviewed here. For simplicity, the discussion in this section is restricted to one dimension.

Consider the functional described by the integral

$$I(v) = \int_a^b F(x, v, v') dx \tag{17}$$

where v is a function of x and v' denotes the derivative of v . The central problem in the calculus of variations is the determination of the function v that gives a minimum or maximum value to this integral, subject to the restrictions

$$\begin{aligned} v(a) &= v_a \\ v(b) &= v_b \end{aligned} \tag{18}$$

Suppose that the minimum of Eq. (17) is achieved for some function $v(x) = u(x)$. We wish to determine the differential equation satisfied by u . Any other function that satisfies the boundary conditions [Eq. (18)] can be written as

$$v(x) = u(x) + \varepsilon h(x) \tag{19}$$

if $h(a) = h(b) = 0$. Moreover, in most variational approaches, the function h is assumed independent of ε . (This restriction is called the case of *weak variations* in the literature [20].) If the function F possesses continuous partial derivatives, an application of Taylor’s theorem gives

$$\begin{aligned} F(x, u + \varepsilon h, u' + \varepsilon h') \\ = F(x, u, u') + \varepsilon \left[h \frac{\partial F(x, u, u')}{\partial u} + h' \frac{\partial F(x, u, u')}{\partial u'} \right] + O(\varepsilon^2) \end{aligned} \tag{20}$$

The first variation of I is denoted by δI , and can be defined by the equation

$$\delta I = \lim_{\varepsilon \rightarrow 0} \frac{I(u + \varepsilon h) - I(u)}{\varepsilon} \tag{21}$$

From Eqs. (17), (20), and (21), the first variation of I is given by

$$\delta I = \int_a^b \left[h \frac{\partial F(x, u, u')}{\partial u} + h' \frac{\partial F(x, u, u')}{\partial u'} \right] dx \tag{22}$$

This “first variation” plays roughly the same role in the calculus of variations that the derivative plays in the standard calculus.

The form of Eq. (22) can be further simplified by applying integration by parts to the second term, and recalling that $h(a) = h(b) = 0$. This procedure gives a final form for δI :

$$\delta I = \int_a^b h \left\{ \frac{\partial F(x, u, u')}{\partial u} - \frac{d}{dx} \left[\frac{\partial F(x, u, u')}{\partial u'} \right] \right\} dx \tag{23}$$

Since the value of I depends linearly on ε , a minimum or maximum of I can be achieved only if $\delta I = 0$ independent of the choice of h . This observation leads directly to a differ-

ential equation first derived by Euler in 1744 [20], now known as the *Euler differential equation*:

$$\frac{\partial F(x, u, u')}{\partial u} - \frac{d}{dx} \left[\frac{\partial F(x, u, u')}{\partial u'} \right] = 0 \tag{24}$$

Much of physics can be formulated variationally, that is, as the minimization of an appropriate functional. The history of modern variational approaches to physics begins roughly with the work of Pierre de Fermat, and major contributions were made by a host of eminent physicists and mathematicians including Isaac Newton, Gottfried Wilhelm von Leibnitz, Johann and Jacob Bernoulli, Jean Le Rond d’Alembert, Joseph-Louis Lagrange, and William Rowan Hamilton [21].

The particular genius of Rayleigh and Ritz was not in this use of the calculus of variations to derive differential equations or formulate physical problems, but to convert it into a practical method for solving differential equations. Specifically, if the solution to a differential equation can be shown to minimize some functional, the Rayleigh–Ritz method approximates the solution through an appeal to the variational principle that describes it. (More generally, the solution of the differential equation may make the functional *stationary*, i.e., make its first variation vanish.) Since the Rayleigh–Ritz approach hinges on the creation of a variational principle, before discussing the method itself, we describe a variational principle useful in the solution of electromagnetic problems.

3.2. Variational Principles for the Scalar Helmholtz Equation

Consider the scalar Helmholtz equation

$$\mathcal{L}u = f \tag{25}$$

where \mathcal{L} is the linear Helmholtz operator

$$\mathcal{L}v = \nabla \cdot (p \nabla v) + k^2 qv \tag{26}$$

u is an unknown function defined on some closed domain Ω , k^2 is a constant, and p , q , and f are known real functions over the domain Ω . (For now, we assume that Ω is three-dimensional, but the derivation presented here can easily be specialized to fewer dimensions.) To completely characterize u , boundary conditions must also be specified on S , the boundary of Ω . To this end, assume that S is split into two nonoverlapping parts S_E and S_N . On S_E , the value of the function is specified; i.e.,

$$u = U \tag{27}$$

on S_E , where U is a given function. On S_N , the boundary condition is assumed to be

$$\frac{\partial u}{\partial n} + au = U' \tag{28}$$

where a and U are given functions, and $\partial u / \partial n$ denotes the outward normal derivative. (Of course, any of the given data, a , U , or U' , can be taken to be zero.)

We now show that the solution to this boundary value problem is the function that satisfies Eq. (27) and makes the functional

$$I(v) = \frac{1}{2} \iiint_{\Omega} [p \nabla v \cdot \nabla v - k^2 q v^2 + 2fv] d\Omega + \frac{1}{2} \iint_{S_N} p v [a v - 2U'] dS \tag{29}$$

stationary. Because the boundary condition of Eq. (28) is contained in the variational principle, it is said to be a *natural boundary condition*. Equation (27), on the other hand, is satisfied only by an explicit restriction of the domain of the functional, and is thus termed an *essential boundary condition*.

Using Eqs. (19) and (21), the first variation of I is given by

$$\delta I = \iint_{\Omega} [p \nabla u \cdot \nabla h - k^2 q u h + f h] d\Omega + \iint_{S_N} h p [a u - U'] dS \tag{30}$$

Now, simple differential identities allow the first term in δI to be simplified, since

$$p \nabla u \cdot \nabla h = \nabla \cdot [h p \nabla u] - h \nabla \cdot [p \nabla u] \tag{31}$$

Substituting this expression into Eq. (30) and applying the divergence theorem allows it to be written as

$$\delta I = - \iiint_{\Omega} h [\nabla \cdot (p \nabla u) + k^2 q u - f] d\Omega + \iint_{S_N} h \left[p \frac{\partial u}{\partial n} + a u - U' \right] dS \tag{32}$$

Because the function h is arbitrary, enforcing $\delta I = 0$ implies that each integral in Eq. (32) vanishes, which in turn implies Eqs. (25) and (28) as was asserted. Note that the application of the essential boundary condition is indeed essential; Eq. (32) implies that if nothing is done on S_E , the variational principle will enforce the condition

$$\frac{\partial u}{\partial n} = 0 \tag{33}$$

Similar variational principles may be derived for the vector Helmholtz equation, and may be found in Refs. 1 and 3.

3.3. Examples of the Rayleigh-Ritz Method for Boundary Value Problems

Now that variational principles have been described, the description of the Rayleigh-Ritz method itself is relatively simple. Suppose that a variational expression $I(v)$ for some differential equation is available. The unknown u is

approximated by a series \tilde{u} of the form

$$u \approx \tilde{u}_N = u_0 + \sum_{i=1}^N x_i u_i \tag{34}$$

where the u_i , $i = 0, \dots, N$, are known functions and the x_i , $i = 1, \dots, N$, are unknown coefficients. If there are essential boundary conditions of the form of Eq. (27), the function u_0 is assumed to satisfy them; if there are no such conditions, u_0 can be dropped. The remaining functions u_i , $i = 1, \dots, N$, satisfy the homogeneous form of Eq. (27), thus ensuring that the approximation of Eq. (34) satisfies the essential boundary conditions. As described in Section 2, substituting Eq. (34) into the functional gives rise to a function of the variables x_i . Stationary points of this functional satisfy the N equations

$$\frac{\partial I(\tilde{u}_N)}{\partial x_i} = 0 \tag{35}$$

which may then be solved to yield the x_i .

As a first simple example of the Rayleigh-Ritz method, consider finding the solution of the differential equation

$$\frac{\partial^2 u}{\partial t^2} = 36t^2 + 12t - 4 \tag{36}$$

subject to the boundary conditions

$$u(1) = u(-1) = 0 \tag{37}$$

The true solution to this problem, as is easily verified, is

$$u(t) = 3t^4 + 2t^3 - 2t^2 - 2t - 1 \tag{38}$$

According to the recipe above, the functional for this problem is given by

$$I(v) = \int_{-1}^1 \left[\frac{1}{2} \left(\frac{dv}{dt} \right)^2 + (36t^2 + 12t - 4)v \right] dx \tag{39}$$

Now, consider trial solutions of the form

$$\tilde{u}_N = \sum_{i=0}^{N-1} x_{i+1} t^i (t^2 - 1) \tag{40}$$

Note that each term in this series satisfies the homogeneous essential boundary conditions of Eq. (37). We examine the solutions given by the approximations \tilde{u}_1, \tilde{u}_2 , and \tilde{u}_3 .

For \tilde{u}_1 , the functional becomes

$$I(\tilde{u}_1) = \frac{4}{3} x_1^2 - \frac{64}{15} x_1 \tag{41}$$

Enforcing the condition of Eq. (35) gives the equation

$$\frac{8}{3} x_1 = \frac{64}{15} \tag{42}$$

Thus, $x_1 = \frac{8}{5}$, and the approximate solution is given by

$$\tilde{u}_1 = \frac{8}{5}t^2 - \frac{8}{5} \tag{43}$$

Using trial function \tilde{u}_2 gives rise to the function

$$I(\tilde{u}_2) = \frac{4}{3}x_1^2 + \frac{4}{5}x_2^2 - \frac{64}{15}x_1 - \frac{16}{5}x_2 \tag{44}$$

The gradient of this function vanishes when

$$\begin{bmatrix} \frac{8}{3} & 0 \\ 0 & \frac{8}{5} \end{bmatrix} \begin{bmatrix} x_1 \\ x_2 \end{bmatrix} = \begin{bmatrix} \frac{64}{15} \\ \frac{16}{5} \end{bmatrix} \tag{45}$$

giving rise to $x_1 = \frac{8}{5}$, $x_2 = 2$, and the approximate solution

$$\tilde{u}_2 = 2t^3 + \frac{8}{5}t^2 - 2t - \frac{8}{5} \tag{46}$$

Finally, using trial function \tilde{u}_3 , the functional becomes the function

$$I(\tilde{u}_3) = \frac{4}{3}x_1^2 + \frac{4}{5}x_2^2 + \frac{4}{105}x_3^2 + \frac{8}{15}x_1x_3 - \frac{64}{15}x_1 - \frac{16}{5}x_2 - \frac{64}{21}x_2 \tag{47}$$

The stationary point of this function occurs at the solution of the equations

$$\begin{bmatrix} \frac{8}{3} & 0 & \frac{8}{15} \\ 0 & \frac{8}{5} & 0 \\ \frac{8}{15} & 0 & \frac{8}{105} \end{bmatrix} \begin{bmatrix} x_1 \\ x_2 \\ x_3 \end{bmatrix} = \begin{bmatrix} \frac{64}{15} \\ \frac{16}{5} \\ \frac{64}{21} \end{bmatrix} \tag{48}$$

which is at the point $x_1 = 1$, $x_2 = 2$, $x_3 = 3$. In particular, $\tilde{u}_3 = u$, the exact solution. The exact solution and the two other trial solutions are plotted in Fig. 1.

A few comments about these results are in order. The error in each result can be computed in the relative L_2 norm; that is, the error in an approximate solution \tilde{u} relative to the true solution can be written as

$$\text{Error} = \frac{\int_{-1}^1 (u - \tilde{u})^2 dt}{\int_{-1}^1 u^2 dt} \tag{49}$$

Using this error criterion, the error in \tilde{u}_1 is about 29.3%, and that in \tilde{u}_2 is 9.6%. Of course, \tilde{u}_3 is exact.

The large error in the first two approximations can be traced to the fact that they simply cannot curve enough to capture the true behavior of the solution. On the other hand, the third approximation is exact because the true solution lies in the space spanned by the basis functions

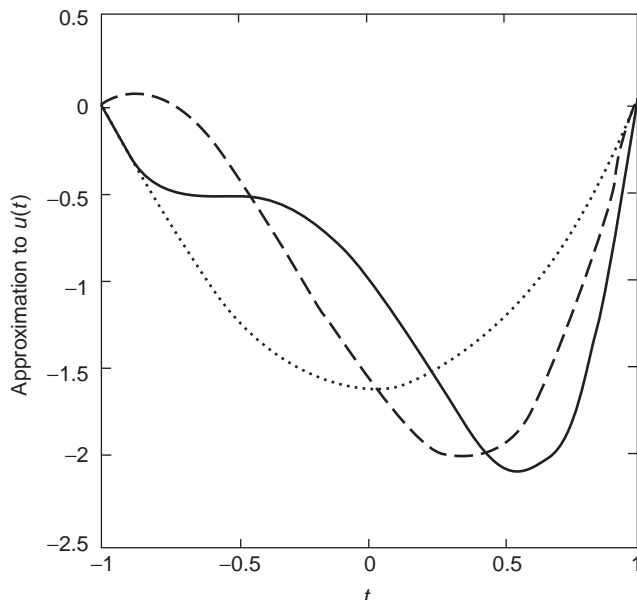


Figure 1. Approximate solutions of the boundary value problem of Eqs. (36) and (37) using the Rayleigh–Ritz method. The dotted line is \tilde{u}_1 , the dashed line is \tilde{u}_2 , and the solid line is $\tilde{u}_3 = u$.

used to construct it; that is, since the exact solution can be represented by \tilde{u}_3 with a proper choice of coefficients, the Rayleigh–Ritz method returns the exact solution. This highlights (in a fairly trivial way) the importance of basis function selection in the Rayleigh–Ritz method; a judicious choice of basis leads to good results fast, while a poor choice of basis may result in a poor approximation. Nonetheless, if a given set of basis functions is complete (i.e., can represent any function as the number of bases becomes large), the result will eventually converge.

The inclusion of inhomogeneous essential conditions creates no major problems. Consider, for instance, the problem of solving Eq. (36), subject to the boundary conditions

$$u(1) = -u(-1) = 1 \tag{50}$$

The inclusion of these boundary conditions necessitates adding a nonzero u_0 function to the trial function of Eq. (40) that satisfies the boundary conditions. The simplest way to satisfy this criterion is to make the new trial function

$$\tilde{u}_N = t + \sum_{i=0}^{N-1} x_{i+1} t^i (t^2 - 1) \tag{51}$$

and repeat the process. Substituting this function into the functional does not alter it in any way except by adding a meaningless value of 2 to the function $I(\tilde{u}_N)$. (The added value is meaningless in that it is annihilated by differentiation in the minimization of the function.) The reason for the simple result is clear; the exact solution to the new boundary value problem is just

$$u(t) = 3t^4 + 2t^3 - 2t^2 - t - 1 \tag{52}$$

which is just the old solution, plus the new term t . Choosing a different function to satisfy Eq. (50) would lead to different results in general, but exact results will always be obtained once the true solution can be expressed exactly in terms of the basis functions. (In particular, if u_0 is chosen to be t^3 instead of t , the solutions \tilde{u}_1 and \tilde{u}_2 will change, but \tilde{u}_3 will still be exact. If instead $u_0 = t^5$, the exact solution will not be obtained until $N = 4$.) In short, inhomogeneous essential boundary conditions do not alter the procedure significantly.

We now examine Eq. (36) under natural boundary conditions. To begin, note that in general Eq. (36) is incompatible with the simplest natural boundary condition, the homogeneous Neumann condition $u'(1) = u'(-1) = 0$. This is because integrating Eq. (36) between -1 and 1 gives

$$u'(1) - u'(-1) = 32 \tag{53}$$

where the homogeneous Neumann boundary condition requires this difference to vanish. The Rayleigh-Ritz method cannot save us from an improperly formulated problem!

Thus, consider Eq. (36) subject to the boundary conditions

$$\begin{aligned} -u'(-1) + u(-1) &= 1 \\ u'(1) - 4u(1) &= 2 \end{aligned} \tag{54}$$

The exact solution to this problem is given by

$$u(t) = 3t^4 + 2t^3 - 2t^2 \tag{55}$$

The functional for this problem can be constructed with reference to Eqs. (25)–(29), but only with some care. For instance, the surface integral in Eq. (29) must be interpreted as merely the value of the integrand at the endpoints. Similarly, the normal derivative in Eq. (28) should be interpreted as the usual derivative of the function at the right endpoint of the interval, and minus the usual derivative at the left endpoint of the interval. [The first boundary condition in Eq. (54) is written in a form that makes this explicit.] With these caveats in mind, the functional to be minimized for this problem is

$$\begin{aligned} I(v) = \int_{-1}^1 \left[\frac{1}{2} \left(\frac{dv}{dt} \right)^2 + (36t^2 + 12t - 4)v \right] dx \\ + \frac{1}{2}v^2(-1) - 2v^2(1) - v(-1) - 2v(1) \end{aligned} \tag{56}$$

For this case, the trial function series will be constructed as

$$\tilde{u}_N = \sum_{i=0}^{N-1} x_{i+1} t^i \tag{57}$$

Substituting this trial function into the functional yields a function of the form

$$I(\tilde{u}_N) = \frac{1}{2} \mathbf{x}^T \mathbf{A} \mathbf{x} - \mathbf{b}^T \mathbf{x} \tag{58}$$

where \mathbf{b} and \mathbf{x} are column vectors of N elements and \mathbf{A} is an $N \times N$ matrix. Specifically, the i th element of \mathbf{x} is x_i , and the i th element of \mathbf{b} is given by the formula

$$[\mathbf{b}]_i = \begin{cases} \frac{i-23}{i+1} & i \text{ even} \\ \frac{3i^2 - 58i + 16}{i^2 + 2i} & i \text{ odd} \end{cases} \tag{59}$$

and the elements of \mathbf{A} are given by

$$[\mathbf{A}]_{ij} = \begin{cases} \frac{2ij - 5i - 5j + 4}{i+j-1} & i+j \text{ even} \\ -5 & i+j \text{ odd} \end{cases} \tag{60}$$

The stationary point of this function occurs when $\mathbf{A}\mathbf{x} = \mathbf{b}$. Solving the set of equations for $N = 2, \dots, 5$ gives the solutions

$$\begin{aligned} \tilde{u}_2 &= 1 + 2t \\ \tilde{u}_3 &= -\frac{3}{5} + 2t + \frac{8}{5}t^2 \\ \tilde{u}_4 &= -\frac{3}{5} + \frac{8}{5}t^2 + 2t^3 \\ \tilde{u}_5 &= u = -2t^2 + 2t^3 + 3t^4 \end{aligned} \tag{61}$$

These solutions are plotted in Fig. 2. As expected, \tilde{u}_5 is exact, but the next best estimate, \tilde{u}_4 , is about 22% in error.

This example further clarifies issues involved both the Rayleigh-Ritz and Galerkin methods. First, problems

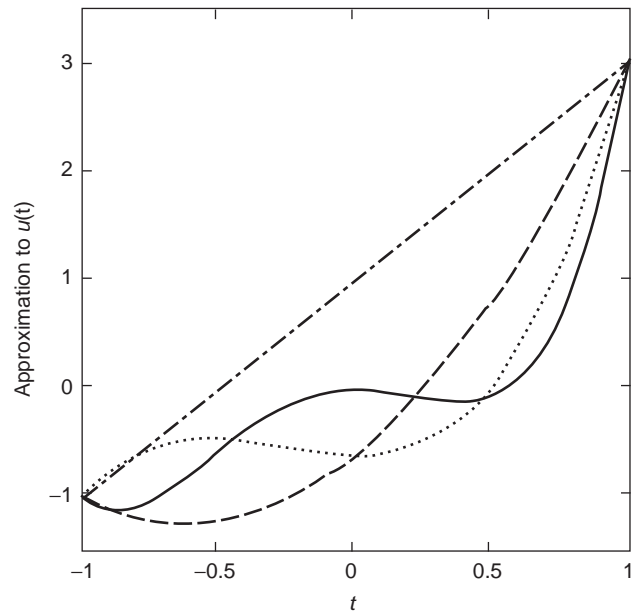


Figure 2. Approximate solutions of the boundary value problem of Eqs. (36) and (54) using the Rayleigh-Ritz method. The dashed-dotted line is \tilde{u}_2 , the dashed line is \tilde{u}_3 , the dotted line is \tilde{u}_4 , and the solid line is $\tilde{u}_5 = u$.

involving natural boundary conditions generally involve more unknowns than do those involving essential boundary conditions. In the cases presented here, it is clear that the exact solution to the differential equation is a fourth-order polynomial. In the case of natural boundary conditions, this implies that the solution has 5 degrees of freedom. (Here we chose the coefficient of each monomial term, but that specific choice is not necessary.) On the other hand, essential boundary conditions limit the choice of acceptable functions by forcing the functions with unknown coefficients to have a value of zero at both ends of the interval. In effect, for a one-dimensional problem, this reduces the number of degrees of freedom by 2. (In this case, the 2 degrees of freedom removed were the purely constant and linear terms, since neither of these terms can satisfy this condition.) In greater numbers of dimensions, the savings can be even more profound.

The second observation that can be made here concerns the choice of basis functions. The monomial basis functions chosen here are a particularly bad choice, in that as the order of the polynomials increases, the functions begin to resemble one another. Because of this, the condition number of the matrix **A** grows rapidly with increasing *N*. Indeed, the only reason that this is not obvious in the example presented is that the exact solution was obtained before the condition number increased too much. If the right-hand side of the differential equation were a higher-order polynomial, or some other arbitrary function, accurate results might require the inclusion of more monomials. Given the chosen basis, however, the inclusion of more monomial terms would vastly increase the condition number of the matrix, and thus potentially decrease the accuracy of the solutions. Figure 3, which plots the condition number of the matrix **A** versus the order of approximation *N*, shows just how serious the problem can become. With only 20 monomials, the condition number is

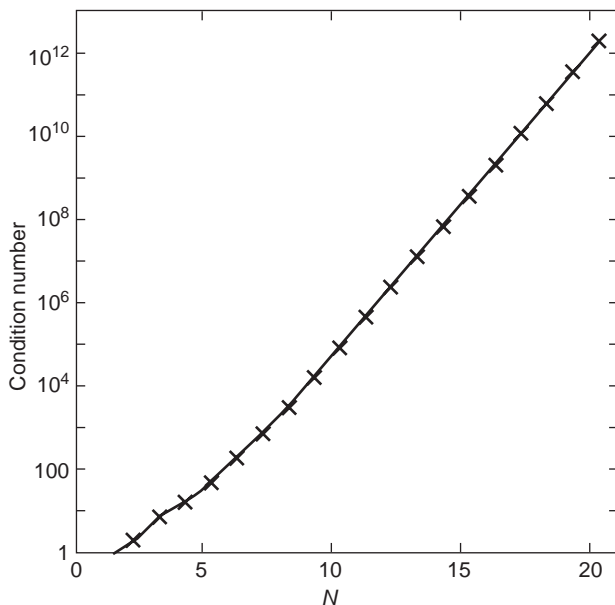


Figure 3. Condition number of the Rayleigh–Ritz matrix **A** in terms of approximation order for a monomial basis.

greater than 10^{12} , so the solution **x** loses 12 digits of accuracy relative to the accuracy with which **b** is computed.

3.4. The Rayleigh–Ritz Method for Eigenvalue Problems

As a final example of the Rayleigh–Ritz method, the fundamentally different eigenvalue problem is studied. We will see in this section, however, that the procedure for eigenvalue problems differs little from that for boundary value problems.

Consider the differential equation

$$\frac{d}{dt} \left(t \frac{du}{dt} \right) + k^2 t u = 0 \tag{62}$$

subject to the boundary conditions

$$u'(0) = u(1) = 0 \tag{63}$$

This equation will have solutions only for particular values of *k* called *eigenvalues*, and associated with each such *k* will be an *eigenfunction*. For Eq. (62), the eigenfunctions and eigenvalues are well known; in particular, the eigenfunctions of the equation are

$$u^m(t) = J_0(k_m t) \tag{64}$$

where J_0 denotes the zeroth-order Bessel function and k_m is its *m*th zero. [The superscript on *u* in Eq. (64) is used only to differentiate the *m*th eigenfunction, which will be denoted by a superscript, and the *m*th basis function, which is denoted by a subscript. The superscript is therefore not an exponent, but no confusion should arise as we will never have a need to exponentiate eigenfunctions.]

Using the recipe of Eqs. (25)–(29) leads to the functional for this problem, which may be written as

$$I(v) = \int_0^1 \left[t \left(\frac{dv}{dt} \right)^2 + k^2 t v^2 \right] dt \tag{65}$$

(The extraneous leading factor of $\frac{1}{2}$ has been dropped.) The trial function employed in this example will be

$$\tilde{u}_N = \sum_{n=1}^N x_n \cos(\kappa_n t) \tag{66}$$

where

$$\kappa_n = \frac{2n - 1}{2} \pi \tag{67}$$

These functions satisfy the essential boundary condition at $t = 1$, and even the natural boundary condition at $t = 0$. Of course, satisfaction of the natural boundary condition is not necessary, but since the problem statement implies that the solution will be an even function of *t*, the chosen basis functions seem a reasonable choice for the representation of the solution. (They are indeed the basis for even function Fourier series.)

Substituting the trial solution into the functional yields the function

$$I(\tilde{u}_N) = \mathbf{x}^T \mathbf{A} \mathbf{x} - k^2 \mathbf{x}^T \mathbf{B} \mathbf{x} \tag{68}$$

where, as usual, the vector \mathbf{x} contains the unknown coefficients x_n , $n = 1, \dots, N$, and \mathbf{A} and \mathbf{B} are $N \times N$ matrices. Defining the Krönercker delta symbol $\delta_{mn} = 0$ for $m \neq n$, and $\delta_{mm} = 1$, the elements of the matrices \mathbf{A} and \mathbf{B} are given by the expressions

$$[\mathbf{A}]_{mn} = \begin{cases} \frac{\kappa_m \kappa_n}{(\kappa_m + \kappa_n)^2} + \delta_{mn} \frac{\kappa_m^2}{4} & \text{for } m + n \text{ even} \\ -\frac{\kappa_m \kappa_n}{(\kappa_m - \kappa_n)^2} & \text{for } m + n \text{ odd} \end{cases} \quad (69)$$

$$[\mathbf{B}]_{mn} = \begin{cases} \frac{\delta_{mn}}{4} - \frac{1}{(\kappa_m + \kappa_n)^2} & \text{for } m + n \text{ even} \\ -\frac{1}{(\kappa_m - \kappa_n)^2} & \text{for } m + n \text{ odd} \end{cases} \quad (70)$$

The extremum of the functional of Eq. (68) occurs when

$$\mathbf{A}\mathbf{x} = k^2 \mathbf{B}\mathbf{x} \quad (71)$$

so the original problem has been reduced to a generalized algebraic eigenvalue problem. The eigenvalues of this problem (which we will denote by $K_{m,N}$) are approximations to the true eigenvalues, which in this case are the roots of the zeroth-order Bessel function. The eigenvectors, on the other hand, represent the weighting coefficients to be substituted into Eq. (66) to approximate the eigenfunctions. Since eigenvectors and eigenfunctions are unique only up to a multiplicative constant, all solutions related here have been scaled so that $\tilde{u}_N(0) = J_0(0) = 1$.

Figure 4 shows the first two approximations to the eigenfunction associated with the smallest eigenvalue returned by the Rayleigh–Ritz method. The true eigenvalue is given (to double precision) by $k_1 = 2.40482555769577$;

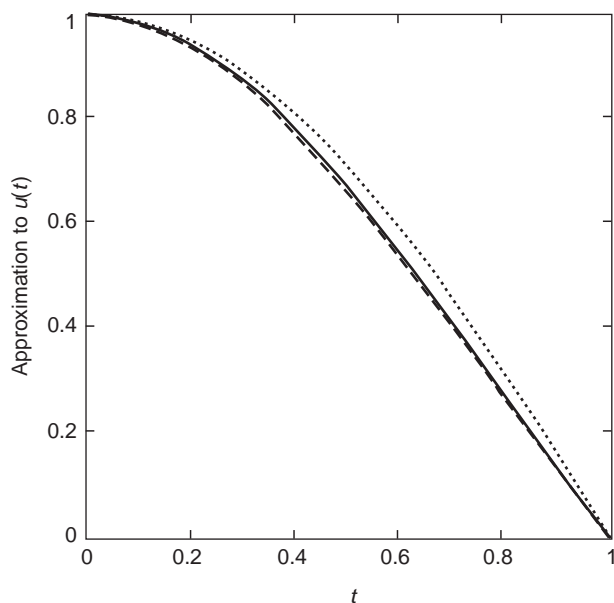


Figure 4. Approximations to $J_0(k_1 x)$: \tilde{u}_1 is shown as a dotted line, \tilde{u}_2 is shown as a dashed line, and $J_0(k_1 x)$ is shown as a solid line.

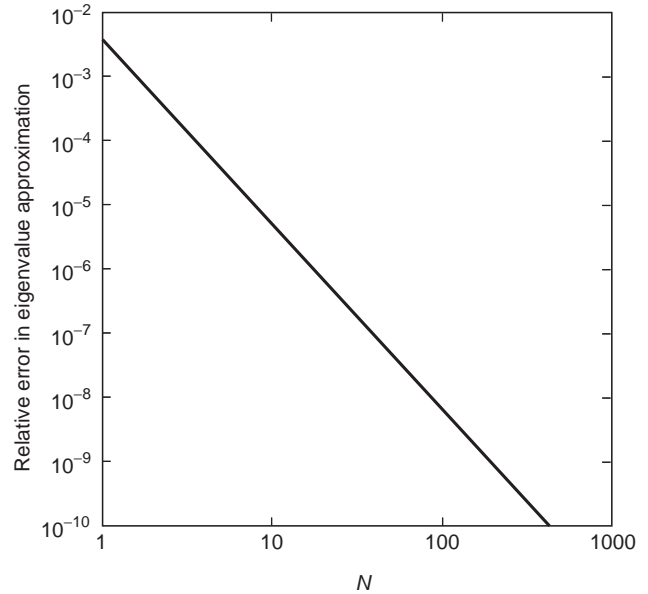


Figure 5. Convergence of the smallest eigenvalue as a function of the order of approximation.

the approximations associated with the two approximations shown in the figure are $K_{1,1} = 2.414$ and $K_{1,2} = 2.406$. These numbers represent relative errors of 0.41% and 0.056%, respectively. In contrast to the previous examples, this example illustrates how quickly the Rayleigh–Ritz method can converge with a good choice of trial function. Figure 5 shows the convergence of the eigenvalue approximation itself as a function of approximation. The order of convergence is nearly cubic.

This example also highlights some of the advantages of the Ritz method relative to Rayleigh’s original method. While Rayleigh’s method provides only an approximation to the smallest eigenvalue, the Ritz method actually provides estimates of all the lowest eigenvalues. For instance, taking the fifth smallest eigenvalue of the algebraic eigenvalue problem results in an approximation of the fifth smallest eigenvalue of the analytic problem. The true value of the fifth eigenvalue is given by $k_5 = 14.93091770848779$, and the first two estimates provided by the Rayleigh–Ritz method are $K_{5,5} = 14.9399$ and $K_{5,6} = 14.9325$, values that contain far less than one-tenth of one percent error.

4. GALERKIN’S METHOD

In this section, Galerkin’s method is described. The method itself is described in Section 4.1, and Section 4.2 discusses its relationship with the Rayleigh–Ritz method. Finally, Section 4.3 describes the weighted-residual method, which is a generalization of the Galerkin method.

4.1. Description of the Method

Galerkin’s method is used to solve equations involving linear operators. The operators may be integral operators, differential operators, or even integrodifferential operators.

For differential operators, the method is strongly related to the Rayleigh–Ritz method (as will be demonstrated in the next section), but it is much simpler to apply. (Indeed, this is the main reason why the Rayleigh–Ritz method takes up more space in this article than the Galerkin method, which is ostensibly the main topic.)

An operator \mathcal{L} is called *linear* if given two functions v and w , and two scalars a and b

$$\mathcal{L}(av + bw) = a\mathcal{L}v + b\mathcal{L}w \tag{72}$$

Galerkin’s method works by projecting the original operator equation, defined on a function space, onto a finite-dimensional vector space. This is accomplished with the help of an inner product. An *inner product* defined on a complex vector space (such as the space of all complex functions of N variables) is a complex scalar function of two vectors (functions) that satisfies certain criteria. If v , w , and s denote functions, and a and b are scalars, the inner product $\langle v, w \rangle$ must be

1. Linear, that is

$$\langle s, av + bw \rangle = a\langle s, v \rangle + b\langle s, w \rangle \tag{73}$$

2. Hermitian, that is

$$\langle v, w \rangle = \langle w, v \rangle^* \tag{74}$$

where the asterisk denotes complex conjugation.

3. Positive-definite, that is

$$\langle v, v \rangle \geq 0 \tag{75}$$

with equality only if $v = 0$ [22].

While this is the commonly accepted mathematical definition of inner products, in practical applications, products that are not positive definite are often used. Most often, such products are not Hermitian, but instead are symmetric:

$$\langle v, w \rangle = \langle w, v \rangle \tag{76}$$

(Generally, such products are also not positive definite.) In this article, we will not distinguish between the two, and refer to any linear and symmetric or Hermitian scalar functional of two functions as an inner product. In particular, over a three-dimensional domain Ω , the most common inner product definitions are

$$\langle v, w \rangle = \iiint_{\Omega} vwd\Omega \tag{77}$$

for scalar functions v and w , and

$$\langle \mathbf{v}, \mathbf{w} \rangle = \iiint_{\Omega} \mathbf{v} \cdot \mathbf{w}d\Omega \tag{78}$$

for vector functions \mathbf{v} and \mathbf{w} . If these products are defined over a real vector space, then the mathematical definition

of inner product is met by these functions. On the other hand, if these products are used over a complex vector space, they are not Hermitian or positive definite. Finally, note that these definitions extend trivially to an arbitrary number of dimensions.

Armed with this definition of inner product, Galerkin’s method is simple to describe. Consider the equation

$$\mathcal{L}u = f \tag{79}$$

where \mathcal{L} is a linear operator, u is an unknown function, and f is a known function. As in the Rayleigh–Ritz method, u is approximated by a series of basis functions of the form

$$u \approx \tilde{u}_N = u_0 + \sum_{i=1}^N x_i u_i \tag{80}$$

where the u_i are called basis functions, and the x_i are unknown basis function coefficients. As in the case of the Rayleigh–Ritz method, the extra function u_0 is included to satisfy inhomogeneous essential boundary conditions; we will ignore it for the time being and discuss it in the next section where boundary conditions are described.

Thus, assuming that there are no inhomogeneous essential boundary conditions, the approximation of Eq. (80) is substituted into Eq. (79). In view of the linearity of the operator, the resulting equation may be written as

$$\sum_{i=1}^N x_i \mathcal{L}u_i = f \tag{81}$$

Unfortunately, this equation is ill-posed; it is one equation in N unknowns. To create a set of N equations that can be solved for the x_i , the inner product of Eq. (81) can be taken with each basis function in turn. This procedure yields

$$\sum_{i=1}^N x_i \langle u_m, \mathcal{L}u_i \rangle = \langle u_m, \mathcal{L}f \rangle \tag{82}$$

for $m = 1, \dots, N$; a set of N equations in N unknowns.

The advantage of this method relative to the Rayleigh–Ritz approach should be obvious—the Galerkin approach does not require the creation of a functional, which may be difficult to find in some circumstances. The disadvantage of the Galerkin approach is that boundary condition application is not as elegant, and the difference between essential and natural boundary conditions is not as clear. Nonetheless, Galerkin’s method and the Rayleigh–Ritz method are closely related, as the discussion in the next section will demonstrate. (As was mentioned in the introduction, the genesis of Galerkin’s method can be found in I. G. Bubnov’s comment that the Rayleigh–Ritz equations could be derived more simply.)

4.2. Boundary Conditions and Relation to Rayleigh–Ritz

To demonstrate the application of boundary conditions in Galerkin’s method, and to elucidate its relation to the Rayleigh–Ritz method, we once again consider the model

problem defined by Eqs. (25)–(28). The first step in the Galerkin method is the creation of a trial function and its substitution into the equation. In this discussion, the trial function will be that given by Eq. (80), where, as usual, we assume that u_0 satisfies the inhomogeneous essential boundary condition on S_E , and that the remaining u_i satisfy the homogeneous version of the same essential boundary condition on S_E . Substituting the basis function series into the differential equation results in the specific equivalent of Eq. (81), a single equation in N unknowns given by

$$\sum_{i=1}^N x_i [\nabla \cdot (p \nabla u_i) + k^2 q u_i] = f - \nabla \cdot (p \nabla u_0) - k^2 q u_0 \quad (83)$$

To derive a set of N equations, this equation is multiplied by each of the functions u_m , $m = 1, \dots, N$, in turn, and integrated over the domain [i.e., the inner product of Eq. (83) is taken with each of the basis functions in turn.] This procedure yields a set of N equations that may be written as

$$\sum_{i=1}^N x_i \iiint_{\Omega} [u_m \nabla \cdot (p \nabla u_i) + k^2 q u_m u_i] d\Omega \quad (84)$$

$$= \iiint_{\Omega} [u_m f + u_m \nabla \cdot (p \nabla u_0) - k^2 q u_m u_0] d\Omega$$

This equation can be simplified using Eq. (31) (with $h = u_m$ and $u = u_i$) and the divergence theorem, resulting in

$$\begin{aligned} & \sum_{i=1}^N x_i \left\{ \iiint_{\Omega} [-p \nabla u_m \cdot \nabla u_i + k^2 q u_m u_i] d\Omega \right. \\ & \left. + \iint_S p u_m \frac{\partial u_i}{\partial n} dS \right\} \\ & = \iiint_{\Omega} [u_m f + p \nabla u_m \cdot \nabla u_0 - k^2 q u_m u_0] d\Omega \\ & - \iint_S p u_m \frac{\partial u_0}{\partial n} dS \end{aligned} \quad (85)$$

Now, the surface integrals in Eq. (85) vanish over S_E since the functions u_m satisfy homogeneous essential boundary conditions there by construction. On the other hand, on S_N , \tilde{u}_N must satisfy the natural boundary condition of Eq. (28). Substituting this equation into Eq. (85) yields

$$\begin{aligned} & \sum_{i=1}^N x_i \left\{ \iiint_{\Omega} [-p \nabla u_m \cdot \nabla u_i + k^2 q u_m u_i] d\Omega \right. \\ & \left. - \iint_{S_N} p a u_m u_i dS \right\} \\ & = \iiint_{\Omega} [u_m f + p \nabla u_m \cdot \nabla u_0 - k^2 q u_m u_0] d\Omega \\ & + \iint_{S_N} p u_m (a u_0 - U') dS \end{aligned} \quad (86)$$

for $m = 1, \dots, N$. This is the final form of the Galerkin equations.

Equation (86) may be related to the Rayleigh–Ritz approach for this problem very simply. Direct substitution of the trial function into the functional of Eq. (29) gives

$$\begin{aligned} I(\tilde{u}_N) = & \frac{1}{2} \sum_{i=1}^N \sum_{m=1}^N x_i x_m \left\{ \iiint_{\Omega} [p \nabla u_i \cdot \nabla u_m - k^2 q u_i u_m] d\Omega \right. \\ & \left. + \iint_{S_N} a p u_i u_m dS \right\} \\ & + \sum_{m=1}^N x_m \left\{ \iiint_{\Omega} [u_m f + p \nabla u_0 \cdot \nabla u_m - k^2 q u_0 u_m] d\Omega \right. \\ & \left. + \iint_{S_N} p u_m (a u_0 - U') dS \right\} \end{aligned} \quad (87)$$

if constant terms involving u_0 alone are ignored. (Such terms will be annihilated by differentiation in the Rayleigh–Ritz procedure.) Differentiating this equation with respect to each unknown and setting the result equal to zero clearly yields the same set of equations as the Galerkin method. Thus, all the examples of Section 2 apply equally well to Galerkin’s method. In particular, all the same integrals will be computed, and the equations derived will be identical (except for possibly a meaningless shared factor that multiplies all of the equations).

The close relationship between the Rayleigh–Ritz and Galerkin methods can be clarified by studying the methods from a geometric/linear algebraic point of view. For this discussion, we will assume that the inner product employed actually satisfies conditions 1–3 listed at the beginning of Section 4.1, and that we are dealing with real functions and operators. In this case, the norm (i.e., length) of a function (vector) can be defined by

$$\|v\|^2 = \langle v, v \rangle \quad (88)$$

Assume further that we are trying to solve Eq. (79), where \mathcal{L} is a *positive definite* operator, that is

$$\langle v, \mathcal{L}v \rangle \geq 0 \quad (89)$$

for all functions v , and equality holds only if $v = 0$. (Many physical problems in which the Rayleigh–Ritz method is applied involve positive definite operators. In particular, many variational principles are derived from energy considerations.)

Given that \mathcal{L} is positive definite, an alternative inner product (called the \mathcal{L} *inner product*) can be defined by the equation

$$\langle u, v \rangle_{\mathcal{L}} = \langle u, \mathcal{L}v \rangle \quad (90)$$

This inner product gives rise to its own norm (the \mathcal{L} norm)

$$\|v\|_{\mathcal{L}}^2 = \langle v, v \rangle_{\mathcal{L}} \quad (91)$$

much as the original inner product induced a norm. Assuming that \tilde{u}_N is a trial function defined in the usual way, we may seek to approximate the solution of Eq. (79) by demanding that the coefficients of \tilde{u}_N be chosen to minimize (half the square of) the \mathcal{L} norm of error given by

$$\begin{aligned} I(\tilde{u}_N) &= \frac{1}{2} \langle (u - \tilde{u}_N), \mathcal{L}(u - \tilde{u}_N) \rangle \\ &= \frac{1}{2} \langle \tilde{u}_N, \mathcal{L}\tilde{u}_N \rangle - \langle \tilde{u}_N, f \rangle + \frac{1}{2} \langle u, \mathcal{L}u \rangle \end{aligned} \quad (92)$$

This is the Rayleigh–Ritz approach.

Actually performing the minimization gives rise to N equations for the x_i , which may be written as

$$\sum_{i=1}^N x_i \langle u_m, \mathcal{L}u_i - f \rangle = 0 \quad (93)$$

for $m = 1, \dots, N$. These are the Galerkin equations. Moreover, Eqs. (93) can be written in the form

$$\langle u_m, (\tilde{u}_N - u) \rangle_{\mathcal{L}} = 0 \quad (94)$$

which shows that the Galerkin method imposes the condition that the error be \mathcal{L} orthogonal to the space spanned by the basis functions. Thus, in short, the equivalence of the Rayleigh–Ritz and Galerkin methods in many situations can be traced to the observation that the shortest distance between a point and a line is given by the orthogonal projection of the point onto the line. In fact, these observations are critical not only to the numerical formulation of electromagnetic problems but also to the creation of iterative solvers (like the conjugate-gradient method) that can be used to solve the equations once they are created [23].

4.3. Weighted-Residual Methods

The Galerkin method is actually a special case of a more general set of numerical techniques called *weighted-residual methods*. Weighted residual methods begin the solution of Eq. (79) in the same way as the Galerkin method—by inserting an appropriate combination of basis functions into the equation and arriving at Eq. (81). Instead of taking the inner product of Eq. (81) with the basis functions, however, weighted-residual methods take the inner product with a set of N testing functions v_m , $m = 1, \dots, N$, resulting in the set of equations

$$\sum_{i=1}^N x_i \langle v_m, \mathcal{L}u_i \rangle = \langle v_m, f \rangle \quad (95)$$

If $v_m = u_m$, Galerkin’s method is recovered.

Two other choices of testing function are worth mentioning. First, if the testing functions are taken to be Dirac delta functions shifted to testing points t_m , that is

$$v_m(t) = \delta(t - t_m) \quad (96)$$

the point collocation method is derived. Specifically, substituting Eq. (96) into Eq. (95) yields a set of equations of the form

$$\sum_{i=1}^N x_i (\mathcal{L}u_i)(t_m) = f(t_m) \quad (97)$$

The point collocation method thus enforces the original operator equation exactly over a finite set of points.

Second, in the least-squares method, the testing functions are chosen to be

$$v_m = \mathcal{L}u_m \quad (98)$$

Using these testing functions leads to a method that minimizes the (usual) norm of the residual. These alternative methods can be useful when the Galerkin method is difficult to apply for one reason or another. In particular, point collocation is often very simple to apply. On the other hand, the least-squares method has the advantage that it always leads to symmetric, positive definite systems of equations.

5. THE FINITE-ELEMENT METHOD AND THE METHOD OF MOMENTS

In this final section, we briefly describe FEM and MoM, the two most widespread applications of Galerkin’s method and the Rayleigh–Ritz method in electromagnetics. No attempt is made to make this discussion in any way complete; other articles in this encyclopedia cover these methods in detail.

The finite-element method is simply the application of the Rayleigh–Ritz or Galerkin method to differential equation problems using subsectional basis functions, that is, basis functions that do not span the entire problem domain. The FEM has a rather long history, as it was first suggested by Richard Courant during World War II [15].

As an example of the finite-element method, we will demonstrate how it can be used to determine the bandgap of a two-dimensional photonic bandgap (PBG) structure. The unit cell of the PBG lies in the x - y plane and is shown in Fig. 6. Unshaded areas correspond to free space, and shaded areas correspond to a material of relative permittivity $\epsilon_r = 13$ and relative permeability $\mu_r = 1$. The differential equation associated with this problem is Eq. (25), with $u = E_z$, the z component of the electric field, $p = 1/\mu_r$, $q = \epsilon_r$, $f = 0$, and $k = \omega/c$, where c is the speed of light in vacuum and ω is the angular frequency of the wave. Because the structure is periodic, the wave must satisfy the Floquet boundary condition, that is

$$\begin{aligned} u(S_R) &= u(S_L) \exp(-jk_x d - jk_y d) \\ u(S_T) &= u(S_B) \exp(-jk_x d - jk_y d) \end{aligned} \quad (99)$$

where d is the length of a side of the unit cell (which will be taken as unity in this example) and k_x and k_y are real numbers. This is an essential boundary condition.

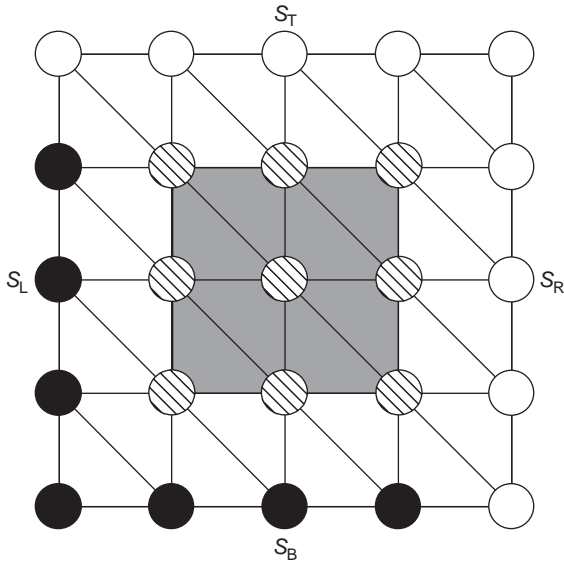


Figure 6. A meshed PBG structure. Circles indicate node locations.

The goal in the solution of this eigenvalue problem is to find the frequencies of propagation allowed for each combination of k_x and k_y , and in particular to determine whether there are any frequency ranges in which propagation is disallowed. (The eigenvalues of such a problem are actually periodic in k_x and k_y , so the search can be accomplished in a finite amount of time.) *Bandgaps* are those ranges of the frequency axis over which propagation is not allowed.

To apply the FEM to this problem, the structure is first meshed with triangles as shown in Fig. 6. A basis function is associated with each node in the mesh that is one at its node and falls off linearly to zero at each node connected to it. In particular, these basis functions are subsectional; they vanish identically on triangles not connected to the associated node.

A set of equations can be created by applying either Galerkin's method or the Rayleigh-Ritz method using these subsectional bases. The essential boundary condition can be enforced by ensuring that nodes on the boundary are related by Eq. (99); this eliminates the unknowns associated with two edges of the mesh. Specifically, the unknowns associated with the white circles in Fig. 6 can be eliminated by expressing their values in terms of the values of the unknowns located at the black circle nodes. In the end, the result of this procedure is a generalized eigenvalue problem for the eigenvalues ω^2 and the associated eigenvectors that represent the electric field of the mode in question. Figure 7 shows the band structure of the lowest two bands for this PBG structure computed by the FEM with 400 unknowns. (The band structure diagram shows the allowed values of ω for each k_x, k_y pair.) A large bandgap is evident.

As a final example of Galerkin's method, we present an example of the method of moments. In computational electromagnetics circles, MoM refers to the use of the weighted-residual method for the solution of integral equations. Here, we will provide an example of Galerkin's method

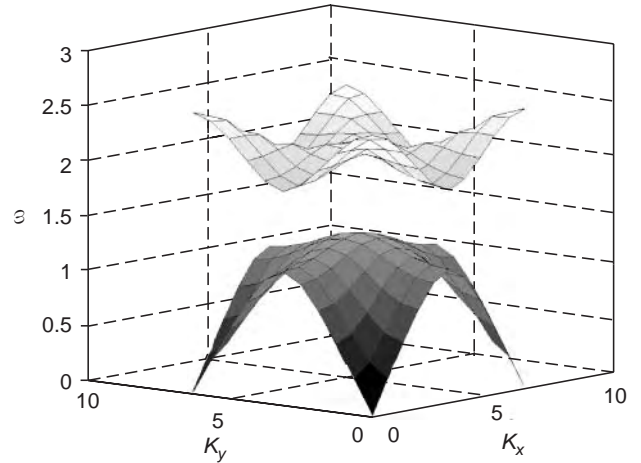


Figure 7. Band structure of the PBG structure of Fig. 6 computed by FEM.

(i.e., the method where the testing functions are chosen to be the basis functions) specifically. In particular, we demonstrate an application of the MoM to scattering from conducting objects.

Thus, let the surface of a perfect conductor situated in free space be denoted by S , and imagine that the conductor is illuminated by an electric field $\mathbf{E}^{\text{inc}}(\mathbf{r})$. (Since the formulation of this problem is standard in the literature, we drop the usual notation of using u as the problem solution, u_i as the basis functions, and so on, in favor of a more standard MoM notation.) This incident field will induce a current $\mathbf{J}(\mathbf{r})$ on the surface of the scatterer, which radiates a scattered field in such a way to exactly cancel the incident electric field tangential to the scatterer. Mathematically, the current must satisfy the electric field integral equation

$$\begin{aligned} \mathbf{E}^{\text{inc}}(\mathbf{r}) = & jk\eta \iint_S \mathbf{J}(\mathbf{r}') \frac{e^{-jk|\mathbf{r}-\mathbf{r}'|}}{4\pi|\mathbf{r}-\mathbf{r}'|} dS' \\ & - \frac{\eta}{jk} \nabla \iint_S [\nabla' \cdot \mathbf{J}(\mathbf{r}')] \frac{e^{-jk|\mathbf{r}-\mathbf{r}'|}}{4\pi|\mathbf{r}-\mathbf{r}'|} dS' \end{aligned} \quad (100)$$

tangential to the surface of the scatter, where η is the impedance of free space, and $k = \omega/c$, where c is the speed of light in vacuum and ω is the angular frequency of the wave. The integral over dS' indicates that \mathbf{r}' is the integration variable, and the prime over the nabla symbol indicated differentiation with respect to \mathbf{r}' .

Assuming that the set of basis functions is denoted by $\mathbf{B}_i(\mathbf{r})$, $i = 1, \dots, N$, and that the inner product used in the formulation of the problem is that of Eq. (78), an application of Galerkin's method gives rise to a matrix equation of the form

$$\mathbf{A}\mathbf{x} = \mathbf{b} \quad (101)$$

where \mathbf{x} is a vector of unknown weighting function coefficients. The elements of \mathbf{b} are given by

$$[\mathbf{b}]_m = \iint_S \mathbf{E}^{\text{inc}}(\mathbf{r}) \cdot \mathbf{B}_m(\mathbf{r}) dS \quad (102)$$

and (if the chosen basis is divergence-conforming [24,25]) the elements of the matrix \mathbf{A} are given by

$$[\mathbf{A}]_{mi} = jk\eta \iint_S \iint_S \mathbf{B}_i(\mathbf{r}') \cdot \mathbf{B}_m(\mathbf{r}') \frac{e^{-jk|\mathbf{r}-\mathbf{r}'|}}{4\pi|\mathbf{r}-\mathbf{r}'|} dS dS' + \frac{\eta}{jk} \iint_S \iint_S [\nabla \cdot \mathbf{B}_i(\mathbf{r}')] [\nabla \cdot \mathbf{B}_m(\mathbf{r})] \times \frac{e^{-jk|\mathbf{r}-\mathbf{r}'|}}{4\pi|\mathbf{r}-\mathbf{r}'|} dS dS' \quad (103)$$

Solving Eq. (101) yields an approximation of the current, which can then be used to compute (for instance) the radar cross section of the object.

This technique was applied to the computation of the radar cross section of a 1-m-diameter sphere at 100 MHz. The sphere was meshed with 32 spherical triangle patches, and the current was discretized into 160 quadratic basis functions on these patches. The geometry model was exact; that is, the sphere was not approximated as a union of flat triangles. The details of the basis functions themselves may be found in Ref. 24; they are generalizations of the well-known linear Rao–Wilton–Glisson basis functions [25]. The radar cross section computed by the MoM technique is shown in Fig. 8, where it is compared to the result returned by the exact analytic solution (Mie series). The two results compare well. While the computation of the matrix elements in this case is far more complicated in this case than in all of the previous cases, in principle this example is a straightforward application of the Galerkin method. Thus, although the integrals in Eqs. (100) and (103) require numerical integration of functions that are often singular, no essential complication is introduced into Galerkin's method.

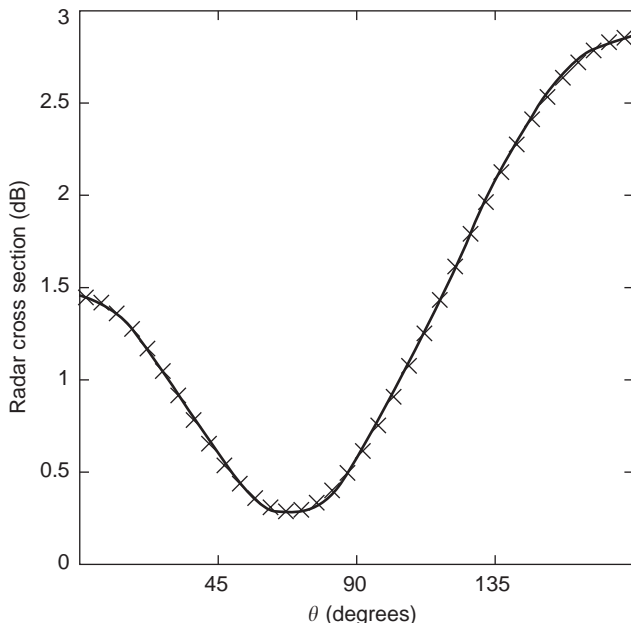


Figure 8. Radar cross section of a 1-m-diameter sphere as computed by the MoM (tickmarked, crossed line) versus Mie series (solid line) at 100 MHz.

BIBLIOGRAPHY

1. J. Jin, *The Finite Element Method in Electromagnetics*, J Wiley, New York, 1993.
2. R. F. Harrington, *Field Computation by Moment Methods*, Robert E. Krieger Publishing, Malabar, FL, 1968.
3. P. P. Silvester and R. L. Ferrari, *Finite Elements for Electrical Engineers*, Cambridge Univ. Press, New York, 1996.
4. E. K. Miller, L. Medgyesi-Mitschang, and E. H. Newman, eds., *Computational Electromagnetics: Frequency-Domain Method of Moments*, IEEE Press, New York, 1992.
5. J. L. Volakis, A. Chatterjee, and L. C. Kempel, *Finite Element Method for Electromagnetics*, IEEE Press, New York, 1998.
6. J. J. H. Wang, *Generalized Moment Methods in Electromagnetics*, Wiley, New York, 1991.
7. G. E. Forsythe and W. R. Wasow, *Finite-Difference Methods for Partial Differential Equations*, Wiley, New York, 1960.
8. G. D. Smith, *Numerical Solution of Partial Differential Equations: Finite Difference Methods*, Oxford Univ. Press, New York, 1978.
9. A. Taflove, *Computational Electrodynamics: The Finite-Difference Time-Domain Method*, Artech House, Boston, 1996.
10. R. Kress, *Linear Integral Equations*, Vol. 82, Springer-Verlag, New York, 1999.
11. L. F. Canino, J. J. Ottusch, M. A. Stalzer, J. L. Visher, and S. M. Wandzura, Numerical solution of the Helmholtz equation in 2D and 3D using a high-order Nyström discretization, *J. Comput. Phys.* **146**(2):627–663 (1998).
12. R. B. Lindsay, *Lord Rayleigh—the Man and His Work*, Pergamon Press, New York, 1970.
13. J. W. Strutt, *The Theory of Sound*, Macmillan, London, 1894.
14. B. N. Parlett, *The Symmetric Eigenvalue Problem*, Society for Industrial and Applied Mathematics, Philadelphia, 1998.
15. R. Courant, Variational methods for the solution of problems of equilibrium and vibrations, *Bull. Am. Math. Soc.* **49**:1–23 (1943).
16. W. Ritz, On a new method for solving variational problems of mathematical physics, *J. Reine Angew. Math.* **135**:1 (1908).
17. W. Ritz, Theory of the transverse oscillations of a square plate with free edges, *Annal. Phys.* **38** (1909).
18. S. G. Mikhlin, *Variational Methods in Mathematical Physics*, Macmillan, New York, 1964.
19. B. G. Galerkin, Rods and plates. Series occurring in various questions concerning the elastic equilibrium of rods and plates, *Vestnik Inzhenerov* **19**:897–908 (1915).
20. C. Fox, *An Introduction to the Calculus of Variations*, Dover, New York, 1987.
21. H. H. Goldstine, *A History of the Calculus of Variations from the 17th through the 19th Century*, Springer-Verlag, New York, 1980.
22. B. D. Reddy, *Introductory Functional Analysis*, Springer-Verlag, New York, 1998.
23. Y. Saad, *Iterative Methods for Large Linear Systems*, Manchester Univ. Press, Manchester, UK, 1996.
24. R. D. Graglia, D. R. Wilton, and A. F. Peterson, Higher order interpolatory vector bases for computational electromagnetics, *IEEE Trans. Anten. Propag.* **45**(3):329–342 (1997).
25. S. M. Rao, D. R. Wilton, and A. W. Glisson, Electromagnetic scattering by surfaces of arbitrary shape, *IEEE Trans. Anten. Propag.* **30**(5):409–418 (1982).

GALLIUM ARSENIDE TECHNOLOGY AND APPLICATIONS

G. F. MANES
University of Florence
Italy

1. INTRODUCTION

Starting from the early 1970s, the increasing request for solid-state devices operating at microwave frequencies lead to investigations of semiconductor structures as alternatives to silicon. The properties of III-V compound materials exhibited favorable characteristics for that purpose, despite inherent limitations in wafer reproducibility and yield. Among various solutions, gallium arsenide generated interest and eventually emerged as the favorite material for high-frequency applications due to the high carrier mobility compared with silicon devices. To produce high-quality gallium arsenide crystals, scientists needed to solve a number of problems, including the need to understand the process in which chemical impurities, introduced either intentionally or unintentionally, are distributed during crystal growth. Operating at higher speed and using less power, electronic devices made from gallium arsenide crystals have several theoretical advantages over silicon.

The advantages in speed and high-frequency performance of GaAs are slightly offset by the manufacturing process limitations of GaAs, in terms of both complexity and reproducibility as opposed to Si. A relevant limitation, for instance, is the maximum wafer dimension (today only 4–6 in. in diameter, compared to the present 12 in. for silicon). This limitation reduces the number of devices per wafer, and thus the final monetary value of each wafer. The size limitation is due to the limited robustness of the bulk material. In addition, the device reliability is much lower than in Si; therefore GaAs is not suitable for very complex circuits. GaAs devices find application at RF and microwave frequencies for both linear and high-speed logic applications. RF devices and ICs are used in consumer electronics to meet specifications beyond Si device capabilities. GaAs microwave devices find extensive use in consumer applications as well in sophisticated warfare electronics. GaAs devices are used in the form of discrete components or microwave monolithic integrated circuits (MMICs). GaAs also exhibits relevant optical properties and finds extensive applications in optoelectronics, including LEDs, laser diodes, and solar cells; this issue, however, will not be addressed in this article.

2. MATERIAL PROPERTIES

Like many other III-V compounds, gallium arsenide crystallizes in the zincblende structure, whose name derives from the ZnS mineral. The primitive cell ($Z=1$) of the zincblende crystal structure is shown in Fig. 1. It can be described as the result of two face-centered cubic (fcc) lattices of gallium (Ga) and arsenic (As) reciprocally pene-

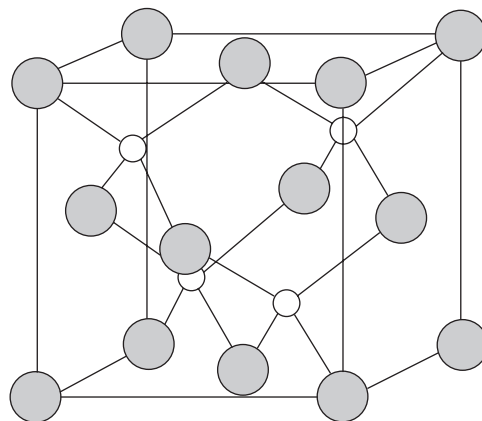


Figure 1. The zincblende primitive cell.

trating and shifted relative to each other by a quarter of the cube diagonal.

Unlike the tetrahedral atomic configuration of silicon and germanium, in the zincblende structure the midpoint between two nearest atoms is no longer a center of inversion. Because of this lack of inversion symmetry, in a gallium arsenide lattice, the directions $[111]$ and $[1\bar{1}\bar{1}]$ are not equivalent. The bonds between nearest Ga and As atoms are in the $[111]$ direction, while the closest equivalent atoms (Ga-Ga or As-As) are in the $[110]$ direction. The $[111]$ plane, which is perpendicular to the $[111]$ direction, is usually known as the *gallium plane*, while the $(\bar{1}\bar{1}\bar{1})$ plane is known as the *arsenic plane*. If the GaAs crystal is cleaved on the (111) plane, the wafer surface is made up of either gallium atoms with one free bond and three bonds with the layer below, or arsenic atoms with three free bonds and only one bond with the layer below. The opposite situation is obtained on the $(\bar{1}\bar{1}\bar{1})$ plane.

Unlike silicon or germanium crystals, which are cleaved on the (111) plane, GaAs crystals are usually cleaved along the (011) or $(01\bar{1})$ plane since, because of the partially heteropolar bonds between gallium and arsenic, the zincblende structure does not easily break along the (111) plane. At $T=300\text{ K}$ the lattice constant of the GaAs crystal is 5.653 \AA and its thermal conductivity is $0.55\text{ W cm}^{-1}\text{ }^{\circ}\text{C}^{-1}$.

The energy band diagram of gallium arsenide at $T=300\text{ K}$ is shown in Fig. 2. Like many other III-V compounds, GaAs is a direct-bandgap material; this means that the top of the valence band (light and heavy holes) and the bottom of the main conduction band valley (the \square valley) are located in the same point in the wavevector space. The conduction band also has two more valleys, one in the $\langle 111 \rangle$ direction and one in the $\langle 100 \rangle$ direction, respectively known as the L valley and the X valley. At room temperature the energy gap E_g between the \square valley and the top of the valence band is 1.42 eV ; in the same conditions the gaps between the top of the valence band and the bottoms of the two secondary valleys of the conduction band are 1.71 eV for the L valley and 1.90 eV for the X valley. The top of the splitoff subband is 0.34 eV below the top of the light- and heavy-hole bands.

All energy values reported are temperature-dependent; in the range $0\text{--}1000\text{ K}$ E_g can be calculated using the

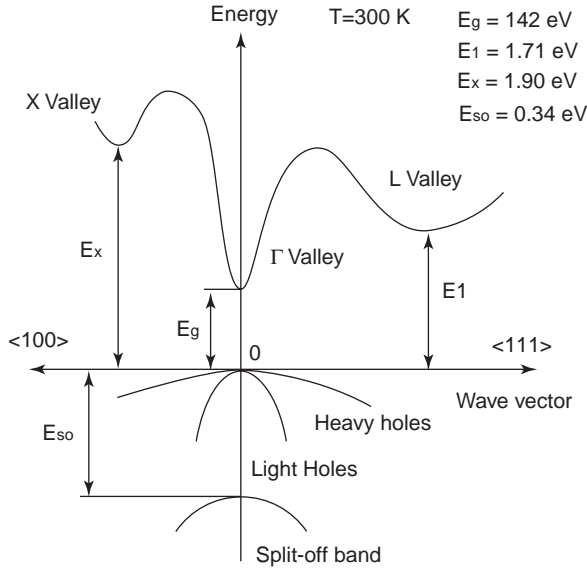


Figure 2. The zincblende primitive cell.

following relation:

$$E_g(T) = 1.519 - 5.405 \times 10^{-4} \cdot \frac{T^2}{T + 204} \text{ (eV)} \quad (1)$$

The intrinsic carrier concentration is given by

$$n_i = (N_C \cdot N_V)^{1/2} \exp\left(-\frac{E_g}{2k_b T}\right) \text{ (cm}^{-3}\text{)} \quad (2)$$

Taking into account the nonparabolic behavior of the Γ valley and the contributions from the X and L valleys, the effective densities of states N_C and N_V can be calculated from the following relations:

$$\begin{aligned} N_C &= 8.63 \times 10^{13} \cdot T^{3/2} [1 - 1.93 \times 10^4 \cdot T \\ &\quad - 4.19 \times 10^8 \cdot T^2 + F_{LX}(T)] \text{ (cm}^{-3}\text{)} \\ F_{LX}(T) &= 21 \cdot \exp\left(-\frac{E_{\Gamma L}}{2k_b T}\right) 44 \cdot \exp\left(-\frac{E_{\Gamma X}}{2k_b T}\right) \\ N_V &= 1.83 \times 10^{15} \cdot T^{3/2} \text{ (cm}^{-3}\text{)} \end{aligned} \quad (3)$$

where $E_{\Gamma L}$ and $E_{\Gamma X}$ are the energy gaps between the main and the two secondary valleys.

The effective masses of carriers are reported in Table 1 ($m_0 = 9.11 \times 10^{-31}$ kg is the electron inertial mass).

Table 1. Effective Masses of Carriers

Conduction band	(Γ valley)	$m_\Gamma = 0.063 m_0$
	(L valley)	$m_L = 0.085 m_0$
	(X valley)	$m_X = 0.085 m_0$
Valence Band	Light holes	$m_{lh} = 0.082 m_0$
	Heavy holes	$m_{hh} = 0.51 m_0$
	Splitoff	$m_{so} = 0.15 m_0$

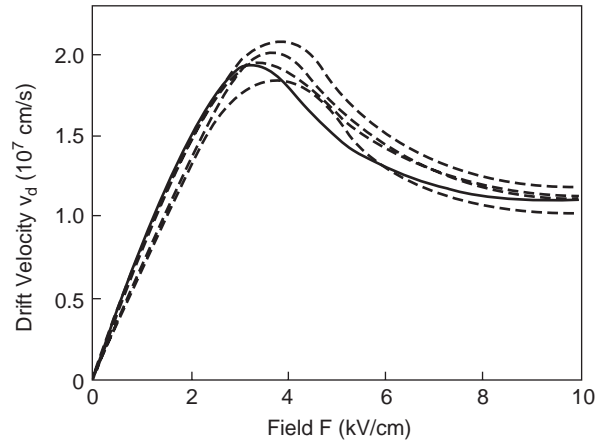


Figure 3. Electric field dependence of the electron drift velocity.

The field dependence of the electron drift velocity is depicted in Fig. 3; the negative differential mobility behavior is due to the increase of the carrier concentration in the L and X valleys for high electric fields. The solid curve was calculated by Pozhela and Reklaitis [*Solid State Electron.* 23(9):927–933 (1980)], dashed and dotted curves are measured data at room temperature.

Modern monolithic devices such as HBTs and HEMTs are based on the properties of wide-bandgap heterojunctions. Figure 4 illustrates the relationship between bandgap and lattice constant for various alloys in the InGaAsP and AlGaAsSb systems.

As can be seen in Fig. 4, gallium arsenide has nearly the same lattice constant of aluminum arsenide (AlAs); at the same time the bandgap difference between the two alloys is quite high (0.8 eV). This implies that the $Al_xGa_{1-x}As$ ternary compound has in any case a lattice

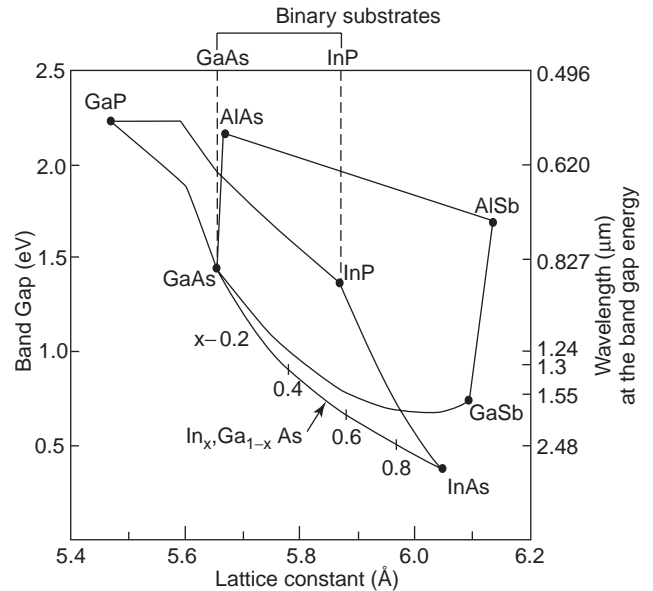


Figure 4. Relationship between bandgap and lattice constant for alloys in the InGaAsP and AlGaAsSb systems. (Figure taken from B. G. Streetman and S. Banerjee, *Solid State Electronic Devices*, Prentice-Hall, 2000.)

constant very close to that of gallium arsenide with a bandgap energy that can be modulated by correctly choosing the alloy composition x .

The properties of the GaAs/AlAs system can be applied to build a wide range of nearly lattice-matched heterojunctions starting from a binary GaAs substrate. The bandgap difference can be further increased by growing a series of $\text{Al}_x\text{Ga}_{1-x}\text{As}$ and $\text{In}_y\text{Ga}_{1-y}\text{As}$ layers on a gallium arsenide substrate, as is done in a GaAs pseudomorphic HEMT. In this case, anyway, the lattice mismatch between GaAs and the $\text{In}_y\text{Ga}_{1-y}\text{As}$ compound quickly rises as the indium alloy composition y is increased.

3. GaAs MMIC FABRICATION

GaAs MMICs are manufactured starting with a wafer of semiconductor material. These wafers are sliced from a large single crystal, known as a *boule*. Boules are grown by the well-known Czochralski crystal growth method, which is substantially the same as the technique used for silicon and other semiconductors. Basically, a small seed crystal is lowered to the surface of the melting material, and then slowly lifted up. In this manner, it draws with it layer by layer of molten material, which cools gradually, resulting in a single crystal with the same crystalline structure as the seed crystal. Actually, growing compound semiconductors is slightly complicated because the vapor pressures of the constituent materials are different. A suitable encapsulate, together with a high pressure of inert gas within the growth chamber, is employed in order to prevent this problem.

After slicing the boules to thin wafers, their surface is smoothed by mechanical and chemical treatments, so that its roughness is reduced to an atomic layer level. The obtained product is the basic material for MMIC microfabrication.

GaAs-based devices need a mesastructure compound by several layers of different material alloys. Their thickness and molar fraction must be known quite accurately. So, process requirements are intrinsically dissimilar from what can be obtained by diffusion doping techniques, which are typically applied in traditional Si-based microcircuit fabrication. Consequently, epitaxial deposition is the most popular and perhaps the only method employed in fabricating GaAs MMICs. In the following sections two main techniques, molecular-beam epitaxy and metallorganic chemical vapor deposition, will be described.

These techniques allow the production of high-quality layers with very abrupt interfaces and good control of thickness, doping, and composition. In fact, they are also compatible with accurate growth measurement systems, such as the reflection high-energy electron diffraction method.

Photolithography and etching are then performed in order to selectively remove material from the sample, resulting in the effective transfer of the design layout to the chip. This kind of technology is not limited to GaAs processing, and its description is beyond the purpose of this section. Multiple metallization layers can be added by

thin-film vacuum evaporation, sputtering, or electroplating; additional sacrificial layers can be grown to allow air-bridge construction. Again, masks are used to control the geometry of the metal film on the device.

4. MOLECULAR-BEAM EPITAXY

Molecular-beam epitaxy (MBE) was developed in the early 1970s as a means of growing high-purity epitaxial layers of compound semiconductors.

The working principle of MBE is shown in Fig. 5. A sample wafer is heated in a chamber, and eventually it is kept in rotation; then, solid sources materials are placed in evaporation cells to provide an angular distribution of atoms or molecules in a beam. Every source is connected to the chamber via a shutter, so that the flux of material can be externally controlled with accuracy. Atoms and molecules combine onto the wafer surface, and epitaxial layers of the desired compound material grow on the sample.

However, some practical issues drastically complicate the construction of a real MBE system. First, the chamber is kept in ultra-high-vacuum (UHV) environment. Actually, the molecular-beam condition that the mean-free path of the particles should exceed the geometric size of the chamber is easily fulfilled if the total pressure does not exceed 10^{-5} torr. Nevertheless, the condition for growing a sufficiently clean epitaxial layer typically requires the partial pressure of the background residual vapor to be less than 10^{-11} torr. Thus, the total pressure is kept as low as reasonably possible—around 10^{-7} torr—and liquid N_2 cryopanel, together with cryopumps, act as a screening around the substrate, minimizing spurious fluxes of atoms and molecules from the chamber walls while reaching the desired level of residual vapor and undesired gas partial pressure. Moreover, the materials of the chamber are chosen so that they minimize the rate of gas evolution (e.g., pyrolytic boron nitride, molybdenum, tantalum) and a special maintenance is applied: a 24-h bakeout of the whole chamber at 200°C after each vent, and heating of the windows at 300°C for a couple of hours to prevent them from being coated.

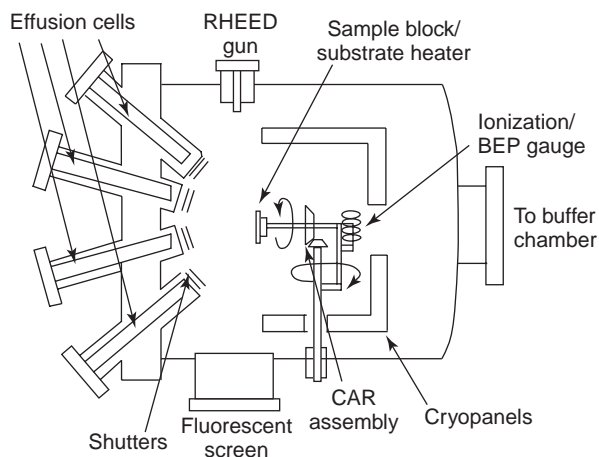


Figure 5. MBE process setup.

Then, a proper temperature has to be chosen for the substrate. Consider one of the key points of MBE, namely, that when particles from the molecular beam reach the sample surface, they are not immediately included in the crystalline structure; instead, they should be able to migrate on the wafer for a relatively long path. In this manner, atoms are allowed to “search” for a minimum energy site, which is always at the edge that rises on a layer when a isle of atoms is forming a new layer because there are forces attracting the atom from both the bottom and the lateral side. This is important since the crystal does not grow randomly, and then grows roughly, but some initial atoms form isles that gradually expand until they coalesce to cover the whole surface. Consequently, the growth proceeds spontaneously layer by layer, resulting in an extremely homogeneous and controllable epitaxial deposition. Now, it is straightforward that the higher the wafer temperature, the longer the migration path of the atoms on its surface. However, looking at the phase diagram of a binary compound, one can conclude that there is a temperature over which the pressure of the more volatile component (in the GaAs case it is arsenic) increases more rapidly, a minimum for a suitable stoichiometry of the solid phase no longer exists, and a liquid gallium phase is created. Hence, a temperature below 630°C is required for GaAs substrates.

The effusion cells are independently heated at accurately controlled temperatures, so that the contained atomic species are able to escape by thermoionic emission. Since the typical rate of growth with MBE is as slow as that around a single monolayer per second, shutters posed in between the sources and the wafer can easily control the composition of the global flux of particles reaching the semiconductor surface, with up to 1% accuracy.

5. METALLORGANIC CHEMICAL VAPOR DEPOSITION

MOCVD (metallorganic chemical vapor deposition) or MOVPE (metallorganic vapor-phase epitaxy) is another widely used method of creating controllable epitaxial layered structures by atomic deposition over a substrate material.

This method involves passing metal oxides in an inert gas across a workpiece to deposit a layer of metal oxide on the surface. MOCVD is utilized largely by the semiconductor industry. As shown in Fig. 6, the substrate wafer is placed on the graphite susceptor inside a reaction vessel and heated by an RF induction heater.

The temperature depends on the type of compounds grown, but it is usually between 500 and 700°C. Growth occurs in an atmosphere of hydrogen at a pressure between 100 and 700 torr. The growth precursors decompose on contact with the hot substrate to form epitaxial layers. Group V precursors are AsH₃ (arsine); while group III are Ga(CH₃)₃ trimethylgallium (TMG). The MOCVD process offers good material distribution capabilities and reproduces fine details with reliable quality. The materials to be coated must be able to withstand the extreme temperatures associated with this process.

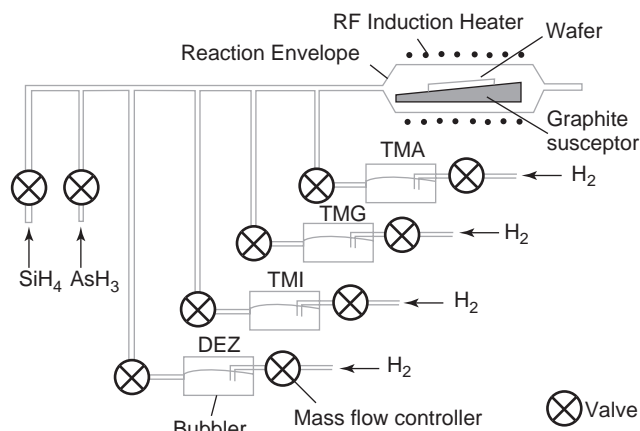


Figure 6. MOCVD process setup.

6. REFLECTION HIGH-ENERGY ELECTRON DIFFRACTION

One of the most useful tools for in situ monitoring of the growth is reflection high-energy electron diffraction (RHEED). It can be used to calibrate growth rates, observe removal of oxides from the surface, calibrate the substrate temperature, monitor the arrangement of the surface atoms, determine the proper arsenic overpressure, give feedback on surface morphology, and provide information about growth kinetics. The layout of the RHEED system, shown in Fig. 7, can be summarized as follows. The RHEED gun emits ~10-keV electrons, which strike the surface at a shallow angle (~0.5–2°), making it a sensitive probe of the semiconductor surface. Electrons reflect from the surface and strike a phosphor screen, forming a pattern consisting of a specular reflection and a diffraction pattern that is indicative of the surface crystallography. A camera monitors the screen and can record instantaneous pictures or measure the intensity of a given pixel as a function of time.

Starting from a flat substrate, the electrons are not scattered greatly and are recorded as an intense beam. As material is deposited on the surface, the atoms create islands of epitaxial growth with a concomitant decrease in the reflectivity of the surface of the material as the electrons are scattered. As the deposition process continues, material builds up on the surface and the islands join together and create new flat surfaces, while the original substrate forms as voids in the newly created material. As yet more material forms, the voids begin to fill up and the reflectivity increases once again, although in reality, the reflectivity does not reach as high a value, since the deposition process is random and the surface never regains the completely flat profile of the initial polished substrate. By monitoring the oscillations in the reflectivity one can estimate the thickness and growth rate of the epitaxial material.

The appearance of the RHEED diffraction pattern can be used to provide qualitative feedback on surface morphology. If the surface is smooth, then the RHEED diffraction patterns appear streaky. If the samples are rough, then the horizontal streaks are more “spotty” and the diffraction pattern is not as clear. An amorphous surface,

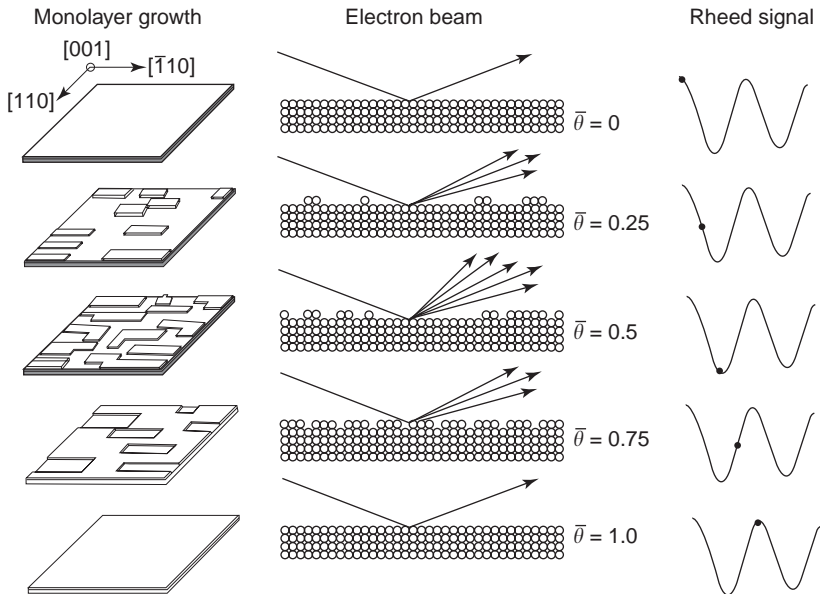


Figure 7. REED in situ growth monitoring technique.

such as an oxide layer, shows a haze instead of a diffraction pattern, and polycrystalline surfaces result in rings circling the straight-through beam. Such information, although only qualitative, can be a useful check of the surface condition.

7. GaAs HIGH-SPEED DEVICES

Gallium arsenide integrated circuit technology has been historically described as the “technology of the future.” Although initially it did not achieve the wide applicability originally predicted, it is now considered a relevant technology for microwave and millimeter-wave applications, and it is a fully accepted and commercially available source for high-speed integrated circuits. The main advantage of GaAs in high-frequency applications is its high electron mobility value. GaAs devices typically show a unity current gain frequency f_T that is 30–70% higher than that of an equivalent silicon transistor, for a given gate length or base width. Similar gainful can be achieved for the unity power gain frequency f_{max} . In addition, AlGaAs, which provides the ability to build lattice-matched and wide-bandgap heterojunctions, allows the device designer to have more freedom for performance optimization.

This feature of the AlGaAs/GaAs system is extremely important for a GaAs heterojunction bipolar transistor (HBT), where a higher emitter bandgap, with respect to the base bandgap material, is used to prevent holes from diffusing from base to emitter. As a result, a higher base doping can be reached, decreasing the base resistance, without degrading current gain. Besides, since undoped GaAs is a semiinsulating material, the parasitic capacitance due to wire interconnects is lower than in silicon technology.

The main GaAs technology drawback is related to the nonoptimal thermal behavior, which makes it more difficult to dissolve the heat generated by dissipated power.

Electrically speaking, the heat generation produces a drain current degradation for FET devices; this phenomenon is usually known as “self-heating”.

The three dominant GaAs high-speed device types are metal Schottky FET (MESFET), modulation doped FET or high-electron-mobility transistor (MODFET, HFET, HEMT), and the bipolar transistor type, known as the *heterojunction bipolar transistor* (HBT).

Besides thermodynamic problems, other drawbacks are observed, related principally to practical aspects, such as the low level of achievable integration, backdating, hysteresis, high $1/f$ noise, and parameter dispersion for MESFET and HEMT devices.

8. GaAs MESFET

The principle of GaAs MESFET transistor operation is similar to that of the simple and well-known silicon JFET, in particular concerning the current control mechanism by means of the voltage applied to the gate. The main difference between a silicon JFET and a GaAs MESFET is that in the former the drain current saturation is achieved at channel pinchoff, while in the latter saturation is induced by the electron velocity saturation. Even if GaAs HEMTs exhibit higher performance levels, GaAs MESFETs, are still commonly used in wireless applications.

GaAs MESFET technology is currently capable of realizing enhancement/depletion-mode integrated circuits of LSI complexity. The cross section of a typical GaAs MESFET is shown in Fig. 8. The maximum f_T of commercially available MESFET for integrated circuits applications is around 15 GHz, and the maximum f_T achieved by the best GaAs MESFET in a research laboratory environment is approximately 80 GHz. Commercially available devices have gate lengths of approximately $0.5\mu\text{m}$ down to $0.1\mu\text{m}$. The typical threshold voltage spread across a 3-in. wafer is 30–40 mV, and local threshold voltage spread,

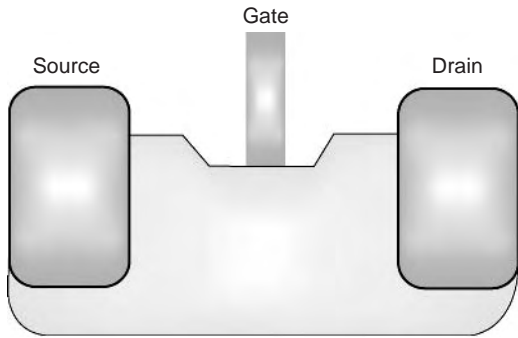


Figure 8. Cross section of a MESFET.

which is important for comparator applications, is 15–20 mV. Because of the Schottky barrier gate, the maximum gate source voltage of GaAs MESFET is typically limited to approximately 0.7 V.

Most commercially available GaAs MESFETs suffer from low-frequency hysteresis effects, which make the design of high-accuracy comparators more difficult. This phenomenon is due to a drop in the high-frequency FET’s drain-to-source resistance, which is also associated with a phase shift, when the device is biased in the saturation region. This behavior produces a time-varying offset voltage or hysteresis, in the I - V relationship of the device, which is added to the DC offset of the comparator, thus reducing its achievable resolution. The hysteresis effect can be reduced by improving the circuit’s design procedures. More recent results obtained by means of improved processing techniques have demonstrated that it can be eliminated.

9. GaAs HEMT

Greater efficiency, along with a lower noise figure and a higher cutoff frequency, can be obtained by using the high-electron-mobility transistor (HEMT; see HEMT cross section in Fig. 9). The principle of operation is based on the concept of modulation doping.

In order to obtain a high-electron-mobility value, which means a high cutoff frequency and a lower noise figure, it is possible to use either a high-electron-mobility semiconductor material such as gallium arsenide or an undoped semiconductor material in which ionized impurity scattering is reduced. A more efficient method is to grow the FET channel using an undoped high-mobility semiconductor material and then increase the concentration of free carriers (which is extremely low at room temperature in an undoped material) by transferring them from an adjacent heavily doped layer, known as the “supply layer”. In this manner it is possible to obtain a high mobility of carriers, since electrons travel in an undoped material, and, at the same time, it is also possible to achieve high carrier concentrations and correspondingly high current densities.

The situation described above can be achieved by means of a heterojunction between two semiconductors with significantly different energy gaps. The wider-band-gap semiconductor is used to grow the heavily doped

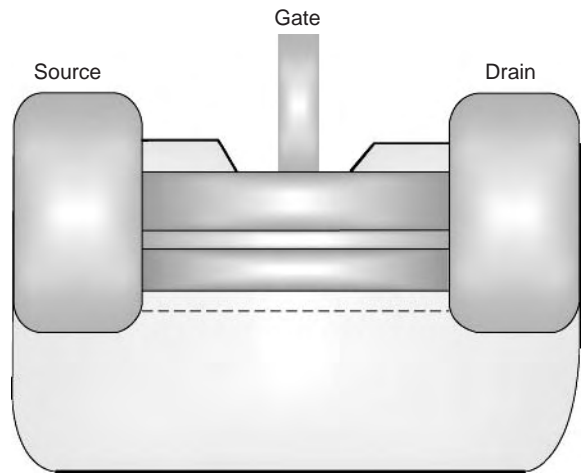


Figure 9. Cross section of a HEMT.

supply layer, while the other alloy, which is intentionally not doped, is used for the FET channel. The electrostatic equilibrium of the heterojunction results in a triangular well at the interface, which confines the electrons in a two-dimensional (2D) electron gas known as 2DEG. The band diagram of this particular type of heterojunction is illustrated in Fig. 10.

At high frequencies, the HEMT structure, using the 2DEG as the current conducting channel, exhibits performance levels higher than those achievable with a conventional MESFET; therefore it is the most suitable transistor structure for microwave and millimeter-wave analog circuits as well as in high-speed digital applications. The first HEMT prototype was demonstrated in 1981 in the AlGaAs/GaAs material system.

The current control mechanism in the HEMT is obtained by tuning the density of electrons in the triangular well. When the gate voltage is modified, both the shape of triangular well and the position of the Fermi level are modified; therefore the number of electrons into the 2DEG is increased or decreased according to the sign of the V_G variation.

The sheet charge density n_s can be expressed as a function of the gate voltage V_G in the following way

$$n_s = \frac{\epsilon}{qd}(V_G - V_{TH}) \tag{4}$$

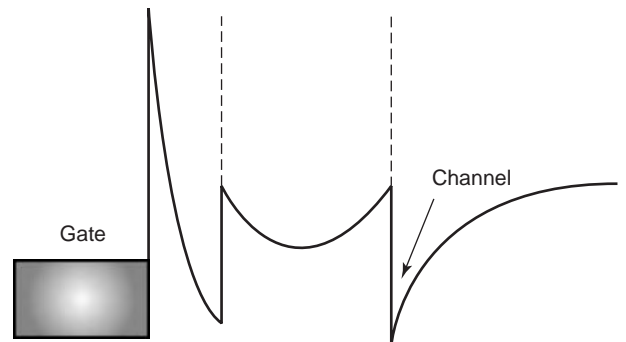


Figure 10. Band diagram of a HEMT.

where ε is the GaAs permittivity, d is the distance between the metal–semiconductor interface (where gate voltage is applied), and V_{TH} is the threshold voltage or pinchoff voltage.

As can be easily understood, n_s is related to the drain current, so that varying the sheet charge density allows the drain current to be controlled. The relationship between the drain current I_D and the gate voltage V_G can be calculated analytically, resulting in the following equation:

$$I_D = \begin{cases} \frac{WC_{OX}\mu_n}{L_G} \left[(V_{GS} - V_T)V_{DS} - \frac{V_{DS}^2}{2} \right] & \text{for } V_{DS} < V_{DS,sat} \\ \frac{WC_{OX}\mu_n}{L_G} \frac{(V_{GS} - V_T)^2}{2} = I_{D,sat} & \text{for } V_{DS} \geq V_{DS,sat} \end{cases} \quad (5)$$

In order to calculate the cutoff frequency, the equivalent circuit of the transistor, shown in Fig. 11, is needed.

Some circuitual components such as capacitances (both intrinsic and extrinsic or parasitic), as well as source and drain input resistances can be calculated. The other elements of the equivalent circuit, such as the transconductance g_m and the drain conductance g_d , can be deduced either from theoretical equations, or from small-signal measurements.

The aim of the analysis is to obtain the h_{21} hybrid parameter expression, which is frequency-dependent; by setting h_{21} to 1, one can calculate the cutoff frequency f_T (i.e., the frequency corresponding to a unit-gain current). Once the proper equivalent circuit has been defined, the same procedure can be used for HBT GaAs-based transistors, because the h_{21} parameter is related to the equivalent circuit and not to the physics behavior of the transistor. The full expression of f_T is

$$f_T = \frac{1}{2\pi \left(\frac{C_{GG,t}}{g_m} + \frac{C_{GG,t}}{g_m} (R_S + R_D)g_d + (R_S + R_D)C_{GD,t} \right)} \quad (6)$$

where $C_{GG,t}$ is related to the charge stored under the gate.

A similar approach can be followed to calculate the maximum oscillation frequency. In this case, however, we

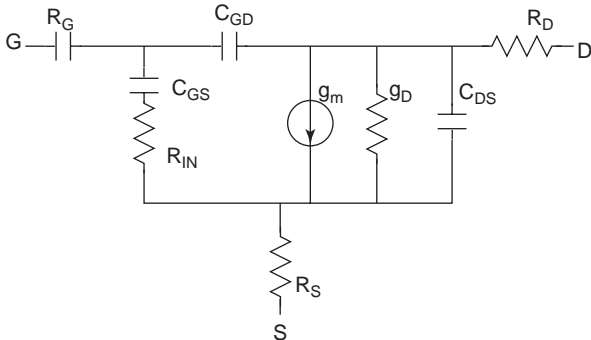


Figure 11. Equivalent circuit of a HEMT.

are interested in deriving the unilateral power gain. Once the unilateral power gain is calculated, we set its value to 1, thus determining the maximum oscillation frequency f_{max} . With reference to the circuit in Fig. 11, the following expression can be derived for f_{max} :

$$f_{max} = \sqrt{\frac{f_T}{8\pi R_G C_{GD,t} \left[1 + \left(\frac{2\pi f_T}{C_{GD,t}} \right) \Psi \right]}} \quad (7)$$

$$\Psi = (R_S + R_D) \frac{C_{GG,t}^2 g_d^2}{g_m^2} + (R_S + R_D) \frac{C_{GG,t} C_{GD,t} g_d}{g_m} + \frac{C_{GG,t}^2 g_d}{g_m^2}$$

$$NF_{min} = 1 + \omega \frac{C_{GS}}{g_m} \left(\frac{R_S + R_G}{R_{IN}} \right)^{1/2} \quad (8)$$

9.1. Output Power

The power performance of a FET, as also of HBT, is determined by the maximum output power P_{out} defined as

$$P_{out} = \frac{1}{8} (I_{max} - I_{min}) (BV_{DS} - V_{knee}) \quad (9)$$

where

$$V_{knee} = V_{DS,sat} \quad (10)$$

$$I_{max} = I_{D,sat}(V_{GS} = 0, V_{DS} = V_{DS,sat}) \quad (11)$$

$$I_{min} = 0$$

The quantities used in these formulas are depicted in Fig. 12.

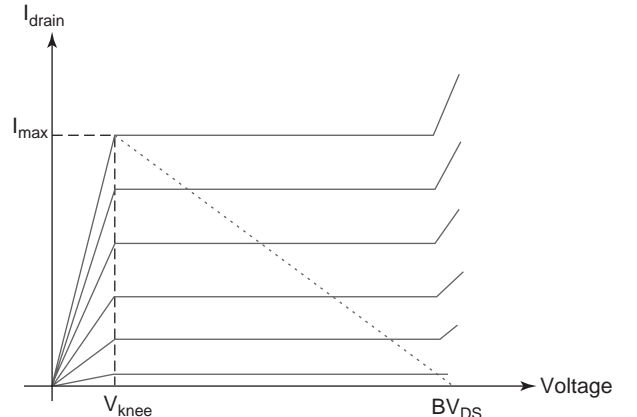


Figure 12. Static I/V characteristic of a HEMT.

The breakdown voltage is given by a semiempirical formula:

$$BV_{DS} = \frac{4.4 \times 10^{13}}{aN_d} \tag{12}$$

where a is the thickness of the channel layer, while N_d is the doping of the supply layer.

10. GaAs HETEROJUNCTION BIPOLAR TRANSISTOR (HBT)

Bipolar transistors, in spite of the advent of field-effect devices (which in Si technology dominate the memory market), continue to play a significant role still at microwave frequencies. The levels of current that can be handled, in fact, is greater than in field-effect devices, leading to both high speed and high power devices.

In field-effect devices, a way to achieve a high cutoff frequency and a low noise figure is to reduce the gate width. This goal, obviously, leads to a more critical lithographic process. For bipolar devices this step is replaced by the precise preparation of the thin base region; appropriate technologies for uniform growth of wafers have been defined to keep bipolar technology competitive.

However, the full fabrication process for bipolar transistors is more complex than for field-effect devices, and this factor has been relevant in making field-effect devices more popular. According to the standard transistor theory, the DC current gain (the ratio between the collector current and the hole current flowing from the base to the emitter) is given by

$$\beta = \left(\frac{n_e v_e}{p_b v_p} \right) \exp\left(\frac{\Delta E_G}{KT} \right) \tag{13}$$

where n_e and p_b are respectively the electron and hole densities in emitter and base, v_e and v_p are the electron and hole effective velocities, and ΔE_G is the difference in bandgap between emitter and base. As can be seen from this relationship, a higher level of gain current can be achieved by increasing the bandgap difference between emitter and base of the transistor. An AlGaAs/GaAs heterojunction, for instance, allows significant improve-

ments in performance; these improvements are summarized below:

- The difference in bandgap is 10 kT, and the exponential factor increases the value of β at room temperature up to 1000 (10–100 is sufficient in practice).
- The doping in the base can be increased significantly; thus the reverse flow in the holes is stopped by the heterojunction, and the lower base resistance provides a higher-speed device.
- The doping in the emitter can be increased without compromising the effect of bandgap narrowing; in turn, this leads to a higher current-handling ability.
- The notch in the conduction band edge can be eliminated by grading down the Al composition in the last few nanometers; this improves the emitter efficiency (see Fig. 13b).

In the transistor design tradeoff, the heterojunction can be used as a further design tool. A thin base, for example, increases the DC current gain (since there is a lower probability of electron–hole recombination in the base), but unfortunately it slows down the device (because of the increased lateral base resistance). A way to avoid this effect, allowed by heterojunctions, is to increase the p doping in order to offset any rise in lateral base resistance. A further advantage of heterojunctions is that the bipolar transistor can operate over a significantly enhanced temperature range, since the heterojunction prevents runaway thermal-based currents (higher temperature range) and because all the doping densities are above the levels at which carriers freeze out at low temperatures (lower temperature range).

If the composition of the base is graded (see Fig. 13b) from 10% Al content at the emitter–base heterojunction up to 100% at the base–collector interface, the electric field at the falling conduction band edge can be used to maintain acceleration of the injected hot electrons. A wider-gap collector can also be used to reduce hole injection from the base to collector when forward-biased (i.e., turned off) and to allow higher voltages to be applied to the collector junction without breakdown or leakage. The main drawback is related to the complex structures associated with the heterojunction bipolar transistor, which leads to a low yield.

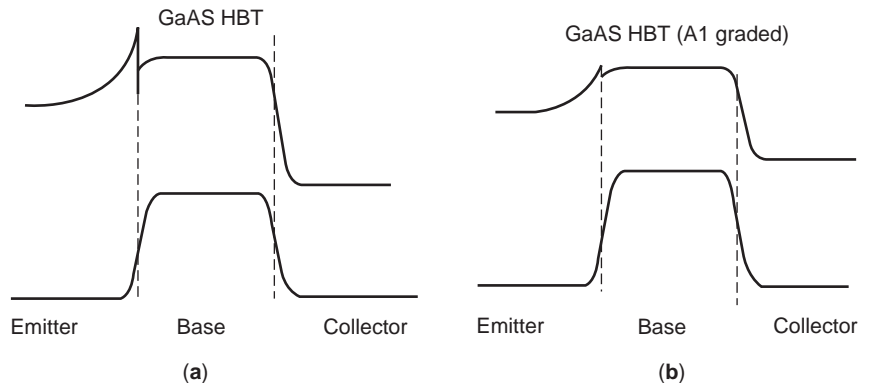


Figure 13. (a) HBT band diagram; (b) Al-graded HBT band diagram.

In digital circuits, the low values of the base resistance and the short electron transit time from emitter to collector enable fast device operation (ON/OFF switching speeds of < 10 ps). The larger bandgap in AlGaAs compared with Si means that larger drive voltages are required for III-V HBTs. In a number of analog circuit configurations, such as amplifiers and high-speed digital-to-analog converters, some of the HBT features are highly desirable to systems designers, particularly the uniformity of the turnon voltage of the emitter-base junction, the absence of trapping effects typical of field-effect devices (where hot electrons are injected into the substrate or into the AlGaAs layer of a heterojunction device), and a low $1/f$ noise. Furthermore, the lower base resistance in the III-V HBTs leads to lower power consumption, when compared with the Si bipolar transistor.

Useful complementary materials for both HEMT and HBT devices are $\text{In}_{0.53}\text{Ga}_{0.47}\text{As}$ and $\text{In}_{0.52}\text{Al}_{0.48}\text{As}$, as they are both lattice-matched to InP. The main advantages offered are

- Reliable technique for the growth of these materials
- Electron mobility 1.6 times higher than in GaAs, resulting in faster devices
- Smaller bandgap (0.75 eV) compared with 1.42 eV for GaAs, leading to a lower turnon voltage, reduced power consumption, and lower voltage supply

A further advantage of the InP substrate is its higher thermal conductivity.

11. APPLICATIONS

High-speed transistors based on gallium arsenide, such as MESFET, HEMT, and HBT, have found wide applications in microwave monolithic integrated circuits (MMICs).

At the early stage of development of GaAs technology, high-speed transistors based on GaAs were used only for defense and space applications because of high-performance system demand; more recently, the huge growth of commercial wireless and fiberoptic communication systems has opened up new application areas for those devices. GaAs MESFET was the first developed high-speed transistor, used for consumer wireless products; a few years later, HEMT and HBT, succeeded it. Mainly III-V based devices are currently used for amplifiers in consumer wireless communications. Initially, when the analog cellular phone market was developing, silicon-based transistors, such as BJT, were exclusively used for power amplifier applications because of their low cost and high-volume production capability. At that time GaAs technology had not yet emerged, so cost and volume requirements could not be met.

By the early 1990s, the GaAs MESFET, which was more efficient, was quickly replacing the Si-based transistor (BJT). The GaAs MESFET manufacturing technology has matured rapidly; cost and manufacturability have become competitive with those of silicon BJTs. In the full-duplex analog cellular phone, output power amplifier noise figures provided by GaAs MESFET has led to

relaxed filtering requirements, enabling a consistent cost reduction, greater integration capability, and improvement efficiency.

In the mid-1990s, cellular phone systems generally ran on digitally modulated schemes such as GSM and CDMA. In a short time the analog cellular phone was replaced by a digital one. Consequently, greater efficiency, lower power consumption, better noise figure, and higher linearity were required; unfortunately the classical MESFET was not able to provide such characteristics. For these reasons a more efficient GaAs-based transistor belonging to the field-effect transistor family, the high-electron-mobility transistor (HEMT), came out. HEMTs, and subsequently pseudomorphic HEMTs, replaced GaAs MESFETs in many application. At the same time, a new bipolar GaAs-based transistor, known as the *heterojunction bipolar transistor* (HBT), was developed. It exhibits greater efficiency than does the common silicon-based bipolar transistor; in many applications GaAs MESFETs were replaced by GaAs HBTs, which shows greater efficiency and smaller size, while providing adequate linearity and low noise figure.

One of the main advantages of HBTs in digital cellular phones, as well as all mobile applications, is that they require only a single polarity power supply, which is an important factor for size and weight reduction.

The most recent research efforts at TRW (Redondo Beach, CA) have shown a new commercially viable technology that monolithically integrates both HEMTs and HBTs in the same MMIC. This technology has potential applications in many applications, including single-chip transmit-receiver circuits, which combine HEMT low-noise front ends with HBT high-linearity output stages along with PIN diode variable gain control.

Acknowledgments

The author gratefully acknowledges the support of A. Cidronali, M. Camprini, and I. Magrini in the preparation of the manuscript. This work was partially supported by the European Project TARGET, Network of Excellence in the VIFW.

FURTHER READING

- M. Shur, *Physics of Semiconductor Devices*, Prentice-Hall, 1990.
- P. H. Ladbrooke, *MMIC Design; GaAs FETs and HEMTs*, Artech House, 1989.
- D. V. Morgan and R. H. Williams, *Physics and Technology of Heterojunction Devices*, IEEE, 1991.
- D. A. Neamen, *Semiconductor Physics and Devices, Basic Principles*, Irwin, 1997.
- K. Heime, *InGaAs Field-Effect Transistors*, RSP—Wiley, 1989.
- B. G. Streetman and S. Banerjee, *Solid State Electronic Devices*, Prentice-Hall, 2000.
- J. S. Yuan, *SiGe, GaAs and InP Heterojunction Bipolar Transistor*, Wiley-Interscience.
- P. Chavarkar and U. Mishra, Field effect transistors: FETs and HEMTs, in *Handbook of Thin Film Devices*, Vol. 1, Chap. 3.

- W. Liu, *Fundamentals of III-V Devices: HBTs, MESFETs, and HFETs/HEMTs*, Wiley.
- P. H. Ladbrooke, *MMIC Design: GaAs FETs and HEMTs*, Artech House.
- P. Roblin, L. Rice, S. Bibyk, and H. Morkoc, Nonlinear parasitic in MODFETs and MODFET I-V characteristics, *IEEE Trans. Electron. Devices* **35**:1207–1214.
- A. Cho, *Film deposition by molecular beam techniques*, *J. Vac. Sci. Technol.* **8**:S31–S38 (1971).
- A. Cho and J. Arthur, Molecular beam epitaxy, *Prog. Solid-State Chem.* **10**:157–192 (1975).
- G. Turner, B. Nechay, and S. Eglash, Frequency-domain analysis of time dependent reflection high-energy electron diffraction intensity data, *J. Vac. Sci. Technol. B* **8**:283–287 (1990).
- C. T. Foxon, MBE growth of GaAs and III-V alloys, *J. Vac. Sci. Technol. B* **1**(2):293–297 (1983).
- J. Neave, B. Joyce, P. Dobson, and N. Norton, Dynamics of film growth of GaAs by MBE from RHEED observations, *Appl. Phys. A* **31**:1–8 (1983).
- P. Cohen, P. Pukite, and J. van Hove, and C. Lent, Reflection high energy electron diffraction studies of epitaxial growth on semiconductor surfaces, *J. Vac. Sci. Technol. B* **3**:1251–1258 (1986).
- T. Block, K. Eyink, D. Neikirk, and B. Streetman, Diffraction condition dependence of RHEED dampening during MBE growth, *SPIE Proc. Epitaxial Growth Process.* **2140**:10–24 (1994).
- M. Ohring, *The Material Science of Thin Films*, Academic Press, 1992.
- G. Petrich, P. Pukite, A. Wowchak, G. Whaley, P. Cohen, and A. Arrot, On the origin of RHEED intensity oscillations, *J. Crystal Growth* **95**:23–27 (1989).
- J. Arthur, "Interaction of Ga and As₂ molecular beams with GaAs surfaces," *J. Appl. Phys.* **39**:4032–4033 (1968).
- R. Fischer, J. Klem, T. Drummond, R. Thorne, W. Kopp, H. Morkoç, and A. Cho, Incorporation rates of gallium and aluminum on GaAs during molecular beam epitaxy at high substrate temperatures, *J. Appl. Phys.* **54**(5):2508–2510 (1983).
- G. Metzger and A. Calawa, Effects of very low growth rates on GaAs grown by molecular beam epitaxy at low substrate temperatures, *Appl. Phys. Lett.* **9**(1):818–820 (1983).
- Y. Horikoshi, M. Kawashima, and H. Yamaguchi, Migration enhanced epitaxy of GaAs and AlGaAs, *Jpn. J. Appl. Phys.* **27**:169–179 (1988).

GALLIUM NITRIDE FOR ELECTRONICS

JONG-WOOK LEE
Kyung Hee University
Korea

ILESANMI ADESIDA
University of Illinois at Urbana-
Champaign

1. INTRODUCTION

The advent of blue light-emitting diodes (LEDs) and short-wavelength blue-violet laser diodes using the III-nitride alloys (AlN, GaN, and InN) have opened up an era of new optical devices that was not possible with the established

III-V material systems based on GaAs, AlAs, GaP, InAs, and related alloys. The direct bandgap and a wide spectrum of bandgap energies (0.7 eV for InN, 3.4 eV for GaN, and 6.2 eV for AlN) of III-nitride semiconductors make them suitable for a wide range of optoelectronic applications. Fundamental breakthroughs in the late 1980s in growth technologies such as improved epitaxial quality using AlN buffers [1,2] and the development of p-type conductivity [3,4] led to the realization of blue light-emitting diodes (LEDs) in 1993 [5,6].

Following the tremendous progress in material quality and device processing, a worldwide market for nitride-based devices has developed. One of the highest profile markets for nitride-based LEDs is in mobile phones, particularly blue LEDs for keypads and white LEDs for the liquid crystal display (LCD) backlight. Nitride-based LEDs also offer great promise for solid-state lighting applications such as architectural lighting, machine vision, illumination for signage, flashlights, and decorative lights. The market for high-brightness LEDs (HB-LEDs) in lighting applications has grown rapidly with an overall market in the billions of dollars [7,8]. Based on continuing positive trends in this dynamic industry, the market for HB-LEDs is projected to grow to ~\$5.0 billion by 2007 [9]. In terms of materials, the market was dominated by InGaN-based devices, which accounted for 68% of total HB-LED sales in 2002. White LEDs are considered very promising for commercial market for general illumination due to progress in lumen output, with higher efficiencies than that of incandescent lamps. With the introduction of blue-violet laser diodes [10], the development of next generation optical storage systems (e.g., DVD drives and recorders), is also underway [11]. Currently, the semiconductor industry is undergoing massive changes which is partly driven by III-nitride semiconductors and associated products.

2. APPLICATIONS OF GALLIUM NITRIDE ELECTRONICS

In addition to their usefulness in optoelectronic applications, GaN-based devices also have excellent electronic properties such as high critical breakdown fields, high saturation velocity, and good thermal conductivity. Many laboratories around the world have demonstrated microwave power performance for GaN devices that are far superior to the performance of other solid-state device technologies. The GaN-based high-electron-mobility transistor (HEMT) is considered an ideal candidate for high-power and high-temperature RF/microwave applications. GaN HEMTs can operate at high speeds, at high power levels, at high temperatures (~500°C), and also in very harsh (i.e., corrosive or high radiation) environments. Electronic systems that can reliably operate under these conditions are currently being sought in industries such as wireless communications, aerospace, automotive, petroleum, and power generation.

Commercial and military applications of GaN-based electronics are numerous and diverse. Power amplifiers (PAs) in the transmitters of 2.5G and 3G cellular base stations are promising and highly competitive market for GaN HEMTs. High-power devices based on GaN clearly

have many advantages in this market over Si and GaAs with the capability of delivering continuous high power levels without stringent cooling requirements. Currently, silicon LDMOS (laterally diffused metal-oxide-semiconductor) is the primary technology in use. However, the LDMOS technology is expected to reach its fundamental limit due to high power and high linearity requirements of next-generation PAs. GaN HEMTs are expected to enter the cellular base-station PA market sooner rather than later. In fact, high-performance wideband UMTS GaN PAs have already been demonstrated [12]. Reliability issues required for widespread commercial usage are yet to be fully addressed.

The automotive and aerospace industry represents another large potential market, where heat-tolerant GaN electronics incorporated in control systems would improve performance and reliability of the overall system. Wide bandgap GaN-based devices would allow bulky hydraulics (e.g., control actuators) and mechanical control systems (e.g., engine-gearbox-driven fuel pumps) to be replaced with solid-state power electronics. Replacement of these systems would reduce the weight and complexity of the overall system.

Radar and satellite-communications links, which operate at microwave frequencies, would benefit from GaN-based electronics as well. GaN electronics can deliver higher power levels per chip area than either Si or GaAs, and thus smaller system components can be realized. In addition, high power (dissipated handling capability allows for smaller cooling systems, so size reductions would significantly lower the overall payload weight and translate into cost savings in delivering satellites into orbit. The petroleum industry seeks to use GaN-based sensors to monitor environmental conditions within an oil well (well logging) where temperatures can be as high as 300°C. Radiation-hardened electronic instrumentation systems based on widegap GaN could also be implemented to directly monitor reactor conditions in nuclear power plants.

Although, GaN-based electronic devices are considered primarily for high-power and high-temperature applications, preliminary results also suggest that they are suitable for microwave low-noise applications. Further improvements in minimum noise figures are expected with optimization of GaN HEMTs. The low noise performance coupled with excellent high voltage capability make GaN HEMTs ideal candidates for robust low-noise amplifiers (LNAs). These properties of GaN HEMTs would eliminate the need for additional protection circuits, thus improving the system noise figure while simplifying overall system design. The excellent microwave power capabilities and the development of low-noise GaN HEMTs provide a path to the realization of highly linear, broadband, and robust transceiver systems.

3. MATERIAL PROPERTIES

The crystal structure of GaN is a hexagonal or wurtzite structure, as shown in Fig. 1, where the bilayers consist of two closely spaced hexagonal layers, one formed by Ga atoms and the other formed by N atoms. The compound

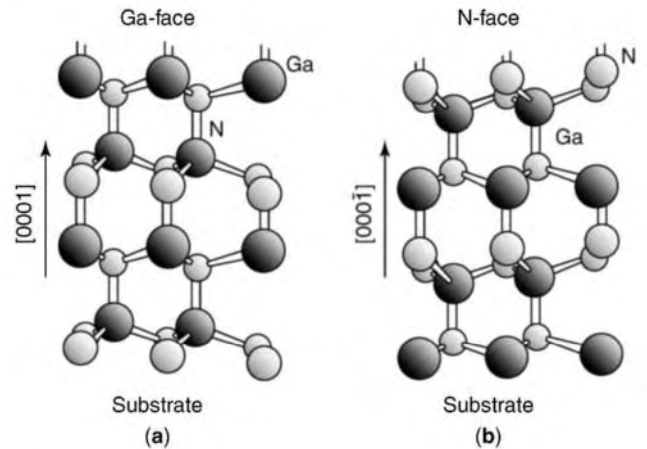


Figure 1. Schematic of (a) Ga-face and (b) N-face wurtzite GaN crystal structures [13].

structure exhibits two different sequences (Ga face and N face) in the atomic layers. The lack of inversion symmetry with the strong ionicity of the covalent bonds leads to the polarization vectors, and these polarization vectors are additive along the *c*-axis of the wurtzite crystal, resulting in macroscopic polarization fields. In AlGaN/GaN hetero-structures, there are two different polarizations: strain-induced (piezoelectric) polarization and zero-strain (spontaneous) polarization. The magnitude and direction of the electric fields associated with these polarization effects depend on the substrate, growth orientation, and nature of the surface (Ga-face or N-face). The most common nitride structures are grown along the [0001] direction with Ga-terminated surface. The high-polarization electric fields in the AlGaN layer induce a high two-dimensional electron gas (2DEG) with very high sheet carrier density at the AlGaN/GaN interface without intentional doping [13]. Due to large piezoelectric constants, the piezoelectric effect is important in determining the charge control model of AlGaN/GaN HEMTs.

As discussed earlier, GaN-based transistors are promising candidates for high-power and high-temperature applications due to the materials' superior electronic properties. Table 1 shows the material parameters for wide-bandgap semiconductors (GaN and 4H-SiC) as well as for Si and GaAs [14–17]. The obvious difference between GaN and conventional semiconductors is the wide bandgap, which results in significantly lower intrinsic carrier density for GaN. This allows GaN-based devices

Table 1. Material Properties of Various Semiconductors

Physical Property/Material	Si	GaAs	4H-SiC	GaN
Bandgap (eV)	1.12	1.43	3.2	3.4
Electron mobility (cm ² /Vs)	1350	8500	800	1500
Peak electron saturation velocity (cm/s) × 10 ⁷	1	1	2	1.5
Breakdown field (V/cm) × 10 ⁵	3	4	32	34
Thermal conductivity (300 K) (W/cmK)	1.5	0.5	3.3	1.3
Dielectric constant	11.8	12.8	9.7	9.5

to operate at much higher temperatures. Also, the material system has high breakdown fields (≥ 3 MV/cm) and high saturation velocity (1.5×10^7 cm/s). Breakdown field is a very important criterion for high-power electronics, since the maximum output power for a class A amplifier can be estimated from the following expression

$$P_{\max} = \frac{(V_{\text{BK}} - V_{\text{knee}})^2}{8R_L},$$

where R_L is the load resistance, V_{BK} is a transistor's breakdown voltage, and V_{knee} is the knee voltage, defined as the voltage at which the transistor current saturates. It is obvious that a high-power output requires high breakdown voltage, which in most cases is directly related to the critical breakdown field. From Table 1, it can be seen that the breakdown field for GaN is much higher than that for GaAs and Si. It means that GaN-based devices can withstand higher bias voltages, thus producing higher total power output.

The current drive capability of AlGaIn/GaN heterostructure is also excellent due to very high sheet carrier density and high saturation velocity. The high conduction band offsets at AlGaIn/GaN interfaces results in high electron mobilities (≥ 2000 cm²/Vs [18]). Because of the strong spontaneous and piezoelectric polarization effects, AlGaIn/GaN heterostructure typically has 2DEG with sheet density values of about 1×10^{13} /cm² with no intentional doping [19]. These values are higher than those seen in AlGaAs/InGaAs and InAlAs/InGaAs heterostructures. In the form of AlGaIn/GaN HEMTs, these transport properties translate to both high current drive capability and high breakdown voltage. High power operation is further facilitated by the use of semiinsulating SiC substrates that are characterized by high thermal conductivity (3.3 W/cmK).

By combining various materials' parameters, the overall potential of any semiconductor material system for high-power, high-frequency performance can be predicted using well-known figures of merit (FoMs). For example, Johnson's figure of merit, $\text{JFoM} = (E_C v_{\text{sat}}/2\pi)^2$ (where E_C is the critical breakdown field and v_{sat} is the saturation velocity) [20], defines the power \times frequency² product for the transistor and determines its output power capability at given frequencies. In addition, Shenai's figure of merit, $Q_{\text{F1}} = \lambda \sigma_A$ (where λ is the thermal conductivity and σ_A is the conductance of the channel) [21], measures the power-handling capability in terms of the dissipated power. Alekseev et al. [22] proposed an extended definition of Shenai's figure of merit, $Q_{\text{FS}} = \lambda_{\text{sub}} \sigma_A$, which takes into account thermal conductivity of the substrate material (sapphire or SiC). Table 2 compares the FoMs calculated for GaN- and GaAs-based devices. It can be seen that GaN is a far more superior material to GaAs for high-power and high-frequency applications.

4. AlGaIn/GaN HEMT OPERATION AND FABRICATION

The basic principle of HEMT operation involves the transfer of electrons from ionized donor impurities in the wider-

Table 2. Comparison of GaN- and GaAs-Based Devices for High-Power and High-Frequency Performance^a

Figures of Merit (FoMs)	GaAs	GaN on Sapphire	GaN on SiC
$\text{JFoM} = (E_C v_{\text{sat}}/2\pi)^2$	1	100	100
$Q_{\text{F1}} = \lambda \sigma_A$	1	22	22
$Q_{\text{FS}} = \lambda_{\text{sub}} \sigma_A$	1	5	76

^aResults are normalized to GaAs.

bandgap semiconductor (e.g., AlGaIn) to form a 2DEG in a potential well at the AlGaIn/GaN hetero-interface. The term "high electron mobility transistor" is used because the structure takes advantage of the superior transport properties (high mobility and velocity) of electrons in the lightly doped semiconductor material (e.g., GaN).

A typical AlGaIn/GaN HEMT structure is shown in Fig. 2; it consists of an AlGaIn barrier layer grown on GaN channel layer. The device structures are mainly grown on sapphire or semiinsulating SiC substrates. Since neither of these substrates is lattice-matched to GaN, an AlN buffer layer is generally used to isolate the channel layer from the substrate. Defects and dislocations occur in the epitaxial layers due to lattice mismatch, with typical dislocation densities on the order of 10^8 – 10^9 /cm². The lattice mismatches of GaN on sapphire and SiC substrates are 13% and 3.1%, respectively; therefore, the GaN crystal quality is better on SiC. As the thermal conductivity of SiC is about 10 times that of sapphire, it is evident that SiC is better suited for high-power and high-temperature applications.

We delineate a typical device fabrication procedure here. The first step for the device fabrication is mesaisolation, which can be etched down to the undoped GaN using Cl₂/Ar plasma in an inductively coupled-plasma reactive-ion etch (ICP-RIE) system. Next, ohmic contacts are formed by rapid thermal annealing of either evaporated Ti/Al/Ti/Au [23] or Ti/Al/Mo/Au [24] in N₂ ambient. A pre-treatment of the ohmic contact area using SiCl₄ plasma in a RIE is performed prior to Ti/Al/Ti/Au (Ti/Al/Mo/Au) metallization. In the case of Ti/Al/Mo/Au ohmic metallization, the surface morphology of the annealed contact is very smooth as well as having low specific contact resistivity. No degradation in contact resistance was observed when the contact was subjected to long-term annealing at

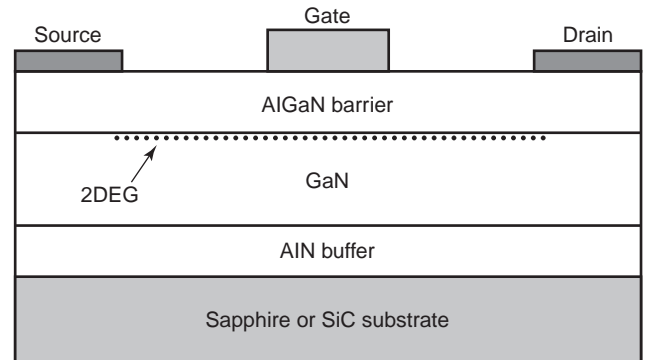


Figure 2. Basic AlGaIn/GaN HEMT structure.

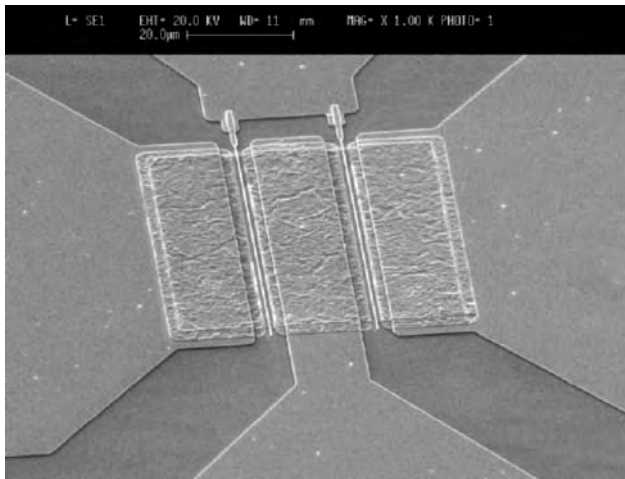


Figure 3. Micrograph of a GaN HEMT.

500°C for 360 h, demonstrating excellent thermal stability. T-shaped gates are defined using a trilayer PMMA/P(MMAMAA)/PMMA and electron-beam lithography. Ni/Au metals are then evaporated for gate metallization. Overlay metallization on ohmic contacts and measurement pads are also deposited during gate formation. Silicon nitride passivation is then deposited. Fig. 3 shows the micrograph of a GaN HEMT.

5. STATE-OF-THE-ART AlGaIn/GaN HEMTs

The first AlGaIn/GaN HEMTs were demonstrated by Khan et al. in 1994 [25]. Transistors with 0.25 μm gate length produced a current density of 60 mA/mm and a transconductance of 27 mS/mm. Since then, dramatic progress has been made in material growth and process technology for AlGaIn/GaN HEMTs. A breakdown voltage as high as 570 V in an AlGaIn/GaN HEMT with a source–drain spacing of 13 μm and a gate length of 0.5 μm using an overlapping gate structure was reported [26]. AlGaIn/GaN HEMTs with current density of 2.1 A/mm have also been reported [27]. A power density as high as 10.7 W/mm at 10 GHz has been achieved on GaN HEMTs [28]; however, their suitability for power applications at frequencies ≥ 30 GHz is currently being limited by the speed of these devices.

5.1. High-Speed Performance

AlGaIn/GaN HEMTs with a unity current gain cutoff frequency (f_T) of 110 GHz and a maximum frequency of oscillation (f_{max}) of > 140 GHz have been demonstrated by reducing the gate length down to 50 nm [29]. However, this reduction of gate length leads to a decrease in breakdown voltage.

To achieve higher performance, indium has been utilized as a surfactant during the growth of AlGaIn/GaN HEMTs [30]. A demonstration of the concept used a MOCVD-grown epilayer which consists of a 100 nm AlN buffer, 2 μm undoped GaN, a 5-nm undoped Al_{0.25}Ga_{0.75}N spacer, a 10-nm Si-doped ($\sim 5 \times 10^{18}/\text{cm}^3$) Al_{0.25}Ga_{0.75}N

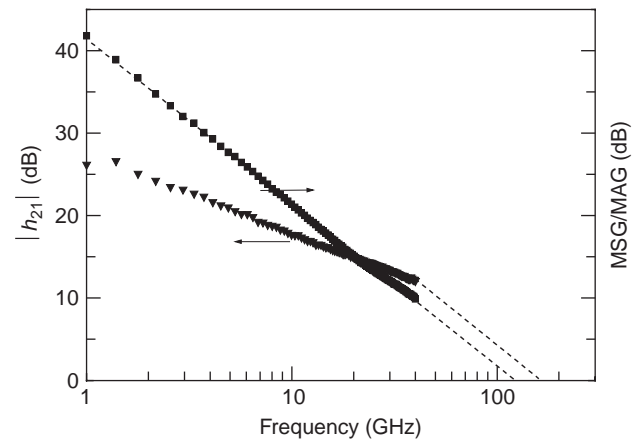


Figure 4. Short-circuit current gain ($|h_{21}|$) and maximum stable/maximum available gain (MSG/MAG) of a 0.12 μm × 100 μm AlGaIn/GaN HEMT on SiC substrates. The device was biased at $V_{DS} = 8$ V and $V_{GS} = -3.95$ V [31].

charge supply layer, and a 10-nm undoped Al_{0.25}Ga_{0.75}N barrier layer. The layer was grown on 4H-SiC. A low-level flux of trimethylindium (TMI) during the growth of the structure helped in improving the surface and interface roughness through the incorporation of trace amounts of indium. Hall measurements showed a sheet carrier concentration of $1.1 \times 10^{13}/\text{cm}^2$ and an electron mobility of 1300 cm²/Vs at room temperature on as-grown wafers.

A device fabricated from this layer demonstrated a typical drain current density of 1.23 A/mm, peak transconductance of 314 mS/mm, and a gate drain breakdown voltage of over 60 V. Figure 4 shows the short-circuit current gain ($|h_{21}|$) and maximum stable gain/maximum available gain (MSG/MAG) derived from on-wafer *S*-parameter measurements as a function of frequency for the 0.12-μm-gate-length device. The effect of pad parasitics was deembedded by conventional *Y*-parameter subtraction. The values of unity current gain cutoff frequency (f_T) and maximum frequency of oscillation (f_{max}) were determined by extrapolation of the $|h_{21}|$ and MSG data at 20 dB/decade. At a drain bias of 8 V and a gate bias of −3.95 V, an f_T of 121 GHz, and an f_{max} of 162 GHz were obtained, which to the best of the authors' knowledge are the highest data ever reported for GaN-based HEMTs [31]. This excellent RF performance is attributed to the high quality of material and also to the optimized device processing.

5.2. High-Power Performance

In terms of power, wide-bandgap AlGaIn/GaN HEMTs on semi-insulating SiC substrates have yielded a continuous-wave (CW) power density of 32 W/mm at 4 GHz and 16.5 W/mm at 10 GHz, and a pulsed power output of 113 W at 1.95 GHz, making them promising candidates for next-generation commercial power amplifier systems [32–34]. Also, more recent millimeter-wave power performance of GaN HEMTs suggests that operation of GaN HEMTs can be extended to K/Ka band. At 20 GHz, 3 W/mm CW power density with 22.5% power-added efficiency

(PAE) has been attained for 0.3- μm -gate-length devices [35] and 6.6 W/mm CW power density with 35% PAE for 0.15- μm -gate-length devices [36]. At 35 GHz, an output power density of 4.13 W/mm with 23% of PAE and 7.54 dB of linear gain were achieved at a drain bias of 30 V [37]. The combined results of power density, PAE, and gain that have been achieved using GaN HEMT technology are impressive. For comparison, silicon-based transistors can efficiently amplify signals up to only 2–3 GHz. GaAs transistors can handle 10 GHz but deliver a power density of less than 1 W/mm at that frequency.

At relatively low frequencies, the field-plated technique have achieved impressive power results [32,33]. Figure 5 shows the measured CW power, gain, and PAE of a modified field-plated device at 10 GHz, where the AlGaIn/GaN HEMTs with an optimized gate structure enabled the device to operate at higher drain biases than did conventional gate structure, yielding improved power levels. Details of the device structure are reported elsewhere by Thompson et al. [33]. Power data were taken on wafer using an automatic load-pull system at room temperature. The large signal performance of a 0.35- μm -gate-length device was measured when the device was biased at a drain-source voltage of 60 V. The device had a saturated output power density of 16.5 W/mm and PAE of 47% as shown in Fig. 5.

State-of-the-art CW power performances at 20 GHz were obtained from a 0.25 $\mu\text{m} \times 100 \mu\text{m}$ AlGaIn/GaN HEMT on 4H-SiC substrates [38]. The devices exhibited high current density, transconductance, and millimeter-wave output power density. The large-signal performance of the device at 20 GHz is shown in Fig. 6. The device was biased with a drain-source voltage of 30 V at a DC drain current of 620 mA/mm. The device had a saturated output power of 6.4 W/mm with an associated gain of 2.9 dB and PAE of 16%. The peak efficiency was 22% with an output power of 5.8 W/mm and gain of 6.1 dB.

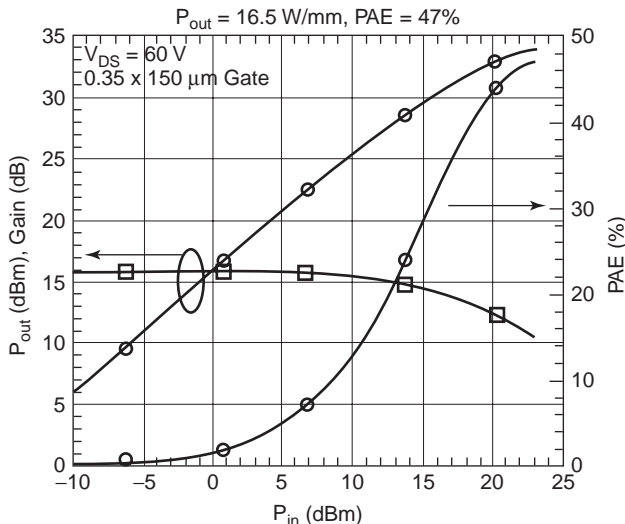


Figure 5. CW power sweep of a 0.35 \times 150- μm field-plated gate device at 10 GHz, demonstrating output power of 16.5 W/mm and PAE of 47% when operated at 60 V drain bias [33].

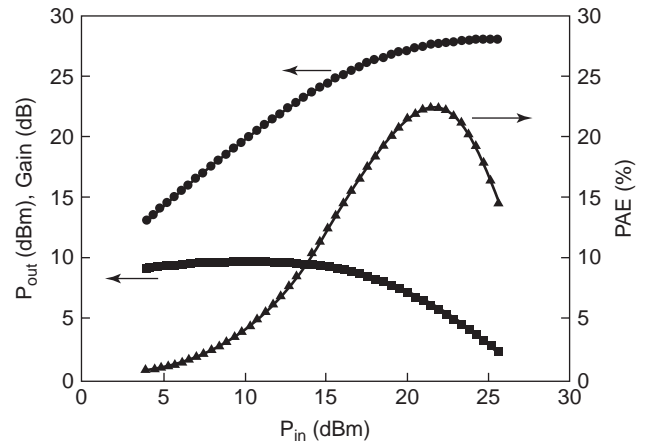


Figure 6. Large-signal performance of a 0.25 \times 100- μm AlGaIn/GaN HEMT on 4H-SiC at 20 GHz when biased with $V_{DS} = 30$ V and $V_{GS} = -1.87$ V, saturated output power was 6.4 W/mm with 2.9 dB gain and 16% PAE [38].

Figure 7 shows the large signal performance of a 0.25 \times 200- μm AlGaIn/GaN HEMT at 30 and 35 GHz [37]. With a drain voltage of 30 V and a drain current of 325 mA/mm, the device had a saturated output power density of 5.43 W/mm at 30 GHz with 9.17 dB gain and PAE of 33%. When the device was tested at the same bias conditions at 35 GHz, the device delivered a remarkable output power of 4.13 W/mm with a peak PAE of 23% and a linear gain of 7.54 dB. This performance vividly demonstrates the potential for very-high-power solid-state amplifiers employing 0.25- μm -gate-length GaN-based HEMTs to replace TWT amplifiers in space-based millimeter-wave communication systems.

The combined results of power density, PAE, and gain that have been achieved to date using GaN HEMT technology are impressive. No other solid-state device technologies have demonstrated these capabilities. Figure 8 shows the various reported power densities over a fre-

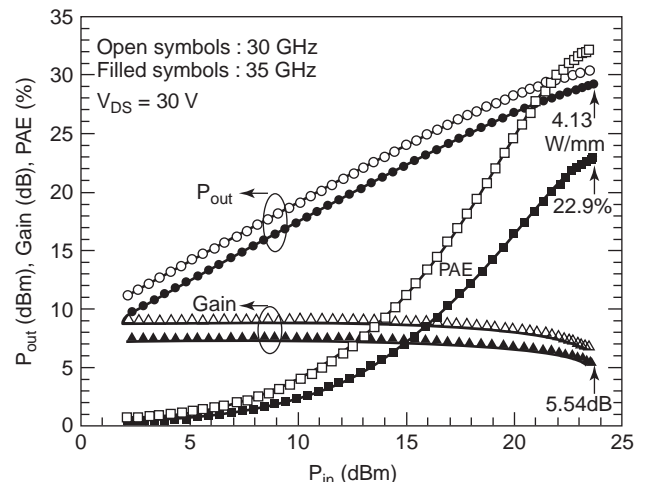


Figure 7. Output power, PAE, and gain as a function of input power of a 0.25 $\mu\text{m} \times 4 \times 50 \mu\text{m}$ AlGaIn/GaN HEMT at 30 and 35 GHz [37].

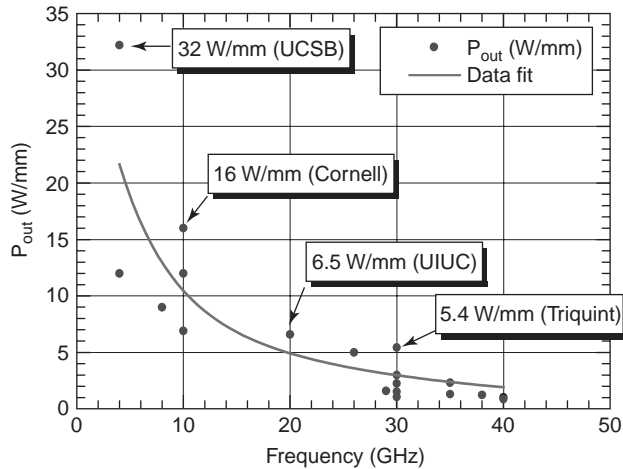


Figure 8. Reported power densities over a frequency range of 4–40 GHz are shown with symbols. The solid line represents a best fit to the points.

quency range of 4–40 GHz. With these results, GaN HEMTs have demonstrated at least an order of magnitude higher power density over the existing Si- and GaAs-based RF and microwave transistor technologies. The excellent material properties of AlGaIn/GaN material system have indeed delivered a new level of microwave power and frequency operation.

5.3. Low-Noise Performance

In parallel with the improvement in power density results, microwave noise performance has also shown rapid improvement. From the first report [39] on the noise characteristics of GaN HEMTs to more recent results [40–42], it has been shown that these devices exhibit promising microwave noise properties. The minimum noise figure of 0.25- μm -gate-length AlGaIn/GaN HEMTs [43] is comparable to the results reported previously for a pseudomorphic GaAs HEMT with similar gate length [44]. The investigation of GaN-based devices for microwave noise applications is of interest because wide-bandgap GaN with its relatively low intrinsic carrier generation and the high breakdown fields provides an enabling technology that can sustain a higher input power and breakdown voltages at higher temperatures than GaAs- and Si-based devices.

Figure 9 shows the measured microwave noise performance of 0.12- μm -gate-length GaN HEMTs on SiC substrate [40]. The minimum noise figure (NF_{min}) and associated gain (G_a) of the devices were measured on wafer using an ATN NP5 noise parameter test set over the 4–18 GHz frequency range. For these measurements, devices were biased at $V_{\text{DS}} = 10\text{ V}$ and $V_{\text{GS}} = -4.8\text{ V}$. The devices exhibited an NF_{min} of 0.77 dB and 0.99 dB at 12 and 18 GHz, respectively. This excellent noise performance is attributed to the higher gains engendered by the smaller gate length and the excellent low leakage Schottky gate characteristics. The current results show significant improvement compared to previously reported 0.25- μm AlGaIn/GaN HEMTs that had minimum noise figures of 1.8 dB [39] and 2.0 dB [42] at 18 GHz, respectively.

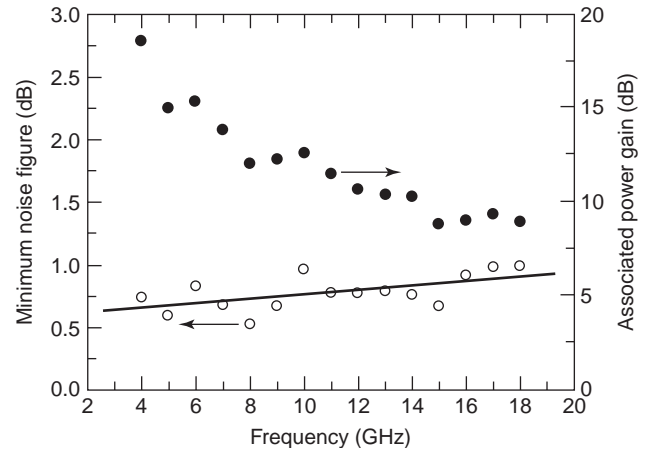


Figure 9. Minimum noise figure (NF_{min}) and associated power gain (G_a) versus frequency for a 0.12 μm AlGaIn/GaN HEMT; the solid line is the modeled minimum noise figure for the extrinsic device; the bias condition was $V_{\text{DS}} = 10\text{ V}$ and $V_{\text{GS}} = -4.8\text{ V}$ [40].

6. GALLIUM NITRIDE RF AND MICROWAVE POWER AMPLIFIERS

6.1. Advantages of GaN-Based Power Amplifiers

High-power-density GaN HEMTs provide many advantages for the realization of power amplifiers: (1) higher output power per unit area needs smaller device size and translates to broader bandwidth for given output power, (2) small device size reduces matching circuit complexity, and (3) efficient heat dissipation through high thermal conductivity of SiC substrates relieves cooling requirement. For high-power amplifiers where multimillimeter-to-centimeter gate peripheries are needed, large impedance transformation ratio limits useful bandwidth for given output power requirement. With higher power density per picofarad of input/output capacitance of GaN HEMTs than devices based on Si and GaAs, multioctave broadband GaN HEMT amplifiers are realizable. Also, small device size for the same output power rating drastically reduces both the input and output impedance transformation ratios, thus simplifying overall matching circuits. For example, let us consider how high-power-density GaN HEMTs can simplify overall amplifier system. Figure 10 shows a conventional amplifier based on InGaAs pHEMTs, which produce a total output power of 4 W at 20 GHz. With the minimum impedance transformation requirement, the output power of an InGaAs-based HEMT MMIC amplifier is limited to about 1 W at 20 GHz. To deliver a total output power of 4 W, external power combining of multiple MMICs is necessary. The external power combining not only adds to assembly cost but also makes the overall system complicated and large. If GaN HEMTs are utilized for the amplifier, a single GaN MMIC can directly produce 4 W at 20 GHz without bulky external power combiners. Thus, using GaN HEMTs provides simple and compact design, which enhances overall system reliability. These advantages are valuable for applications requiring broad bandwidth, high temperature, and high power operation such as in commercial wireless base stations,

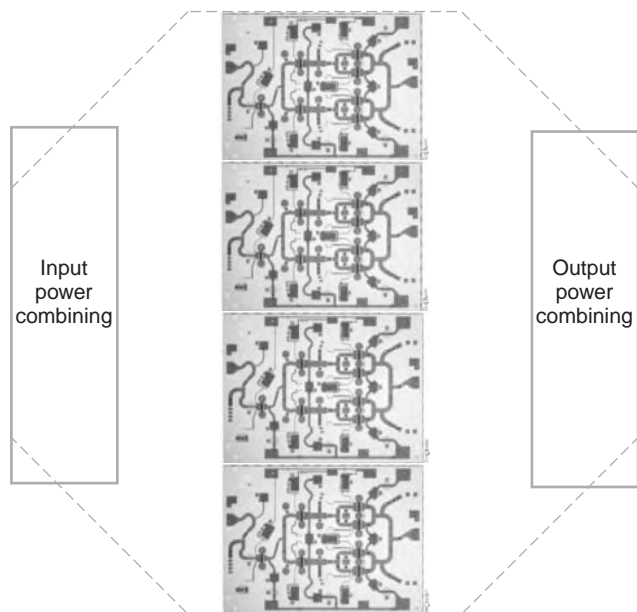


Figure 10. A 20-GHz InGaAs pHEMTs power amplifier system. To deliver overall output power of 4 W, external power combining is required. (From the 6th Widegap III-Nitride Workshop at UCSB; figures of MMIC amplifiers are from Triquint Inc.).

satellite communications, local multipoint distribution system (LMDS), and assorted defense systems.

More recent applications of GaN HEMTs in broadband power amplifiers have included a monolithic nonuniform distributed amplifier with a cascode-connected gain cell [45], an amplifier with *LCR* matching having an input power splitter and an output combiner [46], and a two-stage, reactively matched MMIC amplifier with backside via holes through the SiC substrate [47]. In addition to linear class A operation or nonlinear class AB operation, GaN-based class B amplifiers also have been demonstrated at microwave frequencies. A single-ended class B amplifier employing bandpass filtering at the output resulted in a 36 dBm output with good linearity [48]. In an amplifier with two devices for push-pull operation, a maximum output power of 35 dBm and a PAE of 42% were obtained at 5 GHz [49]. These GaN-based microwave power amplifiers have demonstrated great potential for achieving both high power and broadband performance at microwave frequencies.

6.2. 50-W C-Band GaN HEMT Power Amplifier

A C-band power amplifier is described as an example to show the advantages of using the AlGaN/GaN HEMT for high-power amplifiers [50]. The devices used in the amplifier were 0.6- μm -gate-length GaN HEMTs with maximum drain current of ~ 1 A/mm and a breakdown voltage of 80 V. The power density of a unit device was more than 6 W/mm and a total gate periphery of 8 mm was chosen for the amplifier to achieve 50 W total output power at 6 GHz. The AlGaN/GaN HEMTs typically had an input capacitance of 2.7 pF/mm, similar to that of a GaAs-based HEMT, while the optimum output load was 75 Ω ·mm,

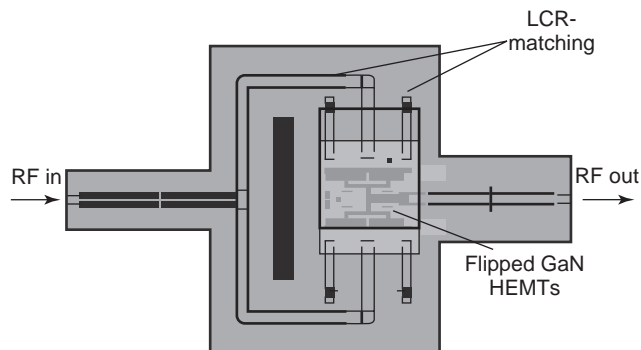


Figure 11. Chip microphotograph of a 50-W GaN-based flip-chip integrated power amplifier incorporating a 8-mm AlGaN/GaN HEMT; die size is about 10×7 mm² [50].

about 2 times that of a GaAs HEMT. Since the GaN HEMT offers 10 times the power density for the same output power, the input transformation ratio is 10 times less, while the transformation ratio is 20 times less than a GaAs HEMT at the output. To achieve 50 W output power using the conventional GaAs-based FET technology (either HEMT or MESFET) the device gate periphery would have to be 80 mm, requiring a challenging input/output impedance transformation ratio.

With the reduced impedance transformation ratio for GaN-based amplifier, an *LCR*-matching network was used to convert the capacitive gate impedance to a real value of $\sim 1.5 \Omega$ within the bandwidth. This was then transformed to the 50 Ω input impedance by an output matching network. At the output, the power load for the 8-mm-wide device was transformed to the 50 W circuit output. The fabricated amplifier is shown in Fig. 11. The circuit was laid out in a coplanar-wave transmission-line system and constructed using a flip-chip integrated-circuit scheme for thermal management and electrical connection. The amplifier exhibited a midband small-signal gain of 14.5 dB when biased at 25 V. Pulsed-power measurement was performed using 0.5 ms pulsewidth and 5% duty cycle. The output power at 6 GHz was 51 W when biased at 39 V with a corresponding power density of 6.4 W/mm. This represents a remarkable power output obtained from a small periphery solid-state FET and simple input/output matching network design.

6.3. Broadband High-Power Cascode GaN HEMT MMICs on SiC Substrates

GaN HEMTs have higher output power per device input/output capacitance ratio than do conventional devices. On the basis of this idea, a broadband high-power cascode GaN HEMT MMIC amplifier with high gain and PAE was fabricated on SiC substrates [45]. Traditionally, distributed amplifiers (DAs) have been used for applications requiring broad bandwidths. DAs offer broadband operation by incorporating gain elements in synthetic lumped-element approximate transmission lines, realized by the transistor capacitances and intervening inductances [51]. This topology allows the addition of transconductance

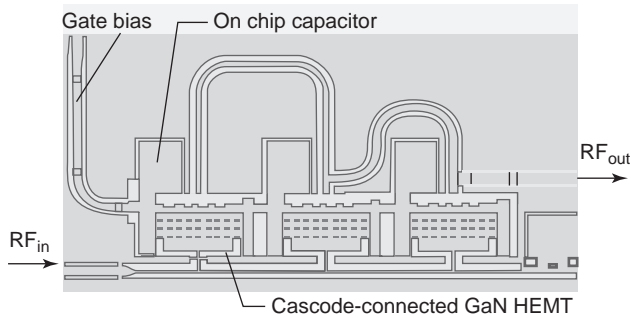


Figure 12. Chip microphotograph of the nonuniform distributed amplifier with cascode-connected GaN HEMTs as gain elements; die size is about $2.5 \times 1.4 \text{ mm}^2$ [45].

without adding device capacitance, thus resulting in excellent gain–bandwidth products.

Figure 12 shows a multioctave broadband GaN HEMT MMIC amplifier fabricated on SiC substrates. It contains three cascode-connected GaN HEMTs as gain elements. Each device has 1 mm of total gate periphery for both the common-source and common-gate devices. The two devices are separated by a 125- μm section of a high-impedance transmission line to further facilitate heat dissipation. Cascode topology reduces the Miller effect, resulting in reduced feedback capacitance. A cascode gain cell exhibited 5 W output power at 8 GHz with a small-signal gain of 19 dB, thus providing high gain and broad bandwidth for the amplifier. All gate CPW line impedances are 80Ω , and the drain-line impedances, from the left- to right-hand sides, are 60Ω , 50Ω , and 30Ω . The drain-line dummy load was removed to prevent power consumption by the synthetic drain-line termination dummy load, thus improving PAE of the amplifier. The gate- and drain-line sections were carefully optimized for optimum power and efficiency using the genetic algorithm method. The resulting amplifier has nonuniform drain-line lengths and impedance to effectively combine output power from three gain elements. The amplifier based on this process yielded a saturated output power of 3–6 W over a DC-to-8 GHz bandwidth with an associated PAE of 13–31%.

6.4. Broadband GaN-Based Flip-Chip Integrated Power Amplifier

With excellent gain–bandwidth product, distributed amplifiers (DAs) are preferred for broadband operation. However, conventional DAs usually exhibit poor output power because nonuniform device loading along the drain line limits effective combining of devices, and also because frequency-dependent attenuation along the gate line supplies limits drive power for the active devices in the later stages.

A new circuit topology employed novel LCR-matching networks in a four-way Wilkinson combiner structure to divide and combine power uniformly from each device. Figure 13 shows a high-power broad band microwave amplifier that used multiple-stage quarter-wavelength transformers for the power combiner to realize the desired bandwidth and impedance transformation ratios [46].

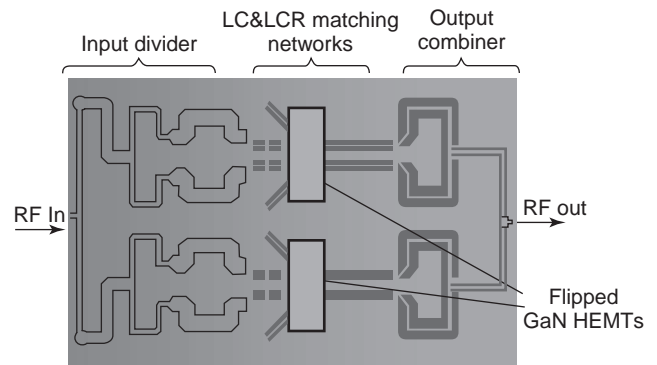


Figure 13. Chip microphotograph of the broadband GaN-HEMT flip-chip integrated power amplifier; die size is about $12 \times 8 \text{ mm}^2$ [46].

Additional LC matching networks were then utilized to reactively compensate for input and output capacitance and provide additional impedance transformation. GaN epitaxial layers grown on sapphire substrates have the advantage of lower cost and availability in larger wafer size than does SiC, but it has poor thermal conductivity. Adequate thermal management was achieved through flip-chip bonding of the device onto a thermally conductive, electrically insulating AlN substrate, which also hosts the matching and combiner networks.

Using devices with $0.7 \mu\text{m}$ gate length and 4 mm gate width, a small-signal gain of 7 dB was obtained over 3–10 GHz bandwidth. A CW output power of 8 W at 9.5 GHz with about 20% PAE was achieved when biased at 24 V, which is a significantly higher output power over the entire bandwidth compared to the results obtained using GaAs-based FET technology.

7. CONCLUSION

This article described the high-speed, high-power, and low-noise performance of GaN HEMTs. Further improvement of device speed, power, and noise figure will be possible with optimization of the GaN HEMT design, growth, and fabrication. In combination with the excellent microwave power capabilities, GaN HEMTs have great potential for other applications such as low noise and high power switching, and will be very attractive for delivering highly linear, broadband, and robust transceiver in future commercial and military communication systems.

Acknowledgment

This work at UIUC was supported by ONR under Contract N00014-01-1-1000 (program monitor: H. Dietrich).

BIBLIOGRAPHY

1. H. Amano, N. Sawaki, I. Akasaki, and Y. Toyoda, Metalorganic vapor phase epitaxial growth of high quality GaN films using an AlN buffer layer, *Appl. Phys. Lett.* **48**: 353–355 (1986).

2. I. Akasaki, H. Amano, Y. Koide, K. Hiramatsu, and N. Sawaki, Effects of AlN buffer layer on crystallographic structure and on electrical and optical properties of GaN and Ga_{1-x}Al_xN grown on sapphire substrate by MOVPE, *J. Cryst. Growth* **98**: 209–219 (1989).
3. H. Amano, M. Kito, K. Hiramatsu, and I. Akasaki, P-type conduction in Mg-doped GaN treated with low-energy electron beam irradiation (LEEBI), *Jpn. J. Appl. Phys.* **28**: L2112–2114 (1989).
4. S. Nakamura, N. Iwasa, M. Senoh, and T. Mukia, Hole compensation mechanism of p-type GaN films, *Jpn. J. Appl. Phys.* **31**:1258–1266 (1992).
5. S. Nakamura, T. Mukai, and M. Senoh, High-power GaN P-N junction blue-light-emitting diodes, *Jpn. J. Appl. Phys.* **30**: L1988–L2001 (1991).
6. S. Nakamura, M. Senoh, and T. Mukai, P-GaN/N-InGaN/N-GaN double heterostructure blue-light-emitting diodes, *Jpn. J. Appl. Phys.* **32**:L8–L11 (1993).
7. T. Whitaker and J. Newey, Things to watch in 2003, *Compound Semiconductors*. **9** (1):23 (2003).
8. HB-LED market reaches \$1.8 billion, *Compound Semiconductors*. **9** (2):17 (2003).
9. High-brightness LEDs 2003–market review and forecast, *Strategies Unlimited* (June 2003).
10. S. Nakamura, M. Senoh, S. Nagahama, N. Iwasa, T. Yamada, T. Matsushita, H. Kiyoku, Y. Sugimoto, T. Kozaki, H. Umemoto, M. Sano, and K. Chocho, High-power, long-lifetime In-GaN/GaN/AlGaN-based laser diodes grown on pure GaN substrates, *Jpn. J. Appl. Phys.* **37**:L309–L312 (1998).
11. J.-W. Lee and I. Adesida, DVD Forum approves blue laser format, *Compound Semiconductors*. **9**(11) (2003).
12. RF micro's nitride operation demos first GaN power amps, *Compound Semiconductors*. **9**(3) (March 2003).
13. O. Ambacher, J. Smart, J. R. Shealy, N. G. Wiemann, K. Chu, M. Murphy, W. J. Schaff, L. F. Eastman, R. Dimitrov, L. Wittmer, M. Stutzman, W. Rieger, and J. Hilsenbeck, Two-dimensional electron gases induced by spontaneous and piezoelectric polarization charges in N- and Ga-face AlGaN/GaN heterostructures, *J. Appl. Phys.* **85**(6):3222–3232 (1999).
14. Y. S. Park, *Semiconductors and Semimetals: SiC Materials and Devices*, Academic Press, New York, 1988, Vol. 52, pp. 195–197.
15. H. Morkoc, S. Strite, G. B. Gao, M. E. Lin, B. Sverdlov, and M. Burns, Large-band-gap SiC, III-V nitride, and II-VI ZnSe-based semiconductor device technologies, *J. Appl. Phys.* **76**: 111–120 (1998).
16. C. E. Weitzel, and K. E. Moore, Silicon carbide and gallium nitride RF power devices, *MRS Symp. Proc.* **483**:111–120 (1998).
17. J. C. Zolper, Junction field effect transistors for high-temperature or high-power electronics, *MRS Symp. Proc.* **483**:83–87 (1998).
18. R. Gaska, J. W. Yang, A. Osinsky, Q. Chen, M. A. Khan, A. O. Orlov, G. L. Snider, and M. S. Shur, Electron transport in AlGaN-GaN heterostructures grown on 6H-SiC substrates, *Appl. Phys. Lett.* **72** (6): 707–709 (1998).
19. L. F. Eastman, V. Tilak, J. Smart, B. M. Green, E. M. Chumbes, R. Dimitrov, H. Kim, O. S. Ambacher, N. Weimann, T. Prunty, M. Murphy, W. J. Scha, and J. R. Shealy, Undoped AlGaN/GaN HEMTs for microwave power amplification, *IEEE Trans. Electron Devices* **48**(3):479–485 (March 2001).
20. E. O. Johnson, Physical limitations on frequency and power parameters of transistors, *RCA Rev.* 163–177 (1965).
21. K. Shenai, R. S. Scott, and B. J. Baliga, Optimum semiconductor for high-power electronic, *IEEE Trans. Electron Devices* **36**(9):1811–1823 (1989).
22. E. Alekseev, D. Pavlidis, N.X. Nguyen, C. Nguyen, and D. E. Grider, Power performance and scalability of AlGaN/GaN power MODFETs, *IEEE Trans. Microwave Theory Tech.* **48**(10):1694–1700 (2000).
23. A. T. Ping, Q. Chen, J. W. Yang, M. A. Khan, and I. Adesida, The effects of reactive ion etching-induced damage on the characteristics of ohmic contacts to n-type GaN, *J. Electron. Mater.* **27**:261–265 (April 1998).
24. V. Kumar, L. Zhou, D. Selvanathan, and I. Adesida, Thermally-stable low-resistance Ti/Al/Mo/Au multilayer ohmic contacts on n-GaN, *J. Appl. Phys.* **92**:1712–1714 (2002).
25. M. A. Khan, J. N. Kuznia, D. T. Olson, W. J. Schaff, J. W. Burm, and M. S. Shur, Microwave performance of a 0.25 μm gate AlGaN/GaN heterostructure field effect transistors, *Appl. Phys. Lett.* **65**(9):1121–1123 (1994).
26. N. Q. Zhang, S. Keller, G. Parish, S. Heikmann, S. P. Denbarrs, and U. K. Mishra, High breakdown GaN HEMT with overlapping gate structure, *IEEE Electron Device Lett.* **21**: 421–423 (Sept. 2000).
27. Q. Chen, J. W. Yang, M. A. Khan, A. T. Ping, and I. Adesida, High transconductance AlGaN/GaN heterostructure field effect transistors on SiC substrates, *Electron. Lett.* **33**:1413–1414 (July 1997).
28. V. Tilak, B. Green, V. Kaper, H. Kim, T. Prunty, J. Smart, J. Shealy, and L. Eastman, Influence of barrier thickness on the high-power performance of AlGaN/GaN HEMTs, *IEEE Electron Device Lett.* **22**: 504–506 (Nov. 2001).
29. M. Micovic, N.X. Nguyen, P. Janke, W. S. Wong, P. Hashimoto, L. M. McCray, and C. Nguyen, GaN/AlGaN high electron mobility transistors with f_T of 110 GHz, *Electron. Lett.* **36**:358–359 (Feb. 2000).
30. M. A. Khan, X. Hu, G. Simin, J. Yang, R. Gaska, and M. S. Shur, AlGaN/GaN metal-oxide-semiconductor heterostructure field effect transistors on SiC substrates, *Appl. Phys. Lett.* **77**:1339–1341 (Aug. 2000).
31. V. Kumar, W. Lu, R. Schwindt, A. Kuliev, G. Simin, J. Yang, M.A. Khan, and I. Adesida, AlGaN/GaN HEMTs on SiC with f_T of over 120 GHz, *IEEE Electron Device Lett.* **23**(8):455–457 (Aug. 2002).
32. Y.-F. Wu, A. Saxler, M. Moore, R. P. Smith, S. Sheppard, P. M. Chavarkar, T. Wisleder, U. K. Mishra, and P. Parikh, 30-W/mm GaN HEMTs by field plate optimization, *IEEE Electron Device Lett.* **25**(3):117–119 (March 2004).
33. R. Thompson, T. Prunty, V. Kaper, and J. R. Shealy, Performance of the AlGaN HEMT structure with a gate extension, *IEEE Trans. Electron Devices* **51**(2):292–295 (Feb. 2004).
34. Y. Ando, Y. Okamoto, H. Miyamoto, N. Hayama, T. Nakayama, K. Kasahara, and M. Kuzuhara, A 110-W AlGaN/GaN heterojunction FET on thinned sapphire substrate, *IEDM Tech. Digest*, Washington, DC, Dec. 2001, pp. 381–384.
35. A. Vescan, R. Dietrich, A. Wieszt, A. Shurr, H. Leier, E. L. Piner, and J. M. Redwing, AlGaN/GaN MODFET's on semi-insulating SiC with 3 W/mm at 20 GHz, *Electron Lett.* **36**: 1234–1236 (July 2000).
36. J. S. Moon, M. Micovic, P. Janke, P. Hashimoto, W.-S. Wong, R. D. Widman, L. McCray, A. Kurdoghlian, and C. Nguyen, GaN/AlGaN HEMT's operating at 20 GHz with continuous-wave

- power density > 6 W/mm, *Electron Lett.* **37**: 528–530 (April 2001).
37. C. Lee, P. Saunier, J. Yang, and M. A. Khan, AlGaIn–GaIn HEMTs on SiC with CW power performance of > 4 W/mm and 23% PAE at 35 GHz, *IEEE Electron Device Lett.* **24** (10): 616–618 (Oct. 2003).
 38. R. S. Schwindt, V. Kumar, A. Kuliev, G. Simin, J. W. Yang, M. A. Khan, M. E. Muir, and I. Adesida, Millimeter-wave high-power 0.25- μ m gate-length AlGaIn/GaN HEMTs on SiC substrates, *IEEE Microwave Wireless Compon. Lett.* **13** (3): 93–95 (March 2003).
 39. A. T. Ping, E. Piner, J. Redwing, M. A. Khan, and I. Adesida, Microwave noise performance of AlGaIn/GaN HEMTs, *Electron Lett.* **36**: 175–176 (2000).
 40. W. Lu, J. Yang, M. A. Khan, and I. Adesida, AlGaIn/GaN HEMTs on SiC with over 100 GHz f_T and low microwave noise, *IEEE Trans. Electron Devices* **48** (3): 581–585 (March 2001).
 41. I. P. Smorchkova, M. Wojtowicz, R. Sandhu, R. Tsai, M. Barsky, C. Namba, P.-S. Liu, R. Dia, M. Truong, D. Ko, J. Wang, H. Wang, and A. Khan, AlGaIn/GaN HEMTs-operation in the K-band and above, *IEEE Trans. Microwave Theory Tech.* **51** (2): 665–668 (Feb. 2003).
 42. W. Lu, V. Kumar, E. L. Piner, and I. Adesida, DC, RF, and microwave noise performances of AlGaIn–GaIn field effect transistors dependence of aluminum concentration, *IEEE Trans. Electron Devices* **50** (4): 1069–1074 (April 2003).
 43. J.-W. Lee, V. Kumar, R. Schwindt, A. Kuliev, R. Birkhahn, D. Gotthold, S. Guo, B. Albert, and I. Adesida, Microwave noise performances of AlGaIn/GaN HEMTs on semi-insulating 6H-SiC substrates, *Electron Lett.* **40** (1): 80–81 (Jan. 2004).
 44. J. Wenger, Quarter-micrometer low-noise pseudomorphic GaAs HEMT's with extremely low dependence of the noise figure on drain-source current, *IEEE Electron Device Lett.* **14** (1): 16–18 (Jan. 1993).
 45. B. M. Green, V. Tilak, S. Lee, H. Kim, J.A. Smart, K. J. Webb, J. R. Shealy, and L. F. Eastman, High-power broad-band AlGaIn/GaN HEMT MMICs on SiC substrates, *IEEE Trans. Microwave Theory Tech.* **49** (12): 2486–2493 (Dec. 2001).
 46. J. J. Xu, S. Keller, G. Parish, S. Heikman, U. K. Mishra, and R. A. York, A 3–10 GHz GaN-based flip-chip integrated broadband power amplifier, *IEEE Trans. Microwave Theory Tech.* **48** (12): 2573–2578 (Dec. 2000).
 47. J. W. Palmour, S. T. Sheppard, R. P. Smith, S. T. Allen, W. L. Pribble, T. J. Smith, Z. Ring, J. J. Sumakeris, A. W. Saxler, and J. W. Milligan, Wide bandgap semiconductor devices and MMICs for RF power applications, *IEDM Tech. Digest*, Washington, DC, Dec. 2001, pp. 385–388.
 48. V. Paidi, S. Xie, R. Coffe, B. Moran, S. Heikman, S. Keller, A. Chini, S. P. DenBaars, U. K. Mishra, S. Long, and M. J. W. Rodwell, High linearity and high efficiency of Class-B power amplifiers in GaN HEMT technology, *IEEE Trans. Microwave Theory Tech.* **51** (2): 643–652 (Feb. 2003).
 49. J.-W. Lee, L. F. Eastman, and K. J. Webb, A gallium nitride push-pull microwave power amplifier, *IEEE Trans. Microwave Theory Tech.* **51** (11): 2243–2249 (Nov. 2003).
 50. Y.-F. Wu, P.M. Chavarkar, M. Moore, P. Parikh, B. P. Keller, and U. K. Mishra, A 50-W AlGaIn/GaN HEMT amplifier, *IEDM Tech. Digest*, 2000, pp. 375–376.
 51. E. L. Ginzton, W. R. Hewlett, J. H. Jasberg, and J. D. Noe, Distributed amplification, *Proc. IRE* **36**: 956–969 (Aug. 1948).

GENERALIZED SCATTERING MATRIX TECHNIQUE

AGOSTINO MONORCHIO

University of Pisa
Pisa, Italy

RAJ MITTRA

Pennsylvania State University
University Park, Pennsylvania

GIULIANO MANARA

University of Pisa
Pisa, Italy

1. INTRODUCTION

Many complex microwave devices can usually be decomposed into a set of elementary waveguide junctions (canonical step discontinuities) that are located at specific transverse reference planes where the waveguide cross section changes abruptly, and are connected through longitudinally uniform waveguide sections. In this context, the mode-matching (MM) technique is capable of providing very accurate results, provided that adequate numbers of higher-order modes—including the evanescent ones—are employed for representation of the field within each elementary waveguiding structure [3,5]. In this approach, the electromagnetic fields within the individual longitudinally uniform waveguide sections are represented as a weighted summation of elementary solutions to Maxwell's equations, and the weight coefficients are obtained by matching the tangential fields at the interfaces of the sections where the structure is discontinuous. A microwave device can be accurately analyzed by using this method, once the equivalent circuits of each of the constituent discontinuities have been obtained [4]. However, a simple characterization of the discontinuities in terms of their conventional fundamental mode scattering parameters (S parameters) cannot recover the full-wave behavior of the device when the interactions between the discontinuities are not negligible—which is a common occurrence. In this event, it becomes essential to include the higher-order modes, generalize the concept of scattering parameters [1], and develop a generalized scattering matrix, which is the subject of discussion in this article.

The article is organized as follows. In Section 2, we review the basic concepts of guided-wave propagation in order to derive a modal representation of the fields. This expansion is represented by an equivalent circuit, which leads to the definition of the generalized admittance matrix (GAM) and the generalized impedance matrix. The modal representation is then rearranged in terms of the incident and reflected waves in order to derive the definition of the generalized scattering matrix (GSM). The next step is to consider the canonical problem of a step discontinuity between two waveguides with dissimilar cross sections, and use this simple canonical problem as the building block for the analysis of more complex geometries constituting multiple cascaded discontinuities, such as filters, matching networks, and directional

couplers. Finally, we present some numerical examples to illustrate the potentials of the GSM technique.

2. MODAL EXPANSION

We begin our discussion of modal expansion by considering the geometry of the problem shown in Fig. 1, specifically, a hollow, lossless, metallic waveguide, with a uniform cross-section and perfectly electric conductor (PEC) type of walls. The structure is uniform along z , which is the direction of propagation in the waveguide. We assume that the guide is filled with a homogeneous and lossless dielectric material, with dielectric permittivity ϵ and magnetic permeability μ .

The solution of the propagation problem is obtained by referring to the source-free Maxwell's equations:

$$\begin{aligned} \nabla \times \underline{E} &= -j\omega\mu\underline{H} \\ \nabla \times \underline{H} &= j\omega\epsilon\underline{E} \end{aligned} \tag{1}$$

The differential equations (1) are a system of six scalar equations with six unknowns. Since the cross section of the waveguide is uniform along the z axis, it is advantageous to split the field solution into two parts—the longitudinal components (E_z, H_z) and the transverse components (\underline{E}_t and \underline{H}_t), as follows:

$$\begin{aligned} \underline{E} &= \underline{E}_t + E_z \underline{i}_z \\ \underline{H} &= \underline{H}_t + H_z \underline{i}_z \end{aligned} \tag{2}$$

The longitudinal and transverse components are interrelated, of course, through Maxwell's equations, and they can be easily derived from each other. This assumption results in a simplification, since we can derive the solution for the only transverse components of the fields, and take advantage of the fact that the longitudinal components are dependent on the latter and vice versa [2].

It can be shown that for the problem at hand, Maxwell's equations can be cast in the form of an eigenvalue problem whose solutions (eigenfunctions) represent a set of elementary configurations (modes) supported by the structure. They constitute a complete set of basis functions for representing the fields in the waveguide. Therefore, we can express the transverse field components as

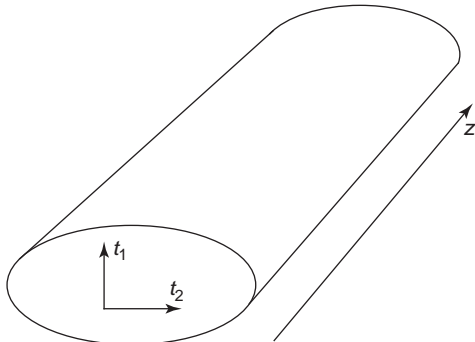


Figure 1. Geometry of a waveguide problem.

summations of modes with complex amplitudes as

$$\underline{E}_t(t_1, t_2; z) = \sum_{m=1}^{\infty} \underline{E}_{t,m}(t_1, t_2; z) \tag{3}$$

$$\underline{H}_t(t_1, t_2; z) = \sum_{m=1}^{\infty} \underline{H}_{t,m}(t_1, t_2; z)$$

where (t_1, t_2) represent the coordinates in the transverse plane as shown in Fig. 1 (in rectangular coordinates $t_1 = x, t_2 = y$).

The separation into longitudinal and transverse components enables us to define three types of modes: (i) transverse electric (TE), for which we have $E_z = 0$ (in this case the electric field is totally transverse: $\underline{E} = \underline{E}_t$); (ii) transverse magnetic (TM), for which we have $H_z = 0$, (i.e., the magnetic field is totally transverse: $\underline{H} = \underline{H}_t$); and (iii) transverse electric and magnetic (TEM), for which we have both E_z and $H_z = 0$.

By invoking the principle of separation of variables, we can represent the electric and the magnetic field components of each mode as a product of a scalar function of z and a vector function of the transverse coordinates that read

$$\underline{E}_{t,m}(t_1, t_2; z) = V_m(z) \underline{e}_m(t_1, t_2) \tag{4}$$

$$\underline{H}_{t,m}(t_1, t_2; z) = I_m(z) \underline{h}_m(t_1, t_2)$$

Following the well-established terminology for waveguiding structures, we refer to the functions \underline{e}_m and \underline{h}_m as the modal vector functions, and to $V_m(z)$ and $I_m(z)$ as the modal scalar functions. The latter satisfy the transmission-line equations (telegraphist's equations), with the standard solution:

$$V_m(z) = V_m^+ e^{-j\beta_m z} + V_m^- e^{+j\beta_m z} \tag{5a}$$

$$I_m(z) = I_m^+ e^{-j\beta_m z} + I_m^- e^{+j\beta_m z} \tag{5b}$$

The modal scalar functions can be interpreted as the equivalent voltages and currents associated with the m th mode of the multimode line—the waveguide. The corresponding modal characteristic impedance for the m th mode is given by

$$Z_{0,m} = \frac{V_m^+}{I_m^+} = -\frac{V_m^-}{I_m^-} \tag{6}$$

and these impedances can be chosen such that they normalize the corresponding modal vector functions. In particular, if we choose:

$$Z_{0,m} = \zeta_{0,m} = \begin{cases} \omega\mu/\beta_m & \text{for TE modes} \\ \beta_m/\omega\epsilon & \text{for TM modes} \end{cases} \tag{7}$$

the modal vector functions are related as follows:

$$\underline{e}_m = \underline{h}_m \times \underline{i}_z \tag{8}$$

The modal vector functions are the solutions of an eigenvalue problem; in particular, we can introduce a potential function φ_m , which satisfies the two-dimensional eigenvalue equation

$$\nabla_t^2 \varphi_m(t_1, t_2) + k_{c,m}^2 \varphi_m(t_1, t_2) = 0 \quad (9)$$

with the following boundary conditions on the contour C of S

$$\varphi_m|_C = 0, \text{ for TE modes} \quad (10a)$$

$$\left. \frac{\partial \varphi_m}{\partial n} \right|_C = 0, \text{ for TM modes} \quad (10b)$$

where $\partial/\partial n$ is the derivative along the outward normal to the contour C . In (9), $k_{c,m}$ is the transverse eigenvalue of the m th mode. The value of the transverse eigenvalue (and, consequently, the final form of the solution φ_m) depends on the geometric shape of the waveguide cross section. Once we have obtained the solution for φ_m , the corresponding vector functions can be evaluated from

$$\underline{e}_m = \begin{cases} \hat{z} \times \nabla_t \varphi_m & \text{for TE modes} \\ -\nabla_t \varphi_m & \text{for TM modes} \end{cases} \quad (11)$$

The wavenumber along the z axis for the m th mode is given by

$$k_z = k_{z\text{TE}} = \sqrt{\omega^2 \epsilon \mu - k_{c,m}^2} \quad (12)$$

An examination of this equation leads to some useful interpretations of the propagation properties of the waveguide. Specifically, we note that the propagation constant β_m in (12) goes to zero at the cutoff frequencies given by

$$\omega_{c,m} = \frac{k_{c,m}}{\sqrt{\mu \epsilon}} \quad (13)$$

For frequencies below the cutoff, the wavenumber is purely imaginary and the corresponding mode is evanescent, with an attenuation constant given by

$$j\beta_m = \alpha_m = \sqrt{k_{c,m}^2 - \omega^2 \epsilon \mu} \quad (14)$$

A TEM mode can be interpreted as a limiting case of a TE or TM mode, with a null transverse eigenvalue k_c . It exists only if the guiding structure consists of at least two parallel electric conductors (i.e., two separated metallic regions on the guiding structure transverse plane). This mode has no cutoff and its propagation constant is identical to that relevant to a uniform plane wave propagating in an unbounded homogeneous medium, with the same electrical characteristics as those of the TEM mode:

$$k_z = k_0 = \omega \sqrt{\epsilon \mu} \quad (15)$$

In contrast to this, the characteristic impedance of the TEM mode depends on both the electric properties of the

medium surrounding the guiding structure and the geometric parameters of the transverse plane.

3. CIRCUIT REPRESENTATIONS OF THE DISCONTINUITIES

In this section, we introduce a formalism that leads to an N -port circuit representation of a waveguiding system [4].

We start by considering a generic discontinuity, with respect to which we define two reference transverse planes T_1 and T_2 (see Fig. 2), where the electric and magnetic fields can be expressed in terms of the modal expansions we have previously introduced. Although, in principle, the modal expansion contains an infinite number of terms, from a practical point of view it is sufficient to truncate it to a finite value. For convenience, we will refer to each of the reference planes as “physical” ports. If we retain N_i modes at the i th “physical” port ($i = 1, 2$) that are sufficient to describe the discontinuity, then we need to know $N_1 + N_2$ modal voltages and currents, implying that an equal number of equations relating the voltages and currents are required, which can be obtained from the Maxwell’s equations. Furthermore, by virtue of the uniqueness theorem, it is sufficient to consider only the tangential components at the interfaces (fields transverse to z) at both the “physical” ports. The discontinuity can therefore be represented by using its multiport equivalent circuit, shown in Fig. 3, where each port is associated with a different mode (“modal” port). Such a network formalism enables us to deal with the voltages and currents—in the same manner as in circuit analysis—instead of working with the electric and magnetic fields.

For the multiport circuit introduced previously, the set of equations relating the voltages and currents can be cast in a more convenient form by expressing all the modal currents as functions of the corresponding voltages. More specifically, we can obtain the following matrix form:

$$\underline{I} = \underline{Y} \underline{V} \quad (16)$$

$$\begin{bmatrix} I_1^{(1)} \\ \vdots \\ I_{N_1}^{(1)} \\ I_1^{(2)} \\ \vdots \\ I_{N_2}^{(2)} \end{bmatrix} = \begin{bmatrix} \underline{Y}_{11} & \underline{Y}_{12} \\ \underline{Y}_{21} & \underline{Y}_{22} \end{bmatrix} \begin{bmatrix} V_1^{(1)} \\ \vdots \\ V_{N_1}^{(1)} \\ V_1^{(2)} \\ \vdots \\ V_{N_2}^{(2)} \end{bmatrix} \quad (17)$$

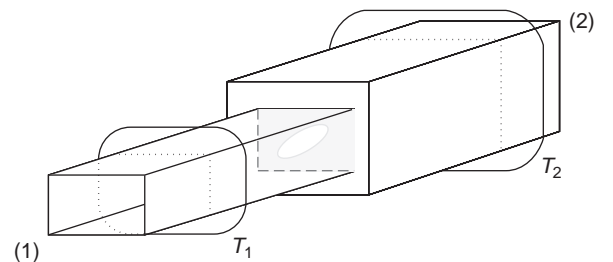


Figure 2. Geometry for representing a waveguide discontinuity.

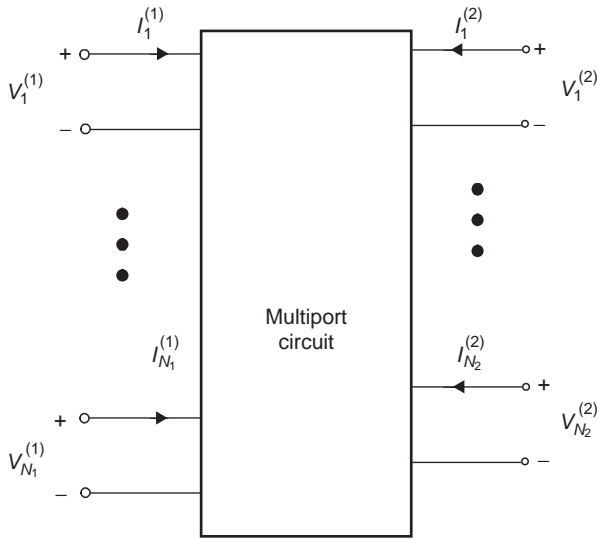


Figure 3. Multiport equivalent circuit to the discontinuity depicted in Fig. 2.

It is important to note that the voltages and currents in these equations are related by the admittance matrix \underline{Y} , which now includes both the evanescent and propagating modes. Consequently, the admittance matrix (17) is more general than the conventional one, which relates only the currents and voltages of the propagating modes. Such a generalization leads to the concept and the definition of a generalized admittance matrix (GAM). In addition, we can divide the modes into two classes: accessible (propagating) and localized (evanescent). If we are interested only in the propagating modes (typically the fundamental modes) at the input and output “physical” ports, then the corresponding admittance matrix has the dimensions of (2×2) , and it can be extracted from the corresponding GAM whose dimensions are $(N_1 + N_2) \times (N_1 + N_2)$. To this end, we consider the equivalent circuit shown in Fig. 4, where all the “modal” ports corresponding to the evanescent modes are matched to their respective characteristic impedances, so that

$$I_m^{(i)} = -Y_{0,m}^{(i)} V_m^{(i)} \quad m = 2, \dots, N_i \quad (18)$$

with

$$Y_{0,m}^{(i)} = 1/Z_{0,m}^{(i)} \quad (19)$$

We can now rearrange and partition the admittance matrix with the objective of separating the entries pertaining to the two fundamental modes (subscript “f”) from to the higher-order evanescent modes (subscript “h”) as follows:

$$\underline{Y} = \begin{bmatrix} \underline{Y}_{ff} & \underline{Y}_{fh} \\ \underline{Y}_{hf} & \underline{Y}_{hh} \end{bmatrix} \quad (20)$$

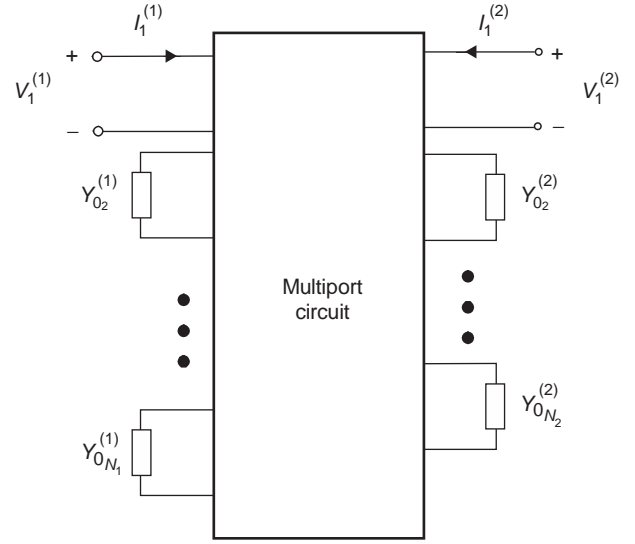


Figure 4. Multiport circuit representation of a waveguide discontinuity for deriving the standard admittance matrix.

The admittance matrix \underline{Y}' of the discontinuity can be expressed as

$$\underline{Y}' = \underline{Y}_{ff} - \underline{Y}_{fh}(\underline{Y}_{hh} + \underline{Y}_{=0})^{-1}\underline{Y}_{hf} \quad (21)$$

where $\underline{Y}_{=0}$ is a diagonal matrix containing the characteristic modal admittances:

$$\underline{Y}_{=0} = \text{diag} [Y_{0,2}^{(1)}, \dots, Y_{0,N_1}^{(1)}, Y_{0,2}^{(2)}, \dots, Y_{0,N_2}^{(2)}] \quad (22)$$

It is important to realize that the higher-order modes, although inaccessible, nevertheless influence the behavior (and the final value of the complex amplitude) of the fundamental modes. We will touch on this aspect again in Section 9 and present some examples to validate the preceding statement.

An alternative description can be obtained by expressing the modal voltages as functions of the modal currents, so that we can obtain an impedance matrix description as follows

$$\underline{V} = \underline{Z}\underline{I} \quad (23)$$

where \underline{Z} is defined as the generalized impedance matrix. In microwave applications, a more useful representation of the electromagnetic field is obtained by working with the incident and reflected wavevectors of the discontinuity, and it is convenient to derive a description that is not tied to the particular type of transmission line feeding the network. Toward this end, we define a normalized modal voltage of the m th mode at the i th port as follows:

$$\hat{V}_m^{(i)} = \frac{V_m^{(i)}}{\sqrt{Z_{0,m}^{(i)}}} \quad (24)$$

Similarly, we can define a normalized modal current of the m th mode at the i th port as

$$\hat{\mathbf{I}}_m^{(i)} = I_m^{(i)} \sqrt{Z_{0,m}^{(i)}} \quad (25)$$

The corresponding voltage and current modal vectors (normalized) are

$$\hat{\mathbf{V}} = [\hat{\mathbf{V}}_m^{(i)}] \quad (26a)$$

$$\hat{\mathbf{I}} = [\hat{\mathbf{I}}_m^{(i)}] \quad (26b)$$

These vectors are related by the normalized impedance matrix $\hat{\underline{\underline{Z}}}$ as

$$\hat{\mathbf{V}} = \hat{\underline{\underline{Z}}} \hat{\mathbf{I}} \quad (27)$$

where the entries of the impedance matrix given above are defined as follows:

$$\hat{Z}_{mn}^{(i,j)} = \frac{Z_{mn}^{(i,j)}}{\sqrt{Z_{0,m}^{(i)}} \sqrt{Z_{0,n}^{(j)}}} \quad (28)$$

The expression in (28) can be interpreted as the normalized mutual impedance between the m th “modal” port at the “physical” port i and the n th “modal” port at the “physical port” j .

A similar normalization can also be applied to the GAM, which can be written as

$$\hat{\mathbf{I}} = \hat{\underline{\underline{Y}}} \hat{\mathbf{V}} \quad (29)$$

The entries of the matrix above are given by

$$\hat{Y}_{mn}^{(i,j)} = \frac{Y_{m,n}^{(i,j)}}{\sqrt{Y_{0,m}^{(i)}} \sqrt{Y_{0,n}^{(j)}}} \quad (30)$$

and they can also be interpreted in a procedure similar to that followed for the impedance matrix elements.

We can now define, at each port, the incident wave amplitude of the m th mode at i th terminal as

$$a_m^{(i)} = \frac{V_m^{+(i)}}{\sqrt{Z_{0,m}^{(i)}}} = I_m^{+(i)} \sqrt{Z} = \frac{V_m^{(i)} + Z_{0,m}^{(i)} I_m^{(i)}}{2\sqrt{Z_{0,m}^{(i)}}} \quad (31)$$

Similarly, the corresponding reflected wave amplitude can also be defined as

$$b_m^{(i)} = \frac{V_m^{-(i)}}{\sqrt{Z_{0,m}^{(i)}}} = -I_m^{-(i)} \sqrt{Z_{0,m}^{(i)}} = \frac{V_m^{(i)} - Z_{0,m}^{(i)} I_m^{(i)}}{2\sqrt{Z_{0,m}^{(i)}}} \quad (32)$$

Finally, using these definitions, we can fully characterize the device in terms of its generalized scattering matrix (GSM) $\underline{\underline{S}}$, which relates the vectors representing the reflected wave and the incident wave amplitudes. The

matrix is defined as

$$\underline{\underline{b}} = \underline{\underline{S}} \underline{\underline{a}} \quad (33)$$

This description in terms of the GSM is equivalent to that in terms of the impedance or admittance matrices. In fact, starting from the following equations

$$\hat{\mathbf{V}} = \underline{\underline{a}} + \underline{\underline{b}} \quad (34a)$$

$$\hat{\mathbf{I}} = \underline{\underline{a}} - \underline{\underline{b}} \quad (34b)$$

we can also write

$$(\underline{\underline{a}} + \underline{\underline{b}}) = \hat{\underline{\underline{Z}}}(\underline{\underline{a}} - \underline{\underline{b}}) \quad (35)$$

Using (33), we obtain the final result

$$\underline{\underline{S}} = (\hat{\underline{\underline{Z}}} + \underline{\underline{1}})^{-1}(\hat{\underline{\underline{Z}}} - \underline{\underline{1}}) = (\underline{\underline{1}} + \hat{\underline{\underline{Y}}})^{-1}(\underline{\underline{1}} - \hat{\underline{\underline{Y}}}) \quad (36)$$

where $\underline{\underline{1}}$ is the unit matrix with dimensions $(N_1 + N_2) \times (N_1 + N_2)$. From knowledge of the GSM of a discontinuity, we can obtain the corresponding admittance and impedance matrices as follows:

$$\hat{\underline{\underline{Y}}} = \hat{\underline{\underline{Z}}}^{-1} = (\underline{\underline{S}} + \underline{\underline{1}})^{-1}(\underline{\underline{1}} - \underline{\underline{S}}) \quad (37)$$

$$\hat{\underline{\underline{Z}}} = \hat{\underline{\underline{Y}}}^{-1} = (\underline{\underline{S}} + \underline{\underline{1}})(\underline{\underline{1}} - \underline{\underline{S}})^{-1} \quad (38)$$

It is important to recognize that, for linear networks, the matrix $\underline{\underline{S}}$ can always be defined, while in some particular situations the matrices $\underline{\underline{Z}}$ and $\underline{\underline{Y}}$ cannot. Moreover, a GSM can always be defined, even if the value of the characteristic impedance of the port is not available.

4. STEP JUNCTION

In this section, we consider the discontinuity problem of a junction between two waveguides with different cross sections S_1 and S_2 . The junction is located at the plane $z = 0$. Let S_C be the common interface, shared by the two waveguides ($S_C = S_1 \cap S_2$) and let S_P be the metallic surface at the interface (for the case shown in Fig. 5, associated with the *boundary enlargement*).

The electromagnetic fields in both the waveguides can be expressed in terms of their respective modes. In particular, by using (4) and (5), we can express the transverse components of the electromagnetic field in the first waveguides (on the left) as a finite summation

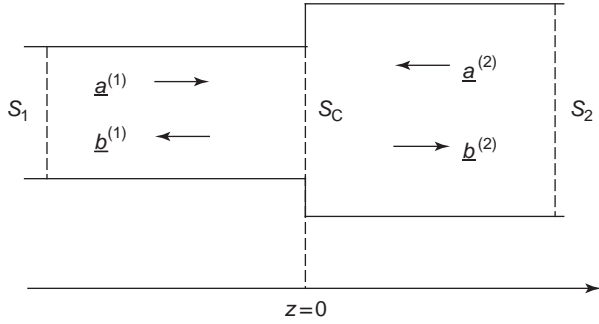


Figure 5. Boundary enlargement problem.

of modes as follows:

$$\left\{ \begin{array}{l} \underline{E}_t^{(1)} = \sum_{m=1}^{N_1} \left(\sqrt{Z_{0,m}^{(1)}} a_m^{(1)} e^{-j\beta_m z} \right. \\ \quad \left. + \sqrt{Z_{0,m}^{(1)}} b_m^{(1)} e^{+j\beta_m z} \right) \underline{e}_m^{(1)}(\underline{t}) \\ \underline{H}_t^{(1)} = \sum_{m=1}^{N_1} \left(\frac{a_m^{(1)}}{\sqrt{Z_{0,m}^{(1)}}} e^{-j\beta_m z} \right. \\ \quad \left. - \frac{b_m^{(1)}}{\sqrt{Z_{0,m}^{(1)}}} e^{+j\beta_m z} \right) \underline{h}_m^{(1)}(\underline{t}) \end{array} \right. \quad (39)$$

Similarly, in the second waveguide (on the right) we have

$$\left\{ \begin{array}{l} \underline{E}_t^{(2)} = \sum_{n=1}^{N_2} \left(\sqrt{Z_{0,n}^{(2)}} a_n^{(2)} e^{+j\beta_n z} \right. \\ \quad \left. + \sqrt{Z_{0,n}^{(2)}} b_n^{(2)} e^{-j\beta_n z} \right) \underline{e}_n^{(2)}(\underline{t}) \\ \underline{H}_t^{(2)} = \sum_{n=1}^{N_2} \left(\frac{a_n^{(2)}}{\sqrt{Z_{0,n}^{(2)}}} e^{+j\beta_n z} \right. \\ \quad \left. - \frac{b_n^{(2)}}{\sqrt{Z_{0,n}^{(2)}}} e^{-j\beta_n z} \right) \underline{h}_n^{(2)}(\underline{t}) \end{array} \right. \quad (40)$$

In these expressions, the wave amplitudes of the modes are the unknowns in this problem that are yet to be determined. As explained in the previous section, a complete characterization of the discontinuity can be obtained if we can relate the $(N_1 + N_2)$ amplitudes of the $a^{(i)}$ incident waves to the corresponding amplitudes of the reflected waves, $b^{(i)}$ ($i = 1, 2$). We can derive these equations by imposing the boundary conditions at the junction, specifically, the continuity of the transverse components of

both the electric and magnetic fields as follows:

$$\left\{ \begin{array}{l} \underline{E}_t^{(2)} = \underline{E}_t^{(1)} \quad \text{at } S_C \\ \underline{E}_t^{(2)} = 0 \quad \text{at } S_P = S_2 \setminus S_1 \\ \underline{H}_t^{(2)} = \underline{H}_t^{(1)} \quad \text{at } S_C \end{array} \right. \quad (41)$$

The simplest way to derive the desired $(N_1 + N_2)$ equations is to impose the continuity condition at $(N_1 + N_2)$ different points. However, such a point-matching technique, although simple from a conceptual point of view, is not very accurate since it imposes the continuity condition only at a finite set of points, and it is better to impose the condition stated above in an integral sense instead. With this in mind, we introduce a definition of the inner product, which must be computed in the process.

5. GSM OF A STEP JUNCTION

In this section, we derive a GSM representation of the step junction, shown in Fig. 5, by using the formulation based on the conservation of complex power [6,7]. However, it can be shown that any relation originating from this formulation is equivalent to the ones derived by matching the transverse electric fields or the transverse magnetic fields at the junction plane. We begin by expressing the transverse electric and magnetic fields at $z = 0$ as

$$\left\{ \begin{array}{l} \underline{E}_t^{(1)}(z=0) = \sum_{m=1}^{N_1} \sqrt{Z_{0,m}^{(1)}} (a_m^{(1)} + b_m^{(1)}) \underline{e}_m^{(1)}(\underline{t}) \\ \underline{H}_t^{(1)}(z=0) = \sum_{m=1}^{N_1} \frac{1}{\sqrt{Z_{0,m}^{(1)}}} (a_m^{(1)} - b_m^{(1)}) \underline{h}_m^{(1)}(\underline{t}) \end{array} \right. \quad (42)$$

$$\left\{ \begin{array}{l} \underline{E}_t^{(2)}(z=0) = \sum_{n=1}^{N_2} \sqrt{Z_{0,n}^{(2)}} (a_n^{(2)} + b_n^{(2)}) \underline{e}_n^{(2)}(\underline{t}) \\ \underline{H}_t^{(2)}(z=0) = \sum_{n=1}^{N_2} \frac{1}{\sqrt{Z_{0,n}^{(2)}}} (a_n^{(2)} - b_n^{(2)}) \underline{h}_n^{(2)}(\underline{t}) \end{array} \right. \quad (43)$$

From the continuity conditions, we have

$$\begin{aligned} \underline{E}_t^{(1)}(z=0) &= \underline{E}_t^{(2)}(z=0) \\ &\Rightarrow \sum_{m=1}^{N_1} \sqrt{Z_{0,m}^{(1)}} (a_m^{(1)} + b_m^{(1)}) \underline{e}_m^{(1)}(\underline{t}) \\ &= \sum_{n=1}^{N_2} \sqrt{Z_{0,n}^{(2)}} (a_n^{(2)} + b_n^{(2)}) \underline{e}_n^{(2)}(\underline{t}) \end{aligned} \quad (44)$$

$$\begin{aligned} \underline{H}_t^{(1)}(z=0) &= \underline{H}_t^{(2)}(z=0) \\ &\Rightarrow \sum_{m=1}^{N_1} \frac{1}{\sqrt{Z_{0,m}^{(1)}}} (a_m^{(1)} - b_m^{(1)}) \underline{h}_m^{(1)}(\underline{t}) \\ &= \sum_{n=1}^{N_2} \frac{1}{\sqrt{Z_{0,n}^{(2)}}} (a_n^{(2)} - b_n^{(2)}) \underline{h}_n^{(2)}(\underline{t}) \end{aligned} \quad (45)$$

Next, we define an inner product between the two functions f_1 and f_2 as

$$\langle f_1, f_2 \rangle = \int_{S_C} f_1(t) \times f_2^*(t) \cdot \hat{z} dS \quad (46)$$

and use this definition to project the continuity equation of the electric (magnetic) field onto each magnetic (electric) modal vector function and the continuity equation. Such a projection guarantees that the continuity is ensured not only at a discrete set of points but also across the junction in an integral sense. In particular, by projecting the first equation onto the eigenfunctions $h_m^{(1)*}$, we have

$$\begin{aligned} & \sum_{m=1}^{N_1} \sqrt{Z_{0,m}^{(1)}} (a_m^{(1)} + b_m^{(1)}) \int_{S_1} (e_m^{(1)} \times h_m^{(1)*}) \cdot d\underline{S} \\ &= \sum_{n=1}^{N_2} \sqrt{Z_{0,n}^{(2)}} (a_n^{(2)} + b_n^{(2)}) \int_{S_1} (e_n^{(2)} \times h_m^{(1)*}) \cdot d\underline{S} \end{aligned} \quad (47)$$

Similarly, by projecting the second equation onto the eigenfunctions $e_n^{(2)*}$, we obtain

$$\begin{aligned} & \sum_{m=1}^{N_1} \frac{1}{\sqrt{Z_{0,m}^{(1)}}} (a_m^{(1)} - b_m^{(1)}) \int_{S_2} (h_m^{(1)} \times e_n^{(2)*}) \cdot d\underline{S} \\ &= \sum_{n=1}^{N_2} \frac{1}{\sqrt{Z_{0,n}^{(2)}}} (a_n^{(2)} - b_n^{(2)}) \int_{S_1} (h_n^{(2)} \times e_n^{(2)*}) \cdot d\underline{S} \end{aligned} \quad (48)$$

By exploiting the orthogonality of the modes at each of the waveguide sections, we can express (47) and (48) in matrix forms as

$$\begin{aligned} & \text{diag} \left\{ \sqrt{Z_{0,m}^{(1)}} \int_{S_1} (e_m^{(1)} \times h_m^{(1)*}) \cdot d\underline{S} \right\} \\ & \times (\underline{a}^{(1)} + \underline{b}^{(1)}) = \underline{A} (\underline{a}^{(2)} + \underline{b}^{(2)}) \end{aligned} \quad (49)$$

$$\begin{aligned} & \underline{B} (\underline{a}^{(1)} - \underline{b}^{(1)}) = \text{diag} \left\{ \frac{1}{\sqrt{Z_{0,n}^{(2)}}} \int_{S_2} (h_n^{(2)} \times e_n^{(2)*}) \cdot d\underline{S} \right\} \\ & \times (\underline{a}^{(2)} - \underline{b}^{(2)}) \end{aligned} \quad (50)$$

The elements of the matrices $\underline{A} (N_1 \times N_2)$ and $\underline{B} (N_2 \times N_1)$ can be written as

$$a_{mn} = \sqrt{Z_{0,n}^{(2)}} \int_{S_1} (e_n^{(2)} \times h_m^{(1)*}) \cdot d\underline{S} \quad (51)$$

$$b_{mn} = \frac{1}{\sqrt{Z_{0,m}^{(1)}}} \int_{S_2} (h_m^{(1)} \times e_n^{(2)*}) \cdot d\underline{S} \quad (52)$$

These matrices have some special properties, and, in order to understand them, we resort to the normalization procedure outlined in Section 2, for which the characteristic impedance of the equivalent transmission line assumes a

unit value:

$$Z_{0,m} \equiv 1 \quad (53)$$

As a consequence, for the corresponding vector functions of each mode, we can write

$$e_m = \zeta_m h_m \times \hat{i}_z, \quad h_m = \frac{1}{\zeta_m} \hat{i}_z \times e_m \quad (54)$$

so that

$$a_{mn} = \frac{1}{\zeta_{0,m}^{(1)*}} \int_{S_C} (e_n^{(2)} \cdot e_m^{(1)*}) \cdot d\underline{S} \quad (55)$$

$$b_{mn} = \frac{1}{\zeta_{0,m}^{(1)}} \int_{S_C} (e_m^{(1)} \cdot e_n^{(2)*}) \cdot d\underline{S} = a_{nm}^* \quad (56)$$

This implies that the following relationship holds:

$$\underline{B} = (\underline{A}^T)^* \quad (57)$$

Thus the matrix B is the conjugate transpose of A . It is worth noting that with a correct choice of the normalization impedance, some interesting and important properties regarding the final form of the GSM can be observed [11].

By defining the following diagonal matrices (power matrices)

$$\begin{aligned} \underline{P} &= \text{diag} \left\{ \frac{1}{\zeta_{0,m}^{(1)*}} \int_{S_1} |e_m^{(1)}|^2 \cdot d\underline{S} \right\} \\ &= \text{diag} \left\{ \zeta_{0,m}^{(1)} \int_{S_1} |h_m^{(1)}|^2 \cdot d\underline{S} \right\} (N_1 \times N_1) \end{aligned} \quad (58)$$

$$\begin{aligned} \underline{Q} &= \text{diag} \left\{ \frac{1}{\zeta_{0,n}^{(2)}} \int_{S_2} |e_n^{(2)}|^2 \cdot d\underline{S} \right\} \\ &= \text{diag} \left\{ \zeta_{0,n}^{(2)*} \int_{S_1} |h_n^{(2)}|^2 \cdot d\underline{S} \right\} (N_2 \times N_2) \end{aligned} \quad (59)$$

Eqs. (49) and (50) can be recast in the following form:

$$\underline{P} (\underline{a}^{(1)} + \underline{b}^{(1)}) = \underline{A} (\underline{a}^{(2)} + \underline{b}^{(2)}) \quad (60)$$

$$(\underline{A}^T)^* (\underline{a}^{(1)} - \underline{b}^{(1)}) = \underline{Q} (\underline{a}^{(2)} - \underline{b}^{(2)}) \quad (61)$$

We can now define the matrices below

$$\begin{aligned} \underline{M}_E &= \underline{P}^{-1} \underline{A} \text{ whose dimensions are} \\ & (N_1 \times N_2) \end{aligned} \quad (62)$$

$$\begin{aligned} \underline{M}_H &= \underline{Q}^{-1} (\underline{A}^T)^* \text{ whose dimensions are} \\ & (N_2 \times N_1) \end{aligned} \quad (63)$$

to derive the final matrix representations:

$$(\underline{a}^{(1)} + \underline{b}^{(1)}) = \underline{M}_E(\underline{a}^{(2)} + \underline{b}^{(2)}) \tag{64}$$

$$\underline{M}_H(\underline{a}^{(1)} - \underline{b}^{(1)}) = (\underline{a}^{(2)} - \underline{b}^{(2)})$$

From (64) we can derive the generalized scattering matrix that relates the vectors \underline{b} and \underline{a}

$$\begin{bmatrix} \underline{b}^{(1)} \\ \underline{b}^{(2)} \end{bmatrix} = \underline{S} \begin{bmatrix} \underline{a}^{(1)} \\ \underline{a}^{(2)} \end{bmatrix} = \begin{bmatrix} \underline{S}_{11} & \underline{S}_{12} \\ \underline{S}_{21} & \underline{S}_{22} \end{bmatrix} \begin{bmatrix} \underline{a}^{(1)} \\ \underline{a}^{(2)} \end{bmatrix} \tag{65}$$

where

$$\begin{cases} \underline{S}_{11} = (\underline{1} + \underline{M}_H \cdot \underline{M}_E)^{-1} \cdot (\underline{1} - \underline{M}_H \cdot \underline{M}_E) \\ \underline{S}_{21} = \underline{M}_E \cdot (\underline{1} + \underline{S}_{11}) \\ \underline{S}_{12} = 2(\underline{1} + \underline{M}_H \cdot \underline{M}_E)^{-1} \cdot \underline{M}_H \\ \underline{S}_{22} = (\underline{M}_E \cdot \underline{S}_{12} - \underline{1}) \end{cases} \tag{66}$$

are the self- and mutual blocks of the GSM.

It should be realized that the computation of the scattering matrix carried out in this manner requires the inversion of an $(N_1 \times N_1)$ matrix for each frequency. Finally, the scattering parameters of the discontinuity can be finally obtained by identifying the first element of each of the submatrices (see Fig. 6) that are

$$\begin{aligned} s_{11} &= \underline{S}_{11}(1, 1), \quad s_{12} = \underline{S}_{12}(1, 1), \\ s_{21} &= \underline{S}_{21}(1, 1), \quad s_{22} = \underline{S}_{22}(1, 1) \end{aligned} \tag{67}$$

For a discussion of the properties of the GSM, the reader is referred to Refs. 8–10.

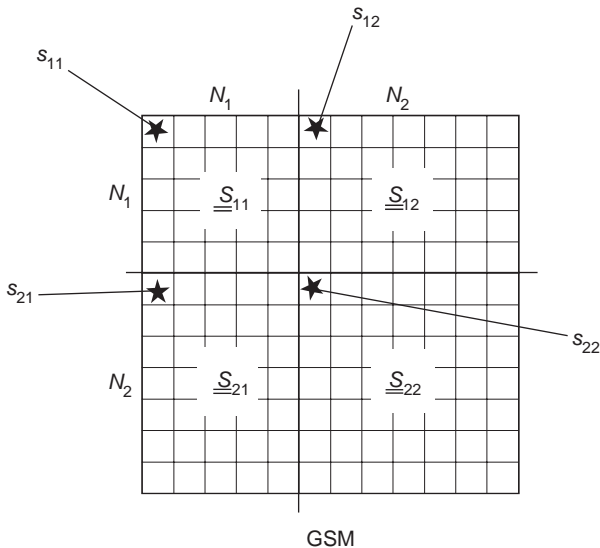


Figure 6. Identification of the scattering parameters of the step discontinuity as entries of the GSM.

6. CASCADING DISCONTINUITIES

A step discontinuity can be viewed as a basic building block for describing more complex configurations. We now consider, as a simple example, the geometry sketched in Fig. 7, where two such discontinuities are separated by a distance L .

The GSM of the uniform waveguide section spanning from $z = 0$ and $z = L$ simply accounts for the phase shift (and/or attenuation) of each mode, as it traverses this section of the guide. This GSM can be written as

$$\underline{S} = \begin{bmatrix} 0 & \underline{D} \\ \underline{D} & 0 \end{bmatrix} \tag{68}$$

where

$$\underline{D} = \text{diag}\{e^{-j\beta_n L}\} \tag{69}$$

The propagating modes only suffer a phase shift, while the evanescent ones are attenuated, since β_n is purely imaginary for the latter. If the distance L is sufficiently large, the evanescent modes originating from the first discontinuity are completely attenuated and do not interact with the second discontinuity; hence they can be neglected.

It is possible to express the wave amplitudes at the second interface in terms of the \underline{S} matrix defined in (8)

$$\begin{bmatrix} \underline{a}^{(2)} \\ \underline{a}_L^{(2)} \end{bmatrix} = \underline{S} \begin{bmatrix} \underline{b}^{(2)} \\ \underline{b}_L^{(2)} \end{bmatrix} = \begin{bmatrix} 0 & \underline{D} \\ \underline{D} & 0 \end{bmatrix} \begin{bmatrix} \underline{b}^{(2)} \\ \underline{b}_L^{(2)} \end{bmatrix} \tag{70}$$

and

$$\begin{aligned} \underline{a}_L^{(2)} &= \underline{D} \underline{b}^{(2)}; \quad \underline{a}^{(2)} \\ &= \underline{D} \underline{b}_L^{(2)} \Rightarrow \underline{b}_L^{(2)} = \underline{D}^{-1} \underline{a}^{(2)} \end{aligned} \tag{71}$$

It is important to note that, in deriving (71), the outgoing waves, transmitted to the right of the first discontinuity, are interpreted as waves incident on the waveguide section located between $z = 0$ and $z = L$. By inserting (71) into (70), we obtain the GSM of the entire configuration, formed by the two discontinuities flanking the waveguide

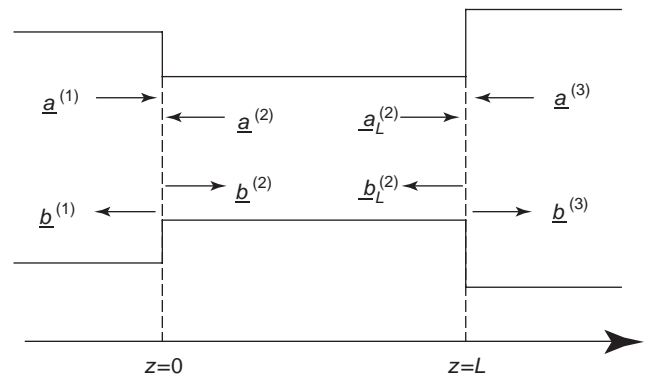


Figure 7. Geometry for analysis of a double-step discontinuity.

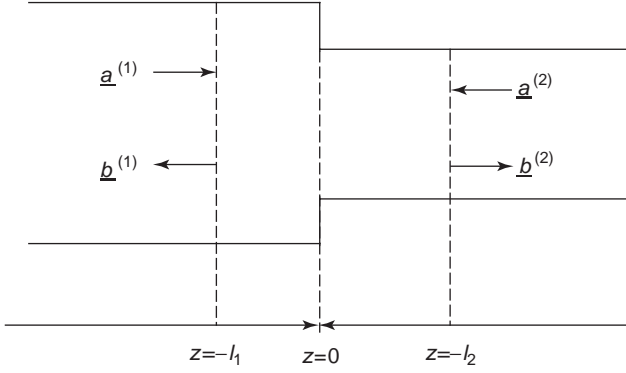


Figure 8. Reference systems at a step discontinuity analyzed through the transmission matrix.

section in between. We can generalize the analysis a bit further and derive the expression for the GSM matrix when we extend the lengths of the waveguide sections at both ends of the discontinuity (see Fig. 8). For this case, the GSM can be expressed as

$$\underline{\underline{S}}' = \underline{\underline{\phi}} \underline{\underline{S}} \underline{\underline{\phi}} = \begin{bmatrix} \underline{\underline{D}}_1 & 0 \\ 0 & \underline{\underline{D}}_2 \end{bmatrix} \underline{\underline{S}} \begin{bmatrix} \underline{\underline{D}}_1 & 0 \\ 0 & \underline{\underline{D}}_2 \end{bmatrix} \quad (72)$$

where

$$\begin{aligned} \underline{\underline{D}}_1 &= \text{diag} \left\{ e^{-j\beta_m^{(1)} l_1} \right\} \\ \underline{\underline{D}}_2 &= \text{diag} \left\{ e^{-j\beta_n^{(2)} l_2} \right\} \end{aligned} \quad (73)$$

To derive the composite solution of this extended geometry case, we need certain connection formulas, which we provide below [11,12]. Given two structures, each of which is characterized by its own GSM $\underline{\underline{S}}^{(1)}$ and $\underline{\underline{S}}^{(2)}$, respectively, we can construct a composite GSM by using the following submatrix blocks [3]

$$\begin{cases} \underline{\underline{S}}_{-11}^{(\text{tot})} = \underline{\underline{S}}_{-11}^{(1)} + \underline{\underline{S}}_{-12}^{(1)} \underline{\underline{S}}_{-11}^{(2)} \underline{\underline{E}} \underline{\underline{S}}_{-21}^{(1)} \\ \underline{\underline{S}}_{-12}^{(\text{tot})} = \underline{\underline{S}}_{-12}^{(1)} \cdot \left(\underline{\underline{1}} + \underline{\underline{S}}_{-12}^{(2)} \underline{\underline{E}} \underline{\underline{S}}_{-22}^{(1)} \right) \underline{\underline{S}}_{-12}^{(2)} \\ \underline{\underline{S}}_{-21}^{(\text{tot})} = \underline{\underline{S}}_{-21}^{(2)} \underline{\underline{E}} \underline{\underline{S}}_{-21}^{(1)} \\ \underline{\underline{S}}_{-22}^{(\text{tot})} = \underline{\underline{S}}_{-22}^{(2)} + \underline{\underline{S}}_{-21}^{(2)} \underline{\underline{E}} \underline{\underline{S}}_{-22}^{(1)} \underline{\underline{S}}_{-22}^{(2)} \end{cases} \quad (74)$$

where

$$\underline{\underline{E}} = \left(\underline{\underline{1}} - \underline{\underline{S}}_{-22}^{(1)} \underline{\underline{S}}_{-11}^{(2)} \right)^{-1} \quad (75)$$

Once again, an inversion is needed to construct the matrix $\underline{\underline{E}}$ in (75), which appears in the expressions given in (74) for the various blocks.

It is important to observe that the expressions in Eqs. (74) and (75) originate from an iterative process that accounts for multiple reflections at both discontinuities. In particular, the modes inside the central section go through a multiple scattering phenomenon that can be

mathematically expressed as a Neumann series with final value given by (74). For an in-depth discussion of this phenomenon, the reader is referred to Ref. 1, where a proof of convergence has been provided.

A more intuitive approach might have been followed, which makes use of an alternative representation in terms of the transmission matrix. It relates the wave amplitudes (both incoming and outgoing) at the first port with those at the second port as follows:

$$\begin{bmatrix} \underline{\underline{a}}^{(1)} \\ \underline{\underline{b}}^{(1)} \end{bmatrix} = \underline{\underline{T}} \begin{bmatrix} \underline{\underline{b}}^{(2)} \\ \underline{\underline{a}}^{(2)} \end{bmatrix} = \begin{bmatrix} \underline{\underline{T}}_{11} & \underline{\underline{T}}_{12} \\ \underline{\underline{T}}_{21} & \underline{\underline{T}}_{22} \end{bmatrix} \begin{bmatrix} \underline{\underline{b}}^{(2)} \\ \underline{\underline{a}}^{(2)} \end{bmatrix} \quad (76)$$

For the cascaded junction, the total transmission matrix can be simply expressed as a product of the single transmission matrices:

$$\underline{\underline{T}}^{\text{tot}} = \underline{\underline{T}}^{(1)} \underline{\underline{T}}^{(2)} \quad (77)$$

However, there are two significant disadvantages when using this approach that we can easily identify. The first one arises from the fact that the wavenumber in the uniform waveguide section between the two step discontinuities exhibits a negative sign with respect to the previous representation, implying that the cutoff modes are mapped into the constituent block matrices with real and positive exponentials. This renders the entries of the final matrix unstable, especially for large n and L . The second difficulty stems from the requirement that we must use an identical number of modes at both ends of the junction, since the use of a different number of modes results in an ill-conditioned matrix. This condition, in turn, suffers from the problem of relative convergence, which will be discussed in the following section.

7. CONVERGENCE CRITERIA

The accuracy of the final results is strongly affected by the truncation of the series used for the modal expansion. Convergence tests are usually performed in order to determine the minimum number of modes required to obtain a certain degree of accuracy; specifically, the number of modes is increased until the final result does not change significantly.

However, an interesting phenomenon can occur when following this procedure; namely, the final results may converge to a value that is strongly dependent on the ratio N_1/N_2 of the total numbers of modes used in the two longitudinally uniform waveguide sections directly connected to the discontinuity. This phenomenon, known as “relative convergence,” may affect the validity of the final results [13,14].

Several different criteria have been presented in the literature to cope with this problem. If we consider the step discontinuity problem reported in Fig. 9, where two rectangular waveguides of the same width and different heights are connected, it is possible to show that a correct result is guaranteed by increasing the number of modes and maintaining the ratio N_1/N_2 approximately equal to

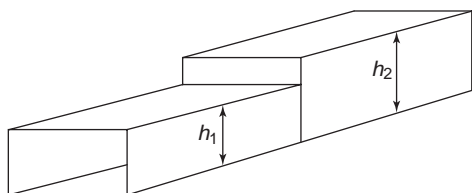


Figure 9. Step discontinuity between two rectangular waveguides of different heights.

the ratio h_1/h_2 . Intuitively, this result can be explained by considering the fact that both modal expansions should be able to follow the same variability of the field at both sides of discontinuity; since the basis functions used in the modal expansions have different periodicities on each side of the junction, the choice of the ratio $N_1/N_2 = h_1/h_2$ leads to the correct behavior of the two final expressions.

For a double step discontinuity (along both height and width), accurate results have been obtained by using the area criterion $N_1/N_2 = A_1/A_2$, where A_1 and A_2 are the cross-sectional areas of the waveguides 1 and 2, respectively. However, this criterion is not as general as a more useful one based on the condition that the maximum values of the transverse eigenvalues for modes at both sides of the discontinuity be the same. This is known as the *spectral criterion*, and it requires that once that the maximum value of the transverse eigenvalue $k_{c,max}$ is fixed, only the modes with $k_c < k_{c,max}$ are to be retained.

8. NUMERICAL EXAMPLES

Numerical results are presented in this section with the objective of demonstrating that the accuracy can be improved by including higher-order modes. As a first example, we consider a single-step discontinuity problem at the junction between a rectangular waveguide (waveguide 1) with dimensions of 10×5 mm, and a smaller rectangular

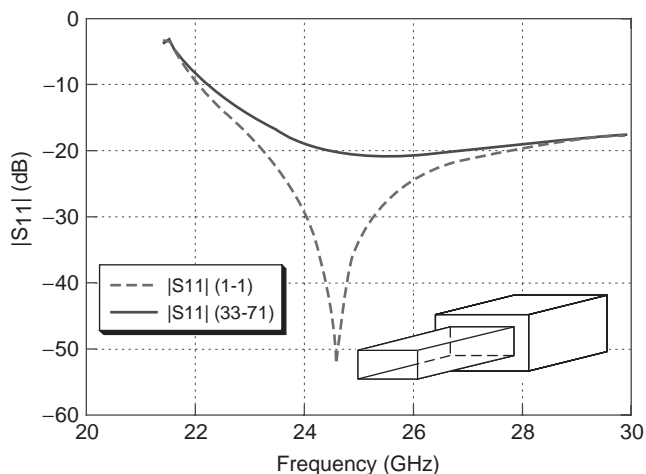


Figure 10. Amplitudes of the S_{11} scattering parameters for the boundary enlargement problem at the junction between two rectangular waveguides with dimensions 7×3.5 mm and 10×5 mm, respectively. The dashed curve is based on the exclusion of the higher order modes.

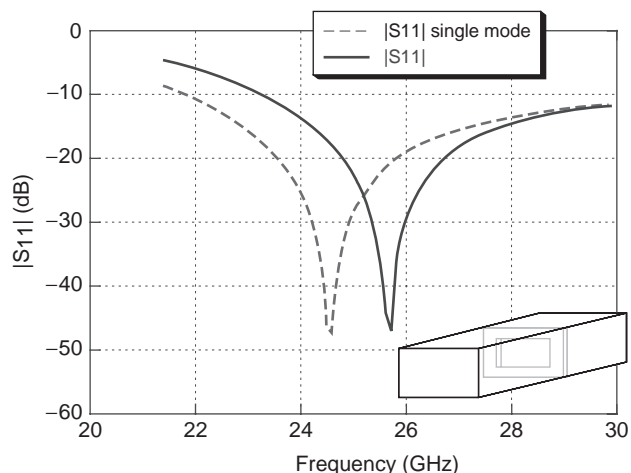


Figure 11. Amplitude of the S_{11} scattering parameter relevant to a thick iris in a rectangular waveguide. The waveguide has dimensions 10×5 mm, whereas the iris has dimensions 7×3.5 mm and a thickness of 2 mm. The dashed line corresponds to the case where the higher-order modes are not included.

waveguide (waveguide 2) whose dimensions are 7×3.5 mm. The single-mode bandwidth of the first waveguide spans from 15 to 30 GHz, whereas the second waveguide exhibits a single-mode bandwidth between 21.42 and 42.84 GHz. The scattering parameter S_{11} of this discontinuity has been calculated by using only the fundamental mode in both the waveguides. These results have been compared with those obtained by calculating the whole GSM of the discontinuity with 71 and 33 modes in the waveguides, respectively. The results are shown in Fig. 10, where the net discrepancy between the two curves clearly demonstrates the importance of including the higher-order modes.

The effects of higher-order modes become even more apparent if we refer to the following problem, where a rectangular iris of finite thickness is considered. This

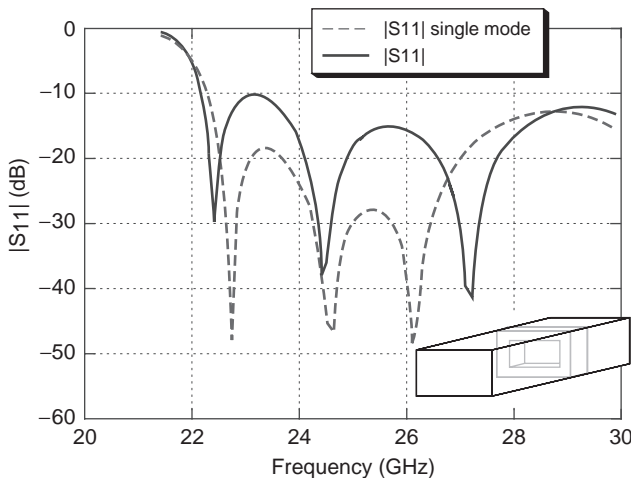


Figure 12. Amplitude of the S_{11} scattering parameter relevant to a thick iris in a rectangular waveguide. The waveguide has dimensions 10×5 mm, whereas the iris has dimensions 7×3.5 mm and a thickness of 5 mm. The dashed line corresponds to the case where the higher-order modes are not included.

problem can be analyzed by following the methodology presented in Section 6, where we cascade the two discontinuity problems and shift the GSM of the first discontinuity toward the second by a length equal to the thickness of the iris. In particular, the results obtained by using only the fundamental modes in the three waveguide sections are shown in Figs. 11 and 12 for two different lengths of the iris, and they are compared with those derived for the same configuration by accounting for the presence of higher-order modes (more precisely, 71 modes are included in the first and third waveguide sections, while 33 modes are retained in the central waveguide section).

BIBLIOGRAPHY

1. R. Mittra and S. W. Lee, *Analytical Techniques in the Theory of Guided Waves*, Macmillan, New York, 1971, pp. 207–217.
2. R. E. Collin, *Field Theory of Guided Waves*, IEEE Press, New York, 1991.
3. J. Uher, J. Bornemann, and U. Rosenberg, *Waveguide Components for Antenna Feed Systems: Theory and CAD*, Artech House, 1993.
4. G. Conciauro, M. Guglielmi, and R. Sorrentino, *Advanced Modal Analysis*, Wiley, 2000.
5. T. Rozzi and M. Mongiardo, *Open Electromagnetic Waveguides*, IEE, London, 1997.
6. R. Safavi-Naini and R. H. Macphie, On solving waveguide junction scattering problems by the conservation of complex power technique, *IEEE Trans. Microwave Theory Tech.* **MTT-29**(4):337–343 (April 1981).
7. S. Omar and K. Schünemann, Transmission matrix representation of finline discontinuities, *IEEE Trans. Microwave Theory Tech.* **MTT-33**:765–770 (Sept. 1985).
8. G. Eleftheriades, A. Omar, L. Katehi, and G. Rebeiz, Some important properties of waveguide junction generalized scattering matrices in the context of the mode matching technique, *IEEE Trans. Microwave Theory Tech.* **42**:1896–1903 (Oct. 1994).
9. M. A. Solano, J. S. Ipiña, Á. Gómez, A. Prieto, and A. Vegas, Comments on “Some important properties of waveguide junction generalized scattering matrices in the context of the mode matching technique,” *IEEE Trans. Microwave Theory Tech.* **49**:1663–1664 (Sept. 2001).
10. A. Morini and T. Rozzi, On the definition of the generalized scattering matrix of a lossless multipoint, *IEEE Trans. Microwave Theory Tech.* **49**:160–165 (Jan. 2001).
11. P. L. Overfelt and D. J. White, Alternate forms of the generalized composite scattering matrix, *IEEE Trans. Microwave Theory Tech.* **37**:1267–1268 (Aug. 1989).
12. T. S. Chu and T. Itoh, Generalized scattering matrix method for analysis of cascaded and offset microstrip step discontinuities, *IEEE Trans. Microwave Theory Tech.* **MTT-34**:280–284 (Feb. 1986).
13. R. Mittra, T. Itoh, and T. Li, Analytical and numerical studies of the relative convergence phenomenon arising in the solution of an integral equation by the moment method, *IEEE Trans. Microwave Theory Tech.* **MTT-20**:96–104 (Feb. 1972).
14. S. W. Lee, W. R. Jones, and J. J. Campbell, Convergence of numerical solutions of iris-type discontinuity problems, *IEEE Trans. Microwave Theory Tech.* **MTT-19**:528–536 (June 1971).

GEOMETRICAL OPTICS

DANILO ERRICOLO
University of Illinois at Chicago
Chicago, Illinois

1. INTRODUCTION

Geometric optics is the simplest theory to explain the formation of images. It represents a useful approximation of more complex theories and, in practical situations, such as the design of optical systems, it provides a useful way to make preliminary assessments. Geometric optics is also important because of the influence it has had on other disciplines, for example, in electrical engineering, on the design of antennas, which is discussed in Section 13. Geometric optics is attractive because it is a simple theory based on rays. However, it also is limited in its applications because it does not include diffraction, which is important to explain more precisely the formation of images and usually requires complex mathematical formulations. Many efforts have been devoted to extend geometric optics to include diffraction while keeping the advantages of a simpler ray theory, which are discussed in Section 14.

Let us consider the location of geometric optics within the realm of optical phenomena. Light is an electromagnetic phenomenon [1], and its propagation may be described in terms of two mutually coupled vectors: the electric and magnetic fields. In practice, many phenomena may be described by simply using only one of these two vector quantities. Hence, this simplification leads to a scalar theory where light is treated as a scalar function and the resulting theory is called *wave optics*. When light propagates around objects that are much larger than its wavelength, the wave nature of light may not be revealed and its propagation may simply be described using rays, and the corresponding theory is called *ray optics* or *geometric optics*. Ray optics is an approximation of wave optics, which, in turn, is a simplification of the electromagnetic theory of optics. All these theories are classical, but there are other light phenomena that are quantum-mechanical, which cannot be explained in terms of the classical electromagnetic theory. The most complete theory that combines quantum-mechanical phenomena with the classical electromagnetic theory is called *quantum electrodynamics* and, in the realm of optics, is referred to as *quantum optics*. The level of complexity of these theories follows their historical development: (1) geometric optics, (2) wave optics, (3) electromagnetic optics, and (4) quantum optics.

Historically, geometric optics was devised to explain the behavior of light. The basic principles of geometric optics that are discussed in this article were all formulated before the year 1900. Some relevant steps in the development of theories related to light follow and are based on Ref. 2; a more complete overview is provided in Ref. 3. The law of reflection was given by the Greek Euclid (ca. 300 B.C.). Refraction was observed by Alexandrian Greeks, but they could not explain it. Abu Ali al-Hasan Ibn al-Haytham (ca. 965–1039), latinized as Alhazen, in

his book on optics [4] gave a detailed description of refraction and investigated reflection from plane and curved surfaces, also known as “Alhazens’ problem.” Optics was put on solid foundation only after the introduction of the experimental method by the Italian Galileo Galilei (1564–1642). We have to wait until the seventeenth century to obtain a mathematical formulation of the law of refraction by the French René Descartes (1596–1650) and the Dutch Willebrod Snell (1580–1626). During the same century, two physical theories of light appeared. One theory was developed by the Dutch physicist Christiaan Huygens (1629–1695) and consisted in a geometric wave theory of light [5]. The other theory was created by the British Sir Isaac Newton (1643–1727), who developed a mechanical theory of propagation of particles [6]. Newton’s theory was accepted for nearly another century only because of his reputation, while Huygens’ theory was ignored.

The seventeenth century gave also birth to experimental discoveries such as interference by the British Robert Boyle (1627–1691) and the British Robert Hooke (1635–1703); the finiteness of the speed of light by the Danish Olaf Römer (1644–1710) and diffraction by the Italian Francesco Maria Grimaldi (1618–1663) and Hooke. After the experimental discoveries, geometric optics appeared as a limited theory of light that was based on four principles: (1) light travels along straight lines in a homogeneous medium, (2) light rays travel out of a source independently, (3) light rays obey the law of reflection, and (4) light rays obey the law of refraction. It is interesting to observe that all these laws follow from a mathematical principle that says nothing about the nature of light. This is principle of least time by the French Pierre de Fermat (1601–1665).

The mathematical theory of geometric optics received its definitive formulation with the work of the Irish Sir William Rowan Hamilton (1805–1865). Hamilton was aware of the works of the French Augustin Jean Fresnel (1788–1827), Huygens, and Newton, but he ignored their works because his goal was to build a mathematical science of optics from which all properties could be deduced. Hamilton’s main idea was the characteristic function. In fact, he showed that from the knowledge of the characteristic function all optical problems involving, for instance, lenses, mirrors, crystals, and propagation in the atmosphere could be solved.

Many scientists pointed out that in order to explain properties of light such as interference, diffraction, and polarization, a wave theory was necessary. Most of the early works on the wave theory of light were driven by an equivalence with waves inside elastic media. Before the work of the British James Clerk Maxwell (1831–1879), it is worth mentioning the results of the Irish James MacCullagh (1809–1847), who introduced differential equations that are closely related to the ones of Maxwell [7]. As of today, the best theory available to explain the behavior of light (with the exception of some problems that are investigated by quantum electrodynamics) is the one that subjects light to an electromagnetic wave that obeys Maxwell’s laws.

As mentioned earlier, geometric optics is an approximate representation. Wavelengths do not come into account, so interference and dispersion cannot be deduced.

Additionally, the vector character of light (i.e., polarization) and diffraction are not incorporated.

2. THE POSTULATES OF GEOMETRIC OPTICS

Geometric optics can be explained using four postulates:

- Light rays travel out of a source independently.
- Inside a homogeneous medium, light rays travel along straight lines.
- Light rays obey the law of reflection.
- Light rays obey the law of refraction.

When light rays propagate inside a homogeneous medium, they travel at a speed $v \leq c_0$, where c_0 is the speed of light in vacuum, and the medium is characterized by the index of refraction

$$n = \frac{c_0}{v} \quad (1)$$

The time taken by a ray of light to travel the geometric distance ℓ is proportional to the product $n\ell$, which is called the *optical path length*.

Let us now consider the simplest kind of optical source, a point source inside a homogeneous medium. Rays emitted from a point source are associated with spherical surfaces, centered at the source, called *wavefronts*. Each wavefront has the property that all its points have the same optical pathlength from the source. Equivalently, all the points that belong to the same wavefront have the same phase. Since there is an equivalence between rays and the associated wavefronts, in what follows we will refer to either rays or wavefronts depending on what is more convenient.

3. THE LAW OF REFLECTION

3.1. Reflection from a Plane Surface

The law of reflection considers a ray that, after interacting with a surface, bounces back to the same medium where it came from. Let us examine a ray with unit vector $\hat{\mathbf{r}}_1$ that is incident on a plane reflecting surface whose unit normal vector is $\hat{\mathbf{v}}$, as shown in Fig. 1. The incident ray $\hat{\mathbf{r}}_1$ and the normal $\hat{\mathbf{v}}$ define the *plane of incidence* that contains the reflected ray unit vector $\hat{\mathbf{r}}_2$. The angle of incidence θ_i and the reflection angle θ_r are related to each other by

$$\theta_i = \theta_r \quad (2)$$

which is the mathematical statement of the law of reflection.

3.2. The Method of Images

The reflected ray $\hat{\mathbf{r}}_2$ appears to an observer O as if it had originated from S' , which is symmetric to S with respect to the plane reflecting surface. The point S' is called the *image of S* and suggests an equivalent method to determine the direction of reflection of a ray incident at P . According to this method, the location P of the reflection point is

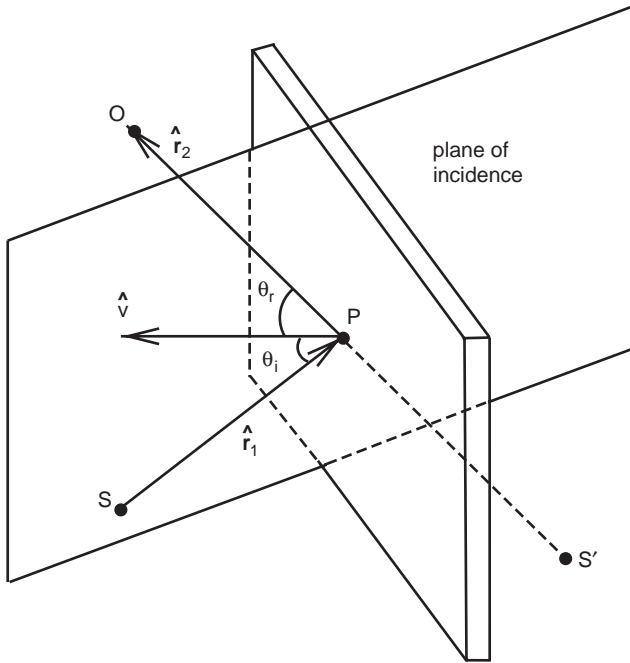


Figure 1. Geometry for the reflection from a plane surface. The plane of incidence defined by the unit vectors $\hat{\mathbf{r}}_1$ and $\hat{\mathbf{v}}$ contains the unit vector $\hat{\mathbf{r}}_2$.

determined by tracing the straight line from S' toward O . The formation of the image of an extended source due to the reflection from a plane surface is easily explained with the method of images. In fact, an observer O will receive rays that appear to have originated from points symmetric to the source, with respect to the plane reflecting source. Hence, in particular, the spherical wavefront originated by a point source will maintain its spherical shape on reflection from a plane interface because all rays associated with the reflected wavefront appear to have originated from the image of the original point source.

3.3. Reflection from a Curved Surface

When the reflecting surface is curved, one can still apply the law of reflection using the formulation (2) provided that the geometry is made locally plane by considering the plane tangent to the curved surface Σ at P , as shown in Fig. 4. In such a case, the plane of incidence contains the normal $\hat{\mathbf{v}}$ to the tangent plane and the angles of incidence and reflection are measured between the normal and the direction of incidence or reflection, respectively. When reflection occurs at a smooth curved surface, it is convenient to present the law of reflection in a compact vector notation. For this purpose, let $\hat{\mathbf{r}}_1$ and $\hat{\mathbf{r}}_2$ be the unit vectors along the directions of the incident and reflected rays and $\hat{\mathbf{v}}$ the unit vector of the normal to the surface at the point of reflection. The law of reflection may be written

$$\hat{\mathbf{r}}_2 = \hat{\mathbf{r}}_1 + \alpha \hat{\mathbf{v}} \quad (3)$$

where the constant α is determined from

$$\alpha = -2\hat{\mathbf{r}}_1 \cdot \hat{\mathbf{v}} \quad (4)$$

Since, according to (3), the unit vector $\hat{\mathbf{r}}_2$ is a linear combination of $\hat{\mathbf{r}}_1$ and $\hat{\mathbf{v}}$, the reflected ray is contained in the plane of incidence. In addition $\hat{\mathbf{r}}_1$ and $\hat{\mathbf{r}}_2$ have the same length, therefore they intersect $\hat{\mathbf{r}}_1 - \hat{\mathbf{r}}_2$ and, hence, $\hat{\mathbf{v}}$ at the same angle. Thus the angle of incidence equals the angle of reflection and

$$\theta_1 = \arccos(\hat{\mathbf{r}}_1 \cdot \hat{\mathbf{v}}) = \arccos(\hat{\mathbf{r}}_2 \cdot \hat{\mathbf{v}}) = \theta_r \quad (5)$$

For practical applications, such as in ray tracing, one is usually given $\hat{\mathbf{r}}_1$ and $\hat{\mathbf{v}}$. Hence, after obtaining α from (4), the direction of the reflected ray is obtained from (3). Further details for reflection from general curved surfaces are given in Refs. 8 and 9.

For a generic curved surface there is no method of images. In fact, for an observer O all rays incident on the curved surface at P will appear to have originated from the images of their sources with respect to the tangent plane at P . However, rays that are reflected at other points will, in general, appear to have originated from images that are different from the previous ones. In particular, a spherical wavefront will not appear to be originated from a single image source on reflection from a curved surface. The reflected wavefront will be, in general, astigmatic.

3.4. Cartesian Reflecting Surfaces

Some conic sections represent *Cartesian reflecting surfaces*; that is, the surfaces form perfect images of point objects upon reflection. These surfaces are the ellipsoid; the paraboloid and the hyperboloid and their cross sections are shown in Fig. 2. The ellipsoid has the property that all rays passing through one focus are reflected at the surface so that the reflected ray passes through the other focus. The paraboloid has the property that rays parallel to its axis are reflected so that they all pass through the focus. For the hyperboloid, rays emitted from one focus are reflected so that they appear to have originated from the other focus. Unfortunately, the relationship that leads to perfect images is valid only for certain points.

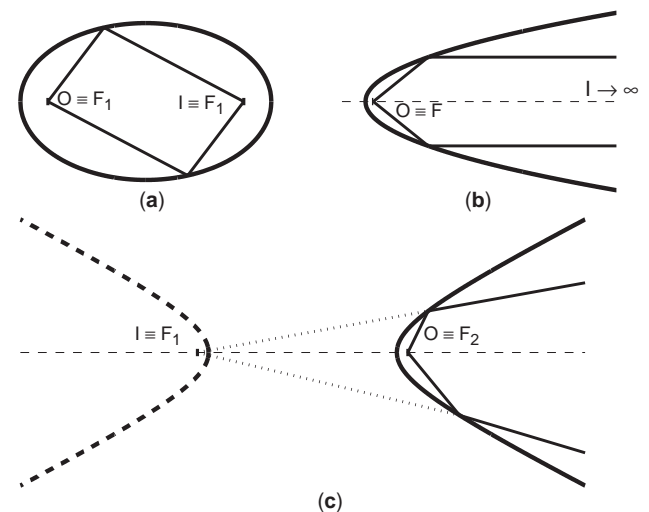


Figure 2. Cross sections of Cartesian reflecting surfaces: (a) ellipsoid; (b) paraboloid; (c) hyperboloid.

4. THE LAW OF REFRACTION

4.1. Refraction from a Plane Surface

The law of refraction considers the passage of a ray from one medium to another. Figure 3 shows the geometry for a ray with unit vector $\hat{\mathbf{r}}_1$ that is incident at P on a plane interface between two media with indices of refraction n_1 and n_2 . As in the case of reflection, one can define a plane of incidence that contains $\hat{\mathbf{r}}_1$ and $\hat{\mathbf{v}}$. The incident ray $\hat{\mathbf{r}}_1$ generates one reflected ray $\hat{\mathbf{r}}$ and a refracted or transmitted ray $\hat{\mathbf{r}}_2$. Both $\hat{\mathbf{r}}$ and $\hat{\mathbf{r}}_2$ are contained in the plane of incidence. The angles of incidence and refraction (or transmission) depend on the properties of the media through their indices of refraction according to

$$n_1 \sin \theta_1 = n_2 \sin \theta_2 \tag{6}$$

which is known as *Snell's law*. Because of Snell's law, the direction of the refracted ray

$$\theta_2 = \arcsin\left(\frac{n_1}{n_2} \sin \theta_1\right) \tag{7}$$

is closer to the normal to the interface when $n_2 > n_1$ and farther away from the normal when $n_2 < n_1$. In particular, when $n_2 < n_1$, the value of the incidence angle θ_1 that causes $\theta_2 = \pi/2$ is called *critical angle* because for $\theta_1 > \theta_c$ there is no refracted ray, a phenomenon known as *total internal reflection*.

4.2. Refraction from a Curved Surface

Refraction from a smooth curved surface is more conveniently expressed using a compact vector notation. Referring to Fig. 4, let $\hat{\mathbf{r}}_1$ and $\hat{\mathbf{r}}_2$ be the unit vectors along the directions of the incident and refracted rays, respectively, and $\hat{\mathbf{v}}$ the unit vector of the normal to the surface at the point of refraction. The law of refraction may then be written as

$$n_2 \hat{\mathbf{r}}_2 = n_1 \hat{\mathbf{r}}_1 - \beta \hat{\mathbf{v}} \tag{8}$$

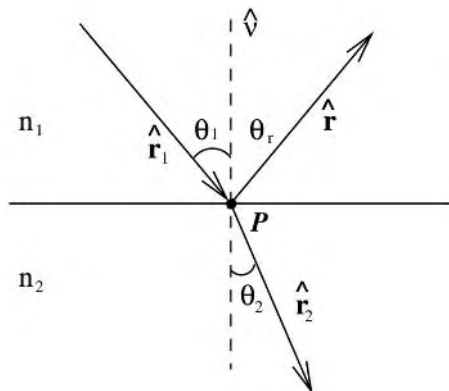


Figure 3. Geometry for the refraction of a ray. The plane of incidence defined by the unit vectors $\hat{\mathbf{r}}_1$ and $\hat{\mathbf{v}}$ contains the unit vector $\hat{\mathbf{r}}_2$ and $\hat{\mathbf{r}}$.

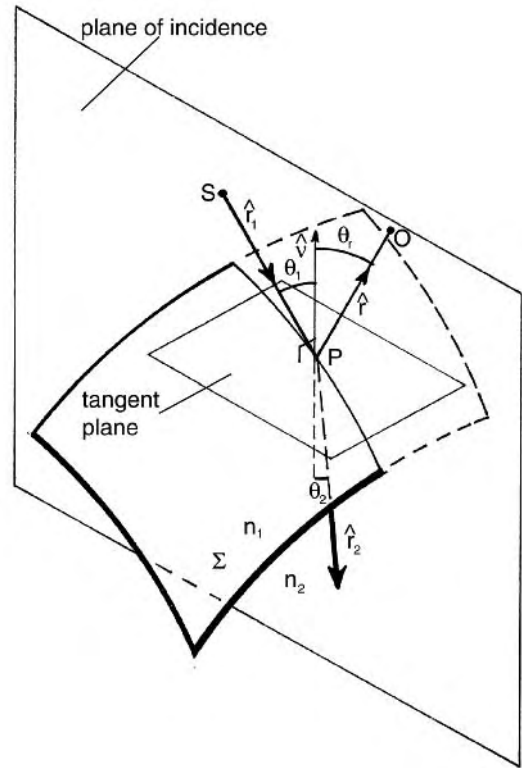


Figure 4. Geometry for the reflection and refraction of a ray from a curved surface.

where the constant β is determined from

$$\beta = n_2 \cos \theta_2 - n_1 \cos \theta_1 \tag{9}$$

and

$$\begin{aligned} \cos \theta_1 &= \hat{\mathbf{r}}_1 \cdot \hat{\mathbf{v}} \\ n_2 \cos \theta_2 &= \sqrt{n_2^2 - n_1^2 + n_1^2 \cos^2 \theta_1} \end{aligned} \tag{10}$$

Equation (8) defines $\hat{\mathbf{r}}_2$ as a linear combination of $\hat{\mathbf{r}}_1$ and $\hat{\mathbf{v}}$ so that the refracted ray is located in the plane of incidence. By taking the cross-product of (8) with $\hat{\mathbf{v}}$, one obtains the usual form of Snell's law

$$n_1 \sin \theta_1 = n_2 \sin \theta_2 \tag{11}$$

(since $|\sin \hat{\mathbf{r}}_1 \times \hat{\mathbf{v}}| = \sin \theta_1$, $|\sin \hat{\mathbf{r}}_2 \times \hat{\mathbf{v}}| = \sin \theta_2$, and $|\sin \hat{\mathbf{v}} \times \hat{\mathbf{v}}| = 0$). In a ray-tracing application, one usually knows $\hat{\mathbf{r}}_1$ and $\hat{\mathbf{v}}$. Then, after evaluating (10), the constant β is obtained from (9) and the direction of the refracted ray is derived from (8). Further details for refraction from general curved surfaces are given in Refs. 8 and 9.

Contrary to the law of reflection, there is no equivalent to the method of images for refraction, even in the case of a

plane interface. In fact, let us consider, for example, rays from a point source S located in a medium 1. Rays from S incident at the interface are refracted into medium 2 along different directions that, when extended back into medium 1, will not intersect all at the same point. Each ray refracted into medium 2 appears to be coming from a different source inside medium 1. Hence this could lead to the formation of multiple images, but the problem is avoided if one observes only a narrow bundle of rays so that they will appear to be coming from the same source. This is the case of a human eye that observes an object under water. Since the pupil captures only a narrow bundle of rays, no multiple images are observed. However, it is possible to find only one image by limiting the consideration to rays that make small angles with the normal $\hat{\nu}$. In fact, when the angles are small, the sine function can be approximated with its argument. Accordingly, the refraction law (6) takes the form

$$n_1\theta_1 = n_2\theta_2 \quad (12)$$

Therefore, referring to Fig. 5, rays that make small angles with the normal appear to an observer O as if they had originated by S' at an apparent depth

$$d' = \frac{n_1}{n_2}d \quad (13)$$

Most optical systems contain spherical surfaces. Similar to the case of refraction at a plane interface, rays in medium 2, originated by a point source in medium 1 and refracted by a spherical surface, do not intersect all at the same point. This is a statement of the fact that spherical surfaces do not produce perfect images. This difficulty of spherical surfaces is overcome, again, by limiting the rays to make small angles with a preferred axis. This results

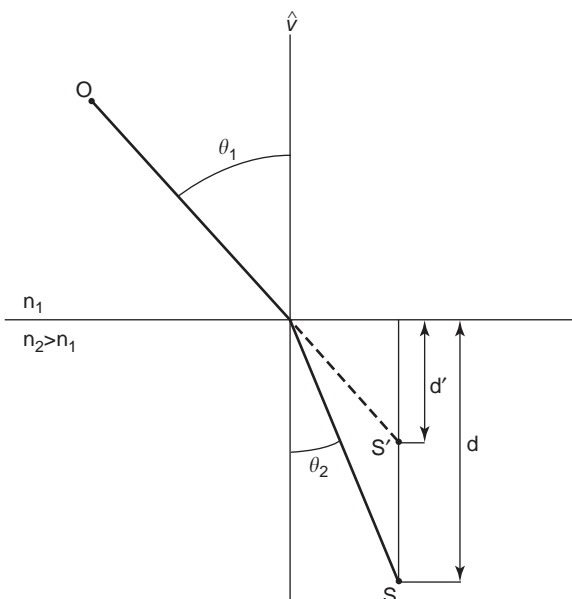


Figure 5. Geometry for the refraction at a plane interface when angles are small.

into the *paraxial approximation*, which is explained in Section 8. Further details of the limitations of spherical surfaces are explained in Section 11. A different approach to the laws of geometric optics is considered next.

5. FERMAT'S PRINCIPLE

The laws of geometric optics may be derived from the purely mathematical Fermat principle. In order to introduce this principle, let us recall that the optical path length of a ray that propagates from point A to point B inside a medium with index of refraction $n(x, y, z)$ is expressed by

$$\int_A^B n(x, y, z) ds \quad (14)$$

According to Fermat's principle, the actual path followed by the ray of light is such that the optical pathlength (14) is stationary in the sense of variational calculus

$$\delta \int_A^B n(x, y, z) ds = 0 \quad (15)$$

where the symbol δ represents the variation. Without going into the formal definition of what a variation is according to variational calculus, the condition (15) may be understood by making a parallelism with ordinary differential calculus and looking at (15) as being a derivative of (14). In particular, if p_0 is the trajectory that satisfies (15), trajectories that are in the neighborhood of p_0 will not change the value of (14) to a first-order approximation. Hence, the trajectory p_0 behaves similarly to a stationary point that may represent either a maximum, a minimum, or an inflection point for the quantity represented by (14). Usually, the trajectory p_0 corresponds to a minimum and, since (14) is proportional to the travel time, the Fermat principle is formulated by saying that light rays travel along paths of least time.

Using Fermat's principle, one can derive the laws of reflection and refraction. For the law of reflection, referring to Fig. 6a, it is easy to prove that the path SPO that satisfies Fermat's principle (15) is shorter than any other path such as SAO . Only for the path SPO , the angles θ_i and θ_r satisfy the law of reflection (2). For the law of refraction, Fig. 6b shows that when the location of a variable point P is chosen so that the path SPO satisfies (15), then the angles θ_1 and θ_2 satisfy the law of refraction (6).

5.1. Principle of Reversibility

The principle of reversibility states that if a ray of light propagating from A to B is reversed in direction, it will follow the same path backward. This property follows from Fermat's principle that does not account for the actual direction of propagation of light.

5.2. Ray Equation

Another consequence of Fermat's principle is the ray equation. If the trajectory of a ray \mathbf{r} is described by the

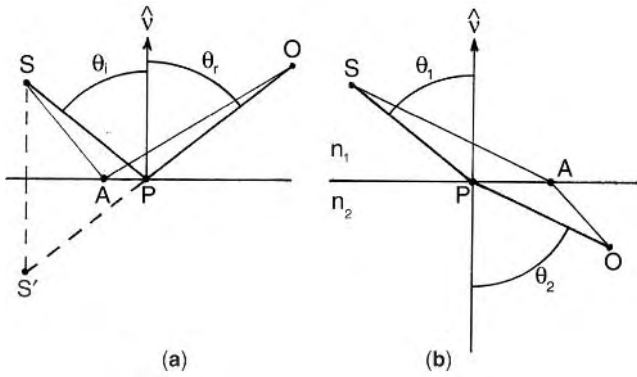


Figure 6. Fermat’s principle: (a) geometry for the reflection of a ray at a plane surface; (b) geometry for the refraction of a ray at a plane interface between two media with different indices of refraction.

coordinates $(x(s), y(s), z(s))$, where s is the length of the trajectory measured from an arbitrary point along the trajectory, it can be shown that the ray equation is

$$\frac{d}{ds} \left(n \frac{dr}{ds} \right) = \nabla n \tag{16}$$

or, equivalently, that the functions $x(s), y(s), z(s)$ must satisfy the partial-differential equations:

$$\frac{d}{ds} \left(n \frac{dx}{ds} \right) = \frac{\partial n}{\partial x}, \frac{d}{ds} \left(n \frac{dy}{ds} \right) = \frac{\partial n}{\partial y}, \frac{d}{ds} \left(n \frac{dz}{ds} \right) = \frac{\partial n}{\partial z} \tag{17}$$

One of the postulates of geometric optics, the rectilinear propagation of rays of light inside a homogeneous medium, follows directly from the ray equation (16). In fact, for a homogeneous medium, $\nabla n = 0$ so that after two integrations, one obtains

$$\mathbf{r} = \mathbf{a}s + \mathbf{b} \tag{18}$$

which is the equation for a straight line where \mathbf{a} and \mathbf{b} are constant vectors. When the medium is not homogeneous, the analytical derivation of the solution of (16) is usually not trivial, but mathematical solutions are possible when the paraxial approximation is made. Accordingly, one assumes that the trajectory is almost parallel to the z axis so that the following two equations are obtained

$$\frac{d}{dz} \left(n \frac{dx}{dz} \right) = \frac{\partial n}{\partial x}, \frac{d}{dz} \left(n \frac{dy}{dz} \right) = \frac{\partial n}{\partial y} \tag{19}$$

5.3. Graded-Index Fiber

Consider a glass fiber cylinder with an index of refraction that depends on the distance from the axis, such as

$$n^2 = n_0^2 [1 - \alpha^2(x^2 + y^2)] \tag{20}$$

When this expression for n is substituted into (19) and the approximation $\alpha^2(x^2 + y^2) \ll 1$ is made, one finds that the components $x(s), y(s)$ of the ray follow the equations

$$\frac{d^2x}{dz^2} = -\alpha^2x, \frac{d^2y}{dz^2} = -\alpha^2y \tag{21}$$

which represent harmonic motions with period $2\pi/\alpha$. Assume that the initial position of a ray is (x_0, y_0) and the initial angle is $(\theta_{x_0}, \theta_{y_0})$. Since this problem has circular symmetry, one may set $x_0 = 0$ without loss of generality. Then the solutions of (21) may be written as follows:

$$x(z) = \frac{\theta_{x_0}}{\alpha} \sin(\alpha z), y(z) = \frac{\theta_{y_0}}{\alpha} \sin(\alpha z) + y_0 \cos(\alpha z) \tag{22}$$

In the particular case of a *meridional ray*, a ray inside a plane that contains the z axis, $\theta_{x_0} = 0$ and the solution (22) shows that the ray will continue to lie in the same plane and will propagate along a sinusoidal trajectory. When $\theta_{y_0} = 0$ and $\theta_{x_0} = \alpha y_0$, then (22) reduces to a helical trajectory on the surface of a cylinder of radius y_0 . In both these cases, the trajectory remains confined within the glass fiber cylinder, which, therefore, operates as a light guide. By changing the initial conditions, other helical trajectories are obtained.

5.4. Spherical Symmetric Media and Lenses

An optical medium with index of refraction that is only a function of the radial distance from the origin is of considerable interest because it makes it possible to determine conditions to obtain perfect images. In fact, if $n = n(r)$, the light ray trajectories are plane curves (similarly to the trajectories of a particle in the field of a central force) and, without loss of generality, one may limit the investigation to trajectories that lie in a plane [11]. Referring to Fig. 7, assume that a unit radius sphere, a spherical lens, is made with material of index of refraction $n = n(r)$ and that the material outside the lens is homogeneous with $n = 1$. The problem consists in finding the functional dependence $n = n(r)$ so that all rays originating

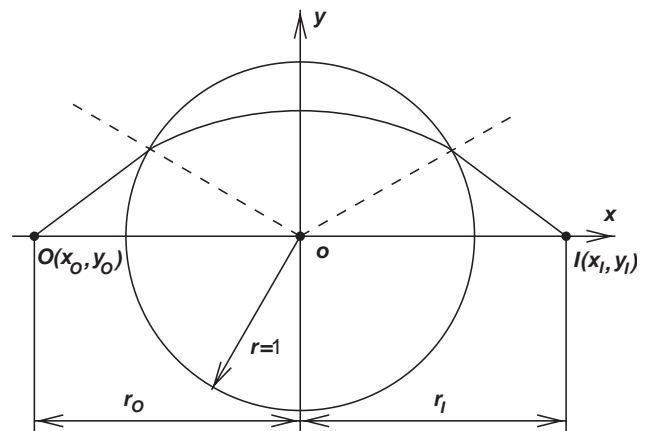


Figure 7. Geometry for the problem of a spherical lens made of a material with index of refraction that is axially nonhomogeneous.

at O and passing through the spherical lens are focused at I . This problem was solved by Luneburg when $n(r)$ is continuous and monotonic in $0 \leq r \leq 1$. Two explicit solutions are *Maxwell's fisheye* and the *standard Luneburg lens*. Maxwell's fisheye images points on the surface of the spherical lens into points that are diametrically opposite on the lens surface, hence $r_O = r_I = 1$ and $n(r) = 2/(1 + r^2)$. The standard Luneburg lens images a point on the surface of the spherical lens at infinity, hence $r_O = 1, r_I = \infty$ and $n(r) = \sqrt{2 - r^2}$. The Luneburg lens and its generalizations find many applications in other disciplines, as mentioned in Section 13.

Now that the laws of geometric optics have been introduced, we will examine what an optical system is and how perfect images are created.

6. DEFINITION OF AN OPTICAL SYSTEM

A source point O inside a medium with index of refraction n generates an infinite number of rays, only a finite number of which, in general, will reach any other point in the medium. If it is possible to find a point I through which an infinite number of rays pass, this point is said to be a stigmatic (or sharp) image of O . An ideal optical system transforms every point O of a three-dimensional region called the *object space* into a stigmatic image I . The collection of all image points is called *image space* [12]. An optical system is composed of a number of refracting and reflecting surfaces and is usually described by neglecting its internal structure and referring to the transformation that it operates, as indicated in Fig. 8. Points that correspond to each other through this transformation are called *conjugate points*. Figure 8 shows a *real* object because rays propagate out of an actual source. Similarly, the image I of the point O is real because it is formed by rays converging at one location. An image may also be *virtual*. This occurs when the rays forming the image appear to have originated from a point even though no actual source of light is located at that point. The relationship between the object and the image may be equivalently described using wavefronts. For example, the optical system of Fig. 8, transforms a wavefront diverging out of O into a wavefront converging at I . In the case of a virtual image, its wavefront appears to be diverging out of a point where no

actual source of light is located [13]. When O describes a curve C_O in the object space, I will describe a conjugate curve C_I in the image space. In general, the conjugate curves are not similar to each other. However, if every curve C_O is geometrically similar to its conjugate curve C_I , the imaging between the two spaces is perfect and so is the optical system.

To determine the transformation operated by an optical system, a sufficient knowledge of its internal structure is required. The numerical analysis of a given optical system is carried out by considering a point $O \equiv (x_O, y_O)$ of a certain plane $z = z_O$, the *object plane*. An appropriate number of rays, which originate at O , are traced through the system with the goal of finding the intersections (x_I, y_I) in another plane $z = z_I$, the *image plane*. The ray tracing operations are carried out using the laws of reflection and refraction described earlier. If the optical system is perfect, these rays intersect the image plane at the ideal image point

$$x_I = Mx_O, y_I = My_O \tag{23}$$

where M is a constant of the optical system that depends only on the choice of the object plane and is called *magnification*. Hence, a perfect image is a scaled replica of the object.

In all that follows, we assume that rays normally propagate from left to right. The first optical system that is examined in more detail is the surface that separates two media with different indices of refraction.

7. CARTESIAN REFRACTING SURFACES

Spherical refracting surfaces do not provide a unique image of a point object, unless rays are restricted to make small angles with the optical axis. In order to obtain a unique image of a point object without imposing restrictions on the rays, the shape of the refracting surface must be changed. Referring to Fig. 9, the surface Σ is determined so that each ray that originated at O and refracted at P passes through I . Hence, the refracting surface Σ represents a perfect optical system according to the previous definition. The shape of Σ is obtained by applying Fermat's principle and requesting that for each point

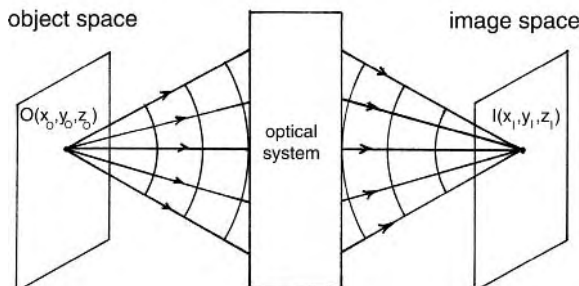


Figure 8. Optical system and conjugate points.

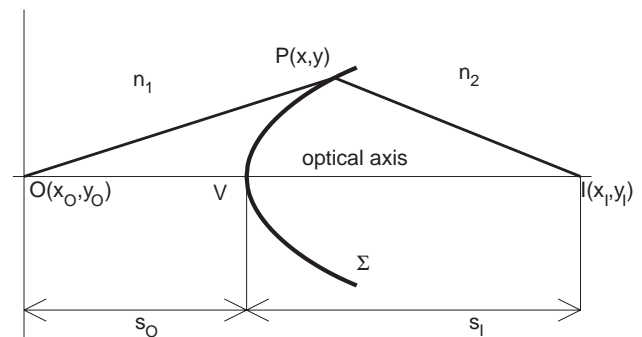


Figure 9. Geometry for a surface that refracts O into I . Note that the surface Σ is not spherical.

$P(x, y)$ on Σ , the path length $O \rightarrow P \rightarrow I$ be the same, i.e.:

$$\begin{aligned} & n_1 \sqrt{(x - x_0)^2 + (y - y_0)^2} \\ & + n_2 \sqrt{(x - x_I)^2 + (y - y_I)^2} \\ & = n_1 s_O + n_2 s_I \end{aligned} \tag{24}$$

This results in an algebraic curve of the fourth order, known as *Cartesian oval*, which is shown in Fig. 9. In practice, one would like to have the object and the image in the same medium and this is not accomplished by a single refracting surface. However, lenses provide a solution since rays passing through a lens undergo two refractions and the image appears outside the lens in the same medium of the object. Now the problem is to determine the appropriate shape of each refracting surface of the lens. Of particular interest are Cartesian refracting surfaces that refract rays from a point object into parallel rays. These parallel rays then will be refracted at the second surface of the lens to form the image. Figure 10a shows an ellipsoidal surface that refracts rays from O into parallel rays when $n_2 < n_1$, while Fig. 10b shows a hyperbolic surface that refracts rays from O into parallel rays when $n_2 > n_1$. It is important to understand that these surfaces provide perfect images only for object points O at very specific locations.

Most actual optical systems contain spherical reflecting and refracting surfaces because they are easy to manufacture. In order to obtain images from these systems, rays must be limited to make small angles with the optical axis. These rays are called *paraxial* and are the topic of the next section.

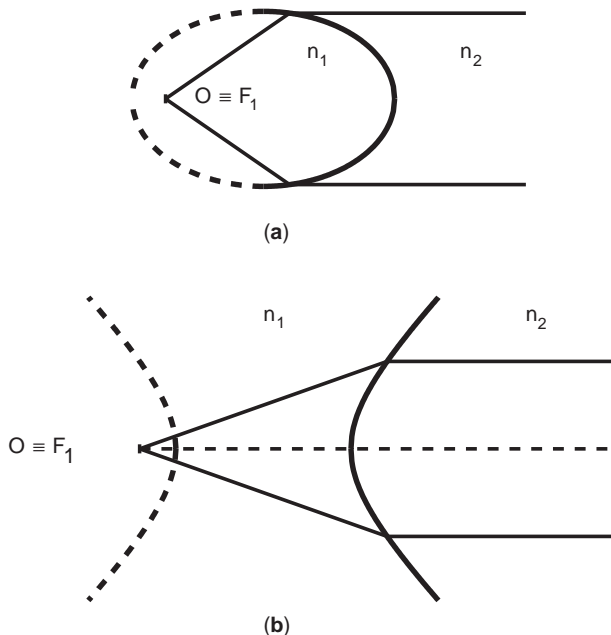


Figure 10. Cross sections of Cartesian refracting surfaces: (a) ellipsoidal surface that images O at infinity when $n_2 < n_1$; (b) hyperbolic surface that images O at infinity when $n_2 > n_1$.

8. PARAXIAL APPROXIMATION

Most optical systems contain spherical surfaces. When the centers of curvature of all these surfaces are aligned along an axis, the system is said to be *centered* and the axis is called the *optical axis*. If light rays travel almost parallel and at a short lateral distance from the optical axis, it is possible to make simplifications so that the laws of reflection and refraction applied to spherical surfaces take simpler forms. Approximations made assuming that rays are almost parallel to the optical axis are referred to as *paraxial approximations* or *Gaussian optics*. If an angle θ satisfies $|\theta| \ll 1$ because of the paraxial approximation, the following simplifications approximations are made

$$\sin \theta \simeq \tan \theta \simeq \theta, \cos \theta \simeq 1 \tag{25}$$

and, in particular, Snell's law becomes

$$n_1 \theta_1 = n_2 \theta_2 \tag{26}$$

8.1. Reflection at a Spherical Mirror

As a first application of the paraxial approximation, the reflection at a spherical mirror, shown in Fig. 11, is considered. To obtain the location of the image, at least two straight lines must be drawn. The first line goes from the tip P of the object to the center of curvature C because this line does not change direction on reflection. The second line is drawn from the tip P of the object to the vertex V , so that it is easy to determine the direction of the reflected ray. The intersection of these two lines determines the tip

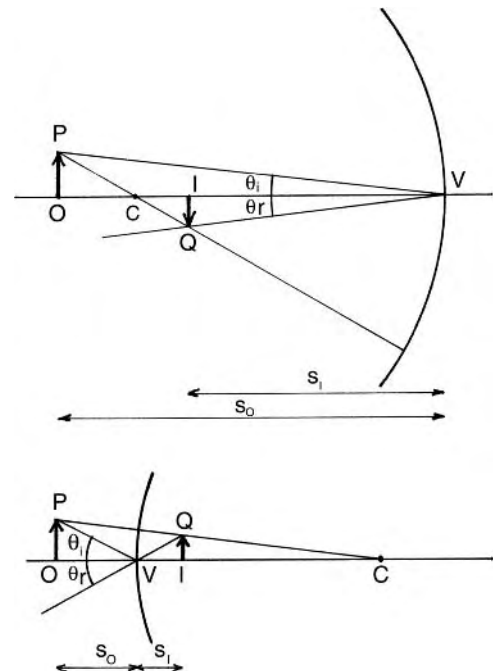


Figure 11. Construction of the images for a concave and a convex spherical mirror.

Q of the image from which the whole virtual image is found. The locations of object and image are determined by using the paraxial approximation and the similarities between the triangles OPC , IQC and OPV , IQV , which yield

$$\frac{1}{s_O} + \frac{1}{s_I} = \frac{1}{f} \tag{27}$$

where f is the focal distance of the mirror, defined as

$$f = -\frac{R}{2} \begin{cases} > 0, & \text{concave mirror} \\ < 0, & \text{convex mirror} \end{cases} \tag{28}$$

The distances s_O and s_I are measured with a sign convention that assumes propagation of light from left to right. A real object (image) is located to the left of V and corresponds to a positive value for s_O (s_I). When the object (image) is virtual, it is located to the right of V and s_O (s_I) is negative. For this geometry, the lateral magnification of the image is

$$m = -\frac{s_I}{s_O} \tag{29}$$

where the negative sign used to obtain a positive number m , due to the sign convention on the distances.

8.2. Refraction at a Spherical Surface

A second application of the paraxial approximation is the refraction from a spherical surface, shown in Fig. 12. Similar to the reflection from a mirror, a minimum of two lines must be drawn to find the location of the image. The first line is traced from the tip P of the object to the center of curvature C , because this line is not deflected. The second line is drawn from the tip P of the object to the vertex V and then continues inside the medium n_2 with an angle θ_2 with respect to the normal at V . These two lines intersect at Q , which gives the location of the image. Application of the paraxial approximation and use of the similarity between triangles OPC and CIQ yields

$$\frac{n_1}{s_O} + \frac{n_2}{s_I} = \frac{n_2 - n_1}{R} \tag{30}$$

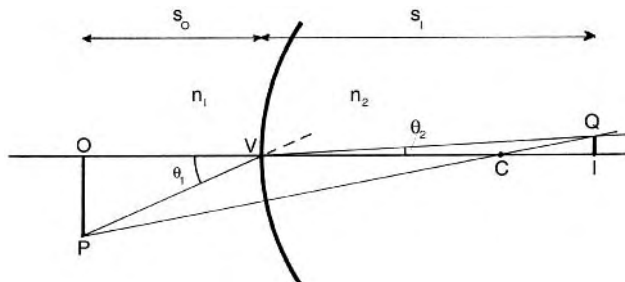


Figure 12. Construction of the image at a spherical refracting surface.

where the radius of curvature R is positive for a convex spherical surface. s_O and s_I are positive for real and negative for virtual object and images, respectively. The lateral magnification is given by

$$m = -\frac{n_1 s_I}{n_2 s_O} \tag{31}$$

8.3. The Thin Lens

The relationship just found for a spherical refractive surface may be used to obtain the equation of a *thin lens*, which is made of two spherical refractive surfaces that are separated by a negligible distance. Specifically, assuming that light propagates inside a medium of refractive index n_1 , crosses a refractive spherical interface with radius of curvature R_1 , enters a medium of index n_2 , crosses a spherical interface with radius of curvature R_2 and, finally, enters back into the medium with index n_1 , one obtains the *lensmaker* equation

$$\frac{1}{s_O} + \frac{1}{s_I} = \frac{1}{f} \tag{32}$$

where s_O and s_I are the object and image distances, respectively, which are measured from the plane of the thin lens. In the previous equation, the focal distance f is

$$\frac{1}{f} = \frac{n_2 - n_1}{n_1} \left(\frac{1}{R_1} - \frac{1}{R_2} \right) \tag{33}$$

The lensmaker equation also may be written in a form that emphasizes the curvatures of the wavefronts. In fact, referring to Fig. 13, a spherical wave that expands from O has a curvature, or *vergence*, $V = 1/s_O$ when it reaches the plane of the lens. The lens is characterized by a refracting power $P = 1/f$ that changes the curvature of the wavefront from V to $V' = 1/s_I$ when the wavefront enters the image space to the right of the lens. With these definitions, the alternative form of the lensmaker equation is

$$V + V' = P \tag{34}$$

and its terms have units of *diopeters*, i.e. the inverse of a length, when the distances are measured in meters.

When two or more thin lenses are attached together, their refractive powers add. So n thin lenses with focal

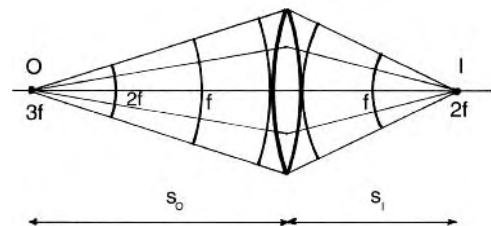


Figure 13. Interpretation of the lensmaker equation in terms of wavefront curvature.

distances f_1, \dots, f_n correspond to one thin lens with equivalent focal length f such that

$$\frac{1}{f} = \frac{1}{f_1} + \dots + \frac{1}{f_n} \quad (35)$$

or with a refractive power

$$P = P_1 + \dots + P_n \quad (36)$$

Many optical systems are designed, at least initially, using paraxial approximations. In fact, paraxial optics relationships are very useful in the analysis of optical systems with many elements, provided that these relationships are cast according to the method discussed in the next section.

9. RAY TRANSFER MATRICES

The analysis of a complex optical system may be carried out by the repeated application of the laws of geometric optics. However, this operation becomes cumbersome even for systems constituted only by a few elements. Fortunately, the paraxial approximation leads to a formalism that describes the passage of a ray through an optical system in terms of simple matrix multiplications. This formalism, known as *matrix optics*, is valid under the paraxial or Gaussian optics approximation and is limited to rays that travel in a single plane; hence it is applicable to systems that have a planar geometry or to meridional rays in circular symmetric systems.

Referring to Fig. 14, at any plane perpendicular to the optical axis, a ray is described by its position y and angle θ , so that the ray at the output plane z_2 is related to the ray at the input plane z_1 by the linear equations:

$$y_2 = Ay_1 + B\theta_1 \quad (37)$$

$$\theta_2 = Cy_1 + D\theta_1 \quad (38)$$

These two equations may be cast in matrix form as

$$\begin{bmatrix} y_2 \\ \theta_2 \end{bmatrix} = \begin{bmatrix} A & B \\ C & D \end{bmatrix} \begin{bmatrix} y_1 \\ \theta_1 \end{bmatrix} \quad (39)$$

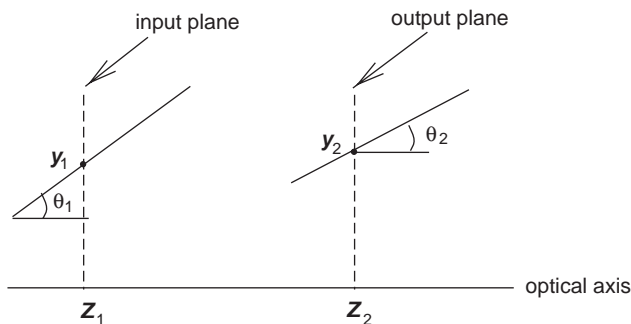


Figure 14. Geometry for the matrix description of a ray.

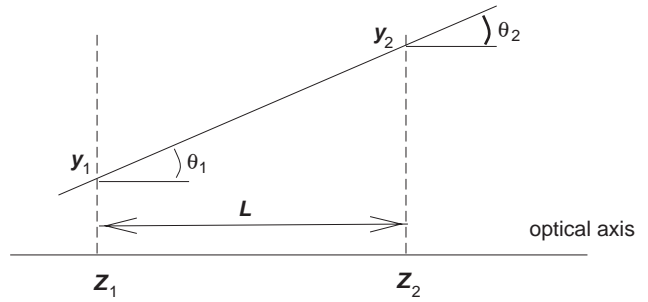


Figure 15. Geometry for the translation matrix.

where the matrix with elements A, B, C, D is called *ray-transfer matrix* or *ABCD matrix*. We now are going to consider the ray transfer matrices for some optical systems.

1. *Translation Matrix.* The simplest optical system is the free space between two planes. Referring to Fig. 15, the matrix that describes the propagation is

$$M = \begin{bmatrix} 1 & L \\ 0 & 1 \end{bmatrix} \quad (40)$$

2. *Reflection at a Spherical Interface.* The geometry for the reflection at a spherical interface is described in Fig. 16, which corresponds to the matrix

$$M = \begin{bmatrix} 1 & 0 \\ \frac{2}{R} & 1 \end{bmatrix} \quad (41)$$

Note that the same sign convention applies to all angles both before and after reflection. Rays pointing upward are associated with positive angles while rays pointing downward are associated with negative angles.

3. *Reflection at a Planar Surface.* This matrix may be derived from the previous one in the limiting case that the

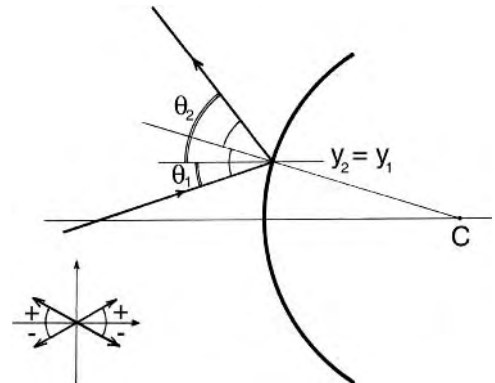


Figure 16. Geometry for the reflection from a spherical interface and sign convention for the angles.

curvature $R \rightarrow \infty$. In such a case, one obtains

$$M = \begin{bmatrix} 1 & 0 \\ 0 & 1 \end{bmatrix} \tag{42}$$

4. *Refraction at a Spherical Interface.* The geometry for this case is given in Fig. 17, and the corresponding matrix is

$$M = \begin{bmatrix} 1 & 0 \\ \frac{n_1 - n_2}{Rn_2} & \frac{n_1}{n_2} \end{bmatrix} \tag{43}$$

5. *Refraction at a Plane Interface.* This is a special case that may be derived when the curvature $R \rightarrow \infty$, which yields

$$M = \begin{bmatrix} 1 & 0 \\ 0 & \frac{n_1}{n_2} \end{bmatrix} \tag{44}$$

6. *Thin-Lens Matrix.* The matrices reported above may be used to derive the ray transfer matrix for a thin lens. In fact, by considering the product of two matrices representing the refraction from a spherical surface, one obtains

$$M = \begin{bmatrix} 1 & 0 \\ \frac{n_2 - n_1}{R_2n_1} & \frac{n_2}{n_1} \end{bmatrix} \begin{bmatrix} 1 & 0 \\ \frac{n_1 - n_2}{R_1n_2} & \frac{n_1}{n_2} \end{bmatrix} \tag{45}$$

$$= \begin{bmatrix} 1 & 0 \\ -\frac{1}{f} & 1 \end{bmatrix}$$

where the focal length f is given by (33). The thin-lens matrix is an example of an optical system that is studied

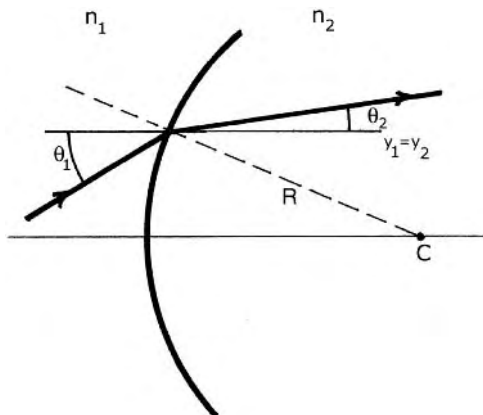


Figure 17. Geometry for the refraction from a spherical interface.

by cascading the matrices of simpler optical systems. In doing so, it is important to observe that if a ray passes through optical elements characterized by the matrices M_1, \dots, M_n , the overall transformation is represented by a matrix given by the product

$$M = M_n M_{n-1} \dots M_1, \tag{46}$$

Thus, the order of the matrices at the right hand side of the previous equation is inverse to the order followed by the ray to go through the elements of the system. One property of ray matrices is that their determinant is always equal to the ratio of the indices of refraction of the first and final media. This property may be used as a necessary condition to verify if a system matrix is computed correctly. Further details on matrix optics are found in the literature [1,8,10,14].

9.1. Cardinal Points of an Optical System

The characteristics of an optical system may be derived from the knowledge of its six *cardinal* points, which are illustrated in Fig. 18: two focal points F_1 and F_2 , two nodal points N_1 and N_2 , and two principal points Q_1 and Q_2 . *Focal points* are the locations where rays parallel to the optical axis converge. The intersections of rays entering the system with those leaving the system define the principal surfaces, which are usually spherical and centered on the object and the image. In the paraxial approximation, these surfaces are planes and are referred to as *principal planes*. Their intersections with the optical axis defines the *principal points*. *Nodal points* are located on the optical axis and have the property that a ray directed through one of them leaves the system from the other nodal point along a

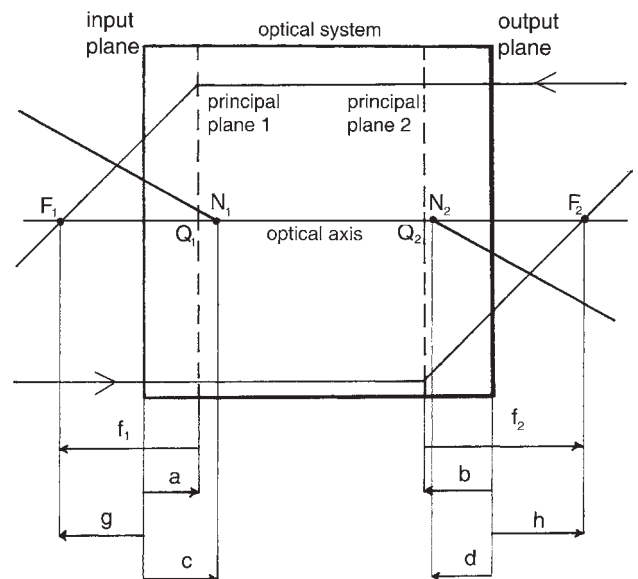


Figure 18. The six cardinal points of an optical system; the principal planes and distances relative to both input/output and principal planes.

direction parallel to the one of the first ray. The expressions “*first focal, principal, and nodal points*” refer to cardinal points defined by rays entering the system from the right. Conversely, “*second cardinal points*” are defined by rays entering the system from the left. The principal planes 1 and 2 are used as references to measure the distances within an optical system [15].

9.2. Meaning of Elements of ABCD Matrix

There are some interesting implications when the elements of the ray transfer matrix go to zero. Referring to (38), when $D = 0$, we obtain $\theta_2 = Cy_1$ regardless of θ_1 . So all rays that enter the system at y_1 will leave with the same angle θ_2 . Hence the input plane of a system with $D = 0$ is first focal plane.

When $A = 0$, from (37), $y_2 = B\theta_1$ hence input rays parallel to each other will leave the system passing by the point at y_2 . Therefore, the output plane of a system with $A = 0$ is the second focal plane of the system.

When $B = 0$, from (37), $y_2 = Ay_1$ so all rays entering the system at y_1 leave the system at y_2 . Hence the input and output planes are conjugate and $A = y_2/y_1$ represents the linear magnification.

When $C = 0$, from (38), $\theta_2 = D\theta_1$ so all rays parallel to the θ_1 direction will leave the system parallel to each other along θ_2 with an angular magnification $D = \theta_2/\theta_1$. Such a system is called *telescopic* because a telescope admits parallel rays and returns parallel rays.

The characteristics of an optical system are determined from its six cardinal points. Under the paraxial approximation, the elements of the ABCD matrix determine the characteristics of the system as well. Thus, there must be a relationship between the cardinal points and the ABCD matrix. This relationship is summarized in Table 1, where the symbols used for the distances are defined in Fig. 18.

Table 1. Relationship between Cardinal Points, Ray Matrix Elements, and Distances Shown in Fig. 18

Relative to Input and Output Reference Planes	
$g = \frac{D}{C}$	
$h = -\frac{A}{C}$	
$a = \frac{D - n_0/n_f}{C}$	
$b = \frac{1 - A}{C}$	
$c = \frac{D - 1}{C}$	
$d = \frac{n_0/n_f - A}{C}$	
Relative to Principal Planes	
$f_1 = g - a = \frac{n_0/n_f}{C}$	
$f_2 = h - b = -\frac{1}{C}$	

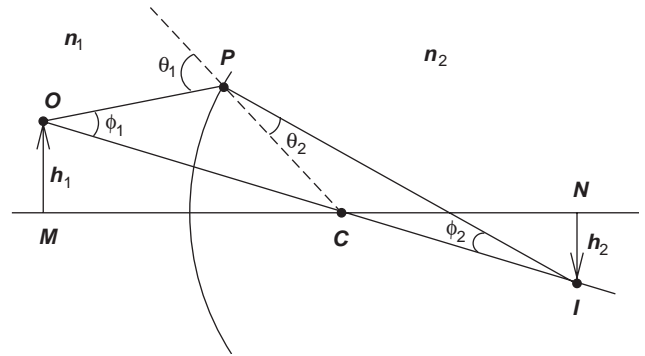


Figure 19. Geometry for the refraction from a spherical surface when the paraxial approximation is removed.

Let us now move away from paraxial rays and consider a general result, involving spherical surfaces, attributed to the German Ernst Abbe (1840–1905).

10. REFRACTION AT A SPHERICAL INTERFACE

Let us consider refraction from a spherical surface when the paraxial approximation is abandoned. Referring to Fig. 19, a small object near the axis is considered and its image is obtained by tracing two rays. The first ray, OC, passes through the center of curvature of the lens, so that it is not deflected. The second ray, OP is refracted and intersects the first ray at I. By simple considerations using the triangles OPC, PCI and the similarity between the triangles MOC, CNI one finds the following relationship

$$n_1 h_1 \sin \phi_1 = n_2 h_2 \sin \phi_2 \tag{47}$$

which is called the *Abbe sine condition*. In the paraxial approximation, the angles ϕ_1 and ϕ_2 are small so that the Abbe sine condition is simplified into

$$n_1 h_1 \phi_1 = n_2 h_2 \phi_2 \tag{48}$$

which is also known as the *Lagrange theorem*. For a centered optical system, with many refracting surfaces, the quantities $n_i h_i \sin \phi_i$ or, in the paraxial case, $n_i h_i \phi_i$ are invariant, which constitutes an important property. The Abbe sine condition is used in the one of Seidel’s aberrations.

11. ABERRATIONS

The paraxial approximation is valid for rays that travel very close to the axis of an optical system and leads to the formation of perfect images. In practical optical systems there are apertures, rays are not necessarily paraxial and departures from perfect images are observed. These departures are called *aberrations*, and practical optical systems are corrected to minimize aberrations so that images that are as close as possible to the ideal ones are obtained. To understand the origin of aberrations, let us consider an optical system that images a point source. Under the

paraxial approximation, the ideal wavefront at the exit pupil of an optical system is spherical and is obtained from linear expressions that result from the following trigonometric expansions

$$\begin{aligned} \sin x &= x - \frac{x^3}{3!} + \frac{x^5}{5!} + \dots + (-1)^n \frac{x^{2n+1}}{(2n+1)!} \\ \cos x &= 1 - \frac{x^2}{2!} + \frac{x^4}{4!} + \dots + (-1)^n \frac{x^{2n}}{(2n)!} \end{aligned} \tag{49}$$

when they are stopped at the first term. When higher order terms are included, aberrations appear. In particular, if the expansions (49) are stopped at terms of order no larger than x^3 , one obtains the third-order aberration theory originally developed by the German mathematician Ludwig Von Seidel (1821–1896). According to his theory, there are five aberrations for monochromatic illumination: *spherical aberration*, *coma*, *astigmatism*, *curvature of field* and *distortion*. If nonmonochromatic illumination is considered, the *chromatic aberration* is the sixth Seidel aberration. A further refined theory considers terms up to the order of x^5 , but for most practical applications Seidel theory is sufficiently accurate. The theory of aberrations is described, among others, elsewhere in the literature [9–11,13,15–19].

11.1. Third-Order Theory

Figure 20 shows a generic optical system that creates the actual wavefront S_2 and the ideal wavefront S_1 . The actual ray forms an image L along the optical axis and the image T in the plane of the ideal paraxial image, while the ideal ray forms an image at I . There are different ways to measure the aberration. One may refer to the longitudinal aberration LI , the transverse, or lateral aberration TI or the difference PQ of the wavefront position. Since most optical systems contain spherical surfaces, the aberrations of spherical surfaces are studied in great detail when the object is either a point along the optical axis or a point off the optical axis. For a point object O located on the optical axis, the aberration is measured as shown in Fig. 21 by the optical path difference between the shortest ray, OVI , and another ray refracted at P , OPI . The aberration according

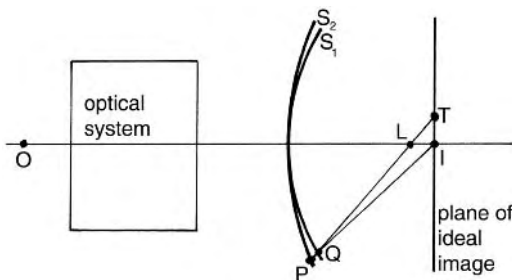


Figure 20. Difference between the ideal wavefront S_1 and the actual wavefront S_2 and various measures for the aberration.

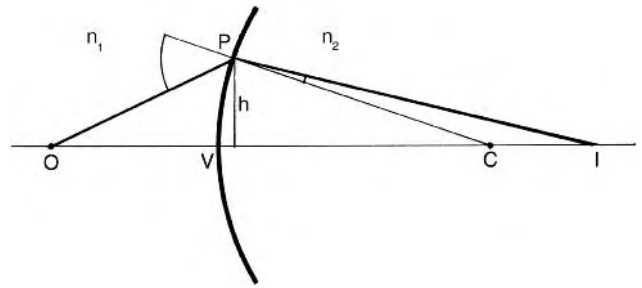


Figure 21. Geometry for the reflection at a spherical interface.

to the third-order theory, is given by the difference

$$a(P) = \overline{OCI} - \overline{OPI} = ch^4 \tag{50}$$

where c is a proportionality constant.

For an object point O located off axis, as shown in Fig. 22, the aberration measured as the difference between the shortest ray and another ray diffracted at P is given by

$$a(P) = \overline{OCI} - \overline{OPI} \tag{51}$$

However, all practical optical systems have an aperture or pupil or stop that is usually centered along the optical axis. Hence, a beam of rays out of O is not symmetrical with respect to OC because of the presence of the aperture. As a result of this lack of symmetry, the measure of the aberrations for points located off axis leads to four (additional) Seidel aberrations. Referring to Fig. 22, it is found that

$$\begin{aligned} a(P) &= C_{040}r^4 + C_{131}h_I r^3 \cos \theta + C_{222}h_I^2 r^2 \cos^2 \theta \\ &+ C_{220}h_I^2 r^2 + C_{311}h_I^3 r \cos \theta \end{aligned} \tag{52}$$

where the subscripts of the coefficients represents powers of h_I , r , $\cos \theta$, respectively. The terms that appear in (52)

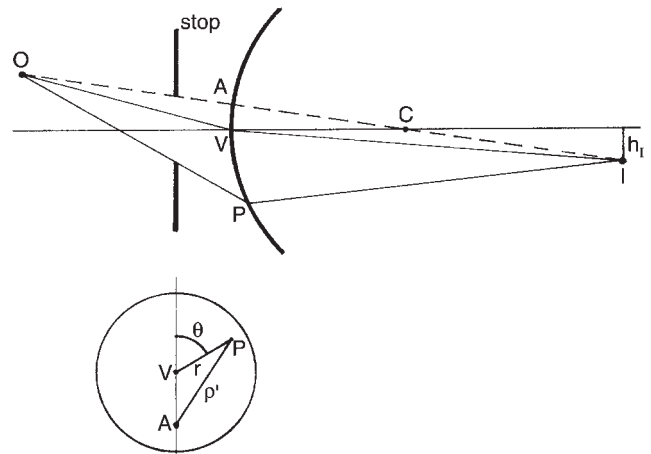


Figure 22. Geometry for refraction of an off-axis point O by a spherical surface. The presence of a stop breaks the symmetry around the shortest ray OCI .

represent

$$\begin{aligned}
 S_1 &= C_{040}r^4 && \text{spherical aberration} \\
 S_2 &= C_{131}h_I r^3 \cos \theta && \text{coma} \\
 S_3 &= C_{222}h_I^2 r^2 \cos^2 \theta && \text{astigmatism} \\
 S_4 &= C_{220}h_I^2 r^2 && \text{curvature of field} \\
 S_5 &= C_{311}h_I^3 r \cos \theta && \text{distortion}
 \end{aligned}
 \tag{53}$$

Each one of these aberrations is described in the following as if they were the only aberration present.

11.2. Spherical Aberration

Spherical aberration is the variation of the focal length with the aperture and is the only aberration, among $S_1 - S_5$ indicated in (53), that does not depend upon h_I so it always exists. In particular, it may exist when combinations of spherical surfaces occur. Most optical instruments use parallel rays, so it is customary to measure, for comparison purposes, the aberration due to parallel rays. Figure 23 illustrates how spherical aberration results into different focal points F_0, F_1, F_2, F_3 depending on the diameter r of the zone of the lens where the beam of parallel rays is incident. The spherical aberration of a lens is reduced by changing the radii of curvature of the two spherical surfaces of the lens. In fact, since the focal length of the lens is given by (33), it is possible to change the values of the index of refraction n, R_1 and R_2 without altering the focal length f .

As an example, Fig. 24 shows lenses with the same focal length but different shape. The shape of a thin-lens may be characterized by the *Coddington shape factor*

$$\zeta = \frac{R_2 + R_1}{R_2 - R_1}
 \tag{54}$$

and by changing ζ the spherical aberration may be reduced but not completely eliminated. It is possible to completely eliminate spherical aberration from a single lens by aspherizing it. However, such an aspherized lens will be free from spherical aberrations only for a particular object distance, so such a process is justified for only a few special instruments.

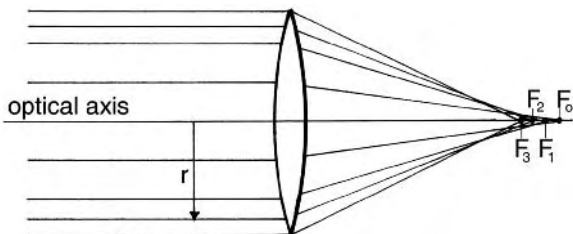


Figure 23. Spherical aberration of a lens that produces different images depending on the diameter h of the zone of the lens.

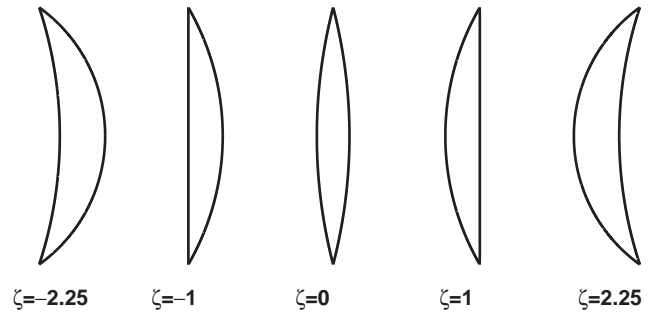


Figure 24. Lenses with same focal length but different Coddington shape factors.

11.3. Coma

Coma is the variation of magnification with the aperture and is nonsymmetric with respect to the optical axis because it depends on $\cos \theta$. Figure 25 shows how this aberration affects a set of parallel rays that are refracted by a thin lens. The ray through the center of the lens V is focused at V' , while the rays through the edges of the lens P are focused at P' . Hence, the magnification is different depending on which part of the lens the rays go through.

More specifically, referring to Fig. 26, each ring-shaped area of the lens forms a so-called comatic circle. Within each ring-shaped zone of the lens, rays contribute to different parts of the comatic circle. For example, rays contained in the sagittal plane determine the top part of the comatic circle, whereas rays contained in the tangential plane determine the bottom of the comatic circle. Each comatic circle increases in radius as the radius of the originating zone on the lens increases. The superposition of all comatic circles, shown in the bottom right corner of Fig. 25, is a comet-like figure from which the name coma for this aberration is derived.

In Section 10, we saw that rays making wide angles with the optical axis must satisfy the Abbe sine condition (47). This relation may be rearranged to point out the lateral magnification as

$$\frac{h_2}{h_1} = -\frac{n_1 \sin \varphi_1}{n_2 \sin \varphi_2}
 \tag{55}$$

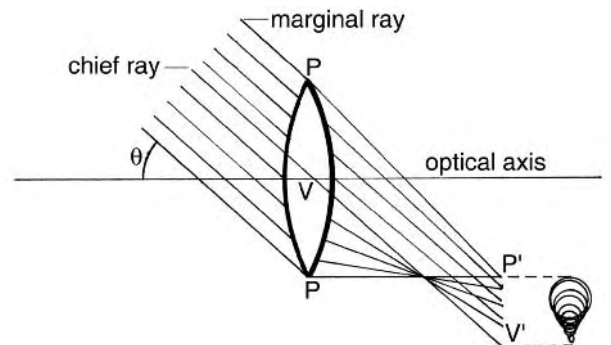


Figure 25. A set of parallel rays generates a superposition of comatic circles of different radii.

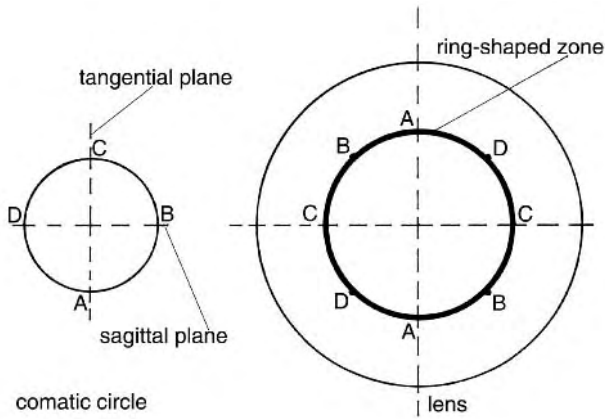


Figure 26. Detail of the contribution of a ring-shaped zone of a lens to the creation of a comatic circle. Rays through the tangential plane of the lens contribute to the bottom of the comatic circle, and rays through the sagittal plane of the lens contribute to the top of the comatic circle.

Hence, to prevent coma, the lateral magnification must be the same for all zones of a lens:

$$\frac{\sin \phi_1}{\sin \phi_2} = \text{const} \tag{56}$$

Similar to spherical aberration, coma may be reduced by changing the shape of a lens. In particular, it is possible to prove that coma is absent when

$$\zeta = \left(\frac{2n^2 - n - 1}{n + 1} \right) \frac{s_O - s_I}{s_O + s_I} \tag{57}$$

An optical system that is free of both spherical aberration and coma is called *aplanatic*.

11.4. Astigmatism

Astigmatism is explained with the help of Fig. 27 that shows an object point *O* and two beams of rays that are obliquely incident on the lens. The rays contained in the vertical, or tangential, plane *tt'* focus along the horizontal caustic line *T*, while the rays contained in the horizontal, or sagittal, plane *ss'* cross along the vertical caustic line *S*.

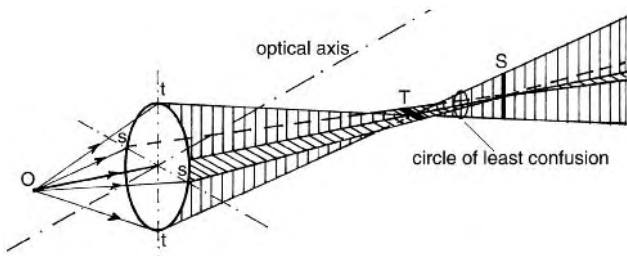


Figure 27. Formation of an astigmatic image. A fan of rays in the sagittal, or horizontal, *ss'* plane focuses along the vertical line *S*, while a fan of rays in the tangential, or vertical, plane *tt'* focuses along the horizontal line *T*.

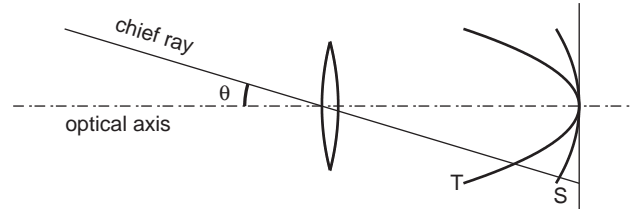


Figure 28. Cross sections of the paraboloidal surfaces *S* and *T*.

Normally, the image of a point is a point, but, when astigmatism is present, the image takes the form of two separate lines. Between *T* and *S* the cross section of the beam is approximately circular and constitutes the *circle of least confusion* for the image of *O*. When the angle θ is varied, *S* and *T* describe curved surfaces that are paraboloids of revolution whose cross sections are indicated in Fig. 28. The amount of astigmatism is measured by the distance between these two surfaces along the chief ray (a ray that passes through the center of the aperture of an optical system). If the astigmatism is removed, the surfaces *S* and *T* coincide with each other and result into the *Petzval surface* (named after Joseph Max Petzval [1807–1891], a Hungarian optician and mathematician).

11.5. Curvature of Field

Even if the first three aberrations are removed, the image is formed on the curved Petzval surface and, hence, the focal surface is curved, which leads to the curvature of the field. This is understood by referring to Fig. 29, which shows the location of an ideal image *IQ* of the object *OP*. According to Fermat’s principle, for *IQ* to be an image, the distances *s_I* and *s_Q* must be identical. Since this cannot happen for an extended object *OP*, the image is formed along the curved surface *RS*. A simple way to obtain flattening of the image field is by means of a stop that prevents oblique chief rays from penetrating the lens center.

11.6. Distortion

This aberration is caused by a different lateral magnification for points located at different distances from the optical axis. The common shapes of distorted images are shown in Fig. 30, where part (a) represents the undistorted image of a wire mesh object; part (b) shows barrel distortion, which is characterized by a smaller magnification at the edges of the field; and part (c) shows pincushion distortion that is characterized by a greater magnification

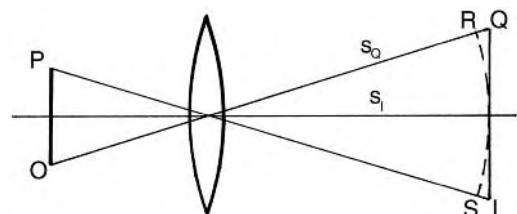


Figure 29. Geometry for the formation of the image of an extended object that shows the curvature of field.

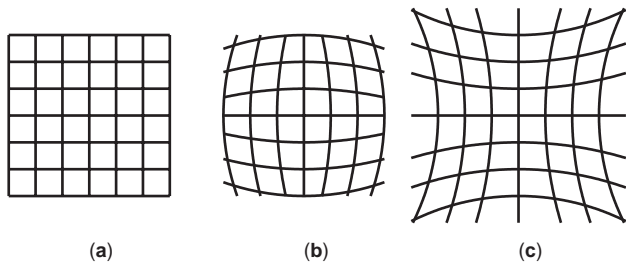


Figure 30. Example of distorted images. The correct image of a wire mesh object is shown in (a), while (b) represents an image affected by barrel distortion, and (c) depicts an image affected by pincushion distortion.

toward the edges of the field. As an example of an optical system that is free from distortion is the pinhole camera, shown in Fig. 31, for which

$$\frac{\tan \theta'}{\tan \theta} = \text{const} \tag{58}$$

11.7. Chromatic Aberration

The previous five aberrations occur for monochromatic light; when nonmonochromatic light is used, the variation of the index of refraction with the frequency of light causes chromatic aberration, which results in the creation of one image per color present in the illumination. Normally, the index of refraction is larger at higher frequencies, so that, for a thin lens, the focal distance (33) is shorter at higher frequencies. Figure 32a shows the variation in focal distance for the image of the same object that is illuminated with white light and located at large distance from the lens along the optical axis. The axial distance between the images *V* and *R* is the longitudinal chromatic aberration. There is also a lateral chromatic aberration, shown in Fig. 32b, for the image of an off-axis object. One of the simplest methods to correct chromatic aberration is to put in contact two lenses made of different materials and with different powers, as shown in the achromatic doublet of Fig. 32c. The powers are chosen with opposite sign and different magnitudes so that the net power is either

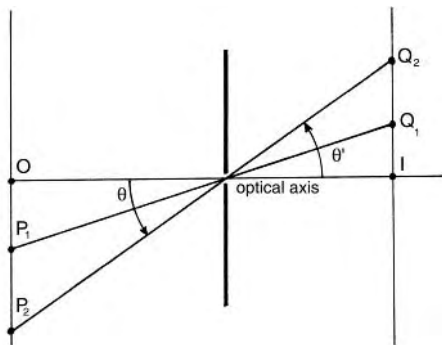


Figure 31. A pinhole camera provides a lateral magnification that is constant.

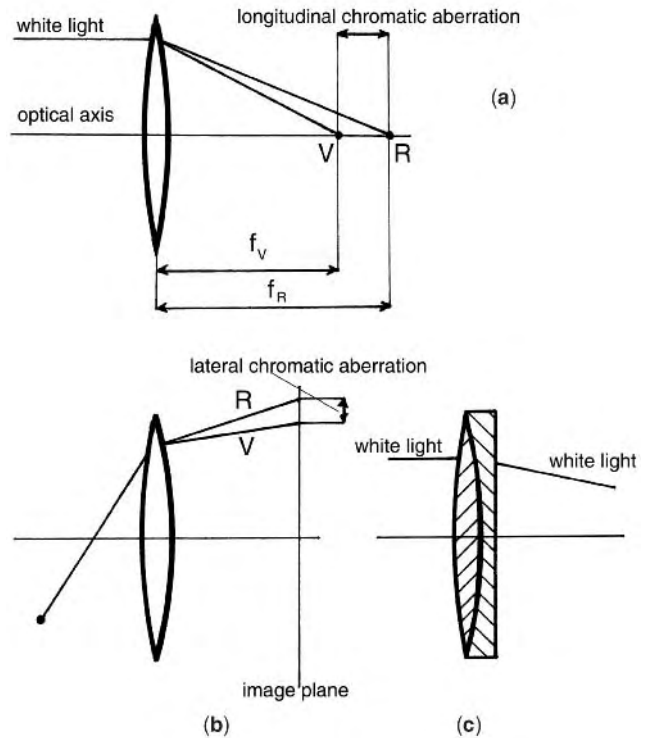


Figure 32. (a) Longitudinal chromatic aberration resulting from different focal distances for different colors for the images of an object located along the optical axis and at large distance from the lens; (b) lateral chromatic aberration for an object located off the optical axis; (c) achromatic doublet that removes chromatic aberration.

positive or negative. The materials and the shapes of the lenses are chosen so that the dispersion of one lens compensates for the dispersion of the other and, within a certain frequency interval, the doublet is not affected by chromatic aberration.

12. RELATIONSHIP BETWEEN GEOMETRIC OPTICS AND ELECTROMAGNETIC THEORY

12.1. Eikonal Equation

An elegant introduction to geometrical optics and its relationship to the electromagnetic theory is found in Refs. 2 and 12, from which part of the material contained in this section is based.

The German Gustav Kirchhoff (1824–1887) made the first significant effort to derive geometrical optics from a wave theory. He expressed mathematically the principle of Huygens, which resulted in the Kirchhoff–Huygens principle. Even though the Kirchhoff–Huygens principle contains some mathematical inconsistencies, it is remarkable that it is successful in so many applications. In particular, in 1882 Kirchhoff [20] showed that when the wavelength $\lambda \rightarrow 0$, the field given by the Kirchhoff integral in the presence of an obstacle approaches the prediction obtained from geometrical optics: the existence of a sharp transition

between dark and lit regions. Eventually, the point of view of geometric optics as a limiting case of the electromagnetic theory when $\lambda \rightarrow 0$ became accepted.

Sommerfeld and Runge [21] provided the most accepted argument to show the connection between geometric optics and electromagnetic theory. They assumed that a scalar function $u(x, y, z)$ represents the complex amplitude of a component of the electric field \mathbf{E} , which, in the monochromatic case, satisfies the Helmholtz scalar equation

$$\nabla^2 u(x, y, z) + k^2 u(x, y, z) = 0 \quad (59)$$

where ∇^2 is the laplacian operator, $k = k_0 n = \sqrt{\epsilon \mu} \omega / c = 2\pi / \lambda$ is the wavevector, ω is the angular frequency, and the medium is assumed to be linear, isotropic and described by a permittivity ϵ and a permeability μ , which may be functions of the position. Sommerfeld and Runge assumed that the functional form of $u(x, y, z)$ was a generalization of a plane wave

$$u(x, y, z) = A(x, y, z) e^{jk_0 \Psi(x, y, z)} \quad (60)$$

where A is the amplitude of u and $k_0 \Psi$ is the phase. In particular, $\Psi(x, y, z)$ is a real scalar called *eikonal function* and surfaces along which $\Psi(x, y, z) = \text{const}$ are the wavefronts of the electromagnetic field. It is also assumed that A and Ψ do not vary rapidly with changes in the position. When (60) is substituted into (59), it is obtained that

$$k_0^2 (n^2 - |\nabla \Psi|^2) A + \nabla^2 A + j k_0 (2\nabla \Psi \cdot \nabla A + A \nabla^2 \Psi) = 0 \quad (61)$$

which requires that both real and imaginary part be independently zero. The condition on the real part yields

$$|\nabla \Psi|^2 = n^2 + \left(\frac{\lambda}{2\pi}\right)^2 \frac{\nabla^2 A}{A} \quad (62)$$

In the limit of $\lambda \rightarrow 0$, the last term of the previous equation vanishes, which leaves the so-called eikonal equation:

$$|\nabla \Psi|^2 = n^2 \quad (63)$$

The eikonal equation is at the basis of geometric optics, and its solutions define the wavefronts. In the following, it is shown that the ray equation (16) may be obtained from the eikonal equation. For this purpose, let us observe that $\hat{\mathbf{t}} = \nabla \Psi / n$ defines a unit vector that is perpendicular to the surfaces $\Psi = \text{const}$ (because of the meaning of the gradient of Ψ) and consider a trajectory $\mathbf{r} = \mathbf{r}(s)$ that admits $\hat{\mathbf{t}}$ as its tangent unit vector, where s measures the length of the trajectory from an arbitrary point along it. Then, it is possible to write

$$n \hat{\mathbf{t}} = n \frac{d\mathbf{r}}{ds} = \nabla \Psi \quad (64)$$

from which ray trajectories could be derived from the knowledge of Ψ . With a few more steps, the dependence on Ψ is removed from the previous equation. In fact, the directional derivative along $\mathbf{r}(s)$ of the previous equation

yields

$$\begin{aligned} \frac{d}{ds} \left(n \frac{d\mathbf{r}}{ds} \right) &= \frac{d}{ds} (\nabla \Psi) = \frac{d\mathbf{r}}{ds} \cdot \nabla (\nabla \Psi) = \frac{\nabla \Psi}{n} \cdot \nabla (\nabla \Psi) \\ &= \frac{1}{2n} \nabla (|\nabla \Psi|^2) = \frac{1}{2n} \nabla n^2 = \nabla n \end{aligned} \quad (65)$$

So, finally, one obtains the ray equation (16) that was independently derived from Fermat's principle. Therefore, the path to point out the relationship between the electromagnetic theory and geometric optics occurs in three steps: (1) one shows that when $\lambda \rightarrow 0$ (high-frequency approximation) the description of the electromagnetic field provided by (60) leads to the eikonal equation (63); (2) one observes that the eikonal equation defines surfaces $\Psi = \text{const}$ that are perpendicular to the ray trajectories; and (3) the ray equation (16) is derived from the eikonal equation.

Classical geometric optics provides a description of light phenomena that is based only on the geometric concept of a ray. However, in order to use geometric optics to make quantitative statements, this theory needs to be extended to introduce the concepts of amplitude, phase, and polarization. These extensions are explored in the following two sections, which are based on Ref. 22.

12.2. Amplitude Relation

The notion of light intensity may be introduced into the classical geometric optics by imposing the conservation of the energy flux inside a tube of rays. For example, let us consider the isotropic spherical wavefront shown in Fig. 33, where two different cross sections of areas dA_0 and dA are located at some reference points $s=0$ and s , respectively. The radiation density S_0 at $s=0$ and S at s

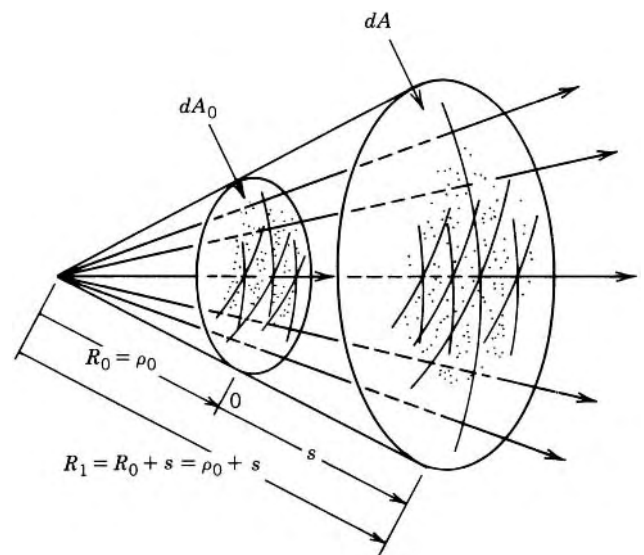


Figure 33. Tube of rays for an isotropic spherical source. (Constantine A. Balanis, *Advanced Engineering Electromagnetics*, copyright ©1989 by John Wiley & Sons, Inc. This material is used by permission of John Wiley & Sons, Inc.)

are related by

$$S_0 dA = S dA \tag{66}$$

because it is assumed that no energy flows through the lateral side of the cylinder. For an electromagnetic wave in the far-zone field of the source, the relationship between the electric field $\mathbf{E}(\mathbf{r}, \theta, \varphi)$ and the radiation density $S(r, \theta, \varphi)$ is

$$S(r, \theta, \varphi) = \frac{1}{2\eta} |\mathbf{E}(r, \theta, \varphi)|^2 \tag{67}$$

Hence, combining the last two equations, one obtains

$$\frac{|\mathbf{E}|}{|\mathbf{E}_0|} = \sqrt{\frac{dA_0}{dA}} \tag{68}$$

The shape of the eikonal surface combined with this equation determines how the amplitude of the electric field changes between eikonal surfaces. As an example, let us consider the astigmatic eikonal surface, which is more general than a spherical one, shown in Fig. 34. For such a surface, the amplitude of the electric field on one surface relative to another varies according to [22]

$$\frac{|\mathbf{E}|}{|\mathbf{E}_0|} = \sqrt{\frac{dA_0}{dA}} = \sqrt{\frac{\rho_1 \rho_2}{(\rho_1 + s)(\rho_2 + s)}} \tag{69}$$

This equation reduces to

$$\frac{|\mathbf{E}|}{|\mathbf{E}_0|} = 1 \tag{70}$$

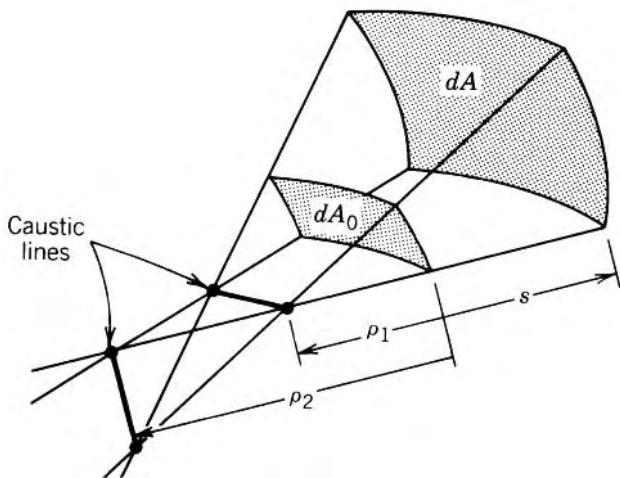


Figure 34. Astigmatic tube of rays. (Constantine A. Balanis, *Advanced Engineering Electromagnetics*, copyright © 1989 by John Wiley & Sons, Inc. This material is used by permission of John Wiley & Sons, Inc.)

for a plane wave, which corresponds to $\rho_1 = \rho_2 = \infty$. Equation (69) reduces to

$$\frac{|\mathbf{E}|}{|\mathbf{E}_0|} = \sqrt{\frac{dA_0}{dA}} = \sqrt{\frac{\rho_0}{\rho_0 + s}} \tag{71}$$

for a cylindrical wavefront, which corresponds to $\rho_1 = \rho_0, \rho_2 = \infty$. For a spherical wavefront, which corresponds to $\rho_1 = \rho_2 = \rho_0$, Eq. (69) becomes

$$\frac{|\mathbf{E}|}{|\mathbf{E}_0|} = \sqrt{\frac{dA_0}{dA}} = \sqrt{\frac{\rho_0}{\rho_0 + s}} \tag{72}$$

The relationship (69)–(72) define the correct way to relate to the amplitudes of the electric field at one surface relative to another, when the frequency ω is sufficiently large. However, these relationships do not include phase and polarization.

12.3. Phase and Polarization

Phase and polarization may be introduced into classical geometric optics using the approach of Luneburg [11] and Kline [23], which is referred to as *Luneburg–Kline high-frequency expansion*. According to their approach, when the frequency ω is sufficiently large, the electric field may be written using the following series:

$$\mathbf{E}(x, y, z, \omega) = e^{-j\beta_0 \Psi(x, y, z)} \sum_{m=0}^{\infty} \frac{\mathbf{E}_m(x, y, z)}{(j\omega)^m} \tag{73}$$

If we limit our attention only to solutions that (1) are of the first order (i.e., $m = 0$) and (2) take the form

$$\mathbf{E}(s) = e^{-j\beta_0 \Psi(s)} \mathbf{E}(s = 0) \tag{74}$$

we can prove [2] that for the geometry of Fig. 34

$$\mathbf{E} = \mathbf{E}_0 e^{-jk_0 \Psi(0)} \sqrt{\frac{\rho_1 \rho_2}{(\rho_1 + s)(\rho_2 + s)}} e^{-jk_0 s} \tag{75}$$

where $s = 0$ is the reference point. Equation (75) provides the extended geometric optics description of an electric field where the polarization comes from the vector \mathbf{E}_0 at an arbitrary reference point $s = 0$ along a trajectory described by a normal to the eikonal surface Ψ . The initial phase is given by $e^{-jk_0 \Psi(0)}$. The amplitude varies according to the square-root term, for an astigmatic wavefront, and the last exponential term accounts for the appropriate phase delay. When $s = -\rho_1$ or $s = -\rho_2$, Eq. (75) is singular because these are the locations of the two caustic lines shown in Fig. 34; hence this equation should not be used at caustics or very close to them.

13. APPLICATION OF GEOMETRIC OPTICS TO THE DESIGN OF ANTENNAS

The Cartesian surfaces described in Section 3 have properties that are exploited in the design of a class of antennas called *reflector antennas*. To understand how basic geometrical optics concepts are transferred to the operation of these antennas, let us refer to Fig. 35. In Section 3, we mentioned that rays emitted from a point source located at the focus F become parallel to the axis z after a reflection on the parabolic surface. Hence the circular wavefront out of F is transformed into a plane wavefront. The same conclusion may be obtained directly from the definition of a parabola. The parabola is the locus of points P that have the same distance from a straight line, the directrix d , and a point, the focus F , which yields

$$FP = GP \quad (76)$$

Consider the line MN , which is perpendicular to the axis z , and its intersection W with a ray reflected at P . One can write

$$FP + PW = FP + (GW - GP) = GW \quad (77)$$

Thus, since the path length $FP + PW$ is the same for all points P on the parabola, the line MN is a wavefront. Additionally, the image of the focus is the directrix because the wavefront at W appears to have originated at G .

In practice, the parabola shown in Fig. 35 must be terminated somewhere, such as at points A and B indicated in the figure. This geometry should be interpreted as the cross section of two antennas: the paraboloidal and the cylindrical parabolic reflectors. A paraboloid is obtained by the rotation of a parabola around its axis. If an isotropic source is located in the focus of the parabola, the portion of the spherical wavefront that is captured by the paraboloid is transformed into a plane wavefront. The cylindrical parabolic reflector has a line source located in the focus

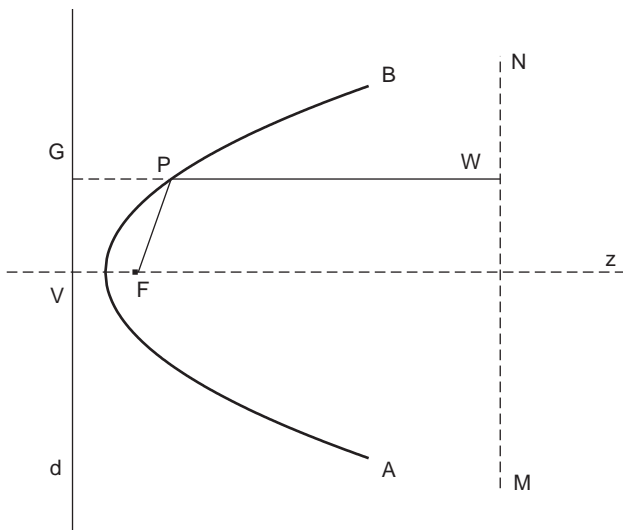


Figure 35. A parabola.

and transforms a cylindrical wavefront into a plane wavefront. For both antennas, the power due to a source is concentrated mostly along the direction of the axis. For both antennas, the actual field received by an observer along the axis is the superposition of a plane wavefront and the direct field from the source. Improvements on the design of reflector antennas include the use of subreflectors. For example, in the Cassegrain design a hyperbolic subreflector faces the main parabolic reflector with the advantage of an overall more compact design because the feedpoint is moved closer to the vertex of the parabola [24]. Similar to optical elements with spherical surfaces, reflector antennas also are affected by aberrations.

Another result of geometric optics that finds application in the design of antennas is the Luneburg lens introduced in Section 5.4. In view of the relationship between electromagnetic theory and geometric optics, it is important to point out that many results from geometric optics are useful for the design of systems that operates at frequencies different from those of visible light. Such a perspective that unites optical principles with the design of microwave antennas are provided in Refs. 25 and 26.

14. EXTENSION OF GEOMETRIC OPTICS TO INCLUDE DIFFRACTION PHENOMENA

Ray tracing, which stems from geometric optics, is not only used for the design of optical systems but also has applications in other engineering fields. For example, many applications related to computer graphics are based on ray tracing [27], and software is available to write programs that exploit ray tracing [28].

The link between geometric optics and electromagnetic theory not only is a topic of academic interest but also proves useful in many engineering applications. Ray tracing is a very convenient way to simplify the complex problem of the propagation of a wavefront. In fact, many electromagnetic problems are simplified by making a high-frequency approximation that reduces the complex study of the propagation of a wavefront to the simpler ray tracing of the normal to the wavefronts. Electromagnetic problems that benefit from ray theories include the computation of radar cross sections and diffraction by objects and predictions of the path loss for radiocommunications [29].

The ray tracing that is derived from geometric optics is concerned only with the direction of propagation of the normal to the wavefront. For an electromagnetic application, other quantities such as polarization and the intensity associated with the wavefront are also important. While polarization is easily accounted for, a correct evaluation of the intensity requires an extension of geometric optics to account for diffraction. Hence many efforts have been devoted to the development of extensions to geometric optics [30]. Without going into the details of these extensions, which would be beyond the purpose of this article on geometric optics, only few of these efforts are mentioned. Keller [31] developed a theory that includes diffraction by formulating a generalization of Fermat's principle. Keller's geometric theory of diffraction (GTD) was later improved by uniform theories such as the

uniform theory of diffraction (UTD) of Kouyoumjian and Pathak [32,33] and the uniform asymptotic theory (UAT) of electromagnetic diffraction by Lee and Deschamps [34]. These theories may fail near caustics, so more recently Tiberio et al. [35] developed the incremental theory of diffraction (ITD), which avoids problems near caustics and presents other advantages.

BIBLIOGRAPHY

1. B. E. A. Saleh and M. C. Teich, *Fundamental of Photonics*, Wiley, New York, 1991.
2. M. Kline and I. W. Kay, *Electromagnetic Theory and Geometrical Optics*, Interscience, New York, 1965.
3. E. T. Whittaker, *A History of the Theories of Aether and Electricity*, T. Nelson and Sons, London and Edinburgh, 1953.
4. A. I. Sabra, *The Optics of Ibn Al-Haytham*, The Warburg Institute, Univ. London, 1989.
5. C. Huygens, *Treatise on Light*, Univ. Chicago Press, Chicago, 1962; reprint of London 1912 edition, translated into English by Silvanus P. Thompson.
6. I. Newton, *Opticks or a Treatise of the Reflections, Refractions, Inflections and the Colours of Light*, Dover Publications, New York, 1952.
7. J. C. Maxwell, *A Treatise on Electricity and Magnetism*, Oxford, 1873.
8. M. V. Klein, *Optics*, Wiley, New York, 1970.
9. M. Herzberger, *Modern Geometrical Optics*, Interscience, New York, 1958.
10. F. L. Pedrotti and L. S. Pedrotti, *Introduction to Optics*, Prentice-Hall, Upper Saddle River, NJ, 1993.
11. R. K. Luneburg, *Mathematical Theory of Optics*, Univ. California Press, Berkeley and Los Angeles, 1966.
12. M. Born and E. Wolf, *Principles of Optics*, Pergamon Press, London, 1965.
13. B. Rossi, *Optics*, Addison-Wesley, Reading, MA, 1957.
14. A. E. Siegman, *Lasers*, University Science Books, Mill Valley, CA, 1986.
15. W. J. Smith, *Modern Optical Engineering*, McGraw-Hill, New York, 2000.
16. F. A. Jenkins and H. E. White, *Fundamental of Optics*, 4th ed., McGraw-Hill, New York, 1976.
17. Y. Matsui and K. Nariai, *Fundamentals of Practical Aberration Theory*, World Scientific, Singapore, 1993.
18. W. H. A. Fincham and M. H. Freeman, *Optics*, 9th ed., Butterworths, London, 1980.
19. M. Cagnet, M. Françon, and J. C. Thierri, *Atlas of Optical Phenomena*, Springer-Verlag, Berlin, 1962.
20. G. R. Kirchhoff, Zur theories der lichtstrahlen, *Ann. Phys.* **2**:663 (1883).
21. A. Sommerfeld and J. Runge, Anwendung der vektorrechnung auf die grundlagen der geometrischen optik, *Ann. Phys.* **35**:277–298 (1911).
22. C. A. Balanis, *Advanced Engineering Electromagnetics*, Wiley, New York, 1989.
23. M. Kline, An asymptotic solution of Maxwell's equations, in *The Theory of Electromagnetic Waves*, Interscience, New York, 1951.
24. J. D. Kraus, *Antennas*, McGraw-Hill, Boston, 1988.
25. S. Cornbleet, *Microwave Optics*, Academic Press, London, 1976.
26. S. Cornbleet, *Microwave and Optical Ray Geometry*, Wiley-Interscience, New York, 1984.
27. A. S. Glassner, ed., *An Introduction to Ray Tracing*, Academic Press, 1989.
28. N. P. Wilt, *Object Oriented Ray Tracing in C++*, Wiley, 1994.
29. D. Erricolo and P. L. E. Uslenghi, Two-dimensional simulator for propagation in urban environments, *IEEE Trans. Vehic. Technol.* **50**(4):1158–1168 (July 2001).
30. L. B. Felsen and N. Marcuvitz, *Radiation and Scattering of Waves*, *IEEE Press*, Piscataway, NJ, 1994.
31. J. B. Keller, Geometrical theory of diffraction, *J. Opt. Soc. Am.* **52**:116–130 (1962).
32. R. G. Kouyoumjian and P. H. Pathak, A uniform geometrical theory of diffraction for an edge in a perfectly conducting surface, *Proc. IEEE*, **62**(11):1448–1461 (Nov. 1974).
33. D. A. McNamara, C. W. I. Pistorius, and J. A. G. Malherbe, *Introduction to the Uniform Geometrical Theory of Diffraction*, Artech House, Boston–London, 1990.
34. S.-W. Lee and G. Deschamps, A uniform asymptotic theory of electromagnetic diffraction by a curved wedge, *IEEE Trans. Antennas Propag.* **24**(1):25–34 (Jan. 1976).
35. R. Tiberio, A. Toccafondi, A. Polemi, and S. Maci, Incremental theory of diffraction: a new-improved formulation, *IEEE Trans. Antennas Propag.* **52**(9):2234–2243 (Sept. 2004).

GE-SI ALLOYS AND DEVICES

PETER RUSSE
JOHANN-FRIEDRICH LUY
Munich Technical University
Germany

1. INTRODUCTION

Silicon–germanium heterojunction bipolar transistors (HBTs) [1–3] extend the frequency limits of silicon-based technology. In the SiGe HBT, the base region is formed by an epitaxially grown SiGe layer between the adjacent silicon layers. Because of the lower bandgap of the base region also existing in the case of high base doping, a high emitter efficiency is achieved. This allows a HBT design with small base width and a low base series resistance. The heterojunction bipolar transistor was first suggested in 1957 by Kroemer [4]. A first suggestion for a SiGe-base heterojunction bipolar transistor (HBT) for high-frequency applications was made in 1977 [5]. SiGe technology has been pushed mainly as a commercial technology by IBM, DaimlerChrysler/TEMIC and Infineon. Commercially available HBTs exhibit f_T values greater than 50 GHz and f_{max} values in excess of 70 GHz, a minimum noise figure below 0.7 dB at 2 GHz, $1/f$ noise corner frequencies below 500 Hz, and a reliability comparable to Si devices [2]. Future trends in SiGe technology point toward the integration of more complex circuits, technology efforts to facilitate easier manufacturing and speed increase beyond $f_T = 200$ GHz [6]. The silicon–germanium heterojunction bipolar transistor enabled the breakthrough of silicon-based

MMIC (monolithic millimeter-wave integrated circuit) technology [1,6]. Amplifiers and tunable oscillators or with maximum operation frequencies beyond 80 GHz become feasible. Infineon's SiGe bipolar production technology B7HF is capable for high-volume production [7]. SiGe HBTs with transit frequencies f_T above 200 GHz and maximum oscillation frequencies of $f_{\max} = 338$ GHz already have been realized [8–11].

Also, the suitability of CMOS devices for RF applications continuously improves [3]. With 0.25- μm technology, f_T values are as high as 40 GHz and should double roughly every 3 years if trends continue [12,13]. A K-band traveling-wave amplifier as well as a 17-GHz traveling-wave oscillator have already been realized with CMOS devices [12]; 70-nm CMOS have cutoff frequencies reaching 150 GHz and an inverter gate delay time around 15 ps at a supply voltage of 1.5 V [14]. The short gate delay time makes CMOS circuits suitable for future broadband multimedia applications.

SiGe/Si-MODFETs (*modulation-doped field-effect transistors*) are high electron mobility transistors [15]. The material system GeSi is the only one that exhibits symmetric transport properties for complementary n- and p-channel devices. For both channel types an f_{\max} of 100 GHz has already been achieved. Silicon-germanium MODFETs have a significant high-frequency potential [16]. The introduction of SiGe allows the realization of n- and p-type hetero-FETs (MOSFETs), both with enhanced performance. Maximum oscillation frequencies of more than 100 GHz have been obtained with n- and p-MOSFETs.

A further improvement of the RF properties of silicon-based devices will result from the introduction of copper technology. As semiconductor devices are scaled down to the submicron region, interconnection losses are becoming a limiting factor. In submicrometer technology, copper interconnects will exhibit lower resistivity and better reliability than aluminium interconnects. Copper reduces line and via resistances by at least 50%, increases the maximum current density by a factor of 2.5–3.0, and maintains the same leakage current properties as the Al interconnects. The damascene process enables the fabrication of submicrometer copper interconnects [17,18].

New device concepts try to exploit unavoidable delay times and drift fields in heterojunction devices in order to generate a resonant behavior of the device at frequencies beyond the current gain cutoff frequency [19–21].

Silicon as a substrate for millimeter-wave monolithically integrated circuits was suggested in 1981 by RCA [22]. Since 1986 in the field of silicon *monolithic millimeter-wave integrated circuits* (SIMMWICs) there have been research activities at the former AEG-Telefunken Research Institute (now DaimlerChrysler Research Center) and at the Technische Universität München [23–29]. Up to now SIMMWICs for frequencies up to above 100 GHz already have been fabricated, and the suitability of silicon as the base material for monolithic integrated millimeterwave circuits has been successfully demonstrated. Monolithic integration of solid-state devices provides the possibility of low-cost production, improved reliability, small size and light weight, and easy assembly.

The linear passive parts of SIMMWICs may be realized in planar circuit technology. The fundamental transmission-line structures used SIMMWIC design are microstrip lines, slotlines, coplanar lines, coplanar striplines, and microshield lines. Based on these fundamental geometric structures, the planar circuit elements are designed. These planar circuit elements include transmission-line discontinuities, planar resonators and antennas as the basic structures.

In the frequency region above 60 GHz, SIMMWICs with dimensions of only a few millimeters may also include planar antenna structures. The integration of the antenna structures allows the direct coupling of SIMMWICs to the radiation field.

Monolithic integrated millimeterwave circuits based on silicon and SiGe will give new options for millimeter-wave sensor and communication applications. Compared with microwave-based systems, millimeter-wave-based systems offer the following advantages:

- Availability of broader frequency bands
- Higher gain and smaller dimensions of antennas
- Lower weight and smaller size of the components
- Higher resolution for sensor applications
- Atmospheric attenuation that may prevent interference between cells

A broad application of millimeter waves in sensors and communications has been hampered up to now because of the high costs of millimeter-wave components. This situation may change in the future with the availability of low-cost monolithic integrated components based on a silicon and SiGe technology.

2. SILICON AS THE BASE MATERIAL

Table 1 compares the data for Si and GaAs. At 90 GHz, the dielectric loss tangents of Si and GaAs are within the same order of magnitude, and for microwave circuits, silicon substrates with a specific resistance of $10,000 \Omega \cdot \text{cm}$ are available. For this material, the conductor losses due to the skin effect dominate the loss contributions of planar circuits, whereas the substrate losses in the silicon account only for a minor part. The electron mobility of GaAs is 6 times higher than the electron mobility of Si. This yields a correspondingly higher f_T value for bipolar transistors and field effect transistors. On the other hand, the

Table 1. Parameters of Si and GaAs

	Si	GaAs
Dielectric constant	$\epsilon_r = 11.7$	$\epsilon_r = 12.9$
Specific resistance	$> 10^4 \Omega \cdot \text{cm}$	$> 10^6 \Omega \cdot \text{cm}$
Dielectric loss		
Factor (90 GHz)	1.3×10^{-3}	0.7×10^{-3}
Thermal conditions	$1.45 \text{ W cm}^{-1} \text{ K}^{-1}$	$0.46 \text{ W cm}^{-1} \text{ K}^{-1}$
Electron mobility	$700 \text{ cm}^2/\text{V} \cdot \text{s}$	$4300 \text{ cm}^2/\text{V} \cdot \text{s}$
High field drift velocity	10^7 cm/s	$6 \cdot 10^6 \text{ cm/s}$
Density	2.33 g/cm^3	5.32 g/cm^3

high field drift velocity of Si and GaAs are in the same order. The thermal conductivity of silicon is 3 times higher than the thermal conductivity of GaAs. From this point of view, silicon is advantageous for power circuits. Silicon and germanium can be mixed in alloys with arbitrary mixing ratios because of their identical lattice structure and their similar lattice constants. The atoms are distributed statistically on free places and the lattice structure is maintained. The lattice constant a_{SiGe} can be calculated by the linear interpolation between the lattice constants a_{Si} of silicon (0.5431 nm) and a_{Ge} of germanium (0.5658 nm):

$$a_{\text{Si}_{1-x}\text{Ge}_x} = (1-x)a_{\text{Si}} + xa_{\text{Ge}} \quad (1)$$

For the realization of npn heterojunction bipolar transistors, the pseudomorphic growth of strained $\text{Si}_{1-x}\text{Ge}_x$ layers without misfit dislocations is of essential importance. Strained SiGe layers may be grown epitaxially on silicon substrate. If the thickness of the epitaxial layers is kept below a critical thickness, then the mismatch between the alloy and the silicon substrate is accommodated elastically. The strain grows with increasing lattice mismatch and germanium content [30,31]. The lattice mismatch is defined as

$$\eta = \frac{a_{\text{Si}_{1-x}\text{Ge}_x} - a_{\text{Si}}}{a_{\text{Si}}} \quad (2)$$

and the lattice mismatch between pure germanium and silicon is 4.2%.

Figure 1 shows that the energy gap of the alloy is dependent not only on the germanium content but also on the strain situation. The conduction band minima in unstrained silicon correspond to sixfold degenerate valleys located along {100} directions in k space. In case of strain, the sixfold degenerate conduction band valleys are separated and the four valleys oriented normal to the heterojunction are lowered in energy and the remaining two valleys are raised in energy. The overall bandgap shrinkage is increased over that of unstrained material with the same germanium content.

A unified SiGe/SIMMWIC technology uses this band-gap engineering to develop SiGe HBTs, MODFETs, and MOSFETs [28]. This unified technology also allows the fabrication of Schottky diodes, IMPATT diodes, and PIN diodes (Fig. 2).

3. ELECTRONIC DEVICES

3.1. SiGe-Base HBTs

Although silicon bipolar transistors with transient frequencies above 50 GHz are possible in principle, these devices would exhibit too high a base resistance and too low a breakdown voltage. A promising device for millimeter-wave applications is the SiGe base heterojunction bipolar transistor (HBT) [1]. The heterojunction bipolar transistor first has been suggested in 1957 by Kroemer [4]. A first suggestion for a SiGe-base HBT for high-frequency applications was made in 1977 [1,5]. Detailed investigations of

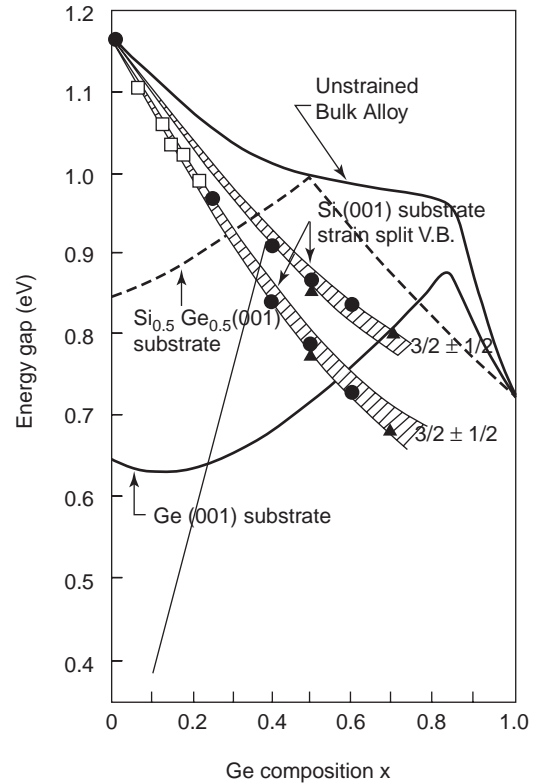


Figure 1. Energy gap in $\text{Si}_{1-x}\text{Ge}_x$ layers as a function of the Ge composition x .

the millimeterwave SiGe-base HBT have been presented [32–40].

In SiGe HBT, the base region is formed by an epitaxially grown SiGe layer between the adjacent silicon layers. With increased germanium content in the base, the band-gap of the base region is reduced. Because of the lower band gap of the base region also in the case of high base doping a high emitter efficiency is achieved. The base of a HBT can thus be more heavily doped than the base of a silicon bipolar transistor to reduce the base resistance without the negative impact on the current amplification. Figure 3 shows the cross section of a heterojunction bipolar transistor. The HBTs are fabricated using a self-aligned emitter–base structure together with selective epitaxial growth of the SiGe-base layer. Figure 4 shows a SiGe HBT embedded in a coplanar line crossing.

The effect of reduced barrier for the electron injection from the emitter into the base and the corresponding design freedom regarding the emitter and the base doping becomes evident if the current gain of a bipolar junction transistor is compared with the current gain of a heterojunction bipolar transistor. The current gain β of a conventional bipolar transistor is given by

$$\beta = \frac{D_{nE}N_Ew_E}{D_{pB}P_Bw_B} \quad (3)$$

where D_{nE} and D_{pB} are the diffusion constants of electrons and holes in the emitter and base regions respectively, N_E

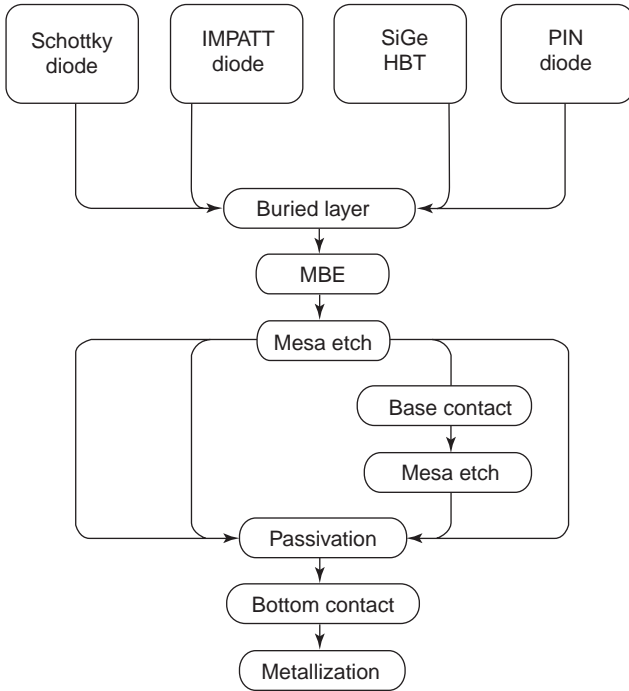


Figure 2. Technology.

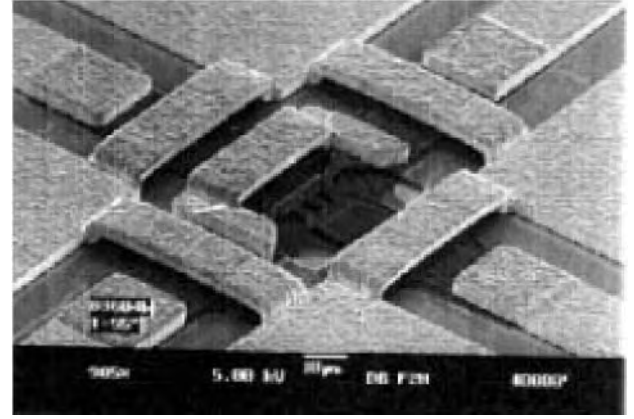


Figure 4. SiGe-HBT in coplanar line crossing.

and P_B are the emitter and base doping concentrations, w_E is the emitter thickness, and w_B is the base thickness. For the HBT after Kroemer [4] the current gain β is given by

$$\beta = \frac{D_{nE} N_E w_E}{D_{pB} P_B w_B} e^{\Delta E/kT} \quad (4)$$

where ΔE is the bandgap difference between Si and SiGe. The exponential dependence of the minority carrier injection rate across the emitter–base barrier on the band gap difference yields for a Ge content of 20% a value of the exponential term of more than 1000. Thus a high base efficiency is obtained even in the case of a high emitter doping. Due to the high base doping, low base sheet resistances with base widths down to 10 nm are attainable. A typical high-frequency silicon bipolar transistor with a base width of less than 100 nm exhibits base sheet resistances in the order of 10 k Ω /□, whereas SiGe HBTs reach base sheet resistances as low as 1 k Ω /□ for a 20-nm-

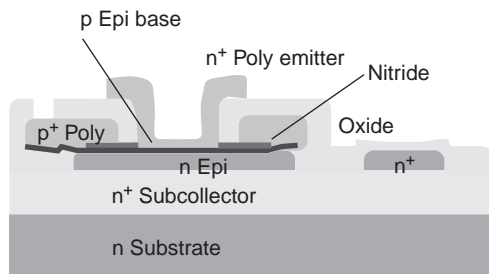


Figure 3. Cross section of SiGe HBT.

doped base [28]. Therefore, a high current gain and a low base resistance are possible due to extremely low base width.

The unity current gain cutoff frequency f_T is given by [2]

$$f_T = [r_e(C_{eb} + C_{cb} + \tau_b + \tau_e + \tau_c)]^{-1} \quad (5)$$

where C_{eb} and C_{cb} are the emitter–base and collector–base depletion capacitances; τ_b , τ_e , and τ_c are the base, emitter, and collector transit times, respectively; and the emitter resistance r_e is given by

$$r_e = \frac{kT}{eI_c} \quad (6)$$

In bipolar junction transistors (BJTs), f_T is usually limited by the base transit time τ_b given by

$$\tau_{b,Si} = \frac{w_b^2}{2D_{nb}} \quad (7)$$

where D_{nb} is the electron diffusivity in the base region and w_b is the base width. In the SiGe HBT the Ge grading across the base decreases τ_b by [2]

$$\frac{\tau_{b,SiGe}}{\tau_{b,Si}} = \frac{2}{\tilde{\eta}} \frac{kT}{\Delta E_{g,Ge(grade)}} \left\{ 1 - \frac{kT}{\Delta E_{g,Ge(grade)}} \left[1 - e^{-\Delta E_{g,Ge(grade)}/kT} \right] \right\} \quad (8)$$

where the bandgap grading term $\Delta E_{g,Ge(grade)}$ is given by

$$\Delta E_{g,Ge(grade)} = \Delta E_{g,Ge(w_b)} - \Delta E_{g,Ge(0)} \quad (9)$$

and

$$\tilde{\eta} = \frac{D_{nb(SiGe)}}{D_{nb(Si)}} \quad (10)$$

The maximum oscillation frequency f_{max} of the HBT is given by

$$f_{max} = \sqrt{\frac{f_T}{8\pi C_{bc} r_b}} \tag{11}$$

where f_T is the transit frequency, r_b is the base resistance, and C_{bc} is the base collector capacity. In SiGe HBTs the lower bandgap allows for high base doping and therefore low base resistance. That increases f_{max} .

The fabrication of a heterojunction bipolar SiGe transistor with f_T values above 200 GHz has already been reported [1,8–11,28,35,41]. For most circuit applications, f_{max} is the more important parameter [1,28] and coplanar MMICs based on SiGe HBTs with f_{max} values as high as 338 GHz are under development [8,10,42–44].

For an efficient circuit design an accurate large-signal transistor model is required. Gummel and Poon introduced a bipolar transistor model based on a charge-control relation, derived from basic physical considerations, linking the dominant component of collector current, emitter and collector junction voltages, and base charge [45,46]. The equivalent circuit of the Gummel–Poon model is depicted in Fig. 5. The Gummel–Poon model is the basis for most advanced nonlinear BJT models; however, it is not suitable for reliable design of circuits operating at either high current densities or low voltages. Several authors proposed large-signal models for the SiGe heterojunction bipolar transistor [47–50].

The physics-based compact bipolar transistor model HICUM (high-current model) uses the small-signal parameters, such as the depletion capacitances and the transit times, as basic variables, which are described accurately as a nonlinear function of bias, temperature, and geometry. This results in continuously differentiable relations for charges and transfer current and accurate modeling of the large-signal switching behavior, including harmonic distortion at high frequencies [51,52]. A detailed description of the HICUM model can be found in Ref. 53. The so-called vertical bipolar intercompany (VBIC) model was developed as an industry standard to improve defi-

ciencies of the SPICE Gummel–Poon model that have become apparent over time because of the advances in BJT process technology. The VBIC model is still based on the Gummel–Poon formulation; however, it includes improved modeling of the Early effect, quasisaturation, substrate and oxide parasitics, avalanche multiplication, and temperature behavior [54]. A VBIC model for the analysis of two-tone intermodulation distortion behavior of SiGe HBTs takes into account all important effects for accurate modeling of large-signal behavior, including self-heating, weak-avalanche multiplication, quasisaturation effects, and all device capacitances [55].

The SGH (SiGe HBT) large-signal model combines elements of the VBIC and HICUM models [56,57]. Figure 6 shows the equivalent circuit of the SGH model. The SGH model accurately describes the SiGe HBT behavior up to 40 GHz. In the SGH model the transport current

$$I_{CC} = \frac{I_f - I_r}{q_b} \tag{12}$$

is related to the normalized stored charge q_b , given by

$$q_b = q_1 + q_2 \tag{13}$$

with

$$q_1 = \frac{Q_{p0} + HJE \cdot Q_{je} + HJC \cdot Q_{jc}}{Q_{p0}} \tag{14}$$

$$q_2 = \frac{Q_{f0} + HE \cdot Q_{fe} + HC \cdot f_c \cdot Q_{f0} + Q_{fb}}{Q_{p0}} \tag{15}$$

The coefficients HJE , HJC , HE , and HC , introduced similarly to the HICOM model parameters, are determined by parameter extraction. The empirical smoothing function f_c is given by

$$f_c = \left(\frac{V_{cc}}{VHC} \right)^{NHC} \tag{16}$$

where VHC and NHC are determined by parameter extraction. The default smoothing function is $f_c = 1$.

For an accurate simulation of the intermodulation performance of semiconductor devices, the modeling of the

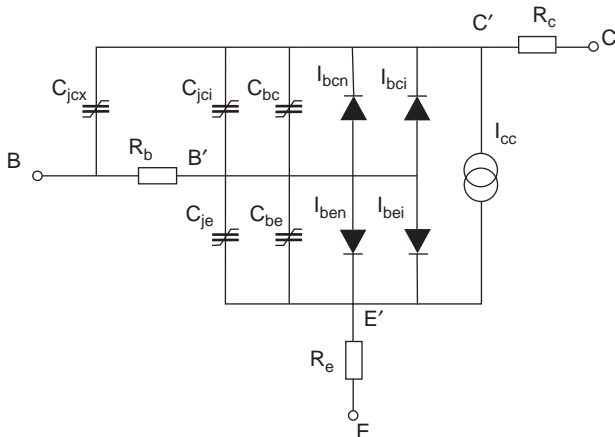


Figure 5. Gummel–Poon transistor model.

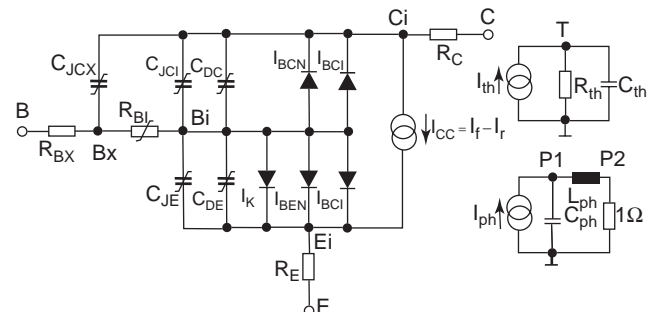


Figure 6. SiGe HBT large-signal equivalent circuit [56].

dynamic self-heating is required [58]. A method to extract the thermal time constants of HBTs from *S*-parameter data has been given by Sinnesbichler and Olbrich [59].

The noise figure of a bipolar transistor may be approximated by [60]

$$F = 1 + \frac{1}{R_s} \left[r_b + \frac{r_e}{2} + \left(\frac{1}{\beta} + \frac{f^2}{f_T^2} \right) \frac{r_b^2 + R_s^2}{2r_e} \right] \quad (17)$$

where *F* is the noise figure, *R_s* is the source impedance, and β is the current gain. The high *f_T* and the low base resistance of SiGe HBTs yield a low noise figure. SiGe HBT noise figures as low as 0.5 dB at 2 GHz, 0.9 dB at 10 GHz, and 2 dB at 20 GHz have been reported [61].

Low-frequency noise in active devices is a serious design constraint for millimeter-wave oscillator and mixer applications. Since the low-frequency noise is upconverted by the inherent nonlinearities of the active device, the low-frequency noise of the active device has to be minimized. The low-frequency noise in millimeter-wave Si/SiGe HBTs has been investigated [62–64]. For a SiGe HBT with an *f_T* of 43 GHz, Cressler et al. have reported a corner frequency of 373 Hz for the 1/*f* noise at a bias current of 2.25 μA [64]. However in real circuit applications, the bias currents are at least one order of magnitude higher. Usually the corner frequency increases proportional to the square of the bias current.

An accurate extraction method for the 1/*f* noise parameters of BJTs and FETs is presented in Ref. 65. Figure 7 shows the BJT equivalent circuit with input and output terminations and noise sources. Combining the nonlinear large-signal models with the noise models allows nonlinear noise modeling. This is a requirement for accurate phase noise modeling of oscillators.

3.2. Si/SiGe-Hetero FETs

Si/SiGe heterostructure technology may also be combined with Si CMOS technology [36,66]. Most of the Si/SiGe-hetero-FETs (MOSFETs) are of the modulation-doped type. These so-called MODFETs exhibit a thin quantum-well layer with a thickness of 5–30 nm. Within the quantum-well layer, a two-dimensional electron or hole gas with collision-free carriers exists. The n-quantum wells are Si layers, whereas the p-quantum wells are formed by SiGe

15 nm Si	Cap
40 nm Si _{0.7} Ge _{0.3}	Cap spacer
12 nm Si _{0.7} Ge _{0.3}	n ⁺ doping
10 nm Si _{0.7} Ge _{0.3}	spacer
25 nm Si	2 DEG (Si)
0.5 μm Si _{0.7} Ge _{0.3}	Buffer
1.5 μm Si _{1-x} Ge _x	X=0.3 X=0.05 Graded buffer
Si	Substrate

Figure 8. Layer structure of a n-type Si/SiGe-hetero FET.

layers. Figure 8 shows the layer structure of a n-type Si-channel Si/SiGe MOSFET.

The introduction of SiGe in field effect transistors allows the realization of n- and p-type hetero-FETs. Tensile-strained Si films on strain-relieved SiGe buffer layers enable the formation of electron quantum wells that exhibit enhanced electron mobilities. Compressively strained SiGe or even pure Ge layers can be used to create two-dimensional hole channels. The combination of n- and p-SiGe MOSFETs and a complementary circuit arrangement promises the realization of a novel hetero-CMOS generation [36,67]. This approach requires a proper SiGe buffer layer.

The epitaxial layers for n-type MODFETs—deposited on a high resistivity substrate—start with a relaxed buffer whose Ge content is linearly graded to 40–50%. The core of the layer structure is the 7–10-nm tensile-strained Si channel embedded into undoped Si_{1-x}Ge_x spacers that separate the carrier supply layers from the channel (Fig. 9a). Because of a Ge content of 40–50% in the SiGe layers, a high conduction band offset of 0.24 eV is achieved and the quantum well enables electron mobilities up to 2800 cm²/V·s [68]. Schottky or junction gates may be realized. The p-type MODFET employs a Ge channel (Fig. 9b). A double-sided doped Ge channel is on top of an artificial Si_{0.4}Ge_{0.6} substrate, accomplished by the compositionally graded strain relieved buffer. With the layer design values given in Fig. 9b, a 2D hole gas mobility of 1870 cm²/V·s is extracted from magnetic-field-dependent Hall measurements.

The RF performance is defined by *f_T* extrapolated from the current gain *h₂₁* and by *f_{max}* extrapolated from the maximum available gain or the unilateral gain. For n-Si channel MODFETs, *f_T* = 65 GHz and *f_{max}* = 120 GHz (non-deembedded still 110 GHz) for technologically relaxed gate lengths around 0.2 μm are reported [68,69]. For p-Ge

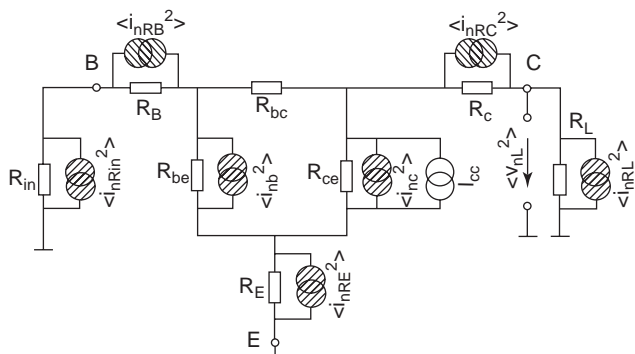


Figure 7. BJT equivalent circuit with noise sources [65].

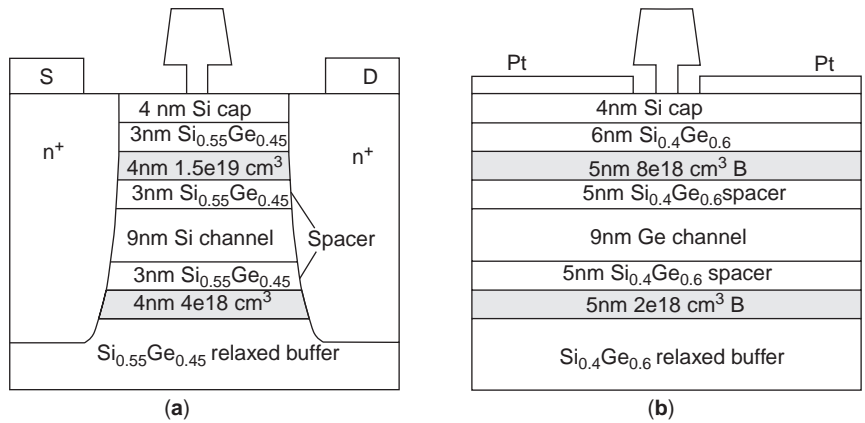


Figure 9. Layers of (a) n-type Si/SiGe MOD-FET and (b) p-type Ge channel MODFET.

channel MODFETs the f_T is up to 70 GHz and f_{max} values up to 135 GHz are reported [70,71].

The SiGe MOSFETs are still not yet optimized. Most of the MOSFET devices reported so far are mesalike. Preferably source and drain implantation is used. Pads are mostly arranged on field oxide, however, the cutoff frequencies of MOSFETs are already a factor of >2 above those of traditional Si MOSFETs, owing to their much higher mobilities. Furthermore the frequency level of n- and p-MOSFETs are very similar, which supports the potential of SiGe for the novel HCMOS generation.

3.3. Future Device Concepts

Future development of SiGe MMICs for operation up to 100 GHz stimulates the search for even faster transistors. A first approach might be to change the base SiGe profile from a box-shaped to a triangular curvature. A small improvement in f_{max} can be expected. However, due to a rough estimation, f_{max} values should be a factor of 5 higher than the operational frequency. Therefore, about 300 GHz f_{max} is required for 60-GHz SiGe MMICs. The pure HBT principle will not be sufficient to reach these frequencies. Improvements are expected from a transition to a metal base transistor or a camel-type transistor. Another promising concept was proposed by Luryi [19,20]: a transistor with an active behavior beyond the cutoff frequencies. The combination of a graded base layer enforcing coherent carrier transport and a base layer thickness designed to yield a transit-time-induced phase shift of $3\pi/2$ lead to a resonancelike behavior at elevated frequencies above f_{max} , the resonance phase transistor (RPT).

The overall phase of the collector current in a bipolar transistor is composed of an injection phase angle $\varphi = \varphi_E + \varphi_B$ with an emitter-base transit angle $\varphi_E = \omega\tau_E$ and $\varphi_B = \omega\tau_B$, respectively, and the drift delay $\theta = \omega\tau_C$ in the base-collector junction. At frequencies below the cutoff frequency, the phase delay of the collector current is less than $\sim 60^\circ$, as

$$\varphi + \theta = \varphi_E + \varphi_B + \theta = 2\pi f(\tau_E + \tau_B + \tau_C) \text{ for } f/f_T < 1 \quad (18)$$

In common transistor operation the phase of the collector current increases with decreasing current gain, taking a

maximum value around 60° at frequencies close to the cutoff frequency. However, at further increased phase delay, the output resistance of the transistor may become negative and result in renewed active behavior at higher frequencies. Such renewed active behavior was previously discussed on the basis of transit time effects using properly delayed injection of carriers into the base-collector space charge [19,20,72,73].

In SiGe four grading steps in a 200-nm base are suitable, considering the limitations given by the critical thickness and the germanium content as well as the requirements given by the energy steps to obtain coherent carrier transport [21]. After first experimental reports on the increase of the unilateral gain at frequencies larger than f_T [74], the RPT effect has been proven experimentally. A current amplification of 6.5 dB was measured at a frequency of $7 f_T = 40$ GHz for an RPT structure with a base layer thickness of 120 nm [75]. The measured current gain is depicted in Fig. 10.

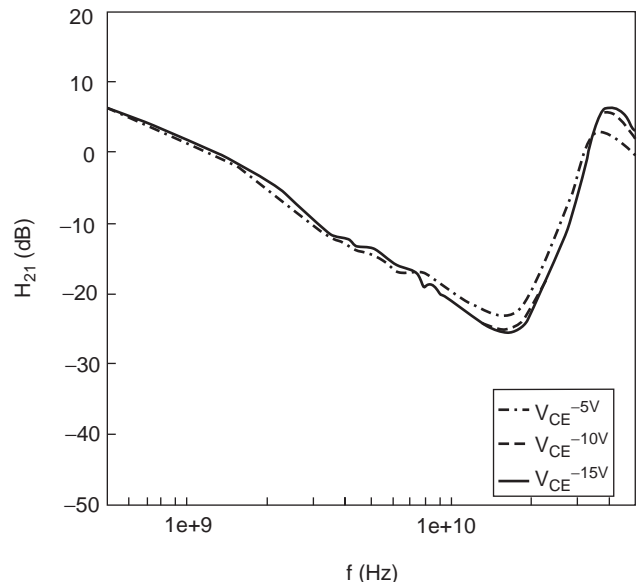


Figure 10. Unilateral gain of a RPT test transistor deduced from S-parameter measurements between 100 MHz and 40 GHz.

A totally different approach to enhance the injection phase angle, proposed in 1998, uses counter-phase injection via resonant tunneling in a double barrier base structure [21]. The initial concept of resonance phase amplification using delayed injection basically subsists on keeping the base transport factor sufficiently high.

4. APPLICATIONS

Numerous examples of Si/SiGe-based monolithically integrated RF chips of high performance have been presented in the literature. A SiGe differential transimpedance amplifier with 50 GHz bandwidth for application as baseband amplifier in 40-Gbps (gigabits per second) Fiberoptic receivers already has been reported [76]. A monolithic integrated 40-Gbps clock and data recovery circuit with a 1 : 4 demultiplexer has also been realized in SiGe HBT technology [77] and a 40-Gbps 2 : 1 multiplexer and 1 : 2 demultiplexer, in 120 nm CMOS technology [78].

Monolithic integrated HBT oscillators with oscillation frequencies up to 74 GHz have been reported [79–81]. A 47-GHz MMIC SiGe HBT oscillator with an output power of 13.1 dBm, an efficiency of 13.6%, and a phase noise of -99.31 dBc/Hz at 100 kHz off carrier has already been realized [82]. The oscillator was realized on high-resistivity silicon ($\rho > 5000 \Omega \cdot \text{cm}$) in coplanar line technology. Applying the push–push principle, a hybrid SiGe HBT microstrip transmission-line oscillator with an output power of $+1$ dBm at 58 GHz and a single-sideband phase noise of -108 dBc/Hz at an offset frequency of 1 MHz [57,83] and a monolithic integrated 150 GHz SiGe HBT push–push VCO with -5 dBm output power at 150 GHz and 30 GHz tuning range [84] already have been realized. Figure 11 shows a 27 GHz SiGe HBT voltage-controlled oscillator in microstrip technology designed by DASA and fabricated by DaimlerChrysler Research. The oscillator exhibits an output power of $+1$ dBm and a SSB phase noise of -112 dBc/Hz at 1 MHz offset. In Fig. 12 a 38-GHz SiGe HBT harmonic mixer fabricated by DaimlerChrysler Research is depicted. A local oscillator input signal at 4.75 GHz is required. The conversion loss amounts 23 dB. The mixer

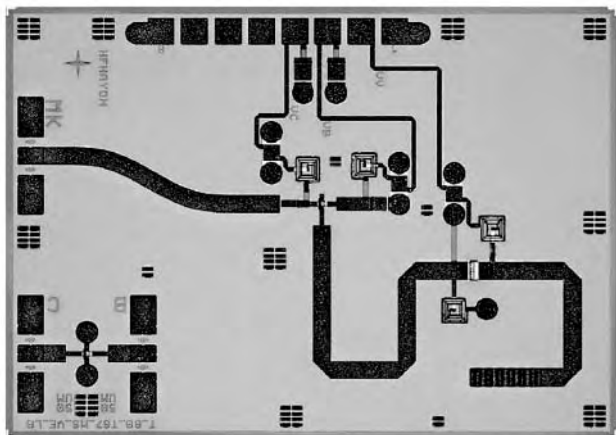


Figure 11. A 27-GHz SiGe HBT VCO. (This figure is available in full color at <http://www.mrw.interscience.wiley.com/erfme>.)

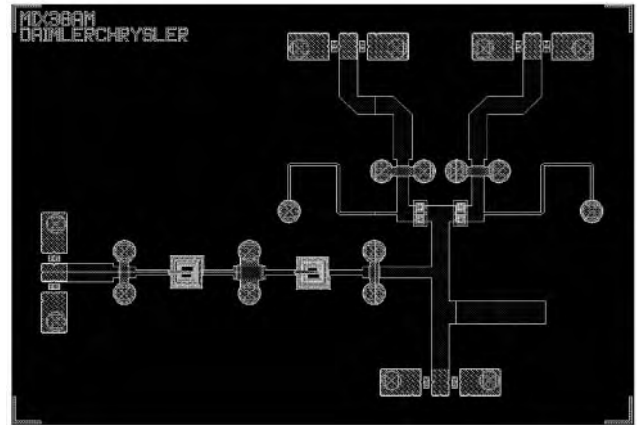


Figure 12. A 38-GHz SiGe HBT harmonic mixer. (This figure is available in full color at <http://www.mrw.interscience.wiley.com/erfme>.)

delivers an IF output signal at 1.33 GHz. The first active integrated K-band antenna on high-resistivity silicon substrate employing a Si/SiGe HBT has been presented [85,86]. Microstrip structures represent the resonating and radiating circuits. The HBT was mounted using the flip-chip technique. An output power of 20 dBm at 24 GHz has been achieved.

5. CONCLUSIONS

The performance of SiGe MMICs has to be viewed under the consideration of competing approaches, especially CMOS. K-band low-noise amplifiers using a $0.18\text{-}\mu\text{m}$ CMOS technology with operating frequencies of ≤ 24 GHz, a gain of > 12 dB, and a noise figure of 5.6 dB have been reported [87]. At 26 GHz still 8.9 dB of gain and a noise figure of 6.9 dB are obtained. The current consumption is 30 mA from a 1.8 V power supply. This results represent the highest operation frequencies reported for low-noise amplifiers in a standard CMOS process.

These results have to be compared with the latest SiGe device and circuit results. Cutoff frequencies are now approaching 400 GHz, and the circuit performance at W-band frequencies approaches or even exceeds that of III–V MMICs [81]. The most important advantage of SiGe MMIC concepts is probably the possible cointegration of low-noise, high current building blocks (e.g., oscillators) with CMOS circuits in order to realize complete single-chip solutions.

The availability of SiGe HBTs with transit frequencies above 200 GHz and even higher maximum oscillation frequencies [8–11] will allow the development of silicon-based monolithic integrated circuits for operation frequencies above 100 GHz. Areas of application include millimeter-wave communications and sensorics [88,89] and also mixed-digital/analog applications at millimeter-wave frequencies [90]. In digital fiberoptic receivers Schottky diode demultiplexers [91] in connection with SiGe HBT push–push oscillators for clock recovery may allow to realize electronic demultiplexers for bit rates of ≤ 160 Gbps in the future. Monolithic integrated millimeterwave sensors an communication front-end circuits may also include

antenna structures. An active SIMMWIC antenna for vehicular technology in the frequency range around 76.5 GHz already has been presented [92]. This active antenna acts as a transceiver and is well suited for low-cost integrated sensor systems for automotive applications.

BIBLIOGRAPHY

1. A. Gruhle, SiGe heterojunction bipolar transistors, in J.-F. Luy and P. Russer, eds., *Silicon-Based Millimeter-Wave Devices*, Springer Series in Electronics and Photonics, Vol. 2, Springer, 1994, pp. 149–192.
2. J. Cressler, SiGe HBT technology: A new contender for Si-based rf and microwave circuit applications, *IEEE Trans. Microwave Theory Tech.* **46**:572–589 (May 1998).
3. B. Meyerson, Silicon:germanium-based mixed-signal technology for optimization of wired and wireless telecommunications, *IBM J. Res. Devel.* **44**:391–407 (May 2000).
4. H. Kroemer, Theory of a wide-gap emitter for transistors, *Proc. IRE* **45**(11):1535–1537 (1957).
5. E. Kasper and P. Russer, *Verfahren zur Herstellung von bipolaren Hochfrequenzschaltungen*, German (Patent) Disclosure P2719464.5, (April 1977).
6. E. Kasper and J. Eberhardt, Physics of future ultra high speed transistors part 1: HBT, *Proc. 29th European Microwave Conf.* Munich, Oct. 1999, Vol. 1, pp. 151–154.
7. W. Klein and B.-U. Klepser, 75 GHz bipolar production technology for the 21st century, *Proc. 29th European Solid-State Device Research Conf. (ESSDERC'99)*, Leuven, Belgium, 1999, pp. 88–94.
8. G. Freeman, S. R. J. B. Jagannathan, Z. Yang, F. Guarin, and A. Joseph, Device scaling and application trends for over 200 GHz SiGe HBTs, *2003 Topical Meeting on Silicon Monolithic Integrated Circuits in RF Systems Digest*, Grainau, April 9–11, 2003, pp. 6–9.
9. M. Schwerd, M. Seck, T. Huttner, T. Böttner, S. Drexler, B. Hasler, A. Mitchell, H. Helneder, H. Körner, V. Kubrak, M. Schrenk, and R. Lachner, A manufacturable 0.35 μm 150 GHz f_T SiGe:C bipolar RF technology, *2003 Topical Meeting on Silicon Monolithic Integrated Circuits in RF Systems Digest*, Grainau, April 9–11, 2003, pp. 6–9.
10. B. Jagannathan, M. Khater, F. Pagette, J.-S. Rieh, D. Angell, H. Chen, J. Florkey, F. Golan, D. Greenberg, R. Groves, and S. Jeng, Self-aligned site NPN transistors with 285 GHz f_{max} and 207 GHz f_T in a manufacturable technology, *IEEE Electron. Devices Lett.* **23**:258–260 (May 2002).
11. B. Jagannathan, M. Meghelli, K. Chan, J.-S. Reih, K. Schonenberg, D. Ahlgren, S. Subbanna, and G. Freeman, 3.9 ps SiGe HBT ECL ring oscillator and transistor design for minimum gate delay, *IEEE Electron. Devices Lett.* **24**:324–326 (May 2003).
12. T. Lee, CMOS RF: (still) no longer oxymoron, *1999 IEEE Radio Frequency Integrated Circuits (RFIC) Symp. Digest*, Anaheim, CA, June 1999, pp. 3–6.
13. T. Lee, CMOS RF integrated circuits: Past, present and future, *Proc. 29th European Microwave Conf.* Munich, Oct. 1999, Vol. 3, pp. 12–19.
14. H.-S. P. Wong, D. Frank, P. Solomon, C. Wann, and J. Welsler, Nanoscale CMOS, *Proc. IEEE*. **87**:537–570 (April 1999).
15. E. Kasper and G. Reitmann, Physics of future ultra high speed transistors part 2: New concepts, *Proc. 29th European Microwave Conf.* Munich, Oct. 1999, Vol. 1, pp. 155–157.
16. U. König, SiGe/Si-bipolar and quantum well transistors, results and prospects, *Mat. Res. Soc. Symp. Proc.* **282**:387–399 (1993).
17. C. Ryu, K.-W. Kwon, A. L. Loke, H. Lee, T. Nogami, V. Dubin, R. Kavari, G. Ray, and S. Wong, Microstructure and reliability of copper interconnects, *IEEE Trans. Electron. Devices*, **46**:1113–1120 (June 1999).
18. H. Helneder, H. Körner, A. Mitchell, M. Schwerd, and U. Seidel, Comparison of copper damascene and aluminum re metalization in BICMOS technology, in paper presented at materials for Advanced Metallization Conf. Stresa, Italy, March 2000; reprinted in *Microelectron. Eng.* (2001).
19. S. Luryi, A. Grinberg, and V. Gorfinkel, Heterostructure bipolar transistor with enhanced forward diffusion of minority carriers, *Appl. Phys. Lett.* **63**:1537–1540 (1993).
20. S. Luryi, Ultrafast operation of heterostructure bipolar transistors resulting from coherent base transport of minority carriers, *Proc. ISDRS*, Charlottesville, 1993, pp. 59–64.
21. H. Jorke, J. Weller, and J.-F. Luy, A new transistor concept for operating Si/SiGe devices at frequencies above 60 GHz, *Proc. 1998 Advanced Research Workshop Future Trends in Microelectronics: Off the Beaten Path*, Ile des Embiez, France, 1998.
22. A. Rosen, M. Caulton, P. Stabile, A. M. Gombar, W. M. Janton, C. P. Wu, J. F. Corboy, and C. W. Magee, Silicon as a millimeter-wave monolithically integrated substrate, *RCA Rev.* **42**:633–660 (Dec. 1981).
23. K. M. Strohm, J. Büchler, P. Russer, and E. Kasper, Silicon high resistivity substrate millimeter-wave technology, *IEEE Microwave and Millimeter-Wave Monolithic Circuits Symp. Digest*, Baltimore, MD, June 4–5, 1986, pp. 93–97.
24. J. Büchler, E. Kasper, P. Russer, and K. M. Strohm, Silicon high-resistivity-substrate millimeter-wave technology, *IEEE Trans. Microwave Theory Tech.* **34**:1516–1521 (Dec. 1986).
25. J.-F. Luy and P. Russer, *Silicon-based Millimeter-wave Devices*, Springer Series in Electronics and Photonics, Vol. 32, Springer, 1994.
26. P. Russer and E. Biebl, Fundamentals, in J.-F. Luy and P. Russer, eds., *Silicon-Based Millimeter-Wave Devices*, Springer Series in Electronics and Photonics, Vol. 32, Springer, 1994, pp. 149–192.
27. J. Buechler, Silicon millimeter-wave integrated circuits, in J.-F. Luy and P. Russer, eds., *Silicon-Based Millimeter-Wave Devices*, Springer Series in Electronics and Photonics, Vol. 32, Springer, 1994, pp. 149–192.
28. J.-F. Luy, K. M. Strohm, H.-E. Sasse, A. Schüppen, J. Büchler, M. Wollitzer, A. Gruhle, F. Schäffler, U. Güttich, and A. Klaassen, Si/SiGe MMICs, *IEEE Trans. Microwave Theory Tech.* **43**:705–714 (April 1995).
29. P. Russer, Si and SiGe millimeter-wave integrated circuits, *IEEE Trans. Microwave Theory Tech.* **46**:590–603 (May 1998).
30. R. People, Indirect band gap of coherently strained $\text{Ge}_x\text{Si}_{1-x}$ bulk alloys on (001) silicon substrates, *Phys. Rev.* **32**(2):1405–1410 (1985).
31. R. People, Physics and applications of $\text{Ge}_x\text{Si}_{1-x}$ /Si strained layer heterostructures, *IEEE J. Quantum Electron.* **36**:1696–1705 (Sept. 1986).
32. S. A. Campbell and A. Gopinath, Possibility of silicon monolithic millimeterwave integrated circuits, in *1989 IEEE MTT-S Int. Microwave Symp. Dig.*, (Long Beach, CA), June 1989, pp. 817–819.
33. M. K. M. Willander, Optimized frequency characteristics of Si/SiGe heterojunction and conventional bipolar transistors. *Solid-State Electron.* **33**(2):199–204 (1990).

34. T. Won and H. Morkoc, High-speed performance of Si/Si_{1-x}Ge_x heterojunction bipolar transistors, *IEEE Electron. Device Lett.* **10**(1):33–35 (1989).
35. G. L. Patton, J. H. Comfort, B. S. Meyerson, E. F. Crabbe, G. J. Scilla, E. de Fresart, J. M. C. Stork, J. Y.-C. Sun, D. L. Harame, and J. N. Burghartz, 75-GHz f_T . SiGe-base heterojunction bipolar transistors, *IEEE Electron. Device Lett.* **11**:171–173 (Jan. 1990).
36. U. König and H. Dämbkes, SiGe HBTs and MOSFETs, *Solid-State Electron.* **38**(9):1595–1602 (1995).
37. D. L. Harame, J. H. Comfort, J. D. Cressler, E. Crabbé, J. Y.-C. Sun, B. S. Meyerson, and T. Tice, Si/SiGe epitaxial-base transistors—Part I: Materials, properties, physics, and circuits, *IEEE Trans. Electron. Devices* **42**:455–468 (March 1995).
38. D. L. Harame, J. H. Comfort, J. D. Cressler, E. Crabbé, J. Y.-C. Sun, B. S. Meyerson, and T. Tice, Si/SiGe epitaxial-base transistor—Part II: Process integration and analog applications, *IEEE Trans. Electron. Devices* **42**:469–482 (March 1995).
39. R. J. E. Hueting, J. W. Slotboom, A. Pruijboom, W. B. de Boer, C. E. Timmering, and N. E. B. Cowern, On the optimization of SiGe-base bipolar transistors, *IEEE Trans. Electron. Devices* **43**:1518–1523 (Sept. 1996).
40. D. Behammer, J. N. Albers, U. König, D. Temmler, and D. Knoll, Si/SiGe HBTs for applications in low power ICs, *Solid-State Electron.* **39**(4):471–480 (1996).
41. E. F. Crabbe, B. S. Meyerson, J. M. C. Stork, and D. I. Harame, Vertical profile optimization of very high frequency epitaxial Si- and SiGe-base bipolar transistors, *1993 IEDM Tech. Digest*, 1993, pp. 73–86.
42. R. Doerner, J. Gerdes, C. Rheinfelder, F. J. Schmückle, W. Heinrich, and K. S. F. S. J.-F. Luy, Modelling of passive elements for coplanar SiGe MMICs, in *1995 IEEE MTT-S Int. Microwave Symp. Digest*, Orlando, FL, May 1995, pp. 1187–1190.
43. K. M. Strohm, J.-F. Luy, F. Schäffler, H. Jorke, H. Kibbel, C. Rheinfelder, R. Doerner, J. Gerdes, F. J. Schmückle, and W. Heinrich, Coplanar Ka-band SiGe-MMIC amplifier, *Electron. Lett.* **31**:1353–1354 (Aug. 1995).
44. K. M. Strohm and J.-F. Luy, Silicon-germanium bipolar technology for RF and microwave applications, *Proc. Microwave & Radio Frequency Conf.*, London, Sept. 30–Oct. 2, 1997, pp. 340–345.
45. H. Gummel and H. Poon, A compact bipolar transistor model, *Proc. 1970 IEEE Int. Solid-State Circuits Conf.* Feb. 1970, pp. 78–79.
46. H. Gummel and H. Poon, An integral charge control model of bipolar transistors, *Bell Syst. Tech. J.* **49**:827–853 (May–June 1970).
47. S. Bruce et al., Development, implementation and verification of a physics-based Si/SiGe HBT model for millimeter-wave nonlinear circuit simulation, *Proc. 26th European Microwave Conf.* Prague, 1996, pp. 903–905.
48. C. Rheinfelder, M. Rudolph, R. Beißwanger, and W. Heinrich, Nonlinear modeling of SiGe HBTs up to 50 GHz, *1997 Int. Microwave Symp. Digest*, Denver, June 1997, pp. 877–880.
49. M. Friedrich and H.-M. Rein, Analytical current-voltage relations for compact SiGe HBT models. Part I: The “idealized” HBT, *IEEE Trans. Electron. Devices* **46**:1384–1393 (July 1999).
50. M. Friedrich and H.-M. Rein, Analytical current-voltage relations for compact SiGe HBT models. Part II: Application to practical HBTs, *IEEE Trans. Electron. Devices* **46**:1394–1401 (July 1999).
51. M. Schröter and T.-Y. Lee, Physics-based minority charge and transit time modeling for bipolar transistors, *IEEE Trans. Electron. Devices* **46**:288–300 (Feb. 1999).
52. M. Schröter Staying current with hicum, *IEEE Circ. Devices Mag.* **18**:16–25 (May 2002).
53. M. Schröter, HICUM/Level2 model equations (online).
54. C. McAndrew, J. Seitchik, D. Bowers, M. Dunn, M. Foisy, I. Getreu, M. McSwain, S. Moinian, J. Parker, D. Roulston, M. Schroter, P. van Wijnen, and L. Wagner, VBIC95, the vertical bipolar inter-company model, *IEEE J. Solid-State Circ.* **31**:1476–1483 (Oct. 1996).
55. M. Ramana Murty, K. M. Newton, S. Sweeney, D. Sheridan, and D. Harame, Implementation of a scalable and statistical VBIC model for large-signal and intermodulation distortion analysis of SiGe HBTs, *2002 Int. Microwave Symp. Digest*, Seattle, June 2002, pp. 2165–2168.
56. F. Sinnesbichler and G. Olbrich, Accurate large-signal modeling of SiGe HBTs, *2000 Int. Microwave Symp. Digest*, Boston, June 2000, pp. 749–752.
57. F. Sinnesbichler, Hybrid millimeter-wave push–push oscillators using silicon-germanium HBTs, *IEEE Trans. Microwave Theory Tech.* **51**(2):422–430 (2003).
58. Y. Zhu, J. Twynam, M. Yagura, M. Hasegawa, T. Hasegawa, Y. Eguchi, A. Yamada, E. Suematsu, K. Sakuno, H. Sato, and N. Hashizume, Analytical model for electrical and thermal transients of self-heating semiconductor devices, *IEEE Trans. Microwave Theory Tech.* **46**:2258–2263 (Dec. 1998).
59. F. Sinnesbichler and G. Olbrich, Thermal time constant extraction for HBTs from S-parameter measurements, *Int. J. Electron. Commun. (AEÜ)* **57**(3):181–184 (2003).
60. C. D. Motchenbacher and F. C. Fitchen, *Low-Noise Electronic Design*, Wiley, New York, 1973.
61. U. König, A. Gruhle, and A. Schüppen, SiGe devices and circuits: Where are the advantages over III/V?. *Proc. 1995 IEEE GaAs IC Symp.* 1995, pp. 15–17.
62. R. Plana, L. Escotte, J. P. Roux, J. G. A. Gruhle, and H. Kibbel, 1/f noise in self-aligned Si/SiGe heterojunction bipolar transistor, *IEEE Electron. Device Lett.* **16**:58–60 (Feb. 1995).
63. R. Plana, B. V. Haaren, J. P. Roux, L. E. A. Gruhle, H. Dietrich, J. Graffeuil, K. S. F. Schäffler, and J.-F. Luy, Low-frequency noise in millimeter-wave Si/SiGe heterojunction bipolar transistors, *1995 IEEE MTT-S Int. Microwave Symp. Digest*, Orlando, FL, May 1995, pp. 1187–1190.
64. J. D. Cressler, L. Vempati, J. A. Babcock, R. C. Jaeger, and D. L. Harame, Low-frequency noise characteristics of UHV/CVD epitaxial Si- and SiGe-base bipolar transistors, *IEEE Electron. Devices Lett.* **17**:13–15 (Jan. 1996).
65. F. Sinnesbichler, M. Fischer, and G. Olbrich, Accurate extraction method for 1/f-noise parameters used in Gummel-Poon type bipolar junction transistor models, *1998 Int. Microwave Symp. Digest*, Baltimore, June 1998, pp. 1345–1348.
66. R. Hagelauer, T. Ostermann, U. König, M. Glück, and G. Höck, Performance estimation of Si/SiGe hetero-CMOS circuits, *Electron. Lett.* **33**:208–210 (Jan. 1997).
67. S. Sadek and K. Ismail, Si/SiGe CMOS possibilities, *Solid-State Electron.* **38**:1731–1734 (1995).
68. T. Hackbarth, G. Hck, H. Herzog, and M. Zeuner, Strain relieved SiGe buffers for Si-based heterostructure field effect transistors, *J. Cryst. Growth* **201/202**:734–738 (1999).

69. M. Zeuner, T. Hackbarth, G. Höck, D. Behammer, and U. König, High-frequency SiGe-n-MODFET for microwave applications, *IEEE Microwave Guided Wave Lett.* 410–412 (Oct. 1999).
70. G. Hock, T. Hackbarth, H.-J. Herzog, M. Enciso, F. Aniel, P. Crozat, R. Adde, E. Kohn, and U. König, 0.1 μm gate length p -type $\text{Ge/Si}_{0.4}\text{Ge}_{0.6}$ MODFET with 135 GHz f_{max} , *Electron. Lett.* **36**:1428–1429 (Aug. 2000).
71. M. Enciso, F. Aniel, P. Crozat, R. Adde, M. Zeuner, A. Fox, and T. Hackbarth, 0.3 dB minimum noise figure at 2.5 GHz of 0.13 μm $\text{Ge/Si}_{0.58}\text{Ge}_{0.42}$ n -MODFETs, *Electron. Lett.* **37**:1089–1090 (Aug. 2001).
72. G. Wright, Small-signal theory of the transistor transit-time oscillator (translator), *Solid State Electron.* **22**:399–407 (1979).
73. A. Grinberg and S. Luryi, Coherent transistor, *IEEE Trans. Electron. Devices* **40**:1512–1520 (1993).
74. J. Weller, H. Jorke, K. Strohm, J.-F. Luy, H. Kibbel, H.-J. Herzog, and R. Sauer, Assessment of transport parameters for the design of high speed Si/SiGe HBTs with compositionally graded base, *Thin Solid Films* **336**:137–140 (1998).
75. R. Wanner, G. Olbrich, H. Jorke, J.-F. Luy, S. Heim, E. Kaspe, and P. Russer, Experimental verification of the resonance phase transistor concept.
76. J. Weiner, A. Leven, V. Houtsma, Y. Baeyens, Y.-K. Chen, P. Paschke, Y. Yang, F. J. W.-J. Sung, A. Tate, R. Reyes, R. Kopf, and N. Weimann, SiGe differential transimpedance amplifier with 50-GHz bandwidth, *IEEE J. Solid-State Circ.* **38**:1512–1517 (Sept. 2003).
77. M. Reinhold, C. Dorschky, E. Rose, R. Pulella, P. Mayer, F. Kunz, Y. Baeyens, T. Link, and J.-P. Mattia, A fully integrated 40-Gb/s clock and data recovery IC with 1:4 DEMUX in SiGe technology, *IEEE J. Solid-State Circ.* **36**:1937–1945 (Dec. 2001).
78. D. Kehrer, H.-D. Wohlmuth, H. Knapp, M. Wurzer, and A. Scholz, 40-Gb/s 2:1 multiplexer and 1:2 demultiplexer in 120-nm standard CMOS, *IEEE J. Solid-State Circ.* **38**:1830–1837 (Nov. 2003).
79. F. Beisswanger, U. Gütlich, and C. Rheinfelder, Microstrip and coplanar SiGe-MMIC oscillators, in *European Microwave Conf.*, Prague, 1996, pp. 588–592.
80. H. Li and H.-M. Rein, Millimeter-wave VCOs with wide tuning range and low phase noise, fully integrated in a SiGe bipolar production technology, *IEEE J. Solid-State Circ.* 184–191 (Feb. 2003).
81. H. Li, H.-M. Rein, R.-E. Makon, and M. Schwerd, Wide-band VCOs in SiGe production technology operating up to about 70 GHz, *IEEE Microwave Wireless Compon. Lett.* 425–427 (Oct. 2003).
82. C. Rheinfelder, K. Strohm, L. Metzger, H. Kibbel, J.-F. Luy, and W. Heinrich, 47 GHz SiGe-MMIC oscillator, *1999 Int. Microwave Symp. Digest*, Anaheim, CA, June 1999, pp. 5–8.
83. F. Sinnesbichler, B. Hautz, and G. Olbrich, Low phase noise 58 GHz SiGe HBT push-push oscillator with simultaneous 29 GHz output, *2000 Int. Microwave Symp. Digest*, Boston, June 2000, pp. 11–16.
84. Y. Baeyens and Y. Chen, A monolithic integrated 150 GHz SiGe HBT push-push VCO with simultaneous differential v-band output, *2003 Int. Microwave Symp. Digest*, Philadelphia, June 2003, pp. 877–880.
85. M. Kaleja, A. Grübl, F. Sinnesbichler, G. Olbrich, K.-M. Strohm, J.-F. Luy, and E. Biebl, Application of Si/SiGe HBTs in active integrated antennas, *2000 Topical Meeting on Silicon Monolithic Integrated Circuits in RF Systems Digest*, Garmisch, April 26–28, 2000, pp. 64–66.
86. M. Kaleja, A. Grübl, F. Sinnesbichler, G. R. Olbrich, K. Strohm, J. Luy, and E. Biebl, Si/SiGe hbt active integrated antenna on high resistivity silicon substrate, *2000 Int. Microwave Symp. Digest*, Boston, June 2000, pp. 1899–1902.
87. K.-W. Yu, Y.-L. Lu, D.-C. Chang, V. Liang, and M. Chang, K-band low-noise amplifiers using 0.18 μm CMOS technology, *IEEE Microwave Wireless Compon. Lett.* **14**:106–108 (March 2004).
88. W. Menzel, Future applications, in J.-F. Luy and P. Russer, eds., *Silicon-Based Millimeter-Wave Devices*, Springer Series in Electronics and Photonics, Vol. 32, Springer, 1994, pp. 323–338.
89. M. Steinhauer, H. Irion, M. Schott, M. Thiel, H.-O. Ruoss, and W. Heinrich, SiGe-Based Circuits for Sensor Applications beyond 100 GHz, *2004 Int. Microwave Symp. Digest*, Fort Worth, TX, June 2004, pp. 223–226.
90. J. Block, T. Meister, H. Knapp, D. Zoschg, H. Schafer, K. Aufinger, M. Wurzer, S. Boguth, M. Franosch, R. Stengl, R. Schreiter, M. Rast, and L. Treitinger, SiGe bipolar technology for mixed digital and analogue RF applications, *Electron Devices Meeting 2000, IEDM Tech. Digest*, Dec. 2000, pp. 745–748.
91. J. Choi, C.-J. Weiske, G. Olbrich, and P. Russer, 'Flip-chip bonded Si Schottky sampling circuits for high speed demultiplexers,' *2003 Int. Microwave Symp. Digest*, Philadelphia, June 2003, pp. 1515–1518.
92. M. Singer, K. M. Strohm, J.-F. Luy, and E. M. Biebl, Active SIMMWIC-antenna for automotive applications, *1997 Int. Microwave Symp. Digest*, Denver, June 1997, pp. 1265–1268.

GRATINGS, GRATING ANTENNAS

CHRISTOPHER T. RODENBECK
KAI CHANG
Texas A&M University
College Station, Texas

A *grating* is an array of parallel obstructions separated from one another at a distance comparable to a wavelength. When an electromagnetic wave is incident upon a grating, it scatters to one or more specific angles determined by the spacing of the grating and the frequency of the wave. Since this effect is a diffraction phenomenon, gratings are often also referred to as *diffraction gratings*.

One of the most important uses of the diffraction grating is as an antenna for millimeter-wave through optical frequencies. This type of diffraction grating is the primary focus of this article. In integrated optics, grating antennas are used to couple power into and out of dielectric waveguides. For millimeter-wave systems, grating antennas have received attention for several key advantages that they have in comparison with other

conventional microwave antennas. They have low radiation losses, they are inexpensive and easy to fabricate, and they are planar. There is also considerable interest in using grating antennas to implement low-cost beam steering at millimeter-wave frequencies.

This article examines gratings and grating antennas in a series of five sections. Each of these sections is presented in such a way that it may be read independently from the others. An overview of the historical development of diffraction gratings is presented. The fundamental principles behind grating diffraction are explained in a manner suitable for those with an RF/microwave background. A clear design procedure for grating antennas is offered, along with an extensive reference list for those interested in further study. Some of the latest and most impressive applications of millimeter-wave gratings are described. The article then concludes with a brief discussion of the future of this field.

1. HISTORICAL OVERVIEW

Despite its fundamental importance, the early origins of the diffraction grating are a remarkable tale of discovery and rediscovery. An intense period of research into optical technology had begun during the early 1600s following the invention of the telescope by the Dutch. During that century, the fundamental principles of refraction and diffraction were discovered and applied to numerous optical components such as lenses, mirrors, reflectors, slits, pinholes, etc. Gratings, however, were not invented until a much later date.

The first discovery of the diffraction grating occurred in Philadelphia in 1785. Francis Hopkinson, one of the signers of the Declaration of Independence, held a finely woven silk handkerchief up to a bright light and observed the interference pattern produced by the light passing through the fabric. Hopkinson consulted his friend David Rittenhouse, a self-trained physicist. Recognizing the phenomenon as a diffraction effect, Rittenhouse designed his own diffraction grating made of human hairs wound around two fine screws. He then used the device to measure the approximate wavelength of visible light. Hailing his invention in an American scientific journal, Rittenhouse exclaimed that “new and interesting discoveries may be made respecting the properties of this wonderful substance, light, which animates all nature in the eyes of man, and perhaps, above all things, disposes him to acknowledge the Creator’s bounty” [1–3].

Since few researchers of that era read American scientific journals, Thomas Young of London had the opportunity to re-invent the diffraction grating in 1803. Young used his invention to measure the wavelengths of the various visible colors, but his main objective was to lend support to his view that light is a wave rather than a particle. Opponents of the wave theory attacked Young’s work, labeling it as “destitute of every species of merit” [3,4]. The practical importance of Young’s invention was thus unfortunately lost amid the then viscous debate concerning the nature of light.

The grating would be discovered for the final time by Joseph von Fraunhofer in 1821. Fraunhofer had earlier established an optical company in Bavaria that produced optical components of the highest quality. After unexpectedly observing grating diffraction during an experiment, Fraunhofer built increasingly precise gratings, ultimately etching the profile of a grating directly onto the surface of a glass plate. Using this arrangement, Fraunhofer was able to separate visible light into the different colors and measure their wavelengths. Although his primary objective was to use the device to make precise optical measurements and thereby improve his company’s products, Fraunhofer did popularize additional uses for optical gratings, including chemical spectroscopy and astronomical observation [1–4]. After his death, the diffraction grating eventually became an indispensable component of optics. As one researcher put it in 1960, “It is difficult to point to another single device that has brought more important information to every field of science than the diffraction grating” [3].

The first use of gratings at radiofrequencies came during Heinrich Hertz’ revolutionary experiments in 1887–1891. Hertz used a narrowly spaced wire grating in order to test the polarization of his “electric waves” [5,6]. Shortly after Hertz’ death in 1894, Chandra Bose of Calcutta built an impressive 60-GHz transmitter and receiver. During these experiments, Bose used a diffraction grating to measure the wavelength of his millimeter-wave source [7]. Subsequent decades saw rapid progress in the area of RF/microwave antennas and arrays. Early researchers in this area were heavily influenced by their familiarity with the already well-known diffraction grating. This is not surprising since gratings and array antennas are both governed by the same fundamental principles of wave interference. In fact, the designation “grating lobe” is still commonly used to refer to the additional maxima emitted by an array of widely spaced antennas.

The first grating antennas were developed and popularized at optical frequencies during the 1970s. Researchers at IBM etched a grating profile along the surface of a dielectric waveguide and used the device to transmit and receive laser light [8]. Called a grating “coupler,” this optical antenna is used in integrated optics for coupling optical power into and out of dielectric waveguides. In 1977, Tatsuo Itoh demonstrated the first microwave grating antenna at 15 GHz [9]. Shortly afterward, a team of researchers at the U.S. Army Communications-Electronics Command presented the development of a 60-GHz grating antenna fabricated along a silicon dielectric waveguide [10–14]. The design established the grating antenna as a new kind of low-loss low-cost antenna for millimeter-wave frequencies. This work captured the interest of researchers worldwide. Progress was rapid and was aided by inherent similarities between grating antennas and earlier traveling-wave antennas designed at lower microwave frequencies [15–17]. With increasing contemporary interest in the commercial and military applications of millimeter waves, much of the early research on grating antennas is now receiving renewed attention. And what is more, new and exciting applications of this antenna continue to be developed and are beginning to find

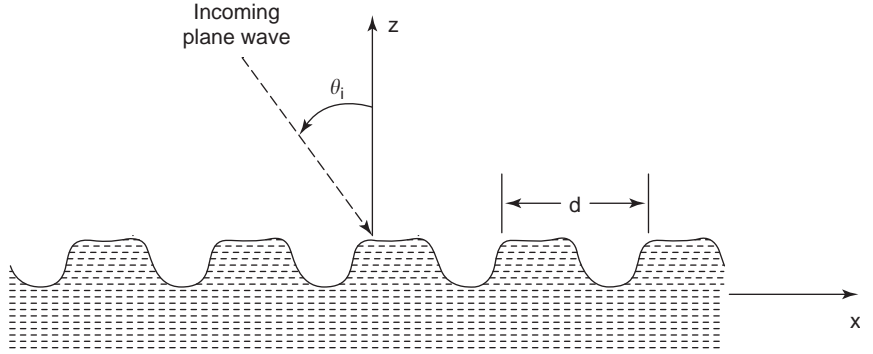


Figure 1. A generalized reflection grating of periodicity d illuminated by a plane wave incident at the angle θ_i .

commercial success for a wide range of millimeter-wave applications.

2. FUNDAMENTAL PRINCIPLES

The early investigators who popularized gratings were able to grasp the underlying principles of grating diffraction even before those principles had been formalized. Grating diffraction can in fact be accurately explained by an analogy between light and sound [1]:

If a sudden sharp noise such as is made by clapping the hands together is reflected from a high flight of steps, the sound comes back to us as a musical note; in other words, the steps impress the element of periodicity upon the reflected disturbance, each step throwing off an echo wave.

Sound incident on the staircase scatters in different directions. Those directions are determined by the step spacing and by the wavelength of each tone. In the case of a grating, an electromagnetic wave incident on a periodic interface scatters in a direction determined by the grating spacing and frequency of the wave.

This section presents a brief description of the fundamental principles behind grating diffraction. The discussion draws on material found in the literature [3,18–21] and is crafted in a manner suited for those with an RF/microwave background.

To begin with, consider the generalized two-dimensional grating interface shown in Fig. 1. The structure is infinite and periodic in the x direction and is excited by a plane wave incident at the angle θ_i . Since the grating interface is periodic in x , this suggests that the scattered field can be expanded in terms of a Fourier series

$$F_s(x, z) = \left[\sum_{n=-\infty}^{\infty} F_n(z) e^{-j(2n\pi/d)x} \right] e^{-jk_0(\sin \theta_i)x} \quad (1)$$

where $F_n(z)$ is the unknown Fourier coefficient for the n th-space harmonic $e^{-j(2n\pi/d)x}$. The $e^{-jk_0(\sin \theta_i)x}$ term outside the expansion accounts for the phase distribution of the incident field along the surface of the grating interface. Bring-

ing that term within the expansion simplifies (1) to

$$F_s(x, z) = \sum_{n=-\infty}^{\infty} F_n(z) e^{-jk_{x,n}x} \quad (2a)$$

where

$$k_{x,n} = k_0 \sin \theta_i + \frac{2\pi n}{d} = k_0 \sin \theta_n \quad (2b)$$

and θ_n denotes the angle of radiation for the n th-space harmonic. Equation (2b) is the well-known “grating equation.” By convention, θ_i and θ_n are defined so that θ_i is positive in the reverse quadrant and θ_n is positive in the forward quadrant.

Since the scattered field must satisfy the Helmholtz equation

$$\nabla^2 F_s(x, z) + k_0^2 F_s(x, z) = 0 \quad (3)$$

it is possible to define

$$k_{z,n} = \pm \sqrt{k_0^2 - k_{x,n}^2} = k_0 \cos \theta_n \quad (4)$$

where the sign is chosen to satisfy the radiation condition. The wavevector for the scattered field can now be expressed in terms of the unit vectors \mathbf{u}_x and \mathbf{u}_z :

$$\mathbf{k}_n = k_{x,n} \mathbf{u}_x + k_{z,n} \mathbf{u}_z = k_0 \sin \theta_n \mathbf{u}_x + k_0 \cos \theta_n \mathbf{u}_z \quad (5)$$

The incident wavevector likewise has the following form:

$$\mathbf{k}_i = k_0 \sin \theta_i \mathbf{u}_x - k_0 \cos \theta_i \mathbf{u}_z \quad (6)$$

For a given incident angle θ_i and grating spacing d , it is possible to plot the incident and scattered wavevectors from (5) and (6) on an illustrative diagram. An example is shown in Fig. 2. The incident wavevector \mathbf{k}_i arrives at an angle θ_i , and the wavevector \mathbf{k}_0 scatters in an equal and opposite direction θ_0 . All the radiating wavevectors lie together on a unit circle of radius k_0 , with each vector pointing in its direction of radiation. All the nonradiating wavevectors lie outside this circle. These nonradiating or *evanescent* modes decay exponentially away from the

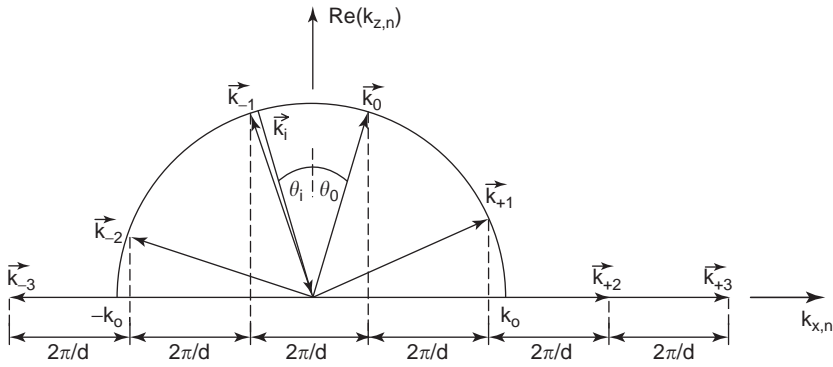


Figure 2. Diagram illustrating the incident and scattered wavevectors from a hypothetical reflection grating.

surface of the grating. What makes this diagram especially useful is that it gives the designer the ability to visualize how changing θ_i or d changes how many modes radiate and in which direction each radiates.

In the case of a grating antenna, the grating interface lies along the surface of a dielectric waveguide, and the grating is excited by the signal propagating within that waveguide. The grating equation (2b) should then be rewritten as

$$\text{Re}(k_{x,n}) = \text{Re}(k_{x,0}) + \frac{2\pi n}{d} = k_0 \sin \theta_n \quad (7)$$

where $k_{x,0}$ is the propagation constant within the dielectric waveguide. $k_{x,0}$ is actually a complex number with the imaginary part describing the rate of radiation along the antenna [21]. The imaginary part of $k_{x,0}$ is disregarded, however, when calculating the number and directions of the radiating space harmonics. Furthermore, the real part of $k_{x,0}$ is typically calculated with good accuracy as the propagation constant along the dielectric waveguide without any grating present.

A plot similar to Fig. 2 can be produced using (7) to determine the scattered wavevectors from the expression in (5). An example case is shown in Fig. 3. The fundamental wavevector \mathbf{k}_0 points in the positive direction along the ordinate axis with a magnitude equal to $\text{Re}(k_{x,0})$. Each radiating space harmonic lies on the unit circle and corresponds to a beam radiated by the antenna. Although

grating antennas are typically designed so that only the $n = -1$ beam radiates, this example shows two radiating beams. The $n = -1$ beam is radiating in the forward quadrant ($\theta > 0^\circ$) and the $n = -2$ beam, in the reverse quadrant ($\theta < 0^\circ$). This diagram can be useful for designing a grating so that a single main beam radiates in some desired direction.

3. ANTENNA DESIGN AND ANALYSIS

The grating antenna is a type of leaky-wave antenna. A leaky-wave antenna is essentially a waveguiding structure perturbed either continuously or periodically so that it leaks power all along its length [22]. In the case of a grating antenna, the waveguiding structure is a dielectric waveguide perturbed by a periodic grating placed along its surface. The conventional configuration is shown in Fig. 4. A periodic array of transverse strips is arranged along the surface of a dielectric waveguide, in this case a dielectric image line. The strips can be either metallic or dielectric. These strips form a grating that perturbs the signal traveling along the guide. If the antenna is designed correctly, the grating excites a single leaky mode above the surface of the guide to create a directive beam of radiation in the far field. The radiated beam is fan-shaped, with narrow beamwidth in the array-effect dimension.

The procedure for designing a grating antenna encompasses four key steps. This section provides a complete

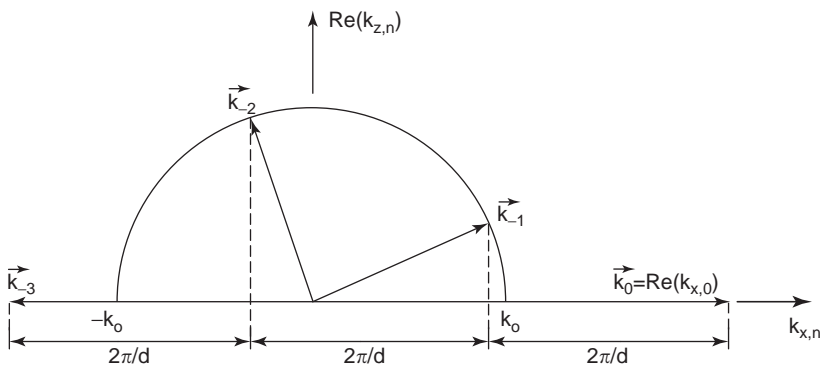


Figure 3. Diagram illustrating the wavevectors along a hypothetical grating antenna.

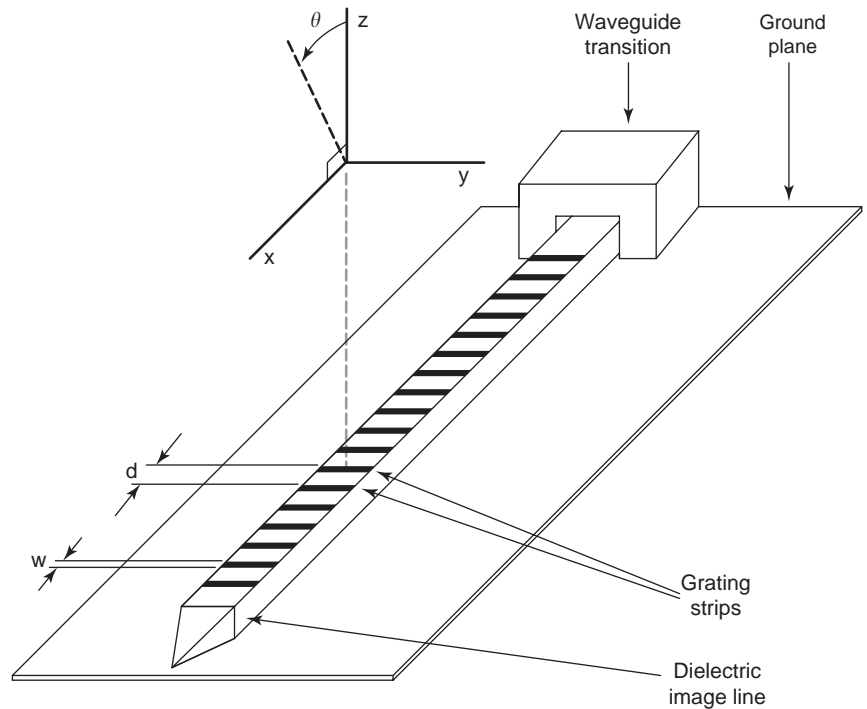


Figure 4. Configuration of a conventional grating antenna.

description for each of those steps. Additional references are also provided for the reader who wishes to explore more advanced topics related to the design and analysis of this class of antenna.

Step 1. The aspect ratio and dielectric constant of the dielectric waveguide must be chosen so that only one mode can propagate within the guide over the antenna's desired frequency range. This requires that the designer calculate the propagation constants and cutoff frequencies within the guide for each potential dielectric waveguide design. There are several options for performing this sort of calculation. Rigorous methods are available [23], but they are not popular since they involve the solution of a large set of coupled, transcendental equations. For low-dielectric-constant guides, simple effective dielectric constant (EDC) methods can be used with good accuracy [23]. An especially accurate EDC method has been developed for dielectric image line [24]. For high-dielectric-constant guides, full-wave electromagnetic simulation should be used to determine the guided wavelength.

In general, greater antenna directivity can be achieved using a wide guide rather than a narrow guide of the same length. However, this factor must be balanced against other considerations, such as the available single-mode bandwidth in the guide and the mechanism used to feed the guide. Using a high-dielectric-constant material also has certain advantages, to be discussed later, but these too must be balanced against other considerations, such as the availability of high-dielectric-constant substrates with reasonably low loss in the chosen frequency range and by the undesirable dispersion in the guided and leaky modes

that can occur along high dielectric constant guides [25,26].

Step 2. The dielectric waveguide must be excited at the intended frequency of operation. This can be accomplished by directly integrating a signal source into the dielectric guide [27–32] or by manufacturing a transition between the dielectric guide and another type of transmission line. Although a waveguide transition is shown in Fig. 4, other transitions, including microstrip, CPW, and slot transitions, are also available [21,23,33–37]. In every case, the transition should be carefully designed to limit spurious radiation and surface-wave excitation, which have the potential to spoil an otherwise good antenna design by increasing the sidelobes above an acceptable level [22].

It is important to note that the method of excitation determines the polarization of the far-field radiation pattern. Dielectric waveguides can, in general, be excited so that one or both of two orthogonal degenerate fundamental modes propagate [23]. For a rectangular dielectric guide like the image line shown in Fig. 4, the primary field components under E -wave excitation are H_y , E_x , and E_z , and the antenna's E plane is located in the x - z plane. Under H -wave excitation, the primary field components are E_y , H_z , and H_x , and the H plane is located in the x - z plane. Using other conventions present in the literature, it is also possible to designate E -wave excitation along the guide in Fig. 4 as TM-to- z excitation or simply as TM excitation, as E_{mn}^z excitation, or as TE or "perpendicular-polarized" excitation (since the E field is "perpendicular" to the strips). Likewise, H -wave excitation can be referred to as TE-to- z , TE, E_{mn}^y , TM, or "parallel-polarized." For an

image line, E -wave excitation is generally preferred since the presence of the ground plane shorts out most of the power that could couple to the H -wave modes. Recent patents indicate that it may also be possible to intentionally excite both degenerate modes in a dielectric waveguide in order to create dual polarization or even circular polarization [38,39].

Step 3. The next step in the design process is to determine the periodic spacing between the grating strips. For thin

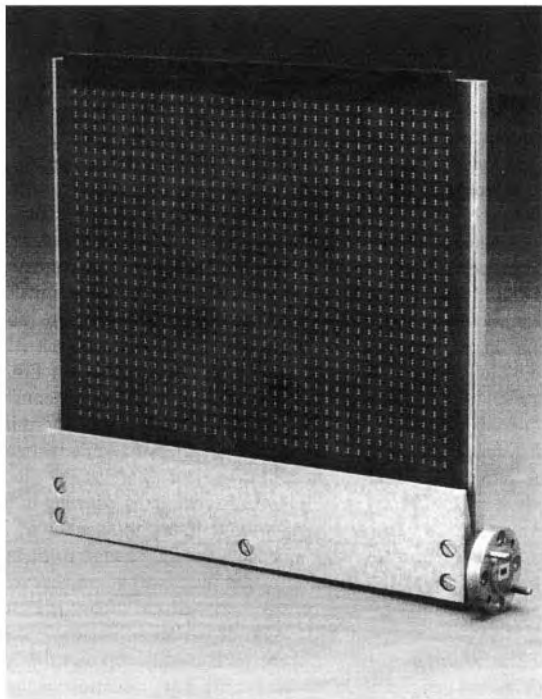
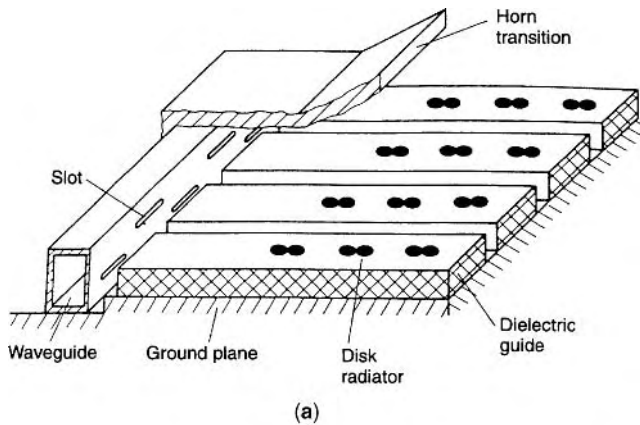


Figure 5. Array of periodic dielectric antennas designed for radiation in the broadside direction: (a) array configuration; (b) finished device for 65-GHz band. The element antennas are fed by a resonant slotted waveguide array with a horn transition. (From Solbach, [66], © 1985 EW Communications. Reprinted with permission of publisher from MSN & CT. All rights reserved.)

metal strips or thin dielectric strips, the presence of a grating along the dielectric guide has only a negligible effect on the propagation constant within the guide itself. In this case, the angle of radiation in the direction forward from broadside can be calculated at any given frequency of excitation as a simple function of the guide wavelength λ_g and strip spacing d

$$\theta_n = \arcsin\left(\frac{\lambda_0}{\lambda_g} + \frac{n\lambda_0}{d}\right), \left|\frac{\lambda_0}{\lambda_g} + \frac{n\lambda_0}{d}\right| \leq 1 \quad (7a)$$

where λ_0 is the free-space wavelength and n , the space harmonic ($0, \pm 1, \pm 2, \dots$), is chosen as -1 for single-beam operation [40]. In principle, the permissible range of values for θ_{-1} extends both forward and reverse of broadside, across the entire $\pm 90^\circ$ range. But as is the case with most planar antenna arrays, grating antennas do not radiate well beyond the $\pm 60^\circ$ range. There are other limitations as well. Bragg reflection occurs if $d = \lambda_g$ [9]. This prevents the antenna from radiating well for $\theta_{-1} = 0^\circ$ unless a more elaborate grating pattern [23,41,42] is used. In addition, it is difficult to achieve a sufficiently high effective relative dielectric constant along an image line or other open dielectric guide in order to prohibit appearance of the $n = -2$ grating lobe for increasingly positive values of θ_{-1} while still maintaining single-mode bandwidth along the guide. Unusually high dielectric constants ($\epsilon_r > 20$) are required, with associated tradeoffs in performance and implementation [25,26,43]. Choosing a main beam angle in the $\theta_{-1} > 0^\circ$ range is thus typically limited by the propagation of the $n = -2$ space harmonic.

Step 4. The final design step is to choose the strip widths and antenna length. The widths of the strips determine the rate of radiation along the antenna, and the antenna length determines how much power is left unradiated at the end of the antenna. Narrow strips radiate too little, leaving a substantial amount of power unradiated at the end of even a long antenna. Excessively wide strips radiate too much power during the first few strips, causing the effective aperture of the antenna to be too small and the sidelobes to be large [33]. In both cases, antenna efficiency can suffer. A popular compromise is to gradually increase the widths of the strips away from the input to the antenna.

Designing the strip widths can be done by experiment, by analysis, or even by rules of thumb. Several such rules of thumb are available in the literature. For the case of dielectric-strip gratings, perturbational analysis can be used to argue that $w = 0.5d$ is an optimal strip width [40,44]. In the case of a metal-strip grating, researchers determined by experiment that maximum radiation for a particular design occurred when $w = 0.4\lambda_g$ [33]. They then used this finding to formulate a very conservative empirical guideline for designing a tapered distribution of strip widths along their antenna.

Analytical approaches are generally preferred in antenna design. To analytically design a grating antenna

requires an analysis that is capable of relating the design parameters (viz., the strip width, interelement spacing, dielectric constant, etc.) to the radiation rate along the surface of the antenna. Once the radiation rate is known, the far-field pattern can easily be calculated using the spatial Fourier transform [40]. Unfortunately, calculating the radiation rate along a grating antenna is typically considered an involved process [21]. For the dielectric strip gratings commonly used in integrated optics, commercial software and curve fit models [45] are available. For metallic strip gratings, several rapid analytical procedures are available for the limiting cases of narrow strip gratings and narrow slot gratings. (See Refs. 17, 46, and 47 and the references cited in those papers.) Practical designs, however, typically use strips whose widths fall between those two limiting cases. Recently, a simple spectral-domain approach has been proposed that is capable of analyzing metal gratings composed of strips that are neither narrow nor wide [48]. Many more rigorous numerical methods are also available, with varying levels of rigor and computational effort for each approach. These methods include mode-matching techniques [49,50], waveguide models [51], rigorous network formulations [52], and full-wave simulation [53,54]. An excellent and timely overview of various approaches and their relative merits is provided in Ref. 3 for both metal and dielectric strip gratings. The reader is warned to investigate each approach since the literature does contain references to inaccurate and even erroneous approaches for analyzing grating antennas.

Experimental design can be a particularly expedient approach in the case of metal-strip gratings. Multiple sets of gratings can be etched onto a single thin dielectric film [55–57]. Thin dielectric films made from materials such as RT-Duroid have low loss at millimeter-wave frequencies

and can be easily etched using conventional photolithography. The film can then be extended across the surface of the dielectric guide, allowing the designer to rapidly test the radiation rate for each of the sets of grating strips. This information can then be used together with the spatial Fourier transform to determine a favorable distribution of strip widths in order to achieve a desired far-field pattern.

When the distribution of strip widths and the radiation rate along the antenna are being determined, the length of the antenna must also be chosen so that only a certain fraction of the input power remains unradiated at the end of the dielectric guide. If the amount of unradiated power is too large, antenna efficiency is low. For an antenna of length L , the total efficiency η can be expressed as

$$\eta = \int_0^L 2\alpha(x)e^{-2(\alpha(x) + \alpha_L)x} dx \quad (8)$$

where $\alpha(x)$ is the radiation rate along the grating and α_L accounts for conductor and dielectric losses [15]. If the radiation rate is uniform along the antenna and much larger than the loss factors, the efficiency can be approximated for design purposes as $1 - e^{-2\alpha_L L}$. If a substantial portion of the input power is to be left unradiated, the dielectric guide should be terminated in a matched load or with absorbing material, or else the wasted power will reflect from the end of the antenna and radiate as a sidelobe.

4. APPLICATIONS

The chief purpose of this section is not to present a comprehensive review of all applications of gratings and

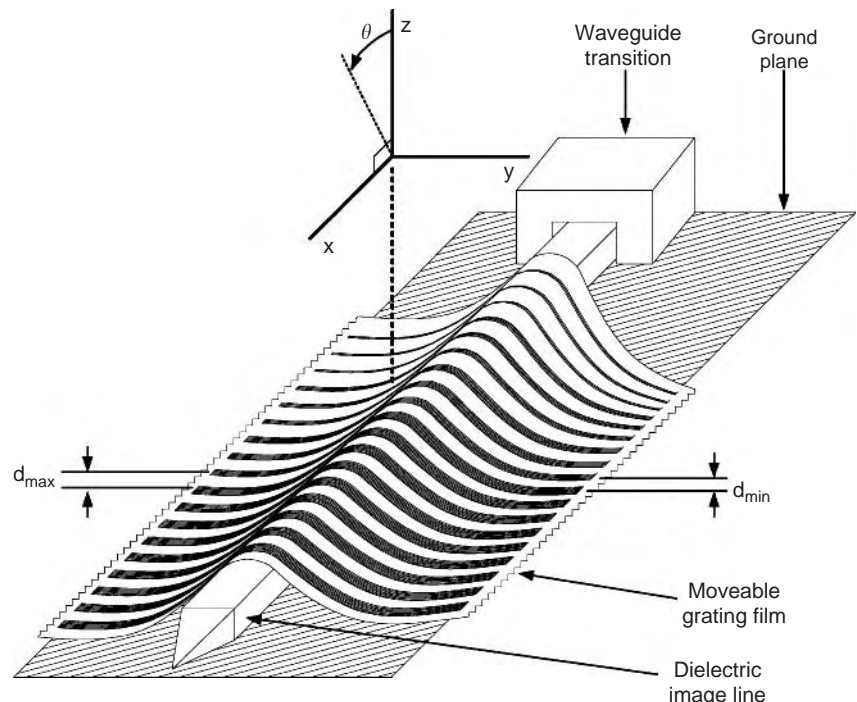


Figure 6. A low-cost reconfigurable grating antenna.

grating antennas. Instead, the objective is to capture the reader's interest and identify the major applications of gratings. A special emphasis is given to antenna applications at millimeter-wave frequencies.

4.1. Array Antennas

Grating antennas are based on dielectric waveguide technology. Unlike printed-circuit transmission lines, dielectric waveguides exhibit low loss even at very high millimeter-wave frequencies. Unlike rectangular metal waveguides, dielectric waveguides are easily fabricated and compatible with mass production at frequencies through W band and beyond. Dielectric waveguides are thus ideal candidates for feeding millimeter-wave antenna arrays. Diffraction gratings are perhaps the most natural and inexpensive implementation of an array antenna to be based on this class of transmission line.

A conventional grating antenna is shown in Fig. 4. Many variations on this configuration are possible. The strips can be metal [10] or dielectric [40]. The strips can be replaced with slots, grooves, or cavities in the ground plane [23]. These strips, slots, and other perturbations don't necessarily have to be rectangular; they can also be circular. Their cross sections can be "blazed" or nonrectangular [3]. In addition, the perturbations can be made self-similar to allow broadside radiation [23,41]. If desired, the image line can also be replaced with another type of dielectric waveguide, such as insular image guide, nonradiative dielectric (NRD) guide, inverted-strip dielectric guide, or rectangular dielectric waveguide [23]. Gratings fabricated on circular dielectric waveguides can radiate omnidirectionally [58]. Gratings based on rotated strips can radiate circular polarization [59,60].

Several methods are available for increasing the gain of a grating antenna. The gain in the nonarray plane can be increased by embedding the dielectric guide within a trough [61] or flared trough [33] or by placing the guide in proximity to a parabolic reflector [39]. Pencil-beam radiation can be achieved by etching a two-dimensional grating on a surface-wave-excited dielectric slab [62–64]. This kind of grating is designated a "hologram" or "holographic antenna." This is a matter of nomenclature, however, since the standard grating antenna is itself a type of hologram. Other research has demonstrated unconventional circular and linear polarized pencil-beam antennas fed by NRD gratings [65]. Planar arrays of grating antennas can also be formed to increase the directivity of the beam [42]. One planar grating array, shown in Fig. 5, radiates a broadside beam at 65 GHz with a total efficiency, including the power divider and feed losses, of 27% [66].

4.2. Scanning Antennas

A wide array of consumer wireless applications are anticipated at millimeter-wave frequencies [48,55]. Many of these emerging applications require the ability to track a user or moving target. Unfortunately, conventional technology for steering and redirecting millimeter-wave

wireless signals is often prohibitively expensive for consumer applications. Rotating antennas use RF gimbal feeds that require precision machining and costly maintenance. Millimeter-wave phased arrays, on the other hand, are often exuberantly expensive, requiring exotic technologies and extensive supporting electronic equipment. In order to reduce the cost and broaden the commercial applications millimeter-wave frequencies, considerable research is currently directed at developing low-cost scanning antennas and phased arrays for the Ka band and above. Several approaches based on the grating arrays are under investigation, including

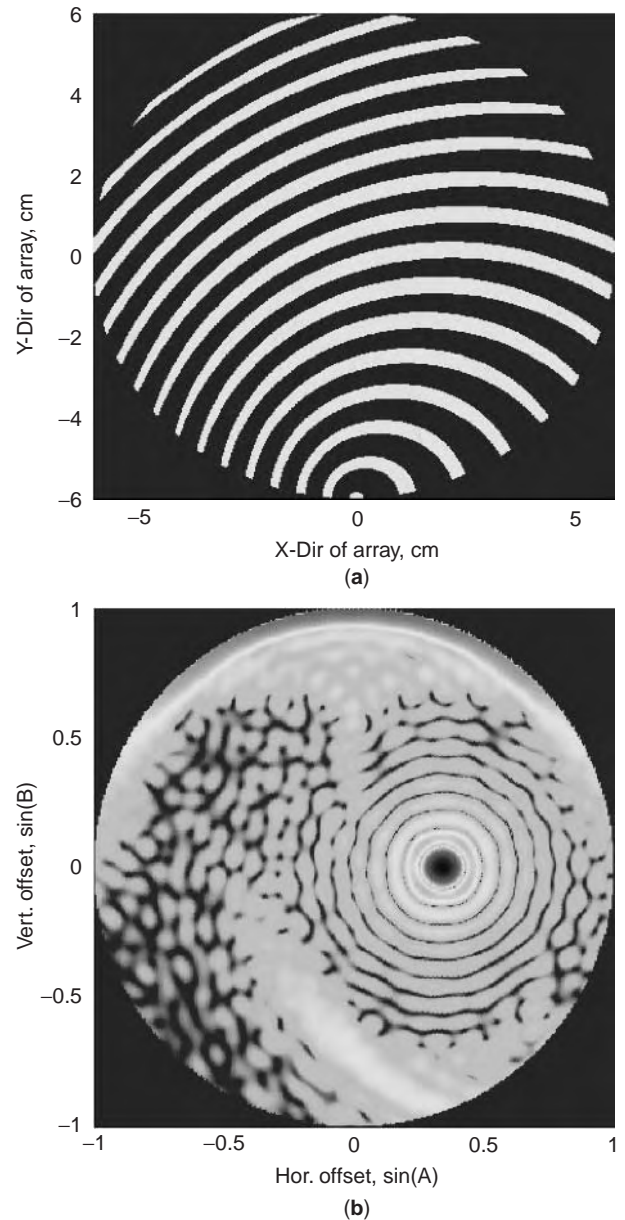


Figure 7. Electronically reconfigurable holographic antenna: (a) conducting regions formed on a silicon wafer; (b) corresponding far-field radiation pattern. (Courtesy of Dr. A. Fathy, University of Tennessee.) (This figure is available in full color at <http://www.mrw.interscience.wiley.com/erfme>.)

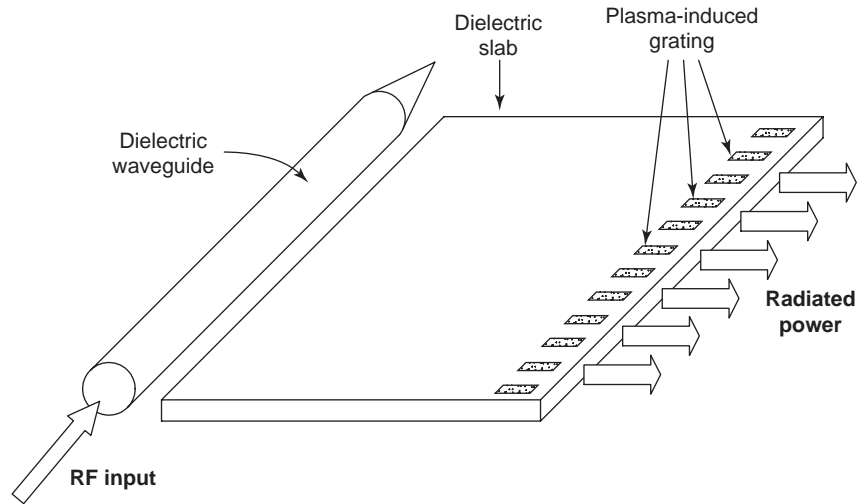


Figure 8. A commercially available optically controlled grating antenna.

electromechanical, electronic, and electrooptic. Some of these approaches are also classified as “reconfigurable antennas” since the central tactic is often to provide beam steering by reconfiguring the aperture of the grating.

Figure 6 illustrates a simple scanning antenna that can be electromechanically reconfigured to provide low-cost millimeter-wave beam steering [67]. A thin movable dielectric film is extended across a stationary dielectric image line. Continuous metal grating strips are etched along the underside of the film, with the strips depicted as visible in the figure. The spacing between the metal strips varies linearly along the length of the film from d_{\max} to d_{\min} . Scrolling the film along the image line shifts the film in the y direction, steering a highly directive fan-shaped beam of radiation along the angle θ . As illustrated in the figure, the widths of the strips themselves are designed to increase away from the input to the guide in order to gradually perturb the signal as it is launched along the image line. The prototype configuration shown in Fig. 1 is able to achieve 53° beam steering at 35 GHz. An innovative, bidirectionally excited design achieves $\pm 50^\circ$ scanning across the complete 35–40 GHz range [48,57]. A key advantage of this approach is that the mechanical motion is inertialess and completely external to the millimeter-wave feed. Thin steel sheets may also be used. In either case, only a simple DC motor is required to spool the grating layer along the surface of the dielectric guide. Another electromechanical approach is to form a grating antenna from a spring coiled around a dielectric waveguide [68]. Flexing the spring provides beam steering. Several interesting electromechanically scanning grating antennas are now available commercially and are disclosed in a U.S. patent [39].

Other researchers are developing electronically scanned grating antennas by integrating PIN diodes into the grating structure. In Refs. 13 and 14, a PIN diode integrated into the sidewall of a grating antenna is used to modulate the propagation constant within the dielectric guide in order to steer the beam. In Ref. 69, PIN diodes are integrated into the grating strips themselves in order to switch the radiated beam between one of two scan states.

Most impressively, in Ref. 64, an array of PIN diodes are integrated onto the back of a silicon wafer in order to create a dynamically reconfigurable hologram. Holographic antennas are the two-dimensional analog of grating antennas. Figure 7 illustrates the conducting pattern formed by the PIN diodes on the silicon wafer and the corresponding far-field pattern.

Optical and ferroelectric scanning grating antennas are also a topic of investigation [70–75]. In many cases, however, the experimental results require improvement in order for the systems to find broad acceptance. Figure 8 illustrates the configuration of one design [74]. A circular dielectric waveguide is coupled to a semiconducting dielectric slab. Laser light illuminates the surface of the dielectric slab in order to create islands of conducting plasma on the surface. The spacing between these islands can be changed in order to steer the mainbeam angle of the radiated beam. Ferroelectric scanning grating antennas are also commercially available at frequencies from 10 to 76 GHz [75].

4.3. Other Applications

Many other uses for millimeter-wave gratings do exist. For example, on the circuit level gratings can be used as resonators for notch filters or for oscillators [9,76]. Closely spaced gratings are often used as polarizers in grid amplifiers [77]. In the far-field zone, millimeter-wave gratings are used for as spectrometry [7,78], spatial filtering and beam-shaping [79], spatial power combining and dividing [80–82], and remote beam control [83–85]. These applications for gratings are likely to increase in importance as millimeter-wave technology becomes more and more common.

5. CONCLUSION

Interest in millimeter-wave technology has been building steadily since the mid-1970s. Today, several applications have already become established; numerous others are quickly emerging. These new millimeter-wave wireless systems require inexpensive, mass-producible, low-loss

antenna arrays. Grating antennas meet these demands at frequencies up through the W band and beyond.

This article began with an examination of the historical background of gratings and grating antennas. The fundamental principles underlying their operation were clearly described, and an antenna design procedure was presented. The article ended with a survey of some of the most interesting applications to date for millimeter-wave gratings.

Acknowledgments

The authors wish to thank Prof. R. Nevels of Texas A&M University for graciously opening to them his extensive personal notes on periodic structures. They also kindly appreciate the assistance of Dr. A. Fathy at the University of Tennessee, of President H. Rutstein at Dorado International Corp., and of Ms. T. Quintana at Waveband Corp.

BIBLIOGRAPHY

- G. K. Sweetnam, *The Command of Light*, American Philosophical Society, Philadelphia: 2000.
- M. C. Huntley, *Diffraction Gratings*, Academic Press, New York, 1982.
- E. G. Loewen and E. Popov, *Diffraction Gratings and Applications*, Marcel Dekker, New York, 1997.
- E. Hecht, *Optics*, 3rd ed., Addison-Wesley, New York, 1998.
- H. Hertz, *Electric Waves*, Macmillan, London, 1893.
- D. Pozar, *Microwave Engineering*, Wiley, New York, 1990.
- J. C. Bose, On the determination of the wavelength of electric radiation by a diffraction grating, *Proc. Roy. Soc.* **60**:167–178 (1897).
- M. L. Dakss, L. Kuhn, P. F. Heidrich, and B. A. Scott, Grating coupler for efficient excitation of optical guided waves in thin films, *Appl. Phys. Lett.* **16**(12):523–525 (June 1970).
- T. Itoh, Application of gratings in a dielectric waveguide for leaky-wave antennas and band-reject filters, *IEEE Trans. Microwave Theory Tech.* **25**(12):1134–1137 (Dec. 1977).
- K. L. Klohn, R. E. Horn, H. Jacobs, and E. Freibergs, silicon waveguide frequency scanning linear array antenna, *IEEE Trans. Microwave Theory Tech.* **26**(10):764–773 (Oct. 1978).
- S. T. Peng and F. Schwering, Dielectric grating antennas, R&D Tech. Report CORADCOM 78-3, U.S. Army CORADCOM, Ft. Monmouth, NJ, 1978.
- K. L. Klohn, R. E. Horn, H. Jacobs, and E. Freibergs, Silicon waveguide frequency scanning linear array antenna, *IEEE Trans. Microwave Theory Tech.* **26**(10):764–773 (Oct. 1978).
- R. E. Horn, H. Jacobs, E. Freibergs, and K. L. Klohn, Electronic modulated beam-steerable silicon waveguide array antenna, *IEEE Trans. Microwave Theory Tech.* **28**(6):647–653 (June 1980).
- R. E. Horn, H. Jacobs, E. Freibergs, and K. L. Klohn, Single-frequency electronic-modulated analog line scanning using a dielectric antenna, *IEEE Trans. Microwave Theory Tech.* **30**(5):816–820 (May 1982).
- C. H. Walter, *Traveling Wave Antennas*, McGraw-Hill, New York, 1965.
- R. C. Honey, A flush-mounted leaky-wave antenna with predictable patterns, *IEEE Trans. Anten. Propag.* **7**(4):320–329 (Oct. 1959).
- J. Jacobsen, Analytical, numerical, and experimental investigation of guided waves on a periodically strip-loaded dielectric slab, *IEEE Trans. Anten. Propag.* **18**(3):379–388 (May 1970).
- R. D. Nevels, Periodic structures (personal notes), Texas A&M Univ.
- S. T. Peng, T. Tamir, and H. L. Bertoni, Theory of periodic dielectric waveguides, *IEEE Trans. Microwave Theory Tech.* **23**(1):123–133 (Jan. 1975).
- S. T. Peng, T. Tamir, and H. L. Bertoni, Correction to “Theory of periodic dielectric waveguides,” *IEEE Trans. Microwave Theory Tech.* **24**(8):542 (Aug. 1976).
- P. Bhartia and I. J. Bahl, *Millimeter Wave Engineering*, Wiley, New York, 1984.
- A. A. Oliner, Leaky-wave antennas, in R. C. Johnson, ed., *Antenna Engineering Handbook*, 3rd ed., McGraw-Hill, New York, 1993.
- S. K. Koul, *Millimeter Wave and Optical Dielectric Integrated Guides and Circuits*, Wiley, New York, 1997.
- R. M. Knox and P. P. Toullos, Integrated circuits for the millimeter through optical frequency range, *Proc. Symp. Submillimeter Waves*, New York, March 1970, pp. 497–516.
- M. Guglielmi, *Radiation from a Metal Strip Grating on a Dielectric Slab*, Ph.D. dissertation, Polytechnic Univ., New York, March 1986, pp. 131–152.
- M. Guglielmi and A. A. Oliner, A practical theory for dielectric image guide leaky-wave antennas loaded by periodic metal strips, *Proc. European Microwave Conf.*, Rome, Italy, Sept. 1987, pp. 549–554.
- R. E. Horn, H. Jacobs, and E. Freibergs, Millimeter-wave oscillators using image-line or microstrip waveguides, *IEEE Trans. Microwave Theory Tech.* **34**(2):285–288 (Feb. 1986).
- R. Frolich and J. Litva, Beam-steerable active array antenna, *Electron. Lett.* **28**(2):184–185 (Jan. 1992).
- A. M. Kirk and K. Chang, Integrated image line steerable active antennas, *Int. J. Infrared Millimeter Waves* **13**(6): 841–851 (June 1992).
- J. J. Potoczniak, H. Jacobs, C. M. Lo Casio, and G. Novick, Power combiner with gunn diode oscillators, *IEEE Trans. Microwave Theory Tech.* **82**(5):724–728 (May 1982).
- Z. W. Li and W. Menzel, A 61 GHz doppler radar using an inverted strip dielectric waveguide, *IEEE MTT-S Int. Microwave Symp. Digest*, Albuquerque, NM, June 1992, pp. 629–632.
- R. E. Lehmann, N. H. Sun, and J. K. Butler, Integrated Q-band MMIC diffraction grating transmitter, *Proc. 1996 IEEE Int. Symp. Antennas Propagation*, Baltimore, MD, July 1996, pp. 2188–2191.
- T. T. Trinh, R. Mittra, and R. J. Paleta, Jr., Horn image-guide leaky wave antenna, *IEEE Trans. Microwave Theory Tech.* **29**(12):1310–1314 (Dec. 1981).
- A. Basu and T. Itoh, Dielectric waveguide-based leaky-wave antenna at 212 GHz, *IEEE Trans. Anten. Propag.* **46**(11):1665–1673 (Nov. 1998).
- K. Solbach, Slots in dielectric image line as mode launchers and circuit elements, *IEEE Trans. Microwave Theory Tech.* **29**(1):10–16 (Jan. 1981).
- H. Tehrani, M. Li, and K. Chang, Broadband microstrip to dielectric image line transitions, *IEEE Microwave Guided Wave Lett.* **10**(10):409–411 (Oct. 2000).
- A. Scharly, G. C. Dalman, and C. A. Lee, *Dielectric Waveguide-to-Coplanar Transmission Line Transitions*, U.S. Patent 5,225,797 (July 1993).

38. V. Manasson, L. Sadovnik, and V. Yepishin, *Antenna with a Plasma Grating*, U.S. Patent 5,982,334 (Nov. 1999).
39. V. Manasson and L. Sadovnik, *Scanning Antenna Including a Dielectric Waveguide and a Rotatable Cylinder Coupled Thereto*, U.S. Patent 6,211,836 B1 (April 2001).
40. F. K. Schwing and S. T. Peng, Design of dielectric grating antennas for millimeter-wave applications, *IEEE Trans. Microwave Theory Tech.* **31**(2):199–209 (Feb. 1983).
41. M. Guglielmi and D. R. Jackson, Broadside radiation from periodic leaky-wave antennas, *IEEE Trans. Anten. Propag.* **41**(1):31–37 (Jan. 1993).
42. K. Solbach, Review of dielectric image line antennas, in K. L. Button, ed., *Infrared and Millimeter Waves*, Vol. 15, Academic Press, Orlando, FL, 1986.
43. S. Kobayashi, R. Lampe, R. Mittra, and S. Ray, Dielectric rod leaky-wave antennas for millimeter-wave applications, *IEEE Trans. Anten. Propag.* **29**(5):822–824 (Sept. 1981).
44. T. Tamir and S. T. Peng, Analysis and design of grating couplers, *Appl. Phys.* **14**:235–254 (Nov. 1977).
45. H. Nishihara, M. Haruna, and T. Suhara, *Optical Integrated Circuits*, McGraw-Hill, New York, 1989, pp. 62–95.
46. R. Mittra and R. Kastner, A spectral domain approach for computing the radiation characteristics of a leaky-wave antenna for millimeter waves, *IEEE Trans. Anten. Propag.* **29**(4):652–654 (July 1981).
47. M. Guglielmi and A. A. Oliner, Multimode network description of a planar periodic metal-strip grating at a dielectric interface—Part II: Small-aperture and small-obstacle solutions, *IEEE Trans. Microwave Theory Tech.* **37**(3):542–552 (March 1989).
48. C. T. Rodenbeck, M. Li, and K. Chang, Design and analysis of a reconfigurable dual-beam grating antenna for low-cost millimeter-wave beam-steering, *IEEE Trans. Anten. Propag.* (in press).
49. R. Petit, *Electromagnetic Theory of Gratings*, Springer-Verlag, New York, 1980.
50. J. A. Encinar, Mode-matching and point-matching techniques applied to the analysis of metal-strip-loaded dielectric antennas, *IEEE Trans. Anten. Propag.* **38**(9):1405–1412 (Sept. 1990).
51. M. Ghomi, B. Lejay, J. L. Amalric, and H. Baudrand, Radiation characteristics of uniform and nonuniform dielectric leaky-wave antennas, *IEEE Trans. Anten. Propag.* **41**(9):1177–1186 (Sept. 1993).
52. M. Guglielmi and H. Hochstadt, Multimode network description of a planar periodic metal-strip grating at a dielectric interface—Part III: Rigorous solution, *IEEE Trans. Microwave Theory Tech.* **37**(5):902–909 (May 1989).
53. S. D. Gedney, J. F. Lee, and R. Mittra, A combined FEM/MoM approach to analyze the plane wave diffraction by arbitrary gratings, *IEEE Trans. Microwave Theory Tech.* **40**(2):363–370 (Feb. 1992).
54. M. Chen, B. Houshmand, and T. Itoh, FDTD analysis of a metal-strip-loaded dielectric leaky-wave antenna, *IEEE Trans. Anten. Propag.* **45**(8):1294–1301 (Aug. 1997).
55. C. T. Rodenbeck, M. Li, and K. Chang, A novel millimeter-wave beam-steering technique using a dielectric-image lined grating film, *IEEE Trans. Anten. Propag.* **51**(9):2203–2209 (Sept. 2003).
56. C. T. Rodenbeck, M. Li, and K. Chang, A novel millimeter-wave beam-steering technique using a dielectric-image lined grating film, *P. IEEE MTT-S Int. Microwave Symp. Digest*, Phoenix, AZ, May 2001, pp. 267–270.
57. C. T. Rodenbeck, M. Li, and K. Chang, A novel multibeam grating antenna with applications to low-cost millimeter-wave beam-steering, *Proc. IEEE MTT-S Int. Microwave Symp. Digest*, Seattle, June 2002, pp. 57–60.
58. F. Schwing and A. A. Oliner, Millimeter-wave antennas, in Y. T. Lo, ed., *Antenna Handbook*, Van Nostrand-Reinhold, New York, 1988, Chap. 17.
59. T. Hori and T. Itanami, Circularly polarized linear array antenna using a dielectric image line, *IEEE Trans. Microwave Theory Tech.* **29**(9):967–970 (Sept. 1981).
60. C. T. Rodenbeck, M. Li, and K. Chang, Circular-polarized reconfigurable grating antenna for low-cost millimeter-wave beam-steering, *IEEE Trans. Anten. Propag.* (in press).
61. T. Itoh and B. Adelseck, Trapped image-guide leaky-wave antennas for millimeter-wave applications, *IEEE Trans. Anten. Propag.* **30**(5):505–509 (May 1982).
62. P. Checcacci, V. Russo, and A. Scheggi, Holographic antennas, *IEEE Trans. Anten. Propag.* **18**(6):811–813 (Nov. 1970).
63. K. Levis, A. Ittipiboon, A. Petosa, L. Roy, and P. Berini, Ka-band dipole holographic antennas, *IEE Proc. Microwave Anten. Propag.* **148**(2):129–132 (April 2001).
64. A. E. Fathy, A. Rosen, H. S. Owen, F. McGinty, D. J. McGee, G. C. Taylor, R. Amantea, P. K. Swain, S. M. Perlow, and M. ElSherbiny, Silicon-based reconfigurable antennas—concepts, analysis, implementation, and feasibility, *IEEE Trans. Microwave Theory Tech.* **51**(6):1650–1661 (June 2003).
65. K. Maamria, T. Wagatsuma, and T. Yoneyama, Leaky NRD guide as a feeder for microwave planar antennas, *IEEE Trans. Anten. Propag.* **41**(12):1680–1686 (Dec. 1993).
66. R. J. Mailloux, F. K. Schwing, A. A. Oliner, and J. W. Mink, Antennas III: Array, millimeter wave, and integrated antennas, in K. Chang, ed., *Handbook of Microwave and Optical Components*, Vol. 1, Wiley, New York, 1989, Chap. 12, p. 726.
67. C. T. Rodenbeck, M. Li, and K. Chang, *System and Method for Millimeter-Wave Beam Steering Using a Grating Film Fed by Dielectric Integrated Guide*, U.S. Patent 60,292,369 (Provisional) (May 2001).
68. M. R. Seiler and B. M. Mathena, Millimeter-wave beam steering using “diffraction electronics,” *IEEE Trans. Anten. Propag.* **32**(9):987–990 (Sept. 1984).
69. L. Huang, J. C. Chiao, and M. P. De Lisio, An electronically switchable leaky wave antenna, *IEEE Trans. Anten. Propag.* **48**(11):1769–1772 (Nov. 2000).
70. A. Rosen, R. Amantea, P. J. Stabile, A. E. Fathy, D. B. Gilbert, D. W. Bechtel, W. M. Janton, F. J. McGinty, J. K. Butler, and G. A. Evans, Investigation of active antenna arrays at 60 GHz, *IEEE Trans. Microwave Theory Tech.* **43**(9):2117–2125 (Sept. 1995).
71. A. Alphones and M. Tsutsumi, Leaky wave radiation from a periodically photoexcited semiconductor slab waveguide, *IEEE Trans. Microwave Theory Tech.* **43**(9):2435–2441 (Sept. 1995).
72. A. Alphones and M. Tsutsumi, Leaky wave radiation of millimeter waves by photoinduced plasma grating in a semiconductor slab, *IEE Proc. Microwave Anten. Propag.* **146**(1):77–83 (Feb. 1999).
73. H. Maheri, M. Tsutsumi, and N. Kumagai, Experimental studies of magnetically scannable leaky-wave antennas having a corrugated ferrite slab/dielectric layer structure, *IEEE Trans. Anten. Propag.* **36**(7):911–917 (July 1988).

74. V. A. Manasson, L. S. Sadovnik, V. A. Yepishin, and D. Mark-er, An optically controlled mmw beam-steering antenna based on a novel architecture, *IEEE Trans. Microwave Theory Tech.* **45**(8):1497–1500 (Aug. 1997).
75. H. Rutstein, private communication, June 2002.
76. T. Itoh and F. J. Hsu, Distributed bragg reflector gunn oscillators for dielectric millimeter-wave integrated circuits, *IEEE Trans. Microwave Theory Tech.* **82**(5):724–728 (May 1982).
77. J. A. Navarro and K. Chang, *Integrated Active Antennas and Spatial Power Combining*, Wiley, New York, 1996.
78. K. B. Mallory, R. H. Miller, and P.A. Szente, A simple grating system millimeter and submillimeter wavelength separation, *IEEE Trans. Microwave Theory Tech.* **11**(5):433–434 (Sept. 1963).
79. J. Meltaus, J. Salo, E. Noponen, M. M. Salomaa, V. Viikari, A. Lonnqvist, T. Koskinen, J. Saily, J. Hakli, J. Ala-Laurinaho, J. Mallat, and A. V. Raisanen, Millimeter-wave beam shaping using holograms, *IEEE Trans. Microwave Theory Tech.* **51**(4):1274–1280 (April 2003).
80. B. Schumann, M. Hoft, M. Saglam, H. L. Hartnagel, and R. Judaschke, A 5 element 450 GHz HBV frequency tripler, *IEEE MTT-S Int. Microwave Symp. Digest*, Philadelphia, June 2003, pp. 759–762.
81. M. Hoft, J. Weinzierl, and R. Judaschke, Broadband analysis of a D-band holographic power combining circuit, *2001 IEEE MTT-S Int. Microwave Symp. Digest*, Phoenix, AZ, May 2003, pp. 1407–1410.
82. M. Shahabadi and K. Schunemann, Millimeter-wave holographic power splitting/combining, *IEEE Trans. Microwave Theory Tech.* **45**(12):2316–2323 (Dec. 1997).
83. V. A. Manasson, L. S. Sadovnik, A. Moussessian, and D. B. Rutledge, Millimeter-wave diffraction by a photo-induced plasma grating, *IEEE Trans. Microwave Theory Tech.* **43**(9):2288–2290 (Sept. 1995).
84. W. Platte, S. Ruppik, and M. Guetschow, Optically induced mask-controlled time-variable periodic microwave structures, *IEEE Trans. Microwave Theory Tech.* **48**(5):846–851 (May 2000).
85. G. F. Brand, Remote millimeter-wave beam control by the illumination of a semiconductor, *IEEE Trans. Microwave Theory Tech.* **48**(5):855–857 (May 2000).

GREEN'S FUNCTION METHODS

JIAN-MING JIN
 WENG CHO CHEW
 University of Illinois at Urbana-
 Champaign

The Green's function method is a powerful techniques for solving boundary value problems. Green's function was named after George Green (1793–1841), who developed a general method to obtain solutions of Poisson's equation in potential theory. This method was described in an essay by Green entitled "On the application of mathematical analysis to the theories of electricity and magnetism," published in 1828.

To illustrate the Green's function method, consider the electric potential produced by a point electric charge q_1

placed at \mathbf{r}_1 in an unbounded homogeneous free space. It is well known from the elementary theory of electricity [1] that this potential at \mathbf{r} is given by

$$\phi_1(\mathbf{r}) = \frac{q_1}{4\pi\epsilon|\mathbf{r} - \mathbf{r}_1|} \quad (1)$$

where $|\mathbf{r} - \mathbf{r}_1|$ denotes the distance between the points \mathbf{r} and \mathbf{r}_1 and ϵ is a constant called the *permittivity*. If there is another point charge q_2 placed at \mathbf{r}_2 , the potential produced by this charge is

$$\phi_2(\mathbf{r}) = \frac{q_2}{4\pi\epsilon|\mathbf{r} - \mathbf{r}_2|} \quad (2)$$

The total potential produced by q_1 and q_2 is then the linear superposition of ϕ_1 and ϕ_2 :

$$\phi(\mathbf{r}) = \phi_1(\mathbf{r}) + \phi_2(\mathbf{r}) = \frac{q_1}{4\pi\epsilon|\mathbf{r} - \mathbf{r}_1|} + \frac{q_2}{4\pi\epsilon|\mathbf{r} - \mathbf{r}_2|} \quad (3)$$

If there are N point charges in the space, the total potential is given by

$$\phi(\mathbf{r}) = \sum_{i=1}^N \phi_i(\mathbf{r}) = \sum_{i=1}^N \frac{q_i}{4\pi\epsilon|\mathbf{r} - \mathbf{r}_i|} \quad (4)$$

where Σ denotes the summation over all point charges and ϕ_i denotes the potential due to the i th point charge placed at \mathbf{r}_i . The procedure described above is known as the principle of linear superposition.

Next, consider the electric potential produced by a volume electric charge whose charge density is denoted by $\rho(\mathbf{r})$. To find the potential, we divide the volume of the charge into many small cubes. The charge within each small cube is then given by

$$q_i \approx \rho(\mathbf{r}_i)\Delta V_i \quad (5)$$

where \mathbf{r}_i denotes the center of the i th cube and ΔV_i denotes the volume of the cube. Since each cube is very small, it can be approximated as a point charge, whose potential is given by

$$\phi_i(\mathbf{r}) \approx \frac{q_i}{4\pi\epsilon|\mathbf{r} - \mathbf{r}_i|} \approx \frac{\rho(\mathbf{r}_i)\Delta V_i}{4\pi\epsilon|\mathbf{r} - \mathbf{r}_i|} \quad (6)$$

According to the principle to linear superposition, the total potential is then given by

$$\phi(\mathbf{r}) = \sum_{i=1}^N \phi_i(\mathbf{r}) \approx \sum_{i=1}^N \frac{\rho(\mathbf{r}_i)\Delta V_i}{4\pi\epsilon|\mathbf{r} - \mathbf{r}_i|} \quad (7)$$

Clearly, the approximation improves as the volume is divided into smaller cubes. In the limit when $\Delta V_i \rightarrow 0$, Eq. (7) becomes exact. Hence, one obtains

$$\phi(\mathbf{r}) = \lim_{\Delta V_i \rightarrow 0} \sum_{i=1}^{\infty} \frac{\rho(\mathbf{r}_i)\Delta V_i}{4\pi\epsilon|\mathbf{r} - \mathbf{r}_i|} \quad (8)$$

which can be written in the integral form as

$$\phi(\mathbf{r}) = \int_V \frac{\rho(\mathbf{r}') dV'}{4\pi\epsilon|\mathbf{r} - \mathbf{r}'|} \tag{9}$$

where V denotes the volume of the electric charge.

The potential produced by a point source of unit strength is called *Green's function*. In the example above, the Green's function is

$$G(\mathbf{r}, \mathbf{r}') = \frac{1}{4\pi\epsilon|\mathbf{r} - \mathbf{r}'|} \tag{10}$$

and the total potential can then be written as

$$\phi(\mathbf{r}) = \int_V \rho(\mathbf{r}') G(\mathbf{r}, \mathbf{r}') dV' \tag{11}$$

It is clear that the Green's function method treats an arbitrary source for the potential as a linear superposition of weighted point sources. It then finds the potential as the corresponding linear superposition of the potentials produced by the point sources.

Obviously, once the Green's function corresponding to the potential due to a point source is found, the potential produced by an arbitrary distribution of sources can be obtained easily. Therefore, for a specific boundary value problem, instead of finding the potential for each new source encountered by solving Poisson's equation repeatedly, one can find the Green's function for that problem only once and obtain solutions to any sources by the principle of linear superposition. The procedure of finding Green's function is usually much simpler than finding the solution to an arbitrary source. To a large extent, a Green's function plays the same role as an impulse response of a linear circuit system. The system response to any input function can be determined by convolving the input function with the impulse response of the system. The Green's function method has since been expanded to deal with a large number of different partial-differential equations.

In electrodynamics, both the source (electric current density) and the response (electric or magnetic field) are vectors, each of which has three components. Since each component of an electric current density can produce all three components of the electric or magnetic field, one has nine Green functions that relate the response to the source. This unwieldiness can be alleviated by introducing the concept of the dyadic Green function. A dyadic Green function, which can be expressed as a 3×3 matrix, can be considered as a compact representation of the nine scalar Green's functions. The first use of dyadic Green's function was made by Julian Schwinger. The subject was also covered by Morse and Feshbach [2] in their well-known treatise on the methods of theoretical physics. A more comprehensive treatment of the dyadic Green functions in electromagnetic theory was presented by Tai [3], who has done much original work on this topic. In his well-known book, Tai derived dyadic Green's functions for variety of electromagnetic problems of practical importance.

Discussions on dyadic Green's functions can be found in Collin [4], Kong [5], and Chew [6].

As shall be shown later, the Green's function method not only provides a solution to many boundary value problems involving canonical geometries but also leads to integral equations for problems involving more complex geometries. These integral equations form the basis for a numerical solution of complex boundary value problems.

1. SCALAR GREEN'S FUNCTIONS

When both the source and response are scalar functions, the corresponding Green's function is also scalar and, hence, the name scalar Green's function.

1.1. The Delta Function

Since the Green's function method is based on the representation of an arbitrary source by the superposition of point sources, the mathematical representation of a point source will first be described. Consider an electric charge of unit strength located at point \mathbf{r}' . When the volume of the charge approaches zero, the charge density can be described by a function

$$\delta(\mathbf{r} - \mathbf{r}') = \begin{cases} \infty & \text{for } \mathbf{r} = \mathbf{r}' \\ 0 & \text{for } \mathbf{r} \neq \mathbf{r}' \end{cases} \tag{12}$$

Since the total charge remains at unity

$$\int_V \delta(\mathbf{r} - \mathbf{r}') dV = \begin{cases} 1 & \text{for } \mathbf{r}' \text{ in } V \\ 0 & \text{for } \mathbf{r}' \text{ not in } V \end{cases} \tag{13}$$

The function defined in Eqs. (12) and (13) is known as the *Dirac delta function*, named after P. A. M. Dirac. Clearly, given an arbitrary function $f(\mathbf{r})$, which is continuous at $\mathbf{r} = \mathbf{r}'$, we obtain

$$\int_V f(\mathbf{r}) \delta(\mathbf{r} - \mathbf{r}') dV = \begin{cases} f(\mathbf{r}') & \text{for } \mathbf{r}' \text{ in } V \\ 0 & \text{for } \mathbf{r}' \text{ not in } V \end{cases} \tag{14}$$

This expression represents a volume source $f(\mathbf{r}')$ as a linear superposition of an infinite number of point sources $\delta(\mathbf{r} - \mathbf{r}')$.

In one dimension, the delta function can be considered as the limit of a function

$$\delta(x - x') = \lim_{\epsilon \rightarrow 0} u_\epsilon(x - x') \tag{15}$$

where $u_\epsilon(x - x')$ is called a *delta family*. It can be a rectangular function of width ϵ and height $1/\epsilon$, or a triangular function of width 2ϵ and height $1/\epsilon$, or a Gaussian function $e^{-(x-x')^2/2\epsilon^2}/\epsilon\sqrt{2\pi}$, all centered at $x = x'$. The important feature of the delta function is not its shape, but the fact that its effective width approaches zero, while its area remains

at unity, that is

$$\int_a^b \delta(x - x') dx = \begin{cases} 1 & \text{for } x' \text{ in } (a, b) \\ 0 & \text{for } x' \text{ not in } (a, b) \end{cases} \quad (16)$$

such that

$$\int_a^b f(x) \delta(x - x') dx = \begin{cases} f(x') & \text{for } x' \text{ in } (a, b) \\ 0 & \text{for } x' \text{ not in } (a, b) \end{cases} \quad (17)$$

The delta function so defined is not a function in the classical sense. For this reason, it is called a symbolic or generalized function [7].

Clearly, the delta function is a symmetric function

$$\delta(x - x') = \delta(x' - x) \quad (18)$$

The three-dimensional delta function in the rectangular, cylindrical, and spherical coordinate systems is related to the one-dimensional delta function by

$$\delta(\mathbf{r} - \mathbf{r}') = \delta(x - x') \delta(y - y') \delta(z - z') \quad (19)$$

$$\delta(\mathbf{r} - \mathbf{r}') = \frac{\delta(\rho - \rho') \delta(\phi - \phi') \delta(z - z')}{\rho} \quad (20)$$

$$\delta(\mathbf{r} - \mathbf{r}') = \frac{\delta(r - r') \delta(\theta - \theta') \delta(\phi - \phi')}{r^2 \sin \theta} \quad (21)$$

All of these above satisfy Eq. (13).

1.2. One-Dimensional Green's Function

To introduce the concept of Green's function in one dimension, consider an infinitely long transmission line with a distributed current source $K(x)$ (3), as illustrated in Fig. 1. Using Kirchhoff's voltage and current laws, one finds the relations between the voltage and current as

$$\frac{dV(x)}{dx} + (j\omega L + R)I(x) = 0 \quad (22)$$

$$\frac{dI(x)}{dx} + (j\omega C + G)V(x) = K(x) \quad (23)$$

where ω denotes the angular frequency and L , C , R , and G are the inductance, capacitance, resistance, and conduc-

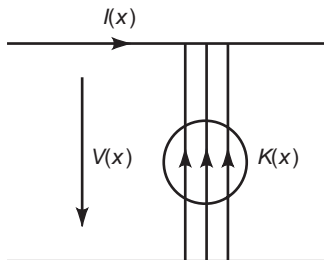


Figure 1. An infinitely long transmission line excited by a distributed current source.

tance of the transmission line per unit length. Eliminating $I(x)$ in Eqs. (22) and (23), one obtains the differential equation for the voltage as

$$\frac{d^2V(x)}{dx^2} - \gamma^2V(x) = -(j\omega L + R)K(x) \quad (24)$$

where $\gamma^2 = (j\omega L + R)(j\omega C + G)$. Since the line is infinitely long, there is no reflected wave; hence, $V(x)$ satisfies the boundary conditions

$$\frac{dV(x)}{dx} + \gamma V(x) = 0 \quad \text{for } x \rightarrow \infty \quad (25)$$

$$\frac{dV(x)}{dx} - \gamma V(x) = 0 \quad \text{for } x \rightarrow -\infty \quad (26)$$

Since these boundary conditions are imposed when $|x| \rightarrow \infty$, they are also called *radiation conditions*.

Instead of solving for $V(x)$ directly from Eqs. (24)–(26), one can consider the solution of the following differential equation

$$\frac{d^2g_0(x, x')}{dx^2} - \gamma^2g_0(x, x') = -\delta(x - x') \quad (27)$$

where $g_0(x)$ satisfies the same radiation condition as $V(x)$. Since $g_0(x, x')$ is a point source response and $V(x)$ in Eq. (24) is due to the source $(j\omega L + R)K(x)$, according to the principle of linear superposition, $V(x)$ can be expressed as a convolution of $g_0(x, x')$ with $(j\omega L + R)K(x)$:

$$V(x) = \int_{-\infty}^{\infty} (j\omega L + R)K(x')g_0(x, x') dx' \quad (28)$$

It is evident that once we obtain $g_0(x, x')$, the voltage on the transmission line can be evaluated via a simple integration using Eq. (28).

To find $g_0(x, x')$, note that since

$$\frac{d^2g_0(x, x')}{dx^2} - \gamma^2g_0(x, x') = 0 \quad \text{for } x > x' \text{ or } x < x' \quad (29)$$

one has

$$g_0(x, x') = Ae^{-\gamma x} \quad \text{for } x > x' \quad (30)$$

$$g_0(x, x') = Be^{\gamma x} \quad \text{for } x < x' \quad (31)$$

where the radiation conditions in Eqs. (25) and (26) were used to determine the sign in front of γ . To determine the unknown coefficients A and B , consider Eq. (27). First, note that $g_0(x, x')$ must be continuous at $x = x'$, that is

$$g_0(x, x')|_{x=x'+0} = g_0(x, x')|_{x=x'-0} \quad (32)$$

where $x = x' + 0$ stands for the right-hand side of x' and $x = x' - 0$ stands for the left-hand side of x' since a discontinuity in $g_0(x, x')$ at $x = x'$ would result in a derivative on $\delta(x - x')$ on the left-hand side of Eq. (27). Next, integrate Eq. (27) over the region from $x' - \varepsilon$ to $x' + \varepsilon$ and in the limit

when $\varepsilon \rightarrow 0$

$$\left. \frac{dg_0(x, x')}{dx} \right|_{x=x'+0} - \left. \frac{dg_0(x, x')}{dx} \right|_{x=x'-0} = -1 \tag{33}$$

Applying these two conditions to Eqs. (30) and (31), one finds

$$g_0(x, x') = \frac{1}{2\gamma} e^{-\gamma(x-x')} \text{ for } x > x' \tag{34}$$

$$g_0(x, x') = \frac{1}{2\gamma} e^{\gamma(x-x')} \text{ for } x < x' \tag{35}$$

or, more compactly

$$g_0(x, x') = \frac{1}{2\gamma} e^{-\gamma|x-x'|} \tag{36}$$

This is the Green function for the infinitely long transmission line.

1.3. Two- and Three-Dimensional Green's Function

Consider the electric and magnetic fields produced by a time-harmonic electric source whose current density is denoted by $\mathbf{J}(\mathbf{r})$ and charge density is denoted by $\rho(\mathbf{r})$. These fields satisfy Maxwell's equations given by (1)

$$\nabla \times \mathbf{E}(\mathbf{r}) = -j\omega\mathbf{B}(\mathbf{r}) \tag{37}$$

$$\nabla \times \mathbf{H}(\mathbf{r}) = j\omega\mathbf{D}(\mathbf{r}) + \mathbf{J}(\mathbf{r}) \tag{38}$$

$$\nabla \cdot \mathbf{D}(\mathbf{r}) = \rho(\mathbf{r}) \tag{39}$$

$$\nabla \cdot \mathbf{B}(\mathbf{r}) = 0 \tag{40}$$

and the constitutive relations given by $\mathbf{B} = \mu\mathbf{H}$ and $\mathbf{D} = \varepsilon\mathbf{E}$, where μ is the magnetic permeability and ε is the electric permittivity. Again, assume that the space is homogeneous. Taking the curl of Eq. (37), one has

$$\nabla \times \nabla \times \mathbf{E}(\mathbf{r}) = -j\omega\mu\nabla \times \mathbf{H}(\mathbf{r}) \tag{41}$$

Using Eq. (38) in Eq. (41), one obtains

$$\nabla \times \nabla \times \mathbf{E}(\mathbf{r}) - k^2\mathbf{E}(\mathbf{r}) = -j\omega\mu\mathbf{J}(\mathbf{r}) \tag{42}$$

where $k^2 = \omega^2\mu\varepsilon$. Since $\nabla \times \nabla \times \mathbf{E} = \nabla(\nabla \cdot \mathbf{E}) - \nabla^2\mathbf{E}$, Eq. (42) can be written as

$$\nabla^2\mathbf{E}(\mathbf{r}) + k^2\mathbf{E}(\mathbf{r}) = j\omega\mu\mathbf{J}(\mathbf{r}) + \frac{1}{\varepsilon}\nabla\rho(\mathbf{r}) \tag{43}$$

where Eq. (39) has been applied. Similarly, one obtains the equation for \mathbf{H} as

$$\nabla^2\mathbf{H}(\mathbf{r}) + k^2\mathbf{H}(\mathbf{r}) = -\nabla \times \mathbf{J}(\mathbf{r}) \tag{44}$$

Equations (43) and (44) are inhomogeneous Helmholtz wave equations.

If one uses ϕ to represent each component of \mathbf{E} or \mathbf{H} in a Cartesian coordinate system, then ϕ satisfies the inhomogeneous Helmholtz equation

$$\nabla^2\phi(\mathbf{r}) + k^2\phi(\mathbf{r}) = -f(\mathbf{r}) \tag{45}$$

where $\phi(\mathbf{r})$ propagates in an infinite unbounded space, there is no reflected wave. Hence, $\phi(\mathbf{r})$ satisfies the radiation condition

$$r\left(\frac{\partial\phi}{\partial r} + jk\phi\right) = 0 \text{ for } r \rightarrow \infty \tag{46}$$

where r represents the radial variable in spherical coordinates. Instead of solving for $\phi(\mathbf{r})$ directly from Eqs. (45) and (46) for each $f(\mathbf{r})$, one first finds its Green function, which is the solution of the following partial-differential equation

$$\nabla^2G_0(\mathbf{r}, \mathbf{r}') + k^2G_0(\mathbf{r}, \mathbf{r}') = -\delta(\mathbf{r} - \mathbf{r}') \tag{47}$$

subject to the radiation condition in Eq. (46). If G_0 can be found, using the principle of linear superposition, one obtains

$$\phi(\mathbf{r}) = \int_V G_0(\mathbf{r}, \mathbf{r}')f(\mathbf{r}')dV' \tag{48}$$

where V is the support of $f(\mathbf{r})$, which is the volume having nonzero $f(\mathbf{r})$.

To find G_0 , we introduce a new coordinate system with its origin located at \mathbf{r}' . Thus, the problem has a spherical symmetry with respect to this point. Equation (47) then becomes

$$\frac{1}{r_1^2} \frac{d}{dr_1} \left[r_1^2 \frac{dG_0(\mathbf{r}_1, 0)}{dr_1} \right] + k^2G_0(\mathbf{r}_1, 0) = -\delta(\mathbf{r}_1) \tag{49}$$

where $\mathbf{r}_1 = \mathbf{r} - \mathbf{r}'$. When $r_1 \neq 0$, Eq. (49) can be written as

$$\frac{d^2[r_1G_0(\mathbf{r}_1, 0)]}{dr_1^2} + k^2r_1G_0(\mathbf{r}_1, 0) = 0 \tag{50}$$

which has a well-known solution

$$r_1G_0(\mathbf{r}_1, 0) = Ae^{-jkr_1} \text{ or } G_0(\mathbf{r}_1, 0) = A \frac{e^{-jkr_1}}{r_1} \tag{51}$$

The sign in the exponent is chosen such that Eq. (51) satisfies the radiation condition in Eq. (46). To determine the unknown coefficient A , substitute Eq. (51) into Eq. (49) and integrate over a small sphere centered at $\mathbf{r}_1 = 0$ with its radius $\varepsilon \rightarrow 0$. The result is $A = (4\pi)^{-1}$. Therefore

$$G_0(\mathbf{r}_1, 0) = \frac{e^{-jkr_1}}{4\pi r_1} \tag{52}$$

and in the original coordinates, it becomes

$$G_0(\mathbf{r}, \mathbf{r}') = \frac{e^{-jk|\mathbf{r}-\mathbf{r}'|}}{4\pi|\mathbf{r}-\mathbf{r}'|} \quad (53)$$

Following the same procedure, one can obtain the two-dimensional Green function for the Helmholtz equation as

$$G_0(\rho, \rho') = \frac{1}{4j} H_0^{(2)}(k|\rho - \rho'|) \quad (54)$$

where $\rho = x\hat{x} + y\hat{y}$ and $H_0^{(2)}(k|\rho - \rho'|)$ is the zeroth-order Hankel function of the second kind.

When one deals with the static electric field, Maxwell's equations for $\mathbf{E}(\mathbf{r})$ reduce to

$$\nabla \times \mathbf{E}(\mathbf{r}) = 0 \quad \text{and} \quad \nabla \cdot \mathbf{E}(\mathbf{r}) = \frac{\rho(\mathbf{r})}{\varepsilon} \quad (55)$$

These two equations can be solved conveniently by introducing the electric potential $\phi(\mathbf{r})$, which is defined as

$$\mathbf{E}(\mathbf{r}) = -\nabla\phi(\mathbf{r}) \quad (56)$$

The first equation in Eq. (55) is automatically satisfied because of the identity $\nabla \times \nabla\phi(\mathbf{r}) \equiv 0$. Substituting Eq. (56) into the second equation in Eq. (55), one obtains

$$\nabla^2\phi(\mathbf{r}) = -\frac{\rho(\mathbf{r})}{\varepsilon} \quad (57)$$

This equation is Poisson's equation, which can be considered as a special case of Eq. (45) with $k=0$.

Using the procedure described in this section, one obtains the three-dimensional Green function for Poisson's equation as

$$G_0(\mathbf{r}, \mathbf{r}') = \frac{1}{4\pi|\mathbf{r}-\mathbf{r}'|} \quad (58)$$

and the two-dimensional Green function as

$$G_0(\rho, \rho') = -\frac{1}{2\pi} \ln|\rho - \rho'| \quad (59)$$

1.4. Classification of Green's Functions

The Green functions derived above are for the infinite unbounded space where no other objects are present. They are called the *free-space Green's functions* and are denoted by the subscript 0. When the region of interest is bounded, one then has to consider boundary conditions for Green's function. Different boundary conditions lead to different Green's functions. For this reason, Green's functions are classified into three categories: Green's functions of the first, second, and third kind [3].

Green's function of the first kind, denoted by G_1 , satisfies the Dirichlet boundary condition, that is

$$G_0(\mathbf{r}, \mathbf{r}') = 0 \quad \text{for } \mathbf{r} \text{ on } S \quad (60)$$

where S denotes the boundary of the problem. For a half-space with an infinite ground plane coincident with the $z=0$ plane, the Green's function of the first kind for Poisson's equation is given by

$$G_0(\mathbf{r}, \mathbf{r}') = G_0(\mathbf{r}, \mathbf{r}') + G_0(\mathbf{r}, \mathbf{r}'_i) = \frac{1}{4\pi|\mathbf{r}-\mathbf{r}'|} - \frac{1}{4\pi|\mathbf{r}-\mathbf{r}'_i|} \quad (61)$$

where $\mathbf{r}'_i = \mathbf{r}' - 2z'\hat{z} = x'\hat{x} + y'\hat{y} - z'\hat{z}$. This result can be derived conveniently using the method of images. It is easy to see that the Dirichlet boundary condition is satisfied by $G_1(\mathbf{r}, \mathbf{r}')$ in the $z=0$ plane.

The Green's function of the second kind, denoted by G_2 , satisfies the Neumann boundary condition, that is

$$\frac{\partial G_2(\mathbf{r}, \mathbf{r}')}{\partial n} = 0 \quad \text{for } \mathbf{r} \text{ on } S \quad (62)$$

where S denotes the boundary of the problem and $\partial/\partial n$ denotes the normal derivative. For a half space with an infinite magnetic (symmetry) plane coincident with the $z=0$ plane, the Green's function of the second kind for Poisson's equation is given by

$$G_2(\mathbf{r}, \mathbf{r}') = G_0(\mathbf{r}, \mathbf{r}') + G_0(\mathbf{r}, \mathbf{r}'_i) = \frac{1}{4\pi|\mathbf{r}-\mathbf{r}'|} + \frac{1}{4\pi|\mathbf{r}-\mathbf{r}'_i|} \quad (63)$$

where \mathbf{r}'_i is the same as the one in Eq. (61). It satisfies the Neumann boundary condition in the $z=0$ plane.

The Green's function of the third kind is defined for problems involving two or more media. It can be denoted as $G^{(ij)}(\mathbf{r}, \mathbf{r}')$, where i indicates the medium where the field point \mathbf{r} is located and j indicates the medium where the source point \mathbf{r}' is located. Consider, for example, a potential problem involving two half-spaces. The upper half-space (medium 1) above $z=0$ has a permittivity of ε_1 , and the lower half-space (medium 2) has a permittivity of ε_2 . The Green's function for Poisson's equation is given by (8)

$$G^{(11)}(\mathbf{r}, \mathbf{r}') = G_0(\mathbf{r}, \mathbf{r}') - \frac{\varepsilon_2 - \varepsilon_1}{\varepsilon_2 + \varepsilon_1} G_0(\mathbf{r}, \mathbf{r}'_i) = \frac{1}{4\pi|\mathbf{r}-\mathbf{r}'|} - \frac{\varepsilon_2 - \varepsilon_1}{\varepsilon_2 + \varepsilon_1} \frac{1}{4\pi|\mathbf{r}-\mathbf{r}'_i|} \quad (64)$$

and

$$G^{(21)}(\mathbf{r}, \mathbf{r}') = \frac{2\varepsilon_2}{\varepsilon_2 + \varepsilon_1} G_0(\mathbf{r}, \mathbf{r}') = \frac{2\varepsilon_2}{\varepsilon_2 + \varepsilon_1} \frac{1}{4\pi|\mathbf{r}-\mathbf{r}'|} \quad (65)$$

Exchanging ε_1 and ε_2 in $G^{(11)}$ and $G^{(21)}$, one obtains the expressions for $G^{(22)}$ and $G^{(12)}$, respectively. This method

of obtaining the Green's functions of the third kind works only for Poisson's equation, but not for the Helmholtz equation because the standard image method is not applicable to the Helmholtz equation in this case.

1.5. Eigenfunction Expansion

In addition to the conventional method described earlier, another general method for deriving Green's functions is the method of Ohm-Rayleigh or the method of eigenfunction expansion [3]. In this section, one rederives the Green functions in Eq. (36) and Eq. (53) to illustrate the process of the Ohm-Rayleigh method.

Consider first the solution of Eq. (27). Expand $g_0(x, x')$ in terms of a Fourier integral

$$g_0(x, x') = \int_{-\infty}^{\infty} A(h)e^{ihx}dh \tag{66}$$

The e^{ihx} , which is the solution of the homogeneous differential equation $d^2\psi(x)/dx^2 + h^2\psi(x) = 0$, is called the *eigenfunction* and h^2 is the corresponding *eigenvalue*. Therefore, Eq. (66) can be considered as the eigenfunction expansion of $g_0(x, x')$. To determine $A(h)$, substitute Eqs. (66) into Eq. (27) and note that

$$\delta(x - x') = \frac{1}{2\pi} \int_{-\infty}^{\infty} e^{jh(x-x')}dh \tag{67}$$

This yields

$$A(h) = \frac{e^{-jh x'}}{2\pi(h^2 + \gamma^2)} \tag{68}$$

Hence, we obtain

$$g_0(x, x') = \frac{1}{2\pi} \int_{-\infty}^{\infty} \frac{e^{jh(x-x')}}{h^2 + \gamma^2} dh \tag{69}$$

This is known as the *spectral representation* of $g_0(x, x')$. The integral in this equation can be evaluated using Cauchy's residue theorem [9]. For this, one needs to form a closed contour for the integral in Eq. (69). In order to satisfy the boundary conditions in Eqs. (25) and (26), for $x - x' > 0$ the infinite integration path must be closed in the upper half-plane and for $x - x' < 0$ the infinite path must be closed in the lower half-plane, as shown in Fig. 2. The application of Cauchy's residue theorem yields

$$g_0(x, x') = \frac{1}{2\gamma} \begin{cases} e^{-\gamma(x-x')} & \text{for } x > x' \\ e^{\gamma(x-x')} & \text{for } x < x' \end{cases} \tag{70}$$

which is the same as Eqs. (34) and (35).

Next, consider the solution of Eq. (47). First expand $G_0(\mathbf{r}, \mathbf{r}')$ in terms of Fourier integrals

$$G_0(\mathbf{r}, \mathbf{r}') = \int_{-\infty}^{\infty} A(\mathbf{h})e^{i\mathbf{h}\cdot\mathbf{r}}d\mathbf{h} \tag{71}$$

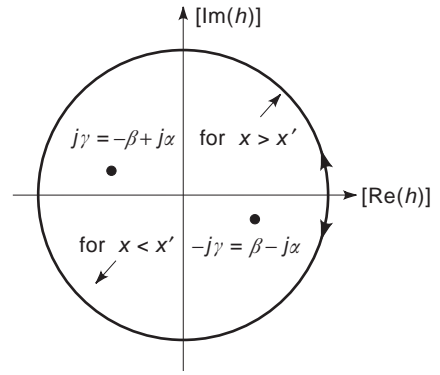


Figure 2. Locations of the two poles in the complex plane and the closed contours for integration.

where $\mathbf{h} = h_x\hat{x} + h_y\hat{y} + h_z\hat{z}$. The $e^{i\mathbf{h}\cdot\mathbf{r}}$, which is the solution of the homogeneous partial differential equation $\nabla^2\psi(\mathbf{r}) + h^2\psi(\mathbf{r}) = 0$, is called the *eigenfunction* and $h^2 = |\mathbf{h}|^2$ is the corresponding *eigenvalue*. Again, Eq. (71) can be considered as the eigenfunction expansion of $G_0(\mathbf{r}, \mathbf{r}')$. Substituting Eq. (71) into Eq. (47), and noting that

$$\delta(\mathbf{r} - \mathbf{r}') = \frac{1}{(2\pi)^3} \int_{-\infty}^{\infty} e^{i\mathbf{h}\cdot(\mathbf{r}-\mathbf{r}')}d\mathbf{h} \tag{72}$$

one finds

$$A(\mathbf{h}) = \frac{e^{-j\mathbf{h}\cdot\mathbf{r}'}}{(2\pi)^3(h^2 - k^2)} \tag{73}$$

Therefore

$$G_0(\mathbf{r}, \mathbf{r}') = \frac{1}{(2\pi)^3} \int_{-\infty}^{\infty} \frac{e^{i\mathbf{h}\cdot(\mathbf{r}-\mathbf{r}')}}{h^2 - k^2}d\mathbf{h} \tag{74}$$

This is the spectral representation of the three-dimensional Green function. To evaluate the spectral integral, let

$$h_x = h \sin \theta \cos \varphi, \quad h_y = h \sin \theta \sin \varphi, \quad h_z = h \cos \theta \tag{75}$$

so that

$$d\mathbf{h} = h^2 \sin \theta dh d\theta d\varphi \tag{76}$$

Furthermore, because of the spherical symmetry of G_0 with respect to the point \mathbf{r}' , the value of G_0 is independent of the direction of $\mathbf{r} - \mathbf{r}'$. Therefore, one can choose an arbitrary $\mathbf{r} - \mathbf{r}'$ for the evaluation of G_0 . If one chooses the direction of $\mathbf{r} - \mathbf{r}'$ to coincide with the z direction, Eq. (74)

may be written as

$$\begin{aligned}
 G_0(\mathbf{r}, \mathbf{r}') &= \frac{1}{(2\pi)^3} \int_0^\infty \int_0^\pi \int_0^{2\pi} \frac{e^{jh \cos \theta |\mathbf{r}-\mathbf{r}'|}}{h^2 - k^2} h^2 \sin \theta \, dh \, d\theta \, d\varphi \\
 &= \frac{j}{(2\pi)^2 |\mathbf{r}-\mathbf{r}'|} \int_0^\infty [e^{-jh|\mathbf{r}-\mathbf{r}'|} - e^{jh|\mathbf{r}-\mathbf{r}'|}] \frac{h \, dh}{h^2 - k^2} \\
 &= \frac{j}{(2\pi)^2 |\mathbf{r}-\mathbf{r}'|} \int_0^\infty \frac{h e^{-jh|\mathbf{r}-\mathbf{r}'|}}{h^2 - k^2} \, dh \quad (77)
 \end{aligned}$$

This integral can now be evaluated using Cauchy's residue theorem. The integral has two poles: one at $h = k$ and the other at $h = -k$. Although the problem considered here is lossless, treat it as a limiting case of lossy problem for which k has a small negative imaginary part. Consequently, the pole at $h = k$ is on the lower side of the real axis and the pole at $h = -k$ is on the upper side of the real axis. In order to satisfy the radiation condition in Eq. (46), the infinite integration path must be closed in the lower half-plane, as shown in Fig. 3. Applying Cauchy's residue theorem, one obtains

$$G_0(\mathbf{r}, \mathbf{r}') = \frac{e^{-jk|\mathbf{r}-\mathbf{r}'|}}{4\pi |\mathbf{r}-\mathbf{r}'|} \quad (78)$$

which is the same as Eq. (53).

Finally, note that, although the process of the Ohm-Rayleigh method is more involved than the conventional method, it is more general and can be used to find Green's functions in many problems.

1.6. Green's Functions in a Bounded Region

As can be seen in the preceding section, the spectrum (eigenvalue) for infinite-space problems is continuous and, as a result, the spectral representation of the Green function involves spectral integrals. When the region of interest is finite, the spectrum will be discrete. To demonstrate this fact, consider a grounded rectangular cavity of dimension $a \times b \times d$, depicted in Fig. 4. The Green's function for Poisson's equation satisfies the partial differential

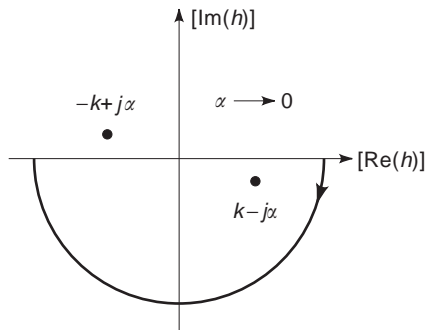


Figure 3. Locations of the two poles in the complex plane and the closed contour for integration.

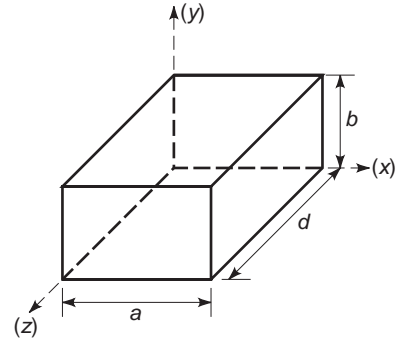


Figure 4. A grounded rectangular cavity.

equation

$$\nabla^2 G_1(\mathbf{r}, \mathbf{r}') = -\delta(\mathbf{r} - \mathbf{r}') \quad (79)$$

and the Dirichlet boundary condition

$$G_1(\mathbf{r}, \mathbf{r}') = 0 \quad \text{for } \mathbf{r} \text{ on cavity walls} \quad (80)$$

This Green's function can be derived in a number of different ways, such as the conventional method, the method of images, and the Ohm-Rayleigh method. Here, the Ohm-Rayleigh method is employed. First, consider the solution of

$$\nabla^2 \psi + h^2 \psi = 0 \quad (81)$$

subject to the condition in Eq. (80). Using the method of separation of variables, one finds

$$\psi_{mnp} = \sin \frac{m\pi x}{a} \sin \frac{n\pi y}{b} \sin \frac{p\pi z}{d} \quad (82)$$

which is the eigenfunction of Eq. (81) with eigenvalue $h^2 = (m\pi/a)^2 + (n\pi/b)^2 + (p\pi/d)^2$. This can be used to expand G_1 :

$$G_1(\mathbf{r}, \mathbf{r}') = \sum_{m=1}^{\infty} \sum_{n=1}^{\infty} \sum_{p=1}^{\infty} A_{mnp} \sin \frac{m\pi x}{a} \sin \frac{n\pi y}{b} \sin \frac{p\pi z}{d} \quad (83)$$

Substituting this expression into Eq. (79), one has

$$\begin{aligned}
 \sum_{m=1}^{\infty} \sum_{n=1}^{\infty} \sum_{p=1}^{\infty} A_{mnp} h^2 \sin \frac{m\pi x}{a} \sin \frac{n\pi y}{b} \sin \frac{p\pi z}{d} \\
 = \delta(x - x') \delta(y - y') \delta(z - z') \quad (84)
 \end{aligned}$$

The coefficient A_{mnp} can be determined by multiplying both sides by $\sin(m'\pi x/a)$, $\sin(n'\pi y/b)$, and $\sin(p'\pi z/d)$ and

integrating over x, y and z . The result is

$$G_1(\mathbf{r}, \mathbf{r}') = \sum_{m=1}^{\infty} \sum_{n=1}^{\infty} \sum_{p=1}^{\infty} \frac{8}{abd h^2} \sin \frac{m\pi x}{a} \sin \frac{m\pi x'}{a} \sin \frac{n\pi y}{b} \sin \frac{n\pi y'}{b} \sin \frac{p\pi z}{d} \sin \frac{p\pi z'}{d} \tag{85}$$

The triple summation can be reduced to a double summation using the formula [4]

$$\sum_{p=1}^{\infty} \frac{1}{h^2} \sin \frac{p\pi z}{d} \sin \frac{p\pi z'}{d} = \frac{d}{2k_c \sinh k_c d} \sinh k_c z_{<} \sinh k_c (d - z_{>}) \tag{86}$$

where $k_c = \sqrt{(m\pi/a)^2 + (n\pi/b)^2}$, $z_{<} = z$ when $z < z'$, and $z_{<} = z'$ when $z' < z$, and $z_{>} = z$ when $z > z'$, and $z_{>} = z'$ when $z' > z$. As a result, Eq. (85) becomes

$$G_1(\mathbf{r}, \mathbf{r}') = \sum_{m=1}^{\infty} \sum_{n=1}^{\infty} \frac{4}{ab} \sin \frac{m\pi x}{a} \sin \frac{m\pi x'}{a} \sin \frac{n\pi y}{b} \sin \frac{\sinh k_c z_{<} \sinh k_c (d - z_{>})}{k_c \sinh k_c d} \tag{87}$$

Next, consider the problem of a parallel-plate waveguide, which is finite in the y direction and infinite in the x and z directions, as shown in Fig. 5. Assuming that the source is uniform in the z direction, Green's function of the first kind for the Helmholtz equation satisfies the partial-differential equation

$$\nabla^2 G_1(\rho, \rho') + k^2 G_1(\rho, \rho') = -\delta(\rho - \rho') \tag{88}$$

and the boundary conditions

$$G_1(\rho, \rho') = 0 \text{ for } y = 0, b \tag{89}$$

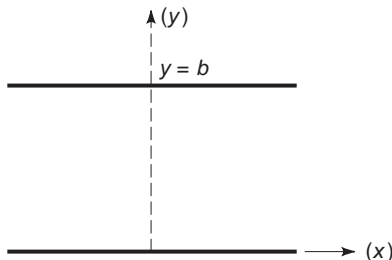


Figure 5. A parallel-plate waveguide.

and the radiation conditions

$$\frac{\partial G_1(\rho, \rho')}{\partial x} + jk G_1(\rho, \rho') = 0 \text{ for } x \rightarrow \infty \tag{90}$$

$$\frac{\partial G_1(\rho, \rho')}{\partial x} - jk G_1(\rho, \rho') = 0 \text{ for } x \rightarrow -\infty \tag{91}$$

The eigenfunction for this problem is found as

$$\psi_n(h_x) = e^{jh_x x} \sin \frac{n\pi y}{b} \tag{92}$$

from which G_1 can be expanded as

$$G_1(\rho, \rho') = \int_{-\infty}^{\infty} \sum_{n=1}^{\infty} A_n(h_x) e^{jh_x x} \sin \frac{n\pi y}{b} dh_x \tag{93}$$

Substituting this expression into Eq. (88), one obtains

$$\int_{-\infty}^{\infty} \sum_{n=1}^{\infty} A_n(h_x) \left[k^2 - h_x^2 - \left(\frac{n\pi}{b} \right)^2 \right] e^{jh_x x} \sin \frac{n\pi y}{b} dh_x = -\delta(x - x') \delta(y - y') \tag{94}$$

The coefficient $A_n(h_x)$ can be determined by multiplying both sides by $e^{jh_x x} \sin(n\pi y/b)$ and integrating over x and y . The result is

$$G_1(\rho, \rho') = \frac{1}{\pi b} \int_{-\infty}^{\infty} \sum_{n=1}^{\infty} \left[h_x^2 + \left(\frac{n\pi}{b} \right)^2 - k^2 \right]^{-1} e^{jh_x(x-x')} \sin \frac{n\pi y}{b} \sin \frac{n\pi y'}{b} dh_x \tag{95}$$

Using Cauchy's residue theorem, one can evaluate the spectral integral in a similar manner to that for the transmission line case, yielding

$$G_1(\rho, \rho') = \frac{1}{b} \sum_{n=1}^{\infty} \frac{1}{\gamma_x} e^{-\gamma_x |x-x'|} \sin \frac{n\pi y}{b} \sin \frac{n\pi y'}{b} \tag{96}$$

where $\gamma_x = \sqrt{(n\pi/b)^2 - k^2}$.

1.7. Scalar Integral Equations

Originally, Green's function methods were developed for finding the general solution of a boundary value problem whose Green function can be derived. For many practical problems, the Green function cannot be derived. As a result, one must resort to a numerical method for the solution of the problem. One such numerical method is based on an integral equation derived using the Green's function method.

To demonstrate the formulation of integral equations, consider the problem of a scalar wave produced by a source $f(\mathbf{r})$ in the presence of an arbitrarily shaped object immersed in an infinite medium, as illustrated in Fig. 6. Exterior to the object, the wavefunction $\phi(\mathbf{r})$ satisfies the inhomogeneous Helmholtz equation in Eq. (45) and the

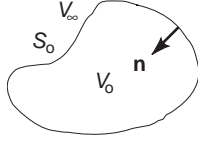


Figure 6. An object occupying volume V_0 .

radiation boundary condition in Eq. (46). Since the object has an arbitrary shape, no closed-form Green function can be found for this problem. However, one can establish an integral equation for this problem using the free-space Green function given in Eq. (53), which is the solution of Eq. (47) under the condition in Eq. (46).

First, multiply Eq. (45) with G_0 , Eq. (47) with ϕ , and integrate the difference of the resultant equations over the entire exterior volume, yielding

$$\begin{aligned} & \int_{V_\infty} [G_0(\mathbf{r}, \mathbf{r}') \nabla^2 \phi(\mathbf{r}) - \phi(\mathbf{r}) \nabla^2 G_0(\mathbf{r}, \mathbf{r}')] dV \\ &= - \int_{V_s} G_0(\mathbf{r}, \mathbf{r}') f(\mathbf{r}) dV + \int_{V_\infty} \phi(\mathbf{r}) \delta(\mathbf{r} - \mathbf{r}') dV \end{aligned} \quad (97)$$

where V_∞ denotes the infinite space exterior to the object and V_s denotes the support of $f(\mathbf{r})$. Applying the second scalar Green's theorem (1)

$$\int_V (a \nabla^2 b - b \nabla^2 a) dV = \int_S \left(a \frac{\partial b}{\partial n} - b \frac{\partial a}{\partial n} \right) dS \quad (98)$$

where S denotes the surface enclosing V , one obtains

$$\begin{aligned} & \int_{S_0 + S_\infty} \left[G_0(\mathbf{r}, \mathbf{r}') \frac{\partial \phi(\mathbf{r})}{\partial n} - \phi(\mathbf{r}) \frac{\partial G_0(\mathbf{r}, \mathbf{r}')}{\partial n} \right] dS \\ & - \int_{V_\infty} \phi(\mathbf{r}) \delta(\mathbf{r} - \mathbf{r}') dV \\ &= - \int_{V_s} G_0(\mathbf{r}, \mathbf{r}') f(\mathbf{r}) dV \end{aligned} \quad (99)$$

where S_0 denotes the surface of the object and S_∞ denotes a spherical surface with a radius approaching infinity. Since both G_0 and ϕ satisfy Eq. (46), the surface integral over S_∞ vanishes. Consequently, one has

$$\begin{aligned} & \int_{S_0} \left[G_0(\mathbf{r}, \mathbf{r}') \frac{\partial \phi(\mathbf{r})}{\partial n} - \phi(\mathbf{r}) \frac{\partial G_0(\mathbf{r}, \mathbf{r}')}{\partial n} \right] dS \\ & - \int_{V_\infty} \phi(\mathbf{r}) \delta(\mathbf{r} - \mathbf{r}') dV = - \int_{V_s} G_0(\mathbf{r}, \mathbf{r}') f(\mathbf{r}) dV \end{aligned} \quad (100)$$

where the normal unit vector on S_0 points toward the interior of the object. Using Eq. (14), one obtains

$$\begin{aligned} & \int_{S_0} \left[G_0(\mathbf{r}, \mathbf{r}') \frac{\partial \phi(\mathbf{r})}{\partial n} - \phi(\mathbf{r}) \frac{\partial G_0(\mathbf{r}, \mathbf{r}')}{\partial n} \right] dS \\ & + \int_{V_s} G_0(\mathbf{r}, \mathbf{r}') f(\mathbf{r}) dV \\ &= \begin{cases} \phi(\mathbf{r}') & \text{for } \mathbf{r}' \text{ in } V_\infty \\ 0 & \text{for } \mathbf{r}' \text{ in } V_0 \end{cases} \end{aligned} \quad (101)$$

where V_0 denotes the volume of the object. Exchanging \mathbf{r} and \mathbf{r}' and using the symmetry property of G_0 [i.e., $G_0(\mathbf{r}', \mathbf{r}) = G_0(\mathbf{r}, \mathbf{r}')$], one has

$$\begin{aligned} & \int_{S_0} \left[G_0(\mathbf{r}, \mathbf{r}') \frac{\partial \phi(\mathbf{r})}{\partial n'} - \phi(\mathbf{r}) \frac{\partial G_0(\mathbf{r}, \mathbf{r}')}{\partial n'} \right] dS' \\ & + \int_{V_s} G_0(\mathbf{r}, \mathbf{r}') f(\mathbf{r}') dV' \\ &= \begin{cases} \phi(\mathbf{r}) & \text{for } \mathbf{r} \text{ in } V_\infty \\ 0 & \text{for } \mathbf{r} \text{ in } V_0 \end{cases} \end{aligned} \quad (102)$$

Equation (102) is an important result, which has several implications. First, notice that when the object is absent, the surface integral vanishes. Hence

$$\phi(\mathbf{r}) = \int_{V_s} G_0(\mathbf{r}, \mathbf{r}') f(\mathbf{r}') dV' \quad (103)$$

which is the same as Eq. (48). This may be called the *incident field impinging on the object* and be denoted as $\phi^{\text{inc}}(\mathbf{r})$. Second, when there is no source in V_∞ , Eq. (102) become

$$\phi(\mathbf{r}) = \int_{S_0} \left[G_0(\mathbf{r}, \mathbf{r}') \frac{\partial \phi(\mathbf{r}')}{\partial n'} - \phi(\mathbf{r}') \frac{\partial G_0(\mathbf{r}, \mathbf{r}')}{\partial n'} \right] dS' \quad (104)$$

for \mathbf{r} in V_∞ . Since there is no source in V_∞ , the field on S_0 must be produced by the source inside S_0 . This equation indicates that the field in a source-free region can be calculated by applying knowledge of the potential and its normal derivative on the surface enclosing the region. This is the mathematical representation of the well-known Huygens' principle for a scalar wave.

Equation (102) also provides the foundation to establish an integral equation for ϕ and $\partial\phi/\partial n$ on the surface of the object. If the object is impenetrable with a hard surface where ϕ satisfies the boundary condition

$$\phi(\mathbf{r}) = 0 \quad \text{for } \mathbf{r} \text{ on } S_0 \quad (105)$$

Eq. (102) becomes

$$\begin{aligned} \phi^{\text{inc}}(\mathbf{r}) + \int_{S_o} \mathbf{G}_0(\mathbf{r}, \mathbf{r}') \frac{\partial \phi(\mathbf{r}')}{\partial \mathbf{n}'} dS' \\ = \begin{cases} \phi(\mathbf{r}) & \text{for } \mathbf{r} \text{ in } V_\infty \\ 0 & \text{for } \mathbf{r} \text{ in } V_o \end{cases} \end{aligned} \quad (106)$$

Applying this equation on S_o , one obtains

$$\int_{S_o} G_0(\mathbf{r}, \mathbf{r}') \frac{\partial \phi(\mathbf{r}')}{\partial n'} dS' = -\phi^{\text{inc}}(\mathbf{r}) \text{ for } \mathbf{r} \text{ on } S_o \quad (107)$$

which is the integral equation for $\partial\phi/\partial n$ on S_o .

If the object is impenetrable with a soft surface where ϕ satisfies the boundary condition

$$\frac{\partial \phi(\mathbf{r})}{\partial n} = 0 \text{ for } \mathbf{r} \text{ on } S_o \quad (108)$$

Eq. (102) becomes

$$\begin{aligned} \phi^{\text{inc}}(\mathbf{r}) \\ - \int_{S_o} \phi(\mathbf{r}') \frac{\partial G_0(\mathbf{r}, \mathbf{r}')}{\partial n'} dS' = \begin{cases} \phi(\mathbf{r}) & \text{for } \mathbf{r} \text{ in } V_\infty \\ 0 & \text{for } \mathbf{r} \text{ in } V_o \end{cases} \end{aligned} \quad (109)$$

Applying this equation on S_o , one obtains

$$\frac{1}{2} \phi(\mathbf{r}) + \int_{S_o} \phi(\mathbf{r}') \frac{\partial G_0(\mathbf{r}, \mathbf{r}')}{\partial n'} dS' = \phi^{\text{inc}}(\mathbf{r}) \text{ for } \mathbf{r} \text{ on } S_o \quad (110)$$

where \int denotes the integral excluding the contribution from the singular point, which is known as the *principal-value integral*. This result is obtained as follows. The integral over S_o in Eq. (109) is divided into an integral over a small circular disk with center at \mathbf{r} plus the remaining integral, which is represented as a principal-value integral in the limit as the area of the isolated disk approaches zero. If \mathbf{r} approaches S_o from the outside, the integral over the vanishingly small disk can be evaluated to give $-\phi(\mathbf{r})/2$. If \mathbf{r} approaches S_o from the inside, the integral gives $\phi(\mathbf{r})/2$. In either case, one obtains Eq. (110), which is the integral equation for ϕ on S_o .

If the object is penetrable and homogeneous, apply Eq. (102) on S_o to obtain

$$\begin{aligned} \frac{1}{2} \phi(\mathbf{r}) - \int_{S_o} [G_0(\mathbf{r}, \mathbf{r}') \frac{\partial \phi(\mathbf{r}')}{\partial n'} - \phi(\mathbf{r}') \frac{\partial G_0(\mathbf{r}, \mathbf{r}')}{\partial n'}] dS' \\ = \phi^{\text{inc}}(\mathbf{r}) \text{ for } \mathbf{r} \text{ on } S_o \end{aligned} \quad (111)$$

To solve for ϕ and $\partial\phi/\partial n$ on S_o , another equation is needed, which can be derived by considering the interior of the object. The wavefunction inside the object satisfies the Helmholtz equation

$$\nabla^2 \phi(\mathbf{r}) + \tilde{k}^2 \phi(\mathbf{r}) = 0 \quad (112)$$

where \tilde{k} characterizes the property of the object. Multiplying this equation by the Green function for unbounded space filled with material characterized by \tilde{k}

$$\tilde{G}_0(\mathbf{r}, \mathbf{r}') = \frac{e^{-j\tilde{k}|\mathbf{r}-\mathbf{r}'|}}{4\pi|\mathbf{r}-\mathbf{r}'|} \quad (113)$$

and applying a similar derivation as before, one has

$$\begin{aligned} - \int_{S_o} \left[\tilde{G}_0(\mathbf{r}, \mathbf{r}') \frac{\partial \phi(\mathbf{r}')}{\partial n'} - \phi(\mathbf{r}') \frac{\partial \tilde{G}_0(\mathbf{r}, \mathbf{r}')}{\partial n'} \right] dS' \\ = \begin{cases} 0 & \text{for } \mathbf{r} \text{ in } V_\infty \\ \phi(\mathbf{r}) & \text{for } \mathbf{r} \text{ in } V_o \end{cases} \end{aligned} \quad (114)$$

When this is applied on S_o , one obtains the second integral equation

$$\begin{aligned} \frac{1}{2} \phi(\mathbf{r}) + \int_{S_o} \left[\tilde{G}_0(\mathbf{r}, \mathbf{r}') \frac{\partial \phi(\mathbf{r}')}{\partial n'} - \phi(\mathbf{r}') \frac{\partial \tilde{G}_0(\mathbf{r}, \mathbf{r}')}{\partial n'} \right] \\ \cdot dS' = 0 \text{ for } \mathbf{r} \text{ on } S_o \end{aligned} \quad (115)$$

which can be used together with Eq. (111) for a numerical solution of ϕ and $\partial\phi/\partial n$ on S_o .

If the object is penetrable and inhomogeneous, the wavefunction still satisfies Eq. (112); however, \tilde{k} now is a function of \mathbf{r} . In this case, one can write Eqs. (45) and (112) in one equation:

$$\nabla^2 \phi(\mathbf{r}) + k^2 \phi(\mathbf{r}) = -f(\mathbf{r}) - [\tilde{k}^2(\mathbf{r}) - k^2] \phi(\mathbf{r}) \quad (116)$$

Multiplying this equation by G_0 and integrating over the infinite volume, one obtains

$$\begin{aligned} \phi(\mathbf{r}) - \int_{V_o} [\tilde{k}^2(\mathbf{r}') - k^2] G_0(\mathbf{r}, \mathbf{r}') \phi(\mathbf{r}') dV' \\ = \int_{V_s} G_0(\mathbf{r}, \mathbf{r}') f(\mathbf{r}') dV' \end{aligned} \quad (117)$$

This is the integral equation that can be used to solve for ϕ in V_o . Unlike the previous integral equations, this equation involves the volume integral. For this reason, it is often referred to as the *volume integral equation*, whereas the previous ones are often referred to as the *surface integral equations*. Integral equations for more complicated objects may involve both volume and surface integrals [10].

2. DYADIC GREEN'S FUNCTIONS

When both the source and response are vector functions, the corresponding Green function is a dyad; hence, the term, *dyadic Green function*.

2.1. Definition of Dyad

A dyad, denoted by $\bar{\mathbf{D}}$, is formed by two vectors:

$$\bar{\mathbf{D}} = \mathbf{A}\mathbf{B} \quad (118)$$

This entity by itself does not have any physical interpretation as a vector. However, when it acts on another vector, the result becomes meaningful. The major role of a dyad is that its scalar product with a vector produces another vector of different magnitude and direction. For example, its anterior scalar product with vector \mathbf{C} yields

$$\mathbf{C} \cdot \bar{\mathbf{D}} = (\mathbf{C} \cdot \mathbf{A})\mathbf{B} \quad (119)$$

which is a vector. Its posterior scalar product with vector \mathbf{C} yields

$$\bar{\mathbf{D}} \cdot \mathbf{C} = \mathbf{A}(\mathbf{B} \cdot \mathbf{C}) \quad (120)$$

which is also a vector. Apparently, the resulting vectors in Eqs. (119) and (120) are different. In addition to the two scalar products, there are two vector products. The anterior vector product is defined as

$$\mathbf{C} \times \bar{\mathbf{D}} = (\mathbf{C} \times \mathbf{A})\mathbf{B} \quad (121)$$

and the posterior vector product is defined as

$$\bar{\mathbf{D}} \times \mathbf{C} = \mathbf{A}(\mathbf{B} \times \mathbf{C}) \quad (122)$$

Clearly, these products are dyads.

The dyad defined in Eq. (118) is a special entity, since it contains only six independent components, three in each of the two vectors. A more general dyad, also called a tensor, is defined as

$$\bar{\mathbf{D}} = \mathbf{D}_x \hat{x} + \mathbf{D}_y \hat{y} + \mathbf{D}_z \hat{z} \quad (123)$$

where \mathbf{D}_x , \mathbf{D}_y , and \mathbf{D}_z are vectors. Therefore, Eq. (123) can be expressed as

$$\begin{aligned} \bar{\mathbf{D}} = & D_{xx} \hat{x}\hat{x} + D_{yx} \hat{y}\hat{x} + D_{zx} \hat{z}\hat{x} + D_{xy} \hat{x}\hat{y} + D_{yy} \hat{y}\hat{y} + D_{zy} \hat{z}\hat{y} \\ & + D_{xz} \hat{x}\hat{z} + D_{yz} \hat{y}\hat{z} + D_{zz} \hat{z}\hat{z} \end{aligned} \quad (124)$$

which contains nine independent components.

A special dyad is called the unit dyad or identity dyad, defined as

$$\bar{\mathbf{I}} = \hat{x}\hat{x} + \hat{y}\hat{y} + \hat{z}\hat{z} \quad (125)$$

It is evident that

$$\mathbf{C} \cdot \bar{\mathbf{I}} = \bar{\mathbf{I}} \cdot \mathbf{C} = \mathbf{C} \quad (126)$$

2.2. Free-Space Dyadic Green's Functions

Consider the electric and magnetic fields produced by an electric current source $\mathbf{J}(\mathbf{r})$ in an unbounded space. Maxwell's equation for this problem are given in Eqs. (37)–(40),

which lead to Eq. (42), reproduced here as

$$\nabla \times \nabla \times \mathbf{E}(\mathbf{r}) - k^2 \mathbf{E}(\mathbf{r}) = -j\omega\mu \mathbf{J}(\mathbf{r}) \quad (127)$$

This is the vector wave equation, which is the analog of the scalar Helmholtz wave equation. It describes electromagnetic wave phenomena that are very pervasive in modern technologies, such as in communication, microwave, and computer chip technologies.

Just as in the scalar case, one can derive a dyadic Green function $\bar{\mathbf{G}}_{e0}$, whose end result is to relate $\mathbf{E}(\mathbf{r})$ and $\mathbf{J}(\mathbf{r})$ by

$$\mathbf{E}(\mathbf{r}) = -j\omega\mu \int_V \bar{\mathbf{G}}_{e0}(\mathbf{r}, \mathbf{r}') \cdot \mathbf{J}(\mathbf{r}') dV' \quad (128)$$

where V is the support of the current $\mathbf{J}(\mathbf{r})$. Using Eq. (128) in Eq. (127), one obtains

$$\begin{aligned} & -j\omega\mu \int_V \nabla \times \nabla \times \bar{\mathbf{G}}_{e0}(\mathbf{r}, \mathbf{r}') \cdot \mathbf{J}(\mathbf{r}') dV' \\ & + j\omega\mu k^2 \int_V \bar{\mathbf{G}}_{e0}(\mathbf{r}, \mathbf{r}') \cdot \mathbf{J}(\mathbf{r}') dV' \\ & = -j\omega\mu \mathbf{J}(\mathbf{r}) = -j\omega\mu \int_V \bar{\mathbf{I}}\delta(\mathbf{r} - \mathbf{r}') \cdot \mathbf{J}(\mathbf{r}') dV' \end{aligned} \quad (129)$$

For arbitrary $\mathbf{J}(\mathbf{r})$, this could be satisfied only if

$$\nabla \times \nabla \times \bar{\mathbf{G}}_{e0}(\mathbf{r}, \mathbf{r}') - k^2 \bar{\mathbf{G}}_{e0}(\mathbf{r}, \mathbf{r}') = \bar{\mathbf{I}}\delta(\mathbf{r} - \mathbf{r}') \quad (130)$$

where $\bar{\mathbf{G}}_{e0}(\mathbf{r}, \mathbf{r}')$ is the dyadic Green function of the electric type that relates vector field \mathbf{E} to vector current \mathbf{J} .

Taking the curl of Eq. (128) and using Maxwell's equations, one obtains

$$\begin{aligned} \mathbf{H}(\mathbf{r}) &= \int_V \nabla \times \bar{\mathbf{G}}_{e0}(\mathbf{r}, \mathbf{r}') \cdot \mathbf{J}(\mathbf{r}') dV' \\ &= \int_V \bar{\mathbf{G}}_{m0}(\mathbf{r}, \mathbf{r}') \cdot \mathbf{J}(\mathbf{r}') dV' \end{aligned} \quad (131)$$

where $\bar{\mathbf{G}}_{m0}(\mathbf{r}, \mathbf{r}') = \nabla \times \bar{\mathbf{G}}_{e0}(\mathbf{r}, \mathbf{r}')$ is the dyadic Green's function of the magnetic type. It satisfies the equation

$$\nabla \times \nabla \times \bar{\mathbf{G}}_{m0}(\mathbf{r}, \mathbf{r}') - k^2 \bar{\mathbf{G}}_{m0}(\mathbf{r}, \mathbf{r}') = \nabla \times [\bar{\mathbf{I}}\delta(\mathbf{r} - \mathbf{r}')] \quad (132)$$

Therefore, the task of finding the dyadic Green function of the electric type is reduced to the task of solving Eq. (130). Equation (130) can be made less difficult by taking the posterior scalar product with an arbitrary vector \mathbf{a} , yielding

$$\nabla \times \nabla \times \bar{\mathbf{G}}_{e0}(\mathbf{r}, \mathbf{r}') \cdot \mathbf{a} - k^2 \bar{\mathbf{G}}_{e0}(\mathbf{r}, \mathbf{r}') \cdot \mathbf{a} = \mathbf{a}\delta(\mathbf{r} - \mathbf{r}') \quad (133)$$

Recognizing that $\bar{\mathbf{G}}_{e0}(\mathbf{r}, \mathbf{r}') \cdot \mathbf{a}$ represents a vector, one may use the vector identity $\nabla \times \nabla \times \mathbf{A} = \nabla(\nabla \cdot \mathbf{A}) - \nabla^2 \mathbf{A}$ to find

$$\begin{aligned} & -\nabla^2 \bar{\mathbf{G}}_{e0}(\mathbf{r}, \mathbf{r}') \cdot \mathbf{a} - k^2 \bar{\mathbf{G}}_{e0}(\mathbf{r}, \mathbf{r}') \cdot \mathbf{a} \\ & = \mathbf{a}\delta(\mathbf{r} - \mathbf{r}') - \nabla[\nabla \cdot \bar{\mathbf{G}}_{e0}(\mathbf{r}, \mathbf{r}') \cdot \mathbf{a}] \end{aligned} \quad (134)$$

Taking the divergence of Eq. (133) and making use of the fact that $\nabla \cdot (\nabla \times \mathbf{A}) \equiv 0$, it can be seen that

$$\nabla \cdot \overline{\mathbf{G}}_{e0}(\mathbf{r}, \mathbf{r}') \cdot \mathbf{a} = -\frac{1}{k^2} \nabla \cdot [\mathbf{a} \delta(\mathbf{r} - \mathbf{r}')] \quad (135)$$

Using this in Eq. (134), one obtains

$$\begin{aligned} \nabla^2 \overline{\mathbf{G}}_{e0}(\mathbf{r}, \mathbf{r}') \cdot \mathbf{a} + k^2 \overline{\mathbf{G}}_{e0}(\mathbf{r}, \mathbf{r}') \cdot \mathbf{a} = \\ - \left(1 + \frac{\nabla \nabla \cdot}{k^2} \right) [\mathbf{a} \delta(\mathbf{r} - \mathbf{r}')] \end{aligned} \quad (136)$$

By making use of the fact that

$$\nabla^2 G_0(\mathbf{r}, \mathbf{r}') + k^2 G_0(\mathbf{r}, \mathbf{r}') = -\delta(\mathbf{r} - \mathbf{r}') \quad (137)$$

and the fact the $1 + \nabla \nabla \cdot / k^2$ is a linear operator that commutes with ∇^2 , it can be deduced that

$$\overline{\mathbf{G}}_{e0}(\mathbf{r}, \mathbf{r}') \cdot \mathbf{a} = \left(1 + \frac{\nabla \nabla \cdot}{k^2} \right) [\mathbf{a} G_0(\mathbf{r}, \mathbf{r}')] \quad (138)$$

Writing this as

$$\overline{\mathbf{G}}_{e0}(\mathbf{r}, \mathbf{r}') \cdot \mathbf{a} = \left(\overline{\mathbf{I}} + \frac{\nabla \nabla}{k^2} \right) G_0(\mathbf{r}, \mathbf{r}') \cdot \mathbf{a} \quad (139)$$

and since \mathbf{a} is an arbitrary vector, one deduces that

$$\overline{\mathbf{G}}_{e0}(\mathbf{r}, \mathbf{r}') = \left(\overline{\mathbf{I}} + \frac{\nabla \nabla}{k^2} \right) G_0(\mathbf{r}, \mathbf{r}') \quad (140)$$

The free-space dyadic Green function of the magnetic type can be derived as

$$\begin{aligned} \overline{\mathbf{G}}_{m0}(\mathbf{r}, \mathbf{r}') &= \nabla \times \overline{\mathbf{G}}_{e0}(\mathbf{r}, \mathbf{r}') = \nabla \times [\overline{\mathbf{I}} G_0(\mathbf{r}, \mathbf{r}')] \\ &= \nabla G_0(\mathbf{r}, \mathbf{r}') \times \overline{\mathbf{I}} \end{aligned} \quad (141)$$

This is the explicit representation of the dyadic Green's function in terms of the scalar Green's function $G_0(\mathbf{r}, \mathbf{r}')$. It is to be noted that the aforementioned relationship between the dyadic Green function and the scalar Green function $G_0(\mathbf{r}, \mathbf{r}')$ is valid only for a homogeneous unbounded space such as a free space. Such a relation does not hold true in a cavity, waveguide, or half-space. For example, the dyadic Green's functions for a half-space (above $z = 0$) are given by [3]

$$\begin{aligned} \overline{\mathbf{G}}_{e1}(\mathbf{r}, \mathbf{r}') &= \left(\overline{\mathbf{I}} - \frac{\nabla \nabla'}{k^2} \right) [G_0(\mathbf{r}, \mathbf{r}') \\ &- G_0(\mathbf{r}, \mathbf{r}'_i)] + 2\hat{z}\hat{z}G_0(\mathbf{r}, \mathbf{r}'_i) \end{aligned} \quad (142)$$

and

$$\overline{\mathbf{G}}_{m2}(\mathbf{r}, \mathbf{r}') = \nabla G_0(\mathbf{r}, \mathbf{r}') \times \overline{\mathbf{I}} + \nabla G_0(\mathbf{r}, \mathbf{r}'_i) \times \overline{\mathbf{I}}_i \quad (143)$$

where $\mathbf{r}'_i = x'\hat{x} + y'\hat{y} - z'\hat{z}$ and $\overline{\mathbf{I}}_i = -\overline{\mathbf{I}} + 2\hat{z}\hat{z}$. It can be verified that $\overline{\mathbf{G}}_{e1}(\mathbf{r}, \mathbf{r}')$ and $\overline{\mathbf{G}}_{m2}(\mathbf{r}, \mathbf{r}')$ satisfy the boundary

conditions

$$\hat{z} \times \overline{\mathbf{G}}_{e1}(\mathbf{r}, \mathbf{r}') = 0 \text{ for } z = 0 \quad (144)$$

and

$$\hat{z} \times \nabla \times \overline{\mathbf{G}}_{m2}(\mathbf{r}, \mathbf{r}') = 0 \text{ for } z = 0 \quad (145)$$

respectively. For this reason, $\overline{\mathbf{G}}_{e1}(\mathbf{r}, \mathbf{r}')$ is called the "electric-type dyadic Green function of the first kind" and $\overline{\mathbf{G}}_{m2}(\mathbf{r}, \mathbf{r}')$ is called the "magnetic-type dyadic Green's function of the second kind". The classification of dyadic Green's functions is similar to that of scalar Green's functions.

2.3. Eigenfunction Expansion

As in the scalar case, the Ohm-Rayleigh method or the method of eigenfunction expansion is a general method to derive dyadic Green function [3]. For vector problems, the eigenfunctions are vector functions, known as vector wavefunctions. There are three kinds of vector wavefunctions [1], defined by

$$\mathbf{L}(\mathbf{r}) = \nabla \psi(\mathbf{r}) \quad (146)$$

$$\mathbf{M}(\mathbf{r}) = \nabla \times [c\psi(\mathbf{r})] \quad (147)$$

$$\mathbf{N}(\mathbf{r}) = \frac{1}{\kappa} \nabla \times \mathbf{M}(\mathbf{r}) \quad (148)$$

where \mathbf{c} is a vector called the "pilot vector" and ψ satisfies that homogeneous Helmholtz wave equation

$$\nabla^2 \psi(\mathbf{r}) + \kappa^2 \psi(\mathbf{r}) = 0 \quad (149)$$

It can be shown that, \mathbf{L} , \mathbf{M} , and \mathbf{N} satisfy the vector equations

$$\nabla^2 \mathbf{L}(\mathbf{r}) + \kappa^2 \mathbf{L}(\mathbf{r}) = 0 \quad (150)$$

$$\nabla \times \nabla \times \mathbf{M}(\mathbf{r}) - \kappa^2 \mathbf{M}(\mathbf{r}) = 0 \quad (151)$$

$$\nabla \times \nabla \times \mathbf{N}(\mathbf{r}) - \kappa^2 \mathbf{N}(\mathbf{r}) = 0 \quad (152)$$

and \mathbf{M} can be expressed in terms of \mathbf{N} as

$$\mathbf{M}(\mathbf{r}) = \frac{1}{\kappa} \nabla \times \mathbf{N}(\mathbf{r}) \quad (153)$$

Since $\nabla \times \mathbf{L}(\mathbf{r}) = \nabla \times \nabla \psi(\mathbf{r}) = 0$, \mathbf{L} is the irrotational vector wavefunction. Since $\nabla \cdot \mathbf{M}(\mathbf{r}) = 0$ and $\nabla \cdot \mathbf{N}(\mathbf{r}) = 0$, \mathbf{M} and \mathbf{N} are the solenoidal vector wavefunctions.

For a rectangular waveguide illustrated in Fig. 7, ψ is given by

$$\psi_{mn}(h, \mathbf{r}) = \left\{ \begin{array}{l} \cos k_x x \cos k_y y \\ \sin k_x x \sin k_y y \end{array} \right\} e^{-jhz} \quad (154)$$

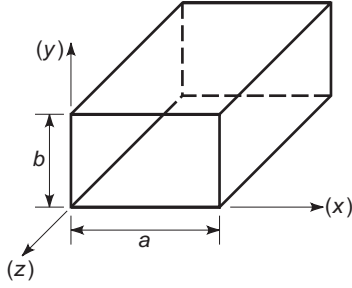


Figure 7. A rectangular waveguide.

where $k_x = m\pi/a$ and $k_y = n\pi/b$. The vector wavefunctions \mathbf{L} , \mathbf{M} , and \mathbf{N} are given by

$$\mathbf{L}_{\sigma mn}^e(h, \mathbf{r}) = \nabla \psi_{\sigma mn}^e(h, \mathbf{r}) \quad (155)$$

$$\mathbf{M}_{\sigma mn}^e(h, \mathbf{r}) = \nabla \times [\hat{\mathbf{z}} \psi_{\sigma mn}^e(h, \mathbf{r})] \quad (156)$$

$$\mathbf{N}_{\sigma mn}^e(h, \mathbf{r}) = \frac{1}{\kappa} \nabla \times \nabla \times [\hat{\mathbf{z}} \psi_{\sigma mn}^e(h, \mathbf{r})] \quad (157)$$

where the pilot vector is $\mathbf{c} = \hat{\mathbf{z}}$. This causes \mathbf{M} to be transverse to $\hat{\mathbf{z}}$.

The vector wavefunctions are always orthogonal to each other. For those in a rectangular waveguide, it can be shown

$$\int_V \mathbf{U}_{\sigma mn}^e(h, \mathbf{r}) \cdot \mathbf{V}_{\sigma' m' n'}^e(-h', \mathbf{r}) dV = 0 \quad (158)$$

where $\mathbf{U}, \mathbf{V} = \mathbf{L}, \mathbf{M}, \mathbf{N}$, except when $\mathbf{U}_{\sigma mn}^e(h, \mathbf{r}) = \mathbf{V}_{\sigma mn}^e(h, \mathbf{r})$. They form a complete set and, therefore, can be employed to expand any vector functions.

The electric-type dyadic Green's function of the first kind satisfies the equation

$$\nabla \times \nabla \times \bar{\mathbf{G}}_{e1}(\mathbf{r}, \mathbf{r}') - k^2 \bar{\mathbf{G}}_{e1}(\mathbf{r}, \mathbf{r}') \equiv \bar{\mathbf{I}} \delta(\mathbf{r} - \mathbf{r}') \quad (159)$$

and the boundary condition

$$\hat{\mathbf{n}} \times \bar{\mathbf{G}}_{e1}(\mathbf{r}, \mathbf{r}') = 0 \quad \text{on the waveguide walls} \quad (160)$$

It is clear that only \mathbf{L}_{omn} , \mathbf{M}_{emn} , and \mathbf{N}_{omn} satisfy Eq. (160) and, therefore, can be used to expand $\bar{\mathbf{G}}_{e1}$:

$$\begin{aligned} \bar{\mathbf{G}}_{e1}(\mathbf{r}, \mathbf{r}') = & \int_{-\infty}^{\infty} \sum_{m,n} [\mathbf{L}_{omn}(h, \mathbf{r}) \mathbf{A}_{omn}(h) + \mathbf{M}_{emn}(h, \mathbf{r}) \mathbf{B}_{emn}(h) \\ & + \mathbf{N}_{omn}(h, \mathbf{r}) \mathbf{C}_{omn}(h)] dh \end{aligned} \quad (161)$$

Substituting this expansion into Eq. (159), one obtains

$$\begin{aligned} & \int_{-\infty}^{\infty} \sum_{m,n} \{-k^2 \mathbf{L}_{omn}(h, \mathbf{r}) \mathbf{A}_{omn}(h) \\ & + (\kappa^2 - \kappa'^2) [\mathbf{M}_{emn}(h, \mathbf{r}) \mathbf{B}_{emn}(h)] \\ & + \mathbf{N}_{omn}(h, \mathbf{r}) \mathbf{C}_{omn}(h)\} dh = \bar{\mathbf{I}} \delta(\mathbf{r} - \mathbf{r}') \end{aligned} \quad (162)$$

Taking the anterior scalar product of Eq. (162) with $\mathbf{L}_{om'n'}$ ($-h'$, \mathbf{r}), $\mathbf{M}_{em'n'}$ ($-h'$, \mathbf{r}), and $\mathbf{N}_{om'n'}$ ($-h'$, \mathbf{r}), respectively, integrating over the entire volume of the waveguide, and applying the orthogonal relation in Eq. (158), one can find

$$\mathbf{A}_{omn}(h) = -\frac{k_{cmn}^2}{k^2 \kappa'^2} C_{mn} \mathbf{L}_{omn}(-h, \mathbf{r}') \quad (163)$$

$$\mathbf{B}_{emn}(h) = \frac{1}{\kappa^2 - \kappa'^2} C_{mn} \mathbf{M}_{emn}(-h, \mathbf{r}') \quad (164)$$

$$\mathbf{C}_{emn}(h) = \frac{1}{\kappa^2 - \kappa'^2} C_{mn} \mathbf{N}_{omn}(-h, \mathbf{r}') \quad (165)$$

where $k_{cmn}^2 = k_x^2 + k_y^2$ and $C_{mn} = (2 - \delta_0) / (\pi a b k_{cmn}^2)$ with $\delta_0 = 1$ when $m = 0$ or $n = 0$ and $\delta_0 = 0$, where m and n are nonzero. Therefore

$$\begin{aligned} \bar{\mathbf{G}}_{e1}(\mathbf{r}, \mathbf{r}') = & \int_{-\infty}^{\infty} \sum_{m,n} C_{mn} \left\{ -\frac{k_{cmn}^2}{k^2 \kappa'^2} \mathbf{L}_{omn}(h, \mathbf{r}) \mathbf{L}_{omn}(-h, \mathbf{r}') \right. \\ & + \frac{1}{\kappa^2 - \kappa'^2} [\mathbf{M}_{emn}(h, \mathbf{r}) \mathbf{M}_{emn}(-h, \mathbf{r}') \\ & \left. + \mathbf{N}_{omn}(h, \mathbf{r}) \mathbf{N}_{omn}(-h, \mathbf{r}') \right\} dh \end{aligned} \quad (166)$$

Through some mathematical manipulations and the application of Cauchy's residue theorem [3], one can simplify Eq. (166) as

$$\begin{aligned} \bar{\mathbf{G}}_{e1}(\mathbf{r}, \mathbf{r}') = & -\frac{1}{k^2} \hat{\mathbf{z}} \hat{\mathbf{z}} \delta(\mathbf{r} - \mathbf{r}') - \frac{j}{ab} \sum_{m,n} \frac{2 - \delta_0}{k_{cmn}^2 k_{gmn}} \\ & [\mathbf{M}_{emn}(\pm k_{gmn}, \mathbf{r}) \mathbf{M}_{emn}(\pm k_{gmn}, \mathbf{r}) \mathbf{M}_{emn}(\mp k_{gmn}, \mathbf{r}') \\ & \mathbf{N}_{omn}(\pm k_{gmn}, \mathbf{r}) \mathbf{N}_{omn}(\mp k_{gmn}, \mathbf{r}')] \quad z \geq z' \end{aligned} \quad (167)$$

where $k_{gmn} = \sqrt{k^2 - k_{cmn}^2}$.

In addition to the method described above, Tai [3] proposed the method of $\bar{\mathbf{G}}_m$, in which $\bar{\mathbf{G}}_m$ is derived first and $\bar{\mathbf{G}}_e$ is then derived from $\nabla \times \bar{\mathbf{G}}_m = \bar{\mathbf{I}} \delta(\mathbf{r} - \mathbf{r}') + k^2 \bar{\mathbf{G}}_e$. Since $\bar{\mathbf{G}}_m$ is completely solenoidal, its expansion requires only \mathbf{M} and \mathbf{N} and, therefore, the derivation becomes simpler.

The Ohm-Rayleigh method can be used to derive a variety of dyadic Green's functions. Table 1 lists the problems for which the dyadic Green's functions have been derived.

Table 1. Problems with Available Dyadic Green Functions

Geometry of Problem	References
Parallel-plate waveguide	3
Rectangular waveguide	3,11
Rectangular waveguide with two dielectrics	3,12
Cylindrical waveguide	3,13,14
Coaxial waveguide	3,15
Rectangular cavity	3,16
Cylindrical cavity	3,13,17
Spherical cavity	3,18
Circular conducting cylinder	3
Circular dielectric cylinder	3
Circular coated cylinder	3
Elliptical conducting cylinder	3
Conducting wedge and half-sheet	3
Conducting sphere and cone	3
Homogeneous and inhomogeneous spheres	3
Planar layered medium	3,5,6
Planar anisotropic layered medium	19
Conductor-backed layered medium	20–22
Cylindrically layered medium	6,23
Spherically layered medium	3,6,24
Moving medium	3,25,26

2.4. Vector Integral Equations

Consider the problem of the electric and magnetic fields produced by an electric current source $\mathbf{J}(\mathbf{r})$ in the presence of an arbitrarily shaped object immersed in an infinite homogeneous medium (see Fig. 6). Exterior to the object, the electric field satisfies the vector wave equation in Eq. (127), and the radiation condition at infinity is given by

$$r[\nabla \times \mathbf{E}(\mathbf{r}) + jk\hat{\mathbf{r}} \times \mathbf{E}(\mathbf{r})] = 0 \text{ for } r \rightarrow \infty \quad (168)$$

Multiplying Eq. (127) by $\bar{\mathbf{G}}_{e0}(\mathbf{r}, \mathbf{r}')$, Eq. (130) by $\mathbf{E}(\mathbf{r})$, and integrating the difference of the resultant equations over the exterior region, one obtains

$$\begin{aligned} & \int_{V_\infty} \{[\nabla \times \nabla \times \mathbf{E}(\mathbf{r})] \cdot \bar{\mathbf{G}}_{e0}(\mathbf{r}, \mathbf{r}') - \mathbf{E}(\mathbf{r}) \cdot [\nabla \times \nabla \times \bar{\mathbf{G}}_{e0}(\mathbf{r}, \mathbf{r}')]\} dV \\ &= -j\omega\mu \int_{V_s} \mathbf{J}(\mathbf{r}) \cdot \bar{\mathbf{G}}_{e0}(\mathbf{r}, \mathbf{r}') dV - \int_{V_\infty} \mathbf{E}(\mathbf{r}) \cdot \bar{\mathbf{I}}\delta(\mathbf{r} - \mathbf{r}') dV \end{aligned} \quad (169)$$

where V_∞ denotes the infinite space exterior to the object and V_s denotes the support of $\mathbf{J}(\mathbf{r})$. Applying the vector dyadic Green's second identity [27]

$$\begin{aligned} & \int_V [(\nabla \times \nabla \times \mathbf{A}) \cdot \bar{\mathbf{D}} - \mathbf{A} \cdot (\nabla \times \nabla \times \bar{\mathbf{D}})] dV \\ &= \int_S [(\hat{\mathbf{n}} \times \mathbf{A}) \cdot (\nabla \times \bar{\mathbf{D}}) + (\hat{\mathbf{n}} \times \nabla \times \mathbf{A}) \cdot \bar{\mathbf{D}}] dS \end{aligned} \quad (170)$$

where V is a volume enclosed by S , one has

$$\begin{aligned} & \int_{S_0 + S_\infty} \{[\hat{\mathbf{n}} \times \mathbf{E}(\mathbf{r})] \cdot [\nabla \times \bar{\mathbf{G}}_{e0}(\mathbf{r}, \mathbf{r}')] \\ &+ \hat{\mathbf{n}} \times \nabla \times \mathbf{E}(\mathbf{r}) \cdot \bar{\mathbf{G}}_{e0}(\mathbf{r}, \mathbf{r}')\} dS \\ &= -j\omega\mu \int_{V_s} \mathbf{J}(\mathbf{r}) \cdot \bar{\mathbf{G}}_{e0}(\mathbf{r}, \mathbf{r}') dV - \int_{V_\infty} \mathbf{E}(\mathbf{r}) \delta(\mathbf{r} - \mathbf{r}') dV \end{aligned} \quad (171)$$

where S_0 denotes the surface of the object, S_∞ denotes a large spherical surface whose radius approaches infinity, and $\hat{\mathbf{n}}$ is the normal unit vector pointing away from V_∞ . Since both $\mathbf{E}(\mathbf{r})$ and $\bar{\mathbf{G}}_{e0}(\mathbf{r}, \mathbf{r}')$ satisfy the radiation condition, the surface integral over S_∞ vanishes. As a result, we obtain

$$\begin{aligned} & - \int_{S_0} \{[\hat{\mathbf{n}} \times \mathbf{E}(\mathbf{r})] \cdot [\nabla \times \bar{\mathbf{G}}_{e0}(\mathbf{r}, \mathbf{r}')] \\ &+ [\hat{\mathbf{n}} \times \nabla \times \mathbf{E}(\mathbf{r})] \cdot \bar{\mathbf{G}}_{e0}(\mathbf{r}, \mathbf{r}')\} dS \\ &- j\omega\mu \int_{V_s} \mathbf{J}(\mathbf{r}) \cdot \bar{\mathbf{G}}_{e0}(\mathbf{r}, \mathbf{r}') dV = \begin{cases} \mathbf{E}(\mathbf{r}') & \text{for } \mathbf{r}' \text{ in } V_\infty \\ 0 & \text{for } \mathbf{r}' \text{ in } V_0 \end{cases} \end{aligned} \quad (172)$$

which can also be written as

$$\begin{aligned} & - \int_{S_0} \{[\nabla \times \bar{\mathbf{G}}_{e0}(\mathbf{r}, \mathbf{r}')] \cdot [\hat{\mathbf{n}}' \times \mathbf{E}(\mathbf{r}')] \\ &- j\omega\mu \bar{\mathbf{G}}_{e0}(\mathbf{r}, \mathbf{r}') \cdot [\hat{\mathbf{n}}' \times \mathbf{H}(\mathbf{r}')] \} dS' \\ &- j\omega\mu \int_{V_s} \bar{\mathbf{G}}_{e0}(\mathbf{r}, \mathbf{r}') \cdot \mathbf{J}(\mathbf{r}') dV' = \begin{cases} \mathbf{E}(\mathbf{r}) & \text{for } \mathbf{r} \text{ in } V_\infty \\ 0 & \text{for } \mathbf{r} \text{ in } V_0 \end{cases} \end{aligned} \quad (173)$$

where V_0 denotes the volume of the object.

Similar to Eq. (102) in the scalar case, Eq. (173) is an important result, which has several implications. First, notice that when the object is absent, the surface integral vanishes. Hence

$$\mathbf{E}(\mathbf{r}) = -j\omega\mu \int_{V_s} \bar{\mathbf{G}}_{e0}(\mathbf{r}, \mathbf{r}') \cdot \mathbf{J}(\mathbf{r}') dV' \quad (174)$$

where is the same as Eq. (128). This can be regarded as the incident field and denoted as $\mathbf{E}^{\text{inc}}(\mathbf{r})$. Second, when there is no source in V_∞ , Eq. (173) becomes

$$\begin{aligned} \mathbf{E}(\mathbf{r}) = & - \int_{S_0} \{[\nabla \times \bar{\mathbf{G}}_{e0}(\mathbf{r}, \mathbf{r}')] [\hat{\mathbf{n}}' \times \mathbf{E}(\mathbf{r}')] \cdot -j\omega\mu \bar{\mathbf{G}}_{e0}(\mathbf{r}, \mathbf{r}') \\ & \cdot [\hat{\mathbf{n}}' \times \mathbf{H}(\mathbf{r}')] \} dS' \end{aligned} \quad (175)$$

for \mathbf{r} in V_∞ . Since there is no source in V_∞ , the field on S_0 must be produced by the source inside S_0 . This equation indicates that the field in a source-free region can be calculated from knowledge of the tangential electric and

magnetic fields on the surface enclosing the region. This is the mathematical representation of the well-known Huygens' principle for a vector field.

Equation (173) also provides the foundation to establish an integral equation for $\hat{n} \times \mathbf{E}$ and $\hat{n} \times \mathbf{H}$ on the surface of the object. If the object is a perfect conductor, $\hat{n} \times \mathbf{E}(\mathbf{r}) = 0$ for \mathbf{r} on S_o . Consequently, Eq. (173) becomes

$$\mathbf{E}(\mathbf{r}) = \mathbf{E}^{\text{inc}}(\mathbf{r}) + j\omega\mu \int_{S_o} \bar{\mathbf{G}}_{e0}(\mathbf{r}, \mathbf{r}') \cdot [\hat{n}' \times \mathbf{H}(\mathbf{r}')] dS' \quad (176)$$

for \mathbf{r} in V_∞ . Substituting this into $\hat{n} \times \mathbf{E}(\mathbf{r}) = 0$ for \mathbf{r} on S_o , we obtain an integral equation, which can be solved for $\hat{n} \times \mathbf{H}(\mathbf{r})$.

If the object is a homogeneous body, one can derive another integral representation for the field inside S_o using the unbounded-space dyadic Green's function for the interior medium. When this and Eq. (173) are applied at S_o , one obtains two integral equations, which can be solved for $\hat{n} \times \mathbf{E}(\mathbf{r})$ and $\hat{n} \times \mathbf{H}(\mathbf{r})$.

If the object is an inhomogeneous dielectric body, the electric field satisfies the vector wave equation

$$\nabla \times \nabla \times \mathbf{E}(\mathbf{r}) - \tilde{k}^2(\mathbf{r})\mathbf{E}(\mathbf{r}) = -j\omega\mu\mathbf{J}(\mathbf{r}) \quad (177)$$

This can be written as

$$\begin{aligned} \nabla \times \nabla \times \mathbf{E}(\mathbf{r}) - k^2\mathbf{E}(\mathbf{r}) &= -j\omega\mu\mathbf{J}(\mathbf{r}) + [\tilde{k}^2(\mathbf{r}) \\ &- k^2]\mathbf{E}(\mathbf{r}) \end{aligned} \quad (178)$$

Multiplying Eq. (177) by $\bar{\mathbf{G}}_{e0}(\mathbf{r}, \mathbf{r}')$ and integrating the resultant equation over the entire space, one obtains

$$\mathbf{E}(\mathbf{r}) = \mathbf{E}^{\text{inc}}(\mathbf{r}) + \int_{V_o} \bar{\mathbf{G}}_{e0}(\mathbf{r}, \mathbf{r}') \cdot [\tilde{k}^2(\mathbf{r}') - k^2]\mathbf{E}(\mathbf{r}') dV' \quad (179)$$

This is the mathematical representation of the volume equivalence principle. It provides a volume integral equation that can be solved for $\mathbf{E}(\mathbf{r})$.

We note that the formulation described in this section can be repeated for the magnetic field in a similar manner. As a result, different integral equations exist for the same problem, which provide different approaches to the solution of the problem.

2.5. Singularity of the Dyadic Green's Function

As shown in Eq. (128), the electric field produced by the current \mathbf{J} in an unbounded space can be written as

$$\mathbf{E}(\mathbf{r}) = -j\omega\mu \int_V \bar{\mathbf{G}}_{e0}(\mathbf{r}, \mathbf{r}') \cdot \mathbf{J}(\mathbf{r}') dV' \quad (180)$$

where $\bar{\mathbf{G}}_{e0}(\mathbf{r}, \mathbf{r}')$ is defined by Eq. (140). Many electromagneticists have tried to fathom the meaning of Eq. (180). Strictly speaking, the integral does not converge because of the $1/|\mathbf{r} - \mathbf{r}'|$ singularity in $G_0(\mathbf{r}, \mathbf{r}')$. After being operated upon by the double ∇ operator in Eq. (140), $\bar{\mathbf{G}}_{e0}(\mathbf{r}, \mathbf{r}')$

contains terms of the form $1/|\mathbf{r} - \mathbf{r}'|^3$, rendering the integral in Eq. (180) ill-defined. A remedy to this is to rewrite Eq. (180) as

$$\mathbf{E}(\mathbf{r}) = -j\omega\mu \left(\bar{\mathbf{I}} + \frac{\nabla\nabla}{k^2} \right) \cdot \int_V G_0(\mathbf{r}, \mathbf{r}') \mathbf{J}(\mathbf{r}') dV' \quad (181)$$

This equation is well defined for all \mathbf{r} and \mathbf{r}' , but lacks the compactness of Eq. (180).

Equation (180) can be made meaningful in a generalized function sense. To this end, one defines $\bar{\mathbf{G}}_{e0}(\mathbf{r}, \mathbf{r}')$ as a generalized function

$$\bar{\mathbf{G}}_{e0}(\mathbf{r}, \mathbf{r}') = PV\bar{\mathbf{G}}_{e0}(\mathbf{r}, \mathbf{r}') - \frac{\bar{\mathbf{L}}\delta(\mathbf{r} - \mathbf{r}')}{k^2} \quad (182)$$

where PV implies the invocation of a principal volume integral whose value depends on the shape of the principal volume chosen. For the sake of uniqueness, $\bar{\mathbf{L}}$ also depends on the shape of the principal volume. A principal volume integral is defined as

$$\begin{aligned} \int_V PV\bar{\mathbf{G}}_{e0}(\mathbf{r}, \mathbf{r}') \cdot \mathbf{J}(\mathbf{r}') dV' &= PV \int_V \bar{\mathbf{G}}_{e0}(\mathbf{r}, \mathbf{r}') \cdot \mathbf{J}(\mathbf{r}') dV' \\ &= \lim_{V_\delta \rightarrow 0} \int_{V-V_\delta} \bar{\mathbf{G}}_{e0}(\mathbf{r}, \mathbf{r}') \cdot \mathbf{J}(\mathbf{r}') dV' \end{aligned} \quad (183)$$

where V_δ is the exclusion volume. Unfortunately, even though the integral above converges, its value is nonunique in the sense that it depends on the shape of V_δ . The nonuniqueness in the first term of Eq. (182) is rectified by the choice of a shape-dependent $\bar{\mathbf{L}}$. The volume of $\bar{\mathbf{L}}$ in Eq. (182) for various exclusion volumes is given by [28–33].

$$\bar{\mathbf{L}} = \frac{\bar{\mathbf{I}}}{3} \text{ for spheres and cubes} \quad (184)$$

$$\bar{\mathbf{L}} = \hat{z}\hat{z} \text{ for disks perpendicular to the } z \text{ axis} \quad (185)$$

$$\bar{\mathbf{L}} = \frac{\hat{x}\hat{x} + \hat{y}\hat{y}}{2} \text{ for needles parallel to the } z \text{ axis} \quad (186)$$

To understand how these $\bar{\mathbf{L}}$ values are derived, one can start with the classically legitimate Eq. (181) and split the integral into two terms with the definition of a principal volume integral:

$$\begin{aligned} \mathbf{E}(\mathbf{r}) &= -j\omega\mu \lim_{V_\delta \rightarrow 0} \left(\bar{\mathbf{I}} + \frac{\nabla\nabla}{k^2} \right) \cdot \int_{V-V_\delta} G_0(\mathbf{r}, \mathbf{r}') \mathbf{J}(\mathbf{r}') dV' \\ &\quad - j\omega\mu \lim_{V_\delta \rightarrow 0} \left(\bar{\mathbf{I}} + \frac{\nabla\nabla}{k^2} \right) \cdot \int_{V_\delta} G_0(\mathbf{r}, \mathbf{r}') \mathbf{J}(\mathbf{r}') dV' \end{aligned} \quad (187)$$

In the first term, $V_\delta > 0$ and hence, it is legitimate to exchange the order of differentiation and integration so that it becomes the first term of Eq. (182). In the second term in Eq. (187), the term that does not allow the exchange of the order of integration and differentiation is the term involving the $\nabla\nabla$ operator. Focusing on it more carefully, one has

$$\begin{aligned} & \lim_{V_\delta \rightarrow 0} \nabla\nabla \cdot \int_{V_\delta} G_0(\mathbf{r}, \mathbf{r}') \mathbf{J}(\mathbf{r}') dV' \\ &= \lim_{V_\delta \rightarrow 0} \nabla \left[\int_{V_\delta} G_0(\mathbf{r}, \mathbf{r}') \nabla' \cdot \mathbf{J}(\mathbf{r}') dV' \right. \\ & \quad \left. - \int_{S_\delta} \hat{\mathbf{n}}' \cdot \mathbf{J}(\mathbf{r}') G_0(\mathbf{r}, \mathbf{r}') dS' \right] \end{aligned} \quad (188)$$

To arrive at this, one has made use of the fact that $\nabla G_0(\mathbf{r}, \mathbf{r}') = -\nabla' G_0(\mathbf{r} - \mathbf{r}')$, and $[\nabla' G_0(\mathbf{r}, \mathbf{r}') \cdot \mathbf{J}(\mathbf{r}')] = \nabla' \cdot [G_0(\mathbf{r}, \mathbf{r}') \mathbf{J}(\mathbf{r}')] - G_0(\mathbf{r}, \mathbf{r}') \nabla' \cdot \mathbf{J}(\mathbf{r}')$. Using Gauss' theorem on the term involving $\nabla' \cdot [G_0(\mathbf{r}, \mathbf{r}') \mathbf{J}(\mathbf{r}')]$ finally gives rise to Eq. (188). The first integral on the right-hand side of Eq. (188) vanishes since if $\mathbf{J}(\mathbf{r}')$ is regular, $\nabla' \cdot \mathbf{J}(\mathbf{r}') = \rho(\mathbf{r}')/j\omega$ is also regular and the integral is finally proportional to V_δ . In the second integral, S_δ is the surface bounding V_δ . Hence, $\hat{\mathbf{n}}' \cdot \mathbf{J}(\mathbf{r}')$ is the surface charge on S_δ due to the sudden truncation of $\mathbf{J}(\mathbf{r}')$ within the volume V_δ . This integral gives the potential observed within V_δ due to this surface charge, and it is non zero even when $V_\delta \rightarrow 0$. The gradient (outside the brackets) in turn yields the field generated by this surface charge. In other words, surface charges of opposite polarities on the wall of an infinitesimally small volume always generate a finite field within the small volume. This fact is also intimately related to the scale invariant nature of the Laplace equation which is Maxwell's equations at low frequency.

BIBLIOGRAPHY

1. J. A. Stratton, *Electromagnetic Theory*, McGraw-Hill, New York, 1941.
2. P. M. Morse and H. Feshbach, *Methods of Theoretical Physics*, McGraw-Hill, New York, 1953.
3. C. T. Tai, *Dyadic Green Functions in Electromagnetic Theory*, 2nd ed., IEEE Press, New York, 1994.
4. R. E. Collin, *Field Theory of Guided Waves*, 2nd ed., IEEE Press, New York, 1991.
5. J. A. Kong, *Electromagnetic Wave Theory*, 2nd ed., Wiley, New York, 1990.
6. W. C. Chew, *Waves and Fields in Inhomogeneous Media*, IEEE Press, New York, 1995.
7. I. M. Gel'fand and G. E. Shilov, *Generalized Functions*, Academic Press, New York, 1964.
8. J. D. Jackson, *Classical Electrodynamics*, 2nd ed., Wiley, New York, 1975.
9. E. T. Copson, *Theory of Functions of a Complex Variable*, Oxford Univ. Press, London, 1948.
10. J. M. Jin, V. V. Liepa, and C. T. Tai, A volume-surface integral equation for electro-magnetic scattering by inhomogeneous cylinders, *J. Electromagn. Waves Appl.* **2**:573–588 (1988).
11. C. T. Tai, On the eigenfunction expansion of dyadic Green's functions, *Proc. IEEE* **61**:480–481 (1973).
12. C. T. Tai, Dyadic Green's functions for a rectangular waveguide filled with two dielectrics, *J. Electromagn. Waves Appl.* **2**:245–253 (1988).
13. M. Kisluk, The dyadic Green's functions for cylindrical waveguides and cavities *IEEE Trans. Microwave Theory Tech.* **28**:894–898 (1980).
14. V. Daniel, New expressions of dyadic Green's function in uniform waveguide with perfectly conducting walls, *IEEE Trans. Anten. Propag.* **30**:487–499 (1982).
15. C. T. Tai, Dyadic Green's functions for a coaxial line, *IEEE Trans. Anten. Propag.* **31**:355–358 (1983).
16. C. T. Tai and P. Rozenfeld, Different representations of dyadic Green's functions for a rectangular cavity, *IEEE Trans. Microwave Theory Tech.* **24**:597–601 (1976).
17. S. Zhang and J. M. Jin, Derivation of dyadic Green's functions for cylindrical cavities by image method, *Acta Electronica Sinica*, **12**(5):21–26 (1984).
18. R. E. Collin, Dyadic Green's function expansion in spherical coordinates, *Electromagnetics*, **6**:183–207 (1986).
19. J. K. Lee and J. A. Kong, Dyadic Green's functions for layered anisotropic medium, *Electromagnetics*, **3**:111–130 (1983).
20. J. S. Bagby and D. P. Nyquist, Dyadic Green's functions for integrated electronic and optical circuits, *IEEE Trans. Microwave, Theory Tech.* **35**:206–210 (1987).
21. L. Vegni, R. Cicchetti, and P. Capcec, Spectral dyadic Green's function formulation for planar integrated structures, *IEEE Trans. Anten. Propag.* **36**:1057–1065 (1988).
22. P. Bernardi and R. Cicchetti, Dyadic Green's functions for conductor-backed layered structures excited by arbitrary tri-dimensional sources, *IEEE Trans. Microwave Theory Tech.* **42**:1474–1483 (1994).
23. Z. Xiang and Y. Lu, Electromagnetic dyadic Green's function in cylindrically multilayered media, *IEEE Trans. Microwave Theory Tech.* **44**:614–621 (1996).
24. L. W. Li et al., Electromagnetic dyadic Green's function in spherically multilayered media, *IEEE Trans. Microwave Theory Tech.* **42**:2302–2309 (1994).
25. C. T. Tai, The dyadic Green's function for a moving isotropic medium, *IEEE Trans. Anten. Propag.* **13**:322–323 (1965).
26. C. Stubenrauch and C. T. Tai, Dyadic Green's function for cylindrical waveguide with moving medium, *Appl. Sci.* **25**:281–289 (1971).
27. C. T. Tai, *Generalized Vector and Dyadic Analysis*, 2nd ed., IEEE Press, New York, 1997.
28. J. Van Bladel, Some remarks on Green's dyadic for infinite space, *IEEE Trans. Anten. Propag.* **9**:563–566 (1961).
29. K. M. Chen, A simple physical picture of tensor Green's function in source region, *Proc. IEEE*, **65**:1202–1204 (1977).
30. A. W. Johnson, A. Q. Howard, and D. G. Dudley, On the irrotational component of the electric Green's dyadic, *Radio Sci.* **14**:961–967 (1979).
31. A. D. Yaghjian, Electric dyadic Green's functions in the source region, *Proc. IEEE*, **68**:248–263 (1980).
32. S. W. Lee et al., Singularity in Green's function and its numerical evaluation, *IEEE Trans. Anten. Propag.* **22**:311–317 (1980).
33. W. C. Chew, Some observations on the spatial and eigenfunction representations of dyadic Green's function, *IEEE Trans. Anten. Propag.* **37**:1322–1327 (1989).

GROUND PENETRATING RADAR

DAVID J. DANIELS
ERA Technology
Surrey, United Kingdom

1. INTRODUCTION

Ground penetrating radar (GPR) is a nondestructive measurement technique, which uses electromagnetic waves to locate targets or interfaces buried within a visually opaque substance or Earth material.

GPR is also termed *ground probing, surface penetrating* (SPR), or subsurface radar. A GPR transmits a regular sequence of low-power packets of electromagnetic energy into the material or ground, and receives and detects the weak reflected signal from the buried target. The energy is in the form of either a very short-duration impulse, a sweep over a range of frequencies, radiation of noise over a defined band, or a pseudorandom coded sequence of pulses. Most GPR systems, which all need to comply with the relevant national and international regulations regarding radio transmitters, operate within the range of frequencies from 10 MHz to 10 GHz and can have a bandwidth of several GHz. GPR systems are a special class of ultra-wideband (UWB) radar systems. The typical average radiated power is in the order of a thousandth of a watt. The receiver is highly sensitive and can detect reflected signals of less than one millionth, of one millionth, of a watt. The topic of radar system design is covered in many texts, and useful information relating to GPR will be found in several texts [1–7].

The buried target can be a conductor, a dielectric, or combinations of both. The surrounding host material can be soil, Earth materials, wood, rocks, ice, fresh water, or manmade (synthetic) materials such as concrete or brick. A typical GPR achieves a range of up to a few meters, but some special systems can penetrate up to hundreds of meters or even kilometers. A few GPR systems have been operated from aircraft and from satellites to image geologic features buried beneath the Sahara Desert as well as measuring the depth of the (Earth's) Moon and features on Mars or comets.

The range of the GPR in the ground is limited because of the absorption that the signal undergoes, while it travels, on its two-way path, through the ground material. GPR works well through materials such as granite, dry sand, snow, ice, and freshwater, but will not penetrate certain clays that are high in salt content or saltwater because of the high absorption of electromagnetic energy of such materials. In air, the GPR signal travels at the speed of light, but is slowed down in ground materials by their dielectric constant; hence true range needs calibrating for each material. GPR will not penetrate metal because of the latter's conductivity.

There are now a number of commercially available equipments, and the technique is gradually developing in scope and capability. GPR has also been used successfully to provide forensic information in the course of criminal investigations, detect buried mines, survey roads,

detect utilities, measure geophysical strata, and in other applications. Many GPR systems are handheld, but systems can be used on vehicles for rapid survey, by means of an array of antennas. Other GPR systems are designed to be inserted into boreholes to provide images of the intervening rock. Typical GPR system attributes are given in Table 1.

Most GPR systems use separate, human-portable, transmit and receive antennas, which are placed on the surface of the ground and moved in a known pattern over the surface of the ground or material under investigation, and an image can be generated, in real time, on a display either in gray scale or in color. By systematically surveying the area in a regular grid pattern, a radar image of the ground can be built up. GPR images are displayed either as two-dimensional representations, using horizontal (x or y) and depth (z) axes or a horizontal plane representation (x , y) at a given depth (z) or as a three-dimensional reconstruction. GPR data may be classified as *A scan*, *B scan*, or *C scan* depending on the plane of image. *A scan* is a measurement at a single fixed point in space and is displayed in amplitude (y) and range (x). *B scan* is a representation usually in grayscale or color-coded image intensity of a plane (x , z or y , z) of scan, while *C scan* represents a horizontal plane (x , y) at a given depth (z). Alternatively, the GPR may be designed to provide an audible warning of target presence.

The radar image is very different from an optical image because the wavelengths of the illuminating radiation are similar in dimension to those of the target. This results in a much lower definition in the GPR image and one that is highly dependent on the propagation characteristics of the ground. The beam pattern of the antenna is widely spread in the dielectric, and this degrades the spatial resolution of the image, unless corrected. Refraction and anisotropic characteristics of the ground may also distort the image. For some longer-range systems, synthetic aperture techniques processing techniques are used to optimise the resolution of the image.

Unprocessed GPR images often show “bright spots” caused by multiple internal reflections as well as a distortion of the aspect ratio of the image of the target caused by variations in the velocity of propagation. Symmetric targets, such as spheres or pipes, cause migration of the reflected energy to a hyperbolic pattern. GPR images can be processed to compensate for these effects, and this is usually carried out offline. A GPR can be designed to detect specific targets such as interfaces in roads, pipes, and

Table 1. Characteristics of GPR System

Pulse Duration (ns)	Center Frequency (mHz)	Target Depth (m)	Depth Resolution (m)
0.5	2000	<0.25	0.025
1.0	1000	<0.5	0.05
2.0	500	<1.0	0.1
4.0	250	<2.0	0.2
8.0	125	<4.0	0.4
16.0	63	<8.0	0.8
32.0	31	<16.0	1.6

cables and localized objects such as cubes, spheres, and cylinders. GPR is capable of detecting features many hundreds of years old; hence a prospective site should remain unexcavated, prior to survey, so as to preserve its information and aid interpretation of the GPR image.

2. PHYSICS OF PROPAGATION

2.1. Introduction

Maxwell's equations are the foundation for the consideration of the propagation of electromagnetic waves. In free space the magnetic susceptibility and electric permittivity are constants; that is, they are independent of frequency and the medium is not dispersive. In a dielectric with zero loss tangent, no losses due to attenuation are encountered and hence there is no consideration of the attenuation, which occurs in real dielectric media.

If an alternating electric field is applied to a material, the individual molecules will be induced to rotate in an oscillatory manner about an axis through their centers, the inertia of the molecules preventing them from responding instantaneously. Similar translational effects can occur. The polarization produced by an applied field (such as a propagating radar wave) is closely related to the thermal mobility of the molecules and is, therefore, strongly temperature-dependent. In general, the relaxation time (which may be expressed as a relaxation frequency) depends on activation energy, the natural frequency of oscillation of the polarized particles, and temperature. Relaxation frequencies vary widely between different materials.

For example, maximum absorption occurs at very low frequencies in ice (10^3 Hz), whereas it takes place in the microwave region in water (10^6 – 10^{10} Hz); thus the effects of this phenomenon can have a direct bearing on the dielectric properties of materials at the frequencies employed by surface penetrating radars, especially if moisture is present within a material. There are a number of other mechanisms that cause a separation of positively and negatively charged ions resulting in electric polarization. These mechanisms can be associated with ionic atmospheres surrounding colloidal particles (particularly clay minerals), absorbed water and pore effects, as well as interfacial phenomenon between particles. The general form of the model that describes the frequency dependence of such systems is the Debye [8] relaxation equation

$$\epsilon' - i\epsilon'' = \epsilon_\infty + \frac{\epsilon_s - \epsilon_\infty}{1 + i\omega\tau}$$

where

- ϵ' = real part of the dielectric permittivity
- ϵ'' = imaginary part of the dielectric permittivity
- ϵ_∞ = high-frequency limiting value of the permittivity
- ϵ_s = low-frequency limiting value of the permittivity
- ω = radian frequency ($= 2\pi f$)
- τ = relaxation time constant

The frequency of maximum movement and loss occurs at $\omega = 1/\tau$.

In general, single relaxations are rarely observed in natural systems. Instead, there are distributions of relaxations corresponding to distributions of size scales that influence movement of charge. There are several equations describing such distributed systems, with the most common experimental observations in agreement with the model from Cole and Cole [9]

$$\epsilon' - i\epsilon'' = \epsilon_\infty + \frac{\epsilon_s - \epsilon_\infty}{1 + (i\omega\tau)^\alpha}$$

where α describes the breadth of the time constant distribution, from a single relaxation, $\alpha=1$, to an infinitely broad distribution, $\alpha=0$, with a common process. Different polarization processes may be described by a series of Cole–Cole equations with different values of α and other parameters.

The electromagnetic properties of a buried target must be different from those of the surrounding soil or material, and this means that to a first order its relative dielectric constant should be significantly lesser or greater than the host soil. Typically, most soils exhibit a relative dielectric constant, which ranges between 2 and 25. Freshwater has a relative dielectric constant of approximately 80. It should be noted that the ground and surface are quite likely to be inhomogeneous and contain inclusions of other rocks of various size as well as manmade debris. This suggests that the signal to clutter performance of the sensor is likely to be an important performance factor. Clutter may be regarded as any radar return that is not associated with the intended target and needs to be carefully defined.

2.2. Attenuation

Electromagnetic waves propagating through natural media experience losses, to both the electric (E) and magnetic (H) fields. This causes attenuation of the original electromagnetic wave. Plane waves are good approximations to real waves in many practical situations. More complicated electromagnetic wavefronts can be considered as a superimposition of plane waves, and this method may be used to gain an insight into more complex situations. For most soils of interest in ground penetrating radar the magnetic response is weak and need not be considered as a complex quantity, unlike the permittivity and conductivity. However, in certain soil types such as those derived from volcanic rocks or otherwise high in iron content, full consideration of the magnetic properties is necessary. In the case of lossy dielectric materials, both conduction and dielectric effects cause absorption of electromagnetic radiation.

The electromagnetic material properties that describe such a coupled system are in the complex propagation constant or circular wavenumber

$$\gamma = ik = \alpha + i\beta$$

where

- γ = propagation constant
- k = circular wavenumber
- α = attenuation constant (Np/m) (nepers per meter)
- $k^2 = \omega(\mu' - i\mu'')(\omega(\epsilon' - i\epsilon'') + i\sigma)$
- β = phase constant (rads/m)

with

$$\alpha = \omega \sqrt{\frac{(\mu'\epsilon' - \mu''(\epsilon'' + \frac{\sigma}{\omega}))^2 + (\mu''\epsilon' + \mu'(\epsilon'' + \frac{\sigma}{\omega}))^2}{2}}$$

$$\beta = \omega \sqrt{\frac{(\mu'\epsilon' - \mu''(\epsilon'' + \frac{\sigma}{\omega}))^2 + (\mu''\epsilon' + \mu'(\epsilon'' + \frac{\sigma}{\omega}))^2 + (\mu'\epsilon' - \mu''(\epsilon'' + \frac{\sigma}{\omega}))}{2}}$$

The field at a distance z from the source is given by

$$E(z, t) = E_0 e^{-\alpha z} e^{j(\omega t - \beta z)}$$

The wavelength λ in the medium is given in meters, and the frequency f is expressed in hertz:

$$\lambda = \frac{2\pi}{\beta} = \frac{v}{f}$$

The losses in such systems are described in terms of tangents of loss angles δ between fields and fluxes:

$$\tan \delta_e = \frac{\epsilon''}{\epsilon'} + \frac{\sigma}{\omega\epsilon'}$$

The electrical loss tangent represents the sum of the charge transport and polarization relaxation losses, and the phase angle between electric field and current density. The skin depth or attenuation length is $1/\alpha(\text{m})$; the distance electromagnetic energy travels while being attenuated by $1/e$ in amplitude. This distance is known as the *skin depth* d and provides an initial guide to the useful penetration depth of a ground penetrating radar system, although in some media the useful range may be greater.

In a lossy conducting dielectric the parameters associated with susceptibility can be rearranged to give

$$\alpha = \omega \sqrt{\left(\frac{\mu\epsilon'}{2} \left(\sqrt{1 + \left(\frac{\epsilon'}{\epsilon''}\right)^2} - 1\right)\right)}$$

$$\beta = \omega \sqrt{\left(\frac{\mu\epsilon'}{2} \left(\sqrt{1 + \left(\frac{\epsilon'}{\epsilon''}\right)^2} + 1\right)\right)}$$

and where the losses are low, then

$$\tan \delta_e = \frac{\sigma}{\omega\epsilon'}$$

This article has not considered the electromagnetic and magnetic loss tangent, and these may need to be considered in special cases.

It can be seen from the expressions above that the attenuation constant of a material is, to a first order, linearly related (in dB/m) to frequency. It is not sufficient to consider only the low-frequency conductivity when attempting to determine the loss tangent over the frequency range 10^7 – 10^{10} Hz. In the case of a material that is dry and relatively lossless, it may be reasonable to consider that $\tan \delta$

is constant over that frequency range. However, for materials that are wet and lossy such an approximation is invalid. There are, nevertheless, a number of other factors, that influence the effective penetration depth, notably the strength of reflection from the target sought, and the degree of clutter suppression of which the system is capable.

A first-order estimate of the various contributions to signal loss can be carried out using the standard radar range equation, although this is only applicable for far-field conditions and thus has restrictions:

$$P_r = \frac{P_t A G \sigma k}{(4\pi R^2)^2} e^{-\alpha 2R}$$

where

- P_t = transmitted power in watts
- P_r = received power in watts
- A = antenna gain
- G = antenna effective aperture
- R = range in meters
- σ = target radar cross section
- k = calibration coefficient

The cumulative losses include the transmission coefficients into the ground, the spreading losses describe the R^{-4} losses for a target of 1 m^2 , and the attenuation losses are for a soil with a ϵ_r of 9 and $\tan \delta$ of 0.1. Fixed losses include the transmission losses into the soil and the reflection loss from the target. In Fig. 1 the first meter (1 m) has not been plotted, as the radar range equation is not an accurate model in this range and the purpose of the explanation is to provide a basic introduction to first-order signal estimation.

2.3. Velocity

The velocity of propagation of electromagnetic waves in free space is approximately $3 \times 10^8 \text{ m/s}$ ($2.997925 \times 10^8 \text{ m/s}$),

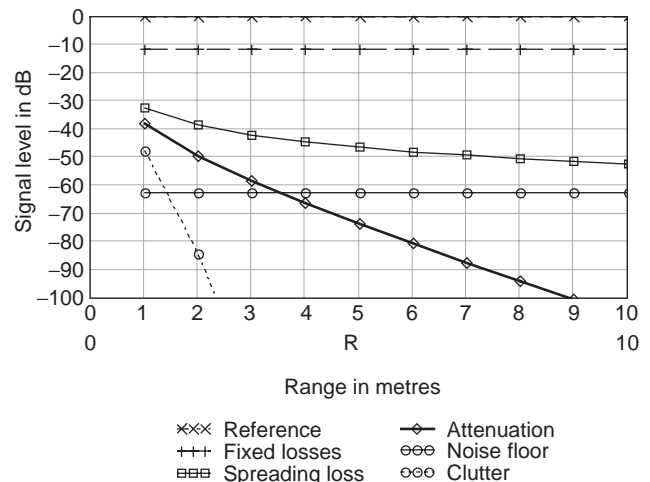


Figure 1. Graph of the typical losses encountered at 100 MHz by a GPR probing into the ground. (This figure is available in full color at <http://www.mrw.interscience.wiley.com/erfme>.)

but slows in a material depending on its relative permittivity and relative magnetic permeability. The velocity of propagation of electromagnetic waves in a soil with a value for ϵ_r of 9 would be slowed to 1.10^8 m/s. The time to a target at a range of 1 m is therefore 20 ns, and GPR systems operate at time ranges between a few nanoseconds up to 200 ns, although some systems for probing through ice may use ranges up to several tens of milliseconds.

In general, it is not possible to make a reliable estimate of propagation velocity or relative permittivity in a medium from a single measurement without trial holing or other supplementary information. Even in the case where a measurement is carried out at one location, it is often found that significant variations in velocity will occur within comparatively short distances from the original location. This can lead to significant errors in the estimation of depths of reflectors. One procedure that overcomes this limitation is known as *common-depth-point surveying*, which utilizes two antennas in bistatic operation at a number of transmit and receive positions. The velocity of propagation is also slowed by $\tan \delta$ and ϵ_r and assumes $\mu_r = 1$ and is given by

$$v = c \frac{\epsilon'}{2\epsilon_0} \sqrt{\left(\sqrt{1 + \left(\frac{\epsilon'}{\epsilon''}\right)^2} - 1 \right)}$$

It is also possible to derive velocity from multiple measurements scanning over a target, but this works well only in relatively uncluttered situations where the media has no anisotropic characteristics.

2.4. Reflection

In any estimation of received signal level it is necessary to consider the coefficients of reflection and transmission, as the wave passes through the dielectric to the target and Snell's laws describe the associated angles of incidence, reflection, transmission, and refraction. Where lossy materials are involved, complex angles of refraction may occur, unlike the simple classical case, and polarization and the Stoke's matrix may also be required for oriented high-aspect-ratio features such as pipes, wires, and fractures. The intrinsic impedance η of a medium is the relationship between the electric field E and the magnetic field H and is a complex quantity given by

$$\eta = \sqrt{\frac{-j\omega\mu}{\sigma - j\omega\epsilon}}$$

At the boundary between two media, some energy will be reflected and the remainder transmitted. The reflected field strength is described by the reflection coefficient r

$$r = \frac{\eta_2 - \eta_1}{\eta_2 + \eta_1}$$

where η_1 and η_2 are the impedances of media 1 and 2, respectively.

The reflection coefficient has a positive value when $\eta_2 > \eta_1$, such as where an air-filled void exists in a dielectric material. The effect on a pulse waveform is to change the phase of the reflected wavelet so that targets with relative dielectric constants different from those of the host material show different phase patterns of the reflected signal. However, the propagation dielectric of the host material, and the geometric characteristics of the target and its dielectric parameters affect the amplitude of the reflected signal.

2.5. Polarization

A complete description of the radar scattering cross section of a target includes a description of its polarization scattering characteristics. The polarizing properties of targets are described by the Stokes parameters, and the polarization coordinates can be represented on the Poincaré sphere. All of these are well described in standard texts. In summary, these descriptions allow the state of an electromagnetic wave to be described in terms of linear, elliptical, and circular polarization (left-handed or right-handed). It is well known that linear targets as depolarizing features and a linearly polarized crossed dipole antenna rotated about an axis normal to a linear target produces a sinusoidal variation in received signal. However, the null points are a distinct disadvantage because the operator is required to make two separate, axially rotated measurements at every point to be sure of detecting pipes at unknown orientations. An attractive technique is to radiate a circularly polarized wave, which automatically rotates the polarized vector in space and hence removes the direction of signal nulls.

2.6. Dispersion

The frequency-dependent nature of the dielectric properties of the material causes the phase velocity of the component frequencies of a wideband signal to suffer differential propagation values. Hence, there will be variation in the velocity of propagation with frequency. Dielectrics exhibiting this phenomenon are termed *dispersive*. In this situation, the different frequency components within a broadband radar pulse would travel at slightly different speeds, causing the pulse shape to change with time. However, the propagation characteristics of octave band radar signals remain largely unaffected by dispersion. In many instances, the potential variation in the velocity of wave propagation over the frequency range of interest is small and will be ignored.

2.7. Clutter

A major difficulty for operation of GPR systems is the presence of clutter within the material. *Clutter* is defined as sources of unwanted reflections that occur within the effective bandwidth and search window of the radar and present as spatially coherent reflectors. The definition of clutter depends heavily on the intended target. The operator of a GPR system searching for pipes may classify the interfaces between road layers as clutter, whereas the operator of a system measuring road layer thickness might

consider pipes and cables as sources of clutter. Careful definition and understanding are critically important in selecting and operating the best system and processing algorithms. Clutter can completely obscure the buried target and a proper understanding of its source and impact on the radar is essential.

2.8. Depth Resolution

Normally the range, or in the case of GPR, the depth resolution, of a radar is defined by considering the case of targets with identical radar scattering cross sections. In the case of Gaussian pulses, resolution can be achieved at pulse separations between 1.25 and 1.5 of the pulsewidth and can be defined by the Rayleigh criteria for resolution. Essentially, range resolution is defined by the bandwidth of the received signal. A receiver bandwidth in excess of 500 MHz and typically 1 GHz is required to provide a typical resolution of 5–20 cm, depending on the relative permittivity of the material.

When a number of features may be present, a signal having a larger bandwidth is required to be able to distinguish between the various targets and to show the detailed structure of a target. In this context it is the bandwidth of the received signal that is important, rather than that of the transmitted wavelet. The material acts a lowpass filter that modifies the transmitted spectrum in accordance with the electrical properties of the propagating medium. There are some applications of subsurface radar, such as road layer thickness measurement, where the feature of interest is a single interface. Under such circumstances, it is possible to determine the depth sufficiently accurately by measuring the elapsed time between the leading edge of the received wavelet provided the propagation velocity is accurately known.

Although a greater depth resolution is achieved in wetter materials for a given transmitted bandwidth, Earth materials with significant water content tend to have higher attenuation properties. This characteristic reduces the effective bandwidth, tending to balance out the change so that within certain bounds the resolution is approximately independent of loss within the propagating material.

Where interfaces are spaced more closely than a half-wavelength, the reflected signal from one interface will become convolved with that from the other. In such circumstances, some form of deconvolution processing would be required in order to recognize the responses from the individual interfaces and to enable them to be characterized and traced. Such processing is seldom carried out during standard commercial radar surveys.

It should be noted that the Rayleigh criteria for range resolution are less appropriate for the case of a weak target adjacent to strong target. For example, if the amplitude of the weak target is -20 dB relative to that of the strong target, different criteria are needed. Thus the resolution at the -20 dB amplitude level may be a more relevant criterion on which to assess the merits of competing system designs. This is because of the need to detect targets of low radar cross section in close proximity to targets of high radar cross section.

It can be shown [10] that for equivalent main 3 dB bandwidths, a radar design using a time-domain, direct receiver has a considerably better resolution at the -20 dB level than does a frequency-domain radar. This is primarily because the receiver of the frequency-domain radar cross-correlates the received signal. In essence, resolution has been achieved at the expense of signal-to-noise ratio, but this may not be so relevant to attenuation-limited operation.

2.9. Plan Resolution

The plan resolution of a subsurface radar system is important when localized targets are sought and when there is a need to distinguish between more than one at the same depth. Where the requirement is for location accuracy, which is primarily a topographic surveying function, the system requirement is less demanding.

The *plan resolution* is defined by the characteristics of the antenna and the signal processing employed. In general, to achieve an acceptable plan resolution, one must employ a high-gain antenna. This necessitates transmission of a sufficiently large aperture at the lowest frequency. To achieve small antenna dimensions and high gain therefore requires the use of a high carrier frequency, which may not penetrate the material to sufficient depth. When selecting equipment for a particular application, it is necessary to compromise between plan resolution, size of antenna, the scope for signal processing, and the ability to penetrate the material. Plan resolution improves as attenuation increases, provided there is sufficient signal to discriminate under the prevailing clutter conditions. In low-attenuation media the resolution obtained by the horizontal scanning technique is degraded, but under these conditions the use of advanced signal processing techniques becomes feasible and synthetic aperture techniques can dramatically increase the plan resolution. These techniques typically require measurements to be made using transmitter/receiver pairs at a number of antenna positions to generate a synthetic aperture or focus the image. Unlike conventional radars, which generally use a single antenna, most ground penetrating radar systems use separate transmit and receive antennas in what has been termed a *bistatic mode*.

3. PROPERTIES OF MATERIALS

Determination of the dielectric properties of Earth materials remains largely experimental. Rocks, soils, and concrete are complex materials composed of many different minerals in widely varying proportions, and their dielectric parameters may differ greatly even within materials, that are nominally similar. Most Earth materials contain moisture, usually with some measure of salinity. Since the relative permittivity of water is in the order of 80, even small amounts of moisture cause a significant increase of the relative permittivity of the material. A large number of workers have investigated the relationships between the physical, chemical, and mechanical properties of materials and their electrical and in particular microwave properties. In general, they have sought to develop

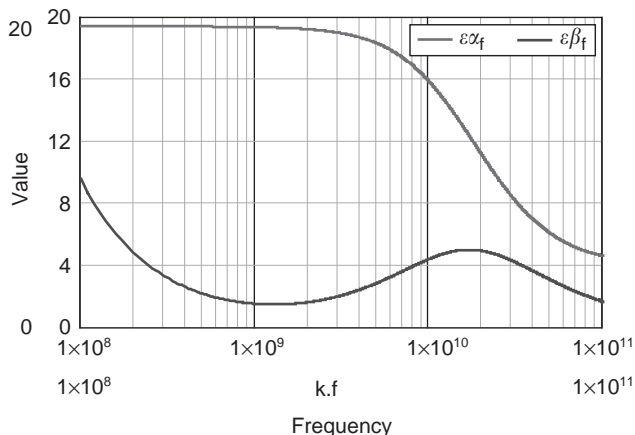


Figure 2. Real and imaginary dielectric losses plotted as a function of frequency for a typical Earth material with specified fractions of water, sand, silt, and clay. (This figure is available in full color at <http://www.mrw.interscience.wiley.com/erfme>.)

suitable models to link the properties of the material to its electromagnetic parameters. Such models provide a basis for understanding the behavior of electromagnetic waves within these media. The real and imaginary dielectric losses as a function of frequency can be plotted over a wide frequency range, and a typical result is shown in Fig. 2.

Information on the geologic properties of Earth soils can be found in the *Digital Soil Map of the World and Derived Soil Properties CD* © published by the Food and Agriculture Organisation of the United Nations. This enables the 10 map sheets of the world to be classified in terms of parameters such as pH, organic carbon content,

carbon/nitrogen ratio, clay mineralogy, soil depth, soil moisture capacity, and soil drainage class. Such information is useful in assessing the potential of RF techniques and particularly GPR for particular geographic regions.

There are two benefits to understanding soil properties in relation to GPR. (1) to understand the applicability of GPR to particular soils and hence the possibility of using GPR to detect buried targets such as pipe, cables, and landmines and (2) to use GPR to characterise soils and soil properties.

GPR can provide a detailed map of the subsurface, which, combined with traditional soil survey methods, can provide information on the type, lateral extent, and depth of the soil; the water table; and the layering and features of the soil and hence its local geology and history.

Since the mid-1970s GPR has been used in the united states by the Department of Agriculture–Natural Resources Conservation Service (USDA-NRCS) as a quality control tool for soil mapping and investigations. The use of GPR in soil survey activities has provided information about the soil resource that would have been unobtainable by other means or would have been uneconomic to obtain. An example of the results of this work is shown in Fig. 3.

4. GPR SYSTEMS

The choice of system design is to a large extent governed by the type of target, the resolution required, and the anticipated ground attenuation and clutter. The depth range of the radar system is likely to be primarily defined by the soil attenuation, once a particular frequency range has

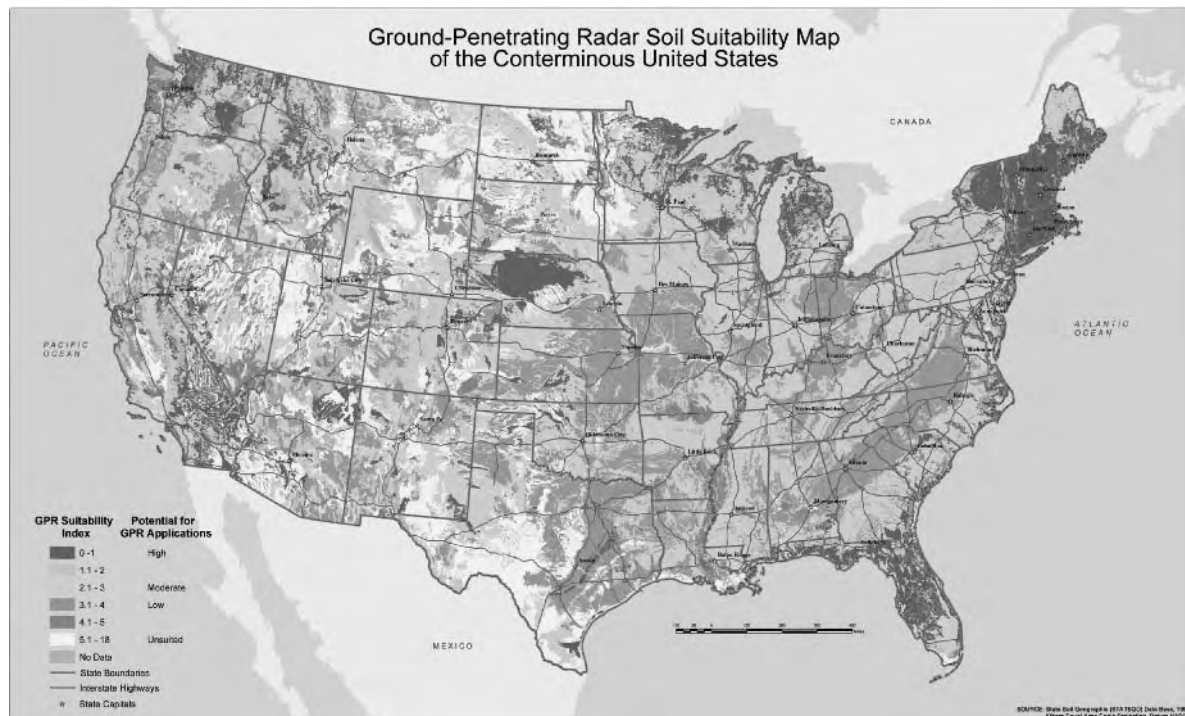


Figure 3. Soil suitability map for GPR applications in the United States. (Courtesy of USDA-NRCS.) (This figure is available in full color at <http://www.mrw.interscience.wiley.com/erfme>.)

been chosen. However, it can be shown that considerable variations (10–30 dB) in the sensitivity of competing system designs actually translate to relatively small changes in depth performance in lossy soils.

The selection of a suitable waveform for transmission, at least in terms of resolution, can be considered a function of the duration of the complex envelope of the measured signal. The output from most ultrawideband radar systems can be compared in terms of a time-domain representation of the waveform. Almost all types of radar can be assessed not just by their signal-to-noise and signal-to-clutter ratios but also by comparing their inherent range sensitivity. Such a procedure reveals the characteristics that control radar performance. The design of a GPR system is defined by the modulation technique and time-domain, frequency-domain, and noise-domain radar designs are most likely to be encountered.

The frequency-domain, matched-filter, radar receiver provides an optimum linear processing of radar in the presence of noise. The radar signal is processed by a receiver that cross-correlates the received waveform with a suitably time-delayed version of the transmitted waveform. The output results in a compressed pulse in which the amplitude of the latter and its position in delay time is related to the target radar characteristic. This type of receiver is widely used to process chirp, stepped-frequency, coded, and noise waveforms, and the design of such waveforms is extensively described in the literature. Time-domain radar systems are simpler in design and use a sampling receiver to downconvert the radar signals from the nanosecond timeframe to a millisecond timeframe that is easier to postprocess. However, a real disadvantage of the sampling receiver is its limited dynamic range and high noise floor.

A key parameter for most radar systems is the mean power. For portable, close-in radars the capacity of the power sources limits the radiated power. The frequency-domain radar transmits, on a repetitive basis, a nominally constant amplitude signal whose frequency increases in a linear progression from the lowest to the highest values. However, shaping of the envelope of the radiated signal reduces the mean power compared with the instantaneous peak value. The time-domain radar transmits, on a repetitive basis, a short-duration impulse. Consequently the peak power is significantly greater than the mean power. This is not the case with noise radar, whose radiated power per unit bandwidth is optimally low compared with the frequency-domain and time-domain designs.

5. MODULATION TECHNIQUES

There are three basic modulation techniques: time-domain, frequency-domain, and noise-coded radar.

5.1. Time-Domain Radar

Most commercially available ground probing radar systems use short pulses or impulses such as the Ricker wavelet shown in Fig. 4. The high-speed sequential sampling approach used to acquire RF waveforms produces a low SNR because the spectrum of the sampling pulse is a

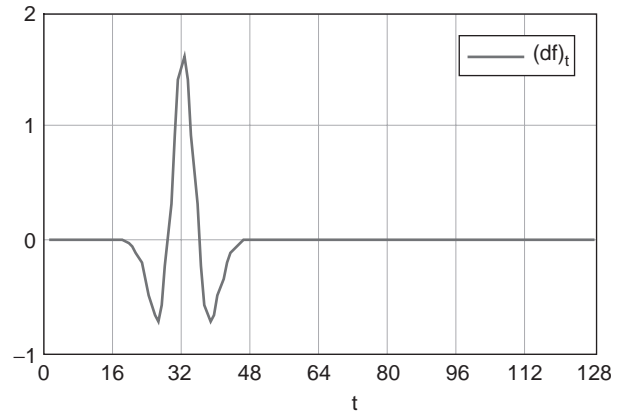


Figure 4. Ricker wavelet (amplitude vs. time).

poor match for that of the received pulse. In general, the dynamic range of the sampling receiver is typically 60 dB, without time varying gain, and with time varying gain is equivalent to 90 dB or more. Signal averaging can increase the effective sensitivity by the amount of averaging, and this can be typically 10–30 dB. The overall dynamic range is set largely by the ratio of the mean power to the effective receiver sensitivity and can extend up to 150 dB. The antennas that can be used are limited to linear phase designs such as resistively loaded dipoles, TEM horns, or impulse radiating antennas (IRAs) unless the dispersive properties of the antenna used are compensated by suitable post-processing filtering.

5.2. Frequency-Domain Radar

The main potential advantages of the frequency-domain radar are the wider dynamic range, lower noise figure, and higher mean powers that can be radiated. There are two main types of frequency-domain radar: frequency-modulated carrier wave (FMCW) and stepped-frequency carrier wave (SFCW). FMCW radar transmits a continuously changing carrier frequency by means of a voltage-controlled oscillator (VCO) over a chosen frequency range on a repetitive basis as shown in Fig. 5. The received signal is mixed with a sample of the transmitted waveform and results in a difference frequency that is related to the phase of the received signal; hence its time delay and hence range of the target. The difference frequency or intermediate frequency (IF) must be derived from an I/Q mixer pair if the information equivalent to a time-domain representation is required, as a single-ended mixer provides only the modulus of the time-domain waveform. The FMCW radar system is particularly sensitive to certain parameters. In particular, it requires a high degree of linearity of frequency sweep with time to avoid spectral widening of the IF and hence degradation of system resolution. An assessment of the sensitivity of sidelobe level to linearity was made by Dennis and Gibbs [11], who showed the ratio of sidelobe to peak level was dependent on the sweep linearity. Practically the effect of a nonlinearity of a few percent is to cause significant sidelobes.

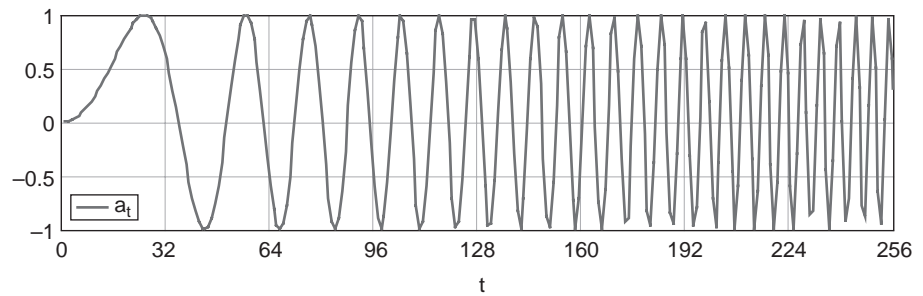


Figure 5. Typical FMCW transmitted swept waveform (amplitude vs. time).

The SFCW radar transmits a series of incremental frequencies and stores the received IF signal to then carry out a fast Fourier transform (FFT) reconstruction of the time-domain equivalent waveform. The SFCW has found many applications, and the impact of mobile communications technology has had a significant impact on reducing the cost of radar components for this design. Two forms of the synthesized radar can be considered. The first and simplest system is stepped-frequency continuous-wave radar. The second form is more complex in that each individual frequency is appropriately weighted in amplitude and phase prior to transmission. Normally the radar is calibrated to establish a reference plane for measurement as well as to reduce the effect of variations in the frequency characteristics of components and antennas.

A much wider class of antenna is available for use by the designer of frequency-domain radars. The sensitivity of the receiver is much better than the time-domain equivalent, simply by virtue of its lower bandwidth and hence lower thermal noise. Typically, a sensitivity of 120 dBm is found, and a system dynamic range of 180 dB is feasible. However, the FMCW ground probing radar system is particularly sensitive to certain parameters. In particular, it requires a high degree of linearity of frequency sweep with time to avoid spectral widening of the IF and hence degradation of the system resolution.

The main potential advantages of a stepped-frequency or FMCW ground probing radar are its ability to adjust the range of frequencies of operation to suit the material and targets and electromagnetic environment under investigation if the antenna has an adequate passband of frequencies. It can radiate a higher mean power level per spectral line, and its ability to integrate the received signal level improves the system sensitivity. The calibration of the radar does, of course, depend on stable system characteristics and antenna parameters that are invariant with the spacing of the front surface and the antenna. Although on first consideration frequency-domain radars should offer a sensitivity superior to that of time-domain radars, because of their lower receiver bandwidth and, hence thermal noise, both the type of receiver and the range sidelobes of the radiated spectrum may result in an equivalent or worse sensitivity in terms of range resolution as discussed above.

5.3. Noise or PseudoRandom Coded Radar

More recently, work has been carried out on noise modulation and pseudorandom coded modulation techniques for

GPR. The main advantage of these methods is that the energy transmitted is spread more evenly over the spectrum than with any other modulation method, and hence the likelihood of interference to other users of the spectrum is minimized. In addition, the chances of other users of, say, mobile phones interfering with the GPR operator are also reduced. The mean power is the lowest of any of the modulation schemes, and this is helpful in meeting regulatory requirements.

The transmitted signal has noiselike characteristics, and the received signal is cross-correlated with a sample of the transmitted signal. The range of the target is given by the time position of the cross-correlated signal and the amplitude by the peak of the cross-correlated signal. Control of the cross-correlation sidelobes is vital to achieve good range resolution, and the sidelobes are affected by the antenna and system characteristics as well as the duration and randomness of the transmitted waveform. Further information is given by Narayan et al. [12] and Sachs et al. [13].

6. ANTENNAS

In the ultrawideband case the radar antennas are considered in terms of their transfer function rather than their gains or effective apertures. In many cases separate transmit and receive antennas are used; hence their transfer functions may not be identical. The type of antenna that is used with ultrawideband radar has an important role in defining the performance of the radar.

The types of antenna that are useful to the designer of ultrawideband radar fall into two groups: dispersive antennas and nondispersive antennas. However, in principle, all antennas are dispersive to some extent. Examples of dispersive antennas that have been used in ultrawideband radar are the exponential spiral, the Archimedean spiral, the logarithmic planar antenna, the Vivaldi antenna, slot antennas, and the exponential horn. The impulse response of this class of antenna is extended, and generally results in a "chirp" waveform if the input is an impulse. Examples of nondispersive antennas are the TEM horn; the bicone; the bowtie; the resistive, lumped-element loaded antenna; and the continuously, resistively loaded antenna. The input voltage driving function to the terminals of the antenna in an impulse radar is typically a Gaussian pulse, and this requires the impulse response of the antenna to be extremely short, mainly to prevent the antenna from distorting the input function and generating

time sidelobes. These time sidelobes would obscure targets that are close in range to the target of interest; in other words, the resolution of the radar can become degraded if the impulse response of the antenna is significantly extended.

Element antennas are characterized by linear polarization, low directivity, and relatively limited bandwidth unless either end loading or distributed loading techniques are employed, in which case bandwidth is increased at the expense of radiation efficiency. Horn antennas have found most use with FMCW ultrawideband radars where the generally higher frequency of operation and relaxation of the requirement for linear phase response permit the consideration of this class of antenna. FMCW ultrawideband radars have used an offset paraboloid fed by a ridged horn. This arrangement was designed to focus the radiation into the ground at a slant angle to reduce the level of the reflection from the ground. Care needs to be taken in such arrangements to minimize the effect of back- and sidelobes from the feed antenna, which can easily generate reflection from the ground surface.

One method of radiating circular polarization is to use an equiangular spiral antenna. The dispersive nature of this type of antenna causes an increase in the duration of the transmitted waveforms, and the radiated pulse takes the form of a “chirp” in which high frequencies are radiated first, followed by the low frequencies. This effect, however, may be compensated by a “spiking” filter, which may take the form of a conventional matched filter or a more sophisticated filter such as Wiener filter.

7. SIGNAL AND IMAGE PROCESSING

The most basic GPR data record is an *A* scan, and an example is shown in Fig. 6. An *A* scan provides an amplitude–time record of a single measurement over a target. Only amplitude range information is plotted. Ground penetrating radar is generally used in such a way as to generate a sequence of *A* scans related to the survey position on the ground surface. This sequence can be termed a *B* scan, and an example is shown in Fig. 7. This effectively

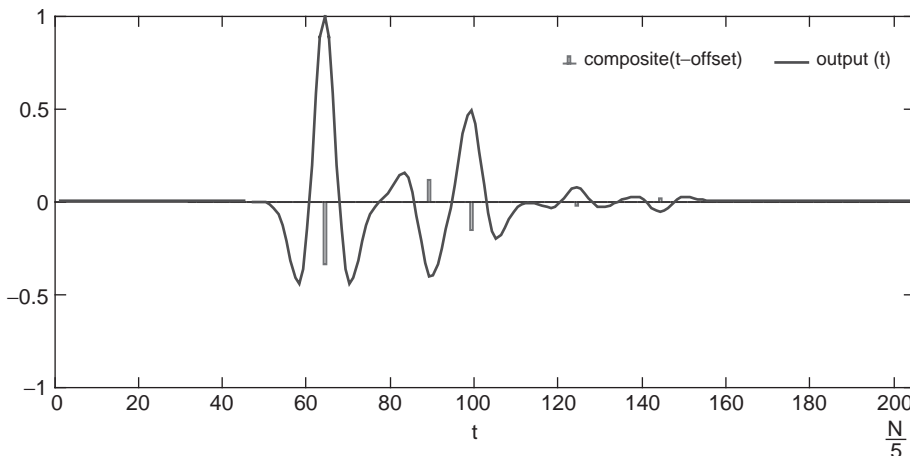


Figure 6. Typical example of GPR *A* scan (amplitude/time-modeled data).

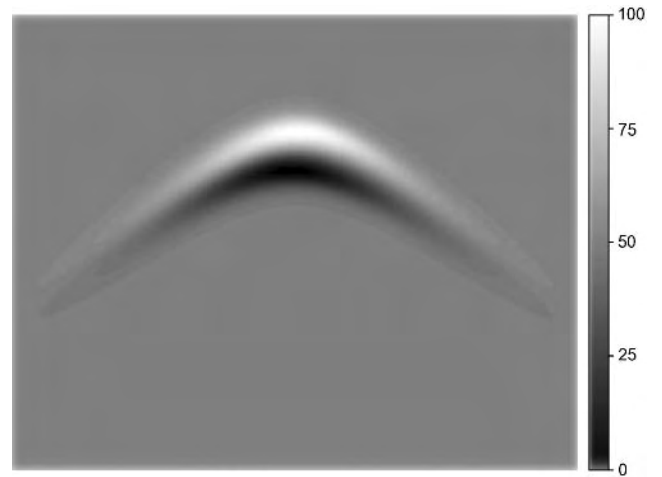


Figure 7. Typical example of *B* scan (y, z axis, gray scale image of modeled data).

represents on one axis (z) depth and the orthogonal axis (x or y) linear position. The amplitude of the signal may be shown as a series of overlapping signals or alternatively a “wiggle plot” (borrowed from the seismic terminology) or a grayscale coded intensity plot or a pseudocolor image. In the modeled example shown, the hyperbolic spreading of the target spatial response can be seen. As shown in Fig. 8, a *C* scan consists of a plan view (x, y plane over a defined range of depth z).

As the antennas generally used for surface penetrating radars have a poor directivity, the pattern of the reflected waveform in the *B* scan represented the spatial convolution of the antenna pattern with the point source of the target. This pattern may be deconvolved using any of the following processes: synthetic aperture processing, conjugate gradient methods, and reverse time migration. Many of these techniques work well on isolated targets such as pipes, which have well defined geometric boundaries. The situation is more difficult with stratified layers and, of course, anisotropic materials. When a focused image of the buried object is created, whether as a *B* or *C* scan (area at a particular range of depths), it is necessary to interpret

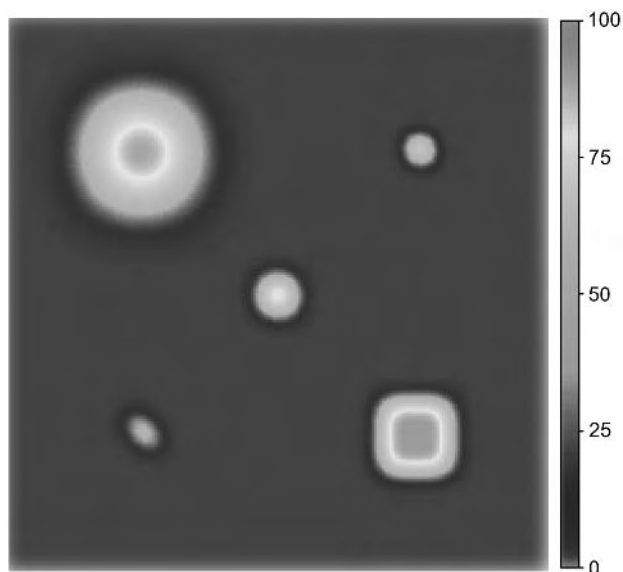


Figure 8. Typical example of *C* scan (x - y plane at defined z -range color image of modeled data of buried landmines). (This figure is available in full color at <http://www.mrw.interscience.wiley.com/erfme>.)

the radar image as being generated by a physical structure. This is not always easy in the case of a cluttered image, and a great deal still depends on the field experience of the operator.

Automated methods based on standard image processing methods (mask filtering), image matching, and similar methods, as well as methods based on neural networks, have been investigated. The variability of ground conditions, as well as the physics of EM wave propagation and reflection, must be carefully taken into account in generating pattern libraries. For example, the depth image of a void is always apparently smaller than the void's physical size; corner reflectors of any reasonable size generate large, apparently discontinuous reflection images; and conductive targets, which reverberate by means of stored energy, create extended-depth images. The image of a buried target generated by a subsurface radar will not, of course, correspond to the target's geometric representation. The fundamental reasons for this are related to the ratio of the wavelength of the radiation and the physical dimensions of the target. In most cases for surface penetrating radar, the ratio is close to unity. This compares very differently with an optical image, which is obtained with wavelengths such that the ratio is considerably greater than unity. In ground penetrating radar, applications, the effect of combinations of scattering planes, for example, the corner reflector, can cause "bright spots," in the image and variations in the velocity of propagation can cause dilation of the aspect ratio of the image. While many images can be focused to reduce the effect of antenna beamspeading, regeneration of a geometric model is a much more complex procedure and is rarely attempted.

The general objective of signal processing as applied to ground penetrating radar is to present either an image that can readily be interpreted by the operator or to classify the target return with respect to a known test

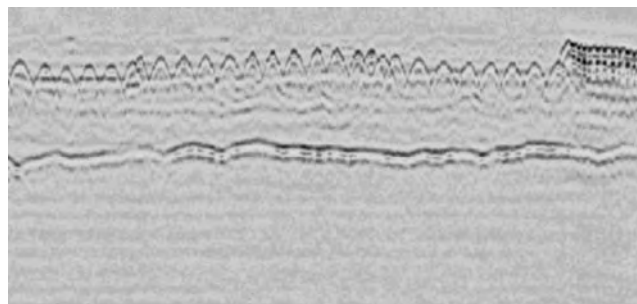


Figure 9. GPR data from reinforced-concrete roadway taken with 1-GHz SPR radar system at 50-ns time window and 3 m horizontal distance. (Courtesy of ERA Technology.) (This figure is available in full color at <http://www.mrw.interscience.wiley.com/erfme>.)

procedure or template. While much work has been carried out on 3D SAR processing, there is a tendency for this to be restricted to situations where the customer is prepared to pay for the additional information.

The general processing problem encountered in dealing with ground penetrating radar data is in the widest sense the extraction of a localized wavelet function from a time series that displays time-domain characteristics very similar to those of the wavelet. This time series is generated by signals from the ground and other reflecting surfaces, as well as internally from the radar system. Unlike conventional radar systems in which the target can generally be regarded as being in motion compared with the clutter, in the ground penetrating radar case, the target and the clutter are spatially fixed and the radar antenna is moved with respect to the environment.

It is assumed that data are recorded to an adequate resolution and bandwidth. Most antennas used in surface penetrating applications have a limited low-frequency response and tend to act as highpass filters effectively differentiating the applied impulse, hence creating a wavelet. In the case of antennas operated in close proximity to the ground, the antenna characteristics may vary as a result of changes in the ground surface electrical parameters. Any processing scheme that relies on invariant antenna parameters should take into account the mode of operation of the antennas and the degree of stability that is practically realizable. This is a particular issue for GPR and needs careful attention to reduce the effect of antenna-ground surface interaction.

Alternative methods of processing are associated with identifying target resonances using singularity expansion methods (SEMs) to evaluate the target response. Early research using Prony methods encountered difficulties due to the ill-conditioned nature of natural frequency extraction from noisy data.

Some of the ancillary requirements of an operational subsurface radar system need to be considered. There is a need for an accurate, small-scale, low-cost position referencing system for use with radar for subsurface survey techniques. It is important that data can be related to a true geographic reference particularly when filed on digital mapping systems and used to define areas of safe working. It is necessary to provide some means of scanning the antenna. Obviously a basic approach is the

handheld device, but this places some limitations on the signal processing strategies.

Another consideration is the plane of polarization of the electromagnetic energy. For targets with one large area dimension such as a pipe, the radar cross-scattering section will be larger when the polarization vector is in line with the pipe. This means that any area that is surveyed with, say, parallel dipoles must be surveyed in orthogonal directions to ensure that no targets are missed. The same principle also relates to crossed dipole antennas.

8. APPLICATIONS

8.1. Introduction

It is possible to provide only a brief summary of the wide variety of the applications for GPR, which has in some cases become an established and routine method of subsurface investigation. In other applications, such as borehole detection, the technique is under development, whereas in others, such as mine detection, basic research is being carried out, although some equipment is now being used in field trials. GPR, in the hands of an expert, provides a safe and noninvasive method of conducting speculative searches without the need for unnecessary disruption and excavation.

GPR has significantly improved the efficiency of the exploratory work that is fundamental to the construction and civil engineering industries, the police and forensic sectors, security/intelligence forces, and archaeological surveys.

GPR has been very successfully used in forensic investigations. The most notorious cases are in the United Kingdom in 1994, when the gravesites, under concrete and in the house of Fred West, of the victims of the serial murderer, were pinpointed. In Belgium, the gravesites of the victims of the pedophile Dutroux were detected in 1996.

Archaeological applications of GPR have been varied, ranging from attempts to detect the Ark to the exploration of Egyptian (see Fig. 10) and North American Indian sites as well as castles and monasteries in Europe. The quality of the radar image can be exceptionally good, although correct understanding normally requires joint interpretation by the archaeologists and radar specialists see (Fig. 11).

Abandoned antipersonnel landmines and unexploded ordnance are a major hindrance to the recovery of many countries from war. Their effect on the civilian population is disastrous, and major efforts are being made by the international community to eliminate the problem. Most detection is done with metal detectors, which respond to the large amount of metallic debris in abandoned battlefield areas and hence have difficulty in detecting the minimum metal or plastic, mine. GPR technology is being applied to this problem as a means of reducing the false-alarm rate and providing improved detection of low-metal-content mines. An example of data gathered from a 4-m wide GPR 32-channel array is shown in Fig. 12.

GPR has been used for surveying many different types of geologic strata ranging from exploration of the Arctic

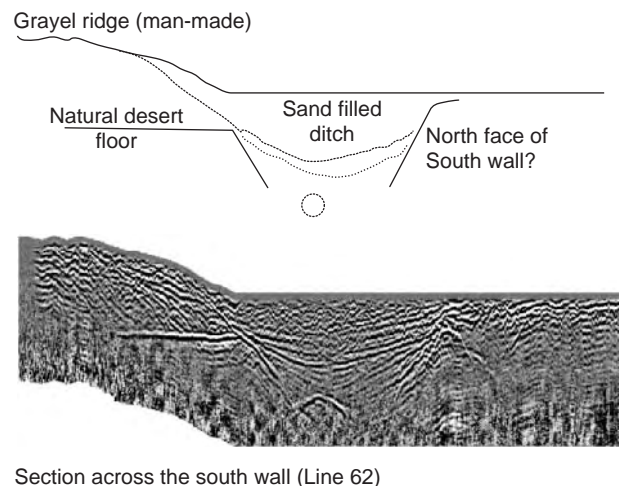


Figure 10. GPR system in use for archaeological surveying in Saqqara, Egypt. (Courtesy of ERA Technology.)

and Antarctic icecaps and the permafrost regions of North America, to mapping of granite, limestone, marble, and other hard rocks as well as geophysical strata.

The thickness of the various layers of a road can be measured using radar techniques. The great advantage is that this method is nondestructive and high-speed (>40 km/h) and can be applied dynamically to achieve a continuous profile or rolling map. The accuracy of calibration tends to reduce as a function of depth because of the attenuation characteristics of the ground. The accuracy may be quite high (i.e., a few millimeters) for the surface wearing course but will degrade to centimeters at depths of 1 m. An example is shown in Fig. 9.

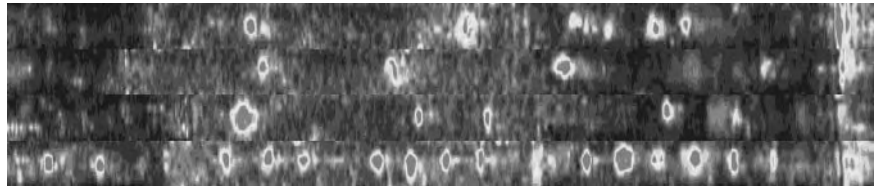
While most GPR systems are used in close proximity to the ground, airborne systems have been able to map ice formations and glaciers, and penetrate through forest canopy. Airborne GPR, processed using synthetic aperture techniques, has been used to detect buried metallic mines from a height of several hundred meters. In addition, the SIR-C satellite SAR radar has imaged buried artefacts in desert conditions, and the JPL Website <http://southport>.



Section across the south wall (Line 62)

Figure 11. Radar cross section through buried wall (horizontal 15 m; vertical 3.5 m). (Courtesy of ERA Technology.)

Figure 12. Radar plan image of buried AT mines (4m swathe width; 10m survey length). (Courtesy of ERA Technology.) (This figure is available in full color at <http://www.mrw.interscience.wiley.com/erfme>.)



jpl.nasa.gov/sir-c/ is an important source of radar imagery.

A list of the applications is given below, and the reader can find further information from the literature and publications referenced:

- Archaeological investigations
- Bridge deck analysis
- Borehole inspection
- Building condition assessment
- Contaminated-land investigation
- Detection of buried mines (antipersonnel and antitank)
- Evaluation of reinforced concrete
- Forensic investigations
- Geophysical investigations
- Medical imaging
- Pipes and cable detection
- Planetary exploration
- Rail track and bed inspection
- Remote sensing from aircraft and satellites
- Road condition survey
- Security applications
- Snow, ice, and glaciers
- Timber condition
- Tunnel linings
- Wall condition

Readers are encouraged to review the applications described in the following sources.

8.2. GPR Conferences

GPR 2000—Gold Coast, Australia 8th Int. Conf. Ground Penetrating Radar, David Noon, University of Queensland; email noon@cssip.uq.edu.au.

GPR '98—Lawrence, Kansas, USA 7th Int. Conf. Ground Penetrating Radar Dr. Richard Plumb, Univ. Kansas; email rplumb@binghamton.edu.

GPR '96—Sendai, Japan 6th Int. Conf. Ground Penetrating Radar, Prof. Motoyuki Sato, Tohoku Univ. email sato@cneas.tohoku.ac.jp.

GPR '94—Kitchener, Ontario Canada 5th Int. Conf. Ground Penetrating Radar, David Redman, Sensors & Software; email dr@sensoft.ca.

GPR '92—Rovaniemi, Finland 4th Int. Conf. Ground Penetrating Radar, Pauli Hanninen, Geological Survey of Finland.

GPR '90—Lakewood, Colorado (USA) 3rd Int. Conf. Ground Penetrating Radar, Prof. Gary Olhoeft, Colorado School of Mines; email golhoeft@mines.edu.

1988—Gainesville, Florida (USA) 2nd Int. Symp. Geotechnical Applications of Ground Penetrating Radar, Mary Collins, Univ. Florida; email mec@gnu.ifas.ufl.edu.

1986—Tifton, Georgia (USA) 1st Int. Conf. Geotechnical Applications of Ground Penetrating Radar.

8.3. International Workshops on Advanced GPR

IWA GPR Delft 01, 1st Int. Workshop on Advanced Ground Penetrating Radar (International Workshop), proceedings published in *Subsurface Sensing Technologies and Applications* (Kluwer Academic Publishers).

IWA GPR Delft 03, 2nd Int. Workshop on Advanced Ground Penetrating Radar (International Workshop), Weblink <http://irctr.et.tudelft.nl/IWAGPR/>.

8.4. Institution of Electrical Engineers (UK)

See also Radar 2002; <http://www.iee.org/Publish/Digests/conf2002.cfm>.

See the IEE Proceedings of Radar, Sonar, and Navigation; Weblink <http://ioj.iee.org.uk/journals/ip-rsn>.

See Edinburgh MD96, Detection of Abandoned Landmines (Main Past Conf.); Weblink <http://www.iee.org/Publish/Digests/conf1996.cfm>.

See Edinburgh MD98, 2nd Int. Conf. Detection of Abandoned Landmines (Main Past Conf.); Weblink <http://www.iee.org/Publish/Digests/conf1998.cfm>.

8.5. Institution of Electrical and Electronic Engineers (USA)

See proceedings particularly of the societies for

Antennas and Propagation; <http://www.ieeeaps.org/>.
Aerospace and Electronic Systems; <http://ewh.ieee.org/soc/aes/>.

For Radar conferences, see also <http://www.ewh.ieee.org/soc/aes/Conferences.html>.

Geoscience and Remote Sensing; <http://www.ewh.ieee.org/soc/grss/>.

Microwave Theory and Transactions; <http://www.mtt.org/>.

8.6. SPIE Conferences

SPIE Orlando—SPIE Detection and Remediation Technologies for Mines and Minelike Targets 1995 to 2003; <http://spie.org/app/conferences/index.cfm?fuseaction=archive&year=2002>.

8.7. Geophysics

<http://www.geo-online.org/>.

8.8. Subsurface Sensing Technologies and Applications

<http://www.kluweronline.com/issn/1566-0184>.

8.9. Literature on GPR Applications

D. J. Daniels, *Ground Penetrating Radar*, IEE Radar Sonar Navigation and Avionics Series, Vol. 6, 1996.

M. Skolnik, *Introduction to Radar Systems*, 2nd ed., McGraw-Hill, 1981.

S. Cloude, *Introduction to Electromagnetic Wave Propagation and Antennas*, UCL Press, 1995.

J. Hunter, C. Roberts, and A. Martin, *Studies in Crime: An Introduction to Forensic Archaeology*, B. T. Batsford Ltd. 1996.

9. REGULATION

All countries require that GPR systems be properly regulated and operated in accordance with national and international requirements. Users should consult with their national authorities to determine the regulatory environment.

Within the European Union (EU) there are two main considerations governing the use of ground penetrating radar (GPR): (1) the use of the equipment as a deliberate radiofrequency radiator and (2) usage as equipment that must satisfy the EMC requirements of the EU. The ETSI regulatory body is in the process of drafting specifications, and information can be found at <http://www.etsi.org> that will cover the use of such equipment as a deliberate radiofrequency radiator. Planned legislation and an ETSI product specification at some undefined time in the future means that this equipment will eventually need to conform to the R&TTE directive. In the short term until a new product specification is introduced and formally published in the *Official Journal of the European Communities*, the EMC directive should be applied. All equipment, including ultrawideband radar or ground probing radar, must be CE marked to demonstrate that it satisfies the relevant directives of the European Union. The CE mark may be applied only when the requirements of all other relevant EU directives, such as safety, have also been demonstrated.

In the United States the FCC Website <http://www.fcc.gov/aboutus.html> provided the following information in February 2002:

Feb 2002 Washington, D.C.—The Federal Communication Commission (FCC) adopted today a First Report and Order that permits the marketing and operation of certain types of new products incorporating ultra-wideband (“UWB”)

technology. UWB technology holds great promise for a vast array of new applications that have the potential to provide significant benefits for public safety, businesses and consumers in a variety of applications such as radar imaging of objects buried under the ground or behind walls and short-range, high-speed data transmissions.

UWB devices operate by employing very narrow or short duration pulses that result in very large or wideband transmission bandwidths. With appropriate technical standards, UWB devices can operate using spectrum occupied by existing radio services without causing interference, thereby permitting scarce spectrum resources to be used more efficiently. This First Report and Order (“Order”) includes standards designed to ensure that existing and planned radio services, particularly safety services, are adequately protected. The FCC will act vigorously to enforce the rules and act quickly on any reports of interference.

The standards adopted today represent a cautious first step with UWB technology. These standards are based in large measure on standards that the National Telecommunications and Information Administration (“NTIA”) believes are necessary to protect against interference to vital federal government operations. Since there is no production UWB equipment available and there is little operational experience with the impact of UWB on other radio services, the Commission chose in this First Report and Order to err on the side of conservatism in setting emission limits when there were unresolved interference issues. The Commission intends within the next six to twelve months to review the standards for UWB devices and issue a further notice of proposed rule making to explore more flexible standards and address the operation of additional types of UWB operations and technology.

Ground Penetrating Radar Systems: GPR’s must be operated below 960 MHz or in the frequency band 3.1–10.6 GHz. GPR’s operate only when in contact with or within close proximity of, the ground for the purpose of detecting or obtaining the images of buried objects. The energy from the GPR is intentionally directed down into the ground for this purpose. Operation is restricted to law enforcement, fire and rescue organizations, to scientific research institutions, to commercial mining companies, and to construction companies.

It is understood that waivers have been granted to certain operators and the FCC are in the process of reviewing the policy announced in 2002. In February 2003 the following announcement was made:

In response to the petitions, the Commission amended the rules to facilitate the operation of through-wall imaging systems by law enforcement, emergency rescue and firefighter personnel in emergency situations; eliminated the requirement that GPR’s and wall imaging systems operate with their – 10 dB bandwidths below 960 MHz or above 3.1 GHz; specified the limitations on who may operate ground penetrating radar (GPR) systems and wall imaging systems and for what purposes; eliminated the requirement for non-hand held GPR’s to employ a dead man switch; clarified the coordination requirements for imaging devices; and clarified the rules regarding emissions produced by digital circuitry used by UWB transmitters.

For more information, see <http://www.g-p-r.com/>.

10. SUMMARY

Advances in the performance and design of lightweight and compact GPR radar sensors have been significant since the mid-1990s because of the impact of the telecommunications industry and availability of affordable high-power computing; the volume of published papers and conferences, some devoted entirely to GPR, has risen considerably since then. Inevitably there have been some claims for GPR capability that are simply outside the realms of known physics and unfortunately have been accepted by some sections of the media. Tuley et al. [14] give an excellent review of one such claim. There has also been some duplication of basic research. However, developments in the field of noise and pseudorandom coded [15] modulation techniques together with better signal and image processing algorithms as well as spinoff from improved microwave technology originating from the telecommunications industry will have a significant impact on GPR in the future.

It is reasonable to conclude that GPR is now an established branch of science. It has links to electronic engineering, mathematics, signal processing, geophysics, civil engineering, structural engineering, archaeology, forensic science planetary exploration, as well as unexploded ordnance (UXO) clearance and mining. GPR has achieved academic recognition as well as commercial impact and seems set to continue its impact into all branches of human activity where buried objects are sought.

BIBLIOGRAPHY

1. D. J. Daniels, *Ground Penetrating Radar*, 2nd ed., IEE Radar Sonar Navigation and Avionics Series, London, 2004.
2. C. E. Cook and M. Bernfeld, *Radar Signals, An Introduction to Theory and Application*, Artech House, Norwood, MA, 1993, p. 9.
3. M. Skolnik, *Radar Handbook*, 2nd ed., McGraw-Hill, New York, 1985, Chap. 10.
4. F. Nathanson, *Radar Design Principles*, SciTech Publishing, 1969, Chap. 8, pp. 276–318.
5. D. R. Wehner, *High Resolution Radar*, Artech House, Norwood, MA, Chap. 4.
6. G. Galati, *Advanced Radar Techniques and Systems*, IEE Radar Sonar Navigation and Avionics Series, London, 1994, Vol. 4, p. 104.
7. L. Y. Astanin and A. A. Kostylev, *Ultra-Wideband Radar Measurements Systems*, IEE Radar Sonar Navigation and Avionics Series, London, 1997, Vol. 7, Chap. 1.
8. P. Debye, *Polar Molecules*, Chemical Catalog Co., New York, 1929.
9. K. S. Cole and R. S. Cole, Dispersion and absorption in dielectrics, I, alternating current characteristics, *J. Phys. Chem.* **9**: 341–351 (1941).
10. D. J. Daniels, Resolution of UWB signals, *IEE Proc. Radar Sonar and Navig.* **146**:189–194 (Aug. 1999).
11. P. Dennis and S. E. Gibbs, Solid-state linear FMCW systems—their promise and their problems, *Proc. IEEE Int. Microwave Conf.*, Atlanta, 1974, pp. 340–345.
12. R. M. Narayanan, Y. Xu, P. D. Hoffmeyer, and J. O. Curtis, Design, performance, and applications of a coherent random noise radar, *Opt. Eng.* **37**(6):1855–1869 (June 1998).
13. J. Sachs, P. Peyerl, F. Tkac, and M. Kmec, Digital ultra-wide-band-sensor electronics integrated in SiGe-technology, *Proc. EuMC*, Milan (Italy), Sept. 2002, Vol. II, pp. 539–542.
14. M. T. Tuley, J. M. Ralston, F. S. Rotondo, A. M. Andrews, and E. M. Rosen, Evaluation of EarthRadar unexploded ordnance testing at Fort A.P. Hill, Virginia, *IEEE Aerospace Electron. Syst. Mag.* **17**(5):10–12 (May 2002).
15. J. Sachs and P. Peyerl, Chip integrated UWB radar electronics, *Proc. 3rd DTIF Workshop on Ground Penetrating Radar in Support of Humanitarian Demining, JRC*, Ispra (Italy), Sept. 2002.

GUIDED ELECTROMAGNETIC WAVES

WILLIAM T. JOINES
Duke University

Closed-form solutions for TEM, TM, and TE waves in guiding structures are obtained from Maxwell's equations. Propagation parameters, frequency ranges, broadbanding techniques, and design examples are presented. Dielectric waveguides for microwave and optical frequencies are also presented.

1. MAXWELL'S EQUATIONS

Maxwell's equations in differential form, as determined from Faraday's, Ampere's, and Gauss' laws, respectively, are

$$\nabla \times \mathbf{E} = -\frac{\partial \mathbf{B}}{\partial t} \quad (1)$$

$$\nabla \times \mathbf{H} = \mathbf{J} + \frac{\partial \mathbf{D}}{\partial t} \quad (2)$$

$$\nabla \cdot \mathbf{D} = \rho \quad (3)$$

$$\nabla \cdot \mathbf{B} = 0 \quad (4)$$

In these equations, \mathbf{E} is the electric field intensity in V/m, \mathbf{H} is the magnetic field intensity in A/m, $\mathbf{D} = \epsilon \mathbf{E}$ is the electric flux density in C/m², ϵ is the electric permittivity in F/m, $\mathbf{J} = \sigma \mathbf{E}$ is the conduction current density in A/m², σ is the electrical conductivity in S/m, ρ is electric charge density in C/m³, $\mathbf{B} = \mu \mathbf{H}$ is the magnetic flux density in Wb/m² (or tesla) and μ is the magnetic permeability in H/m.

2. PROPAGATING SINE WAVES AND THE WAVE EQUATION

For signals oscillating sinusoidally in time it is convenient to represent the time variation as $e^{j\omega t}$. Thus, the electro-

magnetic fields are expressed as $\mathbf{E}(x, y, z, t) = \mathbf{E}(x, y, z)e^{j\omega t}$, and $\mathbf{H}(x, y, z, t) = \mathbf{H}(x, y, z)e^{j\omega t}$. Substituting these expressions into the differential form of Maxwell's equations given in (1)–(4) yields the sinusoidal steady-state form as

$$\nabla \times \mathbf{E} = -j\omega\mu\mathbf{H} \quad (5)$$

$$\nabla \times \mathbf{H} = (\sigma + j\omega\epsilon)\mathbf{E} \quad (6)$$

$$\nabla \cdot \mathbf{D} = \rho \quad (7)$$

$$\nabla \cdot \mathbf{B} = 0 \quad (8)$$

where the last two equations are unchanged since no time derivative is involved.

A wave equation for \mathbf{E} and \mathbf{H} is derived by taking the curl of both sides of (5) and (6), and then using the vector identity

$$\nabla \times \nabla \times \mathbf{E} = \nabla(\nabla \cdot \mathbf{E}) - \nabla^2 \mathbf{E} \quad (9)$$

Thus, from (5), (6), and (9), we obtain

$$\nabla \times \nabla \times \mathbf{E} = -j\omega\mu(\nabla \times \mathbf{H}) \quad (10)$$

and

$$\nabla(\nabla \cdot \mathbf{E}) - \nabla^2 \mathbf{E} = -j\omega\mu(\sigma + j\omega\epsilon)\mathbf{E} \quad (11)$$

If in the region of interest, $\rho = 0$, and $\epsilon \neq \epsilon(x, y, z)$, then from (7), $\nabla \cdot \mathbf{E} = 0$, and (11) takes a convenient form of the wave equation as

$$\nabla^2 \mathbf{E} = j\omega\mu(\sigma + j\omega\epsilon)\mathbf{E} = \gamma^2 \mathbf{E} \quad (12)$$

A similar procedure, starting with the curl of both sides of (6), yields an identical equation involving \mathbf{H} as

$$\nabla^2 \mathbf{H} = j\omega\mu(\sigma + j\omega\epsilon)\mathbf{H} = \gamma^2 \mathbf{H} \quad (13)$$

In (12) and (13), we obtain

$$\gamma = \sqrt{j\omega\mu(\sigma + j\omega\epsilon)} = \alpha + j\beta \quad (14)$$

where γ is the propagation constant, α is the attenuation constant, and β is the phase constant, all expressed per unit length.

Solutions to the wave equations for \mathbf{E} and \mathbf{H} may be obtained most conveniently by separation of variables, as shown in the next section.

3. SOLUTIONS FOR TEM, TM, AND TE WAVES [1,2]

Allowing all polarizations of \mathbf{E} in rectangular coordinates, (12) may be expressed as

$$\nabla^2(E_x\hat{x} + E_y\hat{y} + E_z\hat{z}) = \gamma^2(E_x\hat{x} + E_y\hat{y} + E_z\hat{z}) \quad (15)$$

where \hat{x} , \hat{y} , and \hat{z} are unit vectors. Thus, a typical term is

$$\nabla^2 E_z = \gamma^2 E_z \quad (16)$$

Substituting the separated-variable solution $E_z(x, y, z) = X(x)Y(y)Z(z)$ into (16), and dividing by XYZ , produces the result

$$\frac{1}{X} \frac{d^2 X}{dx^2} + \frac{1}{Y} \frac{d^2 Y}{dy^2} + \frac{1}{Z} \frac{d^2 Z}{dz^2} = \gamma^2 = -k_x^2 - k_y^2 - k_z^2 \quad (17)$$

From (17), it will be convenient to let

$$k_z^2 = -(\gamma^2 + k_x^2 + k_y^2) = -\Gamma^2 \quad (18)$$

or

$$\Gamma = \sqrt{\gamma^2 + k_x^2 + k_y^2} \quad (19)$$

where the propagation constants k_x , k_y , and Γ are to be determined.

Equating terms in (17) yields three ordinary differential equations that have the implied solutions indicated in the following:

$$\frac{d^2 X}{dx^2} + k_x^2 X = 0 \rightarrow X(x) = A_1 \cos k_x x + B_1 \sin k_x x \quad (20)$$

$$\frac{d^2 Y}{dy^2} + k_y^2 Y = 0 \rightarrow Y(y) = A_2 \cos k_y y + B_2 \sin k_y y \quad (21)$$

$$\frac{d^2 Z}{dz^2} - \Gamma^2 Z = 0 \rightarrow Z(z) = A_3 e^{-\Gamma z} + B_3 e^{\Gamma z} \quad (22)$$

We express a sinusoidally time-varying, z -polarized wave propagating in the $+z$ direction as

$$E_z(x, y, z, t) = E_z(x, y, z)e^{j\omega t} = X(x)Y(y)e^{j\omega t - \Gamma z} \quad (23)$$

and all the other components of E and H are expressed in a similar form.

In (23), in order to produce the term $e^{j(\omega t - |\Gamma|z)}$ necessary for wave propagation to occur, Γ must be imaginary. Taking the dielectric material through which the wave propagates to be perfect ($\sigma = 0$), then $\gamma^2 = j\omega\mu(\sigma + j\omega\epsilon) = -\omega^2\mu\epsilon$. The propagation condition is

$$\Gamma = \sqrt{\gamma^2 + k_x^2 + k_y^2} = j\sqrt{\omega^2\mu\epsilon - k_x^2 - k_y^2} = j\beta_g \quad (24)$$

and wave propagation occurs if β_g (the phase constant of the wave-guiding structure) is real. At $\beta_g = 0$, no propagation occurs, which defines a cutoff frequency

$$f_c = \frac{\omega_c}{2\pi} = \frac{1}{2\pi\sqrt{\mu\epsilon}} \sqrt{k_x^2 + k_y^2} \quad (25)$$

Substituting (25) into (24) yields

$$\Gamma = j\sqrt{\omega^2\mu\epsilon - \omega_c^2\mu\epsilon} = j\omega\sqrt{\mu\epsilon} \sqrt{1 - \left(\frac{f_c}{f}\right)^2} = j\beta_g \quad (26)$$

These parameters will be examined further for different wave-guiding structures.

All of the field solutions, expressed in the form $XYe^{-\Gamma z}$, satisfy the wave equation, and the solutions must also satisfy the boundary conditions imposed by the guiding structure. For guided waves, the basic wave types are transverse electromagnetic (TEM) waves, transverse magnetic (TM) waves, and transverse electric (TE) waves. For propagation guided in the z direction, a TEM wave has components of \mathbf{E} and \mathbf{H} that are perpendicular (or transverse) to the z axis, and thus by definition, $E_z = H_z = 0$. A TM wave has components of \mathbf{H} perpendicular to the z axis, but by definition, $H_z = 0$. A TE wave has components of \mathbf{E} perpendicular to the z axis, but by definition, $E_z = 0$. These wave types and polarizations are illustrated in Fig. 1, where the TE and TM waves are guided by reflecting rays at specific angles (θ) between the parallel metal plates at $x = 0$ and $x = a$.

The guiding structures may take on a variety of forms, but two important ones are diagramed in Fig. 2: Fig. 2a is a parallel-plate transmission line with plate separation a and width w ; Fig. 2b is a rectangular waveguide with inside width a and height b . Within the parallel-plate line depicted in Figs. 1 and 2a, a TEM wave can propagate at all frequencies, and TM and TE waves can propagate at all frequencies above a certain cutoff frequency (f_c) that will be determined later. Within the closed structure of the rectangular waveguide, TM and TE waves can propagate at all frequencies above their cutoff frequencies (f_c differs for TM and TE waves in the closed waveguide), but TEM waves cannot exist within the closed waveguide.

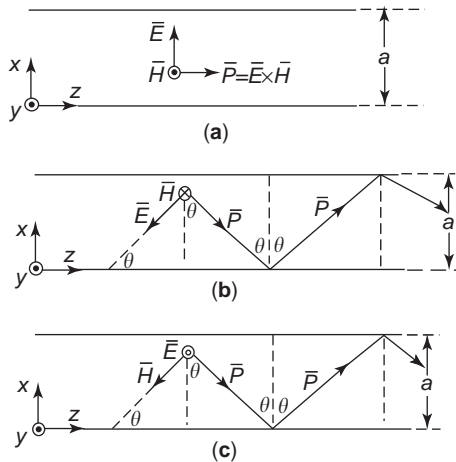


Figure 1. Waves guided between parallel metal plates spaced a distance a apart: (a) TEM waves— $\mathbf{E} = E_x\hat{x}$, $\mathbf{H} = H_y\hat{y}$, $E_z = 0$; (b) TM waves— $\mathbf{E} = -E_x\hat{x} - E_z\hat{z}$, $\mathbf{H} = -H_y\hat{y}$, $H_z = 0$; (c) TE waves— $\mathbf{E} = E_y\hat{y}$, $\mathbf{H} = -H_x\hat{x} - H_z\hat{z}$, $E_z = 0$.

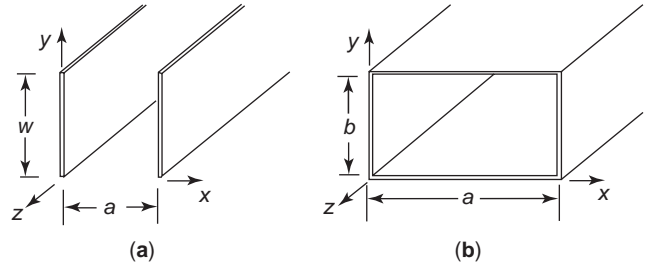


Figure 2. Two important structures for guiding waves: (a) parallel-plate line of width w and spacing a ; (b) closed rectangular waveguide of inside width a and height b .

3.1. Transverse Electromagnetic (TEM) Waves

To show that TEM waves cannot exist, and therefore propagate, within the rectangular waveguide, proceed to solve for a propagating wave as if one may exist. Assume solutions of the form $XYe^{-\Gamma z}$ for E_x , E_y , H_x , and H_y , take $E_z = H_z = 0$ by definition, and substitute the assumed solutions into Maxwell's curl equations. First, $\nabla \times \mathbf{E} = -j\omega\mu\mathbf{H}$ yields

$$0 + \Gamma E_y = -j\omega\mu H_x \quad (27)$$

$$-\Gamma E_x + 0 = -j\omega\mu H_y \quad (28)$$

$$\frac{\partial E_y}{\partial x} - \frac{\partial E_x}{\partial y} = 0 \quad (29)$$

and $\nabla \times \mathbf{H} = (\sigma + j\omega\epsilon)\mathbf{E}$ yields

$$0 + \Gamma H_y = (\sigma + j\omega\epsilon) E_x \quad (30)$$

$$-\Gamma H_x + 0 = (\sigma + j\omega\epsilon) E_y \quad (31)$$

$$\frac{\partial H_y}{\partial x} - \frac{\partial H_x}{\partial y} = 0 \quad (32)$$

where the common term $e^{-\Gamma z}$ has been canceled in each equation.

From (27), (28), (30), and (31), we obtain

$$-\frac{E_y}{H_x} = \frac{E_x}{H_y} = \frac{j\omega\mu}{\Gamma} = \frac{\Gamma}{\sigma + j\omega\epsilon} \quad (33)$$

Therefore, $\Gamma^2 = j\omega\mu(\sigma + j\omega\epsilon) = \gamma^2$, and $k_x = k_y = 0$, which allows no variation of \mathbf{E} and \mathbf{H} in the x - y plane. Thus, boundary conditions cannot be satisfied within the closed structure, and TEM waves cannot exist.

Since $\Gamma^2 = \gamma^2$ for TEM waves, the wave equations for E_x and H_y within the parallel-plate transmission line are

$$\frac{d^2 E_x}{dz^2} = \gamma^2 E_x \quad \text{and} \quad \frac{d^2 H_y}{dz^2} = \gamma^2 H_y \quad (34)$$

If $w \gg a$ for the parallel-plate line, then E_x and H_y represent uniform fields between the plates. By applying Faraday's law between the conducting plates, and Ampere's law around the plates, the fields are related to the voltage

and current at any point z by

$$E_x = \frac{V(z)}{a} \quad \text{and} \quad H_y = \frac{I(z)}{w} \quad (35)$$

Thus, $V(z)$ and $I(z)$ also satisfy the wave equation, and for waves propagating in the $+z$ direction they have the solutions

$$V(z) = Ae^{-\gamma z} \quad \text{and} \quad I(z) = \frac{A}{Z_0} e^{-\gamma z} \quad (36)$$

where A is a constant and Z_0 is the characteristic impedance of the transmission line. As in (33), since $E_x/H_y = \eta$, the intrinsic impedance of the material between the plates, it is easily determined from foregoing relations that

$$Z_0 = \frac{V(z)}{I(z)} = \frac{E_x a}{H_y w} = \frac{a}{w} \eta = \frac{a}{w} \sqrt{\frac{j\omega\mu}{\sigma + j\omega\epsilon}} \quad (37)$$

for the parallel-plate line considered here.

3.2. Transverse Magnetic (TM) Waves

Returning to the rectangular waveguide of width a and height b , since $H_z = 0$ by definition for TM waves, select $E_z = XYe^{-\Gamma z}$ as a solution that cannot vanish if a solution does exist. Assuming solutions of the form $XYe^{-\Gamma z}$ for E_x , E_y , H_x , and H_y , substitute the assumed solutions into Maxwell's curl equations. First, $\nabla \times \mathbf{E} = -j\omega\mu\mathbf{H}$ yields

$$\frac{\partial E_z}{\partial y} + \Gamma E_y = -j\omega\mu H_x \quad (38)$$

$$-\Gamma E_x - \frac{\partial E_z}{\partial x} = -j\omega\mu H_y \quad (39)$$

$$\frac{\partial E_y}{\partial x} - \frac{\partial E_x}{\partial y} = 0 \quad (40)$$

and $\nabla \times \mathbf{H} = (\sigma + j\omega\epsilon)\mathbf{E}$ yields

$$0 + \Gamma H_y = (\sigma + j\omega\epsilon)E_x \quad (41)$$

$$-\Gamma H_x + 0 = (\sigma + j\omega\epsilon)E_y \quad (42)$$

$$\frac{\partial H_y}{\partial x} - \frac{\partial H_x}{\partial y} = (\sigma + j\omega\epsilon)E_z \quad (43)$$

The common term $e^{-\Gamma z}$ has been canceled in each equation.

From (41) and (42)

$$-\frac{E_y}{H_x} = \frac{E_x}{H_y} = \frac{\Gamma}{\sigma + j\omega\epsilon} = Z_0 \quad (44)$$

which defines Z_0 as the characteristic impedance of TM waves in the rectangular waveguide. Using this definition of Z_0 , and the curl equations, all the field components may be expressed in terms of the one-component solution E_z .

Substituting (42) into (38) and using (44), we obtain

$$H_x = \frac{\partial E_z / \partial y}{\Gamma Z_0 - j\omega\mu} \quad (45)$$

Substituting (41) into (39) and using (44), we obtain

$$H_y = \frac{-\partial E_z / \partial x}{\Gamma Z_0 - j\omega\mu} \quad (46)$$

The remaining components are

$$E_x = Z_0 H_y, \quad E_y = -Z_0 H_x, \quad \text{and} \quad H_z = 0 \quad (47)$$

Again, the assumed solution for E_z is

$$E_z = XYe^{-\Gamma z} = (A_1 \cos k_x x + B_1 \sin k_x x) \times (A_2 \cos k_y y + B_2 \sin k_y y) e^{-\Gamma z} \quad (48)$$

and the boundary conditions are that $E_z = 0$ on each wall of the waveguide. Letting $E_z(0, y) = 0$ and $E_z(x, 0) = 0$ requires that $A_1 = 0$ and $A_2 = 0$. The remaining sinusoidal terms will satisfy the conditions $E_z(a, y) = 0$ and $E_z(x, b) = 0$ if

$$k_x = \frac{m\pi}{a} \quad \text{and} \quad k_y = \frac{n\pi}{b} \quad (49)$$

where m and n are integers, including zero. Thus, the solution for E_z is

$$E_z(x, y, z, t) = E_{mn} \sin \frac{m\pi x}{a} \sin \frac{n\pi y}{b} e^{-\Gamma z} e^{j\omega t} \quad (50)$$

Depending on the choice of integers m and n , different cross-sectional field patterns may occur in the x - y plane. These different modes are designated by TM_{mn} . Observe from (50) that the TM_{23} mode (for example) has two half-sine-wave variations in the x direction and three half-sine-wave variations in the y direction. The lowest-order mode that can propagate is the TM_{11} , since the TM_{10} and the TM_{01} modes render $E_z = 0$ in (50).

In (50), as stated earlier, wave propagation occurs if Γ is imaginary. Taking the dielectric material (usually air) filling the waveguide to be perfect ($\sigma = 0$), then $\gamma^2 = j\omega\mu(\sigma + j\omega\epsilon) = -\omega^2\mu\epsilon$, and

$$\begin{aligned} \Gamma &= \sqrt{\gamma^2 + k_x^2 + k_y^2} \\ &= j\sqrt{\omega^2\mu\epsilon - \left(\frac{m\pi}{a}\right)^2 - \left(\frac{n\pi}{b}\right)^2} = j\beta_g \end{aligned} \quad (51)$$

Thus, wave propagation occurs at frequencies above the cutoff frequency

$$f_c = \frac{\omega_c}{2\pi} = \frac{1}{2\pi\sqrt{\mu\varepsilon}} \sqrt{\left(\frac{m\pi}{a}\right)^2 + \left(\frac{n\pi}{b}\right)^2} \quad (52)$$

$$= v \sqrt{\left(\frac{m}{2a}\right)^2 + \left(\frac{n}{2b}\right)^2}$$

The cutoff frequency of the TM_{11} (lowest-order) mode is

$$f_c = \frac{v}{2a} \sqrt{1 + \left(\frac{a}{b}\right)^2} \quad (53)$$

Note that if the dimension b approaches infinity, and the parallel sides remain a distance a apart, the cutoff frequency for all TM modes in (52) becomes

$$f_c = \frac{mv}{2a} \quad (54)$$

3.3. Transverse Electric (TE) Waves

For TE waves within the rectangular waveguide of width a and height b , since $E_z = 0$ by definition, select $H_z = XYe^{-\Gamma z}$ as a solution that cannot vanish if a solution does exist. Assuming solutions of the form $XYe^{-\Gamma z}$ for E_x , E_y , H_x , and H_y , substitute the assumed solutions into Maxwell's curl equations. First, $\nabla \times \mathbf{E} = -j\omega\mu\mathbf{H}$ yields

$$0 + \Gamma E_y = -j\omega\mu H_x \quad (55)$$

$$-\Gamma E_x + 0 = -j\omega\mu H_y \quad (56)$$

$$\frac{\partial E_y}{\partial x} - \frac{\partial E_x}{\partial y} = -j\omega\mu H_z \quad (57)$$

and $\nabla \times \mathbf{H} = (\sigma + j\omega\varepsilon)\mathbf{E}$ yields (assuming $\sigma = 0$ for a perfect dielectric medium)

$$\frac{\partial H_z}{\partial y} + \Gamma H_y = j\omega\varepsilon E_x \quad (58)$$

$$-\Gamma H_x - \frac{\partial H_z}{\partial x} = j\omega\varepsilon E_y \quad (59)$$

$$\frac{\partial H_y}{\partial x} - \frac{\partial H_x}{\partial y} = 0 \quad (60)$$

The common term $e^{-\Gamma z}$ has been canceled in each equation.

The characteristic impedance of TE waves is defined from (55) and (56) as

$$-\frac{E_y}{H_x} = \frac{E_x}{H_y} = \frac{j\omega\mu}{\Gamma} = Z_0 \quad (61)$$

Using this definition of Z_0 in (58) and (59) yields

$$\frac{\partial H_z}{\partial y} = j\omega\varepsilon E_x - \frac{\Gamma E_x}{Z_0} = \left(j\omega\varepsilon - \frac{\Gamma}{Z_0}\right) E_x \quad (62)$$

$$\frac{\partial H_z}{\partial x} = -j\omega\varepsilon E_y + \frac{\Gamma E_y}{Z_0} = -\left(j\omega\varepsilon - \frac{\Gamma}{Z_0}\right) E_y \quad (63)$$

For the rectangular waveguide under consideration, $E_x = 0$ at $y = 0$ and $y = b$, and $E_y = 0$ at $x = 0$ and $x = a$. Thus, from (62) and (63), we obtain

$$\frac{\partial H_z}{\partial y} = 0 \quad \text{at } y = 0 \quad \text{and } y = b \quad (64)$$

and

$$\frac{\partial H_z}{\partial x} = 0 \quad \text{at } x = 0 \quad \text{and } x = a \quad (65)$$

are appropriate boundary conditions since H_z cannot vanish if a solution exists.

Applying the boundary conditions to the assumed solution

$$H_z = XYe^{-\Gamma z} = (A_1 \cos k_x x + B_1 \sin k_x x) \times (A_2 \cos k_y y + B_2 \sin k_y y) e^{-\Gamma z} \quad (66)$$

yields

$$H_z = H_{mn} \cos \frac{m\pi x}{a} \cos \frac{n\pi y}{b} e^{-\Gamma z} \quad (67)$$

where $k_x = m\pi/a$, $k_y = n\pi/b$, and m and n are integers corresponding to the mode variations in the x - y plane.

The remaining components of the TE waves are obtained as follows: From (62), we obtain

$$E_x = \frac{\frac{\partial H_z}{\partial y}}{j\omega\varepsilon - \frac{\Gamma}{Z_0}} = \frac{-k_x H_{mn} \cos k_x x \sin k_y y e^{-\Gamma z}}{j\omega\varepsilon - \frac{\Gamma}{Z_0}} \quad (68)$$

From (63)

$$E_y = \frac{\frac{\partial H_z}{\partial x}}{-j\omega\varepsilon + \frac{\Gamma}{Z_0}} = \frac{k_x H_{mn} \sin k_x x \cos k_y y e^{-\Gamma z}}{j\omega\varepsilon - \frac{\Gamma}{Z_0}} \quad (69)$$

From (61)

$$H_x = -\frac{E_y}{Z_0} \quad (70)$$

and

$$H_y = \frac{E_x}{Z_0} \quad (71)$$

If $a > b$ for the rectangular waveguide, the mode of lowest order is the TE_{10} , which has the cutoff frequency $f_c = v/2a$ and the field components

$$H_z = H_{10} \cos \frac{\pi x}{a} e^{-\Gamma z} \quad (72)$$

$$E_y = -j\eta \frac{2a}{\lambda} H_{10} \sin \frac{\pi x}{a} e^{-\Gamma z} = E_{10} \sin \frac{\pi x}{a} e^{-\Gamma z} \quad (73)$$

$$H_x = -\frac{E_y}{Z_0} \quad (74)$$

$$E_x = H_y = E_z = 0 \quad (75)$$

The cutoff frequency of the TE_{10} mode is

$$f_c = \frac{v}{2a} \sqrt{m^2 + n^2 \left(\frac{a}{b}\right)^2} = \frac{v}{2a} \quad (76)$$

Again, TE and TM waves share the same general expressions for propagation constant (Γ) and cutoff frequency (f_c), as expressed in Eqs. (24), (25), (51), and (52). For the two wave types, Γ and f_c differ in the choice of the integer mode numbers m and n . However, if the dimension b goes to infinity, creating a parallel-plate waveguide, then Γ and f_c are the same for both TE and TM waves. The characteristic impedance differs for the two wave types, as $Z_0 = \Gamma/(j\omega\epsilon) = \eta\sqrt{1 - (f_c/f)^2}$ for TM waves, and $Z_0 = j\omega\mu/\Gamma = \eta/\sqrt{1 - (f_c/f)^2}$ for TE waves, where $\eta = \sqrt{\mu/\epsilon}$ is the intrinsic impedance of the medium filling the guide. Thus, as frequency is increased from f_c to ∞ , Z_0 increases from 0 up to η for TM waves and decreases from ∞ down to η for TE waves.

For $f < f_c$, Γ is real, and the propagation term $e^{j\omega t - \Gamma z}$ from the wave equation becomes $e^{j\omega t - \alpha_g z}$, or

$$\Gamma = \omega\sqrt{\mu\epsilon}\sqrt{(f_c/f)^2 - 1} = \alpha_g \quad (77)$$

At operating frequencies below cutoff for the waveguide, the waves are attenuated by the factor α_g as they evanesce or diffuse along the guide in the z direction with no real wave propagation occurring. A waveguide below cutoff may be used as an attenuator. For example, if $f = 10$ GHz and $f_c = 13.12$ GHz (corresponding to $a = 0.45$ in. or 11.43 mm in an air-filled, TE_{10} waveguide), then $\alpha_g = 1.78$ Np/cm, or 15.46 dB/cm. Thus, the length is adjusted to yield a desired attenuation.

For $f < f_c$, the characteristic impedances are imaginary, as $Z_0 = \Gamma/(j\omega\epsilon) = -j\eta\sqrt{(f_c/f)^2 - 1}$ for TM waves, and $Z_0 = j\omega\mu/\Gamma = j\eta/\sqrt{(f_c/f)^2 - 1}$ for TE waves. This puts the transverse components of \mathbf{E} and \mathbf{H} 90° out of time phase, and tells us once again that time-average power cannot be transferred as a propagating wave. Thus, energy transfer along the guide is by evanescence or diffusion.

4. INTERPRETING Z_0 FOR TEM, TM, AND TE WAVES

Taking the propagation medium to be a lossless dielectric ($\sigma = 0$), the intrinsic impedance of the medium is $\eta = \sqrt{\mu/\epsilon}$. For TEM waves propagating in the z direction, the characteristic impedance is

$$Z_0 = \frac{V(z)}{I(z)} = \eta F(g) = \frac{E_x}{H_y} F(g) \quad (78)$$

where, as in Fig. 2a, the geometry function $F(g) = a/w$ for two parallel conducting strips of width w , separation a , and $w \gg a$; and $F(g) = (1/2\pi) \ln(b/a)$ for a coaxial line, if a is the inner conductor radius and b is the inner radius of the outer conductor.

For TM waves guided in the z direction, the characteristic impedance is

$$\begin{aligned} Z_0 &= \frac{\Gamma}{j\omega\epsilon} = \frac{j\omega\sqrt{\mu\epsilon}}{j\omega\epsilon} \sqrt{1 - \left(\frac{f_c}{f}\right)^2} \\ &= \eta \sqrt{1 - \left(\frac{f_c}{f}\right)^2} \end{aligned} \quad (79)$$

From a raypath diagram of the guided TM wave, as in Fig. 1b, Z_0 may also be determined as

$$Z_0 = \frac{E_x}{H_y} = \frac{E \sin \theta}{H} = \eta \sin \theta = \eta \sqrt{1 - \cos^2 \theta} \quad (80)$$

But, $\beta_z = \beta \sin \theta$ and $\beta_x = \beta \cos \theta$, and Z_0 becomes

$$Z_0 = \eta \frac{\lambda}{\lambda_z} = \eta \sqrt{1 - \left(\frac{\lambda}{\lambda_x}\right)^2} = \eta \sqrt{1 - \left(\frac{f_c}{f}\right)^2} \quad (81)$$

where $\lambda_z = \lambda_g$ is the wavelength along the direction of propagation or the wavelength along the guide, and $\lambda_x = \lambda_c$ is the cutoff wavelength.

For TE waves guided in the z direction, the characteristic impedance is

$$Z_0 = \frac{j\omega\mu}{\Gamma} = \frac{j\omega\mu}{j\omega\sqrt{\mu\epsilon}\sqrt{1 - \left(\frac{f_c}{f}\right)^2}} = \frac{\eta}{\sqrt{1 - \left(\frac{f_c}{f}\right)^2}} \quad (82)$$

From a raypath diagram of the guided TE wave, as in Fig. 1c, Z_0 may also be determined as

$$Z_0 = -\frac{E_y}{H_x} = \frac{E}{H \sin \theta} = \frac{\eta}{\sin \theta} = \frac{\eta}{\sqrt{1 - \cos^2 \theta}} \quad (83)$$

Again, $\beta_z = \beta \sin \theta$ and $\beta_x = \beta \cos \theta$, and Z_0 for TE waves becomes

$$Z_0 = \eta \frac{\lambda_z}{\lambda} = \frac{\eta}{\sqrt{1 - \left(\frac{\lambda}{\lambda_x}\right)^2}} = \frac{\eta}{\sqrt{1 - \left(\frac{f_c}{f}\right)^2}} \quad (84)$$

Table 1. Comparison Equations and Properties of TM, TE, and TEM Waves

TM Waves	TE Waves	TEM Waves
$H_z = 0$	$E_z = 0$	$E_z = H_z = 0$
$\Gamma = \sqrt{-\omega^2 \mu \epsilon + k_x^2 + k_y^2}$	$\Gamma = \sqrt{-\omega^2 \mu \epsilon + k_x^2 + k_y^2}$	$\gamma = \sqrt{-\omega^2 \mu \epsilon} = j\omega \sqrt{\mu \epsilon}$
$f_c = \frac{v}{2\pi} \sqrt{k_x^2 + k_y^2}$	$f_c = \frac{v}{2\pi} \sqrt{k_x^2 + k_y^2}$	$f_c = 0$
$\lambda_c = \frac{v}{f_c} = \frac{2\pi}{\sqrt{k_x^2 + k_y^2}}$	$\lambda_c = \frac{v}{f_c} = \frac{2\pi}{\sqrt{k_x^2 + k_y^2}}$	$\lambda_c = \infty$
$\beta_g = \sqrt{\omega^2 \mu \epsilon - (k_x^2 + k_y^2)}$	$\beta_g = \sqrt{\omega^2 \mu \epsilon - (k_x^2 + k_y^2)}$	$\beta = \omega \sqrt{\mu \epsilon}$
$\beta_g = \frac{2\pi}{\lambda} \sqrt{1 - \left(\frac{\lambda}{\lambda_c}\right)^2}$	$\beta_g = \frac{2\pi}{\lambda} \sqrt{1 - \left(\frac{\lambda}{\lambda_c}\right)^2}$	$\beta = \frac{2\pi}{\lambda}$
$\lambda_g = \frac{2\pi}{\beta_g} = \frac{\lambda}{\sqrt{1 - (\lambda/\lambda_c)^2}}$	$\lambda_g = \frac{2\pi}{\beta_g} = \frac{\lambda}{\sqrt{1 - (\lambda/\lambda_c)^2}}$	λ
$Z_0 = \frac{\Gamma}{j\omega \epsilon} = \eta \sqrt{1 - (\lambda/\lambda_c)^2}$	$Z_0 = \frac{j\omega \mu}{\Gamma} = \frac{\eta}{\sqrt{1 - (\lambda/\lambda_c)^2}}$	η
$v_g = \frac{\omega}{\beta_g}$	$v_g = \frac{\omega}{\beta_g}$	$v = \frac{\omega}{\beta}$
$Z(z) = Z_0 \frac{Z_L + jZ_0 \tan \beta_g z}{Z_0 + jZ_L \tan \beta_g z}$	$Z(z) = Z_0 \frac{Z_L + jZ_0 \tan \beta_g z}{Z_0 + jZ_L \tan \beta_g z}$	$Z(z) = Z_0 \frac{Z_L + jZ_0 \tan \beta z}{Z_0 + jZ_L \tan \beta z}$

and again, $\lambda_z = \lambda_g$ is the wavelength along the guide, and $\lambda_x = \lambda_c$ is the cutoff wavelength.

For convenient reference, selected equations, properties and parameters of waveguiding structures are collected in Table 1 and 2.

5. FREQUENCY BANDWIDTH OF WAVEGUIDES

As discussed in earlier sections, waveguides operate at frequencies above a specific cutoff frequency, and they may be subject to higher-order modes (higher than the funda-

Table 2. Features of Some Commercially Available Rectangular Waveguides

EIA Designation	Inside Dimensions $a \times b$ (in.)	Cutoff f_c (MHz)	Range for TE ₁₀ (MHz)	CW Power Rating (MW)
WR1150	11.5 × 5.75	513	640–960	35.00–53.80
WR975	9.75 × 4.875	605	750–1120	27.00–38.50
WR770	7.70 × 3.85	766	960–1450	17.20–24.10
WR650	6.50 × 3.25	908	1120–1700	11.90–17.20
WR510	5.10 × 2.55	1157	1450–2200	7.50–10.70
WR430	4.30 × 2.15	1372	1700–2600	5.20–7.50
WR340	3.40 × 1.70	1735	2200–3300	3.40–4.71
WR284	2.84 × 1.34	2077	2600–3950	2.18–3.10
WR229	2.29 × 1.145	2590	3300–4900	1.56–2.14
WR187	1.87 × 0.87	3155	3950–5850	0.94–1.32
WR159	1.59 × 0.76	3710	4900–7050	0.75–0.98
WR137	1.37 × 0.62	4307	5850–8200	0.55–0.70
WR112	1.12 × 0.50	5260	7050–10000	0.36–0.45
WR90	0.90 × 0.40	6560	8200–12400	0.21–0.29
WR75	0.75 × 0.37	7867	9833–14950	0.19–0.27
WR62	0.62 × 0.31	9516	11900–18080	0.16–0.22
WR42	0.42 × 0.17	14047	17560–26690	—
WR28	0.28 × 0.14	21071	26340–40035	—
WR19	0.188 × 0.094	31383	39230–59630	—
WR15	0.148 × 0.074	39865	49830–75740	—
WR10	0.100 × 0.050	59000	73750–112100	—
WR8	0.080 × 0.040	73750	92200–140125	—
WR6	0.065 × 0.0325	90769	113460–172460	—
WR5	0.051 × 0.0255	115686	144600–220000	—

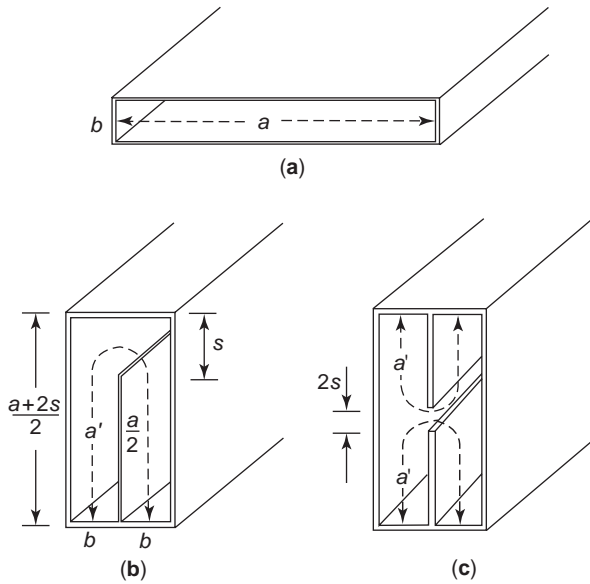


Figure 3. (a) The cutoff frequency of TE₁₀-mode waveguide is lowered by increasing the width a ; (b) the waveguide in (a) is folded for a more compact structure, and the new equivalent width is a' ; (c) a double-ridged version of (b), imaged along the horizontal bisector, has the same operating frequencies and bandwidth as in (b).

mental mode). Single-mode propagation is necessary for efficient transmission and detection of signal information on the carrier wave, and, of course, more information may be sent if the bandwidth is as large as possible. These restrictions may be troublesome at times, but there are ways to avoid most of the trouble.

5.1. Lowering the Cutoff Frequency of Waveguides

The bandwidth of a rectangular waveguide operating in the TE₁₀ mode is generally taken to be $1.25f_c \leq f \leq 1.90f_c$, where $f_c = v/2a$ is the TE₁₀-mode cutoff frequency. This is the choice because $f_1 = 1.25f_c$ is a convenient distance above $f = f_c$ (where $Z_0 = \infty$) and $f_2 = 1.90f_c$ is conveniently less than $f = 2f_c$ (where the first higher-order mode, TE₀₂, occurs if $2b < a$). Thus, the operating bandwidth is $f_2 - f_1 = 0.65f_c$.

To increase the bandwidth, we first lower the cutoff frequency of the TE₁₀ mode waveguide by increasing the wide dimension a in $f_c = v/2a$, as in Fig. 3a. To accommodate a large increase in the width a , the waveguide is folded such that the width is now $2b$ and the height is $(a + 2s)/2$, as in Fig. 3b.

In Fig. 3, the dotted path a' is longer than a because of the fringing capacitance across the gap s . The fringing capacitance is [3]

$$C_f = \epsilon \frac{4}{\pi} \ln \left(\coth \frac{\pi s}{2b} \right) \quad (85)$$

which is equivalent to a length increase given by

$$C_f = \epsilon \frac{2\Delta a}{b} \quad (86)$$

Thus

$$a' = a + 2\Delta a = a + \frac{4b}{\pi} \ln \left(\coth \frac{\pi s}{2b} \right) \quad (87)$$

In (87), if $s = 0.2b$ and $b = 0.5a$, then $a' = 1.715a$, and the resulting lower cutoff frequency for the TE₁₀ mode is $f'_c = v/2a' = f_c/1.715 = 0.583f_c$. The lower operating frequency is $f'_1 = 1.25f'_c = 0.729f_c$. The upper operating frequency remains the same at $f'_2 = f_2 = 1.90f_c$, since the electric field of the TE₂₀ mode is zero across the gap s and little or no fringing capacitance occurs to increase the pathlength. Thus, the new operating bandwidth is $f'_2 - f'_1 = (1.90 - 0.729)f_c = 1.171f_c$, rather than $0.65f_c$.

Example 1. Given $a = 12.5$ cm, $b = 0.5a = 6.25$ cm, and $s = 0.2b = 1.25$ cm, determine the operating frequencies and bandwidth for exclusive TE₁₀ mode operation in (a) the rectangular waveguide and (b) the folded rectangular waveguide in Fig. 3b.

Solution: (a) For the rectangular waveguide

$$f_c = \frac{v}{2a} = \frac{3 \times 10^8}{0.25} = 1200 \text{ MHz} \quad (88)$$

$$f_1 = 1.25f_c = 1500 \text{ MHz} \quad (89)$$

$$f_2 = 1.90f_c = 2280 \text{ MHz} \quad (90)$$

$$\text{BW} = f_2 - f_1 = 780 \text{ MHz} \quad (91)$$

(b) For the folded rectangular waveguide in Fig. 3b, we obtain

$$f'_c = \frac{v}{2a'} = 0.583f_c = 700 \text{ MHz} \quad (92)$$

$$f'_1 = 1.25f'_c = 875 \text{ MHz} \quad (93)$$

$$f'_2 = f_2 = 1.90f_c = 2280 \text{ MHz} \quad (94)$$

$$\text{BW} = f'_2 - f'_1 = 1405 \text{ MHz} \quad (95)$$

The folded waveguide considered here is more commonly known as a single-ridged waveguide with a ridge thickness approaching zero ($t \cong 0$). A double-ridged version using the same configuration (same operating frequencies and bandwidth as in Fig. 3b) is shown in Fig. 3c. More commonly used relative dimensions are shown in Figs. 4a and 4b for single-ridged and double-ridged waveguides, respectively [4]. Another variation on the same theme is the T-septum waveguide, single and double, as shown in Figs. 4c and 4d [5–7].

6. DIELECTRIC WAVEGUIDES

An electromagnetic wave is guided by a dielectric material [8] of permittivity ϵ_1 surrounded by another dielectric material of permittivity ϵ_2 , where $\epsilon_1 > \epsilon_2$, as illustrated in

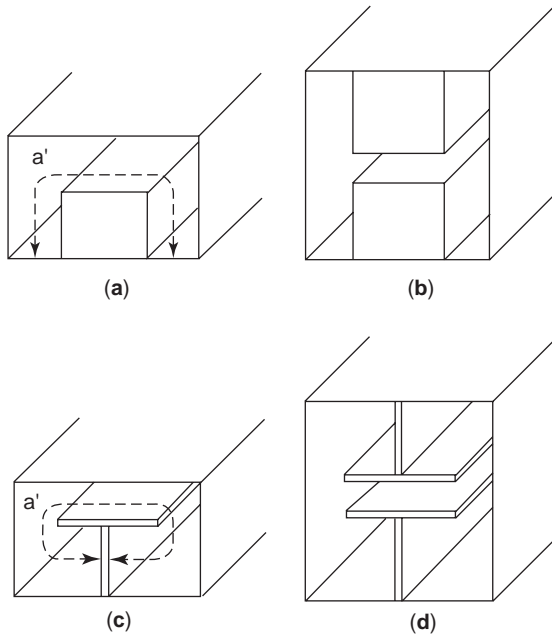


Figure 4. More commonly used relative dimensions for (a) a single-ridged waveguide and (b) a double-ridged waveguide. Other variants are (c) the single T-septum waveguide and (d) the double T-septum waveguide.

Fig. 5a and the top view along the propagation direction in Fig. 5c. If θ is the angle of the guided ray to the interface normal, and ϕ is the angle to the normal interface of any ray that transmits into material 2, then by Snell's law of refraction

$$\sqrt{\epsilon_1} \sin \theta = \sqrt{\epsilon_2} \sin \phi \quad (96)$$

Requiring $\phi = 90^\circ$ for total internal reflection yields

$$\theta = \sin^{-1} \sqrt{\frac{\epsilon_2}{\epsilon_1}} \triangleq \theta_c \quad (97)$$

Thus, with $\epsilon_1 > \epsilon_2$, the wave is guided along material 1 for all angles $\theta \geq \theta_c$. While most of the guided wave is in material 1, part of the wave protrudes into material 2 and propagates along the interface.

For TE waves, $E_x = 0$, $E_z = 0$, and

$$\mathbf{E} = \hat{y}E_y(x)e^{-j\beta z} = \hat{y}E_y(x, z) \quad (98)$$

where $\beta = \omega\sqrt{\mu\epsilon_e}$ is the propagation constant of the guided wave that propagates through an effective permittivity that has the range: $\epsilon_2 \leq \epsilon_e \leq \epsilon_1$. Note that $\partial\mathbf{E}/\partial z = -j\beta\mathbf{E}$, and $\partial\mathbf{E}/\partial y = 0$, but $\partial\mathbf{E}/\partial x \neq 0$, since the permittivity changes along the x dimension. Substituting these specifications into Maxwell's curl equations yields

$$\frac{\partial E_y}{\partial x} = -j\omega\mu H_z \quad (99)$$

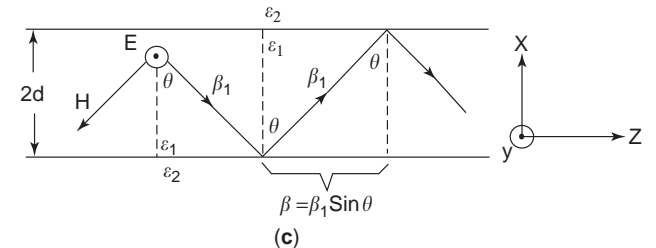
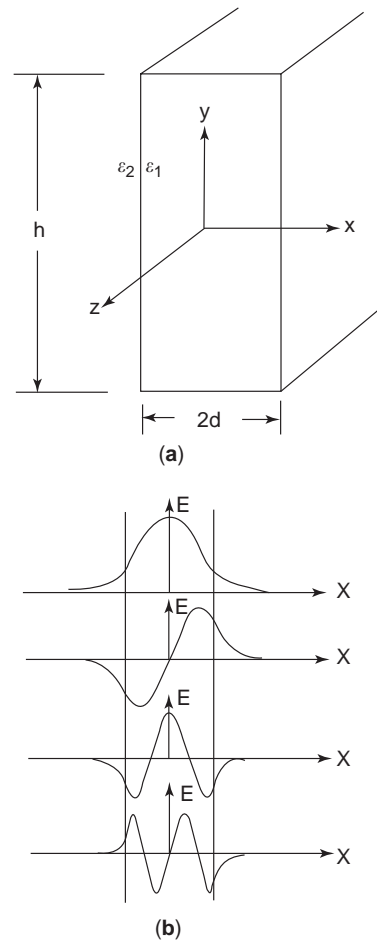


Figure 5. (a) Dielectric waveguide of permittivity ϵ_1 surrounded by permittivity ϵ_2 , where $\epsilon_1 > \epsilon_2$ and $2d \ll h$; (b) electric field distributions along x for the first two even modes (cosine terms) and the first two odd modes (sine terms)—as in Fig. 6, the phase angle from center to edge $\beta_{1x}d$ in increasing mode order is $0 < \beta_{1x}d < \pi/2$, $\pi/2 < \beta_{1x}d < \pi$, $\pi < \beta_{1x}d < 3\pi/2$, and $3\pi/2 < \beta_{1x}d < 2\pi$; (c) a TE wave guided in the z direction between the sides $2d$ apart.

and

$$j\beta E_y = -j\omega\mu H_x \quad (100)$$

from $\nabla \times \mathbf{E} = -j\omega\mu\mathbf{H}$, and

$$-j\beta H_x - \frac{\partial H_z}{\partial x} = j\omega\epsilon E_y \quad (101)$$

from $\nabla \times \mathbf{H} = j\omega\epsilon\mathbf{E}$.

Substituting (99) and (100) into (101) yields

$$\frac{\partial^2 E_y}{\partial x^2} = (\beta^2 - \omega^2 \mu \epsilon) E_y \quad (102)$$

which is valid in both material 1 and material 2 and has the general solution

$$E_y = A_i e^{-\sqrt{\beta^2 - \omega^2 \mu \epsilon} x} \quad (103)$$

Thus, in material 1 ($\epsilon_1 > \epsilon_2$), we obtain

$$\begin{aligned} E_y &= A_i e^{-\sqrt{\beta^2 - \omega^2 \mu \epsilon_1} x} = A_i e^{-j \sqrt{\omega^2 \mu \epsilon_1 - \beta^2} x} \\ &= A_i e^{-j \beta_{1x} x} = A \cos \beta_{1x} x + B \sin \beta_{1x} x \end{aligned} \quad (104)$$

where

$$\beta_{1x}^2 = \omega^2 \mu \epsilon_1 - \beta^2 = \beta_1^2 - \beta^2 \quad (105)$$

The $\cos \beta_{1x} x$ and $\sin \beta_{1x} x$ solutions in (104) allow harmonic modes of the propagating wave across the x dimension in material 1. In material 2 ($\epsilon_2 < \epsilon_1$)

$$E_y = A_i e^{-\sqrt{\beta^2 - \omega^2 \mu \epsilon_2} x} = C e^{-\alpha_2 x} \quad (106)$$

where

$$\alpha_2^2 = \beta^2 - \omega^2 \mu \epsilon_2 = \beta^2 - \beta_2^2 \quad (107)$$

which shows that E_y decreases exponentially in the x direction.

Tangential components of E and H must be continuous across the interface between materials 1 and 2, and this condition is used to determine additional characteristics of the propagating modes. Equating E_y terms at $x = d$, and using the $E_y = A \cos \beta_{1x} x$ solution from (104), we obtain

$$A \cos \beta_{1x} d = C e^{-\alpha_2 d} \quad (108)$$

or

$$C = A e^{\alpha_2 d} \cos \beta_{1x} d \quad (109)$$

Thus, in material 2 at $x \geq d$, we have

$$\begin{aligned} E_y &= (A e^{\alpha_2 d} \cos \beta_{1x} d) e^{-\alpha_2 x} \\ &= (A \cos \beta_{1x} d) e^{-\alpha_2 (x-d)} \end{aligned} \quad (110)$$

Equating $H_{1z} = H_{2z}$ at $x = d$ by using $\partial E_y / \partial x = -j \omega \mu H_z$ as given by (99), we obtain

$$H_{1z} = \frac{1}{-j \omega \mu} \frac{\partial}{\partial x} (A \cos \beta_{1x} x) = \frac{\beta_{1x} A}{j \omega \mu} \sin \beta_{1x} x \quad (111)$$

$$H_{2z} = \frac{1}{-j \omega \mu} \frac{\partial}{\partial x} (C e^{-\alpha_2 x}) = \frac{\alpha_2 C}{j \omega \mu} e^{-\alpha_2 x} \quad (112)$$

and at $x = d$

$$\begin{aligned} \beta_{1x} A \sin \beta_{1x} d &= \alpha_2 C e^{-\alpha_2 d} \\ &= \alpha_2 (A e^{\alpha_2 d} \cos \beta_{1x} d) e^{-\alpha_2 d} \end{aligned} \quad (113)$$

or

$$\tan \beta_{1x} d = \frac{\alpha_2}{\beta_{1x}} \quad (114)$$

is obtained for the choice $E_y = A \cos \beta_{1x} x$ in material 1. If the equally valid $E_y = B \sin \beta_{1x} x$ had been chosen as the solution in material 1, the result of matching tangential fields at $x = d$ would have been

$$\tan \beta_{1x} d = -\frac{\beta_{1x}}{\alpha_2} \quad (115)$$

The electric field distributions along the x dimension for the first four modes, two even (cosine terms), and two odd (sine terms), are shown in Fig. 5b. Note the corresponding phase angle $\beta_{1x} d$ from center to edge for each mode as listed in the caption for Fig. 5b. These phase angles and the propagating modes that are allowed may be determined by graphically solving the transcendental eigenvalue equations $\tan \beta_{1x} d = \alpha_2 / \beta_{1x}$ and $\tan \beta_{1x} d = -\beta_{1x} / \alpha_2$.

From the expressions defined earlier, $\alpha_2^2 = \beta^2 - \omega^2 \mu \epsilon_2$ and $\beta_{1x}^2 = \omega^2 \mu \epsilon_1 - \beta^2$, express

$$\frac{\alpha_2}{\beta_{1x}} = \sqrt{\frac{\omega^2 \mu (\epsilon_1 - \epsilon_2)}{\beta_{1x}^2} - 1} \quad (116)$$

Next, define and then substitute the term

$$\begin{aligned} V &\triangleq \sqrt{\omega^2 \mu (\epsilon_1 - \epsilon_2) d^2} = \omega d \sqrt{\mu \epsilon_0} \sqrt{\epsilon_{1r} - \epsilon_{2r}} \\ &= \frac{\omega d}{c} \sqrt{\epsilon_{1r} - \epsilon_{2r}} = \frac{2\pi d}{\lambda_0} \sqrt{\epsilon_{1r} - \epsilon_{2r}} \end{aligned} \quad (117)$$

to obtain

$$\tan \beta_{1x} d = \frac{\alpha_2}{\beta_{1x}} = \sqrt{\left(\frac{V}{\beta_{1x} d}\right)^2 - 1} \quad (118)$$

for the even modes, and

$$\tan \beta_{1x} d = -\frac{\beta_{1x}}{\alpha_2} = \frac{-1}{\sqrt{\left(\frac{V}{\beta_{1x} d}\right)^2 - 1}} \quad (119)$$

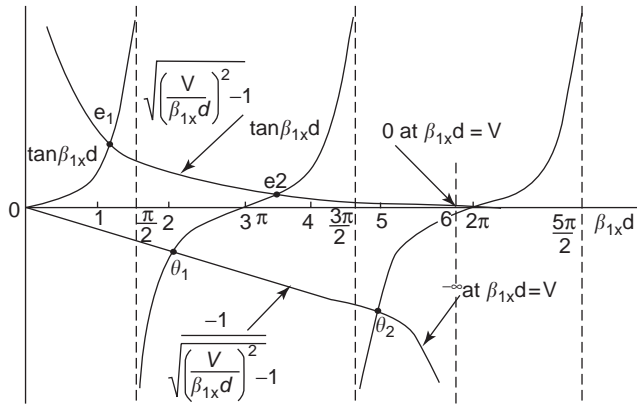


Figure 6. First and last terms of (118) and (119) plotted against $\beta_{1x}d$ for the case when $V = 6$. For this value of V , two even modes and two odd modes are allowed to propagate.

for the odd modes. The operating frequency and the parameters of the dielectric waveguide set the value of V (called the *normalized frequency*). The first and last terms of (118) and (119) are plotted against $\beta_{1x}d$, and the particular points of the curves give the allowed modes and the particular value of $\beta_{1x}d$ for that mode. An example is plotted in Fig. 6 for the case when $V = 6$. For this value of V , two even modes and two odd modes are allowed to propagate. Observe from the plot that if $V < 3\pi/2$, only three modes could propagate (two evens and one odd). Also, if $V < \pi/2$, only one mode could propagate (the lowest-order even mode).

Example 2. A dielectric sheet of thickness $2d = 0.002$ m and permittivity $\epsilon_1 = 3.25\epsilon_0$ is surrounded by air ($\epsilon_2 = \epsilon_0$). (a) Over what range of operating frequencies will no more than three modes propagate? (b) Over what range of operating frequencies will only one mode propagate?

Solution:

$$V = \frac{2\pi fd}{c} \sqrt{\epsilon_{1r} - \epsilon_{2r}}$$

$$= \frac{2\pi f \cdot 0.001}{3 \times 10^8} \sqrt{3.25 - 1} = \pi f \times 10^{-11}$$

(a) For $\pi f \times 10^{-11} < 3\pi/2$, three modes propagate in the range $f < 150$ GHz.

(b) For $\pi f \times 10^{-11} < \pi/2$, only one mode propagates in the range $f < 50$ GHz.

As indicated earlier, β , the propagation constant of waves or modes that are guided in the z direction, lies within the range $\beta_2 \leq \beta \leq \beta_1$, where $\beta_1 = \omega\sqrt{\mu_0\epsilon_1}$ and $\beta_2 = \omega\sqrt{\mu_0\epsilon_2}$. Also, the raypaths of guided waves may have θ angles that lie within the range $\theta_c \leq \theta \leq 90^\circ$, where $\theta_c = \sin^{-1} \sqrt{\epsilon_2/\epsilon_1}$ is the angle of the critical ray and $\theta = 90^\circ$ is the angle of the axial ray. So, how do the angles of the raypaths relate to the propagation constant of modes or waves? From the raypath diagram in Fig. 5c, the propa-

gation constant of modes guided in the z direction is

$$\beta = \beta_1 \sin \theta = \omega\sqrt{\mu_0\epsilon_1} \sin \theta \tag{120}$$

For axial rays ($\theta = 90^\circ$)

$$\beta = \beta_1 = \omega\sqrt{\mu_0\epsilon_1} \tag{121}$$

This is the largest value of β , and it occurs at the highest operating frequency of a particular mode, since β is directly proportional to frequency.

For rays at $\theta = \theta_c$, we obtain

$$\beta = \omega\sqrt{\mu_0\epsilon_1} \sqrt{\frac{\epsilon_2}{\epsilon_1}} = \omega\sqrt{\mu_0\epsilon_2} = \beta_2 \tag{122}$$

This is the smallest value of β , and it occurs at the lowest operating frequency of a particular mode. Also, at $\theta = \theta_c$ where $\beta = \beta_2$, we have from (105)

$$\beta_{1x}^2 = \omega^2 \mu \epsilon_1 - \beta^2 = \omega^2 \mu \epsilon_1 - \omega^2 \mu \epsilon_2 \tag{123}$$

or

$$\beta_{1x} = \omega\sqrt{\mu\sqrt{\epsilon_1 - \epsilon_2}} = \frac{V}{d} \tag{124}$$

Thus, rays at $\theta = \theta_c$ within a particular mode have $\beta_{1x}d = V$, which is at the point of extinction or cutoff for the mode. The relationships discussed above are indicated on the plot of β versus radian frequency ω in Fig. 7. Note from the plot that at a single operating frequency, many different modes may be propagating, and the highest-order modes have ray paths at $\theta = \theta_c$, while the lowest-order modes have axial rays ($\theta = 90^\circ$).

Example 3. (a) A dielectric waveguide has $\epsilon_{1r} = 2.34$, $\epsilon_{2r} = 2.28$, $d = 5 \mu\text{m}$ and $f = 318.31$ THz, which yields a normalized frequency of $V = (\omega d/c)\sqrt{\epsilon_{1r} - \epsilon_{2r}} = 8.22$. The

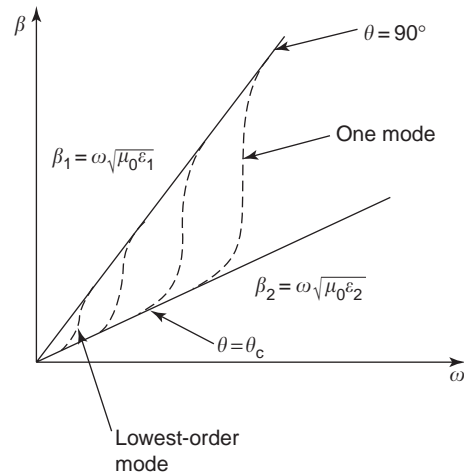


Figure 7. Plot of β versus radian frequency ω . Note from the plot that at a single operating frequency, many different modes may be propagating, and the highest-order modes have raypaths near the critical angle, while the lowest-order modes are nearly axial.

eigenvalues of each propagating mode are $\beta_{1x}d = 1.400, 2.491, 4.179, 5.543, 6.865, \text{ and } 8.045$. Find the propagation angle (θ to the interface normal) for each mode. (b) Is the raypath of the highest-order mode near the critical angle ($\theta = \theta_c$) or near the axial angle ($\theta = 90^\circ$)?

Solution: The propagation constant along a ray path within the waveguide is

$$\beta_1 = \omega\sqrt{\mu_0\epsilon_1} = \frac{\omega\sqrt{\epsilon_{1r}}}{c} = \frac{1.02 \times 10^7}{\text{m}} \quad (125)$$

The propagation constant along the x direction is $\beta_{1x} = \beta_1 \cos \theta_1$, where from the data, we have

$$\beta_{1x} = \frac{0.28, 0.498, 0.8358, 1.1086, 1.373, 1.609 \times 10^6}{\text{m}} \quad (126)$$

Thus

$$\theta = \cos^{-1} \frac{\beta_{1x}}{\beta_1} = 88.43^\circ, 87.20^\circ, 85.30^\circ, 83.76^\circ, 82.26^\circ, 80.92^\circ \quad (127)$$

Observe that the highest-order mode is near the critical angle, $\theta_c = \sin^{-1} \frac{1.51}{1.53} = 80.72^\circ$, and the lowest-order mode is nearly axial (90°).

Example 4. (a) A dielectric waveguide has $\epsilon_{1r} = 2.19$ and $\epsilon_{2r} = 2.16$. For single-mode propagation at the following wavelengths (in air), $\lambda_0 = 1.3, 1.4, 1.5, 1.6 \mu\text{m}$, the eigenvalues are $\beta_{1x}d = 0.9336, 0.9027, 0.8734, 0.8456$, respectively. Find the propagation angle (θ to the interface normal) for each wavelength if $d = 1.89 \mu\text{m}$. (b) Is the shortest wavelength closest to the critical ray ($\theta = \theta_c$) or to the axial ray ($\theta = 90^\circ$)?

Solution: The normalized frequency (V) in the order of increasing wavelength (in μm) is

$$V = \frac{2\pi d}{\lambda} \sqrt{\epsilon_{1r} - \epsilon_{2r}} = \frac{2.042}{\lambda_0} \quad (128)$$

$$= 1.5708, 1.4586, 1.3613, 1.2763$$

Using this result, the eigenvalue at each wavelength is found by solving

$$\tan \beta_{1x}d = \sqrt{\left(\frac{V}{\beta_{1x}d}\right)^2 - 1} = \sqrt{\left(\frac{2.042}{\lambda\beta_{1x}d}\right)^2 - 1} \quad (129)$$

to yield $\beta_{1x}d = 0.9336, 0.9027, 0.8734, 0.8456$, and $\beta_{1x} = (0.4940, 0.4776, 0.4621, 0.4474) \times 10^6/\text{m}$. At each wavelength, $\beta_1 = 2\pi\sqrt{\epsilon_{1r}}/\lambda_0 = 7.1532, 6.6422, 6.1994, 5.8119 \times 10^6/\text{m}$.

Thus

$$\theta = \cos^{-1} \frac{\beta_{1x}}{\beta_1} = 86.04^\circ, 85.88^\circ, 85.72^\circ, 85.58^\circ \quad (130)$$

in the order of increasing wavelength. Note that the shortest wavelength is closest to the axial ray ($\theta = 90^\circ$), and the longest wavelength is closest to the critical ray ($\theta = \theta_c = 83.34^\circ$).

Acknowledgement

This work was supported in part by the National Cancer Institute under PHS Grant 2 pol CA42745-17.

BIBLIOGRAPHY

1. S. Ramo, J. R. Whinnery, and T. Van Duzer, 3rd ed., *Fields and Waves in Communication Electronics*, Wiley, New York, 1994.
2. P. Rizzi, *Microwave Engineering Passive Circuits*, Prentice-Hall, Englewood Cliffs, NJ, 1988.
3. S. B. Cohn, Problems in strip transmission lines, *IRE Trans. Microwave Theory Tech.* **3**:119–126 (March 1955).
4. S. Hopfer, The design of ridged waveguides, *IEEE Trans. Microwave Theory Tech.* **3**:20–29 (Oct. 1955).
5. Y. Zhang and W. T. Joines, Some properties of T-septum waveguides, *IEEE Trans. Microwave Theory Tech.* **35**:769–775 (Aug. 1987).
6. Y. Zhang and W. T. Joines, Attenuation and power-handling capacity of T-septum waveguides, *IEEE Trans. Microwave Theory Tech.* **35**:858–861 (Sept. 1987).
7. G. G. Mazumder and P. K. Saha, Rectangular waveguide with T-shaped septa, *IEEE Trans. Microwave Theory Tech.* **35**:201–204 (Feb. 1987).
8. W. B. Jones, *Introduction to Optical Fiber Communication Systems*, Oxford Univ. Press, New York, 1988.

GUNN OR TRANSFERRED-ELECTRON DEVICES AND CIRCUITS

HERIBERT EISELE
University of Leeds
Leeds, United Kingdom

1. GENERAL

Among all solid-state microwave devices, transferred-electron devices (TEDs), often called *Gunn devices*, are quite unique in that they utilize specific bulk-material properties of certain semiconductors. They are unipolar devices and, generally, do not exhibit the distinctive diode characteristic of p-n (positive-negative) junctions as seen, for example, in other two-terminal microwave devices such as impact ionization avalanche transit-time (IMPATT) or tunnel injection transit-time (TUNNETT) diodes. Originally, TED structures and circuits were developed for both

amplifier and oscillator applications. However, rapid progress in high-speed and high-frequency three-terminal devices with excellent noise performance has practically been eliminating TEDs from all low-noise preamplifier applications up to the high-millimeter-wave frequencies. Additionally, oscillators or amplifiers with three-terminal devices continue to reach higher and higher frequencies and offer similar or even higher radiofrequency (RF) output power levels and direct-current (DC)-to-RF conversion efficiencies compared to the most powerful two-terminal devices such as IMPATT diodes. TEDs in oscillator applications are characterized by low-noise and medium-RF output power P_{RF} . Therefore, they are well suited for local oscillators in sensitive heterodyne receivers and for transmitters at operating frequencies above 30 GHz.

2. PRINCIPLES OF OPERATION

The transferred-electron effect only depends on a specific band structure of the semiconductor material and, therefore, is present in the bulk material. Several materials, mainly in groups III–V and II–VI compound semiconductors and listed in Table 1 [1–3] exhibit such a band structure. These semiconductor materials have more than one energy minimum (i.e., valley in the conduction band) and meet the following criteria, which were proposed independently by Ridley and Watkins [4] as well as Hilsum [5] (RWH):

1. At least two valleys must be present in the conduction band.
2. The minimum (minima) of the upper valley(s) must be several times the thermal energy of electrons above the minimum of the lowest (= main) valley in the conduction band for electrons to reside initially in the lowest valley.
3. The energy difference (ΔE) between the minimum (minima) of the upper valley(s) and the minimum of the main valley in the conduction band must be less

than the energy bandgap E_g to avoid the onset of significant impact ionization in such a device.

4. The transfer of electrons from one conduction band valley to another must require much less time than one period of the intended operating frequency.
5. The effective masses and densities of states in the upper valley(s) must be considerably higher than in the main valley. As a consequence of the higher effective masses, mobilities in the upper valley(s) must be much lower than in the main valley.

For the principles of operation, a homogeneous bulk semiconductor material and a simplified band structure as shown in Fig. 1 are assumed. Electrons at low energies initially reside in the main valley of the conduction band, where a low effective mass corresponds to a high mobility μ_1 . When electrons acquire more energy (e.g., under an electric field \mathcal{E}), most of them still remain in the main valley if $\mathcal{E} < \mathcal{E}_{th}$, where \mathcal{E}_{th} is referred to as the *threshold electric field*. As electrons acquire even more energy (for $\mathcal{E} > \mathcal{E}_{th}$), many of them are scattered (“transferred”) into the upper valley, where a higher effective mass corresponds to a lower mobility μ_2 [1]. For an electric field \mathcal{E} , assumed to be constant in the bulk material, an average electron velocity v_{avg} and average mobility μ_{avg} can be defined as

$$v_{avg} = \frac{n_1\mu_1 + n_2\mu_2}{n_1 + n_2} \mathcal{E} = \mu_{avg} \mathcal{E} \tag{1}$$

where n_1 and n_2 denote the number of electrons in the lower and upper valleys, respectively. Since n_1 decreases and n_2 increases, v_{avg} decreases as shown in Fig. 2. At large energies [i.e., high electric fields ($\mathcal{E} \gg \mathcal{E}_{th}$)], most of the electrons are transferred to the upper valley and $n_1 \ll n_2$. Therefore, after reaching the minimum value, the average drift velocity again increases for higher electric fields. The decrease in the average drift velocity for $\mathcal{E} > \mathcal{E}_{th}$ generates a region of negative differential

Table 1. Semiconductor Materials Related to the Transferred-Electron Effect

Semiconductor	E_g (eV)	Valley Separation		\mathcal{E}_T (kV/cm)	v_p (10^7 cm/s)	T (K)
		Between	ΔE (eV)			
GaAs	1.42	Γ and L	0.31 (0.33)	3.2–3.5	2.2–2.3	300
InP	1.35	Γ and L	0.53 (0.45)	10–12	2.5–2.8	300
Ge	0.74	L and Γ	0.18	2.3	1.4	77
CdTe	1.50	Γ and L	0.51	11	1.5	300
InAs	0.36	Γ and L	1.28/0.87	1.6/2.5	3.6	300
InSb	0.28 (0.18)	Γ and L	0.41	0.6	5.0	77
ZnSe	2.60	Γ and L	—	38	1.5	300
Ga _{0.5} In _{0.5} Sb	0.36	Γ and L	0.36	0.6	2.5	300
Ga _{0.3} In _{0.7} Sb	0.24	Γ and L	—	0.6	2.9	300
In _{0.53} Ga _{0.47} As	0.76	Γ and L	0.55	3–4	2.9	300
InAs _{0.2} P _{0.8}	1.10	Γ and L	0.95	5.7	2.7	300
Ga _{0.13} In _{0.87} As _{0.37} P _{0.63}	1.05	Γ and L	—	5.5–8.6	1.2	300
GaN	3.36	Γ and X	1.5	80–160	2.5–4.5	300
Ga _{0.5} Al _{0.5} N	4.77	Γ and X	0.44	>70	2.5	300

Source: Data From Refs. 1–3.

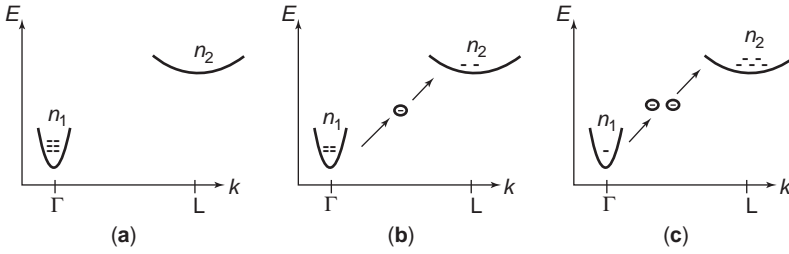


Figure 1. Simplified energy-band diagram for a direct two-valley semiconductor showing electron transfer: (a) electron distribution for $\mathcal{E} < \mathcal{E}_{th}$; (b) electron distribution for $\mathcal{E} > \mathcal{E}_{th}$; (c) electron distribution for $\mathcal{E} \gg \mathcal{E}_{th}$.

mobility μ_{diff} with

$$\mu_{diff} = \frac{dv_{avg}}{d\mathcal{E}} \quad (2)$$

If electrons in the upper valley reach a region where the electric field \mathcal{E} drops below \mathcal{E}_{th} , they lose energy and significantly more of them are scattered back to the main valley.

James B. Gunn was the first to observe current oscillations experimentally in bulk GaAs and InP [6,7], which were subsequently explained by this transferred-electron effect [8]. As a result, the term *Gunn device* quickly became common for this type of device. Out of more than 10 semiconductor materials known for the transferred-electron effect, only GaAs and InP have so far found widespread use in system applications. GaAs and InP have three valleys in the conduction band, and at the doping concentrations required for operation at millimeter-wave frequencies, high-field mobilities are considerably lower than the low-field mobilities. As a consequence of two upper valleys and additional scattering mechanisms, the electron drift velocity v monotonically decreases for electric fields above \mathcal{E}_{th} . Figure 3 shows simplified band structure diagrams for GaAs and InP, and Fig. 4 their respective velocity–electric field profiles. Table 2 [9–11] summarizes the relevant material characteristics of GaAs and InP. The finite time it takes for electrons to gain or lose energy in an electric field causes a fundamental physical frequency limit in these devices. This frequency limit

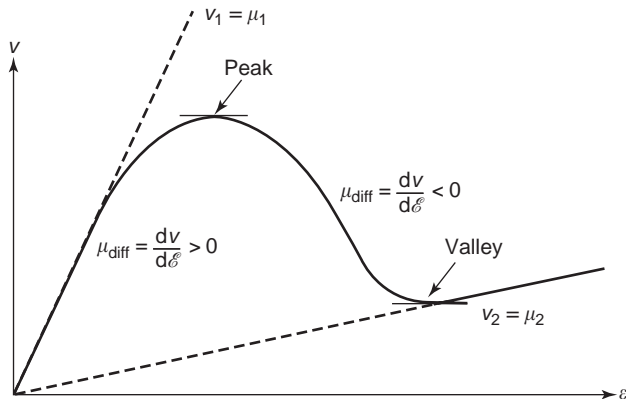


Figure 2. Velocity–electric field profile for the two-valley semiconductor of Fig. 1.

was originally thought to be approximately 100 and 200 GHz [9–11] for TEDs based on the GaAs and InP material systems, respectively. However, more recent theoretical and experimental work indicates a significantly higher frequency limit in InP-based TEDs.

Except for some rare conditions in devices at lower microwave frequencies, the bulk negative differential mobility alone does not cause a static negative differential resistance (NDR) to be used for RF power generation. A mechanism based on the negative differential mobility results in a dynamic negative resistance as shown next. In a region of bulk semiconductor material under uniform conditions (doping concentration N_D , electric field \mathcal{E} , average differential mobility μ_{diff}), any space charge inhomogeneity $Q_S(x,t)$ traveling at the velocity v grows or decays following an exponential law that can be derived from Maxwell's equations:

$$Q_S(x,t) = Q_S(x - vt, 0) \exp\left(-\frac{t}{\tau}\right) \quad (3)$$

where

$$\tau = \frac{\epsilon_s}{\sigma} = \frac{\epsilon_s}{qN_D\mu_{diff}} \quad (4)$$

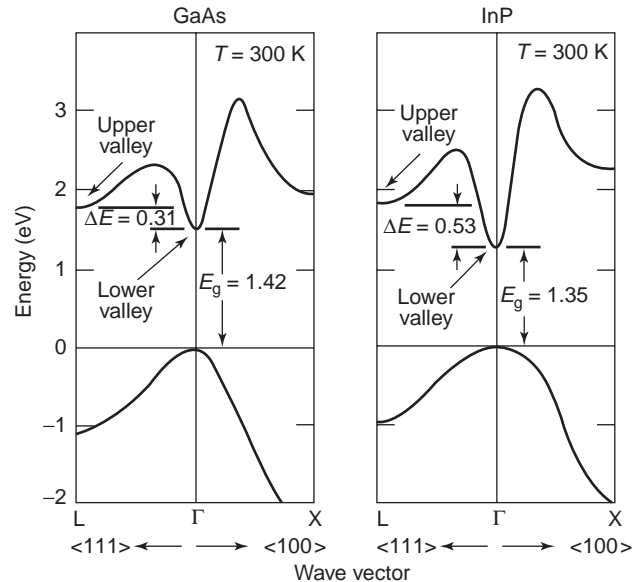


Figure 3. Simplified band diagram for the three-valley semiconductor materials GaAs and InP.

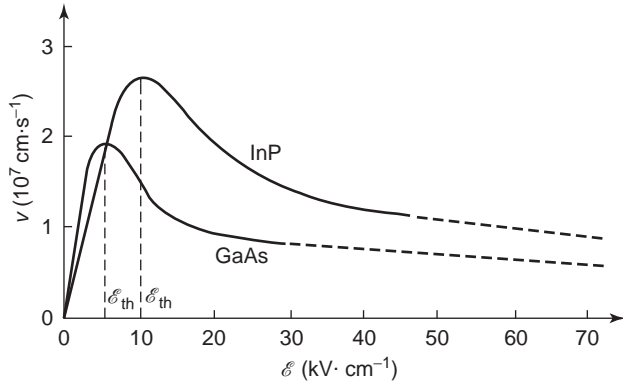


Figure 4. Velocity–field profile for the three-valley semiconductor materials GaAs and InP.

where, q denotes the elementary charge; σ and ϵ_s denote specific conductivity and dielectric constant of the material, respectively. At low electric fields \mathcal{E} , where $\mu_{\text{diff}} > 0$, the charge inhomogeneity decays with $\tau = \tau_D$, the dielectric relaxation time, and at higher electric fields, where $\mu_{\text{diff}} < 0$, a charge inhomogeneity can grow. This charge inhomogeneity reaches a significant level only if the growth factor for the maximum traveled distance l , the length of the active region of the device, is very large. Therefore the condition

$$\frac{l}{v|\tau|} = \frac{lqN_D|\mu_{\text{diff}}|}{\epsilon_s v} > 1 \tag{5}$$

must be satisfied, which corresponds to

$$N_D l > 1 \times 10^{12} \text{ cm}^{-2} \tag{6}$$

for both GaAs and InP.

Table 2. Semiconductor Material Characteristics Relevant to GaAs and InP TEDs^a

Properties	Semiconductor	
	GaAs	InP
Energy gap (eV)	1.42	1.34
Low-field mobility (at 500 K) (cm ² V ⁻¹ s ⁻¹)	5000	3000
Thermal conductivity (Wcm ⁻¹ K ⁻¹)	0.37–0.54	0.68–0.80
Velocity peak-to-valley ratio	2.2	3.5
Threshold field E_{th} (kV/cm)	3.5	10.5
Breakdown field (at $N_D = 10^{16} \text{ cm}^{-3}$) (kV/cm)	400	500
Effective transit velocity v_T (cm/s)	0.7×10^7	1.2×10^7
Temperature dependence of v_T (K ⁻¹)	-0.0015	-0.001
Diffusion coefficient-mobility ratio at $2E_{\text{th}}$ (cm ² /s)	72	142
Energy relaxation time due to collisions (ps)	0.4–0.6	0.2–0.3
Intervalley relaxation time (ps)	—	0.25
Acceleration–deceleration time (ps) (inertial energy time constant)	1.5	0.75

Source: After Wandinger Ref. 9, Fank et al. [10], and Eddison [11].
^aAt a temperature of 300 K unless noted otherwise.

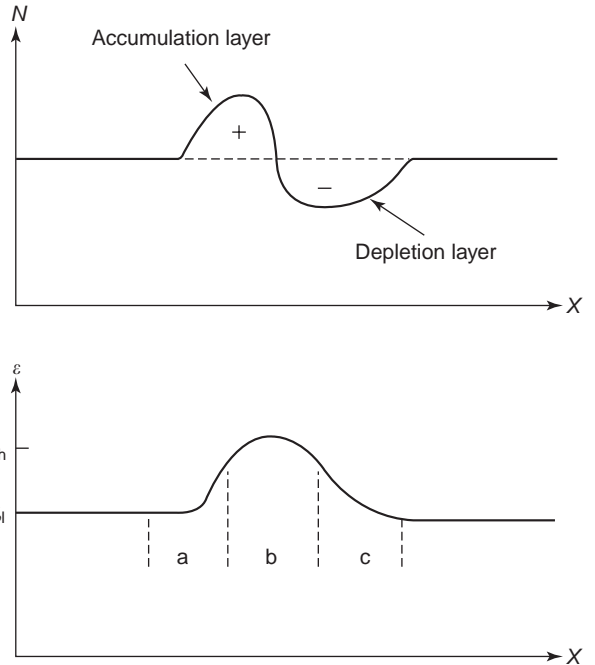


Figure 5. Carrier concentrations and electric field profile for a dipole domain.

Typical Gunn devices at millimeter-wave frequencies have $N_D l$ products between $1 \times 10^{12} \text{ cm}^{-2}$ and $3 \times 10^{12} \text{ cm}^{-2}$, and doping concentrations N_D in the active region exceed 10^{15} cm^{-3} . For $N_D > 10^{15} \text{ cm}^{-3}$, space charge inhomogeneities typically grow into so-called dipole domains where accumulation and depletion layers are lumped together. Figure 5 shows the carrier distribution and electric-field profile for such a dipole domain under uniform conditions. Electrons in the low-field region travel at a constant v_T for a constant electric field \mathcal{E}_1 . Electrons in region a are accelerated by the higher electric field until they reach region b , where they are transferred to the upper valley and slow down to be trapped in this accumulation region. Electrons in region c lose energy and are transferred back to the lower valley. Their average velocity now is higher than the average velocity in region b , thus region c is depleted of electrons. After a domain forms at the cathode, grows, and propagates through the active region, the voltage drop across the domain increases and, under a constant bias voltage, lowers the voltage drop outside the domain. This voltage drop is equivalent to a reduction in the electric field \mathcal{E}_1 outside the domain and generally prevents formation of new domains in the active region. It also limits the growth of the existing domain because fewer electrons are trapped in the accumulation layer or escape the depletion layer. Domains reaching the anode collapse and induce a current flow in the external circuit. A phase difference occurs between this current flow and the applied RF voltage and, at the right frequency, this phase difference corresponds to a dynamic negative resistance and causes RF power generation in an appropriate RF circuit.

Distinct modes of operation have been investigated and described for TEDs at microwave frequencies [12].

However, as is shown next, at millimeter-wave frequencies finite intervalley transfer and domain formation times reach a significant fraction of the RF cycle. In such a case, domains form, grow, and suppress formation of new domains, but may never reach the stable state before they reach the anode as described above. Therefore, modes get blurred, and devices generally operate in a near transit-time mode, where the operating frequency f_{op} is given by

$$\frac{1}{T} = f_{op} = \frac{v_T}{l} \quad (7)$$

The effective transit velocity $v_T = v(\mathcal{E}_1) = v_D(\mathcal{E}_h)$ can be determined from Butcher's equal-area rule [13], which is

$$\int_{\mathcal{E}_1}^{\mathcal{E}_h} [v(\mathcal{E}) - v_D] d\mathcal{E} = 0 \quad (8)$$

for a constant diffusion coefficient throughout the active region and is illustrated in Fig. 6.

If the operating frequency f_{op} differs somewhat from Eq. (7), the domain reaches the anode prematurely or is delayed. Similar to the operation of transit-time diodes, the current pulse from the collapsing domain still causes a negative resistance and generates RF power. Therefore, operation over a broad bandwidth can be achieved. Additionally, higher bias voltages increase electric fields in the device, and higher electric fields reduce the domain velocity v_D , as seen in Fig. 6. At higher electric fields, electrons also acquire the energy for intervalley transfer over a shorter distance as is described in more detail in a subsequent section. Consequently, the portion of the active region where domains form and travel is increased. Lower v_D and longer domain travel distance correspond to a lower optimum f_{op} .

Figure 7 gives an overview of typical structures and schematic doping profiles for TEDs that yielded (Figs. 7a, 7b, 7d, 7e) or are expected to yield (Fig. 7c) excellent RF performance in oscillators. The three-zone flat-doping and the two-zone flat-doping structures were the first to be exploited because they are easy to grow in more classical growth systems such as liquid-phase or vapor-phase epitaxy (LPE or VPE). The three-zone flat-doping structure [14] consists of the n^- -doped active region sandwiched between the highly doped n^+ regions for the ohmic contacts. Since low-ohmic alloyed contacts can be formed on

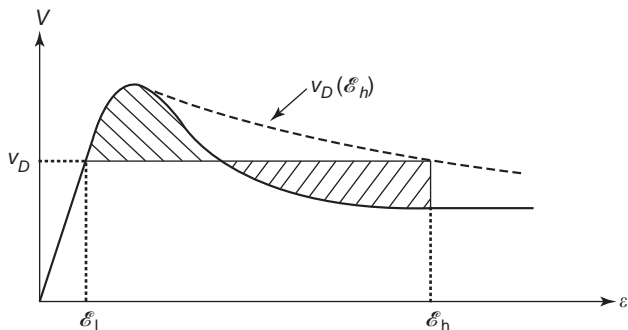


Figure 6. Equal-area rule for TEDs.

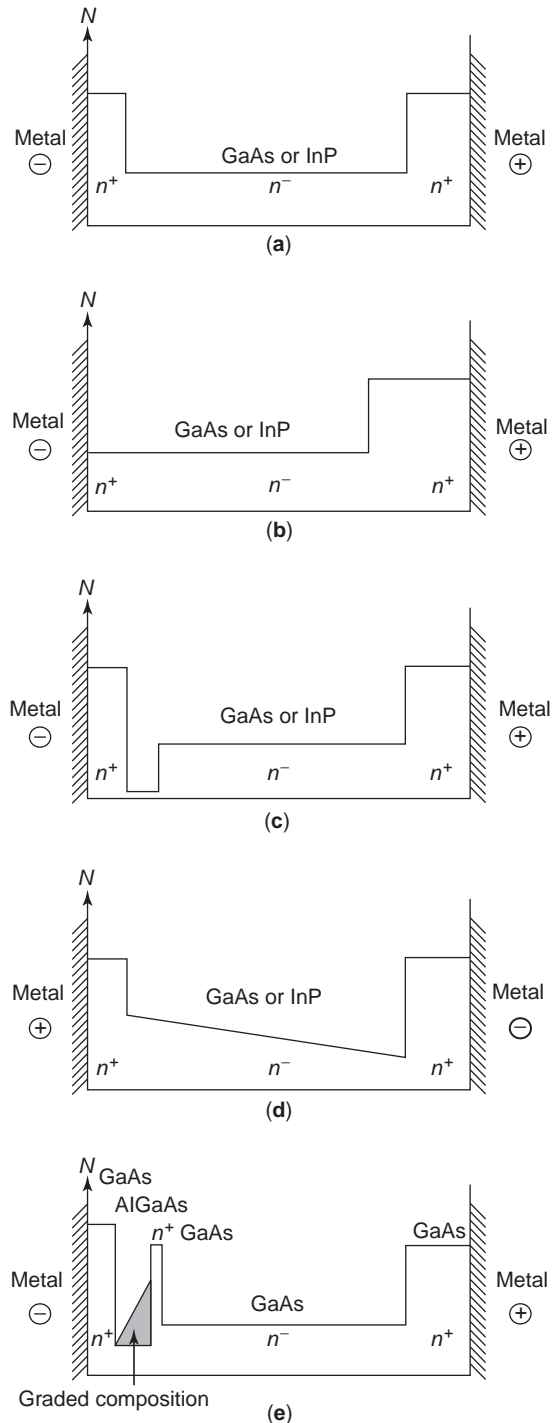


Figure 7. Different device structures for TEDs: (a) three-zone flat doping; (b) two-zone flat doping; (c) three-zone flat doping with cathode notch; (d) three-zone graded doping; (e) heterojunction barrier cathode.

n -type GaAs and InP, the highly doped region on the cathode side can be omitted and just a two-zone, flat-doping structure needs to be grown by VPE or LPE.

The advent of advanced growth techniques such as molecular-beam epitaxy (MBE), metallorganic chemical vapor deposition (MOCVD), metallorganic molecular-beam

epitaxy (MOMBE), and chemical-beam epitaxy (CBE) has allowed more complicated structures to be grown. Using these growth techniques, graded-doping profiles and heterojunction barriers as shown in Fig. 7 can be incorporated into the device structures and suitably tailored to optimize device performance at a particular frequency or to extend the frequency limit of TEDs. Computer simulations [11,15,16] have revealed that in a three-zone flat-doping structure, “cold” electrons with low energies enter the active region from the contact zone at the cathode and require some time to acquire enough energy before they transfer to the upper valley. The results of such Monte Carlo simulations [16] at a frequency of 95 GHz are illustrated in Fig. 8 for a three-zone flat-doping structure in InP with a doping of $1 \times 10^{16} \text{ cm}^{-3}$ in the active region. The finite-energy relaxation times, which are shown in Fig. 9 as a function of the electron energy in GaAs and InP,

create a huge so-called “dead space” at the beginning of the 1.7- μm -long active region. As can be seen from Fig. 8c, the average energy E of electrons within the dead space does not reach the threshold energy E_{th} for intervalley transfer, and electrons reside mostly in the main valley. Therefore, the differential mobility remains positive, and space charge inhomogeneities are prevented from growing, which is illustrated in Fig. 8b with insignificant electron accumulation within the dead space. As a consequence, the resistance of the device $R(x)$ [i.e., the real part of $\mathbf{Z}(x)$] as a function of the position x

$$\mathbf{Z}(x) = R(x) + j\mathbf{X}(x) = \frac{\int_0^x \mathcal{E}(x') dx'}{\frac{A}{l} \int_0^x \mathbf{J}(x') dx'} \quad (9)$$

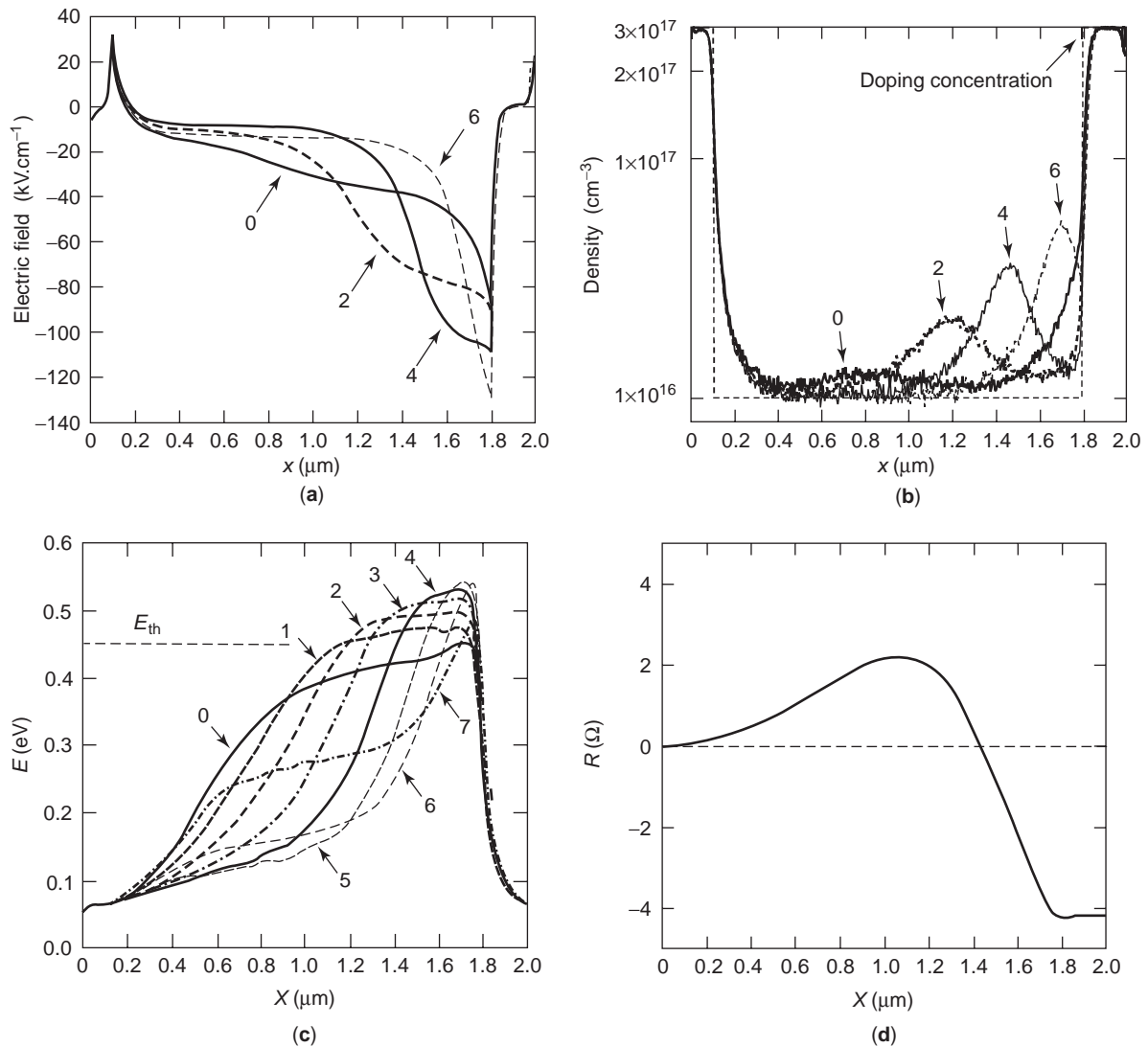


Figure 8. Evolution of (a) electric field, (b) electron density, (c) average electron energy E , and (d) diode resistance R against position x (active region 0.1–1.8 μm): $f = 95 \text{ GHz}$, $V_{\text{rf}} = 1.0 \text{ V}$, $V_{\text{bias}} = 5.0 \text{ V}$, $I_{\text{bias}} = 474 \text{ mA}$, $T = 500 \text{ K}$. The graphs in parts (a), and (b) show the electric field and the electron density, respectively, at $\omega t = n\pi/4$, $n = 0, 2, 4, 6$, and part (c) shows the electron energy profile at $\omega t = n\pi/4$, $n = 0 \dots 7$, during one RF cycle.

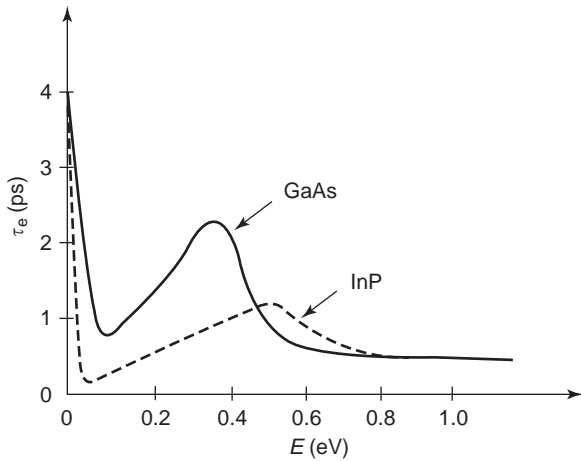


Figure 9. Energy relaxation times τ_e in GaAs and InP against electron energy E . (After Rolland et al. [15].)

remains positive for a large fraction of the active region and contributes to losses in this dead-space region, whereas a negative resistance contributes to the RF power generation only for a small fraction of the active region. In Eq. (9), A and J , denote the device area and total current density, respectively. In addition to this dead-space region, the peak electric field occurs near the anode, and, at a high DC bias, the electric field may reach values for the onset of avalanche breakdown. The energy-dependent energy relaxation times of Fig. 9 lead to effective transfer time constants as shown in Table 2 for GaAs and InP. Fundamental frequency limits of 100 GHz for GaAs and 200 GHz for InP TEDs were originally estimated from these effective transfer time constants and considered hard limits. However, in subsequent sections, some solutions that help reduce the dead-space region or have been demonstrated to extend the useful frequency range even far beyond these fundamental frequency limits are presented and discussed.

3. FABRICATION TECHNOLOGIES

TEDs are characterized by low to medium DC-to-RF conversion efficiencies ranging from approximately more than 15% down to less than 1%. As a consequence, most of the DC input power P_{DC} , namely, $P_{DC} - P_{RF}$, needs to be dissipated as heat in the device. In most cases, one of the metal contacts near the active region of the device also acts as the heatsink; therefore, TEDs for millimeter-wave frequencies generally are mesa-type devices. Additionally, operation at these frequencies requires thin devices to reduce losses in the substrate resulting from the skin effect. The integrated heatsink technology is the most widespread for devices at millimeter-wave frequencies. To reduce losses in the substrate, most of it needs to be removed during fabrication.

In early fabrication technologies, vapor-phase epitaxy (VPE) provided the layer structures. As a first step in processing, a few small holes (or grooves) across the sample

were etched through the epitaxial layers down into the substrate. An appropriate depth of the holes was chosen to gauge the thickness during substrate removal. The advent of more advanced growth techniques, such as MBE, MOMBE, MOCVD, and CBE, allows the incorporation of a lattice-matched, stop-etch layer between the substrate and the epitaxial layers of the device. This way, the substrate is completely removed, and precise control of the mesa height and, consequently, the device diameter is achieved. Fabrication technologies for substrateless devices on integral heatsinks or on diamond heatsinks for better heat removal have been developed and described in the literature. Selective etching technologies in the GaAs and InP material systems [16–18] employ as etch-stop layers lattice-matched $\text{Ga}_x\text{Al}_{1-x}\text{As}$ ($x < 0.4$) and $\text{In}_{0.53}\text{Ga}_{0.47}\text{As}$ layers, respectively. Improved yield, reproducibility, and performance characterize these substrateless devices.

Figure 10 summarizes the basic steps of these fabrication technologies. The batch fabrication of InP TEDs on integral heatsinks serves as an example [16]. In the first step, the metallization for the n-ohmic contact (Ni/Ge/Au/Ti/Au) is evaporated or sputtered onto the surface. A thick gold layer is then electroplated onto this metallization to form the integral heatsink. The sample is mounted on a carrier to provide additional mechanical support and protect the heatsink during the subsequent processing steps. The substrate is removed in a selective etchant of diluted hydrochloric acid [16], which does not attack the $\text{In}_{0.53}\text{Ga}_{0.47}\text{As}$ etch-stop layer. Good ohmic contacts can be formed on n-type InP or, with lower specific contact resistance ρ_c , on n-type $\text{In}_{0.53}\text{Ga}_{0.47}\text{As}$. Therefore, this $\text{In}_{0.53}\text{Ga}_{0.47}\text{As}$ layer need not be removed, but may be etched away selectively in a standard solution of phosphoric or sulfuric acid, hydrogen peroxide, and water as indicated in Fig. 10. Such a solution does not attack InP. A photolithography step defines the openings on this InP surface (or $\text{In}_{0.53}\text{Ga}_{0.47}\text{As}$ surface if left in place), where the metallization (Ni/Ge/Au/Ti/Au) for the other n-ohmic contacts on the second heavily n^+ -doped layer is deposited. Excess metal outside the contacts is lifted off with the photoresist and, using another photolithography step, the contacts are selectively electroplated with several micrometers of gold to form a good bonding pad. The contact pad acts as a mask when the mesa of the diode is etched in a nonselective etch. After the sample has been removed from the carrier, the contacts are annealed, and the sample is diced into individual diodes. Diodes are then mounted in packages for appropriate RF circuits.

4. DEVICE PACKAGES, OSCILLATOR CIRCUITS, AND RF PERFORMANCE

Figure 11a shows a typical TED package. It consists of a gold-plated threaded copper puck (which can be screwed into the RF circuit), an alumina ring, and a top lid for a hermetic seal. The device is soldered or thermocompression-bonded onto a pedestal inside the ring, and gold straps are then thermocompression-bonded onto the device and the top metallization of the alumina ring. The height and diameter of the ring depend on the operating

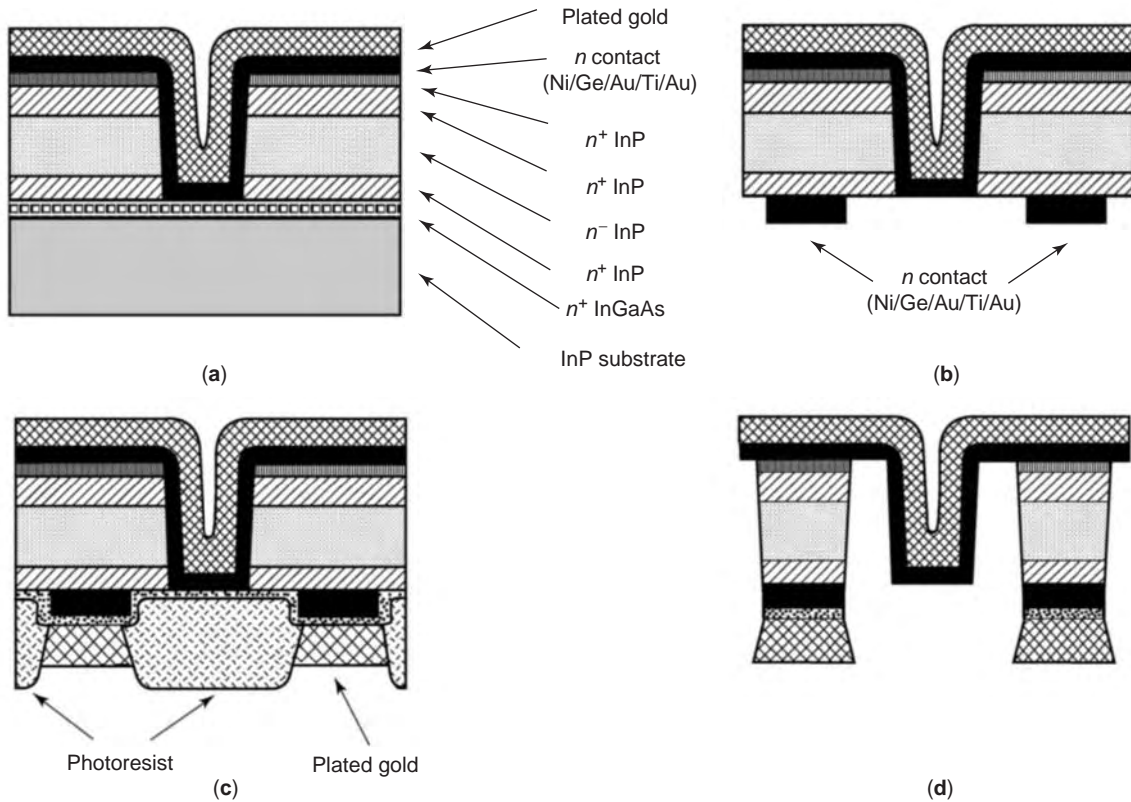


Figure 10. Steps in the fabrication of InP TEDs on integral heatsinks: (a) Island definition, N-ohmic evaporation and gold plating of heatsink ($\approx 20\ \mu\text{m}$); (b) substrate thinning, etch-stop layer removal, and second N-ohmic evaporation; (c) gold plating of ohmic contacts; (d) final devices after annealing and mesa etch. (After Kamoua et al. [16].)

frequency as well as the device, and typical values are given in Fig. 11a. This type of package is used up to frequencies of 94 GHz, and its parasitic elements can be approximated by lumped elements as illustrated in Fig. 11b. Different ribbon configurations are chosen to minimize the influence of the parasitic inductance L_p , which is the highest for just one gold strap across and the lowest for the “star” configuration. The useful frequency range of the package can be extended to 140 GHz and higher if the alumina ring is replaced by a quartz ring for a lower parasitic capacitance C_p . However, new devices for frequencies above 100 GHz are still being developed, and, for research purposes, a low-parasitic open package with two or four standoffs at the highest millimeter- and up to submillimeter-wave frequencies is also often employed [18,19].

The heat-flow resistance R_{th} from the active layer of the device to the package causes an average temperature increase ΔT_{op} in the active layer

$$\Delta T_{op} = R_{th}(P_{DC} - P_{RF}) \tag{10}$$

Too high an active layer temperature degrades the RF performance as well as the device reliability and lifetime [11]. A larger valley separation of 0.53 eV in InP than in GaAs (see Fig. 3) reduces the temperature dependence of

the transfer mechanism as well as the temperature-dependence of the effective transit velocity v_T (see Table 2). As a result, DC-to-RF conversion efficiencies and oscillation frequencies are generally less temperature-dependent in InP Gunn devices. However, the higher threshold electric field of 10.5 kV/cm in InP (see Table 2) requires higher bias voltages than those applied at GaAs devices of the same length. Therefore, RF power levels are thermally limited at low microwave frequencies, where long active regions need to be used. As a further consequence, InP TEDs are more likely to benefit from reduced heat-flow resistances [11]. Figure 12 compares the estimated [20] heat-flow resistances of W-band (75–110 GHz) and D-band (110–170 GHz) InP Gunn devices on integral and diamond heatsinks as well as some measured values for devices on integral heatsinks [21–23]. Examples of how significantly diamond heatsinks improve the RF performance of both GaAs and InP Gunn devices are provided in the sections on device structures.

Many different circuit configurations for oscillators with TEDs have been investigated. At millimeter-wave frequencies, waveguide circuits are quite common. Although excellent results were reported from a few transferred-electron oscillators (TEO) in microstrip circuits [10,11,24–26], the vast majority of the state-of-the-art results were obtained in waveguide circuits. These results, summarized in Fig. 13, include the performance of different

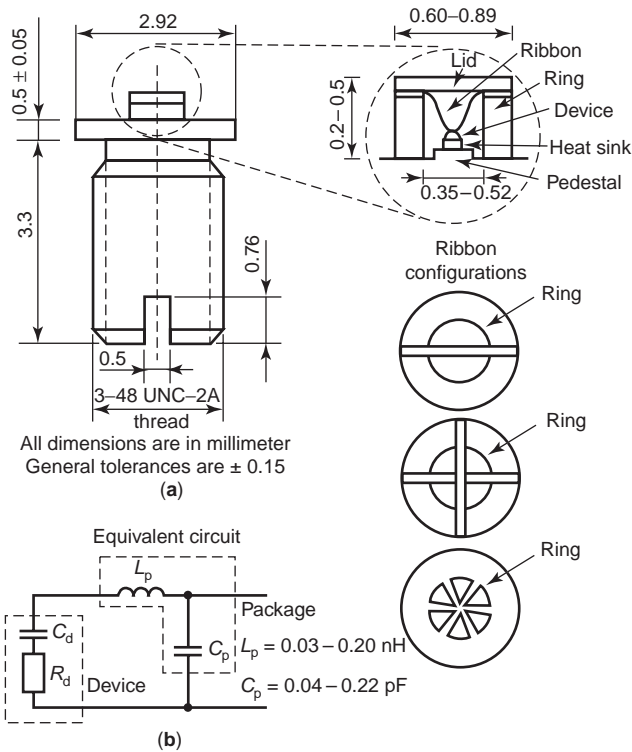


Figure 11. (a) Hermetically sealed package for millimeter-wave TEDs; (b) equivalent circuit of the parasitic elements.

device structures as illustrated in Fig. 7. Examples for the RF performance of individual device structures are given in the subsequent sections. An overview of typical configurations for waveguide circuits [27,28] is shown in Fig. 14. Examples of oscillator circuits using coaxial lines at microwave frequencies can be found in Ref. 1.

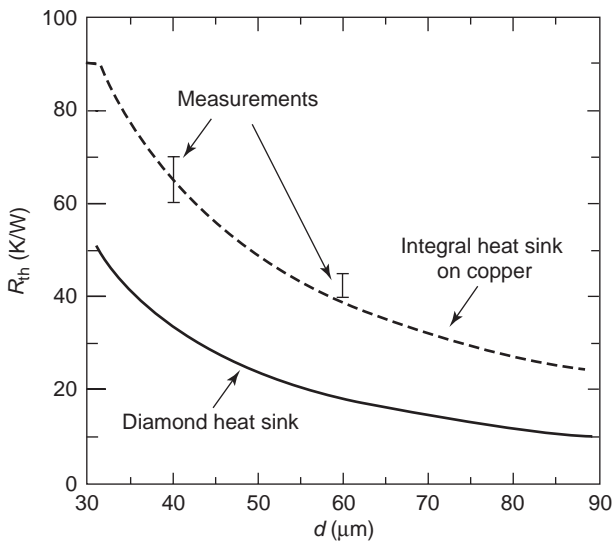


Figure 12. Estimated and measured [21–23] heat-flow resistances R_{th} of InP TEDs on integral heatsinks and estimated R_{th} of InP TEDs on diamond heatsinks against device diameter d ; estimates based on the spreading approximation [20].

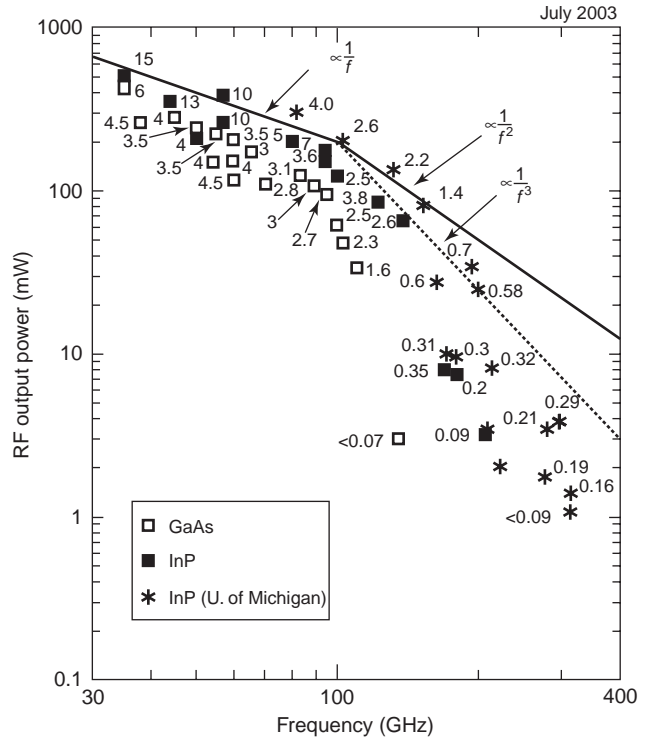


Figure 13. State-of-the-art RF power levels from TEDs under CW operation in the frequency range of 30–400 GHz. Numbers next to the symbols denote DC-to-RF conversion efficiencies in percent.

5. DEVICE STRUCTURES

5.1. Ohmic Cathode Contacts

TEDs with ohmic contacts on both heavily n-doped regions of the structure of Fig. 7a (flat-doping profile) are the simplest structure, easy to fabricate, but characterized by low DC-to-RF efficiencies. These devices are typically operated in a full-height waveguide cavity with a resonant cap on top of the device package, and this configuration is illustrated in Fig. 14e. Modifications of this configuration include the use of a reduced-height waveguide or a mechanism for adjusting the position of the resonant cap and the device package with respect to the bottom of the waveguide. Fundamental-mode operation of Gunn devices in a reduced-height postcoupled waveguide cavity was reported up to millimeter-wave frequencies, for instance, for a GaAs Gunn device at 84 GHz [29] and an InP Gunn device at 126 GHz [30]. RF power levels (and corresponding DC-to-RF conversion efficiencies) of 420 mW (6%) at 35 GHz [19], 280 mW at 45 GHz [19], 150 mW at 60 GHz, and 110 mW (2.8%) at 70 GHz [31] were reported from flat-profile GaAs Gunn devices in the fundamental mode.

A sharp decline in the DC-to-RF conversion efficiencies of devices operating in the fundamental-mode presages the abovementioned frequency limits for GaAs or InP Gunn devices. However, this frequency limit can be extended by the extraction of higher harmonics from the inherently nonlinear Gunn device. Second-harmonic power extraction has proved most successful in a slightly

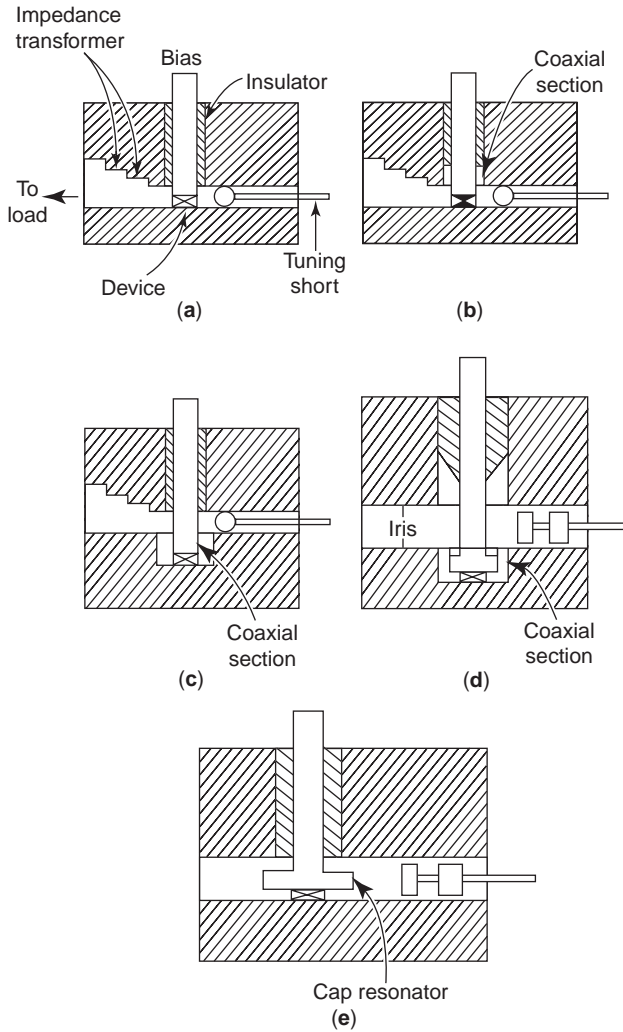


Figure 14. Examples of waveguide circuits for TED oscillators. (After Kuno [27].)

modified version of a resonant-cap, full-height waveguide cavity. The size of the waveguide is appropriate for the second-harmonic frequency, but impedes wave propagation at the fundamental frequency. If in such a circuit the fringe capacitance of the cap and the device capacitance together resonate with the inductance of the bias post (see Fig. 14e) at half the output frequency, this signal cannot propagate, and the termination of the device is almost purely reactive at the fundamental frequency. This reactive termination causes a large voltage swing in the device and, as a result, strong nonlinear operation. A cap of appropriate size together with the coaxial post provides impedance matching into the waveguide at the second-harmonic frequency, and a waveguide backshort at one side of the cavity provides power tuning. The resonant circuit at the fundamental frequency is decoupled from the load, which corresponds to Q values typically higher than those in fundamental-mode operation. As results, reduced frequency pulling with load changes or improved frequency stability may be observed. However, more complicated circuits with precise mechanical dimensions are

necessary if wide-range frequency tuning is to be implemented. As an example for second-harmonic power extraction, RF power levels (and DC-to-RF conversion efficiencies) of 123 mW (3.1%) at 83 GHz, 96 mW (2.7%) at 94 GHz were measured with GaAs Gunn devices [31].

The advantages of InP can be clearly seen at millimeter-wave frequencies with short active regions where lower inertial energy time constants lead to a much higher fundamental frequency limit. RF power levels (and corresponding DC-to-RF conversion efficiencies) of 200 mW (5%) at 80 GHz and 150 mW (3.5%) at 94 GHz [22] in the fundamental mode as well as 7 mW at 180 GHz and 3.2 mW at 206 GHz [32] in a second-harmonic mode were reported from similar flat-doping InP Gunn devices on integral heatsinks.

RF power stability against package temperature typically ranges from -0.02 to -0.06 dB/°C as quoted by various manufacturers for commercially available GaAs Gunn devices (see also Ref. 11). Conversely, values of around -0.013 dB/°C [11] or as low as -0.005 dB/°C [21,22] were reported from InP Gunn devices.

The more complex structures of Figs. 7c–7e also employ ohmic cathode contacts at the anode and cathode, but device characteristics and RF performance are discussed separately in subsequent sections.

5.2. Current-Limiting Cathode Contacts

A partially annealed ohmic contact significantly reduces the typical Schottky barrier height of metals on the semiconductors GaAs and InP (0.6–0.9 eV), but still leaves a small barrier (<200 meV). If such a contact is formed on the cathode side of the two-zone structure (see Fig. 7b) and is reverse-biased, this barrier causes a high-field region at the cathode contact of the device under bias. Electrons injected over this barrier enter the active region at a higher energy and, under this high electric field, transfer faster into the upper valleys. This faster transfer reduces the dead space. The shallow Schottky barrier also limits the current flow into the active region at the cathode. Thermionic emission and thermionic field emission contribute to the current flow, and, in this case, the current density J_c as a function of the voltage V_c across the barrier can be approximated by

$$J_c(V_c) = J_r \left\{ \exp\left(-\frac{qV_c}{rkT}\right) - \exp\left[\frac{(1-r)qV_c}{kT}\right] \right\} \quad (11)$$

where $J_r = A^*T^2 \exp(-q\phi_{Bn}/kT)$ is the saturation current; k , T , r , A^* , and $q\phi_{Bn}$ denote the Boltzmann constant, absolute temperature, ideality factor, effective Richardson constant, and effective barrier height on n-type material, respectively [1]. Current limiting as a boundary condition at the cathode causes the electrons in the active region of the device to approximate the current valley condition [15,33] for a saturated electron velocity v_s and a doping concentration N_D

$$\int_0^T J(t) dt = J_0 = N_D q v_s \quad (12)$$

with large space charge waves superimposed on an almost constant electric field throughout the active region [15]. This mode of operation yields high RF power levels in the fundamental mode as well as a second-harmonic mode. Corresponding DC-to-RF conversion efficiencies are typically the highest reported to date. RF power levels (and DC-to-RF conversion efficiencies) of more than 500 mW (15%) at 35 GHz, more than 350 mW (13%) at 44 GHz and 380 mW (10.6%) at 57 GHz [19,34] in the fundamental mode as well as 175 mW (7%) at 94 GHz and 65 mW (2.6%) at 138 GHz [23,35] in a second-harmonic mode were achieved using this technology. These devices are on integral heatsinks, and still higher RF power levels are expected from devices on diamond heatsinks. Devices on integral heatsinks with high RF power levels are also commercially available.

Equation (11) expresses the strong temperature dependence that is inherent in the current flow through a shallow Schottky barrier in the reverse direction [1]. However, the high-efficiency mode reduces DC input requirements and provides higher RF impedance levels. As a consequence, larger device diameters can be used, which have lower heat-flow resistances (see Fig. 12). In turn, lower heat-flow resistances R_{th} entail lower active-layer temperatures T_{op} [see Eq. (10)]. The typical temperature increase ΔT_{op} remains below 100 K at maximum RF output power [23,34], and low operating active-layer temperatures ensure reliability and excellent temperature stability over wide temperature ranges of -30 to $+70^\circ\text{C}$ for devices at 56 GHz [34] and 94 GHz [34,35] as well as of 0 – 50°C for devices at 140 GHz [23]. The temperature-dependent performance of a D-band InP Gunn device in Fig. 15 serves as an example.

5.3. Graded Active Region

A doping profile with a lower doping concentration N_D at the cathode and a linear grading toward a higher N_D at the anode as shown in Fig. 7d decreases the peak electric field near the anode to a large extent and increases the electric field near the cathode [16]. Both effects are beneficial to the device operation, and enhance the DC-to-RF conversion efficiency as well as the RF output power of the device. A lower electric field near the anode reduces the power dissipation in this region and also allows higher bias voltages without the onset of impact ionization and avalanche breakdown. A higher electric field near the cathode causes a larger fraction of the electrons to transfer to the upper valleys over a shorter distance, which is equivalent to a shorter dead-space region. This is illustrated in Fig. 16, which compares domain formation in a flat-profile (Fig. 16a) and a graded-profile (Fig. 16b) TED structure, both with a $1.0\text{-}\mu\text{m}$ -long active region. Accumulation domains form in the flat-profile structure, whereas dipole domains form in the graded-profile structure. A higher fraction of electrons in the upper valleys slightly lowers the average electron velocity throughout the active region; as a consequence, the graded-profile structure operates at lower current densities compared to a flat-profile structure of a similar (average) doping concentration. In fact, a lower average electron velocity and shorter dead

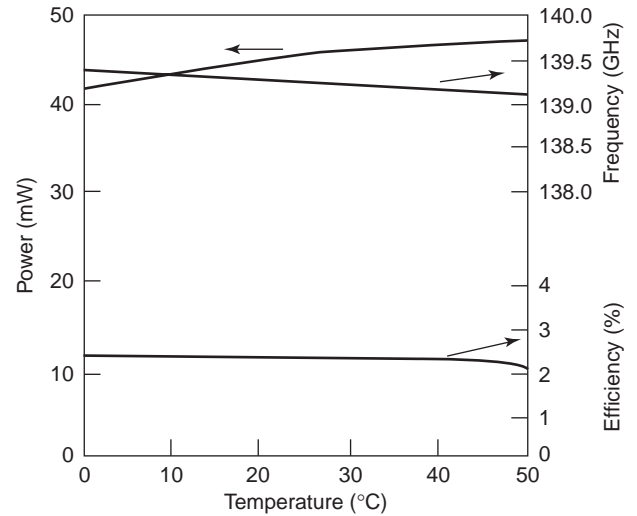


Figure 15. Measured RF performance of a D-band InP Gunn device against ambient temperature. (After Crowley et al. [23].)

space may somewhat decrease the optimum operating frequency f_{op} for the same device length l . However, more efficient device operation extends the upper frequency limit and allows shorter active regions. Similar to the three zone structures of Fig. 7a, the structures with graded-doping profiles have ohmic contacts at anode and cathode; therefore, they are easy to fabricate. They were investigated in both InP and GaAs material systems.

RF power levels (and DC-to-RF conversion efficiencies) of 345 mW (6.8%) at 31.2 GHz and 325 mW (6.6%) at 34.9 GHz from devices on integral heatsinks [36] and 210 mW (3.5%) around 60 GHz from devices on diamond heatsinks [37] were achieved in the GaAs material system. The devices on diamond heatsinks showed operating active-layer temperatures below 150°C and fundamental-mode operation up to 84 GHz (33 mW and 1.7%) [38]. Devices from InP material with properly designed [16,39] graded-doping profiles yielded the highest RF power levels reported for any Gunn device to date. Fundamental-mode operation was demonstrated up to 165 GHz, and RF power levels that exceeded 310 mW at 82 GHz [40], 200 mW at 103 GHz, 130 mW around 132 GHz, 80 mW at 152 GHz, and 25 mW at 163 GHz [41] were obtained from devices on diamond heatsinks [30]. As an example, DC-to-RF conversion efficiencies exceeded 4% at 82 GHz [39,40] and 2.3% between 102 and 132 GHz [42].

As illustrated in Fig. 17, the InP Gunn devices on diamond heatsinks allow single-mode operation over a wide range of DC input power levels. Excellent tuning behavior was also observed, which can be expected from operation in the fundamental mode. This tuning behavior over a range of more than 4.5 GHz is shown in Fig. 18 for the device of Fig. 17 near maximum DC bias. The oscillation frequency changes almost linearly with the position of the backshort, which is the only tuning element in this full-height waveguide resonant cap cavity (see Fig. 14e for a schematic). Improved DC-to-RF conversion efficiencies reduce the DC input power requirements for the same RF power levels, and, similar to devices with current-limiting

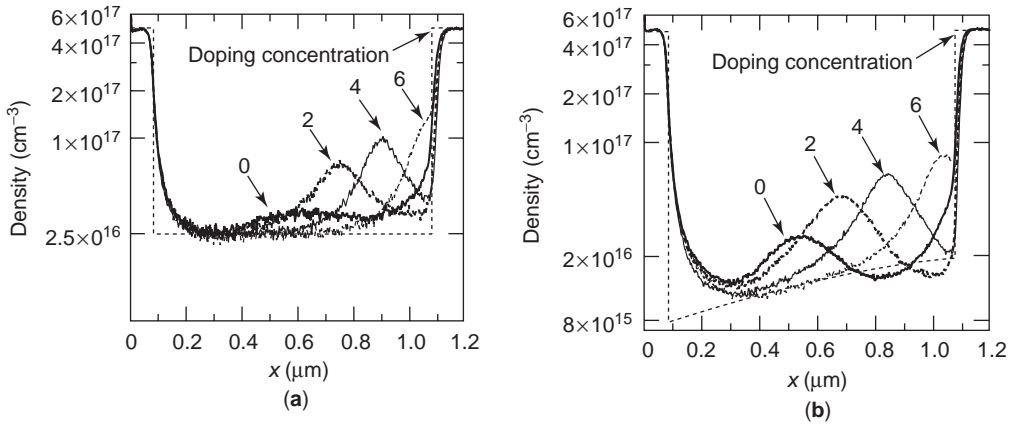


Figure 16. Evolution of electron density against position x (active region $0.1\text{--}1.1\ \mu\text{m}$) for a flat-profile (a) and graded-profile (b) TED structure at $f = 130\ \text{GHz}$ and $ot = n^{\pi/4}$, $n = 0, 2, 4, 6$, during one RF cycle.

cathode contacts, lower the operating active-layer temperatures, in particular on diamond heatsinks [30,38].

InP Gunn devices with a graded-doping profile yielded the highest RF power levels from any Gunn device not only in the fundamental mode but, for the same graded-doping profile, also in a second-harmonic mode. Examples are the RF power levels of 1.8 and 1.1 mW at second-harmonic frequencies of 280 GHz and 315 GHz, respectively [41,43] (see inset of Fig. 17 for the doping profile) as well as 34 mW at 193 GHz and 26 mW at 199 GHz [40,44]. When the graded-doping profile is optimized just for second-harmonic power extraction, even higher RF power levels of, for example, more than 3.5 mW around 300 GHz

are generated and, as indicated in Fig. 13, RF power generation is observed up to at least 325 GHz [40,45].

5.4. Injection over a Homo- or Heterojunction Barrier

Injection of electrons with an energy higher than that at thermal equilibrium (i.e., “hot” electrons) over a barrier reduces the dead space in the active region. Several concepts (e.g., planar-doped barrier, camel cathode, and heterojunction barriers) have been investigated in the GaAs/AlGaAs material system to improve efficiency, but also to eliminate cold-start problems in GaAs Gunn devices. Injection over a heterojunction barrier has proved the most

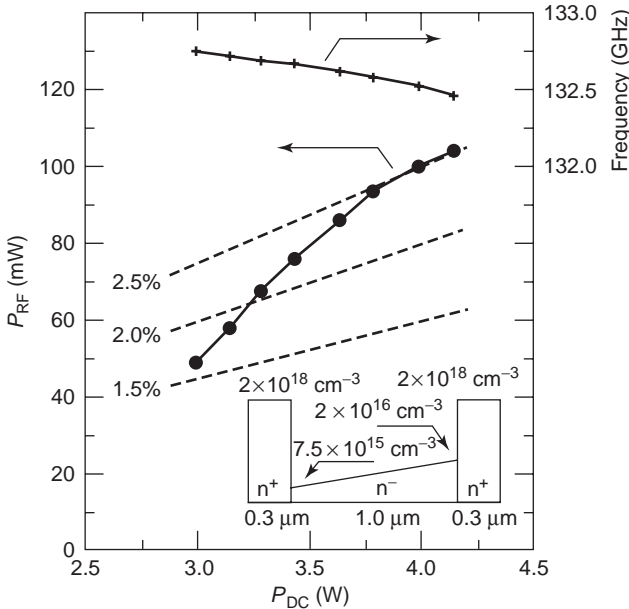


Figure 17. Bias-dependent RF characteristics of a D-band InP Gunn device (●: output power, +: oscillation frequency, ---: lines of constant efficiency). *Inset:* Nominal doping profile. (After Eisele and Haddad [30].)

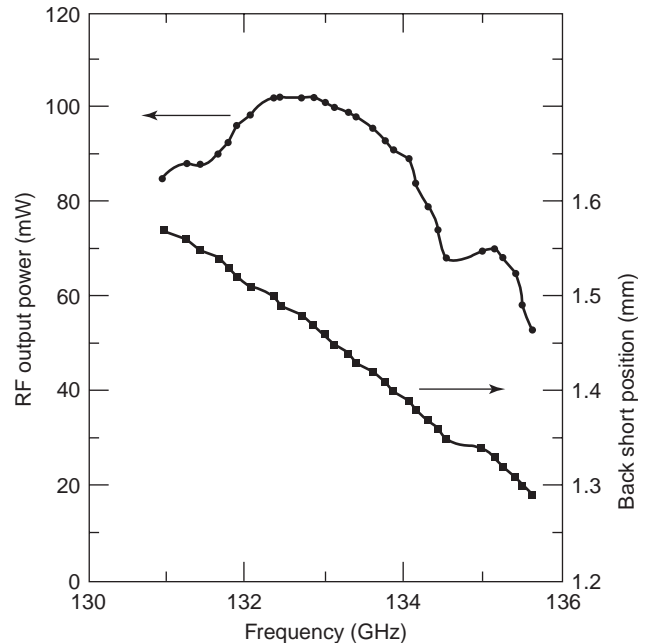


Figure 18. Mechanical tuning characteristic for the D-band InP Gunn device of Fig. 17 close to maximum applied bias.

successful and was experimentally investigated in the AlGaAs/GaAs system with improved efficiencies and upper frequency limits [29,46]. Figure 19 shows the band diagrams of isotype heterojunctions in the lattice-matched GaAs/Al_xGa_{1-x}As and InP/In_xGa_{1-x}As_yP_{1-y} material systems. In both material systems, layers can be grown lattice-matched over a wide composition range and, thus, bandgap or conduction-band offset can be tailored suitably.

Linear composition grading from the GaAs to the wider-bandgap AlGaAs eliminates the first barrier, and the doping spike as shown in Fig. 7e at the beginning of the active region (GaAs) reduces or eliminates the notch at the interface from the AlGaAs layer to the GaAs region. At the proper bias level, “hot” electrons are now ballistically launched into the active region from an approximately 200-meV-high step in the conduction band. The optimization of such a design requires advanced simulation schemes, such as ensemble Monte Carlo techniques. Using a reduced-height post-coupled waveguide cavity (see Fig. 14b for a schematic) for the oscillator, an RF output power of 71 mW with a corresponding DC-to-RF conversion efficiency of 2.8% was measured in the fundamental mode at 77.6 GHz. Low-noise operation of such a Gunn device was achieved at least up to 84 GHz [29]. As a characteristic of fundamental-mode operation [30], a wide tuning bandwidth of more than 6 GHz was observed by simply adjusting the position of the backshort [29].

In contrast to the GaAs/AlGaAs material system, lattice-matched InGaAsP has a smaller bandgap than does InP as illustrated in Fig. 19. Therefore, electrons cannot be ballistically launched into the active region. However, a wide composition range in the InGaAsP material system can be grown lattice-matched to InP. This wide composition range allows a wide range in the bandgap and conduction-band offset to be implemented. As a consequence, the proper current-limiting injection at the cathode can be designed. Theoretical investigations predict a significant improvement in DC-to-RF conversion efficiencies at W-band and D-band frequencies [33,47] while preserving the higher frequency limit of InP compared to GaAs.

In summary, different schemes for “accelerating” electrons and transferring them faster to the upper valleys can be incorporated into a device design. Shorter transfer times reduce the dead space, improve the DC-to-RF conversion efficiency, and allow for a shorter active region to achieve a higher operating frequency. However, a reduced dead space effectively increases the transit time and actually lowers the optimum operating frequency f_{op} for an active region of the same length l . Finite valley transfer times still impose some physical upper frequency limit. Additionally, if electrons gain too much energy and/or the active region is too short, the long energy relaxation time prevents the electrons from losing enough energy to transfer back to the lower valley. No domains can form in such a structure, the dynamic resistance between the two device terminals remains positive for all frequencies, and no RF power is generated.

6. NOISE

The noise in the output spectrum of an oscillator consists of fluctuations in RF amplitude (AM noise) and oscillation frequency (FM noise). However, FM noise generally dominates in Gunn devices and can be described as effective frequency modulation Δf_{rms} versus frequency f_m off the oscillation frequency f_o . It corresponds to the noise-to-carrier ratio $N/C|_{FM}$ as, for example, seen on a spectrum analyzer

$$\left. \frac{N}{C} \right|_{FM} = \frac{\Delta f_{rms}^2}{2f_m^2} \quad (13)$$

To compare the noise performance of different oscillators, including those with other two-terminal devices on a more equitable basis, the FM noise measure M [48] is more appropriate

$$M = \frac{\Delta f_{rms}^2 Q^2}{f_o^2 k T_0 B} P_{RF} \quad (14)$$

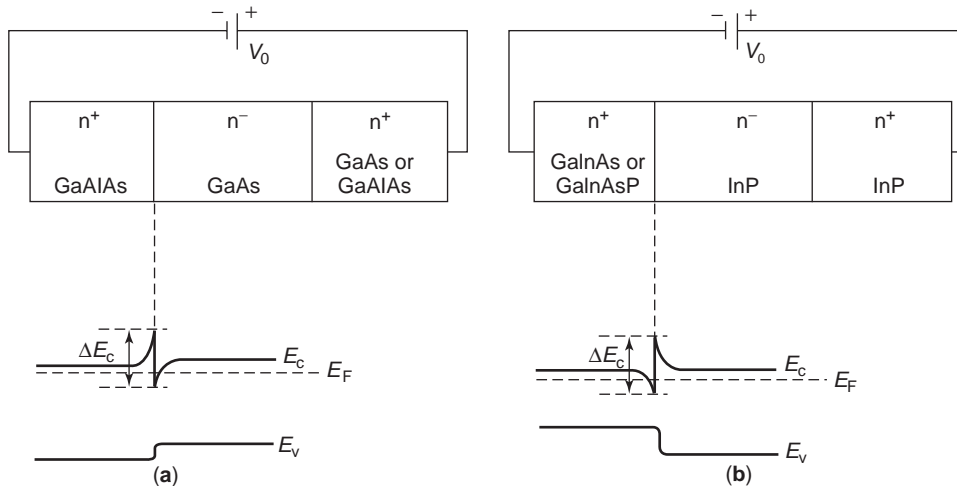


Figure 19. Band diagram of isotype heterojunctions in GaAs/AlGaAs and InP/InGaAsP at zero bias. (After Friscourt et al. [33].)

where T_0 is the absolute temperature and B is the measurement bandwidth. The loaded Q factor of the oscillator circuit is determined in a waveguide setup as illustrated in Fig. 20a. The sweep oscillator injects a signal at the power level P_i into the oscillator under test (OUT), and the maximum continuous frequency range Δf_s over which the OUT remains injection-locked with the sweep oscillator is determined [48]:

$$Q = \frac{2f_o}{\Delta f_s} \left(\frac{P_i}{P_{RF}} \right)^{1/2} \tag{15}$$

An alternative is also shown in Fig. 20b. The signal from the OUT is reflected at a tunable low-loss short and injected back as P_i through the coupler into the OUT. If the position of the short is moved by more than half of the guide wavelength λ_g , the oscillation frequency continuously changes from a lower to an upper limit. This maximum tuning range (i.e., the self-injection locking range) is now Δf_s in Eq. (15).

Thermal noise of electrons is the dominant effect in Gunn devices. If a TED is designed (using subcritical $N_D l < 1 \times 10^{12} \text{ cm}^{-2}$) for and operated in the amplifier mode [1], the small-signal noise measure M approaches the asymptotic limit M_0

$$M_0 = \frac{qD}{k|\mu_{diff}|T_0} \tag{16}$$

where the ratio of the diffusion coefficient D and the differential mobility μ_{diff} is the crucial factor. InP shows an advantage of 142/72 (approximately 3 dB; see Table 2) over GaAs. If an equivalent differential mobility μ_{eff} is introduced for the oscillator mode (critical $N_D l > 1 \times 10^{12} \text{ cm}^{-2}$) with the device conductance per unit area G_D

$$\mu_{eff} = \frac{|G_D|}{qN_D} \tag{17}$$

the large-signal noise measure M can be defined as

$$M = \frac{qD}{k\mu_{eff}T_0} \tag{18}$$

The noise performance of Gunn devices near the carrier is dominated by flicker noise components with typical corner frequencies in the range of 100 kHz–1 MHz. As predicted by Eq. (13), the phase noise decreases by -20 dB per decade at higher off-carrier frequencies f_m . Table 3 summarizes typical results from GaAs and InP Gunn devices [24,29,30,39,41,44,49].

Although Eq. (18) predicts lower values of M for oscillators with InP Gunn devices, experimental results indicate little difference between the two. Figure 21 [50] compares the FM noise measure M of Gunn devices with that of other two-terminal devices in the frequency range of 75–155 GHz. This figure highlights the low-noise

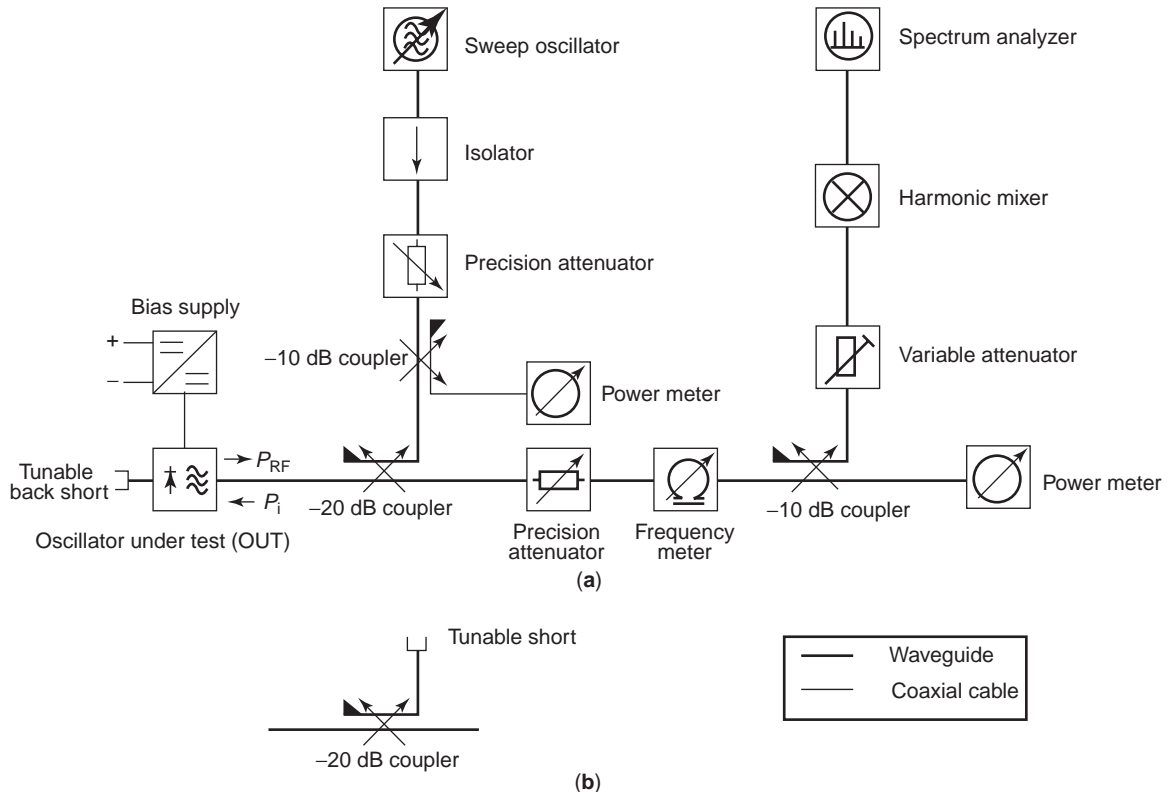


Figure 20. Waveguide test setup to determine the injection locking range Δf_s and Q factor of a transferred-electron oscillator: (a) using injection locking with a sweep oscillator; (b) using self-injection locking.

Table 3. Phase Noise of Free-Running Oscillators using GaAs or InP Millimeter-Wave Gunn Devices

Material System	Phase Noise (dBc/Hz)	Off-Carrier Frequency (kHz)	Oscillation Frequency (GHz)	RF Output Power (mW)	Ref.
GaAs	< -80 ^a	100	77	>40 ^a	29
GaAs	-70	100	80	55	24
GaAs	-100	1,000	80	55	24
GaAs	-120	10,000	80	55	24
GaAs	-80	100	94	10	49
GaAs	-105	1,000	94	10	49
InP	-75	100	94	20	49
InP	-100	1,000	94	20	49
InP	< -110	500	81	126	39
InP	< -110	500	103	180	41
InP	< -108	500	132	120	30
InP	< -103	500	151	58	30
InP	< -94	500	199	19	44

^aReported as typical value, corresponding RF output power not mentioned.

characteristics of TEDs, where the large-signal FM noise measure of both GaAs and InP Gunn devices typically remains below 25 dB [11,24,30,49,51]. Some InP devices with current-limiting contacts show excess flicker noise components near the carrier frequency f_0 . Oscillators with Gunn devices in a second-harmonic mode yield lower values for the phase noise, but they yield similar values for the noise measure because much higher Q values are achieved in a circuit without a resistive load at the fundamental frequency.

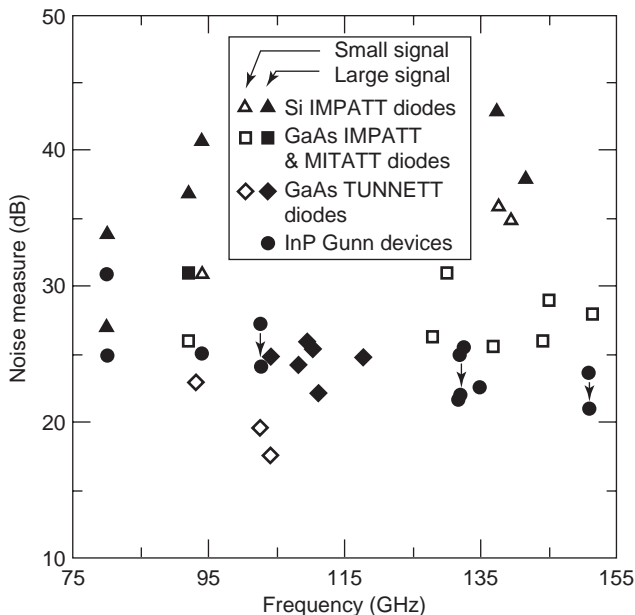


Figure 21. Comparison of the FM noise measure M in free-running oscillators with different two-terminal devices at millimeter-wave frequencies of 75–155 GHz. (After Eisele and Haddad [50].)

7. FUTURE TRENDS

7.1. More Power and Higher Operating Frequencies with INP TEDs

Fundamental-mode operation up to 165 GHz was demonstrated with InP Gunn devices. Therefore, InP or InP with heterojunction barriers are promising material systems not only for device structures that exhibit improved performance in the fundamental mode at frequencies around or above 100 GHz but also for other device structures that generate significant RF power levels up to submillimeter-wave frequencies in a second-harmonic mode. In all these devices, proper heat management is one of the important factors, and employment of the appropriate diamond heat-sink technologies is mandatory for maximum RF output power as well as reliable long-term operation. Power-combining techniques [28,52] can be employed to increase the available RF power levels. As examples, four InP Gunn devices in a power-combiner circuit delivered an RF power of 260 mW to the load in CW operation at 98.6 GHz [11,53], and two devices each on diamond heatsinks yielded more than 300 mW at 103 GHz [42] or more than 125 mW at 152 GHz [41].

Structures with a flat-doping profile, ohmic contacts at cathode and anode, but with a doping notch near the cathode, were originally investigated for low-noise microwave and millimeter-wave amplifier applications [11], but have now emerged as quite promising candidates for efficient second-harmonic power extraction at J-band (220–325 GHz) frequencies and above [39,45]. Figure 22a compares the predicted RF performance of two different doping profiles in the active region of InP Gunn devices in a second-harmonic mode as shown in Fig. 22b [45]. In all simulations, the predicted operating temperatures were kept similar and below 420 K to ensure a fair comparison and, much more importantly, reliable long-term operation of fabricated devices on diamond heatsinks. The improvements are even more pronounced at frequencies above 300 GHz, where initial Monte Carlo simulation results indicate an improvement in RF output power by a factor of 2–3 compared to structures with a graded-doping profile. RF power levels of more than 7 mW at 360 GHz and 4.7 mW at 500 GHz are predicted for structures with a doping notch as opposed to 5 and 2.6 mW, respectively, for structures with a graded-doping profile at the same frequencies [45]. These performance improvements are attributed to a faster transfer of electrons to the upper valleys near the cathode and, as a comparison in Fig. 23 indicates, a rather flat electric field profile throughout most of the active region [39,45] of the structure with a notch in the doping profile.

7.2. New Material Systems

Wide-bandgap materials such as GaN and AlGaN are also regarded as promising for high-power Gunn devices. Favorable material parameters, for example, are higher critical electric fields for avalanche breakdown, higher thermal conductivities, higher permissible operating temperatures, and expected higher carrier drift velocities. However, high threshold electric fields E_{th} and

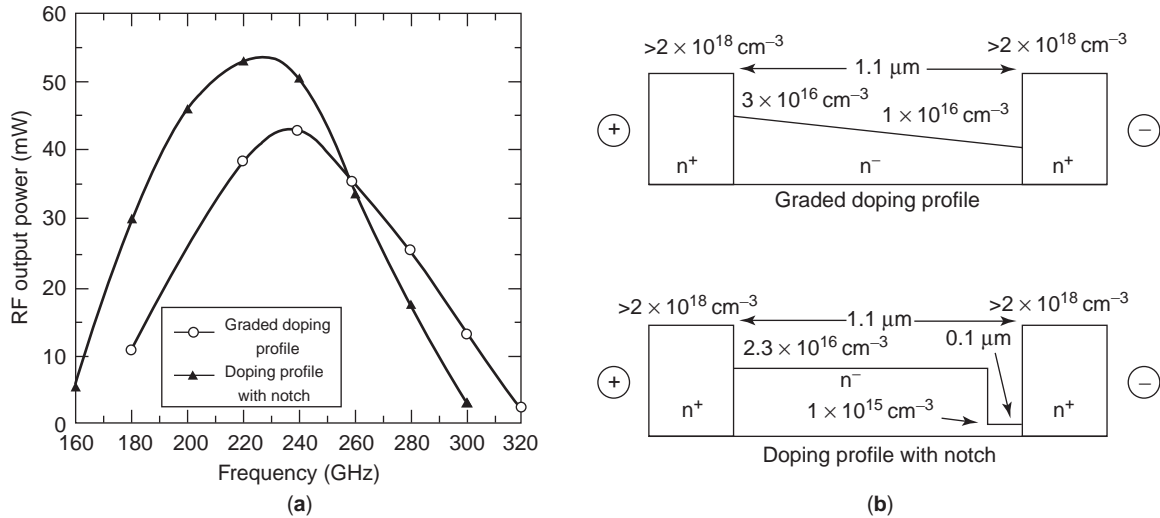


Figure 22. Comparison of predicted RF power level from InP Gunn devices with doping profiles optimized for second-harmonic power extraction.

consequently higher DC bias voltages may result in severe thermal limitations of the device performance [54]. Furthermore, major improvements in material quality or availability and in fabrication technologies are needed before devices for system applications can be developed.

7.3. Circuit Integration

Waveguide circuits are, in general, rugged, can dissipate heat easily, and offer high Q values. Therefore, they are the preferred circuits to obtain the maximum RF output power. However, they are bulky and in most cases must be machined, assembled, and tested individually, which prohibits low-cost mass production. Therefore, high-volume production for system applications such as wireless communication (high-speed data transmission) or collision avoidance radar in automobiles must be based on quite

different approaches. Both hybrid and monolithic integration were attempted with Gunn devices. Hybrid microstrip-line oscillators with InP Gunn devices exhibited excellent performance. RF power levels (with corresponding DC-to-RF conversion efficiencies) of 52 mW (3.5%) at 94 GHz [25], but also 40 mW (1.4%) at 81 GHz [11,24] and > 200 mW (>7.5%) around 35.5 GHz [10,35] were measured and are considered comparable to values from similar Gunn devices in waveguide circuits. Hybrid integration of a GaAs Gunn device for automotive applications at 77 GHz was also demonstrated [26]. The thermal conductivity of the semiconductor materials InP and GaAs is rather low (0.68 and 0.46 W cm⁻¹K⁻¹, respectively) when compared to metals or diamond (20 W cm⁻¹K⁻¹ at room temperature). Therefore, fully monolithic integration of low-efficiency Gunn devices at millimeter-wave frequencies encounters severe thermal

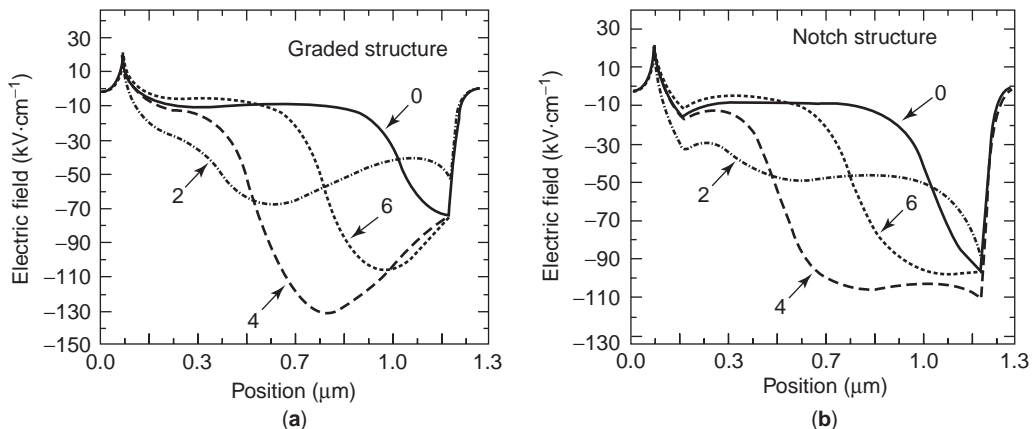


Figure 23. Evolution of electric field against position x (active region 0.1–1.2 μm) for a graded-profile (a) and a flat-profile with notch (b) TED structure at the fundamental frequency $f = 120$ GHz and $\omega t = n\pi/4$, $n = 0, 2, 4, 6$, during one RF cycle.

limitations. A summary of reports on integration of Gunn devices at frequencies up to approximately 68 GHz can be found elsewhere [28].

BIBLIOGRAPHY

1. S. M. Sze, *Physics of Semiconductor Devices*, 2nd ed., Wiley, New York, 1981.
2. U. V. Bhapkar and M. S. Shur, Monte Carlo calculation of velocity-field characteristics of wurtzite GaN, *J. Appl. Phys.* **82**(4):1649–1655 (1997).
3. S. Krishnamurthy, M. van Schilfgaarde, A. Sher, and A.-B. Chen, Bandstructure effect on high-field transport in GaN and GaAlN, *Appl. Phys. Lett.* **71**(14):1999–2001 (1997).
4. B. K. Ridley and T. B. Watkins, The possibility of negative resistance effects in semiconductors, *Proc. Phys. Soc. Lond.* **78**:293–304 (1961).
5. C. Hilsum, Transferred electron amplifiers and oscillators, *Proc. Inst. Radio Eng.* **50**:185–189 (1962).
6. J. B. Gunn, Microwave oscillation of current in III-V semiconductors, *Solid-State Commun.* **1**:88–91 (1963).
7. J. B. Gunn, Instabilities of current in III-V semiconductors, *IBM J. Res. Devel.* **8**:141–159 (1964).
8. H. Kroemer, Theory of the Gunn effect, *Proc. IEEE* **52**:1736 (1964).
9. L. Wandering, mm-Wave InP Gunn devices: Status and trends, *Microwave J.* **24**(3):71–78 (1981).
10. B. Fank, J. Crowley, D. Tringali, and L. Wandering, Basics and recent applications of high-efficiency millimeter wave InP Gunn diodes, *Proc. 1st Int. Conf. Indium Phosphide and Related Materials for Advanced Electronic and Optical Devices*, Norman, OK, March 20–23, 1989; *SPIE* **1144**:534–546 (1989).
11. I. G. Eddison, Indium phosphide and gallium arsenide transferred-electron devices, in *Infrared and Millimeter Waves*, Vol. 11, *Millimeter Components and Techniques, Part III*, Academic Press, Orlando, FL, 1984, pp. 1–59.
12. J. A. Copeland, LSA oscillator-diode theory, *J. Appl. Phys.* **38**:3096–3101 (1967).
13. P. N. Butcher, Theory of stable domain propagation in the Gunn effect, *Phys. Lett.* **19**:546–547 (1965).
14. J. F. Caldwell and F. E. Rosztoecz, Gallium arsenide Gunn diodes for millimeter-wave and microwave frequencies, *Proc. 4th Int. Symp. GaAs and Related Compounds*, Denver, CO, 1972.
15. P. A. Rolland, M. R. Friscourt, D. Lippens, C. Dalle, and J. L. Nieruchalski, Millimeter wave solid-state power sources, *Proc. Int. Workshop on Millimeter Waves*, Rome, April 2–4, 1986, pp. 125–177.
16. R. Kamoua, H. Eisele, and G. I. Haddad, D-band (110–170 GHz) InP Gunn devices, *Solid-State Electron.* **36**:1547–1555 (1993).
17. H. Eisele, Selective etching technology for 94-GHz GaAs IMPATT diodes on diamond heatsinks, *Solid-State Electron.* **32**:253–257 (1989).
18. H. Eisele and G. I. Haddad, D-band InP Gunn devices with second-harmonic power extraction up to 290 GHz, *Electron. Lett.* **30**:1950–1951 (1994).
19. Y. E. Ma, Millimeter-wave active solid-state devices, *Millimeter Wave Technol. III*; *SPIE* **544**:95–102 (1985).
20. L. W. Holway and M. G. Adlerstein, Approximate formulas for the thermal resistance of IMPATT diodes compared with computer calculations, *IEEE Trans. Electron Devices* **ED-24**:156–159 (1977).
21. M. A. di Forte-Poisson, C. Brylinski, G. Colomer, D. Osselin, S. Hersee, J. P. Duchemin, F. Azan, D. Lechevallier, and J. Lacombe, High-power high-efficiency LP-MOCVD InP Gunn diodes for 94 GHz, *Electron. Lett.* **20**:1061–1062 (1984).
22. M. A. di Forte-Poisson, C. Brylinski, N. Proust, D. Pons, M. Secoué, P. Arsène Henry, M. Calligaro, and J. Lacombe, LP-MOCVD InP Gunn devices developed for 94 GHz millimeter range operation, *Proc. 1st Int. Conf. Indium Phosphide and Related Materials for Advanced Electronic and Optical Devices*, Norman, OK, March 20–23, 1989; *SPIE* **1144**:551–560 (1989).
23. J. D. Crowley, C. Hang, R. E. Dalrymple, D. R. Tringali, F. B. Fank, L. Wandering, and H. B. Wallace, 140 GHz indium phosphide Gunn diode, *Electron. Lett.* **30**:499–500 (1994).
24. D. C. Smith, T. J. Simmons, and M. R. B. Jones, A comparison of the performance of millimeter-wave semiconductor oscillator devices and circuits, *Digest of the 1983 IEEE MTT-S Int. Microwave Symp.*, May 31–June 3, 1983, Boston, pp. 127–129.
25. C. Kim, C. Dunnrowicz, J. Crowley, B. Fank, and L. Wandering, Millimeter-wave tunable microstrip InP Gunn oscillators, *Microwave J.* **32**(4):91–102 (1989).
26. N. Priestley, K. Newsome, I. Dale, and P. Norton, A Gunn diode based surface mount 77 GHz oscillator for automotive applications, *2002 IEEE MTT-S Int. Microwave Symp. Digest*, June 2–7, 2002, Seattle, pp. 1863–1866.
27. H. J. Kuno, IMPATT devices for generation of millimeter waves, in K. Button, ed., *Infrared and Millimeter Waves*, Academic Press, New York, Vol. 1, 1979, Chapter 2.
28. K. Chang, *Handbook of Microwave and Optical Components*, Vol. 2, Wiley, New York, 1990.
29. I. Dale, J. R. P. Stephens, and J. Bird, Fundamental-mode graded-gap Gunn diode operation at 77 and 84 GHz, *Proc. Microwaves 94*, London, Oct. 25–27, 1994, pp. 248–251.
30. H. Eisele and G. I. Haddad, High-performance InP Gunn devices for fundamental-mode operation in D-band (110–170 GHz), *IEEE Microwave Guided Wave Lett.* **MGWL-5**:385–387 (1995).
31. S. J. J. Teng and R. E. Goldwasser, High-performance second-harmonic operation W-band GaAs Gunn diodes, *IEEE Electron Device Lett.* **EDL-10**:412–414 (1989).
32. A. Rydberg, High efficiency and output power from second- and third-harmonic millimeter-wave InP-TED oscillators at frequencies above 170 GHz, *IEEE Electron Device Lett.* **EDL-11**:439–441 (1990).
33. M.-R. Friscourt, P.-A. Rolland, and M. Pernisek, Heterojunction cathode contact transferred-electron oscillators, *IEEE Electron Device Lett.* **EDL-6**:497–499 (1985).
34. B. Fank, J. Crowley, and C. Hang, InP Gunn diode sources, *Millimeter Wave Technol. III*; *SPIE* **544**:22–28 (1985).
35. J. D. Crowley, R. E. Dalrymple, C. Hang, D. R. Tringali, F. B. Fank, and L. Wandering, InP Gunn diodes serve millimeter-wave applications, *Microwaves RF* **33**(3):143–146 (1994).
36. J. Ondria and R. L. Ross, Improved performance of fundamental and second-harmonic mmw oscillators through active doping concentration contouring, *1987 IEEE MTT-S Digest*, 1987, pp. 977–980.
37. T. Hisatsugu, S. Yamamura, S. Yokogawa, Y. Hirachi, A. Miura, and A. Shibatomi, A 160-mW 65-GHz Gunn diode, *Technical Digest 1976 Int. Electron Device Meeting*, Washington, DC, Dec. 6–8, 1976, pp. 94–97.

38. K. Akamatsu, A. Yokohata, S. Kato, N. Ohkuba, and M. Ohmori, High-efficiency millimeter-wave GaAs Gunn diodes operating in the fundamental mode, *Digest 19th Int. Conf. Infrared and Millimeter Waves*, Sendai, Japan, Oct. 17–20, 1994, pp. 89–90.
39. H. Eisele and R. Kamoua, InP Gunn devices for low-noise and high-performance oscillators in the 80–400 GHz frequency range, *2001 IEEE 19th Int. Conf. Terahertz Electronics Proc.*, Charlottesville, Virginia, VA, Oct. 15–16, 2001.
40. H. Eisele, Conventional and novel approaches to RF power generation with two-terminal devices at terahertz frequencies, invited paper, *2002 IEEE 10th Int. Conf. Terahertz Electronics Proc.*, Cambridge, UK, Sept. 9–10, 2002, pp. 13–18.
41. H. Eisele, A. Rydberg, and G. I. Haddad, Recent advances in the performance of InP Gunn devices and GaAs TUNNETT diodes for the 100–300-GHz frequency range and above, *Special Issue on Terahertz Electronics, IEEE Trans. Microwave Theory Tech.* **MTT-48**(4):626–631 (2000).
42. H. Eisele and G. I. Haddad, Efficient power combining with D-band (110–170 GHz) InP Gunn devices in fundamental-mode operation, *IEEE Microwave Guided Wave Lett.* **MGWL-8**:24–26 (1998).
43. H. Eisele, Second-harmonic power extraction from InP Gunn devices with more than 1 mW in 200–320 GHz frequency range, *Electron. Lett.* **34**(25):2412–2413 (1998).
44. H. Eisele, High performance InP Gunn devices with 34 mW at 193 GHz, *Electron. Lett.* **38**(16):923–924 (2002).
45. R. Kamoua and H. Eisele, Theoretical and experimental comparison of optimized doping profiles for high-performance InP Gunn devices at 220–500 GHz, *2003 IEEE MTT-S Int. Microwave Symp. Digest*, Philadelphia, June 8–13, 2003, pp. 907–910.
46. N. R. Couch, H. Spooner, P. H. Beton, M. J. Kelly, M. E. Lee, P. K. Rees, and T. M. Kerr, High-performance, graded AlGaAs injector, GaAs Gunn diodes at 94 GHz, *IEEE Electron Device Lett.* **EDL-10**:288–290 (1989).
47. R. Kamoua, Heterojunction D-band (110–170 GHz) InP Gunn devices, *Solid-State Electron.* **37**:269–274 (1994).
48. K. Kurokawa, Noise in synchronized oscillators, *IEEE Trans. Microwave Theory Tech.* **MTT-16**:234–240 (1968).
49. C. Dalle, P. A. Rolland, and G. Lleti, Flat doping profile double-drift silicon IMPATT for reliable cw high-power high-efficiency generation in the 94-GHz-window, *IEEE Trans. Electron Devices* **ED-37**:227–236 (1990).
50. H. Eisele and G. I. Haddad, Two-terminal millimeter-wave sources, *IEEE Trans. Microwave Theory Tech.* **MTT-46**:739–746 (1998).
51. D. M. Brookbanks, A. M. Howard, and M. R. B. Jones, Si IMPATTs exhibit low noise at mm-waves, *Microwaves RF* **22**(2):68–72 (1983).
52. K. Chang and C. Sun, Millimeter-wave power-combining techniques, *IEEE Trans. Microwave Theory Tech.* **MTT-31**:91–107 (1983).
53. J. J. Sowers, J. D. Crowley, and F. B. Fank, CW InP Gunn diode power combining at 90 GHz, *Digest 1982 IEEE MTT-S Int. Microwave Symp.*, Dallas, TX, June 15–17, 1982, pp. 503–505.
54. R. Kamoua, Y. Zhu, and Y. Corcoran, Potential of GaN Gunn devices for high power generation above 200 GHz, *Proc. Conf. Wide-Bandgap Electronic Devices*, April 24–27, 2000, Vol. MRS 622, pp. 261–266.

FURTHER READING

- E. L. Holzman and R. S. Roberston, *Solid-State Microwave Power Oscillator Design*, Artech House, Boston, 1992.
- S. M. Sze, *High-Speed Semiconductor Devices*, Wiley, New York, 1990.
- S. M. Sze, *Modern Semiconductor Device Physics*, Wiley, New York, 1998.
- K. S. Yngvesson, *Microwave Semiconductor Devices*, Kluwer Academic Publishers, Boston, 1991.
- J. G. Webster, ed., *Encyclopedia of Electrical and Electronics Engineering*, Wiley, New York, 1999.
- R. E. Miles, P. Harrison, and D. Lippens, *Terahertz Sources and Systems*, NATO Science Series, Series II: Mathematics, Physics, and Chemistry, Vol. 27, Kluwer Academic Publishers, Dordrecht, 2001.
- T. Pearsall, InP: *Properties, Processing, and Applications*, IEE, Stevenage, UK, 1999.

GYRATORS

DOUGLAS R. FREY
Lehigh University

1. DEFINITION

A *gyrator* is a nonreciprocal electrical network. It is capable of transforming signals or energy represented in terms of one electrical quantity, such as voltage or magnetic field, to another electrical quantity that may be of similar type or of a complementary type, such as current or electric field. Such networks are quite useful in electronic systems, since one often wishes to design systems with a limited set of component types or with restrictions regarding certain physical parameters.

2. HISTORICAL USAGE

Tellegen first proposed the idea of a gyrator in his original work in 1948 [1]. In this paper he explained that resistors, capacitors, inductors, and ideal transformers were the four basic circuit building blocks. However, these elements are all reciprocal and could, therefore, only be expected to go into the creation of reciprocal networks. *Reciprocal networks* are those networks whose impedance (or admittance) matrices are symmetrical. In order to realize nonreciprocal networks, one would need a nonreciprocal building block. Tellegen proposed such a network, calling it a gyrator. This name was given because the equations produced for an electrical network with a gyrator were identical to those of a mechanical gyrostatic network. As time went on other researchers [2–5] picked up on the idea and began to look for circuit realizations for this abstract functional block. In addition, over the years other systems, such as microwave circulators, have been recognized as being analogous to gyrators, which helps in the understanding of these systems.

3. THE BASICS OF TWO-PORT GYRATORS

3.1. Introduction to Two-Ports and Passivity

A gyrator is a special type of electrical two-port network. Electrical two-port networks are any circuits where one can identify two ports, or simply, two pairs of nodes to which one might consider the connection of two pairs of wires. One of the nodes at each port may be in common—for example, ground may be common to both ports. Additionally, a bipolar transistor may be considered a two-port, where port 1 is the base-emitter node pair, and port 2 is the collector-emitter node pair.

Except for trivial cases, every two-port possesses a mathematical description relating the port voltages, V_1 and V_2 , and associated port currents, I_1 and I_2 . Figure 1 shows the standard reference labeling for the voltages and currents of a two-port. Notice that the port currents are defined as flowing into the + voltage reference for each port. These sign conventions make the definition of power regarding a two-port more precise. Specifically, the power as a function of time $P(t)$ delivered to a two-port is given by $P(t) = V_1(t)I_1(t) + V_2(t)I_2(t)$, which is analogous to the definition in a one-port—that is, a two-terminal element. A two-port network is *lossless* when the average power $P(t)$ delivered to the network is zero. A network is called *passive* if the average power delivered to the network is positive. Active networks are those networks where $P(t)$ is negative on average. In general, the power delivered to a network can be positive or negative instantaneously, regardless of its passivity. For example, a capacitor in a resonant circuit alternately sinks and sources power instantaneously, despite its lossless average power consumption. Power can be defined just as easily in the frequency domain, again in a way analogous to one-ports. The Fourier transform of power $P(\omega)$ as a function of frequency is given by $P(\omega) = V_1(\omega)I_1(\omega)^* + V_2(\omega)I_2(\omega)^*$, where the * indicates complex conjugation.

The general description for a two-port is given by a relation between its port voltages and currents. One such description is the so-called y -parameter model given by

$$\begin{bmatrix} I_1 \\ I_2 \end{bmatrix} = \begin{bmatrix} y_{11} & y_{12} \\ y_{21} & y_{22} \end{bmatrix} \begin{bmatrix} V_1 \\ V_2 \end{bmatrix} \Rightarrow \mathbf{I} = \mathbf{YV} \quad (1)$$

Equation (1) defines the port current and port voltage vectors, \mathbf{I} and \mathbf{V} , respectively, in addition to the y -parameter matrix, \mathbf{Y} . By inverting this vector equation, one relates the port voltages to the port currents with z parameters. Specifically

$$\begin{bmatrix} V_1 \\ V_2 \end{bmatrix} = \begin{bmatrix} z_{11} & z_{12} \\ z_{21} & z_{22} \end{bmatrix} \begin{bmatrix} I_1 \\ I_2 \end{bmatrix} \Rightarrow \mathbf{V} = \mathbf{ZI} \quad (2)$$

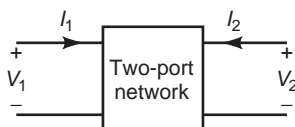


Figure 1. Basic two-port model.

where Z is the z -parameter matrix for the two-port. Using models of the type shown in Eqs. (1) and (2), two-ports can be compared by their two-port parameters—for example, y parameters. Two-ports characterized by symmetric y -parameter matrices (equivalently z -parameter matrices) are called *reciprocal*. Networks possessing this reciprocity are not necessarily lossless, but can always be realized with reciprocal physical elements. Note that one-ports (two terminal elements) are always reciprocal. The concept of a two-port can be extended in an obvious way to N -ports by considering the voltage-current relationship measured using N pairs of terminals or, equivalently, N -ports.

3.2. Mathematical Two-Port Definition of a Gyrator

In the context of this discussion, a gyrator is simply a special case of a linear two-port. While there are many possible two-port descriptions, the most common way of writing the basic equations relating the port parameters in a gyrator is as follows:

$$I_2 = gV_1; \quad I_1 = -gV_2 \quad (3)$$

Using these equations it is simple to write the y -parameter two-port description for a gyrator as

$$\begin{bmatrix} I_1 \\ I_2 \end{bmatrix} = \begin{bmatrix} 0 & -g \\ g & 0 \end{bmatrix} \begin{bmatrix} V_1 \\ V_2 \end{bmatrix} \Rightarrow \mathbf{I} = \mathbf{YV} \quad (4)$$

This suggests that a gyrator can be implemented with voltage-controlled current sources, having gains of g and $-g$, respectively. By inverting the relations in Eq. (3), one obtains a gyrator formulation based on current-controlled voltage sources. Specifically

$$\mathbf{V} = \begin{bmatrix} V_1 \\ V_2 \end{bmatrix} = \begin{bmatrix} 0 & -r \\ r & 0 \end{bmatrix} \begin{bmatrix} I_1 \\ I_2 \end{bmatrix} = \mathbf{ZI}; \quad r = 1/g \quad (5)$$

where the z -parameter matrix Z is just the inverse of the y -parameter matrix \mathbf{Y} . Since it is most convenient to realize practical voltage-controlled current source networks, as opposed to current-controlled voltage source networks, the formulation in Eq. (4) is generally preferred. For theoretical purposes, of course, both formulations are useful. Using Eq. (4) it is simple to show that a gyrator is a lossless electrical network. Specifically, we obtain

$$\begin{aligned} P = \mathbf{V}^T \mathbf{I} &= \begin{vmatrix} V_1 & V_2 \\ I_1 & I_2 \end{vmatrix} = \begin{vmatrix} V_1 & V_2 \\ g & 0 \end{vmatrix} \begin{vmatrix} 0 & -g \\ g & 0 \end{vmatrix} \begin{vmatrix} V_1 \\ V_2 \end{vmatrix} \\ &= V_2 V_1 - V_1 V_2 = 0 \end{aligned} \quad (6)$$

The fact that gyrators are, in theory, lossless makes them attractive in filter synthesis, and this will become clear later.

3.3. Properties of Gytrators

Gytrators possess several properties that make these circuits interesting for use in electronics. A first property is that these two-ports are not reciprocal networks, since their y -parameter matrices are not symmetric. In fact, these matrices are skew symmetric. It is well known to circuit theorists that nonreciprocal networks cannot be realized with only passive components—that is resistors, capacitors, and inductors. This means that gytrators are strictly active networks that must, therefore, be realized with active components, such as transistors or operational amplifiers. Two-port gytrators have been given their own circuit symbol, which is shown in Fig. 2. The gyration constant, g is built into the symbol.

Perhaps the most important property of a gytrator is its ability to transform admittances into impedances. Specifically, when an admittance is connected to one port of a gytrator, the impedance looking into the other port is exactly a scaled version of that admittance. The derivation can be accomplished with the help of Fig. 3, where Z_{load} is the impedance attached to port 2, Y_{load} is its reciprocal—that is, the admittance attached to port 2—and Z_{input} is the impedance seen looking into port 1. We have

$$Z_{load} = \frac{V_2}{-I_2};$$

$$Z_{input} = \frac{V_1}{I_1} = \frac{I_2/g}{-gV_2} = \frac{1}{g^2} \frac{1}{Z_{load}} = \frac{1}{g^2} Y_{load}$$

The gyration constant g determines the scale factor, but the nature of the input impedance is determined by the admittance attached to port 2. Therefore, if a capacitor is attached to port 2, then we have

$$Z_{input} = \frac{1}{g^2} sC = sL_{eq}; \quad L_{eq} = \frac{C}{g^2}$$

This simple relation explains the vast majority of the gytrator’s popularity in electronic design. It shows that a capacitor can be used to replace an inductor in a circuit with the help of a gytrator. Since inductors are rarely desirable in electronic circuits operating below about 1 GHz, this idea is quite appealing. Capacitors and gytrators are conveniently realized within integrated circuits.

Filter synthesis based on the inductor simulation already described is usually done by starting with an RLC (resistor, inductor, capacitor) prototype, and replacing the inductors with capacitor–gytrator combinations. Consider the following example of a very simple second-order bandpass filter shown in Fig. 4. After replacing the inductor with a gytrator/capacitor combination, the filter is realized solely using RC (resistor, capacitor) passive elements, as shown in Fig. 5. Some original related work appears in

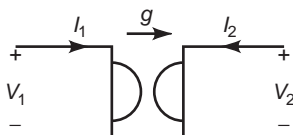


Figure 2. Electrical circuit symbol for a gytrator.

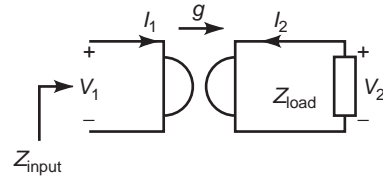


Figure 3. Reflecting load impedance with a gytrator.

Refs. 6 and 7. Furthermore, the filter can be tuned electronically if the gyration constant can be varied electronically. An electronically tunable filter using gytrators will be shown later.

A byproduct of the property under discussion is that series and parallel circuits may be interchanged with the help of a gytrator. Suppose one port, say, port 2, of a gytrator is loaded with a parallel combination of elements. The admittance of this combination is the sum of the admittances of each of the elements. At the other port, port 1, the input impedance will be a scaled version of this admittance; hence, a sum of impedances. Since the composite input impedance seen at port 1 is given by a sum of impedances, it must be equivalent to a series combination of elements. Therefore, the gytrator converts a parallel network into a series network. Using similar logic, it becomes clear that a series network connected to port 2 will be reflected as a parallel network looking into port 1 (these results are summarized next):

$$Y_{load} = \sum_{k=1}^N Y_k \Rightarrow Z_{input} = \frac{Y_{load}}{g^2}$$

$$= \sum_{k=1}^N \frac{Y_k}{g^2} = \sum_{k=1}^N Z_{in-k}$$

$$Z_{load} = \sum_{k=1}^N Z_k \Rightarrow Y_{input} \tag{9}$$

$$= \frac{1}{Y_{load}/g^2} = g^2 Z_{load}$$

$$= \sum_{k=1}^N g^2 Z_k = \sum_{k=1}^N Y_{in-k}$$

4. CIRCUIT REALIZATIONS FOR GYRATORS

4.1. The 2G_m Cell Realization

The realization of gytrators in electronic form is quite simple; however, as usual, different circuit realizations are

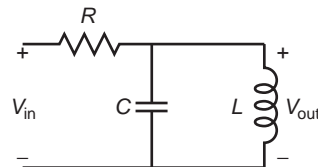


Figure 4. Bandpass filter.

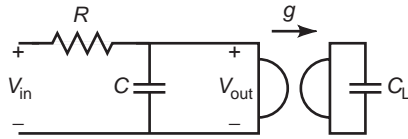


Figure 5. Bandpass filter with inductor replaced by gyrator/capacitor.

preferable to others, depending on the application. To begin, consider the simplest generic realization consisting of a pair of transconductance amplifiers, as shown in Fig. 6. Each transconductance amplifier is assumed to have infinite input and output impedance, with an output current equal to the transconductance $G_m = g$, times the input voltage applied to the + and - terminals. The circuit shown in Fig. 6 satisfies the basic two-port relations for a gyrator, given by Eq. (3).

The circuit of Fig. 6 does not implement the most general form of a gyrator, since both ports of the gyrator realization in the figure have ground in common. Therefore, only ground-referenced impedances may be transformed as described elsewhere in this article. This limitation stems from the fact that the transconductors in Fig. 6 have single-ended outputs. If differential input/differential output transconductors are used, then a general floating gyrator realization is created—that is, a gyrator whose ports need not be referenced in any way to ground.

Unfortunately, the realization of fully differential gyrators is not easy. In general, this realization requires more circuitry and the management of common-mode signals. Figure 7 shows how a floating gyrator can be realized using single-ended transconductors; however, this circuit suffers from common-mode problems. An analysis of this structure yields the following results:

$$\begin{aligned}
 I_{2+} &= -gV_{1+}; \quad I_{2-} = -gV_{1-}; \quad I_{1+} = gV_{2+}; \quad I_{1-} = gV_{2-} \\
 \Rightarrow I_2 = I_{2+} &= -I_{2-} = -g(V_{1+} - V_{1-}) = -gV_1 \quad (10) \\
 I_1 = I_{1+} &= -I_{1-} = g(V_{2+} - V_{2-}) = gV_2
 \end{aligned}$$

The crucial assumption embodied in Eq. (10) is that + and - currents are equal and opposite one another. This can happen only if the + and - input voltages at the ports are exactly equal and opposite. Since this special case cannot be relied on in practice, additional circuitry must be added to deal with any common-mode current component. To do this compensation, more transconductors can be added to process the average voltage at each port. As

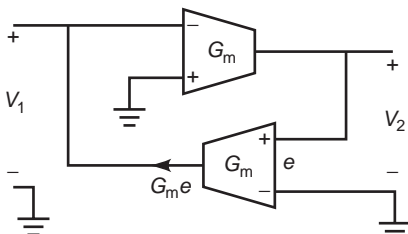


Figure 6. Realization of gyrator using transconductance amplifiers.

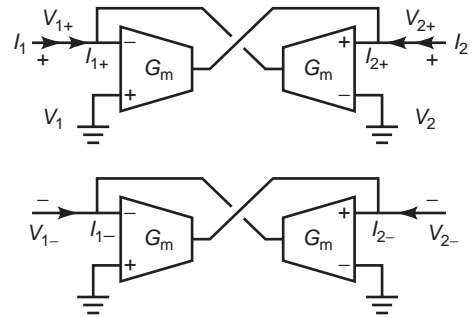


Figure 7. Floating-gyrator implementation.

one might expect, this additional circuitry is an unwelcome addition to the design. As a result, this idea is rarely found in practical designs.

There is an alternative for the simulation of a floating inductor using gyrators. A pair of gyrators is used with a grounded impedance Z_{load} as shown in Fig. 8. The equations describing this system are given by

$$\begin{aligned}
 I_2 &= gV_1; \quad I_1 = -gV_2; \quad I_4 = gV_3; \quad I_3 = -gV_4 \\
 V_{load} &= V_2 = V_3; \quad I_{load} = -(I_2 + I_3) \\
 V_{input} &= V_1 - V_4; \quad I_{input} = I_1 = -I_4 \\
 Z_{input} &= \frac{V_{input}}{I_{input}} = \frac{V_1 - V_4}{I_1} = \frac{I_2/g - I_3/(-g)}{-gV_2} \quad (11) \\
 &= \frac{1}{g^2} \frac{I_2 + I_3}{-V_2} = \frac{1}{g^2} \frac{I_{load}}{V_{load}} \\
 &= \frac{1}{g^2 Z_{load}} = \frac{1}{g^2} Y_{load}
 \end{aligned}$$

Clearly, if a grounded capacitor is used as the grounded load in Fig. 8, then a floating simulated inductor is realized. The obvious benefit of this realization is that it requires only single-ended transconductance amplifiers, configured as in Fig. 6, and a grounded internal load to obtain a floating input port. Observe that no common-mode problems exist with this realization since common-mode signals at the input port cause canceling currents at the grounded port. Even in practice, with unmatched gyrators, there is a negative-feedback effect regarding common-mode errors that is highly desirable. The network of Fig. 8 is the preferred realization of floating inductors using capacitors and gyrators. Reference 8 represents some original work in this area.

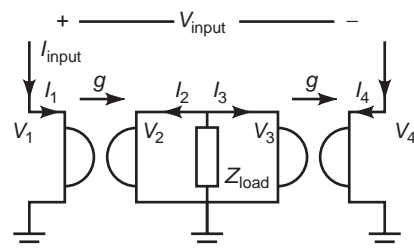


Figure 8. Floating-gyrator realization.

4.2. Realization with Operational Amplifiers

Gyrators may be realized with operational amplifiers; however, modifications must be made to account for the fact that these are voltage-controlled voltage sources. A voltage-controlled current source (VCCS) may be created using an op amp, as is well known, using the circuit of Fig. 9. A gyrator can then be realized with a second VCCS preceded by an inverter, recalling that the gains in different directions have opposite signs. A more clever variation of this idea is shown in Fig. 10, where only two op amps are required to implement the entire gyrator. Of course, this gyrator is ground-referenced as, for example, is the one in Fig. 6. Floating-gyrator structures can be implemented using the ideas stated, and similarly, a floating inductor may be synthesized via a pair of ground-referenced gyrators implemented with op amps and a grounded capacitor. References 6 and 7 give more discussion of the topics in the last two sections.

4.3. Other Realizations

Gyrators may be realized with any active circuitry that can implement either a VCCS or a CCVS (current-controlled voltage source). For example, a simple transistor-level realization for a gyrator appears in Fig. 11. $Q_1 - Q_3$ create a first transconductance amplifier, and Q_4 implements an inverting transconductance amplifier. The signal levels must be restricted with such an implementation due to the nonlinearity of the transistor junctions.

Alternatively, the transconductance amplifiers constituting the gyrator may be implemented using operational transconductance amplifiers (OTAs). OTAs are essentially bipolar differential pairs loaded with current sources in such a way as to create a nearly ideal transconductance amplifier. An example of an integrated version of an OTA is the LM3080 integrated circuit manufactured by National Semiconductor Corp. of Santa Clara, CA. An important feature of OTAs is that their transconductance can be tuned over a wide range by varying a control current. As a result, gyrators made using OTAs are electronically tunable. This is quite desirable in applications where one wishes to electronically tune a filter. An example of this capability is given later.

Of course, there are limitations imposed by the use of OTAs since these circuits are not ideal in practice.

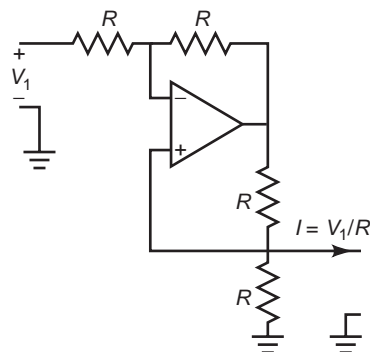


Figure 9. VCCS realization using an op amp.

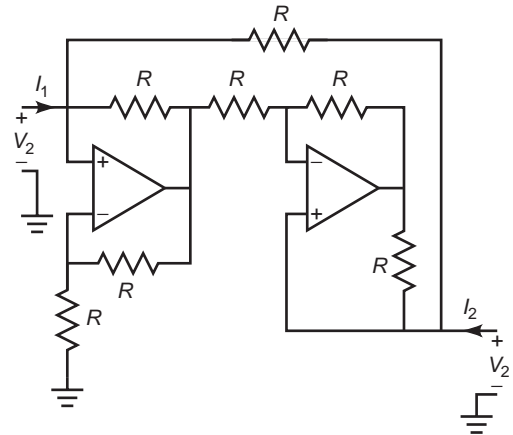


Figure 10. Gyrator realization using op amps.

Specifically, they suffer from finite input and output impedance, and these impedances vary as a function of the transconductance. As a result, the tuning range of OTA tuned filters can be limited. Furthermore, at higher frequencies the complexity of OTAs introduces an unwanted phase shift, which degrades the behavior of the gyrator, as well as compromising the usable tuning range. Finally, these circuits become quite nonlinear for inputs above a few tens of millivolts, which limits the dynamic range of the resulting filters.

5. FILTER REALIZATION USING GYRATORS

This section considers the general problem of filter synthesis based on gyrators. Basically, synthesis with gyrators involves either the substitution of inductors, in the practical case, or the partition of state equations.

5.1. Replacement of Inductors in Ladder Networks

The replacement of inductors in filters has already been implied. In this section, the idea is generalized. Consider the case where a prototype passive RLC filter has been specified. This is usually done, starting from a filter specification, using filter design tables or software to produce one of a variety of passive filter structures. Special cases will be considered in the discussion that follows. All other cases are obvious variations.

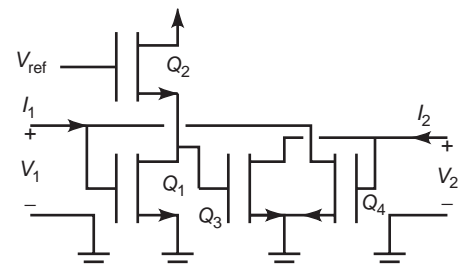


Figure 11. Transistor realization of a gyrator.

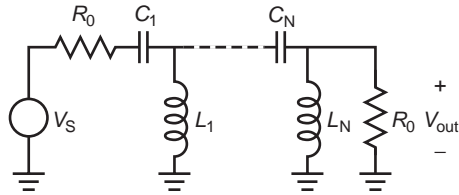


Figure 12. Doubly terminated passive ladder highpass filter.

The first case considered is that of a doubly terminated highpass RLC ladder network, shown schematically in Fig. 12. It is desirable to replace the grounded inductors with gyrator/capacitor combinations. Given the prototype design values for the inductors L_k , for $k = 1$ through N , one simply replaces each grounded inductor with one gyrator terminated with a capacitance C_k , given by the formula

$$C_k = g_k^2 L_k \quad (12)$$

where g_k represents the gyration constant for the k th gyrator. In practice, all gyration constants might be chosen to be equal for reasons of simplicity in the circuit design, and possibly for the purpose of optimizing noise and distortion performance. The resulting gyrator-based implementation is now an active filter containing $2N$ capacitors and N gyrators.

The doubly terminated lowpass filter structure obtained by swapping the positions of the inductors and the capacitors in the highpass filter of Fig. 12 is the dual-filter network to that shown previously. Again, each of the inductors can be replaced by a gyrator loaded by a capacitor, whose value is computed using Eq. (12). However, this time the gyrator structures will have to be the floating implementation described later. The complexity, in principle, of the final realization will equal that of the highpass example; however, each of the gyrators will require twice as much circuitry for its realization, therefore, the final circuit implementation will require considerably more circuitry as N gets larger.

A more complex filter variation is that of a bandpass RLC filter. A doubly terminated bandpass filter can be created starting from the highpass prototype of Fig. 12 by replacing each grounded inductor with a grounded parallel combination of a capacitor and inductor, and each series capacitor with a series combination of a capacitor and an inductor. The resulting filter is of order $4N$, instead of $2N$, as it must be to realize a bandpass equivalent. Again, gyrators may be used to replace each inductor, using methods like Eq. (12). Half of the inductors may be replaced using simple ground referenced gyrators, while the rest must be realized using the floating version.

An interesting final variation of this idea is demonstrated using the notch (bandstop) filter of Fig. 13. Here, the grounded inductor can be replaced by a gyrator and a grounded capacitor as outlined above. An alternative approach is to replace the grounded series LC (inductor, capacitor) combination using a gyrator loaded by a grounded parallel LC combination as shown in Fig. 14. Then replace the grounded inductor with another gyrator and a grounded

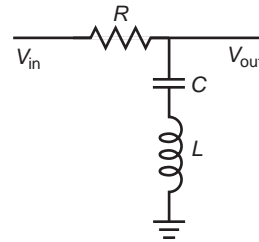


Figure 13. RLC notch filter.

capacitor. This is shown in Fig. 15. While this idea may seem to be wasteful in terms of component count, it shows how to exploit the property described elsewhere in this article regarding the conversion of series impedances combinations to parallel impedance combinations. In addition, this circuit has practical value since the pair of gyrators now allows two parameters to be tuned in this active filter realization. Specifically, the filter design equations are given as follows:

$$\begin{aligned} \frac{V_{out}}{V_e} = H(s) &= \frac{s^2 + \omega_0^2}{s^2 + (\omega_0/Q)s + \omega_0^2}; \\ \omega_0 &= \frac{1}{\sqrt{LC}}; \quad Q = \frac{1}{R} \sqrt{\frac{L}{C}} \\ C &= g_1^2 L_p = \frac{g_1^2}{g_2^2} C_L; \\ L &= \frac{1}{g_1^2} C_p \Rightarrow \omega_0 = \frac{g_2}{\sqrt{C_L C_p}} \\ Q &= \frac{g_2}{R g_1^2} \sqrt{\frac{C_p}{C_L}} \end{aligned} \quad (13)$$

Using this result, it is easy to see that both the notch frequency ω_0 and the sharpness of the notch, proportional to Q , can be controlled independently using only the gyration constants, g_1 and g_2 . Using an OTA implementation of the gyrators as discussed elsewhere, this tuning is relatively simple.

5.2. Synthesis Based on Gyrators

Clearly, the inductor replacement strategy described above could be applied in reverse to replace capacitors with inductors; however, this is not a good option in practical cases. This is because capacitors are easier to realize at frequencies below 1 GHz_z, and capacitors are of generally higher quality than inductors in this range of

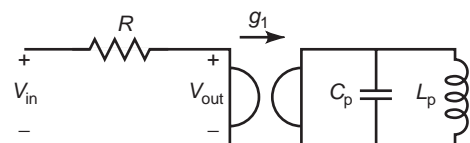


Figure 14. Gyrator-based parallel-to-series conversion.

frequencies. Although inductors may be of greater interest at very high frequencies, the use of gyrators at very high frequencies is limited by the nonideal behavior of the active circuitry used to realize them. It is of interest to note here that, as with any active circuit, there is excess phase shift introduced by the transconductors at high frequencies, causing the gyrators to take on complex gyration constants at high frequencies, as suggested later in the article. Furthermore, the finite output impedance of the transconductors limits there available DC gain. The net result of these effects is to cause simulated inductors to exhibit a reduced Q at both the low and high end of the frequency spectrum. In some situations this may introduce instability; however, this can be compensated for by careful design.

Another option exists for the generic design of active filters using gyrators. This option can be exercised by casting the equations for a given filter in the G_m - C format. This is done by writing the state equations for the desired filter in the standard form

$$\frac{d}{dt} \mathbf{x} = \mathbf{A}\mathbf{x} + \mathbf{b}u; \quad y = \mathbf{c}^T \mathbf{x} + du; \tag{14}$$

$$H(s) = \frac{y}{u} = \mathbf{c}^T (s\mathbf{I} - \mathbf{A})^{-1} \mathbf{b} + d$$

where $\mathbf{x} = (x_1, x_2, \dots, x_N)^T$

where the input u and the output y are assumed scalars, \mathbf{x} is the $(N \times 1)$ -state vector, \mathbf{A} is the N by N state matrix, \mathbf{b} and \mathbf{c}^T are N dimensional vectors, and d is a scalar. Now assume that the input, u , is a voltage, and let each of the state variables x_k be equated to the voltage v_k on some grounded capacitor C_k . The derivative of this voltage, times the capacitance value, is equal to the current in the respective capacitor. Using this idea the state equations may be converted into current equations of the form

$$C \frac{d}{dt} \mathbf{v} = \mathbf{i}_C = \mathbf{C}\mathbf{A}\mathbf{v} + \mathbf{C}\mathbf{b}u = \mathbf{G}_m \mathbf{v} + \mathbf{g}_{m0}u$$

$$\Rightarrow \begin{array}{c} C_1 \dot{v}_1 \\ C_2 \dot{v}_2 \\ \vdots \\ C_N \dot{v}_N \end{array} = \begin{array}{c} i_{C1} \\ i_{C2} \\ \vdots \\ i_{CN} \end{array} \tag{15}$$

$$= \begin{array}{cccc|c} g_{m11} & g_{m12} & \cdots & g_{m1N} & v_1 \\ g_{m21} & g_{m22} & \cdots & g_{m2N} & v_2 \\ \vdots & \vdots & \vdots & \vdots & \vdots \\ g_{mN1} & g_{mN2} & \cdots & g_{mNN} & v_N \end{array} + \begin{array}{c} g_{m01} \\ g_{m02} \\ \vdots \\ g_{m0N} \end{array} u$$

where $C = \text{diag}(C_1, C_2, \dots, C_N)$

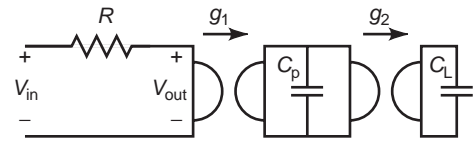


Figure 15. Replacement of series LC with two gyrators and two capacitors.

where the dot above a variable denotes time differentiation. The realization of a filter based on these equations produces a filter composed of grounded capacitors, with transconductance amplifiers bridging between the capacitor nodes and the input. The class of G_m - C filters, sometimes referred to as “OTA- C filters”, is based exclusively on this formulation.

A gyrator-based synthesis is possible by partitioning the G_m matrix into symmetric and skew symmetric matrices. The idea is best described by an example. Suppose that a second-order version of the g_m - C formulation is given. The G_m matrix can always be decomposed as follows

$$G_m = \begin{array}{cc|c} g_{m11} & g_{m12} & \\ \hline g_{m21} & g_{m22} & \end{array} = G_{m1} + G_{m2} \tag{16}$$

$$= \begin{array}{cc|c} g_{m11} & g_{m12} + g & \\ \hline g_{m21} - g & g_{m22} & \end{array} + \begin{array}{cc|c} 0 & -g & \\ \hline g & 0 & \end{array}$$

where the off-diagonal elements of G_{m1} are equal, making this a symmetric matrix. Clearly, G_{m2} is a skew symmetric matrix. With this partitioning of the transconductance matrix, it is possible to realize the system in Eq. (16) using one reciprocal two-port, characterized by G_{m1} , and a second two-port, characterized by G_{m2} , that is a gyrator. Figure 16 shows the realization associated with this decomposition assuming a single input term in Eq. (15) and a special case for the output—that is, $g_{m02} = 0$ and $y = x_1 = v_1$. The reciprocal two-port can often be realized only with resistors, but in general may require active circuitry.

This special case considered can be further explained with a specific example. Suppose the second order system of Eq. (16) is the bandpass filter described with the

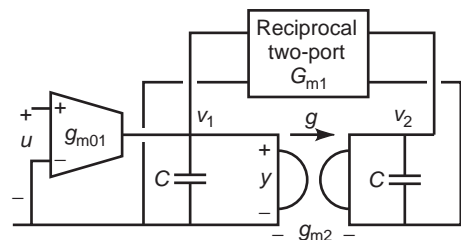


Figure 16. Generic synthesis of a second order G_m - C filter.

following state space description:

$$\begin{aligned} \begin{vmatrix} \dot{x}_1 \\ \dot{x}_2 \end{vmatrix} &= \begin{vmatrix} -\omega_0/Q & -\omega_0 \\ \omega_0 & 0 \end{vmatrix} \begin{vmatrix} x_1 \\ x_2 \end{vmatrix} \\ &+ \begin{vmatrix} \omega_0 \\ 0 \end{vmatrix} u; \quad y = \begin{vmatrix} 1 & 0 \end{vmatrix} \begin{vmatrix} x_1 \\ x_2 \end{vmatrix} \\ H(s) &= \begin{vmatrix} 1 & 0 \end{vmatrix} \begin{vmatrix} s + \omega_0/Q & \omega_0 \\ -\omega_0 & s \end{vmatrix}^{-1} \begin{vmatrix} \omega_0 \\ 0 \end{vmatrix} \\ &= \frac{s\omega_0}{s^2 + s\omega_0/Q + \omega_0^2} \end{aligned} \quad (17)$$

Let us now assume that the input u is a voltage denoted by v_{in} . By equating the state variables, x_1 and x_2 , to respective voltages, v_1 and v_2 , and scaling each equation by the same capacitance value C for convenience, one obtains

$$\begin{aligned} \begin{vmatrix} C\dot{v}_1 \\ C\dot{v}_2 \end{vmatrix} &= \begin{vmatrix} -C\omega_0/Q & -C\omega_0 \\ C\omega_0 & 0 \end{vmatrix} \begin{vmatrix} v_1 \\ v_2 \end{vmatrix} + \begin{vmatrix} C\omega_0 \\ 0 \end{vmatrix} v_{in} \\ &= \begin{vmatrix} -C\omega_0/Q & 0 \\ 0 & 0 \end{vmatrix} \begin{vmatrix} v_1 \\ v_2 \end{vmatrix} + \begin{vmatrix} 0 & -C\omega_0 \\ C\omega_0 & 0 \end{vmatrix} \begin{vmatrix} v_1 \\ v_2 \end{vmatrix} + \begin{vmatrix} C\omega_0 \\ 0 \end{vmatrix} v_{in} \\ &= G_{m1}\mathbf{v} + G_{m2}\mathbf{v} + \mathbf{g}_m v_{in} \end{aligned} \quad (18)$$

$$\text{where } \mathbf{v} = \begin{vmatrix} v_1 \\ v_2 \end{vmatrix}$$

Recognizing that $C\omega_0$ has units of conductance, one may easily realize this bandpass filter with only a resistor, implementing G_{m1} , a gyrator, implementing G_{m2} , and a transconductance amplifier realizing the nonzero term in \mathbf{g}_m . This realization is shown in Fig. 17, where $g_{m01} = C\omega_0$ and $R = Q/C\omega_0$. Observe that this realization is essentially the same as that obtained by replacing the grounded inductor in the bandpass filter of Fig. 4 with a gyrator/capacitor combination.

The generalization of this synthesis technique to arbitrary-order systems is straightforward, although cumbersome. In this case, the G_m matrix is again partitioned into symmetric and skew symmetric matrices; however, each related off-diagonal pair of elements in the skew symmetric G_{m2} matrix must be realized with a separate gyrator.

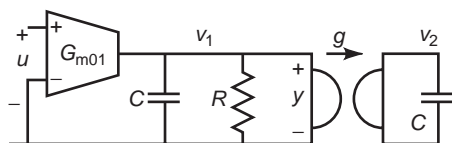


Figure 17. General synthesis realization for a bandpass filter.

This will not be much of a problem if the matrix is sparse, which can often be arranged in setting up the state equations. The N -port gyrator described in, for example, Refs. 9 and 10 can be used to realize the entire G_{m2} matrix at one time.

6. ADVANCED TOPICS

6.1. Energy and Initial Conditions

Gyrators have already been shown to be lossless two-ports. This idea can be extended to show a duality between the energy stored on a capacitor and the energy stored in an inductor. Suppose that a capacitor, of value C , is connected to one port of a gyrator. Further suppose that this capacitor is charged to a voltage V . Then the energy stored in this capacitor is given by $\frac{1}{2}CV^2$. As described earlier, the impedance seen looking into the other port of the gyrator is an equivalent inductor. Given the lossless nature of the gyrator, this equivalent inductor should be expected to have the same apparent stored energy. However, in the case of an inductor the energy stored is $\frac{1}{2}LI^2$, where I is the current flowing in the inductor. A capacitor is in equilibrium with an open circuit across it, and an inductor is in equilibrium with a short circuit across it. Hence, by short-circuiting the port of the gyrator opposite the capacitor, a current flows that will be equal to the equilibrium current in the equivalent inductor. The following analysis shows that the stored energy in the equivalent inductor equals that actually stored on the capacitor:

$$\frac{1}{2}LI^2 = \frac{1}{2} \frac{C}{g^2} (gV)^2 = \frac{1}{2} CV^2 \quad (19)$$

The natural consequence of this energy relationship is that the current at the inductive port cannot change instantaneously, since the voltage at the capacitive port cannot change instantaneously. Hence, initial conditions can be readily translated from one port to another. These facts demonstrate that the gyrator is truly an energy conservative two-port, satisfying any intuition take one might have regarding its operation.

6.2. Nonideal Effects

Gyrators, in practice, cannot be made to be ideal. Therefore, practical gyrators are not lossless. Instead they introduce small losses into the system. This is explained by modifying the y -parameter matrix for the gyrator to include diagonal terms. With these terms the two-port is no longer lossless, as is clear from this analysis:

$$\begin{aligned} \mathbf{I} = \mathbf{YV} &= \begin{vmatrix} g_{11} & -g \\ g & g_{22} \end{vmatrix} \mathbf{V} = \mathbf{GV} \\ \Rightarrow \mathbf{V}^T \mathbf{I} &= \mathbf{V}^T \mathbf{GV} = g_{11} V_1^2 + g_{22} V_2^2 \end{aligned} \quad (20)$$

If the diagonal elements, g_{11} and g_{22} , are both positive, then the two-port described in the equation is lossy, since

the power delivered to this two-port must be positive. In practice, the loss terms arise naturally from the fact that the transconductors comprising the gyrator are nonideal. For example, the input/output impedance of the transconductors will not be infinite in a practical device. In this case, g_{11} and g_{22} are the nonzero input admittance of the transconductors.

Furthermore, the transfer characteristics will not in general be ideal. As an example, consider the case of the gyrator realized using op amps as in Fig. 10. Suppose that the op amps have a finite gain A . Then the y -parameter matrix can be derived, and is found to be

$$Y = \begin{vmatrix} g_0 & -G \\ G - \delta G & g_0 \end{vmatrix}$$

where $G = \frac{1}{R}$; $g_0 = 2(1 - K)G$
 $\delta G = 2(1 - K^2)G$; $K = \frac{1}{1 + 2/A}$

where A is the open-loop voltage gain of the operational amplifiers. Notice that this Y matrix corresponds to an ideal gyrator when A becomes infinite. Also observe that the finite gain of the op amps has caused the y -parameter matrix to no longer be skew symmetric, which in itself adds loss to the system. Hence, in general, practical gyrators exhibit loss and asymmetry—that is, they lack skew symmetry—in their transfer characteristics.

Another possibility, considering Eq. (20), is for the diagonal elements, g_{11} and g_{22} , to be purely imaginary. In this case, the power computed in Eq. (20) is imaginary, which translates to purely reactive power. When dissipated power is purely reactive, no average power is dissipated. Hence, a gyrator with purely imaginary diagonal elements is still lossless. Such a device could be synthesized by adding reactive elements in series or parallel with the ports of the gyrator, since the diagonal elements, g_{11} and g_{22} , amount to the input admittance looking into the respective ports of the gyrator. Furthermore, stray capacitance or inductance associated with the inputs or the active circuitry making up the gyrator does not contribute to loss.

6.3. The Hall Effect Device and Isolators

It has been observed that Hall effect devices implement a lossy gyrator. This is because the physics of these devices is such that the two electric field controlled ports behave as a pair as if they were a gyrator with loss—that is, g_{11} and g_{22} in Eq. (20) are nonzero and not purely imaginary. The physics of such devices is explained in Ref. 11.

Figure 18 shows an interesting usage for a Hall effect gyrator, and in fact any lossy gyrator. In the figure, a gyrator, assumed to have the y -parameter matrix of Eq. (20), has bridging components, R_{p1} and R_{p2} , added around it. Then a pair of sources, V_{S1} and V_{S2} , with respective source resistance, R_{S1} and R_{S2} , are attached as shown. With a little effort the response of this circuit from the sources to

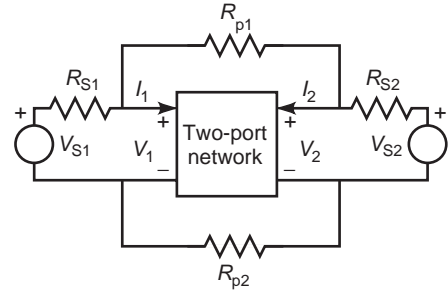


Figure 18. Connection for a lossy gyrator to implement an isolator.

the port voltages of the gyrator can be found to be

$$\begin{vmatrix} V_1 \\ V_2 \end{vmatrix} = \alpha \begin{vmatrix} G_{S1}(g_{22} + G_{S2} + G_P) & -G_{S2}(G_P + g) \\ G_{S1}(G_P - g) & G_{S2}(g_{11} + G_{S1} + G_P) \end{vmatrix} \begin{vmatrix} V_1 \\ V_2 \end{vmatrix}$$

where $\alpha = (g_{11} + G_{S1} + G_P)(g_{22} + G_{S2} + G_P) + G_P^2 - g^2$

$$G_P = G_{P1} + G_{P2}$$

(22)

By choosing the sum of the bridging elements equal to gyration constant g , the response at port 2 can be made totally independent of V_{S1} , as opposed to the response at port 1, which will depend on both sources. This creates a circuit called an *isolator*, which can be found in various applications, especially microwaves and optics.

6.4. Multiport and Gyrators

The concept of a gyrator need not be restricted solely to two-port networks. In fact, an N -port gyrator can be contrived as a natural extension of the two-port gyrator. As one might expect, the N -port gyrator must inherit the key properties of the two-port type. It must be a nonreciprocal lossless network; it must also reflect impedances in a way similar to the two-port gyrator. In general, N -port gyrators have not found use in electrical systems. For a detailed discussion of such networks, refer to Refs. 9 and 10.

There is one special case, however, of an N -port complex gyrator, for $N = 3$, which has found extensive use in microwave systems—namely, the circulator. While practical circulators are quite complex structures, electrically speaking, they can be viewed over a certain range of frequency to be an approximately lossless three-port complex gyrator. Reference 12 describes the three-port y -parameter matrix for a circulator. Specifically

$$Y = \begin{vmatrix} \alpha & \beta & \gamma \\ -\beta^* & \alpha & \beta \\ -\gamma^* & -\beta^* & \alpha \end{vmatrix} \tag{23}$$

where the superscript $*$ denotes complex conjugation. It is referred to as being complex since the lower triangular matrix part of Y is the negative of the conjugate transpose of the upper triangular part. The power P delivered to a

three-port having this y -parameter matrix is given by

$$P = \begin{vmatrix} \alpha & \beta & \gamma \\ -\beta^* & \alpha & \beta \\ -\gamma^* & -\beta^* & \alpha \end{vmatrix} \begin{vmatrix} V_1 \\ V_2 \\ V_3 \end{vmatrix} \quad (24)$$

$$= \alpha(V_1^2 + V_2^2 + V_3^2) + (\beta - \beta^*)(V_1V_2 + V_2V_3) + (\gamma - \gamma^*)V_1V_3$$

As suggested, this power can be made purely reactive if all the coefficients multiplying the voltage products are purely imaginary. This condition is always met if α is imaginary, since the real parts of β and γ cancel in the final result. Hence, the circulator described by this equation is a lossless three-port given purely imaginary values for α . The circulator is interesting in that the transfer characteristics from port to port when driven by sources—for example, V_{S1} , V_{S2} , and V_{S3} —is similar to the isolator previously described. Specifically, V_{S1} does not affect the port 2 voltage, V_{S2} does not affect the port 3 voltage, and V_{S3} does not affect the port 1 voltage. More details of the design and use of circulators is given in Ref. 13.

BIBLIOGRAPHY

1. B. D. H. Tellegen, The gyrator, a new circuit network element, *Phillips Research Report*, 1948, Vol. 3, pp. 81–101.
2. A. Antonou, Realization of gyrators using operational amplifiers, and their use in RC -active network synthesis, *Proc. IEE* **116**:1838–1850 (1969).
3. S. Singer, Loss-free gyrator realization, *IEEE Trans. Circ. Syst.* **35**:26–34 (Jan. 1988).
4. Y. P. Tsividis and J. O. Voorman, *Integrated Continuous-Time Filters: Principles, Design, and Applications*, IEEE Press, Piscataway, NJ, 1993.
5. H. Y. Lam, *Analog and Digital Filters: Design and Realization*, Prentice-Hall, Englewood Cliffs, NJ, 1979.
6. R. S. H. Riordan, Simulated inductors using differential amplifiers, *Electron. Lett.* **3**:50–51 (1967).
7. D. F. Sheahan and H. J. Orchard, Bandpass filter realisation using gyrators, *Electron. Lett.* **3**(1):40–42 (1967).
8. D. F. Sheahan, Gyrator-floatation circuit, *Electron. Lett.* **3**(1):39–40 (1967).
9. Synthesis of active RC systems with a multiport gyrator and a defined structure, *IEEE Trans. Circ. Syst.* **CAS-27**:191–199 (1980).
10. A. G. J. Holt and R. L. Linggard, The multiterminal gyrator, *Proc. IEEE* **56**:1354–1355 (1968).
11. A. G. Milnes, *Semiconductor Devices and Integrated Electronics*, Van Nostrand-Reinhold, New York, 1980.
12. R. H. Knerr, A proposed lumped-element switching circulator principle, *IEEE Trans. Microwave Theory Tech.* **MTT-20**:396–401 (1972).
13. J. Helszajn, Synthesis of octave-band quarter-wave coupled semitracking stripline junction circulators, *IEEE Trans. Microwave Theory Tech.* **43**:573–581 (1995).

GYROTRONS

R. LAWRENCE IVES
Calabazas Creek Research, Inc.
Saratoga, California

1. INTRODUCTION

The gyrotron is a vacuum tube capable of delivering high levels of radiofrequency (RF) power at frequencies from several gigahertz (GHz) to more than 200 GHz, which covers most of the microwave and millimeter-wave bands. Because of the structure of the RF fields in the cavity, the magnitude of the electric fields and the RF losses in the cavity walls are much lower in gyrotrons than in most microwave and millimeter-wave vacuum devices. As the RF frequency increases, it is not necessary to reduce the size of the cavity and output waveguide. For these reasons, the gyrotron is the principal RF device for delivering high levels of RF power in this frequency range.

Gyrotrons typically require a very high magnetic field to provide the electron cyclotron motion for power extraction, and most gyrotrons above 30 GHz require a superconducting magnet. Until recently (as of 2003), this significantly increased system cost and complexity, limiting applications for these devices. Recent advances in cryogen-free magnets are eliminating the requirement for liquid cryogenics and allowing additional applications. Gyrotrons also have a narrow RF bandwidth, typically around 0.1%. Historically, narrow bandwidth and the overmoded nature of the gyrotron limited their use as amplifiers, so almost all high-power gyrotrons are oscillators. Research on high-power gyroamplifiers is in progress at several locations around the world, and bandwidths of 7% and higher have been achieved [1], increasing their potential use for high-power, high-resolution radar [2]. Gyrokystrons are also being developed to drive high-power accelerators, which do not require large bandwidths [3,4].

Gyrotrons are used for electron cyclotron resonance heating (ECRH), electron cyclotron current drive (ECCD), and diagnostic measurements in fusion plasma devices. They are also being used for industrial heating applications such as ceramic sintering. Figure 1 shows a photograph of Dr. Howard Jory, one of the pioneers in gyrotron development, holding a 28-GHz, 10-kW continuous-wave (CW) harmonic gyrotron used for industrial heating. Behind him is a 110-GHz gyrotron, rated at approximately 450 kW CW, used for electron cyclotron resonance heating. Communications and Power Industries, Inc. in Palo Alto, CA manufactures both devices.

Research on gyro-type devices began in the 1950s, when the astrophysicist R. Q. Twiss described an amplifying mechanism for monochromatic radiation of angular frequency ω from stimulated emission of an ensemble of electrons [5]. Twiss' formula predicted amplification for Cerenkov radiation and for cyclotron radiation. Working independently, Schneider described the stimulated emission of radiation from electrons in a magnetic field in 1959 using a quantum-mechanical model [6]. Also in 1959,

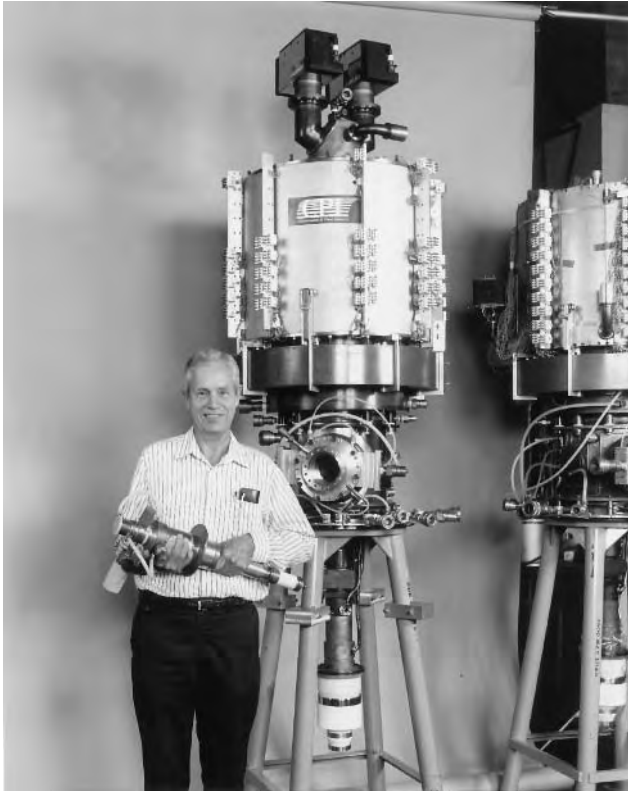


Figure 1. Dr. Howard Jory holds a 28-GHz, 10-kW CW harmonic gyrotron used for industrial heating. Behind him is a 110-GHz, 450-kW CW, 1-MW pulsed, gyrotron used for electron cyclotron heating of fusion plasmas.

Gapanov described this mechanism using a classical approach [7].

The first experimental results describing a fast-wave cyclotron interaction were reported by R.H. Pantell in 1959 [8]. His device produced radiation between 2.5 and 4.0 GHz from a 1-kV, 3- μ A electron beam. A number of additional experiments were reported during the early 1960s [9–12], but the experiment that confirmed the cyclotron maser interaction was performed by Hirshfield and Wachtel in 1964 [13].

During the mid to late 1960s, major advances were made by scientists in the Soviet Union, although much of this work went unreported in the Western world because of the political climate at the time [14]. Soviet scientists embarked on a major program to develop megawatt gyrotrons and made major advances in electron mode selection, open resonators and waveguides [15], ray tracing to optimize the interaction between the electron beam and the RF wave in the circuit, and high-cross-section cavities utilizing whispering gallery modes [16]. “Whispering gallery modes” are transverse electric modes where the number of azimuthal field variations significantly exceeds the number of radial field variations. Use of these modes was further facilitated by the development by Vlasov et al. of a quasioptical device for converting the whispering gallery waveguide mode into a Gaussian mode that can be propagated in a narrow wave beam without waveguides [17].

An equally important Soviet development was the magnetron injection gun, which generates the required electron beam for efficient gyrotron operation.

For a more complete historical description of gyrotron development, the reader is referred to three publications that cover the subject in more detail [18–20]. The reader is also referred to a listing of journals in the bibliography that contain most of the published work in this area.

2. BASIC THEORY OF OPERATION

Gyrotrons exploit the negative mass instability to achieve azimuthal bunching of a cycloding electron beam. A transverse electric field in the cavity modifies the energy of the electrons such that higher-energy electrons gyrate more slowly around the magnetic flux lines than do lower-energy electrons. A schematic cross section of a gyrotron beam is shown in Fig. 2. The gyrotron beam is a hollow electron beam with individual electrons rotating at the cyclotron frequency around magnetic field lines with orbit diameters equal to twice the Larmour radius. The Larmour radius is given by

$$R_1 = \frac{\gamma m v_{\perp}}{e B_0}$$

where $\gamma = (1 - v_{\perp}^2/c^2 - v_z^2/c^2)^{-1/2}$ is the relativistic factor, m is the rest mass of the electron, v_{\perp} is the velocity of the electron in the plane perpendicular to the gyrotron axis, v_z is the electron velocity in the axial direction, e is the charge of the electron, and B_0 is the applied magnetic field parallel to the gyrotron axis.

Figure 3 more closely examines the effect of the electric field on the individual electrons in a cyclotron orbit when the frequency of the electric field is equal to the cyclotron

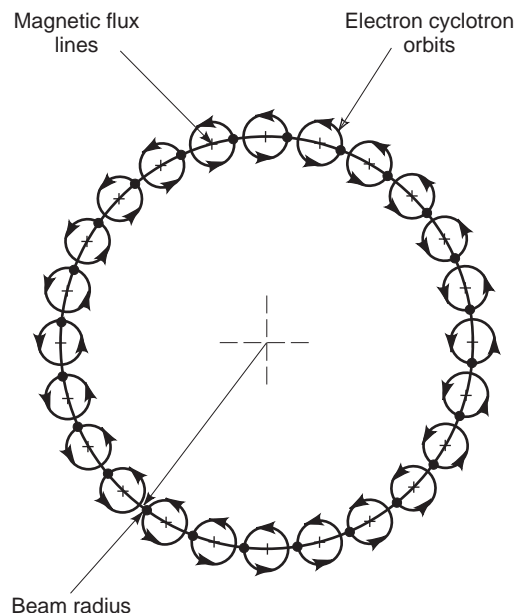


Figure 2. The cylindrical electron beam of the gyrotron consists of electrons orbiting around magnetic flux lines.

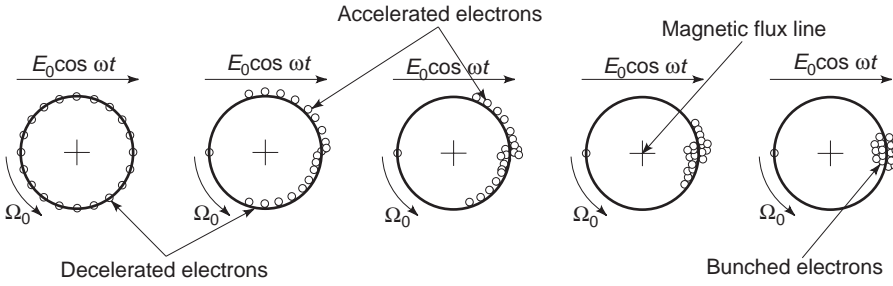


Figure 3. The cavity electric field interacts with the electrons orbiting around the magnetic flux lines. Each diagram illustrates an integral number of cyclotron periods later in time as the electrons traverse the cavity. The force on the electrons is given by $\vec{F} = -e\vec{E}$.

frequency. The cyclotron frequency is given by

$$\Omega = \frac{eB_0}{\gamma mc}$$

The electric field components have the form

$$E_\theta = E_0 J'_m(k_\perp r) \sin k_z z \cos m\theta$$

$$E_r = \frac{m}{k_\perp r} J_m(k_\perp r) \sin k_z z \sin m\theta$$

where E_θ and E_r are the azimuthal and radial components of the electric field, respectively; J_m and J'_m are the Bessel function and Bessel function derivative, respectively; m is the azimuthal mode number of the electric field; $k_\perp = X'_{mn}/r_0$, where X'_{mn} is the n th root of the corresponding Bessel function derivative and r_0 is the circuit radius; and $k_z = p\pi/L$, where p is the axial mode number of the circuit field (typically = 1) and L is the cavity length.

In Fig. 3, each successive image is an integral number of RF periods later in time as the electrons traverse the cavity. Electrons accelerated by the electric field gain energy and, as a result of the relativistic mass increase, their angular velocity decreases as γ increases. Conversely, electrons decelerated by the electric field lose energy and gain angular velocity. This causes azimuthal bunching of the electrons, sometimes referred to as the *cyclotron resonance maser* (CRM) instability.

If the frequency of the electric field exceeds the cyclotron frequency, the bunch will eventually fall back in phase and more electrons will undergo deceleration than acceleration, as shown in Fig. 4. This will result in transfer of energy from the electrons to the electric field. Optimized performance of gyrotrons requires careful design of the circuit geometry and control of the magnetic field. The circuit geometry affects the strength and profile of the electric field. The magnetic field affects the location of the beam and the amount of transverse energy available for transfer to the electric field. In many cases the magnetic field is tapered, that is, it is modified in strength through the cavity, to optimize the efficiency of power extraction.

Harmonic gyrotrons operate at a multiple of the cyclotron frequency. As the harmonic number increases, beam placement becomes more critical and the theoretical efficiency decreases. The advantage of harmonic gyrotrons is that the magnitude of the magnetic field is $1/n$ times that

required for nonharmonic operation. This can eliminate the need for a superconducting magnet or, at least, significantly reduce the cost.

For a more complete description of gyrotron theory, both linear and nonlinear, the reader is referred to several excellent publications on the subject [20–22].

3. BASIC COMPONENTS

Figure 5 shows a schematic layout of a typical gyrotron oscillator. The basic components are an electron gun, input beam tunnel, circuit, output taper, collector, window, and magnets. There are numerous variations of each of these components, depending on the operating characteristics of the gyrotron. The discussion that follows describes the most common types of components, including their purpose and performance characteristics.

3.1. Electron Gun

The function of the electron gun is to produce the electron beam required for interaction with the desired operating mode in the circuit. The gun must produce an electron beam that will be located at the proper radius for efficient interaction with the cavity electric fields and must contain most of its energy in cyclotron motion. Gyrotrons employ a magnetron injection gun (MIG) that emits electrons into a region of crossed electric and magnetic fields. This geometric configuration causes the individual electrons to spiral around the magnetic field lines as they are accelerated by

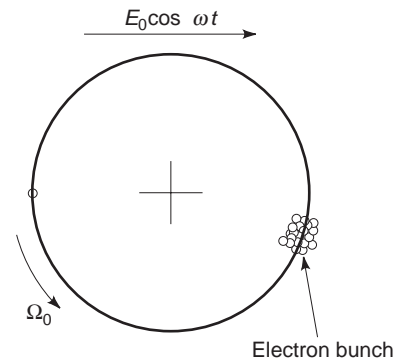


Figure 4. When $\omega > \Omega_0$, more electrons will be decelerated than accelerated, resulting in transfer of energy to the electric field.

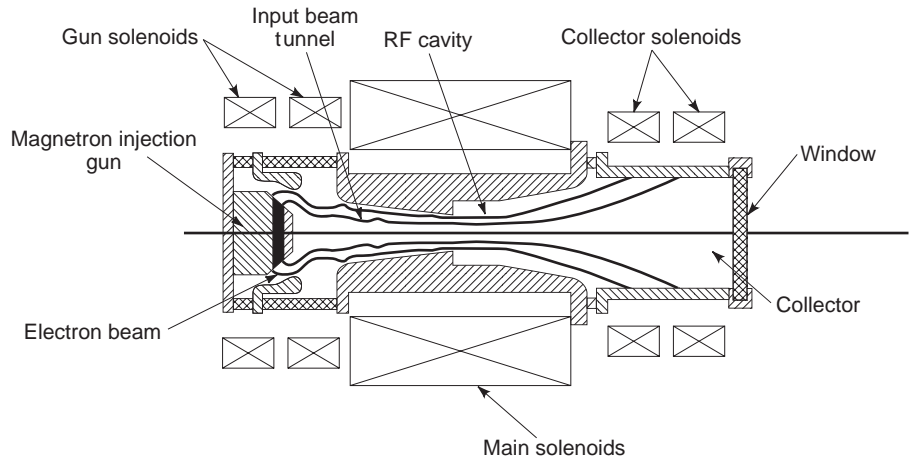


Figure 5. The basic components of a typical gyrotron are the electron gun, beam tunnel, cavity, output beam tunnel, collector, window, and magnet solenoids.

the electric field toward the circuit. This development was pioneered in the Soviet Union in the 1970s and made rapid development of gyrotrons possible [23].

Gyrotron cathodes typically operate temperature-limited, which means that the amount of current emitted from the cathode is determined primarily by the temperature of the emitting surface. The reader is referred to the excellent treatment of cathode emission mechanisms presented by Gilmour [24]. Typical cathode temperatures range between 950 and 1000°C.

Gyrotron guns come in two basic types, modulated (mod) anode and diode. A mod anode gun contains an electrode near the emitting surface to modulate the electron beam; that is, it uses an applied voltage to modify the characteristics of the beam. This electrode is maintained at a voltage between the cathode and ground and can have a significant effect on the beam characteristics and hence the performance of the gyrotron. By varying the voltage on this electrode, the user can control the output power by varying the amount of transverse energy that is present in the electron beam. Most commercially available gyrotron oscillators using mod anode guns operate at cathode voltages between -60 and -80 kV with mod anode voltages ranging from 15 kV up to about 30 kV above cathode potential.

A diode gun possesses no intermediate electrode, so the cathode voltage or the magnetic field controls gyrotron operation. Because the cathode power supply must also supply the current in the beam, it cannot be modified as easily as a mod anode supply, so diode guns typically operate where RF power is turned on or off by pulsing of the cathode power supply. For applications where it is not necessary to modify the operating characteristics of the tube, this represents a lower cost gyrotron and power supply configuration.

3.2. Magnetic Solenoids

The circuit requires an electron beam where the electrons are orbiting the magnetic field lines at a frequency near that of the RF frequency of the cavity. For gyrotrons operating at frequencies above 30 GHz, this typically requires a superconducting solenoid. An exception can occur

if the circuit is operating at a harmonic of the cyclotron frequency. The requirement of a superconducting solenoid limits applications for gyrotrons to those where the additional weight and complexity do not present a severe burden. Recent development of cryogen-free, superconducting magnets is now allowing mobile or airborne applications [25].

In addition to the solenoids required to produce the cavity magnetic field, other solenoids can be present around the electron gun and collector regions. Solenoids around the electron gun modify the amount of transverse energy in the beam or its size in the circuit. These coils are typically operated at room temperature because the fields in the electron gun are usually a few hundred Gauss. The ratio of the magnetic field magnitude in the circuit to that in the electron gun is referred to as the *beam compression*. This value plays an important role in the design of the electron gun and the combination of electric and magnetic fields required for efficient circuit interaction. Beam compressions of 10–20 are typical.

Solenoids around the collector are used to distribute the power deposited by the electron beam exiting from the circuit. The fringing magnetic fields from superconducting coils impose a magnetic field in the collector that is higher than in other linear beam tubes. This field prevents the electrons from spreading as a result of space charge and results in a relatively thin beam of electrons impacting a small region of the collector. This can result in excessive localized heating of the surface and possible destruction of the gyrotron. The collector coils are used to “buck” the field from the main solenoid and spread the electron impact area over a larger region of the collector. In some more advanced applications, an oscillating power supply drives one or more solenoids to sweep the beam back and forth along the collector surface.

3.3. Beam Tunnel

The beam tunnel must perform two important functions. First, it must prevent RF fields from the circuit from traveling back toward the electron gun. RF fields in the electron gun can severely affect the electron beam and cause excessive current on the body of the tube or the mod anode. It can also result in heating of the cathode emitter,

which will affect the beam current. Either condition will adversely affect tube operation.

The second function of the beam tunnel is to prevent parasitic oscillations between gun and circuit. Parasitic oscillations result in excessive body or mod anode current and can prevent tube operation. In some cases, dielectric material with a high RF loss is used to load out any electromagnetic fields present.

3.4. Circuit

The RF circuit typically consists of a right circular cylinder whose radius a is chosen such that

$$a = \frac{cX'_{mn}}{2\pi f}$$

where X'_{mn} is the n th root of the Bessel function derivative for the TE_{mn} cavity mode, c is the speed of light, and f is the operating frequency. The cavity mode depends primarily on the desired RF frequency and output power level. The application for the tube can also play an important role. The first commercial gyrotrons used TE_{01} , TE_{02} , or TE_{03} modes because they were reasonably close to the fundamental mode, did not couple to nonsymmetric modes that could travel down the beam tunnel toward the electron gun, and had very low RF loss in the circuit walls. More than 100 gyrotrons at frequencies between 28 and 100 GHz and power levels up to 340 kW CW were produced by Varian Associates, Inc. (now Communications and Power Industries, Inc.) from 1978 through 1990. These tubes were used for electron cyclotron resonance heating (ECRH) of plasmas in magnetic confinement fusion research. Gyrotrons of this type were also developed in Germany, China, Japan, France, and Russia [26].

As the demand for higher-power tubes increased, gyrotrons that used whispering gallery modes were developed. Whispering gallery modes allow the electron beam to be larger and minimize mode competition from other circuit modes. These modes also have reasonable RF power dissipation in the circuit.

Designers of high-power gyrotrons must balance a large number of factors to achieve a circuit configuration that will provide the power and frequency required with reasonable efficiency while avoiding parasitic mode competition, instabilities, and excessive RF power densities on the circuit walls. For additional information on the design of high-power gyrotron circuits, the reader is referred to the article by Kreisler et al. [27].

3.5. Output Taper

Most gyrotron circuits are open-ended toward the collector, and the RF power diffracts into the output taper. The output taper is usually a shallow, tapered section of circular waveguide that terminates the circuit interaction and transmits the RF power toward the collector. The waveguide radial dimensions must be increased in such a way that the purity of the output mode is not compromised. For gyrotrons where the RF power is extracted along the axis of the tube, the output taper continues to

increase in the radial dimension until the desired collector radius is achieved. The requirement to maintain mode purity often conflicts with the necessity of achieving the collector radius within a reasonable distance. The size of the collector is driven by the necessity to dissipate the spent electron beam without incurring excessive power densities on the walls, which could lead to melting or loss of vacuum integrity.

For gyrotrons with average RF power levels exceeding 200 kW, particularly those employing whispering gallery circuit modes, it is more expedient to extract the RF power radially to allow more flexibility in the collector design. For these tubes, the output taper transmits the circuit power to an RF launcher/antenna for eventual extraction from the vacuum envelope. This eliminates further requirements on the output taper to maintain mode purity and allows the designer more freedom in transitioning to the collector region.

3.6. Collector

Typical linear beam devices rely on termination of the magnetic field and space charge depression to spread the spent electron beam in the collector. Most of these devices employ an iron polepiece to terminate the magnetic field at the entrance to the collector. While this works well for solid electron beams, it does not apply to gyrotrons. Because of the high magnetic fields required in gyrotrons, this is rarely practical, particularly when superconducting solenoids are used.

Forces imposed by nearby iron on the superconducting coils would dramatically increase the complexity and cost of the magnet. As a result, sufficient magnetic fields exist in the collector to limit spreading of the electron beam from space charge forces. In addition, the beam used in gyrotrons is typically a thin cylindrical beam with high current density. This also exacerbates the problem of beam dissipation in the collector. Power densities up to 500 W/cm² are typical; 1000 W/cm² is considered the upper limit.

For gyrotrons at lower average power levels, these complications may not be a critical issue. For these devices, the output taper conducts the RF power to the collector with high mode purity, and the collector also serves as the output waveguide. In some cases, a downtaper is employed at the end of the collector to reduce the tube diameter before the output window. For these devices, the designer must also be concerned about modes that can be trapped in the collector between the uptaper from the circuit and the downtaper to the window.

For gyrotrons exceeding 500 kW of average power, radial RF power extraction is almost always employed. The size of the collector can be based on the dissipation requirements of the spent beam alone. As a result, collectors for high-power gyrotrons often constitute a major portion of the device. In Fig. 1, the collector of the 500-kW CW gyrotron behind Dr. Jory begins above the output window. The designer must balance low power densities with the increasing size, weight, and cost of large collectors.

Considerable research is now in progress to implement collector voltage depression to improve the total efficiency

of the gyrotron while simultaneously reducing the thermal power dissipation. The efficiency of the RF circuit is typically 30–40%; therefore, most of the incident beam power is dissipated in the collector. For a 1-MW CW gyrotron, approximately 2 MW of thermal power must be dissipated by the collector. To reduce this thermal power and improve the gyrotron efficiency, a voltage can be applied to the collector that is between that of the electron gun and the RF circuit. This slows the electrons and reduces the incident power. Since the total gyrotron input power is proportional to the voltage difference between the electron gun and the collector, this also increases the net efficiency. The amount of voltage depression that can be applied depends on the energy of the electrons following RF power extraction in the circuit. Voltage depression that exceeds the energy of the electrons will lead to reflection of the beam back toward the electron gun or circuit. This will lead to excessive heating, loading of the power supplies, or loss of interaction efficiency. Most gyrotrons in development today implement voltage depression to increase the total efficiency to approximately 50%.

Additional increases in efficiency can be achieved by introducing collectors with multiple electrodes at varying voltages and sorting the energy of the incident electrons using carefully designed magnetic fields. This allows additional increase in depression voltage for the higher-energy electrons while still avoiding reflection of slower ones. A two-stage depressed collector is currently being developed and is predicted to increase the overall efficiency of gyrotrons to more than 55% [28,29].

3.7. RF Launcher System

The RF launcher system converts the circular cavity/waveguide mode to a quasioptical Gaussian mode. This development was pioneered in the Soviet Union and allows transmission of the RF beam with very low loss using a series of metallic mirrors. Modern computer codes and integration with computer numerically controlled (CNC) mills and lathes allow precise control of the RF beam. Modern designs convert the power from the circuit into the desired Gaussian mode with greater than 95% efficiency. More advanced computer codes are in development that could increase the efficiency to more than 98% [30]. The conversion of the waveguide mode to a quasioptical Gaussian mode also results in a more convenient RF mode for most user applications.

Figure 6 shows a typical RF launcher configuration consisting of a waveguide launcher and two mirrors internal to the gyrotron. The exit angle of the RF power from the launcher is at the waveguide bounce angle, and the mirrors concentrate the power into a small circular beam and tailor the distribution of power within the beam as required by the output window.

3.8. Output Window

Until recently, the output power of gyrotrons was limited by the capabilities of the output window. The RF power produced in the high-vacuum region inside the gyrotron is extracted from the device through a dielectric window.

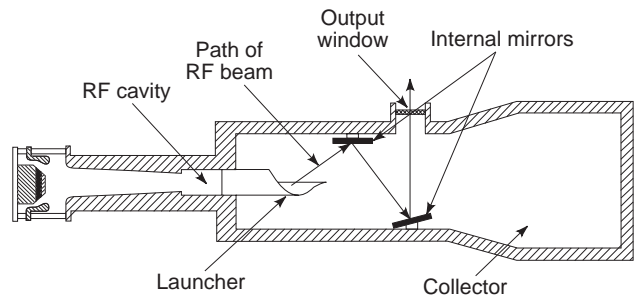


Figure 6. The Gaussian mode launcher converts the waveguide mode to a quasioptical beam, and the internal mirrors shape the RF beam profile.

The window must provide a vacuum interface while transmitting the RF power from the gyrotron into an external waveguide that may, or may not, be under vacuum. Some of the RF power transmitted through the window is absorbed and results in heating of the dielectric material. The window structure must be sufficiently cooled to prevent destruction from thermal stresses.

For gyrotrons producing power levels less than 500 kW continuously, common window materials include alumina and sapphire; however, beryllia oxide, boron nitrite, silicon nitride, and other materials have been used in special devices. At higher average power levels, the thermal characteristics of standard materials is such that the heat deposited in the ceramic cannot be adequately removed by cooling around the edges as in most linear beam devices. Figure 7 shows a schematic diagram of a double disk window that uses a dielectric fluid to convectively face cool the disks.

Development of chemical-vapor-deposited (CVD) diamond windows eliminated thermal stresses as a limiting factor in gyrotrons [31]. CVD diamond is significantly stronger, and has a higher thermal conductivity and much lower RF loss than do other available materials

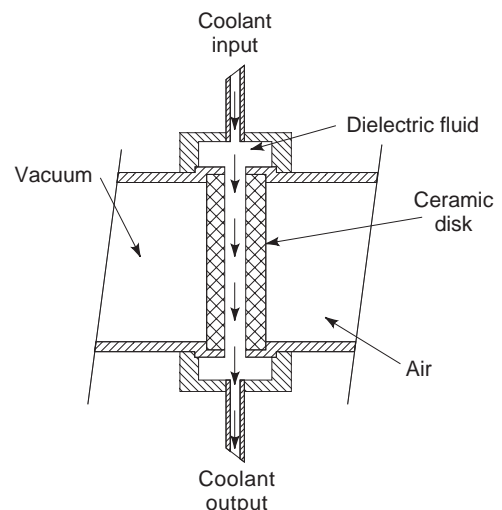


Figure 7. In the double-disk window, a dielectric fluid flows between the ceramic disks for enhanced cooling.

[32]. Consequently, it has become the window material used in all high-power gyrotrons. Unfortunately, the CVD manufacturing process is time-consuming and expensive. Currently, window ceramics for gyrotrons producing 1 MW or more of continuous power cost in excess of \$100,000. Efforts are underway to develop more efficient and less expensive methods for producing these windows.

4. AMPLIFIERS

While most gyro devices are oscillators, research is in progress to develop gyroamplifiers as drivers for linear accelerators [33,34] and for high-frequency, high-resolution radar [35]. While oscillator design is relatively straightforward, amplifier design presents several challenges. Since the circuits are typically overmoded, it becomes more difficult to prevent RF leakage through the drift regions between cavities. Also, the high cavity Q factors characteristic of gyrotron output cavities limit the bandwidth that can be achieved. While several amplifier configurations have been studied, the gyroklystron and the gyro-TWT (traveling-wave tube) have achieved the most success.

The gyroklystron consists of two or more cavities separated by drift spaces too small to propagate the operating mode. An azimuthal drift is imposed on the electrons by a sinusoidal energy modulation in the first cavity. These drifts are enhanced by intermediate buncher cavities, and the output cavity extracts the power from the azimuthally bunched electron beam. Most gyroklystrons employ cavity modes that are above the fundamental TE_{11} circular waveguide mode. Extreme care must be used to ensure that any RF power converted from the cavity mode to the TE_{11} mode is not allowed to propagate through the drift spaces and cause spurious oscillations. This also limits the circuit modes that can be used to those close to the fundamental (typically TE_{01} or TE_{02}) circuit modes. Gyroklystron bandwidths of 7% have been achieved with saturated gain of 20–40 dB. Operating efficiencies greater than 30% are common. An advanced, high-power, millimeter-wave radar system is currently under development by the U.S. Naval Research Laboratory that uses a 94-GHz gyroklystron with a 700 MHz bandwidth, 10% duty factor, and a saturated gain of 33 dB [1]. The device will be used for tactical radar applications, studies of cloud physics, propagation, and forward and backscatter studies [2].

In the gyro-TWT, an azimuthally bunched helical beam interacts with a traveling wave. If the periodicity and velocity of the electron bunches are such that synchronism occurs between the electrons and the traveling wave, cumulative bunching and energy extraction can occur. These amplifiers have considerably larger bandwidths than do gyroklystrons; however, they operate at lower efficiency (<20%) and generally produce less power.

Research has also been performed on gyro backward-wave oscillators, gyrotwistrons, and gyropeniotrons. The reader is referred to the Further Reading list at the end of this article for information on these devices.

5. CURRENT STATE OF THE ART

Gyrotrons are currently in development in several countries around the world, including Russia, Germany, France, Japan, and the United States. Currently, the highest-power gyrotron is a device jointly developed by Germany, France, and Switzerland to produce 1 MW of RF power in pulses lasting several minutes. The device, shown in Fig. 8, operates at 140 GHz and will be used in the stellerator Wendlestein 7-X currently under construction at IPP Greifswald, Germany. A total of 10 MW of RF power will be required for electron cyclotron heating of the stellerator plasma. Researchers recently reported achieving 850 kW in 3-min pulses, which were partially limited by the available power supply [36]. The gyrotron has also produced 970 kW for 11.8 s. Communications and Power Industries, Inc. in the United States produced several 1-MW, 10-s gyrotrons at 110 GHz. These are used for electron cyclotron heating of the DIII-D tokamak at General Atomics in San Diego, CA.

The current state of the art in gyroklystrons is the 94-GHz device built by Communications and Power Industries, Inc. for the WARLOCK radar system. This device produces a peak power of 100 kW and 10 kW of average power.



Figure 8. A 140-GHz, 1-MW gyrotron under development for the stellerator Wendlestein 7-X currently under construction at IPP Greifswald, Germany.

6. FUTURE DEVELOPMENT

Most gyrotron research is focused on increasing the output power, primarily for ECRH and ECCD of fusion plasmas. It is anticipated that several tens of megawatts of RF power will be required for heating these plasmas. It is desirable to maximize the output power of the individual gyrotrons to reduce the number of gyrotrons required. The current goal is to develop gyrotrons producing 1–2 MW of CW power at frequencies between 100 and 170 GHz.

Researchers in the United States are developing a 1.5-MW, long-pulse gyrotron operating at 110 GHz. This device will be used for electron cyclotron heating of the DIII-D tokamak operated by General Atomics in San Diego, CA. The gyrotron will use a conventional cylindrical cavity, diode electron gun, and a depressed collector.

As the required output power increases, the size of the cavity must increase to maintain and handle the RF currents in the walls. Increasing the cavity size increases the number of RF modes that can be excited, thereby increasing problems with mode competition. Above 1.5 MW, it becomes more attractive to utilize a coaxial cavity to decrease the number of competing modes. Researchers in Germany are developing a 2-MW coaxial gyrotron at 170 GHz for anticipated heating requirements for the next generation of fusion experiments. The device incorporates a depressed collector and quasioptical output [37]. Additional complications are introduced by the center conductor, which must be supported, aligned, and cooled within the vacuum envelope of the gyrotron.

Research is in progress to develop step-tunable gyrotrons for operation over increased frequency ranges. Since the gyrotron frequency is partially determined by the magnetic field, it becomes possible to use this characteristic to excite operating modes at different frequencies. As the magnitude of the magnetic field is varied, different operating modes are excited. The frequency of the gyrotron jumps to the resonant frequency of that particular mode [38,39]. A problem arises, however, with designing a ceramic window capable of operating over the required range of frequencies. Several alternatives are under development, including Brewster angle windows.

Amplifier research is focused on developing gyroamplifiers for high-resolution radar and for high-power linear accelerators. Current research goals for radar applications include bandwidth enhancement, increased efficiency, increased output power, and gains exceeding 30 dB. Accelerator applications do not require large bandwidths, but peak powers exceeding 100 MW at frequencies between 11 and 20 GHz and 10 MW devices at W band will be required. Figure 9 shows a 10-MW gyrokyklystron designed to operate at 91.392 GHz that is currently under development. High efficiency and reasonable gain will be major goals. Advances in gyrotron components, such as windows, electron guns, launcher systems, and depressed collectors, will also be applicable to amplifier development.

Research is in progress to develop gyrotrons for industrial heating applications, particularly for sintering of fine-grain ceramics. Studies indicate that microwave and millimeter sintering can produce extremely high heating rates or selective heating in multiphase systems, leading



Figure 9. A 10-MW, 91-GHz gyrokyklystron under development for high-power accelerator research.

to novel ceramic materials with compositions and microstructures not possible using standard techniques [40]. Several experiments are in progress to develop sources for these applications [41,42]. It is anticipated that other applications will materialize when efficient, cost effective sources are available.

BIBLIOGRAPHY

1. M. Blank, K. Felch, B. G. James, P. Borchard, P. Cahalan, T. S. Chu, H. Jory, B. G. Danly, B. Levush, J. P. Calame, K. T. Nguyen, and D. E. Pershing, Development and demonstration of high-average power W-band gyro-amplifiers for radar applications, *IEEE Trans. Plasma Sci.* **30**(3) (June 2002).
2. B. G. Danly, J. Cheung, V. Gregers-Hansen, G. Linde, and M. Ngo, WARLOC: A high-power millimeter wave radar, *Proc. 27th Int. Conf. Infrared and Millimeter Waves*, San Diego, CA, Sept. 2002, pp. 233–234.
3. J. M. Neilson, R. L. Ives, M. Read, M. Mizuhara, T. Robinson, D. Marsden, W. Lawson, and B. Hogan, Development status of a 10 MW, 91 GHz gyrokyklystron, *Proc. 27th Int. Conf. Infrared and Millimeter Waves*, San Diego, CA, Sept. 2002, pp. 237–238.
4. W. Lawson, B. Hogan, E. S. Gouveia, B. Huebschman, and V. L. Granatstein, Improved design of a frequency-doubling KU-Band gyrokyklystron experiment, *Proc. 27th. Int. Conf.*

- Infrared and Millimeter Waves*, San Diego, CA, Sept. 2002, pp. 203–204
5. R. O. Twiss, Radiation transfer and the possibility of negative absorption in radio astronomy, *Austral. J. Phys.* **11** (1958).
 6. J. Schneider, Stimulated emission of radiation by relativistic electrons in a magnetic field, *Phys. Rev. Lett.* **2** (1959).
 7. A. V. Gaponov, Interaction between electron fluxes and electromagnetic waves in waveguides, *Izv. Vyssh. Uchebn. Zaved. Radiofizika* **2** (1959).
 8. R. H. Pantell, Electron beam interaction with fast waves, *Proc. Symp. Millimeter Waves, Microwave Res. Inst. Symp. Ser.* **9** (1959).
 9. K. K. Chow and R. H. Pantell, The cyclotron resonance backward wave oscillator, *Proc. IRE* **48**(11) (1960).
 10. I. B. Bott, Tunable sources of millimeter and submillimeter wave radiation, *Proc. IEEE* **52**(3) (1964).
 11. I. B. Bott, A powerful source of millimeter wavelength electromagnetic radiation, *Phys. Lett.* **14**(4) (1965).
 12. J. Feinsten, Research on electronic interaction with the fields of mirror resonators, *Proc. 5th Int. Congress on Microwave Tubes*, 1964.
 13. J. L. Hirschfield and J. M. Wachtel, Electron cyclotron maser, *Phys. Rev. Lett.* **12**(19) (1964).
 14. M. I. Petelin, Relativism in microwave electronics, *Proc. 22nd Int. Conf. Infrared and Millimeter Waves*, Wintergreen, VA, July 1997.
 15. L. A. Vaynshteyn, Open resonators and open waveguides, *Sovetskoye Radio* (1966).
 16. Y. V. Bykov et al., paper presented at VII Inter-collegiate Conf. SHF Electronics, Tomsk, 1972.
 17. S. N. Vlasov, L. I. Zagryadskaya, and M. I. Petelin, Transformation of a whispering gallery mode, propagating in a circular waveguide, into a beam of waves. *Radio Eng. Electron. Phys.* **20** (Oct. 1975).
 18. V. A. Flyagin, A. V. Gaponov, M. I. Petelin, and V. K. Yulpatov, *IEEE Trans. Microwave Theory Tech.* **MTT-25**:512–521 (1977).
 19. J. L. Hirshfield and V. L. Granatstein, The electron cyclotron maser—an historical survey, *IEEE Trans. Microwave Theory Tech.* **MTT-25**(6) (June 1977).
 20. J. L. Hirshfield, Gyrotrons, *Infrared and Millimeter Waves*, Vol. 1, Academic Press, 1979, Chapter 1.
 21. R. S. Symons and H. R. Jory, Cyclotron resonance devices, *Adv. Electron. Electron Phys.* **55** (1981).
 22. J. M. Baird, Gyrotron theory, in V. L. Granatstein and Alexoff, eds., *High Power Microwave Sources*, Artech House, Norwood, MA, 1987.
 23. V. A. Flyagin, A. V. Gaponov, M. I. Petelin, and V. K. Yulpatov, The gyrotron, *IEEE Trans. Microwave Theory Tech.* **MTT-25**:514–521 (1977).
 24. A. S. Gilmour, *Principles of Traveling Wave Tubes*, Artech House, Boston, MA, 1994, pp. 103–149.
 25. K. Hackett and C. W. Beason, Active denial technology, *AFRL Technol. Horiz.*, 9–10 (Sept. 2001).
 26. M. Thumm, *State-of-the-Art of High Power Gyro-Devices and Free Electron Masers, Update 1995*, Forschungszentrum Karlsruhe, ITP, Assoc. (FZK-Euratom Postfach 3640, D-676021 Karlsruhe, Germany).
 27. K. E. Kreischer, B. Danly, T. B. Schutter, and R. J. Temkin, The design of megawatt gyrotrons, *IEEE Trans. Plasma Sci.* **PS-13**(6) (Dec. 1985).
 28. A. Singh, S. Rajapatirana, Y. Men, V. L. Granatstein, R. L. Ives, and A. J. Anatolak, Design of a multistage depressed collector system for 1-MW CW gyrotrons—Part I: Trajectory control of primary and secondary electrons in a two-stage depressed collector, *IEEE Trans. Plasma Sci.* **27**(2): 490–502 (April 1999).
 29. R. L. Ives, A. Singh, M. Mizuhara, R. Schumacher, J. Neilson, M. Gaudreau, J. Casey, and V. L. Granatstein, Design of a multistage depressed collector system for 1MW CW gyrotrons—Part II: System considerations, *IEEE Trans. Plasma Sci.* **27**(2):503–511 (April 1999).
 30. L. Neilson and R. Bunger, Surface integral equation analysis of quasi-optical launchers using the fast multipole method, *Proc. 27th Int. Conf. Infrared and Millimeter Waves*, San Diego, CA, Sept. 2002, pp. 119–120.
 31. K. Sakamoto, A. Kasugai, M. Tsuneoka, K. Takahashi, and T. Imai, High power 170 GHz gyrotron with synthetic diamond window, *Rev. Sci. Instrum.* **70**(1):208–212 (Jan. 1999).
 32. M. Thumm, Development of output windows for high-power long-pulse gyrotrons and EC wave applications, *Int. J. Infrared Millimeter Waves* **19**:3–14 (1998).
 33. V. L. Granatstein and W. Lawson, Gyro-amplifiers as candidate RF drivers for TeV linear colliders, *IEEE Trans. Plasma Sci.* **24**(3) (June 1996).
 34. J. Cheng, X. Xu, W. Lawson, J. P. Calame, M. Castle, B. P. Hogan, V. L. Granatstein, G. S. Nusinovich, and M. Reiser, Experimental studies of a high-power, x-band coaxial gyro-klystron, *IEEE Trans. Plasma Sci.* **PS-27**:1175–1187 (1999).
 35. B. G. Danly, M. Blank, J. P. Calame, B. Levush, K. Nguyen, D. Pershing, J. Petillo, T. A. Hargraves, R. B. True, A. J. Theiss, G. R. Good, K. Felch, T. S. Chu, H. Jory, P. Borchard, B. G. James, W. G. Lawson, and T. M. Antonsen, Development of a W-Band gyro-klystron for radar applications, *Conf. Digest 23rd Int. Conf. Infrared and Millimeter Waves*, Colchester, UK, Sept. 1998, pp. 32–33.
 36. G. Dammertz, S. Alberti, et al., Progress of the 1MW, 140 GHz, CW gyrotron for W7-X, *Proc. 27th Int. Conf. Infrared and Millimeter Waves*, San Diego, CA, Sept. 2002, pp. 3–4.
 37. B. Piosczyk, A. Arnold, H. Budig, G. Dammertz, O. Dumbrajs, O. Drumm, M. V. Kartikeyan, M. Kuntz, M. Thumm, and X. Yang, Experimental results and technical requirements for a 2 MW CW 170 GHz coaxial cavity gyrotron, *Proc. 27th Int. Conf. Infrared and Millimeter Waves*, San Diego, CA, Sept. 2002, pp. 7–8.
 38. T. Idehara, I. Ogawa, S. Mitsudo, M. Pereyaslavets, N. Nishida, and K. Yoshida, Development of frequency tunable, medium power gyrotrons as submillimeter wave radiation sources, *IEEE Trans. Plasma Sci.* **PS-27**:340–354 (1999).
 39. V. E. Zapevalov, S. S. Bogdashov, A. V. Chirkov, G. G. Denisov, A. N. Kuffin, et al., Optimization of the frequency step tunable 105–170 GHz 1 MW gyrotron prototype, *Proc. 27th Int. Conf. Infrared and Millimeter Waves*, San Diego, CA, Sept. 2002, pp. 1–2.
 40. J. P. Calame, Y. Carmel, D. Gershon, and E. Pert, The microwave sintering of ceramics: New insights, models, and applications based on realistic ceramic microstructures, *Proc. 22nd Int. Conf. Infrared and Millimeter Waves*, Wintergreen, VA, July 1997.
 41. I. I. Antakov, I. G. Facheve, V. I. Kurbatov, E. V. Sokolov, E. A. Solujanova, and E. V. Zasytkin, A KA-Band and W-Band 10kW CW high efficiency gyrotrons for materials processing, *Proc. 3rd Int. Workshop on Strong Microwaves in Plasmas*, Moscow/St. Petersburg, August 1996.

42. A. W. Fliflet, R. P. Fischer, A. K. Kinkead, and R.W. Bruce, Pulsed 35 GHz gyrotron with overmoded applicator for sintering experiments, *Microwave Process. Mat. V.* **430** (1996).

FURTHER READING

The following periodicals contain most of the publications related to gyrotron research and development:

IEEE Transactions on Plasma Science
IEEE Transactions on Microwave Theory and Techniques
International Journal of Electronics
International Journal of Infrared and Millimeter Wave Proceedings of the International Conference on Infrared and Millimeter Waves (yearly)
Proceedings of the International Conference on Plasma Sciences (yearly)
Izv. Vyssh. Uchebn. Zaved. Izvestiya Vysshikh Uchebnykh Zavedni

Additional sources of information are listed below.

- R. B. Miller, *An Introduction to the Physics of Intense Charged Particle Beams*, Plenum Press, New York and London, 1982, pp. 238–249.
- H. R. Jory, E. Lien, and R. S. Symons, *Final Report of Millimeter Wave Study Program*, performed for Oak Ridge National Laboratory on Order Y-12 11Y-499438V, Varian Associates, Inc., Palo Alto, CA, 1975.
- K. R. Chu, *Theory of Electron Cyclotron Maser Interactions in a Cavity at the Harmonic Frequencies*, NRL Memorandum Report 3672, Naval Research Laboratory, Washington, DC, 1977.
- R. S. Symons and H. R. Jory, Small-signal theory of gyrotrons and gyrokystrons, *Proc. 7th Symp. Engineering Problems in Fusion Research*, 1977.
- H. R. Jory, F. I. Friedlander, S. J. Hegji, J. P. Shively, and R. S. Symons, Gyrotrons for high-power millimeter wave generation, *Proc. 7th Symp. Engineering Problems in Fusion Research*, 1977.
- V. L. Bratman, M. A. Moiseev, M. I. Petelin, and R. E. Erm, Theory of gyrotrons with a nonfixed structure of the high frequency field, *Izv. Vyssh. Uchebn. Zaved. Radiofiz.* **16**(4) (1973).
- A. V. Gaponov, A. L. Goldenberg, D. P. Grigorev, I. M. Orlova, T. B. Pankratova, and M. I. Petelin, Induced synchrotron radiation of electrons in cavity resonators, *Sov. Phys. JETP Lett.* **2**(9) (1965).

- M. Caplan and C. Thorington, Improved computer modeling of magnetron injection guns for gyrotrons, *Int. J. Electron.* **51** (1998).
- J. Neilson, P. E. Latham, M. Caplan, and W. Lawson, Determination of the resonant frequency in a complex cavity using scattering matrix formulation, *IEEE Trans. Microwave Theory Tech.* **37** (1989).
- V. A. Flyagin and G. S. Nusinovich, Gyrotron oscillators, *Proc. IEEE* **76** (1988).
- K. Felch, H. Huey, and H. Jory, Gyrotrons for ECH applications, *J. Fusion Energy* **9**(1) (1990).
- Y. V. Bykov, A. L. Goldenberg, L. V. Nikolaev, M. M. Ofitserov, and M. I. Petelin, Experimental investigations of a gyrotron with whispering gallery modes, *Izv. Vyssh. Uchebn. Zaved. Radiofiz.* **18**(10):1544–1546 (1975).
- J. B. Mead, Millimeter wave radars for atmospheric remote sensing, *Proc. 22nd Int. Conf. Infrared and Millimeter Waves*, Wintergreen, VA, July 1997.

PENIOTRONS

- G. Dohler, *Int. J. Electron.* **56**:617–627 (1984).
- P. Vitello, *IEEE Trans. Microwave Theory Tech.* **32**:917–921 (1984).
- L. Zhou, M. Jiang, H. Guo, and Y. He, *Int. J. Electron.* **57**:1065–1075 (1984).

AMPLIFIERS

- K. R. Chu and A. T. Drobot, *Theory and Single Wave Simulation of the Gyrotron Traveling Wave Amplifier Operating at Cyclotron Harmonics*, NRL Memorandum Report 3788, Naval Research Laboratory, Washington, DC, 1978.
- K. R. Chu, A. T. Drobot, V. L. Granatstein, and J. L. Seftor, Characteristics and optimum operating parameters of a gyrotron traveling wave amplifier, *IEEE Trans. Microwave Theory Tech.* **27**(2):178–187 (1979).
- G. G. Denisov, V. L. Bratman, A. D. R. Phelps, and V. Samsonov, Gyro-TWT with a helical operating waveguide: New possibilities to enhance efficiency and frequency bandwidth, *Proc. 22nd Int. Conf. Infrared and Millimeter Waves*, Wintergreen, VA, July 1997.
- Q. S. Wang, D. B. McDermott, and N. C. Luhmann, Operation of a stable 200 kW second-harmonic gyro-TWT amplifier, *IEEE Trans. Plasma Sci.* **24**(3):700–706 (1996).
- E. V. Zasytkin, B. Levush, M. Blank, E. V. Sokolav, and I. I. Antakov, Study of X-band three stage gyrotwystron amplifier, *Proc. 22nd Int. Conf. Infrared and Millimeter Waves*, Wintergreen, VA, July 1997.

HANKEL TRANSFORMS

M. RAHMAN

The object of this article is to introduce integral transform of a particular type, called the *Hankel transform*, and to illustrate the *use* of this method by means of examples. The treatment is that of a review article and as such is not meant to be exhaustive; its aim is to give a concatenated account of known results rather than present new ones. The emphasis throughout is on those results that are of frequent occurrence in boundary value problems of mathematical physics, but some indication is also given for possible theoretical investigations.

Proofs are either omitted entirely or only the key steps are outlined. Readers interested in rigorous proofs of some of the statements in this article are referred to the books by Sneddon [1,2], Davies [3], Andrews and Shivamoggi [4], and Zayed [5].

The organization of the article is as follows. In the first section, we illustrate the motivation behind introducing the Hankel transform and then give a precise definition of the Hankel transform and its inversion. The next two sections are devoted to the derivation of some basic properties of Hankel transforms. In the following section, we explore the connection between Fourier and Hankel transforms. Parseval's relation for Hankel transforms is then deduced. We next introduce the modified operator of Hankel transforms. An overview of Erdelyi-Kober operators and their generalization by Sneddon and Cooke is given. We then derive Beltrami-type relations and give a brief account of their generalization by Sneddon. An extensive account is given of the applications of Erdelyi-Kober and Cooke operators to dual, triple, and quadruple integral equations involving Hankel transforms. A number of issues that arise in connection with applications of Hankel transforms to many physical problems is then addressed. For the convenience of the readers, a compendium is given in the last section of the basic theorems and formulas of Hankel transforms that are of frequent occurrence in applications.

1. THE HANKEL TRANSFORM

The Hankel transform arises naturally as a result of using the method of separation of variables to boundary value problems of mathematical physics in cylindrical coordinates, for example, boundary value problems for the Laplace and Helmholtz equations involving half-spaces and regions bounded by parallel planes. In general, application of this technique is relevant to problems leading to the integration of equations of the type

$$\frac{\partial^2 \phi}{\partial r^2} + \frac{1}{r} \frac{\partial \phi}{\partial r} - \frac{v^2}{r^2} \phi + L\phi = f(r, \dots)$$

where L is a linear operator that does not contain r , and $f(r, \dots)$ is a prescribed function.

To illustrate this, let us consider the axisymmetric solution $\phi(r, z)$ of Laplace's equation

$$\frac{\partial^2 \phi}{\partial r^2} + \frac{1}{r} \frac{\partial \phi}{\partial r} + \frac{\partial^2 \phi}{\partial z^2} = 0 \tag{1}$$

in the half-space $r > 0, z > 0$, which satisfies the boundary condition

$$\phi(r, 0) = f(r) \tag{2}$$

where $f(r)$ is a prescribed function of r .

In addition, the solution of the problem must satisfy the regularity conditions so that the field decays as $R \rightarrow \infty$, where $R = \sqrt{r^2 + z^2}$.

Assuming that the solution can be represented in the separated-variable form

$$\phi(r, z) = \phi_1(r)\phi_2(z)$$

we find that Eq. (1) reduces to

$$\frac{1}{\phi_1} \frac{d^2 \phi_1}{dr^2} + \frac{1}{\phi_1 r} \frac{d\phi_1}{dr} = -\frac{1}{\phi_2} \frac{d^2 \phi_2}{dz^2} \tag{3}$$

Since the left-hand side of Eq. (3) depends only on r while the right-hand side only on z , we conclude that they must be equal to a constant, say, $\lambda = -s^2$, where s is a real quantity. Thus, we obtain two ordinary differential equations

$$\begin{aligned} \frac{d^2 \phi_1}{dr^2} + \frac{1}{r} \frac{d\phi_1}{dr} + s^2 \phi_1 &= 0 \\ \frac{d\phi_2}{dz^2} - s^2 \phi_2 &= 0 \end{aligned} \tag{4}$$

The first of these equations is that of Bessel [6], whose solution bounded at the origin is

$$\phi_1(r) = A_1(s)J_0(sr)$$

where $A_1(s)$ is an arbitrary function of s and $J_0(sr)$ is the zeroth-order Bessel function of the first kind.

On the other hand, the solution of the second relation of Eq. (4) ensuring a decaying field is given by

$$\phi_2(z) = A_2(s)e^{-sz}$$

Therefore, the solution of Eq. (1) is

$$\phi(r, z) = A(s)J_0(sr)e^{-sz} \tag{5}$$

where $A(s)$ is an arbitrary function of s . Readers can easily verify that the other cases, namely, $\lambda = 0$ and $\lambda = s^2$ (s is a real quantity), must be ignored, since they do not ensure a decaying field as $R \rightarrow \infty$.

The solution of Eq. (5) has the property that, if $s > 0$, $\phi(r, z) \rightarrow 0$ as $R \rightarrow \infty$. By simple superposition, we can therefore construct the solution of the form

$$\phi(r, z) = \int_0^\infty sA(s)J_0(sr)e^{-sz} ds \tag{6}$$

The condition of Eq. (2) will be satisfied if

$$f(r) = \int_0^\infty sA(s)J_0(sr) ds \tag{7}$$

yielding an equation for determining the unknown function $A(s)$. It will be shown later that $A(s)$ is given by the formula

$$A(s) = \int_0^\infty rf(r)J_0(sr) dr \tag{8}$$

which on substitution into Eq. (6) then formally gives the solution of our problem.

The formulas in Eqs. (7) and (8) define a transformation pair called the *Hankel transform of order zero*. We now give a formal definition of the Hankel transform of an arbitrary order of a function.

Given a real function $f(r)$ defined in the interval $(0, \infty)$, suppose that

1. $f(r)$ is piecewise continuous and of bounded variation in every finite subinterval $[a, b]$, where $0 < a < b < \infty$
2. The integral

$$\int_0^\infty \sqrt{r}|f(r)|dr < \infty$$

Then, the *Hankel transform of the v th order* of the function $f(r)$ satisfying the preceding conditions is defined as

$$\tilde{f}_v(s) = \int_0^\infty rf(r)J_v(sr) dr \tag{9}$$

which we shall write as

$$\tilde{f}_v(s) = \mathcal{H}_v[f(r); r \rightarrow s] \tag{10}$$

Sometimes, for the sake of brevity, we shall write this notation as $\mathcal{H}_v[f(r); s]$, $\mathcal{H}_v[f(r)]$, or simply $\mathcal{H}_v f(r)$.

Readers should note that since the kernel of the Hankel transform is the Bessel function, the theory of Hankel transforms relies heavily on the theory of the Bessel functions. Perhaps, for this reason, in some literature, this transform is called Bessel transformation or Fourier-Bessel transformation.

The *Hankel inversion theorem* states that if the function $f(r)$ satisfies the preceding conditions, then

$$\int_0^\infty s\tilde{f}_v(s)J_v(sr) ds = f(r) \tag{11}$$

If the function has a jump discontinuity at a point, then the right-hand side of Eq. (11) should be replaced by the sum

$$\frac{1}{2}[f(r+0) + f(r-0)]$$

We shall not give a proof of the Hankel inversion theorem here. Interested readers are referred to the book by Sneddon [2].

It follows from Eqs. (10) and (11) that

$$f(r) = \int_0^\infty sJ_v(sr) ds \int_0^\infty r_0f(r_0)J_v(sr_0) dr_0 \tag{12}$$

$$0 < r < \infty, \quad v > -\frac{1}{2}$$

Equation (12) is called *Hankel's integral theorem*.

Evidently, Eq. (11) can be written as

$$f(r) = \mathcal{H}_v^{-1}[\tilde{f}_v(s); s \rightarrow r]$$

which, in the notation of Eq. (10), is equivalent to

$$f(r) = \mathcal{H}_v[\tilde{f}_v(s); s \rightarrow r]$$

hence establishing the rule $\mathcal{H}_v = \mathcal{H}_v^{-1}$. Thus, we see that if $v > -\frac{1}{2}$, there is a symmetric relationship between a function and its Hankel transform of order v , in the sense that if $\tilde{f}_v(s)$ is the Hankel transform of order v of a function $f(r)$, then $f(r)$ is the Hankel transform of order v of $\tilde{f}_v(s)$.

Extensive tables have been constructed of the Hankel direct and inverse transforms of functions usually encountered in applications [e.g., 7].

As in the case of other types of integral transforms, the use of Hankel transform has many advantages, for example, it is applicable to both homogeneous and inhomogeneous problems, it simplifies calculations and singles out the purely computational part of the solution, and it allows us to construct an operational calculus for a given kernel by using tables of direct and inverse transforms.

An extensive account of applications of the Hankel transform as well as other integral transforms to problems in mathematical physics was given by Sneddon [1,2,8] and Lebedev et al. [9]. Perhaps it is Sneddon who may quite justifiably be regarded as the most ardent proponent of using the method of integral transforms—in particular, Hankel transform—to various boundary value problems of mathematical physics.

2. SOME ELEMENTARY PROPERTIES OF HANKEL TRANSFORMS

Property 1.

$$\begin{aligned} \mathcal{H}_{-m}[f(r); r \rightarrow s] &= (-1)^m \mathcal{H}_m[f(r); r \rightarrow s] \\ &\times (m = \pm 1, \pm 2, \dots, \pm n, \dots) \end{aligned}$$

Proof of this property follows from the fact that [6]

$$J_{-m}(sr) = (-1)^m J_m(sr)$$

Property 2.

$$\mathcal{H}_v[f(ar); r \rightarrow s] = a^{-2} \mathcal{H}_v\left[f(r); r \rightarrow \frac{s}{a}\right]$$

Proof: By definition, we have

$$\mathcal{H}_v[f(ar); r \rightarrow s] = \int_0^\infty rf(ar) J_v(sr) dr \tag{13}$$

By making a change of variable $ar = \rho$, we reduce the integral in Eq. (13) to the form

$$\begin{aligned} \mathcal{H}_v[f(ar); r \rightarrow s] &= a^{-2} \int_0^\infty \rho f(\rho) J_v(sa^{-1}\rho) d\rho \\ &= a^{-2} \mathcal{H}_v\left[f(r); r \rightarrow \frac{s}{a}\right] \end{aligned}$$

Property 3.

$$\begin{aligned} \mathcal{H}_v[r^{-1}f(r); r \rightarrow s] \\ = \frac{s}{2v} [\tilde{f}_{v-1}(s) + \tilde{f}_{v+1}(s)] \quad (v \neq 0) \end{aligned}$$

Proof: From the recurrence relation for the Bessel functions [6]

$$j_{v-1}(x) - \frac{2v}{x} J_v(x) + J_{v+1}(x) = 0$$

we deduce

$$\begin{aligned} \mathcal{H}_v[r^{-1}f(r); r \rightarrow s] &= \int_0^\infty f(r) J_v(sr) dr \\ &= \frac{s}{2v} \left(\int_0^\infty rf(r) J_{v-1}(sr) dr \right. \\ &\quad \left. + \int_0^\infty rf(r) J_{v+1}(sr) dr \right) \\ &= \frac{s}{2v} [\tilde{f}_{v-1}(s) + \tilde{f}_{v+1}(s)] \end{aligned}$$

Property 4. The shift formula for the Hankel transforms is

$$\mathcal{H}_n[f(r-a)H(r-a); r \rightarrow s] = \sum_{m=-\infty}^\infty \alpha_m \tilde{f}_m(s)$$

where

$$\begin{aligned} \alpha_m &= J_{n-m}(sa) + \frac{1}{2}as[(m+1)^{-1}J_{n-m-1}(sa) \\ &\quad + (m-1)^{-1}J_{n-m+1}(sa)] \end{aligned}$$

Proof of this property is given in the book of Sneddon [2].

It should be mentioned here that it is not possible to obtain a simple shift formula for the Hankel transforms. This is primarily because the addition formula for the Bessel functions, that is, the Neumann–Lommel addition formula [6]

$$J_n(x+y) = \sum_{m=-\infty}^\infty J_m(x)J_{n-m}(y)$$

is much more complicated than the addition formula for the exponential functions e^x and e^{ix} for the Laplace and Fourier transforms.

3. THE HANKEL TRANSFORMS OF DERIVATIVES OF A FUNCTION

In applications of Hankel transforms to physical problems, it is necessary to have expressions for the Hankel transforms of the derivatives of a function or a combination of them, through the Hankel transforms of the function itself. Using the definition of Hankel’s transform and the formula for integrating by parts, we obtain

$$\begin{aligned} \mathcal{H}_v\left[\frac{df}{dr}; s\right] &= \int_0^\infty r \frac{df}{dr} J_v(sr) dr \\ &= [rf(r)J_v(sr)]_0^\infty \\ &\quad - \int_0^\infty \frac{\partial}{\partial r} [rJ_v(sr)] f(r) dr \end{aligned} \tag{14}$$

The first term on the right vanishes provided that the function $f(r)$ is such that

$$\lim_{r \rightarrow 0} r^{v+1}f(r) = 0, \quad \lim_{r \rightarrow \infty} \sqrt{r}f(r) = 0$$

It follows from the arguments leading to the proof of the Hankel inversion theorem [2] that the second of these conditions holds for any $f(r)$ whose Hankel transform exists. Therefore, the first term on the right in Eq. (14) vanishes if

$$f(r) = o(r^{-v-1}), \quad r \rightarrow 0$$

where o is the Landau’s symbol of order.

From the theory of Bessel functions [6,10], we have

$$\begin{aligned} \frac{\partial}{\partial r} [rJ_v(sr)] &= J_v(sr) + rJ'_v(sr) \\ J'_v(sr) &= srJ_{v-1}(sr) - vJ_v(sr) \end{aligned}$$

so that Eq. (14) now takes the following form:

$$\mathcal{H}_v \left[\frac{df}{dr}; r \right] = (v - 1) \int_0^\infty f(r) J_v(sr) dr - s \int_0^\infty rf(r) J_{v-1}(sr) dr \tag{15}$$

However, the integral on the right is the $(v - 1)$ th-order Hankel transform of $f(r)$:

$$\int_0^\infty rf(r) J_{v-1}(sr) dr = \mathcal{H}_{v-1}[f(r); r \rightarrow s]$$

Thus, Eq. (15) takes the form

$$\mathcal{H}_v \left[\frac{df}{dr}; r \rightarrow s \right] = (v - 1) \int_0^\infty f(r) J_v(sr) dr - s \mathcal{H}_{v-1}[f(r); r \rightarrow s] \tag{16}$$

The first term on the right is obviously the v th-order Hankel transform of the function $r^{-1}f(r)$. However, our objective is to express everything in terms of the Hankel transform of the function $f(r)$. This can be achieved by utilizing the following relation [10]:

$$J_v(sr) = \frac{1}{2v} [J_{v-1}(sr) + J_{v+1}(sr)] \tag{17}$$

Inserting Eq. (17) into Eq. (16), after some arrangements, we finally obtain the following important relationship:

$$\begin{aligned} \mathcal{H}_v \left[\frac{df}{dr}; r \rightarrow s \right] &= -s \frac{v+1}{2v} \mathcal{H}_{v-1}[f(r); r \rightarrow s] \\ &+ s \frac{v-1}{2v} \mathcal{H}_{v+1}[f(r); r \rightarrow s] \end{aligned} \tag{18}$$

Expressions for Hankel transforms of the higher derivatives of the function $f(r)$ may be deduced by repeated application of the formula in Eq. (18). For instance, we obtain

$$\begin{aligned} \mathcal{H}_v \left[\frac{d^2f}{dr^2}; r \rightarrow s \right] &= \frac{s^2(v+1)}{4(v-1)} \mathcal{H}_{v-2}[f(r)] \\ &- \frac{s^2(v^2-3)}{2(v^2-1)} \mathcal{H}_v[f(r)] \\ &+ \frac{s^2(v-1)}{4(v+1)} \mathcal{H}_{v+2}[f(r)] \end{aligned} \tag{19}$$

In applications of Hankel transforms to many physical problems, it becomes necessary to have available the

formula for Hankel transform of the differential operator:

$$\mathcal{B}_v = \frac{d^2}{dr^2} + \frac{1}{r} \frac{d}{dr} - \frac{v^2}{r^2}$$

Integrating by parts and assuming that $df/dr = o(r^{-1})$, we find

$$\int_0^\infty r \frac{d^2f}{dr^2} J_v(sr) dr = - \int_0^\infty \frac{df}{dr} \frac{d}{dr} [r J_v(sr)] dr$$

so that

$$\begin{aligned} \int_0^\infty r \left(\frac{d^2f}{dr^2} + \frac{1}{r} \frac{df}{dr} \right) J_v(sr) dr &= -s \int_0^\infty \frac{df}{dr} r J'_v(sr) dr \\ &= s \int_0^\infty f(r) \frac{d}{dr} [r J'_v(sr)] dr \end{aligned} \tag{20}$$

Equation (20) was derived on the assumption that the function $rf(r) \rightarrow 0$ as $r \rightarrow 0$ or ∞ .

We know from the theory of Bessel functions [6,10] that the function $J_v(sr)$ satisfies the differential equation

$$\frac{d}{dr} [r J'_v(sr)] = - \left(s^2 - \frac{v^2}{r^2} \right) r J_v(sr) \tag{21}$$

On substitution of Eq. (21) into Eq. (20), we obtain the following formula:

$$\begin{aligned} \int_0^\infty r \left(\frac{d^2f}{dr^2} + \frac{1}{r} \frac{df}{dr} - \frac{v^2}{r^2} f \right) J_v(sr) dr &= -s^2 \int_0^\infty rf(r) J_v(sr) dr \\ &= -s^2 \mathcal{H}_v[f(r); r \rightarrow s] \end{aligned} \tag{22}$$

An immediate consequence of Eq. (22) is the formula

$$\begin{aligned} \int_0^\infty r \left(\frac{d^2f}{dr^2} + \frac{1}{r} \frac{df}{dr} \right) J_0(sr) dr &= -s^2 \mathcal{H}_0[f(r); r \rightarrow s] \end{aligned} \tag{23}$$

To illustrate the use of the properties of Hankel transforms, let us consider the classic problem of determining the potential at any point in the field induced by an electrified disk of radius a , whose potential is raised to ϕ_0 (ϕ_0 is a constant). The problem is known as *Weber's problem*. A discussion of this problem can be found in the books by Jeans [11] and Smythe [12]. The problem reduces to that of solving Laplace's equation in Eq. (1) with the boundary conditions

$$\begin{aligned} \phi(r, 0) &= \phi_0, \quad 0 \leq r < a \\ \left. \frac{\partial \phi}{\partial z} \right|_{z=0} &= 0, \quad r > a \end{aligned} \tag{24}$$

The second boundary condition in Eq. (24) expresses the symmetry of the field with respect to the plane of the disk, that is, the plane $z = 0$.

To solve the problem, we use the zeroth-order Hankel transform of the function $\phi(r, z)$:

$$\phi(r, z) = \mathcal{H}_0[\tilde{\phi}(s, z); s \rightarrow r] \tag{25}$$

Applying the transformation in Eq. (25) to Eq. (1) and making use of the relation of Eq. (23), we obtain the following ordinary differential equation

$$\frac{d^2 \tilde{\phi}}{dz^2} - s^2 \tilde{\phi} = 0$$

whose solution is

$$\tilde{\phi}(s, z) = A(s)e^{-sz} + B(s)e^{sz} \tag{26}$$

where $A(s)$ and $B(s)$ are some unknown functions of s .

Because of symmetry, it is sufficient to consider the half-space $z \geq 0$ only. Then, since the field must vanish at infinity (regularity conditions), we must set $B = 0$, so that Eq. (26) reduces to

$$\tilde{\phi}(s, z) = A(s)e^{-sz}$$

Therefore, our formal solution of the problem takes the form

$$\phi(r, z) = \mathcal{H}_0[A(s)e^{-sz}; s \rightarrow r] \tag{27}$$

Utilizing the boundary conditions in Eq. (24), we get the following equations to determine the unknown function $A(s)$:

$$\begin{aligned} \mathcal{H}_0[A(s); s \rightarrow r] &= \phi_0, & 0 \leq r < a \\ \mathcal{H}_0[sA(s); s \rightarrow r] &= 0, & r > a \end{aligned}$$

or writing in integral form

$$\begin{aligned} \int_0^\infty sA(s)J_0(sr)ds &= \phi_0, & 0 \leq r < a \\ \int_0^\infty s^2A(s)J_0(sr)ds &= 0, & r > a \end{aligned} \tag{28}$$

Equations of the type in Eq. (28) are called *dual-integral equations*. A systematic treatment of this kind of equations will be discussed later. Here, we give a rather heuristic solution. Gradshteyn and Ryzhik [13] provide the following integrals:

$$\begin{aligned} \int_0^\infty \frac{\sin s}{s} J_0(sr) ds &= \frac{\pi}{2}, & 0 \leq r < a \\ \int_0^\infty (\sin s) J_0(sr) ds &= 0, & r > a \end{aligned} \tag{29}$$

A comparison of Eqs. (28) and with Eqs. (29) shows that the solution for $A(s)$ is

$$A(s) = \frac{2\phi_0}{\pi} \frac{\sin s}{s} \tag{30}$$

Putting Eq. (30) into Eq. (27), we obtain the solution of our problem as

$$\phi(r, z) = \frac{2\phi_0}{\pi} \int_0^\infty \frac{\sin s}{s} J_0(sr) e^{-sz} ds \tag{31}$$

The uniqueness of Eq. (31) follows from the physical contents of the problem.

4. RELATION BETWEEN FOURIER AND HANKEL TRANSFORMS

In this section, the relationship between Hankel and Fourier transforms of a function of two variables is explored. Specifically, we shall see that there exists a close relationship between the double Fourier transform of a function of two variables of a particular type and its Hankel transform.

Consider a function $f(x_1, x_2)$ that is a function of $r = x_1^2 + x_2^2$ only. The double Fourier transform $F(\alpha_1, \alpha_2)$ is

$$\begin{aligned} F(\alpha_1, \alpha_2) &= \frac{1}{2\pi} \int_{-\infty}^\infty \int_{-\infty}^\infty f(\sqrt{x_1^2 + x_2^2}) \\ &\times e^{i(\alpha_1 x_1 + \alpha_2 x_2)} dx_1 dx_2 \end{aligned} \tag{32}$$

If we make the substitutions into Eq. (32)

$$\begin{aligned} x_1 &= r \cos \theta, & x_2 &= r \sin \theta, \\ \alpha_1 &= s \cos \varphi, & \alpha_2 &= s \sin \varphi \end{aligned}$$

then, since

$$dx_1 dx_2 = r dr d\theta, \quad \alpha_1 x_1 + \alpha_2 x_2 = rs \cos(\theta - \varphi)$$

the double integral in Eq. (32) reduces to

$$F(\alpha_1, \alpha_2) = \frac{1}{2\pi} \int_0^\infty r f(r) dr \int_0^{2\pi} e^{irs \cos(\theta - \varphi)} d\theta \tag{33}$$

Since the inner integral on the right is 2π -periodic, it does not depend on φ , that is

$$\int_0^{2\pi} e^{irs \cos(\theta - \varphi)} d\theta = \int_0^{2\pi} e^{irs \cos \theta} d\theta$$

which is equal to $2\pi J_0(rs)$ [6,10], where $s = \sqrt{\alpha_1^2 + \alpha_2^2}$. We therefore see that the function $F(\alpha_1, \alpha_2)$ is a function of s only and may be written as

$$F(s) = \int_0^\infty r f(r) J_0(sr) dr = \mathcal{H}_0[f(r); r \rightarrow s] \tag{34}$$

which, of course, is the zeroth-order Hankel transform of $f(r)$. On the other hand, by the Fourier inversion theorem, we have

$$f(x_1, x_2) = \frac{1}{2\pi} \int_{-\infty}^{\infty} \int_{-\infty}^{\infty} F(\alpha_1, \alpha_2) \times e^{-i(\alpha_1 x_1 + \alpha_2 x_2)} d\alpha_1 d\alpha_2$$

Using the same substitution as before, the preceding expression can be reduced to the following formula:

$$f(r) = \int_0^{\infty} sF(s)J_0(sr) ds = \mathcal{H}_0[F(s); s \rightarrow r] \quad (35)$$

Formulas in Eqs. (34) and (35) obviously express the Hankel inversion theorem in the special case where $v = 0$.

The preceding results can be easily generalized in case of n -dimensional Fourier transforms. If the functions $f(x_1, x_2, \dots, x_n)$ is function only of $r = \sqrt{x_1^2 + x_2^2 + \dots + x_n^2}$, then its Fourier transform $F(\alpha_1, \alpha_2, \dots, \alpha_n)$ is a function of s only where $s = \sqrt{\alpha_1^2 + \alpha_2^2 + \dots + \alpha_n^2}$. More specifically, the following relationship holds:

$$s^{(n-1)/2}F(s) = \int_0^{\infty} r[r^{(n-1)/2}f(r)] \times J_{(n-1)/2}(sr) dr \quad (36)$$

For proof, the readers are referred to the book by Sneddon [1].

It therefore follows from Eq. (36) that $s^{(n-1)/2}F(s)$ is the Hankel transform of order $(n - 1)/2$ of the function $r^{(n-1)/2}f(r)$.

Similarly, by n -dimensional Fourier inversion theorem, it can be shown that

$$r^{(n-1)/2}f(r) = \int_0^{\infty} s[s^{(n-1)/2}F(s)] \times J_{(n-1)/2}(sr) ds \quad (37)$$

If we write

$$\phi(r) = r^{(n-1)/2}f(r), \quad \tilde{\phi}_v(s) = s^{(n-1)/2}F(s),$$

$$v = \frac{n - 1}{2}$$

then Eqs. (36) and (37) take the following form:

$$\tilde{\phi}_v(s) = \int_0^{\infty} r\phi(r)J_v(sr) dr = \mathcal{H}_v[\phi(r); r \rightarrow s]$$

$$\phi(r) = \int_0^{\infty} s\tilde{\phi}_v(s)J_v(sr) ds = \mathcal{H}_v[\tilde{\phi}_v(s); s \rightarrow r]$$

These formulas obviously define the v th-order Hankel transformation pair for the function $\phi(r)$.

5. PARSEVAL'S RELATION FOR HANKEL TRANSFORMS

Suppose that

$$\tilde{f}_v(s) = \mathcal{H}_v[f(r); r \rightarrow s], \quad \tilde{g}_v(s) = \mathcal{H}_v[g(r); r \rightarrow s]$$

Then, putting formally, we obtain the equation

$$\int_0^{\infty} s\tilde{f}_v(s)\tilde{g}_v(s) ds = \int_0^{\infty} s\tilde{f}_v(s) ds \int_0^{\infty} xg(x)J_v(sx) dx \quad (38)$$

$$= \int_0^{\infty} xg(x) dx \int_0^{\infty} s\tilde{f}_v(s)J_v(sx) ds$$

in which the inner integral, by Hankel's inversion theorem, is obviously equal to $f(r)$.

Equation (38) then yields the following formula:

$$\int_0^{\infty} s\tilde{f}_v(s)\tilde{g}_v(s) ds = \int_0^{\infty} xf(x)g(x) dx \quad (39)$$

The expression Eq. (39) is evidently the Parseval relation for the Hankel transform. As in the case of other integral transforms, such a Fourier, Laplace, Mellin, and Kantorovich-Lebedev transforms, Parseval's relation is a very useful tool in many theoretical and practical investigations.

It should be noted here that a general Parseval relation involving Hankel transforms of two functions of different orders does not exist. This is primarily because the Neumann-Rahman formula [6,14] for the product of two first-kind Bessel functions of different orders

$$J_{m+n}(sr)J_n(sr_0)$$

$$= \frac{1}{\pi} \int_0^{\pi} \left\{ \cos(n\varphi)T_m\left(\frac{r-r_0 \cos \varphi}{R}\right) + \frac{r_0 \sin n\varphi \sin \varphi}{R} \right.$$

$$\left. \times U_{m-1}\left(\frac{r-r_0 \cos \varphi}{R}\right) \right\} J_m(R) d\varphi, \quad U_{-1}(\dots) = 0 \quad (40)$$

where $R = \sqrt{r^2 + r_0^2 - 2rr_0 \cos \varphi}$, $T_m(\dots)$ and $U_{m-1}(\dots)$ are the Chebyshev polynomials of the first and second kinds, respectively, is much more complicated than the simplest rule for the product of two exponential functions (kernels of Laplace and Fourier transforms) of different powers.

As an example of application of Parseval's relation in Eq. (39), let us evaluate the integral

$$\mathcal{H}_v[x^{-2}J_v(ax); x \rightarrow s], \quad v > -\frac{1}{2}$$

Taking $f(x) = x^v H(a - x) (a > 0)$ and $g(x) = x^v H(b - x) (b > 0)$, where $\mathcal{H}(\dots)$ is the step function, we have

$$\tilde{f}_v(s) = \int_0^a x^{v+1} J_v(sx) dx;$$

$$\tilde{g}_v(s) = \int_0^b x^{v+1} J_v(sx) dx$$

These integrals are easily evaluated [13] as

$$\begin{aligned} \tilde{f}_v(s) &= \frac{a^{v+1}}{s} J_{v+1}(sa), \\ \tilde{g}_v(s) &= \frac{b^{v+1}}{s} J_{v+1}(sb) \end{aligned}$$

Now, using Parseval's relation in Eq. (39), we obtain

$$\begin{aligned} (ab)^{v+1} \int_0^\infty s^{-1} J_{v+1}(sa) J_{v+1}(sb) ds \\ = \int_0^{\min(a,b)} x^{2v+1} dx \end{aligned}$$

Assuming that $0 < a < b$, we find that (13)

$$\begin{aligned} \int_0^\infty s^{-1} J_{v+1}(sa) J_{v+1}(sb) ds \\ = \frac{1}{2(v+1)} \left(\frac{a}{b}\right)^{v+1} \\ 0 < a < b, v > -\frac{1}{2} \end{aligned}$$

It therefore follows from the preceding equation that

$$\begin{aligned} \mathcal{H}_v [x^{-2} J_{v+1}(ax); x \rightarrow s] \\ = \begin{cases} \frac{1}{2v} \left(\frac{s}{a}\right)^v, & 0 < s < a \\ \frac{1}{2v} \left(\frac{a}{s}\right)^v, & s > a \end{cases} \end{aligned}$$

where, $v > \frac{1}{2}$.

6. THE HANKEL OPERATOR

In many theoretical investigations, it is more convenient to use a modified operator of Hankel transform $S_{\eta,\alpha}$ instead of the operator \mathcal{H}_v . This modified Hankel operator is defined by the formula

$$S_{\eta,\alpha}[f(t); x] = 2^\alpha x^{-\alpha} \mathcal{H}_{2\eta+\alpha}[t^{-\alpha} f(t); t \rightarrow x] \tag{41}$$

so that

$$S_{\eta,\alpha}[f(t); x] = 2^\alpha x^{-\alpha} \int_0^\infty t^{1-\alpha} f(t) J_{2\eta+\alpha}(xt) dt \tag{42}$$

If we write

$$\tilde{f}_{\eta,\alpha}(x) = S_{\eta,\alpha}[f(t); x] \tag{43}$$

then from Eq. (41), we obtain

$$\mathcal{H}_{2\eta+\alpha}[t^{-\alpha} f(t); x] = 2^{-\alpha} x^\alpha \tilde{f}_{\eta,\alpha}(x) \tag{44}$$

Applying Hankel's inversion, we deduce from Eq. (43) that

$$f(t) = 2^{-\alpha} t^\alpha \mathcal{H}_{2\eta+\alpha}[x^\alpha \tilde{f}_{\eta,\alpha}(x); t]$$

or writing out the above expression in full, we obtain

$$f(t) = S_{\eta+\alpha,-\alpha}[\tilde{f}_{\eta,\alpha}(x); t]$$

thus establishing the rule

$$S_{\eta,\alpha}^{-1} = S_{\eta+\alpha,-\alpha} \tag{45}$$

In applications, the following relationship is useful

$$S_{\eta,\alpha} f(x) = 2^{-\lambda} x^\lambda S_{\eta\lambda/2,\alpha+\lambda}[x^\lambda f(x)]$$

the validity of which can be easily proved by writing out both sides of the equation using the definition in Eq. (42).

7. THE ERDELYI-KOBER OPERATORS OF FRACTIONAL INTEGRATION

In this section, we present a brief exposition of the so-called Erdelyi-Kober operators of fractional integrations [15–17] and their generalization due to Sneddon and Erdelyi [8,18] and Cooke [19,20]. We next illustrate applications of these operators to the solution of dual-, triple- and quadruple-integral equations involving Hankel transforms, which arise in many boundary value problems of mathematical physics, especially electrostatics and electromagnetic scattering. The description here closely follows Sneddon [21].

In a series of papers [15–17], Erdelyi and Kober investigated properties of the fractional integral

$$\frac{x^{-\eta-\alpha+1}}{\Gamma(\alpha)} \int_0^x (x-t)^{\alpha-1} t^{\eta-1} f(t) dt \quad (\alpha > 0, \eta > 0)$$

which is a generalization of Riemann's integral

$$\frac{1}{\Gamma(\alpha)} \int_0^x (x-t)^{\alpha-1} f(t) dt$$

and Weyl's integral

$$\frac{x^\alpha}{\Gamma(\alpha)} \int_x^\infty (t-x)^{\alpha-1} t^{-\alpha-\eta} f(t) dt \quad (\alpha > 0, \eta > 0)$$

7.1. Definitions and Basic Results

If $\alpha > 0, \eta > -\frac{1}{2}$, we define the operator $I_{\eta,\alpha}$ by the equation

$$\begin{aligned} I_{\eta,\alpha} f(x) \\ = \frac{2x^{-2\alpha-2\eta}}{\Gamma(\alpha)} \int_0^x (x^2 - u^2)^{\alpha-1} u^{2\eta+1} f(u) du \end{aligned}$$

$I_{\eta,0}$ is the identity operator, and if $\alpha < 0$, we define $I_{\eta,\alpha}$ by the relation

$$I_{\eta,\alpha}f(x) = x^{-2\eta-2\alpha-1}D_x^n x^{2\eta+2\alpha+2n+1}I_{\eta,\alpha+n}f(x)$$

where n is a positive integer such that $0 < \alpha + n < 1$ and D_x is the differential operator

$$D_x = \frac{d}{dx}x^{-1}$$

Similarly, $\alpha > 0, \eta > -\frac{1}{2}$, we define the operator $K_{\eta,\alpha}$ by the equation

$$\begin{aligned} K_{\eta,\alpha}f(x) &= \frac{2x^{2\eta}}{\Gamma(\alpha)} \int_x^\infty (u^2 - x^2)^{\alpha-1} u^{-2\alpha-2\eta+1} f(u) du \end{aligned}$$

$K_{\eta,0}$ is the identity operator, and if $\alpha < 0$, we define $K_{\eta,\alpha}$ by the equation

$$K_{\eta,\alpha}f(x) = (-1)^n x^{2\eta-1} D_x^n x^{2n-2\alpha+1} K_{\eta-n,\alpha+n} f(x)$$

Operators $I_{\eta,\alpha}$ and $K_{\eta,\alpha}$ are called Erdelyi-Kober operators.

We next establish some properties of these operators. If we assume that $\alpha > 0, \beta > 0$, we have

$$\begin{aligned} I_{\eta,\alpha}I_{\eta+\alpha,\beta}f(x) &= \frac{2x^{-2\eta-2\alpha}}{\Gamma(\alpha)} \int_0^x (x^2 - u^2)^{\alpha-1} u^{2\eta+1} du \frac{2u^{-2\eta-2\alpha-2\beta}}{\Gamma(\beta)} \\ &\times \int_0^u (u^2 - t^2)^{\beta-1} t^{2\eta+2\alpha+1} f(t) dt \end{aligned}$$

Interchanging the order of integration and using the result (13)

$$\begin{aligned} &2 \int_t^x (x^2 - u^2)^{\alpha-1} (u^2 - t^2)^{\beta-1} u^{-2\alpha-2\beta+1} du \\ &= \frac{\Gamma(\alpha)\Gamma(\beta)}{\Gamma(\alpha+\beta)} t^{-2\alpha} x^{-2\beta} (x^2 - t^2)^{\alpha+\beta-1} \end{aligned}$$

we obtain

$$\begin{aligned} I_{\eta,\alpha}I_{\eta+\alpha,\beta}f(x) &= \frac{2x^{-2\eta-2\alpha-\beta}}{\Gamma(\alpha+\beta)} \int_0^x t^{2\eta+1} (x^2 - t^2)^{\alpha+\beta-1} f(t) dt \end{aligned}$$

The expression on the right is equal to $I_{\eta,\alpha+\beta}$, which follows from its definition, thus establishing the rule

$$I_{\eta,\alpha}I_{\eta+\alpha,\beta} = I_{\eta,\alpha+\beta} \tag{46}$$

Similarly, it can be shown that

$$K_{\eta,\alpha}K_{\eta+\alpha,\beta} = K_{\eta,\alpha+\beta} \tag{47}$$

The preceding relations are valid for $\alpha > 0, \beta > 0$, but it is a simple exercise to show that they are also valid for negative values of α and β . Also, it can be shown from the theory of integral equations of Abel type [8] that the inverse of the Erdelyi-Kober operators are given by the formulas

$$I_{\eta,\alpha}^{-1} = I_{\eta+\alpha,-\alpha}, \quad K_{\eta,\alpha}^{-1} = K_{\eta+\alpha,-\alpha} \tag{48}$$

The following formulas hold, whose validity can be proved very easily:

$$\begin{aligned} I_{\eta,\alpha}\{x^{2\beta}f(x)\} &= x^{2\beta}I_{\eta+\beta,\alpha}f(x) \\ K_{\eta,\alpha}\{x^{2\beta}f(x)\} &= x^{2\beta}K_{\eta+\beta,\alpha}f(x) \end{aligned}$$

The following relationships hold between the Erdelyi-Kober and Hankel operators:

$$\begin{aligned} I_{\eta+\alpha,\beta}S_{\eta,\alpha} &= S_{\eta,\alpha+\beta}, \quad K_{\eta,\alpha}S_{\eta+\alpha,\beta} = S_{\eta,\alpha+\beta} \\ S_{\eta+\alpha,\beta}S_{\eta,\alpha} &= I_{\eta,\alpha+\beta}, \quad S_{\eta,\alpha}S_{\eta+\alpha,\beta} = K_{\eta,\alpha+\beta} \\ S_{\eta+\alpha,\beta}I_{\eta,\alpha} &= S_{\eta,\alpha+\beta}, \quad S_{\eta,\alpha}K_{\eta+\alpha,\beta} = S_{\eta,\alpha+\beta} \end{aligned} \tag{49}$$

The proofs of these identities are based on the properties of Bessel functions and are given in the book by Davies [3].

7.2. The Cooke Operators

Cooke [19,20] has defined the operators

$$\begin{pmatrix} b \\ a \end{pmatrix} I_{\eta,\alpha}$$

and

$$\begin{pmatrix} d \\ c \end{pmatrix} K_{\eta,\alpha}$$

by the formulas

$$\begin{aligned} &\begin{pmatrix} b \\ a \end{pmatrix} I_{\eta,\alpha}f(x) \\ &= \begin{cases} \frac{2x^{-2\alpha-2\eta}}{\Gamma(\alpha)} \int_a^b (x^2 - u^2)^{\alpha-1} u^{2\eta+1} f(u) du, & \alpha > 0 \\ f(x), & \alpha = 0 \\ \frac{x^{-2\alpha-2\eta-1}}{\Gamma(1+\alpha)} \frac{d}{dx} \int_a^b (x^2 - u^2)^\alpha u^{2\eta+1} f(u) du, & -1 < \alpha < 0 \end{cases} \end{aligned} \tag{50}$$

for $0 < a < b < \infty$ and

$$\begin{aligned} & \begin{pmatrix} d \\ c \end{pmatrix} K_{\eta,\alpha} f(x) \\ &= \begin{cases} \frac{2x^{2\eta}}{\Gamma(\alpha)} \int_c^d (u^2 - x^2)^{\alpha-1} u^{-2\alpha-2\eta+1} f(u) du, & \alpha > 0 \\ f(x), & \alpha = 0 \\ \frac{-x^{2\eta-1}}{\Gamma(1+\alpha)} \frac{d}{dx} \int_c^d (u^2 - x^2)^\alpha u^{-2\alpha-2\eta+1} f(u) du, & -1 < \alpha < 0 \end{cases} \end{aligned} \tag{51}$$

for $0 < x < c < d$. It will be observed that these operators are related to the Erdelyi-Kober operators by the relations

$$\begin{pmatrix} x \\ 0 \end{pmatrix} I_{\eta,\alpha} = I_{\eta,\alpha}, \quad \begin{pmatrix} \infty \\ x \end{pmatrix} K_{\eta,\alpha} = I_{\eta,\alpha}$$

Cook [19,20] also defined the operators L and M by the equations

$$\begin{aligned} & \begin{pmatrix} x & b \\ c & a \end{pmatrix} L_{\eta,\alpha} f(x) = \begin{pmatrix} x \\ c \end{pmatrix} I_{\eta,\alpha}^{-1} \begin{pmatrix} b \\ a \end{pmatrix} I_{\eta,\alpha} f(x) \\ & \begin{pmatrix} d & b \\ x & a \end{pmatrix} M_{\eta,\alpha} f(x) = \begin{pmatrix} d \\ x \end{pmatrix} K_{\eta,\alpha}^{-1} \begin{pmatrix} b \\ a \end{pmatrix} K_{\eta,\alpha} f(x) \end{aligned} \tag{52}$$

and showed that if $a < b < c < x$, then

$$\begin{aligned} & \begin{pmatrix} x & b \\ c & a \end{pmatrix} L_{\eta,\alpha} f(x) = \frac{2 \sin(\pi\alpha)}{\pi} x^{-2\eta} (x^2 - c^2)^{-\alpha} \\ & \quad \times \int_a^b \frac{(c^2 - t^2)^\alpha t^{2\eta+1}}{x^2 - t^2} f(t) dt \end{aligned} \tag{53}$$

and that if $x < d < a < b$, then

$$\begin{aligned} & \begin{pmatrix} d & b \\ x & a \end{pmatrix} M_{\eta,\alpha} f(x) = \frac{2 \sin(\pi\alpha)}{\pi} x^{2\eta+2\alpha} (d^2 - x^2)^{-\alpha} \\ & \quad \times \int_a^b \frac{(t^2 - d^2)^\alpha t^{-2\alpha-2\eta+1}}{t^2 - x^2} f(t) dt \end{aligned} \tag{54}$$

8. BELTRAMI-TYPE RELATIONS

A classic problem of electrostatics concerns that of determining the potential of the electrostatic field due to a circular disk whose potential is prescribed. One way to solve this problem is to determine the charge density q on the disk and then to calculate the potential at any field

point \mathbf{r} by evaluating the integral

$$\int_S \frac{q(\mathbf{R}')}{|\mathbf{R} - \mathbf{R}'|} dS'$$

over the surface of the disk. In the case of axisymmetry, that is, when the prescribed potential $\phi(r)$ is a function of r only, Beltrami [22] showed that the density of the surface charge is given by the formula

$$\begin{aligned} q(r) &= \frac{-1}{\pi r} \frac{d}{dr} \int_r^\infty \frac{xdx}{\sqrt{x^2 - r^2}} \frac{d}{dx} \\ & \quad \times \int_0^x \frac{y\phi(y) dy}{\sqrt{x^2 - y^2}}, \quad 0 \leq r \leq a \end{aligned} \tag{55}$$

where a is the radius of the disk.

Sneddon [23] showed that Beltrami's relation in Eq. (55) is a special case of a general relation between Hankel transforms. In particular, he showed that the expression

$$\mathcal{H}_\mu[s^\delta \mathcal{H}_\nu f(s); r]$$

can be expressed as a double integral involving $f(r)$, which is a generalization of the integral occurring on the right-hand side of Beltrami's relation in Eq. (55). By assigning particular values of the parameters μ , δ , and ν , we can deduce relations that are of interest in the investigations into axisymmetric boundary value problems of potential theory.

If we apply the operator $K_{\eta-\gamma,\gamma}$ to both sides of the first equation of Eqs. (49) and make use of the second relation of Eqs. (49), we obtain

$$K_{\eta-\gamma,\gamma} I_{\eta+\alpha,\beta} S_{\eta,\alpha} = S_{\eta-\gamma,\alpha+\beta+\gamma} \tag{56}$$

Equation (56) can be written in terms of Hankel transforms as follows:

$$\begin{aligned} & \mathcal{H}_{2\eta+\alpha+\beta-\gamma}[t^{-\alpha-\beta-\gamma} f(t); r] \\ &= \left(\frac{r}{2}\right)^{\alpha+\beta+\gamma} K_{\eta-\gamma,\gamma} I_{\eta+\alpha,\beta} 2^\alpha \\ & \quad \times x^{-\alpha} \mathcal{H}_{2\eta+\alpha}[t^{-\alpha} f(t); x] \end{aligned} \tag{57}$$

For $\alpha = 0$ $\beta = (\mu - \nu - \delta)/2, \eta = \nu/2$, Eq. (57) simplifies significantly

$$\begin{aligned} & \mathcal{H}_\mu[s^\delta \tilde{f}(s); r] \\ &= 2^\delta r^\delta K_{(\mu+\delta)/2, (\nu-\mu-\delta)/2} I_{\nu/2, (\mu-\nu-\delta)/2} \tilde{f}(r) \end{aligned} \tag{58}$$

Some special cases of formulas in Eq. (58) are of particular interest. If we set $\mu = \nu$, we obtain

$$\mathcal{H}_\mu[s^\delta \tilde{f}(s); r] = 2^\delta r^{-\delta} K_{(\mu+\delta)/2, -\delta/2} I_{\nu/2, -\delta/2} \tilde{f}(r) \tag{59}$$

Special cases of particular interest are given by assigning $\delta = \pm 1$ to Eq. (59); we then obtain

$$\begin{aligned} \mathcal{H}_v [s\tilde{f}_v(s); r] &= \frac{-2}{\pi} r^{v-1} \frac{d}{dr} \int_r^\infty \frac{x^{1-2v}}{\sqrt{x^2 - r^2}} \frac{d}{dx} \\ &\quad \times \int_0^x \frac{y^{v+1} f(y) dy}{\sqrt{x^2 - y^2}} \quad (v \geq 0) \\ \mathcal{H}_v [s^{-1}\tilde{f}(s); r] &= \frac{2}{\pi} r^v \int_r^\infty \frac{x^{-2v}}{\sqrt{x^2 - r^2}} \\ &\quad \times \int_0^x \frac{y^{v+1} f(y) dy}{\sqrt{x^2 - y^2}} \quad (v \geq 0) \end{aligned} \tag{60}$$

On the other hand, if we put $\mu = v + 1$ in Eq. (59), we obtain the relation

$$\begin{aligned} \mathcal{H}_{v+1} [s^\delta \tilde{f}_v(s); r] \\ = 2^\delta r^{-\delta} K_{(v+\delta+1)/2, (-1-\delta)/2} I_{v/2, (1-\delta)/2} f(r) \end{aligned}$$

The special case $\delta = 1$ corresponds to the well-known formula

$$\mathcal{H}_{v+1} [s\tilde{f}_v(s); r] = -r^v \frac{d}{dr} [r^{-v} f(r)] \tag{61}$$

Expressions corresponding to the particular values 0 and -1 of δ are, respectively,

$$\begin{aligned} \mathcal{H}_{v+1} [\tilde{f}_v(s); r] &= \frac{-2}{\pi} r^v \frac{d}{dr} \int_r^\infty \frac{x^{-2v} dx}{\sqrt{x^2 - r^2}} \int_0^x \frac{y^{v+1} f(y) dy}{\sqrt{x^2 - y^2}} \quad (v \geq 0) \\ \mathcal{H}_{v+1} [s^{-1}\tilde{f}_v(s); r] &= r^{-v-1} \int_0^r u^{v+1} f(u) du \quad (v \geq 0) \end{aligned} \tag{62}$$

Finally, if we set $\mu = v - 1$ in Eq. (59), we obtain the relation

$$\mathcal{H}_{v-1} [s^\delta \tilde{f}_v(s); r] = 2^\delta r^{-\delta} K_{(v-1+\delta)/2, (v-1-\delta)/2} f(r) \tag{63}$$

The most frequently occurring special cases of the formula in Eq. (63) are

$$\begin{aligned} \mathcal{H}_{v-1} [s\tilde{f}_v(s); r] &= r^{-v} \frac{d}{dr} [r^v f(r)] \quad (v \geq 1) \\ \mathcal{H}_{v-1} [\tilde{f}_v(s); r] &= \frac{2}{\pi} r^{v-1} \int_r^\infty \frac{x^{1-2v} dx}{\sqrt{x^2 - r^2}} \frac{d}{dx} \int_0^x \frac{y^{v+1} f(y) dy}{\sqrt{x^2 - y^2}} \\ &\quad (v \geq 1) \\ \mathcal{H}_{v-1} [s^{-1}\tilde{f}_v(s); r] &= r^{v-1} \int_r^\infty x^{1-v} f(x) dx \quad (v \geq 1) \end{aligned} \tag{64}$$

8.1. Beltrami's Relation for an Electrified Disk

As an application of Beltrami-type relations just derived, let us consider the problem of an electrified disk of radius a lying in the plane $z = 0$ with its center at the origin of the

coordinate system. Let the surface charge density be $q(r)$. Then in the half-space $z \geq 0$ the potential of the electrostatic field will be $\phi_+(r, z)$ and in the half-space $z \leq 0$, it will be $\phi_-(r, z)$, where

$$\phi_\pm(r, z) = \mathcal{H}_0 [\tilde{\phi}_0(s) e^{\pm sz}; r]$$

where

$$\tilde{\phi}_0(s) = \mathcal{H}_0 [\phi(r, 0); s]$$

The charge density on the plane $z = 0$ is given by the equation

$$q(r) = \frac{-1}{4\pi} \left(\frac{\partial \phi_+}{\partial z} - \frac{\partial \phi_-}{\partial z} \right)_{z=0}$$

and it immediately follows from this equation that

$$q(r) = \frac{1}{2\pi} \mathcal{H}_0 [s\tilde{\phi}_0(s); r] \tag{65}$$

From the first equation of Eqs. (60) then we deduce Beltrami's relation in Eq. (55). On the other hand, we could write Eq. (65) in the form

$$\phi(r, 0) = 2\pi \mathcal{H}_0 [s^{-1}\tilde{q}_0(s); r]$$

and then using the second relation of Eq. (60) deduce the equation

$$\phi(r, 0) = 4 \int_r^\infty \frac{dx}{\sqrt{x^2 - r^2}} \int_0^{\min(a, x)} \frac{yq(y) dy}{\sqrt{x^2 - y^2}}$$

Interchanging the order of integration, the last equation can be written as

$$\phi(r, 0) = \int_0^a \sigma(y) K(r, y) dy$$

where

$$K(r, y) = 4y \int_{\min(r, y)}^\infty \frac{du}{\sqrt{(u^2 - r^2)(u^2 - y^2)}}$$

9. DUAL-INTEGRAL EQUATIONS INVOLVING HANKEL TRANSFORMS

In the applications of the theory of Hankel transforms to the solution of boundary value problems of mathematical physics, it often happens that the problem may be reduced to the solution of a pair of simultaneous equations of the form

$$\begin{aligned} f(x) &= S_{\mu/2-\alpha, 2\alpha} [1 + k(x)]\psi(x); \\ g(x) &= S_{\nu/2-\beta, 2\beta} \psi(x) \end{aligned} \tag{66}$$

in which

$$f(x) = \begin{cases} f_1(x), & x \in I_1 = \{x : 0 < x < 1\} \\ f_2(x), & x \in I_2 = \{x : 1 < x < \infty\} \end{cases}$$

$$g(x) = \begin{cases} g_1(x), & x \in I_1 = \{x : 0 < x < 1\} \\ g_2(x), & x \in I_2 = \{x : 1 < x < \infty\} \end{cases}$$

The problem is as follows. Knowing the functions $k(x)[k(x) \rightarrow 0, x \rightarrow \infty]$, f_1 , and g_2 , is it possible to find the functions ψ , f_2 , and g_1 ? In the following, we consider the special case where $k(x) = 0$, but it is straightforward to generalize the results for $k(x) \neq 0$.

To solve the problem, Sneddon proposed the following trial solution:

$$\psi(x) = S_{\nu/2 + \beta, \mu/2 - \nu/2 - \alpha - \beta} h(x) \tag{67}$$

Putting Eq. (67) into Eqs. (65), we obtain

$$S_{\mu/2 - \alpha, 2\alpha} S_{\nu/2 + \beta, \mu/2 - \nu/2 - \alpha - \beta} h = f$$

$$S_{\nu/2 - \beta, 2\beta} S_{\nu/2 + \beta, \mu/2 - \nu/2 - \alpha - \beta} h = g$$

which can be rewritten, using the third and fourth relations of Eq. (49), as

$$I_{\nu/2 + \beta, \nu/2 - \nu/2 + \alpha - \beta} h = f$$

$$K_{\nu/2 - \beta, \mu/2 - \nu/2 - \alpha + \beta} h = g$$

when

$$h = I_{\nu/2 + \beta, \mu/2 - \nu/2 + \alpha - \beta}^{-1} f \tag{68}$$

$$h = K_{\nu/2 - \beta, \mu/2 - \nu/2 - \alpha + \beta}^{-1} g$$

Writing Eqs. (68) on the intervals I_1 and I_2 , we have

$$h_1(x) = \begin{pmatrix} x \\ 0 \end{pmatrix} I_{\nu/2 + \beta, \mu/2 - \nu/2 + \alpha - \beta}^{-1} f_1$$

$$h_2(x) = \begin{pmatrix} 1 \\ 0 \end{pmatrix} I_{\nu/2 + \beta, \mu/2 - \nu/2 + \alpha - \beta}^{-1} f_1$$

$$+ \begin{pmatrix} x \\ 1 \end{pmatrix} I_{\nu/2 + \beta, \mu/2 - \nu/2 + \alpha - \beta}^{-1} f_2$$

$$h_2(x) = \begin{pmatrix} \infty \\ x \end{pmatrix} K_{\nu/2 - \beta, \mu/2 - \nu/2 - \alpha + \beta}^{-1} g_2$$

$$h_1(x) = \begin{pmatrix} \infty \\ 1 \end{pmatrix} K_{\nu/2 - \beta, \mu/2 - \nu/2 - \alpha + \beta}^{-1} g_2$$

$$+ \begin{pmatrix} 1 \\ x \end{pmatrix} K_{\nu/2 - \beta, \mu/2 - \nu/2 - \alpha + \beta}^{-1} g_1 \tag{69}$$

Putting the first and third equations of Eqs. (69) into Eq. (67), we obtain the solution for $\psi(x)$. On the other hand, from the second and third equations of Eqs. (69), we deduce that

$$\begin{pmatrix} x \\ 1 \end{pmatrix} I_{\nu/2 + \beta, \mu/2 - \nu/2 + \alpha - \beta}^{-1} f_2$$

$$= \begin{pmatrix} \infty \\ x \end{pmatrix} K_{\nu/2 - \beta, \mu/2 - \nu/2 - \alpha + \beta}^{-1} g_2$$

$$- \begin{pmatrix} 1 \\ 0 \end{pmatrix} I_{\nu/2 + \beta, \mu/2 - \nu/2 + \alpha - \beta}^{-1} f_1$$

whence it follows by use of the L operator defined by Eq. (53) that

$$f_2 = \begin{pmatrix} x \\ 1 \end{pmatrix} I_{\nu/2 + \beta, \mu/2 - \nu/2 + \alpha - \beta}$$

$$\times \begin{pmatrix} \infty \\ x \end{pmatrix} K_{\nu/2 - \beta, \mu/2 - \nu/2 - \alpha + \beta}^{-1} g_2 \tag{70}$$

$$- \begin{pmatrix} x & 1 \\ 1 & 0 \end{pmatrix} L_{\nu/2 + \alpha, \nu/2 - \mu/2 + \beta - \alpha} f_1$$

Thus, f_2 is determined. Similarly, using the first and fourth equations of Eqs. (68), we obtain for g_1 the formula

$$g_1 = \begin{pmatrix} 1 \\ x \end{pmatrix} K_{\nu/2 - \beta, \mu/2 - \nu/2 - \alpha + \beta} I_{\nu/2 + \beta, \mu/2 - \nu/2 + \alpha - \beta} f_1$$

$$- \begin{pmatrix} 1 & \infty \\ x & 1 \end{pmatrix} M_{\nu/2 - \beta, \mu/2 - \nu/2 - \alpha + \beta} g_2 \tag{71}$$

Thus, the first two equations in Eqs. (69) and Eqs. (70) and (71) give the complete solution to our problem. The same procedure, applied to the case where $k(x) \neq 0$, yields

$$h_1 + E(x) = \begin{pmatrix} x \\ 0 \end{pmatrix} I^{-1} f_1 \quad (x \in I_1)$$

$$h_2 + E(x) = \begin{pmatrix} 1 \\ 0 \end{pmatrix} I^{-1} f_1 + \begin{pmatrix} x \\ 1 \end{pmatrix} I^{-1} f_2 \quad (x \in I_2)$$

$$\begin{aligned}
 h_2 &= \begin{pmatrix} \infty \\ x \end{pmatrix} K^{-1}g_2 \quad (x \in I_2) \\
 h_1 &= \begin{pmatrix} \infty \\ 1 \end{pmatrix} K^{-1}g_2 + \begin{pmatrix} 1 \\ x \end{pmatrix} K^{-1}g_1 \quad (x \in I_1)
 \end{aligned}
 \tag{72}$$

where

$$\begin{aligned}
 E(x) &= S_{\mu/2-\alpha, \nu/2+\beta+\alpha-\mu/2} \\
 &\times k S_{\nu/2+\beta, \mu/2-\nu/2-\alpha-\beta} h(x)
 \end{aligned}
 \tag{73}$$

The subscripts with the I and K in Eqs. (72) are the same as those in Eqs. (69). Further details are carried out for the special case where $\nu = \mu$, $\beta = 0$, $g_2 = 0$, which is the most frequently occurring case in applications. In this case, we find from Eqs. (72) that $h_2(x) = 0$ and $h_1(x)$ solves the integral equation

$$h_1(x) + E(x) = \begin{pmatrix} x \\ 0 \end{pmatrix} I_{\nu/2, \alpha}^{-1} f_1 \quad (x \in I_1)
 \tag{74}$$

where

$$\begin{aligned}
 E(x) &\equiv S_{\nu/2-\alpha, \alpha} k S_{\nu/2, -\alpha} h(x) \\
 &= 2^\alpha x^{-\alpha} \int_0^\infty t^{1-\alpha} k(t) 2^{-\alpha} t^\alpha J_{\nu-\alpha}(xt) dt \\
 &\int_0^1 u^{1+\alpha} h_1(u) J_{\nu-\alpha}(tu) du
 \end{aligned}$$

and inverting the order of intergration, we have

$$E(x) = x^{-\alpha} \int_0^1 u^{1+\alpha} K(x, u) h_1(u) du
 \tag{75}$$

where

$$K(x, u) = \int_0^\infty t k(t) J_{\nu-\alpha}(xt) J_{\nu-\alpha}(ut) dt
 \tag{76}$$

Since the functions h_1 and h_2 have been determined, it is possible to find the functions ψ , f_2 , and g_1 following the procedure for the case $k(x) = 0$. These details can be found in the papers by Sneddon [8] and Cooke [19,20].

9.1. An Example: Two Coaxial Electrified Circular Disks

The problem of two solid disks, each charged to a uniform potential ϕ_0 , was the subject of numerous research starting with Love's paper [24] (for references, see Cooke [19]). If the disks have different potentials the problem may be reduced to two separate problems, in one of which the potentials are equal and in the other they are equal and opposite. Assume that the disks have the same radii, equal to unity, and are situated in the planes $z = 0$ and $z = h$, where r , θ , and z are cylindrical coordinates. Then, the problem reduces to that of solving

Laplace's equation in Eq. (1) subject to the following boundary conditions:

$$\begin{aligned}
 \phi(r, 0) &= \phi_0, \quad 0 < r < 1 \\
 \phi(r, 0_-) &= \phi(r, 0_+), \quad 0 \leq r < \infty \\
 \frac{\partial \phi}{\partial z} \Big|_{z=0_-} &= \frac{\partial \phi}{\partial z} \Big|_{z=0_+}, \quad r > 1 \\
 \phi(r, h) &= \pm \phi_0, \quad 0 < r < 1 \\
 \phi(r, h_-) &= \phi(r, h_+), \quad 0 \leq r < \infty \\
 \frac{\partial \phi}{\partial z} \Big|_{z=h_-} &= \frac{\partial \phi}{\partial z} \Big|_{z=h_+}, \quad r > 1
 \end{aligned}
 \tag{77}$$

The sign in fourth of the preceding conditions is positive or negative according to whether the disks are of like or unlike potentials ϕ_0 .

The solution of the problem must satisfy the regularity conditions at infinity. Besides, in order to guarantee uniqueness of solution, it must satisfy the *edge condition* [25,26] so that the electric energy stored in any neighborhood of the sharp edge $r = 1$ be finite, which imposes the restriction that the surface charge density not grow more rapidly than $\rho^{-1+\tau}$ with $\tau > 0$ as $\rho \rightarrow 0$, where $\rho = 1 - r$.

It can be shown by using zeroth-order Hankel transform to Laplace's equation in Eq. (1) that the electrostatic field can be represented by the potential function

$$\phi(r, z) = H_0[\phi_0 s^{-1}(e^{-|z|s} + e^{-|z-h|s})A(s); s \rightarrow r]
 \tag{78}$$

which satisfies the second and fifth continuity conditions in Eqs. (77), the sign in Eq. (78) being positive or negative depending on whether the disks are of like or unlike potentials ϕ_0 .

We find that the third and sixth conditions in Eqs. (77) will be satisfied if the function $A(s)$ satisfies the equation

$$\mathcal{H}_0[A(s); s \rightarrow r] = 0, \quad r > 1
 \tag{79}$$

Using the second and fourth boundary conditions in Eqs. (77) and Eqs. (79), we obtain the following dual integral equations:

$$\begin{aligned}
 \mathcal{H}_0[s^{-1}(1 \pm e^{-hs})A(s); s \rightarrow r] &= 1, \quad 0 \leq r < 1 \\
 \mathcal{H}_0[A(s); s \rightarrow r] &= 0, \quad r > 1
 \end{aligned}
 \tag{80}$$

Using the modified operator of Hankel transform, we rewrite Eqs. (80) in the form

$$\begin{aligned}
 S_{-1/2, 1}[1 \pm k(r)]A(r) &= 1, \quad 0 \leq r < 1 \\
 S_{0, 0}A(r) &= 0, \quad r > 1
 \end{aligned}
 \tag{81}$$

where $k(s) = e^{-hs}$. Thus, for our problem

$$\alpha = \frac{1}{2}, \quad \mu = 0, \quad \beta = 0, \quad \nu = 0$$

$$f_1(r) = \frac{r}{2\phi_0}, \quad g_2(r) = 0$$

Therefore, following the procedure outlined in the previous section, we find that $h_2(r) = 0$ and $h_1(r)$ solves the following integral equation

$$h_1(r) + r^{-1/2} \int_0^1 u^{3/2} K(r, u) h_1(u) du$$

$$= \begin{pmatrix} r \\ 0 \end{pmatrix} I_{1/2, -1/2} f_1(r) \quad 0 \leq r < 1 \tag{82}$$

where

$$K(r, u) = \pm \int_0^\infty tk(t) J_{-1/2}(rt) J_{-1/2}(ut) dt$$

Writing $rh_1(r) = H(r)$, we reduce Eq. (82) to the following Fredholm integral equation of the second kind

$$H(r) + \int_0^1 H(u) N(r, u) du$$

$$= \begin{pmatrix} r \\ 0 \end{pmatrix} I_{1/2, -1/2} f_1(r) \tag{83}$$

where

$$N(r, u) = \pm \sqrt{ru} \int_0^\infty tk(t) J_{-1/2}(rt) J_{-1/2}(ut) dt \tag{84}$$

The kernel $N(r, u)$ in Eq. (84) can be evaluated in closed form:

$$N(r, u) = \pm \left(\frac{1}{(r+u)^2 + h^2} + \frac{1}{(r-u)^2 + h^2} \right) \tag{85}$$

The integral equation defined by Eqs. (83) and (85) can be solved numerically.

The surface density at any point of a disk in the plane $z = 0$ is equal to

$$\frac{-1}{4\pi} \left(\frac{\partial \phi}{\partial z} \right)_{z=0}$$

When both sides of the disk are taken into account, this gives for the total charge Q

$$Q = \frac{\phi_0}{2\pi} \int_0^1 2\pi r dr \int_0^\infty A(s) J_0(sr) ds$$

$$= \phi_0 \int_0^1 r g_1(r) dr$$

$$= \phi_0 \int_0^1 r \begin{pmatrix} 1 \\ r \end{pmatrix} K_{0, -1/2} h_1(r) dr \tag{86}$$

$$= -\frac{\phi_0}{\sqrt{\pi}} \int_0^1 dr \frac{d}{dr} \int_x^1 \frac{u^2 h_1(u) du}{\sqrt{u^2 - 1}}$$

$$= \frac{2\phi_0}{\pi} \int_0^1 \frac{u H(u) du}{\sqrt{u^2 - 1}}$$

Once the integral equation in Eq. (83) is solved for $H(r)$, the total charge can be found by evaluating the integral in Eq. (86) numerically and hence the capacity $C = Q/\phi_0$ can be found.

10. TRIPLE-INTEGRAL EQUATIONS INVOLVING HANKEL TRANSFORMS

As an example of the use of Cooke operators, we consider the solution of certain triple-integral equations involving Hankel transforms. The problem consists in finding a function $\Phi(\xi)$ satisfying

$$\int_0^\infty \Phi(\xi) J_\nu(\xi x) d\xi = G_1(x), \quad x \in I_1$$

$$\int_0^\infty \xi^{-2\alpha} [1 + k(\xi)] \Phi(\xi) J_\nu(\xi x) d\xi = F_2(x), \quad x \in I_2 \tag{87}$$

$$\int_0^\infty \Phi(\xi) J_\nu(\xi x) d\xi = G_3(x), \quad x \in I_3$$

where I_j ($j = 1, 2, 3$) denote, respectively, the intervals $(0, a)$, (a, b) and (b, ∞) with $0 < a < b$. The functions G_1 , F_2 , and G_3 are assumed to be prescribed. Assuming that

$$\Phi(\xi) = \xi \psi(\xi), \quad f(x) = \left(\frac{2}{x} \right)^{2\alpha} F(x),$$

$$g(x) = G(x)$$

and using the modified operator of the Hankel transform, we rewrite Eqs. (87) in the form

$$S_{\nu/2 - \alpha, 2\alpha} [1 + k(\xi)] \psi(\xi); x = f(x) \tag{88}$$

$$S_{\nu/2, 0} \psi(\xi) = g(x)$$

We first consider the case where $k = 0$, $g_1 = g_3 = 0$, $|\alpha| < 1$. There are two different ways of solving Eqs. (88), one proposed by Sneddon and the other by Borodachev.

10.1. The Sneddon Trial Solution

Sneddon proposed the following solution for the equations in Eq. (88):

$$\psi = S_{\nu/2, -\alpha} h \tag{89}$$

Then, putting Eq. (89) into Eq. (88), we find that

$$S_{\nu/2,0}\psi = K_{\nu/2,\alpha}h = g(x)$$

$$S_{\nu/2-\alpha,2\alpha}\psi = I_{\nu/2,-\alpha}h = f(x)$$

and solving for h , we obtain

$$h = I_{\nu/2,-\alpha}^{-1}f(x)$$

$$h = K_{\nu/2,\alpha}^{-1}g(x) \tag{90}$$

Now, suppose that $f(x) = f_1(x)$, $x \in I_1$, $f(x) = f_3(x)$, $x \in I_3$, and $g(x) = g_2(x)$, $x \in I_2$. We also write $h(x) = h_j(x)$, $x \in I_j$.

If we evaluate Eqs. (90) on I_3 and use $g_3 = 0$, We deduce that $h_3 = 0$. Similarly, if we evaluate Eq. (90) on I_1 , we have

$$f_1(x) = \begin{pmatrix} x \\ 0 \end{pmatrix} I_{\nu/2,\alpha} h_1(x) \tag{91}$$

and if we evaluate Eq. (90) on I_2 we have

$$h_2 = \begin{pmatrix} a \\ 0 \end{pmatrix} I_{\nu/2,\alpha}^{-1} f_1 + \begin{pmatrix} x \\ a \end{pmatrix} I_{\nu/2,\alpha}^{-1} f_2, \quad x \in I_2 \tag{92}$$

Putting Eq. (92) into Eq. (91) and using the L operator defined by Eq. (53), we obtain

$$h_2 = - \begin{pmatrix} x, & a \\ a, & 0 \end{pmatrix} L_{\nu/2,\alpha} h_1 + \begin{pmatrix} x \\ a \end{pmatrix} I_{\nu/2,\alpha}^{-1} f_2, \quad x \in I_2 \tag{93}$$

Now, evaluating Eq. (90) on I_2 and I_1 , respectively, we obtain the equations

$$g_2 = \begin{pmatrix} b \\ x \end{pmatrix} K_{\nu/2,-\alpha} h_2, \quad h_1 = \begin{pmatrix} b \\ a \end{pmatrix} K_{\nu/2,-\alpha}^{-1} g_2 \tag{94}$$

Putting first of the relation in Eq. (94) into the second and using M operator defined by Eq. (54), we obtain

$$h_1 = - \begin{pmatrix} a, & b \\ x, & a \end{pmatrix} M_{\nu/2,-\alpha} h_2 \quad (x \in I_1) \tag{95}$$

Equations (93) and (95) form a pair of simultaneous equations for the unknown functions h_1 and h_2 , but, by eliminating h_1 between them, we can derive a single Fredholm integral equation of the second kind for h_2 . Solving it, we can determine h_1 using Eq. (95).

The same procedure applied formally to the case in which $k(\xi) \neq 0, g_1 = g_3 = 0, |\alpha| < 1$ leads to the set of

simultaneous equations

$$h_1 + E = k_1(x \in I_1)$$

$$h_2 + E = - \begin{pmatrix} x, & a \\ a, & 0 \end{pmatrix} L_{\nu/2,\alpha} k_1 + \begin{pmatrix} x \\ a \end{pmatrix} I_{\nu/2,\alpha}^{-1} f_2 \quad (x \in I_2) \tag{96}$$

$$h_1 = - \begin{pmatrix} a, & b \\ x, & a \end{pmatrix} M_{\nu/2,-\alpha} h_2 \quad (x \in I_1)$$

where

$$E(x) \equiv S_{\nu/2-\alpha,\alpha} k S_{\nu/2-\alpha} h$$

$$= 2^\alpha x^{-\alpha} \int_0^\infty t^{1-\alpha} k(t) 2^{-\alpha} t^\alpha J_{\nu-\alpha}(xt) dt$$

$$\times \left(\int_0^a u^{1+\alpha} h_1(u) J_{\nu-\alpha}(tu) du \right.$$

$$+ \int_a^b u^{1+\alpha} h_2(u) J_{\nu-\alpha}(tu) du$$

$$\left. + \int_b^\infty u^{1+\alpha} h_3(u) J_{\nu-\alpha}(tu) du \right)$$

and inverting the order of integration in each of the three repeated integrals, we have

$$E(x) = x^{-\alpha} \int_0^\infty u^{1+\alpha} K(x, u) h(u) du \tag{97}$$

where

$$K(x, u) = \int_0^\infty tk(t) J_{\nu-\alpha}(xt) J_{\nu-\alpha}(ut) dt \tag{98}$$

Thus, we have three equations with three unknown h_1, h_2, k_1 . As before $h_3 = 0$. Solving for them, the unknown functions f_1 and f_3 can be found by the formulas

$$f_1 = \begin{pmatrix} x \\ 0 \end{pmatrix} I_{\nu,\alpha} k_1 \tag{99}$$

$$f = I_{\nu/2,\alpha} h + S_{\nu/2-\alpha,2\alpha} k S_{\nu/2,-\alpha} h$$

Equations (93) and (95) to (98) allow us to obtain the complete solution of the problem. (For further details, readers are referred to the papers by Cooke [19,20,27,28]).

10.2. The Borodachev Trial Solution

Borodachev [29] developed a different trial solution to solve the triple integral equations (87). He argued as follows. Assume that the solution of the equations has the form

$$\psi(\xi) = S_{\beta,\gamma} h \tag{100}$$

Eqs. (88), for the case $k(\xi)=0$, may be reduced to the following form

$$I_{\mu_1, \lambda_1} h = f, \quad K_{\mu_2, \lambda_2} h = g$$

which occur when

$$S_{v/2-\alpha} S_{\beta, \gamma} = I_{\mu_1, \lambda_1}, \quad S_{v/2, 0} S_{\beta, \gamma} = K_{\mu_2, \lambda_2} \quad (101)$$

Using the third and fourth relations of Eqs. (49), we infer that

$$\beta + \gamma = \frac{v}{2} - \alpha, \quad \mu_1 = \beta, \quad \lambda_1 = 2\alpha + \gamma$$

$$\beta = \frac{v}{2}, \quad \mu_2 = \frac{v}{2}, \quad \lambda_2 = \gamma$$

which yield

$$\beta = \frac{v}{2}, \quad \gamma = -\alpha, \quad \mu_1 = \frac{v}{2}, \quad \mu_2 = \frac{v}{2},$$

$$\lambda_1 = \alpha, \quad \lambda_2 = -\alpha$$

Thus, in this case Eq. (100) takes the form $\psi = S_{v/2, -\alpha} h$, that is, we have Sneddon's trial solution.

On the other hand, readers might note that Eqs. (88) can be reduced to the form

$$K_{\mu_3, \lambda_3} H = f, \quad I_{\mu_4, \lambda_4} H = g \quad (102)$$

Carrying out calculations similar to the ones done, we have

$$\beta = \frac{v}{2} + \alpha, \quad \gamma = -\alpha, \quad \mu_3 = \frac{v}{2} - \alpha, \quad \mu_4 = \frac{v}{2} + \alpha \quad (103)$$

$$\lambda_3 = \alpha, \quad \lambda_4 = -\alpha$$

Accordingly, in this case

$$\psi = S_{v/2+\alpha, -\alpha} H \quad (104)$$

Equation (104) is called Borodachev's trial solution.

We will now use Borodachev's trial solution to reduce the triple integral equations in Eq. (88) to a Fredholm integral equation of the second kind. Substituting Borodachev's trial solution in Eq. (104) into Eqs. (88), we obtain [see Eqs. (102) and (103)]

$$K_{v/2-\alpha, \alpha} H = f, \quad I_{v/2+\alpha, -\alpha} H = g,$$

whence

$$H = K_{v/2-\alpha, \alpha}^{-1} f, \quad H = I_{v/2+\alpha, -\alpha}^{-1} g \quad (105)$$

As before, for the sake of simplicity, we consider the case where $g_1 = g_3 = 0$. Then writing Eq. (105) for each

interval, we obtain

$$H_1 = \begin{pmatrix} x \\ 0 \end{pmatrix} I_{v/2+\alpha, -\alpha}^{-1} g_1 = 0$$

$$H_2 = \begin{pmatrix} a \\ 0 \end{pmatrix} I_{v/2+\alpha, -\alpha}^{-1} g_1 + \begin{pmatrix} x \\ a \end{pmatrix} I_{v/2+\alpha, -\alpha}^{-1} g_2$$

$$= \begin{pmatrix} x \\ a \end{pmatrix} I_{v/2+\alpha, -\alpha}^{-1} g_2$$

$$H_3 = \begin{pmatrix} a \\ 0 \end{pmatrix} I_{v/2+\alpha, -\alpha}^{-1} g_1 + \begin{pmatrix} b \\ a \end{pmatrix} I_{v/2+\alpha, -\alpha}^{-1} g_2$$

(106)

$$+ \begin{pmatrix} x \\ b \end{pmatrix} I_{v/2+\alpha, -\alpha}^{-1} g_3$$

$$= \begin{pmatrix} b \\ a \end{pmatrix} I_{v/2-\alpha, \alpha}^{-1} g_2$$

$$H_3 = \begin{pmatrix} \infty \\ x \end{pmatrix} K_{v/2-\alpha, \alpha}^{-1} f_3$$

$$H_2 = \begin{pmatrix} \infty \\ b \end{pmatrix} K_{v/2-\alpha, \alpha}^{-1} f_3 + \begin{pmatrix} b \\ x \end{pmatrix} K_{v/2-\alpha, \alpha}^{-1} f_2$$

From the second and fourth formulas in Eqs. (106), we deduce that

$$g_2 = \begin{pmatrix} x \\ a \end{pmatrix} I_{v/2+\alpha, -\alpha} H_2,$$

(107)

$$f_3 = \begin{pmatrix} \infty \\ x \end{pmatrix} K_{v/2-\alpha, \alpha} H_3$$

Substituting Eq. (107) into the third and fifth equations in Eqs. (106) and making use of the operators L and M , we obtain the following system of equations:

$$H_2 = \begin{pmatrix} b \\ x \end{pmatrix} K_{v/2-\alpha, \alpha}^{-1} f_2$$

$$- \begin{pmatrix} b, & \infty \\ x, & b \end{pmatrix} M_{v/2-\alpha, \alpha} H_3 \quad (a < x < b)$$

(108)

$$H_3 = - \begin{pmatrix} x, & b \\ b, & a \end{pmatrix} L_{v/2+\alpha, -\alpha} H_2 \quad (b < x < \infty)$$

Using the definitions of L and M operators, we see that the formulas in Eq. (108) constitute a pair of coupled integral equations, upon solving for which we can find the functions and H_2 and H_3 , while $H_1 = 0$.

Putting the second formula of Eq. (108) into the first equation, we obtain a single-integral equation of the second kind involving only H_2 :

$$H_2(x) = \varphi(x) - \left(\frac{2}{\pi}\right)^2 \int_a^b K(x,y)H_2(y) dy \quad (109)$$

where

$$\begin{aligned} \varphi(x) &= \begin{pmatrix} b \\ x \end{pmatrix} K_{\nu/2, -\alpha} f_2 \\ K(x,y) &= \sin^2(\alpha\pi) \frac{x^\nu y^{1+2\alpha+\nu}}{(b^2 - x^2)^\alpha (b^2 - y^2)^\alpha} \\ &\times \int_0^\infty \frac{t^{1-2\nu-2\alpha}(t^2 - b^2)^{2\alpha}}{(t^2 - x^2)(t^2 - y^2)} dt \\ &\times \left(-\frac{1}{2} < \alpha < 1\right) \end{aligned} \quad (110)$$

10.3. An Example: An Electrified Annular Disk

To illustrate the application of Cooke's and Borodachev's solutions to the set of triple integral equations in Eq. (98), we consider the electrostatic field induced by an annular disk with internal and external radii a and b , respectively, the disk being charged to a potential equal to ϕ_0 . The disk is assumed to lie in the plane $z = 0$.

The solution of the problem must satisfy Laplace's equation in Eq. (1) and the following boundary conditions:

$$\begin{aligned} \phi(r, 0) &= \phi_0, \quad a < r < b \\ \frac{\partial \phi}{\partial z} \Big|_{z=0} &= 0, \quad 0 \leq r < a, \quad b < r < \infty \end{aligned} \quad (111)$$

Furthermore, the solution must satisfy the regularity condition and the edge conditions at the edges $r = a$ and $r = b$. As before, applying zeroth-order Hankel transform to the Eq. (1), it can be shown that the electrostatic potential is given by the equation

$$\phi(r, z) = \phi_0 \mathcal{H}_0[s^{-1}A(s)e^{-sz}, s \rightarrow r] \quad (112)$$

Where $A(s)$ is an unknown function of s to be determined. Equation (112) automatically satisfies the radiation conditions.

Making use of the boundary conditions in Eq. (111), we obtain the following triple-integral equations:

$$S_{-1/2,1}A(r) = f(r), \quad S_{0,0}A(r) = g(r)$$

where $f_2(r) = 2r/\phi_0$, $g_1(r) = 0$, $g_3(r) = 0$. Following Sneddon's trial solution in Eq. (89), we obtain the following Fredholm

integral equation of the second kind:

$$\frac{x^2 - \epsilon^2}{x^2} F(x) = 1 - \left(\frac{2}{\pi}\right)^2 \int_\epsilon^1 K(x,y)F(y) dy \quad (113)$$

where

$$\begin{aligned} x &= \frac{r}{a}, \quad \epsilon = \frac{a}{b}, \quad F(x) = h_2^*(xb) \\ K(x,y) &= \frac{1}{2(x^2 - y^2)} \\ &\times \left(\frac{x^2 - \epsilon^2}{x} \log \frac{x + \epsilon}{x - \epsilon} - \frac{y^2 - \epsilon^2}{y} \log \frac{y + \epsilon}{y - \epsilon} \right) \end{aligned}$$

On the other hand, making use of Borodachev's trial solution in Eq. (104), we obtain the following Fredholm integral equation

$$\frac{1 - x^2}{x^2} G(x) = 1 - \left(\frac{2}{\pi}\right)^2 \int_\epsilon^1 M(x,y)G(y) dy \quad (114)$$

where

$$\begin{aligned} G(x) &= h_2^*(bx), \quad h_2^*(r) = \frac{\sqrt{\pi}r^2}{2\phi_0\sqrt{b^2 - r^2}} h_2(r) \\ M(x,y) &= \frac{1}{2(x^2 - y^2)} \\ &\times \left(\frac{1 - y^2}{y} \log \frac{1 + y}{1 - y} - \frac{1 - x^2}{x} \log \frac{1 + x}{1 - x} \right) \end{aligned} \quad (115)$$

The surface charge density at any point of the disk is

$$\begin{aligned} q &= \frac{-1}{4\pi} \left(\frac{\partial \phi}{\partial z} \right)_{z=0} = \frac{\phi_0}{4\pi} g_2(r) \\ &= \begin{cases} \frac{1}{2\pi^2 r} \frac{d}{dr} \int_a^r \sqrt{\frac{b^2 - u^2}{r^2 - u^2}} h_2^*(u) du, & a < r < b \\ \frac{b\phi_0}{2\pi^2 r} \frac{d}{dr} \int_\epsilon^{r/b} \sqrt{\frac{1 - y^2}{r^2/b^2 - y^2}} G(y) dy, & a < r < b. \end{cases} \end{aligned} \quad (116)$$

Thus, the charge density at any point of the disk can be calculated once the integral equation in Eq. (114) is solved.

Considering both sides of the disk, the total charge is

$$\begin{aligned} Q &= 4\pi \int_a^b r q(r, 0) dr = \frac{2\phi_0 b}{\pi\gamma} \\ \gamma^{-1} &= \int_\epsilon^1 G(y) dy \end{aligned}$$

Whence

$$\phi_0 = \frac{\pi Q \gamma}{2b}$$

so that formula in Eq. (116) takes the form

$$q(r, 0) = \frac{\gamma Q}{2\pi r} \frac{d}{dr} \int_{\varepsilon}^{r/b} \sqrt{\frac{1-y^2}{r^2/b^2 - y^2}} \times G(y) d(y), \quad a < r < b \quad (117)$$

Of great interest is to find the asymptotic representation of the charge density $q(r, 0)$ as $r \rightarrow a + 0$ in the sense of Erdelyi, that is, the first term in the asymptotic expansion of $q(r, 0)$ as $r \rightarrow a + 0$. By letting $r \rightarrow a + 0$ in Eq. (117), we obtain

$$q(r, 0) \approx \frac{Q\omega_a(\varepsilon)}{2\sqrt{2}\pi b^2} \left(\frac{r}{b} - \varepsilon\right)^{-1/2}, \quad r \rightarrow a + 0 \quad (118)$$

where

$$\omega_a(\varepsilon) = \frac{\gamma}{\varepsilon} \sqrt{\frac{1-\varepsilon^2}{\varepsilon}} G(\varepsilon) \quad (119)$$

Performing similar analyses on the Sneddon’s trial solution, it can be shown that the surface charge density exhibits the following behavior as the outer contour of the disk is approached

$$q(r, 0) = \frac{Q\omega_b(\varepsilon)}{\sqrt{2}\pi b^2} \left(1 - \frac{r}{b}\right)^{-1/2}, \quad r \rightarrow b - 0 \quad (120)$$

where

$$\omega_b(\varepsilon) = \gamma \sqrt{1 - \varepsilon^2} F(1) \quad (121)$$

Equations (118)–(121) show that the surface charge density exhibits a square-root singularity as the inner and outer edges of the disk are approached. Thus, edge conditions (Meixner’s conditions) are satisfied.

Integral equations in Eqs. (113) and (114) admit closed-form solutions only in the special case where $\varepsilon = 0$, that is, for the case of a circular disk:

$$F(x) = 1, \quad G(x) = \frac{x}{\pi\sqrt{1-x^2}} \log \frac{1+x}{1-x} \quad (122)$$

In the context of mathematically similar elastic contact problems, Borodachev [29] showed that the values of $G(x)$ do not differ practically in the range $0 \leq \varepsilon \leq 0.5$. Therefore for this range, approximate values of the surface charge density can be calculated by using formulas in Eq. (122) while the intergral equation in Eq. (113) can be solved to find the surface charge density for the range $0.5 < \varepsilon < 1.0$.

Many other application of the triple integral equations considered here to problems of electrostatics are given in Sneddon’s book [8]. It should be noted that using the same approach, it is possible to solve a wide variety of problems concerning diffraction of a plane electromagnetic wave by an annular disk and by a system of coaxial annular disks. Many examples of electromagnetic scattering by objects of

different shapes are analyzed in the books by Bowman et al. [30] and by Uslenghi [31].

11. QUADRUPLE-INTEGRAL EQUATIONS INVOLVING HANKEL TRANSFORMS

We now use Cooke operators to reduce certain quadruple integral equations involving Hankel transforms to a Fredholm integral equation of the second kind or a system of those. The problem is to find a function $\psi(x)$ satisfying the equations

$$\begin{aligned} S_{\nu/2-\alpha, 2\alpha} \psi(x) &= f_1(x), \quad x \in I_1 = \{x : 0 < x < a\} \\ S_{\nu/2-\beta, 2\beta} \psi(x) &= 0, \quad x \in I_2 = \{x : a < x < b\} \\ S_{\nu/2-\alpha, 2\alpha} \psi(x) &= f_3(x), \quad x \in I_3 = \{x : b < x < c\} \\ S_{\nu/2-\beta, 2\beta} \psi(x) &= 0, \quad x \in I_4 = \{x : c < x < \infty\} \end{aligned} \quad (123)$$

Taking a trial solution in the form

$$\psi(x) = S_{\nu/2+\beta, -\alpha-\beta} h(x)$$

and then using the third and fourth relations from Eqs. (49), we obtain

$$\begin{aligned} f(x) &\equiv S_{\nu/2-\alpha, 2\alpha} \psi(x) = I_{\nu/2+\beta, \alpha-\beta} h(x) \\ g(x) &\equiv S_{\nu/2-\beta, 2\beta} \psi(x) = K_{\nu/2-\beta, \beta-\alpha} h(x) \end{aligned} \quad (124)$$

whence

$$\begin{aligned} h(x) &= I_{\nu/2+\beta, \alpha-\beta}^{-1} f(x) \\ h(x) &= K_{\nu/2-\beta, \alpha-\beta}^{-1} g(x) \end{aligned} \quad (125)$$

Writing out Eqs. (125) on $I_j (j = 1, \dots, 4)$, we have

$$\begin{aligned} h_1(x) &= \begin{pmatrix} x \\ 0 \end{pmatrix} I_{\nu/2+\beta, \alpha-\beta}^{-1} f_1 \quad (x \in I_1) \\ h_2(x) &= \begin{pmatrix} a \\ 0 \end{pmatrix} I_{\nu/2+\beta, \alpha-\beta} f_1 \\ &+ \begin{pmatrix} x \\ a \end{pmatrix} I_{\nu/2+\beta, \alpha-\beta}^{-1} f_2 \quad (x \in I_2) \\ h_3(x) &= \begin{pmatrix} a \\ 0 \end{pmatrix} I_{\nu/2+\beta, \alpha-\beta}^{-1} f_1 + \begin{pmatrix} b \\ a \end{pmatrix} I_{\nu/2+\beta, \alpha-\beta}^{-1} f_2 \\ &+ \begin{pmatrix} x \\ b \end{pmatrix} I_{\nu/2+\beta, \alpha-\beta}^{-1} f_3 \quad (x \in I_3) \end{aligned}$$

$$\begin{aligned}
 h_4(x) &= \begin{pmatrix} a \\ 0 \end{pmatrix} I_{\nu/2+\beta,\alpha-\beta}^{-1} f_1 \\
 &+ \begin{pmatrix} b \\ a \end{pmatrix} I_{\nu/2+\beta,\alpha-\beta}^{-1} f_2 + \begin{pmatrix} c \\ b \end{pmatrix} I_{\nu/2+\beta,\alpha-\beta}^{-1} f_3 \\
 &+ \begin{pmatrix} \infty \\ c \end{pmatrix} I_{\nu/2+\beta,\alpha-\beta}^{-1} f_4 \quad (x \in I_4) \\
 h_4(x) &= \begin{pmatrix} \infty \\ x \end{pmatrix} K_{\nu/2-\beta,\alpha-\beta}^{-1} g_4 = 0 \quad (x \in I_4) \\
 h_3(x) &= \begin{pmatrix} c \\ x \end{pmatrix} K_{\nu/2-\beta,\alpha-\beta}^{-1} g_3 \quad (x \in I_3) \\
 h_2(x) &= \begin{pmatrix} c \\ b \end{pmatrix} K_{\nu/2-\beta,\alpha-\beta}^{-1} g_3 \quad (x \in I_2) \\
 h_1(x) &= \begin{pmatrix} c \\ b \end{pmatrix} K_{\nu/2-\beta,\alpha-\beta}^{-1} g_3 \\
 &+ \begin{pmatrix} a \\ x \end{pmatrix} K_{\nu/2-\beta,\alpha-\beta}^{-1} g_1 \quad (x \in I_1)
 \end{aligned} \tag{126}$$

From sixth equation of Eqs. (126), we have

$$g_3 = \begin{pmatrix} c \\ b \end{pmatrix} K_{\nu/2-\beta,\beta-\alpha} h_3$$

which upon substitution into the seventh equation of Eq. (126) yields

$$h_2(x) = - \begin{pmatrix} b, & c \\ x, & b \end{pmatrix} M_{\nu/2-\beta,\beta-\alpha} h_3(x) \tag{127}$$

Writing Eq. (124) on I_3 , we obtain

$$\begin{aligned}
 f_3(x) &= \begin{pmatrix} a \\ 0 \end{pmatrix} I_{\nu/2+\beta,\alpha-\beta} h_1 + \begin{pmatrix} b \\ a \end{pmatrix} I_{\nu/2+\beta,\beta-\alpha} h_2 \\
 &+ \begin{pmatrix} x \\ b \end{pmatrix} I_{\nu/2+\beta,\beta-\alpha} h_3
 \end{aligned} \tag{128}$$

Applying the operator

$$\begin{pmatrix} x \\ b \end{pmatrix} I_{\nu/2+\beta,\beta-\alpha}^{-1}$$

to both sides of Eq. (128), we obtain

$$h_3(x) = \Lambda(x) + \begin{pmatrix} x, & b \\ b, & a \end{pmatrix} L_{\nu/2+\beta,\alpha-\beta} h_2(x) \tag{129}$$

where $\Lambda(x)$ is the known function given by

$$\begin{aligned}
 \Lambda(x) &= \begin{pmatrix} x \\ b \end{pmatrix} I_{\nu/2+\beta,\alpha-\beta}^{-1} f_3(x) \\
 &- \begin{pmatrix} x, & a \\ b, & a \end{pmatrix} L_{\nu/2+\beta,\alpha-\beta} h_2(x)
 \end{aligned} \tag{130}$$

Equations (127) and (129) constitute a pair of coupled integral equations for the determination of the unknown functions h_2 and h_3 , but eliminating h_2 , we obtain a single Fredholm equation of the second kind, namely

$$\begin{aligned}
 h_3(x) + \mu \int_b^c K(x, x_0) h_3(x_0) dx_0 \\
 = \Lambda(x) \quad (b < x < c)
 \end{aligned} \tag{131}$$

where $\mu = (4/\pi^2) \sin^2[\pi(\alpha - \beta)]$ and the kernel is given by the equation

$$\begin{aligned}
 K(x, x_0) \\
 = x^{-\nu-2\beta} (x^2 - b^2)^{\beta-\alpha} (x_0^2 - b^2)^{\beta-\alpha} x_0^{2\alpha-\nu+1} \\
 \times \int_a^b \frac{(b^2 - y^2)^{2\alpha-2\beta} y^{2\nu-2\alpha+2\beta+1}}{(x_0^2 - y^2)(x^2 - y^2)} dy \quad (b < x, x_0 < c)
 \end{aligned} \tag{132}$$

Further details can be found in the article by Sneddon [21] and the references cited therein.

Quadruple integral equations of the type in Eq. (123) arise in many boundary value problems of mathematical physics. For instance, the electrostatic problem of three coplanar circular disks charged to a uniform potential can be reduced to this kind of quadruple integral equations.

Finally, it should be noted that a new set of particular solutions can be derived for the quadruple integral equations of the type in Eq. (123) analogous to Borodachev's trial solution for the triple integral equations in Eq. (88), by assuming

$$\psi(x) = S_{\nu/2+\alpha,-\alpha-\beta} H(x) \tag{133}$$

On substituting Eq. (133) into Eqs. (123), we obtain

$$f(x) = K_{\nu/2-\alpha,\alpha-\beta} H(x)$$

$$g(x) = I_{\nu/2+\alpha,-\alpha+\beta} H(x)$$

12. MISCELLANEOUS

1. There is a generalization of the Hankel integral theorem in Eq. (12), known as Weber's integral [32]

$$f(r) = \int_0^\infty \frac{\varphi_s(r)s ds}{J_v^2(sa) + Y_v^2(sa)} \times \int_0^\infty r_0 f(r_0)\varphi_s(r_0) dr_0 \quad a < r < \infty \tag{134}$$

involving the linear combination

$$\varphi_s(r) = J_v(sa)Y_v(sr) - Y_v(sa)J_v(sr) \tag{135}$$

of Bessel functions of the first and second kinds ($v > -\frac{1}{2}$). A sufficient condition for the validity of the Eq. (133) is that $f(r)$ be piecewise continuous and of bounded variation in every finite subinterval $[\alpha, \beta]$, where $a < \alpha < \beta < \infty$, and the integral

$$\int_a^\infty \sqrt{r}|f(r)|dr < \infty$$

It should be noted that Weber's integral reduces to Hankel's integral in the limit as $a \rightarrow 0$. Derivation of equations in Eqs. (134) and (135) is given in the famous book by Titchmarsh [32]. Properties of Weber's transformation are also similar to those derived for Hankel transforms. Weber's transform is suited for solving equations of the form in Eq. (1) for domains with an excluded circular region. We illustrate the use of Weber's integral by one example.

Given: A cylindrical hole of radius a is drilled in an infinite body, and the walls of the hole are maintained at a temperature T_0 starting from the time $t = 0$. It is required to determine the temperature distribution in the body assuming that the initial temperature is zero. The two-dimensional temperature distribution in the body is governed by the heat conduction equation

$$\frac{1}{r} \frac{\partial}{\partial r} \left(r \frac{\partial T}{\partial r} \right) = \frac{\partial T}{\partial t}, \quad a < r < \infty \tag{136}$$

satisfying the initial condition $T|_{t=0} = 0$ and the boundary and radiation conditions

$$T|_{r=a} = T_0, \quad T|_{r \rightarrow \infty} \rightarrow 0$$

Multiplying both sides of Eq. (136) by $r \varphi_s(r)$ and integrating the resulting expression from a to ∞ , we obtain

$$\frac{d\tilde{T}}{dt} - s^2 \tilde{T} = \frac{2T_0}{\pi} \tag{137}$$

where

$$\tilde{T}(s, t) = \int_a^\infty r \tilde{T}(r, t) \varphi_s(r) dr$$

may be called the *Weber transform* of zeroth order of the function $T(r, t)$. In deriving Eq. (137), use has been made of the relations

$$\varphi_s(a) = 0, \quad \varphi_s'(a) = \frac{2}{\pi a}$$

The solution of Eq. (137) satisfying the boundary condition $\tilde{T}|_{t=0}$ is

$$\tilde{T}(s, t) = \frac{2T_0}{\pi s^2} (1 - e^{-s^2 t})$$

Now, using Weber's inversion, we finally obtain the following formula for the temperature evolution in the body:

$$T(r, t) = \frac{2T_0}{\pi} \int_0^\infty \frac{(1 - e^{-s^2 t}) \varphi_s(r) ds}{s [J_0^2(sa) + Y_0^2(sa)]} \tag{138}$$

Many other practical applications of Weber's integral are given in the book by Lebedev et al. [9].

2. In applications of Hankel transforms to many physical problems, integrals of the following form are encountered:

$$\int_0^\infty s \tilde{f}_n(s) \tilde{F}_m(s) J_{m+n}(sr) ds \tag{139}$$

The need to evaluate such integrals arises in connection with the desire of transforming the solution for the physical quantities given in the space of Hankel Transform domain into the physical space. Using Parseval's relation in Eq. (39), we reduce the integral in Eq. (139) to the form

$$\int_0^\infty s \tilde{f}_n(s) \tilde{F}_m(s) J_{m+n}(sr) ds = \int_0^\infty r_0 f(r_0) \Phi(r_0) dr_0 \tag{140}$$

where

$$\Phi(r_0) = H_n[\tilde{F}_m(s) J_{m+n}(sr); s \rightarrow r_0] = \int_0^\infty s \tilde{F}_m(s) J_{m+n}(sr) J_n(sr_0) dr_0 \tag{141}$$

For the product of Bessel functions in Eq. (141), we use Neumann's formula generalized by Rahman [14], and then interchanging the order of integration, we get

$$\Phi(r_0) = \frac{1}{\pi} \int_0^\pi \left[\cos(n\phi) T_m \left(\frac{r - r_0 \cos \phi}{R} \right) + \frac{r_0 \sin n\phi \sin \phi}{R} U_{m-1} \left(\frac{r - r_0 \cos \phi}{R} \right) \right] F(R) d\phi \tag{142}$$

In specific physical problems, however, the cases where $m = 0$ and $m = 1, n = 0$ are the most frequently encountered

ones. In these cases, formula in Eq. (142) simplifies significantly. For instance, for $m = 0$, we have

$$\Phi(r_0) = \frac{1}{\pi} \int_0^\pi \cos(n\phi) F(R) d\phi$$

while for $m = 1, n = 0$, we have

$$\Phi(r_0) = \frac{1}{\pi} \int_0^\pi \frac{r - r_0 \cos \phi}{R} F(R) d\phi$$

3. An efficient method of solving the integral equation (74) is based on representing the unknown function $h_1(x)$ in the form [33]

$$h_1(x) = x^{v-2\alpha} \sum_{n=0}^\infty a_n P_n^{v-\alpha,0}(1-2x^2) \tag{143}$$

where $P_n^{v-\alpha,0}(1-2x^2)$ is the Jacobi polynomial and a_n are the unknown expansion coefficients to be determined.

Putting the expansion in Eq. (143) into Eq. (73) and considering the orthogonality relationship for the Jacobi polynomials

$$\begin{aligned} & \int_0^1 \frac{P_n^{\alpha,\beta}(1-2x^2) P_m^{\alpha,\beta}(1-2x^2) dx}{2^{-2-\alpha-\beta} x^{-1-2\alpha} (1-x^2)^{-\beta}} \\ &= \frac{2^{\alpha+\beta+1} \Gamma(\alpha+n+1) \Gamma(\beta+n+1)}{n! \Gamma(n+\alpha+\beta+1) (\alpha+\beta+2n+1)} \delta_{mn} \\ & \times (\delta_{mn} - \text{Kr\"{o}necker's delta}) \end{aligned}$$

we obtain the following infinite system of linear algebraic equations:

$$\begin{aligned} & \frac{a_m}{2(1+v-\alpha+2m)} + \sum_{n=0}^\infty a_n K_{mn} = r_m \\ & (m = 0, 1, 2, \dots, \infty) \end{aligned} \tag{144}$$

where

$$\begin{aligned} K_{mn} &= \int_0^\infty t^{-1} k(t) J_{1+v-\alpha+2m}(t) J_{1+v-\alpha+2n}(t) dt \\ r_m &= \int_0^1 x^{1+\alpha} r(x) P_m^{v-\alpha,0}(1-2x^2) dx \end{aligned} \tag{145}$$

A key result that was used to obtain Eqs. (144) and (145) is the following integral [34]:

$$\begin{aligned} & s_{a,-a} [(1-x^2)^{-b} P_n^{a,-b}(1-2x^2)] \\ &= \frac{\Gamma(1-b+n)}{2^{\alpha+b} n! x^{1-a-b}} J_{1+a-b+2n}(x) \end{aligned}$$

The infinite system in Eq. (144) can be solved by truncation for the unknown expansion coefficients a_n . In boundary value problems, often it is often the case that the quantity $g_1(x)$ is of prime importance. For instance, in the

charged disk problems, the function $g_1(x)$ is directly proportional to the surface charge density $q(r, 0)$ ($0 \leq r < a$), which, in turn, is essential for finding the capacitance. Rahman [33] showed that with the representation in Eq. (143), the function g_1 is given by

$$\begin{aligned} g_1(x) &= x^v \sum_{n=0}^\infty a_n \frac{n!}{\Gamma(1-\alpha+n)} \\ & \times (1-x^2)^{-b} P_n^{v-\alpha}(1-2x^2) \end{aligned}$$

The method of solution is certainly preferable to that based on using the numerical quadrature, because it bypasses the arduous job of evaluating Abel integrals numerically. Furthermore, it was shown [34] that the following relation holds:

$$\begin{aligned} & \begin{pmatrix} 1 \\ x \end{pmatrix} K_{v/2,-\alpha} \left(\frac{x^{v-2\alpha}}{(1-x^2)^b} P_n^{v-\alpha,-b}(1-2x^2) \right) \\ &= \frac{\Gamma(1-b+n)}{\Gamma(1-b-\alpha+n)} x^v (1-x^2)^{-b-\alpha} \\ & \times P_n^{v,-b-\alpha}(1-2x^2) \end{aligned} \tag{146}$$

Formula in Eq. (146) gives a class of *spectral relationship* for the operator $K_{v/2,-\alpha}$. It can be seen by writing out Eq. (146) in full that it gives a closed-form expression for a class of Abel integrals involving Jacobi polynomials. It can be used to a polynomial solution to Abel integral equations, which a number of boundary value problems of electrostatics can be reduced to.

4. The methods described in this article for solving dual integral equations are also applicable to a system of those of the form

$$\begin{aligned} S_{\mu_i/2-\alpha,2\alpha} \sum_{j=1}^n c_{ij} \psi_j(x) &= f_i(x), \quad x \in I_1 \\ S_{\nu_i/2-\beta,2\beta} \psi_i(x) &= g_i(x), \quad x \in I_2 \end{aligned}$$

By a systematic use of the properties of Erdelyi-Kober operators Lowndes was able to show that the problem of solving a system of simultaneous equations of this type can be reduced to that of solving a system of simultaneous integral equations. Details of these results can be found in Sneddon's book [8]. To the best of the writer's knowledge, generalization of these results has not yet been attempted for the case of simultaneous triple- and quadruple-integral equations.

5. The theory of Hankel transforms can also be extended to generalized functions or distributions via embedding theory or adjoint method. Interested readers are referred to consult the books by Zayed [5], Zemanian [34,35], and Brychkov and Prudnikov [36].

13. COMPENDIUM OF BASIC FORMULAS

For the sake of convenience of the readers, below we give a compendium of the basic formulas that are of frequent use in applications.

13.1. Definition of Hankel Transforms

$$\begin{aligned} \tilde{f}_v(s) &= \mathcal{H}_v[f(r), r \rightarrow s] = \int_0^\infty r f(r) J_v(sr) dr \\ f(r) &= \mathcal{H}_v[\tilde{f}_v(s), s \rightarrow r] = \int_0^\infty s \tilde{f}_v(s) J_v(sr) dr \end{aligned}$$

13.2. Some Properties of Hankel Transforms

$$\begin{aligned} \mathcal{H}_{-m}[f(r), r \rightarrow s] &= (-1)^m \mathcal{H}_m[f(r), r \rightarrow s] \\ (m = \pm 1, \pm 2, \dots, \pm n, \dots) \\ \mathcal{H}_v[f(ar), r \rightarrow s] &= a^{-2} \mathcal{H}_v\left[f(r), r \rightarrow \frac{s}{a}\right] \\ \mathcal{H}_v[r^{-1}f(r), r \rightarrow s] &= \frac{s}{2v} [\tilde{f}_{v-1}(s) + \tilde{f}_{v+1}(s)] \quad (v \neq 0) \\ \mathcal{H}_n[f(r-a)H(r-a), r \rightarrow s] &= \sum_{m=-\infty}^\infty \alpha_m \tilde{f}_m(s) \\ \alpha_m &= J_{n-m}(sa) + \frac{1}{2}as[(m+1)^{-1}J_{n-m-1}(sa) \\ &\quad + (m-1)^{-1}J_{n-m+1}(sa)] \\ \mathcal{H}_v[\mathcal{B}_v f(r), r \rightarrow s] &= -s^2 \mathcal{H}_v[f(r), r \rightarrow s] \\ \mathcal{B}_v &= \frac{d^2}{dr^2} + \frac{1}{r} \frac{d}{dr} - \frac{v^2}{r^2} \quad (v = 0, 1, \dots) \\ \mathcal{H}_v\left[r^{v-1} \frac{d}{dr} [r^{1-v} f(r), r \rightarrow s]\right] &= -s \mathcal{H}_{v-1}[f(r), r \rightarrow s] \end{aligned}$$

13.3. Parseval's Relation

$$\int_0^{-\infty} s \tilde{f}_v(s) \tilde{g}_v(s) ds = \int_0^\infty r_0 f(r_0) g(r_0) dr_0$$

13.4. Modified Operator of Hankel Transform and Erdelyi-Kober Operators

$$\begin{aligned} I_{\eta,0} &= K_{\eta,0} = I \\ I_{\eta,\alpha} x^{2\beta} f(x) &= x^{2\beta} I_{\eta+\beta,\alpha} f(x) \\ I_{\eta,\alpha} I_{\eta+\alpha,\beta} &= I_{\eta,\alpha+\beta} \\ K_{\eta,\alpha} x^{2\beta} f(x) &= x^{2\beta} K_{\eta-\beta,\alpha} f(x) \\ K_{\eta,\alpha} K_{\eta+\alpha,\beta} &= K_{\eta,\alpha+\beta} \\ I_{\eta,-n} f(x) &= x^{2n-2\eta-1} D_x^n x^{2\eta+1} f(x) \end{aligned}$$

$$\begin{aligned} I_{\eta,\alpha} f(x) &= x^{-2\eta-2n-1} D_x^n x^{2n+2\eta+2\alpha+1} I_{\eta,\alpha+n} f(x) \\ K_{\eta,-n} f(x) &= (-1)^n x^{2\eta-1} D_x^n x^{2n-2\eta+1} f(x) \\ K_{\eta,\alpha} f(x) &= (-1)^n x^{2\eta-1} D_x^n x^{2n-2\eta+1} f(x) K_{\eta-n,\alpha+n} f(x) \end{aligned}$$

$$\begin{aligned} I_{\eta,\alpha}^{-1} &= I_{\eta+\alpha,-\alpha} \\ K_{\eta,\alpha}^{-1} &= K_{\eta+\alpha,-\alpha} \\ S_{\eta,\alpha} f(x) &= 2^\alpha x^{-\alpha} H_{2\eta+\alpha}[t^{-\alpha} f(t), t \rightarrow x] \\ S_{\eta,\alpha}^{-1} &= S_{\eta+\alpha,-\alpha} \\ S_{\eta,\alpha} f(x) &= 2^{-\lambda} x^\lambda S_{\eta\lambda/2,\alpha+\lambda}[x^\lambda f(x)] \\ I_{\eta+\alpha,\beta} S_{\eta,\alpha} &= S_{\eta,\alpha+\beta} \\ K_{\eta,\alpha} S_{\eta+\alpha,\beta} &= S_{\eta,\alpha+\beta} \\ S_{\eta+\alpha,\beta} S_{\eta,\alpha} &= I_{\eta,\alpha+\beta} \\ S_{\eta,\alpha} S_{\eta+\alpha,\beta} &= K_{\eta,\alpha+\beta} \\ S_{\eta+\alpha,\beta} I_{\eta,\alpha} &= S_{\eta,\alpha+\beta} \\ S_{\eta,\alpha} K_{\eta+\alpha,\beta} &= S_{\eta,\alpha+\beta} \end{aligned}$$

13.5. Some Beltrami-Type Relations of Common Occurrence

$$\begin{aligned} \mathcal{H}_0[s^{-1} \tilde{f}_0(s), s \rightarrow r] &= \frac{2}{\pi} \int_r^\infty \frac{dt}{\sqrt{t^2 - r^2}} \int_0^t \frac{xf(x) dx}{\sqrt{t^2 - x^2}} \\ \mathcal{H}_0[s \tilde{f}_0(s), s \rightarrow r] &= \frac{-2}{\pi r} \frac{d}{dr} \int_r^\infty \frac{tdt}{\sqrt{t^2 - r^2}} \frac{d}{dt} \int_0^t \frac{xf(x) dx}{\sqrt{t^2 - x^2}} \end{aligned}$$

13.6. Some Useful Relations

$$\begin{aligned} &\int_0^\infty s \tilde{f}_n(s) \tilde{F}_m(s) J_{m+n}(sr) ds \\ &= \int_0^\infty r_0 f(r_0) \Phi(r_0) dr_0 \\ \Phi(r_0) &= \frac{1}{\pi} \int_0^\pi \left[\cos(n\phi) T_m\left(\frac{r-r_0 \cos \phi}{R}\right) \right. \\ &\quad \left. + \frac{r_0 \sin n\phi \sin n\phi}{R} U_{m-1}\left(\frac{r-r_0 \cos \phi}{R}\right) \right] F(R) d\phi \end{aligned}$$

$$\begin{aligned}
 & J_{m+n}(sr)J_n(sr_0) \\
 &= \frac{1}{\pi} \int_0^\pi \left[\cos(n\phi) T_m \left(\frac{r-r_0 \cos \phi}{R} \right) \right. \\
 &\quad \left. + \frac{r_0 \sin n\phi \sin n\phi}{R} U_{m-1} \left(\frac{r-r_0 \cos \phi}{R} \right) \right] \\
 &\quad \times J_m(sR) d\phi \\
 S_{\eta, -\eta} [(1-x^2)^{-\alpha} P_n^{\eta, -\alpha} (1-2x^2)] \\
 &= \frac{\Gamma(1-\alpha+n)}{2^{\eta+\alpha} n! x^{1-\eta-\alpha}} J_{1+\eta-\alpha+2n}(x) \\
 &\quad \left(\frac{1}{x} \right) K_{\nu/2, -\alpha} \left(\frac{x^{v-2x}}{(1-x^2)^\beta} P_n^{v-\alpha, -\beta} (1-2x^2) \right) \\
 &= \frac{\Gamma(1-\beta+n)}{\Gamma(1-\beta-\alpha+n)} x^\nu (1-x^2)^{-\alpha-\beta} \\
 &\quad \times P_n^{v-\alpha-\beta} (1-2x^2)
 \end{aligned}$$

14. SUGGESTED LITERATURE

Readers interested in rigorous proofs of various aspects of the theory of Hankel transforms are referred to the books by Sneddon [1,2] Davies [3], Andrews and Shivamoggi [4], and Zayed [5] and the papers by Erdelyi (15) and Erdelyi and Kober (16). Many applications of the theory of Hankel transforms to physical problems are given in the books by Sneddon [8] and Lebedev et al. [9]. Fractional integrals and derivatives and their applications to dual-, triple-, and quadruple-integral equations involving Hankel transforms are discussed at greater length in Sneddon [8,21], Cooke [19,20,27,28], Borodachev [29], and Samko et al. [37]. Extension of the theory of Hankel transforms to generalized functions or distributions is presented in the books by Zayed [5], Zemanian [34,35], and Brychkov and Prudnikov [36].

Acknowledgments

The writer wishes to express his deepest gratitude to Professor Raj Mittra (Department of Electrical Engineering, Pennsylvania State University) for his kind response to queries with respect to some of the materials presented herein. He also gratefully acknowledges encouragement from his friends S. Rajeswaran and P. K. Jindal during the period of writing of the article.

BIBLIOGRAPHY

1. I. N. Sneddon, *Fourier Transforms*, McGraw-Hill, New York, 1951.
2. I. N. Sneddon, *The Use of Integral Transforms*, McGraw-Hill, New York, 1972.
3. B. Davies, *Integral Transforms and Their Applications*, Springer-Verlag, Berlin, 1978.

4. L. Andrews and B. Shivamoggi, *Integral Transform for Engineers and Mathematicians*, Macmillan, New York, 1988.
5. A. I. Zayed, *Handbook of Function and Generalized Function Transformations*, CRC Press, Boca Raton, FL, 1996.
6. G. N. Watson, *A Treatise on the Theory of Bessel Functions*, Cambridge Univ. Press, London, 1944.
7. A. Erdelyi et al., *Tables of Integral Transforms*, McGraw-Hill, New York, 1954, Vol. II.
8. I. N. Sneddon, *Mixed Boundary Value Problems in Potential Theory*, North Holland, Amsterdam, 1965.
9. N. N. Lebedev, I. P. Skalskaya, and Ya. S. Ufliand, *Problems of Mathematical Physics*, translated from Russian, Prentice-Hall, Englewood Cliffs, NJ, 1965.
10. A. Erdelyi et al., *Higher Transcendental Functions*, McGraw-Hill, New York, 1953, Vol. II.
11. J. Jeans, *The Mathematical Theory of Electricity and Magnetism*, Cambridge Univ. Press, Cambridge, UK, 1908.
12. W. R. Smythe, *Static and Dynamic Electricity*, McGraw-Hill, New York, 1968.
13. I. S. Gradshteyn and I. M. Ryzhik, *Tables of Integrals, Series and Products*, Academic Press, New York, 1980.
14. M. Rahman, On a generalization of Neumann's formula for the product of two first kind Bessel functions of integral orders, *J. Appl. Math. Mech. ZAMM* **77**(2):156-157 (1997).
15. A. Erdelyi, On fractional integration and its application to the theory of Hankel transforms, *Quart. J. Math. Oxford* **11**:293-303 (1940).
16. A. Erdelyi and H. Kober, Some remarks on Hankel transforms, *Quart. J. Math. Oxford* **11**:212-221 (1940).
17. H. Kober, On fractional integrals and derivatives, *Quart. J. Math. Oxford* **11**:193-211 (1940).
18. A. Erdelyi and I. N. Sneddon, Fractional integration and dual integral equations, *Can. J. Math.* **14**:685-693 (1962).
19. J. C. Cooke, The solution of triple integral equations in operational form, *Quart. J. Mech. Appl. Math.* **18**(Part 3):57-72 (1965).
20. J. C. Cooke, The solution of triple and quadruple integral equations and Fourier-Bessel series, *Quart. J. Mech. Appl. Math.* **25**:247-263 (1972).
21. I. N. Sneddon, The use in mathematical physics of Erdelyi-Kober operators and some of their generalizations, in B. Ross, ed., *Fractional Calculus and Its Applications*, Lecture Notes in Mathematics 457, Springer-Verlag, Berlin, 1975.
22. E. Beltrami, Sulla teoria delle funzione potenziali simmetriche, *Mem. Accad. Sci. Bologna* **22**(IV):462 (1881).
23. I. N. Sneddon, A relation involving Hankel transforms with applications to boundary value problems in potential theory, *J. Appl. Math. Mech.* **14**(1):33-40 (1965).
24. E. R. Love, The electrostatic field of two equal circular coaxial conducting disks, *Quart. J. Math. Mech.* **11**(2):428-451 (1949).
25. J. Meixner, *The Behavior of Electromagnetic Fields at Edges*, Inst. Math. Sci. Research Report EM-72, New York Univ., 1954.
26. R. Mittra and S. W. Lee, *Analytical Techniques in the Theory of Guided Waves*, Macmillan, New York, 1971.
27. J. C. Cooke, Triple integral equations, *Quart. J. Mech. Appl. Math.* **16**:193-203 (1963).
28. J. C. Cooke, Some further triple integral equations, *Proc. Edinburgh Math. Soc.* 303-316 (1963).
29. N. M. Borodachev, On a particular class of solutions of triple integral equations, *J. Appl. Math. Mech. PMM* **40**(4):605-611 (1976).

30. J. J. Bowman, T. B. A. Senior, and P. L. E. Uslenghi, *Electromagnetic and Acoustic Scattering by Simple Shapes*, Wiley, New York, 1970.
31. P. L. E. Uslenghi, *Electromagnetic Scattering*, Academic Press, New York, 1978.
32. E. C. Titchmarsh, *Eigenfunction Expansions Associated with Second-Order Differential Equations*, Oxford Univ. Press, London, 1946, Vol. I.
33. M. Rahman, A note on the polynomial solution of a class of dual integral equations arising in mixed boundary value problems of elasticity, *J. Appl. Math. Phys. ZAMP* **46**(1):107–121 (1995).
34. A. H. Zemanian, *Distribution Theory and Transform Analysis*, McGraw-Hill, New York, 1965.
35. A. H. Zemanian, *Generalized Integral Transforms*, Dover, New York, 1987.
36. Yu. A. Brychkov and A. P. Prudnikov, *Integral Transforms of Generalized Functions* (transl. from Russian), Gordon & Breach, New York, 1989.
37. S. G. Samko, A. A. Kilbas, and O. I. Marichev, *Functional Integrals and Derivatives: Theory and Applications* (transl. from Russian), Gordon & Breach, Philadelphia, 1993.

HARMONIC OSCILLATORS, CIRCUITS

BERNABÉ LINARES-BARRANCO
 ÁNGEL RODRÍGUEZ-VÁZQUEZ
 National Microelectronics
 Center (CNM)

In electronics a harmonic oscillator is an electronic circuit that generates a sinusoidal signal. This signal can either be a voltage, a current, or both. Harmonic oscillators are not restricted to electronics. They can be found in many other disciplines. However, they always can be described by similar mathematical equations. A very familiar harmonic oscillator is the harmonic pendulum, which is found in many high-school physics textbooks. It is a mechanical system consisting of a mass suspended by a fixed-length thread. Figure 1 illustrates this. When mass m is slightly separated from its equilibrium point (so that angle θ in Fig. 1 is sufficiently small) and set free, the earth's gravitational force will make it move toward its resting point. When the mass reaches the resting point it has gained some speed that will make it keep running toward the other side of the equilibrium point, until it stops and comes back. And so it will oscillate from one side of the equilibrium point to the other. What happens is that by initially departing the mass from its equilibrium point, an external agent is increasing its potential energy. When it is set free the action of the earth's gravitational force, together with the constraint imposed by the fixed length thread, will gradually change this initial increase of potential energy into kinetic energy. At the equilibrium point all potential energy supplied initially by the external agent is in form of kinetic energy and speed is maximum. At the points of maximum elongation the kinetic energy (and speed) is zero and the original potential energy is recovered. The

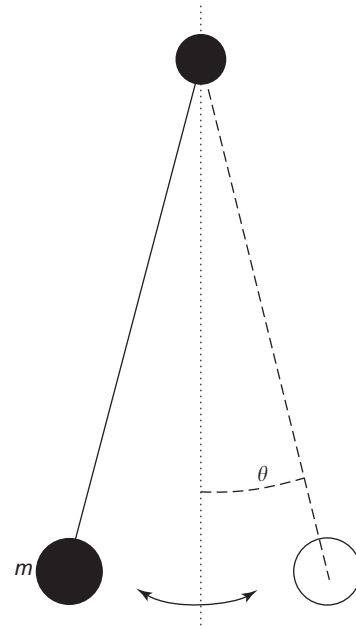


Figure 1. The mechanical pendulum behaves as a harmonic oscillator in the limit of very small maximum angle deviations.

pendulum oscillates at constant frequency and, if there is no friction, it keeps on oscillating indefinitely with constant maximum elongation or amplitude. However, in practice friction cannot be completely suppressed. Consequently, in order to have a pendulum oscillating permanently there must be a way of supplying the energy lost by friction.

In the electronic oscillator there is also a mechanism by which energy of one type is changed into another type (energy can also be of the same type but interchanged between different devices). Figure 2 shows a capacitor connected in parallel with an inductor. At equilibrium there is no voltage across the capacitor and no current through the inductor. However, if by some means, an initial voltage (or equivalently, charge) is supplied to the capacitor, its stored energy increases. The inductor provides a path to discharge the capacitor so that a current builds up through the inductor. However, by the time the capacitor has zero charge the current flowing through the inductor is maximum and the inductor stores all the original capacitor energy in the form of magnetic flux energy. The consequence is that the current keeps flowing through the inductor, charging now the capacitor oppositely, until the current is zero. If there are no resistive losses this process will continue indefinitely; capacitor and inductor continue to interchange their stored energies. The voltage across the capacitor will be sinusoidal in time, and so will be the current through the inductor. The amplitude (or maximum elongation) of the voltage oscillations is equal to the initial voltage supplied to the capacitor. In practice both capacitor and inductor have resistive losses, so that in order to keep the system oscillating indefinitely there must be a way of supplying the energy being lost.

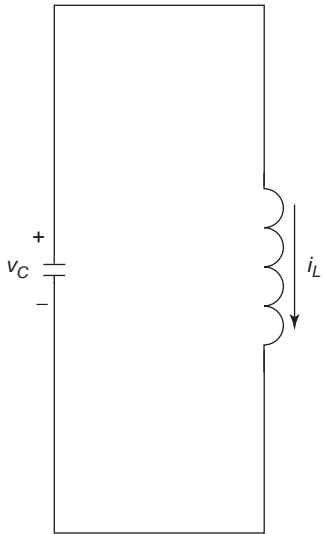


Figure 2. An ideal capacitor connected in parallel with an ideal inductor form a harmonic oscillator.

1. IDEAL RESONATOR MATHEMATICAL MODEL

In Fig. 2 the capacitor voltage v_C and its current i_C are related mathematically by the expression

$$i_C = C \frac{dv_C}{dt} \quad (1)$$

where C is the capacitor's capacitance. For the inductor, its voltage v_L and current i_L are related by

$$v_L = L \frac{di_L}{dt} \quad (2)$$

where L is the inductor's inductance. Besides this, the circuit of Fig. 2 imposes the following topological constraints

$$\begin{aligned} v_C &= v_L \\ i_C &= -i_L \end{aligned} \quad (3)$$

Solving Eqs. (1)–(3) yields

$$\frac{d^2 v_C}{dt^2} + \frac{1}{LC} v_C = 0 \quad (4)$$

The solution to this second-order time-domain differential equation is

$$v_C(t) = v_C(0) \cos(\omega t) - i_L(0) \sqrt{L/C} \sin(\omega t) \quad (5)$$

where $v_C(0)$ is the capacitor voltage at time zero, $i_L(0)$ is the inductor current at time zero, and ω is the angular frequency of the resulting oscillation whose value is

$$\omega = \frac{1}{\sqrt{LC}} \quad (6)$$

Using Eqs. (3), (5), and (6) in Eq. (1) results in

$$i_L(t) = i_L(0) \cos(\omega t) + v_C(0) \sqrt{C/L} \sin(\omega t) \quad (7)$$

By means of basic trigonometric manipulation, Eqs. (5) and (7) can be rewritten as

$$\begin{aligned} v_C(t) &= V_{\max} \cos(\omega t + \varphi) \\ i_L(t) &= V_{\max} \sqrt{C/L} \sin(\omega t + \varphi) \end{aligned} \quad (8)$$

where

$$\begin{aligned} V_{\max} &= \sqrt{v_C^2(0) + i_L^2(0)L/C} \\ \varphi &= \arctan\left(\frac{i_L(0)}{v_C(0)} \sqrt{L/C}\right) \end{aligned} \quad (9)$$

Equation (8) reveals that $v_C(t)$ and $i_L(t)$ have a phase shift of $\pi/2$ radians. This is usually referred to as $v_C(t)$ and $i_L(t)$ being in quadrature, and the resonator in Fig. 2 as being a quadrature resonator or oscillator. Note that the maximum oscillation amplitudes (V_{\max} or $V_{\max} \sqrt{C/L}$, respectively) depend on the initial conditions $v_C(0)$ and $i_L(0) = -C\dot{v}_C(0)$.

Usually, differential equations like Eq. (4) are not solved directly in the time domain but in the frequency domain. For this, let us take the Laplace transform of Eq. (4)

$$s^2 V_C(s) - s v_C(0) - \dot{v}_C(0) + \frac{V_C(s)}{LC} = 0 \quad (10)$$

where $V_C(s)$ is the Laplace transform of $v_C(t)$. Since $i_L(0) = -C\dot{v}_C(0)$, Eq. (10) can be rewritten as

$$V_C(s) = \frac{s}{s^2 + 1/LC} v_C(0) - \frac{1}{s^2 + 1/LC} \frac{i_L(0)}{C} \quad (11)$$

Taking the inverse Laplace transform of Eq. (11) results in Eq. (5). Usually in circuits, the initial conditions involved in the Laplace transform are ignored and Eq. (10) is simplified to

$$s^2 + \frac{1}{LC} = 0 \quad (12)$$

which has the following solutions

$$\begin{aligned} s_1 &= j\omega, \quad s_2 = -j\omega \\ \omega &= \frac{1}{\sqrt{LC}} \end{aligned} \quad (13)$$

Solutions s_1 and s_2 are called the *poles* of the system, and in this case the two poles are complex conjugate and are purely imaginary (their real part is zero). In circuits, people don't take the inverse Laplace transform to know the solution. They know that if a system has a pair of purely

imaginary poles the signals have a sinusoidal steady state whose amplitude depends on the initial conditions.

2. REAL RESONATOR MATHEMATICAL MODEL

As mentioned earlier, the circuit of Fig. 2 is ideal. In practice there will always be resistive losses in the capacitor, in the inductor, or in both. Either introducing a small resistance R_L in series with the inductor, a large resistance R_C in parallel with the capacitor, or both can model this. Solving such a circuit yields the following time-domain differential equation

$$\frac{d^2 v_C(t)}{dt^2} + b \frac{dv_C(t)}{dt} + \omega^2 v_C(t) = 0 \quad (14)$$

with

$$b = \frac{1}{R_C C} + \frac{R_L}{L} \quad (15)$$

$$\omega^2 = \frac{1 + R_L/R_C}{LC}$$

The solution to Eq. (14) is

$$v_C(t) = V_{\max} e^{-bt/2} \cos(\omega_0 t + \rho) \quad (16)$$

where $\omega_0^2 = \omega^2 - (b/2)^2$. Parameters V_{\max} and ρ can be found from the initial conditions $v_C(0)$ and $\dot{v}_C(0)$,

$$V_{\max} = \frac{v_C(0)}{\cos \rho} \quad (17)$$

$$\rho = -\arctan\left(\frac{\dot{v}_C(0) + \frac{b}{2}v_C(0)}{\omega_0 v_C(0)}\right)$$

However, circuit people prefer to solve Eq. (14) in the frequency domain by taking its Laplace transform:

$$s^2 + bs + \omega^2 = 0 \quad (18)$$

The solution to this equation provides the following poles

$$s_1 = -\frac{b}{2} + j\omega \sqrt{1 - \left(\frac{b}{2\omega}\right)^2} = -\frac{b}{2} + j\omega_0 \quad (19)$$

$$s_2 = -\frac{b}{2} - j\omega \sqrt{1 - \left(\frac{b}{2\omega}\right)^2} = -\frac{b}{2} - j\omega_0$$

which are two complex conjugate poles with a negative real part. Circuit people know that when a system has a pair of complex conjugate poles with a negative real part, the system oscillates in a sinusoidal fashion with an amplitude that vanishes after some time. This is what Eq. (16) shows. The amplitude of the oscillations $A(t) = V_{\max} e^{-bt/2}$ decreases exponentially with time. After a few time constants $2/b$ the amplitude is negligible and one can

consider that the system has stopped oscillating. Consequently, in practice, the circuit of Fig. 2 is not useful for building an oscillator.

Imagine that somehow we could make R_L or R_C (or both) negative, so that $b < 0$. A negative resistance behaves as an energy source that replaces the energy dissipated by positive resistances. In this case the poles would have a positive real part and the amplitude of the oscillations

$$A(t) = V_{\max} e^{-bt/2} \quad (20)$$

would increase exponentially in time, assuming $V_{\max} \neq 0$ (due to noise V_{\max} cannot be exactly zero all the time). This would yield an oscillator with initial startup but that would be unstable, because its amplitude would be “out of control.” What circuit designers do to build oscillators with stable amplitude is to make the term b in Eq. (18) depend on the instantaneous oscillation amplitude $A(t)$

$$b(t) = b(A(t)) \quad (21)$$

and in such a way that b increases with A , b is negative for $A = 0$ (to ensure initial startup), and b becomes positive above a certain amplitude. This is called amplitude control. For instance, assume that by adding some special circuitry to Fig. 2 we are able to make

$$b(A) = -b_0 + b_1 A \quad (22)$$

where b_0 and b_1 are positive constants (note that A is always positive). Initially, if $A = 0$, $b = -b_0$ is negative and the real part of the poles is positive: amplitude $A(t)$ increases exponentially with time. As $A(t)$ increases b will eventually become positive (poles with negative real part) and this will decrease the amplitude $A(t)$. The consequence of these two tendencies is that a steady state will be reached for which $b = 0$ and the amplitude is constant. Solving Eq. (22) for $b = 0$ yields the value of the steady state oscillation amplitude A_0 ,

$$A_0 = \frac{b_0}{b_1} \quad (23)$$

Note that, as opposed to the ideal resonator, the steady-state amplitude is independent of any initial conditions.

In general, a harmonic oscillator does not have to be a second order system like the case of Eq. (14) or Eq. (18). It can have any order. What is important is that it has a pair of complex conjugate poles whose real part can be controlled by the oscillation amplitude (so that the real part becomes zero in the steady state), and that the rest of the poles (either complex conjugate or not) have negative real parts. The way b depends on A does not have to be as in Eq. (22). Strictly speaking, the conditions are

$$b(A=0) = -b_0 < 0 \quad \text{for initial startup}$$

$$b > 0 \quad \text{for some } A \quad (24)$$

$$\frac{db(A)}{dA} > 0 \quad \text{for stable amplitude control}$$

This will ensure stable oscillator operation. In what follows we will concentrate on second order systems and will provide two different ways of performing amplitude control.

3. AMPLITUDE CONTROL BY LIMITATION

A very widely used method for oscillator amplitude control is by limitation. This method usually is simple to implement, so simple that many times it is implicit in the components used to build the resonator with initial startup. This makes practical circuits easy to build, although many times people don't understand the underlying amplitude control mechanism.

Let us consider the ideal resonator of Fig. 2 with an additional resistor R_p in parallel to make it real. In order to assure initial startup, let us put a negative resistor in parallel also. Figure 3a shows a very simple way to implement one using a real (positive) resistor and a voltage amplifier of gain larger than one (for example, two). Current I_{in} will be

$$I_{in} = -\frac{V_{in}}{R_n} \tag{25}$$

and the structure resistor–amplifier behaves as a grounded negative resistor of value $-R_n$. Figure 3b shows how to build the amplifier using an operational amplifier and resistors. Connecting this negative resistor in parallel with a positive one of value $R_p = R_n + R_e$ (with $R_e \ll R_n$), the equivalent parallel resistance would be

$$R_{eq} = -\frac{R_n^2}{R_e} \tag{26}$$

which is a very high but negative resistance. Connecting this equivalent resistor in parallel with the ideal resonator of Fig. 2 provides an oscillator with initial startup. This is shown in Fig. 3c.

Because the operational amplifier's output voltage cannot go above its positive power supply V_{DD} or below its negative one V_{SS} , the negative resistance emulator circuit just described works as long as the amplifier output is below V_{DD} and above V_{SS} , or equivalently voltage V_{in} is between $V_{DD}/2$ and $V_{SS}/2$. It is easy to compute the current through R_{eq} as a function of V_{in} taking into account this saturation effect. Figure 3d shows the resulting curve. If $V_{SS}/2 \leq V_{in} \leq V_{DD}/2$ resistor R_{eq} behaves as a negative resistance of high value, but if V_{in} is outside this range the slope of I_{in} versus V_{in} is that of a positive resistance with much smaller value. In order to analyze what happens to the circuit of Fig. 3c when the oscillating amplitude increases beyond $V_{DD}/2$ or $V_{SS}/2$ (whichever is smaller) the concept of describing function can be used.

3.1. Describing Function

Figure 4 shows a sinusoidal signal $x(t)$ applied to a non-linear element $f(x)$ that outputs a distorted signal $y(t)$. Signal $y(t)$ is no longer sinusoidal, but it is periodic.

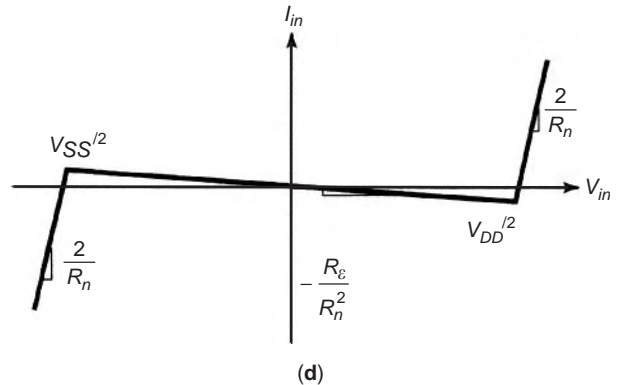
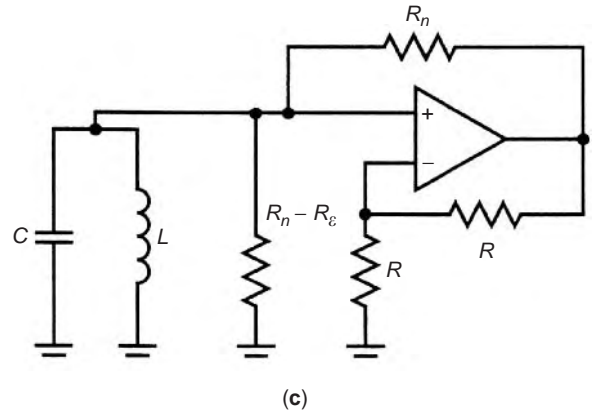
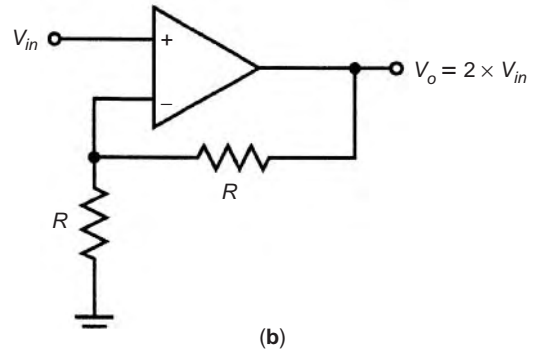
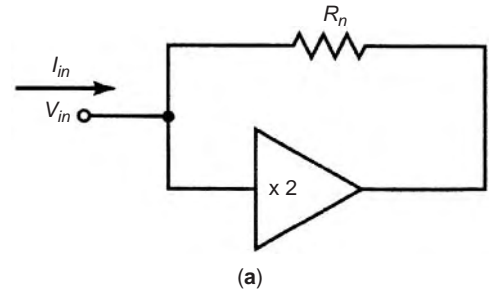


Figure 3. A real harmonic oscillator can be made by adding a negative resistor to a real resonator: (a) a negative resistor can be emulated using a resistor and a voltage amplifier of gain greater than unity; (b) implementation of negative resistor using an operational amplifier and resistors; (c) oscillator composed of capacitor inductor and negative resistor; (d) transfer characteristics of the negative resistor implementation of (b).

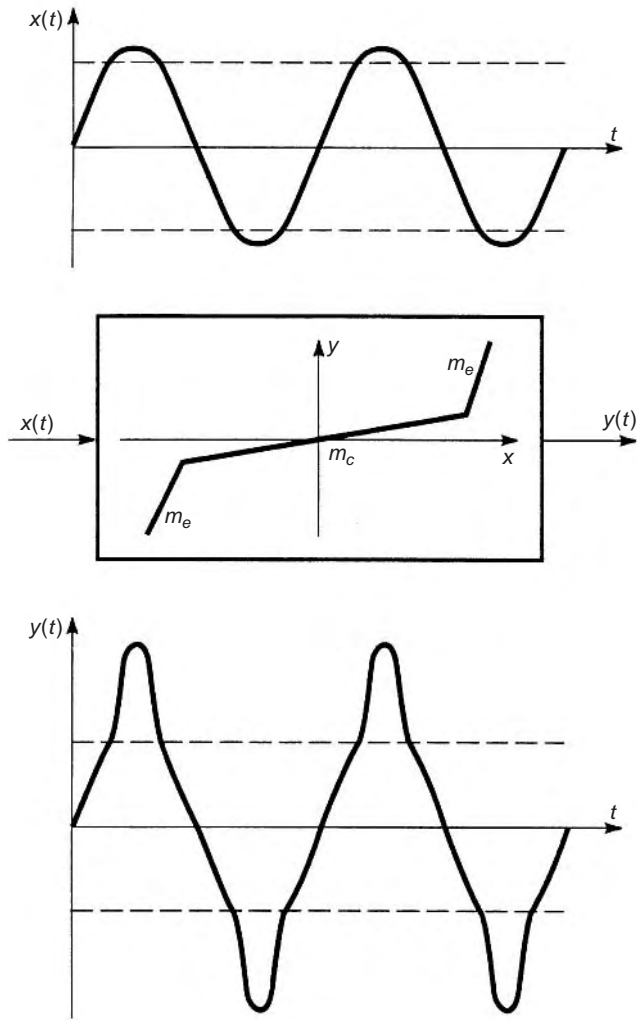


Figure 4. A sinusoidal signal applied to a nonlinear element results, in general, in a distorted output signal.

Consequently, a Fourier series can describe it. The first (or fundamental) harmonic has the same frequency as the input sinusoid, while the others have frequencies which are integer multiples of the first one. If the block of Fig. 4 is used in a system such that the end signals will be approximately sinusoidal (as in a harmonic oscillator) then one can neglect all higher harmonics of the Fourier expansion of $y(t)$ and approximate it using the first or fundamental harmonic only

$$\begin{aligned}
 y(t) &\approx N(A)x(t) \\
 x(t) &= A \sin(\omega t) \\
 N(A) &= \frac{\omega}{\pi A} \int_0^{2\pi/\omega} f(x(t)) \sin(\omega t) dt
 \end{aligned} \tag{27}$$

Note that this approximation makes $y(t)$ to be linear with $x(t)$ so that the nonlinear block in Fig. 4 can be modeled by a linear amplifier of gain $N(A)$. Function $N(A)$ is the “describing” function of the nonlinear element $f(\cdot)$.

This approach is valid for any nonlinear function $f(\cdot)$, but let us consider only piecewise linear functions, as in Figs. 3 and 4, with three pieces: a central linear piece of slope m_c and two external linear pieces of slope m_e . When amplitude A is small enough so that $x(t)$ is always within the central piece then $N(A) = m_c$. When A increases beyond the central piece $N(A)$ will change gradually towards value m_e . In the limit of $A = \infty$ the describing function will be $N(A) = m_e$. Computing the first Fourier term provides the exact expression (let us assume $V_{SS} = -V_{DD}$ for simplicity). If $A \geq V_{DD}/2$

$$N(A) = m_e - 2 \frac{m_e - m_c}{\pi} \left[\sin^{-1} \left(\frac{V_{DD}}{2A} \right) + \frac{V_{DD}}{2A} \sqrt{1 - \left(\frac{V_{DD}}{2A} \right)^2} \right] \tag{28}$$

and if $A \leq V_{DD}/2$

$$N(A) = m_c \tag{29}$$

Applying the describing function method to the nonlinearity of Fig. 3d results in

$$I_{in} = N(A)V_{in} \tag{30}$$

where $N(A) = -R_f/R_n^2$ for $A \leq V_{DD}/2$ and $N(A)$ tends toward $2/R_n$ as it increases beyond $V_{DD}/2$. Since $N(A)$ is continuous and monotonic, there will be a value of A (and only one) for which $N(A) = 0$. Let us call this value A_o . Note that A_o depends only on the shape of the nonlinear function $f(\cdot)$ of Fig. 3d. Equation (29) is the equation of a resistor of value $R_{eq} = 1/N(A)$. For small values of A , $R_{eq} = -R_n^2/R_e$ (high resistance but negative) and the oscillator possesses exponentially increasing amplitude. When A increases beyond $V_{DD}/2$, R_{eq} will become more and more negative until $N(A) = 0$. At this point $A = A_o$, $R_{eq} = \infty$ and we have the ideal resonator. If A increases further, R_{eq} becomes positive and the oscillator presents exponentially decreasing amplitude. This represents a stable amplitude control mechanism such that in the steady state $A = A_o$ and $R_{eq} = \infty$.

3.2. General Formulation

In general, the block diagram of Fig. 5 describes a harmonic oscillator with amplitude control by limitation, where $H(s)$ is a linear block (or filter) and $f(x)$ is the nonlinear element responsible for the amplitude control. Applying the describing function method to the nonlinear block results in

$$y(t) = N(A)x(t) \tag{31}$$

for a time domain description. For a frequency-domain description it would be

$$Y(s) = N(A)X(s) \tag{32}$$

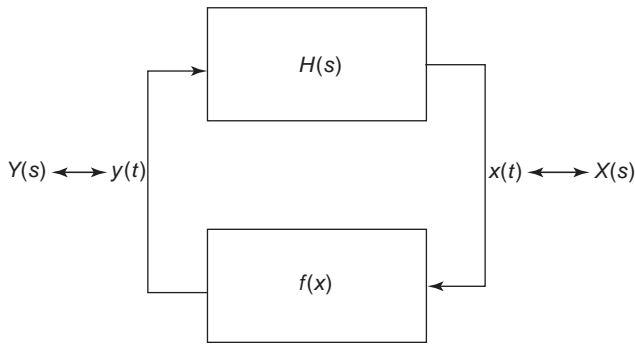


Figure 5. A general block diagram of an oscillator with amplitude control by limitation consists of a linear filter and a nonlinear amplitude controlling element connected in a loop.

On the other hand, input and output of the linear block or filter are related in the frequency domain by

$$X(s) = H(s)Y(s) \tag{33}$$

Equation (32) and (33) result in

$$H(s)N(A) = 1 \tag{34}$$

If $H(s)$ is a second-order block it can be described by

$$H(s) = \frac{a_1s^2 + a_2s + a_3}{s^2 + a_4s + a_5} \tag{35}$$

which together with Eq. (34) yields an equation of the form

$$s^2 + sb + \omega^2 = 0$$

$$b = \frac{a_1 - a_2N(A)}{1 - a_1N(A)} \tag{36}$$

$$\omega^2 = \frac{a_5 - a_3N(A)}{1 - a_1N(A)}$$

For small amplitudes $N(A)$ is equal to some constant (e.g., n_0), and Eq. (36) is called the characteristics equation. It must be assured that $b(A=0) < 0$. This is usually referred to as the *oscillation condition*. For stable amplitude control it should be

$$\frac{db(A)}{dA} > 0 \tag{37}$$

and ω^2 must be kept always positive for all possible values of A . In practice, it is desirable to make in Eq. (35) $a_1 = a_3 = 0$, which will make ω^2 and b not be coupled through a common parameter. This way the oscillation amplitude and frequency can be controlled independently.

3.3. A Practical Example: The Wien Bridge Oscillator

In a practical circuit it is not convenient to rely on inductors because of their limited range of inductance values, high price, and, in VLSI (very large scale integration) design, they are not available unless one operates in the GHz

frequency range. But it is possible to implement the filter function of Fig. 5 without inductors. The Wien bridge oscillator of Fig. 6 is such an example. Figure 6a shows its components: two resistors, two capacitors, and a voltage amplifier of gain k_0 . Figure 6b illustrates an implementation using an op amp and resistors for the voltage amplifier, and Fig. 6c shows its piecewise linear transfer characteristics. Using the describing function, the effective gain of the amplifier $k(A)$ can be expressed as a function of the sinusoidal amplitude A at node v_1

$$k(A) = k_0N(A) \tag{38}$$

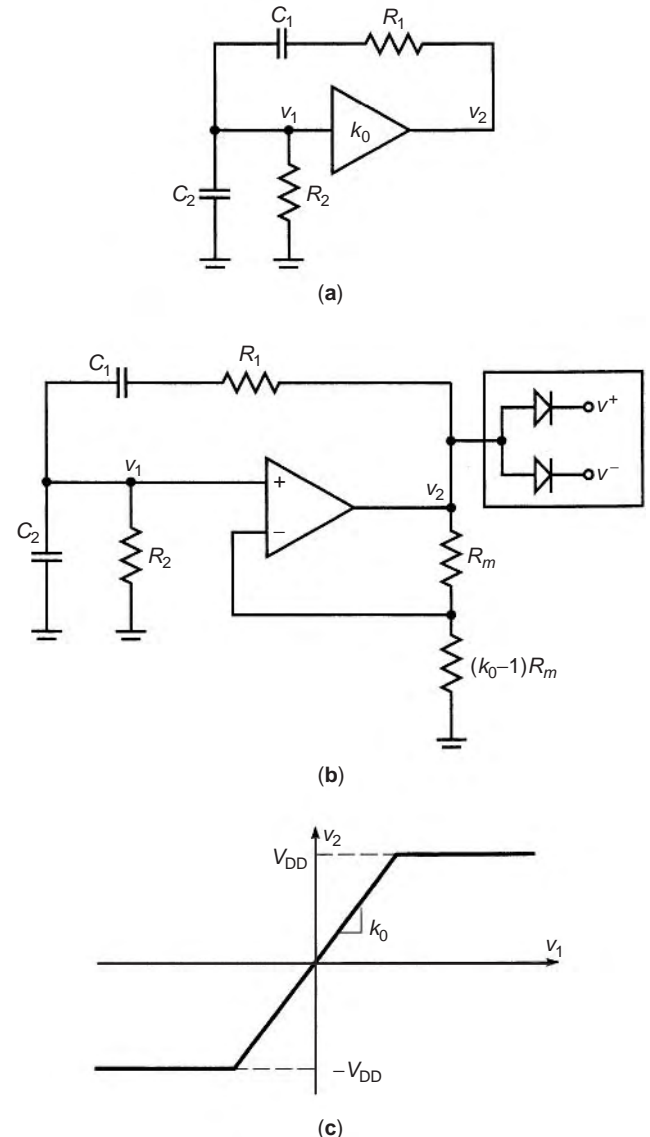


Figure 6. The Wien bridge oscillator is an example of an oscillator that does not require an inductor: (a) it consists of two resistors, two capacitors, and a voltage amplifier circuit; (b) the voltage amplifier can be assembled using an opamp and two resistors; (c) the resulting voltage amplifier has nonlinear transfer characteristics.

where $k_0N(A)$ is the describing function for the function in Fig. 6c and is given by Eq. (28) with $m_c = k_0$, $m_e = 0$, and the breakpoint changes from $V_{DD}/2$ to V_{DD}/k_0 . Consequently, the frequency-domain description of the circuit in Fig. 6a is

$$s^2 + sb + \omega^2 = 0$$

$$b = \frac{1}{R_2C_2} + \frac{1}{R_1C_1} - \frac{k_0N(A) - 1}{R_1C_2} \quad (39)$$

$$\omega^2 = \frac{1}{R_1C_1} \frac{1}{R_2C_2}$$

For initial startup it must be $b < 0$ for $A = 0$. The final amplitude A_0 is obtained by solving $b(A_0) = 0$, and the frequency of the oscillation is ω (in radians per second) or $f = \omega/2\pi$ (in hertz). Optionally, the diodes in Fig. 6b, connected to voltage sources v^+ and v^- , can be added to control the oscillation amplitude. These diodes change the saturation voltage V_{DD} of Fig. 6c, and hence will modify the describing function $N(A)$.

In general, when using amplitude control by limitation, a practical advice is to make $-b_0$ as close as possible to zero but without endangering its sign. This way the nonlinear element will distort very little the final sinusoid, because it needs to use only a small portion of its nonlinear nature to make $b(A)$ become zero. If $-b_0$ is too large the resulting waveform will probably look more like a triangular signal than a sinusoidal one.

4. AMPLITUDE CONTROL BY AUTOMATIC GAIN CONTROL

Let us illustrate the amplitude control by AGC (automatic gain control) using an OTA-C oscillator. An OTA (operational transconductance amplifier) is a device that delivers an output current I_0 proportional to its differential input voltage V_{in} . Figure 7a shows its symbol and Fig. 7b its transfer characteristics. The gain (slope g_m in Fig. 7b) is called the *transconductance*. This gain is electronically tunable through voltage V_{bias} (depending on the technology and the design, the tuning signal can also be a current). Using these devices, the self-starting oscillator of Fig. 7c can be assembled. Note that g_{m1} , g_{m2} , and C_1 emulate an inductance of value $L = C_1/(g_{m1}g_{m2})$, g_{m3} emulates a negative resistance of value $R_3 = -1/g_{m3}$, and g_{m4} emulates a positive one of value $R_4 = 1/g_{m4}$. The characteristics equation of the OTA-C oscillator is

$$s^2 + bs + \omega^2 = 0$$

$$b = \frac{g_{m4} - g_{m3}}{C_2} \quad (40)$$

$$\omega^2 = \frac{g_{m1} g_{m2}}{C_1 C_2}$$

To assure initial startup V_{b3} and V_{b4} must be such that $g_{m3} > g_{m4}$. By making g_{m3} (or g_{m4}) depend on the oscillation amplitude A , an AGC for amplitude control can be

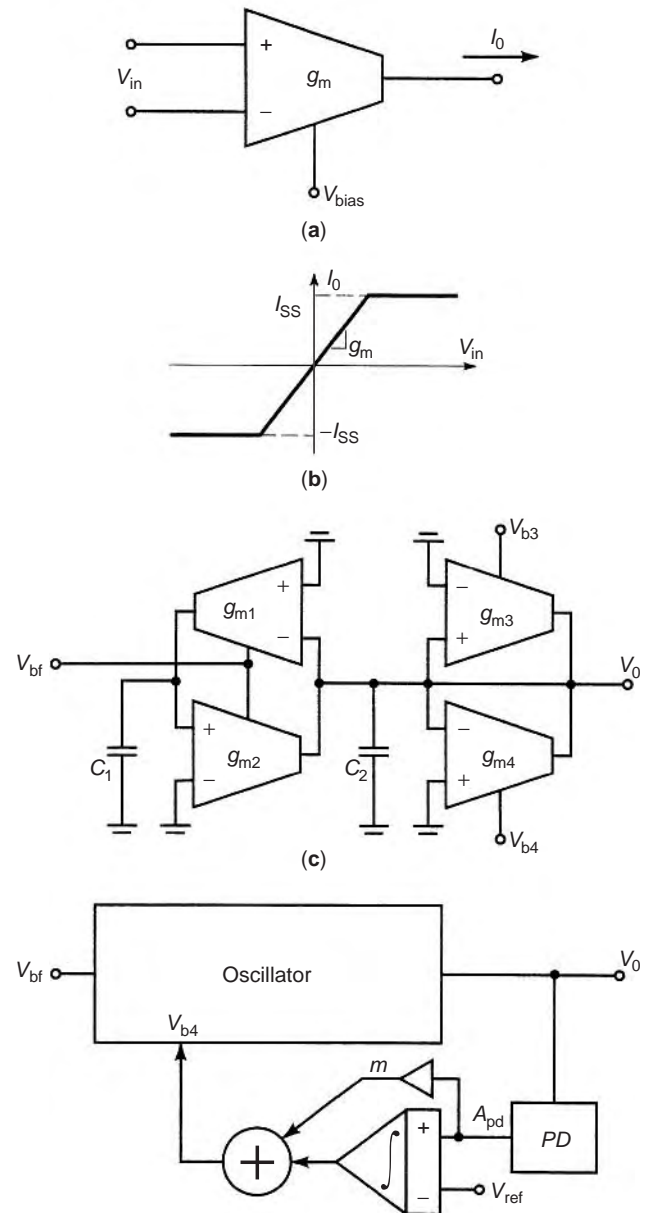


Figure 7. An oscillator with amplitude control by AGC can be made easily with OTAs and capacitors (OTA-C): (a) an OTA delivers an output current proportional to its differential input voltage; (b) it has nonlinear transfer characteristics; (c) a self-starting OTA-C oscillator can be made with four OTAs and two capacitors; (d) the amplitude control by AGC requires an additional peak detector and integrator.

realized. This is illustrated in Fig. 7d, where the box labeled “Oscillator” is the circuit in Fig. 7c, the box labeled “PD” is a peak detector, the large triangle represents a differential input integrator of time constant τ_{AGC} , the small triangle is an amplifier of gain m necessary for stability of the AGC loop, and the circle is a summing circuit. The output of the peak detector $A_{pd}(t)$ follows (with a little delay) $A(t)$, the amplitude of the sinusoid at V_0 . The error signal resulting from subtracting A_{pd} and V_{ref} is integrated and used to control g_{m4} . If $A_{pd} > V_{ref}$ gain g_{m4} will

increase (making b positive, thus decreasing A), and if $A_{pd} < V_{ref}$ gain g_{m4} will decrease (making b negative, thus increasing A). In the steady state $A = A_{pd} = V_{ref}$ and g_{m4} will automatically be adjusted to make $b = 0$. Note that V_{ref} must be such that the node voltages are kept within the linear range of all OTAs, otherwise amplitude control by limitation may be taking place.

OTA-C oscillators are convenient for AGC because their gain can be adjusted electronically. In order to do this for the Wien bridge oscillator of Fig. 6, either a capacitor or a resistor must be made electronically tunable (using a varicap or a JFET). Also, OTA-C oscillators are interesting because they do not need resistors, and this is very attractive for VLSI in CMOS technology where resistors have very poor electrical characteristics and a limited range of values.

4.1. Stability of Automatic Gain Control Loop

An AGC loop for amplitude control, like the one in Fig. 7d, presents a certain dynamic behavior that can be analyzed in order to (1) make sure it is a stable control loop and (2) optimize its time response.

In Fig. 7d the peak detector output $A_{pd}(s)$ can be modeled as a delayed version of $A(s)$

$$A_{pd}(s) = A(s)(1 - s\tau_{pd}) \quad (41)$$

where $A_{pd}(s)$ and $A(s)$ are the Laplace transforms of the small-signal components of $A_{pd}(t)$ and $A(t)$, respectively. Signal $V_{b4}(s)$ [the Laplace transform of the small-signal component of $V_{b4}(t)$], according to Fig. 7d satisfies

$$V_{b4}(s) = \frac{1}{s\tau_{AGC}} [(1 + sm\tau_{AGC})A_{pd}(s) - V_{ref}(s)] \quad (42)$$

and controls parameter b in Eq. (40). Let us assume that $b(t)$ follows instantaneously $V_{b4}(t)$ so that

$$b(s) = \alpha V_{b4}(s) \quad (43)$$

Now what is left in order to close the control loop is to know how the amplitude $A(t)$ (or $A(s)$ in the frequency domain) at node V_0 depends on b .

This dependence can easily be obtained from the time-domain differential equation [like Eq. (14)] in the following way. Assume that $b(t)$ is a time dependent signal that has small changes around $b = 0$ and keeps $A(t)$ approximately constant around A_0 . Then the solution to $V_0(t)$ [or $v_C(t)$ in Eq. (14)] can be written as

$$V_0(t) = A(t) \cos(\omega_0 t + \varphi) \quad (44)$$

where $A(t) = A_0 + a(t)$ and $|a(t)| \ll A_0$. Substituting Eq. (44) into $v_C(t)$ of Eq. (14) yields the following coefficients for the $\cos(\cdot)$ and $\sin(\cdot)$ terms, respectively, which must be iden-

tically zero [if Eq. (44) is indeed a solution for Eq. (14)]:

$$\begin{aligned} \frac{d^2 A(t)}{dt^2} + b(t) \frac{dA(t)}{dt} + b^2(t) \frac{A(t)}{4} &= 0 \\ 2 \frac{dA(t)}{dt} + A(t)b(t) &= 0 \end{aligned} \quad (45)$$

The first equation is not of much use, but from the second it follows that

$$A(t) = A(t_0) e^{-(1/2) \int_{t_0}^t b(t) dt} \quad (46)$$

When the AGC loop is in its steady state $A(t) = A_0 + a(t)$ and the integral is a function that moves above and below zero but is always close to zero. Consequently, the exponential can be approximated by its first-order Taylor expansion resulting in

$$\begin{aligned} A(t) &\approx A(t_0) \left[1 - \frac{1}{2} \int_{t_0}^t b(t) dt \right] \\ \Rightarrow a(t) &\approx -\frac{A(t_0)}{2} \int_{t_0}^t b(t) dt \approx -\frac{A_0}{2} \int_{t_0}^t b(t) dt \end{aligned} \quad (47)$$

In the frequency domain this is

$$A(s) \approx -\frac{A_0}{2s} b(s) \quad (48)$$

From Eqs. (41)–(43) and (48) a loop equation for the AGC control can be written

$$\begin{aligned} A(s) &= \frac{V_{ref}(s)}{s^2 k_1 + s k_2 + 1} \\ k_1 &= \frac{2\tau_{AGC}}{\alpha A_0} - m\tau_{AGC}\tau_{pd} \\ k_2 &= m\tau_{AGC} - \tau_{pd} \end{aligned} \quad (49)$$

This equation represents a stable control system if the poles have negative real part. This is achieved if $k_1 \geq 0$ and $k_2 > 0$. Parameters k_1 and k_2 can also be optimized for optimum amplitude transient response [e.g., after a step response in $V_{ref}(t)$].

5. VOLTAGE-CONTROLLED HARMONIC OSCILLATORS

An oscillator whose frequency can be electronically controlled is required in many applications. Such an oscillator is called a *voltage-controlled oscillator* (VCO), although sometimes the control parameter can also be current.

In the case of the Wien bridge oscillator of Fig. 6 the frequency of oscillation ω is controlled by R_1 , R_2 , C_1 , and C_2 . Changing one or more of these parameters would enable external control of the frequency. In order to have an electronic control there are two options: (1) continuous or analog control and (2) discrete or digital control.

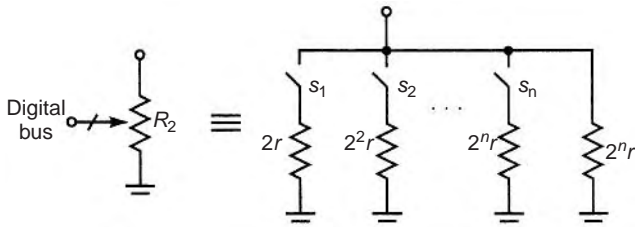


Figure 8. The frequency of the Wien bridge oscillator can be digitally controlled by replacing one of the resistors by a binary-weighted resistor array controlled through a digital databus.

For analog control of the Wien bridge oscillator of Fig. 6 either a voltage-controlled resistor (JFET) or a voltage-controlled capacitor (varicap) is needed. Digital control can easily be implemented by using a binary-weighted array of resistors or capacitors that are switched in and out of the circuit by means of a digital bus. This is exemplified in Fig. 8 for resistor R_2 . Signals s_i are either 0 when the switch is open or 1 when it is closed. This yields

$$\frac{1}{R_2} = \frac{1}{r} \left[\frac{1}{2^n} + \sum_{i=1}^n \frac{s_i}{2^i} \right] = \frac{1}{r} d_n \quad (50)$$

where d_n is a number that ranges from $1/2^n$ to 1 in steps of $1/2^n$. Number d_n is represented in binary format by the bits $\{S_n S_{n-1} \dots S_2 S_1\}$.

The OTA-C oscillator of Fig. 7 is much better suited for analog or continuous control of frequency. If $g_{m1} = g_{m2}$ and $C_1 = C_2$, the frequency is equal to $\omega = 2\pi f = g_{m1}/C_1$. Since voltage V_{bf} in Fig. 7d controls simultaneously g_{m1} and g_{m2} (making them equal), this voltage can be used directly to control the frequency of the VCO.

Whether a VCO is made with OTAs and capacitors, or with resistors, capacitors, and op amps, or uses some other technique, in general it turns out that the frequency does not have a linear dependence on the control voltage. In practical circuits it also happens that if the control voltage is maintained constant, the frequency may change over long periods of time due to temperature changes which cause device and circuit parameters (such as transconductance and resistance) to drift. Both problems can be overcome by introducing a frequency control loop.

6. FREQUENCY-CONTROLLED LOOP

Figure 9a shows the basic concept of frequency-controlled loop for VCOs. It consists of a VCO (e.g., the one in Fig. 7d), a differential input voltage integrator, and a frequency to voltage converter (FVC) circuit. Voltage V_{CO} is now the external control of the VCO frequency. The FVC circuit delivers an output voltage V_{FVC} that depends linearly on the frequency f of its input signal V_{OSC} :

$$V_{FVC} = \rho f + V_{F0} \quad (51)$$

Parameters ρ and V_{F0} must be constants and should not depend on temperature or technological parameters that

change from one prototype to another. If such an FVC is available, the circuit in Fig. 9a would stabilize at $V_{FVC} = V_{CO}$. According to Eq. (51), this means that the resulting oscillation frequency f_0 depends on V_{CO} as

$$f_0 = \frac{V_{CO} - V_{F0}}{\rho} \quad (52)$$

which is linear and temperature-independent.

A possible implementation with OTAs of the FVC is shown in Fig. 9b. It uses two OTAs of transconductance g_o , a capacitor C , a peak detector, a switch, a temperature-independent voltage reference V_{ref} , and a monostable triggered by the oscillating signal V_{OSC} . During each period $T = 1/f$ of signal V_{OSC} the monostable delivers a pulse of constant width t_0 , which must be temperature-independent and well calibrated. Many times it is convenient to add a sine-to-square-wave converter (and even a frequency divider) between V_{OSC} and the monostable. The circuit of Fig. 9b uses three components that are not temperature-independent and may vary over time and from one prototype to another: the two OTAs and the capacitor. However, provided both OTAs have the same transconductance (which is a reasonable assumption for VLSI implementations), the resulting parameters ρ and V_{F0} do not depend on C nor g_o . An example of the time waveforms of $u(t)$ and $v(t)$ of Fig. 9b is shown in Fig 9c. During each

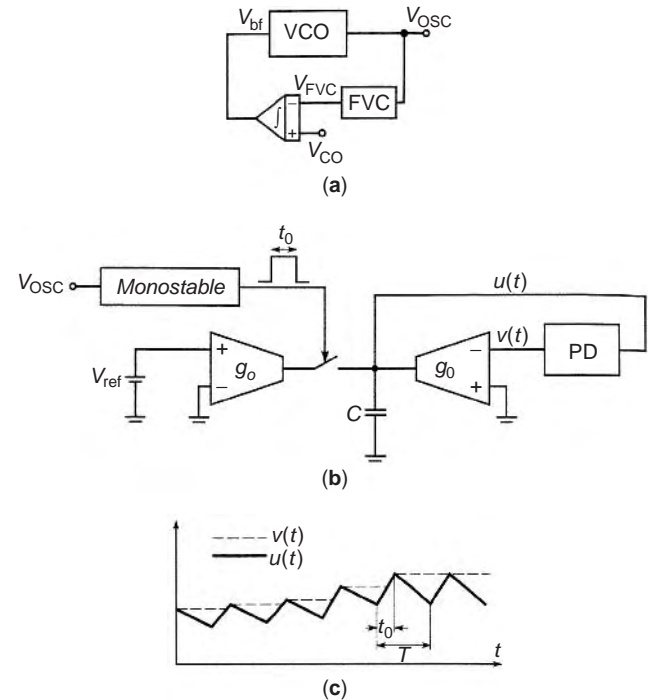


Figure 9. A frequency-controlled loop can provide a linear dependence between tuning voltage and VCO frequency, and can also make this dependence temperature and prototype independent: (a) it can be made by adding a FVC and an integrator to a VCO; (b) the FVC can be made with a calibrated monostable, a reference voltage, a peak detector, two OTAs, a capacitor, and a switch; (c) after a transient the FVC output stabilizes to a steady-state voltage that depends linearly on the input signal frequency.

period T of V_{OSC} the monostable is triggered once, turning the switch ON during a time t_0 . While the switch is in ON state capacitor C is charged by a constant current $g_0(V_{ref}-v(t))$, and when the switch is OFF a constant current of value $-g_0v(t)$ discharges it. The output of the FVC $v(t)$ changes from cycle to cycle but is constant during each cycle. If v_m is its value during one cycle and v_{m+1} for the next one, it follows that

$$u(t+T) = u(t) + \frac{g_0(V_{ref} - v_m)}{C} t_0 - \frac{g_0 v_{m+1}}{C} (T - t_0) \tag{53}$$

where $u(t)$ is taken at one of peaks: $u(t) = v_m$ and $u(t+T) = v_{m+1}$. Consequently, we obtain

$$v_{m+1} = \frac{v_m(C - g_0 t_0) + V_{ref} g_0 t_0}{C + g_0(T - t_0)} \tag{54}$$

In the steady of the FVC $v_{m+1} = v_m$. Applying this condition to Eq. (54) and calling V_{FVC} the stabilized value of v_m yields

$$V_{FVC} = \frac{V_{ref} t_0}{T} = V_{ref} t_0 f \tag{55}$$

Consequently, the circuit of Fig. 9b implements a FVC with $\rho = V_{ref} t_0$ and $V_{F0} = 0$, which both are temperature- and prototype-independent.

7. FURTHER CONSIDERATIONS

The different concepts and considerations mentioned so far have been illustrated with practical circuits using either resistors, capacitors, and op amps, or using OTAs and capacitors. There are many other circuit techniques available that can be used to implement the different blocks and equations needed for stable harmonic oscillator circuits. Some of these techniques could be continuous current mode, switched capacitor, switched current, digital circuit techniques, or even any combination of these techniques.

Depending on the frequency range of the oscillator it may be necessary to consider circuit parasitics that have not been mentioned so far. For example, op amps and OTAs both have nonideal input and output impedances, leakage currents, and most importantly gains that are frequency-dependent. All these parasitics result in modified characteristics equations. A very sensitive parameter to parasitics is the oscillation condition $-b_0$ required for initial startup. Since in practice it is desirable to have $-b_0$ very close to zero but still guarantee its negative sign, it is apparent that parasitics can result in either very negative (resulting in very distorted sinusoids) or positive (resulting in no oscillation) values. Each circuit technique has its own parasitics, and depending on the intended frequency range, they will have a different impact on the final oscillator performance. Consequently, for good oscillator

design the dominant parasitics need to be well known and taken into account.

Another interesting and advanced issue when designing oscillators in distortion. Both amplitude control mechanisms, limitation and AGC, are nonlinear and will introduce some degree of distortion. Is there a way to predict how much distortion will render an oscillator?

7.1. Distortion for Amplitude Control by Automatic Gain Control

In an oscillator with AGC for amplitude control, as in Fig. 7d, the element that introduces most of the distortion is the peak detector. Figure 10 shows examples of peak detectors based on one-phase or half-wave (Fig. 10a), two-phase or full-wave (Fig. 10b), and four-phase (Fig. 10c) rectifying principles. For the four-phase case, either the oscillator should provide two phases with $\pi/2$ shift, or an additional integrator is needed. Peak detectors with more phases can be implemented by linearly combining previous phases. Increasing the number of phases in the peak detector results in faster response [delay τ_{pd} in Eq. (41) is smaller for more phases] and less distortion. However, all phases have to present the same amplitude; otherwise distortion will increase. In practice, as the number of phases increases, it becomes more difficult (due to offsets

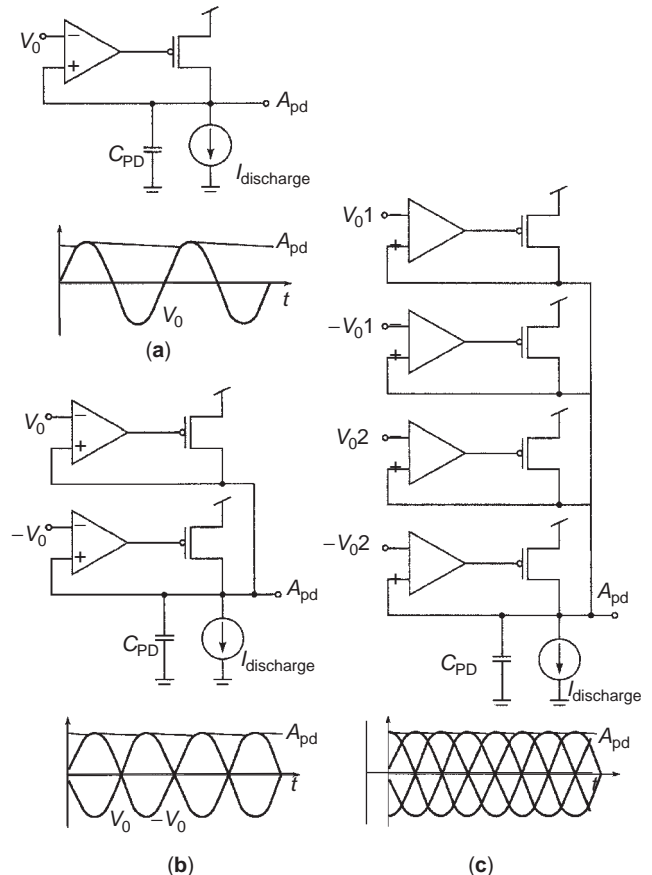


Figure 10. Possible implementations for a peak detector: (a) one phase-based (or half-wave-rectifier based) (b) two phase-based (or full-wave-rectifier-based), and (c) four-phase-based peak detector.

and component mismatch) to keep the amplitude of the phases sufficiently equal.

In the peak detectors of Fig. 10, whenever one of the phases becomes larger than A_{pd} it slightly turns ON its corresponding P transistor injecting a current into C_{PD} until A_{pd} increases sufficiently to turn OFF the P transistor. The discharge current ensures that A_{pd} will follow the amplitude of the oscillations if it decreases. Increasing $I_{discharge}$ results in faster response but higher distortion. Whatever peak detector is used, waveform $A_{pd}(t)$ is not constant nor sinusoidal. It has a shape similar to those shown in Fig. 10. Since $A_{pd}(t)$ is periodic its Fourier series expansion can be computed:

$$A_{pd}(t) = A_0 + \sum_{n=1}^{\infty} a_n \cos(n\omega_0 t + \varphi_n) \quad (56)$$

The high-order harmonic components $\{a_2, a_3, \dots\}$ are those which contribute to distortion at node V_0 (in Fig. 7d). Applying the filtering functions that go from node A_{pd} , through V_{b4} , to V_0 [Eqs. (41)–(43) and (48)] to these higher-order harmonics provides their amplitudes at node V_0 :

$$|A_{on}| = \frac{\alpha A_0}{2\tau_{AGC} n^2 \omega_0^2} |1 + jn\omega_0 m\tau_{AGC}| |1 - jn\omega_0 \tau_{pd}| |a_n| \quad (57)$$

The total harmonic distortion at the output of the oscillator is then defined as

$$\text{THD}(V_0) = \sqrt{\sum_{n=2}^{\infty} \left(\frac{A_{on}}{A_0}\right)^2} \quad (58)$$

7.2. Distortion for Amplitude Control by Limitation

This problem is computationally complicated but can be solved by harmonic balance. Consider the general block diagram of Fig. 5. In the steady state, periodic waveforms $x(t)$ and $y(t)$ can be expressed by their respective Fourier series expansions

$$\begin{aligned} x(t) &= x_1 \cos(\omega_0 t) + \sum_{n=2}^{\infty} x_n \cos(n\omega_0 t + \varphi_n) \\ y(t) &= \sum_{n=1}^{\infty} y_n \cos(n\omega_0 t + \phi_n) \end{aligned} \quad (59)$$

where

$$\begin{aligned} |x_n| &\ll |x_1| \\ |y_n| &\ll |y_1| \end{aligned} \quad (60)$$

In general, this problem is solved numerically for a finite set of harmonics. Let N be the highest harmonic to be computed. Since $f(x(t))$ is also periodic, computing its Fourier series expansion yields that of $y(t)$. Therefore, given a set of parameters for $x(t)$ $\{x_1, \dots, x_N, \varphi_2, \dots, \varphi_N\}$ the set of

parameters $\{y_1, \dots, y_N, \phi_1, \dots, \phi_N\}$ for $y(t)$ can be obtained this way. By applying each component of $y(t)$ (characterized by y_n and ϕ_n) to filter $H(s)$ yields the corresponding component for $x(t)$:

$$\begin{aligned} x_n &= y_n |H(jn\omega_0)| \\ \varphi_n &= \phi_n + \text{phase}(H(jn\omega_0)) \end{aligned} \quad (61)$$

By iterating this procedure until all values x_n, y_n, φ_n , and ϕ_n converge, the distortion of $x(t)$

$$\text{THD}(x) = \sqrt{\sum_{n=2}^N \left(\frac{x_n}{x_1}\right)^2} \quad (62)$$

or $y(t)$

$$\text{THD}(y) = \sqrt{\sum_{n=2}^N \left(\frac{y_n}{y_1}\right)^2} \quad (63)$$

can be predicted.

FURTHER READING

- K. K. Clarke and D. T. Hess, *Communication Circuits: Analysis and Design*, Addison-Wesley, Reading, MA; 1978.
- A. Gelb and W. Vander Velde, *Multiple Input Describing Functions and Nonlinear System Design*, McGraw-Hill, New York, 1968.
- E. J. Hahn, Extended harmonic balanced method, *IEE Proc. Part G, Circ. Devices Syst.* **141**:275–284 (1994).
- B. Linares-Barranco et al., Generation, design and tuning of OTA-C high-frequency sinusoidal oscillators, *IEE Proc. Part G, Circ. Devices Syst.* **139**:557–568 (1992).
- E. Vannerson and K. C. Smith, Fast amplitude stabilization of an RC oscillator, *IEEE J. Solid-State Circ.* **SC-9**:176–179 (1974).

HELICAL ANTENNAS

ARLON T. ADAMS
JAY K. LEE
Syracuse University
Syracuse, New York

1. INTRODUCTION

The helix antenna has a long and fascinating history. It was discovered in 1946 by John Kraus. Since then, new variations have continued to arise even up to the present day. The discovery itself is a very interesting story, which is told in John Kraus' book *Antennas* [1]. It all started with an afternoon lecture at Ohio State University. John Kraus listened as the speaker described the wave-guiding helix used in traveling-wave tubes; he wondered if this interesting helix could be used as an antenna and, after the

talk, he asked the well-known lecturer. The speaker replied emphatically, "No, I've tried it, and it doesn't work." That very evening, John Kraus went down to his basement, wound a seven-turn helical coil one wavelength in circumference and fed it by means of a coaxial line and ground plane (Fig. 1a). He found that it produced a sharp beam of circularly polarized radiation off the open end of the helix. So the helix antenna was born, despite the advice of experts.

1.1. Helical Curves

The helix was well-known in ancient Greece. Geminus described it in the first century B.C. and there are references to earlier work on the helix. The *cylindrical helix* may be defined by considering a right circular cylinder of radius a , whose axis is the z axis. Using a right-handed cylindrical coordinate system (r, ϕ, z) the equations of the helix are

$$x = a \cos \phi; \quad y = a \sin \phi; \quad z = a\phi \tan \alpha \quad (1)$$

where α is the pitch angle of the helix and $2a$ is the diameter. The lines of the cylinder parallel to the z axis, that is, the lines $(r = a, \phi = \phi_0)$ are considered to be the generators of the cylinder. The cylinder is generated by rotating any generator about the z axis. The helix cuts the generators at a constant angle $\pi/2 - \alpha$. It also projects as a sine curve on any plane parallel to the axis, for example, any plane that includes the axis.

Figure 1a shows the wire helix antenna. Parameters are defined as follows:

D is the diameter of helix, which is equal to $2a$.

C is the circumference.

S is the spacing between turns.

α is the pitch angle.

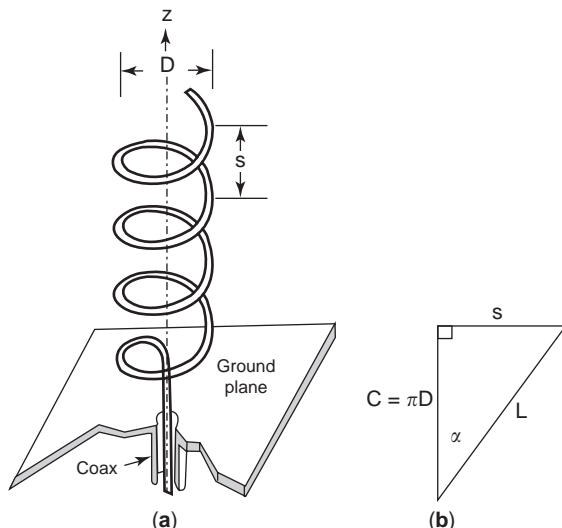


Figure 1. The helical antenna: (a) a helix fed by a coaxial line and a ground plane; (b) one turn of the helix unrolled on a flat plane.

L is the length of one turn.

N is the number of turns.

C_λ , S_λ , and L_λ represent the respective distances in wavelengths such that $C_\lambda = C/\lambda$, and so on. When one turn of the helix is unrolled on a flat plane, the relationships between the spacing S , circumference C , turn length L , and pitch angle α can be obtained from the triangle shown in Fig. 1b as follows:

$$S = C \tan \alpha, \quad \alpha = \tan^{-1} \frac{S}{C}, \quad L = \sqrt{C^2 + S^2} \quad (2)$$

Thus we need only *three* independent parameters, C , α , N , to describe a helix. Note that when $\alpha = 0^\circ$, $S = 0$, and the helix reduces to a planar loop. When $\alpha = 90^\circ$, $C = 0$, and the helix becomes a straight line.

The round-wire helix such as Kraus first built consists of a round wire whose centerline is the helix curve of Eq. (1). The tape helix is a conducting tape of width w , which is wound around a cylinder or a thin cylindrical tube. Its centerline is the helix of Eq. (1). A single-wire helix is called the *monofilar helix*. The double, or *bifilar*, helix is constructed by adding an additional member, which is formed by replacing ϕ with $\phi - \pi$ everywhere in Eq. (1). The *quadrifilar* helix antenna is formed by adding three members; ϕ in Eq. (1) is replaced with $\phi - (\pi/2)$, π , $(3\pi/2)$. A left-handed helix can be formed by using a left-handed coordinate system, or by replacing ϕ in Eq. (1) with $2\pi - \phi$. Figure 1a shows a right-handed helix. There are other helical curves. The *conical helix* lies on the surface of a cone and cuts the radial lines of the cone, the generators, at a constant angle. The *spherical helix* lies on the surface of the sphere and cuts the generators, for example, the longitude lines, at a constant angle.

There are many striking examples of the helix in nature, from some of the smallest to some of the largest objects. Most important of all is the DNA molecule, which is a double helix. The marks on a snail of the family Helicidae resemble a spherical helix. The human ear has a prominent helical ridge. The *Heliconia* is a family of herbs with a helical shape. The helictite is similar to a stalagmite. Some trees have helical bark. Finally, we have the largest of the nebulae, the Helix Nebula. In addition, we see many manmade forms of the helix around us, including automobile springs, spiral staircases, inductance coils, transformer coils, parking lot ramps, automobile antenna coils, and finally, the lowly screw, which is a combination of conical and cylindrical helices.

2. MONOFILAR HELICAL ANTENNA

We first consider the characteristics of a monofilar, or unifilar, helical antenna. In this section we simply call it a helical antenna, implying that it is a *monofilar* helix. The helix commonly operates in two different modes, the normal mode and the axial mode, depending on the electrical size of the helix. When the dimensions of the helix are small compared with a wavelength ($D \ll \lambda$, $NS \ll \lambda$), the maximum radiation is normal (or perpendicular) to the

helix axis. This condition is called the *normal mode*. When the helix circumference is on the order of one wavelength, the maximum radiation is along the helix axis. Thus, this type of operation is called the *axial mode*. The axial mode helix is a broadband antenna. The radiation from this axial-mode helix is close to circular polarization along the axis. There is also a *backfire mode*, which is discussed in a later section.

2.1. Normal-Mode Helix

Let's consider a helix with its axis along the z axis, centered at the origin (Fig. 2a). The geometry of the helix reduces to a loop when the pitch angle α approaches zero and to a straight wire when it approaches 90° . Since the limiting geometries of the helix are a loop and a dipole, the far field radiated by a small helix can be described by the radiation fields of a small loop and a short dipole when dimensions are small compared to a wavelength. The analysis of a small short helix is facilitated by assuming that the helix consists of a number of small loops and short dipoles connected in series as in Fig. 2b. The diameter of the loops is the same as the helix diameter (D) and the length of the dipoles is approximately the same as the spacing (S) between turns of the helix. Because the helix is small and short, the current distribution is assumed to be *uniform* in magnitude and phase over the entire length of the helix. For the same reason, the far-field (Fraunhofer) pattern will be indepen-

dent of the number of turns and thus can be obtained by considering the pattern of a single-turn helix that consists of a single small loop of diameter D and one short dipole of length S .

Assume that the complex amplitude of current is I and the angular frequency is ω . The radiation electric field of the small loop of diameter D has only an E_ϕ component, given by

$$E_\phi = \eta k^2 I A \frac{e^{-jkr}}{4\pi r} \sin \theta \quad (3)$$

where $A = \pi D^2/4$ is the area of the loop, $k = \omega\sqrt{\mu\epsilon}$ is the propagation constant, and $\eta = \sqrt{\mu/\epsilon}$ is the intrinsic impedance. The far field of the short dipole, or the Hertzian dipole of length S , has only an E_θ component, given by

$$E_\theta = j\omega\mu I S \frac{e^{-jkr}}{4\pi r} \sin \theta \quad (4)$$

The total radiation field for one turn is then given by

$$\mathbf{E} = \hat{\mathbf{a}}_\theta E_\theta + \hat{\mathbf{a}}_\phi E_\phi = \{\hat{\mathbf{a}}_j \omega \mu I S + \hat{\mathbf{a}}_\phi \eta k^2 A\} I \frac{e^{-jkr}}{4\pi r} \sin \theta \quad (5)$$

The normalized radiation field pattern $f(\theta)$ of the normal-mode helix is

$$f(\theta) = \sin \theta \quad (6)$$

which is the same as that of the Hertzian dipole and the small loop and is shown in Fig. 2c. The field is zero along the axis (in the endfire direction) and is maximum in the xy plane ($\theta = 90^\circ$), which is normal to the helix axis.

Because E_θ and E_ϕ are 90° out of phase as shown in Eqs. (3) and (4), the radiated wave is elliptically polarized. The axial ratio (AR) of the polarization ellipse of the far field is obtained by dividing the magnitude of Eq. (4) by that of Eq. (3)

$$\text{AR} = \frac{|E_\theta|}{|E_\phi|} = \frac{\omega\mu S}{\eta k^2 \frac{2\pi}{\lambda} A} = \frac{S\lambda}{2\pi A} = \frac{2S\lambda}{(\pi D)^2} \quad (7)$$

where we have used $k = 2\pi/\lambda$, $nk = \omega\mu$. Because E_θ and E_ϕ are 90° out of phase, the polarization ellipse becomes a circle when $|E_\theta| = |E_\phi|$, indicating circular polarization. Setting $\text{AR} = 1$ yields

$$C = \pi D = \sqrt{2S\lambda} \quad \text{or} \quad C_\lambda = \sqrt{2S} \quad (8)$$

Under this condition the radiation field is circularly polarized in *all* directions except of course along the axis where the radiation is zero. The polarization ellipse of the radiation from a helix of constant turn length (L) changes progressively as the pitch angle α is varied. When $\alpha = \tan^{-1}(S/C) = 0$ (the helix reduces to a loop), $\text{AR} = 0$, $E_\theta = 0$, $\mathbf{E} = \hat{\mathbf{a}}_\phi E_\phi$; thus the wave is linearly polarized with horizontal (or perpendicular) polarization. As α increases, the polarization becomes elliptical, with the major axis of the

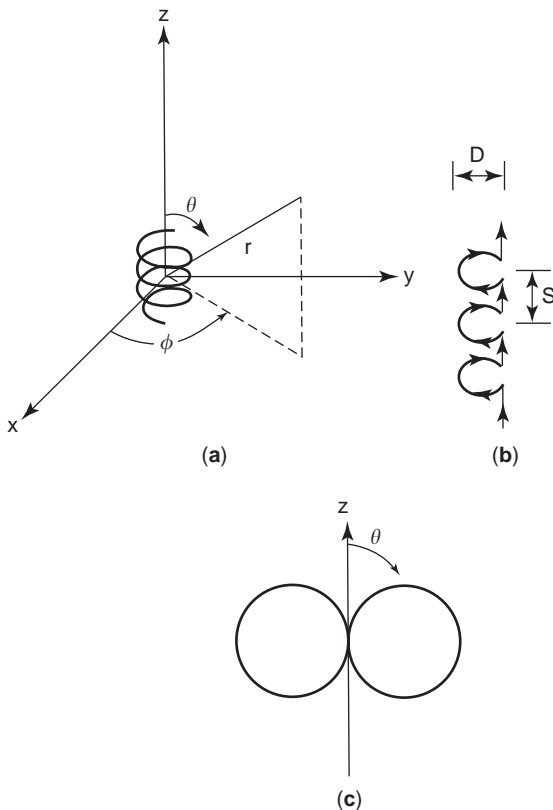


Figure 2. The normal-mode helix: (a) coordinate system; (b) loop-dipole model; (c) beam pattern.

ellipse horizontal. When α reaches a value such that condition (8) is satisfied, $AR=1$, and the polarization is circular. With the help of Eq. (2), the condition (8) leads to the following value of α :

$$\alpha_{CP} = \sin^{-1} \left[\frac{-1 + \sqrt{1 + L_\lambda^2}}{L_\lambda} \right] \quad (9)$$

As α increases further, the polarization again becomes elliptical and the major axis is vertical. Finally, when $\alpha=90^\circ$ (the helix reduces to a dipole), $E_\phi=0$, $\mathbf{E}=\hat{\mathbf{a}}_\theta E_\theta$; thus the polarization is linear with vertical (or parallel) polarization. For small pitch angles ($\alpha \ll 1$), Eq. (9) is simplified to

$$\alpha_{CP} = \frac{C_\lambda}{2} \quad (10)$$

where α_{CP} is expressed in radians. For small pitch angles, circular polarization can occur at frequencies such that the circumference is very small compared to a wavelength ($C_\lambda \ll 1$).

From Eqs. (3) and (4), we note that the loop field E_ϕ and the dipole field E_θ , respectively, are proportional to the second and first powers of frequency. Correspondingly, radiation resistance of loop and dipole are proportional to the fourth and second powers, respectively. Thus, as frequency decreases, the dipole radiation predominates and the beam pattern is linearly polarized. In this linearly polarized frequency range, the normal-mode helix has some interesting properties. Its beam pattern is essentially that associated with the dipoles, that is, a monopole of length NS above a ground plane. Its impedance, however, is significantly affected by the loops.

The normal-mode helix is limited by its size. It has the same restrictions and limitations that apply to any electrically small antenna. But within those restrictions, it has certain advantages over a dipole antenna of the same height. These include a lower frequency for resonance and a larger radiation resistance, because of both the longer path of the helical structure. While the dipole may require additional impedance-matching circuits to achieve resonance, the helix is resonant without supplementary matching elements. Another advantage over the dipole is

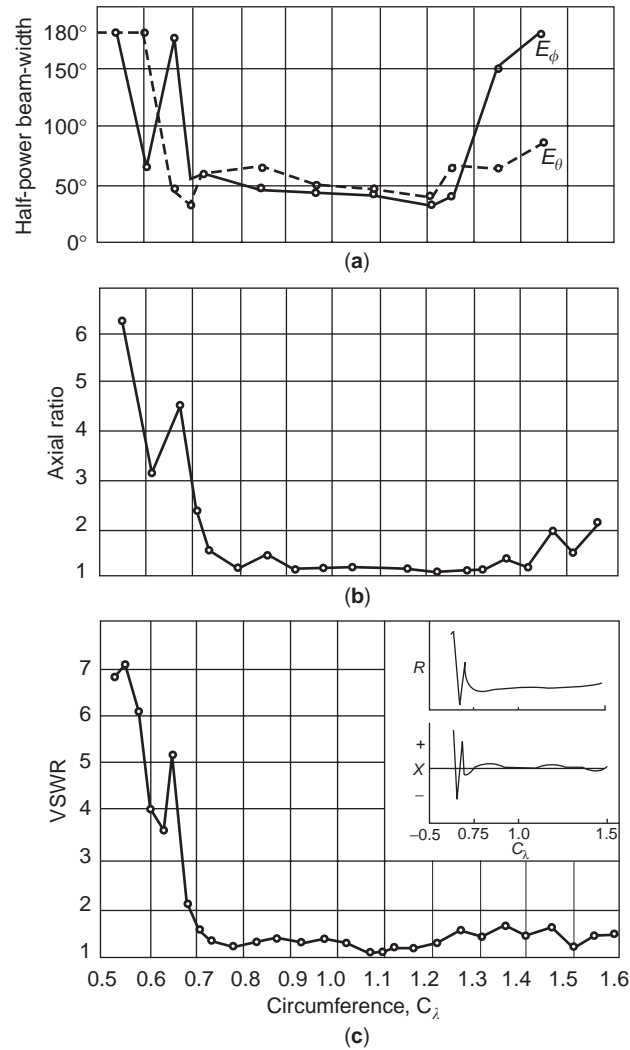


Figure 4. Measured performance of the monofilar axial mode helix: (a) beamwidth; (b) axial ratio; (c) VSWR. (From Kraus [1], © 1988 by McGraw-Hill, Inc. Reprinted with permission of the McGraw-Hill Companies.)

that the helix is flexible and more resilient. The higher radiation resistance, resonant characteristic, and flexibility make the normal-mode helix suitable for small antennas used in mobile communications.

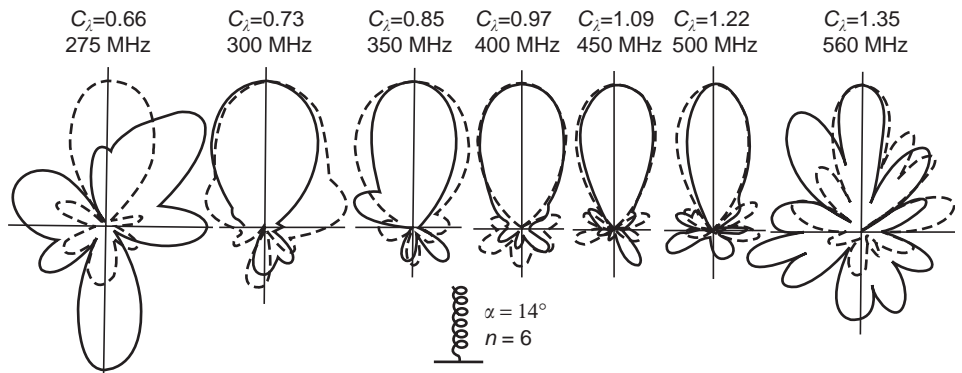


Figure 3. Measured beam patterns of the monofilar axial mode helix. (From Kraus [1], © 1988 by McGraw-Hill, Inc. Reprinted with permission of the McGraw-Hill Companies.)

2.2. Axial-Mode Helix

A very useful mode of operation for the helical antenna is the axial or endfire mode. In this mode the radiation pattern has a single mainbeam along the axis of the helix (+z direction); that is, it is an endfire antenna. Experiments have shown that the axial mode occurs when the circumference of the helix is approximately one wavelength and when the helix has several turns. A primary component of current on the helix is a wave traveling outward from the feed along the wire at approximately the speed of light and the radiation is a beam off the end of the helix. Because the electric field vector rotates around in a circular fashion as does the current on the helix, we expect that the radiation field is circularly polarized along the helix axis. One very important feature of the axial-mode helical antenna is its *broadband* character. As a rule of thumb, the approximate bandwidth for the axial mode is given as follows [2]:

$$\frac{3}{4} < C_\lambda < \frac{4}{3} \quad (11)$$

The bandwidth ratio, the ratio of the upper and lower frequencies, is $\frac{4}{3} \div \frac{3}{4}$ or 1.78, which is close to a 2-1 bandwidth. The helix is usually fed axially or peripherally with the inner conductor of the coaxial line connected to the helix and the outer conductor attached to the ground plane. The ground plane can be made from either solid metal or wire mesh.

2.2.1. Analysis of Radiation Pattern. The axial-mode helix has a circumference of approximately one wavelength, so the current distribution would not be uniform, and we assume that there is an outgoing current wave, traveling along the helical conductor at phase velocity $v = pc$ (where p is the phase velocity relative to the speed of light c in free space). Then

$$I(l) = I_0 e^{-j\beta l} \quad (12)$$

where l is the distance measured along the helix from the beginning of the turn closest to the ground plane, I_0 the input current, $\beta = k/p$ the phase constant of the current wave. When the total length of one turn is approximately a wavelength, the current distribution in Eq. (12) has opposite phase (180° out of phase) on opposite sides of a turn because they are separated by about a half-wavelength. Also the helical coil physically reverses current direction for opposite points. Thus the currents at opposite points of a turn are essentially in phase, giving rise to reinforcement in the far field along the helix axis. We can find the radiation pattern by using the principle of pattern multiplication because a helix with uniform cross section can be considered as an array of N identical elements (or turns). We have a uniformly excited, equally spaced array with spacing S , so the total pattern is the product of the pattern for one turn (the element pattern) and the pattern for an array of N isotropic point sources (an array factor). When the helix is long (say, $NS > \lambda$), the array factor is much sharper than the element pattern and hence determines the shape of the total far-field pattern.

2.2.1.1. Array Factor. The array factor (AF) of a uniformly excited, equally spaced, linear array of N elements is given by

$$\text{AF} = \frac{\sin \frac{N}{2} \psi}{N \sin \frac{\psi}{2}} \quad (13)$$

$$\psi = kS \cos \theta + \delta \quad (14)$$

where θ is an angle measured from the array axis (z axis) and δ is the phase shift between adjacent elements. Explaining the phase relationships of the axial-mode helix is difficult. Begin by finding the phase shift δ required for endfire operation, because we know that the radiation is endfire. For *ordinary endfire*, we find the conditions such that ψ is zero at $\theta = 0^\circ$.

$$\delta = -kS - 2m\pi \quad (m \text{ is an integer}) \quad (15)$$

where the term $(-2m\pi)$ reflects the basic ambiguity of phase. Next we find conditions for *increased directivity Hansen-Woodyard (HW) endfire* [3], since this is an optimum form of endfire:

$$\begin{aligned} \delta &= -kS - 2m\pi - \frac{\pi}{N} \\ &= -2\pi - \left(kS + \frac{\pi}{N}\right) \quad (m = 1) \end{aligned} \quad (16)$$

To be more accurate, the term π/N should be replaced by $2.94/N$ [3]. However, the choice of π/N hardly changes the radiation field [4] and is convenient for expressing other quantities. We have tried the arbitrary choice ($m = 1$) because this term -2π corresponds roughly to one turn of the circumference at midband ($C_\lambda = 1$). Later it will be clear that other choices are not possible solutions. Experiments show [1,5] that the phase shift δ obtained is close to that of Eq. (16) at midband ($C_\lambda = 1$). How does this happen? We have already pointed out that the term (-2π) corresponds roughly to one turn of the circumference. In addition, the length around one turn of the helix is greater than a wavelength ($L_\lambda > 1$) at midband. More importantly, the velocity of travel is less than that of light ($p \approx 0.9$) at midband [5]. These two additional contributions account for the minor term $-(kS + \pi/N)$. Thus the phase at midband is explained. However, the experimental data for δ track Eq. (16) fairly well over the entire bandwidth of the axial mode. How is this possible? We cannot alter our choice of m ; one choice must work for the entire frequency range; and if p remained constant, Eq. (16) could not be satisfied over the entire band. Fortunately, p does vary quite a bit (from 0.73 to 0.97) over the axial-mode frequency range; the result is that HW endfire described by Eq. (16) is tracked quite well over most of the band, falling off a little toward the high end. All in all, this is quite a remarkable story. The phase, so to speak, *locks in* to HW endfire over the bandwidth of almost 2-1. When first reported by Kraus, this was called an *anomalous* phase progression. It still continues to mystify succeeding generations.

To summarize, the phase progression along the helix wire is relatively simple; it corresponds roughly to that of speed of light along the wire. The phase progression in z , which determines the phase difference δ between turns, follows the phase progression of the wire. Taking into account the phase ambiguity (2π), we see that HW endfire is obtained at midband. The relative phase velocity p then changes with frequency just enough to maintain the HW endfire. Another point worth noting is that we have not discussed backfire ($\theta = 180^\circ$) radiation. It does, in fact, occur along with the axial mode but is usually suppressed by the ground plane. It will return, to our advantage, with the multifilar helix:

$$\beta = -\frac{\delta}{L} = \frac{1}{L} \left[kS + 2\pi \left(1 + \frac{1}{2N} \right) \right] = \frac{2\pi}{L} \left(\frac{S}{\lambda} + \frac{2N+1}{2N} \right) \quad (17)$$

$$p = \frac{k}{\beta} = \frac{L_\lambda}{S_\lambda + (2N+1)/2N} \quad (18)$$

Using p as obtained from Eq. (18) to calculate the array factor yields patterns in good agreement with measured patterns. The p value calculated from Eq. (18) is in close agreement with measured values of p [1]. Therefore, it appears that the Hansen–Woodyard increased directivity condition is a good approximation for helices radiating in the axial mode. For a typical case where $C = \lambda$, $\alpha = 14^\circ$, $N = 10$, we find from Eqs. (2) and (18) that $S = C \tan \alpha = 0.249\lambda$, $L = 1.031\lambda$, and $p = 0.79$. Thus the traveling current wave has a phase velocity less than that of free space. Finally, substituting Eq. (16) into Eq. (14) yields

$$\psi = kS(\cos \theta - 1) - \left(2\pi + \frac{\pi}{N} \right) \quad (19)$$

Equations (13) and (19) provide the complete normalized array pattern of the axial-mode helical antenna. For the element pattern we will need an analysis of the radiation from a circular loop, which is covered in the next section.

2.2.2. Circular Loop Radiation. In this section we consider the radiation from a circular loop carrying a current $I(\phi)$. The result is useful in understanding the operation of the helix in both the mono- and multifilar forms. In addition, it will yield an approximate element factor for a single turn of the helix. The loop of radius a is centered at the origin and lies in the xy plane. The current distribution $I(\phi)$ may be represented in terms of a complex Fourier series representation:

$$I(\phi) = \sum_{n=-\infty}^{\infty} I_n e^{jn\phi} \quad (20)$$

Consider the typical term $I_n e^{jn\phi}$ of the current distribution $I(\phi)$. First we evaluate components $A_{\phi n}$, $A_{\theta n}$ of the far-field magnetic vector potential as follows. Directions ϕ, θ are associated with the field point rather than

the source point:

$$A_{\phi n} = \frac{e^{-jkr}}{4\pi r} \int_0^{2\pi} I_n e^{jn\phi'} \cos(\phi - \phi') e^{jka \sin \theta \cos(\phi - \phi')} a d\phi' \quad (21)$$

$$A_{\theta n} = \frac{e^{-jkr}}{4\pi r} \int_0^{2\pi} I_n e^{jn\phi'} [-\sin(\phi' - \phi)] \times \cos \theta e^{jka \sin \theta \cos(\phi - \phi')} a d\phi' \quad (22)$$

To evaluate A_ϕ , we introduce the change of variables $\psi = \phi' - \phi$ and change limits to obtain

$$A_{\phi n} = \frac{e^{jn\phi} e^{-jkr} I_n a}{4\pi r} \int_0^{2\pi} e^{jn\psi} \left(\frac{e^{j\psi} + e^{-j\psi}}{2} \right) e^{j(ka \sin \theta) \cos \psi} d\psi$$

Next, we use the following integral expression for the Bessel function of the first kind $J_m(x)$:

$$\int_0^{2\pi} e^{jx \cos \theta} e^{jm\theta} d\theta = 2\pi j^m J_m(x)$$

A_ϕ is then evaluated directly to obtain

$$A_{\phi n} = \frac{e^{jn\phi} (I_n a) e^{-jkr} j^{n+1}}{4r} [J_{n+1}(ka \sin \theta) - J_{n-1}(ka \sin \theta)] \quad (23)$$

$$E_{\phi n} = -j\omega\mu A_{\phi n} \quad (24)$$

Using similar methods, we obtain the following evaluation of A_θ :

$$A_{\theta n} = \frac{e^{jn\phi} (I_n a) e^{-jkr} j^{n+1} (j \cos \theta)}{4r} [J_{n+1}(ka \sin \theta) \quad (25)$$

$$+ J_{n-1}(ka \sin \theta)]$$

$$E_{\theta n} = -j\omega\mu A_{\theta n} \quad (26)$$

The total fields may, of course, be obtained by adding contributions of all Fourier modes.

Now let's evaluate the far fields along the z axis ($\theta = 0^\circ$, 180°) for each of the separate Fourier modes. We note that $J_n(0) = 0$ ($n \neq 0$) and $J_0(0) = 1$. Evaluating the cases $n = \pm 1$, we find that, along the z axis

$$\frac{E_\phi}{E_\theta} = \pm j \quad (27)$$

In other words, the modes $n = \pm 1$ representing traveling waves yield circular polarization along the z axis. Note that all other traveling-wave modes yield a null on axis. *Of all the Fourier modes, only $n = \pm 1$ radiate in the forward endfire or backfire direction.* For the helix, we define forward or backward radiation as radiation away from or toward the feedpoint, respectively.

This result can also be seen by considering currents around the loop for various modes. For $n = \pm 1$, each current element is matched by its opposite across the loop,

which is in the same direction such as to add along the z axis and to rotate polarization as time progresses. All the other modes cancel along the axis. For even modes, each element is canceled by its opposite across the loop. For odd modes, a group of elements will cancel. For the general odd case n , any group of n elements, each separated by $180^\circ/n$, yields zero contribution. For $n=5$, for example, any group of five elements, each separated by 36° , yields zero contribution.

Any currents on the cylindrical surface may be resolved into ϕ - and z -directed currents. The z -directed currents do not radiate along the axis. Thus, for currents of any direction, *only the $n = \pm 1$ Fourier modes can contribute to endfire or backfire*. These results will be useful when considering multifilar helices.

This discussion makes it easier to understand the operation of the helical antenna. At low frequencies the zeroth mode ($n=0$) is strongly excited because there is little variation of phase around the cylinder on one turn. In addition, the impedance of the higher modes is highly reactive. As frequency increases and C_λ approaches unity, we have one complete cycle around the cylinder on one turn, and we expect the $e^{-j\phi}$ mode to be excited for a right-hand helix. The phase velocity of the helix is lower than that associated with the speed of light, and the impedance of the mode $n = -1$ is reasonable and so the axial mode begins at about $C_\lambda = 0.75$. Similarly, as frequency increases, we expect the mode $n = -2$ to appear; this mode would produce beam pattern deterioration. The axial mode continues until about $C_\lambda = 1.33$.

2.2.2.1. Element Pattern of the Axial-Mode Helix. For the element pattern of one turn of the helix, the current distribution is assumed to be

$$I(\phi') = I_0 e^{-j\beta l} = I_0 e^{-j\beta a \phi'} \quad (28)$$

where $\beta = k/p$, $a = D/2$, and ϕ' is the angle measured from the x axis. For accurate analysis of the element pattern, Eq. (28) should be used to calculate the radiation integral. However, when the helix with several turns operates in the axial mode ($C_\lambda \approx 1$), the array factor dominates the endfire beam pattern and the element pattern provides minor corrections. Thus it suffices to consider the radiation field of a planar loop with $C_\lambda = 1$, instead of a three-dimensional one-turn helix. If we also assume that $p \approx 1$, then

$$I(\phi') \approx I_0 e^{-jka\phi'} = I_0 e^{-j(2\pi/\lambda)\alpha\phi'} \approx I_0 e^{-j\phi'} \quad (29)$$

Using the simple form of the current distribution in Eq. (29), we can easily calculate the radiation fields for the element pattern from Eqs. (23)–(26) for $C_\lambda = 1$ ($n = -1$):

$$E_\phi(\theta, \phi) = C(r)[J_0(\sin \theta) + J_2(\sin \theta)]e^{-j\phi} \quad (30)$$

$$E_\theta(\theta, \phi) = C(r)[J_0(\sin \theta) - J_2(\sin \theta)](j \cos \theta)e^{-j\phi} \quad (31)$$

where $C(r)$ gives the r dependence of the fields. Note that $ka = 1$ when $C_\lambda = 1$. If we plot the radiation patterns of

$|E_\theta|$ and $|E_\phi|$ using Eqs. (30) and (31), we obtain a figure-eight pattern for E_θ with a null at 90° , and a nearly omnidirectional pattern for E_ϕ [6]. From the plot, it is interesting to note that the normalized E_θ can be approximated by $\cos \theta$. We also observe that E_θ and E_ϕ are 90° out of phase. In particular, when $\theta = 0^\circ$, then $|E_\theta| = |E_\phi|$; thus the radiation field is *circularly polarized* in the endfire direction. As one departs from $\theta = 0^\circ$, E_θ decreases more rapidly than does E_ϕ , so the polarization becomes *elliptical*. Finally, it should be noted that Kraus [1] has analyzed the element pattern, by using a single turn of a three-dimensional helix with uniform traveling-wave current.

2.2.3. Beam Patterns. The complete total far-field pattern is given by the product of the array factor shown by Eq. (13) and the element pattern in Eq. (30) or (31). However, the array pattern is much sharper than the element patterns. Thus the total E_θ and E_ϕ patterns are nearly the same, in spite of the difference in the single-turn patterns. The mainlobes of the E_θ and E_ϕ patterns are very similar to those of the array pattern. Therefore, for long helices ($NS > \lambda$), a calculation of only the array factor is sufficient for an approximate pattern of any field component of the helix.

The measured patterns of a six-turn helix with $\alpha = 14^\circ$ as a function of frequency are presented in Fig. 3. Patterns are shown over a range of circumferences from approximately 0.66λ to 1.35λ . The solid patterns are for the horizontally polarized component (E_ϕ) and the dashed for the vertically polarized (E_θ). Both are adjusted to the same maximum. We observe that the endfire beam patterns are preserved over the range of $0.73 < C_\lambda < 1.22$, indicating that the axial-mode helix is a broadband antenna.

2.2.4. Important Parameters. Four important parameters for practical design of an axial-mode helical antenna are (1) beamwidth (BW), (2) gain or directivity, input impedance and axial ratio (AR). They are all functions of the number of turns, the turn spacing (or pitch angle), and the frequency. For a given number of turns, the behavior of the BW, gain, impedance and AR determines the useful *bandwidth*. The nominal center frequency of this bandwidth corresponds to a helix circumference of about 1λ .

2.2.4.1. Beamwidth. On the basis of a large number of measurements, King and Wong [7] give the following quasiempirical formula for the beamwidths:

$$\text{HPBW (half-power beamwidth)} = \frac{K_B}{C_\lambda \sqrt{NS_\lambda}} \text{ (degrees)} \quad (32)$$

where K_B varies from 61 to 70, for $\frac{3}{4} < C_\lambda < \frac{4}{3}$, $12^\circ < \alpha < 15^\circ$, and $8.6 < N < 10$. Note that as N increases, the beamwidth decreases. Figure 4a shows measured HPBW of a six-turn, 14° axial-mode helix as a function of the normalized circumference (C_λ). E_θ is shown dotted as before. We observe that HPBW changes slowly over the range of approximately $0.7 < C_\lambda < 1.25$.

2.2.4.2. Gain. The gain of the axial mode helix can be approximately obtained [8] by

$$G = K_G C_\lambda^2 N S_\lambda \quad (33)$$

where K_G is the gain factor, which depends on the design parameters. King and Wong [7] report that K_G varies from 4.2 to 7.7. Experiments show that the gain is peak when C is slightly larger than 1λ .

2.2.4.3. Axial Ratio. We have shown from the approximate analysis described in a previous section that the radiation field is circularly polarized in the mainbeam direction ($\theta = 0^\circ$), implying $AR = 1$. With a more accurate analysis, including the effect of relative phase velocity for increased directivity, Kraus [1] obtains the axial ratio along the helix axis as follows:

$$AR = \frac{2N + 1}{2N} (\theta = 0^\circ) \quad (34)$$

If N is large, the axial ratio approaches unity and the polarization is nearly circular. For example, for a six-turn helix, $AR = \frac{13}{12} = 1.08$ according to Eq. (34). This axial ratio is independent of frequency or circumference. In Fig. 4b, the measured values of the axial ratio for the six-turn, 14° axial-mode helix are plotted as a function of the circumference (C_λ). We observe that AR is nearly 1 over the range of about $0.73 < C_\lambda < 1.4$. The sense of circular polarization is determined by the sense of the helix windings.

2.2.4.4. Input Impedance. The input impedance of the axial-mode helical antenna is nearly purely resistive. The empirical formulas for the input resistance are given [1] by

$$R_{in} = 140C_\lambda \quad (35)$$

within 20% for the case of axial feed, and

$$R_{in} = \frac{150}{\sqrt{C_\lambda}} \quad (36)$$

within 10% for the case of peripheral feed. Both relations are valid when $0.8 \leq C_\lambda \leq 1.2$, $12^\circ \leq \alpha \leq 14^\circ$ and $N \geq 4$. With a suitable matching section, R_{in} can be made any desired value from 50 to 150 Ω . In the inset of Fig 4c, trends of input resistance R and reactance X are shown as a function of the relative frequency or circumference. Note that R is relatively constant and X is very small for $0.7 < C_\lambda < 1.5$. Figure 4c also shows the voltage standing-wave ratio (VSWR) measured on a 53 Ω coaxial line. We observe that the VSWR nearly remains constant (approximately 1), and equivalently the input impedance of the helix remains unchanged, over the range of about $0.7 < C_\lambda < 1.6$.

2.2.5. Broadband Characteristics. Considering all the characteristics of beam pattern, input impedance, and polarization as a function of circumference, we find that the

performance of the axial-mode helix is satisfactory over the range of about $0.75 < C_\lambda < 1.25$ within the restrictions given on α and N .

Thus the bandwidth, defined by the ratio of upper and lower frequencies, is almost an octave. The broadband characteristics of the helix can be explained by the natural adjustment of the phase velocity. As the helix size C_λ , or equivalently the frequency, varies over a rather wide range, the phase velocity adjusts itself automatically such that the fields from each turn add nearly in phase in the axial direction.

2.3. Variations and Applications of the Helical Antenna

A slight taper on the end of the helix [9,10] reduces the axial ratio at the expense of a slight reduction in gain. Axial ratio is improved both on and off axis. A taper is also used at the input to improve impedance characteristics. A circular cavity backing is sometimes used to reduce the backradiation and increase the forward gain. Dielectric-tube support has been used with the helix antenna. This lowers the frequency for the onset of axial-mode operation and has an effect on the terminal impedance. A solid dielectric core has also been used with the helix (the polyrod helix). A helix with an inner concentric metal core has been used as a TV transmitter [11]. The antenna utilizes higher-order Fourier modes such as $e^{\pm j2\phi}$, $e^{\pm j5\phi}$, which radiate sidefire rather than endfire. This is particularly useful with towers and masts whose circumference is much larger than a wavelength. An array of helices is stacked along the mast to produce the required beam pattern. The helical antenna has often been used as an element in various types of arrays. Large planar arrays of helices have been used in radio astronomy [12]. An array of axial-mode helices has been used for Global Positioning System (GPS) satellite transmitters [1]. Helices are also used as feeds for parabolic dishes. Applications of the helix are legion.

3. MULTIFILAR HELIX ANTENNAS

The helical antenna described in the preceding section may be termed the *monofilar helical antenna*. It is constructed from a single wire, or tape, and fed from a single source. In this section we consider the multifilar helix antenna, which consists of a number of wires or tapes, each of which may be fed from a separate source. The wires may be interleaved as shown in Fig. 5a for the quadrifilar helix. The excitations in all cases discussed is of the form $e^{\pm j\phi}$. Other excitations are certainly possible but have not been thoroughly studied. Many different forms of the multifilar helix have been used, including bifilar, quadrifilar, and octofilar helices. Two distinct classes of multifilar helices have been used: the broadband forward-fire axial mode multifilar helix and the narrowband backfire multifilar helix. For both, the quadrifilar helix has been widely studied and used.

We have already discussed the *Fourier* modes due to a loop of circumferential current. The rigorous consideration of the entire geometry of the helix yields modes with the same ϕ dependence but yields the phase progres-

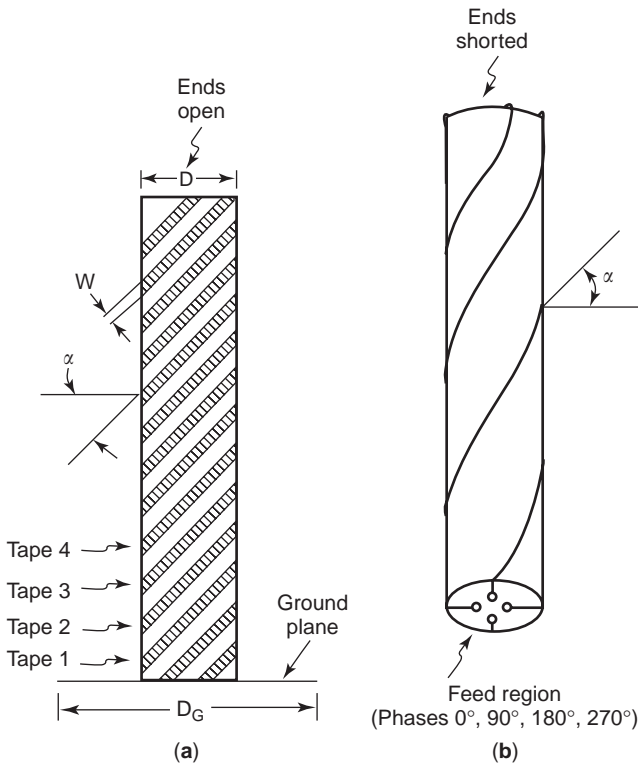


Figure 5. Quadrifilar helical antenna: (a) endfire; (b) backfire.

sion in z as well. Samuel Sensiper [13] carried out this rigorous analysis to determine the real propagation constants of the normal and axial modes. He also determined some of the characteristics of the multifilar helix. Later, Paul Klock [14] found an additional mode with a complex propagation constant. This mode starts with backfire and then splits and scans forward as a conical beam as frequency increases. It operates simultaneously with the axial mode but is usually suppressed by the ground plane. Early experimenters of the multifilar helix showed some improvements over the monofilar helix but did not always recognize that greater bandwidth could be obtained nor how to obtain it, as explained in the following section.

3.1. The Axial-Mode Quadrifilar Helix

Gerst and Worden [15] first described the broadband axial-mode multifilar helix. They pointed out that the frequency range of the axial mode could be extended by (1) adding more wires, (2) using $e^{-j\phi}$ excitation to maintain that mode and suppress others, and (3) increasing the pitch angle α . The technique is readily understood by considering the bifilar helix. First, the two wires are fed 180° out of phase. Consider a cross section perpendicular to the helix axis. We find, in any cross section, two wires 180° apart in space and phase. Only the odd Fourier modes ($e^{jn\phi}$, n odd) are excited. The mode $e^{-j2\phi}$, which may be a culprit in the pattern breakup of the monofilar helix, is suppressed. The mode $e^{-j3\phi}$ is not suppressed, and the bandwidth for the axial mode approaches 3–1. A pitch angle of about 25° – 30° is required. Now consider the quadrifilar helix. A cross section through the right-hand helix

of Fig. 5a displays four wires symmetrically arranged around the periphery, with phases 0° , -90° , -180° , -270° . This $e^{-j\phi}$ excitation suppresses all the even modes, as in the bifilar helix, and mode $e^{-j3\phi}$ as well. Mode $e^{-j5\phi}$ is not suppressed. The bandwidth approaches 5–1. A pitch angle of about 40° is required. In general, with the M -filar helix, mode $e^{-j\phi}$ is excited around the periphery. All other modes up to $e^{-jM\phi}$ are suppressed. The bandwidth lies between M and $M+1$.

Gerst and Worden determined that the frequency range of the multifilar axial mode helix may be approximated as follows [15]:

$$C_{\lambda \min} < C_{\lambda} < C_{\lambda \max} \quad (37a)$$

$$C_{\lambda \min} = \frac{\cos \alpha}{1 + \sin \alpha} \quad (37b)$$

$C_{\lambda \max}$ is the lesser of $C_{\lambda \max 1}$ and $C_{\lambda \max 2}$:

$$C_{\lambda \max 1} = \frac{\cos \alpha}{1 - \sin \alpha} \quad (37c)$$

$$C_{\lambda \max 2} = \frac{M}{2} \cot \alpha \quad (37d)$$

where M is the number of wires. Equation (37) can be used to predict the bandwidth of the axial-mode unifilar or multifilar helix. For example, consider the monofilar helix with $\alpha = 14^\circ$, whose beam patterns and other characteristics are given in Figs. 3 and 4. The figures indicate that the bandwidth is approximately $0.75 < C_{\lambda} < 1.25$ as noted previously. In comparison, Eq. (37) predicts that $C_{\lambda \min} = 0.78$ and $C_{\lambda \max} = 1.25$ for an approximate bandwidth of $0.78 < C_{\lambda} < 1.28$. The two bandwidth ratios are very close. Equation (37) has been applied to bifilar, quadrifilar, and octofilar axial-beam helices, and the results agree well with experiment as shown in Refs. 15–17.

Figure 6 shows the beam patterns of a quadrifilar helix antenna with a ground plane (see Fig. 5a). Pitch angle α is 35° , diameter D is 3 in., antenna length is 24 in., ground-plane diameter D_G is 10 in., and tape width is $\frac{1}{2}$ in. The feed system [16] provides four outputs phased 0° , 90° , 180° , 270° , with each output connected to one of the four wires of the quadrifilar helix antenna. Equations (37b) and (37c) yield $C_{\lambda \min} = 0.52$ and $C_{\lambda \max} = 1.92$ for α is 35° and $M = 4$. Thus the bandwidth of the antenna is given by $0.52 < C_{\lambda} < 1.92$ for a bandwidth ratio of 3.7–1. The progression of the beam patterns may be described as follows. At a frequency somewhat below the lower limit, backfire operation begins, as evidenced by the strong backlobe at $C_{\lambda} = 0.44$. The backlobe decreases rapidly as we approach the lower limit. The axial ratio also decreases rapidly and is less than 2–1 at the lower limit. Other antenna characteristics such as VSWR are also acceptable [17]. The axial mode then predominates over the 3.5–1 bandwidth. The beam pattern narrows steadily, and the directivity increases with frequency. The upper limit occurs at $C_{\lambda} = 1.92$, at a frequency just above that of Fig. 6f. Above the upper limit, beamsplitting occurs at $C_{\lambda} = 2.10$, with a complete pattern breakup at $C_{\lambda} = 2.70$. Thus, with the multifilar

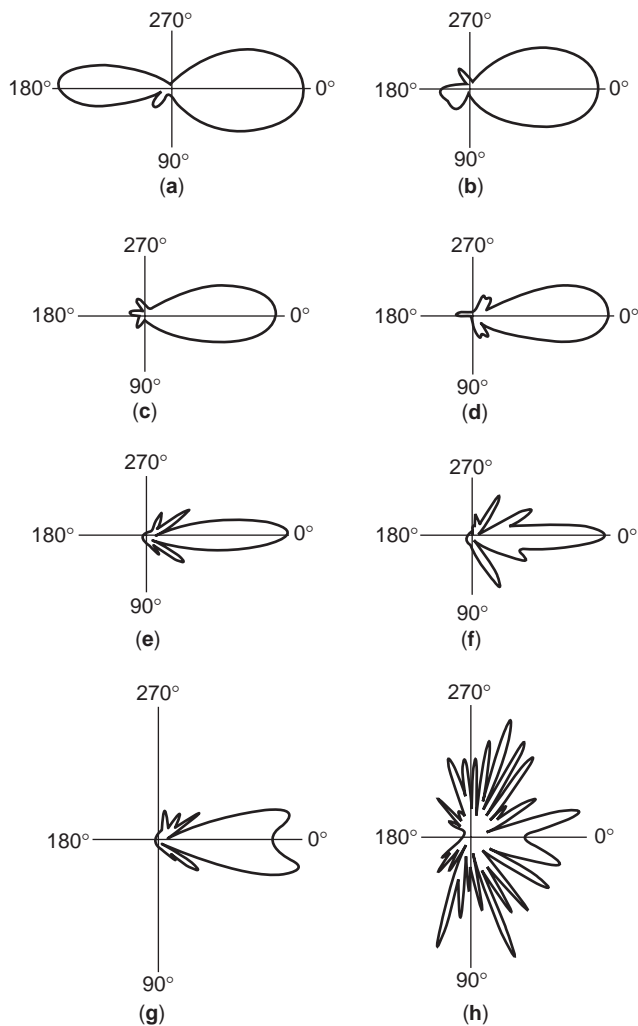


Figure 6. Beam patterns of the axial mode quadrifilar helix antenna: $C_\lambda = 0.44, 0.52, 0.72, 1.1, 1.6, 1.8, 2.1, 2.7$ in (a)–(h), respectively. (From Adams and Lumjiak [17], © 1971 IEEE. Reprinted with permission of IEEE.)

helix, the bandwidth of the axial mode is extended to both lower and higher frequencies as predicted in Eq. (37).

The beam pattern at $C_\lambda = 1.80$ exhibits the undesirable characteristic of high sidelobes. This is caused by the backfire operation, which changes from backfire through sidefire toward endfire as frequency increases. It is sometimes called a “scanning” mode. The quadrifilar helix may also be used in a counterwound version with both right- and left-hand windings. The on-axis polarization is linear rather than circular. The backfire mode is much more effectively suppressed in this version, and the sidelobe levels are much lower. Bandwidths are between 4–1 and 5–1 as shown in Eq. (16). Gerst and Worden [15] describe a 53° pitch angle counterwound octofilar helix with 9–1 bandwidth. The multifilar helix antenna does not radiate in a normal mode at low frequencies because of the phase excitation $0^\circ, 90^\circ, 180^\circ, 270^\circ$ of the windings. The excitation $e^{-j\phi}$ is a supergain excitation at low frequencies ($C_\lambda \ll 1$). Details on the axial multifilar antenna are given in Refs. 15–17 and related references.

3.2. The Backfire Quadrifilar Helix

In the analysis of the circular loops, we noted that, with $e^{\pm j\phi}$, circularly polarized radiation occurs at both $\theta = 0^\circ$ and $\theta = 180^\circ$. To distinguish between these two directions, we need additional information about the helix. A rigorous analysis of the infinite monofilar helix by Paul Klock [14] shows that there are two modes operating simultaneously in the axial-mode region. Both involve $e^{-j\phi}$ excitation for right-hand helices and are circularly polarized on axis. One is the axial mode, and the other is a *backfire* mode, which starts at backfire and scans forward as a conical beam as frequency increases. We may, for purposes of discussion, combine the backfire and forward-scanned operations into a single backfire designation. In the mono- and quadrifilar helices the backfire mode shows up just before the onset of the axial mode. The backfire mode exists along with the axial mode, but is suppressed by the presence of the ground plane. The backfire mode is *favored* over the forward endfire as pitch angle increases. Pitch angles in the $40\text{--}50^\circ$ range with no ground plane show both forward and backward radiation. With no ground plane, the radiation is primarily backfire. For the right-hand helices of Figs. 1 and 5, the endfire radiation is right-handed circularly polarized and the backfire radiation is left-handed circularly polarized.

The backfire bifilar helix was first studied by Patton [18], who carried out extensive theoretical and experimental work. He showed the range of backfire beam patterns obtained with the monofilar and bifilar helices. Later, Charles Kilgus [19] showed that beam pattern improvements could be obtained with the quadrifilar helix. He investigated in detail the shaped conical and cardioid patterns that are obtainable with the backfire quadrifilar helix.

Figure 5b shows the backfire quadrifilar helix. It consists of two bifilar antennas fed 90° out of phase to produce the $e^{-j\phi}$ excitation. No ground plane is required, and the ends of the helices may be shorted (short-circuited) together. The backfire helix is used with pitch angles as high as 60° and 70° . With these high pitch angles, the backfire mode can operate at low frequencies, yielding a small cross section for the antenna.

A typically shaped conical beam is shown in Fig. 7. The beam is very wide for broad sector coverage with a dip or a local maximum (not shown) at the center ($\theta = 180^\circ$). The dip is appropriate for satellite coverage because it can be chosen to yield uniform signal strength at the receiver as the satellite passes. Kilgus [19] shows numerous beam patterns for different designs. The beamwidths vary from 100° to 180° . Directivities of up to 7 dB are observed.

The backfire quadrifilar helix has characteristics that make it especially suitable for many satellite, spacecraft, and navigational applications. It has been used as a transmitter and receiver in satellite communication systems and as a receiver for GPS applications [20]. It has also been considered for cellular phones and new GPS applications [21].

3.3. Smart Antennas

The quadrifilar helix antenna can be used as a “smart” or adaptive antenna. Complex weights are added to its four separate channels. The weights are then adjusted to im-

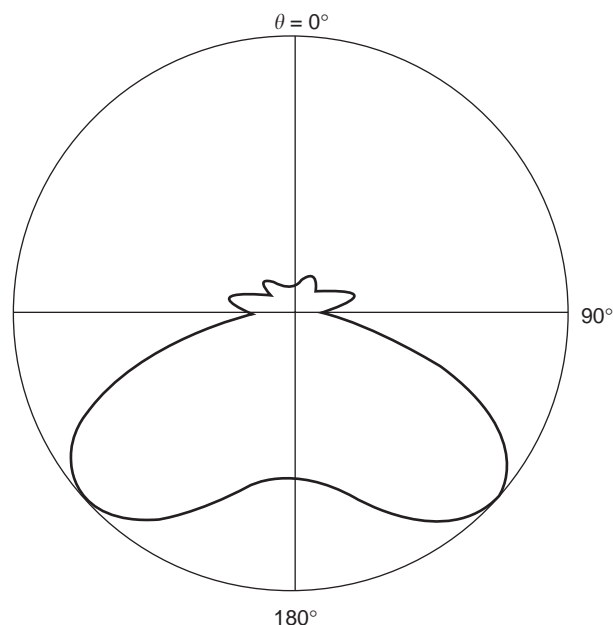


Figure 7. Beam pattern of the backfire quadrifilar helix.

prove selected antenna characteristics [22,23]. The effects of shadowing and multipath, for example, may in some cases be mitigated.

4. HUMAN PROXIMITY EFFECTS

The presence of a human body in close proximity to an antenna may, of course, have significant effects. The human body may absorb radiation. The antenna characteristics may be modified. In particular, handheld antennas with the head and hand very close to the antenna may require a very careful analysis of the situation.

The normal-mode helix antenna has been used for cellular telephone handsets. The antenna is usually electrically small and is *linearly* polarized or nearly so. The head can pick up some radiation but significantly degrades the reception [24]. The axial-mode helix antenna has been proposed for personal satellite communication. This antenna is *circularly* polarized. The head can pick up some radiation and significantly degrades the reception [25].

5. SUMMARY

The helical antenna, first discovered in 1946 by John Kraus, has evolved into many different forms with many different applications. The normal-mode helix has some advantages for low-frequency applications. The broadband, circularly polarized, axial-mode helix radiates forward endfire along its axis. It has been the most widely used of all forms of the helix. The quadrifilar axial-mode helix extends the bandwidth further and can be used as a smart antenna. The backfire quadrifilar helix radiates a broad sector coverage suitable for satellite applications. The presence of a human body in close proximity to handheld antennas may have significant effects on reception.

BIBLIOGRAPHY

1. J. D. Kraus, *Antennas*, 2nd ed., McGraw-Hill, New York, 1988, pp. 265–339.
2. W. L. Stutzman and G. A. Thiele, *Antenna Theory and Design*, 2nd ed., Wiley, New York, 1988, pp. 231–239.
3. W. W. Hansen and J. R. Woodyard, A new principle in directional antenna design, *IRE Proc.* **26**:333–345 (1938).
4. C. A. Balanis, *Antenna Theory: Analysis and Design*, 2nd ed., Wiley, New York, 1997, pp. 271–276.
5. H. Nakano, *Helical and Spiral Antennas: A Numerical Approach*, Wiley, New York, 1987, pp. 123–195.
6. R. S. Elliott, *Antenna Theory and Design*, Prentice-Hall, New York, 1981, pp. 71–78.
7. H. E. King and J. L. Wong, Characteristics of 1 to 8 wavelength uniform helical antennas, *IEEE Trans. Anten. Propag.* **AP-28**:291–296 (1980).
8. E. A. Wolff, *Antenna Analysis*, Wiley, New York, 1967, pp. 437–444.
9. R. C. Johnson and H. Jasik, *Antenna Engineering Handbook*, 2nd ed., McGraw-Hill, New York, 1984, pp. 13-1–13-23.
10. J. L. Wong and H. E. King, Broadband quasi-taper helical antennas, *IEEE Trans. Anten. Propag.* **AP-27**:72–78 (1979).
11. L. O. Krause, Sidefire helix UHF-TV transmitting antenna, *Electronics* **24**:107–119 (Aug. 1951).
12. J. D. Kraus, *Radio Astronomy*, 2nd ed., Cygnus-Quasar, Powell, OH, 1986.
13. S. Sensiper, Electromagnetic wave propagation on helical structures, *Proc. IRE* **43**: 149–161 (1955); also Ph.D. thesis, MIT, 1951.
14. P. W. Klock, *A Study of Wave Propagation of Helices*, Ph.D. thesis, Univ. Illinois, Urbana–Champaign, 1963.
15. C. Gerst and R. A. Worden, Helix antennas take turn for better, *Electronics* **39**:100–110 (Aug. 22, 1966).
16. A. T. Adams, R. K. Greenough, R. F. Wallenberg, A. Mendelovicz, and C. Lumjiak, The quadrifilar helix antenna, *IEEE Trans. Anten. Propag.* **AP-22**:173–178 (1974).
17. A. T. Adams and C. Lumjiak, Optimization of the quadrifilar helix antenna, *IEEE Trans. Anten. Propag.* **AP-19**:547–548 (1971).
18. W. T. Patton, *The Backfire Helical Antenna*, Ph.D. thesis, Univ. Illinois, Urbana–Champaign, 1963.
19. C. C. Kilgus, Shaped-conical radiation pattern performance of the backfire quadrifilar helix, *IEEE Trans. Anten. Propag.* **AP-23**:392–397 (1975).
20. J. M. Tranquilla, S. R. Best, A study of the quadrifilar helix antenna for global positioning system (GPS) applications, *IEEE Trans. Anten. Propag.* **AP-38**:1545–1550 (1990).
21. N. Padros, J. Ortigosa, J. Baker, M. F. Iskander, and B. Thornberg, Comparative study of high-performance GPS receiving antenna designs, *IEEE Trans. Anten. Propag.* **AP-45**:698–706 (1997).
22. M. Cooper, Antennas get smart, *Sci. Am.* **289**:48–55 (2003).
23. S. M. Leach, A. A. Agius, and S. R. Saunders, Intelligent quadrifilar helix antenna, *IEE Proc. Microwave Antennas Propag.* **147**:219–223 (2000).
24. G. Lazzi and O. P. Gandhi, On modeling and personal dosimetry of cellular telephone helical antennas with the FDTD code, *IEEE Trans. Anten. Propag.* **AP-46**:525–530 (1998).
25. J. S. Colburn and Y. Rahmat-Samii, Human proximity effects on circular polarized handset antennas in personal satellite communications, *IEEE Trans. Anten. Propag.* **AP-46**: 813–820 (1998).

HELMHOLTZ EQUATIONS

PIOTR KOWALCZYK
 MICHAŁ MROZOWSKI
 Gdansk University of
 Technology
 Gdansk, Poland

1. INTRODUCTION

The Helmholtz equation¹ is one of the most fundamental equations of mathematical physics widely used in many areas [4,5,16,17], including classical mechanics (waves and vibrations), thermodynamics [28] (diffusion and heat transport), quantum mechanics [24] (for special forms of potential and scattering theory), and finally electricity and magnetism—especially electromagnetic waves—in problems such as radiation, scattering, and guided and unguided waves as well as oscillations in cavities and resonators. The electromagnetic Helmholtz equation is derived from the Maxwell equations under either static or time-harmonic conditions. It allows one to determine how the geometry of a given physical structure interacts with a time-harmonic (or static) electromagnetic field. The solution of the Helmholtz equation provides information such as the resonant frequencies of an electromagnetic cavity, wavelength of waves guided along transmission lines or waveguides, attenuation of an electromagnetic wave due to finite conductivity of a metal or lossy medium, spatial distribution of fields inside electromagnetic structures, radiation loss in open circuits, and field configuration produced by antennas of different shapes or scattered by objects made of various media. This information is essential for design of RF and microwave circuits and systems. The Helmholtz equation has the form of a partial-differential equation involving spatial derivatives, and its solution is influenced by the shape of the structure under investigation (boundary conditions), media properties, and parameters such as frequency. Depending on the problem, the Helmholtz equation is defined in one, two, or three spatial dimensions.

2. SCALAR AND VECTOR HELMHOLTZ EQUATIONS

The Helmholtz equation results from the separation of space and time variables in partial-differential equations such as wave and diffusion equations. In general, it involves vector fields (or functions) and has the following form

$$\nabla^2 \mathbf{M}(\mathbf{r}) + k^2 \mathbf{M}(\mathbf{r}) = 0 \quad (1)$$

¹Hermann Ludwig Ferdinand Helmholtz [born Aug. 31, 1821, Potsdam, Prussia (Germany); died Sept. 8, 1894, Charlottenburg, Berlin, Germany]; German scientist and philosopher who first expressed the relationship between mechanics, heat, light, electricity, and magnetism in the form of the law of conservation of energy [9].

where \mathbf{M} and \mathbf{r} can be vectors² in any multidimensional space and ∇^2 is the vector Laplacian [2,16]. Examples of the physical quantity represented by \mathbf{M} include electric field, magnetic field, or vector potentials. Whenever possible, the problem is reduced to the scalar form

$$\nabla^2 \Phi(\mathbf{r}) + k^2 \Phi(\mathbf{r}) = 0 \quad (2)$$

which is more amenable for analytical and numerical treatment. Here ∇^2 is the scalar Laplacian operator, and the examples of a physical quantity involved are the electric potential, temperature, or acoustic pressure or a wavefunction (in quantum mechanics). The formula for evaluating the scalar Laplacian depends on coordinate system; for instance, in Cartesian coordinates it reads

$$\nabla^2 f(x, y, z) \equiv \frac{\partial^2 f}{\partial x^2} + \frac{\partial^2 f}{\partial y^2} + \frac{\partial^2 f}{\partial z^2} \quad (3)$$

and in spherical coordinates, an analogous formula takes the following form:

$$\begin{aligned} \nabla^2 g(r, \Theta, \phi) \equiv & \frac{\partial^2 g}{\partial r^2} + \frac{2}{r} \frac{\partial g}{\partial r} + \frac{1}{r^2 \sin^2 \phi} \frac{\partial^2 g}{\partial \Theta^2} \\ & + \frac{\cos \phi}{r^2 \sin \phi} \frac{\partial g}{\partial \phi} + \frac{1}{r^2} \frac{\partial^2 g}{\partial \phi^2} \end{aligned} \quad (4)$$

Homogeneous equations (1) and (2) with the right-hand side equal to zero describe the physics of processes that take place when no external excitation is present, such as unforced vibrations.³ If some external force drives the system, this is represented by a source term that appears at the right-hand side of the equation—this is characteristic of nonhomogeneous equations. The nonhomogeneous vector and scalar Helmholtz equation are hence given by

$$\nabla^2 \mathbf{M}(\mathbf{r}) + k^2 \mathbf{M}(\mathbf{r}) = \mathbf{J}(\mathbf{r}) \quad (5)$$

$$\nabla^2 \Phi(\mathbf{r}) + k^2 \Phi(\mathbf{r}) = \rho(\mathbf{r}) \quad (6)$$

These forms of the equation are very general and can represent many physical problems, for instance

- $k = 0$ static problems
- $k^2 > 0$ wave motion and oscillations
- $k^2 < 0$ diffusion and heat transport

In general, the solution to the Helmholtz equation depends on the boundary condition and the value of parameter k . It has to be noted that the solution to the homogeneous or nonhomogeneous equation may not exist for all values of parameter k . In general, the nonhomogeneous equation cannot be solved for values of parameter k

²In this article vector quantities are denoted by bold face.

³An example of unforced vibration is a string that is deflected and then left free to oscillate. The vibrations of the string are not due to a driving force which sustains them but to the initial state of the system.

for which the homogeneous equation is soluble. The Helmholtz equation may be expressed in different coordinate systems, and one usually selects the system that leads to the separation of variables. Separation is particularly important for the analytical treatment of partial-differential equations. The scalar Helmholtz equation is separable in all basic orthogonal coordinate systems [16]. For the vector equation there are fewer coordinate systems where the separation is possible [17].

2.1. Helmholtz Equation from the Wave Motion Perspective

To see the relevance of the Helmholtz equation in investigating wave motion, it is instructive to consider the result of the separation of variables in a one-dimensional wave equation

$$\frac{\partial^2 u}{\partial x^2} - \frac{1}{v^2} \frac{\partial^2 u}{\partial t^2} = 0 \tag{7}$$

where $v^2 > 0$ is the wave velocity squared, t is time, and x is the space variable.

Assuming that $u(x, t)$ can be expressed as $u(x, t) = S(x)T(t)$, we get

$$\frac{d^2 S}{dx^2} - \lambda^2 S(x) = 0 \tag{8}$$

and

$$\frac{d^2 T}{dt^2} - \lambda^2 v^2 T(t) = 0 \tag{9}$$

where λ^2 is the separation constant. In both equations one readily recognizes the form of Eq. (2), namely, of the scalar Helmholtz equation in one dimension. General solutions to these equations for a given $\lambda^2 > 0$ are

$$S(x) = A \cos(\lambda x + \varphi_S) \tag{10}$$

and

$$T(t) = B \cos(\lambda vt + \varphi_T) \tag{11}$$

where A, B and φ_S, φ_T are arbitrary constants.⁴ Function $u(x, t)$ is a product of $S(x)$ and $T(t)$, so, in general, one has to consider products for all λ . In other words, $u(x, t)$ has the form

$$\begin{aligned} u(x, t) &= \int d\lambda AB \cos(\lambda x + \varphi_S) \cos(\lambda vt + \varphi_T) \\ &= \int d\lambda \frac{AB}{2} [\cos(\lambda(x - vt) + \varphi_S - \varphi_T) \\ &\quad + \cos(\lambda(x + vt) + \varphi_S + \varphi_T)] \\ &= E(x - vt) + F(x + vt) \end{aligned} \tag{12}$$

Each term represents a wave, one traveling in the positive and the other in the negative x direction (Fig. 1). This

⁴ $A = A(\lambda), B = B(\lambda), \varphi_S = \varphi_S(\lambda), \varphi_T = \varphi_T(\lambda)$.

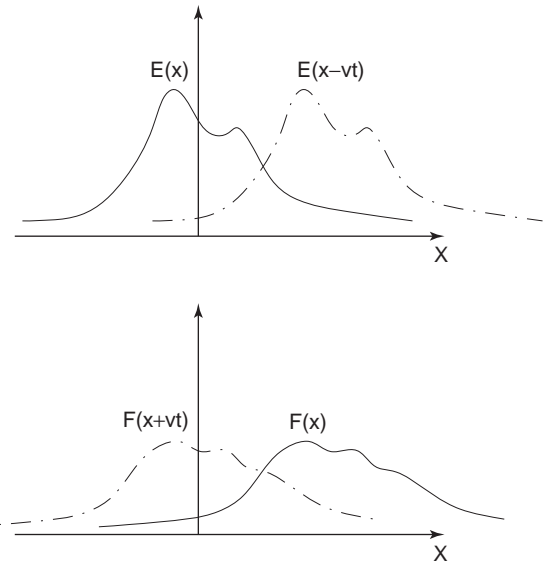


Figure 1. Two waves traveling in opposite directions.

observation is true for higher dimensions and other coordinate systems.

3. HELMHOLTZ EQUATION IN ELECTROMAGNETICS

3.1. Static Problems

Static problems come into play when $k = 0$. In this case the Helmholtz equation transforms into the Laplace or Poisson equation and function $\Phi(\mathbf{r})$ has usually a physical interpretation of the electrostatic or magnetostatic potential. For instance, in electrostatics we have $\nabla \times \mathbf{E}(\mathbf{r}) = 0$ so $\mathbf{E} = -\nabla\phi(\mathbf{r})$. Substituting this relationship into the Gauss law in a homogeneous medium, we get the Poisson equation for the electric charge density $\rho(\mathbf{r})$

$$\nabla^2 \phi(\mathbf{r}) = -\frac{\rho(\mathbf{r})}{\epsilon} \tag{13}$$

which, for $\rho(\mathbf{r}) = 0$, becomes the Laplace equation

$$\nabla^2 \phi(\mathbf{r}) = 0 \tag{14}$$

It is seen that both equations are a particular case ($k = 0$) of the scalar Helmholtz equation.

For $k^2 > 0$ the Helmholtz equation describes wave motion, and hence it is instrumental in investigating radiation and scattering problems, guided and unguided electromagnetic waves, as well as oscillations in cavities.

3.2. One-Dimensional Helmholtz Equation: Transmission Line

One of the most elemental problems whose mathematical model is given by the one-dimensional scalar Helmholtz equation is a transmission line. In the frequency domain, the voltage distribution in an infinitely long transmission line is given by the telegraphist's equation

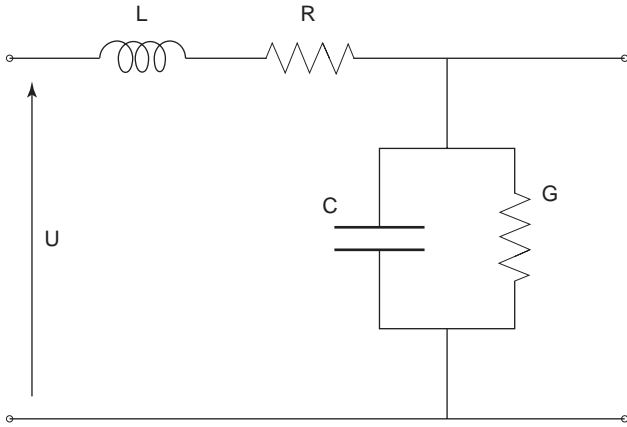


Figure 2. Lumped-element model of a small segment of a transmission line.

[10,20], which reads

$$\frac{\partial^2 U(x)}{\partial x^2} + (\omega^2 LC - j\omega(RC + GL) - RG)U(x) = 0 \tag{15}$$

where ω is the angular frequency, $j = \sqrt{-1}$ is the imaginary unit, and L, R, C, G denote, respectively, the per unit length series inductance, series resistance, shunt capacitance, and the shunt conductance (Fig. 2).

If one denotes $k^2 = \omega^2 LC - j\omega(RC + GL) - RG$, the telegraphist's equation assumes the form of (2), specifically, of the homogeneous Helmholtz equation. For a lossy line k is complex $k = \alpha + j\beta$. The general solution is

$$U(x) = U_0^+ e^{-\alpha x} e^{-j\beta x} + U_0^- e^{\alpha x} e^{j\beta x} \tag{16}$$

In the term $U_0^+ e^{-\alpha x} e^{-j\beta x}$ we recognize a voltage wave traveling in the positive x direction, whereas $U_0^- e^{\alpha x} e^{j\beta x}$ corresponds to a voltage wave going in the opposite sense.

3.3. Electromagnetic Waves: Auxiliary Potentials

Using time-harmonic Maxwell's equations for the isotropic homogeneous media with the source in the form of electric and magnetic currents and charges [2,12]

$$\begin{cases} \nabla \times \mathbf{E}(\mathbf{r}) = -j\omega \mathbf{B}(\mathbf{r}) - \mathbf{J}_m(\mathbf{r}) \\ \nabla \times \mathbf{H}(\mathbf{r}) = j\omega \mathbf{D}(\mathbf{r}) + \mathbf{J}_e(\mathbf{r}) \\ \nabla \cdot \mathbf{D}(\mathbf{r}) = \rho_e(\mathbf{r}) \\ \nabla \cdot \mathbf{B}(\mathbf{r}) = \rho_m(\mathbf{r}) \end{cases} \tag{17}$$

and eliminating the magnetic field $\mathbf{H}(\mathbf{r})$ vector we get a wave equation for the electric field $\mathbf{E}(\mathbf{r})$

$$\nabla^2 \mathbf{E}(\mathbf{r}) + k^2 \mathbf{E}(\mathbf{r}) = j\omega \mu \mathbf{J}_e(\mathbf{r}) + \nabla \times \mathbf{J}_m(\mathbf{r}) + \frac{\nabla \rho_e(\mathbf{r})}{\epsilon} \tag{18}$$

In a similar vein, elimination of the electric field yields

$$\begin{aligned} \nabla^2 \mathbf{H}(\mathbf{r}) + k^2 \mathbf{H}(\mathbf{r}) \\ = j\omega \epsilon \mathbf{J}_m(\mathbf{r}) - \nabla \times \mathbf{J}_e(\mathbf{r}) + \frac{\nabla \rho_m(\mathbf{r})}{\mu} \end{aligned} \tag{19}$$

Equations (18) and (19) both can be regarded as a nonhomogeneous vector Helmholtz equation with $k^2 = \mu \epsilon \omega^2$. In these equations $\nabla \times$ is the curl, $\nabla \cdot$ is the divergence, ∇^2 is the vector Laplacian, $\mathbf{D}(\mathbf{r})$ is the electric flux density, $\mathbf{B}(\mathbf{r})$ is the magnetic flux density, $\rho_e(\mathbf{r})$ and $\rho_m(\mathbf{r})$ are the electric and magnetic charge density, $\mathbf{J}_e(\mathbf{r})$ and $\mathbf{J}_m(\mathbf{r})$ are the electric and magnetic current density, while ϵ and μ stand for the permittivity and permeability of the medium, respectively. It is seen that the right-hand side of these nonhomogeneous Helmholtz equations involves all types of sources. When only electric sources are present, the result is

$$\nabla^2 \mathbf{E}(\mathbf{r}) + \mu \epsilon \omega^2 \mathbf{E}(\mathbf{r}) = j\omega \mu \mathbf{J}_e(\mathbf{r}) + \frac{\nabla \rho_e(\mathbf{r})}{\epsilon} \tag{20}$$

$$\nabla^2 \mathbf{H}(\mathbf{r}) + \mu \epsilon \omega^2 \mathbf{H}(\mathbf{r}) = -\nabla \times \mathbf{J}_e(\mathbf{r}) \tag{21}$$

3.3.1. Vector and Scalar Potentials. Because electric and magnetic fields are, in general, generated by sources consisting of electric and magnetic currents as well as electric and magnetic charges, it is often convenient to operate with auxiliary functions that are related to one type of source. This simplifies the right-hand side of the resulting nonhomogeneous Helmholtz equations. One popular choice [1,14,29] is the generalized electrostatic potential $\varphi_e(\mathbf{r})$ and the vector magnetic potential $\mathbf{A}(\mathbf{r})$. Potential $\mathbf{A}(\mathbf{r})$ is defined as

$$\mathbf{B}(\mathbf{r}) = \nabla \times \mathbf{A}(\mathbf{r}) \tag{22}$$

With these definitions, one gets from Maxwell's equations

$$\nabla \times (\mathbf{E}(\mathbf{r}) + j\omega \mathbf{A}(\mathbf{r})) = 0 \tag{23}$$

This implies

$$\mathbf{E}(\mathbf{r}) = -j\omega \mathbf{A}(\mathbf{r}) - \nabla \varphi_e(\mathbf{r}) \tag{24}$$

where $\varphi_e(\mathbf{r})$ is an arbitrary function.

Imposing the Lorentz gauge

$$\nabla \cdot \mathbf{A}(\mathbf{r}) = -j\omega \varphi_e(\mathbf{r}) \tag{25}$$

we get the following relationships, which have to be satisfied by potentials $\varphi_e(\mathbf{r})$ and $\mathbf{A}(\mathbf{r})$:

$$\nabla^2 \mathbf{A}(\mathbf{r}) + k^2 \mathbf{A}(\mathbf{r}) = -\mu \mathbf{J}_e(\mathbf{r}) \tag{26}$$

$$\nabla^2 \varphi_e(\mathbf{r}) + k^2 \varphi_e(\mathbf{r}) = -\frac{\rho_e(\mathbf{r})}{\epsilon} \tag{27}$$

From these equations it is seen that the electric scalar potential is due to electric charges, whereas the vector magnetic potential is generated by electric currents. In a similar manner one can introduce the magnetic scalar potential $\varphi_m(\mathbf{r})$ and the electric vector potential $\mathbf{F}(\mathbf{r})$, which are due to magnetic charges and currents. Electric vector potential $\mathbf{F}(\mathbf{r})$ is defined as

$$\mathbf{E}(\mathbf{r}) = -\nabla \times \mathbf{F}(\mathbf{r}) \quad (28)$$

which implies that

$$\mathbf{H}(\mathbf{r}) = -j\omega\mathbf{F}(\mathbf{r}) - \nabla\varphi_m(\mathbf{r}) \quad (29)$$

The Lorentz gauge is

$$\nabla \cdot \mathbf{F}(\mathbf{r}) = -j\omega\varphi_m(\mathbf{r}) \quad (30)$$

Considering Faraday's and Gauss' laws with magnetic currents $\mathbf{J}_m(\mathbf{r})$ and charges $\rho_m(\mathbf{r})$, one gets two nonhomogeneous Helmholtz equations that are satisfied by magnetic scalar potential $\varphi_m(\mathbf{r})$ and electric vector potential $\mathbf{F}(\mathbf{r})$ [12]:

$$\nabla^2\mathbf{F}(\mathbf{r}) + k^2\mathbf{F}(\mathbf{r}) = -\mathbf{J}_m(\mathbf{r}) \quad (31)$$

$$\nabla^2\varphi_m(\mathbf{r}) + k^2\varphi_m(\mathbf{r}) = -\frac{\rho_m(\mathbf{r})}{\mu} \quad (32)$$

To sum up, by introducing the auxiliary vector and scalar potential, one gets the Helmholtz equations in a canonical form with each potential associated with one type of the source. Once the potentials have been found the electric and magnetic field can be obtained from [2,12]

$$\mathbf{B}(\mathbf{r}) = \nabla \times \mathbf{A}(\mathbf{r}) - j\omega\mu\mathbf{E}(\mathbf{r}) + \frac{1}{j\omega} \nabla\nabla \cdot \mathbf{F}(\mathbf{r}) \quad (33)$$

$$\mathbf{E}(\mathbf{r}) = -j\omega\mathbf{A}(\mathbf{r}) + \frac{1}{j\omega\mu\epsilon} \nabla\nabla \cdot \mathbf{A}(\mathbf{r}) - \nabla \times \mathbf{F}(\mathbf{r}) \quad (34)$$

3.3.2. Hertz Potentials. There are also other ways to define potential. For instance, one may define the electric potential as [8]

$$\mathbf{H}(\mathbf{r}) = j\omega\epsilon\nabla \times \mathbf{\Pi}_E(\mathbf{r}) \quad (35)$$

For time-harmonic fields there is no significant mathematical difference between this potential and the vector potential introduced previously. However, this choice is popular for investigating, for instance, guided waves, so before proceeding we assume there are no sources in the region of interest. Under this assumption we get from Faraday's law

$$\nabla \times \mathbf{E}(\mathbf{r}) = \mu\epsilon\omega^2\nabla \times \mathbf{\Pi}_E(\mathbf{r}) \quad (36)$$

and hence

$$\mathbf{E}(\mathbf{r}) = \mu\epsilon\omega^2\mathbf{\Pi}_E(\mathbf{r}) + \nabla\psi(\mathbf{r}) \quad (37)$$

where $\psi(\mathbf{r})$ is an arbitrary function.

Assuming

$$\nabla \cdot \mathbf{\Pi}_E(\mathbf{r}) = \psi(\mathbf{r}) \quad (38)$$

and substituting into the Maxwell's equation (Ampère's law), we have

$$\nabla^2\mathbf{\Pi}_E(\mathbf{r}) + \mu\epsilon\omega^2\mathbf{\Pi}_E(\mathbf{r}) = 0 \quad (39)$$

Note that this expression has the form of the homogeneous vector Helmholtz equation. Substituting (38) into (37), one gets the expression for electric field involving only $\mathbf{\Pi}_E(\mathbf{r})$:

$$\begin{aligned} \mathbf{E}(\mathbf{r}) &= \mu\epsilon\omega^2\mathbf{\Pi}_E(\mathbf{r}) + \nabla\nabla \cdot \mathbf{\Pi}_E(\mathbf{r}) \\ &= \nabla \times \nabla \times \mathbf{\Pi}_E(\mathbf{r}) \end{aligned} \quad (40)$$

The magnetic vector potential can be introduced in a similar manner by assuming that

$$\mathbf{E}(\mathbf{r}) = -j\omega\mu\nabla \times \mathbf{\Pi}_H(\mathbf{r}) \quad (41)$$

The potential thus introduced has to fulfill the vector Helmholtz equation

$$\nabla^2\mathbf{\Pi}_H(\mathbf{r}) + \mu\epsilon\omega^2\mathbf{\Pi}_H(\mathbf{r}) = 0 \quad (42)$$

and the magnetic field can be retrieved from

$$\begin{aligned} \mathbf{H}(\mathbf{r}) &= \mu\epsilon\omega^2\mathbf{\Pi}_H(\mathbf{r}) + \nabla\nabla \cdot \mathbf{\Pi}_H(\mathbf{r}) \\ &= \nabla \times \nabla \times \mathbf{\Pi}_H(\mathbf{r}) \end{aligned} \quad (43)$$

3.4. Homogeneous Helmholtz Equation in Electromagnetic Problems

Two of the most important categories of electromagnetic problems involving homogeneous Helmholtz equation are electromagnetic cavities (resonators) and waveguides. For simple cases (structures filled with homogeneous or layered isotropic media), the most elegant approach to the solution, which yields modal field patterns, involves vector potentials. This is because the complete vector field can be found from a single component of vector potential. To illustrate this solution technique, we shall briefly discuss the mathematics related to guided waves based on Hertz potentials.

3.4.1. Cylindrical Waveguides. The problem is expressed by a 2D homogeneous Helmholtz equation. Assume that the wave propagates in the z direction inside a homogeneous and uniform cylinder of arbitrary but homogeneous cross section [8,10]. This type of a hollow-pipe problem can often be solved analytically in a 2D cur-

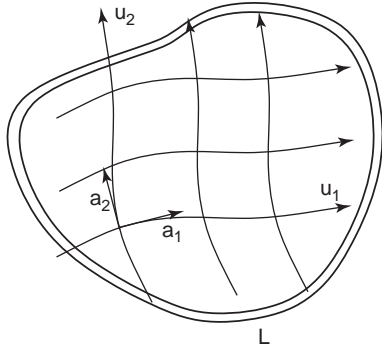


Figure 3. Cross section S of a cylindrical waveguide with the curvilinear system coordinates u_1, u_2 .

vilinear system. It is convenient to choose the coordinate system in such a manner that the waveguide boundary L (Fig. 3) coincides with the constant value surfaces of the system.

We shall consider the Helmholtz equation for electric and magnetic Hertz potential. Because of the uniformity of the structure along the z direction, the potentials have only one component, which, for a perfectly conducting cylinder, has to fulfill either the homogeneous Dirichlet or Neumann boundary conditions on the boundary L . The procedure is identical for electric and magnetic potentials, so we can omit the subscript H or E . When the Hertz potential has only the z component [i.e., $\mathbf{\Pi}(\mathbf{r}) = \Pi(\mathbf{r})\mathbf{a}_z$, where \mathbf{a}_z denotes the unit length vector in the z direction], then the vector Helmholtz equation reduces to the scalar one:

$$\nabla^2 \Pi(\mathbf{r}) + \mu\epsilon\omega^2 \Pi(\mathbf{r}) = 0 \tag{44}$$

Decomposing operator ∇^2 into two terms, ∇_z^2 along the z direction and ∇_t^2 acting on u_1 and u_2 , assuming that $\mathbf{\Pi}(\mathbf{r}) = f(u_1, u_2)g(z)$, and applying the separation of variables technique, one gets

$$\frac{\partial^2 g(z)}{\partial z^2} - \gamma^2 g(z) = 0 \tag{45}$$

and

$$\nabla_t^2 f(u_1, u_2) + \beta^2 f(u_1, u_2) = 0 \tag{46}$$

where $\beta^2 = \gamma^2 + \mu\epsilon\omega^2$, from which it follows that

$$g(z) = G_+ e^{\gamma z} + G_- e^{-\gamma z} \tag{47}$$

where subscript $+/-$ refers to waves propagating in opposite senses. Function $f(u_1, u_2)$ depends on the boundary condition imposed on L . For a complete solution, one has to consider two cases: one with the Dirichlet boundary condition and the other with the Neumann boundary condition. For perfectly conducting cylinders the Dirichlet condition has to be imposed on the electric vector Hertz potential. This leads to the TM modes. The TE modes are obtained by considering the Helmholtz equation for mag-

netic Hertz potential $\mathbf{\Pi}_H(\mathbf{r}) = \Pi_H(\mathbf{r})\mathbf{a}_z$, with the boundary condition $(\partial \mathbf{\Pi}_H(\mathbf{r})/\partial \mathbf{n}) = 0$ on L .

To explain the solution procedure based on the Hertz potential in more detail, it suffices to consider a simple geometry with a rectangular cross section. In this case one assumes the rectangular coordinate system $(u_1, u_2) \rightarrow (x, y)$. If the width and the height of the waveguide are denoted by a and b , respectively, then (using the separation of variables technique for the scalar Helmholtz equation), we get

$$f_{nm}(x, y) = A \cos \frac{\pi n x}{a} \cos \frac{\pi m y}{b} \tag{48}$$

for the Neumann boundary conditions, whereas for the Dirichlet boundary conditions we obtain

$$f_{nm}(x, y) = A \sin \frac{\pi n x}{a} \sin \frac{\pi m y}{b} \tag{49}$$

where

$$\beta_{nm}^2 = \left(\frac{\pi n}{a}\right)^2 + \left(\frac{\pi m}{b}\right)^2 \tag{50}$$

To get the TE modes, we set

$$\mathbf{\Pi}_{H, nm}(\mathbf{r}) = B_{\pm} e^{\pm \gamma_{nm} z} \cos \frac{\pi n x}{a} \cos \frac{\pi m y}{b} \mathbf{a}_z \tag{51}$$

where $\gamma_{nm}^2 = (\pi n/a)^2 + (\pi m/b)^2 - \mu\epsilon\omega^2$. The electric and magnetic fields are then obtained directly from (35) and (40):

$$\begin{aligned} \mathbf{E}_{nm}(\mathbf{r}) = & E_0 \frac{\pi m}{b} e^{\pm \gamma_{nm} z} \cos \frac{\pi n x}{a} \sin \frac{\pi m y}{b} \mathbf{a}_x \\ & - E_0 \frac{\pi n}{a} e^{\pm \gamma_{nm} z} \sin \frac{\pi n x}{a} \cos \frac{\pi m y}{b} \mathbf{a}_y \end{aligned} \tag{52}$$

$$\begin{aligned} \mathbf{H}_{nm}(\mathbf{r}) = & \pm E_0 \frac{\pi n}{a} \frac{j \gamma_{nm}}{\mu \omega} e^{\pm \gamma_{nm} z} \sin \frac{\pi n x}{a} \cos \frac{\pi m y}{b} \mathbf{a}_x \\ & \pm E_0 \frac{j \gamma_{nm}}{\mu \omega} \frac{\pi m}{b} e^{\pm \gamma_{nm} z} \cos \frac{\pi n x}{a} \sin \frac{\pi m y}{b} \mathbf{a}_y \\ & - E_0 \frac{j \beta_{nm}^2}{\mu \omega} e^{\pm \gamma_{nm} z} \cos \frac{\pi n x}{a} \cos \frac{\pi m y}{b} \mathbf{a}_z \end{aligned} \tag{53}$$

Likewise, setting

$$\mathbf{\Pi}_{E, nm}(\mathbf{r}) = B_{\pm} e^{\pm \gamma_{nm} z} \sin \frac{\pi n x}{a} \sin \frac{\pi m y}{b} \mathbf{a}_z \tag{54}$$

and applying relationships (41) and (43), one immediately gets the fields for the TM modes:

$$\begin{aligned} \mathbf{H}_{nm}(\mathbf{r}) = & H_0 \frac{\pi m}{b} e^{\pm\gamma_{nm}z} \sin \frac{\pi n x}{a} \cos \frac{\pi m y}{b} \mathbf{a}_x \\ & - H_0 \frac{\pi n}{a} e^{\pm\gamma_{nm}z} \cos \frac{\pi n x}{a} \sin \frac{\pi m y}{b} \mathbf{a}_y \end{aligned} \quad (55)$$

$$\begin{aligned} \mathbf{E}_{nm}(\mathbf{r}) = & \pm H_0 \frac{\pi n}{a} \frac{j\gamma_{nm}}{\varepsilon\omega} e^{\pm\gamma_{nm}z} \cos \frac{\pi n x}{a} \sin \frac{\pi m y}{b} \mathbf{a}_x \\ & \pm H_0 \frac{j\gamma_{nm}}{\varepsilon\omega} \frac{\pi m}{b} e^{\pm\gamma_{nm}z} \sin \frac{\pi n x}{a} \cos \frac{\pi m y}{b} \mathbf{a}_y \\ & - H_0 \frac{j\beta_{nm}^2}{\varepsilon\omega} e^{\pm\gamma_{nm}z} \sin \frac{\pi n x}{a} \sin \frac{\pi m y}{b} \mathbf{a}_z \end{aligned} \quad (56)$$

For other cross-sections the procedure is analogous. There are other wave guidance problems where the Hertz potentials are instrumental. They include parallel plate or rectangular waveguides loaded with transversely inhomogeneous media including stratified isotropic (Figs. 4a,b) [8,18] or gyrotropic (Fig. 4c) media [18]. For these problems the solution can be obtained by considering the Hertz magnetic or electric potential with a single component that is parallel to the inhomogeneity direction (e.g., normal to the strata). For isotropic media or media with diagonal anisotropy, this leads to the classical Sturm–Liouville equation [16] (in general, a different equation is obtained for magnetic and electric potential) with the Hertz potential as its eigenfunctions. The Sturm–Liouville equation can be regarded as a generalized version of one dimensional Helmholtz equations with variable coefficients. From the two sets of eigenfunctions two families of modes (LSE—the longitudinal section electric modes and LSM—the longitudinal section magnetic modes [8]) are derived from the relationships (41) and (43). Hertz potentials can also be defined for the gyrotropic media. Such generalized Hertz potentials can be used to derive a vector analog of the Sturm–Liouville equation for, for example, a stratified gyromagnetic parallel plate waveguide magnetized perpendicularly to the strata (Fig. 4c) [18].

More complex waveguide geometries, such as cylindrical waveguides loaded with inhomogeneous media (other than the categories described above), in general do not support the TE, TM or LSE, LSM modes. For these problems one has to deal with a much more complex two-dimensional partial-differential equation with coefficients depending on the transverse space coordinates [18]. These equations may be regarded as a generalization of a two-dimensional vector Helmholtz equation.

3.4.2. Cavities (Resonators). Most microwave resonators used in practice are in the form of either empty cavities or cavities loaded with isotropic media. For the latter case the relationships for finding natural fields (modes) and resonance frequencies are obtained by taking the curl of one of the equations Maxwell equations and using the other to eliminate either the electric or magnetic field.

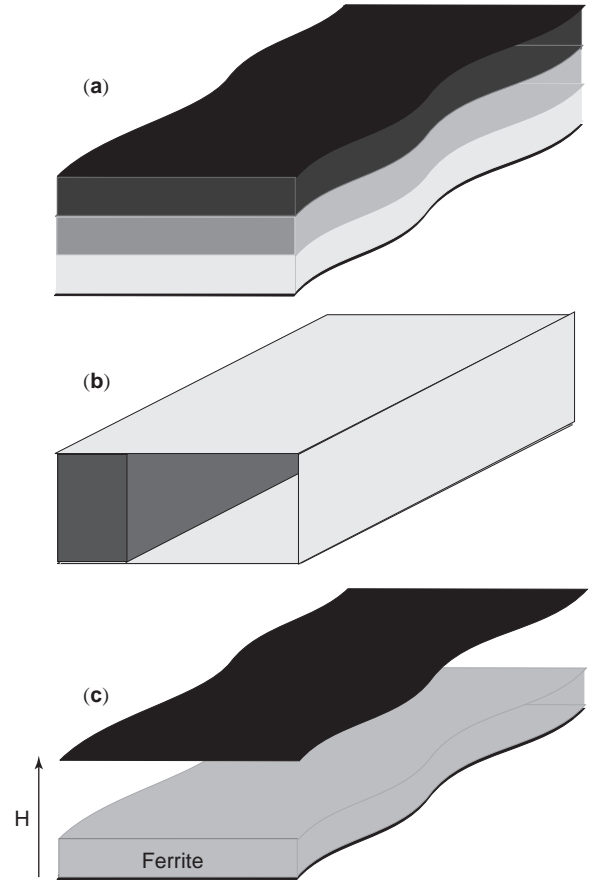


Figure 4. Examples of the stratified waveguiding structures that can be conveniently analyzed using the Hertz potential.

This yields

$$\nabla \times \frac{1}{\mu(\mathbf{r})} \nabla \times \mathbf{E}(\mathbf{r}) - \omega^2 \varepsilon(\mathbf{r}) \mathbf{E}(\mathbf{r}) = 0 \quad (57)$$

and

$$\nabla \times \frac{1}{\varepsilon(\mathbf{r})} \nabla \times \mathbf{H}(\mathbf{r}) - \omega^2 \mu(\mathbf{r}) \mathbf{H}(\mathbf{r}) = 0 \quad (58)$$

In the simplest case of cavities filled with a homogeneous medium and no sources inside the cavity volume, one may use the vector identity $\nabla \times \nabla \times \mathbf{M} = \nabla \nabla \cdot \mathbf{M} - \nabla^2 \mathbf{M}$ and the Gauss law to transform the relations given above to the Helmholtz equations.

$$\nabla^2 \mathbf{E}(\mathbf{r}) + k^2 \mathbf{E}(\mathbf{r}) = 0 \quad (59)$$

$$\nabla^2 \mathbf{H}(\mathbf{r}) + k^2 \mathbf{H}(\mathbf{r}) = 0 \quad (60)$$

These equations can be solved by techniques similar to those used for cylindrical waveguides. The simplest formulation is to use vector potentials instead of fields \mathbf{E} and \mathbf{H} . For homogeneously filled structures the complete field can be derived for a single component of the potential. Since only one component is involved, the technique

involving potentials effectively converts a vector problem to a scalar one. If the volume considered is bounded by a perfectly conducting simply connected boundary, then two scalar Helmholtz equations have to be solved—one for the Neumann condition and the other for homogeneous Dirichlet conditions. One family of solutions gives the TE modes, while the other results in the TM modes.

The scalar Helmholtz equation is also used to find a complete set of vector wavefunctions that are required to represent the field in the cavity with sources. The field in such a cavity consists of two parts [6,12,17]. The first part is irrotational (lamellar), which means that the curl vanishes and the divergence is nonzero; the other part is rotational (solenoidal), and for this part the curl is nonzero and the divergence vanishes. To determine the vector wavefunctions that span both parts, one first solves the scalar Helmholtz equation for both Neumann and homogeneous Dirichlet conditions:

$$\nabla^2\psi(\mathbf{r}) + k^2\psi(\mathbf{r}) = 0 \tag{61}$$

The solution of this equation gives a set of generating functions $\psi = \psi(\mathbf{r})$. The rotational part (consisting of divergence-free wavefunctions) is then obtained by substituting generating functions to the formulas [6]

$$\nabla \times (\psi \mathbf{c}) \tag{62}$$

and

$$\frac{1}{k} \nabla \times \nabla \times (\psi \mathbf{c}) \tag{63}$$

where (c) is called the “piloting vector”. This vector can be chosen in such a way that the vector wavefunctions thus obtained have the field distribution corresponding to the electric or magnetic field associated with relevant TE and TM modes. The lamellar wavefunctions are generated also from ψ by the taking the gradient

$$\nabla\psi(\mathbf{r}) \tag{64}$$

If one uses the generating functions calculated from the scalar Helmholtz equation with the Neumann conditions, then Eq. (64) gives the lamellar vector wavefunctions corresponding to the electric field. Likewise, substituting into (64) generating functions calculated from the scalar Helmholtz equation with the homogeneous Dirichlet conditions, one gets the wavefunctions corresponding to the magnetic field.

4. SOLUTION OF A NONHOMOGENEOUS HELMHOLTZ EQUATION: GREEN’S FUNCTION

4.1. Green’s Function for Scalar Helmholtz Equation

A nonhomogeneous Helmholtz equation can readily be solved if one knows the Green function for the problem at

hand. Let us consider a scalar problem [3,25–27]

$$(\nabla^2 + k^2)\Psi(\mathbf{r}) = f(\mathbf{r}) \tag{65}$$

where $f(\mathbf{r})$ is an excitation. If k^2 belongs to the resolvent set [12], then the solution to this equation can be written in as a sum of two terms

$$\Psi(\mathbf{r}) = \phi(\mathbf{r}) + \psi(\mathbf{r}) \tag{66}$$

where $\psi(\mathbf{r})$ is any particular solution of (65) and $\phi(\mathbf{r})$ is a solution of the homogeneous problem

$$(\nabla^2 + k^2)\phi(\mathbf{r}) = 0 \tag{67}$$

Green’s function $G(\mathbf{r}, \mathbf{r}')$ for the scalar Helmholtz equation satisfies the following relationship

$$(\nabla^2 + k^2)G(\mathbf{r}, \mathbf{r}') = \delta(\mathbf{r} - \mathbf{r}') \tag{68}$$

where $\delta(\mathbf{r} - \mathbf{r}')$ is the Dirac function. If $G(\mathbf{r}, \mathbf{r}')$ is known, then $\psi(\mathbf{r})$ can be found as

$$\psi(\mathbf{r}) = \int_V dV' G(\mathbf{r}, \mathbf{r}') f(\mathbf{r}') \tag{69}$$

In general, finding the Green function for various problems of practical significance is a topic of intensive research [12,13,15], but for open-space configuration, Green’s function for the scalar Helmholtz equation has a simple representation collected [3,21] in Table 1.

For bounded regions, the free-space Green function has to be supplemented with a term $F(\mathbf{r}, \mathbf{r}')$ that fulfills the homogeneous equation

$$(\nabla^2 + k^2)F(\mathbf{r}, \mathbf{r}') = 0 \tag{70}$$

Green’s function for bounded region $G_B(\mathbf{r}, \mathbf{r}')$ becomes

$$G_B(\mathbf{r}, \mathbf{r}') = G_0(\mathbf{r}, \mathbf{r}') + F(\mathbf{r}, \mathbf{r}') \tag{71}$$

The techniques for constructing $F(\mathbf{r}, \mathbf{r}')$ are described in several other sources [2,3,5,21].

4.2. Solution of a Nonhomogeneous Vector Helmholtz Equation: Dyadic Green’s Function

The vector Helmholtz equation is by far more difficult to solve as both the solution and the source have many components. It has to be noted that a particular component of the solution vector may be due to source vector components that are oriented in other directions. In this case the

Table 1. Free-Space Green Functions for the Helmholtz Equation

1D ($x \in \mathbb{R}$)	2D ($\rho \in \mathbb{R}^2$)	3D ($\mathbf{r} \in \mathbb{R}^3$)
$\frac{j}{2k} \exp(-jk x - x')$	$\frac{j}{4k} H_0^{(2)}(k \rho - \rho')^a$	$-\frac{j}{4k} \mathbf{r} - \mathbf{r}' ^{-1} \exp(-jk \mathbf{r} - \mathbf{r}')$

^a $H_0^{(2)}(\cdot)$ is the Hankel function of the second kind.

Green function has to describe this complex excitation–response relationship. A convenient way to do this is by using the dyadic representation. Each component in the dyadic Green function corresponds to the response to a single component of a delta-type vector source. The construction and application of the dyadic Green's function are discussed extensively in the literature [6,29] and often constitute an open research problem. For current planar technologies used in the RF and microwave circuits and antennas, of particular interest are dyadic Green functions involving multilayer and possibly anisotropic substrates [15].

4.3. Application of the Scalar Green Function Technique to a Radiation Problem for a Finite-Length Dipole

An example of a nonhomogeneous problem that can be solved in an elegant way by means of a vector potential formulation of Helmholtz equation and Green's function technique is the derivation of the far-field radiated in open space by a dipole of finite length l [1]. Let us assume an infinitesimally thin dipole is oriented along the z direction and the current distribution is given by

$$\mathbf{I}(z') = I_0 \mathbf{a}_z \begin{cases} \sin\left(k\left(\frac{l}{2} + z'\right)\right), & -\frac{l}{2} < z' < 0 \\ \sin\left(k\left(\frac{l}{2} - z'\right)\right), & 0 < z' < \frac{l}{2} \end{cases} \quad (72)$$

The simplest formulation of the problem is obtained by considering the nonhomogeneous Helmholtz equation for vector potential $\mathbf{A}(\mathbf{r})$. With the source current having only one component, one gets $\mathbf{A}(\mathbf{r}) = A(\mathbf{r})\mathbf{a}_z$, and the vector Helmholtz equation reduces to the scalar one

$$\nabla^2 A(\mathbf{r}) + k^2 A(\mathbf{r}) = -\mu I(z') \nabla(x, y) \quad (73)$$

where $k^2 = \mu\epsilon\omega^2$. To find the solution, one uses the 3D free-space Green function

$$A(\mathbf{r}) = \int_{-l/2}^{+l/2} dz' \mu I(z') \frac{e^{-jkR}}{4\pi R} \quad (74)$$

where $R = \sqrt{(x-x')^2 + (y-y')^2 + (z-z')^2}$. Far from the origin $R \approx r - z' \cos \Theta$ and hence

$$\begin{aligned} A(\mathbf{r}) &= \int_{-l/2}^{+l/2} dz' \mu I(z') \frac{e^{-jkr} e^{jkz' \cos \Theta}}{4\pi r} \\ &= \frac{\mu I_0}{4\pi r} e^{-jkr} \left[\int_{-l/2}^0 dz' e^{jkz' \cos \Theta} \sin\left(\frac{kl}{2} + kz'\right) \right. \\ &\quad \left. + \int_0^{+l/2} dz' e^{jkz' \cos \Theta} \sin\left(\frac{kl}{2} - kz'\right) \right] \end{aligned} \quad (75)$$

Both of these integrals can be integrated using

$$\int dx e^{\alpha x} \sin(\beta x + \gamma) = \frac{e^{\alpha x}}{\alpha^2 + \beta^2} [\alpha \sin(\beta x + \gamma) - \beta \cos(\beta x + \gamma)] \quad (76)$$

After some mathematical manipulations, potential $\mathbf{A}(\mathbf{r})$ takes the form of

$$\mathbf{A}(\mathbf{r}) = \frac{\mu I_0}{2\pi r} \frac{\cos\left(\frac{kl}{2} \cos \Theta\right) - \cos\left(\frac{kl}{2}\right)}{k \sin^2 \Theta} e^{-jkr} \mathbf{a}_z \quad (77)$$

or, in spherical coordinates

$$\begin{aligned} \mathbf{A}(\mathbf{r}) &= \frac{\mu I_0}{2\pi r} \frac{\cos\left(\frac{kl}{2} \cos \Theta\right) - \cos\left(\frac{kl}{2}\right)}{k \sin^2 \Theta} \\ &\quad \times e^{-jkr} (\cos \Theta \mathbf{a}_r - \sin \Theta \mathbf{a}_\Theta) \end{aligned} \quad (78)$$

Using relation (22) and neglecting terms inversely proportional to r^2 (far-field region), the magnetic field takes the following form

$$\mathbf{H}(\mathbf{r}) = \frac{jI_0}{2\pi r} \frac{\cos\left(\frac{kl}{2} \cos \Theta\right) - \cos\left(\frac{kl}{2}\right)}{\sin \Theta} e^{-jkr} \mathbf{a}_\phi \quad (79)$$

Then, the electric field can be obtained from Ampère's law

$$\mathbf{E}(\mathbf{r}) = \frac{j\eta I_0}{2\pi r} \frac{\cos\left(\frac{kl}{2} \cos \Theta\right) - \cos\left(\frac{kl}{2}\right)}{\sin \Theta} e^{-jkr} \mathbf{a}_\Theta \quad (80)$$

where $\eta = \sqrt{\mu/\epsilon}$.

There is also a different way to determine fields generated by a finite-length dipole [1]. As a first step one solves the radiation problem for infinitesimally short dipole of length dl that is placed at the origin. Assuming that the current is constant $\mathbf{I}(z') = I_0 \mathbf{a}_z$, one gets

$$\nabla^2 A(\mathbf{r}) + k^2 A(\mathbf{r}) = -\mu I_0 \quad (81)$$

Using the 3D free-space Green function

$$A(\mathbf{r}) = \int_{-dl/2}^{+dl/2} dz' \mu I_0 \frac{e^{-jkR}}{4\pi R} \quad (82)$$

where $R = \sqrt{(x-x')^2 + (y-y')^2 + (z-z')^2}$. Far from the origin $R \approx r$ and hence

$$A(\mathbf{r}) = \mu I_0 \frac{e^{-jkr}}{4\pi r} dl \quad (83)$$

which, expressed in the spherical coordinates, becomes

$$\mathbf{A}(\mathbf{r}) = \mu I_0 \frac{e^{-jkr}}{4\pi r} dl (\cos \theta \mathbf{a}_r - \sin \theta \mathbf{a}_\theta) \tag{84}$$

The magnetic field is obtained directly from (22) as

$$\mathbf{H}(\mathbf{r}) = \frac{jkI_0 dl \sin \theta}{4\pi r} e^{-jkr} \mathbf{a}_\phi \tag{85}$$

and then

$$\begin{aligned} \mathbf{E}(\mathbf{r}) &= \frac{1}{j\omega\epsilon} \nabla \times \mathbf{H}(\mathbf{r}) \\ &= \frac{jk\eta I_0 dl \sin \theta}{4\pi r} e^{-jkr} \mathbf{a}_\theta \end{aligned} \tag{86}$$

Having obtained the fields for a small dipole one can easily get the solution for a finite-length structure with sinusoidal current distribution. To this end one has to divide the structure into short segments and integrate the contributions from each segment. One finds that for a segment dz located at point z' along z the fields can be expressed as

$$d\mathbf{H}(\mathbf{r}) = \frac{jkI(z')dz' \sin \theta}{4\pi r} e^{-jkr} \mathbf{a}_\theta \tag{87}$$

and

$$d\mathbf{E}(\mathbf{r}) = \frac{jk\eta I(z')dz' \sin \theta}{4\pi r} e^{-jkr} \mathbf{a}_\theta \tag{88}$$

where relationship $R = \sqrt{x^2 + y^2 + (z - z')^2} \approx r - z' \cos \theta$ has been used to derive the formula presented above (Fig. 5).

Assuming the current in the form given by (72) and integrating (87) and (88) over z' , ($z' \in [-l/2, +l/2]$), one finally gets expressions for the magnetic and electric fields, identical to (79) and (80).

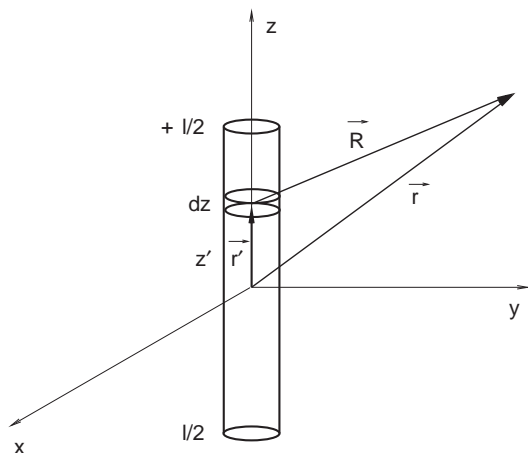


Figure 5. Dipole of finite length l divided into segments dz .

5. NUMERICAL TECHNIQUES FOR SOLVING THE HELMHOLTZ EQUATION

The class of the problems described by the Helmholtz equation that can be solved analytically is very limited so in most cases the only practical approach is to apply numerical methods. Many methods can be used to this end [13,21]; however, two of them have gained the widest acceptance due to generality. For problems where the Green or the dyadic Green function is known, the method of moments is the most popular choice [11,13,30]. More general problems can be handled with the finite-element method [19,22]. The method of moments⁵ transforms an integral equation into a system of linear equations with a dense coefficient matrix (often called the *impedance* or *admittance matrix*). The technique is very powerful as it often allows one to reduce a three-dimensional problem to two dimensions. For this reason the method of moments is very popular for problems such as scattering from perfectly conducting bodies, radiation from wire antennas, slots and patches on multilayered substrates, or planar microwave circuits. On the other hand, because the coefficient matrix is dense, the numerical costs associated with the method of moments increase rapidly with the number of unknowns. The finite-element method solves the Helmholtz equation by discretizing the whole computational space into small volumes and representing the field over each such element by a superposition of functions with local support (typically simple polynomials). By using the variational principle the Helmholtz equation is transformed into, again, the system of linear equation, but this time, due to the local character of the differential operators and local support of functions, the coefficient matrix is highly sparse. This system is then solved by means of iterative methods of numerical linear algebra. The finite-element method is generally used for problems that cannot be easily handled by the method of moments, such as three-dimensional structures of complicated shape involving inhomogeneous media. The current trend is to develop techniques that combine the advantages of both methods or lead to matrix systems having the coefficient matrices that allows one to use faster computational algorithms [7,23]. These new schemes are aimed at handling larger structures or treating objects that contain geometric features that differ significantly in size.

6. OPERATOR FORMULATION

The Helmholtz equation can be put in the framework of the theory of linear operator equations [12,18]. For instance, the homogeneous Helmholtz equation can be

⁵The method of moments is one of the approximate techniques of the functional analysis that can be applied to solve any equation with a linear operator. Variational techniques—such as the finite-element method—can also be formulated in the framework of the method of moments. However, in the computational electromagnetics community, the term “method of moments” is usually associated with a technique for solving the integral equation involving the Green function. This term is used in this article in this (narrower) sense.

recast in the form

$$-\nabla^2\Phi(\mathbf{r}) = \lambda\Phi(\mathbf{r}) \quad (89)$$

Written like that, it can be seen as a spectral (eigenvalue) problem for a linear operator $-\nabla^2$. From this perspective it is seen that the homogeneous Helmholtz equation has the solution only for λ belonging to the spectrum [4,12] of $-\nabla^2$, while for the nonhomogeneous case λ has to be chosen from the resolvent set [12] of this operator. When the problem is defined in the appropriate functional space setting, defined by the inner product and the boundary condition, it can easily be shown that operator $-\nabla^2$ has many useful properties. For instance, for bounded regions with homogeneous Dirichlet conditions, which in electromagnetics corresponds to oscillations in an perfectly conduction cavity, the following is true for problem (89):

1. Operator $-\nabla^2$ is Hermitian and positive definite.
2. Eigenvalues of $-\nabla^2$ are positive.
3. Eigenfunctions are orthogonal and form a complete set.
4. Operator ∇^2 is invariant under certain symmetries.

The operator approach is a very powerful tool of analysis. It allows one to predict the properties of the solution and often provides a uniform way to treat problems formulated in a different manner. For instance, properties 1 and 2 lead to the conclusion that the resonances in a perfectly conducting homogeneous electromagnetic cavity occur only for positive real frequencies. Furthermore, property 3 implies that all modes oscillate independent of one another and that an arbitrary field inside an empty cavity can be decomposed into modes. Finally, property 4 explains why in certain geometries, such as spheres, several modes may oscillate with the same resonant frequency. The operator approach can also be applied to the Helmholtz equation with a source term providing means to construct Green's function and is very instrumental in investigating complex problems [3,12,18].

For instance, Green's function for any Hermitian operator L can be found [3] by first solving the eigenvalue problem:

$$L\Psi(\mathbf{r}) = \Theta\Psi(\mathbf{r}) \quad (90)$$

Once the eigenvalues Θ_n and eigenfunctions $\Psi_n(\mathbf{r})$ have been found, the Green function can be constructed in the form of a series

$$G(\mathbf{r}, \mathbf{r}') = \sum_n \frac{\Psi_n^*(\mathbf{r}')\Psi_n(\mathbf{r})}{\Theta_n} \quad (91)$$

For the scalar Helmholtz equation, $L \equiv \nabla^2 + k^2$, so if the boundary conditions are such that ∇^2 is Hermitian, one can use the eigenvalues and eigenfunctions of Eq. (89), namely, the negative scalar Laplacian: $\Psi(\mathbf{r}) \equiv \Phi(\mathbf{r})$ and

$\Theta_n \equiv k^2 - \lambda_n$. Green's function is then

$$G(\mathbf{r}, \mathbf{r}') = \sum_n \frac{\Phi_n^*(\mathbf{r}')\Phi_n(\mathbf{r})}{k^2 - \lambda_n} \quad (92)$$

BIBLIOGRAPHY

1. C. A. Balanis, *Antenna Theory: Analysis and Design*, Wiley, New York, 1982.
2. C. A. Balanis, *Advanced Engineering Electromagnetics*, Wiley, New York, 1989.
3. G. Barton, *Elements of Green's Functions and Propagation (Potentials, Diffusion, and Waves)*, Clarendon Press, Oxford, 1989.
4. F. W. Byron and R. W. Fuller, *Mathematics of Classical and Quantum Physics*, Vol. 1, Dover, New York, 1969.
5. F. W. Byron and R. W. Fuller, *Mathematics of Classical and Quantum Physics*, Vol. 2, Dover, New York, 1969.
6. C.-T. Tai, *Dyadic Green Functions in Electromagnetic Theory*, IEEE Press, New York, 1994.
7. W. C. Chew, J. M. Jin, E. Michielssen, and J. M. Song, eds., *Fast and Efficient Algorithms in Computational Electromagnetics*, Artech House, Boston, 2001.
8. R. E. Collin, *Field Theory of Guided Waves*, McGraw-Hill, New York, 1960.
9. *Encyclopedia Britannica*, from Encyclopedia Britannica Premium Service; <http://www.britannica.com/eb/article?eu=109225>, Nov. 28, 2003.
10. F. E. Gardiol, *Introduction to Microwaves*, Artech House, Dedham, MA, 1984.
11. R. F. Harrington, *Field Computation by Moment Methods*, Macmillan, New York, 1968.
12. G. W. Hanson and A. B. Yakovlev, *Operator Theory for Electromagnetics*, Springer, New York, 2002.
13. T. Itoh, ed., *Numerical Techniques for Microwave and Millimeter-Wave Passive Structures*, Wiley, New York, 1989.
14. J. D. Jackson, *Classical Electrodynamics*, Wiley, New York, 1975.
15. K. A. Michalski and J. R. Mosig, Multilayered media Green's functions in integral equation formulations, *IEEE Trans. Anten. Propag.* **AP-45**:508–519 (March 1997).
16. P. M. Morse and H. Feshbach, *Methods of Theoretical Physics*, Vol. 1, McGraw-Hill, New York, 1953.
17. P. M. Morse and H. Feshbach, *Methods of Theoretical Physics*, Vol. 2, McGraw-Hill, New York, 1953.
18. M. Mrozowski, *Guided Electromagnetic Waves: Properties and Analysis*, Research Studies Press, Taunton, MA, 1997.
19. G. Pelosi, R. Coccioli, and S. Selleri, *Quick Finite Elements for Electromagnetic Waves*, Artech House, Boston, 1998.
20. D. M. Pozar, *Microwave Engineering*, Wiley, New York, 1998.
21. M. N. O. Sadiku, *Numerical Techniques in Electromagnetics*, CRC Press LLC, Boca Raton, FL, 2001.
22. M. Salazar-Palma, T. K. Sarkar, L. E. Garcia-Castillo, T. Roy, and A. Djordjevic, *Iterative and Self-Adaptive Finite-Elements in Electromagnetic Modeling*, Artech House, Boston, 1998.
23. T. K. Sarkar, M. Salazar-Palma, and M. C. Wicks, *Wavelet Applications in Engineering Electromagnetics*, Artech House, Boston, 2002.
24. L. Schiff, *Quantum Mechanics*, Wiley, New York, 1989.
25. I. Stakgold, *Boundary Value Problems of Mathematical Physics*, Vol. 1, Macmillan, New York, 1967.

26. I. Stakgold, *Boundary Value Problems of Mathematical Physics*, Vol. 2, Macmillan, New York, 1968.
27. D. C. Stinson, *Intermediate Mathematics of Electromagnetics*, Prentice-Hall, Englewood Cliffs, NJ, 1976.
28. A. N. Tikhonov and A. A. Samarskii, *Equations of Mathematical Physics*, Dover, New York, 1963.
29. J. Van Bladel, *Electromagnetic Fields*, McGraw-Hill, New York, 1964.
30. J. J. H. Wang, *Generalized Moment Methods in Electromagnetics. Formulation and Computer Solution of Integral Equations*, Wiley, New York, 1991.

HETEROJUNCTION BIPOLAR TRANSISTOR

JAYASIMHA PRASAD
Maxim
San Jose, California

1. INTRODUCTION

Heterojunction bipolar transistor (HBT) technology has advanced very rapidly since the mid-1980s and has replaced the traditional bipolar transistor in many high-speed applications. An increasing number of commercial HBT products are being introduced into the market almost daily. Foundry services are even available for anyone who wants to design HBT circuits to take advantage of its speed.

The theory behind the HBT is well known and dates back to the time when Shockley invented the transistor [1]. The heterojunction bipolar transistor differs from conventional silicon bipolar junction transistor (BJT) in that at least one of the junctions is formed between dissimilar semiconductor materials and has been widely studied [2–8]. HBTs have been fabricated in III–V semiconductors and silicon. The main advantage of HBTs is an improvement in DC and AC performance. HBT device physics is covered in Section 2.1. The complexities in fabrication of HBTs and reliability issues are discussed in Section 3. The performance of both Si and III–V HBTs are covered in Section 3.6. Some issues in modeling are covered in Section 4. A wide variety of applications are covered in Section 5. Finally, the future of HBT technology is discussed in Section 6.

2. ADVANTAGES OF THE HBT OVER THE BJT

2.1. Wide-Bandgap Emitter

A simple HBT is formed by using a wide-bandgap material for the emitter and a narrow-bandgap material for the base and collector. This is called a *single heterojunction bipolar transistor* (SHBT). If the collector is also made of a wide-bandgap material, then it is called a *double heterojunction bipolar transistor* (DHBT). The difference in bandgap ΔE_g between the two materials is accommodated at the junction by discontinuities in the conduction and valence bands. With abrupt emitter–base junctions, the

band offsets between the wide-bandgap emitter and the narrow-bandgap base lead to a spike ΔE_c in the conduction band and a step ΔE_v in the valence band, as shown in Fig. 1 with the constraint $\Delta E_g = \Delta E_c + \Delta E_v$. The valence band offset prevents the back injection of holes from base to emitter and improves the emitter injection efficiency. On the other hand, the conduction band spike reduces emitter efficiency as the electrons have to surmount that energy to be injected into the base to eventually reach the collector. This also produces a lateral shift of the I_C – V_{CE} curves on the V_{CE} axis by an amount V_{offset} from the origin. In other words, $I_C > 0$ only for $V_{CE} > V_{\text{offset}}$, which is undesirable.

There are two ways to reduce V_{offset} . One is to reduce the conduction band spike, and this can be achieved by smoothly by varying the bandgap of the emitter by varying the composition of the material, in which case ΔE_c almost disappears and the valence band offset ΔE_v approaches ΔE_g as shown in Fig. 2a (dotted lines). The other option is to use a widegap material for the collector (resulting in a symmetric DHBT) and create a conduction band spike at the collector to compensate for the ΔE_c at the emitter. This is illustrated in Fig. 2c (dotted lines).

Thus, under the application of a forward bias, the backward injection of holes into the emitter is reduced by a greater extent than the forward injection of electrons into the base; this leads to two beneficial effects: (1) a reduction in the minority-carrier charge stored in the emitter under forward bias, and hence a reduction in the emitter–base storage capacitance and, consequently, an improvement in high-speed and high-frequency performance; and (2) an improvement in the electron injection efficiency, which impacts directly and favorably on β , the forward common-emitter current gain of the device.

A simple numerical example will illustrate the point. Equations (1) and (2) compare the current gain of a Si BJT with the current gain of an AlGaAs/GaAs HBT. In these equations, we assume that the device has “thin” base and “thin” emitter. We also assume that the base

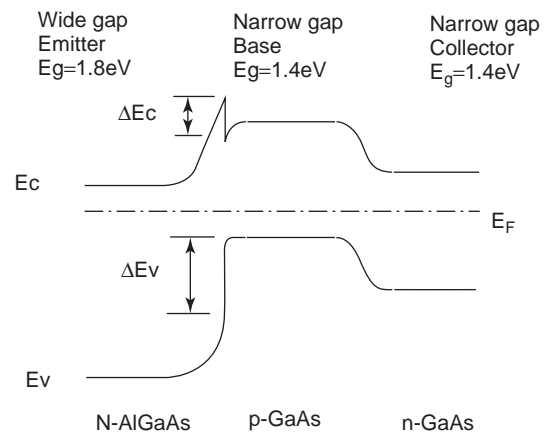


Figure 1. Energy band diagram for a single-heterojunction N-p-n transistor with an emitter having a bandgap wider than that of the base. Let us assume the emitter is doped to 10^{17} cm^{-3} , and the base is doped to 10^{19} cm^{-3} . The hole flow from base to emitter is exponentially reduced by ΔE_v , improving the emitter efficiency.

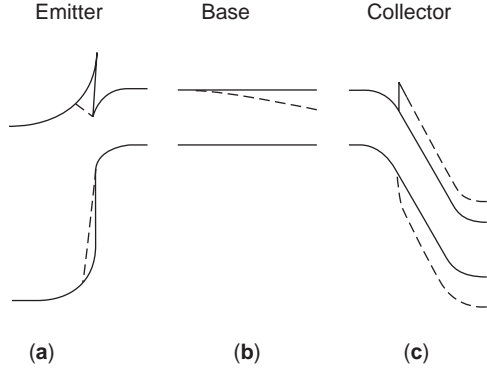


Figure 2. Examples of bandgap engineering in HBT: (a) emitter grading to reduce conduction band spike; (b) base grading to introduce a field to accelerate the electrons; (c) composite collector—a narrow-bandgap collector is used close to the base and a wide-bandgap material is used for the remainder of the collector to improve the breakdown voltage; (d) if all of the collector is made of the same wide-bandgap material as that of the emitter, it is a DHBT. In this case, the conduction band spike occurs exactly at the base–collector junction (not shown) and compensates the ΔE_c at the emitter, reducing the offset voltage V_{offset} . In these figures, the solid lines represent the normal conditions and the dotted lines represent the modifications to the band diagram.

thickness W_B is approximately equal to emitter thickness W_E . D_n and D_p refer to the diffusion constants for electrons and holes, respectively. It is seen that the gain of the HBT is enhanced by the difference in bandgaps between emitter and base:

$$\begin{aligned} \beta(\text{BJT}) &= (N_E W_E D_n / N_B W_B D_p) \\ &= 10^{20}(6.5) / 10^{18}(1.3) = 500 \end{aligned} \quad (1)$$

$$\begin{aligned} \beta(\text{HBT}) &= (N_E W_E D_n / N_B W_B D_p) \exp(\Delta E_g / kT) \\ &= [10^{17}(25) / 10^{19}(5)] 10^5 = 5000 \end{aligned} \quad (2)$$

Additionally, the current gain cutoff frequency f_T is related to transit time of electrons from emitter to collector τ_{EC} by the following relation [6]

$$1/2\pi f_T = \tau_{\text{EC}} = \tau_E + \tau_B + \tau_{\text{CSCR}} + \tau_C \quad (3)$$

where τ_E is the emitter charging time, τ_B is the base transit time, τ_{CSCR} is the transit time in the collector depletion region, and τ_C is the collector charging time. The emitter charging time τ_E has two components; the first is associated with the charge stored in the emitter–base depletion region and the second is due to the holes stored in the emitter as a result of backward-injected holes from the base. In HBTs, the second component is very small, and τ_E can be approximated by the charging time for the emitter–base depletion capacitance C_{BE}

$$\tau_E = C_{\text{BE}}(kT/qI_C) \quad (4)$$

The base transit time in the absence of any electric field in the base is given by

$$\tau_B = (W_B^2/2D_n) + (W_B/v_m) \quad (5)$$

where v_m is the velocity at which the electrons leave the base and $v_m = (kT/2\pi m^*)^{1/2}$.

Typical values for v_m are 5×10^6 cm/s for Si and 1×10^7 for GaAs. If the base has an electric field due to a doping gradient or a bandgap variation, then the carriers move by drift and

$$\tau_B = (W_B^2/\gamma D_n) \quad (6)$$

where γ depends on the electric field present. For a uniform electric field E_0

$$\gamma = 2[1 + (qE_0 W_B/2kT)^{3/2}] \quad (7)$$

Therefore, by creating an electric field, τ_B can be substantially reduced.

The transit time in the collector space charge region is given by

$$\tau_{\text{CSCR}} = W_C/2v_{\text{sat}} \quad (8)$$

where W_C is the collector depletion layer width for a given V_{CB} and v_{sat} is the saturation velocity for electrons. In Si, v_{sat} is 10^7 cm/s. The collector charging time τ_C is the RC time constant of the collector junction capacitance and all the series resistances R_E , R_C and dynamic junction resistance r_e (kT/qI_C).

$$\tau_C = C_{\text{BC}}(R_E + R_C + kT/qI_C) \quad (9)$$

The frequency f_{max} at which the power gain becomes unity is given by

$$f_{\text{max}} = [f_T / (8\pi R_B C_{\text{BC}})]^{1/2} \quad (10)$$

where R_B is the base resistance [9].

Since the reduction in hole flow is large, the emitter doping density N_E can be decreased, and the base doping density N_B can be increased (contrary to that of a BJT), while still maintaining β at an acceptably high value as shown in (2). A lightly doped emitter leads to a reduction in C_{BE} and emitter charging time τ_E , improving f_T , as seen from Eqs. (4) and (3). More importantly, the ability to employ a highly doped base opens up a large number of advantageous possibilities:

1. A reduction in the lateral base resistance R_B , thus improving the power gain at high frequencies, as seen by the expression for f_{max} in Eq. (10)
2. Reduction in emitter–current crowding and also improvement in the noise figure by reducing the thermal noise due to R_B in the base
3. A thinner base in meeting a particular R_B goal, resulting in a shorter base transit time τ_B and, therefore, an improved f_T as seen from Eqs. (6) and (3)

4. A reduction in the collector depletion region encroachments into the base due to heavy doping, leading to higher output conductance and Early voltage, which is often beneficial in analog circuitry, and a reduced susceptibility to device breakdown via punchthrough

It is clear from the discussions above that a HBT gives freedom to independently optimize DC and AC performance. In a BJT, DC and AC parameters are closely coupled and some compromises have to be made in DC performance to meet a given AC performance.

For high-speed digital circuits, bipolar devices are commonly used in two logic families. The current-mode logic (CML) is a simple differential pair with a current source in the emitter leg. The emitter-coupled logic (ECL) is essentially a CML with emitter followers at the outputs. Generally, ECL is faster than CML because of the buffering action of the emitter followers at the expense of additional power dissipation in the emitter followers. The accurate prediction of gate delays of CML and ECL gates is fairly complex and involves several time constants [10]. However, for the purposes of understanding the major factors that contribute to the propagation delay, we can use the approximate expressions given in [11]

$$t_{pd(\text{CML})} = [\tau_{\text{EC}}(R_L + 2R_B)(2C_{\text{BC}} + C_L)]^{0.5} \quad (11)$$

and

$$t_{pd(\text{ECL})} = 1.7 \times [\tau_{\text{EC}}(R_L + 1.4R_B)(3C_{\text{BC}} + C_L)]^{0.5} \quad (12)$$

where R_L is the load resistance and C_L is the parasitic capacitance connected to the output node.

Table 1 shows commonly used material systems, and Table 2 shows the bandgaps and band discontinuities. It is interesting to note from Table 2 that for Si/SiGe system, ΔE_c is almost zero and emitter grading is not necessary.

2.2. Regional Bandgap Engineering

In nearly all the HBTs listed in Table 1, alloy materials are used in some region of the device. By varying the composition of the alloys, it is possible to introduce features that enhance performance of the abrupt-junction HBT.

Table 2. Properties of most Commonly Used Material Systems for HBTs

Material System	E_g (eV)	ΔE_c (eV)	ΔE_v (eV)
$\text{Al}_{0.3}\text{Ga}_{0.7}\text{As}/\text{GaAs}$	1.8/1.42	0.243	0.131
$\text{In}_{0.49}\text{Ga}_{0.51}\text{P}/\text{GaAs}$	1.88/1.42	0.160	0.290
$\text{InP}/\text{In}_{0.53}\text{Ga}_{0.47}\text{As}$	1.35/0.75	0.234	0.366
$\text{Al}_{0.48}\text{In}_{0.52}\text{As}/\text{In}_{0.53}\text{Ga}_{0.47}\text{As}$	1.49/0.75	0.525	0.215
$\text{Si}/\text{Si}_{0.88}\text{Ge}_{0.12}$	1.12/0.99	0.020	0.110

Figure 2 shows some possibilities, which are discussed in the following subsections.

2.2.1. Emitter Grading. Figure 2a illustrates a situation where the wide-bandgap material of the bulk emitter is compositionally graded close to the junction with the base. An example would be an $\text{Al}_x\text{Ga}_{1-x}\text{As}$ emitter with the mole fraction x varied from 0.3 to 0 over a distance of ~ 30 nm from a GaAs base. The diagram depicts a linear grading, as would follow from a linear variation in Al mole fraction. Parabolic grading is also often used. In either case, the objective of the emitter grading is to reduce, or eliminate, the conduction band spike present at abrupt junctions. There are at least two favorable consequences of this. First, because the electron flow across the junction is increased, the collector current and the current gain are enhanced. One advantage of this is a lower turnon voltage—that is, a lower base-emitter bias for a given collector current. This is advantageous for the implementation of HBTs in low-power-consumption circuitry. Second, the ideality factor of the emitter current reduces to unity as thermionic emission takes over from tunneling as the dominant barrier transport mechanism. This fact, when coupled with the increase in emitter current, leads to a lower dynamic emitter resistance and, when coupled with the increase in collector current, leads to an improvement in transconductance. A possible third benefit of a graded emitter is that electrons are injected into the base at near-equilibrium energies, rather than at the elevated kinetic energies possessed by electrons that have tunneled through a high potential barrier, or have been thermionically emitted over it. While these latter “hot” electrons may make a faster transit of the base, they are more likely in GaAs and InP HBTs to be scattered into the lower-mobility, upper-conduction-band valleys on entering the

Table 1. Examples of Material Combinations Frequently Used to Form HBTs with Either a Single Heterojunction (SHBT) or Two Heterojunctions (DHBT)^a

Type	Emitter	Base	Collector	Substrate
SHBT	AlGaAs	GaAs	GaAs	GaAs
SHBT	GaInP	GaAs	GaAs	GaAs
DHBT	AlGaAs	GaAs	AlGaAs	GaAs
SHBT	InP	GaInAs	GaInAs	InP
SHBT	AlInAs	GaInAs	GaInAs	InP
DHBT	AlInAs	GaInAs	InP	InP
SHBT	α -Si	Si	Si	Si
SHBT	SiC	Si	Si	Si
DHBT	Si	SiGe	Si	Si

^aGenerically, the devices are grouped according to the substrate material.

high-field, collector space charge region. Thus, the overall emitter–collector delay time τ_{EC} may in some instances be lower in a graded-junction device.

2.2.2. Base Grading. In base-graded n-p-n HBTs the bandgap is progressively reduced from the emitter to the collector by an appropriate variation in the composition of the base material. As shown in Fig. 2b, the bandgap change is taken up by the conduction band alone. This is because the high hole conductivity precludes any significant variation in the valence band [6].

Thus, the grading has the effect of producing an electric field to aid the passage of electrons across the base. The obvious benefit of this is an improvement in the base transit time τ_B . If, because of the very narrow base that is allowed by having a high base doping density, τ_B is not a major contributor to the overall delay time τ_{EC} , then base grading can be used to achieve an acceptably low value of τ_B in a wider base. The resulting smaller lateral base resistance enables an improvement in f_{max} .

Base grading can also have a beneficial effect on the current gain β ; the reasons for this are twofold:

1. Recombination in the bulk quasineutral base, which can be one of the most significant contributors to the base current, is diminished, with respect to that in a uniform, narrow-bandgap base, because the alloy field increases the electron velocity and, for a given collector current, this means a reduction in the base charge. Of course, this will reduce the base recombination current only if the minority-carrier lifetime is not overly shortened by using an alloy material for the base.
2. Recombination at surface regions of the base is reduced by the tendency of the base alloy field to sweep electrons to the collector—that is, in a direction perpendicular to the base surface. This effect can be particularly beneficial in HBTs with small-dimension emitters, because these devices necessarily have a large emitter perimeter/area ratio.

However, there is a limit to the base grading, beyond which β starts to decrease. Increasing the bandgap of the base material at the emitter–base junction serves to reduce the band offsets, and to make the junction become more and more like a homojunction made from wide-bandgap material. The advantages of a wide-bandgap emitter is lost and current gain degrades to that of a homojunction emitter.

In a wide-bandgap collector DHBT, a further limitation to the permissible amount of base grading is imposed by the need to trade off some of the base grading against the height of the barrier to electron flow into the collector as shown in Fig. 2c. For a given bandgap in the base at the emitter end of the device, decreasing the base bandgap at the collector end increases the amount of base grading, but also increases the barrier to electron flow into the collector. Both β and τ_B are affected by this tradeoff [12].

2.3. Collector Engineering

There are four main motivations for modifying the collector region of a SHBT: (1) to reduce the transit time τ_{CSCR} of electrons in the collector space charge region, (2) to design for a given breakdown voltage BV_{CBO} , (3) to reduce Kirk effect or base pushout effect, and (4) to reduce the collector resistance R_C .

2.3.1. Reduction of τ_{CSCR} . Historically, in bipolar transistors the major transit-time component of τ_{EC} has been τ_B . In modern HBTs, the ability to realize very narrow bases and, to a lesser extent, to implement compositionally graded bases, has led to significant reductions in τ_B , with the result that the dominant transit-related time is τ_{CSCR} . Clearly, reducing the width of the base–collector space charge region W_C would shorten the collector signal delay time, but, if this were accomplished by increasing the collector doping density, then the breakdown voltage and collector junction capacitance C_{BC} would be adversely affected. Trading off speed for improvement in breakdown performance, and vice versa, presents opportunities for novel collector designs. Two structures intended to reduce τ_{CSCR} in GaAs devices are shown in Fig. 3. In the “inverted field” structure of Fig. 3b [12], the field pattern of a conventional collector Fig. 3a is reversed, with the intention of delaying the onset of electron transfer to the lower-mobility, upper conduction bands. This transfer occurs more readily in a conventional collector, as electrons immediately enter a high-field region, in which they are accelerated and rendered more likely to scatter into the upper valleys. This phenomenon is more likely to occur in GaAs than in InP because of the smaller separation between the Γ and L valleys [7]. In the “intrinsic” collector structure shown in Fig. 3c, the high-field zone is restricted to a narrow p^+-n^+ region, and the field remains favorably low in the remaining, weakly doped part of the collector. The first GaAs HBT to register an f_T in excess of 100 GHz was fabricated using such a collector structure [13].

2.3.2. Breakdown Voltage. Turning now to breakdown voltage considerations, the attainment of acceptably high values is difficult in HBTs employing collectors made from

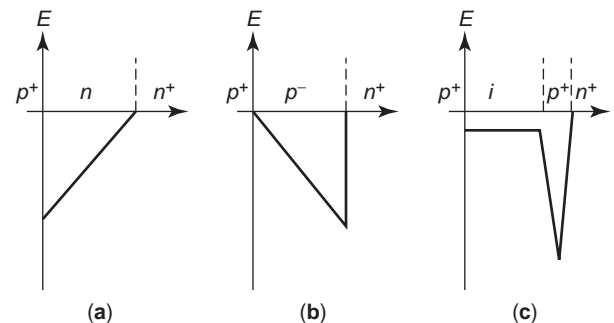


Figure 3. Electric field profiles in different collector structures. The p^+ base is on the left, and the collectors are classified as (a) conventional, (b) inverted, and (c) intrinsic.

narrow-bandgap material, for which the ionization coefficients for electrons and holes are generally high. This is the situation in InP HBTs that have collectors of lattice-matched $\text{In}_{0.53}\text{Ga}_{0.47}\text{As}$, which has a bandgap of only 0.75 eV. Solutions to this problem involve making all, or part, of the bulk of the collector from a wider-bandgap material, such as InP, for which the impact ionization coefficients are low. When all the collector is InP, the device is a DHBT. When the collector comprises GaInAs near the base and then InP for the remainder of the layer, as illustrated in Fig. 2c, the device is labeled as a composite-collector HBT. This design is a refinement of the DHBT, with the objective of using just enough n-GaInAs in the collector to ensure that the conduction band spike at the base-collector junction is reduced below the level of the conduction band in the base. In this way, the stored base charge, which strongly influences τ_B and β , and the collector current are not adversely affected by the presence of the conduction band spike.

2.3.3. Kirk Effect. Of all the aspects of collector design, base pushout or the Kirk effect is the most important design consideration. When the electrons injected into the collector becomes comparable to the background donor concentration, the electric field in the collector first decreases and as the injected carriers continue to increase with collector current density J_C , the field reverses and f_T falls off rapidly. An approximate expression for the critical current density J_K at which the onset of Kirk effect occurs is given by

$$J_K = qv_{\text{sat}}N_C \quad (13)$$

where N_C is the collector doping concentration. Above this current density J_K , the collector-base junction becomes forward-biased and holes are injected into the collector. At this point, the base widens into the collector, τ_B increases and β decreases. Even if the base and emitter are designed properly, if the collector is not at its optimum, the device will not yield the best f_T . To overcome this effect and to meet a given f_T , J_K has to be increased, which requires higher collector doping as predicted by Eq. (13). Higher N_C results in lower BV_{CBO} , lower collector depletion layer width W_C , lower τ_{CSCR} , and higher τ_C , due to higher C_{BC} . To prevent large increases in C_{BC} , selectively implanting the collector just below the emitter is often used in silicon technology. The overall result is that f_T improves at the expense of BV_{CBO} . To regain the some of the lost BV_{CBO} , the collector epitaxial thickness can be increased.

2.3.4. Reduction of R_C . If the collector epitaxial-layer (epi) thickness is increased too much, the undepleted portion of the epi contributes significantly to R_C and τ_C increases. Further, the voltage drop in R_C would cause the collector-base junction to be forward-biased, leading to a drop in f_T with increasing I_C . Attention should be paid to the doping and sheet resistance of the subcollector region as this also contributes to R_C . Therefore, the parameters

N_C , J_K , f_T , and BV_{CBO} have to be optimized for a given application.

3. FABRICATION OF HBTs

HBTs using GaAs or InP substrates, or SiGe base layers, have all progressed beyond the experimental device stage to the point that they are being used in commercial circuits. Examples of the fabrication procedures of HBTs representative of various material systems are discussed in this section.

3.1. AlGaAs/GaAs HBTs

HBTs, at least those of the III-V material variety, are invariably fabricated from a stack of epitaxial layers grown on a semiinsulating substrate (see Table 3), and the devices are built by etching away or implanting unwanted regions. Growing the epitaxial layers on a semiinsulating substrate has the beneficial effect of eliminating the parasitic collector-substrate capacitance, which is present in most silicon BJT structures. It also provides an “inert” platform, which may allow fabrication with equal ease of emitter-up and collector-up structures. Collector-up structures are of interest because the smaller dimension of the collector leads to a reduction in collector-base junction capacitance [14]. A more realistic use of collector-up devices might be as the sole transistor type in exceptionally high-speed ICs [15]. We will now focus on the most frequently used emitter-up HBT structures.

AlGaAs/GaAs HBTs were the first to be fabricated by several companies to take advantage of the high frequency capabilities of these devices [4,5,16]. The bandgap of AlGaAs is given by

$$E_g(x) = 1.424 + 1.247x \quad \text{for } x < 0.45 \quad (14)$$

where x is the Al mole fraction. AlGaAs is lattice-matched to GaAs for a wide range of Al mole fractions. With high electron mobility in AlGaAs, this material is well suited for HBTs. Since LEDs and lasers have been fabricated in this material before, this material system has been well researched. The current gain achieved in this material is about 50–100 (unlike 5000 predicted earlier), due to large surface recombination velocity and significant recombina-

Table 3. Typical Epitaxial-Layer Structure for AlGaAs/GaAs HBTs

Layer	Al Composition	Dopant	Doping (cm^{-3})	Thickness (\AA)
Cap	0	Si	5×10^{18}	1000
Grade	0–0.25	Si	5×10^{17}	300
Emitter	0.25	Si	5×10^{17}	1000
Grade	0.25–0	Si	5×10^{17}	300
Spacer	0	none	—	100
Base	0	Be	2×10^{19}	1000
n ⁻ collector	0	Si	3×10^{16}	5000
n ⁺ collector	0	Si	5×10^{18}	5000
Substrate	0	none	Semiinsulating	—

tion in the emitter–base space charge region. An example of a manufacturable process for AlGaAs/GaAs HBTs from NORTEL is illustrated in Fig. 4 [17]. The epitaxial layers comprising the device, shown in Table 3, can be grown by molecular-beam epitaxy (MBE) or organometallic chemical vapor deposition (OMCVD), and are shown schematically on the figure by the alternating dark and light bands. From the top, the layers are the heavily doped cap to facilitate ohmic contacting to the emitter metal, the emitter, the base, the collector, and the subcollector.

A dummy dielectric emitter (Si_3N_4) is employed for self-alignment to the base metal, which completely surrounds the emitter in this case (see Figs. 4a and 4b). A deep He^+ ion implantation serves to deactivate the collector layer under most of the base metal area, thereby eliminating most of the extrinsic base–collector capacitance. Obtaining a good ohmic contact to the thin, p-type base, without allowing metal penetration through to the collector, is a crucial step. The procedure here is to first etch off the emitter cap and then deposit PdZnPtAuPd, which is then alloyed through the AlGaAs to the p^+ base. The penetration depth during alloying is controlled by the thickness of the Pd layer below the Pt barrier. The next step (Fig. 4c) is to etch off the cap layer between the edge of the base metal

and the emitter stack. This defines the emitter dimensions and, very importantly, leaves an AlGaAs “shelf” layer on top of the base, thereby reducing the surface recombination velocity in this peripheral region. This helps maintain a high β in small-dimension devices. The peripheral region is protected from the subsequent etch, which exposes the subcollector (Fig. 4d), by a SiON sidewall spacer, which also provides alignment tolerance for the emitter metalization. The fabrication sequence is terminated by providing two levels of metal interconnects and a planarizing layer of benzocyclobutene (BCB).

There are many ways to build HBTs, and a simpler process with fewer masks incorporating 1.4-THz Schottky diodes has been described [16]. Generally, Be is used as a p-type base dopant. There were some initial reliability concerns of the device due to dopant migration. These have been resolved and a median time to failure of $>10^8$ h for discrete devices have been shown [18]. Carbon is considered superior to Be in terms of reliability, and most HBTs today employ carbon doping for the base [19–21]. The shift in HBT device parameters is a function of collector current density [22]. The highest reported f_{max} for AlGaAs/GaAs HBT was 350 GHz and this was achieved using a 50 nm base doped to $6 \times 10^{19} \text{ cm}^{-3}$ using carbon [23].

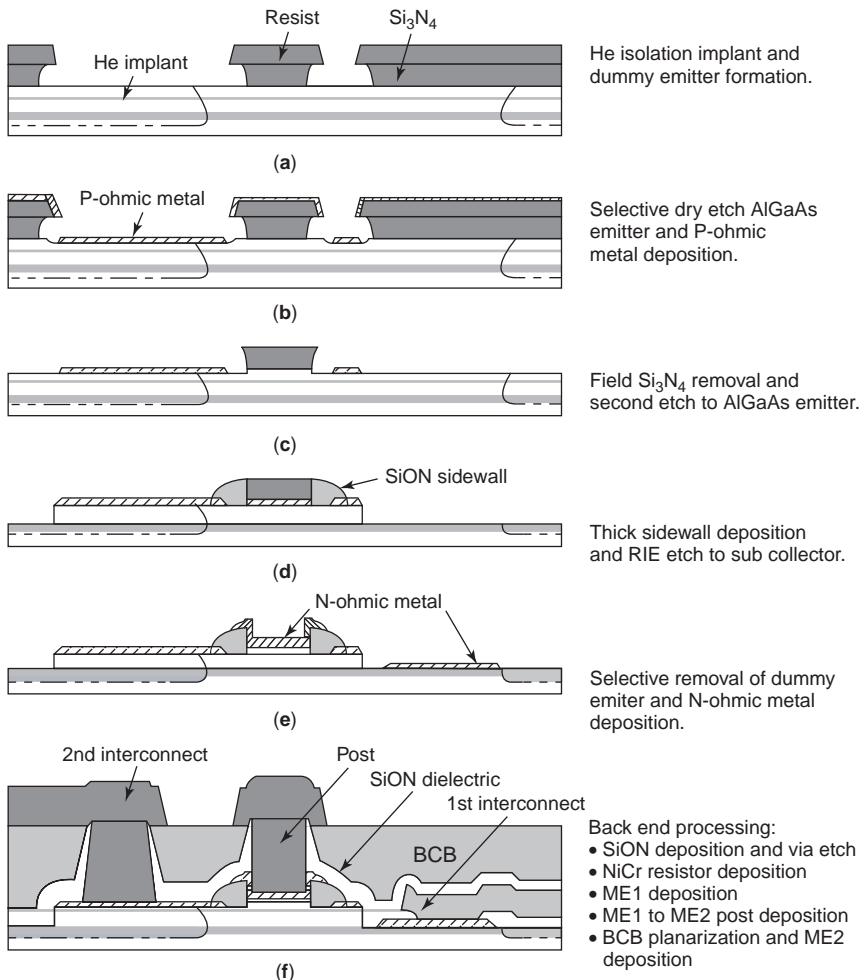


Figure 4. Fabrication sequence for an AlGaAs/GaAs HBT.

3.2. InGaP/GaAs HBTs

A significant event in AlGaAs/GaAs HBT development was the replacement of the AlGaAs emitter by $\text{In}_{0.49}\text{Ga}_{0.51}\text{P}$. Owing to small conduction band offset (0.16 eV) and large valence band offset (0.29 eV), compositional grading of the emitter–base junction is not required (since V_{offset} is small), and this simplifies the epitaxial layer growth. Also, there are selective etchants to etch the InGaP emitter and stop on GaAs base, unlike the case for the AlGaAs/GaAs system [24]. Oxygen complexes, which are often incorporated in aluminum-containing emitters, are less prevalent when using InGaP. This reduces the emitter–base junction recombination current and allows $\beta > 1$ to be maintained down to very low current densities, showing ideal behavior. In fact, InGaP HBTs provide superior current gains compared to AlGaAs HBTs for a given doping profile and almost independent of device size [24,25], due to reduced surface recombination. A first demonstration of a 60-GHz InGaP/GaAs IC technology with 28 ps ECL gate delay was reported in 1993 by Prasad [26]. A YIG-tuned InGaP/GaAs HBT microwave oscillator with low phase noise was first reported in 1994 [27]. The ease of epitaxial growth, simpler fabrication, better temperature stability, lower $1/f$ noise, and improved D.C. properties of InGaP HBTs have led to rapid growth of this technology. Today, InGaP HBTs are widely used for power amplifier applications in cellphones [28,29]. Hitachi has developed a high-speed InGaP HBT IC technology with f_T of 156 GHz and f_{max} of 255 GHz [30]. As described before, carbon doping of the base results in highly reliable devices with no change in the device performance for 10^4 h of operation at a junction temperature of 264°C at $J_C = 2.5 \times 10^4 \text{ A/cm}^2$ [31,32]. The mean time to failure (MTTF) is an order of magnitude better than that for AlGaAs HBTs, suggesting that the InGaP emitter is the best choice for GaAs HBTs [33,34].

3.3. InP/InGaAs HBTs

It is well known that InGaAs, as used for the base material in InP HBTs, has many desirable properties [7]. For example, with respect to GaAs and Si, InGaAs possesses higher electron mobility, higher electron peak velocity, higher electron saturation velocity, and, compared to GaAs, a higher separation of the Γ and L conduction band minima. These properties are very useful for building high-speed devices. Another variation of this device is to use AlInAs emitter instead of InP emitter.

Another beneficial property of InGaAs is its low bandgap (0.75 eV), which results in a higher minority-carrier electron concentration for a given base doping density. When combined with a graded-emitter junction, a significantly lower emitter–base turnon voltage, V_{BE} can be achieved. For example, V_{BE} of InP/InGaAs HBTs is 0.7 V compared to 1.4 V for AlGaAs/GaAs HBTs. A low V_{BE} permits lower supply voltages to be used, resulting in less power consumption and a more favorable gate delay–power product. InGaAs also has a very low surface recombination velocity, which permits achievement of near-ideal I – V characteristics over a large range of forward bias [7].

A typical process sequence for an InP HBT is illustrated schematically in Fig. 5 [35]. Three mesa etches are required: one to define the emitter, one to define the base and collector regions, and one to etch down to the semiinsulating substrate in order to provide device isolation. The mesa etches are necessary because the InP material system lacks an ion implantation damage process capable of rendering GaInAs sufficiently resistive to provide isolation. To reduce the parasitic base–collector capacitance in a mesa structure, the base–collector mesa must be made as small as possible, necessitating tight self-alignment of the base and emitter metallizations. This is achieved by a slight undercutting of the emitter metal contact, which allows this metal to serve as a mask for the medial edge of the subsequently deposited base metal. The etch used in the undercutting must also be selective to avoid destruction of the thin base material; for GaInAs bases, this can present a problem. If the collector is InP, a selective etch can also be used to define the base–collector mesa. If the collector is GaInAs, the same material as the subcollector, then this convenient etch-stop method cannot be employed. However, the etching is less critical than in the

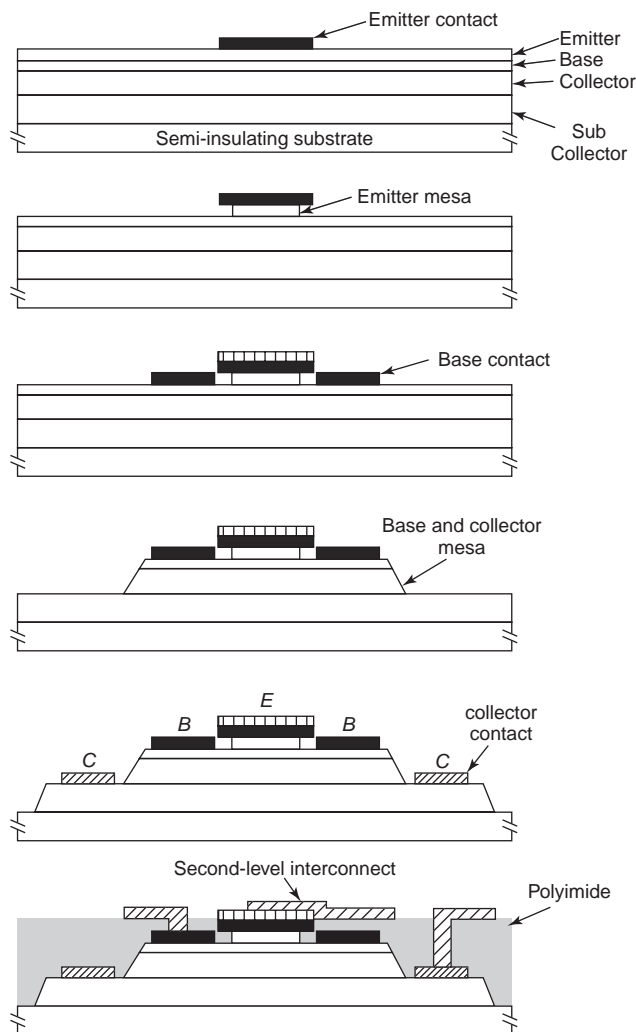


Figure 5. Fabrication sequence for an InP HBT.

case of the emitter mesa formation because the subcollector is relatively thick. The device structure resulting from a triple-mesa process is highly nonplanar, but can be planarized, to facilitate device interconnection and terminal access, by using a suitable polyimide. This coating also provides some passivation of the exposed GaInAs surfaces. The highest reported f_T for InP HBT is 452 GHz [36], and the highest reported f_{max} is 478 GHz [37]. Recently, Vitesse Semiconductor reported a InP DHBD process with f_T and f_{max} of 325 GHz with the lowest CML gate delay of 1.95 ps [126]. Using a transferred-substrate technology, Lee and others have shown a f_{max} of 820 GHz for AlInAs/InGaAs HBT [38]. Reliability studies on InP HBTs have shown that there are no shifts in device parameters based on accelerated tests at 205°C for 6500 h [39,40].

InP technology allows the monolithic integration of long-wavelength photodetectors with HBTs. Inevitably, there are difficulties associated with the simultaneous realization of high-quality optical and electronic devices from a given stack of epitaxial layers. However, in optoelectronic integrated-receiver front ends, for example, good results have been obtained when using the base-collector of an InP HBT as the photodiode [41]. An example of this embodiment is shown in Fig. 6. The top-illuminated photodiode is constructed from the HBT layers by removing the emitter layers and adding an antireflection coating.

3.4. GaN HBTs

There has been a lot of research in GaN materials and devices since the late 1990s. GaN has a bandgap of 3.4 eV, electron saturation velocity of 2×10^7 cm/s, and a high breakdown field of 2 MV/cm. This material is well suited for high breakdown voltage and high temperature applications. A typical GaN HBT would use Si-doped $\text{Al}_{0.15}\text{Ga}_{0.85}\text{N}$ as the emitter ($E_g = 3.85$ eV) and Mg-doped GaN as base and GaN collector grown on sapphire substrate. At this time, GaN HBT technology is not as mature as other HBTs that we have considered so far. The technology suffers from inability to dope the base heavily, very high V_{offset} of 1–5 V

due to high base contact resistance, low current gains (<10), and high collector–emitter leakage [42].

3.5. SiGe HBTs

Unlike the III–V HBTs discussed in the preceding subsections, the starting material for SiGe HBTs are generally p-type silicon substrates. Since the SiGe is the base layer, SiGe HBTs are normally DHBTs. Further, most SiGe HBTs are fabricated by growing a SiGe base layer and depositing a polysilicon layer on top of it to form an emitter, in sharp contrast to III–V HBTs, where all the device layers are grown at once, forming the starting material.

3.5.1. Material Properties. Germanium has a lattice constant of 5.65 Å, whereas silicon has a lattice constant of 5.43 Å. Therefore, the SiGe layer is not lattice-matched to silicon. However, if the epitaxial film is not too thick and the growth temperature is not too high, the SiGe base layer will conform to the Si collector material on which it is grown. Such a layer is referred to as *pseudomorphic* or *coherently strained*. The strain decreases the SiGe bandgap, fortuitously improving the bandgap differential between the base and the subsequently deposited Si emitter, allowing one to build an HBT with tailored bandgap differences. The bandgap of $\text{Si}_{1-x}\text{Ge}_x$ varies according to the relation [43]

$$E_g(x) = 1.124 - 1.22x + 0.88x^2 \quad \text{for } x < 0.6 \quad (15)$$

Furthermore, the strain in the SiGe film breaks the sixfold degeneracy of the conduction band minima and the twofold degeneracy of the valence band maxima; these phenomena can be exploited to improve the electron mobility (reducing τ_B) and the hole mobility (reducing R_B) [6]. The critical thickness—beyond which the SiGe film becomes unstable, and sufficiently defective for the associated rise in recombination centers to render it useless for bipolar applications—is inversely proportional to the Ge content or, for graded SiGe films, to the integrated Ge content. Maintenance of the coherently strained nature of the film,

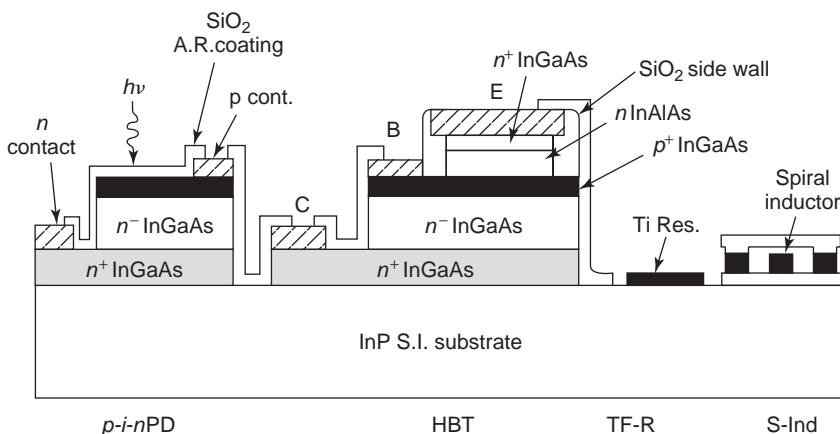


Figure 6. Schematic cross section of the elements of a positive–intrinsic–negative (p-i-n)/HBT OEIC photoreceiver.

by not allowing it to relax and assume its bulk lattice constant, is dependent on minimizing the exposure of the film to subsequent high-temperature environments.

3.5.2. Base Profiles. The constraints imposed by the considerations of SiGe film stability lead to a Si/SiGe HBT fabrication process, which is more complicated than those described previously for III-V HBTs. A review of the procedures used to date to achieve high-performance Si/SiGe HBTs can be found in Refs. 44–46, along with a detailed description of the technology that is employed at IBM to produce HBTs in a manner compatible with standard CMOS processing resulting in a BiCMOS technology. With reference to the HBT base, there are two approaches: (1) using a box SiGe profile with a fixed Ge concentration along with a heavily doped base, similar to the III-V HBTs, where a lightly doped Si emitter is also grown, making it a true HBT (the box profile is used by a few companies, e.g., TEMIC); and (2) using a graded Ge profile (lowest Ge at emitter–base junction and highest Ge at base–collector junction) with a lightly doped base and contact it with a heavily doped polysilicon emitter, which integrates well in standard bipolar process. Here, the speed advantage is due to the accelerating field in the base and the device is a drift base transistor, often abbreviated by the misnomer “HBT”. The graded base approach is widely used in the industry as it has several advantages over the box profile [44].

3.5.3. SiGe Epitaxial Growth. Turning our attention now to the epitaxial (epi) growth of the base, we have two options: (1) nonselective epi and (2) selective epi. In the simplistic nonselective epi, the SiGe base grows as a single crystal on the exposed areas of silicon (where we want the base to be formed) and as polysilicon on oxide. The polysilicon naturally contacts the base and facilitates connection to the base. Also, this polysilicon layer can be used as a resistor if needed. In the selective epi, SiGe base is grown only on the exposed areas of silicon and no growth occurs on the oxide. An additional layer of polysilicon is necessary to contact the base. Each of these techniques has its own advantages and disadvantages.

The SiGe base layers in the HBTs from IBM are grown using a UHV/CVD system, but in this case it is of the hot-wall variety [47]. This equipment has been developed specifically for blanket Si and SiGe epitaxy and is consistent with a low-temperature, commercially feasible process. In this process, hydrogen-passivated Si wafers are admitted to the system, in which a vacuum of around 10^{-9} torr is maintained. The residual gas is predominantly hydrogen; other species, which may be chemically active with silicon, are not present at sufficient partial pressures to violate the hydrogen passivation of the wafer. Films are subsequently deposited under vacuum by CVD at temperatures in the range 400–500°C. Precise dimensional control, of the order of one or two atomic layers, is possible with the UHV/CVD process. Reduced-pressure CVD reactors with pressures of the order of 10 torr are also being used for SiGe epi [48]. These are typically single-wafer machines, unlike the high-vacuum batch reactor described earlier.

3.5.4. SiGe HBT Flow. Here we describe a selective epi technology from NEC, Japan which is geared toward high-performance bipolar circuitry and therefore has the same goal as that of the processes described earlier for III-V HBTs. A partial process sequence is illustrated in Fig. 7 [49,50]. To prepare for the SiGe growth and to begin the emitter definition, the top dielectric film (Si_3N_4) and the large-grain p^+ polysilicon layer shown in Fig. 7a is etched and the edge of the resulting feature is covered with a Si_3N_4 sidewall. The bottom dielectric (SiO_2) is then etched and allowed to laterally undercut the sidewall. From this point on, attention must be paid to the thermal budget, so as not to destroy the pseudomorphic nature of the SiGe base. This layer is grown on the exposed Si substrate, simultaneously with a polysilicon film which descends from the underside of the polysilicon layer exposed by the earlier lateral etch. Growth is stopped when the two growing films touch (see Fig. 7b). Growth is carried out by CVD in a

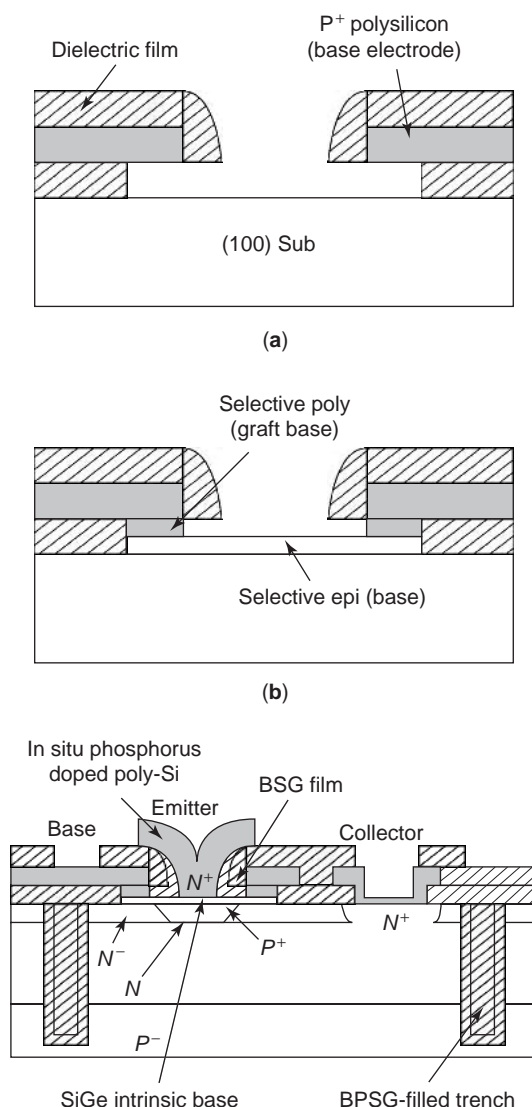


Figure 7. Partial fabrication sequence for SiGe HBT (a) and (b) with the finished device.

cold-wall, ultra-high-vacuum (UHV) system at $\sim 650^\circ\text{C}$. Because films grown by this selective epitaxial growth (SEG) process are very sensitive to the condition of the Si surface, the collector is formed subsequently, using ion implantation. The remaining fabrication steps comprise (1) coating of the Si_3N_4 sidewall with borosilicate glass (BSG), (2) doping of the external SiGe base by driving in boron from the glass at 800°C for 10 min, (3) deposition of phosphorus-doped polysilicon for the emitter, and (4) driving in the emitter at 950°C for 10 s. The finished device, complete with BSG trench isolation, is shown at the bottom of Fig. 7.

3.5.5. SiGe BiCMOS Flow. Most SiGe bipolar processes today incorporate CMOS to take advantage of the high functionality, density, and popularity of several working circuits in standard CMOS. This also helps designing a system on a chip (SoC). In Fig. 8 we show a method of adding bipolar steps to an existing CMOS flow to generate a BiCMOS process flow. The reason for processing the PMOS after the NPN is not to add additional thermal cycles to change the characteristics of the PMOS. It should be noted that if a nonselective epi is used for SiGe base, the SiGe poly layer must be removed from the CMOS areas during base definition. A typical BiCMOS flow with process cross sections is presented in Ref. 45.

One problem associated with thin boron-doped base layers grown by epi is that the dopant diffuses during subsequent device processing, making the base wide and a consequent reduction in f_T , f_{max} , and β . To overcome this problem, the diffusion of boron must be reduced. It has been found that if carbon is added to the SiGe base in concentration of $< 10^{20} \text{ cm}^{-3}$ ($\sim 0.2\%$), the diffusion coefficient of boron is reduced by more than one order of magnitude [51]. Adding carbon to the base thus results in stable DC and AC performance and improved yield. Accelerated testing on SiGe HBTs has shown that the device is very robust and no parametric shifts occur for $> 10^6 \text{ h}$ [52,53].

3.6. Device Performance

The purpose of this subsection is to briefly mention some of the high-performance HBTs that have been reported in the literature and to relate them to the materials constituting the device. Using f_T and f_{max} as figures of merit, Table 4 lists the high-frequency performance of various HBTs reported in the literature. The table also includes data reported in the early 1990s to enable the reader to assess the progress made since that time. It is seen that the InP HBT leads with highest f_T and f_{max} of 370 and 459 GHz, respectively. The highest f_{max} of 820 GHz is obtained on InAlAs/InGaAs HBT transferred to GaAs host substrate and mounted in the collector-up configuration. InGaP HBTs have made a steady progress in f_T from 60 to 156 GHz. The first reported ECL gate delay for InGaP HBT is 28 ps. In the early 1990s, AlGaAs HBTs have shown a f_{max} of 350 GHz. SiGe HBTs have shown performance comparable to III-V HBTs with the lowest CML gate delay of 3.6 ps. More recently, with the regrown emitter process, InP HBTs have shown a f_T of 183 GHz.

The large bandgap of GaAs is also helpful in the attainment of acceptable breakdown voltages. For example, values of BV_{CEO} in the range of 9–15 V are typical of AlGaAs/GaAs HBTs in which the collectors have a doping density of $3 \times 10^{16} \text{ cm}^{-3}$ and thicknesses in the range 300–700 nm. Comparable breakdown voltages in InP HBTs can be obtained only with composite-collector or DHBT structures since the bandgap and breakdown field in InGaAs are smaller than in GaAs. For really high breakdown voltages, InGaP DHBTs are preferred with BV_{CEO} of 47 V [63]. For a given f_T , SiGe HBTs generally have a lower breakdown voltage compared to GaAs HBTs since the collector has to be doped heavily to avoid the Kirk effect.

4. MODELING

The importance of modeling cannot be overemphasized as it forms crucial link between the device physics, device

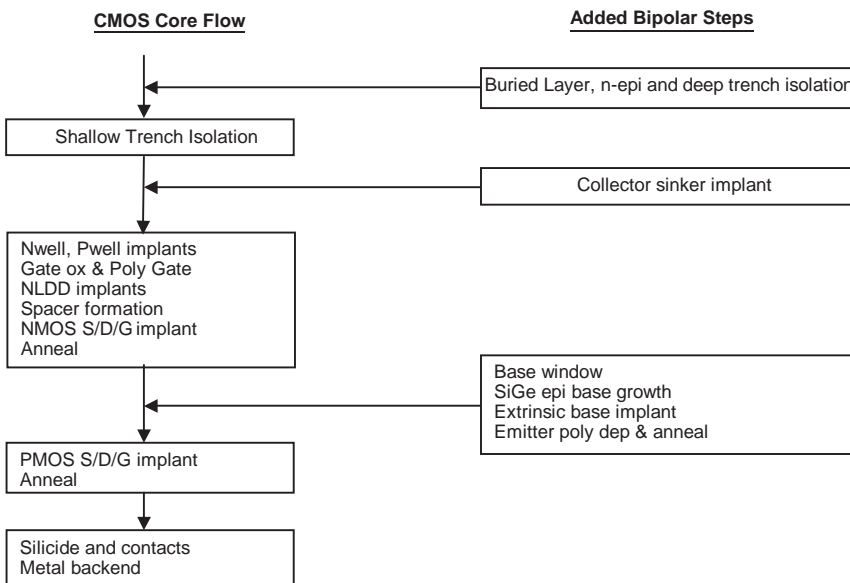


Figure 8. Addition of bipolar steps to a CMOS flow to generate a BiCMOS flow.

Table 4. A Sample of High-Frequency Performance of Various HBTs

Material	Affiliation	f_T (GHz)	f_{max} (GHz)	t_{pd} (ps)	Ref.
InP/InGaAs	UCSB ^a	370	459	—	54
InP/InGaAs	Univ. Illinois, Urbana–Champaign	452	155	—	55
InP/InGaAs	POSTECH, Korea	154	478	—	56
InP/InGaAs	UCSB	183 ^b	165 ^b	—	57
InAlAs/InGaAs	UCSB	300	235	—	58
InAlAs/InGaAs	UCSB	162 ^c	820 ^c	—	38
InGaP/GaAs	Hitachi	156	255	—	30
InGaP/GaAs	Tektronix	60	45	28	26
AlGaAs/GaAs	Rockwell	60	350	—	62
Si/SiGe	IHP, Germany	190	243	3.6	60
Si/SiGe	IBM	180	338	3.9	61
Si/SiGe	IBM	350	170	4.2	59

^aUniversity of California at Santa Barbara.

^bRegrown emitter.

^cTransferred-substrate technology.

structure, process technology, and circuit design. The bipolar compact models have evolved since the Gummel–Poon model to MEXTRAM, high-current model (HICUM), vertical bipolar intercompany (VBIC) model [64–66], and others. Newer models are more complex and take additional computational time, but the advantage is that they are more accurate. This helps in designing complex circuits and better prediction of the performance of a circuit or a system. Some of the newer models have taken into account impact ionization in the collector, quasisaturation, self-heating effects, parasitic substrate transistor effects, and other factors that were not present in the original Gummel–Poon model. A detailed consideration of all these models is beyond the scope of this article. However, in this section, we will present some of the major differences between silicon BJT and HBT models.

4.1. DC and Thermal Effects

Let us now focus on DC properties. III–V HBTs have higher offset voltage (V_{offset}) compared to SiGe or silicon BJT. As mentioned before, V_{BE} for AlGaAs/GaAs and InGaP/GaAs HBT is ~ 1.4 V, whereas V_{BE} for InP/InGaAs and SiGe HBT is close to 0.7 V, comparable to silicon BJT. Due to the presence of the heterojunction at the emitter–base region, the relation between I_C and V_{BE} in a HBT is not as simple as in a BJT, and the ideality factor is greater than unity and varies with V_{BE} . As seen from Eq. (2), the current gain of a HBT decreases with temperature while in a silicon BJT, the current gain increases with temperature. This has to be modeled properly. Typical I_C – V_{CE} characteristics of a silicon BJT slants upward because of (1) lower doping in the base and (2) higher β at higher currents. In HBTs, the I_C – V_{CE} characteristics are generally flat because of higher doping in the base and/or compositional grading across the base. At high currents, the I – V curves droop downward, due to self-heating, which results in a lower current gain and negative Early voltage [67]. Thermal effects are more severe in GaAs HBTs since the thermal conductivity of GaAs is 0.46 W/cm \cdot °C compared to silicon

1.2 W/cm \cdot °C. It should be noted that the thermal effects modeled for DC effects should also model AC thermal effects as it is very important for power amplifier applications.

4.2. AC Effects

Turning our attention now to AC properties, we find that there are new effects in DHBTs. It is well known that at high currents, f_T falls off as a result of the familiar Kirk effect [68], and this also results in a reduction of β with I_C . It is observed that f_T falls off much more rapidly in DHBTs than what is predicted by theory. In addition to the Kirk effect, there is the *heterojunction barrier effect*, which causes this rapid fall of f_T at high currents. In DHBTs, when there is a transition from narrow-bandgap base to wide-bandgap collector, there is a valence band offset at the heterointerface as explained in Fig. 1. Since this barrier is masked by the band bending and the depletion region caused by collector–base (CB) reverse bias, it has negligible effect during low-injection or low-current operation. Under high injection levels, the CB electric field decreases and finally collapses exposing the valence band barrier. This barrier prevents the flow of holes into the collector to maintain charge neutrality when the Kirk effect has set in. These holes pile up at the heterointerface, causing charge imbalance, which results in a conduction band barrier. The conduction band barrier opposes the electron flow into the collector, causing a sudden decrease of f_T [69,70]. This effect is observed in III–V DHBTs and SiGe HBTs. At this point, it is also important to mention another important factor, the *heterojunction barrier effect*, which occurs at low currents as a result of improper base profile design or diffusion of base dopants during subsequent processing, altering the intended base profile. If the transition from narrow-bandgap base to wide-bandgap collector occurs inside a neutral base, parasitic barriers are produced at the conduction band edge, preventing the electron flow into the collector and severely degrading f_T [71,72]. This can be avoided by placing undoped spacers between base and collector. In the case of a SiGe-graded base HBT, if the boron outdiffuses past the Ge profile, it could result in a parasitic conduction band barrier. One method is to set the boron back a certain distance from Ge peak to account for the boron diffusion or use carbon in the base to suppress boron diffusion as explained before.

So far, we have discussed the variation f_T with I_C . We will now consider the variation of f_T with V_{CE} . For a given I_C , as we increase V_{CE} , the collector depletion region width W_C increases and C_{BC} decreases, causing a reduction in τ_C as seen from Eq. (9). This would imply that we have a lower transit time τ_{EC} from Eq. (3) and f_T would increase with increasing V_{CE} . This is what is typically observed in silicon BJTs. However, there is an opposing effect. The transit time in the collector depletion region τ_{CSCR} increases, as seen from Eq. (8). Therefore, the overall variation of f_T with V_{CE} is mixed. Initially, f_T increases with increasing V_{CE} since there is a considerable reduction C_{BC} . Further increase in V_{CE} increases the collector transit time, and f_T decreases with V_{CE} . This has been observed in III–V HBTs. SiGe HBTs do not show this behavior since the collector is very heavily doped.

Since HBTs are increasingly used as power amplifiers in cellphones, the nonlinear behavior such as output power, gain compression, power-added efficiency (PAE), inter-modulation distortion (IMD), and adjacent-channel power ratio (ACPR) have to be modeled for optimizing power amplifier design. Some of the abovementioned effects have been successfully modeled for both III-V and SiGe HBTs [73–78].

4.3. Nonequilibrium Electron Transport

As device dimensions continue to shrink in the never-ending quest for higher speed, transport in the shortened bulk regions of the HBT can no longer be faithfully described by the classical processes of drift and diffusion. The base of modern HBTs is one such region whose width is approaching the length of a mean free path and, therefore, is a region in which quasiballistic transport can be expected to prevail. Quasiballistic transport in the base and velocity overshoot effect in the collector is observed in III-V HBTs. At high values of J_C , the electric field is perturbed by the traveling space charge, leading to very high velocity (even as high as $\sim 7 \times 10^7$ cm/s) near the base-collector junction, leading to very short collector transit time τ_{CSCR} . This results in very high f_T just before onset of the Kirk effect [76–78].

4.4. Parameter Extraction

Once the model is chosen, the next task is to extract device parameters for the model. This task is by no means trivial and creates problems due to the nature of the HBTs and the complexity of the chosen model. For example, the base resistance of a HBT is very low, and conventional DC methods to extract R_B and R_E do not yield correct results [79]. New AC methods have to be used for direct extraction of the model parameters, and there are a variety of papers in the literature [80–82].

5. APPLICATIONS

When AlGaAs/GaAs and SiGe HBTs first came into existence, the main applications were A/D and D/A converters, low-noise amplifiers (LNAs), and power amplifiers. The development and performance of these circuits are described very well in the literature [4–7,45,46]. At the time of this writing, approximately two decades have passed since the first demonstration of these circuits and in the meantime, several new circuits have been developed. Since the applications are widely varied, it will be impossible to cover all of them. We will take a systematic approach to discuss these circuits on the basis of device performance.

5.1. Frequency Dividers

One of the first major building blocks in a digital circuit is the flip-flop, and the speed at which it can be toggled gives a feel for the performance of the circuit. Table 5 shows a summary of various HBT frequency dividers. Static frequency dividers are simple flip-flops. Dynamic frequency dividers make use of a mixer and a lowpass filter in a

Table 5. Summary of Various HBT Frequency Dividers

Material	Affiliation	f (GHz)	Type	Ref.
InP/InGaAs	NTT	150	Dynamic	91
InP/InGaAs	Hughes Research Labs	>100	Static	87
AllnAs/InGaAs	Hughes Research Labs	72.8	Static	88
InGaP/GaAs	Hitachi	39.5	Static	89
InGaP/GaAs	Tektronix	12.5	Static	24
AlGaAs/GaAs	NTT	34.8	Static	90
SiGe	Infineon	110.0	Dynamic	83
SiGe	Infineon	99.0	Dynamic	84
SiGe	IBM	96.0	Static	92
SiGe	Infineon	86.0	Static	83
SiGe	Hitachi	81.0	Static	85
SiGe	Infineon	71.8	Static	86
CMOS 0.18 μm	UCLA	40	Dynamic	93

regenerative loop. The output of the filter is fed back to the mixer so as to generate an output whose frequency is one-half of the input frequency. These generally run at higher frequency, and the output swing is small. In the dynamic frequency dividers, InP HBT from NTT stands tall at a record frequency of 150 GHz. The SiGe counterpart from Infineon is equally impressive, running at 110 GHz.

Coming now to the static dividers, InP HBT from Hughes Research Labs once again sets the record at 100 GHz. On the other hand, a SiGe divider clocking at 96 GHz was reported by IBM at the 2003 GaAs IC Symposium. InGaP HBT dividers have moved from the humble beginning of 12.5 GHz to 39.5 GHz. The emphasis in InGaP HBT technology today is mostly for power amplifiers for cellphones and base stations. Table 5 also shows a 0.18- μm CMOS dynamic frequency divider operating at 40 GHz.

5.2. Oscillators and VCOs

The next circuit that can be benchmarked against the others is a simple oscillator or voltage-controlled oscillator (VCO). Table 6 compares oscillators from various technologies. Shown in the table is also the phase noise at a given offset frequency. The highest-frequency oscillator reported so far operates at 134 GHz, and the transistor used in this oscillator is a InGaP/InGaAs HBT with a f_{max} of 170 GHz. This record is yet to be broken! The SiGe process from Infineon with a f_{max} of 200 GHz has shown a VCO running at 98 GHz. This is the highest reported frequency for an oscillator in silicon-based technology. The next-highest reported frequency for an InP HBT VCO is from TRW running at 62.4 GHz. The very first YIG-tuned InGaP HBT oscillator was reported by Prasad and Haynes [27]. InGaP HBT VCOs are currently running at 34.2 GHz as reported by Hilsenbeck in the 2003 GaAs IC Symposium. A 0.12- μm CMOS VCO from Infineon is running at 51 GHz, which is very good benchmark for a standard CMOS process.

Table 6. Performance Summary of HBT Oscillators and VCOs

Material	Type	Affiliation	f (GHz)	Phase Noise (dBc/Hz)	f_{offset} (MHz)	Ref.
InGaP/InGaAs	Oscillator	Teratec	134	72	1	94
InGaP/GaAs	VCO	FBIH	34.2	108	1	95
InGaP/GaAs	VCO	KAIST	22.3	108	1	96
InGaP/GaAs	YIG oscillator	Tektronix	7.8	135	1	27
InP/InGaAs	VCO	TRW	62.4	104	1	97
SiGe	VCO	Infineon	98.0	97	1	98
SiGe	VCO	IHP	76.0	—	—	99
SiGe	VCO	RUB	46.9	108.5	1	100
CMOS 0.12 μm	VCO	Infineon	51.0	85	1	101

5.3. Power Amplifiers

The superior high-frequency and high-voltage capabilities of HBTs make them very good candidates for RF power amplifiers. The performance levels of power amplifiers and power transistors in different technologies are listed in Table 7. It is clear that InGaP HBTs tend to dominate RF power amplifier market. A 10-W (40-dBm) InGaP DHBT with a gain of 13 dB at 2 GHz and power-added efficiency (PAE) of 50% was reported by Kurpas et al. [63]. An equally good contender for this was a 230-W (53.6-dBm) SiGe power HBT from Northrop–Grumman. This device had a gain of 6.9 dB at 2.8 GHz and a PAE of 46%. For comparison, we have shown a 1-W AlGaAs HBT with 6 dB gain and 72% PAE from Mitsubishi. These high-power transistors are used mainly in power amplifiers for cellphone base stations.

Turning our attention to power amplifiers, we see a 60-GHz power amplifier with 15 dB gain and 13 dBm power output from Sharp built on InGaP HBT technology. We can compare this with a SiGe HBT power amplifier from Infineon operating at 7–18 GHz. This power amplifier has 14 dB gain, 11% PAE, and an output power of 17.5 dBm. A more recent IS-95B power amplifier for cellphones from Skyworks boasts a 27 dB gain and 40% PAE. The data shown in Table 7 represent only a small sample of power amplifiers and power HBTs reported in technical papers and available on the market.

5.4. LNA and Wideband Amplifiers

The most important functional block in a receiver chain is the LNA as it determines the minimum detectable input signal level. Since the HBTs have high current gain, high f_T , and low base resistance, the noise figure of the device is low. Minimum noise figure as low as 0.2 dB and associated

gain of 14 dB at 10 GHz has been reported for SiGe HBTs [108]. Table 8 summarizes LNA and wideband amplifier performance. The SiGe LNA from STMicroelectronics with 22 dB gain and a noise figure (NF) of 1.6 dB operating at 8.2 GHz is a good example of the performance that can be expected from SiGe HBT technology. An example of CMOS LNA built on 0.18 μm technology is also shown in Table 8. At a frequency of 24 GHz, the LNA has a gain of 12.9 dB and noise figure of 5.6 dB. Coming to wideband amplifiers, the highest record is again set by InP HBT. The amplifier boasts a bandwidth of 140–200 GHz and has a gain of 8.5 dB.

5.5. Digital Communication Circuits

In fiberoptic communication systems, several digital circuit blocks can be built with HBTs because of these transistors' superior high-frequency properties. InP HBT is considered to be the best candidate for this purpose since it is a suitable material for the fabrication of OEICs [124]. Beginning with the receiver chain, these include the transimpedance amplifier (TIA), the limiting amplifier, clock and data recovery (CDR), and the demultiplexer (DMUX). On the transmitter chain, we have the multiplexer, the clock multiplication unit, and the voltage driver and the laser modulator. Over the years, the data rates have steadily increased, and we show some recent examples of circuits operating at 40 Gbps. Table 9 shows digital communication circuits fabricated in InP HBT, SiGe HBT, silicon bipolar, and CMOS. We have also included one example of a TIA in InP and SiGe HBT technologies since it is an integral part of the system. It is interesting to note that 50 Gbps 2–1 multiplexer was demonstrated as early as 1996 in silicon bipolar technology. Some of these high-speed circuits were once considered to be only in the realm

Table 7. Performance Summary of HBT Power Amplifiers

Material	Type	Affiliation	f (GHz)	P_{out} (dBm)	Gain (dB)	Power-Added Efficiency (%)	Ref.
InGaP/GaAs	Power HBT	FBIH	2	40	13	50	63
InGaP/GaAs	Power HBT	TI	3	31.8	7	52	28
InGaP/GaAs	PA ^a	Sharp	60	13.0	15	—	102
InGaP/GaAs	WCDMA PA	KAIST	1.9	28	28	40	103
InGaP/GaAs	IS-95B PA	Skyworks	0.837	28	27	40	104
AlGaAs/GaAs	Power HBT	Mitsubishi	12	30	6	72	107
SiGe	Power HBT	Northrop	2.8	53.6	6.9	46	105
SiGe	PA	Infineon	7–18	17.5	14	11	106

^aPower amplifier.

Table 8. Performance Summary of LNA and Wideband Amplifiers

Material	Type	Affiliation	f (GHz)	Gain (dB)	NF (dB)	Ref.
InP/InGaAs	Wideband amplifier	UCSB	140–220	8.5	—	109
SiGe	VG LNA	ETH	16	14.5	3.8	110
SiGe	LNA	STMicro	8.2	22	1.6	111
SiGe	DA LNA	UIUC ^a	0.1–23	14.5	6	112
CMOS 0.18 μm	LNA	UCLA	24	12.9	5.6	113

^aUniversity of Illinois, Urbana–Champaign.

of compound semiconductors. Note that the standard CMOS technology is also advancing rapidly and demonstrating successful 40-Gbps circuits.

6. FUTURE TRENDS AND INDUSTRY OUTLOOK

The heterojunction bipolar transistor has traditionally been the workhorse for ultra-high-speed circuits and will continue to maintain its place at least in the foreseeable future. The HBT is here to stay in spite of the competition from silicon bipolar and deep sub micrometer CMOS. HBTs will dominate in wireless, microwave, fiberoptic communications and test instruments.

The emitter widths of III–V HBTs have scaled down from several micrometers in the mid-1990s to current values of 0.4 μm . On the other hand, the emitter widths of SiGe HBTs have shrunk a lot faster and have reached 0.12 μm . This aggressive scaling of SiGe HBTs is due to the advances in CMOS scaling, lithography, and advanced processes. Base widths will continue to become thin to meet the never-ending need and greed for high f_T . As the base gets thinner, the extrinsic portion of the base also contributes to high R_B . To reduce extrinsic base resistance, a raised extrinsic base (REB) has been employed in 200-GHz SiGe processes [61]. Compared to SiGe HBTs, III–V HBTs will continue to have higher breakdown voltage because of its higher bandgap and breakdown field. The AlGaAs/GaAs HBT, which was dominant at one time, has now been taken over by InGaP HBT. These days, “GaAs HBT” means InGaP HBT, which will play a major role in wireless applications. InP HBT will continue to dominate in high-speed circuits and has a great potential

for developing 160-Gbps fiberoptic communication circuits [124,125].

III–V HBTs have traditionally employed mesa etching of the emitter and a metal liftoff process to form base contacts self-aligned to the emitter. This requires a base (and emitter) that is large enough to be contacted by the ohmic metal and results in high C_{BC} . Higher C_{BC} results in poor device performance, despite the superior material properties of III–V semiconductors. To overcome this problem, regrown emitters are now being used to emulate the double-polytransistor structures in silicon [57].

SiGe HBTs, on the other hand, have used heavily doped polysilicon to form the emitter and contact the SiGe base. This has resulted in lower BV_{EBO} , higher R_E , and a slightly higher $1/f$ noise due to the presence of the interfacial oxide between emitter and base. By using a regrown emitter with the correct amount of doping, BV_{EBO} can be increased and R_E can be decreased [83] with improved $1/f$ noise. Standalone SiGe HBT processes will disappear, and SiGe BiCMOS will be the mainstream process with very high integration levels.

In this fast-moving space age, cost is a deciding factor in making technology decisions. SiGe BiCMOS, which is currently running on 200-mm wafers, with expectations to move to 300-mm wafers, will continue to drive the cost down with improved performance over newer generations. Along with CMOS, BiCMOS offers a very high level of integration and functionality. This fact cannot be denied. Realizing this, many silicon houses (IBM, Infineon, Jazz, National, Maxim, Micrel, Motorola, etc.) have developed their own SiGe processes. For those companies, which do not have their own fabrication facilities, SiGe BiCMOS foundry services are available from IBM, Jazz, TSMC, UMC, and other manufacturers. Comparing this with

Table 9. Performance Summary of Digital Communication Circuits

Material	Circuit	Affiliation	Speed (Gbps)	Ref.
InP/InGaAs	4–1 MUX/DMUX ^a	NTT	40.0	114
InP/InGaAs	CDR ^b /DMUX	Inphi	43.2	115
InP/InGaAs	16–1 MUX	Vitesse	40.0	116
InP/InGaAs	TIA ^c	Vitesse	40.0	117
SiGe	4–1 MUX/DMUX	IBM	50.0	118
SiGe	CDR—Rx/Tx	IBM	43.0	119
SiGe	TIA	Lucent	40.0	120
Si bipolar	2–1 MUX	Siemens	50.0	121
CMOS 0.12 μm	2–1 MUX/DMUX	Infineon	40.0	122
CMOS 0.18 μm	CDR/1–4 DMUX	UCLA	40.0	123

^aMultiplexer/demultiplexer.

^bClock and data recovery.

^cTransimpedance amplifier.

III-V HBTs running on 6- or 4-in. wafers with medium to large-scale integration and higher cost, we find that III-V HBTs have a place in some special applications where SiGe BiCMOS cannot compete. For those competing in the III-V HBT applications who do not have a fabrication facility, foundry services are available from TRW, Knowledge*On, Win Semiconductors, and other companies.

CMOS will continue to catch up with HBTs. However, in applications where $1/f$ noise matters, such as in oscillators, HBTs will dominate. The high-transconductance, high-early-voltage, and high-current-handling capabilities of bipolar technology cannot be ignored. Also, aggressively scaled CMOS can stand only lower supply voltages, and this may be a problem in applications where voltage swing is important. We believe that all the three technologies will coexist and have their own roles to play. It is not too unrealistic for us to witness terahertz transistors in the years to come.

Acknowledgment

The author is deeply grateful to his undergraduate professor, Dr. Sainath, who was instrumental in steering him into the field of semiconductor devices, which was considered a "black art" at that time (and still is!). The author would also like to express his sincere thanks to D. L. Pulfrey for providing an earlier version of this article, which formed a framework on which to build. The author also expresses his heartfelt thanks to the following people for many fruitful discussions on issues pertaining to HBTs: Peter Asbeck, Madhu Gupta, Frank Chang, S. J. Pearton, David Roulston, C. R. Selvakumar, John Cressler, David Hame, Tak Ning, Michael Schroter, Hans-Martin Rein, and the late Greg Stillman. The author was given an opportunity to work and contribute to III-V HBTs at Tektronix with the encouragement and support of Jack Sachitano and Bruce Murdock. Thanks are also due to Reda Razouk (National Semiconductor), Barry Small (Micrel Semiconductor), Viktor Zekeriya, and Vijay Ullal (Maxim) for giving the author an opportunity to contribute to SiGe BiCMOS. Finally, the author would like to thank his wife Chaya and daughter Rama for providing plenty of time during evenings and weekends to complete the deceptively simple task of writing this article.

BIBLIOGRAPHY

- W. Shockley, *Circuit Element Using Semiconductor Material*, U.S. Patent 2,569,347 (1951).
- H. Kroemer, Theory of a wide-gap emitter for transistors, *Proc. IRE* **45**:1535-1538 (1957).
- H. Kroemer, Heterostructure bipolar transistors and integrated circuits, *Proc. IEEE* **70**(1):13-25 (1982).
- P. M. Asbeck, M. F. Chang et al., GaAlAs/GaAs heterojunction bipolar transistors: Issues and prospects for applications, *IEEE Trans. Electron Devices* **36**(10):2032-2042 (1989).
- M. E. Kim, A. K. Oki et al., GaAs heterojunction bipolar transistor device and IC technology for high-performance analog and microwave applications, *IEEE Trans. Microwave Theory Tech.* **MTT-37**(9): 1286-1303 (1989).
- P. M. Asbeck, Bipolar transistors, in S. M. Sze, ed., *High-Speed Semiconductor Devices*, Wiley, New York, 1990, pp. 335-397.
- B. Jalali and S. J. Pearton, eds., *InP HBTs: Growth, Processing and Applications*, Artech House, Boston, 1995, pp. 89-133.
- C. K. Maiti and G. A. Armstrong, *Applications of Silicon-Germanium Heterostructure Devices*, Institute of Physics Publishing, 2001.
- A. P. Laser and D. L. Pulfrey, Reconciliation of methods for estimating f_{max} for microwave heterojunction bipolar transistors, *IEEE Trans. Electron. Devices* **38**:1685-1692 (1991).
- W. Fang, Accurate analytical delay expressions for ECL and CML circuits and their applications to optimizing high-speed bipolar circuits, *IEEE J. Solid State Circ.* **25**(2):572-583 (1990).
- J. M. C. Stork, Bipolar transistor scaling for minimum switching delay and energy dissipation, *IEDM Tech. Digest*, 1988, pp. 550-553.
- O. S. Ang and D. L. Pulfrey, The cut-off frequency of base-graded and junction graded AlGaAs DHBTs, *Solid State Electron.* **34**:1325-1328 (1991).
- T. Ishibashi and Y. Yamauchi, A possible near-ballistic collection in an AlGaAs/GaAs HBT with a modified collector structure, *IEEE Trans. Electron. Devices* **35**:401-404 (1988).
- C. G. Fonstad, Consideration of the relative frequency performance potential of inverted heterojunction n - p - n transistors, *IEEE Electron. Device Lett.* **5**:99-100 (1984).
- B. Agarwal et al., A 277 GHz f_{max} transferred-substrate heterojunction bipolar transistor, *IEEE Electron. Device Lett.* **18**:228-231 (1997).
- S. J. Prasad et al., A 45 GHz AlGaAs/GaAs HBT IC technology, *GaAs IC Symp. Tech. Digest*, 1991, pp. 121-124.
- T. P. Lester et al., A manufacturable process for HBT circuits, *Proc. Int. Symp. GaAs and Related Compounds*, 1993, pp. 449-454.
- D. C. Streit et al., High-reliability GaAs-AlGaAs HBT's by MBE with Be base doping and InGaAs emitter contacts, *IEEE Electron. Device Lett.* **12**:471-473 (1991).
- S. J. Prasad and E. Hultine, Reliability of Carbon doped base AlGaAs/GaAs HBTs as a function of collector current, *MRS Symp. Proc.* **300**: 609-614 (1993).
- S. J. Prasad and E. Hultine, Safe operating current density and failure modes of carbon doped base AlGaAs/GaAs HBTs, *Proc. European Solid-State Device Research Conf. (ESSDERC'93)*, 1993, pp. 643-646.
- D. C. Streit et al., Comparison of MOCVD and MBE for GaAs-AlGaAs HBT manufacturing, *Int. Conf. GaAs Manufacturing Technology Tech. Digest*, 1997, pp. 162-165.
- N. Bovolon, R. Schultheis et al., Analysis of the short-term DC current gain variation during high current density-low temperature stress of AlGaAs/GaAs heterojunction bipolar transistors, *IEEE Trans. Electron. Devices* **47**(2):274-281 (2000).
- W. J. Ho, N. L. Wang et al., Self-aligned, emitter-edge passivated AlGaAs/GaAs heterojunction bipolar transistors with extrapolated maximum oscillation frequency of 350 GHz, *IEEE Trans. Electron. Devices* **39**(11): 2655 (1992).
- S. J. Prasad et al., 35 GHz -Ft. and 26 GHz-Fmax GaInP/GaAs heterojunction bipolar transistors, *IEE Electron. Lett.* **28**(25):2341-2343 (1992).
- W. Liu and S.-K. Fan, Near-ideal I-V characteristics of GaInP/GaAs heterojunction bipolar transistors, *IEEE Electron. Device Lett.* **13**:510-512 (1992).
- S. J. Prasad et al., First demonstration of 60 GHz Ft GaInP/GaAs HBT IC technology with 28 ps ECL gate delay, *IEE Electron. Lett.* **29**(3):320-321 (1993).

27. S. J. Prasad and C. Haynes, First demonstration of a InGaP/GaAs HBT microwave oscillator, *IEEE MTT-S Digest*, 1994, pp. 87–90.
28. W. Liu, E. Beam III, et al., 1.5W CW S-band GaInP/GaAs/GaInP double heterojunction bipolar transistor, *IEEE Electron. Device Lett.* **15**(6):215–217 (1994).
29. T. Iwai, S. Ohara et al., High efficiency and high linearity InGaP/GaAs HBT power amplifiers: Matching techniques of source and load impedance to improve phase distortion and linearity, *IEEE Trans. Electron. Devices* **45**(6):1196–1200 (1998).
30. T. Oka, K. Hirata et al., High-speed small scale InGaP/GaAs HBT technology and its application to integrated circuits, *IEEE Trans. Electron. Devices* **48**(11):2625–2630 (2001).
31. S. R. Bahl, L. H. Camnitz et al., Reliability investigation of InGaP/GaAs heterojunction bipolar transistors, *IEEE Electron. Device Lett.* **17**(9):446–448 (1996).
32. N. Pan, J. Elliott et al., High reliability InGaP/GaAs HBT, *IEEE Electron. Device Lett.* **19**(4):115–117 (1998).
33. T. S. Low, C. P. Hutchinson et al., Migration from an AlGaAs to an InGaP emitter HBT IC process for improved reliability, *GaAs IC Symp. Digest*, 1998, pp. 153–156.
34. M. G. Alderstein and J. M. Gering, Current induced degradation in GaAs HBTs, *IEEE Trans. Electron. Devices* **47**(2):434–439 (2000).
35. M. Hafizi and W. E. Stanchina, Device and circuit fabrication, device characteristics and reliability, in B. Jalali and S. J. Pearton, eds., *InP HBTs: Growth, Processing and Applications*, Artech House, Boston, 1995, pp. 135–194.
36. W. Hafez, J. W. Lai et al., Vertical Scaling of 0.25 μm Emitter InP/InGaAs single heterojunction bipolars with f_T of 452 GHz, *IEEE Electron. Device Lett.* **24**(7):436–438 (2003).
37. D. Yu, K. Lee et al., Ultra high-speed InP-InGaAs SHBTs with f_{max} of 478 GHz, *IEEE Electron. Device Lett.* **24**(6):384–386 (2003).
38. Q. Lee et al., Submicron transferred-substrate heterojunction bipolar transistors, *IEEE Electron. Device Lett.* **20**(8):396–398 (Aug 1999).
39. R. Lee, Accelerated life test results on InGaAs/InP heterojunction bipolar transistors, *GaAs IC Symp. Digest*, 2003, pp. 74–77.
40. S. Bahl, N. Moll et al., Be diffusion in InGaAs/InP heterojunction bipolar transistors, *IEEE Electron. Device Lett.* **21**(7):332–334 (2000).
41. K. Yang et al., Design, modeling and characterization of monolithically integrated InP-based (1.55 μm) high-speed (24 Gb/s) *p-i-n*/HBT front-end photoreceivers, *IEEE J. Lightwave Technol.* **14**:1831–1838 (1996).
42. L. S. McCarthy et al., GaN HBT: Toward an RF device, *IEEE Trans. Electron. Devices* **48**(3):543–551 (2001).
43. R. People, Physics and applications of $\text{Ge}_x\text{Si}_{1-x}/\text{Si}$ strained layer heterostructures, *IEEE J. Quantum Electron.* **22**:1696–1710 (1986).
44. D. L. Harame et al., Si/SiGe epitaxial-base transistors—Part I: Materials, physics and circuits, *IEEE Trans. Electron. Devices* **42**:455–468 (1995).
45. D. L. Harame et al., Si/SiGe epitaxial-base transistors—Part II: Process integration and analog applications, *IEEE Trans. Electron. Devices* **42**(3):469–482 (1995).
46. J. D. Cressler, SiGe HBT Technology; A new contender for Si-based RF and microwave circuit applications, *IEEE Trans. Microwave Theory Tech.* **MTT-46**(5):572–589 (1998).
47. B. S. Meyerson, UHV/CVD growth of Si and SiGe alloys: Chemistry, physics and device applications, *Proc. IEEE* **80**:1592–1608 (1992).
48. C. A. King, J. L. Hoyt et al., Si/Si $_{1-x}$ Ge $_x$ heterojunction bipolar transistors produced by limited reaction processing, *IEEE Electron. Device Lett.* **10**(1):52–54 (1989).
49. F. Sato et al., A super self-aligned selectively grown SiGe Base (SSSB) bipolar transistor fabricated by cold-wall type UHV/CVD technology, *IEEE Trans. Electron. Devices* **41**:1373–1378 (1994).
50. F. Sato et al., Sub-20 ps ECL circuits with high-performance super self-aligned selectively grown SiGe Base (SSSB) bipolar transistors, *IEEE Trans. Electron. Devices* **42**:483–488 (1995).
51. H. J. Osten, D. Knoll et al., Carbon doped SiGe heterojunction bipolar transistors for high frequency applications, *Proc. BCTM Conf.*, 1999, pp. 109–116.
52. J. S. Rieh, K. Watson, F. Guarin, Z. Yang et al., Wafer level forward current reliability analysis of 120 GHz production SiGe HBTs under accelerated current stress, *Proc. Reliability Physics Symp.*, 2002, pp. 184–188.
53. G. Freeman, Z. Yang, F. Guarin et al., Reliability characteristics of 200 GHz f_T 285 GHz f_{max} SiGe HBTs, *GaAs IC Symp. Digest*, 2003, pp. 187–190.
54. Z. Griffith et al., InGaAs-InP Mesa DBHTs with simultaneously high f_T and f_{max} with low Ccb/Ic ratio, *IEEE Electron. Device Lett.* **25**(5):250–252 (2004).
55. W. Hafez et al., Vertical scaling of 0.25 μm emitter InP/InGaAs single heterojunction bipolar transistors with f_T of 452 GHz, *IEEE Electron. Device Lett.* **24**(7):436–438 (2003).
56. D. Yu et al., Ultra high-speed InP-InGaAs SHBTs with f_{max} of 478 GHz, *IEEE Electron. Device Lett.* **24**(6):384–386 (2003).
57. D. Scott et al., A 183 GHz f_T and 165 GHz f_{max} with abrupt InP emitter, *IEEE Electron. Device Lett.* **25**(6):360–362 (2004).
58. Y. Betser, D. Scott et al., InAlAs/InGaAs HBTs with simultaneously high values of f_T and f_{max} for mixed analog/digital applications, *IEEE Electron. Device Lett.* **22**(2):56–58 (2001).
59. J. S. Rieh et al., SiGe HBTs with cut-off frequency of 350 GHz *IEDM Tech. Digest*, 2002, pp. 771–774.
60. H. Rucker et al., SiGe:C BiCMOS technology with 3.6 ps gate delay, *IEDM Tech. Digest*, 2003, pp. 121–124.
61. B. Jagannathan, M. Meghelli, K. Chan, J.-S. Rieh, K. Schonenberg, D. Ahlgren, S. Subbanna, and G. Freeman, 3.9 ps SiGe HBT ECL ring oscillator and transistor design for minimum gate delay, *IEEE Electron. Device Lett.* **24**(5):324–326 (2003).
62. W. J. Ho et al., Self-aligned, emitter-edge passivated AlGaAs/GaAs heterojunction bipolar transistors with extrapolated maximum oscillation frequency of 350 GHz, *IEEE Trans. Electron. Devices* **39**(11):2655 (1992).
63. P. Kurpas, A. Maassdorf et al., 10 W GaInP/GaAs power HBTs for base station applications, *IEDM Tech. Digest*, 2002, pp. 681–684.
64. H. C. de Graaf and F. M. Klassen, *Compact Modeling for Circuit Design*, Springer-Verlag, 1990.
65. J. J. X. Feng et al., A physics-based HBT SPICE model for large-signal applications, *IEEE Trans. Electron. Devices* **42**:8–14 (1995).
66. C. McAndrew, VBIC95, the vertical bipolar inter-company model, *IEEE J. Solid State Circ.* **31**:1476–1483 (1996).
67. W. Liu, *Handbook of III-V Heterojunction Bipolar Transistors*, Wiley, New York, 1998.

68. C. T. Kirk, Theory of transistor cutoff frequency fall of at high current densities, *IEEE Trans. Electron. Devices* **3**:164–170 (1962).
69. S. Tiwari, A new effect at high currents in heterostructure bipolar transistors, *IEEE Electron. Device Lett.* **10**:2105 (1989).
70. Z. Yu, P. E. Cottrell, and R. W. Dutton, Modeling and simulation of high-level injection behavior in double heterojunction bipolar transistors, *Proc. BCTM Conf.*, 1990, pp. 192–195.
71. J. W. Slotboom, G. Streutker et al., Parasitic energy barriers in SiGe HBTs, *IEEE Electron. Device Lett.* **12**(9):486–488 (1991).
72. E. J. Prinz, P. M. Garone et al., The effects of base dopant outdiffusion and undoped SiGe junction spacer layers in Si/SiGe/Si heterojunction bipolar transistors, *IEEE Electron. Device Lett.* **12**(2):42–44 (1991).
73. G.-M. Park and S. Hong, A novel temperature dependent large-signal model of heterojunction bipolar transistor with a unified approach for self-heating and ambient temperature effects, *IEEE Trans. Electron. Devices* **49**(12):2099–2106 (2002).
74. Q. Liang, J. D. Cressler et al., A physics-based high injection transit time model applied to barrier effects in SiGe HBTs, *IEEE Trans. Electron. Devices* **49**(10):1807–1813 (2002).
75. P. Asbeck, III-V HBTs for microwave applications: Technology status and modeling challenges, *Proc. BCTM Conf.*, 2000, pp. 52–57.
76. L. H. Camnitz and N. Moll, *Compound Semiconductor Transistors, Physics and Technology*, IEEE Press, 1993, pp. 21–46.
77. T. Ishibashi, Nonequilibrium electron transport in HBTs, *IEEE Trans. Electron. Devices* **48**(11):2595–2605 (2001).
78. M. Iwamoto, D. E. Root, J. B. Scott, A. Cognata, P. M. Asbeck, B. Hughes, and D. C. D'Avanzo, Large-signal HBT model with improved collector transit time formulation for GaAs and InP technologies, *IEEE MTT Symp. Digest*, June 2003, pp. 635–638.
79. S. J. Prasad, A method of measuring base and emitter resistances of AlGaAs/GaAs HBTs, *Proc. BCTM Conf.*, 1991, pp. 204–207.
80. M. Sotoodeh, L. Sozzi, A. Vinay, A. H. Khalid, Z. Hu, A. A. Rezazadeh, and R. Menozzi, Stepping toward standard methods of small-signal parameter extraction for HBTs, *IEEE Trans. Electron. Devices* **47**(6):1139–1151 (2000).
81. B. Sheinman, E. Wasige, M. Rudolph, R. Doerner, V. Sidorov, and S. Cohen, A peeling algorithm for extraction of the HBT small-signal equivalent circuit, *IEEE Trans. Microwave Theory Tech.* **MTT-50**(12):2804–2810 (2002).
82. M. Dvorak and C. Bolognesi, On the accuracy of direct extraction the heterojunction bipolar transistor equivalent-circuit model parameters C_p , CBC and RE, *IEEE Trans. Microwave Theory Tech.* **MTT-51**(6):1640–1649 (2003).
83. T. F. Meister, H. Schafer et al., SiGe bipolar technology with 3.9 ps gate delay, *Proc. BCTM Conf.*, 2003, pp. 103–106.
84. J. Bock, H. Shafer et al., Sub 5 ps SiGe bipolar technology, *IEDM Tech. Digest*, 2002, pp. 763–766.
85. K. Washio, E. Ohue et al., Ultra-high speed scaled down self-aligned SEG SiGe HBTs, *IEDM Tech. Digest*, 2002, pp. 767–770.
86. M. Wurzer, J. Bock et al., 71.8 GHz static frequency divider in a SiGe bipolar technology, *Proc. BCTM Conf.*, 2002, pp. 216–219.
87. M. Mokhtari, C. Fields et al., 100+ GHz static divide-by-2 circuit in InP-DHBT technology, *IEEE J. Solid State Circ.* **38**(9):1540–1544 (2003).
88. M. Sokolich, C. H. Fields et al., A low-power 72.8 GHz static frequency divider in AlInAs/InGaAs HBT technology, *IEEE J. Solid State Circ.* **36**(9):1328–1334 (2001).
89. T. Oka, K. Hirata et al., High-speed small-scale InGaP/GaAs HBT technology and its application to integrated circuits, *IEEE Trans. Electron. Devices* **48**(11):2625–2630 (2001).
90. Y. Yamauchi, O. Nakajima, K. Nagata, H. Ito, and T. Ishibashi, A 34.8 GHz 1/4 static frequency divider using AlGaAs/GaAs HBTs, *GaAs IC Symp. Digest*, 1989, pp. 121–124.
91. S. Tsunashima, K. Murata, M. Ida et al., A 150 GHz dynamic frequency divider using InP/InGaAs HBTs, *GaAs IC Symp. Digest*, 2003, pp. 284–287.
92. A. Ryljakov and T. Zwick, 96 GHz static frequency divider in SiGe bipolar technology, *GaAs IC Symp. Digest*, 2003, pp. 288–290.
93. J. Lee and B. Razavi, A 40 GHz frequency divider in 0.18 μ m CMOS technology, *IEEE J. Solid State Circ.* **39**(4):594–601 (2004).
94. K. Uchida, I. Aoki et al., 104 and 134 GHz InGaP/InGaAs HBT oscillators, *Proc. GaAs IC Symp.*, 1999, pp. 237–240.
95. J. Hilsenbeck, F. Lenk, W. Heinrich, and J. Wurfl, Low phase noise MMIC VCOs for Ka band applications with improved GaInP/GaAs HBT technology, *GaAs IC Symp. Digest*, 2003, pp. 223–226.
96. J.-G. Kim, D.-H. Baek, S. Jeon et al., A K-Band InGaP/GaAs HBT Balanced MMIC VCO, *IEEE Microwave Wireless Compon. Lett.* **13**(11):478–480 (2003).
97. H. Wang, K.-W. Chang et al., A 62 GHz monolithic InP-based HBT VCO, *IEEE Microwave Guided Wave Lett.* 388–390 (1995).
98. W. Perndl, H. Knapp et al., A 98 GHz voltage controlled oscillator in SiGe bipolar technology, *Proc. BCTM Conf.*, 2003, pp. 67–69.
99. W. Winkler, J. Borngraber et al., 60 GHz and 76 GHz oscillators in 0.25 μ m SiGe:C BiCMOS, *IEEE ISSCC Digest*, 2003, pp. 454–455.
100. H. Li and H.-M. Rein, Millimeter wave VCOs with wide tuning range and low phase noise, fully integrated in a SiGe production technology, *IEEE J. Solid State Circ.* **38**(2):184–191 (2003).
101. M. Tiebout, A 51 GHz VCO in 0.13 μ m CMOS, *ISSCC Digest*, 2002, pp. 372–373.
102. S. Handa, E. Suematsu et al., 60 GHz-band low noise amplifier and power amplifier using InGaP/GaAs HBT technology, *GaAs IC Symp. Digest*, 2003, pp. 227–230.
103. J. Kim, J. Kim et al., An InGaP-GaAs HBT MMIC smart power amplifier for W-CDMA mobile handsets, *IEEE J. Solid State Circ.* **38**(6):905–910 (2003).
104. Y. Yang, K. Choi et al., DC boosting effect of active bias circuits and its optimization for class-AB InGaP-GaAs HBT power amplifiers, *IEEE Trans. Microwave Theory Tech.* **MTT-52**(5):1455–1463 (2004).
105. P. A. Potyraj, K. J. Petrosky et al., A 230 W S-band SiGe heterojunction bipolar transistor, *IEEE Trans. Microwave Theory Tech.* **MTT-42**(11):2392–2397 (1996).
106. W. Bakalski, A. Vasylyev et al., A fully integrated 7–18 GHz power amplifier with on-chip output balun in 75 GHz f_T SiGe bipolar, *Proc. BCTM Conf.*, 2003, pp. 61–64.
107. T. Shimura, M. Sakai et al., 1 W Ku band AlGaAs/GaAs power HBTs with 72% peak power added efficiency, *IEEE Trans. Electron. Devices* **42**(11):1890–1896 (1995).
108. D. R. Greenberg et al., Noise performance of low base resistance 200 GHz SiGe technology, *IEDM Tech. Digest*, 2002, pp. 787–790.

109. M. Urtega, D. Scott et al., G-band (140–220 GHz) InP-based HBT amplifier, *IEEE J. Solid State Circ.* **38**(9):1451–1456 (2003).
110. F. Ellinger and H. Jackel, Low-cost BiCMOS variable gain LNA at Ku-band with ultra-low power consumption, *IEEE Trans. Microwave Theory Tech.* **MTT-52**(2):702–708 (2004).
111. G. Gramegna, A. Magliarisi, and M. Paparo, An 8.2 GHz, 14.4 mW, 1 dB NF SiGe bipolar LNA with DC current reuse, *Proc. BCTM Conf.*, 2003, pp. 49–52.
112. Q. He and M. Feng, Low-power, high-gain and high-linearity SiGe BiCMOS wide-band low-noise amplifier, *IEEE J. Solid State Circ.* **39**(6):956–959 (2004).
113. K. Yu, Y. Lu et al., K-band low-noise amplifiers using 0.18 μm CMOS technology, *IEEE Microwave Wireless Compon. Lett.* **14**(3):106–108 (2004).
114. K. Ishii, H. Nosaka et al., 4-bit multiplexer/demultiplexer chip set for 40-Gbit/s optical communication systems, *IEEE Trans. Microwave Theory Tech.* **MTT-51**(11):2181–2186 (2003).
115. S. Nielsen, J. C. Yen et al., A fully integrated 43.2 Gb/s clock and data recovery and 1:4 demux IC in InP technology, *IEEE J. Solid State Circ.* **38**(12):2341–2346 (2003).
116. A. Hendarman, E. Savaro et al., STS-768 multiplexer with full-rate output data retimer in InP HBT, *IEEE J. Solid State Circ.* **38**(9):1497–1503 (2003).
117. C. Wu and E. A. Sovero, 40 GHz transimpedance amplifier with differential outputs using InP-InGaAs heterojunction bipolar transistors, *IEEE J. Solid State Circ.* **38**(9):1518–1523 (2003).
118. M. Meghelli, A. Rylyakov, and L. Shan, 50 Gb/s SiGe BiCMOS 4:1 multiplexer and 1:4 demultiplexer for serial communication systems, *IEEE J. Solid State Circ.* **37**(12):1790–1794 (2002).
119. M. Meghelli, A. Rylyakov et al., A 0.18 μm SiGe BiCMOS receiver and transmitter chipset for SONET OC-768 transmission systems, *IEEE J. Solid State Circ.* **38**(12):2147–2154 (2003).
120. H. S. Weiner, A. Leven et al., SiGe differential transimpedance amplifier with 50 GHz bandwidth, *IEEE J. Solid State Circ.* **38**(9):1512–1517 (2003).
121. A. Felder, M. Moller et al., 46 Gb/s DEMUX, 50 Gb/s MUX and 30 GHz static frequency divider in silicon bipolar technology, *IEEE J. Solid State Circ.* **31**(4):481–486 (1996).
122. D. Kehrer, H.-D. Wohlmuth et al., 40 Gb/s 2:1 multiplexer and 1:2 demultiplexer in 120 nm standard CMOS, *IEEE J. Solid State Circ.* **38**(11):1830–1837 (2003).
123. J. Lee and B. Razavi, A 40 Gb/s clock and data recovery circuit in 0.18 μm CMOS technology, *IEEE J. Solid State Circ.* **38**(12):2181–2190 (2003).
124. H. Jackel, U. Hammer et al., High speed InP-based HBTs and OEICs, *IEDM Tech. Digest*, 2002, pp. 83–86.
125. J. C. Zopler, Super-scaled InP HBTs for 150 GHz circuits, *IEDM Tech. Digest*, 2003, pp. 709–712.
126. G. He, J. Howard et al., Self-aligned InP DHBT with f_T and f_{max} over 300 GHz in a new manufacturable technology, *IEEE Electron. Device Lett.* **28**(8):520–522 (2004).

HETEROSTRUCTURES DEVICES

VICTOR RYZHII
 University of Aizu
 Japan

All semiconductor devices are made of building blocks, consisting of semiconductor structures with different

properties and supplied by some nonsemiconductor parts. This relates to discrete devices and integrated circuits alike. Junctions of semiconductors doped by different impurities are the most important structures of semiconductor devices. If a junction is formed by regions of the same semiconductor material with one of them doped by acceptor impurities, and the other one by donor impurities, such junction is called the *p-n junction*, or the *p-n homojunction*. Semiconductor structures consisting of homojunctions are known as *homostructures*. More generally, homostructures are defined as semiconductor structures in which doping changes with position. Semiconductor structures with a nonuniform chemical composition are called *heterostructures*. The simplest heterostructure includes a single heterojunction, which is an interface between two different semiconductor materials. The size of the region where the chemical composition changes can be both small (about a few periods of the crystal lattice) and relatively large (comparable with the size of the device). The first case corresponds to so-called abrupt heterostructure, in contrast to graded (or graded-gap) heterostructure, in which the chemical composition and, in turn, the semiconductor energy bandgap change smoothly.

The abrupt heterostructures can be formed by almost all combinations of semiconductor materials, although not all combinations yield heterostructures with desirable properties and quality. Examples of heterostructures include Si–Si_{1-x}Ge, GaAs–Al_xGa_{1-x}As, GaSb–InAs, and other heterostructures. Graded heterostructures are formed by many semiconductor compounds, in particular, A₃B₅ compound system.

The main property of heterostructures used in most heterostructure devices is the nonuniformity of spatial distributions of the bandgap and the edges of the valence and conduction bands. This leads to the formation of the so-called quasi-electric field in heterostructure bulk affecting charge carriers, as has been pointed out in a pioneering paper by H. Kroemer (see, e.g., Ref. 1 and references cited therein). The quasi-electric field in graded heterostructures forces electrons and holes to move in the same direction, despite their opposite charges (Fig. 1). In heterostructures with abrupt heterojunctions, the band offsets can form potential barriers or ramps for electrons and holes, shown in Fig. 2. The band offsets are the result of abrupt variations of the chemical composition. Thus, the

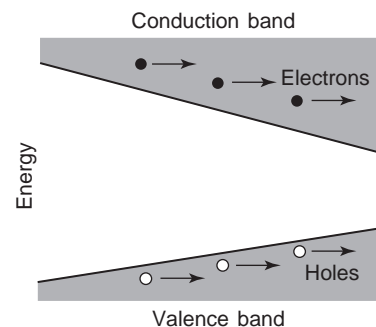


Figure 1. Forces on electrons and holes in a graded-gap heterostructure. The forces in electrons and holes are in the same direction.

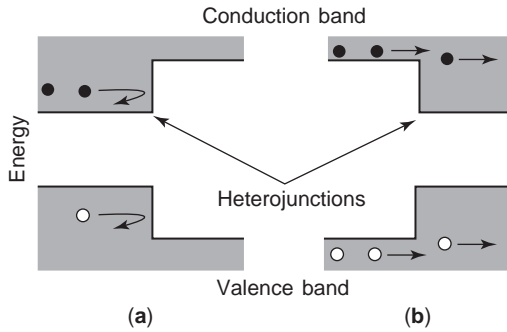


Figure 2. Energy barriers (a) and ramps (b) for electrons and holes in an abrupt heterostructure. Electrons and holes are rejected from the heterojunction if their energy is smaller than the barrier height. They acquire the energy passing the ramp at the heterojunction.

energy of the carriers at the band edges must change as those carriers pass through the heterojunction.

An important practical constraint is the necessity to select materials with small differences in lattice constants at the required fabrication and operating temperatures. A good lattice match is needed to minimize the density of interface states and strain fields at the heterojunction. A heterostructure with a double heterojunction can form a potential well. If such a well is narrow enough, the energy spectrum of electrons (or holes) becomes quantized (Fig. 3), due to the confinement of the latter in the direction perpendicular to the heterojunction plane. Such potential wells are known as *quantum wells* (QWs).

Heterostructures are the elements of many of the most advanced semiconductor devices currently being developed and fabricated. They are essential parts of modern optoelectronic devices, such as semiconductor lasers, light-emitting diodes, and photodetectors with highest performance. Heterostructures are being employed increasingly in high-speed digital and high-frequency analog devices [2,3]. The advantages of heterostructures are that they provide effective control over the states and motions of charge carriers—electrons and holes in active regions of heterostructure-based devices.

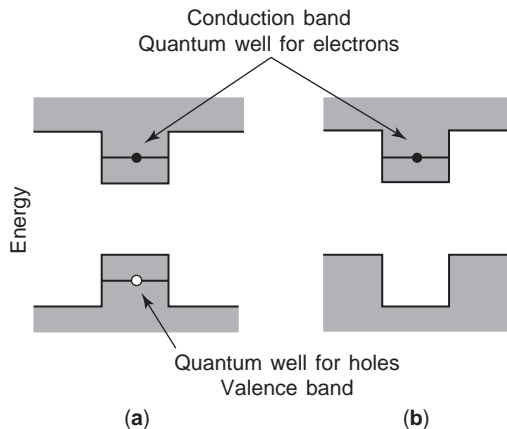


Figure 3. Quantum wells for electron and holes (a) and quantum well for electrons only (b) in double heterostructures.

1. HETEROSTRUCTURE BIPOLAR TRANSISTORS

The principle of a bipolar transistor with heterojunctions is old as the transistor itself. A heterostructure (heterojunction) bipolar transistor (HBT) is the first semiconductor device incorporating heterostructures as it has been patented by W. Shockley as early as 1948. HBTs differ from ordinary bipolar transistors by the utilization of a wide-bandgap semiconductor material for the transistor emitter and, in some cases, for the collector, instead of the same material as for the base. In particular, HBTs are formed by a N-p-n heterostructure with a N-p heterojunction serving as the emitter junction, and a p-n junction for the collector. Such HBTs are single-heterostructure bipolar transistors (SHBTs). SHBTs can be made of P-n-p heterostructures as well. Double heterostructure bipolar transistors (DHBT) consists of both the emitter and collector heterojunctions. They have N-p-N or P-n-P structures. Symbols N and P denote the wide-bandgap semiconductor portions doped by donors and acceptors, respectively, while the symbols n and p correspond to the narrow-bandgap regions with related types of doping.

The basic idea of an HBT is as follows. Consider the energy band structure of an N-p-n HBT with an abrupt or graded-emitter heterojunction, as in Fig. 4. The incorporation of the wide-gap emitter leads to the formation of an additional barrier for the carriers in the base (holes in the example under consideration in Fig. 4) inhibiting their escape to the emitter region. This decreases the current of holes injected from the base into the emitter. A figure of merit for an HBT is the ratio of the collector current I_c to the base current I_b :

$$\beta = \frac{I_c}{I_b} < \frac{I_n}{I_p} \equiv \beta_{\max} \tag{1}$$

Here I_n and I_p are the currents of electrons injected from the emitter into the base and holes injected from the base into the emitter. The ratio of the electron and hole currents, that is, the parameter β_{\max} , is given by the following expression

$$\beta_{\max}^{(HBT)} = \frac{N_e v_{nb}}{p_b v_{pe}} \exp\left(\frac{\epsilon_v}{kT}\right) = \beta_{\max}^{(0)} \exp\left(\frac{\epsilon_v}{kT}\right) \tag{2}$$

for HBTs with an abrupt emitter heterojunction and

$$\beta_{\max}^{(HBT)} = \beta_{\max}^{(0)} \exp\left(\frac{\epsilon_v + \epsilon_c}{kT}\right) \tag{3}$$

in the case of HBTs with a graded heterojunction. Here k is the Boltzmann constant, T is the temperature, N_e and p_b are the electron and hole concentrations in the emitter and the base, respectively, v_{nb} and v_{pe} are the mean velocities of electrons and holes in the related regions, ϵ_v and ϵ_c are the band edge discontinuities related to the valence and conduction bands in the case of an abrupt heterojunction. For a graded heterojunction, ϵ_v and ϵ_c are the fractions of the change of the bandgap in the emitter and base regions related to the valence and conduction bands. In

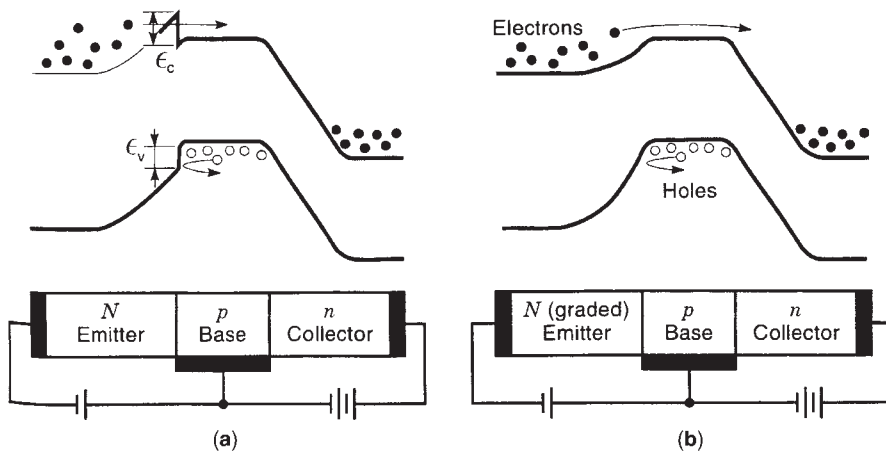


Figure 4. Energy band diagrams of N-p-n HBTs with an abrupt (a) and graded (b) emitter and schematic view of their structure.

the general case $\varepsilon_v + \varepsilon_c = \Delta\varepsilon_g$, where $\Delta\varepsilon_g$ is the difference between the bandgaps in the different parts of the heterostructure. In Eqs. (2) and (3) $\beta_{\max}^{(0)}$ corresponds to a homostructure bipolar transistor ($\varepsilon_v = \varepsilon_c = 0$), with the same doping of all its parts as the HBT under consideration.

For a good transistor, a value β_{\max} should be large. In conventional bipolar transistors the large value of β_{\max} is achieved by significantly higher doping level of the emitter, in comparison to the base ($N_e \gg p_b$). However, very high values of β_{\max} can be realized in HBTs, almost regardless of the doping ratio, due to large value of the exponent in Eqs. (2) and (3). Indeed, if $\Delta\varepsilon_g = 0.2$ eV at $T = 300$ K, one has $\beta_{\max}^{(\text{HBT})} / \beta_{\max}^{(0)} = \exp(\Delta\varepsilon_g / kT) \simeq 3000 \gg 1$. Thus, high β values can be obtained without a high emitter-to-base doping ratio. The increase of the base doping level results in lower base resistance. Simultaneously, a lightly doped emitter region provides smaller capacitance of the emitter. Both high base and low emitter doping promote better high-frequency performance of HBTs, in comparison to homostructure bipolar transistors. This is due to lower base resistance and smaller emitter-base capacitance. High base doping leads to lower noise as well. In addition, high base doping results in higher punch-through voltage.

The conduction band discontinuity in the emitter heterojunction provides the injection of hot electrons from the emitter to the base. If the base is thin enough, the injected electrons can pass it without scattering or enduring a few collisions with impurities and phonons. In the case of such ballistic or near-ballistic transport of electrons in the HBT base, their delay time can be very short. This also contributes to the advantages of HBTs over standard bipolar transistors. Incorporation of the graded-gap base with quasi-electric field yields the acceleration of the injected electrons (or holes) in the base. Such a design provides higher performance as well.

Apart from HBTs with a single heterojunction (usually in the emitter), that is, SHBTs, DHBTs are also considered as prospective components, especially for digital circuits and novel functional devices. The utilization of an additional heterojunction (in the collector) opens up opportunities for separate optimization of the base and the collector—the interchangeability of their functions in some circuits.

The incorporation of more sophisticated heterostructures into the emitter of an HBT or its other parts can substantially extend the diversity of the HBT characteristics. For example, HBTs with a double-barrier heterostructure in the HBT emitter providing resonant-tunneling injection can exhibit N-shape current-voltage characteristics. The utilization of resonant tunneling HBTs (RTHBTs) promises a significant reduction in the logic circuits complexity [4]. HBTs without base contact can be used as phototransistors with very high photoelectric gain, making them rather effective photodetectors for optical fiber communication systems and other applications.

2. HETEROSTRUCTURE HOT-ELECTRON TRANSISTORS

Heterostructure hot-electron transistors (HETs) are made on the base of a double heterojunction structure. Wide-gap regions form the HET emitter and collector. A narrow-bandgap region, sandwiched between the wide-bandgap emitter and collector regions, serves as the HET base. In contrast to HBTs, the HET base is doped by the same type of dopants as the emitter and the collector. Hence HETs are unipolar devices. The energy band diagram of a HET with a N-n-N structure is shown in Fig. 5.

The electron injection from the emitter to the base, and, further, to the collector in HETs with the structure of Fig. 5, is associated with thermionic emission of electrons overcoming the barrier at the N-n interface. Electrons injected from the wide-bandgap emitter have excess kinetic energy in the base. Their motion is directed primarily perpendicular to the heterojunction plane. The directed velocity of electrons significantly exceeds the thermal velocities of both the injected and thermalized electrons in the base. That is why such transistors are called the HETs. The thermalized (or cold) electrons provide electrical neutrality of the base. As the scattering of the injected electrons in the HET base leads to their capture in the latter, and prevents them from the injection into the collector, the electron transport in the base should be either ballistic or near-ballistic.

Different types of HETs have been proposed. The injection of electrons (or holes in P-p-P HETs) from the emitter

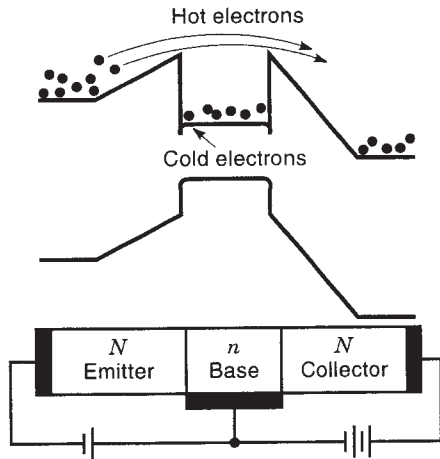


Figure 5. Energy band diagram of a N-n-N HET and schematic view of its structure.

can be associated with thermionic or tunneling processes. The energy band diagram of a HET, with tunneling injection of electrons, is shown in Fig. 6.

The main problem connected with the development of high-performance HETs is the tradeoff between the capture rate of hot electrons into the base, which decreases the HET current gain, and the base resistance, which limits high-speed potentials of HETs. The point is that the enhancement of the base doping level necessary for the lowering of the base resistance leads to the increase of the capture probability of hot electrons, due to the reinforcement of their scattering on donors and cold electrons.

In HETs with a thin base, electrons in the latter can be quantized. The quantization of the electron spectrum in the HET base adds an additional complexity to the HET operation. The existence of a bound state in the electron spectrum can result in significant contribution of resonant tunneling processes to the injection of electrons. Further development of the idea of hot-electron transport resulted in the proposal of a HET with a resonant tunneling emit-

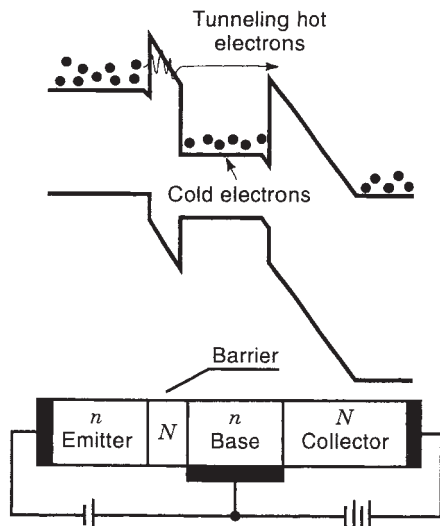


Figure 6. Energy band diagram and structure of a HET with tunneling injection of electrons.

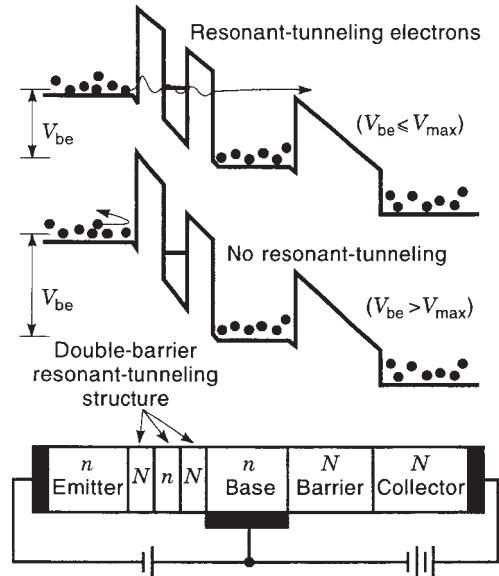


Figure 7. Operational principle and schematic view of the structure of a resonant tunneling HET.

ter. The operation principle of resonant tunneling HETs (RTHETs) is demonstrated in Fig. 7. The most important feature of the RTHET operation is that at some collector-base voltage, the injected electron current has a maximum. The further increase of this voltage leads to a sharp drop of the injected current. Thus, RTHETs are transistors exhibiting negative differential resistance. This property is considered as very promising for future applications in different circuits.

Although HETs of different types are still under investigation, they have no commercial significance, despite very promising features of their characteristics.

3. HETEROSTRUCTURE FIELD-EFFECT TRANSISTORS

Heterostructure field-effect transistors (HFET) are field-effect, three-terminal devices, akin to the metal semiconductor field-effect transistors (MESFETs) with a Schottky gate and metal insulator field-effect transistors (MISFET), taking advantage of electron transport in heterostructure channel. A general name HFET is used for a family of field-effect transistors on the base of different heterostructures. This family includes the modulation-doped field-effect transistor (MODFET), which is also known as the high-electron-mobility transistor (HEMT), the heterostructure insulated-gate field-effect transistor (HIGFET), and some others.

In MODFETs, the wide-bandgap layer beneath the metallic gate is doped, and carriers transfer to the layer of an undoped narrow-gap material. The narrow-bandgap material layer forms the MODFET channel, which is usually undoped. The result of the modulation doping is that electrons (or holes) in the channel are spatially separated from the doped layer. Because of this, they can have extremely high mobility along the heterojunction due to the elimination of impurity scattering. The most common

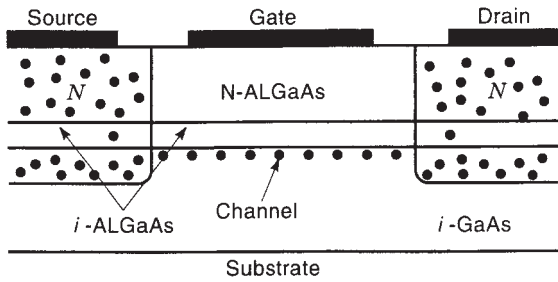


Figure 8. Cross-sectional view of a MODFET with *n*-channel.

MODFETs utilize $Al_xGa_{1-x}As-GaAs$ heterostructures. A typical view of the MODFET structure cross section is shown in Fig. 8.

Electrons (holes) in the MODFET channel are confined by the heterojunction from one side and by the electric potential creating the electric field, forcing them against the heterointerface. Such confinement of electrons may lead to the quantization of their energy spectrum. If the electron confinement is strong, so that the width of the channel is small enough, electrons form a two-dimensional (2D) electron gas, located near the heterojunction. Sometimes, MODFETs with a 2D electron gas in the channel are called the *two-dimensional electron gas field-effect transistors* (TEGFETs).

The MODFET performance is strictly dependent on the thickness and quality of a very thin undoped layer of a wide-gap material, separating the doped region and the narrow-bandgap channel. This so-called spacer is usually made of $i-Al_xGa_{1-x}As$ (see Fig. 8).

HIGFETs differ from MODFETs, in that both the wide-bandgap and the narrow-bandgap layers are undoped. In some HFETs, the narrow-bandgap channel is doped. Such HFETs lose the advantage of high electron mobility. Their operation is similar to that of MISFETs. Along with the HFETs, in which the channel is formed by a heterojunction and an electrostatic barrier, in some HFETs a double heterostructure is used to form the channel. In the latter case, the HFET channel can be a QW, because of strong electron confinement.

4. HETEROSTRUCTURE LASERS AND LIGHT-EMITTING DIODES

First semiconductor lasers began as homostructure devices comprising a p-n homojunction. Today, semiconductor lasers are usually made of a heterostructure, forming a single or multiple QW. The incorporation of a heterostructure and, especially, a QW in the laser structure provides significant advantages of heterostructure laser diodes (HLDs) over lasers with homojunctions [2,5-7]. The same is true for heterostructure light-emitting diodes (HLEDs) as well. The main of such advantages are much lower threshold current of lasing and higher operational temperatures. The implementation of heterostructures in lasers resulted in the development and wide applications of HLDs operating at room temperature.

The energy band diagrams of HLDs are shown in Fig. 9. The wide-bandgap and N and P regions provide the elec-

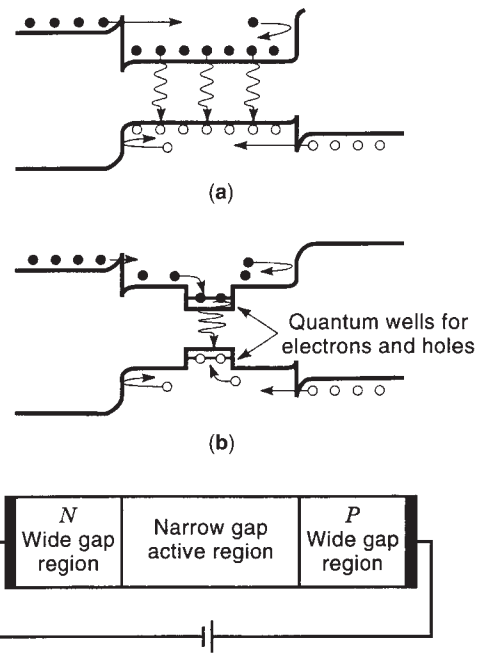


Figure 9. Energy band diagrams of HLDs with a narrow-gap active region (a) and narrow-gap active region with a quantum well (b).

tron and hole injection into a narrow-bandgap active region (Fig. 9).

The lasing power is given by the following equation:

$$P = \frac{\hbar\omega}{e}(I - I_{th}) \tag{4}$$

where $\hbar\omega$ is the energy of the lasing photons, \hbar is the reduced Planck constant, ω is the photon angular frequency, e is the electron charge, I is the pumping current, and I_{th} is the threshold current. The latter is defined by the properties of the HLD structure materials, the HLD geometry, quality of the mirrors reflecting generated radiation or reflecting property of the HLD surfaces serving as the mirrors, and so on.

In HLDs with a QW, electrons and holes are captured in the latter and occupy 2D states. Due to the existence of two barriers, there is the electron-hole confinement within a narrow-gap region. So the barriers prevent the leakage of carriers from the HLD active region. It results in higher electron and hole concentrations in the active narrow-bandgap region, in comparison with homostructure lasers at the same values of the injected current. This means that the threshold concentration of electrons and holes sufficient for the change of the absorption coefficient from negative (absorption of photons with the energies close to the energy gap of the active-region material) to positive (amplification) is achieved at lower injected current. As a result, the injected current corresponding to the threshold of lasing (threshold current I_{th}) reduces if a double heterostructure is used. The incorporation of a more narrow-bandgap layer into the HLD active region, which forms a QW, yields an additional improvement in

the laser performance. Smaller density of states in a QW, due to the 2D nature of the latter, leads to their more full occupation by electrons and holes at given value of the injected current. This effect also contributes to the achievement of the lowest possible threshold current I_{th} .

Apart from the electron-hole confinement, HLDs benefit of the confinement of lasing modes, due to the waveguide effect. This effect (termed *optical confinement*) is connected with the larger crystal lattice refraction index of a narrow-gap part of the HLD structure playing a role of the active region. In homostructure lasers, the effect of optical confinement plays some useful role in reducing the diffraction losses of emitted radiation. In such lasers, the optical confinement is associated with the nonuniformity of the electron and hole concentrations near the p-n junction. In HLDs, the optical confinement is much more effective.

The spectrum of radiation emitted by HLDs and HLEDs is determined primarily by the value of the energy gap of the active region material. The energy of the emitting photons $\hbar\omega$ is close to the energy gap of the active-region semiconductor E_g :

$$\hbar\omega \simeq E_g \quad (5)$$

This equation can be rewritten as

$$\lambda \simeq \frac{2\pi\hbar c}{E_g} \quad (6)$$

where λ is the lasing wavelength and c is the velocity of light in vacuum. If E_g is expressed in electronvolts, the lasing wavelength λ in micrometers according to Eq. (6) is given by $\lambda \simeq 1.24/E_g$. For HLDs with a GaAs active region ($E_g = 1.42$ eV) and $\text{Al}_{1-x}\text{Ga}_x\text{As}$ contact regions, one has $\lambda \simeq 0.87$ μm . Utilizing different semiconductor materials, especially binary, ternary, and quaternary compounds, one may fabricate HLDs and HLEDs operating from mid-infrared to blue range of the spectrum. In HLDs with QWs in the active region, the emitted photons are generated due to the transitions from the electron quantum levels to the hole quantum levels in the QWs (see Fig. 9). In such a case, the effective bandgap defining the energy of the lasing photons E_g^{QW} and their wavelength $\lambda \simeq 2\pi\hbar c/E_g^{\text{QW}}$ depend also on the positions of the quantum levels, with respect to the bottom of the conduction and the top of the valence bands in the QWs. One may obtain

$$\hbar\omega \simeq E_g^{\text{QW}} = E_g + \frac{\pi^2\hbar^2}{2w^2} \left(\frac{1}{m_n} + \frac{1}{m_p} \right) \quad (7)$$

where w is the width of the QW and m_n and m_p are the effective masses of electrons and holes, respectively. Growing the HLD structure with appropriate width of the QW in the action region, one may control the lasing wavelength.

HLDs and HLEDs find numerous applications. They are used in consumer electronics, for example, in CD players, optical communications, navigation devices, and other systems. Thanks to the development of HLDs and HLEDs,

operating in relatively long-wavelength range of spectrum from one side, and heterostructure devices, emitting very short-wavelength light (blue light), their applications can be extended to atmosphere monitoring systems, displays, traffic lights, and so on.

5. QUANTUM-WELL PHOTODETECTORS

Conventional photodetectors utilize the transitions of electrons from the valence band ground state to the conduction band excited state. The photocarriers (electrons and holes) created as a result of such interband transitions produce a photocurrent in photodetectors. To create an electron-hole pair, the photon energy $\hbar\omega$ should be greater than the energy gap E_g of a semiconductor material used for a photodetector. By controlling E_g , one may fabricate photodetectors for different ranges of spectrum. It is possible by using a chemical composition chosen in the proper way. For visible or near-infrared ranges of spectrum, A_3B_5 and some other semiconductor materials are used.

Carrier multiplication, which results from impact ionization initiated by electrons and holes generated due to optical interband transitions at high electric fields across the photodetector active region, is used to achieve internal photoelectric gain and, as a result, higher performance. Avalanche photodiodes (APDs), which utilize impact ionization at bias near the breakdown voltage, can be built using both homo- and heterostructures. Two of the crucial performance characteristics of APDs, the gain-bandwidth product and the excess noise arising from the random nature of the avalanche multiplication of electrons and holes, are determined by the electron and hole ionization coefficients and, what is more important, by the ratio of the latter. One approach to achieving low multiplication noise in APDs is the use of heterojunctions to artificially enhance the ionization rate of either electrons or holes. The most successful APD of this type is the APD with a multiple-QW structure. The point is that, for low-noise and high gain-bandwidth product, the ratio of the electron and hole ionization coefficients k should be either large or small ($k \ll 1$ or $k \gg 1$). It means that a large difference in the ionization rates is necessary. As electrons emerge from the wide-bandgap region between the QWs into the narrow-bandgap portion (into the QW), the discontinuity in the conduction band provides sufficient additional energy to initiate ionization. This enhances the ionization rate of electrons. The ionization rate for holes, on the other hand, is not enhanced to the same degree, since the valence band offset is smaller than that of the conduction band [2,8] in many practically important heterostructures.

Heterostructure APDs with QWs are successfully fabricated in $\text{GaAs-Al}_{1-x}\text{Ga}_x\text{As}$ and $\text{InP-In}_{0.53}\text{Ga}_{0.47}\text{As}$ compound material systems, and some others.

To satisfy the condition $\hbar\omega > E_g$ for very important far- and midinfrared ranges of spectrum, corresponding to wavelengths $\lambda = 2\text{--}20$ μm , semiconductor alloys such as $\text{Hg}_{1-x}\text{Cd}_x\text{Te}$ are used. There are substantial technological difficulties to grow, process, and fabricate photodetectors made of such materials. The transitions from the impurity states to the conduction or valence band can also

be utilized in photodetectors operating in far and near infrared ranges. However, these photodetectors also have some disadvantages.

Quantum-well intersubband photodetectors (QWIPs), based on semiconductor heterostructures, are considered as a very prospective alternative to both $\text{Hg}_{1-x}\text{Cd}_x\text{Te}$ interband photodetectors, as well as impurity photodetectors. QWIPs utilize the intraband electron transitions in the conduction band (in n-type QWIPs) or the intraband hole transitions in the valence band (in p-type QWIPs). By absorbing photons, electrons transfer from the bound states in QWs into states above the barriers between the QWs (continuum states); that is, they transfer between the subbands within a band. Such intersubband transitions result in the occurrence of electrons (holes) in continuum states, where they can freely move, producing a photocurrent. Conventional QWIP consists of a heterostructure with a single or multiple QW, doped either by donors or acceptors. The QW structure is supplied by contact regions of the same type of doping as the QWs. These contacts serve as the QWIP emitter and collector [9]. The conduction band edge profile of the QWIP structure is shown in Fig. 10. Usually QWIPs are made of A_3B_5 or $\text{Si}_{1-x}\text{Ge}_x$ compounds.

QWIPs operate in the range of spectrum, in which the energy of incident photons is sufficient to provide electrons absorbing such photons energy to escape from a QW:

$$\hbar\omega > E_i \quad (8)$$

Here E_i is the ionization energy of the QW, which is the difference between the energy of the barrier top and the bottom of the 2D subband in the QW (see Fig. 10). The ionization energy E_i depends on the depth of the QW, which, in turn, is defined by the difference in the chemical compositions of the barrier and QW materials, and the QW width. Both the depth and width can be easily varied during the QWIP structure growth process, to adjust the range of the sensitivity of the QWIP.

The photoexcited electrons are collected, thereby producing a photocurrent. The escape of electrons from QWs due to their photoexcitation leads to some redistribution of the potential across the QWIP structure and, in turn, to

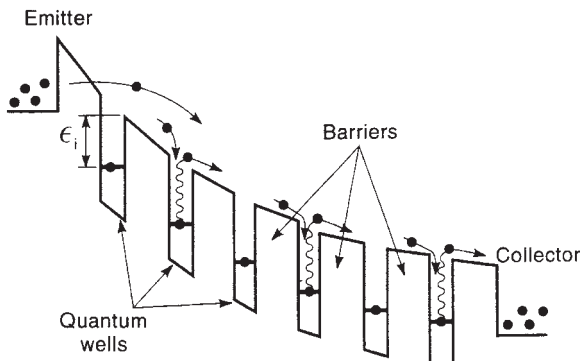


Figure 10. Conduction band edge profiler of a n-type QWIP under biasing voltage. Arrows show injected, captured, and photoexcited electrons.

the increase of the electric field at the QWIP emitter contact. This results in the injection of extra electrons from the emitter. The current created by the injected electrons can significantly exceed the current produced by the photoexcited electrons, so that QWIPs can exhibit a photoelectric gain. The latter can be markedly greater than unity. The photocurrent in a QWIP is given by the following formula:

$$I_{\text{ph}} = \frac{e\sigma \sum \Phi}{p_c} \quad (9)$$

Here σ is the cross section of the electron photoionization from the QW, Σ is the electron sheet concentration in each QW defined by the sheet concentration of donors, Φ is the photon flux, and p_c is the probability of the electron capture into QWs. It is instructive that the photocurrent according to Eq. (9) does not depend on the number of QWs in the QWIP N . Usually the value p_c is small, so that the photoelectric gain $g = (Np_c)^{-1}$ can be large, even in QWIPs with multiple-QW structure. From Eq. (9), one may obtain the following expression for the QWIP responsivity:

$$R = \frac{e\sigma \Sigma}{p_c \hbar\omega} \quad (10)$$

For a QWIP with typical parameters $\sigma = 2 \times 10^{-15} \text{ cm}^2$, $\Sigma = 10^{12} \text{ cm}^{-2}$, $p_c = 0.01\text{--}0.05$, and $\hbar\omega = 0.1 \text{ eV}$ ($\lambda = 12 \mu\text{m}$), from Eq. (10), one has $R = 0.4$ to 2 A/W .

Relatively simpler and cheaper QWIP technology is not the only advantage making QWIPs potential competitors to standard infrared photodetectors. The QWIP advantages are connected also with their intrinsic high-speed operation and the feasibility of their integration with other A_3B_5 and $\text{Si}_{1-x}\text{Ge}_x$ devices.

Despite the novelty of QWIPs, they already find applications as components for infrared imaging devices with large staring arrays of QWIPs.

6. OTHER HETEROSTRUCTURE DEVICES

Among heterostructure devices not discussed above, there are some others that are considered as very prospective in the future. One may point out the real-space transfer transistors (RSTTs) utilizing the real-space transfer of electrons or holes between two semiconductor materials. The RSTT operation requires a heterostructure in which the semiconductor layer with wider energy gap has much reduced mobility. The $\text{GaAs}\text{--}\text{Al}_{1-x}\text{Ga}_x\text{As}$ heterostructures have been used so far largely for the RSTTs. For detailed discussions on RSTTs, readers are referred to Ref. 4.

Solar cells are also an example of devices in which the utilization of heterostructures provides marked advantages. The advantages of heterostructure solar cells (HSCs) over conventional p-n homojunction SCs are as follows [5]: First, HSCs exhibit enhanced short-wavelength response, if the energy gap of the HSC wide-bandgap layer exceeds the energy of photons to be absorbed inside the depletion region in the narrow-bandgap portion. Apart from this, they have lower series resistance, if the wide-bandgap

region is heavily doped without affecting its transparency. In addition, HSCs can exhibit higher radiation tolerance.

Many of novel devices utilize quantum properties of electrons in heterostructures with QWs. As an example, one may mention resonant tunneling diodes (RTDs) for logic and ultra-high-frequency applications [2,10]. Combining RTDs with HBTs or HFETs allows the fabrication of compact high-speed circuits that operate at room temperature. In the early 1990s, the electron intersubband transitions were utilized for laser generation of midinfrared radiation in QW structures, called *quantum cascade lasers* [11]. The intersubband lasers have many potential applications in the midinfrared range of spectrum.

The integration of heterostructures utilizing both intersubband (intraband) and interband transitions open up additional prospects for the development of new functional QW devices. For example, integrated QWIP-LED devices [12] can be used for effective conversion of far- or midinfrared signals or images into near-infrared or, possibly, visible signals and images. In QWIP-LED devices, their QWIP part, utilizing intersubband electron transitions, serves as an element sensitive to infrared radiation. It produces a photocurrent that, being injected into the LED active region, results in the generation of relatively short-wavelength output radiation, due to radiative recombinations of the injected electrons. High-performance discrete devices and pixelless imagers can be fabricated using integrated QWIP-LED heterostructures.

In QWs electrons or holes are spatially confined in one direction. The energy corresponding to their motion in this direction is quantized, while in other directions it can be considered as classical. Advances in microfabrication technology now permit the building of heterostructures, in which electrons and holes are confined in two or even three directions. In the first case, electrons and holes are confined in a narrow-bandgap semiconductor material region extensive in one direction and buried in a wide-bandgap material. In such heterostructures, usually called *quantum wires* (QWRs), the electron (hole) energy spectrum is characterized by two discrete quantum numbers and one continuous quantum number. The latter is the electron (hole) momentum. Thus, electrons and holes in QWRs are propagating as one-dimensional particles. If the region of a narrow-bandgap semiconductor, material has a form of a small "box" electrons, and holes in the narrow-bandgap box exhibit fully discrete energy spectrum. Small boxes of a narrow-bandgap semiconductor surrounded by a wide-bandgap material with discrete energy spectrum are called the "quantum boxes" or "quantum dots" (QDs). QDs are similar to real atoms, because electrons (holes) in them have discrete energy spectrum as it takes place in atoms. A QD is said to be a zero-dimensional structure. However, sizes of QDs are substantially larger than those of real atoms. This is due to large number of atoms of semiconductor material involved in the formation of a QD. The energy spectrum of a QWR or a QD is defined by the difference in the energy gaps of the QWR or QD material from one side, and surrounding material from another. The most crucial are the QWR or QD sizes. If the QD size is small enough, the QD can have the only one quantum level. Usual size of QWRs (in the direction perpendicular

to the direction of classical electron or hole motion) and QDs is about a few nanometers. Due to energy spectra significantly different from those for conventional heterostructures and even for QWs, the one- and zero-dimensional structures constituting QWRs and QDs are very promising for electronic and optoelectronic devices, especially lasers. More detailed description of the QWR and QD properties, and their possible applications, can be found in Refs. 2 and 13.

BIBLIOGRAPHY

1. H. Kroemer, *Proc. IEEE* **70**:13–25 (1992).
2. N. G. Einspruch and W. R. Frensley, eds., *Heterostructures and Quantum Devices*, Academic Press, San Diego, 1994.
3. S. Tiwari, *Compound Semiconductor Device Physics*, Academic Press, San Diego, 1992.
4. S. M. Sze, ed., *High-Speed Semiconductor Devices*, Wiley, New York, 1990.
5. S. M. Sze, *Physics of Semiconductor Devices*, Wiley, New York, 1981.
6. G. P. Agrawal and N. K. Dutta, *Semiconductor Lasers*, Van Nostrand Reinhold, New York, 1993.
7. P. Bhattacharya, *Semiconductor Optoelectronic Devices*, Prentice-Hall, Englewood Cliffs, NJ, 1994.
8. P. Bhattacharya, ed., *Properties of III-V Quantum Wells and Superlattices*, INSPEC, London, 1996.
9. B. F. Levine, Quantum-well infrared photodetectors, *J. Appl. Phys.*, **74**:R1–R81 (1993).
10. H. Mizuta and T. Tanoue, *The Physics and Applications of Resonant Tunneling Diodes*, Cambridge Univ. Press, Cambridge, UK, 1995.
11. J. Faist, F. Capasso, D. L. Sivco, A. L. Hutchinson, and A. Y. Cho, Quantum cascade laser, *Science* **264**:553–557 (1993).
12. V. Ryzhii, H. C. Liu, I. Khmyrova, and M. Ryzhii, Analysis of integrated quantum-well infrared photodetector and light-emitting diode for implementing pixelless imaging devices, *IEEE J. Quantum. Electron.* **33**:1527–1531 (1997).
13. C. Weisbuch and B. Vinter, *Quantum Semiconductor Structures*, Academic Press, San Diego, 1991.

HIGH-FIELD EFFECTS

K. HESS
University of Illinois

Electrons and holes contribute to the charge transport in semiconductors, while ordinary charge transport in metals is restricted to electrons only. Another distinctive feature of semiconductor transport is its inherent non-linearity in high electric fields. It is difficult to generate high electric fields in metals because of their high electrical conductivity and the necessity of the presence of high currents according to Ohm's law. In semiconductors, high fields can exist with current densities of the order of 10^5 A/cm², or even much lower, depending on their conductance, which at low temperatures may approach zero. Ryder [1]

and Shockley [2] noticed that semiconductor electron transport was extremely nonlinear in high electric fields. Strong deviations from the proportionality of current density to fields were measured in germanium at room temperature for fields as small as 1000 V/cm.

High-field transport in semiconductors then became an area of considerable research. It was found that the nonlinear behavior (the deviation from Ohm's law) was due to an elevation of the energy of the charge carriers caused by the accelerating force of the electric field. Interactions with the lattice vibrations lower the energy of the charge carriers as Joule heat is transferred to the crystal lattice. However, electric fields always cause a finite rise of charge carrier energy above the equilibrium energy (corresponding to the temperature of the crystal lattice). This excess energy can sometimes also be described by a temperature, the temperature T_c of the charge carriers, which is larger than the temperature T_L of the crystal lattice. One speaks therefore of *hot-carrier transport* in semiconductors.

The rise in charge carrier energy changes the conductance for two reasons. For one, a higher energy gives rise to significant changes in the interactions of the charge carriers with crystal imperfections that form scattering centers. The scattering rate influences the conductance directly. Increases or decreases of this rate lead to decreases or increases of the conductance, respectively. The second reason for variations in conductance with charge carrier energy arise from changes in the $E(\mathbf{k})$ relation. This function gives the connection between the energy E and the wavevector \mathbf{k} of the charge carriers, which corresponds in classical mechanics to the energy-momentum relation. Since conductance is a sensitive function of $\partial E(\mathbf{k})/\partial k$, it changes with the energy of the electrons (or with T_c whenever a temperature of the carriers is well defined).

The most complete existing theory of high-field transport in semiconductors involves the solution of a Boltzmann-type equation [3]. The use of this equation can be justified by invoking the dephasing of quantum coherence over distances that correspond to the feature sizes of semiconductor structures and devices. Consequently, the charge carriers do behave classically and can, in a way, be understood from the principles of classical mechanics. Quantum mechanics has then only a background role and determines, for example, the effective mass or the velocity of the electrons or gives justification for the existence of holes and hole transport. Fermi's "golden rule" of quantum mechanics is used to calculate the scattering rates and thus represents another quantum contribution. It is also easy to include the Pauli principle in such an equation and thus to approach some properties of a Fermi liquid. However, the assumption of weak perturbational interaction of the particles, which is basic to Boltzmann's derivation, must remain true, and indeed is a good approximation for most of the important semiconductor materials.

The basic phenomena of high field transport are nonlinear conductance [3]; changed responses to magnetic fields [4]; changed high-frequency response, including the dielectric function [5]; and changed confinement in potential wells or at heterojunctions between different semiconductors [6].

In semiconductor devices, the high-field effects are based on the same phenomena. For example, in transistors of the field effect family, the electric fields can be as high as 10^5 V/cm², and the corresponding carrier temperatures may reach $T_c = 10^4$ K [7]. Such temperatures cause changes in the conductivity by orders of magnitude (mostly reductions) [3,5]. Remember that T_c is the temperature of the charge carriers and not of the crystal lattice, which would melt at such temperatures. T_L , the temperature of the crystal lattice, can also be raised, but is usually raised orders of magnitude less. This difference is possible because the systems of electrons and crystal lattice are only weakly coupled. Under certain circumstances the conductance can also be raised by hot-electron phenomena, leading to speed advantages in devices (e.g. velocity overshoot phenomena) [8]. Devices made of semiconductor heterojunctions also exhibit various forms of hot-electron transfer (e.g., real-space transfer) between the different materials. These effects often give rise to a device performance degradation, but also can be used advantageously [6].

In the following, a general theory of high-field transport is developed. The next section describes high-field transport in bulk semiconductors (theory and experimental results), and finally an overview of major effects in devices is given.

1. THE BOLTZMANN EQUATION FOR HIGH-FIELD SEMICONDUCTOR TRANSPORT

The following is a top-down approach to the theory of high-field phenomena. The next section derives a modern Boltzmann equation including the most important quantum effects as derived from the energy band structure. The relevance of the various terms of this equation to hot-electron phenomena are discussed and general ways to obtain solutions are briefly reviewed and referenced. Subsequently a more phenomenological discussion and analytical approximation of several high-field effects is given.

1.1. Derivation of a Modern Boltzmann Equation

The Boltzmann equation derived here is more general than the original equation derived by Boltzmann. The only cases of weakly interacting charge carriers in solids that cannot be understood from this modified equation are those that involve macroscopic feature sizes (e.g., device boundaries) that are smaller than the quantum dephasing length under the given conditions. This dephasing length in silicon at room temperature is of the order of several hundred angstroms, but can be much smaller in high electric fields, approaching 20 Å for electron energies of about 1.5 eV. This means that for conventional devices operating with high fields, hot-electron transport can be understood extremely well with the theory developed below even if the feature sizes are below 100 Å. Quantum effects such as tunneling can often be added to this theory by the Bardeen transfer Hamiltonian formalism [3,9].

The following derivation lacks complete mathematical rigor but is valid under widely varying circumstances. For example, we need not assume conservation of the number

of particles, which is important in that electrons and holes can annihilate each other or can be created by light. We follow Boltzmann, but replace the velocity in seven-dimensional phase space by the wavevector \mathbf{k} in the definition of a distribution function $f(\mathbf{k}, \mathbf{r}, t)$, meaning as usual the probability of finding charge carriers at \mathbf{k}, \mathbf{r} and at time t in the volume elements $d\mathbf{k}, d\mathbf{r}, dt$. Consider then a cube in \mathbf{r} space and in \mathbf{k} space as shown in Fig. 1.

We first calculate how many electrons arrive from the left and enter the cube through the left dy - dz plane, and how many leave at the corresponding plane on the right, all during a time period dt . Since the x -direction travel distance of electrons with velocity \mathbf{v} is $v_x dt$, we have

$$\text{Incoming : } f(\mathbf{k}, \mathbf{r}, t) d\mathbf{k} dy dz v_x dt \tag{1}$$

$$\text{Outgoing : } f(\mathbf{k}, (x + dx, y, z), t) d\mathbf{k} dy dz v_x dt \tag{2}$$

and the net particle gain is

$$\begin{aligned} & -v_x [f(\mathbf{k}, (x + dx, y, z), t) - f(\mathbf{k}, \mathbf{r}, t)] dy dz d\mathbf{k} dt \\ &= -v_x \frac{\partial f}{\partial x} dx dy dz d\mathbf{k} dt \\ &= -\mathbf{v} \cdot \nabla f d\mathbf{k} d\mathbf{r} dt \end{aligned} \tag{3}$$

in three dimensions. Note that the velocity \mathbf{v} here is equal to the group velocity and is related to \mathbf{k} by $\mathbf{v} = \nabla_{\mathbf{k}} E(\mathbf{k})/\hbar$ (3).

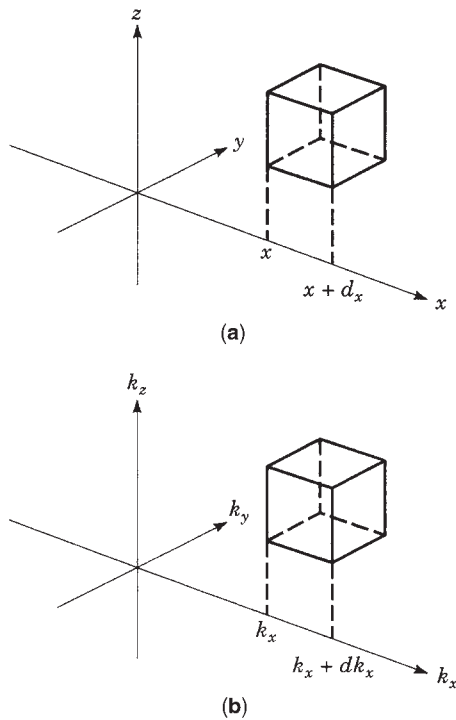


Figure 1. Cubes in (a) \mathbf{r} space and (b) \mathbf{k} space to illustrate the balance of incoming (e.g., into the y - z face) and outgoing (e.g., at $x + dx$) electrons (or change carriers in general). The changes in \mathbf{r} space are due to carrier velocity, those in \mathbf{k} space due to acceleration by a force.

This balance depends on the velocity and \mathbf{k} vector of the electrons and therefore on how “hot” the electrons are. It also describes diffusion, since concentration gradients enter this term. The relation between diffusion and electron heating is actually a complicated one and will be discussed below phenomenologically.

In an analogous manner, we obtain the change of the number of electrons at \mathbf{k} in \mathbf{k} space because of accelerations. Replacing dx by dk_x and so on as illustrated in Fig. 1, and replacing $dx/dt = v_x$ as used in Eq. (1) by dk_x/dt , one gets

$$-\frac{d\mathbf{k}}{dt} \cdot \nabla_{\mathbf{k}} f d\mathbf{k} d\mathbf{r} dt \tag{4}$$

where $d\hbar/dt = -e\mathbf{F}$ (3) and \mathbf{F} is the electric field. This term represents the major energy supply to the electrons and therefore the root cause of the heating and hot-electron effects.

There is still another possibility to change the number of electrons with wavevector \mathbf{k} at \mathbf{r} . The electrons can be scattered and change their wavevector from \mathbf{k} to \mathbf{k}' at a given point \mathbf{r} in real space. Figure 2 shows the two infinitesimal volumes in \mathbf{k} space to illustrate the scattering events. The outgoing (out of state \mathbf{k}) electrons are

$$\text{out} = -\sum_{\mathbf{k}'} S(\mathbf{k}, \mathbf{k}') f(\mathbf{k}, \mathbf{r}, t) d\mathbf{k} d\mathbf{r} dt \tag{5}$$

The factor $f(\mathbf{k}, \mathbf{r}, t)$ is necessary because an electron has first to be in the \mathbf{k} state to be scattered out. In degenerate systems (Fermi statistics), an additional factor $1 - f(\mathbf{k}', \mathbf{r}, t)$ arises from the Pauli principle. The incoming (into the \mathbf{k} state) electrons are

$$\text{in} = \sum_{\mathbf{k}'} S(\mathbf{k}', \mathbf{k}) f(\mathbf{k}', \mathbf{r}, t) d\mathbf{k} d\mathbf{r} dt \tag{6}$$

Again, the Pauli principle will call for a factor $1 - f(\mathbf{k}, \mathbf{r}, t)$. The in and out scatterings lead to a (more or less) random distribution of the \mathbf{k} vector. The energy gained from the

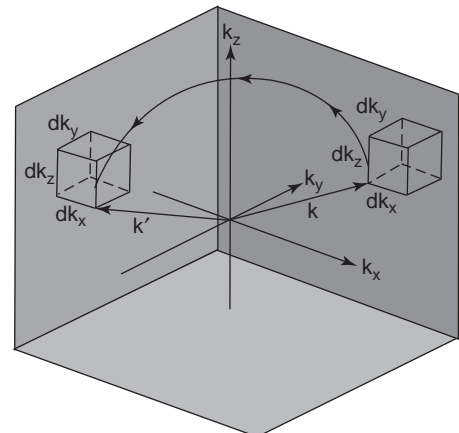


Figure 2. Schematic of a scattering process. The charge carrier scatters from a volume $dk_x dk_y dk_z$ at \mathbf{k} to another such volume at \mathbf{k}' .

field is therefore distributed in \mathbf{k} space and thus receives a random temperaturelike component. The interaction with lattice vibrations is inelastic and also changes the energy (magnitude of \mathbf{k}). This energy loss represents Joule heat and determines, together with the force, the actual average electron energy (temperature).

The Boltzmann equation describes all of these heating-cooling dynamics and is obtained by balancing the particle numbers and the change in f given by the net change of incoming and outgoing particles. Therefore, we have

$$\begin{aligned} \frac{\partial f(\mathbf{k}, \mathbf{r}, t)}{\partial t} = & -\mathbf{v} \cdot \nabla f(\mathbf{k}, \mathbf{r}, t) - \frac{1}{\hbar} \mathbf{F}_0 \cdot \nabla_{\mathbf{k}} f(\mathbf{k}, \mathbf{r}, t) \\ & + \sum_{\mathbf{k}'} [f(\mathbf{k}', \mathbf{r}, t)S(\mathbf{k}', \mathbf{k}) - f(\mathbf{k}, \mathbf{r}, t)S(\mathbf{k}, \mathbf{k}')] \end{aligned} \quad (7)$$

where \mathbf{F}_0 is the force ($-e\mathbf{F}$ for an electric field \mathbf{F}).

If we include the factors arising from the Pauli principle as discussed above, we arrive at

$$\begin{aligned} \frac{\partial f(\mathbf{k}, \mathbf{r}, t)}{\partial t} = & -\frac{1}{\hbar} \nabla_{\mathbf{k}} E(\mathbf{k}) \cdot \nabla f(\mathbf{k}, \mathbf{r}, t) - \frac{1}{\hbar} \mathbf{F}_0 \cdot \nabla_{\mathbf{k}} f(\mathbf{k}, \mathbf{r}, t) \\ & + \sum_{\mathbf{k}'} \{f(\mathbf{k}', \mathbf{r}, t)[1 - f(\mathbf{k}, \mathbf{r}, t)]S(\mathbf{k}', \mathbf{k}) \\ & - f(\mathbf{k}, \mathbf{r}, t)[1 - f(\mathbf{k}', \mathbf{r}, t)]S(\mathbf{k}, \mathbf{k}')\} \end{aligned} \quad (8)$$

This equation is very general and includes automatically, for example, effects of the energy band structure as described by $E(\mathbf{k})$. Of course, it describes transport in one band only [3]. The functional form of this band, however, can be arbitrary. Effects of strain in the solid, for example, need only be included in the band structure and then are automatically taken into account in the distribution function f once the Boltzmann equation is solved. From the distribution function, one can in turn obtain macroscopic quantities such as the electronic current in the usual prescribed way.

To summarize, all terms of this equation have special significance for hot-electron effects. The second term on the right-hand side (RHS) of Eq. (8) represents the driving force, the electric field \mathbf{F} , and signifies the heating of the electrons. The third term on the RHS describes the scattering and how momentum and energy are distributed. This term signifies the influence of hot electrons on the classical conductivity. Electrons are scattered out of a given range of the wavevector \mathbf{k} or scattered into that range from all other possible values of \mathbf{k} , denoted by \mathbf{k}' . This scattering term makes the Boltzmann equation an integrodifferential equation. Therefore, to solve it, one needs a tenfold integral over time, space \mathbf{r} , and \mathbf{k} , as well as \mathbf{k}' . The tenfold numerical integration can probably be done best by Monte Carlo methods, although approximations in lower dimensions may permit the use of computationally more efficient numerics. The first term on the RHS represents space-dependent effects such as diffusion and indicates that the hot-electron diffusion not only is dependent on the heating of the electrons but in turn influences the heating. This term is relevant to the question of how the force heats the electrons. For example, a confining force

that does not give rise to a current (as, e.g., at a potential minimum) may not heat the electrons, since for this case the accelerating drift (second term on RHS) and diffusion (first term on RHS) can cancel exactly [3,10,11].

The energy band structure enters the Boltzmann equation through the $E(\mathbf{k})$ relation in the first term on the RHS. It also enters indirectly through the sum over \mathbf{k} , since this sum includes the density of states. Finally, if one wants to calculate a current, one needs to integrate the product of velocity and distribution function over all \mathbf{k} space, where the velocity is given by $\mathbf{v} = \nabla_{\mathbf{k}} E(\mathbf{k})/\hbar$.

A full solution of the Boltzmann equation as derived above does describe all hot-electron phenomena currently known in semiconductors. It can be and has been achieved numerically in bulk semiconductors [12] and in devices [13]. We refer the reader to these references and to software and explanations available on Websites [14]. Here we continue with discussions of important experimental results in terms of approximate concepts and solutions.

1.2. Approximate Solutions of the Boltzmann Equation and Hot Electrons

Since the Boltzmann equation is an integrodifferential equation, precise and explicit solutions can be found only under very special circumstances. The best-known example is the time-independent solution for homogeneous systems (no space-dependent terms) in the relaxation-time approximation. Under the assumption of weak forces (electric fields), one can write the distribution function as a sum of a function f_0 that is even in the wavevector \mathbf{k} and an odd function f_1 . Assuming that the Pauli terms are negligible, as they are for not too high carrier concentrations, the whole collision integral of Eq. (8) reduces to

$$\text{Collision integral} = f_1/\tau_{\text{tot}} \quad (9)$$

with

$$\frac{1}{\tau_{\text{tot}}} = \sum_{\mathbf{k}'} S(\mathbf{k}, \mathbf{k}') \quad (10)$$

and f_0 is equal to the equilibrium Boltzmann distribution given by

$$f_0 = \exp(E_{\text{F}}/kT_{\text{L}}) \exp(-E/kT_{\text{L}}) \quad (11)$$

The odd part of the distribution function that determines the electric current is then

$$f_1 = -\tau_{\text{tot}} \frac{\mathbf{F}_0}{\hbar} \cdot \nabla_{\mathbf{k}} e^{(E_{\text{F}}-E)/kT} \quad (12)$$

where E_{F} is the Fermi level. The electric current density j is then obtained from

$$j = -\frac{e}{4\pi^3} \int \mathbf{v} f_1 d\mathbf{k} \quad (13)$$

The high field or hot-electron term is neglected in this approach, which describes only low fields and ohmic

behavior. The reason is the approximation of f_0 by the equilibrium distribution. To allow for high electric fields, one needs to solve the full Boltzmann equation or at least the coupled equations resulting for both f_0 and f_1 in the relaxation-time approximation. As described above, the force accelerates the electrons (holes), and the scattering randomizes, thus causing f_0 to contain more energetic electrons and therefore changing its form away from the equilibrium.

As mentioned, the complete solution of Eq. (8) has been achieved by so-called Monte Carlo methods, which are related to the Monte Carlo integration known from numerical mathematics [3,5]. These solutions have been described at length in the literature and form a vast field [5,12–14].

Approximate solutions of the Boltzmann equation for high electric fields are also well known. Of particular importance is the electron temperature approximation, which is described in the next section together with typical experimental results for high field transport in bulk (homogeneous) semiconductors.

2. HOT-ELECTRON EFFECTS IN SEMICONDUCTORS AND APPROXIMATE THEORY

2.1. Electron Temperature and Scattering Rate

A first glimpse of how important hot electrons would be in semiconductor transport was given by the work of Shockley (1951) [2] and Ryder (1953) [1], who found a saturation of the electron current in germanium at electric fields around 1000 V/cm as shown in Fig. 3. This current saturation is basic to hot-electron phenomena and has been shown to arise from the increase of average electron energy $\langle E \rangle$. Under certain assumptions that are approximately satisfied in n-type silicon and germanium for intermediate electric fields [3], one can represent the average energy by a temperature T_c , which, for not too high electron densities, can be approximated

by a Boltzmann-type formula

$$\langle E \rangle = \frac{3}{2} k_B T_c \quad (14)$$

where k_B is Boltzmann's constant. The actual solution of the Boltzmann equation to arrive at the electron temperature concept is involved, and the reader is referred to Ref. 3 for detailed information.

An approximate formula for T_c is [3]

$$T_c \approx T_L \left[1 + \left(\frac{F}{F_c} \right)^2 \right] \quad (15)$$

F_c is a critical electric field that is around 10^4 V/cm for silicon at room temperature. The carrier temperature T_c can therefore become extremely high. For example, at the field $F = 2 \times 10^4$ V/cm, which can easily be reached and indeed is routinely reached in modern transistors, we have $T_c = 1500$ K for $T_L = 300$ K. Such temperatures have indeed been measured by various methods that can sense the electron energy inside the semiconductor [15]. An outside touch does not reveal a temperature increase of the electrons because of the large workfunction that the electrons would need to overcome in order to propagate out of the semiconductor [16]. Equation (11) is not valid for electric fields much higher than 3×10^4 V/cm for silicon because of band structure effects such as non-parabolicity [5]. For very high fields, a full-band Monte Carlo approach is again necessary to calculate the average energy and distribution functions of the electrons reliably.

The rise of the electron temperature (or energy) causes a change in the scattering rate that enters the mobility μ of the charge carriers and therefore the conductivity $\sigma = en\mu$ (n being the carrier concentration). The mobility derives from the relaxation time as defined in Eq. (10) if the scattering in randomizing (independent of the wavevector). Otherwise τ_{tot} needs to be replaced by the so-called momentum relaxation time [3]. This relaxation time usually exhibits a significant energy dependence. For phonon scattering it decreases typically with increasing energy, while for scattering by weakly screened Coulomb charges it increases. The mobility μ is proportional to a weighted energy average of the relaxation time, and the conductivity therefore increases or decreases proportionally.

A typical dependence of the mobility on the electron temperature is then (for the case of scattering by phonons) [3]

$$\mu \approx \mu_0 \left(\frac{T_L}{T_c} \right)^{1/2} \quad (16)$$

where μ_0 is the mobility at zero electric field, that is, for $T_L = T_c$. Using, then, the equation for the current density of a homogeneous semiconductor, $j = en\mu$, one gets from Eqs. (16) and (15)

$$j = en\mu_0 \left(\frac{F}{1 + (F/F_c)^2} \right)^{1/2} \quad (17)$$

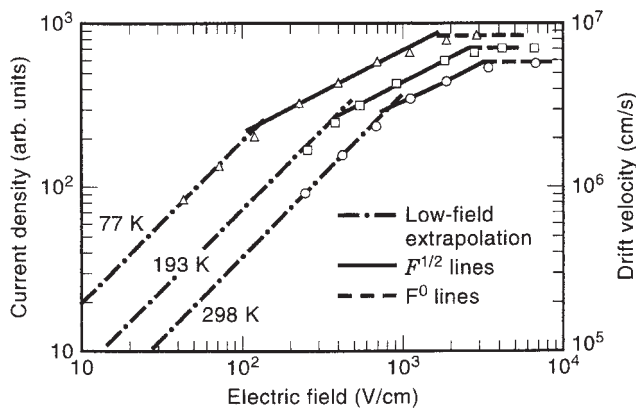


Figure 3. Current density (or drift velocity) versus electric field in bulk n-type germanium for three temperatures (as indicated). Notice the saturation at electric fields above 10^3 V/cm. (After Ref. 1.) Reprinted with permission, © 1953 by the American Physical Society.

This equation shows immediately the essential feature of current saturation (nonlinear transport) at high electric fields and is quite general. For example, the square root in Eq. (16) derives from the density of states. Equation (17) is valid even for a more general density of states; it can be proved easily for any density of states that is proportional to E^p for any $p > 0$. The dependence of the electron phonon scattering rate on the density of states is illustrated in Fig. 9. Note, however, that in devices other scattering mechanisms such as surface roughness scattering are of great importance. Some of these mechanisms are reviewed in Ref. 16.

2.2. Effects of Band Structure and the Gunn Effect

The derivation of Eq. (17) contains only changes in the scattering rate with carrier temperature. As mentioned above, however, the band structure influences not only the scattering rate (via the density of states) but also the velocity v of the electrons, since in the one-band approximation we have [3]

$$\mathbf{v} = \frac{1}{\hbar} \nabla_{\mathbf{k}} E(\mathbf{k}) \quad (18)$$

For the typical band structure of some III–V compounds, this leads to pronounced effects in the current–voltage characteristics. For GaAs, the effective mass is small at low energies ($m^* = 0.067m_0$) and $E(\mathbf{k}) = \hbar^2 k^2 / 2m^*$. Correspondingly, the velocity of electrons becomes very high at moderate energies. However, the band structure changes drastically only 0.3 eV above the conduction band edge, exhibiting there additional minima with much higher effective mass (close to the germanium type conduction), and above 0.5 eV, even higher effective masses (close to the silicon conduction mass). In simple terms, GaAs contains three “highways,” each one becoming available as the energy increases and each one exhibiting higher mass. If the electrons are heated by electric fields, they initially are on the fastest highway, exhibiting a high mobility and conductance. At higher fields they are heated enough to transfer to the germanium like conduction band minimum (highway 2) and at still higher fields to the siliconlike minimum (highway 3). This decreases their speed so drastically that GaAs actually shows a range of negative differential resistance, that is, the current drops as the electric field is increased. This phenomenon leads to the Gunn effect, which manifests itself by high-frequency current oscillations, since the situation of negative differential resistance is not stable [7]. These phenomena have received considerable attention, and a large framework of research exists [7,18].

The current–field characteristic of GaAs is shown in Fig. 4 and compared with the characteristics of silicon (both for electron transport). It is evident that the low-field current behavior of GaAs transforms into silicon like behavior at high electric fields, with a region of negative differential resistance in between. The reader is referred to the literature [3,5,7] for more information.

A word of caution should be added here. There is a lack of direct experimental verification of band structure and

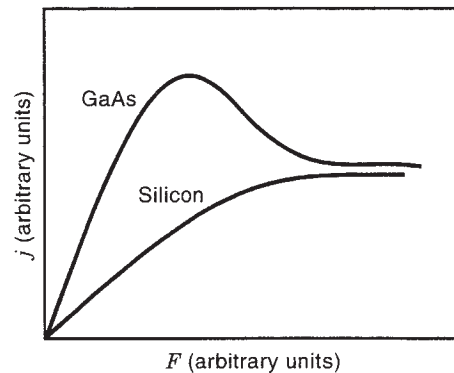


Figure 4. Schematic of current density versus electric field for homogeneous (bulk) GaAs and silicon. Notice the negative differential resistance of GaAs (which leads to instabilities [7] and inhomogeneities of the carrier density). Also note that at very high fields the GaAs and silicon curves approach each other. Depending on temperature and electric field, they can even cross. However, they are always close at very high fields.

related semiconductor parameters for high-field transport. Optical measurements and femtosecond spectroscopy [19] do give detailed information on the density of states.

2.3. Real-Space Transfer

The negative differential resistance of GaAs and the Gunn effect are determined mostly by the structure of the $E(\mathbf{k})$ relation, that is, by effects in \mathbf{k} space. The terms of the Boltzmann equation signifying real-space operations have not been discussed yet. From the discussions following Eq. (8) it is clear, however, that real-space effects complicate hot-electron transport significantly. The prime reason for this complication is the real-space transfer effect [6], which is described here.

The transfer of electrons between two different solids is known from Bethe’s thermionic emission theory [3]. This type of transport includes only electric fields perpendicular to the different layers of semiconductors. However, electric fields parallel to semiconductors can energize the charge carriers (hot-electron effect) and lead to a redistribution of them in the different layers that depends sensitively on the difference of the conduction band edges of the various materials. (Readers not used to solid-state concepts should think of the conduction band edge as the minimum kinetic energy of conduction electrons, which is different in different materials, the electrons thus having different potential energy in each material.) The effect of redistribution of electrons or holes due to electric fields parallel to different layers of semiconductors is called *real-space transfer* (RST) and is shown schematically in Fig. 5. This transfer of electrons (heated by parallel fields) over barriers is more complicated and more difficult to understand than other effects basic to nonlinear semiconductor transport and device operation. The reason is that RST can be visualized only the combination of two concepts related to the energy distribution of electrons. The first concept is that of quasi-Fermi levels [3], and the second is the concept of a charge carrier temperature T_c as already

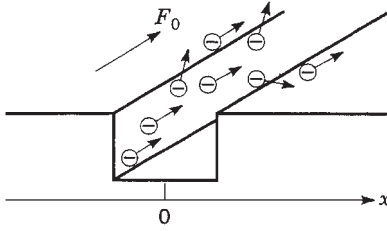


Figure 5. Electrons in a material with lower conduction band edge (e.g., GaAs) neighboring two layers with higher conduction band edge (e.g., AlAs) accelerated by a force F_0 . The electrons gain energy and are scattered and then transfer out of the central material layer, thus exhibiting real-space transfer.

discussed above. For RST problems, both concepts matter, and both the carrier temperature and the quasi-Fermi levels are a function of space coordinate and time.

Imagine, for example, electrons residing in a layer of high-mobility GaAs neighboring, on either side, two layers of low-mobility AlAs (Fig. 5). The GaAs equilibrium distribution function f_0 is

$$f_0 = \exp(-E/kT_L) \quad (19)$$

while in the AlGaAs we have

$$f_0 \propto \exp\left(-\frac{\Delta E_c + E}{kT_L}\right) \quad (20)$$

Here the energy is measured from the GaAs conduction band edge, and ∇E_c is the band edge discontinuity between AlAs and GaAs.

If now the electrons are heated by an external field parallel to the layers, we have to replace T_L in Eqs. (19) and (20) by a space-dependent carrier temperature T_c . It is clear that for $T_c \rightarrow \infty$ the difference between the AlAs and the GaAs population densities vanishes. In other words, the electrons will spread out into the AlAs layers. This also means that even perpendicular to the layers (z direction) a constant Fermi level cannot exist, and E_F has to be replaced by the quasi-Fermi level $E_{QF}(z)$ as the density of electrons becomes a function of $T_c(z)$. This is unusual, since commonly the quasi-Fermi levels differ only in the direction of the applied external voltage V_{ext} (by the amount eV_{ext}). In the present case, a voltage is applied parallel to the layers, the electrons redistribute themselves perpendicularly to the layers, and a field (and voltage perpendicular to the layers) develops owing to the carrier redistribution. Basic to the calculation of this process are the thermionic emission currents [3] of hot electrons from one layer to the other. Since the external voltage is applied parallel to the layers, we have in steady state a precise balance of currents flowing from left to right and right to left, which determines the z -dependent carrier population.

A complication of the theory is presented by the necessity (in most cases) of having to solve Poisson's equation as charge is transferred. For typical parameters of the GaAs-AlAs material system and electric fields of the order of 10^3 to 10^4 V/cm parallel to the layers, one obtains time

constants of the order of picoseconds for the transfer, which gives the RST effect importance for device applications (RST transistors as developed by [6]).

The real-space transfer effect is also of general importance in all situations when electrons are confined in potential wells and parallel fields are applied (and accelerate the charge carriers), even if the electrons do not propagate out of the wells but merely redistribute themselves within each well. This is of relevance for the understanding of the influence of transverse fields (such as the gate field) in a transistor [10]. The RST effect and the spreading of the electrons are then determined by the transverse field. The quantum analog of this classical picture is the redistribution of hot electrons in the different quantized subbands of a quantum well.

2.4. Time Dependences, Velocity Overshoot, and Ballistic Transport

As complex as the considerations of nonlinear transport in \mathbf{r} space and \mathbf{k} space are already, time dependences add to the richness of hot-electron effects. All the discussions above were essentially valid for the steady state only. On short timescales, however, the mode of transport changes its type because of transitions from the ballistic to the overshoot regime and to diffusive transport.

Diffusive transport is the well-known mode for which the mobility is proportional to the average of τ_{tot} . This proportionality implies the validity of the Boltzmann equation, which, as discussed at the beginning, involves the dephasing of the wave function. For times much shorter than τ_{tot} , the transport is essentially *ballistic*, which means that in crystalline semiconductors the accelerations are described by the equation

$$\hbar \frac{d\mathbf{k}}{dt} = -e\mathbf{F} \quad (21)$$

where \mathbf{F} is the electric field and $\hbar\mathbf{k}$ is the crystal momentum. This equation becomes invalid at extremely short times, as described in Ref. 20, but is applicable under most circumstances. Neglecting the basic thermal motion of the electrons (due to T_L), this means that all electrons are accelerated in the direction of the force and gain speed according to Eqs. (18) and (21). Since all electrons move in the same direction, the average velocity is very large compared to the thermal case where electrons move in all directions and have just a small average drift velocity on top of the thermal motion. In high electric fields, and with high values of T_c , the thermal velocity (pointing randomly in all directions) can be as high as 10^8 cm/s, while the saturated drift velocity is (in silicon) a factor of 10 below this value. A visualization of these facts is given in Fig. 6.

The range between the high-velocity ballistic transport and the low-velocity diffusive transport is called the range of velocity overshoot. Imagine transport in a semiconductor switched on at time $t_0 = 0$ by application of a high field F . The electrons are then accelerated ballistically for about 100 fs and may reach a velocity well above 10^7 cm/s (the value of the saturated velocity in silicon and other important semiconductors). Then, as time goes on, scattering

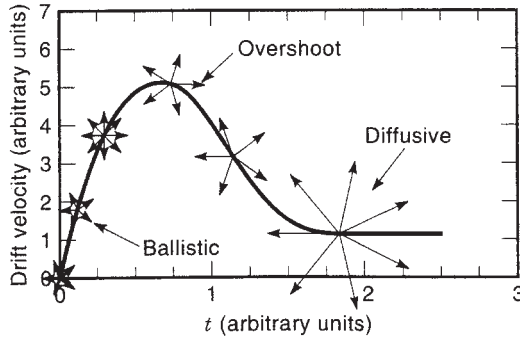


Figure 6. Schematic of the development of average drift velocity versus time, assuming that a high electric field F is suddenly applied at $t=0$. The electrons are accelerated to high velocities and high average drift velocities. Their random velocity (indicated by arrows pointing in all directions) is at first small but is steadily increased because of randomizing scattering. At a certain point the average drift velocity approaches a maximum. From here on the random component of the velocity increases because of the very strong scattering at the high energies that the charge carriers now have, and the average drift velocity decreases. Finally, steady state is reached, where the scatterings and accelerations balance each other. The large random arrows indicate then a high electron temperature, and the drift velocity is saturated (at 10^7 cm/s in silicon).

events randomize the velocity to all directions, which leads, typically after a picosecond or so, to the saturated average velocity. At the times in between, the velocity is higher and exhibits the overshoot. In GaAs these effects are accentuated by the changes in effective mass at high energy, and the overshoot can be considerable [8]. This is shown in Fig. 7.

A similar effect is also achieved for transport in short semiconductor sections sandwiched in between contacts. As soon as the electrons enter the semiconductor from the contact, they are accelerated by high electric fields into the overshoot or even the ballistic regime and leave the semiconductor, entering the second contact, before scattering can randomize their motion. Thus the velocity in short semiconductor diodes can overshoot the saturated value (now for all times), which in some devices gives a speed advantage [22].

2.5. Changes of Carrier Concentration and Hot Electrons: Impact Ionization

Up to now, all the conductivity changes we have discussed have arisen from changes in the carrier velocity and a redistribution of charge carriers in energy. The total number of electrons or holes was not affected by hot-electron effects. There exists, however, an important phenomenon that causes considerable changes of conductance because of changes in the total number of charge carriers. This is the occurrence of impact ionization, the exact inverse of the Auger effect [3]. A heated electron in the conduction band (the same can be argued for holes) gains energy from the applied electric field and collides with an electron in the valence band, lifting this electron up to the conduction band, with the net result of two conduction electrons

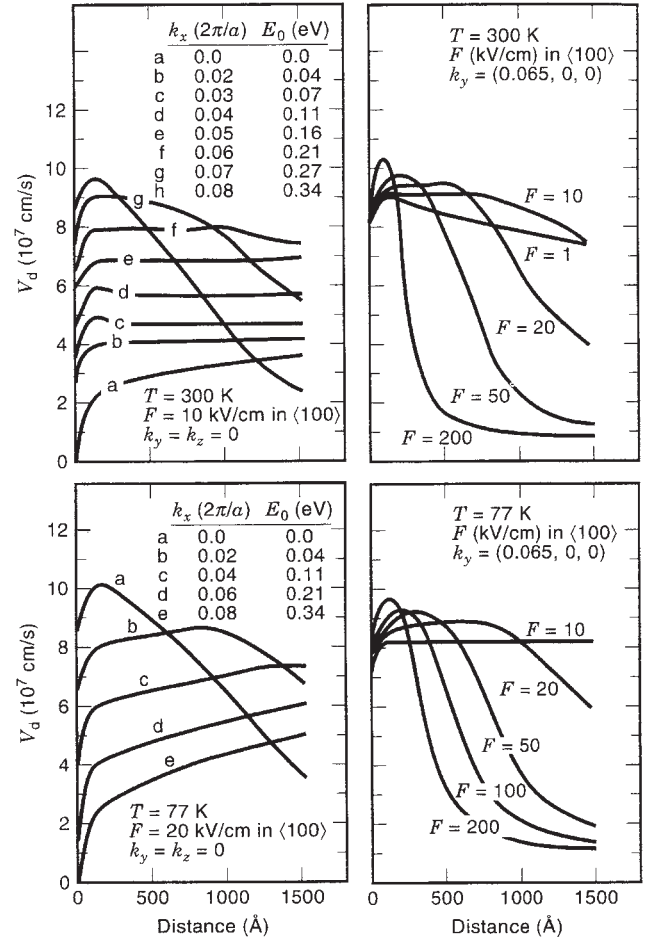


Figure 7. Overshoot of electrons injected with certain wavevectors k_x in the x direction and with certain energies E_0 into GaAs. A field F subsequently accelerates them and leads to velocity overshoot (19).

and a hole. The primary electron and the secondary electron plus hole all now contribute to the conduction, and the electronic current density \mathbf{j} therefore increases with time according to the equation

$$\frac{d\mathbf{j}}{dt} = \alpha_t \mathbf{j} \quad (22)$$

This increase of current with time also gives rise to a spatial increase of the current as

$$\nabla \cdot \mathbf{j} = \alpha_r \mathbf{j} \quad (23)$$

The coefficient α_r is in general a matrix. However, for a constant electric field impact ionization is mostly isotropic and α_r is a scalar [12,23].

We will concentrate, in the following on the theory of α_t . The theory of α_r proceeds very similarly, and one can almost always use $\alpha_t v_d = \alpha_r$, where v_d is the average (drift) velocity of the electrons. The multiplication of electrons (and holes) with time depends physically on two quantities. One is the actual ionization probability, that is, the probability for an electron with given energy to create an

electron-hole pair. This probability per unit time is called the impact ionization rate R_I . The second quantity is the actual probability of having such an electron at a given energy, which is, of course, given by the distribution function. α_t is then the average product of these two probabilities.

$$\alpha_t = \frac{\int_{-\infty}^{\infty} dk R_I f}{\int_{-\infty}^{\infty} dk f} \quad (24)$$

The calculation of R_I involves the quantum mechanics of three particles (two electrons, one hole) in two different bands (conduction and valence) with different (Bloch) wavefunctions and $E(\mathbf{k})$ relations. Even using the approximate "golden rule" of time-dependent perturbation theory involves then a difficult numerical simulation with multiple integrations. Most of the theories of the past are therefore oversimplified and of very limited use, including the formula derived by Keldysh [24]. The only theory in reasonably close agreement with experiments is the Monte Carlo integration of the "golden rule" formulae by Kane [25], the result of which is shown in Fig. 8.

An even greater numerical problem is the calculation of the distribution function entering Eq. (24). The reason is that R_I starts to become appreciably large only at relatively high energies, as shown in Fig. 8. Typically, in silicon, ionization becomes important only for electron energies of 3 eV above the conduction band edge. If this were the average electron energy, it would correspond to a temperature of 24,000 K, which is seldom reached before catastrophic damage occurs. Therefore it is the high-energy

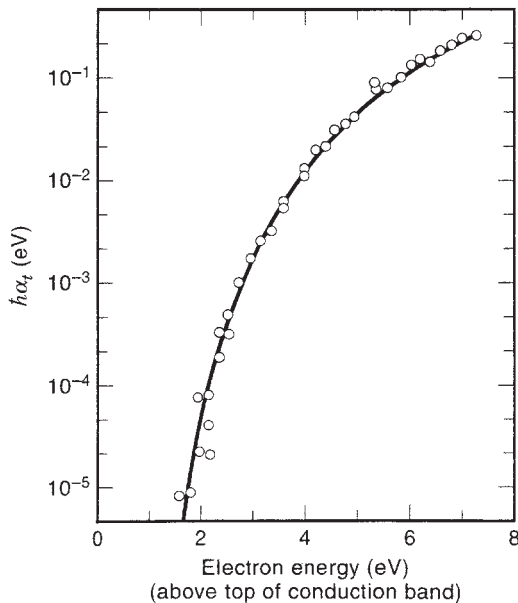


Figure 8. Impact ionization rate α_t (multiplied by \hbar) as a function of conduction electron energy according to the theory of Kane [25]. (Reprinted with permission, © 1967 by the American Physical Society.)

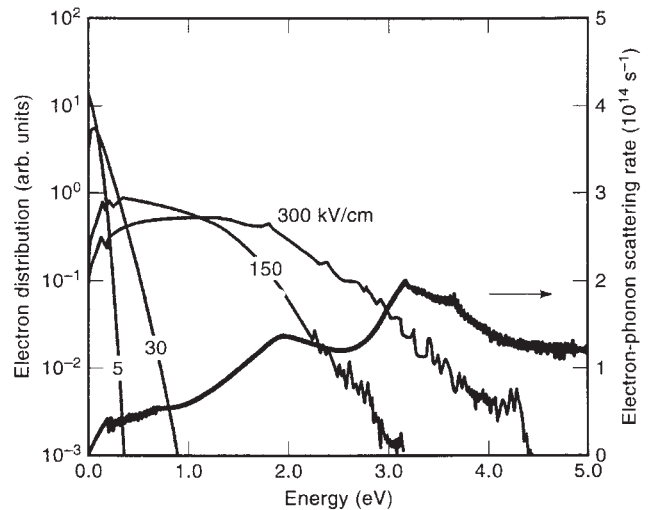


Figure 9. Electron energy distribution as a function of electron energy (in the conduction band), according to Ref. 24, for various constant electric fields. Also shown is the electron-phonon scattering.

tail of the distribution function that matters for impact ionization. This high-energy tail depends sensitively on the band structure and also on spatial and temporal changes of the electric field and can be reliably obtained only from a full-band solution of the Boltzmann equation such as the full-band Monte Carlo [12]. An example of the distribution at high energies is given in Fig. 9 for a constant electric field. Figure 9 also shows the phonon scattering rate in silicon at room temperature as a function of conduction band energies. Note that this rate becomes of the order of 10^{14} s^{-1} at energies above 1.5 eV.

A discussion of all of these complexities and the corresponding results for α_r are given in Refs. 15 and 27. The best results are obtained for theories of R_I à la Kane and

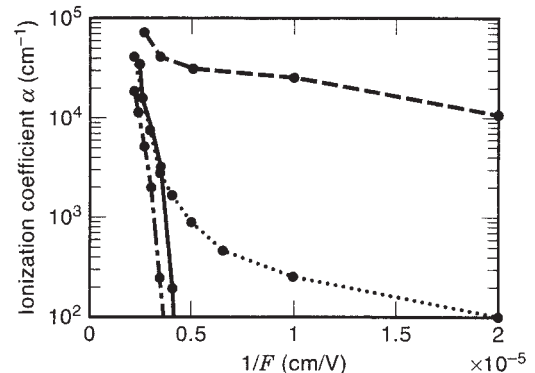


Figure 10. Theoretical electron impact ionization coefficients α_r versus $1/F$ for constant electric fields F and various materials after Bude and Hess [28]. Solid line—GaAs; dashed line—InAs; dotted-dashed line—InP; dotted line— $\text{Ga}_{0.43}\text{In}_{0.57}\text{As}$. The electron ionization coefficient for silicon is roughly a factor of 2 above the coefficient of GaAs. The hole ionization coefficients of GaAs and InP are close to the electron ionization coefficients, while the hole ionization coefficient for silicon is much below the curve for electrons (factors of > 10). (Reprinted with permission, © 1992 by the American Physical Society.)

for distributions from full-band Monte Carlo integrations of the Boltzmann equation (25). Typical theoretical results of α_r are shown in Fig. 10.

The presence of layers of different semiconductors, as occurs in quantum-well structures and superlattices, adds another dimension to the science and engineering of impact ionization and has been discussed extensively in the literature. Examples are given in Refs. 29 and 30.

A simplified approach of great usefulness and parametrized expressions for α_r have been derived by Baraff and others using his theory [7,31]. These are excellent for estimates and for an appreciation of contributory physical parameters. Note, however, that all the simplified analytical expressions given in most textbooks for the threshold, phonon scattering mean free path, and other parameters are quantitatively incorrect and cannot replace the integration of Boltzmann's equation, including the band structure.

3. HOT ELECTRONS IN DEVICES

The special status of hot electrons in semiconductor devices arises from the time and space dependences of electric field and carrier concentrations. These dependences require special care in the theory of average velocity (overshoot, real-space transfer, and transport including abrupt interfaces) and impact ionization. The nonlocality of these effects deserves special attention [32]. Consistency with Gauss law also needs to be satisfied. In fact, numerical solutions of Poisson's equation are a fixed part of any predictive device simulation. The field of hot electrons in devices is therefore a vast one and cannot be reviewed within this limited space. For a general appreciation the reader is referred to discussions of Gunn devices, IMPATT diodes, hot-electron diodes and transistors, real-space transfer devices, and avalanche photodiodes in Ref. 18. All of these devices are based on hot-electron effects. Many of the most important devices, such as metal-oxide-semiconductor field-effect transistors (MOSFETs), involve hot electrons in their operation. Often, hot electrons are felt to cause great disadvantage because they reduce speed (current and velocity saturation), lead to degradation and aging of devices [33], and can cause various instabilities (e.g., through negative differential resistance). However, there are two counts in favor of hot electrons in devices that have led to the continual involvement of hot electrons in chip technology. For one, hot electrons lead to a large scattering rate by phonons as discussed above. This large rate gives rise to dephasing of the wavefunction on the length scale of $0.003\ \mu\text{m}$. Therefore it is possible to reach feature sizes down to $0.1\ \mu\text{m}$ without major transitions from classical to quantum transport. The second point in favor of hot electrons arises from the need for aggressive designs, particularly with respect to switching speed. One needs to use the highest possible current densities, and this means in semiconductors also high electric fields. Frequent predictions that hot-electron effects will be scaled away soon have therefore often not come true. Since hot-electron effects are important in so many devices and of such variable

consequences, we will discuss here only major effects that appear in many variations.

3.1. Hot Electrons in Field-Effect Devices

Field-effect transistors exhibit a large number of hot-electron effects. It has been known since the 1960s [34] that velocity saturation is important in these devices. The saturation was at first only encountered close to the drain, in the so-called pinchoff region [7]. As the device sizes decreased, the velocity saturation spread all over the channel, at least for the highest drain voltages used [7]. This effect reduces some of the figures of merit of the transistors (as, e.g., the transconductance) and was therefore seen as an unwelcome side effect; it was simulated by use of Eqs. (16) and (15) or similar equations but with space-dependent electric fields. This local dependence on a varying electric field is, of course, valid only if the field varies so slowly that the transport is always diffusive without the nonlocal velocity overshoot or ballistic components. These latter effects become important for transistor channel length of the order of $0.1\ \mu\text{m}$ [20]. Then the overshoot effects counteract and undo part of the velocity saturation and generally contribute to higher device speed. This has been proved in MOSFETs, as discussed in Ref. 20.

The documentation of overshoot effects in silicon-based devices is a nontrivial task, since they always appear in connection with velocity degradation in other regions of the devices, and they are small (around a factor of 2 for $T_L = 300\ \text{K}$). Overshoot effects are larger in III-V compound field-effect transistors such as metal-semiconductor transistors (MESFETs). Ordinary MESFETs exhibit much scattering in the conducting channel due to the charged donors or acceptors, in addition to the always present scattering by the polar optical phonons [3,7]. The overshoot effects are therefore more pronounced in modulation-doped field effect transistors (MODFET), which contain the dopants in a layer of a different semiconductor (e.g., AlGaAs) neighboring the channel (e.g., GaAs) as described in Ref. 35. These transistors exhibit, therefore, a significant speed advantage over MESFETs, as shown by numerous works [36,37]. Typical values of the overshoot in such devices, as deduced from Monte Carlo simulations, correspond to those shown in Fig. 7. We note that real-space transfer can, of course, be also of importance in these devices and may reduce some of their advantages.

Impact ionization is an important limiting factor in field-effect transistors, since its presence usually will disturb device operation. The theory of impact ionization in devices proceeds along the lines discussed above. However, nonlocal effects are of great significance because of the presence of rapidly varying electric fields in the conducting channels of field-effect devices. One then needs to allow for dead spaces of the ionization [32,38].

As discussed above, the probability of impact ionization is very small for electron energies below a certain energy in the conduction band. Of course, the minimum energy the electron needs is the energy of the gap E_G . Even above this energy, the threshold for significant ionization is often not reached for energies of 2 or 3 times E_G , as can be seen

from Kane's results in Fig. 8. This energy needs to be reached to start significant ionization.

With a space-dependent electric field $F(z)$ in the z direction, the electron needs to traverse a certain distance d to reach effective threshold. Typically d can be obtained from an equation such as

$$\int_0^d F(z) dz = cE_G \quad (25)$$

where c is a constant determining the effective threshold (normally of the order of 2). Over such a distance, ionization cannot occur, even if the electric field is very high. Ionization in very short field-effect transistors with highly peaked electric fields is therefore smaller than one would expect from an integration of the ionization probability over all fields not counting the dead space of length d . This explains the fact that ionization is not a function of the local electric field alone (nonlocality).

Anisotropies of impact ionization, which have not been found for constant electric fields [23], can occur when ballistic acceleration over short distances is important, mainly because of anisotropies of the effective threshold [39]. These further complicate the simulation of impact ionization in devices. It is the conviction of this author that a quantitative understanding of impact ionization in devices is possible only with a full-band solution of the Boltzmann equation consistent with the solution of Poisson's equation, as can be done with various simulation tools [13,14]. Some of the controversies in the literature can be tracked to oversimplified simulation.

The hot-electron effects discussed above are reversible in the sense that after turning off the electric fields, the hot electrons cool down to the ambient temperature within picoseconds without any structural changes of the crystal lattice. However, hot electrons can also cause structural changes. A particularly well-known hot-electron degradation occurs at the MOSFET interface between the silicon and the silicon dioxide [33]. This damage is linked to the breaking of silicon-hydrogen bonds that are always present at this interface. A clear proof was given by damage measurements involving the isotope deuterium [40]. When the silicon-hydrogen complex was replaced by silicon-deuterium, a much-reduced hot-electron degradation of MOSFETs was found, which has the beneficial effect of increasing the device lifetime [41]. A large framework of experimental and theoretical contributions to this area exists in the literature and is reviewed in Ref. 42.

3.2. Hot Electrons in Quantum-Well Laser Diodes

Hot electrons in quantum-well laser diodes have an origin and consequences different from what they have in field-effect devices. The electrons here are not heated by the electric field but by other electrons propagating into the quantum well and exhibiting suddenly high kinetic energy as shown in Fig. 11. These electrons, originating from outside the well, can now transfer their energy in essentially two ways to the electrons in the quantum well. For one, they can transfer the energy through direct electron-electron interaction (electron-hole interactions can also be

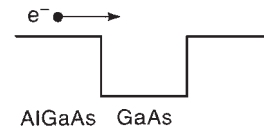


Figure 11. Electron propagating over a semiconductor hetero-junction and acquiring significant kinetic energy (in the GaAs).

important in laser diodes because of the presence of both electrons and holes with approximately equal density). The incoming electron beam therefore heats the quantum-well electrons. Another pathway of energy transfer is by polar optical phonons. Electrons at high energies in the quantum wells emit polar optical phonons (within about 10^{-13} s). These phonons cannot propagate out of the quantum well and decay relatively slowly (typically within 3–10 ps). The phonons therefore accumulate, giving rise to a nonequilibrium (heated) phonon distribution. The quantum-well electrons at low energy can then in turn absorb phonons and heat up themselves. This gives rise to a nonequilibrium electron temperature T_c .

A completely consistent calculation of these effects has been made [43] and shows that the modulation of electron

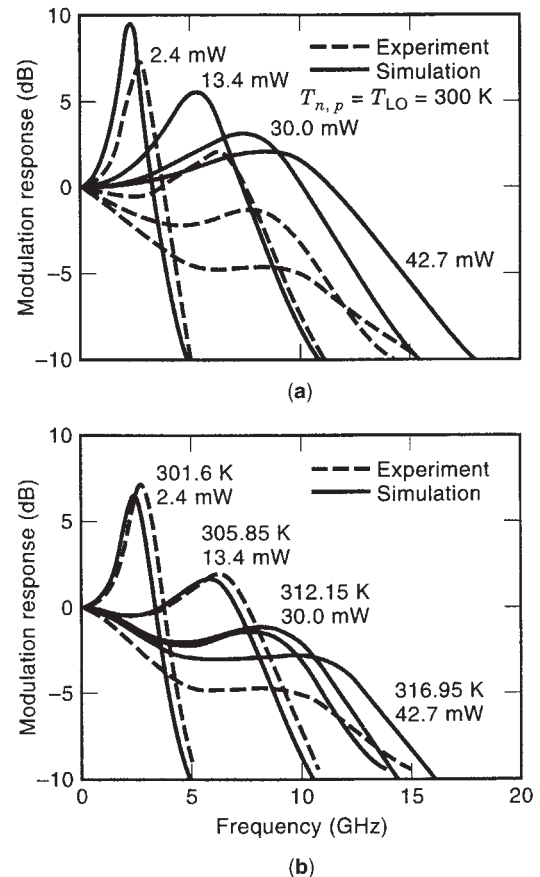


Figure 12. Modulation response of quantum-well laser diodes for various driving currents corresponding to the power indicated: (a) theory without hot-electron effects—the agreement with experiments is weak, particularly at higher power levels; (b) theory including hot-electron effects (temperatures indicated above curves) shows excellent agreement with experiments [38].

density in quantum-well laser diodes is always accompanied by a modulation of the electron temperature and therefore influences the laser performance and modulation response sensitively through very small temperature rises. While field-effect devices operate at electron temperatures of several thousand kelvins caused by the heating of the electric field, laser diodes cease to operate for dynamic electron heating of a few kelvins, as shown in Fig. 12, which depicts the modulation response of a typical semiconductor laser diode. The static heating is also important in lasers and degrades their performance. For the static case electron temperatures around 100 K above room temperature may be tolerated—still much less than the T_c values reached in field-effect devices.

BIBLIOGRAPHY

1. E. J. Ryder, *Phys. Rev.* **90**:766–769 (1953).
2. W. Shockley, *Bell Syst. Tech. J.* **30**:990–1040 (1951); *Solid State Electron.* **2**:35–67 (1961).
3. K. Hess, *Advanced Theory Semiconductor Devices*, Prentice-Hall, Englewood Cliffs, NJ, 1988.
4. G. Bauer, in D. K. Ferry, J. R. Barker, and C. Jacoboni, eds., *Physics of Nonlinear Transport in Semiconductors*, Plenum, New York, 1979, pp. 175–224.
5. D. K. Ferry, *Semiconductors*, Macmillan, New York, 1991, pp. 502–557.
6. Z. S. Gribnikov, K. Hess, and G. A. Kosinovsky, *J. Appl. Phys.* **77**:1337–1373 (1995).
7. S. M. Sze, *Physics of Semiconductor Devices*, Wiley, New York, 1981.
8. J. G. Ruch, *IEEE Trans. Electron. Devices* **ED-19**:652–659 (1972).
9. P. D. Yoder and K. Hess, in N. Balkan, ed., *Negative Differential Resistance and Instabilities in 2-D Semiconductors*, Plenum, New York, 1993, pp. 99–107.
10. K. Brennan and K. Hess, *IEEE Electron. Device Lett.* **7**:86–88 (1986).
11. K. Hess, in N. Balkan, ed., *Hot Electron Physics and Devices*, Oxford Univ. Press, 1997, pp. 13–33.
12. H. Shichijo and K. Hess, *Phys. Rev. B* **23**:4197–4207 (1981).
13. S. E. Laux and M. V. Fischetti, in *Monte Carlo Device Simulation: Full Band and Beyond*, Kluwer Academic, Boston, 1991, pp. 1–26.
14. DEGAS, <http://www.ise.ch>.
15. Z. Selmi et al., *IEDM Tech. Digest*, 1995, pp. 293–296.
16. D. K. Ferry, K. Hess, and P. Vogl, in N. G. Einspruch, ed., *VLSI Electronics*, Vol. 2, Academic Press, New York, 1981, pp. 67–103.
17. H. M. J. Boots et al., *Appl. Phys. Lett.* **57**:2446–2448 (1990).
18. K. K. Ng, *Complete Guide to Semiconductor Devices*, McGraw-Hill, New York, 1995.
19. C. J. Stanton, D. W. Bailey, and K. Hess, *IEEE J. Quantum Electron.* **24**:1614–1627 (1988).
20. G. J. Iafrate and K. Hess, *Proc. IEEE* 519–532 (1988).
21. J. Y. Tang and K. Hess, *IEEE Trans. Electron. Devices* **ED-29**:1906–1910 (1982).
22. M. S. Shur and L. F. Eastman, *IEEE Trans. Electron. Devices* **ED-26**:1677–1683 (1979).
23. G. E. Stillman, V. M. Robbins, and K. Hess, *Proc. 4th Int. Conf. Hot Electrons Semiconductors, Inst. Phys.* **134B/C**:241–246 (1985).
24. L. V. Keldysh, *Soviet Phys. JETP* **21**:1135 (1965).
25. E. O. Kane, *Phys. Rev. B* **159**:624 (1967).
26. P. D. Yoder and K. Hess, *Semiconduct. Sci. Technol.* **9**:852–854 (1994).
27. M. V. Fischetti, S. E. Laux, and E. Crabbe, in K. Hess, J. P. Leburton, and U. Ravaioli, eds., *Hot Carriers in Semiconductors*, Plenum, 1996, New York, pp. 475–480.
28. J. D. Bude and K. Hess, Impact ionization, *J. Appl. Phys.* **72**:3554–3561 (1992); J. D. Bude, K. Hess, and G. J. Iafrate, *Semiconduct. Sci. Technol.* **7**:506–508 (1992); N. Sano, M. Tomizawa, and A. Yoshi, in K. Hess, J. P. Leburton, and U. Ravaioli, eds., *Hot Carriers in Semiconductors*, Plenum, New York, 1996, pp. 337–342.
29. K. Kim, K. Hess, and F. Capasso, *Appl. Phys. Lett.* **51**:508–510 (1987).
30. F. Capasso, *Science* **235**:172 (1987).
31. G. A. Baraff, *Phys. Rev.* **128**:2507–2517 (1962).
32. K. Kim, K. Hess, and F. Capasso, *Appl. Phys. Lett.* **51**:508–510 (1987).
33. C. Hu et al., *IEEE Trans. Electron. Devices* **ED-32**:375–385 (1985).
34. J. A. Cooper and D. F. Nelson, *J. Appl. Phys.* **54**:1445 (1983).
35. T. Mimura, K. Taniguchi, and C. Hamaguchi, *Semiconduct. Sci. Technol.* **7**:379–381 (1992).
36. H. Morkoc and P. M. Solomon, Modulation-doped field-effect transistors, *IEEE Spectrum* **21**(2):28–35 (1984).
37. I. C. Kizilyalli et al., in H. Daemlees, ed., *Modulation-Doped Field-Effect Transistors*, IEEE Press, Piscataway, NJ, 1990, pp. 350–355.
38. J. M. Hightman, I. C. Kizilyalli, and Karl Hess, *IEEE Electron. Device Lett.* **9**:399–401 (1988).
39. T. Kunikiyo, *J. Appl. Phys.* **75**:297 (1994).
40. J. W. Lyding, K. Hess, and I. C. Kizilyalli, *Appl. Phys. Lett.* **68**:2526–2528 (1996).
41. I. C. Kizilyalli, J. W. Lyding, and K. Hess, *IEEE Electron. Device Lett.* **18**:81–83 (1997).
42. E. Takeda, C. Y. Yang, and A. Miura-Hamada, *Hot-Carrier Effects in MOS Devices*, Academic Press, New York, 1995.
43. M. Grupen and K. Hess, *IEEE J. Quantum Electron.* **34**:120–140 (1998).

HIGH-FREQUENCY BROADCASTING

KIM ANDREW ELLIOT

High-frequency (HF) broadcasting, more commonly known as *shortwave broadcasting*, employs the long-distance capabilities of skywave propagation for transmissions over long distances. HF is used for international broadcasting. Some international broadcasters additionally use the mediumwave broadcast band (standard AM) to reach audiences in nearer target countries. HF is also used for domestic broadcasting in countries with large remotely populated regions (e.g., Russia, China, Canada, Australia) and in tropical countries, where the effectiveness of

mediumwave broadcasting is reduced by poor soil conductivity and static from lightning.

International HF broadcast stations generally transmit in a number of languages, including the language of the broadcasting country, plus a selection of major world languages or languages of countries of particular interest to the broadcasting country. For example, the Broadcasting Service of the Kingdom of Saudi Arabia has international HF transmissions in Arabic, Bambara, Bangali, Indonesian, Persian, Somali, Swahili, Turkmen, Turkish, and Urdu—languages of major Islamic populations. Unlike domestic radio, which remains on the air throughout the day, international HF broadcasts in a particular language usually have a duration of a half-hour to 90 min because most international radio stations have a limited number of broadcasters proficient in each language. The fluid nature of the ionosphere also requires that frequencies be changed several times during the day.

1. HISTORY

1.1. Early Years

By the 1920s, the establishment of voice modulation and the discovery of the long-distance properties of the HF frequencies enabled the development of HF broadcasting. In 1927 the Philips company in the Netherlands established a permanent high-frequency broadcasting station to send programs to the Dutch colonies [1]. Soon after, Britain and France began HF broadcasts to their colonies.

During the 1930s, Italy and Germany conducted the first sustained use of radio for international propaganda. Italy transmitted in Arabic to the Middle East in an attempt to turn opinion in that region against the British. Germany broadcast to German communities abroad, adding Spanish, Portuguese, and English to the Americas, and other languages to other targets. The British Broadcasting Corporation (BBC) reacted by supplementing its Empire Service with broadcasts in many of the same languages already transmitted by Germany and Italy [2].

1.2. World War II

Axis broadcasting during World War II had two main strategies. One involved attempts to convince neutral countries to remain neutral or to join with the Axis. The second was to demoralize or confuse the civilian populations or armed forces of countries that had already joined the war against the Axis powers [3]. The BBC countered the Axis broadcasts with a more factual presentation of news. This was also largely the policy of the Voice of America (VoA), created by the United States government in 1942 by consolidating the several private HF broadcast stations that existed in the United States before the war [4].

1.3. The Cold War Years

At the end of World War II, there was a sudden reduction in the amount of international HF broadcasting. However, the advent of the Cold War led to a growth of international broadcasting that was sustained through the 1980s. The Soviet Union's Radio Moscow set the pace with an increas-

ing number of transmitters, transmission hours, and broadcast languages through the Cold War years. All other communist countries, and even some Republics of the Soviet Union, maintained their own international radio services. China's Radio Peking (later, Radio Beijing, and now Voice of China) and its ally Radio Tirana (Albania) were among the largest HF broadcast operations.

From the West, Voice of America and BBC overseas broadcasts expanded. In 1953, West Germany created its Deutsche Welle, which grew to be one of the major international radio services. Also in the early 1950s, the United States created Radio Liberation, later Radio Liberty, directed to the Soviet Union, and Radio Free Europe directed to the other communist countries of Europe. These stations were later merged to form Radio Free Europe/Radio Liberty, Inc.

1.4. The Post-Cold War Period

Radio Moscow, which led the expansion of international broadcasting after World War II, also led the post-Cold War reduction of international broadcasting. In 1990, Radio Moscow broadcast in 61 languages. In 1998, its successor, Voice of Russia, had 33 language services. Western broadcasters also reduced some of their operations and shifted operations from direct HF broadcasts to rebroadcasting within the target country (rebroadcasting is described later). Radio Free Europe/Radio Liberty moved from Munich to Prague. The station closed its Hungarian service and began privatization of its Czech and Polish services. Voice of America HF broadcasts in Russian were reduced from 16 h per day in 1989 to 6 h per week in 1998.

Many of the HF transmitters active during the Cold War are now leased to religious and other radio programmers. In 1997, BBC sold its UK-based HF broadcast transmitters to Merlin Communications International Ltd., which leases the transmitters back to the BBC. Merlin leases spare transmitter time, as do Deutsche Telekom in Germany, Sentech in South Africa, and the transmission companies in many of the former Soviet republics.

Other countries have been considering the future of their international radio services in the post-Cold War era. In late 1996, the Canadian government announced that Radio Canada International would be closed. Public and political support kept the station on the air. In 1997, the Australian government planned to close Radio Australia, the international service of the Australian Broadcasting Corporation. After much debate, Radio Australia remained on the air, but its operations were reduced by about half. Its broadcasts in Cantonese, Thai, and French were dropped, and its main HF transmission site near Darwin was put into mothballs.

The United States has created new international broadcasting services that reflect the shift from the old U.S.–Soviet Cold War theater. Radio Martí to Cuba began broadcasting in 1985. Radio Free Asia was inaugurated in 1997, transmitting to China, Tibet, North Korea, Vietnam, Laos, Cambodia, and Burma (now Myanmar). Congress has allocated funds for new Radio Free Europe/Radio Liberty broadcasts to Iran and Iraq and for a new Radio Democracy for Africa to be operated by the Voice of America.

The use of HF for domestic broadcasting has receded in recent decades. For example, the 1973 *World Radio TV Hand book* listed about 250 stations in the 90-m tropical broadcast band (3200–3400 kHz). The 1998 issue of the *Handbook* lists about 150 stations in that same band [5]. However, investment in domestic HF broadcasting continues in some countries. In 1994, the Zimbabwe Broadcasting Corporation revived its domestic HF broadcasting by putting the first of four new 100 kW HF transmitters into service.

2. PRESENT BROADCASTING ACTIVITY

International radio broadcasting can be divided into three broad types: government-funded, religious, and commercial. Government-financed stations comprise, by far, the

largest share. According to the 1998 *World Radio TV Hand book* [5], some 85 national governments operate international radio stations. Most religious international stations are Protestant evangelical, but there are also Catholic and Islamic stations. Commercial HF international broadcasting has not been successful in selling spot advertisements because of a lack of audience ratings data, but a number of stations make some profit by selling blocks of time to religious and special-interest organizations.

Table 1 shows the top forty international radio stations by frequency hours.

2.1. International Broadcasting from the United States

The United States originates every type of international HF broadcasting. The Voice of America is a government

Table 1. International Radio Broadcasters: Top 40 Stations Ranked by Program Hours per Week^a

	Country	Station	Type ^b	Hours per Week
1	USA	Trans World Radio	R	939
2	United Kingdom	BBC World Service	G	929
3	China	China Radio International	G	893
4	USA	Voice of America	G	870
5	USA	Far East Broadcasting Co	R	809
6	Germany	Deutsche Welle	G	708
7	USA	WWCR	C	672
8	USA	World Harvest Radio	R	665
9	Iran	Voice of the Islamic Republic of Iran	G	637
10	USA	Adventist World Radio	R	618
11	USA	WYFR—Family Radio	R	616
12	Egypt	Radio Cairo/Voice of the Arabs	G	587
13	USA	Radio Free Europe/Radio Liberty	G	553
14	Russia	Voice of Russia	G	539
15	Ecuador	HCJB—Voice of the Andes	R	534
16	India	All India Radio	G	497
17	Japan	NHK World	G	457
18	USA	High Adventure Ministries	R	443
19	France	Radio France Internationale	G	415
20	North Korea	Radio Pyongyang	G	378
21	Turkey	Voice of Turkey	G	375
22	Netherlands	Radio Netherlands	G	369
23	Israel	Kol Israel	G	356
24	USA	WJCR Worldwide	R	336
25	Vatican City	Vatican Radio	R	333
26	Romania	Radio Romania International	G	332
27	South Korea	Radio Korea International	G	322
28	Bulgaria	Radio Bulgaria	G	315
29	USA	WEWN—Worldwide Catholic Ratio	R	301
30	Finland	YLE Radio Finland	G	295
31	Australia	Radio Australia	G	280
32	Switzerland	Swiss Radio International	G	270
33	Spain	Spanish Foreign Radio	G	255
34	Taiwan	Radio Taipei International	G	252
35	Greece	Voice of Greece	G	234
36	Vietnam	Voice of Vietnam	G	231
37	Italy	RAI International	G	218
38	Ukraine	Radio Ukraine International	G	203
39	Poland	Polish Radio Warsaw	G	200
40	Cuba	Radio Havana Cuba	G	195

^aThis table shows program hours rather than frequency hours. Many religious broadcasters transmit in a language on only one frequency. Government-funded international broadcasters use more than one HF frequency per language broadcast, and as such they may have a better chance of delivering an audible signal in the target country or countries. Hours per week include mediumwave and HF transmissions. Program hours reflect simultaneous transmission in more than one language. (Source: BBC Monitoring, World Media Unit.)

^bStation types: G—government-funded; R—religious; C—commercial.

agency (at present part of the U.S. Information Agency) that broadcasts worldwide in 51 languages. Radio Free Europe/Radio Liberty and Radio Free Asia (to China and the other communist countries of Asia, plus Burma) are U.S. government-financed corporations that focus their programming on the domestic affairs of their target countries. The United States also has more than 20 private HF broadcast stations. Some, such as WEWN, Worldwide Catholic Radio in Birmingham, Alabama, are purely religious operations. Others, such as WWCR in Nashville, sell time to religious and special-interest program producers.

2.2. Clandestine Broadcasting

A special category of government-funded HF broadcasting is clandestine broadcasting [6]. These are stations that do not reveal the location of their transmitters or studios. Clandestine stations accompany most wars and revolutions and are used by opposition groups (genuine or contrived by unfriendly countries) to provide an alternative to state-controlled domestic media. Often, a clandestine station claims to be operating from within the target country, as the voice of the people of that country, but actually is transmitting across boundaries. During World War II, the Germans transmitted a “station debunk” on HF to the United States. The station attempted to represent itself as a voice of disenchanting Americans. More recently, opposition groups have been relying less on secret transmitters. Instead, they increasingly lease time from

commercial shortwave transmission companies or disseminate their messages via the Internet. In addition to political clandestine stations, low-powered hobby pirate HF stations are also active, especially in Europe and North America.

2.3. Transmitters and Relays

HF broadcasting requires a significant investment in transmitters and antennas. In the 1990s, HF transmitters typically have power from 100 to 500 kW. Large directional antenna systems are necessary to focus power to the desired target (Fig. 1). Major transmitter manufacturers include Thomcast (France) and Continental (USA, recently merged with Telefunken of Germany).

Despite the long-distance capabilities of HF, attempts to broadcast halfway around the world are generally disappointing. As such, major international radio stations have established relay stations outside their home countries. Until the 1970s, the signals reached the relays by way of HF single-sideband feed transmissions. The signal received by the audience was never better than the weakest HF link. Now, with satellite feeds, transmissions from HF relays begin with a studio-quality signal. A more recent variation of HF relays is transmitter exchanges in which two international stations use each other's transmitters. China Radio International (Beijing) exchanges transmitter time with Radio Canada International, Radio France International, Spanish Foreign Radio, Swiss Radio International, and Voice of Russia.

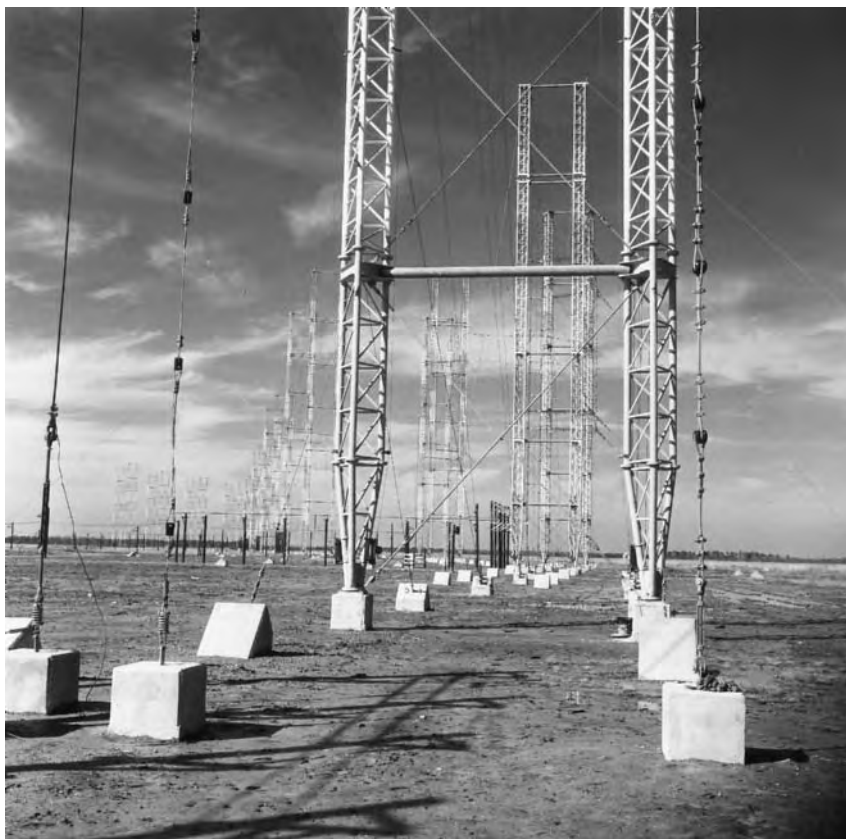


Figure 1. High-frequency broadcast antenna arrays at the Voice of America's Edward R. Murrow transmitting station near Greenville, NC. Guyed masts up to 100 m support arrays of folded dipoles in front of wire reflecting screens. (Courtesy of USIA International Broadcast Bureau.)

Table 2. HF Frequencies Allocated by the International Telecommunications Union for Broadcasting

Frequencies (kHz)	Meter Band	Notes
2300–2495	120	For domestic broadcasting in tropical regions; actually in the “medium frequency” (300–3000-kHz) range
3200–3400	90	For domestic broadcasting in tropical regions
3900–4000	75	Europe and Asia only
4750–5060	60	For domestic broadcasting in tropical regions
5950–6200	49	
7100–7300	41	Eastern Hemisphere only
9500–9990	31	
11,650–12,050	25	
13,600–13,800	22	
15,100–15,600	19	
17,550–17,900	16	
21,450–21,850	13	
25,670–26,100	11	

3. FREQUENCY ASSIGNMENTS

Table 2 shows the HF frequencies allocated for broadcasting. Channels within these bands are spaced 5 kHz apart, that is, 9505, 9510, 9515, and so on. Administrations register frequencies with the Radio Communications Bureau of the International Telecommunications Union that HF broadcast stations within their jurisdictions intend to use. The ITU has a number of procedures for resolving interference. Also useful in preventing interference are frequency coordination meetings held periodically among many international HF broadcasting stations.

Many stations escape interference by broadcasting on frequencies outside (but usually near) the allocated HF broadcast bands. This “out of band” broadcasting is allowed by a provision of the ITU regulations, if users of communications services for which the frequencies are primarily allocated do not complain of interference.

4. PROGRAM CONTENT

HF broadcasters transmit a variety of programs, including news, current affairs analyses and commentaries, cultural and special-interest programs, and music. The most important distinction in programming is propaganda versus a balanced and objective presentation of news and information. One of the pivotal decisions in international broadcasting was that of the BBC not to follow the Axis broadcasters’ propagandistic approach but to maintain the BBC domestic broadcasting policy of (mostly) balanced and factual reportage.

A propagandistic approach to international broadcasting would include one-sided news and current affairs reporting in conjunction with commentaries that are direct attempts to persuade the audience to a certain political viewpoint. This approach, created by the Axis broadcast-

ers before and during World War II, was followed by the international broadcasting of the Communist stations through the 1980s. Propaganda continues to exist—Radio Havana and Radio Pyongyang are two notable examples—but it is less prevalent now that many former communist countries and other dictatorships are experimenting with democracy.

The decision to broadcast balanced, objective news corresponds to the main motivation to listen to foreign broadcasts. Generally, persons seek out foreign broadcasts to get the news and information they want, especially about their own countries and regions, which they cannot get in reliable form from their domestic media. The most important evidence that a balanced presentation of news and information has been more successful than propaganda is that Radio Moscow, during its decades of dominance in terms of broadcast hours, number of languages, and kilowattage, generally had audiences no larger than about 10% the size of those for the BBC World Service or the Voice of America [8]. The international broadcasters of the Western democracies have determined that even if news is embarrassing or negative to their own governments, it attracts audiences and counters the misinformation, disinformation, and withheld information of the state-controlled media in authoritarian countries.

The use of HF broadcasting to transmit music has always been a matter of debate. Some maintain that HF is too unreliable for the enjoyment of music. Many listeners, however, have depended on shortwave for the types of music they wish to hear, but cannot receive from radio stations in their own countries. Willis Conover’s jazz programs on the Voice of America are an important example.

One of the most important programming functions of HF broadcasting is to provide news, information, and entertainment to compatriots living abroad. Virtually all international radio stations transmit in their own languages for emigrants or citizens living or studying in other countries. Often this programming consists of relays of domestic radio programming. This programming fulfills a need—information about the homeland in the language of the homeland—unmet by the domestic broadcasting in the countries where the expatriates live. In 1998, Radio Portugal dropped the last of its foreign-language broadcasts (except for Tetum, a language spoken in former Portuguese East Timor), in favor of a schedule devoted almost exclusively to broadcasts in Portuguese for Lusophone communities worldwide.

5. THE AUDIENCE

Most government-funded international radio stations conduct little or no audience research. They exist largely as a matter of national obligation. So the documentation of an audience is not as vital as for a commercial station, which must provide statistics about its audience to sell advertising.

The largest audience research office is operated by the BBC World Service. The Voice of America, Radio Free Europe/Radio Liberty Inc., Deutsche Welle, and Radio France International also have significant audience

research offices. No global estimate of the number of all international HF broadcast listeners has been attempted because of the impossibility of conducting research in all countries. The best benchmark of the size of the international radio audience is the audience size of the most popular international broadcaster. The BBC estimates that 138 million people listen to BBC World Service at least once a week. This is a conservative estimate because it does not include countries where BBC is unable to commission surveys. Although the estimate includes all listening by way of the BBC's own HF, mediumwave, and FM transmitters, most of the World Service audience still listens via HF [9].

In general, the main predictor of audience size is the nature of the domestic media. Countries that have media that are deficient because of government control, poor economies, or both have the largest international radio audiences.

Some international radio stations cite the volume of audience mail as evidence of an audience. However, there is no reliable way to determine the size of an audience from the number of letters received. Audience mail is more useful to determine audience reaction to programming and reception quality.

A statistic commonly cited in the international broadcasting profession is the existence of 600 million shortwave radios worldwide. This originates from a 1986 study by the Academy for Educational Development [10]. However, an accurate and up-to-date estimate is difficult because of the many radios and "boomboxes" that contain perfunctory shortwave bands. There is no doubt a high mortality rate among these appliances. Radios with shortwave coverage have become less prevalent in general merchandise stores, even in developing countries [11]. In these countries, there is a shift from the number of models with mediumwave and one shortwave band toward those with mediumwave and an FM band.

The quality of shortwave radios varies widely. The typical shortwave available and affordable in a developing country would be a single-conversion model containing a mediumwave band, one or two shortwave bands, and, increasingly, an FM band. Tuning is across large segments of the HF spectrum, from, say 4–12 MHz or 3–22 MHz. Broadcast stations are crowded into the small dial spaces that correspond to the HF broadcast bands. A step up in quality and increasingly available in developing countries are multiband radios that tune only the segments of the HF spectrum devoted to broadcasting, plus mediumwave and FM. This affords better band spread and station separation. Portable shortwave radios with digital frequency readout are less available and more expensive in the developing countries, but they are favored among consumers in the industrialized countries. The highest level receiver is the communications receiver, a tabletop model usually costing from \$700 to more than \$2000. These have digital frequency readout and many technical features that facilitate the reception of marginal signals.

Many of the users of high-end communications receivers are "DXers." DXers are a significant segment of the HF broadcast audience, especially in industrialized countries. The term "DX" comes from the old radiotelegraph abbreviation for "distance." DXing listeners try to receive as

many stations as possible in as many countries as possible. They verify their reception of these stations by sending reception reports and receiving a QSL (another radiotelegraph abbreviation for "confirmation") card.

6. PROBLEMS OF HF BROADCAST RECEPTION

Good, reliable reception of HF broadcasts is limited by the nature of the ionosphere. Conditions of the ionosphere vary day-to-day in weatherlike fashion. They also vary in accordance with the eleven year sunspot cycle. During ebbs in the sunspot cycle, frequencies above, roughly, 12 MHz are less useful for long distance broadcasting. Nearer the peaks of the cycle, the higher HF frequencies become useful, and the lower frequencies remain so. This gives the many international radio broadcasters more room to distribute themselves and avoid interference.

One impediment to good reception is the tendency of many international radio stations to exceed the capabilities of HF. Stations that do not have relay stations or exchange agreements may attempt to send their signals to target countries halfway around the world. These attempts generally produce poor results and, in the process, cause interference in areas short of the target.

Most of the problems of HF reception are of human rather than ionospheric origin. There are too many broadcast stations for the number of frequencies available. Despite some ITU regulation, many stations commence use of frequencies with impunity. As already mentioned, shortwave signals are usually heard outside their target areas. They are not causing interference "on paper," but in reality they are. Interference can be cochannel or adjacent-channel. Theoretically, short-wave stations do not broadcast to the same target on channels less than 10 kHz apart. However, stations 5 kHz apart are heard on any shortwave radio. Often typical inexpensive shortwave radios cannot separate strong signals on adjacent channels.

6.1. Jamming

Most interference is not intentional. Intentional interference is known as jamming. Jamming dates back before World War II. During the Cold War, the Soviet Union maintained an intensive program of jamming the broadcasts of Radio Free Europe, Radio Liberty, the Voice of America, the BBC World Service, and other Western stations. The jamming usually consisted of a raucous buzzing noise. This would be accompanied by a Morse code identifier used by Soviet engineers to track the performance of their jamming transmitters. Because of the tendency of HF signals to be heard better over long distances than shorter distances, skywave jamming is not completely effective in blocking transmissions from abroad. The Soviets remedied this by ringing major cities with HF transmitters close enough to propagate groundwave signals within these cities. Soviet jamming ended in 1989, a manifestation of Mikhail Gorbachev's *glasnost* policy.

Today, China is the country most actively engaged in jamming. China interferes with the broadcasts of the Voice

of America, the U.S. Radio Free Asia, BBC World Service, and transmissions from Taiwan. In addition to noise jamming China transmits overmodulated audio from its domestic radio programs on the frequencies of these external broadcasts. Cuba, North Korea, Vietnam, and Burma (Myanmar) are also presently of recently jamming external broadcasts. Jamming is also often heard from a number of Middle Eastern countries.

7. PROSPECTS FOR HF BROADCASTING

A number of new media technologies are now vying with HF to transmit broadcasts over long distances and across national boundaries. These media are satellite broadcasting, the Internet, and rebroadcasting. Radio was the original medium of international broadcasting because only radio could travel long distances and across national boundaries. New media allow text, graphics, video, and the traditional audio. Most international broadcasters are maintaining most of their efforts in their traditional radio medium. Nevertheless, they will have to decide which medium is most appropriate for each of their broadcasting missions. Since the 1970s or so, international radio broadcasts have consisted largely of news, commentaries, and current affairs talks, with a minimum of production. Such content might more efficiently be transmitted as text.

7.1. Satellite Broadcasting

With terrestrial broadcasting, radio developed first, then television. In satellite broadcasting, television has already started, but direct satellite *radio* systems for domestic and international use are still in development. WorldSpace Corporation of Washington, DC is planning to launch the first of its three direct radio broadcasting satellites in late 1998. The WorldSpace system will transmit radio broadcasts to small receivers in Africa, the Middle East, Asia, the Caribbean, and Latin America. Each WorldSpace satellite will have three beams, each with a capacity of 96 AM-quality channels. The company plans to provide transmissions services for both international and domestic radio broadcasting.

Many international radio broadcasters are already using audio subcarriers of direct-to-home *television* satellite systems. This is most prevalent on the Astra satellite television system in Europe. World Radio Network of London combines the programs of several international radio stations into 24 hour services, using subcarriers of Astra in Europe and other satellites in other parts of the world.

7.2. The Internet

Now the advent of RealAudio and other audiostreaming software it possible for persons to receive foreign broadcasts via the Internet. Audio fidelity is usually not even AM-quality, but reception is more reliable than via HF. An important advantage of Internet audio is that a listener can hear a specific program, say, a weekly half-hour pro-

gram about science, at any convenient time, rather than having to be at the radio at the scheduled time of the program. Some international broadcasters also present "live" streams of their 24-h schedule. The BBC World Service in English is available via Broadcast.com, a commercial World Wide Web service.

At present, however, computers with Internet access are much less common in homes than are shortwave radios, especially in the developing countries, where audiences for international radio are largest. Also, access to certain World Wide Web sets can be interdicted. The Chinese government controls Internet gateways in that country and currently blocks access to some foreign news-oriented sites, including those of the Voice of America and the Cable News Network. Inbound electronic mail is more difficult to stop, and now the Voice of America has a Mandarin-language e-mail news service delivered to computer users in China. This service uses the most popular software in China to convert from ASCII to Chinese characters.

7.3. Rebroadcasting

Now many international broadcasters use satellites to feed complete programs of brief reports to radio stations in the target country, which rebroadcast this content to local audiences. When given the choice, listeners certainly prefer to hear foreign broadcasts via a nearby FM or mediumwave transmitter than by way of a distant and unreliable HF signal. Rebroadcasting also facilitates international television because terrestrial television transmission is limited to relatively short distances and direct-to-home satellite opportunities are still limited and expensive.

To some extent, however, rebroadcasting is a self-negating enterprise. The fact that a country could allow foreign broadcasts to be transmitted from its own territory indicates that the country tolerates a free and diverse domestic media environment. This reduces much of the incentive to listen to foreign broadcasts, whether via local or external transmitters. At present, there is no rebroadcasting (at least of news and current-affairs programs) in some of the most important target countries for international radio such as China, Nigeria, Indonesia, India, and Cuba. During crises, private radio stations are also sometimes banned from rebroadcasting international programs or are themselves taken off the air. The Voice of America, BBC, and Radio France International have experienced a temporary loss of local rebroadcasting during turbulent periods in the Democratic Republic of the Congo, Liberia, Niger, and other countries.

7.4. Digital HF Broadcasting

In the 1980s, it was widely assumed that satellites would replace HF as the medium for international broadcasting. Two events in the 1990s have caused international broadcasters to temper their optimism about the new technologies. BBC World Service Television was broadcast to East Asia, including China, as part of the Star TV service of the AsiaSat satellite. The English-language television service was accompanied by a Mandarin-language translation on

an audio subcarrier. Media entrepreneur Rupert Murdoch purchased Star TV in 1994. Murdoch, pursuing media opportunities in China, yielded to Chinese government pressure and removed BBC World Service Television from the Star TV beam, which reached most of China. BBC's Arabic Television Service was shut down in 1996 when the Saudi-owned Orbit Radio and Television Network, which beamed the service into the Middle East, objected to BBC's coverage of Saudi domestic affairs.

Therefore, international broadcasters are reconsidering the future of HF for international broadcasting. The main incentive for listening to foreign broadcasts is to get news that the audience wants but cannot get from their domestic state-controlled media. Therefore international broadcasting must rely on noninterdictable, direct-to-home media. HF is not encumbered by the politicocommercial links which affect the owners of satellite transponders. And HF transmissions are not as easy to block as World Wide Webpages.

A coalition of international radio broadcasters and manufacturers of HF transmitters and shortwave receivers have formed Digital Radio Mondial (DRM) to develop a system for digital broadcast transmission on HF and in the mediumwave and longwave broadcast bands [12]. The DRM inaugural meeting was held, remarkably, in China at Guangzhou City in March 1998. A DRM statement proclaims that HF digital broadcasting will allow listeners to hear "shortwave programs free of fading and interference." This will require new and, at least initially, more expensive receivers. It remains to be seen if digital transmission will overcome the degradations of HF reception. An important question is whether digital HF transmission will help overcome or facilitate attempts by authoritarian governments to block broadcasts from abroad.

BIBLIOGRAPHY

1. Radio Nederland Wereldomroep, *History in Brief*; available online.
2. D. R. Browne, *International Broadcasting: The Limits of the Limitless Medium*, Praeger, New York, 1982, pp. 48–61.
3. P. E. Jacob, The theory and strategy of Nazi short-wave propaganda, in H. L. Childs and J. B. Whitton, eds., *Propaganda by Short Wave*, Princeton Univ. Press, Princeton, NJ, 1942, pp. 49–108.
4. J. Houseman, *Front and Center*, Simon & Schuster, New York, 1979, pp. 19–104.
5. J. M. Frost, ed., *World Radio TV Handbook*, 27th ed., Billboard, New York, pp. 366–368; Andrew G. Sennitt, ed., *World Radio TV Handbook*, 1998 ed., Billboard, New York, pp. 511–512.
6. K. A. Elliott et al., Unofficial broadcasting for politics, profit, and pleasure, *Gazette* **29** (1982).
7. G. Mansell, *Let Truth Be Told: 50 Years of BBC External Broadcasting*, Weidenfeld & Nicolson, London, 1982, pp. 40–94; A. Walker, *A Skyful of Freedom: 60 Years of the BBC World Service*, Broadside Book, London, 1992, pp. 26–35.

8. G. Mytton and C. Forrester, Audience for international radio broadcasts, *Eur. J. Commun.* **3**:457–481 (1988).
9. Telephone interview with Colin Wilding, research services manager, BBC World Service Marketing & Communications, May 14, 1998.
10. R. S. Fortner, *A Worldwide Radio Receiver Population Analysis*, Academy Educational Development, Washington, DC, 1986.
11. A. Dasgupta, Indian receiver survey 1998, Radio Netherlands Real Radio; available online.
12. Information about Digital Radio Mondial; available online at <http://www.rnw.nl/DRM/>.

FURTHER READING

A description of international and domestic radio broadcasting in all countries, including schedules for HF broadcasts in all broadcast languages, is in the annual *World Radio TV Handbook*, published until 1998 by Billboard Publications. Beginning with the 1999 issue, the book will be published by WRTH Publications, Milton Keynes, UK (editor@wrth.demon.co.uk).

Schedules of English-language HF broadcasts, plus reviews of receivers and other information for the listener is in Lawrence Magne, ed., *Passport to World Bank Radio*, International Broadcasting Services Ltd., Penns Park, PA (<http://www.passport.com>).

Schedules and general articles about HF broadcasting and other radio topics are contained in *Monitoring Times* magazine, published monthly by Grove Enterprises, Brasstown, NC (<http://www.grove-ent.com>). Schedules and information are also published in the monthly *Journal of the North American Shortwave Association* (<http://www.anarc.org/naswa>). English-language HF broadcast schedules are updated weekly by FineWare.

A comprehensive compilation of news about and schedules of world broadcasting stations, including HF broadcasting, is contained in the *World Media* and *Schedules* publications of BBC Monitoring, Reading, England (marketing@mon.bbc.co.uk).

A listing of most of the world's HF broadcast transmitters by country, location, manufacturer, power, date of inauguration, and (if applicable) decommission, is in L. Maes, *Transmitter Documentation Project*, 5th ed., Rijkvevorse, Ludo Maes, Belgium, 1998 (<http://www.ping.be/tdp>). A comprehensive discussion of HF receivers is F. Osterman, *Shortwave Receivers Past and Present: Communications Receivers 1942 to 1977*, 5th ed., Universal Radio Research, Reynoldsburg, OH, 1998 (<http://www.universal-radio.com>).

General descriptions and the history of international broadcasting include D. R. Browne, *International Broadcasting: The Limits of the Limitless Medium*, Praeger, New York, 1982; H. L. Childs and J. B. Whitton, eds., *Propaganda by Short Wave*, Princeton Univ. Press, 1942; M. Nelson: *War of the Black Heavens: Western Broadcasting in the Cold War*, Syracuse Univ. Press, 1997; C. J. Rolo, *Radio Goes to War: The "Fourth Front,"* Putnam, New York, Peter 1942; J. Wood, *History of International Broadcasting*, Peregrinus, London, 1993.

Several World Wide Websites contain information for the shortwave listener about international broadcasting. Among the most useful (with links to other sites) are TRS Consultants (<http://www.trsc.com>), Shortwave/Radio Catalog (<http://itre.ncsu.edu/radio>), Association of North American Radio Clubs (<http://www.anarc.org>), Radio Netherlands Real Radio (<http://www.rnw.nl/realradio/index.html>), and the IBB Monitoring Homepage (<http://voa.his.com/>).

HIGH-FREQUENCY TRANSMISSION LINES

FERNANDO L. TEIXEIRA*
The Ohio State University
Columbus, Ohio

KALADHAR RADHAKRISHNAN
Intel Corporation
Chandler, Arizona

WENG C. CHEW
University of Illinois at
Urbana—Champaign
Urbana, Illinois

1. INTRODUCTION

Transmission lines are used to guide electromagnetic waves from one place to another. They are used for a wide range of applications, and different types of lines are suitable for different applications. The power transmission lines that supply electricity do not transmit signals, but just the power required to run the various electrical devices. As a result, power lines are designed to minimize the various losses incurred in traversing great distances. There are also transmission lines that carry high-frequency signals varying in a nonrepetitive fashion for communication purposes. These are called *high-frequency transmission lines*. The impetus in the design of such lines is to maximize the operable frequency bandwidth and minimize the attenuation of the signals. The former preserves the quality of the signal being transmitted, while the latter increases the spacing between repeater stations, reducing the cost of transmission. Transmission of signals is not limited to physically long lines. Transmission lines are also used to send signals within a computer or to feed an antenna from its source.

1.1. Historical Perspective

The earliest device to use electrical transmission lines was the telegraph. The first message was sent by Morse in the year 1844. By the year 1866, a cable was laid across the Atlantic Ocean, making it possible to send messages across continents. A few years later, with the invention of the telephone, transmission lines with a wider bandwidth were employed. By 1890, as electricity became more important, power lines were developed to transmit power from the generators to the consumers. These lines which use just a simple wire to transmit signals are referred to as *single-wire transmission lines*.

The first experiments involving two-conductor transmission lines were carried out by Heinrich Hertz [1] toward the end of the nineteenth century. His experiments with the coaxial line demonstrated the validity of the electromagnetic theory of Faraday and Maxwell [2]. In 1897, Lord Rayleigh [3] proved mathematically that it is possible to transmit waves through a hollow waveguide of rectangular or circular cross section. A different type of wave propagation based on surface waves was analyzed by

Sommerfeld in 1899 [4]. This work was extended to analyze wave propagation along dielectric cylinders by Hondros and Debye in 1910 [5]. Marconi was the first to demonstrate wireless communication by sending signals across the Atlantic Ocean in 1901. The primary function of transmission lines in wireless communication is in transferring the signal from the transmitter to the antennas.

With the development of the radar in the 1930s, the frequency of the signals were approaching the gigahertz range. At these frequencies, the hollow waveguides provide a more practical, low-loss way of transferring energy. Even though it was theoretically proved that it was possible to transmit waves through a hollow waveguide, no experimental results were forthcoming until the year 1936. It was then that two men, George C. Southworth and Wilmer L. Barrow, independently demonstrated wave transmission through the waveguide [6]. The period during World War II saw a steady growth in both theoretical and experimental work on transmission lines and waveguides as practical communication devices.

After World War II, rectangular waveguides became the dominant waveguiding structure. However, as engineers sought components with larger bandwidths, other structures were investigated. The next major milestone in the history of transmission lines was the development of the microwave printed circuit [7,8]. The microstrip line was introduced to alleviate the bandwidth problem since its fundamental mode operated at all frequencies. The ease of fabrication was another attractive feature of the microstrip line.

By the 1970s, most long-distance communication lines were simple two-conductor transmission lines. As the demand for high capacity and long-distance transmission systems increased, optical fibers were developed to replace the existing copper wire system [9]. Optical fibers had a much wider bandwidth than did the simple coaxial line since they operated at optical frequencies. Their inherent low loss also made it possible to achieve a much higher repeater spacing than conventional copper-based transmission lines.

1.2. Comparison of Transmission Lines

Several factors need to be considered when choosing a transmission line for a particular application. The most important factors to be considered when comparing transmission lines are

1. Frequency range and bandwidth
2. Attenuation
3. Power-handling capability
4. Ease of fabrication

Since there is no single transmission line that gives the optimal performance in all these areas, the line that has the best tradeoff for the given application must be chosen. For low-frequency applications like power transmission, a simple wire can be used to connect the source and the receiver. The frequency range of such lines is limited to low frequencies because they start radiating energy as the frequency is increased. At higher frequencies, the field is

*Corresponding author

Table 1. Comparison of Transmission Lines

Type	Advantages	Disadvantages
Single-wire transmission lines	High power, inexpensive	Low-frequency range, lossy
Coaxial lines	Large bandwidth, small size	Low power, high attenuation
Hollow waveguides	Low attenuation, high power	Limited bandwidth, large size
Optical waveguides	Large bandwidth, low loss	Radiate at bends, low power
Microstrip lines	Large bandwidth, ease of fabrication	Low power, high attenuation

usually transmitted using coaxial lines that consist of a wire inside a cylindrical outer conductor. The outer conductor acts as a shield to minimize radiation losses. Such coaxial lines can be used to send signals up to a few gigahertz. Even though the coaxial lines have large bandwidth, they suffer from high attenuation and low power-handling capability. A hollow metallic waveguide is more efficient at high frequencies because of its high power-handling capability and low attenuation. However, unlike coaxial lines, waveguides have a much smaller bandwidth.

It is also possible to transmit energy through dielectric slabs and rods, without any conducting walls. Such waveguides are referred to as *open* or *dielectric waveguides*. For example, an optical fiber is a dielectric waveguide. As their name suggests, they operate at optical frequencies. Since they operate at such high frequencies, they have a very large bandwidth. They also tend to radiate energy at discontinuities and bends.

The last transmission line to be discussed in this section is the microstrip. A microstrip line consists of a thin metallic strip placed on top of a dielectric substrate that is supported from below by a conducting plate. Just like the coaxial lines, microstrip has a large bandwidth but suffers from high attenuation and low power-handling capability. But their primary advantages are their ease of fabrication and integration with complicated microwave circuits. The properties of the various transmission lines discussed

above are summarized in Table 1. Some of them are illustrated in Fig. 1.

1.2.1. Two-Conductor Transmission Line. Different types of two-conductor transmission lines are available for different applications. The simplest of them is the single-wire transmission line with Earth acting as the implicit ground plane. Such lines are useful for low-frequency applications. At higher frequencies, the radiation losses make it impractical to use a single wire transmission line. At such frequencies, it is desirable to use a coaxial line that consists of a wire surrounded by an external cylindrical conductor. The outer conductor acts as a shield that prevents radiation losses. The principal mode of operation in such lines is the TEM mode: a mode in which both the electric and the magnetic fields are perpendicular to the direction of wave transmission. The TEM mode can propagate at all frequencies, giving the coaxial line a large bandwidth. Besides the coaxial line, there also exists the two-wire balanced line that consists of two identical lines placed next to each other. The twisted-pair transmission line is another type of two-conductor transmission line. In these lines, two insulated wires are twisted together and encased, along with other similar pairs, inside a metallic sheath. These lines are popular for transmission of both analog and digital data. The twisting in the wire reduces low-frequency interference, and the

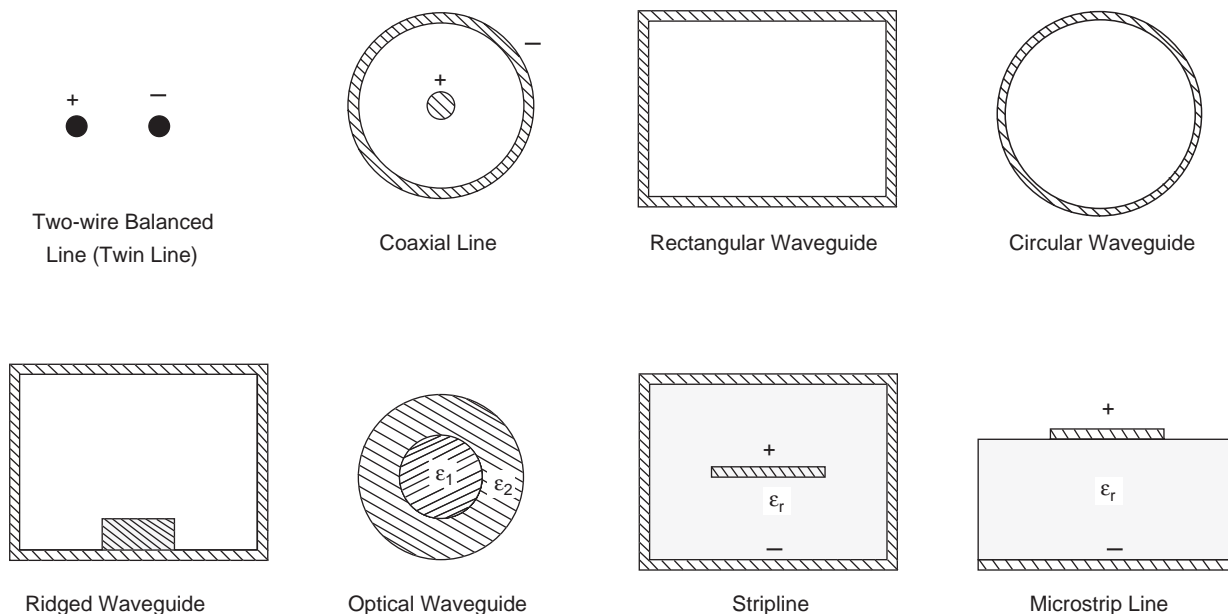


Figure 1. Cross-sectional view of typical transmission line structures.

use of different twist lengths in adjacent pairs reduces crosstalk. The bandwidth of such twisted-pair lines used in transmission of digital signals is presently around 6 MHz.

1.2.2. Hollow Waveguides. Hollow waveguiding structures are more efficient at transmitting high-frequency signals. A simple hollow waveguide is a hollow metallic cylinder filled with air or any dielectric medium. Such waveguides, unlike coaxial lines and other simple transmission lines, do not have a central conductor. As we shall see later, these waveguides cannot support the TEM mode. Instead, the wave propagates by bouncing between the perfectly conducting walls. The modes inside a hollow waveguide can be classified into TE and TM modes. In a TE mode, the electric field is transverse to the direction of propagation. In TM modes, it is the magnetic field that is transverse to the direction of propagation. The TE and TM modes are decoupled from each other. Any arbitrary field distribution within the waveguide can be expressed as a linear combination of a TE component and a TM component. Typically the field inside the waveguide is a combination of several modes. For each waveguide mode, there is a critical frequency below which the waveguide will not propagate that mode. This critical frequency, also known as the *cutoff frequency*, is inversely proportional to the size of the waveguide cross section. Therefore, to propagate low-frequency signals, the waveguide must be made bigger. This tends to restrict the bandwidth of the signal in a waveguide.

1.2.3. Open Waveguides. The simplest form of an open waveguide is the dielectric slab waveguide. It consists of a dielectric coating on top of a ground plane. To simplify the analysis of such a structure, the coating is usually assumed to have an infinite width with no field variation along that direction. For the wave to propagate within a dielectric waveguide, its permittivity should be higher than the permittivity of the surrounding medium. The wave is then guided by total internal reflection. As in the case of hollow waveguides, the field inside a dielectric slab waveguide can also be decomposed into TE and TM modes. However, the field is not localized to the waveguiding structure. Since these waveguides are not enclosed by conducting walls, there exists a residual field outside the slab waveguide. The field outside the guiding structure decays exponentially, and hence the energy is localized to the waveguide.

Apart from the slab waveguides, there also exist circular and rectangular dielectric waveguiding structures. The optical fiber is a simple and very popular example of a circular dielectric waveguide. It has a dramatic impact on modern telecommunications. Dielectric waveguides are also very important in integrated optics and at the shorter millimeter-wave frequencies. Unlike the closed waveguides, the TE and TM modes are coupled to each other in circular and rectangular open waveguides; thus, none of the modes are strictly TE or TM. Instead, the *EH* notation is sometimes used to denote a mode whose TE component dominates over its TM component, and vice versa for the *HE* notation.

1.2.4. Microstrip Lines. Microwave integrated circuit (MIC) transmission lines in general and microstrip lines in particular have become popular for high-frequency applications because of their ease of fabrication and large bandwidth. Moreover, they can be easily integrated with microwave and millimeter-wave integrated circuits. A microstrip line consists of a thin metallic strip on top of a dielectric substrate backed by a ground plane. The dielectric substrate material needs to have a low-loss tangent and a relatively large dielectric constant. The principal mode of operation is not strictly TEM since the dielectric does not uniformly surround the conducting strip. Instead, the fundamental mode is an approximation to the TEM mode and is commonly referred to as the *quasi-TEM mode*. Microstrip lines can be designed for frequencies ranging from a few gigahertz, or even lower, to many tens of gigahertz.

2. PROPAGATION IN GUIDING STRUCTURES

When the transmission lines [10–16] are small in terms of the wavelengths of the transmitted signal, they can be satisfactorily analyzed in terms of circuit theory parameters, such as currents and voltages. In this case, the line is treated using a distributed circuit model. However, as the frequency increases and the operating wavelength becomes comparable with the dimensions of the transmission line, a more general analysis is necessary. The most general approach to study the energy propagation along transmission lines is based on Maxwell's equations. By solving the associated boundary-value problem defined by the geometry and material of the transmission line, one can, in principle, completely characterize the electrical properties of the transmission line. In many cases, an analytical solution is not possible, requiring the use of numerical techniques.

In this section, we shall describe the basic properties of the electromagnetic fields on a transmission-line structure using Maxwell's equations, and discuss how they can give rise to the concepts of current and voltage along the transmission line.

If the regions between the conductors in the transmission line are filled with a homogeneous material, it can support purely transverse electric (TE), transverse magnetic (TM), or transverse electromagnetic (TEM) modes. A TE wave is such that the electric field \mathbf{E} is everywhere transverse to the direction of propagation, which will be assumed to be the z axis. This is equivalent to saying that, in the TE mode, the \mathbf{E} field is completely confined to the transverse plane (cross section) of the waveguide. Analogously, for the TM wave, the magnetic field \mathbf{H} is transverse to z , and for the TEM wave, both fields are transverse to z . If the wave is TEM, it is customary to say that the waveguide is operating in the *transmission-line mode*. (*Note:* The term *transmission line* is occasionally reserved for structures that support the TEM mode. Here, we consider transmission lines as any structure capable of guiding waves; hence, the terms waveguides and transmission lines are used interchangeably.) It can be shown that a

hollow waveguide cannot support a TEM wave. For the transmission-line mode to exist, there needs to have at least two conductors (one of them can be a ground plane). In our analysis, we will assume harmonic fields and adopt the $e^{-i\omega t}$ time convention.

2.1. TE and TM Modes

Because the fields of a general uniform transmission line can be decomposed into TE and TM types, we can characterize the TE wave with the \hat{z} component of the magnetic field or H_z , since $H_z \neq 0$ for this type of wave. Similarly, we can characterize the TM wave with the \hat{z} component of the magnetic field or E_z since $E_z \neq 0$ for this type of wave.

We shall first derive the equations governing the E_z and H_z components of the fields in a uniform transmission line with a general geometry filled with a homogeneous material.

We start from Maxwell's equations

$$\nabla \times \mathbf{E} = i\omega\mu\mathbf{H} \quad (1)$$

$$\nabla \times \mathbf{H} = -i\omega\varepsilon\mathbf{E} \quad (2)$$

and let

$$\mathbf{E} = \mathbf{E}_s + \hat{z}E_z, \quad \mathbf{H} = \mathbf{H}_s + \hat{z}H_z \quad (3)$$

where the subscript s represents the transverse to z components. Substituting Eq. (3) into Eqs. (1) and (2), we have

$$\left(\nabla_s + \hat{z} \frac{\partial}{\partial z}\right) \times (\mathbf{E}_s + \hat{z}E_z) = i\omega\mu(\mathbf{H}_s + \hat{z}H_z) \quad (4)$$

$$\left(\nabla_s + \hat{z} \frac{\partial}{\partial z}\right) \times (\mathbf{H}_s + \hat{z}H_z) = -i\omega\varepsilon(\mathbf{E}_s + \hat{z}E_z) \quad (5)$$

where ∇_s stands for the transversal part of the nabla operator:

$$\nabla_s \equiv \hat{x} \frac{\partial}{\partial x} + \hat{y} \frac{\partial}{\partial y}$$

Equating the s components of Eqs. (4) and (5), we have

$$\nabla_s \times \hat{z}E_z + \frac{\partial}{\partial z} \hat{z} \times \mathbf{E}_s = i\omega\mu\mathbf{H}_s \quad (6)$$

$$\nabla_s \times \hat{z}H_z + \frac{\partial}{\partial z} \hat{z} \times \mathbf{H}_s = -i\omega\varepsilon\mathbf{E}_s \quad (7)$$

Substituting for \mathbf{E}_s from Eq. (7) into Eq. (6), we have

$$\omega^2\mu\varepsilon\mathbf{H}_s = -i\omega\varepsilon\nabla_s \times \hat{z}E_z + \frac{\partial}{\partial z} \hat{z} \times \left(\nabla_s \times \hat{z}H_z + \frac{\partial}{\partial z} \hat{z} \times \mathbf{H}_s\right) \quad (8)$$

Using the vector identities $\hat{z} \times \nabla_s \times \hat{z} = \nabla_s$, $\hat{z} \times \hat{z} \times \mathbf{H}_s = -\mathbf{H}_s$, and assuming that the field has $e^{\pm ik_z z}$

dependence, so that $(\partial^2/\partial z^2) \rightarrow -k_z^2$, we can rewrite Eq. (8) as

$$\mathbf{H}_s = \frac{1}{k^2 - k_z^2} \left[\frac{\partial}{\partial z} \nabla_s H_z + i\omega\varepsilon \hat{z} \times \nabla_s E_z \right] \quad (9)$$

where $k^2 = \omega^2\mu\varepsilon$. By the same token, we have

$$\mathbf{E}_s = \frac{1}{k^2 - k_z^2} \left[\frac{\partial}{\partial z} \nabla_s E_z - i\omega\mu \hat{z} \times \nabla_s H_z \right] \quad (10)$$

The factor k_z is called the *propagation constant*. Equations (9) and (10) allow us to derive all the other components of the field in a waveguide once we know the z components of the field.

If we equate the \hat{z} components of Eqs. (4) and (5), we have

$$\nabla_s \times \mathbf{E}_s = i\omega\mu H_z \quad (11)$$

$$\nabla_s \times \mathbf{H}_s = -i\omega\varepsilon E_z \quad (12)$$

Substituting Eqs. (9) and (10) into Eqs. (11) and (12), we have

$$(\nabla_s^2 + k_s^2)H_z = 0 \quad \text{for TE waves} \quad (13)$$

$$(\nabla_s^2 + k_s^2)E_z = 0 \quad \text{for TM waves} \quad (14)$$

where $k_s^2 = k^2 - k_z^2$. Therefore, H_z and E_z satisfy a two-dimensional scalar wave equation, also known as the *reduced-wave equation*. Once E_z and H_z are solved for from Eqs. (13) and (14), we can derive all the other field components using Eqs. (9) and (10).

2.2. TEM Mode of a Transmission Line

For TEM waves, both E_z and H_z are zero. According to Eqs. (9) and (10), \mathbf{H}_s and \mathbf{E}_s will be nonzero only if $k_z = k$. Therefore, all TEM waves, or TEM modes in a waveguide, have e^{ikz} dependence, where the propagation constant in the guiding structure is equal to that in free space. Furthermore, from Eqs. (11) and (12), we conclude that, for TEM waves

$$\nabla_s \times \mathbf{E}_s = 0, \quad \nabla_s \times \mathbf{H}_s = 0 \quad (15)$$

These equations state that both the \mathbf{E}_s and \mathbf{H}_s are irrotational fields in the xy plane. Any irrotational field can be written as the gradient of a scalar function, as in the case of the electrostatic field $\mathbf{E} = -\nabla\phi$, where ϕ is the electric potential. In other words, \mathbf{E}_s is electrostatic in the xy plane while \mathbf{H}_s is magnetostatic in the xy plane. Hence, we can let

$$\mathbf{E}_s = -\nabla_s \phi_s(x, y)e^{ikhz}, \quad \mathbf{H}_s = -\nabla_s \psi_s(x, y)e^{ikhz} \quad (16)$$

Since $\nabla \cdot \mathbf{E}_s = 0$ and $\nabla \cdot \mathbf{H}_s = 0$ in the waveguide, ϕ_s and ψ_s satisfy Laplace's equations

$$\nabla_s^2 \phi_s(x, y) = 0, \quad \nabla_s^2 \psi_s(x, y) = 0 \quad (17)$$

If we have perfect electric conductors, the boundary conditions are $\hat{\mathbf{n}} \times \mathbf{E}_s = 0$, and $\hat{\mathbf{n}} \cdot \mathbf{H}_s = 0$ on the metallic surfaces. These boundary conditions translate to

$$\phi_s = \text{constant} \quad (18)$$

$$\hat{\mathbf{n}} \cdot \nabla_s \psi_s = \frac{\partial}{\partial n} \psi_s = 0 \quad (19)$$

Equation (18) is known as the *Dirichlet boundary condition*, while Eq. (19) is the *Neumann boundary condition*. The constants in Eq. (18) are the potentials on the conductors, which may differ for different conductors.

At this point, it seems that ϕ_s and ψ_s are decoupled, and hence, the electric field and the magnetic field are independent of each other. This could not be true, as the coupling is expressed in Eqs. (6) and (7) (if we set $E_z = H_z = 0$ for discussing TEM modes). Hence, the coupling of the fields is only through the \hat{z} variation of the fields:

$$\frac{\partial}{\partial z} \hat{z} \times \mathbf{E}_s = i\omega\mu\mathbf{H}_s \quad (20)$$

$$\frac{\partial}{\partial z} \hat{z} \times \mathbf{H}_s = -i\omega\epsilon\mathbf{E}_s \quad (21)$$

Furthermore, from these equations, we deduce that \mathbf{H}_s and \mathbf{E}_s are mutually orthogonal in the TEM mode. Since the fields have e^{ikz} dependence, we conclude that

$$\hat{z} \times \mathbf{E}_s = \sqrt{\frac{\mu}{\epsilon}} \mathbf{H}_s = \eta \mathbf{H}_s \quad (22)$$

if we assume that the wave is propagating in only one direction, then η is also known as the *intrinsic impedance* of the medium, and all TEM waves satisfy Eq. (22).

We can integrate Eq. (20) about a line contour around one of the conductors that made up the transmission line to obtain

$$\frac{\partial}{\partial z} \oint_C \hat{z} \times \mathbf{E}_s \cdot d\mathbf{l} = i\omega\mu \oint_C \mathbf{H}_s \cdot d\mathbf{l} \quad (23)$$

By Ampere's law, we have $\oint_C \mathbf{H}_s \cdot d\mathbf{l} = I$, the total current on one of the conductors. For the left-hand side, we have

$$\begin{aligned} \oint_C \hat{z} \times \mathbf{E}_s \cdot d\mathbf{l} &= - \oint_C d\mathbf{l} \cdot \hat{z} \times \nabla_s \phi_s \\ &= - \int_S dS \hat{z} \cdot \nabla_s \times \hat{z} \times \nabla_s \phi_s. \end{aligned} \quad (24)$$

The second equality follows from Stokes' theorem. Using $\hat{z} \cdot \nabla_s \times \hat{z} \times \nabla_s \phi_s = \nabla_s^2 \phi_s = 0$, we have

$$\oint_C \hat{z} \times \mathbf{E}_s \cdot d\mathbf{l} = - \int_S dS \nabla_s^2 \phi_s \quad (25)$$

$\nabla_s^2 \phi_s = -\rho/\epsilon$, the right-hand side of Eq. (25) evaluates to Q/ϵ , where Q is the total charge per unit length on one conductor. Hence, Eq. (25) becomes

$$\oint_C \hat{z} \times \mathbf{E}_s \cdot d\mathbf{l} = \frac{Q}{\epsilon} \quad (26)$$

Therefore, Eq. (23) becomes

$$\frac{d}{dz} Q = i\omega\mu\epsilon I \quad (27)$$

Since the transverse field is purely static, we can define $Q = CV$, where C is the capacitance per unit length and $V = V_1 - V_2$. Hence, Eq. (27) becomes

$$\frac{d}{dz} V = i\omega \frac{\mu\epsilon}{C} I \quad (28)$$

Since $\mu\epsilon/C$ has the dimension of henries per meter, we can define $L = \mu\epsilon/C$, an inductance per unit length, and Eq. (28) becomes

$$\frac{dV}{dz} = i\omega LI \quad (29)$$

With manipulations similar to $\hat{z} \times (21)$, we obtain

$$\frac{dI}{dz} = i\omega CV \quad (30)$$

Equations (29) and (30) are the telegraphist equations for a transmission line, which can also be derived from a circuits viewpoint.

Since the fields, and hence the voltage and current, have e^{ikz} dependence, where $k = \omega\sqrt{\mu\epsilon} = \omega\sqrt{LC}$, we deduce either from Eq. (29) or (30) that

$$\frac{V}{I} = \sqrt{\frac{L}{C}} = Z_0 \quad (31)$$

if the wave is propagating only in the positive z direction. Z_0 is also known as the *characteristic impedance* of a transmission line. Since C and L are dependent on the geometry of the transmission line, Z_0 is a geometry-dependent impedance. This is unlike η , the intrinsic impedance. It can be easily shown from Eqs. (29) and (30) that

$$\frac{d^2 V}{dz^2} + \omega^2 LCV = 0 \quad (32)$$

$$\frac{d^2 I}{dz^2} + \omega^2 LCI = 0 \quad (33)$$

which are one-dimensional scalar wave equations, whose solutions are given by

$$V(z) = V^+ e^{ikz} + V^- e^{-ikz} \quad (34)$$

$$I(z) = I^+ e^{ikz} - I^- e^{-ikz} \quad (35)$$

These constants are related through $V^+/I^+ = V^-/I^- = Z_0$. The velocity of the wave on the line is given by

$$v = \frac{1}{\sqrt{\mu\epsilon}} = \frac{1}{\sqrt{LC}} \quad (36)$$

The time-average energy stored per unit length in a transmission line for a single propagating wave is given by

$$\langle W_e \rangle = \frac{1}{4} \epsilon \int_S \mathbf{E}_s \cdot \mathbf{E}_s^* dS = \frac{1}{4} \epsilon \int_S (\nabla_s \phi_s)^2 dS \quad (37)$$

$$\langle W_m \rangle = \frac{1}{4} \mu \int_S \mathbf{H}_s \cdot \mathbf{H}_s^* dS = \frac{1}{4} \mu \int_S (\nabla_s \psi_s)^2 dS \quad (38)$$

where $\langle W_e \rangle$ and $\langle W_m \rangle$ are the time average energy stored in the electric field and the magnetic field, respectively. Using the fact that $\nabla \cdot (\phi \nabla \phi) = (\nabla \phi)^2 + \phi \nabla^2 \phi$, we can write

$$\langle W_e \rangle = \frac{1}{4} \epsilon \oint_{C_1+C_2} \phi \frac{\partial}{\partial n} \phi dl = \frac{1}{4} (V_1 - V_2) Q = \frac{1}{4} CV^2 \quad (39)$$

where $V = V_1 - V_2$, $Q = CV$. This equation could also be derived from circuits theory. As we have shown before, $|\mathbf{E}_s| = \sqrt{\frac{\epsilon}{\mu}} |H_s|$; hence the time-average energy stored in the magnetic field is

$$\langle W_m \rangle = \langle W_e \rangle = \frac{1}{4} CV^2 \quad (40)$$

Since $V^2 = Z_0^2 I^2 = \frac{L}{C} I^2$, and $\mu\epsilon = LC$, we can also write

$$\langle W_m \rangle = \frac{1}{4} LI^2 \quad (41)$$

Equation (41) can also be established by circuit theory. It also establishes our definition of L as an inductance per unit length.

The time-average power flow down a transmission line is given by

$$\langle P \rangle = \frac{1}{2} \Re \int_S dS \hat{z} \cdot (\mathbf{E}_s \times \mathbf{H}_s^*) \quad (42)$$

Since $\mathbf{H}_s = \sqrt{(\epsilon/\mu)} \hat{z} \times \mathbf{E}_s$ from Eq. (22), we have

$$\langle P \rangle = \frac{1}{2} \sqrt{\frac{\epsilon}{\mu}} \int_S dS |\mathbf{E}_s|^2 = 2v \langle W_e \rangle = v \langle W_e + W_m \rangle \quad (43)$$

Hence, the time-average stored energy $\langle W_e + W_m \rangle$ moving at velocity v contributes to power flow. Equation (43) is also valid for non-TEM modes and more general (but loss-

less) situations, if v is replaced by v_g , the *group velocity*. The group velocity is defined as $v_g = (dk_z/d\omega)^{-1}$. In the TEM case, $k_z = k = \omega\sqrt{\mu\epsilon}$, so that $v_g = v$. The group velocity is the velocity of energy propagation in a waveguide, and it is also the signal velocity. Equations (29) and (30) can be also derived from a simple circuits model assuming distributed inductances and capacitances along the line.

2.3. Lossy Transmission Lines

To characterize a lossy transmission line, we replace the series impedance per unit length $-i\omega L$ by $-i\omega L + R$, and the shunt admittance per unit length $-i\omega C$ by $-i\omega C + G$, where R is the series resistance per unit length in the conductor, while G is the shunt conductance per unit length in the dielectric insulator. The series resistance results from the finite conductivity of the (imperfect) conductors, while the shunt conductance results from the imperfect insulation of the dielectrics. Usually, the series resistance is a much more important attenuation factor than the shunt conductance.

Figure 2 illustrates the distributed circuit model for the transmission line. Together with L and C , R and G constitute the *primary* transmission-line constants. In contrast, the velocity of propagation v and the characteristic impedance of the line Z_0 are usually called *secondary* constants. The telegraphist equations then become

$$\frac{dV}{dz} = (i\omega L - R)I = -ZI \quad (44)$$

$$\frac{dI}{dz} = (i\omega C - G)V = -YV \quad (45)$$

The characteristic impedance is now

$$Z_0 = \sqrt{\frac{Z}{Y}} \quad (46)$$

while the propagation constant becomes

$$k^2 = -(i\omega L - R)(i\omega C - G), \quad (47)$$

$$k = \omega \sqrt{LC \left(1 + \frac{iR}{\omega L}\right) \left(1 + \frac{iG}{\omega C}\right)}$$

Hence k is complex and the wave e^{ikz} is attenuating. Moreover, with loss, even if the primary constants are independent of frequency, the secondary parameters will be frequency-dependent.

Note that, strictly speaking, when we have a lossy transmission line due to conductor losses, a pure TEM wave cannot exist. This is because the axial current flow meets a resistance, and hence, an axial component of the electric field is necessary now to drive a current in the conductor. Therefore, the field is only quasi-TEM. However, the conductor loss can be regarded as a small perturbation of the perfect conductor case, and the electromagnetic field in the lossy line will not differ much from that of a lossless case.

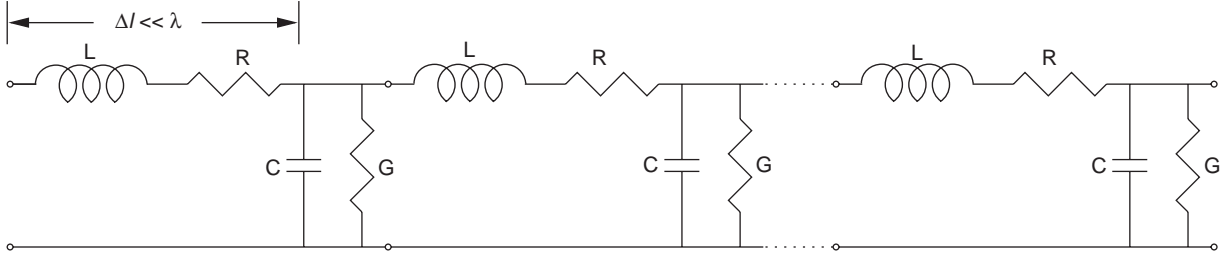


Figure 2. Distributed equivalent circuit representation of a transmission line supporting the TEM mode. Each section Δl is modeled by a resistance R per unit length (Ω/m), an inductance L per unit length (H/m), a capacitance C per unit length (F/m), and a conductance G per unit length (G/m).

The shunt conductance G in a lossy line can be found as follows. If the capacitance per unit length between two conductors is given by the formula

$$C = \epsilon K \quad (48)$$

where K is a geometry-dependent factor, the shunt admittance would be given by $Y = -i\omega C = -i\omega\epsilon K$. If now the dielectric medium is lossy so that $\epsilon = \epsilon' + (i\sigma/\omega)$, then the shunt admittance is given by

$$Y = -i\omega\epsilon'K + \sigma K \quad (49)$$

Hence, we identify $G = \sigma K$. Note that the derivations in Eqs. (20)–(30) hold true even if ϵ is complex. For this reason, Y in Eq. (33) is exact.

The series resistance R can be found by calculating the resistance of the conductor in a perturbative manner when it is lossy. The skin effect will confine the current to flow only on the surface of the conductor. Since the skin depth in a conductor is $\delta = \sqrt{2/\omega\mu\sigma}$, the current is confined to flow in a thinner region at higher frequencies, hence increasing this series resistance.

Another way of calculating transmission-line loss is via a perturbation argument and the use of energy conservation. If a transmission line is lossy such that $k = k' + ik''$, and

$$V, I \sim e^{ik'z - k''z} \quad (50)$$

then, the power flow in a line, which is proportional to $|V|^2$ or $|I|^2$, is

$$P \sim e^{-2k''z} \quad (51)$$

By energy conservation, we obtain

$$\frac{dP}{dz} = -P_d = -2k''P \quad (52)$$

where P_d is the power dissipated per unit length on the line. Therefore, the attenuation constant k'' can be derived to be

$$k'' = \frac{P_d}{2P} \quad (53)$$

if we know P_d . We can assume P to be close to that of a lossless line in using Eq. (53) in a perturbative concept.

2.4. Distributed Parameters

From Eqs. (34) and (35), the impedance of a lossless transmission line at any given point is given by

$$Z(z) = \frac{V(z)}{I(z)} = Z_0 \frac{e^{ikz} + \Gamma_0 e^{-ikz}}{e^{ikz} - \Gamma_0 e^{-ikz}} \quad (54)$$

where $\Gamma_0 = V^-/V^+$ is the reflection coefficient, which can be found by using a known value of $Z(z)$ at some point on the line. For instance, if the line is terminated with a load Z_L at $z = 0$, then $Z(0) = Z_L$ and, substituting in Eq. (54), we have

$$\Gamma_0 = \frac{Z_L - Z_0}{Z_L + Z_0} \quad (55)$$

Furthermore, the line impedance can be written at any location along the line

$$Z(z) = Z_0 \frac{Z_L + iZ_0 \tan \beta z}{Z_0 + iZ_L \tan \beta z} \quad (56)$$

with $z < 0$, while the reflection coefficient everywhere along the line (generalized reflection coefficient) $\Gamma(z)$ is given by Eq. (55) with Z_L substituted by $Z(z)$ above. The representation of the variation of the normalized impedance along the line with the angle of the generalized reflection coefficient, that is, the relation

$$\Gamma = \frac{Z - Z_0}{Z + Z_0}$$

for all Z , such that $\text{Re}[Z] \geq 0$, in the Γ plane, is called the *Smith chart* [17,18]. It provides a useful graphical aid to the analysis of transmission-line and matching problems that are otherwise cumbersome if treated in analytical form.

The addition of two waves, V^+ and V^- , propagating in opposite directions gives rise to a standing-wave pattern along the line. The ratio of the minimum and maximum values of the voltage of the standing-wave pattern defines

the *voltage standing-wave ratio* (VSWR), given by

$$\text{VSWR} = \frac{1 + |\Gamma_0|}{1 - |\Gamma_0|} \tag{57}$$

Transmission lines are usually designed to maximize transmission and minimize reflection over the frequency band of interest. Therefore, in practical design situations, we have $\text{VSWR} \approx 1$.

2.5. Transformation Matrices

In a circuit, a transmission line may interact with other transmission lines, either by design, as in microwave integrated circuits (MICs), or as a result of undesired effects, as in closely packed, high-frequency circuit interconnections [19,20] on computer boards. We use the term *coupling* when such property is desired, or planned by design [21,22]. Coupled integrated transmission lines form the basic building blocks for a series of passive microwave elements such as filters and directional couplers [15]. In the case of an undesired interaction, we usually employ the term *crossstalk*. In both cases, one can analyze the N -transmission-line problem as a general microwave circuit consists of many ports. A convenient way to characterize an N -port network is to describe the network in terms of *impedance matrices* or *admittance matrices*. For example, if the N -port network can be characterized by a voltage-current pair at each port (flowing into), then a column vector of voltages can be defined and also a column vector of currents. We can express a relationship between the voltages and the currents as

$$\mathbf{V} = \begin{bmatrix} V_1 \\ V_2 \\ \vdots \\ V_N \end{bmatrix} = \begin{bmatrix} Z_{11} & Z_{12} & \cdots & Z_{1N} \\ Z_{21} & Z_{22} & \cdots & Z_{2N} \\ \vdots & \vdots & \ddots & \vdots \\ Z_{N1} & Z_{N2} & \cdots & Z_{NN} \end{bmatrix} \begin{bmatrix} I_1 \\ I_2 \\ \vdots \\ I_N \end{bmatrix} = \bar{\mathbf{Z}} \cdot \mathbf{I} \tag{58}$$

By the same token, we can express

$$\mathbf{I} = \bar{\mathbf{Y}} \cdot \mathbf{V} \tag{59}$$

where $\bar{\mathbf{Y}}$ is the admittance matrix, which define the Y parameters. For reciprocal circuits, it can be shown that $\bar{\mathbf{Z}}$ and $\bar{\mathbf{Y}}$ are symmetric matrices, so that there are only three independent matrix elements in a two-port network. For lossless circuits, it can be shown that these matrices have pure imaginary elements.

For high frequencies, however, it is more pertinent to think about waves. Then, at each port, we can define an incident and a reflected wave. For instance, we can define an incident voltage wave V^+ and a reflected voltage wave V^- . A relationship can then be express between the reflected waves at all the ports to the incident waves at all

the ports. This constitutes the *scattering matrix*:

$$\mathbf{V} = \begin{bmatrix} V_1^- \\ V_2^- \\ \vdots \\ V_N^- \end{bmatrix} = \begin{bmatrix} S_{11} & S_{12} & \cdots & S_{1N} \\ S_{21} & S_{22} & \cdots & S_{2N} \\ \vdots & \vdots & \ddots & \vdots \\ S_{N1} & S_{N2} & \cdots & S_{NN} \end{bmatrix} \begin{bmatrix} V_1^+ \\ V_2^+ \\ \vdots \\ V_N^+ \end{bmatrix} = \bar{\mathbf{S}} \cdot \mathbf{V}^+ \tag{60}$$

It can be proved that the matrix $\bar{\mathbf{S}}$ has to be symmetric for reciprocal circuits, and that it has to be unitary if the circuit is lossless. The S_{ij} are called *scattering* or simply *S-parameters*. S parameters are very important in the characterization of a microwave circuits. CAD (computer-aided design) packages for the analysis of complex networks are usually based on the availability of S parameters (or Y parameters) for each of their building blocks (such as the transmission lines).

When one needs to cascade a series of two-port networks, it is more convenient to work with chain matrices or transmission matrices. A voltage-current transmission matrix, usually called an *ABCD matrix*, relates the voltage and current at one port to the voltage and current at the second port.

Written explicitly, we have

$$\begin{bmatrix} V_1 \\ I_1 \end{bmatrix} = \begin{bmatrix} A_1 & B_1 \\ C_1 & D_1 \end{bmatrix} \begin{bmatrix} V_2 \\ I_2 \end{bmatrix} \tag{61}$$

Notice that in the convention for the *ABCD* matrix, the current at port 2 is flowing out of the port rather than into the port. In this manner, if we have a second transmission matrix of a second network that relates V_2, I_2 to V_3, I_3 namely

$$\begin{bmatrix} V_2 \\ I_2 \end{bmatrix} = \begin{bmatrix} A_2 & B_2 \\ C_2 & D_2 \end{bmatrix} \begin{bmatrix} V_3 \\ I_3 \end{bmatrix} \tag{62}$$

then, when these two networks are cascaded together, the resultant transmission matrix is the product of the two matrices

$$\begin{bmatrix} V_2 \\ I_2 \end{bmatrix} = \begin{bmatrix} A_1 & B_1 \\ C_1 & D_1 \end{bmatrix} \begin{bmatrix} A_2 & B_2 \\ C_2 & D_2 \end{bmatrix} \begin{bmatrix} V_3 \\ I_3 \end{bmatrix} \tag{63}$$

For a two port network, it can be shown that

$$A = \frac{Z_{11}}{Z_{12}}, \quad B = \frac{Z_{11}Z_{22} - Z_{12}^2}{Z_{12}} \tag{64a}$$

$$C = \frac{1}{Z_{12}}, \quad D = \frac{Z_{22}}{Z_{12}} \tag{64b}$$

for a reciprocal network. It is also readily verified that

$$AD - BC = 1 \tag{65}$$

for this case. Hence, the determinant of a chain matrix is always 1 for a reciprocal network.

3. HOLLOW WAVEGUIDES

In this section, we will focus on a typical class of high-frequency transmission line, the hollow waveguide [10,23]. Hollow waveguides are specially useful in low-loss and high-power systems, such as the feeding system of an antenna. Hollow waveguides do not support a TEM mode, and the analysis of the previous section deriving the circuit parameters (line and voltage) along the line in terms of the TEM fields does not apply in this case. The absence of a TEM mode in a hollow waveguide can be proved by contradiction as follows. If we assume that it does, then the magnetic field $\mathbf{H} = \mathbf{H}_s$ has to end on itself due to the absence of magnetic charges. It is clear that $\oint_C \mathbf{H}_s \cdot d\mathbf{l} \neq 0$ about any closed contour following the magnetic field lines. This is clearly in violation of Eq. (15) for a TEM mode, which implies that if $\oint \mathbf{H}_s \cdot d\mathbf{l} = 0$ if C does not enclose any conducting current. These two results are contradictory, implying the absence of a TEM mode in a hollow waveguide.

3.1. Rectangular Waveguides

The rectangular waveguide is the most commonly used hollow waveguide. It is illustrated in Fig. 3. By adjusting the aspect ratio, a to b , of the waveguide, one can obtain a good bandwidth for single-mode propagation (the aspect ratio of $\frac{1}{2}$ is used in most practical waveguides). Furthermore, the analysis of this waveguide is the simplest.

3.1.1. TE Modes (H Modes). A TE mode in a rectangular waveguide is characterized by H_z satisfying Eq. (13) with the requisite Neumann boundary condition. An H_z that will satisfy Eq. (13) with $(\partial/\partial n)H_z = 0$ on the waveguide wall is

$$H_z = H_0 \cos\left(\frac{m\pi}{a} x\right) \cos\left(\frac{n\pi}{b} y\right) e^{ik_z z} \quad (66)$$

where $k_s^2 = (m\pi/a)^2 + (n\pi/b)^2$, $k_z = \sqrt{k^2 - k_s^2}$. This last relation is called the *dispersion relation*. A dispersion relation gives the propagation constant as function of frequency: $k_z = k_z(\omega)$. The transverse fields can be found using Eqs. (9) and (10). The mode becomes *evanescent* or

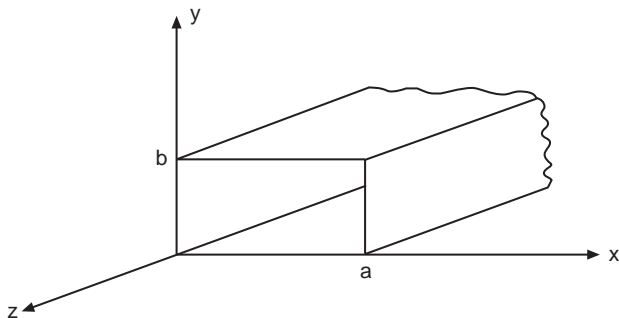


Figure 3. Geometry of a rectangular hollow waveguide.

nonpropagating when $k_s^2 > k^2$, that is, when k_z becomes imaginary. Since $k^2 = \omega^2 \mu \epsilon$, the *cutoff frequency* (i.e., the frequency below which the mode is evanescent) is given by

$$\omega_{mn,c} = \frac{1}{\sqrt{\mu \epsilon}} \left[\left(\frac{m\pi}{a} \right)^2 + \left(\frac{n\pi}{b} \right)^2 \right]^{1/2} \quad (67)$$

The corresponding mode is usually labeled as TE_{mn} (or H_{mn}) mode. Note that this is in marked contrast for the case of TEM propagation. For the TEM mode, no cutoff frequency exists. The wavelength of a wave at ω_c in the medium denoted by μ , ϵ is the cutoff wavelength:

$$\lambda_{mn,c} = \frac{2}{[(m/a)^2 + (n/b)^2]^{1/2}} \quad (68)$$

In waveguide conventions, a is assumed larger than b . Then, the dominant mode (fundamental mode) with the lowest cutoff frequency is the $m=1$, $n=0$ mode, also known as the TE_{10} mode (or H_{10} mode). The TE_{00} mode is nonexistent because, otherwise, $k_s = 0$, and \mathbf{E}_s and \mathbf{H}_s would diverge from Eqs. (9) and (10) when $k_s \rightarrow 0$. The waveguide usually operates at those frequencies where only the fundamental mode can propagate.

3.1.2. TM Modes (E Modes). A TM mode in a rectangular waveguide is characterized by E_z satisfying Eq. (14) with the requisite Dirichlet boundary condition. An E_z that will satisfy Eq. (14) with $E_z = 0$ on the waveguide wall is

$$E_z = E_0 \sin\left(\frac{m\pi}{a} x\right) \sin\left(\frac{n\pi}{b} y\right) e^{ik_z z} \quad (69)$$

where $k_s^2 = (m\pi/a)^2 + (n\pi/b)^2$, $k_z = \sqrt{k^2 - k_s^2}$. The TM_{mn} mode has the same cutoff frequency as the TE_{mn} mode. However, when either $m=0$, or $n=0$, the mode does not exist since $E_z = 0$ then. Therefore, the lowest TM mode is the TM_{11} mode with a cutoff frequency above that of the TE_{10} mode. Given the z components of the fields, all other field components of a waveguide can be derived.

3.2. Circular Waveguides

Certain modes of a circular waveguide have less attenuation from wall loss compared to a rectangular waveguide. Hence, circular waveguides are sometimes preferred over a rectangular waveguide. The geometry of a circular hollow waveguide is illustrated in Fig. 4.

3.2.1. TE Modes (H Modes). The E_z component of a TE mode satisfies Eq. (13) in cylindrical coordinates

$$\left[\frac{1}{\rho} \frac{\partial}{\partial \rho} \rho \frac{\partial}{\partial \rho} + \frac{1}{\rho^2} \frac{\partial^2}{\partial \phi^2} + k_s^2 \right] H_z = 0 \quad (70)$$

with the boundary condition that $(\partial/\partial \rho)H_z = 0$, $\rho = a$, where a is the radius of the waveguide. If we assume that H_z has $e^{\pm in\phi}$, $\sin n\phi$ or $\cos n\phi$ dependence, where n is an integer, we can replace $\partial^2/\partial \phi^2$ by $-n^2$. The solution of

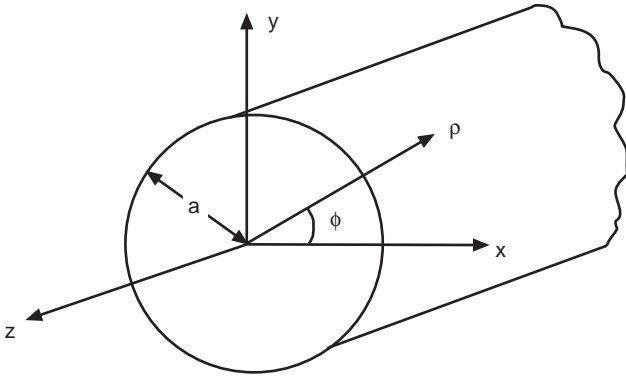


Figure 4. Geometry of a cylindrical hollow waveguide.

Eq. (70) then becomes

$$H_z = H_0 J_n(k_s \rho) e^{\pm i n \phi + i k_z z} \tag{71}$$

where J_n is the Bessel function. We require that $(\partial/\partial\rho)H_z = 0$ at $\rho = a$, implying that

$$J'_n(k_s a) = 0 \tag{72}$$

with $k_z = \sqrt{k^2 - k_s^2}$. If the m th zero of $J'_n(x)$ is defined to be β_{nm} such that $J'_n(\beta_{nm}) = 0$, then the values of possible k_s are

$$k_s = \frac{\beta_{nm}}{a} \tag{73}$$

The subscript n denotes the orders of the Bessel function $J_n(x)$ and the circular harmonic $e^{\pm i n \phi}$. The subscript m denotes the m th zero of $J'_n(x)$ discounting the zero at the origin. The corresponding mode is usually denoted as the TE_{nm} mode. Cutoff occurs when $k = \omega \sqrt{\mu\epsilon} < k_s$. From the tabulated data for β_{nm} , it follows that the TE_{11} modes corresponding to the first zero of $J'_1(x)$ have the lowest cutoff frequency. The cutoff frequency for the TE_{nm} mode is given by

$$\omega_{nm,c} = \frac{1}{\sqrt{\mu\epsilon}} \frac{\beta_{nm}}{a} \tag{74}$$

and the corresponding cutoff wavelength is

$$\lambda_{nm,c} = \frac{2\pi}{\beta_{nm}} a \tag{75}$$

3.2.2. TM Modes (E Modes). Similar to a TE mode, the E_z component of a TM mode has $e^{\pm i n \phi}$ dependence, satisfying the equation

$$\left[\frac{1}{\rho} \frac{\partial}{\partial \rho} \rho \frac{\partial}{\partial \rho} - \frac{n^2}{\rho^2} + k_s^2 \right] E_z = 0 \tag{76}$$

with the boundary condition $E_z(\rho = a) = 0$. Hence

$$E_z = E_0 J_n(k_s \rho) e^{\pm i n \phi + i k_z z} \tag{77}$$

with $J_n(k_s a) = 0$. If we denote the m th zero of $J_n(x)$ by α_{nm} , then k_s has possible values of

$$k_s = \frac{\alpha_{nm}}{a} \tag{78}$$

where the subscript n denotes the order of the Bessel function $J_n(x)$ and the subscript m denotes the m th zero of $J_n(x)$, discounting the zero at the origin. The corresponding mode is known as the TM_{nm} mode. The cutoff frequency of the TM_{nm} mode is given by

$$\omega_{nm,c} = \frac{1}{\sqrt{\mu\epsilon}} \frac{\alpha_{nm}}{a} \tag{79}$$

and the corresponding cutoff wavelength is

$$\lambda_{nm,c} = \frac{2\pi}{\alpha_{nm}} a \tag{80}$$

From the tabulated data for α_{nm} , it follows that the lowest TM mode is the TM_{01} mode, but it has a higher cutoff frequency compared to the TE_{11} mode.

It can also be shown that the TE_{01} mode has the lowest loss at high frequencies. The TE_{01} is axially symmetric with $\mathbf{E} = \phi \mathbf{E}_\phi$. An interesting property of this mode is that, contrary to other modes, the loss decreases monotonically as frequency increases.

The transverse field components of a circular waveguide are easily obtained given the axial components. One disadvantage of circular waveguides is that, because of its circular symmetry, the wave polarization on the transversal plane may change as the wave propagates, as a result of small perturbations. One way to combat this problem is to employ elliptical waveguides [24].

3.3. Other Closed Waveguides

If a metallic waveguide has an arbitrary cross section whose shape does not fall on any of the curvilinear coordinates, one has, in general, to resort to numerical techniques to find the modes and dispersion curves. These will be discussed later. Among these other waveguides, ridge waveguides are commonly used [25,26]. They are attractive because the frequency range of their dominant mode exceeds that of a rectangular waveguide of same external dimensions (the cutoff is lowered). The tradeoff is for an increased loss from the walls.

When a uniform waveguide is filled with inhomogeneous materials [27], the guided modes of the structure cannot be decomposed into TE and TM waves, except for some very special cases. In other words, the E_z and H_z components of the fields are always coupled together. Such modes are also called the *hybrid modes*. This coupling can be shown from Maxwell's equations [10]. The fact that the E_z and H_z waves are in general coupled at a dielectric interface is also known as the *depolarization effect*.

In general, inhomogeneous filled waveguides can be used to make variable phase shifters and attenuators. If the inhomogeneity filling the waveguide is nonreciprocal (like ferrite), then isolators, gyrators, and attenuators can be made.

An example of inhomogeneous filled waveguide is the dielectric-slab-loaded waveguide. The dispersion relation for this structure can be easily derived using the transverse resonance condition [10].

4. OPEN WAVEGUIDES

In an open waveguide [28–32] a wave is guided along a structure, but the field is not enclosed completely in the structure—the field extends to infinity. However, the field decays exponentially away from the guiding structure; hence, the energy of the wave is still localized around the guiding structure. The guiding structure is often filled with inhomogeneous medium. Therefore, many properties of inhomogeneously filled waveguides are also true in open, inhomogeneously filled waveguides.

4.1. Dielectric Waveguides

An example of an open waveguide is a dielectric slab waveguide. The waveguide is made with dielectric coating on a ground plane, or in the case of optical thin-film waveguides, it is a coating of an optically more dense medium on top of an optically less dense substrate, as illustrated in Fig. 5.

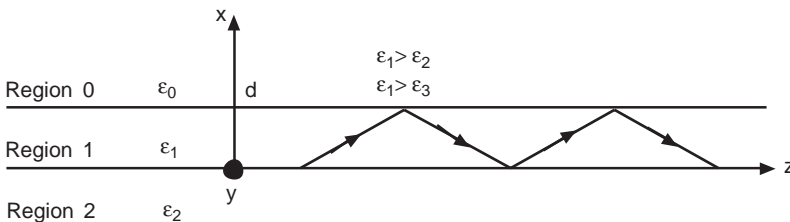
Because of the symmetry of the geometry, we can decompose the field inside such a waveguide into TM and TE types [33]. The mode is guided by total internal reflection. This is possible only if $\epsilon_1 > \epsilon_0$ and $\epsilon_1 > \epsilon_2$. At total internal reflection, the fields in regions 0 and 2 are evanescent, and hence they decay exponentially away from the structure. Therefore, most of the energy of the mode is still trapped and localized in the vicinity of the structure.

If a TM wave is in a dielectric slab, we can write the field in region 1 as

$$\mathbf{H}_1 = \hat{y}[A_1 e^{ik_{1x}x} + B_1 e^{-ik_{1x}x}]e^{ik_z z} \quad (81)$$

Equation (1) has the physical meaning that the wave in region 1 is representable as bouncing waves. At $x = 0$, the upgoing wave is the reflection of the downgoing wave; hence, we have

$$A_1 = R_{12}^{\text{TM}} B_1 \quad (82)$$



where R_{12}^{TM} is the TM reflection coefficient at the 1–2 interface. If there are subsurface layers, R_{12}^{TM} could be the generalized reflection coefficient that includes subsurface reflections. Otherwise, it is just the single interface, Fresnel reflection coefficient for a TM wave. At the upper interface at $x = d$, we require that the downgoing wave be a reflection of the upgoing wave:

$$B_1 e^{-ik_{1x}d} = R_{10}^{\text{TM}} e^{ik_{1x}d} A_1 \quad (83)$$

For nontrivial A_1 and B_1 , Eqs. (82) and (83) imply that

$$1 - R_{10}^{\text{TM}} R_{12}^{\text{TM}} e^{2ik_{1x}d} = 0 \quad (84)$$

This is the guidance condition, sometimes known as the transverse resonance condition for TM modes in a dielectric slab, with

$$R_{ij}^{\text{TM}} = \frac{\epsilon_j k_{ix} - \epsilon_i k_{jx}}{\epsilon_j k_{ix} + \epsilon_i k_{jx}}, \quad k_{ix} = \sqrt{k_i^2 - k_z^2} \quad (85)$$

Because of Eq. (85), the guidance condition expressed by Eq. (84) can be expressed entirely as a function of k_z . We can solve Eq. (84) either graphically or numerically on a computer. Once the value of k_z that satisfies Eq. (84) is found, it can be used in Eq. (82) or (83) to find a relationship between A_1 and B_1 . The fields in region 0 and 2 can be found easily:

$$\mathbf{H}_0 = \hat{y} T_{10}^{\text{TM}} A_1 e^{ik_{0x}(x-d) + ik_z z} \quad (86a)$$

$$\mathbf{H}_2 = \hat{y} T_{12}^{\text{TM}} B_1 e^{-ik_{2x}x + ik_z z} \quad (86b)$$

In other words, the field in region 0 is a consequence of the transmission of the upgoing wave in region 1, while the field in region 2 is a consequence of the transmission of the downgoing wave in region 1. In the above, T_{ij} is a transmission coefficient with

$$T_{ij}^{\text{TM}} = 1 + R_{ij}^{\text{TM}} \quad (87)$$

In order for a mode to be trapped, the field has to decay exponentially in the x direction. Therefore, k_{0x} and k_{2x} have to be purely imaginary. In other words, we can find the values of k_z for guidance only in the ranges $k_z > k_0$ and $k_z > k_2$.

For a symmetric waveguide where regions 0 and 2 are the same, the first few modes of the waveguides are as sketched in Fig. 6. These modes are, in general, better

Figure 5. Geometry of a dielectric slab waveguide. The electromagnetic field is guided by total internal reflection. This is possible only if $\epsilon_1 > \epsilon_2$ and $\epsilon_1 > \epsilon_3$.

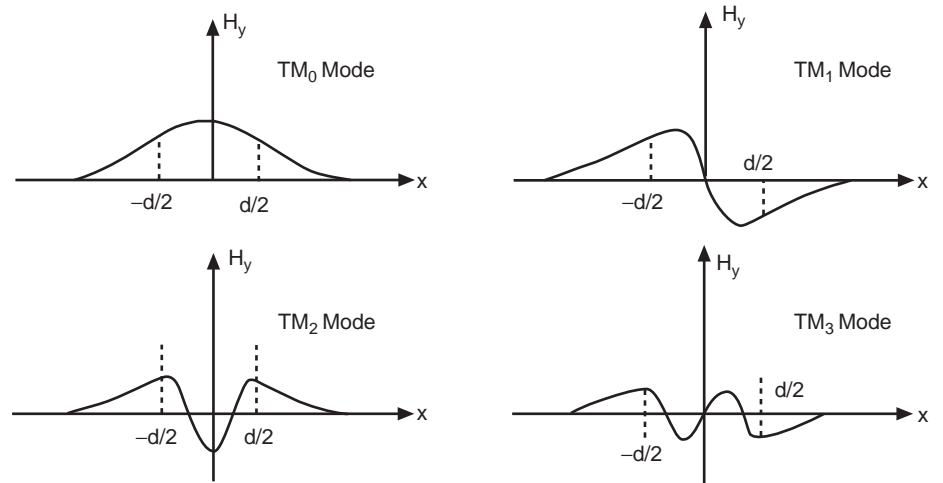


Figure 6. Field distribution for different modes in a dielectric slab waveguide. The amplitude scale is arbitrary. The TM_0 has no cutoff frequency, but the other modes have a finite cutoff frequency.

trapped when the contrast is high between region 1 and regions 0 and 2, or when the frequency is high. We can study the guidance of a TE mode that is the dual of a TM mode in a similar fashion.

By a further manipulation of Eq. (84), and using the definition of Fresnel reflection coefficients, Eq. (84) can be written as

$$\alpha_{0x} \frac{d}{2} = \frac{\varepsilon_0}{\varepsilon_1} k_{1x} \frac{d}{2} \tan\left(\frac{k_{1x}d - m\pi}{2}\right) \quad (88)$$

where $\alpha_{0x} = \sqrt{k_z^2 - k_0^2}$, $k_{1x} = \sqrt{k_1^2 - k_z^2}$, and $m = 1, 2, 3, 4, \dots$. The left-hand side of Eq. (88) can be expressed in terms of the $k_{1x}d$ variable

$$\frac{d}{2} \sqrt{k_z^2 - k_0^2} = \sqrt{(k_1^2 - k_0^2) \left(\frac{d}{2}\right)^2 - \left(\frac{k_{1x}d}{2}\right)^2} \quad (89)$$

which is the equation of a circle. Equation (88) can hence be solved graphically by plotting both sides of Eq. (88) as a function of $k_{1x}d$.

A mode in a dielectric has a part of its energy outside the waveguide and inside the waveguide. Hence, the group velocity of the mode is between that of the slab region and the outer region. When the frequency is very low, the mode is weakly evanescent outside the dielectric slab and the group velocity of a mode is closer to that of the outer region because most of the energy of the mode is outside the waveguide. When the frequency is high, the mode is strongly evanescent outside and most of the energy of the mode is trapped inside the slab. Hence, the group velocity of the mode is close to that of the dielectric slab.

The TM_0 mode has no cutoff, since continuity of the slope and field amplitude can be satisfied for all frequencies, and yet the field is evanescent outside. This is not true of the higher-order modes. For high frequencies, the higher-order modes are well trapped inside the dielectric waveguide. When the frequency is lowered, however, the field may cease to be evanescent outside the dielectric

slab. At the frequency when the field becomes constant outside, we have the cutoff. At frequencies lower than the cutoff frequency, the mode leaks energy to outside the slab, it becomes a leaky mode and is not guided at all.

Many other configurations of dielectric waveguides are possible. Dielectric waveguides found many applications in the millimeter-wave and optical frequency ranges. One problem of these waveguides is the radiation loss incurred at bends and discontinuities. This can be minimized by utilizing a higher dielectric constant, but at the expense of a much smaller size of the structures, which leads to manufacturing problems. Analytical solutions in general are not available for these structures, and a numerical analysis is necessary to find the modes and dispersion relations. Moreover, in these structures, the TE and TM modes are coupled by the boundary conditions at the dielectric boundaries. For this reason, none of the modes are strictly TE or TM, and the *EH* notation is used to denote a mode whose TE component dominates over its TM component, and vice versa for the *HE* notation.

A very popular geometry of dielectric waveguides is the circular dielectric waveguide, which is discussed next.

4.2. Circular Dielectric Waveguide

The geometry of a circular dielectric waveguide is illustrated in Fig. 7. An optical fiber is a kind of circular dielectric waveguide. Usually, an optical fiber has a protective cladding as well. In the ensuing analysis, we will ignore the protective cladding, letting $b \rightarrow \infty$.

In order for a mode to be guided, we require that $\varepsilon_1\mu_1 > \varepsilon_2\mu_2$. In other words, the light velocity in the core region has to be slower than the light velocity in the cladding. The field outside the core region is evanescent for a guided mode. Therefore, letting $b \rightarrow \infty$ affects the guided mode slightly, especially if the mode is tightly bound to the core; hence, it is a good approximation.

In the optical fiber modes, except for the axisymmetric modes, the TE and TM fields are coupled to each other by the boundary conditions as in an inhomogeneously filled waveguide. The z components of the field are solutions to

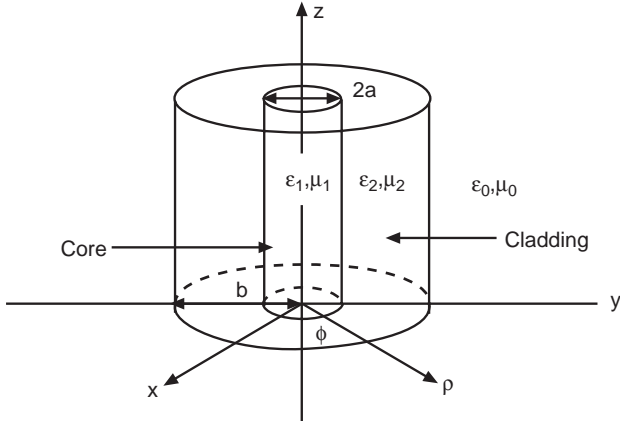


Figure 7. Geometry of a circular dielectric waveguide. To obtain a guided mode, the dielectric constant in the core should be greater than in the cladding, $\epsilon_1 > \epsilon_2$. The field is guided by total internal reflection. An optical fiber is an example of circular dielectric waveguide. In this case, the contrast between the dielectric constants ϵ_1 and ϵ_2 is usually very low.

the wave equation in cylindrical coordinates for each of the homogeneous regions.

We will analyze next the circular dielectric waveguide using the weakly guided approximation [34]. The weakly guided approximation is quite useful in analyzing optical fibers, since the dielectric constant contrast from core to cladding is usually very low.

4.3. Weakly Guided Approximation

Starting from Maxwell's equations, we can derive the vector wave equations governing electromagnetic fields in an inhomogeneous waveguide

$$\nabla \times \mu_r^{-1} \nabla \times \mathbf{E} - \omega^2 \mu_0 \epsilon_0 \epsilon_r \mathbf{E} = 0 \quad (90a)$$

$$\nabla \times \epsilon_r^{-1} \nabla \times \mathbf{H} - \omega^2 \mu_0 \epsilon_0 \mu_r \mathbf{H} = 0 \quad (90b)$$

where $\mu_r = \mu(\mathbf{r})/\mu_0 = f_1(\mathbf{r})$, and $\epsilon_r = \epsilon(\mathbf{r})/\epsilon_0 = f_2(\mathbf{r})$. If we find a solution to Eq. (90a), the solution to the dual problem is obtained by letting $\mathbf{E} \rightarrow -\mathbf{H}$, $\mathbf{H} \rightarrow \mathbf{E}$, $\mu_r \rightarrow \epsilon_r$, $\epsilon_r \rightarrow \mu_r$. However, if $f_1(\mathbf{r}) \neq f_2(\mathbf{r})$, the dual problem corresponds to a different waveguide with $\mu_r = f_2(\mathbf{r})$ and $\epsilon_r = f_1(\mathbf{r})$. In order for a dual problem to be itself, we require that $f_1(\mathbf{r}) = f_2(\mathbf{r})$. If this is the case, then a mode and its dual are degenerate. Therefore, we can associate every mode in a waveguide with a dual mode. However, $f_1(\mathbf{r}) = 1$ usually, while $f_2(\mathbf{r}) \neq 1$; therefore, a mode is not exactly degenerate with its dual.

However, in the case of a weakly guided dielectric waveguide, $\epsilon_r \rightarrow 1$; hence, a mode is nearly degenerate with its dual. Furthermore, we can show that the vector nature of the wave is unimportant. If $\mu_r = 1$, we can rewrite Eqs. (90a) and (90b) as

$$\nabla \times \nabla \times \mathbf{E} - \omega^2 \mu_0 \epsilon_0 \epsilon_r \mathbf{E} = 0 \quad (91a)$$

$$\nabla \times \nabla \times \mathbf{H} - (\nabla \ln \epsilon_r) \times \nabla \times \mathbf{H} - \omega^2 \mu_0 \epsilon_0 \epsilon_r \mathbf{H} = 0 \quad (91b)$$

where $\nabla \ln \epsilon_r = \nabla \epsilon_r / \epsilon_r$ is the effect of the polarization charges at the dielectric interface. If the transverse and longitudinal components of Eqs. (91a) and (91b) are extracted, the following equations ensue:

$$\nabla^2 \mathbf{E}_s + \nabla_s [\nabla_s \ln \epsilon_r \cdot \mathbf{E}_s] + k^2 \mathbf{E}_s = 0 \quad (92a)$$

$$\nabla^2 E_z + ik_z (\nabla_s \ln \epsilon_r) \cdot \mathbf{E}_s + k^2 E_z = 0 \quad (92b)$$

$$\nabla^2 \mathbf{H}_s + (\nabla_s \ln \epsilon_r) \times (\nabla_s \times \mathbf{H}_s) + k^2 \mathbf{H}_s = 0 \quad (93a)$$

$$\begin{aligned} \nabla^2 \mathbf{H}_z + (\nabla_s \ln \epsilon_r) \times (\nabla_s \times \mathbf{H}_z) + (\nabla_s \ln \epsilon_r) \\ \times (\hat{z} ik_z \times \mathbf{H}_s) + k^2 \mathbf{H}_z = 0 \end{aligned} \quad (93b)$$

In the limit when $\epsilon_r \rightarrow 1$, and $\omega \rightarrow \infty$, the polarization charge terms in Eqs. (92a) and (93a), which are proportional to the first derivative of the field, can be ignored with respect to the other terms, yielding

$$\nabla^2 \mathbf{E}_s + k^2 \mathbf{E}_s = 0 \quad (94a)$$

$$\nabla^2 \mathbf{H}_s + k^2 \mathbf{H}_s = 0 \quad (94b)$$

In other words, the wave guidance problem by a fiber of weak contrast in the high-frequency limit reduces to a scalar problem.

In the limit when the contrast $\epsilon_r \rightarrow 1$, the wave that propagates in the fiber is a TEM wave where $E_z = 0$. When $\epsilon_r > 1$, we see from Eq. (92b) that $E_z \sim |\mathbf{E}_s|/\omega$. Therefore, when $\omega \rightarrow \infty$, then $|E_z| \ll |\mathbf{E}_s|$. By the same token, $|H_z| \ll |\mathbf{H}_s|$ when $\omega \rightarrow \infty$. Therefore, when the contrast is very low, and the frequency is very high, the mode is quasi-TEM, and $\nabla_s \cdot \mathbf{E}_s \approx 0$ and $\nabla_s \cdot \mathbf{H}_s \approx 0$.

Equations (94a) and (94b) are equivalent to

$$(\nabla^2 + k^2)\phi = 0 \quad (95)$$

where ϕ is either E_x , E_y , H_x or H_y .

For example, if we assume cylindrical geometry, we can let

$$\phi = \begin{cases} AJ_n(k_{1\rho}\rho)e^{in\phi + ik_z z}, & \rho < a \\ BK_n(\alpha_2\rho)e^{in\phi + ik_z z}, & \rho > a \end{cases} \quad (96)$$

The boundary conditions for ϕ at the interface where $k^2 = \omega^2 \mu_0 \epsilon_0 \epsilon_r$ displays a step discontinuity is

$$\phi_1 = \phi_2 \quad (97a)$$

$$\hat{n} \cdot \nabla \phi_1 = \hat{n} \cdot \nabla \phi_2 \quad (97b)$$

These boundary conditions are derivable from Eq. (95) alone.

Imposing these boundary conditions at $\rho = a$ for the weakly guided dielectric waveguide, whose field is given

by Eq. (96), we have

$$AJ_n(k_{1\rho}a) = BK_n(\alpha_2 a) \quad (98a)$$

$$AK_{1\rho}J'_n(k_{1\rho}a) = B\alpha_2 K'_n(\alpha_2 a) \quad (98b)$$

which yields

$$\frac{k_{1\rho}J'_n(k_{1\rho}a)}{J_n(k_{1\rho}a)} = \frac{\alpha_2 K'_n(\alpha_2 a)}{K_n(\alpha_2 a)} \quad (99)$$

Using the recurrence relationship that $J'_n(x) = -J_{n+1}(x) + \frac{n}{x}J_n(x)$, and that $K'_n(x) = -K_{n+1}(x) + \frac{n}{x}K_n(x)$, we can transform this to

$$\frac{k_{1\rho}J_{n+1}(k_{1\rho}a)}{J_n(k_{1\rho}a)} = \frac{\alpha_2 K_{n+1}(\alpha_2 a)}{K_n(\alpha_2 a)} \quad (100)$$

Similarly, using the recurrence relationship that $J'_n(x) = J_{n-1}(x) - (n/x)J_n(x)$, and $K'_n(x) = -K_{n-1}(x) - (n/x)K_n(x)$, we have

$$\frac{k_{1\rho}J_{n-1}(k_{1\rho}a)}{J_n(k_{1\rho}a)} = -\frac{\alpha_2 K_{n-1}(\alpha_2 a)}{K_n(\alpha_2 a)} \quad (101)$$

We can solve Eq. (11) graphically. The modes thus found are collectively designated the LP_{nm} mode. The lowest order mode is the LP_{01} mode (where LP stands for “linearly polarized”). These LP modes can be shown to be a linear combination of the EH and HE modes mentioned before.

The term “weakly guided dielectric waveguide” is a misnomer. When V is large, a mode can be tightly bound as demonstrated by the phase velocity approaching that of a core. Also, E_x and E_y are not independent of each other since $\nabla_s \cdot \mathbf{E}_s = 0$. The same statement applies to H_x and H_y .

5. MICROWAVE INTEGRATED CIRCUITS (MIC) TRANSMISSION LINES

With the advent of integrated circuits at microwave and millimeter-wave frequencies, microwave integrated circuit (MIC) transmission lines have become increasingly important [15]. They are easily integrated with other microwave integrated circuits, and have a low cost and better reproducibility/reliability than do conventional lines. Some examples are shown in Fig. 8. Not presented on this figure but also representative of MICs lines are the stripline and the inverted microstrip line [11]. Along with some configurations of dielectric waveguides for millimeter waves and integrated optics [29,32], such transmission lines belong to a class usually called *planar transmission lines* because the characteristics of these lines can be determined from the dimensions on a single plane.

5.1. Quasi-TEM Approximation

The usual integrated circuits waveguiding structures cannot support a TEM mode (an exception is the stripline, whose design data can be determined exactly from an electrostatic analysis for the TEM mode), for if they do, the

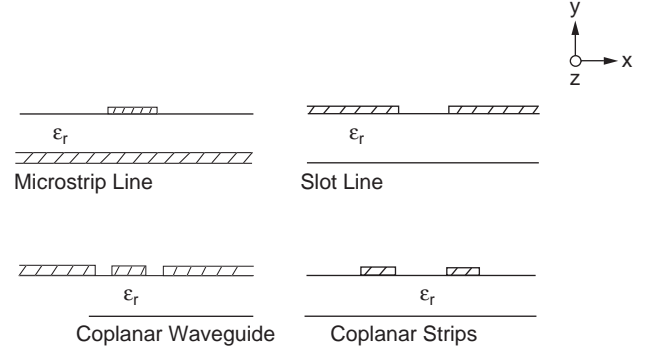


Figure 8. Cross-sectional view of different kinds of microwave integrated circuit (MIC) waveguides.

phase-matching condition will be violated at the interface between the inhomogeneities (i.e, between the two dielectrics). This is because a TEM wave has the same phase velocity of the medium in which the wave is traveling.

However, if the wavelength under consideration is much larger than the transverse structure of the waveguide, we can show that the fundamental mode of such a structure is almost TEM or quasi-TEM. A “fundamental” mode is the mode that is propagating when $\omega \rightarrow 0$ or $\lambda \rightarrow \infty$. The analysis under such assumptions is usually called *quasistatic* analysis.

We can write Maxwell’s equations by separating out the transverse and longitudinal components as

$$\nabla_s \times \mathbf{E}_s = ik\eta \mathbf{H}_z \quad (102)$$

$$\nabla_s \times \mathbf{H}_s = -ik\eta^{-1} \mathbf{E}_z \quad (103)$$

$$\frac{\partial}{\partial z} \hat{z} \times \mathbf{E}_s - \hat{z} \times \nabla_s E_s = ik\eta \mathbf{H}_s \quad (104)$$

$$\frac{\partial}{\partial z} \hat{z} \times \mathbf{H}_s - \hat{z} \times \nabla_s H_z = -ik\eta^{-1} \mathbf{E}_s \quad (105)$$

where $\eta = \sqrt{\mu/\epsilon}$. For a structure whose dominant transverse dimension is much smaller than the wavelength, the transverse variation of the field would be more rapid than the longitudinal variation. The x and y variations will vary on the length scale of δ . To emphasize this fact, we can perform a coordinate stretching transformation by letting

$$x = \delta x', \quad y = \delta y' \quad (106)$$

Under such a coordinate stretching transformation, we obtain

$$\nabla_s \rightarrow \frac{1}{\delta} \nabla'_s \quad (107)$$

Equations (104) and (105) become

$$ik_z \delta \hat{z} \times \mathbf{E}_s - \hat{z} \times \nabla'_s E_z = ik\eta \delta \mathbf{H}_s \quad (108)$$

$$ik_z \delta \hat{z} \times \mathbf{H}_s - \hat{z} \times \nabla'_s H_z = -ik\eta^{-1} \delta \mathbf{E}_s \quad (109)$$

where we have assumed $e^{ik_z z}$ dependence of the field. When $\delta/\lambda \rightarrow 0$, then $k\delta \rightarrow 0$. Since $k_z = \sqrt{k^2 - k_s^2} < k$, we also expect $k_z \delta \rightarrow 0$, when $\delta/\lambda \rightarrow 0$. Therefore, in the long-wavelength limit, we obtain

$$(\mathbf{E}_z, \eta \mathbf{H}_z) \sim O(k\delta)(\mathbf{E}_s, \eta \mathbf{H}_s) \quad (110)$$

In other words, $|E_z| \ll |\mathbf{E}_s|$, $|H_z| \ll |\mathbf{H}_s|$, implying that the field is quasi-TEM. Therefore, we can write Eqs. (102) and (103) as

$$\nabla_s \times \mathbf{E}_s = 0 \quad (111)$$

$$\nabla_s \times \mathbf{H}_s = 0 \quad (112)$$

Taking the divergence of Eqs. (104) and (105) and making use of Eqs. (111) and (112), we have

$$\nabla_s \cdot \epsilon \mathbf{E}_s = 0 \quad (113)$$

$$\nabla_s \cdot \mu \mathbf{H}_s = 0 \quad (114)$$

Consequently, the transverse field of a quasi-TEM mode is essentially static. For this reason, the waveguide can be analyzed as if a TEM mode were propagating on it. We can solve the electrostatic problem to find the line capacitance C of the line. The line inductance L can be obtained by solving the magnetostatic problem. Then, k_z , the axial wavenumber, can be found by

$$k_z = \omega \sqrt{LC} \quad (115)$$

The preceding analysis indicates that when the wavelength is long, the axial variation of the field is slow compared to the transverse variation. The transverse variation of the field has to be such that the field can match the boundary condition on the metallic conductors, which is much smaller in dimension than the wavelength. Hence, the transverse variation of the field must balance itself, resulting in Eqs. (111) to (113), which are the static equations.

5.2. Capacitance and Effective Dielectric Constant of MIC Lines

We shall discuss how the line capacitance of a MIC line, such as a microstrip line, can be found. For other MIC lines, the analysis follows in a similar manner [15]. There is no closed-form solution for such a class of problem. When $\epsilon_r = 1$ (i.e., the conductors are surrounded by homogeneous space and no dielectric interface is present), the structure supports the TEM mode and one may solve such problems by conformal mapping (as in the stripline case) [35]. When $h/w \ll 1$, the problem can be solved by asymptotic matching [36]. However, to get an accurate value of C for all w/h , a numerical analysis is preferable.

To find the line capacitance of the MIC line, one can first solve for the charge distribution on the line. Then, the capacitance can be easily found from the equation $Q = CV$, where Q is the total charge per unit length on the line and V is the voltage applied between the strip and the ground

plane. To find the charge distribution, we can first formulate an integral equation governing the charge distribution, and then solve it by numerical techniques [37]. Approximate closed-form formulas for C_{eff} as a function of line geometry and substrate material are also available [38,39]. A potential ϕ can be defined such that $\mathbf{E}_s = -\nabla_s \phi$ and $\nabla_s^2 \phi = 0$, because \mathbf{E}_s is an electrostatic field in the long-wavelength limit.

To find L , we make use of the fact that if $\epsilon_r = 1$, a pure TEM mode propagates on the MIC line. In this case

$$k_z = k_0 = \omega \sqrt{L_0 C_0} \quad (116)$$

Therefore, L_0 can be found once C_0 , the line capacitance with $\epsilon_r = 1$, is known. C_0 can be also found by solving an integral equation. Since L_0 remains unchanged when $\epsilon_r \neq 1$, we have

$$k_z = \sqrt{\frac{C}{C_0}} k_0 \quad (117)$$

An *effective* relative dielectric constant can be defined such that

$$\epsilon_{\text{eff}} = \frac{C}{C_0} \quad (118)$$

which is a function of frequency. The physical meaning for ϵ_{eff} is simple. It is the dielectric constant with which one can fill the space homogeneously around a MIC line to yield the same line capacitance as the inhomogeneously filled line.

A characteristic impedance can also be defined as

$$Z_0 = \sqrt{\frac{L_0}{C}} = \sqrt{\frac{\mu_0 \epsilon_0}{C_0 C}} = \frac{Z_0^a}{\sqrt{\epsilon_r}} \quad (119)$$

where Z_0^a is the characteristic impedance of the air-filled line.

For the most commonly employed geometries and materials, closed-form empirical formulas for ϵ_{eff} and Z_0 are available for design purposes and easy incorporation into CAD algorithms [39].

5.3. Frequency-Dependent (Full-Wave) Theory of MIC Lines

The quasi-TEM model triumphs in predicting the value of k_z or the phase velocity in the long-wavelength limit. However, k_z is in general frequency-dispersive. To obtain a k_z that is valid at high frequencies as well (above a few GHz), we need to solve the full-wave solution to the MIC line problem. Approximate closed formulas (some essentially empirical formulas, backed up by accurate characterizations) for the frequency-dispersive $\epsilon_{\text{eff}}(\omega)$ (and hence, k_z and C) as a function of the static ϵ_{eff} , geometry, substrate, and frequency are available [39]. These formulas are useful for CAD applications, but have a number of drawbacks, such as being applicable to only a specific class of MIC lines (e.g., those based on alumina substrates) and sometimes requiring accurate static (TEM) data.

On the other hand, numerical methods [37] are the only means of solving the full-wave problem for the general microwave and millimeter-wave transmission-line problem. This is also true for integrated optics waveguides. With the advances in computer technology, these methods have become increasingly important. The most popular numerical methods include the finite-difference and finite-difference time-domain (FD and FDTD) methods, the transmission-line method (TLM), the finite-element method (FEM), the boundary-element method (BEM), the method of lines (MoL), the method of moments (MoM), the beam propagation method (BPM), the effective index method, and the spectral domain approach. There is no such a thing as *the* best universal numerical method available. Each of these methods has its advantages and limitations and is best suited for some given applications. Each has its own variations and improvements. For a discussion of each and example applications, the reader is referred to the texts by Sorrentino [37] and Huang and Kong [40].

BIBLIOGRAPHY

1. H. Hertz, *Electric Waves, Being Researches on the Propagation of Electric Action with Finite Velocity through Space* (transl. D. E. Jones), Macmillan, 1893 and Dover, 1962, New York.
2. J. C. Maxwell, *Electricity and Magnetism*, 1873, p. 385; also in Vol. 2, Section 690, p. 322, Academic Press, New York, 1935.
3. Lord Rayleigh, On the passage of electric waves through tubes, *Phil. Mag.* **43**:125–132 (1897); reprinted in *Collected Papers*, Paper 226, Vol. 4, Cambridge Univ. Press, Cambridge; UK, 1903.
4. A. Sommerfeld, Fortpflanzung elektrodynamischer Wellen an einen zylindrischen Leiter, *Ann. Phys.* **67**(Ser. 3):1223 (1899).
5. D. Hondros and P. Debye, Electromagnetische Wellen an dielectricischen Drähten, *Ann. Phys.* **32**(Ser. 4): 465 (1910).
6. K. S. Packard, The origin of waveguides: A case of multiple rediscovery, *IEEE Trans. Microwave Theory Tech.* **32**(9):961–969 (1984).
7. R. M. Barrett, Microwave printed circuits—the early years, *IEEE Trans. Microwave Theory Tech.* **32**(9):983–990 (1984).
8. H. Howe, Jr., Microwave integrated circuits—an historical perspective, *IEEE Trans. Microwave Theory Tech.* **32**(9):991–996 (1984).
9. T. Ikegami, Survey of telecommunications applications of quantum electronics—progress with optical fiber communications, *Proc. IEEE* **80**(3):411–419 (1992).
10. R. E. Collin, *Field Theory of Guided Waves*, IEEE Press, Piscataway, NJ, 1991.
11. I. J. Bahl, Transmission lines, in K. Chang, ed., *Handbook of Microwave and Optical Components*, Wiley, New York, 1989, pp. 1–59.
12. K. C. Gupta, Transmission-line discontinuities, in K. Chang, ed., *Handbook of Microwave and Optical Components*, Wiley, New York, 1989, pp. 60–117.
13. F. A. Benson and T. M. Benson, *Fields, Waves, and Transmission Lines*, Chapman & Hall, New York, 1991.
14. B. C. Wadell, *Transmission Line Handbook*, Artech House, Norwood, MA, 1991.
15. T. Itoh, ed., *Planar Transmission Line Structures*, IEEE Press, New York, 1987.
16. W. C. Chew, *Theory of Microwaves and Optical Waveguides*, ECE431 Class Notes, Dept. Electrical and Computer Engineering, Univ. Illinois at Urbana—Champaign, 1997.
17. G. Gonzalez, *Microwave Transistor Amplifiers*, 2nd ed., Prentice-Hall, Upper Saddle River, NJ, 1992.
18. P. Magnusson, G. C. Alexander, and V. K. Tripathi, *Transmission Lines and Wave Propagation*, 3rd ed., CRC Press, Boca Raton, FL, 1992.
19. A. Deutsch, G. V. Kopschay, P. J. Restle, H. H. Smith, G. Katopis, W. D. Becker, P. W. Coteus, C. W. Surovic, B. J. Rubin, R. P. Dunner, Jr., T. Gallo, K. A. Jenkins, L. M. Terman, R. H. Dennard, G. A. Sai-Halasz, B. L. Krauter, and D. R. Knebel, When are transmission line effects important for on-chip interconnections? *IEEE Trans. Microwave Theory Tech.* **45**(10):1836–1846 (1997).
20. M. Celik, A. C. Cangellaris, and A. Yagmour, An all-purpose transmission-line model for interconnect simulation in SPICE, *IEEE Trans. Microwave Theory Tech.* **45**(10):1857–1867 (1997).
21. N. Fache, F. Olyslager, and D. De Zutter, *Electromagnetic and Circuit Modelling of Multiconductor Transmission Lines*, Oxford Univ. Press, New York, 1993.
22. J. A. Brandao Faria, *Multiconductor Transmission-line Structures: Modal Analysis Techniques*, Wiley, New York, 1993.
23. R. F. Harrington, *Time-Harmonic Electromagnetic Fields*, McGraw-Hill, New York, 1961.
24. J. Kretzschmar, Wave propagation in hollow conducting elliptical waveguides, *IEEE Trans. Microwave Theory Tech.* **18**(9):547–554 (1970).
25. S. B. Cohn, Properties of ridge wave guide, *Proc. IRE* **35**:783–788 (1947).
26. J. Montgomery, On the complete eigenvalue solution of ridged waveguide, *IEEE Trans. Microwave Theory Tech.* **19**(6):457–555 (1971).
27. P. B. Johns, The solution of inhomogeneous waveguide problems using a transmission-line matrix, *IEEE Trans. Microwave Theory Tech.* **22**(3):209–215 (1974).
28. N. Dagli, Equivalent circuit representation of open guided-wave structures, *IEEE J. Quantum Electron.* **26**(1):98–108 (1990).
29. N. Dagli and C. G. Fonstad, Universal design curves for rib waveguides, *J. Lightwave Technol.* **6**(6):1136–1145 (1988).
30. K. Ogusu, Numerical analysis of the rectangular dielectric waveguide and its modifications, *IEEE Trans. Microwave Theory Tech.* **25**(11):874–885 (1977).
31. W. C. Chew and M. Nasir, A variational analysis of anisotropic, inhomogeneous dielectric waveguides, *IEEE Trans. Microwave Theory Tech.* **37**(4):661–668 (1989).
32. W. C. Chew, Analysis of optical and millimeter wave dielectric waveguides, *J. Electromag. Waves Appl.* **3**(4): 359–377 (1989).
33. W. C. Chew, *Waves and Fields in Inhomogeneous Media*, IEEE Press, Piscataway, NJ, 1995.
34. A. W. Snyder, Asymptotic expression for eigenfunctions and eigenvalues of a dielectric or optical waveguide, *IEEE Trans. Microwave Theory Tech.* **17**(12):1130–1138 (1969).
35. P. Grivet, *The Physics of Transmission Lines at High and Very High Frequencies*, Academic Press, London, 1970.
36. W. C. Chew and J. A. Kong, Asymptotic eigenequations and analytic formulas for the dispersion characteristics of open

wide microstrip lines, *IEEE Trans. Microwave Theory Tech.* **29**(9):933–941 (1981).

37. R. Sorrentino, ed., *Numerical Methods for Passive Microwave and Millimeter Wave Structures*, IEEE Press, New York, 1989.
38. S. Y. Poh, W. C. Chew, and J. A. Kong, Approximate formulas for line capacitance and characteristic impedance of microstrip line, *IEEE Trans. Microwave Theory Tech.* **29**(2):135–142 (1981); correction in *IEEE Trans. Microwave Theory Tech.* **29**(10):1119 (1981).
39. T. Edwards, *Foundations for Microstrip Circuit Design*, 2nd ed., Wiley, New York, 1992.
40. W. P. Huang and J. A. Kong, eds., *Progress in Electromagnetics Research (PIER)*, Vol. 10, *Methods for Modeling and Simulations of Guided-Wave Optoelectronic Devices*, Elsevier, New York, 1995.

HIGH-TEMPERATURE SUPERCONDUCTORS

RAAFAT R. MANSOUR
University of Waterloo
Waterloo, Ontario, Canada

1. INTRODUCTION

Superconductors, as opposed to normal or conventional conductors, have the ability to conduct electrical current with very small resistance, very small power loss, very small generation of heat, and greatly reduced noise levels. The resistance is very small but finite at microwave frequencies and is truly zero at DC. Superconductivity was first understood as a very-low-temperature phenomenon and was explained by John Bardeen, Leon Cooper, and Robert Schrieffer in what has become known as the BCS theory. According to this theory, at a particular low temperature, called the *transition temperature* or *critical temperature* (T_c), the electrons in certain materials pair up and form a single quantum state, acting like a frictionless fluid, and become superconducting.

While conventional low-temperature metallic superconductors have been known since the beginning of the twentieth century, the extremely high cost of refrigeration has limited their use in many applications. Until 1986 researchers could not identify any materials that could become superconducting with a critical temperature higher than 23 K. The materials discovered up to that time, which had critical temperatures lower than 23 K, were commonly known as *low-temperature superconductor* (LTS) materials. A new era in superconductivity began in 1986 with the discovery of a new class of ceramic materials that are superconductive at temperatures as high as 125 K. Referred to as *high-temperature superconductor* (HTS) materials, these materials generally have significant advantages over LTS materials because they can be cooled at economically and commercially feasible temperatures.

Superconductivity is certainly a multidisciplinary field. It spans almost the entire realm of electrical engineering including microwave, power, electronic, and power and computer engineering [1]. In microwave applications, the

HTS technology offers major breakthroughs in performance of components and subsystems. Light weight, small volume, and high performance, which are the properties of the superconducting technology, are also the main drivers in the design and construction of microwave systems. The feasibility of using this technology to design microwave components such as filters, multiplexers, receivers, delay lines, couplers, antennas, and phase shifters with superior performance has been already demonstrated. A review of progress since 1990 is given in three IEEE-MTT Special Issues on HTS microwave applications published in 1991 [2], 1996 [3], and 2000 [4]. Three books have also been published on microwave superconductive devices [5–7].

Although the quest for room-temperature superconductor materials goes on, the quality of today's materials is adequate for the development of advanced superconductive systems with superior RF performance for wireless and space applications. In this article we provide first a brief historical overview summarizing the key development milestones of the technology. We discuss the basic material characteristics, highlighting the unique features that are relevant to microwave applications. We then cover the progress to date in various microwave applications of high-temperature superconductivity.

2. HISTORY AND PHENOMENA OF SUPERCONDUCTIVITY

The history of superconductivity can be divided into two eras. The first era started with H. Kamerlingh Onnes, a Dutch physicist, who successfully liquefied helium in the early twentieth century at around 4.2 K. While investigating the effect of such low temperatures on the properties of various metals in 1911, Onnes observed that the ohmic resistance for mercury vanishes at about 4 K. He made the same discovery with lead and tin shortly after. The progress in understanding superconductivity and in developing superconductors with transition temperatures higher than 4 K was agonizingly slow. By switching from single elements to alloys, researchers were eventually able in 1941 to raise the transition temperature to 15 K, for niobium nitride. It took, however, more than 30 years to further raise the transition temperature to 23 K with the discovery of the niobium germanium alloy in 1973. A number of systems already use low-temperature superconducting devices. A comprehensive review of the applications of low temperature superconductivity is given in a special issue published in January 1973 in the *Proceedings of the IEEE*. The LTS materials are still being used today in various applications. It was not until 1957 that a theory finally emerged to give an acceptable microscopic picture explaining why metals become superconductors at low temperatures. Three physicists at the University of Illinois, John Bardeen, Leon Cooper, and Robert Schrieffer, introduced what is now known as the BCS theory, named after the initial letters of their surnames. The theory was criticized from the start for failing to provide predictions that match experiments. Numerous revisions and even quite different models were proposed.

The second era commenced in 1986 with the discovery of a new class of superconducting materials with a then recordbreaking temperature of 35 K by Alex Muller and George Bednorz of IBM Zurich. The compound was a ceramic with a complex structure: an oxide of lanthanum, barium, and copper. Muller and Bednorz were awarded the 1987 Nobel Prize in Physics for their discovery.

Early in 1987, Paul Chu and his colleagues at the University of Houston reported the real breakthrough in high-temperature superconductivity (HTS), a yttrium–barium–copper–oxide compound ($\text{YBa}_2\text{Cu}_3\text{O}_7$) with a transition temperature of 94 K. The material is commonly known as YBCO. These new materials operate well at 77 K, allowing the use of liquid nitrogen rather than liquid helium. Liquid nitrogen is much cheaper and denser and has a heat vaporization that is 60 times larger than that of liquid helium. The ability to use liquid nitrogen rather than liquid helium reduces the cost of cooling by a factor of 1200.

In December 1987, Hiroshi Maeda’s group at Tsukuba laboratories in Japan reported the bismuth–strontium–calcium–copper–oxides (BiSrCaCuO), which have a T_c of 110 K. The next breakthrough was announced in February 1988 at the World Congress on Superconductivity in Houston. Zhengzhi Sheng and Allen Hermann from the University of Arkansas reported success with a thallium compound (TlBaCaCuO) having a transition temperature of 120 K.

In 1993, Paul Chu’s group at the Texas Center for Superconductivity at the University of Houston announced the discovery of a mercury compound HgBaCaCuO having a transition temperature of 161 K. For the first time, superconductors could conceivably be cooled by the household coolant Freon, which exists in liquid form at 147 K. The stability of this compound is still however, in question since it was developed in a procedure that involves a static pressure of 150,000 atm. It is believed that chemical

substitution may be used to achieve the same result the high pressure is now achieving. Figure 1 summarizes the history of the superconductor materials.

Shortly after the discovery of the YBCO materials at temperature near 90 K, scientists and engineers became very interested in the prospects of employing the HTS technology in the design of microwave components and subsystems. The U.S. Naval Research Laboratory (NRL) established a program known as the “high-temperature superconductivity space experiment” (HTSSE) in 1989. This program was a major catalyst to the development of microwave superconductivity. It consisted of two phases: the focus of the first-phase HTSSE-I (1989–1992) was to develop microwave HTS components such as resonators and filters [8], while the focus of the second phase HTSSE-II (1992–1996) was to develop advanced HTS subsystems [9]. More than 30 organizations from the United States, Canada, and Europe provided devices and subsystems to the HTSSE program [8–11]. The results obtained from this comprehensive research program did conclusively demonstrate that viable and robust HTS subsystems could be developed, fabricated, and cryogenically packaged for both ground and space applications [11].

In addition to the HTSSE program, several other focused programs were led by government agencies in the United States, Japan, Canada, and Europe on advancing HTS microwave technology. In particular, the U.S. Defense Advanced Research Projects Agency (DARPA), which sponsored several research programs in this field [12].

Another key factor that helped advance the development of HTS microwave devices was the rapid progress of the wireless industry in the 1990s. Several startup companies emerged in the United States, Europe, and Japan since the mid-1990s [13–16] with a focus on the commercialization of HTS microwave devices for wireless applications.

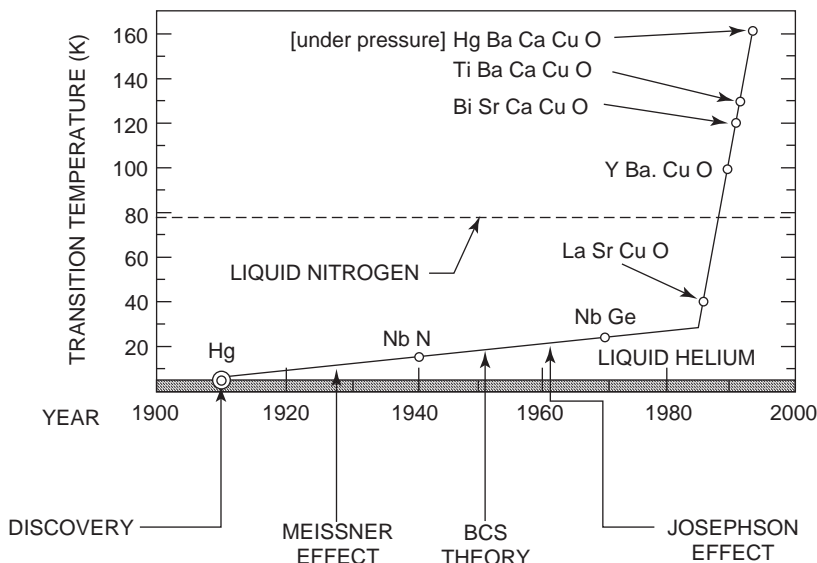


Figure 1. History of superconductor materials.

3. CHARACTERISTICS AND THEORIES OF SUPERCONDUCTORS

Superconductors have unique characteristics that differ from those of normal conductors. A much lower loss can be obtained with superconductors corresponding to lower RF losses. The surface resistance of superconductor materials at microwave frequencies is typically two orders of magnitude smaller than that of normal conductors. While the surface resistance of a normal conductor varies with frequency as $(f)^{1/2}$, that of superconductors varies with frequency as $(f)^2$ [7]. This frequency dependence is seen experimentally and can be easily deduced from theory.

Superconductors have a surface resistance that is dependent on the applied field. The dependence is more pronounced at high levels of fields, leading to nonlinearities and generation of intermodulation products. The nonlinearity exists even at low power levels but is more pronounced at high power levels. Such nonlinear characteristics have a negative impact on the power-handling capability of microwave superconductive devices [17–21]. The same nonlinear characteristics, however, were exploited to develop novel HTS devices such as mixers [7] and nonlinear transmission lines (NLTLs) [22]. Another characteristic of superconductor materials is that they have frequency-independent penetration depth that determines field penetration into the materials rather than the skin depth of normal conductors.

There are two other unique characteristics of superconductor material: the Meissner effect and flux quantization. The Meissner effect relates to the superconductor's ability to expel magnetic field; specifically, superconductors are perfect diamagnets. This characteristic makes it possible to suspend a magnet in midair over a piece of superconductor. The Meissner effect also implies that the transition to the superconducting state is sensitive to the magnetic field, and for increasing magnetic fields the flux first penetrates into and then ultimately destroys the superconducting state. Correspondingly, a superconducting transmission line can be driven into the normal state by a sufficiently large current that exceeds the critical current J_c .

The flux quantization relates to the phenomenon that magnetic field generated from a current circulating in a superconducting loop is quantized. The unit of quantization is known as the fluxon, or flux quantum and is given by 2.07×10^{-15} Wb. The characteristic of flux quantization makes it possible to build extremely sensitive magnetometer devices capable of measuring extremely low

levels of magnetic fields. Such magnetometers are known as *superconductor quantum interference devices* (SQUIDs) [23]. Table 1 summarizes the differences between superconductors and normal conductors.

For microwave applications, the two most important parameters of HTS materials are the surface resistance R_s and the critical current density J_c , which represents the maximum current that can be carried by the superconductor before switching to the normal state. There are several techniques available to measure these two parameters [5–7]. Typical values for R_s and J_c for HTS thin films are 100–200 $\mu\Omega$ and 10^6 A/cm², respectively.

The HTS thin films are deposited on a low loss dielectric substrate and are processed using standard photolithographic techniques. The most widely used substrate is lanthanum aluminate (LaAlO₃) with a dielectric constant of $\epsilon_r = 24$ and a loss tangent of $\tan \delta = 3 \times 10^{-5}$. One challenge with the LaAlO₃ substrate is that its crystal structure exhibits twinning, which makes the substrate effectively inhomogeneous. This can affect the ability to set the frequency correctly in narrowband filter applications. Another commonly used substrate for HTS films is magnesium oxide (MgO) with $\epsilon_r = 9.5$. MgO does not suffer from twinning problems, but on the other hand it does not offer the same miniaturization, which the LaAlO₃ substrate offers, because of its high dielectric constant. Sapphire substrates have also been used with various buffer layers to provide the appropriate lattice match to HTS films. However, the surface resistance R_s and current density J_c are inferior to films on LaAlO₃ or MgO substrates.

Dielectric materials typically exhibit a considerable improvement in loss tangent $\tan \delta$ on cooling to cryogenic temperatures. For example, high-purity sapphire ($\epsilon_r = 9.4$) at X-band frequencies exhibits $\tan \delta$ of 10^{-5} at 300 K and $\tan \delta$ of 10^{-7} at 77 K [24]. MgO and LaAlO₃ exhibit a similar loss tangent improvement at cryogenic temperatures [25] as compared to room-temperature operation. This is considered a fringe benefit of operating at cryogenic temperatures.

The HTS films are deposited on 2- and 3-in. wafers, which can vary in substrate thickness from 0.010 to 0.1 in. (standard substrate thicknesses are 0.01 and 0.02 in.). The HTS films are typically deposited either by laser ablation or by sputtering techniques [26]. Currently, 2- and 3-in.-diameter wafers with HTS films on one or both surfaces are commercially available from various sources at prices that are almost one-tenth the prices of the early 1990s.

The BCS theory deals with superconductors from a microscopic point of view. Two other well-known theories

Table 1. Differences between Superconductors and Normal Conventional Conductors

Characteristic	Normal Conductor	Superconductor
Surface resistance at 77 K and $f = 5$ GHz	5 m Ω (Cu)	0.1 m Ω (TBCCO)
Frequency dependence of surface resistance	$(f)^{1/2}$	$(f)^2$
Field dependence of surface resistance ^a	Constant	$R_s \propto H^2$
Field penetration	Skin depth (δ)	Penetration depth (λ)
Meissner effect	Not applicable	Applicable
Magnetic flux quantization	Not applicable	Applicable

^aThe dependence on magnetic field H is very weak at low levels of H .

were developed to deal with the macroscopic properties of superconductors: the London theory [27] and Ginzburg–Landau (GL) theory [28]. These two theories have been used in conjunction with Maxwell’s equation to model the electromagnetic characteristics of superconductive microwave devices [29–31]. The London theory is based on the two-fluid model [27], which assumes that the current in superconductor is carried by two parallel pathways, one of the normal electrons and one of the superconducting electrons whose densities are a function of temperature. The London theory has been successful in explaining several of the characteristics of superconductor materials. It does not however, take into consideration the field dependence of the constituent parameters of the superconductor materials. The GL theory, on the other hand, is a more comprehensive macroscopic theory that accounts for field dependence allowing the characterization of the nonlinear behavior of the superconductive materials.

4. HTS MICROWAVE FILTERS

Microwave filter networks represent a critical and substantive portion of any communication system. Such a system, whether wireless or satellite, requires filters to separate the signals received into channels for amplification and processing. The phenomenal growth in the telecommunications industry has brought significant advances in filter technology as new communication systems emerged, demanding equipment miniaturization while requiring more stringent filter characteristics. The emergence of the HTS technology has offered the possibility, for the first time, to build filters that can compete with traditional waveguide and dielectric resonator filters not only in size but also in Q (quality factor).

Figure 2 illustrates a pictorial comparison between microwave filters realized using rectangular single-mode waveguide technology, circular dual-mode waveguide technology, dielectric resonator technology, and superconductor technology [32]. Two types of superconductive filters are included in this figure: one using the hybrid

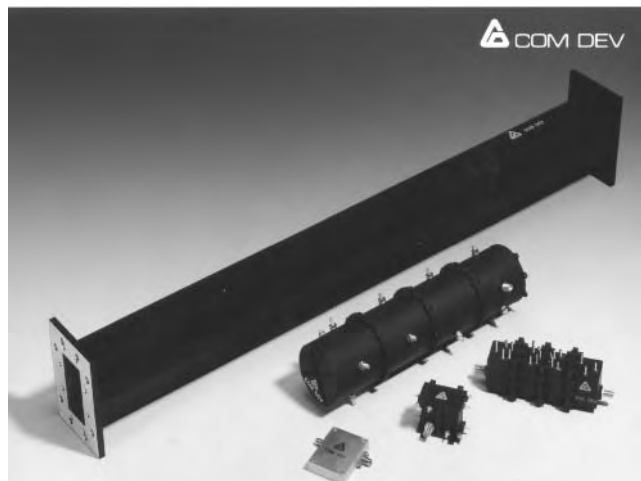


Figure 2. A comparison between various microwave filters.

DR/HTS technology and the other based on HTS thin-film technology. All filters have the same order and are designed to operate at the same center frequency of 4 GHz. It is clear that a significant reduction in size and mass can be achieved with the use of HTS technology.

In addition to size and mass reduction, HTS filters also offer improvement in the in-band insertion loss. The unloaded Q of a microwave resonator in general can be written as $Q_u = (R_s/G + F \tan \delta)^{-1}$, where G is a factor determined by the resonator’s geometry, which typically increases as the resonator dimensions increase, while F is a factor determined by the fraction of the electrical energy of the cavity stored in the dielectric materials; R_s is the surface resistance and $\tan \delta$ is the loss tangent of the dielectric material. It is clear that reducing either R_s or $\tan \delta$ or both of them can increase the unloaded Q_u . Three main types of HTS filter are reported in the literature:

1. HTS thin-film planar filters
2. Hybrid dielectric/HTS filters
3. HTS thick-film-coated filters

In both HTS thin-film planar filters and thick-film-coated filters, the Q improvement is attributed mainly to the reduction of R_s by replacing normal metals with HTS materials. On the other hand, the improvement in Q in hybrid dielectric/HTS filters is attributed to the reduction of R_s as well as to the reduction of the loss tangent of the substrate due to cooling.

4.1. HTS Thin-Film Planar Filters

Planar filters such as stripline, microstrip, and coplanar line filters have been known since the mid-1970s [33]. These filters, however, have very limited applications because of their low Q values. Effectively any known planar filter configuration can be realized in HTS technology by replacing metal films with HTS films. This in turn would increase the filter Q value by several orders of magnitude. For example, a half-wavelength microstrip resonator made of gold films on lanthanum aluminate substrate would typically have an unloaded Q value of 400. Replacing the gold films with HTS films while using the same substrate would provide an HTS resonator with an unloaded Q value of $\sim 30,000$.

The emergence of the HTS technology has created the opportunity for more innovation in planar filter configurations. Several novel filter configurations have been proposed allowing the realization of quite advanced filter functions [34–38]. Figure 3 illustrates a packaged HTS 10-pole elliptic function self-equalized planar filter. The basic building block of this filter is a dual-mode lumped-element resonator, which makes it easy to create elliptic and self-equalization functions [39].

The emergence of several commercial computer software packages for simulation and design of planar circuits in the early 1990s played a key role in advancing the development of HTS planar filters. Even though these commercial packages do not factor in the physical characteristics of the superconductor materials, they

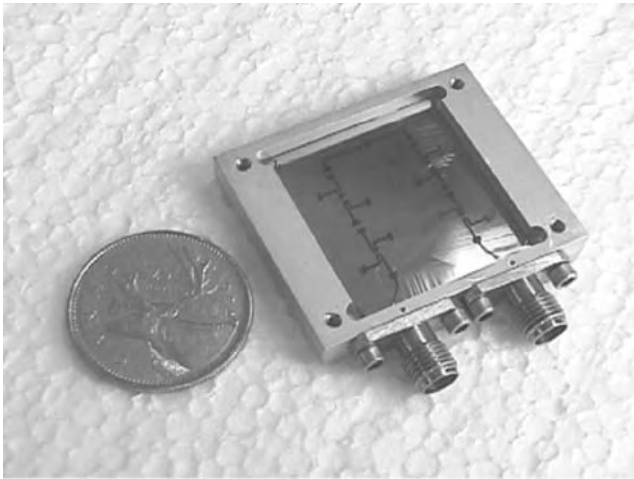


Figure 3. A 10-pole HTS thin-film filter.

have been successfully used in the design of planar HTS filters, particularly for low-power applications.

4.2. Hybrid Dielectric/HTS Filters

For the conventional dielectric resonator shown in Fig. 4a, the tangential electric field of the HEE_{11} mode vanishes at the plane $z=0$ [40]. As a consequence, introducing a conducting wall at this plane will only slightly perturb the field distribution of this mode. Thus the size of the dielectric resonator filter operating in the HEE_{11} mode may be reduced by supporting the resonator directly on a conducting surface (image plate) as shown in Fig. 4c. With the use of dielectric support that fills the whole cavity, further size reduction can be achieved as shown in Fig. 4d.

A normal-conducting image plate, however, significantly degrades the Q of the resonator, which in turn makes the approach unfeasible for high- Q applications. On the other hand, if the image plate is replaced by a surface made of high-temperature superconductor materials, the original unloaded resonator Q will be only slightly affected, allowing the use of this resonator structure to realize compact size filters with a superior loss performance for cryogenic applications [41,42]. The reduction in size is attributed to the use of the image plate, while the improvement in loss performance is attributed to the use of the

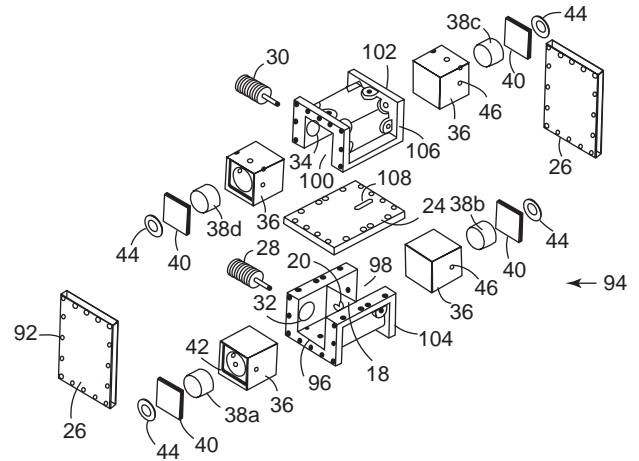


Figure 5. A layout of the eight-pole hybrid DR/HTS filter. The 38s are dielectric resonators; the 40s are HTS wafers diced from a standard 2-in. wafer; the 36s are dielectric supports; the 44s are spring washers; the 26s, 102, and 104, are elements of the filter housing; and the 28s are input/output probes.

HTS image plate as well as to the increase in the unloaded Q of the dielectric resonator as the temperature is lowered from 300 to 77 K.

Several hybrid DR/HTS filters, which utilize the concept illustrated in Fig. 4, were built and tested [21,38, 41,43]. Figure 5 shows a detailed configuration of an eight-pole hybrid DR/HTS filter [29]. The filter consists of four dielectric resonators operating in image-type dual modes. The resonators are supported inside the filter housing using two blocks made of low-loss low-dielectric constant ceramic materials. The HTS material is in the form of

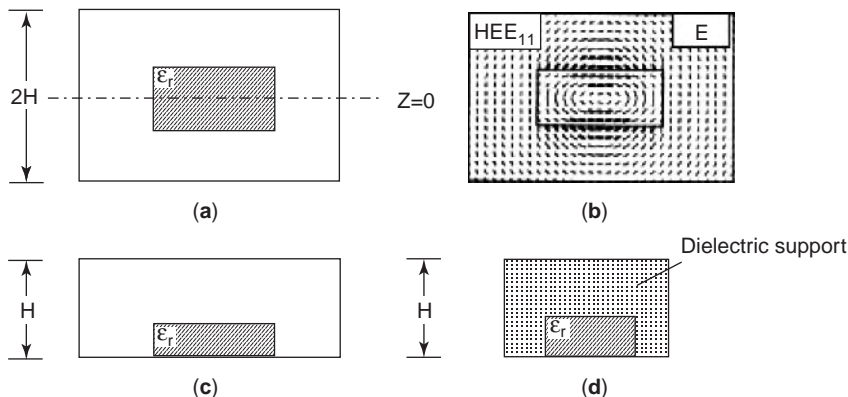


Figure 4. Transition from conventional DR cavity to an image DR cavity: (a) conventional DR resonator; (b) field distribution; (c) image DR resonator; (d) image DR resonator with a DR support.

small wafers (0.5×0.5 in. at C band), which are diced from a standard 2-in. HTS thin film deposited on 0.02-in.-thick wafer of LaAlO_3 . The HTS films are kept in contact with the dielectric resonators using springs and metallic plates bolted to the filter housing. A detailed description of this type of filter is given in [44].

The drawback of hybrid DR/HTS filters is the mechanical design complexity. These filters do, however, have several advantages over their counterparts HTS thin-film planar filters:

1. No etching is required for the HTS material. Etching may reduce the power-handling capability of the HTS material and degrade its surface resistance. The design also eliminates the need to deposit gold contacts, which are required for thin-film filters. Also there is no need to generate circuit and contact masks.
2. In patterned thin-film filters, a good portion of the HTS material is wasted as a result of the etching process, while in hybrid DR/HTS filters the wafer is diced into small pieces called “shorting [short-circuiting] plates.” The wafer is used efficiently.
3. The filter has a good spurious performance. The image plate helps not only in reducing the filter size but also in eliminating spurious modes, making it possible to design filters of this type with a spurious-free window of more than 2 GHz width centered at a frequency of 4 GHz.

4.3. HTS Thick-Film-Coated Filters

Melt-processed YBCO thick films were used to coat three-dimensional structures for microwave applications [45,46]. YBCO thick films typically have a current density of 2000 A/cm^2 and a relatively low value of surface resistance of approximately $0.5 \text{ m}\Omega$ (5 GHz at 77 K). The feasibility of constructing a thick-film YBCO 5.66-GHz cavity resonator operating in TE_{011} modes with unloaded Q values of 715,000 at 77 K has been demonstrated [47]. Measured results of cavities operating at 10 and 7.5 GHz have also been reported [48]. However, the TE_{011} cavities are too bulky to be used at frequencies below $\sim 1\text{--}2$ GHz. At lower frequencies, two resonator structures have been proposed for thick-film coating: coaxial resonators and split-ring resonators [49]. Thick-film coaxial resonators have found limited use because of the need to coat all surfaces in the cavity to achieve reasonably high Q values. On the other hand, the split-ring resonator has been adopted by Illinois Superconductor Corporation to manufacture thick-film HTS filters for wireless applications [51].

Figure 6 illustrates a 3-pole HTS filter employing split-ring resonators coated with HTS thick films. Coupling between resonators is achieved through the use of irises to provide the right coupling between resonators. Details on this type of filter can be found in Ref. 50.

5. CRYOGENIC RECEIVERS

A layout of a typical receiver is shown in Fig. 7. In addition to signal amplification, the receiver typically provides fre-

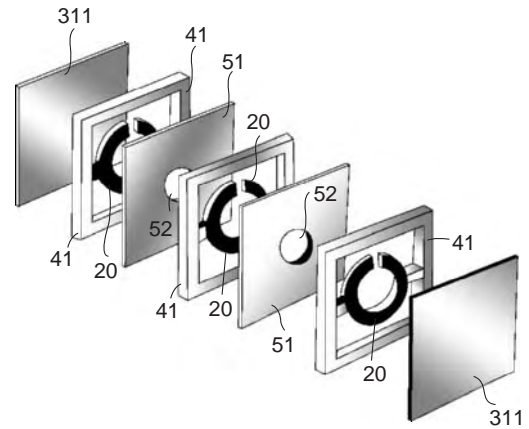


Figure 6. A three-pole filter employing split-ring resonators coated with HTS thick films.

quency conversion to the transmit band. It consists of an input filter, a low-noise amplifier (LNA), an oscillator, and a downconverter. The input filter limits the noise bandwidth and provides a high rejection of out-of-band signals. The insertion loss of this filter is a very critical parameter since it adds directly to the overall noise figure of the receiver. In most applications, these filters are typically built using high- Q filter structures to minimize the insertion loss. For example, a C-band input filter in satellite receivers is typically configured as a cascade of a waveguide lowpass filter and a waveguide bandpass filter. An HTS filter with a similar performance would have $\frac{1}{16}$ th the mass and $\frac{1}{100}$ th the volume of the conventional C-band waveguide input filter. It will also provide a 50% reduction in insertion loss.

The LNA benefits from cryogenic operation in two ways [51,52]. The use of HTS-matching structures results in decreased loss at the input of the LNA, which directly improves the attainable noise figure. Additionally, a fringe benefit of operation at 77 K is the reduction in the inherent noise of the active component. The improvement is more pronounced at high frequencies. Table 2 summarizes the typical measured noise figure results of C-band and Ka-band LNAs. The oscillator could also benefit from using HTS technology by employing high- Q HTS resonator as the frequency-determining element. The benefit in this case would be phase noise reduction. However, cooling the

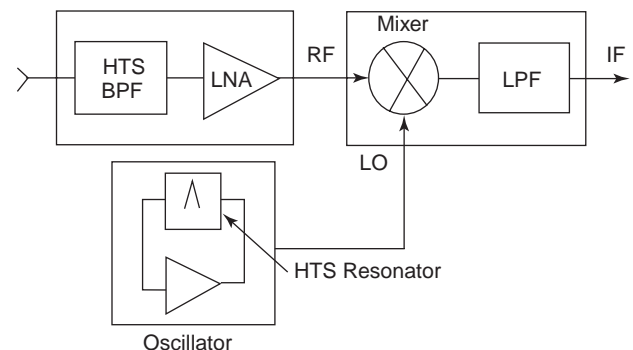


Figure 7. A block diagram for an RF receiver.

Table 2. Measured Noise Figure Results of Ka-Band and C-Band LNAs

Component	Measured Noise Figure	
	At 300 K (dB)	At 77 K (dB)
Ka-band LNA	3.1	0.8
C-band LNA	1.0	0.25

remaining oscillator components will have a negligible impact on overall oscillator performance while adding a large heat load on the system. Therefore the use of cryogenic technology has been limited in most applications to the input filters and the first LNA stage.

6. HTS DELAY LINES

Delay lines are useful devices in realizing transversal filters for analog signal processing applications. Current technologies for delay lines include surface acoustic wave (SAW) devices and electromagnetic coaxial cables in the form of coils. However, the small acoustic wavelength and the minimum achievable linewidth limit the SAW delay devices to low-frequency applications. Electromagnetic coaxial transmission lines with much larger wavelengths can yield much higher frequency limits. On the other hand, coaxial delay lines are bulky and have high insertion losses. Often the use of amplifiers and equalizers is necessary to restore the original signal.

Superconducting delay lines [53–55] offer the highest bandwidth with the lowest loss in highly compact designs. Several HTS planar transmission lines such as striplines and microstrip and coplanar lines could be used to realize delay lines. The high dielectric constant of lanthanum aluminate substrates ($\epsilon_r = 24$) allows a significant amount of delay to be placed on a single substrate, while the low

conductor loss of the HTS material keeps insertion loss to a minimum. Figure 8 illustrates a delay line realized using an HTS coplanar delay line [56]. A 100-ns HTS delay line of this type measures $90 \times 96 \times 12$ mm. A 100-ns delay line realized using RG-141 cables would have a length of 70 ft. Even with a cryocooler, the size and weight reductions offered by the HTS technology are very attractive.

7. ANTENNA AND BEAMFORMING NETWORKS

High-temperature superconductors offer new opportunities for the designers of antenna systems. Examples include antenna-matching elements, feed networks, microstrip antennas, and superdirective arrays [57–59]. In particular, beamforming networks can benefit from HTS technology in areas of both insertion loss reduction and miniaturization. The current designs for beamforming networks use either multilayer stripline technology or coaxial technology. The stripline designs are compact in size but exhibit very high insertion loss. The coaxial designs, on the other hand, exhibit low loss but are known to be very heavy and bulky.

Figure 9 illustrates a layout of an HTS 8×8 Butler matrix designed to operate at L band [59]. The matrix consists of folded thin-film 90° hybrids and delay lines. The size of the overall matrix is $75 \times 50 \times 12$ mm. The HTS Butler matrix is two orders of magnitude smaller than its coaxial counterpart.

8. WIRELESS APPLICATIONS

Mobile communication systems require improved sensitivity and selectivity to support the constant growth in services, increased coverage, and larger numbers of subscribers. Several companies have taken advantage of

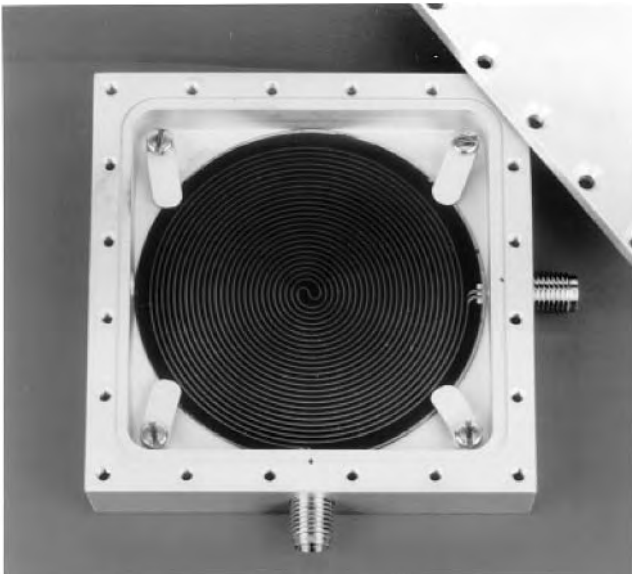


Figure 8. A layout of an HTS delay line.

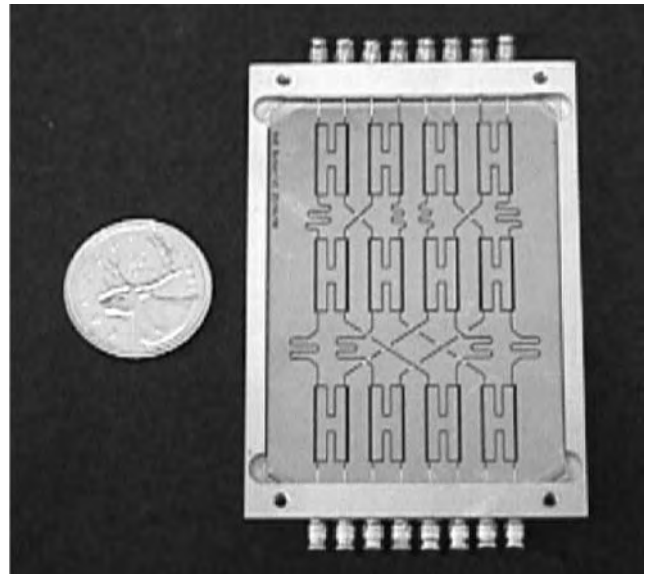


Figure 9. An 8×8 HTS Butler matrix.

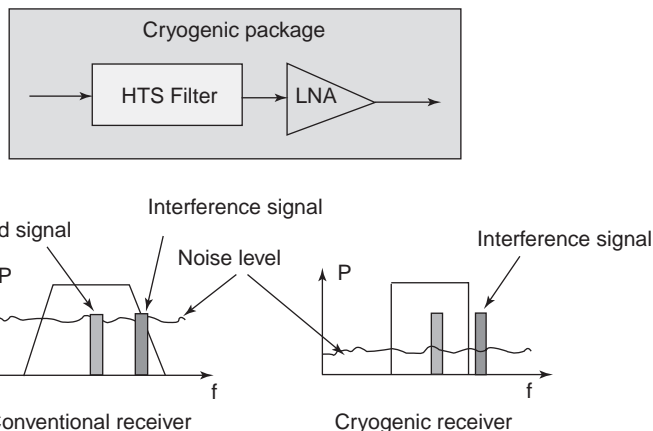


Figure 10. A cryogenic package consisting of an HTS filter and an LNA.

technical innovations in cryoelectronics to address these improvements. Cryoelectronic solutions have matured to the point where numerous field trials under the auspices of both RF equipment manufacturers and PCS carriers have been proved to be successful [60–63].

The performance of wireless base stations can be considerably enhanced by incorporating cryogenic LNAs with high-temperature superconductor filters. The HTS technology presents a viable solution of realizing small-size high-order filters with low insertion loss. The overall size of multiple HTS transceiver chains, including the associated cryocooler, is considerably less than that of an equivalent conventional transceiver.

The capacity and coverage of a base station receiver are determined primarily by the receiver selectivity and sensitivity on the up-link and in part by the base station transmitter power of the downlink. The selectivity can be significantly increased with the use of high-order filters as shown in Fig. 10. However, high-order filters, built using conventional technology, would exhibit a very high pass-band insertion loss, resulting in a reduced signal-to-noise ratio and hence degrading the sensitivity performance of the receiver.

A significant improvement in receiver sensitivity can be achieved by designing the receiver to operate in a cryogenic environment. This virtually eliminates thermal noise from the LNA and potentially improves the filter loss performance. Although conventional dielectric resonator filters can be cooled with some improvement in performance, integrated receivers of this type are too large for tovertop mounting.

The low resistance of the HTS materials makes it possible to use the planar thin-film technology to provide HTS filters that are two orders of magnitude smaller in size than conventional dielectric resonator filters. This significant reduction in physical size makes valuable space available for other required electronic components, enabling service providers to enhance the utilization of existing base stations instead of developing additional base stations. In addition, miniaturization can decrease deployment costs for new base stations, as less real estate is required to support base station. Figure 11 illustrates a comparison between a conventional transceiver and an HTS transceiver [63].

9. SPACE APPLICATIONS

The mass, volume, and power consumption of payload electronic equipment are significant contributors to the overall cost of space systems. HTS technology offers the potential of large reductions in mass and volume of electronic equipment, leading to significant cost reduction of satellite systems [39,64,65]. Today's space segment represents a market of many billions of dollars for commercial and military applications and is growing. HTS technology has the potential to accelerate the development and implementation of new advanced satellite systems. It also represents the potential of performance enhancements of strategic defence communications systems.

Mass reductions have a dramatic impact on the economics of a satellite program because launch costs are related to satellite weight. Similarly, mass reductions can be exploited to increase the capacity (by adding payload electronics) or extending operational life (by increasing station maintenance fuel). As a result, market factors have constantly been pushing hardware suppliers to reduce mass and size of their products.

The current technology for satellite input multiplexers is the dielectric resonator technology. A 60-channel HTS



Figure 11. A comparison between a conventional dielectric resonator transceiver (left) and an HTS transceiver (right).

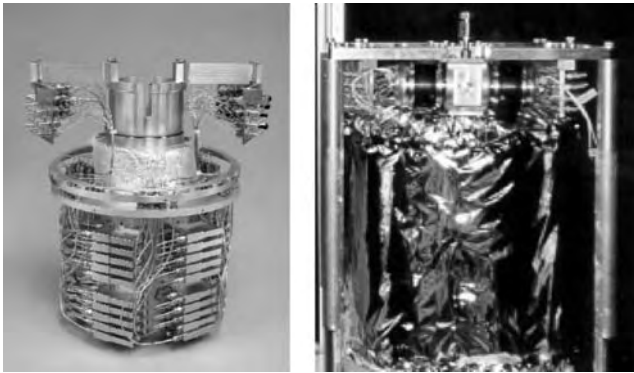


Figure 12. A 60-channel HTS multiplexer integrated with cryocoolers.

multiplexer was built [39] to duplicate the requirements of the Intelsat 8 C-band dielectric resonator multiplexer. The channel filters are 10-pole self-equalized planar HTS thin-film filters of the type shown in Fig. 3.

Figure 12 illustrates the overall 60-channel HTS multiplexer, while Fig. 13 shows the experimental results of four channel HTS filters having bandwidths of 34, 41, 72, and 112 MHz, which meet the bandwidth requirements of the Intelsat 8 program. More than 50% reduction in mass and 50% reduction in size were achieved with the use of HTS technology [39]. It should be mentioned that the reductions in mass and size include the cryogenics (two cryocoolers for redundancy).

There have also been efforts dedicated to the development of high-power HTS output multiplexers [43,65]. Figure 14 illustrates the layouts of a four-channel superconductive C-band output multiplexer and a similar conventional waveguide output multiplexer. For the conventional C-band multiplexer, both the channel filters and the manifold are built using the waveguide technology. For the superconductive multiplexer, the channel filters are hybrid DR/HTS filters, while the manifold is realized using coaxial technology. The superconductive multiplexer

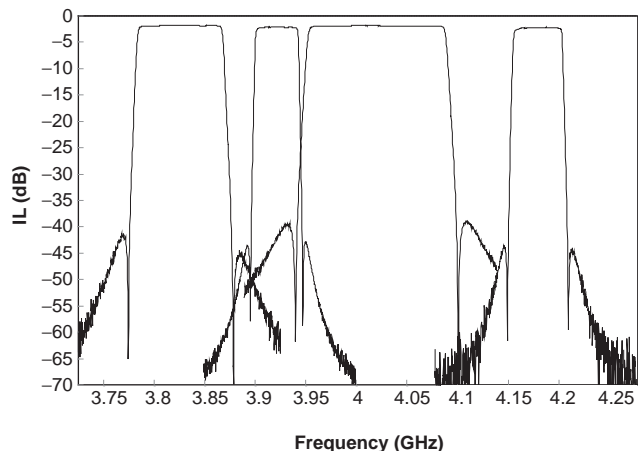


Figure 13. Experimental results of four channels of the HTS 60-channel C-band input multiplexer.

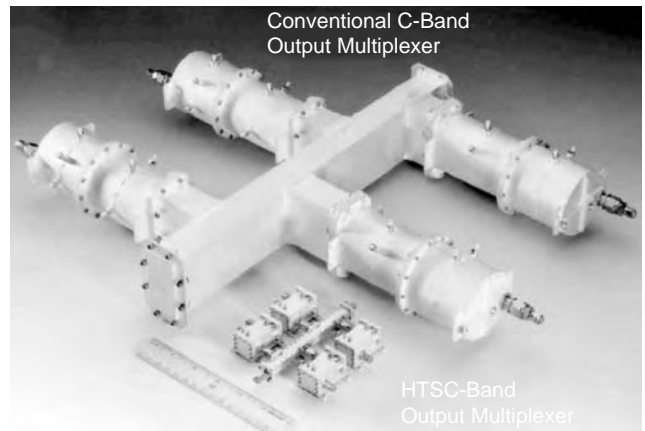


Figure 14. A comparison between a C-band four-channel HTS output multiplexer and its waveguide counterpart.

occupies less than 5% of the volume of the waveguide multiplexer (without the cryocooler).

The potential advantages of using HTS technology in the design of output multiplexers are mass and volume reduction as well as insertion loss improvement. The insertion loss improvement can translate into improvement in satellite EIRP or reduction in the DC power required for power amplifiers. However, the mass penalty of the currently available cryocooler and associated electronic controller may overshadow any advantages gained with the use of HTS technology for high-power-output multiplexer applications [43].

10. CRYOCOOLER TECHNOLOGY AND CRYOPACKAGING

Several cryocooler techniques exist that could meet the temperature needs for microwave HTS devices and subsystems. These techniques can be divided into two main categories: open-cycle and closed-cycle [66]. The open-cycle techniques include cooling with a stored cryogen such as liquid nitrogen or through Joule–Thomson gas expansion. Open-cycle coolers are bulky and dissipate materials, requiring frequent fillup of the cryogen or compressed gas. Therefore, they are ideal for laboratory environments or in applications where regular equipment maintenance is possible.

Closed-cycle coolers are self-contained refrigerators that consume only electrical power, requiring no maintenance over the designed lifetime. Closed-cycle cryocoolers have been primarily developed for infrared devices and military applications. The main design considerations for a closed-cycle cryocooler are DC power consumption, size, and reliability. In particular, the reliability of the cryocooler remains the primary barrier to the widespread commercial acceptance of superconducting devices.

In addition to the cryocooler, it is also essential to provide a cryopackage with a means to mechanically and thermally attach the HTS microwave device to the cold head of the cryocooler within an evacuated enclosure, while providing electrical and RF cabling through the enclosure. One major challenge is to ensure low loss in the

electrical connections without allowing too much heat to travel from the outside room-temperature environment to the HTS component. It is difficult to find commercially available RF cables that can reasonably meet the two conditions described above. For example, having a cable with low conduction heat load requires the use of a small-diameter cable. On the other hand, small-diameter cables typically have a high RF insertion loss. The choice of the RF and electrical connections to the package has a major impact on the size and cooling power of the cryocooler. Another major design issue is to guarantee that the enclosure maintains its vacuum over the operational lifetime of the system. Cryopackaging is typically one of the main issues in the design of microwave HTS subsystems.

11. CONCLUSIONS

The HTS technology offers the potential of large reduction in mass and volume of microwave equipment. It could also provide performance discrimination not attainable with other technologies. The technology has grown very fast and merged with commercial and defense applications. This article has presented a summary of the main HTS microwave applications. I strongly urge newcomers to the field to continue reading about the subject to understand more about the potential challenges and limitations of this revolutionary technology.

BIBLIOGRAPHY

1. Special Tenth Anniversary Plenary Sessions, *IEEE Trans. Appl. Superconduct.* **7**(2):69–145 (June 1997).
2. P. H. Carr and B. R. McAvoy, eds., IEEE-MTT special issue on microwave applications of superconductivity, *IEEE Trans. Microwave Theory Tech.* **MTT-39** (Sept. 1991).
3. M. Nisenoff and W. Meyers, eds., IEEE-MTT special issue on the microwave and millimeter wave applications of high temperature superconductivity, *IEEE Trans. Microwave Theory Tech.* **MTT-44** (July 1996).
4. J. J. Whelehan and G. C. Liang, eds., IEEE-MTT special issue on microwave and communication applications at low temperatures, *IEEE Trans. Microwave Theory Tech.* **MTT-48** (July 2000).
5. H. Weinstock and M. Nisenoff, eds., *Microwave Superconductivity*, Kluwer Academic Publishers, The Netherlands, 2001.
6. M. J. Lancaster, *Passive Microwave Device Applications of High Temperature Superconductors*, Cambridge Univ. Press, Cambridge, MA, 1997.
7. Z. Y. Shen, *High Temperature Superconducting Microwave Circuits*, Artech House, Norwood, MA, 1994.
8. J. C. Ritter, M. Nisenoff, G. Price, and S. A. Wolf, High temperature superconductivity space experiment (HTSSE), *IEEE Trans. Magn.* **27**(2):2533–2537 (March 1991).
9. T. G. Kawecki et al., The high temperature superconductivity space experiment (HTSSE-II) design, *IEEE Trans. Microwave Theory Tech.* **MTT-44**:1198–1212 (July 1996).
10. G. W. Mitschang, Space applications and implications of high temperature superconductivity, *IEEE Trans. Appl. Superconduct.* **8**(2):69–73 (June 1995).
11. M. Nisenoff and W. J. Meyers, On-orbit status of the high temperature superconductivity experiment, *IEEE Appl. Superconduct. Trans.* **11**:799–805 (March 2001).
12. F. Patten, US programs in HTS electronics and radar applications, Workshop on Superconducting Microwave Applications to Mobile Communications, Asia-Pacific Microwave Conf., Yokohama, Japan, Dec. 1998.
13. R. B. Hammond et al., “HTS wireless filters; past, present and future performance” *Microwave J.* **41**:94–107, 1998.
14. A. I. Braginski, “Superconducting electronics coming to market”, *IEEE Trans. Appl. Supercond.*, **9**:2825–2836, 1998.
15. M. J. Rowell, “Recommended directions of research and development in superconducting electronics”, *IEEE Trans. Appl. Supercond.* **9**:2837–2848, 1999.
16. D. G. Smith and V. K. Jain, Superconducting filters for wireless communications; A reappraisal, *IEEE Trans. Appl. Supercond.*, **9**, pp. 4010–4013, 1999.
17. D. E. Oates, A. C. Alfredo, S. M. David, and A. M. Sami, Stripline resonator measurements of Z_s vs H_f in thin films, *IEEE Trans. Microwave Theory Tech.* **MTT-39**:1522–1529 (Sept. 1991).
18. P. P. Nguyen et al., Nonlinear surface impedance for YBCO thin film: Measurements and a coupled-grain model, *Phys. Rev. B*, **48**:6400–6412 (Sept. 1993).
19. C. Wilker et al., Nonlinear effects in high temperature superconductors: 3rd order intercept from harmonic generation, *IEEE Trans. Appl. Superconduct.* **5**(2):1665–1670 (June 1995).
20. O. G. Vendik, I. B. Vendik, and T. B. Samoiloova, Nonlinearity of superconducting transmission line and microstrip resonator, *IEEE Trans. Microwave Theory Tech.* **45**(2):173–178 (Feb. 1997).
21. R. R. Mansour, B. Jolley, S. Ye, F. S. Thomson, and V. Dokas, On the power handling capability of high temperature superconductive filters, *IEEE Trans. Microwave Theory Tech.* **MTT-44**:1322–1338 (July 1996).
22. G. Coutts, R. R. Mansour, and S. K. Chaudhuri, High temperature superconducting nonlinear transmission lines, *IEEE Trans. Microwave Theory Tech.* **MTT-48**:2511–2518 (Dec. 2000).
23. J. Clark, Principles and applications of SQUIDs, *Proc. IEEE* **77**(2):1208–1223 (1989).
24. N. Klein et al., High-Q dielectric resonator devices at cryogenic temperatures, *IEEE Trans. Appl. Superconduct.* **9**(2):3573–3576 (1999).
25. N. Klein et al., Properties and applications of HTS-shielded dielectric resonators: A state-of-the-art report, *IEEE Trans. Microwave Theory Tech.* **44**:1369–1373 (July 1996).
26. J. D. Doss, *Engineer’s Guide to High Temperature Superconductivity*, Wiley, New York, 1989.
27. T. P. Orlando and K. A. Delin, *Foundations of Applied Superconductivity*, Addison-Wesley, Reading, MA, 1991.
28. T. Van Duzer and C. W. Turner, *Principles of Superconductive Devices and Circuits*, Prentice-Hall, Englewood Cliffs, NJ, 1999.
29. C. W. Lam, D. M. Sheen, S. M. Ali, and D. E. Oates, Modeling the nonlinearity of superconducting strip transmission lines, *IEEE Trans. Appl. Superconduct.* **2**(2):58–65 (June 1992).
30. R. M. A. Megahed and S. M. El-Ghazaly, Nonlinear analysis of microwave superconductor devices using full-wave electromagnetic model, *IEEE Trans. Microwave Theory Tech.* **43**(11):2590–2598 (Nov. 1995).

31. J. Kuster, R. Dill, and P. Russer, Filed theory investigation of high-Tc superconducting coplanar waveguide transmission lines and resonators, *IEEE Trans. Microwave Theory Tech.* **39**:1566–1574 (1991).
32. R. R. Mansour et al., Design considerations of superconductive input multiplexers for satellite applications, *IEEE Trans. Microwave Theory Tech.* **MTT-44**:1213–1228 (July 1996).
33. I. Bahl and P. Bhartia, Microwave solid state circuit design, in I. Bahl and P. Bhartia, eds., *Filters and Multiplexers*, Wiley, New York, 1988, Chap. 6.
34. M. Lancaster et al., Miniature superconducting filters, *IEEE Trans. Microwave Theory Tech.* **MTT-44**:1339–1346 (1996).
35. K. F. Raihan, R. Alvarez, J. Costa, and G. Hey-Shipton, Highly selective HTS band pass filter with multiple resonator cross-couplings, *IEEE MTT-S Int. Microwave Symp. Digest*, June 2000, pp. 661–664.
36. S. Ye and R. R. Mansour, A novel split-resonator high power HTS planar filter, *IEEE MTT-S Int. Microwave Symp. Digest*, June 1997, pp. 299–302.
37. G. Tsuzuki, M. Suzuki, and N. Sakakibara, Superconducting filter for IMT-2000 band, *IEEE Trans. Microwave Theory Tech.* **MTT-48**:2519–2525 (Dec. 2000).
38. R. R. Mansour, S. Ye, S. Peik, V. Dokas, and B. Fitzpatrick, Quasi dual-mode resonators, *IEEE Trans. Microwave Theory Tech.* **MTT-48**(12):2476–2482 (Dec. 2000).
39. R. R. Mansour et al., A 60 channel superconductive input multiplexer integrated with pulse-tube cryocoolers, *IEEE Trans. Microwave Theory Tech.* **MTT-48**(7):1171–1180 (July 2000).
40. D. Kajfez and P. Guilon, *Dielectric Resonators*, Artech House, Norwood, MA, 1986.
41. R. R. Mansour, V. Dokas, G. Thomson, W. C. Tang, and C. Kudsia, A C-band superconductive input multiplexer for communications satellites, *IEEE Trans. Microwave Theory Tech.* **MTT-42**:2472–2479 (Dec. 1994).
42. J. A. Curtis and S. J. Fiedziuszko, Hybrid dielectric/HTS resonator and their applications, *IEEE MTT-S Int. Microwave Symp. Digest*, 1991, pp. 447–450.
43. R. R. Mansour, S. Ye, V. Dokas, B. Jolley, W. C. Tang, and C. Kudsia, System integration issues of high power HTS output multiplexers, *IEEE Trans. Microwave Theory Tech.* **MTT-48**:1199–1208 (July 2000).
44. R. R. Mansour and V. Dokas, *Miniaturized Dielectric Resonator Filters and Method of Operation Thereof at Cryogenic Temperatures*, U.S. Patent 5,498,771 (1996).
45. N. M. Alford et al., Low surface resistance in YBCO melt-processed thick films, *Nature* **349**:680 (1991).
46. T. W. Button et al., The processing and properties of high Tc thick films, *IEEE Trans. Magn.* **27**:1434–1437 (1991).
47. T. W. Button and N. M. Alford, High Q YBCO cavities, *Appl. Phys. Lett.* **60**:1378–1380 (1992).
48. T. W. Button et al., Properties and applications of thick film high temperature superconductors, *IEEE Trans. Microwave Theory Tech.* **MTT-44**:1356–1360 (July 1996).
49. W. N. Hardy et al., Split-ring resonator for use in magnetic resonance from 200–2000 MHz, *Rev. Sci. Instrum.* **52**(2):213 (1981).
50. R. D. Lithgow and J. M. Peters, *Electromagnetic Resonant Filter Comprising Cylindrically Curved Split Ring Resonators*, U.S. Patent 6,616,540A (1997).
51. H. H. S. Javadi et al., Jet Propulsion Laboratory/NASA Lewis Research Center space qualified hybrid high temperature superconducting/semiconducting 7.4 GHz, low noise downconverter, *IEEE Trans. Microwave Theory Tech.* **MTT-44**:1279–1288 (July 1996).
52. R. Romano, R. R. Mansour, and F. Thomson, A hybrid superconductive/semiconductive microwave receiver, *IEEE Trans. Appl. Superconduct.* **7**:3067–3070 (June 1997).
53. W. G. Lyons et al., High temperature superconductive wide-band compressive receivers, *IEEE Trans. Microwave Theory Tech.* **MTT-44**:1258–1278 (July 1996).
54. S. H. Talisa et al., High temperature superconducting space-qualified multiplexers and delay lines, *IEEE Trans. Microwave Theory Tech.* **MTT-44**:1229–1239 (July 1996).
55. G. C. Liang et al., Space qualified superconductive digital instantaneous frequency-measurement subsystem, *IEEE Trans. Microwave Theory Tech.* **MTT-44**:1289–1299 (July 1996).
56. D. Oates, Analog devices in military systems, *Microwave Superconductivity*, Chapter 12, Kluwer Academic Publishers, The Netherlands, 2001.
57. H. Chaloupka et al., Miniaturized high temperature superconductor microstrip patch antenna, *IEEE Trans. Microwave Theory Tech.* **MTT-39**:1531–1529 (Sept. 1991).
58. C. Kuester, H. Chaloupka, and J. Knauth, A high temperature superconducting anti-jam GPS antenna array, *Proc. Military Communications Conf., 1999 (MILCOM 1999)*, 1999, Vol. 1, pp. 671–674.
59. S. Peik and R. R. Mansour, High temperature superconductor beam forming network, *IEEE MTT-S Int. Microwave Symp. Digest*, June 1999, pp. 1015–1019.
60. G. Koepl, A receiver front end for wireless base stations, *Microwave J.* **39**(4) (April 1996).
61. G. Koepl, Superconductor improve coverage in wireless network, *Microwave RF* **37**(4):94–107 (April 1998).
62. R. W. Simon, Superconductor filters in wireless base stations, *Commun. Syst. Design* (July 1997).
63. J. P. Simmons and J. Madden, Practical HTS/cryogenic systems for wireless applications, *Microwave J.* (Oct. 1996).
64. J. S. Fiedziuszko, J. A. Curtis, and S. C. Holme, Low-loss multiplexers with planar dual-mode HTS resonators, *IEEE Trans. Microwave Theory Tech.* **MTT-44**:1248–1257 (July 1996).
65. M. Klauda et al., Superconductors and cryogenics for future communication systems, *IEEE Trans. Microwave Theory Tech.* **MTT-48**(7):1227–1239 (July 2000).
66. W. A. Little, Recent advances in low cost cryogenic coolers for electronics, *Proc. Semiconductor Thermal Measurement and Management Symp.*, 2000, pp. 110–111.

HISTORY OF WIRELESS COMMUNICATION

PATT LEGGATT

In the earlier decades of the nineteenth century, magnetic and electric forces were believed to act instantaneously at a distance, a view prevalent in continental Europe and especially in Germany. But the obvious philosophical difficulties inherent in instantaneous action at a distance made this concept less acceptable to a few in the United Kingdom in general and to Michael Faraday in particular.

1. FARADAY'S WAVES

In 1831 Faraday conducted a series of experiments on the magnetic effects of electric currents, during which he made his important discovery of electromagnetic induction, whereby an electric potential was induced in a conductor subjected to a changing magnetic field. In the course of these experiments, Faraday came to the conclusion that magnetic and electrostatic forces were not instantaneously effective at a distance but required a finite time for their transmission. We know now that electromagnetic energy is transmitted at the speed of light, but while continuing his experiments into 1832, Faraday had no means of detecting or measuring the very small time intervals necessary to confirm his theories. Furthermore he suggested, with remarkable intuition, that transmission of such forces took the form of some kind of wave motion. To establish his prior claim to the notion of wave motion, Faraday deposited a written statement in a sealed envelope with the Royal Society in 1832. The envelope was finally opened more than 100 years later in 1937 by the then-president of the Royal Society, and found to contain, *inter alia*, the following words: "I am inclined to compare the diffusion of magnetic forces from a magnetic pole to the vibrations upon the surface of disturbed water, or those of air in the phenomenon of sound."

Faraday, the son of a blacksmith, was a brilliantly imaginative experimenter and theoretician but had only self-taught scientific education and no knowledge of mathematics. Because of this, his theories were regarded with some disdain by many contemporary scientists. However, there was one young mathematician, James Clerk Maxwell, who was most impressed by Faraday's concepts of magnetic fields and lines of force as set out in his paper "Experimental researches in electricity," read to the Royal Society in 1851.

2. MAXWELL'S ANALYSIS

Maxwell already had an interest in this area, triggered while he was at Cambridge by the ideas of William Thomson, afterward to become Lord Kelvin; and Maxwell determined to submit Faraday's concepts to detailed mathematical analysis. As his studies continued, he concentrated his attention on the possible nature of the medium through which electromagnetic forces could be propagated, wishing to devise a mechanical model exhibiting appropriate characteristics. This was a complex task, but by about 1862 he came up with a system of very minute rapidly spinning eddies or vortices, each surrounded by a layer of even more minute particles revolving in a direction opposite to that of the vortices themselves.

The vortices, with their outer layers of particles, could interact with one another in a manner analogous to a train of gear wheels, so that energy imparted to one vortex would be transferred to others and so progress through the medium.

Maxwell devised this mechanical model as one that could exhibit the sort of behavior necessary to embrace

Faraday's concepts of lines of force and wavelike transmission of energy; but it was a convenient model only, and he was not so fanciful as to suggest that it represented anything much related to reality. Nevertheless it served his purpose of enabling rigorous mathematical analysis, culminating in his 1864 paper to the Royal Society, "A dynamical theory of the electro-magnetic field." One of Maxwell's main hopes had been to derive the electromagnetic nature of light and heat, and this was triumphantly achieved in particular by one of the consequences of his theories, that electromagnetic wave propagation would travel at a velocity very close to the value for the speed of light that had been experimentally determined by others at the time.

3. THE MAXWELLIANS

Maxwell's analysis was deeply mathematical, making use of Hamiltonian quaternionic calculus and high-order differential equations, and at the time of his final publication in 1873, there were very few physicists with the intellectual ability to understand it. There were only three of note: Oliver Lodge and Oliver Heaviside in England, and the Irish professor George Francis FitzGerald of Trinity College, Dublin.

In 1873 Oliver Lodge, then a student at University College, London, attended a lecture by Maxwell at a meeting of the British Association and obtained a copy of his *Treatise* published in that year. Lodge did not study this closely until 1876, but when he did he quickly came to realize that Maxwell's equations implied not only the electromagnetic nature of light and heat but also that there could be a whole spectrum of radiation with wavelengths both above and below those of visible light. Lodge was probably the first to appreciate that such electromagnetic waves could perhaps be generated electrically; and in 1879, after Maxwell's death, he began to give serious attention to this possibility.

FitzGerald too was studying Maxwell's theories at about this time and, in a paper to the Royal Dublin Society in 1882, suggested that electromagnetic radiation of about 10 wave-length could be generated by discharging a condenser (Leyden jar) through a circuit of very low resistance and low inductance. Furthermore, he clarified Maxwell's analysis to the extent of showing that the equations also led to the laws of reflection and refraction that had already been developed in the wave theories of light.

Another physicist who contributed significantly in this way was Oliver Heaviside, now best remembered for his 1902 theory of a reflecting ionized layer in the upper atmosphere, which, when physically verified some 20 years later, was named after him. Heaviside was a first-class mathematician and was already interested in Maxwell's papers. He reformulated much of the analyses in appreciably simpler terms, changing Maxwell's rather convoluted systems into notation of his (Heaviside's) own devising. He developed his own operational calculus and vector algebra and although contemporary mathemati-

cians found it difficult to grasp at first, it is in this form that Maxwell's equations are familiar to students of today.

These three adherents and interpreters of the equations called themselves *Maxwellians*. They were scientists, and what was crucial to them was that the electromagnetic radiation implicit in the equations indicated that the unsatisfactory theories of instantaneous action at a distance could be discarded. While the theoretical analyses were their prime interest, they naturally hoped for experimental verification of the real existence of such radiation, and it was Lodge who pursued this most effectively.

4. OLIVER LODGE

Oliver Lodge was born in Staffordshire, England in 1851, the son of a pottery merchant. He received his scientific education at University College, London and while there attended a lecture by James Clerk Maxwell showing that oscillatory electrical discharges resulted in electromagnetic wave radiation propagating with the velocity of light. This fired Lodge with an abiding interest in what was eventually to become *wireless*.

Lodge quickly rose to be an eminent physicist, gaining his D.Sc. degree in 1877 and being appointed Professor of Experimental Physics at the University College of Liverpool in 1881. In 1887 he was elected Fellow of the Royal Society, the highest honor in British science, and he was knighted as Sir Oliver Lodge in 1902. He died at age 89 in 1940.

In 1887 Lodge undertook a series of investigations into lightning discharges and protection against them. He found by experiment that lightning flashes were oscillatory and followed this up with further experiments involving spark discharges from Leyden jars. In early 1888 he developed a famous experiment that he called the *recoil kick*. This involved generating oscillations by discharge of a Leyden jar capacitor into a long pair of wires and observing that a much greater spark would occur at the end of the wires when they were of a suitable length. He correctly surmised that this was due to a standing-wave pattern along the wires with a voltage anti-node at the end. Furthermore, he understood that this condition would be satisfied when the wires were a half-wavelength long (or a multiple of this) and was thus able to determine experimentally the wavelength of the oscillations.

It can be seen therefore that he was conversant with the principles of resonance and tuning—or *syntony* as he called it—saying in 1888, “The natural period of oscillations in the wires will then agree with the oscillation period of the discharging circuit, and the two will vibrate in unison, like a string or a column of air resounding to a reed.”

Although his experiments were largely confined to oscillations along wires, Lodge knew well that the electromagnetic waves were propagated in the space surrounding the wires rather than in the wires themselves. He knew also, being familiar with Clerk Maxwell's mathematical analysis, that the waves would be radiated into space and travel at the speed of light.

Thus we can see that Lodge had demonstrated experimentally the existence of electromagnetic waves as predicted by Maxwell's equations. But he had dealt only with waves guided along wires, since he had not then devised any means of detecting such radiation in free space.

In fact Lodge was not the first to observe electromagnetic waves along wires. In 1870 Wilhelm von Bezold observed such phenomena, detecting the waves by patterns formed by dust particles under the influence of electrostatic fields. However, he did not relate these observations to Maxwell's theories and his work attracted little notice.

5. HEINRICH HERTZ

At the same time that Lodge was undertaking his experiments, there were even more effective investigations being carried out by Heinrich Hertz in Germany. Hertz, the son of a lawyer, was born in February 1857. He turned eventually to science with a year's course at Munich, transferring in 1878 to the University of Berlin. Here he studied under Professor von Helmholtz, who gave much encouragement to one he recognized as an outstanding pupil. Finally, having been awarded his doctorate, Hertz was appointed assistant professor at the Physics Institute of Berlin in 1880.

Hertz had been brought up in the “instantaneous action at a distance” school of thought, but fairly early in his career he was introduced to Maxwell's theories by professor von Helmholtz, who encouraged him to attempt experimental proof of Maxwell's postulated *displacement current* in air or empty space. Hertz did not immediately take this up, but he was intrigued by the possibility that the concepts of displacement currents and electromagnetic waves could fundamentally change action at a distance theories.

A few years later he had been appointed professor at the Technical High School at Karlsruhe and found there in a collection of old physical apparatus a pair of Knochenhauer spirals, flat coils wound in wooden frames. Experimenting casually with these, he noticed that discharging a Leyden jar through one of the coils gave rise to a small spark across the open terminals of the other some distance away. This revived his earlier interests, and he began to devote effort to theoretical clarification of Maxwell's equations. He became increasingly convinced that the equations could indeed give the true explanation of electric and magnetic field phenomena, and by 1884 he wrote “I think we may infer without error that if the choice rests only between the usual system of electromagnetics and Maxwell's, the latter is certainly to be preferred.” But the physical existence of electromagnetic waves, and especially their finite velocity of propagation, needed to be established by practical demonstration, so Hertz undertook a series of experiments culminating in the famous ones of 1887/88 that proved the point beyond all doubt. It is true that others before him had, rather accidentally, observed electromagnetic radiation, notably Mahlon Loomis in the United States in 1872 and David Hughes in England in 1879, but neither of them under-

stood what was happening or were familiar with Maxwell's work.

Hertz's investigations into the subject had involved generation, detection, and measurement of waves in free space, rather than along wires. Lodge generously acknowledged that Hertz experiments were superior to his own and a more convincing proof of the validity of Clerk Maxwell's theories.

After his experiments Hertz undertook further theoretical interpretation and development of the Maxwell concepts, much helped by his correspondence with FitzGerald, Lodge, and Heaviside, which revealed significant earlier work by these Maxwellians that he had not previously heard of. Hertz's papers in 1890 were particularly important in the field of theoretical physics and were influential in setting the scene for the later achievements of Lorentz and Einstein. Hertz died in 1894 at the early age of 36.

Hertz was not primarily an experimentalist seeking to demonstrate the existence of electromagnetic waves. He was a theoretical physicist who conducted his famous experiments as a means of justifying his firm conclusion on a matter of fundamental scientific importance. The waves were not important to Hertz for their own sake; he saw them simply as affording proof that Maxwell's equations gave the true picture and that hitherto accepted theories of action at a distance must therefore be regarded as obsolete.

The three Maxwellians, Lodge, FitzGerald, and Heaviside, were of a like mind. They were satisfied with the fact that Hertz had experimentally demonstrated the real existence of electromagnetic radiation, and neither they nor Hertz himself concerned themselves with any possible practical applications such as communication.

Someone soon did, however; Richard Threlfall, as president of the Australasian Association for the Advancement of Science, proposed in 1890 using Hertzian waves for communication purposes. But no one else saw this as a practical proposition at the time, the range of a few yards achieved by Hertz in his Karlsruhe laboratory not seeming to offer very much.

6. WIRELESS TELEGRAPHY BEGINS WITH MARCONI

Five or six years went by with nothing very significant happening until Hertz' death in 1894. But ironically, this was one further event involving Hertz that had a most profound impact, for in that year the 20-year-old Guglielmo Marconi, on holiday in the Italian Alps, read an obituary describing the work of Hertz. He was immediately inspired to consider whether Hertzian waves might not form the basis of a wireless telegraph communication system, and dedicated himself to this idea for the rest of his life.

At the end of his holiday Marconi returned to the family home in the Villa Griffone near Bologna, and at once commenced experiments in his attic workshop, where he had long since occupied himself with the electrical devices that had fascinated him from boyhood.

It is a well-known story how Marconi improved his apparatus and techniques to achieve greater and greater ranges during 1894/95; how he came to England in 1896 to make further progress; and how he spanned the Atlantic with the letter "S" in Morse in 1901. This story need not be told again here, but Marconi's relationship with Oliver Lodge is perhaps less well known and may usefully be described.

7. LODGE AND COHERERS

Although it was Hertz who first contrived to demonstrate the existence of electromagnetic waves in free space and that they exhibited reflection and refraction in the same way as light, it is true to say that Lodge knew and understood as much or more about the nature and behavior of the waves than did anyone else in the latter years of the nineteenth century.

As already mentioned, Lodge was thoroughly conversant with resonance and tuning, and he also well understood the principles underlying radiation from antennas of various configurations. Although he knew that waves must be radiated into free space, he lacked any means of detecting them; and it was use of the crude, but just adequate, resonant sparkgap detector that enabled Hertz to effect his splendidly successful experiments.

But in 1889, the year after Hertz' demonstrations, Lodge made a discovery that was to prove a crucial step forward on the path to a practical wireless communication system. During his investigations into lightning and the analogous effects of spark discharges from Leyden jars, Lodge observed that two iron spheres or other metal surfaces very close together would at times fuse together to form a conducting path when subjected to a Hertzian wave pulse. He called this arrangement a *coherer*, saying that it formed "an astonishingly sensitive detector of Hertzian waves." Later, in 1893, he was made aware of the work of Edouard Branly in France, who had observed similar cohering effects with a glass tube filled with metal filings. Lodge immediately tried this for himself and found it very much more sensitive than his own iron spheres. In fact the phenomenon of coherence resulting from nearby spark discharges had been independently noticed by others some years earlier, including Guitard in 1850, Varley in 1866, and Onesti in 1874; but these predecessors had not in fact ascribed the effects to Hertzian waves, and neither had Branly in his 1890 experiments. In 1902 Lodge, in conjunction with Alexander Muirhead, invented a new form of coherer in which a knife-edged steel wheel grazed the surface of a small pool of mercury covered with a film of oil: an incoming radio pulse ruptured the thin oil film and allowed low-resistance contact between the steel and the mercury. This type of coherer was at least as sensitive as any other and a good deal more stable in operation.

Lodge did not at the time attempt to put his coherers to practical use, but Marconi used a filings version in his early apparatus. It was this, plus the use of elevated antennas and connection to Earth, which enabled Marconi to develop and steadily improve his equipment to the point

where it could be seen as a workable wireless communication system.

8. LODGE VERSUS MARCONI

Marconi came to England in 1896 as a young man of nearly 22, with little theoretical knowledge of wireless principles but full of enthusiasm and dedication. He had a flair for publicity and in December gave a demonstration to members of the public, carrying a blackbox around the audience that rang a bell whenever a key at the end of the hall was depressed. Representatives of the press were present, and the next day Marconi was headline news, hailed as the inventor of wireless. In fact Marconi was always quite modest and did not claim to be an inventor but rather that he “took up others people’s ideas and inventions and improved them.” But Lodge, and other scientists who had made significant contributions in the field, was naturally indignant about the adulation of a young Italian upstart: Lodge may thus be forgiven his testy comment in later years that “It was stale news to me and to a few others,” but he then added more generously, “But whereas we had been satisfied that it *could* be done, Marconi went on enthusiastically and persistently till he made it a practical success.”

Another area of interplay between Marconi and Lodge was tuning. As already mentioned, Lodge had a full understanding of the principles of resonance and tuning and in May 1897 he applied for a patent on his *syntony* ideas.

Tuning, and the resultant ability to separate one transmission from another, was of course a vital necessity for the development of Marconi’s wireless system and he tried many different circuit arrangements with gradually increasing success. Finally in 1900 his famous “four sevens” patent was granted. It may appear strange that he was granted this patent when Lodge had registered his some years earlier; but it seems that it was not considered that one infringed the other, and it was ruled in court that the two were complementary rather than duplications. Nevertheless the existence of Lodge’s patent was seen as an embarrassment by the Marconi Company, especially when its validity was extended in 1911 by a further 7 years. Accordingly, the Marconi Company negotiated with Lodge and bought his patent for a considerable sum.

9. THE LODGE–MUIRHEAD SYNDICATE

Another source of rivalry was the appearance of the Lodge–Muirhead Syndicate with a competing wireless telegraphy system. Although Lodge was basically uninterested in commercial exploitation of his Hertzian wave experiments and discoveries, such a venture was suggested to him by Dr. Alexander Muirhead after he had attended one of Lodge’s lectures in 1894. This eventually resulted in formation of the Lodge–Muirhead Syndicate in which Lodge provided the scientific ideas and Muirhead—a very able telegraph engineer—the design of practical equipment.

By 1903 the Syndicate was ready with a well-designed and effective system incorporating the Lodge steel–mercury coherer, but they found themselves up against the Marconi Company’s monopoly of coastal stations in the United Kingdom that it had negotiated with Lloyds of London from 1901, and the company’s contracts with many shipping lines for exclusive use of Marconi equipment and operators.

Faced with this situation, the Syndicate could find only limited markets in the military field and in a few overseas countries. So despite its technical excellence, the Lodge–Muirhead system was not a commercial success and was wholly bought out by the Marconi Company in 1911, together with the Lodge tuning patent referred to previously.

10. CONTINUOUS-WAVE TELEGRAPHY

Early radiotelegraphy was effected by spark trains produced as Morse signals by a telegraph key. The spark-induced oscillation bursts making up a dot or dash were randomly phased.

It was realized that continuous wave trains could be advantageous in offering narrower bandwidth transmission and hence the possibility of more precise tuning of transmitter and receiver, and various developments were undertaken to achieve this. The first was Marconi’s synchronous spark discharger wherein multiple sparkgaps on a rotating disk ensured that the oscillations from one gap would be so phased as to continue the oscillations from the preceding gap, giving a reasonable approximation of a continuous wave.

An alternative approach was the Poulsen system, based on earlier work by Duddell, using the negative resistance characteristic of an arc to generate continuous oscillation in a parallel resonant circuit. This was quite widely used by the German Telefunken company for a radiotelephone system, but was not always successful due to the difficulty of maintaining a steady arc discharge.

Another alternative was the high-frequency alternator. Difficulties here arose from the very high rotational speeds necessary to produce even quite modest radio-frequencies; but Ernst Alexanderson of American General Electric designed very successful machines capable of 100 kHz at powers of hundreds of kilowatts. A later development in Germany was the Goldschmidt HF, alternator, which reduced the need for excessive rotational speed by an ingenious system of frequency multiplication within the machine. With suitable coils and pole pieces, and moderate speed, the rotor could produce a frequency of perhaps 15 kHz; this would be induced in the stator, setting up a rotating field therein. The stator field was arranged to rotate in the direction opposite that of the rotor, so that an oscillation of double the frequency, 30 kHz was induced in the stator and $30 + 15 = 45$ kHz in the rotor. This 45 kHz was selected by a tuned filter resulting in a frequency of 60 kHz in the stator; the latter frequency was applied to the aerial for transmission. The Goldschmidt patents were bought up by the Marconi Company in 1913.

A difficulty with any of these machines was to maintain very precise alternator rotational speed, since even a small fluctuation would seriously detract from the potential for exact frequency stability and receiver selectivity. Particularly difficult was avoidance of speed changes with electrical load when the Morse key was operated; and this was compensated to some extent by a subsidiary key contact adjusting the alternator driving motor field when the key was depressed.

A final problem was that a continuous wave would by itself produce no sound in receiver headphones. To render Morse signals audible required the wave to be modulated at audiofrequency. Crude modulation could be provided by a "ticker," a chattering contact that broke up the continuous wave into audiofrequency groups. A better solution was to modulate the signals with a frequency about 1 kHz different from the main carrier to produce an audible "beat" note. This was achieved by Fessenden's heterodyne arrangement or by Goldschmidt's tonewheel.

11. RADIOTELEPHONY

Most early workers were content to communicate in Morse code telegraphy, but Reginald Fessenden, a Canadian working in the United States, considered radiotelephony much preferable. In 1900 he achieved speech transmission over a distance of 1 mi using a spark transmitter with a spark repetition frequency of 10,000/s. But modulating speech on a spark signal has been memorably described as "like printing a newspaper on a roll of stair carpet," and articulation and background noise were very unsatisfactory.

Fessenden realized that a continuous wave carrier was necessary for satisfactory speech modulation, and he initially experimented with arc-based oscillators, but found a HF alternator more satisfactory. On Christmas Eve 1906, and again on New Year's Eve, he successfully transmitted speech and music from his Brant Rock station using a HF alternator. Remarkably, his experimental speech transmissions shortly before these two events were heard by chance at Fessenden's receiving station at Machrihanish in Scotland.

In the very early years of the twentieth century the only radiowave detector was the coherer; but this, which was an ON/OFF device, was suitable only for reception of Morse transmissions. Fessenden sought a continuously operating detector that would be suitable for demodulating speech signals on a continuous-wave carrier, and in 1903 invented his "liquid barretter," an electrolytic gas generator that did indeed respond continuously to the amplitude of a received carrier. This was used in conjunction with his 1906 speech and music transmissions, although by this time the Marconi magnetic detector was also in use and capable of amplitude demodulation, as were Fleming's diode of 1904 and the crystal detectors introduced by Braun, Austen, Pickard, Pierce, and Dunwoody from 1906.

Lee de Forest developed an arc-based radio telephone in 1907/08, which was supplied in some quantity to the U.S. Navy.

12. VACUUM TUBES

On the basis of Thomas Edison's discovery in 1883 of unilateral conduction or electric current between an incandescent filament and an adjacent "plate" electrode, John Ambrose Fleming in England devised his "oscillation valve" in 1904. In 1906 de Forest introduced a third "grid" electrode between filament and plate, thus inventing the triode tube: but he had little understanding of the operating principles of his invention, and it was the detailed studies of Howard Armstrong and Irving Langmuir that developed it into a reliable and practical device by 1915.

Also in 1915, Armstrong developed the regeneration principle and hence the triode oscillator, and this finally fulfilled the need for convenient and stable generation of continuous radiofrequency oscillations that could readily be amplitude modulated for radiotelephony applications. Furthermore, the triode could be configured as a sensitive detector of such signals.

Thus was opened the way to modern electronics and, a few years later, to entertainment broadcasting of speech and music.

FURTHER READING

- M. Adams, *The Race for the Radiotelephone*, AWA Review, Vol. 10, The Antique Wireless Association, Bloomfield, NY, 1996.
- W. J. Baker, *A History of the Marconi Company*, Methuen, London, 1970.
- A. Briggs, *The Golden Age of Wireless*, Oxford Univ. Press, New York, 1965.
- L. Coe, *Wireless Radio: A Brief History*, McFarland, Jefferson, NC, 1996.
- H. M. Dowsett, *Wireless Telegraphy and Broadcasting*, Gresham Publishing, London, 1923.
- H. M. Dowsett, *Handbook of Technical Instruction for Wireless Telegraphists*, The Wireless Press, London, 1925.
- O. E. Dunlap, *Marconi, The Man and His Wireless*, Arno Press, New York, and *The New York Times*, 1971.
- W. H. Eccles, *Continuous Wave Wireless Telegraphy*, Wireless Press, London, 1921.
- J. J. Fahie, *A History of Wireless Telegraphy*, Arno Press, New York, and *The New York Times*, 1971.
- H. M. Fessenden, *Fessenden Builder of Tomorrows*, Arno Press, New York, 1974.
- G. M. Garratt, *The Early History of Radio*, IEE, London, 1994.
- J. V. Hinshaw, *Marconi and His South Wellfleet Wireless*, Chatham Press, Chatham, MA, 1969.
- W. P. Jolly, *Marconi*, Constable, London, 1972.
- T. S. W. Lewis, *Empire of the Air*, Harper Collins, New York, 1991.
- T. L. Mayes, *Wireless Communication in the United States: The Early Development of American Radio Operating Companies*, New England Wireless and Steam Museum, East Greenwich, RI, 1989.
- J. G. O'Hara and W. Pricha, *Hertz and the Maxwellians*, IEE, London, 1987.
- V. J. Phillips, *Early Radio Wave Detectors*, IEE, London, 1980.
- P. Rowlands and J. P. Wilson, *Oliver Lodge and the Invention of Radio*, PD Publications, Liverpool, UK, 1994.
- R. Stanley, *Book of Wireless Telegraphy*, Longmans, London, 1919.

G. E. Sterling, *The Radio Manual*, Van Nostrand, New York, 1928.

G. F. J. Tyne, *Saga of the Vacuum Tube*, Howard W. Sams, Indianapolis, 1977.

HORN ANTENNAS

EDWARD V. JULL
 University of British Columbia
 Vancouver, British Columbia
 Canada

A “horn” antenna is a length of conducting tube, flared at one end, and used for the transmission and reception of electromagnetic waves. For an efficient transition between guided and radiated waves, the horn dimensions must be comparable to the wavelength. Consequently horns are used mostly at centimeter and millimeter wavelengths. At lower or higher frequencies they are inconveniently large or small, respectively. They are most popular at microwave frequencies (3–30 GHz), as antennas of moderate directivity or as feeds for reflectors or elements of arrays.

Since acoustic horns have been in use since prehistoric times, the design of horns as musical instruments was a highly developed art well before the appearance of the first electromagnetic horns. This occurred shortly after Hertz in 1888 first demonstrated the existence of electromagnetic waves. Experimenters placed their sparkgap sources in hollow copper tubes (Figs. 1a, 5a). These tubes acted as highpass filters for microwave and millimeter-wave radiation from the open end. In London in 1897 Chunder Bose used rectangular conducting tubes with “collecting funnels,” or pyramidal horns (Fig. 1d) in his demonstrations at 5 and 25 mm wavelengths [1]. Thus the electromagnetic horn antenna was introduced but this early beginning of microwave invention closed with Marconi’s demonstration that longer wavelengths could be received at greater distances. Horns were too large to be practical at those wavelengths, and it was almost 40 years before microwave horns reappeared with the need for directive antennas for communications and radar. Horns alone were often not sufficiently directive but combined in an array or with a lens (Fig. 4a), or more often a parabolic reflector (Figs. 4b, 4c) highly directive antenna beams are obtained.

1. RADIATING WAVEGUIDES AND HORNS

Horns are normally fed by waveguides supporting only the dominant waveguide mode. For a rectangular waveguide (Fig. 1a) with TE_{01} mode propagation only, these dimensions in wavelengths λ are $\lambda/2 < a < \lambda$ and $b \approx a/2$. Open-ended waveguides have broad radiation patterns, so when used as a feed for a reflector, there is substantial spillover, or radiation missing the reflector and radiation directly backward from the feed. To increase the directivity of a radiating waveguide and its efficiency as a reflector feed, for example, its aperture dimensions must be enlarged, for the beamwidth of an aperture of width $a \gg \lambda$ is proportional to λ/a radians.

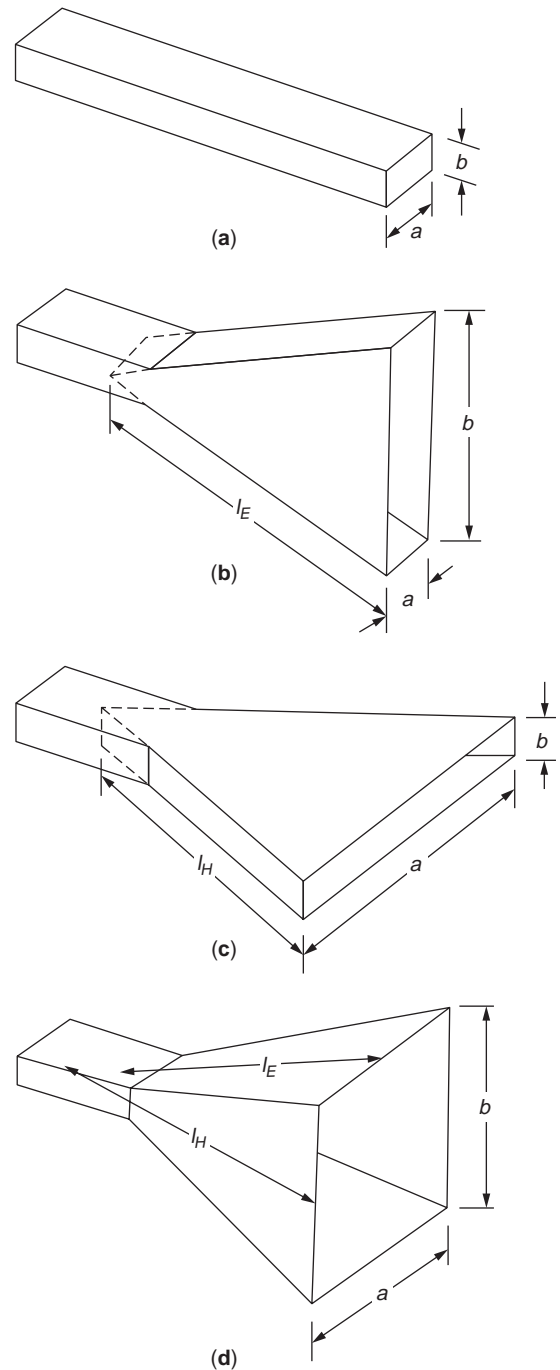


Figure 1. (a) Open-ended rectangular waveguide; (b) E -plane sectoral horn; (c) H -plane sectoral horn; (d) pyramidal horn.

This waveguide enlargement by a flare characterizes horns. The aperture fields of a horn are spherical waves originating at the horn apex (Fig. 2). The path from the horn apex to the aperture plane at a distance x from the aperture center of a horn of slant length ℓ is

$$\rho = ((\ell \cos \alpha)^2 + x^2)^{1/2} \approx \ell \cos \alpha + \frac{x^2}{2\ell \cos \alpha} \quad (1)$$

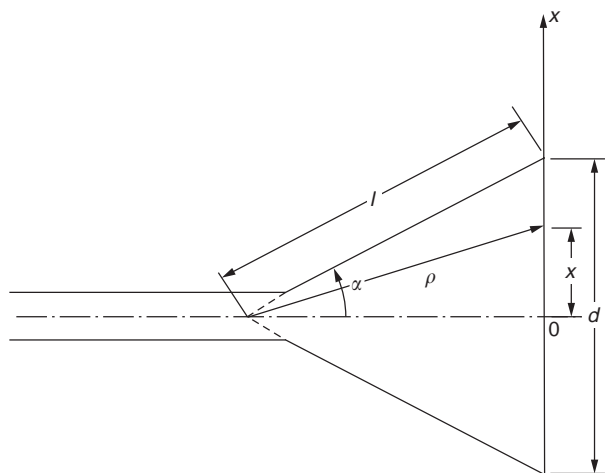


Figure 2. Effect of horn flare on the aperture field phase of a horn.

when $x \ll l \cos \alpha$. Thus the phase variation in radians across the aperture for small flare angles α is approximately $kx^2/(2\ell)$, where $k = 2\pi/\lambda$ is the propagation constant. This quadratic phase variation increases with increasing flare angle, thus reducing directivity increase due to the enlarged aperture dimension. It is convenient to quantify aperture phase variation by the

parameter

$$s = \frac{\ell(1 - \cos \alpha)}{\lambda} \approx \frac{d^2}{8\lambda\ell}, \quad d \ll \ell \tag{2}$$

which is the approximate difference in wavelengths between the distance from the apex to the edge ($x = d/2$) and the center ($x = 0$) of the aperture. The radiation patterns of Figs. 3a, 3b [2] show the effect of increasing s on the E - and H -plane radiation patterns of sectoral and pyramidal horns. The main beam is broadened, the pattern nulls are filled, and the sidelobe levels are raised over those for an in-phase aperture field ($s = 0$). With large flare angles radiation from the extremities of the aperture can be so out of phase with that from the center that the horn directivity decreases with increasing aperture width.

The adverse effects of the flare can be compensated by a lens in the aperture (Fig. 4a), but because that adds to the weight and cost and because bandwidth limitations are introduced by matching the lens surfaces to reduce reflections, it is seldom done. Instead, a combination of aperture width and flare length in wavelengths is chosen that provides maximum axial directivity or minimum beamwidth. This is an “optimum” horn design. To achieve higher directivity or narrower beamwidth for a given aperture width, a longer horn is required.

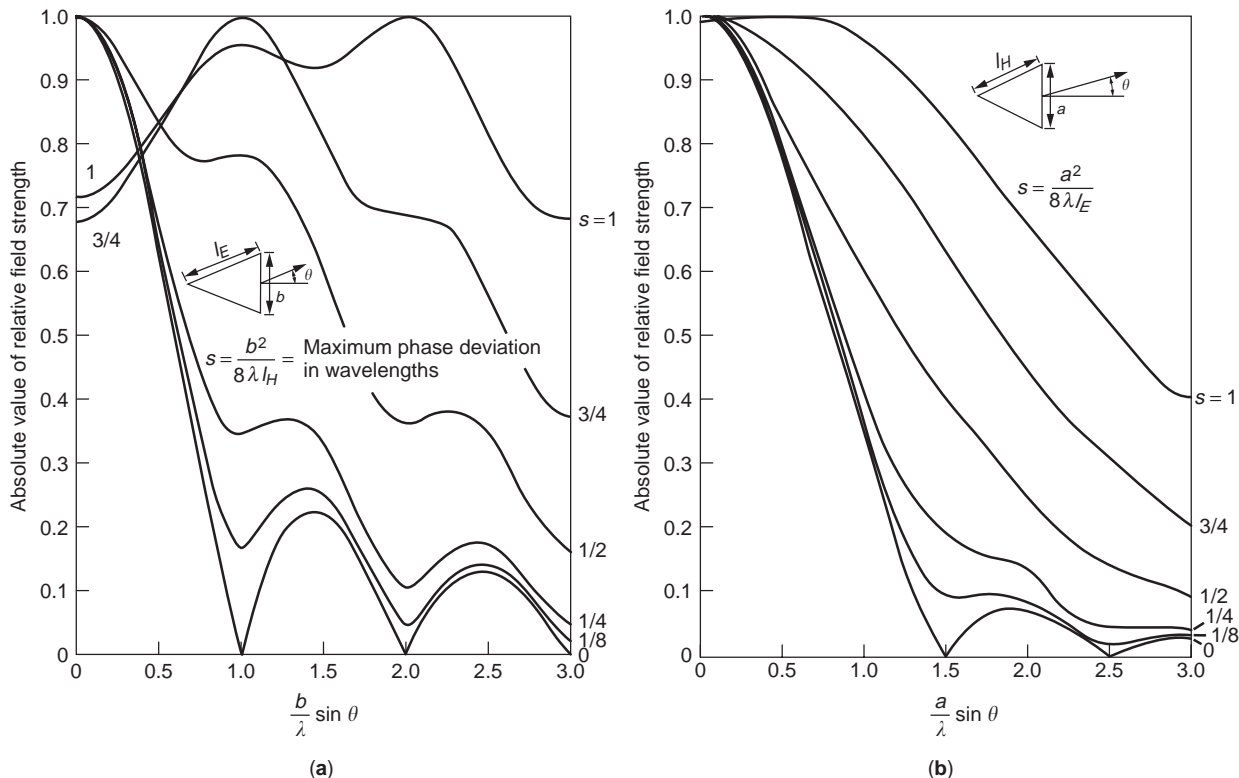


Figure 3. Universal radiation patterns of sectoral and pyramidal horns flared in the (a) E and (b) H planes. The parameter $s = b^2/8\lambda\ell_E$ in (a) and $a^2/8\lambda\ell_H$ in (b); $2\pi s/\lambda$ is the maximum phase difference between the fields at the center and the edge of the aperture. (Copyright 1984, McGraw-Hill, Inc. from Love [2].)

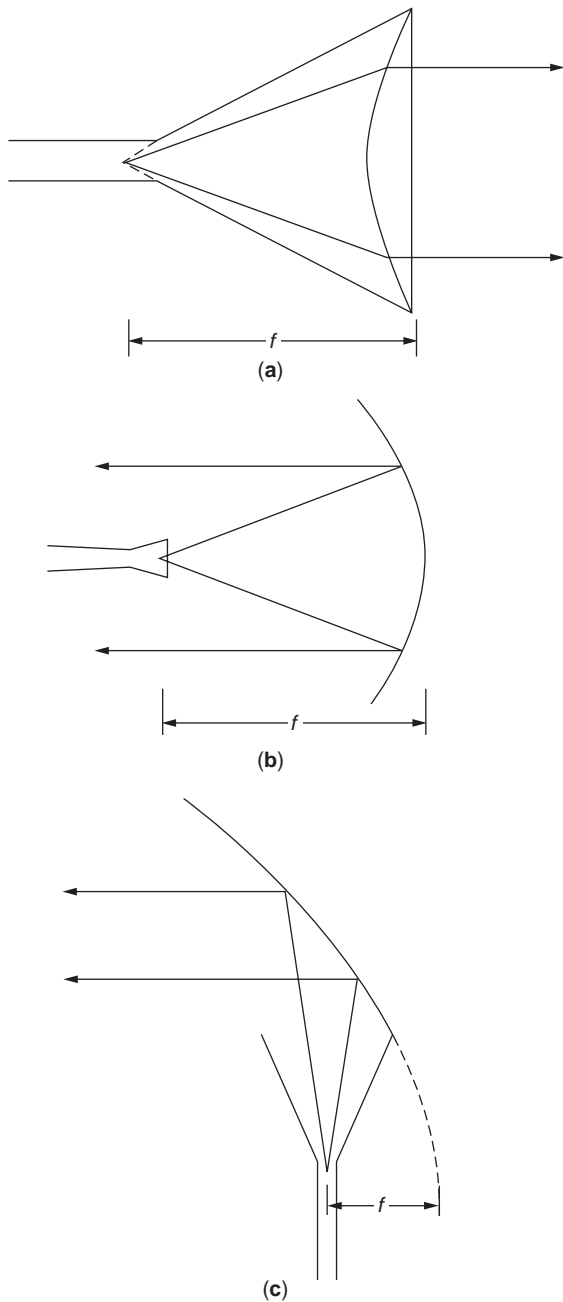


Figure 4. (a) Horn aperture field phase correction by a lens; (b) parabolic reflector fed by a horn; (c) horn reflector antenna (f =focal length of the lens or reflector).

Sectoral horns (Figs. 1b, 1c) are rectangular waveguides flared in one dimension only. The incident waveguide mode becomes a radial cylindrical mode in the flared region of the horn. Since radiation pattern beamwidths are inversely proportional to aperture dimensions in wavelengths, sectoral horns have beams that are narrow in the plane containing the broad dimension. Such fan-shaped beams may be useful for illuminating elongated parabolic reflectors or parabolic cylinder reflectors.

A pyramidal horn (Fig. 1d) is flared in both waveguide dimensions and so is more adaptable both as a reflector feed and on its own. The forward radiation pattern may be

calculated quite accurately from Kirchhoff diffraction theory for all except small horns. The TE_{01} rectangular waveguide mode yields an aperture field uniform in one dimension (in the E plane) and cosinusoidal in the other (the H plane). A comparison of parts (a) and (b) of Fig. 3 shows that this results in a higher sidelobes in the E plane and, for a square aperture, a narrower beam. Pyramidal horns are relatively easily constructed, and for all except small horns their axial gain can be predicted accurately. Consequently, they are used as gain standards at microwave frequencies; that is, they are used to experimentally establish the gain of other microwave antennas by comparing their response to the same illuminating field.

Most of the preceding remarks on open-ended rectangular waveguides and pyramidal horns also apply to open-ended circular waveguides and conical horns (Figs. 5a, 5b). For propagation of the lowest-order mode (TE_{11}) only in a circular waveguide, the interior diameter must be $0.59\lambda < a < 0.77\lambda$. This mode has a uniform aperture field in the E plane and a cosinusoidal distribution in the orthogonal H plane. This appears, modified by a quadratic phase variation introduced by the flare, in the aperture field of the horn. Consequently the E -plane radiation pattern of the horn is narrower, but with higher sidelobes than the H -plane pattern and the radiated beam is elliptical in cross section. In addition, cross-polarized fields appear in pattern lobes outside the principal planes.

2. HORN FEEDS FOR REFLECTORS

Many refinements to horns arise from their use as efficient feeds for parabolic reflectors, particularly in satellite and space communications and radio astronomy. The phase center, where a horn's far radiation field appears to originate, must be placed at the focus of the reflector (Fig. 4b). This phase center is within the horn on the horn axis and depends on the flare angle and aperture distribution. For both rectangular and conical horns the position of the phase center is not the same in the E and H planes, or planes containing the electric and magnetic field vectors, respectively. A phase center can be calculated from the average of the positions of the E - and H -plane phase centers or determined from the position of the feed that maximizes the gain of the reflector antenna.

For efficient aperture illumination the feed horn radiation pattern should approximately match the shape of the aperture, and illuminate it essentially uniformly and with minimal spillover, or radiation missing the reflector. Pyramidal horns may seem suitable for rectangular apertures because their beams are rectangular in cross section, and conical horns may seem a natural choice for a circular aperture, but efficient aperture illumination is not obtained in either case, because their principal plane patterns differ. Both horns have high E -plane pattern sidelobes and low H -plane sidelobes. A dual (TE_{11}/TM_{11})-mode conical horn provides equal E - and H -plane beamwidths and equally low sidelobes, and is an efficient feed for a circular aperture over a narrow frequency band (see Love [3], p. 195; Ref. 3 also contains reprints of most earlier significant papers on horn antennas). A broadband

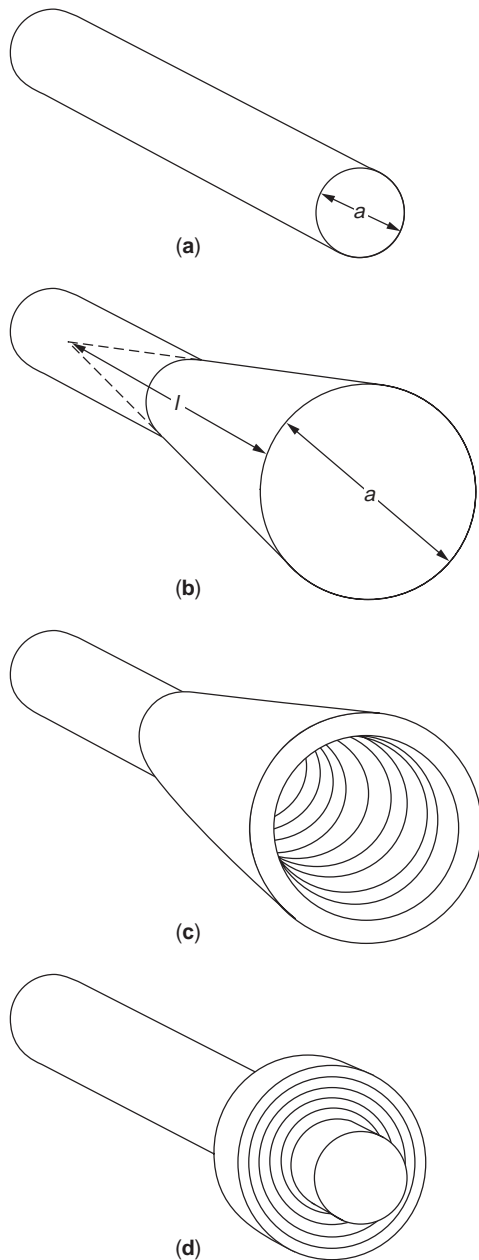


Figure 5. (a) Open-ended circular waveguide; (b) conical horn; (c) corrugated horn; (d) circular waveguide with corrugated flange.

solution achieves an axisymmetric beam with annular corrugations on the interior surfaces of a conical horn (Fig. 5c). These produce a horn aperture field distribution that is approximately cosinusoidal across the conical horn aperture in all directions and hence an axisymmetric radiation pattern with low sidelobes. Such corrugations in the E -plane interior walls only of a pyramidal horn will produce a cosinusoidal E -plane aperture distribution, and consequently similar E -plane and H -plane radiation patterns for a square horn aperture.

A feed for a small circular reflector that is more easily constructed than a corrugated conical horn but with a less axisymmetric radiation pattern, is an open-ended circular

waveguide ringed by a recessed disk of approximately quarter-wavelength-deep corrugations (Fig. 5d). These corrugations suppress backradiation from the feed and so improve the aperture illumination over that of a simple open circular waveguide [3, pp. 181, 226]. Combined with dual-mode excitation, this arrangement provides a simple and efficient feed for a front-fed paraboloidal reflector.

3. RADIATION FROM APERTURES

The far-field radiation pattern of an aperture can be calculated exactly from the Fourier transform of the tangential fields in the entire aperture plane. Either electric or magnetic aperture fields may be used but for apertures in space, a combination of the two gives the best results from the usual assumption that aperture plane fields are confined to the aperture and negligible outside it. This aperture field is assumed to be the undisturbed incident field from the waveguide. For apertures with dimensions larger than several wavelengths, a further simplifying assumption usually made is that the aperture electric and magnetic fields are related as in free space.

3.1. Rectangular Apertures

With the abovementioned assumptions, at a distance much greater than the aperture dimensions, the radiated electric field intensity of a linearly polarized aperture field $E_x(x, y, 0)$ in the coordinates of Fig. 6a is

$$\bar{E}(r, \theta, \phi) = \bar{A}(r, \theta, \phi) \int_{-(b/2)}^{b/2} \int_{-(a/2)}^{a/2} E_x(x, y, 0) e^{j(k_1 x + k_2 y)} dx dy \quad (3)$$

Here

$$\left. \begin{aligned} k_1 &= k \sin \theta \cos \phi \\ k_2 &= k \sin \theta \sin \phi \end{aligned} \right\} \quad (4)$$

and

$$\bar{A}(r, \theta, \phi) = j \frac{e^{-jkr}}{2\lambda r} (1 + \cos \theta) (\hat{\theta} \cos \phi - \hat{\phi} \sin \phi) \quad (5)$$

is a vector defining the angular behavior of the radiation polarization for an aperture in space. For an aperture in a conducting plane, it is more accurate to use

$$\bar{A}(r, \theta, \phi) = j \frac{e^{-jkr}}{\lambda r} (\hat{\theta} \cos \phi - \hat{\phi} \sin \phi \cos \theta) \quad (6)$$

which, since it is based on the aperture plane electric fields only, fully satisfies the assumption of a vanishing tangential field in the aperture plane outside the aperture. Consequently radiation fields of open-ended waveguides and small horns can be calculated accurately from (3) with (6) if they are mounted in a conducting plane. Clearly (5) and (6) differ significantly only for large angles θ off the beam axis.

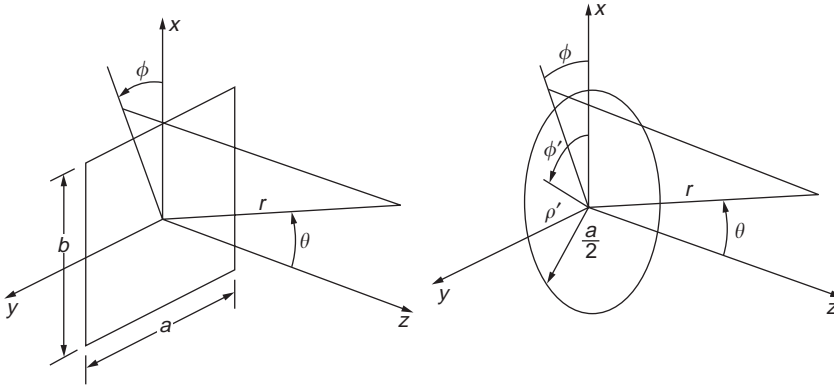


Figure 6. Coordinates for radiation from (a) rectangular and (b) circular apertures.

If the aperture field is separable in the aperture coordinates—that is, if in (3), $E_x(x, y, 0) = E_0 E_1(x) E_2(y)$, where $E_1(x)$ and $E_2(y)$ are field distributions normalized to E_0 , the double integral is the product of two single integrals

$$E(r, \theta, \phi) = \bar{A}(r, \theta, \phi) E_0 F_1(k_1) F_2(k_2) \quad (7)$$

where

$$F_1(k_1) = \int_{-(a/2)}^{a/2} E_1(x) e^{jk_1 x} dx \quad (8)$$

$$F_2(k_2) = \int_{-(b/2)}^{b/2} E_2(y) e^{jk_2 y} dy \quad (9)$$

define the radiation field.

4. OPEN-ENDED WAVEGUIDES

4.1. Rectangular Waveguides

With the TE_{10} waveguide mode the aperture field

$$E_x(x, y, 0) = E_0 \cos \frac{\pi y}{a} \quad (10)$$

in (7) yields the following equations for (8) and (9):

$$F_1(k_1) = b \frac{\sin\left(\frac{k_1 b}{2}\right)}{\frac{k_1 b}{2}} \quad (11)$$

$$F_2(k_2) = a \left(\frac{\cos\left(\frac{k_2 a}{2}\right)}{\pi^2 - (k_2 a)^2} \right) \quad (12)$$

This defines the radiation pattern in the forward hemisphere $-\pi/2 < \theta < \pi/2$, $0 < \phi < 2\pi$. If the aperture is in space, then (5) is used for $\bar{A}(r, \theta, \phi)$, but this is not an accurate solution since the aperture dimensions are not large. Rectangular waveguides mounted in conducting planes use (6) for $\bar{A}(r, \theta, \phi)$ in (7), which then accurately provides the far field. The pattern has a single broad lobe

with no sidelobes. For large apertures plots of the normalized E -plane ($\phi = 0$) and H -plane ($\phi = \pi/2$) patterns of (7) appear in Figs. 3a and 3b for those of a horn with no flare ($s = 0$), but without the factor $(1 + \cos \theta)/2$ from (5) or $\cos \theta$ from (6).

4.2. Circular Waveguides

The dominant TE_{11} mode field in circular waveguide produces an aperture field distribution, which in the aperture coordinates ρ', ϕ' of Fig. 6b is

$$\bar{E}(\rho', \phi') = E_0 \left[\hat{\rho}' \frac{J_1(k_c \rho')}{k_c \rho'} \cos \phi' + \hat{\phi}' J_1'(k_c \rho') \sin \phi' \right] \quad (13)$$

where J_1 is the Bessel function of the first kind and order, J_1' is its derivative with respect to its argument $k_c \rho'$, and $k_c a/2 = 1.841$ is its first root; E_0 is the electric field at the aperture center ($\rho' = 0$). Since (13) is not linearly polarized, its use in (3) provides only part of the total radiated far field. The total field

$$\bar{E}(r, \theta, \phi) = jka E_0 J_1(1.841) \frac{e^{-jkr}}{r} \left\{ \hat{\theta} \cos \phi \frac{J_1\left(\frac{k'a}{2}\right)}{\frac{k'a}{2}} + \hat{\phi} \sin \phi \cos \theta \frac{J_1\left(\frac{k'a}{2}\right)}{1 - \left(\frac{k'a}{3.682}\right)^2} \right\} \quad (14)$$

in which $k' = k \sin \theta$.

In the E and H planes ($\phi = 0$ and $\pi/2$) the cross-polarized fields cancel and the patterns shown in Fig. 14a are similar to those of (11) and (12), respectively, but with slightly broader beams and lower sidelobes for the same aperture dimensions. As with rectangular waveguides, open-ended circular waveguide apertures are insufficiently large for (14) to represent all the radiated fields accurately. In the principal planes ($\phi = 0, \pi/2$), it can give a reasonable approximation for the copolarized fields but fails to accurately represent the cross-polarized field patterns in $\phi = \pi/4$. This is evident from a comparison of

numerical results from approximate and exact solutions [4, p. 233].

5. PYRAMIDAL AND SECTORAL HORNS

5.1. Radiation Patterns

A pyramidal horn fed by a rectangular waveguide supporting the TE_{10} mode has an incident electric field in the aperture of Fig. 6a that is approximately the mode distribution modified by a quadratic phase variation in the two aperture dimensions:

$$E_x(x, y, 0) = E_0 \cos\left(\frac{\pi y}{a}\right) \exp\left(-jk\left(\frac{x^2}{2\ell_E} + \frac{y^2}{2\ell_H}\right)\right) \quad (15)$$

With (15), Eq. (3) becomes

$$\bar{E}(r, \theta, \phi) = \bar{A}(r, \theta, \phi) E_0 I_1(k_1) I_2(k_2) \quad (16)$$

where (5) is used for $\bar{A}(r, \theta, \phi)$ and

$$I_1(k_1) = \int_{-(b/2)}^{b/2} \exp\left(-j\left(\frac{\pi x^2}{\lambda \ell_E} - k_1 x\right)\right) dx \quad (17)$$

$$I_2(k_2) = \int_{-(a/2)}^{a/2} \cos\left(\frac{\pi y}{a}\right) \exp\left(-j\left(\frac{\pi y^2}{\lambda \ell_H} - k_2 y\right)\right) dy \quad (18)$$

The E -plane ($\phi = 0$) and H -plane ($\phi = \pi/2$) radiation patterns are, respectively

$$\frac{E_\theta(r, \theta)}{E_\theta(r, 0)} = \frac{1 + \cos \theta}{2} \frac{I_1(k \sin \theta)}{I_1(0)} \quad (19)$$

$$\frac{E_\theta(r, \theta)}{E_\theta(r, 0)} = \frac{1 + \cos \theta}{2} \frac{I_2(k \sin \theta)}{I_2(0)} \quad (20)$$

These integrals can be reduced to the Fresnel integrals

$$C(u) - jS(u) = \int_0^u e^{-j(\pi/2)t^2} dt \quad (21)$$

which are tabulated and for which computer subroutines are available. For example, we obtain

$$\frac{I_1(k \sin \theta)}{I_1(0)} = \frac{e^{j(\pi \ell_E / \lambda) \sin^2 \theta} C(u_2) - C(u_1) - j[S(u_2) - S(u_1)]}{C(u) - jS(u)} \quad (22)$$

with

$$u = \frac{b}{\sqrt{2\lambda \ell_E}} \quad (23)$$

$$u_1^2 = \pm u - \sqrt{\frac{2\ell_E}{\lambda}} \sin \theta \quad (24)$$

Figure 3a shows plots of the magnitude of (22) for various values of the E -plane flare parameter $s = b^2/8\lambda \ell_E$, while

Fig. 3b shows corresponding plots of $|I_2(k \sin \theta)/I_2(0)|$ for the H -plane flare parameter $s = a^2/8\lambda \ell_H$. For no flare ($s = 0$) the patterns are those of a large open-ended rectangular waveguide supporting only the TE_{10} mode. The effect of the flare is to broaden the mainbeam, raise the sidelobes, and fill the pattern nulls. For larger values of s , there is enhanced pattern beam broadening and eventually a splitting of the mainbeam on its axis.

These curves also represent the radiation patterns of the E/H -plane sectoral horns of Figs. 1b and 1c. For an E -plane sectoral horn ($\ell_H \rightarrow \infty$), the E -plane pattern is given by (19) and the H -plane pattern approximately by (12). For an H -plane sectoral horn ($\ell_E \rightarrow \infty$), the E -plane pattern is given approximately by (11) and the H -plane pattern by (20).

In comparing parts (a) and (b) of Fig. 3 it is evident that E -plane beamwidths of a square aperture are narrower than H -plane beamwidths. For horns of moderate flare angle and optimum horns the E -plane half-power beamwidth is $0.89\lambda/b$ radians and the H -plane half-power beamwidth is $1.22\lambda/a$ radians. E -plane patterns have minimum sidelobes of -13.3 dB below peak power, while H -plane pattern minimum sidelobes levels are -23.1 dB.

The universal patterns of Fig. 3 can also be used to predict the approximate near-field radiation patterns of horns by including the quadratic phase error; which is a first-order effect of finite range r . This is done by including

$$\exp\left(-j\frac{\pi}{r\lambda}(x^2 + y^2)\right) \quad (25)$$

in (15). Then the near-field principal plane patterns of a pyramidal horn are given by (17) and (18) with ℓ_E, ℓ_H replaced by

$$\ell'_H = \frac{r\ell_H}{r + \ell_H} \quad (26)$$

and

$$\ell'_E = \frac{r\ell_E}{r + \ell_E} \quad (27)$$

These near-field effects are analogous to decreasing the flare length of a horn with a fixed aperture width. The mainbeam broadens, nulls are filled in, and sidelobes rise.

5.2. Limitations and Extensions

Results from (16) do not apply to small horns and are limited to the forward direction ($\theta < 90^\circ$). They are most accurate on and around the beam axis ($\theta = 0$), becoming progressively less accurate as θ increases. The simplest method for extending the analysis is by the uniform geometric theory of diffraction [e.g., 3, p. 66], which provides the edge-diffracted fields in the lateral and rear directions, which receive no direct illumination from the aperture. Only the edges normal to the plane of the pattern contribute significantly to the E -plane pattern, but the rear H -plane pattern requires contributions from all four aperture edges and so is difficult to calculate this way.

While the geometry of the pyramidal horn defies rigorous analysis, numerical methods have been used with some success for open waveguides and small horns. For larger horns this approach becomes computationally intensive, but some results from Liu et al. [5] are shown in Fig. 7 and compared with measurements and approximate computations. Their numerical computations and measurements by Nye and Liang [6] of the aperture fields show that higher-order modes need to be added to the dominant mode field of (15) and that the parabolic phase approximation of (1) improves as the aperture size increases.

5.3. Gain

Pyramidal horns are used as gain standards at microwave frequencies because they can be accurately constructed and their axial directive gain reliably predicted from a relatively simple formula. The ratio of axial far-field power density to the average radiated power density

from (16) yields

$$G = G_0 R_E(u) R_H(v, w) \quad (28)$$

where $G_0 = 32ab/(\pi\lambda^2)$ is the gain of an in-phase uniform and cosinusoidal aperture distribution. The reduction of this gain due to the phase variation introduced by the E -plane flare of the horn is

$$R_E(u) = \frac{C^2(u) + S^2(u)}{u^2} \quad (29)$$

where the Fresnel integrals and their argument are defined by (21) and (23). Similarly the gain reduction factor due to the H -plane flare of the horn is

$$R_H(v, w) = \frac{\pi^2}{4} \frac{[C(v) - C(w)]^2 + [S(v) - S(w)]^2}{(v - w)^2} \quad (30)$$

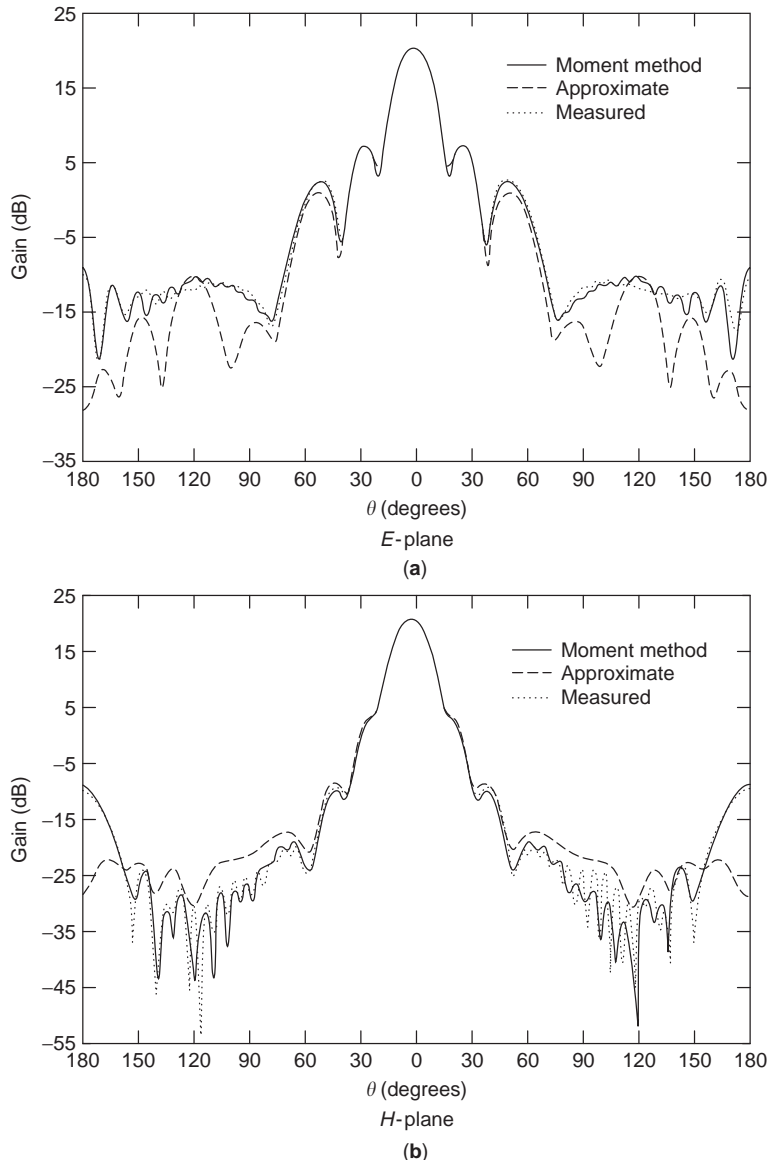


Figure 7. Calculated and measured (a) E -plane and (b) H -plane radiation patterns of a pyramidal horn of dimensions $a = 4.12\lambda$, $b = 3.06\lambda$, $\ell_E = 10.52\lambda$, $\ell_H = 9.70\lambda$ (Copyright 1993, IEEE, from Liu et al. [5].)

where

$$\frac{v}{w} = \pm \frac{a}{\sqrt{2\lambda\ell_H}} + \frac{1}{a} \sqrt{\frac{\lambda\ell_H}{2}} \quad (31)$$

A plot of R_E and R_H in decibels as a function of the parameter $2d^2/\lambda\ell$, where d is the appropriate aperture dimension b or a and ℓ the slant length ℓ_E or ℓ_H , respectively, is shown in Fig. 8. Calculation of the gain from (28) is accurate to about ± 0.1 dB for 22 dB standard gain pyramidal horns: optimum horns with dimensions of at least 5λ . For 18-dB-gain horns, the accuracy is about ± 0.2 dB, and for 15-dB horns, ± 0.5 dB. Since optimum gain pyramidal horns have an aperture efficiency of approximately 50%, the gain is approximately

$$G = 0.5 \frac{4\pi}{\lambda^2} ab \quad (32)$$

For an E -plane sectoral horn $\ell_H \rightarrow \infty$ and $R_H(v, w) \rightarrow 1$ the axial gain is then $G_E = G_0 R_E(u)$, an inaccurate formula because aperture dimension a is less than a wavelength. A result that includes the fact that aperture electric and magnetic fields are not related by free-space conditions and that interaction occurs across the narrow aperture of the horn is

$$G_E = \frac{16ab}{\lambda^2(1 + (\lambda_g/\lambda))} R_E(u') \exp\left[\frac{\pi a}{\lambda} \left(1 - \frac{\lambda}{\lambda_g}\right)\right] \quad (33)$$

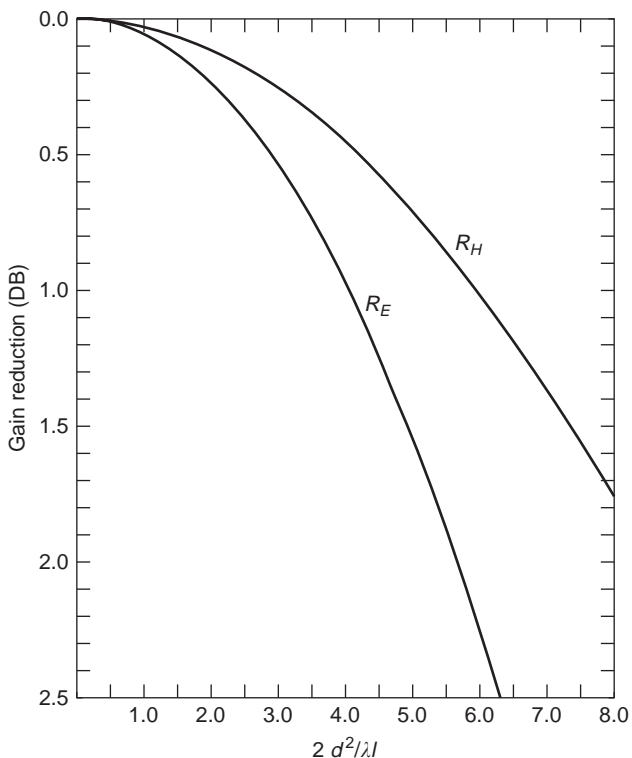


Figure 8. E - and H -plane flare and near-field gain reduction factors R_E and R_H of pyramidal and sectoral horns in decibels. (Copyright 1981, IEE, from Jull [11].)

where

$$u' = \frac{b}{\sqrt{2\lambda_g\ell_E}} \quad (34)$$

and

$$\lambda_g = \frac{\lambda}{\sqrt{1 - (\lambda/2a)^2}} \quad (35)$$

is the guide wavelength. The accuracy of (33) is comparable to that of (28) for the horns of similar b dimension.

The gain of an H -plane sectoral horn, obtained by letting $\ell_E \rightarrow \infty$ so that $R_E(u) \rightarrow 1$, is $G_H = G_0 R_H(v, w)$. It probably is reasonably accurate, but there appears to be no experimental evidence available to verify it.

The near-field gain of pyramidal and sectoral horns can be calculated from the preceding expressions by replacing ℓ_E and ℓ_H by (26) and (27), respectively.

6. CONICAL HORNS

The aperture field of a conical horn fed by a circular waveguide supporting the TE_{11} mode is approximately

$$E(\rho', \phi') \exp\left(\frac{-jk\rho'^2}{2\ell}\right) \quad (36)$$

where $\bar{E}(\rho', \phi')$ is given by (13) and ℓ is the slant length of the horn. Numerical calculation of the radiation patterns is necessary. In the example of Fig. 9 [7] with a flare angle $\alpha = 5^\circ$ and aperture width $a = 4\lambda$, the E -plane ($\phi = 0$)

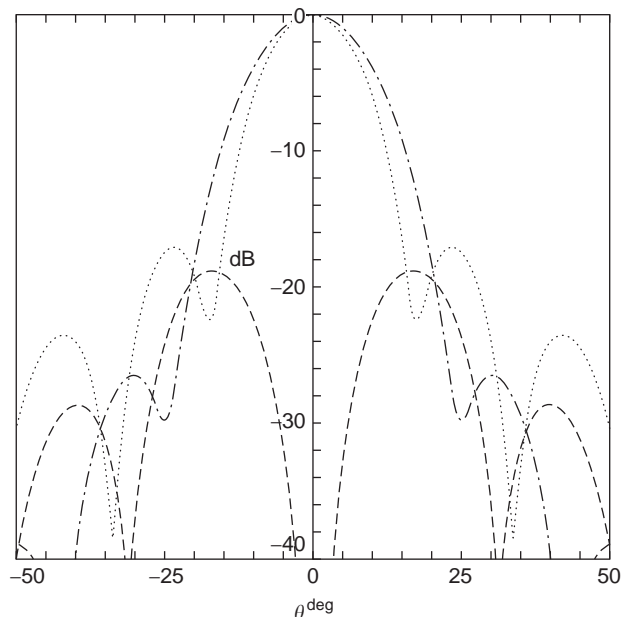


Figure 9. Copolar and cross-polar radiation patterns for a conical horn with dimensions $a = 4\lambda$, $\ell = 23\lambda$ --- E -plane, - - - H -plane - . . . cross-polarization. (Copyright 1994, IEE, from Olver et al. [7].)

pattern is narrower than the H -plane ($\phi = \pi/2$) pattern as in square rectangular horns. The cross-polar ($\phi = \pi/4$) radiation pattern peak level is -18.7 dB relative to the copolar pattern peak levels, a level typical of conical horn apertures large than about 2λ . Smaller conical horns can have more axisymmetric patterns. E - and H -plane patterns have equal beamwidths for an aperture diameter $a = 0.96\lambda$, and cross-polarized fields cancel for $a = 1.15\lambda$. This makes small conical horns efficient as reflector feeds and as array elements with high polarization purity.

Larger conical horns are similar to rectangular horns in their lack of axial pattern symmetry. Optimum gain conical horns have an aperture efficiency of about 54% and half-power beamwidths in the E and H planes of $1.05\lambda/a$ and $1.22\lambda/a$ radians, respectively, for aperture diameters of more than a few wavelengths.

7. MULTIMODE AND CORRUGATED HORNS

Lack of axisymmetric radiation patterns make rectangular and conical horns inefficient reflector feeds. Conical horns also have unacceptably high cross-polarization levels if used as reflector feeds in a system with dual polarization. Multimode and corrugated horns were developed largely to overcome these deficiencies. In a dual-mode horn in [3, p. 195], this is done by exciting the TM_{11} mode, which propagates for circular waveguide diameters $a > 1.22\lambda$, in addition to the TE_{11} mode, which propagates for $a > 0.59\lambda$. The electric field configuration of these modes in a waveguide cross section is shown in Figs. 10a and 10b. Added in phase and in the right proportion, cross-polarized and aperture perimeter fields cancel, while the copolar fields around the aperture center add, yielding the aperture field configuration of Fig. 10c. These mixed mode fields are linearly polarized and taper approximately cosinusoidally radially across the aperture. This yields the essentially linearly polarized and axisymmetric radiation patterns desired.

Partial conversion of TE_{11} to TM_{11} fields can be effected by a step discontinuity in the circular waveguide feed, as

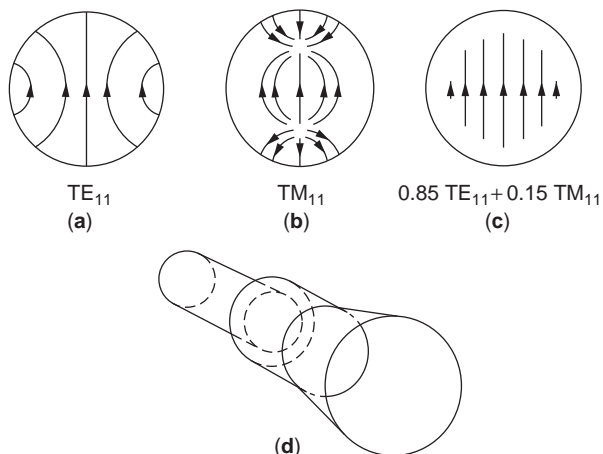


Figure 10. Excitation of axisymmetric linearly polarized aperture fields in a stepped conical horn. (Copyright 1984, McGraw-Hill, Inc. from Love [2].)

in Fig. 10d, or by a circular iris or dielectric ring in the horn. The TM_{11}/TE_{11} amplitude ratio depends on the ratio of waveguide diameters, and the relative phase of the modes depends on the length of larger-diameter circular waveguide and the horn. This dependence limits the frequency bandwidth of the horn to about 5%. A multimode square pyramidal horn has similarly low sidelobe levels in its E - and H -plane radiation patterns because of an essentially cosinusoidal aperture distribution in both E and H planes [2]. This is achieved by excitation of a hybrid TE_{21}/TM_{21} mode either by an E -plane step discontinuity or by changes in the E -plane flare. With their bandwidth very limited, dual-mode horns have largely been replaced by corrugated horns in dual-polarization systems, except where a lack of space may give an advantage to a thin-walled horn.

Corrugated horns have aperture fields similar to those of Fig. 10c and consequently similar radiation patterns, but without the frequency bandwidth limitations of the multimode horn. This is achieved by introducing annular corrugations to the interior walls of a conical horn. There must be sufficient corrugations per wavelength (at least 3) that the annular electric field E_ϕ is essentially zero on the interior walls. The corrugations make the annular magnetic field H_ϕ also vanish. This requires corrugation depths such that short circuits at the bottom of the grooves appear as open circuits at the top, suppressing axial current flow on the interior walls of the horn. This groove depth is $\lambda/4$ on a plane corrugated surface or a curved surface of large radius. For a curved surface of smaller radius, such as near the throat of the horn, the slot depths need to be increased; for example, for a surface radius of 2λ , the depth required is 0.3λ . Usually slots are normal to the conical surface in wide-flare horns but are often perpendicular to the horn axis with small flares. To provide a gradual transition from the TE_{11} mode in the waveguide to a hybrid HE_{11} mode in the aperture, the depth of the first corrugation in the throat should be about 0.5λ so that the surface there resembles that of a conducting cone interior. Propagation in corrugated conical horns can be accurately calculated numerically by mode matching techniques. The aperture field is approximately

$$E_x(\rho') = AJ_0(k_c \rho') \exp\left(\frac{-jk \rho'^2}{2\ell}\right) \quad (37)$$

where $k_c a/2$ is 2.405, the first zero order Bessel function J_0 ; ℓ is the slant length of the horn; and A is a constant. This aperture field is similar to that of Fig. 10c, and the resulting E and H patterns are similarly equal down to about -25 dB. Some universal patterns are shown in Fig. 11. Cross-polarization fields are also about -30 dB from the axial values, but now over a bandwidth of 2–1 or more.

Broadband axisymmetric patterns with low cross-polarization make corrugated horns particularly attractive as feeds for reflectors. Low cross-polarization allows the use of dual polarization to double the capacity of the system. Another notable feature for this application is that the position of the E - and H -plane pattern phase centers coincide. Figure 12 shows the distance of the phase center

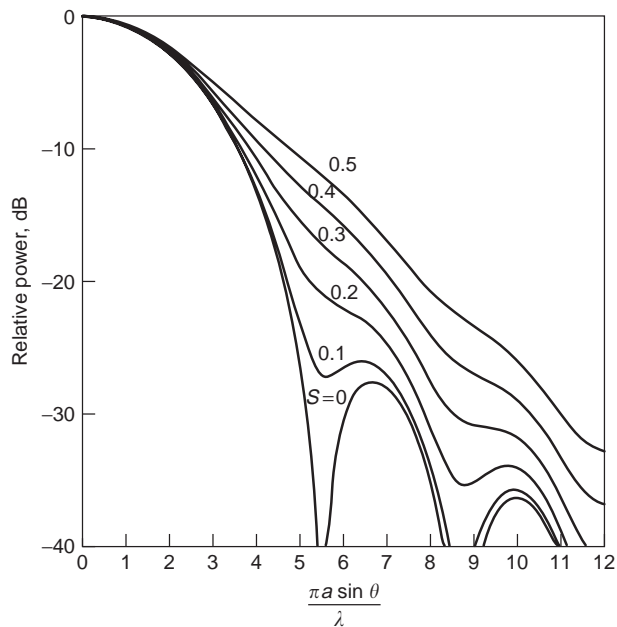


Figure 11. Universal patterns of small-flare-angle corrugated horns as a function of the parameter $s = a^2/8\lambda l$. (Copyright 1984, McGraw-Hill, Inc. from Love [2].)

from the horn apex, divided by the slant length, of small flare angle conical [8] and corrugated [9] horns for values of the phase parameter s given by (2). For a conical horn the E -plane phase center is significantly farther from the aperture than the H -plane phase center. Thus, if a conical horn is used to feed a parabolic reflector, the best location for the feed is approximately midway between the E - and H -plane phase centers. With a corrugated horn such a compromise is not required, so it is inherently more efficient.

Corrugated horns may have wide flare angles, and their aperture size for optimum gain decreases correspondingly.

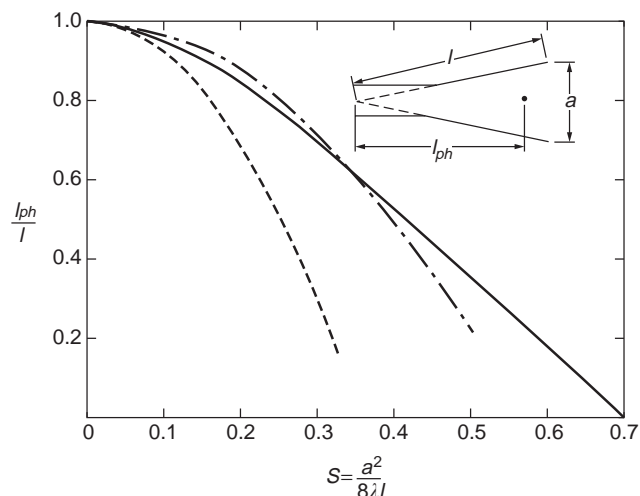


Figure 12. Normalized distance of the phase center from the apex of conical (--- E plane, - · - · - H plane and corrugated (—) horns). (Data from Milligan [8] and Thomas [9].)

For example, with a semiflare angle of 20° , the optimum aperture diameter is about 8λ , whereas for a semiflare angle of 70° it is 2λ . Wide-flare corrugated horns are sometimes called “scalar horns” because of their low cross-polarization levels.

For radio astronomy telescope feeds and other space-science applications, efficient corrugated horns have been made by electroforming techniques for frequencies up to 640 GHz. Their axisymmetric radiation patterns with very low sidelobe levels resemble Gaussian beams, which is often essential at submillimeter wavelengths.

8. PROFILE HORNS

Most corrugated horns are conical with a constant flare angle. Figure 13 shows a profile conical horn in which the flare angle varies as on a sine-squared or similar curve along its length. This arrangement provides a horn shorter than a conical corrugated horn of similar beamwidth, with a better impedance match due to the curved profile at the throat and an essentially in-phase aperture field distribution due to the profile at the aperture. Consequently the aperture efficiency is higher than that of conical corrugated horns. The phase center of the horn is near the aperture center and remains nearly fixed over a wide frequency band. Radiation patterns of a short profile horn similar to that of Fig. 13, but with hyperbolic profile curves, are shown in Fig. 14 [10]. A Gaussian profile curve has also been used. All produce patterns similar to those of a Gaussian beam, such as is radiated from the end of an optical fiber supporting the HE_{11} mode. The performance of this small horn as a feed seems close to ideal, but larger-profile horns may exhibit higher sidelobe levels due to excitation of the HE_{12} mode at the aperture.

9. HORN IMPEDANCE

Antennas must be well matched to their transmission lines to ensure a low level of reflected power. In microwave communications systems levels below -30 dB are commonly required.

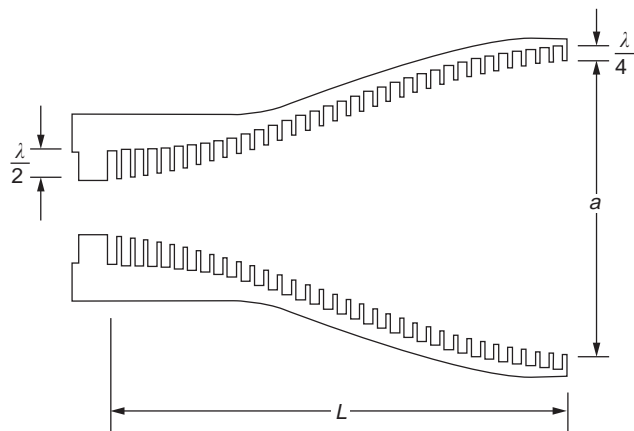


Figure 13. A profile corrugated horn. (Copyright 1994, IEE, from Olver et al. [7].)

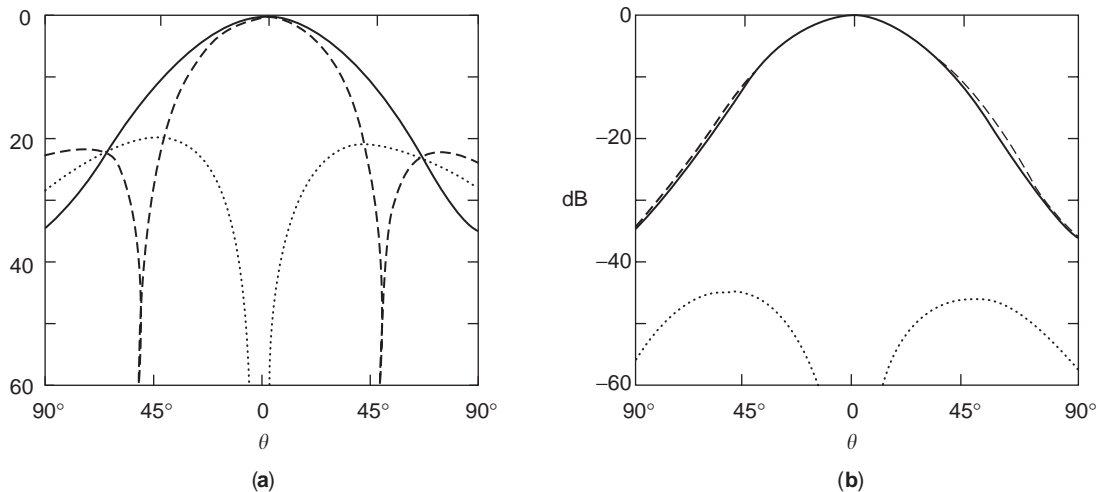


Figure 14. (a) Far field radiation patterns of TE₁₁ mode and (b) radiation patterns of a profile corrugated horn of aperture $a = 15.8$ mm and length $L = 26.7$ mm at 30 GHz (--- E -plane, ____ H -plane cross-polarization). (Copyright 1997, IEEE, from Gonzalo et al. [10].)

The impedance behavior of a horn depends on the mismatch at the waveguide/horn junction and at its aperture. For an E -plane sectoral horn, reflections from these discontinuities are comparable in magnitude, and since they interfere, the total reflection coefficient oscillates with frequency and the input voltage standing-wave ratio (VSWR) may vary from 1.05 at high frequencies to 1.5 at the lowest frequency. With E -plane sectoral horns aperture reflection is much stronger than junction reflection, so their VSWRs increase almost monotonically with decreasing frequency. An inductive iris in the waveguide near the E -plane horn junction can match its discontinuity. A capacitive iris may be similarly used for an H -plane sectoral horn. Aperture reflections in these horns may be matched with dielectric covers.

Pyramidal horns of sufficient size and optimum design tend to be inherently well matched to their waveguide feeds because the E/H -plane aperture and flare discontinuities partially cancel. For example, a 22-dB-gain horn has a VSWR of about 1.04 and an 18 dB horn a VSWR of less than 1.1.

Conical horns fed by circular waveguides supporting the dominant TE₁₁ mode have an impedance behavior similar to that of pyramidal horns of comparable size fed by rectangular waveguides. The waveguide/horn discontinuities of both horns may be matched by an iris placed in the waveguide near the junction. A broader bandwidth match is provided by a curved transition between the interior walls of the waveguide and the horn. Broadband reduction of aperture reflection may be similarly reduced by a curved surface of a few wavelengths' radius. Such "aperture-matched" horns also have lower sidelobe levels and less backradiation in their E -plane patterns than do conventional pyramidal and conical horns. Their H -plane flare patterns are affected little by such aperture matching because the electric field vanishes at the relevant edges.

For dual-mode and corrugated horns there are also negligible fields at the aperture edges and hence little diffraction there. Corrugated horns with initial groove

depths near the throat of about a half-wavelength and which gradually decrease to a quarter-wavelength near the aperture, as in Fig. 13, are well matched at both throat and aperture. For most well-designed corrugated horns a VSWR of less than 1.25 is possible over a frequency range of about 1.5–1. Dual-mode horns using a step discontinuity as in Fig. 10d may have a VSWR of 1.2–1.4. If an iris is required for a match, the frequency bandwidth will, of course, be limited. Conical and pyramidal horns using flare angle changes to generate the higher-order modes can have VSWRs less than 1.03 and require no matching devices.

BIBLIOGRAPHY

1. J. F. Ramsay, Microwave antenna and waveguide techniques before 1900, *Proc. IRE* **46**:405–415 (1958).
2. A. W. Love, Horn antennas, in R. C. Johnson and H. Jasik, eds., *Antenna Engineering Handbook*, 2nd ed., McGraw-Hill, New York, 1984, Chap. 15.
3. A. W. Love, ed., *Electromagnetic Horn Antennas*, IEEE Press, Piscataway, NJ, 1976.
4. R. E. Collin, *Antennas and Radiowave Propagation*, McGraw-Hill, New York, 1985.
5. K. Liu, C. A. Balanis, C. R. Birtcher, and G. C. Barber, Analysis of pyramidal horn antennas using moment methods, *IEEE Trans. Anten. Propag.* **41**:1379–1389 (1993).
6. J. F. Nye and W. Liang, Theory and measurement of the field of a pyramidal horn, *IEEE Trans. Anten. Propag.* **44**:1488–1498 (1996).
7. A. D. Olver, P. J. B. Clarricoats, A. A. Kishk, and L. Shafai, *Microwave Horns and Feeds*, IEE Electromagnetic Waves Series, Vol. 39, IEE, London, 1994.
8. T. Milligan, *Modern Antenna Design*, McGraw-Hill, New York, 1985, Chap. 7.
9. B. MacA. Thomas, Design of corrugated horns, *IEEE Trans. Anten. Propag.* **26**:367–372 (1978).
10. R. Gonzalo, J. Teniente, and C. del Rio, Very short and efficient feeder design from monomode waveguide, *IEEE*

Antennas and Propagation Soc. Int. Symp. Digest, Montreal, 1997, pp. 468–470.

11. E. V. Jull, *Aperture Antennas and Diffraction Theory*, IEE Electromagnetic Waves Series, Vol. 10, IEE, London, 1981.

HTS FILM GROWTH

KOOKRIN CHAR
VLADIMIR MATIJASEVIC
Conductus, Inc.

Thin films of superconductors are of interest primarily for electronics applications. High-performance superconducting thin films are essential, for example, for high-frequency passive devices and Josephson junction circuits. Thin films are also important for fundamental studies of superconducting materials, where specially designed experiments can take advantage of the thin-layer geometry and the capability of layering various combinations of materials, as well as lithographically defining fine features in them. Additionally, there is currently growing interest in using thin-film deposition technology for deposition of thick films on polycrystalline substrates for power applications.

In the decade since the discovery of high-temperature superconductivity (HTS) in cuprate compounds, thin-film materials have played an important role in the evolution of this field. The discovery of HTS has led to a rapid development of many different thin film deposition techniques. HTS thin films are now routinely made in hundreds of laboratories around the world, and thin-film research is actively pursued in areas such as new superconducting materials and epitaxial oxide heterostructures. More recently, advances in deposition processes have brought about the synthesis of larger-area HTS films, making fabrication less expensive and allowing for high-throughput manufacturing of single-superconducting-layer films.

In this article, we review the physical vapor deposition (PVD) techniques most frequently used for HTS thin-film synthesis. Chemical vapor deposition techniques are reviewed in another article of this encyclopedia. Here, we review only the methods and issues that are relevant for film deposition. This does not cover the details of the film growth processes, nor the physical properties of HTS films and their applications. The reader is referred to other references for a more complete discussion of HTS thin films and their applications [1,2].

1. MATERIALS

The HTS material of choice for applications is still $\text{YBa}_2\text{Cu}_3\text{O}_7$ (YBCO), the first cuprate discovered to superconduct above 77 K. There are several compelling reasons why this material is still the most suitable for many of the applications. Some of the fundamental ones are its smaller conduction anisotropy, higher superconducting critical

currents in a magnetic field, and greater chemical stability than in other HTS compounds. However, the most important reason is the ease of fabricating high-quality, single-phase YBCO thin films.

In this review, YBCO will be considered the canonical high- T_c superconductor, and the discussion will be limited to this example, partly for reasons of conciseness and partly because of the prominence of this compound in the HTS community. Additionally, unless otherwise mentioned, one is generally considering growth of *c*-axis-oriented films, i.e. where the CuO_2 layers are parallel to the substrate.

Table 1 reviews the HTS compounds and methods used to date to prepare these thin films. For a review of materials, we refer the reader to Refs. 2 and 3. There has been a substantial effort related to Bi–Sr–Ca–Cu–O thin films (2212 and 2223 phases) by a variety of techniques, particularly in Japan. Some industrial work in the United States has also focused on Tl–Ba–Ca–Cu–O (mostly 2212), primarily for passive electronics applications. One of the obvious reasons for looking at these other compounds is their higher critical temperatures. Nevertheless, the advantages of YBCO have been hard to surpass, particularly at temperatures below 65 K. Substantial thin-film work has also been devoted to La–Sr–Cu–O, Nd–Ce–Cu–O, Hg–Ba–Ca–Cu–O, and infinite-layer compounds, mostly driven by academic interest in basic properties of these HTS materials.

2. THERMODYNAMIC ISSUES

Film growth is inherently a nonequilibrium process. Nevertheless, thermodynamic stability is important as a driving force for the reactions taking place during growth. HTS compounds possess large unit cells that can have additional complications, such as a wealth of metal atom defects and oxygen nonstoichiometries. These complex structures require temperatures for formation close to their melting points, typically (0.8–0.9) T_m , much higher

Table 1. HTS Materials Systems, Methods Used to Fabricate Thin Films, and Applications of the Thin Films

Material	T_c (K)	Thin-Film Deposition Technique	Applications
Y(R)BaCuO 123	85–95	In situ: sputtering, PLD, evaporation, MOCVD; ex situ	RF devices, Josephson Junctions
BiSrCaCuO 2201, 2212, 2223	10–115	In situ: sputtering, PLD, evaporation	Josephson junctions
TlBaCaCuO 1201, 1212, 1223, 2201, 2212, 2223	20–125	1212: in situ sputtering; ex situ	RF devices
HgBaCaCuO 1201, 1212, 1223	95–133	Ex situ	
LaSr(Ba)CuO	20–40	In situ	
NdCeCuO	20–30	In situ	

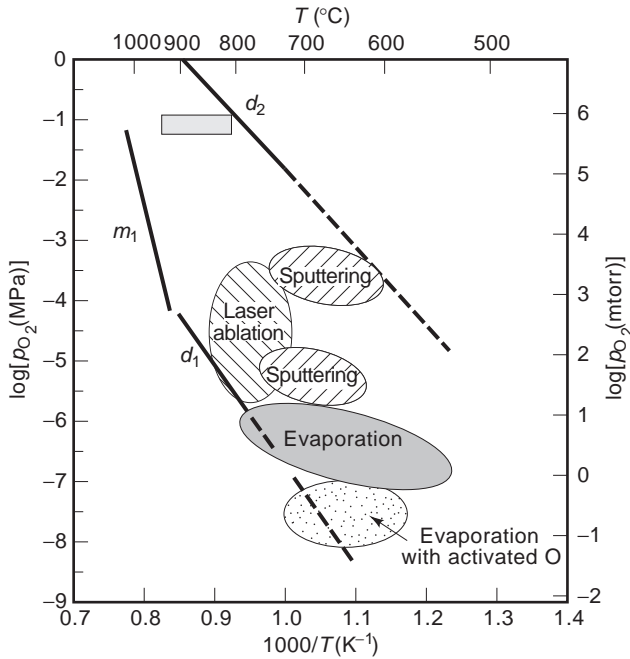


Figure 1. Thermodynamic stability diagram for YBCO in oxygen pressure and temperature. The shaded elliptical areas indicate regimes where in situ film growth for YBCO has been reported successful. The rectangles show ex situ film growth regimes.

than is usual for growth of epitaxial metals and semiconductors. The intricacies of film growth and the thermodynamics of phases produced are certainly not sufficiently well understood at present. Below, we summarize some of the key thermodynamic issues as they are currently accepted.

2.1. Oxygen Stability

HTS compounds are oxides and, as such, require the presence of oxygen during synthesis. Although it is technically possible to deliver oxygen through the substrate, in practice, oxygen is delivered as a gas impinging on the growth surface together with the cation species. Figure 1 shows the pressure–temperature thermodynamic stability diagram for the bulk YBCO compound. One can see from the diagram that a certain minimum pressure must be maintained for the stability of YBCO. Below that oxygen pressure, depicted by the line labeled d_1 , the YBCO compound is not stable and will decompose. For the typical temperatures during film formation, this translates into a minimum oxygen pressure of about 100 mPa (1 mtorr). At higher oxygen pressures, there is another decomposition line for YBCO, labeled d_2 , seldom not reached during in situ growth of thin films. During cooldown of films to room temperature, this second decomposition is seldom observed because it is strongly limited by diffusion kinetics. However, the stability diagram also implies that the YBCO compound is metastable at room temperature and pressure. In fact, most HTS compounds are believed not to be thermodynamically stable at lower temperatures. References 4 and 5 have a more detailed discussion of the YBCO stability lines. Hammond and Bormann [6] argued

that growth of thin films is optimal close to the high-temperature thermodynamic decomposition line of the compound. In fact, the empirical data confirm this, as can be seen also in Fig. 1, where successful film growth regions are denoted. For processes that possess a more reactive form of oxygen, such as atomic oxygen or ozone, the equivalent decomposition line is shifted compared with that in Fig. 1. Such activated oxygen species have been proven helpful for growth of YBCO when the total pressure is lower than about 1 Pa (10 mtorr).

2.2. Compositional Phase Diagram

The HTS compounds contain typically three to five different metal species in addition to oxygen. Some of these materials are line compounds (and this is presumed to be the case for YBCO) and, as such, do not accept a solid solution of atoms in their chemical formula. This means that one will always be synthesizing a number of phases in addition to the desired HTS material. For YBCO, the Gibbs phase rule implies two other compounds as impurity phases. Figure 2 shows the present understanding of the ternary phase diagram for Y–Ba–Cu oxides at the low oxygen pressures relevant for in situ thin-film growth [7,8]. The corners of the triangles define the phases which will be present for any composition in that triangle.

There are some caveats to the description given above. First, as already stated, film growth is not an equilibrium process, and therefore metastable phases could be formed during synthesis. Second, the HTS material that is formed during film growth may not be, and probably is not, exactly like the bulk material. This has now been well documented in the literature for YBCO films. In fact, it is also fairly well established that YBCO film growth does not match exactly the thermodynamic phase diagram shown in Fig. 2. In particular, the Y_2BaCuO_5 phase has not been observed in in situ-grown films. On the other hand, CuO and Y_2O_3 second phases are commonly observed in YBCO films prepared close to 1:2:3 stoichiometry and are not predicted by the phase diagram.

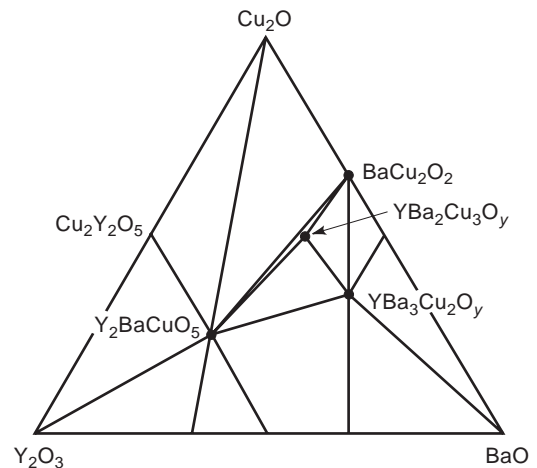


Figure 2. Thermodynamic ternary phase diagram for Y–Ba–Cu oxides at temperatures below 850°C and oxygen pressures below one atmosphere.

3. EPITAXY

Due to the significant anisotropy of the HTS materials, the easy direction for electrical current flow is in the ab plane, along the Cu-O_2 planes. For devices which require current to flow parallel to the substrate, the growth direction of the HTS films has to be in the c -axis direction. In order to achieve c -axis-oriented growth, good epitaxial growth of all grains is necessary. Furthermore, a high-angle, in-plane grain boundary of two c -axis-oriented grains has been found to behave as a superconducting weak link. This implies that one needs to align all grains in the plane of the substrate as well as out of the plane. The requirements of in-plane epitaxy are very well illustrated in the case of yttria-stabilized zirconia (YSZ) substrates where the YBCO films grow in the c direction, but the c axis grains can have two major different orientation in the ab plane, 45° apart [15]. In the case of applications that require the current flow to be perpendicular to the substrate, a -axis growth has been implemented. Many multilayer Josephson devices have been tried in this way; a -axis growth is typically initiated with a lower substrate temperature, which in turn reduces the mobility of ions necessary for the c -axis growth. Because of the lower growth temperature, films are formed that are structurally less perfect. To overcome this problem, many workers have used a technique of starting growth at a lower temperature for a -axis nucleation, making a template, and then raising the temperature for the remainder of film deposition [16].

3.1. Substrates

The most frequently used substrate for fundamental research is SrTiO_3 because of its good thermal and lattice constant match with most HTS materials. However, high dielectric loss, small wafer size, and high cost of SrTiO_3 render it unfavorable for technological applications. LaAlO_3 has emerged as an alternative to SrTiO_3 as a low-loss perovskite substrate, although its critical dielectric properties are not under complete control. MgO substrates, on the other hand, have an even lower loss for microwave applications. However, the reproducibility of the MgO surface quality has been a problem in the earlier days, but more recently, the surface quality has improved. For applications where very low loss is required, MgO is the best HTS substrate at present. MgO and LaAlO_3 are commercially available in wafer sizes larger than 5 cm (2 in.). More conventional substrates such as Si and sapphire have been used and found to be incompatible with thick HTS thin films, mainly due to microcracking in the HTS films resulting from the thermal expansion mismatch between the substrates and the HTS materials. The maximum thickness of YBCO one can grow without significant microcracking is about 50 nm on Si and about 600 nm on sapphire. Table 2 lists the substrates most commonly used today for growth of HTS films. References 17 and 18 more extensively discuss HTS-compatible substrates and buffer layers.

In most cases, excellent epitaxial alignment can be achieved by depositing oxide buffer layers, such as CeO_2 ,

Table 2. Substrates and Buffer Layer for HTS Thin Films

Substrate	Orientation	Buffer Layer
SrTiO_3	(1 0 0)	None CeO_2
LaAlO_3	(1 0 0) Pseudocubic	CeO_2 None
MgO	(1 0 0)	None SrTiO_3
YSZ	(1 0 0)	CeO_2 Y_2O_3
Al_2O_3	(1 $\bar{1}$ 0 2)	CeO_2 MgO
Si	(1 0 0)	$\text{YSZ}/\text{Y}_2\text{O}_3$ YSZ/CeO_2

before HTS growth. The CeO_2 buffer layer has been found to suppress the unwanted a -axis nucleation for the c -axis growth on substrates such as SrTiO_3 and LaAlO_3 . On substrates such as YSZ and r -plane sapphire, the CeO_2 buffer layer promotes in-plane alignment of each c -axis grain, thereby eliminating potential high-angle grain boundaries. In fact, by using an appropriate buffer layer and a seed layer, one can create a process to produce 45° -angle grain boundaries in a controlled fashion. On Si substrates, the YSZ buffer layer was found to grow epitaxially and to be very effective in preventing chemical reaction between HTS materials and Si.

3.2. Ion-Beam-Assisted Deposition

More recently, a new technique, ion-beam-assisted deposition (IBAD), has been implemented to grow HTS layers on polycrystalline substrates. By bombarding the growing film surface with an ion beam incident at a specific angle to the substrate, one is able to achieve partial in-plane crystalline alignment of the deposited material where the substrate has none. Iijima et al. [19] first utilized this technique to grow in plane textured zirconia buffer layers on substrates made of polycrystalline Ni-based alloys. YBCO was then deposited by PLD. Due to the absence of high-angle grain boundaries in YBCO, the critical currents attained are much higher than without the IBAD process. Other groups, including the one at Los Alamos National Laboratory, has followed on this work and achieved critical currents over 10^6 A/cm^2 at 77 K [20]. More recently a group at Stanford University has demonstrated very good IBAD results with 10 nm thick MgO films [21]. While more development is needed to establish whether the IBAD process is a viable one for large-scale applications, it certainly opens up a whole new range of substrate materials for HTS film growth.

4. FILM GROWTH METHODS

Most of the methods currently employed for fabrication of HTS thin films involve formation of the cuprate crystal structure during film deposition. These are usually called "in situ processes," and they will represent most cases covered in this review. Chemical vapor deposition processes, which are also in situ growth, are covered in another

chapter of this volume. Historically, the processes that were developed first, required a postdeposition anneal, or simply postanneal, in order to crystallize the material. Such methods are now less frequently utilized, since they are not well suited for fabrication of multilayer structures and are thus technologically more limiting. However, they are still used for compounds such as TlBaCaCuO or HgBaCaCuO, where the in situ processes are often impractical because of the required high vapor pressures of Hg and Tl. Finally, there are other processes such as sol-gel, plasma spray deposition, and liquid-phase epitaxy that are generally used for fabrication of thick films (thicker than 1 μm); these also will not be covered in this brief review.

4.1. Postanneal Growth Methods

In the postanneal, or ex situ, growth process, the metallic elements are deposited on a substrate in the correct composition as an amorphous or multilayer film, usually in compound form with oxygen and possibly fluorine. Subsequent annealing in air or oxygen at a high temperature, typically $\geq 850^\circ\text{C}$ for YBCO, forms an epitaxial film of the desired HTS phase [9]. A very commonly used postanneal method for growth of YBCO films is achieved by using BaF_2 in the precursor film. Water is then required in the annealing step in order to eliminate the fluorine and start the HTS growth process. Since the critical growth step takes place separately from deposition, the actual technique used to deposit the layers is of secondary importance. Sputtering and evaporation are typically used.

Ex situ methods have initially focused on synthesis under atmospheric oxygen pressure and correspondingly high temperatures. This region of phase space is depicted in Fig. 1 with the rectangle in the upper left corner. Later work has shown that lower-temperature ex situ growth can also be achieved if the oxygen pressure is reduced at the same time (see also the lower rectangle in Fig. 1). Such films grown under lower oxygen pressures were observed to have properties closer to the in situ grown films [10,11].

4.2. In situ Growth Methods

Dominant methods in use today for physical vapor deposition of HTS are sputtering and laser ablation [also referred to as *pulsed-laser deposition* (PLD)]. Both of these methods are most commonly done from a single target and as such, became rather popular mostly because they are relatively simple to implement and fairly reproducible in the films they produce. In addition, targets for PLD are relatively inexpensive and easy to fabricate, and hence, the technique is well suited for investigation of many different materials. Less widespread today, but currently growing in popularity, are coevaporation and molecular beam epitaxy. After the initial slow start in contending with a sufficiently oxidizing environment in high vacuum, evaporation methods have now emerged as an established way to grow high-quality HTS films.

The following is a list of in situ physical vapor deposition techniques used for deposition of HTS compounds,

which will be covered in this review:

1. Sputtering
 - On-axis magnetron
 - Off-axis magnetron
 - Inverted cylindrical magnetron
 - Ion-beam sputtering
2. Laser ablation
 - On-axis
 - Off-axis
 - Laser-MBE
3. Evaporation
 - Flash evaporation
 - Reactive coevaporation
 - Reactive-MBE

For more discussion on various PVD techniques, we also refer the reader to Refs. 12–14.

5. SPUTTERING

Sputtering is a very commonly used technique for metal deposition in semiconductor and magnetic storage industries. As such, it was applied early on to HTS materials. The first event of significance was the use of a single composite target, which became commonplace for HTS materials because of the inherent difficulty of reproducing the metal atom stoichiometry. The major complication compared to more conventional sputtering of metals is the energetic negative-ion (oxygen) bombardment of the substrate, due to the ionic nature of the oxide target. This causes resputtering and degradation of the sample. This has been recognized even before the advent of HTS and has been fully investigated by Rossnagel and Cuomo [22]. Two types of solution emerged: (1) Using a higher gas pressure in order to thermalize the energetic species [23] and (2) off-axis sputtering, where one eliminates the high-energy particles coming directly from the target [24,25]. Figure 3 shows a schematic of the two processes. Other variations include on-axis unbalanced-magnetron sputtering [26] and inverted cylindrical magnetron (ICM) sputtering [27].

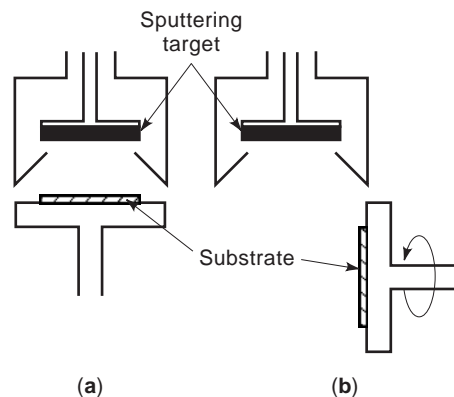


Figure 3. Schematic for the (a) on-axis and (b) off-axis sputter deposition processes.

The energies of ejected atoms from the sputtered targets are in the range of tens of electron volts, and they get scattered by the background Ar and O₂ gas. The angular distribution of each cation species is different, and the *sweet spot* for the proper cation composition is relatively small. In order to cover a 5-cm (2-in.) Wafer uniformly from a single 5-cm target in an off-axis geometry, one has to resort to some sort of scanning method, such as rotation of the wafer. The deposition rate is very low, not only because the deposition rate for oxides is much lower than for metals but also because of the off-axis geometry. It takes several hours to deposit a few hundred nanometers of film. Larger targets and a number of sputter guns depositing simultaneously have been used at several laboratories to increase the deposition rate. When all the deposition conditions are optimum, sputtering has demonstrated a capability to produce YBCO films of excellent crystallinity and surface condition. However, the deposition conditions have to be changed as the targets erode, because the changing target surface geometry results in a different plasma distribution. In addition, the substrate heating method for off-axis sputtering is not as simple as in the case of the off-axis laser ablation or evaporation, which will be described later.

6. LASER ABLATION

Laser ablation, or pulsed-laser deposition (PLD), is a relatively new technique that gained much popularity because it is ideally suited for deposition at a high oxygen pressure. The relative ease of this technique in depositing multicomponent oxides (and nitrides) has made it especially effective in exploring new materials for HTS electronics, such as epitaxial dielectrics or barrier layers. A short-wavelength (170–260-nm) excimer laser is focused onto a rotating target of the material to be deposited. Under the energy of the laser beam (0.1–2 J per pulse), the matter emitted from the target forms a plume that carries it to the substrate at supersonic velocities. In general, a higher gas pressure is required during laser ablation, due to the very high energy of the vaporized material from the surface of the target. The laser plume glows brightly from the target, and deposition is usually done near the end of the plume, about 5 cm away (see Fig. 4). Again, as in the case of sputtering, the various species scatter differently, and therefore the *sweet spot* of the deposition process is relatively small, usually one to two centimeters, depending on the geometry. The deposition rate per laser pulse ranges from a fraction of an angstrom to a few angstroms. The technique was found to be fairly reproducible from the early days and has been used extensively for research and development purposes since 1989. Even though other techniques are potentially more manufacture-friendly, laser ablation is still very actively used for prototyping devices made up of several complex materials, such as superconductors, ferroelectric oxides, and magnetic oxides.

A particular problem associated with PLD is the deposition of micrometer-sized droplets, so-called *boulders*, on the grown film. These particles originate at the target and

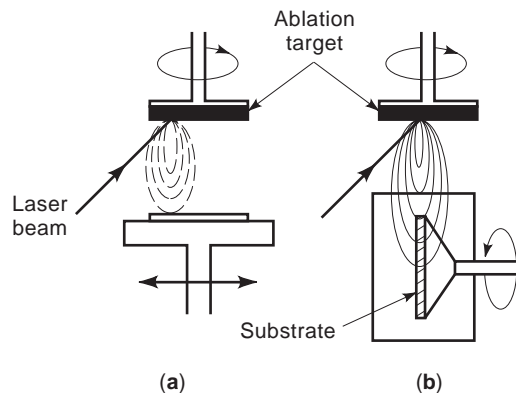


Figure 4. Schematic for the (a) on-axis and (b) off-axis laser ablation processes.

are emitted from the action of the laser pulse. A variety of procedures have been utilized to reduce this problem, so that the boulder density can be very low in the best films. Such procedures include target preparation (such as frequency polishing), defocusing the laser spot, mechanically chopping the plume, and spatially filtering the beam.

Although PLD can produce high deposition rates (up to tens of nanometers per second), the area on which one deposits is small. A straightforward way to increase the deposition area is to scan wafers over the plume either by moving the substrate vertically and horizontally or by rotating the substrate. This method has been tried in several laboratories and is still pursued. Another scheme utilizes a rotating cylindrical target with a linear laser profile to obtain larger deposition areas.

Another major difficulty of these techniques is uniform heating of large wafers. Most of the heating methods for small-area laser ablation have been to mount a substrate on a heated metal surface with silver paste, which is difficult to extend to larger sizes. In order to overcome this difficulty of heating a large wafer, an off-axis laser ablation technique has been developed (see Fig. 4b). A large wafer (5–8 cm) can be mounted parallel to the direction of the plume inside a relatively simple blackbodylike heater. The deposition takes place when the atoms collide with the background pressure and are scattered to the surface of the wafer. By rotating the wafer and selecting an appropriate pressure for the geometry, a fairly uniform deposition was achieved over 5-cm wafers. This technique allows for simultaneous deposition on both surfaces of the wafer, which is an important benefit for microwave applications requiring a ground plane. A drawback of this technique is its low deposition rate because of the off-axis geometry. Typical conditions for deposition of a 5-cm wafer resulted in a deposition rate about a factor of 10 lower than for the on-axis deposition.

By using laser fluence just enough to evaporate a few atomic layers of the target in a low-oxygen environment (less than 10^{-2} Pa $\approx 10^{-4}$ torr) and at the same time using a sequence of metal or metal oxide targets, one can obtain a process similar to molecular-beam epitaxy (MBE) by evaporation, here called “laser MBE.” Some in situ diagnostic tools can then be used to characterize the growth of

the materials. This technique has mainly been used to grow artificially layered superconducting materials, such as the infinite-layered superconductor [28,29].

7. EVAPORATION AND MOLECULAR-BEAM EPITAXY

Deposition of HTS thin films by evaporation follows a tradition of such deposition of metal films. The added complexity here is the required partial pressure of oxygen during growth. One can distinguish several variations in the evaporation approaches: flash evaporation, reactive coevaporation of metals, and sequential deposition by MBE. Except for the first process, these evaporation techniques utilize individual metallic sources. However, in attempting to control individual sources, two difficulties arise. One is the need for very fine control of individual sources, including development of species-specific sensors. The second is the need to work at a low enough pressure to minimize beam scattering and at the same time achieve the highly oxidizing thermodynamic conditions required for the growth of these compounds. For an in situ process, one is confined to work at a pressure of molecular oxygen above 100 mPa (1 mtorr) or to use a more reactive form of oxygen supply than molecular oxygen.

7.1. Flash Evaporation

The simplest approach to evaporation of HTS materials is to evaporate the compound in small batches, namely, in flashes of evaporant material. Since the material does not melt congruently, it is not possible to establish a continuously constant rate of metal fluxes, but for short enough intervals, one can average out the compositional variations. Usually, the evaporant material is a powder of YBCO located in a feed mechanism that drops small quantities onto an evaporation source [30]. In most cases, the films require a postannealing treatment to oxidize the film sufficiently, since the fast deposition does not allow for sufficient incorporation of oxygen. This method is at present less significant.

7.2. Reactive Coevaporation

Historically, the first attempts to make films by evaporation utilized a high molecular oxygen pressure. The problems associated with a high background oxygen pressure are rate control of the individuals species and the degradation of the sources. In order to circumvent this difficulty, several approaches were taken. One was to accommodate a high differential pressure between the sources and the sample by introduction of nozzles in close proximity to the sample. Another method is to utilize a more reactive species for oxygen incorporation, such as atomic oxygen or ozone.

The evaporation technique allows one to tune the composition of the film by adjusting the relative rates of the sources. Several groups have worked over the past years on developing process control for coevaporation and studying YBCO film properties as a function of metal atom composition. Figure 5 shows SEM micrographs of films with various metal compositions. The general finding is

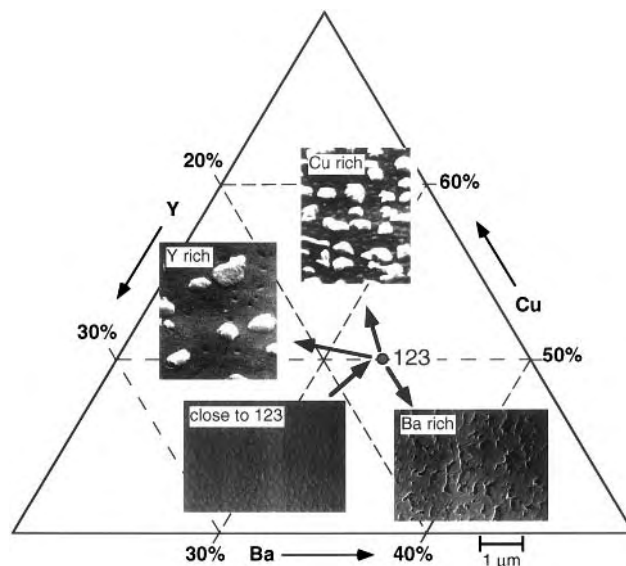


Figure 5. Morphology of YBCO films as a function of their composition during reactive coevaporation.

that films that are grown slightly Y- and Cu-rich have better performance than films with exactly 1:2:3 stoichiometry. This is true for a majority of in situ techniques and not just evaporation. The reasons for this are still not completely clear—in particular, whether it is a materials issue or a process control issue. It is known that superconducting properties of films degrade significantly as one goes into the Ba-rich composition. It is possible that process fluctuations around the desired metal atom stoichiometry are responsible for degradation of films close to 1:2:3 composition.

Probably the most technologically significant advance in HTS thin-film evaporation has been the large-area heater developed for coevaporation by the group of H. Kinder at the Technical University of Munich (Germany) and depicted in Fig. 6. They used a blackbody-type rotating-disk heater, similar to the one used by others in PLD deposition, but they added an *oxidation pocket* [31]. This heater has a narrow slit that allows for a differential pressure between the oxidation pocket and the rest of the chamber of about 1000:1. The deposition and the oxidation processes are therefore separated, and a low pressure in the chamber improves the stability of thermal evaporation sources. Uniform YBCO films were grown on wafers up to

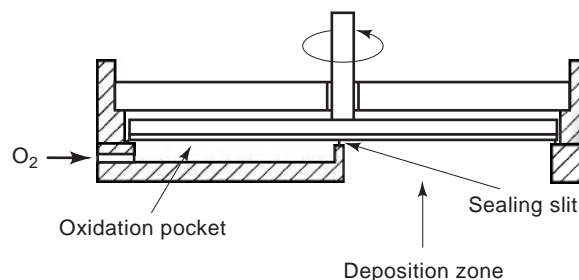


Figure 6. Schematic of the heater for large-area HTS deposition by evaporation.

20 cm in diameter using this technique. More importantly, this method is significantly more cost-effective and has higher throughput than any of the other PVD processes.

7.3. Molecular-Beam Epitaxy

In general, one can distinguish between reactive molecular-beam epitaxy (MBE) approaches to HTS film deposition and mere reactive evaporation by the lower background pressure of the former technique. Another difference is that MBE deposition is usually done sequentially rather than simultaneously. Typically, MBE systems have multiple sources with individual shutters, as well as some in situ monitoring tools (see Fig. 7). Reference 32 has a thorough discussion of relevant issues in reactive MBE of HTS films. The work by a number of groups in this field has focused on careful atomic layering to produce very smooth films, as well as customized growth of new materials and heterostructures containing these phases. The reactive MBE technique also lends itself to careful control of chemical doping of these materials, an issue that is very important for the superconducting properties of the cuprates.

7.4. In situ Monitoring Diagnostics

Evaporation and, especially, MBE, with their inherent low background pressure, lend themselves well to vacuum techniques for in situ deposition monitoring and film diagnostic tools such as reflection high-energy electron diffraction (RHEED). RHEED has been shown to be particularly helpful in controlling deposition of Bi-Sr-Ca-Cu-O films, where the growth occurs in blocks of sub-unit cells, but where many similar phases are possible. RHEED has been less helpful to date in the growth of YBCO, which occurs in blocks of unit cells and where intergrowths are more difficult to tailor, due to the higher stability of the primary phase. Terashima and coworkers [33] have shown that growth of YBCO can exhibit oscilla-

tions in the RHEED pattern commensurate with unit cell deposition, suggesting that growth proceeds in a unit-cell-by-unit-cell fashion, rather than in smaller building blocks. More recently, RHEED has also been extended to high-pressure processes such as PLD [34].

Another area of technological development has been in the use of optical absorption techniques for measurement and control of atomic fluxes. Both hollow-cathode lamp systems [35] and tunable diode lasers [36] have been used to monitor fluxes in situ in close proximity to the substrate. Such monitoring of individual fluxes is a prerequisite for careful control of HTS growth.

8. CONCLUDING REMARKS

In spite of a wealth of research, growth of cuprate films has remained a complicated matter. This is due to the materials' rather complex multicomponent crystal structures. They are prone to a variety of defects and growth morphologies. Much work still remains to be done until films are better understood and more reproducible.

As already described, HTS films are now routinely made with out-of-plane as well as in-plane alignment on single-crystalline substrates. Aligned films are still not routine on polycrystalline substrates, but there has been progress in this area as well. This has been manifested in high critical currents in films, particularly for YBCO. Typical critical currents in good quality YBCO films are over 2×10^6 A/cm² at 77 K and above 10^7 A/cm² at low temperatures. There has been much work in characterizing defect structures, but a good understanding of their influence on physical properties is still lacking. One growth structure that seems to be nearly ubiquitous in YBCO films is the spiral, which forms during growth and at the core of which is a screw dislocation [36]. Figure 8

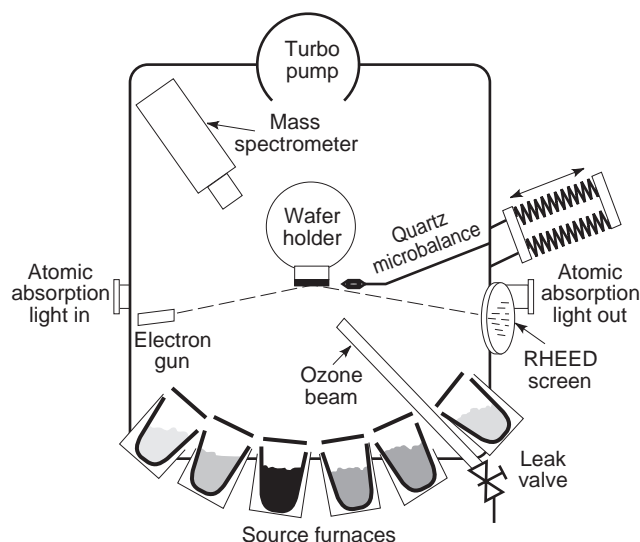


Figure 7. Schematic for the reactive MBE process used in HTS film growth.

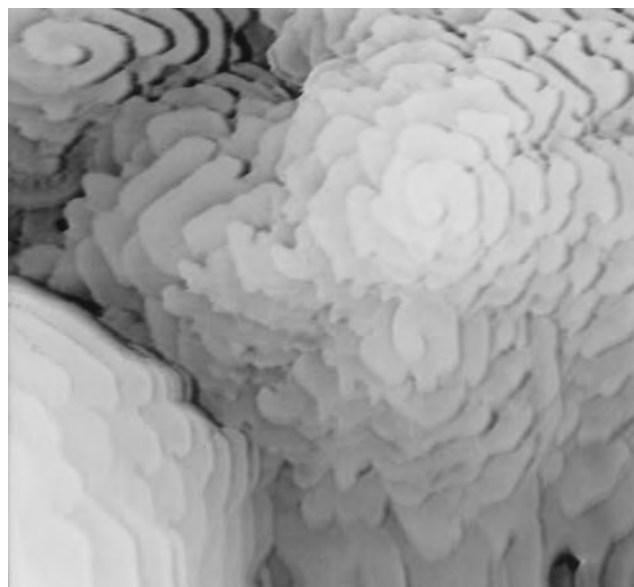


Figure 8. An STM image of a laser ablated YBCO film, showing spiral growth structures. (Image courtesy of Prof. Darrell Schlom.)

shows a scanning tunneling microscopy (STM) image of a surface of a YBCO film with a spiral. Steps in this image have a height of one unit cell of YBCO. Such spirals have been identified as contributing of pinning of vortices, important for high critical currents.

Maximally oxygen-doped YBCO bulk materials, made at higher temperatures than thin films, have a superconducting transition temperature of 92 K and a resistivity of $35 \mu\Omega \cdot \text{cm}$ at 100 K. Although having nominally the same crystal structure as the bulk material, YBCO films often have different electronic properties. For example, lower T_c (85–90 K) and expanded c -axis lattice constants (1.170–1.172 nm) are frequently found in thin films. Additionally, flux-pinning centers appear to be highly dispersed in in situ-grown films of YBCO, although the structural origin of these centers has not yet been identified. It is important to have a close feedback loop between film deposition and structural and electrical characterization in order to further improve HTS films.

Technology for deposition and monitoring of HTS thin films has developed significantly since the late 1980s. At the same time, the materials understanding of film nucleation, growth, and oxide interfaces has started to unfold. Together, these developments in the future will bring new capabilities for HTS film growth.

BIBLIOGRAPHY

- J. M. Rowell, A decade of progress towards a high temperature superconducting electronics technology, *Solid State Commun.* **102**:269–282 (1997).
- T. R. Lemberger, Films of high-temperature oxide superconductors, in D. M. Ginsberg, ed., *Physical Properties of High Temperature Superconductors III*, World Scientific, Singapore, 1992.
- C. P. Poole, H. A. Farach, and R. J. Creswick, *Superconductivity*, Academic Press, San Diego, 1995.
- T. B. Lindemer et al., Decomposition of $\text{YBa}_2\text{Cu}_3\text{O}_{7-x}$ and $\text{YBa}_2\text{Cu}_4\text{O}_8$ for $p_{\text{O}_2} \leq 0.1 \text{ MPa}$, *Physica C* **178**:93 (1991).
- R. K. Williams et al., Oxidation induced decomposition of $\text{YBa}_2\text{Cu}_3\text{O}_{7-x}$, *J. Appl. Phys.* **70**:906–913 (1991).
- R. H. Hammond and R. Bormann, Correlation between the in situ growth conditions of YBCO thin films and the thermodynamic stability criteria, *Physica C* **162–164**:703–704 (1989).
- R. Beyers and B. T. Ahn, Thermodynamic considerations in superconducting oxides, *Rev. Mater. Sci.* **21**:335 (1991).
- P. Karen, O. Braaten, and A. Kjekshus, Chemical phase diagrams for the $\text{YBa}_2\text{Cu}_3\text{O}_7$ family, *Acta Chem. Scand.* **46**:805–840 (1992).
- M. Naito et al., Thin film synthesis of the high T_c oxide superconductor $\text{YBa}_2\text{Cu}_3\text{O}_7$ by electron beam codeposition, *J. Mater. Res.* **2**:713–725 (1987).
- R. Feenstra et al., Effect of oxygen pressure on the synthesis of YBaCuO_{7-x} thin films by post deposition annealing, *J. Appl. Phys.* **69**:6569–6585 (1991).
- J. M. Phillips et al., Comparison of $\text{Ba}_2\text{YCu}_3\text{O}_{7-\delta}$ thin films grown on various perovskite substrates by coevaporation, *J. Mater. Res.* **7**:2650–2657 (1992).
- R. G. Humphreys et al., Physical vapor deposition techniques for the growth of $\text{YBa}_2\text{Cu}_3\text{O}_7$ thin films, *Superconduct. Sci. Technol.* **3**:38–52 (1990).
- J. A. Alarco et al., High quality YBCO thin films—laser deposition, co-evaporation, and device fabrication, *Phys. Scripta* **44**:95–101 (1991).
- C. H. Stoessel et al., Thin-film processing of high- T_c superconductors, *J. Superconduct.* **6**(1):1–17 (1993).
- S. M. Garrison et al., Observation of two in-plane epitaxial states in $\text{YBa}_2\text{Cu}_3\text{O}_{7-\delta}$ films on yttria-stabilized ZrO_2 , *Appl. Phys. Lett.* **58**:2168–2170 (1991).
- H.-U. Habermeier et al., Preparation and properties of YBCO thin films with the c -axis aligned in the film plane, in L. Correria, ed., *High Temperature Superconductor Thin Films*, North-Holland, Amsterdam, 1992, pp. 343–352.
- A. Perrin and M. Sergent, in A. Narlikar, ed., *Studies of High Temperature Superconductors*, Vol. 7, Nova Science Publishers, Commack, NY, 1991.
- J. Qiao and C. Y. Yang, High- T_c superconductors on buffered silicon: Materials properties and device applications, *Mater. Sci. Eng.* **R14**:157–202 (1995).
- Y. Iijima et al., In-plane aligned $\text{YBa}_2\text{Cu}_3\text{O}_{7-x}$ thin films deposited on polycrystalline metallic substrates, *Appl. Phys. Lett.* **60**:769–771 (1992).
- X. D. Wu et al., High current $\text{YBa}_2\text{Cu}_3\text{O}_{7-d}$ thick films on flexible nickel substrates with textured buffer layers, *Appl. Phys. Lett.* **65**:1961–1963 (1994).
- C. P. Wang et al., Deposition of in-plane textured MgO on amorphous Si_3N_4 substrates by ion-beam-assisted deposition and comparisons with ion-beam-assisted deposited yttria-stabilized-zirconia, *Appl. Phys. Lett.* **71**:2955–2957 (1997).
- S. M. Rossnagel and J. J. Cuomo, Negative ion effects during magnetron and ion beam sputtering of $\text{YBa}_2\text{Cu}_3\text{O}_x$, in *Thin Film Processing and Characterization of High-Temperature Superconductors*, American Institute of Physics Conf. Proc. 165, AIP, New York, 1988, pp. 106–113.
- U. Poppe et al., Direct production of crystalline superconducting thin films of $\text{YBa}_2\text{Cu}_3\text{O}_7$ by high-pressure oxygen sputtering, *Solid State Commun.* **66**:661–665 (1988).
- C. B. Eom et al., Synthesis and properties of $\text{YBa}_2\text{Cu}_3\text{O}_7$ thin films grown in situ by 90 degrees off-axis single magnetron sputtering, *Physica C* **171**:354–382 (1990).
- J. R. Gavaler et al., Critical parameters in the single-target sputtering of $\text{YBa}_2\text{Cu}_3\text{O}_7$, *J. Appl. Phys.* **70**:4383–4391 (1991).
- N. Savvides and A. Katsaros, In situ growth of epitaxial YBCO thin films by on-axis unbalanced direct current magnetron sputtering, *Appl. Phys. Lett.* **62**:528–530 (1993).
- X. X. Xi et al., Preparation of $\text{YBa}_2\text{Cu}_3\text{O}_7$ thin films by inverted cylindrical magnetron sputtering, *J. Less-Common Metals* **151**:349–355 (1989).
- T. Kawai et al., Superconducting artificial lattices grown by laser MBE, in L. Correria, ed., *High Temperature Superconductor Thin Films*, North-Holland, Amsterdam, 1992.
- H. Koinuma and M. Yoshimoto, Controlled formation of oxide materials by laser molecular beam epitaxy, *Appl. Surface Sci.* **75**:308–319 (1994).
- Y. Yasuda et al., Y–Ba–Cu–O superconducting thin films prepared by plasma-assisted flash evaporation, *Appl. Phys. Lett.* **55**:307–309 (1989).
- P. Berberich et al., Homogeneous high quality $\text{YBa}_2\text{Cu}_3\text{O}_7$ on 3" and 4" substrates, *Physica C* **219**:497 (1994).
- D. G. Schlom and J. S. Harris, Jr., MBE growth of high T_c superconductors, in R. F. C. Farrow, ed., *Molecular Beam Epitaxy: Applications to Key Materials*, Noyes, Park Ridge, IL, 1995.

33. T. Terashima et al., Reflection high-energy electron diffraction oscillations during epitaxial growth of high-temperature superconducting oxides, *Phys. Rev. Lett.* **65**:2684–2687 (1990).
34. G. J. H. M. Rijnders et al., In situ monitoring during pulsed laser deposition of complex oxides using reflection high energy electron diffraction under high oxygen pressure, *Appl. Phys. Lett.* **70**:1888–1890 (1997).
35. J. N. Eckstein, I. Bozovic, and G. F. Virshup, Atomic layer-by-layer engineering of high- T_c materials and heterostructure devices, *Mater. Res. Soc. Bull.* **19**(9): 44–50 (1994).
36. W. Wang et al., Direct atomic flux measurement of electron-beam evaporated yttrium with a diode-laser-based atomic absorption monitor at 668 nm, *Appl. Phys. Lett.* **71**:31–33 (1997).
37. C. Gerber et al., Screw dislocations in high- T_c films, *Nature* **350**:279–280 (1991).

HYBRID CAD TECHNIQUES

F. ARNDT
University of Bremen
Bremen, Germany

1. INTRODUCTION

To meet the increasing demand for enhanced waveguide components and antennas in wireless terrestrial and satellite-based communications, and for radar applications, accurate *and* efficient CAD tools are required. Due to efforts during the 1990s—the decade of global 3D electromagnetic (EM) field solvers—the task of accurate analysis of components can be considered as being largely solved. Current challenges for CAD software relate to a new quality of efficiency and speed that allow direct, fast component optimizations in order to meet desired specifications within reasonable timeframes.

Many approaches to improve the efficiency of EM-based field solvers have been reported so far, such as reduced-order models (ROMs) applied for finite-element (FE) [1] or finite-difference (FD) [2] methods, fast multipole and adaptive integral methods (FMM, AIM) for method-of-moment (MoM) solutions of scattering and microstrip circuit problems [3–10], or combined subgrid conformal techniques for FD methods [11,12].

The issue discussed in this article is the utilization of advanced hybrid MM/FE/MoM/FD techniques, which typically can go beyond the efficiency possibilities of the involved single methods.

In computational electromagnetics, the idea of combining different variations to “hybrid techniques” or “hybrid methods” to expand their capabilities is not new.

Hybrid techniques have already been utilized long ago for handling electromagnetic scattering and radiating problems for large structures [7,13,14]. Examples are the combination of MoM with an “asymptotic” method [e.g., geometric theory of diffraction (GTD)], [7,13–16], or the combination of FE with the boundary integral equation method [7,17,18].

We apply in our article the “hybrid” notation for combining the fast mode-matching (MM) method with EM-based space or surface discretization methods, such

as the finite-element (FE) and finite-difference (FD) methods and the method-of-moments (MoM), to combine the efficiency of the MM with the flexibility of the FE, MoM, and FD techniques.

Due to its efficiency, the mode-matching (MM) method [19–45] has been widely employed for designing waveguide components, where modal expansions can be derived analytically. For structures that are not separable in Cartesian, cylindrical, or elliptical coordinate systems, FE, FD, or MoM techniques provide the desired flexibility. However, because of rather high requirements concerning central processing unit (CPU) time for the CAD of components using pure FE, MoM, or FD methods, for reasonably fast optimizations of typical industrial components, which often require a high number of iterations to meet given specifications, more efficient techniques are desirable. A very effective approach for solving this problem utilizes hybrid methods based on MM/FE/MoM/FD techniques, hence retaining the specific advantages of all proven EM methods while largely avoiding their disadvantages.

Hybrid mode-matching/method-of-moment (MM/MoM) techniques have been applied for horn antennas for a long time [46,47], where the inner horn structure is calculated by the MM method and the radiation problem is solved by MoM [46–50]. Hybrid MM/FE techniques have been introduced more recently for the analysis of dual-mode filters [51–53]. In these applications, the cross section eigenvalue problem of arbitrarily shaped homogeneous waveguide structures (e.g., cross-iris) is solved by a 2D FE method while the MM is applied for the calculation of the scattering parameters at the discontinuities with arbitrary contour. The full-wave combination of all discontinuities is achieved by the generalized scattering matrix (GSM). A more detailed overview on the MM/FE method is given in Ref. 54. More recent applications describe the MM/FE CAD of waffle-iron, evanescent-mode, and combine filters [55–57], of coaxial feeds [58,59], and the analysis of some discontinuities [60,61]. Modal expansion FDTD and transmission-line matrix (TLM) techniques have been proposed [62,63], and a hybrid MM/FD-FD method has been presented [64]. The extension of hybrid methods to MM/FE/MoM and MM/FE/FD has been presented [65,66], and hybrid techniques exploiting the full efficiency and flexibility spectrum of MM/FE/TransFE/MoM/FD methods have been introduced [67,68].

In this article, we describe the recent state of the art of hybrid MM/FE/MoM/FD techniques employed for the rigorous, efficient CAD and optimization of waveguide components, coupled horns, and waveguide slot array antennas, and discuss some typical applications and advanced aspects. Representative application examples will demonstrate the versatility and computational speed of these hybrid methods. Their accuracy is verified by available measurements or reference calculations.

2. THEORY

2.1. MM/FE Method

A very large class of waveguide components in microwave techniques is typically composed of stepwise homogeneous

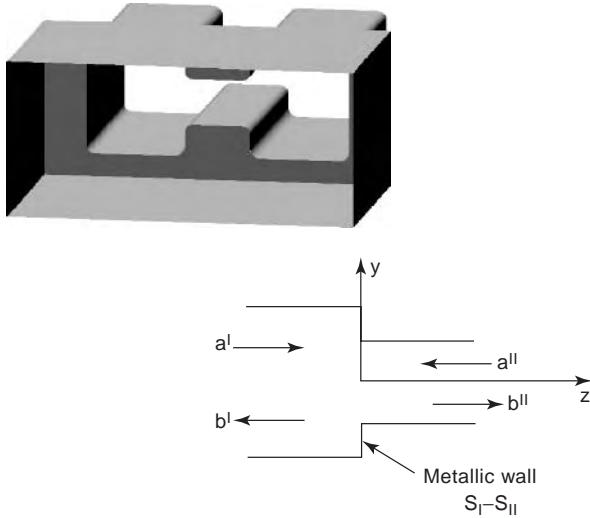


Figure 1. Step discontinuity between two homogeneous waveguides.

waveguide sections (Fig. 1). Because of its high numerical efficiency, the mode-matching (MM) CAD technique has long been advantageously applied for the design of corresponding components such as for iris or metal-insert-coupled filters, junctions, couplers, diplexers, multiplexers, polarizers, transformers, and orthomode transducers [19–45]. An overview of many of the earlier research work in MM techniques is given in Ref. 36.

The basic principle of the MM technique can be elucidated at a step discontinuity (Fig. 1). Matching the tangential \mathbf{E} - and \mathbf{H} -field components along the transverse surface of the general step discontinuity, which is assumed to be located at $z = 0$, yields the relation between the incident and scattered modal wave amplitude coefficients \mathbf{a} and \mathbf{b}

$$\sqrt{Z_i^I}(a_i^I + b_i^I) = \sum_{j=1}^{\infty} C_{ij} \sqrt{Z_j^{II}}(a_j^{II} + b_j^{II}) \quad i = 1 \dots \infty \quad (1)$$

$$\sum_{i=1}^{\infty} C_{ij} \sqrt{Y_i^I}(a_i^I - b_i^I) = \sqrt{Y_j^{II}}(a_j^{II} - b_j^{II}) \quad j = 1 \dots \infty$$

where $Z = 1/Y$ are the modal wave impedances and C_{ij} are the elements of the frequency independent coupling matrix

$$C_{ij} = \int_{S_{II}} \int \mathbf{e}_i^{\text{Tr}} \mathbf{e}_j^{\text{II}} dS = \int_{S_{II}} \int \mathbf{h}_i^{\text{Tr}} \mathbf{h}_j^{\text{II}} dS, \quad (2)$$

\mathbf{e} and \mathbf{h} are the transversal eigenvectors

$$\mathbf{e} = \begin{cases} \mathbf{u}_z \cdot \nabla_t \Psi & \text{TE modes} \\ -\nabla_t \Psi & \text{TM and TEM modes} \end{cases} \quad (3)$$

$$\mathbf{h} = \mathbf{u}_z \times \mathbf{e}$$

with \mathbf{u}_z the unit vector in the z direction, and the potentials Ψ are solutions of the 2D Helmholtz equation

$$\nabla_t^2 \Psi + k_c^2 = 0 \quad (4)$$

in case of TE and/or TM modes, with the separation condition

$$k_c^2 + \beta^2 = k^2 \quad (5)$$

where $j\beta = \gamma$ is the propagation factor and k the free-space wavenumber; $\nabla_t^2 = \nabla^2 - (\partial^2/\partial z^2)$ denotes the transversal Laplace operator. For TEM modes, Ψ are solutions of the Laplacian equation

$$\nabla_t^2 \Psi = 0 \quad (6)$$

The potentials Ψ are suitably normalized

$$\iint_S \nabla_t^T \Psi_i \nabla_t \Psi_j dS = 1 \quad (7)$$

The Dirichlet and Neumann boundary conditions are

$$\begin{aligned} \Psi^{\text{TM}} &= 0 \quad \Gamma_E & \frac{\partial \Psi^{\text{TM}}}{\partial n} &= 0 \quad \Gamma_M \quad (\text{TM modes}) \\ \frac{\partial \Psi^{\text{TE}}}{\partial n} &= 0 \quad \Gamma_E & \Psi^{\text{TE}} &= 0 \quad \Gamma_M \quad (\text{TE modes}) \\ \Psi_i^{\text{TEM}} &= \begin{cases} \text{const} \neq 0 \quad \Gamma_{E,i} \\ 0 \quad \text{else} \quad \Gamma_E \end{cases} & \frac{\partial \Psi_i^{\text{TEM}}}{\partial n} &= 0 \quad \Gamma_M \quad (i\text{th TEM mode}) \end{aligned} \quad (8)$$

where Γ denotes an electric (E) or magnetic (M) wall. Equation (1) is represented in form of a matrix equation

$$\begin{aligned} \mathbf{a}^I + \mathbf{b}^I &= \mathbf{V}(\mathbf{a}^{II} + \mathbf{b}^{II}) \\ \mathbf{V}^T(\mathbf{a}^I - \mathbf{b}^I) &= \mathbf{a}^{II} - \mathbf{b}^{II} \\ \mathbf{V} &= [\sqrt{\mathbf{Y}^I}][\mathbf{C}][\sqrt{\mathbf{Z}^I}] \\ \sqrt{\mathbf{Y}^I} &= \text{diag}(\sqrt{Y^I}) \\ \sqrt{\mathbf{Z}^I} &= \text{diag}(\sqrt{Z^I}) \end{aligned} \quad (9)$$

which can be solved with regard to the amplitudes of \mathbf{b} in order to yield the generalized scattering matrix (GSM)

$$\mathbf{b} = \mathbf{S}\mathbf{a} \quad (10)$$

In case of rectangular, circular, circular coaxial, and elliptical waveguide discontinuities, the cross section eigenvectors required for the MM technique are given

analytically [19–45]. For more general cross sections, the corresponding eigenvalue problem has to be solved numerically, where formulations by a 2D FE method [52–57] are preferred, leading to a fast convergent direct solution without requiring search algorithms that are usually necessary for cross section field matching [69] or for boundary integral equation techniques [70].

2.1.1. 2D FE Scalar Approach (Nodal Elements) for Waveguides with Ideally Conducting Boundaries. Nodal function expansion of scalar potentials achieves—according to the author’s experience—the most efficient approach (and free of spurious modes) for metallic boundaries and homogeneous cross sections, such as for typical waveguide discontinuities shown in Fig. 1.

A standard generalized matrix eigenvalue problem for the considered waveguide cross sections of more general shape is obtained [51,52] as follows

$$[\mathbf{K} - k_c^2 \mathbf{M}] \vec{\Psi} = 0 \tag{11}$$

where

$$\mathbf{K}_{JK} = \int_{\Omega} \int \nabla_t N_J \nabla_t N_K d\Omega$$

$$\mathbf{M}_{JK} = \int_{\Omega} \int N_J N_K d\Omega, \quad \vec{\Psi} = (\Psi_1, \Psi_2, \dots, \Psi_N)^T$$

and the potentials $\vec{\Psi}$ are approximated by their nodal values Ψ_K and first-order Lagrangian interpolation polynomials $N_K(x, y)$ by

$$\Psi(x, y) \approx \sum_K \Psi_K N_K(x, y) \tag{12}$$

The generalized eigenvalue problem (11) is transformed into standard form by a Cholesky separation technique, and is solved iteratively by the Lanczos algorithm after suitable preconditioning, which includes the boundary problem for the TEM wave of coaxial sections as a special case.

Matching the transverse fields at the common interface of the general waveguide step discontinuity leads to the corresponding generalized scattering matrix (GSM) [52,54], which achieves the stable, reliable, and efficient full-wave combination of all involved parts.

2.1.2. Line Integral Formulation of Coupling Integrals. The frequency independent coupling integrals of the MM technique can be formulated in terms of line integrals by using the common definitions of the trans-

versal eigenvectors [54]

$$\begin{aligned} \frac{k_{cII}^2}{k_{cI}^2 - k_{cII}^2} \oint_{\Gamma_{II}} \Psi_{II} \frac{\partial \Psi^I}{\partial n} dc & \quad \text{TE - TE} \\ 0 & \quad \text{TE - TM, TE - TEM} \\ - \oint_{\Gamma_{II}} \Psi_{II} \frac{\partial \Psi^I}{\partial \tau} dc & \quad \text{TM - TE, TEM - TE} \\ \frac{k_{cI}^2}{k_{cI}^2 - k_{cII}^2} \oint_{\Gamma_{II}} \Psi^I \frac{\partial \Psi_{II}}{\partial n} dc & \quad \text{TM - TM} \\ \oint_{\Gamma_{II}} \Psi^I \frac{\partial \Psi_{II}}{\partial n} dc & \quad \text{TM - TEM, TEM - TEM} \\ 0 & \quad \text{TEM - TM} \end{aligned} \tag{13}$$

In case of degenerate modes ($k_{cI} = k_{cII}$), an adequate expression for the limiting case $k_{cI} \rightarrow k_{cII}$ is formulated.

Line integral formulations (13) of coupling integrals are applied for discontinuities, which consist—at least at one port side—of waveguides providing analytical expressions for the eigenvectors. The accuracy is nearly identical to the corresponding area integral formulations, and there is a slight reduction in calculation time concerning the individual coupling integrals.

However, for discontinuities of waveguides with arbitrary cross section on both sides, where the eigenvectors are numerical solutions of the corresponding 2D FE eigenvalue problem, the accuracy of line integral calculations can typically be one order of magnitude lower than for results using area integral formulations. This is due mainly to errors caused by finite discretization in the numerical approximations of the line integral contour. Moreover, the factor $(1 - k_{cI}^2/k_{cII}^2)$, which occurs in the line integral formulations (13), can increase the error still further, since the determination of eigenvalues k_c is also of only limited accuracy. Hence, in such cases, in contrast to the opinion presented in Ref. 61, area integral formulations [54] are preferable.

2.1.3. 2D FE Vector Approach (Edge Elements) for Inhomogeneous Cross Sections. For inhomogeneous cross sections, such as for waveguide structures containing dielectrics (Fig. 2), triangular edge elements for transversal field expansion are preferred because of their useful features such as eliminating spurious modes (which can occur at inhomogeneous cross sections containing dielectrics), closely approximating material boundaries, and reducing effects of singularities.

Following the approach in Refs. 71 and 72, we expand the vector field within a triangular edge element (Fig. 2) as

$$\mathbf{E}^e = \sum_{i=1}^3 \mathbf{N}_i^e E_i^e \tag{14}$$

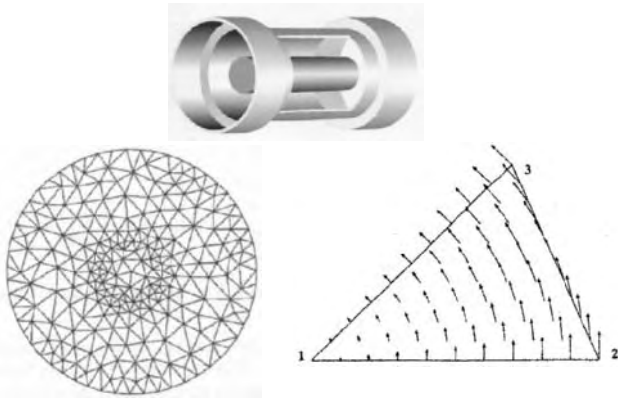


Figure 2. Step discontinuity to waveguide with inhomogeneous cross section (circular waveguide containing dielectric cylinder); mesh; vector basis function for a triangular element.

where E_i^e denotes the tangential field along the i th edge and \mathbf{N} the normalized vector function

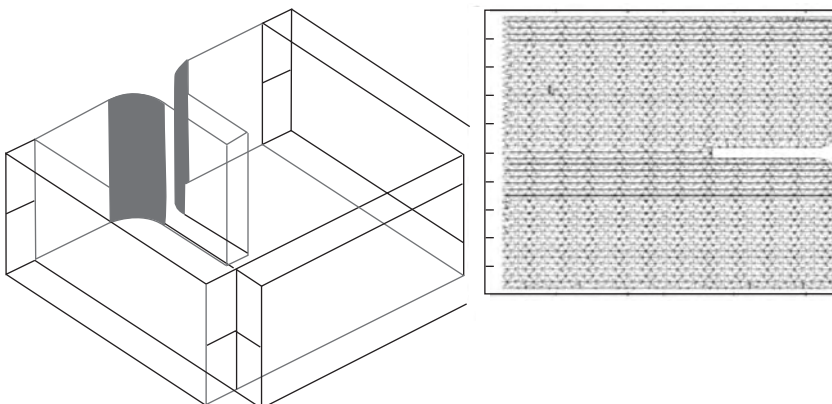
$$\mathbf{N}_i^e = l_i^e (L_i^e \nabla L_j^e - L_j^e \nabla L_i^e) \quad (15)$$

where l_i is the length of i th edge and $L_j(x, y)$ the area coordinate of the j th node [71]. The Ritz procedure [71] is applied to formulate the generalized eigenvalue problem, which is reduced to tridiagonal form by the Lanczos procedure [72,73]. The system of equations arising in each Lanczos iteration step is solved by sparse matrix Cholesky decomposition using the minimum-degree algorithm [73].

It should be noted that in contrast to the opinion expressed in Ref. 60, for homogenous cross sections (containing only metallic boundaries), the scalar nodal element approach [52,54] achieves the most efficient formulation for this kind of problem.

2.2. MM/Transfinite FE Method for Planar Waveguides with Arbitrary Contour

Many waveguide components (such as a T-junction with septum, Fig. 3) are planar in the H or E plane with arbitrary contour. Instead of solving the complete structure by the transfinite element (TransFE) method [74], for



such components, a hybrid MM/TransfiniteFE method is applied [67], which combines again the efficiency and flexibility advantages of the involved methods. For the planar element under consideration, the 2D Helmholtz equation can be expressed by an adequate functional [74]. Its solution area is subdivided into an inner region to be discretized and the port region. The fields are approximated by a suitable set of basis functions, which are solutions of the Helmholtz equation in either the H or in the E plane. Assuming that the fields at the ports are expressed in terms of normalized forward- and backward-traveling modes, an expression containing the modal S parameters can be derived. The resulting equation system is solved by the iterative biconjugate gradient (BCG) procedure.

2.3. MM/MoM Method for Apertures and Arbitrarily Shaped 3D Waveguide Discontinuities

For horn antenna structures with arbitrarily shaped outer contour, and for arbitrary 3D metallic N -port waveguide structures (Fig. 4), a hybrid MM/MoM is advantageously applied [46–50,76]. Enforcing the continuity of the tangential magnetic field at the aperture(s) in the usual way [75–78] yields the following equation for the magnetic surface current density \mathbf{M}

$$\mathbf{H}_t^i = \mathbf{H}_t^I(\mathbf{M}) + \mathbf{H}_t^{II}(\mathbf{M}) \quad (16)$$

where \mathbf{H}_t^i denotes the tangential magnetic field incident from the waveguide side(s), and $\mathbf{H}_t^I, \mathbf{H}_t^{II}$ are the tangential fields in regions I and II, respectively (Fig. 4) caused by the magnetic surface current density.

For the solution of (16), the MoM is employed. The magnetic surface current density on the aperture surface is approximated by Q linear independent basis functions \mathbf{M}_q on S_a

$$\mathbf{M}(\mathbf{r}) = \eta_0 \sum_{q=1}^Q V_q \mathbf{M}_q(\mathbf{r}) \quad (17)$$

where V_q are the expansion coefficients and η_0 denotes the free-space impedance. Introducing a set of $P=Q$ linear

Figure 3. Planar waveguide structure with arbitrarily shaped contour solved by the MM/transfinite FE method. Example: T junction with septum.

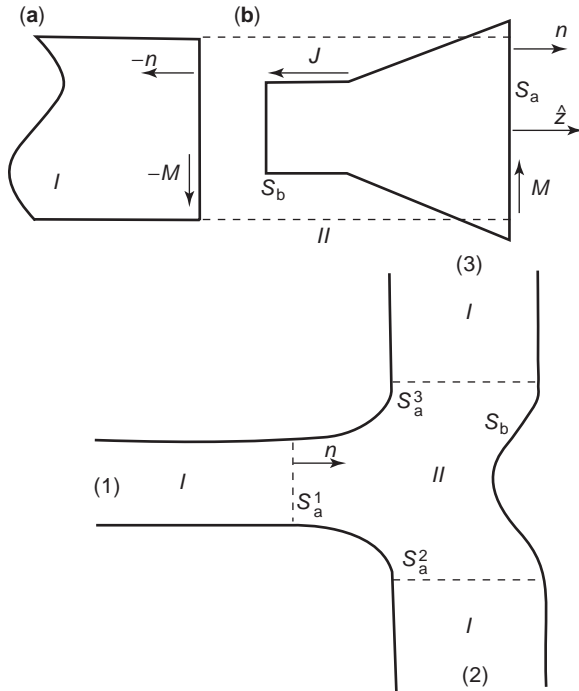


Figure 4. Definitions of regions I and II for the investigated horn and arbitrarily shaped 3D waveguide structures.

independent test functions \mathbf{W}_p on S_a results in a system of linear equations, which leads to the elements of the modal admittance matrix for region I [46,50,76].

Calculation of the admittance matrix for region II is based on the Kirchhoff–Huygens principle. The electromagnetic field is calculated using the magnetic surface current densities on S_a and the electric surface current densities on S_a and S_b :

$$\mathbf{M}(\mathbf{r}) = \begin{cases} -\mathbf{n} \times \mathbf{E}(\mathbf{r}) & \mathbf{r} \text{ on } S_a \\ 0 & \mathbf{r} \text{ on } S_b \end{cases} \quad (18a)$$

$$\mathbf{J}(\mathbf{r}) = \mathbf{n} \times \mathbf{H}(\mathbf{r}) \quad \mathbf{r} \text{ on } S_a \text{ and } S_b \quad (18b)$$

For numerical calculations, the electric field integral equation (EFIE) is preferred:

$$\begin{aligned} \mathbf{E}(\mathbf{r}) = & -\text{rot} \int_S \mathbf{M}(\mathbf{r}') G_0(\mathbf{r}, \mathbf{r}') dS' \\ & + \frac{1}{j\omega\epsilon_0} \text{rot rot} \int_S \mathbf{J}(\mathbf{r}') G_0(\mathbf{r}, \mathbf{r}') dS' \end{aligned} \quad (19)$$

Advantages include the possibility of direct applicability of numerically available eigenvectors \mathbf{e}_i in region I as basis functions $-\mathbf{u}_z \times \mathbf{e}_i$ for the magnetic surface current density. In (19), G_0 is the free-space Green's function, and the electric surface current densities are expanded in

$$\mathbf{J}(\mathbf{r}) = \sum_{s=1}^S I_s \mathbf{J}_s(\mathbf{r}) \quad \mathbf{r} \text{ on } S_a \text{ and } S_b \quad (20)$$

For the electric surface current densities, the Rao–Wilton–Glisson (RWG) basis functions [79] for triangular patches are chosen, which yields the required high flexibility. The Galerkin method is applied for the numerical solution [46–50,76], which results in the modal admittance matrix of region II.

Using the orthonormality of the eigenvectors, the following expression for the scattering coefficients is derived [50,76]

$$s_{ij} = -\eta_0 \sum_{q=1}^Q A_{iq} V_{qj} - \delta_{ij} \quad (21)$$

where V_{qj} is the expansion coefficient for the basis function \mathbf{M}_q for excitation with mode j , δ_{ij} is the Kronecker delta, and

$$A_{iq} = \int_S \mathbf{M}_q \cdot (\hat{\mathbf{z}} \times \mathbf{e}_i) dS \quad (22)$$

2.4. MM/FD Method

For arbitrary 3D structures containing dielectric material, such as the example of Fig. 5, the MM/finite-difference (FD) method is applied. When calculating the structure as a whole, the FD time-domain (FDTD) method is used; when combining parts with the MM, the FD frequency domain (FDFD) method is preferred [109].

Microwave structures, such as filters and feeds, often include dielectric 3D objects of arbitrary shape, as well as areas of rather different field intensities. Hence, the numerical effort for the FD computation can be high for accurate results if no additional refinement approaches are utilized. Several subgrid techniques have been reported [11,12,80–84]. Whereas usual subgrids mostly typically require additional interpolations schemes at the grid interfaces that can reduce flexibility, the literature [11,12,64,80,81,108,109] presents an efficient direct subgrid method without interpolation.

For the corresponding CAD applications described in this article, the direct subgrid FD technique is generalized to include both arbitrarily curved metallic and dielectric surfaces by a formulation based on combining the subgrid with a locally conformal FD algorithm [85] and with a modified intersection approach [86] for arbitrary dielectric

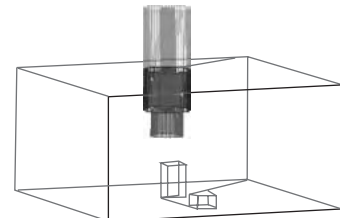


Figure 5. Arbitrary 3D structures containing dielectric material. Example: Lateral coax feed with dielectric coating and compensation posts.

boundaries. The high flexibility of this mesh generator is characterized by the fact that all three techniques can be combined [12] arbitrarily, also at one cell if necessary. For the FDTD, S -parameters are extracted via the matrix pencil method [87,88,105] which reduces the number of involved timesteps as compared with more standard methods.

2.5. Multilevel Fast Multipole Algorithm (MLFMA) and Adaptive Integral Method (AIM)

Matrix equations for N unknowns resulting from MoM solutions [e.g., Eqs. (16)–(20)] require $O(N^2)$ operations when applying standard MoM solutions by using an iterative solver [6,7]. Hence, for a high number of unknowns arising in large-scale problems, such as slot arrays, it is imperative to apply fast integral equation solvers, such as the multilevel fast multipole algorithm (MLFMA) or the adaptive integral method (AIM). The MLFMA allows matrix vector products to be effected in $O(N \log N)$ operations [3–7,10,89]. Applications of MLFMA have been restricted mainly to scattering problems so far. MLFMA applications to apertures with an electric field integral equation (EFIE) approach have been introduced in Refs. 90 and 91; a combined field integral equation (CFIE) MLFMA solution for coupled apertures was presented more recently [92,93].

Fast integral solvers based on the adaptive integral method (AIM) have proved appropriate for large-scale problems [94–98]. The method retains the advantages of the conjugate-gradient fast Fourier transform (CGFFT) technique allowing matrix vector products to be effected in $O(N \log N)$ operations as well as flexible modeling techniques involving adequate basis functions [97]. Applications of AIM have been restricted mainly to scattering problems and microstrip antennas [94–97]. Initial investigations of the applicability of the AIM method to aperture radiating problems, such as slot arrays, have been presented more recently [98,113].

For application to, for example, the slot array problem (Fig. 6), the formulation is subdivided into three calculation steps. In the first step, the MoM is applied to calculate

the integral equation for the radiating aperture(s) within the corresponding external (horn or slot array) structure geometries. The eigenvectors of rectangular and circular apertures are analytically given or can be calculated for arbitrarily shaped apertures by the FE approach [51,54].

In the second step, the AIM is utilized for the efficient solution of the matrix–vector product. The third step comprises the calculation of the radiation field by taking into account the generalized scattering matrix composed of the complete radiating and feed parts. The computation scheme for the example of slot arrays is shown in Fig. 6.

The solution is based on the magnetic field integral equation (MFIE) setup in the aperture areas of the slot array [113]:

$$\hat{z} \times \mathbf{H}^{\text{inc}} + \hat{z} \times \mathbf{H}_1\{-\mathbf{M}_z\} = \hat{z} \times \mathbf{H}_2\{\mathbf{M}_z\} \quad (23)$$

For the solution of (23), the magnetic surface current density is discretized using the aperture eigenvectors \mathbf{e}_j as basis functions

$$\mathbf{M}_z = -\hat{z} \times \sum_j M_j \mathbf{e}_j \quad (24)$$

Scalar multiplication by weighting function and integration over the apertures yields the matrix equation in the usual form [99]

$$\underline{\mathbf{Z}} \cdot \underline{\mathbf{M}} = \underline{\mathbf{I}} \quad (25)$$

with

$$\begin{aligned} (\underline{\mathbf{Z}})_{ij} &= \iint w_i \cdot \mathbf{H}_2\{\mathbf{M}_z\} dA - \iint w_i \cdot \mathbf{H}_1\{-\mathbf{M}_z\} dA, \\ (\underline{\mathbf{I}})_i &= \iint w_i \cdot \mathbf{H}^{\text{inc}} dA, \\ (\underline{\mathbf{M}})_j &= M_j \end{aligned} \quad (26)$$

and the excitation vector

$$(\underline{\mathbf{I}})_i = -2 \iint \hat{z} \cdot (\mathbf{e}_i \times \mathbf{h}^{\text{inc}}) dA. \quad (27)$$

The matrix elements can be formulated in their mixed-potential form, which alleviates the problem with singularities [100]:

$$\begin{aligned} (\underline{\mathbf{Z}})_{ij} &= - \iint \hat{z} \cdot (\mathbf{e}_i \times \mathbf{h}_j) dA - \frac{2jk}{4\pi Z_F} \iint \mathbf{e}_i \cdot \iint \frac{e^{-jkR}}{R} \mathbf{e}_j' dA' dA \\ &\quad - \frac{2}{jk4\pi Z_F} \iint (\hat{z} \cdot \text{rot}_i \mathbf{e}_i) \\ &\quad \iint \frac{e^{-jkR}}{R} (\hat{z} \cdot \text{rot}_i' \mathbf{e}_j') dA' dA. \end{aligned} \quad (28)$$

The principle of the adaptive integral method [94–98] consists in the representation of distributed sources by an

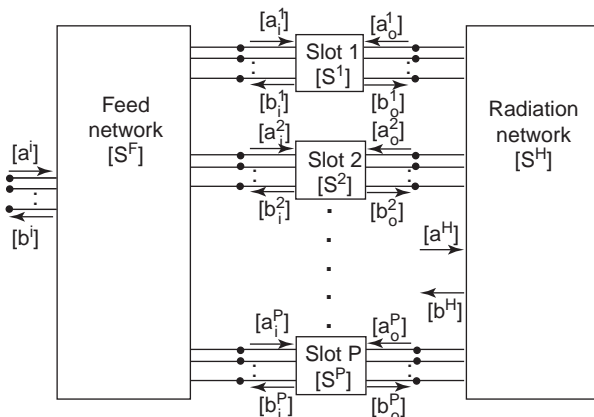


Figure 6. Computation scheme of external and internal couplings of waveguide fed arrays.

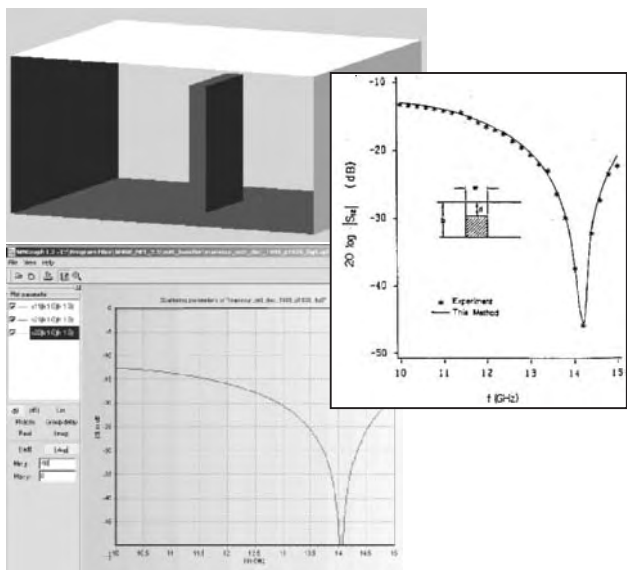


Figure 7. Application of the MM/FE method. Rectangular waveguide with a ridge discontinuity [101]. Waveguide $a = 19.05$ mm, $b = 9.524$ mm; ridge $w = 5.08$ mm, thickness $s = 1.016$ mm, $d = 1.905$ mm. Measurements [101]. Hybrid MM/FE method CPU speed 500 frequency points < 2 s (2-GHz P4 PC, 41 modes): 4 ms per frequency point.

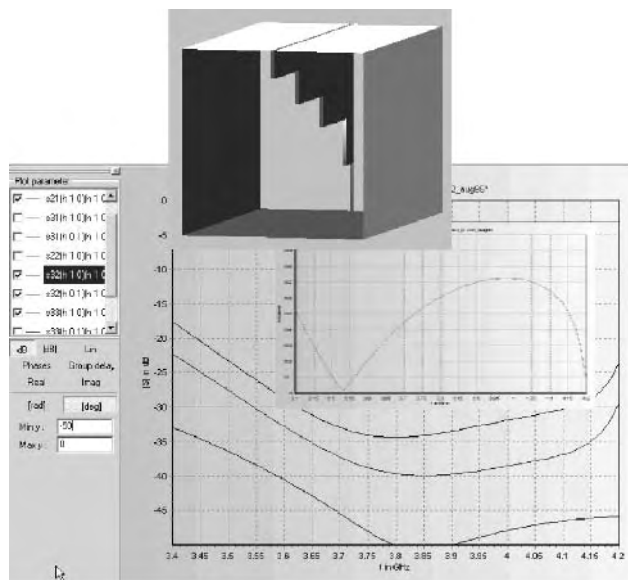


Figure 9. Application of the MM/FE method for direct combination of FE eigenvector sections. Septum polarizer, dimensions according to Ref. 102 (waveguide $a = b = 48.26$ mm). Power split of square waveguide orthogonal modes to rectangular waveguide output ports, H01 return loss, isolation, H10 return loss. Small window: axial ratio. CPU time 34 s, 500 frequency points, with < 0.1 s per frequency point (14 s for eigenvalue problem of the four ridge sections, 20 s MM dynamic calculation for the 500 frequency points), 2-GHz P4 PC, 120 modes.

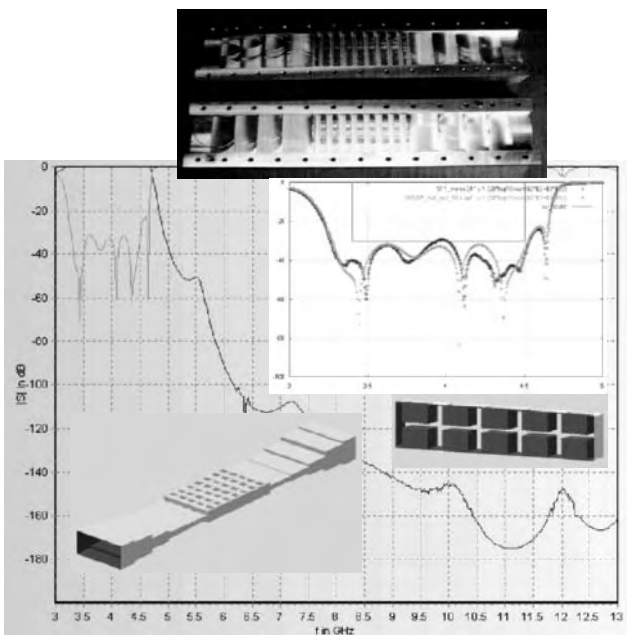


Figure 8. Accuracy and dynamic range of the MM/FE method. Optimized C-band waffle-iron filter; built without tuning screws. CPU speed < 0.1 s per frequency point, 2-GHz P4 PC, 152 modes. [Measured results (boldface return-loss curve in small window) courtesy of Bosch Telecom (now TESAT Spacecom GmbH), F.-J. Goertz, D. Wolk, Backnang, Germany, and Dr. D. Schmitt (now European Space Agency (ESA), Noordwijk, The Netherlands).]

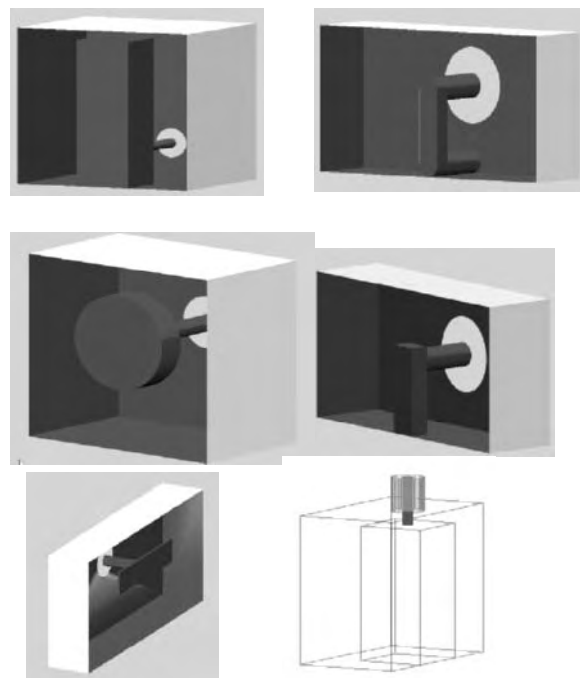


Figure 10. Extending the MM/FE and MM/MoM methods to coaxial structures. Typical feed elements for combine filters: direct post, loop, disk, slope, sheetmetal coupling, transformer coupling.

equidistant mesh of point sources. The electric field strength of the j th wave mode is, for instance, given by

$$\begin{aligned} \mathbf{e}_{xj} &= \sum_n \Lambda_{jn}^x \delta(\vec{r} - \vec{r}_n), \\ \mathbf{e}_{yj} &= \sum_n \Lambda_{jn}^y \delta(\vec{r} - \vec{r}_n), \\ \hat{z} \cdot \text{rot}_t \mathbf{e}_j &= \sum_n \Lambda_{jn}^\phi \delta(\vec{r} - \vec{r}_n) \end{aligned} \tag{29}$$

The weights for mesh points are determined by the identity of the moments. For an aperture with a partial grid of $N_x N_y$ points, we obtain by the requirement

$$\begin{aligned} &\sum_{n_x=0}^{N_x-1} \sum_{n_y=0}^{N_y-1} \Lambda_{n_x n_y}^x (x_{n_x} - x_0)^{m_x} (y_{n_y} - y_0)^{m_y} \\ &= \iint_{A_{pj}} e_x (x - x_0)^{m_x} (y - y_0)^{m_y} dA \\ &\forall 0 \leq m_x < N_x \wedge 0 \leq m_y < N_y \end{aligned} \tag{30}$$

a linear equation system for the weights of the x components of the electric field strength in the equivalent source mesh. For \vec{r}_0 the centerpoint of the aperture leads to minimum numerical effort, although other choices are also possible. This equivalent representation is inserted in (28), and one obtains

$$\begin{aligned} (\underline{Z}^{\text{AIM}})_{ij} &= -\frac{2jk}{4\pi Z_F} \sum_n \sum_{n'} \Lambda_{in}^x g(\vec{r}_n - \vec{r}_{n'}) \Lambda_{jn'}^x \\ &\quad - \frac{2jk}{4\pi Z_F} \sum_n \sum_{n'} \Lambda_{in}^y g(\vec{r}_n - \vec{r}_{n'}) \Lambda_{jn'}^y \\ &\quad - \frac{2}{jk 4\pi Z_F} \sum_n \sum_{n'} \Lambda_{in}^\phi g(\vec{r}_n - \vec{r}_{n'}) \Lambda_{jn'}^\phi \end{aligned} \tag{31}$$

For this expression, application of the fast Fourier transformation (FFT) is possible. For the near couplings, the accuracy of the expression has to be improved by taking into account corrections due to the method of moments.

The matrix is not stored explicitly; hence, an iterative solver has to be applied, which is based on a fast matrix

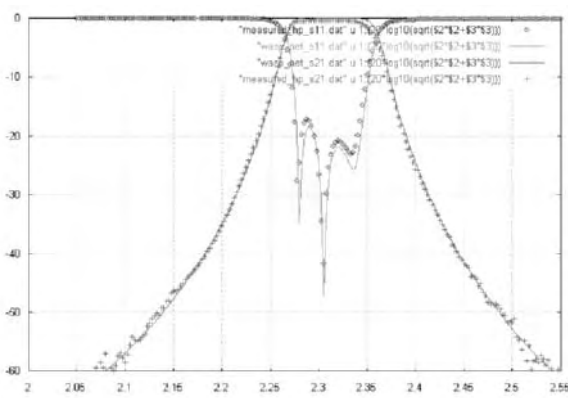


Figure 11. Milled rectangular combline filter for 2.32GHz mid-band frequency without tuning screws. Dimensions (mm): waveguide housing $a = 22.816$, $b = 21.729$; feed SMA, inner conductor height 4.5, distance wall to center first post 10.4, posts 8.928×8.928 , heights 20.35 (1st), 19.96 (2nd), distances (post plane to post plane) 20.47, 23.76 (Mesh refinement in post section factor 5). CPU time 20 s, 200 frequency points (0.1 s per frequency point), 125 modes, 2-GHz P4 PC. (This figure is available in full color at <http://www.mrw.interscience.wiley.com/erfme>.)

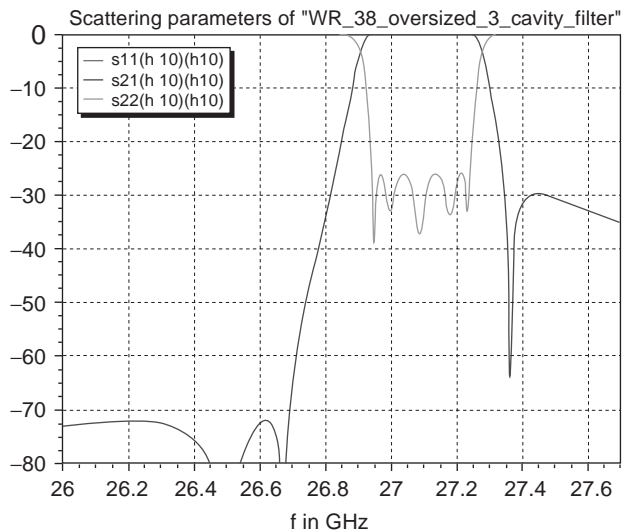
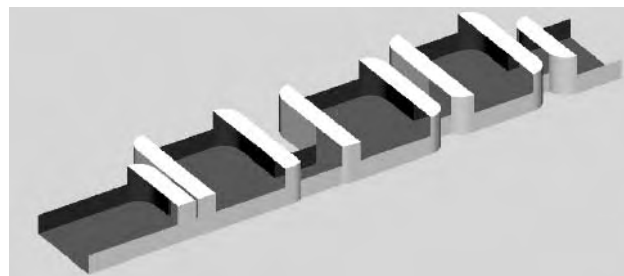


Figure 12. Advanced optimized WR-38 dual-mode filter utilizing TE_{20} -mode excitation in oversized cavities [37]. Application of the MM/transfinite element method for arbitrarily shaped planar structures. CPU time 60 s for 500 frequency points, 34 modes, 2-GHz P4 PC. (This figure is available in full color at <http://www.mrw.interscience.wiley.com/erfme>.)

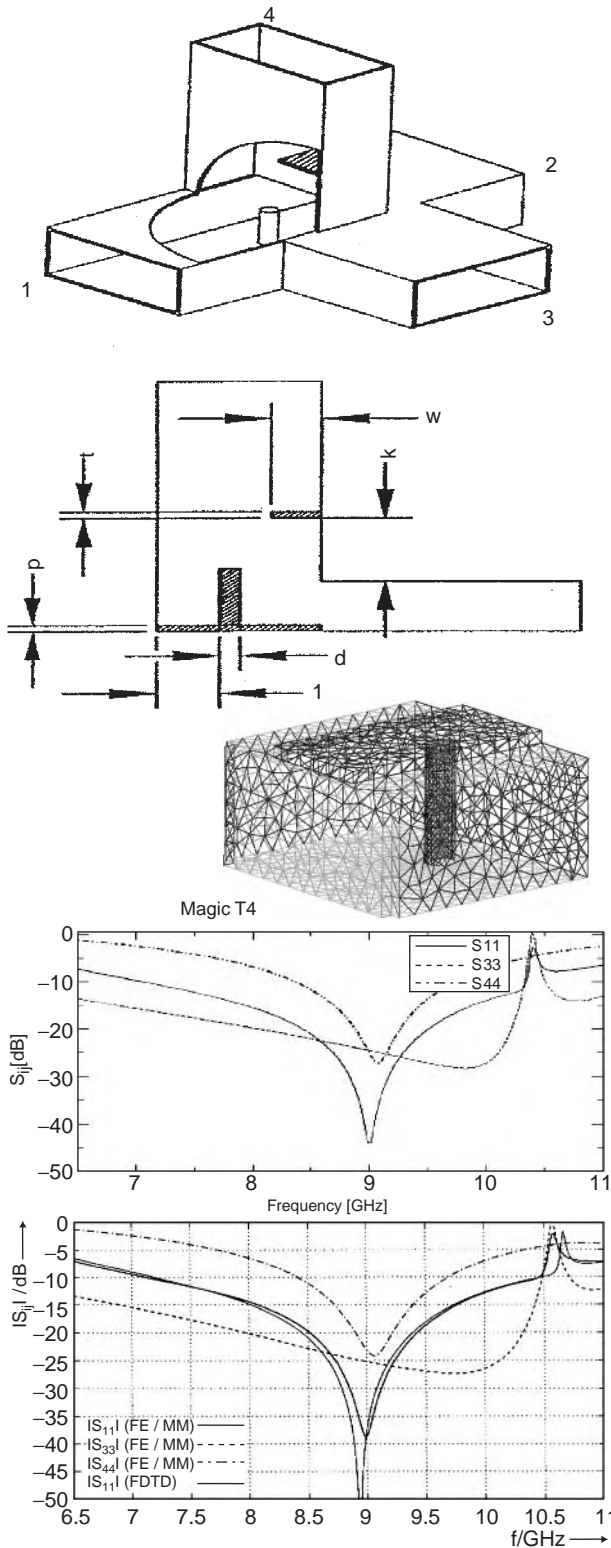
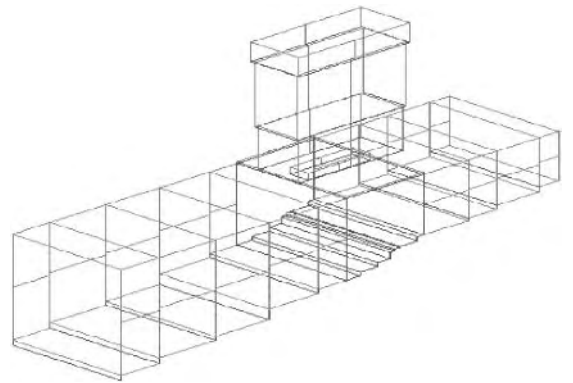


Figure 13. Application of the hybrid MM/MoM method. Compensated magic T, dimensions (mm): waveguide 12.7×25.4 , $l = 8.225$, $d = 3.175$, $k = 3.556$, $w = 8.382$, $t = 0.7937$, $p = 0$, height of post element 12.7. Structure: triangular mesh. MM/MoM results, comparison with MM/FE [59] and FDTD [109] results.



Scattering parameters of "WR112_asymn_Tee_stepped_omt_opt_opt3"

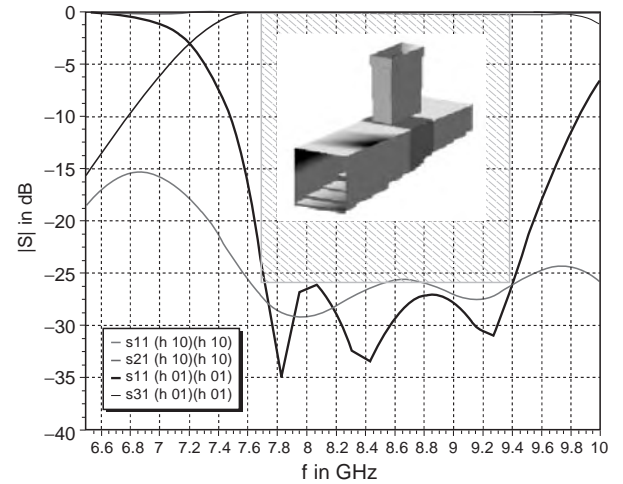


Figure 14. Optimized broadband WR-112 taper/branching ortho-mode transducer (OMT) with stepped T junction in the branching region for improved bandwidth behavior. Return loss of both polarizations. (This figure is available in full color at <http://www.mrw.interscience.wiley.com/erfme>.)

vector product

$$\begin{aligned}
 (\underline{Z} \cdot \underline{M})_i &= (\underline{Z}^{\text{MoM}} \cdot \underline{M})_i - \frac{2jk}{4\pi Z_F} \sum_n \Lambda_{in}^x \mathcal{F}^{-1} \\
 &\times \left\{ \mathcal{F}\{g(\vec{r}_m)\} \mathcal{F} \left\{ \sum_j \Lambda_{jm}^x M_j \right\} \right\}_n \\
 &- \frac{2jk}{4\pi Z_F} \sum_n \Lambda_{in}^y \mathcal{F}^{-1} \left\{ \mathcal{F}\{g(\vec{r}_m)\} \mathcal{F} \left\{ \sum_j \Lambda_{jm}^y M_j \right\} \right\}_n \\
 &- \frac{2}{jk4\pi Z_F} \sum_n \Lambda_{in}^\phi \mathcal{F}^{-1} \left\{ \mathcal{F}\{g(\vec{r}_m)\} \mathcal{F} \left\{ \sum_j \Lambda_{jm}^\phi M_j \right\} \right\}_n
 \end{aligned} \tag{32}$$

3. TYPICAL APPLICATION EXAMPLES

The extremely high CPU speed that can be achieved by applying hybrid methods is demonstrated by a simple example, a rectangular waveguide with a ridge discontinuity (Fig. 7), a structure originally reported in Ref. 101. The hybrid MM/FE method takes less than 2 s for

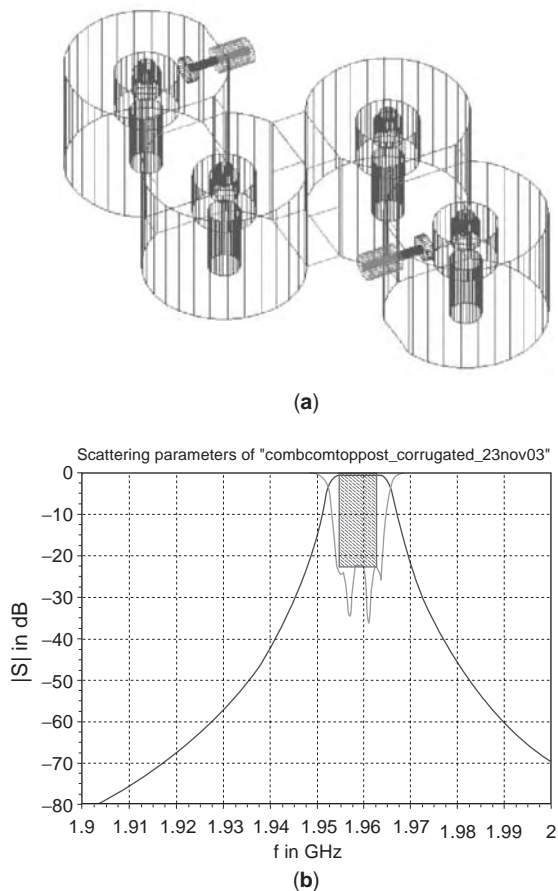


Figure 15. Advanced combline filter with rounded cavities and corrugated reentrant resonators directly optimized toward the goal of -23 dB return loss: (a) structure; (b) S -parameter results. (This figure is available in full color at <http://www.mrw.interscience.wiley.com/erfme>.)

500 frequency points (i.e., ~ 4 ms per frequency point, 41 modes, 2-GHz P4 PC), with the time required for the 2D FE eigenvalue solution included.

The excellent accuracy, high dynamic range, and high CPU speed achieved by the MM/FE method are demonstrated by an optimized and measured C-band waffle-iron filter (WR-229) Fig. 8 for space applications. The filter has been fabricated without any tuning screws. The advanced filter utilizing a large gap width for high-power applications has been optimized by applying the evolution strategy [30,54], and has been multipacting tested with >1.5 kW by the European Space Agency (ESA).

The next example, a septum polarizer (Fig. 9), relates to a typical MM/FE application, where the ridge sections (i.e., FE eigenvector sections) are directly connected to each other. Hence—as outlined in Section 2—for the corresponding coupling coefficients, calculations via area integrals are preferred to line integrals in this case. The dimensions are chosen according to Ref. 102, where cross section field-matching has been applied for solution of the eigenvalue problem [103], which is considerably more time-consuming than applying the MM/FE technique because of the search algorithm involved in the MM eigenvalue solution problem.

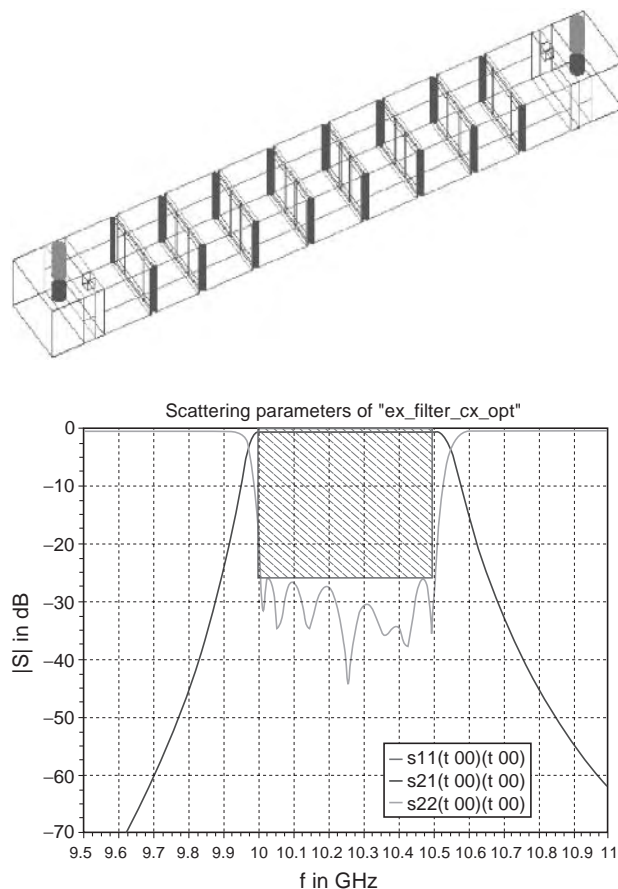


Figure 16. WR-90 H -plane iris seven-resonator filter with rounded corners, fed by topwall SMA connectors. Optimization of the whole filter including the effect of the coax feeds. (This figure is available in full color at <http://www.mrw.interscience.wiley.com/erfme>.)

The MM/FE and MM/MoM methods have been extended for inclusion of typical coaxial feed structures in Fig. 10, where TEM mode expressions (Sections 2.1,2,3) have to be taken into account. This achieves the possibility of fast CAD and optimization of combline and interdigital filters/diplexers with rectangular post elements. The rectangular post structure in combline/interdigital filters can be utilized for low-cost fabrication, such as by computer-controlled milling techniques [110,112] directly, or the rectangular structure can be converted into corresponding circular posts by applying well-known formulas, such as those in Ref. 111, of identical characteristic impedances (square/circular rod between two plates). This yields good starting points for further optimizations by applying, for example, the MM/FD or MM/MoM methods for circular posts.

For accuracy and computing speed verification, a simple direct post-fed four-resonator rectangular combline filter for 2.32 GHz midband frequency has been optimized and fabricated by a computer-controlled milling technique without any tuning screws (Fig. 11). Advanced CAD tools based on these hybrid techniques [68], allow the corresponding data file to be directly and conveniently loaded from the graphical output after optimization. Very good

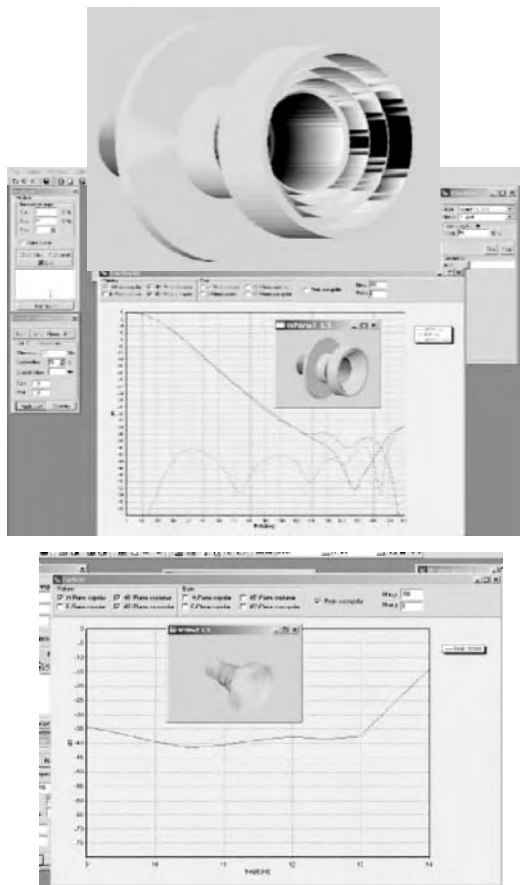


Figure 17. Axially corrugated (“choked”) horn optimized for broadband low cross-polarization. Lower plot shows the peak cross-polarization level as a function of frequency. (This figure is available in full color at <http://www.mrw.interscience.wiley.com/erfme>.)

agreement between theory and measurements can be achieved. For the MM/FE calculation, 125 modes have been taken into account; the CPU speed is 0.1s per frequency point on a 2-GHz P4 PC, which underlines, again, the efficiency of the hybrid MM/FE method also for this class of filters, making their optimization a straightforward task.

An application example for the MM/transfinite FE method for planar waveguides with arbitrary contour is the oversized cavity filter shown in Fig. 12. The TE₂₀ mode excited by offset irises can be controlled to achieve a dual-mode behavior with stopband poles [37].

The application of the MM/MoM method for 3D waveguide structures is demonstrated in Fig. 13 with the example of a magic T compensated by a post and an iris. The CPU speed is about 8 s per frequency point on a 2-GHz P4 PC. Good agreement with reference calculations using the FDTD method [59] and the MM/FE generalized scattering matrix separation (GSMS) technique [105] can be achieved. In this way, rather complicated 3D structures, such as waffle-iron filters with round teeth [76] can be modeled.

Figure 14 demonstrates the application of the MM/MoM technique for an advanced broadband taper/branching orthomode transducer (OMT) with a tapered branch-

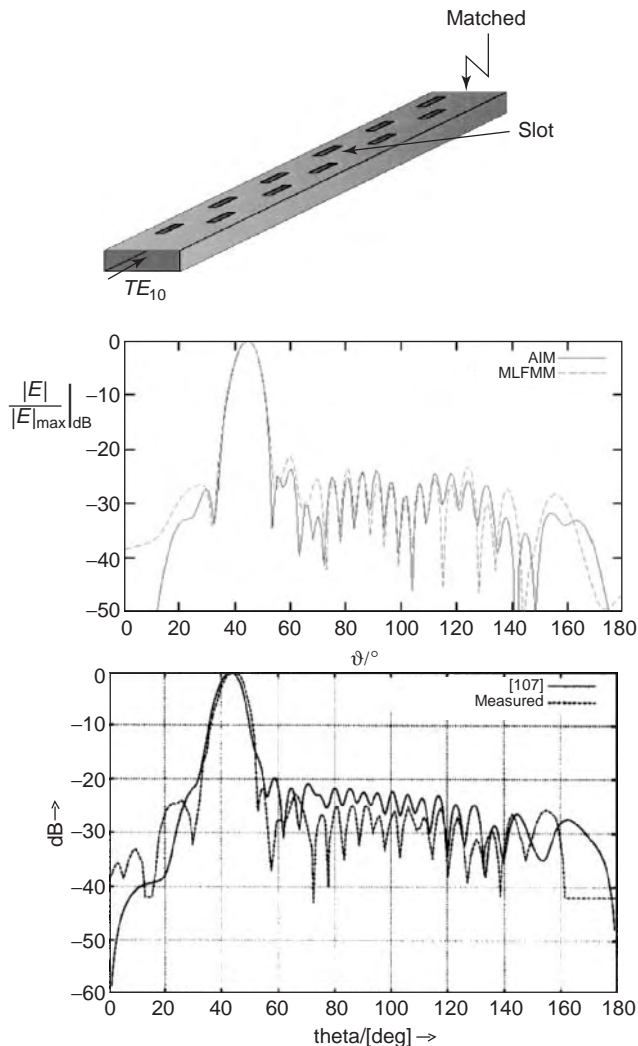


Figure 18. Traveling-wave slot array antenna with 21 slots according to Elliott [107]. Dimensions given in Ref. 102. The author’s own calculation with fast MoM techniques: adaptive integral method (AIM) and multilevel fast multipole method (MLFMM). Comparison with reference calculations [107] and measurements [106]. (This figure is available in full color at <http://www.mrw.interscience.wiley.com/erfme>.)

ing section. The ~20% bandwidth achieved compares well with the usual 10% of more standard designs [104].

The MM/MoM technique can also advantageously be applied for more complicated components such as a comb-line filter with rounded cavities and reentrant resonators for convenient tuning (Fig. 15).

An application example for the hybrid MM/transfinite FE/MoM technique with high practical importance is shown in Fig. 16: a WR-90 H-plane iris filter with rounded corners, fed by a coax standard 50 Ω subminiature version A (SMA) connector transition from the topwall. Because of the high CPU speed (1 s per frequency point, 2-GHz P4 PC, 102 modes), the filter can be directly optimized taking the effect of the coax feed rigorously into account.

An antenna application example of the MM/MoM technique is the design of an axially corrugated (“choked”)

horn (Fig. 17). Because of the consequent utilization of the hybrid technique, the CPU speed achieved (~ 5 s per frequency point, 3-GHz P4 PC) allows the convenient direct optimization toward desired broadband low cross-polarization levels.

Figure 18 shows a traveling-wave slot array antenna with 21 slots in the broad waveguide wall [106]. The utilization of the MM/MoM AIM and MLFMM techniques including the internal coupling provides results that agree well with measurements reported in Ref. 106 and with reference calculations using the more standard MoM spectral-domain technique [107].

4. CONCLUSION

Fast EM-based CAD tools yielding accurate, optimized designs within adequately short response times are indispensable for solving challenging optimization tasks of advanced modern microwave and millimeter-wave component applications. This goal is achieved by hybrid CAD techniques, which typically go beyond the possibilities of single methods, by expanding the capabilities and enhancing the efficiency. The hybrid CAD techniques described here combine advantageously the efficiency of the mode-matching (MM) method with the flexibility of finite-element (FE), finite-difference (FD), and method-of-moments (MoM) techniques. Typical application examples demonstrate their versatility and high calculation speed. The accuracy is verified by available measurements and reference calculations.

BIBLIOGRAPHY

1. J. E. Bracken, D.-K. Sun, and Z. J. Cendes, S-domain methods for simultaneous time and frequency characterization of electromagnetic devices, *IEEE Trans. Microwave Theory Tech.* **MTT-46**:1277–1290 (Sept. 1998).
2. A. S. Rong, H. Yang, X. H. Chen, and A. Cangellaris, Efficient FD-TD modeling of irises/slots in microwave structures and its application to the design of combline filters, *IEEE Trans. Microwave Theory Tech.* **MTT-49**:2266–2275 (Dec. 2001).
3. W. C. Chew, J.-M. Jin, C.-C. Lu, E. Michielssen, and J. M. Song, Fast solution methods in electromagnetics, *IEEE Trans. Anten. Propag.* **AP-45**:533–543 (March 1997).
4. J.-S. Zhao, W. C. Chew, C.-C. Lu, E. Michielssen, and J. Song, Thin-stratified medium fast-multipole algorithm for microstrip structures, *IEEE Trans. Microwave Theory Tech.* **MTT-46**:395–403 (April 1998).
5. F. Ling, C.-F. Wang, and J.-M. Jin, An efficient algorithm for analyzing large-scale microstrip structures using adaptive integral method combined with discrete complex-image method, *IEEE Trans. Microwave Theory Tech.* **MTT-48**:832–839 (May 2000).
6. A. F. Peterson, S. L. Ray, and R. Mittra, *Computational Methods for Electromagnetics*, IEEE Press, New York, 1998.
7. W. C. Chew, J.-M. Jin, E. Michielssen, and J. Song, *Fast and Efficient Algorithms in Computational Electromagnetics*, Artech House, Boston, 2001.
8. R. Coifman, V. Rokhlin, and S. Wandzura, The fast multipole method for the wave equation: A pedestrian prescription, *IEEE Anten. Propag. Mag.* **35**:7–12 (June 1996).
9. E. Bleszynski, M. Bleszynski, and J. Jaroszewicz, AIM: Adaptive integral method for solving large-scale electromagnetic scattering problems, *Radio Sci.* **31**:1225–1251 (Sept.–Oct. 1996).
10. M. F. Gyure and M. A. Stalzer, A prescription for the multi-level Helmholtz FMM, *IEEE Comput. Sci. Eng.* **5**:35–47 (July–Sept. 1998).
11. R. Lotz and F. Arndt, Locally conformed subgrid FD-FD technique for the analysis of 3D waveguide structures with curved metallic objects, *1999 Int. Microwave Symp. Digest*, June 1999, Vol. 3, pp. 1277–1280.
12. F. Arndt, R. Lotz, and J. Ritter, Advanced FD-TD techniques for the CAD of microwave components, *Electromagnetics* **23**:153–168 (Feb.–March 2003).
13. G. A. Thiele and T. H. Newhouse, A hybrid technique for combining moments methods with the geometrical theory of diffraction, *IEEE Trans. Anten. Propag.* **AP-23**:62–69 (Jan. 1975).
14. W. D. Burnside and P. H. Pathak, A summary of hybrid solutions involving moment methods and GTD, in B. J. Strait, ed., *Applications of the Method of Moments to Electromagnetic Fields*, SCEE Press, St. Cloud, FL, 1980.
15. J. J. H. Wang, *Generalized Moment Methods in Electromagnetics*, Wiley, New York, 1991.
16. G. Tiberi, A. Monorchio, G. Manara, and R. Mittra, Hybridizing asymptotic and numerically rigorous techniques for solving electromagnetic scattering problems using the characteristics basis functions, *Int. Antenna and Propagation Symp. Digest*, June 2003, Vol. 3, Session 114.
17. J. Liu and J. M. Jin, A novel hybridization of higher order finite element and boundary integral methods for electromagnetic scattering and radiation problems, *IEEE Trans. Antennas Propag.* **AP-49**:1794–1806 (Dec. 2001).
18. H. Rogier, F. Olyslager, and D. de Zutter, A hybrid finite element integral equation approach for the eigenmode analysis of complex anisotropic dielectric waveguides, *Radio Sci.* **31**:999–1010 (July–Aug. 1996).
19. W. C. Hahn, A new method for the calculation of cavity resonators, *J. Appl. Phys.* **12**:62–68 (Jan. 1941).
20. J. R. Whinnery and H. W. Jamieson, Equivalent circuits for discontinuities in transmission lines, *Proc. IRE.* **32**:98–116 (Feb. 1944).
21. P. J. B. Clarricoats and K. R. Slinn, Numerical solution of waveguide-discontinuity problems, *Proc. IEE.* **114**:878–886 (July 1967).
22. A. Wexler, Solution of waveguide discontinuities by modal analysis, *IEEE Trans. Microwave Theory Tech.* **MTT-15**:508–517 (Sept. 1967).
23. G. L. James, Analysis and design of TE₁₁-to-HE₁₁ corrugated cylindrical waveguide mode converters, *IEEE Trans. Microwave Theory Tech.* **MTT-29**:1059–1066 (Oct. 1981).
24. H. Patzelt and F. Arndt, Double-plane steps in rectangular waveguide and their application for transformers, irises and filters, *IEEE Trans. Microwave Theory Tech.* **MTT-30**:771–777 (May 1982).
25. F. Arndt, D. Ellermann, H. W. Haeusler, and J. Strube, Field theory analysis and numerical synthesis of symmetrical multiple-branch waveguide couplers, *Frequenz* **36**:262–266 (Oct. 1982).
26. F. Arndt, J. Bornemann, D. Grauerholz, and R. Vahldieck, Theory and design of low-insertion loss fin-line filters, *IEEE Trans. Microwave Theory Tech.* **MTT-30**:155–163 (Feb. 1982).

27. R. Vahldieck, J. Bornemann, F. Arndt, and D. Grauerholz, Optimized waveguide E-plane metal insert filters for millimeter-wave applications, *IEEE Trans. Microwave Theory Tech.* **MTT-31**:65–69 (Jan. 1983).
28. F. Arndt, B. Koch, H.-J. Orlok, and N. Schroeder, Field theory design of rectangular waveguide broad-wall metal-insert slot couplers for millimeter-wave applications, *IEEE Trans. Microwave Theory Tech.* **MTT-33**:95–104 (Feb. 1985).
29. U. Tucholke, F. Arndt, and T. Wriedt, Field theory design of square waveguide iris polarizers, *IEEE Trans. Microwave Theory Tech.* **MTT-34**:156–160 (Jan. 1986).
30. H. Schmiedel and F. Arndt, Field theory design of rectangular waveguide multiple-slot narrow wall couplers, *IEEE Trans. Microwave Theory Tech.* **MTT-34**:791–798 (July 1986).
31. J. Dittloff, F. Arndt, and D. Grauerholz, Optimum design of waveguide E-plane stub-loaded phase shifters, *IEEE Trans. Microwave Theory Tech.* **MTT-36**:583–587 (March 1988).
32. J. Dittloff and F. Arndt, Rigorous design of septate E-plane multiplexers with printed circuit elements, *1988 IEEE MTT-S Int. Microwave Symp. Digest*, New York, May 1988, pp. 431–434.
33. J. Dittloff and F. Arndt, Computer-aided design of slit-coupled H-plane T-junction diplexers with E-plane metal-insert filters, *IEEE Trans. Microwave Theory Tech.* **MTT-36**:1833–1840 (Dec. 1988).
34. F. Alessandri, G. Bartolucci, and R. Sorrentino, Admittance matrix formulation of waveguide discontinuity problems: Computer-aided design of branch-guide directional couplers, *IEEE Trans. Microwave Theory Tech.* **MTT-36**:394–403 (Feb. 1988).
35. F. Arndt, J. Dittloff, U. Papziner, D. Fasold, N. Nathrath, and H. Wolf, Rigorous field theory design of compact and light-weight broadband diplexers for satellite communication systems, *Proc. 19th European Microwave Conf.*, London, Sept. 1989, pp. 1214–1219.
36. R. Sorrentino, ed., *Numerical Methods for Passive Microwave and Millimeter Wave Structures*, IEEE Press, New York, 1989.
37. F. Arndt, T. Duschak, U. Papziner, and P. Rolappe, Asymmetric iris coupled cavity filters with stopband poles, *1990 MTT-S Int. Microwave Symp. Digest*, Dallas, May 1990, pp. 215–218.
38. U. Papziner and F. Arndt, Field theoretical computer-aided design of rectangular and circular iris coupled rectangular or circular waveguide cavity filters, *IEEE Trans. Microwave Theory Tech.* **MTT-41**:462–471 (Feb. 1993).
39. M. Guglielmi, G. Gheri, M. Calamia, and G. Pelosi, Rigorous multimodule network representation of inductive steps, *IEEE Trans. Microwave Theory Tech.* **MTT-42**:317–326 (Feb. 1994).
40. A. P. Orfanidis, G. A. Kyriacou, and J. N. Sahalos, A mode-matching technique for the study of circular and coaxial waveguide discontinuities based on closed-form coupling integrals, *IEEE Trans. Microwave Theory Tech.* **MTT-48**:880–883 (May 2000).
41. F. Alessandri, M. Giordano, M. Guglielmi, G. Martirano, and F. Vitulli, A new multiple-tuned six-port Riblet-type directional coupler in rectangular waveguide, *IEEE Trans. Microwave Theory Tech.* **MTT-51**:1441–1448 (May 2003).
42. J. Kocbach and K. Folgero, Design procedure for waveguide filters with cross-couplings, *2002 Int. Microwave Symp. Digest*, June 2002, Vol. 3, pp. 1449–1452.
43. L. Accatino and M. Mongiardo, Hybrid circuit-full-wave computer-aided design of a manifold multiplexers without tuning elements, *IEEE Trans. Microwave Theory Tech.* **MTT-50**:2044–2047 (Sept. 2002).
44. P. Matras, R. Bunger, and F. Arndt, Modal scattering matrix of the general step discontinuity in elliptical waveguides, *IEEE Trans. Microwave Theory Tech.* **MTT-45**:453–458 (March 1997).
45. M. Mongiardo, P. Russer, C. Tomassoni, and L. Felsen, Analysis of N-furcation in elliptical waveguides via the generalized network formulation, *IEEE Trans. Microwave Theory Tech.* **MTT-47**:2473–2478 (Dec. 1999).
46. E. Kühn and V. Hombach, Computer-aided analysis of corrugated horns with axial ring or ring-loaded radial slots, *Proc. Int. Conf. Antennas Propagation (ICAP 83)*—Part I, UK, March 1983, pp. 293–296.
47. K. Wolff, T. Wriedt, F. Arndt, and U. Tucholke, Hybrid field design of square potter horns, *Proc. Int. Conf. Antennas Propagation (ICAP 87)*—Part I, UK, March 1987, pp. 210–213.
48. T. Wriedt, K.-H. Wolff, F. Arndt, and U. Tucholke, Rigorous hybrid field theoretic design of stepped rectangular waveguide mode converters including the horn transitions into half-space, *IEEE Trans. Anten. Propag.* **AP-37**:780–790 (June 1989).
49. K. Liu, C. A. Balanis, and C. R. Birtcher, Analysis of pyramidal horn antennas using moment methods, *IEEE Trans. Anten. Propag.* **AP-41**:1379–1389 (Oct. 1993).
50. R. Bunger, R. Beyer, and F. Arndt, Rigorous combined mode-matching integral equation analysis of horn antennas with arbitrary cross-section, *IEEE Trans. Anten. Propag.* **AP-47**:1641–1648 (Nov. 1999).
51. R. Beyer and F. Arndt, Field theory design of circular waveguide dual-mode filters by a combined mode matching finite element method, *EuMC Int. Microwave Symp. Digest*, Cannes, France, Sept. 1994, pp. 437–442.
52. R. Beyer and F. Arndt, Efficient modal analysis of waveguide filters including the orthogonal mode coupling elements by an MM/FE method, *IEEE Microwave Guided Wave Lett.* **5**:1–3 (Jan. 1995).
53. J. R. Montejo-Garai and J. Zapata, Full-wave design and realization of multicoupled dual-mode circular waveguide filters, *IEEE Trans. Microwave Theory Tech.* **MTT-43**:1290–1297 (June 1995).
54. F. Arndt, R. Beyer, J. M. Reiter, T. Sieverding, and T. Wolf, Automated design of waveguide components using hybrid mode-matching/numerical EM building blocks in optimization-oriented CAD frame-works—state-of-the-art and recent advances, *IEEE Trans. Microwave Theory Tech.* **MTT-45**:747–760 (May 1997).
55. F. Arndt, R. Beyer, W. Hauth, D. Schmitt, and H. Zeh, Cascaded wide stop band waffle-iron filter designed with a MM/FE CAD method, *EuMC Int. Microwave Symp. Digest*, Munich, Germany, Oct. 1999, pp. 186–189.
56. F. Arndt and J. Brandt, Fast hybrid MM/FE CAD tool for the design and optimization of advanced evanescent mode filters, *MIOF Int. Microwaves and Optronics Symp. Digest*, Stuttgart, Germany, May 2001, pp. 369–372.
57. F. Arndt and J. Brandt, MM/FE CAD and optimization of rectangular combline filters, *EuMC Int. Microwave Symp. Digest*, Milan, Italy, Sept. 2002, pp. 335–338.
58. J. Rubio, J. Arroyo, and J. Zapata, Analysis of passive microwave circuits by using a hybrid 2-D and 3-D finite-element mode-matching method, *IEEE Trans. Microwave Theory Tech.* **MTT-47**:1746–1749 (Sept. 1999).

59. R. Beyer and F. Arndt, Efficient MM/FEG SMS technique for the CAD of broadband lateral coax feeds in rectangular waveguide, *IEEE MTT-S Int. Microwave Symp. Digest*, Boston, June 2000, pp. 109–112.
60. D. Arena, M. Ludovico, G. Manara, and A. Monorchio, Analysis of waveguide discontinuities using edge elements in a hybrid mode matching/finite elements approach, *IEEE Microwave Wireless Compon. Lett.* **11**:379–381 (Sept. 2001).
61. V. Crino, C. Tomassoni, and M. Mongiardo, Line-integral formulation of the hybrid MM/FEM technique, in *IEEE MTT-S Int. Microwave Symp. Digest*, Seattle, WA, June 2002, pp. 2033–2036.
62. F. Alimenti, P. Mezzanotte, L. Roselli, and R. Sorrentino, Efficient analysis of waveguide components by FDTD combined with time domain modal expansion, *IEEE Microwave Guided Wave Lett.* **5**:351–353 (Oct. 1995).
63. M. Righi, M. Mongiardo, R. Sorrentino, and W. Hoefler, Efficient TLM diakoptics for separable structures, *Proc. Int. MTT-S*, Atlanta, GA, June 1993, Vol. 1, pp. 425–428.
64. R. Lotz and F. Arndt, FD-FD GSM technique for the CAD and optimization of combline filters, *IEEE MTT-S Int. Microwave Symp. Digest*, Phoenix, May 2001, pp. 1253–1256.
65. F. Arndt and A. Enneking, Hybrid MM/FE/MoM technique for waveguide horn antennas and slot arrays, *Proc. Int. Conf. Electromagnetics in Advanced Applications (ICEAA'01)*, Torino, Italy, Sept. 2001, pp. 569–572.
66. F. Arndt, J. Brandt, and J. Ritter, MM/FE/FD CAD method for the optimization of waveguide filters including structures of arbitrary shape and coax feeds, *EuMC Int. Microwave Symp. Digest*, London, Sept. 2001, pp. 319–322.
67. F. Arndt, J. Brandt, V. Catina, A. Enneking, and J. Ritter, Fast hybrid MM/FE/TransFE/MoM/FD CAD of waveguide components and aperture antennas, *Proc. 18th Annual Review of Progress in Applied Computational Electromagnetics (ACES)*, Monterey, CA, March 2002, pp. 1-15–1-23.
68. MiG, A CAD tool utilizing fast hybrid MM/FE/MoM/FD techniques, *Microwave J. (cover feature article)* **45**:178–182 (Sept. 2002).
69. J. Strube and F. Arndt, Rigorous hybrid-mode analysis of the transition from rectangular waveguide to shielded dielectric image guide, *IEEE Trans. Microwave Theory Tech.* **MTT-33**:391–401 (May 1985).
70. W. Schroeder and M. Guglielmi, Boundary integral equation approach to multi-mode Y-matrix characterization of multi-ridged sections in circular waveguide, *IEEE MTT-S Int. Microwave Symp. Digest*, San Francisco, June 1996, pp. 1849–1852.
71. J. Jin, *The Finite Element Method in Electromagnetics*. Wiley, New York, 1993.
72. O. C. Zienkiewicz, *The Finite Element Method*, McGraw-Hill, Berkshire, UK, 1977.
73. Y. Saad, Numerical methods for large eigenvalue problems, in *Algorithms and Architectures for Advanced Scientific Computing*. Manchester Univ. Press, Manchester, UK, 1992.
74. Z. J. Cendes and J. F. Lee, The transfinite element method for modeling MMIC devices, *IEEE Trans. Microwave Theory Tech.* **MTT-36**:1639–1649 (Dec. 1988).
75. A. Joestingmeier and A. S. Omar, Analysis of inhomogeneously filled cavities coupled to waveguides using the VIE formulation, *IEEE Trans. Microwave Theory Tech.* **MTT-41**:1207–1214 (June/July 1993).
76. R. Bunger and F. Arndt, Moment-method analysis of arbitrary 3D metallic N-port waveguide structures, *IEEE Trans. Microwave Theory Tech.* **MTT-48**:531–537 (April 2000).
77. J. R. Mautz and R. F. Harrington, A generalized network formulation for aperture problems, *IEEE Trans. Anten. Propag.* **AP-24**:870–873 (Nov. 1976).
78. H. Auda and R. F. Harrington, A moment solution for waveguide junction problems, *IEEE Trans. Microwave Theory Tech.* **MTT-31**:515–520 (July 1983).
79. S. M. Rao, D. R. Wilton, and A. W. Glisson, Electromagnetic scattering by surfaces of arbitrary shape, *IEEE Trans. Anten. Propag.* **AP-30**:409–418 (May 1982).
80. J. Ritter and F. Arndt, A generalized 3D subgrid technique for the finite-difference time domain method, *1997 Int. Microwave Symp. Digest*, June 1997, Vol. 3, pp. 1563–1566.
81. R. Lotz, J. Ritter, and F. Arndt, 3D subgrid technique for the finite difference method in the frequency domain, *1998 Int. Microwave Symp. Digest*, June 1998, Vol. 3, pp. 1739–1742.
82. S. S. Zivanovic, K. S. Yee, and K. K. Mei, A subgridding method for the time-domain finite-difference method to solve Maxwell's equations, *IEEE Trans. Microwave Theory Tech.* **MTT-39**:471–479 (March 1991).
83. I. S. Kim and W. J. R. Hoefler, A local mesh refinement algorithm for the time domain finite difference method using Maxwell's curl equations, *IEEE Trans. Microwave Theory Tech.* **MTT-38**:812–815 (June 1990).
84. S. Kapoor, Sub-cellular technique for finite-difference time-domain method, *IEEE Trans. Microwave Theory Tech.* **MTT-45**:673–677 (May 1997).
85. S. Dey and R. Mittra, A locally conformal finite-difference time-domain (FD-TD) algorithm for modeling three-dimensional perfectly conducting objects, *IEEE Microwave Guided Wave Lett.* **7**:273–275 (Sept. 1997).
86. N. Kaneda, B. Houshmand, and T. Itoh, FDTD analysis of dielectric resonators with curved surfaces, *IEEE Trans. Microwave Theory Tech.* **MTT-45**:1645–1649 (Sept. 1997).
87. Y. Hua and T. K. Sarkar, Matrix pencil method for estimating parameters of exponentially damped/undamped sinusoids in noise, *IEEE Trans. Acoust. Speech Signal Process.* **38**:814–824 (May 1990).
88. J. Ritter and F. Arndt, Efficient FD-TD/matrix pencil method for the full-wave scattering parameter analysis of waveguiding structures, *IEEE Trans. Microwave Theory Tech.* **MTT-44**:2450–2456 (Dec. 1996).
89. J. M. Song and W. C. Chew, Multilevel fast-multipole algorithm for solving combined field integral equations of electromagnetic scattering, *Microwave Opt. Tech. Lett.* **10** (1):14–19 (Sept. 1995).
90. R. Bunger and F. Arndt, MLFMM analysis of ridged waveguide horns, *Proc. Millennium Conf. Antennas Propagation (AP2000)*, Davos, Switzerland, April 2000, p. 1418.
91. I. Rullhusen and F. Arndt, MLFMA analysis of coupled rectangular apertures, *Proc. JINA Conf.*, Nice, France, Nov. 2002, pp. 459–462.
92. I. Rullhusen and F. Arndt, Efficient MLFMA analysis of coupled rectangular and circular apertures in a finite screen, *IEEE MTT-S Int. Microwave Symp. Digest*, Philadelphia, June 2003, pp. 1971–1974.
93. I. Rullhusen and F. Arndt, MLFMA analysis of finite aperture arrays including reflector, *IEEE AP-S Int. Symp. Digest*, Columbus, OH, Paper 125.8, June 2003.
94. S. S. Bindiginawale, J. L. Volakis, and H. Anastassin, Scattering from planar structures containing small features using

- the adaptive integral method (AIM), *IEEE Trans. Anten. Propag.* **AP-46**:1867–1878 (Dec. 1998).
95. E. Bleszynski, M. Bleszynski, and T. Jaroszewicz, AIM: Adaptive integral method for solving large scale electromagnetic scattering and radiation problems, *Radio Sci.* **31**:1225–1251 (Sept./Oct. 1996).
 96. F. Ling, C. F. Wang, and J. M. Jin, Application of the adaptive integral method to scattering and radiation analysis of arbitrarily shaped planar structures, *J. Electromagn. Waves Appl.* **12**:1021–1037 (1998).
 97. F. Ling, C. F. Wang, and J. M. Jin, An efficient algorithm for analyzing large-scale microstrip structures using adaptive integral method combined with discrete complex image method, *IEEE Trans. Microwave Theory Tech.* **MTT-48**:832–839 (May 2000).
 98. I. Rullhusen and F. Arndt, AIM analysis of slot arrays, *Proc. Int. Conf. Electromagnetics in Advanced Applications (ICEAA'03)*, Torino (Turin, Italy), Sept. 2003, pp. 321–324.
 99. R. Bunger, R. Beyer, and F. Arndt, Rigorous combined mode-matching integral equation analysis of horn antennas with arbitrary cross section, *IEEE Trans. Anten. Propag.* **AP-47**:1641–1648 (Nov. 1999).
 100. D. R. Wilton, S. M. Rao, A. W. Glisson, D. H. Schaubert, O. M. Al-Bundak, and C. M. Butler, Potential integrals for uniform and linear source distributions on polygonal and polyhedral domains, *IEEE Trans. Anten. Propag.* **AP-32**:276–281 (March 1984).
 101. R. Mansour, R. S. K. Tong, and R. H. McPhie, Simplified description of the field distribution in finlines and ridge waveguides and its application to the analysis of E-plane discontinuities, *IEEE Trans. Microwave Theory Tech.* **MTT-36**:1825–1832 (Dec. 1988).
 102. J. Bornemann and V. A. Labay, Ridge waveguide polarizer with finite and stepped thickness septum, *IEEE Trans. Microwave Theory Tech.* **MTT-43**:1782–1787 (Aug. 1995).
 103. J. Bornemann and F. Arndt, Transverse resonance, standing wave, and resonator formulation of the ridge waveguide eigenvalue problem and its application to the design of E-plane finned waveguide filters, *IEEE Trans. Microwave Theory Tech.* **MTT-38**:1104–1113 (Aug. 1990).
 104. J. Uher, J. Bornemann, and U. Rosenberg, *Waveguide Components for Antenna Feed Systems: Theory and CAD*, Artech House, Boston, 1993.
 105. J. Ritter and F. Arndt, Efficient FD-TD/matrix pencil method for the full-wave scattering parameter analysis of waveguiding structures, *IEEE Trans. Microwave Theory Tech.* **MTT-44**:2450–2456 (Dec. 1996).
 106. R. S. Elliott, On the design of traveling-wave-fed longitudinal shunt slot arrays, *IEEE Trans. Anten. Propag.* **AP-27**:717–720 (Sept. 1979).
 107. A. Enneking, R. Beyer, and F. Arndt, Rigorous analysis of large finite waveguide slot arrays including the mutual internal and external higher-order mode coupling, *AP-S Int. Symp. Digest*, July 2000, pp. 74–77.
 108. R. Lotz, J. Ritter, and F. Arndt, 3D subgrid technique for the finite difference method in the frequency domain, *1998 Int. Microwave Symp. Digest*, June 1998, Vol. 3, pp. 1739–1742.
 109. R. Lotz, J. Ritter, and F. Arndt, Locally conformed subgrid FD-FD technique for the analysis of 3D waveguide structures with curved metallic objects, *1999 Int. Microwave Symp. Digest*, June 1999, Vol. 3, pp. 1277–1280.
 110. A. M. K. Saad, Antipodal ridge evanescent wave-guide filter, *Proc. 17th European Microwave Conf. (EuMC) Proceedings*, Rome, Italy, Sept. 1987, pp. 157–162.
 111. T. S. Saad, *Microwave Engineers' Handbook*, Vol. 1, Dedham, MA, Artech House, 1971.
 112. G. L. Matthaei, L. Young, and E. M. T. Jones, *Microwave Filters, Impedance-Matching Networks, and Coupling Structures*, McGraw-Hill, New York, 1964.
 113. F. Arndt, I. Rullhusen, V. Catina, J. Brandt, and W. Wessel, Fast hybrid mode-matching/integral equation methods for the analysis of slot arrays, *Proc. Int. Symp. on Electromagnetic Theory*, URSI EMTS, Pisa, May 2004, pp. 45–47.

HYBRIDS AND COUPLERS

PRAKASH BHARTIA
Natel Engineering Co., Inc.
Chatsworth, California
PROTAP PRAMANICK
K & L Microwave
Salisbury, Maryland

1. INTRODUCTION

Hybrids and couplers form an indispensable component group in modern MIC technology. With the inventions of planar transmission lines such as stripline, microstrip line, finline, dielectric image line, and their derivatives, hybrid and coupler technology has undergone a substantial change since the mid-1960s as a result of the rapidly growing applications of MICs in the electronic warfare, communications, and radar industries.

Despite the fact that the basic philosophy behind the operation of such couplers remains the same as in couplers designed using conventional transmission lines, their analyses and syntheses are quite involved. This is because most of these lines support hybrid modes due to inhomogeneity in configuration. However, the present-day analysis and synthesis techniques for such hybrids and couplers are believed to have gained maturity.

This article describes the design aspects of planar hybrids and couplers in as self-contained a presentation as possible within a limited space. In what follows in this section, we present the basics of hybrids and couplers and discuss different types of hybrids and couplers and their applications. The next section describes the design of matched hybrid “tees” (Ts), hybrid rings, and 90° hybrids. This is followed by a section on coupled-line couplers, both the TEM and the distributed types, as well as other miscellaneous types of couplers. The final section includes various aspects of coupler design, such as losses and improvement of directivity.

1.1. Basics of Hybrids and Couplers

A hybrid or a directional coupler can in principle be represented as a multiport network. In such a network, the

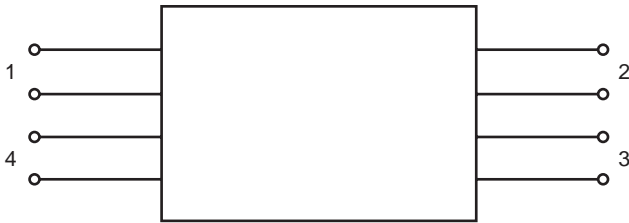


Figure 1. Four-port network.

port into which the electrical power is fed is called the *incident port*. The ports through which the desired amounts of coupled power are extracted are called *coupled ports*, while the rest of the ports are called *isolated ports*. Although hybrids and couplers having up to six ports find applications in many systems, we will restrict ourselves mostly to discussion of four-port networks without loss of generality.

Consider the four-port network shown in Fig. 1. If P_1 is the power fed into port 1 (which is matched to the generator impedance) and P_2 , P_3 , and P_4 are the powers available at the ports 2, 3, and 4, respectively (while each of the ports is terminated by its image impedance), the coupling coefficient is defined as

$$C = -10 \log \left| \frac{P_n}{P_1} \right| \quad n = 3, 4 \quad (1)$$

If port 3 happens to be the desired coupled port, the coupling coefficient is given by

$$C = -10 \log \left| \frac{P_3}{P_1} \right| \text{ dB} \quad (2)$$

If port 4 is the desired uncoupled port, the desired isolation is given by

$$I = -10 \log \left| \frac{P_4}{P_1} \right| \text{ dB} \quad (3)$$

The transmission to the primary port 2 is given by

$$T = 10 \log \left| \frac{P_2}{P_1} \right| \text{ dB} \quad (4)$$

The measure of directivity between the coupled and the uncoupled ports is given by

$$D = I - C \quad (5)$$

As a general practice, the performance of a hybrid or a directional coupler is specified in terms of its coupling, directivity, and the characteristic impedance at the center frequency of its band of operation. These data enable the circuit designer to calculate the structural parameters of the coupler.

1.2. Types of Hybrids and Couplers

Hybrids use directly connected circuit elements. Couplers can be parallel-coupled or aperture-coupled.

Figure 2a shows the simplest form of a hybrid. This is a branchline coupler, consisting of two mainlines coupled by two $\frac{1}{4}\lambda$ line sections spaced $\frac{1}{4}\lambda$ apart, where λ is the wavelength. Such a branchline hybrid can also be in circular form as shown in Fig. 2b. In either case, the total length of all the lines is one wavelength.

Figure 3 shows a parallel-coupled coupler. It consists of two coupled transmission lines. The lines can have any form depending on the application.

A parallel-coupled line coupler (Fig. 4) can be of two types: the TEM type or the distributed type. In the former, the coupled transmission lines support a pure TEM or a quasi-TEM mode. In the latter, the mode supported by the coupled lines are non-TEM in nature. While all of these types of couplers are realized using planar IC technology, there can be another type of coupler using aperture coupling, through some common ground plane (as used in conventional aperture-coupled waveguide couplers as shown in Fig. 5) with two similar or dissimilar types of planar transmission lines.

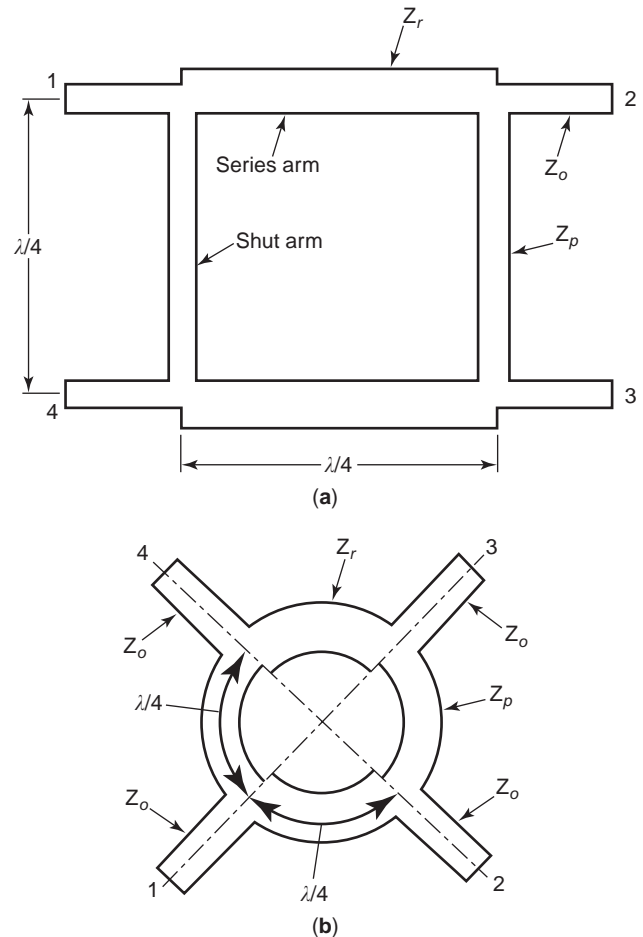


Figure 2. (a) Single-section branchline hybrid; (b) circular form of branchline hybrid.

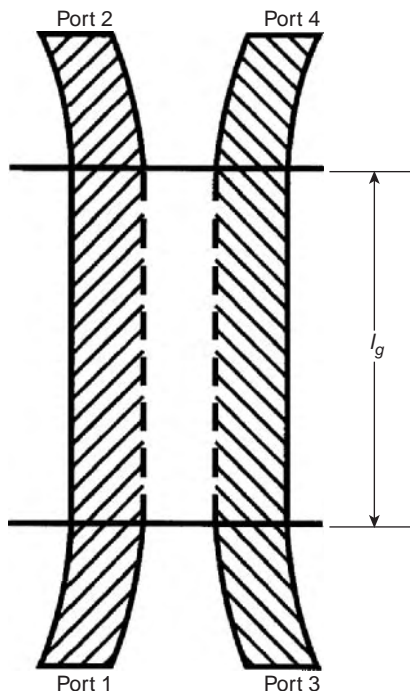


Figure 3. Direct-coupled coupler.

To achieve tighter coupling over a wider bandwidth, multisections of the previously mentioned couplers can be cascaded in tandem (to be discussed in a later section).

1.3. Applications

Virtually all kinds of microwave circuits use hybrids or couplers in one form or another. In general, the areas of application can be divided into two parts:

1. *Passive*—tuners, delay lines, filters, and matching networks (sometimes an array of couplers may be needed for a desired performance of the network).
2. *Active circuits*—used mainly as directional couplers in balanced amplifiers, mixers, attenuators, modulators, discriminators, and phase shifters

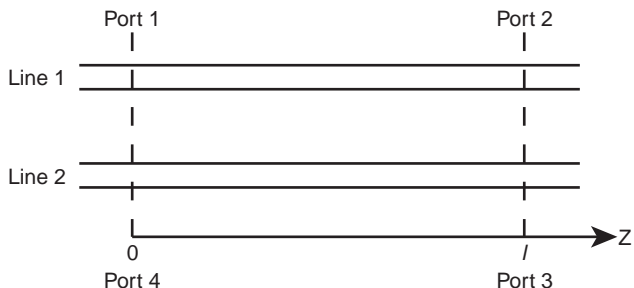


Figure 4. Parallel-coupled line coupler.

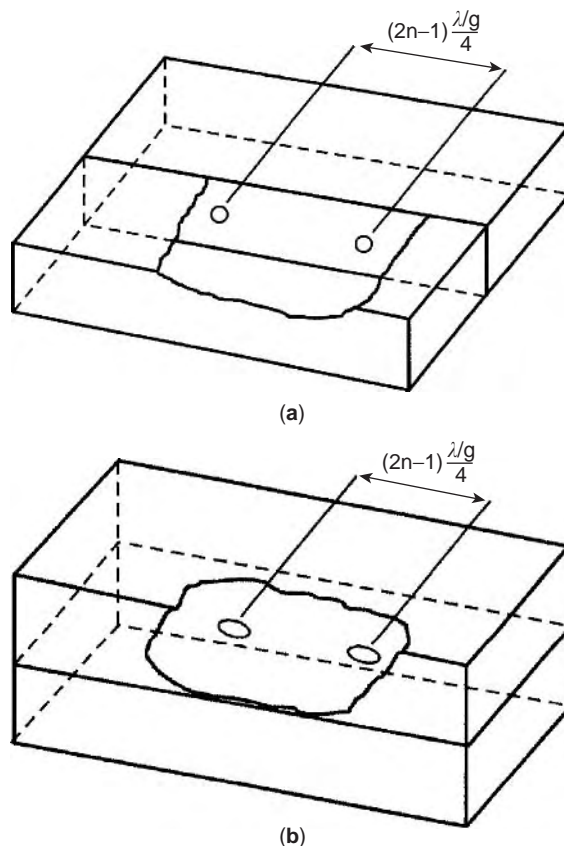


Figure 5. Aperture-coupled couplers: (a) narrow-wall coupling; (b) broad-wall coupling.

2. DESIGN OF HYBRIDS

2.1. 90° Hybrid

The simplest 90° hybrid is the branchline hybrid shown in Fig. 2a. For a certain input power at port 1, under match condition, there will be 90° phase difference between the waves appearing at ports 2 and 3, at the center frequency at which each arm is exactly a quarter-wavelength long. This 90° phase difference varies over ±5° for a 10% change in frequency around the center frequency. The coupling bandwidth is 20%, but its usable bandwidth is limited to 10%, due to an unacceptable change in the isolation over a bandwidth exceeding 10%. Ideally such couplers can be designed for 3–9 dB coupling.

There are three main arm losses in branchline hybrids: losses due to the portion of power coupled to the secondary arm (1) and the power dissipated as a result of dielectric (2) and conductor (3) losses.

Branchline hybrids can be realized using virtually all kinds of planar transmission lines, for example, stripline, microstrip line, slotline, finline, and image line. However, the basic design principle is extremely simple and the same in all cases.

The coupling factor is determined by the ratio of the impedance of the shunt and series arms and is optimized to meet the proper match over the required bandwidth.

For 90° hybrids, the following conditions hold good (see Fig. 2a):

$$\frac{P_2}{P_3} = \left(\frac{Z_0}{Z_p}\right)^2 \quad (6)$$

$$\left(\frac{Z_0}{Z_r}\right)^2 = \left(\frac{Z_0}{Z_p}\right)^2 + 1 \quad (7)$$

Although the two-branch hybrid is the most fundamental structure, it has a very narrow bandwidth. This disadvantage can be overcome by using multisection hybrids, but in most cases, planar transmission lines require too wide a range of impedances for this purpose. These may sometimes be difficult to realize physically. On the other hand, very wide linewidths may require unreasonable aspect ratios at higher frequencies due to shorter wavelengths. The physically unrealizable high-impedance line can be avoided by using a modified hybrid ring [1].

Complete analytical design techniques for such hybrids using Chebyshev and Zolotarev [2,3] functions are available. However, such techniques may sometimes be unsuitable for the design of planar circuits because of the wide impedance range problem, as previously mentioned. Muraguchi et al. [4] presented a computer-aided design technique that is most suitable for an optimum design.

2.2. Ring Form of Branchline Hybrid

This is a circular ring version of the square 90° hybrid described in the previous section. Therefore, the discussion of the previous section is equally valid for hybrid rings. The configuration is shown in Fig. 2b and is particularly advantageous in the realization of microstrip phase detectors and balanced mixers, with all ports matched.

2.3. Matched Hybrid T (Ratrace Hybrid)

A matched hybrid T is a special kind of ring form of the branch-line coupler in which the circumference is an odd multiple of $\frac{3}{2}\lambda$. As a result, the phase response is $0^\circ/180^\circ$. The simplest version of a matched hybrid T is shown in Fig. 6. Ports A–B, B–C, and C–D are separated by 90° , and

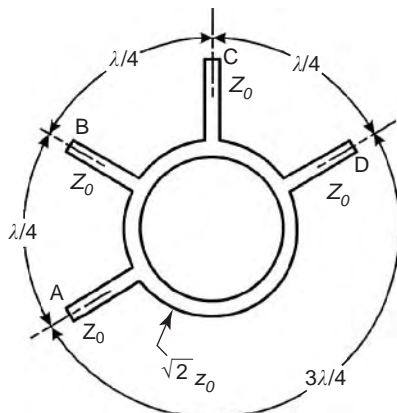


Figure 6. Hybrid ring.

ports A and D are three quarter-wavelengths away from each other.

Because of the impedance and the phase relationships shown in the structure, any power fed into port C splits equally into two parts that add up in phase at ports B and D and out of phase of port A. As a result port A is isolated from the input. Similarly, power fed at port A divides equally between ports B and D with 180° phase difference, and port C remains isolated.

The frequency response of a typical $\frac{3}{2}$ wavelength hybrid T is shown in Figs. 7a and 7b. It is observed that it offers around 20% bandwidth in terms of matching, split, and isolation. Moreover, the 180° phase relationship is much more frequency-sensitive than is the 0° phase relationship. Still, such a response is quite adequate for applications in mixers, SSB (single-side band) generators, and other components.

For high-frequency applications, a circumferential length of $\frac{3}{2}$ wavelengths may pose fabrication difficulties due to unrealizable aspect ratios of the transmission lines. This problem is overcome by having a ring of circumferential length of two wavelengths, where ports A and D are located $\frac{5}{4}\lambda$ away on the ring.

The design of a hybrid amounts to realizing the required transmission-line sections with proper phase velocities and characteristic impedances. Direct synthesis equations can be used in cases of stripline [5], microstrip [6], suspended microstrip, and inverted microstrip [7], which support pure TEM or quasi-TEM modes of propagation.

Realizations of the hybrids using non-TEM transmission lines such as slotline, finline, or image line use iterative techniques with the help of accurate analysis equations [7–9] depending on the mode of propagation. However, closed-form design equations are also available.

Microstrip and stripline hybrids have been realized and successfully used in commercially available microwave-balanced mixers and other circuit components. Development of finline and image-line hybrids are still at the experimental stage [10].

3. COUPLED-LINE DIRECTIONAL COUPLERS

The hybrids described in the previous sections are inherently of narrow bandwidth. Broadbanding of microwave couplers is achieved in a number of different ways, depending on the application.

Broadband couplers are either aperture-coupled or parallel-coupled. Aperture coupling is used very successfully in conventional waveguide techniques for realizing directional couplers with large bandwidths. Although aperture coupling is a convenient way of realizing directional couplers using two different planar transmission lines, directional couplers using the same kind of planar transmission lines are realized more efficiently using parallel coupling.

3.1. Directional Couplers Using Aperture-Coupled Lines

Figure 8 shows a simple two-hole directional coupler. Electromagnetic energy is coupled from the primary guide to

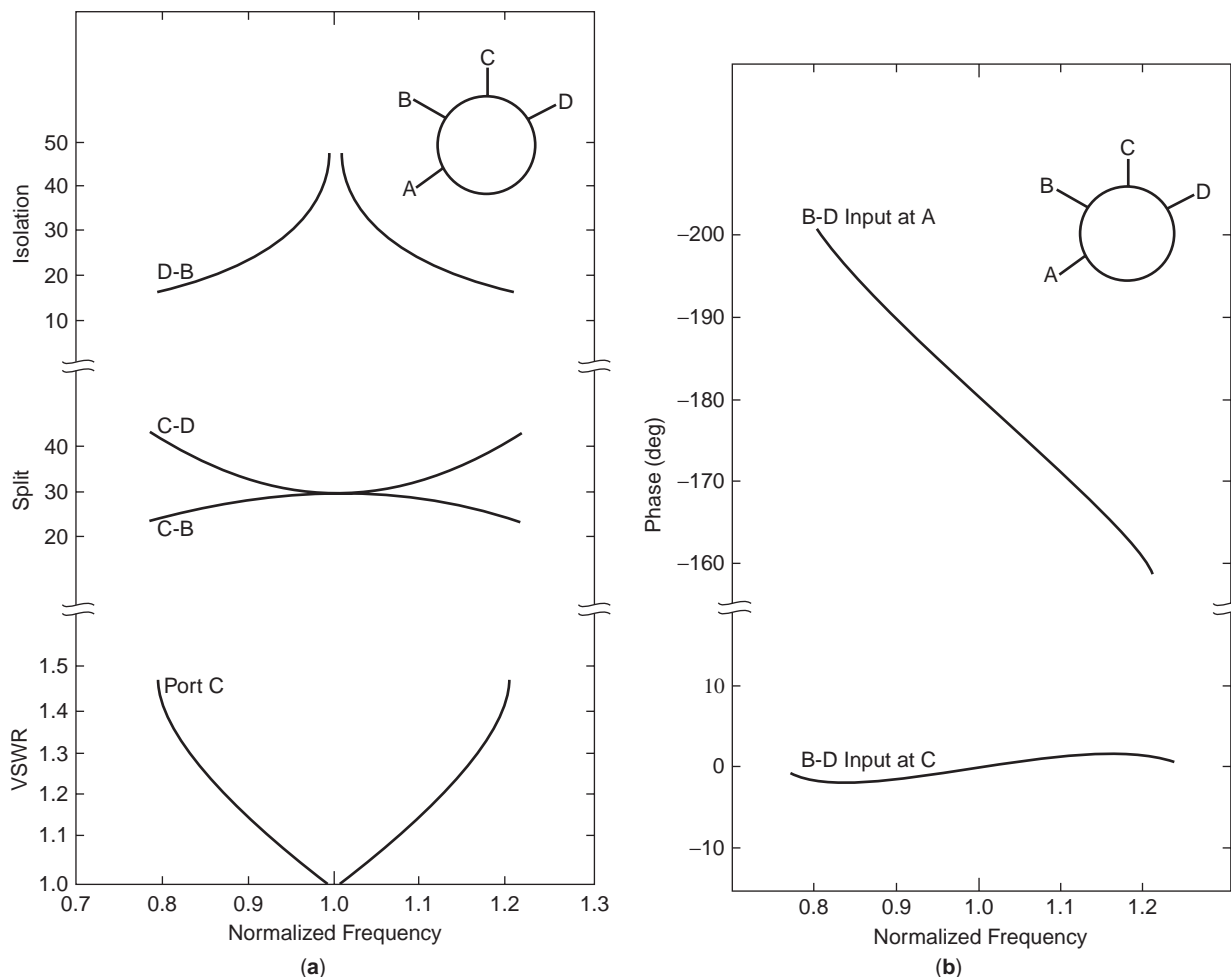


Figure 7. (a) Response curves for $\frac{3}{2}$ ratrace magic T (power split and isolation are expressed in decibels); (b) phase response curves for $\frac{3}{2}$ ratrace magic T.

the secondary guide due to the field radiated by the excited electric and magnetic dipoles generated at the holes by the propagating electromagnetic wave in the primary guide. The holes are spaced such that the round-trip phase shift of a wave through them should be 180° . Therefore the backward-traveling waves in the secondary guide will be completely out of phase to cancel each other at port 3. If the coupled lines have the same propagation constant, then the forward-traveling waves in the secondary guide will be of the same phase regardless of hole spacing and are added at port 4.

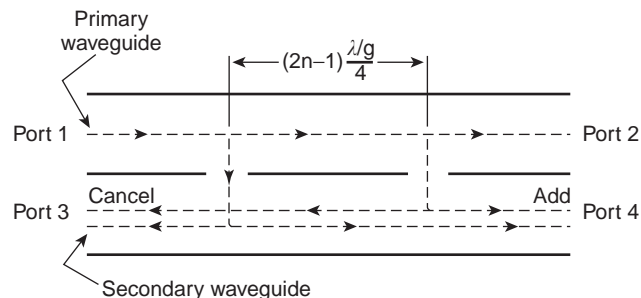


Figure 8. Schematic of a two-aperture directional coupler.

Such aperture-coupled directional couplers can be realized using various kinds of planar transmission-line combinations, for example (1) microstrip–microstrip, (2) microstrip–image line, (3) image line–image line, (4) image line–trough guide, or (5) trough guide–trough guide. Some possible combinations are shown in Fig. 9.

3.2. TEM Line Directional Couplers

When the center conductors of two coaxial lines supporting a pure TEM mode of propagation are brought into close proximity of each other, electromagnetic energy is coupled from one line to the other. This property has given rise to a class of broadband planar directional couplers. Most such couplers use striplines or microstrip lines that support pure TEM or quasi-TEM modes, respectively.

Planar TEM-line directional couplers can be either edge-coupled or broadside-coupled as shown in Figs. 10a and 10b.

In general, such coupled TEM lines support two modes that interact to give rise to the coupling. These are the even and odd modes. Properties of the coupled lines can be evaluated by suitable linear combinations of even and odd modes.

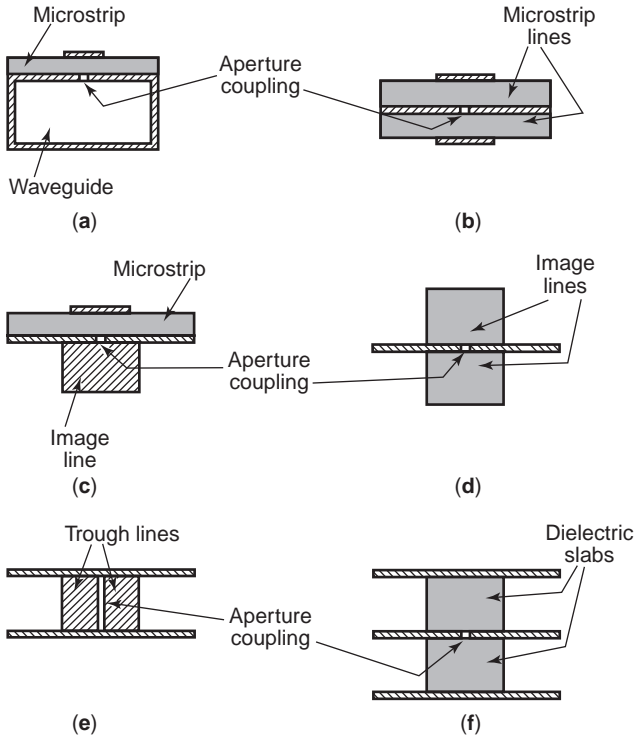


Figure 9. Possible combinations of various aperture-coupled lines: (a) microstrip-waveguide coupling; (b) microstrip-microstrip line; (c) microstrip-image line; (d) image line-image line; (e) trough line-trough line; (f) dielectric guide-dielectric guide.

TEM-line couplers can be reduced to a two-port network as shown in Fig. 11a. There is a plane of symmetry that becomes a perfect magnetic wall for the incident signals of equal amplitude and same phase at ports 1 and 4.

The plane of symmetry becomes a perfect electric wall for the incident signals of equal amplitude but of exactly opposite phases at the same ports. Therefore each mode corresponds to a two-port network as shown in Figs. 11b and 11c for even and odd modes, respectively. Analysis of the directional coupler is accomplished by analyzing these two networks and superimposing the responses as shown in Fig. 11d.

The S -matrix equation of a Four-port symmetric and reciprocal network can be written as

$$\begin{bmatrix} b_1 \\ b_2 \\ b_3 \\ b_4 \end{bmatrix} = \begin{bmatrix} S_{11} & S_{12} & S_{13} & S_{14} \\ S_{12} & S_{11} & S_{14} & S_{13} \\ S_{13} & S_{14} & S_{11} & S_{12} \\ S_{14} & S_{13} & S_{12} & S_{11} \end{bmatrix} \begin{bmatrix} a_1 \\ a_2 \\ a_3 \\ a_4 \end{bmatrix} \quad (8)$$

where

$$S_{11} = \frac{1}{2}(\Gamma_e + \Gamma_o) \quad (9a)$$

$$S_{12} = \frac{1}{2}(T_e + T_o) \quad (9b)$$

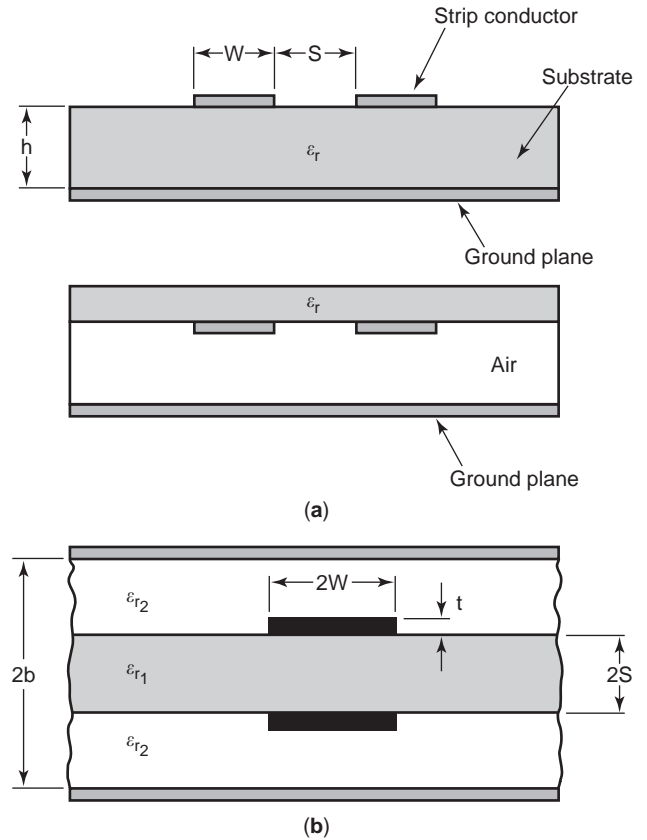


Figure 10. (a) Edge-coupled microstrip lines; (b) broadside-coupled microstrip line.

$$S_{13} = \frac{1}{2}(T_e - T_o) \quad (9c)$$

$$S_{14} = \frac{1}{2}(\Gamma_e - \Gamma_o) \quad (9d)$$

Evaluation of the even- and odd-mode reflection and transmission coefficients is done from the corresponding effective dielectric constants and the characteristic impedances:

$$\Gamma_i = \frac{A_i + B_i/Z_0 - C_i Z_0 - D_i}{A_i + B_i/Z_0 + C_i Z_0 + D_i} \quad (10a)$$

$$T_i = \frac{2}{A_i + B_i/Z_0 - C_i Z_0 + D_i} \quad (10b)$$

where the transmission matrix

$$\begin{bmatrix} A_i & B_i \\ C_i & D_i \end{bmatrix} = \begin{bmatrix} \cos \theta_i & jZ_{0i} \sin \theta_i \\ \frac{j \sin \theta_i}{Z_{0i}} & \cos \theta_i \end{bmatrix} \quad i = e, o \quad (11)$$

Knowing $Z_{0,e}$, θ_e , $Z_{0,o}$, θ_o , and Z_0 and the system characteristic equation, we can calculate the performance of the directional coupler using (9) and (10).

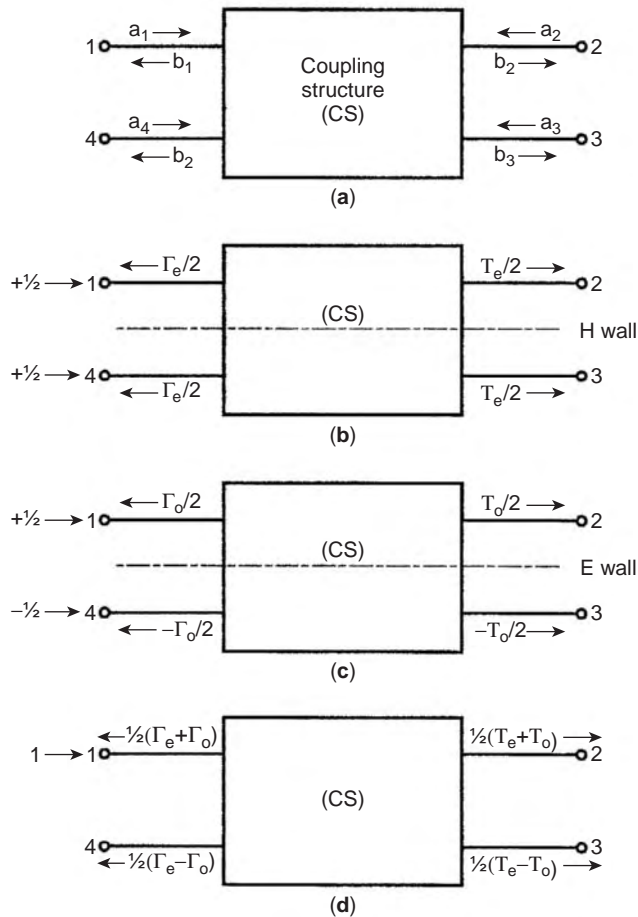


Figure 11. Schematic of directional coupler: (a) wave parameters; (b) even-mode excitation; (c) odd-mode excitation; (d) input excitation.

3.2.1. Coupled TEM Line. For coupling between the purely TEM lines shown in Fig. 12, we have the following special case

$$\theta_e = \theta_o = \theta \tag{12}$$

which means equal, even-, and odd-mode phase velocities, and

$$Z_0 = \sqrt{Z_{0,e}Z_{0,o}} \tag{13}$$

$$\Gamma_e = -\Gamma_o = \frac{j[(Z_{0,e}/Z_{0,o})^{1/2} - (Z_{0,o}/Z_{0,e})^{1/2}] \sin \theta}{\Sigma} \tag{14}$$

where

$$\Sigma = 2 \cos \theta + j \left[\left(\frac{Z_{0,e}}{Z_{0,o}} \right)^{1/2} + \left(\frac{Z_{0,o}}{Z_{0,e}} \right)^{1/2} \right] \sin \theta \tag{15}$$

Substitution of (14) and (15) into (9) gives

$$S_{11} = 0 \tag{16a}$$

$$S_{12} = T_e \tag{16b}$$

$$S_{13} = 0 \tag{16c}$$

$$S_{14} = \Gamma_e \tag{16d}$$

Such couplers, known as *backward-wave couplers*, are in general a quarter-wavelength long at the center frequency or $\theta = \frac{1}{2}\pi$.

From (13) and (14) the coupling coefficient is given by

$$C = -20 \log |S_{14}| = -20 \log \left| \frac{Z_{0,e} - Z_{0,o}}{Z_{0,e} + Z_{0,o}} \right| \text{ dB} \tag{17}$$

Moreover, for a system impedance Z_0 of 50 Ω , the matching condition (condition for a perfect input match) gives

$$Z_0^2 = Z_{0,e}Z_{0,o} \tag{18}$$

Therefore, for a specified coupling C the design equations become

$$Z_{0,e} = Z_0 \left[\frac{1 + 10^{-C/20}}{1 - 10^{-C/20}} \right]^{1/2} \tag{19a}$$

$$Z_{0,o} = Z_0 \left[\frac{1 - 10^{-C/20}}{1 + 10^{-C/20}} \right]^{1/2} \tag{19b}$$

Once $Z_{0,e}$ and $Z_{0,o}$ are known, the physical dimensions of the coupler can be obtained using the equations for coupled TEM transmission lines [6,20].

3.2.2. Coupled Quasi-TEM Line. In coupled quasi-TEM lines, for example, in microstrip, the odd-mode phase velocity is different from the even-mode phase velocity. Therefore, the condition given by (12) does not hold good. However, for weak couplings, (12) can be assumed to be approximately true. Hence the designer may go ahead and determine the initial design using (17)–(19). However, as the coupling gets tighter, the previous equations tend to be less valid. In such a case, the condition for

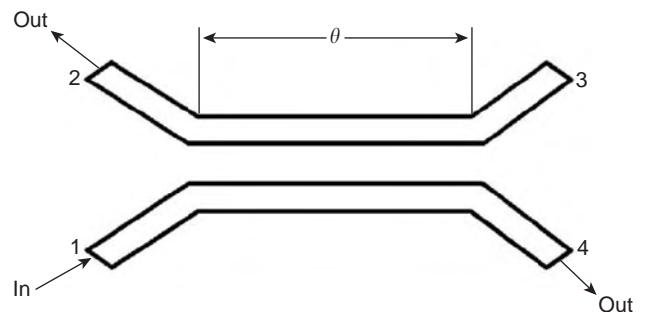


Figure 12. Coupling between two TEM lines.

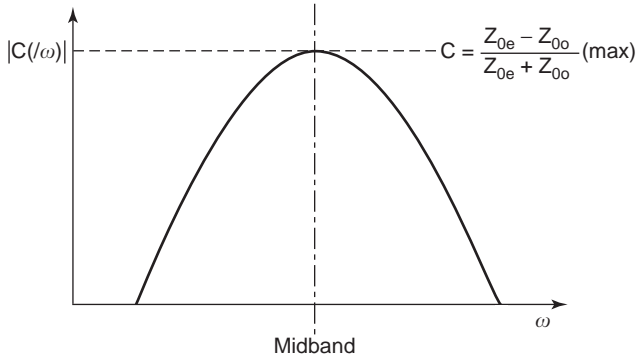


Figure 13. Approximate frequency response of a quasi-TEM line.

input matching becomes

$$Z_0 = \left(\frac{Z_{0,e} \sin \theta_e + Z_{0,o} \sin \theta_o}{Z_{0,e} \sin \theta_o + Z_{0,o} \sin \theta_e} \right)^{1/2} \sqrt{Z_{0,o} Z_{0,e}} \quad (20)$$

and the electrical length at the center frequency is

$$\theta = \frac{1}{2}(\theta_e + \theta_o) = \frac{2\pi}{\lambda_0} \frac{\sqrt{\epsilon_{ee}} + \sqrt{\epsilon_{eo}}}{2} l = 90^\circ \quad (21)$$

where l is the physical length of the coupler.

Single-section quarter-wave parallel-coupled line couplers are used extensively in many applications. They are usually of narrow bandwidth of approximately one octave. To obtain the desired coupling at the band edges, the coupler has to be designed for overcoupling at the center frequency.

3.2.3. Frequency Response of a Single-Section Coupler. Using the analysis equations (9)–(17), it can be shown that the frequency response of the coupling coefficient is given by

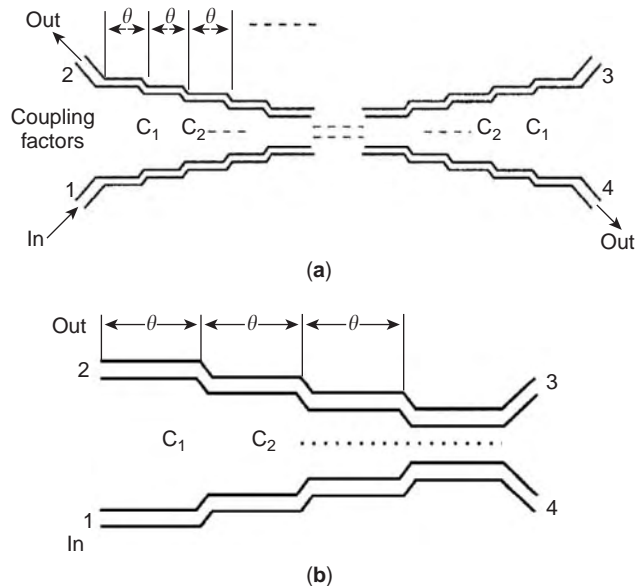


Figure 14. Multisection (a) symmetric and (b) asymmetric couplers.

cient is given by

$$C/(\theta) = \frac{jC \sin \theta}{\sqrt{1 - C^2} \cos \theta + j \sin \theta} \quad (22a)$$

where C is the midband coupling for a matched, loosely coupled coupler. The approximate frequency response of a quasi-TEM coupler is shown in Fig. 13. The response follows Eq. (22a) when the coupled lines support TEM mode.

The general expression for the directivity or the undesired coupling is given by [11]

$$D = \left[\frac{\pi \Delta (1 - |\xi|^2)}{4|\xi|} \right]^2 \quad (22b)$$

where

$$\Delta = \frac{\beta_e - \beta_o}{\beta_o}$$

$$\xi = \left(\frac{\rho_e}{1 + \rho_e^2} \right) - \left(\frac{\rho_o}{1 + \rho_o^2} \right)$$

$$\rho_e = \frac{Z_{0,e} - Z_0}{Z_{0,e} + Z_0} \quad \rho_o = \frac{Z_{0,o} - Z_0}{Z_{0,o} + Z_0}$$

and β_e and β_o are the even- and odd-mode propagation constants, respectively, $D = 0$ for $\beta_e = \beta_o$, that is, for a TEM coupler.

3.2.4. Multisection Couplers for Wider Bandwidth. For many applications, the single-section coupler proves to be of inadequate bandwidth. Therefore, the designer should have recourse to a multisection design. A multisection coupler is a cascaded combination of more than one single-section coupler, each a quarter-wavelength long at the center frequency of the band. The number of sections to be used depends on the tolerable insertion loss, bandwidth, and the available physical space.

Multisection couplers can be either symmetric or asymmetric around the center section, as shown in Fig. 14.

3.2.5. Symmetric Coupler. The symmetric coupler gives 90° phase difference between the direct and the coupled output ports under matched conditions. In what follows we present a direct synthesis technique.

Figure 14a shows a multisection symmetric coupler. The coupling factor for an n -section symmetric coupler with weak coupling can be written as [12]

$$C(\theta) = \left| \frac{V_2}{V_1} \right|$$

$$= C_1 \sin(n\theta) + (C_2 - C_1) \sin[(n-2)\theta] + \dots \quad (23)$$

$$+ (C_i - C_{i-1}) \sin[(n-2i+2)\theta]$$

$$+ (C_{[(n+1)/2]} - C_{[(n-1)/2]}) \sin \theta$$

If the desired coupling response is maximally flat, then C_i must satisfy a set of $\frac{1}{2}(n-1)$ linear equations

obtained from

$$\left[\frac{d^r C(\theta)}{d\theta^r} \right]_{\theta=\pi/2} = 0 \quad r=2, 4, 6, \dots, n-1 \quad (24)$$

Note that n is always an odd integer.

The design concept is based on the fact that the backward-coupled wave of a TEM coupler corresponds to the reflected wave of a quarter-wave filter. Therefore the designer of a TEM-wave coupler has to synthesize only a two port in place of a four port with the reflection coefficient response the same as the desired coupling coefficient response of the four-port directional coupler.

In terms of the midband VSWR R of the quarter-wave filter, the coupling coefficient is given by [12]

$$C_0 = \frac{R-1}{R+1} \quad (25)$$

3.3. Multiconductor Couplers

The interdigital coupler, or multiconductor coupler, invented by Lange [13], has always been a popular component in planar circuits. Figure 15 shows a four-element interdigital coupler, although in certain applications the number of elements may be greater than four. The coupler is usually designed for 3 dB coupling and the output phases are in quadrature. Obviously, the best realization is in the microstrip form.

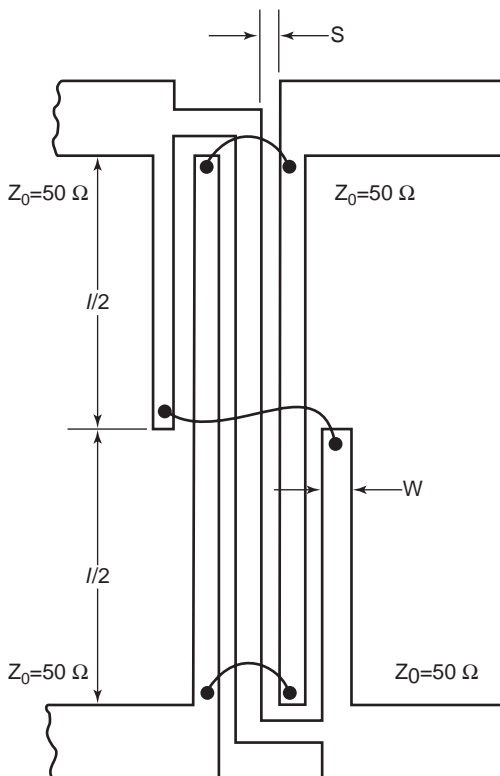


Figure 15. Lange coupler.

An interdigital coupler has advantages because of its small size and relatively large line separation when compared with the two-coupled line device and has a much larger bandwidth when compared with branchline couplers.

Interdigital couplers are used for balanced MIC amplifiers, balanced mixers, and binary power divider trees.

3.3.1. Design of Interdigital Couplers. Kajfez et al. [14] have described a simplified design technique for the interdigital coupler. The proposed technique serves many practical purposes but seems to be inadequate for an accurate design. So far the method due to Presser [15] has been found to be the most accurate and simplest. Moreover, it has the provision for finite stripthickness correction.

Consider the layout shown in Fig. 15. The designer is supplied with the desired coupling coefficient C and the system characteristic impedance Z_0 . The length of the coupled region l has to be a quarter wavelength at the center of the band.

The main design equations for an N element (N even) coupler are written as

$$R = \frac{Z_{0,o}}{Z_{0,e}} \quad (26a)$$

$$C = \frac{(N-1)(1-R^2)}{(N-1)(1+R^2)+2R} \quad (26b)$$

$$Z = \frac{Z_{0,o}}{Z_0} \frac{\sqrt{R[(N-1)+R][(N-1)R+1]}}{1+R} \quad (26c)$$

3.4. Distributed-Type Couplers

Distributed-type coupling takes place between two adjacent transmission lines supporting purely non-TEM modes. For example, distributed-type couplers can be realized using two open dielectric waveguides (or image guides) or finlines.

In general, two distributed-type coupled lines can be represented as shown in Fig. 16. Under the assumption that all four ports are matched and the coupling structure has the length l , the ratio of the fields in the two lines can be shown to be [16]

$$\frac{E_b(l)}{E_a(l)} = \tan\left((\beta_e - \beta_o)\frac{l}{2}\right) \quad (27)$$

where β_e and β_o are the even- and the odd-mode phase constants, respectively.

Therefore for complete transfer of power from line a to line b requires

$$(\beta_e - \beta_o)\frac{L}{2} = \frac{\pi}{2} \quad (28)$$

or

$$L = \frac{\pi}{\beta_e - \beta_o} \quad (29)$$

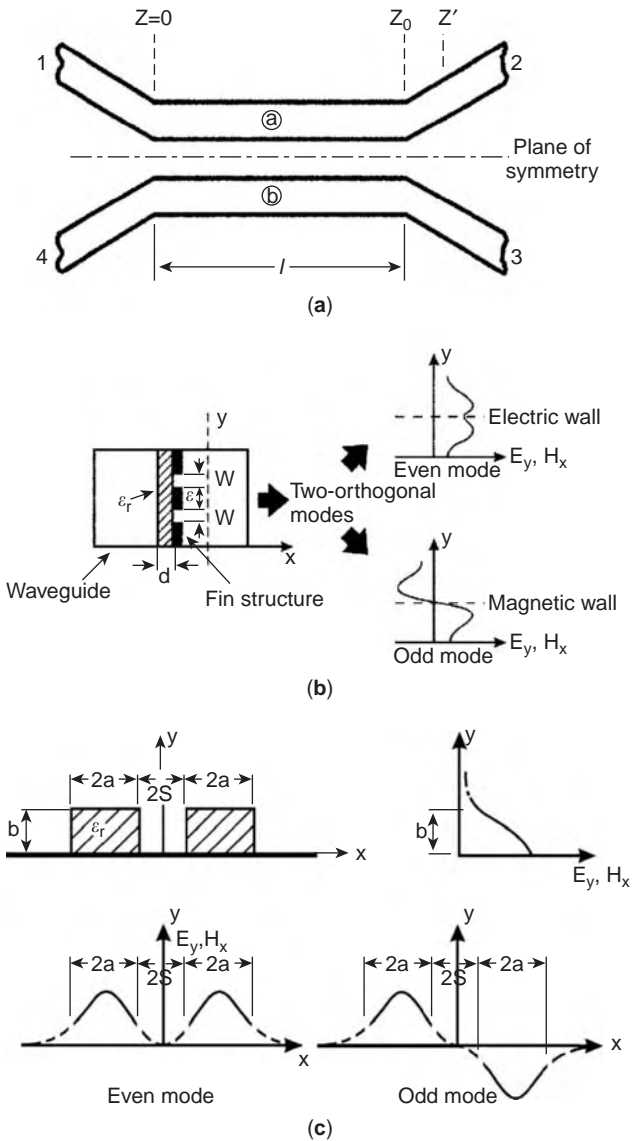


Figure 16. (a) Schematic of distributed coupler; (b) coupled fin-lines and field distributions; (c) coupled image lines and field distributions.

The scattering coefficients of the structure can be written as a function of l normalized by L as

$$|S_{12}| = \left| \cos \left(\frac{\pi l}{2L} \right) \right| \quad (30a)$$

$$|S_{13}| = \left| \sin \left(\frac{\pi l}{2L} \right) \right| \quad (30b)$$

Equation (30b) shows that the required length for 3 dB coupling is one half of L .

The preceding equations are based on the assumptions that the bent portions of the guides have no effect on coupling. Branch junction effects near the bends are negligible, but the assumed uncoupled lines $z \leq 0$ and $z \geq z_0$ do get coupled. This extra coupling can be taken into consideration by

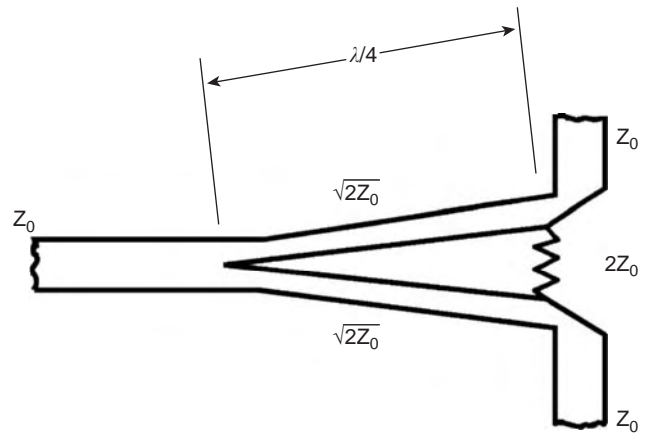


Figure 17. Single-section Wilkinson coupler.

defining the effective length of the coupler as

$$l_{\text{eff}} = l + \frac{2L}{\pi} \int_{z_0}^{z'} [\beta_e(z) - \beta_o(z)] dz \quad (31)$$

The integration limit z' is chosen to be the point at which the coupling is practically negligible.

From the preceding discussions it appears that the design of any distributed coupler requires a precise knowledge of the even- and the odd-mode phase constants of the coupled lines. Figures 16b and 16c show the cross sections of a coupled finlines and image lines, respectively, as examples of two commonly used distributed couplers.

3.5. Wilkinson Couplers, Power Dividers, and Combiners

A Wilkinson coupler [17,18] is a special case of couplers that do not have isolated ports and offer broad bandwidth and equal phase characteristics at each of its output ports. Figure 17 shows the schematic diagram of a Wilkinson coupler. The output port's isolation is obtained by series terminating the output ports. Each quarter-wave line has the characteristic impedance of $\sqrt{2}Z_0$ and the output is terminated by a resistor of $2Z_0 \Omega$, where Z_0 is the system impedance.

A Wilkinson power divider offers a bandwidth of about one octave. The typical frequency response is shown in Fig. 18. An adequately flat response is obtained over more than one octave band, but at the band edges the isolation is affected by the load impedance.

The performance of a Wilkinson coupler can be further improved, depending on the availability of space, by the addition of a $\frac{1}{4}\lambda$ transformer in front of the power division step. The output VSWR of the uncompensated coupler is better than the output VSWR of the compensated circuit.

3.5.1. Multisection Wilkinson Coupler. The octave bandwidth of a single-section coupler proves to be inadequate in many applications; therefore Cohn [18] proposed the use of multisections for bandwidth expansion. The use of multisections makes it possible to obtain a decade bandwidth.

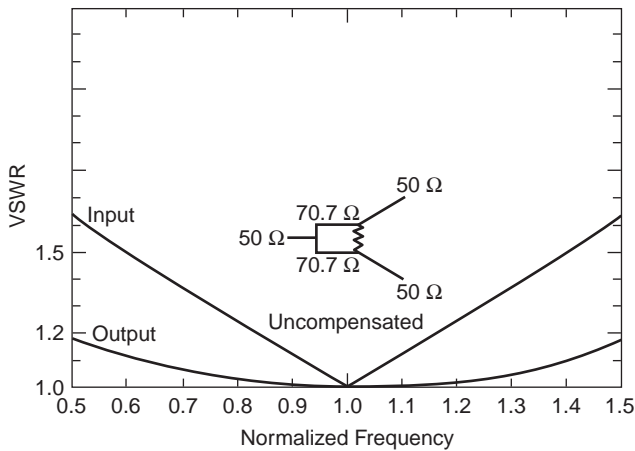


Figure 18. Frequency response of Wilkinson coupler. (After Howe [5]. Reprinted with permission of Artech House.)

A multisection Wilkinson power divider coupler consists of a number of quarter-wave sections with resistive terminations at the end of every section, as shown schematically in Fig. 19. Larger bandwidth and greater isolation are obtained when a large number of sections are used.

The characteristic impedances of the sections are obtained from the normalized impedances for $\frac{1}{4}\lambda$ transformer sections for a 2–1 transformer. This can be done with the help of charts in Ref. 5, which presents design curves up to four sections. Similar figures are also available for higher numbers of sections. Having obtained the impedance of each section, we can obtain values of the terminating resistors for each section.

For a two-section divider the values of the terminating resistors are given by

$$R_2 = \frac{2Z_1Z_2}{[(Z_1 + Z_2)(Z_2 - Z_1 \cot^2 \phi)]^{1/2}} \quad (32a)$$

$$R_1 = \frac{2R_2(Z_1 + Z_2)}{R_2(Z_1 + Z_2) - 2Z_2} \quad (32b)$$

where

$$\phi = \frac{\pi}{2} \left[1 - 0.707 \left(\frac{f_2 - f_1}{f_2 + f_1} \right) \right] \quad (32c)$$

and f_1, f_2 are the upper and lower band edge frequencies of operation.

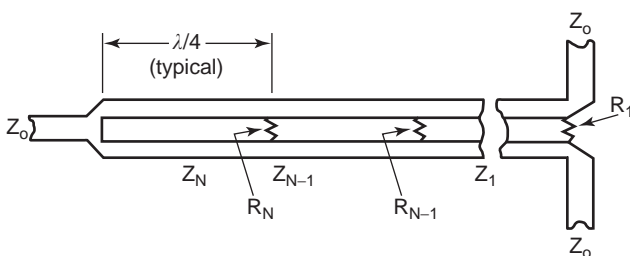


Figure 19. Multisection Wilkinson coupler.

3.6. Other Couplers

3.6.1. Tandem Coupler. The design of a multisection coupler with tight coupling over a broad bandwidth requires some of its sections to have tighter coupling than the overall coupling. This invariably leads to the physically unrealizable spacings between the two conductors or severely reduced directivity due to significant mechanical discontinuities in the sections. To solve this problem, in a restricted physical space, various combinations of symmetric and asymmetric couplers are tandemed [5,19]. Since in the majority of applications, the tightest coupling may be 3 dB, two couplers may be connected in tandem to achieve the goal. Figure 20a shows the symmetric tandem of two 8.34-dB couplers, while Fig. 20b shows the symmetric tandem of two asymmetric couplers. When tandemed, each 8.34-dB coupler gives an overall coupling of 3 dB. This configuration offers high power-handling capability and often represents a good choice, provided the particular application does not require maximum bandwidth with very low loss.

Figure 21 shows the configuration of an asymmetric tandem of symmetric couplers. As in the symmetric tandem of symmetric couplers, the quadrature phase shift is maintained between the outputs.

As is apparent from the interconnections, the 90° phase relationship is maintained in the symmetric case, but in the asymmetric case, the phase relation depends on the number of sections.

4. DESIGN CONSIDERATIONS

4.1. Losses in Hybrids

The total loss in hybrids can be estimated from the combined dielectric and conductor losses in the individual lines. These are obtained using closed-form equations for microstrip- and stripline-type transmissions lines [20].

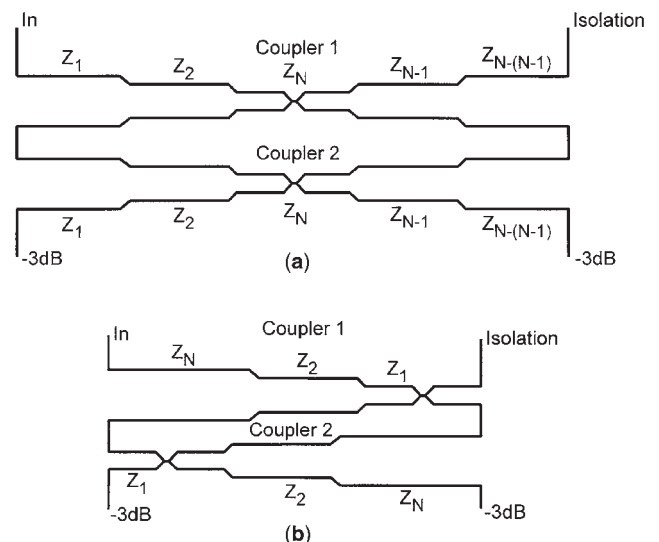


Figure 20. Tandem coupler: (a) Symmetric tandem of symmetric couplers; (b) symmetric tandem of asymmetric couplers.

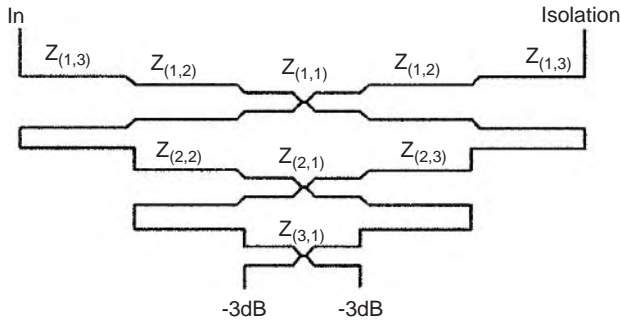


Figure 21. Asymmetric tandem of symmetric coupler.

For other types of transmission lines, numerical techniques are used [21].

The attenuation due to the even mode α_c^e is always less than that due to the odd mode α_c^o . In coupled lines the loss is given by the average of the losses due to even and odd modes. In almost all planar coupled lines the conductor loss greatly exceeds the dielectric loss [20].

As in striplines and microstrip lines, the primary contributors to losses in dielectric-based planar waveguide couplers are the dielectric loss and the metallic loss. Such losses are always computed numerically from the associated field equations [22].

4.2. Directivity Improvement

Because of the inhomogeneity in dielectric structure, the directivity of microstrip couplers offers a poor bandwidth resulting from different odd- and even-mode phase velocities. There are several ways to equalize the phase velocities, which are described as follows.

4.2.1. Use of a Shield. These structures nearly equalize even- and odd-mode phase velocities. The cross section of the structure is shown in Fig. 22. This configuration essentially redistributes the field with a substantial amount of the field in the air-dielectric medium above the coupled strips. For $d = h$ the phase velocities are exactly equal, and each is equal to

$$v_e = v_o = \frac{c}{\sqrt{(\epsilon_r + 1)/2}} \tag{33}$$

Strictly speaking, improvement in directivity is obtained at the cost of manufacturing difficulties in this case.

4.2.2. Use of Lumped Capacitors. Using lumped capacitors at the ends of the coupled section is the simplest way of achieving equal phase velocities. The structure is shown

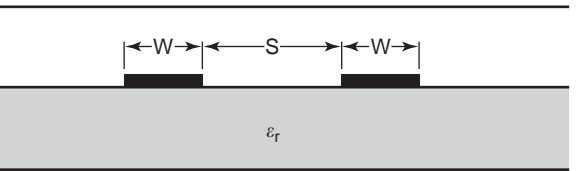
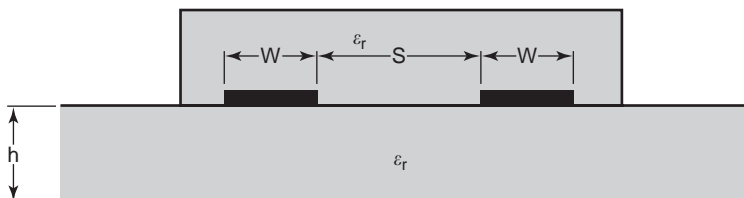


Figure 22. Parallel-coupled microstrip with grounded shield.

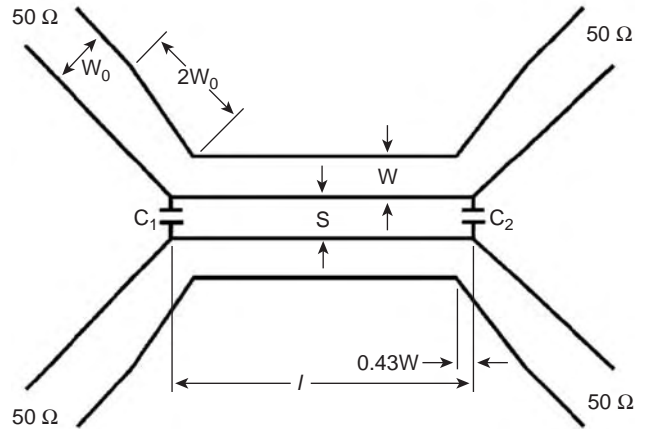


Figure 23. Lumped-capacitor compensation of microstrip coupler.

in Fig. 23. This effectively increases the odd-mode phase angle by [16]

$$\Delta\theta_o = 2\pi f_0(C_1 + C_2)Z_{0,o} \tag{34}$$

where f_0 is the center frequency of the coupled line.

4.2.3. Use of a Dielectric Overlay. The presence of another dielectric layer of the same permittivity as that of the substrate reduces the odd-mode phase velocity to a large extent without considerably affecting the even-mode phase velocity [23]. Thus, by controlling the thickness and width of the overlay, the even- and the odd-mode phase velocities can be equalized within 1% over quite a broad band. As shown in Fig. 24, the overlay covers the two strips where the main coupling takes place. The overlay is bonded with the help of some kind of epoxy. However, this method is practically cumbersome because of its poor repeatability. To overcome this problem a multilayer structure using different dielectric constants materials has been proposed [23].

Figure 24. Parallel-coupled microstrip with overlay compensation.

BIBLIOGRAPHY

1. A. K. Agrawal, and G. F. Mikucki, A printed circuit hybrid ring directional coupler for arbitrary power divisions, *IEEE Trans. Microwave Theory Tech.* **MTT-34**: 1401–1407 (Dec. 1986).
2. R. Levy, Zolotarev branch-guide couplers, *IEEE Trans. Microwave Theory Tech.* **MTT-21**: 95–99 (Feb. 1973).
3. R. Levy, and J. Helszajn, Specific equation for one or two section quarter-wave matching networks for stub resistor loads, *IEEE Trans. Microwave Theory Tech.* **MTT-30**: 55–62 (Jan. 1982).
4. O. Muraguchi, M. Y. Takeshi, and Y. Naito, Optimum design of 3-dB branch line couplers using microstrip lines, *IEEE Trans. Microwave Theory Tech.* **MTT-31**: 674–678 (Aug. 1983).
5. H. Howe, *Stripline Circuit Design*, Artech House, Dedham, MA, 1974.
6. K. C. Gupta, R. Garg, and I. J. Bahl, *Microstrip Lines and Slotlines*, Artech House, Dedham, MA, 1979.
7. P. Pramanick, and P. Bhartia, Analysis and synthesis equations for suspended and inverted microstriplines, *Arch. Elek. Übertragung*, **39**: 323–326 (Sept. 1985).
8. P. Pramanick, and P. Bhartia, Computer aided design models for millimeter wave finlines and suspended substrate microstrip lines, *IEEE Trans. Microwave Theory Tech.* **MTT-33**: 1429–1435 (Dec. 1985).
9. P. Bhartia, and I. J. Bahl, *Millimeter Wave Engineering and Applications*, Wiley, New York, 1984, pp. 300–346.
10. S. K. Koul, private communication, Center for Advanced Research in Electronics, Indian Institute of Technology, New Delhi, India, 1985.
11. T. C. Edwards, *Foundations for Microstrip Circuit Design*, Wiley, New York, 1981, pp. 147–148.
12. G. L. Matthaei, L. Young, and E. M. T. Jomes, *Microwave Filters Impedance Matching Networks and Coupling Structures* (reprinted), Artech House, Dedham, MA, 1980.
13. J. Lange, Interdigitated stripline quadrature hybrid, *IEEE Trans. Microwave Theory Tech.* **MTT-17**: 1150–1151 (Dec. 1969).
14. D. Kajfez, Z. Paunovic, and S. Paulin, Simplified design of Lange coupler, *IEEE Trans. Microwave Theory Tech.* **MTT-26**: 806–808 (Oct. 1978).
15. A. Presser, Interdigitated microstrip coupler design, *IEEE Trans. Microwave Theory Tech.* **MTT-26**: 801–805 (Oct. 1978).
16. P. Bhartia, and I. J. Bahl, *Millimeter Wave Engineering and Applications*, Wiley, New York, 1984, pp. 358–382.
17. E. Wilkinson, An N-way hybrid power divider, *IEEE Trans. Microwave Theory Tech.* **MTT-8**: 116–118 (Jan. 1960).
18. S. B. Cohn, A class of broadband 3-port TEM hybrids, *IEEE Trans. Microwave Theory Tech.* **MTT-16**: 110–118 (Feb. 1968).
19. W. A. Davis, *Microwave Semiconductor Circuit Design*, Van Nostrand, New York, 1983.
20. R. Garg, and I. J. Bahl, Characteristics of coupled microstrip, *IEEE Trans. Microwave Theory Tech.* **MTT-27**: 700–705 (July 1979).
21. T. N. Trinh, and R. Mittra, Suspended H-waveguide and its mm-wave applications, *IEEE Int. Microwave Symp. Digest*, 1983, pp. 305–308.
22. B. Shelad, and B. E. Spielman, Broadband (7–18 GHz) 10-dB overlay coupler for MIC applications, *Electron. Lett.* **11**: 175–176 (April 1975).
23. M. Horno, and F. Medina, Multilayer planar structures for high-directivity directional coupler design, *IEEE Trans. Microwave Theory Tech.* **MTT-34**: 1442–1449 (Dec. 1986).

IMPATT DIODES AND CIRCUITS

JAMES W. McCLYMONDS
Raytheon Systems Company

IMPATT (impact avalanche transit time) diodes have the highest output power of any solid-state device at millimeter-wave frequencies. Significant advances have been made to power-combine these devices efficiently, and IMPATT diode transmitters can now rival the output power per unit volume of vacuum-tube transmitters. IMPATT transmitters have several advantages over tubes, particularly for missile radar applications, so very high-power transmitters are being developed for several military systems. IMPATT diodes are also suited for low-cost commercial applications that require the power of only a few devices.

This article will explain the basic principles for designing IMPATT diode circuits, beginning with the characteristics of the diodes. General circuit principles will be discussed, and calculations of amplifier circuit performance will be illustrated. The general principles then will be applied to several types of single-diode circuits. Last, an approach for building very high-power transmitters with hundreds of diodes will be shown.

Much of the material in this article is drawn from the author's personal experience in designing IMPATT transmitters at Raytheon Systems Company. Many of the diodes and circuits that will be used for illustrations have military applications, so exact performance levels and design details cannot be revealed. However, this article will provide all the fundamental concepts and guidelines to design IMPATT transmitters for many applications.

1. IMPATT DIODE OVERVIEW

As a two-terminal device, an IMPATT diode generates radiofrequency (RF) power by causing the RF current to be approximately 180° out of phase with the RF voltage [1]. This is accomplished by two current delaying mechanisms, avalanche multiplication and transit-time delay, which are the basis for the acronym IMPATT.

Figure 1 shows the doping profile $N(x)$ and electric field profile $E(x)$ of the most common type of IMPATT diode. The two curves are related by Poisson's equation in one dimension:

$$dE/dx = -qN(x)/\epsilon$$

The integral of the electric field over distance (i.e., the area under the curve) is equal to the applied voltage plus the built-in diode potential.

The thin region in the center of the device is called the "avalanche zone". The field is highest there, and avalanche multiplication occurs when a sufficient bias

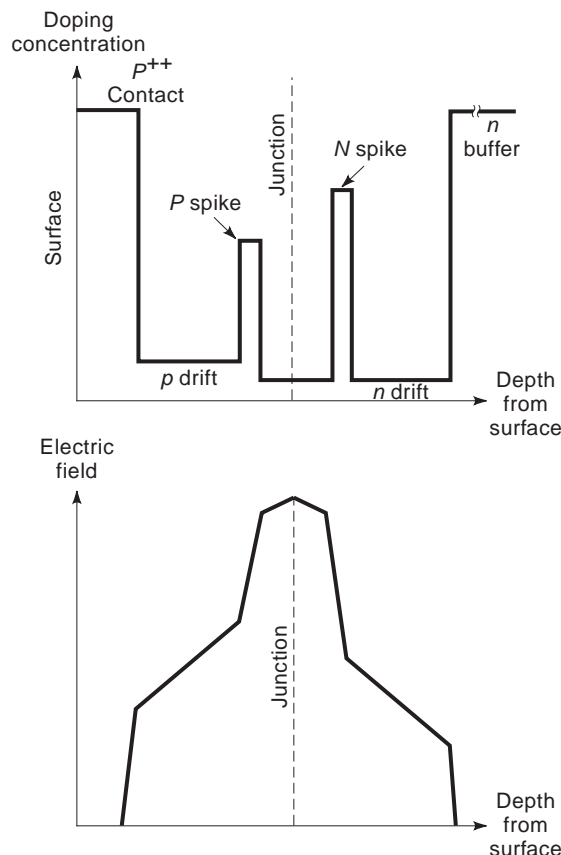


Figure 1. Doping versus depth and electric field versus depth of a double-drift IMPATT diode.

voltage is applied. To the right of the avalanche zone is a thin spike of n-type doping, which causes a large drop in the electric field. On the left side of the avalanche zone is a p-type doping spike that causes a similar drop in the electric field. These doping spikes confine the avalanche process to the thin, high-field avalanche zone.

The IMPATT structure in Fig. 1 also has an n-type drift zone on the right side of the avalanche zone and a p-type drift zone to the left. The doping in these regions is chosen to cause the electric field to slope gradually away from the center of the device. The right side of the device is bounded by a heavily doped n-type contact layer, and the left side is bounded by a p-type contact.

Figure 2 explains how this structure accomplishes the necessary phase delay between the RF voltage and the RF current. The upper graph shows a sinusoidal RF voltage (35 GHz is used in this example) superimposed on a DC bias. The second graph shows the current that leaves the avalanche zone in response to the sinusoidal terminal voltage. Notice that the peak of the avalanche current is delayed by 90° from the peak of the terminal voltage. This phase shift occurs because the avalanching process needs many collisions, each with a very short delay, to generate a significant current. There are few electrons and holes at

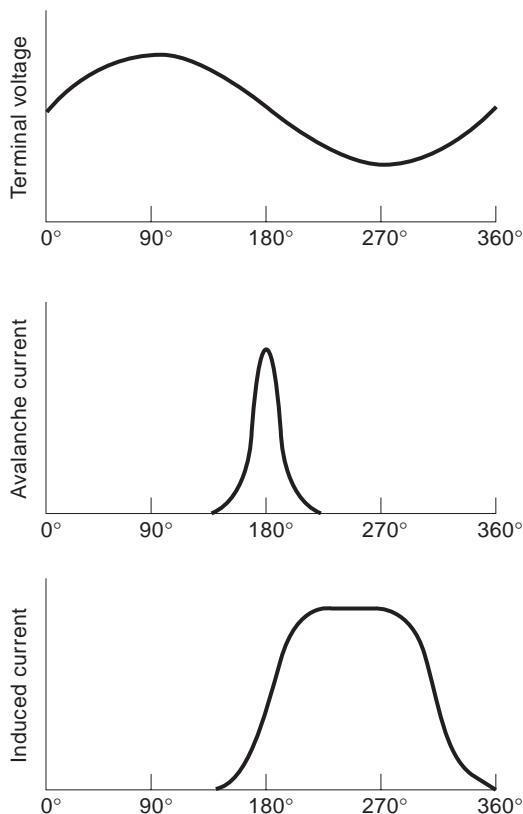


Figure 2. Simplified theory of an IMPATT diode.

the beginning of the cycle, and most of the positive half of the RF cycle is needed for the current to grow exponentially to a significant level. In the second half of the cycle, the electric field is insufficient to sustain the avalanche, and the current quickly decays until the next cycle.

The pulses of electrons and holes that were generated in the avalanche zone during the positive half of the RF cycle flow with constant velocity through the drift zones during the negative half of the cycle. The motion of the large bunch of electrons toward the n contact on the right and the motion of the holes to the left induce the external current shown in the third graph of Fig. 2. Notice that the terminal current is flowing primarily during the negative half-cycle of the terminal voltage (i.e., the diode behaves as a negative resistance at its operating frequency). This causes the IMPATT diode to deliver energy to the external circuit at the frequency of the voltage excitation. The remainder of the bias power that is not converted to RF energy is dissipated in the diode as heat.

The concept of negative resistance is very useful to the circuit designer, who must tailor the impedance of the IMPATT circuit to the impedance of the IMPATT diode to achieve the desired oscillation or amplification. However, to those readers who are not accustomed to this concept, another way to understand the power generation of an IMPATT diode is to consider the power dissipation in the diode relative to the applied DC power. The DC input power is the average DC voltage multiplied by the average DC current, whereas the power dissipation is the time average of the product of the instantaneous voltage and

instantaneous current. These quantities are illustrated in the top and bottom graphs in Fig. 2. The dissipation is about 80% of the DC input power in this illustration, and the remaining 20% emerges from the device as RF power at the frequency of the RF voltage excitation.

Notice in Fig. 2 that the induced current waveform is not centered at 270° where the minimum RF voltage occurs. The length of the induced current pulse can be adjusted by changing the lengths of the drift zones, and the highest efficiency occurs when the induced current pulse is somewhat shorter than 180°.

It is important for a circuit designer to understand that the impedance of an IMPATT diode is a function of the RF voltage amplitude. Figure 3 illustrates the terminal voltage and induced terminal current at three different voltage amplitudes. The upper graph shows the small-signal waveform conditions where both the current and the voltage are sinusoidal. The amplitude of the RF current is proportional to the RF voltage, causing the device impedance (the ratio of the RF voltage to the RF current) to be insensitive to the voltage amplitude. With the medium voltage amplitude shown in the center graph, the current waveform has become distorted, and additional increases in RF voltage will not result in proportional increases in the RF current. Then, under the large-signal conditions shown in the lower graph, the current waveform is nearly a square wave. Additional increases in the RF voltage amplitude cannot cause additional increases in the amplitude of the induced

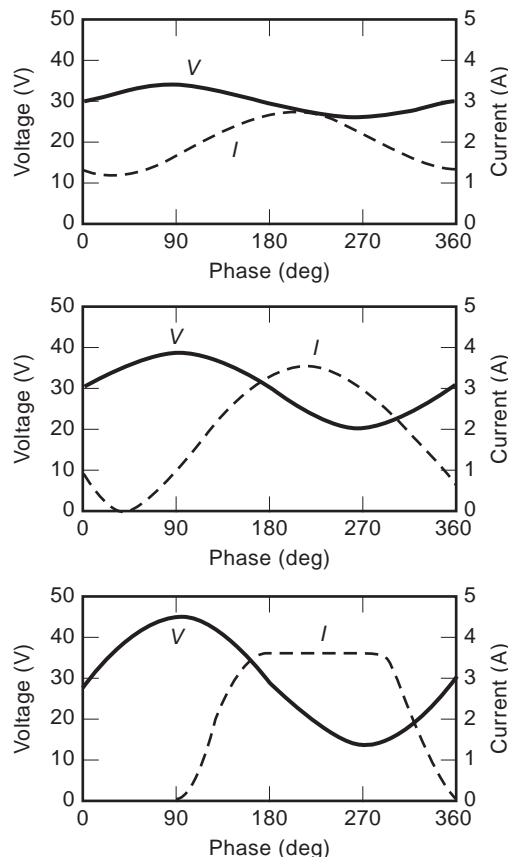


Figure 3. Induced current in an IMPATT diode for low-, medium-, and high-voltage amplitudes.

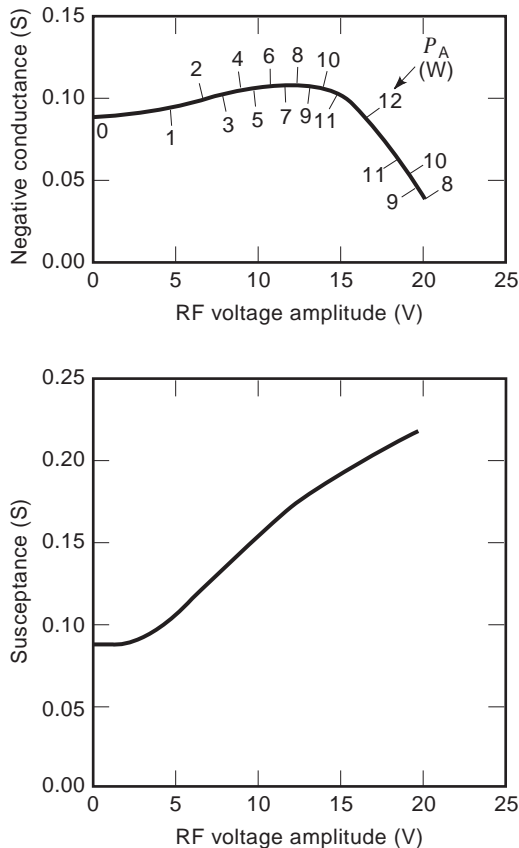


Figure 4. IMPATT diode conductance and susceptance versus RF voltage amplitude.

current because the time average of the current waveform must equal the fixed bias current.

The admittance of the diode at its terminals can be extracted from these waveforms by computing the amplitude of the first harmonic of the current waveform and its phase relative to the RF voltage. Figure 4 shows the conductance and susceptance at the terminals of a 35-GHz IMPATT diode over the range of RF voltages shown in Fig. 3. The susceptance includes the fixed-capacitive susceptance of the diode as well as the portion caused by the currents in Fig. 3.

Several observations about these curves are important to an RF circuit designer. Notice that negative conductance of the diode is considerably lower for high RF voltage amplitudes than for small signals. This will cause gain compression in IMPATT amplifiers. Notice also that the susceptance of the diode is a function of RF voltage amplitude. This will cause the center frequency of an IMPATT amplifier to decrease as the RF signal level increases. It also causes the gain–frequency characteristic of an IMPATT amplifier to drop more rapidly below the center frequency than on the high side of the center frequency. All these observations will be discussed later in this article.

The power P that is generated by an IMPATT diode can be calculated using

$$P = -\frac{1}{2}GV^2$$

where G is the chip conductance (a negative quantity) and V is the RF voltage amplitude.

Figure 4 has tickmarks along the conductance–RF voltage amplitude curve in intervals of 1 W. In this example, the maximum RF power is 12 W at an RF voltage of 16.5 V. At higher RF voltage amplitudes, other physical effects begin to affect the induced current waveform, and the output decreases.

A convenient way for the circuit designer to plot this information is to convert the chip conductance and susceptance data at each tickmark to chip impedance $-Z_C$ as illustrated in Fig. 5. Notice that the negative resistance of an IMPATT diode is relatively low, varying in this case from a small-signal value of -6.4Ω to a large-signal value of -0.8Ω . It is difficult to match low impedance levels like this over a broad frequency range, so IMPATT amplifiers are generally used for systems with fractional bandwidths of 5% or less. Most transmitters require less than 5% bandwidth, so this is not a significant restriction.

The electrical characteristics shown in Figs. 4 and 5 are approximations to the properties of a pulsed Ka-band IMPATT diode. Exact values have not been used because these devices are useful in military systems. The shapes of the curves are qualitatively correct, and they will be used in later sections to explain circuit design principles.

Figure 6 is a cross-sectional drawing of a typical millimeter-wave IMPATT diode package. The chip is thermal-compression-bonded to a diamond heatsink, which gives the best possible heatsinking. The diamond is imbedded in a copper puck to facilitate a good thermal contact to the bottom of the diode package. The chip is surrounded by a ceramic or quartz insulating ring, and beam leads or bonding straps connect the top of the chip to the top of the insulator. A cap is soldered over the top of the ring to provide mechanical protection and an hermetic enclosure.

Figure 7 is a photograph of a Raytheon device in which one-half of the ceramic ring is removed to reveal the internal construction. This type of package can be easily

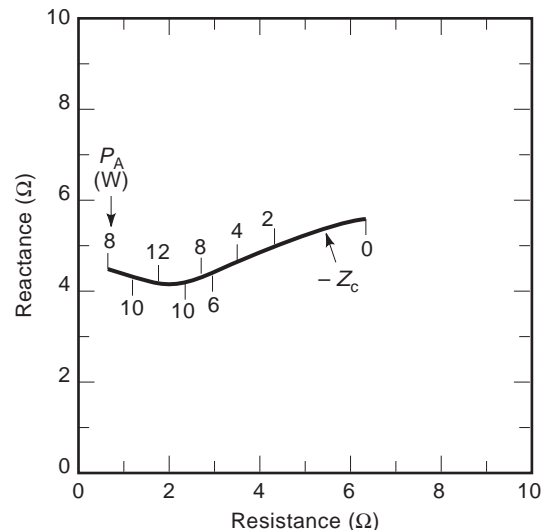


Figure 5. IMPATT diode resistance and reactance as functions of RF power.

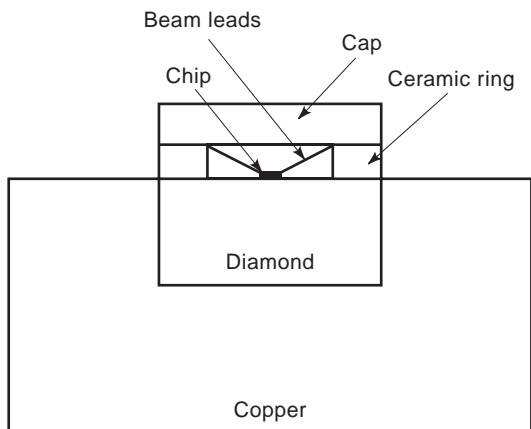


Figure 6. Cross section of an IMPATT diode package.

inserted or removed from an RF circuit, held in place with a copper screw for heat removal. The ring is as small as possible to minimize the electrical transformation through the parasitic inductances and capacitances of the package. Low-cost IMPATT diodes at lower microwave frequencies have a threaded stud in place of the diamond puck.

2. IMPEDANCE MATCHING OF A NEGATIVE-RESISTANCE DEVICE

An IMPATT diode can be used as a stable amplifier, an injection-locked oscillator, or a free-running oscillator. The mode of operation is determined by the load impedance that the RF circuit presents to the IMPATT chip. This section will explain the general principles of IMPATT diode impedance matching to lay a foundation for later discussions of specific circuits.

2.1. Free-Running Oscillator

Figure 8 contains the IMPATT chip impedance curve $-Z_C$ from Fig. 5 (the “device line”) plus a curve of load impe-

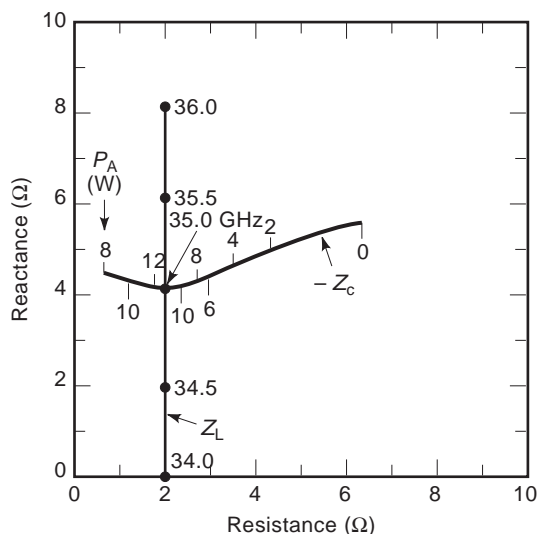


Figure 8. IMPATT device line and load line for an oscillator.

dance versus frequency Z_L (the “load line”). In Fig. 8, we will assume that the impedance of this 35-GHz diode does not change appreciably over a frequency range of 2 GHz (a 6% bandwidth). The load line of the circuit Z_L crosses the device line $-Z_C$ at 35 GHz near the highest power point on the device line. At the intersection, the condition for oscillation is met:

$$Z_C + Z_L = 0$$

If the load line is moved vertically, the frequency of intersection will shift, causing the diode to oscillate at a new frequency. If the load line is moved horizontally, the intersection will occur at a different RF output power level. Moving the load line horizontally also changes the frequency slightly as a result of the slope of the device line.

2.2. Injection-Locked Oscillator

Figure 9 is similar to Fig. 8, but the load line is shifted to the right. The point of intersection occurs at 35.25 GHz on the load line and at less than full power on the device line. In the absence of an RF input signal, the diode will oscillate in this circuit at 35.25 GHz with an output power of about 1 W.

If a 35.25 GHz RF input signal is applied, the power P_A that is added by the diode will combine with the RF input signal P_I to produce an RF output signal P_O that is larger than the input signal

$$P_O = P_I + P_A$$

The gain G of the circuit is the ratio of RF output to RF input

$$G = P_O/P_I$$

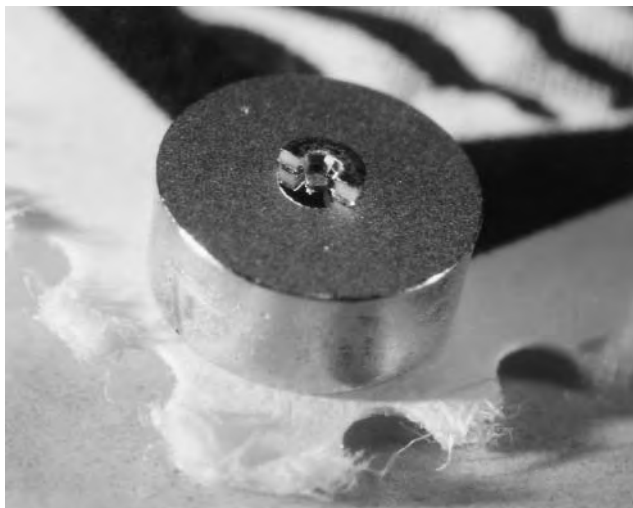


Figure 7. Photograph of an IMPATT diode package.

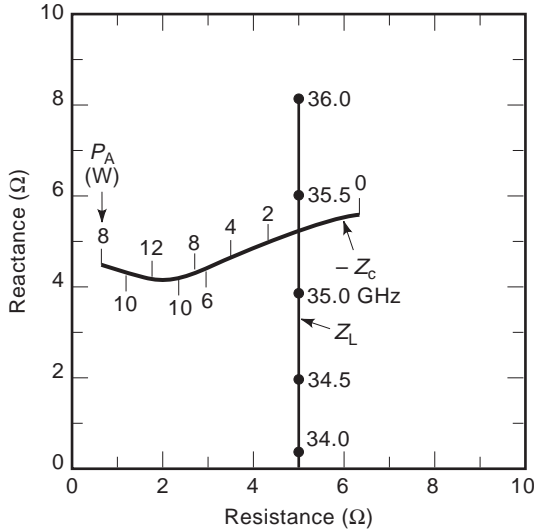


Figure 9. IMPATT device line and load line for an injection-locked oscillator.

These two equations can be combined to solve for both P_O or P_I in terms of P_A and G :

$$P_I = P_A / (G - 1) \quad (1)$$

$$P_O = G P_A / (G - 1) \quad (2)$$

Figure 10 illustrates a simple equivalent circuit for an IMPATT amplifier. A more accurate approach to circuit characterization will be discussed later, but the basic principles can be explained more clearly with this simple model. The model is an LC circuit in series with the IMPATT chip Z_C . The coupling between the resonant circuit and the external load Z_O is an ideal transformer with a turns ratio of n .

The input impedance Z at angular frequency ω of the diode and circuit shown in Fig. 10 is

$$Z = n^2 [Z_C + j\omega L + 1/(j\omega C)]$$

This equation can be further simplified by substituting $j\omega X_L = j\omega L + 1/(j\omega C)$, so that

$$Z = n^2 (Z_C + j\omega X_L) \quad (3)$$

The voltage reflection coefficient Γ from an impedance Z in a transmission line with characteristic impedance Z_0 is

$$\Gamma = (Z - Z_0) / (Z + Z_0) \quad (4)$$

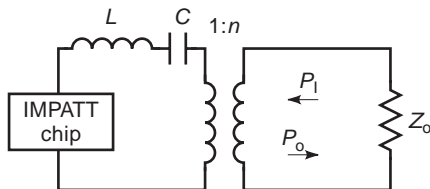


Figure 10. Equivalent circuit for a one-diode IMPATT amplifier.

Substituting Eq. (3) into Eq. (4) and making a few algebraic steps, we obtain

$$\begin{aligned} \Gamma &= [n^2(Z_C + j\omega X_L) - Z_0] / [n^2(Z_C + j\omega X_L) + Z_0] \\ &= [(Z_C + j\omega X_L) - Z_0/n^2] / [(Z_C + j\omega X_L) + Z_0/n^2] \quad (5) \\ &= [Z_C - (Z_0/n^2 - j\omega X_L)] / [Z_C + (Z_0/n^2 + j\omega X_L)] \end{aligned}$$

The load impedance seen by the diode is $Z_L = (Z_0/n^2) + j\omega X_L$ and its complex conjugate is $Z_L^* = (Z_0/n^2) - j\omega X_L$. Substituting these quantities into Eq. (5), we have

$$\Gamma = (Z_C - Z_L^*) / (Z_C + Z_L) \quad (6)$$

The gain of the amplifier is the square of the magnitude of the reflection coefficient

$$G = |\Gamma|^2 = |(Z_C - Z_L^*) / (Z_C + Z_L)|^2 \quad (7)$$

Equations (1), (2), and (7) can be used to construct curves of P_O versus P_I from the data in Fig. 9 using the following procedure:

1. Choose a value of $-Z_C$ on the device line (start at the left end of the device line) and note the added power P_A .
2. Note the value of Z_L from the load line at the frequency of operation.
3. Calculate the gain G using Eq. (7).
4. Calculate the RF input power P_I and RF output power P_O using Eqs. (1) and (2).
5. Repeat this calculation for several other values of $-Z_C$ and draw a curve of P_O versus P_I .

As the choice for $-Z_C$ is moved to the right along the device line toward the intersection of the device line and the load line, the gain of the circuit increases, and the calculated input power decreases. When $-Z_C$ is chosen to be the intersection between the device line and the load line, the gain is infinite, and the RF input power is zero, which is the free-running oscillator condition. Values of $-Z_C$ that are to the right of the intersection point will not result in stable operation, and the injection-locked oscillator will “break lock” [2] from the RF input signal and generate a free-running signal.

Figure 11 shows curves of P_O versus P_I at five different frequencies. All the curves were calculated with the same procedure, but with different values of Z_L from the load line for each of the frequencies. Notice that the curves do not pass through the origin because of the free-running oscillation at 35.25 GHz. At frequencies near 35.25 GHz, P_O increases rapidly for small values of P_I because the gain is very high when $-Z_C$ is close to Z_L [see Eq. (7)]. For larger values of P_I , P_O continues to increase but at a slower rate because the gain is steadily decreasing. This effect is called *gain compression*.

The diagonal lines in Fig. 11 are contours of constant added power. At 35.0 GHz, the maximum added power is

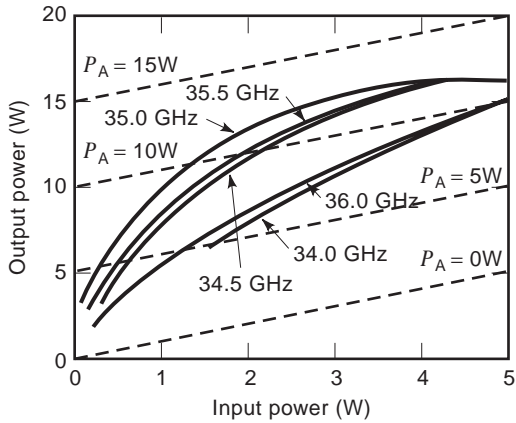


Figure 11. RF output power versus RF input power of an injection-locked oscillator.

12 W, which occurs at an input power of 3 W. For maximum efficiency, the circuit should be designed to operate near this point. Notice, however, that the added power of the circuit is relatively constant over a modest range of input powers. This makes IMPATT circuits tolerant to being underdriven or overdriven.

The data in Fig. 11 show how an injection-locked IMPATT circuit behaves as a function of RF input power at several fixed frequencies, and these are called *drive curves*. Data points from this graph can be replotted such that the RF input power is held constant while the frequency is varied. This is illustrated in Fig. 12, and these are the frequency response curves of the IMPATT circuit. There are several interesting observations regarding these curves. First, the curves are not symmetric because the device line is tilted relative to the load line in Fig. 9. As the RF input drive is decreased, the circuit becomes unlocked at the lower edge of the operating frequency range before it becomes unlocked at the high end of the band.

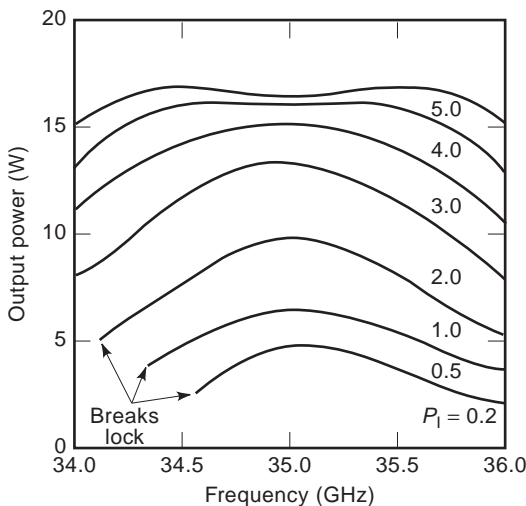


Figure 12. RF output power versus frequency of an injection-locked oscillator.

Another important observation is that the bandwidth of the circuit is greater when the RF input power is higher. When the RF input power is 0.2 W, the gain is high at 35.0 GHz, but it decreases rapidly for other frequencies. When the RF input power is between 3 and 4 W at 35.0 GHz, the circuit adds about 12 W. At 5 W of RF input, the diode is overdriven and only 11 W are added. This saturation behavior causes the output power and gain to be relatively constant over the entire frequency range at the higher drive levels.

2.3. Stable Amplifier

The mode of operation in Figs. 9, 11, and 12 is called *injection-locked*, and the circuit is called an *injection-locked oscillator*. The gain of an injection-locked oscillator as illustrated in Figs. 11 and 12 will increase if the circuit designer moves the device line in Fig. 9 to the left toward the maximum added power point along the device line. This will be accompanied by a corresponding decrease in injection-locking bandwidth. Conversely, the gain will decrease and the bandwidth will increase, if the load line is moved to the right in Fig. 9. If the load line is moved far enough to the right, there is no intersection between the load line and the device line. In this case, the IMPATT circuit will not oscillate if the RF input signal is removed. This type of circuit is called a *stable amplifier*.

Figure 13 illustrates relationship between the device line and the load line for a stable amplifier. The same procedure that was used earlier to calculate the drive curves and frequency response curves can be applied to the stable amplifier case. Figures 14 and 15 illustrate the resulting graphs. Notice that all the curves in Fig. 14 begin at the origin because the output of a stable amplifier is always “locked” to the RF input signal. Both figures show that the gain of the circuit is lower, and Fig. 15 clearly demonstrates an accompanying increase in bandwidth.

The choice of operating mode—oscillator, injection-locked oscillator, or stable amplifier—depends on the

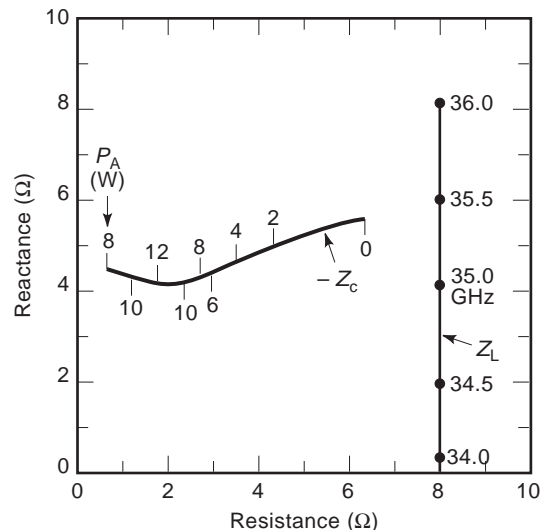


Figure 13. IMPATT device line and load line for a stable amplifier.

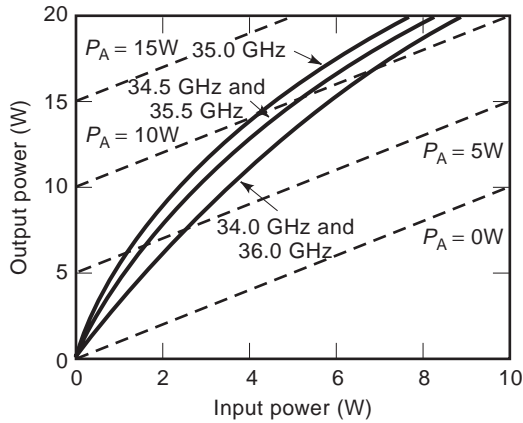


Figure 14. RF output power versus RF input power of a stable amplifier.

application. A free-running oscillator is useful for generating a high-power RF signal with a minimum of hardware. For example, a mechanically tuned oscillator is a good source of RF power for laboratory instrumentation.

An injection-locked oscillator is best for most transmitter applications. Gains of 3–10 dB are typical, and multiple stages can be cascaded for higher overall gain. If the bandwidth requirement is small, fewer stages with higher gain per stage can be used. The drive curve of an injection-locked oscillator is very nonlinear (see Fig. 11), and a multiple-stage transmitter will have many decibels of gain compression. Therefore, injection-locked oscillators are used only with frequency-modulated or phase-modulated signals.

An important application for injection-locked IMPATT amplifiers is pulsed radar systems. The bias current to the IMPATT diodes is turned on and off with the same

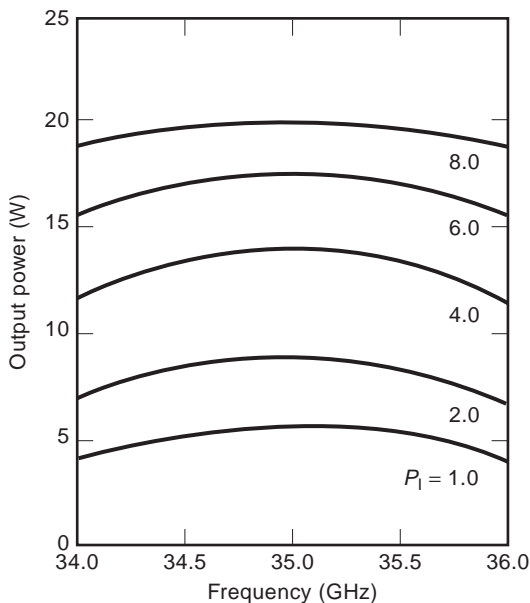


Figure 15. RF output power versus frequency of a stable amplifier.

waveform as the RF input signal. In this way, the IMPATT amplifier does not generate a free-running signal or noise while the radar receiver is detecting the reflected signal from the target. Pulsing the diode bias also reduces the prime power requirement by the duty cycle of the RF waveform.

Stable amplifiers are used when a free-running oscillation cannot be tolerated. A stable IMPATT amplifier might also be chosen for an amplitude-modulated signal if a modest amount of gain compression is acceptable. The use of constant voltage bias instead of constant current bias can be used to produce more linear drive curves [3], but constant voltage bias can also produce parametric instabilities, which will be discussed in a later section.

2.4. Effect of Load Mismatch

One final note of caution for the circuit designer is to provide a good external load for the IMPATT amplifier circuit. In the preceding examples, a perfect matched load Z_0 was assumed. A load impedance other than Z_0 will perturb the circuit impedance seen by the diode, changing the response of the amplifier. In practice, an amplifier circuit will be connected to a circulator to separate the output and input signals, and circulators have a return loss of about –25 dB over a 5% bandwidth.

A convenient way to estimate the effect of load mismatch is to estimate the amplitude of the wave that is reflected from the mismatch. This signal will combine with the intended RF input signal, resulting in a different amplitude. The maximum combined amplitude will occur when the voltage vectors for the two signals are in phase, and the minimum occurs when they are out of phase. The engineer should estimate the maximum and minimum voltage vectors and then calculate the maximum and minimum RF input power to the amplifier circuit.

For example, if an amplifier circuit has a gain of 5 dB and the load to which the circuit is connected has a return loss of 25 dB, the portion of the amplifier output signal that is reflected from the load will be 20 dB (a factor of 0.01) below the intended or nominal RF input signal. The voltage amplitude of a signal is proportional to the square root of its power, so the voltage amplitude of the signal that is reflected from the load will be approximately 0.10 relative to the voltage amplitude of the nominal RF input signal. The maximum RF input occurs when the nominal input signal and the signal that is reflected from the load are in phase:

$$\max P_I \approx (1 + 0.10)^2 \text{ nominal } P_I = 1.21 \text{ nominal } P_I$$

The minimum RF input occurs when the two signals are out of phase:

$$\min P_I \approx (1 - 0.10)^2 \text{ nominal } P_I = 0.81 \text{ nominal } P_I$$

It can be seen that even a good external load causes a modest uncertainty in the RF drive to an amplifier circuit. Fortunately, the gain compression that is evident in the drive curves in Figs. 11 and 14 causes the added power of a high-power IMPATT amplifier to be insensitive to an input

power range of this size. The early stages of a multiple-stage amplifier will be more sensitive to load mismatch, however, because the gains are usually higher, and there is less gain compression when the diodes are operated at lower power levels.

3. PARAMETRIC OSCILLATION

The preceding sections of this article have explained how an IMPATT diode generates negative resistance at the frequency of operation and how the impedance of the circuit must be tailored to the device impedance. An IMPATT diode is very nonlinear when the RF voltage is high, and parametric effects cause it to develop negative resistance over a wide frequency range. This section will explain the origin of the parametric negative resistance and how to design an IMPATT circuit to prevent unwanted oscillations.

3.1. Bias Circuit Oscillation

One source of instability in IMPATT diodes is caused by the decreased power dissipation that occurs when the RF voltage across the diode is increased and the device generates more RF power. The ionization rates in the avalanche zone are higher if the temperature is reduced, so the DC bias current will increase if the voltage is held constant. A runaway condition can occur in an IMPATT oscillator because an increase in the bias current will cause a further increase in the RF voltage amplitude. This type of instability can cause oscillation in the bias input to an IMPATT amplifier or oscillator at frequencies up to ~ 10 MHz. The effect diminishes at higher frequencies because the thermal time constant of the IMPATT chip and package are too long to allow the junction temperature to respond to the changes in dissipated power.

Preventing this form of bias oscillation requires a high-impedance bias current source. When the RF voltage increases incrementally and the dissipated power decreases, the bias voltage will drop incrementally if the current is held constant. The RF properties of the diode are relatively insensitive to small changes in the operating voltage, so there is not a positive-feedback effect as there is in the case of constant voltage bias. The drop in operating voltage that is caused by an increase in RF voltage amplitude is called the *rectification effect* or *backward-bias effect*.

The simplest way to create a high-impedance DC bias source in the laboratory is to insert a noninductive power resistor between the bias input of the IMPATT circuit and a DC power supply. The minimum value of resistance that is needed for stability will need to be determined experimentally, but $100\ \Omega$ is a good starting value. The resistor should consist of a network of lower power, noninductive resistors rather than a single, high-power, wirewound resistor. The "constant current" mode of a power supply should not be used because the response time of the feedback loop within the supply is much too long to protect the diode from a runaway condition.

The primary disadvantage to using a series resistor to make a high-impedance current source is the amount of

heat that is dissipated in the resistor. A better approach is to design a constant current electronic bias circuit with a low-voltage drop (typically 5 V). If a pnp transistor or a p-channel FET is used for the pass transistor in the bias circuit, the bias output will come from the collector or drain and have a relatively high impedance well beyond 10 MHz. If the IMPATT circuit is to be used in a pulsed radar transmitter, the electronic bias circuit must be designed for both high output impedance and fast switching speed.

Another effect occurs at high RF voltage amplitudes when the current leaving the avalanche zone becomes very low between cycles. In IMPATT diodes that are designed for microwave frequencies such as 10 GHz, the avalanche current waveform may reach the saturation current level. If the RF voltage amplitude is increased further, the avalanche current cannot drop below the saturation current level. During the positive half of the RF voltage cycle, the avalanche current builds up too quickly from this lower bound. This will result in a higher peak avalanche current and a higher DC current if the bias voltage is not reduced. This effect is quite strong in low-frequency devices, and it generates negative resistance to several gigahertz. However, this mechanism does not exist in millimeter-wave diodes because there is insufficient time between RF cycles for the avalanche current to drop to the ionization current level.

An IMPATT bias circuit must have a high impedance to several gigahertz to prevent the last type of parametric oscillation. It is particularly important to have low shunt capacitance in the bias circuit of the IMPATT circuit and in the bias supply. There are several comprehensive articles on this subject from the early years of IMPATT research [4,5]. The principles in these articles can be adapted to other types of IMPATT circuits.

3.2. Subharmonic Oscillation

Another type of parametric effect that is common in IMPATT circuits is subharmonic oscillation [6–9]. Simply stated, the IMPATT diode generates broadband negative resistance as a result of the nonlinear behavior of the avalanche process. One form of subharmonic oscillation is a signal at exactly one-half of the fundamental operating frequency. Subharmonic oscillation can also appear as a pair of signals whose frequencies add up to the fundamental frequency.

Subharmonic oscillation is very difficult to prevent because of the very broad frequency range where it can occur, so it is usually present in IMPATT amplifiers. A general approach to minimize the magnitude of subharmonic oscillation is to load the bias port of the IMPATT circuit with a microwave-absorbing material. This load will absorb some of the RF power at the fundamental, but the circuit designer can find creative ways to minimize the lost power.

If the circuit designer uses a high-impedance bias supply, minimizes the shunt capacitance in the bias circuit of the IMPATT circuit and in the bias supply, and also loads the bias port with a microwave absorber, the IMPATT circuit should behave well.

4. TYPES OF IMPATT CIRCUITS

All the general principles of IMPATT diode operation and the RF circuit requirements have been discussed in the previous section of this article. This section will briefly illustrate several types of IMPATT circuits that meet these general requirements.

An IMPATT circuit must present a load resistance of only a few ohms to an IMPATT chip, so a large transformation is required between the characteristic impedance of the RF port of the IMPATT circuit and the chip. In a coaxial transmission line medium, this can be accomplished with a coaxial matching transformer as illustrated in Fig. 16. The low-impedance transformer is created by reducing the diameter of the outer conductor rather than increasing the diameter of the inner conductor because this results in lower parasitic inductance in the mount. The “puck” style of IMPATT package that was illustrated in Figs. 6 and 7 can be easily installed and removed from this kind of diode mount.

The matching transformer (typically $\frac{1}{8}$ th wavelength long because of the parasitic reactance of the package and the mount) is designed to transform the characteristic impedance of the coaxial line (typically 50Ω) to the desired load impedance. Wider bandwidth can be achieved with a two-section transformer. Bias is applied to the center conductor through a bias tee (not shown), and the RF input and output signals are separated by a coaxial circulator (not shown). The circulator should have wide bandwidth to provide RF loading in the subharmonic frequency range.

The top-hat circuit [15], illustrated in Fig. 17, was used extensively in the early years for oscillator testing of IMPATT diodes. The diode is mounted in the floor of a waveguide cavity (a threaded diode package works well with this type of circuit), and a top hat resonator is placed on top of the diode. The region under the top hat is a radial transmission line that transforms the high impedance of the waveguide to the low impedance of the chip. The frequency of oscillation is set primarily by the diameter of the top hat, and the backshort (backward-traveling short circuit) is adjusted to set the cavity resonant frequency to be equal to the top-hat frequency. The load resistance that is seen by the IMPATT diode is set by the spacing between the top hat and the floor of the waveguide. At millimeter-wave frequencies, the diameter of the top hat might be as small as the diameter of the bias pin. An *E-H* tuner or slide-screw tuner can be connected to the waveguide output for fine-tuning. The bias pin contains an RF absorber for parametric stability.

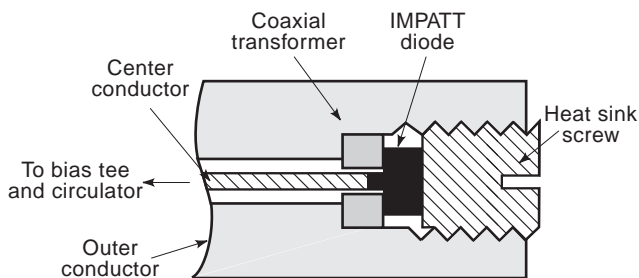


Figure 16. Coaxial circuit.

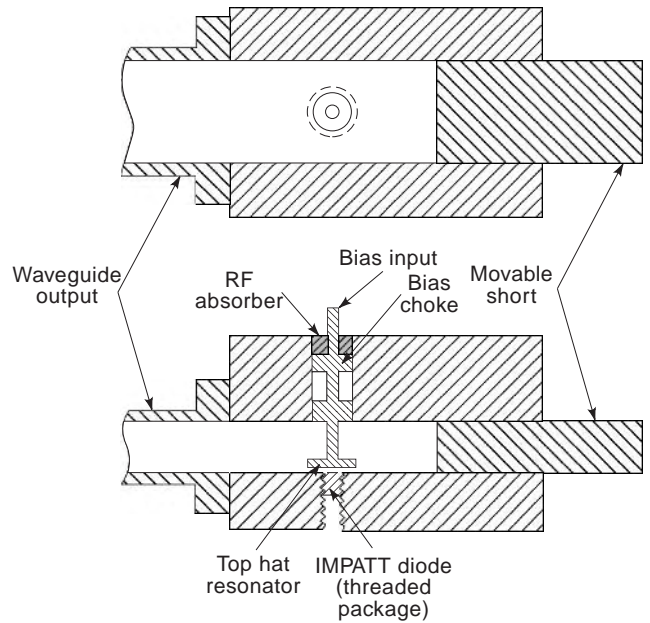


Figure 17. Top-hat circuit.

A very common and useful type of IMPATT circuit is the rectangular Kurokawa circuit [10], which is illustrated in Fig. 18. A resonant cavity is formed in a rectangular waveguide between the movable short circuit at the right and

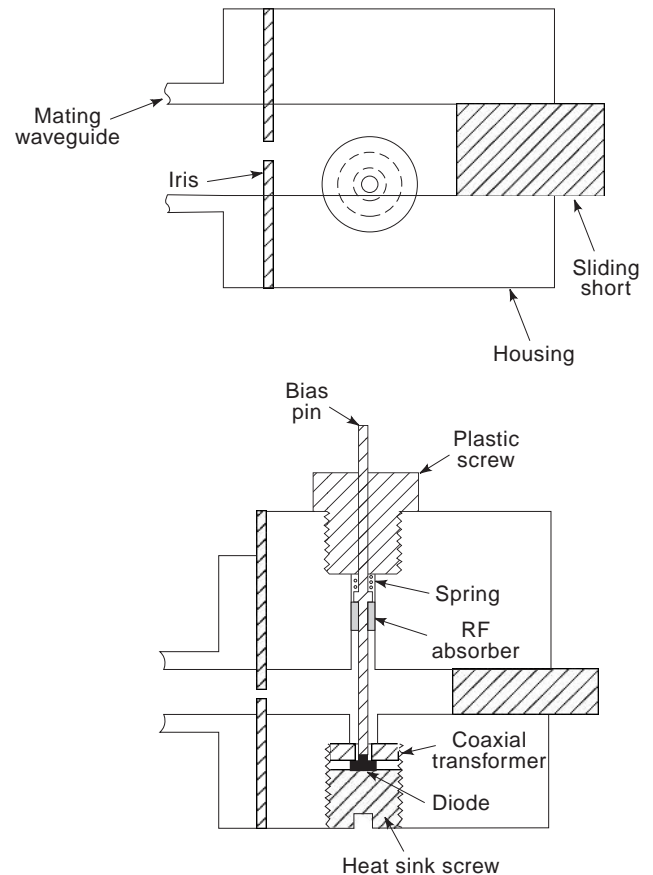


Figure 18. One-diode rectangular Kurokawa circuit.

an iris on the left. A coaxial transmission line passes through the broad walls of the waveguide cavity to which it is magnetically coupled. An IMPATT diode and a matching transformer are located at one end of the coaxial line, and an RF absorber is inserted into the other end. The coaxial transformer is the primary impedance-matching element, and the load resistance and reactance are controlled by the transformer impedance and length, respectively.

The cavity resonance in the rectangular Kurokawa circuit causes a significant perturbation in the diode load impedance near the operating frequency. The movable short circuit is adjusted to make the cavity resonant frequency correspond to the resonant frequency of the diode and matching transformer, and the hole diameter in the iris controls the coupling to the external load. Far from the operating frequency, the cavity has little effect, and the RF absorber helps prevent parametric oscillation.

The Kurokawa circuit is very useful for diode testing because a wide range of load impedances can be achieved with different matching transformers and irises. The RF load in the coaxial line absorbs about 25% of the generated power, but the circuit efficiency can be measured with an automatic network analyzer so that the RF power of the diode can be calculated.

The Kurokawa circuit can be modified to be a power combiner [11] by adding additional coaxial lines as shown in Fig. 19. The pairs of coaxial lines are separated by one-half of a wavelength so that the coupling from the waveguide cavity to each coaxial line is approximately the same.

A variation of this last circuit type is the cylindrical Kurokawa circuit illustrated in Fig. 20. The coaxial lines that contain the diodes are the same as the ones in the

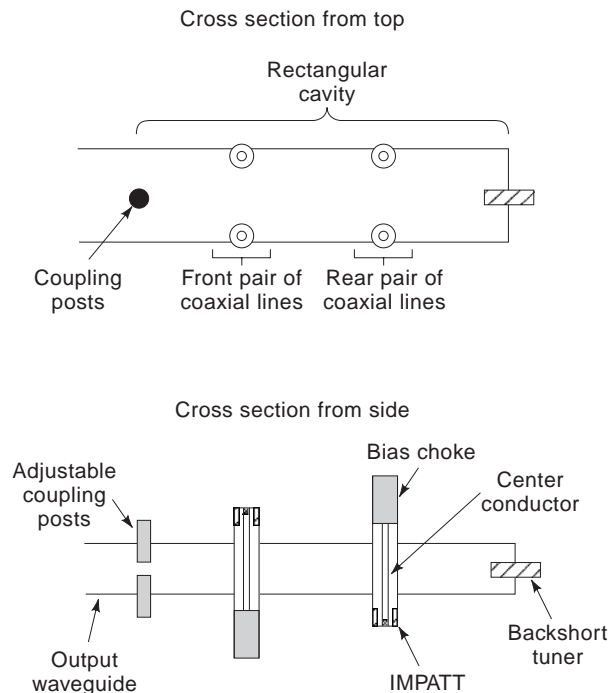


Figure 19. Four-diode rectangular Kurokawa circuit.

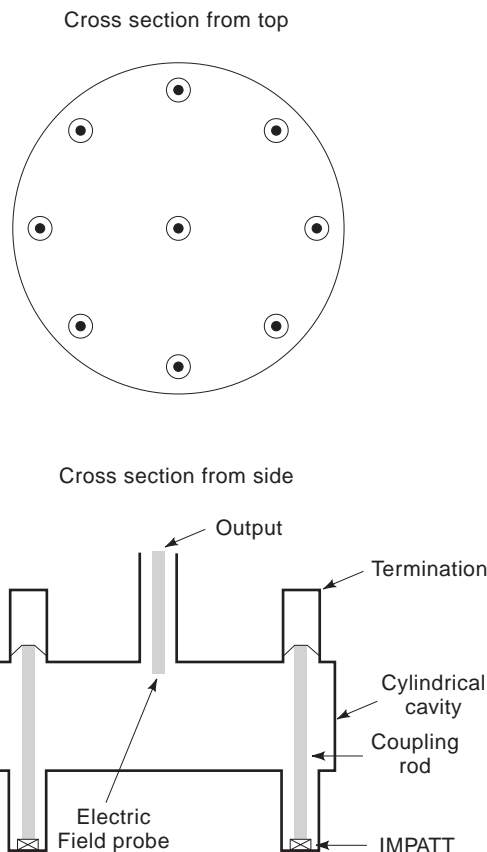


Figure 20. Eight-diode cylindrical Kurokawa circuit.

rectangular Kurokawa, but the cavity is now cylindrical instead of rectangular. The RF output port is a coaxial line in the top of the cavity, and the coupling between the cavity and the external load is adjusted by changing the penetration of the electric field probe.

5. IMPATT CIRCUIT CHARACTERIZATION

The discussion of impedance matching a negative-resistance device used a lossless series resonant equivalent circuit. In practice, an IMPATT circuit is not lossless, nor does its impedance vary with frequency as in this simple model. However, this model is qualitatively correct and useful for the purposes of illustration.

It is not practical to measure directly the load impedance that is seen by an IMPATT diode because the load impedance is only a few ohms and the chip location is inaccessible to a network analyzer. However, those IMPATT circuits where the diode is mounted in a coaxial transmission line can be characterized indirectly with a network analyzer. If the diode and its matching transformer are removed, a network analyzer with a coaxial input can be connected to the circuit. After the two-port *S* parameters of the circuit are measured, an equivalent circuit for the matching transformer and the diode package parasitic reactance can be used to calculate the load impedance at the diode chip. Figure 21 illustrates how a network analyzer

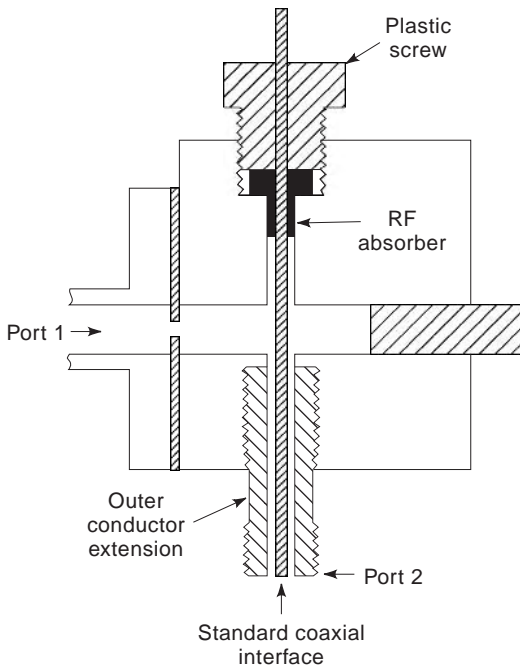


Figure 21. Direct characterization of an IMPATT circuit with a coaxial adapter.

would be used to make this two-port measurement of a one-diode rectangular Kurokawa circuit.

There is another measurement technique that requires only one-port network analyzer measurements. Figure 22 shows a rectangular Kurokawa circuit with the diode and its coaxial transformer removed. These components are replaced by a coaxial short (circuit) and an outer conductor spacer to create an offset short. The reflection coefficient Γ_2 of a load that is attached to port 2 is transformed to Γ_1 at port 1 by the S parameters of the circuit according to the equation

$$\Gamma_1 = S_{11} + S_{21}S_{12}\Gamma_2 / (1 - S_{22}\Gamma_2)$$

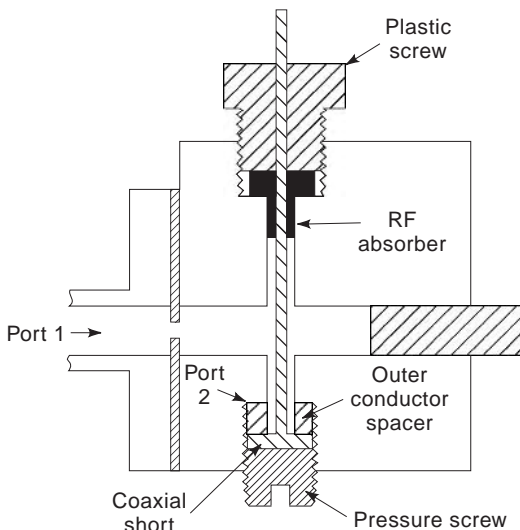


Figure 22. Characterization of an IMPATT circuit by using offset short circuits.

This equation has three unknowns (S_{11} , S_{22} , and the product $S_{21}S_{12}$) that fully describe the circuit at a single frequency. Different values of Γ_2 are created by three offset shorts, and Γ_1 is measured for each one. This gives three simultaneous equations that can be solved for the three unknowns. More accurate results over a wider range of circuit impedance can be obtained by using more than three (typically five to seven) offset shorts and using numerical methods to find a least-squares best fit for the three unknowns. The procedure to calculate the circuit S parameters over a frequency range of interest is easily programmed into a computer that controls an automatic network analyzer.

Figure 23 illustrates the S_{22} of a one-diode rectangular Kurokawa oscillator circuit. The load impedance at the chip was calculated by referring the S_{22} data through an equivalent circuit for the matching transformer and package parasitic reactance. Notice that the load resistance at the chip is nearly constant and the reactance increases linearly with frequency. This impedance-versus-frequency behavior was the basis for choosing a series-resonant equivalent circuit in the earlier discussion on impedance matching. The oscillator circuit efficiency η is the ratio of the power that emerges from the oscillator divided by the power generated by the diode

$$\eta = |S_{21}S_{12}| / (1 - |S_{22}|^2)$$

This relationship is used during IMPATT diode oscillator testing to calculate the RF output power of the diode.

The offset short method for characterizing a circuit has several advantages and disadvantages compared to a direct two-port network analyzer measurement. The offset method can be used to characterize a multiple diode combiner circuit if all the coaxial ports are electrically identical. To do this, the coaxial lines are loaded with identical offset shorts. Network analyzer measurements are taken for three or more sets of these offset shorts, and the data

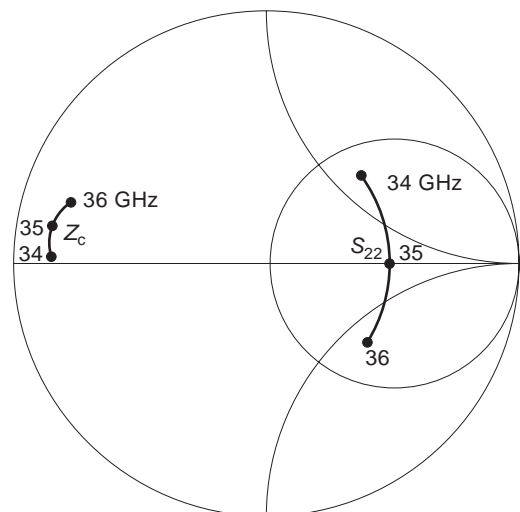


Figure 23. Smith chart impedance plot of the S_{22} and chip load impedance of an oscillator circuit.

are analyzed as if the combiner were a one-diode circuit. The offset short method is also preferable for circuits that operate at high millimeter-wave frequencies where coaxial network analyzer measurements are unfeasible or insufficiently accurate. The disadvantage of the offset method is that it works only when there is good coupling between the coaxial line and the RF output port. Therefore, this method cannot be used to characterize most circuits at frequencies where parametric oscillations occur.

6. TRANSMITTERS USING A COMBINER PLATE

This article has explained the basic principles of IMPATT circuit design. As a conclusion, a new power combining technique that uses the IMPATT circuits discussed earlier will be described.

Many millimeter-wave systems require high-power transmitters, especially missile radar seekers, so an efficient means for combining hundreds of IMPATT diodes is needed. In the 1970s and 1980s, cylindrical Kurokawa power combiners were developed with as many as 60 IMPATT diodes [12]. However, these circuits had limited bandwidth, and the failure of one diode would seriously detune the other devices, resulting in poor graceful degradation.

A new transmitter architecture was invented at Raytheon in the late 1980s that has been applied with great success to many frequency ranges and power levels [13–15]. The basic concept of a combiner plate (16) is illustrated in Fig. 24. The IMPATT diodes are mounted in rectangular Kurokawa “modules,” typically with four devices per module. Many of these modules are then power combined passively by the combiner plate.

The combiner plate consists of two plates with square grooves machined on the mating surfaces. The pattern of grooves is the same on both plates, so a network of rectangular waveguides is formed when the plates are mated. The joint is in the middle of the broad wall of the waveguides where no RF current will cross the joint. This results in very low attenuation within the combiner.

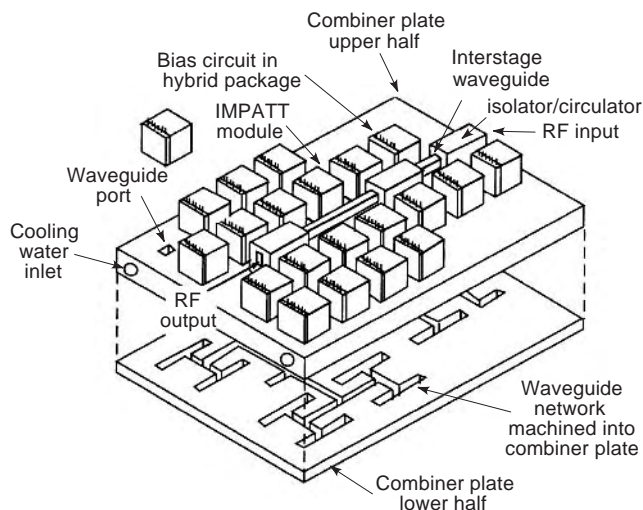


Figure 24. Concept drawing of an IMPATT transmitter using a combiner plate.

The transmitter is designed to use a binary number of IMPATT modules in every stage. Magic tee junctions are built into the waveguide network to split the RF input power to the modules in a stage and then recombine their outputs. Exceptionally good port matches (typically -30 dB return loss) can be achieved with magic tees, so the modules can be integrated with the combiner plate without retuning. This is important for achieving the manufacturing cost goals for these transmitters. The magic tees also permit high isolation (typically -30 dB) between module ports, so this architecture also has very good graceful degradation.

The combiner plate is used as the main mechanical structure of the IMPATT transmitter with most components attached to it. The combiner plate is also the thermal heat sink. Water-cooling passages can be machined into the plate or air-cooling fins attached to the bottom. In missile applications, the thermal mass of the transmitter is adequate to maintain a safe temperature for the few seconds of operation that are required.

The combiner plate architecture has been used to develop very powerful solid state transmitters for military applications. The performance characteristics cannot be reported here, but they generate more power in the same volume as a traveling-wave-tube amplifier. Moreover, solid-state transmitters have lower phase noise, better reliability as a result of graceful degradation, and they do not need high-voltage electronics.

7. CONCLUSIONS AND FUTURE DIRECTIONS

IMPATT transmitters are emerging as the best technology for high-power millimeter-wave applications, displacing even traveling-wave-tube amplifiers. This article has given an overview of the characteristics of IMPATT diodes, the operating principles of IMPATT circuits, descriptions of the most common types of circuits, and how they can be power-combined to make a high-power, multistage transmitter.

As this technology enters large-scale production, there will be pressure to reduce the cost to fabricate and assemble these transmitters. Innovations that might result are hybrid microstrip IMPATT circuits or fully integrated MMIC IMPATTs with their matching circuits. These new IMPATT circuits may appear to be radically different from today's technology, but they will use the same operating principles that were described in this article, only they will be applied to another transmission-line medium.

BIBLIOGRAPHY

1. W. T. Read, A proposed high frequency negative resistance diode, *Bell Syst. Tech. J.* **37**(2):401–446 (1958).
2. R. Adler, A study of locking phenomena in oscillators, *Proc. IRE* **34**:351–357 (1946).
3. J. W. McClymonds, *Linear, High Power IMPATT Amplifiers Using Constant Voltage Bias*, Ph.D. thesis, Dept. Electrical Engineering, Cornell Univ., Ithaca, NY, 1980.
4. C. A. Brackett, The elimination of tuning-induced burnout and bias-circuit oscillations in IMPATT oscillators, *Bell Syst. Tech. J.* **52**(3):271–306 (1973).

5. Y. Hirachi et al., High-power 50 GHz double-drift-region IMPATT oscillators with improved bias circuits for eliminating low-frequency instabilities, *IEEE Trans. Microwave Theory Tech.* **MTT-24**(11):731–737 (1976).
6. M. E. Hines, Large signal noise, frequency conversion, and parametric instabilities in IMPATT diode networks, *Proc. IEEE* **60**(12):1534–1548 (1972).
7. D. F. Peterson, Circuit conditions to prevent second-subharmonic power extraction in periodically driven IMPATT diode networks, *IEEE Trans. Microwave Theory Tech.* **MTT-22**(8):784–790 (1974).
8. W. E. Schroeder, Spurious parametric oscillations in IMPATT diode circuits, *Bell Syst. Tech. J.* **53**(7):1187–1210 (1974).
9. J. Gonda and W. E. Schroeder, IMPATT diode circuit design for parametric stability, *IEEE Trans. Microwave Theory Tech.* **MTT-25**(5):343–352 (1977).
10. F. M. Magalhaes and K. Kurokawa, A single-tuned oscillator for IMPATT characterizations, *Proc. IEEE (Lett.)* **58**:831–832 (1970).
11. K. Kurokawa, The single-cavity multiple-device oscillator, *IEEE Trans. Microwave Theory Tech.* **MTT-19**(10):793–801 (1971).
12. R. Laton, S. Simoes, and L. Wagner, A dual diode TM₀₂₀ cavity for IMPATT diode power combining, *Proc. IEEE-MTTS Int. Microwave Symp.*, Dallas, TX, 1982, pp. 129–131.
13. J. W. McClymonds, GaAs IMPATT diode transmitters, *Workshop Millimeter Wave Power Generation Beam Control*, Univ. of Alabama, Huntsville, 1993.
14. J. W. McClymonds and M. Afendykiw, GaAs IMPATT diode transmitters, *Proc. AIAA Missile Sciences Conf.*, Monterey, CA, 1994.
15. J. W. McClymonds and M. Afendykiw, GaAs IMPATT Diode Transmitters, *AIAA/BMDO Technol. Readiness Conf.*, Natick, MA, 1995.
16. R. M. Carvalho and G. H. Stilgoe, Integrated Waveguide Combiner, US Patent 5229728.

FURTHER READING

- E. L. Holzman and R. S. Robertson, *Solid-State Microwave Power Oscillator Design*, Norwood, MA: Artech House, 1992.
- K. Chang, *Handbook of Microwave and Optical Components, Vol. 2: Microwave Solid State Components*, New York: Wiley, 1990.
- G. I. Haddad, *Avalanche Transit Time Devices*, Norwood, MA: Artech House, 1973.

IMPEDANCE TRANSFORMERS AND MATCHING NETWORKS

KE WU
DOMINIC DESLANDES
YVES CASSIVI
Ecole Polytechnique
Montreal, Quebec, Canada

1. INTRODUCTION

Generally speaking, RF and microwave circuits and systems consist of multiple planar and/or nonplanar

transmission-line sections (passive elements) and active devices (e.g., transistors, diodes) that are interconnected in an appropriate manner in order to achieve specific high-frequency signal processing. In some cases, it is also possible to design a complete microwave system with only passive components. At lower frequencies (e.g., 300 MHz–10 GHz), the circuits usually involve lumped elements such as resistor, inductor, and capacitor to keep circuit dimensions small. At higher frequencies, the quality of lumped elements deteriorates rapidly, and mostly distributed elements are used. In any case, the transmission-line technique is the foundation for designing such microwave elements. In a typical microwave circuit or system, the passive part easily makes up 75% or more of the circuit real estate area. Because of different electromagnetic signal processing techniques involved in each component and also specific requirements for component-to-component signal transfer or transmission, impedance transformers, and/or matching networks are always needed.

The purpose of an impedance transformer is to transform a given impedance to a specific value in view of microwave signal transmission. An impedance-matching network may consist of more than one impedance transformer. Its design goal is to match a given impedance to a prescribed value over a frequency range of interest to ensure maximum power transfer from one place to another (e.g., from a source to a load). Impedance transformers and matching networks are perhaps the most important and most widely used microwave circuit components, which are usually passive. There also exist in practice active and electronically tunable impedance transformers and matching networks for special applications such as broadband or multiband systems design. In this case, semiconductor-based monolithic microwave integrated circuits (MMICs) are a choice of preference. Electrical (active) and/or mechanical (passive) impedance tuners, for example, are widely used in RF and microwave measurement setups, such as load-pull nonlinear and noise characterization systems. Nevertheless, most practical matching networks are fixed (passive) with respect to the center frequency, bandwidth of application, and impedance transformation (impedance ratio). Typical applications include optimizing return loss between an antenna and a low-noise amplifier for receiver, realizing low-noise performances in active circuits, providing conjugate complex matching in amplifier design, and usually matching high-contrast impedance values between a laser diode and its microwave driving circuit for optoelectronic applications.

It is imperative to mention that the definition of impedance may vary from one transmission line to another, and it usually depends on the use or operation of guided-wave mode such as transverse electromagnetic (TEM), transverse electric (TE), or transverse magnetic (TM) mode. Unfortunately, the definition of voltage and current is rather ambiguous and mode-dependent at microwave frequencies. As far as single-mode structures are concerned, this problem may be solved easily with specific definition of impedance that should be consistent for the entire circuit design. This becomes a quite complex issue for multimode non-TEM-mode structures, which still poses a challenge even today in the design of impedance

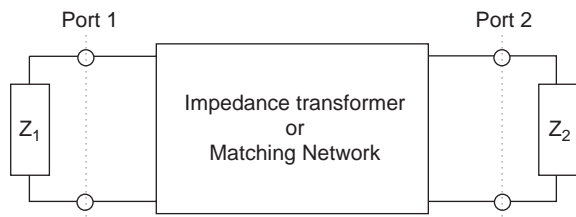


Figure 1. Basic block diagram of a two-port impedance transformer or matching network.

transformer and matching network if the classical network synthesis is used with lumped-element network parameters. This generally requires a full-wave numerical analysis and optimization of the transformer structures. In a practical design, the characteristic impedance of the transformer and matching network depends on the type of transmission line that dictates its achievable impedance range. Further, the type of transmission line used gives preference to either shunt (common voltage) or series (common current) branch connection in the formulation of equivalent circuit or network synthesis. In a microstrip line (MLINE), for example, stubs are best used in shunt-parallel connections.

A basic block diagram of impedance transformers and matching networks is shown in Fig. 1. Various design techniques are available. Techniques based on the Smith chart are popular in connection with the lumped-element network approach. Matching networks may be built from lumped or distributed elements or a combination of both. In the following, we will begin with the description of an impedance-matching network with various techniques of impedance transformers. Practical examples are also shown to highlight application features of those techniques. A comprehensive comparison is made with respect to design parameters and practical specifications. Then, commonly used line-to-line transitions are presented as a special impedance transformer or transition transformer because the impedance matching between two different lines is generally involved in the design. Among such transitions, balun transformers present a special class of microwave passive components that converts the fundamental guided mode from balanced to unbalanced or vice

versa. This is why it is called *balun* (balance-to-unbalance). In this case, the impedance may also be transformed in this line-to-line modal conversion. Usually, a balun structure deals with two different types of transmission-line geometry that are used as input and output of the circuit. A class of balun structures will be described and discussed.

2. IMPEDANCE-MATCHING NETWORK

The purpose of an impedance transformer (commonly called an *impedance-matching network*) is to transform an arbitrary load or a specific value of impedance at one reference plane into a desired value at another reference plane. Usually in the very beginning, the impedance-matching network may be handled in the design as an insert part between two circuits or two components although it is in fact an integrated part of the final circuit. Since the impedance definition may be ambiguous at microwave frequencies for non-TEM-mode transmission lines or high-order modes, the following presentation will be limited to the well-defined impedance cases such as TEM-mode impedance-matching networks. The impedance-matching process allows a circuit of interest to meet a given requirement, such as to minimize the reflection coefficient, minimize the noise, or maximize the output power of an amplifier. The reflection coefficient from a load is given by

$$\Gamma = \frac{Z_L - Z_0}{Z_L + Z_0} \tag{1}$$

where Z_L is the load impedance and Z_0 is the source impedance of the circuit. The circuit is said to be matched when the reflection coefficient is equal to zero, $\Gamma = 0$. To do so, the source and load impedances must be equal, or $Z_L = Z_0$. This condition is the basis for all impedance-matching networks.

Table 1 shows different kinds of impedance-matching networks and their principal characteristics. The element type used, bandwidth, design flexibility, and network complexity are some of the principal aspects that must be considered in the choice of a network topology. Two

Table 1. Lossless Matching Networks and Their Properties

Matching Network	Element Type	Operating Bandwidth	Network Flexibility	Network Complexity	Load Impedance	Design Technique
L network	Lumped	Narrow	Low	Low	Complex	Smith chart or analytical equation
T and Π networks		Medium	Medium	Medium	Complex	Smith chart or analytical equation
Ladder network		Large	High	High	Complex	Synthesis method
Single stub	Distributed	Narrow	Low	Low	Complex	Smith chart
Double stub		Medium	Medium	Medium	Complex	Smith chart
Filter theory		Large	Large	High	Complex	Synthesis method
Quarter-wave transformer		Narrow	None	Low	Real	Analytical equation
Multisection transformer		Large	Medium	High	Real	Synthesis method
Tapered line		Large	Large	High	Real	Analytical equation
Combination	Lumped and distributed	Small to large	Large	Low to High	Complex	Smith chart or Analytical equation

different element types are used in (ideally) lossless matching networks: (1) lumped elements such as inductors and capacitors and (2) distributed elements such as transmission-line sections and open- and short-circuit stubs. Seldom do all the networks provide the same bandwidth. The general rule is that as the number of elements used grows, the bandwidth gets wider up to a maximal value, as will be discussed in Section 2.3. Furthermore, some networks are more flexible than others. When different configurations are available and different element values can be used, much freedom is gained to meet the specifications. On the other hand, this flexibility usually leads to more complex circuits.

Generally, impedance-matching networks can be divided into two different categories: complex load-related matching networks and real load-related matching networks. In the former case, a complex load, $Z_L = R_L + jX_L$, must be transformed into a real load, Z_0 . The latter case is generally used to connect two transmission lines with different impedances, Z_1 and Z_2 . The design of these networks is achieved with different techniques. The Smith chart is still the basic tool for the designer. However, analytical equations are available for some designs, and synthesis methods are applied in the design of multisection matching networks.

2.1. Lumped Elements

With inductors and capacitors, any complex load on the Smith chart can be transformed into real impedance. The special case of a straight reactance cannot be matched with a lossless network. This case will be discussed in Section 2.3. Commercial off-the-shelf lumped elements are popular at low frequencies, up to ~ 3 GHz. Beyond this frequency, parasitic elements are too important to ignore. For MMIC chip circuits, the frequency limit is largely extended and some lumped elements are even designed above 100 GHz.

2.1.1. L Network. The L networks are made up of two reactances, one in series and one in parallel. There are eight different configurations, but none of them can be used to match every load on the Smith chart. However, there is always more than one choice to match a given load. The eight configurations and their matching area on the Smith chart are shown in Fig. 2. The area in gray shows the locations of loads that cannot be matched with the respective network.

The simplest way to design an L network is to use the Smith chart. The method is explained in detail by Gonzalez [1, Chap. 2]. Analytical equations are also available

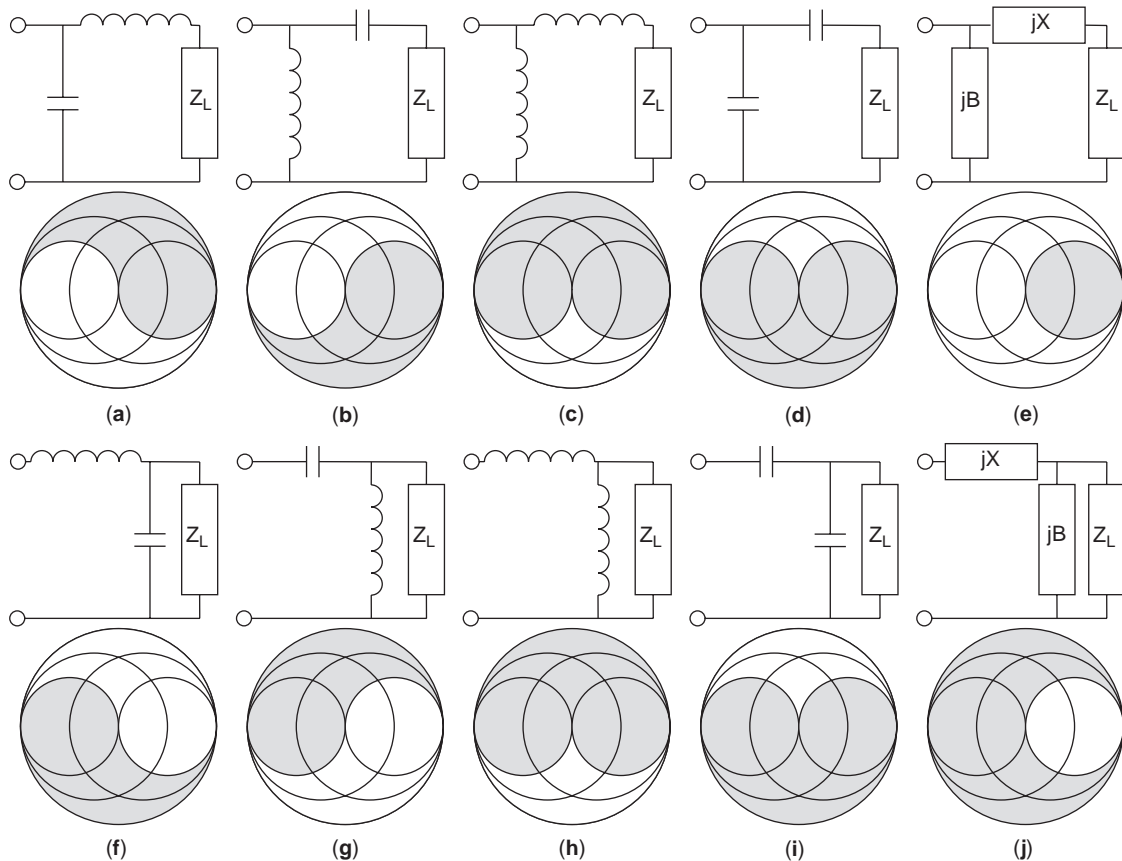


Figure 2. Eight different configurations for the L network: series-parallel (a–d) and parallel-series (f–i). The areas that cannot be matched for a given configuration are shown in gray. Series-parallel and parallel-series are represented in a more general way by diagrams (e) and (j), where the gray area on the Smith chart is associated with the analytical equation.

for this network [2]. In this case, the Smith chart is first divided in two regions delimited by the circle $1 + jx$. If the normalized load, Z_L/Z_0 , falls inside the circle, the circuit shown in Fig. 2j is used. The reactance values are then given by

$$B = \frac{X_L \pm \sqrt{R_L/Z_0} \sqrt{R_L^2 + X_L^2 - Z_0 R_L}}{R_L^2 + X_L^2} \tag{2}$$

$$X = \frac{1}{B} + \frac{X_L Z_0}{R_L} - \frac{Z_0}{B R_L} \tag{3}$$

Equations (2) and (3) indicate that there are always two different networks available to match a load. These two possible choices are the circuits shown in Figs. 2f and 2g. If the normalized load is outside circle $1 + jx$, the circuit in Fig. 2e is used. The reactance values are then calculated by using the following equation:

$$X = \pm \sqrt{R_L(Z_0 - R_L)} - X_L \tag{4}$$

$$B = \pm \frac{\sqrt{(Z_0 - R_L)/R_L}}{Z_0} \tag{5}$$

Once again, these equations suggest that there are always two possible configurations to match a load, thus giving some flexibility to the designer.

2.1.2. T and Π Networks. The T and Π networks are shown in Fig. 3. These networks are essentially L networks in which one element has been added. There are 16 possible configurations that provide much more freedom than do the L networks. This freedom can be used to obtain the desired element values or to control the operating bandwidth. Kuroda’s identities are used to transform an L network into a T or Π network [3]. Furthermore, a T network can be transformed to a Π network, or vice versa, with the following relations:

$$\begin{aligned} Z_A &= \frac{Z_1 Z_2}{Z_1 + Z_2 + Z_3} & Z_1 &= \frac{Z_A Z_B + Z_B Z_C + Z_A Z_C}{Z_C} \\ Z_B &= \frac{Z_1 Z_3}{Z_1 + Z_2 + Z_3} & Z_2 &= \frac{Z_A Z_B + Z_B Z_C + Z_A Z_C}{Z_B} \\ Z_C &= \frac{Z_2 Z_3}{Z_1 + Z_2 + Z_3} & Z_3 &= \frac{Z_A Z_B + Z_B Z_C + Z_A Z_C}{Z_A} \end{aligned} \tag{6}$$

Matching a load with a T or Π network is usually done with the Smith chart. However, analytical expressions are also available for some T networks [3].

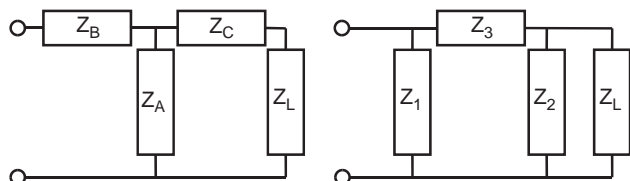


Figure 3. The T and Π matching networks.

2.1.3. Ladder Network. As we have seen, adding an element to the L network increases the degree of freedom in the design. This freedom can be used to improve the bandwidth. As more elements are added, the bandwidth can be increased, but there is a limit, as we will see in Section 2.3. To design a ladder network, synthesis methods should be applied. As in the design of filters, Butterworth or Chebyshev frequency responses can be synthesized for the ladder networks. The technique details are presented in detail in Ref. 4, and are not reproduced in this article.

2.2. Distributed Elements

Most matching networks working at microwave frequencies are designed with distributed elements. Transmission-line sections are easy to fabricate and very flexible, presenting low-loss characteristics. The basic building blocks of distributed matching networks are transmission-line sections, open- and short-circuits stubs. These stubs are theoretically equivalent because a quarter-wavelength line can transform a stub from its open state to its short counterpart and vice versa. In practice, both circuits are quite different from each other. It is not always possible or easy to manufacture a circuit having both stubs with a given technology. With the MLINE technology, for example, an open circuit is easier in the implementation. This is not the case for the rectangular waveguide, where only the short circuit is usable. In all cases, if both stubs are available, the one that requires the shortest physical length should be used in order to minimize the loss and also possibly maximize the bandwidth.

2.2.1. Single-Stub Network. The single-stub network is the most common way to match a load, which has 2 degrees of freedom, namely, the linelength and the stub length. The topology shown in Fig. 4 is a single parallel stub network. The Smith chart is the usual tool in the design of this circuit, and the method has been explained in many references [1,2,4] and will not be repeated here. The network can also be designed with analytical equations. With the parallel stubs, it is easier to work with admittance. The first segment, going from the load to the stub, has admittance equal to Y_0 and an electrical length equal to θ_1 . The admittance looking into the input of the

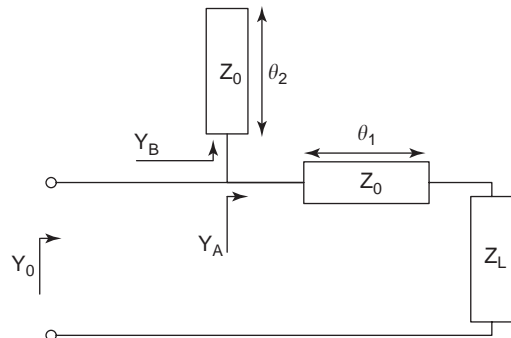


Figure 4. A single-stub matching network.

transmission-line section is

$$Y_A = G_A + jB_A = Y_0 \frac{Y_L + jY_0 \tan \theta_1}{Y_0 + jY_L \tan \theta_1} \quad (7)$$

The electrical length θ_1 must be chosen so as to match the real part of the admittance: $G_A = Y_0$. Then, a parallel stub of admittance Y_0 and electrical length θ_2 is added to cancel out the reactive part. The admittance looking into the input of this stub, for the open/short-circuit case, is

$$\begin{aligned} \text{Open circuit: } Y_B &= jB_B = jY_0 \tan \theta_2 \\ \text{Short circuit: } Y_B &= jB_B = -jY_0 \cot \theta_2 \end{aligned} \quad (8)$$

The electrical length θ_2 must be selected to cancel out the reactive part; thus $B_B = -B_A$ and yields

$$Y_A + Y_B = Y_0 \quad (9)$$

An analytical solution for θ_1 and θ_2 , given in terms of Z_L and Z_0 , is found in Ref. 2. Parallel stubs are easy to design using MLINE. However, there are some transmission lines such as coupled lines, where a serial stub is easier to design. The design steps to match a load are the same when working with a serial stub as with a parallel one, but Eqs. (7)–(9) are calculated with impedance instead of admittance.

2.2.2. Double-Stub Network. With a single-stub network, the length between the load and the stub is a variable related to the value of the load. In some cases it is better to have the stub at a fixed position, for example, in the case of designing a tunable matching network in which the stub length is easier to change than its position. This can be done by using two stubs. The double-stub matching network is widely used to design tuners. The circuit is shown in Fig. 5 with two parallel stubs. Serial stubs are also used in the same way. This type of network cannot match all the loads on the Smith chart. There is always a blind zone that is impossible to match. To minimize this area, the distance between the two stubs must be kept as short as possible. This distance is, however, limited by the physical size of each stub. Furthermore,

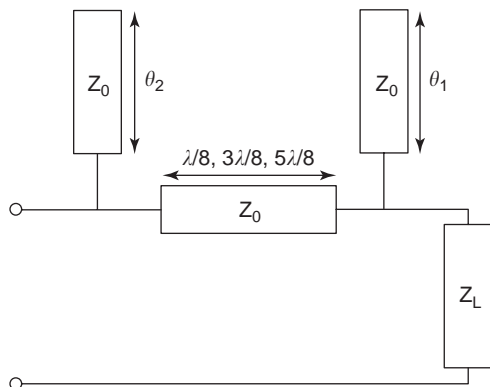


Figure 5. A double-stub matching network.

spacing close to 0, $\lambda/2$, and their multiples are too frequency-sensitive to be of interest. In practice, spacing equal to $\lambda/8$, $3\lambda/8$, or $5\lambda/8$ is usually chosen. The double-matching technique makes use of the Smith chart or analytical equations in finding the length of each stub [2].

2.2.3. Filter Theory for Designing Matching Networks. As can be seen in Section 2.1, increasing the number of elements make it possible to design matching networks with a wider bandwidth. In the same way, multisection distributed-element networks are usually used to improve the bandwidth. Filter synthesis techniques are also applied in the design of such circuits. The reader is referred to Ref. 3 for a complete explanation of the synthesis method.

2.2.4. Quarter-Wave Transformer. All the matching networks presented in the preceding sections can be used to match a complex load. Another class of matching networks is used only to match real loads, presented below. Although those circuits seem limited, they are used largely to connect two transmission lines of different impedances and to design various transitions. The most common network applied to adapt two real impedances is the quarter-wave transformer, as shown in Fig. 6. The impedance looking into the input of the quarter-wave transformer is

$$Z_{\text{IN}} = \frac{Z_m^2}{Z_2} \quad (10)$$

To match both lines, one should have $Z_{\text{IN}} = Z_1$. The quarter-wavelength line impedance must be

$$Z_m = \sqrt{Z_1 Z_2} \quad (11)$$

The bandwidth for this circuit is related to the line impedance at the input and at the output. The closer they are, the wider the bandwidth is. It becomes infinite when the impedances are equal.

2.2.5. Multisection Transformer. With only one section, the bandwidth is limited. As we increase the number of sections, a wider bandwidth is obtained. The multisection transformer can be synthesized with the well-established Butterworth or Chebyshev frequency response. Impedance values for various numbers of sections have already been tabulated [2,4]. The normalized impedance value of each section is available for many Z_2/Z_1 ratios.

2.2.6. Tapered-Line Transformer. If we increase the number of sections to the infinite, a tapered line is formed. However, it has an infinite length, which is not of practical

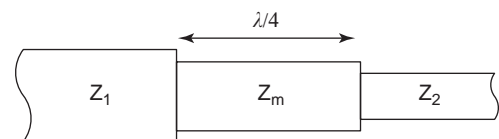


Figure 6. A quarter-wavelength transformer.

value. The tapered line of finite length is still an excellent matching circuit. The simplest taper is the linear one, and it requires very little calculation, but does not provide a wide bandwidth. Exponential taper increases the bandwidth and is still easy to design. Many other tapers have been proposed, such as in the triangular [2], cosine-squared, and parabolic configurations [5]. With all these tapers available for the design, one may wonder which one is the best. The taper proposed by Klopfenstein [6] is optimum in the sense that it provides the shortest length for a given reflection coefficient. However, the Klopfenstein taper presents a step at both ends. Sometimes, these steps are undesirable because they generate high-order modes and radiation loss. The taper proposed by Hecken then becomes optimum [7]. For a desired reflection coefficient, this profile provides the shortest length for a taper without steps.

Although there are many different tapers, the design technique is fundamentally the same for all of them. Let us begin with a topology shown in Fig. 7. The tapered line design is always done at the lowest frequency of interest. In the first step, the impedance variation as a function of the position $Z(z)$ is formulated. The impedance variations, for the most common tapers, are listed in Table 2. Knowing the impedance, one can evaluate the reflection coefficient as a function of the taper length using the following equation:

$$\Gamma = \frac{1}{2} \int_{z=0}^L e^{-2j\beta z} \frac{d}{dz} \ln \left(\frac{Z(z)}{Z_1} \right) dz \quad (12)$$

Analytical values for the linear [8], the exponential [2], the triangular [2], the Klopfenstein [6], and the Hecken [7] tapers have been obtained and they are available in the literature. If we know the reflection coefficient for an arbitrary length, we can find the minimum length providing a desired reflection coefficient. With this length L and the equations in Table 2, the impedance variation as a function of the position z is then calculated. The impedance taper must then be transformed to a physical taper. Computing the impedance at several points and then finding the physical dimensions from this impedance is the standard method used to generate the dimensions of the taper. The number of points must be large enough to obtain a smooth and continuous taper.

2.3. Fano's Criterion

In Sections 2.1.3 and 2.2.3, a multielement network that was used to improve the bandwidth was described. However, what is the maximum achievable bandwidth? Bode's [9] work and Fano's [10] work have answered this question. For a lossless matching network, the reflection

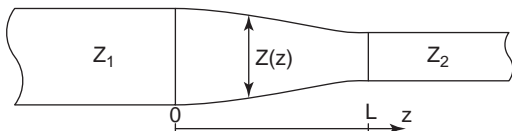


Figure 7. Impedance transformer design with the tapered line.

Table 2. Tapered-line Impedance Z as a Function of Position z (with Taper Length L)

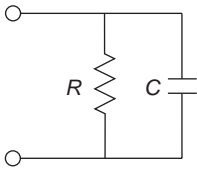
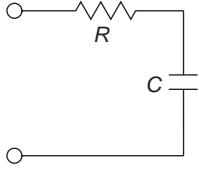
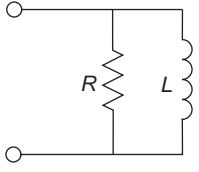
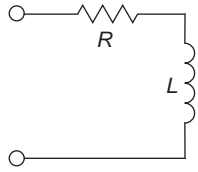
Taper	$Z(z)$
Linear	$Z(z) = Z_1 + \frac{z}{L}(Z_2 - Z_1)$
Exponential	$Z(z) = Z_1 e^{az}$ $a = \frac{1}{L} \ln \left(\frac{Z_2}{Z_1} \right)$
Triangular	$Z(z) = Z_1 e^{2(z/L)^2 \ln(Z_2/Z_1)}$ for $0 \leq z \leq L/2$ $Z(z) = Z_1 e^{(4z/L - 2z^2/L^2 - 1) \ln(Z_2/Z_1)}$ for $L/2 \leq z \leq L$
Cosine-squared	$Z(z) = Z_1 \cos^2 az$ $a = \frac{1}{L} \cos^{-1} \left(\frac{Z_2}{Z_1} \right)$
Parabolic	$Z(z) = (\sqrt{Z_1} + az)^2$ $a = \frac{1}{L} (\sqrt{Z_2} - \sqrt{Z_1})$
Klopfenstein	$\ln(Z(z)) = \frac{1}{2} \ln(Z_1 Z_2) + \frac{\Gamma_0}{\cosh A} A^2 \phi \left(2 \frac{z}{L} - 1, A \right)$ $A = \cosh^{-1} \left(\frac{\Gamma_0}{\Gamma_m} \right), \quad \Gamma_0 = \frac{Z_2 - Z_1}{Z_2 + Z_1}$ $\phi(x, A) = -\phi(-x, A) = \int_0^x \frac{I_1(A\sqrt{1-y^2})}{A\sqrt{1-y^2}} dy$ $I_1(x)$ = first-kind modified Bessel function Γ_m = maximum desired reflection coefficient
Hecken	$\ln(Z(z)) = \frac{1}{2} \ln(Z_1 Z_2) + \frac{1}{2} \ln \left(\frac{Z_1}{Z_2} \right) \psi \left(2 \frac{z}{L} - 1, B \right)$ $B = \sqrt{(\beta L)^2 - 6.523}$ $\psi(x, A) = -\psi(-x, A) = \frac{B}{\sinh B} \int_0^x \frac{I_0(B\sqrt{1-y^2})}{\sqrt{1-y^2}} dy$ $I_0(x)$ = first-kind modified Bessel function β = propagation constant at lowest frequency

coefficient and the bandwidth are related to each other by the following equation

$$\int_0^\infty \ln \frac{1}{|\Gamma(\omega)|} d\omega \leq K \quad (13)$$

where K is a constant related to the load. Equation (13) shows that the area under the reflection coefficient is smaller or equal to a constant K . The value of K for the RC and RL loads is tabulated in Table 3, where ω_0 is the center frequency of the matching bandwidth. Several observations can be made from this equation: (1) a perfect matching, $\Gamma = 0$, can be obtained at only a finite number of frequencies. It is impossible to have a perfect matching over a frequency band; (2) the bandwidth can be increased at the expense of the reflection coefficient—bandwidth and reflection coefficient are exchangeable quantities when matching a load; and (3) if the load is purely resistive, for example, the capacitance is equal to zero in a parallel RC network; the value of K goes to infinity. Thus, multi-section or the tapered-line transformers have an infinite theoretical bandwidth. However, the number of section or the length also increases to infinity. Finally, if the quality factor is infinite, for example, the resistance is infinite in the parallel RC network, the value of K is equal to zero. A reactive load cannot be matched with a lossless network. Incidentally, if the quality factor of the load increases, the maximum area under the reflection curve decreases.

Table 3. K Values for RC and RL Networks

Load Type			
			
$K = \frac{\pi}{RC}$	$K = \pi\omega_0^2 RC$	$K = \frac{\pi\omega_0^2 L}{R}$	$K = \frac{\pi R}{L}$

2.4. Other Types of Impedance Transformer and Matching Networks

There are many other variations of matching networks. A single transmission line can be used as a matching network with proper impedance and length [11]. With this technique, however, only 25% of the Smith chart can be matched. This region can be increased up to 75% if two serial transmission lines instead of a single one are used [12]. Analytical expressions are available for design of the required length and impedance [13]. There are also a broad range of combinations between different matching networks. A quarter-wavelength line can be used with parallel stubs [14]. The respective advantages of lumped and distributed matching networks can also be combined [15]. The coupled line provides the same behavior as does a quarter-wavelength transformer [16]. The hybrid coupler is also a basic building block to design matching networks in a single section [17] or a multiple section [18]. Special impedance-matching networks, some of which have more recently emerged with respect to the development of novel RF and microwave technologies, are described below.

2.4.1. Tunable Matching Networks. The matching networks that we have presented so far are used to match a fixed load. Sometimes, the impedance of the load changes and a tunable matching network becomes necessary. Tunable matching networks can be divided into two categories: adaptative tunable matching networks and selective tunable matching networks. In the former case, the tunable matching network makes it possible to keep a good matching over a variable condition. This variation may come from manufacturing tolerance, temperature change, aging effects, and interaction with the surroundings (detuning effects), to name only a few examples. In the latter case, the matching network is used to select an appropriate value, such as a frequency band in a filter, a particular gain in an amplifier, an operating frequency in an oscillator, or a beaming angle in a scanning beam antenna. Such a tunable matching network is then an effective tool to accomplish critical tasks. The adaptative or selective networks are mostly designed using three categories of elements: varactor diodes, RF microelectromechanical systems (MEMS), and ferrite or ferroelectric materials. Principal characteristics of these elements are

briefly explained as follows. Ferrites have been widely used and are well documented in the literature and thus are not included here.

2.4.1.1. Varactor Diode Techniques. Semiconductor diodes are used to create variable-capacitance components such as varactors. When a reverse voltage is applied to the diode, a depletion region is created whose thickness can be tuned electronically, thus modifying the capacitance. Varactor diodes have been widely used as tuning elements for more than 40 years. This is a very mature technology with a wide range of commercially available components. The principal limitation in a varactor diode is its low quality factor, which suffers from high series resistance of the diode junction.

2.4.1.2. RF MEMS Techniques. RF MEMS technology has generated significant interest [19–21]. Generally, MEMS are made up of two parts: a mechanical part and an electrical part. The mechanical part contains a mobile section that creates the tuning capability controlled by the electrical part. In the design of a tunable matching network, MEMS are used for variable capacitors, which include parallel-plate and interdigital capacitors. Generally, the tuning range is large with a relatively low voltage.

2.4.1.3. Ferroelectric Techniques. The integration of ferroelectric material such as barium strontium titanate (BST) involving the design of tunable microwave devices is relatively new [22]. Different from the techniques described in Sections 2.4.1.1 and 2.4.1.2, a ferroelectric circuit achieves its tuning capability by modifying its dielectric permittivity with respect to an externally applied electric field. In addition, an unusually high dielectric constant of the ferroelectrics can be used to miniaturize the circuits, which are of critical importance for tunable matching networks at lower microwave frequencies such as the emerging software-defined radio. Metal-insulator-metal (MIM) capacitors are the most common variable devices based on this technology. Other solutions are studied, such as double-stub variable matching networks [23].

2.4.2. Active Matching Networks. When a broadband matching network is required, the above-described passive matching networks are not always the best solutions.

The size of the structure may be prohibitively large because of wavelength limitations, which may pose a challenging problem in the design of MMICs in spite of lumped-element techniques. On the other hand, the passive impedance matching may also be loss-limited for some applications. In the design of a RF driving circuitry for multioctave broadband direct modulation with a very-low-impedance laser, it is rather difficult to use a passive matching network. In this case, an active matching network becomes necessary, which may be made of transistors or MMIC chips. FET transistors operating in a common gate provide a good input match over a wide bandwidth, which has been used, for example, to design multioctave amplifiers [24,25]. Details related to the active matching techniques are beyond the scope of this article, and some references may be found in Ref. 26.

3. TRANSMISSION-LINE TRANSITIONS

The above-described matching techniques allow for a high-quality connection between two different impedance circuits or components of the same microwave transmission structure such as MLINE and waveguides. However,

the connection may be required between two circuits or components made of different transmission structures. In this case, the transmission-line transitions should be used, which possibly involve mode conversion and impedance matching. As we discussed earlier, the impedance definition may vary from line to line, suggesting that the design of such transition structures is much more involved. These transitions are essential for a wide range of microwave circuits such as mixer, filter, and antenna feeder. In most practical cases such as the connection of active elements to low-loss/high-quality waveguide components, the transitions play a vital role in maintaining the performance of the whole circuit.

The design of a transition between two different transmission structures depends on the electromagnetic field or modal configuration of each structure [27]. If the electromagnetic fields or modes have similar profiles, an impedance taper can be designed such that the shape of one transmission line is gradually altered so to physically match that of the other transmission line, as detailed in Section 2.2.6. This seems to be the best option in terms of the insertion loss and bandwidth. If those electromagnetic fields or modes are incompatible, an electromagnetic (noncontact) coupling technique between the two structures is preferred.

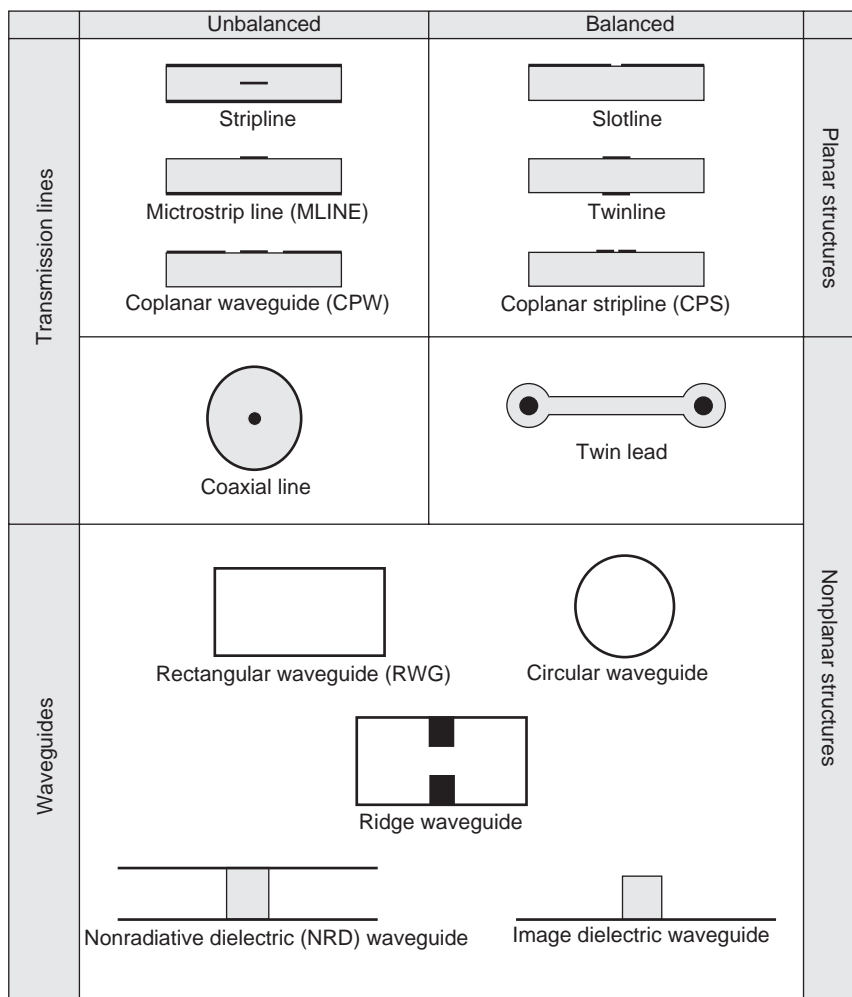


Figure 8. Transmission structure classification.

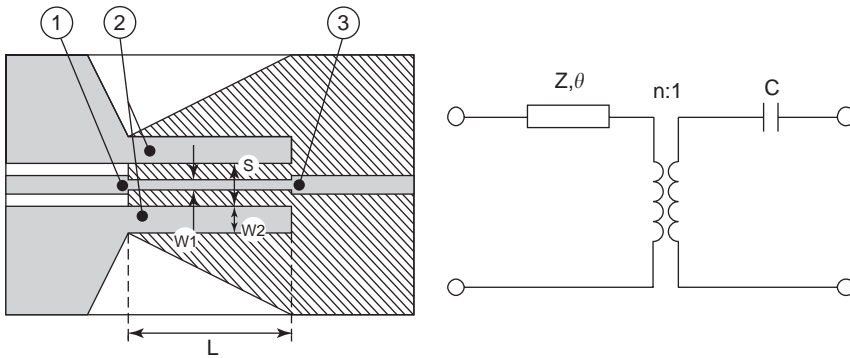


Figure 9. Topology of the MLINE-CPW transition proposed in Ref. 30 with its equivalent model: (1) \Rightarrow CPW; (2) \Rightarrow transformer; (3) \Rightarrow MLINE.

In the following, we begin by classifying the principal transmission structures used in the design of RF, microwave, and millimeter-wave circuits. Then, we will show different examples of transitions design illustrating planar-to-planar transitions and planar-to-nonplanar transitions. We will discuss differences among impedance taper transitions, electromagnetic coupling transitions, and special balanced line-unbalanced line (balun) transitions.

3.1. Transmission Structures

To classify the transmission structures (see Fig. 8), three distinct criteria are used in this article; the first is related to the possible TEM mode transmission lines or non-TEM-mode waveguides. The second looks into the structure whether it is planar or nonplanar. The last one is in connection with balanced and unbalanced topologies, which apply only to TEM-mode transmission lines. A balanced transmission line has by definition a transmission line that has equally distributed resistance, capacitance, inductance, and conductance elements between its conductors. Usually this means that the two conductors of a balanced transmission line are of the same size, opposite to an unbalanced transmission line having a small conductor and a wide ground plane. This also implies that a metallic sheet could be placed in the middle of a balanced line without affecting it, which is analog to the electric symmetry plane (electric wall) that exists in some propagating modes in waveguide. A variety of transmission-line structures are used in RF, microwave and millimeter-wave circuits, many of which are simple derivatives of the basic structures shown in Fig. 8.

3.2. Planar-to-Planar Transitions

Planar-to-planar transitions are very useful in the realization of wideband mixers, printed antennas, measurement setups, and multifunction modules (MFMs). Examples presented in the following subsequent sections constitute the most popular ones.

3.2.1. Microstrip Line (MLINE)-CPW Transition. Transitions between MLINE and CPW have been realized in many ways. For MMIC, a transition between MLINE and CPW is necessary for measurement purposes with CPW probes directly in contact with the circuit wafer. A model

for this transition was developed in Ref. 28. For cases where the MLINE and CPW are placed on opposite sides of the dielectric substrate, a broadband transition without via hole was designed by Lin [29]. For cases where both MLINE and CPW are placed on the same side of the dielectric substrate, Houdart and Aury [30] have proposed a transition using the coupling between the ground planes of the MLINE and CPW. The layout of the transition is illustrated in Fig. 9. A design approach based on the quasi-TEM approximation was proposed.

3.2.2. MLINE-to-Twinline Balun. This transition is particularly useful in the realization of printed dipole antenna array [31–33]. Since both transmission lines have a very similar electromagnetic field orientation, a simple impedance taper between both the lines can be used as shown in Fig. 10. The length L is usually equal to a quarter-wavelength in the middle of the band.

3.2.3. Planar Balun Transitions. In the design of a planar mixer or a planar magic tee, the use of printed Marchand and/or double-Y baluns is necessary for wideband operation and high isolation. Trifunovic and Jokanovic [34] provide an overview of these baluns, which are illustrated in Fig. 11. Marchand type baluns offer bandpass frequency

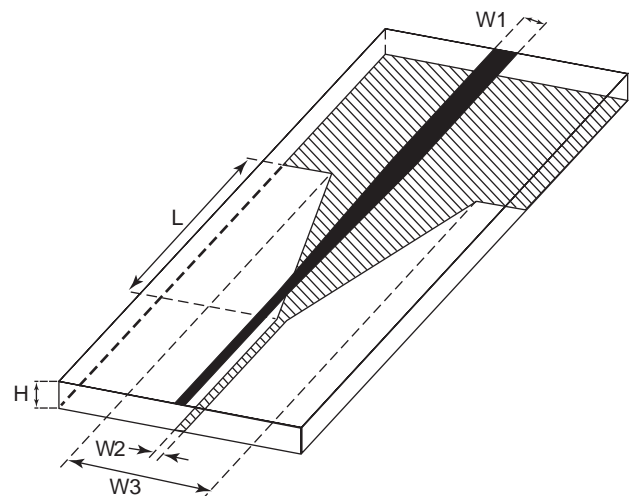


Figure 10. Topology of the MLINE-to-twinline balun.

DOUBLE Y BALUN	MARCHAND BALUNS		
	Second order	Fourth order	
			MLINE - SLOTLINE
			CPW - SLOTLINE
			CPW _{Gap} - CPS

Figure 11. Printed balun topologies.

response. Double-Y baluns could provide allpass frequency response. Because of the limitation on the realization of perfect open and short circuits in planar technologies, the allpass response begins at DC and is limited to a certain maximum frequency. This maximum frequency is designed as a function of the length of open and short circuits of the junction, which in turn depend on the gaps used in the realization of CPW, slotline, or CPS. Note that the use of CPW with a slotline or a CPS allows the realization of uniplanar mixer circuits, which is of great importance in MMIC technology.

3.3. Nonplanar-to-Planar Transitions

Generally, the coaxial-line technology is useful up to 65 GHz. Therefore, transitions between a coaxial line and a planar circuit are very important for circuit measurements and module interconnects. At higher frequencies, transitions between rectangular waveguides and planar circuits are more appropriate. Three typical application examples are described below.

3.3.1. Coaxial Line-to-MLINE Transition. The transition between coaxial line and MLINE is of critical importance in the RF industry. Many types of connector layout are now available for RF and microwave circuit designer. We can divide the most commonly used connectors into three basic types: (1) the inline connector, (2) the through-ground connector, and (3) the top connector (see Fig. 12).

Directly applicable design models are not available for these transitions. A resonance measurement method was used to characterize them [35]. The method is accurate and has been applied to many types of coaxial transition.

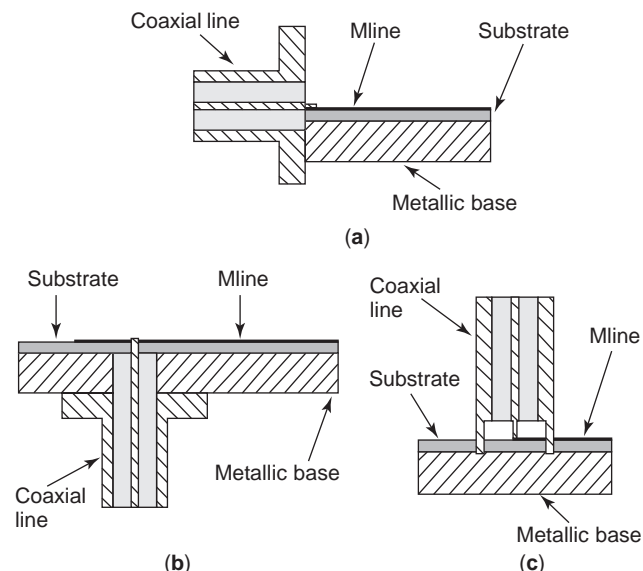


Figure 12. Cutaway view of the three basic coaxial line-to-MLINE transition topologies: (a) inline transition, (b) through-ground transition; (c) top transition.

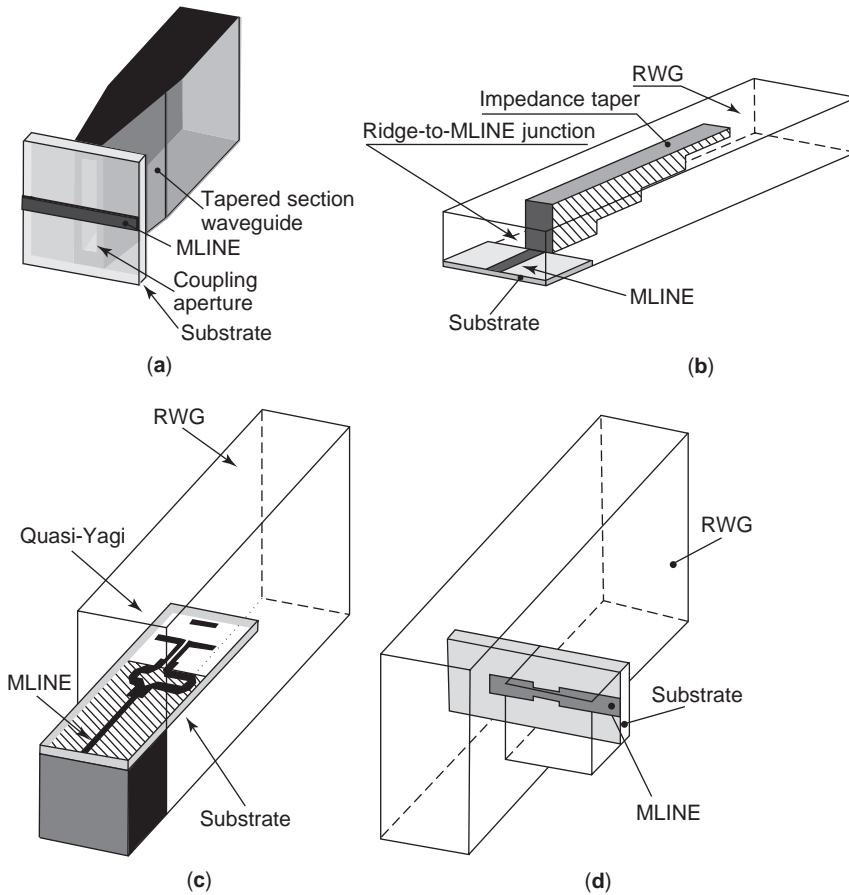


Figure 13. Topology of four different transitions between MLINE and RWG: (a) aperture coupling [40]; (b) ridge waveguide approach [41]; (c) quasi-Yagi antenna in the E plane [43]; (d) E -plane probe [47].

For the through-ground transition, an interesting example was illustrated in Ref. 36.

3.3.2. Rectangular Waveguide (RWG)-to-MLINE Transition. Different strategies have been developed for designing MLINE-to-RWG transitions. The first is an aperture coupling placed at the end of the RWG [37–40]. The second is a complex structure consisting of an MLINE-to-RWG transition through an intermediate ridge waveguide [41,42]. Another configuration uses a printed quasi-Yagi antenna placed at the end of the RWG [43]. It seems that the simplest topology is the use of an MLINE E -plane probe inside the RWG [44–49]. All topologies are illustrated in Fig. 13. All these transition geometries provide a great flexibility in the design process.

Aperture coupling generally tends to be narrowband except for the design in Ref. 40, where the use of a waveguide taper considerably increases the bandwidth. The MLINE–Ridge–RWG transition provides low loss and very wide bandwidth. Nevertheless, its construction is difficult and expensive. The quasi-Yagi antenna transition gives a good bandwidth with acceptable performance. The E -plane probe allows a good performance over a wide bandwidth, but a quarter-wavelength backcavity is necessary in this case.

3.3.3. RWG-to-Slotline (Finline) Transition. The transition between RWG and slotline can be made wideband and low-loss [50–52]. Figure 14 illustrates a general topology

of the transition. A simple geometric design approach can be used for the realization of the transition [51]. On the other hand, a sophisticated optimization algorithm can be used for critical applications where the minimum return loss is required [52].

3.4. Nonplanar-to-Nonplanar Transitions

A large number of useful transitions between nonplanar structures have been studied and developed. Impedance

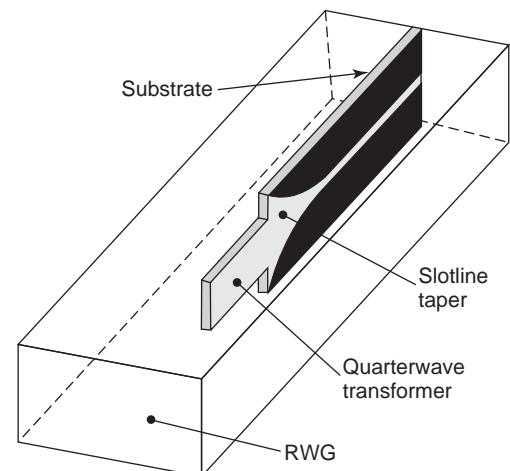


Figure 14. Topology of the RWG-to-slotline transition.

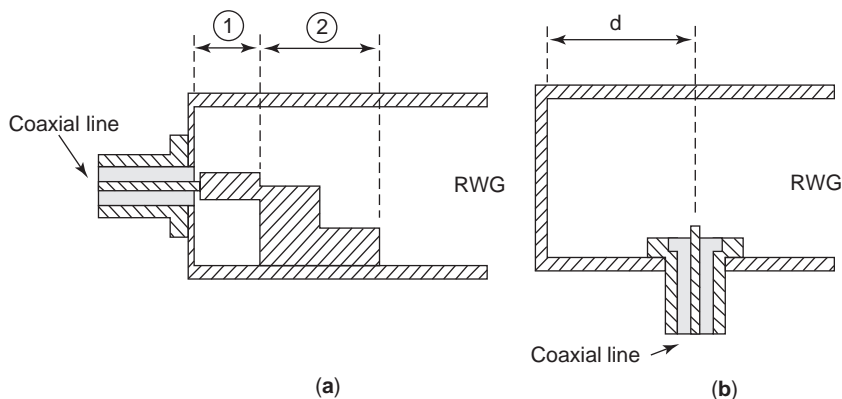


Figure 15. Cutaway view of coaxial line-to-RWG transitions: (a) inline transition using intermediate square coax (1) and ridge waveguide (2) stages; (b) perpendicular wideband transition.

taper can be used effectively when the electromagnetic field orientations (mode profiles) between the two waveguides are similar. Some types of transition make use of a small antenna (loop or monopole), while the others use small-aperture coupling. We illustrate in the following each type of transition with an example.

3.4.1. Coaxial Line-to-RWG Transition. The geometry of the transition between coaxial line and RWG can be designed in two ways, as illustrated in Fig. 15. The first is inline (end-launched) [53,54], meaning that both the coaxial line and the RWG are on the same axis. The second topology places the RWG and the coaxial line perpendicular to each other [55]. The geometry of the transition can be an important criterion of selection in system planning. Usually, the perpendicular type provides the widest bandwidth for the smaller length.

The general topology of inline configuration was described by Chan et al. [53]. This transition can provide wideband operation by using an intermediate ridge waveguide section in the transition. The fabrication cost of this transition limits its application to specific cases.

In the perpendicular configuration using the inner conductor of the coaxial line a quarter-wavelength monopole antenna is contained inside the RWG. It was found [55] that the best topology for the transition was to fix $d = \lambda g/4$ at the average frequency of the RWG and to adjust the

dimensions of the monopole for optimum return loss (see Fig. 15). This provides a $VSWR \leq 1.02$ over the entire useful bandwidth of the RWG.

3.4.2. NRD Guide–RWG Transition. The NRD guide is a special class of low-cost dielectric guide providing superior performance at millimeter-wave frequencies [56]. The hybrid LSM_{10} mode is the preferred mode of operation because of its low-loss characteristics. For the measurement purposes of NRD guide components, a high-performance transition between NRD guide and RWG was developed in Ref. 57. Since the TE_{10} mode of RWG has similar electromagnetic field orientations with reference to the LSM_{10} mode, continuous-impedance tapers [7] are used in the design of the transition as illustrated in Fig. 16. This transition is divided into two sections. The first is a transition between a RWG and a dielectric-filled RWG. The second is between the dielectric-filled RWG and the NRD guide.

BIBLIOGRAPHY

1. G. Gonzalez, *Microwave Transistors Amplifiers, Analysis and Design*, 2nd ed., Prentice-Hall, Englewood Cliffs, NJ, 1997.
2. D. M. Pozar, *Microwave Engineering*, 2nd ed., Wiley, New York, 1998.
3. I. Bahl and P. Bhartia, *Microwave Solid State Circuit Design*, Wiley, New York, 1988.
4. G. Matthaei, L. Young, and E. M. T. Jones, *Microwaves Filters, Impedance-Matching Networks, and Coupling Structures*, Artech House, Norwood, MA, 1980.
5. M. J. Ahmed, Impedance transformation equations for exponential, cosine-squared, and parabolic tapered transmission lines, *IEEE Trans. Microwave Theory Tech.* **MTT-29**(1):67–68 (Jan. 1981).
6. R. W. Klopfenstein, A transmission line taper of improved design, *Proc. IRE* **44**:31–51 (Jan. 1956).
7. R. P. Hecken, A near-optimum matching section without discontinuities, *IEEE Trans. Microwave Theory Tech.* **MTT-20**(11):734–739 (Nov. 1972).
8. A. M. Khilla, Optimum continuous microstrip tapers are amenable to computer-aided design, *Microwave J.* **26**:221–224 (May 1983).
9. H. W. Bode, *Network Analysis and Feedback Amplifier Design*, Van Nostrand, New York, 1945.

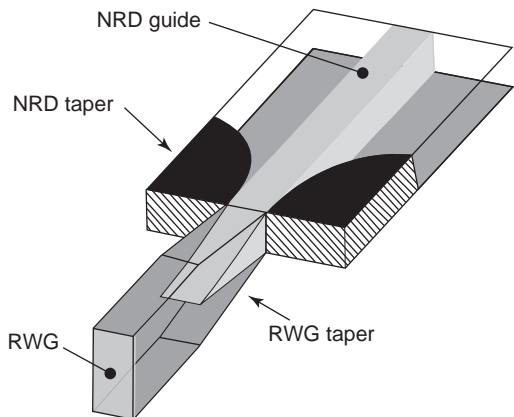


Figure 16. Topology of a typical NRD guide–RWG transition.

10. R. M. Fano, Theoretical limitations on the broad-band matching of arbitrary impedances, *J. Franklin Inst.* **249**:57–83, 139–154 (Jan.–Feb. 1950).
11. R. M. Arnold, Transmission line impedance matching network using smith chart, *IEEE Trans. Microwave Theory Tech.* **MTT-22**:977–978 (Nov. 1974).
12. J. M. Leopoff, Matching: When are two lines better than one? *Microwaves* **20**:74–78 (March 1981).
13. H. Jasik, *Antenna Engineering Handbook*, McGraw-Hill, New York, 1961, Chap. 31.
14. H. A. Atwater, Reflection coefficient transformations for phase-shift circuits, *IEEE Trans. Microwave Theory Tech.* **MTT-28**:563–568 (June 1980).
15. R. Levy, Synthesis of mixed lumped and distributed impedance-transforming filters, *IEEE Trans. Microwave Theory and Tech.* **MTT-20**:223–233 (March 1972).
16. K. Chang, *Handbook of Microwave and Optical Components*, Wiley-Interscience, New York, 1989, Vol. 1, Chap. 3.
17. R. K. Gupta, S. E. Anderson, and W. J. Getsinger, Impedance-transforming 3-dB 90° hybrids, *IEEE Trans. Microwave Theory Tech.* **35**:1303–1307 (Dec. 1987).
18. S. Kumar, C. Tannous, and T. Danshin, A multisection broad-band impedance transforming branch-line hybrid, *IEEE Trans. Microwave Theory Tech.* **43**:2517–2523 (Nov. 1995).
19. G. M. Rebeiz, *RF-MEMS Theory, Design and Technology*, Wiley, New York, 2003.
20. V. K. Varadan, K. J. Vinoy, and K. A. Jose, *RF-MEMS and Their Applications*, Wiley, New York, 2003.
21. H. J. De Los Santos, *RF-MEMS Circuit Design for Wireless Communications*, Artech House, Norwood, MA, 2002.
22. B. Noren, Thin film barium strontium titanate (BST) for a new class of tunable RF components, *Microwave J.* **47**:210–220 (May 2004).
23. A. Deleniv, T. Hu, H. Jantunen, S. Leppavuori, and S. Gevorgian, Tunable ferroelectric components in LTCC technology, *IEEE Int. Microwave Symp. Digest*, June 2003, pp. 1997–2000.
24. V. Pauker and M. Binet, Wideband high gain small size monolithic GaAs FET amplifiers, *IEEE Int. Microwave Symp. Digest*, June 1983, pp. 81–84.
25. W. C. Petersen, D. R. Decker, A. K. Gupta, J. Dully, and D. R. Chen, A monolithic GaAs 0.1 to 10 GHz amplifier, *IEEE Int. Microwave Symp. Digest*, 1981, pp. 354–355.
26. K. B. Niclas, Active matching with common-gate MESFETs, *IEEE Trans. Microwave Theory Tech.* **MTT-33**:492–499 (June 1985).
27. J. S. Izadian and S. M. Izadian, *Microwave Transition Design*, Artech House, Norwood, MA, Dec. 1988.
28. W. Wiatr, D. K. Walker, and D. F. Williams, Coplanar-waveguide-to-microstrip transition model, *IEEE Int. Microwave Symp. Digest*, June 2000, pp. 1797–1800.
29. T.-H. Lin, Via-free broadband microstrip to CPW transition, *Electron. Lett.* **37**(15):960–961 (July 19, 2001).
30. M. Houdart and C. Aury, Various excitation of coplanar waveguide, *IEEE Int. Microwave Symp. Digest*, April 1979, pp. 116–118.
31. S. Dey, C. K. Aanandan, P. Mohanan, and K. G. Nair, Analysis of cavity backed printed dipoles, *Electron. Lett.* **30**(3):173–174 (Feb. 3, 1994).
32. M. Richard, M. Kanda, C. DiNallo, and C. K. Chou, A rugged microstrip tapered balun printed dipole reference for SAR system verification, *IEEE Int. Microwave Symp. Digest*, June 2002, pp. 1743–1746.
33. M. Gans et al., Frequency independent balun, *IEEE Proc.* **53**:647–648 (June 1965).
34. V. Trifunovic and B. Jokanovic, Review of printed marchand and double Y baluns: Characteristics and application, *IEEE Trans. Microwave Theory Tech.* **42**(8):1454–1462 (Aug. 1994).
35. J. Chramiec and J. K. Piotrowski, Novel approach to the characterization of coaxial-to-microstrip transitions, *Proc. 27th European Microwave Conf.*, Sept. 1997, Vol. 2, pp. 697–702.
36. M. Morgan and S. Weinreb, A millimeter-wave perpendicular coax-to-microstrip transition, *IEEE Int. Microwave Symp. Digest*, 2002, pp. 817–820.
37. F. J. Villegas, D. I. Stones, and H. A. Hung, A novel waveguide-to-microstrip transition for millimeter-wave module applications, *IEEE Trans. Microwave Theory Tech.* **47**(1):48–55 (Jan. 1999).
38. L. Hyvonen and A. Hujanen, A compact MMIC-compatible microstrip to waveguide transition, *IEEE Int. Microwave Symp. Digest*, 1996, pp. 875–878.
39. W. Grabherr, B. Huder, and W. Menzel, Microstrip to waveguide transition compatible with mm-wave integrated circuits, *IEEE Trans. Microwave Theory Tech.* **42**(9):1842–1843 (Sept. 1994).
40. M. Davidovitz, Wide-band waveguide-to-microstrip transition and power divider, *IEEE Microwave Guided Wave Lett.* **6**(1):13–15 (Jan. 1996).
41. H.-W. Yao, A. Abdelmonem, J.-F. Liang, K. A. Zaki, A full wave analysis of microstrip-to-waveguide transitions, *IEEE Int. Microwave Symp. Digest*, 1994, pp. 213–216.
42. G. Zarba, G. Bertin, L. Accatino, and P. Besso, An improved approach to implement a microstrip to waveguide transition, *IEEE Antennas and Propagation Society Int. Symp. Digest*, June 1995, Vol. 3, pp. 1502–1505.
43. N. Kaneda, Y. Qian, and T. Itoh, A broad-band microstrip-to-waveguide transition using quasi-yagi antenna, *IEEE Trans. Microwave Theory Tech.* **47**(12):2562–2567 (Dec. 1999).
44. K. W. Kim, C.-H. Na, and D.-S. Woo, New dielectric-covered waveguide-to-microstrip transitions for Ka-band transceivers, *IEEE Int. Microwave Symp. Digest*, 2003, pp. 1115–1118.
45. Y.-C. Leong and S. Wienreb, Full band waveguide-to-microstrip probe transitions, *IEEE Int. Microwave Symp. Digest*, 1999, pp. 1435–1438.
46. S. C. Shi and J. Inatani, A waveguide-to-microstrip transition with a DC/IF return path and an offset probe, *IEEE Trans. Microwave Theory Tech.* **45**(3):442–446 (March 1997).
47. Y.-C. Shih, T.-N. Ton, and L. Q. Bui, Waveguide-to-microstrip transitions for millimeter-wave applications, *IEEE Int. Microwave Symp. Digest*, 1988, pp. 473–475.
48. S.-H. Kim, J.-S. Lim, and J.-H. Choi, Design of a Ku-band microstrip-to-waveguide transition, *IEEE Antennas and Propagation Society Int. Symp. Digest*, June 2002, Vol. 3, pp. 424–427.
49. S. Llorente-Romano, B. P. Dorta-Naranjo, F. Pérez-Martínez, and M. Salazar-Palma, Ka-band waveguide-to-microstrip transition design and implementation, *IEEE Antennas and Propagation Society Int. Symp. Digest*, June 2002, Vol. 3, pp. 404–407.
50. C. J. Verner and W. J. R. Hofer, Quarter-wave matching of waveguide-to-finline transitions, *IEEE Trans. Microwave Theory Tech.* **32**(12):1645–1648 (Dec. 1984).
51. A. Beyer and I. Wolff, Fin-line taper design made easy, *IEEE Int. Microwave Symp. Digest*, 1985, pp. 493–496.

52. C. A. W. Vale and P. Meyer, Designing high-performance finline tapers with vector-based optimization, *IEEE Trans. Microwave Theory Tech.* **47**(12):2467–2472 (Dec. 1999).
53. K. K. Chan, R. Martin, and K. Chadwick, A broadband end launched coaxial-to-waveguide transition for waveguide phased arrays, *IEEE Antennas and Propagation Society Int. Symp. Digest*, June 1998, Vol. 3, pp. 1390–1393.
54. R. Levy and L. W. Hendrick, Analysis and synthesis of in-line coaxial-to-waveguide adapters, *IEEE Int. Microwave Symp. Digest*, 2002, pp. 809–811.
55. F. C. de Ronde, Ideal W.G. to coax transitions using F.B.M. monopole, *IEEE Int. Microwave Symp. Digest*, 1988, pp. 591–594.
56. T. Yoneyama, Millimeter-wave integrated circuits using nonradiative dielectric waveguide, *Electron. Commun. Jpn., Part 2* **74**(2):20–28 (Feb. 1991).
57. J. A. G. Malherbe and J. H. Cloete, A transition from rectangular to nonradiating dielectric waveguide, *IEEE Trans. Microwave Theory Tech.* **33**(6):539–543 (June 1985).

INDIUM PHOSPHIDE (InP)

OSAMU WADA
Kobe University
Japan

1. INTRODUCTION

Indium phosphide (InP) and its related ternary and quaternary alloys grown epitaxially on InP substrates form one of the most important III–V compound semiconductor families because of their broad applications in electronic, microwave, optoelectronic, and photonic devices with high performance and high reliability. This is due primarily to the physical properties intrinsic to this material

system such as the high electron mobility, high saturation velocity, high thermal conductivity, wide selectivity of the bandgap energy suitable for optical communication wavelengths, and high threshold of optical catastrophic degradation. Also the development of practical devices for both electronic and optoelectronic systems have pushed the technical frontiers in material preparation, processing, device designs, fabrication, and also integration to extremely high standards. Operation frequency of more recent InP-based microwave devices is in the range of 100–200 GHz, and operation bit rates of state-of-the-art electronic and optoelectronic digital devices and integrated circuits are in the range of 40–100 Gbps. In extension to these technologies, research is underway to generate and detect terahertz (THz) waves and also to process optical pulse signals in the femtosecond time domain. Thus InP-based materials and devices are prerequisite in establishing technical infrastructure for ubiquitous communication and informatics utilizing electronic, microwave, and photonic technologies. In what follows, we review first the basic material properties of InP-related material systems and then current device technologies for both electronic and photonic applications.

2. GENERAL PROPERTIES OF InP-BASED MATERIALS AND HETEROSTRUCTURES

InP has, like many other III–V compound semiconductors, zincblende structure with a lattice constant a of 0.58687 nm. The relationships between the energy gap E_g and the lattice constant a are summarized in Fig. 1 for various binary and ternary III–V material systems. A variety of ternary and quaternary alloy systems possessing lattice parameters the same as that of InP can be grown on lattice-matched InP substrates without introducing misfit dislocations. A very wide range of bandgap energy

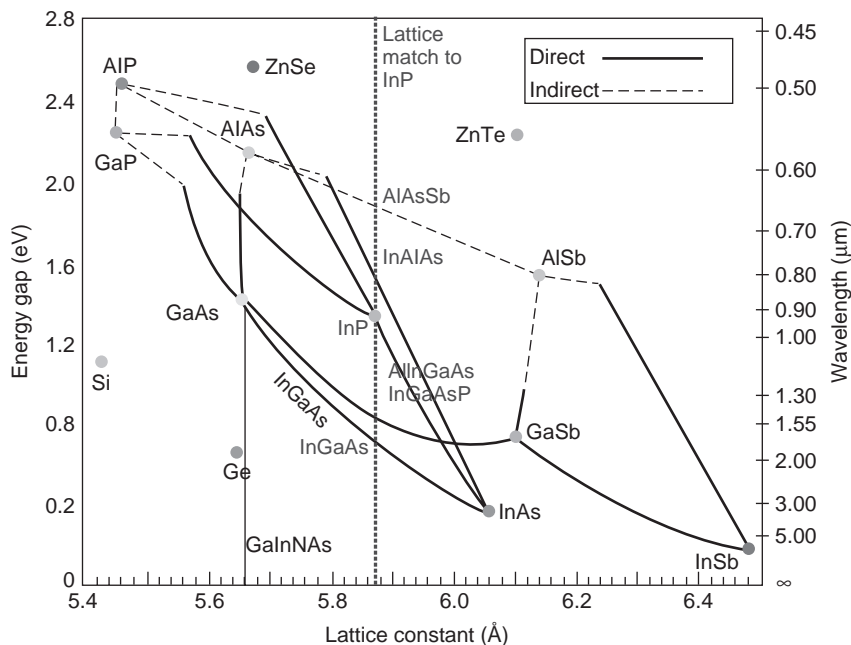


Figure 1. Relationship between energy gap E_g and lattice constant a for various III–V semiconductors.

variation in this alloy system is extremely useful for device applications, particularly for optoelectronic devices in the long-wavelength region covering 1.3–1.55 μm [1,2]. Lattice-mismatched heterointerfaces can be classified into (1) coherently strained or pseudomorphic interfaces free of misfit dislocations, in which the thickness of strained layer is smaller than the “critical thickness” determined from the elastic property of the crystal; and (2) relaxed interfaces where strain is partially or fully relaxed with the introduction of misfit dislocations. Quality of heterointerfaces is strongly dependent on the crystallographic nature of the interface as well as the growth conditions in real interface formation process, including growth interruption and regrowth. InP-based materials are grown epitaxially on InP substrates usually with (100)-oriented surfaces using various epitaxial techniques including metal organic chemical vapor deposition (MOCVD) and chemical-beam epitaxy (CBE) and also molecular-beam epitaxy (MBE) for non-P-containing materials [2]. InP substrates used for device fabrication are in the range of 2–3 in. in diameter, whereas 4-in. substrate growth technology is available for future high-volume production.

The choice of alloy system is important not only for the bandgap energy itself but also for the band discontinuity or lineup at the heterointerface. Figure 2 shows the band lineup (type I) for lattice-matched InP/In_{0.53}Ga_{0.47}As and In_{0.52}Al_{0.48}As/In_{0.53}Ga_{0.47}As heterointerfaces, which are used most widely for electronic and optoelectronic devices, whereas the lattice-matched InP/In_{0.52}Al_{0.48}As heterointerface is of type II staggered lineup [2]. For application of InP-based heterostructures to electronic and optoelectronic devices, alloy composition must be designed for optimizing the band discontinuity for tight carrier confinement. In the optoelectronic device applications, the bandgap energy and refractive index must be designed for the operation wavelength and optical confinement within heterostructure devices. The maximum conduction band discontinuity for lattice-matched interfaces is obtained by AlAsSb/InGaAs heterostructure, which can be

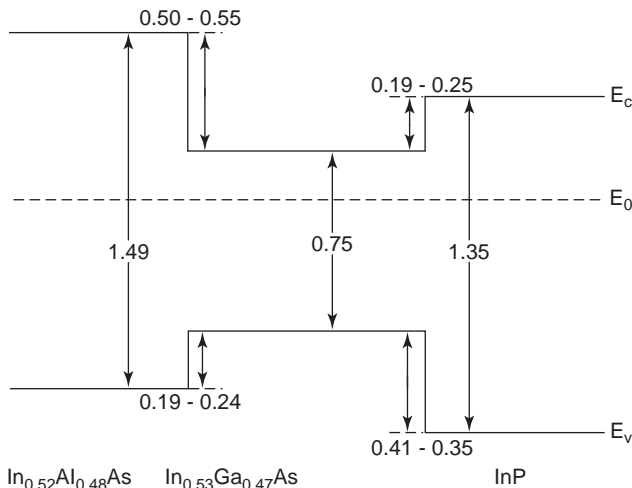


Figure 2. Band lineup for In_{0.52}Al_{0.48}As/In_{0.53}Ga_{0.47}As/InP heterostructure. Units are in eV.

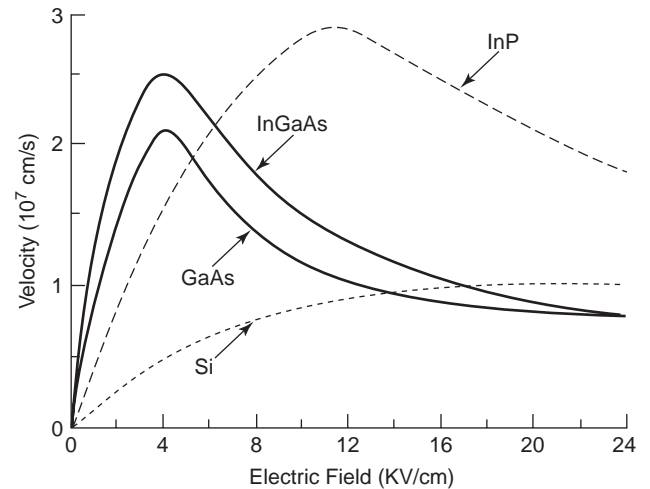


Figure 3. Monte Carlo calculation of velocity–field curves for InP and GaAs. InP has a higher peak velocity and a higher corresponding electric field than does GaAs. (After J. Hayes [3].)

useful for cascade lasers and intersubband transition optical modulators and switches, as will be described later. Another important factor that plays an important role in heterointerface band lineup is strain. For example, uniaxial tensile (compressive) strain is induced to In_xGa_{1-x}As interfacing to InP when x is less (greater) than 0.53, which splits the degenerate valence bands at $k = 0$, which causes the light-hole (heavy-hole) band to lie higher than the heavy-hole (light-hole) band. Such an effect is critical to determine the operation wavelength and polarization properties of optical devices, and also to determine the carrier transit speed and confinement effect in electronic devices.

Figure 3 shows velocity–field characteristics for different semiconductor materials [3]. Low electric field mobility, which is defined by the slope of the velocity–field curve close to the axis, for all III–V compounds exceeds that of Si. Another significant difference in velocity–field characteristics is in that there is a region of negative resistance resulting from the electron dynamics and the band structure. The negative resistance of InP is initiated at a field much higher than that of GaAs, and correspondingly the electron saturation velocity is much higher than in GaAs. This is caused by larger energy separation between Γ and L valleys in InP conduction band [3]. InGaAs ternary alloy shows the highest low-field mobility in excess of 10,000 $\text{cm}^2/\text{V}\cdot\text{s}$ and maximum saturation velocity over 2.4×10^7 cm/s . For a given class of device structures, this can result in lower parasitic resistance, higher current-carrying capacity, and shorter transit time. Unique properties of InP-based materials include a stable surface property, which is well known for lasers under age testing to be much more resistant to facet degradation than for GaAs-based lasers. Low surface recombination velocity and a lower rate of recombination-enhanced defect formation are characteristic to this material system. Such material properties, together with the higher thermal conductivity, InP, and related alloys, may also be suitable for high-power applications.

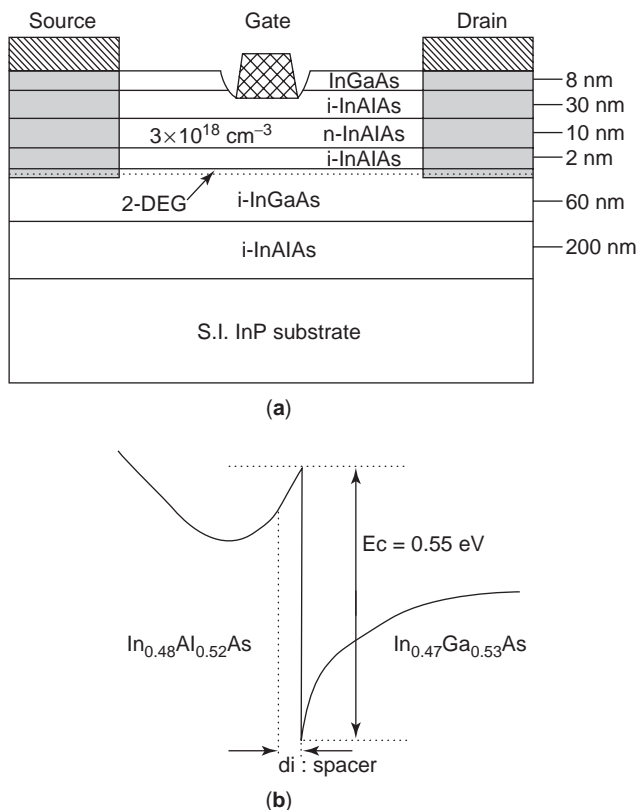


Figure 4. (a) Typical device structure for InGaAs/InAlAs HEMT; (b) energy band diagram for InGaAs/InAlAs HEMT.

3. ELECTRONIC DEVICES AND INTEGRATED CIRCUITS

The most important electronic devices based on InP are high-electron-mobility transistors (HEMTs) and hetero-

bipolar transistors (HBTs). Significant improvement is being made in these discrete devices as well as their monolithic microwave integrated circuits (MMICs). In order to indicate RF and microwave performance of these devices, characteristic parameters such as f_t , f_{max} , and noise figure are used. f_t is defined as the frequency where the current amplification gain equals unity, and is basically determined by the intrinsic device speed. f_{max} is defined as the maximum oscillation frequency, and is influenced by parasitic components such as the gate resistance and drain feedback capacitance. Noise figure is defined by the ratio of noise at the input and output represented in decibels (dB).

InP-based HEMTs using the $In_{0.52}Al_{0.48}As/In_{0.53}Ga_{0.47}As$ 2DEG system were first reported in 1985 [4]. Typical device structure is shown in Fig. 4, together with a band diagram of the 2DEG heterostructure [5]. The performance of HEMTs has improved rapidly since then primarily by shrinking the device size, particularly reducing the gate length down to 100 nm and beyond. Pseudomorphic heterostructure in which the In composition $x > 0.53$ provides lower bandgap energy and enhances the electron drift velocity, conduction band discontinuity ΔE_c , and also sheet carrier density, so that extremely high f_t data have been achieved by more recent developments. Figure 5 shows the structure of such a pseudomorphic ($x = 0.7$) HEMT with a gate length of 25 nm [5]. In reducing the gate length, it is important to avoid the short-channel effect by decreasing the gate-channel distance. The gate-channel distance of only 4 nm has been achieved in this case by introducing the etch-stop layer technique together with the electron-beam-processed two-step recess gate technique. Static I-V and current gain-frequency characteristics are shown in Fig. 6, indicating that $f_t = 562$ GHz. A lattice-matched HEMT with the same structure has exhibited a frequency of 500 GHz [6].

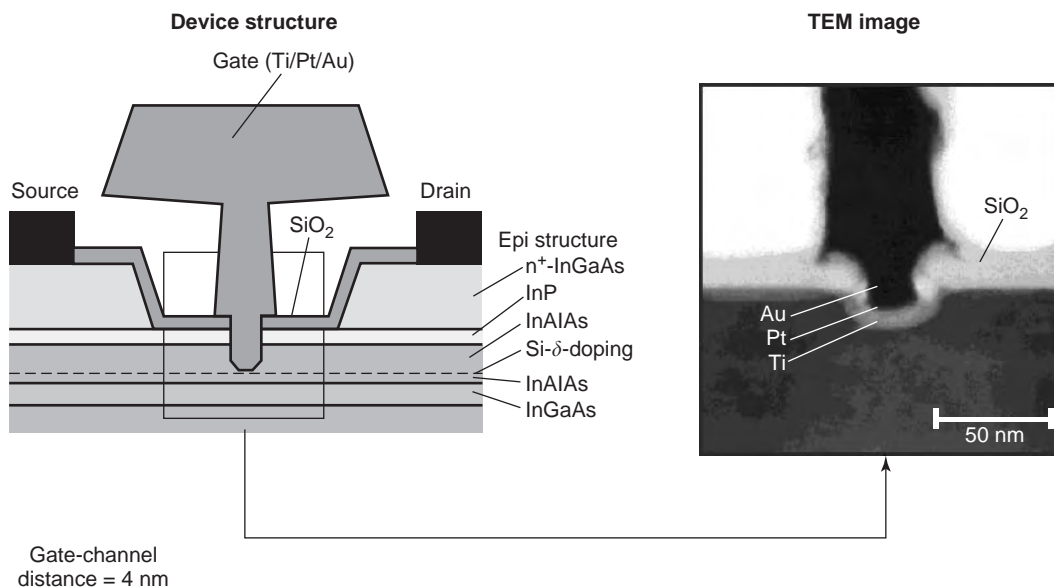


Figure 5. Schematic cross-sectional view of InGaAs/InAlAs HEMT (left) and cross-sectional TEM image around the bottom of the 25-nm-long T-shaped gate. (After A. Endoh et al. [6].) (This figure is available in full color at <http://www.mrw.interscience.wiley.com/erfme>.)

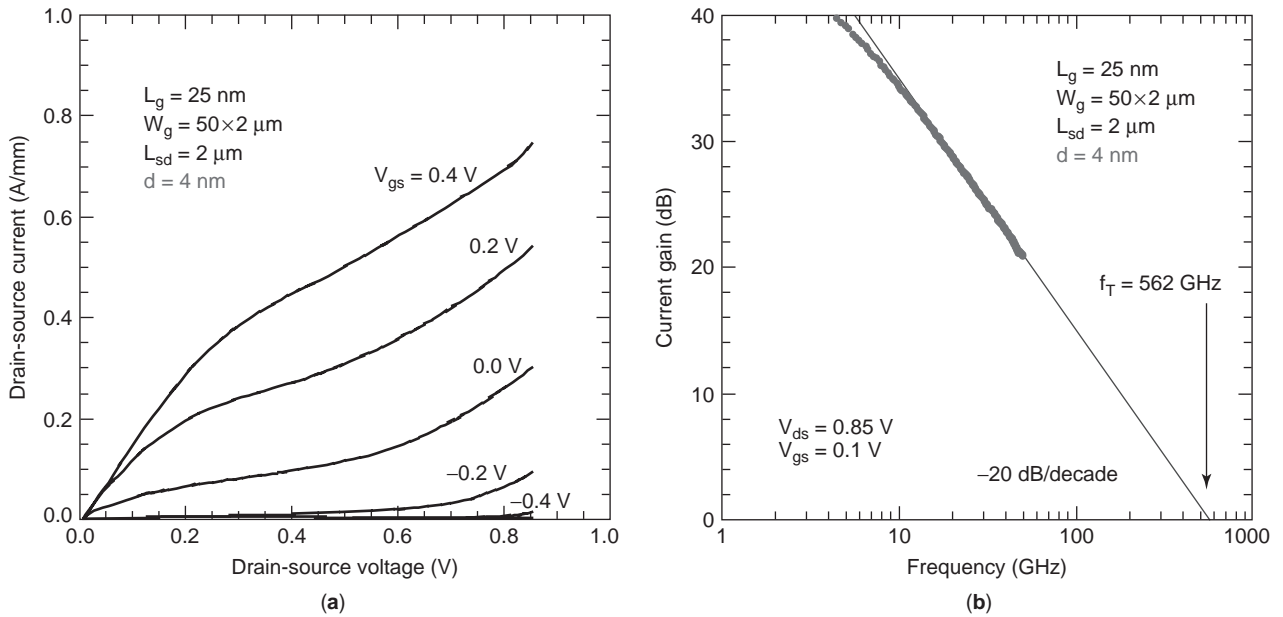


Figure 6. (a) Static current–voltage characteristics and (b) current gain–frequency characteristics of 25-nm-gate pseudomorphic HEMT with gate–channel distance of 4 nm. The maximum DC transconductance is about 1.23 S/mm. The cutoff frequency achieved is 562 GHz. (After A. Endoh et al. [6].) (This figure is available in full color at <http://www.mrw.interscience.wiley.com/erfme>.)

Typical application of InP-based HEMT includes millimeter-wave communication and remote sensing instruments for Earth atmosphere, radio astronomy, medical thermography, and target seekers. Millimeter-wave radar for the automotive collision avoidance system is another key application of InP HEMT MMICs.

For the application to low-noise amplifiers (LNAs), InP HEMTs are intrinsically suitable because of their high transconductance, high f_t , and low source resistance. InP HEMT MMIC, which exhibits 25 dB gain and 3.0 dB noise figure at 102 GHz, and 12 dB gain and less than 6 dB noise figure in the range of 170–200 GHz, has been developed [7]. Also a six-stage coplanar waveguide design MMIC has demonstrated 20 dB average gain with a noise figure of < 6 dB over a range of 160–215 GHz [7]. A high breakdown

voltage is achieved through composite InGaAs–InP channel designs, and a single-chip power amplifier has achieved 16 dB gain and 420 mW output power at 95 GHz with a 20% power-added gain efficiency [7].

Digital ICs based on InP-based HEMTs will be indispensable in developing ultrafast optical communication systems. Device structure and fabrication technique adequate to achieve uniform threshold characteristics over the wafer are essential for digital ICs. Chipsets for 40 Gbps (gigabits per second), including multiplexing (MUX) and demultiplexing (DEMUX) circuits, have been developed [8]. An IC structure with 100-nm-long gates fabricated using double-recess and InP-etch stop-layer techniques is shown in Fig. 7, exhibiting $f_t = 175$ GHz, a threshold voltage of -0.58 V, and the standard deviation

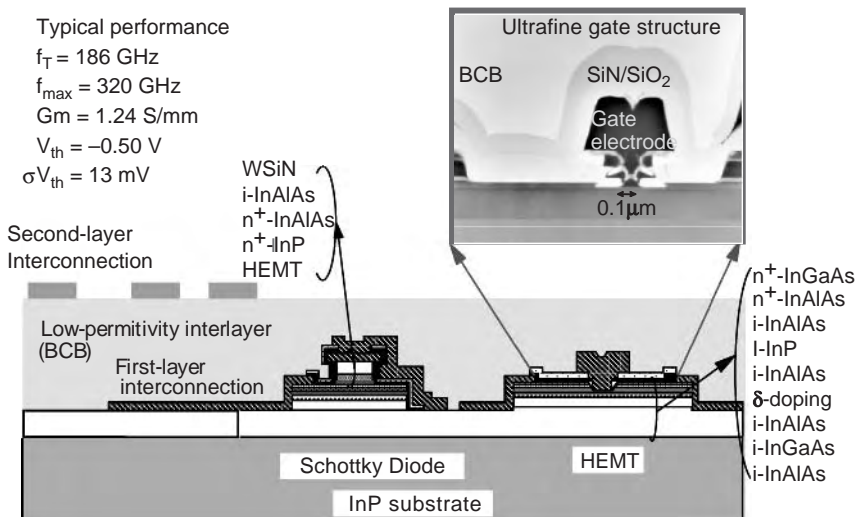


Figure 7. Schematic cross section of InP HEMT IC, incorporating HEMTs, InAlAs Schottky diodes, metal resistors, MIM capacitors, and two-level Au interconnection lines. (After K. Murata et al. [8].) (This figure is available in full color at <http://www.mrw.interscience.wiley.com/erfme>.)

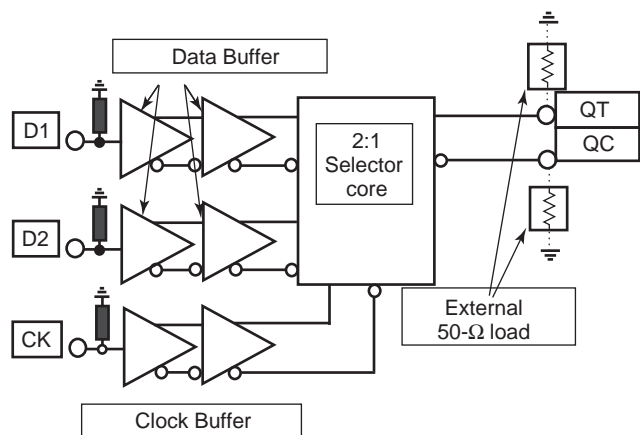
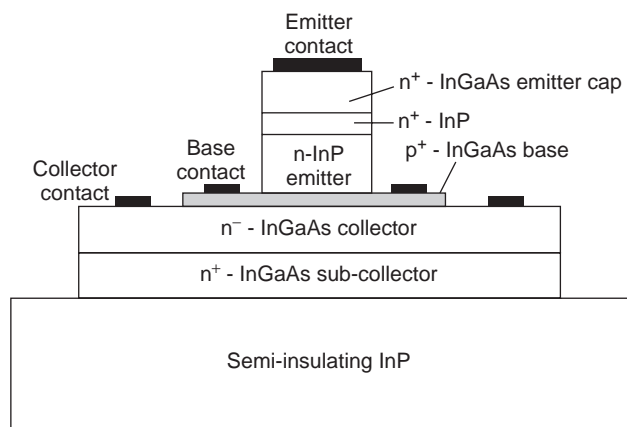


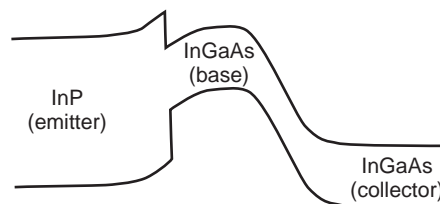
Figure 8. Block diagram of 2-1 selector circuit consisting of 0.1- μm -gate InGaAs/InAlAs HEMT IC. (After K. Murata et al. [9].)

of 36 mV. Figure 8 shows the circuit diagram of a channel selector and Fig. 9, an “eye” diagram demonstrating error-free operation at 100 Gbps [9].

Another important class of InP-based electronic devices is heterojunction bipolar transistors (HBTs). The schematic structure and band diagram of InGaAs/InAlAs HBTs are shown in Figs. 10a and 10b, respectively. HBTs have a great advantage in increasing the current gain by limiting the backward injection of holes into the emitter with the introduction of a wide-bandgap emitter as illustrated in Fig. 10b. This allows significant increase in base doping, resulting in lower base resistance and high base current operation at high speed. Although the Si bipolar has remained very competitive in high-speed applications not only with the superaligned technology but also with inclusion of SiGe HBTs, the highest performance has been recorded by InP-based HBTs. Ultrafast HBTs over 200 GHz are key to next generation analog-to-digital converters and other digital and mixed-signal circuits. The schematic cross-sectional structure of superscaled double-



(a)



(b)

Figure 10. (a) Typical device structure for InGaAs/InAlAs HBT; (b) energy band diagram for InGaAs/InAlAs HBT.

heterojunction HBTs (DHBTs) and important factors for high-speed performance are shown in Fig. 11 [10]. InP-based DHBTs have achieved a combined f_t/f_{max} of 300/300 GHz and 21 dB unilateral power gain at 100 GHz [7,10]. More recent InP-based HBTs involving heavily C-doped GaAsSb base layers have also shown outstanding performance with $f_t = 300$ GHz [10]. InP-based HBT MMICs have been developed for a variety of applications, including an X-band direct synthesizer consisting of 3000 InP HBTs [7].

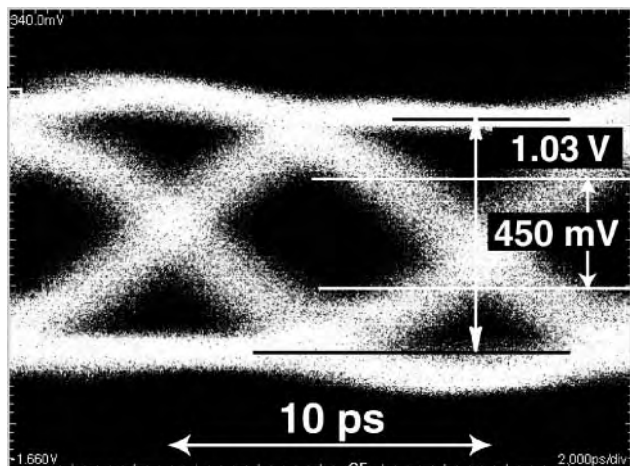


Figure 9. 100-Gbps output waveform of a HEMT 2-1 selector IC. (After K. Murata et al. [9].) (This figure is available in full color at <http://www.mrw.interscience.wiley.com/erfme>.)

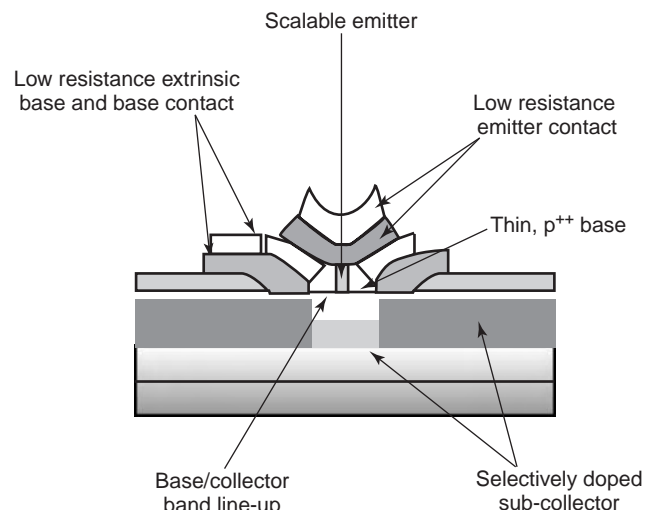


Figure 11. Schematic of a scalable, high-performance, InP HBT for mixed-signal circuits. (After J. C. Zolper [10].)

4. OPTOELECTRONIC DEVICES AND INTEGRATED CIRCUITS

Since the development of low-loss optical fibers at wavelengths $1.3\ \mu\text{m}$ and then $1.55\ \mu\text{m}$, InP-based quaternary alloy systems, particularly the lattice-matched $\text{Ga}_x\text{In}_{1-x}\text{As}_y\text{P}_{1-y}$ system, have become indispensable for light source and photodetector devices for optical communications. Development of erbium-doped fiber amplifiers (EDFAs) and the wavelength-division multiplexing (WDM) technique have improved the throughput and functionality of optical network greatly and also enhanced the importance of InP-based optoelectronic devices. Present InP-based device development covers many different directions. Improvement of device performance in WDM systems and high-speed systems with the bit rate greater than 40 Gbps is being tackled. Another important direction is the development of easy-to-use, compact devices at acceptable cost for further widening the application of optical techniques in communication networks and interconnections within systems. A variety of approaches using new type of devices such as coolerless (uncooled) Fabry-Perot (FP) lasers and vertical cavity surface emitting lasers (VCSELs), and integration of devices are being developed using hybrid and monolithic techniques, including photonic and optoelectronic integrated circuits (PICs and OEICs) [2,11,12]. Another direction required toward the next-generation network enabling support of Tbps (terabits per second)-level throughput is the development of ultrafast devices operating at a bit rate exceeding 100 Gbps, where device operation must be all-optical,

since no electron devices would be able to function at that rate. Some of the current developments are reviewed in the following paragraphs.

Figure 12 shows a $1.3\text{-}\mu\text{m}$ -wavelength InGaAlAs/InP multiple-quantum-well (MQW) distributed-feedback (DFB) laser with ridge waveguide structure [13]. The introduction of an InAlAs cladding layer provides a large conduction band discontinuity, and the insertion of a grating layer in the p-type region eliminates the valence band notch at the heterointerface, enabling uncooled operation up to temperatures of 115°C as shown in Fig. 13. Direct modulation at 10 Gbps has confirmed error-free transmission over 30 km with 20 ps/nm dispersion.

Figure 14 shows a InGaAsP/InP electroabsorption modulator (EAM)-integrated DFB laser for 40 Gbps modulation at $1.55\ \mu\text{m}$ [14]. A short-length ($100\text{-}\mu\text{m}$) EAM with ridge waveguide structure with minimized capacitance has been introduced for widening the modulation bandwidth. The EAM quantum-well number, quantum-well thickness, and detuning against the laser emission wavelength have been optimized for improving the extinction ratio. The eye diagram observed at a bit rate of 40 Gbps demonstrates successful transmission with an extinction ratio greater than 12 dB over a 2-km-long conventional single-mode fiber without dispersion compensation fiber using a drive voltage as low as 3.2 V, as shown in Fig. 15 [15]. Also, a clearly open eye diagram has been observed after transmission in 80-km nonzero dispersion-shifted fiber with dispersion compensation [14].

The photonic integration technique is useful for integrating other devices on InP substrates. Multiple-wavelength

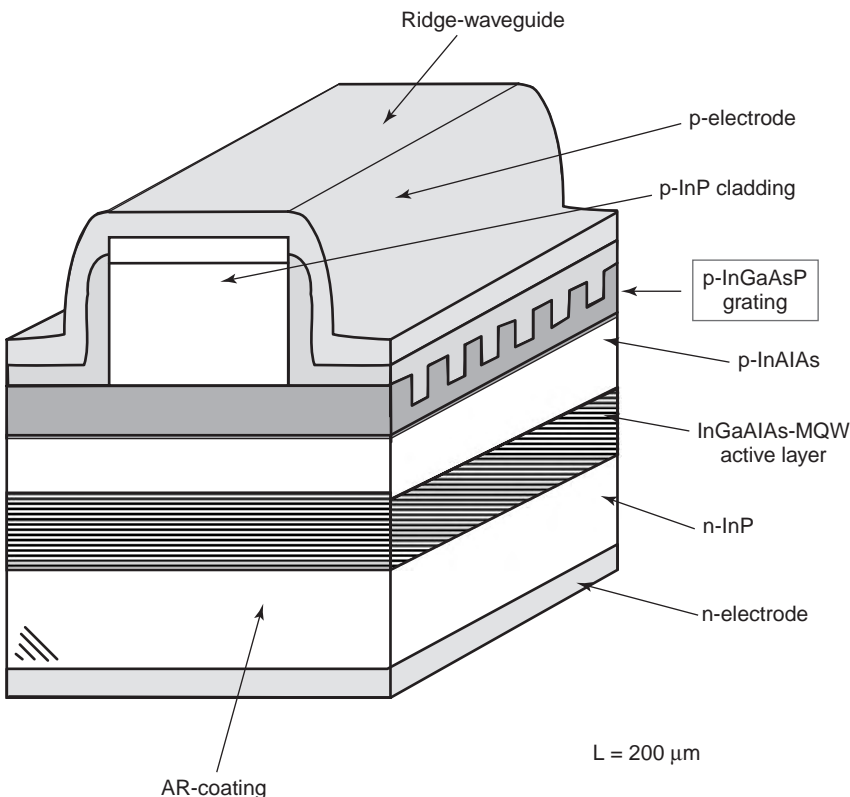


Figure 12. Structure of uncooled $1.3\text{-}\mu\text{m}$ InGaAlAs-MQW DFB laser involving a low-resistance (notch-free) grating layer. (After K. Nakamura et al. [13].)

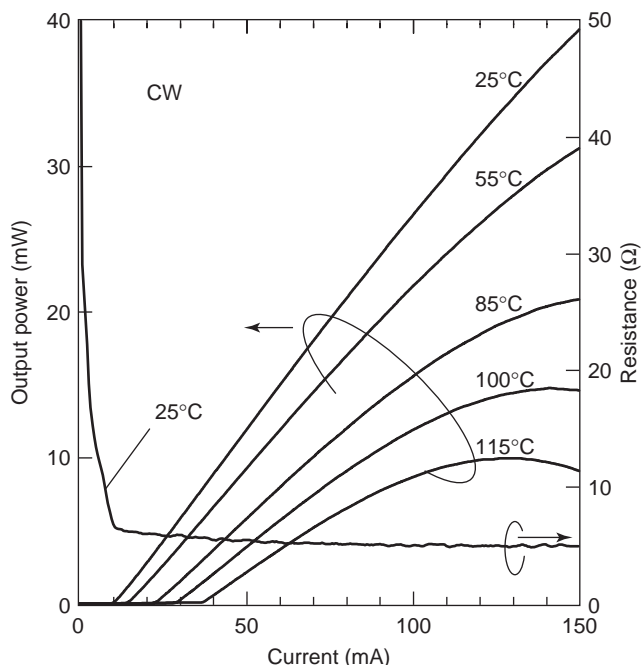


Figure 13. Light output and resistance–current characteristics for uncooled 1.3- μm InGaAlAs-MQW DFB laser. Resistance observed is 30% lower than that of conventional floating-type grating. (After K. Nakamura et al. [13].)

sources, in which distributed Bragg reflector (DBR) lasers with different center wavelengths, an optical coupler, and a semiconductor optical amplifier (SOA) are integrated, and multisection tunable lasers, in which an optical gain, tuning, and phase matching sections are integrated, are typical examples. Figure 16 illustrates the structure of an InGaAsP/InP eight-channel multiwavelength laser exhibiting emission in the 1535–1558 nm wavelength range with high uniformity, high output power (+ 15 dBm), and high single-mode suppression ratio (SMSR > 50 dB) [16].

On the photodetector side, PIN photodiodes (PIN PDs) and avalanche photodiodes (APDs) have been improved in performance by using both the optimization of heterostructure design and the development of integration and packaging techniques. Figure 17 shows the structure of an APD amplifier receiver integrated by using a lensed, flip-chip structure photodiode (PIN PD or APD) and a Si or GaAs preamplifier chip [17]. A monolithic lens formed by the ion etching technique on the InP substrate provides extremely small junction diameter (10–15 μm) but maintaining a very high quantum efficiency, reducing the overall capacitance to improve both the speed and noise performance. High performance of InGaAs/InP APD is represented by a gain–bandwidth product in the range of 30–50 GHz. Using such an APD, the hybrid integrated receiver has shown excellent performance up to 10 Gbps. Monolithic integration of optical receivers has also been developed using mainly PIN PDs and HEMT and HBT amplifier circuits on InP substrates. The more recent PIN/amplifier OEIC receiver bandwidth is in excess of 30 Gbps [18], and is promising for application to not only optical communication systems but also optical interconnections in high-speed electronic systems.

For application to systems at 40 Gbps and beyond, the cutoff frequency of the vertical structure photodiode becomes limited by the carrier transit time, rather than the CR time constant as described in the previous example. Waveguide photodiodes and APDs are being developed for this reason by adopting a structure such as that shown in Fig. 18 [19]. A device with optimized structure (20 μm length) has exhibited a high quantum efficiency (70%) maintaining a speed sufficient to achieve a record gain–bandwidth product of 140 GHz as shown in Fig. 19 [19]. Monolithic OEIC receiver has been developed by integrating a waveguide PIN PD and a 500-nm-gate-length HEMT cascade amplifier, which has exhibited – 22.7 dBm at 40 Gbps [20]. More complicated integrated receivers using OEIC and PIC techniques, including arrayed waveguide grating integrated multichannel photoreceivers,

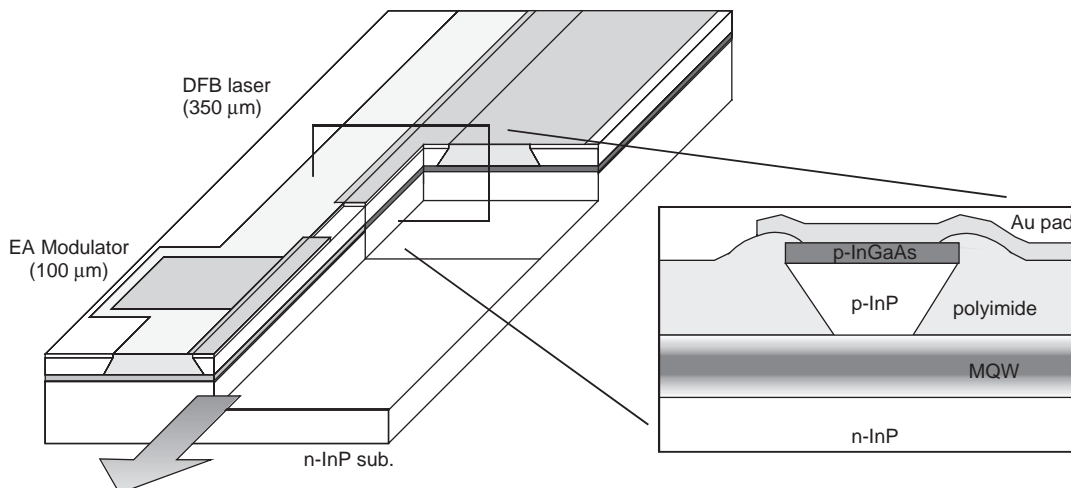


Figure 14. Schematic structure of InGaAsP/InP electroabsorption modulator (EAM)-integrated DFB laser for 40 Gbps modulation at 1.55 μm . (After H. Kawanishi et al. [14].) (This figure is available in full color at <http://www.mrw.interscience.wiley.com/erfme>.)

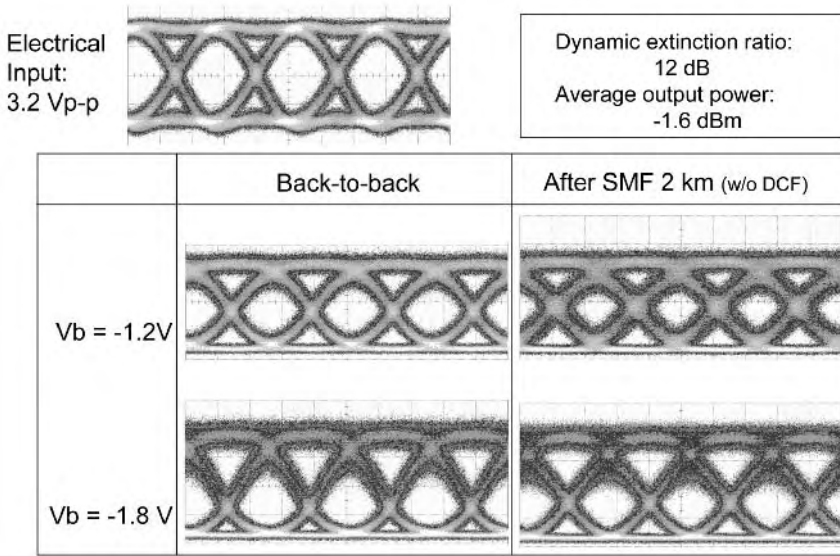


Figure 15. Eye diagram of 40 Gbps NRZ (non-return-to-zero) operation of InGaAsP/InP EAM-integrated DFB laser. (After H. Kawanishi et al. [15].) (This figure is available in full color at <http://www.mrw.interscience.wiley.com/erfme>.)

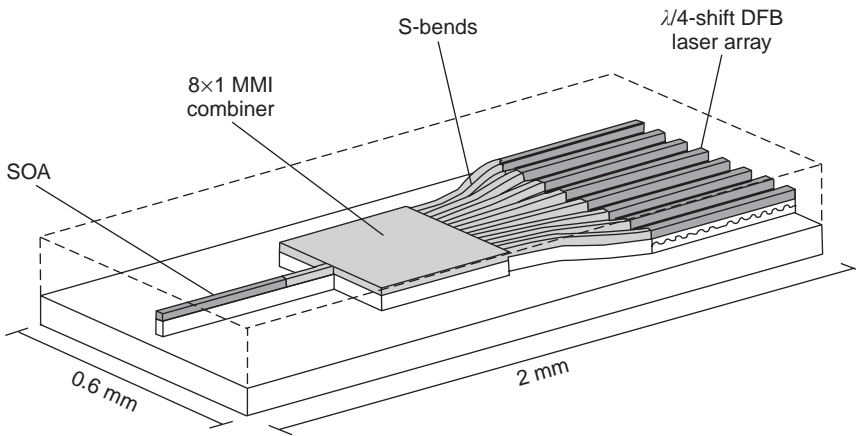


Figure 16. Structure of wavelength-selectable light source integrating eight-channel DFB lasers, multimode interferometer combiner, and a semiconductor optical amplifier on an InP substrate. (After M. Bouda et al. [16].)

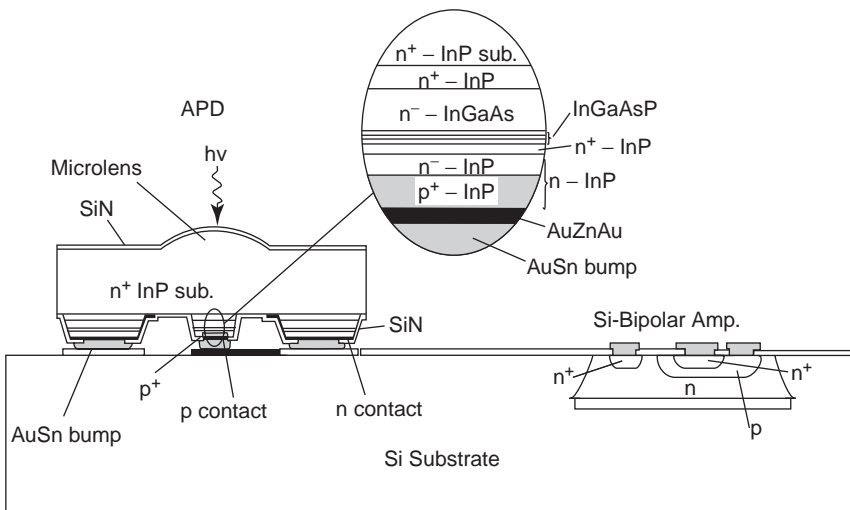


Figure 17. Hybrid integrated APD amplifier receiver using a lensed, flip-chip structure APD and a Si bipolar transistor preamplifier chip [17].

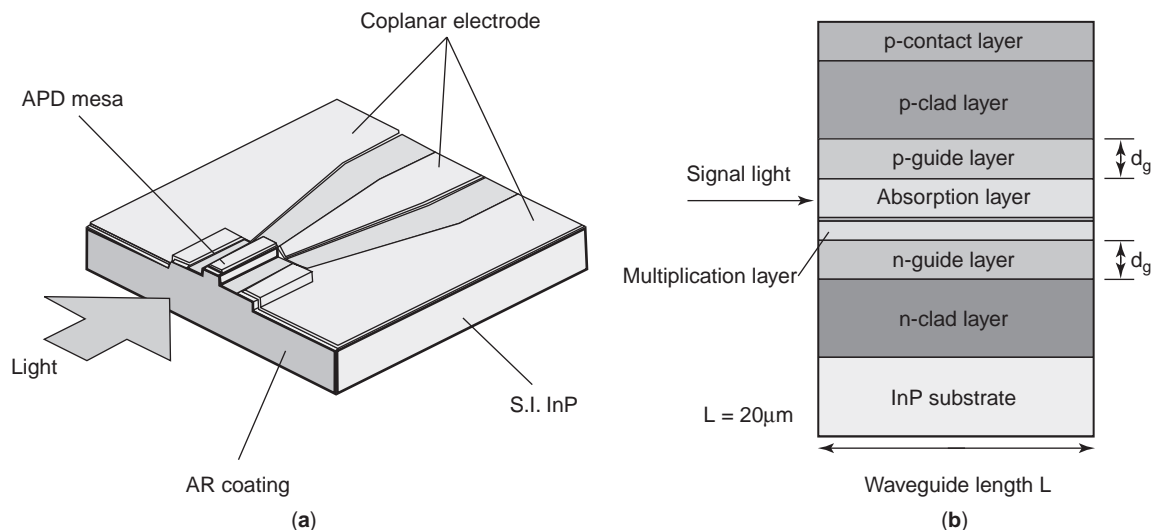


Figure 18. (a) Schematic structure of waveguide APD fabricated on an InP substrate; (b) cross sectional structure of waveguide InGaAs/InAlAs APD incorporating very thin absorption and multiplication layers. (After T. Nakata et al. [19].) (This figure is available in full color at <http://www.mrw.interscience.wiley.com/erfme>.)

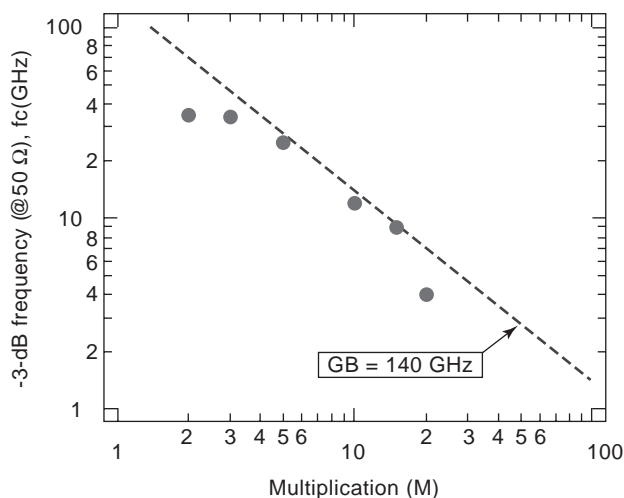


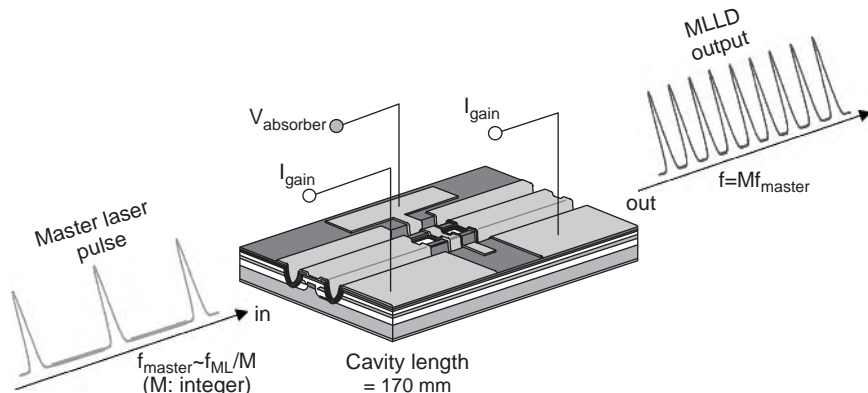
Figure 19. Cutoff frequency versus multiplication characteristics of waveguide APD, indicating a gain-bandwidth product of 140 GHz. (After T. Nakata et al. [19].)

have been also investigated for application to WDM systems [2].

5. ULTRAFAST ALL-OPTICAL DEVICES

Toward the development of ultrafast optical transmission systems with the bit rate beyond 100 Gbps, an optical time-division multiplexing (OTDM) technique based on stable, compact all-optical devices is a prerequisite. The most basic devices required in OTDM systems are ultrafast light sources and all-optical switches [21]. Figure 20 illustrates the structure of a monolithic colliding pulse-mode-locked (CPM) laser, consisting of a pair of optical gain sections sandwiching a saturable absorber section, all formed on an InP substrate by MOCVD [22]. To ensure an extremely high repetition rate (500 GHz) together with a high extinction ratio, a short (174- μm) cavity design, and an ultrafast saturable absorber with graded-index separate confinement heterostructure (GRIN-SCH)

Figure 20. Structure of monolithic colliding pulse-mode-locked (CPM) laser fabricated on an InGaAsP/InP-based multiple quantum-well wafer. A very short cavity length is used for ultrafast operation. Synchronous optical injection locking technique is applied for stabilizing the repetition rate. (After S. Arahira et al. [22].)



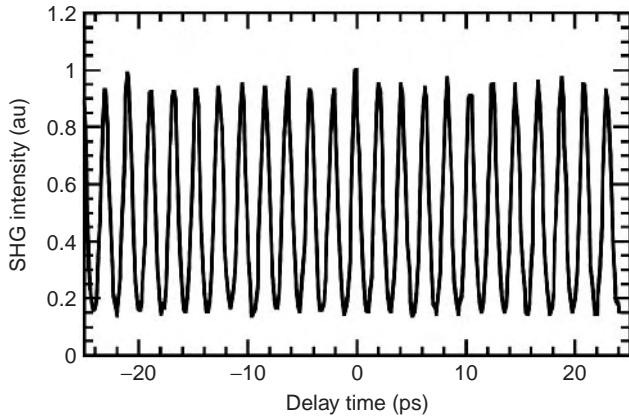


Figure 21. SHG correlation trace of monolithic mode-locked laser, indicating 580 fs half-width pulse generation at 480 GHz repetition rate. (After S. Arahira et al. [22].)

have been adopted. Laser facets have been coated by high-reflectivity (85%) mirrors. Figure 21 shows a second-harmonic generation (SHG) correlation trace of pulses generated by this laser with bias current 78 mA for two sections. Averaged output optical power is 1.6 mW, and the extinction ratio is high, as shown in Fig. 21. Also, low jitter characteristics have been achieved at 480 GHz by applying the synchronous optical injection technique using an external master laser [22].

Ultrafast all-optical switch is another device prerequisite for OTDM systems, and a variety of new materials and devices are being researched currently worldwide. One promising all-optical switch is the InP-based symmetric Mach-Zehnder (SMZ) all-optical switch. The basic structure and operation principle are illustrated in Fig. 22 [23]. The two arms of SMZ switch involve nonlinear waveguides, and they are activated (switched on) by a pair of incoming control light signals with a mutual timeshift of T . When there is no optical phase difference between two arms, no output signal is generated at the output port of the SMZ interferometer. A rectangular pulse can thus be generated at the output port only during the time interval T . Such a device has been fabricated by a hybrid integration technique using two InGaAsP/InP SOAs as nonlinear

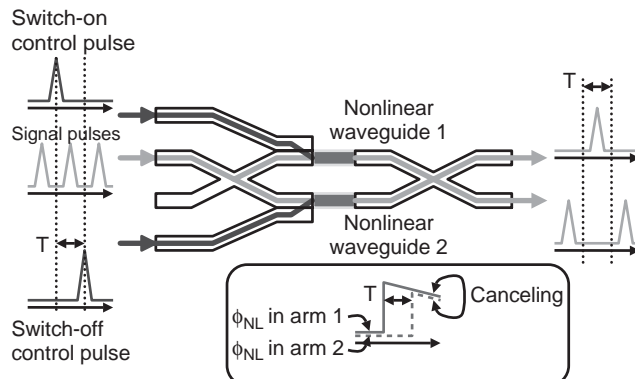


Figure 22. Schematic showing structure and operation of symmetric Mach-Zehnder (SMZ) all-optical switch. (After K. Tajima [23].)

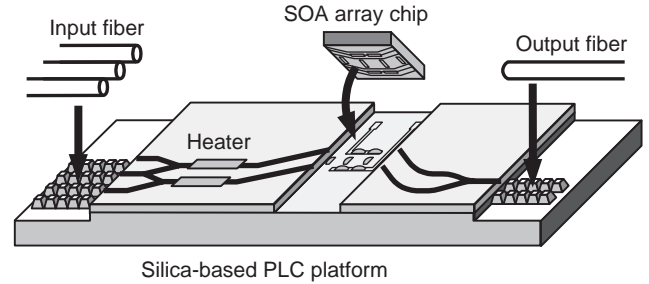


Figure 23. Structure of hybrid-integrated SMZ all-optical switch. (After K. Tajima et al. [24].)

elements and a silica-based planar lightwave circuit (PLC), as shown in Fig. 23. Figure 24 depicts SHG waveforms, clearly demonstrating 168 Gbps–10.5 Gbps DEMUX operation at the signal wavelength of 1560 nm (control wavelength: 1545 nm) [24]. The pulsewidth observed is as narrow as 1–2 ps, and the switching energy intrinsically required for control pulses is as low as 50–80 fJ. Error-free DEMUX operation has also been shown at 336 Gbps–10.5 Gbps [25].

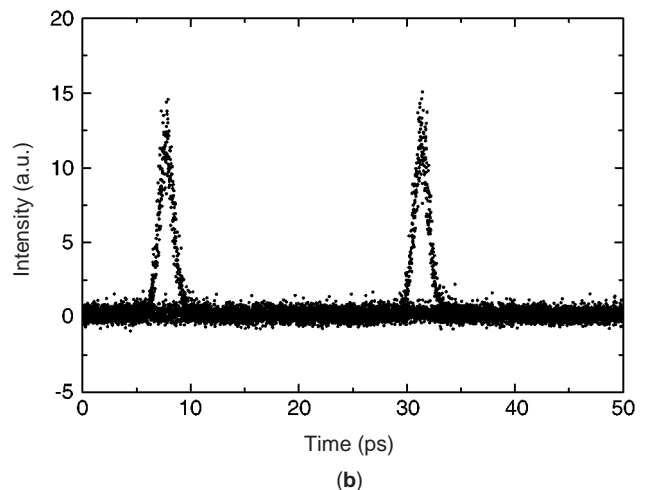
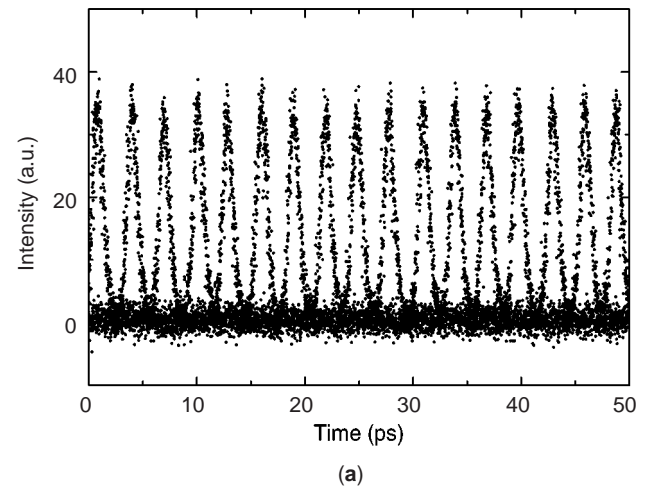


Figure 24. (a) Input and (b) output signal pulses for 168–10.5-Gbps demultiplexing experiment using SMZ all-optical switch. (After S. Nakamura et al. [25].)

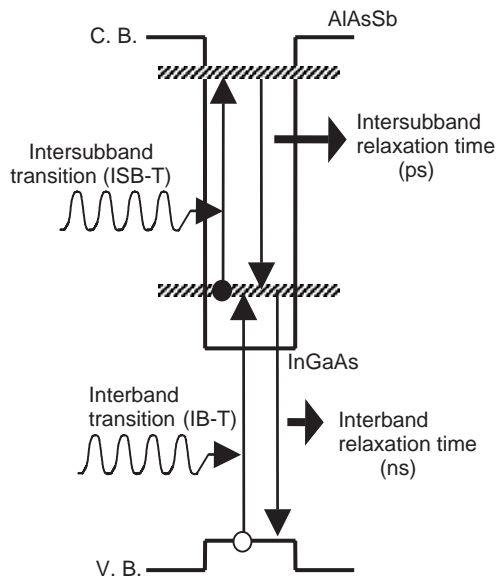


Figure 25. Schematic band diagram showing various transitions in a single quantum well. Ultrafast relaxation is expected for the intersubband transition in contrast to the interband transition.

Other approaches for developing all-optical switches include application of the intersubband transition (ISBT) in quantum-well (QW) structure for modulating the absorption and/or refractive index of a waveguide. Referring to the QW band diagram illustrated in Fig. 25, ISBT in the conduction band can exhibit an ultrafast relaxation time unlimited by the carrier lifetime and high oscillator strength. A wide tunability range is obtained by designing the well width. Figure 26 shows the structure of ridge waveguide ISBT switch incorporating 80 periods of AlAsSb/InGaAs-coupled quantum wells grown on an InP substrate [26]. In order to achieve operation at communication wavelengths, an AlAsSb/InGaAs QW, which has a conduction band discontinuity of 1.6–1.7 eV, has been introduced. Figure 27 shows a pump-probe measurement result demonstrating basic DEMUX operation for a series of four input pulses with an equivalent repetition rate of 1 THz. The operation wavelength is 1.55 μm, and the control energy required is 27 pJ. Further reduction of the

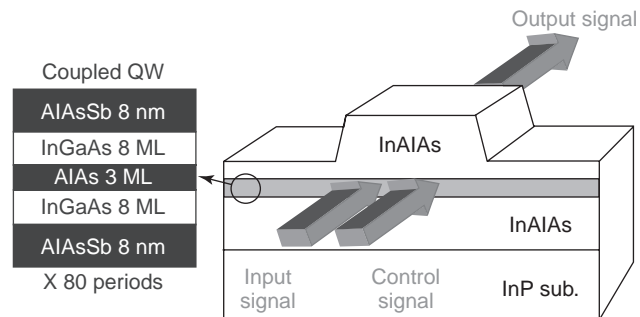


Figure 26. Structure of ridge waveguide switch incorporating InGaAs/AlAsSb coupled double quantum wells. (After T. Akiyama et al. [26].) (This figure is available in full color at <http://www.mrw.interscience.wiley.com/erfme>.)

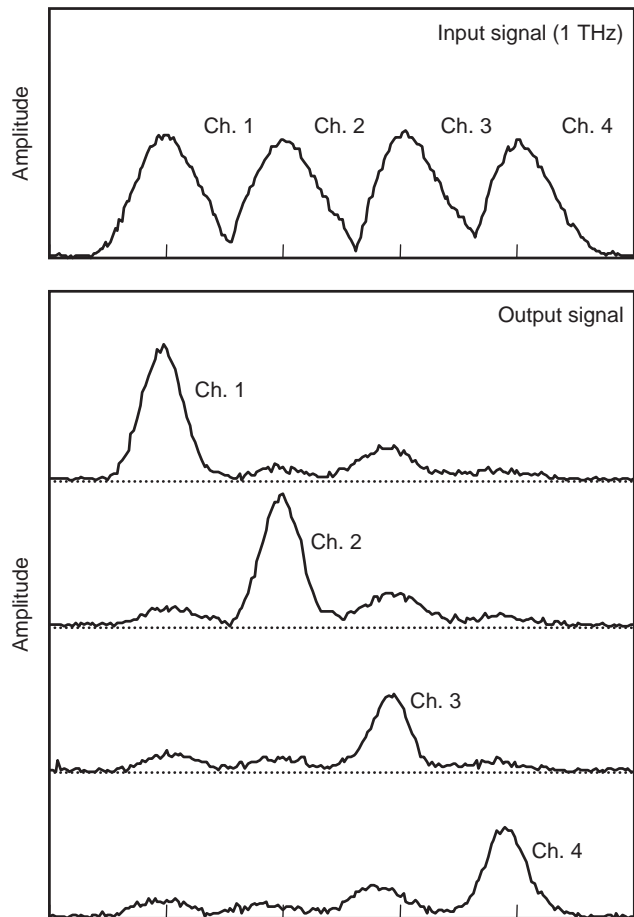


Figure 27. Input and output signal traces of InGaAs/AlAsSb MQW intersubband transition all-optical switch, showing demultiplexing operation at an equivalent repetition rate of 1 THz. (After T. Akiyama et al. [26].)

switching energy is necessary for practical application and the subject of future research [26].

6. SUMMARY

Technologies of InP and related materials have been developed at very rapid rates since the mid-1980s and have already been applied to a variety of real-world devices covering electronic, microwave, and optical areas. This progress is due primarily to the advantageous properties of these materials, and also a very strong market pull, particularly from continuously increasing demands in optical communication systems in the long-wavelength region. Most of the recorded high performance of transistors, lasers, photodiodes, and electronic and optoelectronic integrated circuits has been demonstrated by InP-based materials. Future development planned for InP-based material and device technology includes improvement in operation speed, bandwidth, throughput, and device functions by exploiting novel material physics and device principles using, for example, quantum dots and photonic crystals. Another significant technical challenge to be targeted is the development of low-cost, reliable, easy-to-use

devices and circuits to provide firm infrastructure for ubiquitous communications and information processing. Further progress of integration technology will play an important role in this direction.

Acknowledgment

The author would like to thank T. Enoki (NTT) for his useful suggestions and all the people who have kindly permitted the citation of figures from their publications. A part of the works described here was performed under the management of the Femtosecond Technology Research Association (FESTA) supported by the New Energy and Industrial Technology Development Organization (NEDO).

BIBLIOGRAPHY

1. A. Katz, *Indium Phosphide and Related Materials: Processing, Technology and Devices*, Artech House, 1992; T. P. Pearsall, ed., *GaInAsP Alloy Semiconductors*, Wiley, 1982.
2. O. Wada and H. Hasegawa, eds., *InP-Based Materials and Devices—Physics and Technology*, Wiley, 1999.
3. L. W. James et al., *Phys. Rev. B* **1**:3998–4004 (1970); J. Hayes, Electronics for optoelectronic integrated circuits, in M. Dagenais, R. F. Leheny, and J. Crow, eds., *Integrated Optoelectronics*, Academic Press, 1999, pp. 317–337.
4. U. K. Mishra et al., *IEEE Electron. Device Lett.* **8**:647 (1988).
5. T. P. Lee et al., Long wavelength lasers and IOEIC transmitters, in O. Wada, ed., *Optoelectronic Integration: Physics, Technology and Applications*, Kluwer Academic Publishers, 1994, pp. 144–190.
6. A. Endoh et al., *Jpn. J. Appl. Phys.* **42**:2214–2218 (2003).
7. D. Streit et al., *Proc. 2002 Int. Conf. Indium Phosphide and Related Materials*, (IPRM), 2002, pp. 11–14.
8. K. Murata et al., *IEEE GaAs IC Symp. Tech. Digest*, 2003, pp. 161–164.
9. K. Murata et al., *IEEE GaAs IC Symp.* 2002, pp. 937–939.
10. J. C. Zolper, *Proc. 2002 Int. Conf. Indium Phosphide* (IPRM), 2002, pp. 8–11.
11. O. Wada, ed., *Optoelectronic Integration: Physics, Technology and Applications*, Kluwer Academic Publishers, 1994.
12. M. Dagenais, R. F. Leheny, and J. Crow, eds., *Integrated Optoelectronics*, Academic Press, 1999.
13. K. Nakamura et al., *Proc. 2003 IEEE LEOS Annual Meeting*, 2003, Vol. 1, pp. 348–349.
14. H. Kawanishi et al., *IEEE Photonics Technol. Lett.* **13**:954–956 (2001).
15. H. Kawanishi et al., *OFC 2003 Tech. Digest*, 2003, Vol. 1, pp. 270–271.
16. M. Bouda et al., *OFC 2000 Tech. Digest*, 2000, Tuesday, TuL1-1, pp. 178–180.
17. O. Wada et al., *J. Lightwave Technol.* **9**:9 (1990).
18. G. G. Mekonnen et al., *IEEE Photonics Technol. Lett.* **11**:257–259 (1999).
19. T. Nakata et al., *Proc. ECOC'2002*, 2002, Vol. 4, Paper 10.5.1.
20. K. Takahata et al., *IEEE J. Select. Topics Quantum Electron.* **6**:31–37 (2000).
21. T. Kamiya, F. Saito, H. Yajima, and O. Wada, eds., *Femtosecond Technology—from Basic Research to Application Prospects*, Springer-Verlag, 1999.
22. S. Arahira et al., *Opt. Quantum Electron.* **33**:691 (2001).
23. K. Tajima et al., *Jpn. J. Appl. Phys.* **32**:L1746 (1993).
24. K. Tajima et al., *IEICE Trans. Electron.* **E83-C**:959–965 (2000).
25. S. Nakamura et al., *Abstracts 2002 Int. Workshop on Femtosecond Technology*, Tsukuba, Japan, June 2002, p. 61.
26. T. Akiyama et al., *IEEE Photonics Technol. Lett.* **14**:495 (2002).

INTEGRAL EQUATIONS

S. M. RAO
G. K. GOTHARD
Auburn University
Auburn, Alabama

Mathematics plays a very important role in all the areas of electrical engineering. Whenever we are asked to develop a system or address a problem, the first thing we need to do is to develop a simple model. This simple model often turns out to be a mathematical model. The mathematical model lets us study many important aspects of the problem thoroughly and in an inexpensive manner.

In this article, we deal with an area of mathematics known as *integral equations*. We define an equation as an integral equation when the unknown quantity, specifically, the quantity to be determined, is under an integral sign. Integral equations are usually formulated when it is required to obtain the driving mechanism (input) of a physical system, given the description of the system along with the response function (output). For electrical engineers, the physical system may be an electrical circuit, an electrical machine, or, sometimes, a complex structure such as a fighter aircraft whose electromagnetic signature is the quantity of interest. Similarly, in many situations in electrical engineering, the response function may, simply, be the voltage at some given terminals or the current flowing in a wire.

Several methods are used to solve integral equations [1] using complex mathematics. However, in many practical situations, these methods are inadequate and, quite often, we need to resort to numerical methods to solve these equations. In the following section, we formally introduce *integral equations* using simple mathematical language. We also introduce standard terminology to describe such equations and describe various types of integral equations. In Section 2, we describe a general numerical method, known as *method of moments*, to solve these equations. In Section 3, we present a new technique that makes the method of moments technique computationally more efficient along with a set of numerical results. Note that, although the topic of *integral equations* is really a mathematical subject, we develop the subject using examples from electrical engineering and, in fact, from electromagnetic theory. It must be clearly understood that this way of treatment of the subject does not necessarily preclude the application of the techniques discussed in this article into other areas of engineering.

1. INTEGRAL EQUATIONS

Mathematically speaking, an equation involving the integral of an unknown function of one or more variables is known as an *integral equation*. One of the most common integral equations encountered in electrical engineering is the *convolution integral* given by

$$\int X(\tau)H(t, \tau)d\tau = Y(t) \tag{1}$$

where we note that the response function $Y(t)$ and the system function $H(t, \tau)$ are known and we need to determine the input $X(\tau)$. Of course, if $X(\tau)$ and $H(t, \tau)$ are known and we need to determine $Y(t)$, then Eq. (1) simply represents a integral relationship that can be performed in a straight forward manner. We further note that $H(t, \tau)$ is also commonly known as *impulse response* if Eq. (1) represents the system response of a linear system. In general, in mathematics and in engineering literature, $H(t, \tau)$ is known as *Green's function* or the *kernel function*. We also acknowledge that, for some other physical systems, $Y(t)$ and $X(t)$ may represent the driving force and response functions, respectively.

Next, we note that Eq. (1) is known as *integral equation of first kind*. We also have another type of integral equation given by

$$C_1X(t) + C_2 \int X(\tau)H(t, \tau)d\tau = Y(t) \tag{2}$$

where C_1 and C_2 are constants.

In Eq. (2), we note that the unknown function $X(t)$ appears both inside and outside the integral sign. Such equation is known as the *integral equation of second kind*. Further, we also see in electrical engineering yet another type of integral equation given by

$$C_1 \int X(\tau)H(t, \tau)d\tau + C_2X(t) + C_3 \frac{dX(t)}{dt} = Y(t) \tag{3}$$

which is known as an *integrodifferential equation*.

It may be noted that for a limited number of kernel and response functions, in Eqs. (1)–(3), it is possible to obtain the solution using analytical methods. Several textbooks have been written to discuss the mathematical aspects of the integral equations from analytical point of view [2–4]. However, for a majority of practical problems, these equations can be solved using numerical methods only. Fortunately, in this day and age, we can obtain very accurate numerical solutions owing to the availability of fast digital computers. In the following section, we discuss a general numerical technique, popularly known as *method of moments*, to solve the integral equations (1)–(3).

2. METHOD-OF-MOMENTS SOLUTION

The method-of-moments (MoM) solution procedure was first applied to electromagnetic scattering problems by

Harrington [5]. Consider a linear operator equation given by

$$AX = Y \tag{4}$$

where A represent the integral operator, Y is the known excitation function, and X is the unknown response function to be determined. Now, let X be represented by a set of known functions, termed *basis functions* or *expansion functions* (p_1, p_2, p_3, \dots), in the domain of A as a linear combination:

$$X = \sum_{i=1}^N \alpha_i p_i \tag{5}$$

where the α_i terms are scalars to be determined. Substituting Eq. (5) into Eq. (4), and using the linearity of A , we have

$$\sum_{i=1}^N \alpha_i A p_i = Y \tag{6}$$

where the equality is usually approximate. Let (q_1, q_2, q_3, \dots) define a set of testing functions in the range of A . Now, multiplying Eq. (6) with each q_j and using the linearity property of the inner product, we obtain

$$\sum_{i=1}^N \alpha_i \langle q_j, A p_i \rangle = \langle q_j, Y \rangle \tag{7}$$

for $j = 1, 2, \dots, N$. The set of linear equations represented by Eq. (7) may be solved using simple matrix methods to obtain the unknown coefficients α_j .

The simplicity of the method lies in choosing the proper set of expansion and testing functions to solve the problem at hand. Further, the method provides a most accurate result if properly applied. However, for the integral equation operators, the method generates a dense matrix that may be expensive in terms of computer storage requirements when complex systems are involved. In the following subsections, we discuss the application of the method of moments to some commonly used integral equations in engineering and science.

2.1. Integral Equations without Derivatives

In this section, we develop simple numerical methods to solve integral equations (both first and second kind) applying the method of moments. Further, we restrict our treatment to integral equations with single independent variables (one-dimensional) only. The extension to multiple variables is straightforward and hence is not considered here. The numerical methods are general methods, and thus applicable to variety of practical problems.

Consider an integral equation given by

$$\int_{x'=-w}^w u(x')g(x, x')dx' = f(x) \quad x \in (-w, w) \tag{8}$$

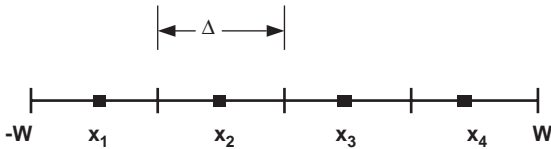


Figure 1. Match points for the integral equation.

in which $u(x)$ is the unknown function to be determined. For the MoM analysis of such problems, we develop a numerical scheme known as the *collocation method*, *sub-domain method*, or *point-matching method*. For this procedure, we first divide the interval $-w$ to w into N equal segments of width Δ as shown in Fig. 1.

The segment centerpoints are given by

$$x_i = -w + (i - 1)\Delta + 0.5\Delta \quad i = 1, 2, \dots, N \quad (9)$$

Note that while defining Eq. (9), we have divided the interval $-w$ to w into equal segments, although this need not be the case in general.

The next step in the MoM solution procedure is to define a suitable set of basis and testing functions. Our research shows that, for this type of problem, namely, the integral equations with no derivatives, the most convenient and simple set of functions are pulse functions with unit amplitude as basis functions and Dirac delta distributions (functions) as testing functions. In the following, we formally define these functions, as shown in Fig. 2, given by

$$p_i(x) = \begin{cases} 1 & x_i - \frac{\Delta}{2} \leq x \leq x_i + \frac{\Delta}{2} \\ 0 & \text{otherwise} \end{cases} \quad (10)$$

and

$$q_j(x) = \delta(x - x_j) \quad (11)$$

Here, we emphasize that Eqs. (10) and (11) are by no means the only set of functions used in practice. It is quite

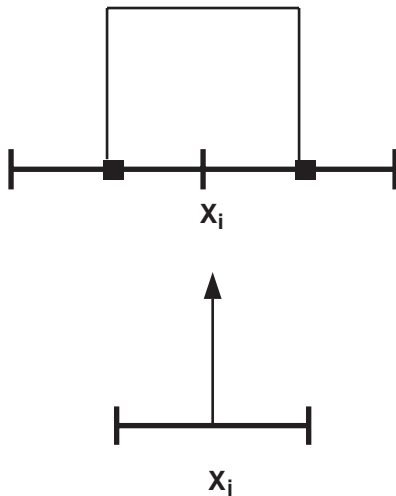


Figure 2. Pulse function and delta function.

possible to define a completely different set of functions as long as these functions satisfy a certain set of conditions [6–8]. Further, it is also possible to carry out an entirely different scheme in which the expansion and testing functions are defined over the whole interval without ever dividing the solution region into subsections. Such numerical schemes are known as *entire-domain methods*. Entire domain methods are known to be mathematically unstable [5], which may be overcome by a suitable choice of testing and basis functions and/or a combination of sub-domain/entire-domain functions [9]. However, we will not present the numerical treatment with entire-domain functions in this work since the subject is still in research stage.

First, we shall consider the testing procedure. Here, we multiply the Eq. (8) by the testing function q_j and integrate over the whole interval to obtain a set of equations given by

$$\int_{x'=-w}^w u(x')g(x_j, x') dx' = f(x_j) \quad j = 1, 2, \dots, N. \quad (12)$$

Observe that, while evaluating Eq. (12), we made use of the well-known properties of the delta distribution (function). Also note that Eq. (12) is actually a set of N equations for each j and that x_j represents the value of the independent variable at the center of the j th subdomain. Further, observe that we are matching the LHS and RHS (left- and right-hand sides) of Eq. (12) at points x_j for $j = 1, 2, \dots, N$. Thus, these points are known also as *match points*.

Next we consider the expansion procedure. Using the basis functions defined in Eq. (10), the unknown quantity $u(x)$ may be written as

$$u(x) = \sum_{i=1}^N \alpha_i p_i \quad (13)$$

where the α terms represent the unknown scalar coefficients. Substituting Eq. (13) into Eq. (12), we have

$$\sum_{i=1}^N \alpha_i \int_{x'=x_i-\Delta/2}^{x_i+\Delta/2} g(x_j, x') dx' = f(x_j) \quad j = 1, 2, \dots, N. \quad (14)$$

Note that Eq. (14) may be written as a matrix equation, given by

$$[Z][I] = [V] \quad (15)$$

where

$$Z_{ji} = \int_{x'=x_i-\Delta/2}^{x_i+\Delta/2} g(x_j, x') dx' \quad (16)$$

$$V_j = f(x_j) \quad (17)$$

and the column vector $[I]$ contains unknown coefficients α . Except for certain special cases, the matrix $[Z]$ is a well-conditioned matrix, and hence the solution of Eq. (15) is

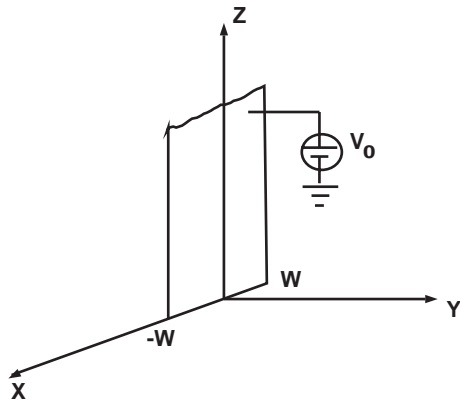


Figure 3. Infinite strip raised to 1 Volt potential.

straightforward. Also, the integrations involved in Eq. (16) may be performed either analytically or numerically depending on the exact nature of the kernel function.

Finally, the numerical method described so far is also known as the *pulse expansion* or *point-matching method*. In the following, we present an example problem based on the procedure described so far.

Example 1. Consider an infinitely long conducting strip of width of 0.1m located symmetrically at the origin as shown in Fig. 3. The strip is raised to a potential of 1V. Note that the reference point (i.e., $V=0$) is at $x = 1$ m. Calculate the charge distribution on the strip.

Solution: Following the basic principles of electrostatics, an integral equation may be developed, given by

$$\int_{x'=-0.05}^{0.05} q_s(x') \ln |x - x'| dx' = 2\pi\epsilon_0 \quad x \in (-0.05, 0.05) \quad (18)$$

where $\epsilon_0 = 8.854e - 12$ is the permittivity of the surrounding medium. Following the numerical procedures described so far, we obtain the elements of the $[Z]$ matrix given by

$$\begin{aligned} Z_{ji} &= \int_{x'=x_i-\Delta/2}^{x_i+\Delta/2} \ln |x_j - x'| dx' \\ &= \Delta - \frac{\Delta}{2} \ln \left| (x_j - x_i)^2 - \left(\frac{\Delta}{2}\right)^2 \right| \\ &\quad - (x_j - x_i) \ln \frac{|x_j - x_i + \Delta/2|}{|x_j - x_i - \Delta/2|} \end{aligned} \quad (19)$$

and the elements of the $[V]$ matrix are

$$V_j = 2\pi\epsilon_0 \quad (20)$$

In Fig. 4, we present the charge distribution for N equal to 10, 50, and 100 obtained by solving the integral equation (18).

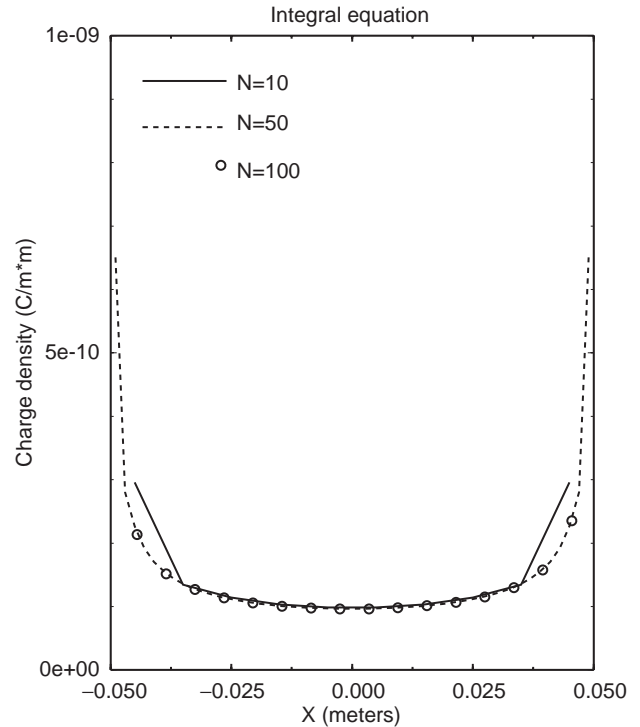


Figure 4. Charge density distribution on the infinite strip.

2.2. Integral Equations With Derivatives

In this section, we develop simple numerical methods to solve integrodifferential equations, that is, integral equations with derivative operators, applying the method of moments. As before, we restrict our treatment to integral equations with a single independent variable (one-dimensional) only. The extension to multiple variables is straightforward and hence is not considered here. The numerical methods are general methods, and thus applicable to variety of practical problems.

We consider two cases in this section: (1) the first-order integrodifferential equation and (2) the second-order integrodifferential equation. Obviously, higher-order derivatives may be handled in a similar manner.

2.2.1. First-Order Integrodifferential Equation. Consider a first-order integrodifferential equation given by

$$\frac{\partial}{\partial x} \int_{x'=-w}^w u(x')g(x,x')dx' = f(x) \quad x \in (-w, w) \quad (21)$$

subject to

$$\int_{x=-w}^w u(x)dx = 0 \quad (22)$$

Equation (22) is also known as *constraining equation*. In variety of situations, constraining equation can be implicitly enforced by a proper choice of basis and/or testing functions. This necessitates a more elaborate construction of basis/testing functions that, although seeming to be complicated, result in an efficient numerical solution. It is

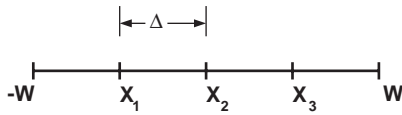


Figure 5. Match points for Integrodifferential equation.

quite easy to see that a straightforward application of the method discussed in the previous section, namely, pulse expansion and point-matching method, results in a $N \times N$ matrix. However, the application of the constraint equation adds one more column to the $[Z]$ matrix, thus making the problem an overdetermined system. Further, other numerical problems, such as stability and nonuniqueness, set in when MoM is applied blindly. Thus, we develop the following numerical procedure for this case.

As before, the interval $(-w, w)$ is divided into N equal segments. But for this case, the match points are labeled in the following way for mathematical convenience as shown in Fig. 5.

$$x_i = -w + i \times \Delta \quad i = 1, 2, \dots, N - 1 \quad (23)$$

In order to enforce the constraining equation (22), we let the basis function to overlap over two subdomains with positive unit height in the first subdomain and negative unit pulse in the second subdomain as shown in Fig. 6.

Thus, mathematically, we define the basis function as

$$p_i(x) = \begin{cases} 1 & x_{i-1} \leq x \leq x_i \\ -1 & x_i \leq x \leq x_{i+1} \\ 0 & \text{otherwise} \end{cases} \quad (24)$$

and express the unknown quantity $u(x)$ as

$$u(x) = \sum_{i=1}^{N-1} \alpha_i p_i \quad (25)$$

Note that, by defining basis functions as in Eq. (24), Eq. (22) is automatically satisfied, which can be proved as

$$\begin{aligned} \int_{x=-w}^w u(x) dx &= \sum_{i=1}^N \alpha_i \int p_i dx \\ &= \sum_{i=1}^N \alpha_i \left[\int_{x_{i-1}}^{x_i} dx - \int_{x_i}^{x_{i+1}} dx \right] \\ &= 0 \end{aligned} \quad (26)$$

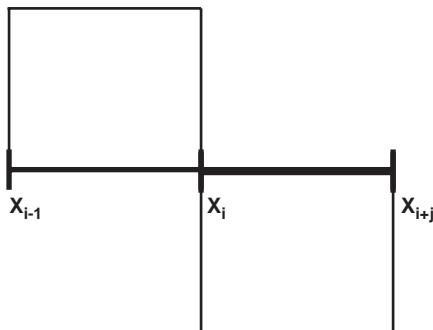


Figure 6. Pulse doublet function.

The functions defined by Eq. (24) are known as *pulse doublet functions*.

Next, we define the testing procedure for this case. Note that we have one derivative on the integral sign. By simple mathematical manipulation, we transform the derivative operator onto the testing function q_j . Using a compact notation

$$\langle f, g \rangle = \int fg dx \quad (27)$$

we can write the integrodifferential equation (21) as

$$\left\langle \frac{\partial v}{\partial x}, q_j \right\rangle = \langle f(x), q_j \rangle \quad (28)$$

where

$$v(x) = \int_{x'=-w}^w u(x')g(x, x')dx' \quad (29)$$

Then, we have

$$\begin{aligned} \left\langle \frac{\partial v}{\partial x}, q_j \right\rangle &= \int \frac{\partial v}{\partial x} q_j dx \\ &= [q_j v] - \int \frac{\partial q_j}{\partial x} v dx \end{aligned} \quad (30)$$

The first term in the Eq. (30) can be set to zero if $q_j = 0$ at the ends of the subdomain.

Keeping this procedure in mind, we select the testing functions in such a way that when the derivative is transformed onto the testing function, the result must be a delta distribution (function). A unit pulse function, as shown in Fig. 7, has this property whose derivative happens to be two delta distributions on either end of the pulse.

Thus, for first-order integrodifferential equations, we choose the testing function q_j as

$$q_j(x) = \begin{cases} 1 & x_j - \frac{\Delta}{2} \leq x \leq x_j + \frac{\Delta}{2} \\ 0 & \text{otherwise} \end{cases} \quad (31)$$

The numerical procedure may be best illustrated by the following example.

Example 2. Consider an infinitely long conducting strip of width 1 m, as shown in Fig. 3, is immersed in a electrostatic field. Calculate the charge distribution on the strip.

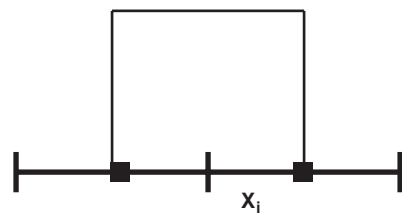


Figure 7. Pulse-testing function.

Solution: Following the basic principles of electrostatics, and applying the electric field boundary condition on perfect conducting bodies, an integral equation may be developed, given by

$$\frac{\partial}{\partial x} \int_{x'=-w}^w q_s(x') \ln|x-x'| dx' = 2\pi\epsilon \mathbf{a}_x \cdot \mathbf{E}^i \quad x \in (-w, w) \quad (32)$$

subject to

$$\int_{x=-w}^w q_s(x) dx = 0 \quad (33)$$

where \mathbf{E}^i , q_s , and \mathbf{a}_x are the impressed electric field, charge density, and the x -directed unit vector, respectively. For the numerical solution, we divide the interval $(-w, w)$ into N subdomains of width Δ and label the match points as shown in Fig. 5. Note that when the interval is divided into N divisions, we actually have $N-1$ match points.

Defining the testing functions by Eq. (31), and carrying out the mathematical steps outlined in Eq. (30), we get

$$\int_{x'=-w}^w q_s(x') \ln\left|x_j + \frac{\Delta}{2} - x'\right| dx' - \int_{x'=-w}^w q_s(x') \ln\left|x_j - \frac{\Delta}{2} - x'\right| dx' = 2\pi\epsilon \Delta \mathbf{a}_x \cdot \mathbf{E}^i(x_j) \quad (34)$$

for $j = 1, 2, \dots, N-1$.

Next, we apply the expansion procedure. By selecting the basis functions as described in Eq. (25), the constraining equation (33) is automatically enforced. Thus, applying the method of moments procedure, we obtain $[Z][I] = [V]$, where

$$\begin{aligned} Z_{ji} = & \int_{x_{i-1}}^{x_i} \ln\left|x_j + \frac{\Delta}{2} - x'\right| dx' \\ & - \int_{x_i}^{x_{i+1}} \ln\left|x_j + \frac{\Delta}{2} - x'\right| dx' \\ & - \int_{x_{i-1}}^{x_i} \ln\left|x_j - \frac{\Delta}{2} - x'\right| dx' \\ & + \int_{x_i}^{x_{i+1}} \ln\left|x_j - \frac{\Delta}{2} - x'\right| dx' \end{aligned} \quad (35)$$

and

$$V_j = 2\pi\epsilon \Delta \mathbf{a}_x \cdot \mathbf{E}^i(x_j) \quad (36)$$

In Fig. 8, we present the charge distribution for N equal to 10, 50, and 100 obtained by solving the integrodifferential equation (32). Note that, in this procedure, the dimension of the system matrix is $N-1$.

2.2.2. Second-Order Integrodifferential Equation. In this section, we consider techniques for solving the integrodif-

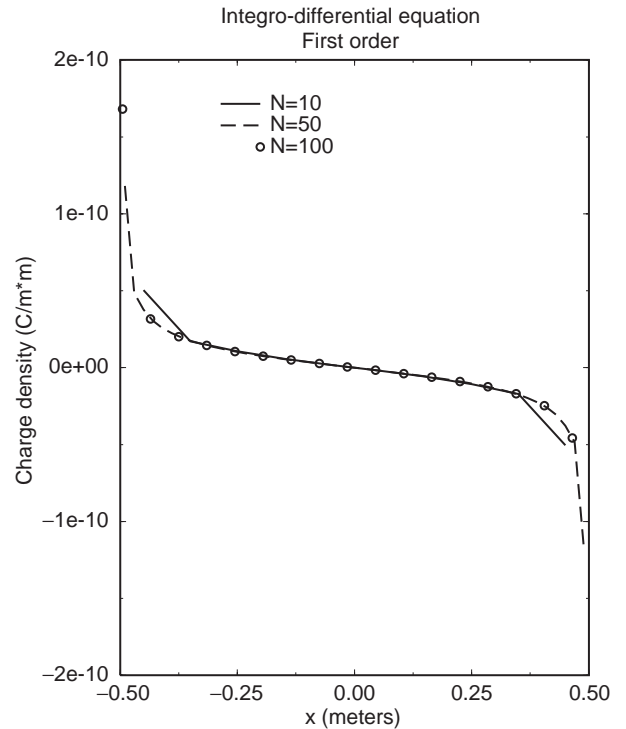


Figure 8. Charge density distribution on the infinite strip immersed in electric field $\mathbf{E}^i = \mathbf{a}_x$.

ferential equation

$$\frac{\partial^2}{\partial x^2} \int_{x'=-w}^w u(x') g(x, x') dx' = f(x) \quad x \in (-w, w) \quad (37)$$

where the unknown function $u(x)$ must satisfy the boundary conditions $u(w) = u(-w) = 0$.

These types of integral equations usually appear in electromagnetic and acoustic scattering problems; the most common is the dipole antenna problem in antenna engineering. Further, the treatment of the second-order integrodifferential equation, coupled with the treatment of first-order derivatives, provides a solution procedure for handling higher-order derivatives.

We begin our analysis by re-writing the integrodifferential equation (37) in the following form:

$$\frac{\partial}{\partial x} \int_{x'=-w}^w u(x') \frac{\partial g(x, x')}{\partial x} dx' = f(x) \quad x \in (-w, w) \quad (38)$$

For almost all mathematical problems in engineering, there exists a definite relationship between $\partial g/\partial x$ and $\partial g/\partial x'$. In fact, for electromagnetic (EM) and acoustic scattering problems, we have $\partial g/\partial x = -(\partial g/\partial x')$. Using this relationship, we can write Eq. (38), at least for EM and acoustic problems, as

$$\frac{\partial}{\partial x} \int_{x'=-w}^w \frac{\partial u(x')}{\partial x'} g(x, x') dx' = f(x) \quad x \in (-w, w) \quad (39)$$

Now, we have an integrodifferential equation of first order that we already know how to handle. At first, we divide the interval $(-w, w)$ into N segments and label $N-1$ match points as shown in Fig. 5. The definition of testing functions and the testing procedure are identical to those of the first-order integrodifferential equation and hence need not be repeated again. However, we need to look more closely at the basis functions.

Note that, for the case of first-order integrodifferential equations, we defined the “pulse doublet” as the expansion function and obtained the solution for the unknown function. In the present case we can do the same thing, if we define the *antiderivative* of the pulse doublet as the expansion function. Following this logic, we define the basis functions for the solution of second order integrodifferential equation as

$$p_i(x) = \begin{cases} 1 - \frac{x_i - x}{\Delta} & x_{i-1} \leq x \leq x_i \\ 1 + \frac{x_i - x}{\Delta} & x_i \leq x \leq x_{i+1} \\ 0 & \text{otherwise} \end{cases} \quad (40)$$

The functions described in Eq. (40), and shown in Fig. 9, are popularly known as *triangle functions*, which are linear piecewise.

Thus, to solve the second-order integrodifferential equation, we employ triangle function expansion and pulse function testing. We describe the numerical procedure using the following example.

Example 3. Consider a finite-length straight wire with radius $a = 0.001\lambda$ and length $2h = 0.5\lambda$ illuminated by an electromagnetic plane wave (wavelength λ) as shown in Fig. 10. Calculate the current induced on the wire.

Solution: Since the radius a is very small compared to λ and h , we can use the thin-wire theory [10] to formulate the integrodifferential equation. Following the mathematical procedures described by Jones [11], we derive the following integral equation, given by

$$\begin{aligned} & \frac{\partial}{\partial z} \int_{z'=-h}^h \frac{\partial I(z')}{\partial z'} G(z-z') dz' \\ & + k^2 \int_{z'=-h}^h I(z') G(z-z') dz' \\ & = -j \frac{4\pi k}{\eta} E_z^i(z) \quad z \in (-h, h) \end{aligned} \quad (41)$$

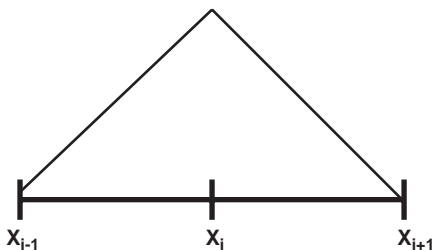


Figure 9. Triangle basis function.

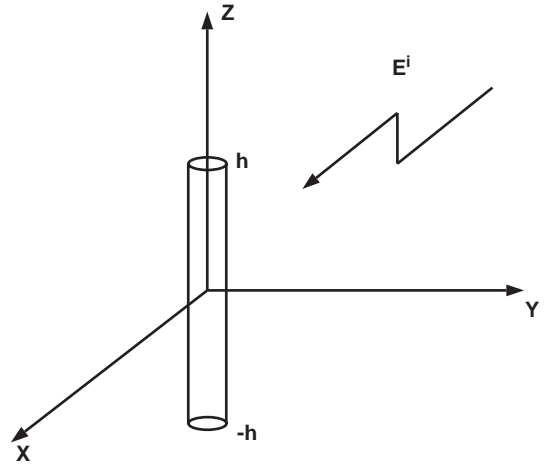


Figure 10. Straight wire illuminated by a plane wave.

where

$$G(z-z') = \frac{e^{-jkR}}{R} \quad (42)$$

and

$$R = \sqrt{(z-z')^2 + a^2} \quad (43)$$

In Eqs. (41)–(43), I is the unknown current induced on the wire, $E_z^i(z)$ is the z component of the incident plane wave, $k = 2\pi/\lambda$ is the wavenumber, and η is the wave impedance of the surrounding medium.

First, divide the wire region $(-h, h)$ into N equal segments, labeling $N-1$ match points as shown in Fig. 5. Next, for this problem, we choose the expansion functions p_i defined in Eq. (40) to express the unknown current I and the testing functions q_j defined in Eq. (31).

Thus, we have

$$I = \sum_{i=1}^{N-1} \alpha_i p_i \quad (44)$$

Next, we consider the testing procedure. By following the same procedures of the previous section on the first-order integrodifferential equation, the testing procedure yields

$$\begin{aligned} & \int_{z'=-h}^h \frac{\partial I(z')}{\partial z'} G\left(z_j + \frac{\Delta}{2} - z'\right) dz' \\ & - \int_{z'=-h}^h \frac{\partial I(z')}{\partial z'} G\left(z_j - \frac{\Delta}{2} - z'\right) dz' \\ & + \Delta k^2 \int_{z'=-h}^h I(z') G(z_j - z') dz' \\ & = -j \frac{4\pi k \Delta}{\eta} E_z^i(z_j) \end{aligned} \quad (45)$$

for $j = 1, 2, \dots, N-1$. Note that, in Eq. (45), the integrations on the second term and the right-hand side of the Eq. (41) are approximated by a simple one-point rule.

Substituting the expansion equation (44) into Eq. (45), we obtain the matrix equation $[(1/\Delta)[Z^a] + (k^2\Delta)[Z^b]] [I] = [V]$, where the matrix elements are:

$$Z_{ji}^a = \int_{z_{i-1}}^{z_i} G\left(z_j + \frac{\Delta}{2} - z'\right) dz' - \int_{z_i}^{z_{i+1}} G\left(z_j + \frac{\Delta}{2} - z'\right) dz' - \int_{z_{i-1}}^{z_i} G\left(z_j - \frac{\Delta}{2} - z'\right) dz' + \int_{z_i}^{z_{i+1}} G\left(z_j - \frac{\Delta}{2} - z'\right) dz' \tag{46}$$

$$Z_{ji}^b = \int_{z_{i-1}}^{z_i} \left\{1 - \frac{z_i - z}{\Delta}\right\} G(z_j - z') dz' + \int_{z_i}^{z_{i+1}} \left\{1 + \frac{z_i - z}{\Delta}\right\} G(z_j - z') dz' \tag{47}$$

and

$$v_j = -j \frac{4\pi k \Delta}{\eta} E_z^i(z_j) \tag{48}$$

The integrations involved in Eqs. (46) and (47) may be carried out using the methods discussed in [12].

In Fig. 11, we present the current induced on a half-wave dipole wire scatterer due to a unit-amplitude,

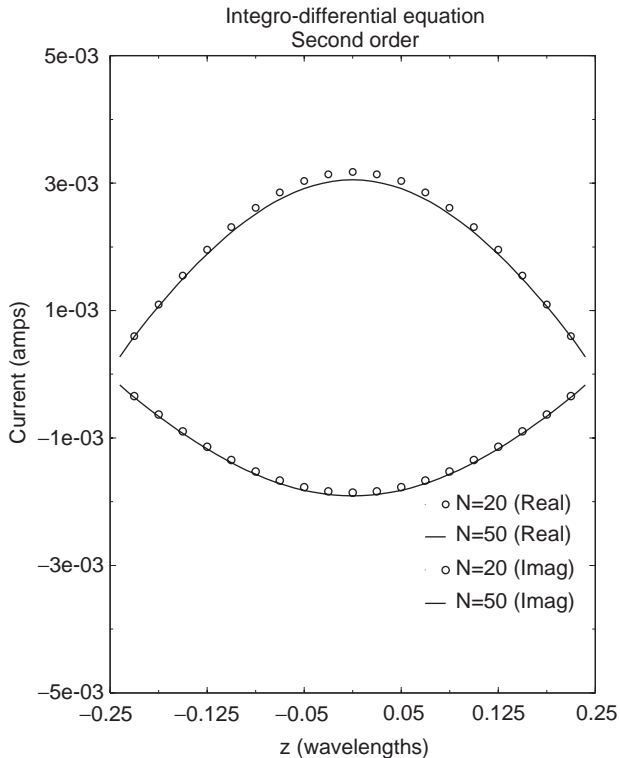


Figure 11. Current induced on the wire scatterer.

normally incident plane wave for N equal to 20 and 50 divisions obtained by using Eqs. (46)–(48).

2.3. Integral Equations with More Variables

In the previous subsection, we discussed numerical methods applying the method of moments to handle integral and integrodifferential equations with one independent variable. Extension to the multivariable case is straightforward and follows the same numerical procedures discussed so far. For example, for the two-variable case, that is, the xy plane, the solution region may be divided into square or rectangular cells, and one can construct the basis and testing functions using the methods discussed in the previous section [13]. For a more general situation, the solution region can be divided into triangular subdomains along with suitable basis and testing functions [14,15]. Efficient solutions have been obtained for very complex problems using these methods in electromagnetics and acoustics [16–19], and it is quite possible that these methods found applications in other areas of engineering. Finally, we discussed primarily only boundary-value problems in this work, but solutions have also been obtained for initial-value problems [20–28] using the same methods. An extensive application of method of moments to electromagnetic scattering problems may be obtained from Miller et al. [29].

3. SPARSE-MATRIX METHODS

One major problem with MoM is the generation of a dense matrix and for complex problems; the dimension of this matrix can be prohibitively large. Usually, for electromagnetic and acoustic scattering problems, it is necessary to divide the solution region into subdomains small enough to yield accurate results. By “small enough,” we mean about 200–300 subdomains per square wavelength. In usual practice, we may typically solve for several thousand unknowns for large, complex problems. This requirement quickly becomes expensive, in terms of computational resources, and may even become impossible to handle. Hence, we look for alternate schemes to reduce the computational resources by generating a sparse matrix instead of a full matrix.

The generation of a sparse matrix in the method of moment solution procedure may be achieved in one of two ways: (1) by defining a special set of basis functions to represent the unknown quantity or (2) by handling the influence of the kernel function in a novel way. The use of well-known wavelet-type basis functions to provide the required sparsity belong to the former category [30], and application of the fast multipole method (FMM) belongs to the latter category [31]. So far, the wavelet-type basis functions have been applied to integral equations with one variable only, and it remains to be seen how these functions can be utilized for two or more variable case. In contrast, in the FMM scheme, the matrix-vector product is carried out in a novel way, and this seem to work well for more complex problems. Unfortunately, the FMM is a complicated scheme, and any reasonable summary of the method is beyond the scope of the present article.

There is also yet another scheme, known as *impedance matrix localization* (IML) scheme, which achieves modest sparsity for simple problems [32]. Note that the kernel function is, in general, a decaying function with respect to the distance between the source and observation points. Thus, with increasing distances, the influence of a given source becomes negligible at a sufficiently distant observation point and may actually be set to zero. The IML scheme cleverly exploits this fact. However, there is a certain degree of arbitrariness in this scheme and seems to work for simple problems only.

A newer method, known as the *generalized sparse-matrix reduction* (GSMR), scheme has been proposed and seems to improve on the IML method. The basic concept utilized in the GSMR technique may be qualitatively illustrated as follows. Following similar procedures of the MoM, a moment matrix is also generated in the GSMR method. However, in contrast to the conventional moment method where interaction is computed from each and every cell on other cells, only the interaction from the self-cell and few neighboring cells is computed in the GSMR technique. In fact, for single-variable problems (wire scatterer and two-dimensional, infinite cylinders) only the self-term and two neighboring terms on either side of the self-cell are generated in this technique. This implies that the moment matrix for the GSMR technique is essentially sparse. Further, the effect of nonself-terms is taken into account by defining a set of linearly independent functions over the entire structure. In mathematical terms, for single variable problems, the procedure may be described as follows:

Let $[Z]$ represent the moment matrix for a given problem generated by using appropriate basis and weighting functions. Note that, for well-defined problems with proper choice of basis and testing functions, the moment matrix is well conditioned and diagonally strong. The j th row of the moment matrix may be written as

$$\sum_{i=1}^N Z_{j,i} I_i = V_j \quad (49)$$

where all the matrix elements $Z_{j,i}$ are nonzero. In the new GSMR technique, the j th row is modified as

$$\sum_{i=j-1}^{j+1} \alpha_{j,i} Z_{j,i} I_i = \Gamma_j V_j \quad (50)$$

where $\alpha_{j,j-1}$, $\alpha_{j,j}$, $\alpha_{j,j+1}$, and Γ_j are the unknown coefficients and the remaining terms in the row are set to zero. Further, dividing by $Z_{j,j}$, Eq. (50) may be rewritten as

$$\sum_{i=j-1}^{j+1} \beta_{j,i} I_i = \gamma_j V_j \quad (51)$$

which may be expressed, using the matrix notation, as

$$[\beta][I] = [V] \quad (52)$$

where $[\beta]$ is a sparse matrix with, at most, three nonzero elements per row.

On a close examination of Eq. (52), it is obvious that one needs to reconstruct the $[\beta]$ matrix. This task may be accomplished by first setting $\gamma_j = 1$ for $j = 1, \dots, N$ in Eq. (51).

Next, define three linearly independent functions, $I^{(1)}$, $I^{(2)}$, and $I^{(3)}$, over the entire domain of the problem. These functions may be regarded as source distributions. For the examples we discuss below, these functions are assumed to be a constant, $\cos(kl)$ and $\sin(kl)$, where $k = (2\pi/\lambda)$ is the wavenumber and l is the parameter measured along the length of the independent variable in the integral equation.

The next step in the GSMR technique is to compute the corresponding response functions, $V^{(1)}$, $V^{(2)}$, and $V^{(3)}$. This task may be easily accomplished by using the assumed source distributions $I^{(1)}$, $I^{(2)}$, and $I^{(3)}$, and utilizing Green's function for the problem.

Once we have $I^{(1)}$, $I^{(2)}$, $I^{(3)}$, $V^{(1)}$, $V^{(2)}$, and $V^{(3)}$, we may construct the $[\beta]$ matrix as follows:

- For any j , sample $I^{(1)}$, $I^{(2)}$, and $I^{(3)}$ at locations $j-1$, j , and $j+1$, $V^{(1)}$, $V^{(2)}$, and $V^{(3)}$ at location j , and write the following system of equations:

$$\begin{aligned} \beta_{j,j-1} I_{j-1}^{(1)} + \beta_{j,j} I_j^{(1)} + \beta_{j,j+1} I_{j+1}^{(1)} &= V_j^{(1)} \\ \beta_{j,j-1} I_{j-1}^{(2)} + \beta_{j,j} I_j^{(2)} + \beta_{j,j+1} I_{j+1}^{(2)} &= V_j^{(2)} \\ \beta_{j,j-1} I_{j-1}^{(3)} + \beta_{j,j} I_j^{(3)} + \beta_{j,j+1} I_{j+1}^{(3)} &= V_j^{(3)} \end{aligned} \quad (53)$$

- Solve Eq. (54) to obtain $\beta_{j,j-1}$, $\beta_{j,j}$, and $\beta_{j,j+1}$ and store in the j th row of the $[\beta]$ matrix.
- Repeat the previous two steps for all values of j .

Further, note that for $j=1$ and $j=N$, we select $\beta_{1,N}$, $\beta_{1,1}$, and $\beta_{1,2}$, and $\beta_{N,N-1}$, $\beta_{N,N}$, and $\beta_{N,1}$, respectively.

Once all the coefficients for each row are computed, we have successfully generated the new matrix representation for the integral equation. Finally, Eq. (52) may be solved efficiently using iterative methods such as the conjugate gradient method [33] or the GMRES [generalized minimal residual (algorithm)] method [34] since we are dealing with sparse matrices.

Example 4. Consider a 10λ straight wire, with 0.001λ radius, illuminated by a normally incident plane wave. The matrix sizes for the MoM and GSMR method are 149×149 and 149×3 , respectively. The results are shown in Fig. 12, and the comparison is excellent.

Example 5. Consider the case of a circular loop located in the $z=0$ plane with center at the origin. The loop is illuminated by an x -polarized plane wave traveling along the z axis. Figure 13 shows the results for $ka=150$, where k and a are the wavenumber and the radius of the loop, respectively. The matrix sizes for the MoM and the GSMR technique are 1800×1800 and 1800×3 , respectively. It is evident from the figure that the results compare very well

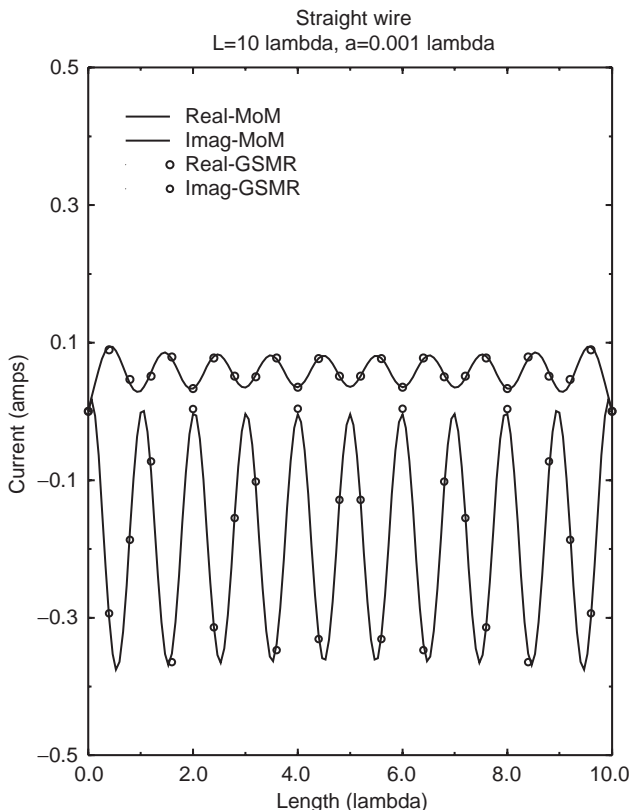


Figure 12. Current induced on the 10λ wire scatterer.

with each other. This example clearly illustrates the applicability of the GSMR method for truly large bodies.

Example 6. Finally, we present the case of an infinitely long, conducting strip illuminated by a transverse magnetic (TM) incident electromagnetic plane wave. The derivation of the governing integral equation for this problem may be found in the text by Harrington [5]. Figure 14 shows the current density induced on a 150λ bent strip

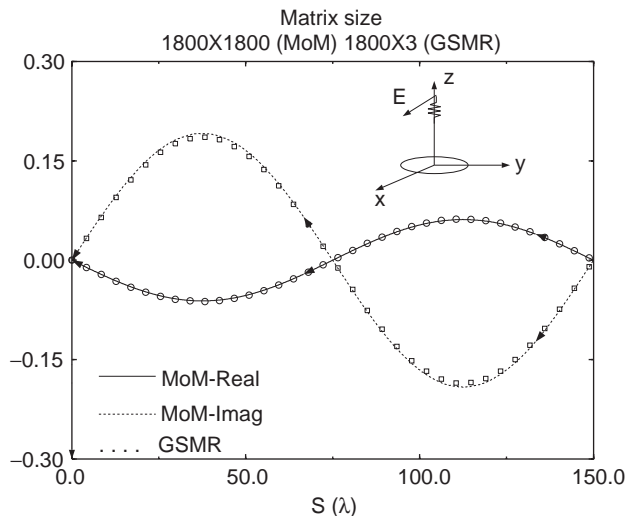


Figure 13. Current induced on the circular loop.

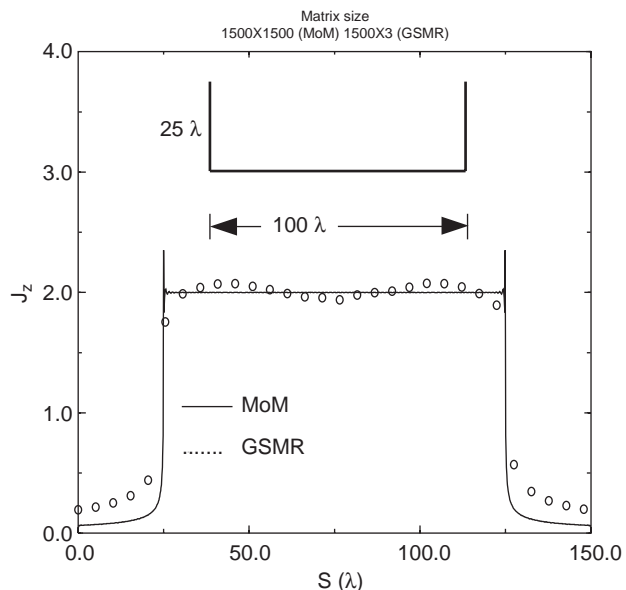


Figure 14. Current induced on the conducting bent strip by a TM incident plane wave. The cross section of the strip is shown in the inset.

obtained by applying MoM and GSMR techniques. The comparison between both methods is reasonably accurate for both cases as evident from the figure.

Finally, before closing the discussion on GSMR technique, the existence of $[\beta]$ matrix may be explained in the following way. It may be noted that the moment matrix generated in the conventional MoM solution procedure is a representation of the unique relationship that exists between the source and the response. This relationship is specified in mathematical terms via Green's function along with the boundary conditions. Further, this relationship holds for any source distribution and response function as long as the response function is derived utilizing Green's function satisfying the appropriate boundary conditions. Since the $[\beta]$ matrix is developed using this unique relationship, Eq. (52) must represent a discretized form of the operator equation. Further, it should be noted that, although the operator equation is unique, the matrix representation is *not necessarily* unique. This is quite obvious since different basis and testing functions result in a different matrix representation. Also, one can perform elementary row and column operations on the given system of equations and arrive at another representation of the same operator equation. However, as a word of caution, it may be noted that the GSMR technique is a recent concept and has been tested only on some simple problems. It is obvious that the procedure needs to be validated for more complex geometries. Presently, work is in progress to apply the GSMR technique to some of these cases.

BIBLIOGRAPHY

1. W. Pogorzelski, *Integral Equations and Their Applications*, Vols. I-III, Pergamon Press, New York, 1966.

2. B. L. Moiseiwitsch, *Integral Equations*, Longman, New York, 1977.
3. A. C. Pipkin, *A Course on Integral Equations*, Springer-Verlag, New York, 1991.
4. I. Stakgold, *Green's Functions and Boundary Value Problems*, J Wiley, New York, 1979.
5. R. F. Harrington, *Field Computation by Moment Methods*, Macmillan, New York, 1968.
6. T. K. Sarkar, A note on the choice of weighting functions in the method of moments, *IEEE Trans. Anten. Propag.* **33**:436–441 (1985).
7. T. K. Sarkar, A. R. Djordjevic, and E. Arvas, On the choice of expansion and weighting functions in the method of moments, *IEEE Trans. Anten. Propag.* **33**:988–996 (1985).
8. A. R. Djordjevic and T. K. Sarkar, A theorem on the moment methods, *IEEE Trans. Anten. Propag.* **35**:353–355 (1987).
9. J. M. Bornholdt and L. N. Medgyesi-Mitschang, Mixed domain Galerkin expansions in scattering problems, *IEEE Trans. Anten. Propag.* **36**:216–227 (1988).
10. R. W. P. King, *The Theory of Linear Antennas*, Harvard Univ. Press, Cambridge, MA, 1956.
11. D. S. Jones, *Methods in Electromagnetic Wave Propagation*, Clarendon, Oxford, 1979.
12. D. R. Wilton, S. M. Rao, A. W. Glisson, D. H. Schaubert, O. M. Al-Bundak, and C. M. Butler, Potential integrals for uniform and linear source distributions on polygonal and polyhedral domains, *IEEE Trans. Anten. Propag.* **32**:276–281 (March 1984).
13. A. W. Glisson and D. R. Wilton, Simple and efficient numerical methods for problems of electromagnetic radiation and scattering from surfaces, *IEEE Trans. Anten. Propag.* **28**:593–603 1980.
14. S. M. Rao, A. W. Glisson, D. R. Wilton, and B. S. Vidula, A simple numerical solution procedure for statics problems involving arbitrary shaped surfaces, *IEEE Trans. Anten. Propag.* **27**:604–608 (1979).
15. S. M. Rao, D. R. Wilton, and A. W. Glisson, Electromagnetic scattering by surfaces of arbitrary shape, *IEEE Trans. Anten. Propag.* **30**:409–418 (1982).
16. S. M. Rao and P. K. Raju, Application of the method of moments to acoustic scattering from multiple bodies of arbitrary shape, *J. Acoust. Soc. Am.* **86**:1143–1148 (1989).
17. P. K. Raju, S. M. Rao, and S. P. Sun, Application of the method of moments to acoustic scattering from multiple infinitely long fluid filled cylinders, *Comput. Struct.* **39**:129–134 (1991).
18. S. M. Rao and B. S. Sridhara, Application of the method of moments to acoustic scattering from arbitrary shaped rigid bodies coated with loss-less, shearless materials of arbitrary thickness, *J. Acoust. Soc. Am.* **90**:1601–1607 (Sept. 1991).
19. S. M. Rao and B. S. Sridhara, Acoustic Scattering from arbitrarily shaped multiple bodies in half space: Method of moments solution, *J. Acoust. Soc. Am.* **91**:652–657 (Feb. 1992).
20. C. L. Bennett, *A Technique for Computing Approximate Electromagnetic Impulse Response of Conducting Bodies*, Ph.D. thesis, Purdue Univ., Lafayette, IN, 1968.
21. S. M. Rao, T. K. Sarkar, and S. A. Dianat, The application of the conjugate gradient method to the solution of transient electromagnetic scattering from thin wires, *Radio Sci.* **19**:1319–1326 (Sept.–Oct. 1984).
22. S. M. Rao, T. K. Sarkar, and S. A. Dianat, A novel technique to the solution of transient electromagnetic scattering from thin wires, *IEEE Trans. Anten. Propag.* **34**:630–634 (May 1986).
23. S. M. Rao and D. R. Wilton, Transient scattering by conducting surfaces of arbitrary shape, *IEEE Trans. Anten. Propag.* **39**:56–61 (Jan. 1991).
24. D. A. Vechinski and S. M. Rao, Transient scattering from dielectric cylinders—*E*-field, *H*-field, and combined field solutions, *Radio Sci.* **27**:611–622 (Sept.–Oct. 1992).
25. D. A. Vechinski and S. M. Rao, Transient scattering from two-dimensional dielectric cylinders of arbitrary shape, *IEEE Trans. Anten. Propag.* **40**:1054–1060 (Sept. 1992).
26. D. A. Vechinski and S. M. Rao, Transient scattering by conducting cylinders—TE case, *IEEE Trans. Anten. Propag.* **40**:1103–1106 (Sept. 1992).
27. D. A. Vechinski and S. M. Rao, A stable procedure to calculate the transient scattering by conducting surfaces of arbitrary shape, *IEEE Trans. Anten. Propag.* **40**:661–665 (June 1992).
28. D. A. Vechinski, S. M. Rao, and T. K. Sarkar, Transient scattering from three-dimensional arbitrarily shaped dielectric bodies, *J. Opt. Soc. Am.* **11**:1458–1470 (April 1994).
29. E. K. Miller, L. Medgyesi-Mitschang, and E. H. Newman, *Computational Electromagnetics—Frequency-Domain Method of Moments*, IEEE Press, New York, 1992.
30. B. Z. Steinberg and Y. Leviatan, On the use of wavelet expansions in the method of moments, *IEEE Trans. Anten. Propag.* **41**:610–619 (May 1993).
31. R. Coifman, V. Rokhlin, and S. Wandzura, The fast multipole method: A pedestrian prescription, *IEEE AP-S Mag.* **35**:7–12 (1993).
32. F. X. Canning, Improved impedance matrix localization method, *IEEE Trans. Anten. Propag.* **41**:659–667 (May 1993).
33. M. Hestenes and E. Stiefel, Method of conjugate gradients for solving linear systems, *J. Res. Nat. Bur. Stand.* **49**:409–436 (1952).
34. Y. Saad and M. H. Schultz, GMRES: A generalized minimal residual algorithm for solving nonsymmetric linear systems, *SIAM J. Sci. Stat. Comput.* **7**:856–869 (1986).

INTEGRATED ANTENNA SYSTEMS

KYOHEI FUJIMOTO
University of Tsukuba
Japan

1. GENERAL

An antenna system is ordinarily designed independently from transmitter or receiver circuitry, to which the antenna is connected by a transmission line (Fig. 1a). Unlike such an ordinary antenna system, an *integrated antenna system* (IAS) incorporates components, either passive, active, or both, into the antenna structure (Fig. 1b) [1]. The term *integration* here implies unification of an antenna and device or circuitry so that the performance of the antenna system is determined by both the antenna and the integrated device or circuitry. By means of integration, one can expect either improvement or modification of the antenna characteristics, or enhancement of antenna performance due to the addition of functions introduced by the integration.

2. B. L. Moiseiwitsch, *Integral Equations*, Longman, New York, 1977.
3. A. C. Pipkin, *A Course on Integral Equations*, Springer-Verlag, New York, 1991.
4. I. Stakgold, *Green's Functions and Boundary Value Problems*, J Wiley, New York, 1979.
5. R. F. Harrington, *Field Computation by Moment Methods*, Macmillan, New York, 1968.
6. T. K. Sarkar, A note on the choice of weighting functions in the method of moments, *IEEE Trans. Anten. Propag.* **33**:436–441 (1985).
7. T. K. Sarkar, A. R. Djordjevic, and E. Arvas, On the choice of expansion and weighting functions in the method of moments, *IEEE Trans. Anten. Propag.* **33**:988–996 (1985).
8. A. R. Djordjevic and T. K. Sarkar, A theorem on the moment methods, *IEEE Trans. Anten. Propag.* **35**:353–355 (1987).
9. J. M. Bornholdt and L. N. Medgyesi-Mitschang, Mixed domain Galerkin expansions in scattering problems, *IEEE Trans. Anten. Propag.* **36**:216–227 (1988).
10. R. W. P. King, *The Theory of Linear Antennas*, Harvard Univ. Press, Cambridge, MA, 1956.
11. D. S. Jones, *Methods in Electromagnetic Wave Propagation*, Clarendon, Oxford, 1979.
12. D. R. Wilton, S. M. Rao, A. W. Glisson, D. H. Schaubert, O. M. Al-Bundak, and C. M. Butler, Potential integrals for uniform and linear source distributions on polygonal and polyhedral domains, *IEEE Trans. Anten. Propag.* **32**:276–281 (March 1984).
13. A. W. Glisson and D. R. Wilton, Simple and efficient numerical methods for problems of electromagnetic radiation and scattering from surfaces, *IEEE Trans. Anten. Propag.* **28**:593–603 1980.
14. S. M. Rao, A. W. Glisson, D. R. Wilton, and B. S. Vidula, A simple numerical solution procedure for statics problems involving arbitrary shaped surfaces, *IEEE Trans. Anten. Propag.* **27**:604–608 (1979).
15. S. M. Rao, D. R. Wilton, and A. W. Glisson, Electromagnetic scattering by surfaces of arbitrary shape, *IEEE Trans. Anten. Propag.* **30**:409–418 (1982).
16. S. M. Rao and P. K. Raju, Application of the method of moments to acoustic scattering from multiple bodies of arbitrary shape, *J. Acoust. Soc. Am.* **86**:1143–1148 (1989).
17. P. K. Raju, S. M. Rao, and S. P. Sun, Application of the method of moments to acoustic scattering from multiple infinitely long fluid filled cylinders, *Comput. Struct.* **39**:129–134 (1991).
18. S. M. Rao and B. S. Sridhara, Application of the method of moments to acoustic scattering from arbitrary shaped rigid bodies coated with loss-less, shearless materials of arbitrary thickness, *J. Acoust. Soc. Am.* **90**:1601–1607 (Sept. 1991).
19. S. M. Rao and B. S. Sridhara, Acoustic Scattering from arbitrarily shaped multiple bodies in half space: Method of moments solution, *J. Acoust. Soc. Am.* **91**:652–657 (Feb. 1992).
20. C. L. Bennett, *A Technique for Computing Approximate Electromagnetic Impulse Response of Conducting Bodies*, Ph.D. thesis, Purdue Univ., Lafayette, IN, 1968.
21. S. M. Rao, T. K. Sarkar, and S. A. Dianat, The application of the conjugate gradient method to the solution of transient electromagnetic scattering from thin wires, *Radio Sci.* **19**:1319–1326 (Sept.–Oct. 1984).
22. S. M. Rao, T. K. Sarkar, and S. A. Dianat, A novel technique to the solution of transient electromagnetic scattering from thin wires, *IEEE Trans. Anten. Propag.* **34**:630–634 (May 1986).
23. S. M. Rao and D. R. Wilton, Transient scattering by conducting surfaces of arbitrary shape, *IEEE Trans. Anten. Propag.* **39**:56–61 (Jan. 1991).
24. D. A. Vechinski and S. M. Rao, Transient scattering from dielectric cylinders—*E*-field, *H*-field, and combined field solutions, *Radio Sci.* **27**:611–622 (Sept.–Oct. 1992).
25. D. A. Vechinski and S. M. Rao, Transient scattering from two-dimensional dielectric cylinders of arbitrary shape, *IEEE Trans. Anten. Propag.* **40**:1054–1060 (Sept. 1992).
26. D. A. Vechinski and S. M. Rao, Transient scattering by conducting cylinders—TE case, *IEEE Trans. Anten. Propag.* **40**:1103–1106 (Sept. 1992).
27. D. A. Vechinski and S. M. Rao, A stable procedure to calculate the transient scattering by conducting surfaces of arbitrary shape, *IEEE Trans. Anten. Propag.* **40**:661–665 (June 1992).
28. D. A. Vechinski, S. M. Rao, and T. K. Sarkar, Transient scattering from three-dimensional arbitrarily shaped dielectric bodies, *J. Opt. Soc. Am.* **11**:1458–1470 (April 1994).
29. E. K. Miller, L. Medgyesi-Mitschang, and E. H. Newman, *Computational Electromagnetics—Frequency-Domain Method of Moments*, IEEE Press, New York, 1992.
30. B. Z. Steinberg and Y. Leviatan, On the use of wavelet expansions in the method of moments, *IEEE Trans. Anten. Propag.* **41**:610–619 (May 1993).
31. R. Coifman, V. Rokhlin, and S. Wandzura, The fast multipole method: A pedestrian prescription, *IEEE AP-S Mag.* **35**:7–12 (1993).
32. F. X. Canning, Improved impedance matrix localization method, *IEEE Trans. Anten. Propag.* **41**:659–667 (May 1993).
33. M. Hestenes and E. Stiefel, Method of conjugate gradients for solving linear systems, *J. Res. Nat. Bur. Stand.* **49**:409–436 (1952).
34. Y. Saad and M. H. Schultz, GMRES: A generalized minimal residual algorithm for solving nonsymmetric linear systems, *SIAM J. Sci. Stat. Comput.* **7**:856–869 (1986).

INTEGRATED ANTENNA SYSTEMS

KYOHEI FUJIMOTO
University of Tsukuba
Japan

1. GENERAL

An antenna system is ordinarily designed independently from transmitter or receiver circuitry, to which the antenna is connected by a transmission line (Fig. 1a). Unlike such an ordinary antenna system, an *integrated antenna system* (IAS) incorporates components, either passive, active, or both, into the antenna structure (Fig. 1b) [1]. The term *integration* here implies unification of an antenna and device or circuitry so that the performance of the antenna system is determined by both the antenna and the integrated device or circuitry. By means of integration, one can expect either improvement or modification of the antenna characteristics, or enhancement of antenna performance due to the addition of functions introduced by the integration.

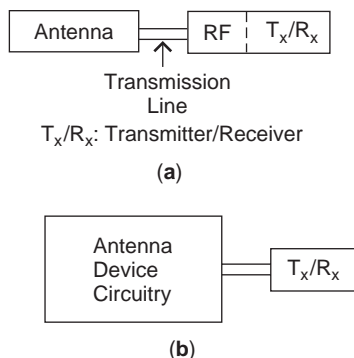


Figure 1. Conventional antenna system and integrated antenna systems.

When an active device or circuitry is integrated, IAS is referred to as *active IAS* (AIAS) and when a passive device or circuitry is integrated, as *passive IAS* (PIAS) (Fig. 2).

The terms *active antenna* (AA) [2,3] and *active integrated antenna* (AIA) [4] are also used interchangeably with IAS. AA has been used since the early 1960s as the most popular term, whereas active integrated antenna has been used mainly for planar AIAS, which is integrated in planar structures such as patches, microstrip substrates, and microwave integrated circuit (MIC) modules [4]. Another term, *integrated active antenna* (IAA) [5], has also been used for AIAS. In Ref. 5, active integration and passive integration are distinguished from each other and termed AIA and *passive integrated antenna* (PIA), respectively [6].

A number of features in the IAS are noted:

1. Compact and low loss structure may be realized by incorporating a circuitry directly into an antenna, thus dispensing with connecting cable between antenna and circuitry, which may be part of the RF front end of a transmitter or receiver.
2. Improvement of the antenna characteristics or enhancement of the antenna performance may be achieved as a consequence of the integration.
3. Realization of an antenna system, which can perform improved or modified functions due to the integrated device or circuitry in addition to the inherent antenna performance, is possible.
4. The inherent antenna characteristics such as linear, reciprocal, and time-invariable, may be changed to nonlinear, nonreciprocal, and time-variable, respectively. Thereby, creation of new antenna systems, which would never be achieved by the conventional concept, may become possible.

I A S	(Passive)	PIAS		PIA
	(Active)	AA	AIAS IAA	AIA (Planar structure)

Figure 2. Integrated antenna system terminology.

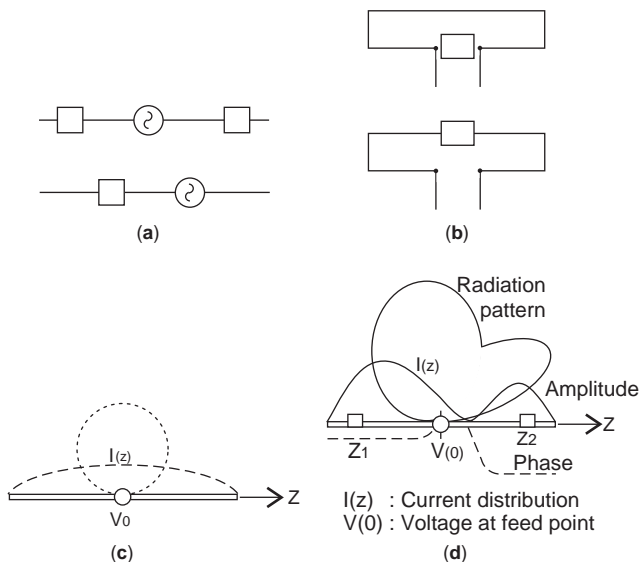


Figure 3. Basic dipole IAS structures: (a) dipole IAS; (b) folded dipole IAS; (c) dipole antenna and the current distribution; (d) current distribution and radiation pattern of dipole IAS.

One can use any type of antenna in order to constitute an IAS. Linear elements such as monopole, dipole, and loop were used mainly in the early stages of IAS development. Use of planar antennas such as printed and microstrip antennas (MSAs) began in the 1980s and application of the microwave monolithic integrated circuit (MMIC) module to IAS technology appeared in the 1990s. Arrays were first used in the early 1960s; however, intensive use began in the mid-1990s when they were applied to power combiners and as phased arrays.

Devices used for integration are also full of variety; various types of solid-state devices such as diodes and transistors are applied to AIAS and impedance components (R , C , and L) and diodes, for PIAS.

The objective of IAS development in the early 1960s was mostly to achieve gain in small antennas and in turn reduction of antenna size by integration of an amplifier into an antenna. Other functional antennas such as frequency conversion, pattern control, and pattern synthesis were studied in addition to the amplifier antennas. Later, the IAS concept was applied to array structures, in which power combiners and phased arrays were particularly significant. The successful application of spatial power combiners in microwave (MW), millimeter-wave (MMW), and

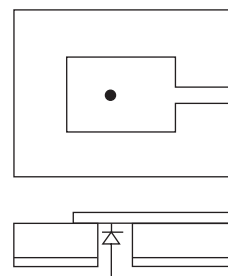


Figure 4. Varactor-diode integrated patch antenna.

sub-millimeter-wave (SMMW) regions was attributed to the incorporation of IAS. IAS was ideally suited for power combiners, which require a number of distributed sources, for which small, compact, low-power-consumption and low-cost devices such as IAS is preferred. IAS is also advantageous since power deficits in solid-state oscillation were overcome by using a number of IAS devices as the distributed array sources, and thus high-efficiency radiation was accomplished. IAS was instrumental in developing a variety of power combiners and phased arrays that brought various types of functional antenna systems, which perform such functions as oscillation, multiplying, mixing, beamscanning, beamsteering, and frequency conversion. Other IASs that have been used in practice so far are receivers, transceivers, and sensors. Some typical integrated antenna systems are illustrated in the following figures.

Figure 3a shows some dipole antennas in which an integrated device is shown by a blackbox, which may be a part of the RF front end of the transmitter (Tx) or the receiver (Rx). As is shown in the figure, no transmission line and conventional matching are used between the dipole and the blackbox. By dispensing with the connection cable between the antenna and the RF front end, loss in the

transmission line can be avoided, noise performance may possibly be improved, input impedance may be varied to have wide frequency band, and the antenna structure can be made compact and/or planar. When an amplifier circuitry is used in the blackbox, IAS works as an amplifier antenna and the gain can be increased.

Figure 3b shows two types of folded-dipole IAS, in which a blackbox depicts an integrated device. The input impedance of the antenna can be varied by varying parameters in the blackbox, enabling one to obtain wideband characteristics. By adjusting the integrated circuit parameters, thus varying the phase of the current distributions on the dipole, radiation patterns can be varied. Unidirectional radiation pattern is an example.

Figure 3c depicts a dipole along with the current distribution and the radiation pattern. Figure 3d shows a dipole IAS, where two impedance components Z_1 and Z_2 are integrated, thereby producing asymmetric current distribution on the antenna element that produces variation in the radiation pattern. This type of IAS has a feature in that neither changing antenna dimensions nor moving the antenna element is necessary for beamshifting, beamscanning, or beamsteering.

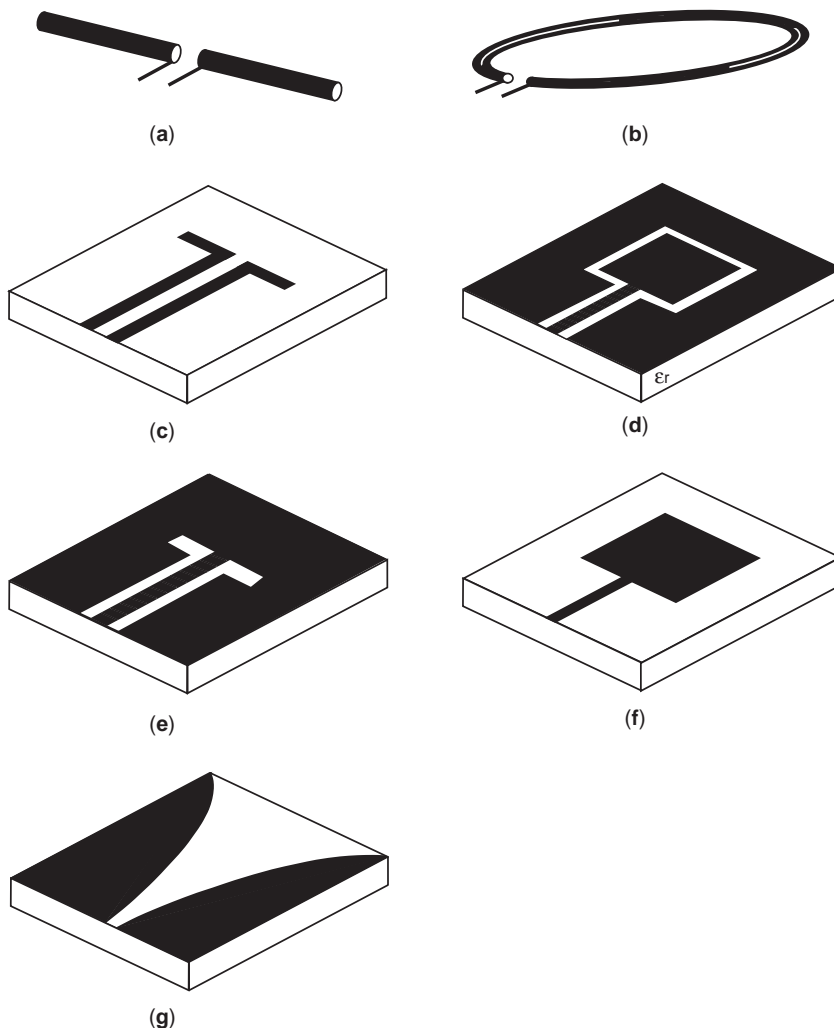


Figure 5. Various antenna structures as the base of IAS: (a) dipole; (b) loop; (c) planar dipole; (d) slot dipole; (e) slot loop; (f) microstrip patch; (g) tapered slot.

In Fig. 4, a patch antenna integrated with a varactor-diode is shown. The resonance frequency can be controlled by varying parameters of the varactor circuit with variation of the bias voltage to the circuit. Change in the resonance frequency results in change in the operating bandwidth and radiation pattern.

By integration of functions such as mixing, oscillation, and phase control, antennas performing such functions as well as radiation can be developed. By integrating an amplifier into a small antenna, the gain can be increased. This in turn suggests the possibility of producing a small antenna while keeping the gain unchanged.

Figure 5 illustrates typical antenna types used as the base of IAS. Practical examples are a bowtie mixer antenna (Fig. 6a), a unidirectional loop IAS (Fig. 6b), an oscillator patch antenna (Fig. 6c), a notch receiver IAS (Fig. 6d), a slot loop mixer IAS (Fig. 6e), a cross-slot IAS for polarization control (Fig. 6f), and a slot array IAS for pattern synthesis (Fig. 6g).

Early power combiners used open-cavity resonators such as that shown in Fig. 7a. However, since IAS was considered ideally suited for the distributed power sources in the power combiners, IAS application to the power combiners was widely current. Figure 7b depicts the basic structure of the power combiner with distributed power sources in an IAS array. Grid oscillators have also been applied to the power combiners as shown in Fig. 7c.

IAS is constituted on not only a simple planar structure but also layered, three-dimensional (3D), or multistage structures. Examples of various IAS structures are shown in Fig. 8.

Design concepts of integrated antenna systems differ from those of the conventional antenna systems. Conventionally, antennas have been designed almost independently from transmitter or receiver, to which the antenna is connected, whereas the IAS is designed en bloc; in the design the integrated devices are combined with the antenna structure, with the result that IAS performance

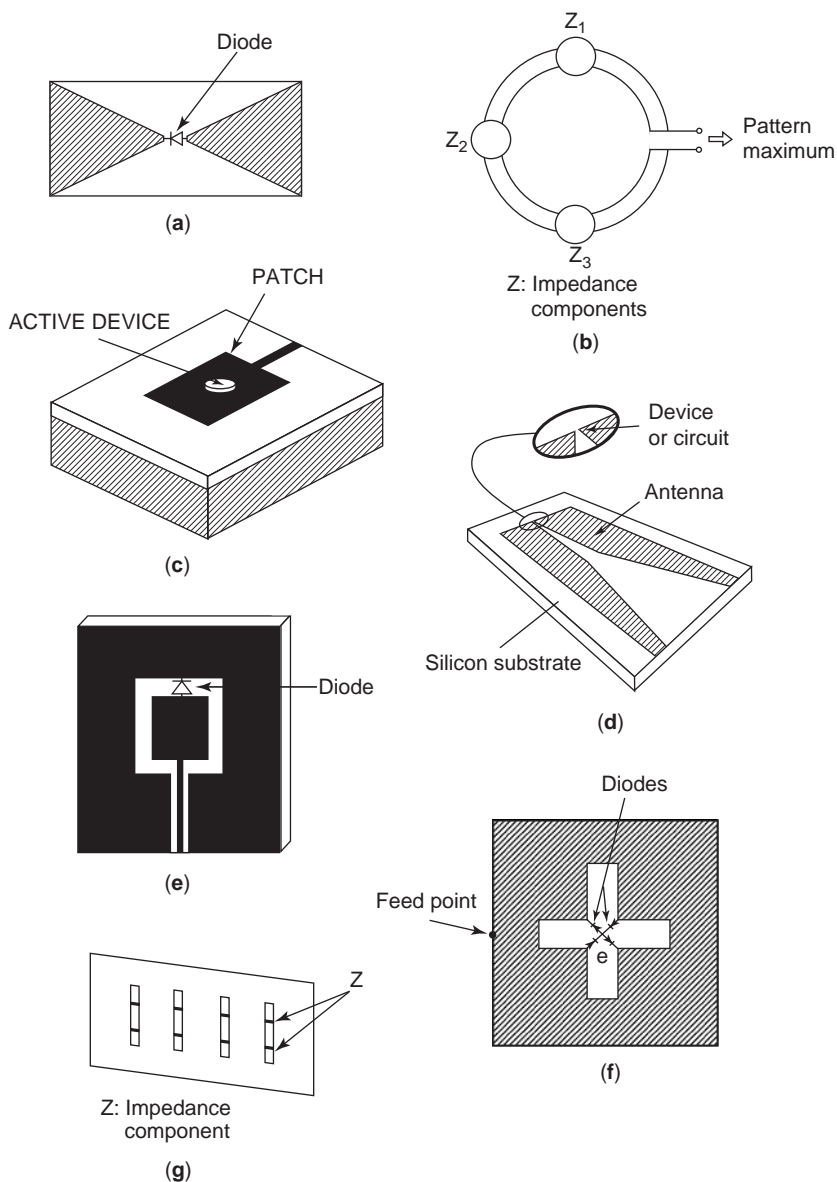


Figure 6. Practical examples of IAS: (a) bowtie mixer antenna; (b) unidirectional loop IAS; (c) oscillator patch antenna; (d) notch receiver IAS; (e) slot-loop mixer IAS; (f) cross-slot IAS; (g) slot array.

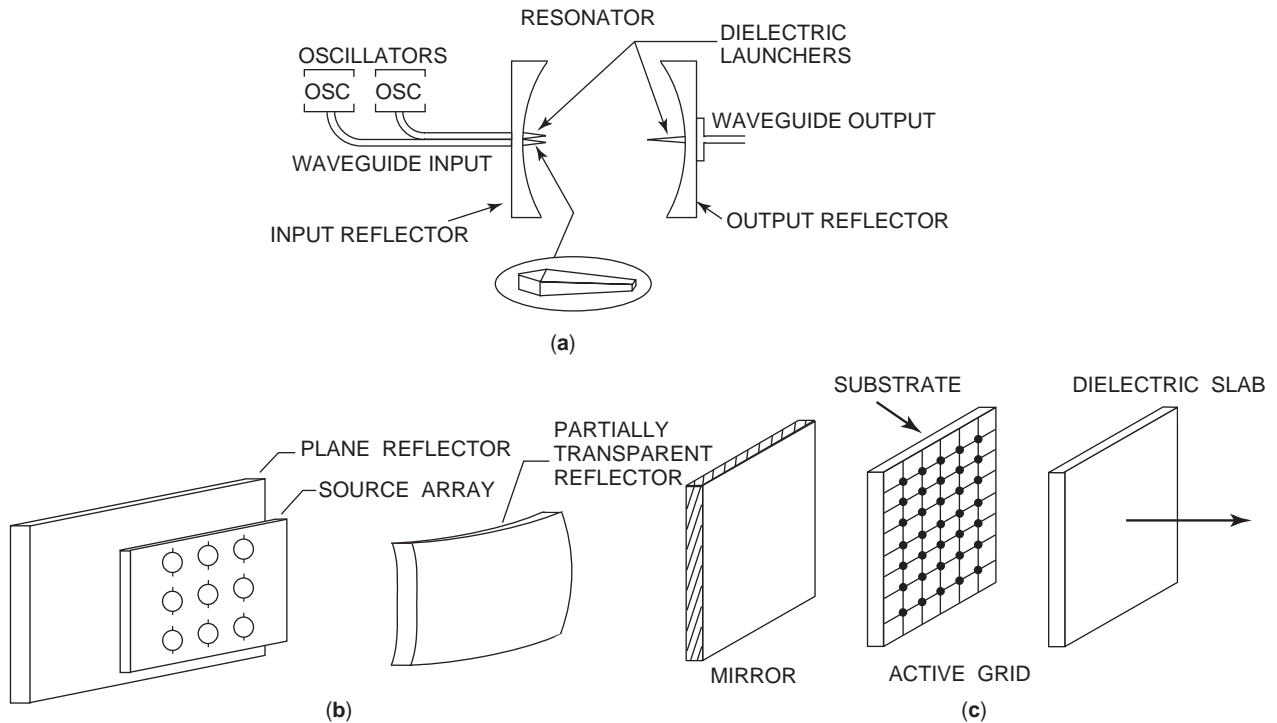


Figure 7. Power combiner: (a) Early power combiner with open cavity; (b) power combiner with distributed power sources; (c) power combiner with grid oscillators. (From Refs. 5, 46 and 48, with permission from Wiley and IEEE.)

depends on both the antenna and the integrated devices, which may be a part of the transmitter or the receiver.

When IAS is designed, one should ideally have the appropriate knowledge and techniques that are associated with all IAS components: antennas, devices, circuitry, and systems. However, experts in some fields might not be versed in what is outside their own fields. In such cases, cooperative efforts of antenna engineers with engineers outside their fields and vice versa should be necessary.

Although both active and passive integration can be implemented, the active integration may have higher potential for application than passive integration because it may flexibly vary or modify antenna performance so that a variety of functional antenna systems can more easily be realized.

Initial work on IAS began in 1960. Early-stage IAS involved mainly active antennas (AAs), in which transistors and tunnel diodes (Esaki diodes) were used as the integrated devices. Most of that AA effort was focused on increasing the gain in small antennas by integrating the amplifier and in turn realizing small antennas. Other attempts to achieve wideband antennas, frequency conversion antenna, radiation pattern synthesis, and pattern control by electronic means, and so forth, were made from the early 1960s through the mid-1970s.

The concept of IAS, including both passive and active integration in order to implement functions such as beam-shaping and control into an antenna system and performing pattern synthesis, was discussed in 1970. Until the mid-1970s, height reduction of antennas or making an antenna smaller by incorporating active integration was still a major subject; however, pattern shaping, beamsteering, and synthesis using both active and passive integra-

tion have gained ground. In the late 1970s, use of patch antennas, instead of linear elements, for IAS began.

Beginning in the 1980s, IAS has made remarkable progress along with progress in solid-state devices in high-frequency regions, especially microwave (MW) and millimeter-wave (MMW) regions. Up to the early 1980s, there was a limitation in the availability of solid-state devices that could perform with low noise and high power capability in MW and MMW regions. Application of IAS shifted to arrays and promoted development of the power combining technique, in which distributed-array sources using IAS were employed. With the use of a number of IAS sources in the power combiners, efficient radiation was accomplished, as the power deficiency of solid-state devices was overcome. IAS was instrumental in advancing the power combiners. Integrated circuit (IC) structure was well suited as the base of IAS, and MMIC structure was also used to compose IAS in a planar, compact, low-loss, and low-power-consumption structure. These IASs, of two-dimensional (2D) or three-dimensional (3D) structure, had accelerated development of novel small, compact, planar, and yet sophisticated functional IAS, including power combiners.

2. TERMINOLOGY

The “active antenna” (AA) [2,3] has been used to express active IAS (AIAS) since the early 1960s. In early days of IAS, AA was simply considered as an antenna in which the power source or head amplifier was closely associated with the radiating or receiving element. With the advancements of IAS technology, this sort of narrow understanding has gradually disappeared. Two other terms are used

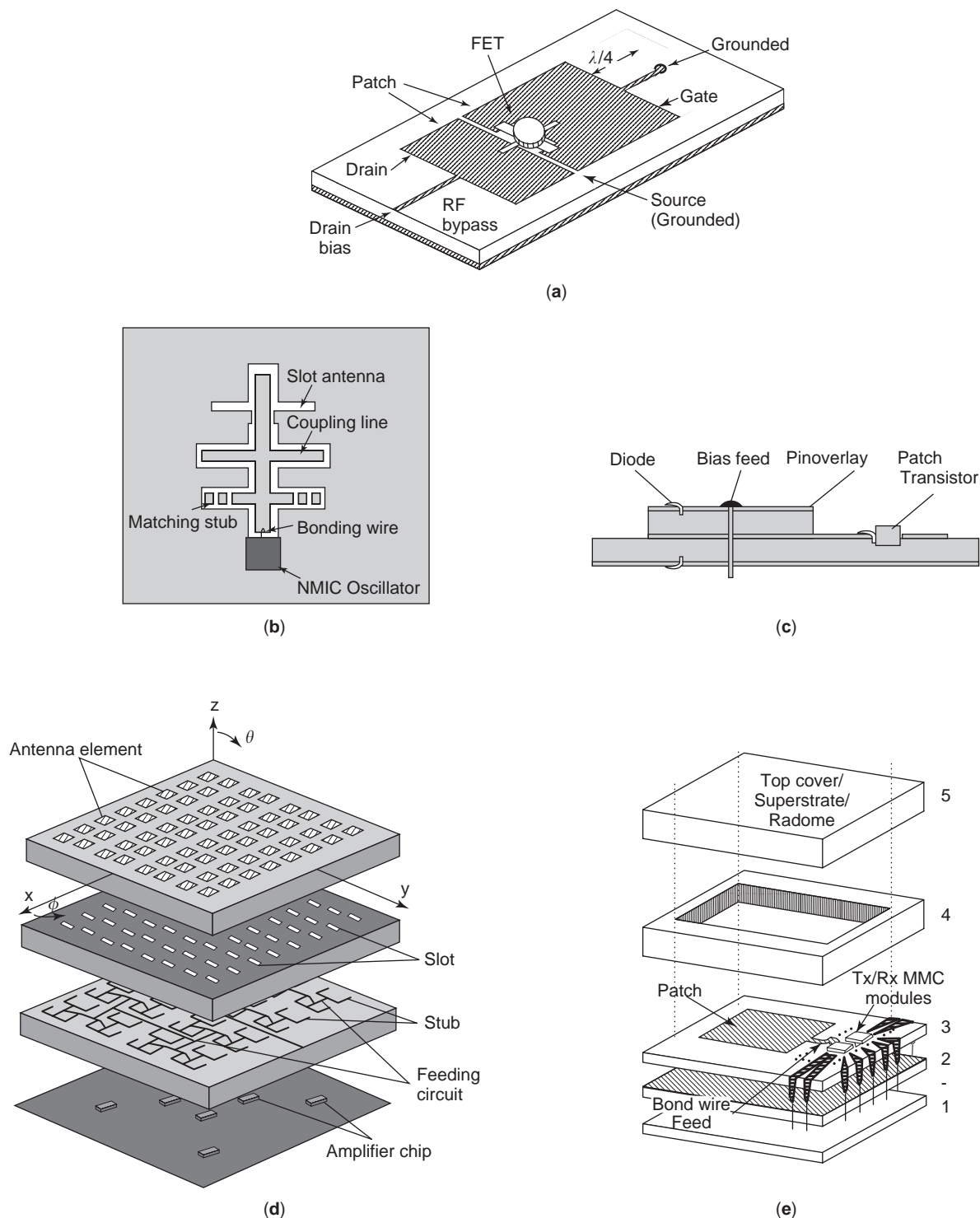


Figure 8. IAS structures: (a) planar structure; (b) MMIC structure; (c) double-layered structure; (d) packaged structure; (e) multistage structure. ((a) from Refs. 5 and 48 with permission from Wiley and IEE; (b) from Ref. 113 with permission from Wiley and IEICE; (d) from Ref. 12 with permission from IEICE; and (e) from Ref. 82 with permission from IEICE, respectively.)

interchangeably with AA: active integrated antennas (AIAs) [4] and integrated active antennas (IAAs) [5]. Both AIA and IAA should be understood to mean AIAS; however, AIA is mainly taken for planar IAS or printed or MIC-based IAS [4]. The term IAA is seldom used by itself,

but with a prefix, in expressions such as diode integrated active antenna and transistor integrated active antenna [5]. For a time “loading” was used instead of “integration”; for example, diode-loaded active antenna. Navarro and Chang [5] define IAS by differentiating active integration

space domain defines relationships between the EM fields E and H and the current distributions J on the antenna system. These relationships are expressed as

$$E = L [J] \tag{1}$$

and

$$J = L^{-1}[E] \tag{2}$$

where L is the operator and L^{-1} is the inverse operator; the overhead bar denotes a vector quantity, and $[]$ denotes matrix.

The immittance domain defines the relationships between the current distributions J and the circuit parameters V and I . These are expressed by using either the impedance matrix $[Z]$ or the admittance matrix $[Y]$ as

$$[V] = [Z][I] \tag{3}$$

or

$$[I] = [Y][V] \tag{4}$$

where the parameters are treated as scalar quantities. This domain is essentially linear, reciprocal, and time-invariable. By integrating devices, either passive, active, or both, into an antenna system, the parameters in the immittance domain are varied, and thus so are the currents J . As a result, the antenna performance is modified, or a new function is implemented into the antenna system.

When an active device is integrated, the immittance domain becomes active in nature, and so does the IAS. If the integrated device is nonlinear, or time-variable, the immittance domain and thus the IAS also become nonlinear or time-variable (Fig. 11). This is one of the most important concepts of the IAS; that is, the fundamental nature of the antenna system may be changed as a consequence of integration, in by which creation of a new antenna system unachievable by conventional antenna technology may become possible.

When functional devices or circuits such as amplifier, oscillator, and mixer, are integrated, the immittance domain and thus an antenna will perform such functions in addition to the performances as a radiator. With addition of the amplifying function, for example, antenna gain can be increased. Increase in the antenna gain without change in the antenna size in turn may be used to decrease the antenna size while keeping the antenna gain unchanged. The bandwidth of a small antenna may be increased by means of integration that can transform the antenna impedance to satisfy the matching requirement for the wide frequency band. Antenna structures having conjugate, complementary, and dual modes may be created by

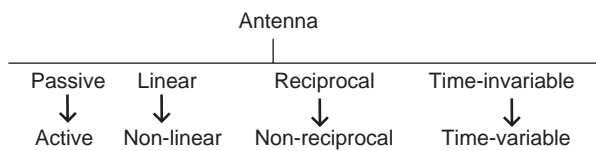


Figure 11. Physical nature of an antenna.

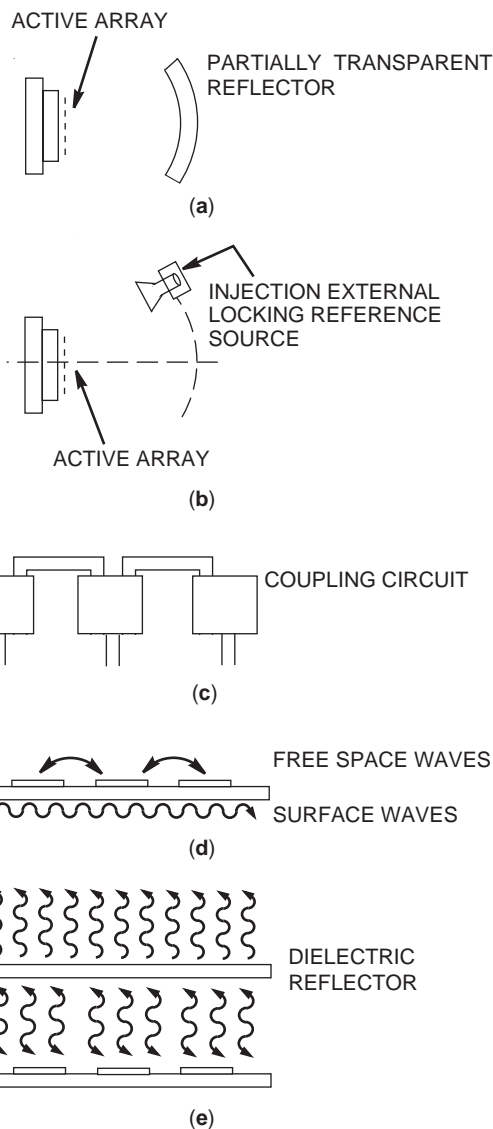


Figure 12. Synchronization methods: (a) open cavity; (b) external source; (c) external coupling; (d) mutual coupling; (e) rectifier-enhanced coupling. (From Ref. 5 with permission from Wiley.)

integrating either active or passive devices into an antenna system.

An antenna into which an oscillator is integrated, for example, may become a high efficiency transmitting antenna or oscillating antenna, which is useful for application not only to a transmitter but also for power combining

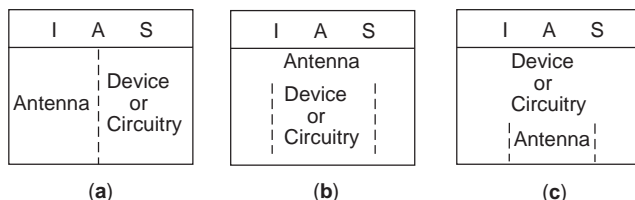


Figure 13. Integration structures of IAS: (a) antenna and circuit in series structure; (b) circuit into antenna structure; (c) antenna into circuit structure (AIA).

and pattern control, beamshaping and so forth, when it is arranged in an array structure. Close implementation of an oscillator into an antenna system reduces the loss in the cable or feedline, which connects the antenna to the transmitter, and thus the efficiency degradation can be mitigated. Integration of mixing function, as another example, will create a mixer antenna, a direct-conversion antenna-receiver system, in which frequency is converted from radiofrequency to the baseband. This direct-conversion antenna-receiver system is useful for small, compact, mobile terminals.

A distinction of IAS from an ordinary antenna system can be clearly recognized in the variation of current distributions on the antenna system due to the integration that will lead to change in the antenna characteristics

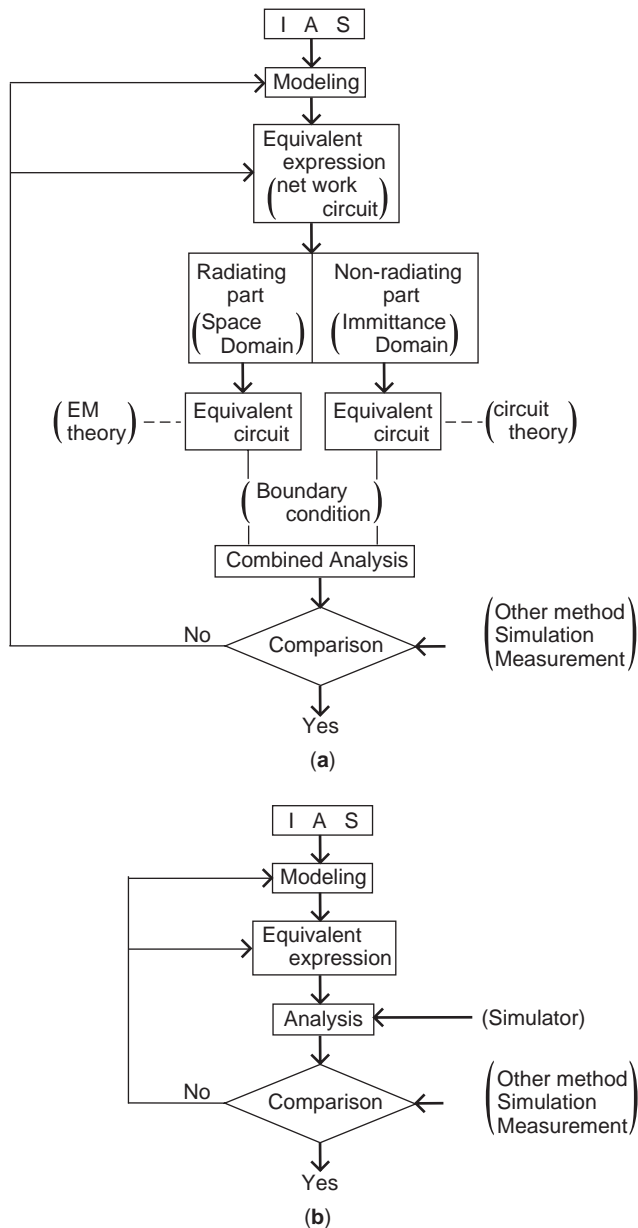


Figure 14. IAS analysis/design procedure for (a) IAS and (b) simple IAS.

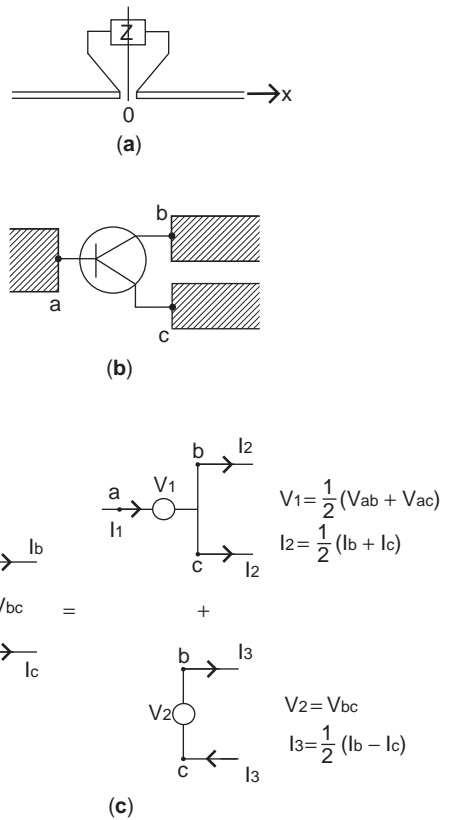


Figure 15. Treatment of integration as loading.

or performance. In general, antenna performance is determined by factors such as the antenna structure, dimensions, and feeding method. When an antenna characteristic—for instance, the impedance—must be changed in order to obtain an appropriate matching condition for a certain bandwidth, the conventional method is to design antenna configuration, dimensions, and so on to accomplish the desired bandwidth. When beamscanning is required, a sharp beam antenna is generally rotated. On the contrary, the antenna impedance can be varied by integrating some components into the antenna structure. This integration attributes the change in impedance to the variation in current distributions in the antenna structure (Fig. 9). In a similar way, radiation patterns can be varied by means of integration, causing variation in current distributions, in turn producing variation in radiation patterns. An example has been shown in Fig. 3d, where current distribution on an antenna element is changed by integration of a device, resulting in shifting of the beam direction. An essential concept of IAS is to vary current distributions on the antenna system by integration so that the desired antenna characteristics or performance levels will be achieved.

In AIA here, which is generally constituted on a MIC substrate, integration is not the main purpose for varying the current distributions on the antenna structure, but rather for implementing MIC functions into either an antenna or vice versa (antenna functions into MIC). Nevertheless, current distributions on the antenna element would in most cases be varied as a result of integration

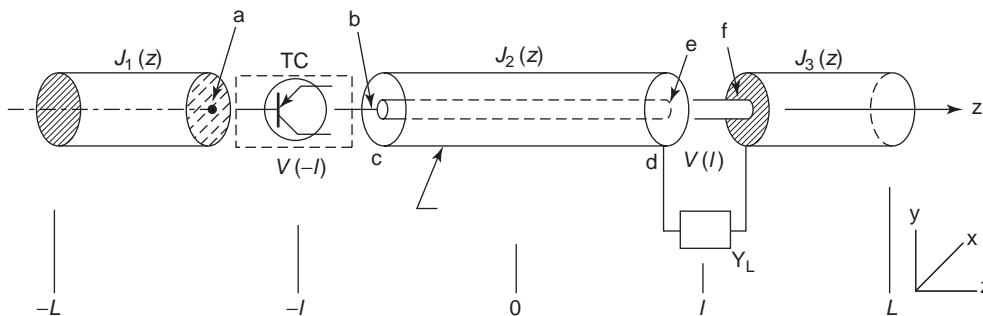


Figure 16. Dipole antenna integrated with a transistor (DAT).

because of interaction between the antenna and the circuitry or vice versa, which is caused by electromagnetic (EM) coupling between the antenna and the circuitry, due to their close physical proximity. In turn, in some areas on the circuitry, radiation currents might be induced as a result of the EM coupling. These components, which are normally nonradiating, then act as a part of the radiator and assist to either enhance or reduce the radiation. These interactions may result in either modification or degradation of the circuit functions and the radiation performance as well. In designing IAS, very careful considerations of these interactions is necessary.

5. A BRIEF HISTORY

There is a view that the antenna used in Hertz' first experiment in 1888 to verify the existence of EM waves was a type of IAS. The Hertz antenna [8] was a loop that was directly combined with an induction coil to produce a high potential at the loop terminals with the resonance condition. Hence the loop was classified as a type of IAS.

Another antenna, a monopole antenna [9] introduced in 1928, is also considered to be a type of IAS. In this

antenna, an amplifier circuit is directly connected to the antenna terminals so that the antenna is in resonance condition and radiates efficiently.

Although these antennas seem to have IAS characteristics, they were not intentionally designed as IAS. The substantial work on the IAS started in early 1960 with the active IAS. Some initial work had been done by Frost and Pedinof. Frost developed an active cylindrical dipole [10], in which a parametric diode was integrated, and discussed the parametric amplification and radiation pattern control by means of parametric excitation to the dipole antenna. In his antenna, a tunnel diode was integrated into a slot antenna, and some transmission gain was reported [11].

The most notable work was done by researchers at Technische Hochschule Munchen (THM), Germany, and the Ohio State University (OSU; USA) from early 1960. At THM, Lindenmeier, Landstorfer, Flachenecker, and their colleagues, under the direction of Prof. Meinke worked mostly on small antennas by integrating a diode or a transistor into an antenna structure [2,12-14]. Later, Landstorfer discussed noise and bandwidth limitation of AA in MW regions [15], and Lindenmeier extended his work to include improvement of receiver performance by using AA [16].

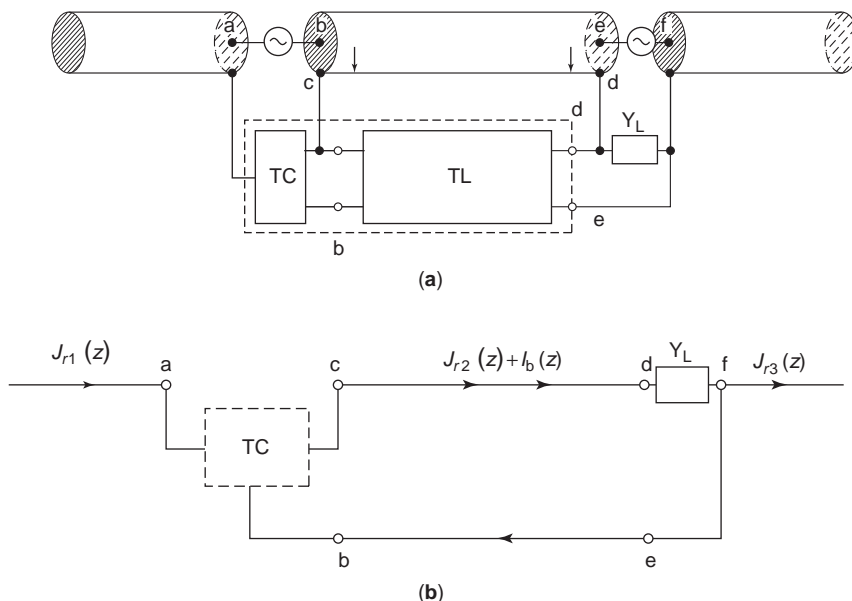


Figure 17. Equivalent expressions of DAT: (a) equivalent model of DAT; (b) equivalent circuit of DAT. (From Refs. 89a and 89b with permission from Research Studies Press and IEICE, respectively.)

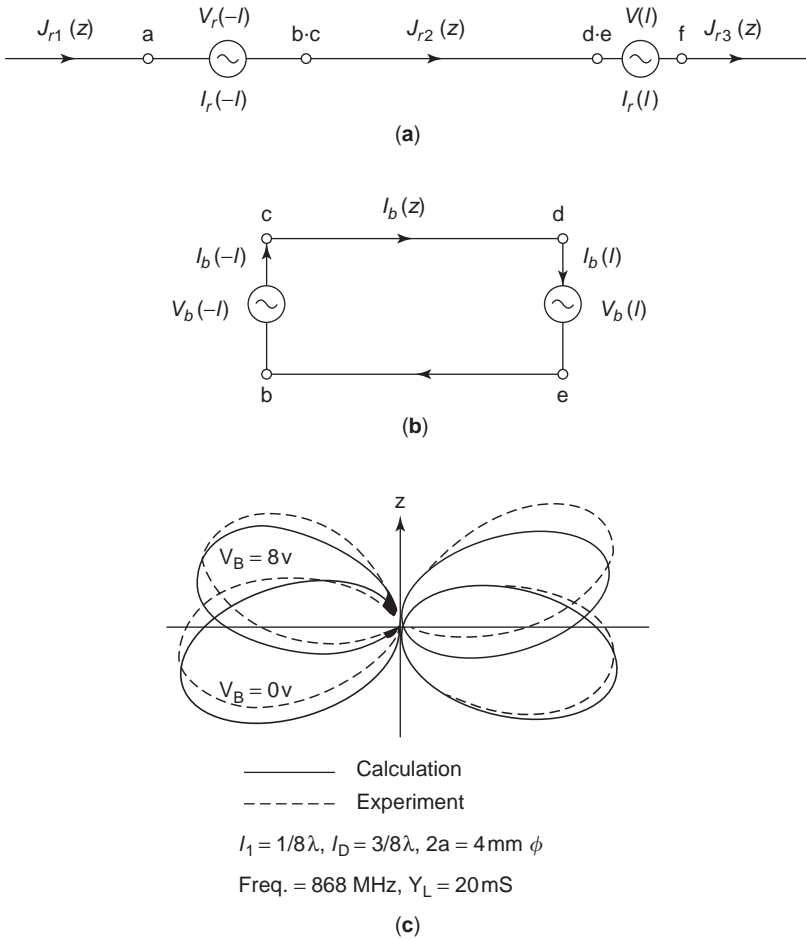


Figure 18. Equivalent-circuit expressions of DAT: (a) radiating part (space domain); (b) nonradiating part (immittance domain); (c) radiation patterns (calculated result). (From Ref. 89a with permission from Research Studies Press.)

Meanwhile, researchers at OSU and Copeland, Robertson, and their colleagues under Prof. Walter did pioneering work on various types of AAs with functions such as amplification and mixing, and wideband characteristics [17,18]. They demonstrated several AAs, one of which is referred to as an *antennafer*, where the amplifier function is integrated with an antenna, and another, referred to as an *antennaverter*, where the converter function is integrated. In these IAS designs, tunnel diode (or Esaki diode) and transistors were used as the active devices, while dipole, traveling-wave structure, and conical-spiral configurations were used as the antenna elements. One of their colleagues, Fujimoto, had shown extensive treatment of Esaki diode integrated dipoles [19,20]. More significant work done at OSU was on antenna synthesis by using an antennafer array, which was

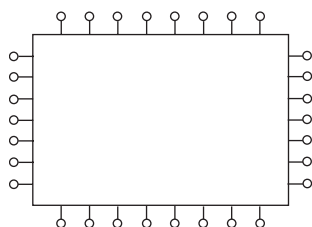


Figure 19. Multiport expression of a patch IAS.

demonstrated by Copeland and Robertson both theoretically and experimentally [21].

In an early stage of IAS research and development, integration of an amplifier into an antenna seemed to be main issue, because gain increase in small antennas was taken as the most interesting subject. By integrating an amplifier into the antenna structure, the loss observed between antenna terminals and RF circuitry was compensated by the amplifier gain. This results in increasing the gain of an antenna and also improves the radiation efficiency. However, there was a noise problem at that time in solid-state devices in high-frequency regions that had degraded the SNR (signal-to-noise ratio) performance of IAS, although the output signal power was increased because of the amplifier gain. Thus there were some arguments on

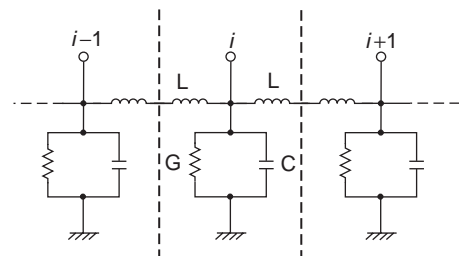


Figure 20. Equivalent expression of edge parameters. (From Ref. 91 with permission from Wiley.)

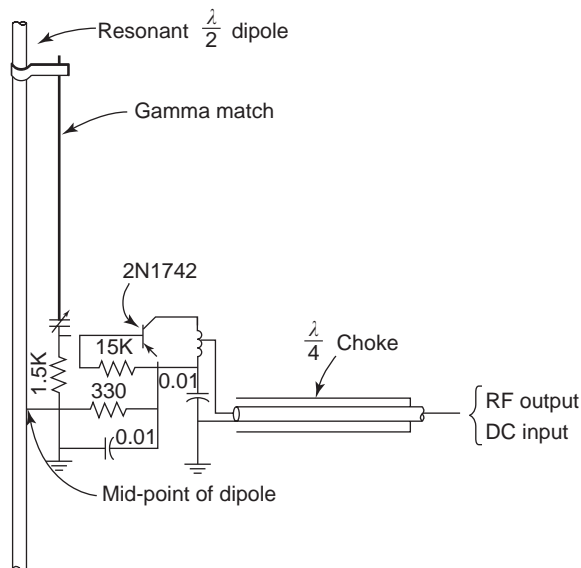


Figure 21. Antennafier (variable gain). (From Ref. 21 with permission from IEEE.)

the significance of AA with the rather narrow understanding that AA was merely an amplifier antenna.

In 1970, treatment of the IAS was discussed [1], clarifying the concept of IAS to extend inclusion of passive integration as well as active integration so that various new antenna systems could be realized as the consequence of either passive or active integration.

From late 1960s to the mid-1970s, numerous studies applying either passive or active integration to modify antenna performance were undertaken to achieve beam-shifting [22], a unidirectional pattern [23], beam control [24], and wideband performance [25]. Antennas with a variety of configurations such as loop [26], dipole [27], monopole [28], inverted L [29], ferrite coil [30], and dipole array [31] were used as the base of the IAS. Meanwhile, the small antenna, to which the IAS concept was applied, was still the main subject of research until the late 1970s. Maclean and Ramsdale analyzed performance of the active loop dipole antenna for both transmitting and receiving [27]. They also worked on the receiving dipole for height reduction [32] and SNR performance [33]. Daniel et al. discussed the wideband performance of a transistor-loaded folded dipole [25]. They also treated mutual coupling in an array using passive/active dipoles [34] and showed its reduction in superdirective arrays [35]. Anderson worked on an array that used transistor-loaded dipoles [36] and discussed the reduction of frequency dependence in an array [37].

Other examples of transistor-integrated small antenna are an indoor TV receiving antenna [38] and an inverted-L antenna for a portable receiver [29]. These active antennas were commercialized and used in practice. One more interesting antenna is a parametric excitation ferrite antenna [30], which achieved 10 dB excess *S/N* gain over a ferrite antenna of the same size. It should be noted that this is a really “active” antenna, as the ferrite element itself as a radiator is made active. In general AIAS function,

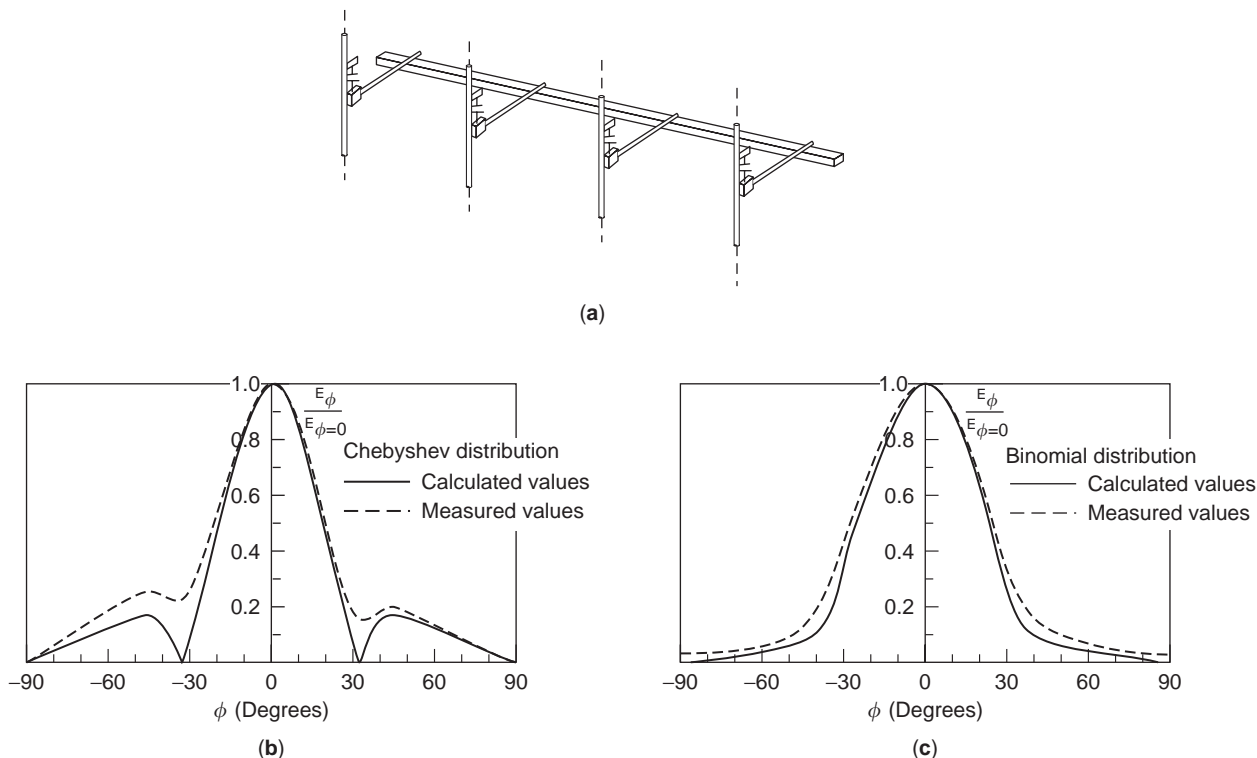


Figure 22. Pattern synthesis with antennafier array: (a) a four-element variable-gain antennafier array; (b) synthesized 15-dB Chebyshev pattern; (c) synthesized binomial pattern. (From Ref. 21 with permission from IEEE.)

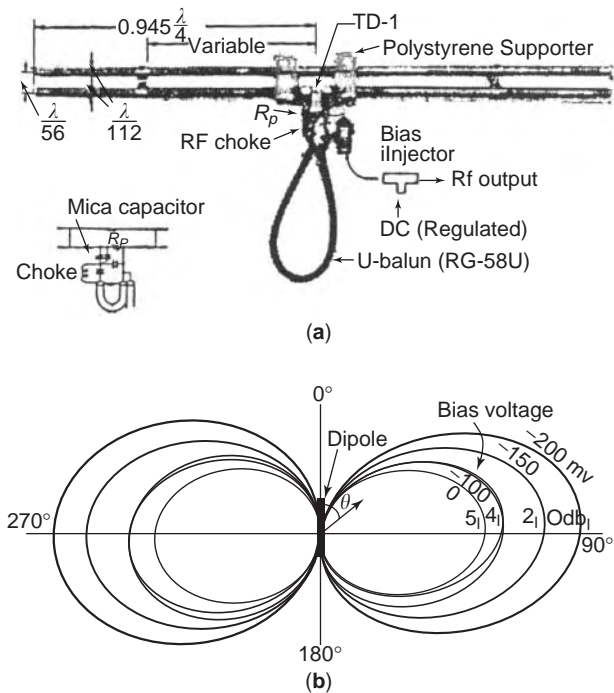


Figure 23. H-shaped dipole IAS: (a) antenna integrated with a tunnel diode; (b) receiving patterns. (From Refs. 19 and 20 with permission from IEICE and IEEE, respectively.)

the radiator itself is inherently passive, even though it is called as an “active antenna.”

Since the early 1980s, progress in IAS was accelerated by the availability of solid-state devices at higher frequency regions and also by progress in antenna technology. A planar IAS first appeared in 1980, replacing the linear IAS. This was an AA embedded on a microstrip antenna (MSA) in which a barrier injection transit time (BARITT) diode was integrated [39]. Solid-state devices used in those days included the BARITT diode [40], the Gunn diode [41], the impact ionization avalanche transit-time (IMPATT) diode [42], and the field-effect transistor (FET) [43]. These devices gradually became available after the mid-1980s.

Methods of integration in IAS have evolved with the use of integrated circuit (IC) structure and further evolved to the hybrid IC. Later, the microwave monolithic integrated circuit (MMIC) became available. The MMIC technique brought further sophistication in the functional IAS that was eventually embedded in two-dimensional (2D) or 3D MMICs [44].

The trend of using a single IAS shifted to an IAS array in the mid-1980s. In one particular array, reactance components were integrated and pattern synthesis was accomplished [45]. Applications of IAS to power combining and phased array were the main focuses of R&D. The power combining was first proposed by Mink [46], who analyzed the possibility of using arrays of millimeter-wave devices in open resonators for power combining. The spatial power combiners use distributed sources, which radiate power freely in space. These sources are synchronized by means of mutual coupling, an external circuit network, an extra source, or an open cavity. When an open cavity is used, array sources are synchronized through the

open-resonator mode. Hence this technology is called the *quasioptical technique* because of its similarity to Fabry–Perot laser applications in optical frequency.

Young and Stephan applied the quasioptical technique to an array in which open-cavity resonator was replaced by distributed oscillator sources, and demonstrated a beamsteering array [47]. Active IAS was instrumental in the application of power combiners such as those capable of generating the power produced by the array of many solid-state devices and combined in free space, compensating the combination loss limitation and generating efficient radiation. Using IASs as individual sources of array elements, the power deficiency due to inherent low-power solid-state devices in MW and MMW regions was overcome, as the power was enhanced by combining the individual powers of sources in space. The injection locking and phase-locked-loop (PLL) techniques were applied to synchronous operation of free-running oscillators in arrays. Typical phase locking methods are shown schematically in Fig. 12, illustrating

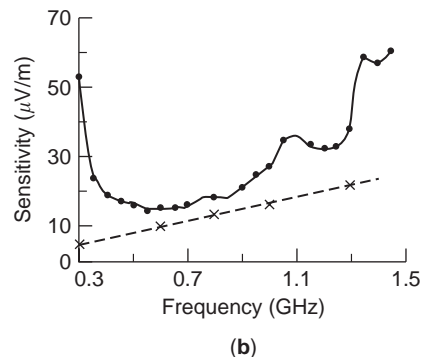
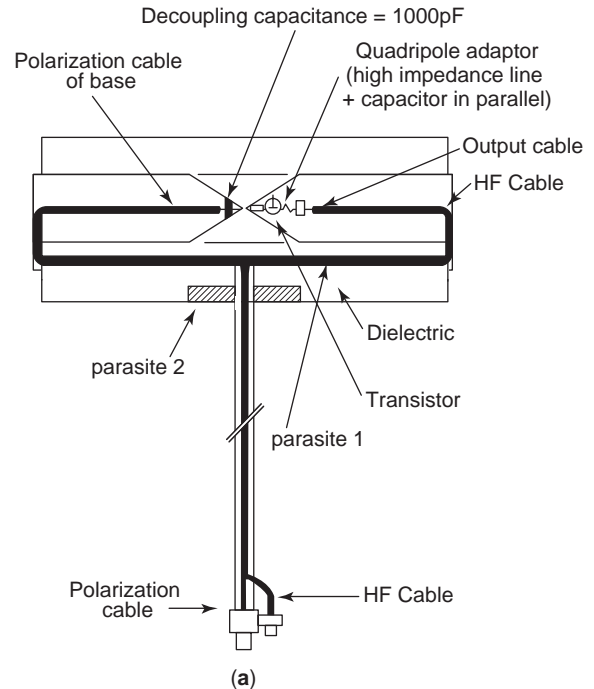


Figure 24. Folded-dipole IAS: (a) antenna integrated with a transistor circuit; (b) frequency characteristics. (From Ref. 25 with permission from IEEE.)

the open-cavity method (a), use of external locking reference source (b), use of mutual coupling using free-space waves (c), mutual coupling by means of surface waves (d), and use of a reflector to enhance coupling (e), thereby increasing output. Various types of power combiners were developed [48,49]. Functional antenna systems that perform beam control, beamsteering, beamscanning, and so forth, have also been achieved by applying IAS to phased arrays.

In power combining, the grid is used as alternative method to AIA. The grid consists of small, planar AA modules. Early grid arrays used diodes, which converted energy into DC power in a microwave wireless link [50]. This type of antenna system is called “rectifying antenna” or “rectenna.” Since the grid structure is suitable for quasi-optical power combining, it was applied to not only power combiners but also quasi-optical oscillators, amplifiers, mixers, multipliers, phase shifters, and switches.

Popovic and Rutledge introduced first a grid oscillator used in quasi-optical power combining [51]. In this oscillator, the Gunn diode was used; however, it was later replaced by the metal–semiconductor field–effect transistor (MESFET) in order to increase efficiency [52]. Since then, many investigators have worked on grid oscillators [53,54]. For instance, Popovic reported analyses of the planar grid oscillator [55], the 3D power combiner [56], the quasi-optical VCO [57], and the multielement grid oscillator [58]. Prior to development of these arrays, beam control by means of a single-dipole IAS had been accomplished [59,60].

From the mid-1980s to 1990, a variety of further advanced active integrated antenna (AIA) designs were developed. The AIA in this era attributed its progress to advances in array antenna technology in addition to MW and MMW solid-state devices and MMIC technologies [61,62]. In an AIA, the antenna is placed on the same substrate of MMIC so that the antenna and circuitry could be directly connected and losses ordinarily existing between them be reduced. In conjunction with the quasi-optical power combining technique, the IAS array could enhance system performance; specifically, power output or SNR could be increased, as a number of solid-state sources contribute to increase the power output and reduce the losses associated with circuitry and transmission lines. MMIC can serve as the base for such individual sources.

Examples of IAS in those days can be seen in amplifier antennas [63,64], mixers [65], beamsteering [66], beam-scanning [67], and other features in microwave antenna systems.

Itoh has investigated and demonstrated a number of IAS arrays [49]. He has shown some practical applications of IAS such as a transceiver [68] and transponder [69]. Chang and Navarro have also shown a variety of IAS designs [48]. Chang first demonstrated the FET integrated active patch [70] and worked on many spatial power combiners [71,72] and other IASs.

Meanwhile, Hall showed analysis and design of circuit antenna modules, in which the microwave or radiofrequency circuit is integrated with a radiator [73]. In addition, he described a detailed treatment of IAS, including

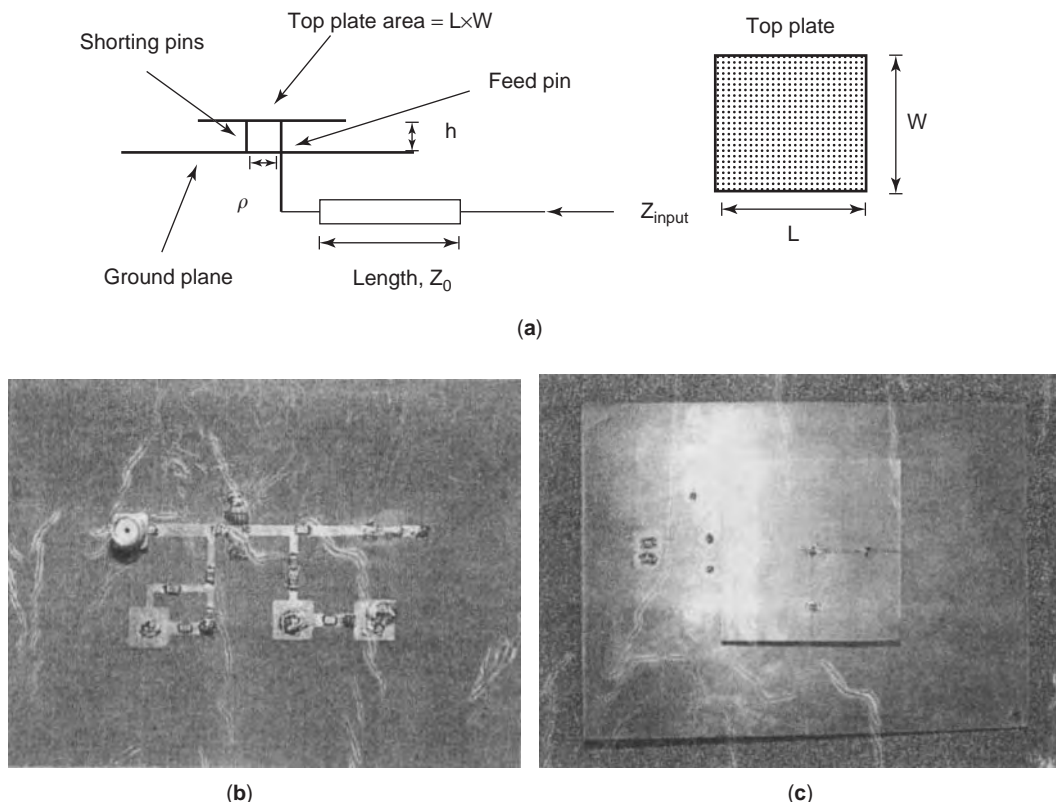


Figure 25. Active PIFA: (a) schematic expression; (b) amplifier circuit (side 1); (c) PIFA (side 2). (From Ref. 88 with permission from IEEE.)

the CAD process, the circuit-simulator based-method, and the multiport network method [73]. He had shown integration techniques with the aid of hybrid IC, MMIC, or other packaging methods. One example was an MMIC-type GaAs oscillating patch for 30 GHz [74] and another was a multilayer-type packaging IAS at 2.45 GHz (Fig. 8d) [75], which did not use MMIC structure, but was fabricated by a hybrid method, mounting a patch on the same substrate with circuits.

In the early stage of AIA arrays, diodes (i.e., two-terminal devices) were most commonly used; however, since diodes generally have disadvantages of low power, low DC-RF efficiency, and inconvenience in integrating into a circuitry, transistors (i.e., three-terminal devices) were gradually regarded as the preferable component to be integrated into IAS. Typical transistors widely used in those days were the HEMT (high-electron-mobility transistor) [76] and the HBT (heterojunction bipolar transistor) [77]. These advantages of transistors over two-terminal diodes include high gain, high DC-to-RF efficiency, low noise, and planar structure that is easily integrated in MMW regions.

HEMT has higher power efficiency and lower noise than does MESFET, while HBT can improve SNR and power efficiency as compared with other diodes such as the PIN diode.

In the current era of (2000 and beyond), much more advanced MMIC technology, higher-frequency solid-state devices, and refined precise processing of circuit structure have become accessible to develop further complicated and sophisticated IAS. Quasioptical and grid array techniques have also been utilized to produce a number of functional antennas. The current trend in IAS development has gradually shifted toward promoting practical applications rather than basic investigation. The direct-conversion antenna [78], circulator antenna [79], polarization-controllable MSA [80], mixer array [81], multistage amplifier array [82], retrodirective array [83], self-oscillating mixer [84], reflectarray [85], transceiver [86], RF tag [87], and active PIFA (planar inverted-F antenna) [88], are typical examples.

6. ANALYSIS AND DESIGN OF IAS

Because of the integrated structure of an antenna with circuitry, analysis of IAS requires special attention beyond that needed for treating the ordinary antenna system. The analysis method depends on the type of IAS; one is for the IAS, in which antenna and circuitry functions interact through the transmission structure connecting them (Fig. 13a), and another is for a different type of IAS (Fig. 13b), in which the circuitry is integrated within the antenna structure in such a way that the IC and the antenna cannot be clearly treated separately in terms of each individual function. The concepts are similar; however, there is yet another type of IAS (Fig. 13c) in which an antenna is integrated into a circuit structure; for example, a MIC structure is the base of the IAS (Fig. 8b). In this type of IAS, integration of antenna system functions is a major design objective (Fig. 9). Almost all AIA design types belong to this type of IAS.

In either case, the analysis must be done in steps starting with modeling of an IAS and representing it with a network or an equivalent circuit, if possible (Fig. 14a). Then the network model or the equivalent-circuit model is divided into two; one part relates to radiation (i.e., the space domain), and another part deals with nonradiation

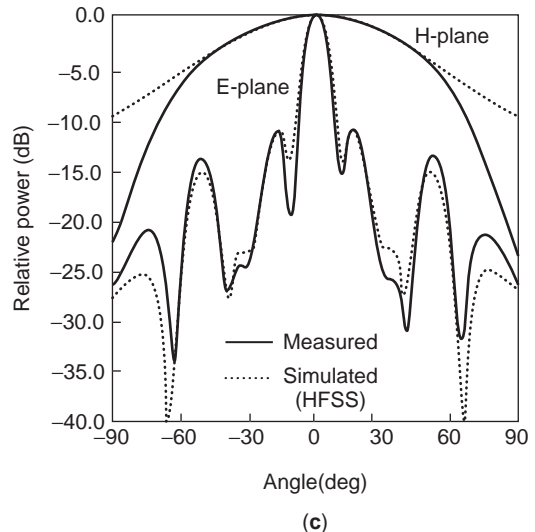
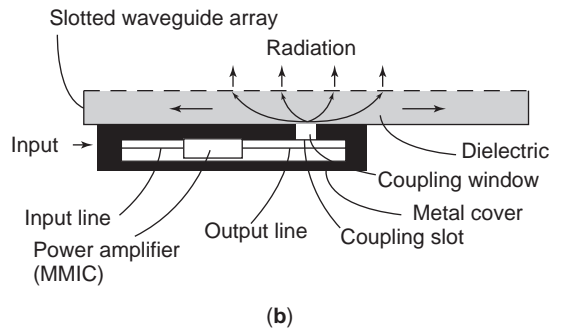
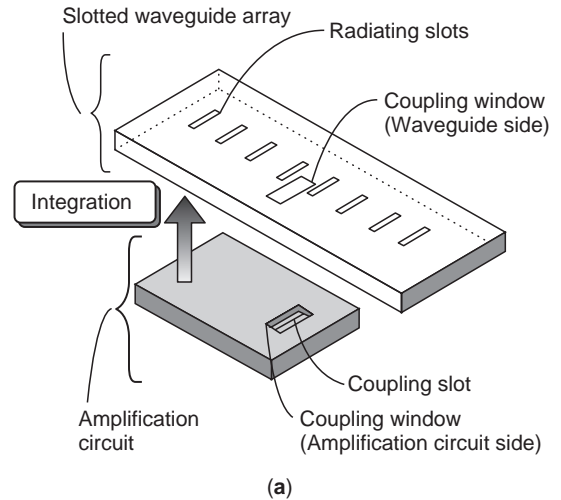


Figure 26. Slot amplifier array: (a) exploded view; (b) cross-sectional view; (c) radiation patterns. (From Ref. 92 with permission from IEICE.)

(i.e., the immittance domain). This approach is advantageous in representing interaction of the antenna to the circuitry or vice versa, which is caused by the physical interconnection and the EM coupling between the antenna and the circuitry. Such interaction is usually difficult to treat since it cannot be observed explicitly. However, it can be included in the network or equivalent-circuit representation. Depending on how such an interaction is classified, it is included in either the radiation (space-domain) or nonradiation (immittance-domain) part.

EM theory is applied to the space domain in order to obtain the field parameters that correspond to antenna performances such as radiation patterns, and the circuit theory is applied to the immittance domain to identify the parameters that correspond to the antenna characteristics such as impedance and bandwidth. Analysis may be made by directly applying the simulator to the equivalent expression of IAS when the IAS has a simple structure (Fig. 14b).

EM formulation of the space domain depends on the type of antenna. Linear antennas can be treated with the conventional integral equations, by which field parameters are obtained using Green's function weighted with

currents on the antenna structure. The method of moments (MoM) is often used to solve this sort of field problem. Equivalent circuits of the integrated devices, consisting of either two or three terminals, are inserted in the antenna structure. Dimensions of the integrated devices are considered to be small enough to prevent interruption of antenna performance. When MoM is used, the equivalent-circuit components representing the integrated device are treated as a load at the point $z=0$, where the device Z is located (Fig. 15a). When a three-terminal device such as a transistor is used (Fig. 15b), the terminal where the device is located can be divided into two parts as shown in Fig. 15c. Then analysis can be made by using parameters shown in the figure.

Either small- or large-signal representation of the active device is used, depending on the signal level. If the high signal level is taken into consideration, in some cases nonlinear treatment of the system is required.

Planar antennas such as MSA and patch antennas can be represented by a model using the equivalent circuit, the transmission-line, and the cavity concept [73], which is not necessarily applicable to linear structures. The equivalent

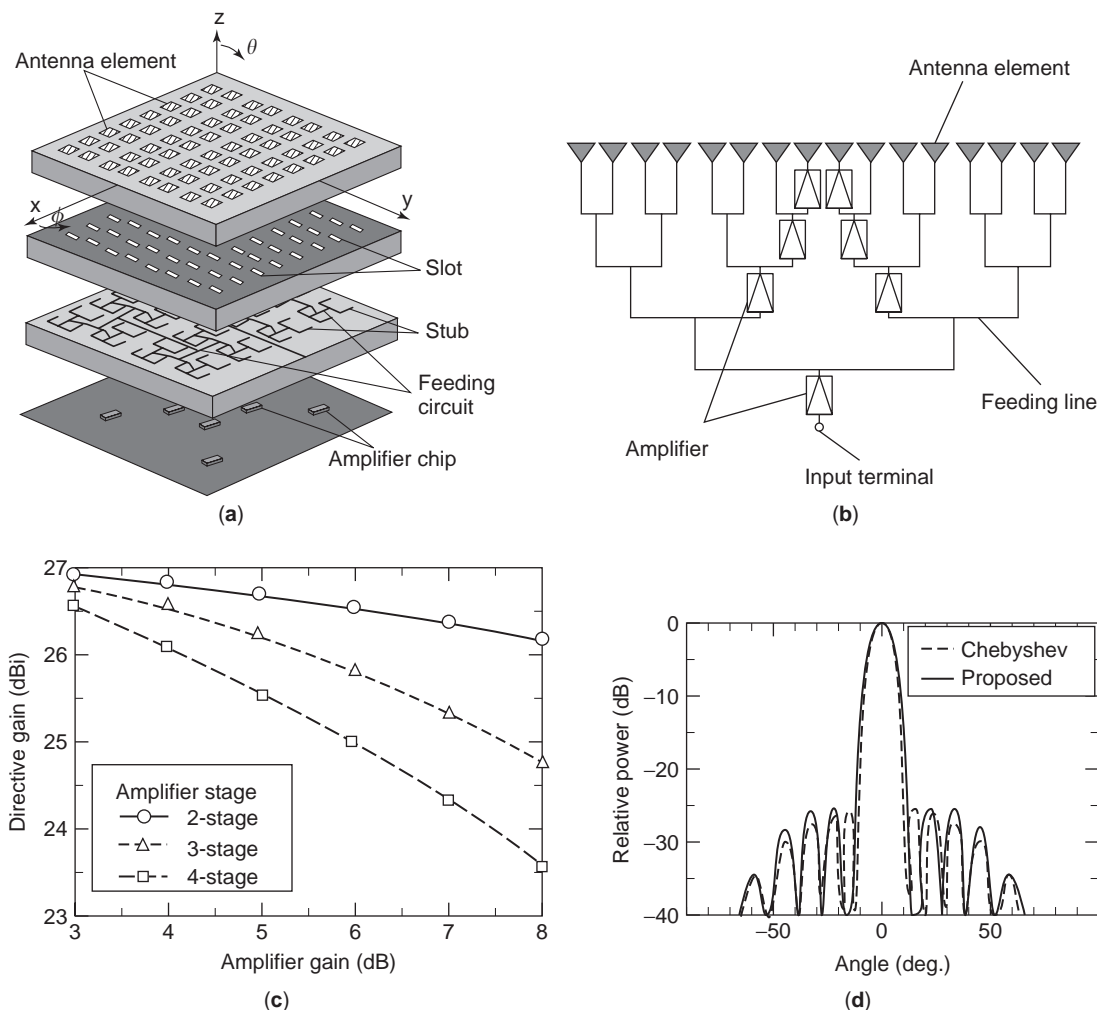


Figure 27. Multistage amplifier IAS: (a) antenna structure; (b) array structure with amplifier; (c) directive gain versus amplifier gain; (d) H -plane radiation patterns. (From Ref. 82 with permission from IEICE.)

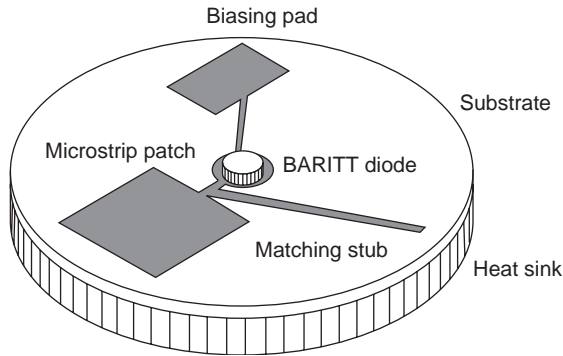


Figure 28. Barrier injection transit time (BARITT) diode integrated oscillator patch antenna. (From Refs. 5 and 39 with permission from Wiley and IEEE, respectively.)

circuit of the planar antenna can be constructed by using parameters obtained by either measurement or simulation of the antenna. The circuitry or device to be integrated, which is also modeled with an equivalent circuit, is included in the equivalent antenna model without difficulty. The transmission-line model is convenient for designing patch antennas; however, assumption of uniform field distributions on the patch edge and attention to the direction of current flow on the patch are necessary. On the contrary, the cavity model is more convenient as compared with other modeling such as the equivalent circuit and transmission line. Since a cavity is a resonator and the field inside the cavity can be obtained by rather simple EM formulation and the field at the open edge is found as the source of radiation. Integration of circuitry or device is effected with the parallel combination of the impedance at the site of integration. This provides more accurate results regardless of the geometries of the patch structure as compared with the results obtained using other models.

For the immittance domain, the conventional circuit theory is applied generally to analyze IAS in the lower-frequency regions such as VHF and UHF. The network modeling or equivalent-circuit representation in the MW and MMW regions warrants some special consideration.

Parameters in each domain are combined with boundary conditions at the terminals where they are connected, and the field parameters and the circuit parameters each are obtained as the result of analysis with respect to either antenna performance or characteristics. The results are usually compared with the results obtained by either simulation or experiment. When discrepancies are found between the two methods, the analysis should be repeated from the beginning.

The strategy used to obtain the field and circuit parameters is similar to cases where network modeling is used. EM simulators may be used to obtain the field parameters E and H from the electric/magnetic currents J/M on the antenna structure. Typical EM simulators are MoM, FDTD (finite-difference time-domain method), and IE3D and so forth. When materials other than metal are used for the substrate, HFSS may be applied.

In the case of AIA, where an antenna is integrated onto a planar structure like MIC, integration is not the prime objective for obtaining variation in current distributions

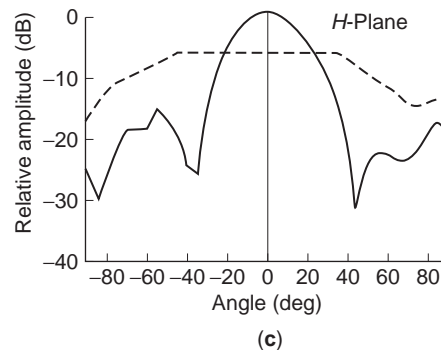
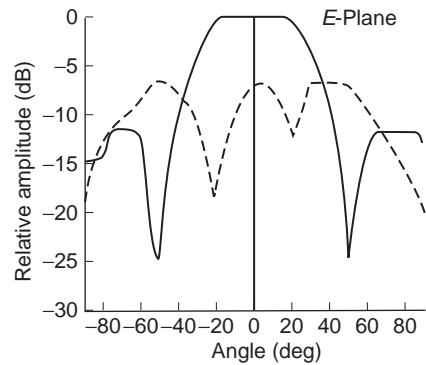
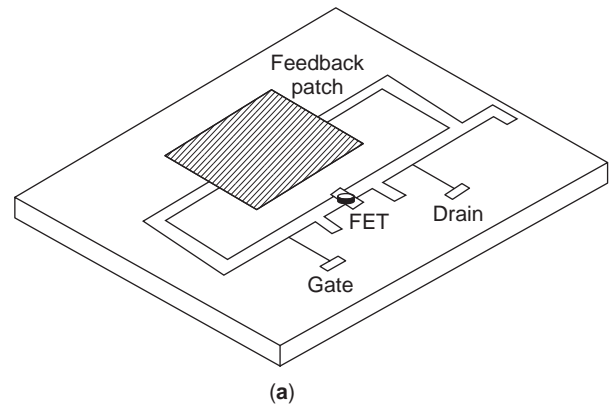


Figure 29. FET-integrated oscillator patch antenna: (a) antenna configuration; (b) radiation pattern (E -plane); (c) radiation pattern (H -plane). (From Refs. 5 and 43 with permission from Wiley and IEE, respectively.)

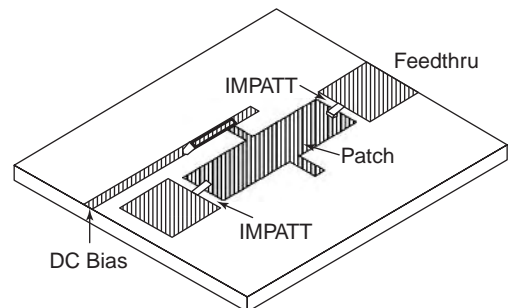


Figure 30. IMPATT diode integrated oscillator MSA. (From Refs. 5 and 62 with permission from Wiley and IEEE, respectively.)

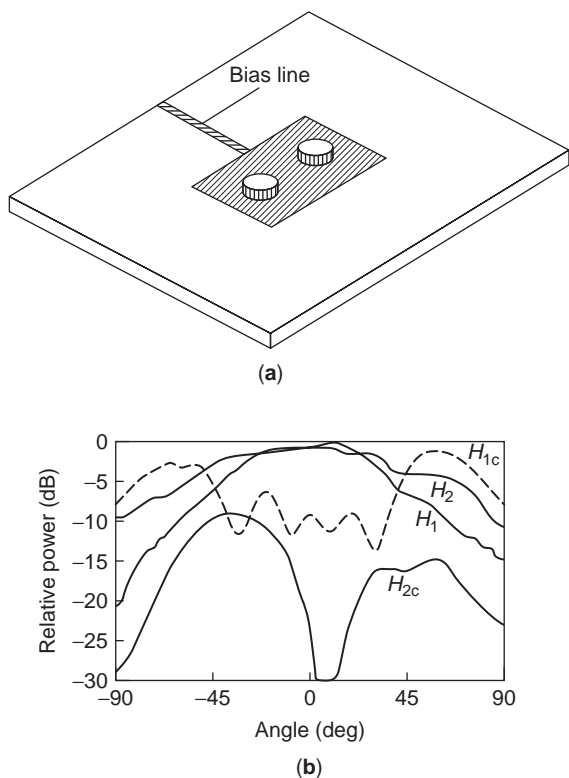


Figure 31. Gunn-diode integrated oscillator MSA: (a) antenna configuration; (b) radiation patterns. (From Refs. 5 and 94 with permission from Wiley and IEE, respectively.)

on the antenna structure, but it does provide the functions, and either modification or enhancement of the antenna performance is obtained thereby. Hence, the AIA may often be modeled by a network in which the radiating part can be represented separately from the nonradiating part relatively easily, so that the space domain and the immittance domain, respectively, can be treated comparatively easily. However, in some cases the radiating and nonradiating parts cannot be clearly differentiated. The degree of distinction depends on the MIC structure and the integration status, particularly in case of 2D or 3D structure. In this case, modeling of the antenna system and hence the analysis is not performed easily.

For instance, an MSA-based IAS, which is fed through an active device without using the transmission line and

hence the functions of the antenna and in which the active circuitry components interact through the transmission structure, network representation can be used for the analysis. The integrated device is formulated by an equivalent circuit consisting of some lumped constants and loaded on the antenna terminals.

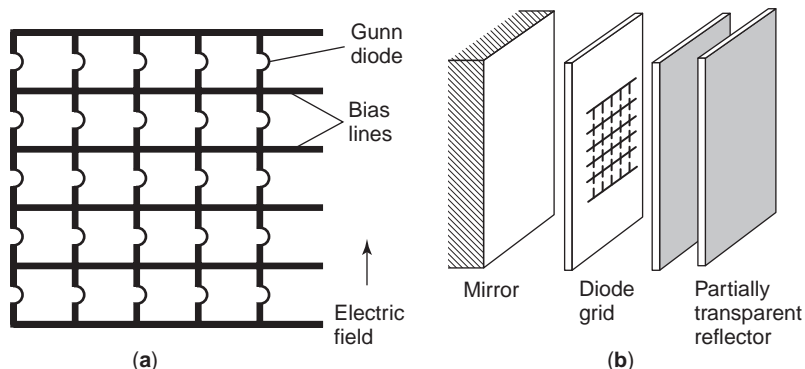
In general IAS structure, a concurrent approach is required in which the EM theory and circuit theory are combined because of the blurred distinction between the antenna and the circuitry. There are two approaches: (1) using the network representation and (2) performing simulation, combining the EM simulator with the circuit simulator. In the network approach, the model in most cases is expressed by a multiport network, involving interaction between the antenna and the circuitry, including integrated devices. When an antenna has more than one radiation source, mutual coupling among the components is also expressed by connecting multiport terminals.

Appropriate modeling is essential for the analysis. Even with an appropriate model, in many cases analysis is hardly possible because the model would be so complicated that the solution could be very difficult or impossible to obtain.

Selection of appropriate EM and circuit simulators is essential. When an IAS is represented by an appropriate equivalent model, a simulator may be applied even at the beginning of the analysis. Typical frequency-domain simulators are MoM and IE3D based on MoM, whereas FDTD and TLM (transmission line matrix method) are typical time-domain simulators. Each has its own advantages and disadvantages. Selection of the simulator depends on the antenna structure, application, and objectives. Methods of incorporating certain elements of network analysis in EM simulation algorithms have become available as a useful tool for the analysis of IAS. Both frequency-domain and time-domain simulators can be used. Selection of these depends on not only the IAS structure but also speed, accuracy, and ease of the analysis method.

Design of the IAS is based on the analysis. Appropriate CAD can be used for the design of both antenna and circuitry, if available. Results of the analysis will further assist in optimization of the design. When the IAS is designed, the knowledge and techniques involved in antennas, circuitry, network, devices, including IC, MIC, and MMIC, are necessary. However, since experts

Figure 32. Gunn diode integrated grid: (a) front view of grid; (b) quasioptical oscillator configuration. (From Refs. 5 and 51 with permission from Wiley and IEEE, respectively.)



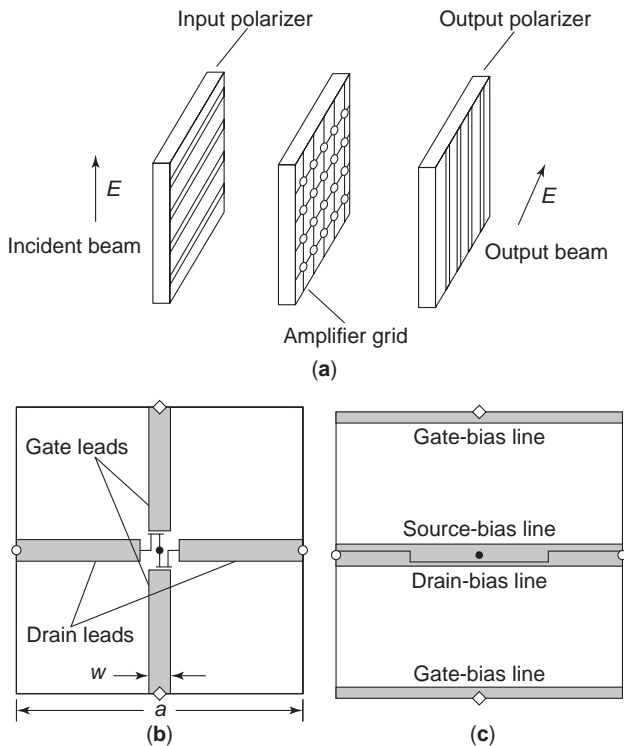


Figure 33. Grid amplifier: (a) MESFET-integrated grid amplifier; (b) unit cell of amplifier (front view); (c) unit cell of amplifier (back view). (From Refs. 5 and 98 with permission from Wiley and IEEE, respectively.)

in the field of antennas might not necessarily be expert in components outside of their fields of expertise, cooperative work between engineers in different fields is required.

6.1. Analysis Using Network Model and Equivalent Circuit

6.1.1. Dipole Loaded with Transistor Circuit. Here a dipole on which a transistor circuit (TC) is integrated is taken as an example [89a,89b]. Figure 16 depicts the model in which a coaxial line is used in the middle part of the dipole to supply the bias voltage to the TC. This IAS is

referred to as “DAT” (dipole antenna integrated with a transistor). This DAT is used only for a receiving case, where the receiving pattern is controlled by electronic means. In principle, the receiving patterns are changed by varying the parameters of the TC by changing its bias voltage, which varies the phase and amplitude of the current distributions on the dipole.

Figures 17a and 17b, respectively, illustrate an equivalent model and a circuit expression of the DAT. This model is further decomposed into a radiating part (space domain) and a nonradiating part (immittance domain), as shown in Figs. 18a and 18b, respectively. The coordinate system and parameters to be used in the analysis are also shown in the figure. The current distributions J on the radiating part can be obtained by solving the ordinary integral equation method. An appropriate EM simulator, such as MoM, can be applied to find the current distributions, which will give the receiving patterns. Regarding the nonradiating part, which consists of a coaxial transmission line (TL) and TC, the TL theory is applied and the circuit parameters are obtained. Then the field parameters and the circuit parameters are combined by applying the boundary conditions at the common terminals of the space domain and the immittance domain (nodes a, b, c, and d, e, f, respectively, in Figs. 18a and 18b). Figure 18c depicts calculated results, giving variation of the receiving patterns according to variation in the bias voltage of the TC.

With integration of a TC, other functions such as pattern shaping and beams scanning can be performed electronically without movement of the antenna. The volume occupied by the TC on the antenna structure should be small enough to prevent interference with the radiation.

6.1.2. MSA Integrated with a Diode. Multiport network modeling of MSA is considered as an extension of the cavity modeling. The inner and outer EM fields of the patch are modeled separately and the patch is treated with the 2D planar network having multiports (Fig. 19) [90]. For a rectangular MSA, for example, a multiport Z-matrix characterization, which represents the inner

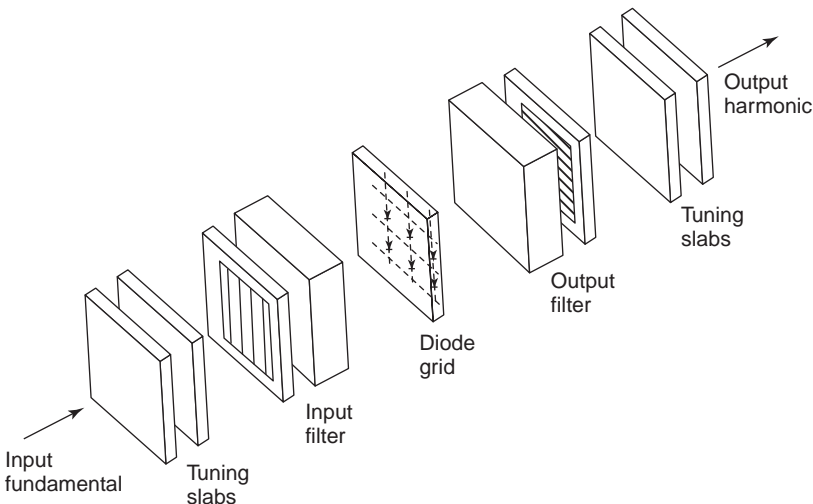


Figure 34. Grid multiplier: quasioptical grid doubler. (From Refs. 5 and 99 with permission from Wiley and IEEE, respectively.)

field of the patch, can be derived by using Green's function as

$$Z_{ij} = \frac{1}{W_i W_j} \int_{W_i} \int_{W_j} G(X_i, Y_i/X_j, X_j) dX dY \quad (5)$$

where $X_i, Y_i, X_j,$ and Y_j denote the locations of the two ports of widths of W_i and $W_j,$ respectively, and G is the impedance Green function for the rectangular patch. This part corresponds to the immittance domain. The outer field of the patch is modeled by an equivalent network consisting of the parallel combination of the capacitance and inductance, which represent the energy stored inside the patch; and the conductance, which represents the power radiated from the patch and the surface waves. Figure 20 depicts an equivalent expression of edge parameters.

The Z matrix of a rectangular MSA is obtained by performing integration given in Eq. (5) using Green's function. The Green function should be known a priori. For a rectangular MSA of thickness $d,$ the length W_X and the width $W_Y,$ which orient along the x and y axes, respectively, the impedance matrix element Z_{pq} for the two ports W_X and W_Y may be expressed as

$$Z_{pq} = \frac{j\omega\mu d}{W_X W_Y} \sum_{m=0}^{\infty} \sum_{n=0}^{\infty} \sigma_m \sigma_n \phi_{mn}(X_a, Y_a) \phi_{mn}(X_b, Y_b) / (k_x^2 + k_y^2 - k^2) \quad (6)$$

where, for ports oriented along the y direction

$$\phi_{mn}(x, y) = \cos(k_x X) \cos(k_y Y) \text{sinc} \frac{k_y W}{2} \quad (7)$$

and for ports oriented along the x direction

$$\phi_{mn}(x, y) = \cos(k_x X) \cos(k_y Y) \sin \frac{k_y W}{2} \quad (8)$$

The function $\text{sinc}(z)$ is defined as $(\sin z)/z$ and other parameters are

$$k_x = \frac{m\pi}{W_X}, \quad k_y = \frac{n\pi}{W_Y} \quad (9)$$

$$\sigma_m = \begin{cases} 1, & m = 0 \\ 2, & n \neq 0 \end{cases} \quad (10)$$

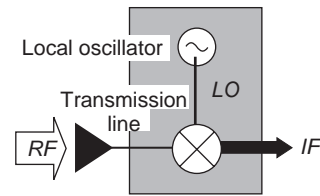
$$k^2 = \omega^2 \mu \epsilon_0 \epsilon_r (1 - j\delta) \quad (11)$$

where δ is the loss tangent of the dielectric and X_a, Y_a and $X_b, Y_b,$ respectively, are locations of the a and the b ports.

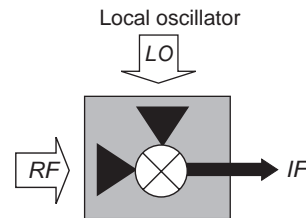
The edge fields of the MSA, which include the radiation field, the surface-wave field, and the fringing fields at the edge, are modeled by the admittance network, which is located between space and the patch network. Figure 20 depicts a part of the admittance network. The edge admittances are assumed to be distributed uniformly over the edge, as the thickness of the MSA is very thin compared with the wavelength and the fields are constant.

With the knowledge of voltages on the edge, the edge admittance can be evaluated. The edge voltage can be found by modal analysis of the fields inside the patch as a cavity.

When a device is integrated into a patch, the impedance at the port where the device is located is changed. The impedance is found by taking a ratio of voltage and current at the terminals where a device is integrated. Equation (6) can be used after modifying it to match the terminal conditions. The main task is to define the terminal conditions adequately, depending on whether it is two-terminal or three-terminal as shown in Fig. 15. When a varactor diode is used, for example, the resonance frequency of the patch can be adjusted by changing the bias voltage of the varactor. The location of the diode is also one of the parameters used to achieve the designed frequency. When a Gunn diode is integrated, as another example, as the diode exhibits a negative resistance at MW frequency regions and thus the DC supply to the diode can be converted to the RF power, the patch can be designed as a transmitting antenna. The impedance at the location of the diode should have the negative resistance of the Gunn



(a) Conventional receiver



(b) Quasi-optical antenna-mixer

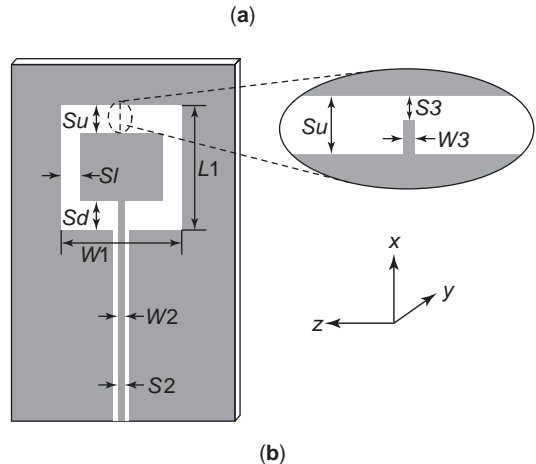


Figure 35. Mixer IAS using a loop slot: (a) principle of quasi-optical mixer; (b) antenna configuration. (From Ref. 81 with permission from IEICE.)

diode. The essential of the design is to determine the patch dimensions and the location of the integration that yields the desired impedance.

6.2. Analysis Using Simulators

Modeling of IAS is the first step, as in the other method of analysis. Whichever model is used, simulators are conveniently applied to perform numerical evaluation, by which the IAS can be designed. Depending on the IAS structure, there are two typical cases: one in which an EM simulator and a circuit simulator are applied separately, and another involving the combined use of these simulators. Usually the EM simulator is applied to the radiating part (the space domain) and the circuit simulator, to the nonradiating part (immittance domain). The results obtained for each part are combined according to the boundary conditions at the interface of the two parts, and the final expressions are obtained. Typically, there are two ways to perform simulation. One is to use lumped circuit elements together with EM formulation, where the circuit element is incorporated into, for instance, the radiating part as additional boundary conditions; another is to combine the EM simulator applied to the passive part of the IAS, including radiating parts, with a network simulator applied to the nonradiating parts, including active devices.

EM simulators such as MoM, FEM (finite-element method), and FDTD are capable of including integrated

devices in the process of simulation as loaded impedances or admittances at the segment of the analysis model, which corresponds to the location of the integration. For this purpose, the integrated devices are represented by the equivalent circuits and incorporated in the simulation model.

Simulation is possible in either the time or frequency domain. In either way, the process involves first modeling the IAS accurately, then selecting appropriate simulators for the problem, and finally combining them with exact boundary conditions. Selection of the simulators depends on speed, complexity, and accuracy of the simulator; ease of incorporating active devices; and the flexibility of treating an arbitrary structure. Table 1 compare some typical simulators [91].

When a complicated IAS structure is treated, particularly the IAS type, in which radiating parts and nonradiating parts cannot be clearly separated, application of a simulator would be very difficult, and analysis often becomes impossible. In many cases simulators cannot be applied because the antenna structure is too complicated to deal with.

7. MAIN APPLICATIONS

7.1. Amplifier IAS

The amplifier IAS was the main subject of R&D in the initial stage of IAS. In those days, linear antenna elements were mostly used. In the 1980s, planar IASs were

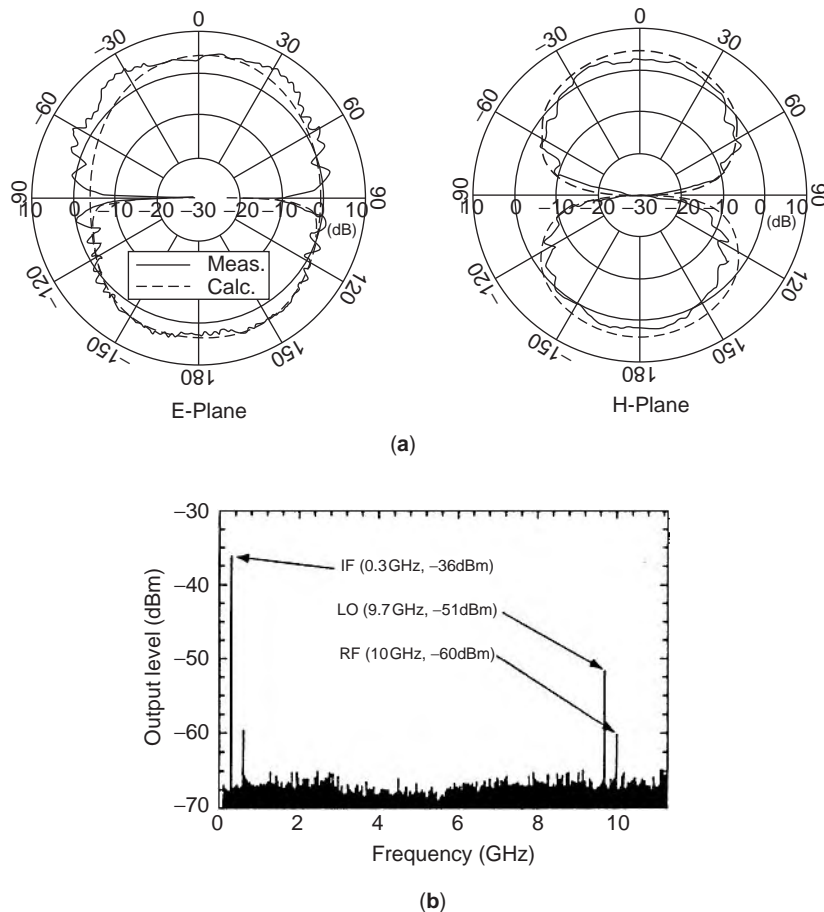


Figure 36. Loop slot mixer IAS performance: (a) radiation patterns; (b) power spectrum showing mixing performance. (From Ref. 81 with permission from IEICE.)

Table 1. Comparison of Simulators

Method	Good Flexibility for Arbitrary Structures	High Speed	Low Complexity	Good Accuracy	Ease of Incorporating Active Device
Equivalent circuit	—	***	***	*	***
Multiport network	*	**	**	**	**
Integral equation	*	*	—	***	*
FDTD	**	—	*	***	*
Finite element	***	—	—	***	*
Transmission line matrix	**	—	*	***	*

—poor *moderate **good ***very good

developed; however, the amplifier IASs did not receive much attention as oscillator IASs until their application to the spatial power combiners was recognized as significant. The spatial power combiners require an array of power sources to which small, compact, and low-power-consumption devices are needed. The amplifier IAS was considered to be the most appropriate device to use as the unit of array power source in spatial power combiners.

The first three examples described next are single-amplifier IASs. The remaining IASs are examples applied to power combiners.

7.1.1. Antennafier. Figure 21 illustrates a schematic diagram of an *antennafier* (the combined term for antenna and amplifier) [17], in which a transistor amplifier is

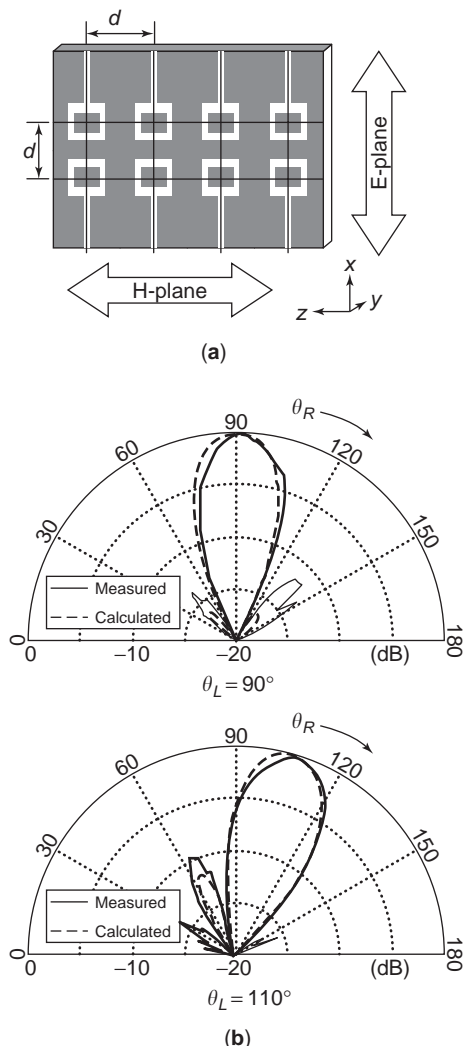


Figure 37. Loop slot mixer IAS array: (a) array structure; (b) beamsteering pattern. (From Ref. 81 with permission from IEICE.)

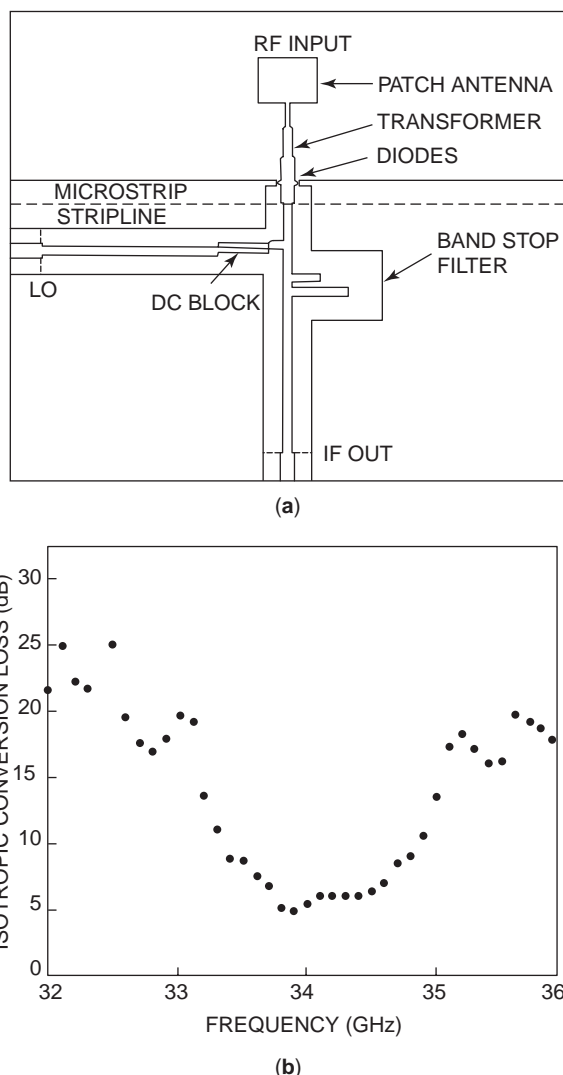


Figure 38. Subharmonic mixer IAS: (a) circuit layout of mixer IAS; (b) conversion loss. (From Refs. 5 and 100 with permission from Wiley and IEEE, respectively.)

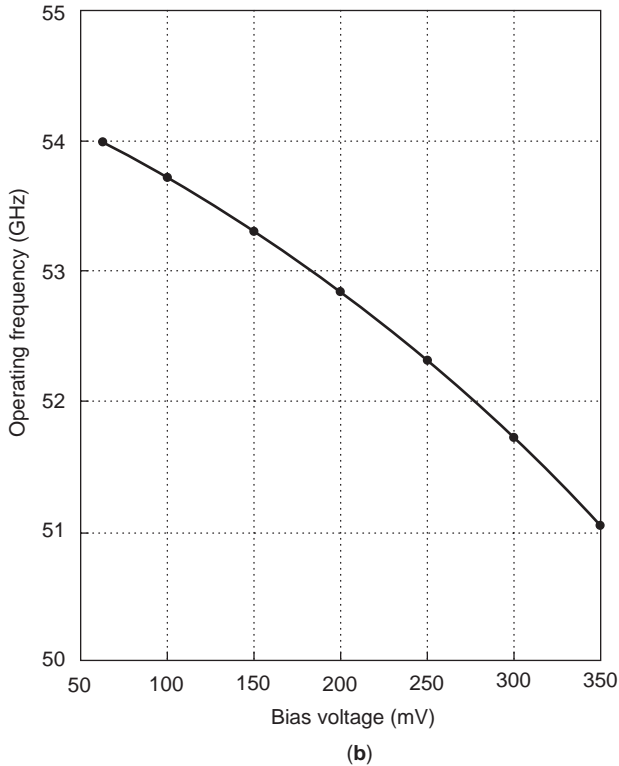
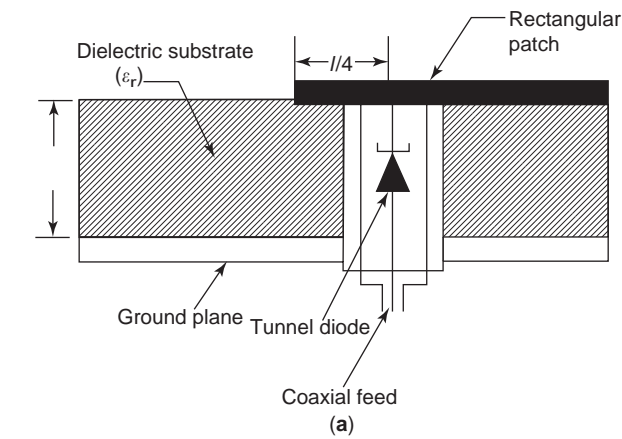


Figure 39. Frequency-tunable rectangular MSA: (a) side view of tunnel diode IAS; (b) frequency versus bias voltage. (From Ref. 101 with permission from IEEE.)

integrated into a dipole antenna. This IAS was introduced in 1964 and hence it seems to be a classical example; however, it may have historical significance, as a variety of IASs evolved following the concept demonstrated by this IAS.

This IAS can be viewed as the receiver front end by itself or used as an element of array, by which the receiving pattern is synthesized. Two types of antennafiers were demonstrated: the fixed-gain device, which exhibited a maximum gain of 12.5 dB; and the variable-gain type (Fig. 21), which had a gain ranging from -20 to +12.5 dB.

In a four-element variable-gain antennafier array (Fig. 22a), synthesis of a 15 dB-Chebyshev pattern and a binomial pattern, respectively, was accomplished as

shown in Figs. 22b and 22c. The patterns were controlled by changing the bias voltage to the integrated amplifier circuit, thus varying the phase and amplitude of the array feeding.

7.1.2. Dipole IAS. H-shaped dipoles, into which a tunnel diode was integrated, were analyzed and design parameters discussed [18,20]. Figures 23a and 23b, respectively, illustrate the model and the receiving patterns, which show a gain increase of 6 dB relative to the passive dipole.

A transistor-integrated folded dipole (Fig. 24a) was shown to have accomplished wideband characteristics (Fig. 24b) [25]. The input impedance was adjusted by means of integration so as to achieve the wide bandwidth.

7.1.3. Active PIFA. A power-FET integrated planar inverted-F antenna (PIFA) was shown to have more than 50% power-added efficiency (PAE) at several frequencies between 1 and 2 GHz. This was achieved by designing the antenna system to obtain the optimum power output by using a class F termination as the load to provide optimum power matching for the FET [88]. Figure 25a shows the schematic expression of an active PIFA; Fig. 21b shows an amplifier circuit (side 1), and Fig. 21c illustrates antenna (side 2).

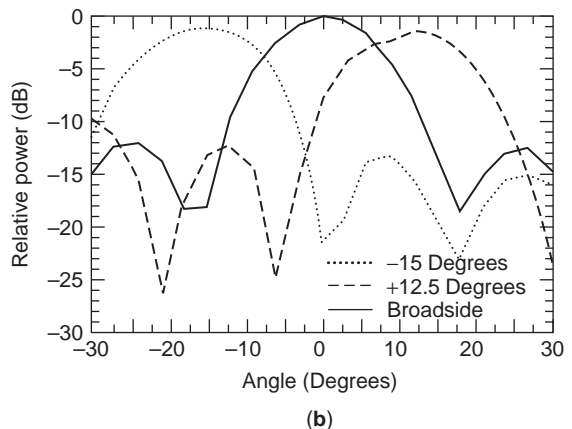
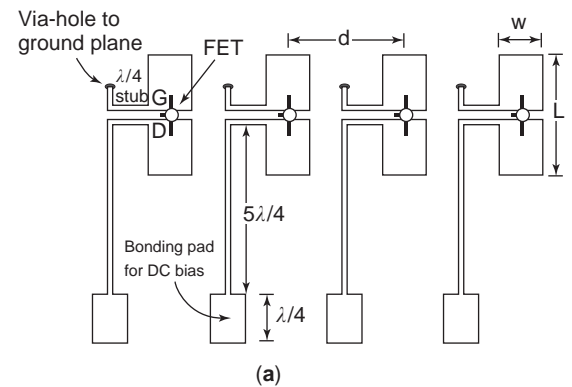


Figure 40. Four-element FET IAS beamscanning array: (a) array configuration; (b) beamscanning performance. (From Refs. 5 and 102 with permission from Wiley and IEEE.)

7.1.4. Slot Amplifier IAS Array. A slot IAS array antenna, to which a MMIC power amplifier is coupled, has been demonstrated [92]. The antenna structure is illustrated in Fig. 26, in an exploded view (a) and a cross-sectional view (b), showing coupling of the amplifier to the array antenna. Analysis was performed first on the slot array on a waveguide using HFSS, and the array performance was experimentally analyzed with a MMIC amplifier coupled to the antenna. Radiation patterns of an eight-element array are shown in Fig. 26c, where a passive slot array pattern is shown for comparison.

7.1.5. Multistage Amplifier IAS. A spatial power combiner based on a multistage structure has been proposed [82]. The antenna system consists of array elements in the first stage, slots in the second stage to couple with antenna elements, and feeding circuitry integrated with amplifiers in the third stage. Figure 27 illustrates the antenna system, showing antenna structure (a) and array structure (b) along with placement of amplifiers. Figure 27c depicts output directive gain versus amplifier gain with the amplifier stage as the parameter, and Fig. 27d shows an *H*-plane radiation pattern.

7.2. Oscillator IAS

Oscillator integrated antenna systems are used either as the front end of a transmitter or a unit of array power

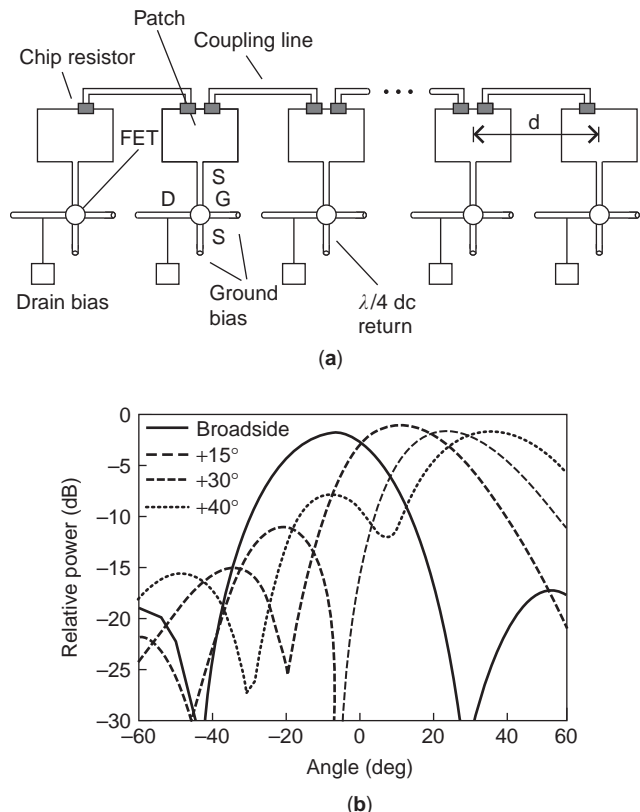


Figure 41. Six-element FET-IAS beamsteering array: (a) array configuration; (b) beamsteering performance. (From Refs. 5 and 113 with permission from Wiley and IEEE, respectively.)

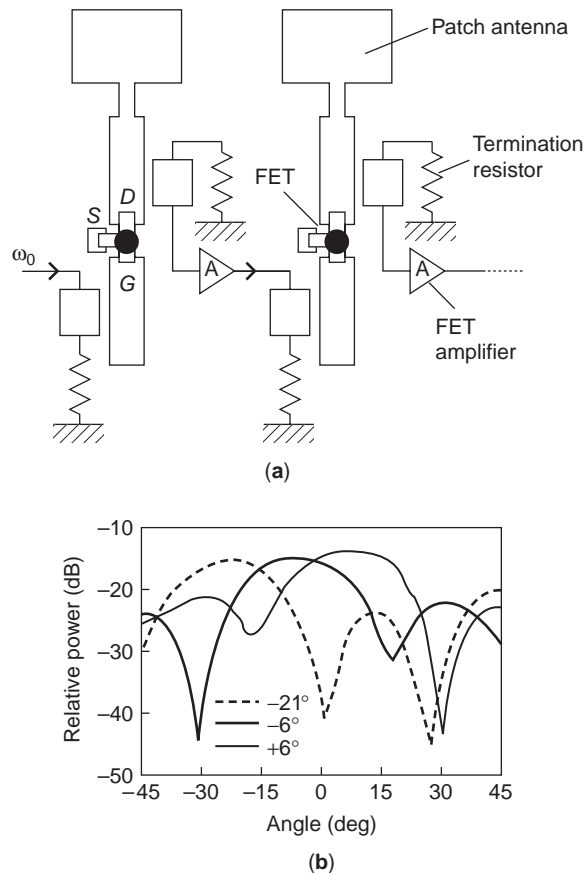


Figure 42. Three-element beamscanning IAS array: (a) part of an array configuration; (b) beamscanning patterns. (From Refs. 5 and 104 with permission from Wiley and IEEE, respectively.)

source in spatial power combiners [93]. Since the spatial power combiners use arrays of distributed power sources in order to achieve efficient and high output radiation in space, small, compact, lightweight, and low-power-consumption devices as the units of array power sources are required. For this purpose, the oscillator IAS is well suited as it meets such requirements.

Two-terminal devices such as IMPATT diodes, Gunn diodes, and tunnel diodes, and also three-terminal devices such as MESFETs, HEMTs, and HBTs, are used for the distributed power source. The two-terminal devices are suitable for high-power applications in MW, MMW, and sub-MMW regions; however, they suffer from relatively low-power DC-RF conversion efficiency. Meanwhile, three-terminal devices provide high gain, high DC-RF conversion efficiency, and low noise figure at MW, MMW, and sub-MMW regions. In addition, they have an advantage in possessing the appropriate structure for integration in a planar structure.

The first oscillating IAS was introduced as a sensor, which consisted of a BARITT diode oscillator and a patch antenna (Fig. 28) [39]. The sensing operation was performed by detecting variation of the operating frequency due to the interaction of its immediate environmental conditions such as temperature and relative motion. This can

be considered as the first application of a patch antenna to the IAS.

Since then, numerous oscillating IASs have been developed [85]. Some examples are described below. Most of them are concerned with the spatial power combiners, and some are constituted in a grid structure.

7.2.1. FET Integrated Oscillator Patch Antenna. The first FET-integrated oscillator patch antenna was demonstrated in 1988 [43]. Figure 29a depicts the IAS in which a patch is shown to be a feedback element for an FET oscillator circuit and a radiator. The IAS operates at 5.7 GHz with a power output of 17 mW. Figures 29b and 29c, respectively, illustrate the *E*-plane and *H*-plane patterns, which also show high cross-polarization levels.

7.2.2. IMPATT Diode Integrated Rectangular MSA. A monolithic IAS was developed as an element of an array of distributed sources in the spatial power combiners [62]. Figure 30 shows an example of two IMPATT diodes that feed the edge of a MSA and have a DC biasing network as well as an open stub for frequency trimming. This IAS operates at 43.3 GHz with an output power of 27 mW at 7.2% DC–RF conversion efficiency.

7.2.3. Gunn Diode Integrated MSA. Figure 31a shows an example of a two-Gunn-diode integrated MSA [94]. Using a MSA designed to resonate at 10 GHz, a Gunn diode oscillator-integrated MSA operates at 10.4 GHz with an output power of 26 mW. Using two Gunn diodes, the

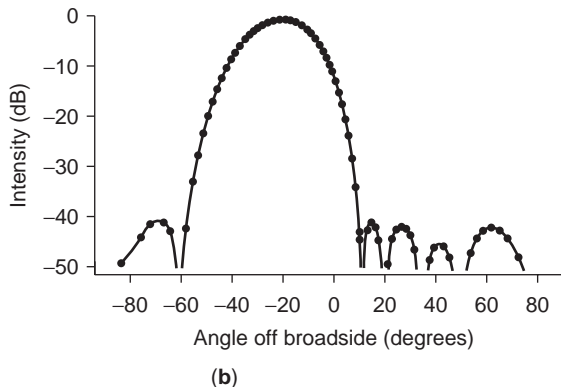
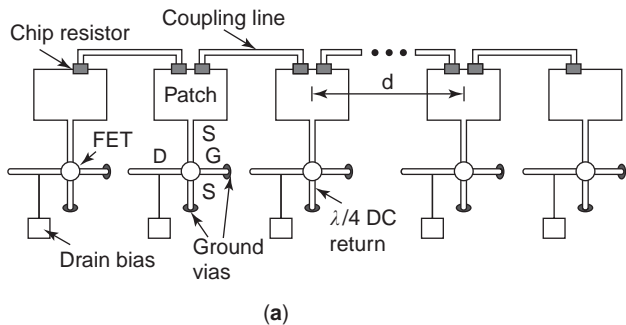


Figure 43. Nonlinear coupled array: (a) array configuration; (b) pattern with reduced sidelobe. (From Ref. 105 with permission from IEEE.)

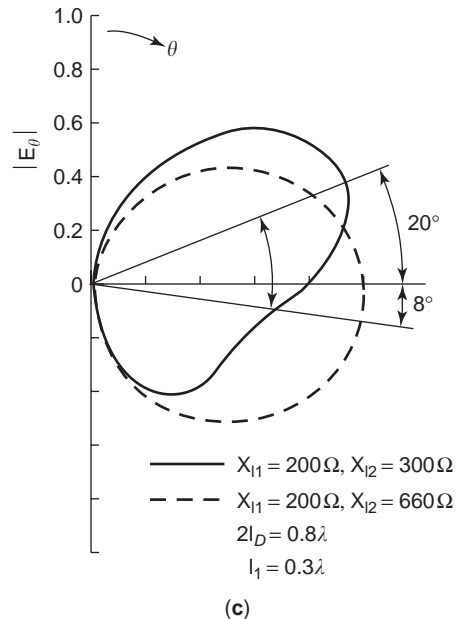
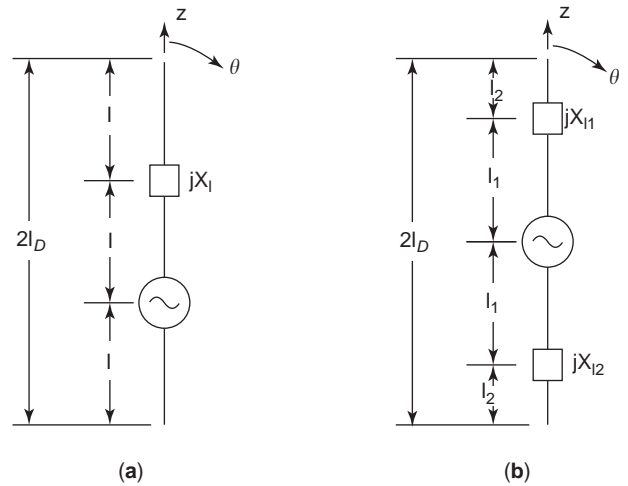


Figure 44. Beam control by a single-dipole antenna: (a) one-reactance component IAS (ORDA); (b) two-reactance component IAS (TRDA); (c) TRDA beamshifting performance. (From Ref. 106 with permission from Research Studies Press.)

output power was increased about twice the operating frequency of 10.7 GHz and lower cross-polarization patterns were achieved as a consequence of the symmetric configuration as compared with a single-Gunn-diode integrated case. Figure 31b illustrates radiation patterns for both single- and double-Gunn integrated cases.

7.3. Grid and IAS

Use of a large grid array in antenna systems traces back to 1960. Grid formats were applied not only to communication antennas, but also to the rectifier antenna, which converts RF energy to DC power in the microwave wireless link, FSS (frequency-selective surface), which provides different transmission and/or reflection properties as

functions of the frequency, polarization of electromagnetic waves in space, and spatial power combiners. The concept of grid has been applied to not only oscillators in spatial power combining but also to amplifiers, mixers, phase shifters, and switching [95].

7.3.1. Grid Oscillator. The first grid oscillator, introduced in 1988 [51], is shown in Fig. 32, illustrating the front view of a Gunn diode integrated grid (a) and a quasi-optical oscillator configuration (b). Active devices are embedded in a two-dimensionally periodic array on a dielectric substrate. The grid array was placed between a mirror and a partially transparent reflector that constitutes a quasi-optical resonator. The grid oscillator operates at 10 GHz.

The grid oscillator differs from that of other spatial power combiners in that the integrated devices in the grid structure are closely arranged with respect to wavelength,

so that strong coupling and collective interaction among these devices create a quasi-optical component. The grid oscillators demonstrated its substantial usefulness in improving power deficiency and radiation efficiency at that time. Various types of grid oscillators were developed since the first grid oscillator was demonstrated [96].

Another example is a MESFET integrated grid oscillator. The Gunn diode was replaced in order to improve the efficiency. A 10×10 FET grid oscillator has also been demonstrated [97].

7.3.2. Grid Amplifier. Grid structure offers advantages of increasing power-handling capability and eliminating losses associated with feed network. A 50-MESFET grid amplifier demonstrated 11 dB gain at 3.3 GHz [98]. Figure 33 illustrates the grid amplifier structure and the unit cell of the grid amplifier (a); and front (on the left)

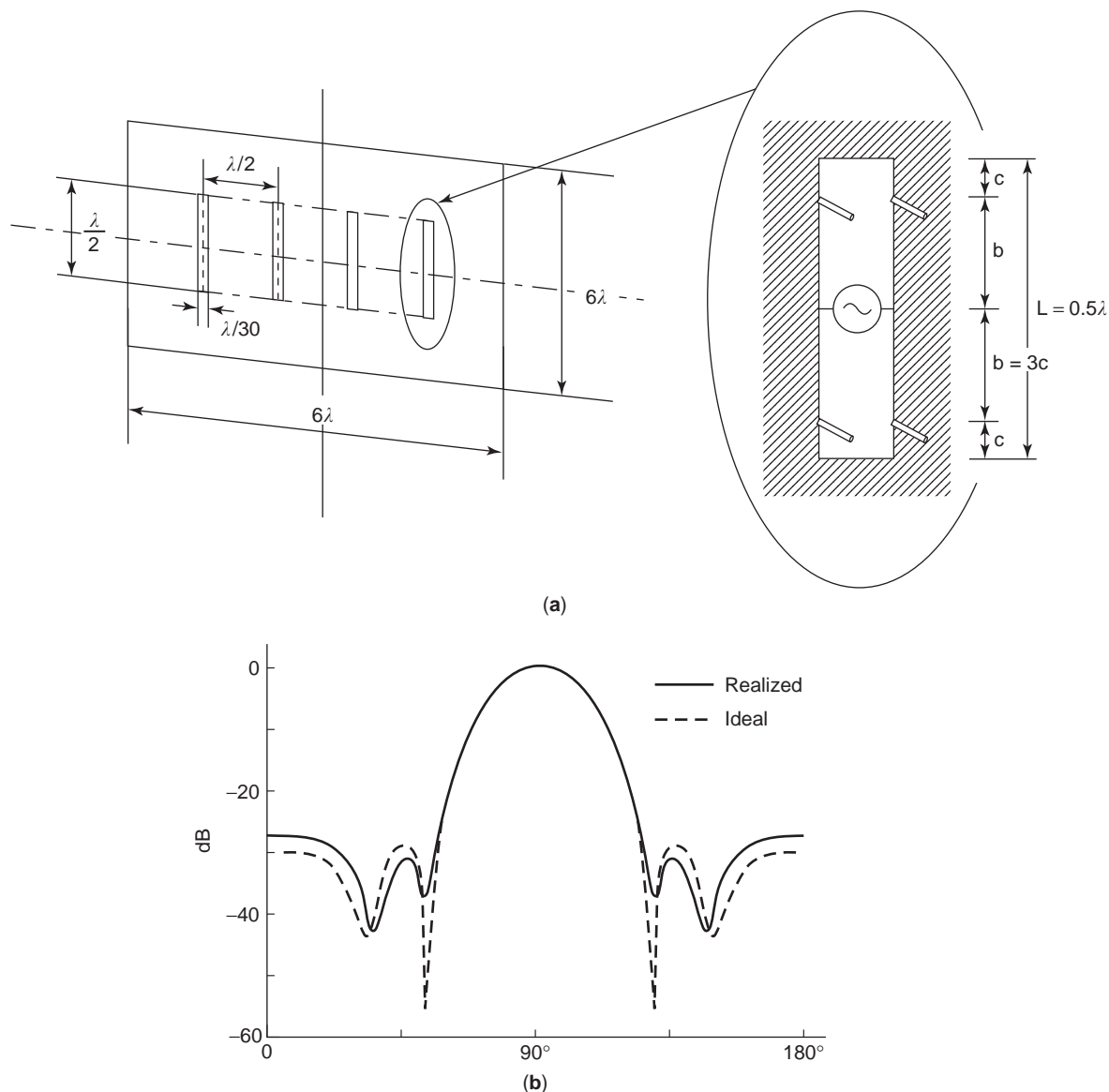


Figure 45. Pattern synthesis by four-slot IAS: (a) array structure; (b) antenna configuration with integrated reactance components (inset); (c) synthesized 30-dB Chebyshev pattern. (From Ref. 45 with permission from IEEE.)

(b) and back (on the right) (c) views. The amplifier accepts a vertically polarized input, amplifies it, and then radiates an asymmetric polarizing output. The unit cell consists of a two-MESFET differential amplifier.

7.3.3. Grid Multiplier. A grid of 1000 Schottky diodes used for frequency doubling [99], producing a power of 0.5 W at 66 GHz with a doubling efficiency of 9.5%, is shown in Fig. 34. The two tuning slabs and two filters were used in order to optimize the fundamental frequency (33 GHz) input to the grid, while similar output filter and tuning slabs were used to match the output.

7.4. Mixer IAS

7.4.1. A Magnetic-Loop Mixer IAS. A mixer IAS, which can perform spatial–optical mixing of RF frequency and a local oscillator within an antenna structure, was proposed by using a loop slot [81]. Figure 35a shows the principle and Fig. 35b, the antenna configuration. The measured antenna parameters are shown in Fig. 36, illustrating radiation patterns at 10 GHz (a) and the power spectrum showing the mixing performance (b). In the measurement, the RF frequency was 10 GHz and the local frequency was 9.7 GHz.

By arraying this IAS unit on a 2D structure (Fig. 37a), beamsteering can be achieved. The basic principle is based on the fact that the direction of an incident RF signal can be shifted by changing either the direction of the local signal or the ratio of the RF frequency and the local frequency. An example beamsteering pattern, measured at the IF frequency, is shown in Fig. 37b.

7.4.2. Subharmonic Mixer IAS. A quasioptical mixer using patch antenna for RF signal, a waveguide for the local signal, and a microstrip for IF is shown in Fig. 38, illustrating the circuit layout (a) and the conversion loss (b) [100]. As the figure shows, the patch antenna, the RF matching network, and the IF output and local oscillator, are integrated on a dielectric substrate. Mixing of 33–36 GHz at RF with 17.6 GHz provides 0–2 GHz IF output. Conversion loss was 5 dB at 34 GHz (Fig. 39b).

7.5. Tunnel Diode Integrated Frequency Tunable MSA

This is an example of a frequency tunable IAS, in which a tunnel diode is integrated and the operating frequency is controlled by the bias voltage in the 51–54 GHz range [101]. Figure 39a depicts the side view of the IAS and Fig. 39b, frequency variation with the bias voltage.

The radiation patterns can also be varied with the bias voltage as the resonance frequency is directly proportional to the bias voltage. The radiation power, beamwidth, and directivity are varied inversely with the increase in bias voltage.

7.6. Beam Control

In a single-antenna system, the radiation pattern can be controlled by the phase control of current distributions on the antenna element. In an array system, a similar concept can be applied to the phase parameters of the array aperture. IAS is useful for this purpose; the current dis-

tributions on an antenna element can be varied by integrating either passive or active devices into the antenna structure so that the radiation patterns can be varied. Similarly, in an array system, phase control of the array feed, and thus radiation pattern control, can be accomplished by integrating either passive or active devices into the array structure. In this case, conventional phase shifters are not necessarily required. The phase control can be performed by other methods such as mutual coupling between array elements, interconnection of array elements by circuitry or external space feeding, and external source excitation (Fig. 12). These phase dynamics can actually be realized in the spatial power combiners, the spatial power combining can serve to not only increase power in space but also provide a method for beam control.

7.6.1. Four-Element FET IAS Array. A four-element beamsteering FET IAS array is shown in Fig. 40, including (a) an array configuration and (b) radiation patterns measured at three different scan angles [102]. A FET using zero-bias gate is integrated into an edge of a patch element to provide oscillation, and the instantaneous phase of each oscillator is varied by the bias voltage, thus producing radiation patterns.

7.6.2. Six-Element FET IAS Array. A six-element beamsteering FET IAS array using a direct-coupling circuit,

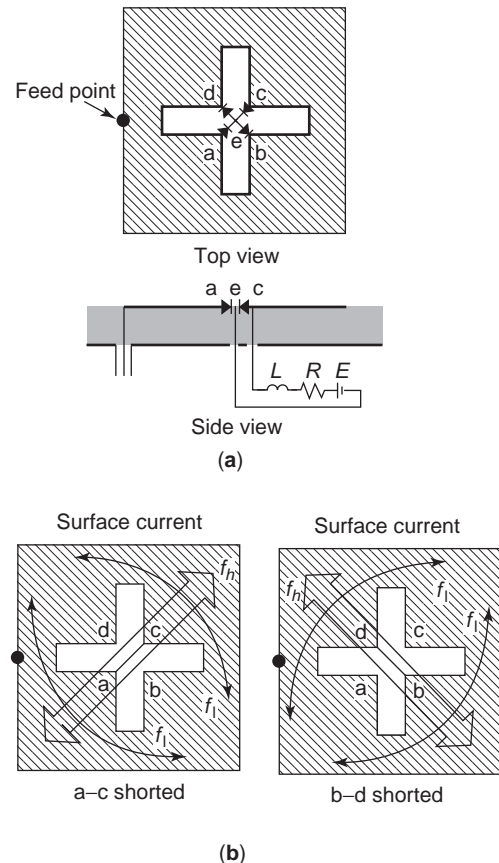


Figure 46. Polarization-controllable IAS: (a) antenna structure; (b) principle of operation. (From Ref. 80 with permission from IEICE.)

which adjusts array element phase, is shown in Fig. 41 [103], including (a) an array configuration and (b) measured radiation patterns, showing continuous scanning from broadside to the scan limit of 40° . The array source is composed of the conventional patch fed at the radiation edge of the microstrip oscillator, which is realized by the lumped-element circuit. The radiation edge on the far side of the patch is used to interinjection lock. The combined sources are interinjection locked at the far side of the radiation patch.

7.6.3. Three-Element Beamsanning IAS Array. Figure 42a shows part of an array configuration employing unilateral injection locking using an amplifier to ensure strong coupling between sources [104]. Beamsanning patterns of a three-element active phased array for three different scan angles are shown in Fig. 42b.

7.6.4. Nonlinear Coupled Array. The active antenna array, with which nonlinear dynamics are combined, is discussed by Meaddows et al. [105], who demonstrated interactions between coupled, nonlinear elements to produce a desired far-field pattern such as beamsteering, reduced sidelobe, and beamforming. An example of a nonlinear array structure producing beamsteering is shown in Fig. 43a. The array is composed of a voltage-controlled oscillator (VCO) connected to a patch radiator, which is coupled with a nearest-neighbor element in the array via a stripline. Beamsteering is realized by varying the varactor bias, which adjusts the freerunning frequency of each oscillator. The sidelobe reduction (Fig. 43b) is

accomplished with a nonlinear coupled array, in which amplitude dynamics were employed along with phase dynamics. It should be noted that beamsteering is accomplished with suppressed sidelobes simultaneously.

7.6.5. Beam Control by a Single IAS. Beamshifting or beamsteering realized by a single antenna element has demonstrated [106]. A 0.8λ dipole was used and asymmetric current distributions on the dipole were accomplished by either type I, where one reactance component is integrated as shown in Fig. 44a, or type II, where two different reactance components are used as shown in Fig. 44b. Beamsteering or beamsanning, if required, can be achieved by varying the impedance of the integrated reactance components electronically. Figure 44c shows a beamshifting pattern obtained by using type II.

7.6.6. Pattern Synthesis. The first pattern synthesis using the IAS array was demonstrated in 1964 [21]. A passive integrated dipole array applied to pattern synthesis was later demonstrated in 1985 by using a four-element array [45], into which reactance components were integrated. Figure 45a shows the antenna structure, and Fig. 45b shows an antenna configuration with integrated reactance components, and Fig. 45c shows a synthesized 30-dB Chebyshev pattern. A reactance component was made with a short-circuited two-wire transmission line as shown in the inset in the figure.

7.6.7. Polarization Control Antenna. A polarization-controllable IAS is developed by using a switching diode

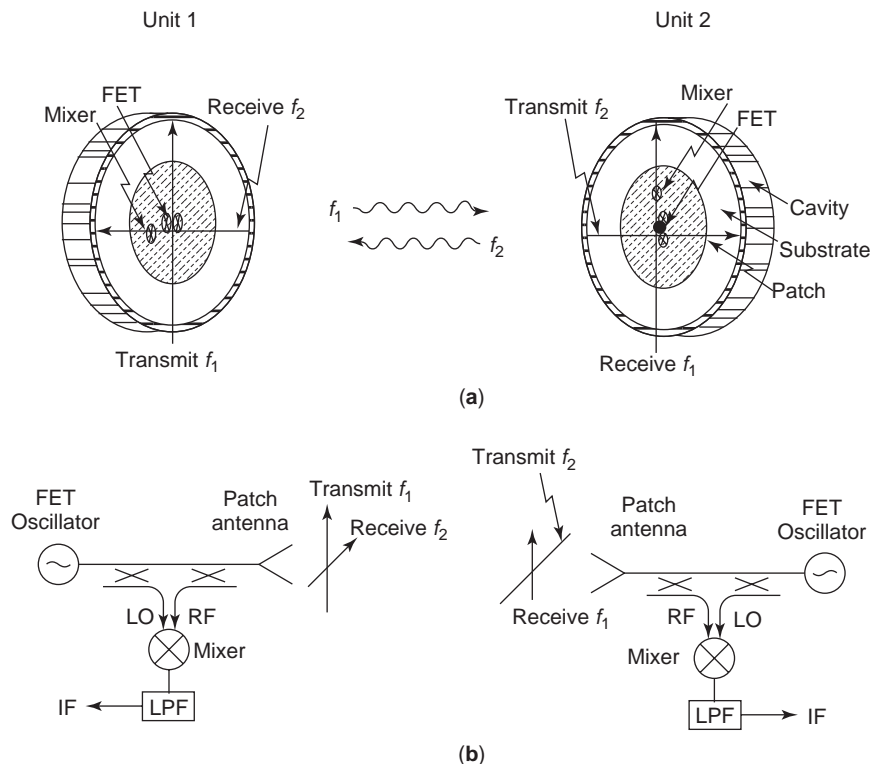


Figure 47. Transceiver: (a) units; (b) operation concept. (From Refs. 5 and 86 with permission from Wiley and IEEE, respectively.)

integrated MSA [80]. Figure 46a shows the antenna structure, which has a cross-slot on the patch surface and Schottky diodes are integrated at the center of these slots. Figure 46b illustrates the principle of operation. Polarization can be varied by changing the current flowing on the patch surface. The antenna operates at two resonance frequencies and produces cross-polarization. The high-frequency current flows in a diagonal direction on the surface, depending on the connection of the diode, while the low-frequency current flows around the cross-slot as shown in Fig. 46b. By changing the bias voltage supplied to the diode, its ON or OFF state can be changed, and thus the direction of the current flow, and thereby polarization of the antenna is changed at each frequency. FDTD is used for the analysis.

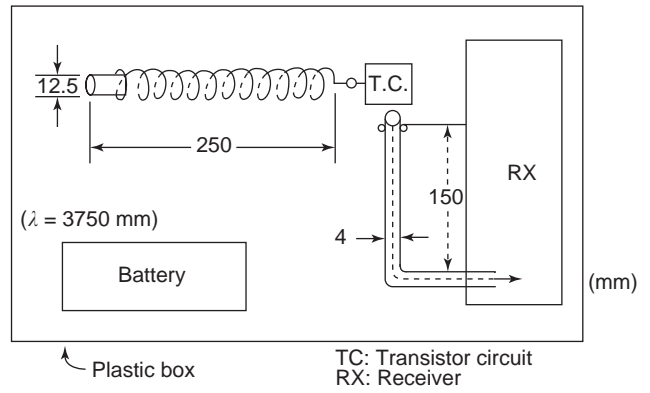


Figure 49. Inverted-L IAS for portable receiver.

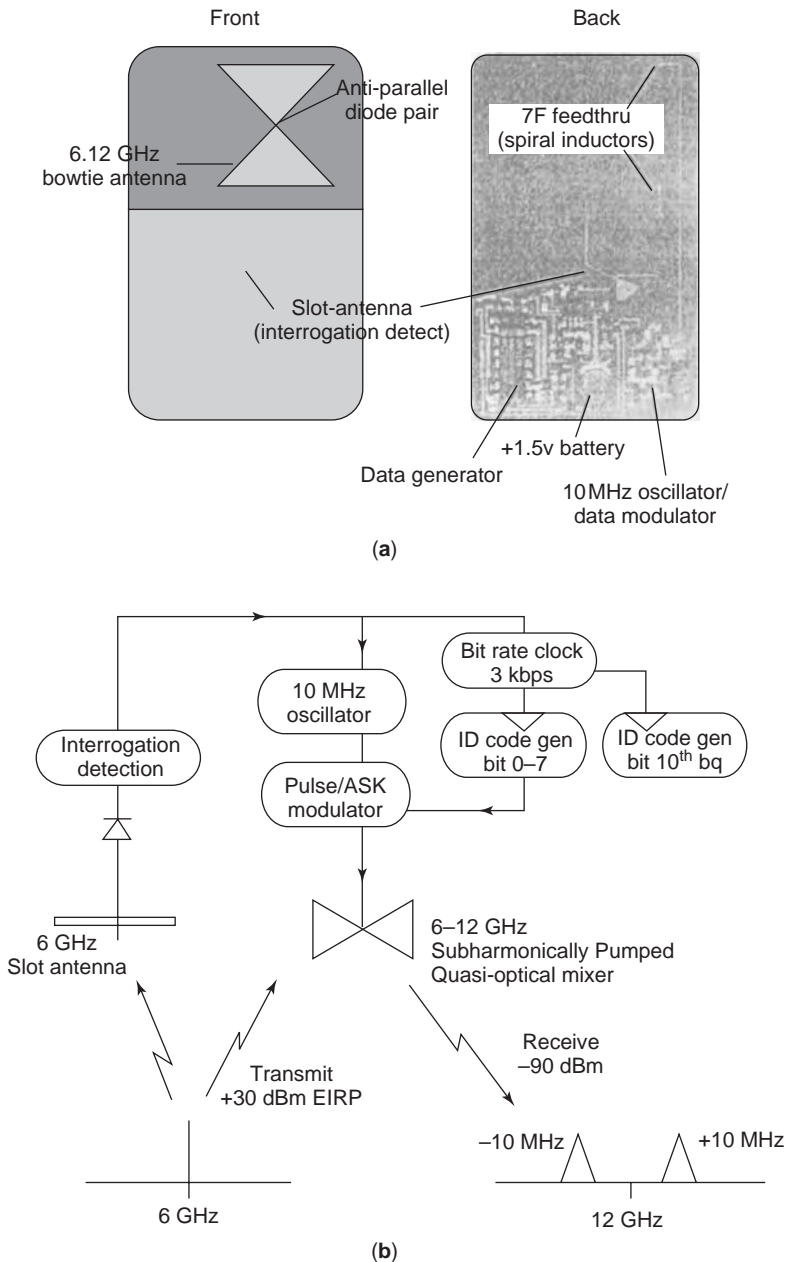


Figure 48. Transponder: (a) card-type transponder (photos); (b) operation concept. (From Ref. 107 with permission from IEEE.)

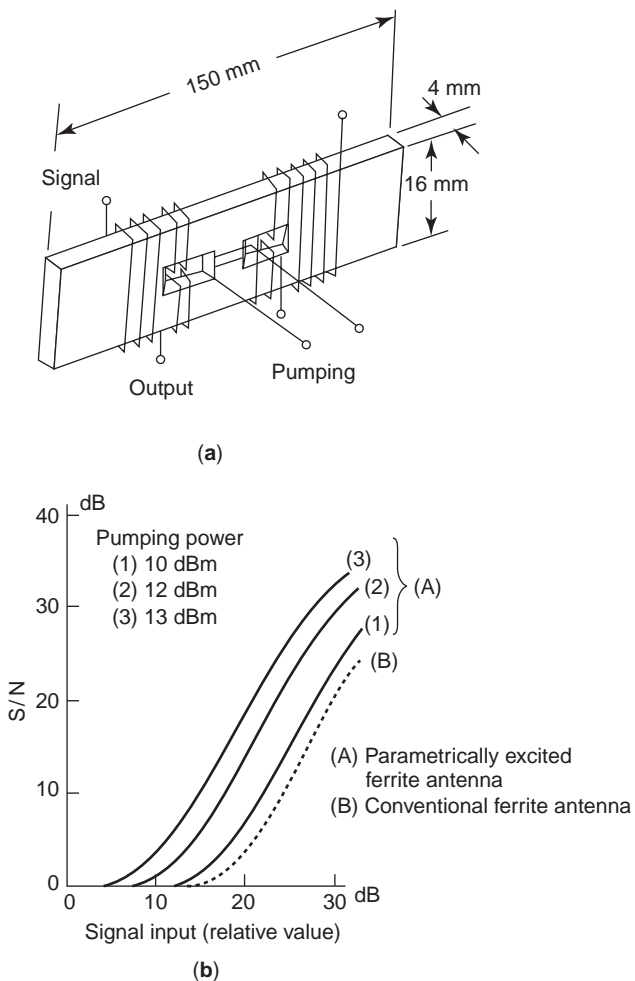


Figure 50. Parametric excitation integrated ferrite antenna: (a) antenna structure; (b) *S/N* gain performance. (From Ref. 30 with permission from IEEE.)

7.7. Transmitter–Receiver IAS

IAS can be applied to either transmitter or receiver systems, depending on integration of functions such as oscillation, amplification, mixing, multiplying, and switching. Integrated antenna systems have various advantages in that they can be designed to be small, compact, and lightweight structures, with low power consumption, and to be congruent or compatible with planar and/or MIC structures. An IAS can be constructed as a single structure and is used as an RF front end of either transmitter or receiver. The packaging can take the form of a simple planar structure using a microstrip substrate or 2D or 3D structure consisting of layered substrates or IC, MIC, and MMIC.

Losses associated with interconnection between antenna and RF front end, dielectrics, circuitry, and other properties can be reduced. Noise performance may also be improved as a result of integration. Utilizing IAS technology in this way, a variety of IAS transmitters or receivers have been developed. Typical applications are to transceivers, transponders, and direct-conversion receivers. Some other applications are rectifier antennas, which convert RF energy to DC power; retrodirective antennas, which control radiation patterns to the same direction of the incoming signal; and reflectarray, which produces any desired direction, including the same direction as the incoming wave.

7.7.1. Transceiver. Figure 47a illustrates the units and Fig. 47b, the operation concept [86]. The FET is integrated into a circular patch to oscillate at C band. The oscillator acts as a transmitter and also as a local-oscillator source, which consumes a portion of the oscillation power. Another diode, a Schottky diode, is integrated within the antenna cavity to function as a mixer by receiving the local-oscillator power. This system uses an RF signal of 6 GHz and a local

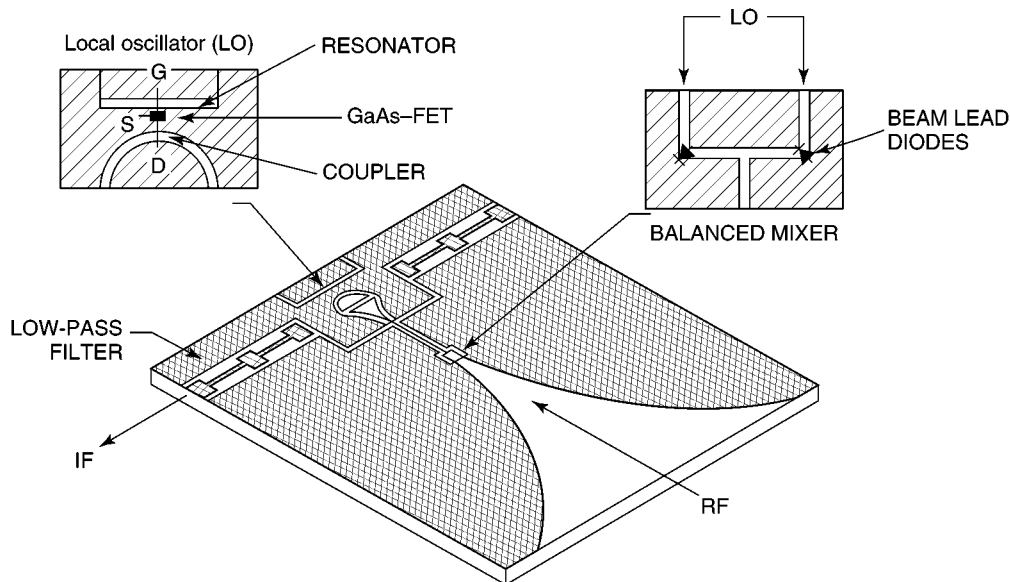


Figure 51. Notch receiver. (From Refs. 5 and 119 with permission from Wiley and IEEE, respectively.)

frequency of 5.8 GHz, equaling an output signal of 0.2 GHz. The features of the transceiver are low cost, small size, compactness, and light weight, as the mixer and oscillator are configured on the same small patch antenna, avoiding interconnecting lines and circuitry.

7.7.2. Transponder. An antenna integrated with a mixer functions as a receiver front end, to which a local oscillator (LO) can be either integrated on the same substrate or supplied externally by a source in free space. Without using a separate LO, a self-oscillating mixer can be used by utilizing a nonlinear property of an oscillating device itself. In millimeter-wave regions, a LO frequency is achieved by subharmonically pumping up from one-half the value required for a conventional mixer, as the LO frequency with sufficient power to drive the mixer can hardly be obtained.

Such a subharmonically pumped mixer quasioptical mixer practically applied to a noncontact identification transponder has been invented [107]. The transponder has a form of ID card supporting a slot antenna, a bowtie (planar triangular dipole) antenna, and transmitter and receiver circuitry (Fig. 48a). Figure 48b illustrates the operational concept. The transponder receives an interrogation signal at 6 GHz by a dipole antenna as the harmonically pumped LO power and responds with an ASK (amplitude shift keying)-modulated ID code around 12 GHz. Antiparallel Schottky diode pairs are mounted at the terminals of the bowtie antenna. It has the quasioptical mixer structure proposed previously for microwave imaging and telemetry by Stephan and Itoh [108].

7.7.3. Receiver

7.7.3.1. Inverted-L IAS. The inverted-L IAS shown in Fig. 49 [29] was installed inside an 80-MHz small portable receiver, which was used practically in the field. A transistor circuit was integrated into the middle of the inverted-L element and S/N gain of 10 dB over the conventionally used monopole antenna of $\sim \frac{1}{3}\lambda$ was obtained.

7.7.3.2. Ferrite IAS. A parametric excitation integrated ferrite antenna [30], (Fig. 50a) was developed. The frequencies of signal, pump, and output were 1, 3, and 2 MHz, respectively, and an S/N gain of >10 dB over that of the same-size ferrite antenna was obtained as a result of parametric excitation to the ferrite antenna (Fig. 50b).

It should be noted that this IAS is a real “active” antenna, because the part that is involves radiation (receiving) in this antenna is “active.” In general AIAS function, the radiator is not really “active,” but inherently passive, even though it is called an “active antenna.”

7.7.3.3. Notch Receiver. To obtain wideband operation, a notch structure was used for an IAS receiver (Fig. 51) [109]. A notch element is integrated with coupled slotlines to complete an RF front end. A GaAs-FET local oscillator with local resonator slot is used to form a balanced mixer. These components are embedded at the site where the notch element begins to taper out.

7.7.3.4. Direct-Conversion Receiver. Figure 52a illustrates a single integrated I/Q (in-phase/quadrature) direct-conversion converter [110], which is composed of a 40-GHz patch antenna, a quadrature mixer, and a local oscillator, all of which are integrated on a planar substrate. The antenna was designed for a 10 dB bandwidth of 1.64 GHz for wideband operation. The quadrature mixer performs direct downconversion for digitally modulated signals. A pair of antiparallel diodes are used for the mixer, which is LO-pumped subharmonically at half of the RF carrier frequency. Figure 52b is a photo of the receiver.

8. OTHER APPLICATIONS

Applications of IASs other than those described above are rectennas and retrodirective antennas. Rectennas

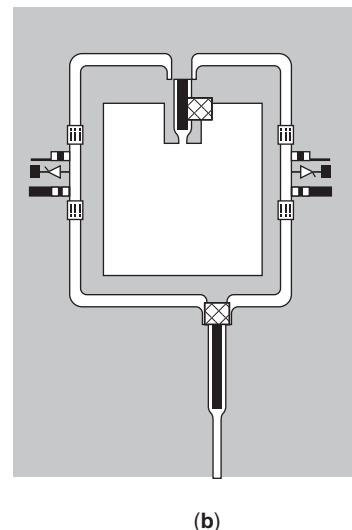
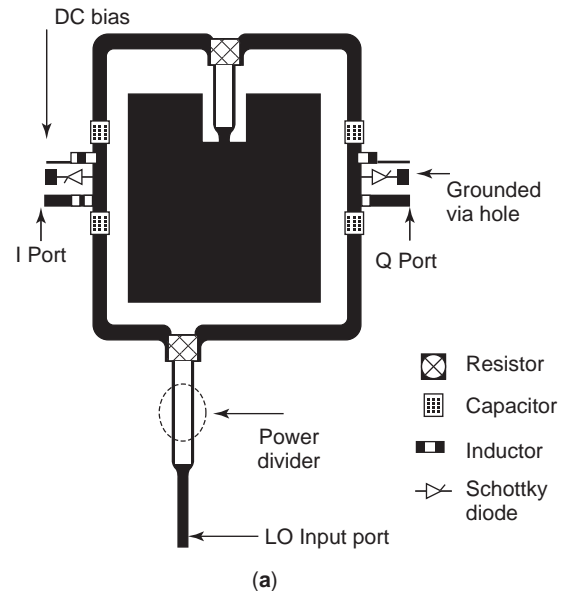


Figure 52. Direct-conversion receiver: (a) I/Q integrated antenna; (b) photo. (From Ref. 112 with permission from IEICE.)

are antenna systems that convert RF energy into DC power in the wireless transmission link. Either a single antenna element, to which a rectifying device is integrated, or an array of rectennas is used for rectennas. The earliest rectennas were developed by Brown [111], who contributed to microwave power transmission as well as rectenna development. Since then many investigators have developed rectennas [112] applying IAS technology.

Retrodirective antennas are antenna systems that reradiate signals back toward the direction of incoming signals. Retrodirective antennas consist of transmitting and receiving antennas and phase conjugation circuitry.

8.1. Rectenna

A 35-GHz rectenna is shown in Fig. 53a [113], consisting of a patch dipole antenna and a diode integrated at the input terminals of the dipole. The conversion efficiency is shown in Fig. 53b, illustrating formats using either a patch or a dipole.

8.2. Retrodirective antenna

A 6-GHz-band planar active retrodirective antenna, using subharmonic mixing for phase conjugation, has been demonstrated [114]. An incoming signal of 5.79 GHz is subharmonically mixed with the local-oscillator output of 2.9 GHz, thereby producing an IF signal of 10 MHz. Antiparallel diode pairs are used in subharmonic phase

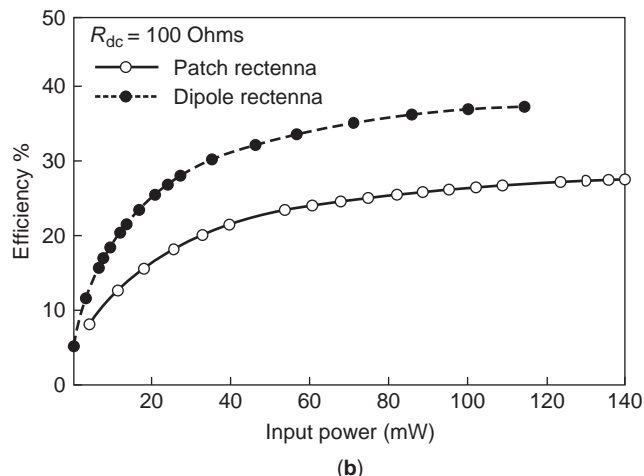
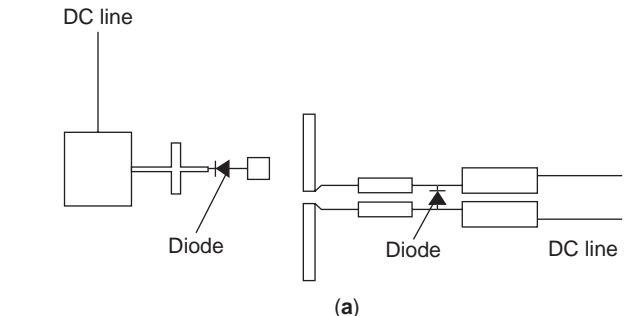


Figure 53. Rectenna: (a) patch rectenna; (b) conversion efficiency. (From Refs. 5 and 111 with permission from Wiley and IEEE, respectively.)

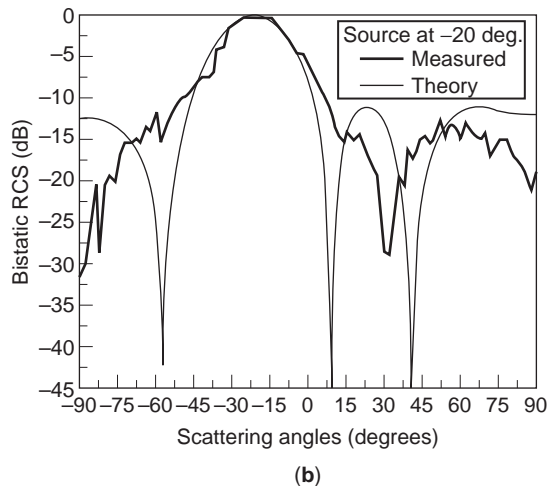
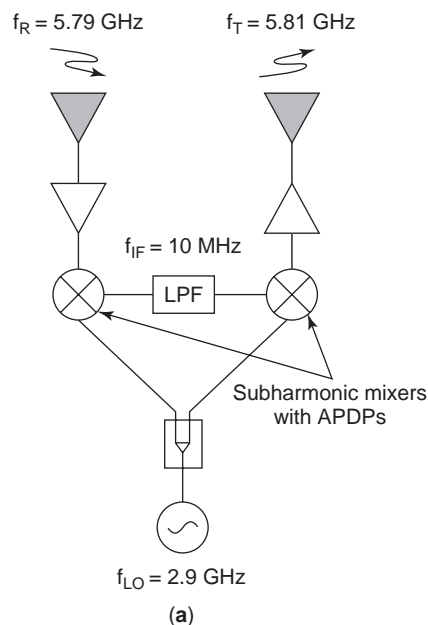


Figure 54. Retrodirective antenna: (a) antenna system; (b) scattering pattern. (From Ref. 113.)

conjugation mixers. The IF frequency is then upconverted with the same local frequency to produce a transmitting frequency of 5.81 GHz. Figure 54a illustrates the antenna system concept, and Fig. 45b shows measured and calculated patterns with an incoming signal on a -20° trajectory. These results verify the advantages of retrodirective performance.

9. PERSPECTIVE

IAS technology and its applications still remain in the process of development. There is no limit to the type of antennas as the base of IAS and also in the integration materials, which include not only solid-state devices but also such components as dielectrics and magnetic materials. The development one may expect in the near future for integrated antenna systems will be integration of metamaterials or left-handed materials into an antenna

system. That would bring small antennas or functional antenna systems, which could never been realized by conventional technology.

IAS technology will promote further advancement of antenna systems in microwave and higher-frequency regions. Integration of materials never used before such as nonreciprocal or nonlinear devices would create new antenna systems with capability beyond the scope of anything available today.

There are various IAS applications. IAS is useful for antenna systems not only in communications but also in other wireless systems such as radar, sensing, control, and broadcasting. In another aspect, application of IAS would offer many advantages in realizing small antennas, including antennas that are functionally as well as electrically small.

BIBLIOGRAPHY

1. K. Fujimoto, A treatment of integrated antenna systems, *IEEE AP-S Int. Symp. Digest*, 1970, pp. 120–123.
2. H. H. Meinke, Active antennas, *Nachrichtentechnische Zeitschrift* **19**:695–705 (1966).
3. A. Mortazawi, T. Itoh, and J. Harvey, *Active Antennas and Quasioptical Arrays*, IEEE Press, 1999.
4. K. Chang, R. A. York, P. S. Hall, and T. Itoh, Active integrated antennas, *IEEE Trans. Anten. Propag.* **50**(3):937–943 (2002).
5. J. A. Navarro and K. Chang, *Integrated Active Antennas and Spatial Power Combining*, Wiley, New York, 1996.
6. J. A. Navarro and K. Chang, *Integrated Active Antennas and Spatial Power Combining*, Wiley, New York, 1996, p. 128.
7. H. Morishita, Y. Kim, and K. Fujimoto, Design concept of antennas for small mobile terminals and the future perspectives, *IEEE Anten. Propag. Mag.* **44**(56):40–41 (Oct. 2002).
8. R. Hertz, *Electric Waves*, Macmillan, 1883.
9. H. A. Wheeler, Small antennas, *IEEE Trans. Anten. Propag.* **23**:462–469 (1975).
10. A. D. Frost, Parametric amplifier antenna, *Proc. IRE* **48**:1163 (1960).
11. M. E. Pedinof, The negative conductor slot amplifier, *IRE Trans. Microwave Theory Tech.* **9**:557–566 (1961).
12. H. H. Meinke, Tunnel diode integrated with microwave antenna systems, *Radio Electron. Eng.* **31**(2):76–80 (1966).
13. H. H. Meinke, *Receiving Antennas Integrated with Transistors*, Progress Report 4, Inst. Hochfrequenz Technische Hochschule, Munich, Germany, 1964.
14. F. M. Landstorfer, Applications and limitation of active aerials at microwave frequencies, *Proc. European Microwave Conf.* 1969, pp. 141–144.
15. H. H. Meinke and F. M. Landstorfer, Noise and bandwidth limitation with transistor antenna, *IEEE AP-S Int. Symp. Digest*, 1968.
16. V. H. Lindenmeier, Einige Beispiele rausharmer transistorierter empfangsantenne, *Nachrichtentechnische Zeitschrift* **7** (1969).
17. J. R. Copeland and W. J. Robertson, Antennaversers and antennafiers, *Electronics* 68–71 (1961).
18. K. Fujimoto, Tunnel diode loaded dipole antenna, *IEEE Trans. Aerospace* **2**:297–307 (1964).
19. K. Fujimoto, Active antennas; tunnel-diode loaded dipole antenna, *Proc. IEEE* **53**:174 (1965).
20. K. Fujimoto, Esaki-diode-loaded dipole antenna, *Trans. IECE Jpn.* **48**(4):242–251 (1964) (in Japanese).
21. W. J. Robertson, J. R. Copeland, and R. Verstraete, Antennafier arrays, *IEEE Trans. Anten. Propag.* **2**:227–233 (1964).
22. K. Fujimoto, A. Henderson, K. Hirasawa, and J. R. James, *Small Antennas*, Research Studies Press, UK, 1987, pp. 152–164.
23. Y. Mikuni and K. Nagai, Uni-directional two-conductor antenna with impedance loading, *Trans. IECE* **55-B**(2):52–59 (1972) (in Japanese).
24. Y. Hiroi and K. Fujimoto, Analysis and design of the electronically-beam-controllable antennas, *IEEE AP-S Int. Symp.* 1971, pp. 241–244.
25. J. P. Daniel, G. Dubost, and J. Rospers, Doublet reception active a large bande a la reception, *Electron. Lett.* **11**(4) (1975).
26. T. Doi and R. Sato, An active antenna based on distribution current source pattern synthesis, *Trans. IECE* **54-B**(10):647–653 (1971) (in Japanese).
27. R. A. Ramsdale and T. S. M. Maclean, Active loop-dipole aerials, *Proc. IEE* **118**(2):1698–1710 (1971).
28. A. P. Anderson and M. M. Dawoud, The performance of transistor fed monopoles in active antennas, *IEEE Trans. Anten. Propag.* **AP-21**:371–374 (1973).
29. K. Fujimoto, A. Henderson, K. Hirasawa, and J. R. James, *Small Antennas*, Research Studies Press, UK, 1987, pp. 130–135.
30. K. Tamura and K. Fujimoto, A parametric-excitation-integrated ferrite antenna, *IEEE Trans. MAG-8* **3**:384 (1972).
31. K. Fujimoto, A. Henderson, K. Hirasawa, and J. R. James, *Small Antennas*, Research Studies Press, UK, 1987, pp. 160–164.
32. R. A. Ramsdale and T. S. M. Maclean, Short range active transmitting antenna with very large height reduction, *IEEE Trans. Anten. Propag.* **23**(3):286–287 (1975).
33. R. A. Ramsdale and T. S. M. Maclean, Signal/noise-ratio performance of loaded wire antennas, *Proc. IEE* **124**(10):841–844 (1977).
34. J. P. Daniel and C. Terre, Mutual coupling between antenna-optimization of transistor parameters in active antenna design, *IEEE Trans. Anten. Propag.* **AP-23**:513–516 (1975).
35. J. P. Daniel, Reduction of mutual coupling between active monopole: Application to super directive receiving array, *IEEE Trans. Anten. Propag.* **AP-25**(6):737–741 (1977).
36. A. P. Anderson, W. B. Davies, M. M. Dawoud, and D. E. Galanakis, Note on transistor-fed active array antennas, *IEEE Trans. Anten. Propag.* **AP-19**:537–539 (1971).
37. M. M. Dawoud and A. P. Anderson, Calculation showing the reduction in the frequency dependence of a two element array antenna fed by microwave transistors, *IEEE Trans. Anten. Propag.* **AP-20**:497–499 (1972).
38. *Development of Active Indoor TV Reception Antenna*, Tech. Report MR722005, Matsushita Communication Ind. Co. Ltd. Japan, Aug. 1972.
39. M. B. Armstrong, R. Brown, F. Rix, and J. A. C. Stewart, Use of microstrip impedance-measurement technique in the design of a BARITT diplex Doppler sensor, *IEEE Trans. Microwave Theory Tech.* **28**(12):1437–1442 (1980).
40. S. P. Kwak and K. P. Welles, Low cost X-bands MIC BARITT sensor, *IEEE Trans. Microwave Theory Tech.* **27**(10):844–847 (1979).
41. G. Morris, H. J. Thomas, and L. D. Fudge, Active patch antenna, *Proc. 1984 Military Microwave Conf.*, London, 1984, pp. 245–249.

42. M. D. Dydyk, Planar radial resonator oscillator, *IEEE MTT-S Int. MW Symp. Digest*, 1986, pp. 167–168.
43. K. Chang, K. Hummer, and G. Gopalakrishnan, Active radiating element using FET source integrated with microstrip patch antenna, *Electron. Lett.* **24**(21):1347–1348 (1989).
44. R. N. Shiroma, B. L. Show, and A. B. Popovic, Three dimensional power combiners, *IEEE MTT-S Int. MW Symp. Digest*, 1994, pp. 831–834.
45. K. Fujimoto and K. Hirasawa, Application of reactance-integrated dipole antenna to array synthesis, *Proc. IEEE 14th Conf. Electrical and Electronic Engineering in Israel*, 1985, Paper 2.3.1.
46. J. W. Mink, Quasi optical power combining of solid state millimeter-wave sensors, *IEEE Trans. Microwave Theory Tech.* **MTT-34**(2):273–279 (1986).
47. S. Young and K. D. Stephan, Stabilization and power combining of planar microwave oscillators with an open resonator, *IEEE MTT-S Int. MW Symp. Digest*, 1987, pp. 185–188.
48. J. A. Navarro and K. Chang, *Integrated Active Antennas and Spatial Power Combining*, Chap. 7–Chap. 9, Wiley, New York, 1996.
49. A. Mortazawi, T. Itoh, and J. Harvey, *Active Antennas and Quasi-Optical Arrays*, IEEE Press, Englewood Cliffs, NJ, 1999.
50. E. M. Sabbagh and R. George, *Microwave Energy Conversion*, WADD Tech. Report, Parts I and II, 1961.
51. Z. B. Popovic and D. B. Rutledge, Diode grid oscillator, *IEEE AP-S Int. Symp. Digest*, 1988, pp. 442–445.
52. Z. B. Popovic, M. Kim, and D. B. Rutledge, Grid oscillator, *Int. J. Infrared Millimeter Waves* **9**(7):647–654 (1988).
53. J. A. Navarro and K. Chang, *Integrated Active Antennas and Spatial Power Combining*, Wiley, New York, 1996, Chap. 8.
54. J. A. Navarro and K. Chang, *Integrated Active Antennas and Spatial Power Combining*, Wiley, New York, 1996, Chaps. 2, 4, and 5.
55. S. C. Bundy and Z. B. Popovic, Analysis of planar grid oscillators, *IEEE MTT-S Int. MW Symp. Digest*, 1994, pp. 827–830.
56. W. A. Shiroma, B. L. Shaw, and Z. B. Popovic, Three-dimensional power combiners, *IEEE MTT-S Int. MW Symp. Digest*, 1994, pp. 831–834.
57. T. Mader, S. Bundy, and Z. B. Popovic, Quasi-optical VCOs, *IEEE Trans. Microwave Theory Tech.* **41**(10):1775–1781 (1993).
58. Z. B. Popovic, R. M. Weikle, M. Kim, and D. B. Rutledge, A 100-MESFET planar grid oscillator, *IEEE Trans. Microwave Theory Tech.* **39**(2):193–200 (1991).
59. Y. Hiroi and K. Fujimoto, Analysis and design of the electronically-beam-controllable antenna, *IEEE AP-S Int. Symp. Digest*, 1972, pp. 241–244.
60. K. Hirasawa and K. Fujimoto, On electronically-beam-controllable dipole antenna, *IEEE AP-S Int. Symp. Digest*, 1980, pp. 692–695.
61. A. Mortazawi, T. Itoh, and J. Harvey, *Active Antennas and Quasi-Optical Arrays*, IEEE Press, Englewood Cliffs, NJ, 1999, Chap. 4.
62. N. Camirelli and B. Bayraktaroglu, Monolithic millimeter-wave IMPATT oscillator and active antenna, *IEEE Trans. Microwave Theory Tech.* **36**(12):1670–1676 (1988).
63. M. Kim, E. A. Sovero, J. B. Hacker, M. D. Delisio, J. C. Chiao, S. J. Lin, D. R. Gragnon, J. J. Rosenberg, and D. B. Rutledge, A 100-element HBT grid amplifier, *IEEE Trans. Microwave Theory Tech.* **43**(10):1762–1771 (1993).
64. D. S. Hernandez, M. Gillick, and I. Robertson, An 18 GHz circularly polarized multilayer active microstrip antenna subarray using MMIC amplifier, *IEEE MTT-S Int. MW Symp. Digest*, 1995, pp. 1099–1102.
65. J. B. Hacker, R. M. Weikle, M. Kim, M. P. Delisio, and D. B. Rutledge, A 100-element planar shottky diode grid mixer, *IEEE Trans. Microwave Theory Tech.* **40**(3):557–582 (1992).
66. R. D. Martinez, and R. C. Compton, Electronic beam steering of active array with phase-locked-loop, *IEEE Microwave Guided Wave Technol. Lett.* **4**:166–168 (1994).
67. S. T. Chew, T. K. Tong, M. C. Wu, and T. Itoh, An active phased array with optical input and beam scanning capability, *IEEE Microwave Guided Wave Technol. Lett.* 205–207 (1994).
68. T. Birkeland and T. Itoh, FET-based planar circuits for quasi-optical sources and transceivers, *IEEE Trans. Microwave Theory Tech.* **37**(9):1452–1459 (1989).
69. K. Cha, S. Kawasaki, and T. Itoh, A microwave non-contact identification transponder using sub-harmonic interrogation, *IEEE MTT-S Int. MW Symp. Digest*, 1994.
70. K. Chang, A. Hummer, and G. Gopalakrishnan, Active radiating element using FET source integrated with microstrip patch antenna, *Electron. Lett.* **24**(21):1347–1348 (1988).
71. K. Hummer and K. Chang, Spatial power combining using active microstrip antenna, *Microwave Opt. Technol. Lett.* **1**(1):8–9 (1988).
72. X. Gao and K. Chang, Network modeling of an aperture coupling between microstrip line and patch antenna for active array applications, *IEEE Trans. Microwave Theory Tech.* **36**(3):505–513 (1988).
73. K. C. Gupta and P. S. Hall, eds., *Analysis and Design of Integrated-Circuit Antenna Modules*, Wiley, New York, 2000.
74. P. S. Hall, Advances in quasi-optical active antennas, *Proc. Microwave and RF Conf.*, 1996, pp. 208–213.
75. C. T. P. Song, P. S. Hall, G. Shiraz, and D. Wake, Packaging technique for gain enhancement of electrically small antennas designed on gallium arsenides, *Electron. Lett.* **36**(18):1524–1525 (2000).
76. A. Sheth, T. Ivanov, A. Balasubramanian, and A. Mortazawi, A nine HEMT spatial amplifier, *IEEE MTT-S Int. MW Symp. Digest*, 1994, pp. 1239–1242.
77. M. Kim, E. A. Sovero, J. B. Hacker, M. P. Delisio, S. J. Li, D. R. Gognon, A. Rosenberg, and D. B. Rutledge, A 100-element HBT grid amplifier, *IEEE Microwave Theory Tech.* **41**(10):1762–1771 (1993).
78. G. Ma, P. S. Hall, P. Gardner, and M. Hajian, Direct-conversion active antenna for modulation and demodulation, *Microwave Opt. Technol. Lett.* **28**(2):89–93 (2001).
79. C. Kallialakis, M. J. Cryan, P. S. Hall, and P. Garner, Analysis and design of integrated active circulator antennas, *IEEE Trans. Microwave Theory Tech.* **48**:1017–1023 (2000).
80. E. Nishiyama, K. Takenaka, and M. Aikawa, Polarization controlled microstrip antenna, *Trans. IEICE* **J85-B**(9):1519–1525 (2002) (in Japanese).
81. H. Saito, T. Nishimura, M. Yamamoto, and K. Itoh, Quasi-optical antenna-mixer array composed of a magnetic loop antenna operated at 10 GHz band, *Trans. IEICE* **J85-B**(9):1493–1500 (2002) (in Japanese).
82. T. Seki, H. Yamamoto, T. Hori, K. Cho, and H. Mizuno, Active integrated array antenna using multi-stage amplifier arrangement method, *Trans. IEICE* **J85-B**(9):1512–1518 (2002) (in Japanese).
83. R. Y. Miyamoto, Y. Qian, and T. Itoh, Active retro-directive array for remote sensing and wireless sensor applications, *IEEE MTT-S Int. MW Symp. Digest*, 2000, pp. 1431–1434.

84. K. D. Park, S. Sakuragawa, and H. Arai, Experimental study for optimizing self-oscillating mixer with electromagnetically coupled antenna element, *Trans. IEICE J85-B(9)*:1542–1548 (2002) (in Japanese).
85. R. W. Clark, G. H. Huff, and J. T. Bernard, An integrated active microstrip reflectarray element with an internal amplifier, *IEEE Trans. Anten. Propag.* **51**(5) (2003).
86. R. Flynt, F. J. Navarro, and K. Chang, Low cost and compact active transceiver for system applications, *IEEE MTT-S Int. MW Symp. Digest*, 1995, pp. 953–956.
87. B. Strassner and K. Chang, Integrated antenna system for wireless RFID tag in monitoring oil drill pipe, *IEEE AP-S Int. Symp. Digest*, 2003, Vol. 1, pp. 208–211.
88. G. Ellis and S. Liw, Active planar inverted-F antennas for wireless applications, *IEEE Trans. Anten. Propag.* **51**(10):2899–2906 (2003).
89. (a) K. Fujimoto, A. Henderson, K. Hirasawa, and J. R. James, *Small Antennas*, Research Studies Press, UK, 1987, pp. 164–181; (b) K. Fujimoto, Integrated antenna systems, *Proc. IEICE* **86**(6):403–408 (2003).
90. K. C. Gupta and P. S. Hall, eds., *Analysis and Design of Integrated Circuit Antenna Modules*, Wiley-Interscience Series, 2000, Chap. 4.
91. K. C. Gupta and P. S. Hall, eds., *Analysis and Design of Integrated Circuit Antenna Modules*, Wiley-Interscience Series, 2000, p. 414.
92. T. Iwasaki and T. Murata, Characteristics of electromagnetic coupling-fed active slot array antenna, *Trans. IEICE J85-B(9)*:1575–1582 (2002) (in Japanese).
93. J. A. Navarro and K. Chang, *Integrated Active Antennas and Spatial Power Combining*, Wiley, New York, 1996, pp. 148–189, 199–210.
94. R. A. York and R. C. Compton, Dual device active patch antenna with improved radiation characteristics, *Electron. Lett.* **28**(11):1019–1021 (1992).
95. J. A. Navarro and K. Chang, *Integrated Active Antennas and Spatial Power Combining*, Wiley, New York, 1996, Chap. 8.
96. J. A. Navarro and K. Chang, *Integrated Active Antennas and Spatial Power Combining*, Wiley, New York, 1996, pp. 199–219.
97. Z. R. Popovic, R. M. Weikle, M. Kim, and D. B. Rutledge, A 100-MESFET planar grid oscillator, *IEEE Trans. Microwave Theory Tech.* **39**(2):193–200 (1991).
98. M. Kim, J. J. Rosenberg, R. P. Smith, R. M. Weikle, J. B. Hacker, M. P. DeLisio, and D. B. Rutledge, A grid amplifier, *IEEE Microwave Guided Wave Lett.* **1**(11):322–324 (1991).
99. C. F. Jou, W. W. Lam, H. Z. Chen, K. S. Stolt, N. C. Luhmann, and D. B. Rutledge, Millimeter-wave diode-grid frequency doubler, *IEEE Trans. Microwave Theory Tech.* **36**(11):1507–1514 (1988).
100. C. M. Jackson, Patch antenna quasi-optical mixers, *Microwave Opt. Technol. Lett.* **1**(12):1–4 (1988).
101. S. Srivastava, B. R. Vishvakarma, and J. A. Ansari, Tunnel diode loaded rectangular microstrip antenna for millimeter range, *IEEE Trans. Anten. Propag.* **51**(4):750–755 (2003).
102. P. Liao and R. A. York, A new phase-shifterless beam scanning technique using arrays of coupled oscillators, *IEEE Trans. Microwave Theory Tech.* **41**(10):1810–1815 (1993).
103. P. Liao and R. A. York, A six-element beam-scanning arrays, *Microwave Guided Wave Lett.* **41**(1):20–22 (1993).
104. J. Lin, S. T. Chew, and T. Itoh, A unilateral injection-locking type active phased array for beam scanning, *IEEE MTT-S Int. MW Symp. Digest*, 1994, pp. 1231–1234.
105. B. K. Meaddows, T. H. Heath, J. D. Neff, E. A. Brown, D. B. Fogliatti, V. In, P. Halsler, S. P. Deweerth, and W. L. Ditto, Non-linear antenna technology, *Proc. IEEE* **90**(5):882–897 (2002).
106. K. Fujimoto, A. Henderson, K. Hirasawa, and J. R. James, *Small Antennas*, Research Studies Press, UK, 1987, pp. 152–164.
107. C. W. Pobanz and T. Itoh, A microwave non-contact identification transponder using subharmonic interrogation, *IEEE MTT Int. Symp. Digest*, 1994, pp. 753–756.
108. K. Stephan and T. Itoh, A planar quasi-optical subharmonically pumped mixer characterized by isotropic conversion loss, *IEEE Trans. Microwave Theory Tech.* **32**:92–102 (1984).
109. U. Guttich, Planar integrated 20 GHz receiver in slot line and coplanar waveguide technique, *Microwave Opt. Technol. Lett.* **2**(11) 1989.
110. K. M. K. H. Leong and T. Itoh, Development in active integrated antennas, *IEEE AP-S Int. Symp. Digest*, 2003, Vol. 1, pp. 212–215.
111. W. C. Brown, The history of power transmission by radio wave, *IEEE Trans. Microwave Theory Tech.* **32**(9):1230–1242 (1984).
112. T. Yoo, J. M. Spadden, and K. Chang, 35 GHz rectenna implemented with a patch and microstrip dipole antenna, *IEEE MTT-S Int. MW Symp. Digest*, 1992, pp. 345–348.
113. S. S. Bharj, R. Camisa, S. Grober, F. Wozniak, and E. Pendelton, High efficiency C-band 1000-element rectenna array for microwave powered applications, *IEEE MTT Int. MW Symp. Digest*, 1992, pp. 301–303.
114. J. Y. Park, K. M. K. H. Leong, G. R. Kim, J. I. Choi, and T. Itoh, Active planar retrodirective array with subharmonic conjugation mixers, *Proc. Asia Pacific Microwave Conf.*, 2003.

INTEGRATED CIRCUITS

N. RANGANATHAN
 RAJU D. VENKATARAMANA
 University of South Florida

The invention of the transistor in 1947 by William Shockley and his colleagues John Bardeen and Walter Brattain at Bell Laboratories, Murray Hill, NJ, launched a new era of integrated circuits (ICs). The transistor concept was based on the discovery that the flow of electric current through a solid semiconductor material like silicon can be controlled by adding impurities appropriately through the implantation processes. The transistor replaced the vacuum tube because of its better reliability, lesser power requirements, and, above all, much smaller size. In the late 1950s, Jack Kilby of Texas Instruments developed the first integrated circuit. The ability to develop flat or planar ICs, which allowed the interconnection of circuits on a single substrate (due to Robert Noyce and Gordon Moore), began the microelectronics revolution. The substrate is the supporting semiconductor material on which the various devices that form the integrated circuit are attached. Researchers developed sophisticated photolithography techniques that helped in the reduction of the minimum feature size, leading to larger circuits being implemented

on a chip. The miniaturization of the transistor led to the development of integrated circuit technology in which several hundreds and thousands of transistors could be integrated on a single silicon die. IC technology led to further developments, such as microprocessors, mainframe computers, and supercomputers.

Since the first integrated circuit was designed following the invention of the transistor, several generations of integrated circuits have come into existence: SSI (small-scale integration) in the early 1960s, MSI (medium-scale integration) in the latter half of the 1960s, and LSI (large-scale integration) in the 1970s. The VLSI (very large scale integration) era began in the 1980s. While the SSI components consisted on the order of 10–100 transistors or devices per integrated circuit package, the MSI chips consisted of anywhere from 100–1000 devices per chip. The LSI components ranged from roughly 1000–20,000 transistors per chip, while the VLSI chips contain on the order of up to 3 million devices. When the chip density increases beyond a few million, the Japanese refer to the technology as ULSI (ultra-large-scale integration), but many in the rest of the world continue to call it VLSI. The driving factor behind integrated circuit technology was the scaling factor, which in turn affected the circuit density within a single packaged chip. In 1965, Gordon Moore predicted that the density of components per integrated circuit would continue to double at regular intervals. Amazingly, this has proved true, with a fair amount of accuracy [1].

Another important factor used in measuring the advances in IC technology is the minimum feature size or the minimum linewidth within an integrated circuit (measured in micrometers). From about $8\mu\text{m}$ in the early 1970s, the minimum feature size has decreased steadily, increasing the chip density or the number of devices that can be packed within a given die size. In the early 1990s, the minimum feature size decreased to about $0.5\mu\text{m}$, and currently 0.3- , 0.25- , and $0.1\text{-}\mu\text{m}$ technologies (also called “deep-submicrometer technologies”) are becoming increasingly common. IC complexity refers, in general, to the increase in chip area (die size), the decrease in minimum feature size, and the increase in chip density. With the increase in IC complexity, the design time and the design automation complexity increase significantly. The advances in IC technology are the result of many factors, such as high-resolution lithography techniques, better processing capabilities, reliability and yield characteristics, sophisticated design automation tools, and accumulated architecture, circuit, and layout design experience.

1. BASIC TECHNOLOGIES

The field of integrated circuits is broad. The various basic technologies commonly known are shown in Fig. 1. The inert substrate processes, further divided as thin and thick film processes, yield devices with good resistive and temperature characteristics. However, they are used mostly in low-volume circuits and in hybrid ICs. The two most popular active substrate materials are silicon and gallium arsenide (GaAs). The silicon processes can be separated into two classes: MOS (the basic device is a metal

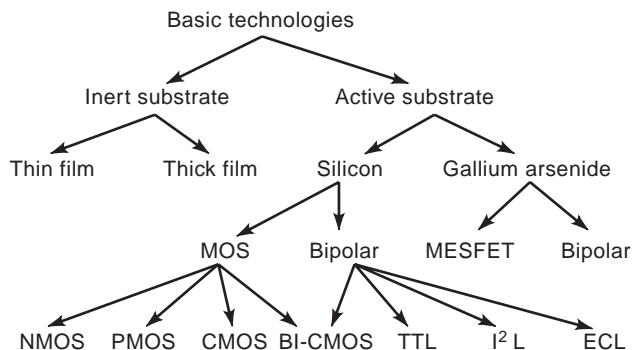


Figure 1. Overview of the basic technologies.

oxide semiconductor field effect transistor) and bipolar (the basic device is bipolar junction transistors). The bipolar process was commonly used in the 1960s and 1970s and yields high-speed circuits with the overhead of high-power dissipation and the disadvantage of low density. The transistor–transistor logic (TTL) family of circuits constitutes the most popular type of bipolar and is still used in many high-volume applications. The emitter-coupled logic (ECL) devices are used for high-speed parts that form the critical path delay of the circuit. The MOS family of processes consists of PMOS, NMOS, CMOS, and BiCMOS. The term *PMOS* refers to a MOS process that uses only p-channel transistors, and *NMOS* refers to a MOS process that uses only n-channel transistors. PMOS is not used much due to its electrical characteristics, which are not as good as the n-channel field-effect transistor (FET), primarily since the mobility of the n-channel material is almost twice compared to the mobility of the p-channel material. Also, the NMOS devices are smaller than the PMOS devices, and thus PMOS do not give good packing density.

CMOS was introduced in the early 1960s; however, it was used only in limited applications, such as watches and calculators. This was primarily due to the fact that CMOS had slower speed, less packing density, and latchup problems although it had a high noise margin and lower power requirements. Thus, NMOS was preferred over CMOS, in general, until the p-channel devices developed began to have similar-characteristics as the nMOS and both the p-channel and n-channel transistors started delivering close to equal amounts of currents with similar transistor sizes. In the 1980s and the 1990s, the need for lower power consumption was the driving factor, and thus CMOS emerged as the leading IC technology [2]. The BiCMOS technology combines both bipolar and CMOS devices in a single process. While CMOS is preferred for logic circuits, BiCMOS is preferred for input/output (I/O) and driver circuits due to its low input impedance and high current driving capability.

Since the 1980s, efforts have been directed toward designing digital ICs using GaAs devices. In many high-resolution radar systems, space systems, high-speed communication circuits, and microwave circuits, the integrated circuits need to operate at speeds beyond several gigahertz (GHz). In silicon technology, it is possible to obtain speeds on the order of up to 10 GHz using ECL

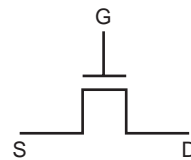
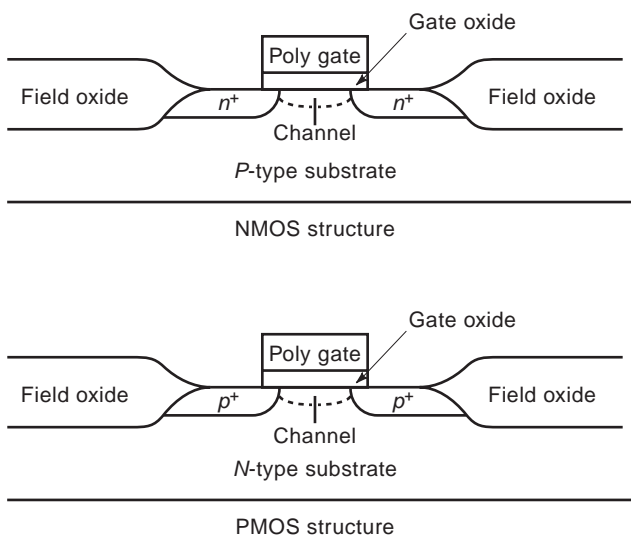
circuits, which is almost pushing the limits of the silicon technology. In GaAs technology, the basic device is the metal semiconductor (Schottky gate) field-effect transistor, called the GaAs MESFET. Given similar conditions, the electrons in n-type GaAs material travel twice faster than in silicon. Thus, the GaAs circuits could function at twice the speed than the silicon ECL circuits for the same minimum feature size. The GaAs material has a larger bandgap and does not need gate oxide material, as in silicon, which makes it immune to radiation effects. Also, the GaAs material has very high resistivity at room temperatures and lower parasitic capacitances, yielding high-quality transistor devices. However, the cost of fabricating large GaAs circuits is significantly high because of its low reliability and yield characteristics (due primarily to the presence of more defects in the material compared to silicon). The fabrication process is complex, expensive, and does not aid scaling. Also, the hole mobility is the same as in silicon, which means that GaAs is not preferable for complementary circuits. Thus, the GaAs technology has not been as successful as initially promised. Since CMOS has been the most dominant technology for integrated circuits, we examine the MOS transistor and its characteristics as a switch in the next section.

2. THE MOS SWITCH

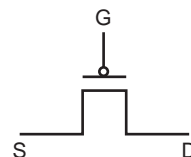
The MOSFET is the basic building block of contemporary CMOS circuits, such as microprocessors and memories. A MOSFET is an unipolar device; that is, current is transported by means of only one type of polarity (electrons in an n type and holes in a p type). In this section, we describe the basic structure of MOSFETS and their operation and provide examples of gates built using MOS devices.

2.1. Structure

The basic structure of a MOSFET (both n and p types) is shown in Fig. 2. We describe the structure of an n-type



NMOS symbol



PMOS symbol

MOSFET (3), (4). It consists of four terminals with a p-type substrate into which two n^+ regions are implanted. The substrate is a silicon wafer that provides stability and support. The region between the two n^+ regions is covered by an insulator, typically polysilicon and a metal contact. This contact forms the gate of the transistor. The insulating layer is required to prevent the flow of current between the semiconductor and the gate. The two n^+ regions form the source and the drain. Due to the symmetry of the structure, the source and the drain are equivalent. The gate input controls the operation of the MOSFET. A bias voltage on the gate causes the formation of a channel between the n^+ regions. This channel causes a connection between the source and drain and is responsible for the flow of the current. The MOSFET is surrounded by a thick oxide, called the “field oxide,” which isolates it from neighboring devices. Reversal of n and p types in the discussion will result in a p-type MOSFET. Typical circuit symbols for n-type and p-type MOSFETS are also shown in Fig. 2.

2.2. Operation

When no gate bias is applied, the drain and the source behave as two pn junctions connected in series in the opposite direction. The only current that flows is the reverse leakage current from the source to the drain. When a positive voltage is applied to the gate, the electrons are attracted and the holes are repelled. This causes the formation of an inversion layer or a channel region. The source and the drain are connected by a conducting n channel through which the current can flow. This voltage-induced channel is formed only when the applied voltage is greater than the threshold voltage V_t . MOS devices that do not conduct when no gate bias is applied are called *enhancement mode* or normally OFF transistors. In nMOS enhancement mode devices, a gate voltage greater than V_t should be applied for channel formation. In pMOS enhancement-mode devices, a negative gate voltage whose magnitude is greater than V_t must be applied. MOS devices that conduct at zero gate bias are called normally ON

Figure 2. Structure of n- and p-type MOSFETS.

or depletion-mode devices. A gate voltage of appropriate polarity depletes the channel of majority carriers and hence turns it off.

Considering an enhancement-mode n-channel transistor, when the bias voltage is above the predefined threshold voltage, the gate acts as a closed switch between the source and drain, the terminals of which become electrically connected. When the gate voltage is cut off, the channel becomes absent, the transistor stops conducting, and the source and the drain channels get electrically disconnected. Similarly, the p-channel transistor conducts when the gate voltage is beneath the threshold voltage and stops conducting when the bias voltage is increased above the threshold. The behavior of the MOS transistor as a switch forms the fundamental basis for implementing digital Boolean circuits using MOS devices.

2.3. Output Characteristics

We describe the basis output characteristics [5,6] of a MOS device in this subsection. There are three regions of operation for a MOS device:

1. Cutoff region
2. Linear region
3. Saturation region

In the cutoff region, no current flows and the device is said to be off. When a bias V_{gs} is applied to the gate such that $V_g > V_t$, the channel is formed. If a small drain voltage V_{ds} is applied, drain current I_{ds} flows from source to drain through the conducting channel. The channel acts like a resistance, and the drain current is proportional to the drain voltage. This is the linear region of operation. As the value of V_{ds} is increased, the channel charge near the drain decreases. The channel is pinched off when $V_{ds} = V_{gs} - V_t$. An increase in V_{ds} beyond the pinchoff value causes little change in the drain current. This is the saturation region of operation of the MOS device. The output characteristics of n- and p-type devices is shown in Fig. 3. The equations that describe the regions of operation can be summarized as follows:

$$0 \text{ if } V_{gs} \leq V_t \text{ (cutoff)}$$

$$I_{ds} = k/2[2(V_{gs} - V_t)V_{ds} - V_{ds}^2]$$

$$\text{If } V_g > V_t, V_{ds} \leq (V_{gs} - V_t) \text{ (linear)}$$

$$k/2(V_{gs} - V_t)^2 \text{ If } V_g > V_t, V_{ds} > (V_{gs} - V_t) \text{ (saturation)}$$

where k is the transconductance parameter of the transistor. A detailed analysis of the structure and operation of MOS devices is described in Refs. 3, 5, 7 and 8.

2.4. CMOS inverter

The basic structure of an inverter is shown in Fig. 4, and the process cross section is shown in Fig. 5. The gates of both the NMOS and the PMOS transistors are connected. The PMOS transistor is connected to the supply voltage V_{dd} , and the NMOS transistor is connected to G_{nd} . When a

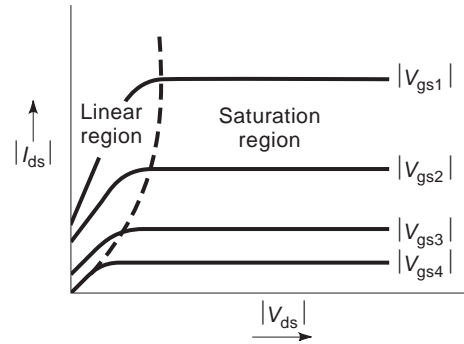


Figure 3. Output characteristics of a MOS transistor.

logical 0 is applied at the input V_{in} , then the PMOS device is on and the output is pulled to V_{dd} . Hence the output is a logical 1. On the other hand, when a logical 1 is applied at the input, then the NMOS transistor is on and the output is pulled to the ground. Hence we have a logical 0. The operating regions of the transistor are shown in Fig. 6. In region I, the n device is off and the p device operates in the linear region. Hence the output is pulled to V_{dd} . In region II, the n and p devices operate in the linear and saturation region depending on the input voltage. In region III, the p device is cut off and the n device is operating in the linear region. The output is pulled to the ground. In region II, when both the transistors are on simultaneously, a short circuit is produced between V_{dd} and G_{nd} . This accounts for the short-circuit power dissipation in CMOS logic.

2.5. Transmission Gate

Consider the device shown in Fig. 7, which represents an NMOS or a PMOS device. By suitably controlling the gate bias, the device can be made to turn on or off. It behaves as an electrical switch that either connects or disconnects the points s and d . An NMOS device is a good switch when it passes a logical 0, and a PMOS is a good switch when it passes a logical 1. In CMOS logic, both the NMOS and PMOS devices operate together. In general, the NMOS transistor pulls down the output node to logical 0, and the PMOS device pulls up a node to logical 1. A transmission gate is obtained by connecting the two in parallel, as shown in Fig. 8. The control signal (say, g) applied to the n-type device is complemented and applied to the p-type device. When g is high, both the transistors are on and

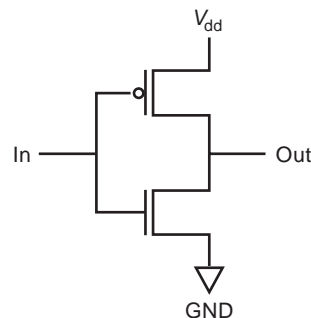


Figure 4. Circuit schematic of an inverter.

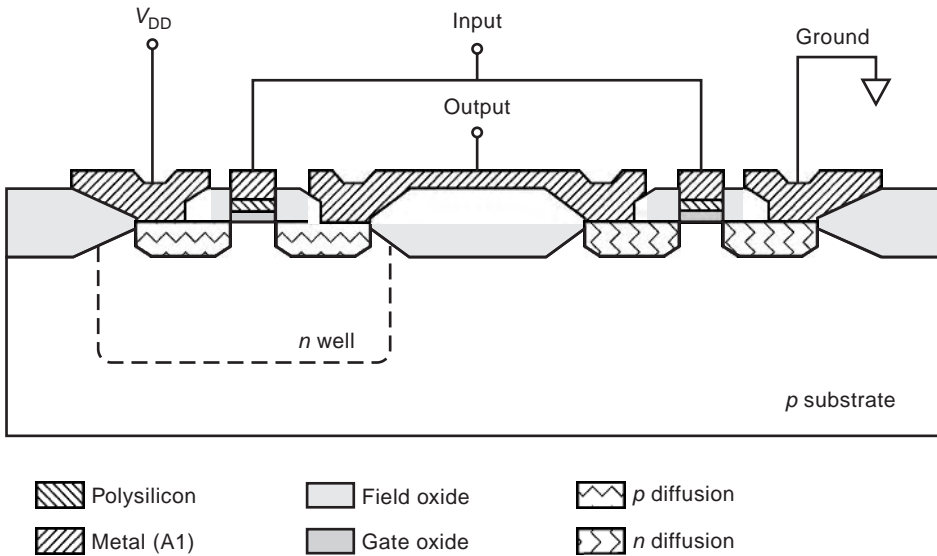


Figure 5. Process cross section of an n-well inverter.

hence a good 1 or a 0 is passed. When g is low, both the devices are off. This is also called a complementary switch, or a C SWITCH [5].

2.6. NAND and NOR Gates

CMOS combinational gates are constructed by connecting the PMOS and NMOS devices in either series or parallel to generate different logical functions. The structures for a two-input NAND and NOR gate are shown in Fig. 9.

2.6.1. NAND Gate. The p devices are connected in parallel, and the n devices are connected in series. When either of the inputs A or B is a logical 0, the output is pulled high to V_{dd} . When both A and B are high, then the output is pulled to the ground. Hence this structure implements the operation $f = (A \cdot B)'$.

2.6.2. NOR Gate. Similarly, in the NOR gate, the p devices are connected in series and the n devices are connected in parallel. When either of the inputs A or B is a logical 1, then the output is pulled to the ground. When

both A and B are low, then the output is pulled to V_{dd} . Hence this structure implements the operation $f = (A + B)'$. The p structure is the logical dual of the n structure. An n input NAND and NOR gate can be constructed in a similar fashion.

3. IC DESIGN METHODOLOGY

To design and realize VLSI circuits, several factors play key roles. The goal of an IC designer is to design a circuit that meets the given specifications and requirements while spending minimum design and development time avoiding design errors. The designed circuit should function correctly and meet the performance requirements, such as delay, timing, power, and size. A robust design methodology has been established over the years, and the design of complex integrated circuits has been made possible essentially because of advances in VLSI design automation. The various stages in the design flow are shown in Fig. 10. The design cycle ranges from the system-level specification and requirements to the end product of a fabricated, packaged, and tested integrated circuit. The basic design methodology is briefly described here, and the various stages are discussed in detail in the following sections using simple examples.

The first step is to determine the system-level specifications, such as the overall functionality, size, power, performance, cost, application environment, IC fabrication process, technology, and chip-level and board-level

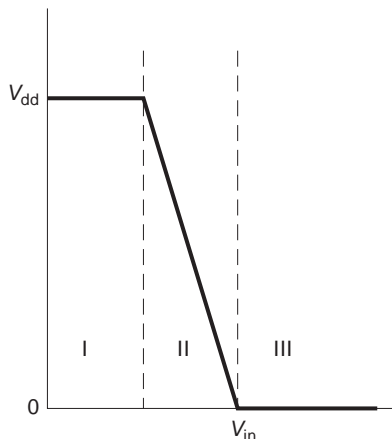


Figure 6. Operating regions of the transistor.

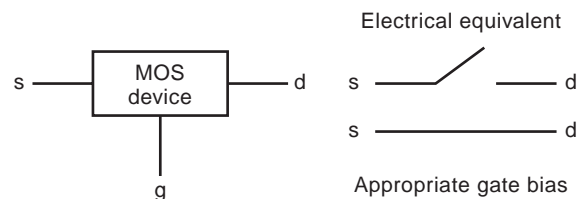


Figure 7. A MOS device as a switch.

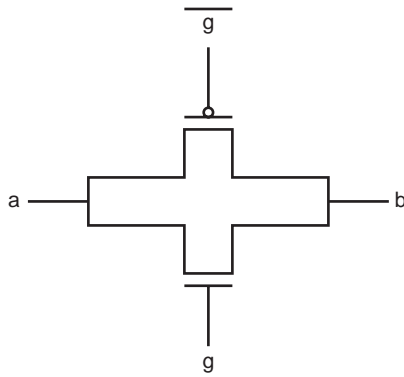


Figure 8. Transmission gate.

interfaces required. There are several tradeoffs to be considered. The next step is the functional design and description, in which the system is partitioned into functional modules and the functionality of the different modules and their interfaces to each other are considered. The issues to be considered are regularity and modularity of structures, subsystem design, data flow organization, hierarchical design approach, cell types, geometric placements, and communication between the different blocks.

Once the functionality of the various modules is determined, the architectural design of the modules is pursued. Many design alternatives are considered toward optimization. This stage also includes the design of any hardware algorithms to be mapped onto architectures. A behavior-level description of the architecture is obtained and verified using extensive simulations, often with an iterative process. This stage is critical in obtaining an efficient circuit in the end and for simplifying the steps in some of the following stages. In the logic design stage, the architectural blocks are converted into corresponding gate-level logic designs, Boolean minimization is performed, and logic simulation is used to verify the design at this level. In some design flows, the circuit could be synthesized from the logic level by using gate-level libraries (this is referred to as *logic synthesis*). The logic

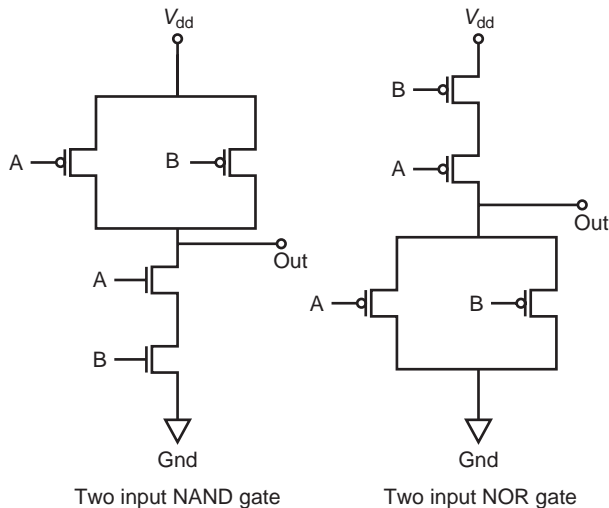


Figure 9. Two-input NAND and NOR gates.

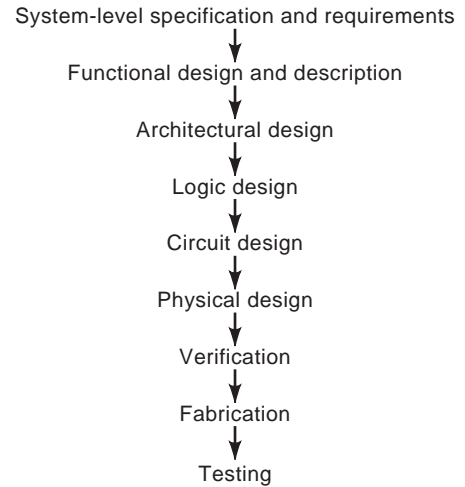


Figure 10. IC design methodology.

design usually includes a conventional logic design approach and a nontraditional design, such as precharge logic. At this stage, gate delays are considered and timing diagrams are derived to verify the synchronization of the various logic modules. The next step is the circuit design stage, which essentially involves converting the logic design modules into a circuit representation. At this stage, the essential factors considered are clocking, switching speeds or delays, switching activity and power requirements, and other electrical characteristics (e.g., resistance, capacitance).

The most complex step in VLSI design automation is the physical design, which includes floorplanning, partitioning, placement, routing, layout, and compaction. This process converts the given circuit design or description into a physical layout that is a geometric representation of the entire circuit. Each step of the physical design by itself is complex and takes significant amounts of iterations and time. The various types of transistors, the interconnecting wires, and contacts between different wires and transistors are represented as different geometric patterns consisting of many layers placed according to several design rules that govern a given fabrication technology and process. The floorplanning step involves higher-level planning of the various components on the layout. The partitioning step converts the overall circuit into smaller blocks to facilitate the other steps. It is usually impractical to synthesize the entire circuit in one step. Thus, logic partitioning is used to divide the given circuit into a smaller number of blocks, which can be individually synthesized and compacted. This step considers the size of the blocks, the number of blocks, and the interconnections between the blocks and yields a netlist for each block that can be used in the further design steps.

During the next step, which is the placement of the blocks on the chip layout, the various blocks are placed such that the routing can be completed effectively and the blocks use minimum overall area, avoiding any white spaces. The placement task is iterative in that an initial placement is obtained first and evaluated for area minimization and effective routing possibility, and alternate

arrangements are investigated until a good placement is obtained. The routing task completes the routing of the various interconnections, as specified by the netlists of the different blocks. The goal is to minimize the routing wirelengths and minimize the overall area needed for routing. The routing areas between the various blocks are referred to as *channels* or *switchboxes*. Initially, a global routing is performed in which a channel assignment is determined on the basis of routing requirements, and then a detailed routing step completes the actual point-to-point routing.

The last step in the physical design is the compaction step, which tries to compact the layout in all directions to minimize the layout area. A compact layout leads to less wirelengths, lower capacitances, and more chip density since the chip area is used effectively. The compaction step is usually an interactive and iterative process in which the user can specify certain parameters and check if the compaction can be achieved. The goal of compaction, in general, is to achieve minimum layout area. The entire physical design process is iterative and is performed several times until an efficient layout for the given circuit is obtained.

Once the layout is obtained, design verification needs to be done to ensure that the layout produced functions correctly and meets the specifications and requirements. In this stage, design rule checking is performed on the layout to make sure that the geometric placement and routing rules and the rules regarding the separation of the various layers, the dimensions of the transistors, and the width of the wires are followed correctly. Any design rule violations that occurred during the physical design steps are detected and removed. Then circuit extraction is performed to complete the functional verification of the layout. This step verifies the correctness of the layout produced by the physical design process. After layout verification, the circuit layout is ready to be submitted for fabrication, packaging, and testing. Usually, several dies are produced on a single wafer and the wafer is tested for faulty dies. The correct ones are diced out and packaged in the form of a pin grid array (PGA), dual in-line package (DIP), or any other packaging technology. The packaged chip is tested extensively for functionality, electrical and thermal characteristics, and performance. The process of designing and building an integrated circuit [9] that meets the performance requirements and functions perfectly depends on the efficiency of the design automation tools.

4. CIRCUIT DESIGN

To create performance optimized designs, two areas have to be addressed to achieve a prescribed behavior: (1) circuit or structural design and (2) layout or physical design. While the layout design is discussed in a later section, this section focuses on the former.

A logic circuit must function correctly and meet the timing requirements. There are several factors that can result in the incorrect functioning of a CMOS logic gate: (1) incorrect or insufficient power supplies, (2) noise on gate inputs, (3) faulty transistors, (4) faulty connections to transistors, (5) incorrect ratios in ratioed logic, and (6)

charge sharing or incorrect clocking in dynamic gates. In any design, there are a certain paths, called *critical paths*, that require attention to timing details since they determine the overall functional frequency. The critical paths are recognized and analyzed using timing analyzer tools and can be dealt with at four levels:

1. Architecture
2. RTL/logic level
3. Circuit level
4. Layout level

Designing an efficient overall functional architecture helps to achieve good performance. To design an efficient architecture, it is important to understand the characteristics of the algorithm being implemented as the architecture. At the register transfer logic (RTL)/logic level, pipelining, the type of gates, and the fanin and the fanout of the gates are to be considered. Fanin is the number of inputs to a logic gate, and fanout is the number of gate inputs that the output of a logic gate drives. Logic synthesis tools can be used to achieve the transformation of the RTL level. From the logic level, the circuit level can be designed to optimize a critical speed path. This is achieved by using different styles of CMOS logic, as explained later in this section. Finally, the speed of a set of logic can be affected by rearranging the physical layout. The following techniques can be used for specific design constraints.

The various CMOS logic structures that can be used to implement circuit designs are as follows:

1. *CMOS Complementary Logic*. The CMOS complementary logic gates are designed as ratioless circuits. In these circuits, the output voltage is not a fraction of the V_{dd} (supply) and the gates are sized to meet the required electrical characteristics of the circuits. The gate consists of two blocks, an n block and a p block, that determine the function of the gate. The p block is a dual of the n block. Thus, an n-input gate will consist of 2^n transistors.
2. *Pseudo-NMOS Logic*. In this logic, the load device is a single p transistor with the gate connected to V_{dd} [5,10]. This is equivalent to replacing the depletion NMOS load in a conventional NMOS gate by a p device. The design of this style of gate [11,12] involves ratioed transistor sizes to ensure proper operation and is shown in Fig. 11. The static power dissipation that occurs whenever the pulldown chain is turned on is a major drawback of this logic style.
3. *Dynamic CMOS Logic*. In the dynamic CMOS logic style, an n-transistor logic structure's output node is precharged to V_{dd} by a p transistor and conditionally discharged by an n transistor connected to V_{ss} [5]. The input capacitance of the gate is the same as the pseudo-NMOS gate. Here, the pullup time is improved by virtue of the active switch, but the pulldown time is increased due to the ground. The disadvantage of this logic structure is that the inputs can only change during the precharge phase

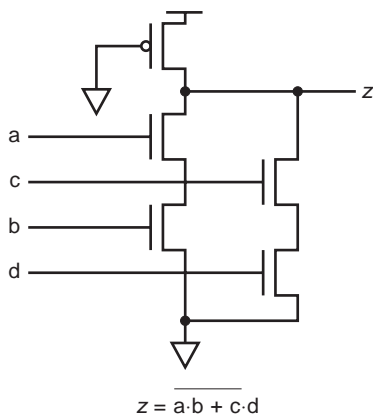


Figure 11. Pseudo-NMOS logic.

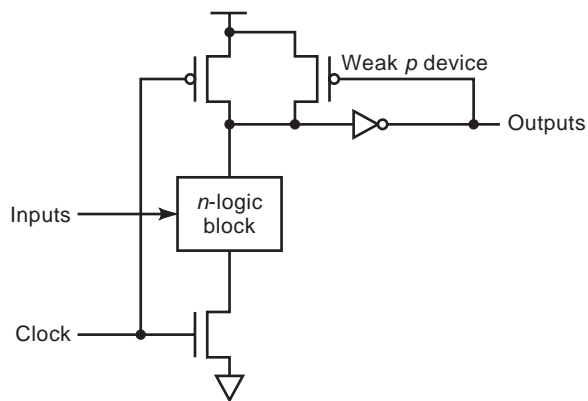


Figure 13. CMOS domino logic.

and must be stable during the evaluate portion of the cycle. Figure 12 depicts this logic style.

4. *Clocked CMOS Logic.* To build CMOS logic gates with low power dissipation [13], this logic structure was proposed. The reduced dynamic power dissipation is realized because of the metal gate CMOS layout considerations. The gates have larger rise and fall times because of the series clocking transistors, but the capacitance is similar to the CMOS complementary gates. This is a recommended strategy for “hot electron” effects, because it places an additional n transistor in series with the logic transistors [14].
5. *CMOS Domino Logic.* This is a modification of the clocked CMOS logic, in which a single clock is used to precharge and evaluate a cascaded set of dynamic logic blocks. This involves incorporating a static CMOS inverter into each logic gate [15], as shown in Fig. 13. During precharge, the output node is charged high, and hence the output of the buffer is low. The transistors in the subsequent logic blocks will be turned off since they are fed by the buffer. When the gate is evaluated, the output will conditionally go low (1–0), causing the buffer to conditionally go high (0–1). Hence, in a cascaded set of logic blocks, each state evaluates and causes the next stage to evaluate, provided the entire sequence can be evaluated in one clock cycle. Therefore, a single clock is used to precharge and evaluate all logic

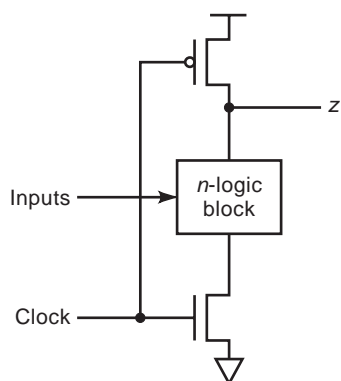


Figure 12. Dynamic CMOS logic.

gates in a block. The disadvantages of this logic are that (1) every gate needs to be buffered, and (2) only noninverting structures can be used.

6. *NP Domino Logic (Zipper CMOS).* This is a further refinement of the domino CMOS [16–18]. Here, the domino buffer is removed, and the cascading of logic blocks is achieved by alternately composed p and n blocks, as is shown in Fig. 14. When the clock is low, all the n-block stages are precharged high while all the p-block stages are precharged low. Some of the advantages of the dynamic logic styles include (1) smaller area than fully static gates, (2) smaller parasitic capacitances, and (3) glitch-free operation if designed carefully.
7. *Cascade Voltage Switch Logic (CVSL).* The CVSL is a differential style of logic requiring both true and complement signals to be routed to gates [19]. Two complementary NMOS structures are constructed and then connected to a pair of cross-coupled p pull-up transistors. The gates here function similarly to the domino logic, but the advantage of this style is the ability to generate any logic expression involving both inverting and noninverting structures. Figure 15 gives a sketch of the CVSL logic style.
8. *Pass Transistor Logic.* Pass transistor logic is popular in NMOS-rich circuits. Formal methods for deriving pass transistor logic for NMOS are presented

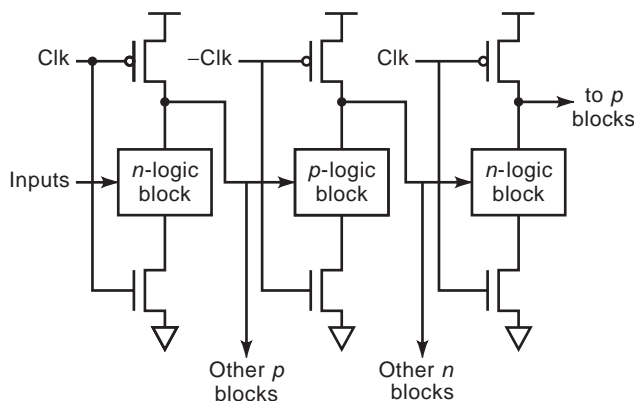


Figure 14. NP domino logic.

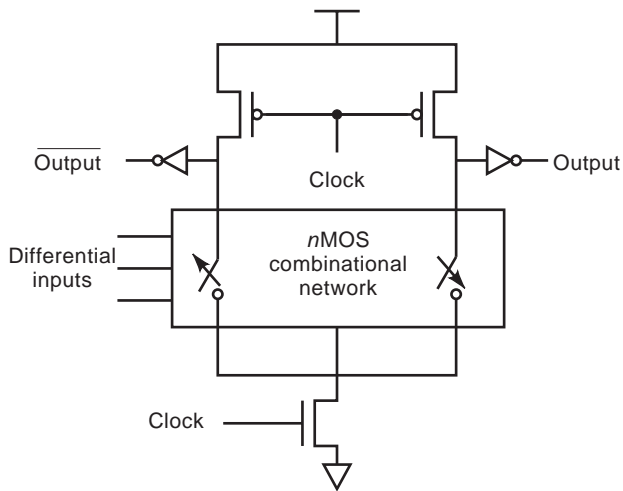


Figure 15. Cascade voltage switch logic.

in Ref. 20. Here, a set of control signals and a set of pass signals are applied to the gates and sources of the n transistor, correspondingly. From these signals, the truth table for any logic equation can be realized.

9. *Source Follower Pullup Logic (SFPL)*. This is similar to the pseudo-NMOS gate except that the pullup is controlled by the inputs [21]. In turn, this leads to the use of smaller pulldown circuits. The SFPL gate style reduces the self-loading of the output and improves the speed of the gate. Therefore, it shows a marked advantage in high-fanin gates.

Using the various design styles, any circuit design can be built in a hierarchical fashion. The basic gates are first built, from which functional blocks like a multiplexer or an adder circuit can be realized. From these basic blocks, more complex circuits can be constructed. Once a design for a specific application has been designed, the functionality of the circuit needs to be verified. Also, other constraints, such as the timing and electrical characteristics, have to be studied before the design can be manufactured. The techniques and tools to achieve this are the subject of the next section.

5. SIMULATION

Simulation is required to verify if a design works the way it should. Simulation can be performed at various levels of abstraction. A circuit can be simulated at the logic level, the switch level, or with reference to the timing. Simulation is a critical procedure before committing the design to silicon. The simulators themselves are available in a wide variety of types [22].

5.1. Logic-Level Simulation

Logic-level simulation occurs at the highest level of abstraction. It uses primitive models of NOT, OR, AND, NOR, and NAND gates. Virtually all digital logic simulators are

event-driven (i.e., a component is evaluated based on when an event occurs on its inputs). Logic simulators are categorized according to the way the delays are modeled in the circuit: (1) unit delay simulators, in which each component is assumed to have a delay of one time unit; and (2) variable-delay simulators, which allow components to have arbitrary delays. While the former helps in simulating the functionality of the circuit the latter allows for more accurate modeling of the fast-changing nodes.

The timing is normally specified in terms of an inertial delay and a load-dependent delay, as follows

$$T_{\text{gate}} = T_{\text{intrinsic}} + C_{\text{load}} \times T_{\text{load}}$$

where

$$T_{\text{gate}} = \text{delay of the gate}$$

$$T_{\text{intrinsic}} = \text{intrinsic gate delay}$$

$$C_{\text{load}} = \text{actual load in some units (pF)}$$

$$T_{\text{load}} = \text{delay per load in some units (ns/pF)}$$

Earlier logic simulators used preprogrammed models for the gates, which forced the user to describe the system in terms of these models. In modern simulators, programming primitives are provided that allow the user to write models for the components. The two most popular digital simulation systems in use today are VHDL and Verilog.

5.2. Circuit-Level Simulation

The most detailed and accurate simulation technique is referred to as *circuit analysis*. Circuit analysis simulators operate at the circuit level. Simulation programs typically solve a complex set of matrix equations that relate the circuit voltages, currents, and resistances. They provide accurate results but require long simulation times. If N is the number of nonlinear devices in the circuit, then the simulation time is typically proportional to N^m , where m is between 1 and 2. Simulation programs are useful in verifying small circuits in detail but are unrealistic for verifying complex VLSI designs. They are based on transistor models and hence should not be assumed to accurately predict the performance of designs. The basic sources of error include (1) inaccuracies in the MOS model parameters, (2) an inappropriate MOS model, and (3) inaccuracies in parasitic capacitances and resistances. The circuit analysis programs widely used are the SPICE program, developed at the University of California at Berkeley [23], and the ASTAP program from IBM [24]. HSPICE [25] is the commercial variant of these programs. The SPICE program provides various levels of modeling. The simple models are optimized for speed, while the complex ones are used to get accurate solutions. As the feature size of the processes is reduced, the models used for the transistors are no longer valid and hence the simulators cannot predict the performance accurately unless new models are used.

5.3. Switch-Level Simulation

Switch-level simulation is simulation performed at the lowest level of abstraction. These simulators model transistors as switches to merge the logic-level and circuit-level simulation techniques. Although logic-level simulators also model transistors as switches, the unidirectional logic gate model cannot model charge sharing, which is a result of the bidirectionality of the MOS transistor. Hence, we assume that all wires have capacitance, since we need to locate charge-sharing bugs. RSIM [26] is an example of a switch-level simulator with timing. In RSIM, CMOS gates are modeled as either pullup or pulldown structures, for which the program calculates a resistance to power or ground. The output capacitance of the gate is used with the resistance to predict the risetime and the falltime of a gate.

5.4. Timing Simulators

Timing simulators allow simple nonmatrix calculations to be employed to solve for circuit behavior. This involves making approximations about the circuit, and hence accuracy is less than that of simulators like SPICE. The advantage is the execution time, which is over two orders of magnitude less than for SPICE. Timing simulator implementations typically use MOS-model equations or table lookup methods. Examples of these simulators are given in Ref. 27.

5.5. Mixed-Mode Simulators

Mixed-mode simulators are available commercially today and merge the aforementioned different simulation techniques. Each circuit block can be simulated in the appropriate mode.

The results of the simulation analysis are fed back to the design stage, where the design is tuned to incorporate the deviations. Once the circuit is perfected and the simulation results are satisfactory, the design can be fabricated. To do this, we need to generate a geometric layout of the transistors and the electrical connections between them. This has been a subject of intense research over the last decade and continues to be so. The following section introduces this problem and presents some of the well-known techniques for solving it.

6. LAYOUT

The layout design is considered a prescription for preparing the photomasks used in the fabrication of ICs [5]. There is a set of rules, called the *design rules*, used for the layout; these serve as the link between the circuit and the process engineer. The physical design engineer, in addition to knowledge of the components and the rules of the layout, needs strategies to fit the layouts together with other circuits and provide good electrical properties. The main objective is to obtain circuits with optimum yield in as small an area as possible without sacrificing reliability.

The starting point for the layout is a circuit schematic. Figure 2 depicts the schematic symbols for n-type and p-type transistors. The circuit schematic is treated as a

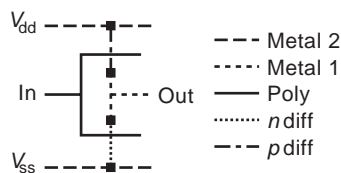


Figure 16. Stick diagram of the inverter.

specification for which we must implement the transistors and connections between them in the layout. The circuit schematic of an inverter is shown in Fig. 4. We need to generate the exact layout of the transistors of this schematic, which can then be used to build the photomask for the fabrication of the inverter. Generating a complete layout in terms of rectangles for a complex system can be overwhelming, although at some point we need to generate it. Hence designers use an abstraction between the traditional transistor schematic and the full layout to help organize the layout for complex systems. This abstraction is called a *stick diagram*. Figure 16 shows the stick diagram for the inverter schematic. As can be seen, the stick diagram represents the rectangles in the layout as lines, which represent wires and component symbols. Stick diagrams are not exact models of the layouts but let us evaluate a candidate design with relatively little effort. Area and aspect ratio are difficult to estimate from stick diagrams.

6.1. Design Rules

Design rules for a layout [28] specify to the designer certain geometric constraints on the layout artwork so that the patterns on the processed wafer will preserve the topology and geometry of the designs. These help to prevent separate, isolated features from accidentally short-circuiting, or thin features from opening, or contacts from slipping outside the area to be contacted. They represent a tolerance that ensures very high probability of correct fabrication and subsequent operation of the IC. The design rules address primarily two issues.

1. The geometric reproduction of features that can be reproduced by the maskmaking and lithographical process
2. The interaction among the different layers

Several approaches can be used to describe the design rules. These include the micron rules, stated at some micrometer resolution, and the lambda (λ)-based rules. The former are given as a list of minimum feature sizes and spacings for all masks in a process, which is the usual style for the industry. Mead and Conway [29] popularized the λ -based approach, where λ is process-dependent and is defined as the maximum distance by which a geometric feature on any one layer can stray from another feature. The advantage of the λ -based approach is that by defining λ properly the design itself can be made independent of both the process and fabrication house, and the design can be rescaled. The goal is to devise rules that are simple, constant in time, applicable to many processes,

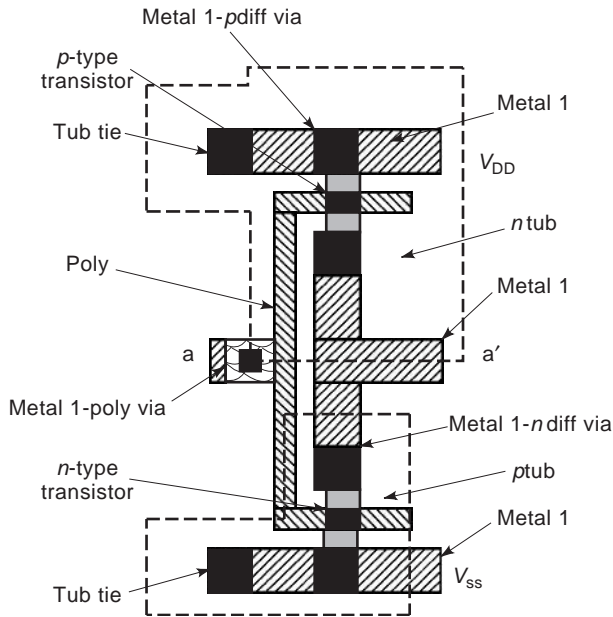


Figure 17. Transistor layout of the inverter.

standardized among many institutions, and have a small number of exceptions for specific processes. Figure 17 gives the layout of the inverter, with the design rules specified.

To design and verify layouts, different computer-aided design (CAD) tools can be used. The most important of these are the layout editors [30], design rule checkers, and circuit extractors. The editor is an interactive graphic program that allows us to create and delete layout elements. Most editors work on hierarchical layouts, but some editors, like Berekely's Magic tool [31], work on a symbolic layout. The latter include somewhat more detail than the stick diagram but are still more abstract than the pure layout. The design rule checker, or DRC, programs look for design rule violations in the layouts. Magic has an online design rule checking. The circuit extractor is an extension of the DRC programs. While the DRC must identify transistors and vias to ensure proper checks, the circuit extractor performs a complete job of component and wire extraction. It produces a netlist, which lists the transistors in the layouts and the electric nets that connect their terminals.

6.2. Physical Design

From the circuit design of a certain application and the design rules of a specific process, the physical design problem is to generate a geometric layout of the transistors of the circuit design conforming to the specified design rules. From this layout, photomasks can be generated that will be used in the fabrication process. To achieve this, the different modules of the design need to be placed first and then electrical connections between them realized through the metal layers. For instance, a two-layer metallization would allow the designer to lay out metal both vertically and horizontally on the floorplan. Whenever the wire

changes direction, a via can be used to connect the two metal layers. Due to the complexity of this problem, most authors treat module placement and the routing between modules as two separate problems, although they are related critically. Also, in former days, when designs were less complex, design was done by hand. Now we require sophisticated tools for this process.

6.2.1. Placement. Placement is the task of placing modules adjacent to each other to minimize area or cycle time. The literature consists of a number of different placement algorithms that have been proposed [32–35]. Most algorithms partition the problem into smaller parts and then combine them, or start with a random placement solution and then refine it to reach the optimal. The modules are usually considered as rectangular boxes with specified dimensions. The algorithms then use different approaches to fit these boxes in a minimal area or to optimize them to certain other constraints. For instance, consider a certain number of modules with specific dimensions and a given area in which to fit them. This is similar to the bin-packing algorithm. After the placement step, the different modules are placed in an optimal fashion and the electrical connections between them need to be realized.

6.2.2. Routing. Once the modules have been placed, we need to create space for the electrical connections between them. To keep the area of the floorplan minimal, the first consideration is to determine the shortest path between nodes, although a cost-based approach may also be used. The cost is defined to include an estimate of the congestion, number of available wire tracks in a local area, individual or overall wirelength, and so on. Since the problem is a complex one, the strategy is to split the problem into global or loose routing and local or detailed routing. Global routing is a preliminary step, in which each net is assigned to a particular routing area, and the goal is to make 100% assignment of nets to routing regions while minimizing the total wirelength. Detailed routing then determines the exact route for each net within the global route. There are a number of approaches to both of these problems.

6.2.2.1. Global Routing. Global routing [36] is performed using a wirelength criterion, because all timing critical nets must be routed with minimum wirelength. The routing area itself can be divided into disjoint rectangular areas, which can be classified by their topology. A two-sided channel is a rectangular routing area with no obstruction inside and with pins on two parallel sides. A switch box is a rectangular routing area with no obstructions and signals entering and leaving through all four sides [37]. The focus in this problem is only to create space between the modules for all the nets and not to determine the exact route. The algorithms proceed by routing one net at a time, choosing the shortest possible path. Since there is a lot of dependency among the nets, different heuristics are used to generate the least possible routing space in which to route the nets. Once space is created for all the nets, the exact route of each net can be determined.

6.2.2.2. Detailed Routing. Detailed routing is usually done by either a maze search or a line search algorithm. The maze-running algorithm [38,39] proposed by Lee and Moore finds the shortest path between any two points. For this, the layout is divided into a grid of nodes, in which each node is weighted by its distance from the source of the wire to be routed. The route that requires the smallest number of squares is then chosen. If a solution exists, this algorithm will find it, but an excessive amount of memory is required to achieve this. In the line search algorithm, vertical and horizontal lines are drawn from the source and the target, followed by horizontal or vertical lines that intersect the original lines. This is repeated until the source and target meet. There are also a number of other heuristic algorithms that exploit different characteristics of the design to generate optimal routing solutions. Genetic algorithms and simulated annealing approaches to this problem have gained importance in recent years.

An introduction to the various algorithms that have been proposed for layouts can be found in Ref. 40. Once the layout has been determined and the photomasks made, the circuit can go to the fabrication plant for processing.

7. FABRICATION

The section describes the approach used in building integrated circuits on monolithic pieces of silicon. The process involves the fabrication of successive layers of insulating, conducting, and semiconducting materials, which have to be patterned to perform specific functions. The fabrication therefore must be executed in a specific sequence, which constitutes an IC process flow. The manufacturing process itself is a complex interrelationship of chemistry, physics, material science, thermodynamics, and statistics.

Semiconducting materials, as the name suggests, are neither good conductors nor good insulators. While there are many semiconducting elements, silicon is chosen primarily for manufacturing ICs because it exhibits few useful properties. Silicon devices can be built with a maximum operating temperature of about 150°C, due to the smaller leakage currents as a result of the large bandgap of silicon (1.1 eV). IC planar processing requires the capability to fabricate a passivation layer on the semiconductor surface. The oxide of silicon, SiO₂, which could act as such a layer, is easy to form and is chemically stable. The controlled addition of specific impurities makes it possible to alter the characteristics of silicon. For these reasons, silicon is almost exclusively used for fabricating microelectronic components.

7.1. Silicon Material Technology

Beach sand is first refined to obtain semiconductor-grade silicon. This is then reduced to obtain electronic-grade polysilicon in the form of long, slender rods. Single-crystal silicon is grown from this by the Czochralski (CZ) or float-zone (FZ) methods. In CZ growth, single crystal ingots are pulled from molten silicon contained in a crucible. For VLSI applications, CZ silicon is preferred because it can better withstand thermal stresses (41) and offers an in-

ternal gettering mechanism than can remove unwanted impurities from the device structures on wafer surfaces (42). FZ crystals are grown without any contact to a container or crucible and hence can attain higher purity and resistivity than CZ silicon. Most high-voltage, high-power devices are fabricated on FZ silicon. The single crystal ingot is then subjected to a complex sequence of shaping and polishing, known as *wafering*, to produce starting material suitable for fabricating semiconductor devices. This involves the following steps:

1. The single-crystal ingot undergoes routine evaluation of resistivity, impurity content, crystal perfection size, and weight.
2. Since ingots are not perfectly round, they are shaped to the desired form and dimension.
3. The ingots are then sawed to produce silicon slices. The operation defines the surface orientation, thickness, taper, and bow of the slice.
4. To bring all the slices to within the specified thickness tolerance, lapping and grinding steps are employed.
5. The edges of the slices are then rounded to reduce substantially the incidence of chipping during normal wafer handling.
6. A chemico-mechanical polishing [43] step is then used to produce the highly reflective and scratch- and damage-free surface on one side of the wafer.
7. Most VLSI process technologies also require an epitaxial layer, which is grown by a chemical vapor deposition process.

The most obvious trend in silicon material technology is the increasing size of the silicon wafers. The use of these larger-diameter wafers presents major challenges to semiconductor manufacturers. Several procedures have been investigated to increase axial impurity uniformity. These include the use of double crucibles, continuous-liquid-feed (CLF) systems [44], magnetic Czochralski growth (MCZG) [44,45], and controlled evaporation from the melt.

7.2. Epitaxial Layer

The epitaxial growth process is a means of depositing a single-crystal film with the same crystal orientation as the underlying substrate. This can be achieved from the vapor phase, liquid phase, or solid phase. Vapor-phase epitaxy has the widest acceptance in silicon processing, since excellent control of the impurity concentration and crystalline perfection can be achieved. Epitaxial processes are used for the fabrication of advanced CMOS VLSI circuits, because epitaxial processes minimize latchup effects. Also in the epitaxial layer, doping concentration can be accurately controlled, and the layer can be made oxygen/carbon-free. Epitaxial deposition is a chemical vapor deposition process [46]. The four major chemical sources of silicon used commercially for this deposition are (1) silicon tetrachloride (SiCl₄), (2) trichlorosilane (SiHCl₃), (3) dichlorosilane (SiH₂Cl₂), and (4) silane (SiH₄). Depending

on particular deposition conditions and film requirements, one of these sources can be used.

7.3. Doping silicon

The active circuit elements of the IC are formed within the silicon substrate. To construct these elements, we need to create localized n-type and p-type regions by adding the appropriate dopant atoms. The process of introducing controlled amounts of impurities into the lattice of the monocrystalline silicon is known as *doping*. Dopants can be introduced selectively into the silicon using two techniques: diffusion and ion implantation.

7.3.1. Diffusion. The process by which a species moves as a result of the presence of a chemical gradient is referred to as *diffusion*. Diffusion is a time- and temperature-dependent process. To achieve maximum control, most diffusions are performed in two steps. The first step is predeposition [47], which takes place at a furnace temperature and controls the amount of impurity that is introduced. The second step, the drive-in step [47], controls the desired depth of diffusion.

7.3.1.1. Predeposition. In predisposition, the impurity atoms are made available at the surface of the wafer. The atoms of the desired element in the form of a solution of controlled viscosity can be spun on the wafer, in the same manner as the photoresist. For these spinon dopants, the viscosity and the spin rate are used to control the desired dopant film thickness. The wafer is then subjected to a selected high temperature to complete the predeposition diffusion. The impurity atoms can also be made available by employing a low-temperature chemical vapor deposition process in which the dopant is introduced as a gaseous compound—usually in the presence of nitrogen as a diluent. The oxygen concentration must be carefully controlled in this operation to prevent oxidation of the silicon surface of the wafer.

7.3.1.2. Drive-in. After predeposition the dopant wafer is subjected to an elevated temperature. During this step, the atoms further diffuse into the silicon crystal lattice. The rate of diffusion is controlled by the temperature employed. The concentration of the dopant atoms is maximum at the wafer surface and reduces as the silicon substrate is penetrated further. As the atoms migrate during the diffusion, this concentration changes. Hence a specific dopant profile can be achieved by controlling the diffusion process. The dopant drive-in is usually performed in an oxidizing temperature to grow a protective layer of SiO_2 over the newly diffused area.

7.3.2. Ion Implantation. Ion implantation is a process in which energetic, charged atoms or molecules are directly introduced into the substrate. Ion implantation [48,49] is superior to the chemical doping methods discussed previously. The most important advantage of this process is its ability to control more precisely the number of implanted dopant atoms into substrates. Using this method, the lateral diffusion is reduced considerably compared to the

chemical doping methods. Ion implantation is a low-temperature process, and the parameters that control the ion implantation are amenable to automatic control. After this process the wafer is subjected to annealing to activate the dopant electrically. There are some limitations to this process. Since the wafer is bombarded with dopant atoms, the material structure of the target is damaged. The throughput is typically lower than in the diffusion doping process. Additionally, the equipment used causes safety hazards to operating personnel.

7.4. Photolithography

Photolithography is the most critical step in the fabrication sequence. It determines the minimum feature size that can be realized on silicon and is a photoengraving process that accurately transfers the circuit patterns to the wafer. Lithography [50,51] involves the patterning of metals, dielectrics, and semiconductors. The photoresist material is first spin-coated on the wafer substrate. It performs two important functions: (1) precise pattern formation and (2) protection of the substrate during etch. The most important property of the photoresist is that its solubility in certain solvents is greatly affected by exposure to ultraviolet radiation. The resist layer is then exposed to ultraviolet light. Patterns can be transferred to the wafer using either positive or negative masking techniques. The required pattern is formed when the wafer undergoes the development step. After development, the undesired material is removed by wet or dry etching.

Resolution of the lithography process is important to this process step. It specifies the ability to print minimum size images consistently under conditions of reasonable manufacturing variation. Therefore, lithographic processes with submicrometer resolution must be available to build devices with submicrometer features. The resolution is limited by a number of factors, including (1) hardware, (2) optical properties of the resist material, and (3) process characteristics [52].

Most IC processes require 5–10 patterns. Each one of them needs to be aligned precisely with those already on the wafer. Typically, the alignment distance between two patterns is less than $0.2\ \mu\text{m}$ across the entire area of the wafer. The initial alignment is made with respect to the crystal lattice structure of the wafer, and subsequent patterns are aligned with the existing ones. Earlier, mask alignment was done using *contact printing* [53,54], in which the mask is held just off the wafer and visually aligned. The mask is then pressed into contact with the wafer and impinged with ultraviolet light. There is a variation of this technique called *proximity printing*, in which the mask is held slightly above the wafer during exposure. Hard contact printing was preferred because it reduced the diffraction of light, but it led to a number of yield and production problems. So the projection alignment and exposure system was developed, in which the mask and wafer never touch and an optical system projects and aligns the mask onto the wafer. Since there is no damage to the mask or photoresist, the mask life is virtually unlimited. VLSI devices use projection alignment as the standard production method.

7.5. Junction Isolation

When fabricating silicon ICs, it must be possible to isolate the devices from one another. These devices can then be connected through specific electrical paths to obtain the desired circuit configuration. From this perspective, the isolation technology is one of the critical aspects of IC fabrication. For different IC types, like NMOS, CMOS, and bipolar, a variety of techniques have been developed for device isolation. The most important technique developed was termed LOCoS, for *local oxidation of silicon*. This involves the formation of semirecessed oxide in the nonactive or field areas of the substrate. With the advent of submicron-size device geometries, alternative approaches for isolation were needed. Modified LOCoS processes, trench isolation, and selective epitaxial isolation were among the newer approaches adopted.

7.5.1. LOCoS. To isolate MOS transistors, it is necessary to prevent the formation of channels in the field regions. This implies that a large value of V_T is required in the field region, in practice about 3–4 V above the supply voltage. Two ways to increase the field voltage are to increase the field oxide thickness and raise the doping beneath the field oxide. Thicker field oxide regions cause high enough threshold voltages but unfortunately lead to step coverage problems, and hence thinner field oxide regions are preferred. Therefore, the doping under the field oxide region is increased to realize higher threshold voltages. Nevertheless, the field oxide is made 7–10 times thicker than the gate oxide. Following this, in the channel-stop implant step, ion implantation is used to increase the doping under the field oxide. Until about 1970, the thick field oxide was grown using the *grow-oxide-and-etch* approach, in which the oxide is grown over the entire wafer and then etched over the active regions. Two disadvantages of this approach prevented it from being used for VLSI applications: (1) field oxide steps have sharp upper corners, which poses a problem to the subsequent metallization steps; and (2) channel-stop implant must be performed before the oxide is grown. In another approach, the oxide is selectively grown over the desired field regions. This process was introduced by Appels and Kooi in 1970 [55] and is widely used in the industry. This process is performed by preventing the oxidation of the active regions by covering them with a thin layer of silicon nitride. After etching the silicon nitride layer, the channel-stop dopant can be implanted selectively. The process, has a number of limitations for submicrometer devices. The most important of these is the formation of the “bird’s beak,” which is a lateral extension of the field oxide into the active areas of the device. The LOCoS bird’s beak creates other problems as junctions become shallower in CMOS ICs. The LOCoS process was therefore modified in several ways to overcome these limitations: (1) etched-back LOCoS, (2) polybuffered LOCoS, and (3) sealed-interface local oxidation (SILO) [56].

7.5.2. Non-LOCoS Isolation Technologies. There have been non-LOCoS isolation technologies for VLSI and ultra-large-scale integration (ULSI) applications. The

most prominent of these is *trench* isolation technology. Trench technologies are classified into three categories: (1) shallow trenches ($<1\mu\text{m}$), (2) moderate depth trenches ($1\text{--}3\mu\text{m}$), and (3) deep, narrow trenches ($>3\mu\text{m}$ deep, $<2\mu\text{m}$ wide). Shallow trenches are used primarily for isolated devices of the same type and hence are considered a replacement to LOCoS. The buried oxide (BOX) [57] isolation technology uses shallow trenches refilled with a silicon dioxide layer, which is etched back to yield a planar surface. This technique eliminates the bird’s beak of LOCoS. The basic BOX technique has certain drawbacks for which the technique is modified.

7.6. Metallization

This subsection describes the contact technology to realize the connections between devices, and how the different metal layers are connected to realize the circuit structure.

7.6.1. Contact Technology. Isolated active-device regions in the single-crystal substrate are connected through high-conductivity, thin-film structures that are fabricated over the silicon dioxide that covers the surface. An opening in the SiO_2 must be provided to allow *contacts* between the conductor film and the Si substrate. The technology involved in etching these contacts is referred to as *contact technology*. These contacts affect the circuit behavior because of the parasitic resistances that exist in the path between the metal to Si substrate and the region where the actual transistor action begins. Conventional contact fabrication involves the fabrication of a contact to silicon at locations where the silicon dioxide has been etched to form a window. It involves the following steps:

1. In regions where contacts are to be made, the silicon substrate is heavily doped.
2. A window or *contact hole* is etched in the oxide that passivates the silicon surface.
3. The silicon surface is cleaned to remove the thin native-oxide layer that is formed rapidly when the surface is exposed to an oxygen-containing ambient.
4. The metal film is deposited on the wafer and makes contact with silicon wherever contact holes were created. Aluminum is the most commonly used metal film.
5. After depositing the metal, the contact structure is subjected to a thermal cycle known as *sintering* or *annealing*. This helps in bringing the Si and metal into intimate contact.

Al is desired as an interconnect material because its resistivity, $2.7\mu\Omega\cdot\text{cm}$, is very low, and it offers excellent compatibility with SiO_2 . Al reacts with SiO_2 to form Al_2O_3 , through which the Al can diffuse to reach the Si, forming an intimate AlOSi contact. But using pure Al has certain disadvantages. Since Al is polycrystalline in nature, its grain boundaries offer very fast diffusion paths for the Si at temperatures above 400°C . Hence, if a large volume of Al is available, a significant quantity of the Si can diffuse into Al. As a result, the Al from the film moves rapidly to

fill in the voids created by the migrating Si, which leads to large leakage currents or electrically shorting the circuit. This effect is referred to as *junction spiking* [58]. To prevent junction spiking, different techniques are used:

1. Add approximately 1% of Si to Al.
2. Add a diffusion barrier to prevent Si from diffusing into Al.
3. Decrease sintering temperature, but this increases contact resistance.
4. Add a “barrier” metal to the contact hole [59].

Of these techniques, the most commonly used is the barrier metal. The idea is to block or hinder Al from intermixing with Si. There are three main types of contact barrier metallurgies: (1) sacrificial barrier, (2) passive barrier, and (3) stuffed barrier.

The use of Al has its own problems; the most important is its high resistivity and electromigration. There is also the problem with “hillock” formation. Hillocks are formed as a result of the thermal expansion mismatch among Al, SiO₂, and Si. As the wafer is cooled, thermal expansion mismatch forms stresses (usually compressive), which forms these hillocks. Therefore, copper metallization has been gaining importance. Copper is preferred over Al because it has a low resistivity (1.2 μΩ · cm) and is resistant to electromigration. In fact, copper is added in small quantities to Al to reduce the electromigration problem of Al. However, there are some real problems with copper that need to be addressed before it can replace Al:

1. Cu is a terrible contaminant in Si. It has a very high diffusivity in Si and causes junction leakage, which degrades the gate oxide integrity (GOI).
2. Cu diffuses and drifts easily through SiO₂. Hence, Cu needs to be encapsulated for use in metallization.
3. Cu oxidizes to CuO easily.
4. The etch chemistry for Cu is highly contaminated, and the wafers need to be held at higher temperatures.

Typical process steps involved in the fabrication of a 0.8-μm LOCoS n-well inverter are as follows:

1. Wafer: 1×10^{15} to 1×10^{16} CZ(p) with (100) crystal orientation. Epitaxial layer required because of latchup. The thickness is 2–16 μm with 5×10^{15} .
2. Grown screen oxide layer, with the thickness in the range 400–1000.
3. Expose the n-well photo on the wafer.
4. n-well ion implant. Use $1 \times 10^{13}/\text{cm}^2$ phosphorous. The voltage used is 60 keV–2 MeV.
5. n-well drive-in. This step is carried out at 1050–1100°C for 2–6 h. This activates the dopant atoms. The drive-in depth is around 1–10 μm.
6. Perform LOCoS process.
 - a. Strip wafer.
 - b. Pad oxide. Thickness is 100–400.
 - c. Pad nitride. Thickness is 1000–2000. LPCVD silicon nitride is used.
 - d. Expose the diffusion photo on the wafer.
 - e. Etch the nitride layer.
 - f. Expose the block field (BF) photo. This is the inverse of the n-well photo and prevents the formation of the parasitic transistors between adjacent transistors.
 - g. Field ion implantation. $1 \times 10^{13}/\text{cm}^2$ boron at 60 keV.
 - h. Strip the BF and the resist layer.
 - i. Grow the field oxide. The thickness is about 4000–6000 of SiO₂. The process used is a pyro process at 900–1050°C for 3–6 h.
 - j. Strip the pad nitride layer by dipping the wafer in H₃PO₄.
 - k. Strip the pad oxide layer by dipping the wafer in 50 : 1 HF.
7. Grow a sacrificial oxide layer and strip it. The thickness is about 600–1000. The sacrificial oxide layer eats into the bare silicon, thus exposing fresh silicon area on which the device can be grown.
8. Grow a sacrificial gate oxide layer. Here the thickness is about 80–130. This layer protects the gate when the V_T implant is done.
9. V_T implant. Two masks, one for the n region and one for the p region, are used. The concentration is 1×10^{11} to $1 \times 10^{12}/\text{cm}^2$ at 5–30 keV.
10. Strip the sacrificial gate oxide layer using a 50 : 1 HF solution.
11. Grow the gate oxide layer. Typical thickness is 80–130. The gate oxide layer is grown at 800–900°C for 20 min.
12. Polysilicon is deposited all over the wafer. LPCVD silane is used at 620°C for a blanket deposition. The typical thickness is 2500–4000.
13. Polysilicon doping is done by ion implantation using 5×10^{15} phosphorous.
14. The polysilicon etch is a very critical photo/etch process.
 - l. Polysilicon photo is exposed on the wafer.
 - m. Reactive-ion etch (RIE) is used to etch the polysilicon.
 - n. The resist is stripped.
15. Diffusion processing
 - o. Mask the p regions.
 - p. Perform n⁺ source/drain ion implantation using $5 \times 10^{15}/\text{cm}^2$ As⁷⁵ at 40 keV. As is used because it is slow and does not diffuse deep into the silicon substrate.
 - q. Perform n⁺ anneal at 900°C for 15 min to activate the dopant.
 - r. Strip the resist.
 - s. Mask the n⁺ regions.
 - t. Perform p⁺ source/drain ion implantation using $1 \times 10^{15}/\text{cm}^2$ BF₂/B¹¹ at 5–20 keV.
 - u. Source/drain anneal at 900°C for 30 min in an oxidizing atmosphere. This is a rapid thermal process.
 - v. Strip the resist off.

16. Interlevel dielectric. Borophosphosilicon glass (BPSG) is used because it flows well. Typical thickness is 5000–8000. A 900°C reflow anneal is also performed.
17. The contact photo is exposed on the wafer. This is critical to the layout density.
18. The contacts are etched using RIE.
19. After etching, the contact resist is stripped off.
20. Metallization. Ti barrier metallurgy is used. The actual contact is made with an alloy of Al/Cu/Si with percentages 98%, 1%, and 1%, respectively. The Al alloy is sputtered onto the wafer. The typical thickness is about 1.2 μm.
21. The metal 1 layer photo is exposed.
22. Metal 1 etch.
23. Strip resist.
24. Foaming gas anneal is performed to improve the mobility of the electrons and relieve stress on the wafer.

The inverter is finally fabricated. Figure 5 describes the process cross section of this inverter after the various steps have been performed.

8. TESTING

Testing is a critical factor in the design of circuits. The purpose of testing is to verify conformance to the product definition. To understand the complexity of this problem, consider a combinational circuit with n inputs. A sequence of 2^n inputs must be applied and observed to test the circuit exhaustively. Since the number of inputs are high for VLSI circuits, testing the chip exhaustively is impossible. Hence, this becomes an area of importance to circuit design. There are three main areas that need to be addressed to solve this problem:

1. Test generation
2. Test verification
3. Design for testability

Test generation corresponds to the problem of generating a minimum number of tests to verify the behavior of a circuit. The problem of test verification, which is commonly gauged by performing fault simulations, involves evaluating measures of the effectiveness of a given set of test vectors. Circuits can also be designed for testability.

8.1. Test Generation

Test generation [60] involves the search for a sequence of input vectors that allow faults to be detected at the primary device outputs. VLSI circuits are typically characterized by buried flip-flops, asynchronous circuits, indeterminate states, complex clock conditions, multiple switching of inputs simultaneously, and nonfunctional inputs. Due to these factors, an intimate knowledge of the internal circuit details is essential to develop efficient test strategies. The goal of a test generation strategy [61,62] is

multifold: (1) chip design verification in conjunction with the designer, (2) incorporation of the customer's specification and patterns into the manufacturing test program, and (3) fault detection by fault simulation methods.

8.2. Test Verification

Test verification [63] involves calculating measures for how efficient the test vectors for a given circuit are. This is often accomplished by using fault models [64]. Fault simulation requires a good circuit simulator to be efficient and is hence closely related to logic simulation and timing analysis. While the logic simulator verifies the functionality of a design and ensures that the timing constraints are met, the fault simulator tells the designer if enough analysis has been performed to justify committing the design to silicon. In fault simulation, the true value of a circuit and its behavior under possible faults is simulated. The fault model is a hypothesis based on an abstract model of the circuit, conformed to some precise real physical defects. To begin with, the simulator generates a fault list that identifies all the faults to be modeled. Then a set of test vectors is simulated against the fault-free and faulty models. Those faults that cause an erroneous signal at an output pin are considered as detected faults. Now the fault coverage of the test vector set can be computed as the number of faults detected over the total number of faults modeled.

The most widely used fault model is the single stuck-at fault model. This model assumes that all faults occur because of the shorting of a signal node with the power rail. A number of faults can be detected by this model, but a major disadvantage of this model is its assumption that all faults appear as stuck-at faults. The limitations of this model have led to the increased use of other models, like the stuck-open [65] and bridging fault models [66]. The former can occur in a CMOS transistor or at the connection to a transistor. The bridging faults are short circuits that occur between signal lines. These represent a frequent source of failure in CMOS ICs. A majority of the random defects are manifested as timing delay faults in static CMOS ICs. These are faults in which the increased propagation delay causes gates to exceed their rated specifications. The statically designed circuits have a transient power supply that peaks when the gates are switching and then settles to a low current value in the quiescent state. The quiescent power supply current [67], known as I_{DDQ} , can be used as an effective test to detect leakage paths due to defects in the processing. The measured I_{DDQ} of a defect-free CMOS IC is approximately 20 nA. Most physical defects will elevate I_{DDQ} by one to five orders of magnitude. Thus the I_{DDQ} testing approach can be used to detect short circuits not detectable by the single stuck-at fault model.

There are several other ways of applying logic and fault simulation to testing:

1. *Toggle Testing*. This is the cheapest, simplest, and least time-consuming method of applying simulation to testing. Toggle testing provides a testability measure by tracking the activity of circuit nodes. From a

set of vectors, the method identifies those parts of the network that exhibit no activity. Since the test vectors do not affect these nodes, faults occurring here cannot be detected by the fault simulator.

2. *Fault Simulation of Functional Tests.* The outputs of the functional simulator can be used in the design process as an effective design analysis tool. The lists of detectable and undetectable faults generated by the simulator can be used to locate problems in the design and correct them. This results in substantial savings in development and manufacturing.
3. *Fault Simulation after New Test Vector Generation.* High-quality testing in a reasonable time-frame would require an efficient test pattern generation system and a fault simulator. Test vectors are first generated to detect specific faults, and the fault simulator determines the quality of the vector set. In this scenario, it becomes important to fault simulate after every new test vector is generated in order to catch multiple faults. Accelerated fault simulation is faster than test pattern generation.

8.3. Design for Testability

Design for testability commonly refers to those design techniques that produce designs for which tests can be generated by known methods. The advantage of these techniques are (1) reduced test generation cost, (2) reduced testing cost, (3) high-quality product, and (4) effective use of computer-aided design tools. The key to designing circuits that are testable are two concepts, controllability and observability. *Controllability* is defined as the ability to set and reset every node that is internal to the circuit. *Observability* is defined as the ability to observe either directly or indirectly the state of any node in the circuit. There are programs like SCOAP [68] that, given a circuit structure, can calculate the ability to control or observe internal circuit nodes. The concepts involved in design for testability can be categorized as follows: (1) ad hoc testing, (2) scan-based test techniques, and (3) built-in self-test (BIST).

8.3.1. Ad Hoc Testing. Ad hoc testing comprises techniques that reduce the combinational explosion of testing. Common techniques partition the circuit structure and add test points. A long counter is an example of a circuit that can be partitioned and tested with fewer test vectors. Another technique is the use of a bus in a bus-oriented system for testing. The common approaches can be classified as (1) partitioning techniques, (2) adding test points, (3) using multiplexers, and (4) providing for easy state reset.

8.3.2. Scan-Based Test Techniques. Scan-based approaches stem from the basic tenets of controllability and observability. The most popular approach is the level-sensitive scan design, or LSSD, approach, introduced by IBM [69]. This technique is illustrated in Fig. 18. Circuits designed on the basis of this approach operate in two

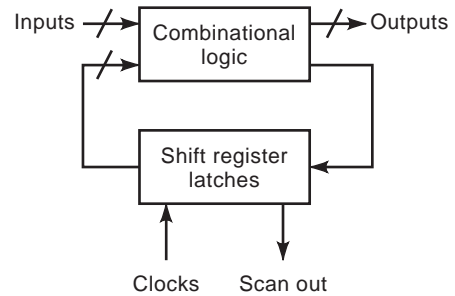


Figure 18. Level-sensitive scan design.

modes: normal mode and test mode. In the normal mode of operation, the shift register latches act as regular storage latches. In the test mode, these latches are connected sequentially and data can be shifted in or out of the circuit. Thus, a known sequence of data (controllability) can be input to the circuit, and the results can be shifted out of the circuit using the registers (observability). The primary disadvantage of this approach is the increased complexity of the circuit design and the increased external pin count. The serial scan approach is similar to the LSSD, but the design of the shift register latch is simplified to obtain faster circuits. For most circuit designs, only the input and output register need be made scannable. This technique makes the designer responsible for deciding which registers need to be scanned and is called the *partial serial scan technique* [70]. The *parallel scan* [71] approach is an extension of the serial scan in which the registers are arranged in a sort of a grid, where on a particular column all the registers have a common read/write signal. The registers that fall on a particular row have common data lines. Therefore, the output of a register can be observed by enabling the corresponding column and providing the appropriate address. Data can also be written into these registers in a similar fashion.

8.3.3. Built-in Self-Test. Signature analysis [72] or cyclic redundancy checking can be used to incorporate a built-in self-test module in a circuit. This involves the use of a linear feedback shift register, as depicted in Fig. 19. The value in the register will be a function of the value and number of latch inputs and the counting function of the signature analyzer. The good part of the circuit will have a particular number or signature in the register, while the faulty portion will have a different number. The signature analysis approach can be merged with the level-sensitive scan design approach to create a structure called a built-in logic block observation, or BILBO [73]. Yet

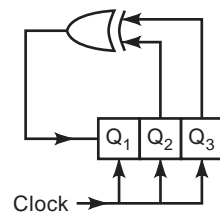


Figure 19. Linear feedback shift register.

another approach to the built-in test is the design for autonomous test, in which the circuit is partitioned into smaller structures that are tested exhaustively. The partitioning method involves the use of multiplexers. The syndrome testing method, in which all possible inputs are applied and the number of 1s at the outputs is counted, is also a test method that requires exhaustive testing. The resultant value is compared to that of a known good machine.

8.4. Other Tests

So far we have discussed techniques for testing logic structures and gates. But we need testing approaches at the chip level and the system level also. Most approaches for testing chips rely on the aforementioned techniques. Memories, for instance, can use the built-in self-test techniques effectively. Random logic is usually tested by full serial scan or parallel scan methods. At the system level, traditionally the "bed of nails" testers have been used to probe points of interest. But with the increasing complexity of designs, system designers require a standard to test chips at the board level. This standard is the IEEE 1149 boundary scan [74] architecture. ICs that are designed on the basis of this standard enable complete testing of the board. The following types of tests can be performed in a unified framework: (1) connectivity test between components, (2) sampling and setting chip I/Os, and (3) distribution and collection of built-in self-test results.

BIBLIOGRAPHY

- R. S. Schaller, Moore's law: Past, present and future, *IEEE Spectrum* **34**(6):52–59 (June 1997).
- J. Y. Chen, CMOS—the emerging technology, *IEEE Circ. Devices Mag.* **2**(2):16–31 (1986).
- S. Wolf and R. N. Tauber, *Silicon Processing for the VLSI Era: Process Integration*, Vol. 2, Lattice Press, Sunset Beach, CA, 1986.
- D. Kahng and M. M. Atalla, Silicon-silicon dioxide field induced surface devices, *Proc. IRE Solid State Devices Res. Conf.*, Carnegie Inst. Technology, Pittsburgh, PA, 1960.
- N. H. E. Weste and K. Esharaghian, *Principles of CMOS VLSI Design*, 2nd ed., Addison-Wesley, Reading, MA, 1993.
- H. C. Pao and C. T. Shah, Effects of diffusion current on characteristics of metal-oxide (insulator)-semiconductor transistors (MOST), *Solid State Electron.* **9**:927–937 (1966).
- S. M. Sze, *Physics of Semiconductor Devices*, Wiley, New York, 1981.
- D. A. Hodges and H. G. Jackson, *Analysis and Design of Digital Integrated Circuits*, McGraw-Hill, New York, 1983.
- P. K. Chatterjee, Gigabit age microelectronics and their manufacture, *IEEE Trans. VLSI Syst.* **1**:7–21 (1993).
- C.-Y. Wu, J.-S. Wang, and M.-K. Tsai, The analysis and design of CMOS multidrain logic and stacked multidrain logic, *IEEE JSSC* **SC-22**:47–56 (1987).
- M. G. Johnson, A symmetric CMOS NOR gate for high speed applications, *IEEE JSSC* **SC-23**:1233–1236 (1988).
- K. J. Schultz, R. J. Francis, and K. C. Smith, Ganged CMOS: Trading standby power for speed, *IEEE JSSC* **SC-25**:870–873 (1990).
- Y. Susuki, K. Odagawa, and T. Abe, Clocked CMOS calculator circuitry, *IEEE JSSC* **SC-8**:462–469 (1973).
- T. Sakurai et al., Hot-carrier generation in submicrometer VLSI environment, *IEEE JSSC* **SC-21**:187–191 (1986).
- R. H. Krambeck, C. M. Lee, and H. S. Law, High-speed compact circuits with CMOS, *IEEE JSSC* **SC-17**:614–619 (1982).
- V. Friedman and S. Liu, Dynamic logic CMOS circuits, *IEEE JSSC* **SC-19**:263–266 (1984).
- N. F. Gonclaves and H. J. DeMan, NORA: A racefree dynamic CMOS technique for pipelined logic structures, *IEEE JSSC* **SC-18**:261–266 (1983).
- C. M. Lee and E. W. Szeto, Zipper CMOS, *IEEE Circ. Devices* **2**(3):101–107 (1986).
- L. G. Heller et al., Cascade voltage switch logic: A differential CMOS logic family, *Proc. IEEE Int. Solid State Circuits Conf.*, San Francisco, CA, Feb. 16–17, 1984.
- T. D. Simon, A fast static CMOS NOR gate, in T. Knight and J. Savage, eds., *Proc. 1992 Brown/MIT Conf. Advanced Res. VLSI Parallel Syst.*, MIT Press, Cambridge, MA, 1992, pp. 180–192.
- D. Radhakrishnan, S. R. Whitaker, and G. K. Maki, Formal design procedures for pass transistor switching circuits, *IEEE JSSC* **SC-20**:531–536 (1985).
- C. J. Terman, in W. Fichtner and M. Morf, eds., *Simulation Tools for VLSI, VLSI CAD Tools and Applications*, Kluwer, Norwell, MA, 1987, Chap. 3.
- L. W. Nagel, *SPICE2: A Computer Program to Simulate Semiconductor Circuits*, Memo ERL-M520, Dept. Electrical Engineering & Computer Science, Univ. California, Berkeley, May 9, 1975.
- W. T. Weeks et al., Algorithms for ATSA— a network analysis program, *IEEE Trans. Circ. Theory* **CT-20**:628–634 (1973).
- HSPICE User's Manual H9001*, Meta-Software, Campbell, CA, 1990.
- C. Terman, Timing simulation for large digital MOS circuits, in A. Sangiovanni-Vincentelli, ed., *Advances in Computer-aided Engineering Design*, Vol. 1, JAI Press, Greenwich, CT, 1984, pp. 1–91.
- J. White and A. Sangiovanni-Vincentelli, *Relaxation Techniques for the simulation of VLSI Circuits*, Hingham, MA, Kluwer, 1987.
- R. F. Lyon, Simplified design rules for VLSI layouts, *LAMBDA*, **II**(1) (1981).
- C. A. Mead and L. A. Conway, *Introduction to VLSI Systems*, Addison-Wesley, Reading, MA, 1980.
- S. M. Rubin, *Computer Aids for VLSI Design*, Addison-Wesley, Reading, MA, 1987, Chap. 11.
- J. K. Ousterhout et al., Magic: A VLSI layout system, *Proc. 21st Design Autom. Conf.*, 1984, pp. 152–159.
- U. Lauther, A min-cut placement algorithm for general cell assemblies based on a graph, *Proc. 16th Design Autom. Conf.*, 1979, pp. 1–10.
- E. S. Kuh, Recent advances in VLSI layouts, *Proc. IEEE* **78**:237–263 (1990).
- S. Kirkpatrick, C. Gelatt, and M. Vecchi, Optimization by simulated annealing, *Science* **220**(4598):671–680 (1983).
- C. Sechen and A. Sangiovanni-Vincentelli, TimberWolf 3.2: A new standard cell placement and global routing package, *Proc. 23rd Design Autom. Conf.*, Las Vegas, NV, 1986, pp. 432–439.
- G. W. Clow, A global routing algorithm for general cells, *Proc. 21st Design Autom. Conf.*, Albuquerque, NM, 1984, pp. 45–50.

37. G. Dupenloup, A wire routing scheme for double layer cell-layers, *Proc. 21st Design Autom. Conf.*, Albuquerque, NM, 1984, pp. 32–35.
38. E. F. Moore, The shortest path through a maze, *Proc. Int. Symp. Switching Theory*, Vol. 1, Harvard Univ. Press, 1959, pp. 285–292.
39. C. Y. Lee, An algorithm for path connection and its applications, *IRE Trans. Electron. Comput.* 346–365 (Sept. 1961).
40. T. Lengauer, *Combinatorial Algorithms for Integrated Circuit Layouts*, Wiley, New York, 1981.
41. J. Doerschel and F. G. Kirscht, Differences in plastic deformation behavior of CZ and FZ grown Si crystals, *Phys. Status Solid* **A64**:K85–K88 (1981).
42. W. Zuhlechner and D. Huber, *Czochralski Grown Silicon, Crystals*, Vol. 8, Springer-Verlag, Berlin, 1982.
43. D. Biddle, Characterizing semiconductor wafer topography, *Microelectron. Manuf. Test.* **15**:15–25 (1985).
44. G. Fiegl, Recent advances and future directions in CZ-silicon crystal growth technology, *Solid State Technol.* **26**(8):121–131 (1983).
45. T. Suzuki et al., CZ silicon growth in a transverse magnetic field, in *Semiconductor Silicon 1981*, Electrochemical Society, Pennington, NJ, 1981, pp. 90–93.
46. J. Bloem and L. J. Gillig, Epitaxial growth by chemical vapor deposition, in N. G. Einspruch and H. Huff eds., *VLSI Electronics*, Vol. 12, Academic Press, Orlando, FL, 1985, Chap. 3, pp. 89–139.
47. S. Wolf and R. N. Tauber, *Silicon Processing for the VLSI Era: Process Technology*, Lattice Press, Sunset Beach, CA, 1986.
48. P. Burggraaf, Ion implantation in wafer fabrication, *Semiconductor Int.* **39**:39–48 (1981).
49. H. Glawishing and N. Noack, Ion implantation system concepts, in J. F. Ziegler, ed., *Ion Implantation, Science and Technology*, Academic Press, Orlando, FL, 1984, pp. 313–373.
50. L. F. Thompson and M. J. Bowden, The lithographic process: The physics, in L. F. Thompson, C. G. Willson, and M. S. Bowden, eds., *Introduction to Microlithography*, American Chemical Society, Advances in Chemistry Series Vol. 219, 1983, pp. 15–85.
51. M. C. King, Principles of optical lithography, in N. G. Einspruch, ed., *VLSI Electronics Micro Structure Science*, Vol. 1, Academic Press, New York, 1981.
52. P. S. Gwozdz, Positive vs. negative: A photoresist analysis, *SPIE Proc. Semiconduct. Lithogr. VI* **275**:156–182 (1981).
53. D. J. Elliot, *Integrated Circuit Fabrication Technology*, McGraw-Hill, New York, 1982, Chap. 8.
54. R. C. Braken and S. A. Rizvi, Microlithography in semiconductor device processing, in N. G. Einspruch and G. B. Larabee, eds., *VLSI Electronics—Microstructure Science*, Vol. 6, Academic Press, Orlando, FL, 1983, pp. 256–291.
55. E. Kooi and J. A. Appels, Semiconductor silicon 1973, in H. R. Huff and R. Burgess, eds., *The Electrochemistry Symp. Series*, Princeton, NJ, 1973, pp. 860–876.
56. P. Deroux-Dauphin and J. P. Gonchond, Physical and electrical characterization of a SILO isolation structure, *IEEE Trans. Electron. Devices* **ED-32**(11):2392–2398 (1985).
57. M. Mikoshiba, A new trench isolation technology as a replacement of LOCOS, *IEDM Tech. Digest*, 1984, pp. 578–581.
58. Y. Pauleau, Interconnect materials for VLSI circuits: Part II: Metal to silicon contacts, *Solid-State Technol.* **30**(4):155–162 (1987).
59. M. A. Nicolet and M. Bartur, Diffusion barriers in layered contact structures, *J. Vac. Sci. Technol.* **19**(3):786–793 (1981).
60. V. D. Agrawal and S. C. Seth, *Tutorial: Test Generation for VLSI Chips*, IEEE Computer Society Press, Los Alamitos, CA, 1988.
61. S. T. Chakradhar, M. L. Bushnell, and V. D. Agrawal, Toward massively parallel automatic test generation, *IEEE Trans. CAD* **9**:981–994 (1990).
62. J. D. Calhoun and F. Brglez, A framework and method for hierarchical test generation, *IEEE Trans. CAD* **11**:598–608 (1988).
63. H. K. Reghbati, *Tutorial: VLSI Testing and Validation Techniques*, IEEE Computer Society Press, Los Alamitos, CA, 1985.
64. W. Malay, Realistic fault modeling for VLSI testing, *IEEE/ACM Proc. 24th IEEE Design Autom. Conf.*, Miami Beach, FL, 1987, pp. 173–180.
65. A. P. Jayasumana, Y. K. Malaiya, and R. Rajsuman, Design of CMOS circuits for stuck-open fault testability, *IEEE JSSC* **26**(1):58–61 (1991).
66. J. M. Acken, Testing for bridging faults (shorts) in CMOS circuits, *Proc. 20th IEEE/ACM Design Autom. Conf.*, Miami Beach, FL, 1983, pp. 717–718.
67. K. Lee and M. A. Breuer, Design and test rules for CMOS circuits to facilitate IDDQ testing of bridging faults, *IEEE Trans. CAD* **11**:659–670 (1992).
68. L. H. Goldstein and E. L. Thigpen, SCOAP: Sandia controllability/observability analysis program, *Proc. 17th Design Autom. Conf.*, 1980, pp. 190–196.
69. E. B. Eichelberger and T. W. Williams, A logic design structure for LSI testing, *J. Design Autom. Fault Tolerant Comput.* **2**(2):165–178 (1978).
70. R. Gupta, R. Gupta, and M. A. Breuer, An efficient implementation of the BALLAST partial scan architecture, *Proc. IFIP Int. VLSI'89 Conf.*, Munich, 1990, pp. 133–142.
71. H. Ando, Testing VLSI with random access scan, *IEEE/ACM Digest Papers COMPCON 80*, February 1980, pp. 50–52.
72. R. A. Frohwerk, Signature analysis—a new digital field service method, *Hewlett-Packard J.* **28**(9):2–8 (1977).
73. B. Koenemann, J. Mucha, and G. Zwiehoff, Built-in logic block observation techniques, *Digest 1979 IEEE Test Conf.*, Oct. 1979, pp. 37–41.
74. *IEEE Standard 1149.1: IEEE Standard Test Access Port and Boundary-Scan Architecture*, IEEE Standards Board, New York, 1994.

FURTHER READING

- A. Mukherjee, *Introduction to nMOS and CMOS VLSI Systems Design*, Prentice-Hall, Englewood Cliffs, NJ, 1986.
- L. A. Glasser and D. W. Dobberpuhl, *The Design and Analysis of VLSI Circuits*, Addison-Wesley, Reading, MA, 1985.
- M. Annaratone, *Digital CMOS Circuit Design*, Kluwer, Norwell, MA, 1986.
- M. Shoji, *CMOS Digital Circuit Technology*, Prentice-Hall, Englewood Cliffs, NJ, 1988.
- D. A. Pucknell and K. Eshraghian, *Basic VLSI Design: Systems and Circuits*, Prentice-Hall of Australia Ltd., Sydney, 1988.
- W. Wolf, *Modern VLSI Design: A System Approach*, Prentice-Hall, Englewood Cliffs, NJ, 1994.

- J. Schroeter, *Surviving the ASIC Experience*, Prentice-Hall, Englewood Cliffs, NJ, 1992.
- J. M. Rabaey and M. Pedram, *Low Power Design Methodologies*, Kluwer, Boston, 1996.
- S. M. Kang and Y. Leblebici, *CMOS Digital Integrated Circuits*, McGraw-Hill, New York, 1996.
- C. Y. Chang, S. M. Sze, *ULSI Technology*, McGraw-Hill, New York, 1996.
- N. Sherwani, *Algorithms for VLSI Physical Design Automation*, Kluwer, Boston, 1993.
- R. L. Gieger, P. E. Allen, and N. R. Strader, *VLSI Design Techniques for Analog and Digital Circuits*, McGraw-Hill, New York, 1990.
- L. J. Herbst, *Integrated Circuit Engineering*, Oxford Univ. Press, London, 1996.
- M. S. Smith, *Application Specific Integrated Circuits*, Addison-Wesley, Reading, MA, 1997.

INTEGRO-DIFFERENTIAL EQUATIONS

MANUEL GARCIA
Lawrence Livermore National
Laboratory
Livermore, California

1. INTRODUCTION

This article focuses on methods of solution. The aim is to show how a student or engineer can manipulate an integrodifferential problem into a form that is simple to calculate. Few of these equations yield analytical solutions. The direct numerical approach of using finite differences for derivatives and sums for integrals relies on the capability of the computer and on the stability of the numerical algorithm. The methods described in this article aim to improve the stability of the eventual calculation by removing derivatives, and to minimize repetitive calculations (nested loops). These techniques make it possible to solve realistic problems with modest personal computers.

An integrodifferential equation describes the influence of an accumulation of points on the value and dynamics of each individual member of the collection. These equations are a balance between a quantity, its derivatives, and its integrals. The most significant applications of integrodifferential equations are in modeling the impact of heredity and the dynamics of systems out of equilibrium. Heredity problems in engineering include analyzing fluid and heat flow, mechanical stress, and the accumulation of residual charge for materials with memory. The study of nonequilibrium systems is based on kinetic theory, where the properties of a gas are calculated as the average of individual molecular collisions. Integrodifferential equations are applied in biology and economics as well as in physics and engineering.

A differential equation describes the dynamics of a quantity. It is a balance between the values of the quantity and its various rates of change *at a given moment*. One such balance is between the acceleration of a particle and

the action of external forces, classical Newtonian mechanics. Basic examples are the one-dimensional mass–spring–damper equation and its electrical analog, the resistor–inductor–capacitor (*RLC*) circuit equation. These specific differential models each conserve a global quantity; for the mechanical example it is momentum, for the electrical example it is current. The implicit assumption in the differential description is that the future state of a system does not depend on its history. Erosion, fatigue, wear, failure, experience, heredity, evolution, karma—all these words express some observation about the impact of past dynamics on future dynamics. One example is the failure of mechanical components subjected to repetitive stress. Engineers routinely calculate the amount of twist of a metal bar subjected to a specific torque. If we assume this phenomenon to be purely differential, then the same amount of torque will always produce the same amount of twist. In reality, metal subjected to repeated strain experiences fatigue. Eventually the application of the same torque produces a different twist, perhaps a catastrophic event. The metal inherits a degradation of its elasticity, an integral of the history of deflections. This effect caused the breakup of two de Havilland Comet jet airliners during flight in 1954. The engineers of the day were unaware that the aluminum fuselage would experience metal fatigue as a result of the frequent cycles of cabin pressurization.

An integral equation describes the influence of all points in a field upon the value of any particular point. Integral equations express an equilibrium. The points can be spatial for a field of stress in a surface or rod, or they can be instants of time in an orbital trajectory, or they can be individual molecules in a gas in which the field is a statistical distribution of molecular velocities. When external conditions change suddenly so that the system is out of balance, energy or information must flow within the system to rearrange it into a new equilibrium. Describing this nonequilibrium process requires differential terms in addition to the original integral equation. Instantaneous equilibration is often assumed in engineering applications, for instance, in thermodynamics, and integrodifferential equations are avoided. However, the sharpening of technology into much smaller space and timescales has required more exacting physical models that account for nonequilibrium dynamics. This technological trend drives the continuing interest in solving integrodifferential equations.

A method is described for transforming integrodifferential equations with linear derivatives into purely integral forms, which are then solved by iteration. Knowledge of an approximate solution speeds the convergence of iteration. One method of developing such approximate solutions is described in the section that follows. By the very nature of approximation, such methods depend on the specifics of the particular integrodifferential equation. It is best to view the development of the approximate solutions in the sample analysis as an example of the attitude and reasoning that may prove useful in other problems. After the discussion of linear equations a nonlinear system with hereditary effects is described. This nonlinear system describes the conflict between populations of predators and prey. This system is reduced to a single nonlinear integral equation for which an iterated

solution is found. However, a much easier calculation of the solution is possible with an approximate equation developed from the nonlinear integral. This approximation recognizes the effect of the hereditary integral and casts the problem as a type of recursion formula $\{x(t) = f[x(t - \Delta t), t]\}$, eliminating the need for any iteration. A discussion of physical applications of integrodifferential equations concludes the article.

2. A SAMPLE ANALYSIS

Consider the following linear, first-order, homogeneous integrodifferential equation for unknown function $y(x)$:

$$\frac{dy(x)}{dx} = - \int_{x-\alpha}^{x+\beta} \frac{p(\xi)}{a(x)} y(\xi) d\xi \tag{1}$$

We will use this equation to demonstrate how a solution may be attempted. Both α and β are positive constants. This particular equation has a separable kernel

$$K(\xi, x) = \frac{p(\xi)}{a(x)} \tag{2}$$

and we suppose that $a(x)$ is not zero in the domain of interest. Can Eq. (1) be cast as a purely differential, or purely integral equation? If so, it may be possible to transform it to a standard form and solve it by established techniques. In this section we will look first at the effect of differentiating Eq. (1), then we will seek an approximate solution directly from the integrodifferential form, then we will transform Eq. (1) into a purely integral form, and finally we will show specific examples.

Differentiating Eq. (1) results in

$$a(x)y''(x) + a'(x)y'(x) = p(x - \alpha)y(x - \alpha) - p(x + \beta)y(x + \beta) \tag{3}$$

where primes refer to differentiation with respect to x . In Eq. (3) derivatives of y at x depend on values of y at positions to either side of x . This form is a differential-difference equation. References 1 and 2 describe this type of equation. From Eq. (3), $y(x - \alpha)$ can be cast as depending on itself at higher x

$$y(x - \alpha) = \frac{a(x)y''(x) + a'(x)y'(x) + p(x + \beta)y(x + \beta)}{p(x - \alpha)} \tag{4}$$

This form of the equation is the basis of a numerical solution in cases where it is known that $y(x)$ decays exponentially with respect to positive x . Above a given coordinate, say x_2 , y is assumed to be small and its derivatives are assumed to be zero. A solution is constructed for $x < x_2$ using Eq. (4). In a range $x < x_1$, where $x_1 < x_2$, the function $y(x)$ is exponentially larger than the starting value assumed, and $y(x)$ is considered an accurate solution. Care must be taken in the numerical treatment of the derivatives, and this is most directly accomplished by using closely spaced points and higher-order differences. If the kernel is not separable, then differentiation will not

remove the integral. It will now contain the derivative of the kernel with respect to x , $K'(\xi, x)$.

Let us assume that $y(x)$ is a positive function that decays exponentially with respect to positive x . In this case both $a(x)$ and $p(x)$ are positive over the range of interest, $x_0 \leq x < \infty$. Let us seek a solution in the form

$$y(x) = \exp \left[- \int_{x_0}^x B(\eta) d\eta \right] \tag{5}$$

where x_0 is a reference coordinate where $y = 1$, an initial condition. Note that $-y'/y = B$. Divide Eq. (1) by $y(x)$ and use Eq. (5):

$$a(x)B(x) = \int_{x-\alpha}^{x+\beta} p(\xi) \exp \left[- \int_x^\xi B(\eta) d\eta \right] d\xi \tag{6}$$

Note that in Eq. (6) it is the ratio $y(\xi)/y(x)$ that appears in the integral with $p(\xi)$, and this ratio is given by the exponential involving $B(\eta)$. Given an estimate of function B , call it B_0 , Eq. (6) can be used to find a possibly more accurate estimate B_1 by the method of successive approximations. This method, also known as the *method of Picard*, uses a prior iterant within the integral (B_0) to find a next iterant (B_1) from the equation. References 3 and 4 describe the validity and use of this method.

If the method of successive approximations converges to a solution, then the exact nature of the initial iterant B_0 is unimportant. However, the more accurately B_0 portrays the actual solution $B(x)$, the fewer iterants need to be calculated. We now seek an initial iterant from Eq. (6) by making whatever assumptions simplify this problem, while at the same time being mindful to avoid a trivial result by being too hasty. For the moment we will assume that $p(x)$ is weakly dependent on x within any band $(x - \alpha, x + \beta)$, and that $B(\xi)$ remains of the same order of magnitude for $(x - \alpha \leq \xi \leq x + \beta)$. The following approximations cascade from Eq. (6) by using these assumptions:

$$\begin{aligned} a(x)B_0(x) &\approx \int_{x-\alpha}^{x+\beta} p(\xi) e^{-B_0(x)(\xi-x)} d\xi \approx p(x) \int_{x-\alpha}^{x+\beta} e^{-B_0(x)(\xi-x)} d\xi \\ &\approx \frac{p(x)}{-B_0(x)} \int_{x-\alpha}^{x+\beta} e^{-B_0(x)(\xi-x)} [-B_0(x)] d\xi \\ &\approx \frac{p(x)}{B_0(x)} [e^{2B_0(x)} - e^{-\beta B_0(x)}] \end{aligned} \tag{7}$$

$$B_0(x) = \sqrt{\frac{p(x)}{a(x)} e^{2B_0(x)} [1 - e^{-(\alpha+\beta)B_0(x)}]} \tag{8}$$

For a small $B_0(x)$ such that both $B_0(x)(\alpha + \beta) < 1$ and $B_0(x)\alpha < 1$, then

$$B_0(x) = \frac{p(x)}{a(x)} (\alpha + \beta) \tag{8a}$$

which is found by expanding the exponentials in Eq. (8). Note that to be consistent, $p(x)/a(x)$ must be less than

$(\alpha + \beta)^{-2}$. For $B_0(x)$ such that $B_0(x)(\alpha + \beta) > 1$ while $B_0(x)\alpha < 1$, which implies $\beta \gg \alpha$, then

$$B_0(x) = \sqrt{\frac{p(x)}{a(x)}} \tag{8b}$$

This case is consistent with $1/(\alpha + \beta) < \sqrt{p(x)/a(x)} < 1/\alpha$. Finally, for $B_0(x)$ such that both $B_0(x)(\alpha + \beta) > 1$ and $B_0(x)\alpha > 1$, then $B_0(x)$ is the root of a transcendental equation

$$B_0(x) = \sqrt{\frac{p(x)}{a(x)} e^{2B_0(x)}} \tag{8c}$$

If none of Eqs. (8a)–(8c) are applicable, then $B_0(x)$ must be found as a root of Eq. (8). The corresponding initial iterant $y_0(x)$ for Eq. (1) is given by using the appropriate result from Eqs. (8) or (8a)–(8c) in definition (5). The example shown below uses the simplest case, Eq. (8a):

$$y_0(x) = \exp \left[-(\alpha + \beta) \int_{x_0}^x \frac{p(\eta)}{a(\eta)} d\eta \right] \tag{9}$$

It is very important to capture the functional nature of $p(x)$ within the integral of Eq. (7). In the preceding, $p(x)$ was assumed to be very weakly dependent on x over the interval $(x - \alpha, x + \beta)$ in a manner similar to a constant or $\log(x)$. If instead, $p(x) = p_0(x)x$, where $p_0(x)$ is a weak function of x as used here, then the results in place of Eq. (8) are as follows:

$$B_0(x) = \sqrt[3]{\frac{p_0(x)}{a(x)} e^{2B_0(x)} \{1 + B_0(x)(x - \alpha) - [1 + B_0(x)(x + \beta)]e^{-(\alpha + \beta)B_0(x)}\}} \tag{10}$$

The case of small $B_0(x)$ corresponding to Eq. (8a) is now

$$B_0(x) = \frac{p_0(x)}{a(x)} (\alpha + \beta) \left(x + \frac{\beta^2 - \alpha^2}{(\alpha + \beta)} \right) \tag{10a}$$

Note the additional linear factor in comparison to Eq. (8a). It is essential to retain that factor of $p(x)$ with significant variation within the integral of Eq. (7). We will only use the simplest B_0 and y_0 , derived as Eqs. (8a) and (9), respectively, to illustrate a first iterant with Eq. (11)

$$a(x)B_1(x) = \int_{x-\alpha}^{x+\beta} p(\xi) \exp \left[-(\alpha + \beta) \int_x^\xi \frac{p(\eta)}{a(\eta)} d\eta \right] d\xi \tag{11}$$

and a $y_1(x)$ can be constructed from the $B_1(x)$ of Eq. (11). A $y_1(x)$ can also be written explicitly from the integral of Eq. (1) by using $y_0(x)$

$$y_1(x) = y(x_0) - \int_{x_0}^x \int_{\xi-\alpha}^{\xi+\beta} \frac{p(\eta)}{a(\xi)} y_0(\eta) d\eta d\xi \tag{12}$$

Recall that $y(x_0) = 1$ in this particular case. Whether the first iterant sought is B_1 from Eq. (11) or y_1 from Eq. (12), a

double integration is required after the zeroth iterants B_0 and y_0 are calculated. It would be very discouraging to do all this work and then find that our iteration was diverging. An effort to reduce repetitive integration follows.

Equation (12) is a purely integral form of Eq. (1) when the subscripts on y are removed and $y(x_0)$ is arbitrary. By reversing the order of integration it is possible to reformulate this equation as a single integration over the unknown $y(\eta)$ with a new kernel

$$\begin{aligned} y(x) - y(x_0) &= - \int_{x_0}^x \int_{\xi-\alpha}^{\xi+\beta} \frac{p(\eta)}{a(\xi)} y(\eta) d\eta d\xi \\ &= - \int_{x_0-\alpha}^{x+\beta} p(\eta) M(\eta, x) y(\eta) d\eta \end{aligned} \tag{13}$$

The new kernel factor $M(\eta, x)$ is given below for this example. The method of reversing the order of integration and generating kernels of this type will be described in Section 3:

$$\begin{aligned} M(\eta, x) &= \left\{ \int_{x_0}^{\eta+\alpha} \frac{d\xi}{a(\xi)}; [x_0 - \alpha] \leq \eta \right. \\ &\quad \left. < [\min(x_0 + \beta, \min(x_0 + \alpha + \beta, x) - \alpha)] \right\} \\ &\quad + \left\{ \int_{x_0}^x \frac{d\xi}{a(\xi)}; \min[x_0 + \beta, \min(x_0 + \alpha + \beta, x) - \alpha] \right. \\ &\quad \left. \leq \eta < [x_0 + \beta] \right\} \\ &\quad + \left\{ \int_{\eta-\beta}^{\min(\eta+\alpha, x)} \frac{d\xi}{a(\xi)}; [x_0 + \beta] \leq \eta \leq [x + \beta] \right\} \end{aligned} \tag{14}$$

The function $\min(a, b, \dots)$, used in $M(\eta, x)$, selects the minimum of its arguments. $M(\eta, x)$ is the sum of three terms, each defined over a different range of η , and these ranges are functions of x . The new kernel $K(\eta, x) = p(\eta)M(\eta, x)$ can be calculated once from known functions $a(x)$ and $p(x)$, and by the explicit operations of Eq. (14). The derivation of Eqs. (13) and (14) proceeds directly from Eq. (1), without requiring any specialized assumptions, as were used in the development of B_0 . Now the original integrodifferential equation has been transformed into a purely integral form, a Volterra equation (variable upper limit) of the second kind [inhomogeneous if $y(x_0) \neq 0$]. The method of successive approximations applied to Eq. (13) proceeds more quickly because each iterant of $y(x)$ is now the result of a single integration.

Two specific numerical examples follow. In both cases $a(x) = a_0x$, and $p(x) = p_0x$, where a_0 and p_0 are constants. Solutions are sought in the range $[(x_0 = 1) \leq x \leq (x_1 = 3)]$, although calculations must consider the wider range $(1 - \alpha, 3 + \beta)$. In these cases $y(1) = 1$. $B_0(x)$ is found as the root of Eq. (10), and a $y_0(x)$ is calculated from Eq. (5). The kernel $K(\eta, x) = p(\eta)M(\eta, x)$ is calculated on the basis of Eq. (14). Two iterants, y_1 and y_2 , are then found by the method of successive approximations from Eq. (13). Figure 1 shows y_0, y_1 , and y_2 for $a_0 = 1, p_0 = 8, \alpha = 0$, and $\beta = 1.45$. Iterants y_0 and y_1 are quite smooth; with y_2 the

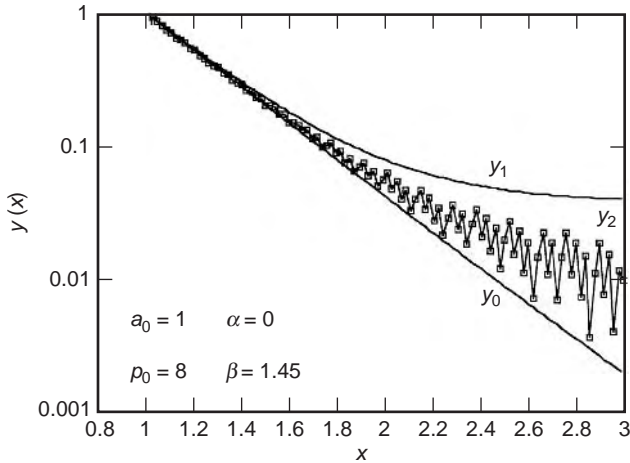


Figure 1. Three iterants for the $y(x)$ of Eq. (1) when $a(x)=x$, $p(x)=8x$, $\alpha=0$, and $\beta=1.45$. The zeroth iterant $y_0(x)$ is found by an approximation to its logarithmic derivative $B_0 = -\{d\ln[y_0(x)]/dx\}$ that is given by Eq. (10). The iteration is applied to Eq. (13), which is a single integral form of Eq. (1) with a new kernel $p(\eta)M(\eta,x)$ that is described by Eq. (14). Convergence is rapid. This function decays by two orders of magnitude for $1 \leq x \leq 3$. The relative error is comparable to $y(x)$ at low amplitude. This error diminishes as more points are used (point locations shown for y_2).

point-to-point numerical noise becomes noticeable (point locations are shown for y_2). This noise diminishes as more closely spaced points are used. In this case $y(x)$ has a rapid exponential decay. A second case has $a_0=1$, $p_0=0.08$, $\alpha=0.55$, and $\beta=1.45$. Figure 2 shows the three iterants of y , which decay gently with x . In both cases y_0 and y_1 bracket y_2 . Figures 3 and 4 show the kernel $K(\eta, x)$ for the first case (both appear similar). Two views are given to help visualize this surface over the full range of the calculation.

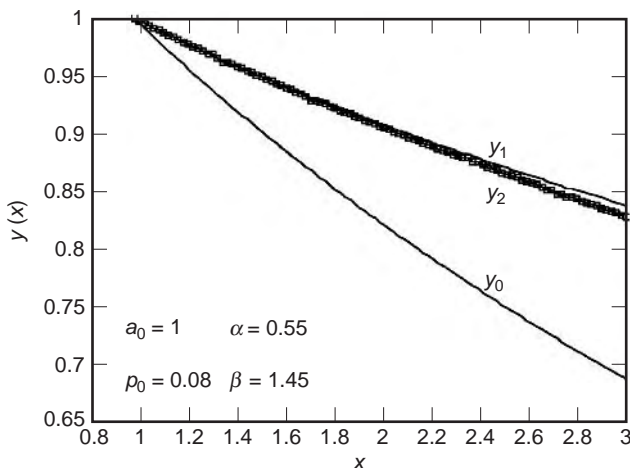


Figure 2. Three iterants for the $y(x)$ of Eq. (1) when $a(x)=x$, $p(x)=0.08x$, $\alpha=0.55$, and $\beta=1.45$. Another case similar to that of Fig. 1. Here the function decays very gently, and the relative error is small.

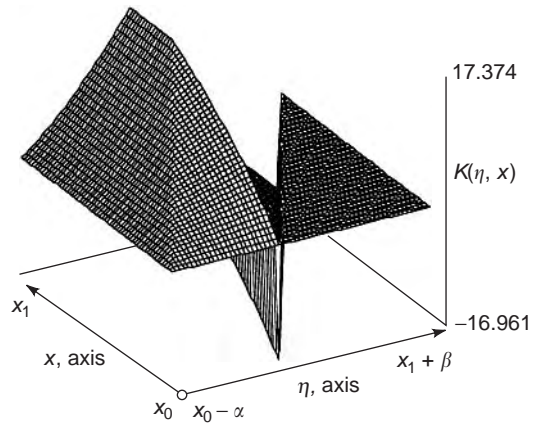


Figure 3. A surface plot of $K(\eta,x)=p(\eta)M(\eta,x)$, the kernel used in the example of Fig. 1. The kernel for the second example has the same shape but is of different magnitude. This view extends over the full area of the calculation in the (η,x) plane. The problem has been converted to an integral equation with single integration and a known kernel.

3. LINEAR EQUATIONS

Casting a linear, first-order integrodifferential equation into a simple integral form is very useful because then it can be solved by the method of successive approximations. This transformation involves switching the order of integration of a double integral, an operation mentioned without explanation in Section 2. This transformation will be illustrated for the following equation:

$$\frac{dy(x)}{dx} + b(x)y(x) + c(x) = \int_{x-\alpha}^{x+\beta} K_1(\xi,x)y(\xi)d\xi + \int_{x_0}^x K_2(\xi,x)y(\xi)d\xi \tag{15}$$

We assume that over the domain of interest, $x_0 \leq x \leq x_1$, none of b, c, K_1 , and K_2 become infinite. Also, α and β are positive constants. The labels $V_1(x)$ and $V_2(x)$ will be used to represent the integrals over K_1 and K_2 , respectively.

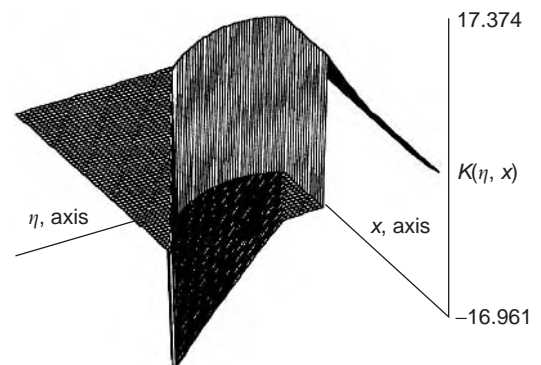


Figure 4. A surface plot of $K(\eta,x)=p(\eta)M(\eta,x)$ seen from a different orientation. This view shows features of the surface that are hidden in Fig. 3. This example shows that integral equations can have smooth solutions even with discontinuous kernels.

Now Eq. (15) is seen as a linear, first-order differential equation with an inhomogeneous term $V_1(x) + V_2(x) - c(x)$. This is formally integrated to

$$y(x) = e^{-\int_{x_0}^x b(\gamma)d\gamma} \left\{ y(x_0) + \int_{x_0}^x [V_1(\xi) + V_2(\xi) - c(\xi)] e^{\int_{x_0}^{\xi} b(\gamma)d\gamma} d\xi \right\} \tag{16}$$

$$y(x) = y(x_0) e^{-\int_{x_0}^x b(\gamma)d\gamma} - \int_{x_0}^x c(\xi) e^{-\int_{\xi}^x b(\gamma)d\gamma} d\xi + \int_{x_0}^x \int_{\xi-\alpha}^{\xi+\beta} e^{-\int_{\xi}^x b(\gamma)d\gamma} K_1(\eta, \xi) y(\eta) d\eta d\xi + \int_{x_0}^x \int_{x_0}^{\xi} e^{-\int_{\xi}^x b(\gamma)d\gamma} K_2(\eta, \xi) y(\eta) d\eta d\xi \tag{17}$$

The order of double integration will now be reversed. This is done to achieve single integral forms $\int M(\eta, x) y(\eta) d\eta$ with kernels $M(\eta, x)$ that are integrals of known functions. The K_1 and K_2 integrations of Eq. (17) occur over specific areas of the (η, ξ) plane determined by the limits. Figure 5 is a schematic of the area of integration for K_1 . Figure 6 is a similar schematic for K_2 . In Figs. 5 and 6 these integrations would be visualized as progressing horizontally through the respective areas (see arrows). To reverse the order of integration is to progress vertically through the integral areas (see vertical hatching). The original double integrals could each become sums of several “reversed”

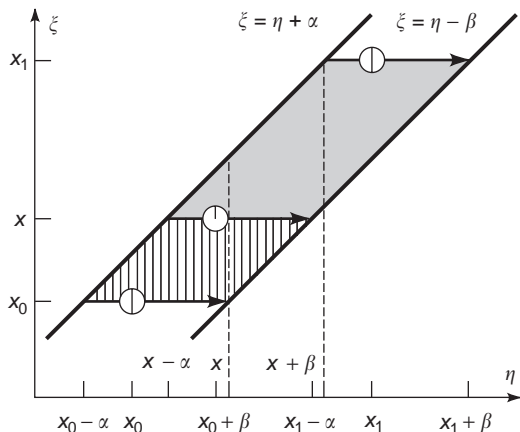


Figure 5. The area where double integration with the K_1 kernel is reversed. Horizontal arrows show the original direction of integration across the area. Reversed integration is shown by vertical hatching. As x moves up the ξ axis from x_0 to x_1 , the horizontal arrow from $\eta = x - \alpha$ to $\eta = x + \beta$ moves vertically through the integration area. Reversed integration is done below this rising arrow. Here vertical integration proceeds in sections as η moves from limits $x_0 - \alpha$ to $x_1 + \beta$ (the new outer integral). ξ is integrated successively from: x_0 to the $\eta + \alpha$ boundary line, x_0 to x , the $\eta - \beta$ boundary line to the $\eta + \alpha$ boundary line, and the $\eta - \beta$ boundary line to x (the new inner integral). The limits are conditional statements because the transitions between vertical sections depend on the slant and width of the area.

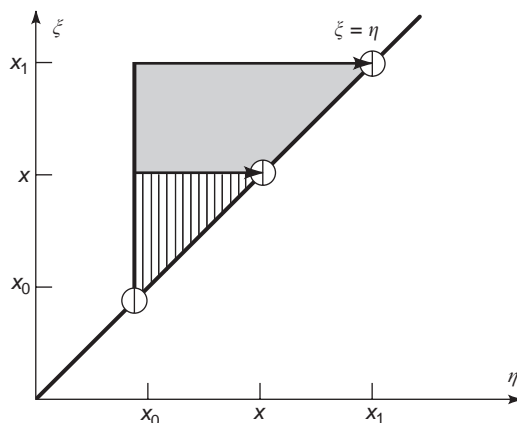


Figure 6. The area where double integration with the K_2 kernel is reversed. The original integration of $x_0 \leq \xi \leq x$ and $x_0 \leq \eta \leq \xi$ is reversed to $x_0 \leq \eta \leq x$ and $\eta \leq \xi \leq x$.

terms. Each of the new, reversed double integrals would account for a portion of the original (η, ξ) area. The limits of the reversed integrals could be conditional statements that depend on the shape of the area boundary. The result here is shown as Eqs. (18) through (22):

$$y(x) = y(x_0) e^{-\int_{x_0}^x b(\gamma)d\gamma} - \int_{x_0}^x c(\xi) e^{-\int_{\xi}^x b(\gamma)d\gamma} d\xi + I_1(x) + I_2(x) \tag{18}$$

$$I_1(x) = \int_{x_0-\alpha}^{\min[x^*-\alpha, x_0+\beta]} \int_{x_0}^{\eta+\alpha} \dots d\xi d\eta + \int_{\min[x^*-\alpha, x_0+\beta]}^{x_0+\beta} \int_{x_0}^x \dots d\xi d\eta + \int_{x_0+\beta}^{x+\beta} \int_{\eta-\beta}^{\min[\eta+\alpha, x]} \dots d\xi d\eta \tag{19}$$

where the integrands are

$$e^{-\int_{\xi}^{x^*} b(\gamma)d\gamma} K_1(\eta, \xi) y(\eta)$$

for the first term of I_1 , and

$$e^{-\int_{\xi}^x b(\gamma)d\gamma} K_1(\eta, \xi) y(\eta) \tag{20}$$

for the last two terms of I_1 . The function x^* is defined as

$$x^* = \min[x, (x_0 + \alpha + \beta)] \tag{21}$$

Finally, for I_2 , we obtain

$$I_2(x) = \int_{x_0}^x y(\eta) \left\{ \int_{\eta}^x e^{-\int_{\xi}^x b(\gamma)d\gamma} K_2(\eta, \xi) d\xi \right\} d\eta \tag{22}$$

The original equation is now in a purely integral form with single integrations. New kernels, $M_1(\eta, x)$ (three terms)

and $M_2(\eta, x)$, are defined as integrals of the products of an integrating factor and original kernels $K_1(\eta, \zeta)$ and $K_2(\eta, \zeta)$, respectively. The sample analysis describes solving a particular equation from this point.

Linear integrodifferential equations with second-order derivatives can be transformed into a Volterra form in a manner similar to first-order equations. Consider the following second-order equation with the same integrals V_1 and V_2 as in Eq. (16):

$$\frac{d^2y(x)}{dx^2} + b(x)\frac{dy(x)}{dx} + c(x)y(x) + d(x) = V_1(x) + V_2(x) \quad (23)$$

Define the function $p(x) = dy(x)/dx$. Now Eq. (23) becomes a linear, first-order equation for $p(x)$ with inhomogeneous term $V_1(x) + V_2(x) - d(x) - c(x)y(x)$. This is integrated once for $p(x)$ by using an integrating factor $\exp[\int b(x)dx]$, and specifying an initial condition $p(x_0)$. The result for $p(x)$ is integrated from x_0 to x , yielding $y(x) - y(x_0)$

$$\begin{aligned} y(x) = & y(x_0) + p(x_0) \int_{x_0}^x e^{-\int_{x_0}^{\eta} b(\gamma)d\gamma} d\zeta \\ & - \int_{x_0}^x \int_{x_0}^{\zeta} d(\eta) e^{-\int_{\eta}^{\zeta} b(\gamma)d\gamma} d\eta d\zeta \\ & + \int_{x_0}^x \int_{x_0}^{\zeta} [V_1(\eta) + V_2(\eta) - c(\eta)y(\eta)] e^{-\int_{\eta}^{\zeta} b(\gamma)d\gamma} d\eta d\zeta \end{aligned} \quad (24)$$

The first three terms after the equal sign in Eq. (24) are all known, the fourth term contains $y(x)$ within double and triple integrals. Let $f(x, x_0)$ represent the sum of the three known terms in Eq. (24) and $H(x, \eta)$ represent the integral factor

$$H(x, \eta) = \int_{\eta}^x e^{-\int_{\eta}^{\zeta} b(\gamma)d\gamma} d\zeta \quad (25)$$

Using these definitions, and Eq. (21) for x^* , the form of Eq. (24) with only single integrals is

$$\begin{aligned} y(x) = & f(x, x_0) + \int_{x_0-\alpha}^{\min[(x^*-\alpha), (x_0+\beta)]} \\ & y(\zeta) \left\{ \int_{x_0}^{\zeta+\alpha} H(x^*, \eta) K_1(\zeta, \eta) d\eta \right\} d\zeta \\ & + \int_{\min[(x^*-\alpha), (x_0+\beta)]}^{x_0+\beta} y(\zeta) \left\{ \int_{x_0}^x H(x, \eta) K_1(\zeta, \eta) d\eta \right\} d\zeta \\ & + \int_{x_0+\beta}^{x+\beta} y(\zeta) \left\{ \int_{\zeta-\beta}^{\min[(\zeta+\alpha), x]} H(x, \eta) K_1(\zeta, \eta) d\eta \right\} d\zeta \\ & + \int_{x_0}^x y(\zeta) \left\{ \int_{\zeta}^x H(x, \eta) K_2(\zeta, \eta) d\eta \right\} d\zeta \\ & - \int_{x_0}^x y(\zeta) c(\zeta) H(x, \zeta) d\zeta \end{aligned} \quad (26)$$

The five integrals shown for Eq. (26) can be combined into a single integration from $(x_0 - \alpha)$ to $(x + \beta)$ by multiplying each kernel with a difference of Heaviside unit step functions to define limits. This was done to calculate examples from Eq. (14) in the sample analysis.

The linear equations discussed in the preceding have all described initial value problems. If boundary values are placed on $y(x)$ or its first derivative at two points (x_0, x_1) , then the solution of a second-order equation is based on the characteristic functions, or eigenfunctions, of the differential part of the equation. A solution of the form $y(x) = C_0y_0(x) + C_1y_1(x) + C_2y_2(x) + \dots$ is assumed, where the y_i are eigenfunctions corresponding to the eigenvalues λ_i . The coefficients C_i are found in exactly the same way as in boundary value problems involving nonhomogeneous differential equations. The three steps to the solution are (1) substitute the eigenfunction expansion into Eq. (23), (2) multiply by a particular eigenfunction y_i to solve for its coefficient C_i , and (3) integrate over the interval (x_0, x_1) . In purely differential problems the result is a series of equations, one for each of the coefficients C_i . For integrodifferential equations the result is a series of equations linking each coefficient to a weighted sum of coefficients, $C_i = \sum w_n C_n$. The weights w_n result from integration and may be difficult to calculate. This matrix relationship among the coefficients reflects the nature of the original equation. The magnitude C_i of each mode $y_i(x)$ is linked to the magnitudes of the other modes in solution $y(x)$ by the integrals involving K_1 and K_2 .

4. VOLTERRA ANIMALS

Volterra introduced the following system of coupled, non-linear, first-order, integrodifferential equations to describe the dynamics of survival for a population of predators $y(t)$ and a population of prey $x(t)$:

$$\begin{aligned} \left[\frac{1}{x(t)} \right] \frac{dx(t)}{dt} = & a(t) - b(t)y(t) - \int_c^t K_y(t, s)y(s)ds \\ \left[\frac{1}{y(t)} \right] \frac{dy(t)}{dt} = & -\alpha(t) + \beta(t)x(t) + \int_c^t K_x(t, s)x(s)ds \end{aligned} \quad (27)$$

These equations show rates of population growth that are dependent on three factors: herd size or predator density, encounters between species, and hereditary influences. Prey $x(t)$ are adversely affected by encounters with predators, $-b(t)x(t)y(t)$, and by evolutionary improvements in these predators, $-x(t)\int K_y(t, s)y(s)ds$. Predators are adversely affected by too high a population of their own kind, $-\alpha(t)y(t)$. Reference 4 discusses this system in detail. The hereditary integral is described for heredity coefficients (K_x and K_y) of the form $K(t - s)$ under various names; it is the “renewal equation” in Ref. 2, “convolution” in Ref. 3, the “superposition integral” in Ref. 5, and an integral with a “displacement kernel” in Ref. 6. We will describe an approximate method of solution for Eq. (27) that makes few assumptions about the coefficients a, b, α , and β , or the kernels K_x and K_y .

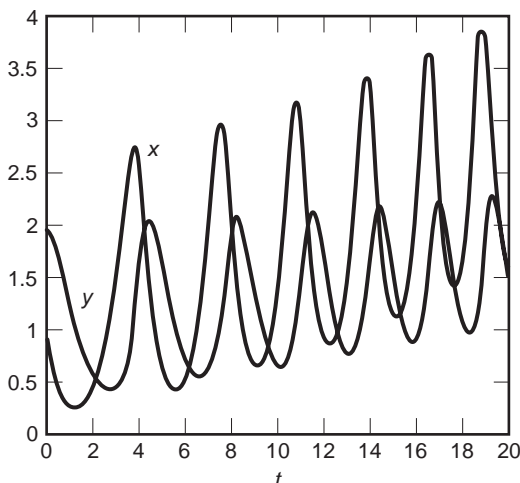


Figure 7. Population histories of predators $y(t)$ and prey $x(t)$ from the Volterra model of Eq. (27) with $a = b = 2$, $\alpha = \beta = 1$, $K_x = K_y = -0.05$, $c = 0$, $y(c) = 2$, and $x(c) = 1$. In this example heredity causes the populations to increase, diverge, and cycle more often.

Figure 7 is a particular example of Eqs. (27) for $0 \leq t \leq 20$, $c = 0$ (“the creation”), $a = b = 2$, $\alpha = \beta = 1$, $K_x = K_y = -0.05$, and initial conditions $x(0) = 1$ and $y(0) = 2$. Figure 8 is a phase diagram for this case where the initial conditions and the direction of time’s arrow are indicated. Without hereditary influences ($K_x = K_y = 0$), the nonlinear, purely differential system has a periodic trajectory that is a noncircular closed path on the xy phase plane (a “vortex cycle”). In general, neither $x(t)$ nor $y(t)$ can be expressed in terms of elementary functions. The effect of the hereditary integrals is to cause a “drift” in the solutions, seen as a rising trend for this example. Additional long-term effects for this case are a diminishing impact of predators (y) on prey (x) and a shortening of the time between cycles.

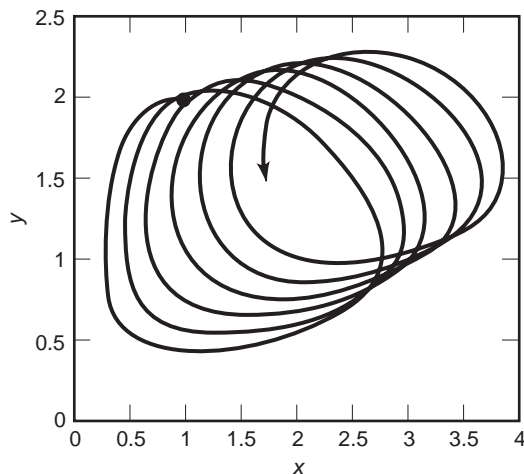


Figure 8. Phase diagram for the Volterra model example of Fig. 7. If heredity coefficients K_x and K_y are zero, then this curve is a closed noncircular path called a *vortex cycle*. The initial point and the direction of time’s arrow are shown. Heredity causes a drift in the cyclic action.

Converging or diverging populations that either grow or diminish can clearly be simulated by changing the magnitudes and the signs of the coefficients and kernels. More interesting effects arise when these factors are time dependent.

Equations (27) are integrated once

$$\begin{aligned} \ln \left[\frac{x(t)}{x_c} \right] &= \int_c^t a(s) ds \\ &\quad - \int_c^t b(s)y(s) ds - \int_c^t \int_c^s K_y(s,u)y(u) du ds \\ \ln \left[\frac{y(t)}{y_c} \right] &= - \int_c^t \alpha(s) ds + \int_c^t \beta(s)x(s) ds \\ &\quad + \int_c^t \int_c^s K_x(s,u)x(u) du ds \end{aligned} \tag{28}$$

The order of double integration is reversed, and then the following functions are defined:

$$\begin{aligned} A(t) &= \int_c^t a(s) ds \\ \Lambda(t) &= \int_c^t \alpha(s) ds \\ M_x(t,u) &= \int_u^t K_x(s,u) ds \\ M_y(t,u) &= \int_u^t K_y(s,u) ds \end{aligned} \tag{29}$$

Now the equations are

$$\begin{aligned} \ln \left[\frac{x(t)}{x_c} \right] &= A(t) - \int_c^t [b(u) + M_y(t,u)]y(u) du \\ \ln \left[\frac{y(t)}{y_c} \right] &= -\Lambda(t) + \int_c^t [\beta(u) + M_x(t,u)]x(u) du \end{aligned} \tag{30}$$

The equation for $y(t)$ is substituted into the equation for $x(t)$, yielding

$$\begin{aligned} \ln \left[\frac{x(t)}{x_c} \right] &= A(t) - y_c \int_c^t [b(u) + M_y(t,u)] \\ &\quad \times e^{-\Lambda(u) + \int_c^u [\beta(w) + M_x(u,w)]x(w) dw} du \end{aligned} \tag{31}$$

The nonlinear equation for $x(t)$ would appear to be an excellent form on which to apply the method of successive approximations. Figure 9 is a display of 23 successive approximations to Eq. (31) for the specific example described in Figs. 7 and 8; 41 points are used in this calculation, and the range is restricted to $0 \leq t \leq 10$. The zeroth iterant is $x_c = 1$ for the entire range, and calculated values of $x(t)$ larger than $6x_c$ are reset to x_c . The solution is seen to chip its way into the unknown like a pickax repeatedly driven

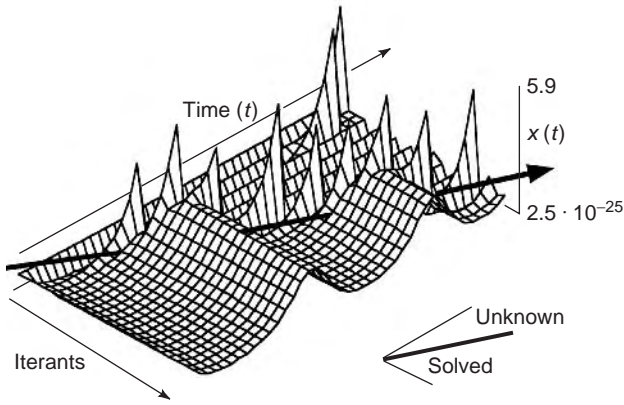


Figure 9. A sequence of successive approximations to Eq. (31) for the case shown in Figs. 7 and 8. Equation (31) is a nonlinear integral form of the Volterra predator and prey model. Each iterant builds up the solution sequentially, even though iteration occurs over the full time interval ($0 \leq t \leq 10$ in these calculations of 23 iterants). This is because the derivative of the solution at the present moment depends on the integral of its history. The iteration had an upper limit of 6 times the initial condition; any point calculated above this limit was reset to the initial condition. A better method of calculation is based only on prior events.

into concrete. This is because the derivative of the solution at its leading edge depends on the integral of its history, so each iterant only advances the solution a small amount in time. It would be more efficient to calculate a solution by advancing forward in time rather than iterating over the entire time domain. The calculation of $x(t)$ requires iteration because $x(t)$ appears on both sides of Eq. (31). If $x(t)$ could be shown to depend only on its history, and not also on its present value, then the solution would be a recursion formula and calculations would be speedier. A solution of this type is achieved by assuming that $x(t) \approx x(t - \Delta t)$ for Δt sufficiently small. The integral in Eq. (31) is split into two terms, the first with limits $c \leq u \leq t - \Delta t$, and the second with limits $t - \Delta t \leq u \leq t$. The second integral is now approximated by a two-point trapezoid rule [$2 \times \text{integral}/\Delta t = \text{integrand}(t) + \text{integrand}(t - \Delta t)$]. The trapezoid rule integrand at t has the form

$$L_y(t, t)e^{-\Lambda(t) + \int_c^t L_x(t, w)x(w)dw} \tag{32}$$

where $L_y(t, u) = b(u) + M_y(t, u)$ and $L_x(t, u) = \beta(u) + M_x(t, u)$. The two-point trapezoid approximation is used again for the integral in Eq. (32), which now has the form

$$\begin{aligned} & \{L_y(t, t)e^{-\Lambda(t) + \int_c^{t-\Delta t} L_x(t, w)x(w)dw}\} e^{\int_{t-\Delta t}^t L_x(t, w)x(w)dw} \\ & \approx \{ \dots \} e^{(\Delta t/2)[L_x(t, t)x(t) + L_x(t, t-\Delta t)x(t-\Delta t)]} \\ & \approx \{ \dots \} e^{(\Delta t/2)[L_x(t, t) + L_x(t, t-\Delta t)]x(t-\Delta t)} \end{aligned} \tag{33}$$

The resulting approximation in place of Eq. (31) is

$$\begin{aligned} \ln \left[\frac{x(t)}{x_c} \right] = & A(t) - y_c \int_c^{t-\Delta t} L_y(t, u)e^{-\Lambda(u) + \int_c^u L_x(u, w)x(w)dw} du \\ & - \frac{y_c \Delta t}{2} L_y(t, t - \Delta t)e^{-\Lambda(t-\Delta t) + \int_c^{t-\Delta t} L_x(t-\Delta t, w)x(w)dw} \\ & - \left\{ \frac{y_c \Delta t}{2} L_y(t, t)e^{-\Lambda(t) + \int_c^{t-\Delta t} L_x(t, w)x(w)dw} \right\} \\ & \times e^{(\Delta t/2)[L_x(t, t) + L_x(t, t-\Delta t)]x(t-\Delta t)} \end{aligned} \tag{34}$$

Note that for $\Delta t = 0$ we recover the original equation. Here the calculation is an explicit operation moving forward in time. This result makes it much easier to calculate the example shown in Figs. 7 and 8 than by iteration (161 points span the range $0 \leq t \leq 20$).

5. APPLICATIONS

Equation (1) in the sample analysis section is a form of the Boltzmann equation for the drift of a cloud of electrons along a constant electric field through a uniform molecular gas. Physical quantities are as follows: x is electron kinetic energy in units of eV, $y(x)$ is the distribution function of electron kinetic energy in units of $\text{eV}^{-3/2}$, $a(x) = a_0 x = (1/3)(E/N)^2(x/Q)$, E is the electric field in V/cm, N is the particle density of the gas in cm^{-3} , Q is the electron-molecule elastic collision cross section in cm^2 , $p(x) = p_0 x = Sx$, S is the electron-molecule inelastic collision cross section in cm^2 , $\alpha = 0$, $B_0(x)$ is an approximation for the logarithmic derivative of $y(x)$, β is large so $\beta B_0(x) > 1$, and $x B_0(x) > 1$ (this model of electron kinetics is for energies x above the range of thermal motion, $x \gg 0.03 \text{ eV}$). Both Q and S are assumed to be only mildly dependent on x . $B_0(x)$ is given by Eq. (10) and then $y_0(x)$ is

$$y_0(x) = \exp \left\{ - \int_0^x \frac{\sqrt{3Q(\xi)S(\xi)}}{E/N} d\xi \right\} \tag{35}$$

Typical parameters in experiments might be $Q = 10^{-15}$, $S = 3 \times 10^{-16}$, $E = 1000$, and $N = 10^{18}$. Good approximations for distribution functions of electron energy in nitrogen mixtures have been calculated from this result by using cross-section data. Literature on the Boltzmann equation is vast. The pervasive approximation is that the system is never far from thermal equilibrium $f_0(x)$ ("Maxwellian" distribution), so that the nonequilibrium solution $f(x)$ is a perturbation given by an expansion $f(x) = f_0(x)(1 + \phi_1(x) + \phi_2(x) + \dots)$, where succeeding terms are of smaller magnitude. The full development of this Chapman-Enskog method is quite involved (see Ref. 7). The electron energy distribution may be far from thermal equilibrium with the gas molecules in an electric discharge because of the high electric fields. A Chapman-Enskog expansion for electrons might require the calculation of many terms. The alternative is to expand the electron distribution function in a series of spherical harmonics

defined by an axis aligned with the electric field. This creates a sequence of linked equations. Once the zeroth-order equation is solved for the leading term of the expansion, then the first-order term can be solved, and so on. The zeroth term describes the average energy of an isotropic cloud of electrons, and the first term describes the drift of this cloud along the field, a current. The result given by Eq. (35) is an approximation to the isotropic part of the electron distribution. References 8–10 describe kinetic theory and the mathematics of the Boltzmann equation. References 11–13 describe the theory for electrons in a gas.

The mechanical constitutive equation of a material relates the stress tensor to the deformation tensor for a solid, and to the rate of strain tensor for a fluid. Many engineering materials are characterized by linear isotropic constitutive relations: the generalized Hooke’s law for solids; and the Newtonian fluid. Technology is rapidly increasing the application of nonlinear “engineered” solids and plastic “rheological” fluids. These materials can have stress dependent on the deformation and rate of strain in a nonlinear way, on higher velocity derivatives, on anisotropies of their internal structure, and on the history of their deformation and motion. In the most general case the constitutive relation is an integrodifferential equation that relates stress to the entire history of the material. One example follows:

$$m \frac{d^2u(t)}{dt^2} + au(t) + \int_0^t K(t-s) \frac{du(s)}{ds} ds = q(t) \quad (36)$$

This is a mass–spring–damper equation with heredity in the damping term. Here u is distance, t is time, m is mass, a is the spring constant, K is a renewal kernel, and q is a forcing term. References 14 and 15 describe this equation. Reference 2 shows how to solve linear, constant-coefficient renewal equations with Laplace transforms. The solution of Eq. (36) by the methods of this article is

$$\begin{aligned} mu(t) = & u(0) \left[m + \int_0^t \int_0^s K(x) dx ds \right] \\ & + mp(0)t + \int_0^t (t-s)q(s)ds \\ & - \int_0^t u(s) \left\{ a(t-s) + \int_0^{t-s} K(x) dx \right\} ds \end{aligned} \quad (37)$$

where $u(0)$ and $p(0)$ are the initial conditions of the displacement u and its first derivative $p = du/dt$. Note that the kernel is a function of one variable. For $K = q = 0$ the problem collapses to a harmonic oscillator, and it is easy to show that $\sin(\sqrt{a/m}t)$ is a solution of the reduced form of Eq. (37). Volterra had shown that kernels of the type $K(t-s)$ produce periodic solutions [4,16,17]. In general we can expect heredity to alter the frequency of oscillations, to introduce a damping, and to shift the mean position, all during the course of time.

An integrodifferential equation for heat transfer occurs when the constitutive relation between heat flux and temperature gradient in the material is a hereditary integral.

In a similar way, an integrodifferential equation describes the evolution of an electric field in the vicinity of a non-conducting material dielectric with a memory of its charging history (a “Maxwell–Hopkinson dielectric”). These and other applications are described in Ref. 18, a mathematician’s treatise on integrodifferential equations.

The technological application of mechanics with heredity and of nonequilibrium kinetics is likely to drive future efforts to improve the solution of integrodifferential problems. These problems arise in the development of non-equilibrium processes, such as plasma–chemical reactors for modifying material surfaces, and in the development of synthetic materials with engineered physical properties. Another thrust to solving these equations is the desire to improve our understanding of natural phenomena and materials. It is not hard to imagine that natural flows like lava or glaciers, and natural cycles like climate and weather, can have a hereditary factor. It would be interesting to have a method for easily estimating a distant cycle time average of a quantity influenced by heredity, be it metal fatigue or species extinction.

BIBLIOGRAPHY

1. B. Sherman, The difference-differential equation of electron energy distribution in a gas, *J. Math. Anal. Appl.* **1**:342–354 (1960).
2. R. Bellman and K. L. Cooke, *Differential-Difference Equations*, Academic Press, New York, 1963.
3. F. B. Hildebrand, *Methods of Applied Mathematics*, 2nd ed., Prentice-Hall, Englewood Cliffs, NJ, 1965.
4. H. T. Davis, *Introduction to Nonlinear Differential and Integral Equations*, United States Atomic Energy Commission, USGPO, Washington, DC, 1960; Dover, New York, 1962.
5. F. B. Hildebrand, *Advanced Calculus for Applications*, Prentice-Hall, Englewood Cliffs, NJ, 1962.
6. J. Matthews and R. L. Walker, *Mathematical Methods of Physics*, 2nd ed., W. A. Benjamin, Menlo Park, CA, 1970.
7. S. Chapman and T. G. Cowling, *The Mathematical Theory of Non-Uniform Gases*, 3rd ed., Cambridge Univ. Press, London, 1970.
8. T. I. Gombosi, *Gaskinetic Theory*, Cambridge Univ. Press, New York, 1994.
9. C. Cercignani, *Mathematical Methods in Kinetic Theory*, 2nd ed., Plenum Press, New York, 1990.
10. C. Cercignani, *Theory and Application of the Boltzmann Equation*, Elsevier, New York, 1975.
11. T. Holstein, Energy distribution of electrons in high frequency gas discharges, *Phys. Rev.* **70**(5/6) (1946).
12. W. L. Nighan, Electron energy distributions and collision rates in electrically excited N₂, CO, CO₂, *Phys. Rev. A* **2**(5):1989–2000 (1970).
13. B. E. Cherrington, *Gaseous Electronics and Gas Lasers*, Pergamon Press, New York, 1979.
14. E. Volterra, On elastic continua with hereditary characteristics. *J. Appl. Mech.* **18**:273–279 (1951).
15. V. Volterra, Sur la théorie mathématique des phénomènes héréditaires, *J. Math. Pures Appl.* **7**:249–298 (1928).

16. V. Volterra, *Leçons sur les équations intégrales et les équations integro-différentielles*, Gauthier-Villars, Paris, 1913.
17. V. Volterra, *Leçons sur la théorie mathématique de la lutte pour la vie*, Gauthier-Villars, Paris, 1931.
18. F. Bloom, *Ill-Posed Problems for Integrodifferential Equations in Mechanics and Electromagnetic Theory*, SIAM, Philadelphia, 1981.

INTERMEDIATE-FREQUENCY AMPLIFIERS

H. R. WALKER
Pegasus Data Systems, Inc.
Edison, New Jersey

The intermediate-frequency (IF) amplifier is the circuitry used to process the information bearing signal between the first converter, or mixer, and the decision making circuit, or detector. It can consist of a very few or a great many component parts. Generally, it consists of an amplifying stage or device to provide gain, plus a bandpass filter, or filters, to limit the frequency band to be passed. The signal to be processed can be audio, video, digital, or pulsed, using amplitude modulation, frequency modulation, phase modulation, or combinations thereof. Several examples are shown in Figs. 13–19.

Bandpass IF amplifiers are also used in radio transmitters to limit the occupied bandwidth of the transmitted signal. Certain modulation methods create a very broad frequency spectrum, which can interfere with adjacent channels. Regulatory agencies, such as the FCC (Federal Communications Commission), require that these out-of-band signals be reduced below a certain permissible level, so they must undergo processing through a bandwidth-limiting filter and amplifier at the transmitter.

For each application there are certain design restrictions or rules that must be followed to achieve optimum results.

1. GENERAL IF AMPLIFIER FUNCTIONS AND RESTRICTIONS

The five basic IF amplifier functions and requirements are as follows:

1. *Image Rejection.* The mixer stages in a superhetrodyne receiver can convert any frequency below or above the local oscillator frequency to an intermediate frequency. Only one of these frequencies is desired. The intermediate frequency must be chosen so that undesirable frequencies or images are removed by the RF amplifier filter (prefiltering) and are rejected by the mixer. This may mean that two or three different intermediate frequencies must be used within the same receiver. The intermediate frequencies in common use range from 0 Hz to approximately 2.0 GHz.

2. *Selectivity.* Selectivity is required to reject as much as possible of any adjacent channel interfering signal. Generally this means attempting to obtain a bandpass

filter characteristic as close to that of the ideal filter as possible that will pass the necessary *Nyquist bandwidth* (the baseband bandwidth from 0 Hz to the highest frequency to be passed) without introducing harmful amplitude or phase distortion.

3. *Gain.* Gain is required to amplify a weak signal to a useful level for the decisionmaking circuit. This gain must be provided by means of a stable amplifier that introduces a minimum of noise, so as not to degrade the receiver *noise figure*. All circuit input and output impedances should be properly matched for optimum power transfer and circuit stability.

4. *Automatic Gain Control.* The amplifier gain must vary automatically with signal strength so that the decisionmaking circuit receives a signal of as nearly constant level as possible. The stages of the IF amplifier must not be overdriven, or go into limiting, until after the last bandpass filter, to prevent “splattering,” or broadening and distortion of the signal.

5. *Linearity.* The amplifier should be linear in phase or amplitude to prevent distortion of the recovered information. AM receivers should be linear in amplitude, while FM or PM receivers should be linear in phase. Some modulation methods can tolerate more linearity distortion than others.

2. SELECTING THE INTERMEDIATE FREQUENCY

Image rejection and signal selectivity are the primary reasons for selecting an intermediate frequency. Most currently manufactured bandpass filters of the crystal, or resonator type, have become standardized so that the designer can obtain off-the-shelf components at reasonable cost for these standard frequencies. The standard AM broadcast receiver utilizes a 455-MHz IF filter because extensive experience has shown that this will reject all but the strongest images. Assume the desired signal is at 600 kHz. A local oscillator operating at 1055 kHz will have an image frequency at 1510 kHz, which the RF input filter can easily reject. Similarly, an FM receiver operating at 90.1 MHz with an intermediate frequency of 10.7 MHz will have an image at 111.5 MHz, which will be rejected by the RF amplifier. In both of these cases, a single intermediate frequency can be used.

A receiver operating at 450 MHz will require two Intermediate frequencies obtained by using first and second mixers, as in Fig. 16. The first IF amplifier may consist of a relatively broadband filter operating at 10.7 or 21.4 MHz, followed by a second converter and IF stage operating at 455 kHz. The first IF filter is narrow enough to reject any 455-kHz images, and the second IF filter is a narrowband filter that passes only the desired signal bandwidth. If the 455-kHz filter had been used as the first IF filter, the 450-MHz RF filter, which is relatively broad, would not have eliminated the image frequency, which is 455 kHz above or below the local oscillator (LO) frequency.

Television receivers use a video intermediate frequency of approximately 45 MHz, since this permits a relatively broad RF filter to pass the broadband TV signal, while still

16. V. Volterra, *Leçons sur les équations intégrales et les équations integro-différentielles*, Gauthier-Villars, Paris, 1913.
17. V. Volterra, *Leçons sur la théorie mathématique de la lutte pour la vie*, Gauthier-Villars, Paris, 1931.
18. F. Bloom, *Ill-Posed Problems for Integrodifferential Equations in Mechanics and Electromagnetic Theory*, SIAM, Philadelphia, 1981.

INTERMEDIATE-FREQUENCY AMPLIFIERS

H. R. WALKER
Pegasus Data Systems, Inc.
Edison, New Jersey

The intermediate-frequency (IF) amplifier is the circuitry used to process the information bearing signal between the first converter, or mixer, and the decision making circuit, or detector. It can consist of a very few or a great many component parts. Generally, it consists of an amplifying stage or device to provide gain, plus a bandpass filter, or filters, to limit the frequency band to be passed. The signal to be processed can be audio, video, digital, or pulsed, using amplitude modulation, frequency modulation, phase modulation, or combinations thereof. Several examples are shown in Figs. 13–19.

Bandpass IF amplifiers are also used in radio transmitters to limit the occupied bandwidth of the transmitted signal. Certain modulation methods create a very broad frequency spectrum, which can interfere with adjacent channels. Regulatory agencies, such as the FCC (Federal Communications Commission), require that these out-of-band signals be reduced below a certain permissible level, so they must undergo processing through a bandwidth-limiting filter and amplifier at the transmitter.

For each application there are certain design restrictions or rules that must be followed to achieve optimum results.

1. GENERAL IF AMPLIFIER FUNCTIONS AND RESTRICTIONS

The five basic IF amplifier functions and requirements are as follows:

1. *Image Rejection.* The mixer stages in a superhetrodyne receiver can convert any frequency below or above the local oscillator frequency to an intermediate frequency. Only one of these frequencies is desired. The intermediate frequency must be chosen so that undesirable frequencies or images are removed by the RF amplifier filter (prefiltering) and are rejected by the mixer. This may mean that two or three different intermediate frequencies must be used within the same receiver. The intermediate frequencies in common use range from 0 Hz to approximately 2.0 GHz.

2. *Selectivity.* Selectivity is required to reject as much as possible of any adjacent channel interfering signal. Generally this means attempting to obtain a bandpass

filter characteristic as close to that of the ideal filter as possible that will pass the necessary *Nyquist bandwidth* (the baseband bandwidth from 0 Hz to the highest frequency to be passed) without introducing harmful amplitude or phase distortion.

3. *Gain.* Gain is required to amplify a weak signal to a useful level for the decisionmaking circuit. This gain must be provided by means of a stable amplifier that introduces a minimum of noise, so as not to degrade the receiver *noise figure*. All circuit input and output impedances should be properly matched for optimum power transfer and circuit stability.

4. *Automatic Gain Control.* The amplifier gain must vary automatically with signal strength so that the decisionmaking circuit receives a signal of as nearly constant level as possible. The stages of the IF amplifier must not be overdriven, or go into limiting, until after the last bandpass filter, to prevent “splattering,” or broadening and distortion of the signal.

5. *Linearity.* The amplifier should be linear in phase or amplitude to prevent distortion of the recovered information. AM receivers should be linear in amplitude, while FM or PM receivers should be linear in phase. Some modulation methods can tolerate more linearity distortion than others.

2. SELECTING THE INTERMEDIATE FREQUENCY

Image rejection and signal selectivity are the primary reasons for selecting an intermediate frequency. Most currently manufactured bandpass filters of the crystal, or resonator type, have become standardized so that the designer can obtain off-the-shelf components at reasonable cost for these standard frequencies. The standard AM broadcast receiver utilizes a 455-MHz IF filter because extensive experience has shown that this will reject all but the strongest images. Assume the desired signal is at 600 kHz. A local oscillator operating at 1055 kHz will have an image frequency at 1510 kHz, which the RF input filter can easily reject. Similarly, an FM receiver operating at 90.1 MHz with an intermediate frequency of 10.7 MHz will have an image at 111.5 MHz, which will be rejected by the RF amplifier. In both of these cases, a single intermediate frequency can be used.

A receiver operating at 450 MHz will require two Intermediate frequencies obtained by using first and second mixers, as in Fig. 16. The first IF amplifier may consist of a relatively broadband filter operating at 10.7 or 21.4 MHz, followed by a second converter and IF stage operating at 455 kHz. The first IF filter is narrow enough to reject any 455-kHz images, and the second IF filter is a narrowband filter that passes only the desired signal bandwidth. If the 455-kHz filter had been used as the first IF filter, the 450-MHz RF filter, which is relatively broad, would not have eliminated the image frequency, which is 455 kHz above or below the local oscillator (LO) frequency.

Television receivers use a video intermediate frequency of approximately 45 MHz, since this permits a relatively broad RF filter to pass the broadband TV signal, while still

rejecting the images. The video signal from the IF amplifier is AM, with an FM sound carrier riding on it. Television sound is generally obtained from a beat, or difference frequency between the video and sound carriers, which is at 4.5 MHz.

Satellite receivers use a broadband first intermediate frequency covering a frequency block from 900 MHz to 2.1 GHz. This is done by means of a *low-noise block* (LNB) converter. The second mixer is made tunable so that any frequency in the block can be converted to the second intermediate frequency, which is usually fixed at 70 or 140 MHz. The second intermediate frequency, which drives the detector, has a narrower bandwidth to reduce noise and reject adjacent channel interference.

Crystal, ceramic resonator, and SAW filters are massed produced at relatively low cost for the frequencies mentioned above, so that most consumer products employ one or more of the abovementioned standard frequencies and standard mass-produced filters.

3. SELECTIVITY

Carson’s rule, and the Nyquist sampling theorem on which it is based, state that a certain bandwidth is required to transmit a signal undistorted. The necessary bandwidth for an AM signal is given as follows:

$$BW = 2f_m \tag{1}$$

Thus an AM broadcast receiver will require 10 kHz of bandwidth to pass a 5 kHz = f_m audio tone. (f_m = Frequency of modulation.) In data transmission systems, the frequency f_m corresponding to the data rate f_b , is $f_m = \frac{1}{2} f_b$. The data clock frequency is twice the frequency of the data in ones and zeros. This means that a baud rate f_b of 9,600 bits per second (bps) will require a bandwidth of 9.6 kHz.

For FM, the necessary bandwidth required for transmission is

$$BW = 2(f_m + \Delta f) \tag{2}$$

A 15-kHz audio tone (= f_m) and an FM transmitter being deviated with a modulation index of 5 will require 2 (15 + (15 × 5)) = 180 kHz of bandwidth. Δf is (5 × 15) and f_m is 15 kHz. Narrowband FM, or phase modulation (PM) (with a modulation index of < 0.7), is somewhat different in that the bandwidth actually required is the same as that for AM. This is due to the fact the higher J_n Bessel products are missing [Eq. (1) applies].

These values are for *double-sideband transmission*. Single-sideband transmission will require half as much bandwidth. The required baseband bandwidth is the same as the value for f_m . This is also known as the *Nyquist bandwidth*, or the minimum bandwidth that can carry the signal undistorted at baseband.

Ideally, the IF filter, or the equivalent baseband filter, need pass only this bandwidth and no more. This requires the use of an “ideal” bandpass or lowpass filter, which does not exist in practice, but can be approached by various means. The filter must be as narrow as conditions permit

to reduce the noise bandwidth and any adjacent channel interference, since noise power rises linearly with increasing filter bandwidth [14]:

$$\frac{S_o}{N_o} = \beta^2 \frac{\text{bit rate}}{\text{filter BW}} \frac{S_i}{N_i} \tag{3a}$$

$$\frac{S_o}{N_o} = \text{modulation} \times \frac{\text{gain}}{\text{loss}} \times \text{processing gain} \frac{S_i}{N_i} \tag{3b}$$

These two equations show a generalized relationship between the signal-to-noise ratio (SNR) at the receiver input and the SNR at the receiver output. The term β^2 represents a gain, or loss, in power due to the modulation method. In FM or PM it is the modulation angle. The term [(bit rate)/(filter bandwidth)] is generally known as *processing gain*. Narrowing the bandwidth improves the S_o/N_o ratio, but this improvement is not always available, depending on the modulation method. The Nyquist bandwidth rules state that it should be (symbol rate)/BW = 1.

Pulse modulation, as in radar (radio detection and ranging), generally requires a much broader filter bandwidth than the other modulation methods. A condition called *envelope delay* or *group delay* must also be observed. This is discussed later along with the transfer functions of the filters. For optimum results, the filter bandwidth (Δf) must be equal to [1/(pulsewidth)]. If the filter bandwidth is too narrow, the amplitude detected is reduced and the SNR is adversely affected. In this case, the processing gain is ideally = 1 [14].

$$\begin{aligned} \frac{S_o}{N_o} &= (\text{processing gain}) \frac{S_i}{N_i} \\ &= \frac{E_b}{N_o} \end{aligned} \tag{4}$$

4. GAIN

The IF amplifier must provide sufficient gain to raise a weak signal at the RF input to the level required, or desired, by the decisionmaking circuit or detector. This receiver gain can vary from 0 up to 130 dB, most of which is usually provided by the IF amplifier. The RF amplifier and mixer circuits preceding the IF amplifier usually provide ≥ 20 dB of gain so that the IF amplifier generally contributes little to the receiver noise figure. (See NOISE FIGURE article elsewhere in this encyclopedia.) Amplifiers with very high gain have a tendency to oscillate; hence two different intermediate frequencies may be used to reduce the gain on any one frequency, or more of the gain may be obtained from the RF section.

Gain is provided by an amplifying device, such as a transistor, or vacuum tube (in older equipment). These devices have input and output impedances of a complex nature that must be matched to the filtering circuits for best power transfer, stability, and lowest noise. Current practice is often to use a “gain stage,” which consists of multiple amplifying devices in an integrated circuit

package. These packages often contain the mixer stages and detectors as well.

5. AUTOMATIC GAIN CONTROL

Receivers must respond to a wide range of input levels while maintaining a nearly constant level at the detector or decisionmaking circuit. The user or operator does not wish to manually adjust the gain to obtain a constant sound or picture level when changing stations. This function is performed by detecting the output level of the IF amplifier and correcting it by means of a feedback circuit that adjusts the gain to keep the level as constant as possible. Since this detected level can vary rapidly, it is passed through a lowpass filter [usually an RC (resistance × capacitance) pair] to integrate or slow down the changes, then amplified by a DC (direct-current) amplifier and applied to an IF amplifier circuit or gain stage that has variable gain characteristics. Some receivers, such as those used in an automobile, require relatively rapid acting AGC circuits, while fixed receivers can use a much slower AGC time constant. Dual-gate field-effect transistors use the second gate to control the gain. Bipolar or single-gate field-effect transistors vary the gain by means of a bias voltage or current applied to the input terminal along with the signal. Special integrated circuit gain stages for IF amplification are available, such as the Motorola MC1350, which both amplify and provide a variable gain control function.

6. FILTERS FOR IF AMPLIFIERS

Except for block conversions, which convert wide frequency bandwidths, such as those used on satellite receivers, IF amplifiers in general use a narrow bandpass, or a low-pass filter, to limit the bandwidth to the Nyquist bandwidth. Block conversion, on the other hand, can use a highpass-lowpass filter pair, where the bandwidth to be passed lies between the high and low cutoff frequencies.

The traditional bandpass filter requires one or more resonant elements. Although the actual resonator may be a coil and capacitor, ceramic resonator, or SAW filter, the principles are basically the same. Digital filters, which do not use resonators, have been employed more recently. These will be discussed later in brief. They are discussed in more detail elsewhere in this encyclopedia.

The inductance/capacitance resonator was the first used, and is still a comparison standard. Figures 1a and 1b show series resonant circuits, and Fig. 1c shows a parallel resonant circuit. These circuits will pass a signal at the resonant peak and reject a signal off resonance. Resistances R_s and R_p are naturally occurring losses that reduce the circuit efficiency. Figure 2 shows the universal resonance curve, which is applicable to both series and parallel resonant circuits. It is important to note that the signal rejection never goes to a zero level in the area of interest, but reaches an asymptotic value between 0.1 and 0.2 or about -17 dB. If it is necessary to reject a signal on the shoulders of this curve by 60 dB, then four cascaded stages of this filter must be used to obtain the necessary

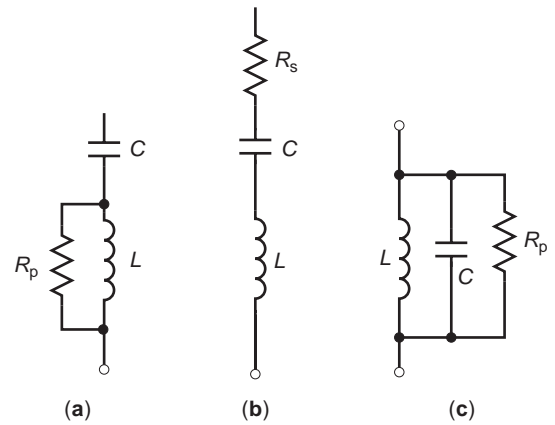


Figure 1. Series (a,b) and parallel (c) resonant circuits.

rejection. Note also that there is a nonlinear phase shift that reaches a maximum in the area of interest, then changes to $\pm 70^\circ$. When stages are cascaded, this phase shift is multiplied by the number of stages. A nonlinear phase shift can cause distortion in FM receivers. The phase shift curve plotted is for a parallel resonant circuit. The phase reverses for a series circuit. The phase at any point on the curve is obtained by plotting horizontally from the vertical amplitude/phase scale: $\alpha = Q$ (cycles off resonance/resonant frequency).

A frequency f_0 at which the response of a parallel resonant LC filter is a maximum, that is, the point at which the parallel impedance is a maximum, is defined as a pole. A frequency at which the impedance is a minimum, as in the series LC circuit, is defined as a zero. Thus the assumed four cascaded stages above would constitute a four-pole filter, since it contains four resonant poles. The frequency of resonance is given by Eq. (5); this is the frequency at which $[X_c = 1/-j\omega C]$ and $[X_L = j\omega L]$ are equal:

$$f_0 = \frac{1}{2\pi(LC)^{1/2}} \tag{5}$$

The bandwidth that an analog LC filter can pass is altered by the circuit efficiency, or circuit Q, given in Eqs. (6).

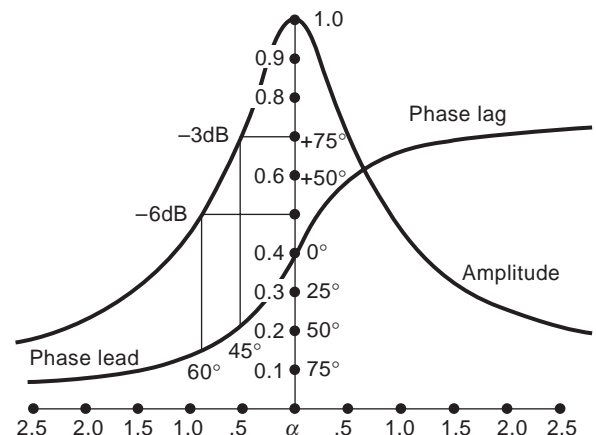


Figure 2. Universal resonance curve (BT = bandwidth × bit period).

Generally the bandwidth is specified as the bandwidth between the -3 dB points, where the phase shift is $\pm 45^\circ$.

$$Q = \frac{X_c}{R_s} \text{ for a series circuit} \tag{6a}$$

$$Q = \frac{R_p}{X_c} \text{ for a parallel circuit} \tag{6b}$$

$$Q = \frac{f_0}{3 \text{ dB BW}} \tag{6c}$$

For simplicity in analyzing the following circuits, the Q determining R will be assumed to be a parallel resistance R_p across the inductance.

Figure 3 shows a typical IF amplifier stage as used in earlier transistor radios [1,2]. In this circuit R_p (the total shunting resistive load) is actually three resistances in parallel; one is the equivalent R_p of the coil itself (representing the coil losses), another is the input resistance of the following stage, as reflected, and the third is the output resistance of the driving transistor as reflected. It cannot be assumed that the resulting coil Q , and hence the selectivity of the circuit, is that of the unloaded coil and capacitor alone. Dual-gate field effect transistors have the highest shunting resistance values, bipolar transistors the lowest. The gain can be varied by increasing or decreasing the bias voltage V_b applied to the input terminal.

Manufacturers of amplifying devices often provide the impedances, or admittances of their products on their data sheets. Formerly this was done in the form of h parameters. The more common practice today is to provide the information in the form of S parameters. These values can be converted to impedances and admittances, but the manual process is rather complicated. An easier method is to use the various software programs (see Available

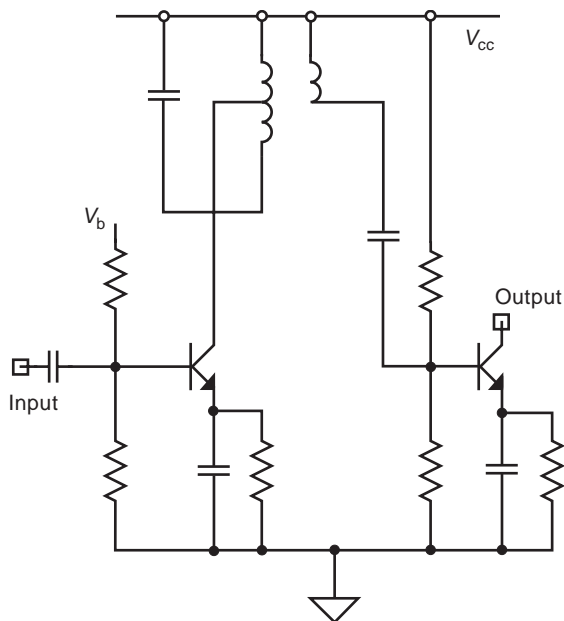
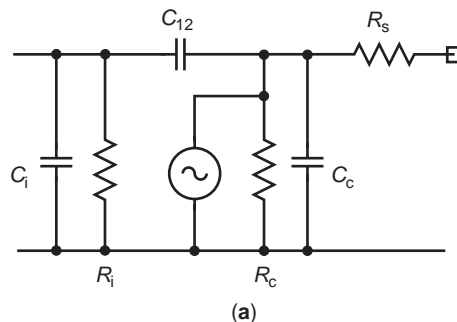
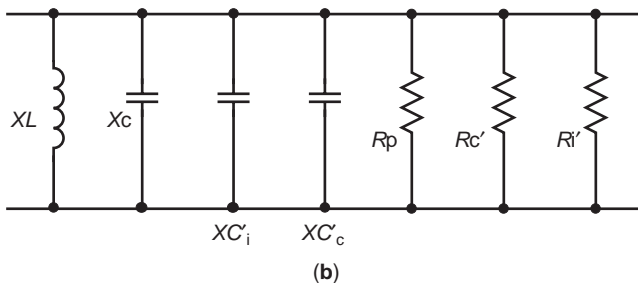


Figure 3. Typical IF amplifier stage.



(a)



(b)

Figure 4. Equivalent circuit of transistor as seen by tuned LC.

Software section at end of this article) to make the conversion. Matrix algebra, h and S parameters are discussed elsewhere in this encyclopedia and also in the Refs. 3 and 4 in this article. Unfortunately, S parameters for bandpass filters are rarely available.

Figure 4a shows the equivalent circuit of the transistor as the tuned LC “sees” it. The transistor amplifies a current, which is passed through a relatively low driving resistance R_s , to the outside. At the same time, the attached LC sees an equivalent shunting resistance R_c and capacitance C_c , which must be added in parallel to R_p , L , and C . The input to the following stage, assumed to be an identical transistor, will have a relatively low shunting resistance R_i , and capacitance C_i , which must be added. Unless the added capacitances are large compared to the resonant C , they merely add to it without greatly detuning the circuit. When tuned, the total C plus L will determine the frequency and the resulting total R_p will determine the Q of the LC circuit, and hence the bandwidth. Thus the complex components can be tuned out and the remaining design problem consists of matching the real or resistive part of the input and output impedances to the best advantage.

The desired end result is to couple the output of the driving stage to the input of the following stage with the least loss by matching the differing impedances. An additional desired result is to narrow the band of frequencies passed by means of a filter. These objectives are accomplished by transforming the input and output impedances to a higher or lower shunting impedance that maintains the desired bandpass characteristic of the filter. A low driving or load impedance can be stepped up to become a very high impedance, which maintains the circuit Q at the desired value.

Impedance matching enables the designer to change the actual impedance to a different apparent value, which

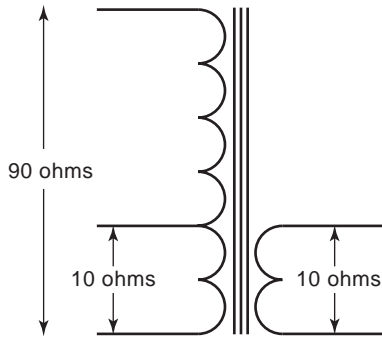


Figure 5. Impedance matching by transformer action.

is optimum for the circuit. Figure 5 shows how impedances are matched by transformer action. A transformer with a 3:1 turns ratio is shown as an example. The output impedance relative to the input impedance is given by Eq. (7), where N_i and N_o are the input and output numbers of turns on the winding.

$$\frac{Z_i}{Z_o} = \sqrt{\frac{N_i}{N_o}} \tag{7}$$

Thus 90 Ω at the input is seen as 10 Ω at the output with a 3:1 stepdown turns ratio. The automatic transformer (tapped coil in Fig. 5) has the same relationship.

When all the reactances and resistances from the tuned circuit and the transistor input and output as modified by the stepup/stepdown process of the impedance-matching networks are added, the network in Fig. 4b results. Calculation of the resonant frequency and circuit Q from these reactances and resistances in parallel is complicated unless they are converted to admittances. Software is available at reasonable cost to perform these calculations (see Available Software section at end of this article).

Stock, or mass-produced IF transformers, which are used to provide bandpass filtering as well as impedance matching, seldom have the desired turns ratio to match the impedances properly. An additional Z -matched circuit using capacitors enables the available transformers to match almost any impedance while preserving the circuit Q . This capacitor divider circuit is often used instead of a tapped coil or transformer as shown in Fig. 6.

The formulas used to calculate the matching conditions using capacitors are more complex than those used for transformer coupling, since there are more variables. In this circuit R_i is assumed to be lower than R_p . Although R_p

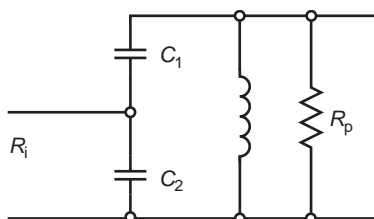


Figure 6. Lowering of total shunting by transformer action.

is the equivalent parallel resistance of the LC circuit in Fig. 6, it could also be the reduced resistance or reflected R_{p2} at a transformer tap. N in these equations is equal to the loaded resonator Q , or to a lower arbitrary value if total shunting R_p is lowered by transformer action as in Fig. 6, or if the component ratios become unwieldy [12]:

$$X_{C2} = \frac{R_i}{\left[\frac{R_i(N^2 + 1)}{R_p - 1} \right]^{1/2}} \tag{8}$$

$$X_{C1} = \frac{R_p N}{N^2 + 1} \left(1 - \frac{R_i}{NX_{C2}} \right) \tag{9}$$

$$X_{C2} \approx \sqrt{\frac{R_i R_p}{Q}} \tag{10}$$

$$X_{C1} \approx \frac{R_p}{Q} = X_L \tag{11}$$

Equations (8) and (9) calculate the reactances of the two capacitors. Note that NX_L is the same as QX_L . Starting with a value of $N = Q$, find X_{C1} , then X_{C2} .

If N is large in Eq. (8), the equations reduce to the approximate values in Eqs. (10) and (11). Unless Q is less than 10, these approximate equations are accurate enough for general use. As an example, let $R_i = 100 \Omega$ and $R_p = 10,000 \Omega$ with $Q = 100$. Then, using Eq. (11), X_{C2} becomes 10Ω and X_{C1} becomes 100Ω . C_2 is approximately 10 times larger than C_1 . Note the similarity of this ratio to Eq. (7). If a transformer is involved, N becomes much smaller and the full formulas (8) and (9) should be used.

Equations (8)–(10) apply for $R_i < R_p$ and $N > (R_p/R_i - 1)^{1/2}$.

7. DOUBLE-TUNED CIRCUITS

When two identical LC circuits are coupled together as shown in Fig. 7, a number of responses are possible as shown in Fig. 8. The amplitude response depends on the coupling coefficient K . Undercoupling results in a two-pole filter with the sharpest selectivity. Critical coupling results in the narrowest bandwidth with the highest gain. Transitional coupling is slightly greater than critical coupling and results in a flat-topped response with a wider

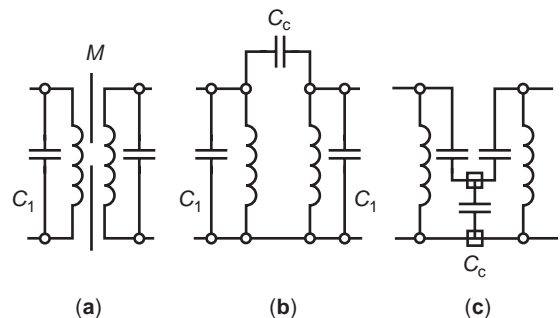


Figure 7. Coupling of identical LC circuits.

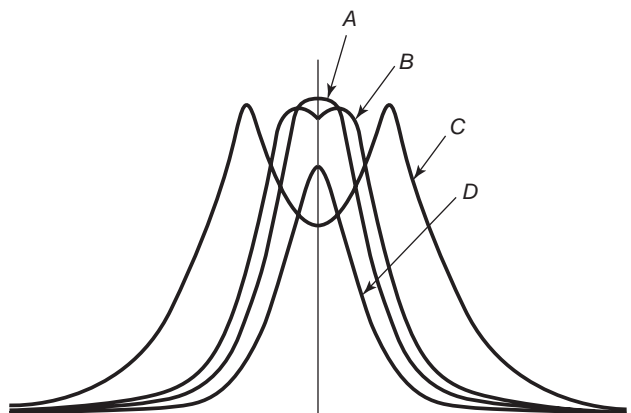


Figure 8. Results of *LC* circuit coupling: critical (curve A); transitional (curve B); overcoupled (curve C); undercoupled (curve D).

bandwidth. Overcoupling results in a double-humped response with sharper skirts and broad bandwidth. The coupling coefficient can be calculated using Eqs. (12). Equation (12a) applies to mutual inductive coupling and (12b)–(12d), to capacitive coupling.

$$K = \frac{M}{\sqrt{L_1 L_2}} \tag{12a}$$

$$K_c = \frac{1}{\sqrt{Q_1 Q_2}} \tag{12b}$$

$$K = \sqrt{\frac{C_c}{C_c + C_1}} \tag{12c}$$

$$K = \sqrt{\frac{C_1}{C_c + C_1}} \tag{12d}$$

Equation (12a) calculates the coupling coefficient for two identical *LC* tuned circuits that are coupled together by leakage inductance (Fig. 7a), often obtained by using shielded coils with holes in the sides of the shield cans to allow the magnetic fields to interact. The size of the hole determines the value of the mutual inductance *M*. Since this is difficult to control, a coupling capacitor is often used as shown in Figs. 7b and 7c. The critical coupling value is

given by Eq. (12b). The coupling coefficients for Figs. 7b and 7c are given in Eqs. (12c) and (12d).

The amplitude response curves in Fig. 8 do not yield any information as to the phase shifts that take place through the filter. In AM circuits, phase is generally of little concern, with most attention paid to the amplitude ripple and linearity. In FM circuits, nonlinear phase shift or a related term, *differential group delay*, becomes more of a problem and efforts are made to keep the phase shift as linear as possible. In data transmission circuits using phase modulation, or amplitude modulation, any nonlinearity must be avoided. For these reasons, the coupling coefficients are carefully adjusted and cascaded IF amplifier stages are used to get the desired transfer function for the IF amplifier.

8. CASCADING IF AMPLIFIER STAGES AND FILTERS

All filtering actions that take place between the RF input of the receiver and the decisionmaking circuit are parts of the IF amplifier bandpass filter. Since the final decision-making circuit is at baseband, or 0 Hz, all filtering prior to the decisionmaking circuit is part of the IF bandpass filtering, which should be treated as a whole.

A single *LC* circuit seldom has the desired bandpass characteristic for an IF amplifier. Cascading IF amplifier stages with differing coupling and *Q* values enables the designer to obtain the desired transfer response. One combination of *LC* filters uses an overcoupled double-tuned stage followed by a single-tuned stage with a lower *Q*. The result is a three-pole filter with relatively steep skirt slopes. Cascading these stages results in filters with responses resembling Butterworth, Chebyshev, elliptical, or equal-ripple filters, which are noted for their rejection of adjacent channel interference (see Figs. 9 and 10).

When additional filtering is required at baseband, simple *RC* filters, lowpass *LC* filters, or digital finite impulse response (FIR) filters are used. These and other filters are discussed in greater detail elsewhere in this encyclopedia.

9. CRYSTAL AND CERAMIC FILTERS

Figure 10a shows the equivalent circuit of a crystal or a ceramic resonator. These devices have both a pole and a

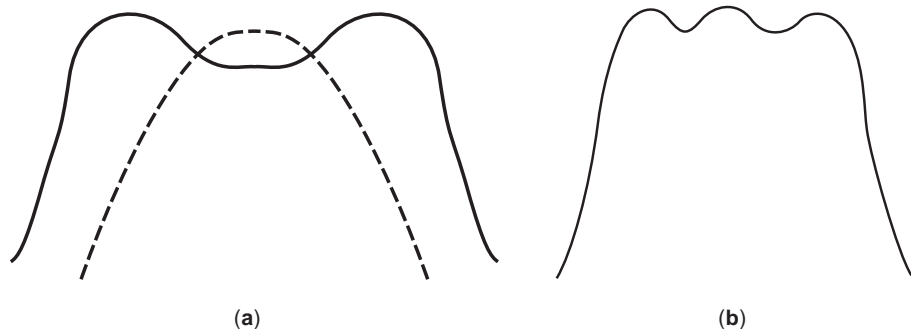


Figure 9. Curves resulting from cascading IF amplifier stages.

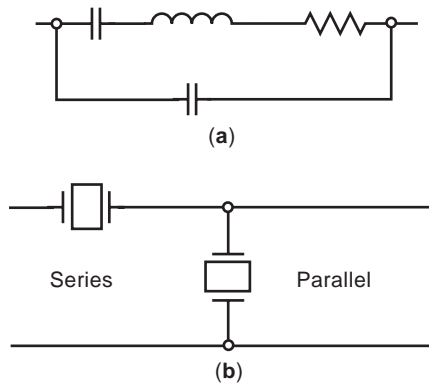


Figure 10. Equivalent circuit of a crystal or ceramic resonator.

zero that are located relatively close to each other in frequency. Quartz crystals have Q values ranging from 2000 to 10,000 depending on the mechanical loading of the crystal. Ceramic resonators usually have Q values between 100 and 2000. The higher the Q , the narrower the filter bandpass. When two of these devices are connected as shown in Fig. 10b, the result is a bandpass filter with steep skirts as shown in Figure 11. These resonators are used in pairs to create a two-pole filter, which can then be combined in a single container with other pairs, to create a filter with as many as eight or more poles. They usually have excellent adjacent-channel rejection characteristics.

When using these devices, care must be taken to carefully match the specified impedance. Any impedance mismatch can seriously alter the response curve of the filter. The impedance-matching techniques discussed previously will enable the designer to obtain a very close match, which will optimize the circuit performance. Typical input and output impedances range from 50 to 4000 Ω . Crystal filter manufacturers often build in transformer or other tuned matching circuits so that the user does not need to provide a matching circuit outside the crystal filter.

SAW (surface acoustic wave) filters utilize a crystal oscillating in a longitudinal mode with many fingers or taps placed along the surface. They can be made with very broad bandpass characteristics, which makes them well suited for TV IF amplifiers, spread-spectrum IF filters, and other uses requiring a wide RF bandwidth. They have losses, which are typically about 8–20 dB, so they must

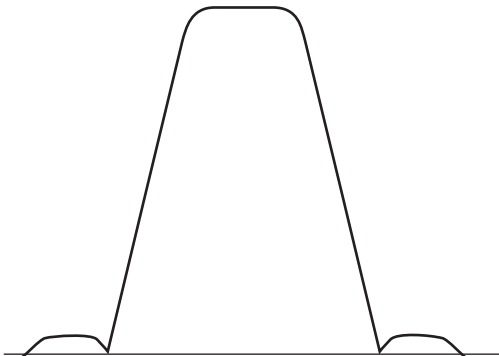


Figure 11. Steep-skirted bandpass filter.

have amplifiers with adequate gain ahead of them if the receiver noise figure is not to be degraded. They are not suitable for use in ultranarrowband or low-frequency applications. The group delay quoted in the specifications is usually the *differential group delay* and not the actual group delay, which is much higher.

10. BASEBAND IF FILTERING

IF bandpass filters with specific response characteristics are sometimes very difficult to obtain, whereas the desired characteristic is easily and inexpensively obtainable at baseband. This concept is often applied to transmitters where a sharp-baseband-cutoff filter can be obtained using simple components, such as the switched filter. An 8-pole equivalent at baseband becomes a 16-pole filter at the modulation intermediate frequency. For example, a sharp-cutoff filter for voice with a 4-kHz audio cutoff results in a bandpass filter 8 kHz wide at RF after modulation, with the same sharp cutoff. The same cutoff characteristics at RF would be almost impossible to obtain in a crystal filter, which would also be very costly and beyond the manufacturing budget for a low-cost transmitter such as a cordless telephone. By using baseband filtering, a poor-quality RF filter that only rejects the opposite image can be used. Similarly, a wideband, or poor-quality IF filter, can be used ahead of a detector, if the undesired signal components can be filtered off after detection at baseband, by using a sharp-cutoff filter.

Switched-capacitor filters are available as packaged integrated circuits that can be used at baseband and some lower intermediate frequencies. They have internal operational amplifiers with a switched feedback capacitor, the combinations of which determine the filter characteristics. Since they are dependent on the speed of the operational amplifiers and the values of the feedback capacitors, they seldom function much above 100 kHz. They can be configured as Bessel, equal-ripple, and Butterworth filters. Typical of this type of filter are the LTC1060 family manufactured by Linear Technology Corporation (a) and the MAX274 from Maxim (b) [see items (a) and (b) in Available Software list at end of this article].¹ As Bessel filters they perform well out to about 0.7 times the cutoff bandwidth, after which the phase changes rapidly and the Bessel characteristic is lost.

Digital signal processing (DSP) at baseband is widely used to reduce the component count and size of the baseband filters in very small radio receivers, such as cordless and cellular telephones. Almost any desired filter response can be obtained from DSP and FIR filters without using inductors and capacitors, which would require factory tuning (c,d).

Separate FIR filters have a flat group delay response and are the best choice for FM or PM filtering, or filters at baseband. Commercially available software design

¹In the remainder of this article, all lowercase letters in parentheses refer to entries in the Available Software list following the Bibliography. Numbers in brackets refer to Bibliography entries (references) as usual.

packages permit the design of trial circuits to investigate phase shift and group delay (e,f).

Unfortunately, digital filtering of any type is frequency-limited. The filter must use a sampling rate that is much higher than the frequency to be passed. To use a digital filter, such as a FIR filter, or DSP as a bandpass filter at 10.7 MHz, requires an analog-to-digital converter (ADC) operating at 160 MHz or higher. Filtering at baseband means the sampling rate can be much lower.

11. AMPLIFYING DEVICES FOR IF AMPLIFIERS

Transistors in one form or another have become the standard for IF amplifiers. The single bipolar or field-effect transistor used as an individual component, was formerly the preferred device. For very-high-Q circuits, the dual-gate FET performs best, since it is the most stable and offers the lowest shunt resistance. Single-gate FET devices often have too much drain to gate capacitance for good stability. Modern bipolar transistors usually have good stability, but lower shunt resistances than dual-gate FETs. Stability is discussed later in this section.

Monolithic amplifiers [MMIC (monolithic microwave integrated circuit) devices] are stable and have good gain, but the shunt load impedance is too low for most bandpass filters other than a crystal or SAW filter matched to 50Ω.

The most recent practice for IF amplifiers is to use integrated circuit blocks containing more than one transistor in a gain stage. These are then packaged together in an integrated circuit with other circuit components to form an almost complete radio. Integrated circuits of this type are shown below.

12. TYPICAL CONSUMER IF AMPLIFIERS

Consumer radio and TV equipment is mass-produced for the lowest possible cost consistent with reasonable quality. Manufacturers of integrated circuits now produce single-chip IF amplifiers that can be combined with mass-produced stock filters to produce a uniform product with a minimum of adjustment and tuning on the assembly line. In the examples that follow, some circuit components inside and outside the IC have been omitted to emphasize the IF amplifier sections.

Figure 12 shows a single-chip AM receiver that uses the Philips TDA1072 [7] integrated circuit and ceramic IF filters at 455 kHz. The input impedance of the ceramic filter is too low to match the output impedance of the mixer, so a tuned matching transformer is used to both reduce the passed bandwidth (prefilter) and match the impedances. The input impedance of the IF amplifier was designed to match the average impedance of the ceramic filters available. This integrated circuit has a built in automatic gain control that keeps the received audio output level relatively constant at 250 mV as long as the input signal level to the chip exceeds 30 μV.

Figure 13 shows a single-chip FM radio based on the Phillips NE605 integrated circuit (g) that uses ceramic IF filters at 10.7 MHz. The input and output impedance of the

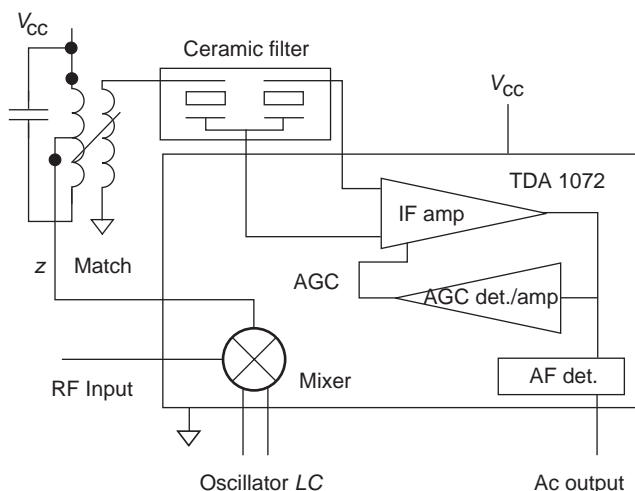


Figure 12. Layout of a single-chip AM receiver.

IF amplifier sections is approximately 1500Ω, to match the ceramic filter impedance, so no matching transformer is required. The audio output is maintained level at 175 mV for all signal levels at the input level from -110 to 0 dBm. An automatic frequency control (AFC) voltage can be obtained from the quadrature detector output. This circuit can also be used for narrow-angle phase modulation if a crystal discriminator is used for a phase reference at the quadrature input.

AGC is available from all FM integrated circuits so that the gain of the mixer and RF stages can be controlled at a level that does not allow these stages to be saturated by a strong incoming signal. Saturation, or nonlinearity before filtering, results in undesirable signal spreading. The NE605 has a “received-signal strength indicator” (RSSI) output that can be amplified and inverted if necessary to provide an AGC voltage, or current, for the RF amplifier and mixer.

Figure 14 shows a TV IF amplifier using the Motorola MC44301/2 video IF integrated circuit (h) with a SAW filter at 45 MHz. The SAW filter bandpass is made

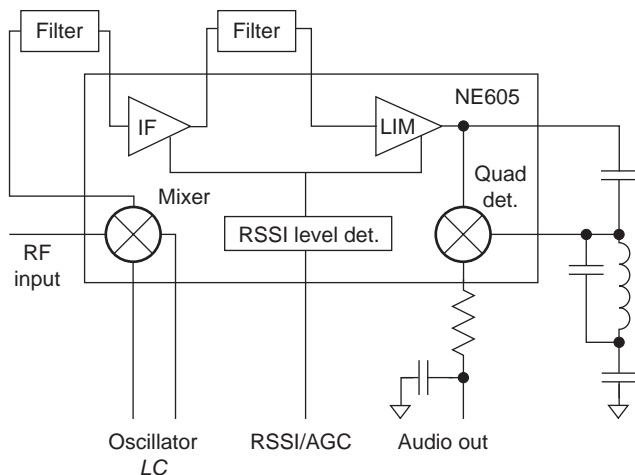


Figure 13. Configuration of a single-chip FM radio.

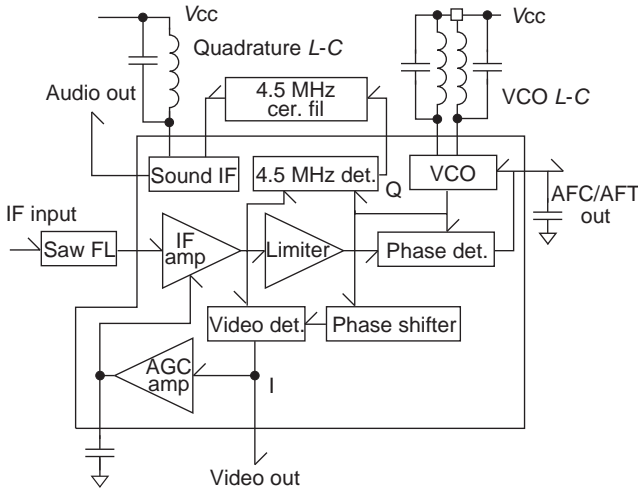


Figure 14. Layout of a television IF amplifier.

approximately 6 MHz wide to pass the video and sound. The circuit has both automatic frequency control (AFC) and automatic gain control (AGC) features built in. Unlike the IF amplifiers used for AM and FM audio broadcast applications, the TV IF amplifier includes a phase-locked loop (PLL) and synchronous detector that locks the frequency of an internal oscillator to the intermediate frequency. This locked, or synchronous, oscillator output is then mixed with the information-bearing portion of the signal to create a baseband signal.

The system shown in Fig. 14 is one of a family of 0-Hz IF amplifiers, are becoming more popular in wireless designs, since they permit most or additional signal processing at baseband. In Fig. 14, the video and sound carriers are both passed by the SAW filter. They beat together at 4.5 MHz in the detector, providing a second IF stage with the sound information. This 4.5-MHz IF information is then filtered by a ceramic bandpass filter approximately 50 kHz wide to remove any video components, limited and detected as a standard FM signal to provide the TV sound. The video portion, consisting of signals from 15 kHz to approximately 4.25 MHz, is then further processed to separate the color information at 3.58 MHz from the black-and-white information. The video output level is detected to provide the AGC voltage.

The phase-locked oscillator, operating at the intermediate frequency, can also be used to provide automatic frequency control to the first mixer stage local oscillator.

Figure 15 shows a dual-conversion receiver in a single integrated circuit for communications use, utilizing the Motorola MC13135 integrated circuit (h). When the receiver is operated at 450 or 850 MHz, as was mentioned above, single-conversion IF stages do not offer the necessary image rejection. This receiver is for narrow-band FM as opposed to wideband FM for entertainment purposes. The first IF filter is a low-cost ceramic filter at 10.7 MHz. The second filter is a multipole crystal or ceramic filter with a bandpass just wide enough to pass the signal with a small FM deviation ratio. Receivers of this type can be used with 12.5 and 25 kHz of channel separation for voice-quality audio. Analog cellular

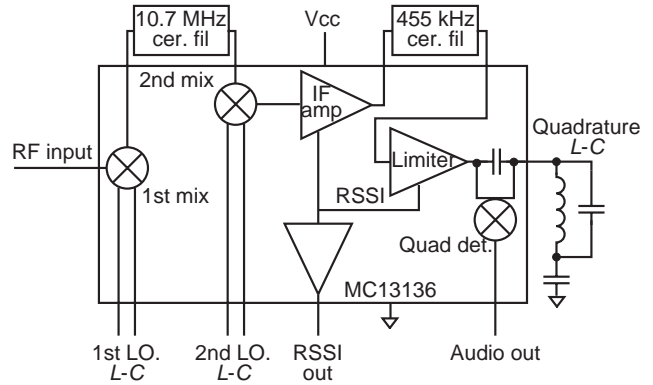


Figure 15. Configuration of a dual-conversion receiver in a single IC.

telephones, aircraft, marine, police, and taxicab radios are typical examples.

13. DIRECT CONVERSION AND OSCILLATING FILTERS

Direct conversion converts the RF frequency directly to baseband by using a local oscillator at the RF carrier frequency. The TV IF amplifier with the detector circuit given in Fig. 14 illustrates some of the reasons. Conversion to baseband can occur at the intermediate frequency or directly from the RF frequency.

There is a noticeable trend in integrated circuit design to utilize synchronous detection [5] with the carrier restored by means of a phase-locked loop, as shown in Fig. 14, or by means of regenerative IF amplifiers [6], to accomplish several desirable features that cannot be obtained from the classical circuits with square-law detectors.

In the case of direct RF-to-baseband conversion, there is no IF stage in the usual sense, and all filtering occurs at baseband. For this reason direct-conversion receivers are referred to as *zero-hertz (0-Hz) IF radios*. Integrated circuits for direct RF conversion are available that operate well above 2.1 GHz at the RF input. The Maxim 2820 (b) and the AMD1771 (i) are examples. DSP and FIR filters are the preferred lowpass filters at baseband, where they are referred to as “windows”.

It was discovered in the 1940s that the performance of a TV receiver could be improved by using a reconstructed synchronous or exalted carrier, as occurs in the TV IF amplifier depicted in Fig. 14. The carrier is reduced by vestigial sideband filtering at the transmitter and contains undesirable AM and PM signal components. By causing an oscillator to be locked to, or to be synchronized with the carrier, and then to be used by the detector, a significant improvement in the received signal can be achieved. Prior to using circuits of this type, the intercarrier sound at 4.5 MHz in earlier TV sets had a characteristic 60 Hz buzz due to the AM and PM on the carrier. By substituting the recovered synchronous carrier instead, this buzz was removed. Figure 14 illustrates an example.

The earliest direct-conversion receivers using locked oscillators or synchronous detectors were built in the

1920s, when they were known as *synchrodyne* or *homodyne* receivers. The theory is relatively simple. A signal from the RF amplifier is coupled to an oscillator, causing a beat or difference frequency. As the frequencies of the two sources come closer together, the oscillator is pulled to match the incoming signal and locks to it. The lock range depends on the strength of the incoming signal. The two signals are then mixed to provide a signal at baseband, which can be further filtered by means of a lowpass filter. In this way, a relatively broad RF filter can be used, while the resulting AM signal bandwidth after detection and baseband filtering can be very narrow. The Q of the oscillator tank circuit rises dramatically with oscillation so that Q values of 6000–10,000 are not unusual and selectivity is greatly improved. AGC can be obtained from the audio signal to maintain an input signal level that is constant to ensure a good lock range. An undesirable characteristic is the whistle or squeal that occurs between stations. Later receivers used a squelch circuit to make the signal audible only after locking has occurred. High-quality receivers for entertainment and communications use were produced in the 1990s using this principle. They offer higher sensitivity, better fidelity, and more controlled response. Integrated circuits for receivers of this type (direct conversion) are now being produced for paging, wi-fi (wireless fidelity), direct-broadcast TV, and cellular and cordless telephones. The Maxim 2820 (b) and the AMD 1771 (i) are examples.

Oscillating filters and phase-locked loops are similar in principle. An intermediate frequency is applied to a phase/frequency detector that compares the intermediate frequency with the oscillator frequency. An error voltage is created that changes the oscillator frequency to match, or become coherent with, that of the incoming IF carrier frequency. In some cases the phase-locked loop signal is 90° out of phase with the carrier, so a phase shifter is used to restore the phase and make the signal from the oscillator coherent in phase with the incoming signal. (See Figs. 14 and 18, where phase-locked loops and phase shifters are employed.)

Synchronous oscillators and phase-locked loops not only extend the lower signal-to-noise ratio but also have a bandwidth filtering effect. The noise bandwidth of the PLL filter is the loop bandwidth, while the actual signal filter bandwidth is the lock range of the PLL, which is much greater. Figure 16 shows the amplitude and linear phase response of a synchronous oscillator. The PLL is not always the optimum circuit for this use because its frequency/phase-tracking response is that of the loop filter.

The locked oscillator [6] performs much better than the PLL since it has a loop bandwidth equal to the lock range without sacrificing noise bandwidth, although with some phase distortion. Some authors hold that the synchronous oscillator and locked oscillator are variations of the PLL in which the phase detection occurs in the nonlinear region of the oscillating device and the voltage-controlled oscillator (VCO) frequency change characteristic comes from the biasing of the oscillator.

Both the PLL and the locked oscillator can introduce phase distortion in the detected signal if the feedback loop is nonlinear. A later circuit shown in Fig. 17 has two

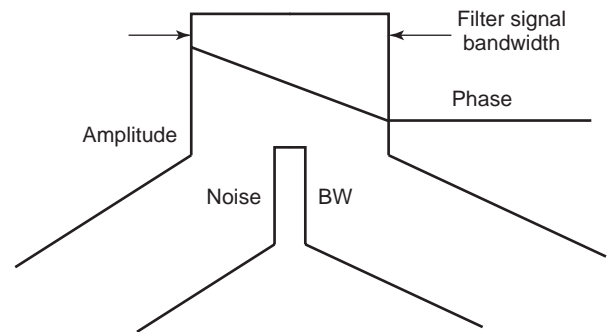


Figure 16. Amplitude and linear phase response of a synchronous oscillator.

feedback loops and is considered to be nearly free of phase distortion [5]. This circuit has the amplitude/phase response given in Fig. 16.

Phase-locked loops have been used for many years for FM filtering, amplification, and detection. They are in common use with satellite communications links for audio and video reception. A 74HC4046 phase-locked loop integrated circuit operating at 10.7 MHz (the FM intermediate frequency) can be used to make an FM receiver for broadcast use [7]. The phase-locked loop extends the lower signal-to-noise limit of the FM receiver by several decibels while simultaneously limiting bandwidth selectivity to the lock range of the PLL. The detected audio signal is taken from the loop filter.

14. AM STEREO (C-QUAM)

AM stereo radio is another application of the phase-locked oscillator at the intermediate frequency. AM stereo radio is dependent on two programs being transmitted at the same time at the same frequency. They arrive at the receiver detector circuitry through a common IF amplifier

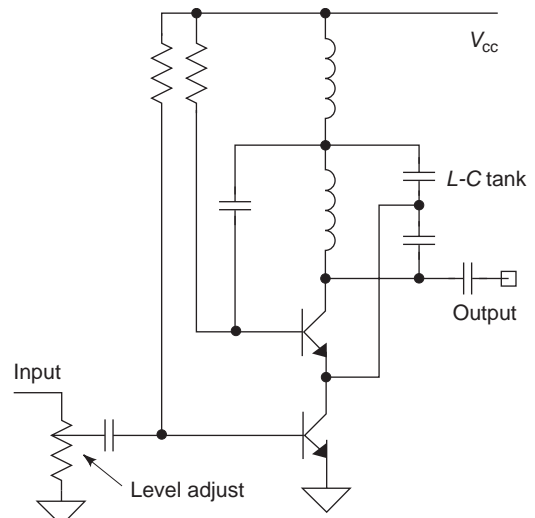


Figure 17. Circuit with same amplitude and phase response as in Fig. 16 but with two feedback loops and markedly decreased phase distortion.

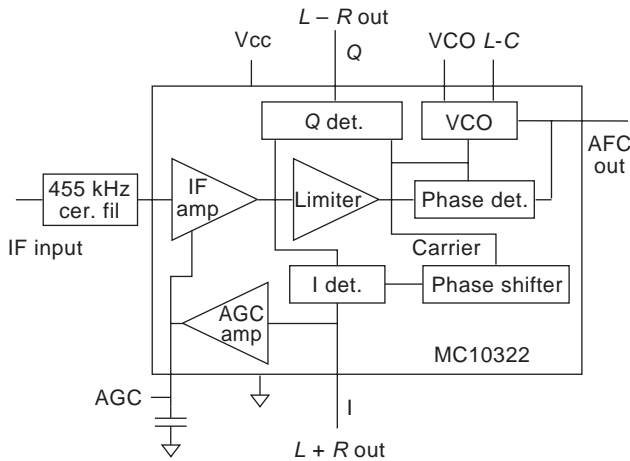


Figure 18. Simplified block diagram of the C-QUAM receiver.

operating at 455 kHz. The normal program heard by all listeners is the $L+R$ program. The stereo information ($L-R$) is transmitted at the same frequency, but in quadrature phase to the $L+R$ program. Quadrature, or orthogonal transmission, is used because the orthogonal channels do not interfere with one another.

Each program section requires a reference carrier, that is coherent with its own sideband data. The $L+R$ program, which has a carrier, may use an ordinary square-law detector or a synchronous detector. This is the program heard over monaural radios. To obtain the $L-R$ program that is transmitted without a carrier, a phase-locked loop is used at the intermediate frequency to lock a voltage controlled oscillator to the carrier of the $L+R$ program. This carrier is then shifted 90° in phase and becomes the reference carrier for the $L-R$ segment. The output of the PLL has the proper phase for the $L-R$ detector, so no phase shifting is necessary. The $L-R$ detector is a coherent or synchronous detector that ignores the orthogonal $L+R$ information. By adding, then inverting and adding, the left and right channels are separated. Figure 18 shows a simplified block diagram of the C-QUAM receiver.

The Motorola MC1032X (h) series of integrated circuits are designed for AM stereo use. The MC10322 and MC10325 have most of the components required, including the IF amplifiers, for a complete AM stereo receiver in two integrated circuit packages.

15. SUBCARRIERS

Subcarriers are used to carry two or more signals on the same carrier. They differ from the orthogonal signals used with C-QUAM in that they are carried as separate signals superimposed over the main carrier information, as in the video sound carrier shown in Fig. 14. In Fig. 14, a frequency-modulated subcarrier at 4.5 MHz is carried on top of the main video signal information, which extends from 0 to 4.25 MHz. This is an example of an AM/FM subcarrier. Nondigital satellites utilize a frequency-modulated video carrier with as many as 12 subcarriers at frequen-

cies ranging from 4.5 to 8.0 MHz. Normal FM stereo broadcasting utilizes a FM/AM subcarrier at 38 kHz to carry the $L-R$ portion of the stereo program. FM stations frequently carry additional subcarriers at 67 and 92 kHz. These FM/FM subcarriers are used to carry background music, ethnic audio programs, and digital data.

To detect a subcarrier, the signal is first reduced to baseband, then a bandpass filter is used that separates only the subcarrier frequencies. The subcarrier frequencies are then passed to a second detector, which must be of the type appropriate for the subcarrier modulation. This can be seen in Fig. 14, where a 4.5-MHz filter is used. This is followed by a limiter and quadrature detector, which is appropriate for the FM signal. In the case of a 67-kHz FM/FM subcarrier, the filter is 15 kHz wide at 67 kHz. Detection can be accomplished by a discriminator, quadrature detector, or PLL.

16. CELLULAR AND CORDLESS TELEPHONES

Analog cellular telephones employ the circuits shown in Figs. 13 and 15. Digital telephones utilizing Gaussian minimum shift keying (GMSK) also use these circuits. Digital telephones using quadrature amplitude modulation (QAM) or phase shift keying (PSK) employ circuits similar to that used for C-QUAM with digital filtering and signal processing instead of audio filtering at baseband. The PLL used for digital receivers is a more complex circuit known as the *Costas loop*, which is necessary to restore a coherent carrier for digital data recovery. Some cellular phones are dual-mode; that is, they can transmit and receive analog voice or digital GMSK modulation using circuits similar to those shown in Figs. 13 and 15.

17. NEUTRALIZATION, FEEDBACK, AND AMPLIFIER STABILITY

Earlier transistors and triode vacuum tubes had considerable capacitance between the output element (collector or plate) and the input side of the device (see Fig. 4). Feedback due to this capacitance is multiplied by the gain of the stage so that enough signal from the output was often coupled back to the input to cause the stage to oscillate unintentionally, as opposed to the planned oscillation of the locked oscillator, synchronous oscillator, or PLL. To prevent this, feedback of an opposite phase was deliberately introduced to cancel the undesired feed back. A neutralized IF amplifier is shown in Fig. 19. Transistors and integrated circuits made since 1985 are rarely unstable and generally do not require neutralization unless seriously mismatched. A better solution than neutralization is usually to improve the matching of the components and the circuit layout.

By carefully controlling the feedback, a regenerative IF amplifier can be constructed that operates on the verge of oscillation. This greatly increases the Q of the tuned circuit, thus narrowing the IF bandwidth. Circuits of this type were once used in communication receivers for

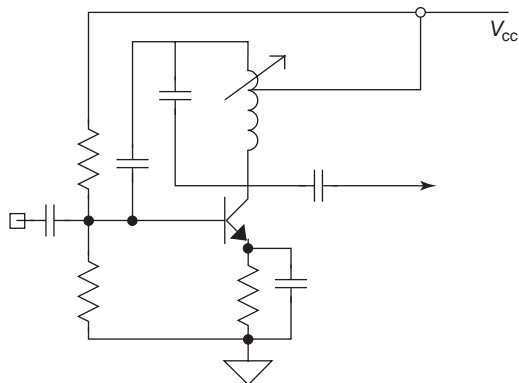


Figure 19. Configuration of a neutralized IF amplifier.

commercial and amateur use, where they were referred to as “ Q multipliers.”

The maximum stable gain (MSG) that can be achieved from a potentially unstable amplifier stage without neutralization is obtainable from the S parameters and can be calculated from Eq. (13). This equation assumes that the input and output impedances are matched and there is little or no scattering reflection at either the input or output. The stability factor K , usually given with the S parameters, must be > 1 . A failure to match the impedances can result in an unstable amplifier, but does not necessarily do so. A higher gain can be obtained, but at the risk of instability.

$$K = \text{MSG} = \frac{S_{21}}{S_{12}} \quad (13)$$

In addition to impedance mismatch, the most frequent cause of amplifier instability, or oscillation, is poor circuit-board layout or inadequate grounding and shielding, not the device parameters. The wiring, whether printed or handwired, forms inductive or capacitive coupling loops between the input and output terminals of the amplifying device. This is particularly noticeable when high-gain ICs such as the NE605 are used. These integrated circuits have IF gains of > 100 dB and require very careful board layouts for best results. Undesirable feedback can greatly decrease the usable gain of the circuit.

18. SOFTWARE RADIO

Digital radios, or radios based on digital signal processing (DSP), offer some technical advantages over their analog predecessors. Digital radios can be used not only for digital modulation but also for AM and FM. One receiver can simultaneously detect both digital and analog modulation; thus they can be used for cellular telephones in environments where multiple modulation standards are used. As a class, they belong to the 0-Hz intermediate-frequency group.

The typical receiver consists of a conventional RF front end and a mixer stage that converts the signal to a lower frequency, as in the dual conversion radios discussed above (Fig. 16). The signal at this stage is broadband in

nature, but not broadband enough to include the image frequencies. The signal is then fed to an analog-to-digital converter (ADC), which is sampled at several times f_m . This converts the portion of interest of the signal to baseband (or 0 Hz) instead of a higher intermediate frequency. The actual filtering to remove unwanted interfering signals then takes place at baseband, using digital filtering. Digital signal processing and decimation are covered elsewhere in this work. The ADC (c) performs the same functions as do the oscillating detectors shown above.

Noise figure, amplification, and AGC considerations of the first IF amplifier are the same as those for a conventional receiver. The ADC and the DSP filters function best with a constant signal input level.

The term “software radio” has been adopted because the tuning function is done in software by changing the sampling frequency at the ADC. The sampling frequency is obtained from a digitally controlled frequency synthesizer instead of tuned LC circuits.

19. SPREAD-SPECTRUM RADIOS

The spread-spectrum receiver also uses a conventional front end with a wideband first IF stage. The same conditions apply as to software radios and dual-conversion receivers. The first IF stage must have the necessary bandwidth to accommodate the spread bandwidth, amplify it with minimum added noise, and match the output to the despreading circuitry. Spread-spectrum technology is covered elsewhere in this encyclopedia. While usually associated with digital reception, spread-spectrum technology can also be used for analog audio.

20. ORTHOGONAL FREQUENCY-DIVISION MULTIPLEXING (OFDM) AND CODED OFDM (COFDM)

These modulation methods could be considered similar to spread-spectrum techniques, or to methods requiring dual conversion, in that they use a very broad spectrum as a first level, followed by a narrowband filter to extract an individual channel. SAW filters are generally used at RF, while second-stage processing can use digital filtering, as in the software radio, or be done at baseband.

21. TRANSFER FUNCTIONS

The amplitude response, plotted relative to frequency of a filter, is usually given in terms of the transfer function $H(f)$. Some typical transfer functions are as follows. For the LC filter of Fig. 2

$$H_{LC}(f) = \exp - \frac{Q\omega t}{2} \quad (14)$$

The LaPlace transform equivalent is

$$H(s) = \frac{K}{s^2 + Bs + \omega_0^2} \quad (15)$$

A similar curve obtainable with digital filters is the Gaussian filter:

$$H_{\text{Gauss}}(f) = \exp -1.38 \left[\frac{1}{(BT)^2} \right] \quad (16)$$

A generalized Nyquist IF filter bandpass spectrum is seen in Fig. 20.

In Fig. 20 the centerline represents either the carrier frequency, or 0 Hz. The portion of the spectrum to the right of the centerline is the baseband response, while both extremes represent the RF double-sideband response with the carrier at the center. The B region is the baseband response of an “ideal” filter, which does not exist in practice. Practical filters have a rolloff, or excess bandwidth, shown in α . Outside the desired bandpass, there is a “comeback” in region C . The “ideal” filter has no rolloff and no comeback. The region B is the required Nyquist bandwidth.

Multilevel digital modulation methods such as quadrature amplitude modulation (QAM) and multiple phase shift keying (MPSK) require filters that are free of amplitude and phase distortion within the Nyquist bandwidth, then having a rolloff α as abrupt as reasonably possible outside that distortion-free bandwidth. The optimum filter for this is considered to be the *raised-cosine filter*, so called because the region after the uniform response is half-cycle of a cosine wave squared (cosine raised to second power). The transfer function for the raised-cosine filter is as follows. In the central bandpass region B , we obtain

$$H(f) = 1 \quad \text{for} \quad |f| > -f_m(1 - \alpha), \quad (17)$$

$$\text{or} \quad < f_m(1 + \alpha) \quad (\text{or } \pm f_m)$$

When $\alpha = 0$, the filter is said to be the “ideal” filter. In the transition region α ; since $\cos 2A = \cos^2 A - 1$ or $1 + \cos 2A = \cos^2 A = 0$ elsewhere, we obtain the following forms of Eq. (17):

1. $H(f) = \cos^2[(\pi|f|T)/2\alpha] - \pi(1 - \alpha)/4\alpha$, for $-f_m(1 - \alpha) < |f| < f_m(1 + \alpha)$
2. $H(f) = \frac{1}{2} \{1 + \cos [(\pi|f|T)/\alpha] - \pi(1 - \alpha)/2\alpha\}$

In practice, there is always some comeback as seen in region C .

Figure 20 shows the double-sided RF bandwidth when the center reference is the carrier. The right-hand side is

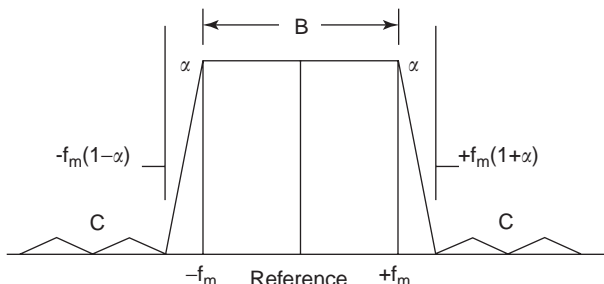


Figure 20. A simplified Nyquist filter bandpass spectrum (from Sklar [13] and Feher [14]).

the baseband bandwidth with the reference at 0 Hz. When used as a lowpass filter at baseband, the filter is referred to as a “window.” There are many rolloff curves associated with windows, which are realizable with DSPs or field-programmable gated arrays (FPGAs) used as FIR filters. Designing an RF bandpass filter with these rolloff curves is very difficult; therefore, the preferred practice is to do the filtering at baseband where numerous windowing curves are available.

Some popular rolloff curves for FIR filters used as “windows” are the Bartlett, Blackman, Hamming, Hanning, Elexix, Truncated Sinc/x, and Kaiser. These are usually realized by changing the multipliers in the 2 of Eq. (17) [above; after text following Eq. (17)] form of the raised-cosine equation. For example, using this form of Eq. (17), the Hamming window has the equation $H(f) = \{0.54 + 0.46\cos[(\pi|f|T)/\alpha] - \pi(1 - \alpha)/2\alpha\}$. The “ideal” filter shape ($\alpha = 0$) at baseband is called a “rectangular” window.

22. GROUP DELAY, ENVELOPE DELAY, AND RISE TIME

The group delay for conventional filters is traditionally calculated to be [11]:

$$T_g = \frac{\Delta\Phi}{2\pi\Delta f} \quad (18)$$

For LC or Gaussian filters (Fig. 2), this is

$$T_g = \frac{1}{(4\Delta f)} \quad \text{and} \quad T_g = \frac{Q\Delta\Phi}{\omega} \quad (19)$$

Obviously, a very narrow bandwidth filter $[\Delta f]$ has a very large group delay, which will adversely affect pulse modulation.

There is an associated equation for the risetime of the conventional filter: $T_r = 0.7/B$, where B is the 3-dB bandwidth $[\Delta f]$ of the filter. This is the time interval from 10% to 90% on the RC curve. Bandwidth, risetime, and sampling rate are mathematically linked.

A radar system with a narrow pulse must have a RC risetime that allows the pulse to pass. This necessarily means a very broad filter bandwidth and an accompanying high noise level.

Two-level modulation methods, such as BPSK, QPSK, GMSK, NBFS, and NBPM (binary, quadrature, Gaussian minimum shift keying and narrowband frequency and phase modulation), can use a narrower-than-usual bandpass filter. The bandpass can be as low as $0.2[\Delta f]$ in Eqs. (18) and (19).

Refer to Fig. 2 and Eq. (4), which demonstrate a reduction of the output level of the high-frequency portion of the signal (sidebands) that pass through the filter and a simultaneously reduction of the noise power bandwidth. The result is an overall S_o/N_o improvement. The notation BT is used for this concept $B = \text{bandwidth}$ and $T = \text{bit period} = 1/f_b$. The value of T is fixed, but B can be altered. The effect is to raise the processing gain in Eq. (4) by $1/BT$.

Certain newer modulation concepts (ultranarrowband) require a filter that does not conform to the group delay

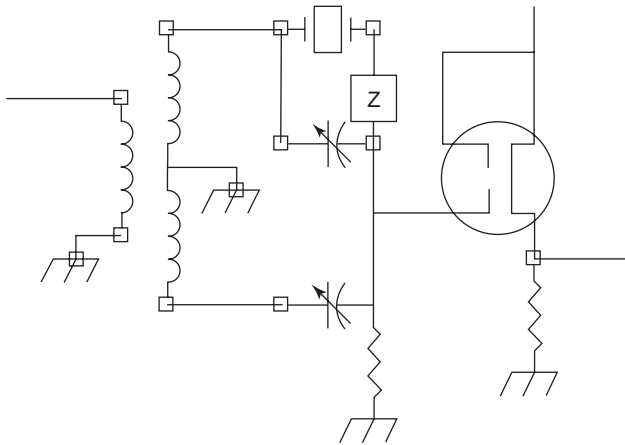


Figure 21. Circuit of a half-lattice (bridge-type) filter with near-zero group delay to a single-pulsed frequency (from Chen [12]).

equation [Eq. (18)]. These so called *zero-group-delay filters* have a very narrow bandwidth with almost instantaneous pulse response at a single frequency. Figure 21 shows the circuit of a half-lattice, or bridge-type, filter, that has near-zero group delay to a single-pulsed frequency. At the parallel resonant frequency of the crystal, the crystal appears to have a very high resistance and the signal passes via the phasing capacitor in the opposite bridge arm. This circuit has a frequency response similar to that of the universal curve (Fig. 2) with shoulders that extend from 0 Hz to infinity. Therefore, it must be used together with pre-filters to narrow the total noise bandwidth. A small capacitor or inductor can be used at z to extend the tuning range of the crystal [11].

23. COMPUTER-AIDED DESIGN AND ENGINEERING

Digital filters are easily designed using commercially available software packages and information provided by the IC manufacturers (d-g, l).

For IF filter design using discrete components, the admittances rather than the impedances are easiest to use, since most components are in parallel as shown in the equivalent circuit of Fig. 4b. Unfortunately, most available data are in the form of S parameters, which are very difficult to convert manually to impedances or admittances. Parameters for the filters are rarely available, so calculated values based on assumed input and output impedances must be used unless test equipment capable of measuring return losses or standing waves is available, in which case the S parameters can be measured or calculated.

Smith and Linville charts have been used by some authors to design IF amplifiers, but these methods are not totally satisfactory for IF amplifier design, since a high- Q circuit has its plot near the outer edge of the circle and changes are difficult to observe. The network admittance values shown in Fig. 4 would be used.

Computer-aided programs for linear or analog designs, such as the various "SPICE" programs are readily available (j). Other programs which concentrate specifically on

filter design (f, k-m) can simplify the filter design. They have outputs that then interface with the SPICE programs if desired. Most semiconductor manufacturers provide scattering parameters (S parameters) or SPICE input data on disk for use with these programs. Some design software sources are listed below (after the Bibliography). Some of the IF amplifier integrated circuit manufacturers also provide software specific to their products.

BIBLIOGRAPHY

(References 8, 9, 10, and 13 contains applicable software).

1. J. M. Pettit and M. M. McWhorter, *Electronic Amplifier Circuits*, McGraw-Hill, New York, 1961.
2. W. Th. Hettterscheid, *Transistor Bandpass Amplifiers*, Philips Technical Library, N.V. Philips, Netherlands/Philips Semiconductors, 1964.
3. Roy Hejhall, *RF Small Signal Design Using Two-Port Parameters*, Motorola Applications Note AN 215A.
4. F. Davis, *Matching Network Designs with Computer Solutions*, Motorola Applications Note AN 267.
5. V. Uzunoglu and M. White, Synchronous oscillators and coherent phase locked oscillators, *IEEE Trans. Circuits Syst.* **36**(7) (1989).
6. H. R. Walker, Regenerative IF amplifiers improve noise bandwidth, *Microwaves RF Mag.* (Dec. 1995, Jan. 1996).
7. R. E. Best, *Phase Locked Loops*, McGraw-Hill, New York, 1984.
8. R. W. Goody, *P-Spice for Windows*, Prentice-Hall, Englewood Cliffs, NJ, 2001.
9. M. E. Herniter, *MicroSim P-Spice*, Prentice-Hall, Englewood Cliffs, NJ, 2000.
10. J. Keown, *Orcad PSpice and Circuit Analysis*, Prentice-Hall, Englewood Cliffs, NJ, 2001.
11. W.-K. Chen, *The Circuits and Filters Handbook*, IEEE Press, New York, 1995.
12. *ARRL Handbook*, Amateur Radio Relay League, Newington, CT, 2000.
13. B. Sklar, *Digital Communications*, Prentice-Hall, Englewood Cliffs, NJ, 2001. (Contains the Elanix SysView design software on CD.)
14. K. Feher, *Wireless Digital Communications*, Prentice-Hall, Englewood Cliffs, NJ, 1995.

AVAILABLE SOFTWARE

The following companies are representative of those providing packaged IF amplifiers as integrated circuits #, and those offering development software packages *.

- (a) #*Linear Technology Corporation, 720 Sycamore Drive, Milpitas, CA 95035 (www.linear-tech.com).
- (b) #Maxim Integrated Products, 120 San Gabriel Drive, Sunnyvale, CA 94086 (www.maxim-ic.com).
- (c) #*Analog Devices, One Technology Way, P.O. Box 9106, Norwood, MA 02062 (www.analog.com).
- (d) *#Texas Instruments, P.O. Box 954, Santa Clarita CA 91380 (www.ti.com/sc or www.ti.com/sc/expressdsp).
- (e) #*Altera Corp., 101 Innovation Drive, San Jose, CA 95134 (www.altera.com).

- (f) *#Xilinx, Inc., 2100 Logic Drive, San Jose, CA 95124 (www.xilinx.com).
- (g) *# Philips Semiconductors, 811 E. Arques Avenue, P.O. Box 3409; Sunnyvale, CA 94088 (www.semiconductors.philips.com).
- (h) *#Motorola Literature Distribution Center, P.O. Box 5405; Denver, CO 80217 (www.motorola.com/semiconductors/ or www.Design-net.com).
- (i) *#AMD, One AMD Place, P.O. Box 3453; Sunnyvale, CA 94088 (www.amd.com).
- (j) *MicroSim Corp., 20 Fairbanks, Irvine, CA 92618 (www.orcad.com).
- (k) *Eagleware Corp., 1750 Mountain Glen, Stone Mountain, GA 30087 (www.eagleware.com).
- (l) *Elanix Inc., 5655 Lindero Canyon Road, Suite 721, Westlake Village, CA 91362 (www.elanix.com).
- (m) *The Math Works (MatLab), 3 Apple Hill Drive, Natick, MA 01760-2098 (www.mathworks.com).
- (n) *Intusoft, P.O. Box 710, San Pedro, CA 90733 (www.intusoft.com).
- (o) *#Hewlett-Packard Company, P.O. Box 58199, Santa Clara, CA 95052 (www.hp.com).
- (p) *Z Domain Technologies, 555 Sun Valley Drive, Roswell, GA 30076 (www.zdt.com/~dsp).
- (q) #Rockwell Semiconductor Systems, 4311 Jamboree Road, Newport Beach, CA 92660 (www.rockwell.com).
- (r) #RF Micro Devices, 7628 Thorndike Road, Greensboro, NC 27409-9421 (www.rfmd.com).

INTERMODULATION

JOSÉ CARLOS PEDRO
University of Aveiro
Portugal

1. INTRODUCTION

1.1. What Is Intermodulation Distortion?

Although the term *intermodulation* is used by some authors to describe a specific manifestation of nonlinear distortion, in this text we will adopt the wide-sense meaning of intermodulation as any form of nonlinear distortion, unless otherwise explicitly stated. So, it is convenient to start an introduction to intermodulation by saying a few words about distortion.

In the field of telecommunication systems, distortion is understood as any form of signal impairment. In this way, distortion takes the broad sense of all differences between the received and the transmitted information signals, specifically, those added or signal-dependent perturbations.

In the first set of added, or signal-independent, perturbations, we should include random noise and deterministic interferences. Typical examples of the former are the always present thermal noise or shot noise of electronic circuits. The second could be illustrated by some man-made (synthetic) repetitive impulsive noise or simply another telecommunications channel that shares the

same transmission medium but that does not carry any useful information.

The set of signal-dependent perturbations can also be divided into two major parts—linear distortion and nonlinear distortion—according to whether what distinguishes the received signal from its transmitted version is due to a linear or a nonlinear process. The reason for this organization stands in the easiness with which we correct linear distortion and the difficulty we have in dealing with nonlinearity. In fact, since linear distortion describes all differences in time-domain waveform, or frequency-domain spectrum, as the ones caused by any usual filter or dispersive transmission medium, it can be corrected by another inverse filter, with a methodology usually known as *pre- or postequalization*. On the other hand, nonlinear distortion cannot be corrected this way, remaining nowadays as a very tough engineering problem.

So, from a purely theoretical point of view, what distinguishes linear distortion from nonlinear distortion is simply the essence of the mapping corresponding to the telecommunication system, from the signal source to the detected signal. If that mapping responds to scaled versions of two different signals with two scaled versions of the responses to these two signals, when they are processed individually, we say that our transmission system obeys superposition, and is thus linear [1]. In any other case, we say that the system is a source of nonlinear distortion. Nonlinear distortion can, therefore, manifest itself in many different forms that range from the obvious signal clipping of saturated amplifiers, to the almost unnoticeable total harmonic distortion present in our high-fidelity audio amplifiers.

Because nonlinear distortion is a property not shared by our more familiar linear systems, we could think of it as something visible only in some special-purpose systems or poorly designed circuits. Unfortunately, that is not the case. To a greater or lesser extent, nonlinear distortion is present in the vast majority of electronic systems. Because nonlinear distortion is associated with PN and PIN diodes or varactors [2], it is found in many control devices such as solid-state switches, controlled attenuators, phase shifters, or tunable filters—and, because of the recognized nonlinearity of magnetic-core inductors, it can also arise from other passive filters and duplexers. However, probably more surprising, is the fact that it can even arise from devices usually assumed as linear.

One example is the nonlinear distortion produced by some RF MEM (radiofrequency micromachined electro-mechanical) switches [3]. Another is *passive intermodulation* (PIM), which is frequently observed when loose connections, or junctions made of different metals or of similar but oxidized metals are subject to high power levels [4]. So, PIM is generated in many RF connectors, antennas, antenna pylons, wire fences, and other components. Finally, intermodulation can even arise from our supposedly linear electronic circuits as it is inherent to the operation of all electronic active transducers. To understand this, let us take the example of the general amplifier described in Fig. 1.

Because our amplifier is a physical system, it must obey energy conservation, which implies that the sum of all

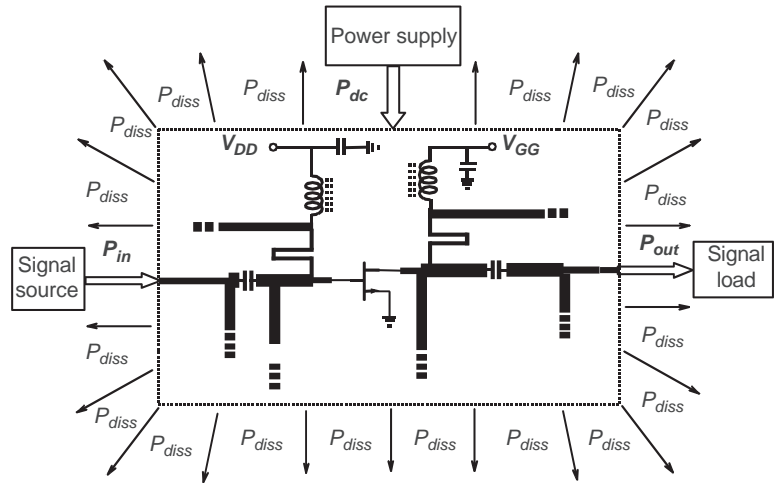


Figure 1. Conceptual amplifier showing input/output power relations.

forms of input power—either signal power P_{in} or DC supply power P_{DC} —must equal the sum of all forms of output power, whether it is signal power delivered to the load P_{out} or dissipated power P_{diss} such as heat or harmonic distortion:

$$P_{in} + P_{DC} = P_{out} + P_{diss} \tag{1}$$

On the other hand, we know that output signal power should be a scaled replica of the input signal power, defining, in this way, a certain amplifier power gain:

$$G_P \equiv \frac{P_{out}}{P_{in}} \tag{2}$$

However, (1) also implies that

$$G_P = 1 + \frac{P_{DC} - P_{diss}}{P_{in}} \tag{3}$$

which shows that no amplifier that relies on a real supply of finite power can keep its gain constant for any increasing input signal level. Sooner or later, it will have to show gain compression, presenting, therefore, nonlinearity.

1.2. Characterizing Intermodulation Distortion

After this brief introduction to the concept of intermodulation distortion, let us now see in more detail which forms of distortion it describes. For that, we will assume a simple system represented by the following cubic model:

$$y(t) = a_1x(t - \tau_1) + a_2x(t - \tau_2)^2 + a_3x(t - \tau_3)^3 + \dots \tag{4}$$

in which the input $x(t)$ is nonlinearly transformed into an output $y(t)$. Note that this system not only shows nonlinearity as it also has memory, since it does not respond instantaneously to the input, but to certain past versions of it. This dynamic behavior is due to the presence of the delays τ_1 , τ_2 , and τ_3 .

1.2.1. Single-Tone Distortion Characterization. Supposing the input is initially composed of one amplitude $A(t)$

and phase $\theta(t)$ modulated RF carrier of frequency ω_c

$$x(t) = A(t) \cos[\omega_c t + \theta(t)] \tag{5}$$

the output will be composed of three sets of terms, say, $y_1(t)$, $y_2(t)$, and $y_3(t)$, each one corresponding to a certain polynomial degree. Illustrations of the time-domain waveforms and frequency-domain spectra of the input $x(t)$ and output $y(t)$ are depicted in Figs. 2a and 2b and in Fig. 3a and 3b, respectively.

The first term of the output is given by

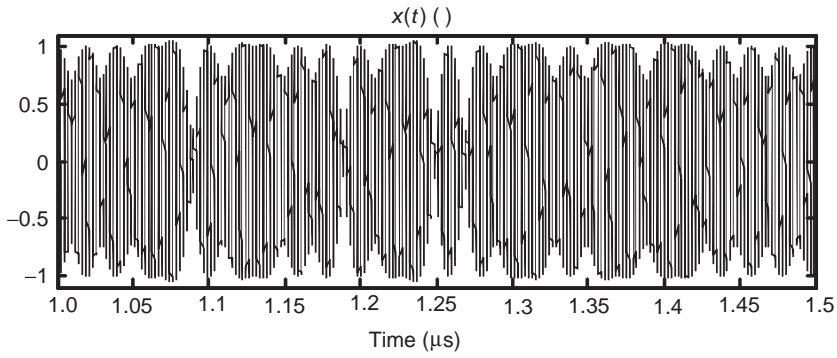
$$y_1(t) = a_1A(t - \tau_1) \cos[\omega_c t + \theta(t - \tau_1) - \phi_1] \tag{6}$$

(where $\phi_1 = \omega_c \tau_1$) and corresponds to the expected linear response. Note that it includes exactly the same frequency components already present at the input.

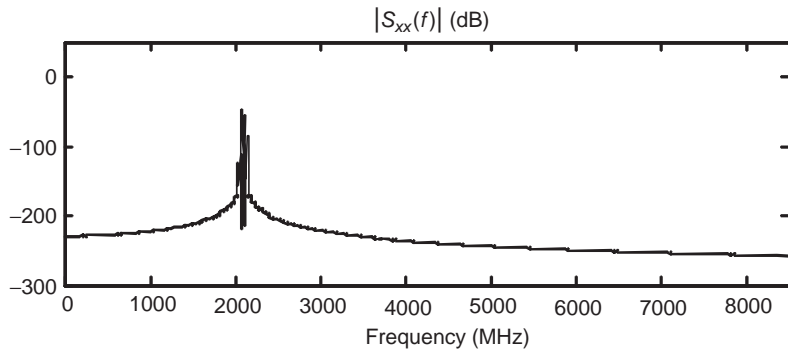
The second term

$$y_2(t) = \frac{1}{2}a_2A(t - \tau_2)^2 + \frac{1}{2}a_2A(t - \tau_2)^2 \cos[2\omega_c t + 2\theta(t - \tau_2) - 2\phi_2] \tag{7}$$

(where $\phi_2 = \omega_c \tau_2$) involves baseband products whose frequency falls near DC and some other products whose frequencies are located around the second harmonic, $2\omega_c$. The first ones consist of second-order intermodulation products of the form $\omega_x = \omega_1 - \omega_2$ (in which ω_x is the resulting frequency, while ω_1 and ω_2 are any two distinct frequencies already present at the input), and describe the demodulation generally provided by even-order nonlinearities. When $\omega_1 = \omega_2$, then $\omega_x = 0$, and the terms fall exactly at DC. So, they also describe the circuit's DC bias shift. Because they are what is sought in AC to DC converters, in amplifiers they model the variation of the $y(t)$ mean value from the quiescent point, to the mean value shown in presence of a significant RF excitation—the large-signal bias point. The second type of even-order products is again second-order intermodulation distortion whose frequency now falls at $\omega_x = \omega_1 + \omega_2$. For $\omega_1 = \omega_2$,

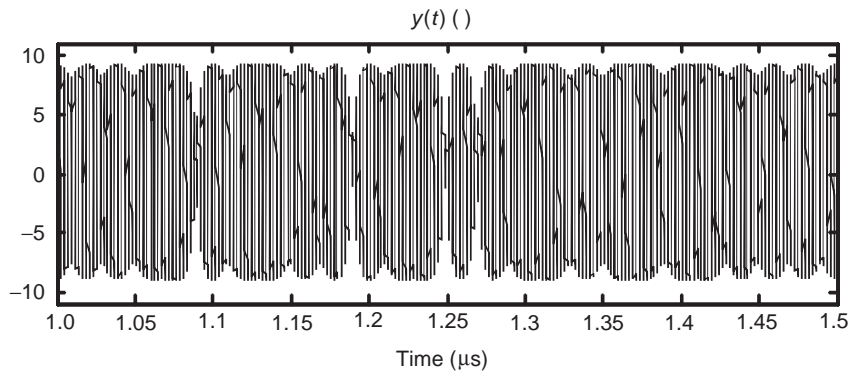


(a)

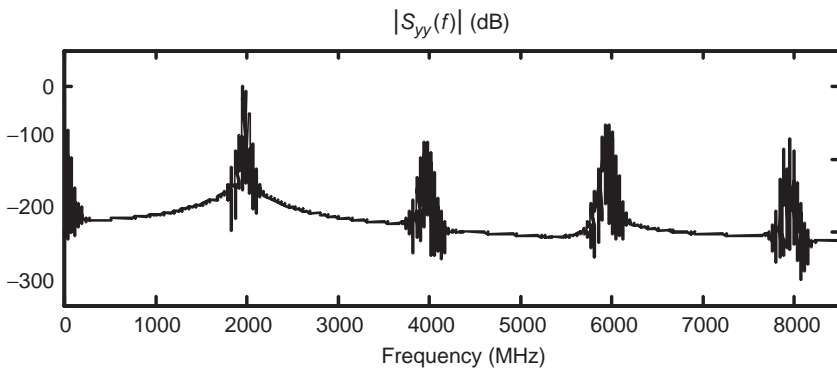


(b)

Figure 2. (a) Time-domain waveform of the input signal $x(t)$; (b) corresponding frequency-domain spectrum.



(a)



(b)

Figure 3. (a) Time-domain waveform of the output signal $y(t)$; (b) corresponding frequency-domain spectrum.

then $\omega_x = 2\omega_1$, and the products are known as second-order harmonic distortion.

Finally, the third term is

$$y_3(t) = \frac{3}{4}a_3A(t - \tau_3)^3 \cos[\omega_c t + \theta(t - \tau_3) - \phi_3] + \frac{1}{4}a_3A(t - \tau_3)^3 \cos[3\omega_c t + 3\theta(t - \tau_3) - 3\phi_3] \quad (8)$$

(where $\phi_3 = \omega_c \tau_3$) and also involves two different sets of products located near the input frequency band (or fundamental band) ω_c and the third harmonic $3\omega_c$.

As are the even-order products, the third-order products falling near the third harmonic $3\omega_c$ are classified as out-of-band products. Appearing at $\omega_x = \omega_1 + \omega_2 + \omega_3$, that is, out of the fundamental signal band in RF systems of narrow bandpass characteristics, these products seldom constitute a major source of nonlinear signal impairment as they can be easily filtered out. Note, however, that they may also constitute in-band products in ultra-wide-band systems such as cable television (CATV).

Third-order products falling exactly over, or in the vicinity of ω_c , in which the resulting frequencies can be either $\omega_x = \omega_1 + \omega_2 - \omega_3$, $\omega_x = 2\omega_1 - \omega_2$, or even $\omega_x = \omega_1$ (whether they arise from the combination of three distinct, two equal and one different, or three equal input frequencies, respectively), are obviously called *in-band products*. Contrary to the products treated above, they cannot be eliminated by linear filtering, constituting the principal object of intermodulation distortion studies in microwave and wireless systems. In fact, some authors even reserve the term *intermodulation distortion* for this particular form of nonlinear signal perturbation.

To analyze these in-band distortion products in more detail, we will now consider two different situations of system memory. In the first case, it is assumed that the time delays of (4) are due only to the active device's reactive components or to the input and output matching networks. In this way, they may be comparable to the RF carrier period, but negligible when compared to the much slower modulation timescale. Therefore, the in-band products can be approximated by

$$\frac{3}{4}a_3A(t)^3 \cos[\omega_c t + \theta(t) - \phi_3] \quad (9)$$

which shows that, although the system kept its dynamic behavior to the RF carrier, it became memoryless (i.e., responds instantaneously) to the modulation envelope. Since general amplitude and phase modulations have frequency components that start at DC, we have already seen that these products include spectral lines falling exactly over the ones already present at the input, and some other new components named as spectral regrowth.

The third-order signal components that are coincident with the input are given by $\omega_x = \omega_1 + \omega_1 - \omega_1 = \omega_1 + (\omega_1 - \omega_1) = \omega_1$ and can be understood as being generated by mixing second-order products at DC with first-order (or linear) ones. Except for their associated gain, which is no longer a_1 , but $\frac{3}{4}a_3$ multiplied by the input amplitude-averaged power A^2 , these products are indistinguishable from the linear components of (6). They carry the same information content, and are, therefore, termed *signal-correlated products*. Although, in a strict sense, they should be considered as nonlinear distortion products (as their signal power rises at a slope of 3 dB/dB against the 1 dB/dB that characterizes truly linear components), from an information content viewpoint, they may also be considered as linear products. In fact, since, for a constant-input-averaged power, they cannot be distinguished from the first-order components, it all happens as if the amplifier had remained linear but with a gain that changed from its small-signal value of $G = a_1 \exp(-j\phi_1)$ to an amplitude-dependent large-signal gain of $G(A) = a_1 \exp(-j\phi_1) + (3/4)A^2 a_3 \exp(-j\phi_3)$. So, input amplitude signal variations [or amplitude modulation (AM)] produce different output amplitude variations, according to the so-called amplifier AM-AM conversion. But, since the gain is also characterized by a certain phase, it is obvious that input amplitude signal variations will also generate output phase variations. In conclusion, and as illustrated in Figs. 4a and 4b, the amplifier will show not only AM-AM but also AM-PM conversion.

Figure 5 depicts a possible block diagram of a laboratory setup intended to measure these static AM-AM and AM-PM characteristics [6]. As shown, it relies on a usual microwave vector network analyzer whose signal source is swept in power.

As a curious aside from this analysis, we should point out that, although our nonlinearity manifests a signal amplitude-dependent gain, it is completely insensitive to

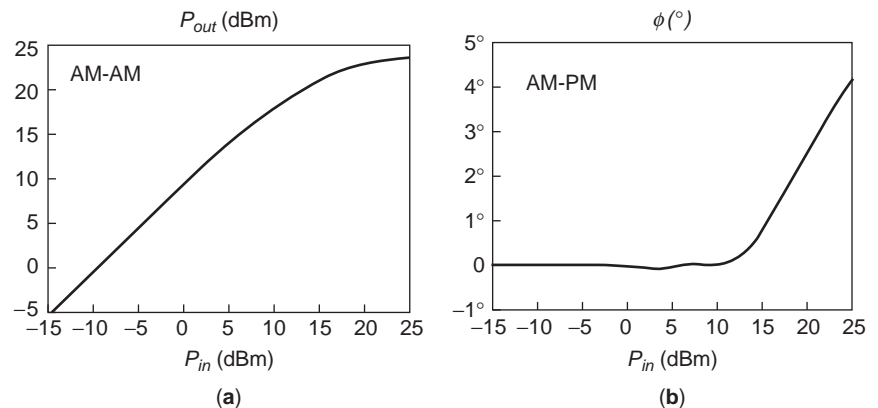


Figure 4. (a) Amplifier's AM-AM conversion; (b) AM-PM conversion.

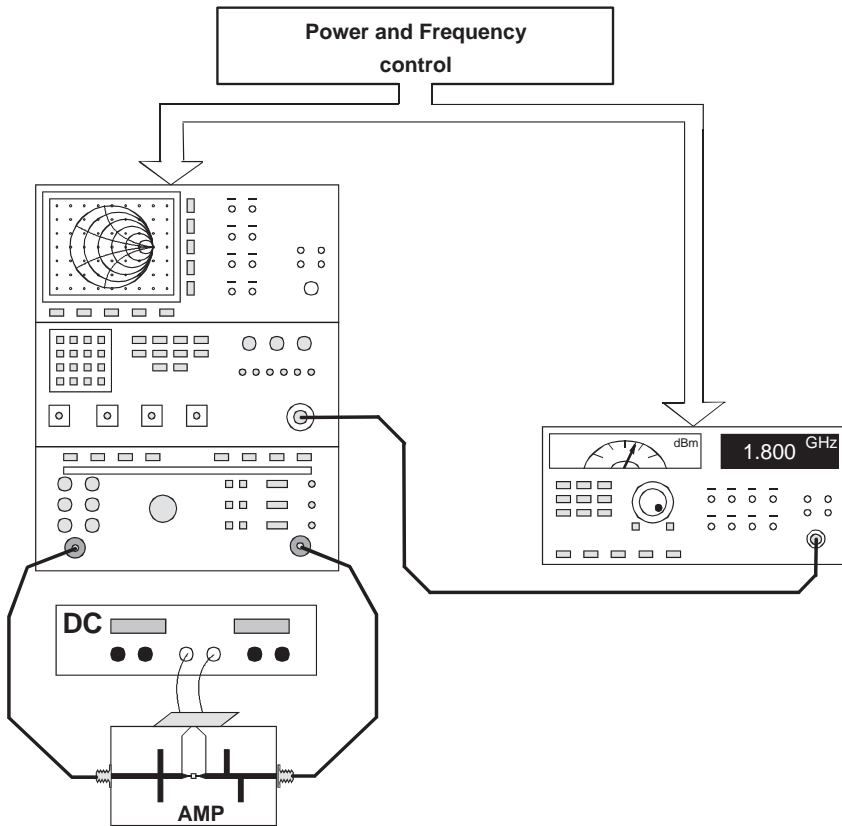


Figure 5. AM-AM and AM-PM characterization setup based on a microwave vector network analyzer.

the input signal phase. In fact, as can be concluded from (9), the bandpass characteristics of our amplifier would be completely transparent to a phase-modulated signal of constant amplitude, in the sense that the phase information present at the output would be exactly equal to the phase information present at its input.

In the second case, it is supposed that, beyond the usual time constants of the order of the RF carrier period, our system may even present time delays, τ_1' , τ_2' , and τ_3' , comparable to the modulation period (e.g., determined by the bias circuitry, active-device charge carrier traps, self-heating). Such time constants are no longer irrelevant for the envelope evolution with time, and the system is said to present long-term or envelope memory effects. The

in-band output distortion becomes

$$\frac{3}{4} a_3 A (t - \tau_3')^3 \cos[\omega_c t + \theta(t - \tau_3') - \phi_3'] \quad (10)$$

and the output envelope will show a phase shift that is dynamically dependent on the rate of amplitude variations. In this case, the output AM-AM or AM-PM is no longer static, and dynamic (or hysteretic) AM-AM and AM-PM conversions are observed, as shown in Figs. 6a and 6b.

This shows that, if our nonlinear system only presents short-term memory effects, and thus is memoryless for the envelope, it may be characterized by a set of gain and

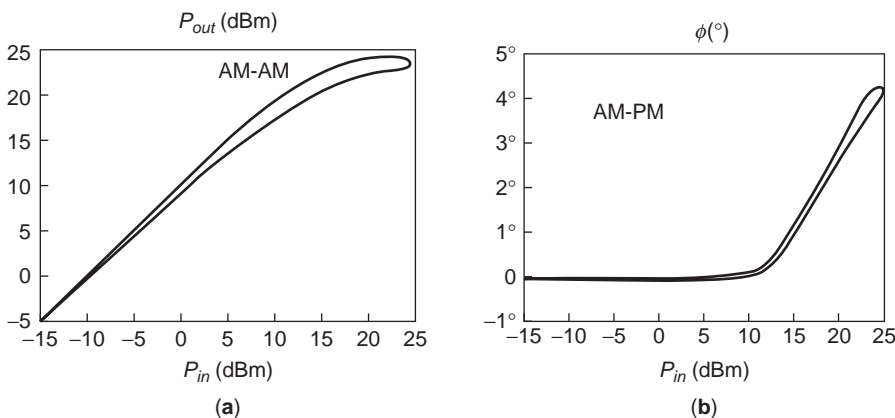


Figure 6. Typical hysteretic AM-AM (a) and AM-PM (b) characteristics shown by nonlinear dynamic amplifiers suffering from both short-term and long-term memory effects.

phase shift tests made with a sinusoidal, or CW (continuous-wave), excitation with swept amplitude and, eventually, with varying frequency. However, if the system is also dynamic to the envelope, then the observed AM-AM/AM-PM varies with the speed of the input amplitude sweep, and such a test becomes questionable. Since each of the tested CW signals can be seen as a carrier modulated by a constant (DC) envelope, it becomes obvious that we cannot fully characterize a dynamic system using only these simple DC excitations.

Moreover, it is clear that testing in-band intermodulation products with a CW signal will never be an easy task, as the output will only have signal-correlated components where $\omega_x = \omega_c$, which all overlap onto the usually much higher linear output. Obviously, in-band intermodulation characterization requires more complex stimuli.

1.2.2. Two-Tone Distortion Characterization. One way to increase the complexity of our test signal is to use a two-tone excitation:

$$x(t) = A_1 \cos(\omega_1 t) + A_2 \cos(\omega_2 t) \tag{11}$$

The in-band output components of (4) when subject to this new stimulus will be

$$\begin{aligned} & a_1 A_1 \cos[\omega_1 t - \phi_{110}] + a_1 A_2 \cos(\omega_2 t - \phi_{101}) \\ & + \frac{3}{4} a_3 A_1^2 A_2 \cos[(2\omega_1 - \omega_2)t - \phi_{32-1}] \\ & + \left[\frac{3}{4} a_3 A_1^3 + \frac{6}{4} a_3 A_1 A_2^2 \right] \cos[\omega_1 t - \phi_{310}] \\ & + \left[\frac{6}{4} a_3 A_1^2 A_2 + \frac{3}{4} a_3 A_2^3 \right] \cos(\omega_2 t - \phi_{301}) \\ & + \frac{3}{4} a_3 A_1 A_2^2 \cos[(2\omega_2 - \omega_1)t - \phi_{3-12}] \end{aligned} \tag{12}$$

Beyond the expected linear components arising at ω_1 and ω_2 , (12) is also composed of other third-order products at ω_1 , ω_2 , $2\omega_1 - \omega_2$, and $2\omega_2 - \omega_1$. They constitute again the signal-correlated (ω_1 and ω_2) and signal-uncorrelated ($2\omega_1 - \omega_2$ and $2\omega_2 - \omega_1$) components. The terms at ω_1 (ω_2) that are dependent only on A_1 (A_2) constitute the AM-AM/AM-PM conversion discussed above. But now there are some new terms at ω_1 (ω_2) whose amplitude is also controlled by A_2 (A_1). They model two different, but obviously related, nonlinear effects. One is cross-modulation, a nonlinear effect in which amplitude modulation of one RF carrier is converted into amplitude modulation of the other; the other is known as *desensitization*, the loss of receiver sensitivity to one signal when in presence of an incoming strong perturbation (e.g., a jammer).

The terms at $2\omega_1 - \omega_2$ and $2\omega_2 - \omega_1$ are spectral regrowth components that appear as sidebands located side by side to the fundamentals at a distance equal to their frequency separation $\omega_2 - \omega_1$. These in-band intermodulation distortion (IMD) sidebands rise at a constant slope of 3 dB per dB of input level rise, until higher-order components (in the case of our polynomial model, output con-

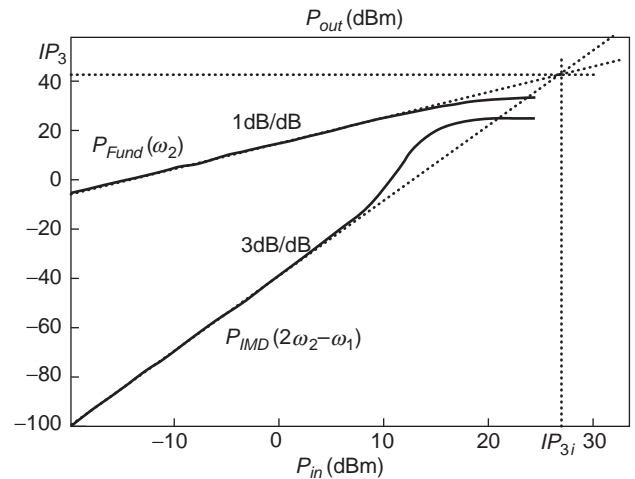


Figure 7. Typical fundamental and third-order intermodulation power versus input power plots. Note the definition of the extrapolated third-order intercept point IP_3 .

tributions due to higher-degree terms) show up. Since first-order components rise at a slope of only 1 dB per dB, we could conceive of an extrapolated (never reached in practice) output power where the output IMD and fundamentals would take the same value. As illustrated in Fig. 7, this is the so-called third-order intercept point IP_3 .

Although meaningful only for small-signal regimes, where the fundamental and IMD components follow their idealized straight-line characteristics, IP_3 is still the most widely used (some times erroneously) intermodulation distortion figure of merit.

Figure 8 shows a block diagram of the most popular laboratory setup used for two-tone intermodulation tests. It relies on a two-tone generator of high-spectral purity, and a high-dynamic range microwave spectrum analyzer.

Although, for many years, two-tone intermodulation characterization has been restricted to these amplitude measurements, more recently we have seen an increasing interest to also identify the IMD components' phase. The reason for this can be traced to the efforts devoted to extract behavioral models capable of representing the device's IMD characteristics and to the design of amplifier linearizers that must be effective even when the main nonlinear device presents long-term memory effects. In fact, since most of the linearizers can be understood as auxiliary circuits capable of generating IMD components that will cancel the ones arising from the main amplifier, it is obvious that those linearizing circuits must be designed to meet both IMD amplitude and phase requirements.

Unfortunately, the first problem that arises when trying to measure the IMD components' phase is that, despite phase is a relative entity, we have no phase reference for IMD. Contrary to what happens to the output fundamentals in which we can refer their phases to the phases at the input (usually arbitrarily assumed zero), the problem is that now there are no input components at the IMD frequencies. So, we first need to create a reference signal at that IMD frequency. That is usually done with a

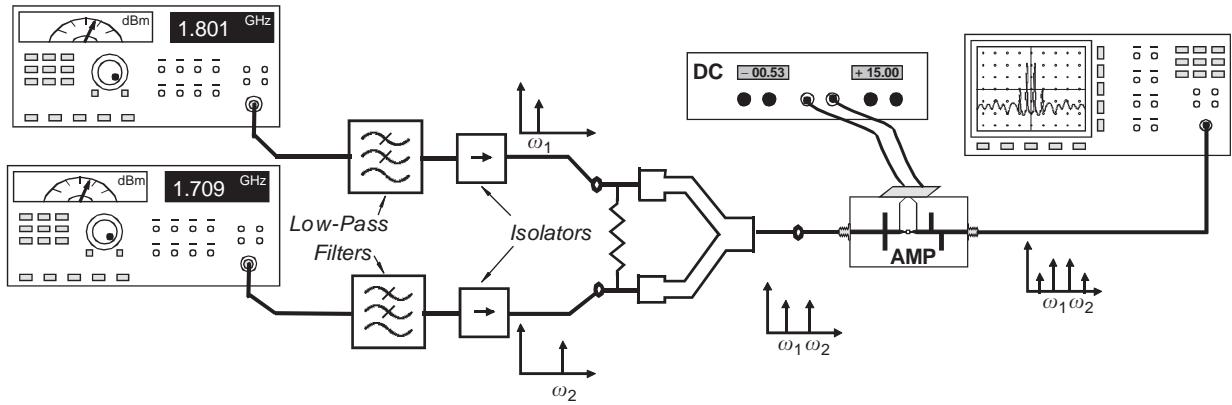


Figure 8. The most popular laboratory setup used for two-tone intermodulation tests.

reference nonlinearity; thus IMD phase measurement results become relative to the reference nonlinearity used in the setup. For example, in the setup depicted in Fig. 9, the reference nonlinearity is based in the nonlinear characteristic of broadband Schottky diodes, and the phase value is acquired from the variable phase shift necessary to balance the device under test (DUT) and reference arms.

1.2.3. Multitone Distortion Characterization. For completeness, let us now briefly introduce intermodulation characterization under multitone excitations. A detailed analysis of this important and up-to-date subject can be found in various references [e.g. 5,6].

First, we will assume that our stimulus can be described as a sum of Q sinusoids of different frequencies:

$$x(t) = \sum_{q=1}^Q A_q \cos(\omega_q t) = \frac{1}{2} \sum_{q=-Q}^Q A_q e^{j\omega_q t} \quad (13)$$

The output of a general power series such as (4) to the excitation of (13) will be

$$y(t) = \sum_{n=1}^N y_n(t) \quad (14a)$$

where each of the orders can be expressed as

$$y_n(t) = \frac{1}{2^n} a_n \left[\sum_{q=-Q}^Q A_q e^{j\omega_q t} \right]^n$$

$$= \frac{1}{2^n} a_n \sum_{q_1=-Q}^Q \cdots \sum_{q_n=-Q}^Q A_{q_1} \cdots A_{q_n} e^{j(\omega_{q_1} + \cdots + \omega_{q_n})t} \quad (14b)$$

which contains various frequencies at $\omega_x = \omega_{q_1} + \cdots + \omega_{q_n}$, originating from many different mixing products.

Since there is, in general, more than one mixing product—that is, more than one combination of input frequencies—falling at the same frequency, the calculation of their output amplitude requires that first we are able to determine the number of those different combinations. One systematic way to do this is to recognize that their frequencies must obey [7]

$$\omega_{n,v} = \omega_{q_1} + \cdots + \omega_{q_n} = m_{-Q}\omega_{-Q} + \cdots + m_{-1}\omega_{-1} + m_1\omega_1 + \cdots + m_Q\omega_Q \quad (15)$$

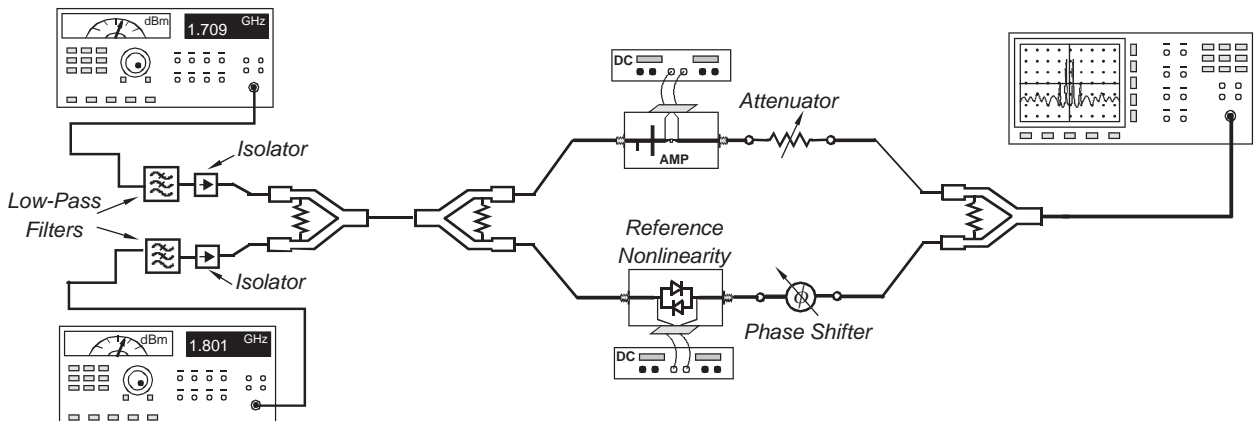


Figure 9. Possible IMD phase measurement setup based on a reference nonlinearity, a spectrum analyzer, and an IMD cancellation loop.

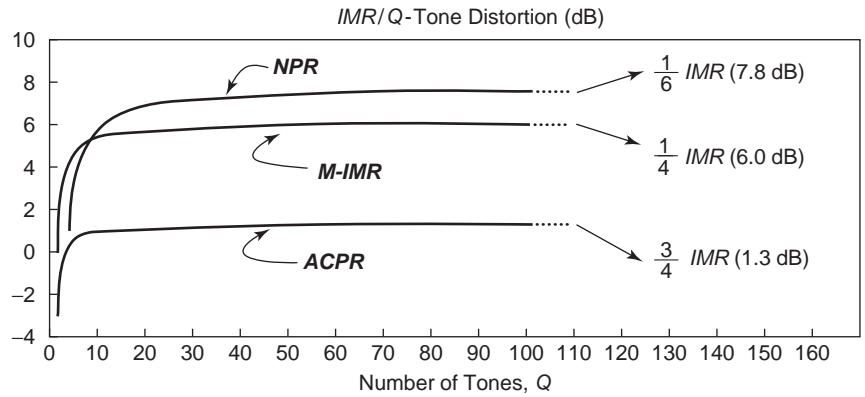


Figure 10. Ratio of two-tone IMR to NPR, M-IMR and ACPR versus the number of tones Q for a memoryless cubic polynomial.

where

$$\sum_{q=-Q}^Q m_q = m_{-Q} + \dots + m_{-1} + m_1 + \dots + m_Q = n \quad (16)$$

defining the following mixing vector:

$$\mathbf{v} = [m_{-Q} \dots m_{-1} m_1 \dots m_Q] \quad (17)$$

Then, the number of different ways of generating the same mixing vector is given by the multinomial coefficient [7]:

$$t_{n,v} = \frac{n!}{m_{-Q}! \dots m_{-1}! m_1! \dots m_Q!} \quad (18)$$

These Q -tone distortion components allow a generalization of the two-tone signal-to-intermodulation distortion ratio [IMR; sometimes also known as carrier-to-IMD ratio (C/I)] to various multitone distortion figures of merit. One of these is defined as the ratio between the constant-amplitude output fundamental signals and the highest sideband IMD component (M -IMR).

Another measure is the ratio between integrated fundamental output power and integrated upper or lower sideband distortion. As this sideband spectral regrowth falls exactly over the location of a potentially present adjacent channel, it is called the *adjacent-channel power ratio* (ACPR).

Finally, a measure of the ratio of the fundamentals to the signal-uncorrelated distortion components that fall exactly among the fundamental components is given by the so-called noise-power-ratio (NPR). The reason for this denomination comes from the fact that, although that figure of merit is being introduced in this text for a multitone excitation, it was traditionally measured with a bandlimited white-noise stimulus—a generalized multi-tone excitation with an infinite number of tones.

Besides all these figures are measures of nonlinear effects that share a common physical origin, and it has not been easy to relate them, except for very particular situations. First, we [5] presented relations between various multitone distortion figures and IMR, obtained for a third-degree polynomial memoryless model. Then,

Boulejfen et al. [8] extended those results for a fifth-degree polynomial. As a summary of these results, Fig. 10 presents the ratio of IMR to the above-defined multi-tone distortion figures versus the number of tones Q for a memoryless cubic polynomial.

A laboratory setup for multitone distortion tests is similar to the one already shown for two-tone tests, except, obviously, with respect to the signal generator [6]. However, since a NPR test focuses on the distortion that falls exactly over the output fundamentals, something must be done to separate the desired distortion components from the much higher fundamental signals. The usual way to solve that problem consists in creating a very narrow measurement window within the input signal bandwidth. This is accomplished by either shutting down a few input tones—when a multitone signal generator is used—or introducing a notch filter between the bandlimited white-noise generator and the nonlinear device under test [6].

2. CAD TOOLS FOR INTERMODULATION DISTORTION PREDICTION

Because intermodulation distortion is a nonlinear effect, any attempt to predict its behavior by hand for even the most simple practical circuits or devices becomes extremely difficult, if not impossible. So, intermodulation distortion prediction relies heavily on good device models and appropriate computer simulation algorithms. Unfortunately, these subjects are so vast that we have to restrict this text to a first guiding overview. So, we will concentrate our discussion on a set of criteria for model quality (for this specific purpose) and give some hints concerning usual simulation tools.

2.1. Nonlinear Device Modeling for Distortion Analysis: General Considerations

Starting with nonlinear device models, we can divide them into four general groups: (1) physical and empirical models and (2) global and local models.

Physical models are mathematical descriptions of the internal device operation that are drawn from the knowledge of the device’s geometric and physical structure, and

from the application of a certain set of basic physics laws. Although relying on extremely complex formulations that require an enormous number of parameters and are computationally expensive to evaluate, they can provide much better accuracy than the empirical models as they necessarily mimic the basic device operation. On the other hand, empirical models do not require any information about the internal structure of the device, relying completely on input–output behavioral observations. Hence, they are also known as blackbox models or behavioral models.

Typical examples of physical models are the Schottky diode equation and the device models described by a set of coupled partial-differential equations of electric potential, charge, and charge carrier mobility. Examples of purely behavioral models are the linear scattering matrix, table-based device models, or even the abovementioned AM–AM/AM–PM models.

Local models can be distinguished from global models for their approximation range. Because they are behavioral in nature, they constitute two different compromises between the domain of fitting and the level of accuracy. While local models are very good in representing mild nonlinear behavior in the vicinity of some quiescent point, global models are conceived as valid for any possible operation regime, but at the expense of an increased error. It is therefore natural that they are also known as *small-signal* or *large-signal models*, respectively. The Gummel–Poon model of BJTs, the quadratic model of FETs, or an AM–AM/AM–PM representation are examples of global models, while the poor extrapolation capability usually associated with polynomial approximators tends to grant them a distinct local behavior. For example, the cubic polynomial that could be extracted from the third-order intercept point is necessarily a local model valid only for small-signal excitation levels.

The polynomial example given above is not accidental as it plays a fundamental role in all nonlinear distortion analysis. In fact, for some unique reason we began this article using exactly the same polynomial of expression (4). As we then concluded, if the model is a polynomial, we have a direct and easy way to calculate the various intermodulation products to any signal that can be described as a sum of sinusoids. Furthermore, by simply selecting its coefficients, we can tailor the polynomial for very different approximation goals. To understand that, let us use an illustration example. Figures 11 and 12 depict the approximation of one typical transfer function characteristic by two different polynomials: a Taylor series and a Chebyshev polynomial series, both of 10th degree.

As seen from Figs. 11a and 11b, the coefficients of the Chebyshev polynomial were selected so that the polynomial could produce an optimum approximation to the response of our original nonlinearity to a sinusoid of 1.5 V peak amplitude, centered at a quiescent point of 0 V (something close to what is found in typical class AB power amplification regimes).

On the other hand, the coefficients of the Taylor series were taken as the appropriately scaled derivatives of the nonlinearity at the same quiescent voltage of 0 V. It constitutes, therefore, the optimum polynomial approxi-

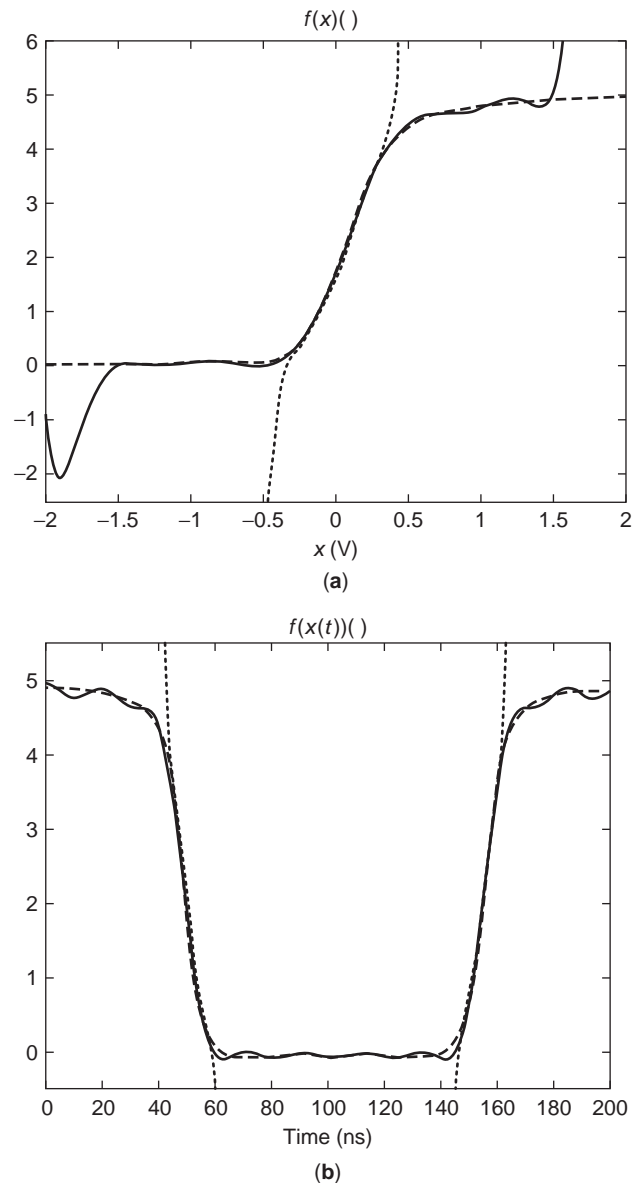


Figure 11. (a) Nonlinear memoryless transfer function, $f(x)$ (---) and its 10th-order Taylor series approximation around $x = 0$ V (---) and Chebyshev polynomial optimized for a sinusoidal input amplitude of $A = 1.5$ V (—); (b) time-domain waveform of the output of the transfer function $f[x(t)]$ (---) and of its 10th-order Taylor series approximation (---) and Chebyshev polynomial (—), when excited by a CW input of amplitude $A = 1.5$ V.

mation to the nonlinear response to any signal of infinitesimal input amplitude (see Fig. 11a).

When excited by sinusoids of variable amplitude, the output DC component (Fig. 12a), the fundamental component (Fig. 12b), and the second- and third-harmonic distortion components (Figs. 12c and 12d, respectively) reveal that these two polynomial approximators present, indeed, very distinct properties.

The Taylor series is clearly a local approximator that produces optimum results in the vicinity of the quiescent point, but then suffers from a catastrophic degradation when the excitation exceeds ~ 0.3 V of amplitude. On the

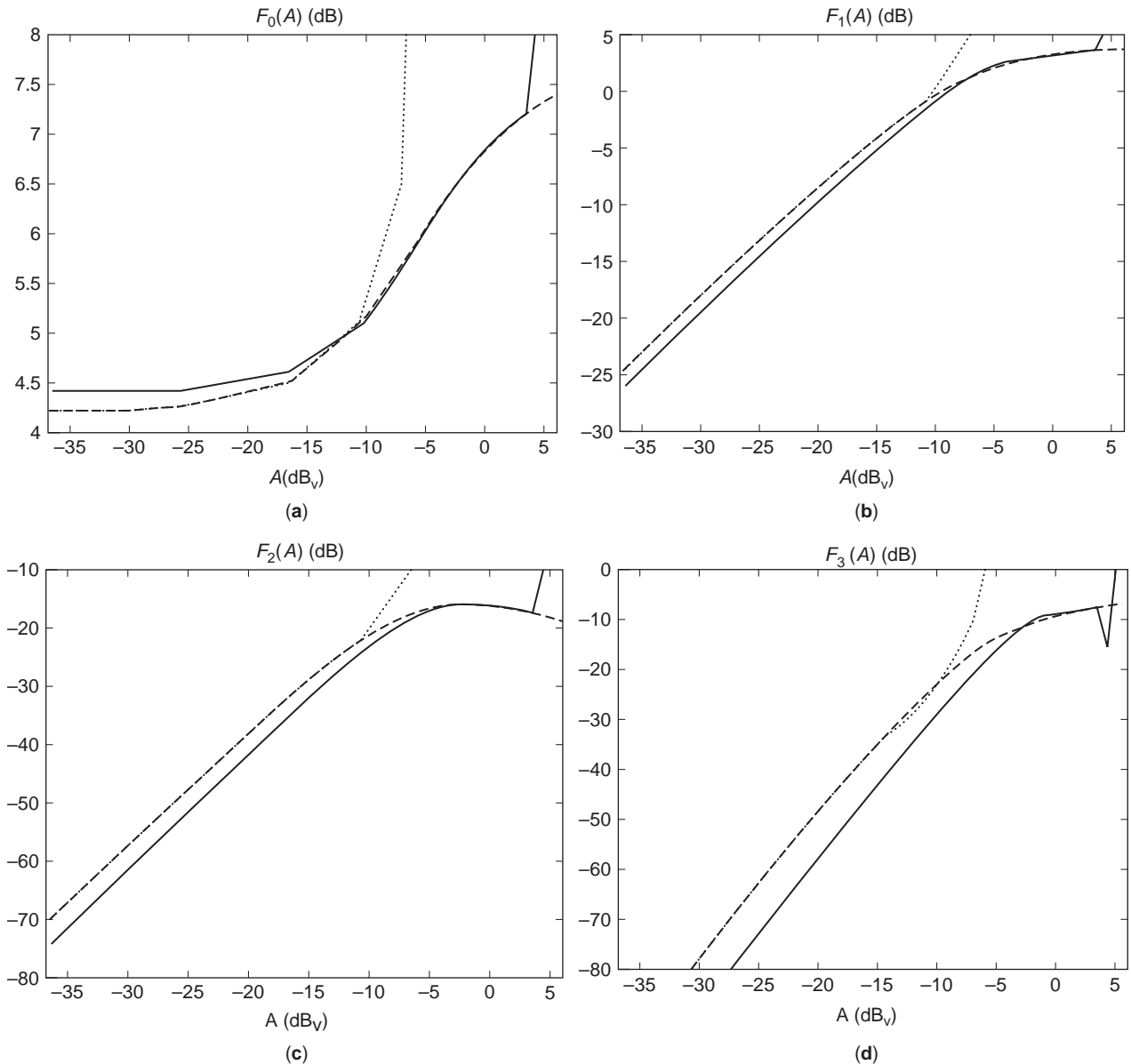


Figure 12. (a) DC component of the output of the transfer function $f[x(t)]$ (---) of its 10th-order Taylor series approximation (···) and Chebyshev polynomial (—), when excited by a CW input of amplitude $0.015\text{ V} < A < 1.95\text{ V}$; (b) fundamental component of output of transfer function $f[x(t)]$ (---) of its 10th-order Taylor series approximation (···) and Chebyshev polynomial (—), when excited by a CW input of amplitude $0.015\text{ V} < A < 1.95\text{ V}$; (c) second-harmonic component of output of transfer function $f[x(t)]$ (---) of its 10th-order Taylor series approximation (···) and Chebyshev polynomial (—), when excited by a CW input of amplitude $0.015\text{ V} < A < 1.95\text{ V}$; (d) third-harmonic component of output of unit transfer function $f[x(t)]$ (---) and its 10th-order Taylor series approximation (···) and Chebyshev polynomial (—), when excited by a CW input of amplitude $0.015\text{ V} < A < 1.95\text{ V}$.

contrary, the Chebyshev series is worse at those small-signal levels, but performs much better up to excitation amplitudes of 1.5 V . It behaves, therefore, as a global approximator. (In fact, the Chebyshev series is still a local approximator whose domain is no longer defined around the fixed quiescent point of 0 V , but around a new generalized dynamic quiescent point imposed by an input sinusoid of 1.5 V amplitude.) As any other mean-square error approximator, the Chebyshev polynomial wanders around the original nonlinearity (see Figs. 11a and 11b), obviously

failing the higher-order derivatives of the function. This is why, contrary to the Taylor series, which, by construction, osculates these derivatives, the Chebyshev series does not show good small-signal distortion behavior.

What we have just seen in this example is common to almost all empirical models and results in an important message as far as intermodulation distortion calculations are concerned. Simultaneously reproducing the device's mild nonlinear details (local characteristics) and the general trends (global properties) is so difficult that we should

never trust an empirical model unless we have guarantees that it was specifically tested for nonlinear distortion.

2.2. Nonlinear Models for Distortion Analysis at the Circuit Level

To perform intermodulation analysis at the circuit level, that is, to compute the distortion arising from a certain electronic circuit subject to a specific bandpass RF input signal stimulus, the device must be represented by some equivalent-circuit model [6]. This is the normal modeling requirement for using either time-marching algorithms, like the ones used by SPICE, or frequency-domain simulators, such as the harmonic-balance solvers. Such equivalent circuits have topologies and parameter sets usually supported from both physical and empirical data.

Linear, or bias-independent, elements are usually extracted from a broadband small-signal AC characterization. Nonlinear elements can be either voltage-controlled current sources (nonlinear device currents) $i(v)$, voltage-controlled electric charge sources (nonlinear capacitances) $q(v)$, or current-controlled magnetic flux sources (nonlinear inductances) $\phi(i)$. Each of these is assumed to be described by a static, or memoryless, function of its controlling variable(s), which can, again, be supported by both physical device knowledge or by empirical observations. Mostly in this latter case, it is the selection of these functions that determines the quality of the model for nonlinear distortion predictions. A small mean-square error between measured and modeled data in the whole range of device operation guarantees good global properties, but says nothing about local properties. To be able to also provide good predictability under small-signal regimes, the model must osculate at least the first three derivatives of the actual device function, which requires special model extraction procedures.

Although those derivatives can be obtained from successive differentiation of measured $i(v)$, $q(v)$, or $\phi(i)$ data, this is not recommended for at least two important reasons: (1) since most of the microwave transistors show low-frequency dispersion effects, differentiating DC data may not lead to the real AC behavior; and (2) the aggravation of measurement noise produced by numerical

differentiation. If we rely on averages (data integration) to reduce random measurement errors, it is natural to expect an aggravation of those errors if we go backward, that is, numerically differentiating measurement data. So, the best way to obtain these device derivatives is to measure entities that directly depend on them; and one good example of those entities is exactly the harmonic or intermodulation distortion produced by the device under a CW or a two-tone excitation.

As an example, the laboratory setup depicted in Fig. 13 uses exactly this principle to acquire the nine coefficients of the Taylor series expansion of the drain–source current of a FET:

$$i_{ds}(v_{ds}, v_{ds}) = G_m v_{gs} + G_{ds} v_{ds} + G_{m2} v_{gs}^2 + G_{md} v_{gs} v_{ds} + G_{d2} v_{ds}^2 + G_{m3} v_{gs}^3 + G_{m2d} v_{gs}^2 v_{ds} + G_{md2} v_{gs} v_{ds}^2 + G_{d3} v_{ds}^3 \quad (19)$$

Exciting the FET at the gate side with a sinusoid of frequency ω_1 and at the drain side with a sinusoid of frequency ω_2 allows the extraction of G_m from the output current component at ω_1 , G_{ds} from the component at ω_2 , G_{m2} from the component at $2\omega_1$, G_{md} from the component at $\omega_1 + \omega_2$, G_{d2} from the component at $2\omega_2$, and so on. Unfortunately, the actual procedure is not that simple. Although the unilateral properties presented by microwave FETs at low frequencies guarantee that v_{gs} will have only the ω_1 component, the requirement that the device is terminated at the drain side by a nonnull impedance determines that v_{ds} will have components at ω_1 , at ω_2 , and at all their mixing products. This impedes the orthogonal (or one-to-one) extraction just explained, demanding the solution of a 2×2 linear system for G_m and G_{ds} ; a 3×3 linear system for G_{m2} , G_{md} , and G_{d2} ; and a 4×4 linear system for extracting G_{m3} , G_{m2d} , G_{md2} , and G_{d3} [9]. Since the concept supporting this setup is general, it can be extended to other nonlinear current sources present in any nonlinear device equivalent-circuit model, or even to charge sources [10].

As an illustrative example, Fig. 14 shows all nine coefficients of (19) extracted with the setup of Fig. 13,

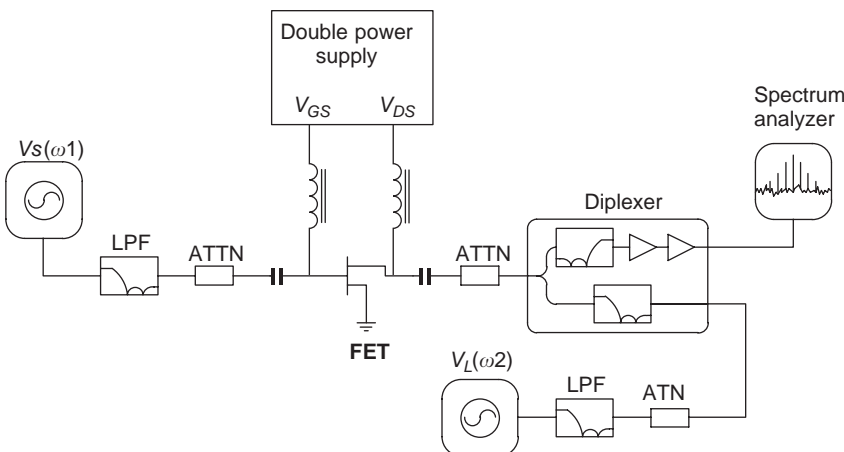


Figure 13. Laboratory setup used to extract the Taylor series coefficients of a bidimensional nonlinearity such as the $i_{ds}(v_{GS}, v_{DS})$ of a FET.

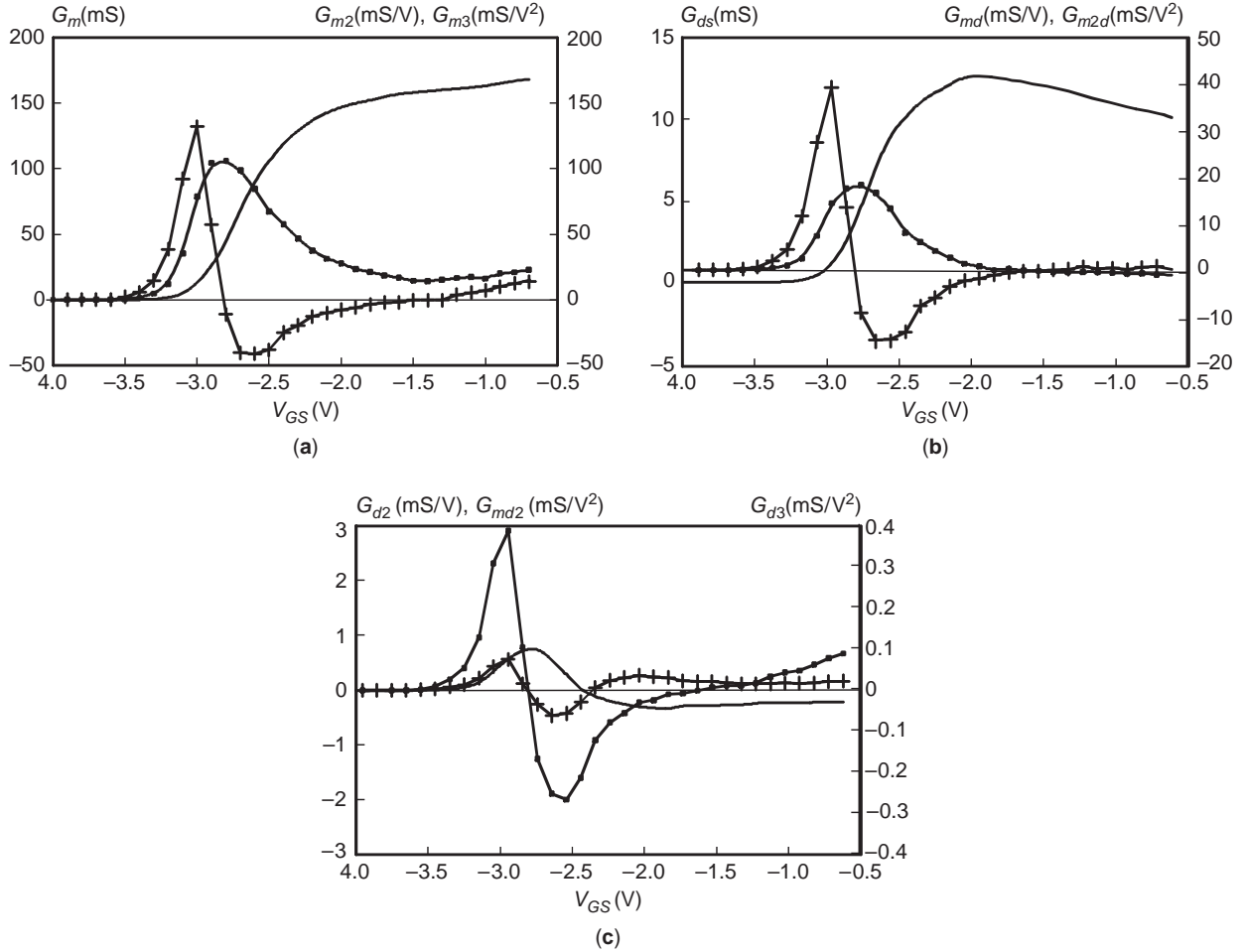


Figure 14. Taylor series coefficients of the bidimensional voltage-controlled $i_{DS}(v_{GS}, v_{DS})$ current source of a GaAs MESFET for a constant V_{DS} in the saturation zone: (a) G_m (—), G_{m2} (—●—), and G_{m3} (—+—); (b) G_{ds} (—), G_{md} (—●—) and G_{md2} (—+—); (c) G_{d2} (—), G_{md2} (—●—), and G_{d3} (—+—).

from a medium-power microwave GaAs MESFET biased in the saturation region.

2.3. Nonlinear Models for Distortion Analysis at the System Level

Although system simulation for the modulated bandpass RF signals has already taken the first steps, system simulation at the complex envelope level is, by far, the most usual way to assess distortion performance of entire communication systems. It assumes that the amplitude/phase-modulated RF signal of (5) can be given by

$$\begin{aligned} x(t) &= A(t) \cos[\omega_c t + \theta(t)] \\ &= \text{Re}[A(t)e^{j\theta(t)}e^{j\omega_c t}] = \text{Re}[\tilde{x}(t)e^{j\omega_c t}] \end{aligned} \quad (20)$$

in which $\tilde{x}(t)$ is the complex envelope—the lowpass equivalent signal of $x(t)$ [11]—and that we are interested only in the system's in-band characteristics. Thus, the object of the analysis ceases to be the real bandpass RF-modulated signal to become only the complex lowpass envelope. In

this way, a significant improvement in simulation efficiency is achieved because time-domain simulations no longer need to be carried on with sampling rates imposed by the RF carrier and its harmonics, but only by the much slower envelope. So, the models required for these envelope-level system simulators are lowpass complex equivalent behavioral models of the original bandpass RF components [11]. They are, therefore, single-input/single-output maps, which may be either linear or nonlinear.

Linear maps are easily implemented as gain factors in the memoryless case, or as finite or infinite impulse responses, FIR or IIR, digital filters [11,12], when in presence of dynamic elements.

A linear dynamic complex envelope filter whose frequency response function is $\tilde{H}(j\tilde{\omega})$ can be directly derived from the corresponding circuit level filter $H(j\omega)$ by simply going through the following bandpass–lowpass transformation [11]

$$\tilde{H}(j\tilde{\omega}) = H[j(\tilde{\omega} + \omega_c)]u(\tilde{\omega} + \omega_c) \quad (21)$$

where $u(\omega)$ is the unity step function.

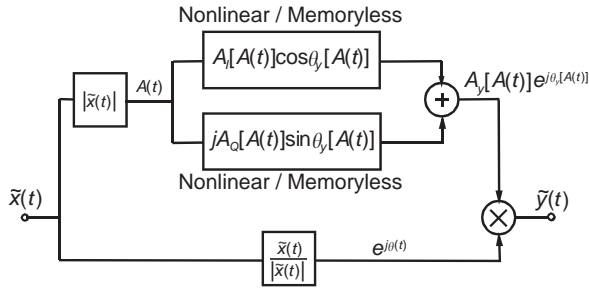


Figure 15. AM–AM and AM–PM memoryless lowpass equivalent behavioral model known as the *Saleh quadrature model*.

2.3.1. Memoryless AM–AM/AM–PM Models. In their most basic form, nonlinear complex envelope models simply try to describe the amplitude-dependent memoryless nonlinear effects observed for the amplitude and phase modulation content. They are the AM–AM/AM–PM models discussed above, and of which the quadrature Saleh model of Fig. 15 is one of the most widely known [13].

When modeled as a polynomial nonlinearity, this AM–AM/AM–PM model can include only odd-degree $(2n + 1)$ terms involving n negative carrier frequencies plus $(n + 1)$ positive ones [11]

$$\hat{y}(t) = \sum_{n=0}^{(N-1)/2} \frac{p_{2n+1}}{2^{2n}} \binom{2n+1}{n+1} \hat{x}(t) |\hat{x}(t)|^{2n} \quad (22)$$

where $\binom{m}{r}$ stands for the number of different combinations of r elements taken from a population of size m and p_{2n+1} are the polynomial coefficients, now having real and imaginary parts.

2.3.2. Dynamic AM–AM/AM–PM Models. As already seen in the introduction, when the system presents memory not only to the RF signal (as indicated by the AM–PM effect) but also to the slowly varying lowpass envelope, this AM–AM/AM–PM model becomes unsatisfactory and a true dynamic model is required. For example, one possibility for such an extension could be to make the in-phase $A_I(\cdot)$ and quadrature $A_Q(\cdot)$ static nonlinear functions dependent not on the amplitude envelope but on some dynamic version of it. In this way, the AM–AM and

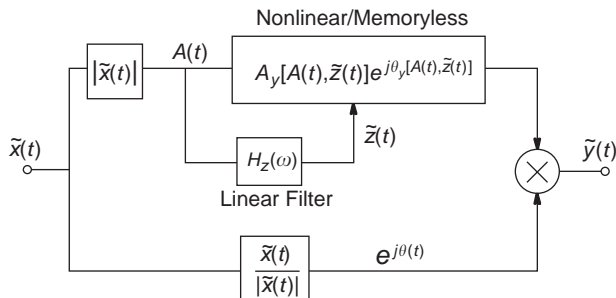


Figure 16. An AM–AM/AM–PM model in which the amplifier is modeled as a dynamic gain function of the envelope amplitude.



Figure 17. A three-box, or Wiener–Hammerstein, lowpass equivalent model.

AM–PM conversions would no longer be instantaneous functions of $A(t)$, but, as shown in Fig. 16, become instantaneous functions of an auxiliary dynamic variable $\tilde{z}(t)$, and thus dynamically varying with $A(t)$.

2.3.3. Memoryless Nonlinearity: Linear Filter Cascade Models. Beyond the methods described above, several other approximated topologies have been tried for building nonlinear dynamic models [14]. Some of those, like the two- or three-box models shown in Fig. 17, deserve mention because of their practical relevance. In fact, they somehow mimic the internal structure of typical RF devices (as microwave power amplifiers), which are usually constituted by a broadband (memoryless) nonlinear active device sandwiched between two linear dynamic input and output matching networks.

As shown in Fig. 17, these two- or three-box nonlinear dynamic models can be cascades of a linear filter followed by the measured memoryless AM–AM/AM–PM nonlinearity (known as the *Wiener model*), be cascades of this AM–AM/AM–PM memoryless nonlinearity followed by a linear filter (the *Hammerstein model*), or even be constituted by a combination of both (the *Wiener–Hammerstein model*). Other parallel combinations of memoryless nonlinearities and linear filters also became popular when an optimal extraction procedure was shown to be practically possible [15].

2.3.4. General Nonlinear Dynamic Models. Unfortunately, these three-box models become hopelessly inaccurate when the dynamic effects presented to the envelope are not due to the bandwidth limitations of the linear matching networks, but are intrinsically mixed with the nonlinearity [14]. That is the case, for example, with wireless power amplifiers whose nonlinear dynamic effects cannot obviously arise from bandwidth limitations—the RF signal can have bandwidths as narrow as 1% or 0.01%, but from the active device self-heating or from reactive (to the envelope) bias paths. In such cases, more general nonlinear dynamic models, as the ones briefly explained in the following paragraphs, must be attempted.

When the lowpass equivalent system is stable, continuous, and of fading memory (i.e., its response cannot keep memory from an infinitely remote past), mathematics operator theory has shown that its response $\hat{y}(t)$ to any input $\hat{x}(t)$ can be approximated, within any desired error margin, by

$$\hat{y}(s) = f_{\text{NL}}[\hat{x}(s), \hat{x}(s-1), \dots, \hat{x}(s-Q)] \quad (23)$$

where $f_{\text{NL}}(\cdot)$ is a $(Q + 1)$ -to-one static nonlinear function, s is the time instant in which the output is being calculated; $\hat{x}(s-1), \dots, \hat{x}(s-Q)$ are delayed, or past versions of the

input; $\tilde{x}(s)$; and Q is the system's finite memory span. Indeed, expression (23) simply states that the system output at a certain instant can be calculated as the nonlinear combination of the input at that instant and all its past versions within the memory span. There are basically two ways of implementing this nonlinear and dynamic input-output mapping, depending on whether $f_{NL}(\cdot)$ is approximated by a $(Q + 1)$ -to-one polynomial or by a neural network: polynomial filters [12] and artificial neural networks (ANNs) [16].

In the first case, (23) becomes

$$\tilde{y}(s) = \sum_{n=1}^N \tilde{y}_n(s) \tag{24a}$$

where

$$\begin{aligned} \tilde{y}_n(s) = & \sum_{q_1=0}^Q \cdots \sum_{q_{2n+1}=0}^Q \tilde{h}_{2n+1}(q_1, \dots, q_{2n+1}) \tilde{x}(s - q_1) \\ & \cdots \tilde{x}(s - q_{n+1}) \tilde{x}(s - q_{n+2})^* \cdots \tilde{x}(s - q_{2n+1})^* \end{aligned} \tag{24b}$$

Such a dynamic polynomial formulation (also known as a *Volterra filter* [12]) presents two important advantages:

1. Its various output components can be traced to a particular coefficient or term. Therefore, it leads to useful concepts as nonlinear order and gives insights into parameter extraction. In fact, this

immediately allows model implementations such as the ones depicted in Figs. 18a and 18b for the first- and third-order outputs, $\tilde{y}_1(s)$ and $\tilde{y}_3(s)$, respectively.

2. The second advantage, shared with all polynomial approximators, is that the formulation is linear in the parameters (although obviously nonlinear in the inputs). Thus, it allows a direct model parameter extraction based on the solution of a system of simultaneous linear equations.

Unfortunately, it also presents an important disadvantage. Like any other polynomial approximator, it is a local model.

It is mostly this drawback that justifies the alternative ANN formulation. A single hidden-layer ANN can be expressed as [16]

$$\tilde{u}_k(s) = \sum_{q=0}^Q [w_k(q)\tilde{x}(s - q)] + b_k \tag{25a}$$

$$\tilde{y}(s) = b_o + \sum_{k=1}^K w_o(k)f_o[\tilde{u}_k(s)] \tag{25b}$$

in which the $w_k(q)$ and $w_o(k)$ are weighting factors and b_o and b_k are bias values, constituting the model parameter set. $f_o(\cdot)$ are static single-input/single-output nonlinear functions (the so-called activating functions) of sigmoid shape. Because a sigmoid is an output-bounded function, an ANN is well behaved for all inputs.

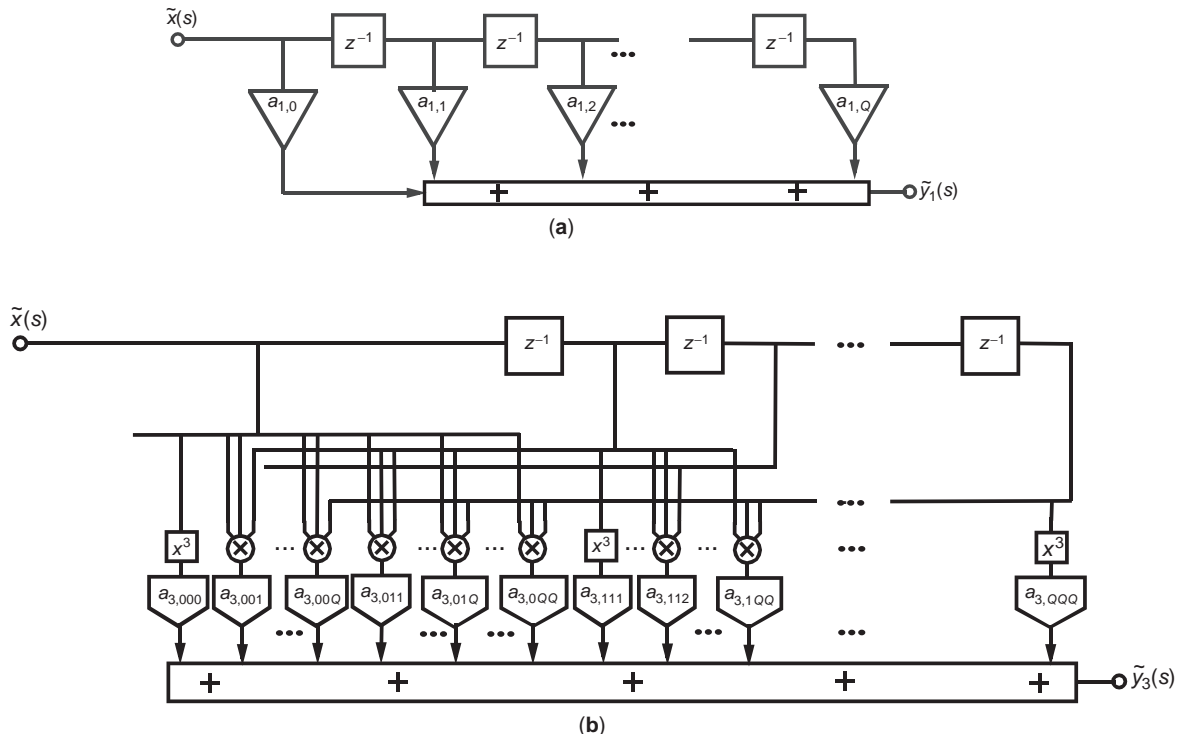


Figure 18. Implementation examples of first- (a) and third- (b) order kernels of a general polynomial filter.

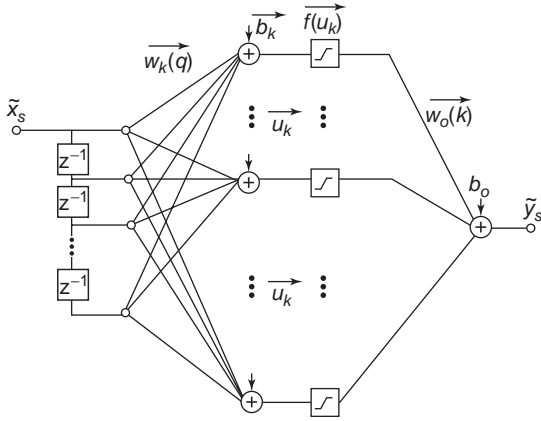


Figure 19. Implementation of a nonlinear dynamic artificial neural network.

A direct implementation of a dynamic ANN is shown in Fig. 19. However, recognizing that (25a) constitutes a biased linear FIR filter, whose bias is b_k and impulse response is $w_k(\cdot)$, this dynamic ANN can also be implemented as a set of parallel branches of the Wiener type, as depicted in Fig. 20 [14].

Unfortunately, since all terms of the ANN are similar, there is no way to identify relations between the system's output properties and any particular ANN terms. Furthermore, as the model is now also nonlinear for the $w_k(q)$ and b_k parameters, the parameter extraction process must rely on some form of optimization. This optimization process, called "ANN training," is known to give results that are highly dependent on the input–output training data. Moreover, there is no guarantee that the parameter set found is unique or even optimum, which can constitute a severe limitation to the model's predictability.

2.4. A Glimpse of Nonlinear Simulation Algorithms for Distortion Prediction

In circuit-level simulators [17], the mathematical representation of the circuit is built by substituting each electronic element with its constitutive relation [e.g., a linear resistor can be represented as Ohm's law, $i = v/R$; a nonlinear resistor would be given by a voltage-controlled

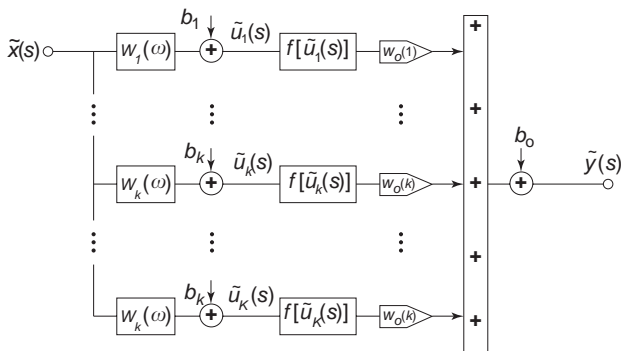


Figure 20. Alternative implementation of the model of Fig. 19, in which the ANN is rebuilt as a parallel combination of several biased linear filter/memoryless nonlinearity branches.

current source, $i(v)$; while a capacitor would be given by a linear or nonlinear charge, $q(v)$] and then applying Kirchhoff's current and voltage laws to the complete circuit. This leads to a system of ordinary nonlinear differential equations (ODEs) in time such as

$$\mathbf{i}[\mathbf{y}(t)] + \frac{d\mathbf{q}[\mathbf{y}(t)]}{dt} = \mathbf{x}(t) \quad (26)$$

where $\mathbf{x}(t)$ and $\mathbf{y}(t)$ stand for the time-domain waveform of the excitation and the state-variable vectors, respectively; $\mathbf{i}[\mathbf{y}(t)]$ represents memoryless linear or nonlinear elements, while $\mathbf{q}[\mathbf{y}(t)]$ models memoryless linear or nonlinear charges (capacitors) or fluxes (inductors). The objective of the simulation is to find the $\mathbf{y}(t)$ circuit solution vector given a known $\mathbf{x}(t)$ input excitation.

On the other hand, system-level simulators are usually implemented as either event-driven or envelope-driven machines. In both cases the simulator treats the system in the time domain, computing a set of time samples of the information signal.

Event-driven machines operate at a very high logic level, in which the information is simply a set of successive logic states. They are, therefore, state flow simulators, without enough subsystem description detail to allow distortion calculations.

Envelope-driven simulators operate with the analogue complex envelope. Hence, they do not handle the true bandpass RF blocks but simply their complex lowpass equivalents. Nevertheless, since these blocks are still nonlinear dynamic blocks, the lowpass equivalent system mathematical representation will again be an ordinary differential equation similar to (26) with the only difference that now both the excitation vector $\mathbf{x}(t)$ and the state variable vector $\mathbf{y}(t)$ are, in general, complex entities.

So, except for the type of signals handled, an ODE such as (26) can be used to represent bandpass RF circuits, bandpass RF systems, or even complex lowpass equivalent systems.

2.4.1. Time-Domain Techniques. The most intuitive way to solve (26) is to covert it into a difference equation

$$\mathbf{i}[\mathbf{y}(s)] + \frac{\mathbf{q}[\mathbf{y}(s)] - \mathbf{q}[\mathbf{y}(s-1)]}{T_s} = \mathbf{x}(s) \quad (27a)$$

or

$$\mathbf{i}[\mathbf{y}(s)]T_s + \mathbf{q}[\mathbf{y}(s)] = \mathbf{x}(s)T_s + \mathbf{q}[\mathbf{y}(s-1)] \quad (27b)$$

in which T_s is the sampling period, and then determine all time samples of $\mathbf{y}(t)$, $\mathbf{y}(s)$, starting from a known initial state $\mathbf{y}(0)$. Because we are integrating the nonlinear ODE in a set of discretized timesteps, this is known as *timestep integration*, and constitutes the basic approach adopted in all time-domain circuit simulators (time-marching machines) such as SPICE, or system simulators like Simulink¹.

¹Simulink is a general-purpose system simulation package that is supported by the Matlab scientific computation software platform.

Although timestep integration is still the nonlinear analysis method of wider acceptance, it suffers from several disadvantages in the RF distortion circuit simulation field. First, since it was conceived to compute the circuit’s transient response, while our interest normally resides in the steady state, it becomes quite inefficient as it has to wait until all transients have vanished. Also, by operating in the time domain, it cannot handle linear elements having a frequency-domain description, such as dispersive distributed transmission media. Finally, even if that drawback is circumvented (e.g., by approximating these elements by lumped networks of reduced order), the necessity of operating in the time domain, while the input and resulting signals are usually handled in frequency domain, would end up in all difficulties associated with the discrete Fourier transform (DFT), namely, spectral leakage when transforming quasiperiodic multitone signals. Fortunately, some time-domain alternatives to the initial timestep integration method, like the “shooting Newton” [17], can bypass the transient response, therefore obviating the waste of time needed to let it vanish.

Furthermore, time-domain methods benefit from two important advantages: (1) since they rely on the SPICE simulator engine, they are well known and available in many electronic design automation tools; and (2) as they use time as a natural continuation parameter [17], they are especially suitable for supporting strong nonlinear regimes. Envelope-driven system-level simulators must handle the information envelopes, which are aperiodic by nature. So, timestep integration does not suffer from the inefficiency attributed to the calculation of the periodic steady-state response, becoming the obvious choice in solving (26).

2.4.2. Frequency-Domain Techniques. Frequency-domain techniques no longer seek a set of time samples of the circuit output or the state variables’ waveforms but a spectral representation of them. In their most simple form, they assume that both the steady state of the excitation and the ODE solution are periodic in time, so that they can be expanded in a truncated DFT of $(2K + 1)$ frequency points. For example, the state variables vector would be represented by

$$\mathbf{y}(t) = \sum_{k=-K}^K \mathbf{Y}(k\omega_0) e^{jk\omega_0 t} \tag{28}$$

Since, in the frequency domain, time-domain derivatives are transformed into products by $j\omega$, substituting (28) into (26) leads to

$$\mathbf{I}[\mathbf{Y}(\omega)] + j\Omega\mathbf{Q}[\mathbf{Y}(\omega)] = \mathbf{X}(\omega) \tag{29}$$

which is a nonlinear algebraic function in the DFT coefficients $\mathbf{Y}(k\omega_0)$. The orthogonality between different frequency components provided by the DFT determines that, despite its appearance, this is not a single equation but can be expanded in a set of $(2K + 1)$ equations, each of these must be fulfilled for its harmonic component; in other words, the LHS and RHS (left- and right-hand side)

components must be in equilibrium, which is why (29) is known as the “harmonic-balance equation.”

Since this harmonic-balance (HB) technique computes the periodic steady state directly, it circumvents most of the disadvantages attributed to time-marching techniques. Its only drawbacks are that, depending on the DFT, it can handle only moderate nonlinear regimes, where the $\mathbf{y}(t)$ can be described by a relatively small number of harmonics, and that it requires both the excitation and the vector of state variables to be periodic. As we have already seen in Section 1, the excitations used for intermodulation distortion analysis are often of the two-tone or multitone type. In general, the frequencies of these tones do not constitute any harmonic set (they cannot be made harmonics of a common fundamental), and the corresponding waveform is aperiodic. (Such multitone signals are actually said to be quasiperiodic waveforms.) One way to circumvent this problem consists in imagining that a multitone time-domain waveform is evolving, not in the natural time t , but in a number of artificial timescales equal to the number of nonharmonically related tones, τ_1, \dots, τ_Q . For example, for a two-tone regime, the ODE in time becomes a multirate partial-differential equation (MPDE) in τ_1 and τ_2 :

$$\mathbf{i}[\mathbf{y}(\tau_1, \tau_2)] + \frac{\partial \mathbf{q}[\mathbf{y}(\tau_1, \tau_2)]}{\partial \tau_1} + \frac{\partial \mathbf{q}[\mathbf{y}(\tau_1, \tau_2)]}{\partial \tau_2} = \mathbf{x}(\tau_1, \tau_2) \tag{30}$$

Since $\mathbf{y}(\tau_1, \tau_2)$ is now double-periodic in τ_1 and τ_2 , it admits a bidimensional Fourier expansion

$$\mathbf{y}(\tau_1, \tau_2) = \sum_{k_1=-K}^K \sum_{k_2=-K}^K \mathbf{Y}(k_1\omega_1, k_2\omega_2) e^{j(k_1\omega_1\tau_1 + k_2\omega_2\tau_2)} \tag{31}$$

which, substituted in (30), results in a new bidimensional HB equation. This is the technique known as the *multi-dimensional discrete Fourier transform harmonic-balance* (MDFT HB).

2.4.3. Time-Domain/Frequency-Domain Hybrid Techniques. When the excitation is a RF carrier of frequency ω_c , modulated by some independent baseband modulation signal, like the one expressed in (5), it can be again conceived as varying according to two independent timescales: one, τ_1 , with fast evolution, for the carrier; and another, τ_2 , slower, for the modulation. So, the circuit can again be described by a bidimensional MPDE such as (30). If we now recognize that this regime is periodic for the carrier but aperiodic for the modulation, we immediately conclude that simulation efficiency would be maximized if we treated the carrier evolution in τ_1 in the frequency domain, but kept the baseband evolution τ_2 in time. This supposes a solution in which the vector of state variables is decomposed in a τ_2 time-varying Fourier series

$$\mathbf{y}(\tau_1, \tau_2) = \sum_{k=-K}^K \mathbf{Y}(k\omega_c, \tau_2) e^{j(k\omega_c\tau_1)} \tag{32}$$

which, substituted in (30), leads to

$$\begin{aligned} \mathbf{I}[\mathbf{Y}(k\omega_c, \tau_2)] + j\Omega_c \mathbf{Q}[\mathbf{Y}(k\omega_c, \tau_2)] \\ + \frac{\partial \mathbf{Q}[\mathbf{Y}(k\omega_c, \tau_2)]}{\partial \tau_2} = \mathbf{X}(k\omega_c, \tau_2) \end{aligned} \quad (33)$$

Solving (33) for the envelope, with a timestep integration scheme, and for the carrier, with harmonic balance, leads to the following recursive HB equation:

$$\begin{aligned} \mathbf{I}[\mathbf{Y}(k\omega_c, s)]T_s + j\Omega_c \mathbf{Q}[\mathbf{Y}(k\omega_c, s)]T_s + \mathbf{Q}[\mathbf{Y}(k\omega_c, s)] \\ = \mathbf{X}(k\omega_c, s)T_s + \mathbf{Q}[\mathbf{Y}(k\omega_c, s-1)] \end{aligned} \quad (34)$$

By handling the RF signal components in the frequency domain and the envelope in the time domain, (34) is particularly appropriate to bridge the gap between circuit and envelope-driven system simulation. In fact, we can conceive of a simulator in which all except a few circuits of a communication system are treated as system-level complex equivalent lowpass behavioral input–output blocks—for maximized computational efficiency—while the remaining circuits are treated at the RF bandpass circuit level—for maximum accuracy.

2.4.4. Volterra Series. Although the Volterra series method is not very widely used outside the intermodulation prediction field, it plays a determinant role for the analysis and design of very-low-distortion circuits.

In comparison with the previously mentioned methods, Volterra series no longer tries to find a solution in an iterative and numerical way, but seeks for an analytic solution of a polynomial approximation of the original circuit or system. In fact, it assumes that if the nonlinearities of the original circuit or system can be decomposed in a Taylor series around a certain fixed quiescent point

$$\mathbf{i}(\mathbf{y}) = \mathbf{g}_1 \mathbf{y} + \mathbf{g}_2 \mathbf{y}^2 + \mathbf{g}_3 \mathbf{y}^3 \quad (35)$$

$$\mathbf{q}(\mathbf{y}) = \mathbf{c}_1 \mathbf{y} + \mathbf{c}_2 \mathbf{y}^2 + \mathbf{c}_3 \mathbf{y}^3 \quad (36)$$

then, the solution can be approximated by the following functional series in the time domain:

$$\begin{aligned} \mathbf{y}(t) &= \mathbf{y}_1(t) + \mathbf{y}_2(t) + \mathbf{y}_3(t) \\ &= \int_{-\infty}^{\infty} \mathbf{h}_1(\tau) \mathbf{x}(t - \tau) d\tau \\ &+ \int_{-\infty}^{\infty} \int_{-\infty}^{\infty} \mathbf{h}_2(\tau_1, \tau_2) \mathbf{x}(t - \tau_1) \mathbf{x}(t - \tau_2) d\tau_1 d\tau_2 \\ &+ \int_{-\infty}^{\infty} \int_{-\infty}^{\infty} \int_{-\infty}^{\infty} \mathbf{h}_3(\tau_1, \tau_2, \tau_3) \mathbf{x}(t - \tau_1) \\ &\times \mathbf{x}(t - \tau_2) \mathbf{x}(t - \tau_3) d\tau_1 d\tau_2 d\tau_3 \end{aligned} \quad (37)$$

If the excitation can be expressed as a frequency-domain sum of complex exponentials (possibly, but not necessarily,

harmonically related sinusoids)

$$\mathbf{x}(t) = \sum_{q=-Q}^Q \mathbf{X}(\omega_q) e^{j\omega_q t} \quad (38)$$

then we obtain a frequency-domain version of (37)

$$\begin{aligned} \mathbf{y}(t) &= \sum_{q=-Q}^Q \mathbf{H}_1(\omega) \mathbf{X}(\omega_q) e^{j\omega_q t} \\ &+ \sum_{q_1=-Q}^Q \sum_{q_2=-Q}^Q \mathbf{H}_2(\omega_{q_1}, \omega_{q_2}) \mathbf{X}(\omega_{q_1}) \mathbf{X}(\omega_{q_2}) e^{j(\omega_{q_1} + \omega_{q_2})t} \\ &+ \sum_{q_1=-Q}^Q \sum_{q_2=-Q}^Q \sum_{q_3=-Q}^Q \mathbf{H}_3(\omega_{q_1}, \omega_{q_2}, \omega_{q_3}) \\ &\times \mathbf{X}(\omega_{q_1}) \mathbf{X}(\omega_{q_2}) \mathbf{X}(\omega_{q_3}) e^{j(\omega_{q_1} + \omega_{q_2} + \omega_{q_3})t} \end{aligned} \quad (39)$$

in which the $\mathbf{h}_n(\tau_1, \dots, \tau_n)$ of (37) and the $\mathbf{H}_n(\omega_1, \dots, \omega_n)$ of (39) are the n th-order impulse responses and the n th-order nonlinear transfer functions, respectively. Each of these sets can be obtained from the other by the direct application of a n -dimensional Fourier transform pair.

The Volterra series method consists in determining the set of $\mathbf{h}_n(\cdot)$ or of $\mathbf{H}_n(\cdot)$ (as occurs with conventional linear systems, the frequency-domain version is usually preferred), which then becomes a true nonlinear dynamic model of the system. In fact, note that if one knows all the $\mathbf{H}_n(\omega_1, \dots, \omega_n)$ of a circuit or system, up to a certain order, one immediately knows its response up to that order [from (39)] to any multitone input represented by (38).

To show how these nonlinear transfer functions can be determined, let us consider again the general circuit or system described by the ODE of (26). Substituting (35), (36), and (39) into (26), and assuming that the input is now a first-order elementary excitation of

$$\mathbf{x}(t) = e^{j\omega t} \quad (40)$$

the orthogonality of the complex exponentials leads us to the conclusion that $\mathbf{H}_1(\omega)$ must be given by

$$\mathbf{H}_1(\omega) = \frac{1}{\mathbf{g}_1 + j\omega \mathbf{c}_1} \quad (41)$$

In fact, this $\mathbf{H}_1(\omega)$ is merely the usual transfer function of the linear circuit or system obtained from a linearization around the quiescent point.

To obtain the second-order nonlinear transfer function, we would now assume that the system is excited by a second-order elementary excitation of

$$\mathbf{x}(t) = e^{j\omega_1 t} + e^{j\omega_2 t} \quad (42)$$

Substituting (35), (36), (39), and (42) into (26), and collecting components in the second-order mixing product of

$\omega_1 + \omega_2$ would lead to

$$\mathbf{H}_2(\omega_1, \omega_2) = -\frac{\mathbf{g}_2 + j(\omega_1 + \omega_2)\mathbf{c}_2}{\mathbf{g}_1 + j(\omega_1 + \omega_2)\mathbf{c}_1} \mathbf{H}_1(\omega_1)\mathbf{H}_1(\omega_2) \quad (43)$$

Similarly, the calculation of the third-order nonlinear transfer function assumes an input of

$$\mathbf{x}(t) = e^{j\omega_1 t} + e^{j\omega_2 t} + e^{j\omega_3 t} \quad (44)$$

and leads to

$$\begin{aligned} \mathbf{H}_3(\omega_1, \omega_2, \omega_3) = & -\frac{2}{3} \frac{\mathbf{g}_2 + j(\omega_1 + \omega_2 + \omega_3)\mathbf{c}_2}{\mathbf{g}_1 + j(\omega_1 + \omega_2 + \omega_3)\mathbf{c}_1} \\ & \times [\mathbf{H}_1(\omega_1)\mathbf{H}_2(\omega_2, \omega_3) + \mathbf{H}_1(\omega_2) \\ & \times \mathbf{H}_2(\omega_1, \omega_3) + \mathbf{H}_1(\omega_3)\mathbf{H}_2(\omega_1, \omega_2)] \quad (45) \\ & -\frac{\mathbf{g}_3 + j(\omega_1 + \omega_2 + \omega_3)\mathbf{c}_3}{\mathbf{g}_1 + j(\omega_1 + \omega_2 + \omega_3)\mathbf{c}_1} \\ & \times \mathbf{H}_1(\omega_1)\mathbf{H}_1(\omega_2)\mathbf{H}_1(\omega_3) \end{aligned}$$

The terms $-\frac{2}{3}[\mathbf{g}_2 + j(\omega_1 + \omega_2)\mathbf{c}_2]\mathbf{H}_1(\omega_1)\mathbf{H}_1(\omega_2)$ in (43) and the terms

$$\begin{aligned} & -\frac{2}{3}[\mathbf{g}_2 + j(\omega_1 + \omega_2 + \omega_3)\mathbf{c}_2] \\ & \times [\mathbf{H}_1(\omega_1)\mathbf{H}_2(\omega_2, \omega_3) + \mathbf{H}_1(\omega_2)\mathbf{H}_2(\omega_1, \omega_3) \\ & + \mathbf{H}_1(\omega_3)\mathbf{H}_2(\omega_1, \omega_2)] \end{aligned}$$

$$\text{and } -\frac{1}{3}[\mathbf{g}_3 + j(\omega_1 + \omega_2 + \omega_3)\mathbf{c}_3]\mathbf{H}_1(\omega_1)\mathbf{H}_1(\omega_2)\mathbf{H}_1(\omega_3)$$

in (45) are known as the *elementary second-order* and *third-order nonlinear sources*, respectively. In fact, comparing (43) and (45) with (41), we immediately conclude that for the calculation of first-, second-, and third-order solutions, what we have been doing was to always analyze the same linearized version of the original ODE with the appropriate elementary nonlinear sources at ω for first order, at $\omega_1 + \omega_2$ for second order, and at $\omega_1 + \omega_2 + \omega_3$ for third order. That is why the method of Volterra series analysis is known to solve a forced n th-order nonlinear dynamic problem, solving n times the same linear problem, with the appropriate (1st, 2nd, ..., n th)-order forcing functions, in a recursive way. As it is based on a polynomial approximation of the nonlinearities, the Volterra series is a local model restricted to small-signal levels, or mildly nonlinear regimes. In practice, it can be used only for calculating the distortion in nonsaturated mixers, small-signal amplifiers, or nonsaturated power amplifiers, that is, well below the 1-dB compression point. However, because it is a closed-form nonlinear model, it provides qualitative information on the nonlinear circuit or system's operation, giving, for instance, insight into the physical origins of nonlinear distortion, and can be directly used for circuit and system's design.

3. INTERMODULATION DISTORTION IN SMALL-SIGNAL AMPLIFIERS

First, let us clarify the meaning of “small-signal amplifiers,” as most of us would expect no appreciable nonlinear distortion from these circuits. This term is used to distinguish low-noise or high-gain amplifiers from the essentially different power amplifiers, treated in the next section. While the small-signal amplifiers referred to here always supposedly operate in highly backed-off class A regimes, power amplifiers are operated close to saturation, usually even in strongly nonlinear modes as class AB, B, or C.

So, now, one question comes to our minds: “What are the mechanisms capable of causing significant nonlinear distortion in small-signal amplifiers?” To advance with an answer, let us consider the case of the low-noise amplifier of a wireless communication receiver front end. This is a circuit that faces, beyond the very weak desired channel, many other incoming channels present in the same communication system's band. For example, a low-noise front end of a handset can be simultaneously excited by the desired channel coming from a remote base station, and by another channel coming from a nearby transmitter handset. Since the ratio of distances between our receiver and the base station, and our receiver and the perturbing transmitter, can easily be on the order of several kilometers to one meter, the ratio of incoming powers can be higher than 10^8 to 1. Therefore, the signal-to-perturbation ratio can be as poor as -70 or -80 dB, and, if it is true that a desired signal of, say, -70 dBm cannot generate any significant nonlinear distortion, that is no longer the case for the $+10$ dBm perturbation.

Indeed, as seen in Section 1, this high-level perturbation can produce nonlinear distortion sidebands falling over the desired channel, cross-modulation, and desensitization. These effects are illustrated in Fig. 21 and can constitute a severe limitation to the performance of RF front ends. In fact, they allow the definition of a very important signal fidelity figure of merit, the dynamic range, which is the ratio between the amplitudes of the highest and lowest incoming detectable signals that still guarantee the specified signal-to-noise ratio SNR. The lowest-amplitude detectable signal—the receiver's sensitivity S_i —is the one that stands the desired SNR over the noise floor. The highest-amplitude detectable signal, P_{\max} , is defined as the one that generates a nonlinear distortion perturbation whose power equals the noise floor. So

$$\text{DR} \equiv \frac{P_{\max}}{S_i} \quad \text{or} \quad \text{DR}_{\text{dB}} \equiv P_{\max_{\text{dBm}}} - S_{i_{\text{dBm}}} \quad (46)$$

where DR is the dynamic range.

Since signal excursions appearing at the nonlinear active device are always kept much smaller than the applied DC voltages and currents, the amplifier can be approximately described by a local model. For example, considering the ideal (low-frequency) situation in which the only nonlinear effects can be attributed to the $i_{\text{ds}}(v_{\text{gs}}, v_{\text{ds}})$ current of a FET, the amplifier would be described by the equivalent circuit depicted in Fig. 22,

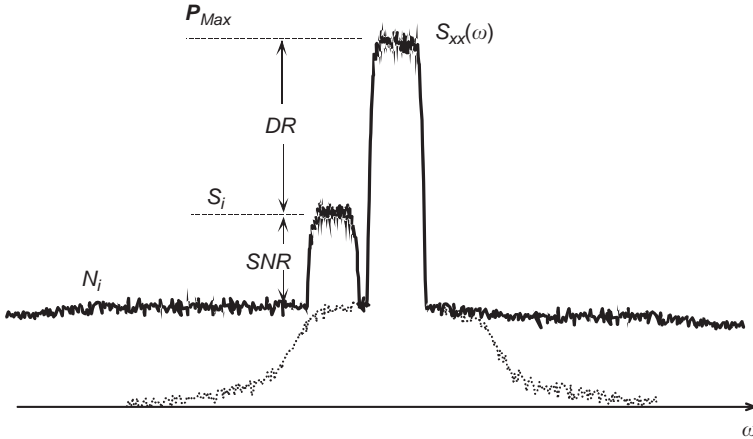


Figure 21. Nonlinear distortion impairments in a mildly nonlinear receiver system: illustration of the concepts of receiver's desensitization and dynamic range.

while the nonlinearity would be represented by the Taylor series of (19).

Although the model shown in Fig. 22 is very simplified, it will already give us some insight onto the mechanisms controlling IMD generation in these small-signal amplifiers. For that, we will first redraw this circuit as the one of Fig. 23 over which a Volterra series analysis will then be performed.

Note that ports 1 and 2 in Fig. 23 handle the amplifier's input and output, respectively, but were defined after the terminal admittances Y_S and Y_L were incorporated into the main circuit. port 3 serves to define v_{gs} , one of the control voltages of the i_{ds} nonlinearity, and port 4 serves to define v_{ds} , the other control voltage. Furthermore, since Fig. 23 is the linearized equivalent-circuit version of the original circuit of Fig. 22, its only $i_{ds}(v_{gs}, v_{ds})$ components are the first-order ones: $G_m v_{gs}$ and $G_{ds} v_{ds}$. All the other nonlinear terms of (19) will behave as nonlinear sources that will be incorporated as independent current sources applied to port 4 [6,7].

Assuming that the equivalent Norton current excitation corresponds to a narrowband two-tone stimulus, this circuit can be represented by the following $[Z]$ matrix and input and output boundary conditions:

$$\begin{bmatrix} V_1(\omega) \\ V_2(\omega) \\ V_3(\omega) \\ V_4(\omega) \end{bmatrix} = \begin{bmatrix} Z_{11} & Z_{12} & Z_{13} & Z_{14} \\ Z_{21} & Z_{22} & Z_{23} & Z_{24} \\ Z_{31} & Z_{32} & Z_{33} & Z_{34} \\ Z_{41} & Z_{42} & Z_{43} & Z_{44} \end{bmatrix} \cdot \begin{bmatrix} I_1(\omega) \\ I_2(\omega) \\ I_3(\omega) \\ I_4(\omega) \end{bmatrix} \quad (47a)$$

$$I_1(\omega) = I_s(\omega) : i_s(t) = I_{s1} \cos(\omega_1 t) + I_{s2} \cos(\omega_2 t) \quad (47b)$$

$$I_2(\omega) = 0 \quad (47c)$$

$$I_3(\omega) = 0 \quad (47d)$$

If the two-tones are closely separated in frequency, the circuit reactances are similar for all in-band products. So, using ω_0 as the center frequency [$\omega_0 = (\omega_1 + \omega_2)/2$], $Z_{ij}(\omega_1) \approx Z_{ij}(\omega_2) \approx Z_{ij}(2\omega_1 - \omega_2) \approx Z_{ij}(2\omega_2 - \omega_1) \approx Z_{ij}(\omega_0)$ for any $i, j = 1, 2, 3, 4$.

After determining the linear equivalent-circuit $[Z]$ matrix, the nonlinear currents' method of Volterra series analysis [6,7] proceeds by determining first-order control voltages $V_{3,1}(\omega_0)$ and $V_{4,1}(\omega_0)$ ($q = 1, 2$) and first-order output voltage $V_{2,1}(\omega_0)$, from the excitation $I_s(\omega_0)$:

$$V_{gs,1}(\omega_1), V_{gs,1}(\omega_2) : V_{3,1}(\omega_0) = Z_{31}(\omega_0) \frac{I_s(\omega_0)}{2} \quad (48a)$$

$$V_{ds,1}(\omega_1), V_{ds,1}(\omega_2) : V_{4,1}(\omega_0) = Z_{41}(\omega_0) \frac{I_s(\omega_0)}{2} \quad (48b)$$

$$V_{L,1}(\omega_1), V_{L,1}(\omega_2) : V_{2,1}(\omega_0) = Z_{21}(\omega_0) \frac{I_s(\omega_0)}{2} \quad (49)$$

From these first-order control variables, the second-order nonlinear current of i_{ds} at $\omega_1 - \omega_2 \equiv \Delta\omega$ and $\omega_1 + \omega_2 \equiv \Sigma\omega$,

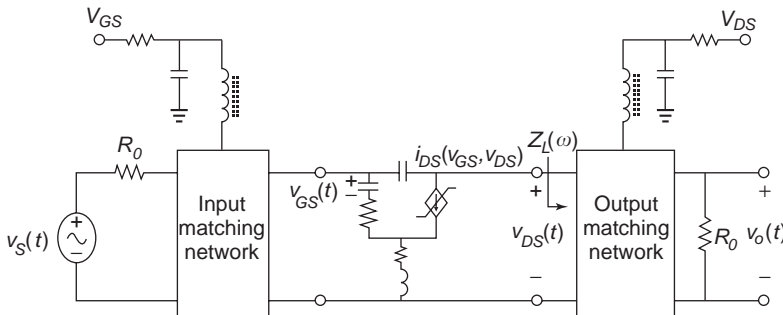


Figure 22. Model of a mildly nonlinear amplifier for small-signal distortion studies.

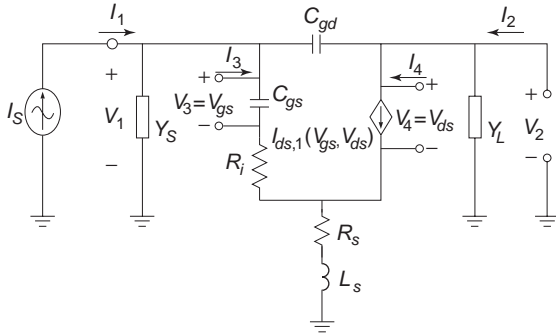


Figure 23. Linearized equivalent-circuit model of a FET-based mildly nonlinear amplifier used in Volterra series calculations.

$I_{4,2}(\omega)$ should now be determined:

$$I_{4,2}(\Delta\omega) = -[2G_{m2}|Z_{31}(\omega_0)|^2 + G_{md}Z_{31}(\omega_0)Z_{41}(\omega_0)^* + G_{md}Z_{31}(\omega_0)^*Z_{41}(\omega_0) + 2G_{d2}|Z_{41}(\omega_0)|^2] \frac{|I_S|^2}{4} \quad (50)$$

$$I_{4,2}(\Sigma\omega) = -2[G_{m2}Z_{31}(\omega_0)^2 + G_{md}Z_{31}(\omega_0)Z_{41}(\omega_0) + G_{d2}Z_{41}(\omega_0)^2] \frac{I_S^2}{4} \quad (51)$$

Then, the linear circuit should be analyzed again for this new second-order current source, determining the second-order control voltages at the difference $\omega_1 - \omega_2 \equiv \Delta\omega$ and sum $\omega_1 + \omega_2 \equiv \Sigma\omega$ frequencies, $V_{3,2}(\omega)$ and $V_{4,2}(\omega)$:

$$V_{3,2}(\Delta\omega) = Z_{34}(\Delta\omega)I_{4,2}(\Delta\omega) \quad (52)$$

$$V_{3,2}(\Sigma\omega) = Z_{33}(\Sigma\omega)I_{3,2}(\Sigma\omega) + Z_{34}(\Sigma\omega)I_{4,2}(\Sigma\omega) \quad (53)$$

$$V_{4,2}(\Delta\omega) = Z_{44}(\Delta\omega)I_{4,2}(\Delta\omega) \quad (54)$$

$$V_{4,2}(\Sigma\omega) = Z_{43}(\Sigma\omega)I_{3,2}(\Sigma\omega) + Z_{44}(\Sigma\omega)I_{4,2}(\Sigma\omega) \quad (55)$$

The last step consists in calculating the third-order nonlinear current of i_{ds} at $2\omega_1 - \omega_2$, $I_{4,3}(2\omega_1 - \omega_2)$ from first- and second-order control voltages $V_{3,1}(\omega)$, $V_{3,2}(\omega)$, $V_{4,1}(\omega)$, and $V_{4,2}(\omega)$:

$$\begin{aligned} I_{4,3}(2\omega_1 - \omega_2) = & -[2G_{m2}Z_{31}(\omega_0)^*Z_{34}(2\omega_0)I_{4,2}(2\omega_0) \\ & + G_{md}Z_{31}(\omega_0)^*Z_{44}(2\omega_0)I_{4,2}(2\omega_0) \\ & + G_{md}Z_{41}(\omega_0)^*Z_{34}(2\omega_0)I_{4,2}(2\omega_0) \\ & + 2G_{d2}Z_{41}(\omega_0)^*Z_{44}(2\omega_0)I_{4,2}(2\omega_0)] \frac{I_S^*}{2} \\ & - [2G_{m2}Z_{31}(\omega_0)Z_{34}(\Delta\omega)I_{4,2}(\Delta\omega) \\ & + G_{md}Z_{31}(\omega_0)Z_{44}(\Delta\omega)I_{4,2}(\Delta\omega) \\ & + G_{md}Z_{41}(\omega_0)Z_{34}(\Delta\omega)I_{4,2}(\Delta\omega) \\ & + 2G_{d2}Z_{41}(\omega_0)Z_{44}(\Delta\omega)I_{4,2}(\Delta\omega)] \frac{I_S}{2} \end{aligned}$$

$$\begin{aligned} & -[3G_{m3}Z_{31}(\omega_0)|Z_{31}(\omega_0)|^2 \\ & + G_{m2d}Z_{31}(\omega_0)^2Z_{41}(\omega_0)^* \\ & + 2G_{m2d}|Z_{31}(\omega_0)|^2Z_{41}(\omega_0) \\ & + G_{md2}Z_{31}(\omega_0)^*Z_{41}(\omega_0)^2 \\ & + 2G_{md2}Z_{31}(\omega_0)|Z_{41}(\omega_0)|^2 \\ & + 3G_{d3}Z_{41}(\omega_0)|Z_{41}(\omega_0)|^2] \frac{I_S|I_S|^2}{8} \quad (56) \end{aligned}$$

and then, finally, determine third-order output voltage at the IMD frequency $2\omega_1 - \omega_2$:

$$V_{2,3}(2\omega_1 - \omega_2) = Z_{24}(\omega_0)I_{4,3}(2\omega_1 - \omega_2) \quad (57)$$

Now we are in a position to calculate the amplifier's signal-to-IMD ratio (IMR) by first determining output power at the fundamental

$$P_L = \frac{1}{2}G_L(\omega_0)|V_L(\omega_0)|^2 = \frac{1}{2}G_L(\omega_0)|Z_{21}(\omega_0)|^2|I_S|^2 \quad (58)$$

and IMD components

$$P_{L_3} = 2G_L(\omega_0)|V_{2,3}(2\omega_1 - \omega_2)|^2 \quad (59)$$

where $G_L(\omega)$ is the real part of load admittance $Y_L(\omega)$. A full expression for this IMR would be very complex. But, under the assumptions that internal feedback is negligible [$Z_{34}(\omega) \approx 0$] and that both second-harmonic and $\omega_1 - \omega_2$ distortion will be very small (usually verified in small-signal amplifiers), it can be approximated by

$$\begin{aligned} \text{IMR} \approx & 16 \left| \frac{A_v(\omega_0)}{Z_D(\omega_0)} \right|^2 \cdot |3G_{m3} + G_{m2d}A_v(\omega_0)^* \\ & + 2G_{m2d}A_v(\omega_0) + G_{md2}A_v(\omega_0)^2 \\ & + 2G_{md2}|A_v(\omega_0)|^2 \\ & + 3G_{d3}A_v(\omega_0)|A_v(\omega_0)|^2|^{-2}|V_S|^{-4} \end{aligned} \quad (60)$$

where $Z_D(\omega) \equiv 1/[G_{ds} + Y_L(\omega)]$, $A_v(\omega)$ is the intrinsic voltage gain defined by $A_v(\omega) \equiv V_{ds}(\omega)/V_{gs}(\omega)$, and V_S is the voltage amplitude of the signal source, $V_S(\omega) = Z_S(\omega)I_S(\omega)$.

If we now study the variation of various third-order current components with V_{GS} bias, as shown in Fig. 24 for a typical general-purpose small-signal MESFET, we conclude that there are two very good points of IMD performance, the so-called small-signal IMD "sweet spots." The first one is located at the FET's threshold voltage [6] and thus has a very small associated power gain. The other is located in high- V_{GS} regions, and although it may not correspond to very good noise figures, it is definitely useful for designing high-gain, highly linear small-signal amplifiers. Unfortunately, this latter small-signal IMD "sweet spot" is a peculiarity of only some GaAs MESFETs, and was never observed on HEMTs, MOSFETs or BJTs.

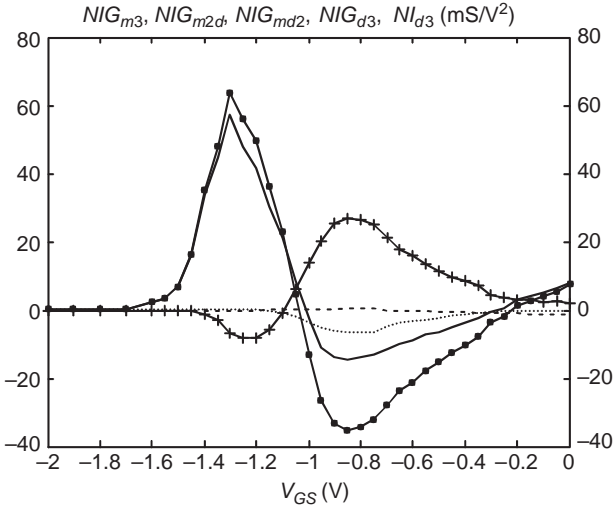


Figure 24. Magnitude of total $i_{ds}(v_{gs}, v_{ds})$ third-order current components $N_{I_{d3}}$ (—) and its various components due to G_{m3} $N_{IG_{m3}}$ (—●—), G_{m2d} $N_{IG_{m2d}}$ (—+—), G_{md2} $N_{IG_{md2}}$ (···), and G_{d3} $N_{IG_{d3}}$ (---) as a function of V_{GS} bias.

Turning now our attention to the IMR variation with source impedance, we can conclude that since P_L can also be given by $P_L = \frac{1}{2} G_L(\omega_0) |A_v(\omega_0)|^2 |V_S|^2$, Eq. (60) confirms the empirical observation that, for constant output power, third-order distortion in FET-based small-signal amplifiers is almost independent of input termination $Z_S(\omega)$.

As far as the IMR variation with load impedance is concerned, Fig. 24 and (60) indicate that, for typical V_{GS} bias, the nonlinear current contributions of G_{m3} and G_{m2d} have effects on IMR that are important but, fortunately, opposite in sign. Since $N_{IG_{m2d}}$ is proportional to voltage gain, and thus to $Z_L(\omega)$, this implies that a maximization of voltage gain can also be beneficial to IMR. This hypothesis was indeed fully confirmed by the measured and simulated IMR_3 load-pull data [9], showing that an optimum $Z_L(\omega)$ really exists and it tends to coincide with the one that maximizes small-signal voltage and power gains in MESFET-based small-signal amplifiers [6,9].

Since BJTs and HBTs have mildly nonlinear characteristics that are completely different from those of FETs, these results cannot be directly extrapolated to bipolar-based small-signal amplifiers. For example, while the most important nonlinearity source, $i_{DS}(v_{GS}, v_{DS})$, is located at the FET's output, in bipolars it is manifested in both the input, $i_B(v_{BE}, v_{CE})$, and the output, $i_C(v_{BE}, v_{CE})$ [6].

4. INTERMODULATION DISTORTION IN HIGH-POWER AMPLIFIERS

Let us now turn our attention to power amplifiers (PAs). Contrary to small-signal amplifiers where noise figure and gain are of primary concern, power amplifiers are designed for high output power P_{out} and power-added efficiency (PAE).

In a well-designed PA, maximum output power is determined by the loadline (load impedance termination)

and available output signal excursion. Power-added efficiency is dependent mostly on the PA operation class (quiescent point) and on a convenient output voltage and current waveform shaping, specifically, selection of harmonic terminations. Therefore, it seems that little is left for optimizing intermodulation distortion. Fortunately, as we will see, that is not necessarily the case.

Since real devices do not present abrupt turnon points, it is difficult to precisely define the PA operation class. So, to prevent any ambiguity in the following discussion, we will first define classes A, AB, B, and C. Taking into account the discussion in Ref. 6, we will adopt the following definitions: (1) the turnon bias V_T is defined as the input quiescent point to which the turnon small-signal IMD “sweet spot” corresponds (see Fig. 24); (2) biasing the device below V_T corresponds to class C ($G_{m3} > 0$); (3) biasing it exactly at V_T corresponds to class B ($G_{m3} = 0$); and (4) biasing it above V_T will determine the usual class AB or class A ($G_{m3} < 0$).

The first design step to be taken when designing a PA is to decide whether precedence should be given to PAE or to IMD specs, as they generally lead to opposite design solutions. The traditional PA design rules state that a PA optimized for IMD requires unsaturated class A operation; that is, the device should be biased and always kept comfortably inside the linear amplification zone (saturation region of FETs and the active region of BJTs or HBTs).

On the other hand, a PA optimized for PAE is usually biased near class B or slightly into class C—that is, with a quiescent point where output voltage is halfway between knee voltage and breakdown, and output current is close to turnon—and then is allowed to be driven into saturation. This leads to saturated classes such as classes E and F [18]. Unfortunately, as such operation classes achieve their high efficiencies by operating the active device in an almost switching mode, their associated nonlinear distortion is also huge. In fact, recognizing that a switching power amplifier turns any waveform into a constant-amplitude square wave, it is easy to conclude that those class E or F PAs cannot be used when the amplitude of the RF-modulated signal also carries information content (modulation formats of non-constant-amplitude envelope).

The basic goal when designing linear PAs is to get class B PAE with class A IMD—and, although this is seldom possible, there are some particular PA features that provide a means to escape from this apparent deadend. One that has been receiving a great deal of attention is the so-called large-signal IMD sweet spots [19]. Contrary to their small-signal counterparts studied above, which were associated to a particular quiescent point and found effective only at very-small-signal levels, these are peculiar points of the IMD–input power characteristic (see Fig. 25) where only a few decibels of output-power backoff (and thus a few percent of efficiency degradation) can lead to astonishingly high levels of IMD reduction.

To understand how this curious effect takes place, we need to abandon our small-signal local model, since, for the signal levels where these large-signal IMD sweet spots are observed, the Taylor expansion of (19) presents an unacceptable error or simply may not converge. Instead, we are

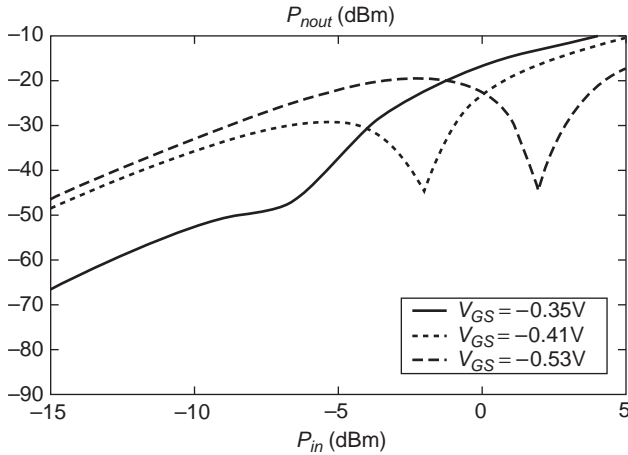


Figure 25. Different IMD versus P_{in} patterns showing large-signal IMD “sweet spots” for a HEMT device.

forced to rely on qualitative solutions of approximated global models. For that, we will transform the bidimensional dependence of (19) on the input and output control voltages, $v_{GS}(t)$ and $v_{DS}(t)$, into a one-dimensional model, generating in this way an equivalent single-input/single-output transfer function (TF), $i_{DS}[v_{GS}(t)]$. This assumes an output boundary condition imposed by load impedance, $Z_L(\omega)$, $V_{ds}(\omega) = V_{DC} - Z_L(\omega)I_{ds}(\omega)$, where V_{DC} is the applied output quiescent voltage, beyond knowledge of the active device nonlinear model $i_{DS}[v_{GS}(t), v_{DS}(t)]$.

In order to describe, with enough generality, the global nonlinearities of the device, we will also consider that turnon can be represented by an exponential of input voltage. This method is commonly adopted to represent subthreshold conduction in FETs, and is even more faithful for describing $i_C(v_{BE})$ in common-base or common-emitter bipolar devices. Then, for increasing v_{GS} voltages, it is assumed that the FET passes through a nearly quadratic zone, which, because of short-channel effects, tends to become linear for even higher v_{GS} . This $i_{DS}(v_{GS})$ behavior was shown to be well reproduced by the following empirical expression [20]

$$i_{DS}(v_{GS}) = \beta \frac{[smt(v_{GS})]^2}{1 + \theta smt(v_{GS})} \quad (61a)$$

where $smt(v_{GS})$ is a smooth turnon function of v_{GS} given by

$$smt(v_{GS}) = K_V \ln\left(1 + e^{\frac{v_{GS}}{K_V}}\right) \quad (61b)$$

and β , θ and K_V are empirical scaling parameters.

If we now take the output boundary into account, $i_{DS}(v_{DS})$ will be almost unchanged unless v_{GS} is so high that $R_L \cdot i_{DS}$ becomes close to V_{DC} . There, v_{DS} is so small that the FET enters the triode region (the saturation region for a bipolar based PA). v_{GS} rapidly loses control over i_{DS} , and the TF saturates (the PA enters into strong compression). So, the global transfer characteristic $i_{DS}(v_{GS})$ presents a distinct sigmoid shape.

Assuming again a two-tone stimulus, several qualitative conclusions may be drawn for large-signal operation. One of the most important is that when the amplifier is driven into harder and harder nonlinear regimes, its gain goes into compression, which means that the phase of the in-band nonlinear distortion components must oppose those of the fundamentals. So, PA energy balance considerations derived in Section 1 show that the large-signal asymptotic phase value of the IMD sidebands, at $2\omega_1 - \omega_2$ and $2\omega_2 - \omega_1$, must tend to a constant value of 180° [19].

On the other hand, we also know that small-signal IMD phase is determined by the sign of the TF local derivatives, determined by the active device’s quiescent point. As seen above, G_{m3} is positive below V_T (class C operation), is null exactly at V_T (class B) and is negative above V_T (classes AB and A). So, since small-signal IMD sign can be made positive, and tends to negative values in the large-signal asymptotic regime, the Bolzano–Weierstrass theorem guarantees the existence of at least one IMD null somewhere in between. This will be observed as a more or less pronounced notch in an $IMD-P_{in}$ plot, constituting a large-signal IMD sweet spot.

From these general conclusions it is clear that the existence of a large-signal IMD sweet spot depends on the small-signal IMD phase and on the physical effects that determine large-signal gain compression. So, each operation class will have its own particular IMD behavior.

Under class C, $V_{GS} < V_T$, $G_{m3} > 0$, the PA presents gain expansion and a high IMD level with 0° phase. When the signal excursion reaches a strong nonlinearity as the gate–channel junction conduction, gate–channel breakdown, or, more likely, the saturation–triode region transition, the PA enters into compression and an IMD notch is observed. So, a large-signal IMD sweet spot should be expected for class C amplifiers when the signal excursion is at the onset of saturation, not far from the PA’s 1-dB compression point. Although the PAE is not yet at its maximum, it may present an interesting value.

In class A, $V_{GS} > V_T$, $G_{m3} < 0$, the PA starts at small signal with almost unnoticeable gain compression and a very small level of IMD with 180° phase. As this phase is maintained when the device enters strong compression, no IMD sweet spot will be generated. Thus, and unless the PA is biased above the small-signal IMD sweet spot found for high V_{GS} bias in certain MESFETs [9], no large-signal IMD sweet spot will be observed. On the contrary, a sudden increase of IMD power at the on-set of saturation is the usual outcome of class A PAs.

In class AB, where V_{GS} is only slightly higher than V_T and $G_{m3} < 0$, the PA again shows a very shallow gain compression and a low-level IMD of 180° phase. Hence, similar to what was concluded for class A operation, no IMD sweet spot should be expected. Nevertheless, depending on the abruptness of turnon and succeeding linearization of the TF characteristic, it can be shown that a transition from 180° to 0° IMD phase can occur at lower values of output power [20,21] generating an IMD sweet spot. At this stage, the circuit begins to behave as a class C PA, with 0° IMD phase and gain expansion. Consequently, a new IMD sweet spot will have to occur at large signal when gain compression will finally take place. In

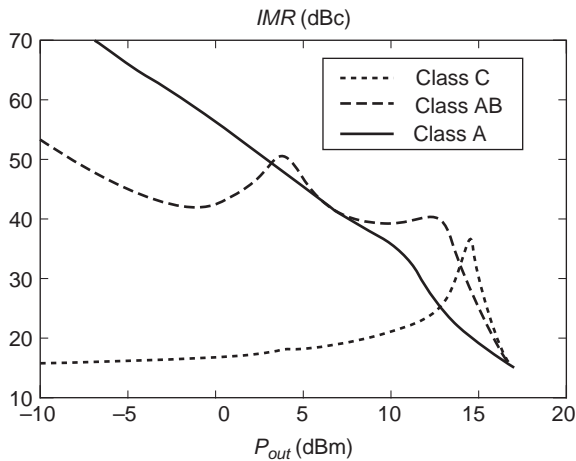


Figure 26. IMR versus P_{out} power plots of typical MOSFET-based PAs at the three operation classes studied: C (· · ·), AB (- - -) and A (—).

summary, depending on the actual device’s transfer characteristic and on the adopted quiescent point, class AB may be significantly different from class A in that it may even present two IMD sweet spots, one for small to moderate levels of P_{in} and another for the onset of saturation.

When the device is biased for class B (i.e., $V_{GS} = V_T$ and $G_{m3} = 0$), there is no small-signal IMD to be compensated by the large-signal distortion behavior. The PA presents very low levels of small-signal distortion (remember that it was biased at a small-signal IMD sweet spot) and then presents a sudden rise of distortion power at the onset of saturation. To illustrate the results of this analysis, Fig. 26 shows three IMR– P_{in} patterns typically observed in MOSFET-based PAs biased for classes A, AB, and C, respectively.

To close this qualitative analysis, let us draw some conclusions about the dependence of large-signal IMD sweet spots on impedance terminations. Starting with source impedance, it is intuitive to realize that, because the $i_{DS}(v_{GS}, v_{DS})$ nonlinearity is located at the output, the large-signal IMD behavior will be mostly invariant with

$Z_S(\omega)$, as was the case studied earlier for small-signal amplifiers. Note that this conclusion may not be extrapolated to bipolar based amplifiers, in which there is an input nonlinearity due to the base–emitter junction, and an output nonlinearity due to the active-to-saturation region transition [6,22].

As seen from the small-signal Volterra series analysis above, the dependence of i_{DS} on v_{DS} should also produce its own impact on the large-signal IMD sweet spot, via $Z_L(\omega)$. In fact, since these sweet spots were related to the output signal excursion that crosses the saturation-to-triode region transition, and as the loadline slope determines that signal level (see Fig. 27), it should be expected that the P_{in} for which the IMD sweet spot is observed will be strongly dependent on load termination. This is illustrated in Figs. 27a and 27b, where a shift of the simulated IMD sweet-spot position is evident when loadline slope $1/R_L$ is varied.

Furthermore, if the PA output is not perfectly matched, the intrinsic load impedance actually presented to the nonlinear current source may have a certain nonnull phase. The output-induced large-signal distortion components will no longer be in exact opposite phase with the small-signal ones, and the previously observed large-signal IMD sweet spots cease to be sharp dips of IMD power to become more or less smooth valleys.

Further conclusions can also be drawn about the impact of out-of-band terminations on the large-signal IMD sweet spots [6,22]. As was seen above from the small-signal analysis, the presence of even-order mixing products—which, as we have already seen, can be remixed with the fundamentals—will generate new odd-order products. But, contrary to the small-signal case in which it was assumed that the quasilinear operation of the amplifier would determine a minor effect to these indirect odd-order products, that is no longer valid for a PA, and its analysis becomes again much more complex:

1. Efficiency considerations may have previously dictated a certain second-harmonic termination. Further, if in most usual situations we seek a squared output voltage waveform, that is, without even-order harmonics, there are situations (e.g., the

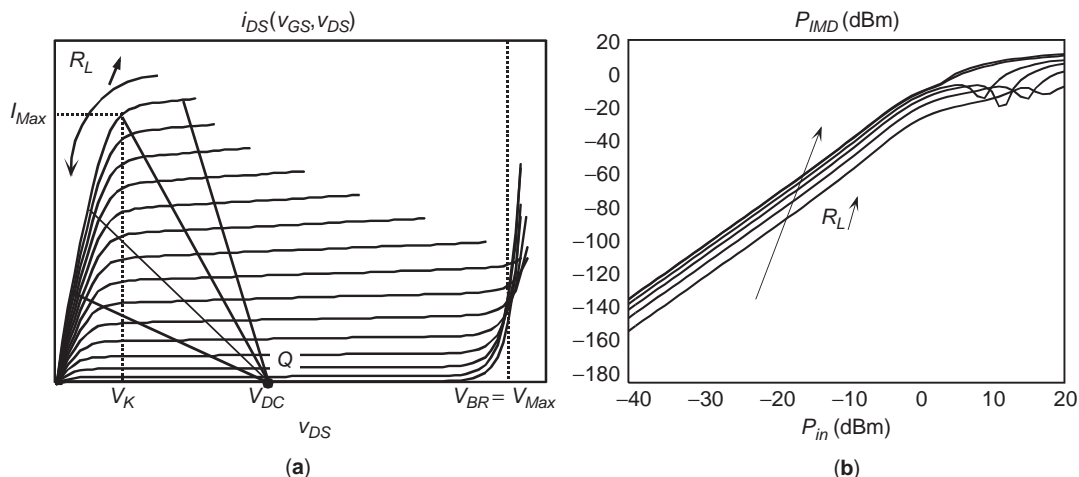


Figure 27. Impact of PA loadline slope $1/R_L$ on large-signal IMD “sweet spots”.

so-called inverse class F [18,23]) in which those even harmonics are indeed maximized.

2. If, in small-signal amplifiers, there would be no difficulty in designing bias networks presenting a very low impedance to the modulation baseband ($\omega_2 - \omega_1$), in PAs that is again incomparably more difficult. Indeed, as output currents may be on the order of several amperes, any parasitic resistance or inductance may immediately develop a nonnegligible output voltage.
3. There will be even additional, contributing baseband reactances in PAs from more or less unexpected physical origins. That is the case of trap-induced low-frequency dispersion presented by some microwave active devices [24], and dynamic self-heating, common to almost all PAs [25].

Depending on the phase of the out-of-band terminations, these new indirect odd-order products may have a phase that either reinforces or reduces the directly generated IMD. As far as the even-harmonics-induced products are concerned, since the modulation bandwidth (or the two-tone separation $\Delta\omega$) is usually much smaller than the PA bandwidth, it may be assumed that $Z_L(2\omega_1) \approx Z_L(2\omega_2) \approx Z_L(2\omega_0)$. So, no important IMD behavior variation within the bandwidth should be expected; that is, the indirect odd-order distortion products may reduce, reinforce, or be in quadrature with the direct ones, but their impact will be the same along the whole modulation bandwidth.

The situation regarding the baseband-induced products is completely different. Now, $Z_L(\Delta\omega)$ may vary significantly within the modulation bandwidth, especially if the bias networks present resonances. Therefore, it is likely that IMD power will vary within that bandwidth, and the amplifier will show (undesirable) long-term memory effects. Moreover, the complex conjugate symmetry of load impedance requires that the imaginary part of $Z_L(\omega_2 - \omega_1)$ have a sign opposite that of $Z_L(\omega_1 - \omega_2)$. So, if some other odd-order products (e.g., the ones due to the presence of second harmonics) also have significant imaginary parts, their addition will even produce asymmetric IMD sidebands [22].

These strange IMD effects have received a lot of attention more recently as their induced long-term memory immensely complicates the design of PA linearizers. Fortunately, since direct static IMD usually dominates this indirect dynamic distortion, those long-term memory effects are seldom noticed. They would be evident only if the

direct static odd-order products were reduced. Unfortunately, IMD sweet spots are, by nature, exactly one of these situations, and so the selection of these out-of-band impedances should not be overlooked during the PA design and implementation phases.

5. INTERMODULATION DISTORTION IN MICROWAVE AND RF MIXERS

A mixer can be viewed as a special kind of amplifier in which the bias supply no longer provides a constant voltage or current, but one that varies in time—the local oscillator. In the same way, an amplifier is a device where the constant quiescent point is perturbed by a certain dynamic signal; a mixer is a similar device where the local-oscillator (LO) time-varying “quiescent point” is perturbed by a dynamic radiofrequency (RF) excitation. Assuming that the mixer is operated in an unsaturated mode, as is the case of most practical interest, the RF signal level is much smaller than the LO level, and the mixer can be analyzed, for the RF signal, as a mild nonlinearity. Thus, it admits a low-degree polynomial expansion in the vicinity of the time-varying LO quiescent point. That constitutes the standard large-signal/small-signal analysis of mixers [7,26]. Mixer distortion analysis can thus follow exactly the one already carried out for small-signal amplifiers, with the exception that now we must start by determining the strong nonlinear regime imposed by the LO and, eventually, some DC bias. The voltage and current waveforms calculated in this way constitute the time-varying quiescent point. Despite the sinusoidal form of the LO excitation, the device’s strong nonlinearities will determine a periodic regime composed by the LO frequency ω_{LO} and its harmonics. So, referring to the illustrative case of the active FET mixer depicted in Fig. 28, the time-varying quiescent voltages that control the FET’s $i_{DS}(v_{GS}, v_{DS})$ nonlinearity will be given by

$$v_{GS}(t) = \sum_{k=-K}^K V_{gs}(k\omega_{LO})e^{jk\omega_{LO}t} \tag{62a}$$

$$v_{DS}(t) = \sum_{k=-K}^K V_{ds}(k\omega_{LO})e^{jk\omega_{LO}t} \tag{62b}$$

Then, the nonlinearity must be approximated by a local polynomial model. For instance, a Taylor series such as

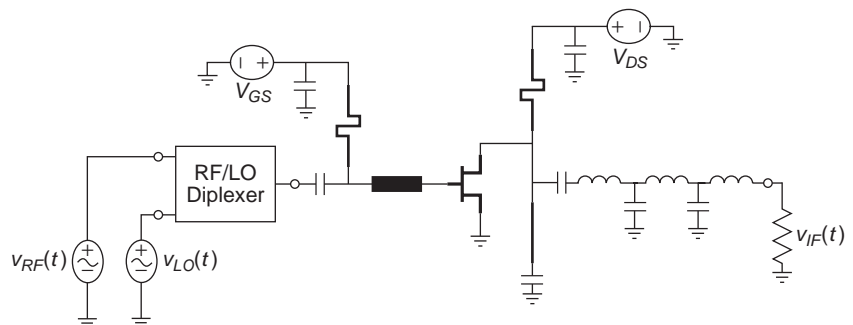


Figure 28. Simplified schematic of the active FET mixer used in the mixer distortion analysis.

(19), in the vicinity of this time-varying LO quiescent point, $[v_{GS}(t), v_{DS}(t)]$, where the small-signal component, $i_{ds}(v_{gs}, v_{ds})$, is determined by the small-signal RF excitation. Since the coefficients of such Taylor series depend on the control voltages $v_{GS}(t)$ and $v_{DS}(t)$, they will also be time-variant:

$$\begin{aligned} i_{ds}(v_{gs}, v_{ds}) = & G_m(t)v_{gs}(t) + G_{ds}(t)v_{ds}(t) \\ & + G_{m2}(t)v_{gs}(t)^2 + G_{md}(t)v_{gs}(t)v_{ds}(t) \\ & + G_{d2}(t)v_{ds}(t)^2 + G_{m3}(t)v_{gs}(t)^3 \\ & + G_{m2d}(t)v_{gs}(t)^2v_{ds}(t) + G_{md2}(t)v_{gs}(t)v_{ds}(t)^2 \\ & + G_{d3}(t)v_{ds}(t)^3 \end{aligned} \quad (63)$$

As $v_{GS}(t)$ and $v_{DS}(t)$ are periodic, the coefficients of (63) are again periodic obeying a Fourier expansion of the form

$$g(t) = \sum_{k=-K}^K G(k\omega_{LO})e^{jk\omega_{LO}t} \quad (64)$$

Assuming that the RF signal is a two-tone signal

$$v_{RF}(t) = V_{RF} \cos(\omega_1 t) + V_{RF} \cos(\omega_2 t) \quad (65)$$

(in which we consider, without any lack of generality, that $\omega_1 < \omega_2 < \omega_{LO}$), the small-signal components of $v_{GS}(t)$, $v_{DS}(t) - v_{gs}(t)$, $v_{ds}(t)$ – are again two-tone signals. Substituting (64) and (65) in (63) determines a small-signal current $i_{ds}(t)$, whose components obey $k\omega_{LO} \pm m_1\omega_{RF_1} \pm m_2\omega_{RF_2}$ (k is any integer number and $m_1, m_2 \in \{-3, -2, -1, 0, 1, 2, 3\}$, $|m_1| + |m_2| \leq 3$) and thus include the input tone frequencies at $\omega_{RF_{1,2}}$ ($k=0$), the intermediate frequencies IF at $\omega_{IF_{1,2}} = \omega_{LO} - \omega_{RF_{1,2}}$ ($k=1$), its second and third harmonics at $2\omega_{IF_{1,2}} = 2\omega_{LO} - 2\omega_{RF_{1,2}}$ ($k=2$), and $3\omega_{IF_{1,2}} = 3\omega_{LO} - 3\omega_{RF_{1,2}}$ ($k=3$), respectively, and second- and third-order intermodulation products at $\omega_{IF_{2A}} = \omega_{IF_2} - \omega_{IF_1} = \omega_{RF_2} - \omega_{RF_1}$ ($k=0$) and $\omega_{IF_3} = 2\omega_{IF_2} - \omega_{IF_1} = \omega_{LO} - (2\omega_{RF_2} - \omega_{RF_1})$ ($k=1$), respectively.

One surprising conclusion that may be drawn from this analysis is that, contrary to an amplifier in which a single Taylor coefficient determines both n th-order harmonics and intermodulation products, in a mixer, for example, the baseband second-order products are determined by the DC component of the Fourier expansion of a coefficient while the second harmonic is determined by the component at $2\omega_{LO}$. Similarly, it is the ω_{LO} Fourier component that determines the in-band third-order products, while the third harmonic is controlled by the Fourier component at $3\omega_{LO}$. Therefore, contrary to what happens in a memoryless amplifier, the behavior of the harmonics of a memoryless mixer may say nothing about the behavior of the corresponding in-band distortion products. A detailed analysis of the distortion arising in a mixer is quite laborious and requires a full small-signal/large-signal analysis using the conversion matrix formalism [6,7,26]. However, some qualitative insight can already be obtained

if we consider the ideal situation of a unilateral gate mixer (total absence of feedback) where the input is tuned for ω_{RF} and ω_{LO} and the output is tuned for ω_{IF} . $v_{gs}(t)$ will have only ω_{RF} components, while $v_{ds}(t)$ will have only the resulting ω_{IF} components and its in-band distortion products ω_{IF_3} .

In such an ideal case the FET's $i_{ds}(t)$ current component at the IF fundamental frequencies will be given by

$$\begin{aligned} I_{ds}(\omega_{IF}) \approx & G_{m1}V_{gs}(-\omega_{IM}) \\ & + G_{m-1}V_{gs}(\omega_{RF}) + G_{ds0}V_{ds}(\omega_{IF}) \end{aligned} \quad (66)$$

where G_{m_k} and G_{ds_k} stand for the k th-order harmonic of the Fourier expansion of $G_m(t)$ and $G_{ds}(t)$, as expressed by (64), and $V_{gs}(\omega)$ and $V_{ds}(\omega)$ represent the $v_{gs}(t)$ and $v_{ds}(t)$ components at ω . ω_{IM} is the so-called image frequency. Because it is symmetrically located near the RF components, taking ω_{LO} as the symmetry axis (since, in the present case, $\omega_{RF} = \omega_{LO} - \omega_{IF}$, then $\omega_{IM} = \omega_{LO} + \omega_{IF}$), it will be also converted to the IF output, thus constituting additive interference.

If now the third-order intermodulation product components of $i_{ds}(t)$, $I_{ds}(\omega_{IF_3})$, were calculated, we would have

$$I_{ds3}(\omega_{IF_3}) \approx G_{m3-1}V_{gs}^3(2\omega_{RF_1} - \omega_{RF_2}) \quad (67)$$

in which $V_{gs}^3(2\omega_{RF_1} - \omega_{RF_2})$ stands for the terms at ω_{IF_3} that result from the frequency-domain convolutions of $V_{gs}(\omega) * V_{gs}(\omega) * V_{gs}(\omega)$ or the time-domain products of $v_{gs}(t)^3$. Expressions (66) and (67) show that a mixer designed for high linearity, namely, one in which conversion gain is maximized and IMD is minimized, requires a (V_{GS}, V_{DS}) bias point and a LO drive level that maximize first-order Fourier component of the time-varying transconductance $G_m(t)$ and minimize first-order Fourier component of $G_{m3}(t)$. Unfortunately, these are conflicting requirements since maximizing G_{m1} or G_{m-1} means searching for a $G_m(t)$ waveform of highest amplitude and odd symmetry, while reducing G_{m3-1} implies reducing $G_{m3}(t)$ swing and a $G_{m3}(t)$ waveform of even symmetry, which, as we will see next, cannot be accomplished simultaneously. So, a compromise should be sought in terms of conversion gain and linearity optimization.

To illustrate this simplified analysis, Fig. 29a shows three $G_m(t)$ waveforms for three distinct V_{GS} bias points, Fig. 29b shows the corresponding $G_{m3}(t)$ waveforms, and, finally, Fig. 29c shows the resulting conversion gain and IMD ratio $[I_{ds}(\omega_{IF})/I_{ds}(\omega_{IF_3})]$ for the whole range of V_{GS} bias.

As stated above, there is indeed a compromise between linearity and conversion gain. Although very high IMR values can be obtained for particular bias points, none of them coincides with the zone of highest conversion gain. In a typical sigmoidal $G_m(v_{GS})$ (such that depicted in Fig. 14a), conversion efficiency is optimized when the FET is biased for maximum $G_m(v_{GS})$ variation, that is, for the $G_{m2}(v_{GS})$ peak. Unfortunately, that maximized variation of $G_m(v_{GS})$ is accompanied by an also nearly ideal odd symmetry of $G_{m3}(v_{GS})$, which is responsible for the

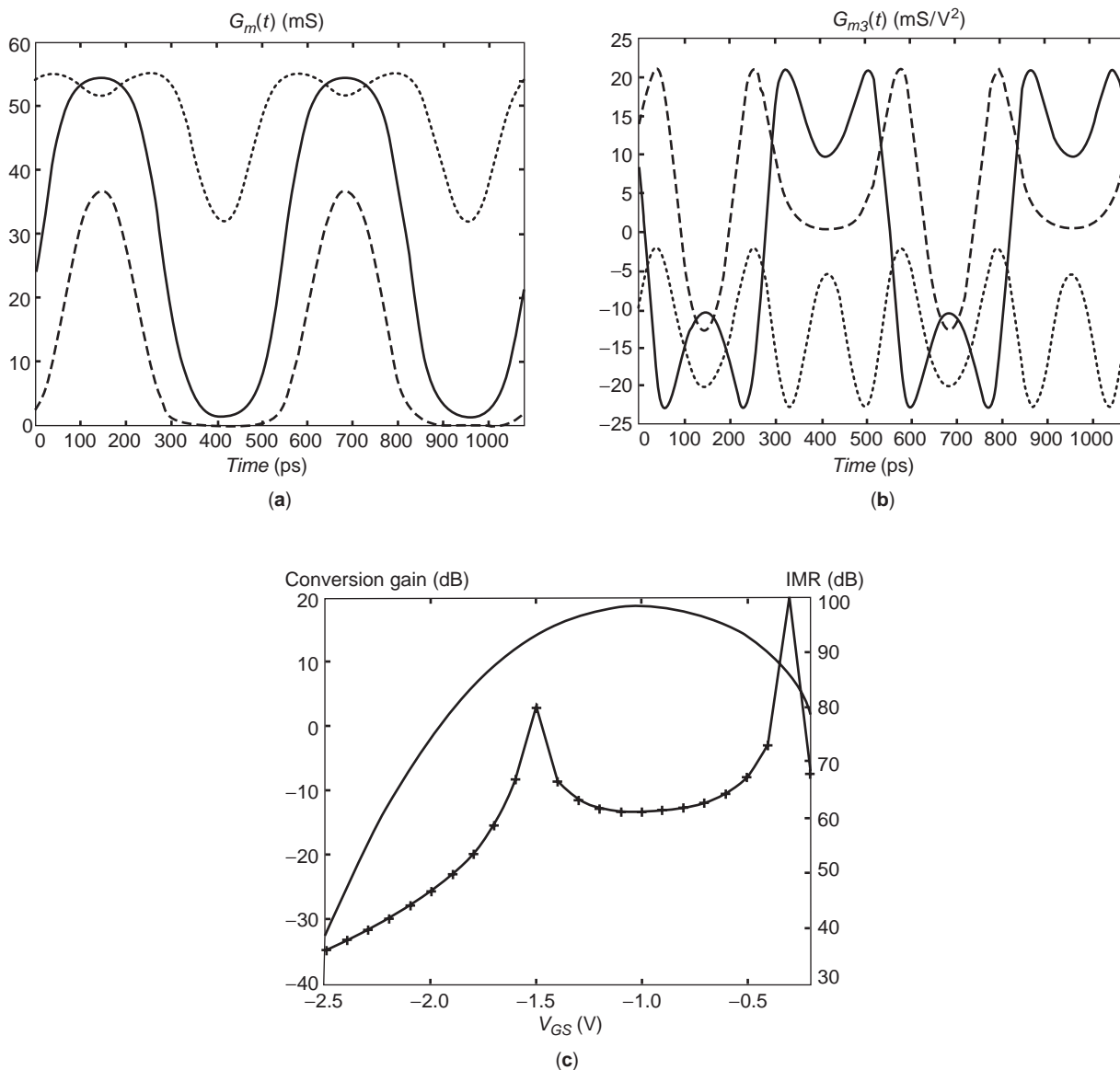


Figure 29. (a) Time-domain waveforms of $G_m(t)$ for three different V_{GS} bias points: $V_{GS} = -1.5$ V (- - -), $V_{GS} = -1.0$ V (—), and $V_{GS} = -0.6$ V (· · ·); (b) corresponding time-domain waveforms of $G_{m3}(t)$ for the same three V_{GS} bias points; (c) conversion gain (—) and IMD ratio (-+-) for the whole range of the FET's V_{GS} bias.

observed IMD impairment. Furthermore, this simplified analysis also shows that, as was previously studied for amplifiers, IMD behavior of mixers strongly depends on the actual shape of the device's nonlinearity. (For example, the very sharp peaks of IMR shown in Fig. 29c are due to the ideal symmetric sigmoidal model used for the simulated FET's transconductance.) So, different devices will show quite distinct IMR patterns, impeding a straightforward extrapolation of these active FET mixer results to diode mixers [6,27] or even resistive FET mixers [28,29].

6. CONCLUSIONS

This article showed that the study of nonlinear distortion mechanisms is a subject of fundamental interest that

spreads through almost all microwave and RF signal processing circuits and systems. Involving various scientific disciplines that range from the physical level of the active-device modeling, to the circuit and system's level of communication links, it requires a broad range of microwave knowledge. Hence, and despite the now more than 40 years of continued progress, intermodulation distortion is still an exciting and challenging field of strong active research both in industry and academia.

Acknowledgements

The author would like to express his gratitude to several of his colleagues and graduate students who contributed with some of the knowledge presented in this article. Of

these, Nuno B. Carvalho, Jose A. Garcia, and Christian Fager deserve a special mention.

BIBLIOGRAPHY

1. L. Chua, C. A. Desoer, and E. S. Kuh, *Linear and Nonlinear Circuits*, McGraw-Hill, 1987.
2. R. H. Caverly, Distortion modeling of PIN diode switches and attenuators, *IEEE Int. Microwave Symp. Digest*, 2004, pp. 957–960.
3. L. Dussopt and G. M. Rebeiz, Intermodulation distortion and power handling in RF MEMS switches, varactors, and tunable filters, *IEEE Trans. Microwave Theory Tech.* **MTT-51**:1247–1256 (2003).
4. P. Liu, Passive intermodulation interference in communication systems, *Electron. Commun. Eng. J.* **2**:109–118 (1990).
5. J. C. Pedro and N. B. Carvalho, On the use of multi-tone techniques for assessing RF components' intermodulation distortion, *IEEE Trans. Microwave Theory Tech.* **MTT-47**:2393–2402 (1999).
6. J. C. Pedro and N. B. Carvalho, *Intermodulation Distortion in Microwave and Wireless Circuits*, Artech House, Norwood, MA, 2003.
7. S. A. Maas, *Nonlinear Microwave and RF Circuits*, 2nd ed., Artech House, Norwood, MA, 2003.
8. N. Boulejfen, A. Harguem, and F. A. Ghannouchi, New closed-form expressions for the prediction of multitone intermodulation distortion in fifth-order nonlinear RF circuits/systems, *IEEE Trans. Microwave Theory Tech.* **MTT-52**:121–132 (2004).
9. J. C. Pedro and J. Perez, Accurate simulation of GaAs MESFET's intermodulation distortion using a new drain-source current model, *IEEE Trans. Microwave Theory and Tech.* **MTT-42**:25–33 (1994).
10. J. A. Garcia, A. Mediavilla, J. C. Pedro, N. B. Carvalho, A. Tazón, and J. L. Garcia, Characterizing the gate to source nonlinear capacitor role on GaAs FET IMD performance, *IEEE Trans. Microwave Theory Tech.* **MTT-46**:2344–2355 (1998).
11. M. C. Jeruchim, P. Balaban, and K. S. Shanmugan, *Simulation of Communication Systems—Modeling, Methodology and Techniques*, 2nd ed., Kluwer Academic/Plenum, New York, 2000.
12. V. Mathews and G. Sicuranza, *Polynomial Signal Processing*, Wiley, New York, 2000.
13. A. Saleh, Frequency-independent and frequency-dependent nonlinear models of TWT amplifiers, *IEEE Trans. Commun.* **COM-29**:1715–1720 (1981).
14. J. C. Pedro and S. A. Maas, A comparative overview of microwave and wireless power amplifier behavioral modeling approaches, *IEEE Trans. Microwave Theory Tech.* (in press).
15. C. P. Silva, C. J. Clark, A. A. Moulthrop, and M. S. Muha, Optimal-filter approach for nonlinear power amplifier modeling and equalization, *IEEE Int. Microwave Symp. Digest*, 2000, pp. 437–440.
16. Q. J. Zhang and K. C. Gupta, *Neural Networks for RF and Microwave Design*, Artech House, Norwood, MA, 2000.
17. K. Kundert, J. White, and A. Sangiovanni-Vicentelli, *Steady-State Methods for Simulating Analog and Microwave Circuits*, Kluwer Academic Publishers, Norwell, MA, 1990.
18. S. C. Cripps, *RF Power Amplifiers for Wireless Communications*, Artech House, Norwood, MA, 1999.
19. N. B. Carvalho and J. C. Pedro, Large and small signal IMD behavior of microwave power amplifiers, *IEEE Trans. Microwave Theory Tech.* **MTT-47**:2364–2374 (1999).
20. C. Fager, J. C. Pedro, N. B. Carvalho, and H. Zirath, Prediction of IMD in LDMOS transistor amplifiers using a new large-signal model, *IEEE Trans. Microwave Theory Tech.* **MTT-50**:2834–2842 (2002).
21. C. Fager, J. C. Pedro, N. B. Carvalho, H. Zirath, F. Fortes, and M. J. Rosário, A comprehensive analysis of IMD behavior in RF CMOS power amplifiers, *IEEE J. Solid State Circ.* **JSSC-39**:24–34 (2004).
22. N. B. Carvalho and J. C. Pedro, A comprehensive explanation of distortion sideband asymmetries, *IEEE Trans. Microwave Theory Tech.* **MTT-50**:2090–2101 (2002).
23. L. R. Gomes and J. C. Pedro, Design rules for highly efficient power amplifiers driven by low voltage supplies, *Proc. 29th European Microwave Conf.*, 1999, Vol. II, pp. 267–270.
24. J. M. Golio, M. G. Miller, G. N. Maracas, and D. A. Johnson, Frequency-dependent electrical characteristics of GaAs MESFETs, *IEEE Trans. Electron. Devices* **ED-37**:1217–1227 (1990).
25. R. Anholt, *Electrical and Thermal Characterization of MESFETs, HEMTs, and HBTs*, Artech House, Norwood, MA, 1995.
26. S. A. Maas, *Microwave Mixers*, Artech House, Norwood, MA, 1986.
27. S. A. Maas, Two-tone intermodulation in diode mixers, *IEEE Trans. Microwave Theory Tech.* **MTT-35**:307–314 (1987).
28. S. Maas, A GaAs MESFET mixer with very low intermodulation, *IEEE Trans. Microwave Theory Tech.* **MTT-35**:425–429 (1987).
29. J. A. Garcia, J. C. Pedro, M. L. de La Fuente, N. B. Carvalho, A. Mediavilla, and A. Tazón, Resistive FET mixer conversion loss and IMD optimization by selective drain bias, *IEEE Trans. Microwave Theory Tech.* **MTT-47**:2382–2392 (1999).

INTERMODULATION MEASUREMENT

MUHAMMAD TAHER
 ABUELMA'ATTI
 King Fahd University of
 Petroleum and Minerals
 Dhahran, Saudi Arabia

1. INTRODUCTION

Virtually all electronic circuits and systems exhibit nonlinear input–output transfer characteristic. Mixers, frequency multipliers, modulators, and square-law detectors represent examples of intentional class members, while linear power amplifiers, active filters, and microwave transmitters, in which nonlinearity represents an undesirable deviation of the system from ideal, linear operation, are examples of unintentional members.

Whenever a number of signals of differing frequencies pass through a nonlinear device, energy is transferred to frequencies that are sums and differences of the original frequencies. These are the intermodulation products (IMPs). In such cases, the instantaneous level of one signal may effectively modulate the level of another signal;

hence the term *intermodulation*. In a transmitting system, the results of excessive intermodulation are unwanted signals that may cause interference. In a receiver, internally generated intermodulation can hinder reception of the desired signals. It is interesting to note that the ear's cochlea has a similar nonlinear response and produces sums and differences of the input frequencies in the same way, particularly with loud sounds [1].

It has also been found that passive components, normally considered to be linear, can also generate IMPs. A variety of situations can arise in which nonlinear resistance junctions can be formed at metallic mating surfaces. Such junctions may result from salt or chemical depositions or from corrosion. The result is sometimes known as the "rusty bolt effect" because rusted bolts in structures have been known to exhibit such nonlinearities. This phenomenon is referred to as *passive intermodulation* (PIM). Sources of PIM include waveguides, directional couplers, duplexers, and antennas [2–6].

Intermodulation may also occur at the amplifier–loud-speaker interface [7], or in general as a result of the nonlinear interaction between the input signal of a two-port and a signal injected to the output port and propagating into the input via a feedback network [8]. Externally induced transmitter intermodulation, also known as *reverse intermodulation*, *backward intermodulation*, and *antenna-induced intermodulation*, is the mixing of a carrier frequency with one or more interfering signals in a transmitter's final stage [9]. Moreover, lack of screening of open-wire transmission lines can result in significant coupling to adjacent lines frequently giving rise to intermodulation products [10]. Furthermore, intermodulation may arise when an array of receiving antennas is illuminated with a transient impulsive electromagnetic plane wave [11].

In discussing the sources of IMPs it is convenient to divide nonlinear mechanisms yielding IMPs into two principal forms. The first is due to a nonlinear amplitude input/output characteristic (AM/AM), which causes amplitude compression with increasing input amplitude. The second mechanism occurs because of the variation of phase shift through the device, or the system, as the input amplitude is changed (AM/PM).

Depending on the signal characteristics, sources of IMPs can be divided into two categories: (1) static nonlinearity, depending solely on the amplitude of the signal, and (2) dynamic nonlinearity, depending not only on the amplitude but also on the time properties or frequency composition of the signal.

Static nonlinearities usually encountered in electronic circuits and systems can be classified into clipping, crossover, and soft nonlinearities [12] as shown in Fig. 1. Among the hard nonlinearities of clipping (which is significant near maximum input amplitudes) and crossover (significant mostly at small input amplitudes), the soft nonlinearity is usually the most important in the transfer characteristic of an electronic circuit. If the frequency content or the time properties of the input signal affect the transfer characteristic of the circuit or the system, the resulting nonlinearities may be called *dynamic*. Intermodulation products resulting from dynamic nonlinearities are

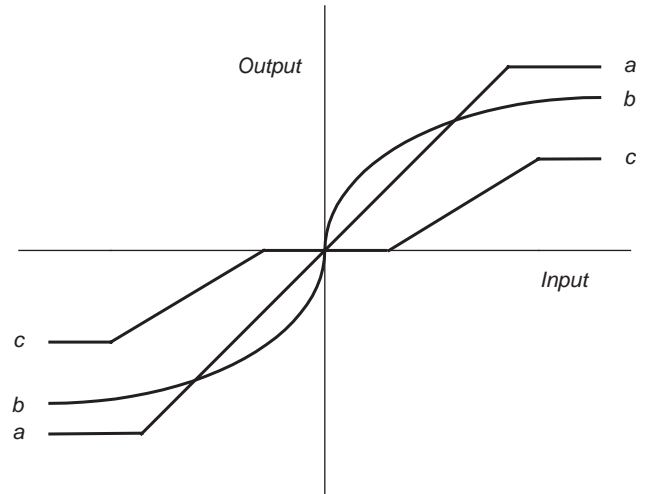


Figure 1. Different types of static nonlinearities: (a) clipping; (b) soft; (c) crossover.

referred to as *transient intermodulation* (TIM), *slew-induced distortion* (SID), or *dynamic intermodulation distortion* (DIM) [13–16].

2. SIMPLE INTERMODULATION THEORY

IMP occurs when two or more signals exist simultaneously in a nonlinear environment. In general, if N signals with frequencies f_1 to f_N are combined in a static nonlinearity, the output will contain spectral components at frequencies given by

$$\sum_{n=1}^N k_n f_n$$

where k_n is a positive integer, a negative integer, or zero, and $\sum_{n=1}^N |k_n|$ is the order of the IMP. Even with a small number of input signals N , a very large number of IMPs are generated. Fortunately, not all products are equally troublesome. Depending on the system involved, some of these IMPs can be neglected since they will be filtered out at some point. For example, most of the communication systems operate over a limited frequency band. Thus, IMPs falling out of the band will be attenuated. Moreover, amplitudes of the IMPs generally decrease with the order of the products, and high-order products can often be neglected. Low-order intermodulation components such as the second-order component $f_m - f_n$ and $f_m + f_n$ and the third-order components occurring at frequencies $2f_m - f_n$ and $f_m + f_n - f_q$ are usually the most troublesome, having the largest magnitudes and/or lying close to the originating frequencies, making their removal by filtering practically difficult. However, a salient characteristic of PIM, as distinguished from the conventional IM counterpart, discussed above, is that the PIMs causing trouble are of a high order, say, 11th–21st.

Analysis of nonlinear systems differs from that of linear systems in several respects: (1) there is no single analytical approach that is generally applicable (such as Fourier

or Laplace transforms in linear systems); (2) closed-form analytical solutions of nonlinear equations are not ordinarily possible; and (3) there is rarely sufficient information available to enable a set of equations that accurately model the system to be derived. These factors preclude the exact analytical determination of nonlinear effects, such as IMPs, in the general case. In order to get anything done at all, it is usually necessary to make various simplifying assumptions and then use an approximate model that will provide results of acceptable accuracy for the problem in hand.

A simple approach, therefore, is to use frequency-domain techniques that provide a separate solution for each frequency present in the output. In general, such methods are (1) centered around a description of the nonlinear mechanism by a continuous function type of characteristic, for example, a polynomial or a Fourier series representation of the output in terms of the input; and (2) based on the simplifying assumption that this characteristic does not vary with frequency, in other words, that it is a memoryless characteristic.

Memoryless nonlinear circuits are often modeled with a power series of the form

$$V_{\text{out}} = \sum_{n=0}^N k_n V_i^n \quad (1)$$

The first coefficient, k_0 , represents the DC offset in the circuit. The second coefficient, k_1 , is the gain of the circuit associated with linear circuit theory. The remaining coefficients, k_2 and above, represent the nonlinear behavior of the circuit. If the circuit were completely linear, all the coefficients except k_1 would be zero.

The model can be simplified by ignoring the terms that come after the k_3 term. For soft nonlinearities, the size of k_n decreases rapidly as n gets larger. For many applications the reduced model of Eq. (2) is sufficient, since the second-order and third-order effects dominate. However, many devices, circuits, and systems present difficulties for the polynomial approximation:

$$V_{\text{out}} = k_0 + k_1 V_i + k_2 V_i^2 + k_3 V_i^3 \quad (2)$$

Assuming that the input signal is a two-tone of the form

$$V_i = V_1 \cos \omega_1 t + V_2 \cos \omega_2 t \quad (3)$$

then combining Eqs. (2) and (3), yields

$$\begin{aligned} V_{\text{out}} = & a_0 + b_1 \cos \omega_1 t + c_1 \cos \omega_2 t + b_2 \cos 2\omega_1 t \\ & + c_2 \cos 2\omega_2 t + b_3 \cos(\omega_1 + \omega_2)t + c_3 \cos(\omega_1 - \omega_2)t \\ & + b_4 \cos 3\omega_1 t + c_4 \cos 3\omega_2 t + b_5(\cos(2\omega_1 + \omega_2)t \\ & + \cos(2\omega_1 - \omega_2)t) + c_5(\cos(2\omega_2 + \omega_1)t \\ & + \cos(2\omega_2 - \omega_1)t) \end{aligned} \quad (4)$$

where

$$\begin{aligned} a_0 &= k_0 + \frac{k_2}{2}(V_1^2 + V_2^2) \\ b_1 &= k_1 V_1 + \frac{3}{4}k_3 V_1^3 + \frac{3}{2}k_3 V_1 V_2^2 \\ c_1 &= k_1 V_2 + \frac{3}{4}k_3 V_2^3 + \frac{3}{2}k_3 V_1^2 V_2 \\ b_2 &= \frac{1}{2}k_2 V_1^2 \\ c_2 &= \frac{1}{2}k_2 V_2^2 \\ b_3 &= c_3 = k_2 V_1 V_2 \\ b_4 &= \frac{1}{4}k_3 V_1^3 \\ c_4 &= \frac{1}{4}k_3 V_2^3 \\ b_5 &= \frac{3}{4}k_3 V_1^2 V_2 \\ c_5 &= \frac{3}{4}k_3 V_1 V_2^2 \end{aligned}$$

For equal-amplitude input tones, Eq. (4) shows that the second-order terms, of amplitudes b_2, c_2, b_3, c_3 will be increased 2 dB in amplitude when input tones are increased by 1 dB. The third-order terms, of amplitudes b_4, c_4, b_5, c_5 , are increased by 3 dB in amplitude when the input tones are increased by 1 dB.

While Eq. (1) is adequate, and widely used, to predict the intermodulation performance of a wide range of devices, circuits, and systems, it seldom can be used. Examples include, but are not restricted to, prediction of spectral regrowth in digital communication systems, transient intermodulation and frequency-dependent nonlinearities, and passive intermodulation.

3. SPECTRAL REGROWTH

When a modulated signal passes through a nonlinear device, its bandwidth is broadened by odd-order nonlinearities. This phenomenon, called *spectral regrowth* or *spectral regeneration*, is a result of mixing products (intermodulation) between the individual frequency components of the spectrum [17]. The spectral regrowth can be classified in the two following categories: (1) in-band intermodulations and (2) out-of-band intermodulations. The first cannot be eliminated by linear filtering and are responsible for the signal-to-noise ratio degradation and, consequently, for the bit error rate (BER) degradation in digital communication systems. The second generates the interference between adjacent channels and can be filtered out at the nonlinear device output with certain output power penalty that is caused by the filter insertion losses. This spectral regrowth causes adjacent-channel

interference (ACI), which is measured by the adjacent-channel power ratio (ACPR).

The ACPR is the power in the main channel divided by the power in the lower plus upper adjacent channels. Considering just the lower channel yields $ACPR_{lower}$ and the upper channel alone yields $ACPR_{upper}$. Analog cellular radio uses frequency or phase modulation, and the ACPR is adequately characterized by intermodulation distortion of discrete tones. Typically, third-order intermodulation product (IMP3) generation, in a two-tone test, is adequate to describe spectral regrowth. Thus, distortion in analog radio is accurately modeled using discrete-tone steady-state simulation. Digital radio, however, uses complex modulation, and adjacent-channel distortion has little relationship to intermodulation in a two-tone test [18,19]. A modulated input signal applied to radiofrequency (RF) electronics in digital radio is a sophisticated waveform resulting from coding, filtering, and quadrature generation. Neither can it be represented by a small number of discrete tones (or frequencies), nor can the waveform be represented in a simple analytic form. Thus, in digital radio, ACPR is more difficult to predict than one- or two-tone responses since it depends not only on the intrinsic nonlinear behavior of the device (e.g. amplifier) but also on the encoding method (i.e., the statistics of the input stream) and the modulation format being used. The only way the input stream can conveniently and accurately be represented is by its statistics, and transforming these using an appropriate behavioral model provides accurate and efficient modeling of ACPR [20]. While in Ref. 20 the input signal is assumed Gaussian, digital communication signals are often far from being Gaussian. In Ref. 21 the input is assumed stationary but not necessarily Gaussian.

ACPR is, therefore, defined differently in the various wireless standards. The main difference is the way in which adjacent-channel power affects the performance of another wireless receiver for which the offending signal is cochannel interference [20]. In general the ACPR can be defined as [20]

$$ACPR = \frac{\int_{f_3}^{f_4} S(f)df}{\int_{f_1}^{f_2} S(f)df} \quad (5)$$

where $S(f)$ is the power spectral density (PSD) of a signal whose channel allocation is between frequencies f_1 and f_2 , and its adjacent channel occupies frequencies between f_3 and f_4 . Regulatory authorities impose strict constraints on ACPR and accurate methods of its determination are of particular interest to those involved in wireless system design.

4. SIMPLE TRANSIENT INTERMODULATION THEORY

To illustrate how TIM distortion arises, consider a differential amplifier with negative feedback applied between the output and the inverting input and a voltage step applied to the noninverting input. If the open-loop gain of the amplifier were flat and the time delay through it were zero, the voltage step would instantaneously propagate undis-

torted through the amplifier, back through the feedback loop, and into the inverting input, where it would be subtracted from the input signal, and the difference signal, which is a voltage step occurring at the same time that the input voltage does, would be amplified by the amplifier. However, this is not the case when the open-loop gain of the amplifier is not flat and the time delay through it is not zero. When the voltage step occurs, the limited high-frequency response of the amplifier prevents the appearance of a signal at the amplifier output terminal until the internal capacitors of the amplifier can charge or discharge. This causes the momentary absence of a feedback signal at the inverting input to the amplifier, possibly causing the amplifier to severely overload until the feedback signal arrives.

If the input signal to the differential amplifier is formed of a sine wave superimposed on a square wave, the amplifier will exhibit the same response to the abrupt level changes in the square wave as it did to the voltage step discussed above. During the momentary absence of the feedback when the square wave changes level, the amplifier can either saturate or cut off. If this occurs, the sine wave momentarily disappears from the signal at the output terminal of the amplifier, or it momentarily decreases in amplitude. This happens because the saturated or cut-off amplifier appears as a short circuit or open circuit, respectively, to the sine wave, and this component of the input signal is interrupted from the output signal, thus resulting in TIM [16].

A point to be noted is that if the term were understood literally, this would imply transients of both high and low frequencies and/or high or low operating levels, in other words, all transients. In actual practice, however, TIM occurs only for signals with simultaneous high level and high frequencies—not lower levels or lower frequencies. The key parameter of such signals is that they are characterized by high signal slopes, not just high frequencies or high levels. Neither high frequencies nor high levels in themselves necessarily result in distortion, unless their combination is such that a high effective signal slope is produced. TIM is actually generated when the signal slope approaches or exceeds the amplifier slew rate. This can happen for either transient or steady-state signals. Thus, a more easily understood term to what actually happens would be one that relates both slew rate and signal slope. A more descriptive term to describe the mechanism would, therefore, be the slew-induced distortion (SID); other descriptive variations of this term are “slew rate distortion” or “slewing distortion” [22].

Because of the complexity of the mechanism resulting in TIM, especially handling the frequency dependence of the amplifier nonlinearity and incorporation of the feedback, Eq. (1) cannot be used to predict the TIM performance of nonlinear devices, and recourse to other analytical techniques, for example, Volterra series or harmonic balance analysis, would be inevitable.

5. VOLTERRA SERIES AND HARMONIC BALANCE ANALYSIS

Volterra series describes a system with frequency-dependent nonlinearity in a way that is equivalent to the

manner in which Taylor series approximates an analytic function. Depending on the amplitude of the exciting signal, a nonlinear system can be described by a truncated Volterra series. Similar to the Taylor series representation, for very high amplitudes the Volterra series diverges. Volterra series describe the output of a nonlinear system as the sum of the response of a first-order operator, a second-order one, a third-order one, and so on [23]. Every operator is described in either the time domain or the frequency domain with a kind of transfer function called a *Volterra kernel*.

In Volterra series analysis the nonlinear circuit is treated purely as an AC problem. Assuming that none of the input signals are harmonically related, an iterative solution can be applied for circuits not operated under distortion saturation conditions. First the circuit is solved for the input signals. These results are then used to calculate the second-order distortion products, and these are treated as generators at a different frequency to the input signals and the network is again solved. This is then repeated for higher-order distortion products. This leads to extremely fast calculation of distortion behavior. Simulation at higher power levels can be achieved by feeding back contributions from higher-order distortion products [24]. The use of Volterra series to characterize the output as a function of the input [25,26] can, therefore, provide closed-form expressions for all the distortion products of a frequency-dependent nonlinearity excited by a multisinusoidal signal.

However, techniques using Volterra series suffer from the disadvantage that a complex mathematical procedure is required to obtain a closed-form expression for the output amplitude associated with a single component of the output spectrum. Moreover, the problem of obtaining output products of orders higher than the third becomes prohibitively difficult unless it may be assumed that higher-order contributions vanish rapidly [27]. The Volterra series approach is, therefore, most applicable to mild nonlinearities where low-order Volterra kernels can adequately model the circuit behavior. With appropriate assumptions and simplifications, many useful features of the Volterra series technique can be used to find approximate expressions for TIM (SID). These are quite accurate for relatively small distortion conditions [28,29].

Alternatively, most RF and microwave circuit analysis are based on the harmonic balance analysis [30]. The harmonic balance technique works by processing the linear part of the circuit in the frequency domain and the nonlinear part in the time domain. Computation in the frequency domain is very fast and efficient, especially for frequency-selective components such as transmission lines and resonant circuits. Computations in the time domain are followed by Fourier transform. Harmonic balance analysis can, therefore, handle intermodulation distortion provided there are not too many excitation tones. In the harmonic balance technique an initial estimate is required for the final waveshape, and this is refined interactively during analysis. The harmonic balance method computes the response of a nonlinear circuit by iteration, and the final result is a list of numbers that do not indicate which nonlinearities in the circuit are mainly

responsible for the observed nonlinear behavior. Hence such a method is suitable for verification of circuits that have already been designed. This method does not present information from which designers can derive which circuit parameters or circuit elements they have to modify in order to obtain the required specifications [31]. While Volterra series analysis can provide such information, it is applicable only to weak nonlinearities.

While viewed as a universal solution, and has been widely used, the harmonic balance analysis may be unnecessarily slow, cumbersome, and prone to subtle errors [32], especially for weak nonlinearities or when a nonlinear device is excited by very small signals. Volterra series analysis is generally more accurate than harmonic balance for these types of problems, and it is several orders of magnitude faster than a harmonic balance analysis [32]. Moreover, Volterra series analysis integrates well with linear analysis tools, supporting simultaneous optimization of several parameters of the nonlinear system. Therefore, Volterra theory appears to be an ideal tool for circuits and systems that are not strongly nonlinear but have aspects of linear and nonlinear circuits [32]. However, Volterra series analysis becomes very cumbersome above third-order products, and for products above fifth order, it loses most of its advantages over the harmonic balance analysis. The major disadvantage of Volterra series is the occasional difficulty in deciding whether the limitations to weakly nonlinear operation have been exceeded.

In fact, Volterra-series analysis and the harmonic balance technique complement each other [32]. Thus, while the Volterra series analysis works well in those cases where harmonic balance works poorly, the harmonic balance works well where the Volterra series works poorly. Volterra series analysis is, therefore, not appropriate for mixers, frequency multipliers, saturated power amplifiers, and similar strongly driven and/or hard nonlinearities. Volterra series analysis is suitable for small-signal amplifiers, phase shifters, attenuators, and similar small-signal and/or soft nonlinearities.

Another technique for analyzing nonlinear systems is the describing function. This approach can yield closed-form expressions for a feedback system that contains an isolated static nonlinearity in the feedback loop [33]. Since it is not possible to map all nonlinear circuits and systems to such a feedback system, the describing function method has restricted applications.

6. PASSIVE INTERMODULATION (PIM)

While the concept of intermodulation in active devices such as amplifiers, filters, and mixers is familiar and well documented, the effects of intermodulation in passive components such as directional couplers, cables, coaxial connectors, power splitters, antennas, and electromechanical and solid-state programmable attenuators are less familiar and less documented. More recently, evidence has emerged that PIM has an impact in other system equipment, such as amplifiers and extenders, fiber nodes, and interface units [34]. Poor mechanical contact, dissimilar metals in direct contact, ferrous content in the conductors,

debris within the connector, poor surface finish, corrosion, vibration, and temperature variations are among the many possible causes of PIM. The sources of PIM have been studied extensively; see Refs. 35–43 and the references cited therein. Similar to the intermodulation products in active devices, PIM is generated when two or more RF signals pass through RF passive devices having nonlinear characteristics [41,42]. Generally the nonlinearities of RF passive devices consist of contact nonlinearity and material nonlinearity [43]. *Contact nonlinearity* refers to all metal contact nonlinearities causing nonlinear current–voltage behavior, such as the tunneling effect, micro-discharge, and contact resistance. *Material nonlinearity* refers to the bulk material itself. Magneto-resistivity of the transmission line, thermal resistivity, and nonlinear hysteresis of ferromagnetic material are good examples [43]. PIM generation in RF passive devices is caused by the simultaneous appearance of one or more of these PIM sources, and the overall performance is often dominated by one principal PIM source [43]. In the case of antennas, PIM is generated not only by the same PIM sources as in general RF passive components but also by the external working environment, such as conducting metal materials.

Over the years Eq. (1) was used to describe the nonlinear current/voltage conduction characteristics of passive components, (see, e.g., Refs. 37–39 and the references cited therein). While this approach results in simple expressions for the magnitudes of the harmonics and intermodulation products resulting from multisinusoidal excitations, it suffers from the following shortcomings. In order to predict high-order harmonic or intermodulation product magnitudes, it is necessary to determine coefficients of terms of similar order in the polynomial. A prerequisite to obtaining coefficients of high-order polynomial terms is measurement of output products of the same order. For example, to obtain the coefficients of a fifth-order polynomial, it is necessary to measure the output fifth-order components. With increasing use of narrowband components in multicouplers used in base stations of mobile radio systems, it becomes difficult to determine high-order coefficients in the nonlinear characteristic because the measured high-order product amplitudes from which they are computed are influenced to an unknown extent by the system selectivity [44]. To overcome these problems, an exponential method has been used to predict the intermodulation arising from corrosion [45].

7. INTERMODULATION CHARACTERIZATION

Although it is important to understand the origin of intermodulation and the engineering techniques for avoiding it, it is equally important to be able to characterize it objectively, preferably in a way that correlates well with the subjective perception of the intermodulation. The ability to characterize an imperfection in this way is an important step toward eliminating it as a system performance degradation.

Several techniques for characterizing intermodulation distortion have been proposed. While some of these

techniques measure the total intermodulation distortion, others distinguish between the various intermodulation products. The latter are preferred, for subjective perception of intermodulation shows that equal amounts of total intermodulation distortion differ widely in their effect according to how the total is made up.

Depending on the signal characteristics, techniques for characterization of intermodulation distortion can be classified into two categories: (1) *steady-state techniques*, where characterization is performed on the assumption that the input to the system under consideration is a multisinusoidal signal, and (2) *dynamic techniques*, where characterization is performed on the assumption that the input to the system under consideration is formed of a sinusoidal signal superimposed on another signal characterized by rapid changes of state, for example, a square wave or a sawtooth wave. While steady-state techniques can be used to characterize both RF and audio systems, dynamic techniques are generally used for characterizing only audio systems.

7.1. Steady-State Techniques

7.1.1. The Intercept Point. Increasing the signal level at the input to a weakly nonlinear device will cause the IMPs to increase at the output. In fact, the increase in IMP amplitudes is faster than the increase in the output version of the input signal. For increasing fundamental input power, the fundamental output power increases in a linear manner, according to the gain or loss of the device. At some point, gain compression occurs and the fundamental output power no longer increases with input power. The output power of the second-order intermodulation products also increases with fundamental input power, but at a faster rate. Recall that, according to the simple intermodulation theory, the second-order intermodulation changes by 2 dB per 1 dB of change in the fundamental. Similarly, the third-order intermodulation changes by 3 dB per 1 dB of change in the fundamental. Thus, on a logarithmic scale, as shown in Fig. 2, the lines representing the second- and third-order intermodulation products have twice and three times, respectively, the slope of the fundamental line.

If there were no gain compression, the fundamental input power could be increased until the second-order intermodulation eventually caught up with it, and the two output power levels would be equal. This point is referred to as the *second-order intercept point* (IP2). The third-order intermodulation product also increases faster than the fundamental, and those two lines will intersect at the third-order intercept point (IP3). Rarely can either of these two points be measured directly, due to the gain compression of the fundamental. Instead, the intercept points are extrapolated from measurements of the fundamental and intermodulation products at power levels below the point where gain compression occurs. The intercept points are usually specified in dBm and may refer to either the output or the input; the two points will differ by the gain of the system under consideration. The second-order and third-order intercept points are figures of merit that are independent of the signal level.

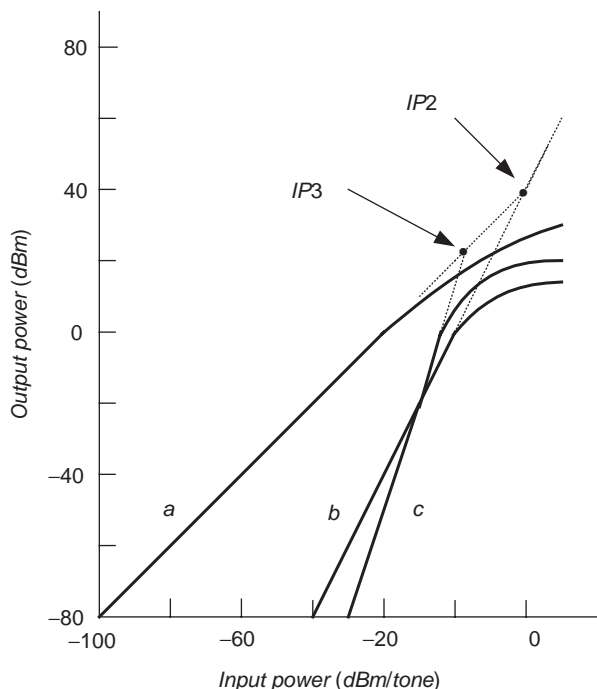


Figure 2. Third-order and second-order intercept points are determined by extending the fundamental, the second- and the third-order intermodulation transfer function lines: (a) Fundamental transfer function, slope = 1; (b) second-order intermodulation, slope = 2; (c) third-order intermodulation, slope = 3. IP3—third-order intercept point; IP2—second-order intercept point.

Therefore, the intermodulation performance of two different systems can be compared quite easily if their intercept points are known [46].

Using the intercept point it is easy to calculate the relative intermodulation level corresponding to a given input signal level. In fact, the difference between the level of the second-order intermodulation and the fundamental signal level is the same as the difference between the fundamental signal level and the intercept point. Thus, if the second-order intercept point is +15 dBm and the fundamental signal level is -10 dBm (both referred to the output of the device), the difference between these two values is 25 dB. Therefore, the second-order intermodulation products will be 25 dB below the fundamental, or -35 dBm. So the intercept point allows easy conversion between fundamental signal level and the intermodulation level.

The difference between the level of the third-order intermodulation products and the fundamental signal level is twice the difference between the fundamental signal level and the third-order intercept point. (Note that the second-order intercept point is not the same as the third-order intercept point.) Suppose that the third-order intercept point is +5 dBm and the fundamental signal is -25 dBm, both referred to the output of the device. The difference between the intercept point and the fundamental is 30 dB, so the third-order intermodulation products will be 2 times 30 dB down from the fundamental. The relative distortion level is -60 dB, and the absolute power of the intermodulation products is -85 dBm.

It is important, however, to note that the preceding analyses assume that the second-order and third-order intermodulation curves have slopes of 2 and 3 dB/dB, respectively. Thus, theoretically, the intercept points are not functions of the input power level. If a power sweep is performed, it is expected that the intercept points will remain constant. The intercept points can, therefore, be calculated from measurements at only one power level. However, if the input signal exceeds a certain limit, the amplitudes of the output fundamentals and the resulting intermodulation products will start to saturate, and the intercept points will usually drop off, indicating an invalid measurement. It is essential to know this limit. It is particularly useful for high-dynamic-range circuits and systems with relatively low output powers where the intermodulation is low, but only for signals that are low enough. Expanding the model of Eq. (2) to include fourth- and fifth-order terms [47] can achieve this.

Moreover, at low power levels, the intercept points will start to change as the noise floor of the measuring instrument, usually a spectrum analyzer, is approached, thus indicating an invalid measurement. It is important, therefore, to look at the variation of the intercept points as functions of power as this provides a good way of checking the valid measurement range.

7.1.2. Two-Tone Test. The two-tone test is extensively used in characterizing a wide range of devices. Magnetic tapes [48]; microwave and millimeter-wave diode detectors [49]; analog-to-digital converters [50,51]; gamma correctors [52]; and electrical components such as resistors, capacitors, inductors, as well as contacts of switches, connectors, and relays [53] are a few examples. The two-tone test is also used to characterize the performance of the basilar membrane of the cochlea [54].

The two-tone test can also be used to determine the transfer characteristic of a nonlinear device modeled by the polynomial approximation of Eq. (2). With the input formed of two properly selected frequencies ω_1 and ω_2 , and if the second-order and third-order intermodulation products are measured separately, it is possible to find, from the measured data, the coefficients of the quadratic and cubic terms k_2 and k_3 , respectively, in the polynomial approximation of Eq. (2). If in addition, the IMPs are measured at two sets of values of ω_1 and ω_2 , it is possible to identify the dominant physical nonlinear process from the variation of IMPs with test frequencies [13].

The two-tone test can also be used to determine the complex transfer characteristic of a nonlinear device exhibiting AM/AM nonlinearity only with fixed phase shift between the output and the input. In this case a complete set of measurement for all the two-tone intermodulation products produced by the nonlinearity at two different power levels is necessary [55]. If the device under consideration exhibits both AM/AM and AM/PM nonlinearities, then determination of a unique set of polynomial coefficients requires a complete set of intermodulation measurements at three different power levels [55]. The set obtained at the highest power level will decide the amplitude range within which the characterization will be valid.

According to the basic assumption that the nonlinearities are represented by polynomials, high-accuracy representation of the device characteristics will require difficult accurate measurements of higher-order intermodulation products, in addition to increased complications and considerable efforts involved in the analysis [55]. Another difficulty from which this method suffers arises from the necessity of measuring complete sets of two-tone intermodulation products spread over a relatively wide frequency range, which consequently may impose stringent specifications on the measuring instruments and techniques if accurate measurements are to be achieved.

In the two-tone test the inband IMPs are used to describe a device, a circuit or a system nonlinearity. Measurements are made in or near the frequency range of interest. In this test, the input signal consists of two frequencies, ω_1 and ω_2 of equal amplitude and a fixed amount of frequency spacing. At the output of the circuit or the system under test the amplitudes of the third-order intermodulation products $2\omega_1 - \omega_2$ and $2\omega_2 - \omega_1$ are measured. The *intermodulation distortion* is defined as the ratio between the root sum square of the intermodulation products and the root sum square of the twin-tone amplitudes.

Unless a wave analyzer or a spectrum analyzer is available, the implementation of the two-tone test invariably require amplification of the whole output spectrum to obtain components ω_1 and ω_2 on a normalized value (100%). Then, ω_1 and ω_2 are suppressed, and the remaining components $2\omega_1 - \omega_2$ and $2\omega_2 - \omega_1$ are measured with an AC voltmeter or oscilloscope. Especially at audiofrequencies, this approach requires steep filters, one set of filters for each set of ω_1 and ω_2 . For the same reason $\omega_2 - \omega_1$ cannot be too low, so it will never be a really narrowband system. This narrowband aspect is particularly important for higher frequencies, where equalizers, in the reproduction audio channel, may give unequal amplification of the components in the spectrum [56]. In the audiofrequency range several versions of the two-tone test are available [56–59].

7.1.3. Three-Tone Test. In this test, again, specific inband IMPs are selected to characterize the overall system nonlinearities [60]. The more even spectral distribution and flexibility, while still allowing discrete frequency evaluation, make this an attractive test for multifrequency systems such as communication and cable television systems. In this test three equal-amplitude tones are applied to the input of the nonlinear system under consideration. Thus

$$V_i = V(\cos \omega_1 t + \cos \omega_2 t + \cos \omega_3 t) \quad (6)$$

Combining Eqs. (2) and (6), and using simple trigonometric identities, it is easy to show that the third-order term, $k_3 V_i^3$ will contribute, to the output spectrum, the following:

1. Three components at frequencies ω_1 , ω_2 and ω_3 each with amplitude given by

$$A_1 = \frac{15}{4} k_3 V^3 \quad (7)$$

2. Three components at frequencies $3\omega_1$, $3\omega_2$, $3\omega_3$ each with amplitude given by

$$A_3 = \frac{1}{4} k_3 V^3 \quad (8)$$

3. Twelve components at frequencies $2\omega_m \pm \omega_n$, $m, n = 1-3$, each with amplitude given by

$$A_{21} = \frac{3}{4} k_3 V^3 \quad (9)$$

4. Four components at frequencies $\omega_m \pm \omega_n \pm \omega_p$, $m, n, p = 1-3$, each with amplitude given by

$$A_{111} = \frac{3}{2} k_3 V^3 \quad (10)$$

Equations (9) and (10) show that an intermodulation product of frequency $\omega_m \pm \omega_n \pm \omega_p$ is 6 dB higher in level than an intermodulation product of frequency $2\omega_m \pm \omega_n$. *Intermodulation distortion* is defined as the ratio between the amplitude of one of the intermodulation products of frequency $\omega_m \pm \omega_n \pm \omega_p$ and the amplitude of one of the three output tones. In this test the choice of frequencies $\omega_1, \omega_2, \omega_3$ used to perform the measurement is important. This is because a system's intermodulation performance may not be constant over its operating frequency range.

The three-tone test is widely used to characterize the performance of RF amplifiers used in television broadcast transposers, where the vision carrier, color subcarrier, and sound carrier frequency components interact in the presence of amplifier nonlinearities. If the three frequency components are represented as single frequencies (ω the vision carrier, ω_{sc} the color subcarrier, and ω_s the sound carrier with amplitudes V_v , V_{sc} , and V_s , respectively), then the input signal can be expressed as

$$V_i = V_v \cos \omega_v t + V_{sc} \cos \omega_{sc} t + V_s \cos \omega_s t \quad (11)$$

Combining Eqs. (2) and (11), and using simple trigonometric identities, it is easy to show that the third-order term of Eq. (2) produces, among others, two in-band intermodulation components given by

$$\begin{aligned} V_{ip} = & \frac{3}{2} k_3 V_v V_{sc} V_s \cos(\omega_v + \omega_s - \omega_{sc})t \\ & + \frac{3}{4} k_3 V_s V_{sc}^2 \cos(2\omega_{sc} - \omega_s)t \end{aligned} \quad (12)$$

Intermodulation performance of the transposer is measured by taking the transposer out of service and using the three-tone simulation of a composite video and sound signal, given by Eq. (11), as its input. The three levels and frequencies vary from system to system. Typical levels, below the peak synchronous pulse level, are $V_v = -6$ dB, $V_{sc} = 17$ dB, and $V_s = -10$ dB. Under these conditions, the first term of Eq. (12) is the most visible, and the second term will be much lower in amplitude, typically 17 dB less. Using a spectrum analyzer, the relative amplitude of the major in-band intermodulation is measured and

referenced to the level of peak synchronous pulse. Usually, the permissible level of the major in-band intermodulation component is -53 dB below the reference level. This three-tone test method is slow and requires spectrum analyzers with relatively wide dynamic ranges. Moreover, it measures the system performance at one luminance level and one chrominance level. Thus, it does not test the system over its full operating range [61].

The inadequacy of the internationally accepted three-tone test method can be overcome by using a modified colorbar test signal [61]. The colorbars are applied to the transposer via a test transmitter. The colorbars and sound carrier therefore apply the three tones to the transposer, changing levels in rapid succession. With suitable processing, based on sampling the demodulated colorbar signal for short intervals corresponding to a selected color, intermodulation levels can be measured simultaneously at seven different luminance levels and can be shown in histogram form [61].

7.1.4. Noise Power Ratio (NPR) Test. In the NPR test, the input to the device under test is obtained from a white-noise source that is bandlimited to the instantaneous frequency range of interest. This emulates a situation with many simultaneous input signals. Provided that none of the signals dominate, according to the central-limit theorem, the resulting voltage obtained when many uncorrelated signals are added will approach a Gaussian distribution. True white noise covers a frequency range of interest continuously, unlike discrete signals.

The NPR test measures the amount of intermodulation products power between two frequency ranges of white Gaussian noise. A white-noise generator is used with its output frequency range limited by a bandpass filter according to the bandwidth of the device under test. A quiet channel is formed by a switchable band-reject filter, as shown in Fig. 3. Then, the resulting white-noise signal is applied to the input of the device under test. At the output of the device under test is a receiver which is switch-tuned to the frequency of the band-reject filter used to produce the quiet channel. The NPR test is widely used for evaluating the intermodulation performance of systems whose input signal spectrum distribution can be approximated by that of white noise. However, the NPR may be degraded by the noise floor of the system under test, especially

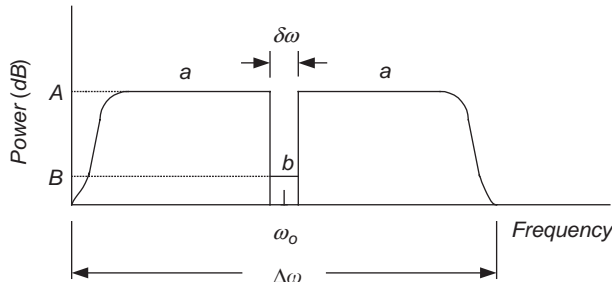


Figure 3. The output spectrum of a noise-power ratio measurement. (a) injected noise; (b) noise and intermodulation generated in the measurement bandwidth $\delta\omega$ by the DUT. $\text{NPR} = A - B$.

under very low loading conditions. It may also be degraded by the distortion products produced under high loading conditions [62].

7.1.5. Cross-Modulation. Cross-modulation occurs when modulation from a single unwanted modulated signal transfers itself across and modulates the wanted signal. Cross-modulation is troublesome primarily if the desired signal is weak and is adjacent to a strong unwanted signal. Even when the carrier of the strong unwanted signal is not passed through the system, the modulation on the undesired carrier will be transferred to the desired carrier. Cross-modulation is, therefore, a special case of intermodulation. Recall that when the input to a non-linear system is formed of a two-tone signal of the form of Eq. (3), then the amplitudes of the output components at frequencies ω_1 and ω_2 will be given by

$$b_1 = k_1 V_1 + \frac{3}{4} k_3 V_1^3 + \frac{3}{2} k_3 V_1 V_2^2 \quad (13)$$

and

$$c_1 = k_1 V_2 + \frac{3}{4} k_3 V_2^3 + \frac{3}{2} k_3 V_1^2 V_2 \quad (14)$$

respectively. Thus, the output obtained at each frequency ω_1 and ω_2 , is dependent on the amplitude of the signal component of the other frequency. If the amplitude of the wanted unmodulated carrier is V_1 and the instantaneous amplitude of the unwanted amplitude-modulated carrier is

$$V_2(t) = V_2(1 + m \cos \omega_m t) \quad (15)$$

then, using Eq. (13), the amplitude of the wanted carrier will be

$$b_1 = k_1 V_1 + \frac{3}{4} k_3 V_1^3 + \frac{3}{2} k_3 V_1 V_2^2 (1 + m \cos \omega_m t)^2 \quad (16)$$

For small values of m and with $k_3 \ll k_1$, Eq. (16) can be approximated by

$$b_1 \cong k_1 V_1 + 3k_3 V_1 V_2^2 m \cos \omega_m t \quad (17)$$

Thus the wanted carrier will be modulated by a modulation index

$$p = 3 \frac{k_3}{k_1} V_2^2 m \quad (18)$$

The cross-modulation factor is then defined as

$$K = \frac{p}{m} \quad (19)$$

Thus, one frequency will be modulated by the modulation of the other frequency. Similar results can be obtained if the unwanted carrier is FM-modulated.

Cross-modulation can be measured as the change in the amplitude of the wanted unmodulated carrier as a function of the amplitude of the unwanted unmodulated carrier. This is the procedure recommended by the NCTA (National Cable Television Association) standard cross-modulation measurement [63]. Alternatively, cross-modulation can be measured using the definition of Eq. (19): measuring percentage modulation that appears on an unmodulated desired carrier due to the presence of an undesired modulated carrier, divided by the percentage modulation on the undesired carrier [64].

Cross-modulation can also be measured using two equal-amplitude carriers. The wanted carrier, ω_2 , is unmodulated while the unwanted carrier, ω_1 , is FM-modulated. The output spectrum clearly shows the frequency deviation of the wanted carrier. Moreover, it can be shown that the frequency deviation of the intermodulation components, of the output spectrum, is larger than that of the original FM-modulated unwanted carrier. For the intermodulation product of frequency $\alpha\omega_1 \pm \beta\omega_2$, the deviation will be multiplied by α . Thus, it may be easier to measure the cross-modulation by measuring the deviation of an intermodulation product rather than the deviation of the wanted unmodulated carrier [65].

7.1.6. Differential Gain. *Differential gain* (DG), a parameter of special interest in color-TV engineering, is conventionally defined as the difference in gain encountered by a low-level high-frequency sinusoid at two stated instantaneous amplitudes of a superimposed slowly varying sweep signal. In video signal transmission, the high-frequency sinusoid represents the chromatic signal and the low-frequency sinusoid represents the luminance signal. Corresponding to the theoretical conditions of the differential measurement, DG measurement is performed by a signal of the form of Eq. (3) with $\omega_2 \gg \omega_1$ and $V_2 \rightarrow 0.0$ at $V_1 = 0.0$ and X [66]. Therefore, recalling that when the input to a nonlinear system is formed of a two-tone signal of the form of Eq. (3), the amplitude of the output component at frequency ω_2 will be given by

$$c_1 = k_1 V_2 + \frac{3}{4} k_3 V_2^3 + \frac{3}{2} k_3 V_1^2 V_2 \quad (20)$$

Thus, DG can be expressed as

$$DG = 1 - \frac{k_1 + \frac{3}{4} k_3 V_2^2}{k_1 + \frac{3}{4} k_3 V_2^2 + \frac{3}{2} k_3 X^2} \quad (21)$$

DG can, therefore, be considered to some extent as a measure of the intermodulation performance of a system under test.

7.1.7. Dynamic Range. *Dynamic range* can be defined as the amplitude range over which a circuit or a system can operate without performance degradation. The minimum amplitude is dictated by the input thermal noise and the noise contributed by the system. The maximum amplitude is dictated by the distortion mechanisms of the system under consideration. In general, the amount of

tolerable distortion will depend on the type of signal and the system under test. However, for the purpose of an objective definition the maximum amplitude will be considered the input signal level at which the intermodulation distortion is equal to the minimum amplitude [67]. The dynamic range can, therefore, be considered to some extent as a measure of the intermodulation performance of a system under test.

A useful working definition of the dynamic range is that it is (1) two-thirds of the difference in level between the noise floor and the intercept point in a 3 kHz bandwidth [68] or (2) the difference between the fundamental response input level and the third-order response input as measured along the noise floor (sometimes defined as 3 dB bandwidth above the noise floor) in a 3 kHz bandwidth, as shown in Fig. 4. Reducing the bandwidth improves dynamic range because of the effect on noise.

Because the power level at which distortion becomes intolerable varies with signal type and application, a generic definition has evolved. The upper limit of a network's power span is the level at which the power of one IM product of a specified order is equal to the network's noise floor. The ratio of the noise floor power to the upper-limit signal power is referred to as the network's *dynamic range* (DR). Thus the DR can be determined from [69]

$$DR_n = \frac{n - 1}{n} [IP_{n,in} - MDS] \quad (22)$$

where DR_n is the dynamic range in decibels, n is the order, IP_{in} is the input intercept power in dBm, and MDS is the minimum detectable signal power in dBm.

Alternatively, in receiver circuits the spurious-free dynamic range (SFDR) and the intermodulation-free

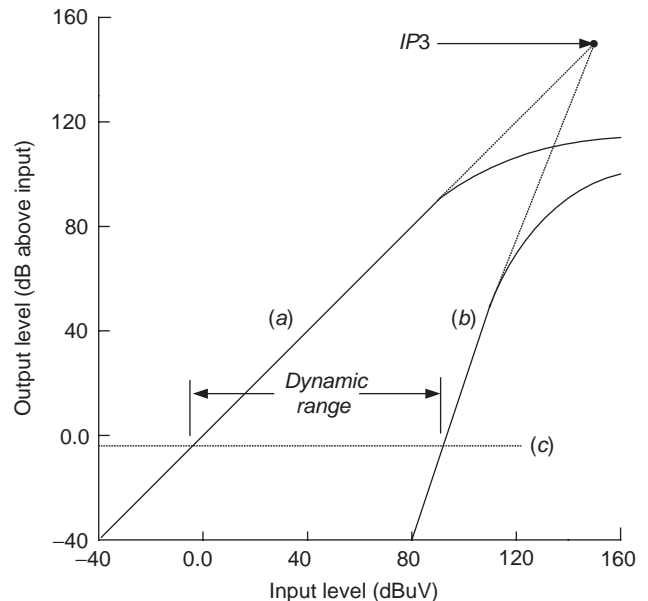


Figure 4. The dynamic range is the difference between the fundamental response input level and the third-order response input as measured along the noise floor: (a) fundamental response; (b) third-order intermodulation response; (c) noise floor.

dynamic range (IFDR) are widely used to quantify the capability of the receiver to listen to a weak station, without disturbance from an intermodulation product generated by strong stations on other frequencies. The SFDR and the IFDR are in fact measures of how strong two signals can be before the level of their intermodulation products can reach the noise floor of the receiver. The SFDR, or the IFDR, is defined as the difference in decibels between the power levels of the third-order intermodulation IM3 (assuming that there is only a third-order non-linearity) and the carrier when the IM3 power level equals the noise floor at a given noise bandwidth. It can be expressed as [70]

$$\text{SFDR} = \frac{2}{3} [\text{IIP3} - \text{EIN} - 10 \log_{10}(\text{NBW})] \quad (23)$$

where IIP3 is the third-order input intercept point, EIN in (dB/Hz) is the equivalent input noise, and NBW (in Hz) is the noise bandwidth.

7.1.8. Adjacent- and Cochannel Power Ratio Tests. In modern telecommunication circuits, signals constituting one or more modulated carriers are handled. Characterization of the intermodulation performance of such circuits cannot, therefore, be performed using two-tone and three-tone input signals; a combination of equally spaced tones—in practice, more than ~ 10 sinusoids [71], with constant power and correlated or uncorrelated phases—would be more appropriate [72].

Because of the nonlinearity of the device under test, intermodulation products will be generated. These intermodulation products can be classified as *adjacent-channel distortion* when their frequencies are located to the right or to the left of the original spectrum, or *cochannel distortion* when their frequencies are located exactly over the original spectrum. The *adjacent-channel power ratio* (ACPR) is defined as the ratio between the total linear output power and the total output power collected in the upper and lower adjacent channels [73]. The *cochannel power ratio* (CCPR) is defined as the ratio between total linear output power and total distortion power collected in the input bandwidth [73]. The *intermodulation distortion ratio* (IMR) is the ratio between the linear output power per tone and the output power of adjacent-channel tones [73].

In fact, the ACPR, CCPR, and IMR distortion measurements are simple extensions of the two-tone intermodulation measurement [74]. However, it is important to first generate a very clean multitone signal. This can be easily achieved using the technique described in Ref. 75.

8. INTERMODULATION MEASUREMENT

8.1. Measurement Equipment

8.1.1. Multitone Tests. A block diagram of the system used for multitone intermodulation measurement is shown in Fig. 5. The multiple-frequency source can be implemented from two or three synthesized sine/square/triangular-wave generators. Amplifier/attenuator pairs

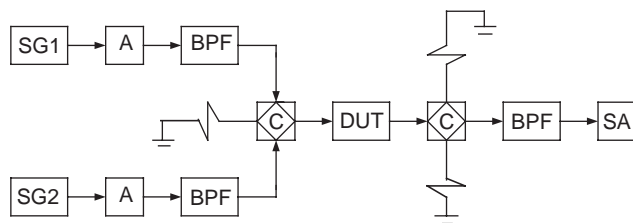


Figure 5. Block diagram of the two-tone test setup; multitone tests require additional signal generators, combiners, amplifiers, and bandpass filters (SG—signal generator; A—amplifier; BPF—bandpass filter; C—combiner; DUT—device under test; SA—spectrum analyzer).

can be added at the output of each generator. Bandpass filters can also be added to suppress the harmonic contents at the output of each generator. For RF measurements, harmonic suppression and isolation between different generators is achieved by using amplifier/circulator combinations and cavity resonators [76]. The synthesized sources are combined using hybrids or combiners of adequate isolation. Spectral purity at this point is crucial to the accuracy of the measurement. The multitone output is fed to the device under test (DUT). The output of the DUT is fed to the spectrum analyzer. For RF measurements, the output of the DUT can be fed to directional couplers. The outputs of the directional couplers are fed to a television oscilloscope and/or a spectrum analyzer.

Alternatively, for audiofrequency measurements, the intermodulation components of interest can be filtered out, using bandpass filters, and fed to AC voltmeters. For audiofrequency measurements, resistive combiners are widely used for combining the outputs of two or more signal generators.

8.1.2. Measurement Using a Microcomputer. Intermodulation can also be measured using a microcomputer [77]. A block diagram of this technique is shown in Fig. 6. This technique is based on measuring the single-tone input-output characteristic of the DUT using a vector voltmeter. The output of the vector voltmeter is fed to a microcomputer that converts it into three digital data lines representing the input amplitude, the output amplitude, and the phase lag between the input and output signals. After storing the data, the microcomputer increments the amplitude of the input signal. After storing all the necessary data, the microcomputer, using a stochastic method, calculates the amplitudes of the intermodulation components of the DUT. Although the procedure reported in Ref. 77 uses a stochastic method for calculating the amplitudes of the intermodulation components resulting from a two-tone input signal, the same procedure can be applied to any number of input tones using different analytic techniques for modeling the nonlinear characteristics of the DUT.

Alternatively, microcomputers can be added to the measurement setup of Fig. 5 to

1. Control the frequencies of the signal sources, especially in the millimeter-wave range, where the

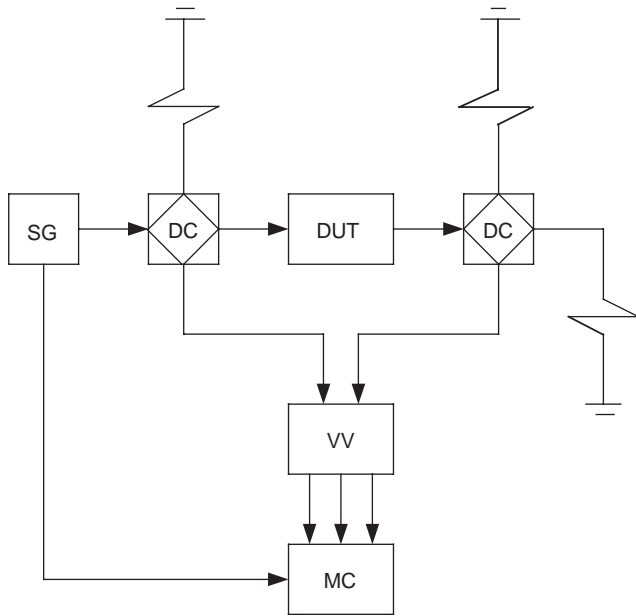


Figure 6. Block diagram of a microcomputer-based intermodulation measurement setup (SG—signal generator; DC—directional coupler; DUT—device under test; VV—vector voltmeter; MC—microcomputer).

difference in frequencies between the signal sources may be less than 0.001 of the base signal frequency [78].

2. Scan the base signal frequency over the measurement range of interest in predefined steps [79].
3. Correct the power from each source so that power delivery to the DUT will be the same across the whole frequency range scanned.
4. Read and calculate the parameters of interest during the measurements [80,81].

8.1.3. Noise Power Ratio Test. Figure 7 shows a block diagram of a noise power ratio test setup [62]. The setup consists of a white-noise generator that applies an accurate level of white Gaussian noise power with known bandwidth (equaling $\Delta\omega$ and centered around ω_0) to the DUT. The output of the DUT is measured with the band-reject filter out. When the band-reject filter, with bandwidth = $\delta\omega$ and centered around ω_0 , is switched in, a narrow band of frequencies is attenuated by about 70 dB, and a quiet channel, of width $\delta\omega$ and centered around ω_0 , is formed as shown in Fig. 3. At the output of the DUT, the noise power is measured in the quiet channel, using a bandpass filter with bandwidth $\delta\omega$ and centered around

Figure 7. Block diagram of the noise power ratio test setup (WNG—white-noise generator; BPF1—bandpass filter with bandwidth $\delta\omega$ centered around ω_0 ; BRF—band-reject filter with bandwidth $\delta\omega$ centered around ω_0 ; DUT—device under test; BPF2—bandpass filter with bandwidth $\delta\omega$ centered around ω_0 ; PM—power meter).

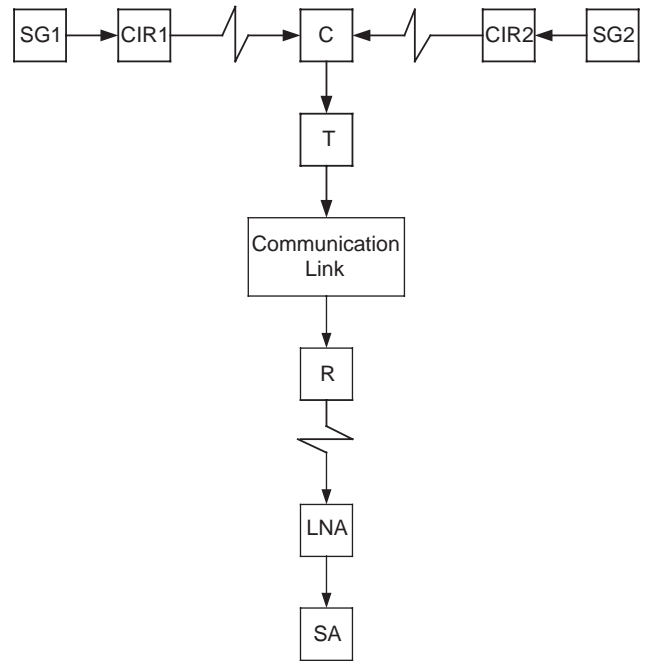
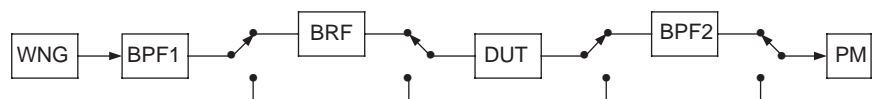


Figure 8. Setup for noise floor and SFDR measurement (SG—signal generator; CIR—circulator; C—combiner; T—transmitter; R—receiver; LNA—low-noise amplifier; SA—spectrum analyzer).

ω_0 . This noise power is due to the thermal noise and the intermodulation introduced by the DUT. The NPR is the ratio between the noise power measured without the band-reject filter inserted before the DUT to that measured with the band-reject filter inserted. The white-noise generator corrects the loading power level for the insertion loss of the band-reject filter.

8.1.4. Noise Floor and SFDR Test. Figure 8 shows a test setup for measurement of noise floor and the SFDR of a communication link [70]. To measure the noise floor of the communication link, the transmitter is switched off. Then the noises of the low-noise amplifier and the spectrum analyzer are measured. Switching the transmitter on increases the noise floor by the transmitter noise and therefore the difference between the two noise measurements is the noise generated by the transmitter.

To measure the SFDR, the input power is decreased until the IM3 level equals the noise floor. Recall that decreasing the input power by 1 dB decreases the IM3 level by 3 dB. However, this is true only if the third-order non-linearity is dominant. Higher-order nonlinearities will contribute to the third-order intermodulation (IM3), and

in such cases the measured SFDR will be different from calculations obtained using Eq. (23).

8.1.5. Externally Induced Intermodulation Test. This is a two-tone test with one signal applied to the input and the other signal applied to the output [9]. A test setup is shown in Fig. 9. Two directional couplers are used to gauge both the forward-carrier power and the intermodulation product levels. Two more directional couplers are added to inject the interfering signal and to measure the actual injected value using the spectrum analyzer.

8.2. Measurement Accuracy

8.2.1. Multitone Tests. For accurate measurements of the intermodulation products using multitone tests, it is essential to reduce, or remove, the nonlinear distortion originating in the signal sources and/or the measurement equipment. Measurement accuracy may, therefore, be affected by the purity of the signal sources, the linearity of the combiners, and the performance of the spectrum analyzer.

8.2.2. Signal Sources. Measurement of the amplitudes of the intermodulation components requires the use of two or more signals. The frequencies of these signals must be noncommensurate. Otherwise, harmonics in one source might interfere with the fundamental(s) of other signal(s) and thus interfere with the desired intermodulation components.

Ideally the signal generators would produce perfect sinusoids, but in reality all signals have imperfections. Of particular interest here is the *spectral purity*, which is a measure of the inherent frequency stability of the signal. Perhaps the most common method used to quantify the

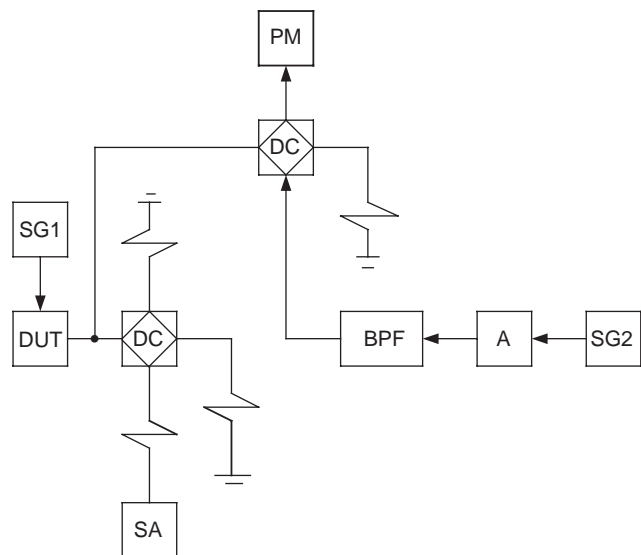


Figure 9. Measurement of externally induced intermodulation can be performed by using two tones: one injected at the input and one injected at the output of the DUT (SG—signal generator; DC—directional coupler; PM—power meter; SA—spectrum analyzer; BPF—bandpass filter; A—amplifier).

spectral purity of a signal generator is its phase noise [82]. In the time domain, the phase noise manifests itself as a jitter in the zero crossings of a sine wave. In the frequency domain, the phase noise appears as sidebands surrounding the original frequency. Thus, mixing with other frequencies, due to the nonlinearities of the DUT, would result in additional intermodulation products. It is, therefore, important to consider the intermodulation due to phase noise when calculating the intermodulation performance of the DUT [83].

Signal generators with automatic level control (ALC) may produce signals with unwanted modulation. The ALC is implemented by rectifying the output signal of the generator and feeding back the resulting DC voltage to drive an amplitude modulator. If a second signal is applied to the output of the signal generator, the detector will produce a signal at the point of difference between the two frequencies. This signal will modulate the generator's output. The frequency of the modulation sidebands will share the same spectral lines as the intermodulation products of interest. Isolating the signal generators and the combiners can minimize such an effect. This can be achieved by ensuring that there is as much attenuation as possible between them.

8.2.3. Combiners. Measurement of intermodulation products is performed by applying to the input of the circuit, or the system, under test a signal consisting of two or more different frequencies obtained from different signal generators. The outputs of the signal generators are, therefore, combined by a combiner. The combiner must provide sufficient isolation between the signal sources to reduce the possibility of producing intermodulation products before the combined input signal is applied to the circuit or the system under test. While resistive combiners are adequate for input signal levels up to a few millivolts, for larger voltage levels the use of power combiners may be inevitable [84]. Insertion of an attenuator in each arm of the combiner helps minimize the distortion components resulting from the interaction between the two signal sources. Such components, if generated, should be at least 80 dB below the fundamental components.

A simple test to determine whether adequate isolation has been achieved can be effected by introducing a variable attenuator between the signal source combiner and the DUT in Fig. 6. This is set to a low value during measurements, but at setup, when IMPs have been located on the spectrum analyzer, increasing the attenuation by 3 dB will result in a reduction in the observed IMP level. If this reduction is only 3 dB, it has to be assumed that the IMP observed has originated in the signal sources, not in the DUT. If, however, the reduction is 6 dB for a second-order IMP or 9 dB for a third-order IMP [see Eq. (4)], then it is safe to assume that the IMP has originated in the DUT or the spectrum analyzer.

Alternatively, a technique that attenuates the parasitic intermodulation products that result from the interaction between the generators of the fundamental components, before the input of the spectrum analyzer, was described in Ref. 85. A block diagram of the technique is shown in Fig. 10. The input to the system under test is formed by

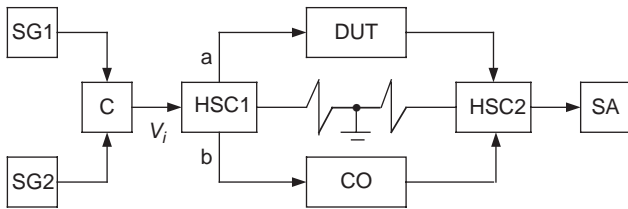


Figure 10. A technique for attenuating the intermodulation products resulting from interaction between the signal generators of the fundamental components (SG—signal generator; C—combiner; DUT—device under test; BRF—band-reject filter; PS—phase shifter; DA—differential amplifier).

combining the outputs of two signal generators at frequencies ω_1 and ω_2 in the combiner. The first hybrid combiner/splitter (HCS1) splits the combined signal into two branches with voltage transfer ratio $a = \alpha$ and $b = \sqrt{1 - \alpha^2}$ at the first and second outputs. Using Eq. (1), and assuming that the system under test and the compensator have identical nonlinear characteristics, the inputs of the second hybrid combiner/splitter (HCS2) can be expressed as

$$V_a = \sum_{n=0}^N k_n (\alpha V_i)^n \quad (24)$$

and

$$V_b = \sum_{n=0}^N k_n (\sqrt{1 - \alpha^2} V_i^n) \quad (25)$$

Using Eqs. (24) and (25), the output of the second hybrid combiner/splitter (HCS2), with voltage transfer ratio opposite in sign and equal to the reciprocal of that of HCS1, can be expressed as

$$V_{\text{out}} = \sum_{n=0}^N -k_n \left(\sqrt{1 - \alpha^2} (\alpha V_i)^n - \alpha (\sqrt{1 - \alpha^2} V_i^n) \right) \quad (26)$$

According to Eq. (26), broadband compensation occurs for the linear components of the combined signal, with $n = 1$. Thus, all the linearly transformed spectral components are eliminated. This is also true for the intermodulation components that may result from the nonlinear interaction between the two signal generators. The output of HCS2 can, therefore, be applied directly to the spectrum analyzer.

This technique does not require complicated high-order selective filters and can attenuate the parasitic intermodulation components and the fundamental frequency components by about 50 dB over a wide range of frequencies differing by 7–10 octaves. However, it requires a compensator with a nonlinear characteristic similar to that of the system under test.

8.2.4. Spectrum Analyzers. Spectrum analyzers are widely used in measuring the intermodulation performance of electronic circuits and systems. Internal circuits of the spectrum analyzers are, themselves, imperfect and

will also produce distortion products [46]. The distortion performance of the analyzers is usually specified by the manufacturers, either directly or lumped into a dynamic range specification. The performance of the analyzer can be stretched, however, if the nature of these distortion products is understood.

Amplitudes of the distortion products, resulting from the internal circuits of the analyzer, can be reduced by reducing the signal levels at the analyzer's input. Thus, using internal and/or external attenuators can reduce the input signal levels to the analyzer and hence reduce its distortion products and improve the intermodulation measurement range of the spectrum analyzer. However, reduced input levels to the analyzer mean reduced signal-to-noise ratio, and the distortion component to be measured may be buried in the noise. While reducing the resolution bandwidth of the analyzer can reduce noise, this may lead to slower sweep rate. Thus, achieving an optimum dynamic range involves tradeoffs between input signal levels and analyzer distortion. Usually, datasheets of analyzers will contain information about noise level in each resolution bandwidth and distortion products generated by the analyzer for each input level. Using this information, one can determine the dynamic range of the analyzer for various input levels [86].

Whenever good selectivity, as well as sensitivity and dynamic range, are of prime importance, test receivers may be used in preference to spectrum analyzers [6]. Alternatively, if the frequencies of the intermodulation components of interest are sufficiently lower (or higher) than the fundamental frequencies, then lowpass (or highpass) filters can be used to remove the fundamental components that would give rise to other nonlinear distortion components in the spectrum analyzer. Attenuation factors of 80 dB or more, at frequencies outside the band of interest, are recommended. The insertion loss of the lowpass (or the highpass) filter should be as small as possible; 0.4 dB or less is recommended.

If the frequency of the intermodulation component of interest is not sufficiently higher (or lower) than the fundamental frequencies, then it would be necessary to have complicated multiple-section high-order filters with amplitude–frequency characteristics that are nearly rectangular. Such filters will change, to some extent, the amplitude of the intermodulation components, and this will complicate calculation of the intermodulation performance of the system under test. A method for compensating for a large fundamental component, thus allowing the measurement of small intermodulation components in its presence, was described in Ref. 87.

A block diagram of the compensation method is shown in Fig. 11. The input to the system under test is formed of one large amplitude signal at frequency ω_1 and one small amplitude signal at frequency ω_2 with $\omega_1 \ll \omega_2$. The output of the system under test contains fundamental components at frequencies ω_1 and ω_2 , and intermodulation components at frequencies $\omega_2 \pm n\omega_1$, $n = 1, 2, \dots, N$. In order to measure the small amplitude intermodulation components, it is necessary to avoid applying to the analyzer the fundamental component at frequency ω_2 . This can be achieved as follows. The output of the system under test is

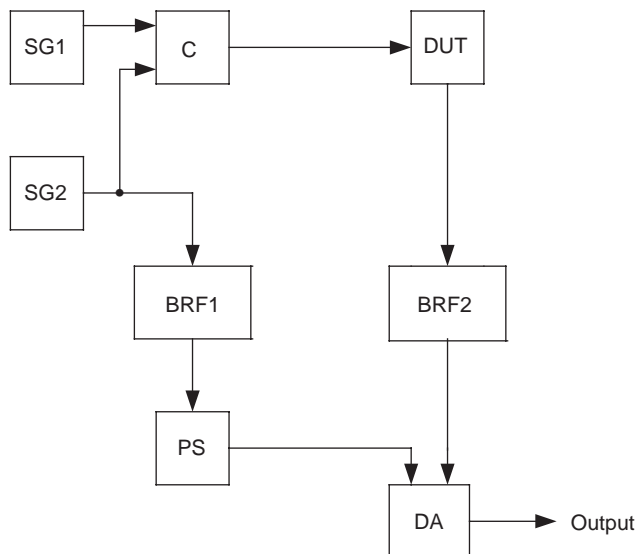


Figure 11. Compensation method for the measurement of small-amplitude intermodulation products in the presence of a large fundamental (SG—signal generator; C—combiner; HSC—hybrid splitter/combiner; DUT—device under test; CO—compensator; SA—spectrum analyzer).

fed to the second band-reject filter BRF2 to suppress the fundamental component at ω_1 . The output of the signal generator of frequency ω_2 is fed to the first band-reject filter BRF1 to suppress any component at frequency ω_1 before reaching the phase shifter through the combiner. The phase shifter compensates, at the frequency ω_2 , the phase shift through the system under test.

Ideally, the voltages of frequency ω_2 at the inputs of the differential amplifier are equal. Thus, the output of the differential amplifier at frequency ω_2 is ideally zero. In practice, the output voltage at ω_2 will be attenuated by 50–60 dB [6]. The output of the differential amplifier, with suppressed fundamental component at frequency ω_2 , can be applied to the spectrum analyzer. This compensation technique, which entails additional filters and matching units, can be used only for broadband measurements with $\omega_1 \ll \omega_2$.

Although spectrum analyzers using digital IF sections may not suffer from the internally generated distortion, discussed above, they may suffer from the relatively low-level distortion products resulting from the analog-to-digital conversion. The amplitudes of these products is usually less sensitive to the amplitude of the signal components.

8.2.5. Noise Power Ratio Test. The accuracy of the noise power ratio (NPR) test is affected mainly by two factors: (1) the noise floor of the amplifier that will dominate under very low loading conditions and (2) the distortion products produced under very high loading conditions. It is, therefore, recommended to sweep the loading between two pre-specified start and stop levels. The NPR is measured at different levels, and the largest measured value of NPR is considered as the worst case.

8.2.6. Microcomputer-Based Tests. Quantization errors associated with the analog-to-digital conversion of the data in microcomputer-based intermodulation test must be taken into account. Measurement errors due to quantization are affected by the length of the binary digits and determine the dynamic range of operation [77].

BIBLIOGRAPHY

1. L. E. Kinsler, A. R. Frey, A. B. Coppens, and J. V. Sanders, *Fundamentals of Acoustics*, Wiley, 1982, pp. 267–268.
2. K. Y. Eng and O.-C. Yue, High-order intermodulation effects in digital satellite channels, *IEEE Trans. Aerospace Electron. Sys.* **AES-17**:438–445 (1981).
3. C. D. Bod, C. S. Guenzer, and C. A. Carosella, Intermodulation generation by electron tunneling through aluminum-oxide films, *Proc. IEEE* **67**:1643–1652 (1979).
4. W. H. Higa, Spurious signals generated by electron tunneling on large reflector antennas, *Proc. IEEE* **63**:306–313 (1975).
5. P. L. Aspden and A. P. Anderson, Identification of passive intermodulation product generation in microwave reflecting surfaces, *IEE Proc. H*, **139**:337–342 (1992).
6. P. L. Liu, A. D. Rawlins, and D. W. Watts, Measurement of intermodulation products generated by structural components, *Electron. Lett.* **24**:1005–1007 (1988).
7. M. Ojala and J. Lammasniemi, Intermodulation at the amplifier-loudspeaker interface, *Wireless World*, **86**:45–47 (Nov. 1980), 42–44, 55 (Dec. 1980).
8. E. M. Cherry and G. K. Cambrell, Output resistance and intermodulation distortion in feedback amplifiers, *J. Audio Eng. Soc.* **30**:178–191 (1982).
9. E. Franke, Test setup gauges externally-induced transmitter IM, *Microwave RF*, **32**:95–98 (April 1993).
10. W. Wharton, S. Metcalfe, and G. C. Platts, *Broadcast Transmission Engineering Practice*, Butterworth-Heinemann, Oxford, UK, 1991, Chapter 5.
11. J. M. Lindsey, L. S. Riggs, and T. H. Shumpert, Intermodulation effects induced on parallel wires by transient excitation, *IEEE Trans. Electromagn. Compat.* **31**:218–222 (1989).
12. M. Ojala, Non-linear distortion in audio amplifiers, *Wireless World* **83**:41–43 (Jan. 1977).
13. E. M. Cherry, Intermodulation distortion in audio amplifiers, *Proc. IREE Conf. Int.*, Australia, 1983, pp. 639–641.
14. W. G. Jung, M. L. Stephens, and C. C. Todd, An overview of SID and TIM—Part I, *Audio* **63**:59–72 (June 1979).
15. R. R. Cordell, Another view of TIM, *Audio* **64**:38–49 (Feb. 1980).
16. W. M. Leach, Transient IM distortion in power amplifiers, *Audio* **59**:34–41 (Feb. 1975).
17. S. A. Mass, Volterra analysis of spectral regrowth, *IEEE Microwave Guided Wave Lett.* **7**:192–193 (1997).
18. J. F. Sevic, M. B. Steer, and A. M. Pavio, Nonlinear analysis methods for the simulation of digital wireless communication systems, *Int. J. Microwave Millimeter-wave Comput. Aid. Design* **6**:197–216 (1996).
19. J. F. Sevic and M. B. Steer, Analysis of GaAs MESFET spectrum regeneration driven by a DQPSK modulated source, *IEEE Int. Microwave Symp. Digest*, June 1995, pp. 1375–1378.
20. K. G. Gard, H. M. Gutierrez, and M. B. Steer, Characterization of spectral regrowth in microwave amplifiers based on

- the nonlinear transformation of a complex Gaussian process, *IEEE Trans. Microwave Theory Tech.* **47**:1059–1069 (1999).
21. G. T. Zhou, Analysis of spectral regrowth of weakly nonlinear amplifiers, *IEEE Commun. Lett.* **4**:357–359 (2000).
 22. W. M. Leach, Suppression of slew rate and transient IM distortions in audio power amplifiers, *J. Audio Eng. Soc.* **25**:466–473 (1977).
 23. M. Schetzen, *The Volterra and Wiener Theories of Nonlinear Systems*, Wiley, New York, 1980.
 24. E. V. D. Eijnde and J. Schoukers, Steady-state analysis of a periodically excited nonlinear system, *IEEE Trans. Circuits Syst.* **37**:232–242 (1990).
 25. S. Naryanan, Transistor distortion analysis using the Volterra series representation, *Bell Sys. Tech. J.* **46**:999–1024 (1967).
 26. D. D. Weitner and J. F. Spina, *Sinusoidal Analysis and Modeling of Weakly Nonlinear Circuits*, Van Nostrand, New York, 1980.
 27. P. Harrop and T. A. C. M. Claasen, Modelling of an FET mixer, *Electron. Lett.* **14**:369–370 (1978).
 28. W. G. Jung, M. L. Stephens, and C. C. Todd, An overview of SID and TIM—Part III, *Audio* **63**:42–59 (Aug. 1979).
 29. M. T. Abuelma'atti, Prediction of the transient intermodulation performance of operational amplifiers, *Int. J. Electron.* **55**:591–602 (1983).
 30. S. A. Mass, *Nonlinear Microwave Circuits*, Arech House, Norwood, MA, 1988.
 31. P. Wambacq and W. Sansen, *Distortion Analysis of Analog Integrated Circuits*, Kluwer Academic Publishers, Boston, 1998.
 32. S. A. Mass, Applying Volterra-series analysis, *Microwave RF* **38**:55–64 (1999).
 33. D. Atherton, *Nonlinear Control Engineering—Describing Function Analysis*, Van Nostrand-Reinhold, New York, 1975.
 34. S. Collins and K. Flynn, Intermodulation characteristics of ferrite-based directional couplers, *Microwave J.* **42**:122–130 (Nov. 1999).
 35. M. Bayrak and F. A. Benson, Intermodulation products from nonlinearities in transmission lines and connectors at microwave frequencies, *Proc. IEE* **122**:361–367 (1975).
 36. M. B. Amin and F. A. Benson, Nonlinear effects in coaxial cables at microwave frequencies, *Electron. Lett.* **13**:768–770 (1977).
 37. K. Y. Eng and O. C. Yue, High-order intermodulation effects in digital satellite channels, *IEEE Trans. Aerospace Electron. Syst.* **AES-17**:438–445 (1981).
 38. P. L. Aspden and A. P. Anderson, Identification of passive intermodulation product generation on microwave reflecting surfaces, *IEE Proc. H* **139**:337–342 (1992).
 39. M. Lang, The intermodulation problem in mobile communications, *Microwave J.* **38**:20–28 (May 1995).
 40. P. L. Lui, A. D. Rawlins, and D. W. Watts, Measurement of intermodulation products generated by structural components, *Electron. Lett.* **24**:1005–1007 (1988).
 41. B. G. M. Helme, Passive intermodulation of ICT components, *Proc. IEE Colloq. Screening Effectiveness Measurements*, 1998, pp. 1/1–1/8.
 42. P. L. Lui and A. D. Rawlins, Passive nonlinearities in antenna systems, *Proc. IEE Colloq. Passive Intermodulation Products in Antennas and Related Structures*, 1989, pp. 6/1–6/7.
 43. J. T. Kim, I.-K. Cho, M. Y. Jeong, and T.-G. Choy, Effects of external PIM sources on antenna PIM measurements, *Electronics and Telecommunication Research Institute (ETRI) J.* **24**:435–442 (Dec. 2002).
 44. J. G. Gardiner and H. Dincer, The measurement and characterisation of non-linear interactions among emissions from communal transmitting sites, *Proc. 2nd Int. Conf. Radio Spectrum Conservation Techniques*, IEE Publication 224, 1983, pp. 39–43.
 45. M. T. Abuelma'atti, Prediction of passive intermodulation arising from corrosion, *IEE Proc. Sci. Meas. Technol.* **150**:30–34 (2003).
 46. R. A. Witte, *Spectrum and Network Measurements*, Prentice-Hall, Englewood Cliffs, NJ, 1991, Chapter 7.
 47. S. Hunziker and W. Baechtold, Simple model for fundamental intermodulation analysis of RF amplifiers and links, *Electron. Lett.* **32**:1826–1827 (1996).
 48. G. A. A. Hueber, B. Nijholt, and H. Tendeloo, Twin-tone tape testing, *J. Audio Eng. Soc.* **24**:542–553 (1976).
 49. J. Li, R. G. Bosisio and K. Wu, A simple dual-tone calibration of diode detectors, *Proc. IEEE Instrumentation and Measurement Technology Conf.*, Hamamatsu, Japan, 1994, pp. 276–279.
 50. J. D. Giacomini, Most ADC systems require intermodulation testing, *Electron. Design* **40**(17):57–65 (1992).
 51. M. Benkais, S. L. Masson, and P. Marchegay, A/D converter characterization by spectral analysis in “dual-tone” mode, *IEEE Trans. Instrum. Meas.* **44**:940–944 (1995).
 52. B. D. Loughlin, Nonlinear amplitude relations and gamma correction, in K. Mclwain and C. Dean, eds., *Principles of Color Television*, Wiley, New York, 1956, pp. 200–256.
 53. M. Kanno and I. Minowa, Application of nonlinearity measuring method using two frequencies to electrical components, *IEEE Trans. Instrum. Meas.* **IM-34**:590–593 (1985).
 54. L. Robles, M. A. Ruggero, and N. C. Rich, Two-tone distortion in the basilar membrane of the cochlea, *Nature* **349**:413–414 (1991).
 55. T. Maseng, On the characterization of a bandpass nonlinearity by two-tone measurements, *IEEE Trans. Commun.* **COM-26**:746–754 (1978).
 56. H. Roering, The twin-tone distortion meter: A new approach, *J. Audio Eng. Soc.* **31**:332–339 (1983).
 57. E. M. Cherry, Amplitude and phase intermodulation distortion, *J. Audio Eng. Soc.* **31**:298–303 (1983).
 58. H. H. Scott, Audible audio distortion, *Electronics* **18**:126 (Jan. 1945).
 59. A. N. Thiele, Measurement of nonlinear distortion in a band-limited system, *J. Audio Eng. Soc.* **31**:443–445 (1983).
 60. G. L. Heiter, Characterization of nonlinearities in microwave devices and systems, *IEEE Trans. Microwave Theory Tech.* **MTT-21**:797–805 (1973).
 61. A. D. Broadhurst, P. F. Bouwer, and A. L. Curle, Measuring television transposer intermodulation distortion, *IEEE Trans. Broadcast.* **34**:344–355 (1988).
 62. B. Hessen-Schmidt, Test set speeds NPR measurements, *Microwaves RF* **33**:126–128 (Jan. 1994).
 63. B. Arnold, Third order intermodulation products in a CATV system, *IEEE Trans. Cable Television* **CATV-2**:67–79 (1977).
 64. O. A. Dogha and M. B. Das, Cross-modulation and intermodulation performance of MOSFET's in tuned high-frequency amplifiers, *Int. J. Electron.* **45**:307–320 (1978).
 65. J. H. Foster and W. E. Kunz, Intermodulation and crossmodulation in travelling-wave tubes, *Proc. Conf. Int. Tubes pour Hyperfrequencies*, Paris, 1964, pp. 75–79.

66. *Differential Phase and Gain at Work*, Hewlett-Packard Application Note 175-1, 1975.
67. J. Smith, *Modern Communication Circuits*, McGraw-Hill, New York, 1987, Chapter 3.
68. J. Dyer, The facts and figures of HF receiver performance, *Electron. World-Wireless World* **99**:1026–1030 (1993).
69. U. L. Rohde and D. P. Newkirk, *RF/Microwave Circuit Design for Wireless Applications*, J. Wiley, New York, 2000.
70. G. Steiner, W. Baechtold, and S. Hunziker, Bidirectional single fibre links for base station remote antenna feeding, *Proc. European Conf. Networks & Optical Communications*, Stuttgart, June 6–9, 2000, Germany, 2000.
71. R. Hajji, F. Beaugreard, and F. Ghannouchi, Multitone power and intermodulation load-pull characterization of microwave transistors suitable for linear SSPA's design, *IEEE Trans. Microwave Theory Tech.* **45**:1093–1099 (1997).
72. N. B. Carvalho and J. C. Pedro, Multi-tone intermodulation distortion performance of 3rd order microwave circuits, *IEEE Int. Microwave Theory and Techniques Symp. Digest*, 1999, pp. 763–766.
73. J. C. Pedro and N. B. Carvalho, On the use of multitone techniques for assessing RF components' intermodulation distortion, *IEEE Trans. Microwave Theory Tech.* **47**:2393–2402 (1999).
74. N. B. Carvalho and J. C. Pedro, Compact formulas to relate ACPR and NPR to two-tone IMR and IP3, *Microwave J.* **42**:70–84 (Dec. 1999).
75. R. Hajji, F. Beaugreard, and F. Ghannouchi, Multi-tone transistor characterization for intermodulation and distortion analysis, *IEEE Int. Microwave Theory and Techniques Symp. Digest*, 1996, pp. 1691–1694.
76. G. Hamer, S. Kazeminejad, and D. P. Howson, Test set for the measurement of IMDs at 900 MHz, *IEE Colloq. Passive Intermodulation Products in Antennas and Related Structures*, IEE Digest 1989/94, London, 1989.
77. T. Sasaki and H. Hataoka, Intermodulation measurement using a microcomputer, *IEEE Trans. Instrum. Meas.* **IM-30**:262–264 (1981).
78. P. A. Morton, R. F. Ormondroyd, J. E. Bowers, and M. S. Demokan, Large-signal harmonic and intermodulation distortions in wide-bandwidth GaInAsP semiconductor lasers, *IEEE J. Quantum Electron.* **25**:1559–1567 (1989).
79. S. Mukherjee, Vector measurement of nonlinear transfer function, *IEEE Trans. Instrum. Meas.* **44**:892–897 (1994).
80. C. Tsironis, Two tone intermodulation measurements using a computer-controlled microwave tuner, *Microwave J.* **32**:161–163 (Oct. 1989).
81. A. A. M. Saleh and M. F. Wazowicz, Efficient, linear amplification of varying-envelope signals using FET's with parabolic transfer characteristics, *IEEE Trans. Microwave Theory Tech.* **MTT-33**:703–710 (1985).
82. B. Cheng, Signal generator spectral purity consideration in RF communications testing, *Microwave J.* **42**:22–32 (Dec. 1999).
83. S. Ciccarelli, Predict receiver IM in the presence of LO phase noise, *Microwaves RF* **35**:86–90 (1996).
84. A. M. Rudkin, ed., *Electronic Test Equipment*, Granada, London, 1981, Chapter 2.
85. Yu. M. Bruk and V. V. Zakharenko, Broadband compensation for dynamic-range measurements by intermodulation, *Instrum. Exp. Tech.* **36**(Part 1)(4):557–562 (1993).
86. *Spectrum Analyzer Series*, Hewlett-Packard Application Note 150-11, 1976.
87. V. G. Frenkel and M. S. Shterengas, Auxiliary unit for a spectrum analyzer when measuring intermodulation distortion, *Meas. Tech.* **32**:385–387 (April 1989).

ITERATIVE METHODS

ROBERT J. BURKHOLDER
JIN-FA LEE
The Ohio State University
Columbus, Ohio

1. INTRODUCTION

Iterative methods are used in RF and microwave engineering to solve complex systems by repeatedly refining an approximate solution until a desired level of accuracy or performance is achieved. In many such problems, an exact solution does not exist and a direct numerical solution may not be feasible because of the very large number of degrees of freedom. Typical applications include the solution of large systems of differential and integral equations that may involve thousands or millions of unknown variables. For these problems it may not be possible to generate and store a full system matrix, and then solve it directly (e.g., by inversion, factorization, or Gauss elimination). Iterative methods only need to apply an operator (or system matrix) to the solution at each iteration. They are particularly well suited for the solution of sparse matrix systems because a large percentage of the operations involved are negligible.

Mathematically, an iterative algorithm starts with an initial approximate solution, and repeatedly applies an operator to the solution to improve its accuracy at each iteration. Eventually the solution should converge to a given level of accuracy. Convergence is the primary issue associated with any iterative method. The solution may converge very slowly if the iterative operator is not well conditioned, or it may even diverge. Figure 1 illustrates the basic iterative loop.

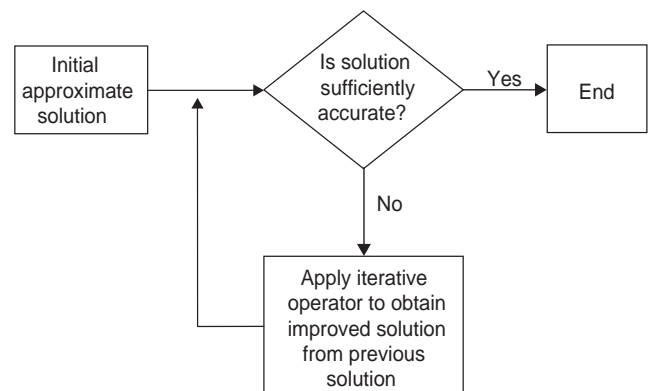


Figure 1. Schematic diagram of an iterative solution.

There are two broad categories of iterative methods: stationary and nonstationary. *Stationary* methods are characterized by an operator that does not change with each iteration. *Classical iterative methods* are included in this category, such as Jacobi and Gauss–Seidel. *Conjugate-gradient methods* are included in the class of nonstationary methods, wherein some parameters in the operator change with each iteration [1].

In general, conjugate-gradient iterative methods have better convergence properties than do classical iterative methods when compared over a wide range of problems. The convergence of classical methods tends to be very problem-dependent. In fact, classical methods are often based on the underlying physics of a particular scenario. For example, a classical iterative algorithm may be designed to model the multiple electromagnetic (EM) wave scattering between two or more objects. Such an algorithm could be very rapidly convergent for that problem, but slowly convergent or even divergent for a different problem. On the other hand, conjugate-gradient methods have theoretically guaranteed convergence if the system matrix is nonsingular, although in practice the limited numerical precision of a computer may cause the algorithm to stall.

The convergence of any iterative method may be improved by altering the formulation so that it is better conditioned. This is referred to as *preconditioning* the operator or system of equations. The accuracy of the solution at each iteration may be gauged in terms of the *residual error*, which is a measure of how well the solution satisfies the original system of equations.

2. HISTORICAL REVIEW OF ITERATIVE METHODS IN ELECTROMAGNETICS

Iterative methods in EM did not become popular until advances in computer technology made it possible to solve large systems of equations. Classical iterative methods were developed to model physical EM interactions between different parts of a geometry. Thiele et al. first developed a hybrid technique to combine physical optics and the method of moments in 1982 [2–4]. The solution iterates between the optically lit region and the shadow region of an arbitrary scattering geometry. This method was extended further and made more general by Hodges and Rahmat-Samii [5], including the interactions between antennas and their supporting platform. Domain decomposition was used by Sullivan and Carin to break up a method-of-moments (MoM) problem into multiple, simpler, solution regions [6]. Iterative method of moments and iterative physical optics have been used to solve multi-bounce problems such as the EM scattering from large open-ended cavities [7,8]. Classical iterative methods have also been applied extensively to compute the scattering from rough surfaces. The forward-backward method developed by Holliday et al. [9], and the method of ordered multiple interactions of Kapp and Brown [10], take advantage of the dominant forward and backward propagation of EM waves over a rough surface. The generalized forward-backward method extended this work to include an obstacle on the rough surface by modifying the matrix

splitting used in the forward-backward method [11]. Comparisons of stationary with nonstationary iterative methods are presented in Refs. 12–14.

The conjugate gradient (CG) method was developed in 1952 by Hestenes and Stiefel [15]. However, like the classical iterative methods, it was not used in the area of electromagnetics until advances in computers made it possible to solve large linear systems. Sarkar and Rao used the CG method to solve method of moments problems in 1984 [16], and Sarkar and Arvas presented a more general CG development for electromagnetics problems in 1985 [17]. The CG-fast Fourier transform method (CG-FFT) became popular for solving quasiplanar geometries in the late 1980s [18,19]. The development of fast integral equation methods, such as the CG-FFT, the fast multipole method [20], the adaptive integral method [21], and the precorrected FFT method [22] gave CG methods a boost. These methods greatly reduce the computational cost of applying the integral equation operator, thereby allowing very large systems of equations to be solved.

3. MATRIX NOTATION FOR ITERATIVE METHODS

The solution of a system of equations with N degrees of freedom, or unknown variables, may be expressed in matrix format as

$$\mathbf{A}x = b \quad (1)$$

where \mathbf{A} is an $N \times N$ system matrix, x is a column vector containing the N unknown coefficients, and b is a known excitation-dependent column vector. The individual elements of this equation may be expressed as

$$b_m = \sum_{n=1}^N A_{mn}x_n \quad (2)$$

This matrix equation is obtained by discretizing the EM operator governing the problem of interest, whether it is from a differential equation or integral equation formulation. The unknown quantity, such as the EM fields or equivalent currents, are expanded into a set of N known basis functions with unknown coefficients comprising the column vector x . The N basis functions are *tested* (or sampled) with N test functions to yield a system of N equations.

The preceding equation for the unknown coefficients may be solved using direct matrix inversion or factorization. However, the *operational complexity* for the direct approach is $O(N^3)$, that is, of order N -cubed. This means that the number of computations necessary to solve the system is proportional to N^3 , which may be too costly when there are thousands or millions of unknowns. Iterative methods have an operational complexity of no more than $O(N^2)$ per iteration, which is the cost of doing one matrix-vector multiplication. So as long as the solution converges quickly, the iterative method is much more efficient.

Iterative methods seek to solve Eq. (1) by successively improving an initial solution to a desired degree of

accuracy. The *residual error* vector is a measure of the accuracy of the solution after k iterations and is defined by

$$r^{(k)} = b - \mathbf{A}x^{(k)} \quad (3)$$

The *residual error norm*, or simply the residual error, is the length of this vector normalized to the length of the excitation vector, $\|r^{(k)}\|/\|b\|$, where $\|r^{(k)}\| = \sqrt{r^{(k)}r^{(k)*}}$. Here, the inner product (or vector product) of two column vectors is Hermitian, defined by

$$ab = \sum_{n=1}^N a_n^* b_n \quad (4)$$

where the $*$ superscript denotes the complex conjugate. (Note: The CG algorithm described later does not use the complex conjugate in the inner product, as will be made apparent.) The residual error tells us how well the solution satisfies the system of equations, and is most often used as the criterion for halting the iterations. The *absolute error* vector is defined by

$$e^{(k)} = x^{(k)} - x \quad (5)$$

where x is the exact solution to (1). The *spectral radius* of a matrix is defined as the magnitude of its largest eigenvalue. This quantity is important for determining convergence of classical iterative methods, whereas the *eigenvalue spectrum* of a matrix determines the convergence of CG methods.

4. CLASSICAL ITERATIVE METHODS

As is apparent from the historical review presented earlier, classical iterative methods are often used to solve problems via a physical decomposition of the geometry, sometimes even using a different solution technique for each region. All of these methods can be cast in the form of *matrix splittings*, where the original system matrix is decomposed in some manner that makes the problem easier to solve. Figure 2 shows some common matrix splittings. We will focus on the lower-upper (LU) triangular splitting. The block-diagonal and banded matrix splittings are extensions of the LU splitting, where the diagonal \mathbf{D} is replaced by the block-diagonal or banded portion of the matrices. Likewise, the hybrid decomposition is a special case of the block-diagonal splitting with only two blocks on the diagonal.

All the matrix splittings of Fig. 2 have the general form $\mathbf{A} = \mathbf{M} - \mathbf{N}$. We may then write an iterative equation from Eq. (1) as

$$\mathbf{M}x^{(k)} = \mathbf{N}x^{(k-1)} + b \quad (6)$$

starting with some initial solution candidate $x^{(0)}$ and solving repeatedly. It is easy to show that if $x^{(k)} = x^{(k-1)}$, then Eq. (1) is satisfied and $x^{(k)} = x$. To solve (6) for $x^{(k)}$, we need \mathbf{M} to be easily invertible or factorizable. Diagonal matrices are trivial to invert, and block-diagonal matrices are

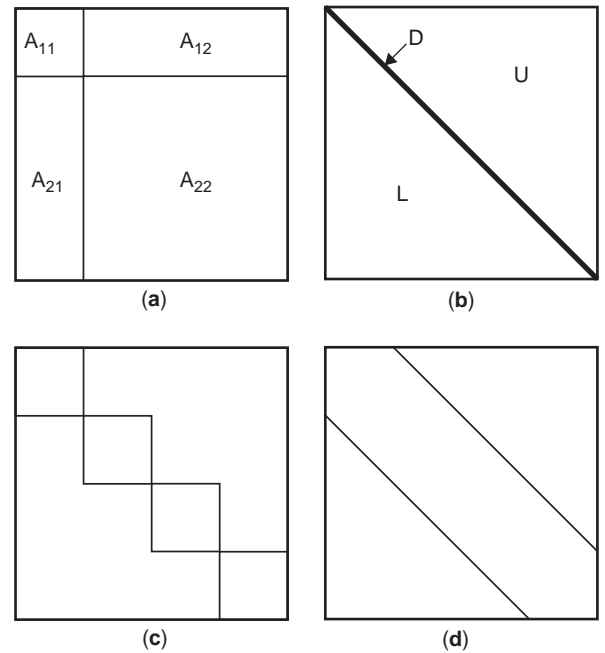


Figure 2. Some common matrix splittings. (a) hybrid decomposition; (b) lower-upper triangular; (c) block-diagonal; (d) banded.

easily inverted by inverting each block independently of the other blocks. Lower triangular and upper triangular matrices are also easy to invert via backward and forward substitutions, respectively [1]. All of these types of inversions are computed much more efficiently than inverting the entire system matrix \mathbf{A} .

The absolute error vector at the k th iteration may be shown to be

$$e^{(k)} = (\mathbf{M}^{-1}\mathbf{N})^k(x^{(0)} - x) \quad (7)$$

Therefore, the spectral radius of the matrix $(\mathbf{M}^{-1}\mathbf{N})$ must be less than unity to guarantee convergence [1]. This ensures that the absolute error approaches zero as k goes to infinity. The residual error vector for the k th iteration may be shown to be

$$r^{(k)} = \mathbf{N}(x^{(k)} - x^{(k-1)})$$

which is easily computed by saving the matrix-vector product $\mathbf{N}x^{(k-1)}$ from the previous iteration. Some common iterative algorithms based on the matrix splittings of Fig. 2 are discussed next.

4.1. Jacobi Iteration

This is the simplest classical iteration algorithm. We choose $\mathbf{M} = \mathbf{D}$ and $\mathbf{N} = -(\mathbf{L} + \mathbf{U})$, so the iterative equation becomes

$$\mathbf{D}x^{(k)} = b - (\mathbf{L} + \mathbf{U})x^{(k-1)} \quad (8)$$

The magnetic field integral equation (MFIE) has this form, which is also used in the iterative physical optics

technique [8]. The operational cost is $O(N^2)$, which is the cost of computing the matrix–vector product $(\mathbf{L} + \mathbf{U})x^{(k-1)}$ on the right-hand side (RHS) of (8).

4.2. Gauss–Seidel Method

This is an improvement over simple Jacobi iteration [1]. Here we choose $\mathbf{M} = \mathbf{D} + \mathbf{L}$ and $\mathbf{N} = -\mathbf{U}$, resulting in

$$(\mathbf{D} + \mathbf{L})x^{(k)} = b - \mathbf{U}x^{(k-1)} \tag{9}$$

This equation is solved using forward substitution. This is easy to see by writing the expression for the individual elements as

$$x_m^{(k)} = \frac{b_m - \sum_{n=1}^{m-1} x_n^{(k)} - \sum_{n=m+1}^N x_n^{(k-1)}}{D_m} \tag{10}$$

The elements $x_m^{(k)}$ are updated sequentially for $m = 1, 2, \dots, N$, so the updated values can be used on the RHS of (10). The convergence of Gauss–Seidel is expected to be somewhat better than Jacobi, and with the same operational cost.

4.3. Symmetric Gauss–Seidel Method

The Gauss–Seidel method can be formulated using forward or backward substitution. A symmetric form of Gauss–Seidel iteration is obtained using both forward and backward substitution in the following two-step algorithm:

$$(\mathbf{D} + \mathbf{L})x^{(k-1/2)} = b - \mathbf{U}x^{(k-1)} \tag{11}$$

$$(\mathbf{D} + \mathbf{U})x^{(k)} = b - \mathbf{L}x^{(k-1/2)}$$

This is the form of the forward–backward method [9], or the method of multiple ordered interactions [10]. This two-step algorithm has the same operational cost of a one-step algorithm because the half-matrix–vector product $\mathbf{L}x^{(k-1/2)}$ is reused in step 2 of each iteration, and $\mathbf{U}x^{(k-1)}$ may be saved from the previous iteration and reused.

4.4. Relaxation

Unless the problem geometry is very well ordered, or the system matrix is strongly diagonally dominant, the classical iterative algorithms above will probably have poor convergence properties. To improve convergence, a *relaxation parameter* [1] (or damping coefficient), ω may be introduced. This is a constant usually in the range $0 < \omega < 2$ such that the relaxed iterative equations reduce to the basic equations above for $\omega = 1$. The relaxed Jacobi iterative equation is given by

$$\mathbf{D}x^{(k)} = \omega b + [(1 - \omega)\mathbf{D} - \omega(\mathbf{L} + \mathbf{U})]x^{(k-1)} \tag{12}$$

It is easy to show that (12) reduces to (8) for $\omega = 1$, and if $x^{(k)} = x^{(k-1)}$ then (1) is satisfied and $x^{(k)} = x$ for any non-zero ω .

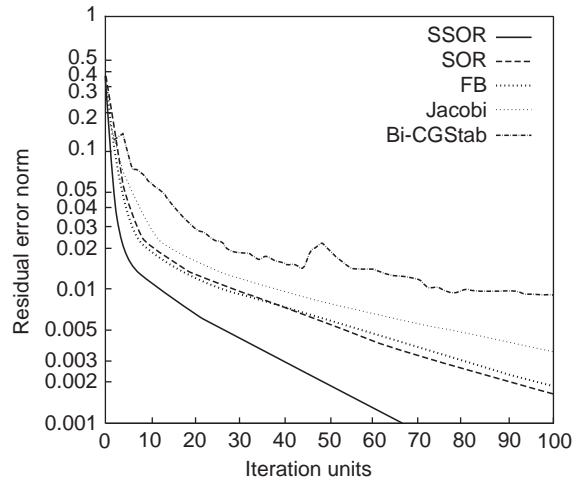
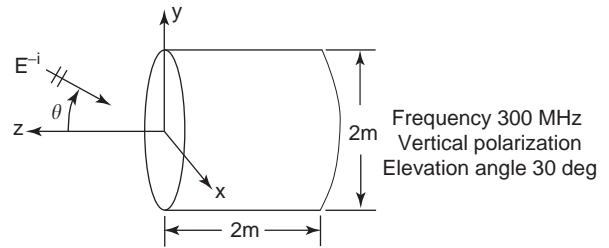


Figure 3. Convergence of classical iterative methods compared with BCGS.

Likewise, the relaxed Gauss–Seidel method, also known as *successive overrelaxation* (SOR) [1], is given by

$$(\mathbf{D} + \omega\mathbf{L})x^{(k)} = \omega b + [(1 - \omega)\mathbf{D} - \omega\mathbf{U}]x^{(k-1)} \tag{13}$$

The relaxed form of symmetric Gauss–Seidel is known as *symmetric successive overrelaxation* (SSOR) [1], and is given by

$$(\mathbf{D} + \omega\mathbf{L})x^{(k-1/2)} = \omega b + [(1 - \omega)\mathbf{D} - \omega\mathbf{U}]x^{(k-1)} \tag{14}$$

$$(\mathbf{D} + \omega\mathbf{U})x^{(k)} = \omega b + [(1 - \omega)\mathbf{D} - \omega\mathbf{L}]x^{(k-1/2)}$$

Figure 3 shows a plot of the convergence of relaxed Jacobi, SOR, SSOR, and the biconjugate gradient stabilized (BCGS) algorithms for the problem of radar scattering from a perfect electrically conducting cylinder computed by the method of moments [14]. For this relatively simple problem, the SSOR method has the best convergence and the BCGS, the worst. However, for more arbitrary geometries the classical iterations may fail to converge, and may eventually diverge.

5. CONJUGATE-GRADIENT (CG) METHODS

CG methods are superior to classical iterative methods in the sense that they are theoretically guaranteed to converge in no more than N iterations if the matrix is

nonsingular. (In practice, the numerical precision of the computer may limit this theoretical convergence.) They are not limited to specific types of problems or physics, and can be used as general matrix solvers. This is achieved by generating a sequence of search vectors that will eventually span the entire N -space. The only difference between the various CG versions is how these search vectors are generated. In general, the search vectors are chosen such that each new vector is linearly independent of all previous vectors, and the residual error is minimized. The basic CG method is applicable only to symmetric systems and is presented here first, followed by two popular methods for nonsymmetric systems, the modified biconjugate gradient (BCG) and the generalized minimum residual (GMRES) methods. An excellent resource for these and other CG algorithms is the *Templates* book [23], for which associated computer subroutines are readily available.

5.1. CG Algorithm for Complex Symmetric Matrices

The basic CG algorithm for solving the complex symmetric matrix equation $\mathbf{A}\tilde{\mathbf{x}} = \tilde{\mathbf{b}}$ is listed below. A complete derivation is included later in this article. *In the following algorithm the vector products are not Hermitian*, that is, there is no complex conjugation as in (4).

Conjugate Gradient Algorithm 1

Initialization:

$$\tilde{\mathbf{v}} = \frac{\tilde{\mathbf{b}}}{\sqrt{\tilde{\mathbf{b}}^T \mathbf{A} \tilde{\mathbf{b}}}}, \quad \tilde{\mathbf{x}} = 0, \quad \tilde{\mathbf{r}} = \tilde{\mathbf{b}}$$

Iteration:

1. $\tilde{\mathbf{x}} = \tilde{\mathbf{x}} + \alpha \tilde{\mathbf{v}}, \alpha = \tilde{\mathbf{v}}^T \tilde{\mathbf{b}}$
2. $\tilde{\mathbf{u}} = \mathbf{A} \tilde{\mathbf{v}}, \tilde{\mathbf{r}} = \tilde{\mathbf{r}} - \alpha \tilde{\mathbf{u}}$
3. Check $\|\tilde{\mathbf{r}}\|/\|\tilde{\mathbf{b}}\| \leq \epsilon$; if yes, then stop, and $\tilde{\mathbf{x}}$ is a good approximation; if no, then continue.
4. $\tilde{\mathbf{p}} = \tilde{\mathbf{r}} - \beta \tilde{\mathbf{v}}, \beta = \tilde{\mathbf{u}}^T \tilde{\mathbf{r}}$
5. $\tilde{\mathbf{v}} = \tilde{\mathbf{p}}/\sqrt{\tilde{\mathbf{p}}^T \mathbf{A} \tilde{\mathbf{p}}}$
6. Go to step 1.

Each iteration of the CG algorithm involves one matrix–vector multiplication, which is at most an $O(N^2)$ operation. The residual error of the solution is checked in step 3. If it is less than some threshold error ϵ , the iterations are halted. This threshold level determines the accuracy of the solution. For most engineering applications a threshold level in the range 0.0001–0.01 yields sufficient accuracy. Of course, greater accuracy requires more iterations, and it is possible for the algorithm to stall before reaching a given threshold. The convergence properties of the CG method are discussed later in this article.

5.2. Modified Biconjugate-Gradient Method for Nonsymmetric Matrices

In solving the magnetic field integral equation or combined field integral equations or many other RF engineering

applications (such as hybrid finite-element/integral equation formulation), we quite often end up with a nonsymmetric matrix equation $\mathbf{A}\tilde{\mathbf{x}} = \tilde{\mathbf{b}}$, where \mathbf{A} is an $N \times N$ complex nonsymmetric matrix. There are many variants of Krylov-based methods for solving this equation; here we shall list the modified BCG method, followed by the GMRES method. *In the following algorithm the vector products are not Hermitian*; that is, there is no complex conjugation as in (4).

Modified BCG Algorithm for Solving Complex Nonsymmetric Matrix Equations

Initialization:

$$\tilde{\mathbf{x}} = \tilde{\mathbf{x}}_T = 0 \quad \tilde{\mathbf{r}} = \tilde{\mathbf{b}} \quad \tilde{\mathbf{r}}_T = \tilde{\mathbf{b}}$$

$$\begin{aligned} \tilde{\mathbf{p}} &= \tilde{\mathbf{r}} & \tilde{\mathbf{p}}_T &= \tilde{\mathbf{r}}_T \\ \tilde{\mathbf{v}} &= \frac{\tilde{\mathbf{p}}}{\sqrt{\tilde{\mathbf{p}}^T \mathbf{A} \tilde{\mathbf{p}}}} & \tilde{\mathbf{v}}_T &= \frac{\tilde{\mathbf{p}}_T}{\sqrt{\tilde{\mathbf{p}}_T^T \mathbf{A}^T \tilde{\mathbf{p}}_T}} \end{aligned}$$

Iteration:

1. $\tilde{\mathbf{x}} = \tilde{\mathbf{x}} + \alpha \tilde{\mathbf{v}} = \tilde{\mathbf{x}} + \left(\tilde{\mathbf{v}}^T \tilde{\mathbf{b}} \right) \tilde{\mathbf{v}}$
2. Compute $\tilde{\mathbf{u}} = \mathbf{A} \tilde{\mathbf{v}}$
 $\tilde{\mathbf{u}}_T = \mathbf{A}^T \tilde{\mathbf{v}}_T$
3. $\tilde{\mathbf{r}} = \tilde{\mathbf{r}} - \alpha \tilde{\mathbf{u}}$
 $\tilde{\mathbf{r}}_T = \tilde{\mathbf{r}}_T - \alpha \tilde{\mathbf{u}}_T$
4. Check convergence. If $\|\tilde{\mathbf{r}}\|/\|\tilde{\mathbf{b}}\| \leq \epsilon$, then stop and $\tilde{\mathbf{x}}$ is a good approximation; if not, continue.
5. $\tilde{\mathbf{p}} = \tilde{\mathbf{r}} - \beta \tilde{\mathbf{v}} \quad \beta = \frac{\tilde{\mathbf{u}}_T^T \tilde{\mathbf{r}}}{\tilde{\mathbf{u}}_T^T \tilde{\mathbf{p}}}$
 $\tilde{\mathbf{p}}_T = \tilde{\mathbf{r}}_T - \beta \tilde{\mathbf{p}}_T \quad \beta_T = \frac{\tilde{\mathbf{u}}^T \tilde{\mathbf{r}}_T}{\tilde{\mathbf{u}}^T \tilde{\mathbf{p}}_T}$
6. $\tilde{\mathbf{v}} = \frac{\tilde{\mathbf{p}}}{\sqrt{\tilde{\mathbf{p}}^T \mathbf{A} \tilde{\mathbf{p}}}}$
 $\tilde{\mathbf{v}}_T = \frac{\tilde{\mathbf{p}}_T}{\sqrt{\tilde{\mathbf{p}}_T^T \mathbf{A}^T \tilde{\mathbf{p}}_T}}$
7. Go to step 1.

In this BCG algorithm it is noted that two matrix–vector products need to be computed for each iteration, one with the original matrix \mathbf{A} and the other with its transpose \mathbf{A}^T . This makes the BCG methods roughly twice as computationally expensive as the CG method for symmetric systems. The difference between the basic BCG and the modified BCG is that the former uses the Hermitian matrix \mathbf{A}^H (i.e., complex conjugate–transpose) instead of the transpose matrix \mathbf{A}^T .

5.3. GMRES Method for Nonsymmetric Matrix Equations

Another useful Krylov space iterative method for nonsymmetric systems is the generalized minimum residual (GMRES) method [24]. Like the CG method, a sequence of linearly independent search vectors is generated. However, unlike the CG method, the entire set of search vectors is saved in memory. Coefficients are found that give the minimum residual error over the complete set of search vectors. In essence, it is a “brute force” CG method. The advantages are that only one matrix–vector product is computed per iteration and the transpose of the matrix is not needed. Furthermore, the GMRES method truly minimizes the residual at each iteration, so its convergence is monotonic. The disadvantage is that all the previous search vectors must be stored in memory. Therefore, the memory requirement grows with the number of iterations. This may not be a problem for dense system matrices for which the matrix storage is generally much larger than the storage of a set of search vectors (depending, of course, on how many search vectors are stored).

To alleviate the memory requirement, the GMRES algorithm may be restarted after a certain number of iterations. The solution vector after one set of iterations is used as the initial solution for the next set of iterations. However, the restarted version of the GMRES algorithm is not guaranteed to converge because the reduced set of expansion vectors may not span the entire solution space. The GMRES algorithm is listed in the third-edition book by Golub and Van Loan [1] and in *Templates* [23]. A simplified algorithm that is conceptually equivalent to GMRES, the generalized conjugate residual (GCR) method [25], is listed below. *In the following algorithm the vector products are Hermitian*, using complex conjugation as in (4).

Generalized Conjugate Residual Algorithm

Initialization: $x = 0$, $r = b$, $p_1 = b$, $u_1 = \mathbf{A}p_1$

Iteration: $k = 1, 2, \dots$

1. $x = x + \alpha p_k$, $\alpha = u_k r / \|u_k\|^2$.
2. $r = r - \alpha u_k$.
3. Check $\|r\| / \|b\| \leq \epsilon$. If yes, then stop, and x is a good approximation; if no, then continue.
4. $\beta_i = \frac{u_i \mathbf{A}r}{\|u_i\|^2}$, for $i = 1, 2, \dots, k$.
5. $p_{k+1} = r - \sum_{i=1}^k \beta_i p_i$.
6. $u_{k+1} = \mathbf{A}r - \sum_{i=1}^k \beta_i u_i$.
7. Go to step 1.

This algorithm is very similar to the basic conjugate-gradient method. Note that only one matrix–vector product is used per iteration (in step 4) if we store all the vectors p_i and u_i for $i = 1, 2, \dots, k$. It is also helpful to store $\|u_i\|^2$ to avoid repeated computation in step 4. If storage becomes excessive, the algorithm may be restarted after the m th iteration starting with $p_1 = p_m$ and $u_1 = u_m$.

6. PRECONDITIONERS FOR ITERATIVE METHODS

The convergence rate of iterative methods, both classical and conjugate-gradient, can be very slow if the system matrix is not *well-conditioned*. As mentioned in the section on classical iterative methods, the convergence of these methods depends on the spectral radius of the iteration matrix ($\mathbf{M}^{-1}\mathbf{N}$). Similarly, the convergence rate of CG methods depends on the spectral properties of the system matrix (see Section 7 for a discussion). Certain formulations in electromagnetics give rise to poorly conditioned systems, such as the electric field integral equation (EFIE). Sometimes the formulation may be altered to give a better conditioned system, such as by converting the EFIE to the combined field integral equation. The choice of basis functions may also affect the conditioning. Alternatively, one may apply a *preconditioner* matrix \mathbf{M} to the original system as

$$\mathbf{M}^{-1}\mathbf{A}x = \mathbf{M}^{-1}b$$

Clearly, if the inverse of \mathbf{M} approximates the inverse of \mathbf{A} , then the solution of this system should be easier, or, mathematically speaking, the matrix $\mathbf{M}^{-1}\mathbf{A}$ should have better spectral properties than the original matrix. The preconditioner may be implemented in any iterative algorithm by replacing matrix–vector products of the form $\mathbf{A}p$ with $\mathbf{M}^{-1}\mathbf{A}p$, and the excitation vector b with $\mathbf{M}^{-1}b$. There are cleverer ways to do this as described in Section 7.

The preconditioner should improve convergence, while its inverse \mathbf{M}^{-1} (or factorization) must be computed efficiently. It is not a coincidence that the preconditioner matrix \mathbf{M} uses the same symbol as the classical iterative matrix splitting \mathbf{M} . In fact, the \mathbf{M} matrix of all of the classical iteration matrix splittings discussed here and shown in Fig. 2 may be used as a preconditioner, namely, diagonal, block-diagonal, lower or upper triangular, and banded. Classical splittings often mimic wave interactions, which make them useful as preconditioners. From the matrix-splitting point of view, we want the matrix \mathbf{M} to contain the “dominant” portion of the system matrix \mathbf{A} . Then the inverse of \mathbf{M} will approximate the inverse of \mathbf{A} , and the iterative algorithm should therefore converge rapidly.

A very effective preconditioner for the EFIE with subsectional basis functions is described in Ref. 26. The preconditioner \mathbf{M} is a sparse version of \mathbf{A} , which contains the matrix entries corresponding to basis interactions within a specified distance. Incomplete factorization is used to compute a sparse factorization of \mathbf{M} . In fact, there is a large class of preconditioners that use incomplete factorization. Some common preconditioning approaches for iterative algorithms are discussed in Refs. 1 and 23.

7. THEORY OF THE BASIC CG METHOD

The basic CG method is applicable only to symmetric systems. Consider the following complex symmetric matrix equation

$$\mathbf{A}x = b \quad (15)$$

where \mathbf{A} is an $N \times N$ complex symmetric matrix, x is the solution column vector, and b is the RHS excitation column vector. Before we derive the CG method, let us try to answer a few related questions first.

A-Conjugate Condition. Given a set of basis column vectors $\{v_0, v_1, \dots, v_{n-1}\}$ with $n < N$, how to determine the *best* approximate solution

$$\tilde{x}_{\text{app}} = \sum_{i=0}^{n-1} c_i \tilde{v}_i \quad (16)$$

that solves (15). The answer is the Galerkin method, or weighted residual. For each column vector, we shall form a residual column vector

$$\tilde{\mathbf{R}} = \tilde{\mathbf{b}} - \mathbf{A}\tilde{x}_{\text{app}} \quad (17)$$

Note also that equation (16) can be written in matrix form as

$$\tilde{x}_{\text{app}} = \mathbf{V}\tilde{\mathbf{c}} \quad (18)$$

$$\mathbf{V} = [\tilde{v}_0 \quad \tilde{v}_1 \quad \cdots \quad \tilde{v}_{n-1}], \quad \tilde{\mathbf{c}} = \begin{bmatrix} c_0 \\ c_1 \\ \vdots \\ c_{n-1} \end{bmatrix}$$

Subsequently, by requiring that the residual vector $\tilde{\mathbf{R}}$ be orthogonal to all the basis vectors is equivalent to solving the coefficient vector $\tilde{\mathbf{c}}$ through the following reduced matrix equation

$$(\mathbf{V}^t \mathbf{A} \mathbf{V}) \tilde{\mathbf{c}} = \mathbf{V}^t \tilde{\mathbf{b}} \quad (19)$$

Let us take a closer look at Eq. (19). If the reduced matrix $\mathbf{V}^t \mathbf{A} \mathbf{V}$ turns out to be an identity matrix, then the coefficients can be simply computed by

$$c_i = v_i \tilde{\mathbf{b}}, \quad v = (\tilde{v})^t \quad (20)$$

What is more is that, as will be seen later in this section, there is no need to store all these basis vectors in order to find the approximate matrix solution \tilde{x}_{app} . Requiring $\mathbf{V}^t \mathbf{A} \mathbf{V} \equiv \mathbf{I}$ implies that the basis vectors need to satisfy

$$v_i \mathbf{A} \tilde{v}_j = \delta_{ij} \quad (21)$$

which is called the *A-conjugate condition*.

Before moving on to derive the CG methods, let's take a few moments to restate what we have discussed in a more fundamental way. You see, as in many applications, to solve equations, whether infinite dimensional problems (integral equation formulations), or finite-dimensional

problems (like matrix equations), the Galerkin method is a very good method of choice. Once again, in applying the Galerkin method, we shall need to establish what the trial and test function spaces are. When the operators are symmetric, some would argue that they need to be positive definite as well, we can simply have both the trial and test functions be the same. The next logical question will be how to generate these basis vectors that span the trial and test function spaces. As basic linear algebra taught us, these basis vectors at least need to be linearly independent, preferably orthonormal. This is where the *A-conjugate condition* comes in. When the operator is symmetric, we can, with some violation when the operator is not positive definite, define the vector inner product as

$$\langle \tilde{v}_i, \tilde{v}_j \rangle = v_i \mathbf{A} \tilde{v}_j \quad (22)$$

As you shall see, different definitions of the “inner product” lead to different variants of CG methods.

For the matrix equation $\mathbf{A}\tilde{x} = \tilde{\mathbf{b}}$ with a nonzero initial solution \tilde{x}_i , it is always possible to solve for the correction equation $\mathbf{A}\tilde{x}' = \tilde{\mathbf{b}}' (= \tilde{\mathbf{b}} - \mathbf{A}\tilde{x}_i)$, and with $\tilde{x} = \tilde{x}' + \tilde{x}_i$. Therefore, without loss of generality, we shall assume that we will solve $\mathbf{A}\tilde{x} = \tilde{\mathbf{b}}$ with initial guess zero. We shall derive the CG method by induction.

$k=0$: With the initial solution $\tilde{x}^{(0)} = 0$, the residual vector is simply $\tilde{r}^{(0)} = \tilde{\mathbf{b}}$. The trial space for solving the matrix equation can now be established as

$$\mathbf{V}_0 = [\tilde{v}_0] = \text{MGS}_A\{\tilde{r}_0\} \quad (23)$$

The notation $\text{MGS}_A\{\tilde{a}_0 \quad \tilde{a}_1 \quad \cdots \quad \tilde{a}_{n-1}\}$ means making an orthonormal basis from the n column vectors, $\tilde{a}_0 \quad \tilde{a}_1 \quad \cdots \quad \tilde{a}_{n-1}$, through the modified Gram-Schmidt (MGS) process and the inner product is defined by the *A-conjugate condition*:

$$\tilde{v}_0 = \frac{\tilde{r}_0}{\sqrt{r_0 \mathbf{A} \tilde{r}_0}} \quad (24)$$

Notice that, in equation (24), we have an expression $r_0 \mathbf{A} \tilde{r}_0$. If the matrix \mathbf{A} is positive definite, the expression $r_0 \mathbf{A} \tilde{r}_0$ will always be a positive nonzero number, thus Eq. (24) will always be valid. Since in our case \mathbf{A} is a complex symmetric matrix, it is possible that $r_0 \mathbf{A} \tilde{r}_0 \equiv 0$ even though $\tilde{r}_0 \neq 0$. This is referred to as “breakdown” in the CG method. Although, in practical computation, it rarely occurs, but when the matrix \mathbf{A} is poorly conditioned, it is possible that $r_0 \mathbf{A} \tilde{r}_0 \approx 0$ and thus causes slow and even failure to converge in the CG process. It should be emphasized here that many researchers object to the use of CG method to non-positive-definite matrix equations; in reality, with good preconditioners (a topic which is of paramount importance) the CG method may be used to solve complex symmetric matrix equations.

$k=1$: The best solution in the trial space $\mathbf{V}_0 = \text{span}\{\tilde{v}_0\}$, from the Galerkin method, for the matrix equation

$\mathbf{A}\tilde{\mathbf{x}} = \tilde{\mathbf{b}}$ is

$$\tilde{\mathbf{x}}^{(1)} = c_0\tilde{\mathbf{v}}_0, \quad c_0 = \nu_0\tilde{\mathbf{b}} \tag{25}$$

Subsequently, the residual vector $\tilde{\mathbf{r}}^{(1)}$ can be obtained as

$$\tilde{\mathbf{r}}^{(1)} = \tilde{\mathbf{b}} - \mathbf{A}\tilde{\mathbf{x}}^{(1)} = \tilde{\mathbf{r}}^{(0)} - c_0\mathbf{A}\tilde{\mathbf{v}}_0 \tag{26}$$

Since the solution is solved through Galerkin method, and $\nu_0\tilde{\mathbf{r}}^{(1)} = 0$, it is certain that $\tilde{\mathbf{r}}^{(1)}$ is linearly independent with vectors from $\mathbf{V}_0 = \text{span}\{\tilde{\mathbf{v}}_0\}$; therefore it would be a good idea to have

$$\mathbf{V}_1 = \mathbf{V}_0 \cup \text{span}\{\tilde{\mathbf{r}}^{(1)}\} = \text{MGS}_A\{\tilde{\mathbf{v}}_0 \quad \tilde{\mathbf{r}}^{(1)}\} \tag{27}$$

Consequently, our new basis vector is determined through the modified Gram-Schmidt (MGS) process:

$$\begin{aligned} \tilde{\mathbf{w}} &= \tilde{\mathbf{r}}^{(1)} - \beta\tilde{\mathbf{v}}_0, \quad \beta = \nu_0\mathbf{A}\tilde{\mathbf{r}}^{(1)} = \nu_0^{(1)}\mathbf{A}\tilde{\mathbf{v}}_0 \\ \tilde{\mathbf{v}}_1 &= \frac{\tilde{\mathbf{w}}}{\sqrt{\nu_0\mathbf{A}\tilde{\mathbf{w}}}} \end{aligned} \tag{28}$$

It is easy to verify that $\nu_0\mathbf{A}\tilde{\mathbf{v}}_1 = \nu_1\mathbf{A}\tilde{\mathbf{v}}_0 = 0$ and $\nu_0\mathbf{A}\tilde{\mathbf{v}}_0 = \nu_1\mathbf{A}\tilde{\mathbf{v}}_1 = 1$. Moreover, we see from equation (26), $\mathbf{A}\tilde{\mathbf{v}}_0 \in \mathbf{V}_1$. To summarize, at $k=1$, we have the following conditions:

1. $\mathbf{V}_1 = \text{span}\{\tilde{\mathbf{v}}_0 \quad \tilde{\mathbf{v}}_1\} = \text{MGS}_A\{\tilde{\mathbf{v}}_0 \quad \tilde{\mathbf{r}}^{(1)}\}$
2. $\mathbf{V}_1^t\mathbf{A}\mathbf{V}_1 = \mathbf{I}$
3. $\mathbf{A}\tilde{\mathbf{v}}_0 \in \mathbf{V}_1$

***k*th iteration:** At this moment, we have the trial space $\mathbf{V}_{k-1} = \text{span}\{\tilde{\mathbf{v}}_0 \quad \tilde{\mathbf{v}}_1 \quad \dots \quad \tilde{\mathbf{v}}_{k-1}\}$ and it satisfies

1. $\nu_i\mathbf{A}\tilde{\mathbf{v}}_j = \delta_{ij}, i, j = 0, 1, \dots, (k-1)$
2. $\mathbf{A}\tilde{\mathbf{v}}_i \in \mathbf{V}_{k-1}, i = 0, 1, \dots, (k-2)$

The best matrix solution in the trial space $\mathbf{V}_{k-1} = \text{span}\{\tilde{\mathbf{v}}_0 \quad \tilde{\mathbf{v}}_1 \quad \dots \quad \tilde{\mathbf{v}}_{k-1}\}$ is then

$$\begin{aligned} \tilde{\mathbf{x}}^{(k)} &= \sum_{i=0}^{k-1} c_i\tilde{\mathbf{v}}_i = \sum_{i=0}^{k-1} \left(\nu_i\tilde{\mathbf{b}}\right)\tilde{\mathbf{v}}_i \\ &= \tilde{\mathbf{x}}^{(k-1)} + \left(\nu_{k-1}\tilde{\mathbf{b}}\right)\tilde{\mathbf{v}}_{k-1} = \tilde{\mathbf{x}}^{(k-1)} + \alpha\tilde{\mathbf{v}}_{k-1} \end{aligned} \tag{29}$$

and of course, the residual vector is computed through

$$\tilde{\mathbf{r}}^{(k)} = \tilde{\mathbf{b}} - \mathbf{A}\tilde{\mathbf{x}}^{(k)} = \tilde{\mathbf{r}}^{(k-1)} - \alpha\mathbf{A}\tilde{\mathbf{v}}_{k-1} \tag{30}$$

From the Galerkin method it follows that

$$\nu_i\tilde{\mathbf{r}}^{(k)} = 0, \quad i = 0, 1, \dots, (k-1) \tag{31}$$

Since $\mathbf{A}\tilde{\mathbf{v}}_i \in \mathbf{V}_{k-1}, i = 0, 1, \dots, (k-2)$, we also have

$$\nu_i\mathbf{A}\tilde{\mathbf{r}}^{(k)} = 0, \quad i = 0, 1, \dots, (k-2) \tag{32}$$

Subsequently, the next basis vector will be computed by

$$\begin{aligned} \tilde{\mathbf{p}} &= \tilde{\mathbf{r}}^{(k)} - \sum_{i=0}^{k-1} \beta_i\tilde{\mathbf{v}}_i = \tilde{\mathbf{r}}^{(k)} - \sum_{i=0}^{k-1} \left(\nu_i\mathbf{A}\tilde{\mathbf{r}}^{(k)}\right)\tilde{\mathbf{v}}_i \\ &= \tilde{\mathbf{r}}^{(k)} - \left(\nu_{k-1}\mathbf{A}\tilde{\mathbf{r}}^{(k)}\right)\tilde{\mathbf{v}}_{k-1} = \tilde{\mathbf{r}}^{(k)} - \beta\tilde{\mathbf{v}}_{k-1} \end{aligned} \tag{33}$$

and

$$\tilde{\mathbf{v}}_k = \frac{\tilde{\mathbf{p}}}{\sqrt{\nu_0\mathbf{A}\tilde{\mathbf{p}}}} \tag{34}$$

Consequently, $\{\tilde{\mathbf{v}}_0 \quad \tilde{\mathbf{v}}_1 \quad \dots \quad \tilde{\mathbf{v}}_k\}$ is an *A*-conjugate basis for the trial space \mathbf{V}_k . This process continues until $\|\tilde{\mathbf{r}}^{(k)}\|$ is very small at a certain iteration *k*; it then implies, for all practical purposes, that $\tilde{\mathbf{x}}^{(k)}$ is the solution to the matrix equation $\mathbf{A}\tilde{\mathbf{x}} = \tilde{\mathbf{b}}$. Note that the process is extremely simple and the recursive nature of the process makes it possible not to store all the basis vectors.

The detailed induction argument above leads directly to the basic CG algorithm 1 listed earlier in this article.

7.1. Convergence Rate of Conjugate-Gradient Methods

There are two features that can make CG converge fast: (1) eigenvalue clusters and (2), a good condition number of the matrix. To see why eigenvalue clusters are good for CG method, let's look at the following theorem.

Theorem 1. Assume that matrix **A**, which is a diagonalizable $N \times N$ symmetric matrix, has only *k* distinctive eigenvalues, namely

$$\begin{aligned} \lambda(\mathbf{A}) &= \left\{ \overbrace{\lambda_0 \quad \lambda_0 \quad \dots \quad \lambda_0}^{n_0} \quad \overbrace{\lambda_1 \quad \lambda_1 \quad \dots \quad \lambda_1}^{n_1} \quad \dots \quad \overbrace{\lambda_{k-1} \quad \lambda_{k-1} \quad \dots \quad \lambda_{k-1}}^{n_{k-1}} \right\} \\ n_0 + n_1 + \dots + n_{k-1} &= N \end{aligned} \tag{35}$$

then the dimension of the Krylov space

$$K_m(\tilde{\mathbf{v}}_0; \mathbf{A}) = \{\tilde{\mathbf{v}}_0 \quad \mathbf{A}\tilde{\mathbf{v}}_0 \quad \dots \quad \mathbf{A}^{m-1}\tilde{\mathbf{v}}_0\} \tag{36}$$

will always be bounded by *k* regardless of the initial vector $\tilde{\mathbf{v}}_0$ and *m*:

$$\dim[K_m(\tilde{\mathbf{v}}_0; \mathbf{A})] \leq k \tag{37}$$

Proof: Let $\tilde{\mathbf{e}}_{p_i}$ be the *i*th eigenvector corresponding to eigenvalue λ_p of the matrix **A**:

$$\mathbf{A}\tilde{\mathbf{e}}_{p_i} = \lambda_p\tilde{\mathbf{e}}_{p_i}; \quad i = 0, 1, \dots, (n_p - 1) \tag{38}$$

Since these eigenvectors form a complete set of basis vectors, any column vector \tilde{v}_0 can be written as a linear combination of these eigenvectors:

$$\tilde{v}_0 = \sum_{p=0}^{k-1} \sum_{i=0}^{n_p-1} c_{p,i} \tilde{e}_{p,i} = \sum_{p=0}^{k-1} \tilde{v}_0^{(p)} \quad (39)$$

$$\tilde{v}_0^{(p)} = \sum_{i=0}^{n_p-1} c_{p,i} \tilde{e}_{p,i}$$

It then follows that

$$\begin{aligned} \mathbf{A}\tilde{v}_0 &= \sum_{p=0}^{k-1} \sum_{i=0}^{n_p-1} \lambda_p c_{p,i} \tilde{e}_{p,i} = \sum_{p=0}^{k-1} \lambda_p \sum_{i=0}^{n_p-1} c_{p,i} \tilde{e}_{p,i} \\ &= \sum_{p=0}^{k-1} \lambda_p \tilde{v}_0^{(p)} \end{aligned} \quad (40)$$

Moreover, we have

$$\mathbf{A}^n \tilde{v}_0 = \sum_{p=0}^{k-1} \lambda_p^n \tilde{v}_0^{(p)} \quad (41)$$

This means that for any Krylov vector $\mathbf{A}^n \tilde{v}_0$, it can always be written as a linear combination of k independent vectors $\tilde{v}_0^{(0)}, \tilde{v}_0^{(1)}, \dots, \tilde{v}_0^{(k-1)}$. Thus, we conclude that

$$\dim[K_m(\tilde{v}_0; \mathbf{A})] = \dim\{\tilde{v}_0 \quad \mathbf{A}\tilde{v}_0 \quad \dots \quad \mathbf{A}^{m-1}\tilde{v}_0\} \leq k \quad (42)$$

regardless of the initial vector and the iteration number m .

Consequently, in applying the CG method, or any Krylov-based methods, to solve a matrix equation with k distinctive eigenvalues, CG converges in at most k iterations.

Next, let's examine the effect of condition number on the convergence rate of the CG methods. To gain more insight, let us assume further that matrix \mathbf{A} is an $N \times N$ symmetric positive definite (SPD) matrix. With this assumption, we can state a fact that at the m th iteration, the CG method produces the same solution as the following minimization problem.

Minimization: Seek $\tilde{\mathbf{x}}^{(m)} \in K_m(\tilde{\mathbf{b}}; \mathbf{A}) = \{\tilde{\mathbf{b}} \quad \mathbf{A}\tilde{\mathbf{b}} \quad \dots \quad \mathbf{A}^{m-1}\tilde{\mathbf{b}}\}$ such that the quadratic form

$$\left(\mathbf{x} - \tilde{\mathbf{x}}^{(m)} \right) \mathbf{A} \left(\mathbf{x} - \tilde{\mathbf{x}}^{(m)} \right) \quad (43)$$

is minimized.

Since \mathbf{A} is SPD, and its eigenvectors form a complete set of basis vectors, we can express the RHS vector $\tilde{\mathbf{b}}$ as

follows:

$$\tilde{\mathbf{b}} = b_0 \tilde{\mathbf{e}}_0 + b_1 \tilde{\mathbf{e}}_1 + \dots + b_{N-1} \tilde{\mathbf{e}}_{N-1} = \sum_{i=0}^{N-1} b_i \tilde{\mathbf{e}}_i \quad (44)$$

It is easy to show then the exact solution $\tilde{\mathbf{x}}$ is

$$\tilde{\mathbf{x}} = \frac{b_0}{\lambda_0} \tilde{\mathbf{e}}_0 + \frac{b_1}{\lambda_1} \tilde{\mathbf{e}}_1 + \dots + \frac{b_{N-1}}{\lambda_{N-1}} \tilde{\mathbf{e}}_{N-1} = \sum_{i=0}^{N-1} \frac{b_i}{\lambda_i} \tilde{\mathbf{e}}_i \quad (45)$$

Furthermore, a general trial vector in the Krylov space in the m th iteration is of the form

$$\begin{aligned} \tilde{v} &= \sum_{i=0}^{m-1} c_i \left(\mathbf{A}^i \tilde{\mathbf{b}} \right) \\ &= \sum_{i=0}^{m-1} (c_0 + c_1 \lambda_i + \dots + c_{m-1} \lambda_i^{m-1}) b_i \tilde{\mathbf{e}}_i \end{aligned} \quad (46)$$

Subsequently

$$\tilde{\mathbf{x}} - \tilde{v} = \sum_{i=0}^{N-1} \frac{1}{\lambda_i} (1 - c_0 \lambda_i - c_1 \lambda_i^2 - \dots - c_{m-1} \lambda_i^m) b_i \tilde{\mathbf{e}}_i \quad (47)$$

and a quadratic functional $F(\tilde{v})$ can be defined as

$$F(\tilde{v}) = (\mathbf{x} - \tilde{v}) \mathbf{A} (\mathbf{x} - \tilde{v}) \quad (48)$$

Substituting (46) and (47) into Eq. (48), we have

$$\begin{aligned} F(\tilde{v}) &= \sum_{i=0}^{N-1} [1 - c_0 \lambda_i - c_1 \lambda_i^2 - \dots - c_{m-1} \lambda_i^m]^2 \frac{1}{\lambda_i} b_i^2 \\ &\leq \max_{\substack{0 \leq i \leq N-1 \\ \lambda_i}} [1 - c_0 \lambda_i - c_1 \lambda_i^2 - \dots - c_{m-1} \lambda_i^m]^2 \sum_{i=0}^{N-1} \frac{1}{\lambda_i} b_i^2 \\ &= \max_{\substack{0 \leq i \leq N-1 \\ \lambda_i}} [1 - c_0 \lambda_i - c_1 \lambda_i^2 - \dots - c_{m-1} \lambda_i^m]^2 \left| \mathbf{x} \mathbf{A} \tilde{\mathbf{x}} \right| \end{aligned} \quad (49)$$

Since the CG solution is the same as the one that minimizes the quadratic functional, we have

$$\begin{aligned} F(\tilde{\mathbf{x}}^{(m)}) &= \min_{\tilde{v} \in K_m(\tilde{\mathbf{b}}; \mathbf{A})} F(\tilde{v}) \leq \left| \mathbf{x} \mathbf{A} \tilde{\mathbf{x}} \right| \min_{\{c_0 \quad c_1 \quad \dots \quad c_{m-1}\}} \\ &\quad \max_{\substack{0 \leq i \leq N-1 \\ \lambda_i}} [1 - c_0 \lambda_i - c_1 \lambda_i^2 - \dots - c_{m-1} \lambda_i^m]^2 \\ &= \left| \mathbf{x} \mathbf{A} \tilde{\mathbf{x}} \right| \min_{P_m(0)=1} \max_{0 \leq i \leq N-1} |P_m(\lambda_i)|^2 \end{aligned} \quad (50)$$

where $P_m(\lambda)$ is the m th polynomial in λ . If we arrange the eigenvalues of \mathbf{A} in ascending manner, namely, $\lambda_0 \leq \lambda_1 \leq \dots \leq \lambda_{N-1}$, then we can replace the best approximation problem on the discrete set with the best

approximation problem on the interval $[\lambda_0 \ \lambda_{N-1}]$. Note that we have

$$\min_{P_m(0)=1} \max_{\lambda_i} |P_m(\lambda_i)| \leq \min_{P_m(0)=1} \max_{\lambda_0 \leq \lambda \leq \lambda_{N-1}} |P_m(\lambda)| \quad (51)$$

The solution to the minmax problem on an interval is known; namely

$$\min_{P_m(0)=1} \max_{\lambda_0 \leq \lambda \leq \lambda_{N-1}} |P_m(\lambda)| = \frac{1}{T_m\left(\frac{\lambda_{N-1} + \lambda_0}{\lambda_{N-1} - \lambda_0}\right)} \max_{\lambda_0 \leq \lambda \leq \lambda_{N-1}} \left| T_m\left(\frac{\lambda_{N-1} + \lambda_0 - 2\lambda}{\lambda_{N-1} - \lambda_0}\right) \right| \quad (52)$$

where $T_m(x) = \frac{1}{2} \left[(x + \sqrt{x^2 - 1})^m + (x - \sqrt{x^2 - 1})^m \right]$ is the Chebyshev polynomial. Also, since $\max_{-1 \leq x \leq 1} |T_m(x)| = 1$ and $-1 \leq [(\lambda_{N-1} + \lambda_0 - 2\lambda)/(\lambda_{N-1} - \lambda_0)] \leq 1$, we then find

$$\begin{aligned} \min_{P_m(0)=1} \max_{\lambda_0 \leq \lambda \leq \lambda_{N-1}} |P_m(\lambda)| &= \frac{1}{T_m\left(\frac{\lambda_{N-1} + \lambda_0}{\lambda_{N-1} - \lambda_0}\right)} \\ &= 2 \frac{\sigma^m}{1 + \sigma^{2m}}; \\ \sigma &= \frac{1 - \sqrt{\frac{\lambda_0}{\lambda_{N-1}}}}{1 + \sqrt{\frac{\lambda_0}{\lambda_{N-1}}}} \end{aligned} \quad (53)$$

In conclusion, the convergence rate of CG method, measured in A norm is

$$\sqrt{(x - x^{(m)}) \mathbf{A} (x - x^{(m)})} \leq 2 \frac{\sigma^m}{1 + \sigma^{2m}} \sqrt{x \mathbf{A} x} \quad (54)$$

7.2. Preconditioned CG method

We conclude the previous section by observing that CG method works well on matrices that are either well-conditioned or have just a few distinct eigenvalues. For many RF engineering applications (such as the electric field integral equation), the system matrix equations are usually not suitable directly for CG method. However, if a proper preconditioning matrix, $\mathbf{M} = \mathbf{C}^t \mathbf{C}$, can be found, then the system matrix can be transformed into

$$\begin{aligned} \mathbf{A} \tilde{\mathbf{x}} = \tilde{\mathbf{b}} &\Rightarrow \mathbf{A}' \tilde{\mathbf{z}} = \tilde{\mathbf{b}}' \\ \mathbf{A}' &= \left((\mathbf{C}^t)^{-1} \mathbf{A} \mathbf{C}^{-1} \right), \tilde{\mathbf{x}} = \mathbf{C} \tilde{\mathbf{z}}, \\ \tilde{\mathbf{b}}' &= (\mathbf{C}^t)^{-1} \tilde{\mathbf{b}} \end{aligned} \quad (55)$$

Applying the CG algorithm 1 to the transformed matrix equation results in the following algorithm.

CG Algorithm 2

Initialization: $\tilde{\mathbf{v}}' = -\frac{\tilde{\mathbf{b}}'}{\sqrt{\tilde{\mathbf{b}}' \mathbf{A}' \tilde{\mathbf{b}}'}}$, $\tilde{\mathbf{z}} = 0, \tilde{\mathbf{r}}' = \tilde{\mathbf{b}}'$
 Iteration:

1. $\tilde{\mathbf{z}} = \tilde{\mathbf{z}} + \alpha \tilde{\mathbf{v}}', \quad \alpha = \underline{v}' \tilde{\mathbf{b}}'.$
2. $\tilde{\mathbf{u}}' = \mathbf{A}' \tilde{\mathbf{v}}', \quad \tilde{\mathbf{r}}' = \tilde{\mathbf{r}}' - \alpha \tilde{\mathbf{u}}'.$
3. Check $\|\tilde{\mathbf{r}}'\| / \|\tilde{\mathbf{b}}'\| \leq \epsilon$. If yes, then stop, and $\tilde{\mathbf{z}}$ is a good approximation; if no, then continue.
4. $\tilde{\mathbf{p}}' = \tilde{\mathbf{r}}' - \beta \tilde{\mathbf{v}}', \quad \beta = \underline{u}' \tilde{\mathbf{r}}'.$
5. $\tilde{\mathbf{v}}' = \tilde{\mathbf{p}}' / \sqrt{\tilde{\mathbf{p}}' \mathbf{A}' \tilde{\mathbf{p}}'}$.
6. Go to step 1.

Of course, once we have $\tilde{\mathbf{z}}$, then we can obtain $\tilde{\mathbf{x}}$ via $\tilde{\mathbf{x}} = \mathbf{C}^{-1} \tilde{\mathbf{z}}$. However, it is possible to avoid explicit reference to the matrix \mathbf{C}^{-1} by defining $\tilde{\mathbf{p}}' = \mathbf{C} \tilde{\mathbf{p}}, \tilde{\mathbf{z}} = \mathbf{C} \tilde{\mathbf{x}}$ and $\tilde{\mathbf{r}}' = (\mathbf{C}^t)^{-1} \tilde{\mathbf{r}}$ in every CG iteration. Indeed, if we substitute these definitions into CG algorithm 2 and recall $\tilde{\mathbf{b}}' = (\mathbf{C}^t)^{-1} \tilde{\mathbf{b}}$, then we obtain

CG Algorithm 3

Initialization:

$$\mathbf{C} \tilde{\mathbf{v}} = \frac{(\mathbf{C}^t)^{-1} \tilde{\mathbf{b}}}{\sqrt{\tilde{\mathbf{b}} (\mathbf{C}^{-1} (\mathbf{C}^t)^{-1}) \mathbf{A} (\mathbf{C}^{-1} (\mathbf{C}^t)^{-1}) \tilde{\mathbf{b}}}}, \quad \tilde{\mathbf{z}} = 0, \tilde{\mathbf{r}} = \tilde{\mathbf{b}}$$

Iteration:

1. $\mathbf{C} \tilde{\mathbf{x}} = \mathbf{C} \tilde{\mathbf{x}} + \alpha \mathbf{C} \tilde{\mathbf{v}}, \quad \alpha = \underline{v} \tilde{\mathbf{b}}.$
2. $(\mathbf{C}^t)^{-1} \tilde{\mathbf{u}} = (\mathbf{C}^t)^{-1} \mathbf{A} \tilde{\mathbf{v}}, \quad (\mathbf{C}^t)^{-1} \tilde{\mathbf{r}} = (\mathbf{C}^t)^{-1} \tilde{\mathbf{r}} - \alpha (\mathbf{C}^t)^{-1} \tilde{\mathbf{u}}.$
3. Check $\|\tilde{\mathbf{r}}'\| / \|\tilde{\mathbf{b}}'\| \leq \epsilon$. If yes, then stop, and $\tilde{\mathbf{x}}$ is a good approximation; if no, then continue.
4. $\mathbf{C} \tilde{\mathbf{p}} = (\mathbf{C}^t)^{-1} \tilde{\mathbf{r}} - \beta \mathbf{C} \tilde{\mathbf{v}}, \quad \beta = \underline{u} \mathbf{C}^{-1} (\mathbf{C}^t)^{-1} \tilde{\mathbf{r}}.$
5. $\mathbf{C} \tilde{\mathbf{v}} = \mathbf{C} \tilde{\mathbf{p}} / \sqrt{\tilde{\mathbf{p}} \mathbf{A} \tilde{\mathbf{p}}}$.
6. Go to step 1.

Finally, the entire algorithm can be simplified by using the preconditioner $\mathbf{M} = \mathbf{C}^t \mathbf{C}$ directly instead of referring to \mathbf{C} or \mathbf{C}^t . This is then the preconditioned CG algorithm.

Preconditioned CG Algorithm

Initialization: $\tilde{\mathbf{z}} = 0, \tilde{\mathbf{r}} = \tilde{\mathbf{b}}, \tilde{\mathbf{p}} = \mathbf{M}^{-1} \tilde{\mathbf{r}}, \tilde{\mathbf{v}} = \tilde{\mathbf{p}} / \sqrt{\tilde{\mathbf{p}} \mathbf{A} \tilde{\mathbf{p}}}$
 Iteration:

1. $\tilde{\mathbf{x}} = \tilde{\mathbf{x}} + \alpha \tilde{\mathbf{v}}, \quad \alpha = \underline{v} \tilde{\mathbf{b}}.$
2. $\tilde{\mathbf{u}} = \mathbf{A} \tilde{\mathbf{v}}, \quad \tilde{\mathbf{r}} = \tilde{\mathbf{r}} - \alpha \tilde{\mathbf{u}}.$
3. Check $\|\tilde{\mathbf{r}}'\| / \|\tilde{\mathbf{b}}'\| \leq \epsilon$. If yes, then stop, and $\tilde{\mathbf{x}}$ is a good approximation; if no, then continue.
4. $\tilde{\mathbf{p}} = \mathbf{M}^{-1} \tilde{\mathbf{r}} - \beta \tilde{\mathbf{v}}, \quad \beta = \underline{u} \mathbf{M}^{-1} \tilde{\mathbf{r}}.$
5. $\tilde{\mathbf{v}} = \tilde{\mathbf{p}} / \sqrt{\tilde{\mathbf{p}} \mathbf{A} \tilde{\mathbf{p}}}$.
6. Go to step 1.

BIBLIOGRAPHY

1. G. H. Golub and C. F. Van Loan, *Matrix Computations*, 3rd ed., Johns Hopkins Univ. Press, Baltimore, 1996.
2. T. J. Kim and G. A. Thiele, A Hybrid diffraction technique—general theory and applications, *IEEE Trans. Anten. Propag.* **30**:888–897 (1982).
3. M. Kaye, P. K. Murthy, and G. A. Thiele, An iterative method for solving scattering problems, *IEEE Trans. Anten. Propag.* **33**:1272–1279 (1985).
4. P. K. Murthy, K. C. Hill, and G. A. Thiele, A hybrid-iterative method for scattering problems, *IEEE Trans. Anten. Propag.* **34**:1173–1180 (1986).
5. R. E. Hodges and Y. Rahmat-Samii, An iterative current-based hybrid method for complex structures, *IEEE Trans. Anten. Propag.* **45**:265–276 (1997).
6. A. Sullivan and L. Carin, Scattering from complex bodies using a combined direct and iterative technique, *IEEE Trans. Anten. Propag.*, **47**:33–39 (1999).
7. D. D. Reuster and G. A. Thiele, A field iterative method for computing the scattered electric fields at the apertures of large perfectly conducting cavities, *IEEE Trans. Anten. Propag.* **43**:286–290 (1995).
8. F. Obelleiro, J. L. Rodriguez, and R. J. Burkholder, An iterative physical optics approach for analyzing the electromagnetic scattering by large open-ended cavities, *IEEE Trans. Anten. Propag.* **43**:356–361 (1995).
9. D. Holliday, L. L. DeRaad, Jr., and G. J. St-Cyr, Forward-backward: A new method for computing low-grazing angle scattering, *IEEE Trans. Anten. Propag.* **44**:722–729 (1996).
10. D. A. Kapp and G. S. Brown, A new numerical method for rough surface scattering calculations, *IEEE Trans. Anten. Propag.* **44**:711–721 (1996).
11. M. R. Pino, L. Landesa, J. L. Rodriguez, F. Obelleiro, and R. J. Burkholder, The generalized forward-backward method for analyzing the scattering from targets on ocean-like rough surfaces, *IEEE Trans. Anten. Propag.* **47**:961–969 (1999).
12. J. C. West and J. M. Sturm, On iterative approaches for electromagnetic rough-surface scattering problems, *IEEE Trans. Anten. Propag.* **47**:1281–1288 (1999).
13. A. R. Clark, A. P. C. Fourie, and D. C. Nitch, Stationary, non-stationary, and hybrid iterative method of moments solution schemes, *IEEE Trans. Anten. Propag.* **49**:1462–1469 (2001).
14. R. J. Burkholder, On the use of classical iterative methods for electromagnetic scattering problems, *Proc. 4th Conf. Electromagnetic and Light Scattering by Nonspherical Particles: Theory and Applications*, Vigo, Spain, Sept. 20–21, 1999, pp. 65–72.
15. M. R. Hestenes and E. Stiefel, Methods of conjugate gradients for solving linear systems, *J. Res. Natl. Bur. Stand.* **49**:409–436 (1952).
16. T. K. Sarkar and S. M. Rao, The application of the conjugate gradient method for the solution of electromagnetic scattering from arbitrary oriented wire antennas, *Trans. Anten. Propag.* **32**:398–403 (1984).
17. T. K. Sarkar and E. Arvas, On a class of finite step iterative methods (conjugate directions) for the solution of an operator equation arising in electromagnetics, *Trans. Anten. Propag.* **33**:1058–1066 (1985).
18. T. K. Sarkar, E. Arvas, and S. M. Rao, Application of FFT and the conjugate gradient method for the solution of electromagnetic radiation from electrically large and small conducting bodies, *Trans. Anten. Propag.* **34**:635–640 (1986).
19. J. D. Collins, J. M. Jin, and J. L. Volakis, A combined finite element-boundary element formulation for solution of 2-dimensional problems via CG-FFT, *Electromagnetics*, **10**:423–437 (1990).
20. R. Coifman, V. Rokhlin, and S. Wandzura, The fast multipole method for the wave equation: A pedestrian prescription, *IEEE Anten. Propag. Mag.* **35**:7–12 (1993).
21. E. Bleszynski, M. Bleszynski, and T. Jaroszewicz, A fast integral equation solver for electromagnetic scattering problems, *Radio Sci.* **31**:1225–1251 (1996).
22. J. R. Phillips and J. White, A precorrected-FFT method for electrostatic analysis of complicated 3D structures, *IEEE Trans. Comput. Aid. Design Integr. Circ. Syst.* **16**:1059–1072 (1997).
23. S. Barnett, M. Berry, T. F. Chan, J. Demmel, J. Donato, J. Dongarra, V. Eijkhout, R. Pozo, C. Romine, and H. van der Vorst, *Templates for the Solution of Linear Systems: Building Blocks for Iterative Methods*, SIAM Publications, Philadelphia, 1993.
24. Y. Saad and M. Schultz, GMRES: A generalized minimal residual algorithm for solving nonsymmetric linear systems, *SIAM J. Sci. Stat. Comput.* **7**:856–869 (1986).
25. S. C. Eisenstat, H. C. Elman, and M. H. Schultz, Variational iteration methods for nonsymmetric systems of linear equations, *SIAM J. Num. Anal.* **20**:345–357 (1983).
26. J.-F. Lee and R. J. Burkholder, Loop star basis functions and a robust preconditioner for EFIE scattering problems, *IEEE Trans. Anten. Propag.* **51**:1855–1863 (2003).

FURTHER READING

- A. F. Peterson, S. L. Ray, and R. Mittra, *Computational Methods for Electromagnetics*, Wiley, New York, 1997 (a good general resource for computational electromagnetics, including the finite-element and finite-difference methods, the method of moments, basis expansions, and solution methods).
- O. Axelsson, *Iterative Solution Methods*, Cambridge Univ. Press, 1996 (a good source for iterative methods, in general). *Matrix Computations* by Golub and Van Loan [1] is an excellent reference on matrix theory, solution of matrix systems, and iterative algorithms.
- The *Templates* book [23] presents many iterative algorithms and their underlying theories, along with a discussion of preconditioners and parallelization; it is available online at http://www.netlib.org/linalg/html_templates/Templates.html, and the associated software may be downloaded from <http://www.netlib.org/templates/>.

ITS RADIO SERVICE STANDARDS AND WIRELESS ACCESS IN VEHICULAR ENVIRONMENTS (ITS-WAVE) AT 5.9 GHz

RAMEZ L. GERGES
IEEE-ITSC Standards
Committee
Goleta, California

1. INTRODUCTION

This article describes ongoing activities to create a new family of standards that supports the emerging Intelligent

Transportation Systems (ITS) and telematics wireless markets. ITS-WAVE is a radiocommunication system intended to provide seamless, interoperable services to surface transportation systems. After an initial overview of the ITS-WAVE family of standards, more emphasis will be given to the radio (lower layers) part of the system, and the use of orthogonal frequency-division multiplexing (OFDM) for the physical layer [1].

1.1. ITS, Telematics, and Wireless Interoperability

The Intelligent Transportation Systems (ITS) initiative was created by Congress in the Intermodal Surface Transportation Efficiency Act of 1991 (ISTEA) to improve the mobility and safety of the surface transportation system. ITS is defined as those systems utilizing synergistic technologies and systems engineering concepts to develop and improve transportation systems of all kinds. Communication and information technologies are at the core of roadside infrastructure and in-vehicle systems. These technologies promise to enhance mobility by improving the way we monitor and manage traffic flow, clear incidents, reduce congestion, and provide alternate routes to travelers. The telematics industry is focused on driver comfort and safety, and while “telematics” in general has meant the blending of computers and telecommunications, it is used within the ITS community with the connotation of “automotive telematics” or the in-vehicle subsystem of ITS.

In 1999, the Federal Communications Commission (FCC) allocated the 5.850–5.925-GHz band for use by the ITS radio service for both public safety and commercial ITS applications. Many standards development organizations (e.g., IEEE, IETF, ISO) are engaged in the process of achieving an end-to-end ITS wireless interoperability. This article addresses Wireless Access in Vehicular Environments (WAVE), which is currently being developed under the IEEE WG 802.11, WAVE Study Group.

1.2. ITS Radio Services

The proposed ITS-WAVE standard addresses broadband wireless communications that operate in a long range (≤ 1000 m) and at a high data rate [27 Mbps (megabits per second)] for all ITS applications. The proposed lower-layer standard currently addresses communications between roadside units and mostly high-speed, but occasionally stopped and slow-moving, vehicles or between high-speed vehicles. The ITS new spectrum will be used to support multiple applications to enhance public safety and transportation mobility and can be categorized as follows:

1. *Public Safety*: The primary use of this band is to offer services such as emergency vehicle signal preemption and announcements for work zones. While the FCC has allocated the 4.9 GHz for communications between *first responders*, the 5.9-GHz band is expected to allow first responders to communicate with the general driving public on roads and freeways.
2. *Mobility*: Services such as electronic toll, vehicle probes, traveler information, and public transporta-

tion integration are expected to enhance the transportation system performance.

3. *Driver Safety*: New features such as support of collision avoidance and warnings for excessive speed and railroad crossings are expected to improve system performance. More recently, vehicle manufacturers and telematics providers have shown interest in the ITS-WAVE standards. There is no other radiocommunication technology that can support the real-time requirements for vehicle-to-vehicle communications.

1.3. ITS-WAVE Development History

Attempts to develop standards for the wireless ITS environment date back to the early 1990s, when California adopted the Title 21 regulation to achieve a common standard for “toll collections.” The dedicated short-range communications (DSRC) standard at 900 MHz, and Title 21 [2], predated the ITS initiative, and addressed only the electronic toll collection; it was not intended to support a national interoperable wireless ITS standard.

The Intermodal Surface Transportation Efficiency Act of 1991 (ISTEA) funded many research ITS programs. In the mid-1990s, the author (then with the New Technology program at Caltrans) initiated some of the first technical studies to develop an integrated wireless communications system for all ITS applications [3]. In 1996, the U.S. National System Architecture identified wireless communications as one of the critical enabling technologies needed to support many of the ITS services. Later, the USDOT funded more studies, and the California Department of Transportation (Caltrans) established the Testbed Center for Interoperability (TCFI) to study and test end-to-end wireless interoperability. In May 1997, the Intelligent Transportation Society of America (ITSA) filed a Petition for Rulemaking, requesting that the FCC allocate 75 MHz of spectrum in the 5.850–5.925-GHz band on a coprimary basis for DSRC-based ITS services. In 1998 at the IEEE-Vehicular Technology Conference, the author suggested to leverage the economical feasibility of the IEEE 802.11 to achieve wireless ITS interoperability [4]. In 1999, the FCC amended Parts 2 and 90 of the Commission’s Rules to allocate the 5.850–5.925-GHz band to the Mobile Service for Dedicated Short Range Communications of Intelligent Transportation Services.¹ The USDOT funded the American Society for Testing and Materials (ASTM) to initiate the standard writing group for the DSRC at 5.9 GHz. In 2000, TCFI tested the first video relay to a moving vehicle at highway speed using OFDM technology.² The successful test paved the way to use broadband technologies for wireless ITS. Later, the ASTM selected the OFDM Forum proposal to use the IEEE 802.11a [5,6] as the basis for the new standard.³ The new DSRC standard is now being

¹ET Docket 98-95, 14 FCC Record 18221.

²Wireless LAN provided the OFDM equipment at 2.4 GHz; Further information is available at <http://www.wi-lan.com>.

³The OFDM-Forum proposal (802.11 RA) suggested changing the physical layer of the IEEE 802.11 to match the requirements of the “road access” environment. (<http://www.ofdm-forum.com>).

Frequency allocations 4.9-5.9 GHz:

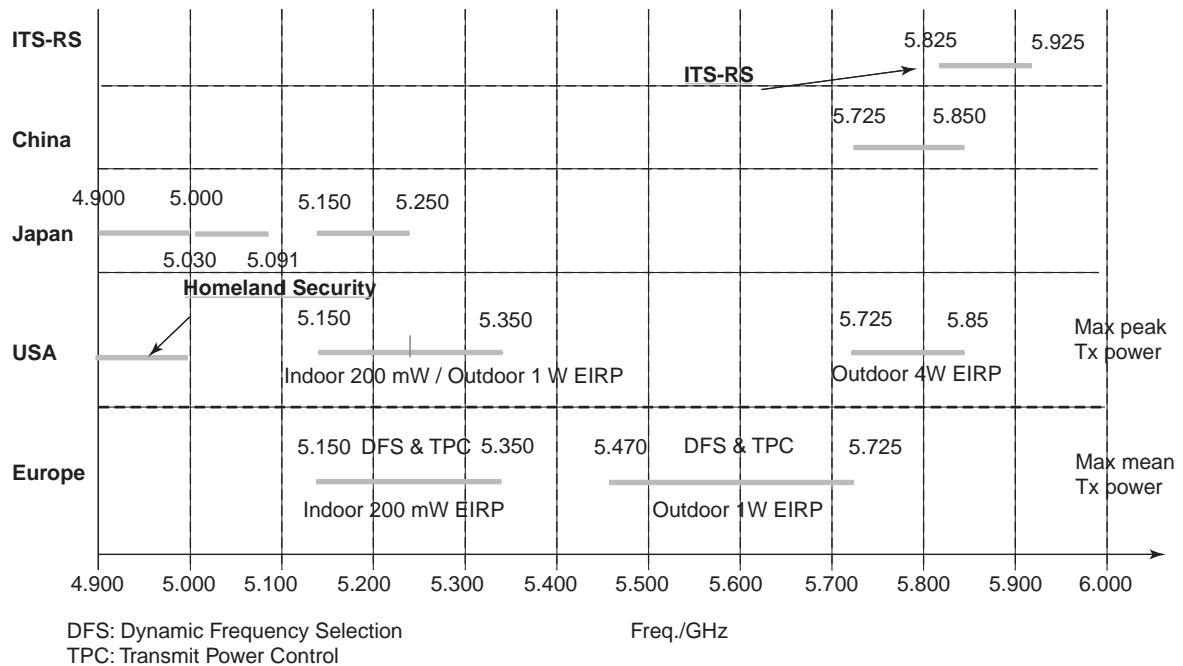


Figure 1. Spectrum allocation at the 5-GHz Band. (This figure is available in full color at <http://www.mrw.interscience.wiley.com/erfme>.)

completed within the IEEE WG 802.11. The Study Group (SG) decided to use the ASTM standard [7] as the basis for the ITS-WAVE proposal.⁴ As the proposed standard is not limited to short-range applications, the SG has named it the *Wireless Access in Vehicular Environments (WAVE)* instead of DSRC. This will also avoid any confusion with the single carrier technology in use in the United States (900-MHz band) or in Japan and Europe (at 5.8 GHz but different standards).

On December 17, 2003 the FCC adopted the rules for the ITS band. It is expected that the new standard (possibly 802.11p) will be completed by the end of 2005.

2. ITS RADIO SERVICES SYSTEM-LEVEL DESCRIPTION

2.1. Spectrum Allocation for ITS, Telematics, and Public Safety

The Broadband ITS Radio Service (ITS-RS) establishes a common framework for providing wireless services in the 5.850–5.925-GHz band. This band is allocated for ITS-RS applications by the FCC.⁵ Figure 1 shows the spectrum allocation in the 4.9–5.9-GHz band. The differences between the ITS-WAVE and the IEEE 802.11 WLAN systems stem from the fact that the ITS-WAVE operates in a licensed band, and it establishes reliable communications

between units operating at full vehicle mobility, a different environment than the indoor WLAN.

These communications may occur with other units that are (1) fixed along the roadside or above the roadway, (2) mounted in other high-speed moving vehicles, (3) mounted in stationary vehicles, (4) mounted on mobile platforms (e.g., watercraft, buoy, or a robotic platform), or (5) portable or handheld. In-vehicle communications units are called *onboard units (OBUs)*. Communication units fixed along the freeways, over the road on gantries or poles, or off the road in private or public areas, are called *roadside units (RSUs)*. The WAVE RSUs may function as stations or as access points (APs) and the WAVE OBUs only have functions consistent with those of stations (STAs). The common function between all RSUs is that these stationary units control access to the radiofrequency medium for OBUs in their communication zone or relinquish control to broadcast data only.

The vehicular mobility environment requires that we design a system that can survive both the time-dispersive (frequency-selective) multipath fading and the frequency-dispersive (time-selective) fading environment. Tests conducted at the Testbed Center For Interoperability (TCFI) at UCSB show that we may encounter up to 400 ns of delay spread and up to 2200 Hz of Doppler spread as explained later. Single-carrier transmission, with a time-domain equalizer, has an inherent limitation due to convergence and tracking problems which arises as the number of taps increase. A coded OFDM (COFDM) approach similar to the IEEE 802.11a/g standard offered a more robust, as well as economically feasible solution

⁴The ASTM E2213-02 was approved but not published because of copyright issues with the IEEE.

⁵Title 47, *Code of Federal Regulations (CFR)*, Part 90, Subpart M.

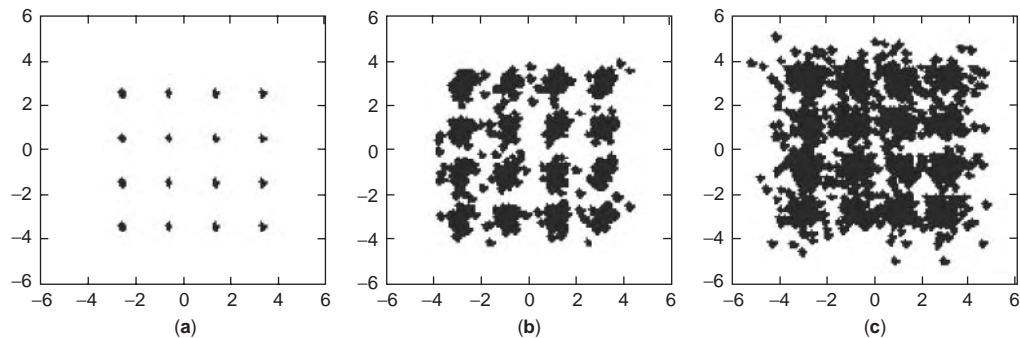


Figure 2. Impact of delay spread. (This figure is available in full color at <http://www.mrw.interscience.wiley.com/erfme>.)

based on the success of the WLAN industry. This economic feasibility also made the COFDM approach a better candidate than the single-carrier transmission with a frequency-domain equalizer. Although, the latter has the same complexity and may have some good features [e.g., avoids the PAPR (peak-to-average power ratio) issues].

The 802.11a scheme would not be able to tolerate the delay spread expected in the WAVE environment. Figure 2 shows the impact of delay spread on a 16-QAM signal constellation for a 64-subcarrier OFDM system [1]. The channel has a two-ray multipath; the second ray is 6 dB lower than the first one: (1) delay spread less than guard time (Fig. 2a), (2) delay spread greater than guard time by 3% of the FFT interval (Fig. 2b), and (3) delay spread greater than guard time by 9% of the FFT interval (Fig. 2c).

We proposed to double the guard interval (GI) to be more multipath-tolerant; in principle, using half the master clock should double the GI and scale down the channel bandwidth to 10 MHz, a desired outcome to increase the number of channels within the allocated spectrum. Of course the maximum data rate will be reduced to 27 Mbps, which is still adequate for demanding ITS applications (e.g., video relay). WLAN chips manufacturers (e.g., Intersil and Atheros) confirmed the feasibility of the approach using their current 802.11a implementations.⁶ It is expected that products with the correct front end operating at 5.9 GHz (10 MHz bandwidth) will be available as the market develops.

In order to accommodate the more dynamic vehicle environment with essentially the same radio technology, and provide priority to public safety communications, the ITS community is proposing a complementing set of standards under the IEEE SCC32. These standards address the upper layers including a different channel structure and access mechanism than that of the IEEE 802.11 as explained later.

2.2. System Architecture and SDO Coordination

The International Standards Organization (ISO) and the IEEE are coordinating their standards development

efforts to achieve ITS wireless interoperability. To this end a common CALM/WAVE architecture has been developed as shown in Figs. 3 and 4.

The current scope of the IEEE-WAVE proposed project is to create an amendment of IEEE 802.11 to support communication between vehicles and the roadside and between vehicles while operating at speeds up to a minimum of 200 km/h for communication ranges up to 1000 m. The amendment will support communications in the 5-GHz bands; specifically, the 5.850–5.925-GHz band within North America with the aim to enhance the mobility and safety of all forms of surface transportation, including rail and maritime transportation. Amendments to the PHY and MAC will be limited to those required to support communications under these operating environments within the 5-GHz bands.

The IEEE SCC32 sponsors the IEEE P1556, DSRC Security and Privacy and the ITS-WAVE (upper layers). The WG P1556 is proposing a dual-certificate system for public safety and vehicle safety to balance security and anonymity requirements. The IEEE WG P1609 architecture adopted IPV6 as the method of handling upper-layer applications. It consists of a series of four standards:

1. P1609.4 defines the channelization approach and considers integration issue with the IEEE 802.11e and IEEE 802.11 h.
2. P1609.3 is based on the IPv6 specification and may include a broad range of supporting standards defined by the Internet Engineering Task Force (IETF). It defines IPv6 addressing and configuration issues, network services (e.g., WAVE router advertisement), and all the WAVE management entities needed for registration and “service table” exchanges.
3. P1609.2 defines applications services.
4. P1609.1 defines a resource manager for onboard units (OBUs).

The ISO-Transport Information & Control (TC204) Working Group 16 is developing standards for wide-area wireless communications for transport information and control. ISO-TC204-WG16 is developing the communication air interface for long and medium range (or short media) (CALM) architecture. The CALM scope includes

⁶WLAN products from Intersil are now part of Conexant (<http://www.conexant.com>), Atheros (<http://www.atheros.com>).

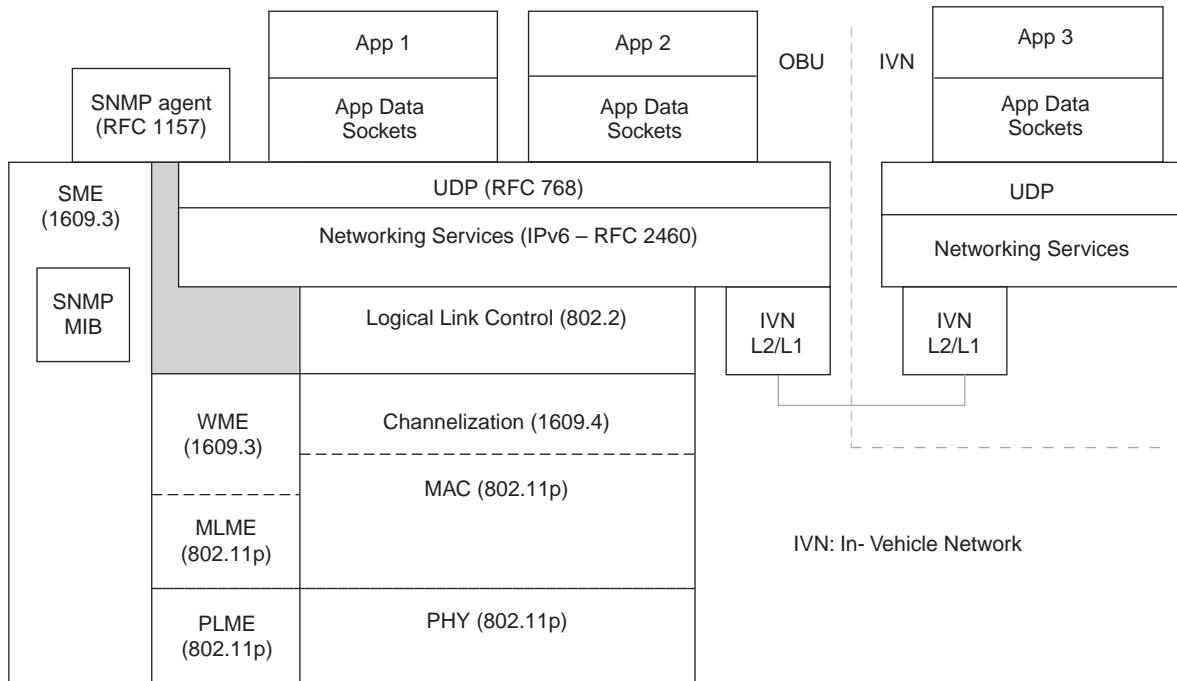


Figure 3. Wave architecture.

communications between fixed sites and switching between communication media (e.g., 3G cellular and WAVE), as well as issues such as handover and mobility management. CALM mandates end-to-end system interoperability at all levels. CALM-M5 is adopting the IEEE-WAVE proposal for the lower layers at 5 GHz.

2.3. Basic Concept of Operation

The ITS-WAVE typically consists of two types of radio devices. The first type is always used while stationary, usually permanently mounted along the roadside, and is referred to as the *roadside unit* (RSU). The second is

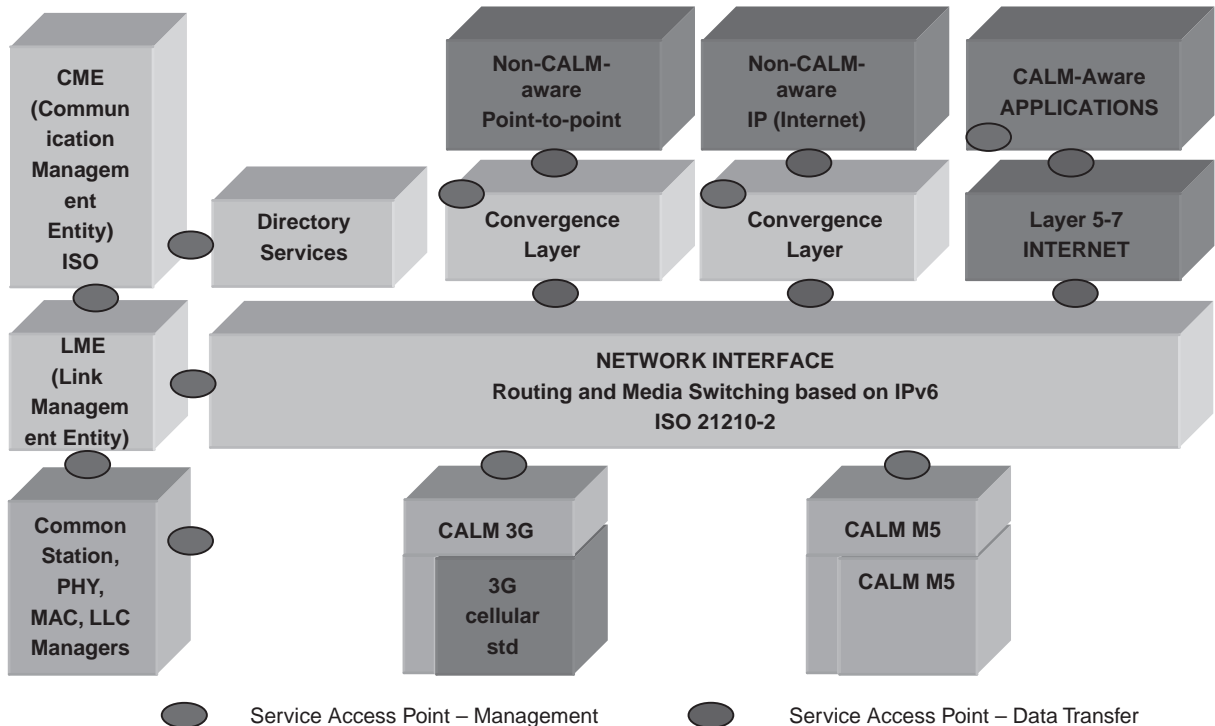


Figure 4. CALM architecture. (This figure is available in full color at <http://www.mrw.interscience.wiley.com/erfme>.)

mobile, mounted on board vehicles, and is referred to as the *onboard unit* (OBU). Three types of communication are supported: a command/response type between a service provider and a service user, a broadcast to listener, and a peer-to-peer type that does not identify either device as controlling the actions of the other. OBUs and RSUs can initiate both types of communication. The command/response type includes various forms of transactions between a service provider and a user of that service. To ensure scalable interoperability between ITS-WAVE units, the proposed standards define two levels of implementations. A minimal implementation only supports the lower layers, those below the network layer, and will be referred to as a “WAVE radio.” An implementation that has the full ITS-WAVE protocol stack is referred to as a “WAVE device.” Multiple devices interact with each other through the Networking Services (IEEE P1609).

Figure 5 represents the current ITS-WAVE band plan. The ITS-WAVE uses a “control channel” and any of six “service channels”. Licensing of both roadside RSUs and OBUs are necessary to prevent unauthorized use of the control channel. OBUs should be licensed by rule, since these devices are mobile and can operate nationwide, communicating with any other ITS-WAVE devices within range.

The onboard units (OBUs) are required to listen on the control channel every few hundred milliseconds, in order to check for public safety messages. The messages on the control channel are of variable length, but are generally kept short, to permit maximum access to the channel. Control channel access will be performed via a standard IEEE 802.11a, *Multiple Access with Collision Avoidance* (CSMA/CA). By default, all devices when turned on are tuned to the control channel. If an ITS-WAVE device

desires to transmit, but detects another message being broadcast on the control channel, it must wait before attempting to transmit. A request to send (RTS) is initiated, and time is granted first to high priority (public safety) broadcasts, then to lower-priority transmissions. The same control channel is used for roadside-to-vehicle, vehicle-to-roadside, and vehicle-to-vehicle communications. “Control channel interval” and “service channel interval” are controlled by RSU beacon frames. Since the control channel will be fixed throughout the nation, all ITS-WAVE devices will be able to access those services in an interoperable matter.

A registration process must occur before a WAVE device can be considered “ready for operation”; the RSU broadcasts beacon frames that include the “provider service table” (PST) and the “WAVE router advertisement” (WRA) on the control channel. Application initialization procedures are based on SNMP, and the designated service channel, priority, and power level are indicated in the PST. At the end of the application initialization state, the RSU commands the OBU to switch to the designated service channel. The RSU, now on the service channel, receives UDP datagrams sent by the OBU. The RSU routes datagrams to and from the applications indicated by the global IPv6.

The description above is included to give an idea about the basic concept of operations, with the understanding that the proposed standards are now under development. The P1609.3, 1609.4, and the P1556 are currently the most critical part of the WAVE family of standards as they require integration and coordination with many other standards such as IEEE 802.11e/h/i and many of the IETF recommendations.

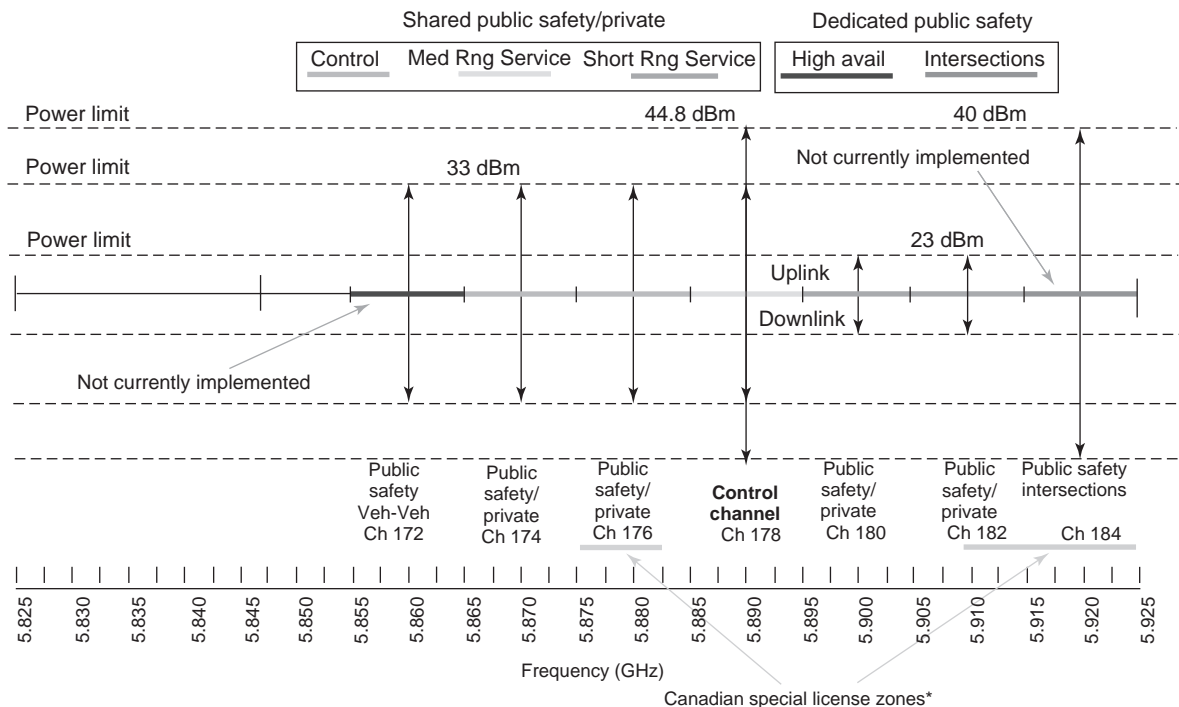


Figure 5. ITS-wave band plan. (This figure is available in full color at <http://www.mrw.interscience.wiley.com/erfme>.)

It is expected that WAVE radios that implement only the lower layers will develop first, as they leverage the existing IEEE 802.11a standard and chip technology.

3. DESIGNING FOR WIRELESS VEHICULAR ENVIRONMENTS

3.1. Channel Impairments

There is extensive literature on different statistical models of the communication channels at different frequency bands [8]. However, limited data of actual field measurements for vehicle–vehicle and vehicle–roadside communications are available at the ITS-WAVE frequency band. Statistical models include large-scale path loss models and small-scale fading models:

1. Large-scale propagation models characterize the mean received power over large transmitter–receiver separation distances. It is used to estimate radio coverage area of a transmitter.
2. Small-scale (fading) models characterize the rapid fluctuations of the received signal strength and phase over a very short distance. Multipath structure (power delay profile) is used to measure and describe the fading effects.

Both large- and small-scale fading models are needed for packet error rate characterization.

3.1.1. Time-Dispersive (Frequency-Selective) Multipath Fading Channel. A *time-dispersive channel* is defined as a channel for which the delay spread is much wider than the signal duration. The classification of a channel as time dispersive is therefore dependent on the data rate of the system. For a single carrier, high-data-rate systems, time-dispersive channels are commonly encountered. This type of fading is often referred to as *frequency-selective* because the signal may be simultaneously faded at one frequency and not at another. OFDM is robust against delay spread by design because of the longer symbol time and the fact that each subcarrier experiences a flat-fading channel. Similar to the IEEE 802.11a, the insertion of guard interval, and the use of forward error correction (FEC) are essential design elements to the coded OFDM scheme employed in the WAVE physical layer. This multipath rejection capability was one of the main reasons for selecting COFDM instead of a single-carrier system, especially for ITS applications that operate at longer ranges and at high data rates.

Short-range systems typically experience significantly smaller delay spreads than does a longer-range system. Previous studies show that 90% RMS (root-mean-square) delay spread is less than 100 ns for typical short-range applications (e.g., toll collection) in urban environments.⁷ RMS delay spread could be up to 300 ns [9,10] in a non-line-of-sight (NLoS) heavy-multipath environment, as may be expected in a freeway urban environment.

⁷For transmit–receive (Tx/Rx) separation of 30–300 m, both LoS and NLoS (Xiongwen, et.; IEEE JSAC 2002).

In order for subcarriers to perceive a flat-fading channel, the bandwidth (subcarrier spacing) must be less than the “coherence bandwidth” (\mathbf{B}_c) of the channel.⁸ \mathbf{B}_c is the bandwidth of the channel variation in frequency and is defined [8] as

$$\mathbf{B}_c = 1/5 \sigma$$

where σ is the RMS delay spread of the channel. The ITS-WAVE has a subcarrier spacing (bandwidth) of 156 kHz, and each subcarrier will encounter flat fading as long as $\sigma < 100$ ns (for range < 300 m). For long ranges (large delay spread), the pilot channels are available to estimate the channel in the frequency domain if they are well structured. In order to use the pilots for channel estimation, the pilot spacing in frequency has to be less than \mathbf{B}_c (~ 2 MHz for $\sigma = 500$ ns). This may not be the case using the current pilot structure of the IEEE 802.11a (pilot spacing = 14×156 kHz = 2.18 MHz $> \mathbf{B}_c$). Interpolation of pilot subcarrier in the current structure may not be sufficient to track the frequency selective fades. It is expected that the first generation WAVE radios, those using modified 802.11a chips, will be limited in range and may not be suitable for long-range public safety applications.

3.1.2. Frequency-Dispersive (Time-Selective) Fading Channel. Frequency-dispersive channels are classified as channels that have a Doppler spread larger than the channel bandwidth. Doppler spread is a direct result of multiple Doppler shifts which are caused by motion of the transmit and/or receive antenna. Doppler shifts can also result from reflections off of moving objects.⁹ Distortion of the power spectrum of the received signal results from Doppler spread, which can be approximated by the Doppler spread \mathbf{B}_d

$$\mathbf{B}_d = \mathbf{f}_m \cdot \cos \alpha$$

where $\mathbf{f}_m = v \cdot \mathbf{f}_c / c$, where v is the vehicle speed in m/s, \mathbf{f}_c is the carrier frequency in Hz, c is the speed of light in m/s, and α is the angle between the direction of vehicle travel and the ray of the communication path. In the case of the ITS-WAVE where vehicle speeds of ≤ 120 mph (193 km/h) must be supported (public safety), the maximum Doppler shift for a vehicle traveling directly toward the roadside antenna would be about 1100 Hz at 5.9 GHz, and much less for vehicle–vehicle communication (two vehicles heading in the same directions).

Time-selective fading caused by Doppler spread is described by the coherence time (\mathbf{T}_c) of the channel. \mathbf{T}_c represents the duration over which the channel characteristics do not change significantly, and is defined [8] as

$$\mathbf{T}_c = 0.423 / \mathbf{f}_m$$

⁸ \mathbf{B}_c is defined as the bandwidth over which the frequency correlation function is above 0.5.

⁹If a sinusoidal signal is transmitted over a fading channel (commonly referred to as a *constant wave*), the Doppler spread \mathbf{B}_d is defined as the range of frequencies over which the received Doppler spectrum is essentially nonzero.

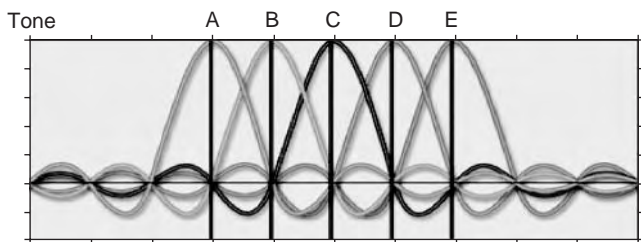


Figure 6. Subcarrier Orthogonality in OFDM systems. (This figure is available in full color at <http://www.mrw.interscience.wiley.com/erfme>.)

At a vehicle speed of 120 mph and a frequency of 5.9 GHz, $T_c = 400 \mu s$. When using pilot symbols at the start of a packet, the assumption is that channel variations during the rest of the packet are negligible. This limits the packet duration to less than T_c , and places an upper limit on the packet size. At a data rate of 3 Mbps, $\frac{1}{2}$ -code-rate BPSK-modulated signal, the maximum packet size¹⁰ is 135 bytes. Although this suggests that higher-order modulation would give better performance, as their transmission time is shorter, these modulation schemes degrade more in the presence of channel impairment.

3.2. The ITS-WAVE Physical Layer

The ITS-WAVE physical layer is based on using the robustness of the coded orthogonal frequency-division multiplexing (OFDM) signal to achieve the required performance in the wireless vehicular environments. OFDM is a special case of multicarrier modulation (MCM), which is the principle of transmitting data by dividing the data-stream into several parallel bitstreams and modulating each bitstream onto individual subcarriers. Each subcarrier is a narrowband signal, resulting in long bit intervals. High data rates are achieved by using multiple orthogonal subcarriers for a single data transmission. The OFDM system differs from traditional MCM in that the spectra of the subcarriers were allowed to overlap under the restriction that they were all mutually orthogonal. An orthogonal relationship between subcarriers is achieved if there are integer numbers of subcarrier frequency cycles over the symbol interval. This orthogonality guarantees that each subcarrier has a null at the center frequency of all other subcarriers as shown in Fig. 6.

Orthogonality is achieved with precision by modulating the subcarriers with a discrete Fourier transform (DFT), which is implemented in hardware with the fast Fourier transform (FFT). By transmitting several symbols in parallel, the symbol duration is increased proportionately, which reduces the effects of intersymbol interference (ISI) caused by the dispersive fading environment. Additional multipath rejection and resistance to intercarrier interference (ICI) is realized by cyclically extending each symbol on each subcarrier. Rather than using an empty guard space, a cyclic extension of the OFDM symbol is used to

¹⁰Packet duration = $[10(16 + 2)(80 + 1)(80 + 135)(8)(2/48)(80)] \times 100 \text{ ns} = 400 \mu s$.

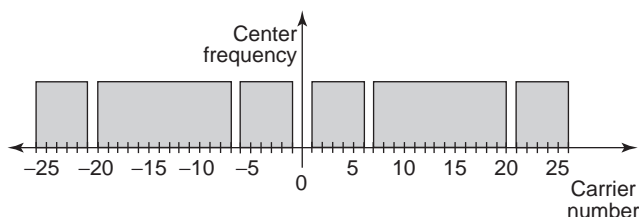


Figure 7. Structure of an Operating Channel.

ensure that delayed replicas of the OFDM symbol will always have an integer number of cycles within the FFT interval. This effectively converts the linear convolution of the channel to a circular one, as long as the cyclic prefix (CP) is longer than the impulse response of the channel. The penalty of using a CP is loss of signal energy proportional to the length of the CP. In order to avoid excessive bit errors on individual subcarriers that are in a deep fade, forward error control (FEC) is typically applied.

The ITS-WAVE physical layer organizes the spectrum into operating channels. Each 10-MHz channel is composed of 52 subcarriers. Four of the subcarriers are used as pilot carriers for monitoring path shifts and ICI, while the other 48 subcarriers are used to transmit data symbols. Subcarriers are spaced 156.25 kHz apart, giving a total bandwidth of 8.8 MHz. The composite waveform, consisting of all 52 subcarriers, is upconverted to one of the seven channels between 5.850 and 5.925 GHz. As shown in Fig. 7, channels are numbered from -26 to 26. Subcarrier 0 is not used for signal processing reasons, and pilot subcarriers are assigned to subcarriers -21, -7, 7, and 21. To avoid strong spectral lines in the Fourier transform, the pilot subcarriers transmit a fixed bit sequence as specified in the IEEE 802.11a using a conservative modulation technique. Table 1 compares the ITS-WAVE and the IEEE 802.11a parameters. Table 2 lists ITS-WAVE baseband modulation values.

3.2.1. Structure of the WAVE Physical Layer. The physical layer is structured as two sublayers: the physical-layer convergence procedure (PLCP) sublayer and the physical-medium-dependent (PMD) sublayer. The PLCP communicates to MAC via primitives through the physical-layer service access point (SAP); it prepares the PLCP protocol data unit (PPDU) shown in Fig. 8. The PPDU provides for asynchronous transfer of the MAC protocol data unit (MPDU) between stations. The PMD provides

Table 1. Comparison of 802.11a and ITS-WAVE Parameters

Parameter	802.11a	ITS-WAVE
Channel bandwidth (MHz)	20	10
Subcarrier spacing (kHz)	312.5	156.25
T_{FFT} (μs)	3.2	6.4
T_{GI} (ns)	800	1600
T_{SYM} (μs)	4	8
Channel symbol rate (Mpsps)	12	6
Minimum data rate (BPSK) (Mbps)	6	3.0
Maximum data rate (64-QAM) (Mbps)	54	27

Table 2. ITS-WAVE Baseband Modulation

Data Rate (Mbps)	Code Rate	Modulation	N_CBPS	N_DBPS
3	$\frac{1}{2}$	BPSK	48	24
4.5	$\frac{3}{4}$	BPSK	48	36
6	$\frac{1}{2}$	QPSK	96	48
9	$\frac{3}{4}$	QPSK	96	72
24	$\frac{1}{2}$	16-QAM	192	96
18	$\frac{3}{4}$	16-QAM	192	144
24	$\frac{3}{5}$	64-QAM	288	192
27	$\frac{3}{4}$	64-QAM	288	216

actual transmission and reception of the physical layer entities via the wireless medium, interfaces directly to the medium, and provides modulation and demodulation of the transmission frame.

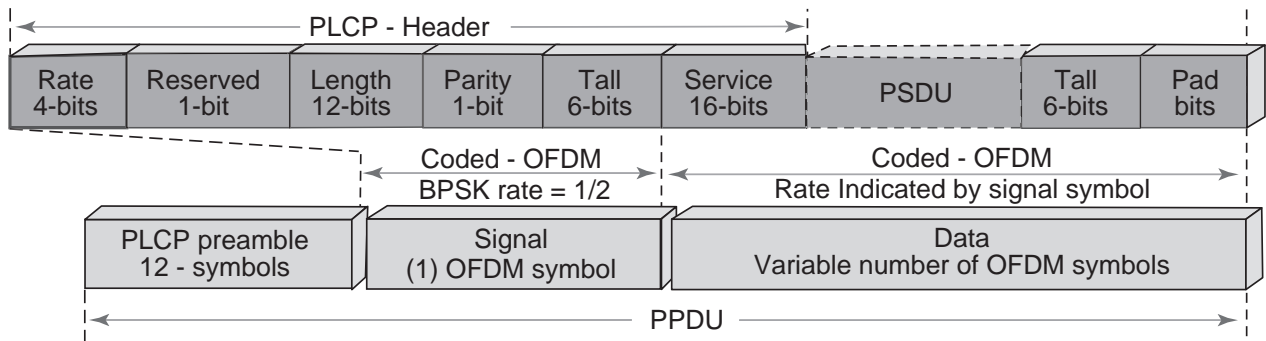
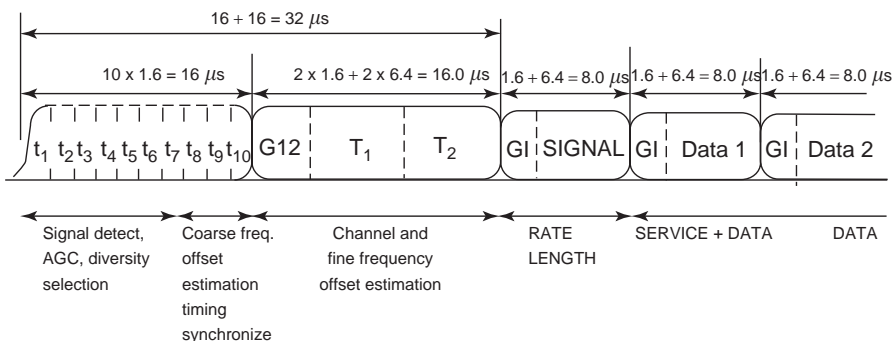
3.2.2. Roles of Preamble, Training Sequences, and Pilots. The ITS-WAVE specifies a preamble at the start of every packet as shown in Fig. 9.

The PLCP preamble consists of 10 short training symbols, each of which is $1.6\ \mu\text{s}$, followed by two long training symbols, each of which is $6.4\ \mu\text{s}$ including a $3.2\text{-}\mu\text{s}$ prefix that precedes the long training symbol. The long training sequence contains a guard interval, T_{GI2} , and two long training symbols, each $6.4\ \mu\text{s}$ in duration. The short symbols are used by the receiver for synchronization [signal detection, AGC (automatic gain control), diversity selection, frequency offset estimation, and timing synchronization]. The long symbols are used to fine-tune the frequency

offset and channel estimates. This training sequence is transmitted over all 52 subcarriers and is QPSK-modulated. In terms of algorithmic complexity, carrier frequency offset and timing recovery are by far the most difficult to determine. The phase-locked-loop (PLL) on the radio subsystem is responsible only for maintaining the 5-ppm voltage-controlled oscillator (VCO) requirement. Digital signal processing is used, independent of the VCO, to remove the carrier frequency offset. It is important to note that once the carrier frequency offset is determined by the digital baseband hardware, there is no time to provide a feedback signal to the WAVE radio's VCO since a PLL network will take too long to eliminate the offset. The training sequences are followed by the SIGNAL symbol, which is a single BPSK-modulated OFDM data symbol containing information about the packet such as data rate.

After preamble transmission, any common frequency offset is tracked via the four pilot subcarriers as shown in Fig. 10. It is not necessary to use pilots to estimate the channel as long as the channel remains fairly stationary over the duration of a single packet. The four pilot signals facilitate coherent detection throughout the duration of the packet. The remaining subcarriers carry the data body of the packet. The pilot spacing is selected to be less than the coherent bandwidth of the channel, as explained later.

3.2.3. ITS-WAVE Performance Issues. The performance of an OFDM receiver is affected by several factors, most of which fall into the categories of hardware limitations and channel impairments. Hardware limitations,

**Figure 8.** PPDU frame.**Figure 9.** ITS-WAVE PLCP structure.

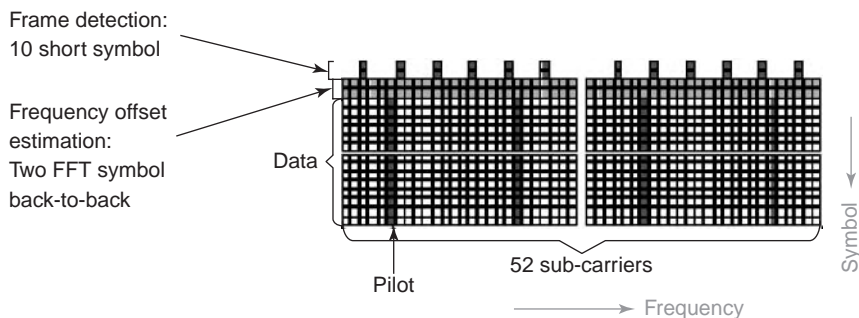


Figure 10. Pilot structure. (This figure is available in full color at <http://www.mrw.interscience.wiley.com/erfme>.)

particularly clock accuracy and oscillator stability, affect the synchronization accuracy of the receiver. The channel impairments discussed in Section 3.1 include “delay spread” and “Doppler spread,” which result in frequency-selective fading and time-selective fading, respectively.

OFDM is extremely sensitive to receiver synchronization imperfections, which can cause degradation of system throughput and performance. The overlap between sub-carriers leads to a system that is extremely sensitive to imperfections in carrier frequency synchronization. Also, multiplexing symbols onto multiple subcarriers results in a system that is extremely sensitive to imperfections in timing synchronization. This requires that the receiver architecture be structured to correct for frequency, timing, and sampling. Figure 11 is a simplified block diagram [1] depicting the major processing modules associated with the ITS-WAVE physical layer.

3.2.3.1. Synchronization. Synchronization is a big hurdle in OFDM systems. The ITS-WAVE physical layer uses

the same synchronization scheme as in the IEEE 802.11a; it usually consists of three processes:

1. Frame detection
2. Carrier frequency offset estimation and correction
3. Sampling error correction

Frame detection is used to determine the symbol boundary so that correct samples of the symbol frame can be taken. The first 10 short symbols are identical and are used for frame detection. The received signal is correlated with the known short-symbol waveform that produces correlation peaks. The received signal is also correlated with itself with a delay of one short symbol, which creates a plateau for the length of 10 short symbols. If the correlation peaks are within the plateau, the last peak is used as the position from where the start of the next symbol is determined.

Frequency offset estimation uses the long training symbols, which are two FFT symbols back-to-back. The

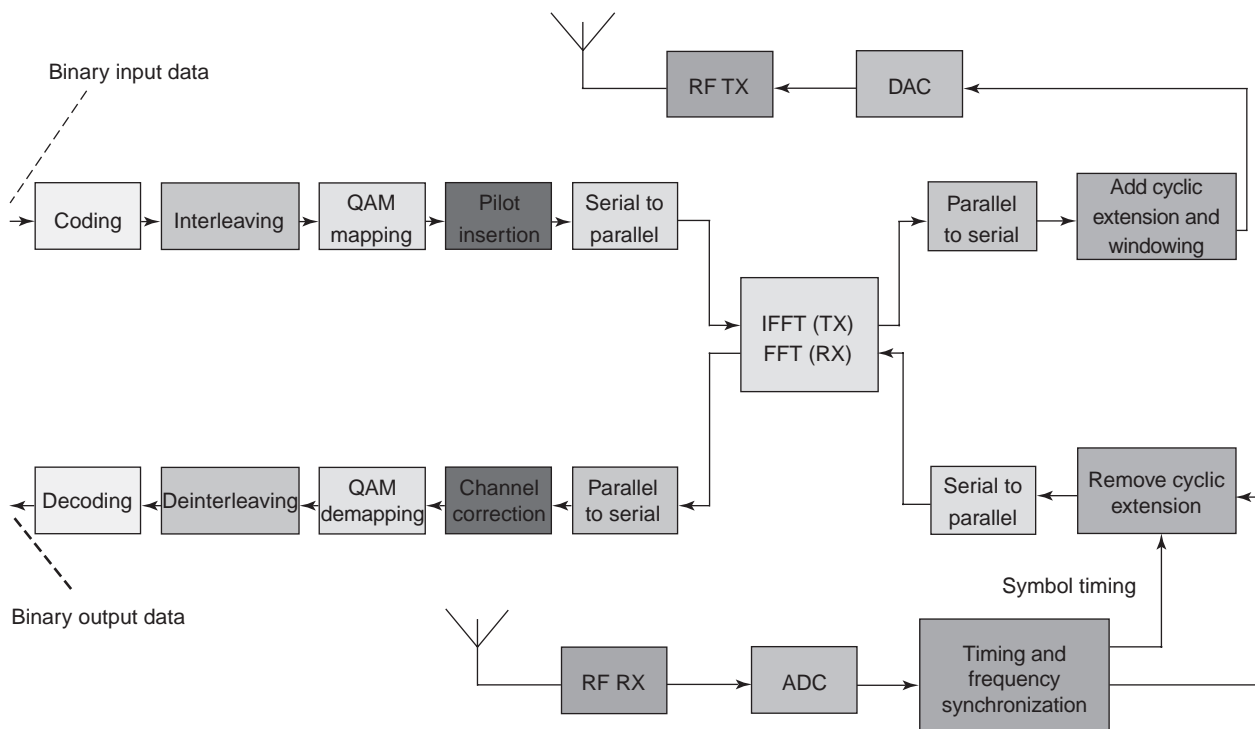


Figure 11. Basic OFDM block diagram.

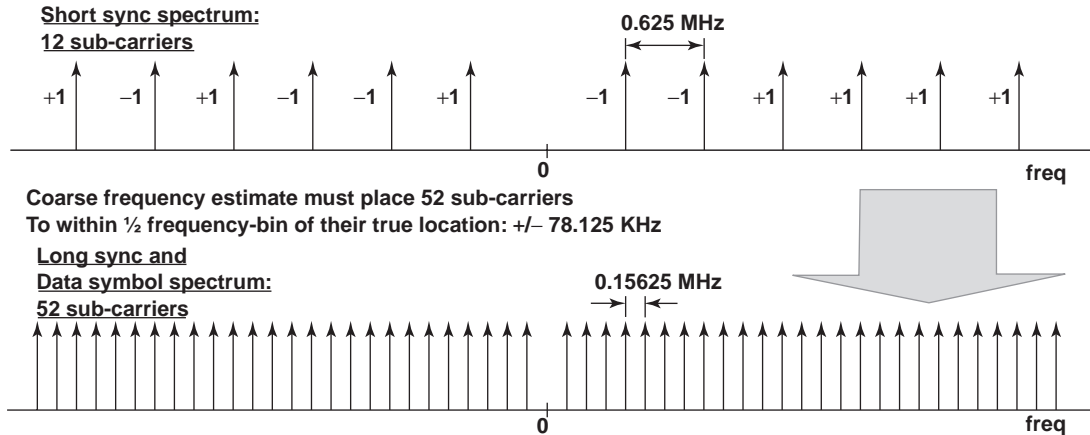


Figure 12. Carrier frequency offset.

corresponding chips of the two FFT symbols are then correlated to estimate the frequency offset. Channel estimation uses the same two OFDM symbols as the frequency offset estimation. Once the frame start is detected, frequency offset is estimated and signal samples are compensated, the two long symbols are transformed into frequency domain by FFT. After performing FFT on the preambles, the frequency-domain values are compared with the known preamble values to determine the channel response.

3.2.3.2. Carrier Frequency Offset. The ITS-WAVE (like the 802.11a) specifies that the carrier frequency and symbol clock be derived off the same oscillator. This allows the receiver to compute symbol clock drift directly from the carrier frequency offset (e.g., ppm error). Frequency synchronization must be applied before the FFT. Without a carrier frequency offset, the peak of any subcarrier corresponds to the zero crossings of all other subcarriers. When there is a random frequency offset, there is no longer an integer number of cycles over T_{FFT} , resulting in ICI. The degradation in SNR that occurs due to random frequency offset is approximated by D [1] in decibels

$$D \approx \frac{10}{3 \ln 10} (\pi \Delta F T_{\text{FFT}})^2 \frac{E_s}{N_0}$$

ΔF is the frequency offset and W ($= 1/T_{\text{FFT}}$) is the bandwidth of the composite OFDM waveform (subcarrier spacing). In essence, any carrier frequency offset results in a shift of the received signal in the frequency domain. This frequency error results in energy spillover between subcarriers, resulting in loss of their mutual orthogonality. The approximation states that the degradation increases with the square of normalized frequency offset. The major tradeoffs encountered when selecting an appropriate carrier frequency offset correction algorithm include speed, accuracy, and performance under noisy conditions.

Short training symbols can recognize offsets as high as 312.5 kHz [$\frac{1}{2} \times (1/1.6 \mu\text{s})$]. However, their short duration results in reduced accuracy since they produce only 16-point FFT samples per symbol. Although there are 10

short training symbols, 5 or 6 are consumed during RSSI, AGC, and timing recovery. Long training symbols provide a much more accurate estimate of the frequency offset since they produce 4 times as many FFT points compared to the short training symbol. However, their long extent limits the discernable frequency offset to 78 kHz [$\frac{1}{2} \times (1/6.4 \mu\text{s})$] as shown in Fig. 12. Noise imparts variance on the final offset estimate, thereby mitigating its accuracy.

3.2.3.3. Symbol Timing. Errors in symbol timing synchronization manifest as ISI and nonuniform phase shift to the constellation points. Both of these effects naturally lead to degradation of bit error rate (BER). The fast Fourier transform (FFT) demodulation process accumulates over exactly one 6.4- μs OFDM interval. If the start of the symbol time is not accurately established, the FFT demodulation process will operate on two adjacent symbols leading to ISI as shown in Fig. 13. Coarse synchronization can resolve to within half the sampling period and remove ISI. However, the residual sampling time offsets must be identified, or a nonuniform phase shift will be imparted to the constellation points.

The 6.4- μs FFT window is divided up into 64 time instants separated by 100 ns. Each point of the FFT is computed at a rate of 10 Msps (megasamples, i.e., 10,000 samples, per second), which corresponds to 64 discrete frequency-domain samples of the composite 6.4- μs symbol. Since these 64 samples are 100 ns apart [$T_s = 100 \text{ ns}$], the

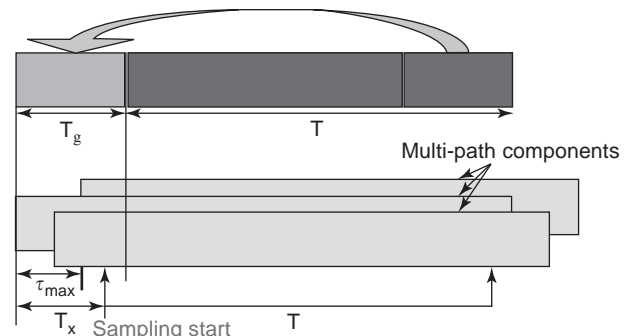


Figure 13. ISI and sampling-time offset. (This figure is available in full color at <http://www.mrw.interscience.wiley.com/erfme>.)

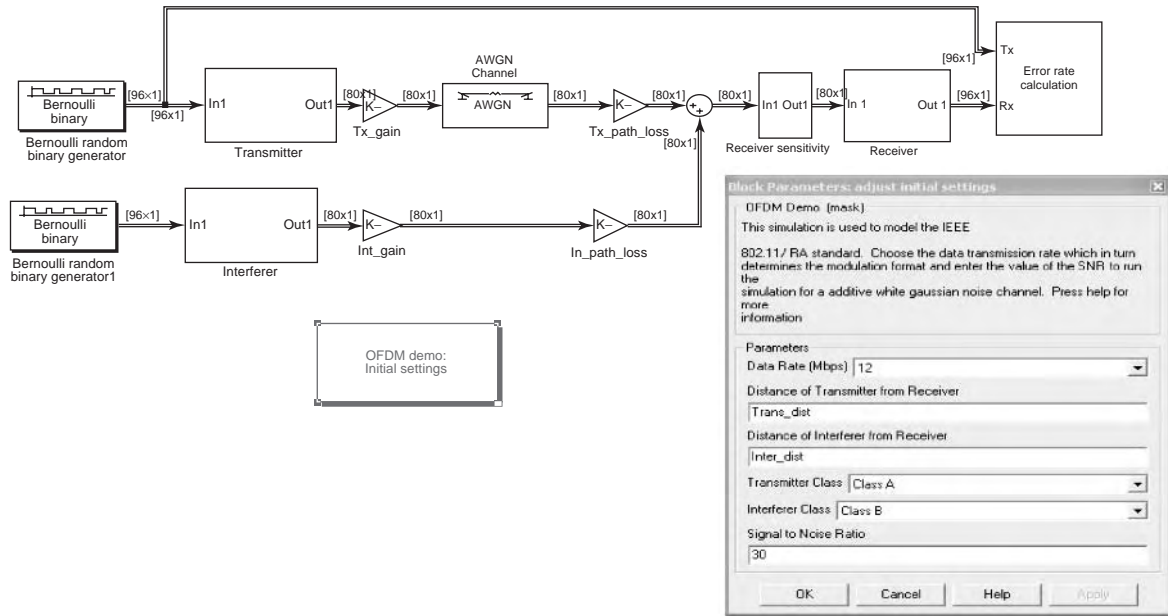


Figure 14. Enhanced simulation model. (This figure is available in full color at <http://www.mrw.interscience.wiley.com/erfme>.)

range of the maximum detectable sampling offset ranges from -50 to $+50$ ns. This sampling time offset manifests itself in the frequency domain as a phase shift, which is proportional to the subcarrier frequency. Subcarriers at the high end of the frequency range are affected disproportionately relative to those subcarriers at the low end. The effect of this phase shift on BER can be devastating, as symbols that map to subcarriers at the edges will experience a phase shift that rotates the constellation point out of its reliable detection region.

Sampling frequency offset does not negatively impact performance on a “symbol per symbol” basis. However, it can have harmful effects over large numbers of symbols. The ITS-WAVE proposal calls out a 5 ppm static center frequency offset from the VCO for analog-to-digital/digital-to-analog clocks and carrier VCOs. At 10 MHz, a 5 ppm figure corresponds to a 50 Hz offset, which means that one of the clocks is toggling 50 Hz faster than the other. In the period of one 10-MHz clock (100 ns), one clock will advance past the other by 0.5 psc. If we take into account the number of samples per symbol and the number of symbols in a large packet, we find that over a time span of 50 symbols the sampling instants for symbols will have shifted by 2 ns.¹¹ This timeshift will manifest itself in the frequency domain as a phase shift proportional to the subcarrier frequency. This is clearly a receiver steady-state issue, and can’t be detected during training. During receiver tracking, this offset is taken care of by processing the pilots and feeding back corrections to an interpolator.

3.2.4. ITS-WAVE Adjacent-channel and Cochannel Interference. Effects of adjacent-channel and cochannel interference has been studied using simulation [11], a Simulink

model developed to evaluate these types of interference as shown in Fig. 14.

In the model shown in Fig. 14 we consider the type of the device and apply the corresponding spectrum mask as

Table 3. ITS-WAVE Device Class Spectral Mask

Device Class	± 4.5 MHz Offset	± 5 MHz Offset	± 5.5 MHz Offset	± 10 MHz Offset	± 15 MHz Offset
A	0	-10	-20	-28	-40
B	0	-16	-20	-28	-40
C	0	-26	-32	-40	-50
D	0	-35	-45	-55	-65

Table 4. ITS-WAVE Classes and Transmit Power Levels

Device Class	Maximum Device Output Power (dBm)
A	0
B	10
C	20
D	28.8

Table 5. ITS-WAVE Receiver Sensitivity

Data Rate (Mbps)	Minimum Sensitivity (dBm)
3	-85
4.5	-84
6	-82
9	-80
12	-77
18	-70
24	-69
27	-67

¹¹0.5 psc/sample \times 80 samples/symbol \times 50 symbols = 2 ns.

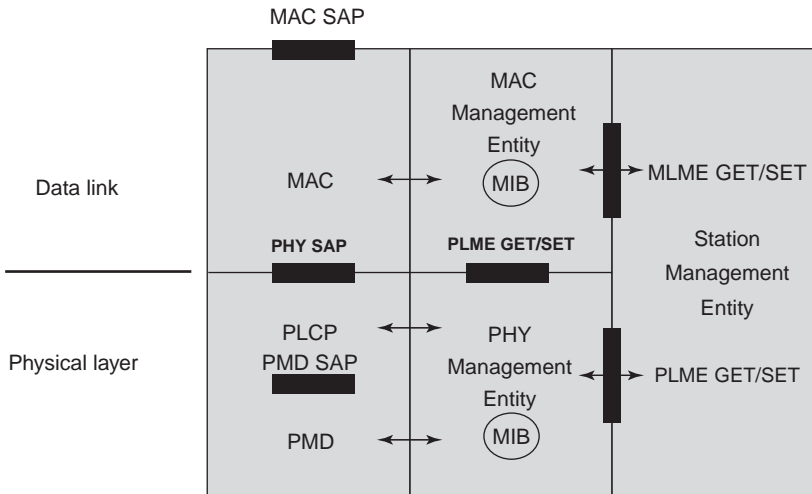


Figure 15. GET and SET operations.

given in Table 3. The model also considers the fact that the devices operate at the maximum power output according to Table 4, which reflects the increase of the out-of-band attenuation for higher power devices. The model takes into account the minimum receiver sensitivity as per Table 5. The channel path loss is modeled according to the two-segment model with a breakpoint of 164 m as given by

$$L(d)_{\text{dB}} = 20 \log(d) + 43.05 \quad (d < 164 \text{ m})$$

$$L(d)_{\text{dB}} = 40 \log(d) - 1.263 \quad (d \geq 164 \text{ m})$$

This is typical for models that use ray tracing [12], where the path loss is generally proportional to $1/d^2$ before the breakpoint and $1/d^4$ after the breakpoint. The breakpoint represents the point at which the first Fresnel zone touches the ground, wherein the reflected ray off the surface of the ground cancels some of the power of the direct ray. The breakpoint is approximated by $d_{\text{bp}} \cong (4h_t h_r)/\lambda$, where h_t is the transmit antenna height and h_r is the receive antenna height.

3.3. The ITS-WAVE MAC Layer

Generally, for reliable system operation, the MAC must be properly designed to match the physical layer so that its impairments do not cause undue degradation at higher layers. The IEEE 802.11 MAC is a very complex protocol; it took over 10 years of development with the support of dozens of corporations developing products for the WLAN market. The ITS-WAVE Study Group intends to use the IEEE 802.11a MAC without modification, except for changes to the management information base (MIB). The management information specific to each layer is represented as a MIB for that layer. The generic model across the management SAPs is to allow the SAP user entity to either GET the value of a MIB attribute, or to SET the value of a MIB attribute. The invocation of a SET.request primitive may require that the layer entity perform

certain defined actions. Figure 15 depicts these generic primitives.

4. CHALLENGES AND FUTURE DEVELOPMENTS

4.1. Validation, Verification, and Testing

Developing the ITS-WAVE family of standards is a complex task, and the fact that these standards will be supporting safety applications makes validation, verification, testing, and system integration critical steps for developing this market. The USDOT has begun this process through funding the Vehicle Safety Communications Consortium (VSCC) and other industry participants. At the Caltrans Testbed Center For Interoperability (TCFI), we have developed lab and field infrastructure [11] in order to support these activities as the standards mature. Figure 16 shows data collected over the air using Agilent's equipment (VSG, VXI, and PSA) at TCFI. In addition, we have demonstrated passing data between the test equipment and the simulation tool (Simulink). Validation of the MAC layer will be a special challenge; currently we are experimenting with Telelogic's TAU G2, which supports both the Specifications and Description Language (SDL) and the Unified Modeling Language (UML).¹² SDL is an ITU formal language that was used to describe the original IEEE 802.11 MAC specifications.

4.2. System Integration: The Santa Barbara Radio Access Network

Beyond the development of the ITS-WAVE family of standards and the availability of telematics products, the development of the ITS wireless market will require reliable roadside infrastructure [13]. This infrastructure requires feeder and backhaul networks that may use both fixed wireless and landline networks. Figure 17 shows one such infrastructure that has passed the planning stage: Santa Barbara's Radio Access Network (RAN) [14]. The RF planning of 28 sites has been completed, and some sites are

¹²Further information is available at <http://www.telelogic.com>.

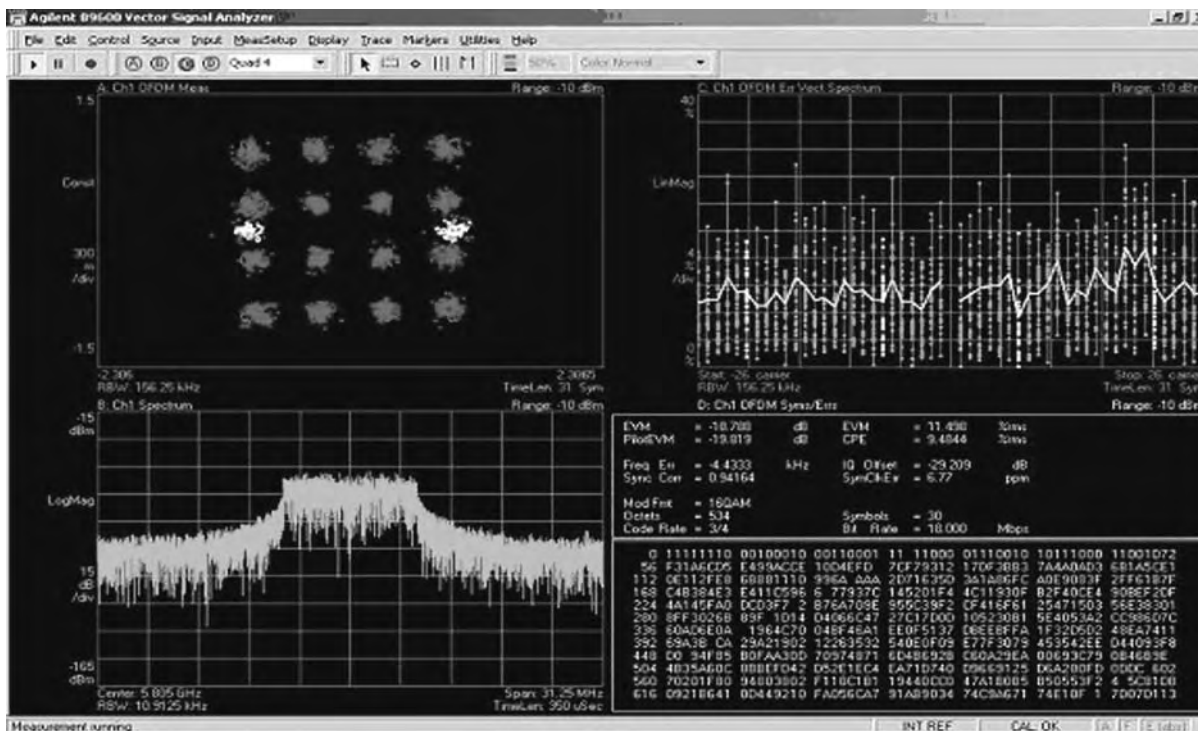


Figure 16. Over-the-air ITS-WAVE signal—18 Mbps. (This figure is available in full color at <http://www.mrw.interscience.wiley.com/erfme>.)

being installed through the collaboration of Caltrans, local governments, and the university (UCSB). SB-RAN is currently part of a new proposal to develop a public safety testbed, which addresses wireless infrastructure interoperability (WII) issues for both the “first responder” (4.9 GHz) and the ITS (5.9-GHz) bands.

4.3. Observations and Future Developments

While WAVE standards efforts are progressing within the IEEE, there are remaining questions yet to be answered regarding many issues such as the following:

- Security architecture (P1556 and 802.11i)
- Multiple-channel devices and the current “concept of operations”
- Interference mitigation in a real environment

- MAC extension and its relation to IEEE 802.11e/h
- “Pilot structure” and its impact on dedicated public safety channels
- Fast handover
- IP-based internetworking
- Wireless infrastructure interoperability

As we move from the descriptive phase of the standard development to the performance and testing phases, the need for better protocol development tools will continue to be a challenge.

Roadside system integration issues are rarely addressed in the wireless ITS community. Issues such as cost-effective feeder and backhaul networks to support the wireless infrastructure are considered implementation issues and are outside the scope of the national efforts.

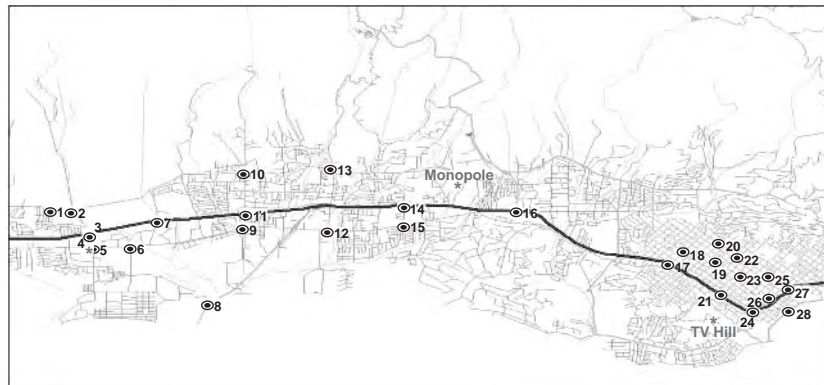


Figure 17. Santa Barbara’s RAN site locations. (This figure is available in full color at <http://www.mrw.interscience.wiley.com/erfme>.)

Presently, the ITS industry is addressing market-enabling applications such as vehicle safety and toll applications. The more general ITS “public safety” applications such as work-zone safety (WZS), public protection disaster relief (PPDR), and homeland security, are assumed to be the role of public agencies.

The potential gains from considering advanced technologies such as software-defined radios (SDR), and multiple-input/multiple-output (MIMO) systems have not yet been investigated for wireless ITS applications.

5. SUMMARY AND CONCLUSION

This article examined the emerging ITS-WAVE family of standards, with emphasis on the mobile vehicle environment and the lower-layer standard. Our findings confirmed the validity of adopting the IEEE 802.11a as the basis for the broadband wireless ITS standard. The OFDM Forum proposal, originally submitted to the ASTM for wireless road access, is now well understood and it has been accepted by the ITS industry.

The physical-layer, proposal is ready for standardization with the exception of the new pilot structure issue. Long-range dedicated public safety cannot be realized without resolving this issue. The data-link layer proves to be more challenging, as we integrate other IEEE standards (e.g., 802.11e/h/i).

As new devices and systems are introduced, there will be a need for demonstration projects, testing standards, compliance certification, and performance benchmarks.

Acronyms

AGC	Automatic gain control
ASTM	American Society for Testing and Materials
BER	Bit error rate
BPSK	Binary phase shift keying
CALM	Communications air interface for long and medium range
Caltrans	California Department of Transportation
CFR	Code of Federal Regulations
CP	Cyclic prefix
CSMA/CA	Multiple access with collision avoidance
DFT	Discrete Fourier transform
DoT	Department of Transportation
DSRC	Dedicated short-range communications
FCC	Federal Communications Commission
FFT	Fast Fourier transform
ICI	Intercarrier interference
IEEE	Institute of Electrical and Electronics Engineers
IETF	Internet Engineering Task Force
ISI	Intersymbol interference
ISO	International Standards Organization
ISTEA	Intermodal Surface Transportation Efficiency Act of 1991
ITS	Intelligent Transportation Systems
ITSA	Intelligent Transportation Society of America
ITS-RS	ITS Radio Services

ITU	International Telecommunication Union
MAC	Medium access control
MCM	Multicarrier modulation
MIB	Management information base
MME	MAC management entity
MPDU	MAC protocol data unit
Msp/s	Megasymbol per second
OBUs	Onboard units
OFDM	Orthogonal frequency-division multiplexing
OMG	Object Management Group
PAPR	Peak-to-average power ratio
PER	Packet error rate
PHY	Physical layer (OSI)
PLCP	Physical-layer convergence procedure
PMD	Physical-medium-dependent
PPDR	Public protection disaster relief
PPDU	PLCP protocol data unit
PSA	Power spectral analyzer
QAM	Quadrature amplitude modulation
QPSK	Quadrature phase shift keying
RAN	Radio access network
RSSI	Received signal strength indicator
RSUs	Roadside units
SAP	Service access point
SDL	Specification(s) and Description Language
SDO	Standards development organization
SNMP	Simple Network Management Protocol
SNR	Signal-to-noise ratio
TCP/IP	Transmissions Control Protocol/Internet Protocol
UCSB	University of California, Santa Barbara
UML	Unified Modeling Language
UNII	Unlicensed national information infrastructure
VSA	Vector spectrum analyzer
VSCC	Vehicle Safety Communications Consortium
WAVE	Wireless Access in Vehicular Environments
WG	Work Group 802.11—WLAN standards
802.11	
WII	Wireless infrastructure interoperability
WLAN	Wireless local-area network
WZS	Work-zone safety

BIBLIOGRAPHY

1. R. Van Nee and R. Prasad, *OFDM for Wireless Multimedia Communications*, Artech House, Boston, 2000.
2. R. Gerges, *Communications Technologies for IVHS*, UCLA, 1994.
3. A. Polydoros, R. Gerges et al, Integrated layer packet radio study for AHS, *Proc. 3rd IEEE Mediterranean Symp. New Directions in Control and Automation*, Cypress, July 1995.
4. R. Gerges, Wireless communications and spectrum requirements for ITS, Paper presented at IEEE Vehicular Technology Conf. Ottawa, May 1998.
5. IEEE 802.11 [full title: *Information Technology—Telecommunications and Information Exchange between Systems—Local and Metropolitan Area Networks—Specific Requirements—*

- Part 11: *Wireless LAN Medium Access Control (MAC) and Physical Layer (PHY) Specifications*], ANSI/IEEE Std 802.11, 1999 edition.
6. IEEE 802.11a (full title: *Supplement to IEEE Standard for Information Technology—Telecommunications and information exchange between systems—Local and Metropolitan Area Networks—Specific Requirements—Part 11: Wireless LAN Medium Access Control (MAC) and Physical Layer (PHY) Specifications, High-Speed Physical Layer in the 5 GHz Band*), IEEE Std 802.11a-1999.
 7. ASTM E2213-02, *Standard Specification for Telecommunications and Information Exchange between Roadside and Vehicle Systems—5 GHz Band Dedicated Short Range Communications (DSRC) Medium Access Control (MAC) and Physical Layer (PHY)*.
 8. T. S. Rappaport, *Wireless Communications Principles and Practice*, Prentice-Hall, Englewood Cliffs, NJ, 2002.
 9. A. Bohdanowicz, *Wide Band Indoor and Outdoor Radio Channel Measurements at 17 GHz*, Uicom Technical Report/2000/2, Feb. 2000.
 10. H. Steendam, and M. Moeneclaey, Analysis and optimization of the performance of OFDM on frequency-selective times-selective fading channels, *IEEE Trans. Commun.* (Dec. 1999).
 11. R. Gerges, *Investigation of Broadband ITS-Radio Services at 5.9 GHz*, Final Report to Battelle—IPAS Program, UCSB-TCFI, Nov. 1, 2003.
 12. *DSRC Physical Channel Characterization*, Interim Report to Caltrans TCFI, TechnoCom Corp., April 2000.
 13. T. Maehata et al., *DSRC Using OFDM for Roadside-Vehicle Communication System*, Radio Communications Technology Group, Sumitomo Electric Industries.
 14. R. Gerges, UCSB-TCFI 65V250 A3 Task Order 301, Interim Report, 2000.

KLYSTRON

PAUL J. TALLERICO
Los Alamos National Laboratory

The klystron is a very successful high-power microwave amplifier since it has good gain, over 40 dB; good efficiency, above 50%; good life expectancy, above 30,000 h, output power up to 150 MW pulsed for several microseconds, or 1.3 MW CW, and reasonable bandwidth of 5% to 15% (measured at rates slower than the response times of the cavities), but the instantaneous bandwidth is generally under a few percent. The klystron can be designed to operate with a center frequency between 200 MHz and 40 GHz, but the bandwidth of a single klystron is usually small. The lower frequency limit occurs only because of the impracticably large size of the klystron at large wavelengths, and the upper frequency limit arises from the difficulties in scaling the device with wavelength. The optimum frequency range for the high-power (above 100 kW) klystron is from 300 MHz to perhaps 20 GHz, but a few kilowatts of peak power can still be obtained up to 100 GHz. Special versions of the klystron—the extended-interaction klystron and the hybrid klystron–traveling-wave amplifier—can provide several kilowatts power over 100 GHz.

1. OPERATION PRINCIPLE

The klystron is a vacuum electron device for transforming DC energy into RF energy, and it may be either an oscillator or an amplifier. In the past, small reflex klystron oscillators were used as local oscillators in microwave receivers, but these oscillators are not used in modern equipment. Therefore the amplifier klystron is emphasized in this article. The klystron was invented in 1938 by the Varian brothers [1,2] to utilize the finite transit time of electrons in motion (which is a severe impediment to the operation of most electron devices at microwave frequencies) and thereby obtain previously impossible levels of microwave power. The klystron is called a *linear beam device*, since the fields that influence the electron motion are predominantly in the same direction as the electron motion. As the frequency is raised for all electron devices, the transit time of the electrons eventually causes low efficiency and poor operation. The basic idea is to start with an unbunched, moderate velocity electron beam in a magnetic system such that the beam translates along an axis with minimal radial spreading. If two RF cavities are also along this axis, the first one can be driven by an external RF source (the input cavity), and the second can serve as a source (the output cavity) of microwave power. This power is obtained from the kinetic energy of the electron beam, which comes from the DC power supply. Figure 1 shows a simplified drawing of a four-cavity klystron. If we arrange

the various cavity voltages and phases such that the beam is converted in tight bunches that cross the output gap periodically, we would expect to convert a significant portion of the electron-beam energy into microwaves. Tuning the intermediate cavities to frequencies above the operating frequency makes the induced voltage and phase correct to maximize the bunching.

The principle of operation is called *velocity modulation*. The electrons are emitted in a continuous stream at the cathode, and accelerated to a moderate velocity by the DC fields in the electron gun. We want the electrons to arrive at the output gap in short bunches, so these bunches can be slowed down by the fields in the output cavity. In this manner, energy from the power supply is converted into microwave energy in the output cavity. In a gridded vacuum tube, the control grid is used to convert a continuous stream of electrons from a cathode into bunches, but the grid only works well when the time the electrons take to move from the cathode to the grid is small compared to an RF period. The input cavity in the klystron has an RF voltage that makes a field that oscillates with time along the axis. The klystron is designed so that the first electrons in each period are slowed down, and the last electrons in each period are accelerated, while the electrons near the center of the period are left alone (the E field is a cosine wave, in this example). As the initially uniform density beam drifts down the axis, the faster electrons at the rear catch up to the slower electrons from the front, and, if the dimensions are correct, the fast, slow, and average velocity electrons arrive at the output gap center at the same time. Of course, with a continuum of electrons in the bunches cavity, and in the presence of the unavoidable electron repulsion (space charge) effects, the bunched beam is only more temporally concentrated in the output cavity, and the electrons remain distributed in time. Thus, the beam is density modulated at the output gap, and a careful analysis (see below) shows that the velocity and density modulation are cosine and sine waves, respectively.

Several of the reasons for the klystron's importance in RF power generation may be seen from Fig. 1. The major

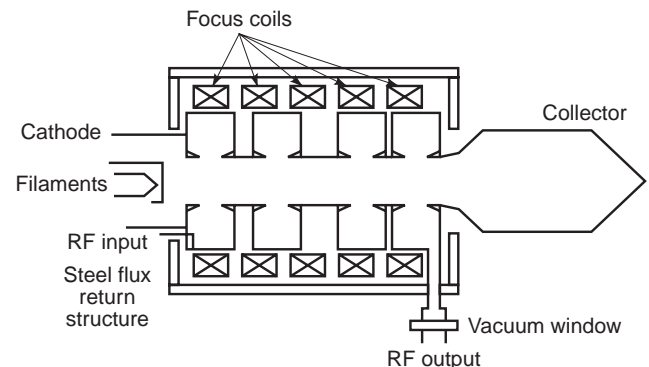


Figure 1. Simplified sketch of a four-cavity klystron. The klystron body is at ground potential, and a high voltage, negative polarity power supply is attached to the cathode.

advantage is that the klystron is naturally made of three main components: the electron gun (on the left), the RF interaction section, and the collector, on the right. Each component has only a simple function, and can be designed almost independently of the other parts. Thus, there are essentially no RF fields in the electron-gun region, so it is designed to make a good, laminar, and uniform electron beam. Similarly, the RF section is composed of several resonant cavities that are designed to optimize the gain and efficiency of power conversion. Significant heat is developed in the collector area, and this can be designed to safely dissipate large amounts of heat, since there are no DC and only minimal RF fields in this region. When power is expensive, the heat in the collector may be reduced by designing a multiple-stage depressed collector, so that the fields in the collector sort the electrons in the spent beam, and the beam is collected at several potentials, thereby reducing the heat produced and the power consumed. There are mechanical problems introduced by the complexity of the multiple-stage depressed collector, and the power supply becomes more complicated, so this technique is used only where power is expensive, such as satellite and airborne applications. Depressed collectors are also used in UHF television transmitters, where the electrical power costs can be a significant portion of the annual operating costs, since these transmitters operate for 24 h per day with peak output powers at or above 50 kW.

2. APPLICATIONS OF THE KLYSTRON

The major uses of the klystron are in UHF television transmitters, particle accelerators, communication system uplinks, and radar. There are several thousand UHF television transmitters in the world, and a majority of the higher-power ones, above 50 kW, use the klystron as the final amplifier. The more modern UHF television transmitters use either klystrones or depressed-collector klystrons to save energy. The latter are discussed subsequently. The most common particle accelerator is the electron linear accelerator, and about five thousand are used for tumor treatment and medical diagnoses in the world. About half of the newer, higher power medical accelerators are driven by klystrons, while the lower powered half are driven by magnetron oscillators. Particle accelerators for nuclear science are generally powered by klystrons, and a review is given in Ref. 3. Indeed, the modern, high-power klystron [4] was developed to power the Stanford Linear Accelerator, which is the world's highest-energy electron accelerator. The development of the high-power klystron started at Stanford after World War II, and the power levels of pulsed klystrons were increased from 30 kW to over 50 MW over a few decades. The linear particle accelerators for nuclear physics are usually even more powerful than the medical accelerators, and klystrons are the most popular vacuum devices used for these applications. This is especially true for large, high-power accelerators. The largest linear electron accelerator is the Stanford Linear Accelerator, and it uses 320 of the 50 MW peak power klystrons at 2856 MHz and 3 μ s pulses at repetition rates

as high as 360 Hz. The highest powered proton linear accelerator is at the Los Alamos Neutron Science Center, where 44 of the 1.25-MW-peak klystrons operate at 805 MHz with 1 ms pulses at a 120 Hz repetition rate.

The role of the klystron in radar is diminishing, since the klystron is best suited for large, high-power transmitters. However, the air traffic control system use klystrons in airport radar, and klystrons are also used in weather radar. Thus, there are over 2000 radar klystrons in operation, but many radar applications now use many small amplifiers, whose phase can be controlled to electronically steer the radar beam. This combination can still give moderate to large output powers, and the steering can be done electronically, so it is very rapid.

Another market is the satellite uplink transmitters, whose numbers are about 7000. Most of these have klystron amplifiers, but some of the newer ones use traveling-wave amplifiers as their final amplifier. The traveling-wave amplifier has a greater bandwidth, and it can be smaller, so it is becoming the amplifier of choice for this application.

3. DESIGN METHODS

The design methods depend on the klystron component, corresponding to the labels in Fig. 1. Each section of the klystron may be designed almost independently of the other sections, which simplifies the design and optimization processes.

3.1. Electron Gun

The first section is the electron gun, and its design is a DC problem, complicated by large space charge fields. The cathode is space-charge-limited, so the emission follows a Child–Langmuir law, with the current proportional to the 1.5th power of the cathode to anode voltage, and the proportionality constant is called the perveance, P . Thus, the cathode current is given by the expression

$$I = PV_A^{3/2} \quad (1)$$

where V_A is the anode voltage. The modern electron gun was invented by J. R. Pierce [5], but his methods provide only a starting point for the design. A good electron gun has laminar (noncrossing) trajectories, and a relatively uniform cathode current density. The gun must also have the correct current at the design voltage, and the electric fields in the gun must be low enough so that sparking very rarely occurs. The peak and average current density at the cathode must be low enough so the cathode life is satisfactory. The detailed design of the electron gun is accomplished with Poisson equation solvers that solve Poisson's equation for the electric (and magnetic) static fields, and the Lorentz force equations with finite-element or finite difference methods. Three-dimensional computations are sometimes required to account for grids or other nonsymmetric features. Another constraint on the gun design is that the beam radius at the entrance to the RF interaction region must be small

relative to the operating wavelength. For good performance, the normalized radius of the beam $k_r b$ must be in the range of 0.5 to 1.0, where b is the beam radius at the entrance to the RF region, and the radial propagation constant is

$$k_r = \frac{\omega}{u_0 \gamma_0} \quad (2)$$

where ω is the radian frequency of operation, γ_0 is the relativistic mass ratio for the electron, and u_0 is the velocity of the electron beam corresponding to the average beam voltage V_0 . For low-beam currents, the average beam voltage is the anode voltage, but the space charge fields of the beam at higher currents reduce the beam's kinetic energy. The mass ratio is essentially unity for low beam voltages, and in general, is given by

$$\gamma_0 = 1 + \frac{\eta V_0}{c^2} \quad (3)$$

where c is the velocity of light and η is the magnitude of the electronic charge-to-mass ratio. If we assume that the charge density in the beam is constant, we can use Gauss' law to show that the voltage at the beam center V_c is

$$V_A - V_c = \frac{I}{2\pi\epsilon_0 u_0} \left(\frac{1}{2} - \ln(b/a) \right) \quad (4)$$

where a is the radius of the beam tunnel and ϵ_0 is the permittivity of free space.

The simplest klystron electron gun produces a solid cylindrical beam, with the cathode at a negative voltage and the anode at ground potential. This design is best for short-pulse applications, where the high-voltage pulse comes from a pulse transformer. An advantage of this design is that the gun is as simple as possible; it is a diode. This simplicity has two advantages: (1) the parts count is minimum, and this helps cost and reliability; and (2) the fields in the gun region can be minimized for any given peak output power with this design. The second type of electron gun has a modulating anode, and both types are shown in Fig. 2. This electron gun may be called a *triode type*, since there is now a second anode and a second insulator in the gun. In operation, voltage of the modulating anode controls the beam current. The modulating anode is a complication in the design, and it is used either for long-pulse applications for pulses above 0.5 ms (where the pulse transformer becomes very large), or for high-efficiency operation, where the beam current is adjusted to optimize the efficiency for a given operating cathode voltage and output power. The modulation anode becomes the anode of the gun, and the voltage between the modulating anode and the anode forms a lens that must be accounted for in the design. The modulating anode aperture is made thick enough so that when it is at the cathode potential, only negligible current flows in the klystron. The cathode is usually shaped to be a segment of a sphere for a solid beam, but it can have a conical shape to produce a hollow beam. This is the magnetron injection gun, and it also is shown in Fig. 2. Hollow-beam klystrons have some

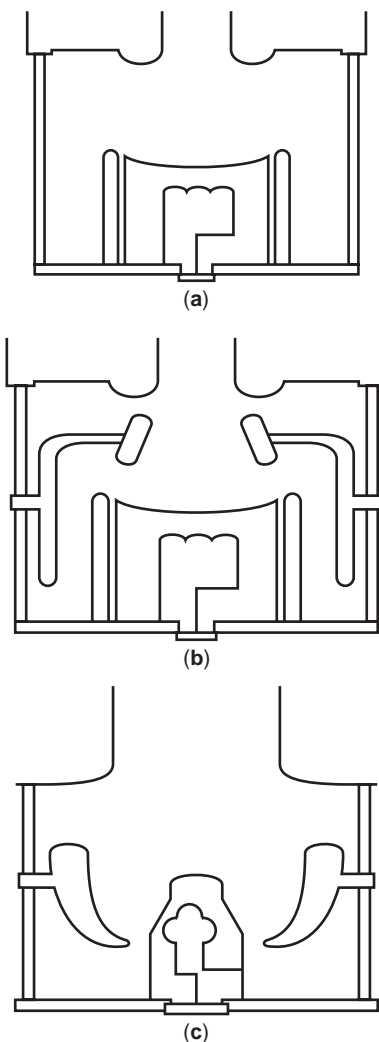


Figure 2. The three types of klystron electron guns: (a) the diode gun; (b) the modulating-anode gun; (c) the magnetron injection gun. The high-voltage insulators are shown shaded.

advantages, including higher perveance and potentially higher efficiency, but the magnetron injection gun can be noisy, since the electrons circulate around the cathode, and influence the emission.

3.2. RF Cavities

The RF cavities must be designed for a high R/Q ratio (which is a measure of the efficiency of the interaction compared to the stored energy in the cavity), good coupling to the beam, and the correct resonant and harmonic frequencies. The input and output cavities are generally tuned close to the operating frequency, and the remaining cavities are tuned for the desired bandwidth and efficiency, as determined either by experiment, or by specially written, nonlinear, large-signal klystron software. Most of the intermediate cavities are tuned above the operation frequency to maximize efficiency, and the detuning increases towards the output cavity. The cavity shape is called reentrant, since this shape puts most of the electric fields in the beam region. Typical reentrant cavity shapes

are shown in Fig. 1. The cavities are each designed for a particular frequency, but mechanical tuners are usually included to compensate for manufacturing tolerances. Some klystrons, especially those for UHF TV transmitters, are designed so the tuners may be adjusted by the final customer, to change the center frequency (TV channel) on demand. Another subtlety of the cavity design is that it is unwise to make the geometry too similar from cavity to cavity. If the cavities all have the same geometry, the higher order cavity modes are likely to overlap, and this increases the probability of exciting significant harmonic voltages with the harmonics of the beam current. The highest R/Q ratio is when the gap is centered in the cavity, but the gaps are often offset by varying amounts, which slightly reduces the R/Q ratio, but that also significantly alters the harmonic frequencies. Remember that the designer is trying to achieve perfect delta-function bunches of current, and thus the amplitude of all the harmonic currents may be up to twice the DC component. Thus, low impedance at the first few harmonics of the beam current is another requirement on the cavities. Low impedance at the higher harmonics is not important, since the coupling of the cavity fields to the beam is generally small for high harmonics.

3.3. The Magnetic Circuit

The magnetic circuit is designed to keep the beam confined. Most klystrons have an axial magnetic focusing field (supplied by either a solenoid or permanent magnets) that counteracts the radial repulsive force on the electron beam. A focus solenoid is shown schematically in Fig. 1. The focus coils and their return circuits can be heavy and rather expensive in a pulsed klystron, and the power dissipated in the focus coils can be several kilowatts. Research is under way to make short-pulsed, high-power klystrons with permanent magnetic focusing, to eliminate this loss of energy and the weight and expense of the focus coils and their power supplies. Permanent magnet systems are also used with either a single magnet or periodic focusing, and the reader should see TRAVELING-WAVE TUBE for more information on periodic focusing systems. Permanent-magnet focusing is used on several commercial medium power (up to 5 kW) klystrons in the 1.5–3 GHz frequency range.

At the gun end, the magnetic field is designed to be parallel with the electron trajectories, so the trajectories are unchanged by the field. The magnetic field balances the space charge forces, and the magnetic field required by the unbunched beam is given by the relation

$$\omega_c^2 = \frac{2\omega_p^2}{\gamma_0(1-K)} \quad (5)$$

where $\omega_c = \eta B_{z0}$ is the cyclotron frequency, B_{z0} is the axial magnetic field at the entrance to the RF interaction region, where the beam has a minimum diameter

$$\omega_p = \sqrt{\frac{\eta\rho_0}{\epsilon_0}}$$

is the free-space plasma frequency, ρ_0 is the space charge density at the beam minimum, and K is the square of the ratio of the magnetic flux at the cathode to the magnetic flux at the beam minimum. The range of K is from 0 to 1, with $K=0$ being called the Brillouin flow case, after its inventor, and K approaching 1 is the confined flow case, where the electrons follow lines of constant magnetic flux, and no radial motion is possible. The higher values of K make the beam more resistant to radial spreading, and are used at high frequencies. The Brillouin case is difficult to achieve, since flux lines from the focus magnet tend to link the cathode, but it can be achieved approximately with a bucking coil whose excitation is adjusted to null the magnetic field at the cathode surface. As the beam bunches, the radial space charge forces grow, and the axial magnetic field increases by a factor of ~ 2 at its peak near the center of the output gap. The magnetic field then drops quickly to cause the beam to rapidly expand into the collector. With careful design, including use of Poisson equation solvers, all these requirements can be realized with a single set of coils and magnetic pole pieces connected with a single power supply.

It is also possible to transport the electron beam through the klystron with an array of electrostatic lenses. Electrostatic focusing was investigated seriously for satellite transmitters when designers thought that the only solution for satellite broadcasting to earth was with 500–1000-W transmitters on the satellite. Several prototype, lightweight, electrostatic-focused klystrons were designed and built, but improvements in the receiver noise figure rendered these higher-powered transmitters obsolete before they were ever deployed in space.

3.4. Collector

The collector's function is to stop the beam and transfer the heat produced by this action to a cooling media. The most stressful operation for the collector is the case with no RF signal applied to the klystron. In this case, the entire beam power is dissipated in the collector. In its basic form, the collector is a hollow cylinder terminated in a cone, that is part of the overall vacuum envelope. The exterior has a cooling jacket, generally with water as the coolant, and lead shielding is used with the higher powered klystrons, since the electrons produce X rays when they are suddenly stopped. The maximum power density must be limited to 500–1000 W/cm², depending on the cooling method, with the former applying to turbulent flow cooling, and the latter for mixed-phase water cooling, where steam is generated at the outside of the collector, but rapidly condenses in the cooling stream. Copper, because of its high thermal conductivity, is the most common collector material, but key parts of the collector are often made of stainless steel, to strengthen the assembly.

For pulsed klystrons, it is desirable to have the collector capable of being isolated from the rest of the klystron with a ceramic joint. This allows the precise monitoring of the body current, and the body current may be monitored to protect the klystron. Many klystrons dissipate 3–10% of the beam power in the body, and this component is not usually designed to dissipate much power.

3.5. The Depressed Collector

Only the kinetic energy of the moving electrons can be converted into microwave energy. After the beam has gone through the output gap, its remaining energy is converted into heat when the electrons strike the collector surface. However, a majority of this energy may be recovered by designing an array of electrodes at carefully selected potentials to form the collector. This is called a *multistage depressed collector*, and it is used in spaceborne and television transmitters to reduce the energy demands on the power supply. A schematic of a depressed collector is shown in Fig. 3. The voltages on the figure follow the inequality $V_c < V_1 < V_2 < V_3 < V_4$, where V_c is the cathode voltage. In practice, V_4 may be only a few percent of the cathode voltage, thus, when no signal is applied to the klystron, all the current is collected on the lowest collector, and the power supply has to provide only a few percent of the normal beam power. The electrostatic fields in the collector region sort out the electrons by their kinetic energy. Consider a case with three energy levels in the spent beam. The electrons with the most energy are intercepted at potential that is close to the cathode, while the electrons with a lower kinetic energy are intercepted at a potential that is between the cathode and the anode, and those with the lowest kinetic energy are intercepted at the anode potential. The kinetic energy of the high-energy electron classes is reduced by the work done moving to a more negative potential, so the heat produced at the collector is reduced, as is the power from the power supply. In this example klystron, the power supply must produce three more voltages, in between the cathode and anode potential, so the power supply is more complicated. However, when energy must be conserved, the depressed collector can save energy. The energy that can be recovered by the depressed collector increases with the number of stages, or potentials, in the collector, but so does the complexity of the power supply.

There are three practical problems of the depressed collector that should be addressed. First, the collector segments must have a low secondary emission ratio, since secondary electron current will travel to a higher potential, and absorb energy from the power supply. Second, the electrons should all hit the collector segments where the electric field will push any secondary electrons back into

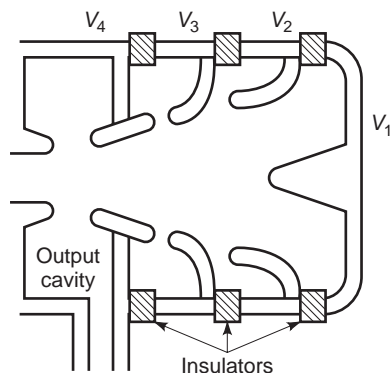


Figure 3. Schematic diagram of a depressed collector with four potentials.

the emitting electrode. Third, the insulators and cooling system must be carefully designed, so only acceptably small amounts of RF radiation are emitted into the space surrounding the collector. The beam in the collector is partially bunched, and it can deliver real RF power to the collector and its circuitry.

High-power (>50-kW), high-efficiency klystrons have not been produced with depressed collectors, since in this type of klystron, some electrons are almost stopped in the output gap, so if there is a potential barrier in the collector, these very slow electrons can be returned to the RF interaction region, and cause the klystron to be unstable. However, depressed collector klystrons are commercially available for the UHF television band to the 50 kW level.

3.6. Mechanical Considerations

The major mechanical requirements are that the klystron have a good vacuum, be strong enough to withstand the stresses of handling and from the water system, and the mechanical design must be repairable. The klystron must also withstand the thermal stresses involved in normal operation and during the bakeout process, which is a 450–600°C bake for 2–3 days for a large klystron. To allow repairs, the klystron often has weld flanges between cavities and at the collector and electron gun. The design must also have no trapped volumes, so it can be outgassed during the bakeout. Materials consistent with high vacuum must also be used, such as oxygen-free, high-conductivity copper, stainless steel, and tungsten and tantalum in the gun area. The RF window is generally made of high-purity aluminum or beryllium oxides, both of which have low losses, and which can be brazed to thin metal membranes for attachment to the klystron.

4. LIMITATIONS OF THE KLYSTRON

4.1. Efficiency

The maximum efficiency obtainable with a klystron remains an open question. For decades, the 58% result mentioned previously was considered the maximum theoretical limit, but numerical calculations involving second harmonic cavities, first published by Lien [6], showed that 70% to 75% efficiencies may be obtainable. The early experimental results [7,8] showed that the new numerical results were essentially correct, but it was several years before the first commercial klystron with over 60% efficiency was produced. The maximum efficiency achieved to date is 76%, in an S-band, 100-kW CW klystron [9] designed for industrial heating. However, for the highest efficiencies, the klystron's bandwidth, gain, and even stability are reduced, due to electrons that are returned from the output gap. Most of the high-efficiency klystrons have a second-harmonic cavity to optimize the shape of the bunch, and the S-band record klystron referred to previously has two second-harmonic cavities. Unfortunately, space charge effects reduce the klystron efficiency, so for high efficiency, the klystron must be designed with low beam current, and low perveance P , which is a geometric factor of the electron gun. Based on results of large signal

calculations and on experimental data, the optimized efficiency of klystron is estimated as [10]

$$\eta_e = 0.82 - 0.228P \cdot 10^6 \quad (6)$$

Thus, it is plausible that 80% efficiencies may be available in the future, provided that the market is large enough to support the necessary research. There will likely be more than one harmonic cavity in 80% efficient klystron. Equation (6) is an expression for the electronic efficiency which neglects the losses in the output cavity, which are also a function of the perveance or the operating voltage. While these losses are usually small, for very low perveance they become proportionately larger, and cannot be neglected.

4.2. Power

The maximum power that may be obtained from the klystron is limited by arcing considerations in the region of the electron gun, the output cavity, or the output window. At the highest peak powers, there is an inverse correlation between maximum peak output power and pulse length, since both pulse voltage and RF breakdown depend on pulsewidth. In the submicrosecond region, klystrons have been made with field-emission cathodes and up to 15 GW [11] output powers. For pulse lengths of a few microseconds, the peak power is limited to about 150 MW [12]. In the CW regime, the record peak power is 1.3 MW [13], and only slow progress has been made in raising this power from the first practical 1 MW CW klystron in 1989 or earlier. The effect of pulselength on the peak power obtainable from a given klystron often varies as the pulselength to the $-\frac{1}{2}$ th power. Representative state-of-the-art peak powers are 150 MW for 3 μ s, 20 MW for 15 μ s, and 5 MW for 1000 μ s. This is typical of short and medium pulsed klystrons.

For the highest peak powers, the output cavity electric fields must be minimized. The first step to reduce these fields is to round the cavity noses more, but this also reduces the interaction impedance. Major improvements in the output fields are obtained by separating the output cavity into two or more coupled cavities, separated by a short drift space. With two cavities, for example, the voltage of each cavity is reduced to 50% of the single cavity value, and so the fields are reduced also by this same 50%. The ohmic losses in the output cavity are proportional to the square of the cavity voltage, so the losses for the two-cavity system will each be only be 25% of the original single cavity, and the total ohmic losses will be 50% for the two-cavity system compared to the single cavity solution.

4.3. Frequency

The beam dynamics allow frequency scaling in the klystron, so that if all the dimensions are changes by a factor k' , the klystron will operate with the same characteristics at a new frequency, f/k' . However, if k' is less than unity, all the current and power densities in the new klystron will be $1/k'^2$ as high, so this limits the power available at high frequency. Both peak and average power then scale as f^{-2} . Hence, the optimum frequency range for the klystron is

from 0.5 to perhaps 20 GHz. Reduced power klystrons are available at up to 100 GHz. The low frequency limit occurs because of the massive size of a low-frequency klystron. With solid beams of ordinary perveance (between 0.75 and 2.0×10^{-6}) the low frequency limit is about 200 MHz. Hollow or multiple beams may permit a reduction in this lower limit, since with higher currents we have a slower electron velocity and therefore a smaller klystron.

The extended interaction klystron uses a set of coupled cavities to replace each cavity in the klystron. Amplifiers can be made with the extended interaction technique at frequencies up to 100 GHz. For even high-frequency operation, the gyroresonant principle must be used, and the gyroklystron is discussed further in the gyrotron section.

4.4. Bandwidth

The bandwidth of the klystron is relatively small, since there are five or more tuned cavities in the klystron. The loaded Q 's of these cavities depend on their shape, the frequency, and the beam current, since the beam loading is the most important factor in determining the cavity loading. The designer has very little control over these variables; the shape is always reentrant, with a gap that does not exceed one radian; the frequency is set by the application, so only the beam current can be controlled. The beam current follows Eq. (1). The output power P_o depends on the electronic efficiency and the power in the klystron beam, $P_o = \eta_e P V_A^{5/2}$. Since the beam loading is proportional to I , one achieves high bandwidth by increasing the beam current, for a given power, but this reduces the overall efficiency. In practice, klystrons with high (above 65%) efficiency tend to have 1 dB bandwidths of about $\pm 1\%$, and if the perveance is increased, the efficiency drops to under 50%, but the 1 dB bandwidth can be increased to 15% [14], even for klystrons at the 1 MW power level. Large bandwidths are easier to obtain in the klystron with high-output powers, since the beam impedance decreases as the operating voltage increases. The DC beam resistance is given by the relation, $R_o = 1/(PP_o^{0.2})$, and this is proportional to the maximum fractional bandwidth. Thus, wideband klystrons must either have high perveance, or high output power. Up to 10 cavities may be used, and optimally tuned to increase the bandwidth, and multiple resonances are designed into the output cavity and its coupling system. The klystron is not suited for wideband low-power applications, and the bandwidth, even for high-power devices, is limited to 15–20%. The cluster cavity concept [15], where each cavity is replaced by a set of closely spaced cavities, has the potential to make improvements in both bandwidth and efficiency, and devices with up to 25% bandwidth should be possible with this concept. A wideband, cluster cavity klystron would have as many as 15 cavities, and it would be more expensive than a conventional klystron, but the bandwidth could be significantly greater.

4.5. Gain

The klystron generally has a gain of 40–60 dB, with the lower gain corresponding to either a few cavities or wide bandwidth. In narrowband applications, gains over 60 dB

are possible, but the stability may suffer. At the higher frequencies, above 10 GHz, gain is more difficult to achieve, since the coupling function to the gap is not favorable.

4.6. Noise

The major noise sources in the klystron are (1) shot noise from the electron beam, (2) resistor noise from the input circuit, and (3) noise from the cathode temperature. The shot noise in a diode is given by the relation

$$\langle i_n^2 \rangle = 2eIBF(\theta) \quad (7)$$

where e is the electronic charge, B is the klystron bandwidth, and

$$F(\theta) = \frac{4}{\theta} [\theta^2 + 2(1 - \cos \theta - \theta \sin \theta)] \quad (8)$$

and the transit angle of the diode is

$$\theta = \frac{2\omega L_d}{u_0} \quad (9)$$

where L_d is the distance from the diode cathode to the anode. This value of the rms noise in the current is reduced by space charge effects, but the noise is proportional to the klystron current. Hence, high-power klystrons often have relatively high noise, with a noise figure of 30 dB being typical. When the klystron is used as a low-noise amplifier, it must be operated at low beam current. Even with low beam current, the klystron typically has a 6 dB noise figure, which is much higher than the few tenths of a dB that is possible with a good solid-state amplifier.

5. KLYSTRON VARIATIONS

Several physical variations of the conventional, solid cylindrical-beam klystron have been studied, including the sheet-beam [16], hollow-beam [17], and the multiple-beam [18] klystron. The cluster klystron [19] is a variation of the multiple beam klystron for very high output power where several beams are put in the same vacuum envelope, but they feed a common output cavity. These designs spread out the beam to reduce the adverse effects of space charge. Both the hollow-beam and multiple-beam klystron have been demonstrated, but the latter is under active development and is discussed here. The fundamental concepts include all klystron cavity gaps have a radial variation of the electric fields, so it is better to have all the electrons at one radius; and by spreading out the electron beam, the potential depression formed by the space charge will be minimized, so the variation in kinetic energy in the beam is minimized. In the interaction with the output gap, only the beam's kinetic energy can be converted to microwave power, the potential energy can be recovered only by using a multiple-stage depressed collector [20], which reduces the energy of the collected electrons. This in turn, reduces

the power from the power supply, but does not increase the output power of the klystron.

Another variant of the klystron is a hybrid of the traveling-wave amplifier (used as the input section) and the klystron output section (or vice versa). This type of amplifier can easily achieve 10–15% bandwidth, high output power, and good gain. The extended-interaction klystron has an RF structure that consists of several coupled cavities, rather than single cavities. With this technology, monotron oscillators can be built to produce 1 kW at frequencies up to 325 GHz, and amplifiers can be made up to 100 GHz.

5.1. Relativistic Klystron

Since the electron has a rest mass of 511 keV, relativistic effects start to appear at only 50 kV, so most high-power klystrons have relativistic effects in their detailed design. However, the term *relativistic klystron* is applied only to those klystrons operating at or above 500 kV, where relativistic effects are extremely important. The relativistic factor for klystron scaling with voltage is $\gamma_0^{3/2}$, so for a given frequency, the length becomes very long for high-voltage operation, or for γ significantly larger than unity. Thus, the relativistic klystrons often exploit a *gating effect* of an electron beam that is very near the space charge propagation limit. The propagation limit occurs when the potential depression because the beam's space charge is so high that all the kinetic energy is converted into potential energy, and the beam stops. This limiting current depends on the geometry of the beam and the surrounding drift tunnel or cavity. The limiting current for a solid beam of radius b in a drift tunnel of radius a is [21]

$$I_{\max} = \frac{4\pi\epsilon_0 mc^3}{e} \frac{(\gamma_0^{2/3} - 1)^{3/2}}{1 + 2 \ln(a/b)} \quad (10)$$

where m is the rest mass of the electron and the first ratio on the right-hand side is the Alfvén current, which is 17.1 kA for electrons.

The beam current in the relativistic klystron is generally a few tenths of this limiting current, while for conventional klystrons the current is often less than one tenth of the limiting current, but it increases with beam voltage. By operating fairly close to the current limit and carefully controlling the transverse geometry, the bunching distances for the relativistic klystron may be drastically reduced from the classic formulas given later, which do not include the gating effect. To obtain such high current, the relativistic klystrons often utilize field emission cathodes, which limits their performance to pulselengths below 1 μ s and limits the repetition rate for the pulse per minute range. The formidable output power of around a gigawatt can be produced, but the efficiency is generally only 20%, because the beam motion during the short pulse is not as uniform and laminar as is possible with lower current beams.

Many variations of the relativistic klystron are possible, and some of the most successful to date have been the virtual cathode or vircator family of devices [22].

5.2. Reflex Klystron

The reflex klystron has a reflector electrode after the first cavity, so the electrons pass through the cavity, are reflected by the electrostatic field from the reflector, and transverse the cavity again in the reverse direction. The beam is velocity modulated by the cavity in the first pass, and the beam will be bunched in $n + \frac{3}{4}$ RF periods, where n is any positive integer, including zero. By varying the potential of the reflector, we can adjust the time the electrons spend in the reflector region, and this changes the frequency of the oscillator. Hence, the device is inherently electronically tunable, so it has been applied primarily as a local oscillator, at the milliwatt power levels. High output powers are possible, but the device has lower efficiency than the conventional klystron, since the bunch geometry cannot be optimized in the reflex case.

5.3. Monotron Oscillator

The monotron is another single-cavity oscillator. The fundamental principle is that the impedance that the unbunched beam presents to a cavity is negative for long-transit angles, and the magnitude of this negative impedance varies linearly with the beam current. Hence, if the cavity and beam are properly designed, the real part of the cavity impedance can be negative and the cavity will oscillate, extracting power from the beam. One pitfall of klystron design is that a cavity, or more often, an inadvertent resonator in the electron-gun region, may start to oscillate at the klystron's design current, due to a monotron oscillation. The designer must know the impedance seen by the beam as a function of frequency, and remove the oscillation possibilities by reducing the Q of the unwanted peaks. This is especially important for high-current beams.

6. THEORY

There are two different limiting small-signal theories of the klystron that are each valid in their own small-signal regions. But the klystron is a very nonlinear device, and one must resort to numerical calculations to predict the efficiency, large-signal gain, and the phase and amplitude transfer functions of the klystron.

6.1. Small-Signal Theory

There are two simple theories of klystron operation, Webster's ballistic theory [23] and the space charge wave theory [24]. The ballistic theory is valid in the limit of small-space-charge forces. The principal result of the theory, when applied to a two-cavity klystron, is that the n th harmonic current amplitude is

$$\left| \frac{i_n}{I_0} \right| = 2\alpha J_n \left(n \frac{\alpha M \theta_d}{2} \right) \quad (11)$$

where I_0 is the DC beam current, J_n is the n th-order Bessel function, α is the ratio of the voltage at the input gap to the DC beam voltage (V_0), M is the gap coupling

coefficient, a number less than 1 that expresses the efficiency of the RF fields in the input gap in coupling to the beam, and $\theta_d = \omega L/u_0$ is the drift distance (in radians of transit time) between the center of the input and output cavities. For the highly idealized case of a gridded planar gap, $M = [\sin(L_g/2)]/[L_g/2]$, where L_g is the distance between the grids, measured in radians. If we assume an output gap with its value of M and α , then the electronic efficiency (the ratio of the RF energy produced to the beam's kinetic energy) may be written as

$$\eta_e = M_2 \alpha_2 J_1 \left(\frac{\alpha M \theta}{2} \right) \quad (12)$$

where the subscript 2 refers to the output cavity. When $M_2 \alpha_2 = 1$, the effective gap voltage experienced by an electron equals the DC beam voltage, and electrons will begin to be reflected from the output gap, and this can cause instabilities due to the electronic feedback. The first maximum of J_1 is approximately 0.584. Thus, the limiting value of klystron efficiency is half the current bunching ratio, or 58%. For several decades after the invention of the klystron, no klystron produced 58% efficiency, but the modern klystron can have an efficiency of up to 76%, and even higher with development.

The bandwidth and frequency response of the klystron was first calculated with the space charge wave theory. The space charge wave theory of the klystron is valid when the gap voltages are small and space charge forces are high. The bunching in the klystron can be explained as a result of two waves carried by the electron beam, a current wave, and a velocity wave. These waves obey a transmission-line equation, and are sinusoidal with distance and time for the usual case of an unaccelerated beam [25]. The voltage at the input gap modulates the velocity of the electrons as they cross the gap (and thus initiates a current wave), and in the drift space the velocity modulation is converted to current modulation. These modulation waves are a result of longitudinal plasma oscillations of the electrons, but it is complicated because the magnetic field and boundary conditions in the drift tubes also affect this plasma frequency. The result of this theory is that each cavity gap in the klystron excites a current and a velocity wave on the beam. The first cavity is driven by an external source (the drive signal), which excites a current wave plus a small velocity wave, due to the finite axial extent of the gap fields. The current wave is a sine wave with distance, so it grows. This wave interacts with the second cavity impedance and produces a larger voltage in the second cavity compared to the input cavity, provided that the second cavity is tuned reasonably close to resonance. This cavity voltage excites a second current and velocity wave, which adds to the original waves from the first cavity, and the process is repeated at each cavity. If we neglect the small velocity waves and concentrate on the current waves, then the standing waves set up by an input gap are of the form [26]

$$\frac{u_1}{u_0} = \frac{\alpha M}{2} \cos Z_1 \quad (13)$$

and

$$\frac{i_1}{I_0} = -j \frac{\alpha M}{2\omega_p/\omega} \sin Z_1 \quad (14)$$

where $Z_1 = (R\omega_p z)/(u_0)$ is the axial distance measured in reduced-plasma radians. The plasma reduction factor R is a measure of the reduction in the plasma frequency by the combined effects of the drift tunnel and the magnetic focus field. The plasma frequency is the free-space oscillation of electron density variations, for a one-dimensional situation. In the klystron, the space charge fields are two-dimensional, and a significant fraction of the space charge electric fields terminate on the drift tunnel walls, rather than on electron scarcity regions. The net result is that the actual plasma frequency, $\omega_q = R\omega_p$, is usually about one-tenth of the free-space value. The value of ω_p/ω is almost always less than unity, and this ratio usually is a few times 0.1. Thus, the current wave is generally 3–10 times larger than the velocity wave, which is often neglected. The small-signal bandwidth of the klystron may be determined by calculating the waves that begin at each cavity, due to the voltage produced in that cavity by the prior cavities. However, the electron beam itself loads down each cavity with a capacitive and a resistive component that are in parallel with the usual L , C , and R parallel elements that represent the cavity at the detuned short plane. If the gaps were gridded, the conductance $G = G_b + jB_b$ supplied by the beam to the gap is calculated from the subsequent relations.

$$\frac{G_b}{G_0} = 1 - \frac{\cos L_g}{L_g^2} - \frac{\sin L_g}{2L_g} \quad (15)$$

and

$$\frac{B_b}{G_0} = \frac{\sin L_g}{L_g^2} - 1 + \frac{\cos L_g}{2L_g} \quad (16)$$

where G_0 is I_0/V_0 , the DC beam conductance. These small-signal equations are easily programmed on small computers, and are widely used to estimate the bandwidth of klystron designs. Note that when designing a wideband klystron, there are frequencies at which the response from the current waves discussed previously is very small. The total response is the sum of the responses from the current waves and from the small velocity waves that have been neglected. Under these conditions, the velocity waves cannot be neglected.

6.2. Large-Signal Simulation

Since the klystron is such a nonlinear device, with many parameters, the linear theories cannot be used to predict the overall efficiency or the power that is intercepted along the klystron body, and large-signal nonlinear computer programs must be used to optimize the efficiency. The first large-signal klystron analysis was performed by Webber in 1958 [27]. For the next decade, the early klystron simulations were not very accurate, with about 10–15%

errors, since the theory was not self-consistent. The force equations were written for both gap and drift regions, with approximate expressions for the space charge. Electrons were tracked through a series of cavities and drift regions, but the amplitudes and phases of the gap fields were estimated by circuit equations that basically came from the linear space charge wave theory, where the beam current is assumed to be unaffected by the cavity fields. These amplitudes and phases were not necessarily correct, since the beam's current at large gap fields is altered by the gap fields. The necessity of iterating this procedure was first published by Kageyama et al. in 1977 [28]. The older methods were still used to estimate the voltages and fields in each cavity, but in addition, for each cavity, the induced current is calculated from Ramo's induced current theorem [29], which states the equivalence of the electrical energy change in a circuit to the work done by the particles on fields. For the klystron, the general form of the induced current is

$$i_i(t) = \frac{\int_V J(t) \cdot E(t) dV}{V_g(t)} \quad (17)$$

where the space charge current is given by J , the electric field E is only that due to the cavity, V_g is the gap voltage, and V is the entire volume over which there are cavity fields. One next takes a Fourier component of this time function to get the appropriate frequency component of the induced current.

Once the last electron leaves a particular gap, the induced current is finally known, and the gap voltage and phase are recalculated, using the Fourier component at the appropriate frequency. The old and new complex gap voltages are averaged, and used for the next iteration of the beam through this gap. After a few such cycles, the new fields and phase are very close to the previous estimates, and the cavity parameters are then established. Then, the next drift space calculation is performed, and the process continues in the next gap, until the output gap is reached. The output gap is special because the output gap voltage is often greater than the beam voltage, and the optimum loading of the cavity is not known a priori. The difference between the beam current at the entrance to the cavity and the induced current in the output cavity is very large, since the output cavity voltage is so great. The optimum coupling between the output cavity and the external load must also be found empirically (with a large-signal computer program), by varying the Q of the output cavity. The output cavity is a parallel RLC circuit (when viewed from the waveguide plane of the detuned short), and the beam is a current source, while the load being driven by the klystron is coupled to the output cavity by an iris, or a loop at low frequencies. This coupling iris can be represented by a transformer. The schematic is shown in Fig. 4. For the simple case where the load is purely resistive, the coupling iris may be ignored, and the combination of the iris and the load resistor can be replaced by a resistor transformed to the primary of the transformer, which is then in parallel with the RLC circuit. Refinements of the

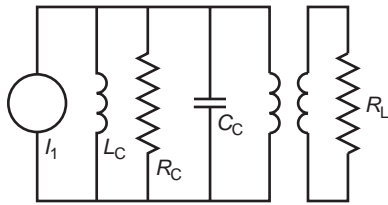


Figure 4. The equivalent circuit for the output cavity (the passive elements on the left of the transformer), the coupling transformer, the klystron's load impedance, and a modulated beam (the current generator) in this cavity.

method include using a wave equation solver to obtain accurate calculations of the cavity field distributions, and iterating over more than one cavity at a time when there are reflected electrons. These calculations must be repeated for each drive level, load on the klystron, and frequency, and so they are time consuming for large-bandwidth klystrons.

One of the most difficult calculations of the large-signal klystron programs is the evaluation of the space charge forces. There are basically two methods for calculating these forces. The earliest method is to calculate the Green function for the charged particle being followed, while accounting for the particular boundary conditions. For example, the Green's function fields at the point r, z for a unit-charged ring of radius r' and position z' , moving with velocity u_0 along the z axis, and contained in a conductive cylinder of radius a are [30]

$$E_r(r, z; r', z') = \frac{\gamma_0}{2\pi\epsilon_0 a^2} \sum_{l=1}^{\infty} \frac{J_0(v_l r) J_0(v_l r')}{J_1^2(v_l a)} e^{(-v_l \gamma_0 |z-z'|)} \quad (18a)$$

$$E_z(r, z; r', z') = \frac{\text{sgn}(z-z')}{2\pi\epsilon_0 a^2} \sum_{l=1}^{\infty} \frac{J_0(v_l r) J_0(v_l r')}{J_1^2(v_l a)} e^{(-v_l \gamma_0 |z-z'|)} \quad (18b)$$

and

$$B_\theta(r, z; r', z') = \frac{u_0}{c^2} E_r(r, z; r', z') \quad (18c)$$

where the eigenvalues are the roots of $J_0(v_l a) = 0$. A finite approximation to the infinite series is only calculated once, at the start of each problem. There are two major difficulties with using these equations in a computer code. The first is that the space charge fields are added in a point-by-point manner, so the time spent calculating the fields grows with n , the number of particles, as n^2 . This places a practical limit of around 100–300 particles with this method, for a personal computer. The other problem is more fundamental; these equations were derived by using a Lorentz transformation of the static fields of a moving charge into the laboratory frame. The γ_0 and u terms in the equations depend on this velocity. For most of the klystron, the particles move with an almost constant velocity, so this approximation is not bad, but in the penultimate and output cavities, there is a large spread of velocity, and Eqs. (18) lose their accuracy.

An alternative method of calculating the space charge fields is to directly integrate Maxwell's equations, with the bunched beam as a driving force. This method is called the particle-in-cell method, and a grid is set up over the klystron interaction area. The beam currents are averaged over the grid, and discretized versions of the curl equations are integrated to find the time derivatives of the fields. The major advantages of this method are that the method is valid for any distribution of particle velocity, and the computation time grows much more slowly, only as $n \log(n)$. A reference to the particle-in-cell method as applied to klystrons is Ref. 31, and a general reference to the particle in cell method is Ref. 32.

BIBLIOGRAPHY

1. R. H. Varian and S. F. Varian, A high-frequency oscillator and amplifier, *J. Appl. Phys.* **10**:321–327 (1939).
2. E. L. Ginzton, The \$100 idea, *IEEE Spectrum* **12**(2):30–39 (1975).
3. P. B. Wilson, Development and advances in conventional high-power RF systems, *Proc. 1995 Particle Accelerator Conf.*, 1995, pp. 1483–1488.
4. M. Chodorow et al., Design and performance of a high-power pulsed klystron, *Proc. IRE* 1584–1602 (1953).
5. J. R. Pierce, *Theory and Design of Electron Beams*, 2nd ed., Van Nostrand, New York, 1954.
6. E. Lien, High-efficiency klystron amplifier, *Proc. 8th Int. Microwave Optical Generation Amplification Conf.*, Amsterdam, 1970.
7. P. J. Tallerico, High performance klystrons for accelerator applications, *IEEE Trans. Nucl. Sci.* **NS-18**:257–259 (1971).
8. E. L. Lien, High efficiency klystron amplifier, Paper 14.4, *IEEE Int. Electron Devices Meeting*, Washington, DC, 1969.
9. S. Arai et al., 2.45 GHz, 100 kW, high efficiency klystron, *Nippon Electron. Comput. J* **46**(3):145–149 (1993).
10. P. Tallerico et al., Techniques for maintaining design efficiency when operating klystron amplifiers at levels below the maximum output power, *IEEE Trans. Electron. Devices* **ED-42**:780–784 (1995).
11. M. Friedman and V. Serlin, Present and future developments of high power relativistic klystron amplifiers, *Proc. SPIE Int. Soc. Opt. Eng.* H. E. Brandt, (ed.) **1872**:2–7 (1992).
12. D. Sprehn, R. M. Phillips, and G. Caryotakis, Performance of a 150-MW S-band klystron, *Proc. AIP Pulsed RF Sources for Linear Colliders Conf.*, 1994, Vol. 337, pp. 43–49.
13. H. Frischholz, The LEP II RF power generation system, *Proc. 1993 Particle Accelerator Conf.*, Washington, DC, 1993, pp. 1247–1249.
14. G. Faillon, G. Egloff, and C. Farvet, Very broad bandwidth klystron amplifiers, paper presented at the Int. Radar Colloquium, Versailles, April 1989; A. Auberdiac, C. Bearzatto, and G. Faillon, A Wideband 3 MW peak S-band klystron, paper presented at 1984 IEEE Int. Electron. Device Meeting, 1984, pp. 656–658.
15. R. S. Symons and J. R. M. Vaughan, Linear theory of the cluster-cavity klystron, *IEEE Trans. Plasma Sci.* **22**:713–718 (1994).
16. K. Eppley, W. Herrmannsfeldt, and R. H. Miller, Design of a wiggler-focused, sheet beam, X-band klystron, *Proc. 1987 Particle Accelerator Conf.*, 1987, pp. 1809–1814.

17. E. K. Demmel, Some studies on a high-perveance hollow-beam klystron, *IEEE Trans. Electron. Devices* **ED-11**:66–73 (1964).
18. E. A. Gelvich et al., The new generation of high-power multiple multiple-beam klystrons, *IEEE Trans. Microwave Theory Tech.* **MTT-41**:15–19 (1993).
19. R. B. Palmer et al., Status of the BLN-MIT-SLAC cluster klystron project, *Proc. AIP Pulsed RF Sources Linear Colliders Conf.*, 1994, Vol. 337, pp. 94–102.
20. R. S. Symons, Depressed collector klystrons for high-efficiency UHF television, *1982 Natl. Assoc. Broadcasters Convention* Dallas, 1982.
21. S. Humphries, Jr., *Charged Particle Beams*, Wiley, New York, 1990, p. 209.
22. V. L. Granatstein and I. Alexeff, *High-Power Microwave Sources*, Artech House, Boston, 1987, Chapters 13 and 14.
23. D. I. Webster, Cathode-ray bunching, *J. Appl. Phys.* **10**:501–508 (1939).
24. S. Ramo, Space charge and field waves on electron beams, *Phys. Rev.* **56**:276 (1939).
25. S. Bloom and R. W. Peter, Transmission-line analog of a modulated electron beam, *RCA Rev.* **15**(3):95–112 (1954).
26. A. H. W. Beck, *Space-Charge Waves and Slow Electromagnetic Waves*, Pergamon, New York, 1958.
27. S. E. Webber, Large-signal analysis of the multicavity klystron, *IRE Trans. Electron. Devices* **ED-5**:306 (1958).
28. T. Kageyama, Y. Morizumi, and E. Watanabe, A large-signal analysis of broad-band klystrons and its design application, *IEEE Trans. Electron. Devices* **59**(1) (1976).
29. S. Ramo, Currents induced by electron motion, *Proc. IRE* 584–585 (1939).
30. P. J. Tallerico and J. E. Rowe, Relativistic effects in the traveling-wave amplifier, *IEEE Trans. Electron. Devices* 549–561 (1970).
31. B. E. Carlsten and P. Ferguson, Large-signal klystron calculations using KLSC, *Proc. 1997 Particle Accelerator Conf.*, Vancouver, Canada, 1997.
32. C. K. Birdsall and A. B. Langdon, *Plasma Physics via Computer Simulations*, McGraw-Hill, New York, 1985.

LEAKY MODES AND HIGH-FREQUENCY EFFECTS IN MICROWAVE INTEGRATED CIRCUITS

FRANCISCO MESA

University of Seville
Seville, Spain

DAVID R. JACKSON

University of Houston
Houston, Texas

1. INTRODUCTION

This article investigates the high-frequency effects that occur when sources or discontinuities are present on printed-circuit transmission lines. Although many of the conclusions are general, the analysis and the results will focus on microstrip and stripline types of transmission lines, where there is a single-strip conductor that is within a layered structure that may contain either one or two ground planes. Examples include the microstrip structure shown in Fig. 1a, the covered microstrip shown in Fig. 1b, and the stripline structure that has an airgap over the

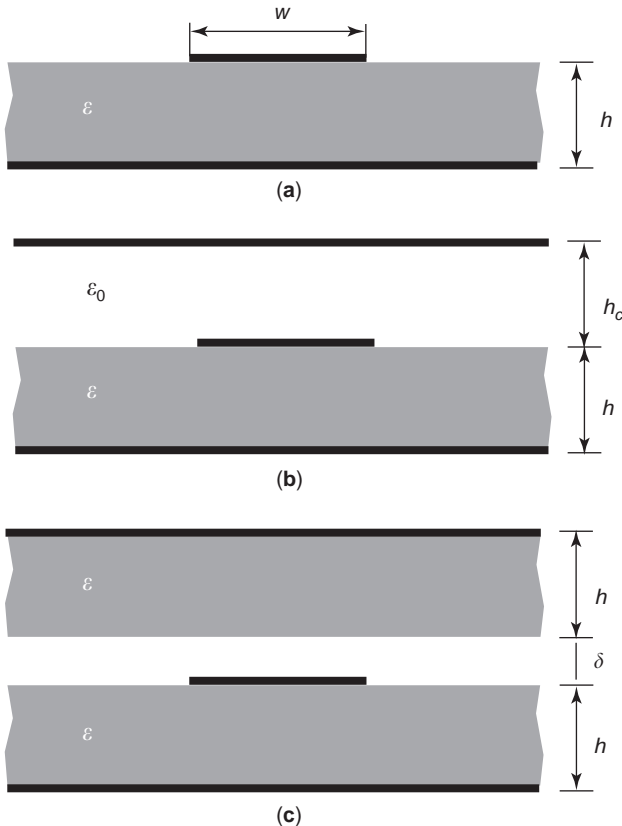


Figure 1. Cross sections of (a) a microstrip line, (b) a covered microstrip, and (c) stripline with an airgap.

strip conductor, as shown in Fig. 1c. (Later in the article, the analysis will be extended to include coupling between two strip conductors, so that the crosstalk current induced on a passive microstrip line from coupling to an adjacent active microstrip line can be studied.)

The analysis and results will focus on the current and fields that are excited when a gap voltage source is located at the origin ($z=0$) on an infinite structure, where the strip conductor extends from $-\infty$ to ∞ , as shown in Fig. 2. This source model allows for a semianalytical treatment of the problem in the spectral domain, which greatly simplifies the solution. Other types of sources may be considered, however. Many of the conclusions also apply to discontinuities on the line (bends, junctions, etc.), although such discontinuity problems are not specifically treated here.

One of the main goals of the article is to examine the nature of the current on the transmission line that is excited by the gap voltage source, and explore what types of spurious effects occur at high frequency. It is well known that at low frequency, simple transmission line theory may be used to adequately predict the current on the strip conductor. In particular, the current $I(z)$ predicted by simple transmission-line theory is

$$I(z) = \frac{1}{2Z_0} e^{-jk_z^{\text{BM}}|z|} \quad (1)$$

where Z_0 is the characteristic impedance of the line and k_z^{BM} is the propagation wavenumber of the transmission-line mode, which is also called a “bound mode” (BM) of propagation, since the fields of this mode decay transversely away from the structure (in the $\pm x$ direction), and hence are bound to the guiding structure.

At high frequency, simple transmission-line theory is no longer adequate to accurately predict the current excited by the gap source, for various reasons. First, it should be noted that the definition of the characteristic impedance Z_0 is not unique at high frequency [1]. Second, at high frequency, the current on the strip is not solely that of the bound transmission-line mode (as assumed in the above equation), but it also consists of a “continuous spectrum” (CS) part, which is not predicted by transmission-line theory, and which becomes more important as the frequency increases. The analysis presented here allows for an accurate calculation of the bound-mode amplitude that is excited by the gap source at any frequency, even when the bound-mode current is not the dominant current on the line. The bound mode current has the form

$$I(z) = A_{\text{BM}} e^{-jk_z^{\text{BM}}|z|} \quad (2)$$

where the modal amplitude A_{BM} is determined by a residue in the complex plane, as explained later.

The semianalytical treatment presented here allows for a calculation of the CS current, which may become very

important at high frequencies. The method also provides a convenient description of the physics of the CS current. In particular, the CS current includes the effects of leaky modes, which are modes that radiate (leak energy) as they propagate. The leakage may be of two types. In one case the leakage occurs into the fundamental mode of the substrate, which is either a surface-wave mode or a parallel-plate mode, depending on whether there are one or two ground planes. (When only a single ground plane is present, the structure will be called “open,” since the structure is open to free space. When there are two ground planes, the structure will be called “closed.”) Assuming that only a single substrate mode is above cutoff (the usual case), the leakage will occur into the fundamental TM_0 mode of the substrate. In the other case, which only occurs on open structures, the leakage occurs into both the TM_0 substrate mode and into space. In either case, a leaky-mode (LM) current has the form

$$I(z) = A_{LM} e^{-jk_z^{LM}|z|} \quad (3)$$

where the propagation wavenumber $k_z^{LM} = \beta - j\alpha$ of the leaky mode is complex as a result of radiation loss. The excitation of a leaky mode may cause considerable spurious effects, including power loss, interference with the desired bound mode, and crosstalk with neighboring circuit components. The semianalytical treatment presented here allows for a calculation of the excitation of any leaky modes that are part of the CS current. In the representation used here (and explained later), leaky modes appear explicitly as part of the continuous spectrum if the modes are “physical,” meaning that the leakage mechanism of the mode (either into the substrate or into both the substrate and into space) is consistent with the phase constant of the leaky mode.

The analysis also reveals that the CS current on the strip conductor consists not only of leaky modes but also of a component called the “residual-wave current.” The residual-wave (RW) current is the leftover, or residual, part of the CS current that is not representable as a sum of physical leaky-mode (LM) currents. When no physical leaky modes are present, the RW current is identically the same as the CS current. When physical leaky modes are present, the CS current consists of both the LM and the RW currents. In either case, the RW current may become important at high frequency. The analysis further shows that the RW current consists, in general, of two parts. One part is called the “ TM_0 RW current,” and exists for both open and closed structures. The second type, called the “ k_0 RW current,” exists only for open structures. An asymptotic analysis shows that for large distances z from the source, the TM_0 RW current behaves as

$$I_{RW}^{TM_0}(z) = A_{RW}^{TM_0} \frac{1}{|z|^{3/2}} e^{-jk_{TM_0}|z|} \quad (4)$$

where k_{TM_0} is the wavenumber of the TM_0 substrate mode, while the k_0 RW current behaves as

$$I_{RW}^{k_0}(z) = A_{RW}^{k_0} \frac{1}{|z|^2} e^{-jk_0|z|} \quad (5)$$

where k_0 is the wavenumber of free space.

Section 2 provides a detailed description of the semi-analytical method of analysis that is used to calculate the strip current and the consistent BM, LM, and RW components. The analysis shows how the total strip current is representable as a sum of BM and CS currents, and also how the CS current can be represented as a sum of physical LM currents together with RW currents.

In Section 3, results will be presented to show the types of spurious effects that can occur for the various types of printed-circuit transmission-line structures in Fig. 1, due to the LM currents and the RW currents.

Section 4 extends the analysis and the results of the previous sections by considering the calculation of the crosstalk current that is excited on a passive (victim) line, when a gap voltage source is present on an excited line. It is shown that simple transmission-line theory can predict the crosstalk current accurately at low frequency, using an even/odd-mode analysis. However, at high frequency, the CS current becomes important, and the crosstalk current cannot be adequately described by simple transmission-line theory.

Section 5 examines the nature of the crosstalk field that surrounds a printed-circuit transmission line, when it is excited by a gap voltage source. It is seen that at low frequency the field decays away from the line fairly rapidly, but at high frequency this is not the case. When physical leaky modes are present, very strong focused radiation may occur in a specific direction, leading to very high crosstalk fields.

Section 6 concludes the article by summarizing the most important observations and conclusions that are obtained from the study of the printed-circuit transmission line excited by a gap voltage source.

2. ANALYSIS FOR CURRENT EXCITED BY A GAP SOURCE

This section describes the theory underlying the computation of the current excited on the strip conductor of an infinite printed-circuit line by a gap voltage source on the line as shown in Fig. 2. The substrate is a lossless dielectric that can be layered and an optional metallic wall can cover the line (in which case the structure is referred to as a “closed” structure, since it is closed vertically, and radiation into space is prohibited). The line is assumed to be infinite along the longitudinal direction (z) and the conductors are infinitesimally thin and perfectly conducting. (Although only lossless striplike lines will be considered here, the present approach can be extended to lossy and/or slotlike lines with some modifications.) The basic ideas of the theory will be exposed in this section in connection with a single microstrip line. Section 4 will treat the current excited on a pair of coupled microstrip lines.

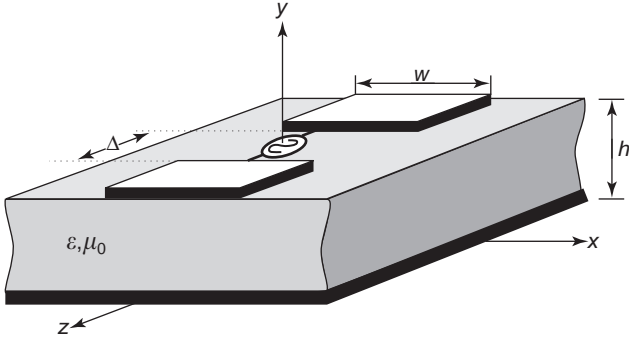


Figure 2. Geometry of an infinite microstrip line excited by a gap voltage source at $z=0$.

In order to compute the surface current on the strip conductor, $\mathbf{J}_s = J_x \hat{\mathbf{x}} + J_z \hat{\mathbf{z}}$, the following electric field integral equation (EFIE) has to be solved:

$$\mathbf{E}_t[\mathbf{J}_s(x, z)] = \mathbf{E}_t^{\text{gap}}(x, z) \quad (6)$$

where $\mathbf{E}_t^{\text{gap}}$ is the tangential electric field impressed in the gap (where the “t” subscript denotes “tangential”) to model the gap voltage source. This impressed electric field is equated to the field that is computed from the strip current using the transverse part of the corresponding dyadic Green’s function of the layered structure at the strip interface, $\bar{\mathbf{G}}_t(x, z; x', z') = G_{xx} \hat{\mathbf{x}}\hat{\mathbf{x}} + G_{xz}(\hat{\mathbf{x}}\hat{\mathbf{z}} + \hat{\mathbf{z}}\hat{\mathbf{x}}) + G_{zz} \hat{\mathbf{z}}\hat{\mathbf{z}}$, as the following convolution product

$$\mathbf{E}_t(x, z) = \int_{-\infty}^{\infty} \int_{-w/2}^{w/2} \bar{\mathbf{G}}_t(x - x', z - z') \cdot \mathbf{J}_s(x', z') dx' dz' \quad (7)$$

where the translational symmetry of the grounded substrate in the tangential plane has been incorporated. The impressed field is assumed to be

$$\mathbf{E}_t^{\text{gap}}(x, z) = -\frac{1}{\Delta} \text{rect}\left(\frac{x}{w/2}\right) \text{rect}\left(\frac{z}{\Delta/2}\right) \hat{\mathbf{z}} \quad (8)$$

in order to give a uniform gap field that corresponds to homogeneous voltage drop of 1 V along the gap (Δ denotes the longitudinal width of the gap, and $\text{rect}(x) = 1$ if $|x| \leq 1$ and is zero otherwise). For future use it is convenient to note that the z Fourier transform of the impressed gap field, $\tilde{\mathbf{E}}_z^{\text{gap}}(x, k_z)$, of (8) is given by

$$\tilde{\mathbf{E}}_z^{\text{gap}}(x, k_z) = -\text{rect}\left(\frac{x}{w/2}\right) \text{sinc}\left(\frac{k_z \Delta}{2}\right) \quad (9)$$

where $\text{sinc}(x) = \sin(x)/x$. (In the present notation, $\tilde{A}(k_z)$ denotes the Fourier transform of $A(x)$ for any function A .)

Next, the EFIE is solved by means of Galerkin’s method [2], for which the unknown induced current density on the strip has to be expanded in basis functions. First, and for simplicity of explanation, the current density will be expanded using only one basis function. The extension to

include multiple basis function will be discussed afterward.

2.1. Single Basis Function

If only a single basis function is employed to expand the induced current density on the strip, $\mathbf{J}_s(x, z)$ will have only a longitudinal component, J_{sz} , which can be represented by

$$J_{sz}(x, z) = T(x)I(z) \quad (10)$$

where $T(x)$ denotes the transverse profile, which is normalized to give

$$\int_{-w/2}^{w/2} T(x) dx = 1 \quad (11)$$

so that $I(z)$ actually represents the longitudinal current on the line at a distance z from the source. Specifically, the following basis function has been chosen

$$T(x) = \frac{\text{rect}\left(\frac{x}{w/2}\right)}{\pi \sqrt{\left(\frac{w}{2}\right)^2 - x^2}} \quad (12)$$

which will give a good approximation for narrow strips. The EFIE (6) can be then written as

$$\int_{-\infty}^{\infty} \int_{-w/2}^{w/2} G_{zz}(x - x', z - z') T(x') I(z') dx' dz' = \mathbf{E}_z^{\text{gap}}(x, z) \quad (13)$$

The application of the longitudinal inverse Fourier transform

$$I(z) = \frac{1}{2\pi} \int_{-\infty}^{\infty} \tilde{I}(k_z) e^{-jk_z z} dk_z \quad (14)$$

to the integral equation above (or alternatively, taking the Fourier transform of both sides with respect to z) leads to

$$\begin{aligned} \tilde{I}(k_z) \int_{-w/2}^{w/2} \tilde{G}_{zz}(x - x', k_z) T(x') dx' \\ = \text{rect}\left(\frac{x}{w/2}\right) \tilde{\mathbf{E}}_z^{\text{gap}}(k_z) \end{aligned} \quad (15)$$

The tilde above the Green’s function indicates here a 1D Fourier transform with respect to z . If Galerkin’s method is now applied, (15) can be finally expressed as

$$\begin{aligned} \tilde{I}(k_z) \int_{-w/2}^{w/2} T(x) \int_{-w/2}^{w/2} \tilde{G}_{zz}(x - x', k_z) T(x') dx' dx \\ = \left[\int_{-w/2}^{w/2} T(x) dx \right] \tilde{\mathbf{E}}_z^{\text{gap}}(k_z) \end{aligned} \quad (16)$$

which, after taking into account (11), allows this to be written as

$$\tilde{I}(k_z) = \frac{\tilde{\mathbf{E}}_z^{\text{gap}}(k_z)}{D(k_z)} \quad (17)$$

with

$$D(k_z) = \int_{-w/2}^{w/2} T(x) \int_{-w/2}^{w/2} \tilde{\mathbf{G}}_{zz}(x-x', k_z) T(x') dx' dx \quad (18)$$

It should be noted that $D(k_z)$ actually represents a function whose zeros are the modal propagation constants (k_z^M) of the infinite microstrip line. A careful study of the singularities of this function in the complex k_z plane will be presented later in this section.

Two common techniques have been commonly used in the literature to compute integrals such as $D(k_z)$: the spectral-domain approach (SDA) [3,4] and the discrete complex images technique (DCIT) [5–7]. Each is discussed further below.

2.1.1. Spectral-Domain Analysis. As is well known, the use of the SDA is motivated by the fact that the dyadic Green's function can be obtained in closed form (or by means of certain algorithms) in the spectral domain [8–10]. Thus, assuming that $\tilde{\mathbf{G}}_{zz}(k_x, k_z)$ is known in closed form, $D(k_z)$ can be expressed analytically in terms of a spectral-domain integral involving this Green's function. (The tilde over the Green's function indicates here a 2D Fourier transform of the Green's function.) This is accomplished by first expressing the inner integral in Eq. (18) as an inverse Fourier transform of the Fourier transform (in x), noting the convolutional nature of the integral, and then performing the outer integral in x in closed form, resulting in the Fourier transform of the function $T(x)$. The result is (assuming that $T(x)$ is an even function)

$$D(k_z) = \frac{1}{2\pi} \int_{C_{kx}} \tilde{\mathbf{G}}_{zz}(k_x, k_z) \tilde{T}^2(k_x) dk_x \quad (19)$$

where C_{kx} is an appropriate inverse Fourier transform path from minus infinity to infinity in the complex k_x plane [11–13].

Since the preceding integral has to be computed many times to obtain the current profile given by (14), it is very convenient to minimize as much as possible the intensive numerical effort required to compute (19). Different strategies have been proposed in the literature to speed up the overall computation of similar integrals, and one that has been found particularly efficient is the extraction of an asymptotic behavior that can be further expressed in closed form. This involves splitting the integral (19) into two integrals

$$D(k_z) = D^s(k_z) + D^\infty(k_z) \quad (20)$$

where

$$D^s(k_z) = \int_{C_{kx}} \left[\tilde{\mathbf{G}}_{zz}(k_x, k_z) - \tilde{\mathbf{G}}_{zz}^\infty(k_x, k_z) \right] \tilde{T}^2(k_x) dk_x \quad (21)$$

$$D^\infty(k_z) = \int_{-\infty}^{\infty} \tilde{\mathbf{G}}_{zz}^\infty(k_x, k_z) \tilde{T}^2(k_x) dk_x \quad (22)$$

so that $D^s(k_z)$ can be computed with low computational effort. An asymptotic expression for the spectral-domain Green function is

$$\tilde{\mathbf{G}}_{zz}^\infty(k_x, k_z) = - \left(\frac{j\omega\mu_0}{2} + \frac{1}{2j\omega\epsilon_m} k_z^2 \right) \frac{|k_x|}{k_x^2 + k_0^2} \quad (23)$$

(where k_0 is the free-space wavenumber). Use of this expression leads to a closed-form expression for $D^\infty(k_z)$ [14,15].

2.1.2. Discrete Complex Images Technique. One of the main numerical disadvantages of the spectral-domain technique is that obtaining the longitudinal current profile from Eq. (14) requires numerically evaluating the integral (21) with infinite limits for each value of k_z . This drawback can be considerably alleviated if the discrete complex images technique (DCIT) is used to obtain a closed-form expression for the Green's function in the spatial domain. This procedure has been employed elsewhere [7,16,17] to deal with 2D printed lines when Eq. (6) is posed as a mixed potential integral equation (MPIE) [18]. It is worth mentioning that the integrals to be repeatedly computed are double definite integrals with nonsingular integrands (except at the strip edges) that can be very efficiently computed by low order Gauss–Chebyshev quadratures [17]. Our experience shows that this scheme reduces the CPU time at least 5 times when compared to that required by the SDA.

2.1.3. Multiple Basis Functions. The procedure shown in the previous section is numerically accurate only for those situations where the transverse component of the current density can be neglected (which is usually found at low frequencies and/or for narrow strips). In general, however, an expansion with multiple basis functions is required. For this purpose, the current density on the strip is assumed to be (with q even and p odd)

$$J_z(x, z) = \sum_{q=0}^{N_f} T_q^z(x) I_q^z(z) \quad (24)$$

$$J_x(x, z) = \sum_{p=1}^{N_f} T_p^x(x) I_p^x(z) \quad (25)$$

where $T_p^z(x)$ and $T_q^x(x)$ are, respectively, the basis functions used to expand the transverse profile of the z and x components of the current density, and $I_p^z(z)$ and $I_q^x(z)$ are the corresponding unknown coefficient functions accounting

for the longitudinal profile of the current density. The term N_f denotes the maximum order of the basis functions. The transverse profile is accounted for by the usual Chebyshev polynomials of the first and second kinds [$T_n(\cdot)$ and $U_m(\cdot)$, respectively] weighted by the proper edge condition, namely

$$T_q^z(x) = (2 - \delta_{q0}) \frac{2}{w\pi} \frac{T_q(2x/w)}{\sqrt{1 - \left(\frac{2x}{w}\right)^2}} \quad (26)$$

$$T_p^x(x) = \frac{4}{w\pi} j U_p(2x/w) \sqrt{1 - \left(\frac{2x}{w}\right)^2} \quad (27)$$

where δ_{mn} is the Krönecker delta. The use of this expansion in the EFIE, after using Galerkin's method and applying the longitudinal Fourier transform, leads to the following linear equation system

$$\begin{bmatrix} \Gamma_{pp'}^{xx}(k_z) & \Gamma_{pq'}^{xz}(k_z) \\ \Gamma_{qp'}^{zx}(k_z) & \Gamma_{qq'}^{zz}(k_z) \end{bmatrix} \cdot \begin{bmatrix} \tilde{I}_p^x(k_z) \\ \tilde{I}_q^z(k_z) \end{bmatrix} = \begin{bmatrix} [0] \\ [\tilde{b}_q^z(k_z)] \end{bmatrix} \quad (28)$$

where

$$\Gamma_{pp'}^{xx}(k_z) = \int_{-w/2}^{w/2} [T_p^x(x)] \int_{-w/2}^{w/2} \tilde{G}_{xx}(x, x', k_z) T_{p'}^x(x') dx' dx \quad (29a)$$

$$\Gamma_{pq'}^{xz}(k_z) = \int_{-w/2}^{w/2} [T_p^x(x)] \int_{-w/2}^{w/2} \tilde{G}_{xz}(x, x', k_z) T_{q'}^z(x') dx' dx \quad (29b)$$

$$\Gamma_{qp'}^{zx}(k_z) = \int_{-w/2}^{w/2} [T_q^z(x)] \int_{-w/2}^{w/2} \tilde{G}_{zx}(x, x', k_z) T_{p'}^x(x') dx' dx \quad (29c)$$

$$\Gamma_{qq'}^{zz}(k_z) = \int_{-w/2}^{w/2} [T_q^z(x)] \int_{-w/2}^{w/2} \tilde{G}_{zz}(x, x', k_z) T_{q'}^z(x') dx' dx \quad (29d)$$

$$\tilde{b}_q^z(k_z) = \tilde{E}_z^{\text{gap}}(k_z) \delta_{q0} \quad (29e)$$

The current along the line can be obtained finally as

$$I(z) = \int_{-w/2}^{w/2} J_z(x, z) dx = \sum_{q=0}^{N_f} I_q^z(z) \int_{-w/2}^{w/2} T_q^z(x) dx \quad (30)$$

which can be recognized as simply $I(z) = I_0^z(z)$ because of the normalization condition imposed on the basis functions. Therefore

$$I(z) = \frac{1}{2\pi} \int_{C_{kz}} \tilde{I}_0^z(k_z) e^{-jk_z z} dk_z \quad (31)$$

The coefficients of the Galerkin matrix (29a)–(29d) can be numerically obtained by using the SDA or the DCIT techniques discussed in the previous sections, since the introduction of multiple basis functions does not affect the asymptotic or singular behavior of the corresponding integrals.

2.2. The Complex k_z Plane

It has been shown above that the computation of the current on the strip $I(z)$ requires an inverse Fourier transform given, in general, by Eq. (31). It is well known that the study of the singularities of the integrand of any complex spectral integral gives very valuable information about the integral itself [19]. In this way, references have shown [12,13,20–22] that a study of the integrand of (31) in the complex k_z plane provides a deep and very useful physical insight into the nature of the current excited on the line, and furthermore, how to decompose the current into its constituent parts. Since the $\exp(-jk_z z)$ function is fully analytic in the entire k_z plane, any singularity of the integrand comes necessarily from $\tilde{I}_0^z(k_z) \equiv \tilde{I}(k_z)$, and therefore the present study will focus on the poles and branch points of this latter function.

Looking at the form of $\tilde{I}(k_z)$ given in (17), it can be recognized that the numerator will not show any singularity in the k_z plane since $\tilde{E}_z^{\text{gap}}(k_z)$ is the Fourier transform of a bounded function. Thus, the pole singularities of $\tilde{I}(k_z)$ will come from the zeros of the denominator $D(k_z)$ (for the case of multiple basis functions, this function will be the determinant of the Galerkin matrix), which have been previously identified as the propagation wavenumbers for modes on the infinite line. Also, the branch points of $D(k_z)$ will be the branchpoint singularities of $\tilde{I}(k_z)$.

The discussion above shows that the nature of the complex k_z plane defined by $\tilde{I}(k_z)$ is fully determined by the function $D(k_z)$. This function can be rewritten in general (also for multiple basis functions) as

$$D(k_z) = \int_{C_{kx}} Q(k_x, k_z) dk_x \quad (32)$$

where $Q(k_x, k_z)$ involves the spectral-domain Green function (SDGF). The expression given in Eq. (19) for $D(k_z)$ makes apparent that its singularities are themselves determined by both the singularities of the SDGF and the corresponding integration path C_{kx} in the complex transverse wavenumber plane (k_x).

There are two types of singularities in the complex k_z plane: poles and branchpoints. Poles correspond to guided modes that exist on the printed-circuit transmission line, and the residues at the corresponding pole locations determine the amplitudes of the modes that get launched by the gap voltage source, including both bound and leaky

modes. During a path deformation to the steepest-descent path (discussed later), the bound-mode poles are always captured, and hence the bound-mode currents always appear explicitly in the final expression for the current. Leaky-mode poles may or may not be captured, however. Leaky modes whose poles are captured are said to be “physical” leaky modes, and these currents appear explicitly in the final expression for the current. Leaky modes whose poles are not captured do not appear explicitly in the final expression for the current, and are said to be “nonphysical.” However, these nonphysical poles may still have an influence on the total current, by virtue of their proximity to the steepest-descent path. This will be particularly true when a nonphysical pole is close to being physical, so that the pole is close to the steepest-descent path.

Branchpoints in the k_z plane arise because of a non-uniqueness in the evaluation of the integral (32). In particular, different paths of integration in the complex k_x plane may be used for the path C_{k_x} . These different paths may detour around the pole and/or branchpoint singularities of the SDGF in different ways, resulting in different values for the integral. This corresponds to $D(k_z)$ being a multiple-valued function of k_z . Mathematically, this may be conveniently viewed as the complex k_z plane corresponding to a Riemann surface. On each sheet of the surface a different path of integration is used in the k_x plane to evaluate the integral in Eq. (32).

The SDGF for an open structure such as microstrip has singularities at particular points in the transverse wavenumber k_t plane, where $k_t^2 = k_x^2 + k_z^2$. This results in corresponding singularities at the following locations in the complex k_x plane [13,23–25]:

1. *Branchpoints* at $k_x = \pm k_{xb}$, where $k_t^2 = k_{xb}^2 + k_z^2 = k_0^2$
2. *Proper poles* at $k_x = \pm k_{xp}$, where $k_t^2 = k_{xp}^2 + k_z^2 = k_{sw}^2$, where k_{sw} is the propagation constant for a proper surface wave of the background layered structure
3. *Improper poles* at $k_x = \pm k_{xi}$, where $k_t^2 = k_{xi}^2 + k_z^2 = k_{imp}^2$, where k_{imp} is the propagation constant of an improper mode of the background layered structure

The improper modes of the background layered structure can be classified as either improper surface-wave modes, if the propagation constant k_{imp} is purely real, or as complex leaky modes, if k_{imp} is complex. (An improper surface-wave mode is never regarded as a physical mode. A complex improper leaky mode is regarded as being physical if the phase constant of the mode is less than k_0 , so that the radiating leaky mode is a fast wave with respect to free space [26,27].)

A careful study of the integration paths in the k_x plane, and their evolution as the point k_z moves in the complex k_z plane, reveals that branchpoints in the complex k_z plane occur at the following locations:

1. Branchpoints at $k_{zb}^p = \pm k_{TM_0}$, where k_{TM_0} is the wavenumber of the TM_0 surface-wave (or parallel-plate) mode of the background layered structure (it

is assumed here that only the TM_0 mode is above cutoff).

2. Branchpoints at $k_{zb}^i = \pm k_{imp}$, where k_{imp} is the wavenumber of an improper (improper real or complex leaky) mode of the background layered structure.
3. Branchpoints at $k_{zb}^0 = \pm k_0$, where k_0 is the free-space wavenumber.

The branchpoints at k_{zb}^p and k_{zb}^i give rise to a double-valued function of k_z (corresponding to two sheets of the k_z Riemann surface), since circling these branchpoints twice gives back the original function $D(k_z)$ at the starting point in the k_z plane. Thus, the path of integration in the k_x plane in integral (32) evolves back to the original path when the point k_z moves twice around the branchpoint back to the original path.

The branchpoints at $k_{zb}^0 = \pm k_0$ have a logarithmic character in the sense that there are an infinite number of sheets associated with these branchpoints; that is, each time the branchpoint is circled in the k_z plane, the path of integration in the k_x plane changes, and never returns to the original path after a finite number of encirclements of the branchpoint. The original path of integration lies in the sheet that is denoted as the “zero” sheet, for which the path of integration in the k_x plane stays on the top (proper) sheet of the k_x Riemann surface.

As shown in Ref. 13, the branchpoints corresponding to the improper modes of the background structure at $k_{zb}^i = k_{imp}$ do not appear on the zero sheet of the $\pm k_0$ branchpoints on the k_z Riemann surface (such branchpoints appear only on the odd sheets of the $\pm k_0$ branchpoints). The original path of integration C_{k_z} , which stays on the zero sheet, thus sees the branchpoints only at $k_{zb}^0 = \pm k_0$ and $k_{zb}^p = \pm k_{TM_0}$. The branchpoints at $\pm k_{TM_0}$ appear only on the even sheets of the $\pm k_0$ branch points, including the zero sheet.

The complex k_z plane for the case of an open structure such as microstrip line is shown in Fig. 3. The branchpoints at $\pm k_0$ and at $\pm k_{TM_0}$ are shown. To aid in the understanding of the branchpoints and the k_z Riemann surface, an example is given to connect the location of

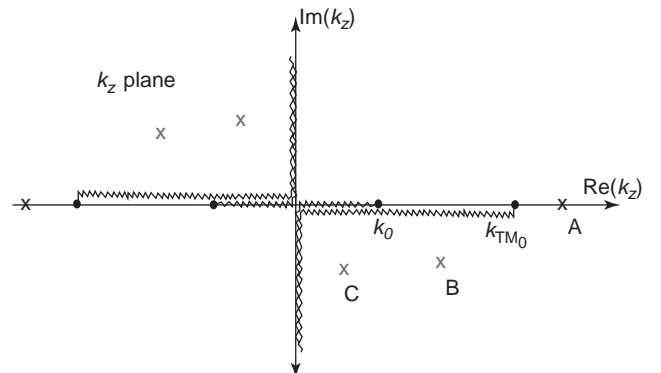


Figure 3. The k_z plane showing two pairs of branchpoints at $\pm k_0$ and $\pm k_{TM_0}$, a pair of proper poles at $\pm A$, and two pairs of leaky poles at $\pm B$ and $\pm C$.

the k_z point on the Riemann surface with the corresponding path of integration in the k_x plane. Three points are shown in the complex k_z plane, labeled as A , B , and C . The corresponding paths of integration in the k_x plane are shown in Figs. 4a, 4b, and 4c.

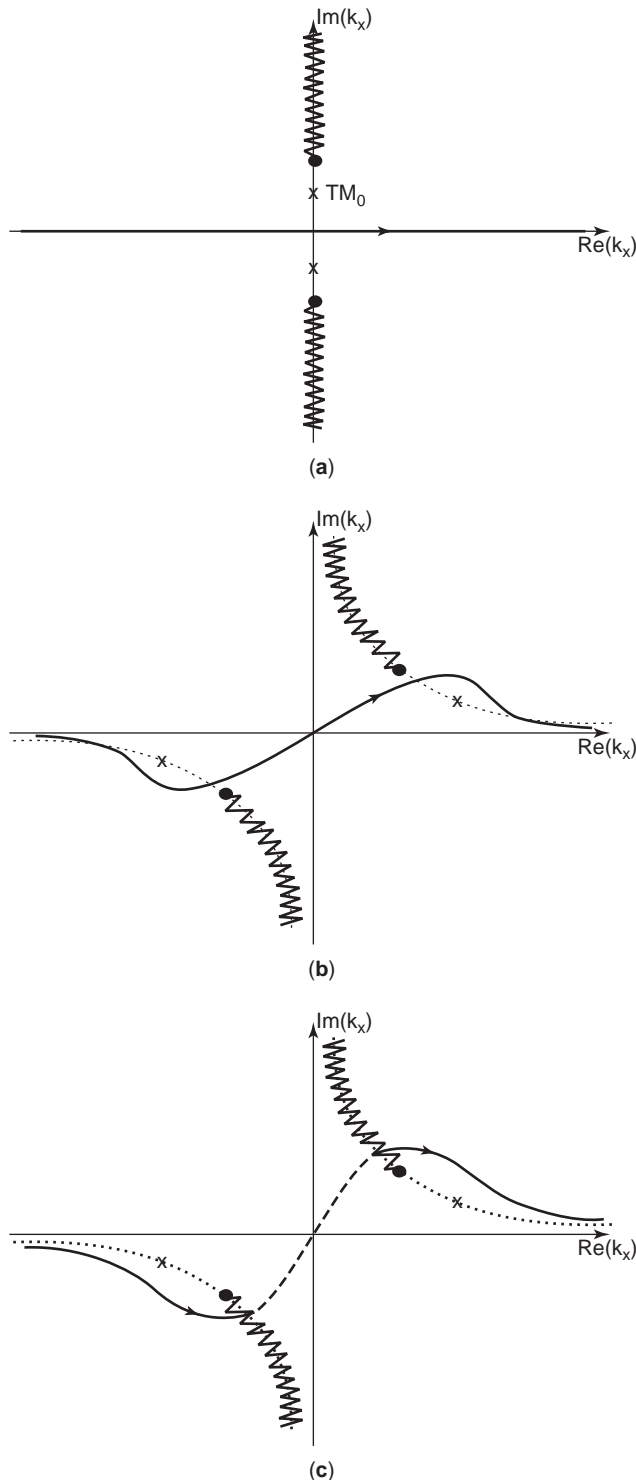


Figure 4. Integration paths in the transverse wavenumber complex plane (k_x) corresponding to (a) point A , (b) point B , and (c) point C in Fig. 6.

Point A is located on the real axis of the k_z plane, and is assumed to be on the zero sheet of the branchpoints at $\pm k_0$ and also the top sheet of the branchpoints at $\pm k_{TM_0}$. (The original path of integration C_{kz} is on this sheet.) This point corresponds to a path of integration that stays along the real axis in the k_x plane, shown in Fig. 4a, without detouring around any pole or branchpoint singularities of the SDGF.

Point B is assumed to lie on the zero sheet of the $\pm k_0$ branchpoints, and the bottom sheet of the $\pm k_{TM_0}$ branchpoints. Such a point is obtained by starting from point A , then moving into the first quadrant of the k_z plane, and then moving down, crossing the real axis between k_0 and k_{TM_0} . In doing so, the branchcut from the k_{TM_0} branchpoint is crossed, to enter the lower sheet of this branchpoint on the k_z Riemann surface. The corresponding path in the k_x plane detours around the TM_0 poles of the SDGF located at $\pm k_{xp}$, but stays on the top sheet of the Riemann surface in the k_x plane.

Point C is assumed to be on the lower (-1) sheet of the k_0 branchpoints on the k_z Riemann surface. Such a point is obtained by starting from point A , then moving into the first quadrant of the k_z plane, and then moving down, crossing the real axis between the origin and k_0 . In doing so, the branchcut from the k_0 branchpoint is crossed, to enter the lower sheet of this branchpoint on the k_z Riemann surface. (As soon as this branchcut is crossed, the branchpoints at $\pm k_{TM_0}$ no longer appear, since these branchpoints appear only on the even sheets of the $\pm k_0$ branchpoints.) The corresponding path of integration crosses through the branchcuts of the SDGF in the k_x plane and lies partly on the improper lower sheet of the k_x Riemann surface. The path also detours around the TM_0 surface-wave poles of the SDGF.

For covered structures such as covered microstrip, the only branchpoints that occur are those at the wavenumbers of the parallel-plate modes of the background structure. Assuming that only the TM_0 parallel-plate mode is above cutoff, there will be one pair of branchpoints on the real k_z axis at $k_{zb} = \pm k_{TM_0}$. There will also be an infinite number of branchpoints on the imaginary axes, corresponding to the wavenumbers of the evanescent parallel-plate modes. The complex k_z plane for a covered structure is shown in Fig. 5.

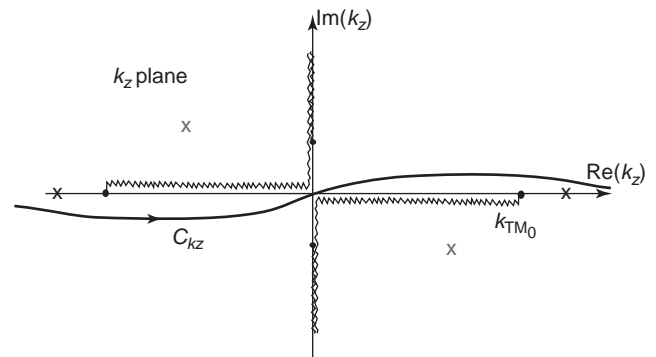


Figure 5. The k_z plane showing a pair of branchpoints at $\pm k_{TM_0}$, a pair (out of an infinite number) of branchpoints on the imaginary axis, and two pairs of poles.

2.3. Decomposition of the Total Current

When computing the fields of a simple source such as a dipole in the presence of a grounded dielectric slab, the existence of square-root-type branchpoints at $\pm k_0$ in the integrand of the corresponding Fourier integral is related to radiation in the free space, namely, to its continuous spectrum [23,24]. This principle holds for more complicated systems, such as the gap source on the microstrip line, discussed here. The existence of branchpoints is related to mechanisms of radiation. Thus, for the microstrip line under study, the fact that $\tilde{I}(k_z)$ has multiple pairs of branchpoints indicates that radiation can take place by means of different mechanisms (or, in other words, that the continuous spectrum will have different components). Specifically, the $\pm k_0$ branchpoints are related to radiation into free space, and the branchpoints at $\pm k_{\text{TM}_0}$ are related to radiation in the form of surface waves or parallel-plate modes of the background waveguide.

In addition to branchpoints, $\tilde{I}(k_z)$ also has pole singularities that originate from the roots of $D(k_z)$. It is well known that $D(k_z)$ has an infinite number of roots: a finite set corresponding to bound (proper) modes and an infinite set of leaky (improper) modes [28–35]. Specifically, the different poles of $\tilde{I}(k_z)$ are located as follows:

- *Bound modes*—the poles lie on the zero sheet with respect to the $\pm k_0$ branchpoints and on the top (proper) sheet with respect to the $\pm k_{\text{TM}_0}$ branchpoints.
- *Surface-wave leaky modes*—the poles lie on the zero sheet with respect to $\pm k_0$ branchpoints and on the bottom (improper) sheet with respect to the $\pm k_{\text{TM}_0}$ branchpoints.
- *Surface and space-wave leaky modes*—the poles lie on the -1 sheet of the $\pm k_0$ branchpoints.

A typical diagram of the integration path C_{kz} to compute $I(z)$ together with some relevant singularities of $\tilde{I}(k_z)$ is shown in Fig. 6. The path is equivalent to a real-axis path that runs from $-\infty$ to ∞ , detouring around the branchpoint singularities and also the bound mode poles on the real axis.

With an understanding of the complex k_z plane, it is now possible to discuss the physical significance of a

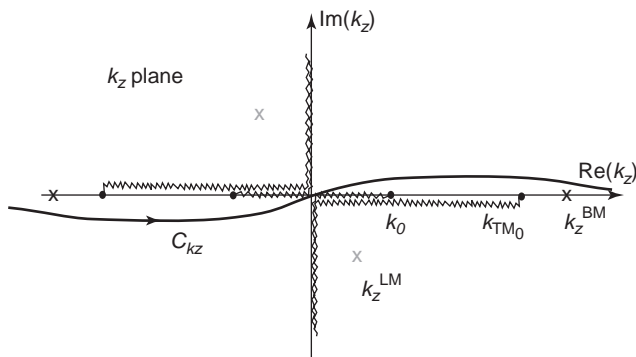


Figure 6. The k_z plane showing the integration path C_{kz} , two pairs of branchpoints at $\pm k_0$ and $\pm k_{\text{TM}_0}$, a pair of proper poles at $\pm k_{\text{TM}_0}^{\text{BM}}$, and a pair of leaky poles at $\pm k_z^{\text{LM}}$.

particular mode. This physical significance can be defined by the degree of excitation of this mode from a realistic source. A mode that is physically significant should be excited by a suitable finite source, which implies that the current $I(z)$ on the line will then have a component that closely resembles the current of the mode. (If a particular mode is excited with a sufficient amplitude, this modal component may dominate the total line current.)

One possible “measure” of the relative significance of each microstrip mode can be obtained by looking at the “distance” from the corresponding pole in the k_z plane to the integration contour C_{kz} on the Riemann surface. The term “distance” here refers to distance on the Riemann surface. For example, two points on the opposite sides of a branchcut, both on the same sheet, will not be “close” to one another, regardless of how geometrically close they are together. Two geometrically close points on either side of a branchcut will be close on the Riemann surface if they are located on different sheets, such that there is a continuous connection between the two points.

Since the k_z^{BM} pole on the real axis corresponding to a bound mode is on the same sheet as the integration path C_{kz} , this pole is always close to the path of integration, and is therefore always physically significant. For the leaky-mode poles, however, the poles may or may not be close to the integration path, depending on which sheet they are located, and the value of the phase constant β of each mode. The physical significance of a leaky mode can be summarized concisely by saying that a mode can have physical significance only if the mode satisfies what is denoted as the *path consistency condition* (PCC). This condition (which was called the “condition of leakage” in Ref. 32) states that the path of integration in the k_x plane used to obtain a particular leaky-mode solution should be *consistent* with the phase constant β of the leaky mode that is obtained by using the given path. For example, if the path in the k_x plane used to obtain a leaky mode is the one shown in Fig. 4b, which corresponds to leakage into the TM_0 mode but not into space, the resulting leaky mode will be physically significant (or “physical”) provided the phase constant of the leaky mode is in the range $k_0 < \beta < k_{\text{TM}_0}$. If the path in the k_x plane used to obtain a leaky mode is the one shown in Fig. 4c, which corresponds to leakage into both the TM_0 mode and into space, the resulting leaky mode will be physically significant (or “physical”) provided the phase constant of the leaky mode is in the range $\beta < k_0$.

This physical significance of a leaky mode is directly related to the closeness of the corresponding pole to the path C_{kz} on the Riemann surface. For example, consider a leaky-mode pole located as shown in Fig. 6, to the left of the branchpoint k_0 ; that is, $\Re(k_{zp}) < k_0$. Such a leaky mode is close to the path C_{kz} if it is on the -1 sheet of the $\pm k_0$ branchpoints. This means that the path of integration in the k_x plane is that shown in Fig. 4c. Similarly, if a leaky-mode pole is located in the region $k_0 < \Re(k_{zp}) < k_{\text{TM}_0}$, the pole is close to the path C_{kz} if the pole is on the zero sheet of the $\pm k_0$ branchpoints, and the bottom sheet of the $\pm k_{\text{TM}_0}$ branchpoints.

A more mathematical way of determining the physical significance of the leaky modes, which also provide

additional insight into the nature of the current and fields excited by the source, is to deform the original integration path C_{kz} to a vertical set of steepest-descent paths (SDPs) [23,24,36]. Figure 7 illustrates this for the case of an open structure such as microstrip (for $z > 0$).

Figure 7a shows how the original C_{kz} path may be first deformed into a path C_{BC} detouring around all the branchcuts (the TM_0 and k_0 branchcuts) and a set of residue contributions C_{BM} from paths that encircle all of the bound-modes poles on the positive real axis (in the figure only one bound mode is assumed). The total current (TC) on the strip can be decomposed as

$$I(z) = -j \operatorname{Res}\{\tilde{I}(k_z^{BM})\}e^{-jk_z^{BM}z} + \frac{1}{2\pi} \int_{C_{BC}} \tilde{I}(k_z) e^{-jk_z z} dk_z \quad (33)$$

$$= I_{BM}(z) + I_{CS}(z) \quad (34)$$

where the residue contribution around C_{BM} accounts for the launching amplitude of the bound-mode (BM) current from the gap source and the integral around C_{BC} defines the continuous-spectrum (CS) current on the line that is induced by the gap source. It is interesting to note that standard transmission-line theory only predicts the BM

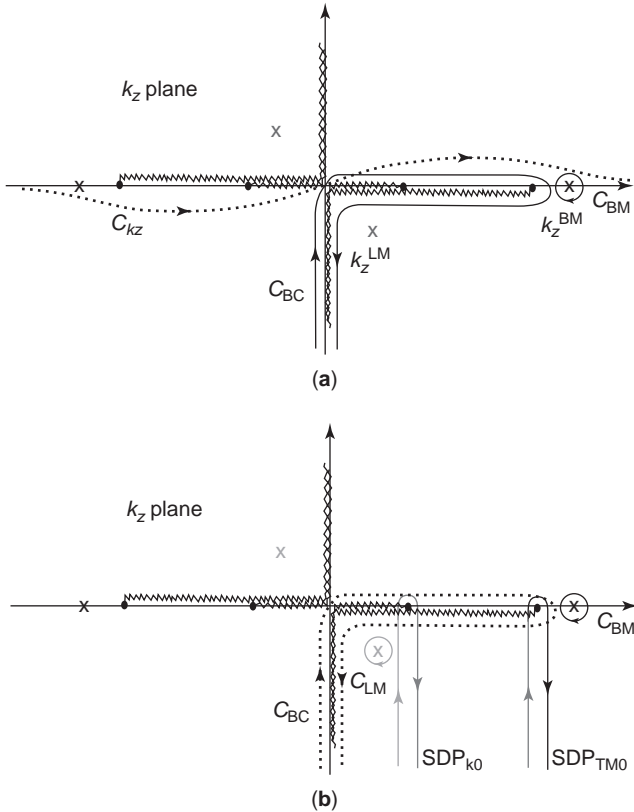


Figure 7. (a) Complex k_z plane showing the integration path C_{kz} , an integration path C_{BC} around the branch cuts, and a residue path C_{BM} around the BM pole; (b) complex k_z plane showing the path deformation of C_{kz} to a set of vertical SDPs, a residue path around the captured LM pole k_z^{LM} , and a residue path C_{BM} around the BM pole.

current and not the CS current, which is a consequence of the full-wave modeling of the complete current spectrum due to the gap source. This latter current usually increases with frequency and is responsible for spurious effects observed in the line current, as shown later.

The CS current can be further decomposed by deforming the C_{BC} path to a set of vertical SDPs as shown in Fig. 7b. In this deformation some leaky-mode (LM) poles may be captured and therefore will appear explicitly in the final decomposition of the strip current. In particular, a leaky-mode pole will be captured if the leaky mode is a physical one, satisfying the path consistency condition described previously. The residue contribution of the captured LM poles will define the launching amplitude of the *physical* leaky modes. Nonphysical leaky-mode poles will not give an explicit contribution to the leaky-mode current (defined from the residues of the captured poles), but the possible influence of such poles is automatically included in the calculation of the “residual wave” (RW) currents, which are the contributions from the path integrations along the two vertical SDP paths. The RW currents represent that part of the CS current that is not represented explicitly by the sum of the physical LM currents. The total strip current can therefore be expressed as

$$I(z) = I_{BM}(z) + I_{LM}(z) + I_{RW}^{TM_0}(z) + I_{RW}^{k_0}(z) + \sum_i I_{RW}^i(z) \quad (35)$$

where

$$I_{BM}(z) = -j \operatorname{Res}\{\tilde{I}(k_z^{BM})\}e^{-jk_z^{BM}z} \quad (36a)$$

$$I_{LM}(z) = -j \operatorname{Res}\{\tilde{I}(k_z^{LM})\}e^{-jk_z^{LM}z} \quad (36b)$$

$$I_{RW}^{TM_0}(z) = \frac{1}{2\pi} \int_{SDP_{TM_0}} \tilde{I}(k_z) e^{-jk_z z} dk_z \quad (36c)$$

$$I_{RW}^{k_0}(z) = \frac{1}{2\pi} \int_{SDP_{k_0}} \tilde{I}(k_z) e^{-jk_z z} dk_z \quad (36d)$$

$$I_{RW}^i(z) = \frac{1}{2\pi} \int_{SDP_i} \tilde{I}(k_z) e^{-jk_z z} dk_z \quad (36e)$$

The first term represents the currents of the bound modes that are launched by the gap source. Usually there is only one, and this is the desired transmission-line mode. The second term represents the sum of all physical leaky modes, from the residues of the captured poles. In general, there may be two types of physical leaky modes, those that leak into only the TM_0 mode, and those that leak into both the TM_0 modes and into space. The next term is the TM_0 RW current, arising from the path integration along the vertical SDP path that descends downward from the branchpoint at $k_{zb} = k_{TM_0}$. The next term is the k_0 RW current that arises from the path integration along the vertical SDP path that descends downward from the branchpoint at $k_{zb} = k_0$. The last series term is a set of

RW currents that comes from SDP paths (not shown in Fig. 7b) that descend from branchpoints associated with improper complex modes of the background structure. These RW currents are included whenever the phase constants of the corresponding improper modes of the background structure are less than k_0 , so that the branchpoints are intercepted by the path deformation. These RW currents are usually negligible because of the large imaginary part of the corresponding branchpoints.

Although the TM_0 and k_0 RW currents do not have closed-form expressions, it is possible to evaluate their asymptotic behaviors for large z [21,36]. The calculation shows that the TM_0 RW current behaves as

$$I_{RW}^{TM_0}(z) \sim A_{RW}^{TM_0} \frac{e^{-jk_{TM_0}z}}{(k_{TM_0}z)^{3/2}} \quad (37)$$

and the k_0 RW current as

$$I_{RW}^{k_0}(z) \sim A_{RW}^{k_0} \frac{e^{-jk_0z}}{(k_0z)^2} \quad (38)$$

3. RESULTS FOR THE CURRENT EXCITED BY A GAP SOURCE

In this section results will be presented for the three structures shown in Fig. 1, to illustrate the types of spurious effects that may be observed in the current excited by a gap voltage source on a printed-circuit transmission line. The three structures are microstrip, covered microstrip, and stripline with an airgap. In each case plots of the total current are presented, along with plots of the bound mode and continuous-spectrum currents. When physical leaky modes are present, the continuous-spectrum (CS) current is decomposed into the leaky-mode (LM) and residual-wave (RW) parts, and these are shown.

3.1. Microstrip

For the microstrip structure of Fig. 1a, the current excited by the gap source consists of a BM current and a CS current. The CS current consists of any physical leaky modes that exist at the frequency of interest, together with a RW current, which consists of both the TM_0 RW current and the k_0 RW current.

In all the cases presented, the only physical leaky mode that is found to exist is one that leaks into the TM_0 surface-wave mode, and not into space. Such a leaky mode is physical, and hence is included in the composition of the CS current, if $k_0 < \beta < k_{TM_0}$. Results are presented for both a moderate-permittivity substrate and a high-permittivity substrate [21].

Results are first presented for the case of a moderate permittivity substrate, $\epsilon_r = 2.2$, for several different values of w/h , corresponding to different characteristic impedances. The substrate thickness is $h = 1.0$ mm in all cases.

Figure 8 shows the dispersion plot for a narrow line, with $w/h = 0.333$. For this dimension, the low-frequency characteristic impedance is 145.8 Ω . A plot of the normal-

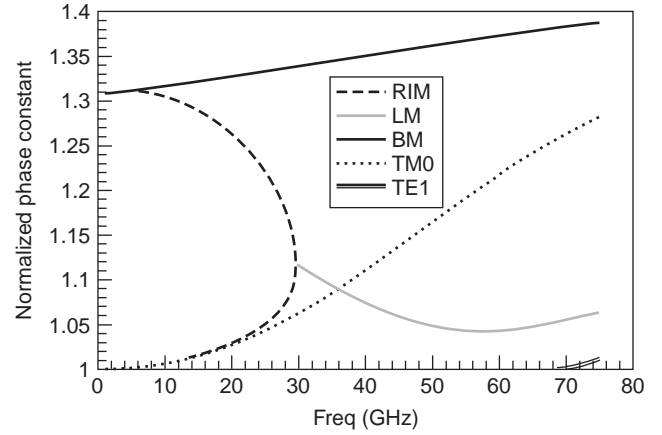


Figure 8. Normalized phase constants (normalized by k_0) versus frequency, for a microstrip line with a moderate substrate permittivity ($\epsilon_r = 2.2$) and a small strip width ($w = 0.333$ mm, $h = 1.0$ mm). The bound mode (BM) is shown along with the leaky mode (LM) and the TM_0 and TE_1 surface-wave modes. At low frequency there is no leaky mode, only a pair of improper real modes (RIM). (This figure is available in full color at <http://www.mrw.interscience.wiley.com/erfme>.)

ized phase constant of the bound mode is shown, along with a plot for the leaky mode. Also, for reference, a plot of the normalized phase constants for the TM_0 and TE_1 surface-wave modes of the grounded substrate are included. It is observed that leakage begins at 30 GHz. Above this frequency a leaky mode with a complex propagation wavenumber exists on the microstrip line. The leaky mode leaks into the TM_0 surface-wave mode of the grounded substrate. The leaky mode is an EH_0 mode, meaning that the transverse profile of the current closely resembles the expected quasi-TEM shape function. Below 30 GHz there is no leaky mode, only a pair of improper real modes (modes that are improper, but with a real propagation wavenumber). The leaky mode becomes physical above about 35 GHz, where it crosses the TM_0 dispersion line to become a fast wave with respect to the TM_0 surface wave.

Figure 9 shows the total current on the strip versus normalized distance from the source, for various frequencies. In this figure, and in all subsequent results, the length of the gap source is taken as $\Delta = 0.1\lambda_0$. It is seen in Fig. 9 that the total current is increasingly oscillatory as the frequency increases. This is due to the interference between the BM and CS currents. At low frequency, only the BM current is significant, and the current level is essentially flat with distance from the source. As the frequency increases, the amplitude of the CS current also increases, resulting in a stronger interference effect.

Figure 10 shows the dispersion plots for the case of a moderate strip width, $w/h = 1$. For this case the low-frequency characteristic impedance is 95.2 Ω . Comparing with Fig. 8, it is seen that leakage begins at a lower frequency for this wider strip, although the lowering in frequency is not dramatic. The leakage starts at about 27 GHz, with the leaky mode becoming physical at about 33 GHz, where the phase constant crosses the TM_0 dispersion curve. The leaky mode is not physical between approximately 47 and 70 GHz, where the dispersion curve

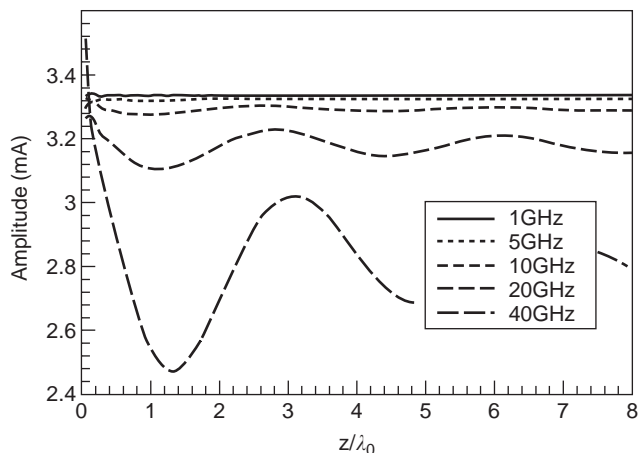


Figure 9. The total strip current versus distance from the source, for the case of Fig. 8. Results are shown for various frequencies.

is below the unity line, so that $\beta < k_0$. In this frequency range a physical leaky mode would be one that leaks into both the TM_0 surface-wave mode of the substrate and into space. However, no such physical leaky mode is found.

Figure 11 shows the current on the strip at various frequencies, for the case of moderate strip width. Comparing with Fig. 9, it is seen that the level of spurious oscillations is roughly the same, although the overall level of the current is higher for the wider strip case, because a wider strip corresponds to a smaller characteristic impedance, and hence the bound mode is excited with a larger amplitude. However, the CS current is also excited with a larger amplitude, giving roughly the same level of oscillations in the total current.

Figure 12 gives the dispersion behavior for a wide-strip case, where $w/h = 3$. For this case the low-frequency characteristic impedance is 51.1Ω . It is seen that the trend of a lower leakage frequency continues, with leakage now

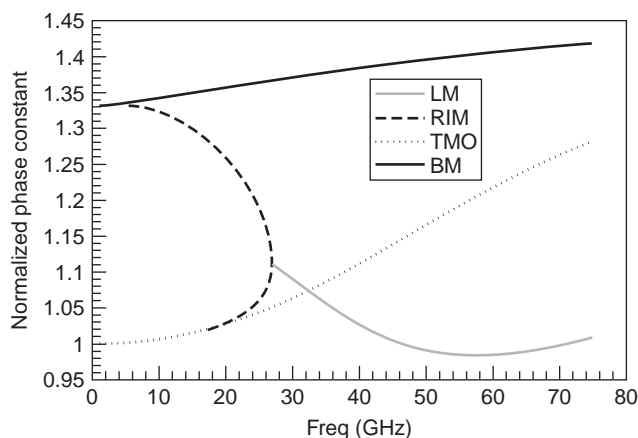


Figure 10. Normalized phase constants (normalized by k_0) versus frequency, for a microstrip line with a moderate substrate permittivity ($\epsilon_r = 2.2$) and a moderate strip width ($w = 1.0$ mm, $h = 1.0$ mm). The bound mode (BM) is shown along with the leaky mode (LM) and the TM_0 surface-wave mode. At low frequency there is no leaky mode, only a pair of improper real modes (RIM). (This figure is available in full color at <http://www.mrw.interscience.wiley.com/erfme>.)

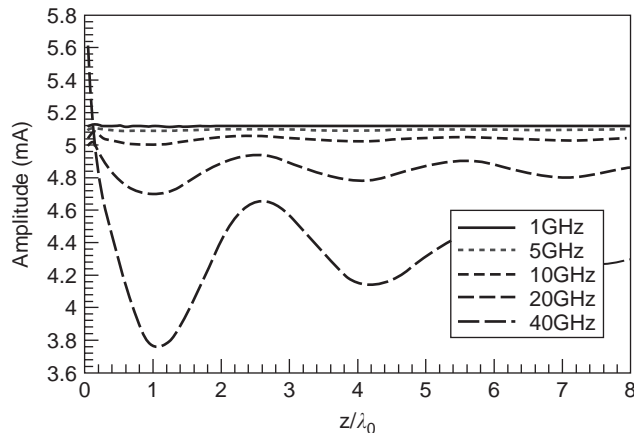


Figure 11. The total strip current versus distance from the source, for the case of Fig. 10. Results are shown for various frequencies. (This figure is available in full color at <http://www.mrw.interscience.wiley.com/erfme>.)

beginning at about 23 GHz, and the leaky mode becoming physical at about 27 GHz. The leaky mode is once again nonphysical in a particular high-frequency region, from about 33 to 64 GHz.

The current plots in Fig. 13 for the wide-strip case show a continuing increase in the overall current level, as expected. As with the other cases, the level of the spurious oscillations increases with frequency. However, for this wider strip case an interesting new effect is also observed. At a high frequency of 70 GHz, the oscillations decay extremely slowly with distance from the source. In fact, out to eight wavelengths from the source, there is no noticeable decay in the oscillation amplitude of Fig. 13. This is because the CS current decays very slowly with distance in this case. The effect has been examined in detail in Ref. 22, where it is shown that the effect is due to a leaky-mode pole

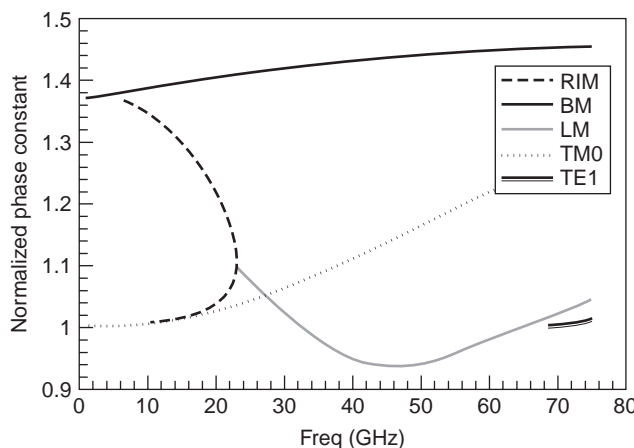


Figure 12. Normalized phase constants (normalized by k_0) versus frequency, for a microstrip line with a moderate substrate permittivity ($\epsilon_r = 2.2$) and a large strip width ($w = 3.0$ mm, $h = 1.0$ mm). The bound mode (BM) is shown along with the leaky mode (LM) and the TM_0 and TE_1 surface-wave modes. At low frequency there is no leaky mode, only a pair of improper real modes (RIM). (This figure is available in full color at <http://www.mrw.interscience.wiley.com/erfme>.)

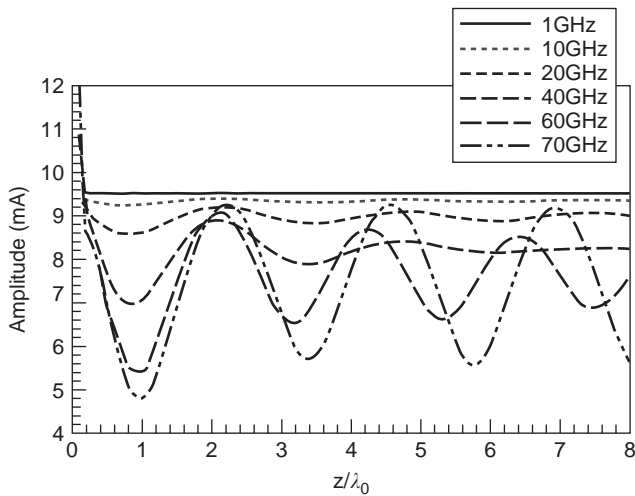


Figure 13. The total strip current versus distance from the source, for the case of Fig. 12. Results are shown for various frequencies. (This figure is available in full color at <http://www.mrw.interscience.wiley.com/erfme>.)

approaching the branchpoint at k_0 in the complex k_z plane. The frequency at which this effect occurs is given approximately for wide strips by the following empirical formula [22]:

$$k_0 \sqrt{\epsilon_r} w = 2\pi \quad (39)$$

In Fig. 14, the current is investigated in more detail for the case of moderate strip width ($w/h = 1$), at a frequency of 20 GHz. Part (a) of this figure shows the total current and its constituent parts, the BM and CS currents; part (b) shows the CS current resolved into its constituent components, the k_0 RW current and the TM_0 RW current. There is no physical leaky mode at this frequency (see Fig. 10), so the CS current is simply the sum of the two RW currents. The TM_0 RW current is the stronger of the two residual waves, although the amplitudes are somewhat comparable. At 40 GHz the situation changes in that a physical leaky mode now exists (see Fig. 10). At this higher frequency the oscillations in the total strip current are larger, as seen in Fig. 15a, because the magnitude of the CS current is larger at this higher frequency. In Fig. 15b, the CS current is shown with its three components, the leaky-mode current, the k_0 RW current, and the TM_0 RW current. Close to the source, the LM current is the strongest. However, because the LM current decays exponentially with distance, the two RW currents become dominant for larger distances. The TM_0 RW current is the more dominant of the two, as for the 20-GHz case. The presence of the physical leaky mode causes the level of spurious oscillation to be quite significant close to the source in the 40-GHz case, much larger than in the 20-GHz case. Farther away from the source the level of spurious oscillation is still slightly larger in the 40-GHz case, but the increase is not as dramatic.

Figure 16 shows the dispersion behavior for a microstrip with a high-permittivity substrate ($\epsilon_r = 10.2$) and a moderate strip width ($w/h = 1$). (The leaky-mode solution is plotted up to 37.5 GHz, which is already well within the

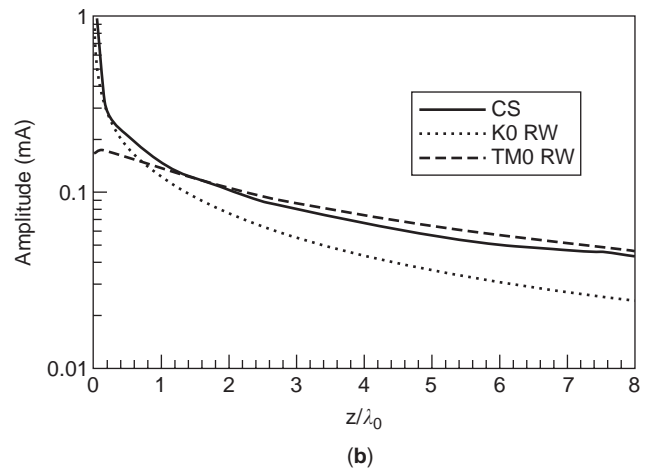
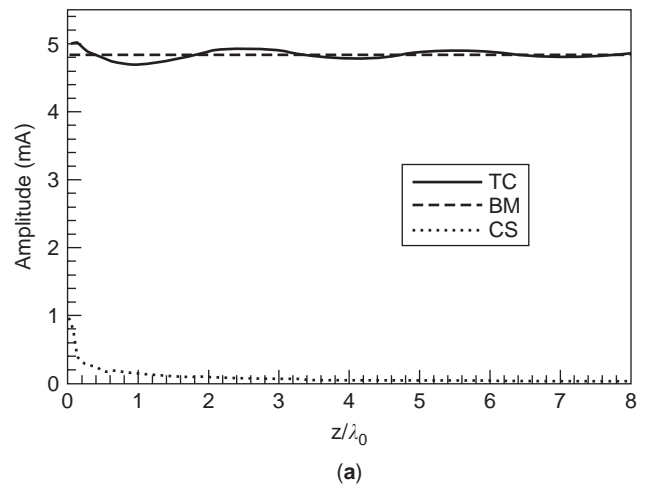
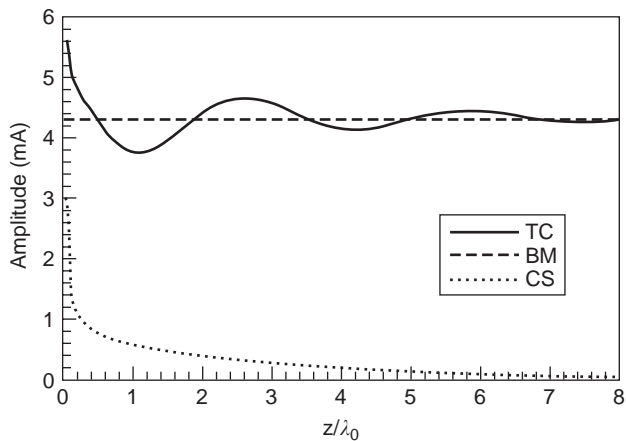


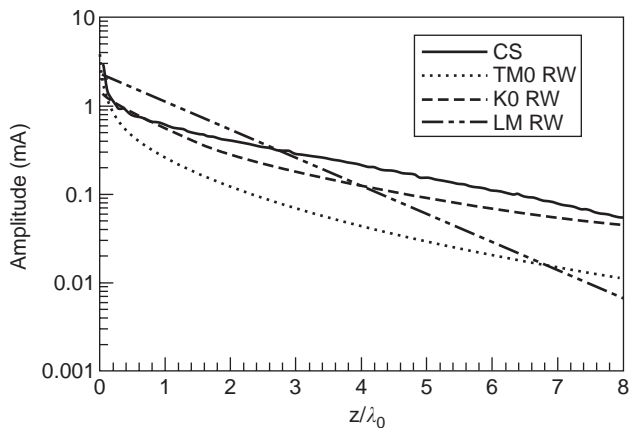
Figure 14. Strip currents for the case of a moderate substrate permittivity ($\epsilon_r = 2.2$) and moderate strip width ($w = h = 1.0$ mm) at 20 GHz: (a) total current and its constituent parts, the bound-mode and continuous-spectrum currents; (b) continuous-spectrum current and its constituent parts, the TM_0 residual-wave current and k_0 residual-wave currents.

nonphysical region.) Comparing with Fig. 10, it is seen that the higher permittivity has lowered the frequency at which leakage begins. At about 24 GHz a second surface-wave mode, the TE_1 mode, begin to propagate, and the dispersion curve for this mode is included in the plot. Above this frequency, there will be a third propagating RW current, corresponding to the TE_1 branchpoint on the real axis in the complex k_z plane.

Figure 17 shows the current versus distance from the source for this high-permittivity case. The level of spurious oscillations in the strip current increases with frequency, as for the moderate-permittivity case of Fig. 11. Figure 18a shows the total strip current at 20 GHz for the case of Fig. 16 along with its components, the BM and CS currents. In Fig. 18b it is seen that a physical leaky mode dominates the CS current near the source, although the k_0 RW and TM_0 RW currents are not negligible, even near the source. Because of the exponential decay of this leaky mode, the oscillations in the total strip current die out fairly quickly with distance.



(a)



(b)

Figure 15. The strip currents for the case of a moderate substrate permittivity ($\epsilon_r = 2.2$) and moderate strip width ($w = h = 1.0$ mm) at 40 GHz: (a) total current and its constituent parts, the bound-mode and continuous-spectrum currents; (b) continuous-spectrum current and its constituent parts—the leaky-mode current, the TM_0 residual-wave, and k_0 residual-wave currents.

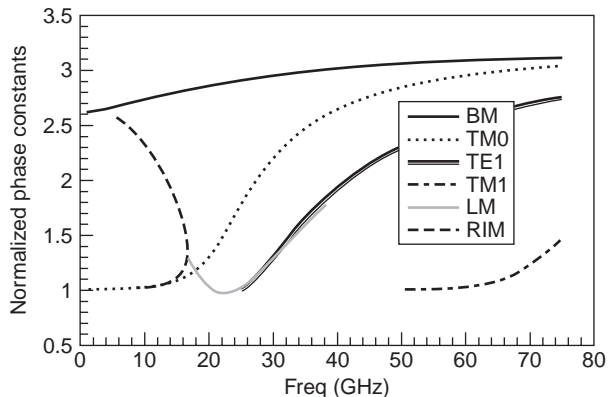


Figure 16. Normalized phase constants (normalized by k_0) versus frequency, for a microstrip line with a high substrate permittivity ($\epsilon_r = 10.2$) and a moderate strip width ($w = h = 1.0$ mm). The bound mode (BM) is shown along with the leaky mode (LM) and the TM_0 and TE_1 surface-wave modes. At low frequency there is no leaky mode, only a pair of improper real modes (RIM). (This figure is available in full color at <http://www.mrw.interscience.wiley.com/erfme>.)

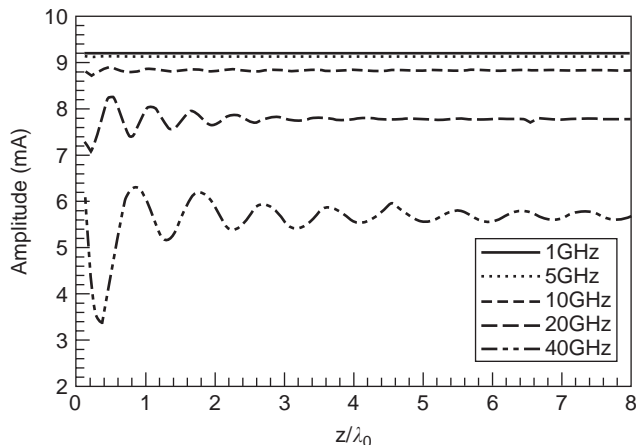
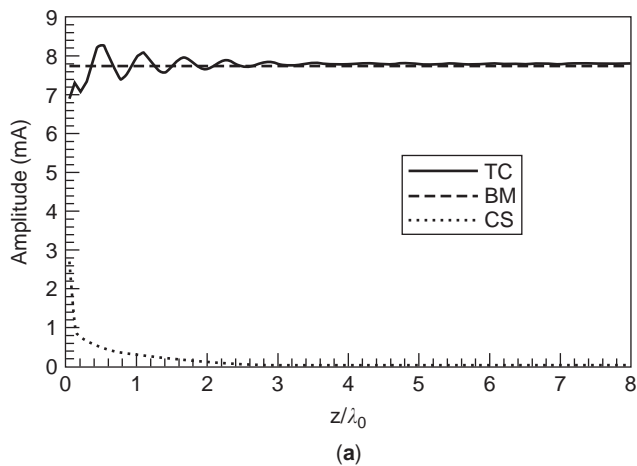
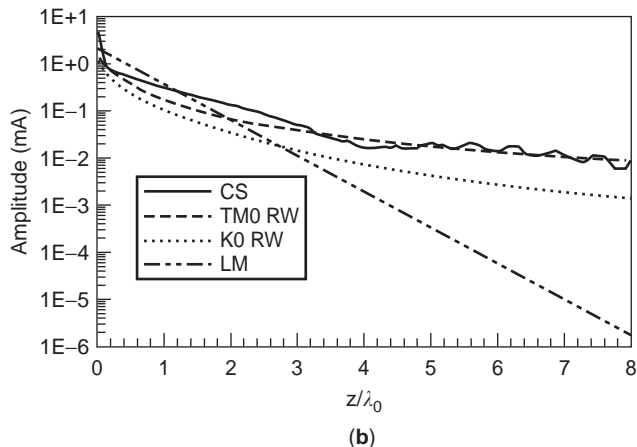


Figure 17. The total strip current versus distance from the source, for the case of Fig. 16. Results are shown for various frequencies.



(a)



(b)

Figure 18. Strip currents for the high-permittivity case of Fig. 16 at 20 GHz: (a) the total current and its constituent parts, the bound-mode and continuous-spectrum currents; (b) the continuous-spectrum current and its constituent parts—a leaky mode current together with TM_0 residual-wave and k_0 residual-wave currents.

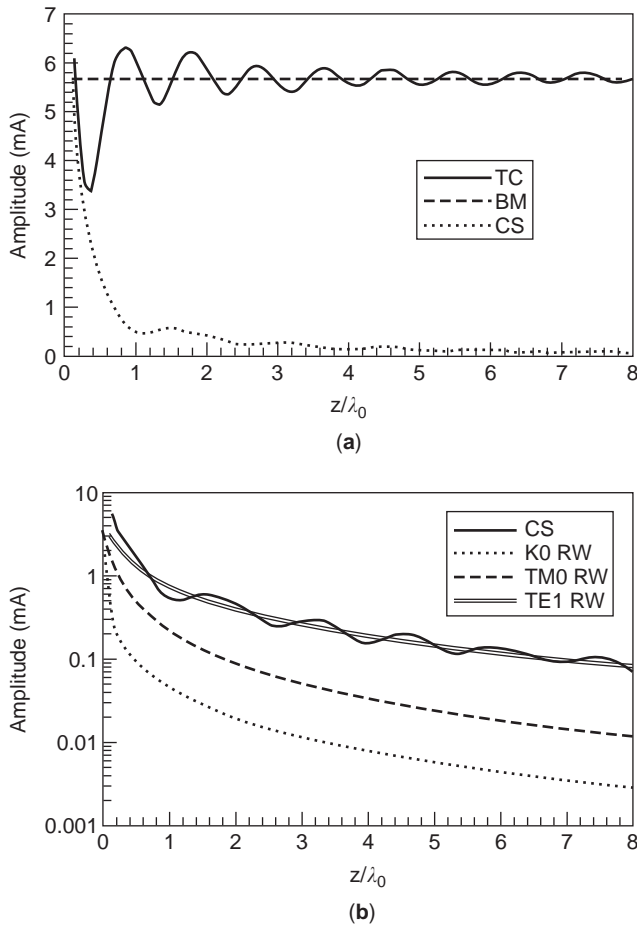


Figure 19. Strip currents for the high-permittivity case of Fig. 16 at 40 GHz: (a) the total current and its constituent parts, the bound-mode and continuous-spectrum currents; (b) the continuous-spectrum current and its constituent parts—a leaky mode current together with TM_0 residual-wave, TE_1 residual-wave, and k_0 residual-wave currents.

At 40 GHz, the oscillations become stronger, as seen in Fig. 19. As before, the CS current is responsible for the oscillations, as seen in Fig. 19a. However, the strong CS current is not due to the excitation of a leaky mode, as was the case for the moderate-permittivity substrate at 40 GHz (Fig. 15). For the higher-permittivity substrate at 40 GHz, the leaky mode shown in Fig. 16 is not physical, since its dispersion curve is lower than that of the TE_1 surface-wave dispersion curve (while this leaky mode has leakage only into the TM_0 surface-wave mode). Furthermore, no physical leaky mode that leaks into both the TM_0 and TE_1 surface-wave modes is found at this frequency. Figure 19b shows that the strong CS current is due to the TE_1 RW current. The TE_1 RW current is very strong because the dispersion curve for the leaky mode is only slightly below that for the TE_1 surface-wave mode. The leaky mode is therefore only slightly into the nonphysical region. Mathematically, this means that even though the LM pole is not captured by the path deformation to the steepest-descent paths from the branchpoints, the LM pole is close to the TE_1 branch point, and thus makes its influence felt in the TE_1 RW current.

3.2. Covered Microstrip

In practice, microstrip lines are often used in microwave circuits that are placed into packages of some type. It is therefore important to determine the influence of the top and sidewalls of a package on the possible leakage behavior of various transmission lines. The effects of a top cover, as shown in Fig. 1b, is investigated here. The addition of a top cover still allows the same method of analysis to be used as for the open microstrip structure, as discussed in Section 2. Because of the cover, leakage may only occur into the TM_0 parallel-plate substrate mode, and not into free space (it is assumed here that only the TM_0 substrate mode is above cutoff). Furthermore, there is only one type of residual current, the TM_0 RW current.

One of the most important conclusions, demonstrated from the results below, is that the presence of the top cover lowers the frequency at which leakage begins. This is because the top cover significantly raises the dispersion plot of the TM_0 mode, while influencing the dispersion plot of the guided mode to a lesser degree. Hence, physical leakage begins at a lower frequency with the top cover.

Furthermore, it is demonstrated that the top cover also increases the overall amplitude of the CS current. Hence, spurious effects significantly increase due to the presence of the top cover.

Figure 20 presents a dispersion plot for a moderate permittivity substrate ($\epsilon_r = 2.2$) and a strip-width:substrate-height ratio of $w/h = 1$, for uncovered microstrip. This result is the same as that shown in Fig. 10, except that the result is plotted in a normalized form, versus the electrical thickness of the substrate h/λ_0 . (Although the result in Fig. 10 is plotted against frequency using fixed dimensions in millimeters instead of plotting versus normalized electrical substrate thickness, the result is just as general, since it can be directly converted into a result for normalized substrate thickness, following the style of Ref. 37.) For the uncovered microstrip, the splitting point (the frequency at which leakage first begins as a nonphysical leaky mode) is at about $h/\lambda_0 = 0.09$, and the frequency at which the leaky mode enters the physical fast-wave region is at about $h/\lambda_0 = 0.11$. Clearly, physical leakage on

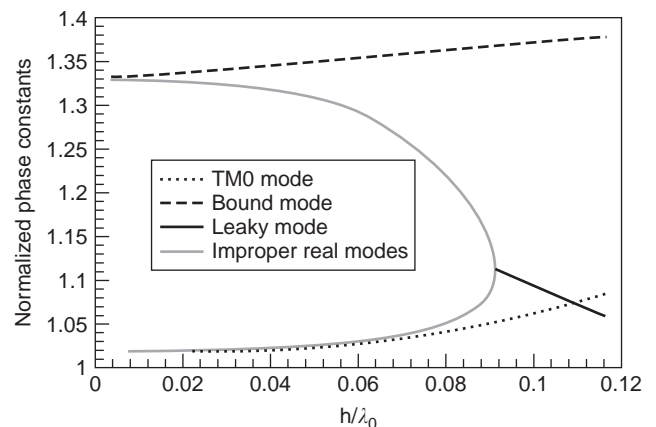


Figure 20. Dispersion plot showing the normalized phase constant versus normalized frequency for an open microstrip line ($w/h = 1.0$, $\epsilon_r = 2.2$).

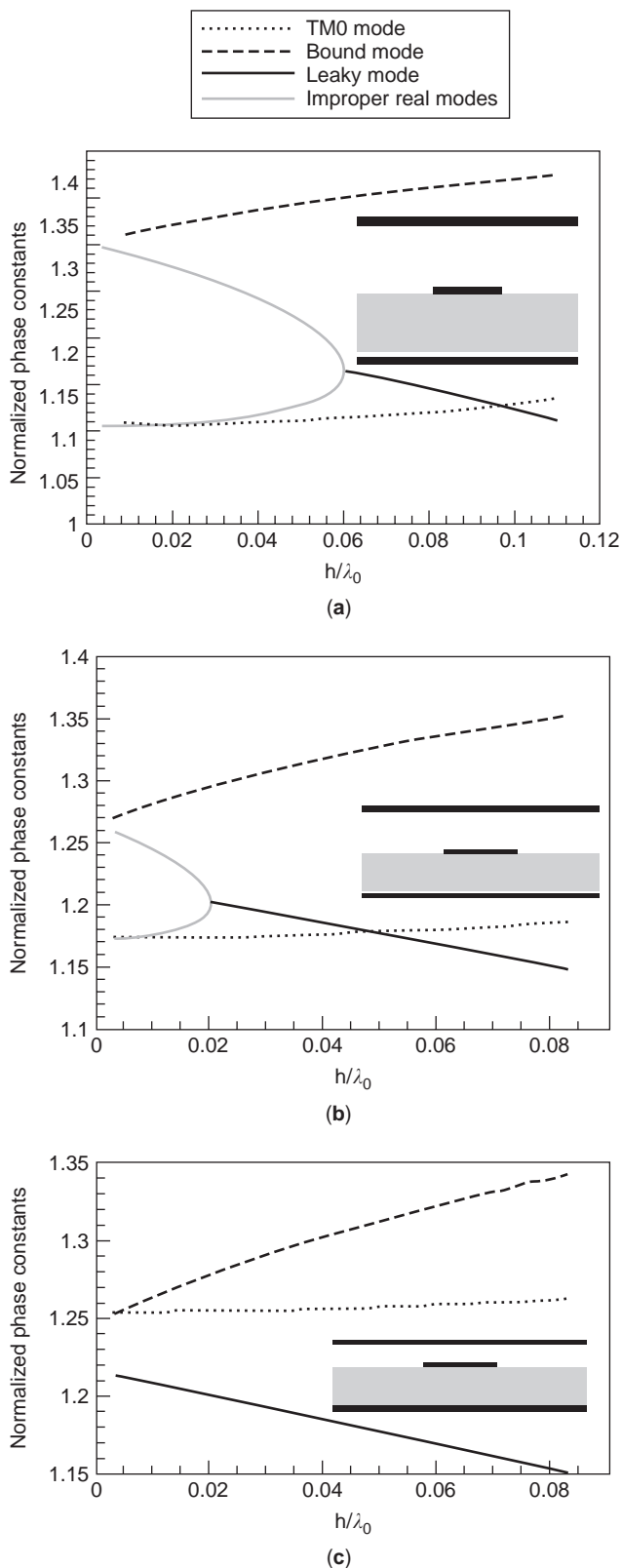


Figure 21. Dispersion plot showing the normalized phase constant versus normalized frequency for a covered microstrip line ($w/h = 1.0$, $\epsilon_r = 2.2$). The cover heights are (a) $h_c/h = 2.0$, (b) $h_c/h = 1.0$, and (c) $h_c/h = 0.5$.

typical microstrip lines occurs only for high frequencies or thicker substrates.

Figures 21a–21c show the dispersion curves for cover heights of $h_c/h = 2.0$, 1.0, and 0.5, respectively, showing the changes in the dispersion plots as the top cover is brought successively nearer to the strip.

For a cover height $h_c/h = 1.0$, the frequency at which leakage begins is approximately $h/\lambda_0 = 0.02$. When the cover height is reduced still further to $h_c/h = 0.05$, leakage now occurs at all frequencies. These results clearly demonstrate that for smaller cover heights the potential exists for spurious effects such as crosstalk and power loss due to the leaky mode. An investigation into the current excited on the strip by a gap voltage source, presented next, will confirm this.

Figure 22 shows a plot of the current for the uncovered case of Fig. 20, at a moderate frequency ($h/\lambda_0 = 0.04$). At this frequency we may note from Fig. 20 that there is no leaky mode, so that the continuous spectrum consists only of the residual wave. From Fig. 22 it is seen that the CS current is very small, and that the total strip current is essentially the same as that of only the bound mode. The residual wave is therefore very small. At this moderate frequency the continuous spectrum is small enough that no serious spurious effects are observed. Of course, significant spurious effects will be observed at higher frequencies, as demonstrated in Section 3.1, but at this relatively low frequency the spurious effects are quite small.

Figure 23 shows a plot of the current for the same moderate-permittivity case as in Fig. 22, but for a cover height of $h_c/h = 1.0$. The normalized frequency is $h/\lambda_0 = 0.02$ (half of the value used in Fig. 22). Even though the frequency is half that used in the uncovered case, the spurious oscillations are clearly much more severe. From Fig. 21b it is seen that the leaky mode is not physical at this frequency, so the CS current consists entirely of the RW current. Hence, one conclusion is that the presence of a top cover increases the amplitude of the RW current.

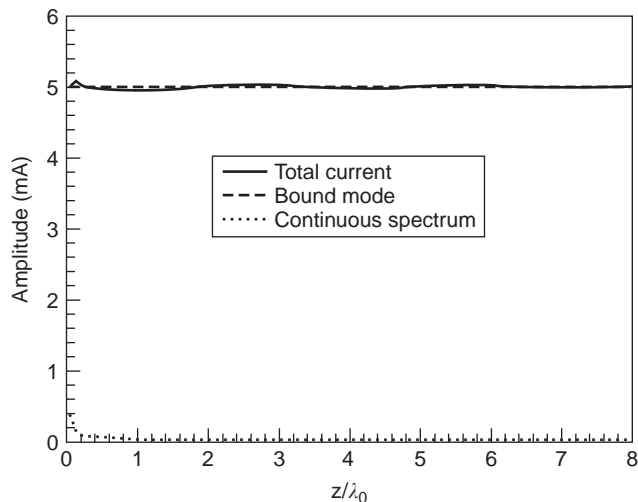


Figure 22. Plots of the total current, BM current, and CS current on an uncovered microstrip line versus normalized distance from the delta gap voltage source at $h/\lambda_0 = 0.04$ ($w/h = 1.0$, $\epsilon_r = 2.2$).

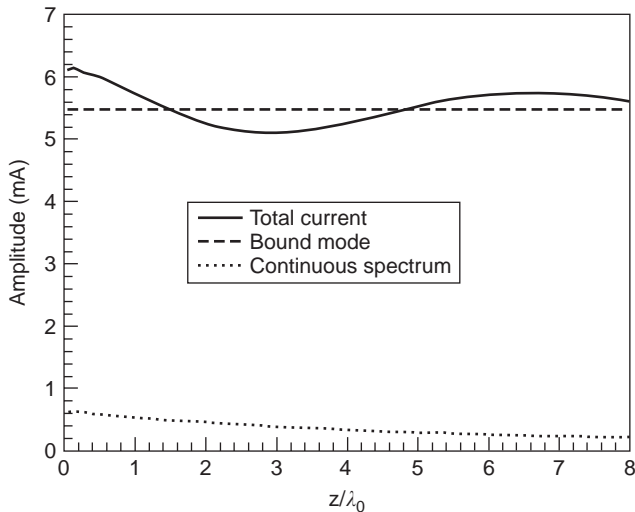


Figure 23. Plots of the total current, BM current, and CS current on a covered microstrip line versus normalized distance from the delta gap voltage source at $h/\lambda_0 = 0.02$ ($h_c/h = 1.0$, $w/h = 1.0$, $\epsilon_r = 2.2$).

Figure 24a shows the current for the case of a smaller cover height, $h_c/h = 0.5$, at the same normalized frequency of $h/\lambda_0 = 0.02$. All other parameters remain the same as in Fig. 23. (See Fig. 21c for a dispersion plot.) This figure reveals two important aspects about the effects of reducing the cover height:

1. The level of oscillation in the total current has increased significantly, compared to that in Fig. 23, which corresponds to the same frequency. This is partly because lowering the cover height has decreased the amplitude of the bound mode, but even more importantly, it has dramatically increased the amplitude of the CS current. Part (b) of Fig. 24 shows that the leaky mode is now the main component of the CS current.
2. Comparing Figs. 24b and 23, it is also seen that the RW current is somewhat stronger for the lower cover height. (In Fig. 23 there is no physical leaky mode at this frequency, so the RW current is the same as the CS current.) However, the main reason why the CS current is significantly larger in Fig. 24 is the presence of the very strong leaky mode. Hence, lowering the top cover both increases the amplitude of the RW current and also results in the excitation of a strong LM current.

3.3. Stripline with an Airgap

The stripline structure is one of the most well known and widely used printed-circuit transmission-line structures. A homogeneous stripline structure will support only a TEM mode of propagation, and no leaky modes. This is because the substrate between the two ground planes is homogeneous. However, during manufacture, an airgap may be inadvertently introduced, resulting in the airgap

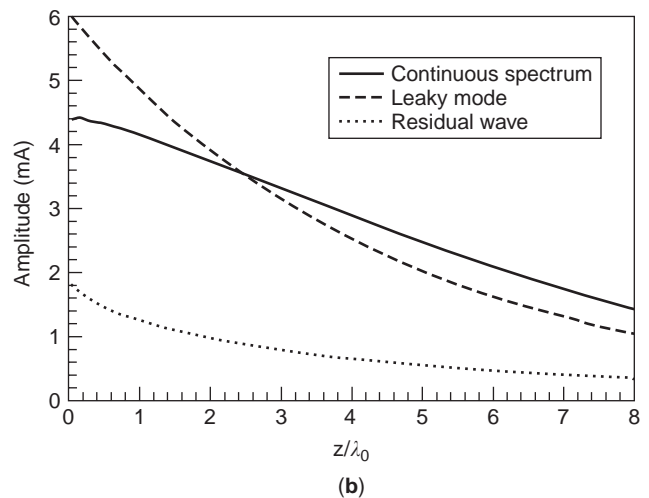
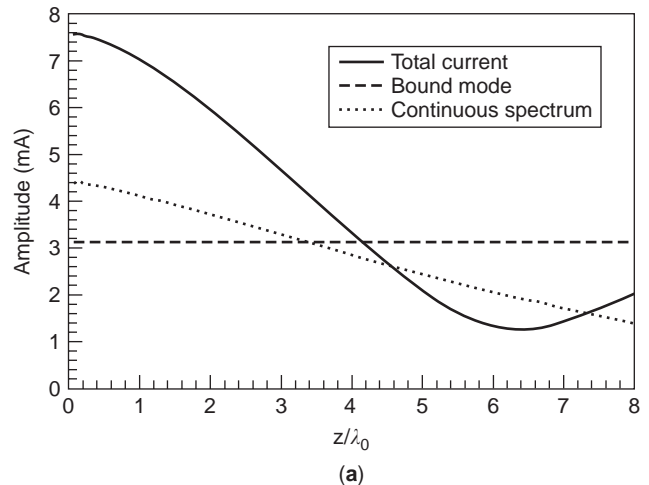


Figure 24. (a) Plot of the total current, BM current, and CS current on a covered microstrip line versus distance from the delta gap voltage source, for $\epsilon_r = 2.2$, $w/h = 1.0$, and a cover height of $h_c/h = 0.5$, with normalized frequency $h/\lambda_0 = 0.02$; (b) the CS current is shown along with its constituent parts: the LM current and the TM_0 RW current.

stripline structure shown in Fig. 1c. It has been known for some time that airgaps within stripline packages can degrade the performance of the stripline, although the fundamental reasons were perhaps not clear. It is shown here that the airgap lowers the phase constant of the dominant quasi-TEM stripline mode below that of the TM_0 parallel-plate mode of the (now inhomogeneous) background structure. This causes the stripline mode to become a physical leaky mode. This means that the stripline mode used for signal transmission will suffer from power loss due to leakage, as well as crosstalk and other effects due to leakage into the TM_0 mode.

When a small airgap is present, it is shown that there is a bound mode present, as well as the leaky mode. However, the bound mode is one that has the field characteristics of a parallel-plate type of mode. In fact, as the airgap thickness tends to zero, the bound mode evolves into a TEM parallel-plate mode. A conventional stripline feed

would predominantly excite the leaky mode, since this is the mode that resembles the TEM stripline mode that would exist with no airgap. However, a practical feed will also excite the bound-mode field to some extent, more so as the airgap thickness increases, since the fields of the leaky and bound modes tend to become less distinct as the airgap thickness increases. The fact that both a leaky mode and a bound mode are excited means that spurious oscillations will occur in the strip current, as was observed in the results presented for the previous two structures, microstrip and covered microstrip. This interference explains the experimental observation in Ref. 11, which was subsequently investigated more thoroughly in [20], where a very sharp and pronounced spurious dip in the transmission (S_{21}) response was observed at a specific frequency, using the airgap stripline. The spurious dip that was observed was attributed to interference between the bound mode and the leaky mode, and this is proved by an examination of the currents excited by a gap voltage source.

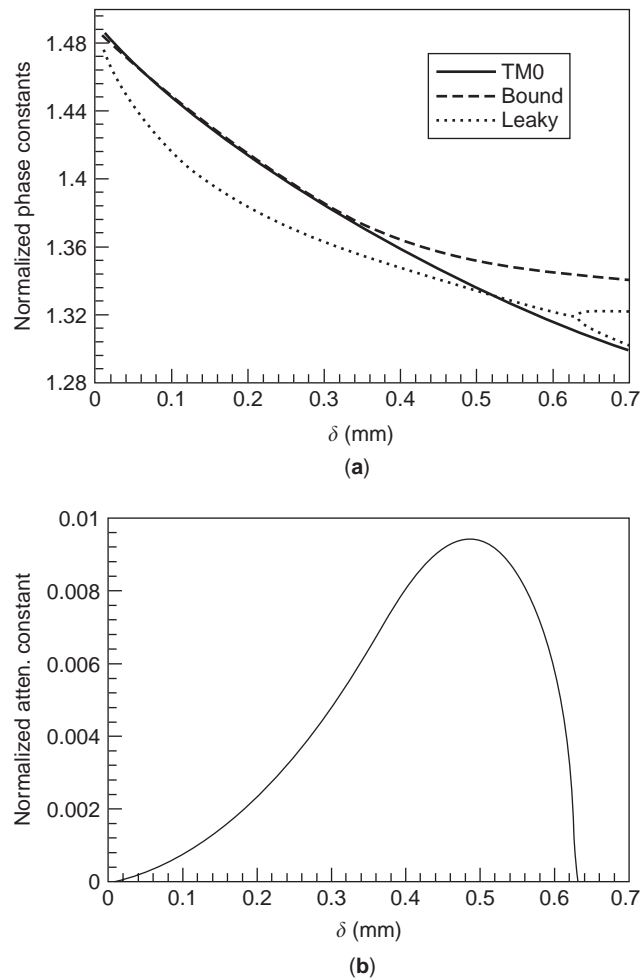


Figure 25. (a) The normalized phase constants of the bound mode, leaky mode, and TM₀ mode of the parallel-plate background structure, versus airgap thickness at 3.0 GHz; (b) the normalized attenuation constant of the leaky mode ($h = 1.0$ mm, $w = 1.0$ mm, $\epsilon_r = 2.2$).

The normalized phase and attenuation constants at 30 GHz are plotted with respect to the airgap thickness in Figs. 25a and 25b, respectively. It is seen from part (a) that the LM will be a physical mode (a fast-wave solution with respect to the TM₀ parallel-plate mode) for an airgap thickness less than 0.5 mm. The physical validity of the leaky mode is gradually lost as the airgap thickness increases beyond this value.

For an airgap thickness of $\delta = 0.3$ mm, plots of the total current as well as the BM and CS currents are shown in Fig. 26a. Figure 26b shows the CS current and its two constituent parts, the LM current and the RW current. For this airgap thickness, Fig. 26a shows that the CS current is much more strongly excited than the BM current. Moreover, the curves in Fig. 26b show that the CS current is almost entirely accounted for by the LM current. This is because the leaky mode is physical for this airgap thickness, and because the field of the leaky mode resembles that of the usual TEM stripline mode, and hence is excited quite strongly by the gap voltage source. The dip in the

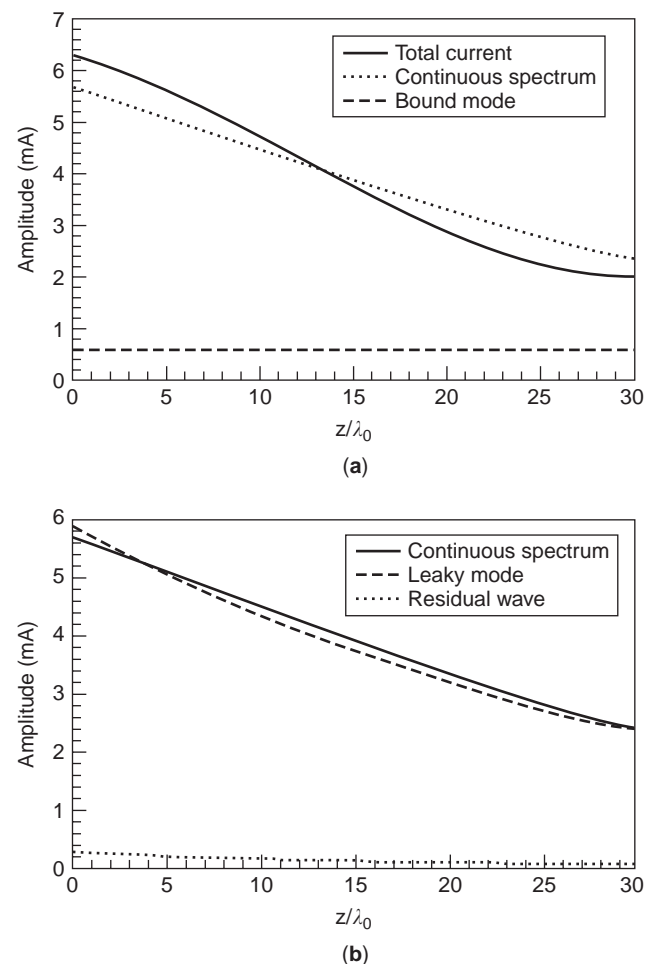


Figure 26. Plots of the total current, bound-mode current, and continuous-spectrum current versus distance from the delta gap source for the structure of Fig. 25 with an airgap thickness of 0.3 mm; (b) plots of the continuous-spectrum, leaky-mode, and residual-wave currents.

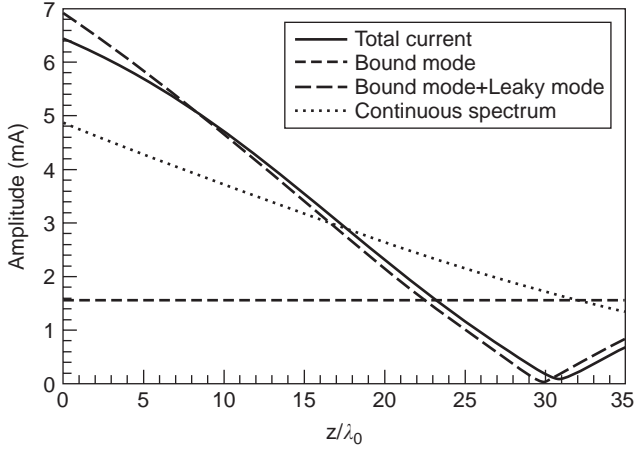


Figure 27. The same type of plot as in Fig. 26a but for an airgap thickness of 0.353 mm, which results in an almost a perfect destructive interference between the bound-mode and continuous-spectrum currents at $z \approx 32\lambda_0$.

amplitude of the total current at about 25 wavelengths from the source is due to the destructive interference between the BM and CS currents, which have an approximate 180° phase difference at this distance. Because the LM current dominates the CS current, it is concluded that the dip in the total current magnitude is due to a destructive interference between the bound and leaky modes that are excited by the source.

At the point of destructive interference, the amplitudes of the leaky and bound modes are not necessarily equal, and this explains why the dip in the total current does not extend completely to zero in Fig. 26a at $z = 25\lambda_0$. However, by correct selection of the airgap thickness, the amplitudes of the two modes can be made equal, resulting in an essentially complete destructive interference. A smaller airgap thickness will cause the amplitude of the leaky mode to dominate the amplitude of the bound mode at the point of destructive interference, while a larger airgap thickness will cause the amplitude of the bound mode to dominate. A critical airgap thickness thus exists that equalizes the two amplitudes at the interference point. This is demonstrated in Fig. 27 for airgap thickness of $\delta = 0.353$ mm. For this case there is an almost perfect cancellation of the total current on the strip at $z = 32\lambda_0$, pointing out how the simultaneous presence of the LM and the BM currents can significantly distort the expected transmission behavior of the line.

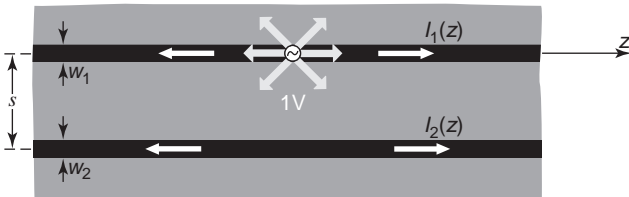


Figure 28. Top view of a pair of coupled microstrip lines. Line 1 is fed by a gap voltage source, causing a crosstalk current in line 2.

4. CROSSTALK BETWEEN TWO MICROSTRIP LINES

This section investigates the current excited on a pair of coupled microstrip lines when one of the lines (the source line, i.e., line 1) is excited by a gap voltage source (see Fig. 28) [38]. The *crosstalk current* is defined as the current induced on line 2 (the victim line, which is passive). At low frequency the current on the two lines is well predicted by standard transmission-line theory, which gives the following expressions for the current on each strip

$$I_1^{\text{TLT}}(z) = \frac{1}{4} \left(\frac{1}{Z_0^e} e^{-jk_z^e z} + \frac{1}{Z_0^o} e^{-jk_z^o z} \right) \quad (40)$$

$$I_2^{\text{TLT}}(z) = \frac{1}{4} \left(\frac{1}{Z_0^e} e^{-jk_z^e z} - \frac{1}{Z_0^o} e^{-jk_z^o z} \right) \quad (41)$$

where Z_0^e and Z_0^o are the frequency-dependent even-mode and odd-mode characteristic impedances and k_z^e and k_z^o are the corresponding wavenumbers. However, simple transmission-line theory fails to predict the effects of the continuous spectrum, and ignores all radiation effects. It will be seen that the CS current can be predominant at high frequency, and can thus be a source of undesirable spurious effects that can ruin the performance of microwave circuitry involving neighboring printed-circuit lines.

4.1. Formulation for the Currents

The same concepts presented in Section 2 apply to the present case, with some extension to account for the fact that currents now exist on two lines. One important feature of the present structure is that the currents do not show any symmetry about the center of either line, and thus a multiple-basis function expansion is necessary in practice to model these currents. Thus, the surface current can be expanded, similarly to (24) and (25), as

$$J_z^{(l)}(x, z) = \sum_{q=0}^{N_f} T_{l,q}^z(x) I_{l,q}^z(z) \quad (42)$$

$$J_x^{(l)}(x, z) = \sum_{p=1}^{N_f} T_{l,p}^x(x) I_{l,p}^x(z) \quad (43)$$

where the subscript $l = 1, 2$ is now added to denote the strip conductor (the integers q and p are no longer even and odd, respectively, as they were for the case of a single strip).

However, with the aim of keeping the explanation of the problem as simple as possible, only a single longitudinal basis function will be used on each line in the following explanation. This implies that the surface current on each line is expanded as $J_z^{(1)}(x, z) = T_1(x)I_1(z)$ and $J_z^{(2)}(x, z) = T_2(x)I_2(z)$ and thus the EFIE can be written as

$$E_z^{(1)}[T_1(x)I_1(z)] + E_z^{(1)}[T_2(x)I_2(z)] = E_z^{\text{gap}}(z) \quad (44)$$

$$E_z^{(2)}[T_1(x)I_1(z)] + E_z^{(2)}[T_2(x)I_2(z)] = 0 \quad (45)$$

The Galerkin testing procedure combined with the application of the inverse longitudinal Fourier transform leads to the following system of equations

$$\begin{aligned} \tilde{I}_1(k_z) \int_{w_1} T_1(x) E_z^{(1)} [T_1(x) e^{-jk_z z}] dx + \tilde{I}_2(k_z) \\ \int_{w_1} T_1(x) E_z^{(1)} [T_2(x) e^{-jk_z z}] dx = \tilde{E}_z^{\text{gap}}(k_z) e^{-jk_z z} \end{aligned} \quad (46)$$

$$\begin{aligned} \tilde{I}_1(k_z) \int_{w_2} T_2(x) E_z^{(2)} [T_1(x) e^{-jk_z z}] dx + \tilde{I}_2(k_z) \\ \int_{w_2} T_2(x) E_z^{(2)} [T_2(x) e^{-jk_z z}] dx = 0 \end{aligned} \quad (47)$$

which can be rewritten as

$$\begin{bmatrix} Z_{11}(k_z) & Z_{12}(k_z) \\ Z_{21}(k_z) & Z_{22}(k_z) \end{bmatrix} \begin{bmatrix} \tilde{I}_1(k_z) \\ \tilde{I}_2(k_z) \end{bmatrix} = \begin{bmatrix} \tilde{E}_z^{\text{gap}}(k_z) \\ 0 \end{bmatrix} \quad (48)$$

where the $Z_{ij}(k_z)$ coefficients ($i, j = 1, 2$) have the following form:

- *Space Domain:*

$$Z_{ij}(k_z) = \int_{w_i} \int_{w_j} T_i(x) \tilde{G}_{zz}(x - x'; k_z) T_j(x') dx' dx \quad (49)$$

- *Spectral Domain:*

$$Z_{ij}(k_z) = \frac{1}{2\pi} \int_{C_{kx}} \tilde{T}_i(-k_x) \tilde{G}_{zz}(k_x, k_z) \tilde{T}_j(k_x) e^{-jk_x s(1-\delta_{ij})} dk_x \quad (50)$$

The form given in (49) will be used when the DCIT is used with the corresponding MPIE in the space domain, and expression (50) is used when the EFIE is solved using the SDA approach.

Following the same rationale as in Section 2, the total current on the lines is given by $I_1(z) = I_{1,0}^z(z)$ and $I_2(z) = I_{2,0}^z(z)$, which are given in terms of their corresponding longitudinal Fourier transforms as

$$I_l(z) = \frac{1}{2\pi} \int_{C_{kz}} \tilde{I}_{l,0}^z(k_z) e^{-jk_z z} dk_z, \quad l = 1, 2 \quad (51)$$

4.2. Results

The theory presented above (using multiple basis functions) has been implemented in a computer code to study the crosstalk current in line 2, $I_2(z)$, for a pair of coupled microstrip lines when line 1 is excited by a 1-V gap voltage source.

Figure 29 shows the crosstalk current for two microstrip lines at various frequencies (low, medium, and high frequencies) and a wide separation between the lines

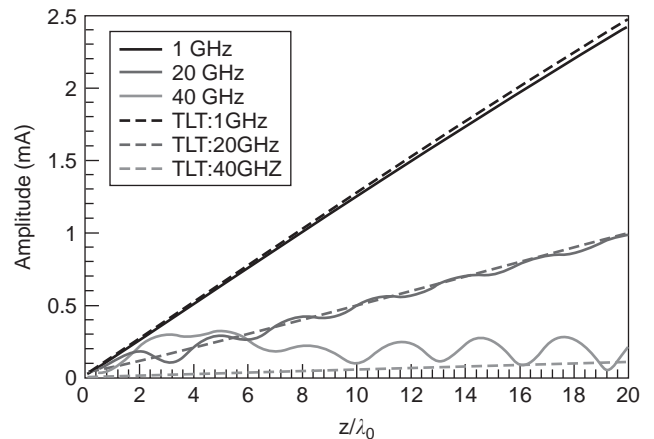


Figure 29. Crosstalk current $I_2(z)$ versus z/λ_0 for $\epsilon_r = 2.2$, $s/h = 10.0$, $w_1 = w_2 = h = 1.0$ mm. Both the total current and the transmission-line theory (TLT) currents are plotted for three different frequencies.

($s/h = 10$). The crosstalk current is plotted versus distance z from the origin (the source is at $z = 0$ on line 1). Both the total current (TC) numerically obtained from (51) and the transmission-line theory (TLT) current given by (41) are shown. The curves show that, at the low frequency of 1 GHz ($h/\lambda_0 \approx 0.003$), transmission-line theory predicts very accurately the crosstalk current. At 20 GHz ($h/\lambda_0 \approx 0.065$) there is overall agreement, but the exact crosstalk current shows a noticeable oscillation, which is due to the presence of the CS current. At 40 GHz ($h/\lambda_0 \approx 0.13$) the CS current has become strong enough that there is no agreement at all between the exact and the TLT currents.

It is interesting to note that at low frequency, for a large line separation, the crosstalk current exhibits an almost perfectly linear growth with distance z . This is explainable from Eq. (41), which may be rewritten as

$$\begin{aligned} I_2^{\text{TLT}}(z) = \frac{1}{4} \left(\frac{1}{Z_0^e} - \frac{1}{Z_0^o} \right) e^{-jk_z^a z} \\ + \frac{j}{2Z_0^o} e^{-jk_z^a z} \sin(\Delta k_z z / 2) \end{aligned} \quad (52)$$

where $k_z^a = (k_z^e + k_z^o)/2$ is the average of the two bound-mode wavenumbers and $\Delta k_z = k_z^e - k_z^o$ is their difference. As the line separation increases, the even- and odd-mode characteristic impedances and wavenumbers approach each other, making the first term in Eq. (52) negligible and the second term approximately linear.

To explore the nature of the spurious behavior of $I_2(z)$ at high frequency (40 GHz), Fig. 30 shows the decomposition of this current in terms of its constituent parts, the BM and the CS currents. The TLT current predicted by Eq. (52) is also shown for comparison. It is seen that the CS current is significantly stronger than the BM current, confirming that the CS current is responsible for the spurious effects. It is also interesting to note that the TLT current predicts fairly accurately the actual BM current

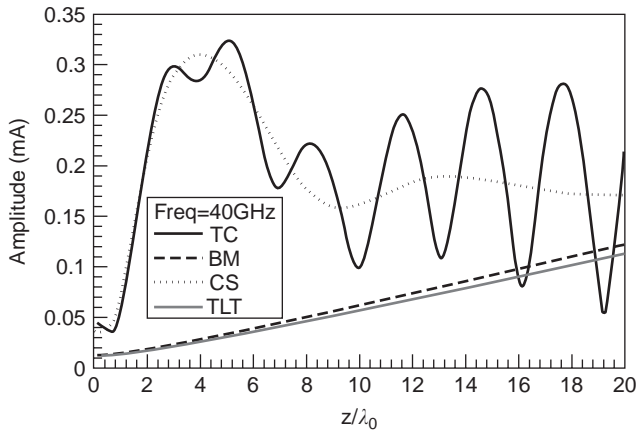


Figure 30. Total crosstalk current $I_2(z)$ and its constituent parts versus z/λ_0 for $\epsilon_r = 2.2$, $s/h = 10.0$, $w_1 = w_2 = h = 1.0$ mm at 40 GHz.

on the line. Thus, transmission-line theory predicts accurately the amplitude of the BM currents on the line, which in the exact theory comes from the residues at the two BM poles in the complex k_z plane. Transmission-line theory does not account for the CS current, however, so the TLT current is far from the actual current on the line.

It is also interesting to note from Fig. 29 that for low to moderate frequencies, the crosstalk current *decreases* as the frequency increases. This is because the even- and odd-mode wavenumbers become more nearly equal as the frequency increases. As seen from Eq. (52), this results in the crosstalk current $I_2(z)$ becoming smaller. However, when the frequency becomes very high, the crosstalk current increases with frequency, due to the increase of the CS current. This is illustrated by Fig. 31, which shows that at 80 GHz the crosstalk current has significantly increased from 40 GHz.

For large line separations, the CS current strongly dominates the crosstalk current at high frequencies. This is illustrated by Fig. 32, which shows that at 80 GHz, the total crosstalk current and the CS component

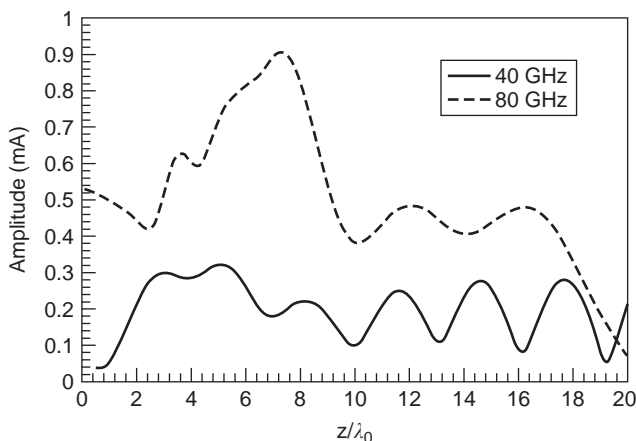


Figure 31. Comparison of the total crosstalk current $I_2(z)$ versus z/λ_0 for $\epsilon_r = 2.2$, $s/h = 10.0$, $w_1 = w_2 = h = 1.0$ mm at 40 and 80 GHz.

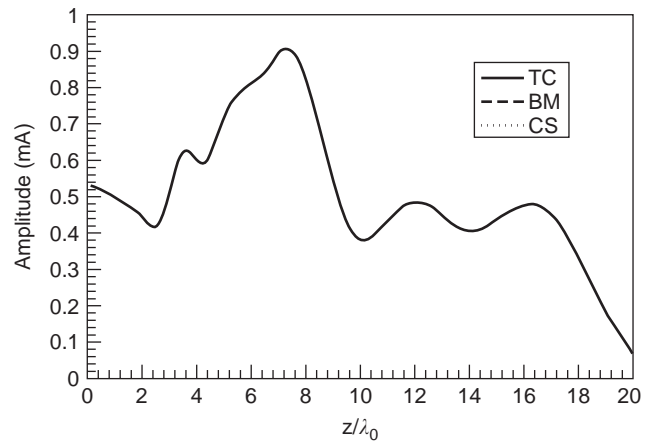


Figure 32. Total crosstalk current $I_2(z)$ and its constituent parts versus z/λ_0 for $\epsilon_r = 2.2$, $s/h = 10.0$, $w_1 = w_2 = h = 1.0$ mm at 80 GHz. The TC and CS curves are indistinguishable, while the BM curve is essentially zero.

of the crosstalk current are essentially indistinguishable. Physically, this is because for large line separation and high frequency, the crosstalk current is due mainly to radiation from the source line into the TM_0 parallel-plate mode, as opposed to quasistatic coupling. Radiation from the source line mainly induces a CS current on the victim line, instead of a bound mode, since the bound modes have wavenumbers that are larger than that of the TM_0 parallel-plate mode, and hence cannot couple to the TM_0 parallel-plate radiation.

The behavior of the high-frequency crosstalk current for various line separations is shown in Fig. 33. For a small line separation ($s/h = 2$), the crosstalk current is well accounted for by TLT model, but this good agreement worsens as the line separation increases. This fact can be added to the predominant quasistatic nature of the crosstalk coupling for small separation between the lines, which is accounted for by the TLT model. As the frequency

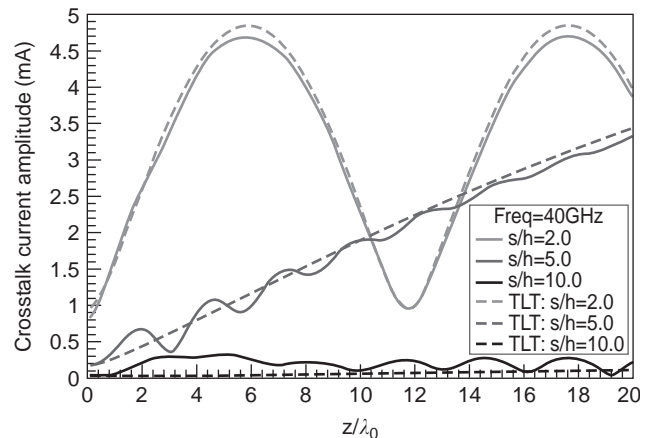


Figure 33. Total crosstalk and transmission-line theory (TLT) currents versus z/λ_0 for various line separations: $s/h = 2, 5, 10$; $\epsilon_r = 2.2$, $w_1 = w_2 = h = 1.0$ mm, frequency = 40 GHz.

increases, the TLT model loses accuracy as the CS current becomes stronger. It is clear by comparing Figs. 29 and 33 that as the line separation increases, the frequency at which the CS current becomes appreciable decreases. Hence, simple transmission-line theory loses accuracy at lower frequencies when the line separation is larger.

5. CROSSTALK FIELDS

In this section, the fields radiated by the currents on the strip conductor of a printed-circuit transmission line are examined, to see how crosstalk fields may be produced, especially at high frequency, due to the radiation from the currents that are induced on the strip conductor excited by a gap voltage source [39,40].

The structure that is examined is the covered microstrip structure of Fig. 1b. The currents on this structure that are produced by a gap voltage source have already been examined in some detail in Section 3.2, where it was shown that the total current consists of a bound-mode (BM) transmission-line mode together with a continuous-spectrum (CS) current. The CS current consists of a physical leaky-mode (LM) current, when such a mode exists, together with a TM₀ residual-wave (RW) current. Hence, there are a maximum of three different types of currents on the line, the BM, LM, and RW currents.

The BM current is normally regarded as a nonradiating type of current, since the fields are bound to the guiding structure. Indeed, for such a mode propagating on an infinite line, there would be no radiation and no power loss (assuming lossless conductors and dielectric). However, the 1-V gap voltage source at $z=0$ is a discontinuity, and radiation in general occurs from discontinuities. In particular, the current in Eq. (2) has a slope discontinuity (a discontinuity in the derivative) at $z=0$. Because of this discontinuity, the BM current will produce a radiation field, with radiation occurring into the TM₀ parallel-plate substrate mode. As shown in the results below, the level of this radiation increases with frequency.

The RW current increases with frequency, as demonstrated in Section 3.2. This current is a rather complicated function of distance z from the source, although asymptotically it propagates with a wavenumber of k_{TM_0} , as shown in Eq. (4). For this reason, the radiation from this current is somewhat endfire directed, concentrated more toward the direction of the strip axis, as will be shown in the results below. However, the radiation is somewhat diffuse, since the current is actually composed of a continuous spectrum of wavenumbers.

When a physical LM current exists on the line, the radiation from this current is typically directive, in the form of a beam, since the LM current has a single wavenumber β that is less than k_{TM_0} . The LM current may thus be responsible for significant crosstalk fields in the direction of this beam. This will be demonstrated in the results presented below.

5.1. Calculation of Crosstalk Fields

To calculate the crosstalk field, it is first assumed that only radiation into the TM₀ parallel-plate mode is significant.

All of the other higher-order parallel-plate modes are assumed to be sufficiently far below cutoff that these fields decay very rapidly away from the strip current, and hence are negligible at any significant distance away from the strip (in practice, more than a half-wavelength or so). Hence, the crosstalk field is assumed to be the field of the TM₀ parallel-plate mode that is produced by the current on the strip conductor. To calculate this field, the field of a unit amplitude infinitesimal electric dipole in the z direction on top of the substrate at $x=0, z=0, y=h$ is considered. The TM₀ field from the dipole has the following form in cylindrical (ρ, ϕ, y) coordinates:

$$E_y(\rho, \phi, y) = Af(y)H_1^{(2)}(k_{TM_0}\rho) \cos \phi \tag{53}$$

where, for $0 < y < h$, we obtain

$$f(y) = \cos(k_{y1}y) \tag{54}$$

with

$$k_{y1} = (k_1^2 - k_{TM_0}^2)^{1/2} \tag{55}$$

where k_1 is the wavenumber in the substrate. The constant A can be determined by spectral-domain techniques, but the value is not important here.

The field from the strip current is found by integrating over the strip current, using the above mentioned dipole field as a Green's function. Assuming the line width to be small relative to a wavelength, the integral has the following form

$$E_y(x, y, z) = Af(y) \int_{-\infty}^{\infty} I(z')H_1^{(2)}(k_{TM_0}\rho') \cos \phi' dz' \tag{56}$$

where

$$\rho' = \sqrt{x^2 + (z - z')^2} \tag{57}$$

$$\tan(\phi') = \frac{x}{z - z'} \tag{58}$$

Integrating across the substrate height, the voltage drop between the strip and the ground plane at any point is

$$V_h(x, z) = -Ah \operatorname{sinc}(k_{y1}h) \int_{-\infty}^{\infty} I(z')H_1^{(2)}(k_{TM_0}\rho') \cos \phi' dz' \tag{59}$$

The integral can be accelerated by using a technique such as the Shanks transform [41].

5.2. Results

All the cases presented in this section are for a covered microstrip with $\epsilon_r = 2.2$ and $w = h$, with a cover height $h_c = h$. The dispersion plot for this structure is shown in

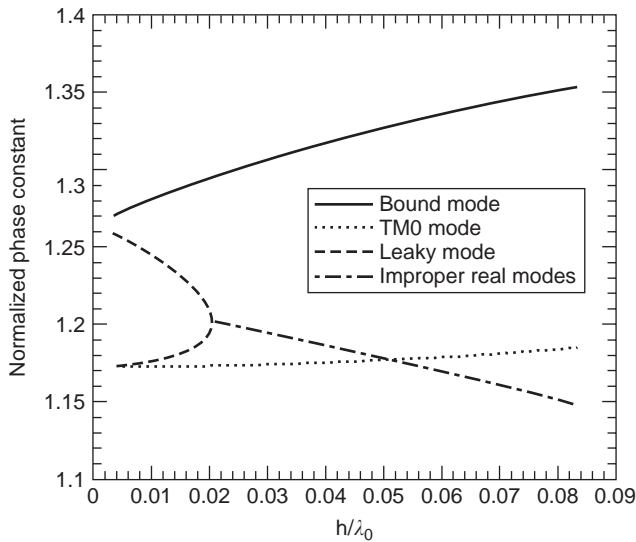


Figure 34. Dispersion plot showing the normalized phase constants (β/k_0) versus normalized frequency (h/λ_0) for a covered microstrip ($h_c = h$, $w = h$, $\epsilon_r = 2.2$)

Fig. 34. This figure shows three distinct regions of behavior. In the first region, $h/\lambda_0 < 0.021$, there is no leaky mode; only a pair of nonphysical improper real modes exist, in addition to the bound mode. In the region $0.021 < h/\lambda_0 < 0.052$, a leaky mode exists, but it is nonphysical (since the wavenumber of the leaky mode is larger than that of the TM_0 parallel-plate mode). In the region $h/\lambda_0 > 0.052$ the leaky mode is physical. Results will be shown for each region to illustrate how the field surrounding the strip behaves.

The first case is that for $h/\lambda_0 = 0.005$. For this low-frequency case, the operating point is well inside the nonphysical spectral-gap region in the dispersion plot of Fig. 34. As a result of the low frequency, the continuous-spectrum current is very small, as shown in Fig. 35. The

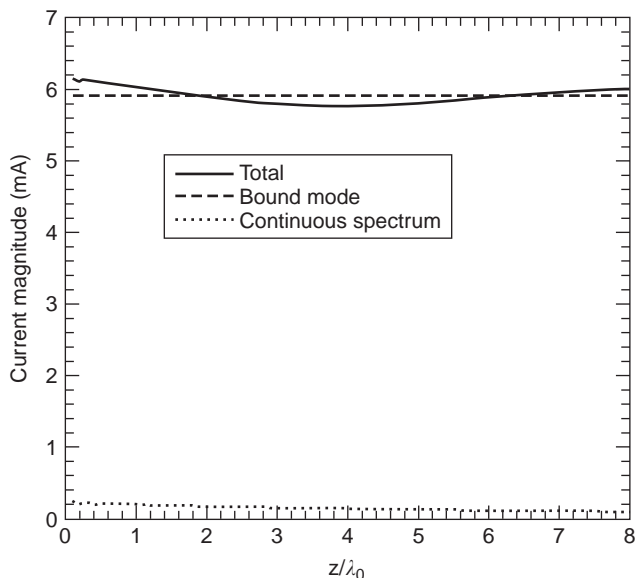


Figure 35. Strip current for a covered microstrip at a normalized frequency of $h/\lambda_0 = 0.005$ ($h_c = h$, $w = h$, $\epsilon_r = 2.2$).

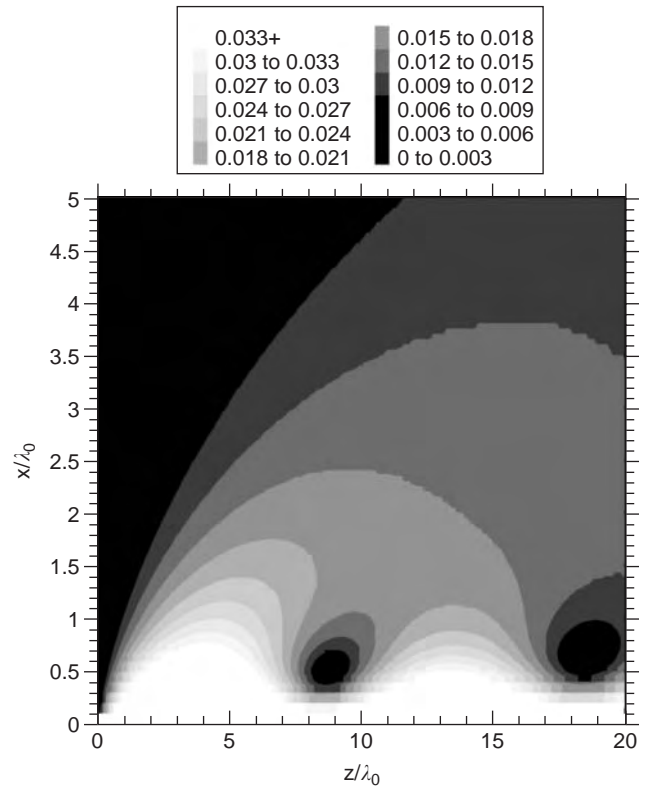


Figure 36. Normalized substrate voltage for the covered microstrip of Fig. 35. (This figure is available in full color at <http://www.mrw.interscience.wiley.com/erfme>.)

oscillations in the total current due to the interference between the BM and CS currents are apparent, although they are small in amplitude, since the CS current is quite small compared with the BM current. Figure 36 shows a plot of the field surrounding the strip for this case. The field is fairly diffuse away from the strip, with noticeable oscillations close to the strip as the observation distance z increases. This oscillation is due to an interference between two components that make up the overall field produced by the BM current. One component is the field due to a bound mode propagating on an infinite line. This field propagates in the z direction with the wavenumber of the bound mode, and decays exponentially away from the line. The second component is a radiation type of field that propagates radially with a wavenumber k_{TM_0} and decays as $1/\sqrt{\rho}$, and arises because of the slope discontinuity of the BM current at the origin.

Figure 37 shows the current components at a higher frequency of $h/\lambda_0 = 0.04$. At this frequency the leaky mode exists, but is nonphysical. Figure 37 shows that at this higher frequency the CS current has become significant, because of the strong RW current that now exists. Figure 38 shows that the field surrounding the strip has begun to become more directive in shape, although the field is still somewhat diffuse.

Figure 39 shows the current components at a still higher frequency of $h/\lambda_0 = 0.08$. At this frequency the leaky mode exists and is physical. Because of the physical LM current, the CS current is now quite strong. Figure 40

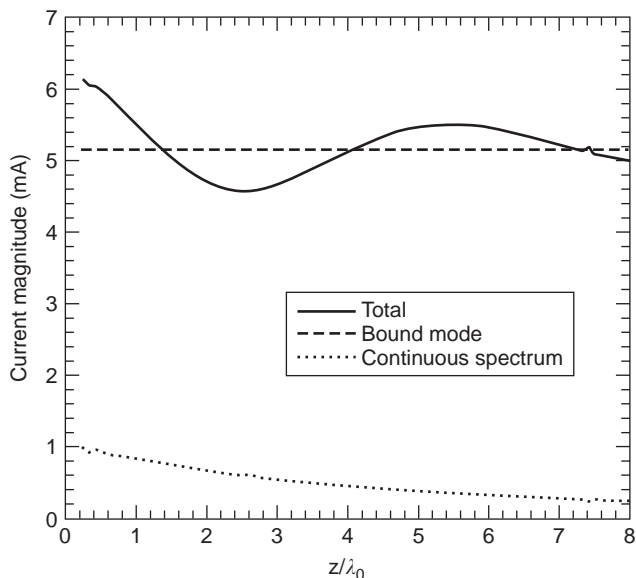


Figure 37. Strip current for a covered microstrip at a normalized frequency of $h/\lambda_0 = 0.04$ ($h_c = h, w = h, \epsilon_r = 2.2$).

shows that the field surrounding the strip has begun to assume a beamlike shape, due to the radiation of the LM current. The overall level of the field is also higher. Clearly, significant crosstalk could occur with circuit components that are placed within the beamlike region of strong leakage fields. The angle of leakage of the leaky mode,

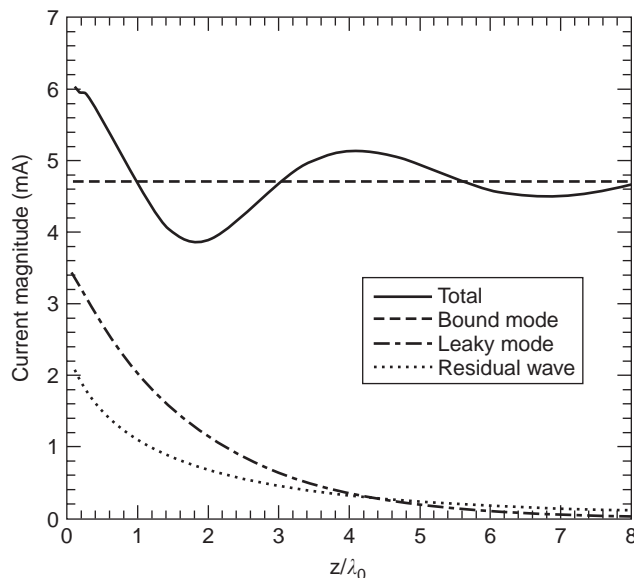


Figure 39. Strip current for a covered microstrip at a normalized frequency of $h/\lambda_0 = 0.08$ ($h_c = h, w = h, \epsilon_r = 2.2$).

measured from the strip axis, is given approximately (for small attenuation constants) as

$$\phi_0 = \cos^{-1}\left(\frac{\beta}{k_{TM_0}}\right) \tag{60}$$

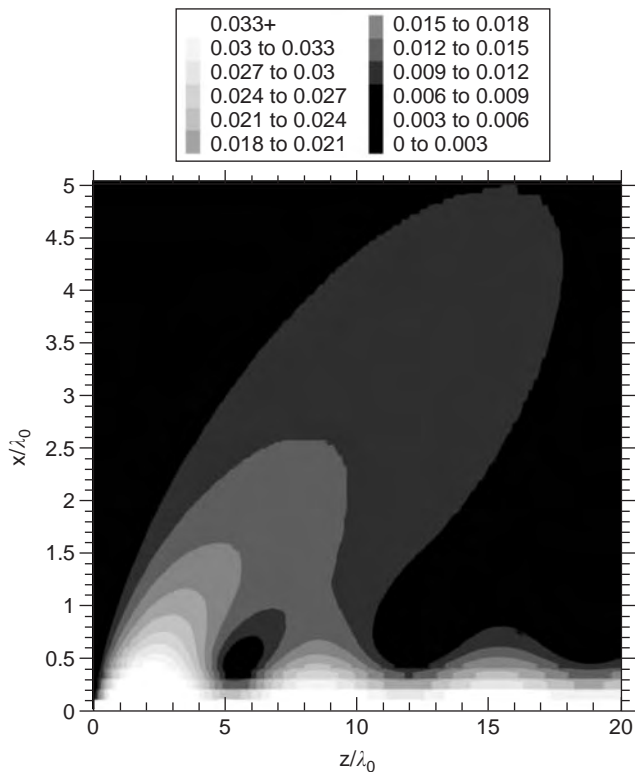


Figure 38. Normalized substrate voltage for the covered microstrip of Fig. 37. (This figure is available in full color at <http://www.mrw.interscience.wiley.com/erfme>.)

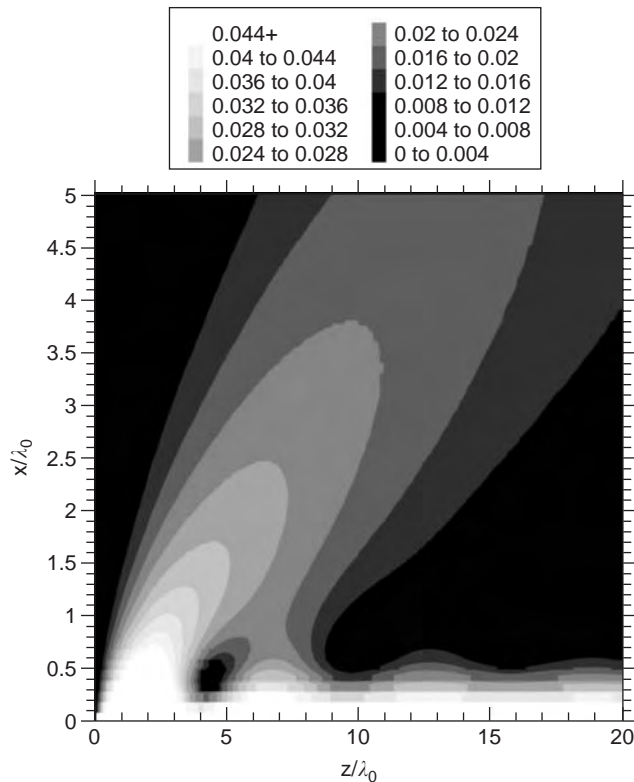


Figure 40. Normalized substrate voltage for the covered microstrip of Fig. 39. (This figure is available in full color at <http://www.mrw.interscience.wiley.com/erfme>.)

where β is the phase constant of the leaky mode. This equation actually predicts the leakage angle for a leaky mode existing by itself on an infinite line, with a small attenuation constant. The predicted leakage angle from this equation is $\sim 13.5^\circ$, whereas the actual beam angle in Fig. 40 is $\sim 18^\circ$. The discrepancy is caused by several factors: (1) the attenuation constant of the leaky mode is not zero, as is assumed in Eq. (60); and (2) the total field consists of the BM and RW fields in addition to the LM field. Finally, the direction of maximum radiation for the field radiated by the LM current of Eq. (3) is not the same as the direction of leakage for a leaky mode on an infinite line, since the field radiated by the LM current of Eq. (3) consists of a source discontinuity radiation term due to the slope discontinuity of the current at the origin.

6. CONCLUSIONS

This article has examined the nature of the current and fields excited by gap voltage source on an infinite printed-circuit transmission line, in order to ascertain the nature of the current and to show what types of spurious effects may be produced at high frequency. Three particular structures have been examined: microstrip, covered microstrip, and stripline with an airgap above the strip conductor.

A semianalytical method for determining the strip current has been used, based on a Fourier transform of the current in the longitudinal (z) direction. The strip current is thus expressed as an inverse Fourier transform integral in the complex longitudinal wavenumber (k_z) plane. This method provides an accurate calculation of the strip current, as well as physical insight into the nature of the current on the strip. In particular, deforming the original path of integration in the k_z plane allows for a convenient decomposition of the total strip current into a sum of constituent parts.

It was shown that the total current consists of a bound-mode (BM) current together with a continuous-spectrum (CS) current. The BM current corresponds to the usual transmission-line mode, whose fields are bound to the strip region, decaying away from the strip in the transverse (x) direction. The amplitude of the BM current is accurately calculated at any frequency by taking the residue in the k_z plane at the BM pole. The amplitude of the BM current obtained this way is accurate even for high frequencies, where the definition of the characteristic impedance becomes ambiguous. The CS current is, generally speaking, a high-frequency radiation type of current whose existence cannot be predicted by simple transmission-line theory.

The CS current consists of two types of current. The first is a set of any physical leaky-mode currents. A "physical" leaky mode is defined here as one that satisfies a "path consistency condition," meaning that the nature of the leakage (as determined by the path of integration in the transverse wavenumber (k_x) plane used to calculate the wavenumber of the leaky mode) is consistent with the phase constant of the leaky mode. For open structures such as microstrip, there are two types of leaky modes that

may in principle be physical. One type has leakage into only the TM_0 surface-wave mode of the grounded substrate (assuming here that only the TM_0 mode is above cutoff). This type of leaky mode is physical when the phase constant of the leaky mode is less than the wavenumber of the TM_0 surface-wave mode, and greater than the wavenumber of free space. The second type of leaky mode, which can exist on open (uncovered) structures, has leakage into both the TM_0 surface-wave mode and also into space. This type of leaky mode is physical when the phase constant of the leaky mode is less than the wavenumber k_0 of free space. For the cases presented here, only the first type of physical leaky mode has been found to exist for the parameters used in the results. For closed structures (meaning that a ground plane exists both above and below the structure) such as covered microstrip, only the first type of leaky mode can exist.

The second type of current that makes up the CS current is the "residual-wave" (RW) current. This current physically represents the current that is left over when the physical leaky-mode currents are removed from the CS current. For open structures such as microstrip, the RW current consists of a sum of two different RW currents: a TM_0 RW current and a k_0 RW current. Mathematically, these currents arise from the corresponding branchpoints in the complex k_z plane, at the locations of the TM_0 surface-wave wavenumber and the k_0 wavenumber, respectively. Although there is no closed-form expression available for these currents, an asymptotic analysis reveals how they behave for large distances z from the source. The TM_0 RW current propagates with the wavenumber of the TM_0 surface-wave mode, and decays with distance along the strip as $z^{-3/2}$. The k_0 RW current propagates with the wavenumber k_0 of free space, and decays with distance along the strip as z^{-2} . For a closed structure such as covered microstrip, only the TM_0 RW current exists.

Hence, for an open structure such as microstrip, the strip current produced by the gap voltage source consists of a sum of five possible current waves:

1. The bound-mode (transmission-line mode) current
2. A physical leaky mode (if any) that leaks into the TM_0 substrate mode
3. A physical leaky mode (if any) that leaks into both the TM_0 substrate mode and into space
4. A TM_0 residual-wave current, which asymptotically propagates with the wavenumber of the TM_0 mode and decays as $z^{-3/2}$
5. A k_0 residual-wave current, which asymptotically propagates with the wavenumber of free space and decays as z^{-2}

For a closed structure such as covered microstrip, only currents 1, 2, and 4 exist.

For microstrip, only the desired BM current exists at low frequency. However, as the frequency increases, the CS current becomes increasingly important. For moderate frequencies, the CS increases in amplitude as the frequency increases because the RW current increases in

amplitude with frequency. For high frequencies a leaky mode (having leakage into the TM_0 surface-wave mode) becomes physical, and the CS current becomes very significant above this frequency. This frequency occurs roughly when the substrate is a tenth of a wavelength thick electrically in the dielectric. As the frequency increases, a significant oscillation is observed in a plot of the strip current versus the distance z from the source. This oscillation is due to an interference between the desired BM current and the CS current.

For covered microstrip, the oscillations in the strip current also increase with frequency, since the CS current increases with frequency. However, the effect of the top cover also significantly increases the magnitude of the spurious oscillation. This is due to two effects: (1) as the top cover is lowered toward the microstrip line, the amplitude of the RW current increases; and (2) even more importantly, as the top cover is lowered, the frequency at which a physical leaky mode exists is lowered. In fact, for a sufficiently small cover height, a physical leaky mode exists at all frequencies. Therefore, even at low frequencies, a significant oscillation in the strip current may be observed when the cover height is sufficiently small, due to the leaky mode. For a certain value of the cover height, a complete destructive interference will occur between the leaky mode and the bound mode at some distance from the source; that is, the two currents will have an equal amplitude and a 180° phase difference at some distance z from the source. At this point on the line the total current will essentially have a complete null.

Homogeneous stripline supports only the desired TEM mode of propagation. However, during manufacture, an airgap may be inadvertently introduced above the strip conductor. It has been known for many years that such an airgap may lead to poor performance, although the reasons were, perhaps, not completely clear. It was shown here that the presence of the airgap causes the TEM stripline mode to become a leaky mode. For a small airgap the leaky mode still resembles the usual TEM stripline mode, but the mode now has a complex wavenumber due to leakage loss (leakage into the TM_0 parallel-plate mode of the background airgap structure). This results in power loss as the mode propagates, which is in addition to any attenuation due to conductor or dielectric loss. In addition to the quasi-TEM leaky mode, there is also a bound mode that exists on the structure with a small airgap, but the bound mode has a field configuration that resembles that of a parallel-plate mode, and is thus only weakly excited by the gap source (or by a conventional stripline connector, in practice). The bound mode does not attenuate with distance from the source, however, and thus a significant interference may occur between the quasi-TEM leaky mode and the bound mode at some distance from the source. This results in a spurious dip in the observed transmission response (S_{12}) of the transmission line at a particular distance from the source (or at a particular frequency, if the distance is fixed).

The analysis and results were extended to the case of two coupled microstrip lines, where a gap voltage source was placed on one line (the source line) and the current that was produced on the second line (the victim line) was

examined. It was concluded that at low frequency, an even/odd-mode transmission-line analysis is sufficient to determine the crosstalk current on the victim line. Interestingly, for larger line separation, and low frequency, the crosstalk current displays an almost linear behavior, growing linearly with distance z on the line away from the origin (where the gap source is placed on the source line). This is explainable from simple transmission-line theory. At higher frequency, the CS current becomes important, and simple transmission-line theory is no longer adequate to predict the crosstalk current. For large line separation and higher frequencies, the main component of the crosstalk current is in fact the CS current.

Finally, the field surrounding a printed-circuit transmission line that is excited by a gap voltage source was examined, and results were shown for the case of a covered microstrip line (with a moderate cover height). The nature of this field is important for understanding the crosstalk that may occur with other circuit components placed in the package near the printed-circuit transmission line. At low frequency, it is mainly the bound mode that is excited on the line. However, because of the discontinuity in the derivative of the current (slope discontinuity) at the source location, there is radiation from the BM current. The total field from the BM current, when plotted along the z direction parallel to the strip, is an oscillatory one. This is because the field from the BM current physically consists of two parts: (1) the field of the bound mode itself, which decays exponentially away from the strip, and (2) the radiation from the slope discontinuity in the BM current at the origin.

As the frequency increases, the RW current becomes appreciable, and the crosstalk fields become stronger and extend out to distances farther from the line. The crosstalk field is fairly diffuse, however. As the frequency increases past the point where a leaky mode becomes physical, the crosstalk field begins to assume a beamlike shape, due to radiation from the leaky-mode current, which is directed at a particular leakage angle. At these higher frequencies, crosstalk may be especially severe for circuit components that are in the direction of the leakage radiation.

BIBLIOGRAPHY

1. N. Fachè, F. Olyslager, and D. De Zutter, *Electromagnetic and Circuit Modelling of Multiconductor Transmission Lines*, Oxford Engineering Science Series, Vol. 35, Clarendon Press, Oxford, 1993.
2. R. F. Harrington, *Time-harmonic Electromagnetic Fields*, McGraw-Hill, New York, 1961.
3. T. Itoh, *Numerical Techniques for Microwave and Millimeter-Wave Passive Structures*, J Wiley, New York, 1989.
4. D. Mirshekar-Syahkal, *Spectral Domain Method for Microwave Integrated Circuits*, J Wiley, New York, 1990.
5. Y. L. Chow, J. J. Yang, D. G. Fang, and G. E. Howard, A closed-form spatial Green's function for the thick microstrip substrate, *IEEE Trans. Microwave Theory Tech.* **39**:588-592 (1991).

6. R. A. Kipp and C. H. Chan, Complex image method for sources in bounded regions of multilayer structures, *IEEE Trans. Microwave Theory Tech.* **42**:860–865 (1994).
7. J. Bernal, F. Mesa, and F. Medina, 2-D analysis of leakage in printed-circuit lines using discrete complex-images technique, *IEEE Trans. Microwave Theory Tech.* **50**:1895–1900 (2002).
8. T. Itoh, Spectral domain immittance approach for dispersion characteristics of generalized printed transmission lines, *IEEE Trans. Microwave Theory Tech.* **28**:733–736 (1980).
9. N. K. Das and D. M. Pozar, A generalized spectral-domain Green's function for multilayer dielectric substrates with application to multilayer transmission lines, *IEEE Trans. Microwave Theory Tech.* **35**:326–335 (1987).
10. F. Mesa, R. Marqués, and M. Horno, A general algorithm for computing the bidimensional spectral dyadic Green's function: The equivalent boundary method (EBM), *IEEE Trans. Microwave Theory Tech.* **39**:1640–1649 (1991).
11. D. Nghiem, J. Williams, D. R. Jackson, and A. A. Oliner, Leakage of the dominant mode on stripline with a small air gap, *IEEE Trans. Microwave Theory Tech.* **43**:2549–2556 (1995).
12. C. Di Nallo, F. Mesa, and D. R. Jackson, Excitation of leaky modes on multilayer stripline structures, *IEEE Trans. Microwave Theory Tech.* **46**:1062–1071 (1998).
13. F. Mesa, C. Di Nallo, and D. R. Jackson, The theory of surface-wave and space-wave leaky mode excitation on microstrip lines, *IEEE Trans. Microwave Theory Tech.* **47**:207–215 (1999).
14. S. Amari, R. Vahldieck, and J. Bornemann, Using selective asymptotics to accelerate dispersion analysis of microstrip lines, *IEEE Trans. Microwave Theory Tech.* **46**:1024–1027 (1998).
15. M. Abramowitz and I. A. Stegun, *Handbook of Mathematical Functions*, Dover, New York, 1972.
16. E. A. Soliman, P. Pieters, E. Beyne, and G. A. E. Vandebosch, Numerically efficient method for multislotted transmission lines in layered media—application to multislotted lines in mcm-d technology, *IEEE Trans. Microwave Theory Tech.* **47**:1782–1787 (1999).
17. J. Bernal, F. Medina, R. R. Boix, and M. Horno, Fast full-wave analysis of multistrip transmission lines based on mpie and complex image theory, *IEEE Trans. Microwave Theory Tech.* **48**:445–452 (2000).
18. K. A. Michaski and D. Zheng, Electromagnetic scattering and radiation by surfaces of arbitrary shape in layered media, Part I: Theory, *IEEE Trans. Microwave Theory Tech.* **38**:335–344 (1990).
19. P. M. Morse and H. Feshbach, *Method of Theoretical Physics*, McGraw-Hill, New York, 1953.
20. M. J. Freire, F. Mesa, D. R. Jackson, and A. A. Oliner, Spurious transmission effects due to the excitation of the bound mode and the continuous spectrum on stripline with an air gap, *IEEE Trans. Microwave Theory Tech.* **47**:2493–2502 (1999).
21. F. Mesa, D. R. Jackson, and M. J. Freire, High-frequency leaky-mode excitation on a microstrip line, *IEEE Trans. Microwave Theory Tech.* **49**:2206–2215 (2001).
22. F. Mesa and D. R. Jackson, The danger of high-frequency spurious effects on wide microstrip line, *IEEE Trans. Microwave Theory Tech.* **50**:2679–2689 (2002).
23. R. E. Collin, *Field Theory of Guided Waves*, 2nd ed., IEEE Press, New York, 1991.
24. L. B. Felsen and N. Marcuvitz, *Radiation and Scattering of Waves*, Prentice-Hall, New York, 1973.
25. R. Marqués and F. Mesa, Spectral domain analysis of higher order leaky modes in microstrip lines: A new spectral-gap effect, *J. Electromagn. Wave Appl.* **11**:1367–1384 (1997).
26. T. Tamir and A. A. Oliner, Guided complex waves, Part I: Fields at an interface, *Proc. IEE Microwaves Opt. Anten. H* **110**(1):310–324 (1963).
27. T. Tamir and A. A. Oliner, Guided complex waves, Part II: Relation to radiation patterns, *Proc. IEE Microwaves Opt. Anten. H* **110**(1):325–334 (1963).
28. A. A. Oliner, Leakage from higher modes on microstrip line with application to antennas, *Radio Sci.* **22**:907–912 (1987).
29. K. A. Michaski and D. Zheng, Rigorous analysis of open microstrip lines of arbitrary cross section in bound and leaky regimes, *IEEE Trans. Microwave Theory Tech.* **37**:2005–2010 (1989).
30. N. K. Das and D. M. Pozar, Full-wave spectral-domain computation of material, radiation, and guided wave losses in infinite multilayered printed transmission lines, *IEEE Trans. Microwave Theory Tech.* **39**:54–63 (1991).
31. H. Shigesawa, M. Tsuji, and A. A. Oliner, Dominant mode power leakage from printed-circuit waveguide, *Radio Sci.* **26**:559–564 (1991).
32. D. Nghiem, J. Williams, D. R. Jackson, and A. A. Oliner, Proper and improper dominant mode solutions for a stripline with an airgap, *Radio Sci.* **28**:1163–1180 (1993).
33. F. Mesa and R. Marqués, Integral representation of spatial Green's function and spectral domain analysis of leaky covered strip-like lines, *IEEE Trans. Microwave Theory Tech.* **43**:828–837 (1995).
34. H. Shigesawa, M. Tsuji, and A. A. Oliner, A simultaneous propagation of bound and leaky dominant modes on printed-circuit lines: A new general effect, *IEEE Trans. Microwave Theory Tech.* **43**:3007–3019 (1995).
35. D. Nghiem, J. Williams, D. R. Jackson, and A. A. Oliner, Existence of a leaky dominant mode on microstrip line with an isotropic substrate: Theory and measurements, *IEEE Trans. Microwave Theory Tech.* **44**:1710–1715 (1996).
36. D. R. Jackson, F. Mesa, M. J. Freire, D. P. Nyquist, and C. Di Nallo, The role of the steepest-descent path in the excitation of leaky modes on stripline structures, *Radio Sci.* **35**:495–510 (2000).
37. F. Mesa, A. A. Oliner, D. R. Jackson, and M. J. Freire, The influence of a top cover on the leakage from microstrip lines, *IEEE Trans. Microwave Theory Tech.* **48**:2240–2248 (2000).
38. J. Bernal, F. Mesa, R. Rodríguez-Berral, and D. R. Jackson, High frequency crosstalk between two microstrip lines, *IEEE Int. Microwave Symp. Digest* pp. 813–816 (2003).
39. W. L. Langston, J. T. Williams, D. R. Jackson, and F. Mesa, Spurious radiation from a practical source on a covered microstrip line, *IEEE Trans. Microwave Theory Tech.* **49**:2216–2226 (2001).
40. W. L. Langston, J. T. Williams, D. R. Jackson, and F. Mesa, Fundamental properties of radiation from a leaky mode excited on a planar transmission line, *IEEE Trans. Microwave Theory Tech.* **51**:2366–2377 (2003).
41. C. M. Bender and S. A. Orszag, *Advanced Mathematical Methods for Scientists and Engineers*, McGraw-Hill, New York, 1978.

LEAKY-WAVE ANTENNAS

ALESSANDRO GALLI
 FABRIZIO FREZZA
 PAOLO LAMPARIELLO
 "La Sapienza" University of
 Rome
 Italy

1. FUNDAMENTAL CONCEPTS

1.1. Definition

According to the IEEE Standard 145-1993, a *leaky-wave antenna* (LWA) is "an antenna that couples power in small increments per unit length either continuously or discretely, from a traveling wave structure to free space."

The basic behavior of LWAs can efficiently be described by means of a particular type of wave, that is the *leaky wave*, which can propagate in open waveguiding structures and describes a gradual loss of power towards the external environment (*leakage*).

1.2. Basic Radiation Features

LWAs belong to the class of traveling-wave antennas for which the illumination is produced by a wave that propagates along a guiding structure [1–3]. If compared with the wavelength, a single LWA typically is *long* in the propagation direction (z), while its cross section usually is of the order of the wavelength (see, as reference, the first two examples in Fig. 1). Therefore, a LWA radiates along its length and is generally excited from one input of an open

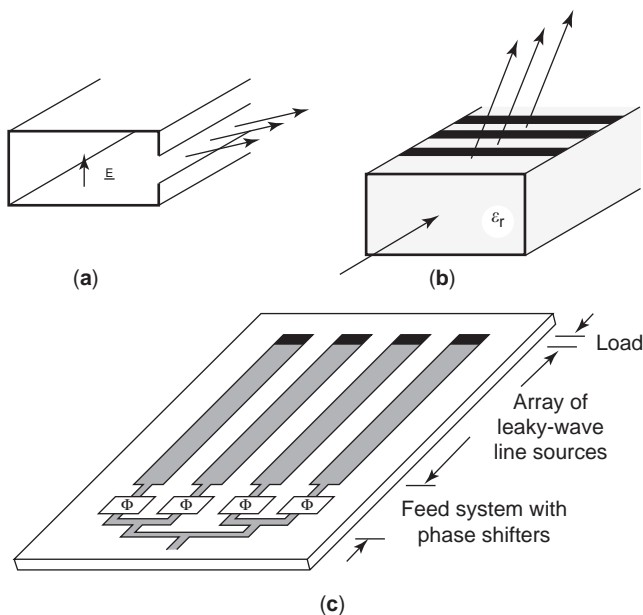


Figure 1. Basic structures of leaky-wave antennas (LWAs): (a) uniform LWAs—geometry derivable by a partially open metallic rectangular waveguide; (b) periodic LWAs—geometry derivable by a strip-loaded dielectric-rod waveguide; (c) LWA arrays—a printed topology based on microstrip.

guiding structure by a traveling wave, which propagates mainly in a longitudinal direction (e.g., $+z$) and is attenuated due to the power leakage toward the external (air) region, thus leaving a negligible field at the termination of the line. In a harmonic regime [assuming an $\exp(j\omega t)$ time dependence], the longitudinal behavior of such a wave can be characterized by a complex propagation constant of the type $k_z = \beta_z - j\alpha_z$ [3–5], where β_z is the *phase constant* and α_z is the *attenuation constant* of the *leaky wave* (when only power loss due to radiation is taken into account, α_z is also termed *leakage constant*). As discussed later, the knowledge of the complex propagation constant of this leaky wave allows for a straightforward description of the main radiation features of LWAs.

Usually the radiation pattern of a single LWA excited at one end has a typical *fan* shape; in the *elevation* (or *zenith*) plane it presents a *narrow beam* scannable by varying the *frequency*, while in the *cross* (or *azimuth*) plane usually it presents a wider beam due to a smaller transverse aperture. Multidirectional excitation is also possible, as can occur in planar dielectric structures excited by local sources (dipoles or slots) able to produce conical beams.

In general, *beamshaping* is achievable by means of suitable longitudinal variations of the structure (and of the consequent equivalent aperture distribution); the proper modulation of geometric parameters (*tapering*) allows for flexible control of the *radiation pattern*. In some cases, in order to obtain a particular beam shaping or a physical matching with mounting curved surfaces, LWAs can be designed with certain amounts of *curvature* along their lengths [6]. *Broadbeam* LWAs have also been proposed using *straight* lengths with suitable longitudinal modulation of both phase and leakage constants [7].

For ordinary LWAs the *frequency-dependent scanning* properties in the elevation plane are related to the kind of the waveguiding structure employed, which can be classified as either of *uniform* (Fig. 1a) or of *periodic* type (Fig. 1b) [1,2]. In LWAs derived by waveguides that are longitudinally *uniform*, the structure maintains a fixed transverse geometry (with possible continuous smooth modulation of the shape in the z direction); this type of radiators typically allows for angular scanning in one quadrant, from around broadside toward one endfire (i.e., the "forward" one, concordant with the wave propagation direction). In LWAs derived by waveguides that are longitudinally *periodic*, the structure along z is periodically loaded with suitable modifications or discontinuities, at intervals that are usually short with respect to the wavelength; this type of radiator allows for a wider angular scanning, in both the forward and backward quadrants. However, for different reasons, limitations in such scanning ranges generally exist for both the types of structures. A scan range in both quadrants may also be accomplished by properly using nonreciprocal anisotropic media.

When a *pencil beam* is desired with possible *two-dimensional* (2D) scanning, both in elevation and cross planes, a *linear phased array* of juxtaposed LWAs may be employed, capable to furnish a wider equivalent aperture also in the transverse direction [8,9] (see Fig. 1c). LWA arrays are in general constituted by a linear configuration

of sources (i.e., one-dimensional elements), instead of planar ones of standard arrays (i.e., two-dimensional elements). For such LWA arrays the pointed-beam scanning is achievable by varying both the *frequency* for the *elevation* plane and the usual *phase shift* between elements for the *cross* plane.

1.3. Applications

Since LWAs are derived by partially open waveguides, they present a number of distinctive features as radiators, including (1) capability of designing a wide variety of aperture distributions and consequent flexibility for beam shaping through tapering; (2) possible use as wideband radiators that allow for large angular scanning by varying frequency instead of using mechanical or electronic means; (3) achievement of very narrow beams, often with good polarization purity; (4) simplicity of feeding and economy for 2D scannable pencil-beam arrays, due to the reduced number of phase shifters; (5) handling of high-power amounts at microwaves, particularly for structures derived by metallic waveguides; (6) easy integration of planar LWAs with microwave integrated circuit (MIC) technology; (7) reduction of some bulk problems, due to usual small profiles in the cross sections; and good physical matching with unconventional mounting geometries.

LWAs are used mainly for microwaves and millimeter waves. The fundamental studies were presented during the 1940s and 1950s, basically for aerospace control applications; since then, a wide number of different solutions for LWAs have been proposed in connection with changing requirements and constraints. Also the applicability of this type of antennas has been widened, involving various aspects of monitoring, remote sensing, wireless local area network (WLAN) communications, and so forth.

2. OPERATION PRINCIPLES

2.1. Leaky Waves in Open Structures

It is known that, in order to describe radiation of a source from an open waveguiding structure, the evaluation of the field through a *spectral representation* (i.e., including a sum of a finite number of guided modes and an integral contribution of the *continuous spectrum*) can be very difficult and cumbersome to quantify in many practical circumstances. In well-designed LWAs the radiation field can be evaluated accurately in much a simpler fashion by considering the contribution due to the presence of just one mode of *complex* type, that is a *leaky wave* of the open guide.

In general, the *characteristic dispersion equation* for a waveguide (whose solution furnishes the propagation constants k_z of the *modes* as a function of *geometry* and *frequency*) presents discrete eigenvalues, which in open waveguides can also assume complex values, thus giving rise to solutions of the type $k_z = \beta_z - j\alpha_z$. It is seen that these complex solutions are in general *nonspectral*, that is the relevant modal fields violate the radiation condition (they attenuate along the propagation direction but exponentially increase in a transverse direction away from the

structure). Actually, when properly excited by a source at a finite section, such a complex wave assumes its physical validity within an angular sector close to the equivalent aperture of the open guiding structure, and the relevant field distribution is able to furnish a fundamental contribution to the evaluation of the near field. Since the far field is achieved by a simple Fourier transform of the field on the aperture, a *leaky wave* can definitively furnish a highly convergent and efficient quantification of the *radiation of the open structure*, as an advantageous alternative to a continuous spectrum evaluation.

When a leaky wave exists and can also be efficiently excited by a source in a structure based on an open waveguide, it therefore can describe simply but accurately the radiation phenomena of the structure, which is therefore termed a *leaky-wave antenna*.

2.2. Phase and Leakage Constants

Evaluation of the *complex eigensolutions* for open waveguides depends on the physical parameters involved (frequency and geometry) and is generally achievable with *numerical methods*. Among them, the transverse resonance technique [10] is one of the most used approaches for either rigorous or approximate evaluations, according to the antenna topology. When separation of variables does not strictly hold, other numerical methods can anyway be employed to accurately determine the complex eigensolutions of the involved open waveguides. The most appropriate choice depends on several factors related to the computational features of the methods, the geometry of the open-type structures, and other variables. Among the various possibilities, integral equation techniques (such as boundary element method, or spectral-domain approaches for planar structures) are well suited to calculate complex eigensolutions also for involved topologies.

A typical behavior of the real and imaginary parts of the longitudinal wavenumber k_z of a leaky wave supported by an open guide is illustrated in Fig. 2, specifically with respect to the dispersion curves of the normalized parameters β_z/k_0 (Fig. 2a) and α_z/k_0 (Fig. 2b) versus frequency f (where k_0 is the free-space wavenumber). Radiation of LW structures can occur approximately inside the frequency range where the wave becomes fast ($\beta_z/k_0 < 1$), and power can therefore leak out from the guiding structure toward the outside air region in the typical form of an inhomogeneous plane wave [4,5]. The valid frequency range for effective LWA applications is actually where, as the frequency decreases, β_z/k_0 diminishes monotonically from unity toward rather low values; in this region, to have an efficient directive beam, α_z/k_0 should assume rather limited values (e.g., typically α_z/k_0 varies from about 10^{-1} to 10^{-3} , as will be discussed further). As the frequency decreases further, a sudden rise of α_z/k_0 can generally be found, which describes the predominance of reactive phenomena instead of radiative ones, while β_z/k_0 can present a flat zone with approximately constant low values before showing a further steep rise as frequency goes to zero: in these ranges, radiative effects can no longer be represented by the leaky wave and the structures usually cannot work well as antennas.

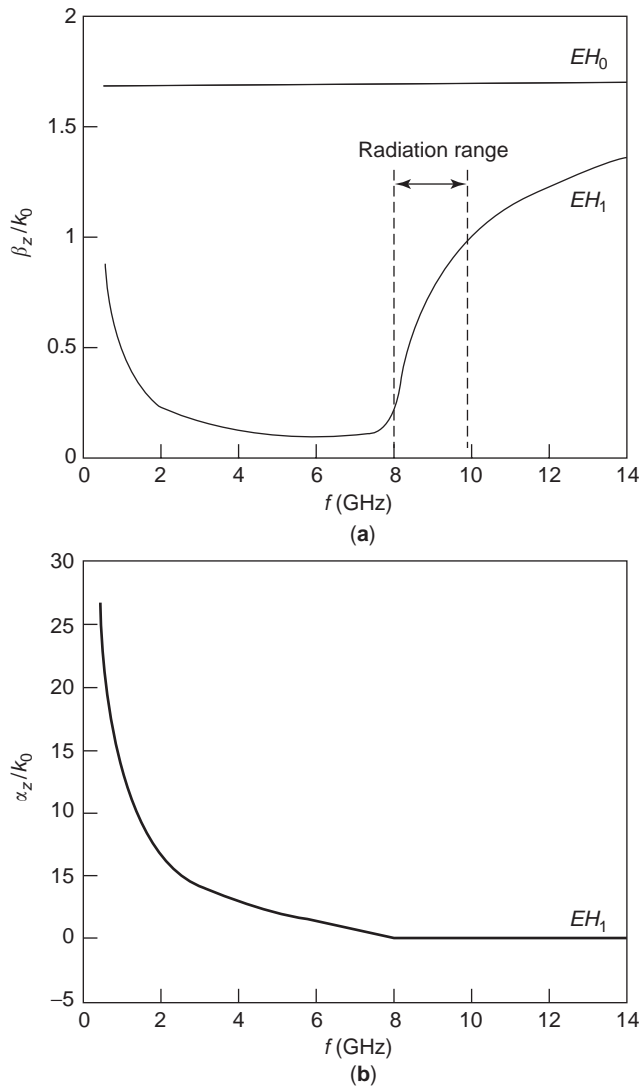


Figure 2. Typical dispersion behavior of the leaky-mode complex wavenumber: (a) normalized phase β_z/k_0 and (b) leakage α_z/k_0 constants versus frequency f for an open waveguide (microstrip operating the EH_1 mode).

It is worth remembering that in planar structures that are also transversely open, a different type of leakage can occur, too, associated with the propagation of complex waves that carry away power from a source in the *lateral* region inside the substrate (*surface waves*), instead of toward the upper-air region (*space waves*); the waves in the substrate do not give useful contributions to a LWA far-field radiation but describe power that leaks out in the stratified structures and accounts for typical *interference* and crosstalk effects in planar circuits [8,11].

2.3. Behavior of a Leaky-Wave Antenna

As stated above, LWAs are described by an inhomogeneous fast wave, which propagates on an equivalent aperture losing power towards free-space with a leakage amount that is usually rather limited for a sufficiently directive beam. The simplest LWA geometry for this purpose is

derivable by a closed metallic waveguide in which a suitable “small” aperture is introduced longitudinally in order to calculate a continuous power loss along its length, as shown in Fig. 3a for a rectangular guide with a slit cut on a sidewall. This structure, besides having a historical importance as the first proposed LWA in 1940 [1–3], can be taken as a reference structure for explaining the basic behavior of LWAs in terms of a waveguide description.

In fact, in this structure a leaky wave can be considered as excited by a standard incident mode for the closed rectangular waveguide, that is, the dominant TE_{10} , which travels in the $+z$ direction with a known phase constant β_{0z} for a fixed choice of the physical parameters (geometry and frequency). For a sufficiently small geometric perturbation due to the slit, the phase constant is changed just “slightly” to a value represented by β_z , and a “low” leakage rate α_z also originates; as mentioned, this accounts for the longitudinal attenuation due to the wave that is no longer confined and flows also in the outside region. The propagating field inside the waveguide and in the proximity of its aperture is therefore described by the complex longitudinal wavenumber $k_z = \beta_z - j\alpha_z$, whose specific quantification depends on the physical parameters of the structure.

In this case the leakage phenomenon is assumed along $+z$ ($\beta_z > 0$ and $\alpha_z > 0$), and by supposing that the vertical field variations are almost negligible ($k_y \cong 0$), it is easily seen that, from the general separation condition for waveguides ($k_0^2 = \omega^2 \mu_0 \epsilon_0 = k_t^2 + k_z^2 \cong k_x^2 + k_z^2$), the horizontal wavenumber is also complex

$$k_x = \beta_x - j\alpha_x, \quad (1)$$

with $\beta_x > 0$ and $\alpha_x < 0$, since $\beta_x \alpha_x = -\beta_z \alpha_z$ results. Therefore a plane wave of inhomogeneous type exists, having a complex propagation vector \mathbf{k} of the type

$$\begin{aligned} \mathbf{k} &= \boldsymbol{\beta} - j\boldsymbol{\alpha} \\ \boldsymbol{\beta} &= \beta_x \mathbf{x}_0 + \beta_z \mathbf{z}_0 \\ \boldsymbol{\alpha} &= \alpha_x \mathbf{x}_0 + \alpha_z \mathbf{z}_0 \end{aligned} \quad (2)$$

with the phase vector $\boldsymbol{\beta}$ directed at an angle that describes the outgoing of power from the guide to the external, and the attenuation (leakage) vector $\boldsymbol{\alpha}$ that is perpendicular to $\boldsymbol{\beta}$, and represents attenuation along z and amplification along x . Consequently, the field has a spatial dependence of the type

$$\exp[-j(\beta_x x + \beta_z z)] \exp[|\alpha_x| x - \alpha_z z] \quad (3)$$

Therefore, this plane wave travels at an angle $\theta = \sin^{-1}(\beta_z/|\boldsymbol{\beta}|)$ with respect to broadside carrying out power, and its amplitude is transversely increasing as expected in a leaky wave. It should be noted that the pointing direction angle θ of the leaky wave is usually expressed under the approximate form $\theta \cong \sin^{-1}(\beta_z/k_0)$, since in general the leakage constant is numerically negligible with respect to the phase constant. The nature of the propagation vector is sketched in Fig. 3b, while the

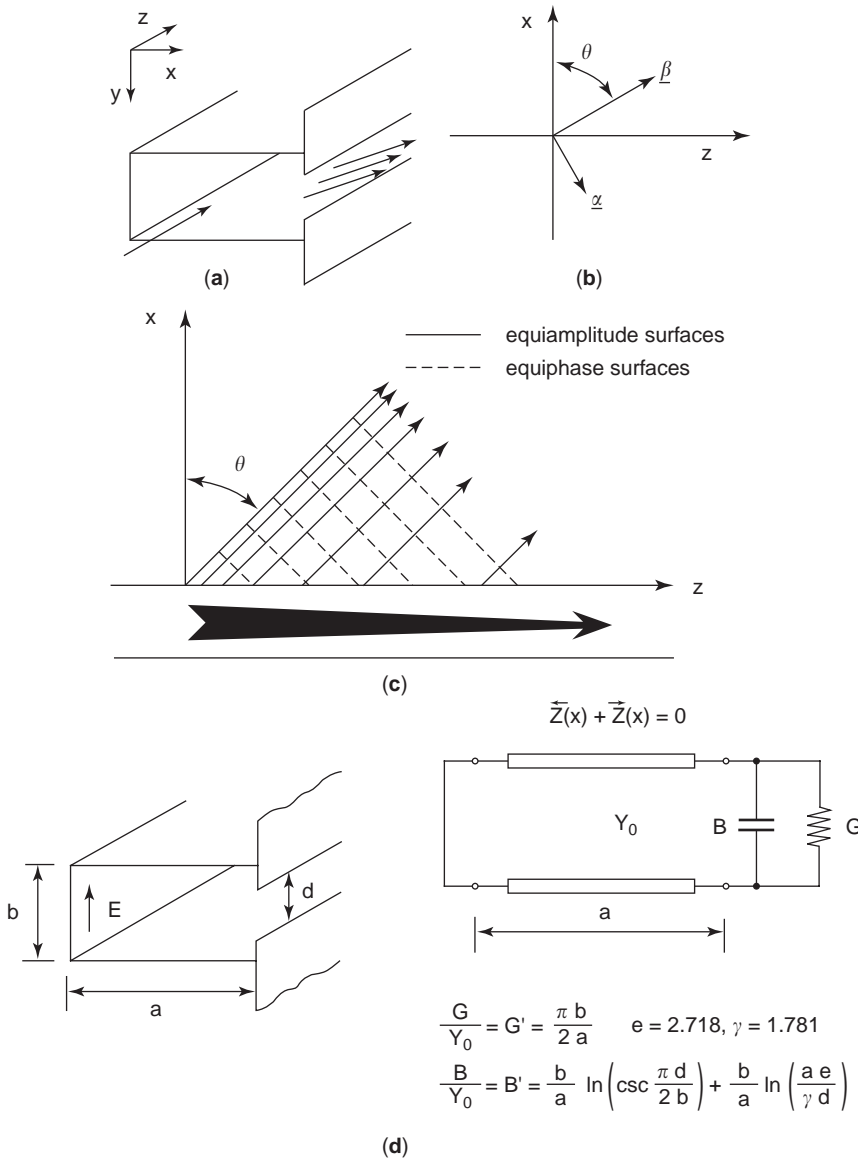


Figure 3. LWA derived by a sidewall slit rectangular waveguide; (a) geometry of the structure; (b) nature of the propagation vector of the inhomogeneous plane leaky wave (phase and attenuation vectors); (c) equiphas and equiamplitude planes of the leaky wave with the relevant leakage phenomenon along the guide; (d) equivalent transverse-resonance network, resonance conditions, and network parameters for evaluation of leaky-wave complex wavenumbers as a function of the physical parameters involved.

distribution of equiphas and equiamplitude surfaces with the decreasing power flow along the guide is represented in Fig. 3c. It should be recalled that, even though the leaky wave has a nonspectral nature, the field generated from a source located at a finite distance along z still satisfies the radiation condition, since the field increases transversely only in a limited sector given by angles greater than the θ value describing the direction of power leakage [4,5].

A quantitative description of the behavior of this LWA can be achieved with a simple evaluation of the complex eigenvalue derivable as a modification of the dominant mode by employing, for example, a transverse resonance technique. To this aim, it is required a characterization of the slit aperture in the sidewall as a circuit element in the equivalent transmission line. For the quantification of such discontinuities, a great deal of work has been deve-

loped, basically through variational methods [8,10]. The solution of the relevant resonance equation in the complex plane for the perturbed dominant mode describes the leaky-wave behavior; for example, in Fig. 3d the equivalent network for the LWA considered here is shown, through which k_z is determined as a function of the physical parameters of the antenna.

3. DESIGN PROCEDURES

3.1. Basic Radiative Features

For a basic LWA constituted by a single nontapered open guiding structure, the fundamental parameters given by pointing direction and beamwidth are simply determined as a function of k_z and other few basic quantities. In

$$\vec{Z}(x) + \vec{Z}(x) = 0$$

$$\frac{G}{Y_0} = G' = \frac{\pi b}{2 a} \quad e = 2.718, \gamma = 1.781$$

$$\frac{B}{Y_0} = B' = \frac{b}{a} \ln \left(\csc \frac{\pi d}{2 b} \right) + \frac{b}{a} \ln \left(\frac{a e}{\gamma d} \right)$$

(d)

particular, as seen before, the beam maximum *direction* θ_m is mainly related to the normalized phase constant according to the simple relationship:

$$\sin \theta_m \cong \beta_z/k_0 \tag{4}$$

Since β_z has a dispersive behavior, as is typical of waveguiding structures, a change in the frequency yields a beam scanning. Typically, as the frequency is increased from the cutoff, the pointing angle varies its direction from around the broadside ($\theta_m = 0^\circ$), toward the forward endfire ($\theta_m = 90^\circ$).

Regarding the *beamwidth*, we recall that the leakage constant α_z quantifies the rate of power loss along the line due to the radiation, thus influencing primarily the effective dimension of the equivalent aperture for the line source; in fact, the more α_z increases, the more the actual illumination length reduces (and the less the beamwidth is focused). A basic link between the leakage constant and the antenna length L derives from the specification of the radiation efficiency η , expressible in LWAs as $\eta = [P(0) - P(L)]/P(0)$, where $P(0)$ is the input power delivered to the structure and $P(L)$ is the output power left at the end section. The link between leakage rate and length is generally dependent on the desired radiation pattern and therefore on the aperture distribution. Referring to a uniform-section LWA, where α_z is independent of z , we obtain $\eta = 1 - \exp(-2\alpha_z L)$. It should also be noted that, for narrowbeam applications, a very high increase in efficiency should require an extreme prolongation of the line source; actually, in LWAs it typically radiates around 90% or at most 95% of the input power, where the remaining power at the termination is absorbed by a matched load to avoid a backlobe of radiation due to the reflected wave. Once the efficiency is chosen, a fixed link therefore exists between the relative length in terms of wavelengths L/λ_0 and the normalized leakage constant α_z/k_0 . For a uniform-section LWA, an inverse proportionality relationship between L and α_z is found to be of the type:

$$\begin{aligned} L/\lambda_0 &\cong c/(\alpha_z/k_0) \\ c &= (1/4\pi) \ln [1/(1 - \eta)] \end{aligned} \tag{5}$$

where c is related to the value of the desired efficiency (e.g., for 90% of efficiency it is $c = 0.185$). For a tapered section, since α_z depends on z , the link between efficiency, length, and leakage rate is related to the chosen illumination and is more complicated.

In order to achieve narrow beams in the elevation angle, the effective longitudinal aperture has to be sufficiently wide (usually several wavelengths), and this implies a rather low leakage rate. The half-power (-3 -dB) beam-width $\Delta\theta$ is directly linkable to the normalized antenna length L/λ_0 through an approximate relationship, which also takes into account the contribution of the scan angle [1]

$$\Delta\theta \cong a/[L/\lambda_0 \cos \theta_m] \text{ (rad)} \tag{6}$$

where the proportionality factor a is dependent on the aperture distribution. It has the most reduced value for a constant aperture distribution ($a \cong 0.88$) and increases for tapered distributions (typically, more than unity) [1]. From the previous expression, it is seen that, since $\cos \theta_m \cong k_t/k_0$, the beamwidth can also be expressed as $\Delta\theta \cong 2\pi/(k_t L)$. This means that the beamwidth is, at first approximation, practically constant when the beam is scanned away from broadside by varying the frequency for air-filled LWAs (where k_t is independent of frequency), while it changes for dielectric-filled LWAs (where k_t depends on frequency). The effective aperture is nevertheless reduced for a fixed antenna length as the beam approaches endfire (where the previous expression becomes inaccurate), and $\Delta\theta$ anyway tends in practice to enlarge. It can be seen that for an ideal semiinfinite uniform structure, that is, an antenna aperture from $z = 0$ to $z = L \rightarrow \infty$, the beamwidth is determined by the leakage rate only, since in this case it can be found that $\Delta\theta \cong 2\alpha_z/k_t$. Moreover, in this situation the radiation pattern depends only on β_z and α_z and does not present sidelobes:

$$R(\theta) \approx \frac{\cos^2 \theta}{(\alpha/k_0)^2 + (\beta/k_0 - \sin \theta)^2} \tag{7}$$

For finite antenna lengths, sidelobes are produced and the expression for $R(\theta)$ is more involved. In general the specifications on the sidelobe level are related to the choice of the aperture distribution, whose Fourier transform allows for the derivation of the radiation pattern.

3.2. Scanning Properties

It is seen that, for LWAs derived by partially open air-filled metallic waveguides, the beams scan in theory an angular region from around the broadside ($\beta_z/k_0 \cong 0$) toward one endfire ($\beta_z/k_0 \cong 1$). In practice, around broadside the structure works near the cutoff region of the closed waveguide where reactive effects are increasingly important. Nevertheless, the leaky-wave values for β_z/k_0 cannot be extremely low, and at the same time α_z/k_0 tends to increase too much, adversely affecting the possibility of focusing radiation at broadside. Regarding the behavior at endfire it is seen that, since β_z/k_0 tends to unity asymptotically as the frequency increases, in the unimodal range (where these structures are usually employed) the beam cannot reach so closely the endfire radiation in an air-filled LWA.

A way of improving the angular scanning is to fill these structures with dielectric materials. Thus, since in this case the normalized phase constant approaches the square root of the relative permittivity as the frequency is increased ($\beta_z/k_0 \rightarrow \epsilon_r^{1/2}$), the $\beta_z/k_0 = 1$ value can actually be approached in a much more restricted frequency range. It should be noted that for such dielectric-filled structures the beamwidth may change strongly as a function of frequency and therefore as the pointing angle varies [see comments to Eq. (6)]. Moreover, it should be noted that in many leaky structures (such as the dielectric and printed ones), as the frequency is increased, the leaky-mode solution changes into a guided-mode solution

through an involved “transition region” [2]; in this frequency range, also called the “spectral gap,” the contribution of the leaky wave to the accurate determination of the field tends progressively to decrease, and generally the structure does not work well as a LWA.

As mentioned, while the uniform LWAs usually radiate only in the forward quadrant, with the limits specified above, the LWAs derived from periodically modulated slow-wave guides can start to radiate from the backward endfire in the lower frequency range. The design principles of periodic LWAs are in most part similar to those of uniform LWAs [1,2]. The main difference lies in the characterization of the fast wave that is now associated with a Floquet space harmonic of the periodic guide [1,2]. One can see that if a uniform guide is considered whose operating mode is slow [$\beta_z/k_0 > 1$, e.g., a dielectric waveguide], and a longitudinally periodic discontinuity is properly added (e.g., an array of metal strips or notches, placed at suitable distances p), such periodicity furnishes a field expressible in an infinite number of space harmonics ($\beta_{zn}p = \beta_{z0}p + 2n\pi$), where β_{z0} is the phase constant of the fundamental harmonic, which is slightly varied with respect to the original value β_z of the unperturbed guide. With proper choices of the physical parameters, it is in general possible to make only one harmonic fast (typically, the $n = -1$ one), so that it can radiate as a leaky wave (presence of an additional attenuation constant α_z).

In this case, the phase constant of this fast harmonic can assume both positive and negative values ($-1 < \beta_z/k_0 < 1$), as a function of the parameters involved; in particular, as frequency is increased, the beam starts to radiate from backward endfire toward the broadside. In general, also periodic LWAs can have difficulties in working well in the broadside region, since usually for periodic structures there exists an “open stopband” [1], where the attenuation constant rapidly increases, resulting in a widening beamwidth. As the frequency is further increased after broadside, the beam is then scanned also in the forward quadrant. In periodic LWAs, depending on the choice of the design parameters, additional limitations in the forward scanning behavior could exist when a second harmonic also starts to radiate before the first harmonic reaches its endfire, thus limiting the scanning range of the single beam [1,3].

3.3. Leaky-Wave Arrays

If an increase of directivity in the cross-plane is desired, a simple improvement for LWAs based on long radiating slots can be achieved by a physical enlargement of the transverse aperture (e.g., with a flared transition to enlarge the effective cross-aperture). As said before, a more efficient way to increase directivity in the cross-plane is to use a number of radiators placed side-by-side at suitable lateral distances, thus constituting a linear array: it is then possible to achieve radiation with a focused pencil beam. In addition, if properly phased, these arrays of LWAs allow a 2D scanning of the beam; in the elevation plane, as is typical for LWA's, the scanning is achievable by varying the frequency, while in the cross-plane the scanning is achievable with phase shifters that vary the phase

difference among the single-line sources. As noted, in LWAs only a one-dimensional number of phase shifters is therefore necessary, with particular structural simplicity and economic advantage if compared to all the usual radiators requiring a two-dimensional number of shifters for the scanning. Additional desirable features of such arrays are in general the absence of blindspots and good polarization properties [8,9].

For the analysis of such LW arrays, an efficient method is that one based on the “unit cell” approach [8,9]. In this way, it is possible to derive the behavior of the global structure by referring to a single radiator taking into account the mutual effects due to the presence of all the others. In the equivalent network this is achievable by changing only the description of the radiation termination for a periodic-type array environment (infinite number of linear elements); in particular, an ‘active admittance’ can be quantified, which describes the external radiating region as a function of the geometry and of the scan angle. More sophisticated numerical techniques also allow for accurate analyses of arrays by taking into account the mutual couplings for a finite number of elements.

3.4. Pattern Shaping

In the basic requirements of the LWAs radiation pattern, in addition to the specification for the maximum of the beam direction and for its half-power width, the sidelobe behavior also has a primary importance. In general, it is required to derive the properties of the source in connection with a desired radiation pattern. Since LWAs can be viewed as aperture antennas with a current distribution having a certain illumination $A(z)$, it is possible to obtain the far field through a standard relationship [1–3]:

$$E(\theta) = G(\theta) \int_0^L |A(z')| e^{j \text{Arg}[A(z')]} e^{jk'z' \sin \theta} dz' \quad (8)$$

The radiation pattern for E is expressed in terms of a Fourier transform of the line-source complex current distribution on the aperture multiplied by the pattern of the element current G (e.g., a magnetic dipole).

It is easily seen that if the LWA geometry is kept longitudinally constant, the amplitude distribution has an exponential decay of the type $\exp(-\alpha_z z)$. As is known, this behavior furnishes a quite poor radiation pattern for the sidelobes that are rather high (around -13 dB). It therefore derives that, in conjunction with the choice of a fixed illumination function $A(z)$ giving a desired sidelobe behavior (cosine, square cosine, triangular, Taylor, etc.), the leakage rate has to be modulated along the direction z of the line source: in practice this is achievable by properly modifying the cross section of the LWA structure along z with the so-called tapering procedure. Considering that, for a smoothly tapered antenna, the power radiated per unit length from the antenna aperture is simply related to the aperture distribution [viz., $-dP(z)/dz = 2\alpha_z(z)P(z) = c|A(z)|^2$], a useful analytical expression for $\alpha_z(z)$ as a function of the amplitude $A(z)$, of the line-source length

L , and of the efficiency η is obtainable [1–3]:

$$\alpha_z(z) = \frac{1}{2} \frac{|A(z)|^2}{\frac{1}{\eta} \int_0^L |A(z')|^2 dz' - \int_0^z |A(z')|^2 dz'} \quad (9)$$

From Eq. (9) it is also seen that the more the efficiency is desired high (around unity), the more α_z has to increase towards extremely high values around the terminal section (as mentioned, efficiency in common practice does not exceed 90–95%).

For narrowbeam applications, in the tapering procedure the longitudinal modification of the geometry should be made in an appropriate way in order to affect only the leakage constant, taking into account the fact that the phase constant should conversely be maintained the same (β_z should not depend on z in order to have the correct pointing angle for each elementary current contribution on the aperture).

The pattern shaping procedure requires therefore the knowledge of the phase and leakage constants as a function of the geometric parameters of the chosen structure, and this is achievable, as mentioned, by finding the suitable complex eigensolution with numerical methods. In general, for beam shaping, either when it is required a proper α_z distribution with β_z constant (for narrow beams) or when α_z and β_z have to assume suitable longitudinal patterns (for wide beams), the procedure is strongly simplified if it is possible to find geometric parameters through which the leakage and phase constants are varied as independently as possible. This property is related to the topology characteristics of the waveguiding structure [1,12].

4. REALIZATION

4.1. Types of Leaky-Wave Antennas

The various LWAs topologies that have been investigated in the literature are based on different solutions derived by waveguiding structures. We briefly survey the main classes proposed in the applications:

1. Some LWAs based on *partially open metallic* waveguides are presented in Fig. 4. Figure 4a shows a top wall slitted rectangular guide LWA; Fig. 4b, a stub-loaded rectangular guide LWA; and Fig. 4c, a “stepped” rectangular guide LWA [12]. Many other solutions have been proposed for this class of radiators, based on groove guide, ridge guide, and so on [1].
2. Examples of structures based on *hybrid metallic/dielectric* guides are given in Fig. 5; a basic configuration of nonradiative dielectric (NRD) waveguide can be suitably modified to obtain a foreshortened (Fig. 5a) and asymmetric (Fig. 5b) NRD LWAs [1].
3. Configurations of *printed-circuit* LWAs are shown in Fig. 6; a basic uniform microstrip LWA operating on a leaky higher-order mode is shown in Fig. 6a, a

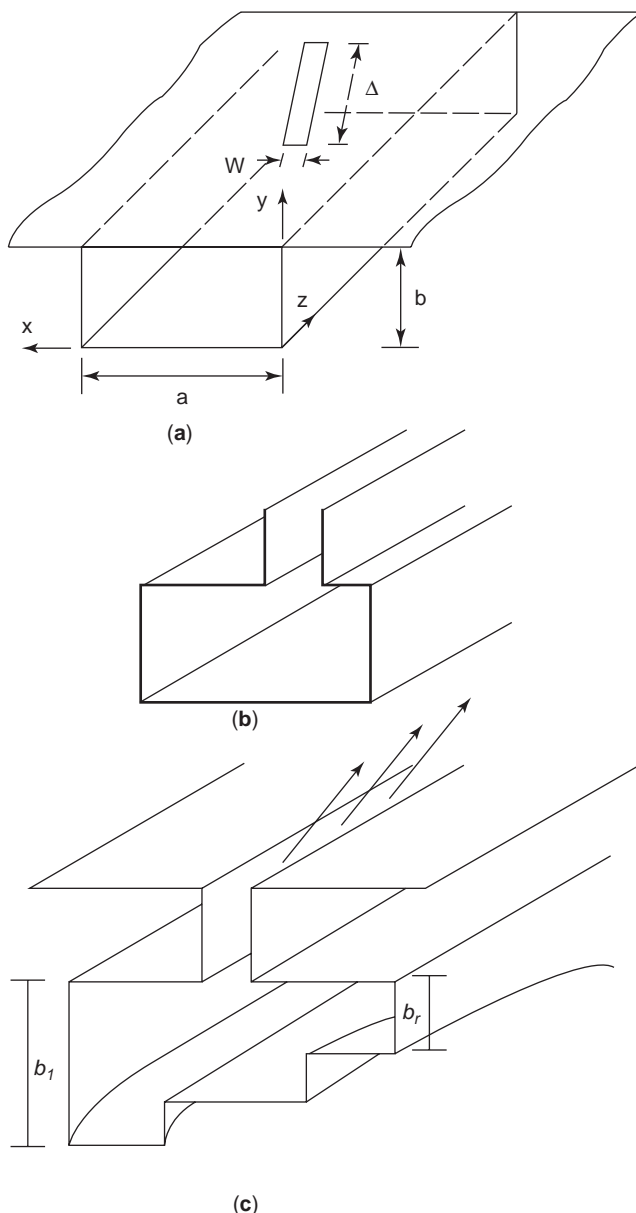


Figure 4. Metallic-guide LWAs: (a) top-wall slitted rectangular guide LWA; (b) stub-loaded rectangular guide LWA; (c) stepped rectangular guide LWA.

periodically loaded microstrip LWA is in Fig. 6b, and a periodical meander microstrip LWA is in Fig. 6c [1].

4. In basic *dielectric* guides, a periodic loading is required in order to isolate a suitable fast-wave space harmonic from the intrinsically slow-wave guiding structure. The most usual periodic perturbation is represented by grating of grooves or metal strips, usually placed in the top surface of the guide (Fig. 7a); also lateral metal patches can be used in hybrid forms (dielectric/microstrip) (Fig. 7b); the reduction of the beamwidth in the cross plane with flared horns has also been employed (Fig. 7c) [1]. All these topologies are good candidates, particularly for

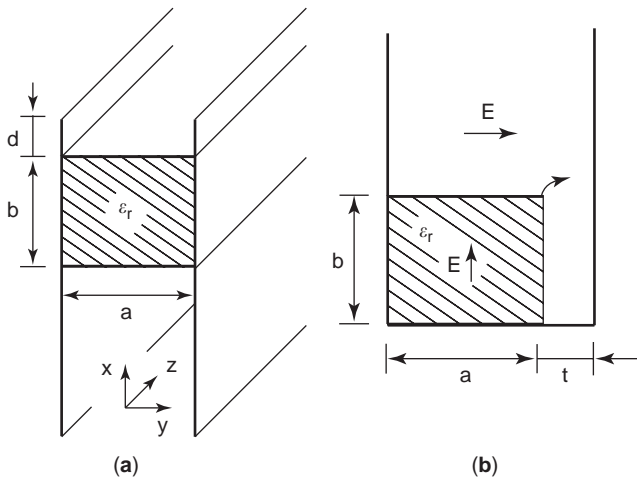


Figure 5. Hybrid metallic/dielectric LWAs: (a) foreshortened nonradiative dielectric (NRD) LWA; (b) asymmetric NRD LWA.

high-frequency applications (millimeter and submillimeter waves), where the use of dielectric instead of metal for the guidance can reduce losses.

- It has to be noted that in uniform planar dielectric LWAs based on a single layer usually present quite high leakage values, with consequent weak capability in focusing radiation. A significant improvement is achievable by properly dimensioning a substrate/superstrate structure (Fig. 8a), where a simple element (dipole or slot) is able to excite a leaky wave giving a conical highly directive beam. This basic topology can be arranged to allow for a very focused pencil beam with a limited number of radiating elements in form of widely spaced array (Fig. 8b).

Feed, Losses, and Manufacture

Feeding LWAs is often quite simple; in particular, for LWAs derived by metal guides, the feed is represented by a continuous transition from the closed structure acting on a suitable guided mode to the related open one acting on a perturbed (leaky) mode. Tapered transitions from the closed to the open structures can be realized to reduce the discontinuity effects and the possible excitation of spurious modes that could arise from abrupt transitions. At the output termination, the introduction of a matched load can strongly decrease the remaining power that, if reflected, should give rise to a backlobe in a direction symmetric to the mainbeam with respect to the broadside. The use of dielectric structures as LWAs can present more difficulties for efficient feeding and coupling, particularly in planar configurations. Attention has to be paid to obtain a “good launching” of the desired leaky wave, avoiding the excitation of additional guided and leaky modes. For planar guides, such as microstrip or layered dielectrics, local coupling elements (such as slot or dipoles) are usually employed to excite the leaky mode from an input line toward the radiating line [9].

Ohmic losses seldom affect the radiative performance of LWAs significantly, since the attenuation due to the leakage of radiated power is generally more influent than the attenuation due to dissipated power in the practical guiding structure. However, since power loss can be excessive as frequency increases, particularly for LWAs based on quasi-closed metal guides, the choice of open guides with dielectrics and a limited use of metal is naturally advisable for millimeter-wave applications.

The general simplicity of LWA structures makes their manufacture usually easy to perform, even though different construction problems can arise depending on the chosen topology and the frequency range. Simple structures are particularly desirable at millimeter waves, due to the

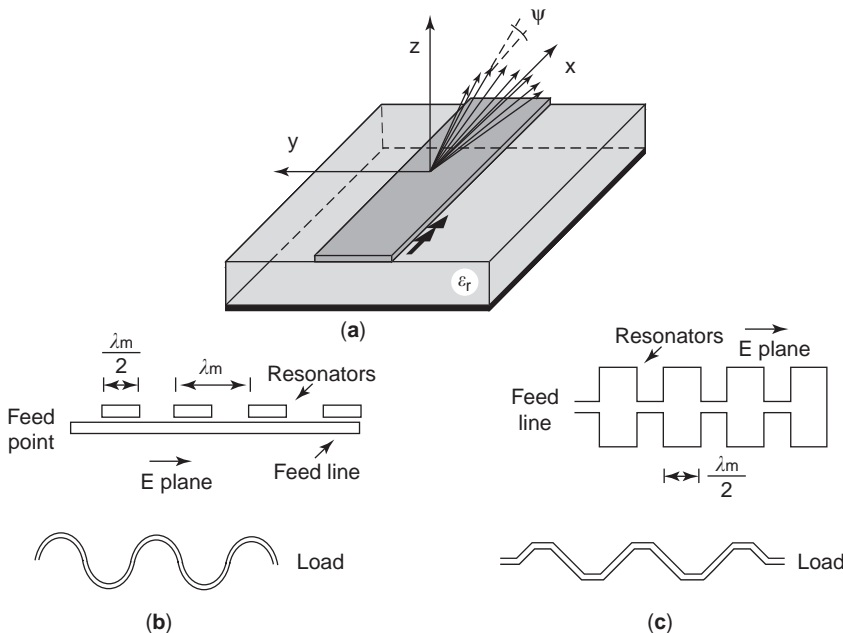


Figure 6. Printed-line LWAs: (a) uniform higher-mode microstrip LWA—space-wave radiation can be associated, for instance, with the strip current distribution of the EH_1 mode, which is leaky in a suitable frequency range; (b) a pair of periodically loaded microstrip LWAs; (c) a pair of periodical meander microstrip LWAs.

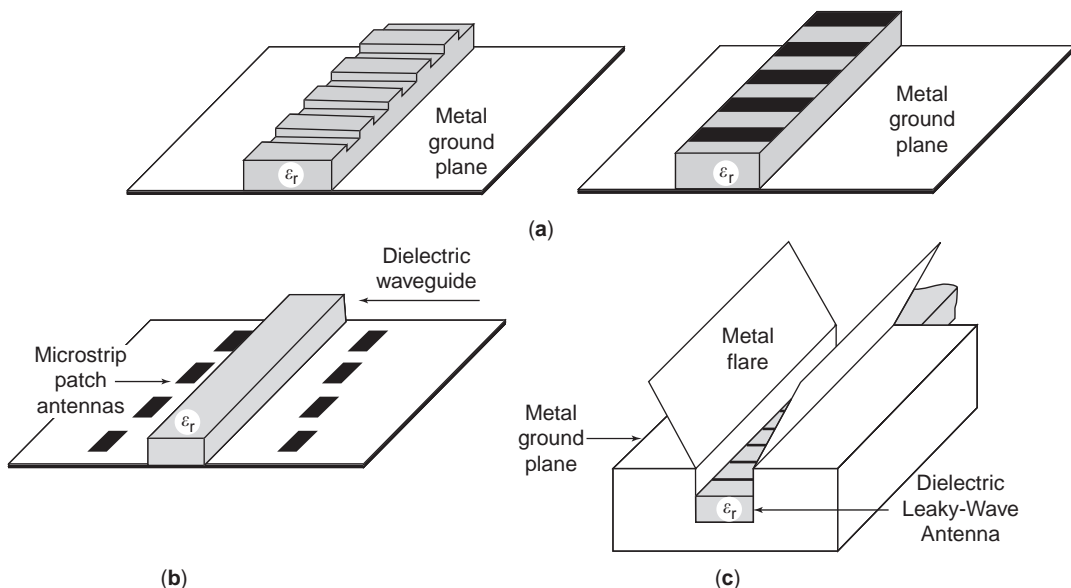


Figure 7. Dielectric-guide LWAs: (a) a pair of periodically loaded dielectric LWAs; (b) dielectric insular guide LWA with metallic patches; (c) dielectric LWA with a flared horn to reduce the cross-plane beamwidth.

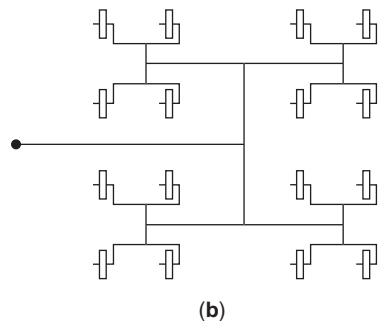
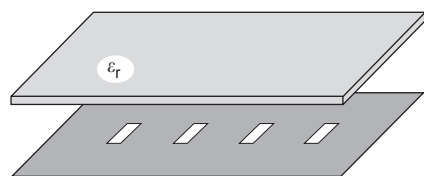
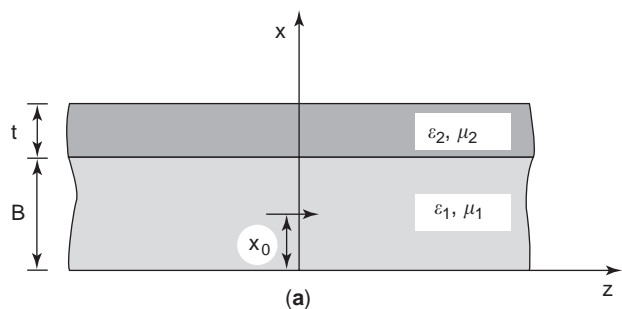


Figure 8. Planar LWAs: (a) layered-dielectric LWA based on a substrate/superstrate structure with an electric-dipole excitation; (b) high-gain LW arrays of widely spaced elements in a substrate/superstrate structure excited through slots: linear and planar configurations.

reduced dimensions. On the other hand, oversimplified shapes seldom allow good control of radiation performance. In particular, a delicate aspect concerns the usually small longitudinal modifications of the geometry related to tapering for beam control. In this case, an accurate determination of the fabrication inaccuracies and tolerances has particular importance to avoid overwhelming the required geometric variations for tapering, thus degrading the improvements of the pattern shaping. Finally, in specific applications, the practical effects of radomes for environmental protection have to be taken into account.

4.2. Measurement Techniques

The radiation properties of LWAs can be tested experimentally through different types of measurement, most of them applicable to aperture antennas. Some basic parameters, such as efficiency and mismatching effects, can be measured directly through the transmission and/or reflection scattering parameters with a network analyzer. Radiation patterns and directivity properties as a function of the observation angles (θ and ϕ in the zenith and azimuth planes, respectively) can be measured for various frequency values with different techniques, on the aperture, in the radiating near field (Fresnel region), and in the far field (Fraunhofer region). In particular, measurements on the aperture are quite easy to perform. A measurement of the field in the close proximity of the aperture can be achieved with a small pickup element (e.g., an electric dipole probe placed parallel to the aperture electric field). Amplitude and phase of the signal received by the probe are thus measurable through a network analyzer, with possible compensation techniques related to the mutual coupling between the current distribution on the aperture and the current probe element. As said, from the determination of

these basic parameters, a complete knowledge of the radiative characteristics is easily achievable in LWAs.

BIBLIOGRAPHY

1. A. A. Oliner, Leaky-wave antennas, in R. C. Johnson, ed., *Antenna Engineering Handbook*, 3rd ed., McGraw-Hill, New York, 1993.
2. R. E. Collin and F. J. Zucker, *Antenna Theory*, Mc-Graw-Hill, New York, 1969.
3. C. H. Walter, *Traveling Wave Antennas*, McGraw-Hill, New York, 1965; Peninsula Publishing, Los Altos, CA, reprint, 1990.
4. T. Tamir and A. A. Oliner, Guided complex waves, Parts I and II, *Proc. IEEE* **110**:310–334 (1963).
5. T. Tamir, Inhomogeneous wave types at planar interfaces: III—Leaky waves, *Optik* **38**:269–297 (1973).
6. I. Ohtera, Diverging/focusing of electromagnetic waves by utilizing the curved leakywave structure: Application to broad-beam antenna for radiating within specified wide-angle, *IEEE Trans. Anten. Propag.* **AP-47**:1470–1475 (1999).
7. P. Burghignoli, F. Frezza, A. Galli, and G. Schettini, Synthesis of broad-beam patterns through leaky-wave antennas with rectilinear geometry, *Anten. Wireless Propag. Lett.* **2**:136–139 (2003).
8. A. A. Oliner, *Scannable Millimeter Wave Arrays*, Final Report on RADC Contract No. F19628-84-K-0025, Polytechnic Univ., New York, 1988.
9. P. Baccarelli, P. Burghignoli, F. Frezza, A. Galli, and P. Lampariello, Novel modal properties and relevant scanning behaviors of phased arrays of microstrip leaky-wave antennas, *IEEE Trans. Anten. Propag.*, **AP-51**:3228–3238 (2003).
10. T. Itoh, ed., *Numerical Techniques for Microwave and Millimeter-Wave Passive Structures*, Wiley, New York, 1989.
11. F. Mesa, C. Di Nallo, and D. R. Jackson, The theory of surface-wave and space-wave leaky-mode excitation on microstrip lines, *IEEE Trans. Microwave Theory Tech.* **MTT-47**:207–215 (1999).
12. C. Di Nallo, F. Frezza, A. Galli, G. Gerosa, and P. Lampariello, Stepped leaky-wave antennas for microwave and millimeter-wave applications, *Ann. Télécommun.* **52**:202–208 (1997).

LEFT-HANDED MATERIALS FOR MICROWAVE DEVICES AND CIRCUITS

CLIFFORD M. KROWNE
Naval Research Laboratory
Washington, DC

1. INTRODUCTION

The use of so-called left-handed materials in the construction of components for physics instruments or electronic devices is an extremely new area to blossom. The materials themselves display a different property of matter compared to ordinary matter relative to the propagation or motion of electromagnetic waves through them. In ordinary matter, through which one sends light, the

energy flow or power travels in the same direction as the phase front or phase motion of the wave. This is not unlike what one would see after dropping a pebble in a pond of water and then observing the ripples. The motion started by initially dropping the pebble in the pond tends to spread out from the point of initial impact where the pebble entered the water surface. As anyone who has seen this phenomenon can attest to, ripples emanate from the initial entry point, and continue in time to spread out, producing increasingly large circles, whose radial distance from the initial entry point increases. One can see that the power flows radially away from the initial point. Also, the phase front of the wave, measured by following a wave crest or trough, also flows radially away from the initial point. So at any given location, the direction of both the power flow and the wave front are the same, or codirectional, and perpendicular to the wave crest, which is in the shape of a circle. If we represent the power flow by a vector, called the *Poynting vector* \mathbf{P} and the phase front by another vector \mathbf{k} at any given location in coordinate space \mathbf{r} , we can say that $\mathbf{P} \cdot \mathbf{k} > 0$, where the dot indicates the multiplication of two vectors, called the *dot product*. Of course, for our example of the pebble in the pond, the problem in computing the dot product is trivial because for any \mathbf{r} location, which in rectilinear coordinates is specified by x , y , and z , \mathbf{P} and \mathbf{k} point in the same direction, and when this occurs, the dot product must both be positive and have a maximum value (Fig. 1a). A more complex situation would be when these two vectors do not point in the same direction (Fig. 1b). This is still not a problem, because we still know how to compute the dot product of two noncollinear vectors. One simply projects one vector onto the other vector, a process that produces the answer $Pk \cos \theta$. Here P is the magnitude of the vector \mathbf{P} , k the magnitude of the vector \mathbf{k} , and θ the angle between them. The cosinusoidal function of θ creates the dot product.

Left-handed materials do not produce positive dot products between the power and phase vectors. Rather, they have $\mathbf{P} \cdot \mathbf{k} < 0$, in apparent contradiction to what we

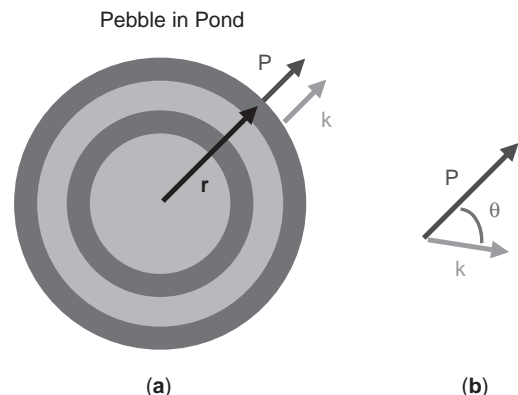


Figure 1. (a) Example of relationship between the power flow vector \mathbf{P} and the phase vector \mathbf{k} for a pebble dropped into a pond at its center—red denotes the location of the crests in the waves emanating from the pond center; (b) nonparallel power \mathbf{P} and phase \mathbf{k} vectors, with an angle θ between them. (This figure is available in full color at <http://www.mrw.interscience.wiley.com/erfme>.)

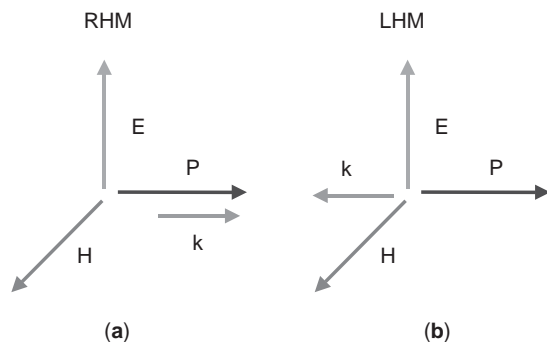


Figure 2. Orientation of the electric \mathbf{E} , magnetic \mathbf{H} , power \mathbf{P} , and phase \mathbf{k} vectors in (a) a right-handed material (RHM) and (b) a left-handed material (LHM). (This figure is available in full color at <http://www.mrw.interscience.wiley.com/erfme>.)

understand to be normal behavior. However, there is nothing fundamental that dictates, on the basis of Maxwell's equations, that the product must always be positive. Since it is known that the Poynting vector is equal to the cross-product of the electric \mathbf{E} and magnetic \mathbf{H} fields, or $\mathbf{E} \times \mathbf{H}$, in normal matter it can be demonstrated that \mathbf{E} , \mathbf{H} , and \mathbf{k} form a right-handed system (see Fig. 2a). Clearly, if \mathbf{k} points oppositely to \mathbf{P} , the triad \mathbf{E} , \mathbf{H} , \mathbf{k} must form a left-handed system (see Fig. 2b); this is how the term "left-handed material" arose. Sometimes left-handed material is abbreviated LHM. Similarly, for ordinary matter, or right-handed material, we can use RHM. Left-handed materials have also been variously referred to as negative-index-of-refraction materials (NIMs or NIRMs), negative-phase-velocity materials (NPVs or NPVMs), backward wave materials (BWMs), and negative permittivity and permeability materials (DNMs or NMs). In the latter acronym, the "D" indicates double because both the permittivity and permeability are simultaneously negative. To see that the dual assignment of negative constitutive parameters of a materials leads to a left-handed arrangement of the vector triad, it is sufficient to examine Maxwell's two curl equations. Index of refraction is a concept arising from optics, and merely gives the ratio between the speed of light in the material in comparison to free space or a vacuum. It is usually denoted by the letter "n."

Interest in left-handed media (LHM) originally arose because of its purported ability in combination with right-handed (RHM) or ordinary media to allow unusual focusing of waves, with possible applications in subwavelength control of optical imaging and negative-index-of-refraction (NIR) behavior leading to new radar uses [1]. Definite proof of NIR has occurred in several laboratories, and there is little question that focusing possibilities exist in the much lower frequency microwave/millimeter wavelength regimes compared to the optical regime, although it is now known that imperfect focusing is the best that can be expected. However, this should present no fundamental stumbling block as long as we do not require perfect focusing performance of imaging systems. Thus, applications can be foreseen in the radiocommunication bands. As far as providing focusing capability at the much higher optical frequencies, that is still an unresolved

question. One unusual property of the LHM in conjunction with RHM is the ability to take diverging or parallel rays of light and focus them with a flat plate of LHM. A normal concave lens will now cause rays of light hitting it from a source to diverge, but a convex lens will focus the light rays. These unusual behaviors of LHM were pointed out in the late 1960s in the Russian physics literature [2]. However, the possibility of backward wave behavior has been known since the 1950s and is available in both the American and British physics and electronics literature. So for half a century or so, something has been known about LHM. The earliest work involved backward wave propagation in traveling-wave tubes [3,4] or microwave or millimeter-wave devices and models using nonreciprocal materials [5] or higher-order modes. This earliest work generally involved propagation in one dimension, or dimensions lower than three, as opposed to the left-handed phenomena occurring in any wave direction. When left-handed behavior occurs in any direction, the property is called *isotropic*, meaning that the behavior is seen for any arbitrary propagation direction. Isotropy is what allows the unlimited focusing property that was discussed in the Russian literature in the late 1960s, and which generated the tremendous interest in the physics community worldwide in the late 1990s.

In contrast to the imaging and radar applications stemming from LHM, potential electronic uses may also exist because new physics of propagation in left-handed media occur in structures compatible with integrated circuits. Treating the LHM as intrinsic with microscopic properties that may be described by constitutive relations relating the displacement field or electric flux density \mathbf{D} and electric field intensity \mathbf{E} (i.e., $\mathbf{D} = \epsilon\mathbf{E}$) and relating the magnetic flux density \mathbf{B} to magnetic field intensity \mathbf{H} , (i.e., $\mathbf{B} = \mu\mathbf{H}$), the electromagnetic fields within guided-wave structures employed in integrated circuits can be studied. Completely new dispersion diagrams and electromagnetic field configurations have been found, and it has been proved that propagation in these devices enables regions of forward and backward waves to exist [6]. Such new propagation behavior is in agreement with more recent macroscopic realizations using lumped/distributed circuit elements to make backward wave circuits [7]. These circuits show that various transmission lines, couplers, and other circuit elements with different or improved characteristics may be produced. It is expected that the same could be done for filters, producing devices with new properties or improved characteristics, since propagating and evanescent frequency bands exist in the dispersion diagram. Additionally, the new electromagnetic field distributions strongly imply that improved isolators and circulators [8] could be constructed using LHM in combination with nonreciprocal materials based on carrier cyclotron motion or spin precession. New control components using reciprocal media are also possible by teaming up LHM with ferroelectric materials [9], for example.

The knowledge that backward waves can be produced from discrete inductor and capacitor arrangements configured as unit cells in a transmission system has been known for a long time, and standard textbooks date back to 1967 [10]. This is the origin of the lumped/distributed

elements mentioned above and employed in circuits made using ordinary materials to obtain the backward wave behavior. Dating even further back is the idea that periodic waveguiding structures, with finite-sized unit cells, require the superposition of an infinite set of discrete modes to determine the field at any given location in the repetition direction, call it z . The result of the superposition is to create what is sometimes referred to as “space harmonics,” a coupled system of modes that together satisfy the periodic boundary conditions of the structure. But what also occurs from this superposition with repetition distance d is a k -frequency f diagram repeated infinitely in reciprocal space of period size $2\pi/d$. If we call k_0 the phase behavior within the basic reciprocal unit cell, then the general phase solution includes all the harmonics, stated mathematically as $k_n = k_0 + 2\pi n/d$, $n = 0, \pm 1, \pm 2, \dots, \pm\infty$ [11]. Thus all periodic circuits and structures have an equal number of forward and backward space harmonics.

We will direct our attention in this article, therefore, to the most original area of left-handed materials and devices, those that utilize intrinsic crystalline properties of the material, as opposed to those using lumped elements consisting of capacitive or inductive sections, or RHM transmission lengths, which has been the approach of more recent work producing backward wave devices and circuits. The easiest way to produce intrinsic LHM crystal-

line properties in a guided-wave device is to choose metallic rods and split rings with gaps and to repeat them in a lattice where the repeat distance is much shorter than the effective wavelength. This arrangement is shown schematically in Fig. 3a, and was used in a different context to produce some of the initial results giving rise to the hope in the physics community that optical focusing could be possible given the proof of principle at microwave frequencies (on the order of 5–15 GHz) [12]. But ideally, one would like to have a single-crystalline substrate of material as in Fig. 3b, at the microscopic level. Barring this possibility, another way to make LHM is to combine a layer of crystalline material that has the desired negative permittivity $\epsilon < 0$ with another layer of crystalline material which has the desired permeability $\mu < 0$. This two-layered structure is shown in Fig. 3c. It is even possible that these uniform layers of material could be amorphous and not crystalline. All that would be needed for this concept to work is that each individual layer be substantially less than the wavelength sampling the combination in the vertical direction [13]. This sampling may be evaluated by hitting the two-layered combination by an incident wave as in Fig. 4a and comparing the reflected and transmitted response to the single-layer case in Fig. 4b. It might even be desirable to make multilayered combinations as in Fig. 3d with alternating layers of negative permittivity $\epsilon < 0$ with

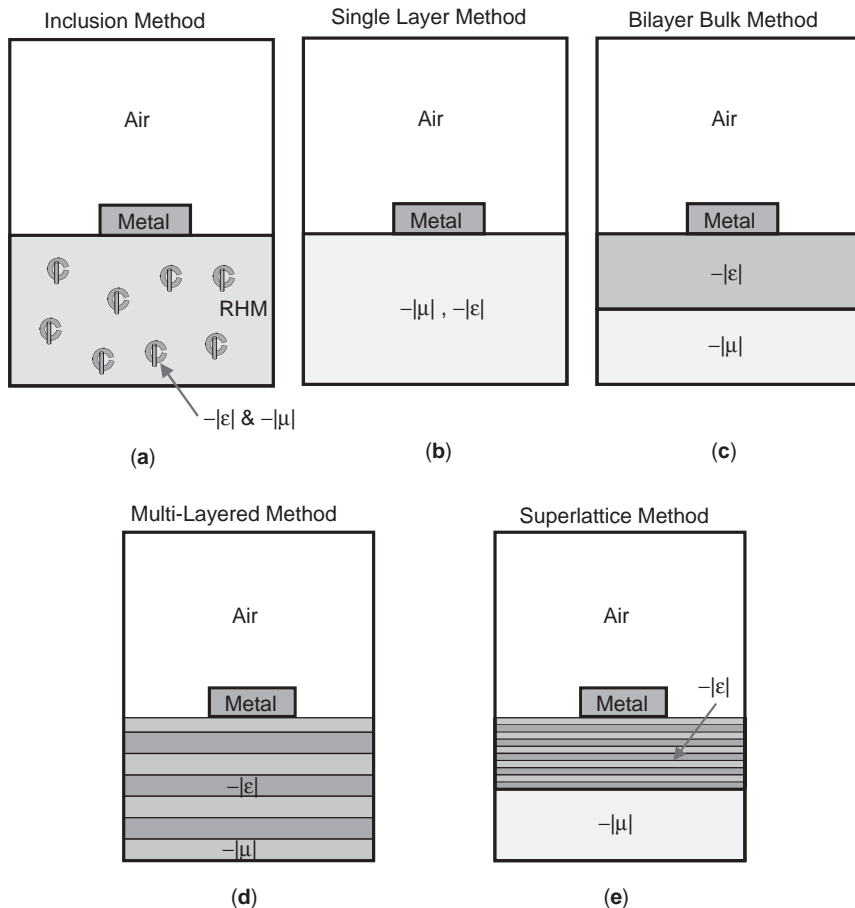


Figure 3. Various arrangements of matter to form intrinsic crystalline double-negative material (DNM) or left-handed material (LHM) from (a) inclusions of metallic rods and split resonator rings in a normal RHM or double-positive material (DPM) host, (b) a single-crystalline substance or a single amorphous substance, (c) a bilayer combination of two materials with one having $\epsilon < 0$ but $\mu > 0$ and the other having $\mu < 0$ but $\epsilon > 0$, (d) multiple stacked bilayers, and (e) a heterostructure or superlattice, which creates one of the two bilayers (or both) from (c). (This figure is available in full color at <http://www.mrw.interscience.wiley.com/erfme>.)

Bilayer Equivalency to Single Layer

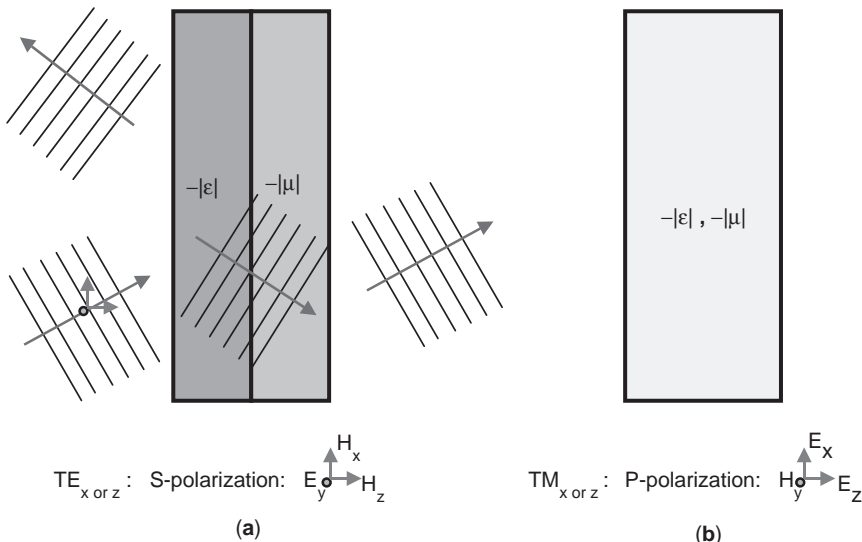


Figure 4. Equivalency of a bilayer and a single DNM or LHM layer is demonstrated using wave transmission (and reflection) of transverse electric (*s*-polarization) or transverse magnetic (*p*-polarization) waves. (This figure is available in full color at <http://www.mrw.interscience.wiley.com/erfme>.)

negative permeability $\mu < 0$. Finally, in an extension of the idea in Fig. 3d, heterostructure or superlattice repetitions of layers could be made on the scale of nanometers to produce to the simultaneous $\epsilon < 0$ and $\mu < 0$, as in Fig. 3e. Fig. 5 shows an ϵ/μ plot for DNM or LHM (in the elliptical region) in comparison to other materials already characterized in terms of their basic physical properties. Roughly speaking, electromagnetic waves can propagate in the first and third quadrants of the chart whereas the waves are evanescent or nonpropagating in the second and fourth quadrants. What material processes will be utilized to combine some of the other materials in the chart into DNM, or what new developments will occur to produce completely new materials for DNM await the future.

Next, the electromagnetic field theory and physics of the DNM will be combined into a governing equation

describing the guided-wave DNM problem. Once the governing equation is found, mathematics is done to cast the problem in terms of a Green's function solution. The Green's function approach finds the solution to the DNM structure as if it were hit by a singularity forcing function (in our case it is actually currents on the guiding strip conductor) on an infinitely narrow strip (such as a wire in two dimensions that forms a point), and then uses this simplified and general function to find the actual solution. From the Green's function for the DNM structure, the electromagnetic fields formulas can be found, and the fields can be computed by using a computer code employing numerical techniques.

2. GOVERNING EQUATION FOR GUIDED-WAVE DNM SUBSTRATE MATERIALS

Maxwell's time-varying equations describe the electromagnetic field behavior in a medium if they are combined with constitutive relationships embedding the physical properties of the medium in them. Maxwell's two curl equations are

$$\nabla \times \mathbf{E}(t, \mathbf{x}) = -\frac{\partial \mathbf{B}(t, \mathbf{x})}{\partial t}; \tag{1}$$

$$\nabla \times \mathbf{H}(t, \mathbf{x}) = \frac{\partial \mathbf{D}(t, \mathbf{x})}{\partial t} + \mathbf{J}(t, \mathbf{x})$$

Constitutive relationships are

$$\mathbf{D}(t, \mathbf{x}) = \bar{\bar{\epsilon}} \mathbf{E}(t, \mathbf{x}) + \bar{\bar{\rho}} \mathbf{H}(t, \mathbf{x}); \tag{2}$$

$$\mathbf{B}(t, \mathbf{x}) = \bar{\bar{\rho}} \mathbf{E}(t, \mathbf{x}) + \bar{\bar{\mu}} \mathbf{H}(t, \mathbf{x})$$

Here $\mathbf{x} = (x_1, x_2, x_3) = (x, y, z)$. Most general NPV medium can have all constitutive tensors in (2) nonzero, including the magnetoelectric or optical activity tensors $\bar{\bar{\rho}}$ and $\bar{\bar{\rho}}'$, as they are sometimes denoted. The formulation is therefore kept

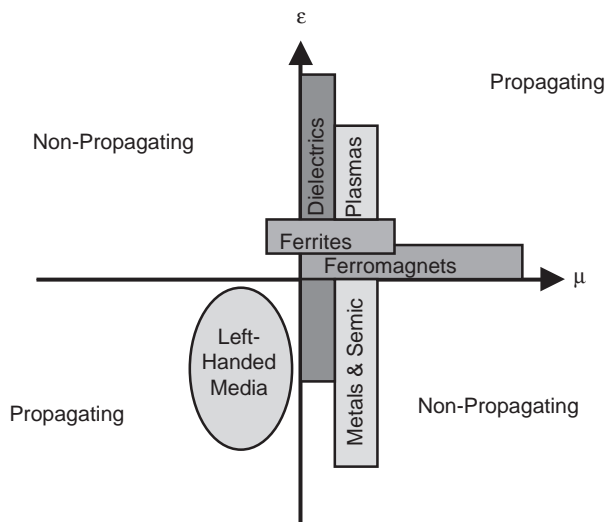


Figure 5. Permittivity ϵ -permeability μ chart showing where DNM or LHM lie in relation to other materials. (This figure is available in full color at <http://www.mrw.interscience.wiley.com/erfme>.)

general in order to retain the most flexibility for studying materials with widely varying physical properties. Because many problems are often transparent in the frequency domain, and because nonharmonic problems can be resolved into a superposition of time-harmonic components, we elect to study here time-harmonic electromagnetic wave propagation through the solid-state LHM-RHM structure (RHM = right-handed-medium, or ordinary medium). Taking the time harmonic variation to be of a form $e^{i\omega t}$, Maxwell's equation become

$$\nabla \times \mathbf{E}(\mathbf{x}) = -i\omega \mathbf{B}(\mathbf{x}); \quad \nabla \times \mathbf{H}(\mathbf{x}) = i\omega \mathbf{D}(\mathbf{x}) + \mathbf{J}(\mathbf{x}) \quad (3)$$

with the constitutive relationships dropping the explicit t dependence

$$\begin{aligned} \mathbf{D}(\mathbf{x}) &= \bar{\bar{\epsilon}}(\omega) \mathbf{E}(\mathbf{x}) + \bar{\bar{\rho}}(\omega) \mathbf{H}(\mathbf{x}); \\ \mathbf{B}(\mathbf{x}) &= \bar{\bar{\rho}}'(\omega) \mathbf{E}(\mathbf{x}) + \bar{\bar{\mu}}(\omega) \mathbf{H}(\mathbf{x}) \end{aligned} \quad (4)$$

Dependence of the constitutive parameters on radian frequency is a well recognized fact, and that is why explicit variation on ω is shown. However, for the study to be conducted here at specific frequencies, we do not need to call out this dependence explicitly. We will be setting, for example, $\bar{\bar{\epsilon}}(\omega) = v$ for $\omega = \omega_v$. Therefore, we set

$$\mathbf{D}(\mathbf{x}) = \bar{\bar{\epsilon}} \mathbf{E}(\mathbf{x}) + \bar{\bar{\rho}} \mathbf{H}(\mathbf{x}); \quad \mathbf{B}(\mathbf{x}) = \bar{\bar{\rho}}' \mathbf{E}(\mathbf{x}) + \bar{\bar{\mu}} \mathbf{H}(\mathbf{x}) \quad (5)$$

and understand it means (2).

Curl equations (1) may be combined into a single governing equation [14]

$$L_T(\mathbf{x}) \mathbf{V}_L(\mathbf{x}) = i\omega \mathbf{V}_R(\mathbf{x}) \quad (6)$$

where the matrix partial differential operator acting on the \mathbf{E} - \mathbf{H} column vector is

$$L_T(\mathbf{x}) = \begin{bmatrix} 0 & L_q(\mathbf{x}) \\ -L_q(\mathbf{x}) & 0 \end{bmatrix} \quad (7)$$

where the quadrant operator is

$$L_q(\mathbf{x}) = \begin{bmatrix} 0 & \frac{\partial}{\partial z} & \frac{\partial}{\partial y} \\ \frac{\partial}{\partial z} & 0 & -\frac{\partial}{\partial x} \\ -\frac{\partial}{\partial y} & \frac{\partial}{\partial x} & 0 \end{bmatrix} \quad (8)$$

Vectors in (6) are

$$\mathbf{V}_L(\mathbf{x}) = \begin{bmatrix} E_x \\ E_y \\ E_z \\ H_x \\ H_y \\ H_z \end{bmatrix} = \begin{bmatrix} \mathbf{E} \\ \mathbf{H} \end{bmatrix}; \quad \mathbf{V}_R(\mathbf{x}) = \begin{bmatrix} D_x \\ D_y \\ D_z \\ B_x \\ B_y \\ B_z \end{bmatrix} = \begin{bmatrix} \mathbf{D} \\ \mathbf{B} \end{bmatrix} \quad (9)$$

Restricting ourselves to a guided-wave structure with the wave traveling in a uniform crosssection in the z direction, that is, where the wave has the form $e^{i\omega t - \gamma z}$, $\gamma = \gamma(\omega)$, simplifies (6)–(8) to

$$L_T(x, y) \mathbf{V}_L(x, y) = i\omega \mathbf{V}_R(x, y) \quad (10a)$$

$$L_T(x, y) = \begin{bmatrix} 0 & L_q(x, y) \\ -L_q(x, y) & 0 \end{bmatrix} \quad (10b)$$

$$L_q(x, y) = \begin{bmatrix} 0 & \gamma & \frac{\partial}{\partial y} \\ -\gamma & 0 & -\frac{\partial}{\partial x} \\ -\frac{\partial}{\partial y} & \frac{\partial}{\partial x} & 0 \end{bmatrix} \quad (10c)$$

Finally, there are certain advantages for approaching the problem in the Fourier transform domain, not the least of which is that real-space convolution integrals reduce to products, and so for the integral equation technique to be applied to a finite enclosed region in the x direction, with layering in the y direction, the finite Fourier transform pair

$$\mathbf{F}(k_x, y) = \int_{-b}^b \mathbf{F}(x, y) e^{-ik_x x} dx; \quad (11a)$$

$$F_i(k_x, y) = \int_{-b}^b F_i(x, y) e^{-ik_x x} dx$$

$$\mathbf{F}(x, y) = \frac{1}{2b} \sum_{k_x=-\infty}^{\infty} \mathbf{F}(k_x, y) e^{ik_x x}; \quad (11b)$$

$$F_i(x, y) = \frac{1}{2b} \sum_{k_x=-\infty}^{\infty} F_i(k_x, y) e^{ik_x x}$$

is applied to the fields, converting (10) into

$$L_T(k_x, y) \mathbf{V}_L(k_x, y) = i\omega \mathbf{V}_R(k_x, y) \quad (12a)$$

$$L_T(k_x, y) = \begin{bmatrix} 0 & L_q(k_x, y) \\ -L_q(k_x, y) & 0 \end{bmatrix} \quad (12b)$$

$$L_q(k_x, y) = \begin{bmatrix} 0 & \gamma & \frac{\partial}{\partial y} \\ -\gamma & 0 & -ik_x \\ -\frac{\partial}{\partial y} & ik_x & 0 \end{bmatrix} \quad (12c)$$

Constitutive relationships (2) can be combined into a supertensor

$$\mathbf{V}_R(t, \mathbf{x}) = \mathbf{M} \mathbf{V}_L(t, \mathbf{x}); \quad \mathbf{M} = \begin{bmatrix} \bar{\bar{\epsilon}} & \bar{\bar{\rho}} \\ \bar{\bar{\rho}}' & \bar{\bar{\mu}} \end{bmatrix} \quad (13)$$

and using the harmonic transformation leading to (5)

$$\mathbf{V}_R(\mathbf{x}) = \mathbf{M}(\omega)\mathbf{V}_L(\mathbf{x}) \quad (14)$$

Characterization of the wave by the complex propagation constant reduces (14) to

$$\mathbf{V}_R(x, y) = \mathbf{M}(\omega)\mathbf{V}_L(x, y) \quad (15)$$

When the finite Fourier transform is applied to (15), we obtain

$$\mathbf{V}_R(k_x, y) = \mathbf{M}(\omega)\mathbf{V}_L(k_x, y) \quad (16)$$

Inserting this formula describing the material physics into electromagnetic equation yields, after eliminating \mathbf{V}_R , the following equation:

$$L_T(k_x, y)\mathbf{V}_L(k_x, y) = i\omega\mathbf{M}(\omega)\mathbf{V}_L(k_x, y) \quad (17)$$

This matrix equation can in principle be solved for the normal-mode eigenvectors and eigenvalues $\gamma = \gamma(\omega)$, realizing that the 1×6 column vectors and the 6×6 operator and material tensor square matrices use the full electromagnetic field component set. However, because we will restrict ourselves to canonical layered structures (layered in the y direction—see in Fig. 6 cross-sectional and top-side views of a DNM or LHM multilayered structure), it is very convenient to extract the perpendicular field components from (17) using rows 2 and 5, which do not possess differential operator $\partial/\partial y$:

$$-\gamma V_4 - ik_x V_6 = i\omega \sum_{i=1}^6 m_{2i} V_i \quad (18a)$$

$$\gamma V_1 + ik_x V_3 = i\omega \sum_{i=1}^6 m_{5i} V_i \quad (18b)$$

Solution of the pair of equations in (18) is

$$V_i = \sum_{j=1}^6 a_{ij}(1 - \delta_{2,j})(1 - \delta_{5,j})V_j; \quad i = 2, 5 \quad (19)$$

where $\delta_{i,j}$ is the Kronecker delta function, or

$$E_y = a_{21}E_x + a_{23}E_z + a_{24}H_x + a_{26}H_z \quad (20a)$$

$$H_y = a_{51}E_x + a_{53}E_z + a_{54}H_x + a_{56}H_z \quad (20b)$$

Here a_{ij} are given by

$$a_{ij} = \frac{a'_{ij}}{D_a} \quad (21)$$

$$D_a = m_{22}m_{55} - m_{25}m_{52} \quad (22)$$

$$a'_{21} = m_{25} \left(m_{51} + \frac{i\gamma}{\omega} \right) - m_{21}m_{55} \quad (23a)$$

$$a'_{23} = m_{25} \left(m_{53} - \frac{k_x}{\omega} \right) - m_{23}m_{55} \quad (23b)$$

$$a'_{24} = m_{25}m_{54} - m_{55} \left(m_{24} - \frac{i\gamma}{\omega} \right) \quad (23c)$$

$$a'_{26} = m_{25}m_{56} - m_{55} \left(m_{26} + \frac{k_x}{\omega} \right) \quad (23d)$$

$$a'_{51} = m_{52}m_{21} - m_{22} \left(m_{51} + \frac{i\gamma}{\omega} \right) \quad (23e)$$

$$a'_{53} = m_{52}m_{23} - m_{22} \left(m_{53} - \frac{k_x}{\omega} \right) \quad (23f)$$

$$a'_{54} = m_{52} \left(m_{24} - \frac{i\gamma}{\omega} \right) - m_{22}m_{54} \quad (23g)$$

$$a'_{56} = m_{52} \left(m_{26} + \frac{k_x}{\omega} \right) - m_{22}m_{56} \quad (23h)$$

Here \mathbf{M} consists of the set $\{m_{ij}\}$ of elements.

The governing equation of the problem can be acquired by realizing that rows 1, 3, 4, and 6 of (17) contain first-order linear differential equations:

$$\gamma V_5 + \frac{dV_6}{dy} = i\omega \sum_{i=1}^6 m_{1i} V_i \quad (24a)$$

$$-\frac{dV_4}{dy} + ik_x V_5 = i\omega \sum_{i=1}^6 m_{3i} V_i \quad (24b)$$

$$-\gamma V_2 - \frac{dV_3}{dy} = i\omega \sum_{i=1}^6 m_{4i} V_i \quad (24c)$$

$$\frac{dV_1}{dy} - ik_x V_2 = i\omega \sum_{i=1}^6 m_{6i} V_i \quad (24d)$$

With the help of (19) to remove V_2 and V_5 from (24), we obtain

$$\frac{d\Phi}{dy} = i\omega \mathbf{R}\Phi \quad (25)$$

$$\Phi = \begin{bmatrix} V_1 \\ V_3 \\ V_4 \\ V_6 \end{bmatrix} = \begin{bmatrix} E_x \\ E_z \\ H_x \\ H_z \end{bmatrix} \quad (26)$$

$$r_{1j} = m_{60} + a_{50}m_{65} + a_{20} \left(m_{62} + \frac{k_x}{\omega} \right) \quad (27a)$$

$$r_{2j} = - \left\{ m_{40} + a_{50}m_{45} + a_{20} \left(m_{42} - \frac{i\gamma}{\omega} \right) \right\} \quad (27b)$$

$$r_{3j} = - \left\{ m_{30} + a_{20}m_{32} + a_{50} \left(m_{35} - \frac{k_x}{\omega} \right) \right\} \quad (27c)$$

$$r_{4j} = m_{10} + a_{20}m_{12} + a_{50} \left(m_{15} + \frac{i\gamma}{\omega} \right) \quad (27d)$$

Here the $\theta(j)$ index on a_{ij} is defined by

$$\theta(j) = \begin{cases} \frac{3}{2}j; & j=2,4 \\ \frac{3j-1}{2}; & j=1,3 \end{cases} \quad (28)$$

Here \mathbf{R} consists of the set $\{r_{ij}\}$ of elements.

The Green's function problem is posed by placing a Dirac delta forcing function

$$\mathbf{J}_{s\delta}(x) = (\hat{x} + \hat{z})\delta(x - x') \quad (29)$$

on the strip conductor (which could be an ordinary metal or a superconductor) and solving the partial-differential equation system in space subject to appropriate boundary and interfacial conditions. Equation (29) says that a surface current of unit delta magnitude is impressed in the x and z directions. This is consistent with the strip having width w in the x direction, infinitesimal extent in the y direction, and extending infinitely in the z direction corresponding to a uniform cross section. Because we have Fourier-transformed the problem into the spectral domain, the impressed delta current now appears as

$$\mathbf{J}_{s\delta}(k_x) = (\hat{x} + \hat{z}) \int_{-b}^b \delta(x - x') e^{-ik_x x'} dx' = (\hat{x} + \hat{z}) e^{-ik_x x'} \quad (30)$$

where $2b$ is the finite width of the enclosure bounding the x extent. Of course, the actual current is a continuous superposition of weighted contributions over the following

strip width:

$$\begin{aligned} \mathbf{J}_s(x) &= \int_{-w/2}^{w/2} [\mathbf{J}_{s,x}(x')\hat{x} + \mathbf{J}_{s,z}(x')\hat{z}] \delta(x - x') dx \\ &= \int_{-w/2}^{w/2} \mathbf{J}_s(x') \delta(x - x') dx \end{aligned} \quad (31)$$

Here we have been using the fact that current exists only on the strip. Equation (31) merely states that scanning the extent of the strip (with the delta function) will reproduce the correct current distribution function. Now one can state that (3) and (14) having assumed a time-harmonic variation, or (10a) and (15) assuming a z -directed propagation constant also, form a complete set of partial-differential equations subject to the interfacial conditions

$$\hat{y} \times (\mathbf{H}^+ - \mathbf{H}^-) = \mathbf{J}_s(x) \quad (32)$$

$$\mathbf{E}_t^+ = \mathbf{E}_t^- \quad (33)$$

and boundary conditions

$$E_y(x, y) = E_z(x, y) = 0; \quad x = \pm b \quad (34a)$$

$$E_x(x, y) = E_z(x, y) = 0; \quad y = 0, h_T \quad (34b)$$

Equation (32), which arose from curl equation (3), says that the tangential \mathbf{H} field above the interface minus that below is related to the surface current at that interface. If we take this interface to be where there are conductor strips, then, $\mathbf{J}_s(x) \neq 0$, but at other interfaces without strips, $\mathbf{J}_s(x) = 0$ and tangential \mathbf{H} field continuity occurs. Equation (33) assures tangential electric field \mathbf{E} continuity at any interface. Equation (34a) enables the finite Fourier transform, and (34b) constrains the device to be fully enclosed with actual (or computational) walls, where h_T is the total vertical structure thickness.

3. GREEN'S FUNCTION FOR DNM MATERIALS

In the Green's function construction, (29) is impressed on the system through (32), which creates the field solution

$$\overline{\overline{\mathbf{G}}}(x, y; x') = F_L[\delta(x - x')] \quad (35)$$

Here the system linear operator F_L takes the delta function $\delta(x - x')$ applied in either the \hat{x} or \hat{z} direction and determines the field component responses, making a two-indexed tensor (dyadic) of size 6×2 . Equation (35) implicitly assumes that a single interface has the delta function source, and this is acceptable because later on when numerical field plots are shown, that will be the situation for the multilayered structures examined. But there is no reason in principle why this formula cannot be extended to multiple forcing function interfaces (this has been done for ordinary media problems in the literature). Multiplying (35) on the right by $\mathbf{J}_s(x')$ and integrating, and because F_L is a linear operator, the current vector along

with the integral operator may be pulled inside it, giving

$$\int_{-b}^b \overline{\overline{\mathbf{G}}}(x, y; x') \cdot \mathbf{J}_s(x') dx' = F_L \left[\int_{-b}^b \mathbf{J}_s(x') \delta(x - x') dx' \right] \quad (36)$$

The left-hand side is the field solution of the problem $\mathbf{F}(x, y)$, and because the argument of the linear operator by (31) is the total vector surface current, (36) yields

$$\mathbf{F}(x, y) = F_L[\mathbf{J}_s(x)] \quad (37)$$

Therefore, with knowledge of $\overline{\overline{\mathbf{G}}}(x, y; x')$, the field solution is immediately known:

$$\mathbf{F}(x, y) = \int_{-b}^b \overline{\overline{\mathbf{G}}}(x, y; x') \cdot \mathbf{J}_s(x') dx' \quad (38)$$

Considering \mathbf{J}_s as a form of a field, as well as \mathbf{F} as a field, makes (36) an integral equation of the homogeneous Fredholm type of the second kind. Neither \mathbf{J}_s nor \mathbf{F} is known. They must be found by solving (38), with the understanding that the kernel $\overline{\overline{\mathbf{G}}}(x, y; x')$ can be acquired before finding the unknowns. Because we will be working in the spectral domain, the integral equation of problem (38) must be converted to this domain also. There are several ways to find the entire field solution, and one effective way, which does not require obtaining the dyadic Green's function over the whole cross-sectional spatial domain, utilizes the fact that the strip is a perfect conductor with

$$\mathbf{E}_t(x, y) = 0 : \quad |x| < w_p, \quad y = y_I \quad (39)$$

A smaller piece of the $\overline{\overline{\mathbf{G}}}$ must be used, $\overline{\overline{\mathbf{G}}}_{EJ}^{xz}$, which relates the driving surface current to the two tangential electric field components. At the $y = y_I$ interface, (38) is then cast into the form

$$\mathbf{E}(x, y_I) = \int_{-b}^b \overline{\overline{\mathbf{G}}}_{EJ}^{xz}(x - x'; y_I) \cdot \mathbf{J}_s(x') dx' \quad (40)$$

Form (40) of the integral equation is a convolution integral of the kernel and the driving surface current. It has the wonderful property that transformation into the spectral domain removes the integral operation. The solution procedure employed requires us to take a finite

Fourier transform of (40)

$$\begin{aligned} \int_{-b}^b \mathbf{E}(x) e^{-ik_x x} dx &= \int_{-b}^b e^{-ik_x x} dx \left\{ \int_{-b}^b \overline{\overline{\mathbf{G}}}_{EJ}^{xz}(x - x') \cdot \mathbf{J}_s(x') dx' \right\} \\ &= \int_{-b}^b \left\{ \int_{-b}^b \overline{\overline{\mathbf{G}}}_{EJ}^{xz}(x - x') e^{-ik_x x} dx \right\} \cdot \mathbf{J}_s(x') dx' \\ &= \int_{-b}^b \left\{ \int_{-b}^b \overline{\overline{\mathbf{G}}}_{EJ}^{xz}(x'') e^{-ik_x(x' + x'')} dx'' \right\} \cdot \mathbf{J}_s(x') dx' \\ &= \int_{-b}^b \left\{ \int_{-b}^b \overline{\overline{\mathbf{G}}}_{EJ}^{xz}(x'') e^{-ik_x x''} dx'' \right\} \cdot \mathbf{J}_s(x') e^{-ik_x x'} dx' \\ &= \left\{ \int_{-b}^b \overline{\overline{\mathbf{G}}}_{EJ}^{xz}(x'') e^{-ik_x x''} dx'' \right\} \cdot \left\{ \int_{-b}^b \mathbf{J}_s(x') e^{-ik_x x'} dx' \right\} \\ &= \overline{\overline{\mathbf{G}}}_{EJ}^{xz}(k_x) \cdot \mathbf{J}_s(k_x) \end{aligned} \quad (41)$$

or

$$\mathbf{E}(k_x) = \overline{\overline{\mathbf{G}}}_{EJ}^{xz}(k_x) \cdot \mathbf{J}_s(k_x) \quad (42)$$

In (41) $x'' = x - x'$, $dx'' = dx$, led to the third step and (11a), to the final step. $\overline{\overline{\mathbf{G}}}_{EJ}$ is given by [15]

$$\begin{aligned} \tilde{\mathbf{G}}_{xx}(k_x, \gamma) &= \frac{P_{13}^{(1)} [P_{24}^{(21)} P_{14}^{(2)} - P_{14}^{(21)} P_{24}^{(2)}]}{P_{14}^{(21)} P_{23}^{(21)} - P_{13}^{(21)} P_{24}^{(21)}} \\ &\quad + \frac{P_{14}^{(1)} [P_{13}^{(21)} P_{24}^{(2)} - P_{23}^{(21)} P_{14}^{(2)}]}{P_{14}^{(21)} P_{23}^{(21)} - P_{13}^{(21)} P_{24}^{(21)}} \end{aligned} \quad (43a)$$

$$\begin{aligned} \tilde{\mathbf{G}}_{xz}(k_x, \gamma) &= -\frac{P_{13}^{(1)} [P_{24}^{(21)} P_{13}^{(2)} - P_{14}^{(21)} P_{23}^{(2)}]}{P_{14}^{(21)} P_{23}^{(21)} - P_{13}^{(21)} P_{24}^{(21)}} \\ &\quad - \frac{P_{14}^{(1)} [P_{13}^{(21)} P_{23}^{(2)} - P_{23}^{(21)} P_{13}^{(2)}]}{P_{14}^{(21)} P_{23}^{(21)} - P_{13}^{(21)} P_{24}^{(21)}} \end{aligned} \quad (43b)$$

$$\begin{aligned} \tilde{\mathbf{G}}_{zx}(k_x, \gamma) &= \frac{P_{23}^{(1)} [P_{24}^{(21)} P_{14}^{(2)} - P_{14}^{(21)} P_{24}^{(2)}]}{P_{14}^{(21)} P_{23}^{(21)} - P_{13}^{(21)} P_{24}^{(21)}} \\ &\quad + \frac{P_{24}^{(1)} [P_{13}^{(21)} P_{24}^{(2)} - P_{23}^{(21)} P_{14}^{(2)}]}{P_{14}^{(21)} P_{23}^{(21)} - P_{13}^{(21)} P_{24}^{(21)}} \end{aligned} \quad (43c)$$

$$\begin{aligned} \tilde{\mathbf{G}}_{zz}(k_x, \gamma) &= -\frac{P_{23}^{(1)} [P_{24}^{(21)} P_{13}^{(2)} - P_{14}^{(21)} P_{23}^{(2)}]}{P_{14}^{(21)} P_{23}^{(21)} - P_{13}^{(21)} P_{24}^{(21)}} \\ &\quad - \frac{P_{24}^{(1)} [P_{13}^{(21)} P_{23}^{(2)} - P_{23}^{(21)} P_{13}^{(2)}]}{P_{14}^{(21)} P_{23}^{(21)} - P_{13}^{(21)} P_{24}^{(21)}} \end{aligned} \quad (43d)$$

with

$$\begin{aligned} P^{(1)} &= P^{(1)}(h_1); \quad P^{(2)} = P^{(2)}(h_2); \\ P^{(21)} &= P^{(2)}(h_2)P^{(1)}(h_1) \end{aligned} \quad (44)$$

$$P(y) = e^{i\omega R y} \quad (45)$$

where h_i is thickness of the i th layer.

4. ELECTROMAGNETIC FIELDS FOR DNM

Formulas (43) were found utilizing (25), which has a solution in the i th layer of

$$\Phi_i = \Phi(y_i) = P^{(i)}(y_i)\Phi_i(h_{T,i}) \quad (46)$$

using the global y coordinate. It is very convenient to convert to the local coordinates y' where for the i th layer now the local coordinate ($h_0 \equiv 0$) is

$$y_i' = y_i - h_{T,i}; \quad h_{T,i} = \sum_{k=0}^{i-1} h_k \quad (47)$$

where $h_{T,i}$ is the total thickness of all the layers prior to the i th layer. In the local coordinate system, (46) appears as

$$\Phi_i = \Phi(y_i') = P^{(i)}(y_i')\Phi_i(0) \quad (48)$$

This equation is applied repeatedly to each layer throughout the structure, exercising caution to impose (32)–(34) in the spectral domain

$$\hat{y} \times [\mathbf{H}^+(k_x, y) - \mathbf{H}^-(k_x, y)] = \mathbf{J}_s(k_x); \quad y = y_I \quad (49)$$

$$\mathbf{E}_t^+(k_x, y) = \mathbf{E}_t^-(k_x, y); \quad y = h_i + h_{T,i} = \sum_{k=0}^i h_k \quad (50)$$

and boundary conditions

$$E_x(k_x, y) = E_z(k_x, y) = 0; \quad y = 0, h_T \quad (51)$$

Boundary conditions on the sidewalls (34a) are converted to the spectral domain in a process that generates the discretization of k_x . The detailed derivation will be given since the whole technique hinges on it.

By (11b), the spatial electric field components $E_{y,z}$ are expressed as

$$E_{y,z}(x, y) = \frac{1}{2b} \sum_{k_x=-\infty}^{\infty} E_{y,z}(k_x, y) e^{ik_x x} \quad (52)$$

Consider first the case where $E_{y,z}(x, y)$ has even symmetry with respect to the x axis. (Symmetry choices will be covered in more detail after the derivation of the discre-

tization k_x values.) For even symmetry, we obtain

$$E_{y,z}(x, y) = E_{y,z}(-x, y) \quad (53)$$

Invoking (52), this becomes

$$\begin{aligned} \frac{1}{2b} \sum_{k_x=-\infty}^{\infty} E_{y,z}(k_x, y) e^{ik_x x} &= \frac{1}{2b} \sum_{k_x=-\infty}^{\infty} E_{y,z}(k_x, y) e^{-ik_x x} \\ &= \frac{1}{2b} \sum_{k_x=+\infty}^{-\infty} E_{y,z}(-k_x, y) e^{ik_x x} \end{aligned} \quad (54a)$$

$$\frac{1}{2b} \sum_{k_x=-\infty}^{\infty} [E_{y,z}(k_x, y) - E_{y,z}(-k_x, y)] e^{ik_x x} = 0 \quad (54b)$$

Equation (54b) is valid for any x if the bracketed term is zero, namely, if

$$E_{y,z}(k_x, y) = E_{y,z}(-k_x, y) \quad (55)$$

Now we must insert this back into the expansion (52), obtaining

$$\begin{aligned} E_{y,z}(x, y) &= \frac{1}{2b} \sum_{k_x=-\infty}^{\infty} E_{y,z}(k_x, y) e^{ik_x x} \\ &= \frac{1}{2b} \sum_{k_x=-\infty}^{0^-} E_{y,z}(k_x, y) e^{ik_x x} + E_{y,z}(0, y) \\ &\quad + \frac{1}{2b} \sum_{k_x=0^+}^{\infty} E_{y,z}(k_x, y) e^{ik_x x} \\ &= \frac{1}{2b} \sum_{k_x=+\infty}^{0^+} E_{y,z}(-k_x, y) e^{-ik_x x} + E_{y,z}(0, y) \\ &\quad + \frac{1}{2b} \sum_{k_x=0^+}^{\infty} E_{y,z}(k_x, y) e^{ik_x x} \\ &= \frac{1}{2b} \sum_{k_x=0^+}^{\infty} E_{y,z}(k_x, y) e^{-ik_x x} + E_{y,z}(0, y) \\ &\quad + \frac{1}{2b} \sum_{k_x=0^+}^{\infty} E_{y,z}(k_x, y) e^{ik_x x} \\ &= \frac{1}{2b} \sum_{k_x=0^+}^{\infty} E_{y,z}(k_x, y) [e^{-ik_x x} + e^{ik_x x}] + E_{y,z}(0, y) \\ &= \frac{1}{b} \sum_{k_x=0^+}^{\infty} E_{y,z}(k_x, y) \cos(k_x x) + E_{y,z}(0, y) \end{aligned} \quad (56)$$

In (56), Eq. (55) was used for the third step. Imposition of boundary condition (34a) forces (56) to obey

$$\frac{1}{b} \sum_{k_x=0^+}^{\infty} E_{y,z}(k_x, y) \cos(k_x x) + E_{y,z}(0, y) = 0 \quad (57)$$

or

$$\cos(k_x b) = 0; \quad E_{y,z}(0, y) = 0 \quad (58)$$

The first constraint in (57) restricts k_x to

$$k_x = \frac{2n-1}{2} \pi; \quad n = 0, \pm 1, \pm 2, \dots \quad (59)$$

showing that $k_x \neq 0$, allowing us to drop the second (57) constraint. For odd symmetry, we obtain

$$E_{y,z}(x, y) = -E_{y,z}(-x, y) \quad (60)$$

Invoking (52), this becomes

$$\begin{aligned} \frac{1}{2b} \sum_{k_x=-\infty}^{\infty} E_{y,z}(k_x, y) e^{ik_x x} &= -\frac{1}{2b} \sum_{k_x=-\infty}^{\infty} E_{y,z}(k_x, y) e^{-ik_x x} \\ &= -\frac{1}{2b} \sum_{k_x=+\infty}^{-\infty} E_{y,z}(-k_x, y) e^{ik_x x} \end{aligned} \quad (61a)$$

$$\frac{1}{2b} \sum_{k_x=-\infty}^{\infty} [E_{y,z}(k_x, y) + E_{y,z}(-k_x, y)] e^{ik_x x} = 0 \quad (61b)$$

Equation (61b) is valid for any x if the bracketed term is zero, namely, if

$$E_{y,z}(k_x, y) = -E_{y,z}(-k_x, y) \quad (62)$$

Now we must insert this back into the expansion (52), obtaining

$$\begin{aligned} E_{y,z}(x, y) &= \frac{1}{2b} \sum_{k_x=-\infty}^{\infty} E_{y,z}(k_x, y) e^{ik_x x} \\ &= \frac{1}{2b} \sum_{k_x=-\infty}^{0^-} E_{y,z}(k_x, y) e^{ik_x x} + E_{y,z}(0, y) \\ &\quad + \frac{1}{2b} \sum_{k_x=0^+}^{\infty} E_{y,z}(k_x, y) e^{ik_x x} \\ &= \frac{1}{2b} \sum_{k_x=+\infty}^{0^+} E_{y,z}(-k_x, y) e^{-ik_x x} + E_{y,z}(0, y) \\ &\quad + \frac{1}{2b} \sum_{k_x=0^+}^{\infty} E_{y,z}(k_x, y) e^{ik_x x} \\ &= -\frac{1}{2b} \sum_{k_x=0^+}^{\infty} E_{y,z}(k_x, y) e^{-ik_x x} + E_{y,z}(0, y) \\ &\quad + \frac{1}{2b} \sum_{k_x=0^+}^{\infty} E_{y,z}(k_x, y) e^{ik_x x} \end{aligned}$$

$$\begin{aligned} &+ \frac{1}{2b} \sum_{k_x=0^+}^{\infty} E_{y,z}(k_x, y) [-e^{-ik_x x} + e^{ik_x x}] + E_{y,z}(0, y) \\ &= \frac{i}{b} \sum_{k_x=0^+}^{\infty} E_{y,z}(k_x, y) \sin(k_x x) + E_{y,z}(0, y) \end{aligned} \quad (63)$$

In (63), Eq. (62) was used in the third step. Imposition of boundary condition (34a) forces (63) to obey

$$\pm \frac{i}{b} \sum_{k_x=0^+}^{\infty} E_{y,z}(k_x, y) \sin(k_x b) + E_{y,z}(0, y) = 0 \quad (64)$$

or

$$\sin(k_x b) = 0; \quad E_{y,z}(0, y) = 0 \quad (65)$$

The first constraint in (65) restricts k_x to

$$k_x = \frac{n}{b} \pi; \quad n = 0, \pm 1, \pm 2, \dots \quad (66)$$

Since the first constraint allows $k_x = 0$, technically the first summation in (64) does not have $n = 0$ in its domain, but by widening its domain to cover $k_x = 0$, the second constraint may be dropped; that is, (64) becomes

$$\pm \frac{i}{b} \sum_{k_x=0}^{\infty} E_{y,z}(k_x, y) \sin(k_x b) = 0 \quad (67)$$

and rule (66) is exact.

Next we treat the origin of the symmetry choices. Go to the harmonic equations (3), and expand them out by components for the simplest case of isotropic DNM, obtaining

$$\begin{aligned} \frac{\partial H_z}{\partial y} - \frac{\partial H_y}{\partial z} &= i\omega \epsilon_{\text{DNM}} E_x + J_x; \\ \frac{\partial H_x}{\partial z} - \frac{\partial H_z}{\partial x} &= i\omega \epsilon_{\text{DNM}} E_y; \end{aligned} \quad (68a)$$

$$\begin{aligned} \frac{\partial H_y}{\partial x} - \frac{\partial H_x}{\partial y} &= i\omega \epsilon_{\text{DNM}} E_z + J_z \\ \frac{\partial E_z}{\partial y} - \frac{\partial E_y}{\partial z} &= -i\omega \mu_{\text{DNM}} H_x; \\ \frac{\partial E_x}{\partial z} - \frac{\partial E_z}{\partial x} &= -i\omega \mu_{\text{DNM}} H_y; \\ \frac{\partial E_y}{\partial x} - \frac{\partial E_x}{\partial y} &= -i\omega \mu_{\text{DNM}} H_z \end{aligned} \quad (68b)$$

Setting $J_z(x, y) = \text{even}$ for the impressed current, we find that (68a) requires that $E_z(x, y) = \text{even}$, $H_y(x, y) = \text{odd}$, and $H_x(x, y) = \text{even}$ in its third equation; $H_z(x, y) = \text{odd}$

and $E_y(x,y)$ = even in its second equation; and $E_x(x,y)$ = odd and $J_x(x,y)$ = odd in its first equation. These selections are consistent with (68b). For $J_z(x,y)$ = odd, all the selections are reversed. Care must be exercised in this process, and one can show that for biaxial DNM, where the $\bar{\epsilon}$ tensor is biaxial, the $\bar{\mu}$ tensor is biaxial, or both, the symmetry choices still hold. This is the case whether the biaxial tensors are principle axis and diagonal, or the crystal is rotated, producing a nondiagonal tensor(s). However, pure symmetry choices are rarely allowed for nonreciprocal materials such as materials employing precessional spin behavior (as in a ceramics with magnetic ions) or cyclotron carrier motion (as in semiconductors with free electrons or holes), which require the superposition of the even and odd symmetry choices.

The surface currents that drive the problem self-consistently can be chosen in a number of ways, as it is necessary to prepare complete sets only of basis functions that are used to construct them. They are selected in the real-space domain to display some advantageous properties, for example, edge singularity behavior due to charge repulsion. For the complete set of cosinusoidal basis functions modified by the edge condition, we have for a strip with even-mode symmetry (determined by the z -component symmetry as just discussed above)

$$J_{zm}(x) = \zeta_{em}(x) = \begin{cases} \frac{\cos\left(\frac{\pi x}{w}[m-1]\right)}{\sqrt{1-(x/w)^2}}; & |x| \leq w \\ 0; & w < |x| \end{cases} \quad (69a)$$

$$J_{xm}(x) = \eta_{em}(x) = \begin{cases} \frac{\sin\left(\frac{\pi x}{w}m\right)}{\sqrt{1-(x/w)^2}}; & |x| \leq w \\ 0; & w < |x| \end{cases} \quad (69b)$$

and for odd-mode symmetry

$$J_{zm}(x) = \zeta_{om}(x) = \begin{cases} \frac{\sin\left(\frac{\pi x}{2w}[2m-1]\right)}{\sqrt{1-(x/w)^2}}; & |x| \leq w \\ 0; & w < |x| \end{cases} \quad (70a)$$

$$J_{xm}(x) = \eta_{om}(x) = \begin{cases} \frac{\cos\left(\frac{\pi x}{2w}[2m-1]\right)}{\sqrt{1-(x/w)^2}}; & |x| \leq w \\ 0; & w < |x| \end{cases} \quad (70b)$$

Superposition of the complete set forms the total surface current [and constitutes the method of moments (MoM) when unknown currents or fields are expanded using basis sets and inner products with weights taken on the structure-governing equation to derive a linear system to

be solved]:

$$J_{x,e}(x) = \sum_{m=1}^{n_x} a_{e,m} \eta_{e,m}(x); \quad J_{z,e}(x) = \sum_{m=1}^{n_z} b_{e,m} \zeta_{e,m}(x) \quad (71a)$$

$$J_{x,o}(x) = \sum_{m=1}^{n_x} a_{o,m} \eta_{o,m}(x); \quad J_{z,o}(x) = \sum_{m=1}^{n_z} b_{o,m} \zeta_{o,m}(x) \quad (71b)$$

Fourier transforming (71) according to (11a) gives

$$J_{x,e}(n) = \sum_{m=1}^{n_x} a_{e,m} \eta_{e,m}(n); \quad (72a)$$

$$J_{z,e}(n) = \sum_{m=1}^{n_z} b_{e,m} \zeta_{e,m}(n)$$

$$J_{x,o}(n) = \sum_{m=1}^{n_x} a_{o,m} \eta_{o,m}(n); \quad (72b)$$

$$J_{z,o}(n) = \sum_{m=1}^{n_z} b_{o,m} \zeta_{o,m}(n)$$

with

$$\zeta_{e,m}(n) = \zeta_{e,m}(k_x[n]) = \frac{\pi w}{2} \{J_0(k_x w + [m-1]\pi) + J_0(k_x w - [m-1]\pi)\} \quad (73a)$$

$$\eta_{e,m}(n) = \eta_{e,m}(k_x[n]) = -\frac{i\pi w}{2} \{J_0(k_x w + m\pi) - J_0(k_x w - m\pi)\} \quad (73b)$$

$$\zeta_{o,m}(n) = \zeta_{o,m}(k_x[n]) = -\frac{i\pi w}{2} \left\{ J_0\left(k_x w + [2m-1]\frac{\pi}{2}\right) - J_0\left(k_x w - [2m-1]\frac{\pi}{2}\right) \right\} \quad (74a)$$

$$\eta_{o,m}(n) = \eta_{o,m}(k_x[n]) = \frac{\pi w}{2} \left\{ J_0\left(k_x w + [2m-1]\frac{\pi}{2}\right) + J_0\left(k_x w - [2m-1]\frac{\pi}{2}\right) \right\} \quad (74b)$$

An exact solution is obtained only when n_x and $n_z \rightarrow \infty$. However, a finite number of them may be used, depending on the propagating eigenmode modeled, to find a reasonably accurate numerical result. In (73) and (74), J_0 denotes the Bessel function of the first kind.

Eigenvalues γ and eigenvectors of the propagating problem can now be found from (42), the interfacial strip equation (drop all interfacial indexes, and use subscripts to label elements)

$$E_x(n, \gamma) = G_{xx}(\gamma, n) J_x(n, \gamma) + G_{xz}(\gamma, n) J_z(n, \gamma) \quad (75)$$

$$E_z(n, \gamma) = G_{zx}(\gamma, n) J_x(n, \gamma) + G_{zz}(\gamma, n) J_z(n, \gamma)$$

by substituting for the surface currents using expression (72a) or (72b) depending on the mode symmetry to be

studied (we drop the explicit mode symmetry type notation since we will treat only one or the other type of pure symmetry solution here):

$$E_x(n, \gamma) = G_{xx}(\gamma, n) \sum_{i=1}^{n_x} a_i \eta_i(n) + G_{xz}(\gamma, n) \sum_{i=1}^{n_z} b_i \zeta_i(n) \quad (76)$$

$$E_z(n, \gamma) = G_{zx}(\gamma, n) \sum_{i=1}^{n_x} a_i \eta_i(n) + G_{zz}(\gamma, n) \sum_{i=1}^{n_z} b_i \zeta_i(n)$$

Next multiply the first equation of (76) by η_j and the second by ζ_j , then summing over the spectral index n (this is the inner product part of the MoM method)

$$\begin{aligned} \sum_{n=-\infty}^{\infty} \eta_j(n) E_x(n, \gamma) &= \sum_{n=-\infty}^{\infty} \left[\eta_j(n) G_{xx}(\gamma, n) \sum_{i=1}^{n_x} a_i(n) \eta_i(n) \right] \\ &+ \sum_{n=-\infty}^{\infty} \left[\eta_j(n) G_{xz}(\gamma, n) \sum_{i=1}^{n_z} b_i(n) \zeta_i(n) \right] \end{aligned}$$

$$\begin{aligned} \sum_{n=-\infty}^{\infty} \zeta_j(n) E_z(n, \gamma) &= \sum_{n=-\infty}^{\infty} \left[\zeta_j(n) G_{zx}(\gamma, n) \sum_{i=1}^{n_x} a_i(n) \eta_i(n) \right] \\ &+ \sum_{n=-\infty}^{\infty} \left[\zeta_j(n) G_{zz}(\gamma, n) \sum_{i=1}^{n_z} b_i(n) \zeta_i(n) \right] \end{aligned} \quad (77)$$

Interchanging the order of the basis function and spectral summations in (77), we obtain

$$\begin{aligned} \sum_{n=-\infty}^{\infty} \eta_j(n) E_x(n, \gamma) &= \sum_{i=1}^{n_x} a_i(n) \left[\sum_{n=-\infty}^{\infty} \eta_j(n) G_{xx}(\gamma, n) \eta_i(n) \right] \\ &+ \sum_{i=1}^{n_z} b_i(n) \left[\sum_{n=-\infty}^{\infty} \eta_j(n) G_{xz}(\gamma, n) \zeta_i(n) \right] \end{aligned}$$

$$\begin{aligned} \sum_{n=-\infty}^{\infty} \zeta_j(n) E_z(n, \gamma) &= \sum_{i=1}^{n_x} a_i(n) \left[\sum_{n=-\infty}^{\infty} \zeta_j(n) G_{zx}(\gamma, n) \eta_i(n) \right] \\ &+ \sum_{i=1}^{n_z} b_i(n) \left[\sum_{n=-\infty}^{\infty} \zeta_j(n) G_{zz}(\gamma, n) \zeta_i(n) \right] \end{aligned} \quad (78)$$

Examine the left-hand sides of this paired set of equations (78):

$$\begin{bmatrix} -1 & 1 \\ 1 & -1 \end{bmatrix} \sum_{n=-\infty}^{\infty} \begin{Bmatrix} \eta_{e,oj} \\ \zeta_{e,oj} \end{Bmatrix} (n) E_{x,z}(n, \gamma)$$

$$\begin{aligned} &= \sum_{n=-\infty}^{\infty} \begin{Bmatrix} \eta_j^* \\ \zeta_j^* \end{Bmatrix} (n) E_{x,z}(n, \gamma) \\ &= \sum_{n=-\infty}^{\infty} \left[\int_{-b}^b \begin{Bmatrix} \eta_j \\ \zeta_j \end{Bmatrix} (x) e^{-ik_x x} dx \right]^* E_{x,z}(n, \gamma) \\ &= \sum_{n=-\infty}^{\infty} \int_{-b}^b \begin{Bmatrix} \eta_j^* \\ \zeta_j^* \end{Bmatrix} (x) e^{ik_x x} dx E_{x,z}(n, \gamma) \\ &= \sum_{n=-\infty}^{\infty} \int_{-b}^b \begin{Bmatrix} \eta_j \\ \zeta_j \end{Bmatrix} (x) e^{ik_x x} dx E_{x,z}(n, \gamma) \\ &= \int_{-b}^b \begin{Bmatrix} \eta_j \\ \zeta_j \end{Bmatrix} (x) \left[\sum_{n=-\infty}^{\infty} E_{x,z}(n, \gamma) e^{ik_x x} \right] dx \\ &= 2b \int_{-b}^b \begin{Bmatrix} \eta_j \\ \zeta_j \end{Bmatrix} (x) E_{x,z}(x, \gamma) dx \\ &= 0 \end{aligned} \quad (79)$$

where the first and second rows in the left-hand side matrix correspond, respectively, to even and odd symmetry. Right-hand equalities in the first, second, fourth, sixth, and last lines used, respectively, (73) and (74), (11a), (69) and (70), (11b), and (40) with (69) and (70). Equation (79) amounts to a Parseval theorem [16] for the problem at hand. Enlisting this theorem, we can rewrite (78) as

$$\begin{aligned} \sum_{i=1}^{n_x} a_i(n) \left[\sum_{n=-\infty}^{\infty} \eta_j(n) G_{xx}(\gamma, n) \eta_i(n) \right] \\ + \sum_{i=1}^{n_z} b_i(n) \left[\sum_{n=-\infty}^{\infty} \eta_j(n) G_{xz}(\gamma, n) \zeta_i(n) \right] &= 0 \\ \sum_{i=1}^{n_x} a_i(n) \left[\sum_{n=-\infty}^{\infty} \zeta_j(n) G_{zx}(\gamma, n) \eta_i(n) \right] \\ + \sum_{i=1}^{n_z} b_i(n) \left[\sum_{n=-\infty}^{\infty} \zeta_j(n) G_{zz}(\gamma, n) \zeta_i(n) \right] &= 0 \end{aligned} \quad (80)$$

Since (80) is valid for any j th basis test function, it may be condensed into the form

$$\begin{aligned} \sum_{i=1}^{n_x} a_i(n) X_{xx}^{ji}(\gamma) + \sum_{i=1}^{n_z} b_i(n) X_{xz}^{ji}(\gamma) &= 0; \quad j = 1, 2, \dots, n_x \\ \sum_{i=1}^{n_x} a_i(n) X_{zx}^{ji}(\gamma) + \sum_{i=1}^{n_z} b_i(n) X_{zz}^{ji}(\gamma) &= 0; \quad j = 1, 2, \dots, n_z \end{aligned} \quad (81)$$

where (this is referred to as the *Galerkin technique* since $\{\eta_i, \zeta_i\} = \{\eta_j, \zeta_j\}$)

$$\begin{aligned} X_{xx}^{ji}(\gamma) &= \sum_{n=-\infty}^{\infty} \eta_j(n) G_{xx}(\gamma, n) \eta_i(n) \\ X_{xz}^{ji}(\gamma) &= \sum_{n=-\infty}^{\infty} \eta_j(n) G_{xz}(\gamma, n) \zeta_i(n) \\ X_{zx}^{ji}(\gamma) &= \sum_{n=-\infty}^{\infty} \zeta_j(n) G_{zx}(\gamma, n) \eta_i(n) \\ X_{zz}^{ji}(\gamma) &= \sum_{n=-\infty}^{\infty} \zeta_j(n) G_{zz}(\gamma, n) \zeta_i(n) \end{aligned} \quad (82)$$

In matrix form, (81) appears as

$$\begin{aligned} \begin{bmatrix} X_{xx} & X_{xz} \\ X_{zx} & X_{zz} \end{bmatrix} \begin{bmatrix} a \\ b \end{bmatrix} = 0; \quad \mathbf{X} \begin{bmatrix} a \\ b \end{bmatrix} = 0; \quad \mathbf{X}\mathbf{v} = 0 \\ \mathbf{X} = \begin{bmatrix} X_{xx} & X_{xz} \\ X_{zx} & X_{zz} \end{bmatrix}; \quad \mathbf{v} = \begin{bmatrix} a \\ b \end{bmatrix} \end{aligned} \quad (83)$$

Once system of equations (83) is solved, then vector \mathbf{v} containing the coefficients needed to construct the surface current, and from them the electromagnetic field, is known, which is the problem eigenvector. The eigenvalue γ is determined from this system also (from the determinant of \mathbf{X} set to zero). From (72), the total vector surface current is obtained:

$$\mathbf{J}(x, y) = \frac{1}{2b} \sum_{n=-n_{\max}}^{n_{\max}} \mathbf{J}(n; y) e^{i\alpha_n x} \quad (84)$$

Once the total surface current is available, the total eigenvector field solution follows from $\overline{\mathbf{G}}_{EJ}^{xz}(x-x'; y_I)$ in

(40) [17]:

$$\begin{aligned} \mathbf{E}(x, y) &= \frac{1}{2b} \sum_{n=-n_{\max}}^{n_{\max}} \mathbf{E}(n; y) e^{i\alpha_n x}, \\ \mathbf{H}(x, y) &= \frac{1}{2b} \sum_{n=-n_{\max}}^{n_{\max}} \mathbf{H}(n; y) e^{i\alpha_n x} \end{aligned} \quad (85)$$

Spectral expansion is truncated at the same maximum number of terms $n = n_{\max}$ for all vector components. Basis function summation limits n_x and n_z for the x and z components ($m = m_{\max}$) [see (72) for the surface current expansion] can be truncated at different values. Current and fields are real physical quantities, so they must be converted through

$$\begin{aligned} \mathbf{J}_p(x, y, z) &= \text{Re}[\mathbf{J}(x, y) e^{i\omega t - \gamma z}], \\ \mathbf{E}_p(x, y, z) &= \text{Re}[\mathbf{E}(x, y) e^{i\omega t - \gamma z}], \\ \mathbf{H}_p(x, y, z) &= \text{Re}[\mathbf{H}(x, y) e^{i\omega t - \gamma z}] \end{aligned} \quad (86)$$

which reasserts both the time and z dependence down the guiding structure. At a particular z plane, say, $z=0$, we may drop the explicit z dependence. And if we don't wish to watch the time evolution of the harmonic wave, which is sufficient for plotting purposes, we may further set $t=0$, and write (86) as

$$\begin{aligned} \mathbf{J}_p(x, y) &= \text{Re}[\mathbf{J}(x, y)]; \\ \mathbf{E}_p(x, y) &= \text{Re}[\mathbf{E}(x, y)]; \\ \mathbf{H}_p(x, y) &= \text{Re}[\mathbf{H}(x, y)] \end{aligned} \quad (87)$$

5. NUMERICAL DETERMINATION OF THE FIELDS FOR DNM

Let us, for the sake of discussion, consider a possible use of DNM or LHM in a combination structure as in Fig. 6, which could indicate where the future may lie with such materials under appropriate development. Figure 6a is a

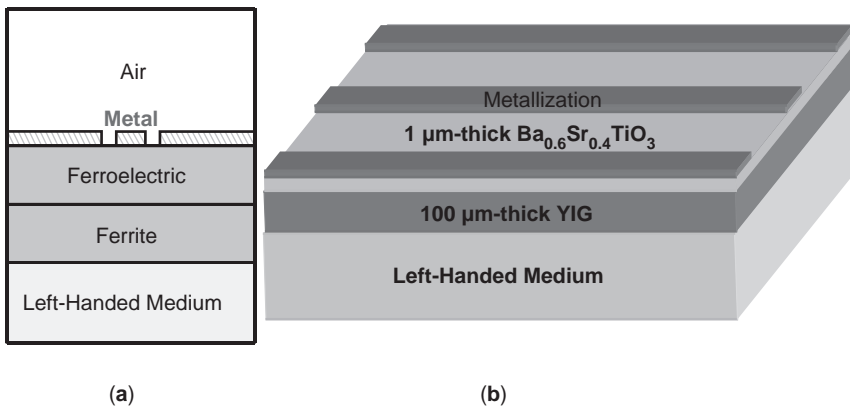


Figure 6. (a) Cross section of a multilayered coplanar structure possessing a ferroelectric material, a ferromagnetic material, and a DNM or LHM; (b) perspective drawing of the structure with possible substances and thicknesses for ferroelectric and ferromagnetic materials. (This figure is available in full color at <http://www.mrw.interscience.wiley.com/erfme>.)

cross-sectional view of metallization in what is commonly referred to as a *coplanar microstrip pattern*. The electric fields go from the inner metal strip to the edges of the wider strips of metal. The wider strips attach to the metal enclosure and so act as ground planes on the surface between the layers of materials and the air above them. The RF electric field tends to go from the inner strip to the outer ground planes. Because the fields are close to the ferroelectric–air interface using this metallization pattern, control of the ferroelectric material’s properties using a static DC voltage bias between the strip and the ground planes allows control component capabilities. In particular, the static DC voltage bias will change the ferroelectric material’s dielectric constant, which will affect the RF propagation. Below the ferroelectric layer is a layer of ferromagnetic material that can be controlled with a static magnetic field bias. The ferromagnetic material’s magnetic properties, through its permeability tensor, are altered by changing the magnetic field bias. Finally, on the bottom is the DNM or LHM, which allows one to change the field line patterns of the prior two layers, thereby adding a further degree of design capability to the structure’s RF performance. Because device impedance varies as $Z = \sqrt{\mu_{\text{eff}}/\epsilon_{\text{eff}}}$, where μ_{eff} and ϵ_{eff} respectively are the effective permeability and permittivity of the device structure, we may express the impedance as $Z = \sqrt{\mu_{\text{eff}}(fm)/\epsilon_{\text{eff}}(fe)}[\text{DNM}]$, which serves to indicate where the major effect of each material is. Clearly, the DNM affects the whole field pattern, and that is why it is to the right of the radical sign, altering the field patterns in both ferroelectric and ferromagnetic materials. Figure 6b shows a topside view of the same structure, with some specific possible materials labeled for the ferroelectric and ferromagnetic substances. Although this structure has been neither built nor modeled, it shows where the research and development could go in the future. However, an experimental structure containing a ferroelectric layer and a ferromagnetic layer was fabricated and tested in 2000 [18].

Before examining a structure compatible with integrated planar circuit technology, the material will be

made less general and complex by eliminating the optical activities (magnetolectric coefficients) in Section 2. Then the factors needed to reconstruct the y components of the transverse electric E_y and magnetic H_y fields become $D_a = \epsilon_{22}\mu_{22}$, $a_{21}' = -\epsilon_{21}\mu_{22}$, $a_{23}' = -\epsilon_{23}\mu_{22}$, $a_{24}' = \mu_{22}i\gamma/\omega$, $a_{26}' = -\mu_{22}k_x/\omega$, $a_{51}' = -\epsilon_{22}i\gamma/\omega$, $a_{53}' = \epsilon_{22}k_x/\omega$, $a_{54}' = -\epsilon_{22}\mu_{21}$, and $a_{56}' = -\epsilon_{22}\eta_{23}$. One notices that the first two factors contain off-diagonal constitutive permittivity tensor elements, the next four contain only diagonal constitutive tensor elements, and the last two contain off-diagonal constitutive permeability tensor elements. Because the discussion below will be limited to biaxial electric and magnetic crystals utilized in the principal axis system, off-diagonal-element-dependent factors will become null, making $a_{21}' = 0$, $a_{23}' = 0$, $a_{54}' = 0$, and $a_{56}' = 0$.

Since microstrip is one of the fundamental building blocks of RF hybrid and integrated circuits, actual numerically determined results will be shown for a structure with a single substrate material, that of a DNM or LHM, and a single microstrip conductor strip. The structure to be modeled is shown in Fig. 7. Figure 7a shows a cross-sectional view, indicating that the device is surrounded by a perfect conducting wall (electric wall), and Fig. 7b shows a perspective view without the obstruction of the enclosure walls. The enclosure walls can be thought of as a computational vehicle for using the numerical procedure described in Sections 2–4, even if the actual device is not inside a conductor box. Since, in general, the LHM or DNM can be anisotropic, the permittivity and permeability of the material are characterized by tensors $\bar{\epsilon}$ and $\bar{\mu}$ (or $[\epsilon]$ and $[\mu]$ in the figure). For our actual DNM study device, however, isotropy will be assumed, making $\bar{\epsilon} = \epsilon I$ and $\bar{\mu} = \mu I$, where $I = \text{identity tensor}$. Because the material is DNM, $\bar{\epsilon} = \epsilon I = -|\epsilon|I$ and $\bar{\mu} = \mu I = -|\mu|I$, where $|\epsilon| = \epsilon_{m,r}\epsilon_0$ and $|\mu| = \mu_{m,r}\mu_0$. Here the subscript “r” denotes relative values to free space, where ϵ_0 and μ_0 are the free-space values of, respectively, the permittivity and permeability. Substrate relative permittivity and permeability magnitude values are set to $\epsilon_{m,r} = 2.5$ and $\mu_{m,r} = 2.5$. Structure dimensions are height $h_T = 5.5$ mm, substrate thickness

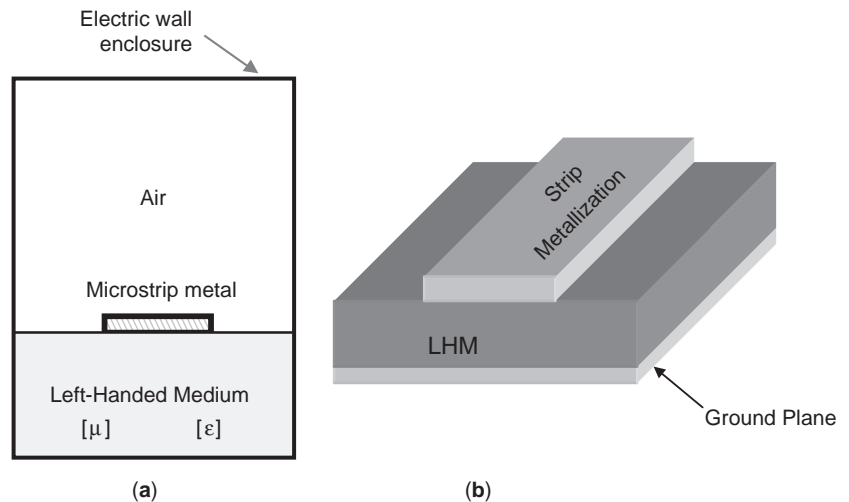


Figure 7. (a) Single microstrip structure using a DNM or LHM substrate—a perfect conductor (electric wall) encloses the device; (b) perspective drawing of the structure, without the encumbrance of the enclosing walls. (This figure is available in full color at <http://www.mrw.interscience.wiley.com/erfme>.)

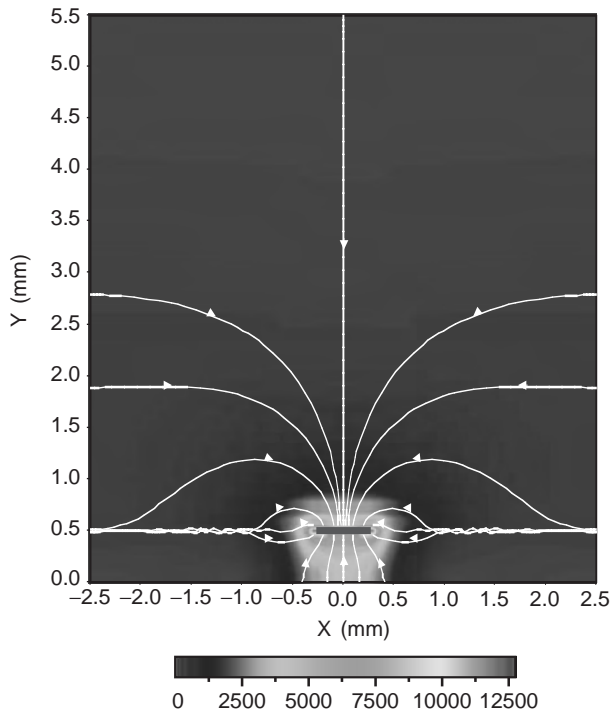


Figure 8. Magnitude plot of electric field E with an overlay of electric field lines of the \mathbf{E} vector is shown for the structure of Fig. 7 at 5 GHz. (This figure is available in full color at <http://www.mrw.interscience.wiley.com/erfme>.)

$h_s = 0.5$ mm, air region thickness $h_a = 5$ mm, box width $B = 2b = 5$ mm, and strip width $w_s = 2w = 0.5$ mm.

Figure 8 shows the electric field magnitude $E = |\mathbf{E}|$ in a color scale plot with the color scale shown below the figure at the frequency of 5 GHz. (This figure and the others to follow, including the associated propagation constants γ , were obtained using $n_x = n_z = 1$ number of surface current basis functions, $n = 200$ Fourier terms, and over 8000 gridpoints for magnitude plots from a computer code. A larger number of n_x , n_z , and n have been examined for plots and propagation constants, but are not discussed here [4,19].) It is a linear scale. Strip location is indicated by a solid dark line at $y = 0.5$ mm, $x = \pm 0.25$ mm. Overlaid on the magnitude plot is a line drawing of \mathbf{E} vector shown in white lines. Electric field direction is also noted by the arrows attached to the lines. The next figure (Fig. 9) shows the magnetic field magnitude $H = |\mathbf{H}|$ in a color scale plot with the color scale again shown below the figure. Once again a line drawing of \mathbf{H} vector is overlaid in white lines on top of the magnitude plot, with \mathbf{H} -field direction indicated by the arrows attached to the lines. In Figs. 9 and 10, we have shown only a limited number of field lines, since in principle one can draw an infinite number of them. In addition, for the electric field lines, we have drawn lines only from the strip, although electric field lines exist elsewhere in the device cross section. Figure 10 extracts from Figs. 9 and 10 the field lines in order to observe them better. Electric field emanation from the strip conductor in terms of the orientation of its vector depends on how the charge resides on the strip, and will vary depending on the

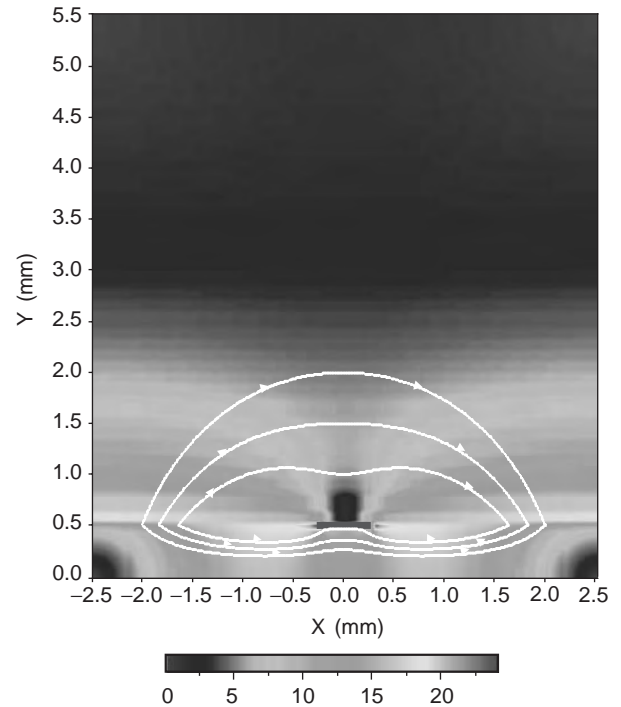


Figure 9. Magnitude plot of magnetic field H with an overlay of magnetic field lines of the \mathbf{H} vector is shown for the structure of Fig. 7 at 5 GHz. (This figure is available in full color at <http://www.mrw.interscience.wiley.com/erfme>.)

mode propagating. Magnetic field-line circulation around the strip conductor is contrary to what one normally expects for ordinary materials. For ordinary materials, the circulation would be either clockwise or counterclockwise, depending on whether the current was flowing,

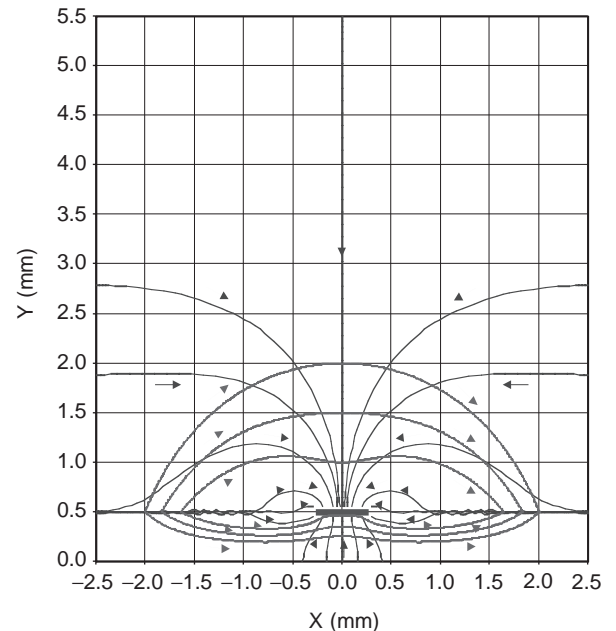


Figure 10. Electric \mathbf{E} and magnetic \mathbf{H} field lines for the structure of Fig. 7 at 5 GHz. (This figure is available in full color at <http://www.mrw.interscience.wiley.com/erfme>.)

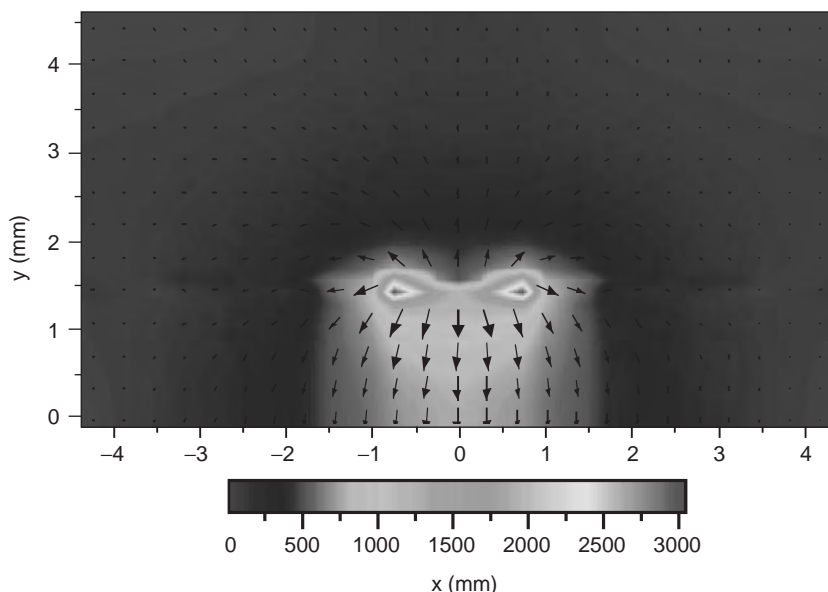


Figure 11. Electric field magnitude E and an overlaid arrow plot giving the electric field vector \mathbf{E} at 15 GHz for a ordinary media structure. (This figure is available in full color at <http://www.mrw.interscience.wiley.com/erfme>.)

respectively, out of or into the paper. But for DNM or LHM in the structure, the behavior changes, as clearly evidenced in Fig. 10.

The propagation constant for the structure at 5 GHz turns out to be entirely real, that is, $\gamma = \alpha + i\beta = i\beta$, where α is the attenuation constant and β is the phase propagation constant, the same quantity that was denoted k in Section 1. Its value at 5 GHz is $\beta = 2.22663$ (relative to the free-space value), and gives the phase behavior in the z direction, perpendicular to the structure cross section. To provide a comparison to other frequencies for this structure, its value at 10 GHz becomes complex and is $\gamma = \alpha + i\beta = 0.939414 + i2.13414$ [17,20]. At 40 GHz it is still complex, ($\gamma = 1.01830 + i1.33370$ [17,20]) and at 80 GHz, it reverts again to being purely a phase, but with two lowest-order fundamental solutions, $\beta = 1.17765$ and $\beta = 1.78861$. Complex γ values at the intermediate millimeter wavelength frequencies mean that the wave is evanescent, or decaying as the wave propagates down the structure. For $\alpha \approx \beta$, it will not take many wavelengths of distance down the guiding structure for the wave to be completely attenuated. However, such wave reduction amplitude control can provide the basis for filtering functions. Now let us return to the discussion of field plots.

For a comparison to an ordinary media structure, Fig. 11 shows the E -field magnitude and an overlaid arrow plot giving the electric field vector \mathbf{E} (arrow length gives the magnitude, while its orientation indicates its direction) at 15 GHz for a somewhat anisotropic device. Its dimensions are total height $h_T = 4.5$ mm, substrate thickness $h_s = 1.5$ mm, air region thickness $h_a = 3$ mm, box width $B = 2b = 8.5$ mm, and strip width $w_s = 2w = 1.5$ mm. The material is pyrolitic boron nitride with diagonal permittivity tensor elements $\epsilon_{xx} = \epsilon_{zz} = 5.12$ and $\epsilon_{yy} = 3.4$. The crystal is oriented so that the structure coordinates and the principal crystal axes match. Although the material's permittivity anisotropy is 33.6% referenced to the dominant diagonal elements, the overall field behavior is indicative of a normal media structure, enough to enable us to

compare it to our demonstration DNM device. Note how the majority of the field magnitude is below the interface. This structure's propagation constant $\gamma = 1.77882$.

This is not the case for our demonstration LHM device, numerically evaluated at 10 GHz and shown in Fig. 12 for the electric \mathbf{E} field. Much of the field is above the interface and to the sides of the strip. Figure 13 shows the magnetic \mathbf{H} field. This figure seems remarkable because the field appears large away from the strip. The ability of the

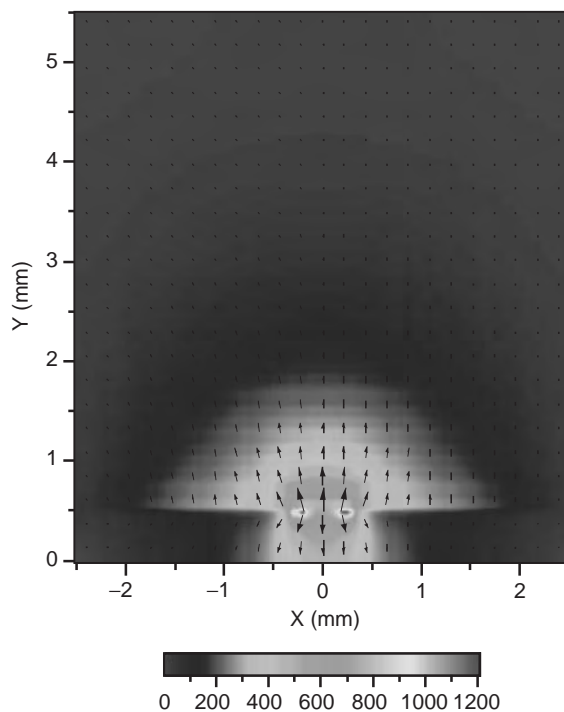


Figure 12. Magnitude plot of the electric field E , with an overlaid arrow plot giving the electric field vector \mathbf{E} , is shown for the structure of Fig. 7 at 10 GHz. (This figure is available in full color at <http://www.mrw.interscience.wiley.com/erfme>.)

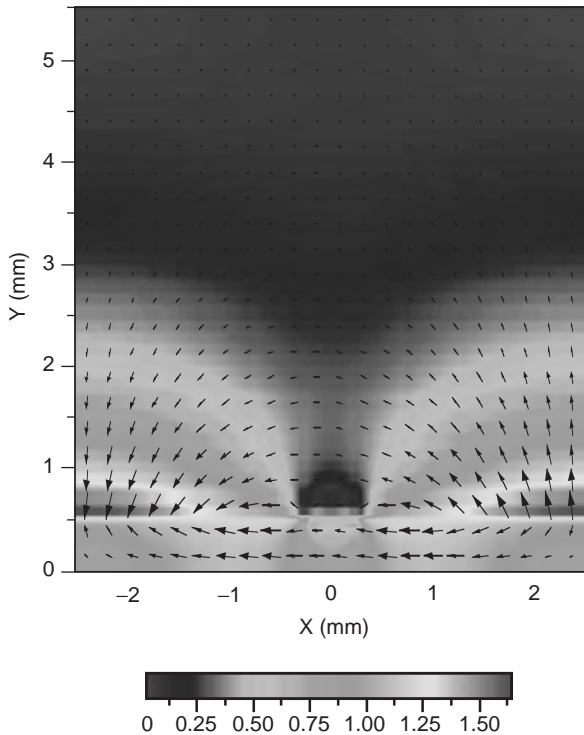


Figure 13. Magnitude plot of the magnetic field H , with an overlaid arrow plot giving the magnetic field vector \mathbf{H} , is shown for the structure of Fig. 7 at 10 GHz. (This figure is available in full color at <http://www.mrw.interscience.wiley.com/erfme>.)

LHM-RHM combination structure to expel the field from the usual regions it is found in and to place it in other regions signals its potential application toward reconfiguring fields in ordinary devices and designing completely new devices.

6. CONCLUSION

There are many fascinating aspects of double-negative materials (DNM) or left-handed materials (LHM) in relation to their physics in guided-wave structures. Likewise, the electronic aspects of using DNM or LHM as substrates based on the new physics of this material could lead to many new devices, modified old ones with additional functionality, or improved old devices. Many microwave components come to mind that could be affected by the use of this new DNM, including transmission lines [21], phase shifters, couplers, power dividers, isolators, circulators, and filters, to name just a few.

BIBLIOGRAPHY

1. For the interested reader seeking more information on focusing and radiating research done using LHM, there are many excellent places to look, including the journals *Physical Review B* and *E*, *Physical Review Letters*, and *Journal of Applied Physics* since 1998; sessions of the June 2003 CLEO/QELS-Conference on Left Handed Materials, session on Optics of Negative Index and Left-Handed Materials at the March 2003 American Physical Society Meeting [in the *APS Bulletin*

- 48, (1), (Part I)]; online April 2003 issue of *Optics Express* (Optical Society of America), special Oct. 2003 issue of the journal *IEEE Transactions of Antennas and Propagation* 51(10) on metamaterials; sessions at the June 2003 IEEE MTT-S International Microwave Symposium on Negative Refractive Index Materials and Applications and on Negative Index Materials and Microwave Applications (Vol. 1 of the *Digest*), and in the 2002 book *Advances in Electromagnetics of Complex Media and Metamaterials*, Part II on metamaterials with negative parameters (and in Parts I and III on related subjects).
2. V. G. Veselago, The electrodynamics of substances with simultaneous negative values of ϵ and μ , *Soviet Phys. USPE-KHI* 10(4):509–514 (Jan.–Feb. 1968).
3. J. F. Gittins, *Power Travelling-Wave Tubes*, American Elsevier, New York, 1965.
4. H. R. Johnson, Backward wave oscillators, *Proc. IRE* 684–697 (1955).
5. M. S. Sodha and N. C. Srivastava, *Microwave Propagation in Ferrimagnetics*, Plenum Press, New York, 1981.
6. C. M. Krowne, Physics of propagation in left-handed guided wave structures at microwave and millimeter wave frequencies, *Phys. Rev. Lett.* 92(5) 053901, (Feb. 3, 2004); also online at Cornell Univ. Archive arXiv.org/abs/physics/0305004, May 5, 2003.
7. C. Caloz and T. Itoh, Novel microwave devices and structures based on the transmission line approach of meta-materials, *IEEE MTT-S Int. Microwave Symp. Digest*, June 2003, Vol. 1, pp. 195–198.
8. C. M. Krowne and R. E. Neidert, Theory and numerical calculations for radially inhomogeneous circular ferrite circulators, *IEEE Trans. Microwave Theory Tech.* 44(3): 419–431 (March 1996).
9. C. M. Krowne, M. Daniel, S. W. Kirchoefer, and J. M. Pond, Anisotropic permittivity and attenuation extraction from phase propagation measurements using an anisotropic full-wave Green's function solver for coplanar ferroelectric thin film devices, *IEEE Trans. Microwave Theory Tech.* 50(2): 537–548 (Feb. 2002).
10. S. Ramo, J. R. Whinnery, and T. Van Duzer, *Fields and Waves in Communication Electronics*, Wiley, New York, 1967.
11. L. Brillouin, *Wave Propagation in Periodic Structures*, Dover, New York, 1953.
12. R. A. Shelby, D. R. Smith, and S. Schultz, Experimental verification of a negative index of refraction, *Science* 292:77–79 (2001).
13. A. Lakhtakia and C. M. Krowne, Restricted equivalence of paired epsilon-negative and mu-negative layers to a negative phase-velocity material (alias left-handed material), *Optik* 114(7): 305–307 (2003); also online at Cornell Univ. [arXiv, physics/0308043](http://arXiv.org/abs/physics/0308043), Aug. 11, 2003.
14. C. M. Krowne, Fourier transformed matrix method of finding propagation characteristics of complex anisotropic layered media, *IEEE Trans. Microwave Theory Tech.* 32(12):1617–1625 (Dec. 1984).
15. A. A. Mostafa, C. M. Krowne, and K. A. Zaki, Numerical spectral matrix method for propagation in general layered media: Application to isotropic and anisotropic substrates, *IEEE Trans. Microwave Theory Tech.* 35(12):1399–1407 (Dec. 1987).
16. C. M. Krowne, A. A. Mostafa, and K. A. Zaki, Slot and microstrip guiding structures using magnetoplasmons for nonreciprocal millimeter wave propagation, *IEEE Trans. Microwave Theory Tech.* 36:1850–1860 (Dec. 1988).

17. C. M. Krowne, Electromagnetic field theory and numerically generated results for propagation in left-handed guided wave single microstrip structures, *IEEE Trans. Microwave Theory Tech.* **51**(12):2269–2283 (Dec. 2003).
18. S. W. Kirchoefer, J. M. Pond, H. S. Newman, W.-J. Kim, and J. S. Horowitz, Ferroelectric-ferrite tunable phase shifters, *IEEE MTT-S Int. Microwave Symp. Digest*, June 2000, Vol. 3, pp. 1359–1362.
19. C. M. Krowne, Physics and electronics of left-handed guided wave devices, American Physical Society March 2003 Meeting, Session K22, Paper 12; in *APS Bull.* **48**(1)(Part I): 580 (March 4, 2003).
20. C. M. Krowne and M. Daniel, Electronic aspects of propagation in left-handed guided wave structures: Electromagnetic-media interactions, *IEEE Int. Microwave Symp. Digest*, June 2003, pp. 309–312.
21. D. R. Jachowski and C. M. Krowne, Frequency dependence of left-handed and right-handed periodic transmission lines, *IEEE Int. Microwave Symp. Digest*, June 2004, Vol. 3, pp. 1831–1834.

LENS ANTENNAS

J. A. G. MALHERBE
University of Pretoria
Pretoria, South Africa

1. LENSES AS ANTENNAS

There are certain, very specific reasons why a lens antenna would be chosen for a given application, and also very specific disadvantages associated with it. They have high directivity and low sidelobe patterns. Lenses are fed from the rear, and consequently there is no aperture blockage. Furthermore, they can be designed to have a minimum of aberrations for off-axis operation, and are therefore ideally suited to multibeam applications. In some instances, extremely wide scan angles can be achieved. Two-dimensional scanning lenses are well suited in application as linefeeds for cylindrical parabolic reflectors for scanning in a single plane.

At the same time, lenses suffer from internal dielectric losses, as well as reflection losses at the surface interfaces. They are often bulky, and have to be mounted by the edges of the antenna. But this disadvantage is a result of the advantage that they have no aperture blockage. These disadvantages are not typical of, for instance, reflector antennas. In spite of the disadvantages, the positive properties of lens antennas make that they are the chosen solution especially where wide scan angles are needed. At the higher microwave and millimeterwave frequencies, size ceases to be a major consideration in the application of lenses.

1.1. Optics and Dielectrics

The electromagnetic spectrum extends from the very low radiofrequencies through the microwave and millimeterwave frequencies to beyond the visible spectrum of light.

All of these wave phenomena can be described by the same set of wave equations, and there is no reason why the principles applicable to optics cannot be extended downward to cover the RF–microwave spectrum. Together with the physical principles and theory, follows devices resulting from the application of the theoretical principles.

Lenses that make use of the refractive phenomena associated with wave motion can be used to collimate electromagnetic radiation in exactly the same way as they do in optical systems.

In optical systems, extensive use is made of the principles of geometrical optics, where propagation is represented as taking place along a straight line or ray, and the same principles will be applied in understanding electromagnetic lenses in the RF and microwave areas. The principles of reflection, refraction, and diffraction are central to the development of lens antennas, although the latter lies beyond the scope of this article.

Two important principles of optics are basic to lens action:

1. The propagation (phase) velocity for wave propagation differs between various media with different relative permittivity. The relative permittivity is directly related to the refractive index of the material, $n = \epsilon_r^{1/2}$. The index of refraction for *natural homogeneous dielectric materials*, is always $n > 1$. It varies from about just over 1 for foam-type plastic dielectrics to between 2 and 4 for plastics, through a wide range from 2 to 80 for mixtures that contain various ceramics.
2. When rays are obliquely incident on the interface between two media, the wave is partially reflected, and partially refracted. Refraction takes place as shown in Fig. 1. Rays will be refracted towards the surface normal PP' at oblique incidence when traveling from a less to a more dense material, and vice versa. This is known as *Snell's law*; it sets the relationship between the angles of incidence and refraction for known values of n . Snell's law is stated as

$$\sin \phi_i = n \sin \phi_t \quad (1)$$

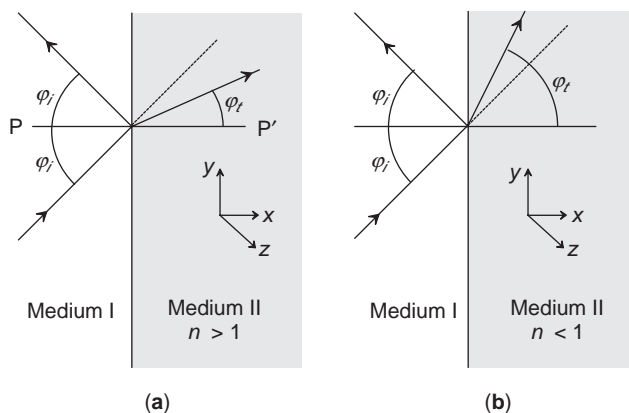


Figure 1. Refraction at an interface between two media.

The statement on natural dielectrics needs expansion. Clearly, most of the materials mentioned, are not *natural* materials in the true sense of the word, but they perform in the same way as natural materials, so we will use the term. There are also a large number of other, constructed and artificial media, for which $n < 1$. Figure 2a, shows a plane wave incident on the interface between free space and a set of *parallel conducting plates*, with the E field parallel to the plates. Providing that the plate separation lies between λ and $\lambda/2$ of the free-space wave, a single mode, the transverse electric (TE) mode, will propagate, with a phase velocity *larger* than that of light in free space.

In effect, this constitutes a medium with $n < 1$, and can be used to construct a lens. If the wave is *not* polarized with the E -field parallel to the plates, as in Fig. 2b, the wave will propagate between the plates in the transverse electromagnetic (TEM) mode, which has the same phase velocity as free space. This is clearly not useful. In the first case, Snell's law is obeyed.

In cases where the wave has a component of velocity normal to the conducting plates, as depicted in Figs. 2c and 2d, the behaviour of the wave in the x - y plane is as described above. In the x - z plane, though, the wave is forced to propagate between the parallel plates. This is termed a constrained wave. In this plane, Snell's law is *not* obeyed.

Waveguides also exhibit the property of a phase velocity different from that of free space. By closely packing waveguides of particular cross section, a synthetic

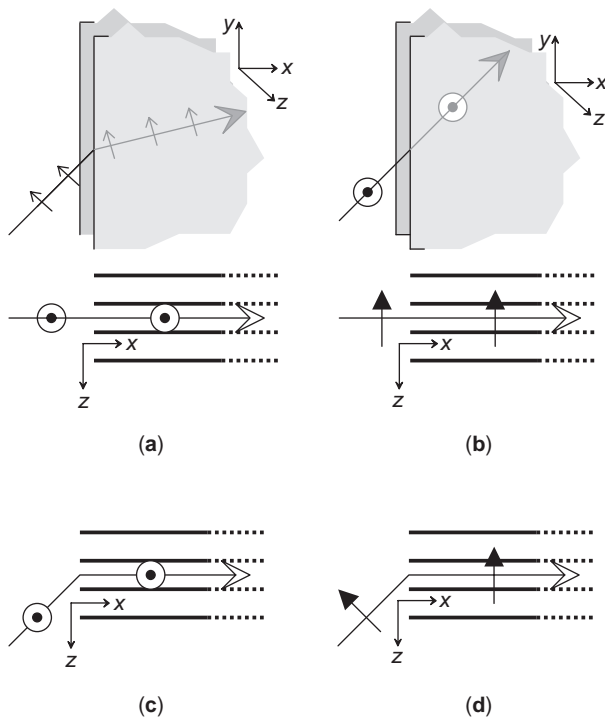


Figure 2. Electromagnetic wave passing through parallel conducting planes: (a, b): Incidence parallel to the plane of the conductors for an E field polarized parallel and normal to the conductors, respectively; (c,d) incidence at an angle to the conductors.

material is created that will have a controlled value of n , and can be applied to the construction of lens antennas. In fact, any device or medium that can be employed to control the phase of a wave over a surface, can be applied as an artificial dielectric medium. In a later section we shall see that even coaxial transmission lines can be applied for this purpose.

A number of synthetic dielectrics have also been developed. They consist variously of plastic bases that have been impregnated with regular lattices of metal spheres, wires, and strips of various cross sections. In some instances, the inclusions are dielectric spheres, or voids such as holes.

In the interest of clarity, we shall discern between *natural dielectrics* when the refractive index $n > 1$, and *artificial dielectrics* if $n < 1$. Synthetic dielectrics will not be treated as examples, and the above definitions will suffice.

1.2. Single-Surface Dielectric Lens

The function of a lens antenna is to collimate all energy radiated from a source. Traveling from the source, all electrical paths to the lens aperture must be of the same length for the rays to add constructively.

In Fig. 3a, the simplest lens is illustrated, where one surface has been chosen to be plane, and the refractive index is $n > 1$. The electrical pathlength of a ray traveling the path FPP' must be the same for P anywhere on the lens surface. Refraction occurs only at the curved surface P , and the rays exit in a direction normal to the plane surface of the lens at P' . The body that satisfies this condition is readily described mathematically, and it turns out that the curved surface of the lens is a hyperbola, with the focus at the origin [1]. Inspection of Fig. 3a leads to the conclusion that the lens can be gainfully increased in size only until the angle subtended by the lens approximates the asymptotes of the hyperbola, and this limits the practical size of the lens.

Because no refraction occurs at plane P' , such lenses are termed *single-surface*. Note that the position of the plane at P' does not enter into any equation, and we are free to make the lens as thick as we like (not that that would be of any advantage). The point being that the lens

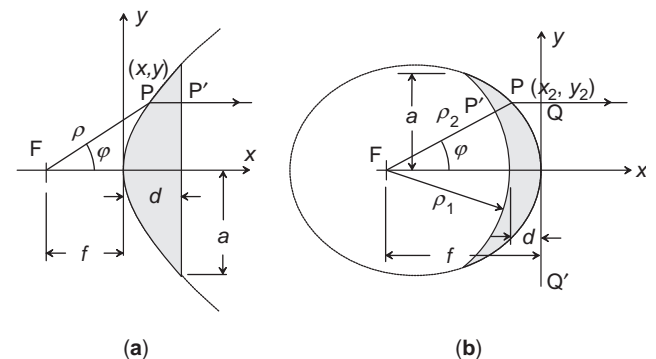


Figure 3. (a) Single-surface dielectric lens with one flat surface; (b) lens with circular arc surface $n > 1$.

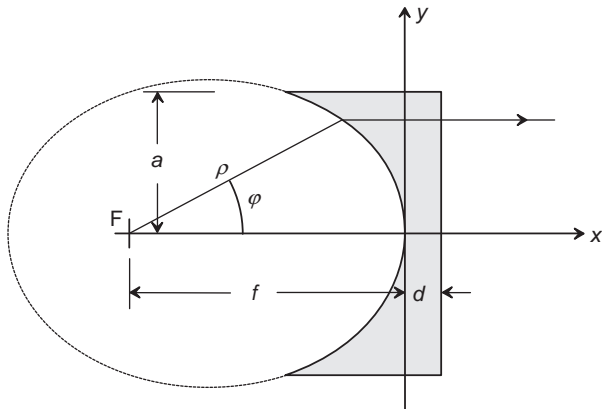


Figure 4. Single-surface lens, with $n < 1$, as for parallel-plate waveguide lenses.

in effect collimates radiation from a less to a denser medium.

An alternative single-surface lens is shown in Fig. 3b. Here the surface P' is chosen to describe an arc of a circle; thus, P' is an equiphase surface with radius ρ_1 , and no refraction occurs there, because incidence is normal to the surface. Once again, we are free to choose the radius as large or as small as we like, because no refraction occurs, and any additional path in the dielectric material is common to all rays. In fact, we may choose the radius to be so small that F lies within the dielectric, and an observer to the right of P will not be able to determine whether F lies in free space, or whether the body to the left of P' is also immersed in the dielectric. For the waves arriving at QQ' to be in phase across the surface, the electrical pathlength $P'PQ$ must be constant. The solution is once again readily found to be that the curve P' must be described by an ellipse, with the focus of the lens at the focal point of the ellipse farthest from QQ' . This lens is the complement of the planoconvex lens described above. It collimates radiation from a dense to a less dense medium.

In Section 1.1, *parallel plates* and *waveguides* as synthetic dielectrics were discussed. Bearing in mind the fact that for these cases the index of refraction, $n < 1$, the wave travels in effect from a more to a less dense material if we keep one surface plane (equiphase). It should therefore not come as a surprise to find that the locus of points describing a parallel-plate lens with one equiphase surface, is an ellipse, as shown in Fig. 4. Note that Snell's law is automatically satisfied in the case of all single-surface lenses.

1.3. Zoned Lenses

The lenses described above present a problem, insofar as that for the practical ranges of refractive index, they are going to be extremely bulky. In order to alleviate both the bulkiness and the dissipation loss through the lens associated with it, the surface of the lens can be *zoned*, that is, subdivided into sections for which the electrical pathlength through each section, is equal *within a wavelength* (or integral number of wavelengths). Waves that travel an integral number of wavelengths further or less, will, of

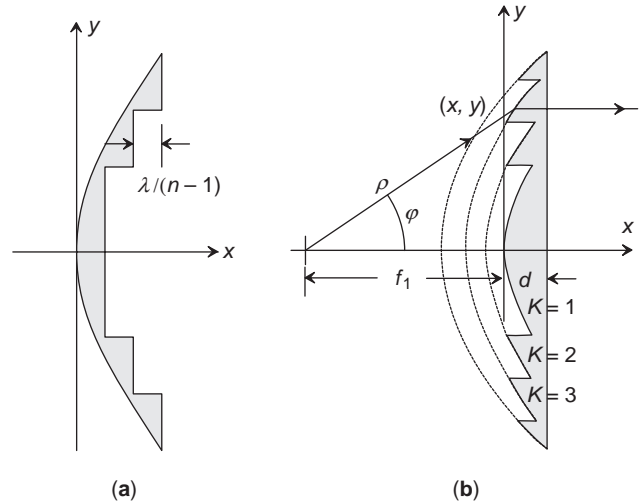
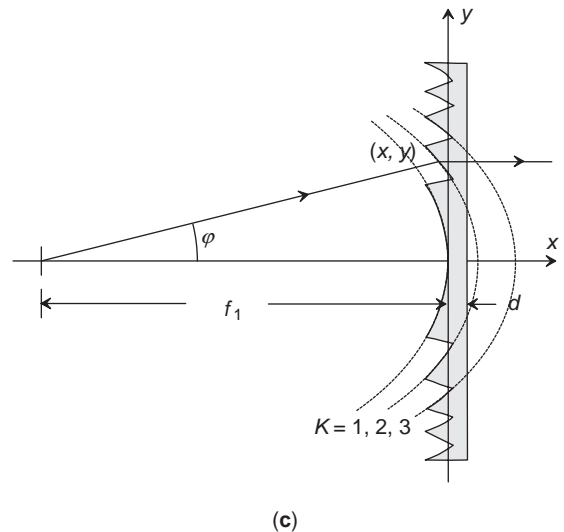


Figure 5. Single-surface lens, $n > 1$, zoned on the planar side (a) and on the convex side (b); artificial dielectric lens with $n < 1$ (c).



course, combine in phase with each other. This is achieved if the steps are equal to $\lambda/(n - 1)$. This is shown in Fig. 5a for zoning on the flat surface of a natural dielectric lens, and in Fig. 5b, where the curved surface of the same lens has been zoned. Zoning for an artificial dielectric lens is shown in Fig. 5c.

In the latter case, each zone is a section of a different ellipse, because as the zoned sections are stepped, the focal distance changes. The zoning exercise is therefore not a simple geometric shift of the lens surface, but a separate lens design for each zone. Fortunately, the mathematics is not complicated, and is given in the next section. Note that this is a frequency-dependent solution, and zoning immediately restricts the useful bandwidth of the antenna.

1.4. Lenses with Two Refracting Surfaces

If the lens has two refracting surfaces (neither of which is equiphase), not only does the equal electrical length

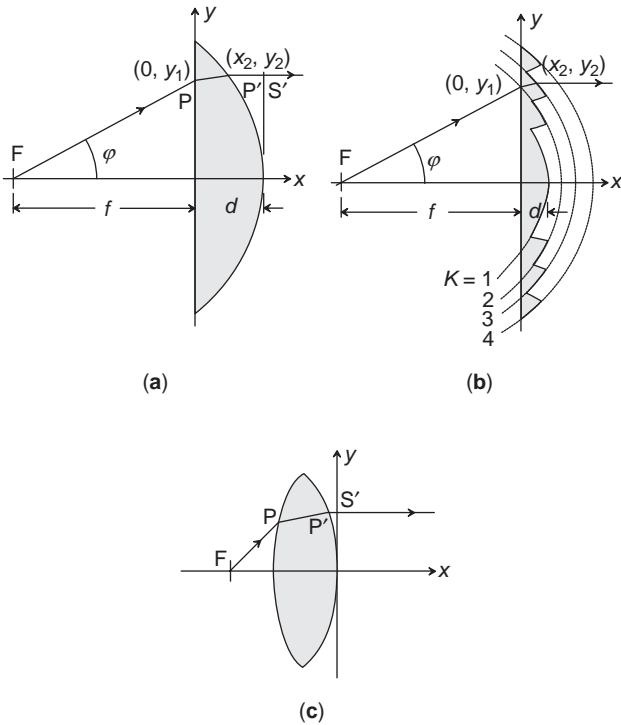


Figure 6. Lenses with two refracting surfaces: (a) one surface plane; (b) the same lens, zoned; (c) both surfaces curved.

condition need to be satisfied, but also Snell's law, at each of the refracting surfaces. In the mathematical analysis for such lenses, it will be found that there are more variables than equations, and it becomes necessary to make assumptions to obtain solutions.

In the lens in Fig. 6a, one of the surfaces has been fixed as planar. This immediately removes one degree of freedom, causing a unique solution to exist, in spite of the fact that also Snell's law needs to be satisfied at both surfaces. The zoned version of the same lens is shown in Fig. 6b. In all other instances (where both surfaces are free, as in Fig. 6c), it is found that there is no unique solution for the surfaces, and a practical design involves choices determined by other considerations [2]. Specific design procedures are discussed in a later section.

1.5. Three-Dimensional Lenses

Up to this point, the lenses studied were described by ray optics and were two-dimensional. In practice, three-dimensional structures are needed, often with specific properties in orthogonal planes. Neglecting the fact that there are end effects when a cylindrical structure is finite, the solution for a cylindrical is identical in cross section to that of the two-dimensional solution. Fig. 7a shows the geometry for a cylindrical lens, fed by a line source, which could typically be a slotted waveguide. The illuminating wavefront is cylindrical.

The rigor of deriving the equations for the geometric surfaces in structures that have some symmetry in a spherical coordinate system can be avoided by simply

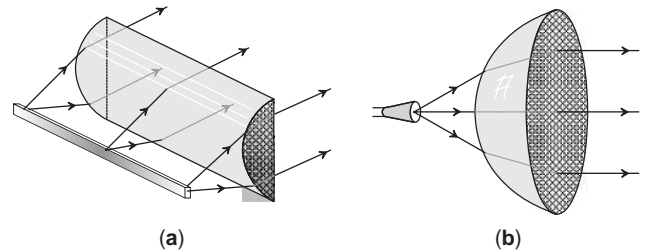


Figure 7. Cylindrical lens fed by a line source (such as a slotted waveguide) and (b) spherical lens fed by a point source, such as a small horn.

rotating the two-dimensional solution about its axis to obtain solutions with rotational rather than translational symmetry. For convenience, these lenses will be called *spherical*, although they are, of course, not spheres. A spherical lens fed by a point source is shown in Fig. 7b. The illuminating wavefront is spherical.

Both these lenses would be constructed of a natural dielectric, $n > 1$, because of their plano-convex shape. For 3D structures with $n < 1$, parallel-plate lenses are popular because of their light weight and low loss, and two possible structures are shown in Fig. 8; dielectric spacers would be used to hold the conducting sheets in place. The structure for a cylindrical lens with the conducting planes in the x - y plane, is shown in Fig. 8a; the E field is also polarized in this plane, and Snell's law is satisfied over the concave area of the lens. In the lens of Fig. 8b, the conducting planes lie in the x - z plane, as does the E field. It is, however, a constrained lens, and Snell's law is not satisfied over the concave face of the lens. For both examples, an appropriate slotted waveguide for forming a linear source is shown.

Figure 9 shows a spherical lens constructed of parallel plates, and fed by a point source. As with lenses constructed from natural dielectrics, the principles of zoning can be applied to the parallel-plate lenses. Arrays of closely packed waveguides of round, rectangular or hexagonal cross section are used as a constraining medium in the construction of waveguide lenses. When the operating frequency of the lens lies within the frequency band of the

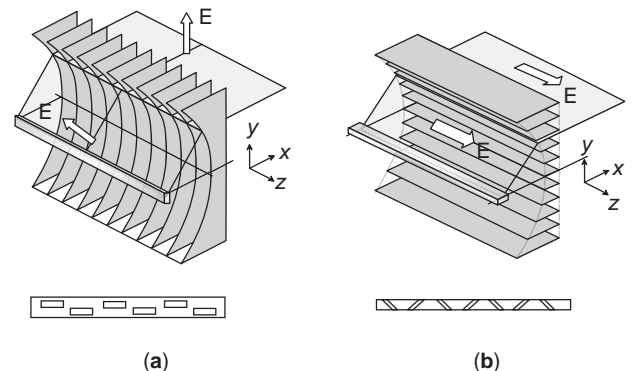


Figure 8. Cylindrical lenses constructed of parallel plates: (a) lens not constrained; (b) lens constrained. An appropriate waveguide linefeed is shown in each case.

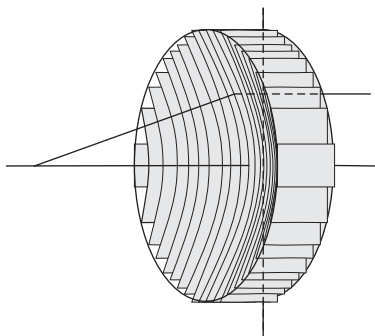


Figure 9. Spherical lens constructed from parallel plates.

waveguide, lenses can be constructed that can be zoned in the same way as the dielectric or parallel plate lenses, and Fig. 10 shows schematically the structure of a zoned rectangular waveguide lens with one planar surface and one concave surface. If the correct dimensions are chosen for the elemental waveguides, the appropriate TE mode will propagate as discussed above, and ensure the correct phase delay through the lens. Waveguide lenses constrain the wave in at least one of the major axes [3]. The major advantage of this type of lens is that, because the elemental waveguides are symmetric about the major axes of the lens, the incident wave can be circularly polarized, without any loss of lens action.

Integrated dielectric lenses, with the source embedded in the dielectric of the lens, have found application in integrated systems, where the lens is mounted directly on top of the stripline or microstrip board that feeds the lens and carries the rest of a microwave circuit. Figure 11 shows an example of such a lens.

1.6. Other Lens Systems

In the areas of application where lenses offer the best solution, it is because of their ability to scan a narrow

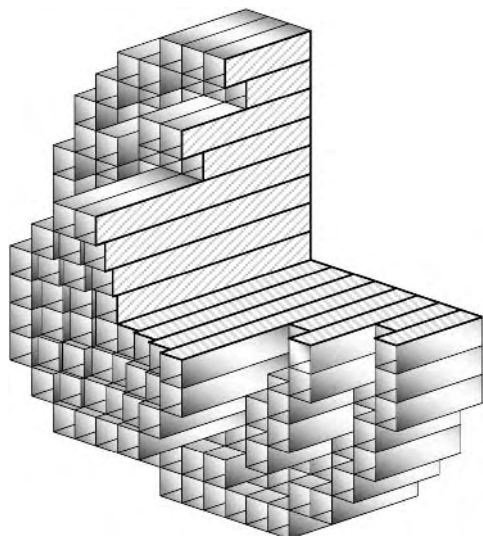


Figure 10. Cross sections through zoned lens of rectangular waveguide.

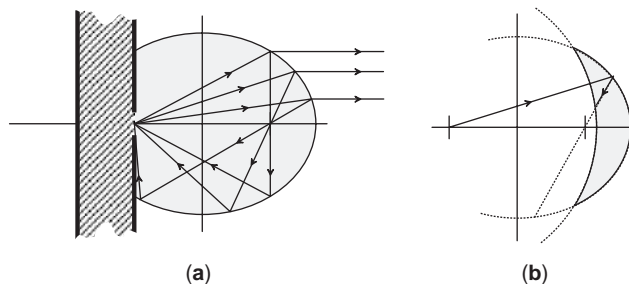


Figure 11. Integrated dielectric lens: (a) the lens is shown on a substrate; (b) thin lens with the same focal length.

beam over a relatively wide angle, that they find regular application. In many instances, substantially more complex lens systems satisfy this need. While a more extensive treatment will be given in Section 3, a brief qualitative description is given here. It will be seen that specific conditions need to be met for a lens to properly collimate the radiation of a source that lies off the focus of the lens. One way to ensure a larger focal area is to design a lens with a multiplicity of focal points. This makes it possible to feed the lens from a number of different points, each corresponding to a new position of the beam of the lens.

1.6.1. Constrained Lens. The constrained lens shown in Fig. 12 has two perfect off-axis focal points, from where the radiation will be collimated in a direction off the main axis of the lens. A source illuminating the lens from anywhere on a circular arc with radius f , and centered at the origin O , will cause the lens to scan in a different direction for each position. Because of these points are not foci, the collimation of the beam will not be perfect, but it will be good enough, provided the source lies between F and F' . By arranging a number of sources on the feed arc, a different beam can be scanned for each of the sources illuminating the lens.

A geometric analysis shows that for two symmetric foci the inner surface of the lens must be an ellipse, with the

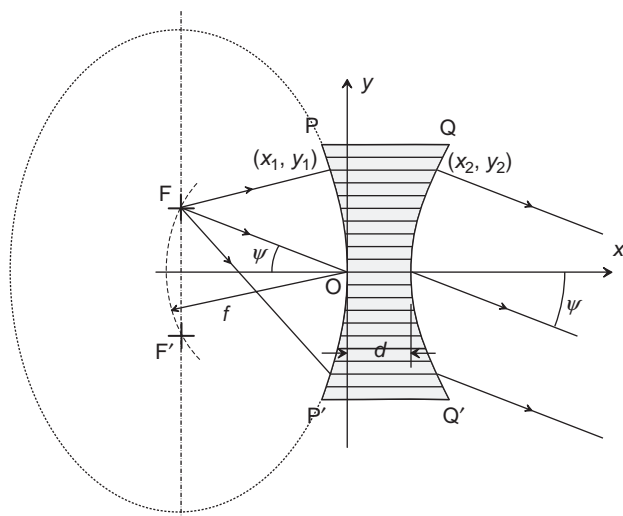


Figure 12. Constrained lens with two symmetric focal points.

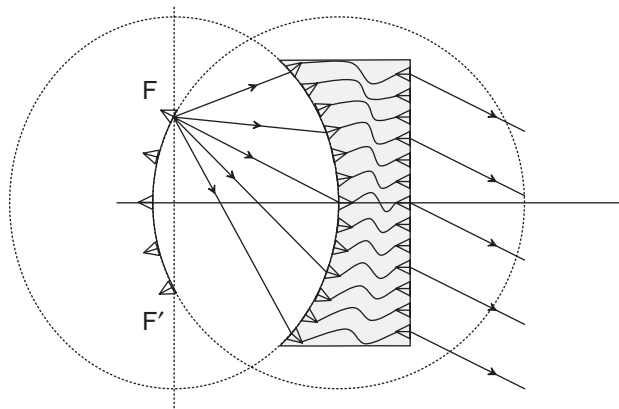


Figure 13. Rotman lens: layout and ray geometry.

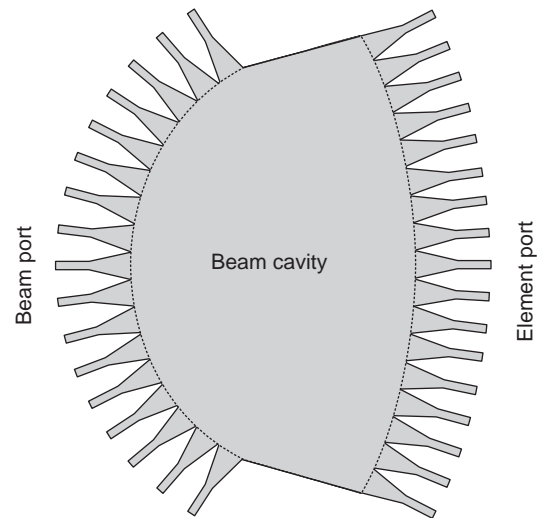


Figure 14. Beam cavity of Rotman lens.

two focal points F and F' on the foci of the ellipse. The construction of the lens would be either as in Fig. 8b, of parallel plates, or of stacked waveguides. The choices that will determine the specific shape of the outer surface of the lens, and other design parameters coupled to it, are discussed in Section 3.2.

1.6.2. The Rotman Lens. In the Rotman lens shown in Fig. 13, the lens consists of a structure that does not have a dielectric per se, not even parallel plates. Each of the two lens surfaces consists of a number of antennas, connected one on one by means of a section of coaxial line. The lengths of the lines determine the phase delay that would normally be associated with the delay through a lens section. The lens is fed from a series of points on a curve FF' as for the constrained lens discussed above; the structure makes it possible to change the outer lens surface shape arbitrarily.

The Rotman lens, of course, is a constrained lens, and originally the lens was constructed of parallel plates that bound the wave between the beam ports (the lens illuminating radiators) and the element ports (the inner surface of the lens). Currently, the most popular form of realization has the beam and element ports constructed of etched tapers, with the inner beam cavity area of stripline, as is shown in Fig. 14.

Because of the stringy transmission lines that connect the two faces of the lens, these lenses are also known as “bootlace lenses”.

1.6.3. The R-2R Lens. Another type of bootlace lens is the R-2R lens shown in Fig. 15. In this lens the feeding curve (the beam port) and the inner face of the lens (the element port) both lie on the same circle of radius R , while the array port containing the radiating elements of the array lie on a circle of radius $2R$. The array elements are connected to the element port elements by transmission lines of equal length, and the lens can scan over a wide angle, free of any distortion.

1.6.4. The Luneburg Lens. A unique and interesting lens, first described by Luneburg [4], is shown in Fig. 16.

The Luneburg lens is a spherically symmetric lens with variable index of refraction, given by $n = (2 - r^2)^{1/2}$ for a sphere of unit radius. When the lens is fed at any point on the surface, it produces a plane wave in a direction diametrically opposite to the feedpoint. In view of the symmetry, moving the feedpoint about the surface results in a scanned beam from a direction diametrically opposite the feedpoint.

Because of the problem of manufacturing a body with a predetermined variation of the dielectric, a number of approximations consisting of discrete shells of fixed dielectric constant are used; these are described in Section 3.4.

1.6.5. Fresnel Zone Plate Lenses. The concept of the Fresnel lens dates from the middle of the nineteenth century, but was until recently (as of 2004) seen as an optical rather than an RF or microwave device. It differs radically from the other lenses described in this article, insofar as it does not make use of the principle of refraction, but rather uses reflection and diffraction.

In its simplest form, the Fresnel lens consists of properly spaced concentric rings of alternately transparent

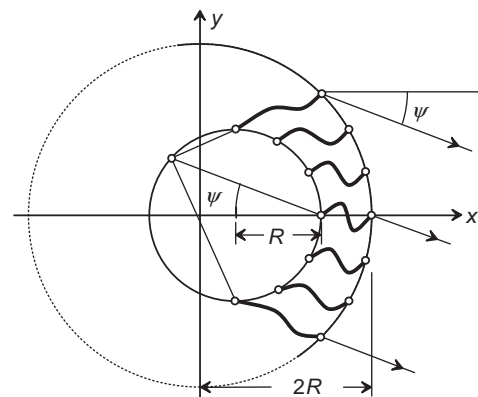


Figure 15. R-2R lens.

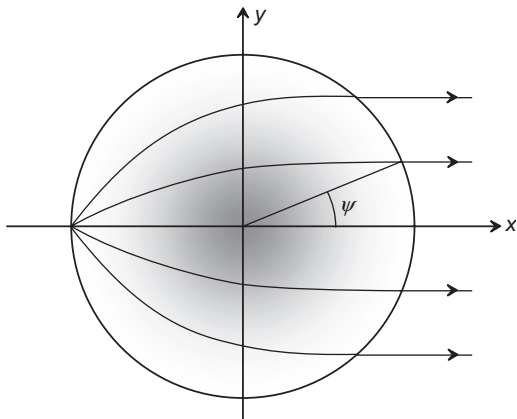


Figure 16. Luneburg lens.

and opaque or reflective material. The sizes of the rings are so chosen that the pathlength from the outside diameter to the focus is one-half wavelength longer than the pathlength to the focus from the inside diameter, as shown in Fig. 17. Energy is reflected and diffracted from the rings in such a way that the forward-scattered components add nominally in phase at the focal point of the plate—at least, their phases will differ by less than half a period. Because of very poor aperture efficiency, practical Fresnel lenses have been developed that are constructed from alternate rings of different dielectrics. Zone plate lenses are attractive solutions when low material weight, low absorption loss and flat lens surfaces are relevant design factors.

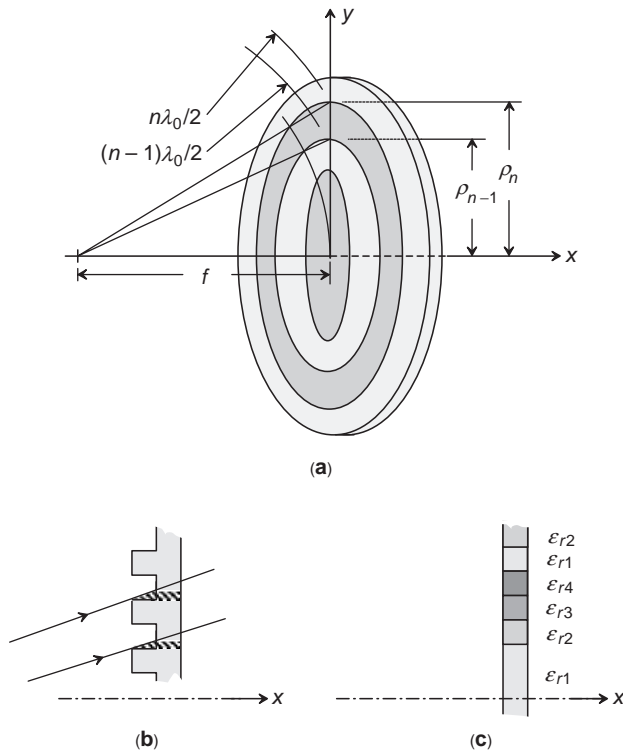


Figure 17. Fresnel lens. Basic structure is shown in (a); shadowing is illustrated in (b). Use of dielectric annuli is illustrated in (c).

2. LENS DESIGN CONSIDERATIONS

This section addresses a number of practical considerations pertaining to the operation of lens antennas, as well as aspects that have to be taken into consideration with the design of such structures.

2.1. Lens Design Equations

The design equations for the lenses described in Section 1, are derived readily from first principles [1,2]:

For the simple planoconvex lens of Fig. 3a

$$\rho = \frac{(n - 1)f}{n \cos \varphi - 1} \tag{2}$$

$$y = \sqrt{(n^2 - 1)x^2 + 2(n - 1)fx} \tag{3}$$

The maximum thickness of the lens is given by

$$d = \frac{1}{(n + 1)} \left(\sqrt{f^2 + \left(\frac{n + 1}{n - 1}\right)a^2} - f \right) \tag{4}$$

For the elliptical lens (Fig. 3b),

$$\rho_1 = f - d \tag{5}$$

$$\rho_2 = \frac{(n - 1)f}{n - \cos \varphi} \tag{6}$$

$$y_1 = \sqrt{(f - t)^2 - (x_1 + f)^2} \tag{7}$$

$$y_2 = \sqrt{-2 \left[\frac{n - 1}{n} \right] fx_2 - \left[\frac{n^2 - 1}{n^2} \right] x_2^2} \tag{8}$$

The central thickness of the lens given by

$$d = \frac{2\rho_1 - \sqrt{4\rho_1^2 - d^2}}{2(n - 1)} \tag{9}$$

For the concave lens with $n < 1$, as shown in Fig. 4, we obtain

$$r = \frac{(1 - n)f}{1 - n \cos \varphi} \tag{10}$$

$$y = \sqrt{2(1 - n)(-x)f - (1 - n^2)x^2} \tag{11}$$

2.2. Zoning: Equations and Effects

The usefulness and purpose of zoning has been discussed in Section 1. Johnson and Jasik [2] give equations that describe the surfaces of zoned lenses.

Referring to the zoned lens of Fig. 5b, we have

$$\rho = \frac{(n-1)f_1 - (K-1)\lambda}{n \cos \varphi - 1} \quad (12)$$

$$y = \sqrt{(n^2-1)x^2 + 2(n-1)f_1x + 2(K-1)\lambda nx + 2f_1(K-1)\lambda + (K-1)^2\lambda^2}$$

$$K = 1, 2, 3, 4, \dots \quad (13)$$

For the zoned concave lens of Fig. 5c, we obtain

$$r = \frac{(1-n)f_1 + (K-1)\lambda}{1 - n \cos \varphi} \quad (14)$$

$$y = \sqrt{2(1-n)(-x)f_1 - (1-n^2)x^2 - 2(K-1)(-x)n\lambda + 2(K-1)f_1\lambda + (K-1)^2\lambda^2},$$

$$K = 1, 2, 3, 4, \dots \quad (15)$$

The lens shown in Fig. 6b has two surfaces, and its zoning equations are given by

$$x_2 = \left\{ \frac{(K-1)\lambda + (n-1)d + f - \sqrt{f^2 + y_1^2}}{n - \sqrt{1 - \frac{y_1^2}{n^2(f^2 + y_1^2)}}} \right\} \quad (16)$$

$$\times \sqrt{1 - \frac{y_1^2}{n^2(f^2 + y_1^2)}}$$

$$y_2 = y_1 \left[1 + \frac{x_2}{\sqrt{n^2(f^2 + y_1^2) - y_1^2}} \right] \quad (17)$$

$$K = 1, 2, 3, 4, \dots$$

Unfortunately, zoning has some disadvantages; Fig. 18a illustrates one of them. If the lens is a zoned single surface, there will be a solid-angle section in which the energy is not refracted into the lens path. This represents loss. On the other hand, for the zoned two-surface lens shown in Fig. 18b, no energy will be lost, but a section of the aperture will not be illuminated. This will cause degradation of sidelobe performance. If the zoning is done in the plane surface of a single-surface lens, it is possible to achieve a situation with no loss or shadowing. However, this represents the more unattractive case, where the lens retains the shape of the large, curved surface, which is mechanically much more difficult to handle (Fig. 18c). A similar situation arises with lenses where $n < 1$, as shown in Fig. 18d. Ultimately, the decision on the shape of the lens will be determined by practical considerations.

The other major disadvantage of zoning affects bandwidth, in that the zoned lens is inherently frequency-sensitive. But as will be seen in Section 2.5 on bandwidth, there can also be an upside to zoning when applied to parallel-plate or waveguide lenses.

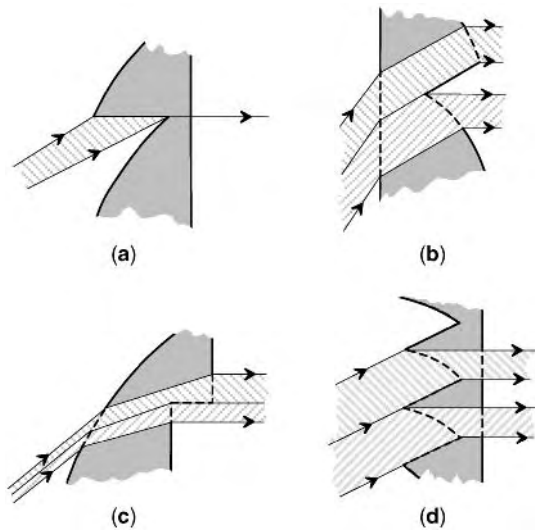


Figure 18. Effects of zoning. Energy in the shaded solid angle in (a) is lost. In (b) there is no loss, but the aperture is shaded. For the stepped lens in (c) there is no loss or shading. Shading in a concave lens is shown in (d).

2.3. Gain and Sidelobe Level

The illumination of the radiating aperture is the primary variable in determining the gain and sidelobe level of an antenna. In certain instances, such as with antenna arrays, extremely intricate field distributions are possible, making for very specific sidelobe performance; associated directly with the sidelobe performance is the gain. Lower sidelobes generally mean a broader beamwidth, and a decrease in gain. Consequently the field in the aperture of the lens is of primary concern.

In the case of a lens with a hyperbolic surface, it has already been pointed out that the maximum size of the lens is limited by the asymptotes. Silver [1] derives an expression for the amplitude distribution over the lens aperture. If the distance from a point on the lens surface to the axis of a spherical lens is given by $r = a \sin \varphi$, and if the source radiates an amplitude of $A(\varphi)$, then the ratio of amplitudes between the source and aperture is given by

$$\frac{A(r)}{A(\varphi)} = \sqrt{\frac{(n \cos \varphi - 1)^3}{f^2(n-1)^2(n - \cos \varphi)}} \quad (18)$$

For the cylindrical hyperbola, the ratio of source to aperture fields is given by

$$\frac{A(y)}{A(\varphi)} = \sqrt{\frac{(n \cos \varphi - 1)^2}{(n-1)f(n - \cos \varphi)}} \quad (19)$$

As the amount of power per unit solid angle radiated from the source is constant, and as the projected area of the lens becomes substantially larger, there will be a severe dropoff of illuminating field toward the edges. In this case, the low edge illumination implies low sidelobe levels and not much can be done to increase the illumination around the edges.

For the lens with an elliptic contour, the corresponding amplitude ratios are

$$\frac{A(r)}{A(\varphi)} = \sqrt{\frac{(n - \cos \varphi)^3}{f^2(n-1)^2(n \cos \varphi - 1)}} \quad (20)$$

and

$$\frac{A(y)}{A(\varphi)} = \sqrt{\frac{(n - \cos \varphi)^2}{(n-1)f(n \cos \varphi - 1)}} \quad (21)$$

For this lens, the limiting variable occurs on the secondary (radiating) side of the lens; the lens cannot be made larger than the largest dimension of the ellipse. In this case, the illumination is substantially stronger at the edges of the lens. Here edge illumination is naturally reduced by practical feeds, such as horns or linear waveguide arrays.

Radiation from the source antenna in any complex antenna system is always designed to illuminate the secondary element with the largest possible portion of the available power. Spillover from the primary radiator represents a loss of gain, and it is usually attempted to ensure that spillover is as small as possible, by choosing an appropriate element or elements for the purpose.

2.4. Reflections and Loss

In the qualitative discussion on lenses so far attention has been given only to the direct ray paths that contribute to the formation of the radiation properties of the antenna. Unfortunately, at each interface between two materials, reflection occurs; such reflections in general do not add in a way that enhances the performance of the antenna.

Consider, for instance, the lens in Fig. 3a. The wave striking the plane interface between the lens and air is partially reflected back into the lens, to retrace along the same path on which it had entered the lens, and is concentrated at the focal point, causing a substantial mismatch at the feedpoint. Similarly, at the circular surface in Fig. 3b, where the first circular wavefront strikes the lens, the wave is partially reflected straight back at the source.

Referring to Fig. 1, for perpendicular polarization, (i.e., the electric field perpendicular to the plane of incidence), the coefficient of reflection at an interface is given by

$$\rho_{\perp} = \frac{E_r}{E_i} = \frac{\cos \varphi_i - \sqrt{n^2 - \sin^2 \varphi_i}}{\cos \varphi_i + \sqrt{n^2 - \sin^2 \varphi_i}} \quad (22)$$

and for parallel polarization

$$\rho_{\parallel} = \frac{E_r}{E_i} = \frac{n^2 \cos \varphi_i - \sqrt{n^2 - \sin^2 \varphi_i}}{n^2 \cos \varphi_i + \sqrt{n^2 - \sin^2 \varphi_i}} \quad (23)$$

where E_r is the reflected field strength and E_i is the incident field.

At perpendicular incidence, the magnitude of the reflected field could be of the order of the surface reflection coefficient for a plane wave. For a dielectric constant of 2.56, $n = 1.6$, this could be as high as -12.7 dB, corresponding to a loss in gain of 0.24 dB.

As in optical instruments, the lens may be coated in a quarter-wavelength layer of index of refraction, $n_l = n^{1/2}$ to ensure a match between the two media. Application at a plane surface is obviously relatively easy, but at a slope the effective thickness in the direction of the incident wave must be used. Certain other devices are employed to either cancel the reflected power, or to concentrate it elsewhere. A slight offset of the feed from the lens axis will focus the reflections at a point outside the feed antenna. In a method similar to zoning, the lens may be split and half of it displaced axially by a quarter-wavelength in the lens medium, causing the reflected power from the two halves to cancel. The two halves will, of course, have focal lengths that differ by a quarter-wavelength in the medium. Other reflections that do not add constructively at the feedpoint may not cause mismatch, but will, of course, represent a loss of power, and thus reduced gain. Johnson and Jasik [2] describe a number of different surface treatments that can be applied to the lens surface in order to affect a quarter-wave match.

Although not caused by reflection, dielectric losses can be lumped conveniently with reflection losses. In the case of natural dielectrics, all materials are lossy to some extent. In some parallel-plate lenses, a dielectric is used to separate the conducting plates; in such arrays both conductive loss and dielectric loss will occur inside the lens. For a zoned dielectric lens, the attenuation through the dielectric is given [2] approximately by $27.3 (\tan \delta) n/(n-1)$ dB, and for a stepped polystyrene lens at 10 GHz, with $\epsilon' = 2.54$ and $\tan \delta = 4.3 \times 10^{-4}$ is about 0.02 dB.

2.5. Bandwidth

A simple dielectric lens would theoretically have infinite bandwidth, and in practice the bandwidth is in fact very large. This is obviously dependent on the material, and if the latter is not dispersive (v is not a function of frequency), the lens will be wideband. On the other hand, parallel-plate and waveguide lenses are extremely dispersive, and will exhibit narrow bandwidth.

As soon as the lens is zoned, though, the structure becomes frequency-dependent, and the effective bandwidth is a function of the number of zones. Conventionally, it is assumed that if an antenna has been designed for a specific radiation pattern, then degradation of the pattern will be acceptable only up to the point where the phase error across the aperture of the antenna amounts to 22.5° or $\lambda/8$. Silver [1] derives that a lens with K zones separated by steps of one wavelength will have a bandwidth of approximately $25/(K-1)$ percent. A lens with six zones (five steps) will have a bandwidth of 5%.

The lenses with $n < 1$ are all dispersive, as discussed in Section 1.1. In practice, the bandwidth limitation caused by the dispersiveness of the lens material is much higher than that caused by zoning. With the same $\lambda/8$ error allowed across the width of the lens, the bandwidth is

given by approximately

$$B \approx \frac{25n_0}{(1+n_0)} \frac{\lambda_0}{(1-n_0)t} \quad (24)$$

where n_0 , λ_0 are, respectively, the refractive index and wavelength at the center frequency and t is the difference in thickness of the lens between the edge and the center.

Because the waveguide or parallel-plate medium is so dispersive, reducing its length by zoning actually increases the useful bandwidth. For K zones, the bandwidth is given approximately by [1]

$$B \approx \frac{25}{(K-1) + \frac{(1+n_0)(1-n_0)t}{n_0 \lambda_0}} \quad (25)$$

Under the assumption that $(1-n_0)t$ is approximately one wavelength at the thickest sections of the lens, we have

$$B \approx \frac{25n_0}{1+Kn_0} \quad (26)$$

Proctor [5] analyses and describes methods of constructing lenses from slot-loaded ridged waveguides. The structures make it possible to improve the scanning ability, and also eliminates the discontinuities associated with zones. The spacing of the plates in a waveguide lens has a critical aspect, in that at each of the plates, diffraction occurs. In order to avoid the diffracted fields adding constructively, the plate spacing must be kept below the value determined by the inequality $\lambda_0/d > 1 + \sin \varphi$, where φ is the angle of incidence of the wave.

2.6. Natural and Artificial Dielectrics

A wide variety of dielectric materials, specifically manufactured for application in microwave applications, are available in the market. These can be divided in a number of classes. Materials with very low dielectric constant are usually some type of foam with a plastic base. Materials with a dielectric constant in the region of 2–4 are mainly plastics. Examples are Teflon ($\epsilon_r = 2.04$), Teflon fiberglass ($\epsilon_r = 2.7$), Plexiglas ($\epsilon_r = 2.56$), and polystyrene ($\epsilon_r = 2.54$). Ceramic materials such as BaZnTa ($\epsilon_r = 30$), BaTiO₃ (barium titanate, $\epsilon_r = 30$), and BaTiO₉ (barium tetratitanate, $\epsilon_r = 38$), [6] are often mixed with plastics. One example of a commercial product is described as a ceramic-filled cross-linked plastic, with dielectric constants available as $\epsilon_r = 3, 4, 5, 6, 7, 8, 9, 10, 12, 15, 20$.

In Section 1, the use of parallel plates as an artificial dielectric was discussed. For the transverse electric (TE) wave (E field parallel to conducting plates), the propagation velocity varies rapidly as the wavelength approaches double the plate spacing:

$$v = \frac{c}{\sqrt{(1 - \lambda/\lambda_c)^2}} \quad (27)$$

In the TE mode, the refractive index is given by

$$n = \sqrt{1 - (\lambda/\lambda_c)^2} \quad (28)$$

where the cutoff wavelength $\lambda_c = 2a$ for a plate separation of a .

For waveguides operating in the TE mode, Equation (28) holds for parallel plates. In this instance, a rectangular waveguide of width a has $\lambda_c = 2a$; a regular hexagon with a between parallel sides has $\lambda_c = 1.792a$, and a circular waveguide with radius a has $\lambda_c = 1.705a$. The application of waveguides in lens design is comprehensively discussed by Rudge [3].

Brown [7] gives an extensive theoretical treatment of artificial dielectrics. They are categorized into two classes—“delay dielectrics” and “phase advance dielectrics”—the derivation of which is self-explanatory. Parallel plates or waveguides are obviously in the second group, because of the value of the refractive index. Also in this group of structures are arrays of metallic rods, as well as perforated metallic plates that are held in position by means of a dielectric supporting medium such as a dielectric foam. Among the delay dielectrics are metallic strips or metallic disks suspended in a substrate. Jasik [8] provides comprehensive information on a wide variety of structures, including those mentioned above. An interesting variation is described by Milne [9], who uses the phase shift (negative below resonance and positive above) of a wave traveling through an array of dipoles, to design the necessary delay structure. Other authors treat the general problem of composite dielectric materials [10,11].

2.7. Aberrations

In optical systems, the main purpose is usually to form an image, either real or virtual. In the functioning of lens antennas, this is not relevant, except to the extent that an image is composed of a collection of points that do not all lie on a single focal point. In a lens antenna the equivalent is that there are sources that illuminate the lens, that lie off the focal point, as well as nonideal characteristics in lens design and performance. Analogous to the aberrations that occur in optical systems, equivalent aberrations occur in lens antennas, and a number of different types of aberration exist; these are comprehensively treated by Lo and Lee [12]. The source of aberrations in lens antennas is a phase error with respect to a reference plane in the aperture of the lens. The phase error could be caused by inherent properties such as the lens not meeting the equal phase path condition or the source being located away from the focus of the lens.

If the phase error across the aperture is linear, it results in the beam squinting off boresight. In practice this is not a problem with lens antennas. Many examples exist in antenna theory of where a quadratic phase error is introduced to an aperture, and the effect of such errors is well known (see, e.g., Ref. 1, Chap. 6.7; Ref. 2, Chap. 2.8; and Ref. 9).

In lens antennas, the most important aberration is coma, because it relates the formation of a properly

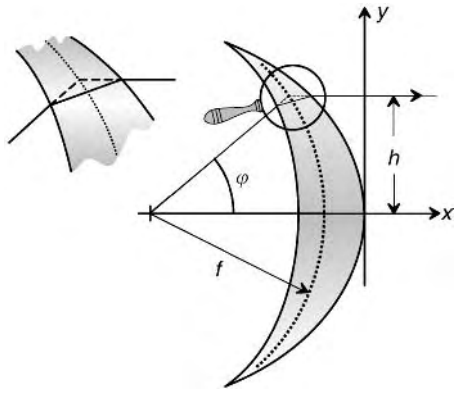


Figure 19. The Abbe sine condition.

collimated beam by a point lying off the focal point. In an 1873 paper, E. Abbe postulated that in order for any optical system to form an image, it must satisfy the condition that the principal surface, defined as the *locus of intersections of the initial and final paths of rays*, is spherical. An optical system satisfying this condition thus acts as a simple spherical lens, and the “Abbe sine condition” is satisfied. Referring to Fig. 19, $h/\sin \varphi = f$. The circular curvature of radius f satisfies the condition, as does the lens shown, because the initial and final rays intersect on the radius f . It is now also clear that the simple planoconvex lens of Fig. 3(a) cannot satisfy this condition.

Note that a simple parabolic mirror does not satisfy the Abbe sine condition, either, since the principal surface is the paraboloid itself. Paraxial rays (rays incident on the mirror and parallel to the optical axis) will focus at a point, but off-axis sources will not. It is possible to meet the Abbe sine condition with two refracting surfaces, as discussed in Section 3.1.

3. WIDE-ANGLE AND SCANNING LENSES

3.1. Wide-Angle Dielectric Lenses

The inability of the lens to collimate properly the radiation from a source offset from the focal axis of the lens is a key element in the performance of a lens designed for wide-angle scanning, and a variety of approaches to improve the scanning properties of dielectric lenses have been developed. The simple hyperboloidal lens is not suitable for substantially displaced feeds in order to scan the mainbeam, and the effects on the lens performance with feed displacement have been analyzed by Kreutel [13]. For small values of the ratio between focal length and diameter f/D and small values of n , coma dominates; with increase in these parameters, astigmatism gradually becomes the dominant aberration.

Making use of thin-lens theory, Rotman [14] develops an analysis in which the zoned lens is approximated by an ideally thin spherical shell. This is applied to evaluate the phase aberrations in the aperture plane of the lens, which are caused by off-axis scanning and deviations from the

design frequency. A set of universal curves, that predict the decrease in directive gain of the lens as function of scan angle and frequency is developed from this theory.

By shaping the lens for aperture distribution control, specific radiation patterns can be achieved through use of the procedure described by Lee [15]. For multiple-beam applications, the design procedure makes it possible to reduce the phase error for off-axis beams by means of coma correction zoning.

A dielectric lens with two refracting surfaces introduces an additional variable, which makes it possible to design a lens with two conjugate off-axis focal points. Peebles [16] describes a procedure for design and analysis of a bifocal dielectric lens with these properties. The lens provides good off-axis performance, and a high-gain radiation pattern over a large field of view. Quadratic phase error is reduced if the feed is constrained along an optimized focal arc. The method of generic curve series has been used [17] to obtain profiles for antennas that have a predetermined aperture amplitude distribution from a given source distribution, or for agreement with the Abbe sine condition.

3.2. Wide-Angle Waveguide Lenses

As has been pointed out for the family of dielectric lenses above, it is possible to obtain wide scan angle performance by ignoring the Abbe sine condition, if two perfect, symmetric off-axis foci are chosen, and illumination of the lens is along a circular path between the two foci. The approach was first proposed by Ruze [18]. For the lens to collimate the radiation, it is found that the inner surface of the lens must be an ellipse, with the foci of the ellipse lying on the chosen focal points of the lens. The problem has three variables (inner and outer surfaces of the lens, and index of refraction), and two variables are fixed by choosing the two foci. This leaves a choice of either the shape of the outer surface, with n to be determined, or, if n is chosen, the outer surface to be determined. It is also possible to choose a third focal point that lies on the axis of the lens.

If the on-axis focal point is chosen, it is chosen such that second-order phase deviation is zero. It is then found that points that lie on an arc of a circle of radius f , centered at the origin O , as shown in Fig. 12, will have good scan performance. Different source antennas, all lying on the arc FF' , will cause beams to be radiated from the lens in different directions.

For the case of a single focal point, the inner surface is described by a circle of radius f ; this forms a sphere when the lens is changed to a 3D body. The outer surface is an ellipsoid described by

$$\frac{y_2^2}{f^2} + \left[\frac{x_2 - d - fn/(1-n)}{fn/(1-n)} \right]^2 = 1 \quad (29)$$

where f is the focal length, n is the refractive index, and d is the minimum thickness of the lens.

If the lens is bifocal, the inner surface is an ellipsoid with focal points at the lens foci, and the surface described

by

$$\frac{y_1^2}{f^2} + \left[\frac{x_1 + f \cos \psi}{f \cos \psi} \right]^2 = 1 \quad (30)$$

The outer surface is also an ellipsoid, described by

$$\frac{y_2^2}{f^2} + \left[\frac{x_2 - d - (nf \cos \psi)/(\cos \psi - n)}{(nf \cos \psi)/(\cos \psi - n)} \right]^2 = 1 \quad (31)$$

The design of a conventional waveguide lens is based on the principle of equal phase delay for the different rays. However, the rays at the edge of the lens have substantially farther to travel than will those in the center, and this inevitably means that, if the frequency changes from the center frequency, the time delay through the lens changes, leading to phase error, and decreased bandwidth. As was pointed out earlier, this situation is alleviated by zoning. Ajioka and Ramsey [19] describe a design procedure that combines constant group delay characteristics with wideband performance.

3.3. Bootlace Lenses

3.3.1. The Rotman Lens. The Rotman lens [20] is one of a family of lenses popularly known as “bootlace lenses”, because of the multitude of transmission lines connecting the inner and outer surfaces of the lens. A brief description of the basic operation of the Rotman lens (as it is usually referred to) was given in Section 1.6. The Rotman lens has two off-axis conjugate focal points and one on-axis focal point. The fact that the shape of the outer surface of the lens can be, in effect, arbitrarily chosen makes it possible to choose four independent conditions to determine the lens parameters. Rotman and Turner select the straight front face of the lens, the two off-axis focal points, and the on-axis focal point. The ray geometry of the lens is shown in Fig. 20. They discuss the merits of different choices for the position of the on-axis focal point.

The lens illustrated is two-dimensional (2D), and cylindrical versions can be constructed by stacking a number of the lenses. Note that the area between the beam and element ports is often referred to as “the lens.” Strictly speaking, the lens comprises the elements in the element port (the inner surface of the lens), the connecting transmission lines, and the radiating array (the outer surface of the lens). The region between the beam port that illuminates the lens, and the element port that forms the inner surface, will be termed the *beam cavity*, and it can be constructed in a variety of media. For the beam and element ports as waveguide horns, the beam cavity can be parallel plates. If the elements of beam and element ports are wideband tapers, stripline or microstrip would be indicated, as is currently common practice. The lens can also be used as a linear scanning feed for a cylindrical reflector, as described by Rotman and Turner.

Musa and Smith [21] describe factors that limit the performance of microstrip lenses compared to parallel-plate lenses. Amongst others, it is necessary to pay specific attention to the design of the beam cavity area. Also, the

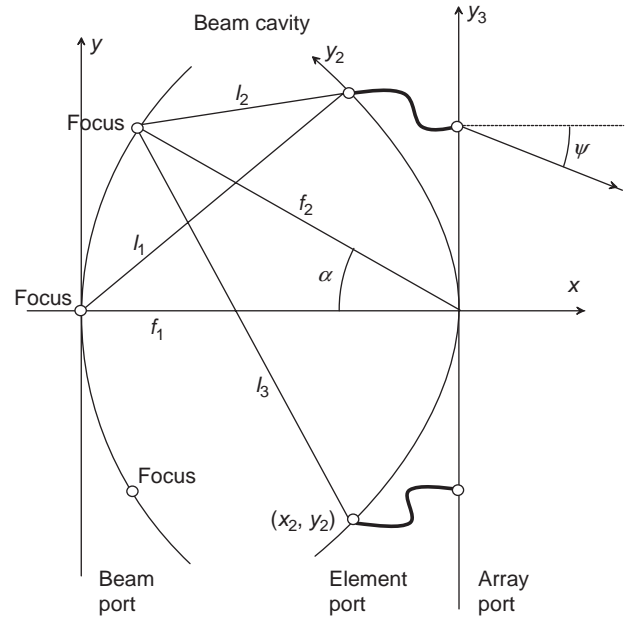


Figure 20. Definitions in the design of a Rotman lens, after Hansen [28]. (With permission, copyright © 1991; IEEE).

direction in which the elements in both ports point should be considered.

A modification to the Rotman lens by Archer [22] has the beam cavity area filled with dielectric. This has the effect of reducing the linear dimensions of the lens by a factor of $n = (\epsilon_r)^{1/2}$. Referring to Fig. 20, if the angle subtended between the focal point and the axis is α and the beam points in a direction ψ , then the ratio of sine of the angles, $\gamma = \sin \psi / \sin \alpha$. For $\gamma > 1$, a design would give large scan angles, while for $\gamma < 1$ the lens will be physically small.

As with any antenna design, the radiation pattern of the antenna is an important parameter, and it is possible to design for predetermined sidelobe patterns. Thomas [23] describes a design in which -30 -dB sidelobe levels were achieved over a 10% bandwidth by the superposition of multiple orthogonal beams; it is shown that the Taylor line source distribution can be described as just such a superposition. Only three beams were sufficient to provide a good approximation to the exact Taylor distribution; the design, however, necessitates a substantial increase in the complexity of the feeding system.

Two or more beams are orthogonal if a signal input to the beam port of one beam gives rise to an output in only that beam, with no signal appearing in any of the other beam patterns or ports. The Rotman and other wide-angle lenses being lenses with multiple beams, this is an important consideration in the design of an antenna, and Hansen [24] explains the effects of nonorthogonality, such as loss of efficiency and changes in sidelobe pattern.

A Rotman lens feed network for a beam forming network implementation employing a 2D stack of Rotman lenses to produce multiple overlapping beams that are scanned in both elevation and azimuth directions is described by Chan and Rao [25]. They present the

development of a compact beamforming network using multiple Rotman lenses having identical design and producing multiple beams with a hexagonal grid. The design of the lens employs dual-port excitations for the beam ports in order to minimize the spillover losses within the lens.

Three-dimensional lenses with two, three, and four perfect focal points are described by Rao [26]. Lenses with more focal points can be scanned to much larger angles in one plane; a tradeoff with the scanning ability in the orthogonal plane exists. In the design procedure described, the lens cross section in the plane in which the focal points lie is first obtained as a 2D solution, and then extended to a three-dimensional (3D) solution by rotating the lens profile around the focal point axis of the lens. In the design procedure proposed in Ref. 27, the planar feed locus of a 2D design is replaced by a curved feed locus optimized to minimize pathlength errors. The design procedure can be extended to a quadrifocal lens with four foci on a circular arc in the plane of the 2D design.

Hansen [24] shows that rotating a Rotman lens to form a symmetric lens does not yield good results and that a circular focus is not possible. The four perfect foci cannot be located with quadrantal symmetry.

3.3.2. Design Procedure. A very substantial body of research and development has been established on the Rotman lens. However, Hansen [28] has published an efficient design procedure that very clearly sets out what the interrelationships between the various choices in the design of Rotman lenses are. The same optical pathlength equality condition as before is applied to the structure of Fig. 20. Note that the position of the focal arc, which contains the three focal points, is not yet specified at this stage. The design equations are repeated here in Hansen’s nomenclature, in order to simplify use of his paper for design purposes.

The problem is defined in terms of the relationship between six basic design parameters, namely, the focal angle α , the focal ratio $\beta = f_2/f_1$, which is the ratio between upper and central focal lengths, the beam angle to ray angle ratio $\gamma = \sin \psi / \sin \alpha$, the maximum beam angle ψ_m , focal length f_1/λ and array element spacing d/λ .

All the dimensions are normalized to the principal focal length, f_1 . The ratio of the upper to central focal length is given by

$$\beta = \frac{f_2}{f_1} \tag{32}$$

as defined previously

$$\gamma = \frac{\sin \psi}{\sin \alpha} \tag{33}$$

A convenient parameter that relates the distance y_3 of any point on the array axis to the principal focal length f_1 is given by

$$\zeta = \frac{y_3 \gamma}{f_1} \tag{34}$$

This parameter controls the portion of the phase and amplitude error that the lens experiences. For a lens with NE radiating elements, spaced a distance d apart, the maximum value that y_3 can have is given by $y_{\max} = (NE - 1)d/2$. Substituting gives

$$\zeta_{\max} = \frac{(NE - 1)\gamma d}{2f_1} \tag{35}$$

An upper limit on ζ occurs when the tangent to the element port curve is vertical; this coincides with $w = 0$. This value of ζ is given by

$$\zeta_{w=0} = \frac{2\sqrt{1 - \beta C}}{S} \sqrt{1 - \frac{1 - \beta C}{S^2}} \tag{36}$$

where $C = \cos \alpha$, $S = \sin \alpha$.

The linelength w that connects the elements on the element port to the array elements is given by the quadratic lens equation

$$a \left(\frac{w}{f_1} \right)^2 + b \frac{w}{f_1} + c = 0, \tag{37}$$

where the coefficients of the equation involve the parameters α , β , and γ and are given by

$$a = 1 - \frac{(1 - \beta)^2}{(1 - \beta C)^2} - \frac{\zeta^2}{\beta^2} \tag{38}$$

$$b = -2 + \frac{2\zeta^2}{\beta} + \frac{2(1 - \beta)}{1 - \beta C} - \frac{\zeta^2 S^2 (1 - \beta)}{(1 - \beta C)^2} \tag{39}$$

$$c = -\zeta^2 + \frac{\zeta^2 S^2}{1 - \beta C} - \frac{\zeta^4 S^4}{4(1 - \beta C)^2} \tag{40}$$

If the maximum beam angle is given by ψ_m , then the maximum allowable array element spacing that will avoid the creation of grating lobes is given by

$$\frac{d}{\lambda} = \frac{1}{\sqrt{2 + \sin \psi_m}} \tag{41}$$

The task at hand is to determine the optimum values for α , β , γ , and f_1/λ .

Hansen sets out the design procedure that amongst others considers the following:

1. The useful range for ζ is roughly from 0.5 to 0.8, and from this a value of β for a given α follows.
2. Six charts in Hansen’s paper [28] show the effect of the choice of variables. It has a bearing on lens width, which in turn affects spillover loss, transmission line loss, amplitude errors, and other parameters.
3. A value of α is chosen that makes the two surfaces of the beam cavity approximately the same height. β has a similar effect to α , and tabulated values for pairs of these two variables are given.

4. Changing γ leaves the port curves relatively unaffected, but the relative positions of the foci change.
5. Changing values of ψ_m spreads the beam ports apart, and determines the maximum element spacing.
6. Changing the focal length changes the separation between the ports, as well as all spacings.
7. Curves showing the effect of parameter choices on phase and amplitude errors are given.
8. Finally, the gain of the lens array can be calculated from [3, Chap. 9]

$$G = \frac{\left| \sum_{n=1}^N A_n \right|^2}{\sum_{n=1}^N \sum_{m=1}^N A_n A_m^* \sin c(n-m)2\pi d/\lambda} \quad (42)$$

where A_n , is the excitation of the array elements.

With the performance parameters frequency range, number of beams, and maximum scan known, the number and spacing of the radiating elements is determined. The maximum value of beam element spacing is limited by the maximum scan angle, and occurs when $d/\lambda = 1/(2 + \sin \psi_m)$. At the center frequency, making use of the guidelines given, α , β , and γ are selected to ensure that the lens meets certain practical and realistic criteria of size and proportion. Once the design parameters have been determined, the gain of the lens can be calculated. It is also possible to make the beam port arc elliptical rather than circular, but Hansen points out that this is not usually warranted, except for very large lenses. The design procedure also includes an evaluation of phase and amplitude errors.

Hansen [24] points out that in practice, bootlace and other lenses are not designed with discrete foci. Rather, the optimum design is a minimax solution for circles of least confusion; that is, aberrations are minimized over the aperture in a sense such as least mean squares. The resultant design produces slightly undefined foci, but better performance. The use of determining the foci, lies in classifying lenses, and developing a sense of how errors are related to lens geometry.

3.3.3. Analysis. The design procedure described above yields the basic dimensions of the lens. However, there are many other aspects that pertain to the physical realization of any given design and make it almost impossible to do a complete design as the result of a sequence of steps. Once the basic design has been achieved, the practical realization of the design needs to be brought into the picture, and to this purpose, analysis methods are very important.

Peterson and Rausch [29] describe an analysis procedure that takes into consideration aspects of the lens design such as the cavity sidewall and port widths, which are parameters not specified by the design procedure. These parameters substantially affect the sidelobe level and insertion loss. The effect of mutual coupling is also included in the analysis procedure. As an example, they quote measured sidelobe levels of -17 dB with straight sidewalls for the beam cavity, while with triangular side-

walls, the sidelobe level improved to -32 dB for a lens with 34 array ports and 19 beam ports. The design sidelobe level was -40 dB, Taylor $n = 3$.

Yuan et al. [30] describe an analysis procedure for Rotman lenses based on a hybrid least-squares finite/transfinite-element method. They point out that most design procedures are based on ray optics, and neglects the effects of port reflections, mutual coupling between elements, and multiple scattering between ports. The procedure used yields the distribution of the electromagnetic fields in the lens, as well as the scattering parameters. They illustrate their procedure by comparing the calculated and measured results for a microstrip Rotman lens with nine beam ports and eight array ports.

3.3.4. The R-2R Lens. The R-2R lens is a bootlace lens in which the radiators on the beam port and element port lie on a circle of diameter R , and where the element ports are connected by equal-length radiators. The properties of the lens are readily derived from the geometry of Fig. 21. If the line OP is extended to intersect the circle $2R$ at Q , then Q defines the position that the array element must have that is connected to the element port at P . If OP subtends an angle of φ with the x axis, then the radius to P will subtend an angle of 2φ . It is clear that, even if the beam port and element port radiators were coincidental, the antenna could not scan more than $\pm 90^\circ$.

In practice, in order to locate the beam and element radiators, the antenna has a restricted scan angle. For cases where extremely wide scan angles are necessary, Clapp [31] has developed a solution making use of four or six physical lenses and hybrid junctions to provide up to 360° scanning.

3.4. The Luneburg Lens

Luneburg [4] solves the problem of determining the index of refraction for a spherical lens that collimates the radiation from any point on the surface of the lens in a direction diametrically opposite. As stated in the introduction, the index of refraction needs to vary as $n = (2-r^2)^{1/2}$. The chief advantages of the Luneburg lens are its ability to scan multiple beams over wide angles, as well as the inherently wide bandwidth. The main disadvantages lie in its bulkiness, and associated weight, and the practical difficulty of manufacturing the varying index of refraction.

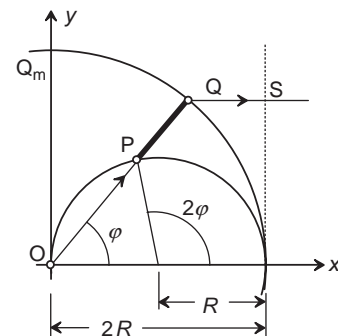


Figure 21. R-2R lens geometry.

The two-dimensional analysis of the Luneburg lens is given by Peeler and Archer [32]. The relationship between the feed pattern and the aperture field is found to be proportional to $(\sec \psi)^{1/2}$, where ψ is the angle subtended with the axis of the lens, inferring that the lens has a very high edge illumination. They describe the performance of a lens constructed by filling the cavity between two parallel-plates with dielectric, and propagating the TE_{10} waveguide mode, which is also a parallel-plate mode. The separation between the plates is varied to obtain the desired variation in effective index of refraction.

The two-dimensional Luneburg lens finds application as source for a parabolic reflector in a scanning antenna [33]. A variety of other structures, all making use of the dispersive properties of propagation between sets of (not parallel) plates function as Luneburg lenses with 2D radiation patterns [34].

Braun [35] derives expressions for the radiation pattern, beamwidth, sidelobe level, and gain of the spherically symmetric Luneburg lens. Because of the high edge illumination of the aperture, the lens has a high gain, and high sidelobe level, typically at -17 dB.

The fact that the index of refraction has to change with radius, presents a problem. If a choice is made that the lens shall have a single index of refraction, then it is possible to have only one point on the lens surface that will support a ray of the same electrical length as the ray through the center, as well as its mirror image. For a lens of diameter 20 wavelengths, and the point of equal electrical length chosen at 30° from the axis of the lens, it is found that the phase error across the lens is 0.1λ , which is quite acceptable [2, Chap. 18-2]. An increase in the lens diameter will increase the phase error.

An alternative is to construct the lens from shells and an inner sphere of different dielectrics [36]. However, the discrete quantization of the lens into steps in the vicinity of a wavelength or more, causes the appearance of grating lobes in the radiation pattern, and should be guarded against.

In a procedure described by Mosallaei and Rahmat-Samii [37], an optimized design procedure is described that strives to minimize the number of dielectric shells. In a radially uniform design, reduction of the number of shells decreases the gain and increases the occurrence of grating lobes. They make use of a genetic algorithm optimizer to determine the optimum layer thickness and permittivity for the desired gain and sidelobe envelope.

Rondineau et al. [38] describe the design, construction, and performance of a spherical lens constructed by slicing the spherical body into $2N$ disks. Each disk then has to approximate the relevant varying index of refraction; this is achieved by drilling holes through the disks. A larger number of holes along the periphery of each disk approximates the low values of n toward the outside of the lens, while toward the center of each disk, the number of holes are reduced, until, for the central disks, the innermost area is left unpenetrated. In the example cited, there were 20 disks constructed of Teflon with $\epsilon_r = 2.04$. The lens diameter was 150 mm, and at 27.5 GHz had a gain of 28.5 dB. The authors provide full information on determining the thickness of the disks, and the number and spacing of the holes.

An interesting variation on the spherical Luneburg lens is the cylindrical Luneburg lens [39]. In instances where the scanning capabilities of the conventional lens are not needed, a cylindrical lens of finite-length forms a useful lens antenna. The lens can be designed to have a focal point on its surface, and is constructed from a number of concentric cylinders; in the example cited, the lens was constructed by including cylindrical voids to obtain the varying dielectric constant.

A study of the Luneburg lens would be incomplete without mentioning its properties as a radar reflector [2,40]. If the lens is partially capped, then energy incident from a direction opposite to the cap will be reflected back from the cap and reradiated in the same direction, functioning as a very effective radar reflector, which has a large radar cross section over a wide angle.

4. INTEGRATED AND PLANE LENSES

4.1. Integrated Dielectric Lenses

Dielectric lenses are very well suited to integration directly onto millimeter and submillimeterwave circuits, but with the growing application of local and indoor wireless networks, are becoming more relevant at microwave frequencies. Typically, the dielectric lens is mounted directly on the microwave integrated circuit substrate that carries the active microwave network, as shown in Fig. 11a [41]. Feeding is done directly by means of dipoles or slots or pairs of slots [42] etched in a metallized area. Typically, this would be a lens that radiates from a more to a less dense dielectric material, and is therefore an ellipsoid of revolution, as was discussed for the dielectric lenses in Section 1.2.

In its most elemental form, the lens is a solid dielectric, and the source is mounted at the far focus of the ellipsoid. This makes for a lens that is very easily mounted, and it eliminates the reflections that occur when the inner surface of the lens is spherical. However, at the same time a new source of serious mismatch is introduced at the source antenna. In the event that the inner surface of an elliptical lens lies between the two foci of the ellipse that describes the outer lens surface, the phenomenon of doubly reflected rays occurs; of this, the "solid" dielectric lens is an example. A ray leaving the source focus point is partially reflected at the lens surface; this reflected energy travels through the second focal point, strikes the surface once again, and is reflected back to the source. This happens for all possible paths in the lens; because of the properties of the ellipse, all rays thus reflected arrive at the source in phase, causing a mismatch. Neto et al. [43] have analyzed the effects of multiple reflections inside an elliptical dielectric lens operating in the millimeterwave area, and make use of physical optics to derive an expression for the input admittance to the lens. As a matter of interest, Fig. 11b illustrates the condition with the inner surface beyond the two foci.

It is possible to alleviate to an extent the effects of multiple reflections by applying a matching layer to the lens surface, bearing in mind that it needs to be tapered away from the apex of the lens. The problems associated

with the analysis of lenses in the millimeterwave and submillimeterwave-region, are addressed by van der Vorst et al., and use is made of a combination of geometric and physical optics in an efficient body of revolution finite-difference time-domain methods [44]. Integrated lenses can be designed to have multiple beams [45].

Indoor wireless communications are becoming increasingly important as technology expands and the cost of integrated microwave circuits drop. Dielectric lenses that produce shaped beams for the reduction of multipath phenomena and predetermined coverage patterns have been designed and evaluated [46].

4.2. Fresnel Zone Plate Lenses

Unfortunately, the simple Fresnel lens described in Section 1.6 has very poor efficiency; figures of 8–15% are common for lenses with alternate opaque and transparent rings. Consequently the reflective or opaque rings are replaced by rings that serve to reverse the phase. Black and Wiltse [47] achieve this phase reversal by making use of annular rings cut into a single dielectric, or by means of layers of different dielectrics, as shown in Fig. 17a. Lenses with annular slots suffer from shadow blockage as depicted in Fig. 17b. Petosa and Ittipiboon [48] describe a lens constructed in such a fashion, and measured an aperture efficiency of 63% for a lens of 194 mm diameter and f/D of 0.25. Note that the diameter of the lens is determined by the number of Fresnel rings, 12 in this case. The gain was 23 dBi.

A method of construction with each full-wave zone of the lens consisting of four quarter-wave subzones, in turn consisting of concentric dielectric rings of equal thickness, but different permittivity, is described by Hristov and Herben [49]. They constructed practical lenses with an aperture efficiency of more than 50% at 60 GHz. In order to achieve the correct phase shift through the rings, the dielectric constants have to be, respectively, $\epsilon_{r1} = 1$, $\epsilon_{r2} = 6.25$, $\epsilon_{r3} = 4$, and $\epsilon_{r4} = 2.25$. This corresponds to phase shifts of $\Delta\Phi_t = 0^\circ, 90^\circ, 180^\circ, 270^\circ$. Full design information is provided in Ref. 49.

An alternative method of constructing a lens without grooves is proposed by Petosa and Ittipiboon [50], who constructed a lens from a single slab of dielectric. The appropriate dielectric constants are realized by perforating the dielectric material. The lens then consists of a slab of dielectric material with annular rings where the material is penetrated by a lattice of holes. The effective dielectric constant for such a medium is given by

$$\epsilon_{\text{eff}} = \epsilon_r(1 - \alpha) + \alpha \quad (43)$$

where α is the filling factor, given by

$$\alpha = \frac{\pi}{2\sqrt{3}} \left(\frac{d}{s} \right)^2 \quad (44)$$

The holes have a diameter of d and lattice spacing s .

Analysis procedures for determining the performance of lenses include the *uniform and geometrical theory of diffraction* for metal ring lenses on dielectric, and in the

case of the quarter-wave planar lens antenna, ray tracing combined with diffraction theory is used.

BIBLIOGRAPHY

1. J. Risser, Lens antennas, in S. Silver, ed., *Microwave Antenna Theory and Design*. MIT Radiation Lab. Ser. Vol.12, McGraw-Hill, New York, 1949, (this text contains a large amount of mathematical detail on all the basic lens types and properties.)
2. R. C. Johnson and H. Jasik, *Antenna Engineering Handbook*, McGraw-Hill, New York, 1984 (treats a wide variety of lens aspects and provides extensive references).
3. A. W. Rudge, K. Milne, A.D. Olver, and P. Knight, eds. *The Handbook of Antenna Design*, Vol. 2, Peter Peregrinus, London; 1983.
4. R. K. Luneburg, *Mathematical Theory of Optics*, Univ. of California Press, Berkeley, CA, 1964.
5. E. K. Proctor, Methods of reducing chromatic aberration in metal-plate microwave lenses, *IEEE Trans. Anten. Propag.* **6**(3):231–239 (July 1958).
6. S.J. Fiedziuszko, I.C. Hunter, T. Itoh, Y. Kobayashi, T. Nishikawa, S.N. Stitzer, and K. Wakino, Dielectric materials, devices, and circuits, *IEEE Trans. Microwave Theory Tech.* **50**(3):706–720 (March 2002).
7. J. Brown, Artificial dielectrics, in J. B. Birks and J. H. Schulman, eds., *Progress in Dielectrics*, Vol. 2, Heywood, London; 1960, pp. 194–225.
8. H. Jasik, *Antenna Engineering Handbook*, McGraw-Hill, New York; 1961 (has an especially complete section on artificial and synthetic dielectrics).
9. R. Milne, Dipole array lens antenna, *IEEE Trans. Anten. Propag.* **30**(4):704–712 (July 1982).
10. W. R. Tinga, W. A. G. Voss, and D.F. Blossey, Generalized approach to multiphase dielectric mixture theory, *J. Appl. Phys.* **44**:3897–3902 (1973).
11. L. S. Taylor, Dielectric properties of mixtures, *IEEE Trans. Anten. Propag.* **13**(6):943–947 (Nov. 1965).
12. J. J. Lee, Lens antennas, in Y. T. Lo and S. W. Lee, eds., *Antenna Handbook*, Vol. II, *Antenna Theory*, Van Nostrand Reinhold, New York; 1993. (Extensive treatment of lenses, especially lens aberrations and taper control lenses).
13. R. W. Kreutel, The hyperboloidal lens with laterally displaced dipole feed, *IEEE Trans. Anten. Propag.* **28**(3):443–450 (July 1980).
14. W. Rotman, Analysis of an EHF aplanatic zoned dielectric lens antenna, *IEEE Trans. Anten. Propag.* **32**(6):611–617 (June 1984).
15. J. J. Lee, Dielectric lens shaping and coma-correction zoning, Part I: Analysis, *IEEE Trans. Anten. Propag.* **31**(1):211–216 (Jan. 1983).
16. A. L. Peebles, A dielectric bifocal lens for multibeam antenna applications, *IEEE Trans. Anten. Propag.* **36**(5):599–606 (May 1988).
17. S. Bishay, S. Cornbleet, and J. Hilton, Lens antennas with amplitude shaping or sine condition, *IEE Proc. H, Microwaves Anten. Propag.* **136**(3):276–279 (June 1989).
18. J. Ruze, Wide-angle metal-plate optics, *IRE Proc.* **38**:53–59 (Jan. 1950).
19. J. S. Ajioka and V. W. Ramsey, An equal group delay waveguide lens, *IEEE Trans. Anten. Propag.* **26**(4):519–527 (July 1978).

20. W. Rotman and R.F. Turner, Wide-angle microwave lens for line source applications, *IEEE Trans. Anten. Propag.* **11**(6):623–632 (Nov. 1963).
21. L. Musa and M. S. Smith, Microstrip port design and sidewall absorption for printed Rotman lenses, *IEE Proc. H, Microwaves Anten. Propag.* **136**(1):53–58 (Feb. 1989).
22. D. Archer, Lens-fed multiple beam arrays, *Microwave J.* 37–42 (Oct. 1975).
23. D. T. Thomas, Multiple beam synthesis of low sidelobe patterns in lens fed arrays, *IEEE Trans. Anten. Propag.* **26**(6):883–886 (Nov. 1978).
24. R. C. Hansen, *Phased Array Antennas*, Wiley, New York; 1998.
25. K. K. Chan and S. K. Rao, Design of a Rotman lens feed network to generate a hexagonal lattice of multiple beams, *IEEE Trans. Anten. Propag.* **50**(8):1099–1108 (Aug. 2002).
26. J. B. L. Rao, Multifocal three-dimensional bootlace lenses, *IEEE Trans. Anten. Propag.* **30**(6):1050–1056 (Nov. 1982).
27. C. M. Rappaport and A. I. Zaghoul, Optimized three-dimensional lenses for wide-angle scanning, *IEEE Trans. Anten. Propag.* **33**(11):1227–1236 (Nov. 1985).
28. R. C. Hansen, Design trades for Rotman lenses, *IEEE Trans. Anten. Propag.* **39**(4):464–472 (April 1991).
29. A. F. Peterson and E. O. Rausch, Scattering matrix integral equation analysis for the design of a waveguide Rotman lens, *IEEE Trans. Anten. Propag.* **47**(5):870–878 (May 1999).
30. N. Yuan, J. S. Kot and A. J. Parfitt, Analysis of Rotman lenses using a hybrid least squares FEM/transfinite element method, *IEE Proc. Microwaves Anten. Propag.* **148**(3):193–198 (June 2001).
31. R. E. Clapp, Extending the R-2R Lens to 360°, *IEEE Trans. Anten. Propag.* **32**(7):661–671 (July 1984).
32. G. D. M. Peeler and D. H. Archer, A two-dimensional microwave Luneburg lens, *Trans. IRE Prof. Group Anten. Propag.* **1**(1):12–23 (July 1953).
33. J. S. Hollis and M. W. Long, A Lunenburg lens scanning system, *IEEE Trans. Anten. Propag.* **5**(1):21–25 (Jan. 1957).
34. G. A. Thiele and R. C. Rudduck, Geodesic lens antennas for low-angle radiation, *IEEE Trans. Anten. Propag.* **13**(4):514–521 (July 1965).
35. E. H. Braun, Radiation characteristics of the spherical Luneburg lens, *IEEE Trans. Anten. Propag.* **4**(2):132–138 (April 1956).
36. G. D. M. Peeler and H. G. Coleman, Microwave stepped-index Luneburg lenses, *IEEE Trans. Anten. Propag.* **6**(2):202–207 (April 1958).
37. H. Mosallaei and Y. Rahmat-Samii, Nonuniform Luneburg and two-shell lens antennas: Radiation characteristics and design optimization, *IEEE Trans. Anten. Propag.* **49**(1):60–69 (Jan. 2001).
38. S. Rondineau, M. Himdi, and J. Sorieux, A sliced spherical Luneburg lens, *IEEE Anten. Wireless Propag. Lett.* **2**:163–166 (2003).
39. K. Kikuchi, Y. Kido, and T. Ogawa, Millimeter wave sensor using cylindrical Luneburg lens with flat sides, *IEEE Trans. Instrum. Meas.* **47**(2):423–425 (April 1998).
40. G. T. Ruck, D. E. Barick, W. D. Stuart and C. K. Krichbaum, *Radar Cross Section Handbook*, Vol. 2, Plenum, New York; 1970, pp. 597–600.
41. G. M. Rebeiz, Millimeter-wave and tetrahertz integrated circuit antenna, *Proc. IEEE*, **80**(11):1748–1770 (Nov. 1992).
42. D. F. Filipovic, S. S. Gearhart, and G. M. Rebeiz, Double-slot antennas on extended hemispherical and elliptical silicon dielectric lenses, *IEEE Trans. Microwave Theory Tech.* **41**(10):1738–1749 (Oct. 1993).
43. A. Neto, L. Borselli, S. Maci, and P. J. I. de Maagt, Input impedance of integrated elliptical lens antennas, *IEE Proc. Microwaves Anten. Propag.* **146**(3):181–186 (June 1999).
44. M. J. M. van der Vorst and P. J. I. de Maagt, Efficient body of revolution finite-difference time-domain modelling of integrated lens antennas, *IEEE Microwave Wireless Compon. Lett.* **12**(7):258–260 (July 2002).
45. X. Wu, G. V. Eleftheriades, and T. E. van Deventer-Perkins, Design and characterization of single- and multiple-beam mm-wave circularly polarized substrate lens antennas for wireless communications, *IEEE Trans. Microwave Theory Tech.* **49**(3):431–441 (March 2001).
46. C. A. Fernandes, Shaped dielectric lenses for wireless millimeter-wave communications, *IEEE Anten. Propag. Mag.* **41**(5):141–150 (Oct. 1999).
47. D. N. Black and J.C. Wiltse, Millimeter-wave characteristics of phase-correcting Fresnel zone plates, *IEEE Trans. Microwave Theory Tech.* **35**(12):1122–1129 (Dec. 1987).
48. A. Petosa and A. Ittipiboon, Shadow blockage effects on the aperture efficiency of dielectric Fresnel lenses, *IEE Proc. Microwaves Anten. Propag.* **147**(6):451–454 (Dec. 2000).
49. H. D. Hristov and M. H. A. J. Herben, Millimeter-wave Fresnel-zone plate lens and antenna, *IEEE Trans. Microwave Theory Tech.* **43**(12):2779–2785 (Dec. 1995).
50. A. Petosa, A. Ittipiboon, and S. Thirakoune, Shadow blockage improvement using a perforated dielectric Fresnel lens, *Proc. 2003 IEEE Antennas and Propagation Society Int. Conf.* Vol. 4, June 22–27, 2003, pp. 514–517.

LINEAR ANTENNAS

ASOKE K. BHATTACHARYYA
Lincoln University

Historically, using a piece of radiating straight wire as an aerial, or antenna, was a natural choice for wireless communications. This radiating piece of straight wire without curvature is the linear antenna. A simple example of a linear antenna is a two-wire transmission line carrying equal currents in opposite directions and hence no resultant radiation. A two-wire transmission line may be bent to create an efficient radiator such as a dipole. The linear antennas have been treated in numerous references. Some of them are in Refs. 1–13. We will describe key features of linear antennas in this article.

1. SOME RELEVANT TERMS

Before we proceed to discuss linear antennas, we need to define and discuss certain terms in accordance with the Institute of Electrical and Electronics Engineers (IEEE) standard definitions of antenna terminology.

20. W. Rotman and R.F. Turner, Wide-angle microwave lens for line source applications, *IEEE Trans. Anten. Propag.* **11**(6):623–632 (Nov. 1963).
21. L. Musa and M. S. Smith, Microstrip port design and sidewall absorption for printed Rotman lenses, *IEE Proc. H, Microwaves Anten. Propag.* **136**(1):53–58 (Feb. 1989).
22. D. Archer, Lens-fed multiple beam arrays, *Microwave J.* 37–42 (Oct. 1975).
23. D. T. Thomas, Multiple beam synthesis of low sidelobe patterns in lens fed arrays, *IEEE Trans. Anten. Propag.* **26**(6):883–886 (Nov. 1978).
24. R. C. Hansen, *Phased Array Antennas*, Wiley, New York; 1998.
25. K. K. Chan and S. K. Rao, Design of a Rotman lens feed network to generate a hexagonal lattice of multiple beams, *IEEE Trans. Anten. Propag.* **50**(8):1099–1108 (Aug. 2002).
26. J. B. L. Rao, Multifocal three-dimensional bootlace lenses, *IEEE Trans. Anten. Propag.* **30**(6):1050–1056 (Nov. 1982).
27. C. M. Rappaport and A. I. Zaghoul, Optimized three-dimensional lenses for wide-angle scanning, *IEEE Trans. Anten. Propag.* **33**(11):1227–1236 (Nov. 1985).
28. R. C. Hansen, Design trades for Rotman lenses, *IEEE Trans. Anten. Propag.* **39**(4):464–472 (April 1991).
29. A. F. Peterson and E. O. Rausch, Scattering matrix integral equation analysis for the design of a waveguide Rotman lens, *IEEE Trans. Anten. Propag.* **47**(5):870–878 (May 1999).
30. N. Yuan, J. S. Kot and A. J. Parfitt, Analysis of Rotman lenses using a hybrid least squares FEM/transfinite element method, *IEE Proc. Microwaves Anten. Propag.* **148**(3):193–198 (June 2001).
31. R. E. Clapp, Extending the R-2R Lens to 360°, *IEEE Trans. Anten. Propag.* **32**(7):661–671 (July 1984).
32. G. D. M. Peeler and D. H. Archer, A two-dimensional microwave Luneburg lens, *Trans. IRE Prof. Group Anten. Propag.* **1**(1):12–23 (July 1953).
33. J. S. Hollis and M. W. Long, A Lunenburg lens scanning system, *IEEE Trans. Anten. Propag.* **5**(1):21–25 (Jan. 1957).
34. G. A. Thiele and R. C. Rudduck, Geodesic lens antennas for low-angle radiation, *IEEE Trans. Anten. Propag.* **13**(4):514–521 (July 1965).
35. E. H. Braun, Radiation characteristics of the spherical Luneburg lens, *IEEE Trans. Anten. Propag.* **4**(2):132–138 (April 1956).
36. G. D. M. Peeler and H. G. Coleman, Microwave stepped-index Luneburg lenses, *IEEE Trans. Anten. Propag.* **6**(2):202–207 (April 1958).
37. H. Mosallaei and Y. Rahmat-Samii, Nonuniform Luneburg and two-shell lens antennas: Radiation characteristics and design optimization, *IEEE Trans. Anten. Propag.* **49**(1):60–69 (Jan. 2001).
38. S. Rondineau, M. Himdi, and J. Sorieux, A sliced spherical Luneburg lens, *IEEE Anten. Wireless Propag. Lett.* **2**:163–166 (2003).
39. K. Kikuchi, Y. Kido, and T. Ogawa, Millimeter wave sensor using cylindrical Luneburg lens with flat sides, *IEEE Trans. Instrum. Meas.* **47**(2):423–425 (April 1998).
40. G. T. Ruck, D. E. Barick, W. D. Stuart and C. K. Krichbaum, *Radar Cross Section Handbook*, Vol. 2, Plenum, New York; 1970, pp. 597–600.
41. G. M. Rebeiz, Millimeter-wave and tetrahertz integrated circuit antenna, *Proc. IEEE*, **80**(11):1748–1770 (Nov. 1992).
42. D. F. Filipovic, S. S. Gearhart, and G. M. Rebeiz, Double-slot antennas on extended hemispherical and elliptical silicon dielectric lenses, *IEEE Trans. Microwave Theory Tech.* **41**(10):1738–1749 (Oct. 1993).
43. A. Neto, L. Borselli, S. Maci, and P. J. I. de Maagt, Input impedance of integrated elliptical lens antennas, *IEE Proc. Microwaves Anten. Propag.* **146**(3):181–186 (June 1999).
44. M. J. M. van der Vorst and P. J. I. de Maagt, Efficient body of revolution finite-difference time-domain modelling of integrated lens antennas, *IEEE Microwave Wireless Compon. Lett.* **12**(7):258–260 (July 2002).
45. X. Wu, G. V. Eleftheriades, and T. E. van Deventer-Perkins, Design and characterization of single- and multiple-beam mm-wave circularly polarized substrate lens antennas for wireless communications, *IEEE Trans. Microwave Theory Tech.* **49**(3):431–441 (March 2001).
46. C. A. Fernandes, Shaped dielectric lenses for wireless millimeter-wave communications, *IEEE Anten. Propag. Mag.* **41**(5):141–150 (Oct. 1999).
47. D. N. Black and J.C. Wiltse, Millimeter-wave characteristics of phase-correcting Fresnel zone plates, *IEEE Trans. Microwave Theory Tech.* **35**(12):1122–1129 (Dec. 1987).
48. A. Petosa and A. Ittipiboon, Shadow blockage effects on the aperture efficiency of dielectric Fresnel lenses, *IEE Proc. Microwaves Anten. Propag.* **147**(6):451–454 (Dec. 2000).
49. H. D. Hristov and M. H. A. J. Herben, Millimeter-wave Fresnel-zone plate lens and antenna, *IEEE Trans. Microwave Theory Tech.* **43**(12):2779–2785 (Dec. 1995).
50. A. Petosa, A. Ittipiboon, and S. Thirakoune, Shadow blockage improvement using a perforated dielectric Fresnel lens, *Proc. 2003 IEEE Antennas and Propagation Society Int. Conf.* Vol. 4, June 22–27, 2003, pp. 514–517.

LINEAR ANTENNAS

ASOKE K. BHATTACHARYYA
Lincoln University

Historically, using a piece of radiating straight wire as an aerial, or antenna, was a natural choice for wireless communications. This radiating piece of straight wire without curvature is the linear antenna. A simple example of a linear antenna is a two-wire transmission line carrying equal currents in opposite directions and hence no resultant radiation. A two-wire transmission line may be bent to create an efficient radiator such as a dipole. The linear antennas have been treated in numerous references. Some of them are in Refs. 1–13. We will describe key features of linear antennas in this article.

1. SOME RELEVANT TERMS

Before we proceed to discuss linear antennas, we need to define and discuss certain terms in accordance with the Institute of Electrical and Electronics Engineers (IEEE) standard definitions of antenna terminology.

1.1. Power Radiated, Radiation Intensity, and Radiation Resistance

Electromagnetic waves, by virtue of their transverse nature, propagate in a direction perpendicular to the plane containing the electric field \mathbf{E} and magnetic field \mathbf{H} . The instantaneous Poynting vector \mathbf{P} , which is a measure of the power density associated with the electromagnetic wave, is given by

$$\mathbf{P} = \mathbf{E} \times \mathbf{H} \quad (1)$$

where \mathbf{P} , \mathbf{E} , and \mathbf{H} are instantaneous Poynting vector in watts per square meter, electric field in V/m, and magnetic field in amperes per meter.

The total power P crossing a sphere enclosing the source (antenna/scatterer) at its center is obtained by integrating the power density over the sphere and is given by

$$P = W \hat{n} \cdot dS = W da \quad (2)$$

where W is the instantaneous power crossing the sphere per unit area held perpendicular to the direction of the flow, \hat{n} is the positive outwardly drawn at the point of incidence, and dS is the unit area arbitrarily oriented at the point of incidence. With $\exp(j\omega t)$ variation assumed, the average power density is given by the time-average Poynting vector \mathbf{P}_{av} :

$$\mathbf{W}_{av}(u, v, w) = \frac{1}{2} \text{Re}(\mathbf{E} \times \mathbf{H}^*) \quad (3)$$

The average radiated power is given by

$$\mathbf{P}_{av} = \frac{1}{2} \iint \text{Re}(\mathbf{E} \times \mathbf{H}^*) da \quad (4)$$

The radiation intensity U is defined by the product of power density \mathbf{P}_{rad} and the square of the far-field range (r) and is expressed as

$$U = r^2 P_{rad} \quad (5)$$

The radiation resistance (R_r) is defined as the positive resistance across which the real power radiated (P_{rad}) can be thought of as being dissipated. The relationship between P_r , R_r , the input resistance, and the current I is

$$R_r = \frac{P_r}{I^2} \quad (6)$$

The input resistance of an antenna is a sum of radiation resistance plus the positive resistance due to ohmic losses.

1.2. Radiation Intensity, Directivity, and Gain

The antenna radiates real power in the far zone in space over a solid angle of 4π radians. The radiation intensity $U(\theta, \phi)$, the real power radiated per unit solid angle, is a product of the radiation intensity P_{rad} , the real power per unit solid area on the surface, multiplied by the square (r^2)

of the distance and is given by

$$U(\theta, \phi) = r^2 P_{rad}(\theta, \phi) \quad (7)$$

The total power can be estimated by integrating the radiation over a large sphere enclosing the antenna over 4π radians:

$$P_{rad} = \int_S U d\Omega = \int_{\theta=0}^{\pi} \int_{\phi=0}^{2\pi} U \sin \theta d\theta d\phi \quad (8)$$

An isotropic source, such as an ideal point source, radiates uniformly in all directions and is independent of θ and ϕ , and the radiation intensity U_0 is related to the real power radiated by the simple formula:

$$U_0 = \frac{P_{rad}}{4\pi} \quad (9)$$

The directivity is a measure of how efficiently the antenna is directing the radiation in space, according to the 1983 IEEE standard [14]. The directivity D , a dimensionless quantity, of an antenna is given by

$$D = \frac{U}{U_0} = \frac{4\pi U}{P_{rad}} \quad (10)$$

The directivity is dependent on the direction. If the direction is not specified, the default is the direction of maximum radiation intensity.

The dimensionless maximum directivity D_{max} , denoted by D_0 , is expressed as

$$D_0 = \frac{U_{max}}{U} = \frac{4\pi U_{max}}{P_{rad}} \quad (11)$$

Many practical antennas work with dual polarizations in mutually perpendicular directions, and then the directivity is defined in that particular direction; the total maximum directivity is a sum of directivities in mutually perpendicular directions and is expressed as

$$D_0 = D_{\parallel} + D_{\perp} \quad (12)$$

The mathematical expressions for D_{\parallel} and D_{\perp} are

$$D_{\parallel} = \frac{4\pi U_{\parallel}}{P_{rad\parallel} + P_{rad\perp}} \quad (13a)$$

$$D_{\perp} = \frac{4\pi U_{\perp}}{P_{rad\parallel} + P_{rad\perp}} \quad (13b)$$

1.3. Antenna Gain and Radiation Efficiency

An antenna is a passive device, but it can be designed to radiate more energy in a desired direction. The gain (G) of

an antenna is defined as

$$G = \frac{\text{radiation intensity in maximum direction of radiation } (U_0)}{\text{radiation intensity of a lossless isotropic source with same input}} \quad (14)$$

All practical antennas have losses, and therefore efficiencies of practical antennas are less than 100%. The antenna efficiency (η) is defined as the ratio of the real power radiated in space by the antenna to the real power input at its feed terminals:

Radiation efficiency (η)

$$= \frac{\text{real power radiated by test antenna } (P_{\text{rad}})}{\text{total real input at antenna feed terminals } (P_{\text{in}})} \quad (15)$$

The antenna efficiency η is related to the directivity D and the gain G through the relationship

$$G = \eta D \quad (16)$$

1.3.1. The Vector and Scalar Potentials and Field Calculations Using Potentials. Most of the time a direct solution of Maxwell's equations subject to the boundary conditions for a practical problem becomes difficult. Therefore, it is customary to use intermediary (or auxiliary) functions, called *potential functions*, to obtain solutions of electromagnetic problems. There are four such functions; two of them are scalar (one electric and one magnetic) and two of them are vector (one electric and one magnetic) potentials.

The magnetic vector potential \mathbf{A} is related to the magnetic flux density through the relation $\mathbf{B} = \nabla \times \mathbf{A}$ and the electric scalar potential V is related to \mathbf{E} and \mathbf{A} through the relation $\mathbf{E} = -\nabla V - \dot{\mathbf{A}}$.

The steps to determine the fields at any point due to the linear antenna are as follows: (1) define the current distribution on the dipole; (2) find expressions for the four potentials; (3) transfer the Cartesian components of the magnetic vector potentials to those in spherical polar coordinates; (4) once the magnetic vector potential is determined, the magnetic field at any point is obtained; and (5) what remains to be done is to use Maxwell's equation to determine the electric fields at any point from the magnetic field obtained.

Before we proceed to determine radiated fields, let us discuss the four potentials for this example. The magnetic current I_m is equal to zero since the wire carries a filamentary electric current and hence the electric vector potential F is zero since it is a function of magnetic current only. In this situation, the magnetic vector potential \mathbf{A} is given by

$$\mathbf{A} = \frac{\mu_0}{4\pi} \int_{-dl/2}^{+dl/2} \mathbf{J}(x', y', z') \frac{\exp(-jkR)}{R} dz' \quad (17)$$

where (x', y', z') are source coordinates, (x, y, z) are the field coordinates, R is the distance between the observation point and any point on the source (Fig. 1). \mathbf{J}_z is the z -directed electric current element, and the linear path C is along the length of the source.

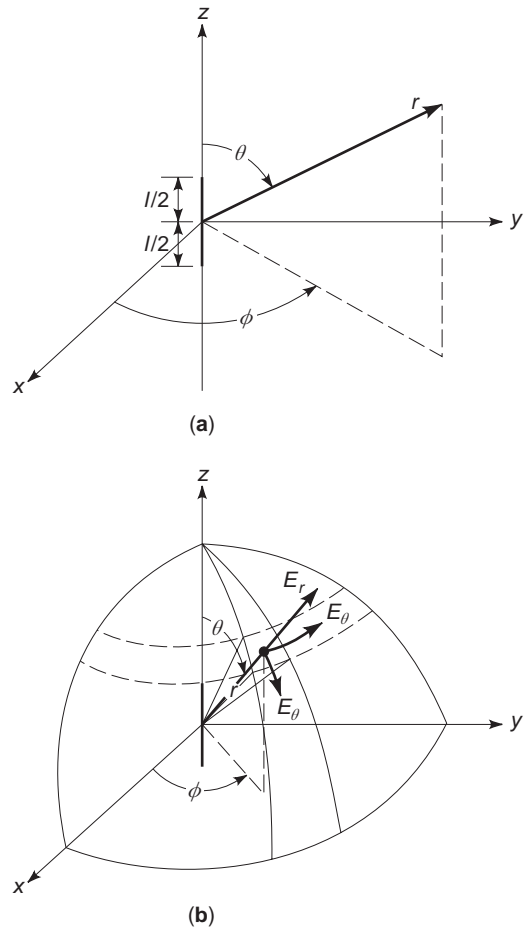


Figure 1. (a) The infinitesimal dipole and (b) its coordinate system. This figure geometrically shows how the field at any observation point from an infinitesimal dipole, which is a building block, can be estimated.

2. THE INFINITESIMAL, OR HERTZIAN, DIPOLE

Before we do the analysis for a practical antenna, namely, a linear antenna, let us establish the analysis procedure for an infinitesimal, elementary, or Hertzian dipole. These are building blocks for more complex antenna systems. Since the dipole is infinitesimal, the current is assumed to be constant.

For the infinitesimal dipole (Fig. 1), the current on the infinitesimal dipole is given by

$$\mathbf{J}_e(x', y', z') = \hat{z} \mathbf{J}_0 \quad (18)$$

where

$x' = y' = 0$, since the length of the dipole is infinitesimal and of length dl

$$R = \sqrt{[(x - x')^2 + (y - y')^2 + (z - z')^2]} \\ = \sqrt{(x^2 + y^2 + z^2)} = r(\text{let})$$

With these, the magnetic vector potential A is given by

$$\begin{aligned} A(x, y, z) &= \hat{z} \frac{\mu_0}{4\pi} \exp(-jkr) dz' \\ &= \hat{z} \frac{\mu_0 I_0 dl}{4\pi r} \exp(-jkr) \text{ for } r \neq 0 \end{aligned} \quad (19)$$

(excluding the source)

The components of A are given by

$$A_r = A_z \cos \theta = \frac{\mu_0 I_0 dl}{4\pi r} \exp(-jkr) \cos \theta \quad (20a)$$

$$A_\theta = -A_z \sin \theta = -\frac{\mu_0 I_0 dl}{4\pi r} \exp(-jkr) \sin \theta \quad (20b)$$

$$A_\phi = 0 \quad (20c)$$

Due to symmetry of the radiating dipole, we have $\partial/\partial\phi = 0$; thus we obtain

$$H = \phi \frac{1}{4\pi r} \left[\frac{\partial}{\partial r}(rA_\phi) - \frac{\partial A_r}{\partial \theta} \right] \quad (21)$$

The expressions for magnetic fields are given by

$$\begin{aligned} H_r &= H_\theta = 0 \\ H_\phi &= j \frac{k_0 I_0 dl}{4\pi r} \left[1 + \frac{1}{jkr} \right] \sin \theta \exp(-jkr) \end{aligned} \quad (22)$$

The electric field can be found from a curl relationship:

$$\mathbf{E} = \frac{1}{j\omega\epsilon} \nabla \times \mathbf{H} \quad (23)$$

This gives the three longitudinal and transverse electric field components as

$$E_r = \frac{\mu_0 I_0 dl}{2\pi r^2} \left[1 + \frac{1}{jkr} \right] \cos \theta \exp(-jkr) \quad (24a)$$

$$E_\theta = j\eta_0 \frac{k_0 I_0 \sin \theta}{4\pi r} \left[1 + \frac{1}{jkr} - \frac{1}{(kr)^2} \right] \exp(-jkr) \quad (24b)$$

$$E_\phi = 0 \quad (24c)$$

2.1. Near and Far Fields

The near-field region are at a close enough distance such that $kr \ll 1$:

$$E_r = -j\eta_0 I_0 dl \frac{\exp(-jkr)}{2\pi k_0 r^3} \cos \theta \quad (25a)$$

$$E_\theta \cong -j\eta_0 I_0 dl \frac{\exp(-jkr)}{4\pi k_0 r^3} \sin \theta \quad (25b)$$

$$H_\phi \cong I_0 dl \frac{\exp(-jkr)}{4\pi r^2} \sin \theta \quad (25c)$$

$$E_\phi = H_r = H_\theta = 0 \quad (25d)$$

Several observations are in order. E_r and E_θ have $(1/r^2)$ variation as distance and therefore decays very fast. These are induction components and die down rapidly with distance. The electric field components E_r and E_θ are in time phase, but the magnetic field component H_ϕ is in time quadrature with them. Therefore, there is no time-average power flow associated with them. Hence, the average power radiated will be zero, and the Poynting vector is imaginary. This can easily be verified by integrating the average power density over a sphere in the near region.

The space surrounding the antenna can be divided into three regions, namely, induction, near-field (Fresnel), and far-field regions. The induction region has $1/r^3$ space variation, the near field has $1/r^2$ variation, and the far field has a $1/r$ variation with distance r .

2.2. Far Field

The far-field expression can be obtained with $kr \gg 1$ and by extracting the $(1/r)$ term and is given by

$$E_\theta = j\eta_0 k_0 I_0 dl \frac{\exp(-jkr)}{4\pi r} \sin \theta \quad (26a)$$

$$E_r = E_\phi = H_r = H_\theta = 0 \quad (26b)$$

$$H_\phi = jk_0 I_0 dl \sin \theta \frac{\exp(-jkr)}{4\pi r} \quad (26c)$$

The intrinsic impedance Z_m of the medium is defined as the ratio of the tangential electric and magnetic fields and is given by

$$Z_m = \frac{E_\theta}{H_\phi} = \eta_m \quad (27)$$

2.3. Intermediate-Field Region

For expression for field components in the intermediate region ($kr > 1$), the reader is referred to any standard text on antennas [1].

2.4. Directivity

The radiation intensity U is given by

$$U = r^2 W_{av} \tag{28}$$

where

$$W_{av} = \frac{1}{2} \text{Re}(\mathbf{E} \times \mathbf{H}^*) \tag{29}$$

and

$$U = \frac{r^2}{2\eta_0} |E_\theta(r, \theta, \phi)|^2 \tag{30}$$

The maximum directivity D_0 turns out to be equal to 1.5.

2.5. Radiation Resistance

The radiation resistance is obtained by dividing total power radiated by the lossless antenna by $|I_0|^2/2$ and is given by

$$R_r = 80\pi^2 \left(\frac{dl}{\lambda}\right)^2 \tag{31}$$

3. THE THIN LINEAR ANTENNA

This section deals with the analysis and properties of a finite-length dipole. The wire is considered to be thin such that tangential currents can be neglected and the current can be considered as only linear. The thin linear antenna and its geometry are shown in Fig. 2. The boundary conditions of the current are that the currents are zero at the two ends and maximum at the center. There is experimental evidence that the current distribution is sinusoidal. The current distributions are for a dipole l and for length varying from $\lambda/2$ to λ . Thick dipoles will be treated in a subsequent section.

3.1. The Current Distribution

The current distribution on the thin dipole is given by

$$\mathbf{I}_x(x' = 0, y' = 0, z') = \begin{cases} \hat{z}I_0 \sin[k(l/2 - z')], & 0 \leq z' \leq l/2 \\ \hat{z}I_0 \sin[k(l/2 + z')], & -l/2 \leq z' \leq 0 \end{cases} \tag{32}$$

The current distributions on the linear dipoles for different lengths are shown in Fig. 3, and Fig. 4 shows the current distributions on a half-wave dipole at different times.

3.1.1. Fields and Radiation Patterns. To determine the field due to the dipole, it can be subdivided into small segments. The field at any point is a superposition of the contributions from each of the segments. Since the wire is

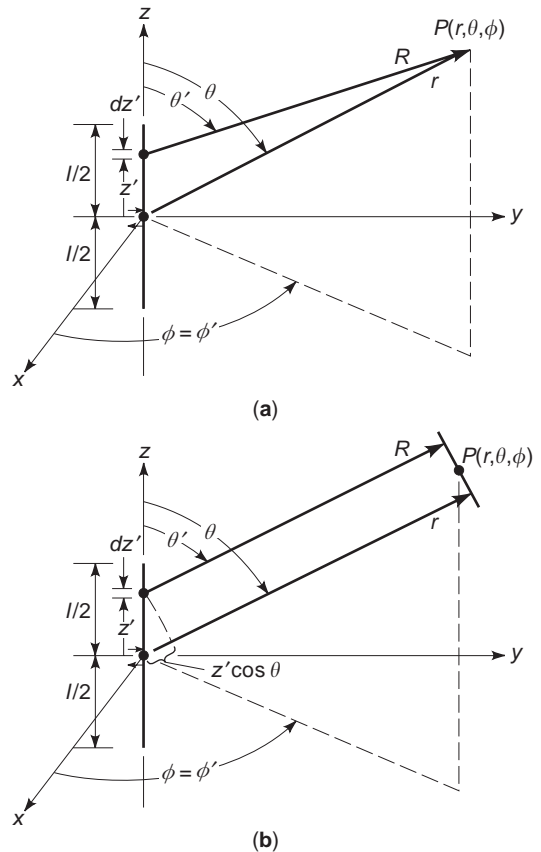


Figure 2. (a) Thin linear antenna and (b) its coordinate system. This figure geometrically shows how the field at any observation point can be formulated using the basic building block, namely, the infinitesimal dipole.

very thin, we have $x' = 0$ and $y' = 0$. The electric and magnetic field components due to the elementary infinitesimal dipole segment of length dz' at an arbitrary point are given by

$$dE_0 = j\eta_0 k_0 I_z(x', y', z') \frac{\exp(-jkR)}{4\pi R} \sin \theta dz' \tag{33a}$$

$$dE_r \cong dE_\phi = dH_r = dH_\theta = 0 \tag{33b}$$

$$dH_\phi \cong jk_0 I_z(x', y', z') \frac{\exp(-jkR)}{4\pi R} \sin \theta dz' \tag{33c}$$

where

$$R = \sqrt{x^2 + y^2 + (z - z')^2} = \sqrt{(r^2 - 2rz' \cos \theta + z'^2)}$$

with

$$r^2 = x^2 + y^2 + z^2, \quad z = r \cos \theta$$

The expression for R can be expanded binomially as

$$R = r - z' \cos \theta + \text{higher-order terms decaying very fast with } r \gg z' \tag{34}$$

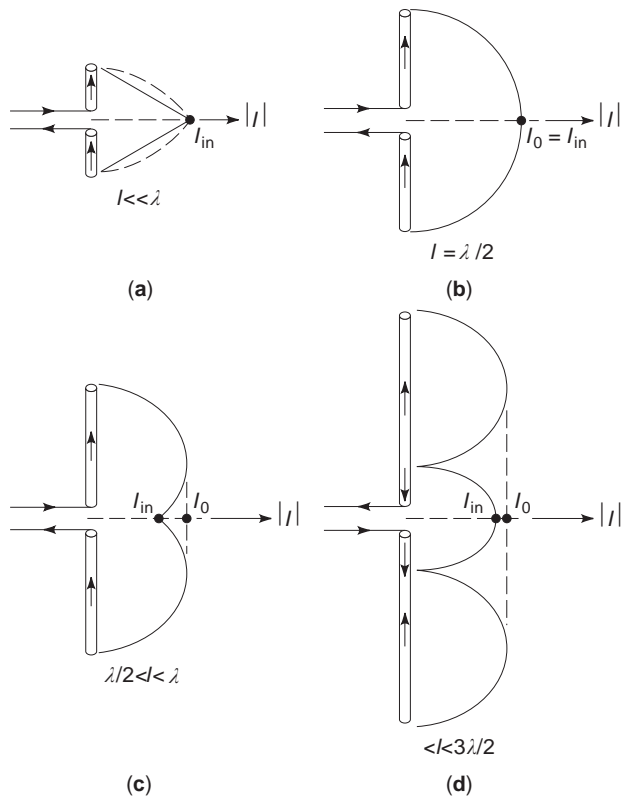


Figure 3. Current distribution on dipoles of different lengths. Different physical lengths of the dipole support different current distributions with varying number of half-sinusoids. This is because at the two ends of the wire, the boundary condition that the current must be zero has to be satisfied.

The total field due to the dipole is obtained by integrating over the whole length. Omitting the straightforward steps, it turns out that the field components E_θ and H_ϕ are given by

$$E_\theta \cong \frac{j\eta_0 I_0}{2\pi} \frac{\exp(-jkr)}{r} \left[\frac{\cos(kl/2 \cos \theta) - \cos(kl/2)}{\sin \theta} \right] \quad (35a)$$

$$H_\phi = E_\theta / \eta_0 \quad (35b)$$

where η_0 is the intrinsic impedance of free space.

To save space we will not describe the derivation of power radiated, which involves $C_i(x)$, $S_i(x)$, and $C_{in}(x)$ functions.

3.1.2. The Radiation Resistance. The resistance can be shown to be given by

$$\begin{aligned} R_r = & \frac{\eta}{2\pi} \{C + \ln(kl) - C(kl) \\ & + \frac{1}{2} \sin(kl) \cdot [S(2kl) - 2S(kl)] \\ & + \frac{1}{2} \cos(kl)[C + \ln(kl/2) \\ & + C(2kl) - 2C(kl)]\} \end{aligned}$$

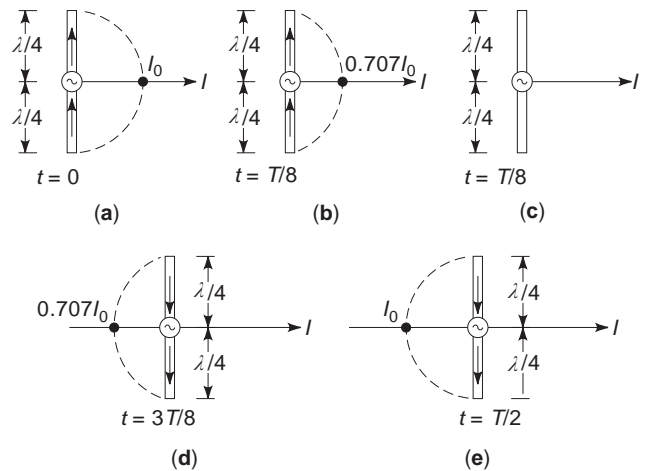


Figure 4. Current distribution on a $\lambda/2$ wire antenna for different times. The current, which is alternating, changes with time. This figure shows the current changes on a half-wavelength wire antenna at different time instants.

where $C(X)$ and $S(X)$ are well-known functions constituting Fresnel integrals (see App. IV in Ref. 1).

4. THE METHOD-OF-MOMENTS SOLUTION

For many practical antennas and scatterers, including linear antennas, the desired current distribution is obtained by numerically solving the integral equations. The method of moments (MoM) is a technique to convert an integral equation to a matrix equation and hence solve the linear system by standard matrix inversion techniques. The MoM is very well documented in the literature [15], and only the basic steps will be briefly discussed below.

The magnetic field integral equation (MFIE) for the unknown current density can be rewritten as an inhomogeneous equation in operator form as follows

$$L(\mathbf{J}_s) = 2\mathbf{n} \times \mathbf{H}(\mathbf{r}) \quad (36)$$

where the right-hand side is a known quantity and $L(\mathbf{J}_s)$ is an integrodifferential linear operator defined as

$$L(\mathbf{J}_s) = \mathbf{J}_s \hat{\mathbf{n}} \times \frac{1}{2\pi} \int_C \mathbf{J}_s(\mathbf{r}') \times \nabla' \mathbf{G} ds' \quad (37)$$

where \mathbf{J}_s is the electric current on the wire and \mathbf{G} is the free-space Green function.

Let us discuss the solution of inhomogeneous scalar equation given by

$$L(f) = g \quad (38)$$

where $f=f(x)$ is the unknown function to be determined, $g(x)$ is a known function and L is a linear operator. The seven steps [16] in obtaining the solution of Eq. (38) are the same as the steps for the solution of Eq. (37).

The steps are as follows:

1. Expand f as

$$f = \sum_{n=1}^N \alpha_n f_n \tag{39}$$

where the α_n values are the unknown coefficients, and the f_n values are known functions of x , known as *expansion*, or *basis*, functions.

2. Using Eq. (38) in Eq. (37), we get

$$\sum_{n=1}^N \alpha_n L(f_n) = g \tag{40}$$

3. Define a suitable inner product $\langle f, g \rangle$ defined in the range L of x :

$$\langle f, g \rangle = \int_D f(x)g(x) dx \tag{41}$$

4. Define a set of testing or weighting functions w_m , $m = 1, 2, \dots, N$, in the range. Taking the inner product of Eq. (40) with each w_m and obtain

$$\sum_{n=1}^N \alpha_n \langle W_m, L(f_n) \rangle = \langle W_m, g \rangle \tag{42}$$

where $m = 1, 2, \dots, N$; $\langle \cdot \rangle$ is the inner product, the product of the two functions integrated over the domain.

5. Express the set of algebraic equations given by Eq. (40) in the matrix form

$$[I_{mn}][\alpha_n] = [g_m] \tag{43a}$$

where the matrix is given by

$$[I_{mn}] = \begin{bmatrix} W_1, L(f_1) & W_1, L(f_2) & \dots & W_1, L(f_N) \\ W_2, L(f_1) & W_2, L(f_2) & \dots & W_2, L(f_N) \\ \dots & \dots & \dots & \dots \\ W_N, L(f_1) & W_N, L(f_2) & \dots & W_N, L(f_N) \end{bmatrix} \tag{43b}$$

where α_N and g_N are the column vectors given by

$$[\alpha_N] = \begin{bmatrix} \alpha_1 \\ \alpha_2 \\ \vdots \\ \alpha_N \end{bmatrix} \tag{44a}$$

$$[g_N] = \begin{bmatrix} \langle W_1, g \rangle \\ \langle W_2, g \rangle \\ \dots \\ \dots \\ \langle W_N, g \rangle \end{bmatrix} \tag{44b}$$

4.1. Moment-Method Solution for Radiation from Thin Wire

Two types of volume integral equations are used for the linear antenna and wire scatterer problem. These are the integral equation of Hallen type and the integral equation of Pocklington type. Hallen's integral equation usually necessitates the postulation of a delta-gap voltage at the feedpoint and also requires the inversion of an $(N + 1)$ -order matrix. The advantages of Pocklington's integral equation is that it is possible to incorporate different source configurations and it requires inversion of a matrix of order N .

For a current-carrying perfectly conducting wire, the Hallen's integral equation obtained by solving the scalar wave equation is given by (1)

$$I_z(z') \frac{\exp(-jkR)}{4\pi R} dz' = -j\sqrt{\epsilon/\mu}[B_1 \cos(kz) + B_2 \sin(kz)] \tag{45}$$

where

$I_z(z')$ = current flowing through elementary length of wire

R = distance of the observation point from elementary length

I = total length of center-fed wire

$\epsilon, \mu, \sigma = 0$ = primary constants of medium in which the antenna is radiating k is the derived secondary constant, namely, the wavevector of the medium

B_1 and B_2 = are constants to be determined

The Pocklington's integral equation is given by

$$I_z(z') \left[\left(\frac{\partial^2}{\partial z^2} + k^2 \right) G(z, z') \right] dz' = -j\omega\epsilon E_z^i \text{ (at } \rho = a) \tag{46}$$

where for thin wire the radius $a \ll \lambda$, the free-space Green function $G(z, z')$ is given by

$$G(z, z') = G(R) = \frac{\exp(-jkR)}{4\pi R} \text{ with } R = \sqrt{a^2 + (z - z')^2} \tag{47}$$

E_z^i = the incident field (this is the source field for antennas and scattered field for scatterers)

The availability of high-speed computers, graphics, and software packages, along with the enormous development of microcomputers, has made electromagnetic numerical computation extremely viable. An attractive feature of numerical methods is their ability to handle arbitrarily shaped and electrically large bodies and bodies with non-uniformity and anisotropy where exact solutions can only at best provide some physical insight. For large problems, it is possible to get a linear system with a minimum set of equations to achieve a certain accuracy.

An account of the area of numerical computation of thin wire problem is well-documented in the literature [1,3,6–13]. As described in Ref. 8, there are many important computational issues involved in thin wire problems. These are (1) segmentation of the structure and the correct number of segments, (2) choice of right current expansion functions, (3) the thin-wire approximation (radius $a \ll \lambda$), (4) roundoff error due to matrix factorization, (5) near-field numerical anomaly, (6) treatment of the junctions of the segments, (7) wire-grid modeling, and (8) computer time required. Also, the errors [7] involved are of concern. There are two types of errors encountered: (1) the physical modeling error, because in the absence of an exact solution for a variety of semicomplex and complex structures, it is the natural departure of the assumed structural details from the actual structure; and (2) the numerical modeling error, since all numerical methods are approximate but sufficiently accurate for the application.

4.2. Formulation

Before we discuss the formulation of the thin-wire integral equation, comments on the expansion functions used in this study are in order. There are broadly two types of expansion functions:

1. *Entire-Domain Functions.* As the name suggests, these functions are defined over the entire integration path C , and the subdomain is defined over pieces on the integration path C . Some of these are Fourier, MacLaurin, Chebyshev, Hermite, Legendre, and so on. Tables available in Richmond’s work [17] and also in Ref. 8 are reproduced in Table 1.

2. *Subdomain Expansion Functions.* Subdomain expansions are attractive, convenient, and less expensive in terms of computer time. This stems from the fact that the current is matched on part of the integration path, whereas for the entire domain the integration is performed over the whole path and for all N terms of the expansions and coefficients determined.

Miller and Deadrick [8] provide a table containing the many basis and weighting functions that have been tested in computer runs. This table also compares the suitability of the use of different functions in different problems. The table is too big to reproduce here, and it is left to the reader to look up. It tabulates the method, integral equation type, basis function, current conditions for interior and end segments, the basis function in terms of unknown for unknown and end segments, weighting function for interior and end segments, number of unknowns, and specific comments on the applicability of the expansion functions.

4.3. The Electric Field Integral Equation and Its Matrix Representation

Figure 5 gives the geometry of the arbitrarily oriented straight wire. The wire is broken into segments, or subsections. The mininumerical electromagnetic code (MININEC) relates the current distribution on the wire due to the incident field E^i , magnetic vector potential \mathbf{A} , and electric scalar potential ϕ are given by

$$-E^i \cdot \hat{t} = -j\omega\mathbf{A} \cdot \hat{t} - \hat{t} \cdot \nabla\phi \tag{48a}$$

where

$$\mathbf{A} = \frac{\mu_0}{4\pi} \int \mathbf{I}(s)\mathbf{S}(s)k(r) ds \tag{48b}$$

$$\phi = \frac{1}{4\omega\epsilon} \int q(s)k(r) ds \tag{48c}$$

Table 1. Entire-Domain Current Expansions Using Different Polynomials

<i>A. The Polynomials</i>					
Fourier: $I(z) = I_1 \cos(\pi x/2) + I_2 \cos(3\pi x/2) + I_3 \cos(5\pi x/2) + \dots$					
MacLaurin: $I(z) = I_1 + I_2 x^2 + I_3 x^4 + \dots$					
Chebyshev: $I(z) = I_1 T_0(x) + I_2 T_2(x) + I_3 T_4(x) + \dots$					
Hermite: $I(z) = I_1 H_0(x) + I_2 H_2(x) + I_3 H_4(x) + \dots$					
Legendre: $I(z) = I_1 P_0(x) + I_2 P_2(x) + I_3 P_3(x) + \dots$					
where $-1/2 \leq x = 2z/L \leq 1/2$					
<i>B. Typical Results for Functions</i>					
$L = 0.5\lambda; a = 0.005\lambda; \theta_i = 90^\circ$					
In	Fourier	MacLaurin	Chebyshev	Hermite	Legendre
1	3.476	3.374	1.7589	8.2929	2.2763
2	0.170	4.037	1.5581	14.3644	2.1005
3	0.085	3.128	0.0319	4.4135	0.0655
4	0.055	4.101	0.0112	0.3453	0.0421
5	0.040	1.871	0.0146	0.0073	0.0322

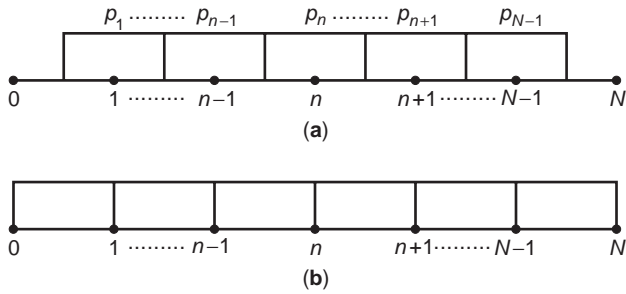


Figure 5. Wire segmentation with pulses for current and charges: (a) unweighted current pulses; (b) unweighted charge representation. The whole length is broken into several segments. Each segment is assigned a pulse, and the pulses represent the assumed current distribution.

t is a unit vector tangential to the wire at any distance along the path of integration which is the length of the wire and $k(R)$ is given by

$$k(R) = \frac{1}{2\pi} \int_{\phi=0}^{2\pi} \frac{\exp(-jkR)}{R} d\phi \quad (49)$$

The continuity equation given below determines the relationship between the charge $q(s)$ and the rate of change of current with distance:

$$q(s) = -\frac{1}{j\omega} \frac{dl}{ds} \quad (50)$$

The MININEC solves the integral equation using the following steps:

1. The wires are divided into small equal segments such that the length of the segment is still large compared to the radius of the wire ($a \ll \lambda$, typically $\frac{1}{100}$ th of a wavelength). The radius vectors $m, n = 0, 1, 2, \dots$ are defined with reference to a global origin.
2. The unit vectors are defined as

$$s_{n+1/2} = \frac{\mathbf{r}_{n+1} - \mathbf{r}_n}{|\mathbf{r}_{n+1} - \mathbf{r}_n|} \quad (51)$$

The testing and expansion functions are pulse functions that are defined by

$$P_n(s) = \begin{cases} 1 & \text{for } s_{n-1/2} < s < s_{n+1/2} \\ 0 & \text{otherwise} \end{cases} \quad (52)$$

where the points $s_{n+1/2}$ and $s_{n+1/2}$ are the segment mid-points and are given by

$$s_{n+1/2} = \frac{s_{n+1} + s_n}{2}, \quad s_{n-1/2} = \frac{s_n - s_{n-1}}{2} \quad (53)$$

In terms of global coordinates, we obtain

$$r_{n+1/2} = \frac{r_{n+1} + r_n}{2}, \quad r_{n-1/2} = \frac{r_n + r_{n-1}}{2} \quad (54)$$

When the pulse functions of Eq. (52) are inserted in parentheses, we obtain

$$\begin{aligned} E^i(s_m) \cdot & \left[\left(\frac{s_m - s_{m-1}}{2} \right) S_{m-1/2} + \left(\frac{s_{m+1} - s_m}{2} \right) S_{m+1/2} \right] \\ = j\omega A(s_m) \cdot & \left[\left(\frac{s_m - s_{m-1}}{2} \right) S_{m-1/2} \right. \\ & \left. + \left(\frac{s_{m+1} - s_m}{2} \right) S_{m+1/2} \right] \end{aligned} \quad (55)$$

The exact kernel treatment developed above is for observation points on source segments. For observation points near but not on the source, a segment has been developed by Wilton, and MININEC has incorporated it (16).

4.4. Expansion of Currents

The currents are expanded in terms of pulse functions as shown in Fig. 5, excluding the endpoints where the currents are chosen as zeros to satisfy boundary conditions at the ends. The current expansion is given by

$$I(s) = \sum_{n=1}^N I_n P_n(s) \quad (56)$$

Using this current expansion in Eq. (48b) and after mathematical manipulations which are available in Ref. 1 and are not detailed here, we get the linear system matrix equation in N unknowns

$$[V_m] = [Z_{mn}] [I_n] \quad (57)$$

where $m, n = 1, 2, \dots, N$, $[Z_{mn}]$ is the square impedance matrix, and $[V_m]$ and $[I_n]$ are applied voltage and current column vectors:

$$\begin{aligned} Z_m = & -\frac{1}{4\pi j\omega\epsilon} \left[k^2 (r_{m+1/2} - r_{m-1/2}) \cdot (s_{n+1/2} \psi_{m,n,n+1/2} \right. \\ & + s_{n-1/2} \psi_{m,n-1/2,n}) - \frac{\psi_{m+1/2,n,n+1}}{s_{n+1} - s_n} + \frac{\psi_{m+1/2,n-1,n}}{s_n - s_{n-1}} \\ & \left. + \frac{\psi_{m-1/2,n,n-1}}{s_{n+1} - s_n} - \frac{\psi_{m-1/2,n-1,n}}{s_n - s_{n-1}} \right] \end{aligned} \quad (58)$$

This matrix has elliptical integrals involved in it. These elliptical integrals can be evaluated numerically.

These equations are valid for any radius other than small, for which the expression for ψ breaks down, and Harrington [19] provided an approximate formula for ψ .

This is given by

$$\psi = \frac{1}{2\pi\Delta s} \ln \left[\Delta \frac{s}{\alpha} \right] - j \frac{k_0}{4\pi} \quad \text{for } m = n \quad (59a)$$

$$= \frac{\exp(-jkr_m)}{4\pi r_m} \quad \text{for } m \neq n \quad (59b)$$

The integral is given by

$$\psi_{m,u,v} = \int k_0(s_m - s') ds' \quad (60)$$

4.5. Inclusion of Nonradiating Structures

4.5.1. The Ground Plane. When the wire structure near the ground plane is assumed to be perfectly conducting, an image is created. The structure and the ground plane is equivalent to the structure and the image.

The voltage and current relationship is given by

$$[V_m] = [Z'_{mn}] [I_n] \quad (61)$$

where

$$Z'_{mn} = Z_{mn} + Z_{m,2N-n+1}$$

4.5.2. Wire Attached to Ground. When a wire is attached to the ground on one or both sides, there will be a residual component of current at one or both ends. In this case, a current pulse is automatically added to the end point in the formulation.

4.5.3. Lumped-Parameter Loading. If an additional complex load is added to the perfectly conducting wire (Fig. 6), there will be an additional voltage drop created at that point if the location of the load ($Z_l = R_l + jX_l$) is at a point of nonzero pulse function. The impedance matrix is modified to

$$[V_m] = [Z'_{mn}] [I_n]$$

where Z'_{mn} is the modified impedance matrix and is given by

$$Z'_{mn} = \begin{cases} Z_{mn} + Z_{load} & \text{for } m = n \\ Z_{mn} & \text{for } m \neq n \end{cases}$$

4.6. Validation of the MININEC code

Extensive work has been reported on the validation of the MININEC. Numerous validation runs have been carried out to meet the following requirements: (1) the segmentation density, (2) thin-wire criteria, (3) small radius calculation, (4) step changes in wire radius, (5) spacing of wires, (6) loop antenna, and (7) monopoles and antennas above ground.

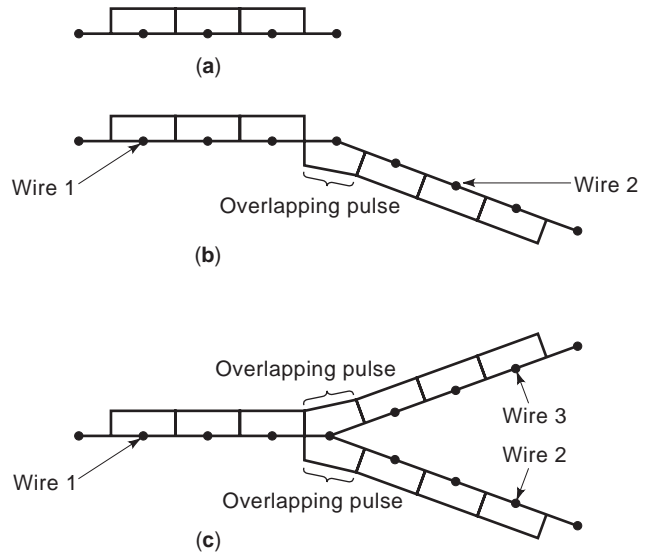


Figure 6. Overlap scheme used at a multiple junction of wires: (a) wire 1 with no end connections; (b) wire 2 overlaps onto wire 1; (c) wire 3 overlaps onto wire 1.

4.7. Operation of Currents—LU Decomposition

The operation is oriented around the menu shown below. Here we describe the DOS version [19,20], but the Windows version is also available [21–23]:

```

MENU
1 -- COMPUTE/DISPLAY CURRENTS
2 -- CHANGE EXCITATION
3 -- CHANGE FREQUENCY
4 -- CHANGE LOADING
5 -- LOAD GEOMETRY
6 -- SELECT OUTPUT DEVICE
7 -- RETURN TO SYSTEM SUPERVISOR
0 -- EXIT TO DOS
SELECTION (1--7 OR 0) ?
    
```

4.8. Some Examples Using MININEC

4.8.1. Tee Antenna. Figure 7 shows the geometry of the tee antenna fed from the base by a coaxial line. The

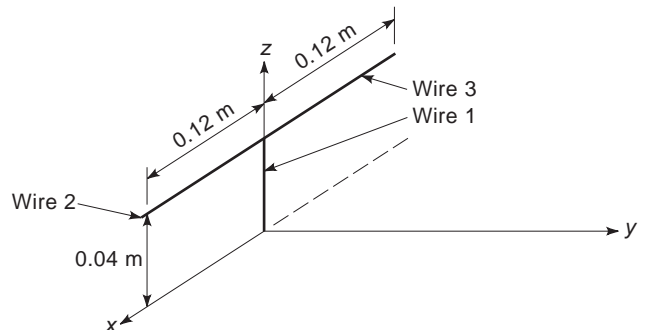


Figure 7. Geometry of the “tee” antenna. Typical dimensions are shown.

impedance calculations of the tee antenna using different computer programs, including CURLU in MININEC and have been compared with measurements [25].

4.8.2. Near and Far Fields. The near- and far-field programs (FIELDS) calculate near and far fields using the current distribution on the structure obtained by integral equation formulations. The current distribution can be computed using three programs: CURLU, CURTE, and CURRO. The current distribution can be computed using perfect and imperfect ground, although the real ground corrections are applied to the far field only. The real ground correction is included in the form of reflection coefficients for parallel and perpendicular polarizations. For details, the reader is referred to Chap. 8 of Ref. 7. The menu is given below. User input(UI) means the user is expected to respond at that point.

```

MENU
1--COMPUTE NEAR FIELDS
2--COMPUTE FAR FIELDS
3--SELECT/CHANGE ENVIRONMENT
4--SELECT/CHANGE CURRENTS FILE
6--RETURN TO SYSTEM SUPERVISOR 7--EXIT TO DOS
SELECTION (1--6 OR 0) ? User Input

NAME OF INPUT CURRENT FILE? User Input (UI)
ELECTRIC OR MAGNETIC NEAR FIELDS (E/M) ? User
  Input
X-COORDINATE Y-COORDINATE
INITIAL VALUE? UI INITIAL VALUE?
INCREMENT? UI INCREMENT?
NO. OF PTS? UI NO. OF PTS?
  Z-COORDINATE
  UI INITIAL VALUE? UI
  UI INCREMENT? UI
  UI NO. OF PTS? UI
PRESENT POWER LEVEL IS : CURRENT VALUE
    
```

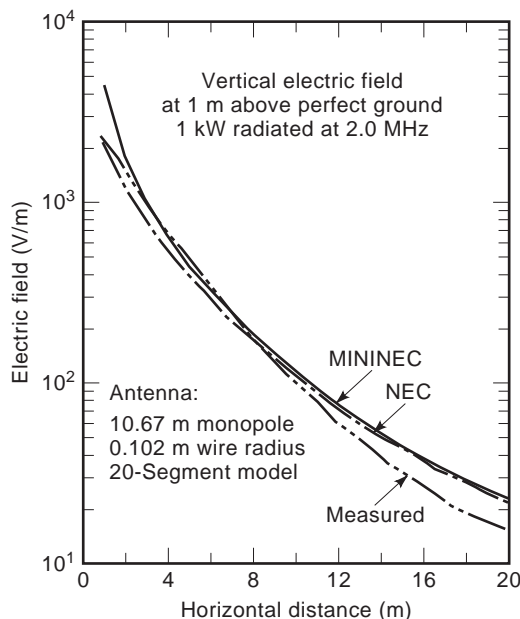


Figure 8. Monopole near fields: E_z versus horizontal distance.

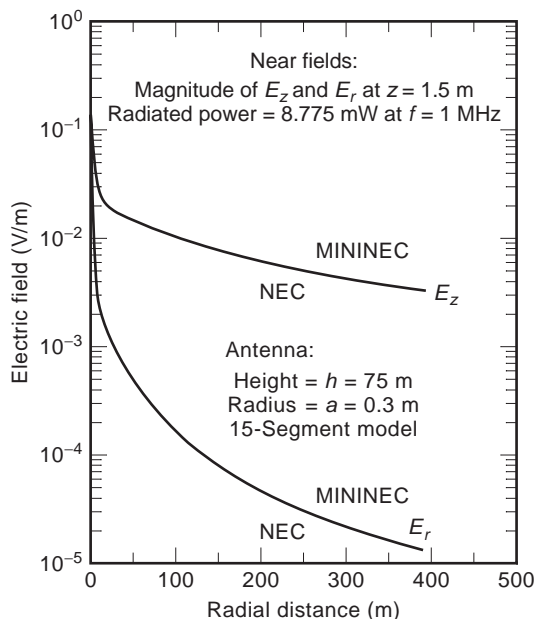


Figure 9. Monopole near fields: electric fields E_z and E_r versus radial distance.

```

CHANGE POWER LEVEL (Y/N) ? UI
NEW POWER LEVEL (WATTS) ? UI
    
```

Once the parameters are specified, the near- and far-field results are printed out in words. Figure 8–15 show the near-field characteristics of the monopole.

5. THE THICK LINEAR ANTENNA

The thin linear antenna is frequency-sensitive. In practical communication scenarios, the transponders use

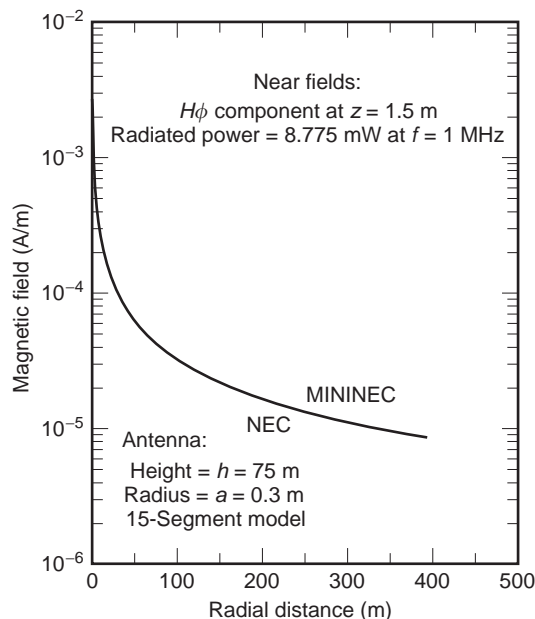


Figure 10. Monopole near fields: H_ϕ versus radial distance.

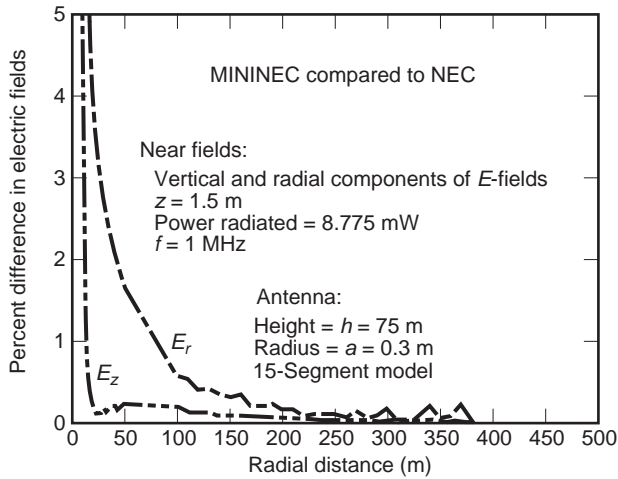


Figure 11. Percentage difference in electric fields E_z and E_r versus radial distance.

wideband signals to increase the channel capacity and therefore needs antennas that can handle a large band of frequencies. One way of increasing the bandwidth is to use electrically thick wires.

A thick cylindrical dipole (Fig. 16) is the inexpensive way to increase the bandwidth of linear antennas. The increase in thickness leads to circumferential component I_ϕ of the otherwise linear current. This can be handled with the integral equation formulation. Figures 17a and 17b, respectively, show the variation of input resistance and reactance of the dipole with $l/2a$ ratios 25 (thick), 50, and 10,000 (thin), where $2a$ is the diameter of the wire.

6. THE SLEEVE DIPOLE

The structure that closely resembles an asymmetric dipole is the sleeve dipole (Fig. 18), which is a base-fed monopole

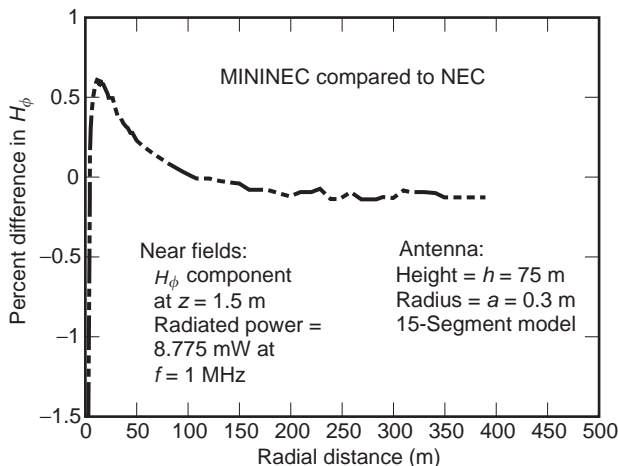


Figure 12. Monopole near fields: percentage difference in H_ϕ versus radial distance.

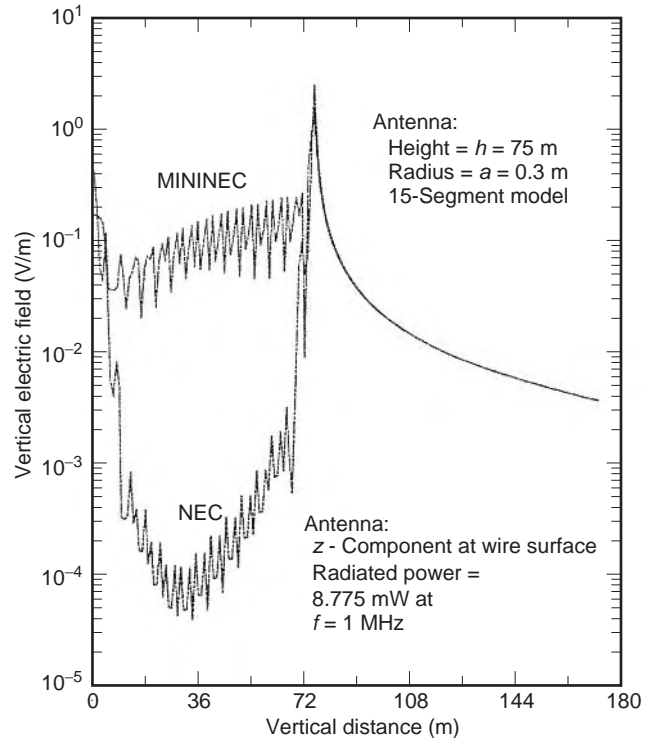


Figure 13. Monopole near fields: vertical electric field versus vertical distance.

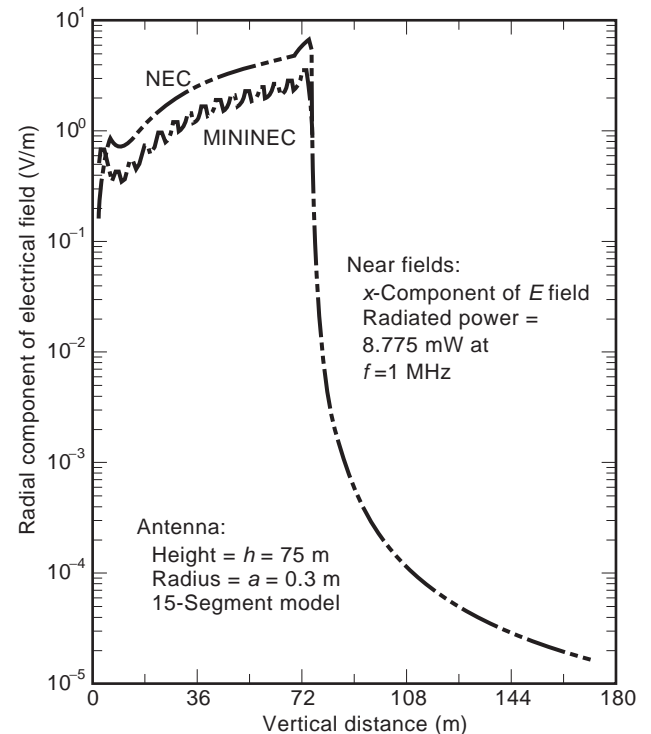


Figure 14. Radial component of electric field at wire surface versus vertical distance.

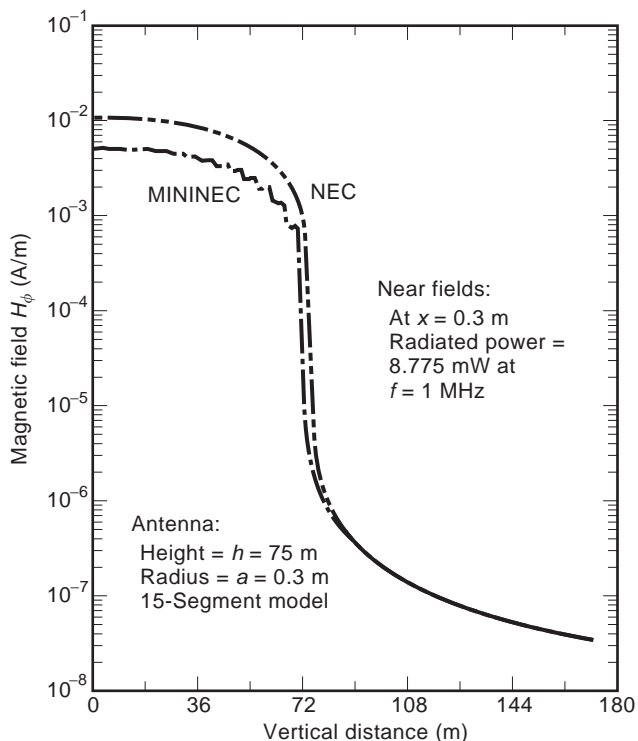


Figure 15. Monopole magnetic field H_ϕ at surface versus vertical distance.

on a ground plane. The outer conductor of the coax line is extended to give wideband characteristics apart from impedance control and mechanical strength. Another way of increasing the bandwidth will be to coat the metal wire

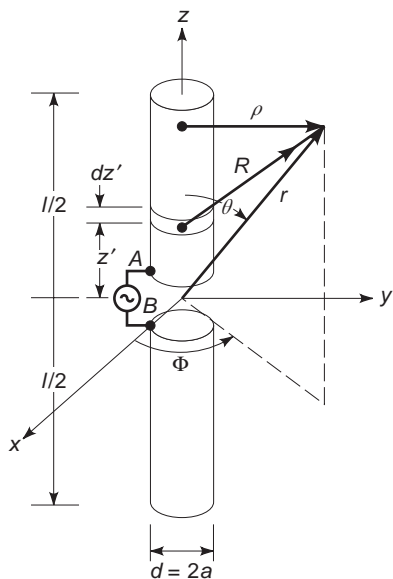


Figure 16. The center-fed thick dipole. A thick dipole has a frequency characteristic over a much wider band than a thin antenna. The diagram shows how such a dipole will receive power from the feeder network.

with a low-loss dielectric or just push the metal wire into a sleeve (a thin dielectric pipe). It can be fed symmetrically, but the problem of impedance matching and using a proper matching network will increase the complexity and cost of the device. For further discussion on sleeve dipoles, the reader is referred to Ref. 1.

7. COMPUTER CODES

7.1. A Summary of Different Available Codes

The following subsections summarize the scope of the codes currently used for linear antenna analysis.

7.1.1. The Electromagnetic Surface Patch Code. The electromagnetic surface patch (ESP) code version IV [26], which uses the method of moments (MoM), is written for the analysis of radiation and scattering from three-dimensional geometries. These geometries include the interconnection of thin wires and perfectly conducting and thin dielectric polygonal plates. This code works for open as well as closed surfaces since the formulation is based on electric field integral equation. It uses polygonal plates modeling, which can generate an object as complex as an aircraft with only 12 polygonal plates. The ESP code is capable of doing the following:

1. It can model an arbitrary thin wire by using a number of piecewise straight segments.
2. It can be model an arbitrary perfectly conducting surface by a combination of polygonal plates. The plates can be of thin dielectric sheets, which have been modeled using impedance approximation.
3. The code incorporates the wire-junction with the restriction that the junction must be at least one-tenth wavelength away from the nearest edge; it can take care of several plates generated from a common edge.

In order to use this code, the user specifies the (x,y,z) coordinates of the corners of each plate by entering the (x,y,z) coordinates of the corners of each plate and the maximum segment size in wavelengths for calculating the MoM modes. The code automatically takes care of the frequency independence of the models.

In summary, the ESP code can treat a variety of geometries: (1) thin wires with finite conductivity and lumped loads, (2) perfectly conducting or thin dielectric polygonal plates (30 wire-plate junctions) at least 0.1λ from the edge of a plate, (3) plate-plate junctions, including several plates of different sizes that intersect along a common edge, and (4) excitation by either a voltage generator or an incident plane wave.

ESP can compute the key characteristics of engineering interest of an antenna, namely, current distributions, antenna input impedance, radiation efficiency, mutual coupling, near- or far-zone radiation patterns for all polarizations, and near- or far-zone back, bistatic, and forward scattering patterns (full scattering matrix). These are still bugs in the ESP code, and new features are being

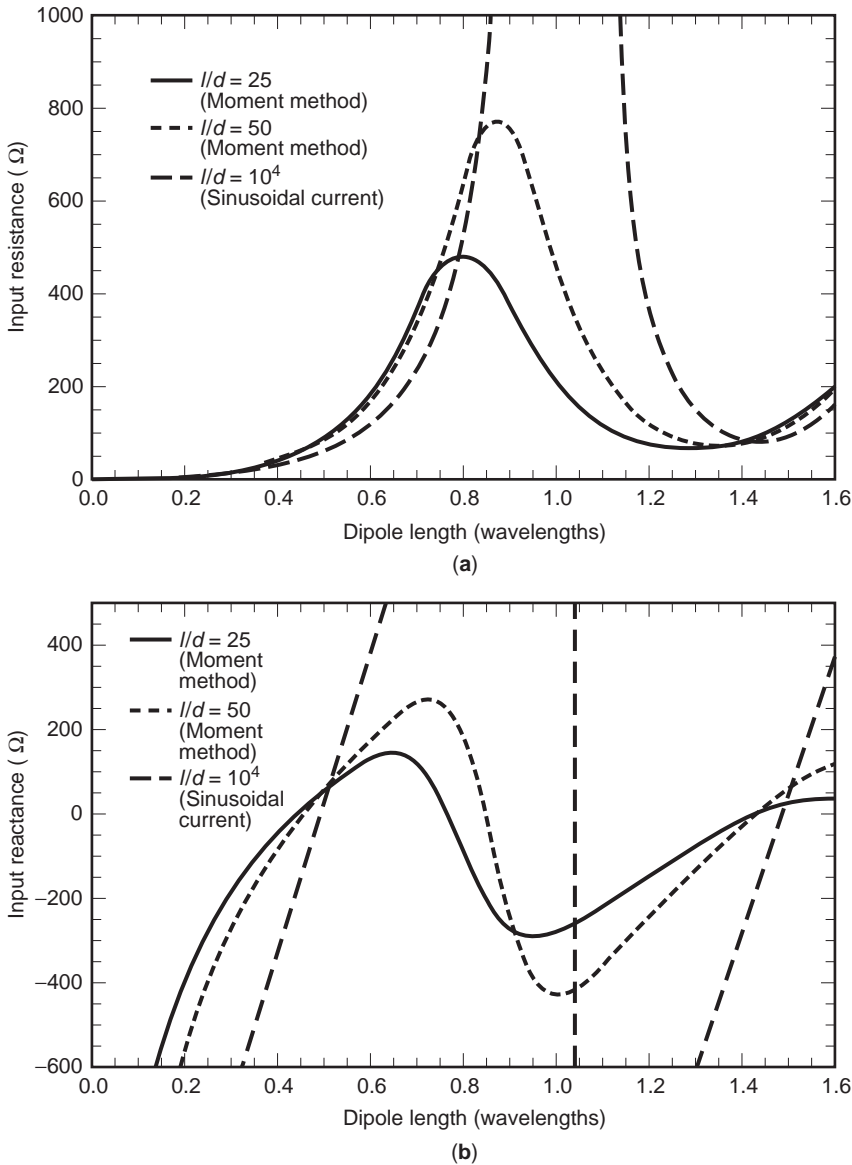


Figure 17. The input impedance of wire dipoles with dipole length in wavelengths: (a) input resistance in ohms; (b) input reactance in ohms. Every antenna presents an input complex impedance at its feed terminals. It is very important to know how the real and imaginary parts of the impedance vary with parameters so that antenna can be matched to the feeder.

added to the codes. Nevertheless, it should be possible to customize the code for a specific application.

7.1.2. The Mininumerical Electromagnetic Code (MININEC). The MININEC [20,21] is a computer program prepared in BASIC language using the method of moments for the analysis of linear antennas. It uses a Galerkin procedure [19] to solve for wire currents using an integral equation formulation that relates the vector and scalar potentials to the electric field. This formulation can easily be programmed for use in microcomputers. The code can solve for impedance and currents on arbitrarily wires including configurations with multiple wire junctions. The code incorporates lumped impedance loading and near-zone electric and magnetic fields when the wire is in free space as well as over a perfectly conducting ground. MININEC is written in a IBM PC-DOS-compatible BASIC language.

8. FEED FOR LINEAR ANTENNAS

In all practical antennas, there exists a mechanism of feeding the antenna to launch the desired current distribution. This requires a finite gap with a nonzero current and alters the normally assumed current distribution. Hence, a correction factor should be introduced to accurately model the feedpoint current. Several methods of feeding half-wave antennas are shown in Figs. 19a–19d. Normally, since the complex input impedance of the dipole is quite different from the real input resistance (under high frequency approximation), there is a need to use a matching network to match the input impedance to the feeder and keeping the voltage standing-wave ratio (VSWR) close to unity in the frequency range of operation. Figure 19a shows the balanced line-type center feed. Figure 19b shows a “delta match” or “shunt feed” feeder that provides a good impedance mismatch and low VSWR

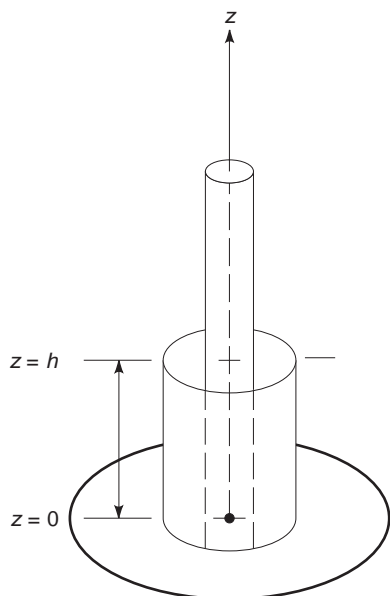


Figure 18. The sleeve dipole. Apart from making the wire thick, another way of increasing the bandwidth of a thin wire is to put it in a sleeve, which is basically a dielectric coating, and terminate by a ground plane on one side.

on the feeder line. The simplest feeding arrangement is the “end feed” (Fig. 19c), where the vertical transmission line radiates energy. The configuration in Fig. 19d can be made efficient by tapping the vertical line at an appropriate location.

To account for the nonzero current at the finite gap feed terminals and consequent distortion in the current distribution.

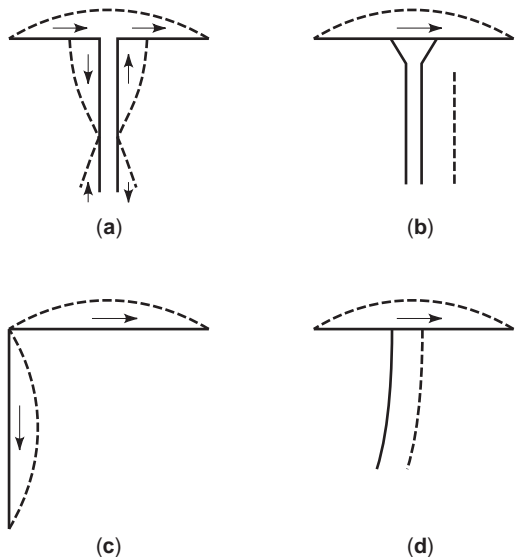


Figure 19. Methods of exciting linear antennas: (a) center feed; (b) delta match or shunt feed; (c) end feed; (d) impedance-matched tapping. Excitation mechanisms are very important in order to launch maximum power. Not shown are matching transformers to ensure maximum power transfer.

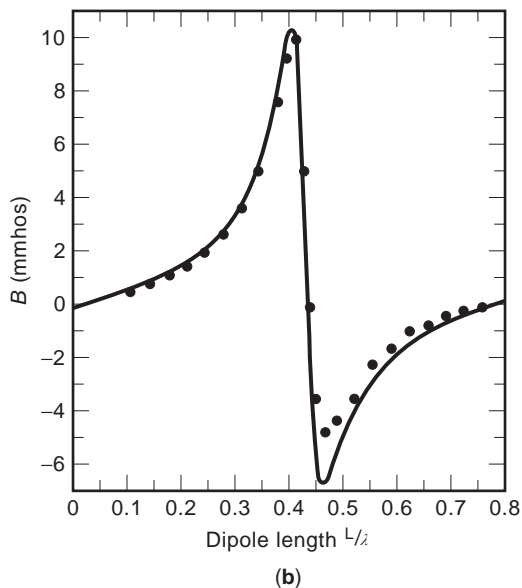
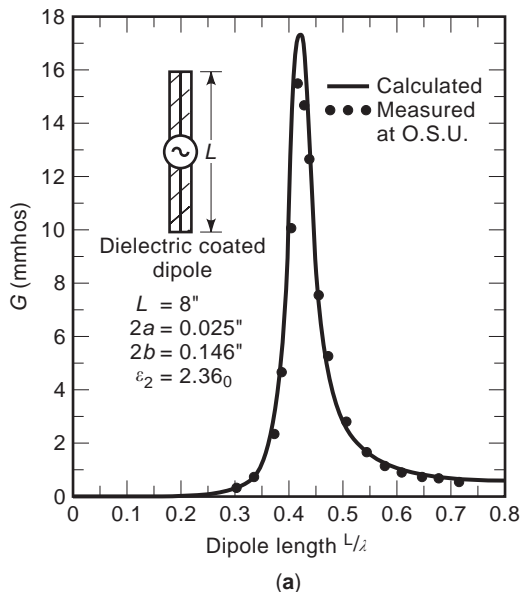


Figure 20. Comparison of measured and calculated admittance values for a coated dipole length $L=8$ in.; $2a=0.025$ in.; $2b=0.146$ in.; $\epsilon_2=2.3\epsilon_0$. The figures show the bandwidth of antennas: (a) conductance; (b) susceptance of an insulated dipole versus length in wavelengths.

The modified current is given by [28]

$$I_z(x', y', z') = \begin{cases} a_z \{ I_0 \sin[k(l/2 - z')] + j\alpha I_0 [\cos(kz') - \cos(kl/2)] \} & \text{for } 0 \leq z' \leq l/2 \\ a_z \{ I_0 \sin[k(l/2 + z')] + j\alpha I_0 [\cos(kz') - \cos(kl/2)] \} & \text{for } -l/2 \leq z' \leq 0 \end{cases} \quad (62)$$

where α = the coefficient dependent on the length of the gap and the antenna. If the radius of the wire and the gap are small the value of this coefficient is small.

For a half-wave dipole, we obtain

$$I_0(x', y', z') = a_z I_0(1 + j\alpha) \cos(kz') \quad \text{for } 0 \leq |z'| \leq \lambda/4$$

The shape of the current does not change for a half-wave dipole, but it does for other lengths, such as a wavelength.

9. BANDWIDTH OF LINEAR ANTENNAS

The bandwidth of an antenna is the frequency range over which the performance of the antennas meets a specific requirement, such as that the gain does not fall below 3 dB of the maximum, or the midfrequency value. There is no unique characterization of bandwidth since the different properties such as input impedance, radiation pattern, polarization, and gain of an antenna vary in entirely different ways in a frequency range. The definition meets the requirement of specific application. Nevertheless, the bandwidth is defined in three different ways: (1) half-power bandwidth is the frequency range within which the gain does not fall by more than 3 dB, (2) the percentage bandwidth normally defined for a narrowband antenna is defined as the bandwidth (the difference between upper and lower frequencies of operation) divided by the center frequency and then multiplied by 100, and (3) for wideband- or frequency-independent antennas it is the ratio of higher and lower frequencies of operation.

The thin linear antenna that we have dealt with in this article is based on the assumption that the radius is small compared with the wavelength of operation. This necessarily means that the current on the wire is linear and has no tangential component. In a practical situation an antenna has to operate in a frequency band. This assumption is no longer valid and the thin linear antenna becomes frequency-sensitive. Therefore, something needs to be done to the thin antenna so that it develops the capability of handling a wide frequency band.

The way of achieving wider bandwidth will be to use electrically thick dipoles or to coat thin metallic wires with lossy dielectrics. A thick dipole and a dielectric coated dipole with their centrally located feeding source are shown in Figs. 20a and 20b, respectively. The effect of coating the thin linear antenna with a layer of electrically and magnetically lossless and lossy material is discussed in two papers in (28) and (29) and summarized in (1). The analytical techniques used is a moment method solution. Two parameters, P and Q [28,29], involving the electrical and magnetic parameters, inner and outer radii, are found to be of interest in moment method solutions and help in designing antenna characteristics using coating of electrically and magnetically lossless and lossy material. They are given by

$$P = \left(\frac{\epsilon_r - 1}{\epsilon_r} \right) \ln \left(\frac{b}{a} \right) \quad (63a)$$

$$Q = (\mu_r - 1) \ln \left(\frac{b}{a} \right) \quad (63b)$$

where a = radius of the thin wire, $b - a$ = thickness of the coating, ϵ_r = the relative permittivity of the coating or the medium in which the thin wire is embedded, and μ_r = relative permeability of the coating or the medium in which the thin wire is embedded.

It turns out that the effects of increasing the real part of both P and Q are to increase the peak value of input impedance, to increase the electric length which lowers the resonant frequency and to reduce the bandwidth of operation. The effects of increasing the imaginary part of P and Q are to decrease the peak value of input impedance, to decrease the electrical length which increases the resonant frequency, and to increase the bandwidth. This means a proper choice of a lossy dielectric with maximum imaginary parts of P and Q and minimum real parts of P and Q can achieve an optimum bandwidth. But this will be at the cost of antenna efficiency because of the lossy coating.

BIBLIOGRAPHY

1. C. A. Balanis, *Antenna Theory: Analysis and Design*, Wiley, New York, 1997.
2. C. A. Balanis, *Advanced Engineering Electromagnetics*, Wiley, New York, 1979, Chap. 12, pp. 670-742.
3. J. Moore and R. Pozer, eds., *Moment Methods in Electromagnetics: Techniques and Applications*, Research Studies Press, Letchworth, UK, 1984; Wiley, New York, 1984.
4. W. A. Imbraile, Applications of the Method of Moments to Thin-Wire Elements, in R. Mittra, ed., *Computer Techniques for Electromagnetics*, Pergamon, New York, 1973, Chap. 1.
5. C. A. Balanis, *Antenna Theory: Analysis and Design*, Wiley, New York, 1997, Chaps. 4 and 8.
6. G. A. Thiele, Wire antenna, in R. Mittra, ed., *Computer Techniques for Electromagnetics*, Pergamon, New York, 1973, Chap. 2, pp. 7-70.
7. J. Rockway et al., *The MININEC System Microcomputer Analysis of Wire Antenna*, Artech House, Norwood, MA, 1988.
8. E. K. Miller and F. J. Deadrick, Some computational aspects of thin-wire modeling, in R. Mittra, ed., *Numerical and Asymptotic Techniques in Electromagnetics*, Springer-Verlag, New York, 1975, Chap. 4, pp. 89-127.
9. J. J. H. Wang, *Electromagnetics: Formulation and Computer Solution of Integral Equation*, Wiley, New York, 1991, Chap. 5.
10. E. K. Miller, L. Medguesi-Mitchang, and E. H. Newman, Thin Wires, *Computational Electromagnetics: Frequency-Domain Method of Moments*, IEEE Press, New York, 1992, Part 3.
11. R. Mittra, ed., *Numerical and Asymptotic in Electromagnetics*, Springer-Verlag, Berlin, 1975.
12. C. A. Balanis, *Advanced Engineering Electromagnetics*, Wiley, New York, 1979, pp. 1-50.
13. K. K. Mei, On the integral equations of thin wire antennas, *IEEE Trans. Anten. Propag.* **AP-13** (1965).
14. C. M. Butler and D. R. Wilton, Analysis of various techniques applied to thin-wire scatterers, *IEEE Trans. Anten. Propag.* **AP-23**:534-540 (1975).

15. G. J. Burke and A. J. Poggio, *Numerical Electromagnetic Code NEC-Method of Moments*, Tech. Document 116, Naval Ocean Systems Center, San Diego, CA, Sept. 6, 1982.
16. IEEE Standard definition for terms for antennas (IEEE Std. 145-1983) *IEEE Trans. Anten. Propag.* **AP-17** (1969); **AP-22** (1974); **AP-31**(Part II) (1983).
17. A. K. Bhattacharyya and D. L. Sengupta, *Radar Cross Section Analysis and Control*, Artech House, Norwood, MA, 1991.
18. J. H. Richmond, *Proc. IRE* **53**:796 (1965).
19. R. F. Harrington, *Field Computation by Moment Methods*, Macmillan, New York, 1968.
20. J. C. Logan and J. W. Rockway, *The New MININEC Version 3: A Mininumerical Electromagnetic Code*, Tech. Document 93B, Naval Ocean Systems Center, San Diego, CA, Sept. 1986.
21. A. J. Julian, J. C. Logan, and J. W. Rockway, *MININEC: A Mininumerical Electromagnetics Code*, NOSC TD 516, Sept. 1982.
22. Windows Version of MININEC, EM Scientific, available by e-mail: emsi@aol.com.
23. Windows versions of NEC2 and NEC4, Nitany-Scientific Available (online), www.nittany-scientific.com.
24. A. R. Djordjevic et al., *AWAS for Windows: Analysis of Wire Antennas and Scatterers—Software and User's Manual*, Artech House, Norwood, MA, 1995.
25. S. Prasad and R. W. P. King, Experimental study of inverted L-, T- and related transmission line antenna, *J. Res. Natl. Bur. Standard-D Ratio Propag.* **65D**(5) (1961).
26. E. H. Newman, *A Users' Manual for Electromagnetic Surface Patch Code ESP, OSUESL*, Dept. Electrical Engineering, Report 713602-1, prepared under Contract DAAG-39-81-K-0020 for the Department of the Army, U.S. Army Res. Office, Res. Triangle Park, NC, July 1981.
27. J. H. Richmond, *Radiation and Scattering by Thin-Wire Structures in the Complex Frequency Domain*, OSU Research Foundation Report RF-2902-10, 1973.
28. S. A. Schelkmooff and H. T. Fris, *Antennas: Theory and Practice*, Wiley, New York, 1952, pp. 229–244, 351–353.
29. J. H. Richmond and E. H. Newman, Dielectric coated wire antennas, *Radio Sci.* **11**(1):13–20 (1976).
30. J. Y. P. Lee and K. G. Balmain, Wire antennas coated with magnetically and electrically lossy material, *Radio Sci.* **14**(3):437–445 (1979).

LOCAL-AREA NETWORKS (LANs)

JOSEPH B. EVANS
University of Kansas
Lawrence, Kansas

Local-area networks (LANs) are data communications networks that are restricted in extent to an office, home,

building, or in some cases, areas as large as a college or university campus. Because of the spectacular growth in networking, LANs can be found deployed in almost every organization. Various established and evolving technologies are used in LANs, based on physical facilities ranging from copper and optical fiber to radio. The characteristics of commonly used LAN technologies will be discussed below.

1. LAN TOPOLOGIES

LANs can be logically organized in several topologies, the most popular of which are the bus, star, and ring.

In the bus structure, illustrated in Fig. 1, nodes (computers, printers, or similar devices) are interconnected to a common, shared physical resource, typically a wire or cable. This topology is inexpensive, since wiring expenses are shared among the nodes. Unfortunately, this scheme involves sharing the limited bandwidth resources of the bus, and can also be somewhat unreliable, as bus failures in the vicinity of one node can affect the others on the same bus. IEEE 802.3 10base5 and 10base5 Ethernet are examples of networking standards based on a bus topology at the physical layer. Despite its shortcomings, this remains a common topology because of the simplicity of deployment. Because of the nature of the wireless medium, it is the topology used by wireless LANs such as those based on IEEE 802.11.

An alternative is the star topology, shown in Fig. 2, in which each node has dedicated resources to some central switching site. This has the advantage of dedicated bandwidth to the interconnection point, but the attendant cabling costs are often higher than those for the bus topologies. Switched Ethernet and asynchronous transfer mode (ATM) are examples of networking standards based on a star topology. There is increasing dependence on star topologies because the limited bandwidth on a cable is not shared and traffic is not subject to internode arbitration delays for access to the medium.

Another option is the ring topology, shown in Fig. 3, in which each node is interconnected to its neighbor. The IEEE 802.5 Token Ring and the Fiber Distributed Data Interface (FDDI) are examples of networking standards based on a ring topology. This topology shares many of the advantages and disadvantages of the bus topology—inexpensive wiring, but with reliability problems if the ring should be broken. Ring-based LANs have been designed to overcome the reliability issues by using counterrotating rings (e.g., FDDI). Depending on the protocols in use, bandwidth in a ring-based network can be reused (since the ring is not physically contiguous), and hence such a

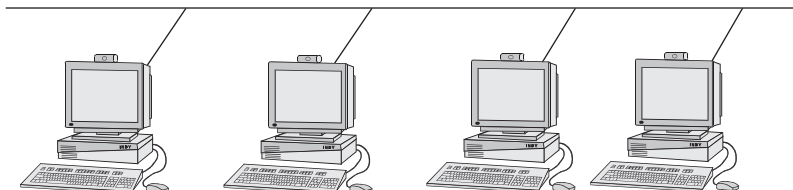


Figure 1. Bus topology.

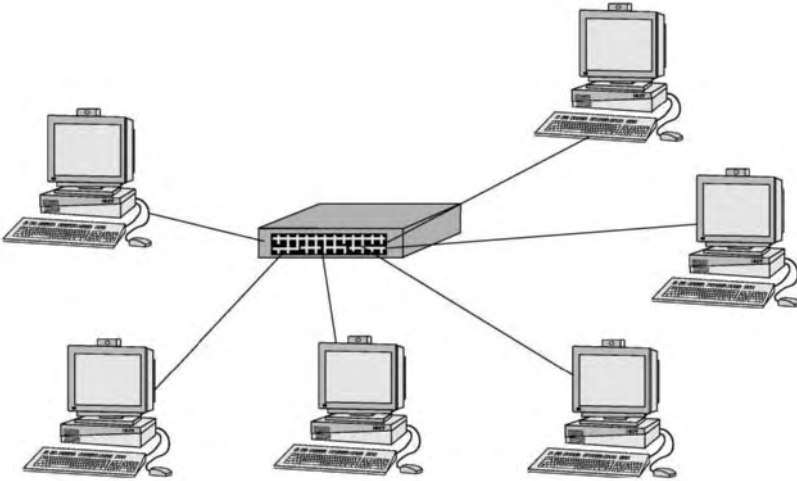


Figure 2. Star topology.

topology can have a capacity greater than the equivalent bus.

2. IEEE 802 LAN STANDARDS

Much of the growth in deployment of LAN technology can be attributed to the standardization of selected technology options, which has enabled multivendor interoperability and has spawned a highly competitive market. The IEEE 802 LAN standards are among the most widely used data protocols yet developed.

The IEEE 802.2 standard specifies the logical link control (LLC) protocols used by the other IEEE LAN standards. IEEE 802.2 allows the lower-level protocols to interface with higher-level protocols in a consistent manner. Using this approach, for example, the Internet Protocol (IP) need not know the type of underlying hardware being used on a particular host, which implies that software can be simplified and made more reliable. Note that

certain other protocol suites (e.g., IP over ATM) use the IEEE LLC SAP (service access point) codes for protocol multiplexing and demultiplexing, so that similar benefits can be obtained. IEEE 802.2 provides several services; which services are used and the extent to which they are used depends on the needs of the other protocols involved.

The IEEE 802.3 standard has been one of the most successful in the IEEE LAN suite. This standard describes the Carrier Sense Multiple Access with Collision Detection (CSMA/CD) protocol that forms the basis for the Ethernet family (note that the 802.3 standard and Ethernet differ slightly, but can be made to interoperate). The IEEE 802.3 standard consists of several related protocols, for different physical media. Included are the original 10base5 standard for CSMA/CD on 50- Ω -thick coaxial cable, the 10base2 standard for lighter 50- Ω coaxial cable, and the 10baseT standard for unshielded twisted-pair cables. No longer commonly used are the 1base5 StarLAN standard and the 10broad36 standard for more widely dispersed networks. Fiber extension options are available for distributed site interconnection (within protocol distance limits). Ethernets can be found in almost all corporate data networks. Although networks based on the 10-Mbps (megabits per second) data rate are still deployed, higher-rate Ethernet protocols are becoming increasingly popular, particularly 100-Mbps Fast Ethernet, Gigabit Ethernet, and most recently 10-Gbps Ethernet. The 100-Mbps and 1-Gbps Ethernet varieties utilize both fiber and copper; the latter are restricted to server rooms and other facilities with small distances between nodes.

The IEEE 802.4 standard specifies the token bus protocol. This protocol has been the basis for several networking technologies, including the MAP/TOP suite. Multiple physical layers are defined for token bus on 75- Ω coaxial cable, including systems at 1, 5, and 10 Mbps. These are all broadband systems. The original 1-Mbps system was quite popular because of its low cost and relative simplicity.

The IEEE 802.5 standard specifies the token ring protocol. This standard was extensively deployed in PC-based networks and became second only to Ethernet in ubiquity, although it is no longer widely used. It uses unshielded

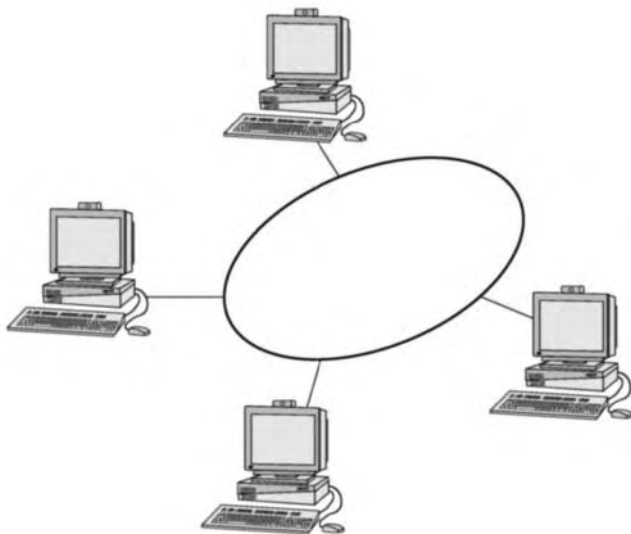


Figure 3. Ring topology.

twisted-pair cabling, with data rates at 4 and 16 Mbps. It has several very desirable features, including robust behavior in the presence of high traffic loads and bounded delay (to transmit) times.

3. PROTOCOL LAYERING

For standardization purposes, networking protocols are most often conceptually partitioned into several layers. In the case of LAN technologies, the physical layer (PHY), media access layer (MAC), and logical link layer (LLC) are commonly specified. The latter two are often grouped together to form the data link layer in standard layering schemes.

3.1. PHY Layer

The PHY, or physical layer, is the lowest layer of a protocol stack. The standards for this layer typically describe the medium to be used (e.g., cable, fiber, wireless), modulation schemes, and encoding schemes used to transmit information across the medium.

The PHY layers of LAN protocols generally fall into two categories: baseband and broadband. A *baseband* PHY layer is one in which the information bearing signals are digital signals, typically encoded using simple level-based keying, Manchester encoding, or differential Manchester encoding. This is the most common type of PHY layer in current LANs, as it is relatively inexpensive and sufficiently robust for most local environments. The disadvantages are distance limitations, typically 100 m to at most 1000 m on copper, and bandwidth no more than about 1 Gbps over copper using current technologies. Baseband techniques may be used over optical fiber at much greater distances and rates, but with the attendant installation and network equipment costs. For typical LAN installations, however, baseband systems on copper are sufficient.

Encoding schemes are another key element of the PHY layer. A variety of encodings, tailored to the physical medium for a given protocol, have been developed. Some typical encodings are depicted in Fig. 4. These can be broadly classed as non-return-to-zero (NRZ) techniques and biphasic techniques.

The conceptually simplest encodings are the NRZ methods. In the NRZ-level approach, for example, zeros (0s) are encoded as low voltage level, and ones (1s) are encoded as a high voltage level. In optical fiber systems, the corresponding encodings may be that ones are the presence of optical power; zeros, the lack of light. In the NRZI (NRZ with invert on ones) approach, a transition (either falling or rising edge) denotes a one, and the lack of a transition signifies a zero.

While simple, the NRZ schemes have several shortcomings. Most significantly, recovery of bit timing at the receiver can be difficult—the moment in time at which to sample a bit to determine whether it is a zero or one is seldom apparent in the presence of noise and other such impairments. A technique that provides an unambiguous timing reference is highly desirable. Furthermore, the occurrence of a long string of zeros or ones can result in an undesirable DC voltage bias on the transmission medium,

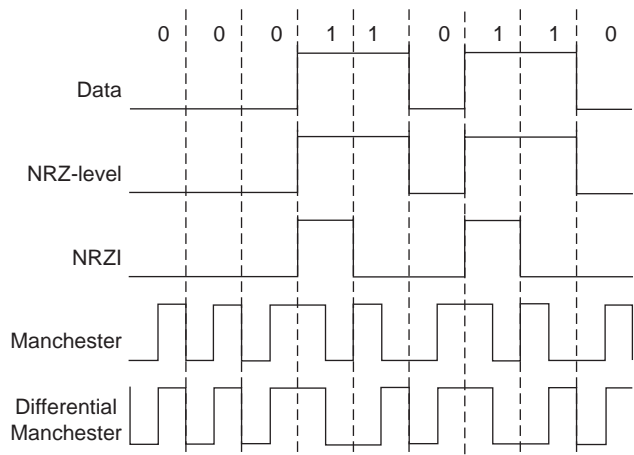


Figure 4. Baseband PHY encoding schemes.

which may cause threshold-related errors and problems with the use of transformers. There are several approaches to resolving these related problems, which center around the need for signal transitions.

The 4B/5B (4-byte/5-byte) and related techniques (4B/6B and 8B/10B are also common) involves guaranteeing sufficient transitions by inserting extra bits into the signal stream. Data symbols, 4 bits in this case, are mapped into a 5-bit code, which is then transmitted using NRZI, for example. This is illustrated in Table 1. An inspection of this table will prove that strings with a maximum of three consecutive zeros are possible, even when codewords are concatenated. Multiple ones are not an issue if NRZI is used for transmission, as ones force a transition to occur. The cost of a 4B/5B mapping, of course, is that only 80% efficiency is possible.

The biphasic encodings are beneficial with respect to signal balance maintenance, and bit timing recovery is particularly easy to implement in this scheme. These are based on signal transitions at a rate double that of the bit rate. A transition (rising edge or falling edge) is guaranteed to occur at the center of the bit period. The absence

Table 1. 4B/5B Encoding

Data Symbol	Codeword
0000	11110
0001	01001
0010	10100
0011	10101
0100	01010
0101	01011
0110	01110
0111	01111
1000	10010
1001	10011
1010	10110
1011	10111
1100	11010
1101	11011
1110	11100
1111	11101

of such a transition can be used as an error detection method.

In Manchester encoding, a zero is encoded as a rising edge at the center of the bit period, and a one as a falling edge at such a time. The encoding mechanism can be implemented as an exclusive-OR operation between the data and the clock. This is the encoding used for most of the original IEEE 802.3 protocols (10base5, 10base2, 10baseT). Differential Manchester encoding uses the mid-period transition for a clocking reference only, and uses the presence (denoting a zero) or absence (denoting a one) of a transition at the beginning of the bit period to encode the information. This is the method used for the IEEE 802.5 token ring standard.

The primary disadvantage of biphase signaling is that transitions happen at twice the data rate, which means that the bandwidth required is greater than that of the equivalent NRZ system, and the hardware need operate twice as quickly. The former is particularly critical in wireless systems.

A broadband PHY layer is one in which the information is coupled into the medium by analog signals, which are modulated by some carrier, and encoded using frequency shift keying (FSK), amplitude shift keying (ASK), phase shift keying (PSK), or some similar scheme. This type of PHY layer is most often used in situations where longer distances need be served or additional bandwidth is required. Much greater bandwidths may be supported on one cable using broadband schemes, as multiple frequencies can be used. The primary disadvantage of the broadband approach is the cost of modulators, demodulators, and the associated analog hardware.

3.2. MAC Layer

The MAC, or media access layer, is used to arbitrate access to the PHY layer. For example, in the case of Ethernet, there is a shared medium (cable) that must be used by several nodes, and only one of the nodes can be permitted to access the cable at a particular time.

The MAC layer influences the effective throughput over a given physical layer and should be efficient in its use of the available bandwidth. This includes minimizing the overhead due to factors such as protocol headers and deadtime between transmissions, while at the same time maximizing the successful transmissions on a busy shared medium network. In addition, the MAC layer is often designed to ensure that errors are not propagated to the higher-layer protocols.

Various MAC schemes have been developed for the LAN protocols. The two most common are the Carrier Sense Multiple Access with Collision Detection (CSMA/CD) protocol used in Ethernet, the token ring protocols, and the token bus protocol.

The CSMA/CD MAC protocol involves detecting the use of the medium by another station by checking the state of the carrier. If a station has data to transmit, it first attempts to verify whether the medium is unused. If it is available, the station transmits. If the medium is not available, the station waits until it becomes idle and

then immediately begins to transmit (note that this is the IEEE 802.3 solution, but other options are possible in the general case of CSMA). The success or failure of transmissions is monitored on the shared medium, and if a transmission is unsuccessful, that is, a collision is detected, the station waits a prescribed random amount of time (binary exponential backoff) and attempts to transmit again. This procedure is repeated until the transmission is successful, or the limit to the number of transmission attempts (16 in IEEE 802.3) is reached. CSMA/CD is simple, inexpensive, and performs well under light loads. Unfortunately, it can perform poorly under heavy loads, and be sensitive to physical layer errors. The CSMA/CD protocol, however, need not be invoked in a full-duplex switched Ethernet network. In a full-duplex switched network, each segment from switch to station or from switch to switch is its own isolated domain, and no collisions that require CSMA/CD can occur.

Token ring protocols use a “token” to arbitrate access to the transmission medium. A token is a small frame that is exchanged between stations in order to gain the right to transmit. If a station has data to transmit, it waits until a token is seen on the medium. This station then modifies the token and appends the necessary fields as well as its data. When this frame returns around the ring to the originating station, it is purged from the medium. When data transmission is complete, the station inserts a new token onto the ring. Token rings support fair, controlled access to the medium, and perform well under heavy load conditions. A disadvantage is the need for careful token maintenance, particular in the presence of errors. Several varieties of token ring exist; some of these will be discussed in subsequent sections.

The token bus protocol is closely related to the token ring, but with an underlying physical bus topology. The token exchange mechanism, however, does in fact use a logical ring for token passing. This logical ring is simply an ordering of stations on the bus. Once the logical ring is in place, token passing can proceed as in a ring-based system. This system provides controlled access to the bus, and is robust under heavy loads. One of the disadvantages of this approach is that ring initialization and maintenance is more complex than in a physical ring—the ordering of stations must be determined through some algorithm, and stations additions and deletions must be managed.

3.3. Logical Link Control (LLC) Layer

The LLC, or logical link control layer, can be viewed as the upper part of the data link layer. It is used to provide data services to the higher layers. In particular, two types of services, connectionless and connection-oriented, are defined. In LANs supporting complex higher layer protocols, such as TCP/IP, only the simplest LLC services are commonly used.

An example of an LLC protocol is the IEEE 802.2 layer. This provides both connectionless and connection-oriented services. The unacknowledged connectionless service provides simple datagram support for the multiplexing and demultiplexing of higher layer protocols. In addition,

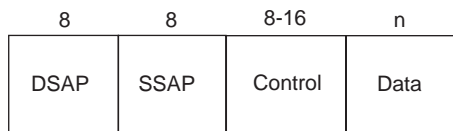


Figure 5. IEEE 802.2 LLC frame format.

a connectionless service with acknowledgments (for monitoring systems, for example) is supported, as well as a connection-oriented service that furnishes flow control and error recovery capabilities based on the lower-layer CRC (cyclic redundancy check) and a “go-back-N” strategy. The IEEE 802.2 LLC frame format is depicted in Fig. 5. The SAP and SSAP (direction and source service access point) fields are used to indicate the service type [e.g., IP or IPX (Internet protocol and internetwork packet exchange)] to higher layers. The control field is used for the LLC service support, including indication of the type of service.

4. ETHERNET (IEEE 802.3)

The Ethernet, and the closely related IEEE 802.3 standard, has been one of the most successful LAN protocols developed to date. This technology is based on CSMA/CD, and takes a variety of forms at the PHY layer. A typical Ethernet installation is depicted in Fig. 6.

The Ethernet frame format is illustrated in Fig. 7. The preamble is used for frame delineation. The destination and source address fields (48 bits each) are globally unique identifiers for each Ethernet adapter, and are used for station-to-station communication, as well as broadcast (all ones) and multicast (the first bit is one). It should be noted that the 48-bit addresses used in Ethernet have become a common feature in IEEE 802-based LANs. The type field (Ethernet) can be used for higher-layer demultiplexing, as in an LLC protocol. The length field (IEEE 802.3) is used to aid in end-of-frame detection. A 32-bit CRC is used for error detection, and is followed by a postamble for end-of-frame detection.

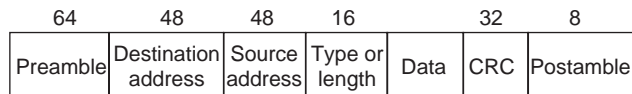


Figure 7. Ethernet frame format.

5. TOKEN-PASSING BUS (IEEE 802.4)

The IEEE 802.4 token bus standard has been widely used in manufacturing systems and early office automation products. Because it is based on a broadband physical medium, it is somewhat more resistant to the low-frequency EM noise that might arise on a factory floor.

A token-passing bus is a LAN with a bus topology that operates on the principle that a token will be received prior to the transmission of data by a station. The token bus frame format includes a preamble, frame control byte for denoting whether a particular frame is a token or data, the destination and source addresses (48 bits, as in 802.3), the data (an LLC frame), a error detection field (CRC-32, as in 802.3), and the postamble.

The token bus operates by first establishing a logical ring that overlays the physical bus topology. Station additions and deletions require reconfiguration of the logical ring. When a token is received, a station is permitted to transmit multiple packets, until its token holding time has expired. The token bus offers optional support for multiple classes of service through the use of complex timer specifications that enable per-class bandwidth guarantees. Support for simpler nontoken stations is included to allow low cost devices to respond to polling requests using this medium.

6. MAP/TOP

MAP is the Manufacturing Automation Protocol developed by General Motors Corporation for communication among automated manufacturing devices, including robotic equipment and the associated controllers. It was primarily designed to support communication between very different sorts of devices, in real time with low, predictable

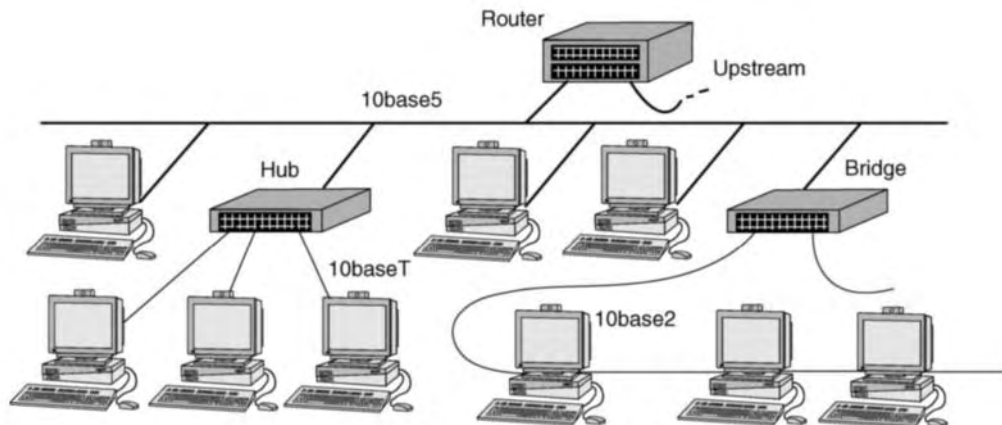


Figure 6. Typical Ethernet installation.

delays. It supports applications as varied as word processing and equipment telemetry (temperature measurement, for example).

TOP is the Technical and Office Protocol developed by Boeing Corporation for communication between office automation devices such as word processing systems and printers. Interoperability between devices from a variety of manufacturers was a key design goal of this protocol.

The MAP/TOP protocol suite is based on the IEEE 802.4 token bus protocols. As such, MAP/TOP networks are often interconnected with some variety of token passing network for ease of interface design.

7. TOKEN RING (IEEE 802.5)

The token ring protocol was widely deployed in networks based on PCs before Ethernet became the dominant LAN technology. Token ring operates on the principle of the exchange of a “token” to a station before it is permitted to transmit. Only one token is allowed on the ring at one time.

The IEEE 802.5 token ring frame formats are illustrated in Fig. 8. The first format is used for token frames, and only includes start and end delimiters, and the access control field with priorities and reservation information. The second format includes start and end delimiters, a frame control word for optional LC support, source and destination addresses (in 802.3 format), the LLC (data) frame, a CRC-32, and a frame status word used by transmitting stations to verify reception.

8. OTHER TOKEN RINGS

Another example of token ring technology in wide use today is the Fiber Distributed Data Interface (FDDI) standard. This technology supports multiple packets on the ring at one time, with rates of 100 Mbps. Provisions are made for multiple service classes (synchronous and asynchronous) with differing throughput and delay requirements. Further, reliability support is provided through the capability for optional redundant counter-rotating rings, which can mask a station or fiber failure.

8.1. Slotted Ring

Slotted-ring technology uses multiple “slots” that rotate around the ring to arbitrate access. Each slot is a small frame that can be marked empty or full. When an empty slot arrives at a station with data to transmit, the slot is marked full and data is injected. The slot is marked empty

when it returns around the ring to its source. A given station cannot transmit again when it has an outstanding slot. The provision for multiple packets from different sources on the ring at one time assists in fair utilization and quality of service support.

The Cambridge ring is an early example of such technology (some claim that it is also the ancestor of the ATM protocols, also based on small fixed frame sizes). A slot contains one octet each for the source and destination addresses, five control bits, and two, four, six, or eight data octets, and thus slot sizes are extremely small. This implies that higher-layer packet data are almost always segmented into small units prior to transmission. Stations could choose not to receive packets from particular sources; some of the control bits support this through response codes. The Cambridge ring was simple to implement, but somewhat wasteful of bandwidth due to the header overhead in such small datagrams.

8.2. Register Insertion Ring

Register insertion rings are a common LAN technology, and can be used to provide high performance through their support for multiple packets on the ring at one time. The register insertion ring uses a small shift register at each station to control forwarding and insertion onto the ring. The shift register is at least as large as the maximum frame size. This allows a station to store a frame as it passes. If the station has no data to send, a passing frame is buffered long enough to determine whether it is destined for the local station. If it is destined locally, a typical implementation will both copy the frame into adapter memory and forward the frame back around the ring in order to support acknowledgments. Transmission when the medium is available is handled by simply copying the data onto the ring. If a frame arrives during this time, it is buffered in the insertion register. The register insertion method provides excellent ring utilization due to the multiple simultaneous packets on the ring without the overhead penalty of the slotted ring. The disadvantage of this technology is that the purge mechanism, that is, the technique used to remove problematic packets from the ring, is generally more complex than in other systems.

9. HYPER CHANNEL, HIPPI, AND FIBRE CHANNEL

A number of LAN protocols are designed for very-high-speed interconnection of computers and their peripherals.

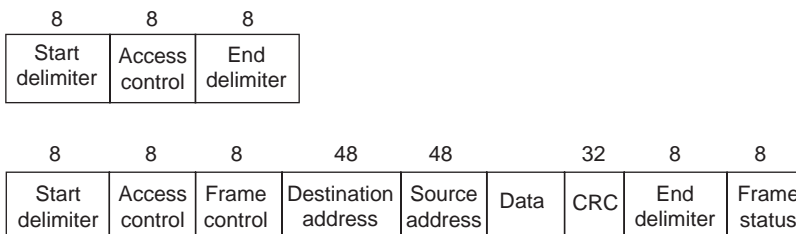


Figure 8. Token ring frame format.

HYPERchannel, developed by Network Systems Corporation, is one of these. This protocol was developed in the mid-1980s for the interconnection of supercomputers and high-performance peripherals, and has been used with Cray and Amdahl systems, among others. It supports data rates of up to 275 Mbps over a variety of physical layers.

HIPPI (high-performance parallel interface) is another of the protocols developed primarily for interconnection of supercomputers. This protocol supports 800-Mbps or 1.6-Gbps links over a large parallel cable, which is either 32 or 64 lines wide and runs at 25 MHz. The distances over which HIPPI can be used is quite limited, but large enough for a typical supercomputer center equipment floor. Interconnection of sites can be accomplished using fiber extension options. Simple flow control features are provided to lessen problems with computers and peripherals of widely different I/O (input/output) bandwidth. Although simple and effective, this flow control scheme does contribute to the problems of extending HIPPI networks over larger distances while maintaining high throughput. In order to build HIPPI networks of nontrivial size, simple switches are used to interconnect devices. These switches are typically not designed to switch between sources and destinations at high rates, as with routers and packet switches, but rather act as interconnection panels that may be reconfigured at reasonable rates for the sharing peripherals.

Fibre Channel is a LAN protocol suite designed for high-speed communication between nodes using optical fiber. Rates of up to 4 Gbps are supported. Fibre Channel is designed to combine the features of channel protocols (such as HIPPI) and switched LAN protocols in order to provide a scalable and reliable interconnection with the high speeds and low latency required for servers and their peripherals in storage-area networks (SANs).

10. OTHER LAN PROTOCOLS

A number of new, flexible, and high-performance LAN protocols have been developed. These developments include FireWire (IEEE 1394) and USB (universal serial bus), high-speed protocol suites based on serial interconnection technology. There are several varieties of FireWire, for example, with support for bandwidths of up to 800 Mbps with up to 63 devices (with no more than 16 cable hops) per bus in the more commonly deployed versions. More recent FireWire standards offer bandwidths up to 1.2 Gbps with continued increases expected. FireWire is most commonly used for interconnection of digital media (video and audio) devices. USB 1.1, a 12-Mbps serial protocol with chaining support, was originally designed primarily as an improvement over traditional serial port technologies. Peripherals such as keyboards and mice now most often use USB, and more exotic USB peripherals such as storage media devices are increasingly commonplace. With the introduction of USB 2.0, which supports speeds of up to 480 Mbps, it is expected that USB video and audio devices will also be widespread.

Asynchronous transfer mode (ATM) technology was also deployed in LANs. ATM is a switch-based technology that uses small packets (53 bytes) called *cells*. Interconnection of nodes is through virtual circuits, which are analogous to circuits in voice telephony. Multiple physical layers are supported, including both copper and fiber infrastructure options. Although ATM is often viewed as a wide-area networking (WAN) technology, it does provide support for features that are not available in other technologies. For example, ATM allows the definition of virtual LANs that provide network administrators with options that are not available in less sophisticated technologies. Virtual or emulated LANs are interconnections of LANs, perhaps widely separated, which are configured to emulate a single local-area network. Furthermore, multiple logical local area networks can be supported over a single physical infrastructure using this capability. Because of its complex administration, ATM LAN deployments have largely been restricted to networks with applications needing its unique capabilities.

11. WIRELESS LANs

Wireless LANs use radio or infrared as the transmission medium, as opposed to the traditional wire or fiber. This has significant advantages, particularly for deployment in older buildings where wiring costs are high, as well as environments in which workers may be moving frequently.

Many of the initial wireless LANs in the United States have used radiofrequencies in one of the ISM (instrumentation, scientific, medical) bands, which generally may be used without individual site licensing subject to restrictions on power output. The data rates on these systems range from tens of kilobits per second to tens of megabits per second, with typical ranges of a few hundreds of meters. Wireless LANs are still evolving, but instances of several standards are now the basis for extremely popular products.

The most significant developments in this area are based on the IEEE 802.11 standard. It is based on a CSMA/CA (CSMA with Collision Avoidance) MAC layer with multiple physical layers, including direct sequence spread spectrum, orthogonal frequency-division multiplexing, frequency-hopping spread spectrum, and infrared. The widely deployed IEEE 802.11b standard provides data rates of 11 Mbps over a range of approximately 100 m in typical radio configurations using the 2.4-GHz ISM band. This has been supplemented by the IEEE 802.11g standard that provides data rates up to 22 Mbps at these same frequencies in a backward compatible manner. The IEEE 802.11a standard provides 54 Mbps rates using radios in the 5-GHz unlicensed bands.

Another wireless local area networking technology that is increasingly popular is Bluetooth. This is intended to be a very-local-area-network, often referred to as a personal-area network, with ranges typically up to only 10 m and data rates below 1 Mbps. This standard also uses the 2.4-GHz ISM frequency band, with frequency hopping spread spectrum. Although Bluetooth is often called a

“cable replacement” technology, it also offers computer-to-computer connectivity within its local region.

Wireless LANs will offer the opportunity to connect all manners of devices such as sensors and instruments to the increasingly pervasive network.

BIBLIOGRAPHY

1. W. Stallings, *Local and Metropolitan Area Networks*, 6th ed., Prentice-Hall, New York, 2000.
2. L. L. Peterson and B. S. Davie, *Computer Networks—a Systems Approach*, 3rd ed., Morgan Kaufmann, San Francisco, 2003.
3. P. T. Davis and C. R. McGuffin, *Wireless Local Area Networks*, McGraw-Hill, New York, 1995.
4. J. Walrand and P. Varaiya, *High Performance Communication Networks*, 2nd ed., Morgan Kaufmann, San Francisco, 1999.
5. J. Wobus, *LAN Technology Scorecard*; available online at <http://www.mcgeoch.com/other/lan-technology.html>, 1999.
6. J. Geier, *Wireless LANs*, Sams Publishing, Indianapolis, 2001.

LOOP ANTENNAS

KAZIMIERZ SIWIAK
TimeDerivative, Inc.
Coral Springs, Florida

The *IEEE Standard Definitions of Terms for Antennas* [1] defines the loop as “an antenna whose configuration is that of a loop,” further noting that “if the current in the loop, or in the multiple parallel turns of the loop, is essentially uniform and the loop circumference is small compared with the wavelength, the radiation pattern approximates that of a magnetic dipole.” That definition and the further note imply the two basic realms of loop antennas: electrically small, and electrically large structures.

There are hundreds of millions of loop antennas currently in use [2] by subscribers of personal communication devices, primarily pagers. Furthermore, loops have appeared as transmitting arrays, like the massive multielement loop array at shortwave station HCJB in Quito, Ecuador, and as fractional wavelength-size tunable HF transmitting antennas. The loop is indeed an important and pervasive communication antenna.

The following analysis of loop antennas reveals that the loop, when small compared with a wavelength, exhibits a radiation resistance proportional to the square of the enclosed area. Extremely low values of radiation resistance are encountered for such loops, and extreme care must be taken to effect efficient antenna designs. Furthermore, when the small loop is implemented as a transmitting resonant circuit, surprisingly high voltages can exist across the resonating capacitor even for modest applied transmitter power levels. The wave impedance in the immediate vicinity of the loop is low, but at close distances

(0.1–2 wavelengths) exceeds the intrinsic free-space impedance before approaching that value.

A loop analysis that applies to loops of arbitrary circular diameter and of arbitrary wire thickness is summarized here. The analysis leads to some detail regarding the current density in the cross section of the wire. Loops of shapes other than circular are less easily analyzed, and are best handled by numerical methods such as moment method described in Ref. 3.

Loops are the antennas of choice in pager receivers, and appear as both ferrite loaded loops and as single-turn rectangular shaped structure within the radio housing. Body-worn loops benefit from a field enhancement due to the resonant behavior of human body with respect to vertically polarized waves. In the high-frequency bands, the loop is used as a series resonant circuit fed by a secondary loop. The structure can be tuned over a very large frequency band while maintaining a relatively constant feedpoint impedance. Large loop arrays consisting of one-wavelength-perimeter square loops have been successfully implemented as high-gain transmitting structures at high-power shortwave stations.

1. ANALYSIS OF LOOP ANTENNAS

Loop antennas, particularly circular loops, were among the first radiating structures analyzed beginning as early as 1897 with Pocklington’s analysis [4] of the thin wire loop excited by a plane wave. Later, Hallén [5] and Storer [6] studied driven loops. All these authors used a Fourier expansion of the loop current, and the latter two authors discovered numerical difficulties with the approach. The difficulties could be avoided, as pointed out by Wu [7], by integrating the Green function over the toroidal surface of the surface of the wire. The present author coauthored an improved theory [8,9] that specifically takes into account the finite dimension of the loop wire and extends the validity of the solution to wires thicker than previously considered. Additionally, the work revealed some detail of the loop current around the loop cross section. Arbitrarily shaped loops, such as triangular loops and square loops, as well as loop arrays, can be conveniently analyzed using numerical methods.

1.1. The Infinitesimal Loop Antenna

The infinitesimal current loop consists of a circulating current I enclosing an infinitesimal surface area S , and is solved by analogy to the infinitesimal dipole. The fields of an elementary loop element of radius b can be written in terms of the loop enclosed area $S = \pi b^2$ and a constant excitation current I (when I is RMS, then the fields are also RMS quantities). The fields are “near” in the sense that the distance parameter r is far smaller than the wavelength, but far larger than the loop dimension $2b$. Hence, this is *not* the *close* near-field region. The term kIS is often called the *loop moment* and is analogous to the similar term Ih associated with the *dipole moment*. The infinitesimally small loop is pictured in Fig. 1a next to its elementary dipole analog (Fig. 1b). The dipole uniform current I flowing over an elemental length h is the dual of a

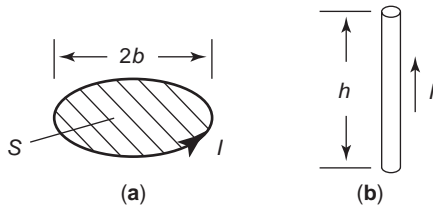


Figure 1. Small-antenna geometry showing (a) the parameters of the infinitesimal loop moment, (b) its elementary dipole dual. Source: After Siwiak [2].

“magnetic current” $M_z S = Ih$ and the surface area is $S = h/k$. The fields due to the infinitesimal loop are then found from the vector and scalar potentials.

1.1.1. Vector and Scalar Potentials. The wave equation, in the form of the inhomogeneous Helmholtz equation, is used here with most of the underlying vector arithmetic omitted (see Refs. 10–12 for more details). For a magnetic current element source, the electric displacement \mathbf{D} is always solenoidal (the field lines do not originate or terminate on sources); that is, in the absence of source charges the divergence is zero

$$\nabla \cdot \mathbf{D} = 0 \quad (1)$$

and the electric displacement field can be represented by the curl of an arbitrary vector \mathbf{F}

$$\mathbf{D} = \varepsilon_0 \mathbf{E} = \nabla \times \mathbf{F} \quad (2)$$

where \mathbf{F} is the vector potential and obeys the vector identity $\nabla \cdot \nabla \times \mathbf{F} = 0$. Using Ampere’s law in the absence of electric sources

$$\nabla \times \mathbf{H} = j\omega \varepsilon_0 \mathbf{E} \quad (3)$$

and with the vector identity $\nabla \times (-\nabla\Phi) = 0$, where Φ represents an arbitrary scalar function of position, it follows that

$$\mathbf{H} = -\nabla\Phi - j\omega \mathbf{F} \quad (4)$$

and for a homogeneous medium, after some manipulation, we get

$$\nabla^2 \mathbf{F} + k^2 \mathbf{F} = -\varepsilon_0 \mathbf{M} + \nabla(\nabla \cdot \mathbf{F} + j\omega \mu_0 \varepsilon_0 \Phi) \quad (5)$$

where k is the wavenumber and $k^2 = \omega^2 \mu_0 \varepsilon_0$. Although Eq. (2) defines the curl of \mathbf{F} , the divergence of \mathbf{F} can be independently defined and the *Lorentz condition* is chosen

$$j\omega \mu_0 \varepsilon_0 \Phi = -\nabla \cdot \mathbf{F} \quad (6)$$

where ∇^2 is the Laplacian operator given by

$$\nabla^2 = \frac{\partial^2}{\partial x^2} + \frac{\partial^2}{\partial y^2} + \frac{\partial^2}{\partial z^2} \quad (7)$$

Substituting the simplification of Eq. (6) into (5) leads to the inhomogeneous Helmholtz equation

$$\nabla^2 \mathbf{F} + k^2 \mathbf{F} = -\varepsilon_0 \mathbf{M} \quad (8)$$

Similarly, using Eqs. (6) and (4), it is seen that

$$\nabla^2 \Phi + k^2 \Phi = 0 \quad (9)$$

Using Eq. (4) and the Lorentz condition of Eq. (6), we can find the electric field solely in terms of the vector potential \mathbf{F} . The utility of that definition becomes apparent when we consider a magnetic current source aligned along a single vector direction, for example, $\mathbf{M} = \mathbf{z}M_z$, for which the vector potential is $\mathbf{F} = \mathbf{z}F_z$, where \mathbf{z} is the unit vector aligned with the z -axis, and Eq. (8) becomes a scalar equation.

1.1.2. Radiation from a Magnetic Current Element. The solution to the wave equation [Eq. (8)] presented here, with the details suppressed, is a spherical wave. The results are used to derive the radiation properties of the infinitesimal current loop as the dual of the infinitesimal current element. The infinitesimal magnetic current element $\mathbf{M} = \mathbf{z}M_z$ located at the origin satisfies a one-dimensional, hence scalar, form of Eq. (8). At points excluding the origin where the infinitesimal current element is located, Eq. (8) is source-free and is written as a function of radial distance r

$$\nabla^2 F_z(r) + k^2 F_z(r) = \frac{1}{r^2} \frac{\partial}{\partial r} \left[r^2 \frac{\partial F_z(r)}{\partial r} \right] + k^2 F_z(r) = 0 \quad (10)$$

which can be reduced to

$$\frac{d^2 F_z(r)}{dr^2} + \frac{2}{r} \frac{dF_z(r)}{dr} + k^2 F_z(r) = 0 \quad (11)$$

Since F_z is a function of only the radial coordinate, the partial derivative in Eq. (10) was replaced with the ordinary derivative. Equation (11) has a solution

$$F_z = C_1 \frac{e^{-jkr}}{r} \quad (12)$$

There is a second solution where the exponent of the phasor quantity is positive; however, we are interested here in outward traveling waves so we discard that solution. In the static case the phasor quantity is unity. The constant C_1 is related to the strength of the source current, and is found by integrating Eq. (8) over the volume including the source, giving

$$C_1 = \frac{\varepsilon_0}{4\pi} kIS \quad (13)$$

and the solution for the vector potential is in the \mathbf{z} unit vector direction

$$\mathbf{F} = \frac{\varepsilon_0}{4\pi} kIS \frac{e^{-jkr}}{r} \mathbf{z} \quad (14)$$

which is an outward propagating spherical wave with increasing phase delay (increasingly negative phase) and with amplitude decreasing as the inverse of distance. We may now solve for the magnetic fields of an infinitesimal current element by inserting Eq. (14) into Eq. (4) with Eq. (6) and then for the electric field by using Eq. (2). The fields, after sufficient manipulation, and for $r \gg kS$, are

$$H_r = \frac{kIS}{2\pi} e^{-jkr} k^2 \left[\frac{j}{(kr)^2} + \frac{1}{(kr)^3} \right] \cos(\theta) \quad (15)$$

$$H_\theta = \frac{kIS}{4\pi} e^{-jkr} k^2 \left[-\frac{1}{kr} + \frac{j}{(kr)^2} + \frac{1}{(kr)^3} \right] \sin(\theta) \quad (16)$$

$$E_\phi = \eta_0 \frac{kIS}{4\pi} e^{-jkr} k^2 \left[\frac{1}{kr} - \frac{j}{(kr)^2} \right] \sin(\theta) \quad (17)$$

where $\eta_0 = c\mu_0 = 376.730313$ is the intrinsic free-space impedance, c is the velocity of propagation (see Ref. 13 for definitions of constants), and I is the loop current.

The equations for the *magnetic* fields H_r and H_θ of the infinitesimal [Eqs. (15) and (16)] loop have exactly the same form as the *electric* fields E_r and E_θ for the infinitesimal dipole, while Eq. (17) for the *electric* field of the loop E_ϕ has exactly the same form as the *magnetic* field H_ϕ of the dipole when the term kIS of the loop expressions is replaced with Ih for the infinitesimal ideal (uniform current element) dipole. In the case where the loop moment kIS is superimposed on, and equals the dipole moment Ih , the fields in all space will be circularly polarized.

Equations (15)–(17) describe a particularly complex field behavior for what is a very idealized selection of sources: a simple linear magnetic current M representing a current loop I encompassing an infinitesimal surface $S = \pi b^2$. Expressions (15)–(17) are valid only in the region sufficiently far ($r \gg kS$) from the region of the magnetic current source M .

1.1.3. The Wave Impedance of Loop Radiation. The *wave impedance* can be defined as ratio of the total energy in the electric field divided by the total energy in the magnetic field. We can study the wave impedance of the loop fields by using Eqs. (15)–(17) for the infinitesimal loop fields, along with their dual quantities for the ideal electric dipole. Figure 2 shows the loop field wave impedance as a function of distance kr from the loop along the direction of maximum far-field radiation. The wave impedance for the elementary dipole is shown for comparison. At distances near $kr = 1$ the wave impedance of loop radiation exceeds $\eta_0 = 376.73\Omega$, the intrinsic free space impedance, while that of the infinitesimal loop is below 376.73Ω . In this region, the electric fields of the loop dominate.

1.1.4. The Radiation Regions of Loops. Inspection of Eqs. (15)–(17) for the loop reveal a very complex field structure. There are components of the fields that vary as the inverse third power of distance r , the inverse square of r , and the inverse of r . In the near field or induction region of the idealized infinitesimal loop, that is, for $kr \ll 1$ (however,

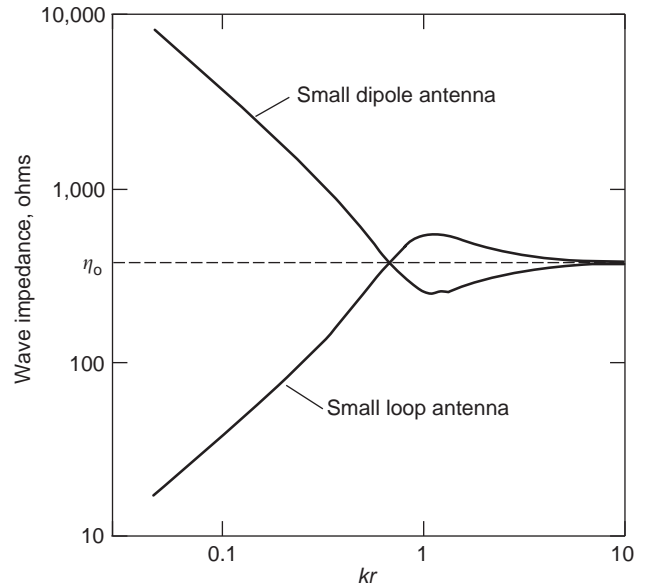


Figure 2. Small loop antenna and dipole antenna wave impedances compared. *Source:* After Siwiak [2].

$r \gg kS$ for the loop and $r \gg h$ for the dipole), the magnetic fields vary as the inverse third power of distance.

The region where kr is nearly unity is part of the radiating near field of the Fresnel zone. The inner boundary of that zone is taken by Jordan [12] to be $r^2 > 0.38D^3/\lambda$ and the outer boundary is $r < 2D^2/\lambda$ where D is the largest dimension of the antenna, here equal to $2b$. The outer boundary criterion is based on a maximum phase error of $\pi/8$. There is a significant radial component of the field in the Fresnel zone.

The far field or Fraunhofer zone is region of the field for which the angular radiation pattern is essentially independent of distance. That region is usually defined as extending from $r < 2D^2/\lambda$ to infinity, and the field amplitudes there are essentially proportional to the inverse of distance from the source. The far-zone behavior is identified with the basic free-space propagation law.

1.1.5. The Induction Zone of Loops. We can study the “induction zone” in comparison to the “far field” by considering “induction zone” coupling which was investigated by Hazeltine [14], and which was applied to low-frequency radio receiver designs of his time. Today the problem might be applied to the design of a miniature radio module where inductors must be oriented for minimum coupling. The problem Hazeltine solved was one of finding the geometric orientation for which two loops in parallel planes have minimum coupling in the induction zone of their near fields and serves to illustrate that the near-field behavior differs fundamentally and significantly from far-field behavior. To study the problem, we invoke the principle of reciprocity which states

$$\int_V [\mathbf{E}_b \cdot \mathbf{J}_a - \mathbf{H}_b \cdot \mathbf{M}_a] dV = \int_V [\mathbf{E}_a \cdot \mathbf{J}_b - \mathbf{H}_a \cdot \mathbf{M}_b] dV \quad (18)$$

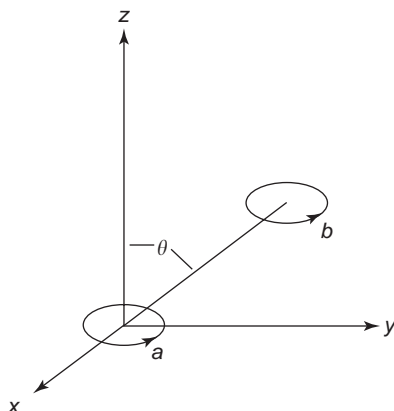


Figure 3. Two small loops in parallel planes and with $\theta = 54.736$ degrees will not couple in their near fields. *Source:* After Siwiak [2].

That is, the reaction on antenna *a* of sources *b* equals the reaction on antenna *b* of sources *a*. For two loops with loop moments parallel to the *z* axis, we want to find the angle θ for which the coupling between the loops vanishes, that is, both sides of Eq. (18) are zero. The reference geometry is shown in Fig. 3. In the case of the loop, there are no electric sources in Eq. (18), so $\mathbf{J}_a = \mathbf{J}_b = 0$, and both \mathbf{M}_a and \mathbf{M}_b are aligned with \mathbf{z} , the unit vector parallel to the *z* axis. Retaining only the inductive field, components and clearing common constants in Eqs. (15) and (17) are placed into (18). We require that $(H_r \mathbf{r} + H_\theta \theta) \mathbf{z} = 0$. Since $\mathbf{r} \cdot \mathbf{z} = -\sin(\theta)$ and $\mathbf{r} \cdot \mathbf{z} = \cos(\theta)$, we are left with $2 \cos^2(\theta) - \sin^2(\theta) = 0$, for which $\theta = 54.736^\circ$. When oriented as shown in Fig. 3, two loops parallel to the *x-y* plane whose centers are displaced by an angle of 54.736° with respect to the *z* axis will not couple in their near fields. To be sure, the angle determined above is “exactly” correct for infinitesimally small loops; however, that angle will be nominally the same for larger loops. Hazeltine [14] used this principle, placing the axes of the inductors in a common plane each at an angle of 54.7° with respect to the normal form the radio chassis, to minimize the coupling between the inductors.

The same principle can be exploited in the design of a metal detector, as depicted in Fig. 4. The loop *a* is driven with an audiofrequency oscillator. Loop *b*, in a parallel plane and displaced so that nominally $\theta = 54.7^\circ$, is connected to a detector that might comprise an audio amplifier that feeds a set of headphones. Any conductive object near loop *a* will disrupt the balance of the system and result in an increased coupling between the two loops, thus indicating the presence of a conducting object near *a*.

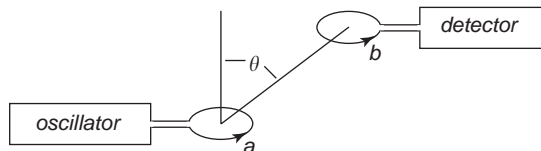


Figure 4. A metal detector employs two loops initially oriented to minimize coupling in their near fields.

1.1.6. The Intermediate and Far-Field Zones of Loops. The loop coupling problem provides us with a way to investigate the intermediate and far-field coupling by applying Eq. (18) with Eqs. (15) and (16) for various loop separations kr . In the far-field region only the H_θ term of the magnetic field survives, and by inspection of Eq. (16), the minimum coupling occurs for $\theta = 0$ or 180° . Figure 5 compares the coupling (normalized to their peak values) for loops in parallel planes whose fields are given by Eqs. (15)–(17). Figure 5 shows the coupling as a function of angle θ for an intermediate region ($kr = 2$) and for the far-field case ($kr = 1000$) in comparison with the induction-zone case ($kr = 0.001$). The patterns are fundamentally and significantly different. The coupling null at $\theta = 54.7^\circ$ is clearly evident for the induction-zone case $kr = 0.001$ and for which the $(1/kr)^3$ terms dominate. Equally evident is the far-field coupling null for parallel loops on a common axis when the $1/kr$ terms dominate. The intermediate zone coupling shows a transitional behavior where all the terms in kr are comparable.

1.1.7. The Directivity and Impedance of Small Loops. The *directive gain* of the small loop can be found from the far-field radially directed Poynting vector in a ratio to the average Poynting vector over the radian sphere:

$$D(\theta, \phi) = \frac{|\mathbf{E} \times \mathbf{H} \cdot \mathbf{r}|}{\frac{1}{4\pi} \int_0^{2\pi} \int_0^\pi |\mathbf{E} \times \mathbf{H} \cdot \mathbf{r}| \sin(\theta) d\theta d\phi} \quad (19)$$

Only the θ component of *H* and the ϕ component of *E* survive into the far-field. Using Eq. (16) for H_θ and (17) for E_ϕ and retaining only the $1/kr$ terms, Eq. (19) yields $D = 1.5 \sin^2(\theta)$ by noting that the functional form of the product of *E* and *H* is simply $\sin^2(\theta)$ and by carrying out the simple integration in the denominator of Eq. (19).

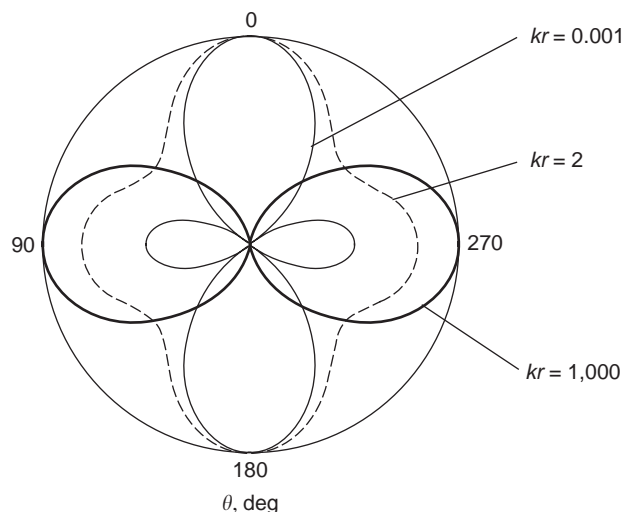


Figure 5. Normalized induction zone, intermediate zone, and far zone coupling between loops in parallel planes. *Source:* After Siwiak [2].

Taking into account the directive gain, the far-field power density P_d in the peak of the pattern is

$$P_d = \frac{1.5 I^2 R_{\text{radiation}}}{4\pi r^2} = H_0^2 \eta_0 = \left[\frac{kS}{4\pi} \frac{k}{r} I \right]^2 \eta_0 \quad (20)$$

for radiated power $I^2 R_{\text{rad}}$; hence, we can solve for the radiation resistance

$$R_{\text{rad}} = \frac{(kS)^2}{6\pi} \eta_0 = \eta_0 \frac{\pi}{6} (kb)^4 \quad (21)$$

for the infinitesimal loop of loop radius b .

When fed by a gap, there is a dipole moment that adds terms not only to the impedance of the loop but also to the close near fields. For the geometry shown in Fig. 6, and using the analysis of King [15], the electrically small loop, having a diameter $2b$ and wire diameter $2a$, exhibits a feedpoint impedance given by

$$\begin{aligned} Z_{\text{loop}} = \eta_0 \frac{\pi}{6} (kb)^4 [1 + 8(kb)^2] \left[1 - \frac{a^2}{b^2} \right] \cdots \\ + j\eta kb \left[\ln \left[\frac{8b}{a} \right] - 2 + \frac{2}{3} (kb)^2 \right] [1 + 2(kb)^2] \end{aligned} \quad (22)$$

including dipole-mode terms valid for $kb \ll 0.1$. The leading term of Eq. (22) is the same as derived in Eq. (21) for the infinitesimal loop. Expression (22) adds the detail of terms considering the dipole moment of the gap-fed loop as well as refinements for loop wire radius a . The small loop antenna is characterized by a radiation resistance that is proportional to the fourth power of the loop radius b . The reactance is inductive and hence is proportional to the antenna radius. It follows that the Q is inversely proportional to the third power of the loop radius, a result that is consistent with the fundamental limit behavior for small antennas.

Using Eq. (22), and ignoring the dipole mode terms and second-order terms in a/b , the unloaded Q of the loop antenna, is

$$Q_{\text{loop}} = \frac{6}{\pi} \frac{\left[\ln \left[\frac{8b}{a} \right] - 2 \right]}{(kb)^3} \quad (23)$$

which for $b/a = 6$ becomes

$$Q_{\text{loop}} = \frac{3.6}{(kb)^3} \quad (24)$$

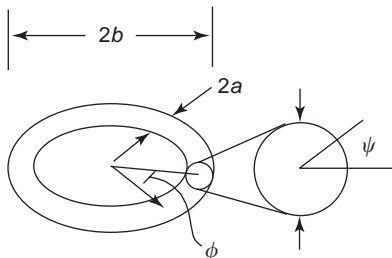


Figure 6. Parameters of the fat wire loop. *Source:* After Siwiak [2].

which has the proper limiting behavior for the small loop radius. The Q of the small loop given by Eq. (23) is indeed larger than the minimum possible $Q_{\text{min}} = (kb)^{-3}$ predicted in Siwiak [2] for a structure of its size. It must be emphasized that the actual Q of such an antenna will be smaller than given by Eq. (24) because of unavoidable dissipative losses not represented in Eq. (22)–(24). We can approach the minimum Q but never be smaller, except by introducing dissipative losses.

1.2. The Gap-Fed Loop

The analysis of arbitrarily fat wire loops follows the method in Ref. 8, shown in simplified form in Ref. 9 and summarized here. The toroid geometry of the loop is expressed in cylindrical coordinates ρ , ϕ , and z with the toroid located symmetrically in the $z = 0$ plane. The relevant geometry is shown in Fig. 6.

1.2.1. Loop Surface Current Density. The current density on the surface of the toroidal surface of the loop is given by

$$J_\phi = \sum_{n=-\infty}^{\infty} \sum_{p=-\infty}^{\infty} A_{n,p} e^{jn\phi} F_p \quad (25)$$

where the functions F_p are symmetric about the z axis and are simple functions of $\cos(n\psi)$, where ψ is in the cross section of the wire as shown in Fig. 6 and is related to the cylindrical coordinate by $z = a \sin(\psi)$. These functions are orthonormalized over the conductor surface using the Gram–Schmidt method described in Ref. 16, yielding

$$F_0 = \frac{1}{2\pi\sqrt{ab}} \quad (26)$$

and

$$F_1 = F_0 \sqrt{\frac{2}{1 - (a/2b)^2}} \left[\cos(\psi) - \frac{a}{2b} \right] \quad (27)$$

The higher-order functions are lengthy but simple functions of $\sin(p\psi)$ and $\cos(p\psi)$.

1.2.2. Scalar and Vector Potentials. The electric field is obtained from the following vector and scalar potentials:

$$\mathbf{E} = -\nabla\Phi - j\omega\mathbf{A} \quad (28)$$

The boundary conditions require that E_ϕ , E_ψ , and E_ρ be zero on the surface of the loop everywhere except at the feed gap $|\phi| \leq \epsilon$. Because this analysis will be limited to wire diameters significantly smaller than a wavelength, the boundary conditions on E_ψ and E_ρ will not be enforced. In the gap $E_\phi = V_0/2\epsilon\rho$, where V_0 is the gap excitation voltage.

The components of the vector potential are simply

$$A_\phi = \frac{1}{4\pi} \int_S \int J_\phi \cos(\phi - \phi') dS \quad (29)$$

and

$$A_\rho = \frac{1}{4\pi} \int_S \int J_\phi \sin(\phi - \phi') dS \quad (30)$$

and the vector potential is

$$\Phi = \frac{j\eta_0}{4\pi k} \int_S \int \frac{1}{\rho} \frac{\partial J_\phi}{\partial \phi} G dS \quad (31)$$

where the value of $dS = [b + a \sin(\psi)]a d\psi$. Green's function G is expressed in terms of cylindrical waves to match the rotational symmetry of the loop

$$G = \frac{1}{2j} \sum_{m=-\infty}^{\infty} e^{-jm(\phi-\phi')} \int_{-\infty}^{\infty} J_m(\rho_1 - v) H_m^{(2)}(\rho_2 - v) e^{-j\zeta(z-z')} d\zeta \quad (32)$$

where

$$\begin{aligned} v &= \sqrt{k^2 + \zeta^2} \\ \rho_1 &= \rho - a \cos(\psi) \\ \rho_2 &= \rho + a \cos(\psi) \end{aligned}$$

and where $J_m(v\rho)$ and $H_m^{(2)}(v\rho)$ are the Bessel and Hankel functions, respectively.

1.2.3. Matching the Boundary Conditions. Expression (8) is now inserted into Eqs. (5)–(8), and the electric field is then found from Eq. (2) and the boundary condition is enforced. For constant ρ on the wire

$$\int_{-\pi}^{\pi} E_\phi e^{jm\phi} d\phi = -\frac{V_0}{\rho} \frac{\sin(m\varepsilon)}{m\varepsilon} \quad (33)$$

This condition is enforced on the wire as many times as there are harmonics in ψ . Truncating the index p as described in Ref. 9 to a small finite number P , we force $E_\phi = 0$ except in the feeding gap along the lines of constant ρ on the surface of the toroid. If we truncate to P , the number of harmonics F_p in ψ , and to M the number of harmonics in ϕ , we find the radiation current by solving M systems of $P \times P$ algebraic equations in $A_{m,p}$. In Ref. 9, $P = 2$ and M in the several hundreds was found to be a reasonable computational task that led to useful solutions.

1.2.4. Loop Fields and Impedance. With the harmonic amplitudes $A_{m,p}$ known, the current density is found from Eq. (1). The electric field is found next from Eq. (2) and the

magnetic field is given by

$$H_\rho = -\frac{\partial A_\phi}{\partial z} \quad (34)$$

$$H_\phi = -\frac{\partial A_\rho}{\partial z} \quad (35)$$

$$H_z = -\frac{\partial A_\phi}{\partial \rho} + \frac{A_\phi}{\rho} - \frac{1}{\rho} \frac{\partial A_\rho}{\partial \rho} \quad (36)$$

The loop current across a section of the wire is found by integrating the function J_ϕ in Eq. (25) around the wire cross section. The loop radiation impedance is then the applied voltage V_0 in the gap divided by the current in the gap. Figure 7 shows the loop feed radiation resistance, and Fig. 8 shows the corresponding loop reactance, as a function of loop radius kr for a thin-wire ($\Omega = 15$) loop and a fat wire ($\Omega = 10$) loop where $\Omega = 2 \ln(2\pi b/a)$. The thin-wire loop has very sharp resonant behavior compared with the fat-wire loop, especially for a half-wavelength-diameter ($kb = 0.5$) structure. The higher resonances are less pronounced for both loops. Fat-wire loops exhibit an interesting behavior in that at a diameter of about a half-wavelength, the reactance is essentially always capacitive and the total impedance remains well behaved.

1.2.5. Small Gap-Fed Loops. The detailed analysis of the fat, gap-fed wire loop, as shown in Refs. 8 and 9, reveals that the current density around the circumference of the wire, angle ψ in Fig. 6, is not constant. An approximation to the current density along the wire circumference for a small diameter loop is

$$J_\phi = \frac{I_\phi}{2\pi a} [1 - 2 \cos(\phi)(kb)^2][1 + Y \cos(\psi)] \quad (37)$$

where I_ϕ is the loop current, which has cosine variation along the loop circumference, and where the variation

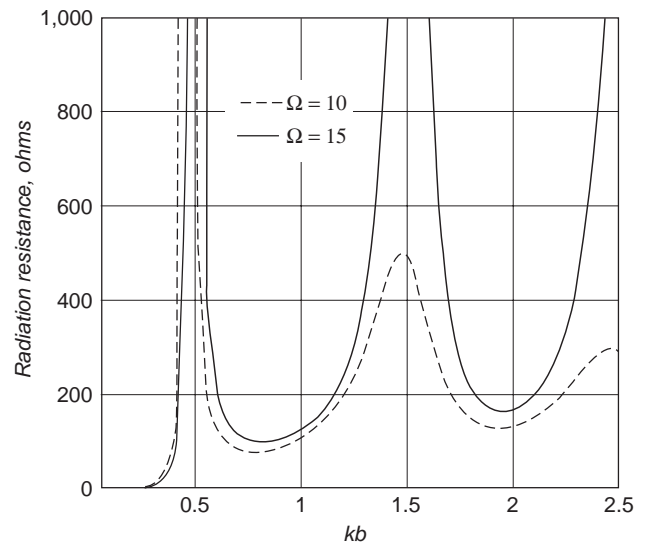


Figure 7. Loop radiation resistance.

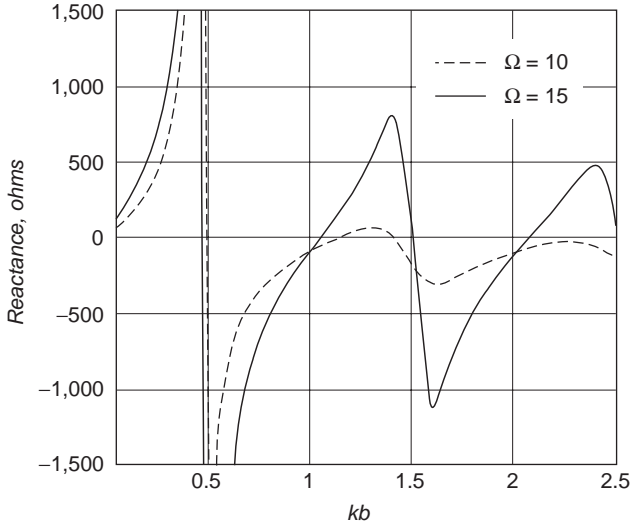


Figure 8. Loop reactance.

around the *wire circumference* is shown as a function of the angle ψ . Y is the ratio of the first-order to the zero-order modes in ϕ , and is not a simple function of loop dimensions a and b , but can be found numerically [2] and from the analysis of the previous section. For the small loop Y is negative and of order a/b , so Eq. (37) predicts that there is current bunching along the inner contour ($\psi = 180^\circ$) of the wire loop. Table 1 gives representative values for Y as a function of a/b .

This increased current density results in a corresponding increase in dissipative losses in the small loop. We can infer that the cross-sectional shape of the conductor formed into a loop antenna will impact the loss performance in a small loop.

The small loop fed with a voltage gap has a charge accumulation at the gap and will exhibit a close near electric field. For a small loop of radius b and centered in the x - y plane, the fields at $(x,y)=(0,0)$ are derived in Ref. 9 and given here as

$$E_\phi = -j \frac{\eta_0 k I}{2} \quad (38)$$

where I is the loop current and

$$H_z = \frac{I}{2b} \quad (39)$$

Table 1. Parameter Y for Various Loop Thickness and $b = 0.01$ Wavelengths

Ω	a/λ	Y
19.899	0.000003	-0.0039
17.491	0.00001	-0.0090
15.294	0.00003	-0.020
12.886	0.0001	-0.048
10.689	0.0003	-0.098
8.2809	0.001	-0.179

Expression (39) is recognized as the classic expression for the static magnetic field within a single-turn solenoid. Note that the electric field given by Eq. (38) does not depend on any loop dimensions, but was derived for an electrically small loop. The wave impedance Z_w at the origin is the ratio of E_ϕ to H_z and from Eqs. (38) and (39) is

$$Z_w = -j\eta_0 kb \quad (40)$$

In addition to providing insight into the behavior of loop probes, Eqs. (38)–(40) are useful in testing the results of numerical codes like the Numerical Electromagnetic Code (NEC) described in Ref. 3, and are often used in the numerical analysis of wire antenna structures.

When the small loop is used as an untuned and unshielded field probe, the current induced in the loop will have a component due to the magnetic field normal to the loop plane as well as a component due to the electric field in the plane of the loop. A measure of sensitivity of the E field to the H field is apparent from expression (40). The electric field to magnetic field sensitivity of a simple small loop probe is proportional to the loop diameter. The small gap-fed loop, then, has a dipole moment, which complicates its use as a purely magnetic field probe.

2. LOOP APPLICATIONS

Loop antennas appear in pager receivers as both ferrite-loaded loops and as single-turn rectangular structures within the radio housing. When worn on the belt, the loop benefits from coupling to the vertically resonant human body. In the high-frequency bands, the loop has been implemented as a series resonant circuit fed by a secondary loop. The structure can be tuned over a very large frequency band while maintaining a relatively constant feedpoint impedance. One-wavelength-perimeter square loops have been successfully implemented as high-gain transmitting structures.

2.1. The Ferrite-Loaded Loop Antenna: A Magnetic Dipole

Let us examine a small ferrite-loaded loop antenna with dimensions, $2h = 2.4$ cm and $2a = 0.4$ cm, and at a wavelength of about $\lambda = 8.6$ m as depicted in Fig. 9. When the permeability of the ferrite is sufficiently high, this antenna behaves like a magnetic dipole. The magnetic fields are strongly confined to the magnetic medium, especially near the midsection of the ferrite rod, and behave as the dual of the electric dipole excited by a triangular current distribution. We can therefore analyze its behavior using a small dipole analysis as shown by Siwiak [2].

The impedance at the midpoint of a short dipole having a current uniformly decreasing from the feed point across its length $2h$ is

$$Z_{\text{dipole}} = \frac{\eta_0}{6\pi} (kh)^2 - j \frac{\eta_0}{2\pi} \left[\ln \left[\frac{2h}{a} \right] - 1 \right] \quad (41)$$

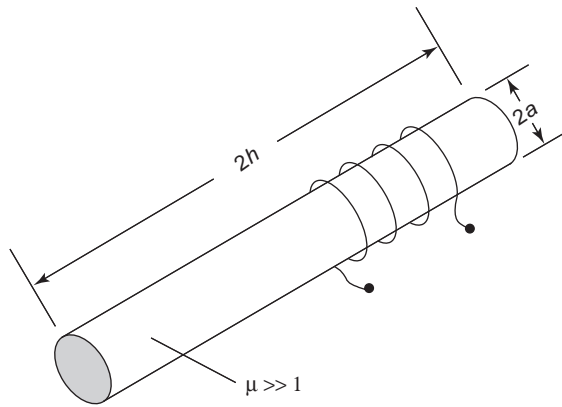


Figure 9. A Ferrite loaded loop antenna. *Source:* After Siwiak [2].

The corresponding unloaded Q of the dipole antenna is

$$Q_{\text{dipole}} = \frac{3 \left[\ln \left[\frac{2h}{a} \right] - 1 \right]}{(kh)^3} \tag{42}$$

Equation (42) has the expected inverse third power with size behavior for small antennas, and for $h/a = 6$

$$Q_{\text{dipole}} = \frac{4.5}{(kh)^3} \tag{43}$$

Comparing the Q for a small dipole given by Eq. (43) with the Q of a small loop of Eq. (24), we see that the loop Q is small even though the same ratio of antenna dimension to wire radius was used. We conclude that the small loop utilizes the smallest sphere that encloses it more efficiently than does the small dipole. Indeed, the thin dipole is essentially a one-dimensional structure, while the small loop is essentially a two-dimensional structure.

We can use Eqs. (41) and (42) for the elementary dipole to examine the ferrite-loaded loop antenna since it resembles a magnetic dipole. The minimum ideal Q of this antenna is given by Eq. (42), 1.0×10^6 . The corresponding bandwidth of such an antenna having no dissipative losses would be $2 \times 35f/Q = 70 \text{ MHz}/1.3 \times 10^6 = 69 \text{ Hz}$. A practical ferrite antenna at this frequency has an actual unloaded Q_A of nearer to 100, as can be inferred from the performance of belt-mounted radios shown in Table 2. Hence, an

Table 2. Paging Receiver Performance Using Loops

Frequency Band (MHz)	Paging Receiver, at Belt Average Gain (dBi)	Field Strength Sensitivity (dB · μV/m)
30–50	–32 to –37	12–17
85	–26	13
160	–19 to –23	10–14
280–300	–16	10
460	–12	12
800–960	–9	18–28

estimate of the actual antenna efficiency is

$$10 \log \frac{Q_A}{Q} = -40 \text{ dB} \tag{44}$$

and the actual resultant 3 dB bandwidth is about 700 kHz. Such an antenna is typical of the type that would be used in a body-mounted paging receiver application. As detailed in Siwiak [2], the body exhibits an average magnetic field enhancement of about 6 dB at this frequency, so the average belt-mounted antenna gain is –34 dBi. This is typical of a front-position body-mounted paging or personal communication receiver performance in this frequency range.

2.2. Body Enhancement in Body-Worn Loops

Loops are often implemented as internal antennas in pager receiver applications spanning the frequency bands from 30 to 960 MHz. Pagers are often worn at belt level, and benefit from the “body enhancement” effect. The standing adult human body resembles a lossy wire antenna that resonates in the range of 40–80 MHz. The frequency response, as seen in Fig. 10, is broad, and for belt-mounted loop antennas polarized in the body axis direction, enhances the loop antenna azimuth-averaged gain at frequencies below ~500 MHz.

The far-field radiation pattern of a body-worn receiver is nearly omnidirectional at very low frequency. As frequency is increased, the pattern behind the body develops a shadow that is manifest as a deepening null with increasing frequency. In the high-frequency limit, there is only a forward lobe with the back half-space essentially completely blocked by the body. For horizontal incident polarization there is no longitudinal body resonance and there is only slight enhancement above 100 MHz.

2.3. The Small Resonated High-Frequency Loop

The simple loop may be resonated with a series capacitor having a magnitude of reactance equal to the loop

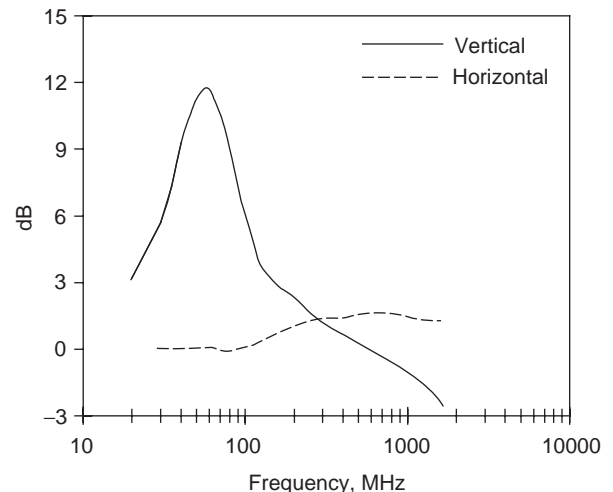


Figure 10. Gain-averaged body-enhanced loop response. *Source:* After Siwiak [2].

reactance, and indeed, is effectively implemented that way for use in the HF bands as discovered by Dunlavy [17]. When fed by a second untuned loop, this antenna will exhibit a nearly constant feedpoint impedance over a 3:1 or 4:1 bandwidth by simply adjusting the capacitor to the desired resonant frequency. The reactive part of the loop impedance is inductive, where the inductance is given by $\text{Im}\{Z_L\} = \omega L$, so ignoring the higher-order terms

$$L = \frac{\eta_0 k b \left[\ln \left[\frac{8b}{a} \right] - 2 \right]}{\omega} \quad (45)$$

which, with the substitution $\eta_0 k / \omega = \mu_0$, becomes

$$L = \mu_0 b \left[\ln \left[\frac{8b}{a} \right] - 2 \right] \quad (46)$$

The capacitance required to resonate this small loop at frequency f is

$$C = \frac{1}{(2\pi f)^2 L} \quad (47)$$

The loop may be coupled to a radio circuit in many different ways, including methods given in Refs. 17 and 18. When used in transmitter applications, the small loop antenna is capable of impressing a substantial voltage across the resonating capacitor. For a power P delivered to a small loop with unloaded Q of Eq. (23) and with resonating the reactance X_C given by the reactive part of Eq. (22), it is easy to show that the peak voltage across the resonating capacitor is

$$V_p = \sqrt{X_C Q P} \quad (48)$$

by recognizing that

$$V_p = \sqrt{2} I_{\text{RMS}} X_C \quad (49)$$

where I_{RMS} is the total RMS loop current

$$I_{\text{RMS}} = \sqrt{\frac{P}{\text{Re}\{Z_{\text{loop}}\}}} \quad (50)$$

along with Q at the resonant frequency in Eq. (23).

Transmitter power levels as low as one watt delivered to a moderately efficient small-diameter ($\lambda/100$) loop can result in peak values of several hundred volts across the resonating capacitor. This is not intuitively expected; the small loop is often viewed as a high-current circuit that is often described as a short-circuited ring. However, because it is usually implemented as a *resonant circuit* with a resonating capacitor, it can also be an extremely high-voltage circuit, as will be shown below. Care must be exercised in selecting the voltage rating of the resonating capacitor even for modest transmitting power levels, just

as care must be taken to keep resistive losses low in the loop structure.

As an example, consider the Q and bandwidth of a small loop antenna, $2b = 10$ cm in diameter, resonated by a series capacitor and operating at 30 MHz. The example loop is constructed of $2a = 1$ -cm-diameter copper tubing with conductivity $\sigma = 5.7 \times 10^7$ S/m. The resistance per unit length of round wire of diameter $2a$ with conductivity σ is

$$R_s = \frac{1}{2\pi a \delta_s \sigma} = \frac{1}{2\pi a} \sqrt{\frac{\omega \mu_0}{2\sigma}} \quad (51)$$

where δ_s is the skin depth for good conductors, ω is the radian frequency, and $\mu_0 = 4\pi \times 10^{-7}$ H/m is the permeability of free space, so $R_s = 0.046 \Omega$. From Eq. (22) the loop impedance is $Z = 0.00792 + j71.41$. Hence the loop efficiency can be found by comparing the loop radiation resistance with loss resistance. The loop efficiency is $R_s / (R_s + \text{Re}\{Z\}) = 0.147$ or 14.7%. From Eqs. (46) and (47) we find the resonating capacitance $C = 74.3 \mu\text{F}$. From Eqs. (48)–(50), we see that if 1 W is supplied to the loop, the peak voltage across the resonating capacitor will be 308 V, and the loop current will be 4.3 A. The *resonated* loop is by no means the “low-impedance structure” that we normally imagine it to be.

2.4. The Rectangular Loop

Pager and other miniature receiver antennas used in the 30–940 MHz frequency range are usually implemented as electrically small rectangular loops. For a rectangle dimensioned $b_1 \times b_2$ of comparable length, and constructed with $2a$ -diameter round wire, the loop impedance is given in Ref. 19 as

$$Z_{\text{rect}} = \frac{\eta_0}{6\pi} (k^2 A)^2 + j \frac{\eta_0}{\pi} \left[b_1 \ln \left[\frac{2A}{a(b_1 + b_c)} \right] + \left[b_2 \ln \left[\frac{2A}{a(b_2 + b_c)} \right] + 2(a + b_c - b_1 - b_2) \right] \right] \quad (52)$$

where $A = b_1 b_2$ and $b_c = (b_1^2 + b_2^2)^{1/2}$. The loss resistance is found by multiplying R_s in Eq. (51) by perimeter length of the loop, $2(b_1 + b_2)$. For a given antenna size the lowest loss occurs for the circular loop.

2.5. The Quad Loop Antenna

The quad loop antenna, sometimes called the “cubical quad,” was developed by Clarence C. Moore in the 1940s as a replacement for a four element parasitic dipole array (Yagi–Uda array). The dipole array exhibited corona arcing at the element tips severe enough to damage the antenna when operated at high power levels (10 kW) in a high-altitude (10,000-f) shortwave broadcasting application in the 25-m band. Moore sought an antenna design with “no tips” that would support extremely high electric field strengths, in order to avoid destructive arcing. His solution was a 1λ -perimeter square loop, later with a loop

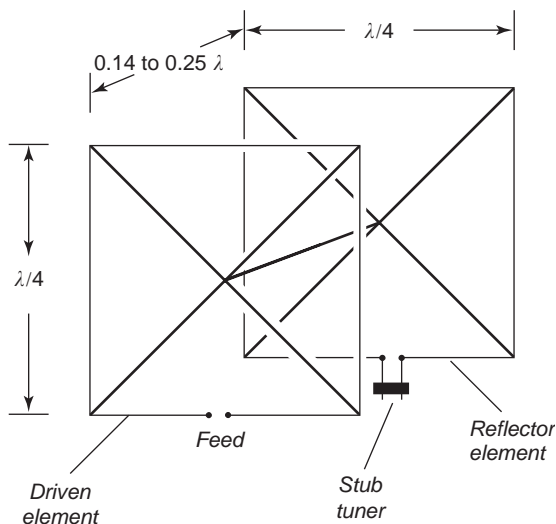


Figure 11. Two element loop array.

director element as shown in Fig. 11. The configuration exhibited no arcing tendencies, and a new shortwave antenna configuration was born.

As pictured in Fig. 11, the driven element is approximately one-quarter wavelength on an edge. Actually, resonance occurs when the antenna perimeter is about 3% greater than a wavelength. The reflector element perimeter is approximately 6% larger than a wavelength, and may be implemented with a stub tuning arrangement. Typical element spacing is 0.14–0.25 wavelength. The directivity of a quad loop is approximately 2 dB greater than that of a Yagi antenna with the same element spacing.

BIBLIOGRAPHY

1. *IEEE Standard Definitions of Terms for Antennas*, IEEE Std 145-1993, SH16279, March 18, 1993.
2. K. Siwiak, *Radiowave Propagation and Antennas for Personal Communications*, 2nd ed., Artech House, Norwood, MA, 1998.
3. G. J. Burke and A. J. Poggio, *Numerical Electromagnetics Code (NEC)—Method of Moments*, Lawrence Livermore Laboratory, NOSC Technical Document 116 (TD 116), Vols. 1 and 2, Jan. 1981.
4. H. C. Pocklington, Electrical oscillations in wires, *Proc. Cambridge Physical Society* London, England, 1897, Vol. 9, pp. 324–333.
5. E. Hallén, Theoretical investigation into transmitting and receiving qualities of antennae, *Nova Acta Regiae Societatis Scientiarum Upsaliensis. Ser. IV*, **II**(4):1–44 (Nov. 4, 1938).
6. J. E. Storer, Impedance of thin-wire loop antennas, *Trans. of AIEE*, **75**:609–619 (Nov. 4, 1965).
7. T. T. Wu, Theory of the thin circular antenna, *J. Math. Phys.* **3**:1301–1304 (Nov.–Dec. 1962).
8. Q. Balzano and K. Siwiak, The near field of annular antennas, *IEEE Trans. Vehic. Technol.* **VT36**(4):173–183 (Nov. 1987).
9. Q. Balzano and K. Siwiak, Radiation of annular antennas, *Correlations, Motorola Eng. Bull.*, (Motorola Inc., Schaumburg, IL), **VI**(2) (winter 1987).

10. C. A. Balanis, *Advanced Engineering Electromagnetics*, Wiley, New York, 1989.
11. R. E. Collin, *Antennas and Radiowave Propagation*, McGraw-Hill, New York, 1985.
12. E. C. Jordan and K. G. Balmain, *Electromagnetic Waves and Radiating Systems*, 2nd ed., Prentice-Hall, Englewood Cliffs, NJ, 1968.
13. *2002 CODATA Recommended Values of the Fundamental Physics Constants*, December 31, 2002, (Online): <http://physics.nist.gov/cuu/Constants/> December 2003.
14. L. A. Hazeltine, *Means for Eliminating Magnetic Coupling between Coils*, US Patent 1,577,421 (March 16, 1926).
15. R. W. P. King and C. W. Harrison, Jr., *Antennas and Waves: A Modern Approach*, MIT Press, Cambridge, MA, 1969.
16. R. Courant and D. Hilbert, *Methods of Mathematical Physics*, Interscience Publishers, New York, 1953.
17. J. H. Dunlavy, Jr., *Wide Range Tunable Transmitting Loop*, US Patent 3,588,905 (June 28, 1971).
18. T. Hart, Small, high-efficiency loop antennas, *QST*, 33–36 (June 1986).
19. K. Fujimoto, A. Henderson, K. Hirasawa, and J. R. James, *Small Antennas*, Wiley, New York, 1987.

LOW NOISE AMPLIFIERS

VIJAY NAIR
Intel Corporation
Hillsboro, Oregon

1. INTRODUCTION

Low-noise amplifiers (LNAs) are one of the most critical components of the today's communication receivers. In wireless systems, the input signal from the antenna first passes through an LNA that provides sufficient gain and noise reduction for the subsequent stages for the RF receiver at the frequency band of interest. This LNA should operate at low voltage, consume very low power, have wide dynamic range, and exhibit excellent low-noise properties. It should also have sufficient linearity for application in systems that employ digital modulation schemes. Very-low-power-consumption low-noise amplifiers are necessary for increasing talk time of wireless communication products. Semiconductor devices having high linearity and better noise figure–gain performance are needed for digital wireless systems. Front-end circuits with good performance have been fabricated using silicon CMOS, BJT, BiCMOS, GaAs MESFET, HFET, HBT, and SiGe technologies [1]. In this article we will discuss the low-noise amplifier design fundamentals, with special emphasis on low-power communication circuits.

2. DEVICE MODELING

A low-noise amplifier consists of transistors to provide the gain and matching circuits to tune the performance at the frequency range of interest. The gain and noise

characteristics of a transistor can be completely specified by the transistor's S -parameters and noise parameters. When an active device, such as a transistor, is employed in a two-port system, the amount of noise that it generates has to be considered carefully. This is often characterized by the ratio of the output signal power to output noise power. A term called *noise factor* is used to express this noise deterioration of the systems. The noise factor F is defined as

$$F = \frac{S/N \text{ power ratio at input}}{S/N \text{ power ratio at output}} \quad (1)$$

where N is noise and S is signal.

If G is the gain of the device, then the signal at the output is given by

$$S_{\text{output}} = GS_{\text{input}} \text{ and the noise at the output is given by } N_{\text{output}} = GN_{\text{input}} + \text{noise generated by the device.}$$

Hence, (1) can be rewritten as

$$F = \frac{N_{\text{output}}}{GN_{\text{input}}} \quad (2)$$

The noise figure in decibels is given by

$$F(\text{dB}) = 10 \log(F) \quad (3)$$

The major sources of noise in active device are thermal noise generated by the resistance and the shot noise generated by the current flowing through the active-device junctions. Noise properties of bipolar transistors can be described by an equivalent circuit as shown in Fig. 1a. Three noise generators are introduced into this common-emitter equivalent circuit to analyze the bipolar transistor noise properties. These noise generators are due to the fluctuations in the DC base current, collector current and thermal noise of the base resistance.

A simple noise equivalent circuit of a common-source FET, as shown in Fig 1b, considers the noise contributions of the gate resistance R_g , source resistance R_s , gate-to-source capacitance C_{gs} , and associated charging resistance R_i . Noise contributions due to other reactive parasitic elements such as the gate and source lead inductance are ignored, since they are negligible.

The noise figure in the presence of the source admittance Y_s can be written as

$$F = F_{\min} + \frac{R_n}{G_s} |Y_s - Y_{\text{opt}}|^2 \quad (4)$$

where $Y_s = G_s + jB_s$, connected at the input port. F_{\min} , R_n , and Y_{opt} characterize the device and are independent of its output terminations [2]. The optimum source admittance, $Y_{\text{opt}} = G_{\text{opt}} + jB_{\text{opt}}$, is that particular value of source admittance Y_s for which the optimum noise factor F_{\min} is realized. Thus the noise performance of the device can be characterized by a set of four noise parameters: the minimum noise figure F_{\min} , the noise resistance R_n , and the optimum source admittance $Y_{\text{opt}} = G_{\text{opt}} + jB_{\text{opt}}$, where G_{opt} and B_{opt} individually affect the noise figure.

Thus (4) can be rewritten as follows:

$$F = F_{\min} + \left(\frac{R_n}{G_s} \right) [(G_s - G_{\text{opt}})^2 + (B_s - B_{\text{opt}})^2] \quad (5)$$

Equation (5) can be converted to arbitrary impedance form as

$$F = F_{\min} + \frac{R_n [(R_{ss} - R_{\text{opt}})^2 + (X_{ss} - X_{\text{opt}})^2]}{R_{ss} (R_{\text{opt}}^2 + X_{\text{opt}}^2)} \quad (6)$$

where

$$Y_s = G_s + jB_s = \frac{1}{Z_s} = \frac{1}{(R_{ss} + jX_{ss})} \quad (7)$$

$$Y_{\text{opt}} = G_{\text{opt}} + jB_{\text{opt}} = \frac{1}{Z_{\text{opt}}} = \frac{1}{R_{\text{opt}} + jX_{\text{opt}}} \quad (8)$$

Thus, knowing the noise parameters F_{\min} , R_n , R_{opt} , and X_{opt} , the noise figure of the device can be calculated using (4) when the device is matched to Z_s instead of Z_{opt} .

3. LOW-NOISE BEHAVIOR OF BJTs AND FETs

The noise behavior of a bipolar device can be analyzed by introducing noise generators due to the fluctuations in the DC base current, collector current, and thermal noise of the base resistance into the common-emitter equivalent circuit shown in Fig. 1a. The mean-square values of these generators are given by [3]

$$i_b^2 = 2qI_b \Delta f \quad (9)$$

$$i_c^2 = 2qI_c \Delta f \quad (10)$$

$$e_b^2 = 4kTr_b \Delta f \quad (11)$$

where i_b is the base current noise generator, i_c is the collector current noise generator, e_b is the thermal noise voltage of the base resistor, I_b is the DC base current, I_c is the dc collector current, Δf is the narrow frequency interval, r_b is the base resistance, q is the electronic charge, k is the Boltzmann constant, and T is the absolute temperature.

Theoretical and experimental study of noise characteristics of a GaAs MESFET were performed by several researchers [4,5]. Fukui [6,7] developed a set of simple analytical expressions for the noise parameters of a MESFET. The Fukui equations shown below are used

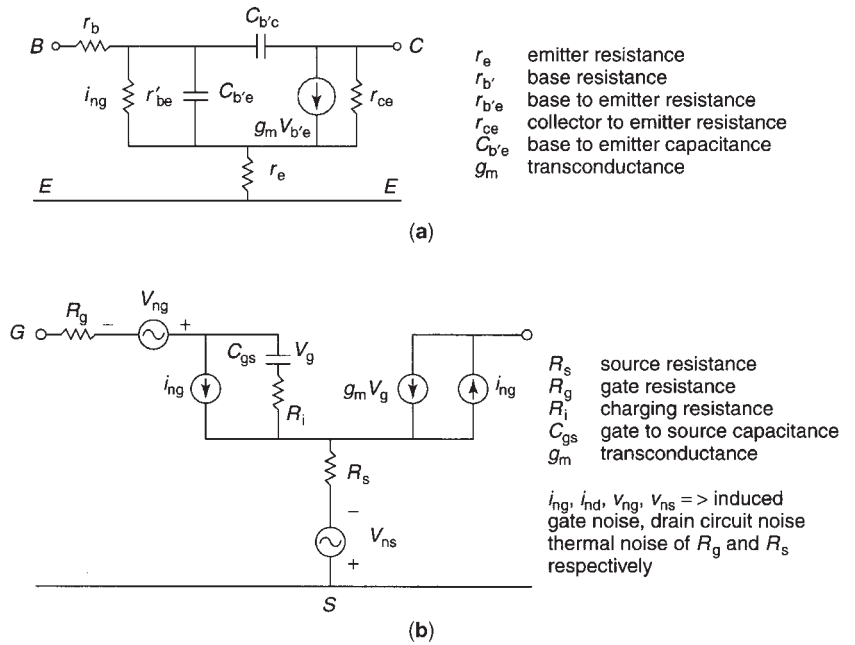


Figure 1. (a) Small-signal equivalent circuit of common-emitter BJT; (b) noise-equivalent circuit of a common-source FET.

extensively to estimate the noise parameters of a device

$$\begin{aligned}
 F_{\min} &= 1 + k_1 f C_{gs} \left(\sqrt{\frac{R_s + R_g}{g_m}} \right) \\
 R_n &= \frac{k_2}{g_m} \\
 R_{\text{opt}} &= k_3 \left[\frac{1}{4g_m} + R_s + R_g \right] \\
 X_{\text{opt}} &= \frac{k_4}{f C_{gs}}
 \end{aligned}
 \tag{12}$$

where k_1 , k_2 , k_3 , and k_4 are fitting factors and f is the operating frequency.

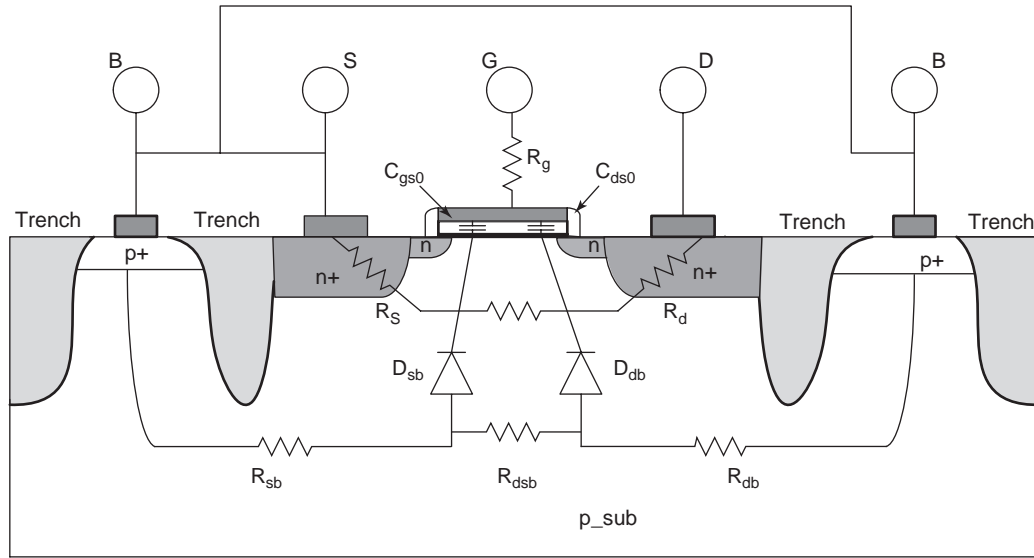
These fitting factors, estimated on the basis of the measured data on microwave transistors, are $k_1 = 0.016$, $k_2 = 0.8$, $k_3 = 2.2$, and $k_4 = 160$, provided the resistance is measured in ohms; transconductance g_m , in siemens; gate-to-source capacitance C_{gs} , in picofarads; and frequency f , in gigahertz. These empirical constants depend on the device manufacturing process and give a good estimate of the capabilities of different types of semiconductor device technologies. These constants have to be determined by measuring the S parameters and noise parameters of the devices.

The noise parameters and the S parameters should be taken into account while choosing a device for a low-noise amplifier design. A method for experimentally determining the noise parameters of a FET is described in Ref. 8. The noise characteristics of heterostructure devices such as HEMT and P-HEMT have been studied by Cappy et al. [9].

Advances in CMOS technology enabled the fabrication of MOSFETs having gate lengths below 100 nm. These devices have realized very high transit frequencies and very low noise figures. CMOS amplifiers with very good low-noise performance have been demonstrated for wireless system applications [10,11]. Figure 2a shows a schematic cross section of a MOSFET that depicts the origin properties of several parasitic elements. Although MOSFETs and MESFETs are very different in their operation and large-signal properties, the small-signal operations are very similar. Therefore theoretical and experimental studies of MESFET behavior can be used to analyze the MOSFET small-signal and high-frequency noise properties. A simplified equivalent circuit of a MOSFET suitable for noise analysis is shown in Fig. 3. Just as in the MESFET, the most important parasitic parameters are the gate resistance R_g , source resistance R_s , channel conductance g_0 , and gate capacitance C_{gs} . The dominant noise sources are the thermal noise associated with the gate noise, source resistance, and channel conductance. A noisy two-port network analysis can be used to study the MOSFET noise properties. Following an analysis similar to MESFET noise analysis, one can show that [12]

$$F_{\min} = 1 + 2\gamma g_{d0} \frac{f}{f_T} \left[\sqrt{\frac{R_g + R_s}{\gamma g_{d0}}} + \frac{f}{f_T} (R_g + R_s) \right]
 \tag{13}$$

where F_{\min} is the minimum noise figure, g_{d0} is the equivalent noise conductance of the channel, γ is a bias-dependent parameter, and R_s and R_g are the source and gate resistances, respectively. Since the second term inside the brackets is typically much smaller than the first, we can



- | | |
|------------------------------------|---|
| B - Base | D _{sb} - Source-to-bulk junction diode |
| S - Source | D _{db} - Drain-to-bulk junction diode |
| D - Drain | R _{ds} - Drain-to-source resistance |
| G - Gate | R _{db} - Drain-to-substrate resistance |
| R _s - Source resistance | R _{sb} - Source-to-substrate resistance |
| R _d - Drain resistance | R _{dsb} - Drain-source to substrate resistance |
| R _g - Gate resistance | C _{gs0} - Gate-source overlap capacitance |
| | C _{ds0} - Gate-drain overlap capacitance |

Figure 2. Small-signal equivalent circuit of a CMOS device showing the origins of the parasitic components. (This figure is available in full color at <http://www.mrw.interscience.wiley.com/erfme>.)

approximate (13) as

$$F_{\min} \approx 1 + 2 \frac{f}{f_T} \sqrt{\gamma g_{d0} (R_g + R_s)} \quad (14)$$

and the optimum reactance is

$$X_{\text{opt}} = \frac{1}{\omega(C_{gs} + C_{gd})} \quad (19)$$

The cutoff frequency f_T is given by

$$f_T = \frac{g_m}{2\pi(C_{gs} + C_{gd})} \quad (15)$$

where g_m is the transconductance of the device and C_{gs} and C_{gd} are the gate-to-source and gate-to-drain capacitances, respectively.

The noise conductance G_n can be written as

$$G_n = \left(\frac{f}{f_T}\right)^2 \gamma g_{d0} \quad (16)$$

The optimum impedance is given by

$$Z_{\text{opt}} = R_{\text{opt}} + X_{\text{opt}} \quad (17)$$

where the optimum resistance is

$$R_{\text{opt}} \approx \frac{f_T}{f} \sqrt{\frac{R_g + R_s}{\gamma g_{d0}}} \quad (18)$$

For low-noise amplifier design, the device should be biased at the minimum noise figure point and the device width should be chosen so that optimum resistance is close to the driving resistance, which is typically 50 Ω. Also note that the minimum noise figure is independent of the gate width. In order to achieve a minimum noise figure, the

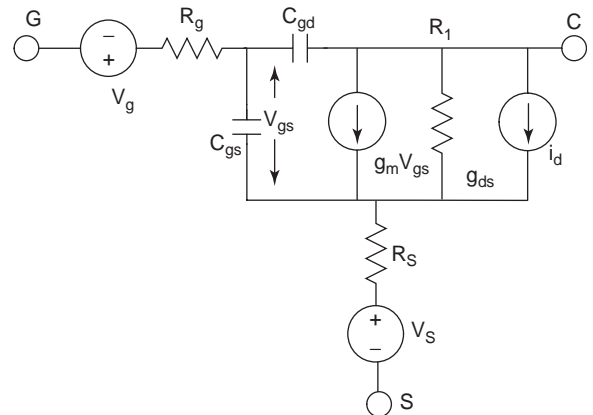


Figure 3. Noise-equivalent circuit of a common-source CMOS.

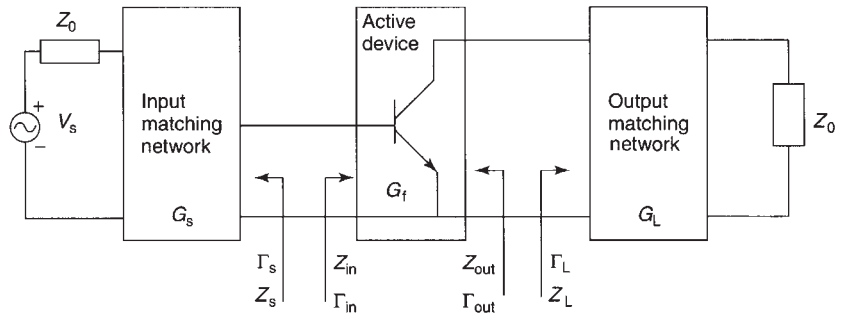


Figure 4. RF amplifier circuit block diagram depicting different power gains and reflection coefficients.

cutoff frequency of the device should be much higher than the operating frequency.

4. AMPLIFIER POWER GAIN EQUATIONS

Many power gain equations are derived from the two-port S parameters of the amplifier. Let us consider the power flow from the source to the load. Figure 4 shows a RF amplifier circuit block diagram depicting the different power gains and reflection coefficients.

The transducer power gain G_T of an amplifier is defined as the ratio of the output power P_L delivered to the load Z_L and the input power P_{avs} available from the source to the network.

$$G_T = G_T(\Gamma_G, \Gamma_L, S) = \frac{P_L}{P_{avs}} \quad (20)$$

This can be expressed in terms of two-port S parameters by

$$G_T = \frac{(1 - |\Gamma_s|^2)|S_{21}|^2(1 - |\Gamma_L|^2)}{|1 - S_{11}\Gamma_s|^2|1 - \Gamma_{out}\Gamma_L|^2} \quad (21)$$

or

$$G_T = \frac{(1 - |\Gamma_s|^2)|S_{21}|^2(1 - |\Gamma_L|^2)}{|1 - \Gamma_{in}\Gamma_s|^2|1 - S_{22}\Gamma_L|^2} \quad (22)$$

where

$$\Gamma_{in} = S_{11} + \frac{S_{12}S_{21}\Gamma_L}{1 - S_{22}\Gamma_L} \quad (23)$$

$$\Gamma_{out} = S_{22} + \frac{S_{12}S_{21}\Gamma_s}{1 - S_{11}\Gamma_s} \quad (24)$$

When both the input and output networks are perfectly matched to the source impedance and the load impedance, respectively, the transducer power gain is given by

$$G_{Tm} = |S_{21}|^2 \quad (25)$$

The unilateral transducer power gain (i.e., $|S_{12}| = 0$) G_{Tu} is given by

$$G_{tu} = \frac{(1 - |\Gamma_s|^2)}{|1 - S_{11}\Gamma_s|^2} |S_{21}|^2 \frac{(1 - |\Gamma_L|^2)}{|1 - S_{22}\Gamma_L|^2} \quad (26)$$

We can rewrite this in the form

$$G_{tu} = G_s G_0 G_L \quad (27)$$

Term G_s , which depends only on the S_{11} parameter of the transistor and the source reflection coefficient, represents the gain or loss of the input matching circuits. Similarly G_L depends on the S_{22} parameter of the transistor and the load reflection coefficient. This represents the gain or loss of the output matching circuits. A block diagram of maximum unilateral gain amplifier is shown in Fig. 5. The middle term depends only on the S_{21} parameter of the transistor.

Maximum unilateral gain $G_{Tu,max}$ is achieved when

$$\Gamma_s = S_{11}^* \quad \text{and} \quad \Gamma_L = S_{22}^* \quad (28)$$

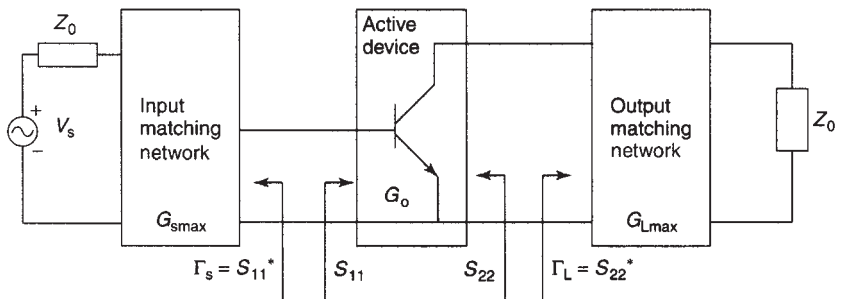


Figure 5. A block diagram of the maximum unilateral gain configuration of an RF amplifier.

and is given by

$$G_{\text{TU max}} = \frac{|S_{21}|^2}{(1 - |S_{11}|^2)(1 - |S_{22}|^2)} \quad (29)$$

5. AMPLIFIER STABILITY

Stability of RF amplifiers is one of the most important criteria in the circuit design. The amplifier stability can be determined from the S parameters, input and output matching networks, and circuit terminations. The amplifier can be conditionally or unconditionally stable. A two-port network as shown in Fig. 4 is unconditionally stable at a given frequency if the input and output resistances (the real part of Z_{in} and Z_{out}) of the device are positive for all passive source and load terminations. This also means that $|\Gamma_s| \leq 1$ and $|\Gamma_L| \leq 1$ in this case. An amplifier is conditionally stable if the real part of input impedance and output impedance of the amplifier are greater than zero for some positive part of real source and load impedances at a specific frequency.

5.1. Stability Circles

The conditions for unconditional stability can be written in terms of reflection coefficients as follows:

$$|\Gamma_s| \leq 1; \quad |\Gamma_L| \leq 1 \quad (30)$$

$$|\Gamma_{\text{in}}| = \left| S_{11} + \frac{S_{12}S_{21}\Gamma_L}{1 - S_{22}\Gamma_L} \right| < 1 \quad (31)$$

$$|\Gamma_{\text{out}}| = \left| S_{22} + \frac{S_{12}S_{21}\Gamma_s}{1 - S_{11}\Gamma_s} \right| < 1 \quad (32)$$

Solutions to these equations give the required conditions for an amplifier to be unconditionally stable. When a two-port network is potentially unstable (or conditionally stable), there may be values of Γ_s and Γ_L for which the real parts of Z_{in} and Z_{out} are positive.

If we set $|\Gamma_{\text{in}}|$ and $|\Gamma_{\text{out}}|$ to unity, a boundary is established beyond which the amplifier becomes unstable. The boundary condition is given by

$$\left| S_{11} + \frac{S_{12}S_{21}\Gamma_L}{1 - S_{22}\Gamma_L} \right| = 1 \quad (33)$$

$$\left| S_{22} + \frac{S_{12}S_{21}\Gamma_s}{1 - S_{11}\Gamma_s} \right| = 1 \quad (34)$$

Solutions to these two equations provide the values of Γ_s and Γ_L . It can be shown that the solutions for Γ_L and Γ_s lie on circles [13]. These circles are known as the *stability*

circles. The equations for these are given by

$$\left| \Gamma_L - \frac{(S_{22} - \Delta S_{11}^*)^*}{|S_{22}|^2 - |\Delta|^2} \right| = \frac{S_{12}S_{21}}{|S_{22}|^2 - |\Delta|^2} \quad (35)$$

$$\left| \Gamma_s - \frac{(S_{11} - \Delta S_{22}^*)^*}{|S_{11}|^2 - |\Delta|^2} \right| = \frac{S_{12}S_{21}}{|S_{11}|^2 - |\Delta|^2} \quad (36)$$

where

$$\Delta = S_{11}S_{22} - S_{12}S_{21} \quad (37)$$

The circles in the Γ_L plane where $|\Gamma_{\text{in}}| = 1$ are called *output stability circles* and the circles in the Γ_s plane where $|\Gamma_{\text{out}}| = 1$, the *input stability circles*. The radii and centers of input stability circles are given by

$$r_s \text{ (radius of } \Gamma_s \text{ circles)} = \left| \frac{S_{12}S_{21}}{|S_{11}|^2 - |\Delta|^2} \right| \quad (38)$$

$$C_s \text{ (center of } \Gamma_s \text{ circles)} = \frac{(S_{11} - \Delta S_{22}^*)^*}{|S_{11}|^2 - |\Delta|^2} \quad (39)$$

The radii and centers of output stability circles are given by

$$R_L \text{ (radius of } \Gamma_L \text{ circles)} = \left| \frac{S_{12}S_{21}}{|S_{22}|^2 - |\Delta|^2} \right| \quad (40)$$

$$C_L \text{ (center of } \Gamma_L \text{ circles)} = \frac{(S_{22} - \Delta S_{11}^*)^*}{|S_{22}|^2 - |\Delta|^2} \quad (41)$$

These equations can be plotted on a Smith chart provided the S parameters of the two-port network are known. Figure 6 illustrates the graphical construction of the stability circles where $|\Gamma_{\text{in}}| = 1$ and $|\Gamma_{\text{out}}| = 1$ in the Γ_L and Γ_s planes, respectively. On one side of the stability circle boundary in the Γ_L plane $|\Gamma_{\text{in}}| < 1$, and on the other side $|\Gamma_{\text{in}}| > 1$.

Similarly, on one side of the stability circle boundary in the Γ_s plane $|\Gamma_{\text{out}}| < 1$, and on the other side $|\Gamma_{\text{out}}| > 1$.

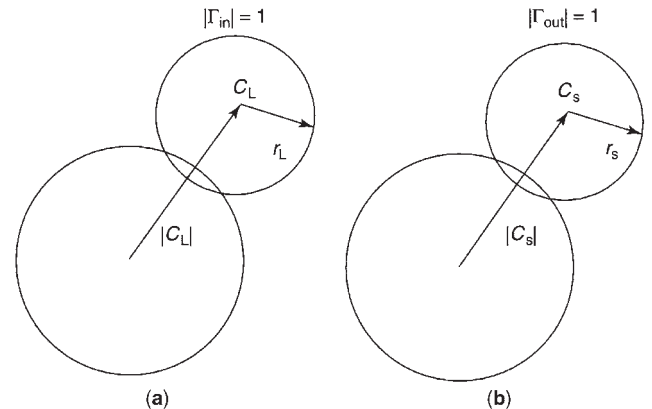


Figure 6. Graphical illustration of construction of stability circles where $|\Gamma_{\text{in}}| = 1$ and $|\Gamma_{\text{out}}| = 1$: (a) Γ_L plane; (b) Γ_s plane.

Stability circles can be plotted on the Smith chart directly. These circles separate the output or input planes into stable or unstable regions. A stability circle plotted on the input plane indicates the values of all the loads that provide negative real part of output impedances. Similarly stability circle plotted on the output plane indicates the values of all the loads that provide negative real parts of input impedances. A *negative real part* of impedance is defined as a reflection coefficient that has a magnitude that is greater than unity. The presence of the negative part of impedances at amplifier input or output causes the amplifier to oscillate. The next step is to determine which area in the Smith chart region is stable:

If $Z_L = Z_0$, then $\Gamma_L = 0$, and $\Gamma_{in} = |S_{11}|$ [from (30)].

If $|S_{11}| < 1$, then $|\Gamma_{in}| < 1$ when $\Gamma_L = 0$.

This means that the center of the Smith chart represents a stable operating point in the Γ_L plane:

If $|S_{11}| > 1$ when $Z_L = Z_0$, then $|\Gamma_{in}| > 1$ when $\Gamma_L = 0$.

This means that the center of the Smith chart represents an unstable operating point. These two cases are shown in Figs. 7a and 7b. The shaded area represents values of Γ_L that produce a stable region. Similarly, Figs. 8a and 8b show stable and unstable regions in the Γ_s plane.

For unconditional stability, any passive source or load impedances in a two-port network must produce stability circles completely outside the Smith chart as shown in Figs. 9a and 9b. The conditions for unconditional stability for all passive loads and sources can be expressed in the form:

$$||C_L| - r_L| > 1 \text{ for } |S_{11}| \tag{42}$$

$$||C_s| - r_s| > 1 \text{ for } |S_{22}| \tag{43}$$

The necessary and sufficient stability conditions can be summarized as follows. A stability factor K for an amplifier can be expressed as

$$K = \frac{1 - |S_{11}|^2 - |S_{22}|^2 + |\Delta|^2}{2|S_{12}S_{21}|} > 1 \tag{44}$$

$$1 - |S_{11}|^2 > |S_{12}S_{21}| \tag{45}$$

$$1 - |S_{22}|^2 > |S_{12}S_{21}| \tag{46}$$

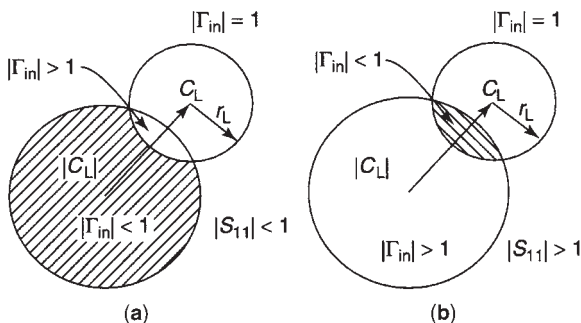


Figure 7. Smith chart showing stable and unstable regions in the Γ_L plane: (a) $|S_{11}| < 1$; (b) $|S_{22}| > 1$. The shaded area represents the stable region.

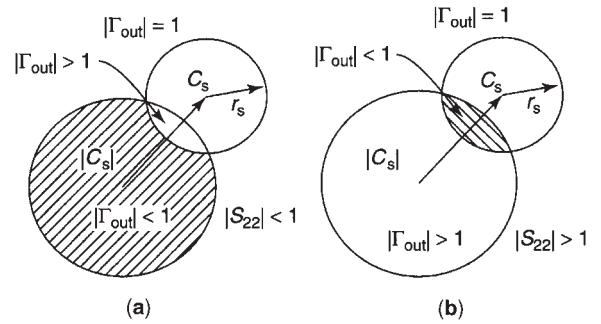


Figure 8. Smith chart showing stable and unstable regions in the Γ_s plane: (a) $|S_{22}| < 1$; (b) $|S_{22}| > 1$. The shaded area represents the stable region.

For unconditional stability

$$K > 1 \tag{47}$$

$$|\Delta| < 1 \tag{48}$$

5.2. Constant-Gain Circles

These are contours mapped on a Smith chart showing the impedance values that produce a constant gain for a given operating condition of an amplifier.

5.2.1. Unilateral Case ($S_{12} = 0$). In the unilateral case, for $\Gamma_s = S_{11}^*$ or $\Gamma_L = S_{22}^*$, the power gain G_s or G_L are at maximum value, and for $|\Gamma_s| = 1$ or $|\Gamma_L| = 1$, the power gain G_s or G_L is zero. A general expression for the G_s and G_L can be written in the following form:

$$G_s = \frac{(1 - |\Gamma_s|^2)}{|1 - S_{11}\Gamma_s|^2} \tag{49}$$

$$G_L = \frac{(1 - |\Gamma_L|^2)}{|1 - S_{22}\Gamma_L|^2} \tag{50}$$

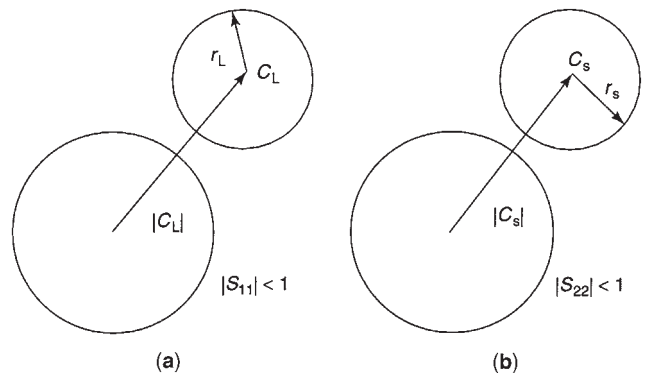


Figure 9. Smith chart showing stability circles for an unconditionally stable amplifier.

A normalized gain factor g_i can be defined as

$$g_i = \frac{G_i}{G_{i\max}} = \frac{(1 - |\Gamma_i|^2)1}{(1 - S_{ii}\Gamma_i^*)} (1 - |S_{ii}|^2) \quad (51)$$

where $i=s$, ($ii=11$), and $i=L$ ($ii=22$). These equations can be rearranged to prove that they represent a family of circles [14]. It is quite often convenient to draw these circles on a Smith chart. The centers of these circles are located on the vector drawn from the center of the Smith chart to the point S_{11}^* or S_{22}^* . The distance from the center of the Smith chart to the center of the constant-gain circles along the vector S_{11}^* for the source side is given by

$$d_s = \frac{g_s |S_{11}|}{1 - |S_{11}|^2 (1 - g_s)} \quad (52)$$

The radius of the constant-gain circles is expressed as

$$r_s = \frac{(1 - |S_{11}|^2) \sqrt{(1 - g_s)}}{1 - |S_{11}|^2 (1 - g_s)} \quad (53)$$

Similar expressions for load-side constant-gain circles can be derived by replacing the S parameters of the signal side with that of the load side.

5.2.2. Simultaneous Conjugate Match: Bilateral Case ($S_{12} \neq 0$). This case occurs when S_{12} cannot be neglected. The transducer power gain is given by Eq. (22). Conditions required for maximum transducer gain are given by

$$\Gamma_{\text{in}} = \Gamma_s^*, \quad \Gamma_{\text{out}} = \Gamma_L^* \quad (54)$$

The simultaneous conjugate match condition thus obtained is shown in Fig. 10.

The gain values Γ_s^* and Γ_L^* can be written as follows:

$$\Gamma_s^* = S_{11} + \frac{S_{12}S_{21}\Gamma_L}{1 - S_{11}\Gamma_L} \quad (55)$$

$$\Gamma_L^* = S_{22} + \frac{S_{12}S_{21}\Gamma_s}{1 - S_{22}\Gamma_s} \quad (56)$$

By solving these last two equations simultaneously, we can get

$$\Gamma_{\text{Ms}} = \frac{B_1 \pm \sqrt{B_1^2 - 4|C_1|^2}}{2C_1} \quad (57)$$

$$\Gamma_{\text{ML}} = \frac{B_2 \pm \sqrt{B_2^2 - 4|C_2|^2}}{2C_2} \quad (58)$$

$$B_1 = 1 + |S_{11}|^2 - |S_{22}|^2 - |\Delta|^2 \quad (59)$$

$$B_2 = 1 + |S_{22}|^2 - |S_{11}|^2 - |\Delta|^2 \quad (60)$$

$$C_1 = S_{11} - \Delta S_{22}^* \quad (61)$$

$$C_2 = S_{22} - \Delta S_{11}^* \quad (62)$$

where Γ_{Ms} and Γ_{ML} are the values of input and output reflection coefficients when the amplifier is conjugate-matched simultaneously.

The maximum transducer power gain, under simultaneous conjugate-matched conditions, is achieved when $\Gamma_s = \Gamma_{\text{Ms}}$ and $\Gamma_L = \Gamma_{\text{ML}}$. Applying these conditions to equation (22), we get

$$G_{\text{t,max}} = \frac{(1 - |\Gamma_{\text{Ms}}|^2)|S_{21}|^2(1 - |\Gamma_{\text{ML}}|^2)}{|(1 - S_{11}\Gamma_{\text{Ms}})(1 - S_{22}\Gamma_{\text{ML}}) - S_{21}S_{12}\Gamma_{\text{Ms}}\Gamma_{\text{ML}}|^2} \quad (63)$$

This can be simplified to

$$G_{\text{t,max}} = \left(\frac{|S_{21}|}{|S_{12}|} \right) (K - \sqrt{K^2 - 1}) \quad (64)$$

where the stability factor K is as defined in (44).

The maximum stable gain G_{msg} , defined as the value of $G_{\text{T,max}}$ when $K=1$, is given by

$$G_{\text{msg}} = \frac{|S_{21}|}{|S_{12}|} \quad (65)$$

This G_{msg} is a figure of merit that represents the maximum value of $G_{\text{T,max}}$.

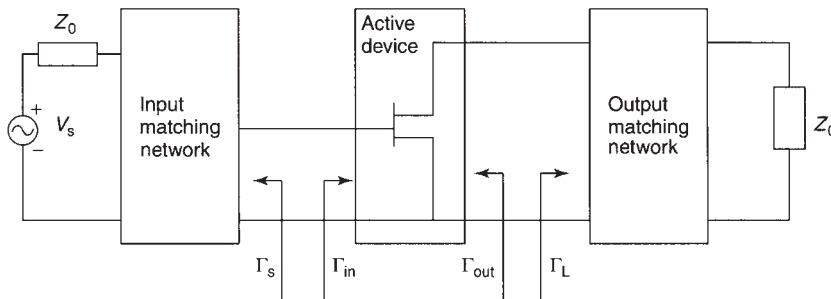


Figure 10. A block diagram of the conjugately matched RF amplifier. (Simultaneous conjugate match is achieved when $\Gamma_{\text{in}} = \Gamma_s^*$ and $\Gamma_{\text{out}} = \Gamma_L^*$.)

5.3. Constant-Noise-Figure Circles

In some applications the major design objective is to obtain the lowest possible noise figure for the circuit. Since minimum noise figure and maximum power gain cannot be obtained simultaneously, constant-noise-figure circles should be plotted on the same Smith chart along with the constant-power-gain circles. The reflection coefficient can then be selected that give the optimum performance in terms of the noise figure and power gain.

The noise figure equation (4) discussed in Section 2 can be rewritten as

$$F = F_{\min} + \frac{r_n}{g_s} (|\bar{Y}_s - \bar{Y}_{\text{opt}}|^2) \quad (66)$$

where r_n is the normalized noise resistance of the two-port network, $\bar{Y}_s = g_s + jb_s$ is the normalized source admittance, and $\bar{Y}_{\text{opt}} = g_{\text{opt}} + jb_{\text{opt}}$ is the normalized source admittance, which results in the minimum noise figure. Usually the normalizing impedance is 50 Ω .

We can express the normalized source admittances \bar{Y}_s and \bar{Y}_{opt} in terms of the source reflection coefficients as

$$\bar{Y}_s = \frac{1 - \Gamma_s}{1 + \Gamma_s} \quad (67)$$

and

$$\bar{Y}_{\text{opt}} = \frac{1 - \Gamma_{\text{opt}}}{1 + \Gamma_{\text{opt}}} \quad (68)$$

Substitution of these quantities into (66) gives the noise figure equations as

$$F = F_{\min} + \frac{4r_n |\Gamma_s - \Gamma_{\text{opt}}|^2}{(1 - |\Gamma_s|^2)(1 + |\Gamma_{\text{opt}}|^2)} \quad (69)$$

The resistance r_n can be found by measuring noise figure for $\Gamma_s = 0$, when a 50 Ω resistance is used. Then

$$r_n = (F_{50} - F_{\min}) \frac{(1 + |\Gamma_{\text{opt}}|^2)}{4|\Gamma_{\text{opt}}|^2} \quad (70)$$

To determine the noise figure circle for a given noise figure F_i , we define a noise figure parameter N_i as

$$N_i = \frac{|\Gamma_s - \Gamma_{\text{opt}}|^2}{1 - |\Gamma_s|^2} = \left(\frac{F_i - F_{\min}}{4r_n} \right) |1 + \Gamma_{\text{opt}}|^2 \quad (71)$$

which can be rewritten in the following form [18]:

$$\left| \Gamma_s - \frac{\Gamma_{\text{opt}}}{1 + N_i} \right|^2 = \frac{N_i^2 + N_i(1 - |\Gamma_{\text{opt}}|^2)}{(1 + N_i)^2} \quad (72)$$

These equations represent a family of circles in terms of N_i . The center of the circle is given by

$$C_F = \frac{\Gamma_{\text{opt}}}{1 + N_i} \quad (73)$$

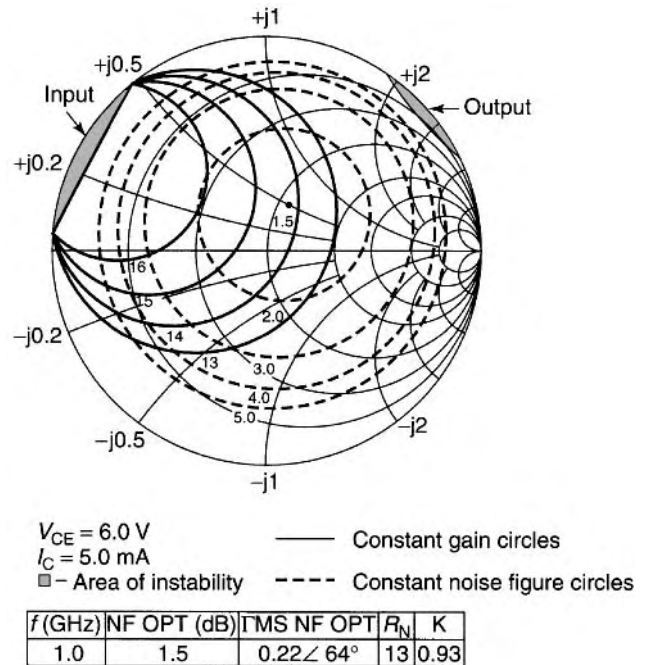


Figure 11. Smith chart showing the constant-gain circles and constant-noise-figure circles for optimum impedance determination. (With permission from Wiley [1].)

and the radius is given by

$$r = \frac{1}{(1 + N_i)} \sqrt{[N_i^2 + N_i(1 - |\Gamma_{\text{opt}}|)]} \quad (74)$$

A set of constant-gain circles and constant-noise-figure circles, as shown in Fig. 11, are drawn on the same Smith chart for the amplifier design. This plot shows the tradeoff between the noise figure and the gain of a device.

6. NARROWBAND AMPLIFIERS

Typical narrowband amplifiers have bandwidth less than 10% of the center frequency. Most of the amplifiers designed for portable communication amplifiers fall into this category. These types of amplifiers can be further divided into maximum power gain amplifiers and low-noise amplifiers. A different design procedure has to be followed for each case.

6.1. Maximum Power Gain Design

From the discussions in Section 5.2.2, the reflection coefficient of the source and load impedance required to conjugately match the amplifier are given by Eqs. (57)–(62). Knowing the values of Γ_{Ms} and Γ_{ML} provided by the device manufacturers, the input-output matching network for the amplifier can be designed.

The source equivalent circuit for maximum power transfer can be written as

$$Z_{\text{in}} = \frac{1 + \Gamma_{Ms}}{1 - \Gamma_{Ms}} \quad (75)$$

where

$$\Gamma_{Ms} = |\Gamma_{Ms}| \cos(\text{ang}(\Gamma_{Ms})) + j|\Gamma_{Ms}| \sin(\text{ang}(\Gamma_{Ms})) \quad (76)$$

The input impedance for minimum noise figure can be written as follows:

$$Z_{in(\text{opt})} = Z_0 \frac{1 - |\Gamma_{Ms}|^2 + j2|\Gamma_{Ms}| \sin(\text{ang}(\Gamma_{Ms}))}{1 + |\Gamma_{Ms}|^2 - 2|\Gamma_{Ms}| \cos(\text{ang}(\Gamma_{Ms}))} \quad (77)$$

The load impedance for maximum power transfer can be written as

$$Z_{out} = Z_0 \frac{1 - |\Gamma_{ML}|^2 + j2|\Gamma_{ML}| \sin(\text{ang}(\Gamma_{ML}))}{1 + |\Gamma_{ML}|^2 - 2|\Gamma_{ML}| \cos(\text{ang}(\Gamma_{ML}))} \quad (78)$$

Once these impedances are determined, CAD tools may be used to compute matching elements of the amplifier.

6.2. Low-Noise Amplifier Design

In this case the minimum noise figure is more important than determining the maximum gain. The noise parameters of the devices are included in the data sheets provided by the vendor or foundry. Figure 12 shows a block diagram of a low-noise narrowband amplifier. The impedances at various points along the circuits are illustrated in this figure. The design procedure is similar to the maximum power gain design, except that we start with the input reflection coefficients for the minimum noise figure. This reflection coefficient is then converted to the equivalent input impedance or admittance. The matching elements are then designed to transform these impedances to $50\ \Omega$.

Let Γ_0 be the optimum reflection coefficient for the minimum noise figure. From Eq. (77), we obtain

$$Z_{opt} = Z_0 \frac{1 - |\Gamma_0|^2 + j2|\Gamma_0| \sin(\text{ang}(\Gamma_0))}{1 + |\Gamma_0|^2 - 2|\Gamma_0| \cos(\text{ang}(\Gamma_0))} \quad (79)$$

We may compute the output impedance computed similarly if we know the load reflection coefficient for the minimum noise figure using Eq. (78).

7. WIDEBAND AMPLIFIER DESIGN

Wideband LNAs have many applications in instrumentation, high-speed microwave, and wireless communication systems. The design methodology for wideband

LNA is more complex than the narrowband amplifiers because of the power gain rolloff characteristics of the device. The matching circuit of the amplifier has to be carefully designed to achieve a constant gain over a broad frequency of interest. The variation in the device S parameters has to be carefully considered. As the frequency increases, the forward gain S_{21} of the device decreases at the rate of 6 dB/octave and the reverse gain S_{12} increases at about the same rate. The input and output impedances S_{11} and S_{22} also vary significantly with frequency.

Several circuit design approaches are employed to achieve the desired broadband characteristics of the amplifier. Broadband amplifier design techniques using negative feedback, compensated impedance matching, and balanced amplifications are discussed in the next section.

7.1. Negative-Feedback Amplifier Design

In this configuration a feedback network is used to compensate for the gain rolloff of the device. Figures 13a and 13b show the shunt feedback amplifier configuration for a bipolar device and a FET, respectively. Similarly, Figs. 14a and 14b show the series feedback configuration for a bipolar device and a FET, respectively. The series feedback enhances the input match of the amplifier, while the shunt feedback flattens the forward gain S_{21} of the amplifier over the frequency range of interest. Typically a resistor is used as the primary feedback element. A capacitor is often added to the shunt feedback circuit to decouple the DC bias of the transistor.

An equivalent circuit of a bipolar transistor can be represented as shown in Fig. 15a and that of a FET, as in Fig. 15b. Other parasitic elements are neglected for simplicity and because their contributions to the amplifier performance are relatively insignificant. The admittance matrix of the network can be written as

$$\begin{bmatrix} I_1 \\ I_2 \end{bmatrix} = \begin{bmatrix} \frac{1}{R_1} & -\frac{1}{R_1} \\ \frac{g_m}{1 + g_m R_2} - \frac{1}{R_1} & \frac{1}{R_1} \end{bmatrix} \begin{bmatrix} V_1 \\ V_2 \end{bmatrix} \quad (80)$$

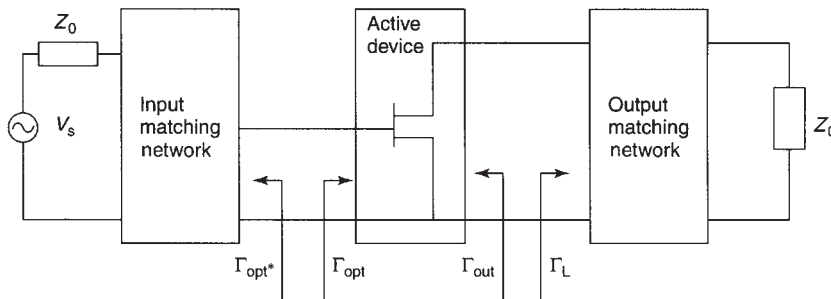


Figure 12. A block diagram of the minimum noise figure narrowband RF amplifier.

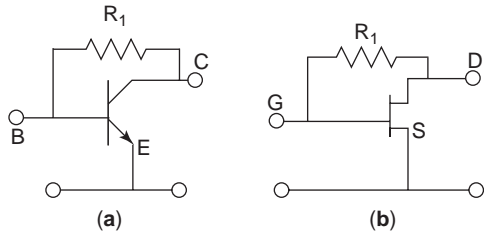


Figure 13. Shunt feedback amplifier: (a) bipolar transistor; (b) FET.

By converting this *Y* parameter equation to *S* parameters, we can get

$$S_{11} = S_{22} = \frac{1}{D} \left[1 - \frac{g_m Z_0^2}{R_1(1 + g_m R_2)} \right] \quad (81)$$

$$S_{21} = \frac{1}{D} \left[\frac{-2g_m Z_0}{(1 + g_m R_2)} + \frac{2Z_0}{R_1} \right] \quad (82)$$

$$S_{12} = \frac{2Z_0}{DR_1} \quad (83)$$

where

$$D = 1 + \frac{2Z_0}{R_1} + \frac{g_m Z_0^2}{R_1(1 + g_m R_2)} \quad (84)$$

For the ideal case of $VSWR = 1$, $S_{11} = S_{22} = 0$

$$1 + g_m R_2 = \frac{g_m Z_0^2}{R_1} \quad (85)$$

or

$$R_2 = \frac{Z_0^2}{R_1} - \frac{1}{g_m} \quad (86)$$

$$S_{21} = \frac{Z_0 - R_1}{Z_0} \quad (87)$$

$$S_{12} = \frac{Z_0}{Z_0 + R_1} \quad (88)$$

Also note that when the transconductance $g_m \gg 1$, we obtain

$$Z_0 = \sqrt{R_2 R_1} \quad (89)$$

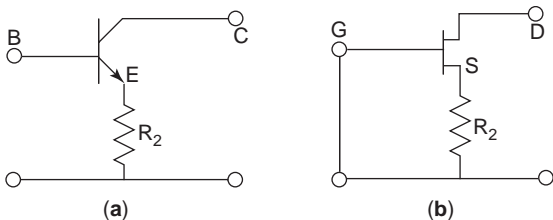


Figure 14. Series feedback amplifier: (a) bipolar transistor; (b) FET.

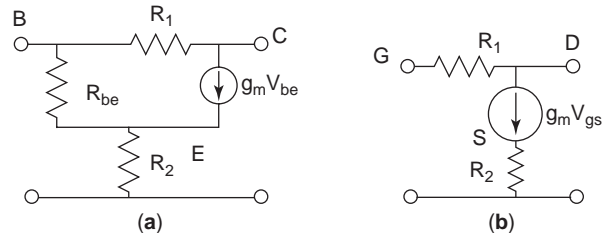


Figure 15. Equivalent circuit of feedback amplifier: (a) bipolar transistor; (b) FET.

Equation (87) shows that S_{21} depends on R_1 only. This shows that gain flattening can be achieved for an amplifier by using parallel feedback.

It can also be seen from Eq. (87) that the minimum transconductance is realized when R_2 is zero:

$$g_m(\min) = \frac{R_1}{Z_0^2} \quad (90)$$

From Eq. (82), it can also be shown that

$$g_m(\min) = \frac{1 - S_{21}}{Z_0^2} \quad (91)$$

$$R_1 = Z_0(1 + |S_{21}|) \quad (92)$$

The phase of S_{21} is an important consideration in negative-feedback amplifier design. At lower frequencies, the phase of S_{21} is close to 180° , but as the operating frequency increases, the phase increases rapidly. The phase difference between the input and output voltages could become zero at some frequency, creating positive feedback. This problem can be avoided by adding a reactive element to the feedback circuit.

7.2. Compensated Matching Technique

In this technique the input and output matching impedances are mismatched to compensate for the variation in the magnitude of S_{21} with frequency. Since the amplifier has to operate over a wide bandwidth, VSWR optimization must cover a wide frequency range. Even though the analytical technique using Smith chart can be used to determine a matching circuit, a more accurate design can be achieved by using computer-aided design procedures.

7.3. Balanced Amplifier Design

It is difficult to achieve good VSWR for broadband amplifiers that employ a compensated matching technique. The mismatching of the input and output impedances causes the VSWR to degrade significantly. Balanced amplifier design can be used to achieve good gain flatness and excellent VSWR. Figure 16 shows the schematic of the balanced amplifier. The input coupler circuit divides input power equally between the amplifier A and B input ports. The output coupler circuit combines the amplified signal from each amplifier. The unused ports of the couplers are terminated at 50Ω impedance to eliminate reflections. In this approach the input and output matching of each amplifier

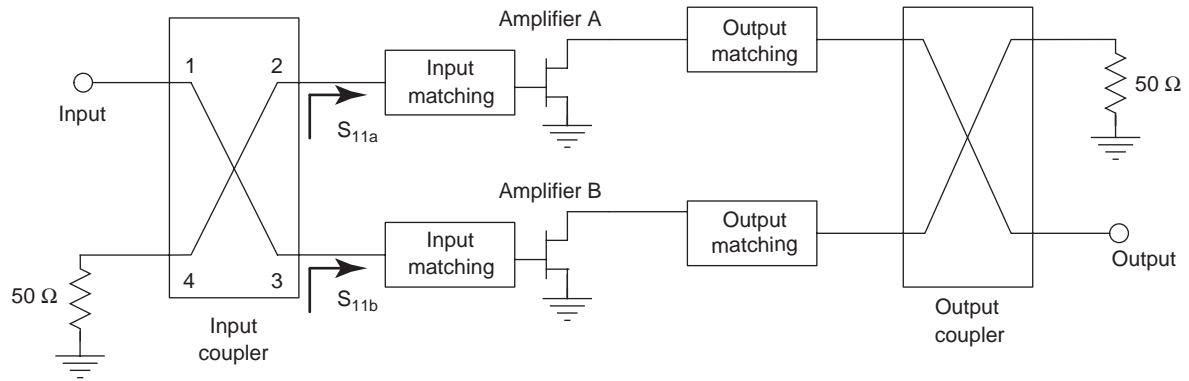


Figure 16. Balanced FET amplifier configuration.

can be mismatched to determine the gain flatness. The combined amplifier will be matched when parallel amplifiers A and B are combined. This will provide excellent VSWR at the input and output of the circuit. The coupler can be realized in many different ways and is discussed elsewhere in this book and in Ref. 1.

For the balanced amplifier that uses a 3-dB coupler, we obtain

$$S_{11} = 0.5[S_{11a} - S_{11b}] \quad (93)$$

$$S_{22} = 0.5[S_{22a} - S_{22b}] \quad (94)$$

The forward power gain is

$$|S_{21}|^2 = 0.25|S_{21a} + S_{21b}|^2 \quad (95)$$

The reverse power loss is

$$|S_{12}|^2 = 0.25|S_{12a} + S_{12b}|^2 \quad (96)$$

The input standing-wave ratio is

$$\text{VSWR}_{\text{in}} = \frac{1 + |S_{11}|}{1 - |S_{11}|} \quad (97)$$

The input standing-wave ratio is

$$\text{VSWR}_{\text{out}} = \frac{1 + |S_{22}|}{1 - |S_{22}|} \quad (98)$$

These types of amplifiers achieve high-gain flatness over a wide range and a high degree of stability and are easy to cascade. However, to achieve this performance, two amplifier chains are required. Hence this amplifier has high power consumption and a larger chip size.

BIBLIOGRAPHY

1. K. Chang, I. Bahl, and V. Nair, *RF and Microwave Circuit and Component Design for Wireless Applications*, Wiley, New York, 2002.
2. IRE standards on methods of measuring noise in linear two-ports, 1959, *Proc. IRE* **48**:60–68 (Jan. 1960).
3. H. Fukui, The noise performance of microwave transistors, *IEEE Trans. Electron. Devices* **ED-13**:329–341 (March 1966).
4. H. Statz, H. A. Haus, and R. A. Pucel, Noise characteristics of gallium arsenide field-effect transistors, *IEEE Trans. Electron. Devices* **ED-21**:549–562 (Sept. 1974).
5. R. A. Pucel, D. J. Massé, and C. F. Krumm, Noise performance of gallium arsenide field-effect transistors, *IEEE J Solid-State Electron.* **SC-11**:243–295 (April 1976).
6. H. Fukui, Design of GaAs MESFET's for broad-band low noise amplifiers, *IEEE Trans. Microwave Theory Tech.* **MTT-27**:643–650 (July 1979).
7. H. Fukui, *IEEE Trans. Microwave Theory Tech.* **MTT-29**:1119 (Oct. 1981).
8. R. Q. Lane, Determination of device noise parameters, *Proc. IEEE* **57**:1461–1462 (Aug. 1969).
9. A. Cappy, M. Schortgen, and G. Salmar, A new method for calculating the noise parameters of MESFET's and TEG-FET's, *IEEE Electron. Device Lett.* **EDL-6**(6):270–272 (June 1985).
10. B. Razavi, A 2.4 GHz CMOS receiver for IEEE 802.11 wireless LANs, *IEEE J. Solid-State Circ.* **34**(10):1382–1385 (Oct. 1999).
11. T. H. Lee, 5-GHz CMOS wireless LANs, *IEEE Trans. Microwave Theory Tech.* **50**(1):268–280 (Jan. 2002).
12. E. Abou-Allam and T. Manku, A low voltage design technique for low noise RF integrated circuits, *Proc. IEEE Int. Symp. Circuits and Systems*, 1998, pp. 373–377.
13. S. Y. Liao, *Microwave Circuit Analysis and Amplifier Design*, Prentice-Hall, Englewood Cliffs, NJ, 1987.
14. G. Gonzalez, *Microwave Transistor Amplifiers, Analysis and Design*, Prentice-Hall, Englewood Cliffs, NJ, 1984.

LOW NOISE AMPLIFIERS: DEVICE NOISE CHARACTERIZATION AND DESIGN

SUNGJAE LEE
 KEVIN J. WEBB
 Purdue University
 West Lafayette, Indiana

1. INTRODUCTION

Receiver sensitivity is limited by noise associated with the elements of the receiver. The most critical element is the

one that first processes the detected signal, usually an amplifier. Therefore, achieving low noise amplifier (LNA) designs is critical in many receiver systems.

Given the input signal-to-noise ratio, the receiver noise, which is the noise added by the receiver component, degrades the signal-to-noise ratio. It is common to use noise figure (F) as a system parameter that characterizes the ability of the component (e.g., the amplifier) to process low-level signals [1]. The noise figure is the ratio of the input to output signal-to-noise ratios, resulting in $F \geq 1$. Assuming that dissipative circuit losses are small, the active device (e.g., the transistor) dominates the receiver noise. An effective receiver amplifier thus requires a suitable low-noise device. It is also important to present an appropriate impedance through matching networks.

The device can be characterized using two-port noise and scattering (S)-parameter measurements. The measurement of the noise figure for various source admittances yields three noise parameters, the minimum noise figure (F_{\min}), the noise resistance (R_n , or conductance G_n), and the optimum source admittance for minimum noise ($Y_{\text{opt}} = G_{\text{opt}} + jB_{\text{opt}}$) [2]. The S -parameter measurements can be used to extract the values for an equivalent-circuit representation for the transistor. The measured noise parameters can then be used to construct a noise equivalent network that, coupled with the device equivalent circuit, can be used to predict the noise performance of this device in, for example, an amplifier configuration, and hence for the design of LNAs.

An empirical relation between the noise figure and the circuit parameters that employs fitting parameters was proposed for GaAs FETs. Fukui describes the dependence of F_{\min} on the operating frequency and the model elements in the equivalent circuit [3]. More quantitative equivalent circuit modeling has been pursued in several works [4–7], where Nyquist noise sources were represented equivalently as temperature or resistance/conductance [8].

Within the active device, there are parasitic noise contributions due to contact metal and contact resistance, along with intrinsic noise mechanisms. Low-noise silicon device technology (e.g., CMOS) has made great strides, showing fairly good performance [9]. However, the lowest-noise-figure device is the high-electron-mobility transistor (HEMT), based on compound semiconductor materials. To first order, a higher-speed device will have lower noise.

2. NOISE FIGURE OF A MULTISTAGE SYSTEM

The analysis of the noise figure in a multistage system demonstrates the importance of good LNA design in receivers. Knowing the noise figure and gain of the individual stages, one can determine the noise figure of the multistage system as [1]

$$F_{\text{tot}} = F_1 + \frac{F_2 - 1}{G_1} + \frac{F_3 - 1}{G_1 G_2} + \dots \quad (1)$$

where the first three stages have gains G_1, G_2, G_3 , and noise figures F_1, F_2, F_3 . Equation (1) clearly shows that the

Table 1. Microwave and Millimeter-Wave Noise Performance (Measured) of GaAs, InP, and GaN-based HEMTs

HEMT (Substrate)	Frequency (GHz)	F_{\min} (dB)	Gate Length (μm)
AlInAs/GaInAs (GaAs) [10]	18	0.48	0.1
AlInAs/GaInAs (InP) [11]	63	0.8	0.2
AlGaN/GaN (SiC) [12]	18	0.75	0.25

noise performance of a multistage system is dominated by the noise figure and the gain of the first stage, since the noise of the later stages is reduced by the gain of the previous stages. Thus, high gain in the first stage (the LNA) reduces the influence of the noise of later stages, making the noise of the first stage critical.

3. NOISE MECHANISMS IN HEMTS

High-gain and low-noise characteristics have made HEMTs the device of choice for building low-noise transistor amplifiers. GaAs-based HEMTs have long been used in microwave low-noise amplifiers [10]. When grown on an InP substrate, GaAs-based HEMTs have demonstrated low noise figure at millimeter-wave frequencies [11]. More recently demonstrated AlGaN/GaN HEMTs on SiC offer promising microwave noise performance [12]. Table 1 summarizes the noise performance achieved with these devices.

One can consider three uncorrelated noise mechanisms in the intrinsic HEMT, associated with velocity fluctuation, gate leakage, and traps, as shown in the schematic of Fig. 1. The velocity fluctuation or diffusion noise is due to electron scatter from the heterojunction, the lattice (phonon), and impurities. This diffusion noise contracts to thermal or Johnson noise if the Einstein relation holds [13]. The bandwidth of this process is proportional to the

HEMT (Substrate)	Frequency	F_{\min}	Gate length
AlInAs/GaInAs (GaAs) [10]	18 GHz	0.48 dB	0.1 μm
AlInAs/GaInAs (InP) [11]	63 GHz	0.8 dB	0.2 μm
AlGaN/GaN (SiC) [12]	18 GHz	0.75 dB	0.25 μm

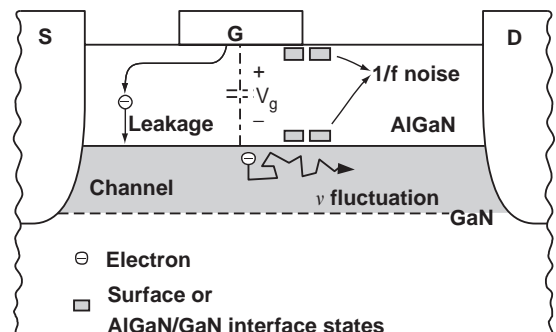


Figure 1. Fundamental noise mechanisms in AlGaN/GaN HEMTs.

inverse of the scattering time, making it frequency-independent (i.e., white noise) in the microwave regime where the device is typically operated. This fundamental noise process results in a drain current noise variance ($\langle |i_d|^2 \rangle$) that will be ideally white and dominated by the channel conduction process. The associated gate voltage variance ($\langle |v_g|^2 \rangle$) is coupled to the channel random process by the gate capacitance (C_{gs}). Physically, one could view this as a random variation in the electric field lines that terminate on the local random variation in channel charge, due to velocity or charge density fluctuation, and the induced gate charge. The line integral of this field gives the gate voltage. A frequency independent $\langle |i_d|^2 \rangle$ will therefore result in $\langle |v_g|^2 \rangle$ being frequency-independent. This model suggests that the correlation between the gate (v_g) and drain (i_d) noise sources will be a function of the degree of electron scatter in the channel, and that it would tend to reduce with increasing channel length.

The gate leakage noise process is associated with electron injection into the channel over the gate Schottky barrier. The randomness of this emission process leads to classical shot noise ($\langle |i|^2 \rangle = 2eI_g A^2/\text{Hz}$, with $e = 1.6 \times 10^{-19} \text{ C}$ and I_g the gate DC current) [13]. This gate leakage noise is also ideally independent of frequency.

Finally, a $1/f^\alpha$ noise process (where $\alpha = 0.5\text{--}2$) occurs as a result of the trapping of electrons in surface states (near the gate) or AlGaIn/GaN interface states (near the channel). This lower frequency noise is particularly important when the device operation is nonlinear, and leads to the noise sidebands on an oscillator signal.

All three of these noise processes will contribute to both the gate and drain noise variances. In addition to the intrinsic noise sources, there is thermal noise associated with various resistances, including source and drain contact resistance and gate finger resistance. All of these parasitic noise sources are uncorrelated with each other and with the intrinsic noise.

4. TWO-PORT NOISE FIGURE

As suggested by Rothe and Dahlke [2], all noise within a linear two-port device can be represented as two equivalent and partially correlated noise sources, and two forms are shown in Fig. 2, with the same two-port device now considered noiseless. In the circuit of Fig. 2(a), the random current i_A and random voltage v_A can be related by

$$i_A = Y_c v_A + i_u \quad (2)$$

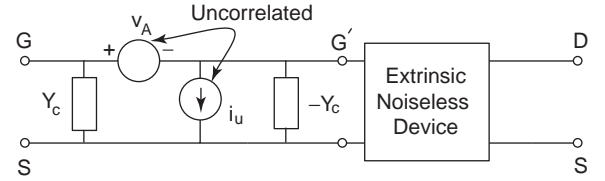
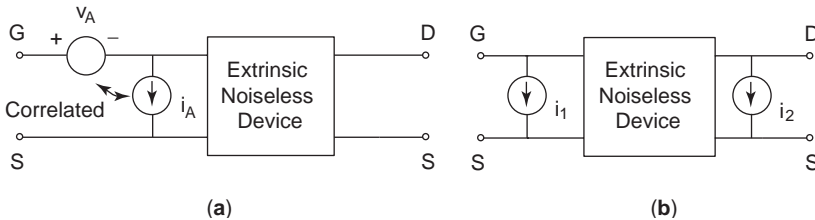


Figure 3. Equivalent noise circuit with two independent noise sources and a correlation admittance ($i_A = Y_c v_A + i_u$).

where v_A and i_u are uncorrelated and $Y_c (= G_c + jB_c)$ is a correlation admittance. In this way, two independent noise sources (v_A, i_u) can be used, as in Fig. 3. This allows the convenient expression of the two-port noise figure and other noise parameters using superposition.

A zero-mean Gaussian noise model is assumed. Also, white noise is assumed over the frequency range of interest. The variance of the noise sources in Fig. 3 can be written using Nyquist's theorem [8] as

$$\langle |v_A|^2 \rangle = 4kT_0 B R_n \quad (3)$$

$$\langle |i_u|^2 \rangle = 4kT_0 B G_n \quad (4)$$

where $\langle \rangle$ denotes the statistical average, k is Boltzmann's constant, T_0 is room temperature (e.g., 290 K), B is the noise bandwidth, and the values of R_n and G_n determine the variances. The two-port noise figure, $F [= 1 + (\langle |i|^2 \rangle_{G'} / \langle |i|^2 \rangle_G)$ in Fig. 3], with source admittance $Y_s (= G_s + jB_s)$, becomes [2]

$$F = 1 + \frac{1}{G_s} [G_n + R_n |Y_s + Y_c|^2] \quad (5)$$

Partial derivatives of (5) with respect to G_s and B_s [$(\partial F / \partial G_s) = 0$, $(\partial F / \partial B_s) = 0$] give the optimum value of Y_s for the minimum F . This optimum input admittance, $Y_{\text{opt}} (= G_{\text{opt}} + jB_{\text{opt}})$, is given by

$$Y_{\text{opt}} = \sqrt{\frac{G_n}{R_n} + G_c^2} + j(-B_c) \quad (6)$$

Substituting $Y_s = Y_{\text{opt}}$ into (5) gives

$$F_{\text{min}} = 1 + 2R_n G_c + 2R_n \sqrt{\frac{G_n}{R_n} + G_c^2} \quad (7)$$

Figure 2. (a) Equivalent noise circuit with noise sources (v_A and i_A) at the input (ABCD representation); (b) equivalent noise circuit with current noise sources (i_1, i_2) at input and output (Y representation).

Rather than expressing F as a function of G_n and Y_c , as in (5), it can be expressed in terms of F_{\min} [using (7)] and Y_{opt} as

$$F = F_{\min} + \frac{R_n}{G_s} |Y_s - Y_{\text{opt}}|^2 \quad (8)$$

A noise-figure meter is commonly used for noise measurements [14–16]. Measurement of the noise figure for various Y_s allows the determination of F_{\min} , R_n , and Y_{opt} in (8) by means of a least-mean-square error fit to $F(Y_s)$ [17]. Then, the parameters G_c , B_c , and G_n can be evaluated from (6) and (7). Measurements of this type are common, and work has been done, for example, to relate the data to noise sources within GaAs, GaN, and CMOS devices [7,18,19].

5. GATE–DRAIN NOISE CORRELATION EFFECT

In the simple FET circuit model of Fig. 4, one can generally anticipate correlation between the gate and drain noise current by capacitive coupling [7]. For example, i_d induces the gate voltage v_g through the transconductance g_m . Then, $v_g = i_d/g_m$ if perfect correlation can be assumed, and $i_g = j\omega C_{gs}v_g = j\omega C_{gs}i_d/g_m$. Finally, $\langle |i_g|^2 \rangle = \omega^2 C_{gs}^2 \langle |i_d|^2 \rangle / g_m^2$. It has been demonstrated experimentally [7] that, in the case of velocity fluctuation, $\langle |i_d|^2 \rangle$ is independent of frequency in the microwave operating range of the transistor (white noise), and $\langle |i_g|^2 \rangle \propto \omega^2$, thus establishing the concept of capacitive coupling between the gate and drain noise. In order to assess the effect of the correlation between i_g and i_d , the correlation coefficient C is defined in normalized form as [4]

$$C = \frac{\langle i_g i_d^* \rangle}{\sqrt{\langle |i_g|^2 \rangle \langle |i_d|^2 \rangle}} \quad (9)$$

With perfect correlation assumed in the ideal noise model of Fig. 4, $C = j1$.

To investigate the influence of C on the total noise, the ideal FET noise model in Fig. 4 is considered with velocity fluctuation noise only, to calculate the minimum noise figure, F_{\min} , in terms of $\langle |i_g|^2 \rangle$, $\langle |i_d|^2 \rangle$, and the correlation coefficient C , by setting $\langle i_g i_d^* \rangle = j|C| \sqrt{\langle |i_g|^2 \rangle \langle |i_d|^2 \rangle}$ (imaginary correlation only). Then, F_{\min} can be expressed

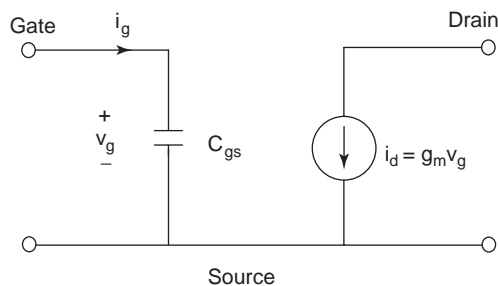


Figure 4. Ideal FET model with white-noise random processes i_d and v_g (i_g).

as [4,7]

$$F_{\min} = 1 + \frac{\sqrt{\langle |i_g|^2 \rangle \langle |i_d|^2 \rangle}}{2kT_0 B g_m} \sqrt{1 - |C|^2} \quad (10)$$

Equation (10) indicates that, with no parasitics, perfect correlation ($|C| = 1$) cancels the noise contribution from $\langle |i_g|^2 \rangle$ and $\langle |i_d|^2 \rangle$ completely, giving $F_{\min} = 1$. Therefore, high correlation ($j1$ is the theoretical maximum) would be desirable for a low-noise device, since correlation is a cancellation term in calculating the total noise of the FET.

6. LOW-NOISE AMPLIFIER DESIGN

There are design tradeoffs between noise figure, gain, and bandwidth. Tradeoffs exist between noise figure and gain because the desired source reflection coefficients for low-noise figure, the optimum being F_{\min} , and maximum available gain values are different. The stability of the LNA circuit is also important. If the transistor used is conditionally unstable, source and load impedances presented by the input and the output matching networks should stabilize the circuit first over all frequencies [20]. Additionally, the linearity performance (third-order intercept point, i.e., IP3) must be adequate to ensure sufficient dynamic range of the receiver system.

Low-noise amplifier design techniques have been investigated by many authors, resulting from various technologies (especially GaAs-based transistors) and circuit architectures. Examples of low-noise amplifiers, including design techniques, can be found in a series of reprint articles edited by Fukui [21]. Computer-aided design synthesis tools provide a convenient platform.

In general, in order to achieve the lowest possible noise figure, the input matching network is designed to provide the source admittance for low-noise figure, and the output matching network is optimized for high gain. The noise parameters F_{\min} , R_n , and Y_{opt} should be determined first for the particular device being used (either from the measurement or given by the manufacturer). Then, these parameters can be used in low-noise transistor amplifier design and simulation with the S parameters.

BIBLIOGRAPHY

1. H. T. Friis, Noise figure of radio receivers, *Proc. IRE* **32**(7):419–422 (July 1944).
2. H. Rothe and W. Dahlke, Theory of noisy fourpoles, *Proc. IRE* **44**:811–818 (June 1956).
3. H. Fukui, The noise performance of microwave transistors, *IEEE Trans. Electron. Devices* **13**:329–341 (March 1966).
4. H. Statz, H. A. Haus, and R. A. Pucel, Noise characteristics of gallium arsenide field-effect transistors, *IEEE Trans. Electron. Devices* **21**:549–562 (Sept. 1974).
5. R. A. Pucel, H. A. Haus, and H. Statz, *Advances in Electronics and Electron Physics*, Vol. 38, Academic Press, New York, 1975.

6. M. W. Pospieszalski, Modeling of noise parameters of MESFET's and MODFET's and their frequency and temperature dependence, *IEEE Trans. Microwave Theory Tech.* **36**(1):1–10 (Jan. 1988).
7. S. Lee, K. J. Webb, V. Tilak, and L. F. Eastman, Intrinsic noise equivalent circuit parameters for AlGaIn/GaN HEMTs, *IEEE Trans. Microwave Theory Tech.* **51**(5):1567–1577 (May 2003).
8. H. Nyquist, Thermal agitation of electric charge in conductors, *Phys. Rev.* **32**:110–113 (July 1928).
9. T. H. Lee, *The Design of CMOS Radio-Frequency Integrated Circuits*, 2nd ed., Cambridge Univ. Press, 2004.
10. M. Kawano, T. Kuzuhara, H. Kawasaki, F. Sasaki, and H. Tokuda, InAlAs/InGaAs metamorphic low-noise HEMT, *IEEE Microwave Guided Wave Lett.* **7**(1):6–8 (Jan. 1997).
11. U. K. Mishra, A. S. Brown, S. E. Rosenbaum, C. E. Hooper, M. W. Pierce, M. J. Delaney, S. Vaughn, and K. White, Microwave performance of AlInAs-GaInAs HEMT's with 0.2- and 0.1- μm gate length, *IEEE Electron. Device Lett.* **9**(12):647–649 (Dec. 1988).
12. J. W. Lee, A. Kuliev, V. Kumar, R. Schwindt, and I. Adesida, Microwave noise characteristics of AlGaIn/GaN HEMTs on SiC substrates for broad-band low-noise amplifiers, *IEEE Microwave Wireless Compon. Lett.* **14**(6):259–261 (June 2004).
13. A. van der Ziel, *Noise in Solid State Devices and Circuits*, Wiley, New York, 1986.
14. A. Przadka, K. J. Webb, and D. B. Janes, Two-port noise and impedance measurements for two-terminal devices with a resonant tunneling diode example, *IEEE Trans. Microwave Theory Tech.* **46**(9):1215–1220 (Sept. 1998).
15. Agilent Technologies, *Fundamentals of RF and Microwave Noise Figure Measurement*, Application Note 57-1.
16. Agilent Technologies, *Noise Figure Measurement Accuracy*, Application Note 57-2.
17. M. Mitama and H. Katoh, An improved computational method for noise parameter measurement, *IEEE Trans. Microwave Theory Tech.* **27**(6):612–615 (June 1979).
18. A. Cappy, Noise modeling and measurement techniques, *IEEE Trans. Microwave Theory Tech.* **36**(1):1–10 (Jan. 1988).
19. P. Heymann, M. Rudolph, H. Prinzler, R. Doerner, L. Klapproth, and G. Bock, Experimental evaluation of microwave field-effect-transistor noise models, *IEEE Trans. Microwave Theory Tech.* **47**(2):156–163 (Feb. 1999).
20. G. Gonzalez, *Microwave Transistor Amplifiers: Analysis and Design*, 2nd ed., Prentice-Hall, Englewood Cliffs, NJ, 1997.
21. H. Fukui, ed., *Low-Noise Microwave Transistors and Amplifiers*, IEEE Press, New York, 1981.

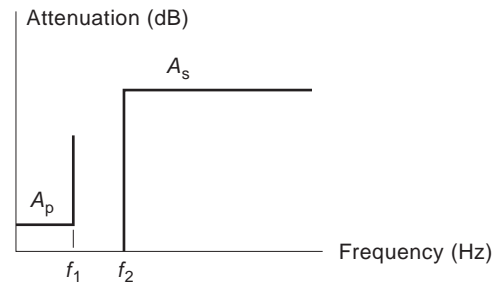


Figure 1. Lowpass filter requirements.

A first-order lowpass filter is shown in Fig. 2. The transfer function is

$$\frac{V_{out}(s)}{V_{in}(s)} = \frac{1}{s + \frac{1}{RC}}$$

The pole-zero diagram is shown in Fig. 3.

An active second-order lowpass filter is shown in Fig. 4. The circuit is known as the *Sallen-Key lowpass circuit*. The transfer function is

$$\frac{V_{out}(s)}{V_{in}(s)} = \frac{\alpha}{s^2 + \left(\frac{1}{R_1C_1} + \frac{1}{R_2C_1} + \frac{1-\alpha}{R_2C_2} \right) s + \frac{1}{R_1R_2C_1C_2}} \quad (1)$$

where $\alpha = 1 + r_2/r_1$. The pole-zero diagram is shown in Fig. 5.

An approach to design a circuit (a lowpass filter) whose frequency response satisfies the lowpass requirements shown in Fig. 1 consists of two steps: approximation of the requirements by a transfer function and synthesis of the transfer function.

There are several approximation methods, for instance, Butterworth, Chebyshev, inverse Chebyshev, and Cauer approximations. A transfer function obtained by one method is different from those obtained by the others, and has different properties. However, the frequency response of each of the transfer functions satisfies the lowpass requirements. The Butterworth approximation method is described below.

Compute the scaling factor k given by the equation below:

$$k = \sqrt{10^{0.1A_p} - 1}$$

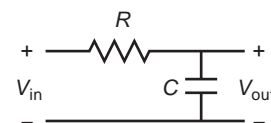


Figure 2. First-order lowpass filter.

LOW-PASS FILTERS

CHIU H. CHOI
University of North Florida
Jacksonville, Florida

A lowpass filter suppresses the high-frequency components of a signal, leaving intact the low-frequency ones. A lowpass filter specification can be expressed as shown in Fig. 1. In the stopband (above f_2 Hz), the attenuation is at least A_s dB. In the passband (below f_1 Hz), the attenuation is at most A_p dB. The band from f_1 to f_2 is called the *transition band*.

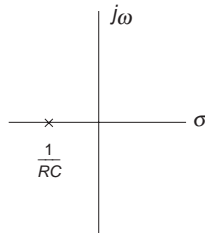


Figure 3. Pole-zero diagram of the first-order lowpass filter.

Next, compute the quantity

$$\frac{\log_{10}\left(\frac{10^{0.1A_s} - 1}{k^2}\right)}{2 \log_{10}\left(\frac{f_2}{f_1}\right)}$$

Choose the order n of the filter to be the smallest integer not smaller than the quantity given above. Solve for all the left-half-plane roots Z_i s of the equation

$$(-1)^n S^{2n} + 1 = 0$$

The Butterworth lowpass transfer function is formed as follows:

$$T_{LP}(s) = \frac{1}{\prod_{i=1}^n (S - Z_i)} \Big|_{s = k^{1/n} s / 2\pi f_1}$$

Example 1. Find the Butterworth transfer function for a lowpass filter with $A_s = 15$ dB, $A_p = 0.5$ dB, $f_1 = 1$ kHz, and $f_2 = 5$ kHz:

$$k = \sqrt{10^{0.1(0.5)} - 1} = 0.35$$

$$\frac{\log_{10}\left(\frac{10^{0.1(15)} - 1}{0.35^2}\right)}{2 \log_{10}\left(\frac{5\text{k}}{1\text{k}}\right)} = 1.72$$

Choose $n = 2$. The left-half-plane roots of the equation

$$(-1)^2 s^{2(2)} + 1 = 0$$

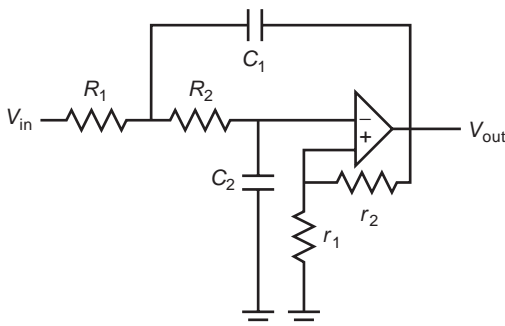


Figure 4. Sallen-Key lowpass circuit.

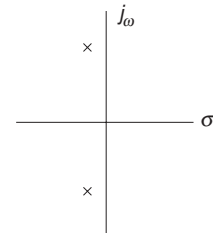


Figure 5. Pole-zero diagram of the Sallen-Key lowpass filter.

are $1/\sqrt{2}(-1 \pm j)$. Therefore, the Butterworth transfer function is

$$T_{LP}(s) = \left. \frac{1}{s^2 + \sqrt{2}s + 1} \right|_{s = \sqrt{0.35} s / 2\pi(1000)}$$

which simplifies to

$$T_{LP}(s) = \frac{1.128 \times 10^8}{s^2 + 1.502 \times 10^4 s + 1.128 \times 10^8}$$

These calculations have all been performed before, and the results and available in tabular and computer program forms.

The Sallen-Key lowpass circuit can be used to realize a second-order lowpass transfer function of the form

$$T(s) = \frac{K}{s^2 + as + b}$$

Compare $T(s)$ with Eq. (1):

$$K = \frac{\alpha}{R_1 R_2 C_1 C_2} \quad a = \frac{1}{R_1 C_1} + \frac{1}{R_2 C_1} + \frac{1 - \alpha}{R_2 C_2}$$

$$b = \frac{1}{R_1 R_2 C_1 C_2}$$

Since there are more unknowns than equations, one can assign values to certain unknowns and then solve for the remaining unknowns. As an example, choose $C_1 = 1$, $C_2 = 1$, $\alpha = 2$. Then

$$K = 2b \quad R_1 = \frac{1}{a} \quad R_2 = \frac{a}{b}$$

The impedance-scaling method can be used to scale the values of R s and C s into the practical ranges.

In general, a higher-order lowpass transfer function obtained by Butterworth and Chebyshev approximations can be factorized into a product of biquadratic functions and possibly one first-order expression. Each of the biquadratic functions can be synthesized by using the Sallen and Key or other lowpass circuits. The first-order transfer function can be realized by an active or passive circuit. By cascading all the biquad and first-order circuits together, the lowpass filter is realized.

FURTHER READING

- G. Daryanani, *Principles of Active Network Synthesis and Design*, Wiley, New York, Wiley, 1976.
- M. E. Van Valkenburg, *Analog Filter Design*, Holt, Rinehart, and Winston, New York, 1982.
- R. W. Daniels, *Approximation Methods for Electronic Filter Design*, McGraw-Hill, New York, 1974.
- G. Morchytz and P. Horn, *Active Filter Design Handbook*, Wiley, New York, 1981.

LOW-POWER BROADCASTING

CHIP MORGAN
 CMBE, Inc.
 Bridport, Vermont

Low-power broadcasting systems are very interesting from a technical perspective for several reasons. Although they appear to be simple to build and easy to design, they can actually be more critical than higher-powered stations. In fact, since the signal is local and likely to receive or cause interference, design and optimization methods for low-power systems can make the difference between a successful operation and a failure.

It is a mistake to think that a low-powered facility cannot perform as well (within its intended coverage area) as a full-powered station. Around the world, there are many facilities operating at low power that provide excellent full-time service to communities every day.

Modern techniques allow some very interesting project work, such as synchronized systems, directional systems to fill in specific areas, and local systems (such as in tunnels, buildings, or temporary high-density populated areas such as stadiums). These techniques also have application for fill-in service for satellite-delivered services as well as terrestrial digital broadcasting.

1. DEFINITIONS

A low-power station is typically a facility with a transmitter power of 1 kW output or less. Although antenna gain plays a large role in the effective radiated power (ERP) of a given facility, it is easier to define the power of a station in general terms by transmitter power. However, when regulating the location and coverage of a given facility, ERP and height above average terrain (HAAT) are often specified.

1.1. Translator

A translator is a radiofrequency (RF) device that retransmits a television or FM signal within a specific broadcast band. The translator alters none of the signal characteristics except frequency and amplitude with a main purpose to extend or fill in the coverage of a transmitted signal. It typically receives a signal, changes its carrier frequency, and then rebroadcasts the changed carrier at

substantially higher levels of radiated energy. A translator is essentially a repeater.

As an example, a broadcast station might have a zone within its trade area that receives a poor signal from its main transmitter. The technical consultant of the station prepares a study to identify the existence of frequencies for a translator. The consultant recommends a site and a specific design.

Listeners and/or viewers within the coverage area of the translator receive primary station programming on a different frequency from the primary station. Thus, the station signal is translated in that area.

1.2. Booster

A booster is an RF device that retransmits a TV or FM signal within a specific broadcast band. It alters none of its characteristics, including frequency or amplitude, with a main purpose to extend or fill in the coverage of a transmitted signal. A booster operates on the same frequency as the primary signal and rebroadcasts it at substantially higher levels of radiated energy. The signal of a booster is the same as the primary station. Boosters are complicated, and a poorly designed or built booster can cause much more harm than good. A booster is an isofrequency transmitter.

As an example, a station might have a location within its trade area that receives a poor signal from its main transmitter. The consultant of the station prepares a study to identify a site with appropriate terrain shielding or to allow the operation of a booster without substantial interference to or from the main signal. Listeners and/or viewers receive the programming from the primary station on the same frequency as the primary station. Thus, the station signal is boosted in that area.

1.3. LPTV

An LPTV (low-power television) station can be defined as one that may operate as a translator or originate programming and operate as a subscription service low-powered TV system intended to serve a local area. It functions as a full-powered TV station, but with reduced output power.

1.4. ITFS, MDS, and MMDS

ITFS (instructional television fixed service), MDS (multi-point distribution service), and MMDS (multichannel MDS) are television transmission systems authorized to provide specific programming to subscribers. Technically, ITFS and MDS are quite similar to each other as well as to broadcast television transmission.

2. GENERAL GUIDELINES

Following are some tips and points to consider when designing a low-power system. Some of these items are simple common sense; others require high-powered computer system analysis to compare options and identify predicted results. These guidelines also apply to high-powered systems. In most cases, low-powered systems have very

stringent requirements due to specific signal challenges. Before designing a system, a complete understanding of all the technical issues will minimize problems. The field is quite complex. For example, propagation and signal analysis is a career unto itself, but understanding the basics will help you identify potential problems in the initial design of a system. Use the services of a professional who designs systems regularly for the best results.

2.1. Location of Antenna in Relation to Population

Locate the transmitting antenna site as close to the target population as possible. Building penetration and received signal strength decreases rapidly as distance between transmitter and receiver increases. RF energy diminishes with the square of the distance. If the transmitter site is distant from the target population, system design is much more critical and difficult.

2.2. Height of Antenna above Population

More antenna height usually means better coverage. However, one should specify an antenna height as high as is needed for the specific requirements, but not any higher. Excessive antenna height leads to unnecessary interference, increased cost of construction and operation, and decreased reliability. The antenna should be just high enough for adequate Fresnel ellipsoid clearance to the target area but not much above that height.

2.3. Fresnel Ellipsoid Clearance of Signal into Target Market

The antenna signal is not a narrow ray of energy like a laser beam. The signal is a noncoherent three-dimensional beam that gets wider as it leaves the transmitting antenna, just like the beam from a flashlight. For maximum received signal strength, all the energy in the Fresnel ellipsoid must pass from the transmitter to the receiver with no obstacles affecting the path of transmission. The receiving antenna works exactly opposite from the transmitting antenna. It gathers energy from a three-dimensional area and narrows it down to the location of the receiver, just as a telescope gathers light from a wide area and focuses it at on small area. At the midpoint of the transmission/reception path, the signal beam is its widest. Therefore, even if you can see the population you want to serve from the transmitter site, the broadcast signal may not be able to reach it due to obstructions below the line-of-sight path.

2.4. Tuning and Installing an Antenna

A transmitting antenna is just as sensitive to its immediate environment as a receiving antenna. If you have ever adjusted a “rabbit ear” antenna on a TV set or the rod antenna on a “boombox,” you understand the concept. A very small change in the antenna orientation or environment has a drastic effect on its performance. Install the antenna and tune it properly from the beginning and the facility will perform as predicted. The supporting structure, the antenna design, and the way the antenna is mounted all affect the quality of the signal.

2.5. Elevation Pattern of an Antenna

There is often population below the height of a transmitting antenna—especially if it is on a tall tower or hill. The elevation pattern of the antenna identifies the amount of signal radiated toward the horizon as well as the amount radiated below the horizon, into low-lying population. The elevation pattern is critical in systems design because control of energy in specific areas can be an important factor in system performance. Conversely, a receiving antenna often receives from a location above its horizontal plane, and the elevation pattern above the horizon is important. The number, spacing, and type of elements in the antenna array typically control the elevation pattern of a wire-type antenna.

2.6. Interference from Adjacent-Channel and Cochannel Stations

Unless the station is located in an area with very few signals, certain portions of the service area will receive interference from other nearby or more powerful transmitters. This can come from stations as far as three channels above or below the carrier frequency. Consider the potential of interference in the design of a facility. Most complaints of poor performance are a result of interference, due to poor signal from the intended transmitter in an area or excessive signal from an interferer or “jammer.”

2.7. Receiver-Induced Third-Order Harmonic Interference

When a receiver is near other transmitters, even if the desired station has a strong local signal, the receiver will overload or “be blanketed” by the relatively higher signal levels of the jamming transmitter. The selectivity (ability to reject strong local interference) of the receiver determines its susceptibility to this kind of interference. In other cases, harmonic mixes occur within the receiver itself, causing the desired signal to be jammed. This situation is receiver-induced third-order harmonic interference.

2.8. Condition of Antenna System

Most transmitters have a test meter that indicates if the antenna has failed to the point that it can harm the transmitter. However, there is typically no accurate test equipment available at a transmission facility to show qualitatively how well the transmitter or antenna is performing. Most antenna complaints are very subjective; you just cannot “get” the station as you used to—it does not sound right or look right any more, and so on. The only way to tell if an antenna is working correctly is to test it with appropriate test equipment used by antenna manufacturers and consultants.

2.9. Quality of Modulation

A commonly overlooked cause of signal problems is poor source material. In this case, no amount of improvement to the antenna or transmission system will correct the problem.

3. LOW-POWER SYSTEM DESIGN

Site selection is the first step in designing a system. The details of the site determine many other design criteria, so an overall review of the impact of any potential site must be exhaustive. Choice of the best site for a transmission system is often a series of compromises. Strike a balance between economical issues, environmental issues, and performance issues of the particular site under review.

In addition to these restrictions, the site must be available; must satisfy all regulatory, practical, and engineering requirements; and must be accessible during the time construction is planned to take place.

The primary technical consideration of site selection is the performance of a transmission system that is located there. Computer analysis should be performed to predict the performance at all intended receiving locations, to predict the interference generated to other operators from the proposed site, and to demonstrate the relative quality of any particular site with others being considered. In addition to the performance of the transmitter(s) located at the proposed site, receiving capability of the primary signal must be possible. This may mean satellite reception, microwave link reception, or off-air reception of the modulating signal.

When using off-air rebroadcast, the site selection is critical. For example, if a booster receives its primary signal from a receiver tuned to the primary FM transmitter, the booster's transmitted signal generally ranges from 90 to 110 dB stronger than the intended input signal. If feedback contamination is to be limited to less than 30 dB, the transmitting antennas and receiving antennas have to have between 120 and 140 dB isolation.

A high degree of shielding between the antennas is required. Sometimes this can be accomplished by terrain or even by a building. Depending on system power levels, a physical separation between highly directional antennas may be enough.

It is good engineering practice to choose a site that is accessible in varying weather conditions. That is, it cannot be subject to factors such as excessive winds, erosion, snow, heat, or water.

3.1. Antennas

Some system designers mistakenly believe that running all the power the license permits and using the largest antenna they get is the best course of action. The problem with higher-gain antennas is that they have small vertical beamwidths that can cause deadspots in the minor lobes due to the nulls in the radiation pattern. Since the major lobe provides the most gain to the detriment of areas near the antenna, signals in the remote areas will likely be excellent, at the cost of local signals. Sometimes, however, this is an intended effect when areas near the antenna are lightly populated.

Beamtilt will not solve a problem caused by insufficient Fresnel ellipsoid clearance ("shadowing"). Antenna tuning will also not solve this kind of problem. If a site has poor performance due to radio shadowing, no amount of manipulation of the antenna system will make a substantial

improvement over a properly operating antenna system. Some operators are willing to pay for minor improvements, but a better use of finances is to analyze carefully a potential site before building it. Examine every proposed system with care to analyze accurately the magnitude of the potential problem areas. Antenna pattern control equals better system performance, less co-channel and adjacent channel interference, and better spectrum utilization.

3.1.1. Transmitting Antennas. There are a number of factors to consider when it comes to designing the antenna system for a low-power operation. Careful attention to materials selected is key. A poor-quality antenna will adversely affect the best system. For omnidirectional usage, use low-power versions of the standard higher-powered transmitting antennas. (They are available in horizontal, vertical, and elliptically polarized models.) Virtually all transmitting and receiving antennas are available in 50- or 75- Ω models. The relationship between the tower and the radiating elements is essential. The best designs are custom tuned for the specific situation.

When designing an antenna system, make sure that antenna and tower manufacturers or owners are kept abreast of any possible problem areas, such as wind resistance, the antenna's postinstallation directivity patterns, and mounting procedures.

Calculate ERP by multiplying the antenna's power gain by the transmitter output in watts less losses (hybrid, coax, duplexer, circulators, etc.). Be aware of the antenna's vertical plane pattern as well as the probable signal levels at various points in the service area, because the measuring gain on VHF antennas is usually set at zero degrees. (The gain at other elevation angles may be considerably less.)

Antenna beamwidth equals the number of degrees between the major lobe half-power points. If it is necessary to have coverage in local *and* distant areas, choose the highest possible antenna location and the antenna configuration that will be the best compromise. A high antenna with no obstructions between the transmission site and the receiving sites is required for consistent service to the intended audience.

If local coverage is of paramount importance, utilize a high-gain antenna with a moderate degree of beamtilt, or lower power and an omnidirectional antenna. This will make the best use of radiated power and reduce interference.

3.1.2. Receiving Antennas for Retransmission. The input signal's delivery to the transmitter is an essential factor in overall system design when retransmitting a signal. A poor-quality input signal makes all the difference in the entire operation of the system.

A simple antenna on a nearby tower is sometimes sufficient for off-air reception. More often, measures that are more intricate are necessary. Sometimes, increasing antenna gain or narrowing the pattern of the arrangement is an option. A 30° horizontal pattern width from a single receiving antenna has been known to allow for reception of an interfering signal. A number of methods can resolve

retransmission reception difficulties, including signal filtering to minimize out-of-band products, antenna-mounted preamplification to increase signal levels, and horizontal and vertical antenna stacking techniques to increase antenna gain and directivity.

The majority of difficulties related to the input signal have to do with weak input signal strength, measured in microvolts on the receiver front panel. Depending on the manufacturer, equipment specifications usually specify that 2–10 μV will result in a good output signal, but those numbers are reflective of equipment capabilities only.

Practical limits at a site tend to be much higher for several reasons. Depending on local conditions, weak signals can result in fades. Upward of 100–300 μV is usual, but even this level of signal can have problems during a fade. Carefully monitoring proposed sites helps avoid the problem from the start. The level of RF noise near a receiving antenna can influence input. Noise levels can be higher than the signal strength of the desired signal. Subsequent filtering or antenna location can help resolve the issue.

In many cases, one must take special measures to ensure that reception and retransmission signals stay clean. A weak signal with poor signal-to-noise ratio is generally the problem. The system's receiving section must contain a superior signal conditioning system, preamp, and receiving antenna to maximize clarity.

4. ANTENNA STACKING

Antenna stacking increases the gain of an antenna array. Stacking can be either horizontal or vertical. Stacking applies in transmission and reception and can be helpful in solving certain reception difficulties.

Vertical antenna stacking influences vertical beamwidth. It is effective in amplifying the gain of the array. Horizontal stacking narrows the array's beamwidth from side to side. If the antennas are in phase, this method adds 3 dB to antenna gain for every doubling of the stack. (A single Yagi antenna has a horizontal acceptance angle of approximately 30° between the 3 dB down points off its front.) Note that horizontal beamwidth decreases considerably and vertical beamwidth remains unaffected.

A variation in stacking resolves certain interference and reception difficulties. There are myriad ways to make use of this technique, including offset antenna arrangements, which allow phase reinforcement off the front of the array and phase cancellation off its rear. The process involves vertical stacking of the antennas (i.e., one antenna forward of another by precisely $\frac{1}{4}\lambda$ at the center frequency of the rejected channel). Use this formula to calculate stacking:

$$D (\text{in.}) = 2951 \text{ divided by frequency of} \\ \text{undesired signal (MHz)}$$

RF signals travel faster in free space than in cable, so connect the rear antenna to the common junction with a short feedline. Then connect the front antenna to the com-

mon junction with a feedline whose length results from the formula multiplied by the velocity of propagation of the cable used, plus the amount of cable that is used for the rearmost antenna.

As another example, set the space from one antenna boom to another so that it will cancel an unwanted signal from a specific forward direction. Install the antennas with the center of each spaced so the unwanted signal is out of phase at the connection between the two antennas, and the interfering signals will negate each other at the combined output.

4.1. Transmitters

Transmitters provide the RF power for the antenna. Proper design of a low-power facility includes selection of the appropriate transmitter for the job. A primary consideration is adequate power in order to achieve desired effective radiated power. The gain of the antenna(s) and the length of the transmission line(s) affect this power level requirement. The available electrical power and the cooling system available at the transmission site also affect the RF power level design. Generally, low-power facilities do not need more complex electrical power systems, such as three-phase power or high-voltage power systems. As in any design, the transmitter should be well designed and easy to maintain and provide diagnostic information about its status and condition.

4.1.1. ITFS and MDS Transmitters. Usually, transmitters for MDS and ITFS rate at 10–100 W visual power and 10% aural capability; 10-W transmitters are typically solid state. Higher-powered transmitters typically operate with vacuum tubes.

Internally and externally diplexed transmitters are widely used. Low-level internal systems work well in uncongested areas due to their ease of use and cost efficiency. Externally diplexed systems reduce cross modulation of video synchronization components onto the aural carrier. They also offer better rejection of products caused by the intermodulation of aural and visual carriers. Aural carrier signal integrity is a considerable element in system performance with multichannel sound and pay television encoding and decoding. Amplitude, phase precorrection methods, and contemporary linear amplifier design ensure good signal performance.

4.1.2. LPTV Transmitters. When choosing an LPTV transmitter, there are a few terms to remember. Linear waveform distortion, called the "2T K factor," measures the distortion of a picture's fine detail. The 2T sine-squared pulse and the 2T bar define the K factor, or actual distortion. The K factor must be less than 3% to meet LPTV standards.

Envelope delay is the delay within the system of the modulation envelope. It is usually a frequency function, with higher frequencies equaling shorter delays. For transmitters, the standard is built on a baseline of the delay within the equipment between 0.05 and 0.2 MHz. For up to 3 MHz, that delay is to be maintained. Past that,

the delay should linearly decrease up to 4.18, so the delay is -170 ns with respect to the baseline at 3.58 MHz.

Differential gain is the difference in gain of the LPTV system's translator for a small, high-frequency signal (chrominance) at two specific levels of a low-frequency signal (luminance) on which the high-frequency signal is superimposed. Differential gain cannot exceed 10% at an average picture level ranging from 10% to 90%.

Differential phase is the difference in the output phase of a signal such as that used in differential gain measurements. It should never exceed 7° past the range of blanking to white.

4.1.3. FM Transmitters. Low-power FM transmitters are usually either a standard FM exciter with lowpass filter or an exciter with a low-power amplifier. Many of the low-power systems are solid state; others operate with vacuum tubes. In a translator or rebroadcast application, several systems are available as complete solutions, with built-in receivers and audio processors. In most cases, the transmitter is simple to install and operate.

4.2. Transmission Lines

Transmission lines play a major role in the design of a low-power system. They provide the connection between the antennas and the equipment—whether transmitters or receivers. It is common for designers to pay little attention to this important part of the design process. In fact, often, low-power systems designers completely forget about the existence of feedline losses. Since these installations operate at low power and are usually on a tight budget, they generally use inexpensive small-diameter coaxial cables. The savings in transmission line costs tend to result in a compromised signal level.

Detailed engineering data are available to allow the user to calculate accurately and compensate for feedline losses. Use the best cable in low-power applications to maximize the power delivered from the transmitter to the antenna or from the antenna to the receiver. The antenna can radiate only the power it receives.

Avoid using a foam-type dielectric cable unless it has a rigid outer connector. Foam dielectric is flexible and has no need for pressurization, but extended exposure to high temperatures can result in migration of center conductors and impedance variations. In some cases, rigid outer conductor foam dielectric cable may be more cost efficient than air dielectric lines if it is installed carefully without sharp bends or kinks. Keep in mind that air dielectric cable, or some alternate means of delivering nitrogen gas, must be provided if the antenna requires pressurization.

An air dielectric transmission-line has a spiral-wound spacer that runs along its length to hold the center conductor in place. It is harder to handle and install than foam because it is so stiff, but it is much sturdier. Air dielectric lines have diameters ranging from $\frac{1}{2}$ in. to 5 in., but the most common sizes for low-power operations are $\frac{7}{8}$ in. and $1\frac{5}{8}$ in.

Here are some important points to remember about coaxial cabling:

The coaxial cable and connector quality is just as important as that of the quality of the system components. All it takes is one bad connector to make a system worthless.

Use a semirigid line for optimum performance. Never use braided cables. If there is any cross-coupling between receiver cables and transmitter cables, all the isolation available will be unusable. Since shield movement can cause noise in systems, secure all flexible cables to keep them safe from strain and unnecessary motion.

Become familiar with the dielectric material, as connectors are the weakest link in every coaxial cable system. Avoid nylon connectors—they can soak up moisture as well as high-frequency RF energy. Polystyrene and Teflon are excellent choices. Only buy superior-quality connectors from a company with a respected name.

Avoid permanently installed adapters. Adapter construction is a compromise providing greater loss and inferior stability than using the correct cable terminations. It can introduce high VSWR into the system, thereby deteriorating overall performance and decreasing isolation.

Above all, pay attention to manufacturer instructions. Just about any good-quality connector works well if protected from cable motion and properly installed.

4.3. Towers

The supporting structure for a low-power antenna may be very short, or it can be 500 m tall. Tower design details are beyond the scope of this article, but it is important for the designer of a low-power system to be aware of various aspects of tower use.

Towers are expensive and dangerous and have a tremendous impact on the surrounding environment. Delays in construction can last for years if proper planning and coordination does not occur. In the initial design phase, use of only the best-quality tower can help avoid many devastating problems in the end.

The loss of a tower can cause more time off the air than the loss of any other major component and can cause severe damage as well. It is essential to give proper attention to the tower supporting any broadcast antenna. While purchasing the best tower money can buy sounds like an expensive proposition, it is nothing compared to the cost of two towers plus any damage resulting from failure.

4.4. Frequency Separation

The strategy of frequency or channel selection for low-power systems, particularly translators, is an art form of itself. According to a common theory, the output frequency of a translator should be as close to the input as possible and ideally an adjacent channel. The reality is that practical and technical issues may preclude this possibility. The majority of quality equipment should be able to operate well on adjacent channels, but there are other more complex issues. For example, operation of a translator on an adjacent frequency always causes interference to the

main station. If the translator is located in the center of a large population, it could actually cause more harm than good.

On the other side of the coin, there is no limit to the frequency separation. Somewhere between the two extremes lies the solution. If maximum quality is the design goal, use at least 2 MHz separation for an FM translator and 60 MHz for a TV translator so that filters and traditional engineering solutions can be used in case of installation difficulties.

4.5. Signal Treatments

If every installation were perfect, there would be no need for signal treatment. The only time when it is unlikely that special treatment for reception or transmission of a signal will be needed is when the facility is located away from all other transmission and reception systems and is not near a populated area. In most of the real world, planning for signal treatment is necessary and important in system design.

4.5.1. Receiving Preamplifiers. Many manufacturers produce tower-mounted preamps with gains ranging from 10 dB to more than 60 dB. Since the received signal may experience increased noise and loss as it travels from the cable to the translator, mount the preamp as close to the antenna as possible. A high-quality amplifier should have no effect on signal reception except to increase amplitude to conquer cable and/or system losses as well as render the signal useful. A preamp with greater gain does not necessarily mean better performance than one with a smaller gain. The reason is that high-gain preamps become more subject to overload as signal input increases. Select a preamp so that installation and input signal requirements are compatible. Overloading during input will result in distortion that can never be “cleaned up” afterward. Moreover, if a preamp experiences a poor signal-to-noise ratio at the input, an equal or slightly worse signal-to-noise ratio will be on the output.

4.5.2. Receiver Filtering. There are many ways to implement filtering. When a low-power receiver is tuned to a frequency near its output, increased out-of-band products result. In early gain stages of receiving equipment, tuning is broader, and a strong first or adjacent second signal may overload the input or mix in the receiver. Increased sharpness of input tuning can result in an increase in system noise.

Traps or bandpass filters at the input or at the tower may help in certain situations. Usually, a bandpass filter attenuates everything but the desired signal and a trap may attenuate a specific signal, causing interference.

4.5.3. Transmitter Filtering. Bandpass cavities are commonly used to reduce a transmitter’s sideband noise. They pass the desired signal with a minimum of loss while sharply attenuating those frequencies that lie above and below the passband.

Notch cavities have a response curve that is the reverse of a bandpass filter—it possesses the same general

configuration. Some people call a notch cavity a “trap filter” or a “reject” because of its ability to pass the desired frequency while it suppresses the rest.

Pass reject (sometimes called “pass notch”) cavities are a combination of the two other cavities. When the interfering frequency is extremely close to the undesired frequency, a pass reject is used.

4.5.4. Combiners. Wireless communications usage increases every day, and tower or system space is becoming more difficult to arrange due to environmental pressures, lack of real estate, and costs. Transmission sites are becoming crowded, and these trends are resulting in a greater need to mix two or more transmitters into one antenna. Combiners do a number of good things at the same time. They filter potential interference and intermodulation, they provide isolation between transmitters, and they allow two or more transmitters to be mixed into one coax run and antenna. Although combiners themselves are relatively expensive, the cost savings to operators of tower sites are high.

Cavity combiners are generally manufactured from inter-cabled bandpass cavities. The isolation is the result of the cavity’s resonant response curve. Sometimes pass reject cavities provide for closer frequency spacing or better isolation.

Advantages of cavity combiners include flexible configuration, cost efficiency, and low insertion loss. Negative features include large size, reduced channel capacity, and possible redesign of a combiner when frequencies are changed or added.

Use a combiner when the frequency spacing between channels is extremely wide. The minimum spacing for the FM band is usually about 1 MHz.

5. INSTALLATION AND TROUBLESHOOTING

Every transmitter site has a potential for problems. While it is impossible to anticipate every conceivable difficulty, proper foresight and planning can help avoid the likelihood of many disasters.

5.1. Boosters

Boosters may experience two kinds of major problems. The first problem is when the booster’s output corrupts the input with the booster’s signal. The second example occurs at a location that receives signals from the booster and the original station.

When isolation between receive and transmit antennas is less than the booster’s overall gain, the result is a power oscillator rather than a power amplifier. Logperiodic antennas rather than omnidirectional antennas are highly recommended. Self-oscillation takes place when the booster is transmitting an unmodulated signal and the booster’s power meter indicates normal operation. Try turning the RF gain control down. If the transmitted signal sounds clean, advance the gain control until the system breaks into oscillation and find a compromise gain setting.

If that does not solve the problem, then the installation is to blame. Disconnect the receive antenna from the down

converter. If the oscillation persists after the antenna is disconnected, there are a few things to do:

The transmission line is carrying energy to the down converter. Burying the interconnecting transmission line underground often resolves the situation.

If there is no energy present at the downconverter end of the transmission line, relocate the transmitting or receiving antennas or both. Or shield the receiving antenna by locating it over the edge of a hill or behind an obstruction such as a water tower. One more solution is to increase the separation between the transmit and receive antennas until the system is stable.

5.2. Translators

If an installed translator fails to operate correctly from the beginning, the cause is nearly always site related. Problems can generally be traced to at least one of the following:

Receive and Transmit Antennas Are Too Close. Translator output power is usually in the millions of microvolts while the input signal is just a few microvolts. Poor translator performance is the result of spacing the antennas a few meters apart because the relatively high-powered output puts too much strain on the receive section. A distance of at least 15 vertical meters is recommended. To ascertain whether antenna separation is the problem, replace the transmit antenna with a dummy load.

Incoming Signal Is Poor-Quality. Translators cannot improve the quality of signal they receive. Some translators are operational with signals from primary stations as much as 160 km away, usually when the elevation is high at the transmit and receive points and low at the transmission path. It is important to monitor the received signal for a good length of time using recording equipment in such cases, since signal quality can come and go.

An Adjacent Channel Is Present. This can be exasperating, because the adjacent channel can sound weak and yet be powerful enough to create distortion in the desired signal. When modulation components overlap on adjacent channels, mixing occurs, resulting in deceptive product generation. The problem can be fixed through special intermediate filters or external filters on the receive antenna.

A High-Powered Station Is Nearby. Serious performance issues can arise when the FM station's output energy mixes with that of the translator. This is a common problem. Tubes and output transistors are not totally linear and thus tend to operate as mixers, producing false signal generation that interferes with sensitive receiving equipment. Because the problem goes away when the translator is shut off, inexperienced technicians tend to blame the translator. The truth is that all translators react this way under the same conditions. The goal is to keep external signals from the final RF stage of the translator. Installing an

isolator in the output transmission line is a cost-efficient way to solve the problem. A second option is to employ a high Q cavity in the output, which bypasses the translator output and rejects the offending signal.

Input and Output Channels Are Too Close in Frequency.

The majority of transmitting equipment (including FM translators) produces spurious emissions extending several megahertz from the principal carrier. These signals possess an infinite amount of signals with the same frequencies as the desired signal so they infiltrate the translator and are amplified. Solve the problem with good antenna and frequency separation, usually with at least 1 MHz between input and output.

Harmonic Problems Cause Interference. The translator's main carrier is almost always the cause. It overburdens the front of the translator or the preamp associated with it. Although the translator suppresses harmonics by at least 60 dB, the seemingly obvious addition of an extra external harmonic filter will not do a bit of good. By placing a bandpass filter into the translator in front of any preamplification, the interfering signal will be too feeble to cause difficulties. Alternatively, try moving the translator installation far enough away that its carrier will not be powerful enough to do harm.

5.3. ITFS and MDS

There are a number of potential RF system difficulties with ITFS and MDS. Both services use 100 W or less per channel, so field intensities are fairly low in contrast to full-service broadcast. The ITFS and MDS services rely heavily on radio line-of-sight coverage, so the use of frequencies greater than 2000 MHz creates a need for better consideration of signal path clearances. The receive system needs a low-noise-figure downconverter (which generally changes a block of the ITFS/MDS band frequency to VHF) and a relatively high-gain antenna. Other problem areas include adjacent-channel and cochannel interference. As the spectrum becomes more crowded, the probability of interference grows in relation. In response, many cities are planning adjacent channel systems. A number of MDS systems, in particular, are already experiencing cochannel interference problems. As the ITFS band grows, so does the likelihood that it, too, will develop problems.

Luckily, a good number of the common engineering principles that solve UHF and VHF broadcast difficulties are proving helpful. Suppressing out-of-band products is essential, as older transmit systems frequently display high levels of lower sideband reinsertion and out-of-band product formation. Externally diplexed linear transmitters and waveguide filters can bring these products to more workable levels. Offset frequency operation can be utilized with relatively high levels of cochannel interference.

The area of best signal coverage is within the areas receiving the entire Fresnel ellipsoid. These areas can extend beyond visible line of sight due to the refraction of electromagnetic waves in the atmosphere. Use a path clearance of at least 0.6 Fresnel zone to avoid excessive diffraction loss due to path obstructions. The formula is as

follows:

$$R = ((\text{wavelength} \times d_1 \times d_2) / (d_1 + d_2))^{1/2}$$

d_1 = the distance from the transmitter to the obstruction

d_2 = the distance from the obstruction to the receiver

Path clearances above 1.3 Fresnel zones can yield multipath propagation, nulls in received levels, and/or picture ghosts in the received pictures. Moving the antenna slightly can help alleviate the problem.

5.4. Spurious Emissions

Looking at the data that come with the translator is a good way to ensure that the system is clean and clear of unwanted emissions, except for harmonic products, which are undetectable by the test data measuring output performance. Low levels of distortion and high signal-to-noise ratios generally indicate clean transmission. The problem with unwanted emissions is that the undesirable products they generate fall inside *and* outside the assigned output channel.

When there are several stations located at one transmitter site where you are receiving interference, there may be harmonic mixes between the other stations that fall on or near your frequency. Sometimes these harmonics originate within the transmitters involved in the mix—and if the spurious harmonic signals are above a certain threshold, they may be in violation of governmental rules. The existence of this type of interference is verified by using a spectrum analyzer at the towers of the offending stations. The source of this kind of interference can be verified only by connecting test equipment to the various transmitters involved.

Most complaints are about interference to nearby television translators. Usually the harmonic stems from the television translator, not the FM translator. Any overloaded amplifier is subject to harmonic generation. Installing a highpass filter at the output of the receive antenna might help. The advantage to going this route is that low loss of the filter does not compromise the integrity of the TV translator. This method could fail if the FM and TV translator antennas are just a few meters apart. If a filter does not work and the antennas are properly spaced, cabinet radiation or power line feedthrough is the culprit.

5.5. Spectrum Analyzers

Spurious emissions are not necessarily transmitter related. Spectrum analyzers can be unreliable when it comes to harmonic measurements if not used properly. Towers and other metallic objects can reradiate signals and cause nonlinear distortion, resulting in spurious emission.

Use a spectrum analyzer to examine the output channel. If the translator datasheet reveals that solid data yet unwanted emissions are present, the cause is usually an adjacent channel. There are several courses of actions to resolve the issue. Use narrowband filters in the IF section of the translator, reduce the signal level of the interfering adjacent channel, or increase the level of the desired channel.

5.6. Desensing

Desensing is the result of brute-power RF transmissions in the surrounding area. It is entirely possible to have a translator operating on 10 μ V, for example, and a 100-kW station 1 km away. Intermodulation occurs when the translator tries in vain to accommodate the lower-level input signal while being hit by the much stronger signal, which runs into the first translator it sees. Filtering on the input line is the best way to solve the problem before the signals mix in the first place. If the site lacks a strong enough input signal to overcome the insertion loss of a selective filter, consider using special preamps designed just for that purpose. Relocating or redesigning the input antenna structure is another viable option. Other methods include raising the receive antenna, adding a preamp to overcome line loss, adding or stacking receive antennas, and relocating receive antennas (or perhaps the entire site).

After translator installation is complete and the power is turned on, there is nothing but hash and noise. But once the translator is off and the receiver is hooked up to the receive antenna, there is no problem. This is because any translator conveys undesirable products as well as the desired modulation. These products possess a wide bandwidth, which is usually several megahertz from the main carrier frequency. Generated products are composed of the energy caused by the random motion of electrons (Johnson noise) and sideband components from the desired modulation. Generally, the undesirable products are quite weak, so they cannot be observed on a spectrum analyzer without suppressing the main carrier. Regardless of whether the undesirable products are modulation components or noise, some of these undesirable products will be in phase between the input and the output of the translator.

5.7. Problem Solving

Providing a filter at the translator's output can solve many problems. The purpose of the filter is to subdue those undesirable products that fall on the translator's input channel, but execution is more difficult than it sounds. Note that the quality factor, known simply as Q , ascertains how lossy the filter will be in operation.

If a translator operates at 100.1 MHz, it would need a filter to prevent undesirable products from falling on the input channel at 102.1 MHz. Two megahertz is the separation factor, so to make sure that no products from output fall on the input, the bandwidth cannot be more than 1 MHz. So $Q = 100.1/1 = 100.1$ is the minimum value. To have a filter with a low insertion loss and a minimum of energy loss, the Q for every element inside the filter has to be 100 times the minimum, or 10,000 times. But the realization of such a Q factor necessitates the use of costly cavity-type filters.

It is much more cost-efficient to use Q factors of around 800 for the filter elements. The filter uses a combination of two techniques: bandstop and bandpass. The bandstop section is a slot about 300 kHz wide, adjusted to the input channel frequency.

The bandpass section passes carrier frequency and useful modulation data. This low-loss device adds more selectivity that optimizes the system's performance. It can also decrease the radiation of out-of-band signals. A good illustration would be between an antenna and transmitter combiner, where the filter's job is to overpower any harmonics originating in the ferrite isolators and downgrade any broadband transmitter noise so that receive sensitivity remains intact. Energy from the translator output that falls on the input frequency is attenuated by approximately 50 dB. Using an example of $5 \mu\text{V}$ worth of undesirable products falling on the input after passing through the filter, the magnitude is reduced by 50 dB ($0.0158 \mu\text{V}$ the $\text{SNR} = 10/0.0158 = 632 = 56 \text{ dB}$). Now performance is excellent.

BIBLIOGRAPHY

1. G. Bostick and R. E. Mohar, *Introduction to Low Power Television Broadcasting*, Communications & Energy Corp., East Syracuse, NY, 1998.
2. G. W. Durling and C. Cuevas, Lower power Ku-band direct to home video broadcasting in rainy regions, *Space Commun.* **12**(3-4):175-184 (1994).
3. K. Nakamura and T. Nakamura, The helical loaded monopole antenna, *Electron. Commun. Jpn., Part 1 (Commun.)* **74**(6):37-41 (1991).
4. G. G. Luetgenau, Low-power television gets solid-state boost, *Microwaves RF* **23**(3):165-171 (1984).
5. International Telecommunication Union. Troisième édition de l'Annexe 1 à l'Accord régional (Genève, 1975): contenant, le plan d'assignations de fréquence pour les stations de radio-diffusion à ondes kilométriques et hectométriques (régions 1 et 3), l'appendice au plan, canaux pour émetteurs de faible puissance, l'appendice 2 au plan, gain de l'antenne (en dB), janvier 1987/Union internationale des télécommunications = third edition of Annex 1 to the Regional agreement (Geneva, 1975): containing, frequency assignment plan for LF/MF broadcasting stations (regions 1 and 3), appendix to the plan, low-power channels, appendix 2 to the plan, antenna gain (dB), January 1987/International Telecommunication Union, Genève: L'Union, 1987.

LOW-TEMPERATURE COFIRE CERAMIC (LTCC) TECHNOLOGY IN RF AND MICROWAVE ENGINEERING

KE-LI WU
The Chinese University of
Hong Kong
Shatin, NT, Hong Kong

1. INTRODUCTION

LTCC is a rapidly developing passive integration and package technology that offers an attractive solution to RF and microwave products in three aspects: (1) embedded passives, (2) packaging and system integration,

and (3) low manufacturing cost for high-volume production, featuring excellent electrical performance at RF and microwave frequencies.

LTCC has distinct advantages in embedded passives and packaging in that it provides a harmonic carrier for ICs (digital and analog) with embedded passives, control and power lines, and functional accessories. As far as interconnect is concerned, LTCC offers the capability of fine pitch on each layer. Since each layer is processed individually, LTCC is more cost-effective than any other sequentially processed technologies.

As shown in Table 1, another advantage of LTCC is its stability and relative insensitivity to environmental stress. The dense structure of a fired ceramic body has very low permeability to moisture, which allows LTCC parts to perform in high humidity without special packaging or protection [1].

The three key areas for LTCC technology are the development of LTCC tape and conductive paste materials; the manufacturing process that leads to high-precision, high-reliability, and low-cost products; and the design technology that needs to take all the necessary electromagnetic couplings and parasitics into account.

In developing dielectric material for an LTCC system, the electrical and thermomechanical aspects must be investigated for enabling the production and usage of reliable components. In the case of RF applications, the dielectric properties such as low-loss tangent [$\tan(\delta)$], permittivity (ϵ_r), and coefficient of thermal expansion (CTE) are important. The typical properties of three major commercial LTCC tape systems are listed in Table 2. After a tape system is developed, matched conductive paste must be developed for different usages such as solderable and wirebondable paste for surface-mounted components and IC dies, solderable paste for BGA (ball grid array) attachment, and conducting paste for inner layer and via filling.

LTCC tapes need to withstand handling and via punching and produce, after lamination and low temperature cofiring, a solid material with the desired properties. A good surface smoothness and compatibility with embedded conductive lines are also essential properties [2].

The current LTCC products can be divided into two major categories: functional components and modules. Chip LC filters, baluns, couplers, and chip antennas are good examples of functional components. On the other hand, modules usually integrate active devices such as IC dies with other required passive components to form a subsystem. In designing LTCC modules or components, electromagnetic phenomena must be taken into account as

Table 1. Performance Characteristics of Dielectric Materials

Materials	Process Temperature (°C)	Expansion Coefficient (ppm/°C)	Moisture Permeability
Polymers	< 200	25-100	Medium to high
Metals	> 600	20-25	Low
Ceramics	800-1700	4-10	Low to medium

Table 2. Typical LTCC Tape Properties

Property	Dupont 951	Dupont 943	Ferro A6M	Ferro A6B	Heraeus CT2000	Heralock HL2000
Color	Blue	Blue	White	Black	Light blue	Light blue
Available fired thickness (mils)	1.7, 3.5, 5.1, 7.8	4.4	3.7, 7.4	3.3, 6.7	0.8, 1.6, 3.1, 4.1, 8.0	3.5 to 3.75
Dielectric constant	7.8	7.5	5.9	6.5	9.1	7.3
Loss tangent (%)	0.15	<0.1	<0.2	<0.5	<0.2	<0.26
Insulation resistance	>10 ¹² Ω per layer	>10 ¹² Ω per layer	>10 ¹² Ω per layer	>10 ¹² Ω per layer	>10 ¹³ Ω · cm	>10 ¹³ Ω · cm
Breakdown voltage	>1000 V per mil	>1000 V per mil	>900 V per mil	>1000 V per mil	>1000 V per mil	>3000 V per mil
Fired density (g/cm ²)	3.1 g/cm ²	3.2 g/cm ²	2.50 g/cm ²	2.50 g/cm ²	2.45 g/cm ²	2.9 g/cm ²
TCE (ppm/°C)	5.8	6.0	7.5	9–10	5.6	6.1
Flexural strength	320 MPa	230 MPa	>210 MPa	>210 MPa	310 MPa	>200 MPa
Thermal conductivity	3.0 W/mK	4.4 W/mK	2.0 W/mK	—	3.0 W/mK	3.0 W/mK
Surface roughness	<0.7 μm	<0.7 μm	—	—	—	<0.7 μm
Flexural strength	28.3 kpsi	33.4 kpsi	17.1 kpsi	17.1 kpsi	310 MPa	>200 MPa
X–Y shrinkage (%)	12.7 ± 0.3	9.5 ± 0.3	15.0 ± 0.2	14.5 ± 0.2	10.6 ± 0.3	0.16–0.24
Z shrinkage (%)	15 ± 0.5	10.3 ± 0.5	25.0 ± 0.5%	35.0 ± 0.5%	16.0 ± 1.5	32.0
Metallizations	Au/Ag-Ag-Au	Au/Ag-Ag-Au	Au/Ag-Ag-Au	Au/Ag-Ag-Au	Au/Ag-Ag-Au	Au/Ag-Ag-Au

accurately as possible. This demands the design tools to incorporate electromagnetic (EM) simulation, in conjunction with the standard circuit-level simulation function for system-level design. Since the LTCC circuit is a multilayer configuration with vias connecting the circuitry on different layers, the EM simulation tools have to be able to handle the current flowing in both horizontal and vertical directions. Additionally, if the thickness of printed conductors is noticeable as compared to the thickness of the dielectric layer, the conductor thickness must be accounted for in an accurate design. The research for effective EM design of LTCC module and design methodologies has attracted a great deal of attention in the field.

2. HISTORY OF LTCC [3]

Like other good invention, LTCC was born of necessity. In 1982, Hughes Aircraft was concerned with developing a process for a group of high complexity multilayer substrates. The solution to this was a dielectric layer that was tape-cast. The tape could be via-punched, filled, and printed with conductor and then fired in place. This process became known as *Ttran* and formed the basis for the three generations of LTCC that we have gone through to date.

The firsthand cast formulations of LTCC tape were based on existing multilayer dielectric pastes from DuPont, ESL, Ferro, and other manufacturers. While made with the most primitive methods to demonstrate the technology and with the aid of some sewing needles for via formation the first real LTCC parts were made in the lab. This grew into the DuPont 851 Green Tape. The dielectric loss of this material at microwave frequencies prompted the development and commercialization of the Ferro A6M system. There were a great deal of refinements and development of additional inks (both metallic and

resistive), and this completed the development of LTCC generation 1.

The environmental movement was key in spurring DuPont to develop the 951 formulation. This eliminated the “made with chlorinated solvents” stigma and allowed continued marketing in Europe and Asia. Improvements in the organic portion of the formulation were made as part of this transition greatly improving produceability and reducing costs. At about the same time Ferro sought to broaden their offering by creating lower cost-versions of their flagship A6M product, including A6C, A6B, and the still available (as of Sept. 2003) A6S.

Nearly concurrent with this effort, Heraeus developed the CT600 and CT800 materials that are nearly equivalent to the Ttran and 951 products. Additionally Heraeus worked toward constrained sintering for “zero shrink” production process. The market for LTCC was growing rapidly during this time with many commercial adoptions in areas such as automotive applications and modules for wireless communication system. The bursting of the Internet and wireless bubbles slowed down the worldwide economy enough to end the development phase of LTCC generation 2 by mid-2001.

Generation 3 of LTCC technology marks the maturing of the LTCC industry. New compositions targeted not at increasing technical merit but lowering system cost. In one instance, Motorola introduced T2000 material, which was designed with its physical properties balanced to have a “zero” T_f . This material has been commercialized by Heraeus as CT2000. Heraeus has also developed this material in a self-constrained version as HL2000 under their HeraLock patent as a way to increase array precision, thus allowing larger arrays for lower assembly cost. Another aspect of LTCC generation 3 is the emergence of low-cost LTCC foundries in the Far East, Taiwan, and mainland China. This further enables low-cost manufacturing but at the same time requires the designer to have the expertise to do the full design and engineering of the product.

3. BASICS OF LTCC DIELECTRIC MATERIALS AND PROCESS

Dielectric materials used for LTCC components must have proper firing, dielectric, and thermomechanical properties so that mechanically reliable multilayer structures with the desired electrical performance can be produced.

Proper firing properties means that the dielectric material has to achieve a dense, nonporous microstructure below 950°C so that it can be cofired with low resistive conductor materials such as silver or copper. As revealed by Table 3, unlike traditional cofired ceramics with firing temperature in excess of 1400°C and only those low conductive with high melting point metals such as tungsten can be embedded, by keeping the firing temperature below 950°C, all the metals with high conductivity can be used.

For commercial LTCC materials, the firing profile is specified accurately in the information given by the manufacturers, and for new dielectric materials, this is an essential part of their development. Figure 1 shows a typical firing profile for LTCCs. Steps 1, 3, and 5 are heating and cooling periods, step 2 is for burning out the organic additives, and step 4 is the actual sintering period. For Heraeus' CT2000, for instance, the recommended firing profile is 3.0°C/min to 100°C, 3.0°C/min to 450°C, 5.5°C/min to 865–875°C, held for 20–30 min. The cooling rate is approximately 6–10°C/min (furnace cooling rate). Firing must be done on flat setter material since the tape will conform to the setter material.

The permittivity of LTCC dielectric is particularly important because the length of a resonator is roughly inversely proportional to the square root of the permittivity. The LTCC materials available commercially have permittivities of 5–10, but higher values (≤ 85) are also available for noncommercial materials.

The number of possible different materials and compositions to decrease the firing temperature of crystalline ceramic is countless. The most common method is to use SiO₂-based glass compositions.

The tape-casting process consists of a slurry preparation and its casting as shown in Fig. 2. The basic formula for the tape casting slurry includes the ceramic powder, solvents, and organic additives. In the fired product the ceramic material is all that remains, and thus the solvents and additives have to be removed in earlier process steps. These ingredients are added only to facilitate the fabrication of the tape with an appropriate thickness and density and to make the tape strong enough for subsequent processing [4].

Table 3. Conductivity and Melting Points for Some Commonly Used Conductors

Conductor	Conductivity σ (S/m)	Melting Point (°C)
Silver (Ag)	6.17×10^7	961
Copper (Cu)	5.8×10^7	1083
Gold (Au)	4.10×10^7	1063
Tungsten (W)	1.815×10^7	3370

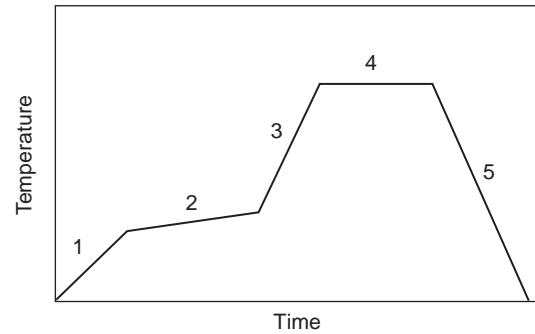


Figure 1. Typical firing profile for LTCC components.

After drying the tape in air, it is further processed to form multilayer components as shown in Fig. 3. The tape is first blanked to size and the required vias are formed using mechanical or laser punching. After via filling and screen printing of the conductive patterns on each separate layer, they are stacked together, laminated, and cofired.

4. LTCC EMBEDDED PASSIVE COMPONENTS

The ability to embed passive elements is one of the most attractive features of LTCC technology. Simple passive elements include inductors, resistors, capacitors, *LC* shunt elements, *LC* series elements, and various functional circuits such as filters. Some common configurations of embedded passive components are listed in Table 4. The main parasitic capacitors in each circuit layout are marked as C_p in the circuit models.

The circular series inductor on a single layer shown in (a) may provide about 10–15% higher *Q* value than its rectangular shaped counterpart shown in (b). The inductors in (c) and (d) are the implementation of the inductors with multilayer windings to increase the inductance value. Usually, the inductor winding layers should be kept as far away from the ground as possible to minimize the loss [5]. To trade off the occupied area and the *Q* value, the ovum-shaped inductor shown in (e) would be a good choice. Capacitors are usually in rectangular shape as shown in (f) and (g). Multilayered interdigital capacitors in (h) are commonly used for high-value capacitance. By combining the basic elements of inductors and capacitors, we can construct various simple functional *LC* networks such as capacitor π network (i), *LC* series network (j), and *LC* resonator tank (k). In constructing the *LC* resonator tank it is wise to lay the inductors above the shunt capacitor to minimize the loss caused by the ground and the parasitic capacitance on the inductor. This guideline is also applicable to the design of the lowpass network (l) and the highpass network (m). In the bandpass filter with one transmission zero (n) [6], the mutual coupling *M* is realized by two side-by-side inductor strips. The mutual coupling *M* in the bandpass filter (o), which has one transmission zero at the lower stopband and a transmission zero at the upper stopband, can be created by a overlapped two inductor strips [7]. It is worth mentioning

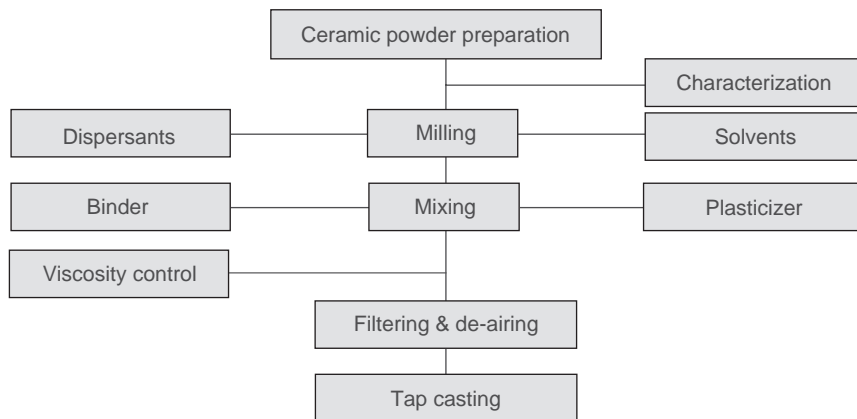


Figure 2. General production process of ceramic tape casting. (This figure is available in full color at <http://www.mrw.interscience.wiley.com/erfme>.)

that in designing high-performance filters, the parasitic coupling between the input and the output must be carefully taken into account [8].

5. LTCC RF MODULES

In most radiofrequency (RF) applications, in order to meet size requirements, a large part of the circuit is usually integrated in a semiconductor die. However, the required functional passive circuits in the system such as filters and baluns form an exception due to the power handling and the requirement for low signal losses. The losses in transmit and receive channels directly influence the power consumption and receiver sensitivity. With this regard, LTCC provides an option to integrate those required high-*Q* passive circuits while providing a packaging substrate to the Si or GaAs IC dies. LTCC enables low-loss stripline designs and geometries realizable with standard screen-printing techniques. In addition, the use of thick-film silver metallization in LTCC substrate ensures lower conductor loss than building circuits on Si or GaAs.

A good example of LTCC modules is the antenna switch diplexer front-end module for GSM/DCS/PCS applica-

tions, in which the diplexer is realized using lowpass and highpass filters. In addition to a lowpass filter at the switch end of DCS band, some elaborately designed resonant circuits are built in the diplexer circuit to trap the second, third, and fourth harmonics. Figure 4a shows the lumped-element model for an LTCC antenna switch diplexer. The 3D layout of a realization of the lumped-element model is illustrated in Fig. 4b with its response shown in Fig. 4c. Due to the strong EM couplings in the embedded passives, an accurate EM modeling and efficient optimization scheme must be used in the design [9].

6. LTCC LAMINATED WAVEGUIDE AT MICROWAVE FREQUENCY

At microwave frequencies, the dielectric loss becomes more significant as compared to the cases in RF frequencies. A part of the loss is contributed by the surface wave. On the other hand, due to the filling effect of a high-dielectric-constant material, some low-loss transmission lines whose dimension is considered as bulky in conventional applications become suitable in LTCC applications. A good example of this type of transmission line is the laminated waveguide [10], a derivation of rectangular

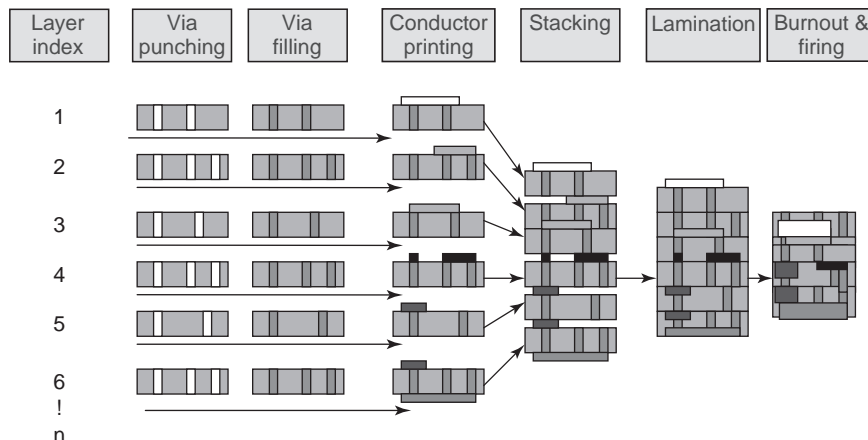

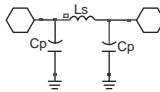

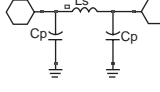
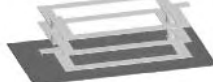
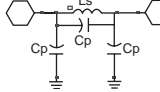

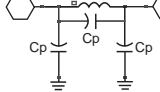

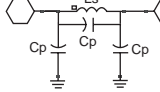

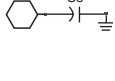

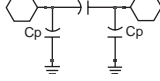

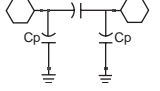

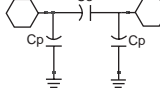

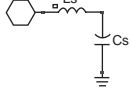

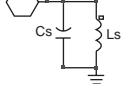

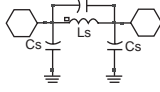

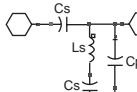

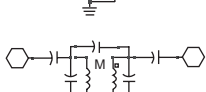

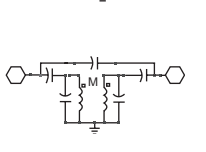


Figure 3. General production process of LTCC multilayer components. (This figure is available in full color at <http://www.mrw.interscience.wiley.com/erfme>.)

Table 4. Basic Passive Components that Can be Embedded in LTCC Substrate and Their Equivalent-Circuit Models

Description	Typical Circuit Layout	Equivalent-Circuit Model
(a) A single-layer circular inductor		
(b) A single-layer rectangular inductor		
(c) A multilayer rectangular inductor		
(d) A multilayer circular inductor		
(e) An ovum-shaped inductor		
(f) A two-layer shunt capacitor		
(g) A single-layer series capacitor		
(h) A four-layer series capacitor		
(i) A capacitor PI network		
(j) An LC series network		
(k) An LC resonator tank		
(l) A low pass network		
(m) A highpass network with one transmission zero		
(n) A bandpass filter with one transmission zero		
(o) A bandpass filter with two transmission zeros		

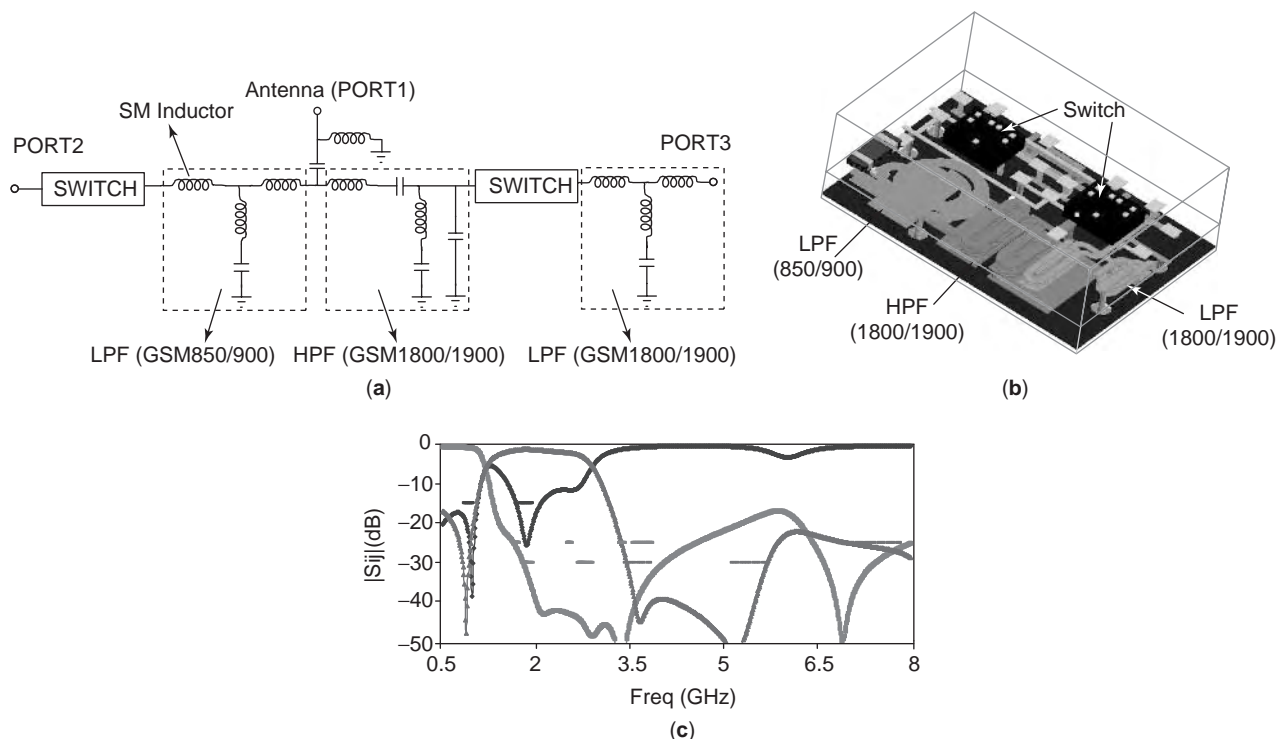


Figure 4. (a) The lumped-element circuit model for an LTCC GSM antenna switch diplexer; (b) layout design of the schematic shown in (a) with size of dimensions $4.5 \times 3.2 \times 0.5 \text{ mm}^3$; (c) response of the antenna switch diplexer. (This figure is available in full color at <http://www.mrw.interscience.wiley.com/erfme>.)

waveguide. As shown in Fig. 5, a laminated waveguide is composed of an LTCC substrate, a pair of main conductive layers on the upper and lower surfaces of the substrate, and a pair of conducting walls formed by a plurality of via holes extending in a thickness direction. The inner conductive layers connecting the via holes play a very important rule in reducing the leakage of electromagnetic waves. The laminated waveguide has also been used in ridge waveguide bandpass filters [11] and surface-mounted bandpass chip filters [12].

In developing an LTCC integrated module at microwave frequencies, people always need to use various transition and packaging structures to connect one type of transmission line to another. For example, some common transitions between laminated waveguide to striplines were proposed in a U.S. patent [13]. A waveguide-

microstrip line transition was proposed in another U.S. patent [14]. A broadband transition between a waveguide and an LTCC laminated waveguide was developed by Huang and Wu [15].

7. CONCLUDING REMARKS

It has been suggested that LTCC as a high-density packaging and passive integration technology offers many benefits over other competing technologies. However, three major limitations need to be mentioned: shrinkage control, strength, and thermal conductivity. These concerns have been addressed by the industry by introducing “zero shrinkage” materials, improving materials, fabrication process, and thermal via/heatsink technology. For high-power applications, LTCC-on-metal (LTCC-M) technology is a good candidate. Another cost-effective way to dissipate heat is the use of cavities in the LTCC structure, allowing access to the underlying heat spreader.

While continuing reduction of material cost, development of a large format process will be another direction toward cutting manufacturing cost.

Today, LTCC products can be found in radar, space, medical, and wireless communication systems; computer hardware; biotechnology; satellite communication; and automobile manufacturing. It is expected that with steady improvement of LTCC materials and process technologies, an increasing number of new applications will appear in our lives.

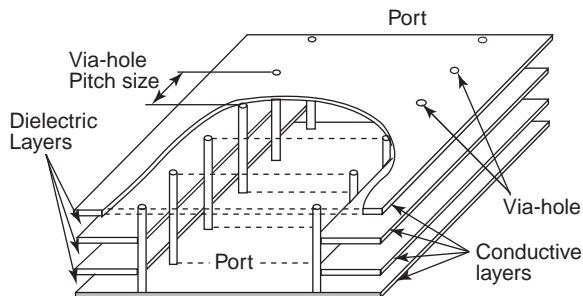


Figure 5. Schematic diagram of laminated waveguide.

BIBLIOGRAPHY

1. R. L. Brown and W. R. Smith, Embedded passive functions for RF and mixed-signal circuits, *Proc. 6th Int. Conf. Multichip Modules*, 1997, pp. 351–356.
2. P. Barnwell, W. Zhang, J. Lebowitz, K. Jones, N. MacDonald, C. Free, and Z. Tian, An investigation of the properties of LTCC materials and compatible conductors for their use in wireless applications, *Proc. Int. Symp. Microelectronics, IMAPS*, Boston, 2000, pp. 659–664.
3. M. Ehlert, private communication, 2003.
4. C. Berry, D. Parlow, T. Vasilov, S. Gurkovich, and A. Bailey, A design of experiment for a tape casting process, *Proc. Int. Symp. Microelectronics, IMAPS*, Boston, 2000, pp. 150–155.
5. A. Sutono, D. Heo, Y.-J. E. Chen, and J. Laskar, High-Q LTCC-based passive library for wireless system-on-package (SOP) module development, *IEEE Trans. Microwave Theory Tech.* **49**(10): 1715–1724 (2001).
6. A. Sutono, J. Laskar, and W. R. Smith, Development of integrated three dimensional Bluetooth image reject filter. *Proc. Int. Microwave Symp.*, IEEE, Vol. 1 2000 11–16.
7. L. K. Yeung, and K.-L. Wu, A compact second-order LTCC band-pass filter with two finite transmission zeros, *IEEE Trans. Microwave Theory Tech.* **51**(2): 337–341 (2003).
8. C.-W. Tang, Y.-C. Lin, and C.-Y. Chang, Realization of transmission zeros in combine filters using an auxiliary inductively coupled ground plane, *IEEE Trans. Microwave Theory Tech.* **51**(10) (2003).
9. K.-L. Wu, Y.-J. Zhao, J. Wang, and M. K. K. Cheng, An effective dynamic coarse model for optimization design of LTCC RF circuits with aggressive space mapping, *IEEE Trans. Microwave Theory Tech.* **52**(1) (2004).
10. H. Uchimura, T. Takenoshita, and M. Fujii, Development of a “laminated waveguide”, *IEEE Trans. Microwave Theory Tech.* **46**(12): 2438–2443 (1998).
11. Y. Rong, K. A. Zaki, M. Hageman, D. Stevens, and J. Gipprich, Low-temperature cofired ceramic (LTCC) ridge waveguide bandpass chip filters, *IEEE Trans. Microwave Theory Tech.* **47**(12): 2317–2324 (1999).
12. J. Hayashi and Y. Nikawa, Improvement of characteristics using cross patch in the LTCC filter, *Proc. Int. Microwave Symp.*, IEEE, 2003, pp. 531–534.
13. H. Uchimura and T. Takenoshita, *Wiring board Equipped with a Line for Transmitting a High Frequency Signal*, U.S. Patent 5,982,256 (1999).
14. H. A. Huang, R. J. Duprey, and R. T. Villeages, *Millimeter-Wave LTCC Package*, U.S. Patent (1999) 5,982,250.
15. Y. Huang and K.-L. Wu, A broadband LTCC integrated transition of laminated waveguide to air-filled waveguide for millimeter wave applications, *IEEE Trans. Microwave Theory Tech.* **51**(5): 1613–1617 (2003).

MAGNETIC FIELD MEASUREMENT

MANFRED STECHER
Rhode & Schwarz GmbH &
Co.KG

1. RELEVANCE OF ELECTROMAGNETIC FIELD MEASUREMENTS

The measurement of electromagnetic (EM) fields is relevant for various purposes: for scientific and technical applications, for radio propagation, for electromagnetic compatibility (EMC) tests (i.e., testing of the immunity of electronic equipment to electromagnetic emissions aiming at the protection of radio reception from radio interference), and for safety reasons (i.e., the protection of persons from excessive field strengths). For radio propagation and EMC measurements, below about 30 MHz a distinction is made between electric and magnetic components of the EM field to be measured. In the area of human safety, this distinction is continued to even higher frequencies.

2. QUANTITIES AND UNITS OF MAGNETIC FIELDS

Especially in the measurement of radio propagation and of radio interference, magnetic field measurements with loop antennas have traditionally been used to determine the received field intensity, which was quantified in units of the electric field strength, namely, in $\mu\text{V/m}$, respectively, in $\text{dB}(\mu\text{V/m})$. For radio propagation this can be justified for far-field conditions where electric field strength E and magnetic field strength H are related via the impedance Z_0 of the free space; $E = HZ_0$ (see also antenna factor definition). Commercial EMC standards in Refs. 1 and 2 specify radiated disturbance measurements below 30 MHz with a loop antenna; however, until 1990 measurement results and limits were expressed in $\text{dB}(\mu\text{V/m})$. Since this measurement is done at less than the far-field distance from the equipment under test (EUT) over a wide frequency range, the use of units of the electric field strength was difficult to justify. Therefore, the CISPR (the International Special Committee on Radio Interference) decided in 1990 to use units of the magnetic field strength $\mu\text{A/m}$, respectively, $\text{dB}(\mu\text{A/m})$.

Guidelines and standards for human exposure to EM fields specify the limits of electric and magnetic fields. In the low-frequency range (i.e., below 1 MHz [3]), limits of the electric field strength are not proportional to limits of the magnetic field strength. Magnetic field limits in frequency ranges below 10 kHz are frequently expressed in units (T and G, for tesla and gauss) of the magnetic flux density B despite the absence of magnetic material in human tissue. Some standards specify magnetic field limits in A/m instead of T (see Ref. 4 in contrast to Ref. 5). For

easier comparison with other applications we therefore convert limits of the magnetic flux density to limits of the magnetic field strength using $H = B/\mu_0$ or $1\text{ T} = 10^7/4\pi\text{ A/m} \approx 0.796 \cdot 10^6\text{ A/m}$ and $1\text{ G} = 79.6\text{ A/m}$. At higher frequency ranges all standards specify limits of the magnetic field strength in A/m. Above 1 MHz the limits of the magnetic field strength are related to limits of the electric field strength via the impedance of the free space. Nevertheless both quantities, electric and magnetic fields, have to be measured, since in the near field the exposition to either magnetic or electric field may be dangerous.

3. RANGE OF MAGNETIC FIELD LEVELS TO BE CONSIDERED FOR MEASUREMENT

In order to show the extremely wide range of magnetic field levels to be measured, we give limits of some national or regional standards. In different frequency ranges and applications magnetic field strength limits vary from as much as 10 MA/m down to less than 1 nA/m (i.e., over 16 decades). This wide range of field strength levels will normally not be covered by one magnetic field meter. Different applications require either broadband or narrowband equipment.

On the high level end there are safety levels and limits of the magnetic field strength for the protection of persons that vary from as much as 4 MA/m (i.e., $4 \times 10^6\text{ A/m}$ corresponding to the specified magnetic flux density of 5 T in nonferrous material) at frequencies below 0.1 Hz, to less than 0.1 A/m at frequencies above 10 MHz (see Fig. 1) [3–6]. These limits of the magnetic field strength are derived from basic limits of the induced body current density (up to 10 MHz), respectively, basic limits of the specific absorption rate (SAR, above 10 MHz). There are also

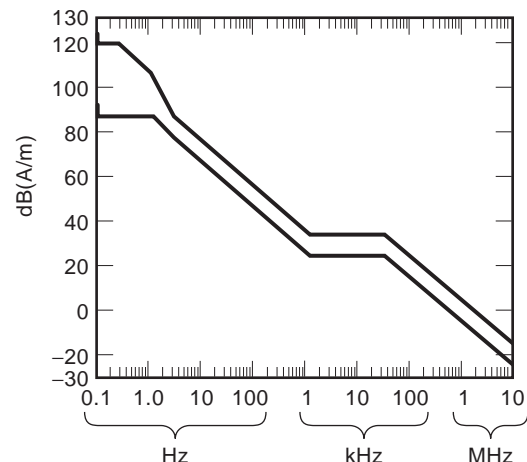


Figure 1. Safety limits of the magnetic field strength derived from the European Prestandard ENV 50166 Parts 1 and 2: 120 dB(A/m) are equivalent to 1 MA/m corresponding to 1.25 T, 0 dB(A/m) are equivalent to 1 A/m.

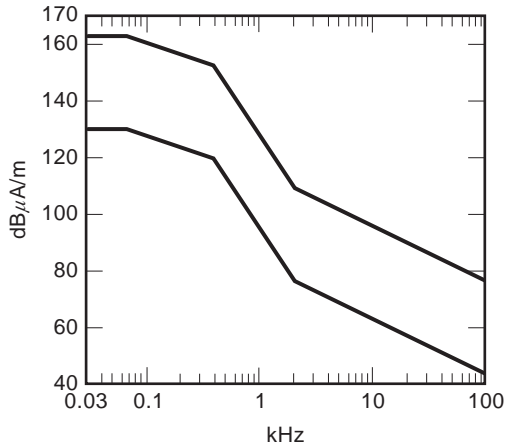


Figure 2. Magnetic field strength limits derived from U.S. MIL-STD-461D RE101 (Navy only) [7]. These limits are originally given in dB(pT) (decibels above 1 pT). The measurement procedure requires a 36-turn shielded loop antenna with a diameter of 13.3 cm. Measurement distance is 7 cm for the upper limit and 50 cm for the lower limit.

derived limits of the electric field strength which are however not of concern here.

By using an approach different from the one of the safety standards, the Swedish standard MPR II, which has become an international de-facto standard for video-display units (VDUs) without scientific proof, specifies limits of the magnetic flux density in two frequency ranges, which are bounded by filters: a limit of 40 nT (≈ 0.032 A/m) in the range from 5 Hz to 2 kHz and a limit of 5 nT (≈ 0.004 A/m) in the range from 2 kHz to 400 kHz.

On the low-level end there are limits for the protection of radio reception and electromagnetic compatibility in some military standards (see Figs. 2 and 3).

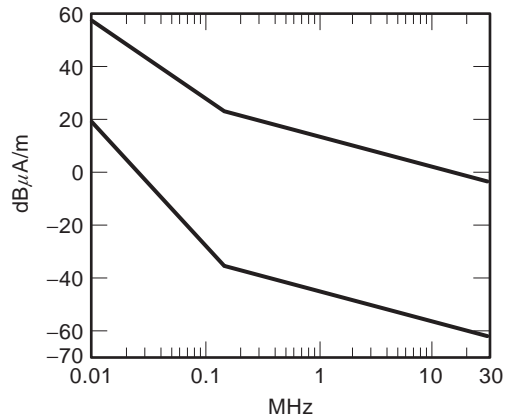


Figure 3. Narrowband emission limits of the magnetic field strength derived from the German military standard VG 95343 Part 22 [8]. This standard gives the limits of $H \cdot Z_0$ in dB(μV/m) of four equipment classes, the emissions have to be measured with a loop antenna calibrated in dB(μV/m) in the near field of the equipment under test (EUT). Therefore, the limits have been converted into dB(μA/m). The lower limits is Class 1, the upper is Class 4.

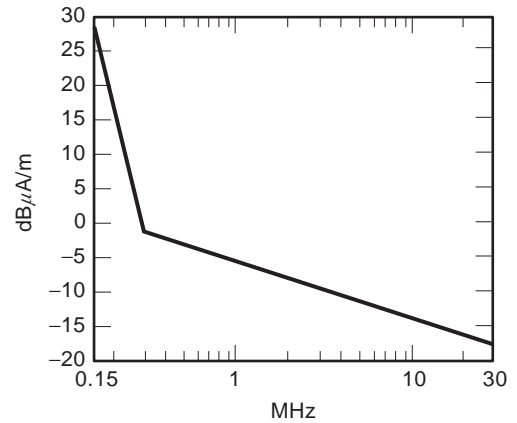


Figure 4. Radiated emission limits for navigational receivers according to draft revision IEC 945 (IEC 80/124/FDIS), originally given in dB(μV/m), for the purpose of this article converted into dB(μA/m).

International and national monitoring of radio signals and the measurement of propagation characteristics require the measurement of low-level magnetic fields down to the order of -30 dB(μA/m): see also subsequent discussions and Refs. 7–9. For the protection of radio reception, international, regional (e.g., European) and national radiated emission limits and measurement procedures have been standardized for industrial, scientific, medical (ISM) and other equipment [1,2,10–12]. An example is given in Fig. 4.

Radiated emission limits of fluorescent lamps and luminaires are specified in a dB(μA) using a large-loop-antenna system (LAS) [10]. For further information, see the text below.

4. EQUIPMENT FOR MAGNETIC FIELD MEASUREMENTS

4.1. Magnetic Field Sensors Others than Loop Antennas

An excellent overview of magnetic field sensors other than loop antennas is given in Ref. 13. Table 1 lists the different types of field sensors that are exploiting different physical principles of operation.

4.2. Magnetic Field Strength Meters with Loop Antennas

Especially for the measurement of radiowave propagation and radiated electromagnetic disturbance pickup devices, the antennas become larger and therefore are used separately from the indicating instrument (see Fig. 5). The instrument is a selective voltmeter, a measuring receiver, or a spectrum analyzer. The sensitivity pattern of a loop antenna can be represented by the surface of two spheres (see Figs. 6 and 7). In order to determine the maximum field strength, the loop antenna has to be turned into the direction of maximum sensitivity.

To obtain an isotropic field sensor, three loops have to be combined in such a way that the three orthogonal components of the magnetic field H_x , H_y , and H_z are combined to fulfill the equation

Table 1. Overview of Different Magnetic Field Sensors, their Underlying Physical Effects, their Applicable Level, and Frequency Ranges from Ref. 13^a

Type	Principles of Operation	Level of Operation	Frequency Range
Search coil magnetometer	Faraday's law of induction	10^{-6} – 10^9 A/m	1 Hz–1 MHz
Flux gate magnetometer	Induction law with hysteresis of magnetic material	10^{-4} – 10^4 A/m	DC–10 kHz
Optically pumped magnetometer	Zeeman effect: splitting of spectral lines of atoms	10^{-6} – 10^2 A/m	DC
Nuclear precession magnetometer	Response of nuclei of atoms to a magnetic field	10^{-5} – 10^2 A/m	DC (upper frequency limited by gating frequency of hydrocarbon fluid)
SQUID magnetometer	Superconducting quantum interference device	10^{-8} – 10^{-2} A/m; speciality: differential field measurements	DC
Hall effect sensor	Hall effect	10^{-1} – 10^5 A/m	DC–1 MHz
Magnetoresistive magnetometer	Magnetoresistive effect	10^{-4} – 10^4 A/m	DC–1 GHz
Magnetodiode	Semiconductor diode with undoped silicon	10^{-2} – 10^3 A/m	DC–1 MHz
Magnetotransistor	Hall and Suhl effects	10^{-3} – 10^3 A/m	DC–1 MHz
Fiberoptic magnetometer	Mach-Zehnder interferometer	10^{-7} – 10^3 A/m	DC–60 kHz
Magneto-optical sensor	Faraday polarization effect	10^2 – 10^9 A/m	DC–1 GHz

^aTo facilitate comparison with values given in text, the values from Ref. 13 have been converted from gauss to A/m.

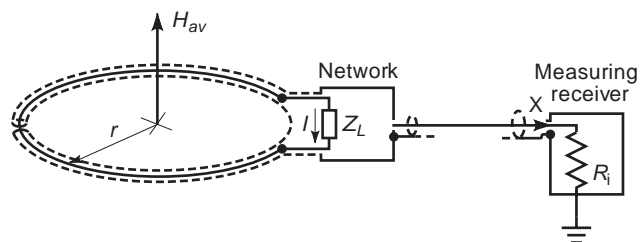


Figure 5. Magnetic field strength measuring loop. The network may consist of a passive or active circuit.

$$H = \sqrt{H_x^2 + H_y^2 + H_z^2}$$

Isotropic performance is, however, only a reality in broadband magnetic field sensors, where each component is detected with a square-law detector and combined subsequently. For the measurement and detection of radio signals isotropic antennas are not available. Hybrids may be used for limited frequency ranges to achieve an omnidirectional azimuthal (not isotropic) pickup.

4.2.1. Antenna Factor Definition. The output voltage V of a loop antenna is proportional to the average magnetic field strength H perpendicular to the loop area. If the antenna output is connected to a measuring receiver or a spectrum analyzer, the set consisting of antenna and receiver forms a selective magnetometer.

The proportionality constant is the antenna factor K_H for the average magnetic field strength H :

$$K_H = \frac{H}{V} \text{ in } \frac{\text{A}}{\text{m}} \frac{1}{\text{V}} = \frac{1}{\Omega \cdot \text{m}} \quad (1a)$$

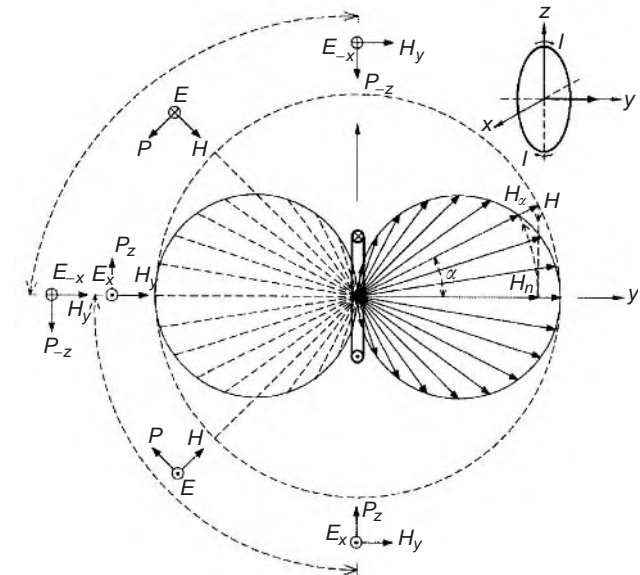


Figure 6. Cross section of a loop antenna sensitivity pattern. The arrow length H_x shows the indicated field strength at an angle α which is a fraction of the original field strength H , with $H_x = H \cos \alpha$.

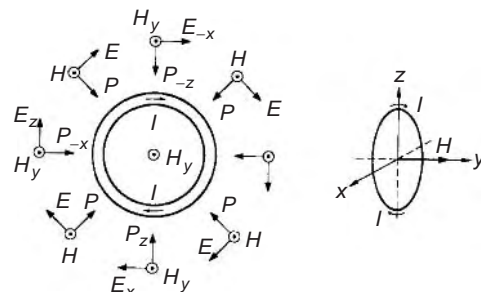


Figure 7. Direction of the field vectors (H , E and P) under far-field conditions.

For the average magnetic flux density B the corresponding proportionality constant is

$$K_B = \frac{B}{V} = \frac{\mu_0 H}{V} = \mu_0 K_H \quad \text{in} \quad \frac{V \cdot s}{A \cdot m} \frac{A}{m} \frac{1}{V} = \frac{V \cdot s}{m^2} \frac{1}{V} = \frac{T}{V} \quad (1b)$$

In the far field, where electric field and magnetic fields are related via the free-space wave impedance Z_0 , the loop antenna can be used to determine the electric field strength E . For this case the proportionality constant is

$$K_E = \frac{E}{V} = \frac{Z_0 H}{V} = Z_0 K_H \quad \text{in} \quad \frac{V}{A} \frac{A}{m} \frac{1}{V} = \frac{1}{m} \quad (1c)$$

In the area of radiowave propagation and radio disturbance measurement, quantities are expressed in logarithmic units. Therefore, the proportionality constants are converted into logarithmic values, too:

$$k_H = 20 \log(K_H) \quad \text{in dB} \left(\frac{1}{\Omega m} \right) \quad (2a)$$

$$k_B = 20 \log(K_B) \quad \text{in dB} \left(\frac{T}{V} \right) \quad (2b)$$

$$k_E = 20 \log(K_E) \quad \text{in dB} \left(\frac{1}{m} \right) \quad (2c)$$

By using logarithmic antenna factors, a field strength level $20 \log(H)$ is obtained in $\text{dB}(\mu\text{A}/\text{m})$ from the measured output voltage level $20 \log(V)$ in $\text{dB}(\mu\text{V})$ by applying the equation: $20 \log(H) = 20 \log(V) + k_H$. The final section of this article describes a method calibrate the antenna factors of circular loop antennas.

4.2.2. Concepts of Magnetic Field Strength Meters. The loop antenna of a magnetic field strength meter may be mounted on the measuring receiver (or used as a separate unit, connected to the measuring receiver) with a coaxial cable. CISPR 16-1, the basic standard for emission measurement instrumentation to commercial (i.e., nonmilitary) standards, requires a loop antenna in the frequency range from 9 kHz to 30 MHz which is completely enclosed by a square having sides 0.6 m in length. For protection against stray pickup of electric fields, loop antennas employ a coaxial shielding structure. For optimum performance, the shielding structure may be arranged symmetrically in two half-circles around a circular loop with a slit between the two halves in order to avoid electric contact between the two shields.

For narrowband magnetic field measurements of radio disturbance, measuring receivers employ standardized bandwidths and weighting detectors in order to produce standardized measurement results for all types of perturbations including impulsive signals. For comparison with the emission limit, usually the quasipeak (QP) detector is to be used.

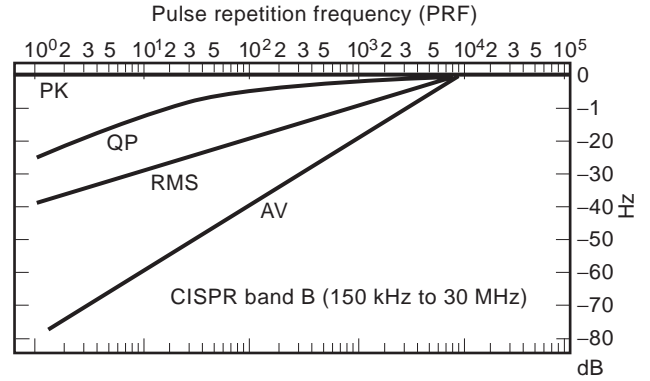


Figure 8. Detector response of a test receiver for impulsive interference as specified in Ref. 1.

To understand the function of a weighting curve in measuring receivers, the following interpretation is given. The test receiver has certain elements that determine a weighting curve (e.g., for the QP detector): the measurement bandwidth, the charge and discharge times of the detector circuit, and the time constant of the meter. When measured with a QP detector, for the frequency range given in Fig. 8, an impulsive signal with a constant impulse strength and a pulse repetition frequency of 100 Hz will cause a meter indication 10 dB above that of the indication when the pulse repetition frequency is 10 Hz. Or, to produce the same indication on the meter as a signal with 100 Hz repetition frequency, the level of the 10-Hz impulsive signal will have to be increased by an amount of 10 dB.

Earlier manually operated field-strength meters achieved high sensitivity by operating the loop at resonance [14]. The sensitivity was raised by the amount of the Q factor of the resonating circuit. One of the latest models that was used up to the 1980s reached a sensitivity of $-60 \text{ dB}(\mu\text{A}/\text{m})$ with a measurement bandwidth of 200 Hz in the frequency range from 100 kHz to 30 MHz [15].

For automated field strength measurement systems, tuning of the loop circuit could no longer be afforded. A broadband active loop employs an output voltage proportional to the short-circuited loop current, thus achieving a flat response of the antenna factor versus frequency [16].

A flat response of the system is also achieved using a current probe that measures the short-circuit current in the large-loop antenna system [LAS] described by Bergervoet and van Veen [9]. It is essentially a magnetic-field-induced current measurement (see subsequent explanations). The highest sensitivity described in the literature for a wideband system was achieved with a specially designed active loop. With additional frequency-dependent switching of elements [17], sensitivity is even better than that of manually operated field strength meters with tuning of the loop circuit. Figure 9 shows the amplitude density of the minimum detectable magnetic field strength H_{Neq} in $\text{dB}(\mu\text{A}/\text{m}\sqrt{\text{Hz}})$ equivalent to the internal electronic noise of the system consisting of antenna and measuring receiver.

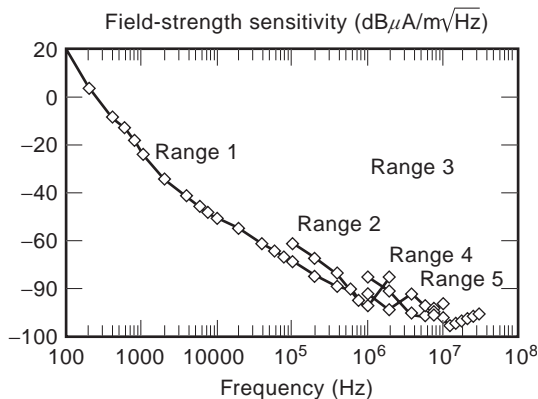


Figure 9. Sensitivity per hertz bandwidth of the active loop [16].

5. MAGNETIC FIELD STRENGTH MEASUREMENT METHODS

5.1. Measurement of Magnetic Fields with Regard to Human Exposure to High EM Fields

Usually, to measure magnetic fields with regard to human exposure to high fields, magnetic field strength meters are using broadband detectors and apply an isotropic response. Modern concepts of low-frequency electric and magnetic field strength meters apply fast Fourier transform (FFT) for proper weighting of the total field with regard to frequency-dependent limits [18,19].

5.2. Use of Loop Antennas for Radiowave Field Strength Measurements up to 30 MHz

ITU-R Recommendation PI.845-1 Annex 1 gives guidance to accurate measurement of radio wave field strengths. Rod antennas are the preferred receiving antennas since they provide omnidirectional azimuthal pickup. The positioning of vertical rod antennas is important, however, since the result is very sensitive to field distortions by obstacles and sensitive to the effects of ground conductivity. It is a well-known fact that measurements with loop antennas are less sensitive to these effects and their calibration is not affected by ground conductivity apart from the fact that the polarization may deviate from horizontal if ground conductivity is poor. Therefore, many organizations use vertical monopoles for signal measurements but standardize results by means of calibration data involving comparisons for selected signals indicated by field strength meters incorporating loop-receiving antennas. Accuracy requirements are given in Ref. 20, general information on equipment and methods of radio monitoring are given in Ref. 21.

5.2.1. Solutions to Problem with Ambients in Commercial EMI Standards. CISPR Class B radiated emission limits in the frequency range from 9 kHz to 30 MHz have been at 34 dB(μV/m) at a distance of 30 m from the EUT for a long time. Moreover, the test setup with EUT and vertical loop antenna required turning of both EUT and the loop antenna to find the maximum emission. On most of the

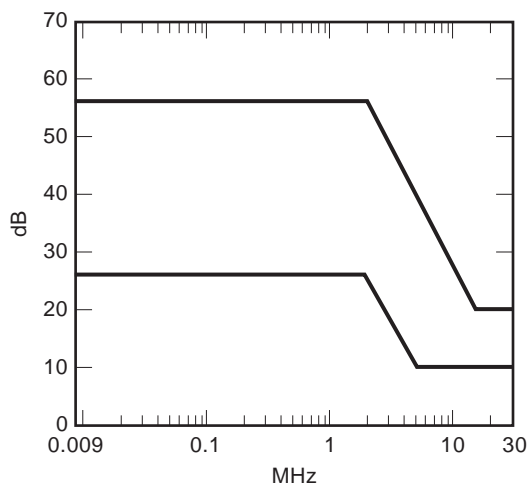


Figure 10. Conversion factors ΔH for the limit of the magnetic field strength from measurement distance 30 m to measurement distances 10 and 3 m above a conducting ground plane according to Ref. 23. The upper curve is for 30–3 m; the lower curve is for 30–10 m distance.

open-area test sites the ambient noise level makes compliance testing almost impossible. This is due to the fact that ambient noise itself is near or above the emission limit. Two different approaches were proposed as a solution to that problem:

1. To reduce the measurement distance from 30 to 10 m or even 3 m. A German group proposed frequency-dependent conversion factors, justified by calculations and an extensive amount of measurements. The conversion factors are given in Fig. 10. In Fig. 10 the slopes between 1.8 and 16 MHz show the transition region from near field, where H is inversely proportional with r^3 or $r^{2.6}$, to far field, where H is inversely proportional with r .
2. To reduce the measurement distance to zero. A Dutch group proposed the large-loop antenna system mentioned previously [9]. With this method the EUT is placed in the center of a loop antenna system, which consists of three mutually perpendicular large-loop antennas (Fig. 11). The magnetic field emitted by the EUT induces currents in the large-loop antennas. Since there are three orthogonal loops, there is no need to rotate either the EUT or the loop antenna system. The current induced in each loop is measured by means of a current probe, which is connected to a CISPR measuring receiver. Since the current is measured, emission limits are given in dB(μA) instead of dB(μA/m). Each loop antenna is constructed of a coaxial cable that contains two slits, positioned symmetrically with respect to the position of the current probe. Each slit is loaded by resistors in order to achieve a frequency response flat to within ± 2 dB in the frequency range from 9 kHz to 30 MHz [9,10]. In order to verify and validate the function of each large loop, a specially designed folded dipole has been developed [9,10]. It

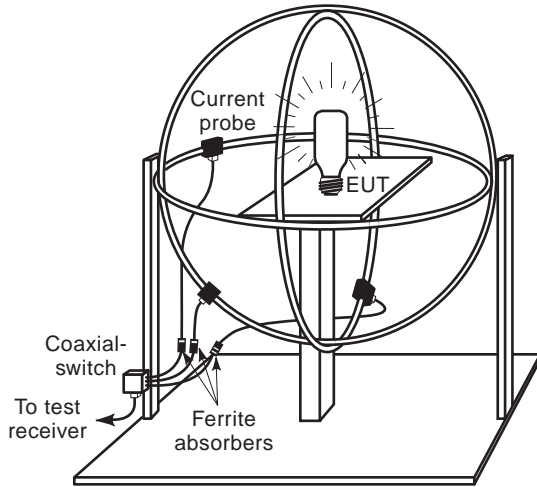


Figure 11. Simplified drawing of a large-loop antenna system with position of the EUT.

produces both a magnetic dipole moment m_H and an electric dipole moment m_E , when a signal is connected to the folded dipole. The folded dipole serves to test large loop antenna for its sensitivity in eight positions.

5.2.2. Problems in the Near-Field–Far-Field Transition Zone. Problems with magnetic field strength measurements in the transition region between near field and far field are discussed in detail in Ref. 22. When a small magnetic dipole is located in the free space, the electromagnetic field in a point $P(r, \theta, \varphi)$ is described by the following three relations (see Fig. 12):

$$H_r = \frac{jk}{2\pi} \frac{m_H \cos \theta}{r^2} \left(1 + \frac{1}{jkr}\right) e^{-jkr} \quad (3a)$$

$$H_\theta = \frac{-k^2}{4\pi} \frac{m_H \sin \theta}{r} \left(1 + \frac{1}{jkr} - \frac{1}{(kr)^2}\right) e^{-jkr} \quad (3b)$$

$$E_\varphi = \frac{Z_0 k^2}{4\pi} \frac{m_H \sin \theta}{r} \left(1 + \frac{1}{jkr}\right) e^{-jkr} \quad (3c)$$

where $k = 2\pi/\lambda$ and $m_H = \pi R_0^2 I_0$ is the magnetic dipole moment, a vector perpendicular to the plane of the dipole. Equations (3a)–(3c) completely describe the electromagnetic field of the magnetic dipole.

Two situations are discussed further: (1) the near field, where r is much smaller than λ but larger than the maximum dimension of the source (i.e., $kr \ll 1$); and (2) the far field, where r is much larger than λ and much larger than the maximum dimension of the source (i.e., $kr \gg 1$).

For the near-field case, where $kr \ll 1$ and using $e^{-jkr} = \cos(kr) - j \sin(kr)$, Eqs. (3a)–(3c) are simplified to

$$H_r = \frac{2m_H \cos \theta}{4\pi r^3} \quad (4a)$$

$$H_\theta = \frac{m_H \sin \theta}{4\pi r^3} \quad (4b)$$

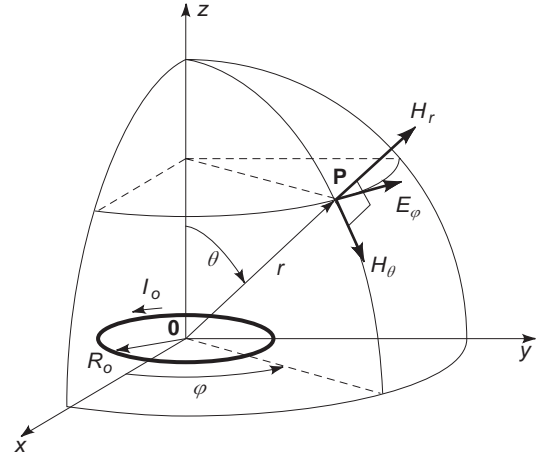


Figure 12. Field components H_r , H_θ , and E_φ in \mathbf{P} at a distance r from the center of the magnetic dipole in the xy plane.

$$E_\varphi = \frac{kZ_0 m_H \sin \theta}{4\pi r^2} \quad (4c)$$

From Eqs. (4a)–(4c) we can see that H_r and H_θ are inversely proportional to r^3 , whereas E_φ is inversely proportional to r^2 .

For the far-field case where $kr \gg 1$, Eqs. (3a)–(3c) are reduced to

$$H_r = \frac{jk m_H \cos \theta}{2\pi r^2} e^{-jkr} \Rightarrow 0 \quad (5a)$$

$$H_\theta = \frac{-k^2 m_H \sin \theta}{4\pi r} e^{-jkr} \quad (5b)$$

$$E_\varphi = \frac{k^2 Z_0 m_H \sin \theta}{4\pi r} e^{-jkr} \quad (5c)$$

From Eqs. (5a)–(5c) one can see that in the far field H_r vanishes in comparison to H_θ and that H_θ and E_φ are inversely proportional to r .

In the frequency range from 9 kHz to 30 MHz, where emission limits have been set, the corresponding wavelength is 33 km–10 m. Since for compliance testing, ambient emissions on an open-area test site require a reduction of the measurement distance to 10 m or even 3 m, measurements are carried out in the near-field zone over a wide frequency range. At the higher frequency range the transition zone and the beginning far field zone are reached. Goedbloed [22] investigated the transition zone and identified the critical condition where H_r and H_θ are equal in magnitude. It occurs where

$$\frac{2m_H}{4\pi r^3} \sqrt{1 + k^2 r^2} = \frac{m_H}{4\pi r^3} \sqrt{1 - k^2 r^2 + k^4 r^4} \quad (6)$$

or where

$$fr = 112.3 \text{ in MHz} \cdot \text{m} \quad (7)$$

For $r = 10$ m, $H_{\theta \max} > H_{r \max}$ at frequencies greater than 11 MHz.

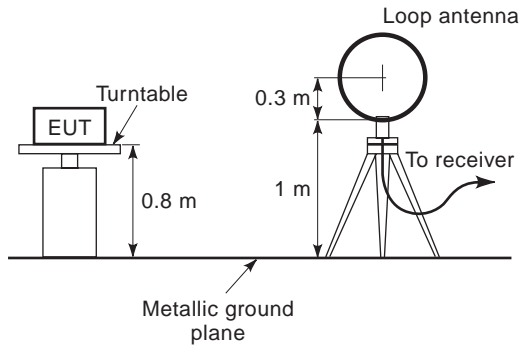


Figure 13. Basic CISPR setup for magnetic field measurements. Both EUT and loop antennas have to be turned round until the maximum indication on the receiver has been found.

The CISPR magnetic field measurement method is illustrated in Fig. 13, with the test setup on a metallic ground plane and the receiving antenna in the vertical plane. In Figs. 14 and 15, two different cases of radiating electrically small magnetic dipoles are illustrated; the first one, with the dipole moment parallel to the ground plane and the second one, with the dipole moment perpendicular to the ground plane. Because of the reflecting ground plane two sources are responsible for the field at the location of the receiving antenna: the original source and the mirror source. The points and crosses drawn in both sources show the direction of the current. In Fig. 14, the currents are equally oriented. In this case the loop antenna detects the radial component $H_{d,r}$ and the direct tangential component $H_{d,\theta} = 0$ since $\theta_d = 0$. Therefore, direct radiation will only contribute if $fd \ll 112 \text{ MHz} \cdot \text{m}$ [see Eq. (7)]. In the case of $fd \gg 112 \text{ MHz} \cdot \text{m}$, the loop antenna will receive direct radiation if it is rotated by 90° . This may be observed frequently in practical measurements: at low frequencies the maximum radiation is found with loop antenna in parallel to the EUT and at high frequencies with the loop antenna oriented perpendicular to the EUT. In addition to these direct components, the indirect radial and tangential components $H_{i,r}$ and $H_{i,\theta}$ are superpositioned in the loop antenna. Assuming near-field conditions it follows from Eqs. (4), that the magnitude of the mag-

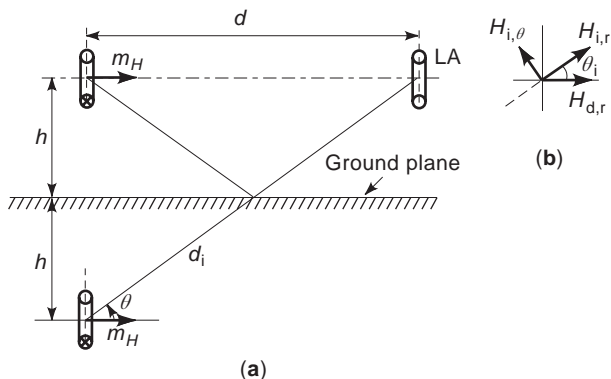


Figure 14. (a) Receiving conditions for a magnetic dipole with a horizontal dipole moment; (b) vectors of the directly and indirectly radiated H -field components.

netic field H_m is given by

$$H_m = H_{d,r} + H_{i,r} \cos \theta_i - H_{i,\theta} \sin \theta_i$$

$$= \frac{m_H}{4\pi d^3} \left(2 + \frac{d^3}{d_1^3} (2 \cos^2 \theta_i - \sin^2 \theta_i) \right) \quad (8)$$

where $d_1 = \sqrt{(2h)^2 + d^2}$ is the distance between the mirror dipole and the loop antenna.

Goedbloed gives a numerical example with $m_H = 4\pi 10^3 \mu\text{A} \cdot \text{m}^2$ (e.g., 100 mA through a circular loop with a diameter of 0.40 m). Using Eq. (8) with $d = 3 \text{ m}$ and $h = 1.3 \text{ m}$ will give $H_m = 38.6 \text{ dB}(\mu\text{A/m})$ with the mirror source and $37.4 \text{ dB}(\mu\text{A/m})$ without the mirror source, which shows that in this case the reflecting ground plane has little influence. The influence of the ground plane is quite different in the case of a vertical dipole moment, specifically, a dipole moment perpendicular to the ground plane as illustrated in Fig. 15. In the case of Fig. 15 the loop antenna does not receive direct radiation at all, as $H_{d,r}(\theta_d = \pi/2) = 0$ and $H_{d,\theta}$ is parallel to the loop antenna. Hence, the received signal is completely determined by the radiation coming from the mirror source, which also means that the result is determined by the quality of the reflecting ground plane. With the reflecting ground plane $H_m = H_{i,r} \sin \theta_i + H_{i,\theta} \cos \theta_i = 27.2 \text{ dB}(\mu\text{A/m})$, whereas without the reflecting ground plane no field strength will be measured. If the loop antenna were positioned horizontally above the ground plane at $h = 1.3 \text{ m}$, then $H_m = H_{d,\theta} + H_{i,r} \cos \theta_i - H_{i,\theta} \sin \theta_i = 32.4 \text{ dB}(\mu\text{A/m})$ and $H_m = 31.4 \text{ dB}(\mu\text{A/m})$ without the reflecting ground plane. Measurements in a shielded room would be even less predictable, since the result would be determined by mirror sources on each side, including the ceiling of the shielded room. Absorbers are not very helpful in the low frequency ranges. From the results, Goedbloed concludes that in order to judge the interference capability of an EUT, the method proposed by Bergervoet and van Veen [9], is an efficient method of magnetic field measurements.

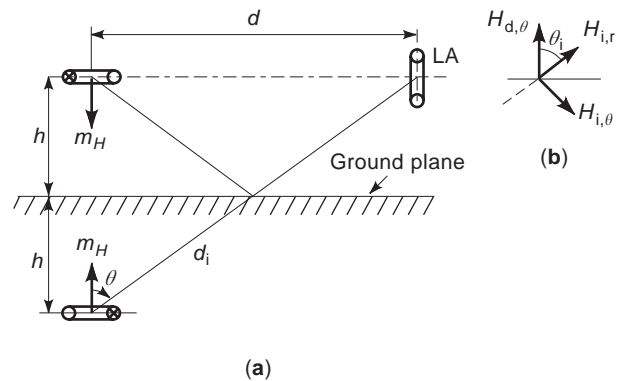


Figure 15. (a) Receiving conditions for a magnetic dipole with a vertical dipole moment, and the receiving loop antenna in the vertical position as specified by the standard; (b) vectors of the indirectly radiated H -field components (no reception of direct radiation).

6. CALIBRATION OF A CIRCULAR LOOP ANTENNA

A time-varying magnetic field at a defined area S can be determined with a calibrated circular loop. For narrow-band magnetic field measurements, a measuring loop consists of an output interface (point \mathbf{X} on Fig. 5), which links the induced current to measuring receiver. It may have a passive or an active network between loop terminals and output. The measuring loop can also include a shielding over the loop circumference against any perturbation of strong and unwanted electric fields. The shielding should be interrupted at a point on the loop circumference.

Generally in the far field that streamlines of magnetic flux are uniform, but in the near field, that is, in the vicinity of the generator of a magnetic field, they depend on the source and its periphery. Figure 19 shows the streamlines of the electromagnetic vectors generated by the transmitting loop \mathbf{L}_1 . In the near field, the spatial distribution of the magnetic flux, $B = \mu_0 H$, over the measuring loop area is not known. Only the normal components of the magnetic flux, averaged over the closed-loop area, can induce a current through the loop conductor.

The measuring loop must have a calibration (conversion) factor or set of factors, that, at each frequency, expresses the relationship between the field strength impinging on the loop and the indication of the measuring receiver. The calibration of a measuring loop requires the generation of a well-defined standard magnetic field on its effective receiving surface. Such a magnetic field is generated by a circular transmitting loop when a defined root-mean-square (RMS) current is passed through its conductor. The unit of the generated or measured magnetic field H_{av} is A/m and therefore is also an RMS value. The subscript "av" strictly indicates the average value of the spatial distribution, not the average over a period of T of a periodic function. This statement is important for near-field calibration and measuring purposes. For far-field measurements the result indicates the RMS value of the magnitude of the uniform field. In the following we discuss the requirements for the near-zone calibration of a measuring loop.

7. CALCULATION OF STANDARD NEAR-ZONE MAGNETIC FIELDS

To generate a standard magnetic field, a transmitting loop \mathbf{L}_1 is positioned coaxial and plane-parallel at a separation distance d from the loop \mathbf{L}_2 , as in Fig. 16. The analytical formula for the calculation of the average magnetic field strength H_{av} in A/m generated by a circular filamentary loop at an axial distance d including the retardation due to the finite propagation time was obtained earlier. The average value of field strength H_{av} was derived from the retarded vector potential A_φ as tangential component on the point P of the periphery of loop \mathbf{L}_2 :

$$H_{av} = \frac{I r_1}{\pi r_2} \int_0^\pi \frac{e^{-j\beta R(\varphi)}}{R(\varphi)} \cos(\varphi) d\varphi \quad (9a)$$

$$R(\varphi) = \sqrt{d^2 + r_1^2 + r_2^2 - 2r_1 r_2 \cos(\varphi)} \quad (9b)$$

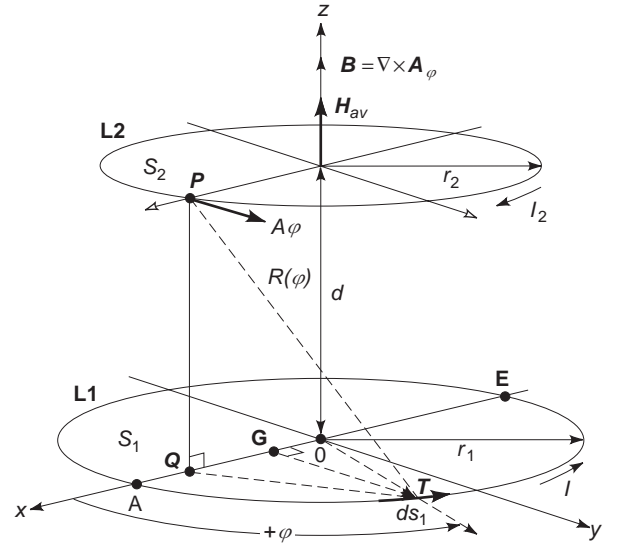


Figure 16. Configuration of two circular loops.

In these equations for the thin circular loop, I is transmitting loop RMS current in amperes, d is distance between the planes of the two coaxial loop antennas in meters, r_1 and r_2 are filamentary loop radii of transmitting and receiving loops in meters, respectively, β is wave-length constant, $\beta = 2\pi/\lambda$, and λ is wavelength in meters.

Equations (9a) and (9b) can be determined by numerical integration. To this end we separate the real and imaginary parts of the integrand using Euler's formula $e^{-j\varphi} = \cos(\varphi) - j \sin(\varphi)$ and rewrite Eq. (9a) as

$$H_{av} = \frac{I r_1}{\pi r_2} (F - jG) \quad (10a)$$

where

$$F = \int_0^\pi \frac{\cos[\beta R(\varphi)]}{R(\varphi)} \cos(\varphi) d\varphi \quad (10b)$$

$$G = \int_0^\pi \frac{\sin[\beta R(\varphi)]}{R(\varphi)} \cos(\varphi) d\varphi \quad (10c)$$

and the magnitude of H_{av} is then obtained as

$$|H_{av}| = \frac{I r_1}{\pi r_2} \sqrt{F^2 + G^2} \quad (10d)$$

It is possible to evaluate the integrals in Eqs. (10) by numerical integration with an appropriate mathematics software on a personal computer. Some mathematics software can directly calculate the complex integral of Eqs. (9).

8. ELECTRICAL PROPERTIES OF CIRCULAR LOOPS

8.1. Current Distribution around a Loop

The current distribution around the transmitting loop is not constant in amplitude and in phase. A standing wave of current exists on the circumference of the loop. We can

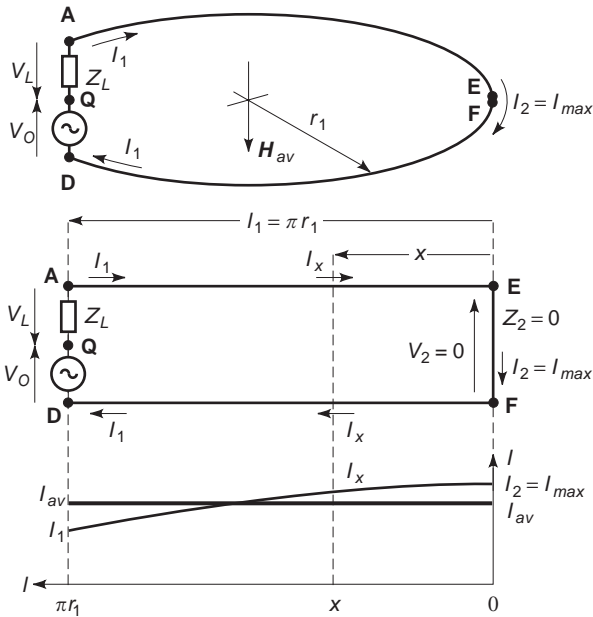


Figure 17. Current distribution on a circular loop.

determine this current distribution along the loop circumference by assuming that the loops circumference $2\pi r_1$ is electrically smaller than the wavelength λ and the loop current is constant in phase around the loop and that the loop is sufficiently loss-free. The single-turn thin loop was considered as a circular balanced transmission line fed at points **A** and **D** and short-circuited at points **E** and **F** (Fig. 17).

In an actual calibration setup the loop current I_1 is specified at the terminals **A** and **D**. The average current was given as a function of input current I_1 of the loop:

$$I_{av} = I_1 \frac{\tan(\beta\pi r_1)}{\beta\pi r_1} \tag{11}$$

The fraction of I_{av}/I_1 from Eq. (11) expressed in dB gives the conditions for determining of the highest frequency f and the radius of the loop r_1 . The deviation of this fraction is plotted in Fig. 18.

The current I in Eqs. (9) must be substituted with I_{av} from Eq. (11). Since Eq. (11) is an approximate expression, it is recommended to keep the radius of the transmitting loop small enough for the highest frequency of calibration to minimize the errors. For the dimensioning of the radius

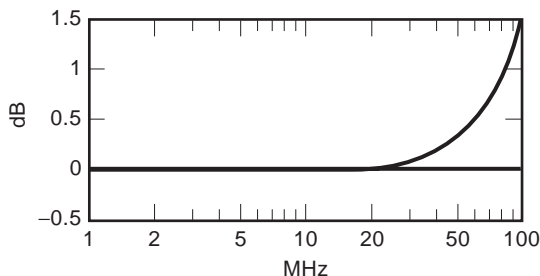


Figure 18. Deviation of I_{av}/I_1 for a loop radius, 0.1 m as $20 \log(I_{av}/I_1)$ in dB versus frequency.

of the receiving loop these conditions are not very important, until the receiving loop is calibrated with an accurately defined standard magnetic field, but the resonance of the loop at higher frequencies must be taken into account.

8.2. Circular Loops with Finite Conductor Radii

A measuring loop can be constructed with one or more winding. The form of the loop is chosen as a circle, because of the simplicity of the theoretical calculation and calibration. The loop conductor has a finite radius. At high frequencies the loop current flows on the conductor surface and it shows the same proximity effect as two parallel, infinitely long cylindrical conductors. Figure 19 shows the cross section of two loops intentionally in exaggerated dimensions. The streamlines of the electric field are orthogonal to the conductor surface of the transmitting loop L_1 and they intersect at points **A** and **A'**. The total conductor current is assumed to flow through an equivalent thin filamentary loop with the radius $a_1 = \sqrt{r_1^2 - c_1^2}$, where $a_1 = \overline{OA} = \overline{OP} = \sqrt{\overline{OQ}^2 - \overline{QP}^2}$. The streamlines of the magnetic field are orthogonal to the streamlines of electric field. The receiving loop L_2 with the finite conductor radius c_2 can encircle a part of magnetic field with its effective circular radius $b_2 = r_2 - c_2$.

The sum of the normal component of vectors H acting on the effective receiving area $S_2 = \pi b_2^2$ induces a current in the conductor of the receiving loop L_2 . This current flows through the filamentary loop with the radius a_2 . The average magnetic field vector H_{av} is defined as the integral of vectors H_n over effective receiving area S_2 , divided by S_2 . The magnetic streamlines, which flow through the

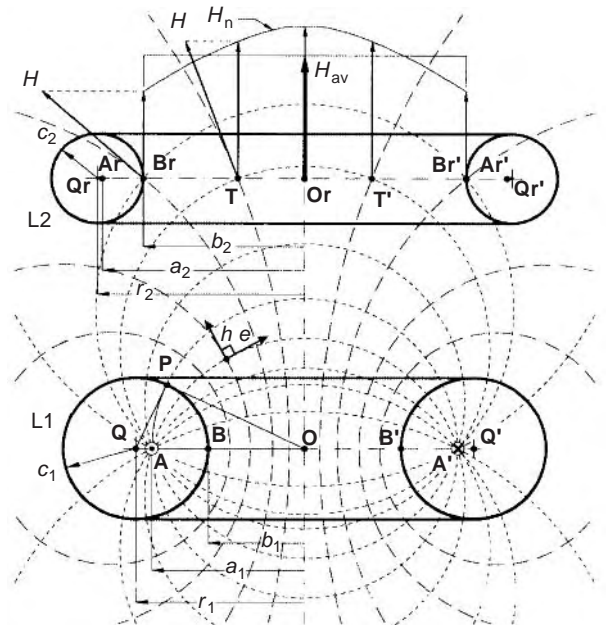


Figure 19. Filamentary loops of two loops with finite conductor radii and orthogonal streamlines of the electromagnetic vectors, produced from transmitting loop L_1 .

conductor and outside of loop \mathbf{L}_2 , cannot induce a current through the conductor along the filamentary loop \mathbf{Ar} , \mathbf{Ar}' , of \mathbf{L}_2 . The equivalent filamentary loop radii a_1 , a_2 and effective circular surface radii b_1 , b_2 can directly be seen from Fig. 19.

The equivalent thin current filament radius a_1 of the transmitting loop \mathbf{L}_1 :

$$a_1 = \sqrt{r_1^2 - c_1^2} \quad (12a)$$

The equivalent thin current filament radius a_2 of the receiving loop \mathbf{L}_2 :

$$a_2 = \sqrt{r_2^2 - c_2^2} \quad (12b)$$

The radius b_1 of the effective receiving circular area of the loop transmitting \mathbf{L}_1 :

$$b_1 = r_1 - c_1 \quad (12c)$$

The radius b_2 of the effective receiving circular area of the receiving loop \mathbf{L}_2 :

$$b_2 = r_2 - c_2 \quad (12d)$$

8.3. Impedance of a Circular Loop

The impedance of a loop can be defined at chosen terminals \mathbf{Q} , \mathbf{D} , as $Z = V/I_1$ (Fig. 17). Using Maxwell's equation with the Faraday's law curl $\mathbf{E} = -j\omega\Phi_m$, we can write the line integrals of the electric intensity \mathbf{E} along the loop conductor through its cross section, along the path joining points \mathbf{D} , \mathbf{Q} , and the load impedance Z_L between the terminals \mathbf{Q} , \mathbf{A} :

$$\int_{(AEFD)} \mathbf{E}_s ds + \int_{(DQ)} \mathbf{E}_s ds + \int_{(QA)} \mathbf{E}_s ds = -j\omega\Phi_m \quad (13a)$$

Here, Φ_m is the magnetic flux. The impressed emf V acting along the path joining points \mathbf{D} and \mathbf{Q} is equal and opposite to the second term of Eq. (13a):

$$V = - \int_{(DQ)} \mathbf{E}_s ds \quad (13b)$$

The impedance of the loop at the terminals \mathbf{D} , \mathbf{Q} can be written from Eqs. (13) dividing with I_1 as

$$\begin{aligned} Z = \frac{V}{I_1} &= \frac{\int_{(AEFD)} \mathbf{E}_s ds}{I_1} + \frac{\int_{(QA)} \mathbf{E}_s ds}{I_1} + \frac{j\omega\Phi_m}{I_1} \\ &= Z_i + Z_L + Z_e \end{aligned} \quad (14)$$

Z_i indicates the internal impedance of the loop conductor. Because of the skin effect, the internal impedance at high frequencies is not resistive. Z_L is a known load or a source impedance on Fig. 17. Z_e is the external impedance of the

loop:

$$Z_e = j\omega \frac{\Phi_m}{I_1} = j\omega \frac{\mu_0 H_{av} S}{I_1} \quad (15a)$$

We can consider that the loop consists of two coaxial and coplanar filamentary loops (i.e., separation distance $d = 0$). The radii a_1 and b_1 are defined in Eqs. (12). The average current I_{av} flows through the filamentary loop with the radius a_1 and generates an average magnetic field strength H_{av} on the effective circular surface $S_1 = \pi b_1^2$ of the filamentary loop with the radius b_1 . From the Eqs. (9) and (11) we can rewrite Eq. (15a), for the loop \mathbf{L}_1 :

$$\begin{aligned} Z_e &= j \frac{\tan(\beta\pi a_1)}{\beta\pi a_1} \mu_0 \omega a_1 b_1 \\ &\times \int_0^\pi \frac{e^{-j\beta R_0(\varphi)}}{R_0(\varphi)} \cos(\varphi) d\varphi \end{aligned} \quad (15b)$$

$$R_0(\varphi) = \sqrt{a_1^2 + b_1^2 - 2a_1 b_1 \cos(\varphi)} \quad (15c)$$

The real and imaginary parts of Z_e are the radiation resistance and the external inductance of loops, respectively:

$$\begin{aligned} \text{Re}(Z_e) &= \frac{\tan(\beta\pi a_1)}{\beta\pi a_1} \mu_0 \omega a_1 b_1 \\ &\times \int_0^\pi \frac{\sin(\beta R_0(\varphi))}{R_0(\varphi)} \cos(\varphi) d\varphi \end{aligned} \quad (15d)$$

$$\begin{aligned} \text{Im}(Z_e) &= \frac{\tan(\beta\pi a_1)}{\beta\pi a_1} \mu_0 \omega a_1 b_1 \\ &\times \int_0^\pi \frac{\cos(\beta R_0(\varphi))}{R_0(\varphi)} \cos(\varphi) d\varphi \end{aligned} \quad (15e)$$

From Eq. (15e) we obtain the external self-inductance:

$$\begin{aligned} L_e &= \frac{\tan(\beta\pi a_1)}{\beta\pi a_1} \mu_0 a_1 b_1 \\ &\times \int_0^\pi \frac{\cos(\beta R_0(\varphi))}{R_0(\varphi)} \cos(\varphi) d\varphi \end{aligned} \quad (15f)$$

Equations (15) include the effect of current distribution on the loop with finite conductor radii.

8.4. Mutual Impedance between Two Circular Loops

The mutual impedance Z_{12} between two loops is defined as

$$Z_{12} = \frac{V_2}{I_1} = \frac{Z_2 I_2}{I_1} \quad (16)$$

The impedance of Z_2 in Eq. (16) can be defined in the same way as Eq. (14):

$$Z_2 = \frac{V_2}{I_2} = Z_{2i} + Z_L + Z_{2e} \quad (17)$$

here Z_{2i} is the internal impedance, Z_L is the load imped-

ance, and Z_{2e} is the external impedance of the second loop \mathbf{L}_2 .

The current ratio I_2 to I_1 in Eq. (16) can be calculated from Eqs. (9),(11), and (12). The current I_1 of the transmit loop with separation distance d :

$$I_1 = \frac{H_{av}\pi b_2}{\frac{\tan(\beta\pi a_1)}{\beta\pi a_1} a_1 \int_0^\pi \frac{e^{-j\beta R_d(\varphi)}}{R_d(\varphi)} \cos(\varphi) d\varphi} \quad (18a)$$

$$R_d(\varphi) = \sqrt{d^2 + a_1^2 + b_2^2 - 2a_1 b_2 \cos(\varphi)} \quad (18b)$$

and the current I_2 of the receive loop for the same H_{av} (here $d = 0$) is

$$I_2 = \frac{H_{av}\pi b_2}{\frac{\tan(\beta\pi a_2)}{\beta\pi a_2} a_2 \int_0^\pi \frac{e^{-j\beta R_0(\varphi)}}{R_0(\varphi)} \cos(\varphi) d\varphi} \quad (18c)$$

$$R_0(\varphi) = \sqrt{a_2^2 + b_2^2 - 2a_2 b_2 \cos(\varphi)} \quad (18d)$$

The general mutual impedance between two loops from Eqs. (16) and (17) is

$$Z_{12} = (Z_{2i} + Z_L + Z_{2e}) \frac{I_2}{I_1} = Z_{12i} + Z_{12L} + Z_{12e} \quad (19a)$$

here Z_{12i} is the mutual internal impedance, Z_{12L} denotes the mutual load impedance, and Z_{12e} is the external mutual impedance.

Arranging Eq. (15b) for Z_{2e} and the current ratio I_2/I_1 from Eqs. (18) external mutual impedance yield

$$Z_{12e} = j \frac{\tan(\beta\pi a_1)}{\beta\pi a_1} \mu_0 \omega a_1 b_2 \times \int_0^\pi \frac{e^{-j\beta R_d(\varphi)}}{R_d(\varphi)} \cos(\varphi) d\varphi \quad (19b)$$

The real part of Z_{12e} may be described as mutual radiation resistance between two loops.

The imaginary part of Z_{12e} divided by ω gives the mutual inductance

$$M_{12e} = \frac{\tan(\beta\pi a_1)}{\beta\pi a_1} \mu_0 a_1 b_2 \times \int_0^\pi \frac{\cos(\beta R_d(\varphi))}{R_d(\varphi)} \cos(\varphi) d\varphi \quad (19c)$$

Equations (19b) and (19c) include the effect of current distribution on the loop with finite conductor radii.

9. DETERMINATION OF THE ANTENNA FACTOR

The antenna factor K is defined as a proportionality constant with necessary conversion of units. K is the ratio of the average magnetic field strength bounded by the loop to

the measured output voltage V_L on the input impedance R_L of the measuring receiver. For evaluation of the antenna factor there are two methods. The first is by calculation of the loop impedances, and the second is with the well-defined standard magnetic field calibration, which will also be needed for the verification of calculated antenna factors [24].

9.1. Determination of the Antenna Factor by Computing from the Loop Impedances

If a measurement loop (e.g., \mathbf{L}_2) has a simple geometric shape and a simple connection to a voltage measuring device with a known load R_L , we can determine the antenna factor by calculation. In the case of unloaded loop from Fig. 17 the open-circuit voltage is

$$V_0 = j\omega\mu_0 H_{av} S_2 \quad (20a)$$

For the case of loaded loop the current is

$$I = \frac{V_0}{Z} = \frac{V_0}{R_L + Z_i + Z_e} \quad (20b)$$

The antenna factor from Eq. (9a) can be written with $V_L = Z_L I$ and Eqs. (20) as

$$K_H = \left| \frac{1}{j\omega\mu_0 S_2} \left(1 + \frac{Z_e}{R_L} + \frac{Z_i}{R_L} \right) \right| \text{ in } \frac{\text{A}}{\text{m}} \frac{1}{\text{V}} \quad (21)$$

The effective loop area is $S_2 = \pi b_2^2$. The external loop impedance Z_e can be calculated with Eqs. (15).

9.2. Standard Magnetic Field Method

In the calibration setup in Fig. 20 we measure the voltages with standard laboratory measuring instrumentation with the $50\ \Omega$ impedance. The device to be calibrated consists at least of a loop and a cable with an output connector. Such a measuring loop can also include a passive or active network between the terminals **C,D** and a coaxial shield on the circular loop conductor against unwanted electric fields, depending on its development and construction. The impedance Z_L at the terminals **C,D** is not accurately measurable. Such a complex loop must be calibrated with the standard magnetic field method. The antenna factor in Eqs. (1) can be defined by measuring of the voltage V_L and the uncertainties between loop terminals **C,D** and measuring receiver are fully calibrated. The attenuation ratio α of the voltages V_2 and V_L can be measured for each frequency:

$$\alpha = \frac{V_2}{V_L} \quad (22)$$

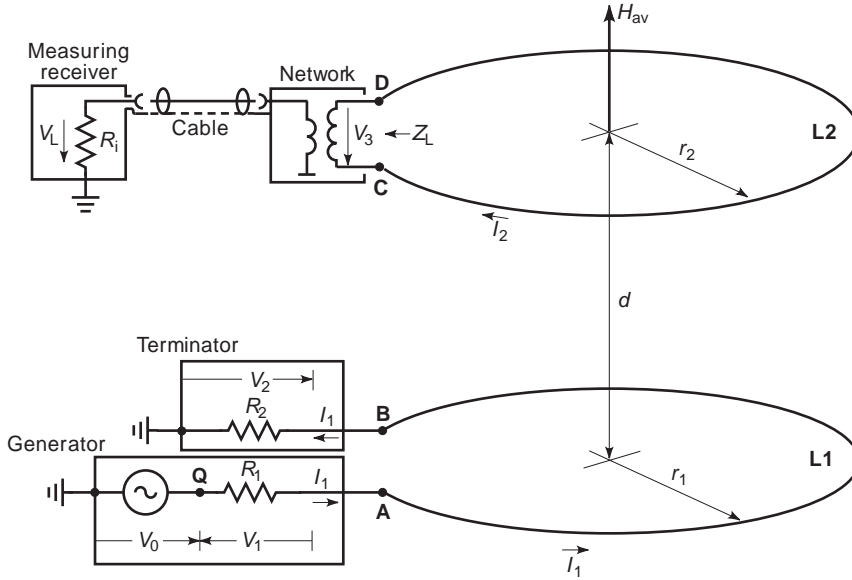


Figure 20. Calibration setup for circular loop antennas.

Using Eqs. (22),(1),(11), and (12), with $V_2 = -I_1 R_2$, and $V_0 = \text{constant}$, Eq. (9a) can be rewritten:

$$K_H = \left| \alpha \frac{1}{R_2} \frac{\tan(\beta\pi a_1)}{\beta\pi a_1} \frac{a_1}{\pi b_2} \times \int_0^\pi \frac{e^{-j\beta R_d(\varphi)}}{R_d(\varphi)} \cos(\varphi) d(\varphi) \right| \quad (23)$$

R_d is defined by Eq. (18b)b. Equation (23) can also be expressed logarithmically

$$k_H = 20 \log(K_H) \text{ in dB} \left(\frac{\text{A}}{\text{m}} \frac{1}{\text{V}} \right)$$

Equation (23) reduces the calibration of the loop to an accurate measurement of attenuation α for each frequency. The other terms of Eq. (23) can be calculated depending on the geometric configuration of the calibration setup at the working frequency band of the measuring loop. The calibration uncertainties are also calculable with the given expressions. The uncertainty of the separation distance d between two loops must be taken into consideration as well. At a separation distance $d < r_1$ the change of the magnetic field is high.

For a calibration setup the separation distance d can be defined as small as possible. However, the effect of the mutual impedance must be taken into account in the calibration process, and a condition to define the separation distance d must be given (Fig. 20). If the second loop is open-circuited, that is the current $I_2 = 0$, the current I_1 is defined only from the impedances of the transmitting loop. In the case of a short-circuited second loop, I_2 is maximum and the value of I_1 will change depending on the supply circuit and loading of the transmitting loop. A current ratio q between these two cases can be defined as the condition of the separation distance d between the two loops.

It is assumed that the generator voltage V_0 is constant. The measuring loop L_2 is terminated by Z_L . For $Z_L = 0$ and $V_{CD} = 0$, one obtains the current I_1 in the transmitting loop as

$$I_{1(Z_L=0)} = \frac{V_0}{R_1 + R_2 + Z_{AB} - \frac{Z_{12}^2}{Z_{CD}}} \quad (24a)$$

and for $Z_L = \infty$, that is, $I_2 = 0$

$$I_{1(Z_L=\infty)} = \frac{V_0}{R_1 + R_2 + Z_{AB}} \quad (24b)$$

The ratio of Eq. (24a) to Eq. (24b) is

$$q \equiv \frac{I_{1(Z_L=0)}}{I_{1(Z_L=\infty)}} = \left| \frac{R_1 + R_2 + Z_{AB}}{R_1 + R_2 + Z_{AB} \left(1 - \frac{Z_{12}^2}{Z_{AB} Z_{CD}} \right)} \right| \quad (25a)$$

here with the coupling factor $k = Z_{12} / \sqrt{Z_{AB} Z_{CD}}$ between two loops:

$$q = \left| \frac{R_1 + R_2 + Z_{AB}}{R_1 + R_2 + Z_{AB}(1 - k^2)} \right| \quad (25b)$$

where $R_1 = R_2 = 50 \Omega$, Z_{AB} , Z_{CD} , and Z_{12} can be calculated from Eqs. (15) and (19). For greater accuracy one must try to keep the ratio q close to unity (e.g., $q = 1.001$).

The influence of the loading of the second loop on the transmitting loop can also be found experimentally. The change of the voltage V_2 at R_2 in Fig. 20 must be considerably small (e.g., < 0.05 dB), while putting a short-circuited measuring loop at the chosen separation distance.

With the determining of K_H or k_H the loop can completely be calibrated up to its 50Ω output. A network analyzer is usually used for the attenuation measurement

instead of a discrete measurement at each frequency with signal generator and measuring receiver. A network analyzer can normalize the frequency characteristic of the transmit loop and gives a quick overview on measured attenuation for the frequency band.

BIBLIOGRAPHY

1. CISPR 16 Specification for radio disturbance and immunity measuring apparatus and methods—Part 1: Radio disturbance and immunity measuring apparatus (8.1993); Part 2: Methods of measurement of disturbances and immunity (11.1996).
2. CISPR 11/2nd edition 1990-09 and EN 55011:07.1992: Limits and methods of measurement of electromagnetic disturbance characteristics of industrial, scientific, and medical (ISM) radio-frequency equipment.
3. *IRPA Guidelines on Protection against Non-Ionizing Radiation*, Pergamon Press, Oxford, UK, 1991.
4. ENV 50166 Part 1:1995—Human Exposure to electromagnetic fields—Low-frequency (0 Hz to 10 kHz) and Part 2:1995—Human exposure to electromagnetic fields—High frequency (10 kHz to 300 GHz).
5. VDE 0848 Part 4 A2:Draft 1992—Safety in electromagnetic fields. Limits for the protection of persons in the frequency range from 0 to 30 kHz and Part 2: Draft 1991—Safety in electromagnetic fields. Protection of persons in the frequency range from 30 kHz to 300 GHz.
6. IEEE standard C95.1-1991: *IEEE Standard for Safety Levels with Respect to Human Exposure to Radio Frequency Electromagnetic Fields, 3 kHz to 300 GHz*.
7. MIL-STD-461D, Jan. 11, 1993: *Requirements for the Control of Electromagnetic Interference Emissions and Susceptibility*, MIL-STD-462D, Jan. 11, 1993: *Measurement of Electromagnetic Interference Characteristics*, DoD, USA.
8. VG 95373 Part 22, Cologne, Germany: Beuth Verlag, 1990.
9. J. R. Bergervoet and H. van Veen, A large loop antenna for magnetic field measurements, *Proc. Int. Symp. EMC*, Zürich, 1989, pp. 29–34.
10. CISPR 15/5th edition 1996-03 and EN 55015:12.1993: Limits and methods of measurement of radio disturbance characteristics of electrical lighting and similar equipment.
11. Draft revision of IEC 945 (IEC 80/124/FDIS): Maritime navigation and radiocommunication equipment and system—General requirements, methods of testing and required test results; identical requirements are given in Draft prETS 300 828/02.1997: EMC for radiotelephone transmitters and receivers for the maritime mobile service operating in the VHF bands, and Draft prETS 300 829/02.1997: EMC for Maritime mobile earth stations (MMES) operating in the 1,5/1,6 GHz bands; providing Low Bit Rate Data Communication (LBRDC) for the global distress and safety system (GMDSS).
12. U.S. FCC *Code of Federal Regulations* (CFR) 47 Part 18. Edition Oct. 1, 1996.
13. J. E. Lenz, A review of magnetic sensors, *Proc. IEEE* **78**(6):973–989 (1990).
14. L. Rohde and F. Spies, Direkt zeigende Feldstärkemesser (Direct indicating field-strength meters), *Z. Technische Physik* **10**(11):439–444 (1938).
15. Datasheet edition 9.72 of Rohde & Schwarz Field-strength Meter HFH (0.1 to 30 MHz).
16. K. Danzeisen, Patentschrift DE 27 48 076 C2, 26.10.1977, Rohde & Schwarz GmbH & Co. KG, POB 801469, D-81614 München.
17. F. Demmel and A. Klein, Messung magnetischer Felder mit extrem hoher Dynamik im Bereich 100 Hz bis 30 MHz (Measurement of magnetic fields with an extremely high dynamic range in the frequency range 100 Hz to 30 MHz), *Proc. EMV '94*, Karlsruhe, 1994, pp. 815–824.
18. CLC/TC111(Sec)61: Sept.1995: Definitions and Methods of Measurement of Low Frequency Magnetic and Electric Fields with Particular Regard to Exposure of Human Beings (Draft 2: August 1995).
19. DKE 764/35-94: Entwurf DIN VDE 0848 Teil 1, Sicherheit in elektrischen, magnetischen und elektromagnetischen Feldern; Mess- und Berechnungsverfahren (Draft DIN VDE 0848 part 1 Safety in electric, magnetic and electromagnetic fields; measurement and calculation methods).
20. Recommendation ITU-R SM 378-5, *Field-Strength Measurements at Monitoring Stations*, SM Series Volume, ITU, Geneva 1994.
21. *Spectrum Monitoring Handbook*, ITU-R, Geneva 1995.
22. J. J. Goedbloed, Magnetic field measurements in the frequency range 9 kHz to 30 MHz; EMC91, ERA Conference, Heathrow, UK, Feb. 1991.
23. J. Kaiser et al., Feldstärkeumrechnung von 30 m auf kürzere Messentfernungen (Conversion of field strength from 30 m to shorter distances), **110**:820–825 (1989).

MAGNETIC MATERIALS

ROBERT B. VAN DOVER
Bell Labs, Lucent Technologies

1. HISTORICAL BACKGROUND

Magnetic materials have been known since ancient times—for example, in 380 B.C.E. Plato wrote [1] of the “stone which Euripides calls a magnet,” which we infer was Fe₃O₄, now known as *magnetite*. The scientific quality of magnetism studies abruptly and dramatically jumped with the publication in 1600 by Gilbert of the classic text *De Magnete* [2]. Quantitative measurements of magnetic materials were enabled by the 1820 discovery by Oersted that an electric current creates a magnetic field. In 1846 Faraday made systematic studies of the attraction and repulsion of materials in a gradient field and classified materials as *diamagnetic* if they are repelled by a region of increased flux density and *paramagnetic* if they are attracted. To this we add *ferromagnetic* (strongly magnetic, like iron) to form the set of three basic classes of magnetic response.

Since the early part of the twentieth century, magnetic materials have been the subject of deep and broad research and development because of their economic and scientific importance, and much of our knowledge is mature. Nevertheless, startling discoveries continue to be made, such as the discovery of Nd–Fe–B permanent magnets and the “giant magneto-resistance” effect in thin-film multilayers.

2. MAGNETIC FIELDS AND THE MAGNETIC RESPONSE OF MATERIALS

The magnetic properties of matter may be viewed as a response to an applied stimulus, namely, the magnetic field strength \mathbf{H} . The macroscopic response of a material is given by its magnetization \mathbf{M} , and the overall field is the sum of the two, called the magnetic induction \mathbf{B} . In a vacuum the magnetization is strictly zero. For this article we adopt SI units, so we have $\mathbf{B} = \mu_0 \mathbf{H}$ in a vacuum, where \mathbf{B} is measured in tesla (Wb/m²), \mathbf{H} is measured in amperes per meter, and by definition $\mu_0 = 4\pi \times 10^{-7}$ H/m². The magnetic response adds directly to the applied field, giving $\mathbf{B} = \mu_0(\mathbf{H} + \mathbf{M})$.

The issue of units in magnetism is perennially vexing. In the past, cgs (Gaussian) units have been commonly used by scientists working with magnetic materials. In that system, \mathbf{B} is measured in gauss, \mathbf{H} in oersteds, and \mathbf{M} in emu/cm³, where emu is short for the uninformative term *electromagnetic unit*. The constitutive relation in Gaussian units is $\mathbf{B} = \mathbf{H} + 4\pi\mathbf{M}$. Important conversion factors to keep in mind are 10^4 Ga = 1 T and 12.5 Oe = 1 kA/m. A definitive discussion of units and dimensions is given in the Appendix of Jackson's *Classical Electrodynamics* [3].

3. TYPES OF MAGNETIC MATERIALS: TAXONOMY

3.1. Basic Families

Two of the basic families of magnetic materials involve a highly linear response (i.e., $\mathbf{M} = \chi\mathbf{H}$, where χ is defined as the magnetic susceptibility). The main magnetic response of all materials is due to the magnetic moment of individual electrons, a property directly connected to their spin. The moment of a single electron is 1 Bohr magneton, $\mu_B = 1.165 \times 10^{-29}$ Wbm. Due to the Pauli principle, in many cases the electrons in an atom are precisely paired with oppositely directed spins, leading to an overall cancellation. Nevertheless, a magnetic response can be discerned in all materials, as observed by Faraday.

3.2. Diamagnetism

Diamagnets have a negative value for χ , that is, the induced moment is opposite to the applied field. The susceptibility is temperature independent and typically small (see Fig. 1). Diamagnetism is due to the effect of a magnetic field on orbital motion of paired electrons about the nucleus (superficially comparable to Lenz' law). The diamagnetic susceptibility of most materials is very small—in the vicinity of -1×10^{-5} . A tabulation of diamagnetic susceptibilities of various atoms, ions, and molecules is given by Carlin [4].

A large negative magnetic susceptibility is characteristic of only one class of materials (namely, superconductors). A type I superconductor in the Meissner state exhibits complete exclusion of magnetic flux from the interior of the sample, $\mathbf{M} = -\mathbf{H}$, or $\mathbf{B} = 0$. Superconductors can also exhibit partial flux penetration, $0 < B < \mu_0 H$. In both cases the spectacular observation of stable levitation is possible, something that cannot be achieved using only

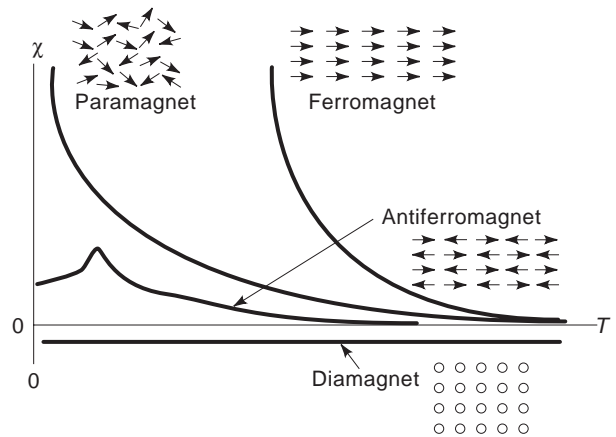


Figure 1. Schematic temperature dependence of the susceptibility of a diamagnet, paramagnet, ferromagnet, and antiferromagnet.

materials with $\chi > 0$ (as prove by Earnshaw's theorem). Note that stable levitation is possible even for bodies that are only weakly diamagnetic given a sufficiently large magnetic field gradient [5].

3.3. Paramagnetism

Paramagnets have a positive value for χ , that is, the induced moment is in the same direction as the applied field. Paramagnetism is due chiefly to the presence of unpaired electrons—either an overall odd number of electrons or an unfilled inner shell. Nuclei can also show paramagnetism, although typically of an extremely small magnitude. The electron gas of a metal is also usually slightly paramagnetic, though exchange coupling can sometimes lead to ordering (e.g., ferromagnetism). Independent unpaired electrons give each atom or molecule a small permanent dipole moment, which tends to be aligned by an external magnetic field. Langevin showed that thermal energy disrupts this alignment, leading to a susceptibility $\chi = Nm^2/3k_B T$, where N is the density of dipoles, m is the moment of each dipole, k_B is the Boltzmann constant, and T is the absolute temperature. Curie and Weiss found that the temperature in this formula should be replaced by $T \rightarrow (T - T_c)$ for materials with an ordering temperature T_c (the “Curie temperature”). The paramagnetic susceptibility of a material can give important insights into its chemistry and physics, but it is an effect of limited engineering significance at present.

3.4. Ferromagnetism

Ferromagnetism is the spontaneous magnetic ordering of the magnetic moments of a material in the absence of an applied magnetic field. Nearly all technologically important magnetic materials exhibit some form of ferromagnetism. In such materials, the magnetic moments of electrons couple together, so that they respond collectively. In this manner it is possible for all magnetic moments in an entire sample to point in the same direction, potentially giving a very strong effect. The details of how the

individual moments couple with each other can be understood in terms of quantum mechanics. There are three types of “exchange” interaction generally found:

- The first is direct exchange, in which an unpaired electron on one atom interacts with other unpaired electrons on atoms immediately adjacent via the Coulomb interaction. This is the strong mechanism that dominates in most metallic magnetic materials, such as Fe, Ni, Co, and their alloys. It results in a positive exchange energy, so the spins on adjacent atoms tend to align parallel.
- The second is indirect exchange, or superexchange, in which the moment of an unpaired electron on one atom polarizes the (paired) electron cloud of a second atom, which in turn interacts with the unpaired electron on a third atom. This is the mechanism that dominates in most oxide materials, such as ferrites. For example, in Fe_3O_4 the Fe ions (with unpaired electrons) interact through O ions (which have only paired electrons). Superexchange creates a negative exchange energy.
- Finally, there is the possibility of interaction between electrons that are not localized but can move freely as in a metal. This interaction, known as the RKKY interaction after its discoverers (Ruderman, Kittel, Kasuya, and Yoshida), is usually weaker than direct exchange. It plays an important role in the behavior known as “giant magnetoresistance” and can result in either a positive or negative exchange energy.

The main properties that characterize ferromagnetic materials are the Curie temperature T_c , the saturation magnetization M_s , the magnetic anisotropy energy K , and the coercive field H_c (see Fig. 2). The first two are intrinsic to a material. The third has both intrinsic and extrinsic factors. The last is extrinsic and depends on the form (microstructure, overall shape, etc.) of the material and will be discussed later.

- The exchange interaction that leads to ferromagnetism can be disrupted by thermal energy. At temperatures above T_c , the disruption is so great that the ferromagnetism ceases, and the material exhibits

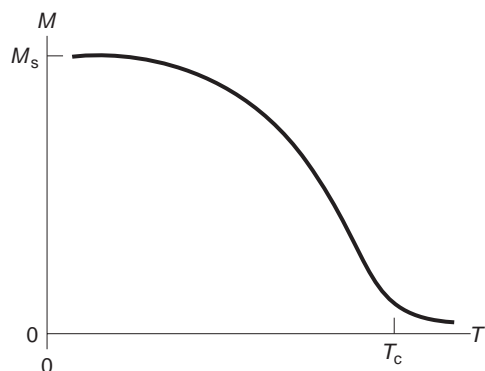


Figure 2. Schematic temperature dependence of the saturation magnetization M_s for a ferromagnet.

only paramagnetism. Thus T_c measures the magnitude of the exchange coupling energy. For example, the T_c of Fe is 770°C while for Co, $T_c = 1115^\circ\text{C}$, and for Ni, $T_c = 354^\circ\text{C}$. The ferromagnetic transition is a second-order phase transition, which means that the order parameter (magnetization) increases continuously from zero as the temperature is lowered below T_c .

- The saturation magnetization is the macroscopic magnetic moment of all of the spins averaged over the volume of the sample. Thus, in a material with many unpaired electrons per atom, M_s will be large (e.g., Fe with $\mu_0 M_s = 2.16\text{ T}$ at room temperature). Conversely, M_s will be much smaller in materials that also contain nonmagnetic atoms or ions (e.g., Fe_3O_4 with $\mu_0 M_s = 0.60\text{ T}$ at room temperature).
- The electron spins couple weakly to their orbital motion in a process known as spin-orbit coupling, a relativistic effect. As a result, the energy of the system depends on the orientation of the spins (i.e., the magnetization) with respect to the orbitals of the atoms (i.e., the orientation of the sample). This results in an intrinsic coupling of the magnetization to the crystal lattice. It leads to magnetic anisotropy—that is, the energy of the system depends on the orientation of the magnetization with respect to the sample. The direction along which the magnetic moment tends to lie is known as the “easy axis.” The magnitude of the anisotropy may be large, as in SmCo_5 permanent magnets that strongly resist demagnetization with $K \sim 10^7\text{ J/m}^3$, or it may be quite small, as in the high-permeability materials $\text{Ni}_{0.8}\text{Fe}_{0.2}$ (Permalloy) or a $\text{Fe}_{0.80}\text{P}_{0.13}\text{C}_{0.07}$ (an amorphous alloy).
- Another source of anisotropy can arise from the shape of the specimen, or from the shape of individual grains within the specimen. This is a local magnetostatic effect, rather than an intrinsic effect, and is called *shape anisotropy* (see Fig. 3). It is an extremely

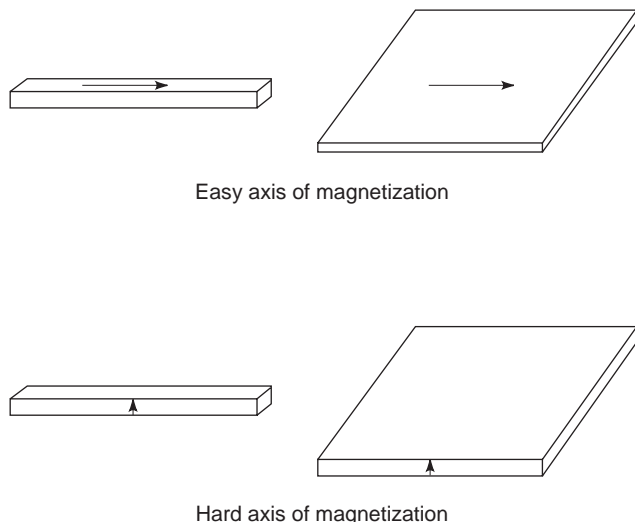


Figure 3. Shape anisotropy quantitatively describes the observation that needles and plates are most easily magnetized along a long dimension.

important factor in any real application. Two extremes are illustrative. A long thin needle (i.e., an acicular particle) can be readily magnetized along its long axis but will require a large field to force the magnetization to be across a short axis. The magnitude of field required is $H_a = M_s/2$ (i.e., $H_a = 8.5 \times 10^5$ A/m for the case of an Fe needle). A flat plate, on the other hand, will require twice that field, $H_a = M_s$, to magnetize it parallel to the normal.

- A third source of anisotropy is due to the magnetostriction of magnetic materials, coupled with stresses in the material. Magnetostriction is the change in dimensions of a sample when the magnetization is aligned along various crystallographic directions; it occurs as a response that minimizes the magneto-crystalline energy. Conversely, when a sample is strained along some crystallographic direction, this contributes to the magnetic anisotropy. This is called *stress anisotropy*. It can be an important effect in low-anisotropy materials that are highly strained, such as almost all thin films.
- The various magnetic anisotropies that may exist in a material all act simultaneously. The best way to analyze their cumulative effect is in terms of the anisotropy energy, which is the sum of all of the energies arising from individual anisotropies. The details of this analysis can be complex; see Bozorth or Brailsford, listed in the Further Reading list, for examples and guidance.

Useful magnetic materials almost inevitably consist mostly of Fe, Co, or Ni or a combination of these three elements, because these are the elements that are ferromagnetic at room temperature and above. A great variety of other elements may be added to form alloys or compounds with specific useful properties, but inevitably a large fraction of Fe, Co, or Ni will be present. When a nonmagnetic metal is alloyed with these elements, M_s and T_c generally decrease rapidly because of dilution. For example, Fig. 4a (Bozorth, pp. 308–309) shows the effect of alloying Ni with Cu (which together form a continuous solid solution), showing the monotonic decrease in M_s with increasing Cu content. Other effects may occur, such as bandstructure effects or the formation of compounds, which will alter the trends with alloying (e.g., formation of Fe_3Al , as shown schematically in Fig. 4b).

Alloying with rare-earth metals is often used in cases where a high intrinsic anisotropy is desired, such as in permanent magnets. The lanthanide rare-earth metals are all highly magnetic because of unpaired electrons in the 4f-shell (inner) orbitals. The T_c of these materials is below room temperature because the exchange interaction between inner orbitals of adjacent atoms is small, but the intrinsic anisotropy is generally large because the spin-orbit interaction is largest in atoms with high atomic number (and therefore highly relativistic orbitals). Adding a small amount of a rare earth can dramatically increase the magnetocrystalline anisotropy of an Fe-, Co-, or Ni-based compound, often with only a modest decrease in T_c and M_s . The modern “rare earth” permanent

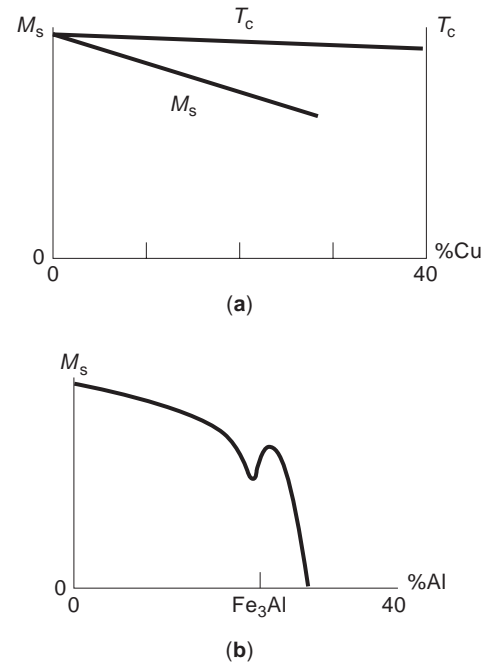


Figure 4. (a) Saturation magnetization and T_c for Fe–Cu alloys, normalized to the values for pure Fe (the monotonic decrease is typical of systems that form a continuous solid solution); (b) saturation magnetization of Fe–Al compositions, normalized to the value for pure Fe. The anomalous behavior near the composition Fe_3Al (25% Al) is due to the formation of the Fe_3Al phase.

magnetic materials use this effect, as in SmCo_5 and $\text{Nd}_2\text{Fe}_{14}\text{B}$.

3.5. Domains and M–H Loops

While positive exchange coupling tends to align all of the spins in the same direction, real materials generally exhibit this uniformly oriented state only if they are very small (<100 nm). Larger samples “demagnetize” by breaking up into magnetic domains. In each domain the local magnetic moments are uniformly aligned, usually along an easy axis. The directions of magnetization of the various domains can balance such that the overall magnetization is zero and the magnetostatic energy is small. When an external field is applied along an easy axis, domains aligned with the field tend to grow, while those antialigned tend to shrink. At high enough field the sample will be forced into single-domain state, and the saturation magnetization will be observed. The formation of domains implies the presence of domain walls—boundaries between adjacent domains—that have increased exchange and anisotropy energies due to misalignment of neighboring spins. The density and orientation of domains in a sample is determined partly by energy balance between the domain wall and magnetostatic terms, but is also strongly affected by nonequilibrium considerations such as domain wall nucleation and pinning. In general, the growth and shrinking of domains (i.e., the motion of domain walls) dissipates energy, so the M – H curve is hysteretic, as shown schematically in Fig. 5.

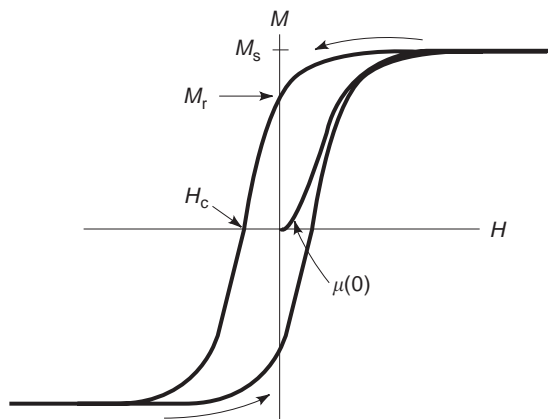


Figure 5. Schematic M - H curve, showing saturation magnetization M_s , remanent magnetization M_r , coercive force H_c , and initial permeability $\mu(0)$ (defined for an initially demagnetized sample, i.e., with $H=0$ and $M=0$).

This hysteretic, sigmoidally shaped M - H curve is very typical of ferromagnetic materials. Four important parameters are immediately evident from examination of the M - H curve:

1. The limiting magnetization is just M_s , the single most important measure of a ferromagnetic material.
2. The slope of the M - H curve at $M=0$ is the small-signal permeability $\mu(0)$, which measures the responsiveness of the magnetic material to an external field when it is close to its demagnetized state. This parameter is particularly important for soft magnetic materials, which use the magnetic material to obtain a flux multiplication by the factor $\mu(0)$. This parameter is determined partly by the magnetic anisotropy that is characteristic of the material but is also affected by factors that impede domain-wall motion, such as physical grain structure, microscopic inclusions, dislocations, or magnitude of the magnetocrystalline anisotropy.
3. The magnetization observed at zero field (after the sample has been fully magnetized) is called the *remanence*, M_r . This is an important parameter for permanent magnets, as it measures the magnitude of M available when the material is isolated. Note that the “squareness ratio,” M_r/M_s , is dominated by extrinsic aspects of the material, such as grain structure and defect, along with underlying anisotropies including the shape of the specimen.
4. The field required to reduce the external magnetization to zero (again, defined only after the sample has first been fully magnetized) is called the “intrinsic coercivity” or coercive field H_c . At this field, the sample is in a multidomain state and the magnetizations from all of the various domains exactly cancel out. The coercive field is an important property for permanent magnets, as it measures the ability of a material to withstand the action of an external magnetic field, whether applied or self-generated. It

is also determined mainly by extrinsic aspects of the material such as grain structure.

The interpretation of M - H loops can often involve subtle aspects of the loop, including directional properties, the approach to saturation, possible nonsigmoidal curving, discrete jumps (known as “Barkhausen jumps”), and so on. These may reflect coherent rotation of spins in a domain when the external field is not aligned with an easy axis or may be due to subtleties of domain wall motion. Development of superior magnetic materials often involves intensive research into these issues, but usually the designers of devices need only focus on a few properties.

3.6. Negative Exchange Interaction

The exchange interaction, as mentioned previously, need not be positive, inducing alignment of adjacent spins. When it is negative, adjacent spins will tend to align antiparallel. This can lead to a variety of behaviors depending on the structure of the material.

3.7. Antiferromagnetism

The simplest configuration that can be obtained with a negative exchange energy is antiferromagnetism, in which the spins on adjacent sites in a unit cell cancel to give no net magnetic moment. A simple example is NiO, which forms in the rock salt (NaCl) structure (see Fig. 6). The ordering temperature for antiferromagnetic materials is called the “Néel temperature”, T_N , after the discoverer of antiferromagnetism, and is analogous to the Curie temperature of a ferromagnet. Above $T_N=250^\circ\text{C}$, NiO is of course, paramagnetic. In the antiferromagnetic state the susceptibility is not negative, as in the case of a diamagnet (which has no permanent dipoles) but is positive, small, and depends on the direction of the external field due to intrinsic magnetocrystalline anisotropy. The details of spin configurations and other properties of antiferromagnets

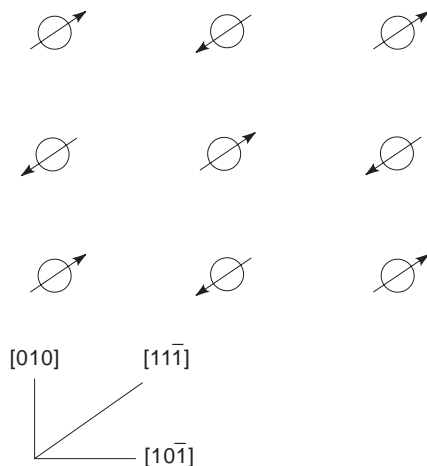


Figure 6. Antiferromagnetic structure of NiO, showing Ni atoms in the $(\bar{1}01)$ plane. The spins are aligned along $[11\bar{1}]$ directions as shown. The magnetic unit cell is twice the length of the crystallographic unit cell.

can be very complicated. Antiferromagnetism is difficult to detect by conventional magnetic measurements. Neutron scattering measurements are typically required to confirm the existence of antiferromagnetism.

Antiferromagnetic materials have been known and understood since the work of Néel beginning in 1932, but there are presently no important applications of bulk antiferromagnetic materials. Thin films ($\sim 1\text{--}100$ nm thick) of antiferromagnetic materials now play an important role in state-of-the-art magnetic recording, specifically in magnetoresistive read heads. The antiferromagnetic thin films are used to magnetically bias the magnetoresistive sensor using a phenomenon called exchange anisotropy: the surface interaction between a ferromagnetic and antiferromagnetic material in intimate contact (see Fig. 7.). Since this is an interfacial phenomenon, its magnitude is only significant when the surface/volume ratio is high, as in a very thin film.

3.8. Ferrimagnetism

In a compound with two magnetic sublattices and antiferromagnetic coupling, the magnetic moments of each sublattice will generally not cancel exactly. Then the material will exhibit an overall magnetization that in many regards will appear exactly like that of a ferromagnet, with a hysteretic $M\text{--}H$ loop, a coercivity, and a remanence. Such materials are called *ferrimagnets*, because the prototypical examples are ferrites. Some properties, such as the temperature dependence of the magnetization, can be radically different from those of ferromagnets. For example, the different temperature dependencies of the magnetization on two sublattices can sometimes lead to exact cancellation of the net magnetization at a particular temperature, called the *compensation temperature* T_{comp} (often denoted T_c , which leads to confusion with the Curie temperature). At that temperature the material behaves as if it were an antiferromagnet.

While ferrimagnets behave in many ways like ferromagnets, the highest saturation flux density in ferrimagnets is typically only about 0.6 T, and they cost significantly more than iron or silicon iron. Their crucial advantage is that they are usually good insulators and therefore are useful at high frequencies due to low eddy-current losses. Three classes of ferromagnetic materials are predominant in applications:

- Garnets have a generic formula of $R_3\text{Fe}_5\text{O}_{12}$, where R represents a lanthanoid (Sc, Y, or lanthanide rare earth). These compounds have a T_c around 275°C and a rather low saturation flux density at room temperature, $B_s = 0.18$ T. They have proven useful for bubble memories because high-quality single-crystal garnets can be prepared, and they continue to be used for UHF applications because they have particularly low losses in that frequency regime.
- Spinel ferrites are an especially large class of materials with a wide range of properties. The generic formula unit is AB_2O_4 , where A is a divalent ion and B is a trivalent ion, usually Fe^{3+} . Most of the useful spinel ferrites are magnetically soft (that is, they have a low anisotropy energy and a high permeability). The prototypical spinel ferrite is Fe_3O_4 , but Zn-substituted MnFe_2O_4 and NiFe_2O_4 are the soft ferrites used in most applications. Another extremely important ferrite is commonly used as a magnetic recording medium—namely, $\gamma\text{-Fe}_2\text{O}_3$, which is a modified spinel in which one in nine Fe sites is systematically vacant.
- Hexagonal ferrites are a much smaller class of materials, but this class includes the important ceramic permanent magnet materials. A typical formula unit for a hard hexagonal ferrite is $\text{BaFe}_9\text{O}_{12}$. These materials have a platelet-type growth habit with a very high uniaxial anisotropy and an easy axis normal to the platelet. This makes it difficult for the magnetization of a platelet to change, which accounts for the hard magnetic properties. The fact that these materials are insulating is often not an important issue since they are used to create a dc magnetic field.

When a magnetic dipole is aligned (e.g., by intrinsic anisotropy) along an axis and a radiofrequency (RF) field is applied perpendicular to that axis, the dipole does not respond simply by oscillating in the direction of the RF field, but it precesses around its axis in accordance with classical mechanics. The precession frequency is commonly expressed as $\omega = \gamma H_{\text{an}}$, where γ is the gyromagnetic constant [$\gamma = 35$ kHz/(A/m) for most materials] and H_{an} is the anisotropy field. If the RF field is at exactly this frequency, the dipole can readily absorb energy from the field (and convert it into heat via coupling to the lattice). This

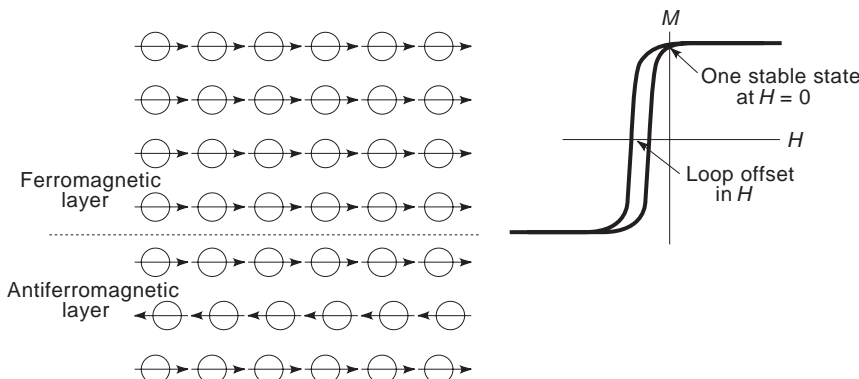


Figure 7. Schematic illustration of exchange anisotropy arising from interface coupling between an antiferromagnetic and ferromagnetic material. The schematic $M\text{--}H$ loop indicates that the loop is offset in H and that with no external field there is only one stable state (namely, the saturated state). That is, at $H = 0$ there can be no domain structure.

phenomenon is known as *ferromagnetic resonance* (FMR), although it is most important in insulating ferrimagnets where eddy currents do not already dominate the losses. Above the FMR frequency the magnetic material has a nonmagnetic response.

At very high frequencies the response of ferrimagnets is not dominated by domain-wall motion, which is sluggish, but by coherent rotation of the spins in the sample. Then the permeability is given simply by $\mu_c = B_s/H_{an}$, so $\omega_{FMR} \mu_c = \gamma B_s$. This equation, known as “Snoek’s law,” says that for a given material, a higher FMR frequency can only be obtained at the cost of a correspondingly smaller permeability. It is a basic limitation to the use of ferromagnetic materials at frequencies above about 10 MHz. Other issues, such as domain-wall resonances, may reduce the maximum frequency even further.

3.9. Metamagnetism

If a large enough magnetic field is applied to an antiferromagnet along an easy axis, the spins that are anti-aligned with the field will suddenly flip their orientation to achieve a lower energy state; that is, for a sufficiently high magnetic field, \mathbf{H} , the magnetostatic energy $\mathbf{m} \cdot \mathbf{H}$ (where \mathbf{m} is the dipole moment of an individual atom) will inevitably outweigh the exchange energy. In some antiferromagnetic materials this flipping can be observed with achievable magnetic fields; it is then called metamagnetism. Note that in principle all antiferromagnets will exhibit this behavior at a high enough field—the distinction is only in whether the required field can be produced in the laboratory.

Antiferromagnets with a relatively low anisotropy energy can exhibit an intermediate state between the antiferromagnetic and metamagnetic states as the field is increased. In this case, application of the field along the easy axis will cause the spins to reorient perpendicular to the magnetic field, and still in an approximately antiferromagnetic configuration, as shown schematically in Fig. 8. This transition is called “spin flopping.”

Neither metamagnetism nor the spin-flop transition are of practical significance in bulk applications of magnetism. However, the metamagnetic transition is an

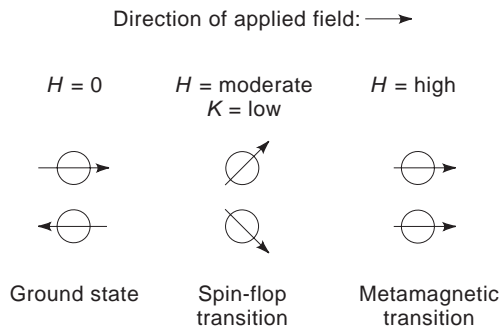


Figure 8. The spin-flop transition and metamagnetic transition in antiferromagnetic materials. The spin-flop transition occurs only in materials with relatively low magnetic anisotropy energy K , binding the spins to the easy axis (in the case, the horizontal axis).

essential feature of the phenomenon of giant magnetoresistance (GMR), which is observed in metallic thin-film ferromagnet/paramagnet multilayers (vide infra).

3.10. Spin Glass State

When a magnetic material has structural disorder, it is sometimes not possible for the exchange interaction among various neighbors to be satisfied, and no long-range orientational order (either ferromagnetic or antiferromagnetic) can be achieved. At low enough temperature such a “frustrated” material will achieve a quasiordered configuration in which the spins are static but aligned in random directions. This is the “spin glass” state. In a given sample, the magnetic properties are found to be history dependent: For example, the saturation magnetization depends on whether the sample was cooled in a magnetic field or in zero field. So-called spin glass materials should not be confused with the metallic glasses discussed later. The nature of the spin glass state has been a productive area of study for physicists for many years, but the phenomenon has no current engineering significance [6].

A related concept is that of “geometric frustration,” which occurs in materials that have triangular site coordination and that therefore are frustrated even in a perfectly ordered material. These materials are presently being explored intensively by physicists, but also have no current engineering significance [7].

3.11. Double-Exchange Materials

Along with the exchange mechanisms listed previously, there is a fourth mechanism, double exchange, that is relevant only to a small class of materials. The prototype material is $(\text{La,Ca})\text{MnO}_3$, a perovskite oxide, in which the Ca substituted for La acts as an electron donor. Electrons hopping from one Mn atom to another do not change their spin orientation during the hop, so the Mn atoms orient ferromagnetically. The most interesting property of these materials is observed in the paramagnetic state—in zero field the Mn spins are randomly oriented, inhabiting electron hopping and yielding a high resistivity. When the Mn spins are partially aligned by applying a large magnetic field, the hopping probability is enhanced, and the resistivity decreases dramatically. At an optimum temperature (near T_c), a resistivity decrease by a factor of 10^5 to 10^6 has been observed at a field of 4 MA/m, a result that has led the effect to be known as colossal magnetoresistance (CMR). The effect is colossal at low temperatures and for only a small temperature range, and it requires very large fields to be applied, so it has not proven useful for engineering applications at present.

3.12. Superparamagnetism

In small single-domain particles of ferromagnetic material, the magnetization tends to align along the easy axis, and the energy barrier required to move the magnetization is on the order of KV , where K is the anisotropy energy density and V is the volume of the particle. For the simple case of uniaxial anisotropy, $\Delta E = KV$. If the thermal energy $k_B T$ is greater than this energy, then fluctuations in the

orientation of the magnetization will lead to zero spontaneous magnetization and a response to an applied field that is analogous to the local moments of a normal paramagnetic material. The effect is seen, for example, in Co particles smaller than about 7.5 nm. The moment of a Co sphere of diameter 7.5 nm is roughly 20,000 times larger than the moment of single Co atom, so the effect is called *superparamagnetism*. While superparamagnetism is not technologically useful itself, it does represent an important limitation to the particle size of future magnetic recording media, and is therefore being intensively investigated.

3.13. Thin Films

Thin films of magnetic materials behave exactly like bulk magnetic materials in most respects, albeit in profoundly different regimes for some parameters. For example, thin films have a demagnetization factor normal to the film and essentially zero demagnetization factor in the plane of the film. Thus it is generally very hard to magnetize a thin film normal to the plane but fairly easy to move the magnetization in the plane. A simple consideration such as this can have wide-ranging implications, from an increased FMR frequency to gross effects on the structure of domain walls (i.e., the transition from conventional Bloch walls to Néel walls as the film thickness is decreased below about 100 nm). Thin films also tend to have stresses that are extremely high compared to stresses in bulk materials—500 MPa values are not uncommon. These stresses couple to the magnetostriction of the material to create a stress anisotropy that can strongly influence the magnetic behavior.

Thin films are used in a wide variety of applications, the most important of which are as media in hard disks and magneto-optic disks, miniature electromagnets in hard-disk write heads, and magnetoresistive sensors in hard-disk read heads.

Thin films inherently possess a unique direction, the growth direction. This is usually the normal, although it can be oblique if the incident atomic flux used to grow the film arrives from an oblique angle. For some materials the growth direction directly leads to a large intrinsic uniaxial anisotropy. For example, in amorphous Tb–Fe one might expect that there would be no anisotropy at all. Instead, films grown with the incident Tb and Fe atoms arriving essentially perpendicular to the substrate exhibit a large intrinsic uniaxial anisotropy oriented along the normal, and with a sense that leads to a perpendicular easy axis. The anisotropy is sufficient to overcome demagnetization, so domains form in which the magnetization is oriented perpendicular to the film. Such materials are used in magneto-optic recording (vide infra) [8].

Some behaviors seen in thin films are either absent or not commonly observed in bulk magnetic materials. An important example is the phenomenon of so-called giant magnetoresistance in thin-film multilayers. These multilayers are typically formed by sequentially depositing metallic ferromagnetic and paramagnetic layers, each ~1–3 nm thick, using sputtering or evaporation in a high-vacuum chamber. Between two and a hundred

layers might be built up in this way. The ferromagnetic layers couple with each other by the RKKY interaction through the paramagnetic metal, so, depending on the thickness of the paramagnetic layer, the interlayer coupling may be antiferromagnetic or ferromagnetic. For example, a film consisting of 100 repeats of 1.0-nm-thick Co adjacent to 0.6-nm-thick Cu exhibits an antiferromagnetic state at zero field; even though each Co layer is individually ferromagnetic, alternate layers have oppositely directed magnetizations. When a moderate field H is applied, the magnetizations of all of the layers align with the external field, producing a metamagnetic transition.

Baibich et al. [9] discovered the most interesting aspect of the metamagnetic transition in metallic multilayers: the effect it has on the resistivity of the sample. The aligned state has a greatly reduced resistivity compared to the antialigned state. The magnetoresistance ratio $[R(H=0) - R(H=H_s)]/R(H=H_s)$ can be as high as ~100% depending on the choice of materials. This is far greater than the highest normal magnetoresistance observed in any material at room temperature; hence the name giant magnetoresistance. It is attributed to spin-dependent scattering of electrons, which is enhanced when magnetizations of adjacent layers are antialigned. This effect is crucial for the highest-performance magnetic disk read heads being currently designed (vide infra) [10].

4. MAGNETIC MATERIALS USED IN APPLICATIONS

Useful magnetic materials are often divided into three categories:

- Soft magnets, in which the magnetization is readily changed with an external field, thereby providing a flux-multiplying effect
- Hard magnets (permanent magnets), which have high coercive fields and therefore resist demagnetization by stray fields including their own
- Magnet recording media, which combine aspects of softness and hardness

4.1. Soft Magnetic Materials

Soft magnetic materials are used in applications such as transformers and inductors. An obvious example would be the iron, known as “electrical steel,” used in transformers for inexpensive power supplies. At frequencies above about 10 kHz, eddy currents limit the use of metallic magnetic materials, so high-resistivity ferrites such as (Mn, Zn)Fe₂O₄ are used.

4.1.1. Permeability. An important property of soft magnetic materials is their relative permeability, nominally defined by $\mu_r = B/\mu_0 H$. Actually, since the $B(H)$ curve is neither linear nor single-valued, a large number of useful permeability parameters can be defined, such as the initial permeability, the maximum permeability, and the anhysteretic permeability. For simplicity, we will consider only the initial small-signal permeability, defined as $\mu(0) \equiv \partial B / \partial H|_{H=0}$. Values from $\mu(0) = 10$ (high-frequency

ferrites) to $\mu(0) = 10,000$ (low-frequency inductors) are typically encountered in applications.

4.1.2. Power Devices. Probably the main use of magnetic materials at present, on a weight basis, is in power transformers. These can range from huge transformers used in substations, to miniature transformers used to convert line voltage to a level suitable for small consumer devices, to small ferrite transformers used in switching power supplies.

Low-frequency power applications almost inevitably employ low Si percentage Fe–Si alloys known as “silicon iron” or “electrical steel.” This is because Fe is by far the cheapest magnetic material available. The coercive field of pure Fe is typically about 80 A/m. The addition of a small amount of Si to Fe lowers the anisotropy, resulting in lower losses and a coercive force of about 40 A/m. It also substantially increases the resistivity, which decreases eddy currents. Eddy currents in transformers are usually further reduced by lamination (i.e., using a stack of Fe–Si plates, each electrically insulated by a coating layer, rather than a single thick piece). The laminations are arranged so that eddy currents are interrupted by the presence of the insulator and forced to circulate only within each lamination (i.e., so that any AC magnetic flux is perpendicular to the normal). Properly designed, the thickness of each plate should be smaller than a skin depth δ , given by $\delta = (2\rho/\omega\mu)^{1/2}$, where ρ is resistivity, ω is the angular frequency of the AC magnetic field, and μ is the permeability. Note that the permeability can also be frequency-dependent.

Improved varieties of silicon iron are prepared using specific sequences of forging (rolling) and annealing to obtain a grain-oriented microstructure. In such materials the crystallographic orientation of individual grains is forced to be aligned over the entire piece. The advantage is that materials with lower losses are obtained, although the material is also somewhat more expensive. At present, most power transformers utilize grain-oriented silicon iron.

The highest-performance materials for low-frequency transformer applications are the metallic glasses, amorphous alloys of Fe and Co with one or more metalloid additions (usually B, C, Si, and P). These materials can have losses that are 10 times smaller than silicon iron and coercive fields below 0.5 A/m. But the saturation flux density is generally ~ 1.5 T, and the materials are substantially more expensive than silicon iron. These negative aspects of metallic glasses have precluded their widespread use.

Power supplies with low weight and volume are highly desirable for some electronic applications, and this can be achieved with the design called “switching” power supplies. An additional benefit is circuit versatility and flexibility, while the main tradeoffs are increased cost and design complexity. A switching power supply uses power electronics [typically metal oxide semiconductor field-effect transistors (MOSFETs)] to chop and rectify power at high frequency, a power transformer or inductor to change the voltage, and control electronics to synchronize and control the system. The frequencies used range from about 50 kHz to a present upper limit of 1 MHz.

At these frequencies, metallic ferromagnets cannot be used as the desirable lamination thickness would be prohibitively small. Fortunately at such high frequencies, the energy that must be stored in the transformer or inductor is correspondingly small for a given power capacity ($E \sim P/\omega$, where E is the maximum stored energy, P is the maximum power, and ω is the angular frequency). Therefore, the cost of the magnetic part need not dominate, especially considering the cost of the electronics involved, so the use of relatively expensive but very high resistivity ferrites is feasible. In most cases an (Mn,Zn)Fe₂O₄ spinel ferrite is chosen as a compromise between saturation flux density, losses, resistivity, and cost. At the highest frequencies, (Ni,Zn)Fe₂O₄ may prove useful, as it has a higher resistivity and therefore is less susceptible to eddy-current losses.

Motors and generators inevitably employ iron or silicon iron to act as a flux concentrator. The armature and stator are commonly constructed of grain-oriented silicon iron, although small motors often employ nonoriented silicon iron or metallic glass materials. As in transformers, the ferromagnetic parts must be laminated to reduce eddy-current losses.

4.1.3. Inductors. Small-signal transformers and inductors are used in a variety of circuit applications, as in impedance-matching and isolation transformers, antennas, and chokes. Signal-level devices do not have to carry substantial power, so they can be small and the cost of materials can easily be outweighed by performance considerations. Thus a wider variety of magnetic materials is used in these devices.

At audiofrequencies and below, transformers and inductors were once commonly used for signal applications. For example, long-distance analog telephone circuits were balanced by the periodic addition of loading coils—inductors designed to match the large distributed capacitance of phonelines. A common choice for the magnetic core in those coils was Permalloy (Ni₈₀Fe₂₀) or a related alloy, and the cores were formed by rolling a long tape into a toroidal core. However, in modern telecommunication systems the analog signals are quickly converted to digital signals at the central exchange and then transmitted by the fiberoptic, satellite, or microwave relay. The need for loading coils is minimal. Similarly, the function of audiofrequency impedance-matching transformers and other inductive electronic components has largely been displaced by more elaborate but much cheaper integrated circuit designs. Low-frequency magnetics are used in modem isolation transformers to provide DC electrical isolation with audio coupling; these are made with either laminated metallic or solid ferrite cores.

At RF frequencies (50 kHz–50 MHz) magnetic cores are widely used; for example, in antennas, RF transformers, chokes, and resonant circuits. The usual choices for magnetic cores are the spinels (Mn,Zn)Fe₂O₄ (up to about 1 MHz) and (Ni,Zn)Fe₂O₄ (up to about 10–50 MHz). The manganese zinc ferrites are cheaper but have a resistivity typically less than 1000 $\Omega \cdot \text{cm}$. Eddy current losses limit their usefulness at high frequencies. The initial permeability is roughly 1000–3000. Nickel zinc ferrites can have

resistivities as high as $10^5 \Omega \cdot \text{cm}$ and initial permeabilities on the order of 1000. Their upper frequency limit is dictated by the need to avoid FMR losses. Material designed for operation above about 10 MHz typically is prepared with moderate porosity to inhibit domain-wall motion and losses associated with domain-wall resonance. The permeability mechanism then is limited to that of coherent rotation of the spins, which implies a much smaller value ($\mu_c \sim M_s/H_k \sim 10\text{--}100$).

Above about 50 MHz, magnetic materials are not commonly used in transformers and inductors, as Snoek's law demands that the permeability be uselessly small in order for the FMR frequency to be sufficiently greater than the frequency of operation. Snoek's law can be circumvented by the use of materials with a large biaxial anisotropy (e.g., the hexagonal magnetoplumbite-type ferrites) or by using thin films with a high saturation magnetization. At present, however, those approaches are not commercially important.

4.1.4. Write Heads. An important application of soft magnetic materials is in the recording heads used in tape and disk systems. Write heads essentially consist of an electromagnet with a toroidal magnetic core and a very small airgap (~ 100 nm to 300 nm). The flux that extends from the airgap, called the "fringing field," is used to magnetize the magnetic medium passing nearby (see Fig. 9). In tape and floppy-disk systems the magnetic medium is in actual contact with the head, while in hard-disk systems the head flies aerodynamically over the spinning medium at a height of 25–75 nm. The maximum magnetic field available for magnetizing the medium is proportional to the saturation magnetization of the head material.

Originally the magnetic recording heads were made from laminated metal alloys, such as Permalloy or Sendust (an alloy of Fe, Si, and Al notable for being magnetically soft and physically very hard), but as recording

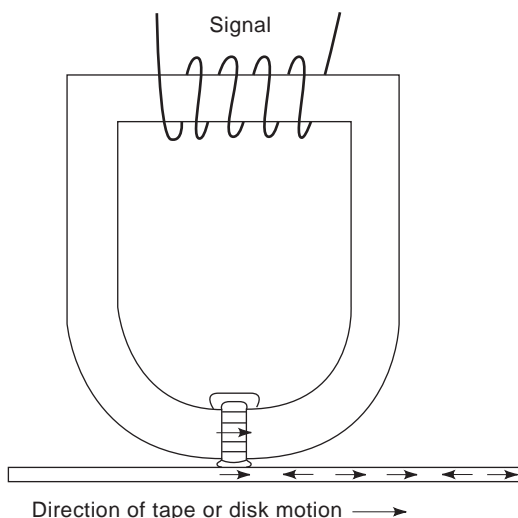


Figure 9. Schematic of a magnetic recording head. Recording is accomplished using the magnetic fringing field (i.e., the field that leaks from the gap).

densities and frequencies increased, an inevitable move was made to ferrite materials. Ferrite heads are made from cast pieces that are carefully polished to form a precise airgap and then are assembled with the driving coil. As recording densities have increased, media with higher coercivities are necessary, so head materials with high saturation magnetization are needed. Unfortunately this is where the ferrites are most deficient, with maximum $B_s \sim 0.6$ T. One approach to obtain improved performance is to add a thin film of relatively high B_s material (such as Permalloy, $B_s = 0.9\text{--}1.1$ T) on the inside edge of the gap of each piece. The thin film acts as a flux concentrator and increases the fringing field significantly. This approach is called the metal-in-gap (MIG) design.

The highest-performance recording heads are constructed using thin films and photolithography. They have the advantage of great precision in layout, leading to extremely narrow pole tips, precise gap widths, and precise placement of the driving coils. Permalloy and related alloys are most commonly used at present, but soft amorphous alloys such as $\text{Co}_{0.85}\text{Nb}_{0.08}\text{Zr}_{0.7}$ offer significant improvements with $B_s \sim 50\%$ greater than Permalloy. The resistivity of the amorphous alloys is in the range $\rho \sim 100 \mu\Omega \cdot \text{cm}$, about fivefold higher than Permalloy, which reduces eddy-current losses, allowing recording at higher frequencies. Further advantage can be obtained by using the recently developed nanocrystalline (grain size $\sim 1\text{--}5$ nm) alloys such as $\text{Fe}_{0.92}\text{Ta}_{0.05}\text{N}_{0.03}$, which have extremely high $B_s \sim 2.0$ T and also have resistivities in the range of $100\text{--}150 \mu\Omega \cdot \text{cm}$. These materials are being vigorously developed for future generations of high-performance recording, especially hard-disk drives.

4.1.5. Read Heads. The same magnetic structure that is used for magnetic recording can also be used for reading the recorded signal. The passage of recorded domains across the gap of the recording head will induce a small voltage on the driving coil, which is amplified and processed. Indeed, this inductive read head is the simplest and cheapest approach to magnetic recording. However, the signal level is very low and limits the performance of hard-disk drives. The present generation of hard disk drives uses a separate magnetic structure (incorporated in a single read/write head) for reading the recorded magnetic signal. The sensor in this device is a magnetoresistive thin film made of Permalloy and biased with a DC current. External flux from the recording medium couples to the Permalloy film, rotating the magnetization with respect to the fixed direction of the DC current. This changes the resistance of the Permalloy [the so-called conventional or anisotropic magnetoresistance effect (AMR)] and therefore the voltage developed across the device. The AMR effect is relatively small, about 5%, but is sufficient to deliver signal superior to that of an inductive head.

Superior performance can be obtained by incorporating materials that exhibit giant magnetoresistance. These can have responses that are about 10-fold higher than AMR materials. So-called spin valves employ the same physical principle as GMR (namely, spin-dependent scattering) in a more highly controlled and responsive magnetic structure. The higher signal output of spin valve read heads, in

conjunction with careful redesign of the entire magnetic recording system (including media, head structure, electronics, signal processing, etc.), can lead to substantial increase in recording density.

4.1.6. Shields. Soft magnetic materials are also used to make magnetic shields, typically used to protect electronic components from magnetic interference or to contain the external field around a component that generates magnetic flux. An example of the former are shields for cathode-ray tubes, such as computer monitors, while an example of the latter are shields for speakers, such as “multimedia” speakers intended for placement close to a (unshielded) monitor. These shields are usually formed from Permalloy and related alloys. Often “Mumetal” is specified for these applications—this originally designated a particular Fe–Ni–Cu alloy but it is now used generically to refer to many high-permeability alloys. Note that RF shields (unlike DC magnetic shields) rely on eddy current screening and use high-conductivity paramagnetic metals such as Cu.

A related application is the use of materials that absorb RF energy. These are typically lossy ferrites and are used in the form of beads threaded on wires, where it is desired to suppress high-frequency signals. Manganese–zinc ferrites are generally used for this purpose, although nickel–zinc is used to obtain the highest cutoff frequencies. Lossy ferrites can also be used as an antiradar coating on military aircraft.

4.2. Hard (Permanent) Magnets

Permanent magnets are used in a wide variety of applications where a static magnetic field is desired. The dominant uses are in speakers and DC motors and as holding magnets. The field available from a given permanent magnet depends on the physical configuration but is limited to B_s , the saturation flux density in the optimum case. Specifically, for a toroidal part with a small airgap (see Fig. 10), the flux density in the gap will be B_s . For Fe this is $B_s = 2.15$ T, while for $\text{Fe}_{0.6}\text{Co}_{0.4}$ it is $B_s = 2.43$ T [11, p. 190], the highest value for any known bulk material. In

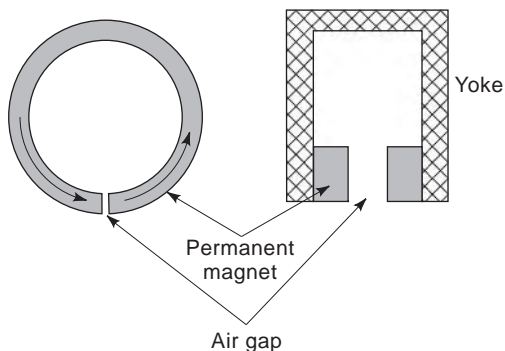


Figure 10. Airgap in magnetic circuits. The gray regions represent permanent magnet material, with the direction of magnetization shown. The hatched region represents soft magnetic material, which is used to complete the magnetic circuit.

less optimum geometries, the available flux density can be greatly reduced, as determined by magnetostatics. For arbitrary-shaped parts, the usual approach is to employ finite-element numerical calculations to infer the flux distribution.

In general, where the design figure of merit is the flux available per unit volume of magnetic material, the corresponding figure of merit for the magnetic material is the energy product $(BH)_{\max}$ [i.e., the largest value measured at any point in the second quadrant (positive B , negative H) of the B – H curve]. This is only a crude way to evaluate the usefulness of a material; nevertheless it is indicative and is commonly quoted by permanent magnet manufacturers. Four main types of permanent magnet materials are commonly used:

- Alnico, a class of Fe–Al–Ni–Co–Cu alloys. The properties of this material are entirely dependent on complex metallurgical processing and microstructural control. Commonly used Alnico materials have $(BH)_{\max} = 50 \times 10^3 \text{ J/m}^3$.
- Barium ferrite, typically $\text{BaO} \cdot (\text{Fe}_2\text{O}_3)_6$, is the standard “ceramic” magnetic material. The typical value $(BH)_{\max} = 25 \times 10^3 \text{ J/m}^3$ is smaller than that of Alnico, but the material is both lower density and cheaper to produce than Alnico and has almost entirely replaced Alnico in highly cost-sensitive applications. The high value of $(BH)_{\max}$ in this and the following materials is due to the very high intrinsic anisotropy.
- Sm–Co is the standard high-performance “rare earth” permanent magnet, with $(BH)_{\max} = 160 \times 10^3 \text{ J/m}^3$. The major disadvantage of this material is its cost.
- Nd–Fe–B, a more recent material, has an even higher value for $(BH)_{\max} = 320 \times 10^3 \text{ J/m}^3$ than Sm–Co, and its value is less expensive. The major disadvantage of this material in some applications is that the T_c is somewhat low, $T_c \sim 150^\circ\text{C}$.

Loudspeakers have long been a dominant application for permanent magnetic materials. The permanent magnet is used to establish a magnetic field in an annular region in which the voice coil is mounted. When a current is driven through the voice coil, an axial force is produced, in accordance with the Lorentz relation, $\mathbf{F} = e\mathbf{v} \times \mathbf{B}$, where \mathbf{F} is the force on an electron, e is the charge on an electron, and \mathbf{v} is the velocity of the electron. Motion of the voice coil is coupled to a speaker cone to move the air efficiently and thereby produce sound waves.

The energy product of a magnetic material is a good figure of merit for speaker applications, since for a given design, a higher-energy product will result in a higher flux density in the annular gap. Most loudspeakers are low-priced components, so the cost of the magnetic material is the other key factor. For this reason, barium ferrite is the dominant material used. In some applications, such as high-performance earphones, the amount of magnetic material is small so materials cost is less critical. In the past, Sm–Co magnets have been used for these applications, though Nd–Fe–B magnets are now clearly the best overall choice.

The materials used for permanent magnets inevitably cost more than silicon iron, so large motors and generators always use soft magnetic materials wound with coils to create the required magnetic field. In small motors, the economics are dominated by the cost of fabrication; the small coils and fine tolerances needed for electromagnet motors outweigh the added cost of permanent magnetic materials. A vast number of small DC motors are produced for a very wide range of applications, from clock motors to the dozens of motors in modern automobiles used to drive windows, locks, seats, windshield wipers, and so on.

An economically important use of permanent magnets is in the low-tech application of holding magnets. These range from decorative magnets for holding notes to a refrigerator door to functional magnets for holding and sealing the refrigerator door shut to strong magnetic chucks for holding ferrous materials for machine-forming operations. In almost all cases cost is paramount, and barium ferrite is used. For some applications the ferrite powder is mixed with a polymer precursor, formed into a tape, and polymerized to form a flexible magnet, albeit with reduced net flux density and therefore reduced holding power.

4.3. Magnetic Recording Media—Intermediate between Soft and Hard

Magnetic recording is a huge business, dominated by the hard disks and floppy disks pervasive in personal computers and by tape recording—audio, video, instrumentation, digital data storage, and so on. The media used in recording are magnetic materials that must have a relatively high coercive force so that they do not spontaneously demagnetize and lose information. But the coercive force cannot be much greater than about 100 kA/m because the leakage flux from the recording head is limited and must nevertheless be sufficient to saturate the medium.

The standard material used in tape and floppy-disk media is gamma iron oxide, $\gamma\text{-Fe}_2\text{O}_3$. It is moderately expensive to prepare (compared to conventional ferrites) because extremely reproducible and controllable properties are required. Acicular (needle-shaped) particles ~ 50 nm in diameter are prepared in order to obtain good recording characteristics. The coercivity of most tapes is about 20–30 kA/m. More recent high-performance formulations use cobalt-modified $\gamma\text{-Fe}_2\text{O}_3$, which has a thin cobalt-rich region on the surface of the particles. This material has an increased coercivity of about 50 kA/m and is routinely used for videotape. In the past, CrO_2 was used as a high-performance medium because it has a higher M_s than $\gamma\text{-Fe}_2\text{O}_3$ and can be prepared with a coercivity as high as 80 kA/m. However, it has a low T_c (only 130°C) and is relatively expensive, so it has been displaced by cobalt-modified $\gamma\text{-Fe}_2\text{O}_3$.

Hard disks used in digital recording are aluminum platters coated with paramagnetic Ni-P or Cr and then a recording medium such as Co-Cr. An extremely thin layer of C is usually then deposited along with an even smaller amount of lubricating fluid, in order to avoid catastrophic head contact with the medium (“head crashes”). The coercivity of hard-disk media is in the range

60–100 kA/m, and the saturation magnetization is about 1000 kA/m.

For many years it was expected that magnetic bubble memory might find a role for data storage in computers. However, bubble memory is slow and expensive compared to hard disks and semiconductor random-access memory (RAM). Its only advantages are that it is mechanically more robust than a hard-disk system, and it is more radiation resistant than semiconductor RAM. Therefore, the only present use for bubble memory is in certain military applications.

Bubble memories store data in cylindrical domains, perpendicular to the surface, that are generated in liquid-phase epitaxy (LPE) grown garnet films. The films are designed to have a large uniaxial anisotropy perpendicular to the film plane and are chosen to meet a number of other criteria. The bubbles are moved around using a rotating external magnetic field created by a miniature electromagnet, and they are detected using a magnetoresistance bridge.

Finally, there is magneto-optic recording. In this scheme data are stored on a plastic disk coated with an amorphous metallic thin film such as $\text{Tb}_{0.2}\text{Fe}_{0.8}$ or similar compositions doped with Dy and Co. They have a large uniaxial anisotropy, with an easy axis perpendicular to the plane of the film, so as with the garnet films designed for magnetic bubble applications, cylindrical domains are stable. Data are written by focusing a laser on the desired spot, which heats the films above its T_c , $\sim 100\text{--}150^\circ\text{C}$. If the film is exposed to a moderate magnetic field while it cools, the heated region will magnetize in the direction of the applied field. Thus alternating regions of, say, north-up and south-up can be written. The data are read with the same laser at lower power to avoid heating, using a polarizer to detect Faraday rotation (i.e., rotation of the polarization of light when it interacts with a magnetic material). This effect is known as *Kerr rotation* when it occurs on reflection from a metallic magnetic surface. The Kerr rotation in a magnetic material is in the opposite sense for regions magnetized north-up versus south-up. The maximum Kerr rotation in Tb-Fe films is rather small, $\sim 0.2^\circ$, which gives a low signal/noise ratio and correspondingly low data rate.

The data density in magneto-optic recording is comparable to that of a conventional CD-ROM but has the great advantage of being endlessly rewriteable. Magneto-optic drives are slower for writing data and more expensive than conventional hard drives, but they confer the advantage of cheap removable media and good archiveability and have found a small but significant market niche.

4.4. Miscellaneous

Along with the three conventional classes of applications for magnetic materials, there are a wide variety of specialized applications, too numerous to list exhaustively.

4.4.1. Nonreciprocal Materials. Some of the most interesting magnetic devices are based on the nonreciprocal propagation of UHF signals in insulating magnetic

materials. The behavior is formally identical to the small optical Faraday rotation observed in some nonferromagnetic materials, but the effect in ferrites can be very large and is commonly used in microwave applications (e.g., in isolators and circulators).

The nonreciprocal phenomena are due to interaction of the incident radiation with the precessing electron spin (see Magnetic resonance). A particularly straightforward case arises when the incident microwaves are circularly polarized with a propagation vector parallel to the easy axis of the magnetic material and at a frequency equal to the natural precession frequency of the electron spins. Then, if the sense of the circular polarization is the same as that of the electron spin precession, energy is readily transferred to the spins and dissipated as loss. If the sense is opposite (corresponding to propagation in the opposite direction), then there is little interaction and the loss is minimized. It is easy to imagine an isolator based on the directionality of this phenomenon, although the practical design of this and other nonreciprocal microwave devices can be very complex. In general, a moderately large external biasing magnet is required to set the FMR frequency equal to the operating frequency (a larger field is required for a higher operating frequency).

Three classes of materials dominate the magnetic materials used for microwave applications—the figure of merit for microwave devices is usually proportional to $1/\Delta H$, where ΔH is the FMR linewidth:

1. The garnet structure ferrites exhibit the highest performance available because they have the lowest FMR linewidths. A typical value for polycrystalline ceramic yttrium iron garnet (YIG) is $\Delta H = 4000$ A/m. Single crystals with linewidths as low as 40 A/m have been reported. Single crystals are relatively expensive but are usually the best choice at low frequencies.
2. The spinel ferrites are useful in a number of cases. Nickel zinc ferrite is particularly useful at high powers because it has a higher T_c than garnets, and it is often used in the range above 10 GHz. Manganese-magnesium ferrites are used in the range of 5–10 GHz because their lower saturation magnetization allows biasing at lower field.
3. The Z-type hexagonal ferrites have a hard axis normal to the basal plane, so the need for external biasing is reduced. They require expensive processing to produce oriented, high-quality ceramics. They are most useful for mm-wave applications.

In general, the key issues in developing materials for microwave applications are related to processing and micro-structure control rather than exploring new compositions. Small grain size is important to minimize losses from domain-wall resonance, to maximize the resistivity, and to make stronger materials that resist the thermal stresses caused by high-power operation. Obtaining a high density is always important, but densification usually is accompanied by grain growth. The art of designing or

choosing a microwave magnetic material is in balancing these conflicting requirements.

4.4.2. Ferrofluids. Ferrofluids are liquid suspensions of magnetic particles coated to avoid agglomeration. Typically the liquid is a hydrocarbon or silicon, and the magnetic particles are ferrites, but a wide range of combinations is possible. The behavior of ferrofluids is unique and scientifically interesting, and ferrofluids are commercially used for such diverse applications as gas-tight seals for rotary shafts, heat transfer agents for loud-speaker voice coils, and damping systems.

BIBLIOGRAPHY

1. Plato, in *The Dialogs of Plato*, transl. B. Jowett, *Great Books of the Western World*, Vol. 7, Benton, Chicago, 1952, p. 144.
2. W. Gilbert, *De Magnete*, transl. P. F. Mottelay, Dover, Mineola, NY, 1958.
3. J. D. Jackson, *Classical Electrodynamics*, Wiley, New York, 1962.
4. R. L. Carlin, *Magnetochemistry*, Springer-Verlag, Berlin, 1986, p. 3.
5. E. H. Brandt, *Science* **243**:349–355 (1989); *Physics World* **10**(4):23–24 (1997).
6. K. Binder and A. P. Young, Spin glasses: Experimental facts, theoretical concepts, and open questions, *Rev. Mod. Phys.* **58**:801–976 (1986).
7. A. P. Ramirez, *Ann. Rev. Mater. Sci.* **24**:453–480 (1994).
8. R. B. van Dover et al., Intrinsic anisotropy of Tb–Fe films prepared by magnetron co-sputtering, *J. Appl. Phys.* **57**:3897–3899 (1985).
9. M. N. Baibich et al., *Phys. Rev. Lett.* **61**:2472–2475 (1988).
10. S. S. P. Parkin, Giant magnetoresistance in magnetic nanostructures, *Ann. Rev. Mater. Sci.* **25**:357–388 (1995).
11. R. M. Bozorth, *Ferromagnetism*, Van Nostrand, New York, 1951.

FURTHER READING

- R. M. Bozorth, *Ferromagnetism*, Van Nostrand, New York, 1951.
- F. N. Bradley, *Materials for Magnetic Functions*, Hayden, New York, 1971.
- F. Brailsford, *Physical Principles of Magnetism*, Van Nostrand, New York, 1966.
- P. Campbell, *Permanent Magnetic Materials and Their Applications*, Cambridge Univ. Press, Cambridge, UK, 1994.
- C. W. Chen, *Soft Magnetic Materials*, North Holland, Amsterdam, 1977; reprinted by Dover, New York, 1986.
- S. Chikazumi and S. H. Charap, *Physics of Magnetism*, Krieger, Malabar, FL, 1964.
- B. D. Cullity, *Introduction to Magnetic Materials*, Addison-Wesley, Reading, MA, 1972.
- D. Jiles, *Introduction to Magnetic Materials*, Chapman & Hall, London, 1991.
- M. M. Schieber, *Experimental Magnetochemistry*, Wiley, New York, 1967.
- J. Smit, H. P. J. Wijn, *Ferrites*, Wiley, New York, 1959.

MAGNETIC MICROWAVE DEVICES

HOTON HOW
Hotech, Inc.
Belmont, Massachusetts

In this article we discuss the following topics on magnetic microwave devices: ferrite junction devices, lumped-element circulators, nonreciprocal resonators, YIG film devices, MSW devices, magneto-optic devices, absorbing/antireflection layers, and nonlinear responses. The article is organized as follows: Section 1 presents a general theoretical background underlying the physics for the operation of ferrite components in microwave devices. Discussions include derivation of the Polder permeability tensor, the effective fields associated with electron spin motion, the general dispersion spectrum and plane-wave solutions for electromagnetic waves propagating in a bulk magnetic medium, magnetostatic waves (MSWs) admitted by the geometry of a yttrium iron garnet (YIG) film, and the nonlinear instabilities for spin waves occurring at high power, including their routes leading to chaos. Section 2 introduces ferrite junction devices, including circulators and isolators. Broadband operation, size reduction, power-handling issues, and other novel applications are discussed in this section. Section 3 delineates the operation of lumped-element circulators in which interport impedances are portrayed. Section 4 defines the effective field associated with a magnetic easy plane from an operation perspective. Section 5 gives an example that ferrite nonreciprocal resonator can be used as a phase shifter whose operation is independent of the derived phase shift angles. Section 6 describes YIG film devices incorporating magnetostatic waves (MSWs), including delay lines, filters, directional couplers, and resonators. Section 7 depicts nonlinear magnetic devices of frequency-selective power limiters, signal-to-noise enhancers, amplitude correctors, and ferrimagnetic echoing devices. Section 8 introduces magnetic solitons, including Bloch domain wall solitons and Microwave magnetic envelope solitons. Section 9 discusses magneto-optic Kerr and Faraday effects, and the operation of magneto-optic Bragg diffraction devices. Finally, design of microwave absorbing layers and antireflection layers is briefly mentioned in Section 10.

1. THEORETICAL BACKGROUND

This section provides a theoretical background underlying the physics that allows for the operation of a magnetic microwave device. A magnetic microwave device generally requires the use of an insulating magnetic ferrite material so that magnetization or spin motion is coupled to Maxwell equations without inducing much eddy-current loss at high frequencies. Also, in order to eliminate domain wall motion, single-domain operation is demanded at RF frequencies, and the ferrite material needs to be magnetized to saturation using an external DC magnetic field. Alternatively, effective fields arising from either the crystalline or shape anisotropy of the ferrite material may be used to fulfill the bias requirement of the magnetic device.

Thus, under small-signal approximations the electromagnetic property of the ferrite is described by a tensor permeability whose nonzero off-diagonal elements permit noble applications of nonreciprocal devices, for example. Most importantly, the permeability tensor can be varied by adjusting the bias field strength, resulting in tunability of the microwave device over frequencies.

A magnetic microwave device is normally operational in the frequency range from 0.1 to 40 GHz or higher, and its performance can be interpreted in terms of the spin/magnetization motion of the ferrite material where coupling to optical/photon modes, elastic/phonon modes, or exchange/magnon modes may be utilized. Depending on the regime of applications, a microwave magnetic device may be distinguished either as a retarded-wave device or a magnetostatic-wave device. The first class of devices includes circulators, isolators, filters, phase shifters, patch antennas, and so on, whose operation requires the magnetization vector to be coupled with the full set of Maxwell equations. The second class consists of mainly high-quality single-crystal YIG film devices where the propagation of magnetization waves involves a wavelength comparable to the film thickness. As such, the displacement currents can be omitted in Maxwell equations. This renders the so-called magnetostatic approximation, which implies that the resultant RF magnetic field can be derived from a scalar potential. Important magnetostatic devices include delay lines, filters, resonators, echo lines, and other nonlinear devices, whose operation complements their low-frequency counterparts below 2 GHz involving surface acoustic wave (SAW) devices.

In the following subsections we first derive the coupling between the magnetization field and the other electromagnetic fields, giving rise to a Polder permeability tensor for the ferrite material under small-signal approximations. Effective fields are then introduced in the equation of motion allowing for coupling of the magnetization field with the other physical fields required for transducer applications. On the basis of the frequency-wavenumber dispersion diagram, the propagation of magnetization waves can be divided into three zones into which magnetic microwave devices are conventionally defined at several regimes. Plane-wave solutions are given describing the propagation of electromagnetic waves in ferrites in the retarded zone. Magnetostatic waves are then discussed, whose dispersion diagrams are described in terms of the bias field configuration relative to the YIG film device geometry. Finally, spin-wave instability is briefly mentioned, delineating the high power threshold that a ferrite device can operate before a cascading energy transfer occurs between the input RF power and the parametric excitation of spin waves.

1.1. Polder Permeability Tensor

In a source-free medium Maxwell equations take the form

$$\begin{aligned}\nabla \times \mathbf{h} &= j\omega\epsilon\mathbf{e}, & \nabla \times \mathbf{e} &= -j\omega\mathbf{b} \\ \nabla \cdot \mathbf{b} &= 0, & \nabla \cdot \mathbf{e} &= 0\end{aligned}\quad (1)$$

where \mathbf{e} and \mathbf{h} are the RF electric and magnetic fields and \mathbf{b} is the RF magnetic induction field. In Eq. (1) ε denotes the permittivity and the time dependence of the RF quantities is assumed to be $\exp(j\omega t)$. For a linear isotropic medium, one may define a constant μ , the permeability, so that \mathbf{b} and \mathbf{h} are linearly proportional to each other:

$$\mathbf{b} = \mu \mathbf{h} \quad (2)$$

This equation holds true if the medium is diamagnetic ($\mu < \mu_0$) or paramagnetic ($\mu > \mu_0$). Here μ_0 denotes the permeability of vacuum. For a ferromagnetic or a ferrimagnetic medium the relationship between \mathbf{b} and \mathbf{h} is neither linear nor isotropic. However, under small-signal approximations the linear relationship between \mathbf{b} and \mathbf{h} may be assumed, provided the scalar permeability needs to be replaced by a tensor. Thus, Eq. (2) becomes

$$\mathbf{b} = \underline{\underline{\mu}} \mathbf{h} = \mathbf{m} + \mathbf{h} \quad (3)$$

where \mathbf{m} denotes the RF magnetization field and $\underline{\underline{\mu}}$ is called the *Polder permeability tensor* [1].

In a magnetic substance the net magnetic dipole moment per volume, or the magnetization vector, denoted as \mathbf{M} , is nonzero as a result of spontaneous magnetization of the material. Denote the angular momentum per volume of the medium to be \mathbf{J} . The time rate change of angular momentum can be equated with the applied torque, and this implies

$$\frac{\partial \mathbf{J}}{\partial t} = \mu_0 \mathbf{M} \times \mathbf{H} \quad (4)$$

where \mathbf{H} denotes the internal magnetic field within the volume. From both classical mechanics and quantum mechanics, the relationship between \mathbf{J} and \mathbf{M} is linear, which can be expressed as

$$\mathbf{M} = \gamma \mathbf{J} \quad (5)$$

where γ is the gyromagnetic ratio, which can be written as

$$\gamma = -\frac{g|e|}{2m_e} \quad (6)$$

where g is the Lande g factor and e and m_e are charge and mass of an electron, respectively. Classically, $g = 1$ for orbital angular momentum, and $g = 2$ for spin angular momentum. Quantum-mechanically, g can take a noninteger value between 1 and 2 due to the interaction between the spin and the orbital motion of the electron [2]. However, for magnetic transition metal ions, Fe, Co, and Ni, the orbital motion of $3d$ electrons is normally quenched and hence $g \approx 2$. This implies $\gamma = -1.76 \times 10^7 \text{ rad (s} \cdot \text{Oe)}^{-1}$ (reciprocal seconds-oersteds). Combining Eqs. (4) and (5), we derive, therefore, the following constitution equation for a magnetic medium:

$$\frac{\partial \mathbf{M}}{\partial t} = \gamma \mu_0 \mathbf{M} \times \mathbf{H} \quad (7)$$

We now assume that the magnetic medium is magnetized to saturation either by an externally applied magnetic field, an internal anisotropy field, or both. Let the saturation magnetization be denoted as M_S . We separate the DC and the RF components of \mathbf{M} and \mathbf{H} as follows:

$$\mathbf{M} = \mathbf{M}_0 + \mathbf{m}, \quad \mathbf{H} = \mathbf{H}_0 + \mathbf{h} \quad (8)$$

Here, capital letters denote DC quantities, and small letters denote RF quantities. Under small-signal assumptions, $|\mathbf{m}| \ll |\mathbf{M}_0| \approx M_S$, $|\mathbf{h}| \ll |\mathbf{H}_0|$, Eq. (7) can be linearized to yield

$$\frac{\partial \mathbf{m}}{\partial t} = \gamma \mu_0 M_S \mathbf{e}_z \times \left(\mathbf{h} - \frac{H_0}{M_S} \mathbf{m} \right) \quad (9)$$

where we have assumed \mathbf{H}_0 , and hence \mathbf{M}_0 , to be along the z axis whose unit vector is denoted as \mathbf{e}_z . From Eqs. (3) and (9), we derive, assuming again the $\exp(j\omega t)$ time dependence

$$\underline{\underline{\mu}} = \mu_0 \begin{pmatrix} \mu & -j\kappa & 0 \\ j\kappa & \mu & 0 \\ 0 & 0 & 1 \end{pmatrix} \quad (10)$$

The Polder tensor elements μ and κ are given as

$$\mu = 1 + \frac{\omega_z \omega_m}{\omega_z^2 - \omega^2} \quad (11)$$

$$\kappa = \frac{\omega \omega_m}{\omega_z^2 - \omega^2} \quad (12)$$

and ω_z and ω_m are defined as

$$\omega_z = |\gamma| H_0 \quad (13)$$

$$\omega_m = |\gamma| \mu_0 M_S \quad (14)$$

Equations (1), (3), and (10) sufficiently describe the general behavior of a linear magnetic microwave device.

1.2. Effective Fields

In Eq. (7) the magnetic field \mathbf{H} is the internal field effectively experienced by electron spins in the magnetic medium. In other words, an effective field is defined if there exist a coupling between the magnetization motion of the medium and the other physical field quantities. The coupling energy density is denoted as $w(\mathbf{M}, \partial \mathbf{M} / \partial x_i)$, which may show dependence on the magnetization \mathbf{M} , the magnetic strains $\partial \mathbf{M} / \partial x_j$, or both. For example, the externally applied magnetic field \mathbf{H}_a can be associated with the Zeeman energy density $w = -\mathbf{H}_a \cdot \mathbf{M}$. For other couplings the resultant effective fields can be derived from the following Lagrangian equations [3,4]:

$$(\mathbf{H}_{\text{eff}})_i = -\frac{\partial w}{\partial M_i} + \sum_{j=1}^3 \frac{\partial}{\partial x_j} \frac{\partial w}{\partial (\partial M_i / \partial x_j)}, \quad i = 1, 2, 3 \quad (15)$$

The associated energy flux is

$$s_i = \sum_{j=1}^3 \frac{-\partial w}{\partial(\partial M_j / \partial x_i)} \frac{\partial M_j}{\partial t}, \quad i = 1, 2, 3 \quad (16)$$

so that

$$\frac{\partial \mathbf{w}}{\partial t} + \nabla \cdot \mathbf{s} = 0 \quad (17)$$

In general, \mathbf{H} in Eq. (7) consists of the following components

$$\mathbf{H} = \mathbf{H}_a + \mathbf{H}_D + \mathbf{H}_A + \mathbf{H}_E + \mathbf{H}_S + \mathbf{h}_{RF} + \mathbf{h}_d + \mathbf{h}_G \quad (18)$$

where

- \mathbf{H}_a = externally applied magnetic field (parallel to the z -axis)
- \mathbf{H}_D = DC demagnetizing field
- $\mathbf{H}_A = (2K/M_S) \mathbf{e}_z$ = uniaxial anisotropy field (along the z -axis)
- $\mathbf{H}_E = (2A/M_S^2) \nabla^2 \mathbf{M}$ = magnetic exchange field
- \mathbf{H}_S = magnetoelastic field
- \mathbf{h}_{rf} = externally applied RF driving field
- \mathbf{h}_d = RF dipolar field
- $\mathbf{h}_G = (-\lambda/\gamma M_S) \partial \mathbf{M} / \partial t$ = Gilbert damping field

where K , A , and λ are, respectively, (uniaxial) anisotropy constant, exchange stiffness, and Gilbert damping constant. We note that although \mathbf{H}_A , \mathbf{H}_E , and \mathbf{H}_S are written in capital letters, they may contain both DC and RF components. In this article we have used \mathbf{H}_0 as \mathbf{H}_a interchangeably in the following discussions. However, it is understood \mathbf{H}_0 can be the externally applied bias magnetic field, or the internal DC magnetic field experienced by electron spins, whichever is applicable.

The DC demagnetizing field \mathbf{H}_D , which results from the shape anisotropy, can be solved analytically only for an ellipsoidally shaped body. In this case a demagnetizing factor tensor $\underline{\underline{N}}_D$ can be calculated so that [1]

$$\mathbf{H}_D = -\underline{\underline{N}}_D \mathbf{M}_0 \quad (19)$$

where \mathbf{M}_0 denotes the DC component of the magnetization vector expressed in Eq. (8). For the limiting case of a thin flat ferrite slab lying on the x - y plane, Eq. (19) becomes

$$\mathbf{H}_D = -\mathbf{M} \cdot \mathbf{e}_z \mathbf{e}_z \quad (20)$$

The definition for \mathbf{H}_A in the list immediately following Eq. (18) denotes the effective field associated with a uniaxial anisotropy. For other anisotropy fields \mathbf{H}_A can be derived from Eq. (15) using the appropriate energy density of the anisotropy. For example, the corresponding energy density for a cubic anisotropy is

$$w_A = K_1(\alpha_1^2 \alpha_2^2 + \alpha_2^2 \alpha_3^2 + \alpha_3^2 \alpha_1^2) + K_2 \alpha_1^2 \alpha_1^2 \alpha_1^2 + \dots \quad (21)$$

where α_i , $i = 1, 2, 3$, is the directional cosine of the magnetization vector \mathbf{M} with respect to the i th cubic axis and K_1 and K_2 are the associated anisotropy constants [5].

Using Eq. (15), the magnetoelastic field can be derived from the following magnetoelastic energy density

$$w_S = b_1(\alpha_1^2 \epsilon_{11} + \alpha_2^2 \epsilon_{22} + \alpha_3^2 \epsilon_{33}) + 2b_2(\alpha_1 \alpha_2 \epsilon_{12} + \alpha_2 \alpha_3 \epsilon_{23} + \alpha_3 \alpha_1 \epsilon_{31}) \quad (22)$$

where the α_i terms, $i = 1, 2, 3$, are the directional cosines of the magnetization vector \mathbf{M} ; the ϵ_{ij} terms, $i, j = 1, 2, 3$, are the strain fields; and b_1 and b_2 are the magnetoelastic coupling constants [3]. The magnetoelastic coupling measures the response with which a strain signal or an acoustic signal interacts with a magnetic signal in a magnetoelastic transducer device, or vice versa.

The dipolar field \mathbf{h}_d denotes the RF field associated with the RF magnetization field \mathbf{m} in Eq. (8), which needs to be solved from Maxwell equations [Eq. (1)] and \mathbf{h}_d relates to \mathbf{m} as follows

$$\mathbf{h}_d = \frac{1}{\gamma} \left(\frac{\underline{\underline{I}}}{\underline{\underline{\mu}}/\underline{\underline{\mu}}_0 - \underline{\underline{I}}} \right) \mathbf{m} \quad (23)$$

where $\underline{\underline{\mu}}$ is the Polder tensor derived in Eq. (10) and earlier in this section and $\underline{\underline{I}}$ denotes the identity tensor. Under magnetostatic approximation, \mathbf{h}_d satisfies the following magnetostatic equations

$$\nabla \cdot \mathbf{h}_d = -\nabla \cdot \mathbf{m} \quad (24)$$

$$\nabla \times \mathbf{h}_d = 0 \quad (25)$$

subject to suitable boundary conditions. Thus, \mathbf{h}_d is solved from \mathbf{m} in almost the same way that the DC demagnetizing field \mathbf{H}_D is solved from \mathbf{M}_0 . In the literature \mathbf{h}_d is sometimes called the RF *demagnetizing field*.

The Gilbert damping field can be effectively accounted for if one replaces H_0 in Eq. (8) by $H_0 + (j\lambda/\gamma\mu_0)\omega$, or, equivalently [1]

$$H_0 \rightarrow H_0 + \frac{j\Delta H}{2} \quad (26)$$

where ΔH denotes the ferromagnetic resonance (FMR) linewidth. The Gilbert damping term is identical to the Landau-Lifshitz form in first order, and is introduced into the equation of motion, Eq. (7), phenomenologically to account for the damping torque experienced by electron spins undergoing precessional motion. Equation (26) describes very well the measured magnetic loss of a magnetic microwave device, provided that the applied RF frequency is not too far away from the frequency at which ΔH was measured. However, the physical meaning of the Gilbert damping, as related to the relaxation processes in the medium, is lacking, as in contrast to the other damping forms, such as the Bloch-Bloembergen damping [1].

Finally, we have to specify the boundary conditions on \mathbf{m} in the presence of an exchange field of \mathbf{H}_E appearing in

Eq. (18). The (direct) exchange coupling is associated with the overlapping integral that relates the spin–spin interaction for two electron spins at neighboring atomic sites. The exchange constant A is larger than 0 for ferromagnetic coupling, and A is smaller than 0 for ferrimagnetic and for antiferromagnetic couplings. The spatial boundary conditions on \mathbf{m} can be derived from the equation of motion, Eq. (7), which requires that the quantity

$$\mu_0 \mathbf{A} \mathbf{M} \times \frac{\partial \mathbf{M}}{\partial \mathbf{n}} \quad (27)$$

needs to be continuous across the ferrite boundaries. Here \mathbf{n} denotes the outward direction normal to the surface of the boundary. The time boundary condition is derived from the energy conservation law. Thus, from Eq. (16) we require the outward energy flux

$$-\mu_0 A \frac{\partial \mathbf{M}}{\partial \mathbf{n}} \cdot \frac{\partial \mathbf{M}}{\partial \mathbf{t}} \quad (28)$$

to be continuous across the material boundaries. However, instead of Eq. (28), it is popular in the literature to use the following spin-pinning condition at the material boundaries:

$$\frac{\partial \mathbf{M}}{\partial \mathbf{t}} = 0 \quad (29)$$

Since A is a microscopic quantity and at the boundary layers the environment there is quite different from that of the bulk, the spin-pinning condition, Eq. (29), might be more realistic than the one representing the macroscopic average, Eq. (28).

1.3. Dispersion Curves for Bulk Modes

Equations (1), (3), and (10) can now be solved for a bulk ferrite medium for plane-wave solutions. The resultant dispersion relation, ω versus k ($= 2\pi/\lambda$), is shown in Fig. 1. Here, k is the wavenumber and λ is the wavelength. In Fig. 1 the k space is conventionally divided into three zones. For the small- k region, $k < k_1$ ($\approx 0.1 \text{ cm}^{-1}$), electron spin motion is strongly coupled with the RF electromagnetic fields so that the full set of Maxwell equations is required to solve the dispersion relations. This region is called the “retarded zone,” and most magnetic microwave devices other than single-crystal YIG films making use of bulk ferrite materials are operational in this region, for example, circulators, isolators, phase shifters, and resonators. The next region consists of intermediate k values, k_1 ($\approx 0.1 \text{ cm}^{-1}$) $< k < k_2$ ($\approx 10^6 \text{ cm}^{-1}$), known as the *magnetostatic-wave zone*. In this region $\omega \ll k(\epsilon\mu_0)^{-1/2}$ and hence the displacement current, $\omega\epsilon\mathbf{e}$, can be ignored in Maxwell equations:

$$\nabla \times \mathbf{h} \approx 0 \quad (30)$$

This equation is called the *magnetostatic approximation*. A magnetostatic wave device usually require the use of a high-quality single-crystal magnetic film such as YIG

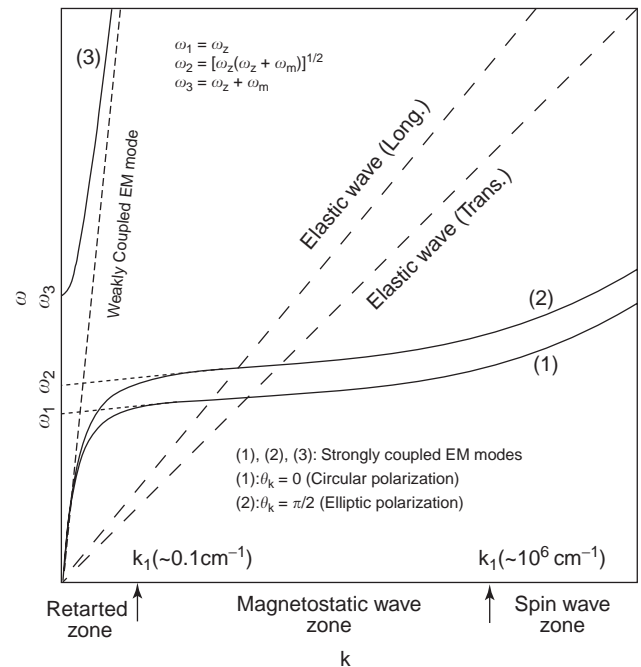


Figure 1. Dispersion curves of the coupled photon–magnon modes. The k space has been divided in three zones for retarded, magnetostatic, and spin-wave modes. Phonon dispersion curves are also shown in the figure.

whose thickness determines the spectrum of the resultant magnetostatic waves prevailing in the device structure. The last region is for $k > k_2$ ($\approx 10^6 \text{ cm}^{-1}$), which is called the *spin-wave zone*. In this region the dispersion curves grow proportional to k^2 , as dictated by the effective exchange field, \mathbf{H}_E , defined following Eq. (18). Although not many practical microwave devices are designed in this region, the spectrum of spin waves is important in the sense that the normal spin precessional motion will break up into spin waves at the onset of instability when a magnetic microwave device is driven beyond a high power threshold. The quadratic dependence of the spin-wave dispersion gives rise to an effective mass for magnons, $m^* = \hbar \delta(2A\omega_m)^{-1}$, where \hbar denotes Planck’s constant.

For a given wave propagation direction \mathbf{k} , Eqs. (1), (3), and (10) imply two plane-wave solutions. Similar to the plane-wave solutions in an isotropic medium, the three vectors, \mathbf{e} , \mathbf{b} , and \mathbf{k} for each mode in an anisotropic magnetic medium, are still mutually perpendicular to each other. However, unlike the isotropic case, the two modes in the magnetic medium are nondegenerate, possessing different effective permeabilities and polarizations. Because of the wrong sense in polarization, one mode is weakly coupled to the photon waves, and hence its dispersion curve represents little departure from that of the (uncoupled) photon modes. This dispersion curve is shown in Fig. 1 as a straight (short) dashed line in the retarded zone. The other mode couples strongly to the photon waves, giving rise to distortion of the dispersion curves in the retarded zone.

For the strongly coupled mode two branches show up, depending on whether the bias magnetic field is applied

above or below FMR. These two branches are shown in Fig. 1 as bottom and top curves, respectively (bias *above* FMR is referred to in the literature as the condition that the bias field is larger than that required by FMR; bias *below* FMR means the reverse. According to this convention, in Fig. 1 the bias-below FMR condition corresponds to the top curve, curve 3, and the bias-above FMR condition corresponds to the bottom curves, curves 1 and 2). The top branch, curve 3 in Fig. 1, lies entirely in the retarded zone and shows very little variation with respect to the wave propagation directions; that is, the propagation of strongly coupled electromagnetic waves biased below FMR is nearly isotropic in the magnetic medium. However, the bottom branch, curves 1 and 2, depends strongly on the wave propagation directions. When \mathbf{k} is parallel to the z axis, the dispersion curve is shown as curve 1 in Fig. 1, and when \mathbf{k} is perpendicular to the z axis, the dispersion curve is shown as curve 2. For other propagation directions, the dispersion curves are distributed between these two curves, and for this reason, the region bounded by curves 1 and 2 in Fig. 1 is usually referred to as the *spin-wave manifold*. In the literature curve 1 is known as the *Kittel mode* and curve 2, the *Voigt mode*. A Kittel mode possess a right-hand circular polarization, whereas a Voigt mode is associated with an elliptic polarization. In Fig. 1 θ_k denotes the angle between \mathbf{k} and the z axis, which is designated as the applied field direction, and ω_1 , ω_2 , and ω_3 are given as

$$\omega_1 = \omega_z \quad (31)$$

$$\omega_2 = [\omega_z(\omega_z + \omega_m)]^{1/2} \quad (32)$$

$$\omega_3 = \omega_z + \omega_m \quad (33)$$

and ω_1 and ω_2 are the limiting values of the magnetostatic modes in the retarded zone (see Fig. 2).

The elastic modes are also shown in Fig. 1 as straight (long) dashed lines. There are two kinds of phonon modes: longitudinal phonons and transverse phonons [6]. In the presence of magnetoelastic coupling, b_1 and b_2 are nonzero in Eq. (22), and the phonon, or acoustic, modes will couple to the spin-wave, or magnon, modes. For the coupled case the dispersion curves of the phonons and the magnons will avoid running across each other in the same fashion that the photon modes and the magnon modes detour each other in the retarded-zone region as shown in Fig. 1 [7]. (If one views the uncoupled dispersion lines of two modes as two intersecting straight lines, the coupled dispersion lines resemble the two branches of a hyperbola using the two intersecting lines as asymptotes.) In Fig. 1 the (uncoupled) magnon modes in the retarded zone are shown as dotted lines, extending curves 1 and 2 smoothly from the magnetostatic-wave zone, intersecting the photon line, and ending at ω_1 and ω_2 of the ω axis (see Fig. 2).

1.4. Plane-Wave Solutions

Plane-wave solutions are needed when performing numerical spectral-domain calculations where a stratified

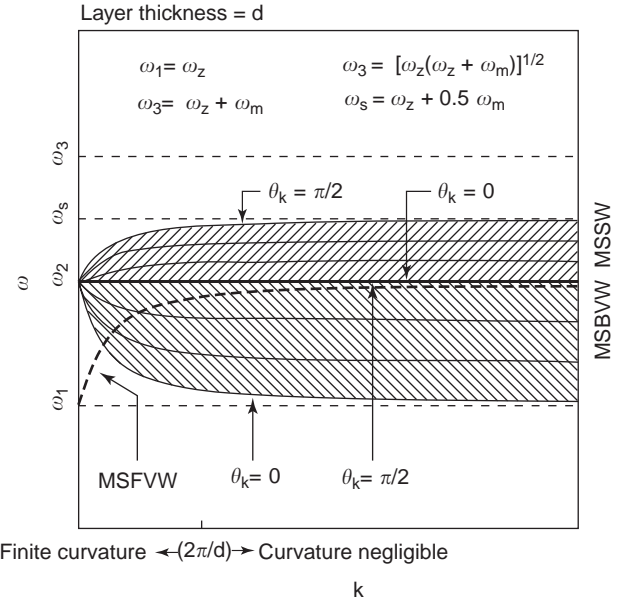


Figure 2. Dispersion curves of magnetostatic waves in a magnetic layer. The MSFVW is shown as a heavy dotted line, rising from ω_1 to ω_2 as k increases from 0 to ∞ . The MSBVW and MSSW are shown hatched depending on the propagation direction of the magnetostatic waves. θ_k denotes the angle between the wave propagation direction and the applied field direction.

structure is considered consisting of dielectric/magnetic layers supporting electromagnetic wave propagation in the retarded zone [8]. We give in this subsection the plane-wave solutions following Maxwell equations, Eq. (1), assuming a Polder permeability tensor, Eqs. (3) and (10)–(14). We consider a bulk ferrite of infinite content (so as not to be bothered by the boundary conditions at infinity) that is biased by an external magnetic field H_0 along an arbitrary direction. Without loss of generality we assume that H_0 is along the z axis [see definition for H_a immediately below Eq. (18)]. Other effective fields can be readily added to H_0 according to Eq. (18). For a given direction of wave propagation, which is specified by a directional cosine vector $(\alpha_1, \alpha_2, \alpha_3)^T$, we have the following dispersion relationship

$$k^2 = \varepsilon_f \mu_0 \mu_{\text{eff}} \omega^2 \quad (34)$$

where ε_f is the permittivity of the ferrite bulk, and the effective (scalar) permeability μ_{eff} can be calculated from

$$\mu_{\text{eff}} =$$

$$1 + \frac{2\alpha_3^2 \omega_m}{(1 + \alpha_3^2)\omega_z + (1 - \alpha_3^2)\omega_m \mp [(1 - \alpha_3^2)^2(\omega_z + \omega_m)^2 + 4\alpha_3^2 \omega^2]^{1/2}} \quad (35)$$

where ω_z and ω_m are as given by Eqs. (13) and (14), respectively. The corresponding RF magnetic field is, within

a multiplication constant

$$h_x = \frac{1}{\gamma} \left[\alpha_1 \alpha_2 \mu_{\text{eff}} \omega j + (1 - \alpha_1^2 \mu_{\text{eff}}^2) \omega_z + \left(1 + \frac{\alpha_3^2 \mu_{\text{eff}}}{1 - \mu_{\text{eff}}} \right) \omega_m \right] \quad (36a)$$

$$h_y = \frac{1}{\gamma} [-(1 - \alpha_2^2 \mu_{\text{eff}}^2) \omega j - \alpha_1 \alpha_2 \mu_{\text{eff}} \omega_z] \quad (36b)$$

$$h_z = \frac{\alpha_3 \mu_{\text{eff}}}{\gamma} \left[\alpha_2 \omega j - \alpha_1 \left(\omega_z + \frac{\omega_m}{1 - \mu_{\text{eff}}} \right) \right] \quad (36c)$$

the RF electric field is

$$e_x = \frac{-\zeta \alpha_3}{\gamma} \left(\omega j - \frac{\alpha_1 \alpha_2 \omega_m \mu_{\text{eff}}}{1 - \mu_{\text{eff}}} \right) \quad (37a)$$

$$e_y = \frac{-\zeta \alpha_3}{\gamma} \left(\omega_z + \frac{(1 - \alpha_2^2 \mu_{\text{eff}}^2) \omega_m}{1 - \mu_{\text{eff}}} \right) \quad (37b)$$

$$e_z = \frac{\zeta}{\gamma} \left[\alpha_2 \omega_z + \alpha_1 \omega j + \alpha_2 \omega_m \left(1 + \frac{\alpha_3^2 \mu_{\text{eff}}}{1 - \mu_{\text{eff}}} \right) \right] \quad (37c)$$

the RF magnetization field is

$$m_x = \frac{\mu_0}{\gamma} [-(1 - \mu_{\text{eff}}) \omega_z - (1 - \alpha_2^2 \mu_{\text{eff}}^2) \omega_m] \quad (38a)$$

$$m_y = \frac{\mu_0}{\gamma} [(1 - \mu_{\text{eff}}) \omega j - \alpha_1 \alpha_2 \mu_{\text{eff}} \omega_m] \quad (38b)$$

$$m_z = 0 \quad (38c)$$

and the RF magnetic induction field is

$$b_x = \frac{\mu_0 \mu_{\text{eff}}}{\gamma} \left[\alpha_1 \alpha_2 \omega j + (1 - \alpha_1^2) \omega_z + \left(\frac{\alpha_3^2}{1 - \mu_{\text{eff}}} + \alpha_2^2 \right) \omega_m \right] \quad (39a)$$

$$b_y = \frac{-\mu_0 \mu_{\text{eff}}}{\gamma} [(1 - \alpha_2^2) \omega j + \alpha_1 \alpha_2 (\omega_z + \omega_m)] \quad (39b)$$

$$b_z = \mu_0 h_z \quad (39c)$$

where

$$\zeta = \left(\frac{\mu_0}{\epsilon_f} \right)^{1/2} \quad (40)$$

Thus, wave propagation in a magnetized ferrite is nondegenerate, assuming different effective permeability values for different modes, resulting in different propagation speeds and polarizations. Similar to the isotropic case, the directions of electric field \mathbf{e} , magnetic induction \mathbf{b} , and wave propagation \mathbf{k} for each mode are mutually perpendicular to each other, as dictated by Maxwell equations; magnetic field \mathbf{h} is no longer aligned with magnetic induction \mathbf{b} , although \mathbf{h} is still required to be perpendicular to the direction of electric field \mathbf{e} . These properties can be readily checked by the above field expressions, Eqs. (36)–(39).

1.5. Magnetostatic Waves in a Magnetic Layer

Wave propagation and dispersion in a magnetic layer can be derived in a manner similar to that shown in Fig. 1 except that boundary conditions need to be explicitly

considered at the layer–air interfaces. For MSW device applications the excited waves have wavelengths in an order comparable to that for the layer thickness. As such, the magnetostatic approximation, Eq. (30), applies, which implies that the RF magnetic field can be derived from a scalar potential, and hence the dispersion calculations are largely simplified. Figure 2 shows such a dispersion diagram. When compared with Fig. 1, we see that in Fig. 2 the retarded zone has been pushed away into the $k=0$ region and the exchange coupling showing k^2 dependence in the large- k region has been neglected. However, the magnetostatic dispersion does not imply horizontal lines, as depicted in the magnetostatic-wave zone of Fig. 1. The finite curvatures of the dispersion curves shown in Fig. 2 are due to the finite thickness of the magnetic layer d , which are restricted roughly to the region bounded by two vertical lines $k=0$ and $k=2\pi/d$ (the vertical line $k=2\pi/d$ is not shown in Fig. 2, although it is understood from the k -axis label).

Magnetostatic waves can be volume waves and surface waves. For a volume wave the RF magnetization varies sinusoidally along the thickness direction, whereas for a surface wave it varies exponentially in this direction. Thus, a volume wave penetrates the whole thickness of the magnetic layer, whereas a surface wave is concentrated near the surface and the film–substrate interface. For a forward wave the dispersion increases monotonically with k so that the group velocity $d\omega/dk$ is positive. This is in contrast with a backward wave where $d\omega/dk$ is negative. Thus, for a forward wave the transmitted power is along the same direction as wave propagation, whereas the power transmitted by a backward wave is opposite to the wave propagation direction.

When the external field is applied normal to the layer plane, magnetostatic waves are generated isotropically with respect to the wave propagation directions lying on the layer plane. This branch of waves is called *magnetostatic forward volume waves* (MSFVWs), whose dispersion is shown in Fig. 2 as a heavy dotted line. The MSFVW mode undergoes uniform precessional motion at the Kittel frequency ω_1 for $k=0$, and the frequency increases thereafter, approaching the bulk limit of the Voigt frequency ω_2 as k goes to infinity. Dispersion of this kind can be readily understood by determining the spin motion occurring in the layer.

However, when the external bias field is applied in the layer, plane anisotropy results in general except at $k=0$, where the uniform precessional motion occurs at the Voigt frequency ω_2 . When k increases further, two kinds of modes are possible: magnetostatic backward volume waves (MSBVWs) and magnetostatic surface waves (MSSWs). Depending on the propagation angle θ_k , MSBVW dispersion will decrease as k increases, approaching the respective bulk-mode limit as k goes to infinity. Therefore, unlike MSFVW, MSBVW occupies a finite area in the dispersion diagram, which is shown hatched between ω_1 and ω_2 in Fig. 2. For device applications, MSBVW is usually launched at $\theta_k=0$; that is, the excited MSBVW is collinear with the applied field direction, since it provides the widest frequency bandwidth among all the MSBVW propagation directions.

For MSSW the dispersion falls within the forbidden area of the bulk modes extending from ω_2 to ω_3 (see Figs. 1 and 2). MSSW dispersions increase as k increases, reaching limiting values at large k . The propagation of MSSW is anisotropic, and the largest dispersion occurs at $\theta_k = \pi/2$, which gives rise to a limiting frequency $\omega_s = \omega_z + 0.5 \omega_m$, known as the *Damon–Eshbach frequency*. The most popularly used MSSW is for $\theta_k = \pi/2$, which requires the MSSW to propagate transverse to the applied field direction and results in the widest frequency band for MSSW device applications.

In Fig. 2 MSFVW and MSBVW are shown only for the lowest-order volume modes. Higher-order volume waves are also possible. A high-order volume wave, which assumes additional nodal points along the thickness of the magnetic layer, will converge to the same frequency as the lower-order waves at large k , except that the curvature of the dispersion curve is reduced. In general magnetostatic waves are generated in single-crystal YIG films epitaxially grown on gadolinium gallium garnet (GGG) substrates. Very often, a dielectric superstrate, for example, alumina, is covered on top of the YIG film to facilitate the excitation of magnetostatic waves. For these situations the dispersion diagram of Fig. 2 remains unchanged. However, when a metal ground plane is placed on top of the superstrate shown in Fig. 3, the dispersion of MSSW, but not MSFVW and MSBVW, will change. The influence of a metal plane is that the MSSW dispersion curve will grow in a convex manner, increasing initially from ω_2 at $k=0$ to a maximum value less than ω_3 followed by decreasing to ω_s as k goes to infinity. When a second metal ground plane is added to the bottom side of the GGG substrate shown in Fig. 3, the propagation of MSSW becomes even nonreciprocal; that is, the dispersion curve is different depending on whether the wave propagation is along the $+k$ or the $-k$ direction. In Fig. 3 magnetostatic waves may be excited by using a microstrip line, consisting of only the top ground plane; or a stripline, consisting of both the top and the bottom ground planes. For a multilayered system containing alternating magnetic and dielectric layers, the bulk and the surface modes form a band structure in almost the same way that atomic energy levels crowded into energy

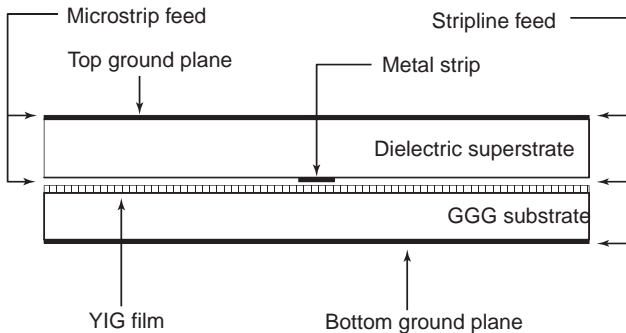


Figure 3. Magnetostatic wave excitation configuration. The YIG film is deposited on top of the GGG substrate. A superstrate can be used to provide microstrip excitation configuration. A bottom ground plane can also be deposited on the GGG substrate to provide stripline excitation configuration.

bands when atoms are brought together to form a periodic lattice [9,10].

Finally, let us discuss the propagation loss of a delay line. When an observer is traveling with the wave down the delay line for a delay time $t = \tau_d$, the electric field is

$$\mathbf{e} = \mathbf{e}_0 \exp[2\pi j(f + j\Delta f)\tau_d] \quad (41)$$

where \mathbf{e}_0 denotes the initial amplitude at $t=0$. This implies that the propagation loss in dB is

$$\alpha = 40\pi(\log_{10} e)\Delta f\tau_d \quad (42)$$

In Eq. (41) f and Δf respectively denote the real and the imaginary parts of frequency. Δf can be related to the linewidth measured with a resonator consisting of the delay line of a finite length but weakly coupled to by an external feeder line circuit. Thus, we have

$$\Delta f = \Delta f_m + \Delta f_d + \Delta f_c \quad (43)$$

where Δf_m , Δf_d , and Δf_c denote, respectively, contributions from magnetic loss, dielectric loss, and conductor loss. As discussed in deriving Eq. (26), Δf_m may be identified as half the FMR linewidth multiplied by a volume filling factor F_m denoting the volume ratio of the ferrite material relative to the total volume enclosing the resonating cavity:

$$\Delta f_m = \frac{F_m |\gamma| \mu_0 \Delta H}{2} \quad (44)$$

The other two linewidths (Δf_d and Δf_c) can be estimated in a similar manner dealing with a dielectric lossy cavity, for example, [11]. If we assume that magnetic loss dominates and approximate $F_m \approx 1$, Eqs. (42) and (44) imply

$$\alpha \approx 76.4\tau_d \Delta H \quad (45)$$

where τ_d is in microseconds and ΔH is in oersteds. Equation (45) was originally derived by Vittoria and Wilsey [12] for an MSW delay line. However, since delay time is measured as group delay, τ_d expressed in Eqs. (41), (42), and (45) will be multiplied by a factor v_g/v_k , where v_g denotes the group velocity ($=d\omega/dk$) and v_k denotes the phase velocity ($=\omega/k$) for wave propagation.

1.6. Spin-Wave Instabilities and Their Route to Chaos

In Fig. 1 the high- k regime where the wave dispersion curves show k^2 dependence is called the *spin-wave zone*. Although spin waves may not be directly exploited for device applications, they are important to influence device performances especially at high power, because they are intimately related to instabilities when a ferrite is excessively excited invoking nonlinearity. The quantized spin-wave particles are called *magnons*, which interact with the quantized electromagnetic-wave particles, or photons, through the nonlinear terms in the equation of motion [Eq. (7) or (61)]. Instabilities occur if energy transfer from the photon modes to the magnon modes, or among magnon modes themselves, becomes unstable [13], rendering

unpredictability resembling the turbulencelike behavior of chaos [14,15].

The concept of spin waves was first introduced by Bloch in 1930 to explain the thermodynamic properties of ferromagnets at low temperatures [16]. Suhl renewed the interest in spin waves and explained the saturation effects observed in ferromagnetic resonance (FMR) experiments [13]. As just stated, the spectrum of spin waves shown in Fig. 1 has proved to play a dominant role in the relaxation processes observed at high power. When an RF field is applied, it drives the spins into precessional motion, which in turn couples with spin-wave propagation, dumping energy into lattice vibration via spin-spin and spin-lattice relaxation processes. The coupling to spin waves must originate from the nonlinear terms in the equation of motion, Eq. (7). The quadratic interaction comes from $\mathbf{h} \times \mathbf{m}$ and the cubic interaction from either $\mathbf{h}\mathbf{m} \cdot \mathbf{m}$ or $\mathbf{m}\mathbf{m} \cdot \mathbf{m}$, inducing the so-called first-order and second-order spin-wave instabilities, respectively. For a spin wave component, \mathbf{m}_k , it induces two \mathbf{h} fields, denoted as \mathbf{h}_E , from the definition for \mathbf{H}_E following Eq. (18), and the dipolar field, \mathbf{h}_d , from Eq. (23). These two \mathbf{h} fields then feed back and couple nonlinearly with the original \mathbf{m}_k field to generate instability if a threshold power is reached. The $\mathbf{m} \cdot \mathbf{m}$ term arises from the constraint that the magnitude of \mathbf{M} needs to be a constant (equal to M_S); that is, in Eq. (8) the longitudinal component M_0 is replaced by

$$M_0 \approx \left(1 - \frac{\mathbf{m} \cdot \mathbf{m}}{2M_S^2}\right) M_S \quad (46)$$

As a consequence, the DC demagnetizing field, if not zero, will add cubic nonlinearity to the equation of motion, giving rise to adverse effects in influencing the spin-wave instability.

Under FMR measurements, the experiments showed a subsidiary absorption at high excitation power that occurs at a DC field less than that required by the resonance condition. Also, as the input power increases, the resonance absorption peak broadened accordingly rendering premature saturation of the main resonance. Suhl [13] showed that the subsidiary peak arises from a spontaneous transfer of energy from the uniform precessional motion of spins to spin waves of half the resonance frequency, $\omega_k = \omega/2$. This instability is caused by the first-order (quadratic) interaction between the dipolar field \mathbf{h}_d and the spin wave \mathbf{m}_k . The second instability responsible for the broadened and declined saturation of the main resonance peak comes from a catastrophic energy transfer from the uniform precessional motion of spins to spin waves of the same frequency $\omega_k = \omega$. This instability is brought about by the second-order (cubic) interaction between the exchange field \mathbf{h}_E and the spin waves, \mathbf{m}_k and \mathbf{m}_k . The resultant input field thresholds for these two instabilities are, respectively [17]

$$h_{SA}^{\text{th}} = \frac{2\Delta H_k}{\omega_m \sin 2\theta_k} \sqrt{(\omega - \omega_z)^2 + \omega_{\Delta H}^2} \quad (47)$$

$$h_{RS}^{\text{th}} = \Delta H \sqrt{\frac{2\Delta H_k}{M \cos 2\theta_k}} \quad (48)$$

where the subscripts SA and RS stand for subsidiary absorption (first-order instability) and resonance saturation (second-order instability), respectively. In Eqs. (47) and (48) ΔH is the FMR linewidth

$$\omega_{\Delta H} = |\gamma| \mu_0 \Delta H_k \quad (49)$$

and ΔH_k is the linewidth of the spin wave that is introduced phenomenologically to parametrize the energy transfer rate from the spin wave \mathbf{m}_k to lattice vibration. Thus, once excited, a spin wave will decay according to the following equation

$$\mathbf{m}_k(t) = \mathbf{m}_k(0) \exp(-\omega_{\Delta H} t) \quad (50)$$

assuming that it does not couple to other magnetic modes.

In addition to Suhl's instabilities, Morgenthaler [17] and Schloemann [18] found that spin waves could also be parametrically excited by an RF field applied parallel to the static field, known as *parallel pumping*, as in contrast to the transverse RF field configuration assumed by FMR measurements. Similar to Suhl's first-order instability, parallel pumping can impose an instability that occurs at a spin-wave frequency equal to half the frequency of the RF pumping signal $\omega_k = \omega/2$. The threshold for parallel pumping instability is

$$h_{PP}^{\text{th}} = \frac{2\Delta H_k \omega}{\omega_m \sin^2 \theta_k} \quad (51)$$

which compare closely in magnitude to h_{SA}^{th} , the threshold for Suhl's first-order instability shown in Eq. (47). In Eq. (51) the subscript PP denotes parallel pumping.

Parallel pumping excites spin waves via the cubic interaction term $\mathbf{h}\mathbf{m} \cdot \mathbf{m}$. However, in contrast to perpendicular pumping assumed by Suhl's instabilities, parallel pumping requires no involvement of the Kittel uniform mode and the pumped photon energy or electromagnetic energy is directly imparted to the creation of two spin-wave magnons of opposite wavevectors $\pm \mathbf{k}$, called *Cooper pair magnons*. For the case of perpendicular pumping, the pump signal is to first induce the Kittel uniform mode followed by conversion into either a single magnon at wavevector \mathbf{k} or Cooper pair magnons at $\pm \mathbf{k}$ for the first-order and the second-order processes, respectively. In Eqs. (47), (48), and (51), θ_k denotes the angle between the wavevector \mathbf{k} and the z axis \mathbf{e}_z . From these three equations, minimum threshold pump fields occur when θ_k equals 0, $\pi/4$, and $\pi/2$ for resonance saturation, subsidiary absorption, and parallel pumping instabilities, respectively. These energy transfer diagrams are shown schematically in Fig. 4, in which the spin-wave band is redrawn from Fig. 1 with the retarded zone omitted, but extended in both $\pm k$ directions. In Fig. 4 the Kittel uniform mode is also shown, whose frequency is

$$\omega_0 = \gamma \{ [H_a + H_A + 4\pi M_s \times (N_x - N_z)] [H_a + H_A + 4\pi M_s (N_y - N_z)]^{1/2} \} \quad (52)$$

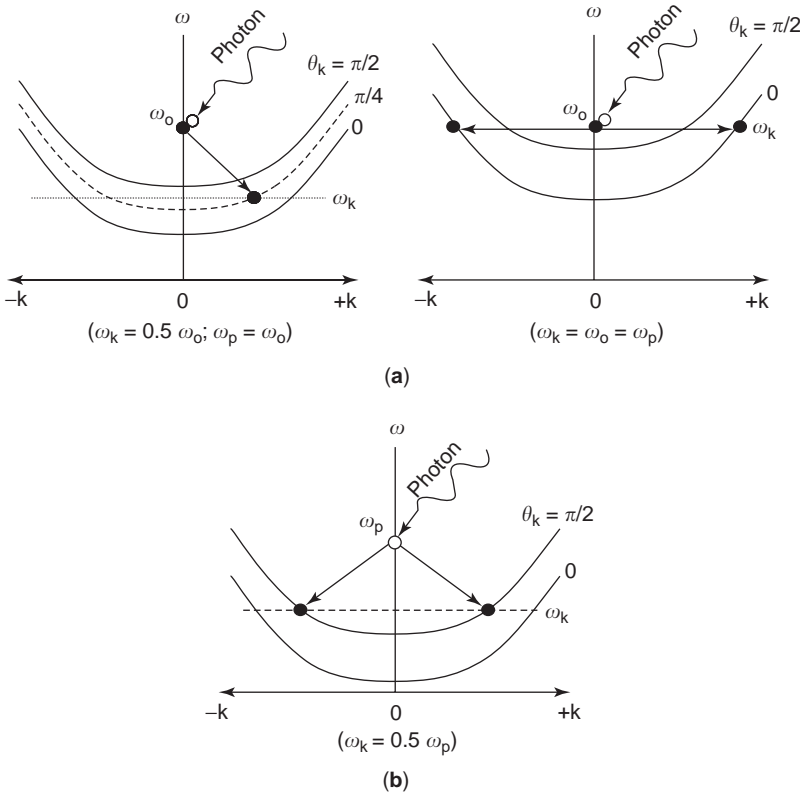


Figure 4. Photo-induced magnon transitions responsible for the observed instabilities for perpendicular pumping [first-order (left) and second order (right)] (a), and parallel pumping (second order) (b) of a nonlinear ferromagnetic spin system.

which can be derived by using the linearized equation Eq. (9) assuming the following dipole field for the uniform precessional mode

$$\mathbf{h}_d = -\underline{N}_D \mathbf{m} \quad (53)$$

see Eqs. (19) and (23). Note that in Fig. 4 Kittel uniform mode is not excited during parallel pumping, since the former requires transverse components of the RF magnetization field that are not able to be supplied by the latter. In Fig. 4 the wavy arrows indicate photon transitions, and solid arrows indicate magnon transitions; only the critical transitions are illustrated in Fig. 4, giving rise to minimum values in the pumping field responsible for the onset of instabilities.

The turbulencelike behavior of magnetic excitations after spin-wave instabilities have set in and their routes to chaos have been studied using the generic numerical analysis [14,15]. The responses of a nonlinear system, such as spins in a ferromagnet, can be totally unpredictable, due to amplification of errors made in the initial states. Such an error amplification mechanism, which is characterized by Lyapunov exponents for trajectories in state space during time evolution, renders randomness to the system's response leading to the violation of the causality principle; namely, the connection between the past and the future of the system is lost after a short transient period. However, in more recent decades, researches have found regularities in irregular systems and randomness appears to have a deterministic underpinning; even the random events

such as water dripping from a leaking faucet has been shown to show similarities with other irrelevant chaotic processes such as stretching and folding a plane (Héno attractor) or kneading a piece of dough (Lorentz attractor). Universal rules have thus been developed that govern the intrinsic structure of a chaotic system or a random process in a manner analogous to the scaling rules developed by using the renormalization group theory for phase transitions observed in condensed-matter physics.

Research in chaos has resulted in a common language suitable for the description of chaotic systems or random processes. This language applies to the universal structure of the limiting curves traced out by trajectories of a dynamic system or process embedded in state space. With dissipation these trajectories will, after a transient period, settle into limiting curves or cycles called *attractors*. If the system or the process is regular with its response predictable, state space trajectories will remain converged and confined all the time and the dimension of the resultant attractor will necessarily be an integer, for example, given by a circle, a torus, or another configuration. However, when chaos or turbulence launches, nearby trajectories in state space diverge and the attractor shows strange behavior, thereby called *strange attractors*. For a strange attractor, its dimension is not an integer and its appearance shows repeated resemblance after it has been continuously magnified, a scenario implied by a fractal. A similar fractal structure can be attributed to the strange basin boundaries separating the domains for different attractors settled in the state space of a chaotic system or process.

The usefulness of the language developed for describing chaos are twofold:

1. It allows a general erratic time-sequenced data or dynamically fluctuating picture to be categorized, according to the appearance of the associated attractors and/or basin boundaries in state space, analogous to the fact that phase transitions are classified according to their order in transformation. As such, routes to chaos can be visualized, and only a few routes have been found available for general random processes or phenomena to follow, including frequency-doubling bifurcation, intermittence, and crises. Similarly, thousands of kinds of phase transitions take place in the physical world, but only a few transformation orders are generally deduced for phase transitions. Universal scaling rules are concluded for both the chaotic/random systems and for the phase transition systems, which describes the rate at which instabilities or critical phenomena are approached by the change in system-pumping parameters or order parameters, respectively.
2. From the dimension or the size of the resultant attractors and/or the basin boundaries in state space, it is possible to determine the degree of randomness or agitation inherent in the chaotic system or process under study, enabling extraction of the maximum amount of information out of irregularity: the larger the entropy or the information content of the system or the process, the more complicated and involved structure will be implied by the strangeness of the attractors and/or the basin boundaries. When the nature of randomness is better known, which is clearly described in terms of the language of chaos, weather prediction and broadcast in the future, say, can then be much more reliable although still perhaps unable to yield 100% accuracy.

It has been shown that spin-wave instabilities resulting from parametric transverse and parallel pumping display chaotic dynamics characterized by the universal routes such as period-doubling bifurcation [14] and subharmonic generation [15]. In general, when the pumping field was increased beyond a threshold value [e.g., see Eq. (47), (48), or (51)], modulation in self-oscillation of the ferrite spin system set in at a low frequency; the amplitude of this low-frequency modulation oscillation grew steadily with pumping power until frequency doubling bifurcation occurred before leading to a full-scale chaotic state. For parallel pumping subharmonic generation routes were also observed from windows of the Feigenbaum scenario [15]. Strange attractors associated with computer-generated time sequences from the nonlinear coupled spin-wave modes, or the so-called two-mode model, showed fractal scenarios common to a generic chaotic system. A scaling parameter $\delta = 4.675$ was found for perpendicular pumping, which is close to the Feigenbaum universal value, indicating the success in adopting the chaotic language in describing the unstable dynamics of the nonlinear spin-wave system [14].

2. FERRITE JUNCTION CIRCULATORS

A *circulator* is defined as a device with ports arranged such that energy entering a port is coupled to that of an adjacent port but not to that of the remaining ports. A ferrite junction circulator has become a versatile microwave device because, in addition to its use as a circulator, it also can be used as an isolator or as a switch. Depending on the bias field direction onto the junction area, either upward or downward, the output ports operate in turn each time an input port is selected, either clockwise or counterclockwise, respectively, so that the junction is said to provide the circulation operation. The three-port version of the ferrite junction circulator, usually called the *Y-junction circulator*, is most commonly used. It can be realized by feeding the junction with three joining transmission lines, including waveguides, striplines, microstrips, CPWs (coplanar waveguides), and slotlines. The waveguide version is usually an *H*-plane junction, although an *E*-plane junction circulator can also be created. The stripline ferrite junction circulator is usually made with coaxial connectors facilitating its use as a discrete component at the UHF, microwave, and millimeter-wave frequencies.

Early experimenters found that waveguide T junctions having a transversely magnetized ferrite slab suitably placed in the junction could, with proper matching and adjustment of the magnetic field, be changed into circulators. The bandwidth of such devices was very narrow. Refinements producing better symmetry were found to broaden the bandwidth so that useful devices were obtained. The first commercial microwave circulator appeared in the early 1950s, while a full theoretical account of its operation was not published until 1962 by Bosma [19,20].

The stripline Y-junction ferrite circulator consists of two ferrite disks filling the space between a metallic center disk and two conducting ground planes. The static magnetic field is applied parallel to the axis of the ferrite disks. In Bosma's theory TEM Voigt modes were assumed propagating clockwise/counterclockwise in the region between the two conductor planes possessing no variation along the applied field direction [19,20]. Magnetic wall boundary conditions were assumed by Bosma at the ferrite disk periphery not adjacent to the circulator ports. Impedance boundary conditions were then imposed on the periphery areas defined by the circulator ports. Under these assumptions the RF magnetic field inside a 2D ferrite junction can be solved analytically, involving Bessel functions of the first kind to be cast in the series form. The circulation conditions were then postulated by Bosma, resulting in two real equations allowing for determination of two circulator design parameters. Bosma chose the radius of the junction R and the dielectric constant of the matching dielectric material surrounding the junction ϵ_d as the two independent parameters [19,20]. Therefore, at the circulation frequency the junction will yield 0 dB insertion loss and infinite isolation with all the input electromagnetic energy dumped into the output port without attenuation. Note that a circulation condition can be formulated only with respect to an ideal lossless junction with perfect impedance matching at all ports.

Fay and Comstock [21] presented a practical model for the operation of a Y-junction circulator. In their treatment the circulator circuit is approximated by a pair of slightly detuned RCL resonators connected in parallel to account for the two counterrotating dipole modes of the ferrite disks in the presence of a bias field. Participation from high orders has thus been ignored. At circulation the two dipole modes are nondegenerate, and the splitting between their (detuned) resonant frequencies Δf is proportional to the resultant gyrotropy $p = \kappa/\mu$ of the junction circuit. Here, κ and μ are the off-diagonal and diagonal elements of the Polder tensor of the ferrite material, respectively [Eqs. (11) and (12)]. Fay and Comstock have shown that it is imperative to incorporate moderate p of the ferrite material to obtain broadband operation of the circulator junction [21].

Fay and Comstock have also proposed RF field patterns responsible for the circulation operation of a ferrite junction [21]. This is shown in Fig. 5, where dipole-mode

excitations are shown as standing waves in an isotropic junction (Fig. 5a), and in a ferrite junction at circulation (Fig. 5b); the junction assumes a thin-disk geometry of a negligible aspect (thickness to diameter) ratio whose periphery is defined by the magnetic wall boundary conditions. In Fig. 5 solid curves with arrows depict RF magnetic field lines, and crosses and dots represent electric lines entering and exiting the junction area, respectively. For an isotropic junction the input field will excite a symmetric field pattern with respect to the output and the isolated ports attaining an equal intensity (Fig. 5a). Energy entering the input port, which has been shown with the most field intensity, will split in two equal halves reaching the output and isolated ports undergoing reciprocal operation. However, for a ferrite junction biased at circulation the dipole pattern of Fig. 5a is rotated 30° counterclockwise such that the input and the output ports are at an equal field intensity; the isolated port is averaged to zero, since an equal number of positive and negative electric field lines appears at the isolated port (Fig. 5b). Thus, electromagnetic energy entering the input port feeds the output port directly, leaving behind the isolated port essentially electronically insulated. The circulator operation is nonreciprocal in the sense that the circulation action takes place in a cyclic order among the three circulator ports, $1 \rightarrow 2$, $2 \rightarrow 3$, $3 \rightarrow 1$, and so forth.

The continuous “frequency tracking” conditions for the operation of a broadband junction circulator were first reported by Wu and Rosenbaum [22], whose design requires the junction to operate below FMR with the magnetization magnetized slightly above saturation. The other design parameters postulated by Wu and Rosenbaum are as follows:

$$\theta = 0.5 \text{ rad} \quad (54)$$

$$\epsilon_d = \epsilon_f \quad (55)$$

$$\omega R(\mu_0 \mu_{\text{eff}} \epsilon_f)^{-1/2} = 1.82 \quad (56)$$

where θ is half the port suspension angle, ϵ_f (ϵ_d) is the permittivity of the ferrite (dielectric matching) material, μ_{eff} ($= 0.556$) is the effective permeability of the ferrite junction, R is the junction radius, μ_0 is the permeability of air, and ω is the angular frequency (at the center of the transmission band). Equation (55) implies that the ferrite and the dielectric-matching material, also called the dielectric-matching “sleeve,” are characterized by the same dielectric constant. Thus, the junction and the sleeve can be conveniently fabricated using the same piece of ferrite, which needs to be magnetized slightly above saturation so as to avoid domain wall loss. As such, there is no need to separately fabricate a dielectric-matching sleeve surrounding the ferrite junction thereby reducing the fabrication costs. The thickness of the junction is not specified by the design, whose value is based on matching of the circulator port impedance:

$$Z_{\text{in}} = \left(\frac{\mu_{\text{eff}}}{\epsilon_f} \right)^{1/2} \quad (57)$$

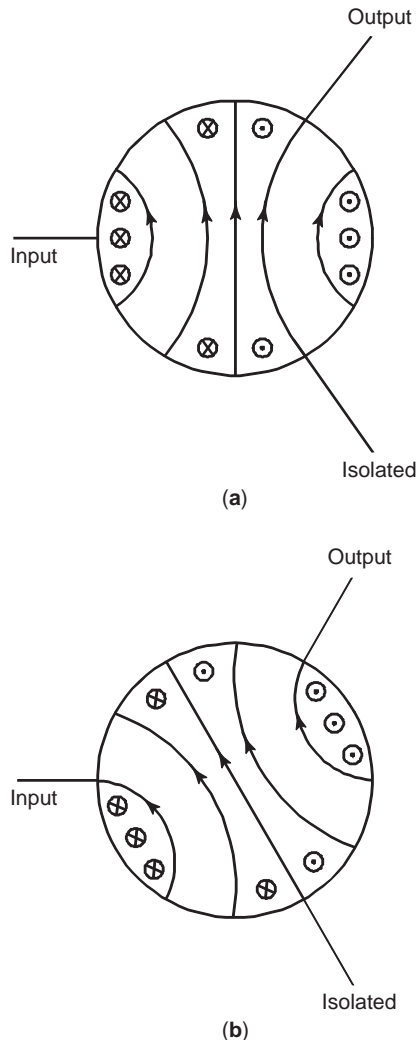


Figure 5. Field pattern for dipole excitations in an isotropic junction (a) and in a ferrite junction at circulation (b). Solid lines represent magnetic field lines; crosses/dots, electric lines entering and exiting the plane of the drawings.

The Wu–Rosenbaum circulator design provides an octave bandwidth extending from ω_m to $2\omega_m$ [22]. Here, $\omega_m = |\gamma| \mu_0 M_S$ and γ is the gyromagnetic ratio and M_S , the saturation magnetization [Eq. (14)].

Schloemann and Blight [23] have improved the Wu–Rosenbaum circulator performance [22] by extending the transmission band at a lower frequency limit. Schloemann and Blight were able to calculate the junction response in the FMR region where the effective permeability becomes a negative number [22]. To proceed, they employed the modified Bessel functions of the first kind to account for the evanescent modes excited during FMR. They also claimed that the measured bandwidth by Wu and Rotenbaum was narrower than that calculated, due to the nonuniform magnetic bias field accidentally introduced with the measurement. To prove their assertion, Schloemann and Blight [23] fabricated two semispherical domes using the same ferrite material as in the junction to cover the junction from above and below so as to ensure a uniform demagnetizing field within the junction area. By so doing, they successfully measured a 3:1 bandwidth for a crystal YIG (yttrium iron garnet) junction circulator (2.8–10.2 GHz) and for a crystal lithium ferrite junction circulator (5.8–18 GHz) [23].

All ferrite circulators are functional utilizing the non-reciprocal property for wave propagation in ferrites, providing low insertion loss and high isolation over a broad frequency band. The bandwidth is proportional to the inverse of the Q value of the cavity resonator formed by the circulator junction, namely, the region of the ferrite bound by metal boundaries at top and bottom and by a magnetic wall at periphery. Typically the bandwidth is about 5–15% of the center frequency, depending on the deployed suspension angle of the ports, unless the frequency-tracking conditions are enforced as postulated by Wu and Rosenbaum [22]. The circulator junction is a low- Q device, since the three coupling ports bestow the junction an open structure, allowing electromagnetic waves to leak from the junction area; the larger the port suspension angle, the broader the transmission bandwidth that will result. It is thus desirable to adopt the Wu–Rosenbaum parameters [Eqs. (54)–(56)] to achieve the broadest transmission band, unless the circulator operation is attempted at high power (or if one attempts to minimize the junction size as discussed later).

To design a circulator junction at high power we must consider the following issues: heat production, intermodulation, spin-wave generation, and thermal stability. There are two kinds of magnetic loss. The first kind is associated with magnetic domain wall motion, and the second kind relates to the intrinsic magnetic relaxation processes underlying the magnon–phonon interactions. To eliminate magnetic loss of the first kind, the ferrite junction needs to be magnetically biased well above saturation. This eliminates residual domains existent with a barely magnetized ferrite junction, thereby reducing heat. For this reason, a power circulator circuit should be biased well above FMR. The second kind of magnetic loss is characterized by a material parameter called *FMR linewidth* (ΔH) Eq. (26). To minimize magnetic loss of the second kind, one prefers to employ low-loss ferrites such as

crystal YIG and lithium ferrite, since these materials have shown the lowest ΔH values at the X-band and at the Ka -band frequencies, respectively.

The second issue relates to nonlinear coupling of electromagnetic signals at high power. This gives rise to intermodulation noise. In a ferrite junction intermodulation noise grows quickly with power, identified as clicking noises in a telephone line, which must be minimized, if not totally eliminated, to ensure quality communication. In the following we argue how intermodulation noise can be minimized in a semiquantitative manner. Let the power be applied to the input port of a circulator junction as

$$P = i^2 Z_{in} \quad (58a)$$

$$= h^2 w^2 Z_{in} \quad (58b)$$

$$= M_s^2 \left(\frac{h}{M_s} \right)^2 4R^2 \sin^2 \theta Z_{in} \quad (58c)$$

$$= M_s^2 |\mu_{eff} - 1|^{-2} \left| \frac{m}{M_s} \right|^2 4R^2 \sin^2 \theta Z_{in} \quad (58d)$$

$$= M_s^2 |\mu_{eff} - 1|^{-2} \delta_m^2 4R^2 \sin^2 \theta Z_{in} \quad (58e)$$

where i denotes the RF current flowing into the input port of impedance Z_{in} , h is the transverse RF magnetic field at the junction edge adjacent to the input port, w is the width of the input port, R is the radius of the junction, θ is half the port suspension angle, μ_{eff} is the effective permeability of the junction defined by

$$\mu_{eff} = 1 + \frac{m}{h} \quad (59)$$

and δ_m denotes the excursion angle of the magnetization vector away from the DC bias field direction, or the deviation or inclination angle of the precessional motion of electron spins in the ferrite junction around the DC bias field direction

$$\delta_m \approx \left| \frac{m}{M_s} \right| \quad (60)$$

where δ_m measures the extent that linear approximation of magnetic excitation remains valid inside the ferrite junction. In other words, if δ_m is large, linear approximation no longer holds true and nonlinear effects become noticeable. As a general rule, the onset of nonlinearity, or intermodulation coupling, is given by

$$\delta_m \leq 0.1 \text{ rad} \quad (61)$$

beyond which nonlinear effects set in, giving rise to appreciable amount of intermodulation noise. In Eq. (58e) δ_m denotes the excursion angle of the magnetization vector near the input port. However, the circulation mode assumes mostly the dipole mode, which implies the largest magnetic excitation near the input and the output ports (see Fig. 5). As such, the threshold condition of Eq. (61), which was derived at the input port, can be applied within

a multiplication constant (≈ 0.6) over the whole junction area, denoting the worst situation invoking the nonlinear interaction. Thus, we define the following parameter F denoting the figure of merit of a power circulator design characteristic of the amount of intermodulation noise as

$$F = 4\pi M_s R \sin \theta Z_{in}^{1/2} \tag{62}$$

by which Eq. (58a) becomes

$$P \propto F^2 \delta_m^2 \tag{63}$$

From Eq. (63) it is understood an effective power circulator design requires the value of F , the figure of merit, to be minimized, so as to yield minimum intermodulation manifested by δ_m under a given power excitation P .

Alternatively, the circulator junction problem at high power can be solved quantitatively, as proposed in [24]. By keeping high-order terms up to the third power of small-field quantities in Eq. (4), Eq. (9) becomes

$$\begin{aligned} \frac{-1}{\gamma} \frac{d\mathbf{m}}{dt} = & \mathbf{e}_z \times [H_{in} \mathbf{m} \\ & - M_s \mathbf{h} - (h_z + 4\pi N_z m_z) \mathbf{m} + m_z \mathbf{h}] \end{aligned} \tag{64}$$

where

$$m_z = M_s - M_z \approx \frac{\mathbf{m} \cdot \mathbf{m}}{2M_s} \tag{65}$$

denotes the z component of the RF magnetization vector that has been neglected in Eq. (9) under the first-order approximation [see Eq. (49)]. In Eq. (64) H_{in} is the internal DC field given by

$$H_{in} = H_0 - 4\pi N_z M_s \tag{66}$$

where H_0 is the applied DC field along the z axis and N_z is the axial demagnetizing factor [see Eq. (18)]. The schematic drawing at the bottom of Fig. 6 illustrates the relationship between intermodulation signals and the applied RF signals, where two RF signals are applied at two nearby carrier frequencies f_1 and f_2 , which are coupled via the (cubic) nonlinear terms in Eq. (64) so as to generate intermodulation signals at $2f_1 - f_2$ and $2f_2 - f_1$. At the top of Fig. 6 the ferrimagnetic amplifying echo signals are also shown; their significance will not be discussed until Section 7, where nonlinear magnetic microwave devices are introduced. Here we want to contrast both phenomena with the same physical origin with which intermodulation and ferrimagnetic echoing are driven by the same cubic nonlinear terms in the equation of motion [Eq. (64)] but with their respective responses expressed in the frequency domain and in the time-domain characteristic of different device applications.

It has been shown [24] that the nonlinear demagnetizing term in Eq. (64) plays a crucial role in bringing in intermodulation noise in a ferrite junction; the larger the demagnetizing field, the larger the intermodulation noise

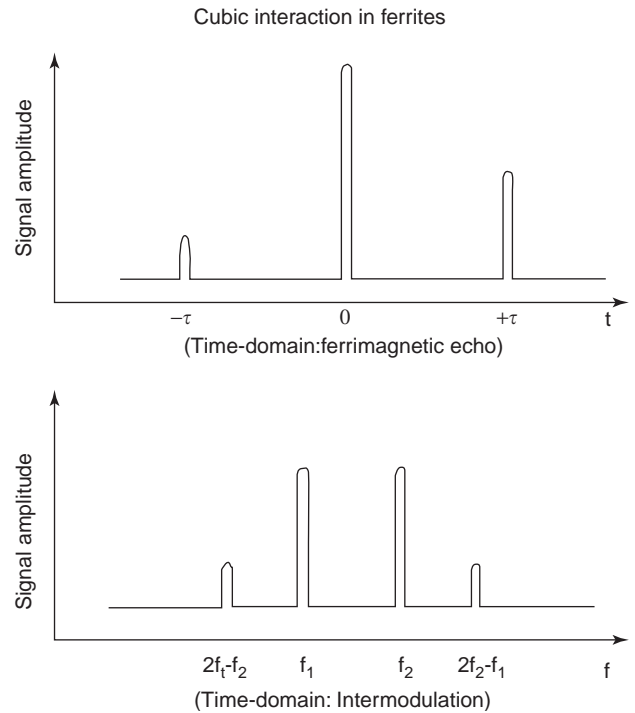


Figure 6. Nonlinear (cubic) coupling in an echo line and in a ferrite junction expressed in time domain and in frequency domain, giving rise to ferrimagnetic echo signals and intermodulation signals, respectively.

will be generated. This suggests the following bias configuration, which is thought to be effective in reducing intermodulation noise. As shown in Fig. 7, the two ferrite junctions implied by a stripline circulator are clamped

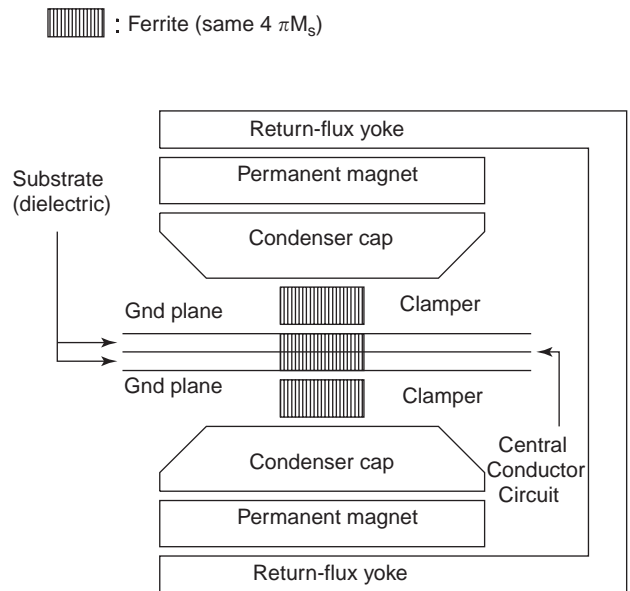


Figure 7. A ferrite junction is clamped between two ferrite cylinders having the same magnetization and cross-sectional area as the junction, and the clamped junction-cylinder assembly is biased by a permanent magnet pair included with flux condenser caps and return contour yoke.

between two cylindrical ferrite poles, which are placed outside the respective ground planes of the stripline circuit having the same saturation magnetization as the junction material and the same cross-sectional area as the junction geometry. While these two ferrite poles have no effect whatsoever in influencing the RF performance of the circulator junctions, they are effective in reducing the DC demagnetizing field within the junction areas so that $4\pi N_z$ in Eq. (64) becomes nearly zero, thereby minimizing intermodulation noise. Here we assume the thickness of the clamping ferrite poles to be much greater than the diameter of the junctions. In Fig. 7 a magnetic yoke (providing magnetic flux closure contour) and condensers (providing magnetic focusing) are used so as to facilitate the bias of the circulator junction circuit incorporating clamping ferrite poles.

We must point out here that the same ferrite clamping technique has been used by the ferrimagnetic echo experiments that reduced the demagnetizing field within an echo line such that an echo gain larger than unity can be realized [25,26]. More detail on ferrimagnetic echo amplification can be found in Section 7. The additional advantage associated with the magnetic bias configuration of Fig. 7 is that it is effective in inhibiting the onset of spin-wave instabilities occurring within the ferrite junction, thereby stabilizing its operation at high power. It is known that the demagnetizing field term in Eq. (64) can adversely affect the spin-wave instabilities at high power [13] and hence must be minimized; see discussion following Eq. (46). This constitutes the third issue, namely, that a ferrite junction to be applied at high power necessitates spin-wave stabilization. Furthermore, besides minimizing spin-waves, reducing the content of magnetostatic surface waves (MSSWs) is also necessary. We know that surface waves are inherent to a guiding structure possessing 2D discontinuities in magnetic or dielectric quantities [8]. In the microstrip geometry surface waves always exist whose modal spectrum depends on the thickness and the dielectric constant of the substrate material; the thicker the substrate and the larger the dielectric constant, the more surface modes will appear [8]. Analogously, one expects MSSWs to abound in a thick ferrite junction showing high saturation magnetization. This situation should be avoided if high power is attempted. Also, a thin ferrite junction facilitates heat removal via conduction so that it favors high-power applications.

The fourth issue on power circulator operation concerns thermal stability. Figure 8 shows four types of magnetization curves exhibited by magnetic materials with qualitatively different temperature dependence. The Q type represents the normal temperature dependence usually observed for metals and alloys. Almost all ferrites (e.g., Mn-Zn ferrite, Ni-Zn ferrite, Co ferrite) and garnets show the R-type temperature dependence. P-type and N-type temperature dependence were observed for some concentration ranges of Ni-Mn-Ti, Ni-Al, and Mn-Fe-Cr ferrites and for garnets in general [27]. In Fig. 8 Q and R types always show a negative slope for their magnetization curves. However, for P and N types the magnetization curves are possible to show a positive slope at certain temperature ranges. If positive slopes occur near room

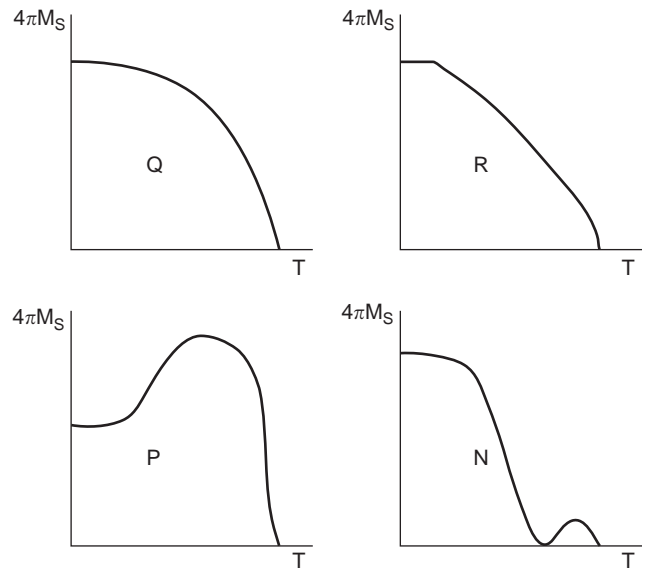


Figure 8. Temperature-dependent magnetization curves: Q type is normally observed for magnetic metals and alloys, and R type for ferrites; both of them show normal temperature dependence. P type and N type occur for some ferrites that show positive slopes at certain temperature ranges near room temperatures; they are termed *temperature-compensated ferrites*.

temperature, the ferrite is then called a *temperature-compensated ferrite*, which provides advantages when the ferrite is used at high power.

When applied at high power, the axial component of the magnetization vector decreases, since the spin's precessional motion dictates the magnetization vector to deviate or incline farther away from the direction of the DC bias field: the more the power applies, the further the deviation or inclination will result [Eq. (60)] in addition to more heat generated in the junction area. This causes the temperature of the junction to rise. However, for a P- or a N- type ferrite, the temperature rise is accompanied by an increase in saturation magnetization, which compensates for the decrease in its axial component expressed in Eq. (46), ensuring that the circulation conditions do not drift away as a result of thermal heating, thereby stabilizing the circulator operation at high power. It is thus clear that temperature-compensated ferrites are preferred when a circulator junction is to be applied at high power.

The size of a ferrite junction can be considerably reduced if the junction is biased above FMR providing directly 50Ω impedance at the junction ports. The advantage of using the bias-below FMR configuration is that it is then possible to realize the frequency-tracking conditions so as to enable the broadband operation of a ferrite junction [22,23]. However, the drawback is that, to invoke a bias-below FMR configuration, the junction acquires a large area, since the junction is then characterized by a relative permeability value considerably smaller than unity (≈ 0.556). In order to reduce the junction size, the junction has to be biased above FMR, utilizing an effective permeability value appreciably larger than unity ($\approx 5-6$). Furthermore, if the circulator design directly

provides $50\ \Omega$ impedance at junction ports, there is no need for transformers, resulting in miniaturization of the circulator circuit at low frequencies. By using these two techniques Hotech has fabricated 5-mm circulator junctions at the ISM (industrial–scientific–medical) band providing 15% bandwidth in transmission. The ISM band includes the frequency ranging from 902 to 928 MHz and from 2.4 to 2.48 GHz, which do not require a FCC (U.S. Federal Communications Commission) license. Even smaller circulator junctions are currently attempted by Hotech incorporating high-dielectric materials so that miniaturized UHF circulators in the order of 1 mm can be potentially fabricated in the future.

A conventional Y-junction circulator utilizes a low-Q resonator that causes the standing modes to couple in and out electromagnetic energy in a nonreciprocal manner [21]. To admit ultrabroadband operation of a circulator junction, one must abandon the conventional standing-mode picture to allow for traveling waves. Broadband two-port isolators using the traveling displacement modes or edge modes were first reported by Hines in 1961 [28]. In Fig. 9 a stripline is fabricated on top of a ferrite substrate and a dissipation pad, such as a thin layer of poor conductor, is deposited at one side of the substrate next to the stripline circuit. The superstrate, which consists of the same ferrite material, stacks above the substrate, and ground planes are attached to the substrate and superstrate at their outer surfaces. Superstrate and ground

planes are not shown in Fig. 9. In the presence of a vertically applied bias magnetic field, wave propagation along the stripline is nonreciprocal: highly transmitting along one direction, but highly attenuating along the other direction. Thus, the RF magnetic field pattern shown as dashed curves in Fig. 7 displaces toward the edge of the stripline in the presence of the bias magnetic field, which is either shifting away from the dissipation pad (top drawing), or onto the dissipation pad (bottom drawing), resulting in little attenuation, or heavy attenuation, respectively. Hynes [28] has shown the operation of an edge-mode isolator providing a 3–1 transmission band, which is about the same bandwidth measured by Schloemann and Blight in 1986 wherein the frequency-tracking conditions were enforced employing the conventional (standing-mode) resonator-type circulator junctions [24].

Edge-mode traveling-wave operation can also be realized by three-port junction geometry. In Fig. 10, three adjoining ports exhibiting a three fold symmetry rather than two aligning ports are shown depositing on top of a triangularly shaped ferrite substrate. Again, a similar superstrate covers the substrate on top and two ground planes are applied at their respective outer surfaces. Superstrate and ground planes are not shown in Fig. 10. To operate, a bias

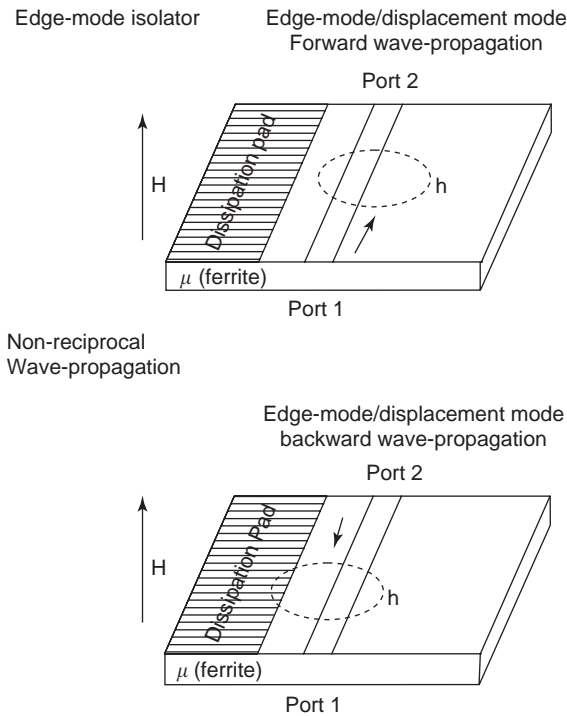


Figure 9. Operation of edge-mode isolator. In the presence of a bias magnetic field, the RF magnetic field pattern is shifted toward the edge of a stripline fabricated using ferrite materials deposited with dissipation pad at one side. As such, propagation of electromagnetic waves along the stripline is nonreciprocal, transmitting along one direction, top, but attenuating along the other direction, bottom.

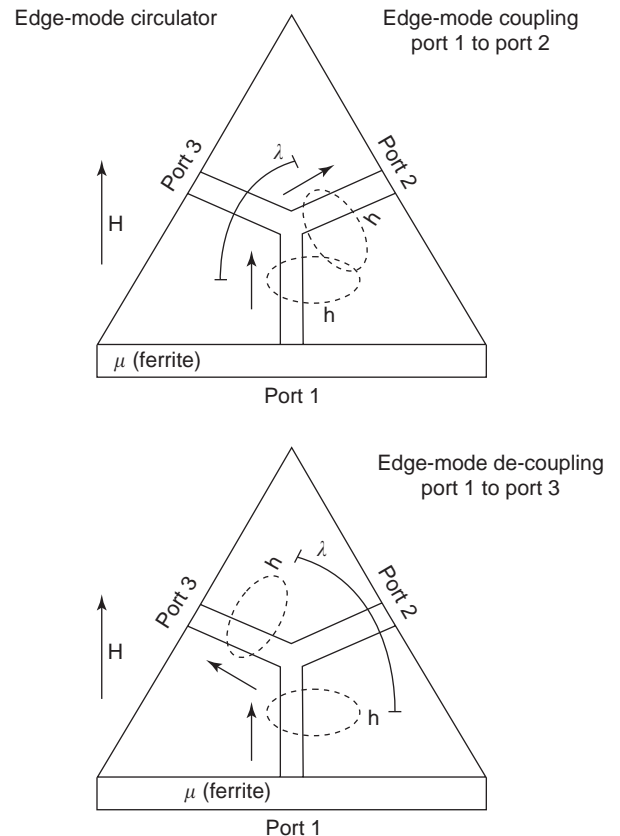


Figure 10. Operation of edge-mode circulator. In the presence of a bias magnetic field, the RF magnetic field pattern shifts toward the edge of a stripline fabricated with ferrite materials, which couples strongly to one joining line (top) but decouples to the other joining line (bottom), resulting in circulation action over a broadband.

magnetic field is applied along the junction thickness direction inducing the displacement modes or the edge modes to propagate in a manner analogous to Hines' isolator circuit shown in Fig. 9. As a consequence, edge modes couple strongly between ports 1 and 2, due to overlapping of their respective propagation electromagnetic waves with phase coherency, but decouple also strongly between ports 1 and 3 due to lack of the required wave overlapping. This results in the desired circulator operation in which electromagnetic signals entering port 1 can exit only from port 2, and so forth. In comparison to Fig. 9, the dissipation pad is not needed by Fig. 10; rather, the wave propagation direction, or the circulation direction, is dictated by the coupling/decoupling mechanism imposed by the ports. In Fig. 10 the dashed curves depict schematically the RF magnetic field pattern illustrating the coupling and decoupling of the propagation waves in ports.

In order to broaden the transmission band of an edge-mode circulator, it is necessary to enforce phase coherency for wave propagation between the input and the output ports across a broad frequency range; that is, phase coherency needs to be maintained over a wavelength distance denoted as λ in Fig. 10. Therefore, high-frequency signals couple more strongly near the center of the junction and low-frequency signals, near the side edge of the junction. Since the operation of a ferrite device requires the magnetization to scale with frequency [this ratio is known as *gyromagnetic ratio*; see Eq. (13)], one expects an ultrabroadband edge-mode circulator to occur if the ferrite junction shows different magnetizations scaled with the propagation wavelengths: large at the center but small at the side edge. This ultrabroadband circulator geometry is shown in Fig. 11, in which a composite substrate is illustrated consisting of five triangular shells of different ferrite materials, labeled as μ_1 to μ_5 , respectively, whose saturation magnetization decreases from center to edge progressively. In Fig. 11 the metal strip has been tapered accordingly from edge to center to accommodate the change in saturation magnetization, assuming that the ferrite materials are characterized by the same dielectric constant. Again, a similar geometry is assumed by the superstrate. Initial studies on circulators of Fig. 11 have shown a 10–1 transmission band. A U.S. utility patent application for ultrabroadband edge-mode circulator operation has been filed by Hotech.

An asymmetric circulator junction can be used as a broad stopband filter [29,30]. Broad stopband filters are required by radome applications protecting the receiver circuits from high-power incidence over a broad frequency band. The traditional filters utilizing coupled resonators can hardly provide the broad stopband operation, since high-order harmonics will inevitably appear at high-order harmonic frequencies. By using an asymmetric ferrite junction it is possible to induce the broad stopband operation. This is seen in Fig. 12, where an asymmetric ferrite junction is shown similar to that in Fig. 5 except that the cyclic symmetry has been removed. Instead, the input and the output ports still show the left-right (image) symmetry so as to allow the circulation conditions to occur. As shown in Fig. 12, at circulation, electromagnetic energy enters the input port and exits from the output port, with

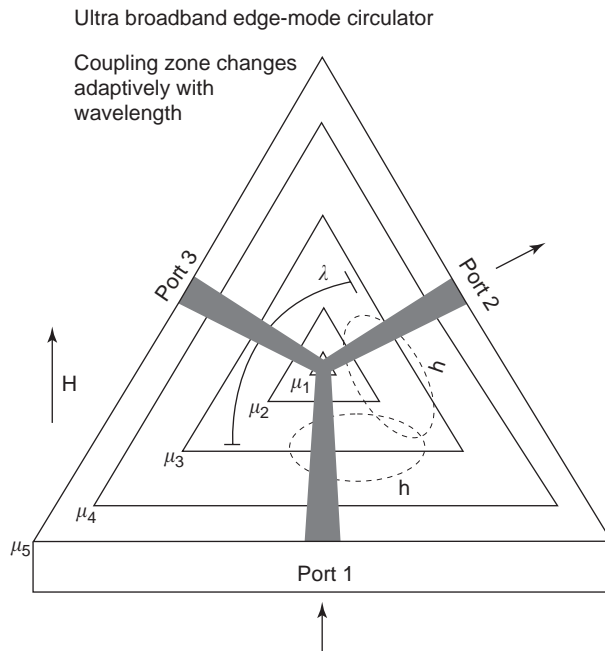


Figure 11. Operation of edge-mode circulator employing a composite substrate/superstrate structure containing five triangularly shaped shells labeled as μ_1 to μ_5 . The magnetization is increased from the side edge μ_5 toward center μ_1 to accommodate the phase-matching requirement to achieve ultrabroadband circulator operation.

the isolated port being connected with a matched dummy load. However, due to the asymmetric arrangement of the ports, high-order harmonics are effectively suppressed, resulting in broad stopband operation as desired. Broad stopband operation revealing a 10–1 bandwidth has been

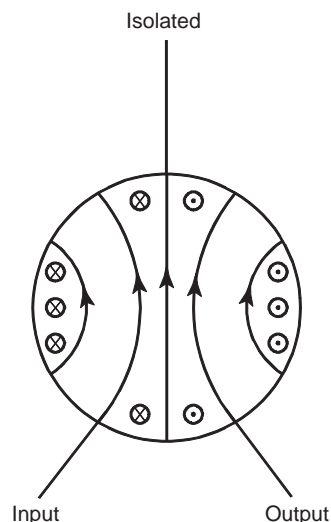


Figure 12. Dipole field pattern for an asymmetric ferrite junction excited at circulation. The field pattern still shows symmetry between the input and the output ports so that energy entering the input port is dumped into the output port, with the isolated port essentially electronically insulated from the input port. Asymmetric junction will provide a broad stopband.

measured by using an asymmetric circulator junction [29,30].

When biased above FMR, a three-port ferrite junction normally shows a transmission band no broader than 15% of its center frequency. However, this bandwidth can be increased if additional tuning ports are added to the junction geometry. This is shown in Fig. 13, where three tuning ports, called tuning “stubs,” have been added to the junction circuit still exhibiting the threefold symmetry of the ports. This allows the circulation conditions to occur as usual. However, the added three tuning stubs are effective in broadening the bandwidth if their length and impedance have been properly designed. It has been shown [31] that the added capacitance from the tuning stubs in Fig. 13 has broadened the bandwidth to 30% of its center frequency when biased above FMR.

Difficulty in using a ferrite substrate is that the bias magnetic field is required to have a magnitude of at least several thousand oersteds to effectively change the permeability of the substrate at X-band frequencies, [e.g., see Eq. (13)]. In order to reduce this bias field requirement, it is desirable to utilize the internal anisotropy field associated with a hexaferrite material to substitute, at least partially, the external field. In a ferrite material exhibiting hexagonal symmetry the internal crystalline anisotropy field can be as high as 50 kOe, admitting device applications even beyond 100 GHz [27]. For a hexaferrite material crystalline anisotropy causes the energy of magnetization direction along the c axis to differ from energies in the directions lying on the ab plane. For an M -type hexaferrite the c axis is an easy axis, and the magnetization vector favors alignment along the c axis. This implies that in an M -type hexaferrite the crystalline anisotropy behaves like an external field aligning the magnetization along the c axis [see the definition for H_A below Eq. (18)].

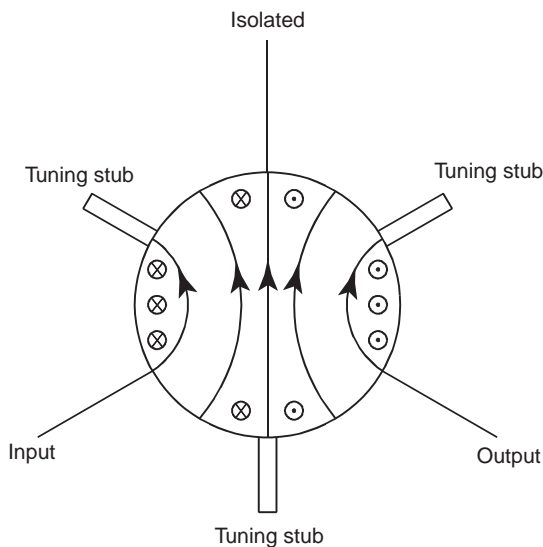


Figure 13. Three additional tuning ports, called *tuning stubs*, are added to a three-port circulator junction. By carefully designing the width and length of the tuning stubs, the added capacitances from the tuning ports can effectively broaden the transmission band.

Important device applications for M -type hexaferrites include circulators and isolators, wherein the easy axes coincide with the thickness direction of the substrates so as to eliminate, or at least reduce, the bias field requirement at high frequencies. Using M -type hexagonal ferrites, barium–strontium magnetoplumbites, a practical self-biasing stripline circulator, has been fabricated at 37 GHz, exhibiting 1 dB insertion loss and 15 dB isolation [32].

The performance of a circulator junction can be numerically simulated by assuming a 2D geometry [33–35]. Dielectric loss can be accounted for by assuming a complex permittivity for the ferrite junction

$$\varepsilon = \varepsilon_0 \varepsilon_r (1 - j \tan \delta) - \frac{j \sigma_f}{\omega} \quad (67)$$

and magnetic loss due to domain-wall motion by a complex permeability

$$\mu = \mu_0 (\mu' + j \mu'') \quad (68)$$

where $\tan \delta$ denotes the dielectric loss tangent, σ_f the conductivity, and ε_r the dielectric constant, and μ' and μ'' are the real and imaginary parts of permeability, respectively. Magnetic loss due to the intrinsic relaxation processes can be included by modifying the bias field to include an imaginary part proportional to the FMR linewidth ΔH [Eq. (26)]. Conductor loss due to imperfect metal boundaries of the ground planes and the stripline central conductor patch can be modeled by using the mean-field theory [36]; that is, the metal boundaries are withdrawn a distance δ_c into the interior of the imperfect metal bulk with the recessed volume to be filled by air [36]. Here δ_c denotes the (complex) skin depth

$$\delta_c = (1 + j) \sqrt{\frac{2}{\omega \mu_0 \sigma}} \quad (69)$$

and σ denotes the conductivity of the metal bulk. This procedure is analogous to Wheeler’s incremental impedance [37,38], and the resultant permittivity of the junction structure, which is viewed as an air–ferrite–air composite, is obtained as an average by using the mean-field theory [36]. As an example, numerical calculations have been applied to a microstrip circulator fabricated on top of an M -type Sc-barium hexaferrite characterized by the following parameters: $4\pi M_s = 2400$ G, $H_A = 19$ kOe, and $\varepsilon_r = 22$. Calculations compared nicely with measurements, shown in Fig. 14. Note that in performing calculations in Fig. 14 no adjustable parameters have been used (Fig. 14 appeared in an internal report from Hotech).

3. LUMPED-ELEMENT CIRCULATORS

The linear dimension of a distributed-element microwave device is comparable to the wavelength of the RF signal propagating in the device, for example, a ferrite junction circulator. At UHF/VHF frequencies the size of a distributed-element device sometimes turns out to be too bulky

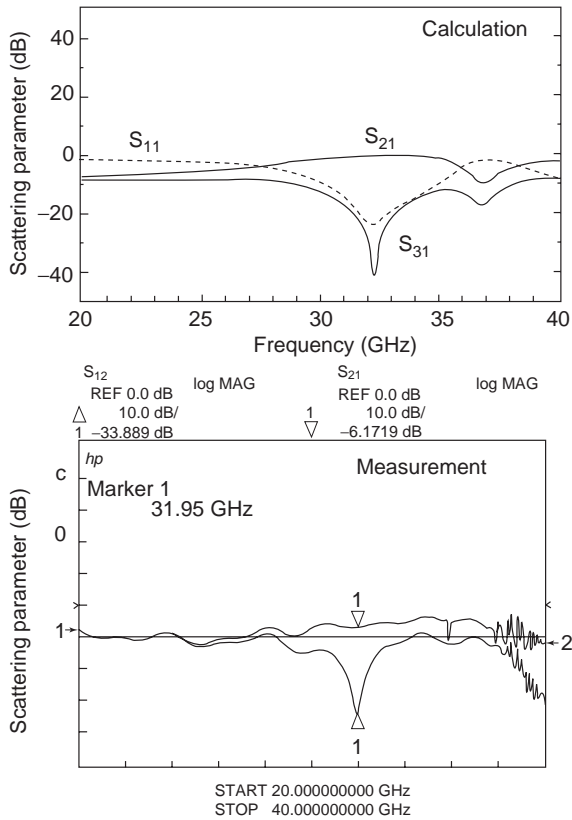


Figure 14. Calculated and measured scattering parameters of a self-biasing hexaferrite circulator.

to be handled practically, and hence the need for lumped-element devices arises. A *lumped-element device* is defined as having a linear dimension much smaller than the wavelength, and its performance can be analyzed in terms of the classical electric components, including resistors, capacitors, and inductors.

The original design of a lumped-element circulator consists of three coils wound around a common ferrite disk/puck intersecting each other at a 120° angle. The modern design makes use of the printed-circuit technique, and the three coils have been replaced by three interwoven microstrips deposited directly on top of the ferrite puck. The other side of the puck is deposited with a copper ground plane. The top view of the circuit is shown in Fig. 15, where the three microstrips intersect each other at 120° angles interwoven to retain the complete threefold symmetry. The importance of the interwoven geometry is that, besides maintaining the cyclic order of the circulator ports as defined by a circulator, interport capacitive coupling can be minimized to facilitate more precise designs of lumped-element circulators. In Fig. 15 the microstrips are grounded at their respective ends to complete the current loops for return paths (shown as heavy arcs in Fig. 15). Matching capacitances are inserted at the entrances of the microstrips to match the input impedance of the circulator to $50\text{-}\Omega$ feeder lines. The DC magnetic field is applied in the direction normal to the ferrite puck surfaces, which is designated as the z axis. A lumped-element circulator usually operates under the bias-above FMR conditions.

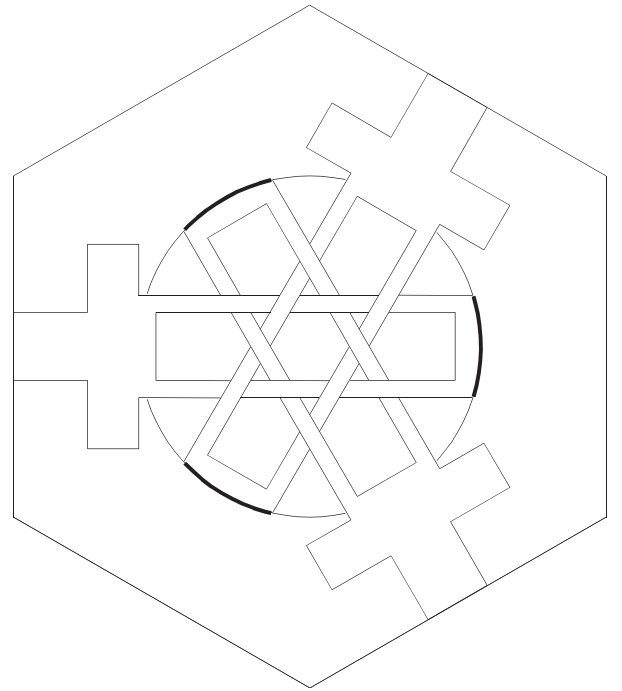


Figure 15. Top view of a lumped-element circulator fabricated using the printing circuit technique. The microstrips are interwoven with each other, rendering a threefold symmetry. The microstrips are electrically grounded on one end and connected with matching capacitances on the other end.

The voltage drop across the k th port microstrip or inductor is

$$\Delta v_k = j\omega \int_{A_k} \mathbf{b} \cdot \mathbf{e}_n da, \quad k = 1, 2, 3 \quad (70)$$

where A_k denotes the area enclosed by the feeding current of the k th strip. To be specific, we define A_k as the area bounded by the line along the center of the k th strip. When a ground plane is used for the current return path, the image strip will be included in conjunction with the original strip to totally specify the current path, and, hence, A_k . In Eq. (70) \mathbf{e}_n denotes the unit vector normal to the surface element da .

When the Polder permeability tensor is used, the \mathbf{b} field in Eq. (70) can be rewritten as

$$\mathbf{b} \cdot \mathbf{e}_n = \mu_0 [\mu \mathbf{h} \cdot \mathbf{e}_n - j\kappa \mathbf{h} \cdot (\mathbf{e}_z \times \mathbf{e}_n)] \quad (71)$$

where \mathbf{e}_z denotes the unit vector along the z axis. Here, μ and κ respectively are the diagonal and off-diagonal elements of the Polder tensor, Eqs. (10)–(12). The \mathbf{h} field can be written as

$$\mathbf{h} = \sum_{k=1}^3 \frac{i_k}{4\pi} \int_{S_k} \frac{d\mathbf{w}}{W_k} \frac{d\ell \times \mathbf{r}}{r^3} \quad (72)$$

where we have assumed the current to flow uniformly in the strips parallel to the length element $d\ell$. The total current in the k th strip is i_k , and W_k denotes the width of the

k th strip not necessarily a constant, for example, for the interwoven strips shown in Fig. 15. The k th strip is defined by the area S_k . In Eq. (72) dw is the width element, and vector \mathbf{r} connects the source point of the current to the observer point. Combining Eqs. (70) and (72), we obtain the following equation

$$\Delta v_i = \sum_{k=1}^3 Z_{ik} i_k \quad (73)$$

where the interport impedance Z_{ik} is given as

$$Z_{ik} = \frac{j\omega\mu_0}{4\pi} \int_{A_i} da' \int_{S_k} \frac{dw''}{W_k} \times \frac{\mu[d\ell'' \times (\mathbf{r}' - \mathbf{r}'')]\mathbf{e}_n - j\kappa[d\ell'' \times (\mathbf{r}' - \mathbf{r}'')] \cdot (\mathbf{e}_z \times \mathbf{e}_n)}{|\mathbf{r}' - \mathbf{r}''|^3} \quad (74)$$

The interport impedance of a cyclic three-port lumped-circuit element circulator can then be written as

$$\underline{\mathbf{Z}} = j\omega L \begin{pmatrix} 1 & \alpha + j\beta & \alpha - j\beta \\ \alpha - j\beta & 1 & \alpha + j\beta \\ \alpha + j\beta & \alpha - j\beta & 1 \end{pmatrix} \quad (75)$$

where

$$L = \frac{\mu\mu_0}{4\pi} \int_{A_1} da' \int_{S_1} \frac{dw'' [(d\ell'' \times (\mathbf{r}' - \mathbf{r}''))\mathbf{e}_n]}{W_1 |\mathbf{r}' - \mathbf{r}''|^3} \quad (76)$$

$$\alpha = \frac{1}{L} \left[\frac{\mu\mu_0}{4\pi} \int_{A_1} da' \int_{S_2} \frac{dw'' [(d\ell'' \times (\mathbf{r}' - \mathbf{r}''))\mathbf{e}_n]}{W_2 |\mathbf{r}' - \mathbf{r}''|^3} \right] \quad (77)$$

$$\beta = \frac{1}{L} \left[\frac{\kappa\mu_0}{4\pi} \int_{A_1} da' \int_{S_2} \frac{dw'' [(d\ell'' \times (\mathbf{r}' - \mathbf{r}'')) \cdot (\mathbf{e}_z \times \mathbf{e}_n)]}{W_2 |\mathbf{r}' - \mathbf{r}''|^3} \right] \quad (78)$$

and

L = self-inductance of each of the current strips

αL = mutual inductance between each pair of the current strips

$\mp j\beta L$ = gyromagnetic inductance between each pair of the current strips

We note that the gyromagnetic component of the interport inductance is nonreciprocal under port exchange. This renders the circulation action for the circulator device. Once the interport impedance matrix is known [Eq. (75)], the circuit of Fig. 15 can then be fully analyzed by using Kirchhoff's law as performed by a classical circuit. Or, one can follow the route adopted by Bosma [19,20] to solve the circulation conditions for a given lumped-element circulator circuit. Literature on lumped-element circulators is cited in Refs. 39 and 40.

4. HEXAFERRITE WITH EASY PLANE

For a Y-type hexaferrite the c axis turns out to be a hard axis and the magnetization vector tends to lie in the ab plane, which is termed the “easy plane”. While it is thought M-type hexaferrite is appropriate for circulator and isolator applications requiring out-of-plane magnetic bias, Y-type hexaferrite is adequate as the substrate material for microwave tunable filters because of its large magnetization and in-plane anisotropy, as well as the ease in use—the demagnetizing field is negligible along the transverse directions of a planar device [41]. Also, elimination of the external magnets represents a significant step toward more compact circuit design, allowing for integration of the device with future semiconductor circuits.

The effective field associated with an easy plane can be derived from using Eqs. (15) and (21). However, this would result in a magnetization–orientation–dependent effective field, as first demonstrated by Schloemann et al. [42], which is in contrast to the conventional concept of a magnetic field [see Eq. (85)]. In the following we define a mean effective field characteristic of the anisotropy of an easy plane from an operational point of view. The precessional motion of the magnetization vector is depicted in Fig. 16 for both cases of an easy axis (top) and an easy plane (bottom). For an easy axis the magnetization vector undergoes a uniform precessional motion around the easy axis, experiencing a uniform torque exerted by the anisotropy, resulting in a constant angular velocity. This is shown in a polar plot at the top of Fig. 17, where the loci of the angular velocity ω traces a circle. However, for the case of an easy plane (Fig. 16, bottom), the precessional motion of the magnetization vector is not uniform. The anisotropy field exerts no torque at all on the magnetization vector at points A and A' lying on the easy plane, and a maximum

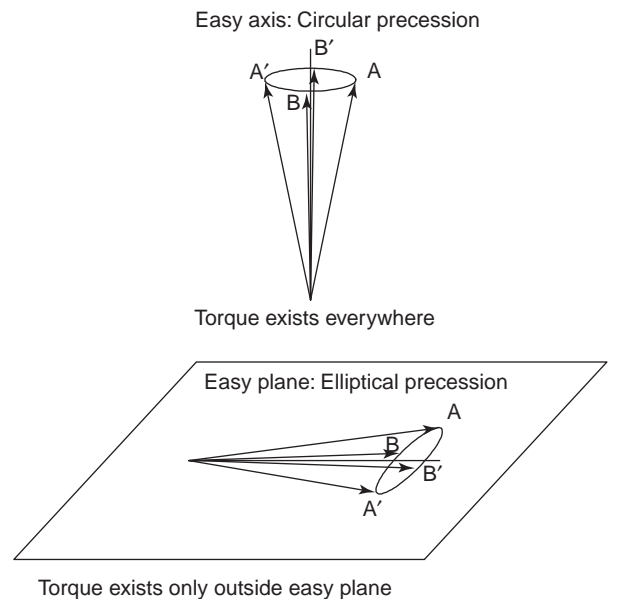


Figure 16. Precessional motion of the magnetization vector around an easy axis (top) and an easy plane (bottom).

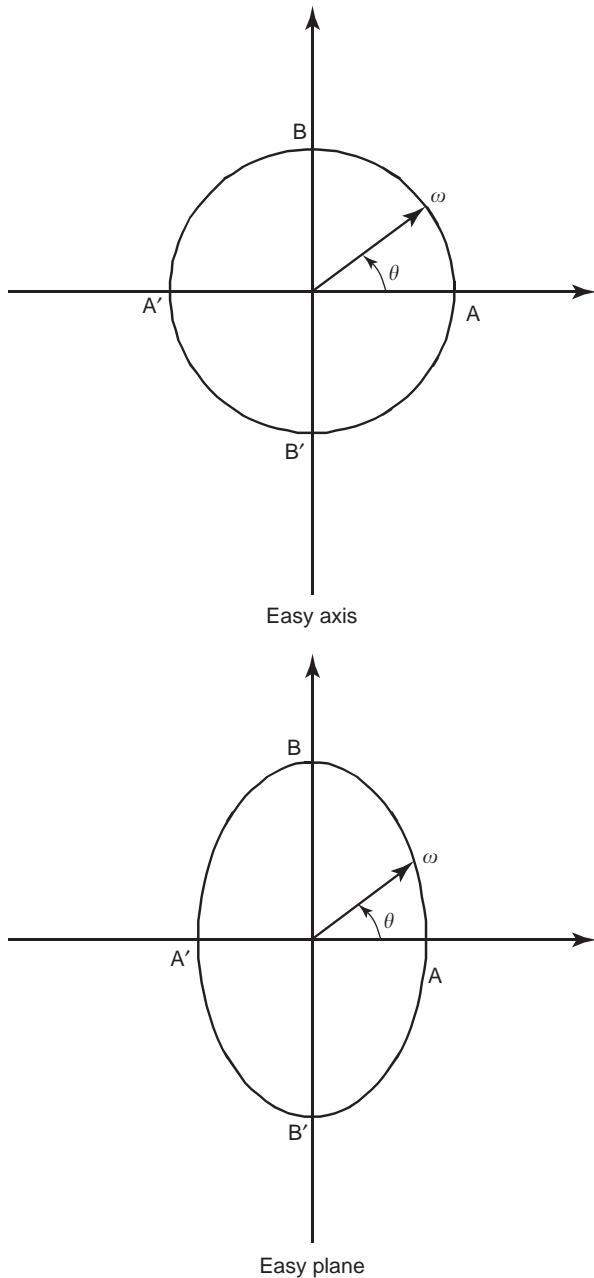


Figure 17. Polar plots of the instantaneous angular velocity of the magnetization vector precessing around an easy axis (top) and an easy plane (bottom).

torque is exerted by the anisotropy at the vertical positions marked as *B* and *B'* at the bottom of Fig. 16. Thus, in the presence of an easy plane the loci of the angular velocity traces out an ellipse, as shown at bottom of Fig. 17, whose semi-major and semi-minor axes are, respectively

$$\omega_{\max} = \gamma(H_0 + H_A), \quad \omega_{\min} = \gamma H_0 \quad (79)$$

Here, H_0 denotes the external field; H_A , the anisotropy field measured by Vibrational Sample Magnetometer (VSM); and γ , the gyromagnetic ratio. The period of the

nonuniform precessional motion is

$$T = \int_0^{2\pi} \frac{d\theta}{\omega} \quad (80)$$

where θ denotes the precessing angle of the magnetization vector shown in Fig. 17. Let this nonuniform magnetization vector precessional motion be associated with an effective internal field H_i whose Larmor frequency γH_i coincides with the period given by Eq. (80):

$$\gamma H_i = \frac{2\pi}{T} \quad (81)$$

We derive, therefore

$$H_i = \left[\frac{\gamma}{2\pi} \int_0^{2\pi} \frac{d\theta}{\omega(\theta)} \right]^{-1} \quad (82)$$

When the functional form of $\omega(\theta)$ is specified as an ellipse in the polar plot whose semi-major and semi-minor axes are given by Eq. (79), respectively, we obtain the following analytic equation from Eq. (82):

$$H_i = [H_0(H_0 + H_A)]^{1/2} \quad (83)$$

Figure 17 shows how the anisotropy field H_A adds to the external field H_0 for both the cases of an easy axis and an easy plane. For a cubic material, or an isotropic material, the anisotropy field is insignificant comparing to H_0 , and the magnetization vector undergoes a uniform precessional motion whose angular velocity is a constant, tracing out a circle of radius γH_0 , denoted as ω_{\min} in Eq. (79). For an easy axis pointing along the *c*-axis of an *M*-type hexaferrite, H_A adds to H_0 arithmetically, wherein the magnetization vector still undergoes a uniform precessional motion whose angular velocity traces out a circle of radius $\gamma(H_0 + H_A)$, denoted as ω_{\max} in Eq. (79). However, for an easy plane coincident with the *ab* plane of a *Y*-type hexaferrite, the magnetization vector no longer performs a uniform precessional motion, and the loci of the angular velocity becomes, instead, an ellipse whose semi-major and semi-minor axes are respectively ω_{\max} and ω_{\min} given by Eq. (79). These three kinds of magnetization vector precessional motions are shown as solid curves in Fig. 18.

Now, Eq. (83) dictates that in the presence of an easy plane the magnetization vector can still be visualized as if it were performing a uniform precessional motion as long as the associated hypothetical motion is characterized by a Larmor frequency whose period is given by Eq. (80). This hypothetical motion is depicted in Fig. 18 as a dashed circle whose radius is γH_i , as specified by Eq. (83). This gives rise to an expression for the effective internal field H_i characteristic of an easy plane, Eq. (83). Note that H_i assumes a magnitude between the two fields corresponding to the isotropic case H_0 and the case of an easy axis $H_0 + H_A$. Actually, H_i happens to be the geometric mean of these two fields: H_0 and $H_0 + H_A$ [Eq. (83)]. In other words,

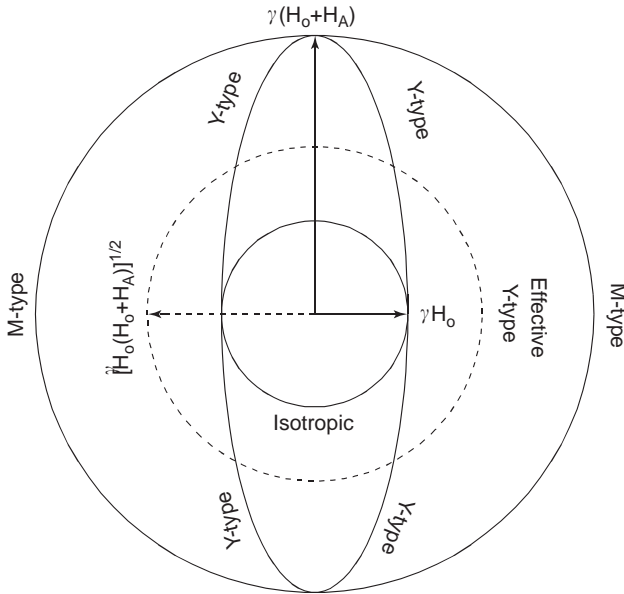


Figure 18. Loci of the angular velocities for an isotropic material, an M-type hexaferrite, and a Y-type hexaferrite, and construction of the effective internal field for the Y-type hexaferrite.

H_i can be constructed in a geometric manner such that in Fig. 18 a hypothetical circle is drawn whose area equals that of an ellipse representing the actual loci of the angular velocity. In this discussion we have assumed the other DC effective fields to be zero, including the DC demagnetizing fields. In case there are nonzero DC fields other than H_0 , they need to be added to H_0 arithmetically before the geometrical construction of H_i giving rise to the total effective internal field in a Y-type hexaferrite exhibiting a magnetic easy plane. The effective field expression [Eq. (83)], applies to wave propagation of arbitrary polarization, as long as the longitudinal component of the magnetization vector does not couple into the precessional motion, as assumed by the small-signal approximation in deriving linearized equations of motion.

By using Eq. (83) the resonant frequency of the uniform mode in a Y-type hexaferrite can be written as

$$\omega_0 = \gamma \{ [H_a + 4\pi M_s(N_x - N_z)][H_a + H_A + 4\pi M_s \times (N_y - N_z)] \}^{1/2} \quad (84)$$

which was derived by Schloemann et al. [42]. However, we must point out that in deriving Eq. (84) those authors have used the following effective field for the planar anisotropy [37]

$$\mathbf{H}_i = \mathbf{e}_A \mathbf{H}_A \cdot \frac{\mathbf{M}}{\mathbf{M}_s} \quad (85)$$

whereas the effective field we used in deriving Eq. (84) is Eq. (83). The difference is that Eq. (83) is a mean effective field, and Eq. (85) is an instantaneous effective field. In Eq. (85) \mathbf{H}_A denotes the anisotropy field along the hard axis whose unit vector is \mathbf{e}_A , and \mathbf{M} is the magnetization vector. In comparison, the corresponding resonant frequency of

Kittel uniform mode for an M-type hexaferrite showing an easy axis is given by Eq. (52). The magnetization properties of an easy-plane Y-type hexaferrite including instability studies and spinwave linewidth measurements are discussed in further Refs. 43–46.

5. FERRITE NONRECIPROCAL RESONATORS

Microwave and millimeter-wave (MMW) devices and systems are becoming increasingly important today for both the defense and the commercial applications. For example, in the collision avoidance industries, low-profile conformal antennas are needed to provide electronically steerable radiations to detect and identify obstacles and extrusions in front of moving vehicles. On navigation the receiver antennas need to follow and trace the motion of GPS (global positioning system) satellites so as to continuously monitor and update their positions. Also, there is a need to create radiation nulls along certain spatial directions for an antenna transmitter/receiver to warrant secure and covert communications. Other applications can be found in target searching/tracking radars for surveillance, satellite communication systems, and TV program broadcasting antennas installed with civilian jet carriers. All of these applications require microwave phase shifters to participate at affordable prices.

Traditional approaches include the use of frequency-agile materials (varactors, ferroelectrics, and ferrites) so that the electrical length of a transmission line, and hence the propagation phase of an electromagnetic signal, can be electronically tuned by applying a voltage, a current, or a magnetic field. Microwave phase shifters thus obtained are expensive, requiring manual tuning or adjustment of the fabricated devices. Furthermore, the resultant phase shifting function is nonuniform, as it is dependent on the derived phase shift angle, since the impedance of the transmission line is inevitably changed accompanying the intended phase shift operation, in addition to the desired change in electrical length. This section introduces an innovative method permitting the phase-shifting function to be realized at microwave frequencies whose operation is independent of the phase shift angles. This method is based on the use of a nonreciprocal ferrite resonator that has been patented by Hotech [47].

For an isotropic resonator showing circular symmetry, for example, an isotropic dielectric microstrip/stripline disk/ring resonator, the excited modes contain both clockwise and counterclockwise rotational modes, because these two mode types are degenerate in frequency, and wave propagation is reciprocal with respect to rotation around the axial direction of the resonator. As such, phases are ambiguous if one attempts to couple out the excited modes from the resonator. This is no longer true for an anisotropic resonator in which the rotational symmetry for wave propagation is removed. As a consequence, the two eigenmodes associated with clockwise and counterclockwise rotations occur at different frequencies, and excitation of one mode excludes the other, and vice versa. This implies that the resonant modes are definite in phase, allowing the resonator to be effectively used as a

phase shifter. Most importantly, the eigenmodes excited in a nonreciprocal resonator are traveling waves, in contrast to the standing eigenmodes excited in a conventional isotropic resonator supporting reciprocal propagation of electromagnetic waves. This traveling-wave nature ensures that when used as a phase shifter, output from a nonreciprocal resonator is uniform or identical in amplitude, except for the desired change in phase, as imposed by the circular symmetry of the resonator circuit.

Among many possible solutions, an explicit example is discussed in this section utilizing a ferrite microstrip/stripline disk/ring resonator [47]. As stated above, in a ferrite disk/ring resonator magnetized along the axial direction the degeneracy between the two counterrotational modes is removed, and the resonant frequencies of these two eigenmodes occur at different frequencies, denoted as f_+ and f_- for the clockwise and the counterclockwise rotational modes, respectively [21]. While the operation of a ferrite junction circulator is designated at a frequency midway between these two frequencies, $f = (f_+ + f_-)/2$ [21], circularly polarized radiations are obtained from the disk/ring resonator if the excitation frequency is located near one of these two frequencies, f_+ or f_- [48]. This implies that at resonance the resonant mode in a ferrite resonator exhibiting circular symmetry consists of only one eigenmode whose phase can thus be determined without ambiguity, allowing the device to be used as a phase shifter.

For a 2D ferrite junction Maxwell equation, Eq. (1) reduces to the following form [19,20]:

$$\left(\frac{\partial^2}{\partial r^2} + \frac{1}{r} \frac{\partial}{\partial r} + \frac{1}{r^2} \frac{\partial^2}{\partial \phi^2} + k^2\right) e_z = 0 \quad (86)$$

$$h_\phi = \frac{j}{\omega \mu_0 \mu_{\text{eff}}} \left(\frac{\partial e_z}{\partial r} - \frac{j\kappa}{\mu} \frac{1}{r} \frac{\partial e_z}{\partial \phi} \right) \quad (87)$$

$$h_r = \frac{-j}{\omega \mu_0 \mu_{\text{eff}}} \left(\frac{1}{r} \frac{\partial e_z}{\partial \phi} + j \frac{\kappa}{\mu} \frac{\partial e_z}{\partial \phi} \right) \quad (88)$$

$$e_r = e_\phi = 0 = h_z \quad (89)$$

Here (r, ϕ, z) are the cylindrical coordinates, k relates to the angular frequency ω by the dispersion relationship [Eq. (37)], and the effective (relative) permeability μ_{eff} is [Eq. (38)]

$$\mu_{\text{eff}} = \frac{\mu^2 - \kappa^2}{\mu} \quad (90)$$

where κ and μ are the Polder permeability tensor elements [Eqs. (10)–(14)]. The normal-mode solution of a thin ferrite disk/ring resonator can thus be solved assuming the magnetic wall boundary conditions at the peripheries, resulting in analytic solutions involving the Bessel and the Neuman functions.

For a disk resonator of radius R , the magnetic wall boundary conditions require

$$h_\phi(R) = 0 \quad \text{for } n = \pm 1, \pm 2, \dots \quad (91)$$

or

$$\left[J'_n(kR) - \frac{\kappa}{\mu} \frac{n J_n(kR)}{kR} \right] = 0 \quad (92)$$

from which the normal-mode frequency ω or k can thus be solved as a function of H_{in} , or H_0 , Eq. (18). For a ferrite ring resonator of inner radius R_1 and outer radius R_2 , the magnetic wall boundary conditions require

$$h_\phi(R_1) = 0, \quad h_\phi(R_2) = 0, \quad \text{for } n = \pm 1, \pm 2, \dots \quad (93)$$

or

$$\left[J'_n(kR_1) - \frac{\kappa}{\mu} \frac{n J_n(kR_1)}{kR_1} \right] + \alpha \left[N'_n(kR_1) - \frac{\kappa}{\mu} \frac{n N_n(kR_1)}{kR_1} \right] = 0 \quad (94)$$

$$\left[J'_n(kR_2) - \frac{\kappa}{\mu} \frac{n J_n(kR_2)}{kR_2} \right] + \alpha \left[N'_n(kR_2) - \frac{\kappa}{\mu} \frac{n N_n(kR_2)}{kR_2} \right] = 0 \quad (95)$$

Here α denotes an unknown mode-mixing parameter. By solving Eqs. (94) and (95) simultaneously, k and α are determined, giving rise to the normal-mode frequency as a function of H_{in} , or H_0 , Eq. (18). In the above equations J_n denotes the Bessel function of order n , and N_n the Neuman function or order n , and $n = 1, 2, 3, \dots$ for the dipole, quadrupole, and octopole modes, respectively.

A gyromagnetic medium, or a ferrite, is characterized by a nonvanishing off-diagonal element of the Polder permeability tensor κ [Eqs. (10) and (12)]. If κ is zero, the medium becomes isotropic, and wave propagation is reciprocal with respect to the wave traveling direction, or the sign of the modal number n in the equations above. For an isotropic medium, Eq. (92) and Eqs. (94) and (95) reduce to those ordinary equations describing the normal-mode solutions of an isotropic disk resonator and ring resonator, respectively. However, if κ is nonzero, wave propagation is nonreciprocal and the normal-mode solutions become dependent on the wave traveling directions, or the sign of the modal number n , as implied by Eq. (92) and Eqs. (94) and (95) for a ferrite disk resonator and ring resonator, respectively. This forms the basis for the operation of a phase shifter using a nonreciprocal ferrite resonator.

Thus, by coupling out the resonant mode selectively from a sequence of positions of the resonator showing circular symmetry, the output phase can be varied, but keeping the output amplitude at a rather constant level. In making this statement we have assumed that the input position is fixed. The reverse also holds true. That is, by keeping the output position fixed, the output phase, but not the amplitude, can be varied if the input position is selectively changed from a sequence of positions showing circular symmetry, exciting the resonant mode with a definite phase. Since the ferrite operation is designed away from ferrimagnetic resonance (FMR), low insertion loss is thus possible. Note that a ferrite junction circulator, which makes use of the standing modes excited inside a ferrite

resonator (rather than the aforementioned traveling waves excited inside a nonreciprocal ferrite phase shifter), has generally shown an insertion loss less than 0.5 dB, and an even smaller insertion loss, say, less than 0.1 dB, can be obtained if the circulator operates over a narrow frequency band. This implies that phase shifts obtained from using a nonreciprocal ferrite resonator can potentially show low insertion loss, if the coupling impedance has been well matched at the input/output ports.

Depending on the speed requirement, the output phase from the ferrite resonator can be coupled out using switches of various kinds, including mechanical switches, optical switches, electronic switches, or electromechanical switches. A mechanical switch might be slow, but it is nevertheless cost-effective. Electronic switches can be fabricated using semiconductor junctions located in close proximity to the resonator ports to be integrated with the other phased-array elements. Microelectromechanical switches (MEMSs) provide high isolation between ports. Optical/superconducting switches are fast devices, and a response time shorter than 1 nsec can be readily achieved.

Phase shifters using ferrite resonators are narrowband devices whose bandwidth is typically 5% of the transmission frequencies. However, one is allowed to vary the bias field magnitude so as to alter the resonant mode of the resonator, resulting in continuous tuning of the transmission frequency. In this sense, phase shifters using ferrite resonators are operational as broadband devices. However, if broadband transmission is not a requirement, the resonator can be fabricated using a self-biasing hexaferrite so that the need for external bias is eliminated. Also, the fabrication of a phase shifter utilizing a ferrite resonator is cost-effective, since, once it is fabricated, there is no need for individual tuning for performance adjustment, because the transmission amplitude is a constant, as implied by the resonator's circular geometry. Phase shifters using ferrite resonators can be fabricated over all the microwave bands, from UHF to millimeter-wave frequencies.

Figure 19 shows an example that a ferrite-ring resonator serves to provide phase shifts invoking a rotating arm as the coupling mechanism. Unlike the other electronic/optical/MEMS coupling mechanisms, a rotating arm gives continuous change in phase shift angles. In Fig. 19 a hole is drilled with the ferrite substrate that constitutes the central hole of the ring resonator, as shown in Fig. 19. In Fig. 19 port 0 is not fixed in position, and is allowed to rotate around an axis at the center of the resonator, contacting loosely, but coupling tightly to, the inner periphery of the ring patch of the conductor circuit of the resonator. Air is used as the substrate material for port 0 so as to facilitate the mechanical motion of the rotating arm intended there. The other end of port 0 is connected to the central conductor of a coaxial cable, which penetrates through the ground plane of the resonator from below, protruding into the hole region formed by the ferrite resonator, joining port 0 and making a 90° angle at the point of joint. This forms a rotating arm, consisting of port 0 and the central conductor of the coax cable, shaped as the letter "L" but upside down. Via a gear assembly, the coax cable, and hence the rotating arm, is loaded into a step motor that drives the rotating arm to perform

rotational motion, as shown in Fig. 19. A rotary joint is used to isolate the rotational motion of the coax cable from the coax launcher, which serves as the entrance for the input signal.

A prototype phase shifter device, whose schematic is shown in Fig. 19, has been fabricated and tested by Hotech. The resonator used garnet G1010 (Trans-Tech, Adamstown, MD) biased by a magnet located under the resonator (Fig. 19). The bias field was measured to be 1050 kOe, and the resonant mode was identified as the 1^+ mode at 3.78 GHz (clockwise rotating dipole mode). The measured transmission phases, as well as amplitudes, are shown in Fig. 20 at the resonant frequency, as a function of the rotating arm positions, normalized with respect to those values when the rotating arm is located along the output port direction (Fig. 19). From Fig. 20 it is seen that

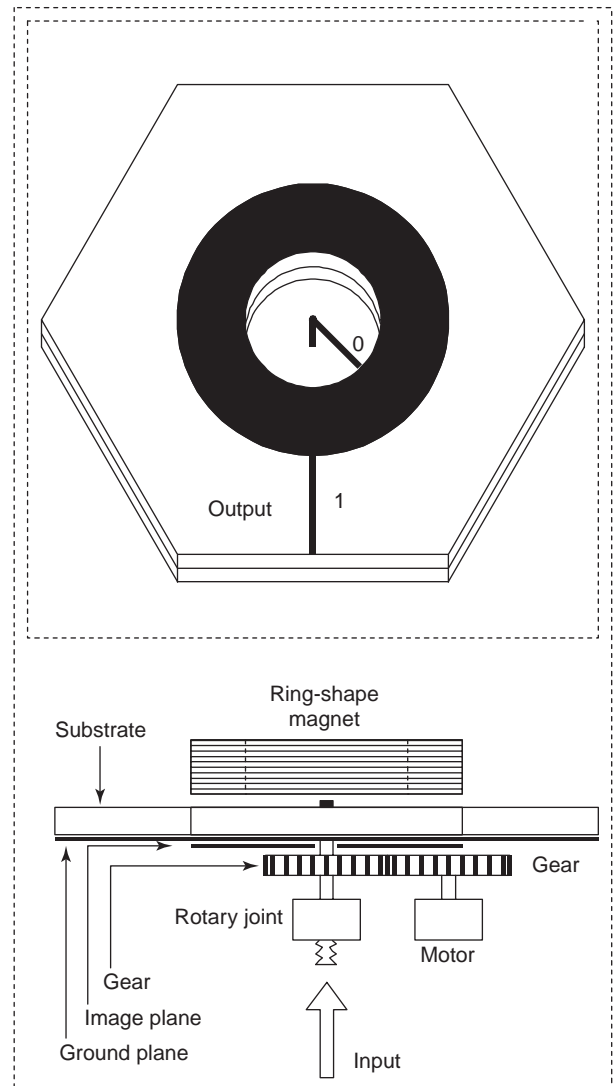


Figure 19. An example of microwave phase shifter construction using a nonreciprocal ferrite resonator. Due to the removed degeneracy in wave propagation, the phase of the resonant mode can thus be uniquely determined. The resonant mode is coupled out via the use of a rotating arm driven by a stepped motor to select the output phase via mechanical means.

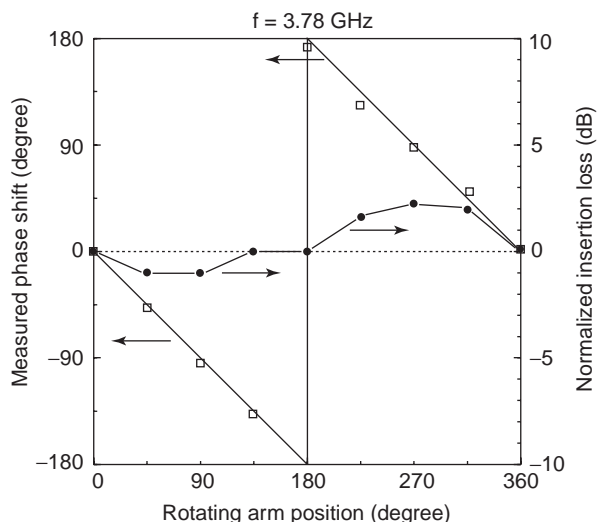


Figure 20. Transmission phase and amplitude at the resonant frequency plotted as a function of the rotating arm position. The measured phase and amplitude values have been normalized with those when the rotating arm is located at the 0° position, that is, when the arm is pointing toward the output port shown in Fig. 15.

the output phase from the phase shifter follows exactly the rotating arm position. Note that in Fig. 20, the measured transmission amplitudes of the phase shifter fluctuate slightly, to an extent of about ±2 dB, due to the imperfection impressed with device fabrication (the rotating arm was fabricated a bit off center). The measured bandwidth of the phase shifter was about 5% of the center transmission frequency, as expected. The minimum insertion loss was measured to be 0.33 dB when the rotating arm was located pointing along a 90° angle (see Fig. 20).

Instead of adopting mechanical means, the phase of the resonant modes excited with the ferrite ring resonator of Fig. 19 can also be coupled in and out using switches, as shown in Fig. 21. Although the construction of a mechanical rotating arm is cost-effective (Fig. (19)), its operation is slow, in the order of milliseconds, suffering from potential problems such as worn-out materials and hence mechanical breakdown. By using electronic switches, the phase shifter becomes more reliable and its response time greatly improves, in the order of microseconds for semiconductor junctions or MEMSs, and nanoseconds for superconducting or optical switches. The phase shifter, circuit shown in Fig. 21 consists of 64/8 switches at the inner/outer ports capable of providing 512 discrete phase angles in operation, if both the inner and outer port switches are under selection at the same time. Most importantly, the input/output ports are all symmetric with respect to one another, ensuring the transmission amplitude from the phase shifter to be uniform and independent of the angle in phase shifting. By applying a magnetic field perpendicular to the ring plane, one can vary the effective permeability of the ferrite resonator, resulting in tuning in the transmission frequencies. The tuning range of an octave band can be readily obtained from UHF to beyond Ka-band frequencies. A U.S. patent for the shifter circuit shown in Fig. 21 is currently pending (Hotech, 2004).

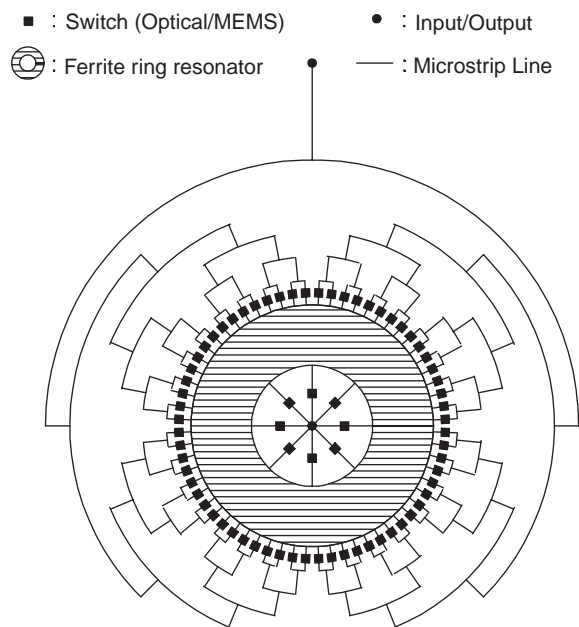


Figure 21. Novel ferrite phase shifter allowing for 512 phase values subject to frequency tuning capability. Isotropic symmetry of the device circuit ensures the phase shifting function to be uniform independent of the derived phase values.

6. MAGNETOSTATIC WAVES AND YIG FILM DEVICES

There exists an ever-increasing demand for signal processing devices that can be used for radar detection, electronics communication, and instrumentation applications. At UHF frequencies surface acoustic wave (SAW) devices have been widely used, providing phase shifting, time delaying, and other analog signal processing functions. However, at higher frequencies (>2 GHz), SAW devices are inefficient because of device fabrication and increased insertion loss. At microwave or even millimeter-wave frequencies signal processing devices have been largely achieved utilizing the newly developed magnetostatic wave (MSW) technology providing similar functional performance as SAW devices. Additional advantages include lower insertion loss, large bandwidth up to 1 GHz, ease of fabrication, frequency tuning, dispersion shaping, and nonlinear operation.

In contrast to SAWs, MSWs are very disperse and can be controlled readily by means of an external magnetic field. In principle, three basic types of MSWs are distinguished: forward volume MSW (MSFVW), backward volume MSW (MSBVW), and surface MSW (MSSW). An MSFVW is excited in the ferrite material, usually a YIG film, magnetized perpendicularly to the film plane. An MSBVW is excited in a YIG film and the magnetization direction is in the film plane along the wave propagation direction. An MSSW is also associated with a transverse magnetization, but the wave propagation is perpendicular to the direction of magnetization. For detailed discussions about excitation and dispersion trends of these three types of MSWs, see text discussion following Fig. 2. All three types of MSWs can be effectively used in fabricating

microwave devices, such as delay lines, tunable filters, phase shifters, resonators, noise suppressers, and amplitude correctors.

In order to reduce wave propagation loss, high-quality single-crystal yttrium iron garnet (YIG) films are usually used for the fabrication of MSW devices. When YIG single-crystal films are epitaxially grown on gadolinium gallium garnet (GGG) substrates, the ferromagnetic resonance (FMR) linewidth ΔH can be as narrow as 0.3 Oe at 9 GHz and 0.6 Oe at 20 GHz. Using Eq. (45), the propagation loss in an MSW delay line is 23 and 46 dB per μs at 9 and 20 GHz, respectively. Therefore, for a typical delay-line application, the propagation loss requiring 200 ns delay will be, respectively, 4.6 and 9.2 dB at 9 and 20 GHz. This compares very favorably with other kinds of delay lines such as a coaxial cable; at 9 GHz, a 200-ns coaxial cable would require a length of 50 m long, resulting in 30 dB loss in propagation.

MSWs are excited within YIG films using either microstrips or striplines as the transducer circuits. The guided electromagnetic modes of the transducers couple with the intrinsic excitations of the YIG films to launch magnetostatic waves traveling down from the input to the output transducers to perform the signal processing functions. In addition to straight microstrip/stripline transducers, meander lines, gratings, and interdigital and unidirectional transducers can also be used to couple in and out the MSW signals. Transducers involving short-circuited and open-circuited microstrip lines are commonly used for broadband MSW device applications. The entire MSSW, MSFVW, or MSBVW frequency band can be excited by using a narrow (10- μm) microstrip transducer. For narrowband devices, meander lines and gratings can be used. These transducers can be designed with 50–75 Ω input impedance over broad frequency bands, and matching circuits can be used to reduce mismatch losses.

In order to reduce spurious reflection of MSWs from the YIG film edges, MSW terminations or absorbers need to be utilized. These terminations can appear in the form of ferrite powders, or iron/permalloy rods, or even recording tapes, or GaAs thin films may be placed at the YIG edges.

However, the simplest way to avoid MSW interference is to cut the YIG edges into angles other than 90° such that the reflected beam is directed away from the active area of the MSW device [49]. Among the many MSW applications discussed in this section, we will briefly discuss the operation of MSW delay lines, filters, directional couplers, and resonators. Other nonlinear and magneto-optic MSW devices will be discussed in Sections 7 and 9, respectively.

6.1. MSW Delay Lines

Figure 22 shows the commonly used flip-over configuration for MSW delay lines. Microstrip lines serving as the transmitter and receiver for MSWs are fabricated using photolithographic technique on top of a dielectric superstrate such as alumina, sapphire, fused silica, or duroid material. The high-quality crystal YIG film epitaxially grown on GGG substrate is brought in contact with the transducers via a spacer layer and the overall dielectric-spacer–YIG–GGG assembly is placed between the poles of the biasing magnet. The biasing magnetic field can be directed either on the YIG film plane parallel to or perpendicular to the microstrip lines, or perpendicular to the YIG film plane, to provide MSBVW, MSSW, or MSFVW delay-line operation, respectively. Therefore, due to the coupling between the electromagnetic waves (EMWs) induced by the microstrip lines and the MSWs, the microstrip transmitter will excite MSWs that travel down the delay-line structure to be picked up by the microstrip receiver. Letting the distance between the transmitter and the receiver be D , the time delay for this device is

$$\tau_d = \frac{D}{v_g} \quad (96)$$

where $v_g = d\omega/dk$ denotes the group delay velocity of MSWs.

Delay-line elements exhibiting a linear dependence of the delay time τ_d on frequency are key components in pulse compression radar, microscan receiver, and Fourier transform systems. In general τ_d is highly dispersive, depending nonlinearly on frequency. There exists various methods that allows τ_d to show linear dependence on

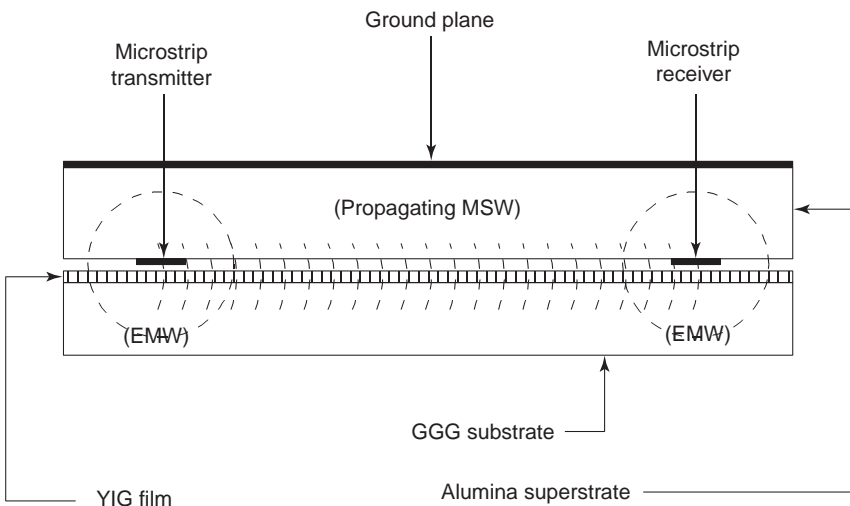


Figure 22. Schematic showing the MSW delay-line configuration. Microstrip transducers are used to couple in and out the MSWs. Depending on the direction of the bias magnetic field, all types of MSWs can be excited and detected using the present circuit configuration.

frequency over broad-frequency bands [50,51]. For example, at X band it is possible to show 1 GHz bandwidth for a linearly dispersion delay line by using a thin YIG film with thickness 20 μm covered with a thin dielectric superstrate of the same thickness [50]. Alternatively, the linear dependence of τ_d on frequency can be obtained by varying the separation distance between the ground plane and the YIG film [51], using the bias field gradients [52], or deploying multiple YIG films [53].

Nondispersive broadband delay lines are potential devices replacing phase shifters at microwave frequencies, providing electronically tuning capability for phased-array antenna and other signal processing component applications. Therefore, we require the time delay τ_d to be independent of the bias field strength and, hence, the frequency over a broad frequency bandwidth. A possible solution to this requirement is to cascade two broadband linearly dispersive delay lines with opposite propagation characteristics; that is, the first device operates for forward volume MSWs and the second, for backward MSWs such that they compensate each other to provide nondispersive dependence on frequencies. Other methods make use of nonuniform bias field [52] and multilayer structure [53], as discussed for the construction of a linearly dispersive delay-line device.

6.2. MSW Filters

Filtering of electronic signals is performed as a frequency-selective process realized in the frequency domain. In principle, any delay-line configuration can be viewed as a frequency filter structure provided that the following features are emphasized: low insertion loss occurring at the passband and high attenuation occurring at the stopbands. The filter characteristics can be feasibly obtained by controlling the transducer dimensions and the YIG/ground-plane separation. While short-circuited straight microstrip lines are generally used as transducers for a broadband filter, multielement grating transducers, such as those shown in Fig. 23, are used to synthesize narrowband filters. As such, narrowband filters of bandwidth 30 MHz tunable from 3 to 7 GHz have been successfully demonstrated [54]. Similarly, by carefully adjusting the width of the short-circuited microstrip transducer and the YIG film thickness, a broadband filter tunable from 0.3 to 12 GHz with stopband rejection better than 45 dB has been shown [55]. The advantage of using a MSW filter is that the passband can be tuned by varying the strength of the bias magnetic field.

6.3. MSW Directional Couplers

Figure 24 shows the schematic of an MSW directional coupler, with which two YIG films are deployed face to face, separated by a dielectric spacer. Ground planes are deposited on the outer sides of the GGG substrates and two multistrip lines are used as transducers, coupling in and out microwave energy through exchange of MSWs. By careful design of the microstrip line spacing as well as the dimensions of the dielectric spacer, the characteristic of a directional coupler can be obtained. Operation at full power coupling is possible [56]; hence, the directional coupler

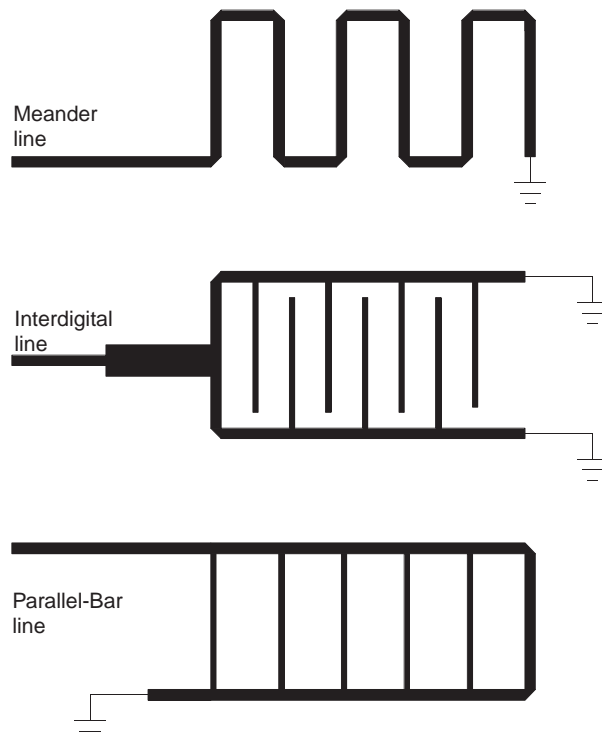


Figure 23. Microstrip circuit showing the geometry for multielement grating transducers used for excitation and receiving MSWs over a narrow frequency band for tunable filter applications.

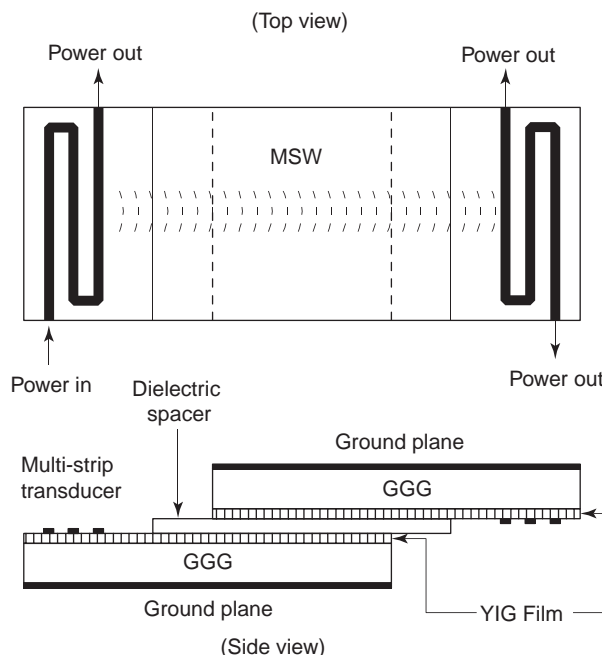


Figure 24. Schematic showing the MSW directional coupler configuration. Microstrip multistrip transducers are used to couple in and out the MSWs. All types of MSWs are possible depending on the bias field direction. The coupling coefficient between the input and output ports can be varied by changing the strength of the bias magnetic field.

can be equivalently used as a bandpass filter. Also, by varying the bias field strength the power transferring coefficient of the directional coupler can be consequently adjusted.

6.4. MSW Resonators

Although the MSW bandpass filters discussed above are useful for many applications, occasionally, considerable signal selectivity may be required over as narrow a pass-band width as possible. For example, tunable MSW resonators can be used as the frequency-selective elements in tunable oscillator circuits in the microwave frequency bands. MSSW resonators can be constructed by placing reflective metal gratings at the edges of the resonating cavity. Alternatively, grooves may be cut on the YIG film surface using wet etching or ion bombardment to form an MSSW cavity. This is shown in Fig. 25, in which two arrays of straight grooves are etched parallel to but on the two sides of the microstrip transducer lines, and, MSSWs, once generated, bounce back and forth indefinitely between these two groove arrays at resonance. As reported by Castera [57], MSSW resonators fabricated in this manner have shown a tuning capability between 2 and 5 GHz, exhibiting a loaded Q of 500 and an off-resonance rejection level of 15 dB.

For MSFVWs the bias magnetic field is perpendicular to the YIG film plane, and hence the propagation of MSFVWs is isotropic in all directions in the film plane. As such, the MSSW resonator shown in Fig. 25 is not suitable for MSFVW applications; it will result in poor off-resonance isolation, since at off resonance the propagation of MSFVWs at slightly tilted angles may still satisfy the

resonance condition. To avoid this drawback, a new configuration that involves two cavities coupled by MSFVWs has been proposed [58], as shown in Fig. 26. Each cavity consists of two etched-groove gratings and a single microstrip transducer. The two cavities are placed at a 90° angle and are coupled by a 45° obliquely oriented gratings capable of deflecting the incident MSW beam by a 90° angle. The resonators reported by Castera and Hartemann [58] exhibited insertion losses between 20 and 32 dB and a loaded Q value of 290–1570 over a tuning range of 2–11 GHz.

The resonator structures discussed so far involve reflection surfaces or mirrors, which is complex in the sense that they require groove or metal-strip arrays to be fabricated on the YIG film surface. To avoid this complexity, it is also possible to directly use the straight edges of the YIG film to form a MSW cavity resonator. Figure 27 shows such a straight-edge resonator (SER) device, where the YIG/GGG resonator, which is of a rectangular shape cut by a dicing saw, is placed on top of the dielectric substrate coupled in and out by the short-circuited microstrip transducers on both sides of the resonator. Depending on the bias field direction, both MSSW and MSFVW SERs can be constructed. Thus, MSSWs propagate along the surface of the YIG film and are reflected back onto the surface at the straight edges. A standing-wave pattern results and a high- Q resonance is obtained. In this manner a MSSW SER has been reported [59], exhibiting an insertion loss of 3.1 dB and a sideband suppression level better than 20 dB tunable from 1 to 22 GHz.

Finally, we consider the MSW structure of Fig. 28, which depicts a one-port resonator circuit. The circuit of Fig. 28 can be fabricated using photolithographic technique, and, hence, cutting of reflective grooves on the YIG film is avoided. In Fig. 28 MSSWs are excited within the metal window coupled in and out via the microstrip transducer. In order to form total reflection of the MSWs at the window boundary, and hence to achieve a high Q value, the geometry of the resonator needs to be carefully designed. The circuit of Fig. 28 allows for operation for all types of MSWs, and simple MSW resonators can be constructed.

7. MAGNETIC MICROWAVE NONLINEAR DEVICES

As discussed in Section 1, nonlinear terms appear in the equation of motion whenever the small-signal assumptions no longer hold true for the magnetization vector. Under these conditions, the magnetization field will couple to itself, resulting in spin-wave interactions between different wavenumbers and frequencies [Eq. (64)]. In this section we discuss how this nonlinear phenomena can be utilized for device applications. Among many important nonlinear devices, we will discuss frequency-selective limiters, signal-to-noise enhancers, amplitude correctors, and ferrimagnetic echoing devices.

7.1. Frequency-Selective Power Limiter

Frequency-selective limiters have been demonstrated using YIG spheres and ferrite slabs in the waveguide, coax,

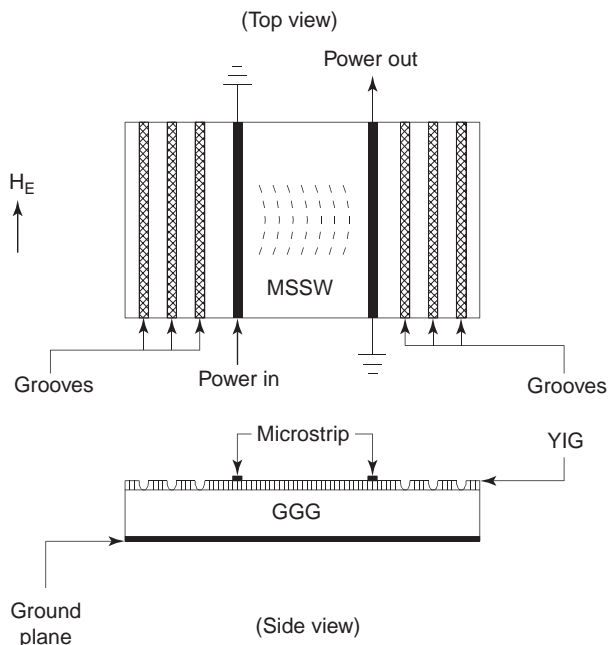


Figure 25. Schematic showing the configuration of an MSSW resonator. Reflecting arrays of grooves are cut on the YIG film surface to form an MSSW cavity resonator. The bias field is applied parallel to the microstrip transducer direction.

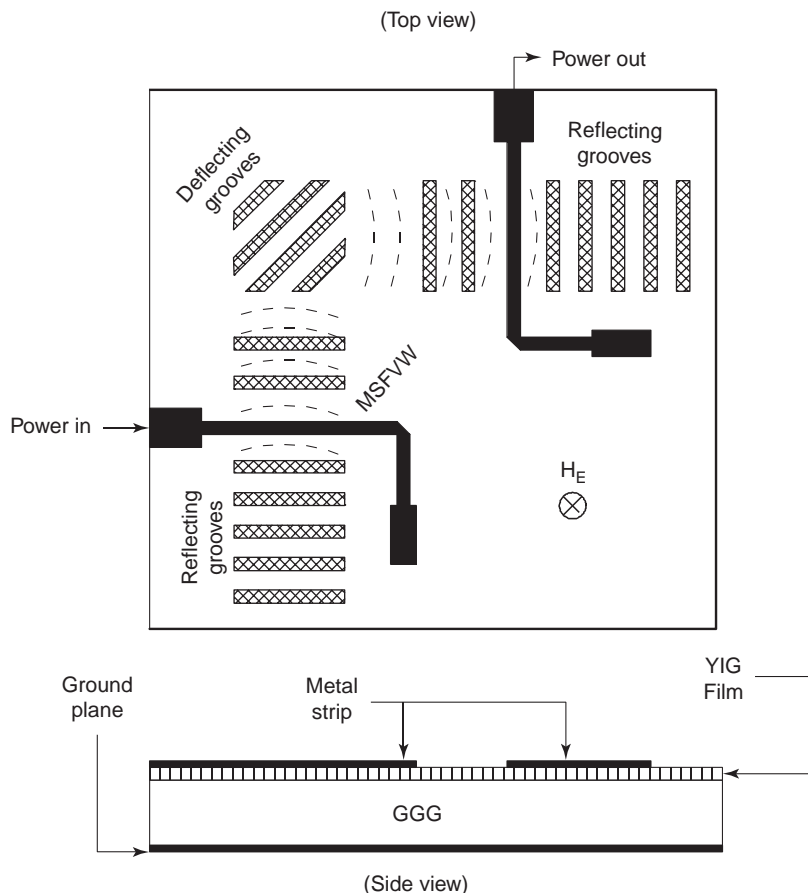


Figure 26. Schematic showing the configuration of an MSFVW resonator. Two cavities are placed at a 90° angle, and are coupled via MSFVWs passing through an obliquely oriented groove grating array. The bias field is applied perpendicular to the YIG film plane.

and stripline configurations [60]. We will discuss here the limiter operation using a single-crystal YIG film arranged in the configuration shown in Fig. 3 of Section 1, except that a meander line is normally used instead of a straight microstrip line. Also, a thick YIG film is preferred, because it implies an abundant spin-wave spectrum allowing the guided electromagnetic waves to react sufficiently with spin waves to induce instability at high power. All types of ferrite frequency-selective limiters operate analogously; when a transmission line is loaded with a ferrite element, the transmitted power cannot exceed a threshold value beyond which catastrophic energy transfer occurs between the guided RF electromagnetic fields and the spin precessional motion. This phenomenon has been discussed in Section 1, and it is generally known as the *Suhl spin-wave instability* [13]. Parallel pumping instability is irrelevant, since it requires the RF magnetic field to be applied parallel to the applied DC field direction, and this is not the case here.

Figure 29 depicts a simple picture explaining the operation of frequency-selective power limiter. As shown at the top left of Fig. 29, the relationship between the input power P_{in} and the output power P_{out} is roughly linear only when P_{in} is smaller than P_{th} , the threshold power. When P_{in} is larger than P_{th} , we observe that P_{out} becomes gradually saturated at P_s , and the excess power, $P_{in} - P_{out}$, couples into spin-wave motion to be ultimately converted

into lattice vibration, and hence dissipated as heat. Thus, when P_{in} is given as a function of frequency, as shown at the bottom left of Fig. 29, the excess power of $P_{in} - P_{th}$ will be removed by the limiter and the resultant output characteristic will be as shown at the top right of Fig. 29. We note that Fig. 29 shows only an idealized operation. In reality, the P_s level shown in the P_{out}/P_{in} diagram is not a constant; it increases slightly with P_{in} when P_{in} exceeds P_{th} . As such, instead of showing chopped-head peaks, the output will consist of rounded-head transmission peaks in the P_{out}/P_{in} diagram shown in Fig. 29.

As an example, in Ref. 61 a 57- μm -thick YIG film was coupled to a 25- μm -wide microstrip meander line of characteristic impedance 50 Ω fabricated on a high-dielectric-constant substrate. This limiter, which operated in the 2–4 GHz range showed a limiting range of 25 dB, a threshold input power level of 0 dBm, and a small-signal loss of 7 dB. The upper frequency limit was not sharply defined, since the limiting power decreased with increasing frequency, but operation up to 8 GHz is possible with this device.

The failure of the limiter device reported by Stizer and Goldie [61] to operate at high frequencies can be explained in terms of the onset condition giving rise to Suhl's spin-wave instabilities. As discussed in Section 1, Suhl's first-order instability occurs for spin waves possessing a frequency equal to half the applied RF frequency. Thus, above 8 GHz, the instability will occur in spin waves of

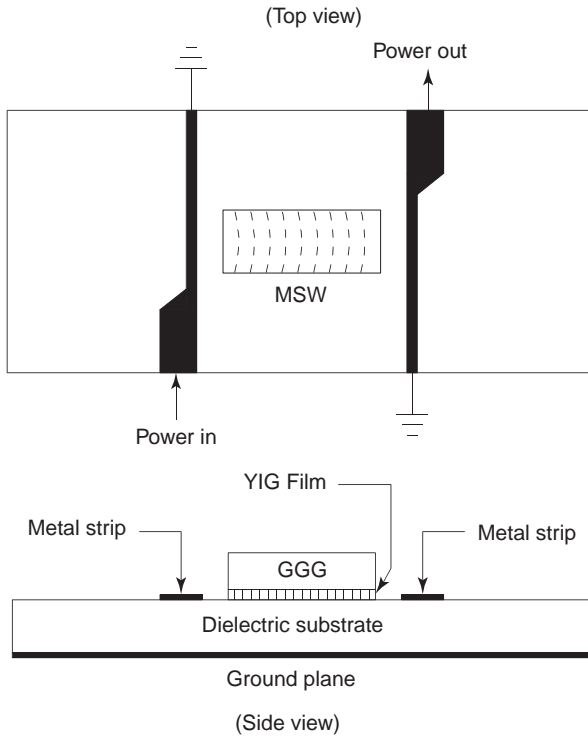


Figure 27. Schematic showing the configuration of a two-port MSW straight-edge resonator. The bias field can be applied perpendicular to the microstrip transducers in the YIG film plane, or perpendicular to the YIG film plane for MSFVW or MSSW operation, respectively.

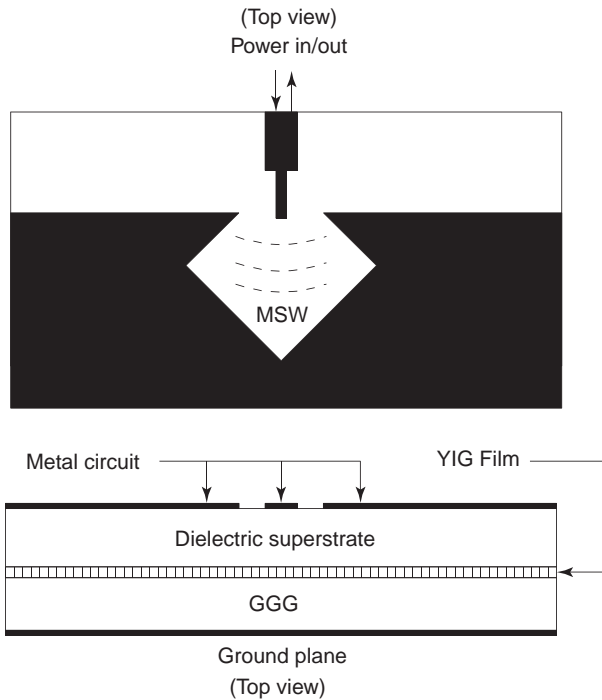


Figure 28. Schematic showing the configuration of a one-port MSW groove-free resonator. The bias field can be applied either perpendicular to the microstrip transducer in the YIG film plane, or perpendicular to the YIG film plane for MSFVW or MSSW operation, respectively.

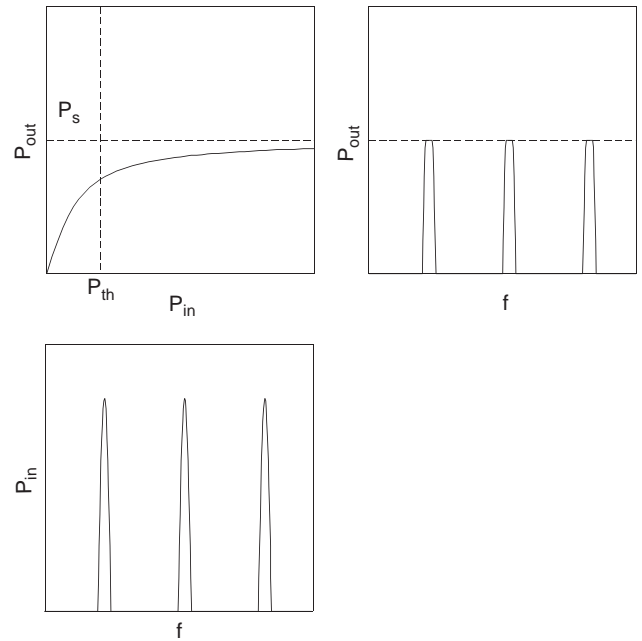


Figure 29. Power transmitted through a nonlinear frequency-selective limiter. Input power spectrum is shown at the bottom left, and the output power spectrum is shown at the top right. The relationship between the input and the output powers is shown at the top left.

frequencies exceeding 4 GHz, which are located above the spin-wave manifold extending the frequency range from 2 to 4 GHz. The second-order spin wave instability, which involves spin waves of the same frequency as the applied RF signals, has a higher threshold and is not used in frequency-selective power limiters. Thus, a power limiter is operational only when half the applied frequency falls within the spin-wave manifold region bounded by the two frequencies ω_1 and ω_2 shown in Fig. 1. Since ω_1 and ω_2 can be tuned by varying the applied field strength, the limiter is therefore termed a *frequency-selective device*.

7.2. Signal-to-Noise Enhancers

Epitaxially grown single-crystal YIG films have been used to fabricate frequency-selective limiters and signal-to-noise enhancers. Although the construction of these two devices is very similar, as shown in Fig. 3, they perform opposite signal processing functions. The limiter presents low attenuation to low-intensity signals and high attenuation to high-intensity signals while the signal-to-noise enhancer attenuates weak signal more severely than strong signals. However, the major difference results from the origin of nonlinearities admitting the operation of these two devices. For a limiter the nonlinear coupling is related to the onset of spin-wave instabilities, whereas the nonlinear behavior of a signal-to-noise enhancer comes from the generation of magnetostatic waves (MSWs). The occurrence of the latter is at a power level much lower than that of the former.

Although a power limiter and a signal-to-noise enhancer are constructed using a configuration similar to that shown in Fig. 3, they are operational under different

physical principles. While the former device requires the insertion loss to increase with input power, the latter requires the insertion loss to decrease with input power. A power limiter circuit will couple most efficiently with spin waves, whereas a signal-to-noise enhancer will avoid this by operating at a frequency ω so that $\omega/2$ is located well beyond the spin-wave manifold region. On the contrary, a signal-to-noise enhancer will couple tightly with magnetostatic waves, for example, MSSW, while for a power limiter this is seldom the case. As a result, meander lines are commonly used in power limiter circuits.

Let us examine the configuration of Fig. 3. Here we assume that the biasing magnetic field is applied parallel to the microstrip direction such that MSSWs are excited propagating perpendicular to the strip. Since the generation of MSSW in this configuration is very efficient, the input RF power is almost entirely consumed for the generation of MSSWs at low input-power levels. However, as the input power increases, the amplitudes of MSSWs increase accordingly until reaching saturation beyond which no more conversion into MSSWs is appreciable. Figure 30 shows that P_{MSSW} increases with the input power P_{in} linearly in the initial region but saturates at large P_{in} . The functional dependence of P_{MSSW} is similar to that of the output power from a limiter device shown in Fig. 29. The output power from the signal-to-noise enhancer is $P_{\text{in}} - P_{\text{MSSW}}$, which is shown as the heavy line in Fig. 30. Thus, from Fig. 30 we conclude that low-intensity signals will be damped more by the generation of MSSWs than high-intensity signals.

The top diagram in Fig. 31 shows the power spectrum output from a signal-to-noise enhancer device based on the input spectrum shown at the bottom of the figure. It is seen in Fig. 30 that noises, appearing at low power levels, are damped out, leaving alone the high-level signals with improved signal-to-noise ratio. Again, Fig. 30 shows an idealized situation in which P_s does not depend on the

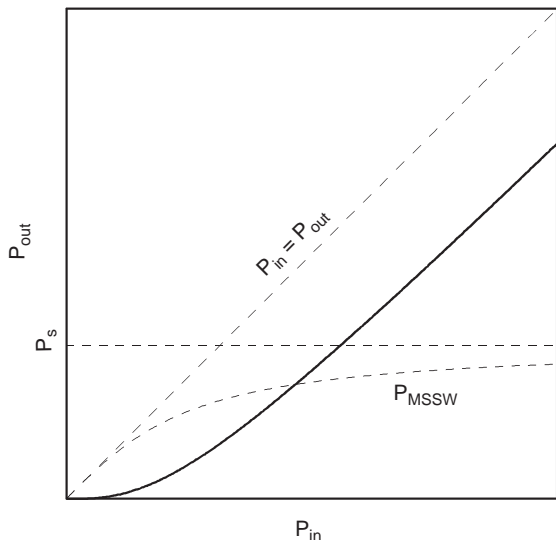


Figure 30. The relationship between the input power P_{in} and the output power P_{out} of a signal-to-noise enhancer. The converted MSSW power P_{MSSW} is also shown, and $P_{\text{out}} = P_{\text{in}} - P_{\text{MSSW}}$.

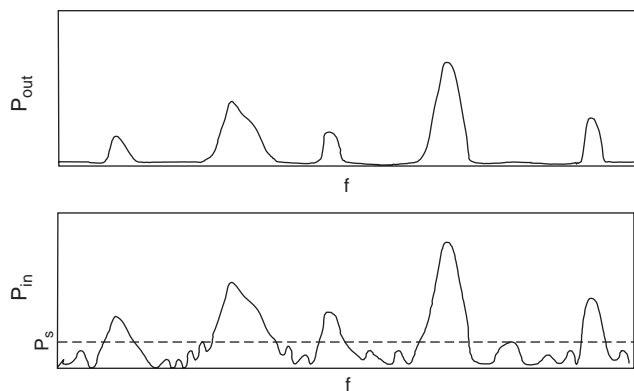


Figure 31. The input power spectrum, bottom, and the output power spectrum, top, applied to and transmitted from a signal-to-noise enhancer, respectively.

input power level P_{in} . In reality P_s will increase slightly with P_{in} when saturation is approached. As an example, Adam and Stizer [62] show a signal-to-noise enhancer device centered at 3.3 GHz with a bandwidth of 800 MHz that exhibited 16 dB less attenuation when the input power increased from -6 to $+10$ dBm.

7.3. Amplitude Correctors

For signal processing at microwave frequencies broadband amplifiers are needed whose characteristics are desired to show linear dependence on the amplitude of the input signals. However, for most power amplifiers including microwave traveling-wave tubes (TWTs), the amplification is deteriorated at high power, resulting in reduced power amplification for high-power input signals. One possible way to resolve this problem is to compensate the input power with a corrector that attenuates more input power at low input power levels. This is exactly the same characteristic that we have discussed for a signal-to-noise enhancer, and, hence, it can be equally used as an amplitude corrector device. It was shown [63] that an amplitude corrector operated at 3 GHz with low and high signal suppression level of 4.2 and 1 dB, respectively, and the threshold power level was 100 mW. This device was equipped with an O-type TWT operating from 2.5 to 3.6 GHz, and corrected output characteristics have thus been obtained.

7.4. Nonlinear Ferrimagnetic Echoing Devices

Echo phenomena are characterized by reradiation of the input signals stored in a nonlinear system through the agitation of a consequently applied pump pulse. Observation of ferrimagnetic echoes was first reported in 1965 by Kaplan in polycrystalline YIG samples [64]. Amplified echoes were thereafter reported in cylinders and truncated spheres of YIG crystals [65] and in single-crystal YIG films [66]. Echo experiments offer a possibility of a novel approach to performing important signal processing functions, such as nondispersive time delay and pulse correlation in the frequency range below 10 GHz. Within the demand of electronic technology advances there is now a

renewed interest in the use of ferrimagnetic echoing devices.

Among many nonlinear systems capable of producing an echoed signal (e.g., cyclotron echo, plasma echo, molecular echo, phonon echo, and spin echo), only ferrimagnetic echo can show amplification. This feature renders the ferrimagnetic echo phenomena in a very unique position for device applications. Ferrimagnetic echo is concerned mainly with the reservoir of the electron spin system provided by a YIG crystal that is nearly the perfect medium for signal storage. Thus, in view of the extremely narrow FMR linewidth (0.3 Oe at X band) the damping action accompanying the spin motion in the YIG crystal is very small; once the spins are put in motion, they will continue the motion indefinitely in time exhibiting very little attenuation. The lifetime of the magnons in a YIG crystal is very long, usually exceeding $1\ \mu\text{s}$. Ferrimagnetic echo signals are shown at the top of Fig. 6 in conjunction with intermodulation signals shown at bottom that are induced by a ferrite junction when excited at high power. We imagine that at the time instant $t = -\tau$ a signal pulse is applied to the YIG crystal setting the spins in precessional motion. Before the spin motion damps out, a pump pulse is applied at the time instant $t = 0$, which is so intense that nonlinear interaction is aroused in the spin system. Due to the (odd) cubic nature of the interaction, the process of time conjugation is recalled, which reverses the timescale for the stored signal such that the spins begin to precess in the opposite direction. As a consequence, at time $t = \tau$ ($\leq 1\ \mu\text{s}$) the original signal pulse recovers, which appears as the image, or replica, of the original signal echoed back by the pump pulse (see Fig. 6, the top diagram).

However, we must emphasize that if the cubic interaction is local in nature, no amplification is possible for the echoed signals, as occurs in the other nonlinear systems involving only isolated echoing sites. For ferrimagnetic echo the nonlinear interaction is brought about by the dipolar field interacting with the nonlocal spin waves showing a long-range dependence (this nonlocal interaction can be described in terms of a Green function whose kernel shows a $1/r$ dependence [25,26], see Eq. (100) below). As such, the echoed signal can show amplification, receiving power from the pump pulse not only to duplicate the signal waveform to result in an echo but also to amplify the echoed signal to high intensity. The amplification gain can be as large as 100, as measured experimentally [64] and calculated theoretically [25,26].

Ferrimagnetic echo experiments are carried out using crystal YIG bulk or thin-film materials in the presence of a high-magnetic-field gradient ($\approx 1\ \text{kOe/cm}$). In order to obtain high amplification gain, the YIG material needs to be clamped between two polycrystalline poles to effectively suppress the demagnetizing field. Theoretically it has been demonstrated that the DC demagnetizing field has adverse effect in reducing the echo gain to zero [25,26]. This result is consistent with Suhl's finding [13] that the DC demagnetizing field is apt to enhance spin-wave instability resulting in subsidiary absorption during microwave resonance measurements.

Finally, we want to point out the similarities between the ferrimagnetic echo signals and the intermodulation

noise observed in a ferrite circulator junction [24]. As shown at bottom of Fig. 6, two RF signals at adjacent frequencies f_1 and f_2 will couple each other to form intermodulation noises at frequencies $2f_1 - f_2$ and $2f_2 - f_1$. Intermodulation signals grow rapidly with power, which may be identified as clicking noises in a telephone line. Actually, both the echoing signals and the intermodulation noises are generated through the same cubic interaction terms in the equation of motion, Eq. (64). The only difference is that echo is a phenomenon in the time domain, whereas intermodulation is manifested in the frequency domain. While the DC demagnetizing field has been shown to have adverse effects in influencing the echo gain in the time domain, it has also been demonstrated that the same demagnetizing field will enhance the intermodulation level in a circulator junction [24]. Therefore, the DC demagnetizing field needs to be suppressed or minimized in nonlinear studies of ferrites applied at high power concerning the phenomena of spin-wave instabilities, the echo gain, and the intermodulation noise.

8. MAGNETIC SOLITONS

It is widely recognized that the study of nonlinear equations and their solutions is of great importance in many areas of physics. Of particular importance are nonlinear wave equations that admit large-amplitude solitary wave or soliton solutions that retain their shape during propagation. Such solutions have received considerable attention by elementary particle physicists since they may be regarded as extended particle-like solutions of nonlinear field equations. The study of solitary waves has proved fruitful in many areas of condensed-matter physics as well, for example, in theories of Bloch walls that separate domains in magnetic materials [3], structural phase transitions [67], liquid helium ^3He [68], 2D fluxons in Josephson weak-link junction [69], and low-temperature charge density wave condensates [70]. Engineering applications prefer solitonlike wavepackets or pulses to be formed in materials allowing the carried information to be transmitted over long distance without experiencing much attenuation and dispersion, such as for the study of optical [71] and microwave [72] magnetic envelope solitons. In this section Bloch wall solitons and magnetic microwave envelope solitons, referred to in general as *magnetic solitons*, are briefly introduced.

The first documented observation of the solitary wave was made in 1834 by the Scottish scientist John Scott Russell [73]. While observing the movement of a canal barge, Scott Russell noticed a novel type of water wave on the surface of the canal, in the form of a long bell-shaped wave that emerged and traveled down the channel—it did not cause rippling of the water, instead it remained stable and localized without change of waveform and diminution of speed over a distance about 2 miles in propagation. This type of water wave is now known as KdV solitons, short-named for Kortweg and de Vries, who first successfully demonstrated the underlying mathematical solutions in 1895. The other two well-known soliton systems are associated with the sine Gordon and the nonlinear Schrödinger

equations, describing the kinetics and dynamics of magnetic Bloch walls and microwave magnetic envelope solitons, respectively, discussed in the section.

In a nonlinear system that admits soliton-like solutions, two kinds of elementary excitations are possible: (1) particles with a finite amplitude in excitation called soliton/antisoliton, or bright/dark solitons, which possesses a finite mass; and (2) massless particles, with an infinitesimal excitation amplitude, called quasiparticles. Examples of solitons/antisolitons are electrons/positrons, and so forth, and quasiparticles are phonons, magnons, photons. Solitons and anti-solitons are topological entities, sometimes called “kinks”, whose waveform shapes are self-balanced so that dispersion imposed by the wave equation cancels exactly the nonlinear contribution from the amplitude of wave excitation. Thus, solitons and antisolitons carry shape integrity along with their motion, retaining their respective waveform shapes after the collision processes, similar to those massive particles observed in the physical world. Furthermore, like particles and antiparticles, a soliton can collide with an antisoliton, resulting in pair annihilation, ending up with radiations in the form of massless particles. Although losses can be readily added to the system, they will not affect the waveform shapes of solitons and antisolitons. Rather, the added loss terms in the equation of motion can merely introduce damping forces impeding the particles’ mobility in their kinetic motion. At a given temperature the thermodynamic quantities of the system, which describe the equilibrium states of solitons/antisolitons and the massless particles, can all be calculated, and phase transition can result at a Currie temperature in a manner analogous to that induced by soft-phonon/displacive modes, as described in Ref. 67. The following section describes domain wall solitons and microwave envelope solitons.

8.1. Magnetic Bloch Wall Soliton

A Bloch wall defines a magnetic transition layer that separates two magnetic domains of opposite magnetization. That is, inside a magnetic Bloch wall the magnetization vector reverses its direction undergoing 180° in-plane rotation in a manner so as to minimize the total free energy imposed by the uniaxial anisotropy and the exchange terms defined for H_A and H_E , respectively, following Eq. (18). Besides Bloch walls, the process of magnetization reversal can also take place by assuming 180° out-of-plane rotation, giving rise to Neel walls, which are not discussed in this section. After applying the Lagrangian equation utilizing the energy densities given by Eq. (15), one obtains the following equation governing the dynamic motion of a magnetic Bloch wall [3]

$$\begin{aligned} \frac{\partial^2 \Psi}{\partial t^2} + \sin \Psi - \frac{\partial^2 \Psi}{\partial x^2} = -f \sin \frac{\Psi}{2} - \Gamma \frac{\partial \Psi}{\partial t} \\ + B \left[\cos \frac{\Psi}{2} \frac{\partial^2 R_y}{\partial x \partial t} + \sin \frac{\Psi}{2} \frac{\partial^2 R_z}{\partial x \partial t} \right] \end{aligned} \quad (97)$$

where ψ denotes twice the azimuthal angle of the magnetization vector swinging away from the easy axis, the z

axis, and R_y and R_z are the y and z components of the displacement fields. In Eq. (97) f , Γ , and B are dimensionless parameters characterizing the magnitudes of the other coupling terms, including the external driving force (the Zeeman field), the Gilbert damping term, and the magnetoelastic constant of the medium, respectively. Here, x denotes the direction normal to the Bloch wall surface. In Eq. (97) the right-hand-side (RHS) terms may be treated as perturbations to the left-hand-side (LHS) terms, which renders the original sine-Gordon equation, describing and defining the unperturbed profile, kinetics, and dynamics of magnetic Bloch wall solitons/anti-solitons. Namely, the first term is associated with the kinetic energy of a sine-Gordon soliton (of a unified mass or inertia), and the second and the third terms are potential energies, arising from the uniaxial anisotropy, and the normalized exchange interaction, respectively. The effects of external magnetic driving f , the Gilbert damping Γ , and the magnetoelastic coupling B in influencing the soliton’s profile and its subsequent motion can thus be calculated [3]. A stability analysis on the mobility of a Bloch wall soliton/anti-soliton has also been performed in Ref. 3, discussed in conjunction with Slonzewski’s formula, which assumed the low-magnetization limits.

8.2. Magnetic Microwave Envelope Soliton

In the absence of an externally applied RF signal field the resultant equation of motion up to the third order in RF magnetization \mathbf{m} is, from Eq. (9)

$$\frac{d\mathbf{m}}{dt} = \gamma \mathbf{e}_z \times \left[H_0 \mathbf{m} - \left(M_s - \frac{\mathbf{m} \cdot \mathbf{m}}{2M_s} \right) \mathbf{h}_d - \left(\frac{2A}{M_s} \right) \nabla^2 \mathbf{m} + \frac{\lambda}{\gamma} \frac{d\mathbf{m}}{dt} \right], \quad (98)$$

where H_0 denotes the externally applied DC magnetic field normalized with respect to M_s , the saturation magnetization, and A and λ denote the exchange stiffness and Gilbert damping constant introduced following Eq. (18), respectively; the nonlinear term comes from Eq. (46) assuming large excursion angle of the magnetization vector away from the z axis, the applied field direction. In Eq. (98) \mathbf{h}_d denotes the dipole field induced by the rf-magnetization \mathbf{m} , all normalized with respect to M_s . Assuming the magnetostatic limit, the relationship between \mathbf{h}_d and \mathbf{m} is specified by Eq. (24). Or

$$\mathbf{h}_d = (1/\mu_0) \nabla \mathfrak{C} \nabla \cdot \mathbf{m} \quad (99)$$

where the Green function operator \mathfrak{C} is defined, upon operation on a regular function $f(\mathbf{r})$ as

$$\mathfrak{C}f(\mathbf{r}) = \int_{\text{all space}} d^3\mathbf{r}' \frac{1}{|\mathbf{r} - \mathbf{r}'|} f(\mathbf{r}') \quad (100)$$

which represents the nonlocal effect characteristics of a dipole field [25,26]. However, if one insists on a local approximation enforcing the dipole field to be equal to the rf

magnetization, or

$$\mathbf{h}_d = (1/\mu_0) \mathbf{m} \quad (101)$$

Eq. (98) becomes

$$\frac{d\phi}{dt} = -j\gamma \left[H_o \phi - \frac{M_S}{\mu_0} \left(1 - \frac{|\phi|^2}{2} \right) \phi - \frac{2A}{M_S} \nabla^2 \phi + \frac{\lambda}{\gamma} \frac{d\phi}{dt} \right], \quad (102)$$

where

$$\phi = (m_x - jm_y)/M_S \quad (103)$$

denotes the (normalized) circularly polarization field. From Eq. (102) one recognizes immediately the (damped) nonlinear Schrödinger equation [73], which admits solutions for microwave magnetic envelope solitons whose existence has been reported by various authors [74–76].

Although we have derived the desired equation of motion characteristic of microwave magnetic envelope solitons [Eq. (102)], caution is needed regarding use of the nonlinear term that was derived on the basis of the local assumption of the dipole field, Eq. (101), which was proposed intuitively without justification. Actually the same local assumption, Eq. (101), was used by Hermann in formulating the ferrimagnetic echo-gain calculations [77]. Although Hermann was able to predict the existence of ferrimagnetic echos, the calculated echo gain factors were two orders smaller than actually measured [64,65], indicating the insufficiency or inadequacy of the local dipole field assumption, Eq. (104). As such, Eq. (102) can pose only limited value; it at best leads to heuristic conclusions that in Eq. (102) the cubic interaction term, due to the large excursion angle of spins performing precessional motion, and dispersion, due to the exchange coupling among spins, constitute the two necessary ingredients for the generation of solitonlike solutions coincident with the nonlinear Schrödinger equation under the very crude assumptions. Only after the nonlocal nature of the dipole field rigorously treated in the equation of motion, can the formulation predict reliable results, Eqs. (99) and (100). Also, Eq. (98) assumes an infinite system for which the boundary conditions have been ignored. In real measurements finite samples such as single-crystal YIG films are normally used in conjunction with the microstrip launcher circuits shown in Fig. 24. As such, boundary conditions need to be included and the demagnetizing field effects to be explicitly considered [Eq. (66)]. The demagnetizing field has been found effective in triggering profound processes in ferrite samples undergoing high-power excitations, as observed in ferrimagnetic echo, intermodulation, and stabilities measurements. More work in these areas is needed.

Two different types of envelope solitons, bright solitons and dark solitons, or solitons and antisolitons, can propagate in nonlinear waveguiding dispersive media. Bright and dark solitons may be classified as dynamical and topological, respectively. The term “dynamical” for bright

solitons means that these pulses are essentially nonlinear wavepackets for which the carrier signal maintains a constant phase over the pulse. The term “topological” denotes the fact that the passage of a single dark soliton modifies the medium or the medium response in some critical way. “Dark envelope” solitons may be described in terms of a carrier signal of constant amplitude that has a dip in amplitude at the soliton position. If this dip goes completely to zero, one has a black soliton. If the minimum power at the dip is nonzero, one has a gray soliton. Dark envelope solitons have a nonzero jump in phase for the carrier signal as one crosses the dip. In the case of black solitons, this jump in phase is exactly 180° .

Observation of self-generated bright and dark microwave magnetic envelope solitons in ferrite films can be found in Refs. 75 and 76, respectively. Interaction between microwave magnetic envelope solitons and between microwave magnetic envelope solitons and continuous magnetostatic waves can be found in Refs. 74 and 78, respectively. Before ending this section, we note that it was generally observed that formulation, propagation, and decay of microwave magnetic envelope solitons were always accompanied by the generation of high-wavenumber spin waves, indicating that the equation of motion of the system is more involved than described by the simple nonlinear Schrödinger equation, Eq. (102), which allows for isolation of stable clean solitons and continuous waves. Thus, a complete description of the nonlinear spin system has to recruit the long-range dipole field, Eqs. (99) and (100), not only to faithfully describe soliton behaviors but also to understand interactions between themselves and between themselves and continuous waves, including the scattering processes involving three magnons and the resultant (modulation) instabilities of the system. These areas are discussed further in Refs. 79–81.

9. MAGNETOOPTIC DEVICES

At optical frequencies the Polder permeability tensor of a ferrite specimen is nearly isotropic with the diagonal element $\mu \approx 1$ and off-diagonal element $\kappa \approx 10^{-5}$, as can be calculated from Eqs. (11) and (12). Although small, the resultant magnetic anisotropy or gyrotropy can be measured using a laser optical beam. On incidence, the reflected and the transmitted beams will carry the magnetization information of the specimen, resulting in not only a rotation in polarization but also a change in reflectivity and transmission. These are called *magneto-optic Kerr* and *Faraday effects* for reflection and transmission measurements, respectively. Kerr and Faraday effects have been used in observing the dynamic processes of domain wall motion in a ferromagnetic metal or a ferrimagnetic insulator sample, respectively [82].

The most important devices utilizing magneto-optic coupling for electronic signal processing applications concern the scattering process between photons and magnons. This process is called *Bragg diffraction*, where in a ferrimagnetic medium a photon of momentum \mathbf{P} is scattered by a magnon of momentum \mathbf{k} , resulting in a photon of momentum $\mathbf{P} + \mathbf{k}$. This interaction is second order in

nature and is described a term of $\gamma\mu_0 \mathbf{m}_k \times \mathbf{h}_P$ included with the right hand side of Eq. (7). Here \mathbf{m}_k denotes the magnetization field of the magnon and \mathbf{h}_P is the magnetic field of the photon. As such, the photon wave is said to be modulated by the magnetization wave, carrying along with it the electronic information after scattering. Because of the nature of a second-order interaction, Bragg diffraction between photons and magnons, or MSWs in a magnetic film, is not very prominent, and only about 4% light diffraction was observed experimentally with a 7-mm interaction length for MSSW excitations approaching saturation [83].

Optical techniques are being increasingly utilized to meet the ever-growing data rate requirements of signal processing and communication applications. A key element to such applications has been acoustooptic modulators based on Bragg diffraction between photons and phonons. A large time–bandwidth product (TBW; i.e., time delay of acoustic signal in traversing the optical beam times signal bandwidth) is usually desirable. However, acoustic waves cannot be efficiently excited at frequencies above 2 GHz. Instead, magneto-optic devices offer the potential of large TBW modulation directly at microwave frequencies. The diffraction of guided optical waves by MSW is analogous to optical diffraction by a SAW and has the potential to enhance a wide variety of integrated optical applications such as spectrum analyzer, optical filters, deflectors, switches, and convolvers.

The basic theories of the MSW–optical interaction, including the development of expressions for optical diffraction efficiency and coupling factor as a function of the MSW power and other relevant parameters, has been derived by Fisher [83]. The theory applies to the collinear configuration, shown in Fig. 32, with the MSW traveling in a direction parallel or antiparallel to the optical beam, as well as to the transverse configuration, shown in Fig. 33, where the MSW travels at a 90° angle to the optical beam. In Figs. 32 and 33 prisms are used to guide optical beams onto the YIG layers that are transparent

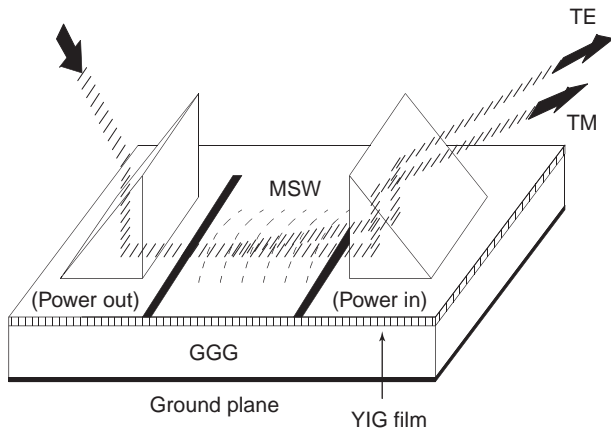


Figure 32. Collinear configuration with codirectional MSW and optical beams. Due to Bragg diffraction between the optical beam and the MSWs, the original TM guided optical beam is scattered into a TE beam with deflected angle of propagation.

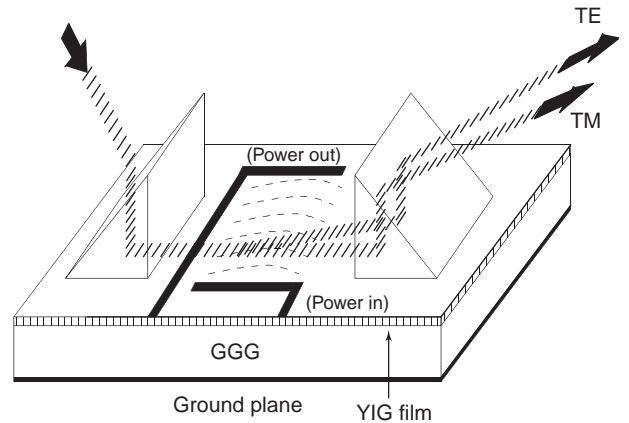


Figure 33. Transverse configuration for MSW and optical beams. Bragg diffraction of the guided optical wave by an MSW induces conversion between orthogonally polarized optical modes.

to lightwave propagation. In Figs. 32 and 33 the MSW configuration may be replaced by the superstrate structure shown in Fig. 3. To achieve good optical properties, the YIG film is usually highly doped, mainly by bismuth. As such, Bragg diffraction of guided optical waves by MSSWs and MSFVWs has been demonstrated in the configurations shown in Figs. 32 and 33, and the conversions between TE and TM modes have been experimentally observed from 1 to 6.5 GHz [83].

In experimental solid-state physics photons are used as instrumentation tools to probe the phonon spectra in solids. This is termed *Brillouin light scattering*. Analogously, Brillouin light scattering can be applied to a ferrite sample to study the magnon or spin-wave spectrum in the presence of solitons as well as to investigate the role of spin waves at the onset of instabilities [84,85]. In a ferrite a photon can create or absorb a magnon. The photon will be scattered in the process; its wavevector will change from \mathbf{k} to \mathbf{k}' and its frequency from ω to ω' . Suppose a magnon is created with a wavevector \mathbf{K} and angular frequency Ω . The kinematics of the collision or scattering event are simple. According to the conservation of energy

$$\omega = \omega' + \Omega \tag{104}$$

and per the wavevector selection rule

$$\mathbf{k} = \mathbf{k}' + \mathbf{K} \tag{105}$$

where, for simplicity, we do not include the possibility that the scattering may be combined with a Bragg diffraction involving a reciprocal lattice vector of the crystalline structure of a ferrite crystal. When ω , ω' , \mathbf{k} , and \mathbf{k}' are known, Ω and \mathbf{K} can thus be determined.

In conclusion, MSW optical devices are currently in an early stage of development, and their basic feasibility has been demonstrated. However, they are expected to lead to a variety of high-performance integrated optical signal processing devices.

10. ANTIREFLECTION LAYERS AND ABSORBING LAYERS

To date microwave or millimeter-wave antireflection layers and absorbing layers are almost exclusively used for radome design applications. Because of the highly classified nature of this topic, not much data have been published in the literature. In this section we discuss only the concepts that lead to the construction of microwave or millimeter-wave antireflection and absorbing layers. No explicit design parameters are given here. By definition, an antireflection/absorbing layer is placed on top of a substrate such that an incident microwave or millimeter-wave beam will be totally transmitted/absorbed when passing across the layer without causing reflection. The layer should be functional over a frequency range as broad as possible to be independent of the incident angle and polarization of the incident beam.

To realize the design of an antireflection layer, we consider first the case of normal incidence of the incident beam. According to the transmission-line theory, one concludes immediately that the first-order solution would require the layer to behave like a quarter-wave transformer. This implies that the layer shall possess a thickness equal to one quarter the wavelength with a characteristic impedance

$$Z_L = (Z_0 Z_S)^{1/2} \quad (106)$$

where

$$Z_0 = \left(\frac{\mu_0}{\epsilon_0} \right)^{1/2} \quad (107)$$

$$Z_S = \left(\frac{\mu_S}{\epsilon_S} \right)^{1/2} \quad (108)$$

where Z_0 (Z_S) is the characteristic impedance of air (substrate) and ϵ_0 (ϵ_S) and μ_0 (μ_S) are the permittivity and permeability of air (substrate), respectively. When broader bandwidth is desired, higher-order solutions are required, and this results in a multilayer system with progressively changing electromagnetic parameters matching the impedance difference between air and substrate.

For an absorbing layer design the air impedance can also be matched by a multilayer system with progressively increasing damping parameters such that the series of the layers satisfies the transformer matching requirement. Thus, we use the same impedance transformer theory for the design of absorbing layers, except that the impedances of the layers are now complex numbers, since the permittivity and permeability of the layers are complex numbers. As such, the incident wave damps out when it passes through the layer system before arriving at the substrate.

When oblique-angle incidence is considered, the impedance transformer theory can be generalized using the transfer matrix technique [41,86]. The present problem is to determine an optimal layer system design allowing for polarization independent operation over a frequency band and angle range on beam incidence as broad as possible. Also, the design task is subject to a very important constraint requiring the thickness of the layers to be

minimal, since at microwave and/or millimeter frequencies a practical layer system should be thin enough compared to the wavelength of the waves propagating in air. The design is in general not a trivial problem, and efficient computer algorithms are needed.

Once an optimal multilayer system is determined, the remaining task is to synthesize it using real materials. Unfortunately, nature does not provide general materials covering the whole range of electromagnetic parameters. Instead, artificial materials need to be developed. The first kind of artificial materials include particle composites where dielectric particles [87], metal-shelled particles [88], ferrite particles [89,90], and graphite powders are embedded in a matrix epoxy such that the effective permittivity, permeability, and/or conductivity of the composite can be controlled over the desired frequency band by adjusting the mixing fraction of the particles.

The second class of artificial materials is quite new; it involves periodic patterns of metal strips or grooves (surface relief gratings) to be fabricated on top of a layer surface. In fact, when electromagnetic waves interact with periodic structures much finer than the wavelength, they do not diffract, but instead reflect and transmit as if they were encountering a nonstructured medium. Effective field theory describes the interaction between electromagnetic waves and such subwavelength structures by representing a region of subwavelength heterogeneity in terms of a homogeneous material possessing a single set of effective electromagnetic parameters: permittivity, permeability, and conductivity [91]. Actually, the antireflection structures consisting of surface relief gratings can be found on the cornea of certain night-flying moths, and the first scientists to investigate antireflection-structured surfaces for application in the visible or near-infrared portion of the spectrum worked to replicate moth eye surfaces [92].

Antireflection means establishing a resonant structure on the substrate surface that is able to “capture” the incident electromagnetic signal forming standing modes so as to dissipate the captured energy, converting it into heat before it reaches the substrate. In this sense an antireflection layer is a sheet of absorbent. Two kinds of resonant structures are possible. Standing modes can be formed along the propagation direction, or the longitudinal direction, of the signal by constructing a quarter-wave transformer [Eq. (106)] or a transformer of high order, as discussed previously. Alternatively, standing modes can be formed along the transverse directions. For example, metal patches or meshes of a diameter equal to one-half the wavelength of the incident electromagnetic waves can be deployed in front of the substrate surface accompanied by an dissipation layer responsible for wave damping. Multiple antireflection layers can be stacked together to jointly capture and damp a broadband signal, thereby realizing the broadband operation.

BIBLIOGRAPHY

1. B. Lax and K. J. Button, *Microwave Ferrites and Ferrimagnetics*, McGraw-Hill, New York, 1962.

2. J. C. Slater, *Quantum Theory of Matter*, 2nd ed., McGraw-Hill, New York, 1972.
3. H. How, R. C. O'Handley, and F. R. Morgenthaler, Soliton theory for realistic domain wall dynamics, *Phys. Rev. B* **40**(7):4809 (1989).
4. C. Vittoria, *Microwave Properties of Magnetic Films*, World Scientific, Singapore, 1993.
5. S. Chikazumi and S. H. Charap, *Physics of Magnetism*, Wiley, New York, 1964.
6. C. Kittel, *Introduction to Solid State Physics*, 4th ed., Wiley, New York, 1971.
7. F. R. Morgenthaler, Dynamic magnetoelastic coupling in ferromagnets and antiferromagnets, *IEEE Trans. Magn.* **Mag-8**(1):130 (1972).
8. H. How, Microstrip antennas, in *Encyclopedia of Electrical and Electronics Engineering*, Wiley, Hoboken, NJ, 2003.
9. H. How and C. Vittoria, Surface retarded modes in multilayered structures: Parallel magnetization, *Phys. Rev. B* **39**(10):6823 (1989).
10. H. How and C. Vittoria, Bulk and surface retarded modes in multilayered structures: Antiparallel magnetization, *Phys. Rev. B* **39**(10):6831 (1989).
11. R. E. Collin, *Foundations for Microwave Engineering*, McGraw-Hill, New York, 1966.
12. C. Vittoria and N. D. Wilsey, Magnetostatic wave propagation losses in an anisotropic insulator, *J. Appl. Phys.* **45**:414 (1974).
13. H. Suhl, The theory of ferromagnetic resonance at high signal powers, *J. Phys. Chem. Solids* **1**:209 (1957).
14. K. Nakamura, S. Ohta, and K. Kawasaki, *J. Phys. C* **15**:L143 (1982).
15. F. M. de Aguiar and S. M. Rezende, Observation of subharmonic routes to chaos in parallel-pumped spin waves in yttrium iron garnet, *Phys. Rev. Lett.* **56**:1070 (1986).
16. F. Bloch, *Z. Physik* **61**:206 (1930); **74**:295 (1932).
17. F. R. Morgenthaler, *J. Appl. Phys.* **31**:95S (1960).
18. E. Shloemann, J. J. Green, and U. Milano, *J. Appl. Phys.* **31**:386S (1960).
19. H. Bosma, On the principle of stripline circulation, *Proc. IEE B* **109**:137 (1962).
20. H. Bosma, On stripline Y-junction at UHF, *IEEE Trans. Microwave Theory Tech.* **MTT-12**:61 (1964).
21. C. E. Fay and R. L. Comstock, Operation of the ferrite junction circulators, *IEEE Trans. Microwave Theory Tech.* **MTT-13**:15 (1965).
22. Y. S. Wu and F. J. Rosenbaum, Wide-band operation of microstrip circulators, *IEEE Trans. Microwave Theory Tech.* **MTT-22**:849 (1974).
23. E. Schloemann and R. E. Blight, Broad-band stripline circulators based on YIG and Li-ferrite single crystals, *IEEE Trans. Microwave Theory Tech.* **MTT-34**:1394 (1986).
24. H. How, T.-M. Fang, C. Vittoria, and R. Schmidt, Non-linear intermodulation coupling in ferrite circulator junctions, *IEEE Trans. Microwave Theory Tech.* **MTT-45**(2):245 (1997).
25. H. How and C. Vittoria, Theory on amplified ferrimagnetic echoes, *Phys. Rev. Lett.* **66**(12):1626 (1991).
26. H. How and C. Vittoria, Amplification factor of echo signals in ferrimagnetic materials, *IEEE Trans. Microwave Theory Tech.* **MTT-39**(11):1828 (1991).
27. W. H. Von Aulock, ed., *Handbook of Microwave Ferrite Materials*, Academic Press, New York, 1965.
28. M. E. Hines, Reciprocal and nonreciprocal modes of propagation in ferrite stripline and microstrip devices, *IEEE Trans. Microwave Theory Tech.* **MTT-19**:442-451 (1961).
29. H. How, C. Vittoria, and C. Carosella, Novel filter design incorporating stripline Y-junction circulators, *IEEE Trans. Microwave Theory Tech.* **MTT-39**(1):40 (1991).
30. H. How, C. Vittoria, and C. Carosella, Experiments on wide-stopband filters utilizing asymmetric circulators, *IEEE Trans. Microwave Theory Tech.* **MTT-40**(1):161 (1992).
31. H. How, R. Schmidt, and C. Vittoria, Design of six-port ferrite junction circulators: Theory and experiments, *IEEE Trans. Microwave Theory Tech.* **MTT-42**(7):1272 (1994).
32. N. Zeina, H. How, and C. Vittoria, Self-biasing circulators operating at Ka band utilizing M-type hexagonal ferrites, *IEEE Trans. Magn.* **Mag-28**(5):3219 (1992).
33. H. How, T. M. Fang, C. Vittoria, and R. Schmidt, "Losses in Stripline/Microstrip Circulators," *IEEE Trans. Microwave Theory Tech.* **MTT-46**(5):543, 1997.
34. H. S. Newman and C. M. Krowne, Analysis of ferrite circulators by 2-D finite-element and recursive Green's function techniques, *IEEE Trans. Microwave Theory Tech.* **MTT-46**(2):167-177 (1998).
35. H. How, S. W. McKnight, S. A. Oliver, P. M. Zavracky, N. E. McGruer, and C. Vittoria, Influence of non-uniform magnetic field on a ferrite junction circulator, *IEEE Trans. Microwave Theory Tech.* **MTT-47**(10), 1982-1989 (1999).
36. H. How, S. A. Oliver, S. W. McKnight, P. M. Zavracky, N. E. McGruer, and C. Vittoria, Theory and experiment of thin-film junction circulator, *IEEE Trans. Microwave Theory Tech.* **MTT-46**:1645-1653 (Nov. 1998).
37. K. C. Gupta, R. Garg, and I. J. Bahl, *Microstrip Lines and Slotline*, Artech, House, Norwood, MA: 1979.
38. H. How, R. Seed, C. Vittoria, D. B. Chrisey, and J. S. Horwitz, Microwave characteristics of superconducting coplanar waveguide resonator, *IEEE Trans. Microwave Theory Tech.* **MTT-41**(3):255 (1993).
39. T. Miura and Y. Konishi, New lumped element circulator by ceramic integrated circuit technology, *IEEE Trans. Broadcast.* **4**(3):101-106 (1995).
40. J. Deutsch and B. Wieser, Resonance isolator and Y-circulator with lumped element at VHF, *IEEE Trans. Magn.* **Mag-2**(3):278-282 (1966).
41. H. How, X. Zuo, E. Hokanson, and C. Vittoria, Calculated and measured characteristics of a microstrip line fabricated on a Y-type hexaferrite substrate, *IEEE Trans. Microwave Theory Tech.* **MTT-50**(5):1280-1288 (2002).
42. E. Schloemann, R. I. Joseph, and I. Bady, Spin-wave instability in hexagonal ferrites with a preferential plane, *J. Appl. Phys.* **34**(3):672 (1963).
43. A. V. Nazarov and C. E. Patton, Effect of large magnetocrystalline anisotropy on the spin wave linewidth in Zn-Y hexagonal ferrite, *J. Appl. Phys.* **93**(11):9195 (2003).
44. R. G. Cox, C. E. Patton, M. A. Wittenauer, P. Kabos, and L. Chen, Spin wave instability in single crystal Zn-Y hexagonal ferrite at 8.93 GHz, *J. Appl. Phys.* **89**(8):4454 (2001).
45. A. V. Nazarov, R. G. Cox, and C. E. Patton, High power microwave properties of Zn-Y hexagonal ferrite-parallel pumping size effects, *J. Appl. Phys.* **92**(7):3890 (2002).
46. S. V. Lebedev, C. E. Patton, and M. A. Wittenauer, Frequency and temperature dependence of the ferromagnetic resonance linewidth in single crystal platelets and pulsed laser deposited films of barium ferrite, *J. Appl. Phys.* **91**(7):4426, (2002).

47. H. How, *Method and Apparatus of Obtaining Phase Shift Using Non-Reciprocal Resonator*, U.S. Patent 6,483,393 (Nov. 19, 2002).
48. D. M. Pozar, Radiation and scattering characteristics of microstrip antennas on normally biased ferrite substrates, *IEEE Trans. Anten. Propag.* **AP-30**:1084 (1992).
49. V. L. Taylor, J. C. Setjares, and C. V. Smith, Jr., MSW terminations, *Proc. IEEE Ultrasonic Symp.* 1980, p. 562.
50. M. R. Daniel, J. D. Adam, and T. W. O'Keeffe, Linearly dispersive delay lines at microwave frequencies using magnetostatic waves, *Proc. IEEE Ultrasonics Symp.* 1979, p. 806.
51. K. W. Chang, J. M. Owens, and R. L. Carter, Linearly dispersive delay control of magnetostatic surface wave by variable ground-plane spacing, *Electron. Lett.* **19**:546 (1983).
52. F. R. Morgenthaler, Field gradient control of magnetostatic waves for microwave signal processing applications, *Proc. RADC Microwave Magnetic Workshop*, 1981, p. 133.
53. L. R. Adkins and H. L. Glass, Dispersion control in magnetostatic delay lines by means of multiple magnetic layer structures, *Proc. IEEE Ultrasonic Symp.* 1980, p. 526.
54. W. S. Ishak and K. W. Chang, Magnetostatic wave devices for microwave signal processing, *Hewlett-Packard J.* **10** (1985).
55. J. D. Adam, An MSW tunable bandpass filter, *Proc. IEEE Ultrasonic Symp.*, 1985, p. 157.
56. J. P. Castera and P. Hartemann, Adjustable magnetostatic surface wave multistrip directional coupler, *Electron. Lett.* **16**:195 (1980).
57. J. P. Castera, New configurations for magnetostatic wave devices, *Proc. IEEE Ultrasonic Symp.* 1980, p. 514.
58. J. P. Castera and P. Hartemann, A multipole magnetostatic wave resonator filter, *IEEE Trans. Magn.* **MAG-18**:1601 (1982).
59. K. W. Chang and W. S. Ishak, Magnetostatic forward volume waves straight-edge resonators, *Proc. IEEE Ultrasonic Symp.* 1986, p. 473.
60. G. S. Uebele, Characteristics of ferrite microwave limiters, *IEEE Trans. Microwave Theory Tech.* **7**:18 (1959).
61. S. N. Stizer, and H. Goldie, A multi-octave frequency selective limiter, *IEEE Digest MTT-S*:326 (1983).
62. J. D. Adam and S. N. Stizer, A magnetostatic signal to noise enhancer, *Appl. Phys. Lett.* **36**:485 (1980).
63. W. S. Ishak, E. Reese, and E. Huijter, Magnetostatic wave devices for UHF band applications, J. P. Parekh, ed., *Circuits Systems Signal Processing*, 1985, Vol. 4, p. 285.
64. D. E. Kaplan, Magnetostatic mode echo in ferromagnetic resonance, *Phys. Rev. Lett.* **14**(8):254 (1965).
65. D. E. Kaplan, R. M. Hill, G. F. Herrmann, Amplified ferrimagnetic echoes, *J. Appl. Phys.* **40**(3):1164 (1969).
66. F. Bucholtz, D. C. Webb, and C. W. Young, Jr., Ferrimagnetic echoes of magnetostatic surface wave modes in ferrite films, *J. Appl. Phys.* **56**(6):1859 (1984).
67. J. A. Krumhansl and J. R. Schieffer, *Phys. Rev. B.* **11**:3535 (1975).
68. K. Maki and P. Kumar, *Phys. Rev. B.* **14**:118 (1976).
69. K. Nakajima, Y. Sawada, and Y. Onodera, *J. Appl. Phys.* **46**:5272 (1975).
70. M. J. Rice, A. R. Bishop, J. A. Krumhansl, and S. E. Trullinger, *Phys. Rev. Lett.* **36**:432 (1976).
71. G. P. Agrawal, *Nonlinear Fiber Optics*, Academic Press, Boston, 1989.
72. B. A. Kalinikos, N. G. Kovshikov, and A. N. Slavin, *Sov. Phys. JETP* **67**:303 (1988).
73. R. K. Dodd, J. C. Eilbeck, J. D. Gibbon, and H. C. Morris, *Solitons and Nonlinear Wave Equations*, Academic Press, London, 1982.
74. K. G. Kovshikov, B. A. Kalinikos, C. E. Patton, E. S. Wright, and J. M. Nash, Formation, propagation, reflection, and collision of microwave envelope solitons in yttrium iron garnet films, *Phys. Rev. B* **54**:15210 (1996).
75. M. M. Scott, B. A. Kalinikos, and C. E. Patton, Self-generation of bright microwave magnetic envelope soliton trains in ferrite films through frequency filtering, *Appl. Phys. Lett.* **78**(7):970 (2001).
76. B. A. Kalinikos, M. M. Scott, and C. E. Patton, Self-generation of fundamental dark Solitons in magnetic films, *Phys. Rev. Lett.* **84**(20):4697 (2000).
77. G. F. Hermann, R. M. Hill, and D. E. Kaplan, *Phys. Rev. B* **2**:2587 (1970).
78. M. M. Scott, Y. K. Fetisov, V. T. Synogach, and C. E. Patton, Suppression of microwave magnetic envelope solitons by continuous wave magnetostatic wave signals, *J. Appl. Phys.* **88**(7):4232 (2000).
79. V. T. Synogach, Y. K. Fetisov, C. Mathieu, and C. E. Patton, Ultrashort microwave pulses generated due to three magnon interactions, *J. Appl. Phys.* **85**(10):2184 (2000).
80. B. A. Kalinikos, N. G. Kovshikov, and A. N. Slavin, Envelope solitons and modulation instability of dipole-exchange magnetization waves in yttrium iron garnet films, *Sov. Phys. JETP* **67**(2):303 (1988).
81. M. M. Scott, B. A. Kalinikos, and C. E. Patton, Spatial recurrence for nonlinear magnetostatic wave excitations, *J. Appl. Phys.* **94**(9):5877 (2003).
82. J. M. Florczak and E. D. Dahlberg, Detecting two magnetization components by the magneto-optical Kerr effect, *J. Appl. Phys.* **67**:7520 (1990).
83. A. D. Fisher, Optical signal processing with magnetostatic waves, in J. P. Parekh, ed., *Circuits Systems Signal Processing*, 1985, Vol. 4, p. 265.
84. H. Y. Zhang, P. Kabos, H. Xia, P. A. Kolodin, and C. E. Patton, Brillouin light scattering observation of the nonlinear spin-wave decay in yttrium iron garnet thin films, *Phys. Rev. B* **61**(1):22 (2000).
85. C. Mathieu, V. T. Synogach, and C. E. Patton, Brillouin light scattering analysis of three-magnon splitting processes in yttrium iron garnet films, *Phys. Rev. B* **67**:10440 (2003).
86. H. How, W. Tian, and C. Vittoria, AC Hall effect in multilayered semiconductors, *J. Lightwave Technol.* **15**(6):1006 (1997).
87. L. Rayleigh, On the influence of obstacles arranged in rectangular order upon the properties of a medium, *Phil. Mag.* **34**:481 (1982).
88. H. How, W. A. Spurgeon, and C. Vittoria, *The Microwave Properties of Conducting Spherical Shells*, Technical Report, U.S. Army Materials Technology Laboratory, MTL TR 90-7, February, 1990.
89. H. How and C. Vittoria, Demagnetizing energy and magnetic permeability tensor of spheroidal magnetic particles dispersed in cubic lattices, *Phys. Rev. B* **43**(10):8094 (1991).
90. H. How and C. Vittoria, The polder tensor of spherical magnetic particles in cubic lattices: An exact solution in multipole expansion, *Phys. Rev. B* **44**(17):9362 (1991).
91. D. H. Raguin and G. M. Morris, Antireflection structured surfaces for the infrared spectral region, *Appl. Opt.* **32**:1154 (1993).
92. P. B. Clapham and M. C. Hutley, Reduction of lens reflection by the "moth eye" principle, *Nature (Lond.)* **244**:281 (1973).

MAGNETIC RESONANCE IMAGING

ANDREW WEBB
 University of Illinois at
 Urbana–Champaign
 Urbana, Illinois

1. INTRODUCTION

Magnetic resonance imaging (MRI) is one of the major radiological diagnostic modalities in the clinic. More than 20 million exams per year are carried out in the United States alone. A large number of academic and commercial laboratories are involved in the development of new hardware, data processing algorithms and applications. Studies can be performed on size scales ranging from humans to single neurons. One factor linking many of the most recent developments in MRI is the trend towards higher static magnetic fields. Higher fields provide many benefits, which will be outlined in this article, but also present considerable challenges in engineering design. Since the “operating frequency” of the system and associated hardware is proportional to the strength of the static magnetic field, high-frequency analysis of system design, as well as the interactions between electromagnetic radiation and the human body are increasingly important areas of research. As shown in Fig. 1, MRI now spans almost the entire radiofrequency spectrum.

The MRI signal arises from protons in the body, primarily water but also lipid. The patient is placed inside a superconducting magnet, which produces a static magnetic field several tens of thousands times stronger than Earth’s magnetic field. Each proton, which is a charged particle with angular momentum, can be considered as acting as a small magnet. The protons align in two configurations, with their magnetic fields aligned either parallel or antiparallel to the direction of the large static magnetic field, with slightly more found in the parallel state. The protons precess around the direction of the static magnetic field, analogously to a spinning gyroscope under the influence of gravity. The frequency of precession is proportional to the strength of the static magnetic field. Application of a weak radiofrequency (RF) field causes the

protons to precess coherently, and the sum of all the magnetic moments of the precessing protons is detected as an induced voltage in a tuned detector coil. Spatial information is encoded into an image using magnetic field gradients [1,2]. These impose a three-dimensional linear variation in the magnetic field present within the patient. As a result of these variations, the precessional frequencies of the protons depend on their position within the body. The frequency and phase of the precessing magnetization are detected by the RF coil, and the analog signal is digitized. An inverse two-dimensional Fourier transform is performed to convert the time-domain signal into the spatial domain to produce the image. By varying data acquisition parameters, differential contrast between soft tissues can be introduced into the image. Figure 2 shows a block diagram of an MRI system. Many of the subsystems are described in detail later in this article.

2. BASIC PRINCIPLES

For this article, only proton MRI will be considered, although useful spatial information from other nuclei such as ²³Na, ¹⁹F, and ³¹P can also be obtained. In proton MRI the signal comes essentially from the protons in water, with a minor component from those in fat. From a quantum mechanical standpoint, the proton possesses two nuclear energy levels, which correspond to the z component of the magnetic moment of the proton being aligned either parallel or antiparallel to the applied static magnetic field, as shown in Fig. 3.

The energy gap between the two energy levels is given by

$$\Delta E = \frac{\gamma \hbar B_0}{2\pi} \tag{1}$$

In order to stimulate transitions between the two energy levels, an oscillating magnetic field must be applied at a frequency ω , such that

$$\frac{\hbar \omega}{2\pi} = \frac{\gamma \hbar B_0}{2\pi} \Rightarrow \omega = \gamma B_0 \tag{2}$$

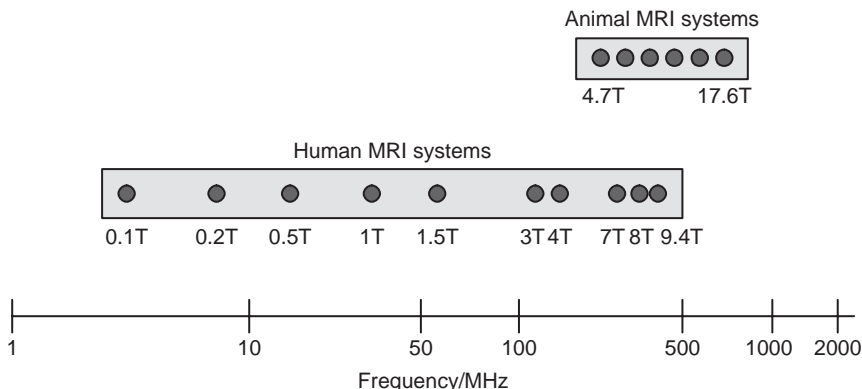


Figure 1. Operating frequencies of human and animal MRI systems. The corresponding static magnetic field strengths are given in tesla (T).

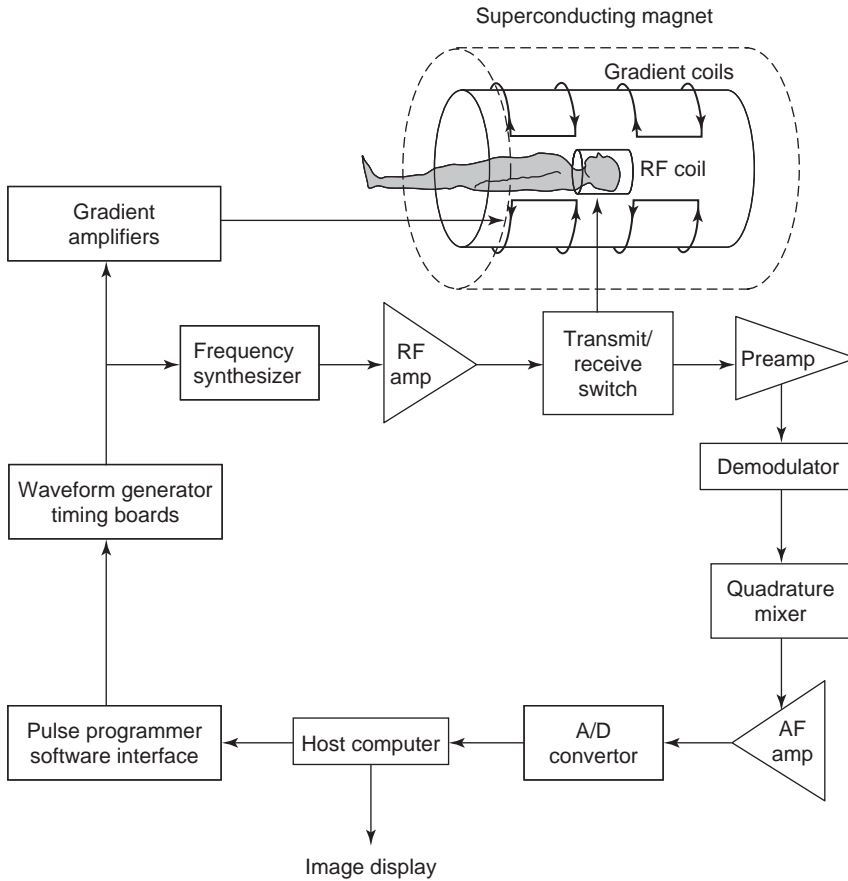


Figure 2. Block diagram of an MRI scanner.

The Boltzmann equation can be used to calculate the relative number of protons in each energy level

$$\frac{N_{\text{antiparallel}}}{N_{\text{parallel}}} = \exp - \left[\frac{\Delta E}{kT} \right] = \exp - \left[\frac{\gamma \hbar B_0}{2\pi kT} \right] \quad (3)$$

where k is the Boltzmann coefficient with a value of 1.38×10^{-23} J/K and T is the temperature measured in degrees Kelvin. Applying the approximation $e^{-x} \approx 1 - x$, we can calculate the net magnetization of the object as

$$M_0 = \frac{\gamma \hbar}{4\pi} (N_{\text{parallel}} - N_{\text{antiparallel}}) = \frac{\gamma^2 \hbar^2 B_0 N_s}{16\pi^2 kT} \quad (4)$$

Therefore, the higher the static magnetic field B_0 , the greater is the equilibrium magnetization, and, as will be seen later, the higher the MRI signal. It is also useful to consider, from a classical description, the motion of the individual magnetic moments. As derived in the previous section, the proton magnetic moment μ is aligned at an angle of 54.7° to the axis of the external magnetic field B_0 . This magnetic field attempts to align the proton magnetic moment parallel to the direction of B_0 , and this action creates a torque C , given by

$$\mathbf{C} = \mu \times \mathbf{B}_0 = i_N |\mu| |B_0| \sin \theta \quad (5)$$

where i_N is a unit vector normal to both μ and \mathbf{B}_0 . The result of the torque is that the proton precesses around the

axis of the magnetic field, keeping a constant angle between μ and \mathbf{B}_0 , at an angular frequency given by

$$\omega = \gamma B_0 \quad (6)$$

where B_0 is universally used to represent \mathbf{B}_0 . Classical mechanics, therefore, shows that the effect of placing a proton in a magnetic field is that it precesses around the axis of that field, at a frequency that is proportional to the strength of the magnetic field. This frequency is termed the *Larmor frequency*.

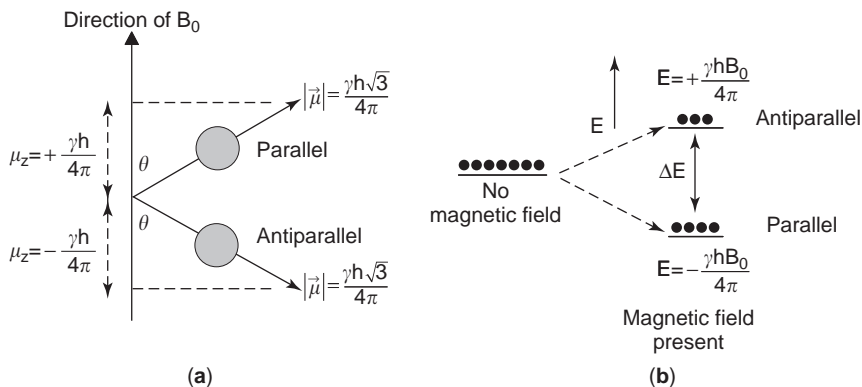
2.1. Application of a Radiofrequency Pulse

Although all of the protons precess around B_0 , they are randomly oriented around a cone, as shown in Fig. 4, and therefore the net magnetization is aligned along the $+z$ axis, that is, there is no transverse component. In order to create a transverse component, an oscillating electromagnetic field (B_1), linearly polarized in the x direction, is applied.

$$B_1 = \hat{x} B_{10} \cos \omega t = \frac{1}{2} B_{10} (\hat{x} \cos \omega t - \hat{y} \sin \omega t) + \frac{1}{2} B_{10} (\hat{x} \cos \omega t + \hat{y} \sin \omega t) \quad (7)$$

where B_{10} is the magnitude of the magnetic field. The right-hand side of Eq. (7) shows that the B_1 field consists

Figure 3. (a) Quantization of the magnitude of the z -component of a proton’s angular momentum means that the z component of the proton’s magnetic moment (μ_z) has two possible physical orientations, parallel and antiparallel, with respect to the direction of the main magnetic field—the value of the angle θ is 54.7° ; (b) in the absence of an external magnetic field, there is only one energy level. When an external magnetic field is present, “Zeeman” splitting results in two energy levels, with more protons occupying the lower energy level, corresponding to the proton magnetic moments being aligned parallel to the main magnetic field, than the higher energy level, corresponding to an antiparallel alignment.



of the sum of two rotating magnetic fields, one rotating clockwise and the other anticlockwise. It can be shown that only the clockwise rotating field interacts with the nuclear spins. Application of the B_1 field at the Larmor frequency rotates the net magnetization M_0 toward the y axis, creating a component of magnetization M_y , given by

$$M_y = M_0 \sin(\gamma B_1 \tau_{B1}) = M_0 \sin \alpha \tag{8}$$

where α is the excitation tip angle. This process of tipping the magnetization is shown in Fig. 4. After the RF pulse, the component of magnetization in the xy plane precesses around B_0 at the Larmor frequency.

2.2. Signal Detection

Signal detection involves placing an RF coil close to the sample. In its simplest form, this coil can be a single loop of wire. Faraday’s law states that, when the magnetic flux enclosed by a loop of wire changes with time, a current is produced in the loop, and a voltage is induced across the

ends of the loop. The induced voltage E is proportional to the negative of the time rate of change of the magnetic flux ($d\phi/dt$):

$$E \propto -\frac{d\phi}{dt} \tag{9}$$

The time-varying magnetic field produced by the precession of the magnetization vectors results in a voltage induced in the RF coil. The requirement for a time-varying magnetic flux is the reason why only precessing magnetization in the xy plane gives rise to an NMR signal; the z component does not precess and therefore produces no voltage. At higher strengths of the B_0 field, the protons precess at a higher frequency [Eq. (6)], and the value of $d\phi/dt$ increases. Therefore, higher magnetic fields produce higher signal not only because of greater nuclear polarizations [Eq. (4)] but also because of the higher voltage induced in the RF coil. Overall, we obtain

$$E \propto \frac{\gamma^2 h^2 B_0 N_s}{16\pi^2 kT} \gamma B_0 \sin \alpha \tag{10}$$

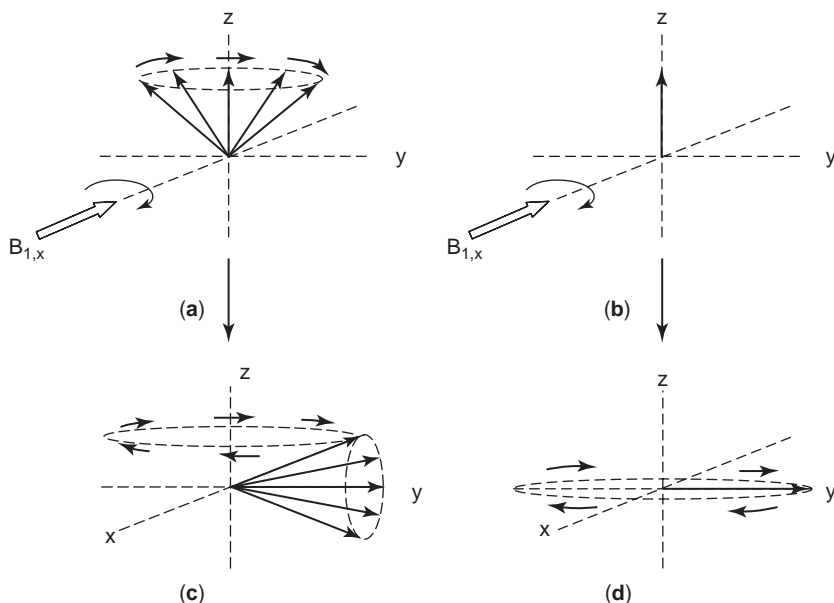


Figure 4. (a) Application of a B_1 field ($B_{1,x}$) along the x axis rotates the individual proton magnetic moments about the x axis toward the y axis; (c) After applying the B_1 field for a certain time duration, the “cone” of magnetic moments has been rotated by 90° (the magnetic moments continue to precess around the B_0 axis); (b,d) the vector model representations of the effect of the B_1 field. The initial longitudinal magnetization (M_z) has been rotated into the transverse plane and has been converted into transverse magnetization (M_y) along the y axis.

2.3. Relaxation

Each of the magnetization components M_z , M_x , and M_y must return to their thermal equilibrium values over time. The time evolutions of M_z , M_x , and M_y are characterized by the Bloch equations [3]

$$\begin{aligned} \frac{dM_x}{dt} &= \gamma M_y \left(B_0 - \frac{\omega}{\gamma} \right) - \frac{M_x}{T_2} \\ \frac{dM_y}{dt} &= \gamma M_z B_1 - \gamma M_x \left(B_0 - \frac{\omega}{\gamma} \right) - \frac{M_y}{T_2} \\ \frac{dM_z}{dt} &= -\gamma M_y B_1 - \frac{M_z - M_0}{T_1} \end{aligned} \quad (11)$$

where T_1 is the spin–lattice relaxation time and governs the z component of magnetization and T_2 is the spin–spin relaxation time governing the transverse component. In the well-known rotating reference frame—a frame of reference where the $x'y'$ axes rotate around B_0 at the Larmor frequency—simple expressions can be obtained for the time evolution of longitudinal and transverse magnetization:

$$M_z(t) = M_z(t=0) + [M_0 - M_z(t=0)](1 - e^{-t/T_1}) \quad (12)$$

$$M_y(t) = M_y(t=0)e^{-t/T_2} \quad (13)$$

$$M_x(t) = M_x(t=0)e^{-t/T_2}$$

As seen later in the article, image contrast depends strongly on the different T_1 and T_2 values for various tissues in the human body.

2.4. Magnetic Field Gradients

Three separate gradient coils are required to encode unambiguously the three spatial dimensions within the body. Since only the z component of the magnetic field interacts with the proton magnetic moments, it is the spatial variation in the z component of the magnetic field which is

important. Image reconstruction is simplified considerably if the magnetic field gradients are linear over the region to be imaged:

$$\frac{\partial B_z}{\partial z} = G_z \quad \frac{\partial B_z}{\partial x} = G_x \quad \frac{\partial B_z}{\partial y} = G_y \quad (14)$$

By convention, for human studies the z direction lies along the head-to-foot axis, the y axis corresponds to the vertical (spine-to-abdomen) direction, and the x axis extends from side to side. The gradient coils are designed (as discussed later in this article) such that there is no additional contribution to the static magnetic field at the isocenter ($z = 0$, $y = 0$, $x = 0$) of the magnet, which means that the magnetic field at this position is simply B_0 . If a gradient G_z is applied, the magnetic field B_z experienced by all nuclei with a common coordinate z is

$$B_z = B_0 + zG_z \quad (15)$$

where G_z has units of tesla (T) per meter or gauss (G) per centimeter (cm). The corresponding precessional frequencies (ω_z) of the protons, as a function of their position in z , is given by

$$\omega_z = \gamma B_z = \gamma(B_0 + zG_z) \quad (16)$$

In the rotating reference frame the precessional frequency is

$$\omega_z = \gamma zG_z \quad (17)$$

Analogous expressions can be obtained for the spatial dependence of the resonant frequencies in the presence of the x and y gradients.

The process of image formation can be broken down into three components: slice selection, phase encoding, and frequency encoding. Examples of common imaging sequences are shown in Fig. 5. In the gradient echo sequence the combination of a frequency-selective 90° pulse

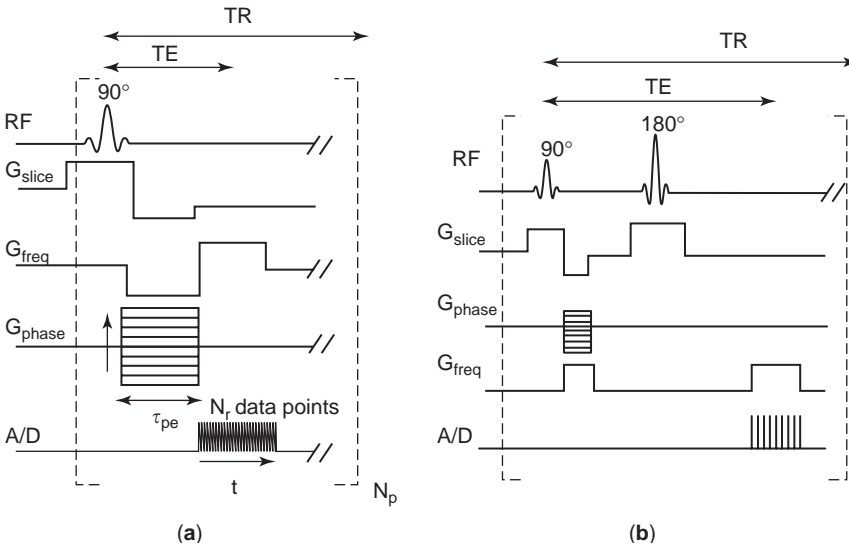
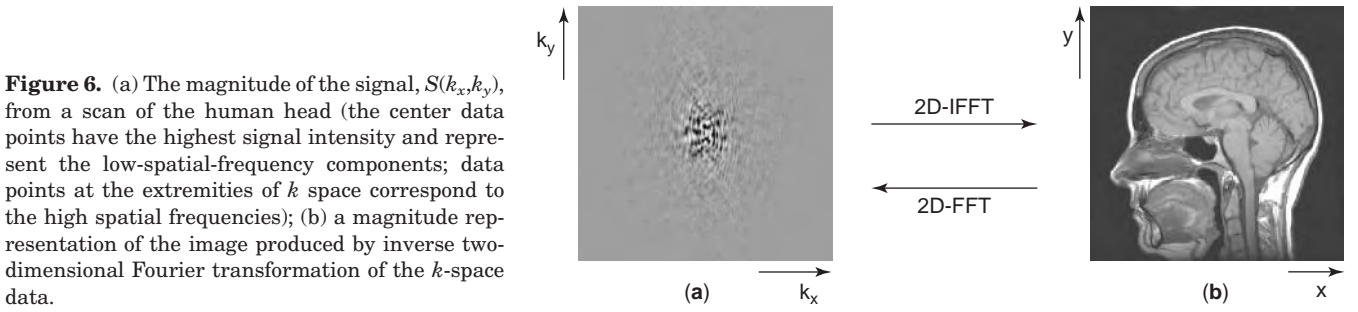


Figure 5. (a) Basic scheme for a gradient-echo imaging sequence and (b) for a spin-echo sequence. In both cases the acquisition matrix size is $N_r \times N_p$ data points.



and the slice gradient tips protons within a thickness $\Delta\omega/\gamma G_{\text{slice}}$, where $\Delta\omega$ is the frequency bandwidth of the pulse, into the transverse plane. Protons outside this slice are not excited. Application of the phase encoding gradient G_{phase} , denoted as the y direction here, imparts a spatially dependent phase shift into the signal. During signal acquisition, the frequency encoding gradient (x direction) generates a spatially dependent precessional frequency in the acquired signal. Overall, ignoring relaxation effects, the detected signal is given by

$$s(G_y, \tau_{\text{pe}}, G_x, t) \propto \int_{\text{slice}} \int_{\text{slice}} \rho(x, y) e^{-j\gamma G_x x t} e^{-j\gamma G_y y \tau_{\text{pe}}} dx dy \quad (18)$$

where $\rho(x, y)$ is the spatially dependent proton density, specifically, the number of protons at a given x, y coordinate. Using the k -space formalism [4], this signal can be expressed as

$$S(k_x, k_y) \propto \int_{\text{slice}} \int_{\text{slice}} \rho(x, y) e^{-j2\pi k_x x} e^{-j2\pi k_y y} dx dy \quad (19)$$

where the two variables k_x and k_y are defined as

$$k_x = \frac{\gamma}{2\pi} G_x t, \quad k_y = \frac{\gamma}{2\pi} G_y \tau_{\text{pe}} \quad (20)$$

This representation of the acquired data is particularly useful since the image can simply be reconstructed by an inverse two-dimensional Fourier transform.

$$\rho(x, y) = \int_{-\infty}^{\infty} \int_{-\infty}^{\infty} S(k_x, k_y) e^{+j2\pi(k_x x + k_y y)} dk_x dk_y \quad (21)$$

The k -space representation of the data is shown in Fig. 6. In the k_x dimension N_r data points are acquired (see Fig. 5). The imaging sequence is repeated N_p times, with the phase encoding gradient incremented for each repetition. This results in N_p lines being acquired in the k_y direction.

If the effects of T_1 and T_2 relaxation are taken into account, it can be shown that in a gradient-echo sequence, the image intensity $I(x, y)$ is given by

$$I(x, y) \propto \frac{\rho(x, y)(1 - e^{-\text{TR}/T_1})e^{-\text{TE}/T_2^*} \sin \alpha}{1 - e^{-\text{TR}/T_1} \cos \alpha} \quad (22)$$

where T_2^* is the spin-spin relaxation time, including the effects of magnetic field inhomogeneity. For a spin-echo imaging sequence, the corresponding expression is

$$I(x, y) \propto \rho(x, y)(1 - e^{-\text{TR}/T_1})e^{-\text{TE}/T_2} \quad (23)$$

The times TR (repetition time) and TE (echo time) within the imaging sequence can be chosen to give different contrasts in the image. For example, Fig. 7 shows the effects of increasing the TE on a simple brain scan.

The ability to produce many different contrast characteristics in images is one of the major advantages of MRI as a clinical diagnostic technique. Clinical applications include brain scanning (for tumors, hematomas, astrocytomas, etc.), musculoskeletal (shoulder, knee, etc.), cardiac, and liver/kidney imaging. Contrast agents such as gadolinium DTPA and superparamagnetic iron oxide are often used to highlight pathological features from surrounding healthy tissue [5]. Detailed descriptions of clinical MRI can be found in Ref. 6.

3. HARDWARE DESIGN

The major hardware components of an MRI system are the magnet, magnetic field gradients, and RF coil, in addition to the receiver. The first three components involve similar analytical methods [7,8] to design, respectively, a homogenous DC static magnetic field, linear spatially dependent rapidly switched magnetic fields, and high-frequency (60–750 MHz) resonators producing a uniform magnetic field.

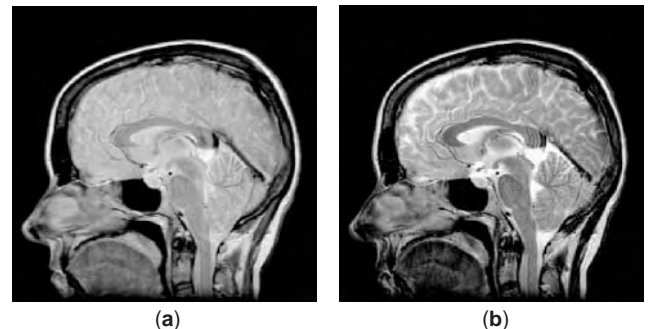


Figure 7. Axial images of the brain acquired at 1.5 T. The image in (a) is acquired with a TE value of 34 ms. Increasing the TE value to 102 ms produces the image in (b).

3.1. Superconducting Magnets

For all imaging studies performed at field strengths above ~ 0.5 T, a superconducting magnet is required. For fields below this, permanent magnets can be used. In either case the critical factors in magnet design are high homogeneity of the field [<1 part per million (ppm) over the sample], and a high degree of temporal stability (<50 Hz drift per hour). Almost all clinical superconducting magnets have a cylindrical bore, approximately 1 m in diameter, which encloses the magnetic field gradients, radiofrequency coil, and patient, as shown in Fig. 1. In order to create high static magnetic fields, it is necessary for the superconductor to carry a large current, and this capability is possessed only by certain alloys, particularly those made from niobium–titanium. Below a critical temperature (9 K) and critical magnetic field (10 T), once current has been fed into such an alloy, this current will run through the wire with constant magnitude essentially indefinitely. The superconducting alloy is formed into multistrand filaments and interspersed within a conducting matrix. This arrangement can support a much higher critical current than a single, large-diameter superconducting wire. The superconducting coils shown in Fig. 8 are housed in a stainless-steel can containing liquid helium at a temperature of 4.2 K. This inner container is surrounded by a series of radiation shields and vacuum vessels to minimize heat transfer to the liquid helium. Liquid nitrogen is used to cool the outside of the vacuum chamber and the radiation shields. Since heat transfer cannot be completely eliminated, liquid nitrogen and liquid helium must be replenished on a regular basis.

The exact placement of the superconducting filaments within the magnet is designed to give the maximum field homogeneity over the patient. The basic design consists of a number of wire helices, or solenoids, of different diameters and separations, each wound along the major axis of the magnet. A typical layout is shown in Fig. 8.

For a single loop of wire, the field can be expressed as

$$B_z(r, \theta) = \sum_{n=0}^{\infty} \left(\frac{r}{r_0}\right)^n B_n P_n(\cos \theta) \quad (24)$$

where r_0 is half the length of the region of interest and $P_n(\cos \theta)$ is the standard Legendre polynomial of degree n . The design problem is to determine the optimum number, spacing, and diameter of wire loops such that the B_n coefficients are zero up to the maximum order. The larger the number of current-carrying elements that are present, the higher the order of the harmonics that can be minimized; however, one constraint is the total length of the magnet.

Slight errors in positioning the wires can lead to significant variations in the field uniformity, in which case the B_z field is given by the complete solution to Laplace's equation. Additional coils of wire are added in series with the main coil as superconducting correction coils. After the magnet has been energized by passing current into the major filament windings, the current can be changed in these correction coils to improve the homogeneity. Fine tuning is performed by using a series of independently wired coils at room temperature, termed "shim coils." The operator can adjust the current in these coils for each clinical examination, and so the magnet homogeneity can be optimized for individual patients.

A strong magnetic field is also present outside the magnet, and this can interfere with any electronic equipment nearby. Machines with moving parts, such as induction motors, or any object with metallic elements must be placed outside the fringe field; this creates an effective "dead space" around the magnet. In many clinical and academic institutions space is limited, and so a reduction in the extent of the "stray" field is highly desirable. "Active shielding" of a magnet uses secondary windings, placed outside the primary magnet windings, with the current traveling in the opposite direction, in order to minimize the fringe field. Clearly, the presence of these secondary windings also reduces the field within the patient, and so an increased current is now needed in the primary windings. The alternative method of "passive magnet shielding" incorporates iron plates into the magnet exterior. The disadvantage of this method of shielding is that the mass of the magnet is increased significantly.

3.2. Magnetic Field Gradient Coils

Three separate "gradient coils" are required to encode the x , y , and z dimensions of the sample. The requirements for gradient coil design are that the gradients are as linear as possible over the region being imaged, that they are efficient in terms of producing high gradients per unit current, and that they have fast switching times for use in rapid imaging sequences. Copper is used as the conductor, with chilled-water cooling to remove the heat generated by the current. Since the gradient coils fit directly inside the bore of the cylindrical superconducting magnet, the geometric design is usually also cylindrical. The simplest configuration for a coil producing a gradient in the z direction is a "Maxwell pair," shown in Fig. 9a, which consists of two separate loops of multiple turns of wire, each loop containing equal currents I flowing in opposite directions. In order to estimate the distance between the two loops that maximizes the linearity of the gradient, the value of B_z is

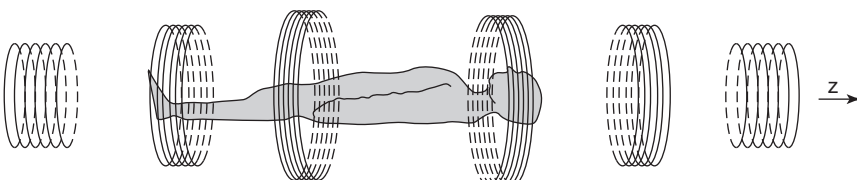


Figure 8. Schematic of the layout of the superconducting wires to produce a homogeneous magnetic field B_z within the patient.

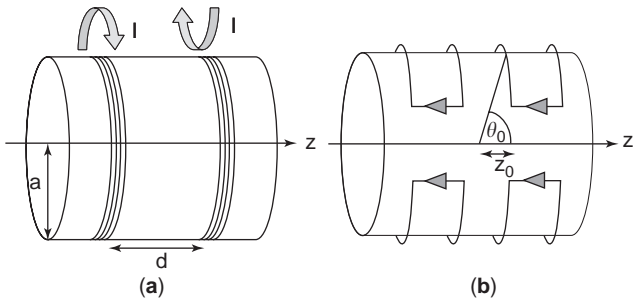


Figure 9. (a) Schematic of a Maxwell gradient set that produces a linear magnetic field gradient in the z direction; (b) schematic of a saddle geometry gradient set producing a linear magnetic field in the y direction.

first calculated

$$B_z = \frac{\mu_0 I a^2}{2[(d/2 - z)^2 + a^2]^{1.5}} - \frac{\mu_0 I a^2}{2[(d/2 + z)^2 + a^2]^{1.5}} \quad (25)$$

where μ_0 is the permeability of free space and a is the radius of the gradient set. The first term that can give a nonlinear contribution is the third derivative, given by

$$\frac{d^3 B_z}{dz^3} = \frac{15\mu_0 I a^2}{2} \left\{ \frac{4(d/2 - z)^3 - 3(d/2 - z)a^2}{[(d/2 - z)^2 + a^2]^{9/2}} + \frac{4(d/2 + z)^3 - 3(d/2 + z)a^2}{[(d/2 + z)^2 + a^2]^{9/2}} \right\} \quad (26)$$

This term becomes zero at a value of $d = a\sqrt{3}$. The magnetic field produced by this gradient coil is zero at the center of the coil, and is linearly dependent on position in the z direction over about one-third of the separation of the two loops. The region over which the gradient is linear can be extended by adding other sets of coils in the axial dimension.

The x - and y -gradient coils are completely independent of the z -gradient coils. The derivation of gradient field linearity for the transverse gradients is somewhat more complicated than for the Maxwell pair. The usual configuration is to use four arcs of wire as shown in Fig. 9b. The wire segments in the z direction do not produce a transverse component to the field, and the four outer arcs provide return paths for the current. The B_z field produced by an arc on a cylinder of radius a is given by

$$B_z(r, \theta, \phi) = \sum_{n=0}^{\infty} \sum_{m=0}^n r^n P_n^m(A_{nm} \cos m\phi + B_{nm} \sin m\phi) P_{nm} \cos \theta \quad (27)$$

If the four inner arcs are placed symmetrically around $z = 0$, then $A_{nm} = 0$ for all m , and $B_{nm} = 0$ if n or m is even. Equation (27) can now be expanded as follows:

$$B_z(r, \theta, \phi) = -B_{11}r \sin \theta \sin \phi + B_{31}r^3 P_3^1 \cos \theta \sin \phi + B_{33}r^3 P_3^3 \cos \theta \sin 3\phi + \dots \quad (28)$$

The first term is a linear function of y , but the other terms are nonlinear. The term in B_{33} can be made zero by setting the angle $\psi = 120^\circ$, and the term in B_{31} can be eliminated by setting $\theta_0 = 21.3^\circ$ for $z_0 = 2.57a$. These results mean that the separation between the arcs along the z axis is ~ 0.8 times the radius of the gradient coil. From symmetry considerations the same basic design can be used for coils producing gradients in the x direction with the geometry simply rotated by 90° .

A second design criterion is that the current in the gradient coils should be switched on and off in the shortest possible time. This reduces the time that must be allowed for gradient stabilization in imaging sequences. This criterion is achieved by minimizing the inductance L of the gradient coils. A related issue is achieving high efficiency η , where η is defined as the gradient strength per unit current at the center of the gradient set. These three criteria (homogeneity, switching speed and efficiency) for judging gradient performance can be combined into a so-called figure of merit β , defined as

$$\beta = \frac{\eta^2}{L \sqrt{\frac{1}{V} \int \left(\frac{B(r)}{B_0(r)} - 1 \right)^2 d^3r}} \quad (29)$$

where $B_0(r)$ is the “desired” magnetic field, $B(r)$ is the actual magnetic field, and V is the volume of interest over which the integral is evaluated.

When the current in the gradient coils is switched rapidly, eddy currents can be induced in nearby conducting surfaces, such as the radiation shield in the magnet. These eddy currents, in turn, produce additional unwanted gradients in the sample that may decay only very slowly, even after the original gradients have been switched off. These eddy currents can result in image artifacts, and are particularly problematic for sensitive measurements of diffusion coefficients and in localized spectroscopy. All gradient coils in commercial MRI systems are now “actively shielded” to reduce the effects of eddy currents. Active shielding uses a second set of coils placed outside the main gradient coils, the effect of which is to minimize the stray gradient fields.

3.3. Radiofrequency Coils for MRI

Radiofrequency coils for MRI differ from conventional antennas in that they are designed to maximize the near-field magnetic energy that is stored in the patient. The desirable properties of such a coil include: (1) a homogeneous B_1 distribution within the patient, (2) minimum electric fields within the patient since these lead to signal-to-noise ratio (SNR) losses and also to an increased specific absorption ratio (SAR; i.e., patient heating), (3) maximum B_1 intensity per unit driving current, and (4) minimum resistive losses in the RF coil.

Since most RF coils are used to image either the brain or torso, the form of the coil is usually cylindrical as shown in Fig. 1. Assuming that this cylinder is infinitely long and carries a surface current J_s , given by

$$J_s = \hat{z} J_0 \sin \phi \quad (30)$$

the field inside the cylinder is given by

$$\begin{aligned}
 B(\rho, \phi) = & -\hat{\rho} \sum_{m=1}^{\infty} m\rho^{m-1}(A_m \cos m\phi + B_m \sin m\phi) \\
 & + \hat{\phi} \sum_{m=1}^{\infty} m\rho^{m-1}(A_m \sin m\phi - B_m \cos m\phi)
 \end{aligned}
 \tag{31}$$

By applying boundary conditions at the cylinder surface (considering the B_1 field created outside the cylinder), all the B_m coefficients must be zero, and the only nonzero A_m coefficient is given by $A_1 = -\mu_0 J_0/2$. Therefore

$$B(\rho, \phi) = \frac{\mu_0 J_0}{2} (\hat{\rho} \cos \phi - \hat{\phi} \sin \phi) = \hat{x} \frac{\mu_0 J_0}{2}
 \tag{32}$$

This shows that a perfectly uniform B_1 field, directed along the x direction, is produced by a sinusoidal current along the surface of a cylinder of infinite length. Of course, this configuration cannot be realized in practice, but the basic tenet of coil design is to approximate this sinusoidal surface current. The most common such realization is called the “birdcage” resonator [9], which is shown in Fig. 10. The resonator is usually constructed in a high-pass configuration, with a series of equidistantly spaced “rungs” and two “end rings.”

The birdcage coil has multiple resonant modes. For an n -rung highpass birdcage the highest-frequency mode is the so-called end-ring mode, the next $n - 2$ modes are each

doubly degenerate (the highest-frequency one produces a homogeneous transverse B_1 field), and there is a single mode at the lowest frequency. Since the birdcage coil has two orthogonal, degenerate homogeneous modes, it can be operated in quadrature; that is, it can produce a circularly polarized B_1 field. This reduces the power required for RF transmission by a factor of 2, and increases the image SNR also by a factor of $\sqrt{2}$. Practical implementation simply involves splitting the transmitter pulse through a quadrature hybrid, the two outputs of which are connected to the coil at feedpoints that are physically 90° apart.

Impedance matching of the coil must be performed in order to ensure maximum power transmission and efficient reception. Since amplifier outputs, transmission cables, and preamplifier input impedances are almost exclusively 50Ω , this is the impedance to which the coil is matched at the Larmor frequency. A balanced impedance-matching network should be used to reduce electric field losses in the sample, and the most common is a standard pi-matching network, with variable capacitors to adjust for different sample-dependent loads. Often, baluns or cabletraps are used to reduce currents traveling on the outside of the transmission cable connecting to the coil.

Noise in MRI originates from the sample and also the RF coil. Coil losses are linearly dependent on the operating frequency, and sample losses in human patients increase as the square of the operating frequency. In general, at low frequencies coil losses are dominant, whereas at high frequencies sample losses are the dominant factor. In all cases it is desirable to minimize the loss

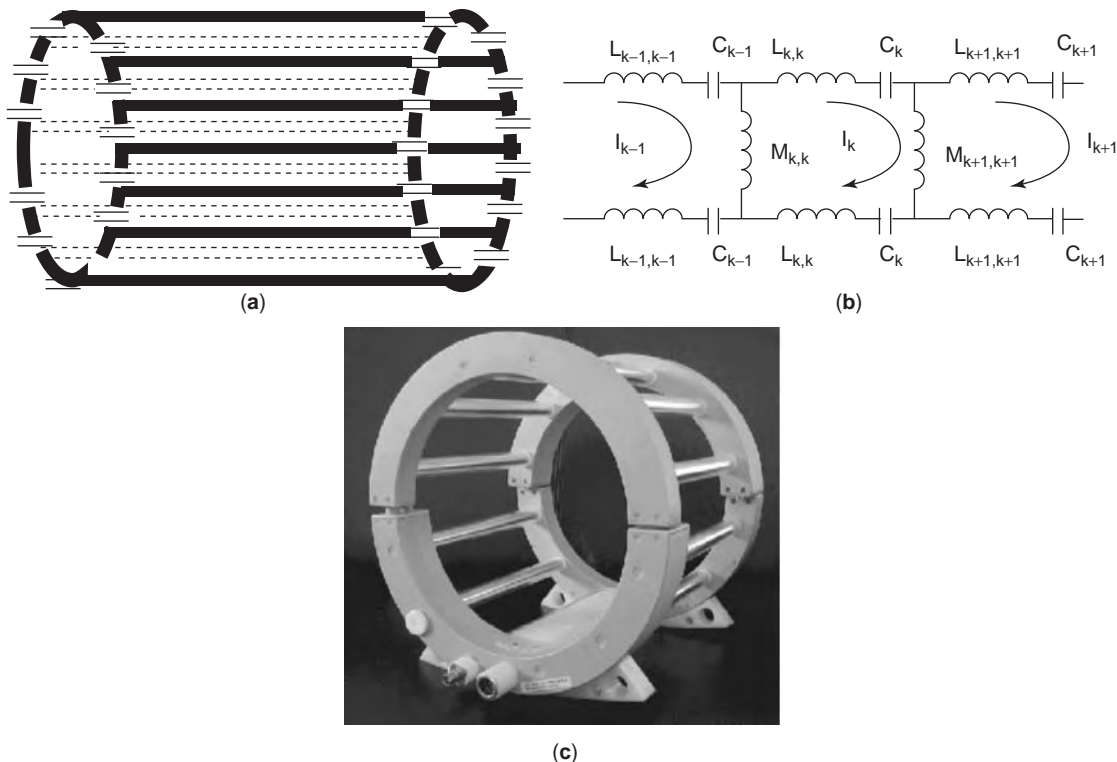


Figure 10. (a) Highpass birdcage coil; (b) equivalent circuit model for the highpass birdcage including the mutual inductance between individual loops; (c) photograph of a 12-leg birdcage coil for a 1.5-T system.

inherent in the coil, that is, to maximize the quality factor Q of the tuned circuit. At high magnetic field strengths the dimensions of the RF coil constitute a substantial fraction of the wavelength of the electromagnetic wave inside the patient. This leads to a number of problematic issues, including increased radiative losses and nonuniform current distribution along the conductors, which reduces the B_1 homogeneity. One way to minimize these effects is to design the coil using distributed capacitance rather than discrete lumped elements. Thus, familiar elements in microwave technology, such as transmission lines and cavities, will potentially play an increasingly important role in the design of high frequency coils. For example, one such design, termed a transverse electromagnetic (TEM) resonator, has been used for human studies up to frequencies of 300 MHz [10].

3.4. Mutually Decoupled Coil Arrays

In many MRI applications, it is not necessary to acquire signal from the entire patient, but only from a localized region. In this case, a small “surface coil” can be placed next to the region of interest. Typically, this surface coil is a simple circular or square loop. Since the B_1 field produced from such a coil is very inhomogeneous, a larger-“volume” coil, such as the birdcage described previously, is used for transmitting a homogeneous B_1 field, and the surface coil is used to receive the signal. Using the small surface coil in this way gives a local SNR much higher than that from the volume coil alone, due to both the high intrinsic sensitivity of the small surface coil and the reduced noise contribution from the patient. However, since there are now two circuits impedance-matched at the same frequency in relatively close proximity, there can be considerable coupling between the two circuits. This coupling must be minimized, and is normally achieved using active detuning of the surface coil during transmission, and the volume coil during signal reception, via PIN diodes.

An extension of the surface coil concept is the design of arrays of mutually decoupled surface coils [11,12], often misleadingly called “phased arrays,” as shown schematically in Fig. 11. The use of many coils requires that the imaging system has multiple receiver channels; as of 2004, most commercial vendors have up to 32 such receiver channels. Each coil in the array is connected to a separate preamplifier and receiver. Using such arrays, much larger imaging fields of view can be covered than with a single small coil, while maintaining the high sensitivity of the individual small surface coils. Image reconstruction is normally implemented using a simple sum-of-squares algorithm. The major engineering challenge is to reduce the coupling between individual coils; this coupling introduces noise correlation into the reconstructed image and reduces the image SNR. Effective coil decoupling can be achieved by optimal overlapping of the coils, a process that minimizes the mutual impedance between neighboring coils, and also by using high-input impedance preamplifiers for each of the coils, which minimizes the currents present in the individual coils, and therefore the intercoil coupling [11].

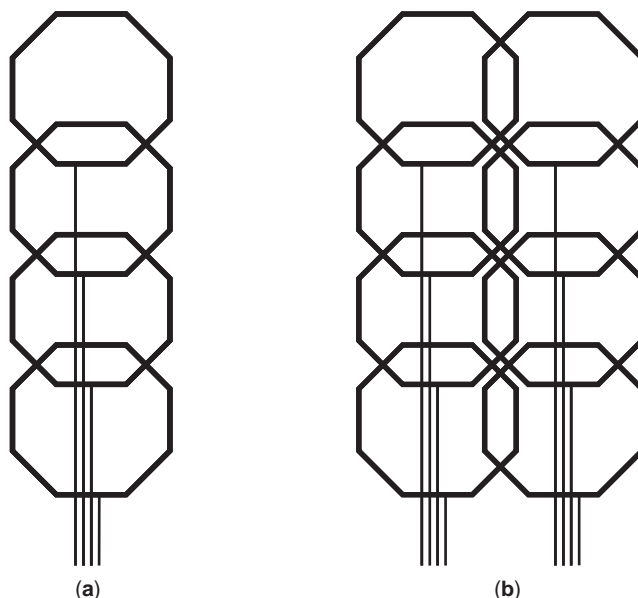


Figure 11. Schematic of a four-element one-dimensional MRI coil array (a) and an eight-element two-dimensional MRI coil array (b).

3.5. The MRI Receiver

The basic elements of an analog MRI receiver chain are a preamplifier, a one- or two-stage demodulator, a quadrature-phase-sensitive detector, lowpass filters, two second-stage audio amplifiers with variable gain, and finally two analog-to-digital converters; the MRI receiver as such is very similar to a conventional superheterodyne radio receiver.

Figure 12 shows the first stage of the receiver chain and the connections to the MRI coil. The purpose of the transmit/receive (Tx/Rx) switch is to ensure that the high-power transmitted RF pulse does not leak into the receiver, and also that during signal reception all of the signal passes to the preamplifier. During transmission of the RF pulse, diodes D_1 and D_2 are turned on and therefore conduct. Diodes D_3 and D_4 are also in ON state, and the quarter-wavelength cable to ground provides a high impedance, preventing current from traveling to the preamplifier. The received signal (typically of the order of millivolts) is several orders of magnitude lower than the transmitted pulse, and so, during signal reception, all diodes are OFF. The transmitter chain presents a high impedance, and all the signal passes through the quarter-wavelength cable to the preamplifier. In certain implementations the quarter-wavelength cable can be replaced by a lumped-element circuit, typically a “pi” network with two capacitors and one inductor. Rather than the single set of diodes shown in the diagram, in practice many sets of diodes are used.

The second stage of the receiver chain is shown in Fig. 13. The first stage demodulates the signal from the Larmor frequency to an intermediate frequency (IF), typically ~ 10.7 MHz. A second demodulation stage to baseband can be used, but most modern scanners directly sample at the intermediate frequency. The signal enters a quadrature mixer to produce real and imaginary

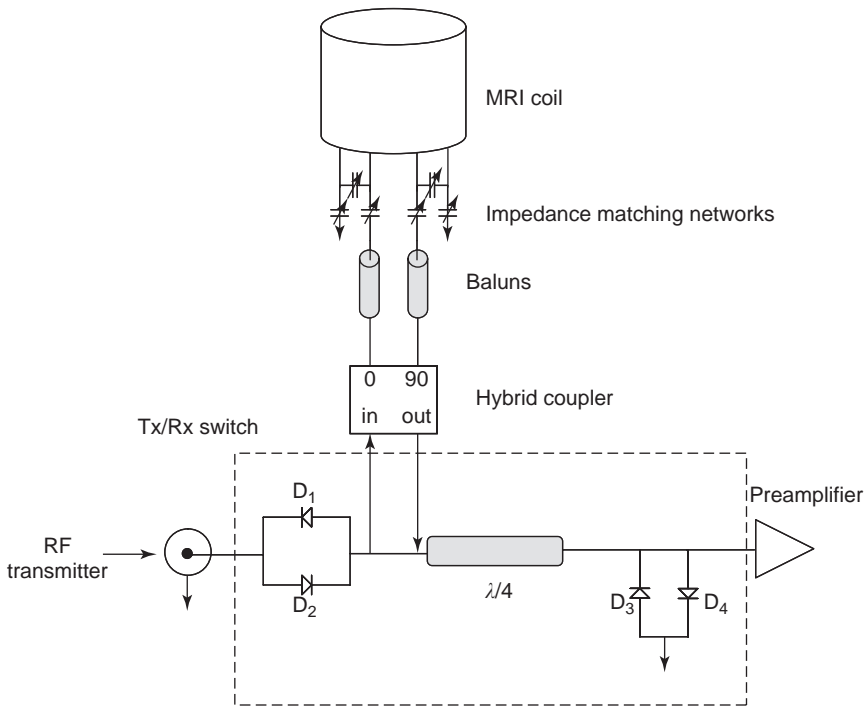


Figure 12. A schematic of the first stage of the receiver chain with a Tx/Rx switch used to isolate the receiver from the transmitter.

outputs. These pass through lowpass filters, the cutoff frequency of which depends on the particular data acquisition parameters used in the image. After final amplification, the signal is digitized, typically with a resolution of 16 bits.

3.6. Direct Digital Synthesis and Digital Detection

The rapid spread of digital transmission and reception in the communication industry has recently been mirrored in the design of MRI systems, in particular the receiver. Using digital filters, for example, enables a much better filter shape than for the analog case. In addition, the data can be oversampled many times, which provides a higher SNR in the reconstructed image. Direct digital synthesis (DDS) has the advantage of faster frequency- and phase-continuous switching than does its analog counterpart. A complete DDS unit is available on-chip (e.g., the AD9854 from Analog Devices, with 48 bit frequency resolution and 14

bit phase resolution). A DDS chip typically consists of an address counter, a lookup table for production of the sine wave at the frequency of interest, and a digital-to-analog converter. Although such chips are currently limited in the highest frequency that can be produced, the image frequency output can potentially be used for such applications.

4. ADVANCED TOPICS

4.1. Parallel Imaging

One of the major limitations of MRI, particularly in comparison with computed tomography and ultrasonic imaging, is the relatively slow data acquisition. The fundamental limits on imaging speed are the time required for current switching in the gradient coils, and the relatively large number of phase encoding steps (typically

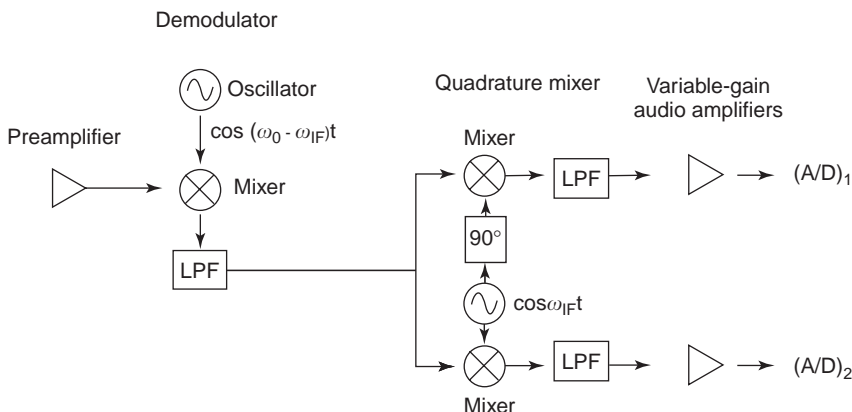


Figure 13. A schematic of the second stage of the receiver chain and analog-to-digital (A/D) conversion, where ω_0 is the Larmor frequency, ω_{IF} the intermediate frequency, and LPF a low-pass filter.

128–256) required for reasonable spatial resolution. More recently, a general class of imaging techniques, termed *parallel imaging*, have been developed that use the spatial information from an array of mutually decoupled coils to reduce the number of acquired phase encoding steps, and therefore increase the imaging speed. Acceleration factors of 4 in one-phase-encoding direction, and up to 10 in two-phase-encoding directions have been achieved.

The basic principle of parallel imaging is that it is possible to reconstruct many lines of k space from a single acquired line. The original method, termed *simultaneous acquisition of spatial harmonics* (SMASH) [13], achieves this by using combinations of signals from an array of surface coils to directly mimic the spatial encoding normally performed by phase encoding. In analogy to Eq. (19), the k -space signal acquired in the p th coil is given by

$$S_p(k_x, k_y) \propto \int_{\text{slice}} \int_{\text{slice}} \rho(x, y) C_p(x, y) e^{-j2\pi k_x x} e^{-j2\pi k_y y} dx dy \quad (33)$$

where $C_p(x, y)$ is the spatial distribution of the RF sensitivity for the p th coil in the array. If the array is constructed appropriately, then a linear combination of the individual coil sensitivities can be used to produce shifts in k_y that are identical to acquiring different phase encoding steps

$$\sum_p n_p^{(m)} S_p(k_x, k_y) \approx \sum_p n_p^{(0)} S_p(k_x, k_y + m\Delta k_y) \quad (34)$$

where m is an integer, either positive or negative. For example, if $m = +1$, then the even lines in k_y space could be acquired, and the odd lines synthesized from the (measured) coil sensitivity profiles, thus reducing the data acquisition time by a factor of 2.

For image reconstruction without artifacts, the SMASH technique relies on accurate knowledge or a good estimate of the relative RF sensitivities of the component coils in the array in order to determine the optimal complex weights $n_p^{(m)}$. Many improvements have been made to the original implementation; for example, the technique known as *generalized autocalibrating partially parallel acquisitions* (GRAPPA) acquires additional autocalibration scan (ACS) lines. Data from multiple lines from all the coils are used to fit ACS lines in a single coil. This fit gives the weights, which are then used to generate the missing k -space lines from that particular coil. After this procedure has been performed for each coil in the array, the full set of images can be combined using an optimal sum-of-squares reconstruction. Using GRAPPA several problems such as sub-optimal image reconstruction, phase cancellation and inexact estimates of coil sensitivities are minimized.

An alternative parallel imaging strategy is the sensitivity encoding (SENSE) method [15], which provides an optimized reconstruction if a perfectly accurate complex coil sensitivity map can be obtained. If the acquired k -space data are reduced by a factor of R by skipping certain k -space lines, then inverse Fourier transformation of the data leads to aliased images from all the coils in the array.

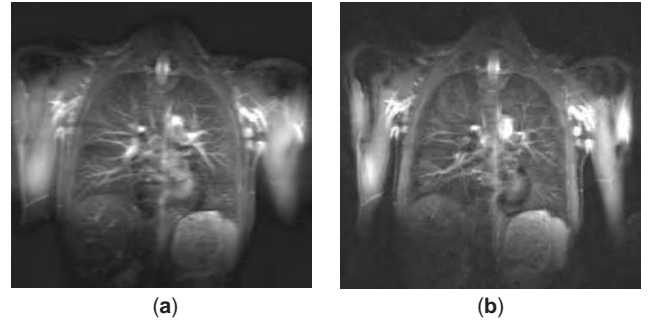


Figure 14. Single-shot inversion recovery HASTE images in the lungs of a healthy volunteer acquired with an eight-element cardiac array: (a) conventional acquisition matrix 128×256 (207 ms imaging time, interecho spacing 2.88 ms); (b) GRAPPA acquisition (acceleration factor 3) with matrix 256×256 (150 ms imaging time, interecho time 0.96 ms). (Reproduced from Ref. 14, copyright 2002, with permission from John Wiley & Sons.)

In order to reconstruct an accurate image of the sample, the true signals and folded signals have to be separated. This can be achieved since, in the image from each individual coil, signal superposition occurs with different weights according to the local coil sensitivities. The unaliased components v of every aliased pixel can be obtained by an appropriate linear combination of the pixel values in the various single-coil images

$$v = (S^H \Psi^{-1} S)^{-1} S^H \Psi^{-1} a \quad (35)$$

where vector v contains the unaliased pixel values, a the aliased values, and S the complex coil sensitivities; the superscript H represents the transposed complex conjugate, and Ψ noise correlation in the receiver channels.

In addition to speeding up data acquisition, partial parallel imaging can also be used to improve image quality in single-shot imaging techniques, where short T_2 values lead to image blurring. An example is shown in Fig. 14.

4.2. Dielectric and Penetration Effects at High Frequencies

As described previously, higher static magnetic fields result in a higher image SNR, and are particularly advantageous in functional magnetic resonance imaging, for example. However, as the Larmor frequency increases, the dimensions of the human patient (head or torso) become a significant fraction of the radiofrequency wavelength, and the B_1 field distribution is distorted significantly by the patient [16,17]. In general, two competing effects arise from the dielectric and conductivity properties of the patient. Materials with a high dielectric constant, for instance water with $\epsilon_r = 80$, reduce the effective wavelength within the patient, and can give rise to dielectric resonances that produce areas of high signal intensity at the center of the object. For a dielectric cylinder with radius a cm and length L cm, the resonant frequency of the $TE_{01\delta}$ mode is given by

$$f_{\text{MHz}} = \frac{3400}{a\sqrt{\epsilon_r}} \left(\frac{a}{L} + 3.45 \right) \quad (36)$$

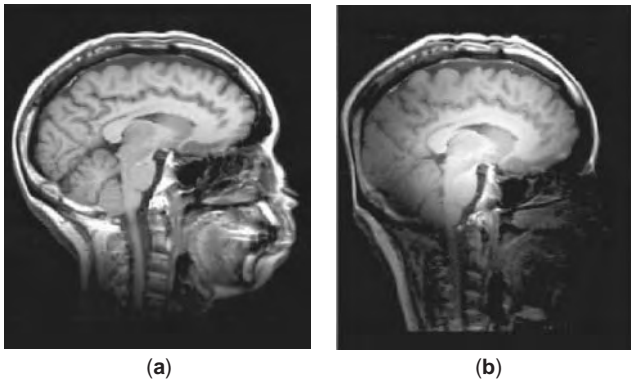


Figure 15. Magnetic resonance images acquired at (a) a field strength of 4 T (proton Larmor frequency 170 MHz) and (b) at a field strength of 7 T (proton Larmor frequency 300 MHz). The presence of a dielectric resonance at the higher field strength is clearly visible. (Reproduced from reference 18, copyright (2001), with permission from John Wiley & Sons.)

The conductivity of the sample, however, dampens this effect and reduces the penetration of the RF field. Since both effects are highly frequency-dependent, the relative effects are manifested very differently at different field strengths. Specifically, the wavelength is given by

$$\lambda = \frac{2\pi}{\sqrt{\omega^2 \mu_0 \epsilon_0 \epsilon_r - j\omega \mu_0 \sigma}} \quad (37)$$

At field strengths up to 7 T, the dominant effect is from the dielectric “focussing,” which is typically seen as a bright area in the center of the patient, as shown in Fig. 15 [18].

BIBLIOGRAPHY

1. P. C. Lauterbur, Image formation by induced local interactions: Examples employing nuclear magnetic resonance, *Nature* **242**:190–191 (1973).
2. P. Mansfield and P. K. Grannell, NMR diffraction in solids, *J. Phys. C Solid State Phys.* **6**:L422–L426 (1973).
3. F. Bloch, Nuclear induction, *Phys. Rev.* **70**:460–474 (1946).
4. S. Ljunggren, A simple graphical representation of Fourier-based imaging methods, *J. Magn. Reson.* **54**:338–343 (1983).
5. W. Krause, ed., *Magnetic Resonance Contrast Agents*, Springer-Verlag, Berlin, 2002.
6. D. D. Stark, and W. G. Bradley, Jr., *Magnetic Resonance imaging*, Vols. 1 and 2, 2nd ed., Mosby-Year Books, 1992.
7. C. -N. Chen and D. I. Hoult, *Biomedical Magnetic Resonance Technology*, Adam Hilger, Bristol and New York, 1989.
8. J. -M. Jin, *Electromagnetic Analysis and Design in Magnetic Resonance Imaging*, CRC Press, Boca Raton, FL, 1998.
9. C. E. Hayes, W. A. Edelstein, J. F. Schenck, O. M. Mueller, and M. Eash, An efficient, highly homogeneous radiofrequency coil for whole-body NMR imaging at 1.5 T, *J. Magn. Reson.* **63**:622–628 (1985).
10. J. T. Vaughan, H. P. Hetherington, J. O. Otu, J. W. Pan, and G. M. Pohost, High frequency volume coils for clinical NMR imaging and spectroscopy. *Magn. Reson. Med.* **32**:206–218 (1994).

11. P. B. Roemer, W. A. Edelstein, C. E. Hayes, S. P. Souza, and O. M. Mueller, The NMR phased array, *Magn. Reson. Med.* **16**:192–225 (1990).
12. S. M. Wright, R. L. Magin, and J. R. Kelton, Arrays of mutually coupled receiver coils: theory and application, *Magn. Reson. Med.* **17**:252–268 (1991).
13. D. K. Sodickson and W. J. Manning, Simultaneous acquisition of spatial harmonics (SMASH): Fast imaging with radiofrequency coil arrays, *Magn. Reson. Med.* **29**:681–688 (1993).
14. M. A. Griswold, P. M. Jakob, R. M. Heidemann, M. Nittka, V. Jellus, J. Wang, B. Kiefer, and A. Haase, Generalized auto-calibrating partially parallel acquisitions (GRAPPA). *Magn. Reson. Med.* **47**:1202–1210 (2002).
15. K. P. Pruessmann, M. Weiger, M. B. Schneidegger, and P. Boesinger, SENSE: Sensitivity encoding for fast MRI, *Magn. Reson. Med.* **42**:952–992 (1999).
16. G. H. Glover, C. E. Hayes, N. J. Pelc, W. A. Edelstein, O. M. Muller, H. R. Hart, C. J. Hardy, M. O'Donnell, and W. D. Barber, Comparison of linear and circular polarization for magnetic resonance imaging, *J. Magn. Reson.* **64**:277–270 (1985).
17. D. I. Hoult, Sensitivity and power deposition in a high-field imaging experiment, *J. Magn. Reson. Imag.* **12**:46–67 (2000).
18. J. T. Vaughan, M. Garwood, C. M. Collins, W. Liu, L. Delabarre, G. Adriany, P. Andersen, H. Merkle, R. Goebel, M. B. Smith, and K. Ugurbil. 7 T vs. 4T: RF power, homogeneity, and signal-to-noise comparison in head images, *Magn. Reson. Med.* **46**:24–30 (2001).

FURTHER READING

- E. M. Haake, R. W. Brown, M. R. Thompson, and R. Venkatesan, *Magnetic Resonance Imaging: Physical Principles and Sequence Design*, Wiley-Liss, 2000.
- Z.-P. Liang, and P. C. Lauterbur, *Principles of Magnetic Resonance Imaging. A Signal Processing Perspective*, IEEE Press Series in Biomedical Engineering, IEEE Press, 2000.
- R. R. Ernst, G. Bodenhausen, and A. Wokaun, *Principles of Nuclear Magnetic Resonance in One and Two Dimensions*, Oxford Science Publications, 1987.
- C. P. Slichter, *Principles of Magnetic Resonance*, Springer-Verlag, 1990.

MAGNETIC SHIELDING

DAVID W. FUGATE
Electric Research and
Management, Inc.
FRANK S. YOUNG
Electric Power Research
Institute

Shielding is the use of specific materials in the form of enclosures of barriers to reduce field levels in some region of space. In traditional usage, *magnetic shielding* refers specifically to shields made of *magnetic* materials like iron and nickel. However, this article is more general because it covers not just traditional magnetic shielding but also

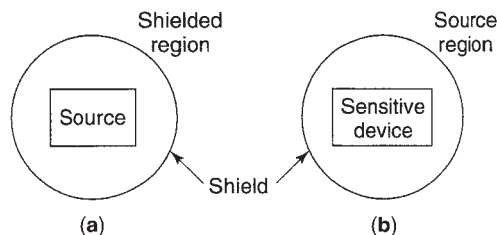


Figure 1. (a) Shielding the source—placing a shield around a field source reduces the fields everywhere outside the shield; (b) shielding the subject—a shield placed around a sensitive device reduces the fields from external sources.

shielding of alternating magnetic fields with conducting materials, such as copper and aluminum. In typical applications, shielding eliminates magnetic field interference with electron microscopes, computer displays (CRTs), sensitive electronics, or other devices affected by magnetic fields.

Although shielding of electric fields is relatively effective with any conducting material, shielding of magnetic fields is more difficult, especially at extremely low frequencies (ELFs). The ELF range is defined as 3 Hz–3 kHz [1]. The selection of proper shield materials, shield geometry, and shield dimensions are all important factors in achieving a specified level of magnetic field reduction. Placing a shield around a magnetic field source, as shown in Fig. 1a, reduces the field magnitude outside the shield, and placing a shield around sensitive equipment, as shown in Fig. 1b, reduces the field magnitude inside the shield. These two options are often called “shielding the source,” or “shielding the subject,” respectively.

Both examples in Fig. 1 illustrate shield geometry. In many applications, it is impractical or impossible (due to physical constraints) to use an enclosure, and open shield geometries, also called *partial shields*, are required. Figure 2 shows two basic partial shield geometries, a flat-plate shield (a), and a channel shield (b). For these configurations, the region where shielding occurs may be limited because the shield does not fully enclose the source or the subject, resulting in *edge effects*. A discussion of the geometric aspects of shielding is contained in Ref. 2.

1. ELF SHIELDING VERSUS HIGH-FREQUENCY SHIELDING

Electric and magnetic fields radiate away from a source at the speed of light c . In the time it takes a source alternating with frequency f to complete one full cycle, these fields have traveled a distance λ , known as the *electromagnetic*



Figure 2. Examples of open shield geometries: (a) flat plate shield, (b) inverted channel shield.

wavelength:

$$\lambda = c/f \quad (1)$$

At distances from a field source on the order of one wavelength and larger, the dominant parts of the electric and magnetic fields are coupled as a propagating electromagnetic wave. If a shield is placed in this region, shielding involves the interaction of electromagnetic waves with the shield materials. Any mathematical description must be based on the full set of Maxwell's equations, which involves calculating both electric and magnetic fields. Shielding of electromagnetic waves is often described in terms of reflection, absorption, and transmission [3]. Because wavelength decreases with increasing frequency, shielding at radio frequencies in the FM band (88–108 MHz) and higher typically involves the interaction of electromagnetic waves with shield materials.

At distances much less than one wavelength, the non-radiating portion of the fields is much larger than the radiating portion. In this region, called the “reactive near-field region,” the coupling between the electric and magnetic fields can be ignored, and the fields may be calculated independently. This is called a quasistatic description. At 3 kHz (the upper end of the ELF band), a wavelength in air is 100 km. Thus, for ELF field sources, one is in the reactive near-field region in all practical cases, and a full electromagnetic solution is not required. Instead, one need focus only on interaction of the magnetic field or the electric field with the shield material, depending on which field is being shielded. In some cases, shielding of the electric field with metallic enclosures is required. This article deals specifically with the shielding of DC and ELF magnetic fields.

2. MAGNETIC FIELDS

Moving electric charges, typically currents in electrical conductors, produce magnetic fields. Magnetic fields are defined by the Lorentz equation as the force acting on a test charge q , moving with velocity \mathbf{v} at a point in space

$$\mathbf{F} = q(\mathbf{v} \times \mu\mathbf{H}) \quad (2)$$

in which \mathbf{H} is the magnetic field strength with units of amperes per meter and μ is the permeability of the medium. By definition of the vector cross-product, the force on a moving charge is at right angles to both the velocity vector and the magnetic field vector. Lorentz forces produce torque in generators and motors and focus electron beams in imaging devices.

Unwanted, or stray magnetic fields deflect electron beams in the same imaging devices, often causing interference problems. Sources that use, distribute, or produce alternating currents, like the 60 Hz currents in a power system, produce magnetic fields that are time-varying at the same frequency.

Magnetic fields are vector fields with magnitude and direction that vary with position relative to their sources. This spatial variation or field *structure* depends on the

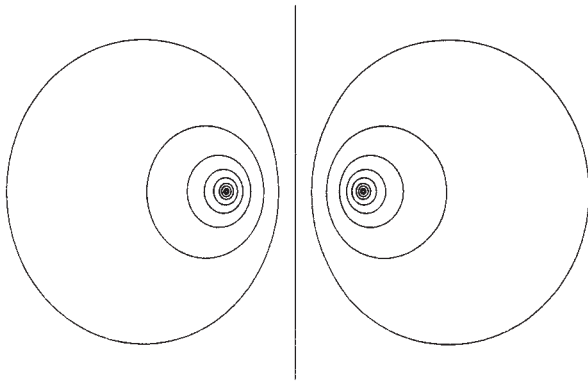


Figure 3. The lines of magnetic flux illustrate the field structure associated with one or more sources. The density of flux lines indicates the relative field strength and the tangent to any line indicates the field direction at that point.

distribution of sources. Equal and opposite currents produce a field structure that can be visualized by plotting lines of magnetic flux, as show in Fig. 3. The spacing between flux lines, or line density, indicates relative field magnitudes, and the tangent to any flux line represents field direction. Another way to visualize field structure is through a vector plot, shown in Fig. 4. Lengths of the arrows represent relative field magnitudes, and the arrows indicate field direction.

Shield performance, or field reduction, is measured by comparing field magnitudes before shielding with the field magnitudes after shielding. In general, field reduction varies with position relative to the source and shield. The shielding factor s is defined as the ratio of the shielded field magnitude \mathbf{B} to the field magnitude \mathbf{B}_0 without the shield present at a point in space:

$$s = |\mathbf{B}|/|\mathbf{B}_0| \tag{3}$$

The shielding factor represents the fraction of the original field magnitude that remains after the shield is in place. A

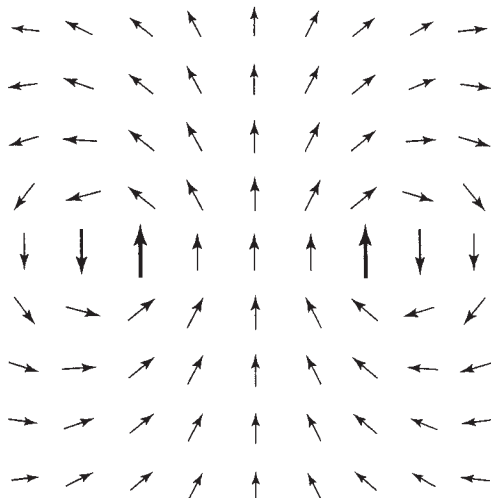


Figure 4. A vector plot graphically illustrates both field strength and direction as a function of position.

shielding factor of zero represents perfect shielding. A shielding factor of one represents no shielding, and shielding factors greater than one occur at locations where the field is increased by the shield. It is incorrect to define the shielding factor as the ratio of the fields on opposite sides of a shield. Shielding factor is often called *shielding effectiveness* (SE), expressed in units of decibels (dB):

$$SE \text{ (dB)} = -20 \log_{10} |\mathbf{B}|/|\mathbf{B}_0| \tag{4}$$

Shielding effectiveness is sometimes alternatively define as the inverse of the shielding factor, the ratio of unshielded to shielded fields at a point, but it is really a matter of preference. For example, a shielding effectiveness of two defined in this manner represents a twofold reduction, that is, the field is halved by the shield and the shielding factor is 0.5. When fields are time-varying, shielding is typically defined as the ratio of RMS magnitudes.

3. SHIELDING MECHANISMS

Although shielding implies a *blocking* action, DC and ELF magnetic field shielding is more aptly described as altering or restructuring magnetic fields by the use of shielding materials. To illustrate this concept, Fig. 5a shows a flux plot of a uniform, horizontal, magnetic field altered (Fig. 5b) by the introduction of a ferromagnetic material.

These are two basic mechanisms by which shield materials alter the spatial distribution of magnetic fields, thus providing shielding. They are the flux-shunting mechanism and the induced-current mechanism [5].

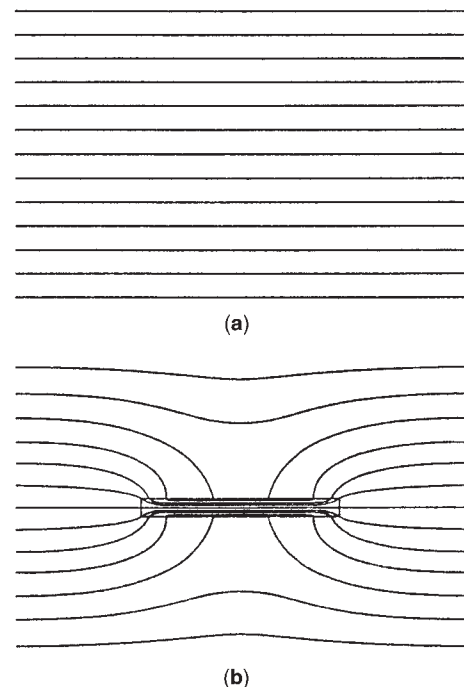


Figure 5. (a) Horizontal uniform field (b) altered by introduction of a ferromagnetic material; illustrates the concept that shielding is the result of induced sources in the shield material.

3.1. Flux Shunting

An externally applied magnetic field induces magnetization in ferromagnetic materials. (All materials have magnetic properties, but in most materials these properties are insignificant. Only ferromagnetic materials have properties that provide shielding of magnetic fields.) Magnetization is the result of electrons acting as magnetic sources at the atomic level. In most matter, these sources cancel one another, but electrons in atoms with unfilled inner shells make a net contribution, giving the atoms a magnetic moment [6]. These atoms spontaneously align into groups called *domains*. Without an external field, domains are randomly oriented and cancel each other. When an external field is applied, the Lorentz forces align some of the domains in the same direction, and together, the domains act as a macroscopic magnetic field source. A familiar magnetic field source is a bar magnet, which exhibits permanent magnetization even without an applied field. Unlike a permanent magnet, most of the magnetization in ferromagnetic shielding materials goes away when the external field is removed.

Basic ferromagnetic elements are iron, nickel, and cobalt, and the most typical ferromagnetic shielding materials are either iron-based or nickel-based alloys (metals). Less common as shielding materials are ferrites such as iron oxide.

Induced magnetization in ferromagnetic materials acts as a secondary magnetic field source, producing fields that add vectorially to the existing fields and change the spatial distribution of magnetic fields in some region of space. The term *flux shunting* comes from the fact that a ferromagnetic shield alters the path of flux lines so that they appear to be *shunted* through the shield and away from the shielded region, as shown by the example in Fig. 6. Flux-shunting shielding is often described in terms of magnetic circuits as providing a low-reluctance path for magnetic flux.

Permeability μ is a measure of the induced magnetization in a material. Thus, permeability is the key property for flux-shunting shielding. The constitutive law

$$\mathbf{B} = \mu \mathbf{H} \quad (5)$$

relates magnetic flux density \mathbf{B} to the magnetic field strength \mathbf{H} . More typically used, relative permeability is

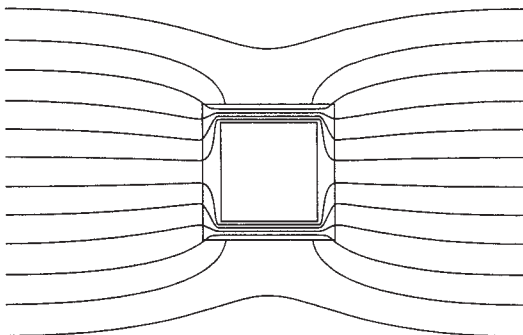


Figure 6. Example of the flux-shunting mechanism. The region inside a ferromagnetic duct is shielded from an external, horizontal magnetic field.

the ratio of permeability in any medium to the permeability of free space, $\mu_r = \mu/\mu_0$. Nonferrous materials have a relative permeability of one, and ferromagnetic materials have relative permeabilities much greater than one, ranging from hundreds to hundreds of thousands. In these materials, permeability is not constant but varies with the applied field \mathbf{H} .

The nonlinear properties of a ferromagnetic material can be seen by plotting flux density \mathbf{B} , as the applied field \mathbf{H} is cycled. Figure 7 shows a generic \mathbf{B} - \mathbf{H} plot that illustrates hysteresis. When the applied field is decreased from a maximum, the flux density does not return along the same curve, and plotting one full cycle forms a hysteretic loop. A whole family of hysteretic loops exists for any ferromagnetic material as the amplitude of field strength \mathbf{H} is varied. The area of a hysteretic loop represents the energy required to rotate magnetic domains through one cycle. Known as *hysteretic losses*, this energy is dissipated as heat in the shield material.

For effective flux-shunting shielding, the flux density in a magnetic material should follow the applied field closely. However, it is obvious from the hysteretic loop of Fig. 7 that \mathbf{B} does not track \mathbf{H} . \mathbf{B} lags \mathbf{H} , as seen by the fact that there is a residual flux density (nonzero \mathbf{B}) when \mathbf{H} has returned to zero and that \mathbf{B} does not return to zero until \mathbf{H} increases in the opposite direction. Thus, *soft* ferromagnetic materials with narrow hysteretic loops are best for shielding, in contrast to *hard* ferromagnetic materials with wide hysteretic loops, typically used as permanent magnets and in applications such as data storage. Hysteretic curves illustrating “soft” and “hard” ferromagnetic materials are shown in Fig. 8.

At very low field levels relative permeability starts at some initial value (initial permeability) increases to a maximum as the applied field is increased, and then decreases, approaching a relative permeability of one as the material saturates, as shown in Fig. 9. Saturation occurs because there is a limit to the magnetization that can be induced in any magnetic material. In Fig. 7, the decreasing slope at the top and bottom of the curves occurs as the limit of total magnetization is reached. When a material saturates, it cannot provide additional shielding.

For shielding alternating magnetic fields via flux shunting, the key property is AC permeability, $\Delta B/\Delta H$ through one cycle. Although Fig. 7 shows a hysteresis

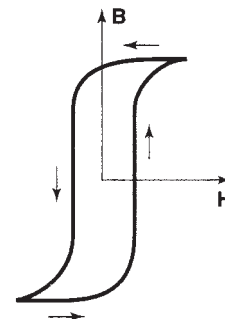


Figure 7. Typical \mathbf{B} - \mathbf{H} curves showing how nonlinear properties of ferromagnetic materials result in a hysteretic loop as the applied field \mathbf{H} is cycled.

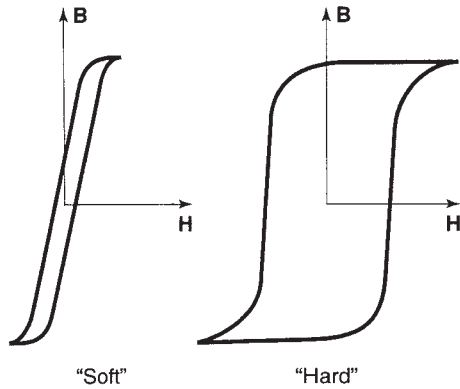


Figure 8. Examples of hysteretic loops for *soft* and *hard* ferromagnetic materials.

curve that swings from near saturation to near saturation in both directions, a hysteresis curve caused by a very small alternating field in the presence of a large DC field might look like Fig. 10. In this case, the ac permeability is less than the DC permeability, B/H . In addition, the DC field creates a constant magnetization that affects the time-varying magnetization. Figure 11 shows how AC permeability for a small alternating field is reduced with increasing DC field. This plot, called a “butterfly” curve, is generated by measuring the AC permeability at different levels of DC field. The DC field is increased from zero to a maximum, reversed to the same maximum in the opposite direction, and then reduced to zero, and the AC permeability is measured at different points to generate the “butterfly” curve. The extent to which the AC permeability is affected depends on the properties of each ferromagnetic material. In general, the better ferromagnetic materials are more sensitive. This type of curve is relevant for shielding small AC fields in the presence of a larger DC field.

To gain an understanding of how flux shunting varies with shield parameters, one can look at the analytical expression for the shielding provided by a ferromagnetic spherical shell with radius a , shield thickness Δ (that is much smaller than the radius), and relative permeability μ_r :

$$s = \frac{3a}{2\mu_r\Delta} \tag{6}$$

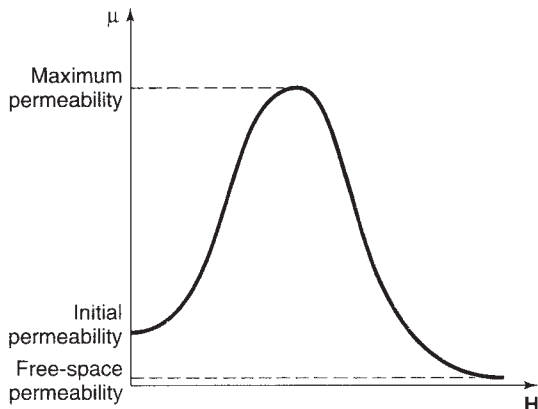


Figure 9. Permeability as a function of applied field strength.

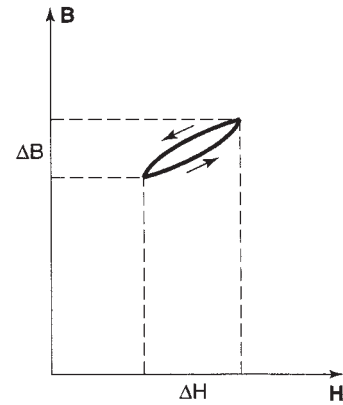


Figure 10. Hysteretic loop formed by a small AC field in the presence of a large DC field.

Equation (6) shows that shielding improves (shielding factor decreases) with increasing relative permeability and increasing shield thickness. It also shows that shielding gets worse with increasing shield radius. From the perspective of magnetic circuits, shielding improves as the reluctance of the flux path through the shield is lowered. Increasing permeability and thickness reduce the reluctance, improving shielding. Increasing shield radius increases reluctance by increasing the pathlength of the magnetic circuit, making shielding worse. In short, the flux-shunting mechanism works best in small, closed-geometry shields.

Flux-shunting shielding has been studied for a long time. A journal article [7] dating back to 1899 describes an effect whereby increased shielding is obtained using nested shells of ferromagnetic material with nonmagnetic materials or air gaps between the ferromagnetic shells. In other words, by changing the shield form a single thick layer to thinner double or triple layers, one can in some cases enhance the shielding effectiveness although using the same amount or even less ferromagnetic material. This effect occurs mainly with configurations where the total shield thickness is within an order of magnitude of the shield radius.

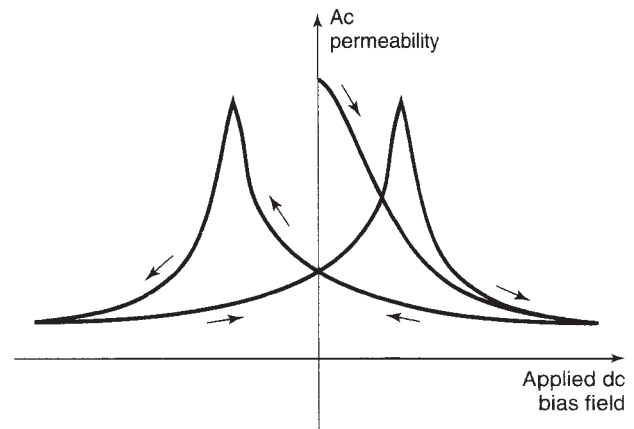


Figure 11. “Butterfly” curve illustrates how the AC permeability changes as a much larger DC field is applied and removed.

Table 1. Properties of Typical Shielding Materials

Name	Material Type	Maximum Relative Permeability	Saturation Flux Density (T)	Conductivity (S/m)	Density (kg/m ³)
Cold-rolled steel	Basic steel	2,000	2.10	1.0 × 10 ⁷	7880
Silicon iron	Electrical steel	7,000	1.97	1.7 × 10 ⁶	7650
45 Permalloy	45%nickel alloy	50,000	1.60	2.2 × 10 ⁶	8170
Mumetal	78%nickel alloy	100,000	0.65	1.6 × 10 ⁶	8580
Copper	High conductivity	1	NA	5.8 × 10 ⁷	8960
Aluminum	High conductivity	1	NA	3.7 × 10 ⁷	2699

From Hoburt (8).

In some cases, a double layer shield is used to avoid saturation of the layer closest to the field source where the fields are strongest. For example, a steel material might be used as the first shield layer, whereas a high-performance nickel alloy is used as the second layer. The steel lowers the field enough that the nickel alloy layer is not saturated. Saturation flux densities of typical shield materials are listed in Table 1.

3.2. Induced-Current Mechanism

Time-varying magnetic flux passing through a shield material induces an electric field in the material according to Faraday’s law:

$$\nabla \times \mathbf{E} = -\frac{\partial \mathbf{B}}{\partial t} \tag{7}$$

In electrically conducting materials, the induced electric field results in circulating currents, or eddy currents, in the shield according to the constitutive relationship

$$\mathbf{J} = \sigma \mathbf{E} \tag{8}$$

where \mathbf{J} is the current density, σ is the material conductivity, and \mathbf{E} is the electric field induced according to Eq. (7). The fields from these induced currents oppose the impinging fields, providing field reductions. Figure 12 shows a flat plate in a uniform field. Induced-current shielding appears to exclude flux lines from the shield, providing field reductions adjacent to the shield on both sides. Because the induced currents are proportional to the time rate of change of the magnetic fields, induced-

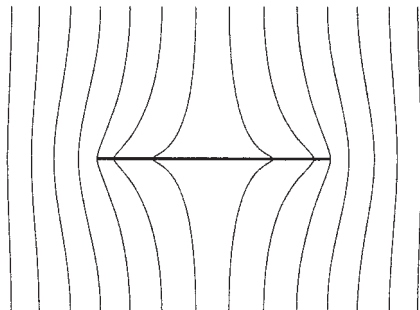


Figure 12. Conducting plate in an alternating vertical field tends to exclude flux from passing through the plate, thus providing shielding.

current shielding improves with increasing frequency. Thus, at higher frequencies, magnetic fields are more easily shielded via the induced-current mechanism. In the limit of infinite conductivity or infinite frequency, flux lines do not penetrate the shield as shown in Fig. 13.

In a conducting shield, the magnetic field and induced-current magnitudes decrease exponentially in the direction of the shield’s thickness with a decay length called the *skin depth* δ

$$\delta = \sqrt{\frac{1}{\pi f \sigma \mu}} \tag{9}$$

which involves not only frequency f and conductivity σ but also permeability μ because it affects the flux density, which induces the circulating currents. Because of exponential decay, shield enclosures with thickness on the order of a skin depth or thicker provide good shielding. For shield thicknesses much less than a skin depth, the induced current densities are constant across a shield thickness. However, significant shielding can still be obtained from thin conducting shields in some situations where the shield is sized properly. In these cases the shielding is a result of induced currents flowing over large loops.

The shielding factor equation for a nonferrous, conducting, spherical shield with radius a , thickness Δ , and conductivity σ provides insight into how these parameters affect the induced-current mechanism:

$$s = \frac{1}{\sqrt{1 + \left(\frac{2\pi f \mu_0 \sigma a \Delta}{3}\right)^2}} \tag{10}$$

Because all parameters are in the denominator of Eq. (10), induced-current shielding improves (shielding factor

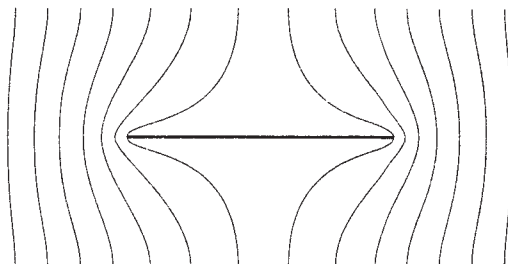


Figure 13. In the limit of zero resistivity or infinite frequency, a conducting shield totally excludes flux lines.

decreases) with increasing frequency f , increasing shield thickness, and increasing shield radius. The effect of shield radius is opposite to that for flux shunting shielding, and although flux shunting shields static fields, the induced-current mechanism does not. In general, induced-current shielding is more effective for larger source shield configurations whereas flux shunting is more effective for smaller shield configurations.

3.3. Combined Shielding Mechanisms

Until now, the shielding mechanisms have been discussed separately. Equations (6) and (10) are the shielding factor equations for flux shunting and induced-current shielding alone. In many shields, both mechanisms are involved. For example, most ferromagnetic materials, being metals, also have significant conductivity in addition to high permeability. Or a shield might be constructed using two materials, one layer of a high permeability material and one layer of a high conductivity material. In these cases both shielding mechanisms contribute to the shielding to an extent that depends on material properties, frequency of the fields, and details of the shield configuration.

To illustrate the combined effect of both shielding mechanisms, Fig. 14 shows the shielding factor, calculated by a method described in Ref. 8, as a function of shield radius for a spherical steel shield in a 60-Hz uniform field. For these calculations steel is assigned a conductivity of 6.76×10^6 S/m, a relative permeability of 180, and the shield thickness of 1 mm is held constant as the shield radius is varied. Flux shunting dominates at the smaller radii, induced-current shielding dominates at the larger radii, and there is a worst-case radius of about 0.4 m, where a transition occurs between the dominant shielding mechanisms.

The combined effect of both flux shunting and induced-current shielding can be exploited with multilayer shields made from alternating ferromagnetic and high-conductivity materials. Also using the method described in Ref. 8, one can explore this type of shield construction. Alternating thin layers of high permeability and high conductivity

perform like a single-layer shield made with a material with enhanced properties.

4. SHIELDING MATERIALS

Basic magnetic field shielding materials can be grouped in two main categories: ferromagnetic materials and high-conductivity materials. For DC magnetic fields, ferromagnetic materials are the only option. They provide shielding through the flux shunting mechanism. For AC magnetic fields, both ferromagnetic and high-conductivity materials may be useful as shielding materials, and both shielding mechanisms operate to an extent determined by the material properties, operating frequency, and shield configuration.

The practical high-conductivity materials are those commonly used as electrical conductors, aluminum and copper. Copper is almost twice as conductive as aluminum, but aluminum is about 3.3 times lighter than copper and generally costs less than copper on a per pound basis. For shielding that depends on the induced-current mechanism, conductivity across a shield is paramount and copper has the advantage that it is easily soldered whereas aluminum is not—it should be welded. Mechanical fasteners can be used for connecting aluminum or copper sheets, but the longevity of these connections is questionable because of corrosion and oxidation.

Although there appears to be a large variety of ferromagnetic shielding materials, most fit into one of five basic types:

- Basic iron or steel—typically produced as coils and sheet for structural uses
- Electrical steels—engineered for good magnetic properties and low losses when used as cores for transformers, motors, and other components
- 40–50% nickel alloys—moderately expensive materials with very good magnetic properties
- 70–80% nickel alloys—highest cost materials with the best magnetic properties, often referred to generically as *mumetal*, although this was originally a trade name.
- Amorphous metals—noncrystalline metallic sheet formed by an ultrarapid quenching process that solidifies the molten metal; the noncrystalline form provides enhanced ferromagnetic properties.

Different manufacturers produce slightly different compositions of these basic materials, and they have different procedures for heat treating, but the percentages of the main elements, iron or nickel, are similar. There are only a few large producers of nickel alloy materials. Shielding manufacturers typically purchase materials from a large producer, heat the materials in a hydrogen atmosphere (hydrogen annealing) to improve the ferromagnetic properties, and then utilize the metal to fabricate a shield enclosure or shield panels. Smaller shields are often annealed after fabrication because the fabrication process may degrade the magnetic properties.

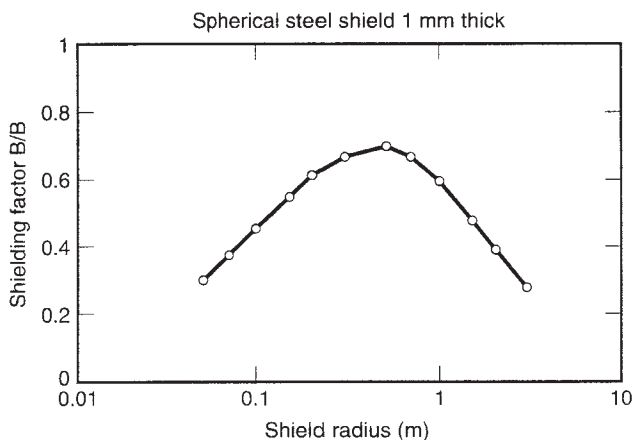


Figure 14. Calculated 60 Hz shielding factor for a spherical steel shell in a uniform magnetic field as a function of shield radius. The shield thickness of one millimeter is held constant.

Important properties for ferromagnetic shield materials are the initial permeability, the maximum permeability, and the magnetic field strength (or flux density) at which the material saturates and further shielding cannot be obtained. Because the ferromagnetic properties are nonlinear, the operating permeability depends on the magnitude of the magnetic field being shielded. In general, increasing magnetic properties go hand in hand with increasing cost, lower saturation levels, and lower conductivity. Table 1 shows nominal values of maximum permeability, saturation flux density, conductivity, and density for basic shielding materials including copper and aluminum [9]. Note that the initial permeabilities of ferromagnetic materials are often one and two orders of magnitude smaller than the maximum permeabilities (see Table 1).

5. SHIELDING CALCULATIONS

Because there are an infinite variety of shield source configurations and a wide variety of shield materials for building effective magnetic field shields, shielding calculations are a key part of practical shield design. Elaborate experiments need not be made to characterize the performance of each unique shield design. Extensive experiments are not only impractical but also unnecessary. However, closed-form analytical expressions exist only for a limited set of ideal shield geometries, such as cylindrical shells, spherical shells, and infinite flat sheets. Even for these ideal shield geometries, the expressions can be quite complicated, especially solutions for shields with more than one material layer. For general shielding calculations, one must either select a simple approximation to obtain an order-of-magnitude shielding estimate or utilize more complex numerical methods to solve the shielding problem.

In high frequency shielding, calculations for plane waves propagating through infinite sheets are used to arrive at shielding estimates. Because the resulting equations are analogous to transmission line equations, this method is often called the *transmission-line approach* [10]. As described previously, this approach is not relevant to ELF shielding except for a limited set of conditions. Reference 8 describes a technique similar to the transmission-line approach, but specifically tailored to ELF magnetic field shielding calculations for ideal shield geometries with multiple layers having different material properties. This method is well suited for calculations involving nested cylindrical or spherical shields or shields constructed from alternating layers of conducting and ferromagnetic materials.

Another technique found in literature is the circuit approach [11]. In this method, typically used to calculate ELF induced-current shielding, the shield enclosure is viewed as a short-circuited turn that can be characterized by an inductance and resistance. This method suffers from the assumption that significant details of field structure for the shielding problem are known a priori to properly set the circuit parameters. This severely limits application of the method.

General modeling of ELF magnetic field shielding amounts to calculating magnetic fields in the presence of

conducting and ferromagnetic materials. The computation must account for induced currents and magnetization throughout the shield material. This involves solutions to the quasistatic form of Maxwell's equations for magnetic fields over a continuum that represents the problem region. In differential form the basic equations to be solved are

$$\nabla \times \mathbf{H} = \mathbf{J} \quad (11)$$

$$\nabla \cdot \mathbf{B} = 0 \quad (12)$$

$$\nabla \times \mathbf{E} = -\frac{\partial \mathbf{B}}{\partial t} \quad (13)$$

along with the constitutive relationships for permeability, Eq. (5), and conductivity, Eq. (8), which describe the macroscopic properties of shield materials. This quasistatic description, which ignores the displacement current term $\partial \mathbf{D} / \partial t$, normally on the right-hand side of Eq. (11), is valid as long as an electromagnetic wavelength is much larger than the largest dimension of the shield. General solutions to these equations are often called *eddy-current* or *magnetic diffusion* solutions. At zero frequency or zero conductivity in the shield, there are no induced currents. Only permeability restructures the magnetic field. This simplification is called the *magnetostatic case*, and solutions must satisfy only Eqs. (11) and (12), along with the constitutive relationship that defines permeability, Eq. (5).

In finding exact solutions to the governing magnetic field equations previously described, one approach is to define a vector potential \mathbf{A} that satisfies Eq. (12):

$$\nabla \times \mathbf{A} = \mathbf{B} \quad (14)$$

Substituting Eq. (14) in Eq. (13), we obtain

$$\mathbf{E} = -\frac{\partial \mathbf{A}}{\partial t} \quad (15)$$

Combining Eqs. (8), (11), (14), (15), and using a vector identity gives the following

$$\nabla^2 \mathbf{A} - \mu \sigma \frac{\partial \mathbf{A}}{\partial t} = -\mu \mathbf{J}_s \quad (16)$$

in which \mathbf{J}_s is the known distribution of source currents producing magnetic fields that require shielding.

When the source currents are sinusoidal, \mathbf{A} and \mathbf{J}_s can be represented as phasors, and the time derivative in Eq. (16) is replaced by $j\omega$:

$$\nabla^2 \mathbf{A} - j\omega \mu \sigma \mathbf{A} = -\mu \mathbf{J}_s \quad (17)$$

When the shield material has zero conductivity or the magnetic fields are constant (zero frequency), Eq. (17) becomes

$$\nabla^2 \mathbf{A} = -\mu \mathbf{J}_s \quad (18)$$

Equation (17) can be used for the general case where a shield provides field reduction through both flux shunting

and induced-current mechanisms. Equation (18) is only for flux shunting. The shielding factor for a specific source shield configuration is determined by first solving for the magnetic vector potential \mathbf{A} without the shield in the problem and then solving for \mathbf{A} with the shield. Using Eq. (14), one calculates the flux densities from both vector potential solutions. Ratios of the field magnitudes as in Eq. (2) define the field reduction provided by the shield as a function of position.

6. NUMERICAL SOLUTIONS FOR SHIELDING

Except for the ideal shield geometries mentioned previously, solving the governing equations requires numerical methods. Two common numerical techniques are the finite-element method and the boundary integral method [12–14].

In the finite-element method, the problem region is subdivided into elements—typically triangles for two-dimensional problems and tetrahedra for three-dimensional problems—that form a *mesh*. The continuous variation of vector potential \mathbf{A} over each element is approximated by a specified basis function. Then the unknowns become the coefficients of the basis function for each element. Variational concepts are used to obtain an approximate solution to the governing partial-differential equation, for example, Eq. (17), across all elements. The net result is a system of algebraic equations that must be solved for the unknowns. Finite-element software is commercially available, and features that provide automatic meshing, graphical pre-processing, and visualization of results make it an accessible and useful general shield calculating tool for some shield problems, especially problems that can be modeled in two dimensions or problems with symmetry about an axis. Figures 3, 5, 6, 12, and 13 were produced with finite-element software.

However, there are weaknesses to the finite-element method. Shield geometries typically involve very thin sheets of materials with much larger length and width dimensions. This, along with the need to accurately model significant changes in field magnitudes across the shield thickness, requires large numbers of elements in the shield region. Shielding problems are also characterized by large regions of air and complicated systems of conductors that are the field sources for the problem. In terms of energy density, the fields in the shielded region are negligible compared with fields near the sources, so one cannot rely on energy as the criterion for determining when an *adequate* solution has been obtained. Finally, solving the partial-differential equations means that the problem region must be bounded and a boundary condition must be specified at the edges. The problem region must be made large enough that the boundary conditions do not affect the solution in the region where shielding is being calculated. This results in more unknowns and a larger problem to solve.

Instead of differential equations, it is also possible to use the integral form of the quasistatic equations. For determining magnetic fields in air due to some distribution of currents, one can derive an integral equation, often

called the *Biot–Savart law*, which gives the magnetic field contribution at a point in space due to a differential *piece* of current density

$$\mathbf{H} = \frac{1}{4\pi} \int_V \frac{\mathbf{J}(\mathbf{r}') \times (\mathbf{r} - \mathbf{r}')}{|\mathbf{r} - \mathbf{r}'|^3} dv' \quad (19)$$

in which $\mathbf{J}(\mathbf{r}')$ is the current density in the problem as a function of position defined by the vector \mathbf{r}' (from the origin to the integration point) and \mathbf{r} defines the point where the magnetic field is being evaluated (vector from origin to the field evaluation point). Integrating over all of the currents in the problem gives the total field at one point in space. This equation is not valid when shield materials, that is, conducting and ferromagnetic materials, are introduced into the problem region. The boundary integral method overcomes this difficulty by replacing the effect of magnetization or induced currents within the materials with equivalent sources at the surface of the materials where discontinuities in material properties occur. In contrast to the finite-element method, only the surfaces are divided into elements. Basis functions are used to approximate a continuous distribution of equivalent sources over these surfaces, and a system of equations is developed in which the unknowns are the coefficients for the basis functions. After solving for the unknown sources on the shield surface, one can then calculate the new magnetic field at any point by combining the contributions of all sources—the original field sources and the induced sources in the shield—to obtain the *shielded* magnetic field distribution.

The key advantages of the boundary integral method are that only the surfaces of the shield need to be subdivided into elements and that the method is ideal for open boundary problems with a large air region. The method is also ideally suited for complex systems of currents. Thus, the boundary-element method is better suited for three-dimensional problems than the finite-element method. The main weakness of the boundary integral method is that it results in a full system of equations that is more difficult to solve than the sparse system produced by the finite-element method. An integral method based on surface elements, developed expressly for solving three-dimensional quasistatic shielding problems, is described in Ref. 15.

The underlying theoretical basis for shield calculations is as old as electricity itself and goes back to Faraday and Maxwell. Although materials science is a rapidly changing area with developments in composite materials and materials processing, the basic materials for shielding of DC and ELF magnetic fields have, for the most part, remained unchanged. For basic shield configurations, calculations are straightforward. However, actual application of shielding requires practical expertise in addition to theoretical knowledge. For example, construction methods used to fabricate a shield from multiple sheets must ensure that conductivity and permeability are maintained across the entire shield surface, especially in critical directions. Edge effects and holes in shields for conduits, doors, windows, and so on degrade shield performance and must be accounted for early in the design process. With proper shield calculating tools and proper construction practices, shields can be designed that attenuate magnetic

fields by factors ranging from 10 to 1000 (shielding factors ranging from 0.100 to 0.001), thus eliminating problems with stray or unwanted magnetic fields.

BIBLIOGRAPHY

1. *IEEE Standard Dictionary of Electrical and Electronics Terms*, ANSI Std 100-1997, 6th ed., IEEE, New York, 1997.
2. L. Hasselgren and J. Luomi, Geometrical aspects of magnetic shielding at extremely low frequencies, *IEEE Trans. Electromagn. Compat.* **37**:409–420 (1995).
3. R. B. Schulz, V. C. Plantz, and D. R. Brush, Shielding theory and practice, *IEEE Trans. Electromagn. Compat.* **30**:187–201 (1988).
4. J. F. Hoburg, Principles of quasistatic magnetic shielding with cylindrical and spherical shields, *IEEE Trans. Electromagn. Compat.* **37**:547–579 (1995).
5. T. Rikitake, *Magnetic and Electromagnetic Shielding*, Reidel, Boston, 1987.
6. R. M. Bozorth, *Ferromagnetism*, IEEE Press, Piscataway, NJ, 1993 Reprint.
7. A. P. Wills, On the magnetic shielding effect of trilamellar spherical and cylindrical shells, *Phys. Rev.* **IX**(4):193–243 (1899).
8. J. F. Hoburg, A computational methodology and results for quasistatic multilayered magnetic shielding, *IEEE Trans. Electromagn. Compat.* **38**:92–103 (1996).
9. R. C. Weast, ed., *Handbook of Chemistry and Physics*, 56th ed., CRC Press, Boca Raton, FL, 1975–1976.
10. S. A. Schelkunoff, *Electromagnetic Waves*, Van Nostrand, New York, 1943.
11. D. A. Miller and J. E. Bridges, Review of circuit approach to calculate shielding effectiveness, *IEEE Trans. Electromagn. Compat.* **EMC-10**:52–62 (1968).
12. P. P. Silvester and R. L. Ferrari, *Finite Elements for Electrical Engineers*, Cambridge Univ. Press, Cambridge, UK, 1983.
13. S. R. Hoole, *Computer-Aided Analysis and Design of Electromagnetic Devices*, Elsevier Science, New York, 1989.
14. R. F. Harrington, *Field Computation by Moment Methods*, Macmillan, New York, 1968.
15. K. C. Lim et al., Integral law descriptions of quasistatic magnetic field shielding by thin conducting plate, *IEEE Trans. Power Deliv.* **12**:1642–1650 (1997).

MAGNETRONS

JOHN M. OSEPCHUK
Concord, Massachusetts
THOMAS E. RUDEN¹
Newton Highlands,
Massachusetts

1. INTRODUCTION

The magnetron is a unique surviving example of an electron tube, or vacuum-electronic device, in the modern age of RF and microwave semiconductor devices. Its definition

is complicated in historical length (back to 1921) and breadth, types, and derived devices. In this review the term “magnetron” usually connotes a source (oscillator) of microwave power, where “microwave” is used to designate frequencies between roughly 300 MHz and 300 GHz. Practical application is dominated by its use in the microwave oven, although a significant number of other military and industrial applications remain.

In the IEEE dictionary (1997 edition), “magnetron” is defined as “An electron tube characterized by the interaction of electrons with the electric field of a circuit element in crossed steady electric and magnetic fields to produce alternating current power output”. If “alternating current” is replaced by RF/microwave, then this definition is roughly equivalent to the one used here with some further caveats. The IEEE definition would apply to amplifiers as well as oscillators. Also, a strict reading would allow its application to a possible class of “cyclotron resonance” devices, which would not generally be termed as *magnetrons*. If the interaction mechanism is restricted to the class of “velocity synchronism,” then the IEEE definition would be apt. It should be noted that in modern technology the term “magnetron” also applies to devices not covered by the IEEE definition but that demonstrably are derived from the basic elements of the magnetron, which are depicted in Fig. 1. A uniform static magnetic field B is applied parallel to a cylindrical (generally) cathode, of radius r_c , which is an effective emitter of electrons when a voltage V_a is applied between the concentric anode, of radius r_a , and the cathode, with conventional polarity. Axial confinement of the electrons is achieved by the presence of end shields or end hats, which are attached to the cathode as depicted in Fig. 1, where the distance between end shields is denoted as L . The anode electrode, of height H in the axial direction, could be merely a solid (generally copper) block, in which case the term “magnetron diode” is used. Alternatively the anode could be made of a circuit, or periodic structure for the purpose of achieving interaction of circuit and electron cloud. The cathode is shown as a uniform cylindrical tube heated by an internal filament (usually tungsten) and thus dubbed an “indirectly heated” cathode. Alternatively, which is the case for most magnetrons in “power applications,” the cathode itself could be directly heated when it itself consists of a tungsten (or thoriated tungsten) helix or coil.

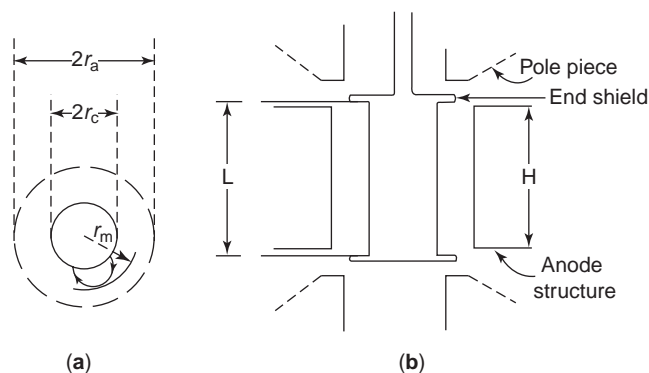


Figure 1. Basic structure of a magnetron: (a) midplane cross section; (b) longitudinal cross section through axis.

¹Section 3,5, and 7 were contributed by Thomas E. Ruden.

fields by factors ranging from 10 to 1000 (shielding factors ranging from 0.100 to 0.001), thus eliminating problems with stray or unwanted magnetic fields.

BIBLIOGRAPHY

1. *IEEE Standard Dictionary of Electrical and Electronics Terms*, ANSI Std 100-1997, 6th ed., IEEE, New York, 1997.
2. L. Hasselgren and J. Luomi, Geometrical aspects of magnetic shielding at extremely low frequencies, *IEEE Trans. Electromagn. Compat.* **37**:409–420 (1995).
3. R. B. Schulz, V. C. Plantz, and D. R. Brush, Shielding theory and practice, *IEEE Trans. Electromagn. Compat.* **30**:187–201 (1988).
4. J. F. Hoburg, Principles of quasistatic magnetic shielding with cylindrical and spherical shields, *IEEE Trans. Electromagn. Compat.* **37**:547–579 (1995).
5. T. Rikitake, *Magnetic and Electromagnetic Shielding*, Reidel, Boston, 1987.
6. R. M. Bozorth, *Ferromagnetism*, IEEE Press, Piscataway, NJ, 1993 Reprint.
7. A. P. Wills, On the magnetic shielding effect of trilamellar spherical and cylindrical shells, *Phys. Rev.* **IX**(4):193–243 (1899).
8. J. F. Hoburg, A computational methodology and results for quasistatic multilayered magnetic shielding, *IEEE Trans. Electromagn. Compat.* **38**:92–103 (1996).
9. R. C. Weast, ed., *Handbook of Chemistry and Physics*, 56th ed., CRC Press, Boca Raton, FL, 1975–1976.
10. S. A. Schelkunoff, *Electromagnetic Waves*, Van Nostrand, New York, 1943.
11. D. A. Miller and J. E. Bridges, Review of circuit approach to calculate shielding effectiveness, *IEEE Trans. Electromagn. Compat.* **EMC-10**:52–62 (1968).
12. P. P. Silvester and R. L. Ferrari, *Finite Elements for Electrical Engineers*, Cambridge Univ. Press, Cambridge, UK, 1983.
13. S. R. Hoole, *Computer-Aided Analysis and Design of Electromagnetic Devices*, Elsevier Science, New York, 1989.
14. R. F. Harrington, *Field Computation by Moment Methods*, Macmillan, New York, 1968.
15. K. C. Lim et al., Integral law descriptions of quasistatic magnetic field shielding by thin conducting plate, *IEEE Trans. Power Deliv.* **12**:1642–1650 (1997).

MAGNETRONS

JOHN M. OSEPCHUK
Concord, Massachusetts
THOMAS E. RUDEN¹
Newton Highlands,
Massachusetts

1. INTRODUCTION

The magnetron is a unique surviving example of an electron tube, or vacuum-electronic device, in the modern age of RF and microwave semiconductor devices. Its definition

is complicated in historical length (back to 1921) and breadth, types, and derived devices. In this review the term “magnetron” usually connotes a source (oscillator) of microwave power, where “microwave” is used to designate frequencies between roughly 300 MHz and 300 GHz. Practical application is dominated by its use in the microwave oven, although a significant number of other military and industrial applications remain.

In the IEEE dictionary (1997 edition), “magnetron” is defined as “An electron tube characterized by the interaction of electrons with the electric field of a circuit element in crossed steady electric and magnetic fields to produce alternating current power output”. If “alternating current” is replaced by RF/microwave, then this definition is roughly equivalent to the one used here with some further caveats. The IEEE definition would apply to amplifiers as well as oscillators. Also, a strict reading would allow its application to a possible class of “cyclotron resonance” devices, which would not generally be termed as *magnetrons*. If the interaction mechanism is restricted to the class of “velocity synchronism,” then the IEEE definition would be apt. It should be noted that in modern technology the term “magnetron” also applies to devices not covered by the IEEE definition but that demonstrably are derived from the basic elements of the magnetron, which are depicted in Fig. 1. A uniform static magnetic field B is applied parallel to a cylindrical (generally) cathode, of radius r_c , which is an effective emitter of electrons when a voltage V_a is applied between the concentric anode, of radius r_a , and the cathode, with conventional polarity. Axial confinement of the electrons is achieved by the presence of end shields or end hats, which are attached to the cathode as depicted in Fig. 1, where the distance between end shields is denoted as L . The anode electrode, of height H in the axial direction, could be merely a solid (generally copper) block, in which case the term “magnetron diode” is used. Alternatively the anode could be made of a circuit, or periodic structure for the purpose of achieving interaction of circuit and electron cloud. The cathode is shown as a uniform cylindrical tube heated by an internal filament (usually tungsten) and thus dubbed an “indirectly heated” cathode. Alternatively, which is the case for most magnetrons in “power applications,” the cathode itself could be directly heated when it itself consists of a tungsten (or thoriated tungsten) helix or coil.

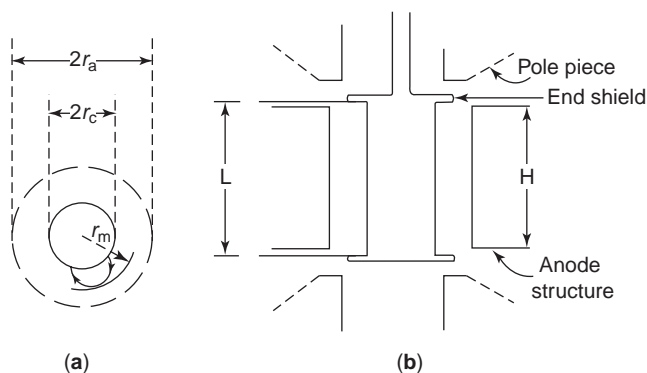


Figure 1. Basic structure of a magnetron: (a) midplane cross section; (b) longitudinal cross section through axis.

¹Section 3,5, and 7 were contributed by Thomas E. Ruden.

The schematic of Fig. 1 applies not only to the magnetron diode and magnetron oscillator but also to a number of derived devices not discussed in detail here. These include the “vac-ion” pump, Penning discharge tubes in which the cathode is reduced only to endplates and “planar magnetrons” used for sputtering and thin-film deposition in the semiconductor industries. Furthermore, even within the class of microwave oscillators there are variations such as the inversion (spatial) of cathode and anode as well as special experimental devices in which the polarity of voltage is reversed—namely, with an interacting periodic structure at or near cathode potential and a positive anode with or without a periodic structure. Ground is at either cathode or anode potential.

2. EARLY HISTORY

In 1921, Dr. A. W. Hull of the General Electric Company published a paper [1] on the magnetron, as depicted in Fig. 1. He studied its basic properties as an electron tube. The key concept he presented was that of the *cutoff* condition, or the boundary of parameters that permit electron flow from cathode to anode and those that do not permit electron flow. This condition was given by the following formula for the Hull cutoff voltage V_{ac} :

$$V_{ac} = (\eta/8)(B)^2(r_a)^2[1 - (r_c/r_a)^2]^2 \quad (1)$$

where MKS units are used, and $\eta = e/m$, the ratio of electron charge to mass, 1.76×10^{11} C/kg (coulombs per kilogram). Neglecting space charge effects and any axial motion (i.e., an assumption of axial uniformity), then, at voltages greater than the cutoff value, an electron will flow directly from cathode to anode, albeit with a curved trajectory, the more so as the magnetic field is increased or voltage decreased. Just at the cutoff condition an electron will just graze the anode and return to the cathode, theoretically with zero energy— that with which it began its trajectory. At anode voltage below the cutoff value the electron trajectories will be confined to some limiting radius r_m , whose value is less than r_a and goes to r_c with decreasing voltage (see the trajectory depicted in Fig. 1).

In the pre-World War II era, little attention was given to the linear version of magnetron devices, but it is useful at this point to point out the simple relation that ensues for cutoff and trajectories in the linear case where r_c and r_a go to infinity and $d = r_a - r_c$, the space between cathode and anode in the linear case. One finds the following for the cutoff voltage in the linear case:

$$V_{ac} = \eta(Bd)^2/2 \quad (2)$$

As shown by Harman [2] after World War II (WWII), the linear case provides a simpler and more easily expressed picture of electron motion, space charge effects, and interaction mechanisms. Thus in crossed fields (a two-dimensional view), E and B , it is found that in general, the average drift velocity of an electron is given by the simple ratio

$$v = E/B \quad (3)$$

and in some cases the trajectory then is a straight line perpendicular to both field directions, with spatial conventions corresponding to a right-hand rule coming from the underlying vector relation $\mathbf{v} = \mathbf{E} \times \mathbf{B}/|B^2|$. In general when the fields are uniform, there will be superimposed on this average drift a quasicycloidal component. For the case where this additional component is cycloidal, the radius of this orbital motion is

$$r = E/B\omega_c \quad (4)$$

where $\omega_c = \eta B$ is the cyclotron frequency corresponding to the magnetic field B . Then, if E is the field between two plates with anode voltage equal to the cutoff value (3), Eqn. (4) reduces to $r = d/2$ or the case of a cycloidal trajectory between cathode and anode at the grazing condition.

More sophisticated later analyses of magnetrons with the static effect of space charge addressed, for example, by Brillouin [3], found that the cutoff relations (1) and (2) remain valid even when space charge is accounted for, at least in the simplest models. In the popular (and neglecting small effects such as axial motion and magnetic field created by the rotating space charge) single-stream model of Brillouin the electron trajectories in the linear case are straight lines parallel to the electrodes and in the cylindrical case circles outside of the cathode. It is found that whatever the space charge distribution $\rho(r)$ is, the potential distribution in the space charge must satisfy the relation

$$V(r) \geq (r\omega_c)^2(1 - r_c^2/r^2)/8\eta \quad (5)$$

and for the single-stream model the equality applies at radii less than r_m , the outer limit of the space charge hub. Thus the anode voltage associated with hub radius r_m is

$$V_a = [\omega_c^2 r_m^2 / 8\eta](1 - r_c^2/r_m^2) \\ [(1 + 2 \ln r_a/r_m)(1 - r_c^2/r_m^2) + 4(\ln r_a/r_m)r_c^2/r_m^2] \quad (6)$$

and the space charge density ρ_0 in the hub is

$$\rho_0 = -(\epsilon_0 \omega_c^2 / 2\eta)(1 + r_c^4/r^4) \quad (7)$$

where ϵ_0 is the dielectric permittivity of free space, 8.86×10^{-12} F/m (farads per meter). The square of the velocity of an electron at radius r is

$$(rd\theta/dt)^2 = 2\eta V(r) = (\omega_c^2 r^2 / 4)(1 - r_c^2/r^2)^2 \quad (8)$$

For the linear case, relations (5)–(8) simplify to the following, respectively, where x is the distance above the lower cathode electrode and x_m denotes the upper boundary of the space charge slipping stream:

$$V(x) \geq (\omega_c x)^2 / 2\eta \quad (9)$$

$$V_a = (d/x_m)(\omega_c x_m)^2 / 2\eta \quad (10)$$

$$\rho_0 = -\epsilon_0 \omega_c^2 / \eta \quad (11)$$

$$v(x)^2 = (\omega_c x)^2 \quad (12)$$

Thus the velocity at the upper edge of the stream x_m is always greater by a factor of 2 than the velocity of an electron without space charge (i.e., $\omega_c x_m$ vs. $\omega_c x_m/2$).

Before WWII the understanding of magnetron space charge did not go much beyond this description with the question of instability and chaos still far in the future for consideration. Nevertheless considerable progress was made in experimental production of magnetron oscillations. At that time these were divided into three categories:

1. *Cyclotron Frequency Oscillations.* In almost any magnetron device evidence of such oscillations can be perceived. In the 1930s various studies showed such oscillations regardless of whether the anode was solid or segmented. The most dramatic report was the production of usable power (for scientific studies) at 50 GHz [4] with powers up to 100 W at low frequencies below 1 GHz. In most cases it was believed that the oscillation was optimum near the cutoff condition where phase sorting could remove unfavorable electrons. This type of oscillation was not pursued much, although it could be considered a precursor of the oscillation type in the modern gyrotron (see GYROTRON article).

2. *Negative-Resistance Oscillations.* This type oscillation occurred when the magnetic field was very high (i.e., $\omega_c \gg \omega$). In this case studies by Kilgore [5] showed favorable electrons performing many gyrations or cycles (at cyclotron frequency) during the transit from cathode to anode. Some commentators suggest that this type is a special case of the more general “traveling wave” oscillations, but in any case applied only to low frequency. More recently, however (see theoretical discussions in Section 5) it appears that there may be some relevance to interaction in relativistic magnetrons.

3. *Traveling-Wave Oscillations.* For many years before World War II many investigators succeeded in producing oscillations in magnetrons where the anode was segmented— for example, into two, four, six, eight, or more segments and various circuits connected to these segments. The theories were not sufficient, but there slowly was an appreciation of the concept of “velocity synchronism” in

which electrons when moving at the same speed as a traveling wave can become phase focused in such a way as to deliver energy to the wave. As depicted in Fig. 2, such a wave that can travel around the anode or interaction space is a “slow wave” supported by “periodic structures” [6,7]. From the principle that electrons in crossed fields move perpendicular to the E field, one can see that certain favorable electrons move toward the anode and give up energy. At the same time unfavorable electrons move a limited distance toward the cathode and possibly gain some energy, which then trigger backbombardment of the cathode, heating and secondary electron emission to add to the presumed thermionic emission. If the circuit, as well as the electron flow, is reentrant, as in the cylindrical magnetron, then oscillations can and should build up.

As documented by Harvey, Guerlac, and others [8,9], all the activity before 1940 resulted in many papers showing traveling-wave oscillations but mostly with modest power of watts up to 100 W and predominantly at low frequency below 1 GHz. The real breakthrough credited as the birth of the microwave magnetron was done in the United Kingdom in response to urgent wartime needs for radars— particularly search and fire control. Boot and Randall [10,11] are credited with this work, which demonstrated the feasibility of generating watts of average power and tens of kilowatts peak power (with microsecond pulses) at high frequencies, around 3 GHz (S band) with good efficiency: 10–50%. The importance of this “cavity magnetron” in winning the war for the United Kingdom and the United States has been well documented [9,12]. Important features introduced by Boot and Randall included the recognition that multiple resonators in a copper block could yield the high Q (low loss) important for extension of performance to higher frequencies (important for radar resolution, etc.). Years later, some decry [13] the credit uniquely given to the British for this development while not recognizing the prior reports of magnetron oscillations in Russia, Germany, Japan, and France. But it has been explained in rebuttal [13] that only when the British demonstrated the breakthrough levels of power at high frequencies was there practical recognition of its importance. Indeed, history [9,12] records the dramatic program to manufacture in large quantity the magnetrons need by the Allies in World War II. (It is ironic that various reports [14] state that in Germany governmental policies in the 1930s and early 1940s had prevented the concentrated attention to high frequencies, which triggered the British milestone.)

An immense amount of research and development on the cavity magnetron for military applications took place during World War II, and unclassified documentation was possible only after then. Concerning the magnetron, that work is described in Volume 8 [15] of the celebrated Radiation Laboratory series of books on radar, microwave technology, and the various associated components such as the magnetron and other devices. As described by Collins [15], many physicists contributed greatly to the theories and experimental magnetron development between 1940 and 1946, and even a bit later. Here we will only summarize the key theoretical principles and experimental results codified during the war effort.

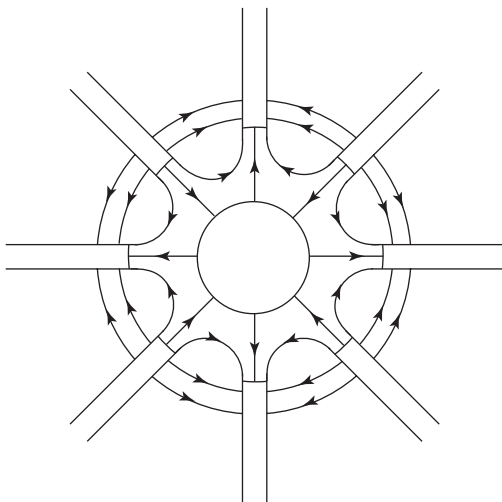


Figure 2. Depiction of RF interaction electric fields in a magnetron.

The copper anode structures consisting of an even number of vanes, or variously shaped resonators were analyzed as reentrant periodic structures with principal modes $n = 0 \cdot \cdot \cdot N/2$ where N is the number of vanes or resonators. For a given mode n there would be $2n$ half-wave fringing fields as depicted in Fig. 2. It was soon found that the best mode of operation was that of the π mode with 180° phase shift between adjacent resonators or cavities and hence $n = N/2$. Also it was found that a “strapping” technique was very effective in providing “mode separation,” allowing stable magnetron operation in that mode.

Key concepts of “instability” voltage and “threshold” voltage were developed [15] by many led by Buneman and Hartree, respectively. The more useful concept is the latter, which describes the minimum voltage at which current can be drawn for a given mode. The Hartree voltage was given by

$$V_H = [\omega B(r_a^2 - r_c^2)/2n](1 - \omega/n\omega_c) \quad (13)$$

where n is the mode number corresponding to the number of periods or wavelengths of the field pattern in the interaction space from the anode structure. In almost all cases the value of n is for the π mode or $n = N/2$, where N is the number of vanes, cavities, or resonators. For the linear case the Hartree voltage becomes

$$V_H = \omega B d / \beta - \omega^2 / 2\eta \beta^2 \quad (14)$$

where $\beta = 2\pi/\lambda$ is the phase parameter for the interacting slow wave where λ is its wavelength or period along the direction of electron or beam flow.

It can be shown that at the Hartree condition in the cylindrical magnetron the azimuthal velocity of the outermost electrons in the space charge hub, is greater than the corresponding azimuthal velocity of the interacting slow wave. This signifies that extra energy must be available for the electrons as they drift radially out from the hub, requiring a continuously increasing azimuthal velocity if the electrons are to stay synchronized with the rotating wave. One speaks of the bunched electron spokes rotating in synchronism with the rotating wave.

For the linear case, however, it can be seen that the voltage for synchronism (or velocity resonance) is the same as the Hartree voltage. Once in synchronism at the outer edge of the sheath of electrons, the electrons or spokes require no increase in velocity along the y direction as they move toward the anode, in the x direction.

We have described the basic concepts underlying the modern microwave magnetron. Later we review practical designs, the use of the “performance chart” and Rieke diagram to describe the magnetron operating results and the actual results achieved in the field during and since World War II. For the most part the magnetron circuit (anode) represents a resonant circuit. Its characterization is required before the full electron cloud-circuit interaction is understood as to its dependence on the load where the output power is delivered and the portrayal of same on the “Rieke diagram”—namely, power and frequency data plotted on the classical “Smith chart” (see SMITH CHART).

3. MICROWAVE MAGNETRONS

3.1. Synopsis of Magnetron and Crossed-Field Amplifier Development

Pre-World War II magnetrons were of the so-called split-anode type [16]. A resonant circuit was formed by coupling the anode segments to a short-circuited Lecher wire transmission line. Operating in the VHF and UHF regions, these magnetrons produced continuous-wave (CW) power of hundreds of watts and could be mechanically tuned over a wide range of frequencies. Short transit time of the electrons from cathode to anode was necessary to obtain efficiencies of 60% and was achieved by the use of a strong magnetic field. Split-anode magnetrons were employed in the early 1940s primarily in radar and UHF electronic countermeasures. It was not practical to use this type of device as a source of high power at microwave frequencies because of the power dissipated in the anode and cathode, and the high magnetic field requirement. However, operation at lower magnetic field and with anodes consisting of multiple electrodes led Posthumous [17] to develop the concept of traveling-wave interaction between the electrons and the RF electric fields developed in the interaction space between cathode and anode. The electrons executed long transit-time orbits, allowing the electrons to efficiently transfer energy from the DC field directly into microwave energy. Traveling-wave interaction formed the basis for the design of high-power, high-frequency magnetrons.

A detailed and descriptive discussion of magnetron development during World War II and the subsequent development of the crossed-field amplifier (CFA) is given in a paper by Brown on the microwave magnetron and its derivatives [18]. Design and performance features of World War II magnetrons are described in a Bell Laboratories paper by Fisk et al. [19], and an MIT Radiation Laboratory Series text edited by Collins [15].

A synopsis of the early magnetron design and its role in crossed-field amplifier development is presented below. Particular crossed-field devices and their performance features are described that influence modern design and applications of magnetrons and crossed-field amplifiers.

3.2. Early Magnetron Design Features that Influence Modern Tube Design

High pulsed power was required at microwave frequencies to meet radar-ranging requirements. In 1939, a compact, mechanically and thermally robust hole and slot anode magnetron resonator was invented. The anode resonator is shown in Fig. 3. Early models of the magnetron employed a large-diameter oxide-type cathode to obtain the necessary electron emission current densities for high power operation. These tubes eventually developed peak power of 100 kW at 10 cm wavelength. However, the anode structure consisting of coupled resonators had multiple resonant frequencies that interfered with the desired oscillation frequency. This problem was resolved by modifying the anode circuit with the addition of metallic conductors called “straps”. Figure 4 shows a typical

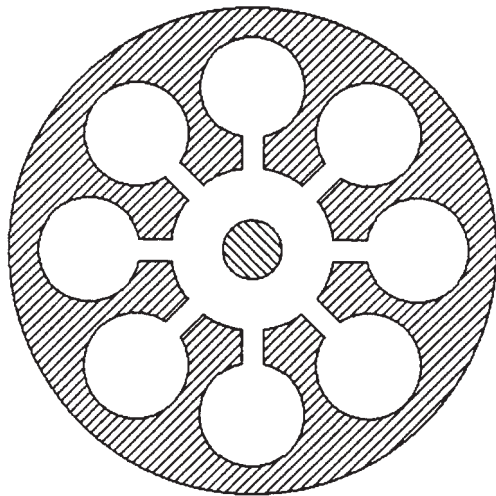


Figure 3. Hole and slot magnetron anode.

early magnetron. The letter I identifies the interaction space between the cathode C and the anode A. The anode resonators are shown as R, and coupling between resonators is increased by the straps S shown electrically connecting alternate resonator cavities. The loop L connected to the end of a coaxial transmission line couples power from the resonator cavity. A second strap, not shown, connects the remaining resonators. Dual strapping was applied to either one end or to both ends of the anode. The effect of strapping was to lower the desired operating frequency and to displace potentially interfering frequencies well above the operating frequency.

Based on the early development work, the design of the anode resonator circuit was modified to include the vane and the slot (wedge) configurations shown in Fig. 5. Both these designs could be strapped as discussed above.

The manufacturing process for the anode block involved machining of OFHC (oxygen-free high-conductivity) copper. This process was time-consuming and costly. An alternate procedure used stamped copper laminations that could be stacked and brazed together with high-conductivity solders. This process was employed for production of tubes with wavelengths of 10-cm tubes and

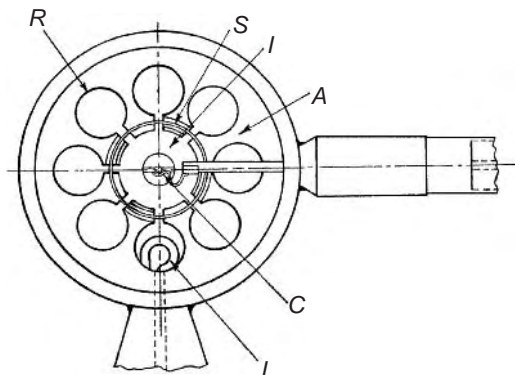
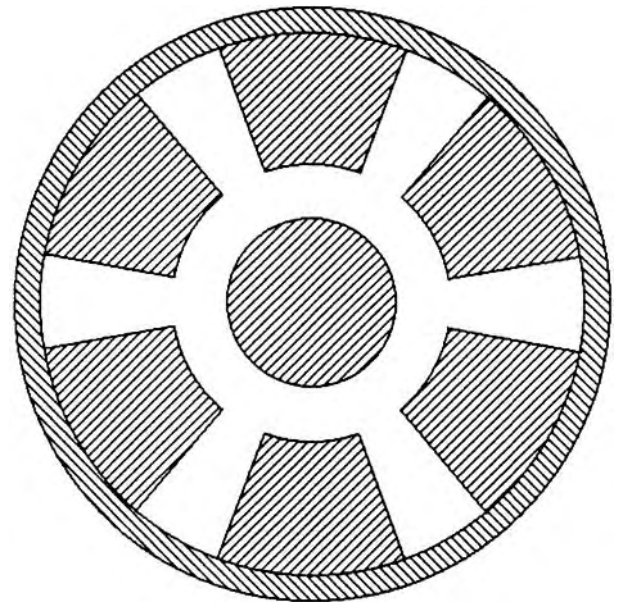
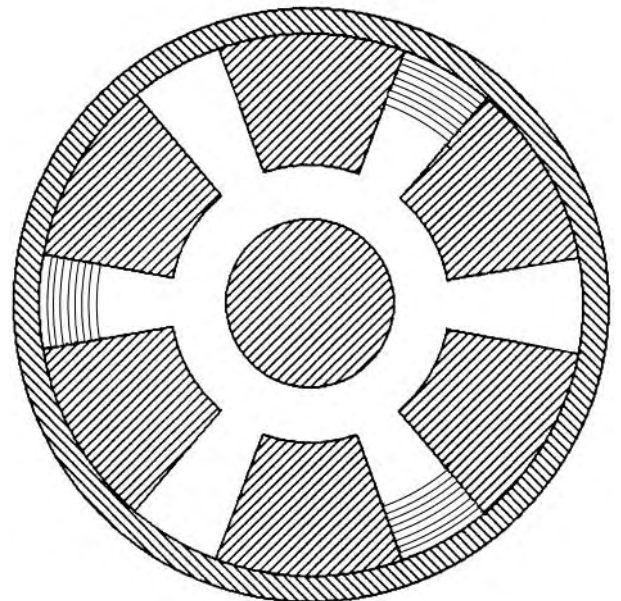


Figure 4. Cross-sectional view of typical hole and slot magnetron anode with straps. (Reproduced from *Microwave Magnetrons*, G.B. Collins, Ed., McGraw-Hill Book Co., Inc., NY, 1948.)



(a)



(b)

Figure 5. Magnetron anode: (a) vane and (b) slot (wedge).

higher. Tubes operating at low wavelength still required machining to meet required tolerances.

Strapped anodes were difficult to fabricate at wavelengths shorter than 10 cm. The strapped anode was replaced by the unstrapped rising sun anode shown in Fig. 6. The rising-sun anode provided adequate frequency separation and could be fabricated at mm wavelengths by using a technique called "hobbing," in which a machine tool is driven into a block of copper to create the rising-sun anode shape.

A large number of fixed-frequency and mechanically tuned magnetrons that incorporated anodes of various designs [15,19] were developed during WWII and oscillated at wavelengths ranging from 40 cm to 10 mm.

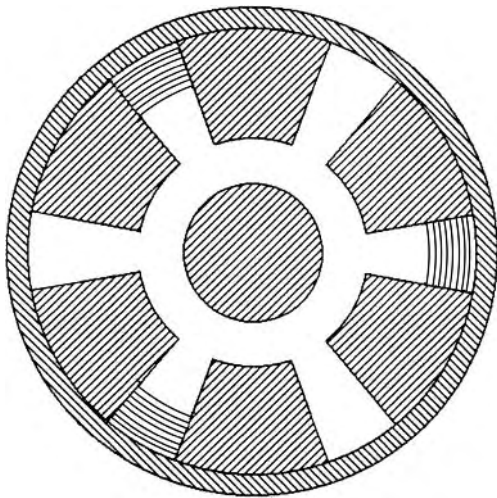


Figure 6. Rising-sun anode.

3.3. Magnetron Tuning Techniques

It was recognized early that tuning of the magnetron was essential for military applications, which required frequency diversity for jamming and general radar applications, including FM altimeters. Tuning was achieved mechanically, electronically, and by voltage tuning [20]. Mechanical tuning involves changing the inductance or capacitance of the anode resonant circuit. This method typically provides a 10% tuning range prior to having mode interference. Nominal shift of frequency can also be obtained either by changing the load impedance of the magnetron or by coupling an external tunable cavity to one or more magnetron cavities.

A variety of other techniques have been used to provide tuning and frequency agility of the magnetron. These include electron-beam tuning of the resonators, change of the permeability of ferrite-loaded transmission lines coupled to the resonators, change of the electrical length of transmission lines coupled to the resonators by means of a multipactor discharge, and piezoelectric tuning [20]. A few examples of magnetron tuning are discussed below.

3.3.1. Voice Coil Tuning Reed. This approach was first incorporated into a low power CW magnetron for use as a frequency-modulated CW radar altimeter. This magnetron is the C-band, 4268–4350-MHz, 1.5-W RK6177 magnetron, which is frequency-modulated at a 300 Hz rate by a vibrating reed driven by a voice coil mechanism [21]. Another device using a voice coil is the frequency-agile MG5272 Ku-band, pulsed coaxial magnetron. This 50-kW peak, 50-W-average power device has a tuning range of 350 MHz and a tuning rate of 700 Hz [22].

3.3.2. Multipactor-Tuned Magnetron. Strapped-vane magnetrons have employed one or more external cavities coupled to individual anode resonators to provide tuning [23]. A modification of this technique is to employ a coaxially tuned circuit inductively coupled to the magnetron having a capacitive section in which an electron

discharge is created between the inner and outer coaxial conductors [24]. RF power coupled from the magnetron excites an electron multipactor discharge within the capacitor volume. The effect of the discharge is to reduce the capacity of this section by about 11%. Magnetron power loss due to the discharge is 5–10%. An X-band multipactor-tuned magnetron MG5286 operates at 22.5 kW with an efficiency of 34%. The tuning range is 9265–9315 MHz [25].

3.4. Coaxial Magnetron and Methods of Tuning

The development of the coaxial magnetron by Feinstein and Collier [26] has had a major impact on the upgrade of commercial and military radars because of its improved spectrum and operational life as compared to the strapped magnetron. In addition, advanced tuning techniques have been applied to this device, further enhancing its overall capability. The coaxial magnetron generally has larger size and weight than does the strapped magnetron to achieve a given power level.

The improved performance was obtained by symmetrically coupling the unstrapped magnetron anode resonators to a TE_{011} mode cavity having a low RF loss. The unloaded Q of the composite anode and cavity is approximately 4 times that of the strapped magnetron, which is a key factor in achieving improved spectrum. Symmetric coupling of the cavity and anode resonators ensured that the anode resonators were excited in the pi mode. The coaxial magnetron structure also has lower power density as compared to the strapped magnetron, thus reducing the tendency for arcing, which affects the performance of high-peak-power magnetrons. A concise description of the coaxial magnetron and performance features is provided by Gerard [27]. The design and performance of a 3-MW S-band coaxial magnetron incorporating mode perturbation techniques to achieve wide tuning range is discussed by Ruden [28], and a field analysis was developed for the mode spectrum of the coaxial magnetron that shows similarity to the mode spectrum of the rising-sun magnetron [29]. The coaxial magnetron has played a major role in the upgrade of existing radars in providing improved spectrum characteristics, enhanced reliability during operation, and exceptionally long operational life. The coaxial magnetron has a number of features that suggest that it may perform well at the multimewatt/gigawatt peak power level. Preliminary work on development a 100-MW relativistic positive anode coaxial magnetron is described in Section 7 on technological developments.

Various methods of tuning the coaxial magnetron are described by Gerard [30]. Slow, motor-driven, mechanical tuning is used to set the magnetron center frequency. A separate motor connected to the cavity tuning plunger is used to “dither” the frequency. At K band the coaxial magnetron is capable of a frequency excursion of 300 MHz at a dither rate of 150 Hz.

Other coaxial magnetrons employ a servocontrolled mechanism to provide accurate and fast frequency response to a variety of input tuning waveshapes, and variable-frequency excursion and tuning rate [31].

3.5. Cathode and Magnet Design

3.5.1. Cathode Design. A variety of cathodes have been used in the magnetron and crossed-field amplifier. The cathode is located directly in, and is integral to, the interaction space, which places unusual design constraints on the cathode. The DC–RF crossed-field interaction results in a percentage of the emitted electrons being returned to the cathode. The kinetic energy of these returning electrons is greater than the thermal energy of the emitted electrons. This is known as “backbombardment” of the cathode, and produces three effects:

1. There is heating of the cathode surface due the energy of the backbombarding electrons, which can result in a significant temperature rise of the cathode. In some magnetrons and CFAs, a precisely controlled change in the heater voltage is required to restore cathode to its original temperature.
2. Depending on the cathode materials, the electron energy may be enough to produce secondary electrons that contribute to the current delivered by the cathode.
3. Depending on the cathode materials and electronic and physical processes, the cathode-emitting surface may be modified by the energy of the returning electrons. Choice of cathode materials and type of cathode is therefore a critical item in magnetron and CFA design.

In general the thermionic emitter type cathodes used in magnetrons are either pure tungsten operating at very high temperatures to achieve the requisite emission densities with long lifetimes, versions of carburized thoriated tungsten operating at lower temperatures and having some reduction of life, or dispenser cathodes operating at much lower temperatures that depend on the constant evolving and migrating of an activating material to the emitting surface to mitigate the effects of evaporation and electron backbombardment.

One of the easiest and least expensive dispenser-type cathodes to manufacture and use is the oxide cathode. This cathode was typically used in low-power CW magnetrons for altimeter and FM transmitters. Originally developed for radio tubes, this cathode through chemical and thermal processes continually replenishes its semiconductor surface with barium ions evolved in the body of the oxide, which in conjunction with the oxide provide emission of electrons at a low temperature. The barium oxide cathode material is frequently used in either a nickel mesh or nickel matrix to enhance its chemical and mechanical properties. The oxide cathode can provide not only CW current but also high peak current at narrow pulsewidth. Currently, the oxide cathode is used in beacon magnetrons for transponder and weather radar applications.

Considerable effort has been devoted over many years to develop fast warmup cathodes for beacon and millimeter-wave magnetrons. In most instances the achievement of fast warmup requires changing many other features of the magnetron design and specifications besides just the

cathode emitter. A recent analysis discusses methods for reducing warmup time and heater power for a “semiindirectly heated” oxide coated cathode [32]. This paper also suggests that materials other than tungsten and molybdenum be used for the cathode heater.

The impregnated type cathode has replaced the oxide cathode in many high-power crossed-field tubes that require long life and wide pulsewidth. The particular type of impregnated cathode used is greatly influenced by the nature of the application of the magnetron or crossed-field amplifier.

Although other methods and materials have been used, in general the impregnated cathode uses a porous matrix of compacted and sintered tungsten into which a suitable barium oxide base compound is impregnated. The emitting surface may be polished or have various other materials deposited on it to stabilize thermionic or secondary emission characteristics. Operating at about 1050°C, this cathode, when applied properly, can supply copious emission for tens of thousands of hours in a crossed-field device.

A paper by Cronin [33] provides basic information on the impregnated cathode and describes various coating methods used to enhance the cathode current density. The impregnated cathode is highly reliable and is extensively used in high-power coaxial magnetrons and crossed-field amplifiers.

General description of cathode types, fabrication, and usage is provided by Gilmour [34], and a complete discussion of cathode fabrication and processing is given by Rosebury [35] and Kohl [36]. Djubua et al. [37] reviews the state of the art of the dispenser cathode to provide current density of 30 A/cm² (amperes per square centimeter) with a life of 10,000 hours for klystron usage. The combination of layered cathode materials and alternate surface coatings is discussed. This technology may be applicable to further improve the performance of cathodes in the magnetron and crossed-field amplifier.

The cathode workhorse for the kilowatt, S-band microwave oven magnetron is the carburized thoriated tungsten helix wire cathode where current density of 1–3 A/cm² is typical depending on whether the device operates CW or pulsed. Carburization reduces the amount of evaporation of thorium leading to enhanced reliability and life. A pure-tungsten cathode helix is used in the higher-power industrial magnetrons. L-band 100-kW CW magnetrons have a life of approximately 10,000 h. Most common failure modes are filament end of life, internal arcing, and moding phenomena. Limited data for L- and S-band 30-kW magnetrons show 6000–8000 h of life with filament end-of-life the most common failure mode [38].

Finally, some cathodes operate on secondary emission. The oxide cathode has a high secondary emission ratio and can provide high current under short pulsewidth conditions. Other secondary emission cathodes can operate stably at reasonably high emission densities and high average power. Pure metal cathodes of tantalum and molybdenum showed some early promise. These materials have been superseded by a cold, secondary emitting platinum cathode that meets the stability and life requirements for both high-CW power generation and combined

high peak and average power generation at wide pulse-widths [39].

Particular applications requiring low-voltage operation of the crossed-field device, long pulse operation dictated the use of metallic oxide films as beryllium oxide. The nature of these emitters is discussed by Shih et al. [40]. The oxide film degrades during operation, and an auxiliary oxygen dispenser is required to allow the oxide film to be continually replaced. This approach has been used successfully in crossed-field amplifiers employed in the AEGIS Weapon System [41].

3.5.2. Magnet Design. The magnetron and crossed-field amplifier have had a long history of using Alnico 5 and 7 magnetic material. Alnico 9 is also used in coaxial magnetrons at L and S band to achieve higher field strength, and to reduce volume and weight. As discussed in Section 7, magnets made of the rare-earth element samarium and cobalt [42] are used in beacon and millimeter-wave magnetrons where exceptionally small volume and low weight, freedom from demagnetization when in proximity to ferrous materials, and high-temperature operation are requirements. The use of temperature compensated samarium-cobalt magnets has achieved essentially zero temperature coefficients and provides long-term stability at 300°C [43]. These magnets have been employed in traveling-wave tubes. Information on usage in crossed-field tubes is not available.

The magnetrons used in microwave ovens typically use low-cost ferrite magnets; changes in temperature can affect the stability of this material.

3.6. Magnetron Performance Chart and Rieke Diagram

The magnetron performance chart shows the relationship between voltage, current, and magnetic field. Specific power data or contours of constant power and constant

efficiency are typically superposed on the voltage-current plot. Regions of high or low noise generation are sometimes identified. Figure 7 is of considerable historical interest in that it shows the “Gauss lines” of voltage versus current for different magnetic field levels for a 25-kW CW magnetron that has used as the base design for higher-power CW magnetrons. Note that as the magnetic field is increased, the efficiency approaches ~85%. This efficiency value includes the electronic conversion efficiency, circuit efficiency, and an efficiency term associated with back-bombardment power to the cathode. Note the wide range of current, which provides high efficiency at a higher than normal magnetic field level. Further investigation is required to establish the maximum efficiency obtainable from the magnetron [140].

The performance chart records the operation of the magnetron into a matched RF load. This chart also provides information on matching the static impedance of the magnetron to the power supply or modulator impedance. The dynamic impedance of the magnetron is of importance relative to the manner in which the magnetron voltage and current are affected by the dynamic impedance of the power supply/modulator. CW magnetrons typically have low dynamic impedance; hence optimum performance is obtained by operation of the magnetron under a condition of constant current. Note the dynamic impedance is sensitive to the heater power and cathode backbombardment power.

At a given magnetic field an increase in magnetron anode voltage produces a change in anode current that is a function of the dynamic impedance of the tube. The voltage and current will increase until a limit in current is reached. The voltage and current may markedly change depending on the nature of the power supply or modulator. This voltage-current change corresponds to a transition of operation into a non- π circuit mode at a different frequency. The current limit is termed a *current-mode boundary*, and the magnetron is said to have moded.

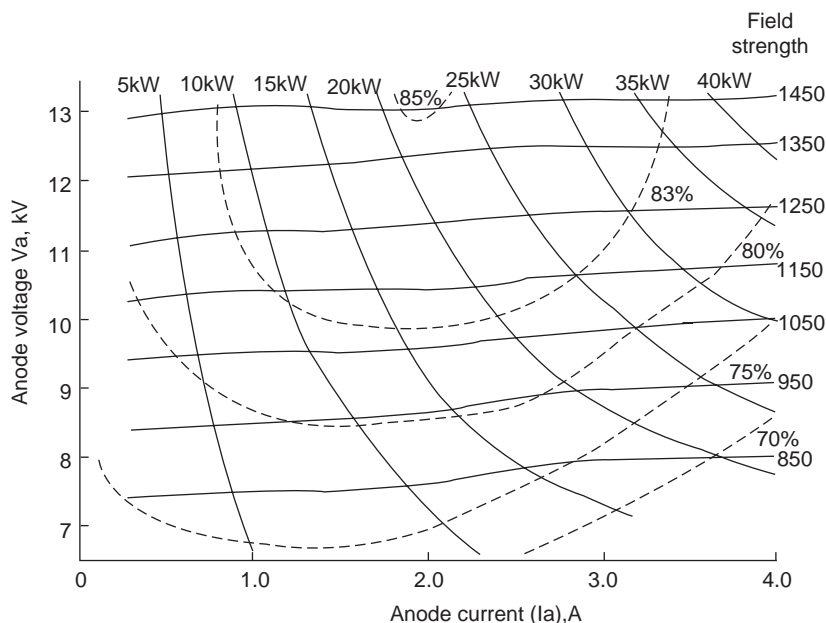


Figure 7. Performance chart: frequency 912 Mc/s, frequency-pulling figure 2.6 Mc/s. (Reproduced with permission from Proc. IEE, 1964, J.R.G. Twisleton, Ref. 56.)

Alternately, the magnetron may undergo a small percentage change in voltage at essentially constant current. This voltage change is accompanied by a shift in frequency. This is termed a “Gauss-line discontinuity,” which causes degradation of the magnetron spectrum.

Moding and the Gauss-line discontinuity can be influenced by the load conditions and is greatly affected by the available cathode emission current. If the maximum available emission current is approached the slope of the voltage-current curve will increase. It has recently been shown by numerical simulation of magnetron operation [79,104] that the magnetron is unstable under this condition. Once the transition into a regime of cathode temperature emission-limited operation has occurred, the magnetron resumes stable operation with typically lower noise generation than that associated with cathode space-charge-limited emission.

The effect of load (microwave oven, plasma reactor, antenna, etc.) mismatch that encompasses variation of both magnitude of load impedance and phase is described by the Rieke diagram, which provides contours of power and frequency as a function of load voltage standing-wave ratio (VSWR) and phase.

The Rieke diagram of Fig. 8 provides a description of the magnetron response to variation of the complex load impedance. Circles of load reflection coefficient or corresponding load VSWR are displayed. The contours of measured constant power output are shown as a function of load VSWR and phase. Note the region of high power corresponds to strong coupling of the magnetron to the load. Matched load is at the center of the diagram and represents zero reflection coefficient or VSWR equal to one. Operation of the magnetron at a power level greater than that at matched load can lead to moding. The region of

high power is called the “sink.” The lines of constant frequency tend to converge in the high-power region of the chart. Small changes in load impedance result in relatively large frequency shifts causing degradation of the spectrum. However, efficiency is high in the sink region.

The low-power region of the chart corresponds to reduced coupling to the load with greater energy storage in the magnetron circuit. While buildup of oscillation is improved in the low-power (antisink) region, the magnitude of the RF fields in the magnetron can lead to arcing and an increase in the missing pulse count. An increase of cathode backbombardment power also occurs in regions of the chart when the output power is less than the matched load power. For a given cathode heater power, the variation in cathode backbombardment power may vary the cathode temperature and thus cathode emission such that the cathode transitions back and forth between space-charge-limited operation and temperature-limited operation.

3.7. Modification of Magnetron Circuit to Create an Amplifier

3.7.1. The Amplitron Crossed-Field Amplifier. From the late 1940s to the early 1950s numerous research activities were in progress to develop a crossed-field amplifier. Magnetron amplifier concepts were in vogue [44], and an offshoot of Warnecke’s work led to the development of the M-type backward-wave oscillator (M-BWO) [45], which provided considerable insight into the crossed-field interaction process. A parallel investigation led to modification of the magnetron anode circuit, which resulted in an amplifying device called the Amplitron invented by Brown [46]. The theory of the Amplitron was developed by Dombrowski [47].

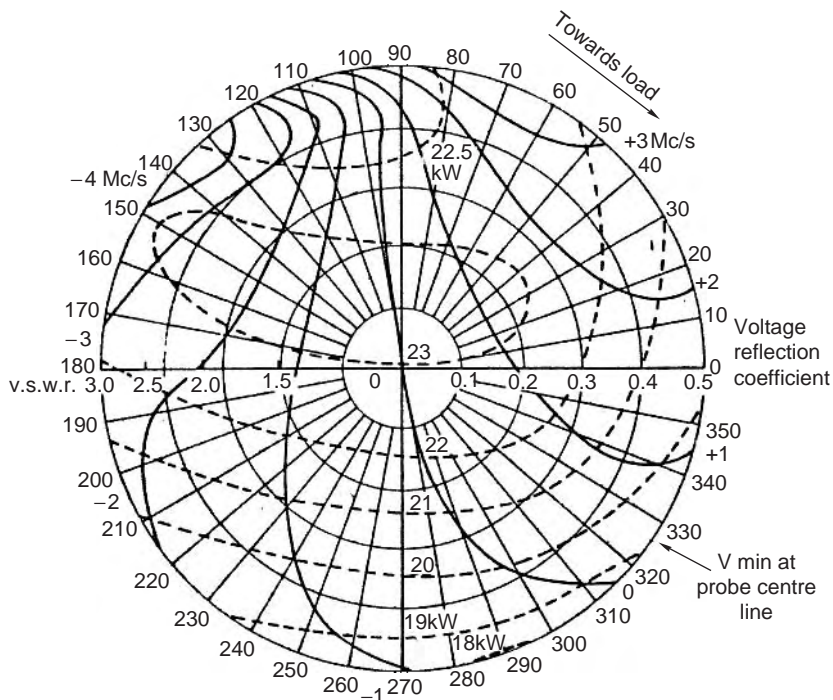


Figure 8. Rieke diagram with series field $V_s = 11.4$ kV, $I_a = 2.35$ A, frequency = 909.6 Mc/s. (Reproduced with permission from Proc. IEE, 1964, J.R.G. Twisleton, Ref. 56.)

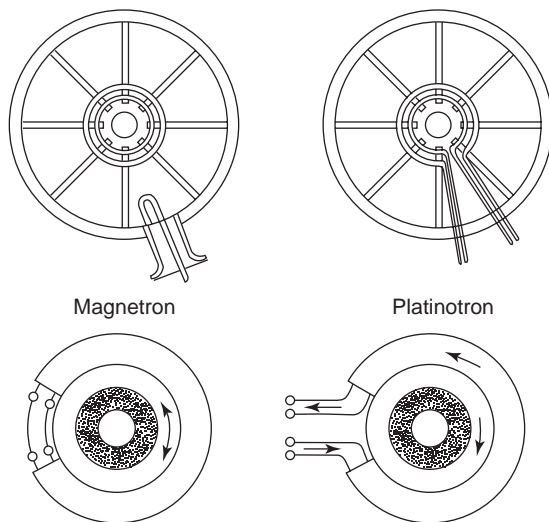


Figure 9. Diagram illustrating the basic difference of construction and operation between the platinotron and the magnetron. (© Proc. IRE, 1957, W.C. Brown, Ref. 46.)

The Amplitron is best described in terms of the magnetron circuit modification as shown in Fig. 9, where the dual strapped circuit is severed. The anode-strap configuration is now representative of a broadband transmission line rather than the resonant structure of the magnetron. The anode vane count for the magnetron is an even number, while for the Amplitron the vane count is odd. The circuit has an input/output terminal. A drive signal impressed on the input is transmitted along the circuit to the output. Electrons created at the cathode rotate about the cathode in a direction opposite that of power flow on the circuit. This device is termed a “backward-wave device.” The power flow on the transmission line creates RF voltages on the anode electrodes. The time-varying electric field created in the interaction space is composed of two fundamental waves, one of which travels in the direction of electron flow. Interaction of this wave with the circulating electron stream is similar to that occurring in the magnetron. The mechanism of power buildup on the circuit is also identical to what occurs in the M-BWO where power flows on the circuit in a direction opposite that of the electron flow. The frequency of the Amplitron is determined by the drive signal and the magnitude of power gain is determined by the impedance of the transmission line.

Of importance is the reentrant nature of the electron stream in the Amplitron. “Reentrant” implies the space charge spokes created by the crossed-field focusing mechanism rotate about the cathode and pass without degradation from the region of low electric field of the input anode electrode to the region of high electric field of the output anode electrode. Typical overall efficiency for the backward wave Amplitron is between 45–80% depending on frequency, magnetic field level, and RF circuit resistive loss associated with the length of the circuit. In some applications the Amplitron can exhibit greater efficiency than the high- Q resonant magnetron due to its broadband, low- Q filter-type RF circuit.

Typical usage of the Amplitron is illustrated by the following examples. The Amplitron was used in the S-band,

CW, FM transmitter in the lunar excursion module of the NASA Apollo program. This Amplitron provided 17 dB of gain, power of 25 W, and operated at an efficiency of 55%. Note this tube employed a standard oxide-coated cathode with a nickel matrix that met the reliability and life requirements of the spaceborne telemetry mission.

For decades the Amplitron was the dedicated pulsed power source for the U.S. FAA Airport Surveillance Radar providing 4.5 MW of peak power at L band and operating at approximately 50% efficiency. An oxide cathode was used that consisted of a coating of barium-strontium oxide supported by a husky nickel sleeve. This cathode provided an operational life of 15,000 h. The drive power for this amplifier was provided by highly frequency-stable, mechanically tuned oscillator version of the Amplitron called the *Stabilotron* [46].

Typical of the many radar systems that have employed the Amplitron are the U.S. Navy 3 D air search SPS-48E and the surface search SPS-67, and the U.S. Army Patriot multifunction phased array radar MPQ-53 [48].

3.7.2. Forward-Wave Crossed-Field Amplifier. One of the many versions of the crossed-field amplifier is the forward-wave crossed-field amplifier. The direction of electron flow in the interaction space is in the same direction as the power flow on the RF circuit; hence the term “forward-wave interaction.” As with backward-wave interaction, the electrons interact with a component of electric field that travels in the same direction as the electron flow; thus the interaction and spoke formation is again similar to that of the magnetron. This device is “nonreentrant” in that a circulating spoke of charge is dispersed as the spoke passes from output to input electrodes. Ideally the dispersed electrons have no residual bunching and carry no modulation into the input region.

A forward-wave crossed-field amplifier is employed in the AN/SPY-1 multifunction, phased-array radar used by the U.S. Navy AEGIS Weapon System [49]. Crossed-field amplifier mean time between failures (MTBF) has reached 45,000 h, compared to a design requirement of 5000 h. As of 1998 the shelf life of AEGIS CFA tubes was ~10–12 years [41].

4. MAGNETRONS FOR POWER APPLICATIONS

The magnetron, per the review in the preceding section, has played a leading role in military and civilian radar applications, primarily in the pulsed mode. In such applications in many cases the magnetron was eventually replaced by magnetron derivatives, such as various forms of the crossed-field amplifier (See Section 7.), by klystrons or traveling-wave tubes (TWTs) and at the lower microwave frequencies by solid-state devices when the radar system is converted to a phased-array system, which uses many lower-power sources instead of one or a few high-power sources. CW applications for the magnetron were first sought in electronic countermeasures but later replaced by M-type backward-wave oscillators (carcinotrons) and TWTs. Magnetrons persisted in applications of beacon magnetrons and marine radar—especially for small boats.

In the 1960s, however, the tube industries in the face of successful replacement of tubes by new semiconductor devices looked for new application areas and recognized [50] the area of noncommunications or non-information-processing applications as a potential new-growth market for tubes. In the main this is equivalent to “power applications” reflecting the fact that tubes generally have much higher power capability than do solid-state devices. Power applications include medical procedures (diathermy, hyperthermia), power transmission as in the solar-satellite power system and microwave heating in the consumer area (the microwave oven), and industrial areas (a variety of tasks from bacon cooking to drying of wood and paper).

The history [51] of microwave heating is centered around the invention and growth of the microwave-oven market for both consumers and commercial sites. The magnetron plays the key role in the history of the microwave oven. The inventor of the microwave oven, Percy Spencer headed the World War II work at Raytheon, which resulted in that one company manufacturing over 80% of the magnetrons in the world in 1946. Naturally he looked for commercial applications of the magnetron following the War; included were the diathermy application, the microwave oven, and even, for a while, microwave relay applications for TV signals. The relatively low weight, size, and cost of the magnetron coupled with its unchallenged potential for efficiency made it the leading candidate for the microwave oven application. After the war, Raytheon successfully proposed to the FCC (Federal Communications Commission) in the United States for a new frequency allocation around 2.45 GHz for heating applications such as diathermy and the microwave oven. At the same time an allocation was made around 915 MHz in response to a request from GE. These two bands have become part of a series of ISM bands [industrial, scientific, and medical (ISM)] recognized by international treaty through the ITU (International Telecommunications Union). The 2.45-GHz band is used throughout the world and specifically is 2.4–2.5 GHz. The 915-MHz band is now 902–928 MHz but is approved for use only in region 1, the Western Hemisphere. Incidental emissions in these ISM bands is limited only by safety regulations and not the much more stringent limits to prevent RFI (radiofrequency interference). The relatively broad width of these bands is necessitated by the properties of inexpensive magnetrons, which include large values of frequency pulling, in response to load variation, large frequency pushing as a function of anode current, and thermal drift as the magnetron temperature varies with time and other parameters, including line voltage.

The magnetron, because of its inherent high efficiency, 90% theoretically and 60–90% in practice, has always been the leading candidate for use in the microwave oven. Early tubes [51] made by Raytheon during 1946–1966, however, still were relatively expensive and heavy—compared to today’s magnetrons. Beginning in the 1960s, contributions from engineers in Japan [52] led to the modern “cooker magnetron.” In the period between 1960 and 1975 the unit cost to OEM (original-equipment manufacturers) microwave oven companies dropped from over \$100 to close to \$10. This represents a cost of about \$0.01/W of microwave

power. The many steps, studies, and innovations by Japanese manufacturers (mainly Toshiba, Matsushita, and Hitachi) have been recorded mostly in papers published in the *Journal of Microwave Power*, published by the International Microwave Power Institute. The potential for further improvement was reviewed in 1995 [52].

By 1995 the characteristics of cooker magnetrons had evolved to essentially a standard design representing a consensus among manufacturers. Figure 10 is a photograph of three typical cooker tubes. As shown their weight is 1–2 lb and size less than a 4-in. cube. Their output powers generally are between 700 and 1000 W with peak anode voltage around 4 kV, peak anode current around 1 A, and a filament voltage around 3.0 V. The internal construction of any cooker magnetron is similar to that shown in Fig. 11 except for the number of vanes, which is now typically only 10. Not shown is the filter box, evident in Fig. 10, which encloses the high-voltage terminals (header) with insertion of series inductors and a shunt capacitance before the external terminals seen in Fig. 10. Ferrite magnets, shown in Fig. 10, provide the magnetic field, which is about 1850 G in the interaction space. The cathode is a carburized thoriated tungsten helix, and the anode structure is a strapped-vane periodic structure. The output is through an antenna shown contacting one vane and transmitting into a rectangular waveguide.

In the microwave oven application the waveguide then transmits the microwave power to the oven cavity and load with the possible utilization of randomizing elements like a rotating antenna, rotating turntable, stirrer, or other components such as multifeed apertures or use of more than one tube per oven. In the early days ferrite circulators were used to protect the magnetron, especially in commercial applications. It, however, has been the standard practice for many years to eliminate any ferrite protection device. The modern cooker tubes, of ceramic metal construction, are rugged enough to withstand such treatment even during no-load operation. The side effects, however, are that the magnetron “sees” a multitude of loads in a stirrer cycle. This and the variables of current and temperature create a complicated matrix of instantaneous operating conditions, which increases greatly the probability for some spurious effect, even if it is for a brief instant.

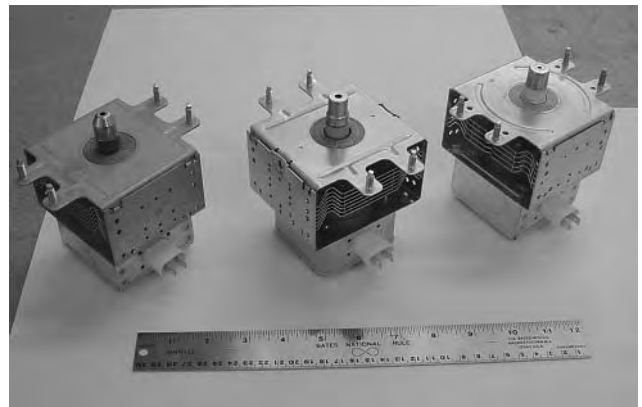


Figure 10. Photograph of several typical modern cooker magnetrons.

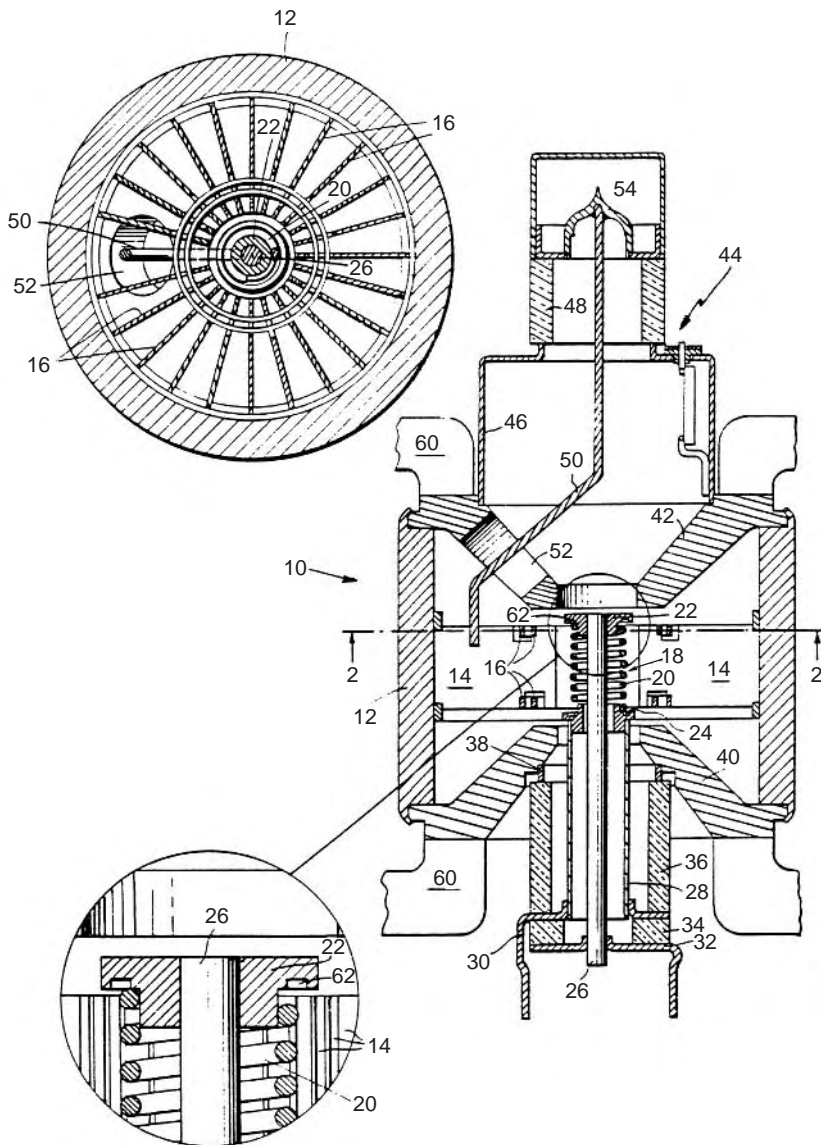


Figure 11. Drawings of typical cooker magnetron construction.

In a 1995 review [53] a comparison of tubes revealed the values shown in Table 1. The cost-reduced 10-vane models retained the approximate values of anode length and cathode length of previous vintage 12 vane tubes (viz., ~0.400 in. for anode length and 0.425 in. for cathode length). Changed were anode diameter, reduced to about 0.350 in. and cathode diameter reduced to about 0.155 in. In addition, the cathode helix wire diameter was reduced by about 20% to 0.020 in.

A very important and distinctive feature of cooker magnetron operation is its AC operation, wherein the tube is subjected to a rectified AC (50 or 60 Hz) voltage of a bit over 4.0 kV peak. This means that, in contradistinction to conventional operation at a DC current, the anode current in the cooker magnetron, each cycle, varies from 0 to a peak of over 1 A. This leads to very important differences in conventional magnetron operation versus that in the microwave oven. Figure 12 depicts typical Gauss lines recorded when a magnetron is operated with steady DC voltage and current. At normal filament voltage one

usually observes the lower Gauss line with significant noise. A higher Gauss line with reduced noise is achieved only after dropping the filament voltage through a critical value of filament voltage. In the AC operation of the cooker magnetron, however (see Fig. 13) the tube each cycle passes on the way up through first a preoscillation region, then a noise region, then a region of discrete spurious sideband oscillations, and finally at high current a region essentially free of noise—at least the noise associated with space charge effects. These regions are also influenced by change in filament voltage as depicted in the oscilloscope photographs in Fig. 14 of Gauss lines, showing at critical values of filament voltage Gauss line discontinuities associated with the boundaries of high-amplitude spurious signals. Figure 15 shows typical instantaneous spectra between 2 and 3 GHz at currents in the three principal regions of anode current

Almost all microwave ovens are operated with “cold start,” meaning that the high voltage (anode) and filament voltage are snapped on simultaneously. Thus, as shown in

Table 1. Summary of Key Tube Dimensions (inches)^a

Vane Number	Tube Type	Anode Diameter	Cathode Diameter	Anode Length	Cathode Length	Wire Diameter	Number of Turns
12	QKH1845	0.400	0.200	0.400	> 0.400	—	—
12	2M107A-78 H	0.416	0.198	0.396	0.425	0.0245	~ 7
12	2M167	0.435	0.205	0.396	0.440	0.024	~ 6.5
12	2M172J	0.397	0.203	0.395	0.420	0.024	~ 6.5
12	OM75A	0.404	0.197	0.396	0.438	0.025	~ 7
12	Sanyo	0.395	0.198	0.357	0.404	—	—
10	2M172AJ(A)	0.357	0.152	0.374	0.413	0.020	~ 8.5
10	2M157A-M10	0.347	0.158	0.394	0.432	0.020	~ 8.5
10	2M107A-304	0.365	0.154	0.386	0.406	0.020	~ 8.5
10	2M214	0.354	—	—	—	—	—
10	2M229	0.346	—	—	—	—	—

^aMeasurements indicate at least ± 0.010 " scatter in cathode axial position with respect to anode. Antenna pole in most tubes is "north," except for Panasonic designs:
 Toshiba: 2M172J, 2M172AJ(A), 2M229
 Hitachi: 2M107A-78 H, 2M107A-304, 2M214
 Panasonic: 2M167, 2M167A-M10, 2M203
 Samsung: OM75A.

Fig. 16, the waveform of anode voltage during cold start shows about a 1.5 s delay before steady cyclic operation is achieved with peak voltage of ~4 kV. Initially the magnetron is subjected to cold-state anode voltage values between 7 and 10 kV and just before full oscillation a ~0.5-s period of complicated moding states and transitions—with operating voltages between 5 and 7.5 kV. There is a small probability of voltage breakdown under the higher cold voltages with subsequent voltage transients generated by the presence of high inductance in power supply transformers. These could be damaging to oven components. Previously there were voltage transients triggered at the end of a spurious mode that occurred just before the moding period, which was the result of an electron discharge from one end shield to the opposite end shield. (This discharge is related to an axial double-stream interaction believed to play a role in the preliminary stages of cold-cathode emission in magnetron diodes [54].) The marking "F" and "FA" on filament leads previously served as a guide for preferred filament polarity for reduced transients of this type. Modern cooker tubes all incorporate the grooves in end shields, (see Fig. 11) as an effective means

of suppressing this spurious mode, making the utility of the F/FA codes academic.

Cooker magnetrons typically encounter only the lower (in terms of filament voltage) mode boundary during normal operation. That boundary, denoted by V_{fm} may typically be below 1 V at the start of life and rises to the normal value of filament voltage around 3.3 V at the end of life. Presumably this deterioration is the result of progressive loss of thorium under complicated processes of sputtering and other gas phenomena, even though the tubes incorporate getters (usually consisting of titanium or Zirconium on the cathode support rod and end shield, made of molybdenum). Less frequently encountered is the upper-mode boundary above which strong spurious sidebands ($f_0 \pm \Delta f$) and baseband signals (Δf) exist with Δf in the range of 200–300 MHz. This spurious modulation, when too strong, causes the magnetron to mode, not at peak current (as is the case for the lower-mode boundary) but at either discontinuity bounding the anode current

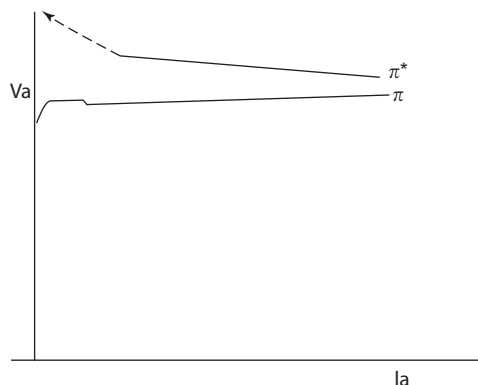


Figure 12. Depiction of low-noise and high-noise Gauss lines (states) in a magnetron when operated with DC anode voltage (taken from old data on CW magnetrons).

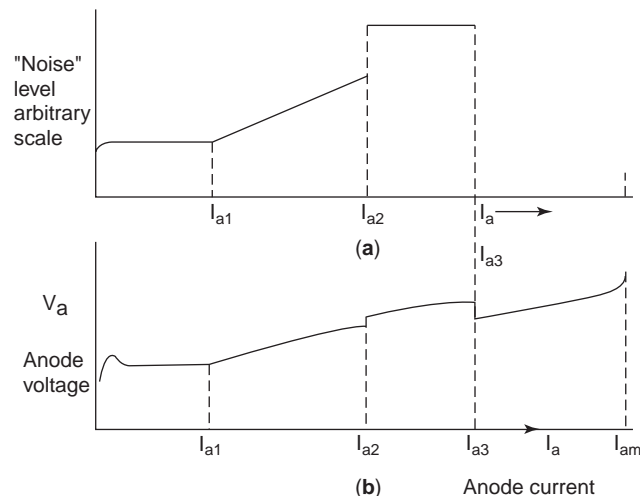


Figure 13. Regions of different noise characteristics during operation of a cooker magnetron with rectified AC voltage.

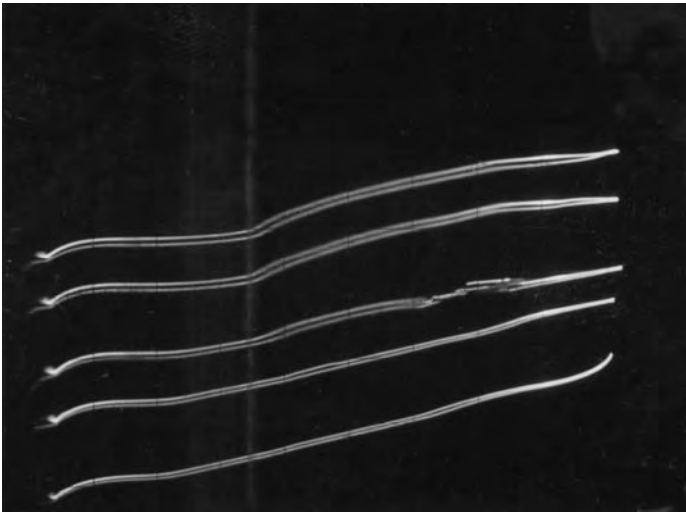


Figure 14. Gauss line traces [50 V/div(division); 0.1 A/div.] of a cooker magnetron at varying filament voltages (1.65, 2.0, 2.5, 3.0, and 3.6 V) showing presence of discontinuities associated with spurious oscillations (traces displaced for viewing purposes).

region of strong spurious. The cause is not too well understood but presumably is associated with excess emission, while the immediate solution is to reduce filament voltage.

Today's cooker magnetrons generally operate around 1 kW with efficiency into a matched load of >70% to permit 50% overall oven efficiency for large loads. The manufacturing volume per year, worldwide, is now (as of 2004)

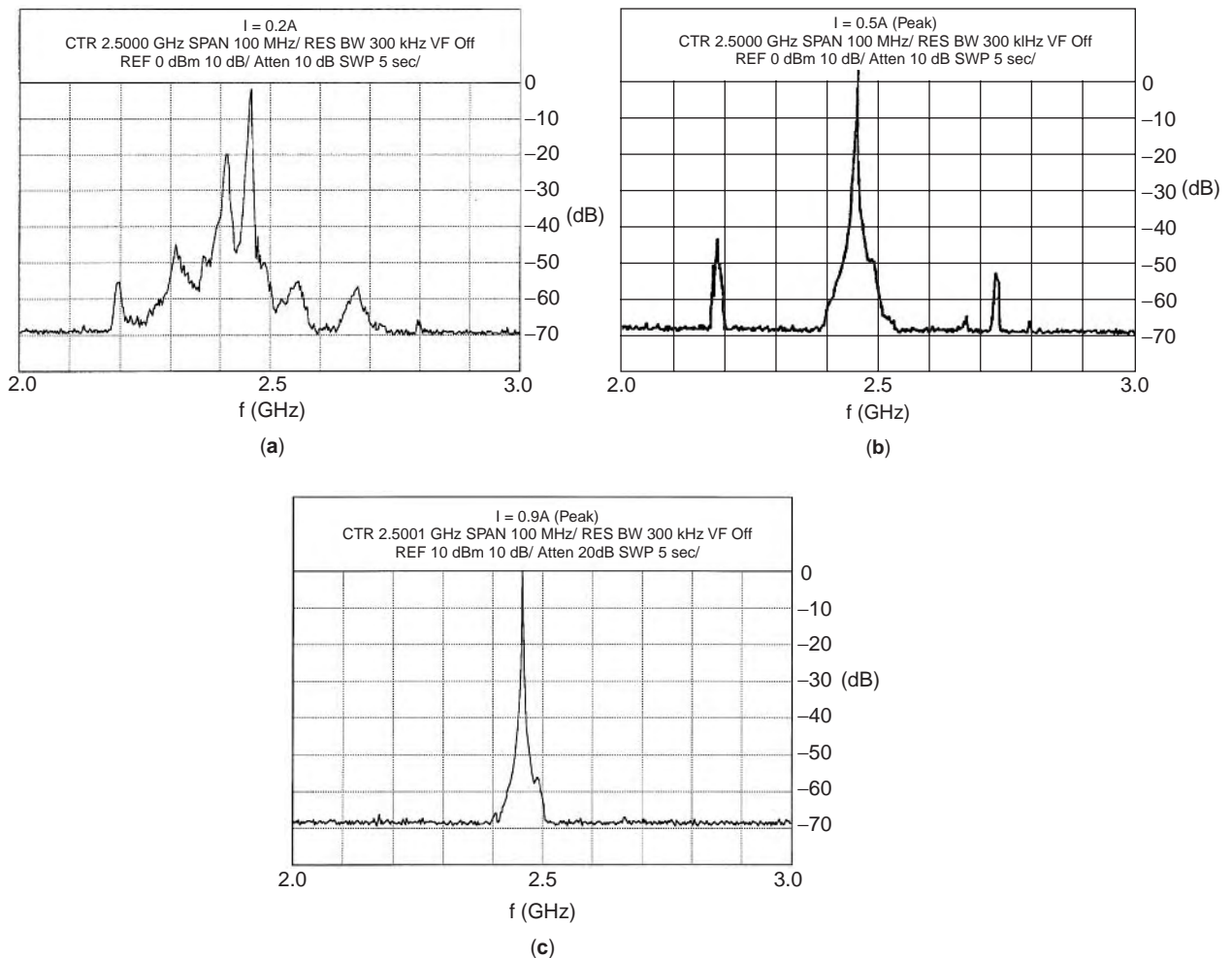


Figure 15. Typical cooker magnetron noise spectra at (a) low currents, (b) moderate currents, and (c) high currents.

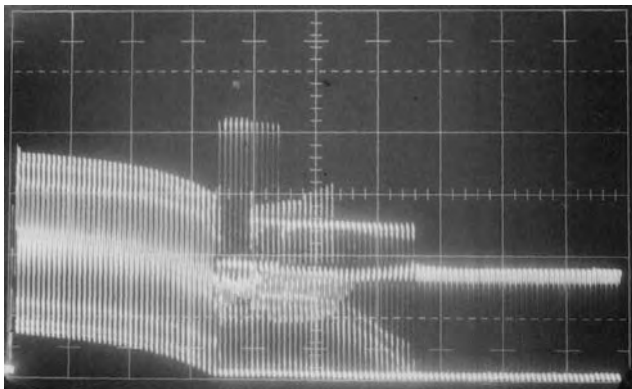


Figure 16. Voltage waveform during cold start of a cooker magnetron. In this case a voltage transient due to end shield emission is present. (2 kV/div; 0.2 s/div).

over 60 million tubes per year. While Japan and Korea are still significant suppliers of cooker magnetrons, the majority are being made in the Third World in China, Indonesia, and Thailand with an unknown production in the former Soviet Union. Large quantity prices are now well below \$10 per tube.

Besides the microwave oven there are some industrial applications of microwave power [55] in which magnetrons play a key role. Some of these, for example, for powering plasma sources of ultraviolet energy, utilize magnetrons at the 2–5 kW level. Although these are not cooker magnetrons, they are closely related in design and performance.

Microwave power applications at power levels below 5 kW are almost all at 2.45 GHz. There are, however, many higher-power applications, up to 100 kW and higher, that operate at 915 MHz. The main uses are in the food industry for meat tempering and bacon cooking [55], although other applications for drying and even some military applications exist. The power source is a magnetron derived from the pioneering work of Twisleton [56] in the 1960s. Today the major suppliers are Burle Industries and California Tube Laboratories (CTL) in the United States, while EEV in the United Kingdom and Istok in Russia also have been suppliers. In Fig. 17 we show a recent photograph of this type of tube. It is large and weighs about 15–20 lb. It is typically operated around 18 kV and 5 A for

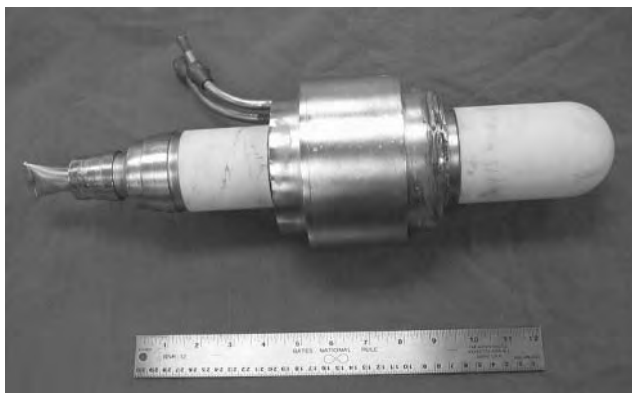


Figure 17. Photograph of a 75-kW 915-MHz magnetron.

75-kW applications with a large solenoid used for the magnetic field, which typically is around 1350 G. The magnetron in this application, in contradistinction to the cooker magnetron, is not operated cold-start, which is clearly impractical at the high voltage and current levels. Instead the cathode, made of tungsten, is preheated at 12 V filament voltage and roughly 100 A and then after start the filament current is programmed to decrease as power increases to, for instance, 75 A at the 75 kW operating point. The conventional supply used with this tube allows anode current to flow through the solenoid. Thus, as power is increased, the current from the separate solenoid current supply is decreased accordingly. The DC voltage is snapped on at start at high Gauss, and then the gauss level is dropped to permit current flow and power output. Typical efficiency is in the mid 80–90% percentage range, while in the laboratory, prototype tubes of the Twisleton variety have shown over 90% efficiency. The cathode is a helix and made of pure tungsten and of roughly 0.400 in. diameter. There is no getter in the tube.

This magnetron is operated in industrial systems only with a ferrite circulator to protect the tube, particularly against “moding,” which can be destructive to the tube. The recommended value of filament voltage versus output power is designed to be adequately separated from both a lower-mode boundary and an upper-mode boundary. The lower-mode boundary is related to inadequate cathode emission. It is believed that the upper-mode boundary is associated with spurious oscillations, as with the cooker tube. Little data exist to confirm this supposition, because of the restrictions involved in experimenting at high power levels. Even though the cathode is pure tungsten, the emission includes contribution from secondary electron emission as well as thermionic emission. The former is not well understood, so considerable variation in lower-mode boundary exists.

A significant field problem with this tube is that of “mag overloads.” Another problem is the methods to restore full power operation after momentary powerdown procedures triggered by arcs in the heating cavities. The mag overloads are not well understood but in the main are “moding” events, sometimes triggered by momentary drops in line voltage in industrial-level voltage lines.

Other magnetrons in industrial applications include tubes at the 600–1000 W level at 915 MHz and tubes at power levels of 5–25 kW at 2.45 GHz. There are also more recent reports of the development of a 1-kW 60% efficiency magnetron in Japan for 5.8 GHz. Little information about these magnetrons is generally available. There is little doubt that useful magnetrons for power applications could be developed over much wider ranges of frequency and power when the economic conditions are appropriate.

5. CROSSED-FIELD DEVICE THEORY AND DEVICE SIMULATION

5.1. Elementary Magnetron Theory

The elements of the magnetron consist of a cathode that emits electrons into a three-dimensional interaction space (r, θ, z) bounded by the cathode of radius r_c and an outer

electrode or anode of radius r_a . A potential difference between the anode and cathode is established by a DC power supply or by a modulator that provides a voltage pulse. The pulse repetition frequency (PRF) multiplied by the pulse length in seconds is called the *duty factor*. This is a measure of the percent time that the device is operating. If the average power delivered to the magnetron is P_{av} watts, then the instantaneous peak power is $P_{av}/(\text{duty factor})$ measured in watts. For continuous-wave (CW) operation, the duty factor is 1.

A magnetic field is applied axially in the z direction, which is in a direction parallel to the anode-cathode surfaces. The electrons emitted from the cathode experience a radial outward force $F = eE$ measured in newtons, where e is the magnitude of the charge on the electron in coulombs and E is the magnitude of the electric field in volts per meter created by the anode-cathode potential difference in volts within the region $(r_a - r_c)$ in meters. A radial inward magnetic force opposes the electric field force and is given by $F = evB$, where v is the azimuth velocity measured in meter per second and B is the applied axial magnetic field measured in teslas. The general motion of an electron within the interaction space is that of an epicycloid with radial acceleration determined by the net force exerted by the electric and magnetic fields; the net force provides the centripetal force $F = mv^2/r$, where m is the mass of the electron in kilograms and r is the radial position of the electron in meters, required for circular motion. The epicycloid motion of the electron consists of an azimuth drift with velocity $v = E/B$ with superposed circular motion with angular velocity $\Omega = v/R$, where R is the radius of the circle; $\Omega = (e/m)B$ is the cyclotron frequency.

The cycloidal motion is termed two-stream motion in that electrons travel outward and then return inward toward the cathode. This motion is modified by the presence of the electrons in that they contribute to the electric field in the interaction space. Thus the motion of the electrons is modified by the density of electrons as a function of radius, azimuth, and axial position such that various configurations of the electron motion can exist. If the number of electrons is minimum, then double-stream motion dominates with electrons traveling radially outward from the cathode and radially inward toward the cathode. This is called the “temperature-limited state” in that for a given cathode temperature the cathode will emit a limited number of electrons. If the number of electrons is large, then the motion of the electrons is greatly modified. A so-called single-stream state may exist when the cumulative effect of all the electrons reduces the electric field at the cathode to zero. The emission from the cathode is termed “space-charge-limited”. Under these conditions all electrons travel in circular orbits about the cathode with azimuth velocity increasing with the radius.

For a given magnetic field and anode voltage, electrons moving on a cycloidal orbit can just graze the anode. The magnetic field is specified as B_0 and the anode voltage as V_0 , and the condition of grazing is termed “cutoff.” Increasing the voltage above V_0 allows electrons to be collected on the anode and the condition is termed “above cutoff.” The device is a diode with current delivered to the anode as a function of the magnetic field and cathode

temperature. If the magnetic field is increased, the electrons can (ideally) no longer reach the anode. This is called a condition of “below cutoff.” In this state we may have the extremes of temperature-limited operation and space-charge-limited operation.

Let us assume in either extreme that we have an aggregate of electrons having a particular azimuth velocity and hence a particular angular velocity at a given radius. These electrons will induce charge on the anode circuit electrodes, which vary with time as the electrons pass by an electrode. The variation of the charge with time creates an induced current in the anode electrode. If, by Fourier analysis of the induced current, a frequency component exists that matches the resonant frequency of the magnetron, an RF voltage will be developed on the anode electrodes. This time-varying voltage will establish electric fields in the interaction space, which can be Fourier-analyzed into azimuth traveling electric field waves in the interaction space. If the electron angular velocity matches the angular velocity of one of these Fourier wave components, then a condition of synchronism is said to exist.

Assume at some radius r_0 that the electron moves with an angular velocity ω that is synchronous with that of the circuit wave. Electrons riding at the positive peak voltage of the wave will experience a force in a direction determined by the vector cross-product of $E_r \times B_z$ such that they will advance toward the zero voltage point of the wave. Electrons riding at the negative voltage of the wave will be retarded in their motion and coalesce about the zero voltage point. Crossed-field bunching of the space charge thus occurs and the angular velocity is constant. In the interaction space electrons at the zero voltage point on the wave will experience an angular component of electric field E_θ due to the circuit wave. The force on the electrons will be in a direction determined by $E_\theta \times B_z$ which is directed toward the anode. The electrons are thus forced radially outward while maintaining approximately constant angular velocity ω_{syn} while the azimuth velocity increases with r . During the radial drift toward the anode, the electrons traverse a potential difference ΔV with available energy $W = q\Delta V$, where q is the transported charge. The change in kinetic energy of the electrons however is $\Delta KE = (m/2)(v_f^2 - v_0^2) = (m/2)(\omega_{syn})^2(r_a^2 - r_0^2)$. It is found that ΔKE is less than W ; thus the potential energy transformed into RF energy is $W - \Delta KE$. The energy exchange mechanism is in contrast to the exchange that occurs in linear beam devices where potential energy is first converted into kinetic energy, which is subsequently converted into RF energy.

5.2. Recent Work on Extending the Theory of Magnetron and Crossed-Field Amplifier

5.2.1. Soliton Theory.

The development of an extension of basic magnetron theory has been minimal in more recent years. Work has been done in the application of soliton theory to the crossed-field device [57]. Early analysis as applied to the crossed-field amplifier in predicting performance was reviewed and found lacking in details [58]. Nonlinear analysis has been pursued by Kaup and Thomas [59] relative to the magnetron and provides

further insight into the complexity of the interaction. Analytical results support some measured data on CFA operation at reduced magnetic fields, which indicates a reduction in noise. This result is supported by measurements on millimeter-wave magnetrons operating at reduced magnetic field that show noise comparable to that of O-type tubes [60].

Usychenko [61] discusses the space charge structure and stability of solitary waves in the crossed-field diode. It is found that stable oscillations exist when the cathode emission is weak. Under high emission conditions the waves are unstable and may result in chaotic behavior of the space charge and excess noise generation. This behavior appears to be related to high noise generation in the magnetron under space-charge-limited operation of the cathode and low-noise generation when the cathode is operated under temperature-limited conditions.

5.2.2. Hartree Threshold Relationship. Lindsay et al. [62] suggested that the Hartree threshold voltage–magnetic field relationship may have a broader interpretation. Usually this relationship has been applied to the voltage–magnetic field relationship that must be met to initiate oscillation in the magnetron. The condition for start of oscillation in the magnetron has experimentally followed closely that predicted by the threshold relationship. It is found by numerical simulation under space-charge-free conditions that electrons can be collected on the anode at anode voltages well below the threshold value. This occurs at normal operating current values and at correspondingly high RF voltage levels. It is probable that the Hartree equation is satisfied under these conditions by the superposition of the reduced anode voltage and the large RF voltage. The range of anode voltage and RF voltage for which the above mentioned threshold condition might hold has not been determined. The extreme conditions for which this rule of thumb may not apply are a minimum RF voltage approximating the start of oscillation-synchronous threshold conditions and a maximum RF voltage approximating the DC anode voltage similar to that occurring in a high-power relativistic magnetron where the RF–electron interaction is highly nonsynchronous.

5.2.3. Radiation Generation in Crossed-Field Devices. An alternate way of looking at the RF generation mechanism in the crossed-field device is considered by Riyopoulos [63,64]. Consistent with elementary theory, electrostatic electron energy is converted into radiation. Total energy and momentum balance during the emission process requires that the change in electron canonical momentum and electrostatic energy be related to a shift of the guiding center location of the electron in a direction perpendicular to the drift velocity of the electron. The incremental change in the electrostatic potential and vector potential due to guiding center shift equal the energy and momentum of the emitted RF quantum. The combined drift plus cyclotron kinetic energy of electron motion are invariant during this interaction process. This analysis is correct to the first order, neglecting second-order effects in E_{rf}/B^2 .

The theory predicts that gain in the CFA is symmetric about the frequency corresponding to that at which perfect

beam–circuit reentrancy occurs. This result is in agreement with Amplitron theory [47] and simulation results [65]. The theory also provides information on the gain per wavelength as a function of the ratio of the height of the space charge hub above the cathode to the anode–cathode spacing.

5.3. Early Crossed-Field Trajectory Calculations; More Recent 2D and 3D Simulations

5.3.1. Analog Computer Computation: Magnetron and Amplitron. In the mid-1950s, prior to the general availability of the digital computer, Feinstein and Kino [66] used an analog computer to solve the equations of motion for electrons in a forward-wave amplifier and an M-type backward-wave oscillator. The computations predicted the performance of these devices under large-signal conditions. It was assumed that the space charge effect on the RF and DC fields could be neglected. Adiabatic motion of the electrons was also assumed. The DC current, generated power, and growth rate of the RF field along the length of the anode circuit were computed.

An alternate approach developed by Brown and described by Zettler et al. [67] employed a large plotting table driven by an analog computer to trace out the x and y positions of an electron in time. The recorder pen was replaced with a probe that sensed electric potentials on a resistive paper sheet placed on the plotting table. The anode–cathode geometry of the magnetron or Amplitron was outlined on the resistive sheet using conductive paint. Assumed RF vane voltages scaled in amplitude and time to give analog voltages were applied to the painted electrodes. Phase shift of the voltage between adjacent vanes was included. The potentials sensed by the probe were used to compute the x and y electric fields for use in solving the equations of motion. The computed x and y position was fed to the plotting table to achieve a closed-loop computation between position coordinates and sensed electric fields. This approach was used by Zettler and Ruden [67] to study the phase focusing mechanism in the magnetron and Amplitron assuming synchronous DC fields and to study the effect of changes of anode vane geometry on efficiency. Use of a slanted anode vane tip designed on the analog trajectory plotting equipment was incorporated into the QK470 magnetron. An efficiency improvement of 5% (absolute) was obtained, and frequency pushing was reduced by an average of 50%. This reduction in pushing provided superior performance of the magnetron in a moving-target-indication (MTI) radar.

Using this same vane shape the efficiency of the QK653 Amplitron, a device used in major airports in the U.S. FAA Air Route Surveillance Radar, was increased by 5–10%.

A round anode vane was also designed and incorporated in the S-band, 400-kW CW power Amplitron. The electronic efficiency of electrons collected on the vane surface was optimized and anode secondary emission energy losses were minimized.

This analog approach was also used to design a broadband VHF Amplitron that employed a single-electron spoke with 10–13 dB of gain occurring over only one guide wavelength of the circuit [68].

5.3.2. Early Self-Consistent Space Charge; 2D Digital Trajectory Calculations in Assumed Space Charge within the Spoke. In 1941 a numerical analysis of the steady-state operation of the magnetron was undertaken by Hartree and Stoner [69]. A relaxation method was employed to adjust the space charge in the interaction space to be consistent with the applied DC electric field, the anode current, and the generated RF electric field. Primary results of the computation were frequency, power, and efficiency. In 1945 self-consistent calculations performed by Tibbs and Wright [70] provided a description of the focusing of the electrons in the interaction space of the magnetron. An instantaneous snapshot of the electrons showed the space charge as having been focused into what were termed “spokes.” This is shown in Fig. 18 for the early British 10-cm, eight-vane, CV 76 magnetron. Although the calculation was run for only one iteration, it was believed that this picture represented steady-state operation.

Further numerical studies of the magnetron had to await the advent of the digital computer. Lehr et al. [71] began a series of computations in 1959 to extend the results of Tibbs and Wright. The computation failed after 36 iterations to converge to a steady-state solution for the imposed condition of space charge limitation of cathode emission. However, a steady-state space charge configuration was obtained under temperature-limited operation of the cathode. Note that magnetrons were normally run in the space charge-limited condition since temperature-limited operation led to degradation of the cathode emission due to ion bombardment of the surface of the oxide cathode. Controversy on operation of the magnetron cathode in the space-charge-limited versus temperature-limited regime had been ongoing since the early 1950s. Experimental confirmation as to the existence of a

low-noise state during temperature-limited operation of an injected-beam amplifier was provided by Little et al. [72]. Noise was high when the cathode was operated in the space-charge-limited state and low when in the temperature-limited state.

Analysis and digital trajectory calculations including space charge effects were made by Dombrowski in 1957 for the magnetron and Amplitron. These computations were based on adiabatic motion of the electrons, which requires constant space charge density within a spoke as predicated by Brown and discussed by Zettler and Dombrowski [67] and employed by Feinstein [66]. An important result of these trajectory calculations was the confirmation that the RF voltage increased linearly along the Amplitron circuit from input to output for a given value of gain as predicted by theory [47] and experimentally measured by Zettler [67]. The trajectory calculations demonstrated that high electronic efficiency occurs in the high-field-output section of the circuit, and provided information on cathode backbombardment power as a function of the assumed space charge distribution in the hub. A movie of the rotating spokes of charge dramatically showed electrons traversing the input-output vanes, thus moving from a low RF potential to a high RF potential region. Because of the inertia of the electrons, the maximum electron collection was not on the output vane but rather occurred downstream from the output. The computed distribution of anode electron collection had excellent agreement with experiment. In addition, details of the electron collection on the cathode were obtained. Information on impact energy, angle of incidence, and spatial distribution of electron collection about the circumference of the cathode provided the impetus to incorporate a cold, secondary emitting platinum cathode into high CW and pulsed power Amplitrons. A paper by Dombrowski and Ruden [73] describes the abovementioned results. Additional information on magnetron and Amplitron calculations can be found in a technical report [74] dealing with self-consistent and adiabatic space charge calculations, analog and digital trajectory calculations, and the early development of a transient space charge simulation program.

5.4. Transient Simulation

Transient calculations of the space charge in the crossed-field device were first applied to the injected-beam crossed-field amplifier by Sedin [75] followed by a magnetron calculation by Yu et al. [76]. Electron-RF wave interaction occurred over a single wavelength and competing circuit modes were not considered. A high degree of turbulence of the space charge was found that had originated in the hub of electrons surrounding the cathode.

Based on the Yu analysis, single moving wavelength particle-in-cell codes were developed by MacDowell [77] for study of the magnetron and the CFA. The magnetron simulations confirmed a turbulent hub condition and the fact that primary and secondary emission dominated states could exist. Turbulence was enhanced when

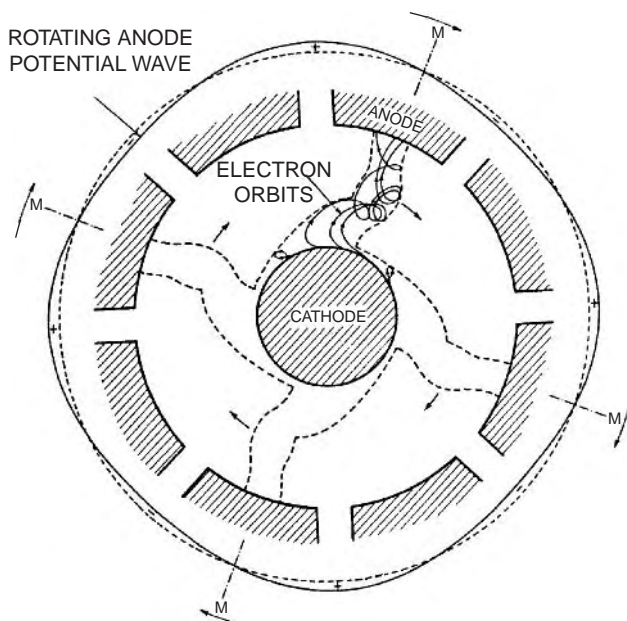


Figure 18. Electron orbits in an eight-segment magnetron. (© IEEE Trans. ED, 1976, H.A.H. Boot and J.T. Randall, Historical notes on the cavity magnetron.)

secondary emission was present; turbulence associated with primary emission was eliminated when a transition was made from the space-charge-limited to the temperature-limited operation of the cathode.

A 2D transient code for the analysis of both the magnetron and the Amplitron was developed by Dombrowski [78]. The code accounted for space charge effects and circuit modes but did not account for electromagnetic modes associated with the volume of the vacuum envelope. A few thousand electrons and timestep of 0.02 RF cycle were used. Simulation results for the 2J32 magnetron were in good agreement with experiment.

This code has been applied to a study of an X-band beacon magnetron [79]. Experimentally this tube showed the Gauss-line discontinuity phenomena. Computationally, the discontinuity occurred at the onset of transition from space-charge-limited operation of the cathode to temperature-limited operation.

Another transient code called MASK was developed by Chernin [80] to study the forward-wave crossed-field amplifier with space charge recirculating in the interaction space between the output and input anode vanes. Circuit properties are handled in a manner similar to that for the Dombrowski code, and the entire interaction space, including a drift space between output and input vanes, is taken into account. This simulation predicts the transition from a high-noise to a low-noise state at a given current level, and a similar discontinuity in voltage as noted above was also observed. Noise was about 20 dB lower than that normally computed for this amplifier design. This reduction of noise was achieved using a primary emitting cathode. The low-noise state was not observed when a secondary emission cathode was used. The results of this simulation are in agreement with measurements made by Ye et al. [81] showing the effect of secondary emission on creating fluctuations of the space charge. It was suggested in this paper that low noise in the crossed-field device might be achieved if the use of the thermionic cathode be reconsidered.

The above-described computations on low-noise, temperature-limited cathode phenomena were highly influenced by a series of measurements made by Brown on the microwave cooking magnetron using a thoriated-tungsten primary emitting cathode. A dramatic reduction of noise was observed by Brown when the cathode was operated in the temperature-limited state [82]. The details of this transition are not understood, but a key observation by Brown indicated that the transition from high to low noise is associated with an increase in anode voltage at a given current, and this appears to be supported by a number of simulations. This phenomenon is believed to be somehow related to the illusive Gauss-line discontinuity problem, where, for the magnetron operating at a given current level, the anode voltage will rise slightly and the magnetron frequency will shift by a few megahertz. The Gauss line discontinuity problem has not been observed in backward-wave Amplitron devices [82]; however, the MASK simulation for the forward-wave CFA shows this anomaly.

Analytic theory and an associated simulation code were used by Schuenemann et al. [83] to compute the steady-state spatial-harmonic operation of a K-band magnetron.

The $\pi/2$ mode of the first backward space-harmonic unit was employed. This mode is of interest for use in millimeter-wave magnetrons as it results in an increase in anode and cathode dimensions with corresponding reduction in power dissipation density. In addition, the strength of the magnetic field is markedly reduced hence minimizing size and weight. The mode separation is large such that a broad tuning range is possible. The computation was made for an 8-mm unstrapped magnetron having a secondary emission cathode that provides for longlived operation at these wavelengths. The anode vane count was 16, and for the $\pi/2$ mode the number of space charge spokes computed was 12 as observed in the interaction space near the anode. An important result was that additional bunching of the space charge occurred near the cathode. Depending on the circuit quality factor Q and level of the RF voltage, the number of bunches near the cathode varied between 4 and 6. The simulation thus predicted the presence of multistable states, the likelihood of which has concerned crossed-field researchers for many years.

Particle simulation studies on optimizing the performance the spatial-harmonic magnetron has concentrated on maximizing of the generated power as a function of the anode resonator dimensions and anode Q [84]. Computations was made for an 8-mm magnetron operating at a magnetic field of 0.5875 T with operation on the backward-wave space-harmonic. The presence of steady-state dual-space-charge configurations was observed in the vicinity of the cathode. The power generated for these two states differed by approximately 3 dB. Further understanding of these phenomena may provide insight into the magnetron problem areas of mode shift, delayed start of oscillation, high-cathode backbombardment at low currents, and noise and spurious signal generation.

5.5. 2D and 3D Electromagnetic Simulation of Crossed-Field Devices

The fully electromagnetic particle-in-cell simulation of the crossed-field device in general solves for electric and magnetic fields created by the charge in the interaction space by solving Maxwell's equations within the volume of the device. The equations of motion include the static magnetic field and account for relativistic effects. The simulation is thus self-consistent in solving both time-dependent and steady-state problems.

The early work of Palevesky et al. [85] on the relativistic magnetron used an electromagnetic code to compute the optimum power generated as function of magnetic field strength at a level somewhat higher than normally employed in S-band magnetrons. The magnetron anode was unstrapped, and it was determined early on that steady-state operation could be obtained in the conventional π mode or 2π mode depending on the cathode diameter. Electromagnetic 2D "Magic" code simulations by Stark et al. [86] and by Weatheral [87] using a single-wavelength, rotating frame-of-reference, 2D code showed that the RF magnetic field had little effect on the interaction process, and that the electron transit time was a fraction of an RF period. When the RF anode voltage is comparable to the applied DC voltage, the interaction is

no longer one of synchronism between the electrons and the RF circuit wave but one of short-transit-time negative-resistance oscillation [16] as proposed by Ruden [88]. Chan et al. [89], using the 2D Magic code to simulate the relativistic magnetron, examined RF output power and electron flow properties, scaling and dependence of emission on fundamental system parameters, and the effect of finite power-supply impedance.

Aspects of phase locking of a rising-sun, L-band, 100-MW pulsed magnetron were studied using the 2D Magic code by Chen et al. [90]. A technique was developed that reveals the dynamical behavior of frequency and phase during the phase-locking process. Without a drive signal, the development of an oscillation takes 50–100 RF cycles and low-level noise is generated during this time interval. With a locking drive signal the power buildup occurs within 20–30 cycles, and noise is almost completely eliminated.

An important application of the 2D Magic code by Jones et al. [91] has been to introduce an analytical expression for a variation of the axial magnetic field in azimuth in the interaction space of the magnetron. This perturbation selectively develops the pi-mode space charge configuration in the vicinity of the cathode. This prebunching action results in rapid buildup of the magnetron oscillation to steady state.

5.6. 3D Simulation

A revision of the Magic code allows analysis of three-dimensional structures and has been applied to the rising-sun magnetron, the strapped magnetron, and the relativistic magnetron. The time to complete a simulation run resulting in a steady-state solution is highly dependent on the number of particles employed; runs of 40–120 h are common such that obtaining the performance of a device over a wide range of operating parameters is rarely practical. It is difficult, therefore, to state whether the simulation truly represents the actual performance of the device. Perhaps limiting the number of particles is an option in obtaining a rough general view of the operation, but in dealing quantitatively with starting processes and noise generation mechanisms, it is probable that fine detail will be required, and hence will require many particles. Users of the code have suggested modifying the code to stop the computation after a number of cycles and then to be able to restart the calculation with a change in operating parameters such as, for example, voltage and magnetic field. This would allow a performance chart to be readily developed from the data.

Kim et al. [92] have used the 3D Magic code to simulate a 250-kW, 28-kV, X-band rising-sun magnetron. A study of the modes of the rising-sun structure showed a discrepancy between an analytic computation and the Magic simulation. The pi-mode frequency agreed with experiment, but experimental data for the other modes were not provided. At the start of oscillation, leakage current to the endspaces was reduced and single-frequency pi-mode oscillation was obtained. No other spoke configurations were reported as occurring during buildup of the oscillation. It is to be noted that the magnitude of the applied magnetic field and the anode voltage are ramped up in time. This

combination of time-varying voltage and magnetic field may inhibit the development of spokes (space charge perturbations) of varying periodicity in azimuth as the space charge hub develops.

The 3D Magic code is capable of analyzing the strapped magnetron. The understanding of the noise-generating mechanisms and the nature of low-noise operation of the microwave oven magnetron and commercial high-power CW magnetrons is important relative to the level of noise within the ISM band and at harmonic frequencies. Results of Kim et al. [93] using the Magic code confirm the pi-mode oscillation, and computed harmonics and higher modes as determined by Magic have been compared to experimental data. The possible competition of the adjacent $\pi - 1$ mode and details on other spurious oscillations are presently not available. Modeling of a high-power CW magnetron with and without straps has been done by Jung et al. [94]. Resonant frequencies, resonant modes, and higher harmonics of the fundamental frequency were identified.

These efforts have been directed mainly at demonstrating the basic performance of the tubes. The important issue of noise mechanisms has not been addressed at this time. This issue is highly dependent on the cathode emission algorithm, and it is not clear whether the present “explosive” and “thermionic” emission algorithms are adequate for the study of noise close to the carrier.

Modeling of a strapped X-band magnetron MG5241 using 3D Magic is discussed in a paper by Ma et al. [95]. Basic resonant frequency computations agreed well with experiment for both cold and hot tests. While experimental-versus-computed agreement was obtained for the input voltage and current, the electronic efficiency did not agree. This problem has been addressed in the simulation by accounting for leakage current due to end-hat emission [96]. Concerns with regard to the cathode electron emission model have also been addressed. The emission models as “explosive emission” and “space-charge-limited emission” are being replaced with a model that can be used to vary the cathode emission density. This later emission model has properties similar to those employed by the Dombrowski magnetron-Amplatron simulation [78]. Unpublished data obtained with the latter simulation code suggest that the starting time of the magnetron is highly dependent on the particular emission model. The space-charge-limited model has a factor of roughly twice the time delay of that of the temperature-limited model. Finally, a major improvement [95] in the 3D Magic code is the modeling of the cathode end hat, and modeling of the actual variation of magnetic field in the interaction space, which has yielded simulation results very different from those for the uniform field. The ability to fully model variations in both the electric and magnetic fields and end-hat geometry that affects electron leakage and confinement in the magnetron is important in the study of noise. (*Note:* Experimental changes in end-hat design and magnetic field uniformity in the region of the cathode endspace have reduced conductive noise in the microwave oven magnetron 2M172A as compared to its predecessor the 2M172 [97].)

Two analyses of the relativistic magnetron have been made using different 3D codes. Arter and Eastwood [98]

developed a 3D PIC code to model a mechanically-tuned rising-sun magnetron design. A comparison of results of the 3D simulation with a 2D simulation showed that maximum efficiency occurs close to the Buneman–Hartree threshold voltage. It is not clear whether this statement holds for conditions approximating negative-resistance oscillation. Simulation time corresponding to onset of oscillation was some 100 ns and computationally quite long, placing a limit on the amount of performance data that can be obtained. The simulations also show mode competition that may terminate operation. This observation may be related to one aspect of the upper current-mode boundary limitation that occurs in many magnetrons and CFAs. The simulations also indicate that one cause of pulse shortening in magnetrons may be related to droop of the voltage pulse. Suggested corrective action would be to tailor the anode voltage to increase during the pulse. Such pulseshaping may have application to the pulse shortening observed in relativistic magnetrons.

The 3D code Quicksilver developed by Lemke et al. [99] has also provided a detailed analysis of operation of the relativistic magnetron. The simulation addressed the reproduction of the experimental results of the Palevsky–Bekefi A6 magnetron [100]. The simulation provided close agreement with experimental results and confirmed that the use of endcaps markedly increases efficiency by reduction of leakage current. The pulse voltage feed to the cathode can be either single-ended or double-ended. From an electromagnetic perspective, potential problems as to the effect of single-versus double-ended voltage feed on the space charge close to the cathode have not been analyzed.

The operation of the relativistic magnetron at voltages substantially above the Buneman–Hartree threshold as compared to nonrelativistic magnetrons appears to suggest that nonsynchronous interaction may be dominant. Design criteria for high efficiency in this regime have not been met [88].

5.7. Analysis of the Crossed-Field Diode

The stability of the space charge in the crossed-field diode has been investigated over several years by researchers at the University of Michigan. Mechanisms that limit the current in a crossed-field gap were analyzed by Christenson and Lau [101] using PDP1, a one-dimensional electrostatic particle-in-cell (PIC) code [102], investigating the transition from laminar to turbulent flow in the space-charge sheath under conditions of cutoff and the excitation of a modulational instability caused by small AC voltages applied across the gap. Christenson et al. [103] also found that crossed-field cycloidal flows are extremely unstable even when the emission current density is a small fraction of the limiting value. A small resistance in the external circuit, a small RF voltage, or a small tilt in the magnetic field would disrupt the cycloidal flow; the end result is always a near-Brillouin state that consists of the classical Brillouin flow superimposed on a turbulent background.

The sensitivity of the crossed-field diode to asymmetry of emission about the cathode surface is illustrated by disturbing the uniform emission with nonemission sites, as shown by Ruden et al. [104]. This simulates nonuniform

emission from the surface of the cathode. It is found that a transition occurs from the stable diode state to one consisting of azimuthally bunched clusters with azimuth periodicity dependent on the time of evolution. This phenomenon is akin to that of the azimuth magnetic field effects described above. As time progresses, the perturbed diode states interact with one another, producing turbulence. This chaotic behavior leads to the creation of streams of secular electrons beyond the crude hub layer. Such bunching and secular electrons have been observed in both 2D electrostatic codes and 2D/3D electromagnetic codes but are not at all understood. These phenomena appear to have some relationship to that described by Schuenemann [83] and may be some what dependent on the model employed for electron emission from the cathode.

Luginsland et al. [105], applying the 3D Magic code to the strapped “cooker” magnetron, extended the 2D simulations described above [91] to show that the periodic placement of permanent magnets about the anode cylinder results in fast startup of the magnetron and demonstrated that under DC operating conditions both sideband spurious signals and noise generated at low anode currents can be eliminated or greatly reduced.

6. THE NOISE PROBLEM

The cooker magnetron is a great success because it is efficient besides being inexpensive. It seems, however, that a concomitant of efficiency is “noise” or an array of spurious signals. This subject has been prominent in all varieties of magnetrons and its derivatives and helped trigger the extensive computer modeling (see Section 5) of amplifier and oscillators derived from the magnetron. Even before World War II it was recognized [8] that the magnetron space charge was unstable without a circuit and that even with a circuit there remained numerous sources of anomalous noise—including discrete signals anywhere in the spectrum.

Many studies [106] of the magnetron diode showed that the magnetron space charge, through its instability, generated signals that were voltage-tunable and corresponded to conditions of “velocity resonance” of n spokes of space charge revolving around the cathode, thus yielding frequencies that obeyed empirical relationships such as

$$f_n = (k/n)(V_a/B) \quad (15)$$

where k is some constant, n is a mode number corresponding to the number of space charge perturbations or “spokes” around the cathode, and V_a and B are the anode voltage and magnetic field, respectively. This space charge instability in crossed fields was dubbed [106] the “diocotron” effect by researchers at CSF (Compagnie Générale de Telegraphie Sans Fil). Those workers in France along with counterparts in the United States [107] found that a satisfying theory could be found for the analogous instabilities in a thin beam moving through crossed fields, but theoretical studies of the full magnetron space charge remain controversial if not intractable to this day. In

addition such linear beam interaction theories were able to predict thresholds for spurious sidebands in M-type backward-wave oscillators (BWO). In this tube the basic issues are exactly when the beam-circuit interaction results in start of oscillations at the desired frequency and when it further allows “spurious” sidebands to be generated. The answers, in terms of “starting currents,” can be derived from the small-signal theories. One finds as beam current is raised first a starting current for the desired oscillation and at some higher starting current (perhaps 2–3 times higher) the generation of sidebands at a frequency Δf , which is of the order of 1–2% of the desired oscillation frequency. At still higher currents the sidebands may begin to show their own sidebands and soon there will be “noise” sidebands in place of discrete coherent spurious signals. This pattern corresponds to the general pattern of modern “chaotic” phenomena [108]. The small-signal theories [106,107] for the thin beam provide a satisfying framework for predicting the regions of current with different “noise.” This theory employs two parameters, one, which we call p , proportional to beam current and another, which we call q , which is proportional to circuit field strength or its “coupling impedance.” One finds that if $q \gg p$, then space charge effects are minimum, but if $p \gg q$, then space charge effects are dominant. No such theory exists for the magnetron (see Section 5). One can perceive, however, the pattern for “chaos” in the magnetron in analogy to the M-type BWO. In Section 4, we showed that as anode current is raised, we pass successively through preoscillation, noise, discrete spurious signals, and finally no-noise or low-noise (“quiet”) regions. Note that this succession with magnetron anode current is inverse to that in the M-BWO with beam current. This is because the true analog in the magnetron to beam current is not anode current but the rotating space charge current. This rotating current and the attendant space charge density is reasonably the highest before start of oscillation (at approximately zero anode current) and then decreases as anode current draws off some of the rotating current.

Space charge effects thus can cause the appearance of many spurious signals and noise in the cooker magnetron, especially because it passes through all regions from preoscillation to the “quiet” state during each cycle. (In contrast, Brown has proposed [82] DC operation of magnetronlike devices in the “quiet” region as a way of minimizing “noise.”)

Besides all the possible signals and noise deriving from space charge effects, there are also a multitude of signals that can result from more conventional electron–circuit interaction, recognizing that the anode structure is characterized by many resonant modes. Furthermore, even though the successful type of interaction in the magnetron is one of “velocity synchronism or resonance,” there are other modes of interaction related to the cyclotron interaction principle. We can most easily discuss the relevant principles by using the language of simple linear beam interaction, where there is a beam moving with velocity v_e and a circuit-supported wave of electric field moving at a speed (phase velocity) v_0 . It is necessary at this point to introduce some notation for this “wave” that derives from modern understanding of periodic structures [6]. When

power is transmitted through or along a periodic structure there is an infinite set of spatial harmonics that make up the total propagating disturbance. Some of these harmonics, which can include the “fundamental” with longest wavelength, propagate in the same direction as the power flow. We call these harmonics or waves “direct” spatial harmonics. There is also a corresponding set of harmonics, which can include the “fundamental” (but not at the same time as the alternate possibility referred to above) that propagate in the direction opposite to the power flow. We call these spatial harmonics “reverse.”

Now in general beam–circuit interaction there is the beam direction, which we will call “forward”; then there is the direction of power flow on the circuit, which we call “forward” if in the same direction as the beam and “backward” if in the direction opposite to the beam. Then there are several alternate resonance or interaction conditions. The first is velocity resonance:

$$V_e = V_0 \text{ or } c/v_e = c/v_0 \quad (16)$$

This corresponds to most conventional interactions in any circuit mode as described in the Hartree voltage relation (14). In addition there are “cyclotron-mode interactions” for which the resonance relations are

$$c/v_0 = c/v_e(1 \pm \lambda/\lambda_c) \quad (17)$$

where $\lambda = c/f$, where f is the operating or interacting frequency and $\lambda_c = c/f_c$, where f_c is the cyclotron frequency.

There are a considerable variety in the possible interactions for which the resonance relations (16) and (17) apply. These are depicted in Fig. 19, which is a $c/v-\lambda$ plot, the equivalent of the more popular ω/β chart, but in which the relations for resonance are more easily pictured. We see that for the velocity resonance condition (16) that the normal situation applies where a forward-wave amplifier exists only with interaction with a direct harmonic wave (FD0) and backward-wave oscillation occurs only with a reverse harmonic (BR0). But equation (17) shows that with the “fast wave” cyclotron resonance case [a minus in Eq. (17) and the downward branch in Fig. 19] we can have forward-wave amplification with a reverse harmonic (FR⁻) as well as backward-wave oscillation with a direct harmonic (BD⁻). We conclude that there is a rich variety of possible resonance interactions that could lead to signal generation in a magnetron during “moding” or even in the presence of the desired oscillation. Classical nonlinear theory [7,15,106] would suggest that the presence of a strong oscillation should suppress buildup of any competing oscillation. This may be true in general when the same interaction mechanism applies for the two competing modes. But because the “cyclotron resonance” is independent or in a sense orthogonal to velocity resonance, the two may possibly coexist. In any case there have been a number of experimental observations of simultaneous oscillations in magnetrons, and certainly they exist at serious “noise” levels of concern to regulators even though they are far from the power level in the π mode.

In addition, some oscillations are connected with endspace resonances. These were observed in early

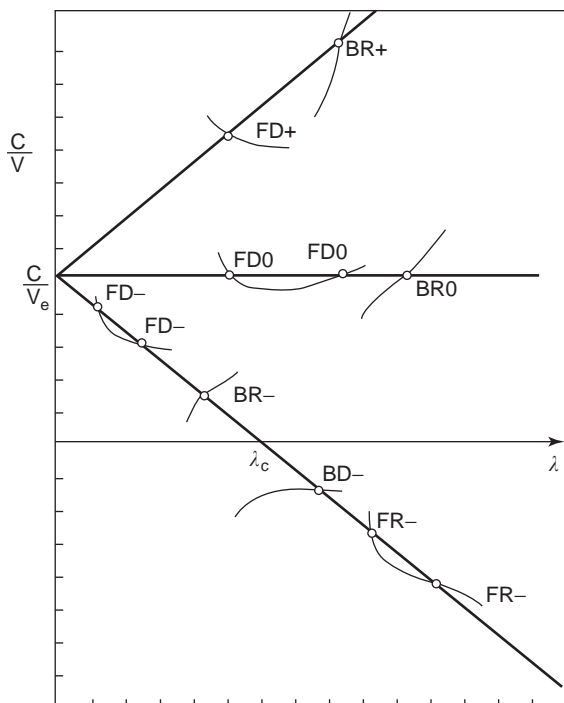


Figure 19. Diagram depicting various interaction modes in a crossed-field tube on the $c/v-\lambda$ chart for periodic structure propagation.

magnetron work [15], and more recently they have been observed as out-of-band signals from cooker magnetrons [109]. Note that these “axial oscillations” tend to strengthen with current up to the peak current while many spurious signals occur only at low or moderate currents.

It is no surprise that the magnetron emits a copious amount of spurious signals and noise across the whole spectrum. In Fig. 20 we see a typical baseband spectrum measured near a microwave oven. Much, if not most, of this energy is associated with spurious space charge phenomena, but not all. Some of it is due to axial oscillations, and some signals defy explanation. In Fig. 21 we see a

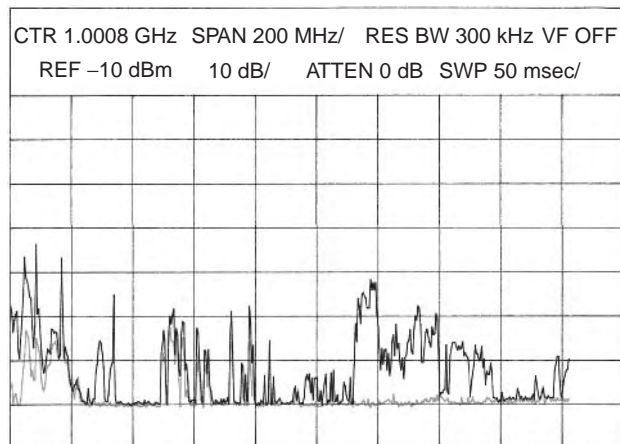


Figure 20. A typical baseband spectrum measured near a modern microwave oven (lower curve is background). (This figure is available in full color at <http://www.mrw.interscience.wiley.com/erfme>.)

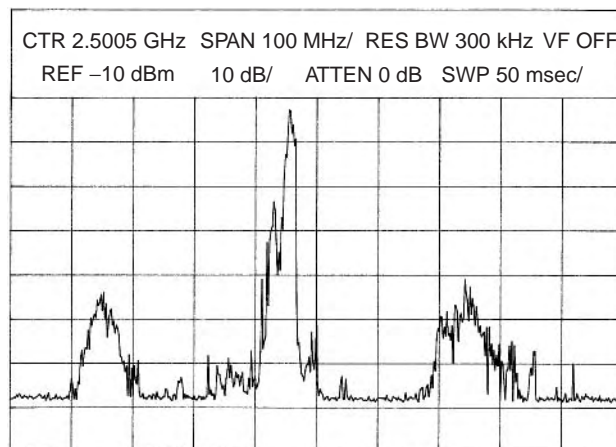


Figure 21. Typical spectrum around 2.45 GHz emitted by a modern microwave oven.

typical spectrum around the main signal at ~ 2.45 GHz. The expected sidebands are in evidence. In Fig. 22 we show a typical result of a compliance test for a microwave oven across the spectrum from 1 to 18 GHz. Only the more prominent signals are shown, signals at harmonic frequencies are expected, but their behavior is not always understood. Other signals are difficult to explain, and in some cases there is reason to believe that parametric interactions [110] may be operating. In Fig. 23 we see a typical waveform for an out-of-band signal, which occurs mostly at low and moderate anode current and thus occurs only during a millisecond or so at the beginning and end of the 50/60-Hz half-cycle when the tube is operating. This opens up the possibility of avoiding interference from the magnetron by transmitting information only when the magnetron is not emitting noise. It should not be forgotten that there are, however, signals, sometimes at peak currents—as in the case of axial oscillations.

The bottom line is that inherently the cooker magnetron is a prolific noise generator that is compounded in the microwave oven application by all variables such as current, stirrer positions, and temperature load changes. For this reason, special attention was devoted to the development of emission limits for microwave ovens. In Tables 2 and 3 we list the limits [111] issued by the CISPR committee of the IEC (International Electrotechnical Committee). Those in Table 2 are for the frequency range below 1 GHz and are quasipeak limits, while Table 3 applies to frequencies above 1 GHz and presents peak limits. While some relaxation is given in the lower sideband region, the limits are tightened elsewhere, particularly around the fifth harmonic, which is close to some satellite TV bands. Note that as of yet, the compliance tests apply only to time after the oven and magnetron have started. The noise and moding signals during the moding period shown in Fig. 16 are not measured or regulated.

Noise and radiofrequency interference are becoming more serious issues as expanding wireless systems [112] develop in the microwave bands above 1 GHz. Of particular concern are the systems that share the ISM band at 2.45 GHz, but there exists RFI potential in many other

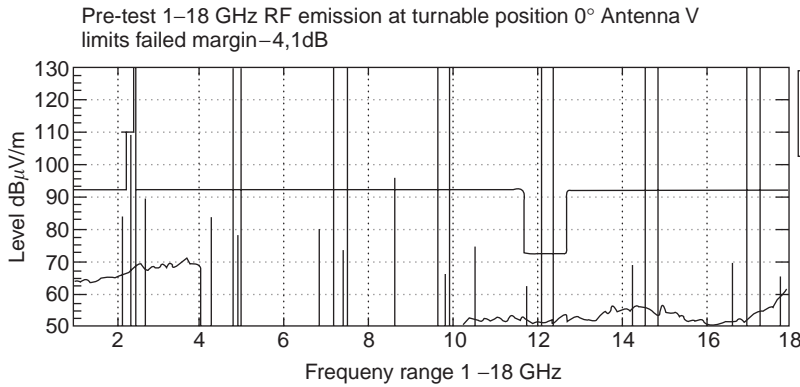


Figure 22. Chart of measured microwave oven emissions in a test for compliance with CISPR 11 limits.

bands—For example, in the satellite radio band located between 2.3 and 2.4 GHz.

Heretofore magnetron developers and manufactures have found no easy solution to the “noise problem,” and it is not likely that one is forthcoming soon. In the meantime oven manufacturers must employ a wide variety of

fixes, sometimes with ingenuity, in the face of such a complex set of phenomena. Note that simple filtering is not the answer, even if it were cost-effective. Filters that reflect energy can also modify the harmonic levels and other signal levels in the magnetron as well. Still a better understanding of the origin of the signals in the magnetron will be helpful, and much work remains in this area.

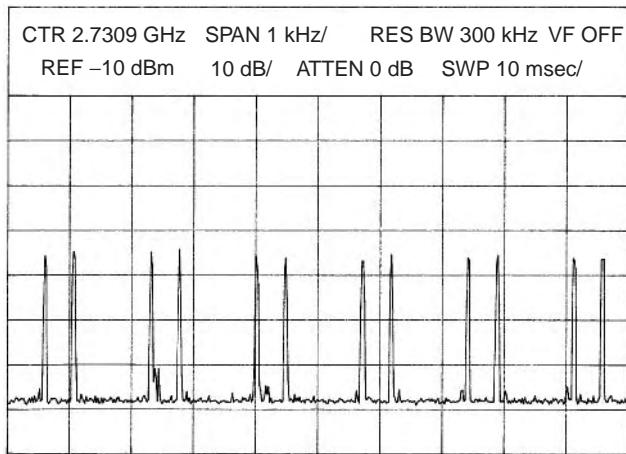


Figure 23. Waveform of a typical out-of-band signal emitted from a microwave oven (spectrum analyzer in line sync condition).

7. TECHNOLOGICAL DEVELOPMENTS

Two devices that have demonstrated excellent performance employ technology that is important in obtaining low-noise operation of the crossed-field device and power generation at millimeter wavelengths. The voltage-tuned magnetron is discussed relative to both noise and a more recent millimeter-wave application, and the beacon magnetron for its high-frequency design features. Both devices have required marked attention to manufacturing details to achieve a high level of performance.

Technology developments for commercial, industrial, and military applications include injection locking of the magnetron, cathode-driven CFA, millimeter-wave tubes and harmonic generation, high peak and average power CFA, relativistic magnetron, and large anode area devices for high-power microwave (HPM) and millimeter-wave applications.

Table 2. CISPR 11 Limits on Microwave Oven Emissions at 10 m, and 0-1 GHz

Frequency Band (MHz)	Electric Field		Magnetic Field
	Quasipeak [dB(μV/m)]	Average [DB(μV/m)]	Quasipeak [dB(μA/m)]
0.15-30	—	—	39 Decreasing linearly with logarithm of frequency to 3
30-80.872	30	25	—
80.872-81.848	50	45	—
81.848-134.786	30	25	—
134.786-136.414	50	45	—
135.414-230	30	25	—
230-1000	37	32	—

Table 3. CISPR 11 Limits on Microwave Oven Emissions^a at 3 m and 1-18 GHz

Frequency Band (GHz)	Field Strength [dB(μV/m)]
	Peak
1-2.3	92
2.3-2.4	110
2.5-5,725	92
5.875-11.7	92
11.7-12.7	73
12.7-18	92
	Average
1-2.4	60
2.5-5.725	60
5.875-18	60

^aOut-of-band emissions limited to 70 dB(μV/m) peak or both peak and average limits listed above; resolution bandwidth of 1 MHz; average measurements with 10 Hz video bandwidth.

7.1. The Voltage-Tuned Magnetron: Past Performance and Potential Application

The voltage-tuned magnetron (VTM) has had application as a low-power, CW, microwave signal source at frequencies extending from 200 MHz to above 10 GHz. At power levels of milliwatts to a few watts, these devices are capable of being tuned over a 2/1 and 3/1 range of frequency. High-power tubes have 10–30% tuning range, which depends on the frequency band. These tubes have been used in electronic countermeasures and as general sources of microwave power for test and evaluation of microwave systems. Typical VTM performance is 400 W (minimum) from 2.7 to 3.5 GHz at 65% efficiency and 100 W from 9 to 10 GHz at about 50% efficiency.

A paper by Weinstein and Winkowski [113] summarized the status of the VTM as of 1977. These devices are magnetically shielded, typically integrated with wideband isolators to permit operation into variable load impedance, can be conduction-cooled as a result of high efficiency, are robust in terms of operation under extreme vibration and shock conditions, generate very low noise, and have excellent shelf life.

To achieve wide tuning, the VTM employs an interdigital anode circuit [114]. The transmission-line circuit is closed on itself in a manner similar to that for the conventional magnetron anode with phase shift of 180° between anode electrodes thus operating in the pi mode. The transmission line can be heavily and uniformly coupled to the load for wide frequency tuning at low power, and nominally coupled for limited tuning at high power.

In the conventional magnetron operating under a condition of space-charge-limited emission an increase in anode voltage produces an increase in anode current. This is accompanied by a small shift in frequency termed “pushing.” In the VTM an electron gun injects electrons axially into the interaction space between a dummy cathode electrode and the anode. The current injected into the interaction space is controlled by adjustment of a voltage applied to a control electrode in the gun. A change in anode voltage at constant anode current produces a change in the azimuth angular velocity of the electrons with an associated increase in frequency such that synchronism is maintained between the rotating electrons and the RF voltage wave supported by the anode circuit. The oscillation frequency is directly proportional to the anode voltage. By sweeping the anode voltage, the frequency can be modulated at rates of 60 MHz. Higher rates can be obtained by aboveground operation of the anode (positive anode operation).

High-power CW tubes with tuning of 10–20% have a spectrum quality that exceeds that obtained from high- Q magnetrons. Limited published data [115] show a noise level of -110 dBc/Hz at 10 kHz offset from the carrier and -150 dBc/Hz extending from 100 kHz to 100 MHz. Other data at 30 MHz offset from the carrier the noise are -160 dBc/Hz and harmonic power -60 dBc [116]. The close-in noise data are consistent with those obtained from the microwave cooker magnetron when operated with a thoriated tungsten cathode operated in the temperature-limited regime. The data suggest that the VTM may be an

ideal vehicle for the study of crossed-field noise generating mechanisms.

It is expected that injection locking of the VTM would further reduce the noise close to the carrier. Since with an injected beam the electron stream is located at large radii, it is probable the locking gain will be higher than that of the conventional magnetron.

A possible application of the VTM principle is to excite multimode microwave cavities for improving the heating or processing of materials and for the generation of large-volume gaseous plasmas. Multikilowatt power can be generated using the vane and strapped S- and C-band magnetron circuits with an axially injected electron beam. The cost of a high-power VTM would be substantially lower than the cost of the traveling-wave tube previously considered for such applications.

Low unit cost, compact size, low weight, excellent spectrum quality, and high reliability under shock and vibration conditions suggest that the VTM is a potential competitor with the beacon magnetron in airborne transponder applications. The VTM should also have application as highly stabilized, tunable oscillator at millimeter wavelengths for radar applications. A high-power, injection-locked harmonic generator is based on the VTM principle is discussed below.

7.2. Beacon Magnetron

The beacon magnetron is a high-frequency, low-peak-power and average-power magnetron optimized for frequency and pulse stability, low jitter, ruggedness, and reliability, which are critical parameters for use in beacon, transponder, fuze, weather, and marine radar applications [117]. This is achieved by design improvements such as making the cathode more rugged, temperature compensation, and output matching to control frequency pulling (change in magnetron frequency with variation of load VSWR). Frequency pushing is controlled by careful interaction space design and by suitably mating the magnetron to the modulator to ensure generation of a flat-top current pulse. Low pulse to pulse frequency jitter and pulse starting-time jitter is obtained by ensuring adequate and uniform cathode emission, careful vacuum processing of the tube, and optimization of the rate of rise of the modulator voltage pulse. Size and weight reduction has been generally achieved with optimizing the design of magnet pole pieces and Alnico magnet location [118].

A design approach presented by Hobbs [119] that provides additional advantages is that of the positive anode magnetron. The magnetron anode is isolated from ground and pulsed positively; the cathode and magnet pole structure are grounded. Axial beam confinement is done by the magnet pole tips now placed closer to the anode. This reduces the amount of magnetic material required to provide the necessary field level and results in improved uniformity of the field. Use of the higher-reluctance Alnico materials or the rare-earth cobalt materials allows placement of the magnet close to the interaction space, reduces energy loss, and again reduces magnet and return path size and weight.

The cathode and the magnet pole tips are at the same DC potential, which allows more accurate centering of the cathode with respect to the anode via the use of thermally insulating spacers near the interaction space. Both electric and magnetic fields in the interaction space are more uniform with the result of reduced starting jitter and lower startup noise, lower frequency pushing, and cleaner spectra. Efficiency is improved by about 5% as compared to the conventional beacon structure. Typical peak power for fixed-tune devices at X band is 1–10 kW at 0.001 duty factor and 0.1–5.0 μ s pulsewidth, and weight and volume are approximately 0.6 lb and 7 in³.

The beacon magnetron design philosophy has been carried over to the millimeter-wave regime. Noise suppression and tuning over a finite frequency range is managed via injection locking as discussed below.

7.3. Injection Locking

Injection locking of the magnetron is the control the frequency of the free-running magnetron oscillation by means of an external drive signal. The magnitude of the locking signal affects the locking bandwidth; specifically, the change of oscillator frequency Δf controllable by the drive frequency is determined by

$$\Delta f = (2f_0/Q_e)[P_{in}/P_{out}]^{1/2} \quad (18)$$

where f_0 is the frequency of the free-running magnetron, the ratio P_{out}/P_{in} is the pseudogain, and Q_e is the external quality factor of the magnetron. Depending on the particular magnetron, the drive power necessary to provide frequency locking can vary from 10 to 30 dB below the carrier. Larger bandwidth is obtained at the higher drive levels. In addition, higher drive reduces both the time to achieve lock from the start of buildup of oscillations, and in the steady-state locked condition the noise level close to the carrier is reduced as compared to that of the free-running oscillator [118].

Data on phase noise–frequency offset from the carrier for a pulsed, 10 W, X-band positive anode magnetron MA2829 was obtained by Hobbs [120]. With a magnetron Q_e of 185 and gain of 10 dB, the coherent bandwidth was 0.34%. From 1 to 100 kHz offset the noise was reasonably flat at -113 dBc/Hz at center frequency while improving at the lower band edge to -115 dBc/Hz and degrading to -100 dBc/Hz at the upper band edge. With a Q_e of 80, corresponding to increased coupling to the load, the coherent bandwidth was increased to 4%. The noise over the same offset range as above was a minimum at -115 dBc/Hz at center frequency. The noise was -111 dBc/Hz at the lower band edge and -108 dBc/Hz at the upper band edge, representing an overall improvement at the lower value of Q_e .

These noise data are consistent with results of English [121] and Garrigus [122] where noise for injection-locked magnetrons lies within the range from -120 to -90 dBc/Hz.

A marked improvement in the noise of the injection locked microwave oven magnetron has been obtained by Brown [123]. The technique employed was to reduce the filament power to the magnetron such that the tube

operated in a temperature-limited emission regime as compared to the conventional a space-charge-limited regime. Historically, prior to 1958 it was recognized that operation of the magnetron had reduced noise when operated with the cathode temperature-limited as compared to the same magnetron operating in the space-charge-limited state. It was also recognized that cathodes available at that time tended to lose emission (*poison*) when operated temperature-limited. Concern on magnetron life and reliability hindered further research at that time. Research on developing a low-noise magnetron operating with space-charge-limited emission was pursued but has not been achieved to date.

The carburized thoriated tungsten cathode employed in the microwave oven magnetron is quite stable under temperature-limited operation. The low-noise performance potentially has application to commercial and industrial magnetrons and to crossed-field devices that might be considered for use in the area of microwave power transmission. CW testing of the oven magnetron at reduced magnetron filament power has shown improved noise performance for both the free-running oscillator and for the injection-locked oscillator (directional magnetron amplifier) with the lowest noise measured when the magnetron frequency is controlled by a drive signal. The measured noise can be as low as -197 dBc/Hz with the imposed conditions of temperature-limited operation of the cathode and the introduction of a cathode impedance that minimizes resonant coupling to the cathode.

A comprehensive historical review of magnetron and crossed-field amplifier noise has been prepared by Brown [123], and details of the experiments and noise measurements have been documented [124].

An approach to increase the locking bandwidth while maintaining the frequency and phase stability of the coherent drive source by the cascading of injection-locked magnetrons has been described [121]. The advantage of cascading is illustrated by the following example.

Example. A basic X-band 1-kW magnetron with a of Q_e 40 and coherent drive source of 10 W provides a 50 MHz locking bandwidth. The bandwidth is adequate to overcome environmental frequency drifts, resulting in a coherent frequency power source such as, for example, missile fuze systems and weather radar. If two magnetrons were cascaded, the 10 W drive source would produce a bandwidth of 158 MHz. It was projected that a fractional bandwidth of 2% at 10–13 dB gain per stage was achievable.

At Ku band the noise output of an injection-locked magnetron chain was less than -105 dBc/Hz. This value is within the general range of injection-locked noise from -120 to -90 dBc/Hz.

7.4. Cathode-Driven Crossed-Field Amplifier

Marked improvement in both gain and noise of the crossed-field amplifier has been obtained with a modified Amplitron experimental device where an RF drive signal is applied to both an anode and cathode slow-wave structure [125]. The standard S-band CFA typically operated at 10–15 dB gain and signal-to-noise ratio (SNR) of 45–50 dB/MHz. The modified S-band CFA provided gain of 20 dB

and noise-level values of 75 dB/MHz, which is comparable to that achieved by injection-locked magnetrons and linear beam devices. The noise level is consistent with that required for high-power radar applications.

These data are consistent with identifying the noise generating regime in the CFA as being related to mechanisms associated with the continuous cathode. The data are also in accord with previously described voltage-tunable magnetron low-noise data where the electron stream is provided by axial injection into the interaction space rather than a concentric anode-cathode geometry.

7.5. Voltage-Tunable Frequency Multiplier

The application of the principles of the voltage-tuned magnetron to achieve frequency multiplication has resulted in a tube design that has potential for millimeter-wave applications. Two VTM-like devices are cascaded within a single vacuum envelope. The coupling between the two circuits is performed by the rotating, bunched, and axially traveling space charge developed in the input VTM section. The input circuit consists of an interdigital line structure coupled to a quasitoroidal resonator. A low- Q composite resonator system is formed that supports a pi-mode voltage distribution on the interdigital fingers. The output structure has a similar circuit, but the number of interdigital fingers is multiplied by the harmonic number [126].

The harmonic operation of the device is dependent on creation of space charge spokes that have high harmonic content, which in turn is dependent on the spatial distribution of the electrons in the spoke. Numerical simulation of the space charge should play a role in determining the space charge harmonic content as a function of the design and operating parameters.

The device can operate in one of two ways: (1) the drive circuit can be allowed to oscillate, and the resultant space charge will drive the output circuit; or (2) alternatively a low-power locking signal can be applied to the drive circuit at the fundamental frequency. This signal is used to control the space charge and frequency of the input device and results in an effective power gain from the output circuit. The phase of the output signal is determined by the phase of the input signal.

An output power of 430 W was obtained in the 10 cm wavelength range when operating at the fourth harmonic of the fundamental frequency of the drive circuit. Gain was 23 dB, electronic efficiency was 52%, and the tube operated over a frequency band of 15%. The frequency was linear with a voltage that is consistent with voltage-tunable magnetron operation.

The pi-mode interdigital circuit provides bandwidth but will have limited average power capability at high frequencies. The use of the unstrapped-vane-type magnetron circuit, which is capable of high average power when operating in a non-pi space-harmonic mode, may be applicable to the dual-circuit VTM concept.

7.6. Millimeter-Wave Sources

7.6.1. Magnetron Millimeter-Wave Sources. Early millimeter-wave magnetrons used the rising-sun anode structure and operated in the pi mode. The Amperex DX287

developed in 1966 generated power at a fixed frequency close to 95 GHz. The tube delivered 10 kW of RF power at pulsewidths between 5 and 200 nanoseconds (ns) and at duty cycles up to 0.0002. Efficiency was about 8%, and using an impregnated type cathode the life was ~ 500 h. The tubes operated stably into a load VSWR of 1.5–1. Permanent, stabilized magnets of ticonal weighing 15 lb were employed [127].

Improvements in the millimeter-wave magnetron have focused on using samarium-cobalt magnet structures to reduce size and weight, cathode design capable of providing the high emission densities compatible with achieving high average power, high reliability, and long life. The EEV MG5294 95 GHz magnetron, delivers 2.5 kW, a 50 ns pulsewidth, and a duty cycle of 0.0002 corresponding to 0.5 W of average power. Maximum load VSWR is 1.3–1; typical test VSWR is 1.15–1. The tube has an overall length of 5.8 in. diameter of 2.6 in. and weight of 2 lb [128].

Substantial progress has also been made since the mid-1990s using the unstrapped magnetron anode operating in a space harmonic of the fundamental [129]. Typical performance at 95 GHz is 4 kW peak power and 2 W average power at a pulse duration of 50–200 ns and a pulse repetition frequency of 5 kHz (maximum). The magnetron is packaged with a solid-state modulator; total volume is 183 in.³ and weight is 8.8 lb. The transmitter is designed for airborne applications. Space-harmonic millimeter-wave magnetrons have also been employed in practical radar systems [130,131].

Research on alternate M-type oscillators at millimeter wavelengths is being carried out by Kulagin and Yeryomka [132]. The RF circuit is that of the unstrapped magnetron with an axial injected large-orbit electron stream. Operation at lower values of magnetic field and voltage is possible when compared to the magnetron operating in the pi mode with small-orbit electron streams originating from the conventional continuous cathode, which is concentric with the anode. Typical analytical results are wavelength of ~ 1.9 mm, anode voltage of 2 kV at a magnetic field of 0.5 T, and efficiency of 12%. Additional reduction in magnetic field is possible by the use of the interaction of the large-orbit stream with an anode space harmonic [133].

Typical applications for millimeter-wave magnetrons as sources are active missile terminal homing systems, detection of small stationary targets, high-resolution surveillance and MTI radar, and lightweight radars in remotely piloted vehicles.

7.6.2. Millimeter-Wave High-Gain Crossed-Field Amplifier. Research was undertaken in the late 1980s by Macmaster and Nichols [134] on a new approach for a crossed-field device to achieve high peak and average power at millimeter wavelengths. The device has a large-area anode consisting of axially aligned, staggered slots in the anode cylinder wall. A continuous cathode is mounted external to and concentric with the anode cylinder creating an inverted crossed-field interaction space. The anode cylinder with a center conductor forms a coaxial TE₀₁-mode waveguide that transforms to circular waveguide at the input and output. The slots couple RF energy from the

interaction space into the waveguide, and power growth occurs within the coaxial waveguide along the length of the anode. At 34 GHz a peak power of 15.5 kW and 140 W of average power was obtained at a gain of 10 dB. To demonstrate somewhat higher average power capability of the circuit and cathode, the tube was operated at 4 kW peak power, 200 W average power, and 8 dB gain. Earlier versions amplified a frequency between 35 and 36.25 GHz at a power of 50 kW peak, 88 W average, and 10 dB gain. Maximum recorded peak and average power was 58 kW at 230 W.

The geometry of this device is such that an RF circuit can be readily located on the cathode to enhance gain and overall performance. A cathode-driven Ka-band device has not been tested.

7.7. The Electromagnetic Amplifying Lens

A very-large-area anode–cathode crossed-field axial gain device with potential for generating exceptionally high peak and average power at millimeter wavelengths is the electromagnetic amplifying lens or “EAL” designed by Brown and Dombrowski [135]. A number of crossed-field tube research programs were carried out in parallel with the EAL design effort [136]. These programs have been briefly reviewed in a paper by Ruden et al. [137]. None of these efforts succeeded in developing a high-frequency, high-power amplifier. As discussed below, the evaluation of the EAL has yet to be completed.

An X-band, 100-MW-peak-power, prototype EAL employing a platinum secondary emitting cathode was fabricated and tested. However, the available drive power required the device to operate at greater than 20 dB gain. The device oscillated at a frequency well removed from the design frequency and failed to amplify. It was estimated that a drive power of 10 MW would be required to achieve a nominal gain of 10 dB. Other techniques that could be used to achieve amplification are the incorporation of an RF drive circuit on the cathode to provide strong RF fields at the cathode, operation of the device in the low-magnetic-field regime to enhance interaction near the anode between the electron stream and the RF circuit, and the use of an axial injected electron beam as in the voltage tuned magnetron to provide a temperature-limited, current-controlled electron beam.

7.8. Magnetron for Medical Applications

A 9.3-GHz magnetron of 1.8 MW peak power has been developed for radiotherapy [138]. The device uses rare-earth magnets, which results in a compact package meeting the system requirements. Lower-frequency magnetrons have been used extensively in this area. Operation of a representative pulsed S-band magnetron as described by Konrad [139] is 2.6 MW peak power and 3.1 kW average with a 4.2 μ s pulse duration, and a tuning range of 9 MHz. Electromagnets are used to provide the magnetic field, and adjustment of field allows operation at various power levels such that the X-ray energy can be varied. Projected need for peak power magnetrons are 3.5 and 6 MW at S band and 2.5 MW at X band. Increased tube reliability and lower unit cost are key manufacturing goals.

7.9. High-Peak- and Average-Power UHF Magnetrons

A paper by Wynn et al. [138] discusses the development of a 915-MHz pulsed magnetron operating at millisecond pulse length and high duty cycle. The magnetron is a strapped device and operates at higher than normal magnetic field levels, which enhance the efficiency of the device [52,140]. Various pulsed tubes have provided the following performance: magnetron with agile tuning of 60 MHz operated at 250 kW peak power at 25 kW average and an efficiency of 85%; fixed-frequency magnetron operation at 600 kW peak power at 300 kW average and 85% efficiency, and 1200 kW peak power at 300 kW average.

A 300-kW CW L-band magnetron, model CWM-300L, whose design was based on the commercially available 75-kW CW magnetron, model CWM-75L, has been developed [141]. The 300-kW tube operates at 32 kV and 10 A. The conversion efficiency is greater than 90%.

7.10. Relativistic Magnetron

In more recent years experimental work on the relativistic magnetron has centered on devices operating at pulsed voltages of a few hundred kilovolts and the generation of peak power from hundreds of kilowatts to gigawatts. A paper by Taylor and Younan [142] discusses the effects of high-power microwave illumination. Topics discussed are electrical effects, effects on electronics, hardening against high-power microwave illumination (including shielding and filtering), and high-power microwave weapons.

The technical status of the relativistic magnetron is reviewed by Saveliev [143]. Design issues as effective anode–cathode gap, uniformity of electron emission, anode–cathode gap closure velocity, voltage–current characteristics as a function of end caps, microwave characteristics as operating frequency and mode structure, and mode competition are discussed.

An alternate relativistic magnetron design is described by Schnitzer et al. [144], which combines coaxial magnetron and positive anode magnetron principles. Operation at 50 MW at 150 ns and 100 MW at 70 ns was achieved. The reduced power density in the structure is proposed as a possible reason for achieving the observed pulse length from a single device. Another cause of pulse shortening under consideration is failure to properly match the impedance of the modulator to the magnetron impedance.

Chen et al. [145] contend that pulse shortening is related to electron bombardment of the anode electrodes with subsequent generation of ions that are accelerated toward the cathode and modify the plasma at the cathode surface. This ion process is in accord with experimental observation of erosion of the platinum cathode surface in both 50–400 kW CW and 25–50 MW pulsed superpower, S-band Amplitron models [146]. The latter pulsed tubes operated at approximately 150 kV, 1–10 μ s pulse width, and average power \leq 200 kW. Axial striations on the cathode surface are observed directly opposite the gaps between anode electrodes. Computation of the ion trajectories showed that the DC fringing electric fields created by the anode electrode system focus the ions and produce the striations on the cathode surface [147]. In addition, electrons created near the anode by gas ionization can result

in electron bombardment of sections of the anode surface. Gas evolution can occur, which enhances vane-to-vane and single-surface anode multipactor, leading to further gas evolution.

The Chen paper also highlights the importance of pre-processing and proper storage of tube parts, and the following of microwave tube industry procedures of vacuum processing of the tube. (Note: Double-vacuum bakeout was standard procedure for the abovementioned superpower Amplitrons).

8. CONCLUSIONS

The magnetron has survived in an era when most electron tubes have been replaced by solid-state devices in modern electronic systems. In particular, the cooker magnetron is the power source for microwave ovens at power levels of 300–3000 W and its manufacturing volume, worldwide, is over 60 million tubes per year. This version of the magnetron preserves the classical strapped-vane anode design of World War II vintage. Because of its low cost and high efficiency (60–90%), it is unlikely to be replaced by other electron devices.

A wide spectrum of related devices is being developed for specialized applications. These include crossed-field amplifiers, voltage-tuned magnetrons, beacon magnetrons, and relativistic magnetrons. Applications range from the classical radar through industrial heating to microwave weapons.

Computer modeling of magnetrons and related tubes has become an extensive activity in many countries, including Russia, Korea, and Japan as well as the United States. Although considerable advances have been made in describing or predicting magnetron performance, computer calculations have not yet mastered the chaotic nature of electron–field interactions in the magnetron. The excess noise feature of magnetrons remains unconquered and very likely will be a potential radiofrequency interference threat to the expanding universe of modern microwave wireless systems.

Large-scale manufacturing of magnetrons has shifted to countries in the Far East such as China, Thailand, Indonesia, and Korea. More limited production and R&D continue in Japan, Russia, the United States, and a few other countries such as the United Kingdom. Trends in the modern global economy determine, in large measure, future R&D and manufacture of magnetrons.

Despite prediction, in the 1960s, of its obsolescence, the magnetron remains one of the electron tubes that survive because of its high efficiency, power capability, and low cost. Future applications remain unpredictable, but many are being explored. Advances in computer modeling will eventually produce success. It remains to be seen whether magnetron noise can be controlled to permit true electromagnetic compatibility in the new era of microwave wireless communications systems.

Acknowledgments

One of the authors, Thomas E. Ruden, wishes to express his appreciation for the technical assistance and helpful

comments provided by Mr. David Hobbs, Microwave Consultant, retired from Microwave Associates, Inc., Burlington, MA. John M. Osepchuk thanks all at Maytag/Amana Appliances who have supported and contributed to this work, particularly Ed Cook and Thomas L. Miller.

BIBLIOGRAPHY

1. A. W. Hull, *Phys. Rev.* **18**:31 (1921).
2. W. W. Harman, *Fundamentals of Electronic Motion*, McGraw-Hill, New York, 1953.
3. L. Brillouin, Practical results from theoretical studies of magnetrons, *Proc. IRE* 216–230 (April 1944).
4. C. E. Cleeton and N. H. Williams, Electromagnetic waves of 1.1 centimeters and the absorption spectra of ammonia, *Phys. Rev.* **40**:234 (1934).
5. G. Ross Kilgore, Recollections of pre-world War II magnetrons and their applications, *IEEE Trans. Electron. Devices* **ED-31**:1593–1595 (Nov. 1984).
6. L. Brillouin, *Wave Propagation in Periodic Structures*, McGraw-Hill, New York, 1946, reprinted by Dover Publications, New York.
7. J. C. Slater, *Microwave Electronics*, Van Nostrand, New York, 1950.
8. A. F. Harvey, *High Frequency Thermionic Tubes*, Wiley, New York, 1943.
9. H. E. Guerlac, *Radar in World War II*, Vols. I and II, American Ins. Physics, New York, 1987.
10. J. T. Randall, The cavity magnetron, *Proc. Phys. Soc.* **58**(Part 3):242–255 (1946).
11. H. A. H. Boot and J. T. Randall, The cavity magnetron, *JIEE (J. Inst. Electric. Eng.)* **93**(Part 3A):928–938 (1946).
12. R. Buder, *The Invention that Won the War*, Simon & Schuster, New York, 1996.
13. Correspondence from J. Fritz and J. M. Osepchuk, *J. Microwave Power* **15**:64–65, 137–138 (1980).
14. J. F. Hull, A Young engineer enters the microwave tube field during World War II, *IEEE Trans. Electron. Devices* **ED-31**:1611–1613 (Nov. 1984).
15. G. B. Collins, *Microwave Magnetrons*, McGraw-Hill, New York, 1948.
16. G. R. Kilgore, Magnetron oscillators for generation of frequencies between 300 and 600 megacycles, *Proc. IRE* **24**:1140–1157 (1936).
17. K. Posthumous, Oscillations in a split anode magnetron, *Wireless Eng.* **12**:126–132 (May 1935).
18. W. C. Brown, The microwave magnetron and its derivatives, *IEEE Trans. Electron. Devices* **ED-31**(11):1595–1605 (Nov. 1984).
19. J. B. Fisk, H. D. Hagstrum, and P. L. Hartman, The magnetron as a generator of centimeter waves, *Bell Syst. Tech. J.* **25**(2):167–348 (April 1946).
20. M. L. Skolnik, *Introduction to Radar Systems*, McGraw-Hill, New York, 1962, pp. 208–211.
21. Ref. 18, p. 1599; Ref. 20, p. 91.
22. *EEV Catalog—Magnetrons*, 12–96 GHz, p. 14.
23. F. E. Vaccaro, Four cavity tunable magnetron, in E. Okress, ed., *Crossed-Field Microwave Devices*, Academic Press, New York, 1961, Vol. 1, pp. 135–148.
24. A. H. Pickering, Electronic tuning of magnetrons, *Microwave J.* 73–78 (July 1979).

25. *EEV Catalog*—Electron tubes, 1988/89; p. 46.
26. J. Feinstein and R. J. Collier, Circular electric mode magnetron, in E. Okress, ed., *Crossed-Field Microwave Devices*, Academic Press, New York, 1961, Vol. 2, pp. 123–134.
27. W. A. Gerard, Coaxial magnetrons, *Microwave J.* 38–39 (March 1965).
28. T. E. Ruden, Design and performance of a one megawatt, 3.1–3.5 GHz coaxial magnetron, *Proc. 9th European Microwave Conf.*, Brighton, UK, Sept. 1979, pp. 731–735.
29. T. E. Ruden and G. E. Dombrowski, A field analysis for identification of spurious modes of the coaxial magnetron, *Proc. 11th European Microwave Conf.*, Amsterdam, The Netherlands, Sept. 1981, pp. 650–654.
30. W. A. Gerard, Frequency-agile coaxial magnetrons, *Microwave J.* 29–33 (March 1973).
31. A. C. Johnson, W. A. Gerard, and R. A. Washburn, Development of a 250 kW, X-band, accusweep magnetron, *Proc. IEDM*, 1991, pp. 601–604.
32. H. K. Dwivedi and D. S. Vendateswarlu, Thermal design considerations for fast warm-up cathodes in mm wave magnetrons, *IEEE Trans. Electron. Devices* **43**(11):2011–2018 (1996).
33. J. L. Cronin, Modern dispenser cathodes, *Proc. IEE* **128** (Part 1)(1):19–31 (Feb. 1981).
34. A. S. Gilmour, Jr., *Microwave Tubes*, Artech House, Dedham, MA, 1986.
35. F. Rosebury, *Handbook of Electron Tube and Vacuum Techniques*, American Inst. Physics, New York, 1993.
36. W. H. Kohl, *Handbook of Materials and Techniques for Vacuum Devices*, American Inst. Physics, New York, 1994.
37. B. Ch. Djubua, O. V. Polivnikova, N. M. Ogoleva, Y. Ding, and J. Peng, The impregnated cathode for high power klystron, *Proc. 2nd Int. IEEE Conf. Microwave and Millimeter Wave Technology*, 2000, pp. 146–148.
38. S. C. Dorak and R. L. Rutherford, L-band magnetron improvements and failure mechanisms, *Proc. 7th Int. Conf. Microwave and High Frequency Heating*, Valencia, Spain, Sept. 1999; R. L. Rutherford, Burle Industries, Inc., Lancaster, PA, personal communication, Feb. 2004.
39. J. F. Skowron, The continuous-cathode (emitting sole) crossed-field amplifier, *Proc. IEEE*. **61**(3):330–356 (March 1975).
40. A. Shih, J. Yater, C. Hor, and R. Abrams, Secondary electron emission properties of oxidized beryllium cfa cathodes, *IEEE Trans. Electron. Devices* **41**(12):2448–2454 (1994).
41. K. Hoffer and M. Moody, A CFD success story—the AEGIS/SPY-1A CFA program, *Proc. 2nd Int. Conf. Crossed-Field Devices and Applications*, Boston, MA, June 1998, pp. 45–47.
42. D. K. Das and W. J. Harrold, Characterization of samarium–cobalt TWT magnets, *IEEE Trans. Magn.* **Mag-7**(2): 281–285 (1971).
43. C. Chen and M. Walmer, *A New Series Of Rare Earth Cobalt Magnet Grades*, Electron Energy Corp. Landsville, PA, April 2003.
44. R. R. Warnecke, W. Kleen, A. Lerbs, O. Döhler, and H. Huber, The magnetron-type traveling-wave amplifier tube, *Proc. IRE* 486–495 (May 1950).
45. R. R. Warnecke, P. Guénard, O. Doehler, and P. Epszstein, The “M”-type carcinotron tube, *Proc. IRE* 413–424 (April 1955).
46. W. C. Brown, Description and operating characteristics of the platinotron—a new microwave tube device, *Proc. IRE* **45**(9):1209–1222 (Sept. 1957).
47. G. E. Dombrowski, Theory of the Amplitron, *IRE Trans. Electron. Devices* **ED-6**(6):419–428 (Oct. 1959).
48. D. Carey and W. Evans, The Patriot Radar in tactical air defense, paper presented at Electronics and Aerospace Systems Conf. Washington, DC, Nov. 1981.
49. J. Williams, An AEGIS radar system perspective of crossed-field devices, *Proc. 2nd Int. Conf. Crossed-Field Devices and Applications*, Boston, MA, June 1998, pp. 2–6.
50. E. W. Herold, The future of the electron tube, *IEEE Spectrum* **2**:49–55 (Jan. 1965).
51. J. M. Osepchuk, A history of microwave heating applications, *IEEE Trans. Microwave Theory Tech.* **MTT-32**:1200–1224 (Sept. 1984).
52. R. Yokayama and A. Yamada, Development status of magnetrons for microwave ovens, *Proc. 31st Microwave Power Symp., IMPI*, Northeastern Univ. Boston, MA, July 1996, pp. 132–135.
53. J. M. Osepchuk, The cooker magnetron as a standard in crossed-field device research, *Proc. 1st Int. Workshop on Crossed-Field Devices*, Univ. Michigan, 1995, pp. 159–177.
54. D. H. Sloan and C. Susskind, Interactions in cold-cathode magnetrons, *Proc. 5th Int. Microwave Tube Congress*, 1964, pp. 311–313.
55. J. M. Osepchuk, Microwave power Applications, *IEEE Trans. Microwave Theory Tech.* **50**(3):975–985 (March 2002).
56. J. R. G. Twisleton, Twenty-kilowatt 890 Mc/s continuous-wave magnetron, *Proc. Inst. Electrical Engineering*, Jan. 1964, pp. 51–56.
57. G. E. Thomas, The nonlinear operation of a microwave crossed-field amplifier, *IEEE Trans. Electron. Devices* **ED-28**(1):27–36 (Jan 1981).
58. T. M. Roberts, Comment on “the non-linear operation of a microwave crossed-field amplifier,” *IEEE Trans. Electron. Devices* **40**(6):1188–1189 (June 1993).
59. D. J. Kaup and G. E. Thomas, Chaotic instabilities and density profiles in a crossed-field electron vacuum device, in H. E. Brandt, ed., *Intense Microwave Pulses*, Vol. VII; see *Proc. SPIE* **4031**:54–64 (2000).
60. G. Ya. Levin, L. A. Semenov, A. Ya. Usikov, and Yu. A. Belov, On the nature of noise and mechanisms of suppressing it in surface-wave magnetrons, *J. Commun. Technol. Electron.* **37**:128–131 (1992).
61. V. G. Usychenko, The space-charge structure and stability of solitary waves in a magnetron diode under reduced electron emission, *J. Commun. Technol. Electron.* **46**(12):1374–1383 (2001).
62. P. A. Lindsay, M. Esterson, and X. Chen, The magnetron “threshold voltage” revisited, *Phys. Plasmas*, **4**(2):463–468 (Feb. 1997).
63. S. Riyopoulos, Stimulated microwave emission from E x B drifting electrons in slow wave cavities: a quantum approach, *Phys. Rev.* **E51**:4930 (1995).
64. S. Riyopoulos, New improved formulae for magnetron characteristic curves, *IEEE Trans. Plasma Sci.* **26**:755 (1998).
65. J. Browning, C. Chan, J. Z. Ye, and T. Ruden, A low frequency crossed-field amplifier for experimental investigations of electron-radio frequency wave interactions, *IEEE Proc. Plasma Sci.* **19**(4):598–606 (Aug. 1991).
66. J. Feinstein and G. S. Kino, The large-signal behavior of crossed-field traveling-wave devices, *Proc. IRE* **45**(10):1364–1373 (Oct. 1957).

67. W. R. Zettler, G. E. Dombrowski, and T. E. Ruden, *Platinotron Research Program*, Final Engineering Report, Contract DA36-039-sc-71173, Oct. 15, 1958.
68. T. E. Ruden and R. F. Bowen, A high power VHF lumped circuit Amplitron, *Proc. 3rd High Power Microwave Tube Symp.* Fort Monmouth, NJ, 1967.
69. D. R. Hartree, *CVD Report*, Mag. 3, 1941; E. C. Stoner, *CVD Report*, Mag. 2, 1941.
70. S. R. Tibbs and F. I. Wright, *CVD Report*, Mag. 41, March 1945.
71. C. G. Lehr, J. W. Lotus, I. Silberman, and R. C. Gunther, Electron trajectories in a magnetron, *J. Electron. Control* **13**: 89–122 (Aug. 1962).
72. R. P. Little, H. M. Ruppel, and S. T. Smith, Beam noise in crossed-field electric and magnetic fields, *J. Appl. Phys.* **29**:1376 (1958).
73. G. E. Dombrowski and T. E. Ruden, Large signal calculation of Amplitron performance, *Proc. 4th Int. Conf. Microwave Tubes*, Schevevningen, The Netherlands, 1962.
74. T. E. Ruden, *Study of Crossed-Field Reentrant Beam Devices*, Final Report Contract 77592, Index SR0080301, Task 9390, Sept. 1965.
75. J. W. Sedin, A large-signal analysis of beam-type crossed-field traveling-wave tubes, *IRE Trans. Electron. Devices*, **ED-9**(1):4–50 (Jan. 1962).
76. S. P. Yu, G. P. Kooyers, and O. Buneman, Time-dependent computer analysis of electron-wave interaction in crossed-fields, *J. Appl. Phys.* **36**(8):2550–2559 (Aug. 1965).
77. H. L. MacDowell, Magnetron simulations using a moving wavelength code, *IEEE Trans. Plasma Sci.* **26**(3):733–754 (June 1998).
78. G. E. Dombrowski, Simulation of magnetrons and crossed-field amplifiers, *IEEE Trans. Electron. Devices* **35**(11):2060–2067 (Nov. 1988).
79. T. E. Ruden, G. E. Dombrowski, D. Hobbs, and G. Boles, Low field magnetron Investigation, *Proc. 20th Int. Conf. Infrared and Millimeter Waves*, Orlando, FL, Dec. 1995, pp. 5–6.
80. D. P. Chernin, Computer simulations of low-noise states in a high power crossed-field amplifier, *Proc. 1st Int. Workshop on Crossed-Field Devices*, Ann Arbor, MI: Aug. 1995, pp. 246–255.
81. J. Z. Ye, R. MacGregor, C. Chan, and T. E. Ruden, Probing space-charge in a crossed-field amplifier, *Proc. 1st Int. Workshop on Crossed-Field Devices*, Ann Arbor, MI: Aug. 1995, pp. 202–211.
82. W. C. Brown, The high signal to noise ratio of the microwave oven magnetron and evidence of a negative feedback loop to control it, *Proc. 1st Int. Workshop on Crossed-Field Devices*, Ann Arbor, MI: Aug. 1995, pp. 178–187.
83. K. Schuenemann, S. V. Sosnytskiy, and D. M. Vavriv, Self-consistent simulation of spatial-harmonic magnetron with cold secondary-emission cathode, *IEEE Trans. Electron. Devices* **48**(5):993–998 (May 2001).
84. K. Schuenemann, A. E. Serebryannikov, S. V. Sosnytskiy, and D. M. Vavriv, Optimizing the spatial-harmonic millimeter-wave magnetron, *Phys. Plasmas* **10**(6):2559–2565 (June 2003).
85. A. Palevsky, G. Bekefi, and A. Drobot, Numerical simulation of oscillating magnetrons, *J. Appl. Phys.* **52**(8):4938–4941 (Aug. 1981).
86. R. A. Stark, H. C. Chen, and H. S. Uhm, Simulation studies of the relativistic magnetron, in H. E. Brandt, ed., *Intense Microwave and Particle Beams*, Vol. II; see *Proc. SPIE* **1407**:128–138 (Jan. 1991).
87. J. C. Weatherall, Numerical simulations of a relativistic magnetron, *IEEE Trans. Plasma Sci.* **18**(3):603–609 (1990).
88. T. E. Ruden, Relativistic magnetron Interaction, *IEEE Conf. Record—Abstracts, Int. Conf. Plasma Science*, Ottawa, Canada, May 1982, p. 63; Relativistic magnetron interaction (Part II), *IEEE Conf. Record—Abstracts, Int. Conf. Plasma Science*, San Diego, CA, May 1983, p. 103.
89. H.-W. Chan, C. Chen, and R. C. Davidson, Numerical study of relativistic magnetrons, *J. Appl. Phys.* **73**(11):7053–7060 (June 1993).
90. X. Chen, M. Esterson, and P. A. Lindsay, Computer modeling of phase locking in magnetrons, *Intensive Microwave Pulses*, Vol. IV; see *Proc. SPIE* **2843**:47–52 (1996); 2-D/3-D magnetron modeling, *Proc. 2nd Conf. Crossed-Field Devices and Applications*, Boston, MA, June 1998, pp. 170–175.
91. M. C. Jones, V. B. Neculaes, W. White, Y. Y. Lau, and R. M. Gilgenbach, Simulation of rapid startup in microwave magnetrons with azimuthally varying axial magnetic fields, *Appl. Phys. Lett.* **84**(6):1016–1018 (2004).
92. H. J. Kim, J. U. Shin, and J. J. Choi, Particle-in-cell code simulations on a rising-sun magnetron oscillator, *IEEE Trans. Plasma Sci.* **30**(3):956–961 (2002).
93. J. I. Kim, G. S. Park, H. J. Ha, and J. C. Shon, Investigation of 10-vane strapped magnetron using three dimensional particle-in-cell simulation, *Conf. Record—Abstracts; Proc. Int. IEEE Conf. Plasma Science*, Jeju, Korea, June 2003, p. 329.
94. S.-S. Jung, Y.-S. Jin, and H.-S. Lee, Study on high-power CW magnetrons for industrial applications, *Conf. Record—Abstracts; Proc. Int. IEEE Conf. Plasma Science*, Jeju, Korea, June 2003, p. 137.
95. L. Ma, X. Chen, M. Esterson, P. A. Lindsay, P. Burleigh, K. Saleem, and D. Wilson, Investigation of an x band experimental magnetron through magic modeling, *IEEE Conf. Record—Abstracts; Proc. Int. IEEE Conf. Plasma Science*, Baltimore, MD, June 2004, p. 177.
96. L. Ma, X. Chen, M. Esterson, P. A. Lindsay, P. Burleigh, and M. Brady, 3-D computer modeling of an experimental x band magnetron, *Proc. 5th IEEE Int. Vacuum Electronics Conf.*, Monterey, CA, April 2004.
97. I. Namba, N. Tashiro, K. Nakai, and H. Saito, A new magnetron (2M172A) from Toshiba, *J. Microwave Power* **19**(3):209–220 (Sept. 1984).
98. W. Arter and J. W. Eastwood, Characterization of relativistic magnetron behavior by 3-D PIC simulation, *IEEE Trans. Plasma Sci.*, **26**(3):714–725 (June 1998).
99. R. W. Lemke, T. C. Genoni, and T. A. Spencer, Three-dimensional particle-in-cell simulation study of the relativistic magnetron, *Phys. Plasmas* **6**(2):603–613 (1999).
100. A. Palevsky and G. Bekefi, Microwave emission from pulsed, relativistic e-beam diodes, II. The multiresonator magnetron, *Phys. Fluids* **22**(5):986–996 (May 1979).
101. P. J. Christenson and Y. Y. Lau, Limiting current in a crossed-field gap, *Phys. Fluids B* **5**(12):4486–4489 (Dec. 1993); Transition to turbulence in a crossed-field gap, *Phys. Plasmas* **1**(12):3725–3727 (Dec. 1994); One-dimensional modulational instability in a crossed-field gap, *Phys. Rev. Lett.* **78**(18):3324–3327 (April 1996).
102. PDP1 (Plasma Device Planar 1 Dimensional), © 1990–1993, Regents of the University of California, Plasma Theory and Simulation Group, Berkeley, CA; electronic mail—*software@eecs.berkeley.edu*; see also J. P. Verboncoeur, M. V. Alves, V. Vahedi, and C. K. Birdsall, *J. Comput. Phys.* 131–321 (1993).

103. P. J. Christenson, D. Chernin, A. Gardener, and Y. Y. Lau, Resistive destabilization of cycloidal electron flow and universality of (near) Brillouin flow in a crossed-field gap, *Phys. Plasmas* **3**:4455–4462 (1996).
104. T. E. Ruden, D. Hobbs, and G. E. Dombrowski, Simulation of 2.45 GHz magnetron oscillator, *IEEE Conf. Record—Abstracts; Proc. Int. IEEE Conf. Plasma Science*, Baltimore, MD, June 2004. p. 176.
105. J. W. Luginsland, Y. Y. Lau, V. B. Neculaes, R. M. Gilgenbach, M. C. Jones, M. H. Frese, and J. J. Watrous, Three-dimensional particle-in cell simulations of rapid start-up in strapped oven magnetrons due to variation in insulating magnetic field, *Appl. Phys. Lett.* **84**(26):5425–5427 (June 2004).
106. E. C. Okress, *Crossed-Field Microwave Devices*, Vols. 1 and 2, Academic Press, New York, 1961.
107. R. W. Gould, Space-charge effects in beam type magnetrons, *J. Appl. Phys.* **28**:599–605 (1957).
108. J. Gleick, *Chaos*, Viking Penguin, New York, 1987.
109. J. M. Osepchuk, Axial energy phenomena in magnetrons, *Proc. CFDA-98; 85–90*, Northeastern Univ., Boston, 1998.
110. O. Doehler and G. Dohler, Parametric oscillations in high-power injected-beam crossed-field amplifiers and TWTs, *IEEE Trans. Electron. Devices* **ED-26**:1602–1608 (Oct. 1979).
111. CISPR/B: *Emission Limits from 1 to 18 GHz*, Int. Special Committee on Radio Interference, Int. Electrotechnical Commission (IEC), Geneva, Switzerland, Amendment CISPR 11, 1999.
112. J. M. Osepchuk, The Bluetooth threat to microwave equipment, *Microwave World* **20**:4–5 (May 1999).
113. M. Weinstein and R. Winkowski, Voltage-tunable magnetron update, *Microwave J.* 75–76 (1977).
114. A. J. Boyd, The mitron: An interdigital voltage-tunable magnetron, *Proc. IRE* **43**:332–338 (March 1955).
115. *Voltage-Tunable Magnetrons*, Tube Dept., General Electric Co., 1967.
116. M. Weinstein, Voltage-tunable magnetron-state of the art, *Microwave J.* 162–166 (1962).
117. New Design Techniques Improve Frequency Stability of Magnetrons, Micronotes, Microwave Assoc., Inc., Burlington, MA, July/Aug. 1968, Vol. 6, p. 1.
118. M. Clark and B. Vyse, Miniature magnetrons for coherent high-duty operation, *Microwave Syst. News Commun. Technol.* 166–171 (May 1988).
119. D. Hobbs, X-band cost effective magnetron for commercial applications, *Power Tube Specialists Conf.* Monterey, CA, March 1976.
120. D. Hobbs, Overview of injection locking magnetrons, *Proc. 2nd Int. Conf. Crossed-Field Devices and Applications*, Boston, MA, June 1998, pp. 111–137.
121. B. English, Magnetrons deliver cost-effective system performance, *Microwaves RF* 67–72 (March 1991).
122. W. E. Garrigus, Phase noise performance of magnetrons, *Microwave J.* 59–73 (July 1973).
123. W. C. Brown, The history of the reentrant beam crossed-field amplifier with emphasis on noise comparison with the magnetron, *Proc. 1st Int. Workshop on Crossed-Field Devices*, Ann Arbor, MI, Aug. 1995, pp. 9–22.
124. W. C. Brown, *A Reporting of Personal Observations of Noise in Magnetrons and CFAs*, Raytheon Co. Internal Report PRP-5504, March 1988.
125. G. H. MacMaster, Current status of crossed-field devices, *Proc. Int. Electron Devices Meeting Tech. Digest*, San Francisco, CA, Dec. 1988, pp. 358–361; Product Feature, Cathode-Driven Crossed-Field Amplifier, *Microwave J.* 208–209 (Feb. 1988).
126. J. O. Meilus and M. J. A. Smith, Two-cascade voltage-tunable magnetron frequency multiplier, *J. Microwaves Optoelectron.* **1**(3):1–12 (Dec. 1998).
127. G. H. Plantinga, A pulsed magnetron for 2.5 mm waves, *Philips Tech. Rev.* **25**(8):217–252 (Aug. 1964) (the DX287 design was based on tube development at 60–120 GHz carried out by Philips Research Laboratory, Eindhoven, The Netherlands).
128. *EEV Catalog*, Magnetrons 12–96 GHz.
129. K. Schuenemann, A. E. Serebryannikov, S. V. Sosnytskiy, and D. M. Vavriv, Optimizing the spatial-harmonic millimeter-wave magnetron, *Phys. Plasmas* **10**(6):2559–2565 (June 2003).
130. A. Belikov, R. Kozhyn, K. Schuenemann, B. Trush, D. Vavriv, and V. Volkov, *German Radar Symposium, GRS 2002*, German Institute of Navigation, Bonn 2002, pp. 571–574.
131. M. Jenett, V. Kazantsev, A. Kurekin, K. Schuenemann, D. Vavriv, V. Vinogradov, and V. Volkov, *IEEE Geoscience and Remote Sensing Symp., IGARSS-99*, Hamburg, 1999, Vol. 5, pp. 2596–2598.
132. O. P. Kulagin and V. D. Yeryomka, Large-orbit m-type oscillator with the adiabatic electron-optical system, *IEEE Trans. Plasma Sci.* **30**(6):2107–2112 (Dec. 2002).
133. O. P. Kulagin and V. D. Yeryomka, The flow forming potential in unconventional magnetrons, *Proc. 5th Int. IEEE Vacuum Electronics Conf.* Monterey, CA, April 2004, pp. 224–225.
134. G. H. Macmaster and L. J. Nichols, Millimeter-wave high gain crossed-field amplifier, *Proc. Int. Electron Devices Meeting IEDM Tech. Digest*, San Francisco, CA, 1990, pp. 963–966.
135. W. C. Brown and G. E. Dombrowski, Analysis of a new crossed-field amplifier, the “EAL,” or electromagnetic amplifying lens, *IRE Trans. Electron Devices* **ED-9**(2):221–228 (March 1962).
136. W. C. Brown, The electromagnetic amplifying lens, progress and potentialities, *Proc. High Power Microwave Tube Symp.* The Hexagon, Fort Monmouth, NJ, Sept. 1962, pp. 74–91.
137. T. E. Ruden, G. E. Dombrowski, D. Hobbs, and G. Boles, Low field magnetron study, *Proc. 1st Int. Workshop on Crossed-Field Devices*, Ann Arbor, MI, Aug. 1995, pp. 66–77.
138. A. Wynn, D. Blank, and P. Campbell, Long pulse and CW magnetron development at 915 and 2450 MHz, and compact X-band 1.8 megawatt magnetron, *Proc. 2nd Int. Conf. Crossed-Field Devices and Applications*, Boston, MA, June 1998, p. 67.
139. G. T. Konrad, Application of magnetrons with medical linear accelerators, *Proc. 1st Int. Workshop on Crossed-Field Devices*, Ann Arbor, MI, August 1995, pp. 89–95.
140. T. E. Ruden, High efficiency concepts for crossed-field devices: Magnetron and Amplitron, *Proc. 2nd Int. Conf. Crossed-Field Devices and Applications*, Boston, MA, June 1998, pp. 232–241. (in Ref. 52 the electronic efficiency of the 2450 MHz cooker magnetron was increased from 74% to 79% using the high magnetic field technique described in this Ruden [140] reference).
141. A. P. Wynn, D. E. Blank, P. E. Campbell, R. R. Lentz, W. T. Main, and S. G. Tantawi, Development of a 300 kW CW L-band industrial heating magnetron, *Proc. 5th Int. IEEE Vacuum Electronics Conf.* Monterey, CA, April 2004, p. 163.

- 142. C. L. Taylor and N. H. Younan, Effects of high power microwave illumination, *Microwave J.* 80–96 (June 1992).
- 143. Y. N. Saveliev, Operation of relativistic rising-sun magnetrons with cathodes of various diameters, *IEEE Trans. Plasma Sci.* 30(3):938–945 (June 2002).
- 144. I. Schnitzer, A. Rosenberg, C. Leibovitz, I. Cohen, M. Botton, and J. Leopold, Evolution of spectral power density in grounded cathode relativistic magnetron, *SPIE* 2843:101–109 (1996).
- 145. X. Chen, M. Esterson, and P. A. Lindsay, Computer simulation of a high power magnetron and possible implications for rf pulse shortening, *IEEE Trans. Plasma Sci.* 26(3):726–732 (June 1998).
- 146. J. F. Skowron, W. C. Brown, and G. H. MacMaster, The super power CW Amplitron, *Microwave J.* 7(10):65–69 (1964); *Ultra High Power Amplitron*, Vol. II, *Pulsed Amplitron Development*, Technical Report RADC-TDR-64–389, Rome Air Development Center, Rome, NY, May 1965.
- 147. T. E. Ruden, *Ion Motion in the Amplitron*, Raytheon Microwave and Power Tube Division, Super Power Programs Laboratory, Spencer Laboratory, Burlington, MA, Memo 63 -11 to J. F. Skowron, March 23, 1963.

MAXWELLIAN CIRCUITS

KENNETH K. MEI
 City University of Hong Kong
 Zhejiang University
 Hangzhou, China

1. INTRODUCTION

The term *circuit* implies the involvement of Kirchhoff’s laws. The name Maxwell is associated with the partial-differential equations of electromagnetic theory. Most of us who have been doing research in electromagnetics believe that Maxwell’s equations are complete, in that they can formulate any problem related to electricity and magnetism including circuit problems, and that Kirchhoff’s theory is a simplified form of Maxwell’s equations, applicable at low frequencies when the circuit components and connecting wires are much smaller than a wavelength. However, a careful search of textbooks and journal papers reveals that many of our colleagues may not agree with these ideas. In fact, the most embarrassing moments for those of us who have taught electromagnetic theory may have been when we realized that the transmission-line equations, which are derived from Kirchhoff’s laws [1,2], have been an integral part of standard textbooks on electromagnetic theory. Indeed, the transmission-line theory is an important part of a course on electromagnetic theory, which students later apply in their careers as microwave engineers. However, deriving transmission-line theory from Kirchhoff’s laws in an electromagnetic textbook is inappropriate, to say the least, because it misleads our students to believe that Kirchhoff’s laws and Maxwell’s equations are really the same. The objectives of this article are (1) to show that some important part is missing from

Kirchhoff’s circuits so that they cannot be used to simulate solutions of Maxwell’s equations except in certain special cases, and (2) that the solutions of Maxwell’s equations of a structure can be simulated by circuits rendered Maxwellian by adding dependent sources, such that the solutions of voltages and currents of the circuits are identical to those of the original problem.

Before we discuss Maxwellian circuits, let’s review the textbook derivation of the transmission-line equation (TLE) from Kirchhoff’s laws, and rederive it from Maxwell’s equations in Sections 2.1 and 2.2.

2. TRANSMISSION-LINE EQUATION

2.1. TLE by Kirchhoff’s Laws

In the traditional derivation of the TLE, a transmission line is segmented into small identical pieces of Δz , and simulated by series inductor and shunt capacitor as shown in Fig. 1, where L and C are inductance per meter and capacitance per meter of the line, which can be calculated from the specific geometry of the line. Using Kirchhoff’s laws, the voltage and current differences between the nodes $i + 1$ and i are found to be

$$\Delta V = -j\omega L\Delta z(I + \Delta I) \tag{1a}$$

$$\Delta I = -j\omega C\Delta zV \tag{1b}$$

As $\Delta z \rightarrow 0$, and neglecting the second-order term, we get the TLE:

$$\frac{dV}{dz} = -j\omega LI \tag{2a}$$

$$\frac{dI}{dz} = -j\omega CV \tag{2b}$$

2.2. TLE by Maxwell’s Equations

Equations (2) can be derived from Maxwell’s equations of the vector and scalar potentials:

$$\nabla V = -j\omega \mathbf{A} - \mathbf{E} \tag{3a}$$

$$\nabla \cdot \mathbf{A} = -j\omega \mu \epsilon V \tag{3b}$$

On a straight conducting wire along the direction z , and assuming that

$$\mathbf{A} \cdot \mathbf{z} = LI \tag{4}$$

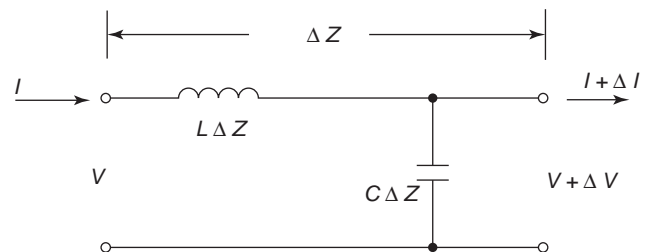


Figure 1. L, C circuit segment used in conventional TLE derivation.

where L is the inductance per meter of the line, which is exact for infinitely long straight wires. Equation (3a) becomes identical to Eq. (2a), since the electric field vanishes along the line. Using the relation

$$\frac{1}{\sqrt{LC}} = v = \frac{1}{\sqrt{\mu\epsilon}} \quad (5)$$

where v is the velocity of propagation, and assume L to be uniform, then, Eq. (3b) becomes the same as Eq. (2b).

2.3. Comparison between Kirchhoff and Maxwell Derivations

While we get identical results from the Kirchhoff and Maxwell theories, there are some differences in the procedures. Specifically, in the derivation by Maxwell's equations, we have to assume that

1. The line is straight and infinite.
2. The inductance and the capacitance per meter are uniform.

These assumptions are absent in Kirchhoff's derivation. This is so because solutions to Maxwell's equations are geometrically specific. Circuits have topology but no geometry; hence Kirchhoff's laws are blind to geometric variation. When L and C are not uniform, Eq. (3b) becomes

$$\frac{dI}{dz} = -j\omega CV - \frac{dL/dz}{L} I \quad (6)$$

The added term in (6) represents the effect of changing geometry in Maxwell's formulation. Since the textbook derivations of the TLE all use Kirchhoff's laws, it is absent from their equations for nonuniform lines. For example, the equations for nonuniform lines in Ref. 1 are

$$\frac{dV(l)}{dl} = -j\omega L(l)I(l) \quad (7a)$$

$$\frac{dI(l)}{dl} = -j\omega C(l)V(l) \quad (7b)$$

where l is the position along a curved line. Using Eqs. 7, the classical textbook [1], for example, went on to obtain the exact solutions to exponential lines. Many inquisitive students have tried to verify their MoM (method of moments) results using those exact solutions and found disappointing results. Of course, they would place the blame on their numerical results. How could one dispute against the exact solution? If the classical textbooks had derived the TLE from Maxwell's equations, such mistakes would not have occurred. Would the added term in Eq. (6) make the equations for a nonuniform line correct? No. As we mentioned earlier, solutions of Maxwell's equations are geometry-specific. So, the approximation of Eq. (4), which is good for a straight and infinite wire, may not apply. In this article, we shall show that wire structures of any shape may be represented by circuits, and are not limited to low frequencies. If the solutions of voltages and currents of a simulating circuit are identical to those of the solutions of the Maxwell's equations of the original

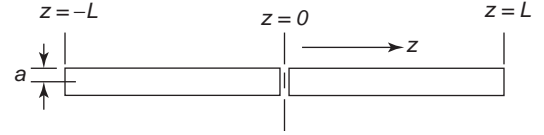


Figure 2. Schematics of a linear dipole

structure, we shall designate it of being *Maxwellian*. To understand the theory of Maxwellian circuits, we need to relate the integral equations of wire structures and differential equations.

3. INTEGRAL EQUATIONS OF WIRE STRUCTURES

The integral equation of a wire structure is derived from Maxwell's equations. The simplest integral equation of a wire structure is that of a straight-wire antenna in free space, driven by an infinitesimally thin gap electric field in the middle of the wire as shown in Fig. 2. The antenna is symmetric: $I(-z) = I(z)$. The simplified geometry will facilitate the ensuing discussions without any loss of generality. The theories can be readily adapted to wire structures of any shape [3].

The integral equation of the current on the antenna in Fig. 2 is

$$\mathbf{L}I(z) = B \cos kz - \frac{jV_0}{2Z_0} \sin k|z| \quad (8)$$

where V_0 is the driving voltage and \mathbf{L} is the integral operator

$$\mathbf{L}I(z) = \int_{-L}^L \mathbf{G}(|z - z'|) I(z') dz' \quad (9)$$

$G|z - z'|$ is the free-space Green function, if the structure is a straight-wire antenna in open air. For wire antennas of other shapes, this should be replaced by an integral of the free-space Green's function [2]. For microstrips of any shape, the integral equation of the thin-wire structure type can still be derived, where $G(|z - z'|)$ would be replaced by a kernel of integrals of a Sommerfeld-type Green dyadic. The constant B is a parameter adjusted to enforce the boundary condition of the vanishing current at the end of the antenna or any other impedance condition at the end of the wire.

4. THE DIFFERENTIAL OPERATOR \mathbf{D}

We have also chosen a delta generator as the source model [4,5] so that the incident field is zero everywhere on the wire except at the gap. Our objective is to find a differential operator \mathbf{D}

$$\mathbf{D}I(l) = \frac{d^2}{dl^2} I + U(l) \frac{d}{dl} I + T(l)I = 0 \quad (10)$$

where $U(l)$ and $T(l)$ are to be found such that the solution of (10) is identical to that of (8). In Eq. (10), the zero on the right-hand side (RHS) is justified because there is no

incident field on the wire owing to the delta source. In fact, for every function of ℓ , there are an infinite number of differential operators that can cause (10) to be zero. We wish to find one that is applicable to all solutions of (8) regardless of the terminating condition at $\ell = L$. Also, the solution of (10) should be the same as that of the integral equation (8) when the same terminating condition is applied. The proofs of the existence and uniqueness of such an operator and its invariance to the terminating conditions are given in the following sections.

Operators are in general not unique, in that the product of the operator of (10) with any other operator should include the same properties of the operator of (10). So, our uniqueness theorem is for \mathbf{D} to be the lowest-order differential operator. It is easy to eliminate a first-order operator as a possible candidate, so the second-order equation of (10) is the next possible candidate.

The theorems to be presented should rely on two assumptions:

1. The inverse operator of the integral operator L exists.
2. The current on the structure can be adequately represented by a complex Fourier series of finite terms.

4.1. Existence Theorem

Let I_i and I_j be two solutions of the integral equation 1 subject to different terminating conditions at $\ell = L$; then there exists a differential operator \mathbf{D} , defined in Eq. (8), such that $\mathbf{D}I_i = 0$ and $\mathbf{D}I_j = 0$.

We can prove the existence theorem by substituting these two solutions into (10) to get two equations from which we can solve for the coefficients U and T . The solutions for U and T should exist and be unique unless the following determinant vanishes:

$$\begin{vmatrix} \frac{dI_i}{d\ell} & I_i \\ \frac{dI_j}{d\ell} & I_j \end{vmatrix} = 0 \tag{11}$$

Vanishing of the determinant (11) means

$$\ln I_i - \ln I_j = \text{constant} \tag{12}$$

In other words, the ratio I_i/I_j must be a constant, which is not possible if I_i and I_j have different terminating conditions. Because a current can be approximated by finite terms of complex Fourier series, then for (4) to be true within a finite nonzero interval of $\Delta\ell$, say, at the neighborhood of a point $\ell = \ell_0$, it should follow that $I_i^{(n)}(\ell_0) = CI_j^{(n)}(\ell_0)$, for $n = 0, 1, 2, \dots, \infty$, where C is a constant. This implies that the Taylor expansions of $I_i(\ell)$ and $CI_j(\ell)$ are identical, which leads to $I_i(\ell) = CI_j(\ell)$ over the entire length of the wire, which again contradicts the assumption of the boundary conditions. Hence, (11) can be true only at discrete points where U and T may be singular but not in a finite interval $\Delta\ell$, and it follows that the existence of a differential operator valid for at least two solutions of (8) is proved.

4.2. Uniqueness Theorem

The differential operator D , defined in Eq. (10), is unique for all solutions of an integral equation shown in Eq. (9).

We can prove the uniqueness theorem by letting I_i and I_j be a pair of solutions of (9) from which we obtain an operator \mathbf{D}_{ij} , and letting L^{-1} be the inverse operator of the integral operator L :

$$\mathbf{D}_{ij}I_{(i)} = \mathbf{D}_{ij}\mathbf{L}^{-1}\left(B_{(i)} \cos k\ell - \frac{jV_0}{2Z_0} \sin k|\ell|\right) = 0 \tag{13}$$

The RHS of (13) must vanish for two different values of B because the left-hand side (LHS) must vanish for both I_i and I_j , which satisfy different terminating conditions. For (13) to vanish for two different values of B , it is necessary that the two terms on the RHS of (13) vanish separately after being operated on by $\mathbf{D}_{ij}\mathbf{L}^{-1}$. It follows that

$$B_{(i)}\mathbf{D}_{ij}\mathbf{L}^{-1} \cos k\ell = 0 \tag{14}$$

Since $B_{(i)}$ govern the terminating conditions and $B_i \neq B_j$, at least one of them does not vanish. Therefore, $\mathbf{D}_{ij}\mathbf{L}^{-1} \cos k\ell = 0$ is independent of the parameter B and $\mathbf{D}_{ij}I_{(i)} = 0$ has to be an invariance of the terminating conditions.

Since \mathbf{D}_{ij} exists and is unique between I_i and I_j , the same is true for \mathbf{D}_{ik} between I_i and I_k . But \mathbf{D}_{ij} is also applicable to I_i and I_k because of its invariance to the terminal condition. It follows that $\mathbf{D}_{ij} = \mathbf{D}_{ik}$. It is thus proved that \mathbf{D} is the same for all solutions I , since \mathbf{D}_{ij} is unique for I_i and I_j and \mathbf{D}_{ik} is unique for I_i and I_k .

4.3. Finding the Operator \mathbf{D} from Numerical Results

The integral equation of the type in (1) is most conveniently solved numerically [2]. To find the operator \mathbf{D} numerically, we assume the wire structure to be subdivided into equal segments, and the values of the currents are found numerically at the middle of each segment. A second-order differential operator may be represented by the linear equation

$$I_{n+1} + a_n I_n + b_n I_{n-1} = 0 \tag{15}$$

at a point n ($n = 1, 2, \dots, N$). Substituting two numerical solutions for I into (15), we can solve for a_n and b_n . The values of U_n and T_n can be obtained readily by comparing (15) to the finite-difference form of (10), which yields

$$U_n = 2 \frac{(1 - b_n)}{(1 + b_n)\Delta\ell}, \quad T_n = \frac{2(1 + a_n + b_n)}{\Delta\ell^2(1 + b_n)} \tag{16}$$

5. OTHER NUMERICAL RESULTS

We have used MoM and the terminating conditions, $I(L) = c$ and $I'(L) = \alpha I(L)$ with various values of c and α to find the current along the wire. Values of coefficients U and T obtained from different pairs of current are all the same, just as the theorem predicts. The values of current, T , and U for a wire antenna with two right angle bends are given in Fig. 3. It is interesting to observe that the value of U is practically zero in the midsection of the straight wire.

The value of T there is the square of the free-space wave-number, which indicates that the current travels along a straight-wire antenna with the velocity of light, almost without attenuation. Most of the radiation, therefore, takes place near the bends and ends of the antenna, where both U and T change drastically. Another interesting feature of the differential equations is that the coefficients U and T are very sensitive functions of the local geometry of the wire. From the currents it is difficult to see where the bends are, but from U and T it is quite obvious where the bends are located. Conversely, the currents are not very sensitive to the errors of the differential equations. Since the functions U and T near the bends are characterized fairly easily, one can make use of their approximations to form the differential equation of the current [6]. Figure 4 shows the values of the current on a rectangular helical antenna as calculated by the MoM and those reconstructed by the differential equation. They are practically identical, just as the theorem has predicted.

5.1. Extraction of Maxwellian Circuit Parameters from Full-Wave Results

One important application of the differential equation formulation is that it is amenable to the extraction of circuit

components from the full-wave results that might be found, for example, by the MoM. Actually, wire antennas and microstrips belong to the same class of problems that can be solved by integral equations of the type in Eq. (8). Circuit parameter extraction is important for IC interconnects, which is done traditionally from static results [7,8] on open transmission systems. Although several researchers have succeeded in obtaining full-wave solutions of microstrips of various shapes [9,10], none has made any attempt to extract circuit parameters from the dynamic results. Using the differential equation of the current, we are able to extract circuit parameters for both transmission and radiating systems at any frequency.

Having shown that the solution of the differential equation (10) truly reproduces the MoM solution, our next step is to split Eq. (10) into two coupled first-order equations involving current and voltage. The general homogeneous first-order linear system of differential equations [11] that can reproduce Eq. (10) may be written in the form

$$\frac{dV}{d\ell} = -j\omega L(\ell)I + \alpha(\ell)V \quad (17)$$

$$\frac{dI}{d\ell} = -j\omega C(\ell)V + \beta(\ell)I \quad (18)$$

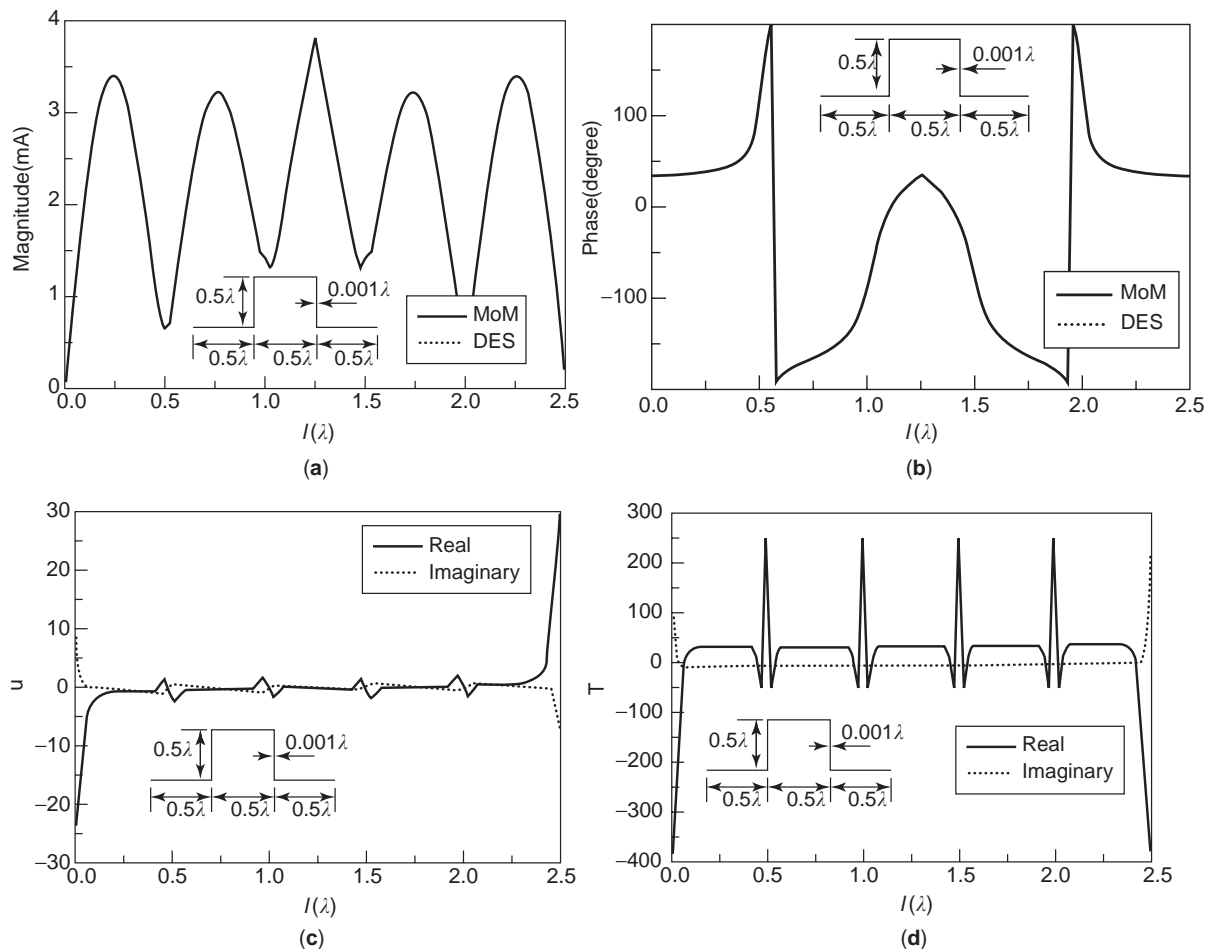


Figure 3. (a) Current $|I|$ on a double-bend wire antenna; (b) phase angle of the current of (a); (c) coefficient $U(\ell)$ of a double-bend wire antenna; (d) coefficient $T(\ell)$ of a double-bend wire antenna.

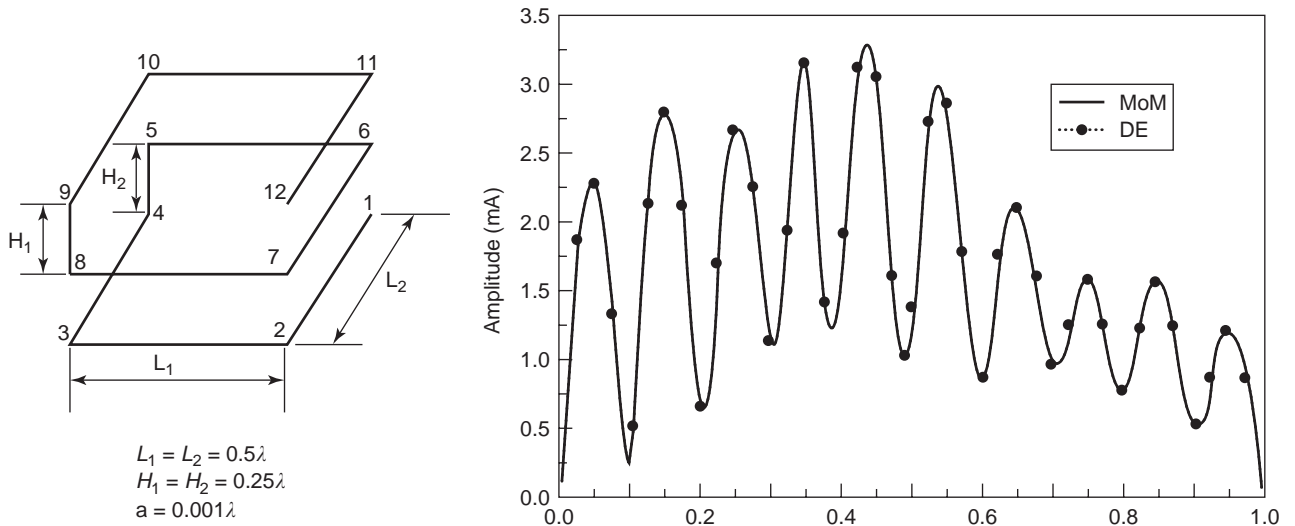


Figure 4. Currents on a rectangular helical antenna driven at node 5, computed by MoM and by solution of the wire differential equation.

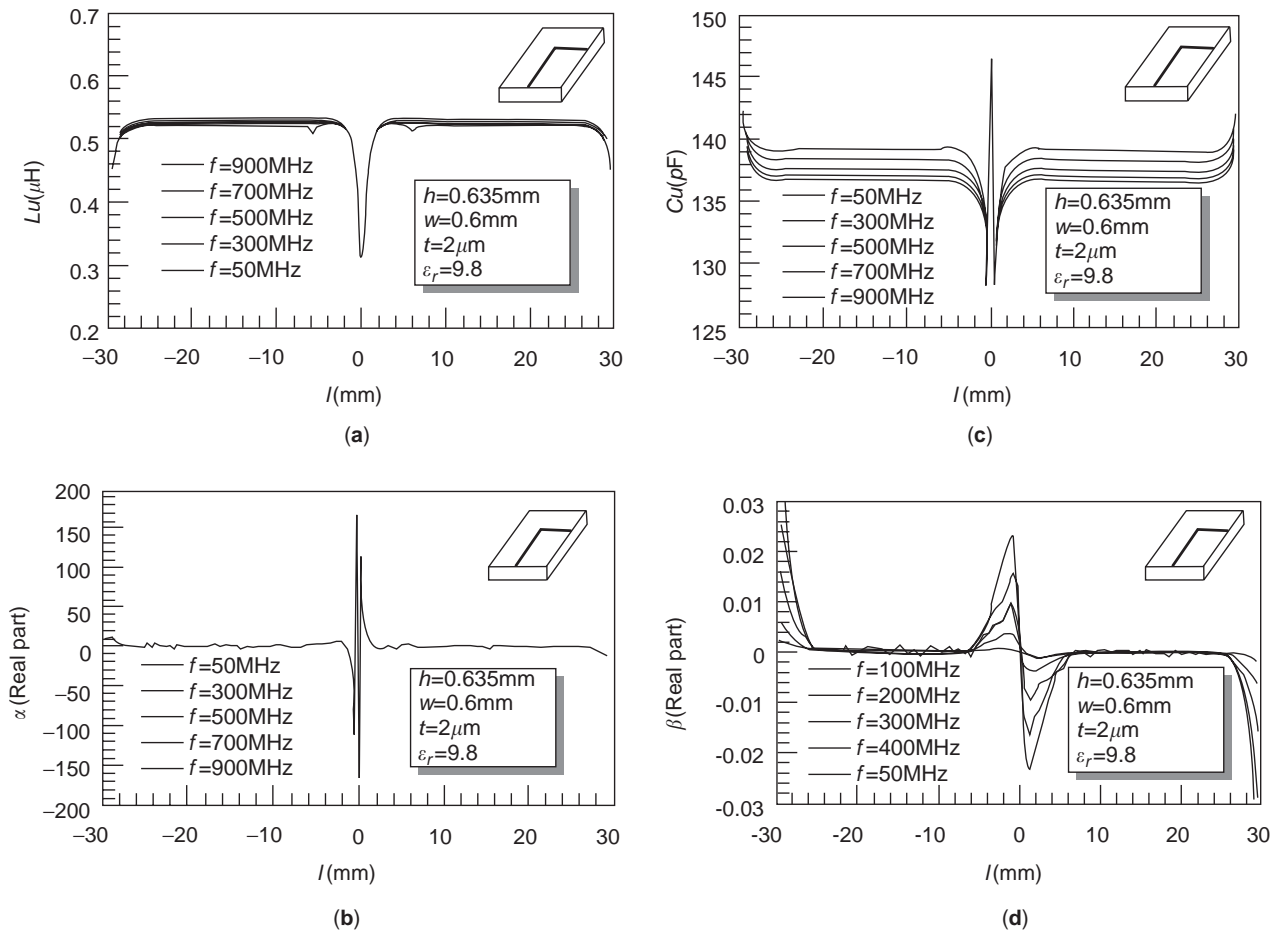


Figure 5. Circuit parameters (a) $L(\ell)$, (b) $\alpha(\ell)$, (c) $C(\ell)$, and (d) $\beta(\ell)$ of a 90° bent microstrip of $\epsilon_r = 9.8$ for $f = 50\text{--}900$ MHz, applicable to all loads.

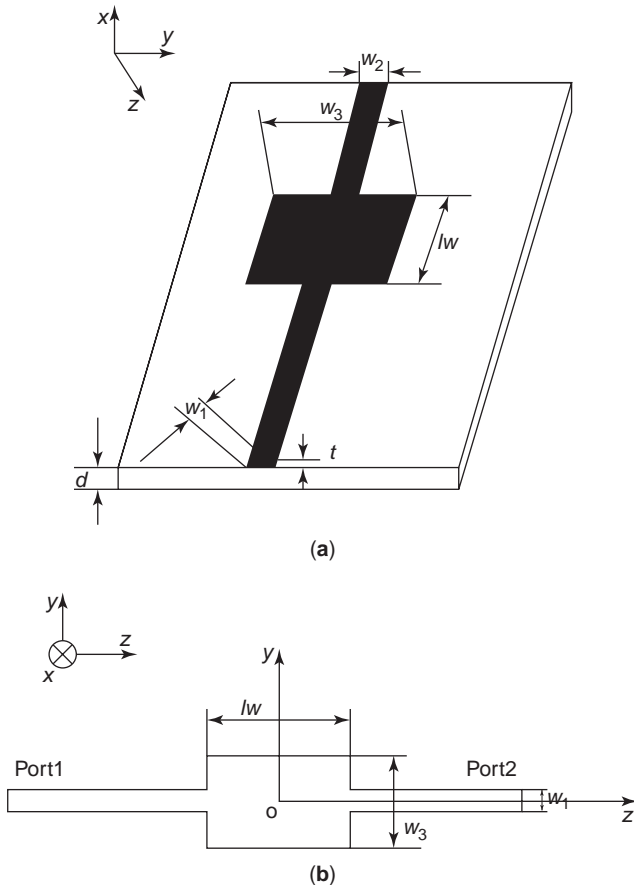


Figure 6. Schematics of a microstrip of double-bend discontinuity.

where the factor $j\omega$ is inserted for convenience in the ensuing discussions relating L and C to circuit elements. Since $I(\ell)$ is found by MoM and $V(\ell)$ can be found from $I(\ell)$, we need two independent solutions of $I(\ell)$ to find L and α from (17), and C and β from (18). After the parameters are found, V may be eliminated from (17) and (18) to get a

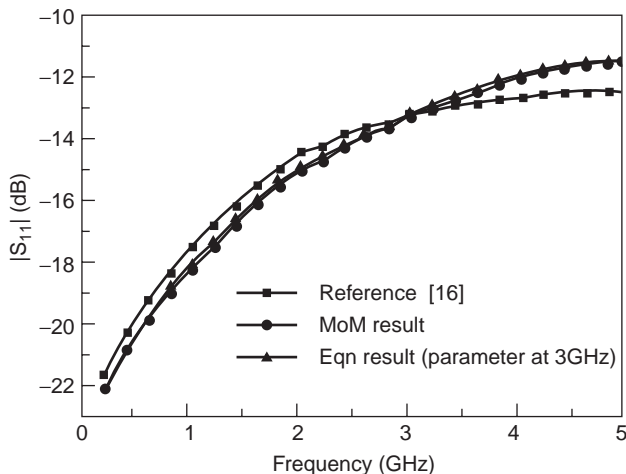


Figure 7. S_{11} of microstrip discontinuities of Fig. 6, computed by Maxwellian circuits with parameter s extracted at 3GHz, and comparison with those by MoM.

second-order differential equation of $I(\ell)$, which, by the uniqueness theorem, should be identical to Eq. (10).

Since D is proved to be invariant to the terminating conditions, so should be the parameters L , C , α , and β , from which we can derive D . The L , C , α , and β are circuit components familiar to circuit engineers, where α and β are parameters of the voltage- and current-dependent sources, respectively. The novelty is that the exact solution of an antenna problem can now be obtained by solving a circuit problem. Since such circuits are formulated via solutions of Maxwell's equations instead of the conventional Kirchhoff's laws, they are termed "Maxwellian circuits."

5.2. Line and Load

In the classical theory of uniform transmission lines, an infinite line is indistinguishable from a finite-length line with a matched load. In this new formulation, we should note that a load has to be different from a line.

The parameters L , C , α , and β are invariants of the load, but they are not invariants of the length or shape of the line. A pure load is defined as a circuit parameter, which does not produce external fields to influence the other parameters of the system. Since a piece of open transmission line is considered to be a radiating or receiving element, it cannot be considered as a pure load. The combination of a load and a transmission line is not a pure load. The attached transmission line must be accounted for in the determination of equivalent-circuit parameters. For the same reason, an antenna is not a pure load unless it can be shown that its radiation has no effect on the transmission system. Because of the variation of the equivalent-circuit parameters near the line termination, an exact matching load may not be easy to find. The conventional matching load, the characteristic impedance, may be a good approximation, but there is no guarantee that it is the optimum.

5.3. Numerical Results on Circuit Parameters

The circuit parameters are not calculated from the second-order differential equations. They are calculated directly from the solutions $I(\ell)$ as mentioned in the previous section. To show the versatility of the theory, we present the circuit parameters of microstrips, where they are most needed.

Figure 5 shows L , C , α , and β of a microstrip with a 90° bend. An interesting feature of these figures is that L and C are now almost independent of frequency. There are small drifting changes, which may be partially attributed to the numerical inaccuracies in the computation. An average value within an operating band may be adequate for most applications. The parameter α is essentially frequency-independent. Only β is dependent on frequency, and our calculations show that its variation is in proportion to ω^2 . Even the ω dependence of β can be avoided if we choose to use a mitered 90° bend. β is independent of ω if the bend is 45° . A 90° bend can be achieved by two 45° bends. β becomes ω dependent when the two varying parts of β overlap, which happens when the inner mitered distance is less than the width of the strip. Using these parameters to solve for the current on the bend microstrip, one should obtain results identical to those from MoM. It is noted

that, in the computation of the parameters, all are considered to be complex, but the results show that all are real. Using these real parameters, one can readily calculate the current of any load. Figure 6 shows the geometry a double-step discontinuity of a microstrip. Figure 7 shows the comparisons of the results calculated by the equivalent circuits and those by MoM of absolute values of S_{11} of the structure. The Maxwellian circuit parameter of Fig. 8 is calculated at 3 GHz. The total time for 20 sample points of calculation using MoM is 1025 s, while the same

calculation using the Maxwellian circuits including one solution of MoM at 3 GHz is 65.87 s.

6. MAXWELLIAN CIRCUITS OF LINEAR ANTENNAS

With the theory of Maxwellian circuits, we can now represent a long dipole by circuits. The only approximation is the discretization in the numerical process. The circuit parameters of a resonant dipole are shown in Fig. 8. There

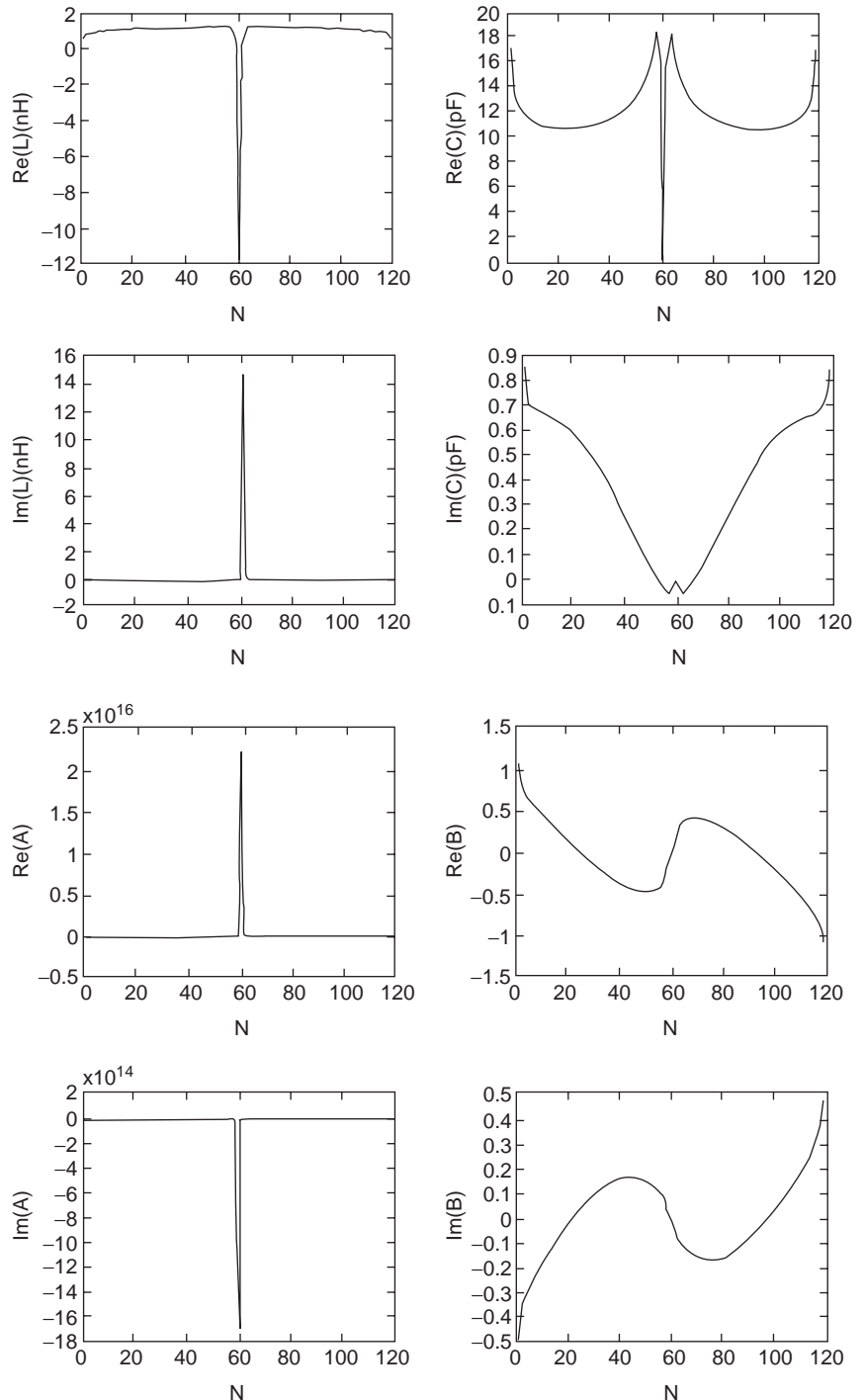


Figure 8. Maxwellian circuit parameters of a resonant dipole.

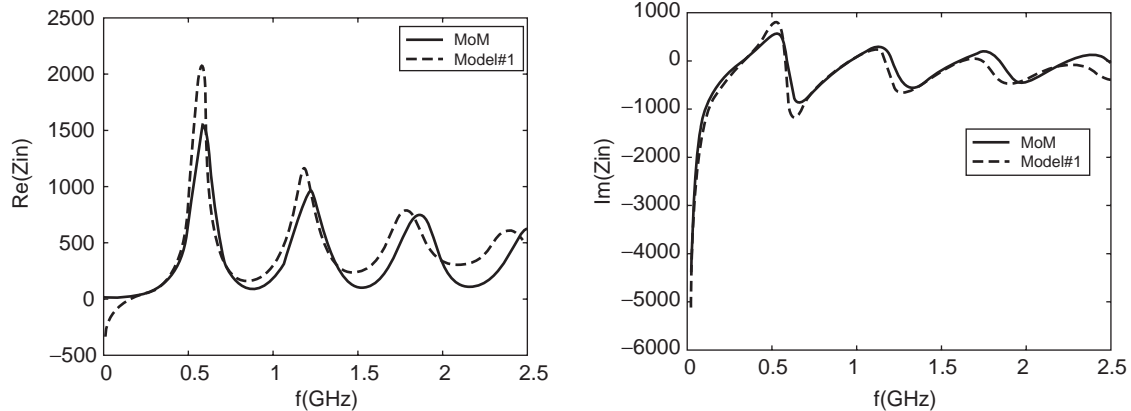


Figure 9. Input impedances of a dipole antenna of the Maxwellian circuits, the parameters of which are extracted at 300 MHz.

are some obvious differences between the parameters of a dipole and those of a transmission line. The parameters α and β of a transmission line are essentially real and appear only near the discontinuity or truncation, but those parameters of the dipole are complex and are spread all over the antenna. The role of those parameters in the radiation process is not exactly known, but one may speculate that they are influential. The input impedances of the equivalent circuits of a dipole, the parameters of which are calculated at 300 MHz, are shown in Fig. 9. Comparing the results of exact MoM calculations, we find the equivalent circuit to be fairly broadband. One may readily broaden the bandwidth by replacing the simple L, C circuits by impedance and an admittance ladder network and match the results at a few frequency points [12].

7. INTERPRETATION OF THE DEPENDENT SOURCES

Without α and β , (17) and (18) are the textbook equations of nonuniform transmission lines [1], which are derived from Kirchhoff's laws. By including the dependent sources, we have essentially modified Kirchhoff's laws, but the physical conditions we have used to replace Kirchhoff's laws are not explicit here. However, the dependent sources α and β are not arbitrary. They are found by fitting the equations to the solutions of Maxwell's equations. The significance lies in the fact that one pair of α and β is sufficient for all solutions of Maxwell's equations of the specific system, which implies that the pair (α, β) is a part of Maxwell's equations. In contrast to Kirchhoff's laws of current conservation, Maxwell's equations stipulate the conservation of charge, so α and β must be there to maintain this physical condition. Another interpretation of the role of the dependent sources is that an open transmission line is not a purely passive system. When a section of line radiates, it behaves like a sink to the system because it takes energy away. Conversely, when a segment of line receives energy from outside, it behaves like a source. So, a section of line can be passive or active depending on the direction of current flow—a role that cannot be fulfilled by an active or passive component. But a dependent source fits naturally. There is very strong evidence to support the claim

that the missing links between a theory based on Maxwell's equations and one based on the laws of circuits are the dependent sources. Without them the model is incomplete and the discrepancies arise as erratic frequency and load dependencies of the circuit parameters. With the dependent sources, the solutions of the equivalent-circuit problem become the same as those of Maxwell's equations for all loads over a wide band of frequencies.

8. FURTHER RESEARCH

The concept of Maxwellian circuit is new. There are only a few published articles on this subject, scattered in journal and conference papers [6,13,14]. The basic theory, presented in this article, is the same as those in Refs. 6 and 13. Reference 14 contains an extension of the theory of Maxwellian circuits to multiwire systems. An extension of the theory from frequency domain to time domain is contained in Ref. 15. The theory is still in its infancy. The direction of further research must depend on the acceptance of the new concept by the microwave and circuit community in either computation or computer-aided design. It is hoped that the theory will soon be extended beyond the thin-wire structures, such as patches and multilayer systems. Since the Maxwellian circuits are obtained from solution of Maxwell's equations, they are only as good as the software that provides the solutions. Most commercial Maxwell's equation solvers provide accurate current densities but not voltages. Thus, the applicability of Maxwellian circuits also depends on the availability of new software, which provides both accurate voltages and currents.

9. CONCLUSION

We have shown that, to every integral equation of the thin wire structure type, there exists a unique second-order differential operator, the solutions of which are identical to those of the integral equation if identical boundary conditions are applied in the solution to the integral and differential equations. Existence and uniqueness theorems are proved. When the second-order differential equations

are rewritten as two first-order differential equations involving voltage and current, equivalent circuits evolve naturally. We have shown that the telegrapher's equations for nonuniform lines, given by most textbooks of electromagnetic field theory, are incomplete. We have appended dependent sources to the equations to make them complete, and the ensuing results are most remarkable. It renders the passive components almost independent of frequency, thus preserving the simple relation between voltage and current of circuit theory without invoking the complicated process of convolution. The dependent sources appear to be the missing link between circuit theory and electromagnetic theory. Only by including them can the currents in a circuit obtained from the solution of equations based on circuit laws be the same as currents obtained from the solution of Maxwell's equations. The theorems and ensuing equivalent circuits have not only improved our physical insights but also accelerated computations because of the broadband nature of the circuit parameters.

BIBLIOGRAPHY

1. S. Ramo, J. R. Whinnery, and T. Van Duzer, *Fields and Waves of Communication Electronics*, 3rd ed., Wiley, 1994.
2. D. Chang, *Field and Wave Electromagnetics*, 2nd ed., Addison-Wesley, 1990.
3. K. K. Mei, On the integral equations of thin wire antennas, *IEEE Trans. Anten. Propag.* **AP-13**(3):374–378 (May 1965).
4. R. E. Collin, *Antennas and Radiowave Propagation*, McGraw-Hill, International Edition, 1985.
5. R. W. P. King, *Theory of Linear Antennas*, Harvard Univ. Press, Cambridge, MA, 1956.
6. K. K. Mei, *Theory of Maxwellian Circuits*, Radio Science Bulletin 305, Sept. 2003, pp. 6–13.
7. P. Silvester and P. Benedek, Equivalent discontinuities capacitance for right-angle bends, T-junctions, and crossings, *IEEE Trans. Microwave Theory Tech.* **MTT-21**: 341–346 (May 1973).
8. W. Sun, W. W. M. Dai, and W. Hong, Fast parameter extraction of general interconnects using geometry independent measured equation of invariance, *IEEE Trans. Microwave Theory Tech.* **MTT-45**(5):827–836 (May 1997).
9. X. Zhang and K. K. Mei, Time-domain finite difference approach to the calculation of the frequency-dependent characteristics of microstrip discontinuities, *IEEE Trans. Microwave Theory Tech.* **MTT-36**(12):1775–1787 (Dec. 1988).
10. W. Harokopos and P. B. Katehi, Characterization of microstrip discontinuities on multilayer dielectric substrates including radiation losses, *IEEE Trans. Microwave Theory Tech.* **MTT-37**(12):2058–2066 (Dec. 1989).
11. I. G. Petrovski, *Ordinary Differential Equations*, English edition transl. by Richard A. Silverman, Dover Publications, 1973.
12. K. K. Mei, Y. Liu, and L. Li, Maxwellian circuits of linear antennas, *IEEE Trans. Anten. Propag.* (in press).
13. K. K. Mei, Existence and uniqueness theorems of equivalent differential operators of thin wire integral equations, *Proc. APMC2001*, Taipei, Taiwan, 2001, Vol. 2(of 3), pp. 453–455 (invited paper).
14. K. K. Mei, Theory of Maxwellian circuits and its applications to multi wire systems, *Proc. Interim Int. Symp. Antennas and Propagation*, Yokosuka, Japan, 2002, pp. 355–361 (invited paper).
15. X. Zhong, *Maxwellian Circuits in Time Domain*, Ph.D. dissertation, Dept. of Electronic Engineering, City Univ. Hong Kong, Kowloon, Hong Kong, SAR, China.
16. Q. Xu, K. J. Webb, and R. Mittra, Study of model solution procedures for microstrip step discontinuities, *IEEE Trans. Microwave Theory Tech.* **MTT-37**:381–386 (Feb. 1989).

MEASUREMENT OF NEAR FIELDS USING A MODULATED SCATTERER

FRED GARDIOL
Swiss Federal Institute of
Technology
Lausanne, Switzerland

1. INTRODUCTION

In the close vicinity of electrical equipment, electronic devices, and antennas, the electric and the magnetic fields often exhibit a complex behavior, in particular when guided, radiated, surface, and leaky waves are simultaneous present. The fields of the different waves combine and may form complicated patterns.

The usual measurement techniques determine signal amplitudes and phases at the ports of a device and in the far field of an antenna. They do not show what happens inside the device itself, or just next to an antenna, how signals travel along transmission lines and across junctions, mysteriously vanishing at some ports, and what parts of an antenna actually contribute to radiation.

For practical purposes, it would be most valuable to know how the fields are distributed in the close vicinity of a device, for instance, to determine the presence of leaks in shielded enclosures, or of hotspots and of potential trouble areas in printed and monolithic circuits. For some large antennas and arrays, the far-field region starts at very large distances, so that measurements have to be made within the near-field region. The far-field behaviour is then derived with the help of mathematical transforms.

One can use a small probe antenna and a receiver to carry out near-field measurements, and this is commonly done in compact antenna test ranges. Unfortunately, the introduction of a probe, together with the transmission line (coaxial line or waveguide) required to connect it to the receiver, perturbs to some extent the measurement, because the presence of metal locally short-circuits the tangential electric field. In addition, the transmission properties of flexible transmission lines vary somewhat with the shape of the line—as the antenna is moved around—and this effect becomes significant at high frequencies. This means that the direct measurements of the fields might yield unreliable data. This can be avoided to some extent by placing the receiving probe far enough

from the element under test, for instance, in the Rayleigh and Fresnel regions of an antenna.

The issue to be resolved is then how can one accurately determine the field distribution that would exist if the probe and its connecting line were not there. Within a complex field environment the answer is by no means obvious, because the field changes with the position of the probe. Only for some simple situations can one determine correction factors to account for its presence.

An indirect measurement approach introduces a small but well-defined perturbing element. Measurements are made with and without this element, and the difference between the two sets of measured values yields the desired information. However, the field distribution must not be significantly modified by the introduction of the element, so that it must remain very small—but at the same time it must also be large enough to produce a detectable response. The two requirements are clearly contradictory! In addition, the need to carry out two sets of measurements tends to be impractical, in particular when one wishes to obtain the distribution of a field component at many locations over a specified region of space.

The perturbing element should be provided with additional information that would attach some kind of “tag” to it, in order to detect its presence more clearly. This is done by applying a modulation by mechanical or electrical means. In this manner, one can discriminate the signal coming from the perturbing element from background reflections and noise. This is the basis of the *modulated scatterer technique* (MST).

The technique was first developed in 1955 by Cullen and Parr [1], with a vibrating and rotating dipole, and by Richmond [2], who electrically modulated a scatterer. At that time measurements had to be carried out manually; they were therefore impractical and time-consuming, and the new technique did not meet with much success.

Since the advent of computers, the measurements can now be completely automated—directed and controlled with the help of dedicated software and directly yielding field plots and associated quantities. The modulated scattering technique now provides a flexible, fast, and efficient way to analyze systems, becoming a useful tool for researchers and designers. Its low invasiveness makes it particularly attractive for particular situations where the element under test must not be disturbed.

The modulated scatterer technique can be used to measure all kinds of antennas and high-frequency printed and monolithic circuits, to test for electromagnetic compatibility, to characterize material properties, and to control industrial processes. In biomedical applications, it plays an important role in microwave tomography. Unfortunately, the information and the results obtained with this technique are widely spread out within the technical publications of the specialized fields involved, and are therefore not easy to locate for “outsiders.” To overcome this hurdle, Bolomey and Gardiol collected the most significant informations related to the modulated scatterer technique and regrouped them within a book, making them more readily available to the general public [3].

2. PRINCIPLE OF OPERATION

When a scatterer is introduced into an electromagnetic field, currents are induced on its metallic parts, which then transmit a scattered signal; thus the scatterer behaves like a radar target. One can use either a short dipole—which couples to the electric field parallel to it—or a small loop, which interacts with the magnetic field perpendicular to the plane of the loop. The scattered field depends on the amplitude of the field at the scatterer location. By moving the scatterer, one can determine the field distribution along a line, over a surface, or within a volume.

When a suitable nonlinear element is placed within the scatterer and a modulating signal applied to it, the scattered field is modulated, and it is then more easy to detect with a receiver tuned at the modulating frequency (coherent detection). In principle, the modulation could be provided by illuminating a photodiode with a laser beam, but this approach proved rather difficult to implement in practice for a mobile scatterer. It is more practical to transmit the modulating signal through an optical fiber illuminating a photodiode (Fig. 1), or still to apply a low-frequency modulation to a mixer diode with high-resistivity wires—in both cases the source of the modulating signal is physically connected to the scatterer, but the dielectric and the highly resistive connections do not significantly affect the electromagnetic field.

The device under test, which may be an antenna or a circuit, creates in its vicinity an electromagnetic field. The

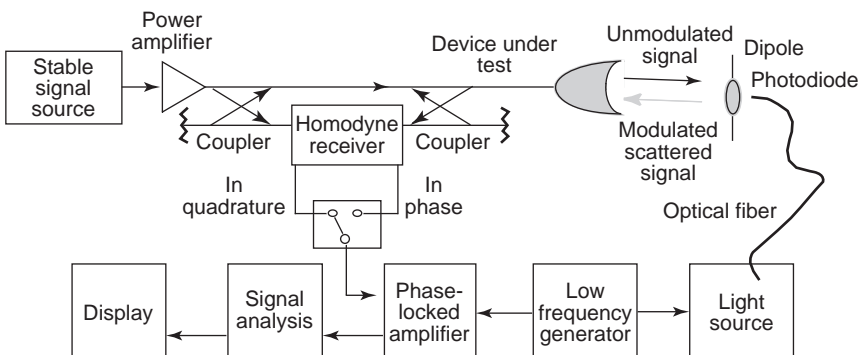


Figure 1. Basic test setup making use of the reflection from a loaded dipole modulated through an optical fiber (monostatic configuration).

scatterer (shown in Fig. 1 as a short dipole loaded by a photodiode) picks up a signal, modulates a portion of it, and reflects it back toward the device under test. The homodyne receiver compares the reflected signal with the signal fed by the source, and provides low-frequency phase and quadrature signals to the phase-locked amplifier. In this way it is possible to retrieve a quantity related to the electric field component parallel to the dipole. When the dipole is replaced by a small loop, the quantity retrieved is related to the magnetic field perpendicular to the plane of the loop.

In the setup of Fig. 1, called *monostatic*, analogously with radar, the same device is used to transmit and to receive, yielding the reflection from the scatterer. The forward and the return signals travel over the same path, so that the transmission factor from the device to the scatterer appears twice in the reflection relationship—a complete mathematical derivation, based on reciprocity and making use of the scattering matrix formulation, is provided in Ref. 3. As a result, the quantity measured in this configuration is proportional to the square of the field component. The amplitude is then determined by taking the square root of the module, but the phase is known only with an uncertainty of $\pm 180^\circ$. This is not too bothersome for field diagnostics, where knowledge of the amplitude of a single field component is generally sufficient to provide the desired information. But the knowledge of the amplitude and phase of two field components is required to determine the antenna pattern with near-to-far-field transformations.

To determine the field pattern over a region of space (line, surface, or volume), the probe is moved, and measurements repeated at a suitable number of locations selected to provide an adequate coverage. A mechanism holding the probe is provided to move it along one, two or three dimensions (not shown in Fig. 1). The probe movement and all the measurements are directed and controlled by a computer, which also treats the information obtained, providing amplitude and phase plots for the electric or magnetic field component considered. When knowledge of more than one field component is desired, it is possible to combine several orthogonal scatterers—but particular care is then required to avoid spurious interactions.

In an alternate approach, transmission and reception functions are treated separately, introducing an additional collector antenna (Fig. 2). By analogy with radar, this

configuration is called *bistatic*. The collector must be placed sufficiently far from the device under test to avoid perturbing the very near field.

In the bistatic configuration, the signal travels only once between the device under test and the scatterer, and therefore the measured values are linearly proportional to the field component (assuming that the transmission from scatterer to collector remains constant during the measurements). This means that the phase is determined without ambiguity, and this configuration is therefore preferred when near-to-far-field transformations are involved later on. This configuration is, however, somewhat more complicated to assemble than the monostatic setup.

Moving the probe from one point to another takes some time, as one must ensure that the probe has reached a stable position when the measurement is taken (residual vibrations would introduce noise, which would be particularly bothersome if it fell within the same frequency range as the modulation). This means that, typically, only a few points can be covered in one second; when measurements are to be made over a large surface, they can become quite time-consuming. This would remain acceptable for simple diagnostic applications, but it would make complete antenna measurements quite impractical.

To reduce the measurement time when many points are involved, the mechanical movement of the scatterer is replaced by electronic switching between many scatterers grouped in an array. Very fast measurements can then be made, but since an array tends to become considerably larger than a single scatterer, its presence will more significantly disturb the field distribution.

Depending on the application considered, arrays of scatterers can lie along a line (one-dimensional scan) or on a surface (two-dimensional scan). They are most often used in a bistatic configuration, as sketched in Fig. 3. In this particular configuration, the modulated scatterers form a linear array, providing a vertical scan, while the antenna under test is rotated for azimuthal scanning [4]. In other measurement setups, the antenna remains steady while two-dimensional scanning is carried out by a surface array of scatterers.

Material measurements are another important field of application of the modulated scatterer technique that also used bistatic array configurations [5]. For instance, one can continuously keep track of manufacturing processes. Three possible schemes are schematically represented in Fig. 4: reflection (for highly lossy and reflecting materials),

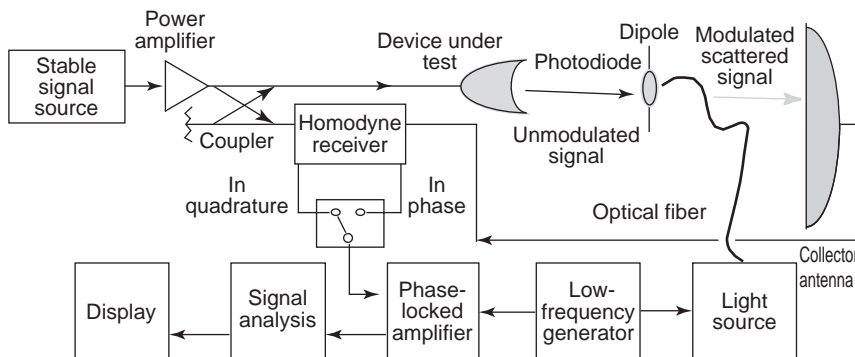


Figure 2. Basic test setup making use of the scattering from a loaded dipole modulated through an optical fiber (bistatic configuration).

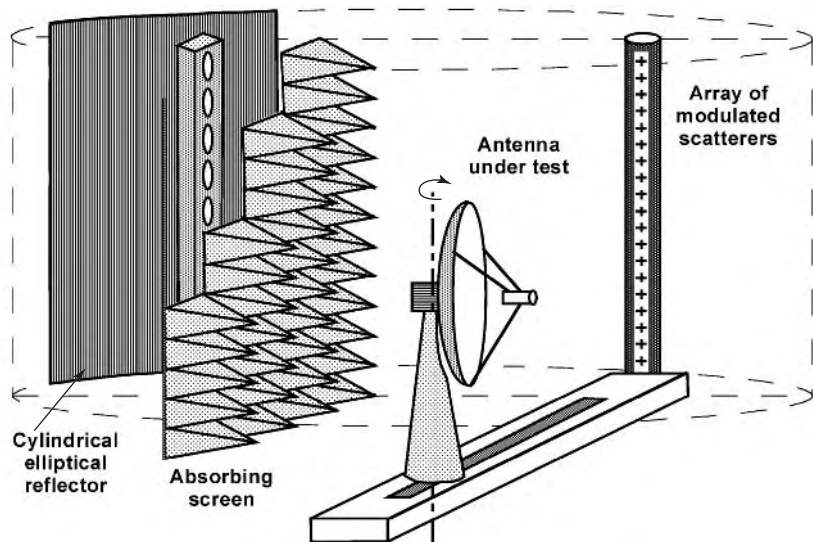


Figure 3. Near-field bistatic test setup making use of a vertical linear array of modulated scatterers while the antenna under test is rotated.

transmission, and double transmission (for transparent materials). Similar arrangements are also used to measure radar cross sections [6] and to detect buried objects.

3. EQUIPMENT

The monostatic mobile probe configuration was implemented at the National Physical Laboratory in Great Britain, where a broadband instrument was designed for operation between 2 and 18 GHz [7]. It was used to analyze the operation of rectangular horn antennas, by measuring the field patterns in the plane of the aperture, and to determine diffraction effects produced in the near-field region by combinations of slits. The measurement results were used to verify existing theories and to validate computer simulations. Considerable work was carried out to characterize close-range interactions between probes and conductor edges.

A similar setup was developed at the Swiss Federal Institute of Technology in Lausanne, Switzerland [8], to measure more particularly microstrip patch antennas and circuits. The project started quite modestly for demon-

stration purposes, making use of material available in the microwave laboratory—except for the homodyne receiver and the scatterers, which were specifically realized for this equipment. High-resistivity wires are used to feed the modulating signal to the scatterer, taking particular

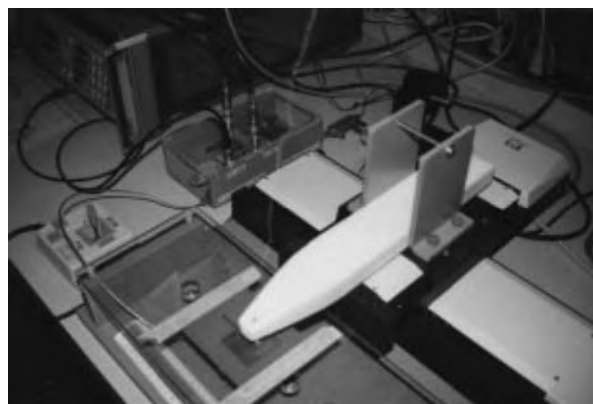


Figure 5. Monostatic measurement setup used for the measurement of printed circuits and antennas at the Swiss Federal Institute of Technology (photo by F. Gardiol).

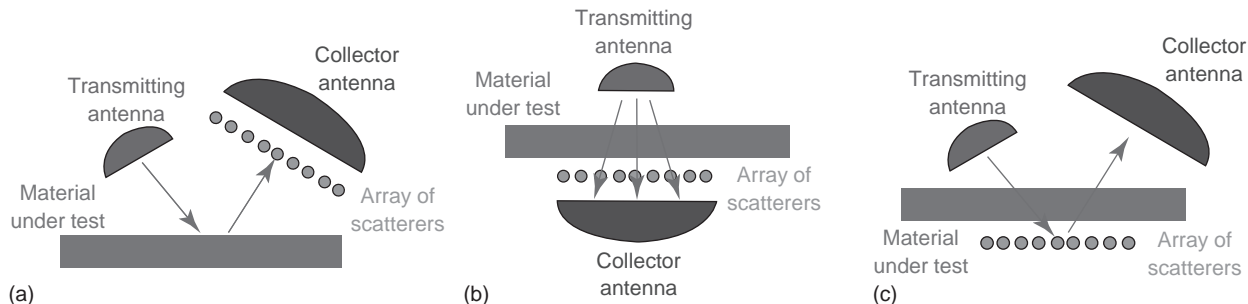


Figure 4. Bistatic configurations for the measurement of materials: (a) reflection; (b) transmission; (c) double transmission.

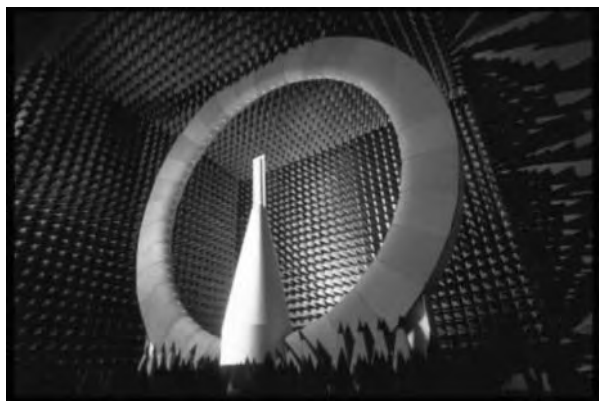


Figure 6. Stargate-64 spherical near-field measurement facility made of a circular array of modulated scatterers. (Courtesy of Satimo Co.)

precautions to avoid high-frequency leakage along the wires (by adding resistors and ferrite beads). A standard x - y plotter was used at first to provide a two-dimensional scan; it was later on replaced by a more sophisticated 3D coordinating table (Fig. 5). The instrument proved quite valuable to design a variety of complex antennas, for which simulation softwares did not always provide satisfactory information.

Along similar lines, a miniaturized probe was developed at the University of Michigan in Ann Arbor, in order to test more specifically microwave monolithic circuits and filters [9]. Both a dipole antenna and a monopole antenna were integrated within the probe, so that vertical and horizontal electrical field components could be measured at the same time.

The development of compact near-field ranges using modulated scatterer arrays to measure large antennas was carried out extensively at Supelec (École Supérieure d'Électricité) near Paris, in France, under the direction of Professor Jean-Charles Bolomey. The various array geometries that can be used in a wide range of situations were carefully analyzed and their respective merits compared: in which cases should one use two-dimensional electronic scanning, in which ones should one combine a one-dimen-

sional electronic scan with a mechanical scan (rotation or translation). Several measurement ranges were built to test large antennas used for military radar and space applications, for instance, at the ESTEC research center of the European Space Agency in Noordwijk, the Netherlands [10]. This research was reported in many technical publications [3].

The complete measurement of an antenna in an modulated scatterer facility takes on the order of 30 s, as compared to one hour or more to achieve the same accuracy in a standard test facility [11]. Since measurements are made in such a short time, one can determine the radiation of a cellular phone together with its user—sitting on the rotating platform. The company SATIMO was actually created to further develop, produce, and sell microwave equipments based on Supelec's inventions, in particular those making use of the modulated scatterer technique. Complete near-field measurement facilities are now commercially available (Fig. 6).

Arrays of modulated scatterers also found applications in the measurement of a wide variety of materials, using the geometries depicted in Fig. 4. Among many others, they control the manufacture of textiles, wooden boards [12], paper, composite materials, and rock fiber [3]. Modulated scatterer arrays are also used to analyze the field distribution within TEM cells used for electromagnetic compatibility (EMC) testing [13], and to detect the presence of buried objects [14].

Last but by no means least, one must mention the important role of modulated scatterer arrays in the field of microwave tomography [15]. A "microwave camera" was developed at Supelec (Fig. 7). Operating at 2.45 GHz, its scatterer array is made of $32 \times 32 = 1024$ short dipoles loaded by pin diodes, which can be individually modulated through a line/row-addressing scheme. The biological target is immersed in a water tank, to optimize the penetration of the beam and to prevent parasitic contributions of waves propagating around the target. Initially developed in the very early 1980s, the camera was constantly updated with the advent of new technology. It provides reconstructed patterns at the rate of 15 images per second, including both acquisition and data processing.

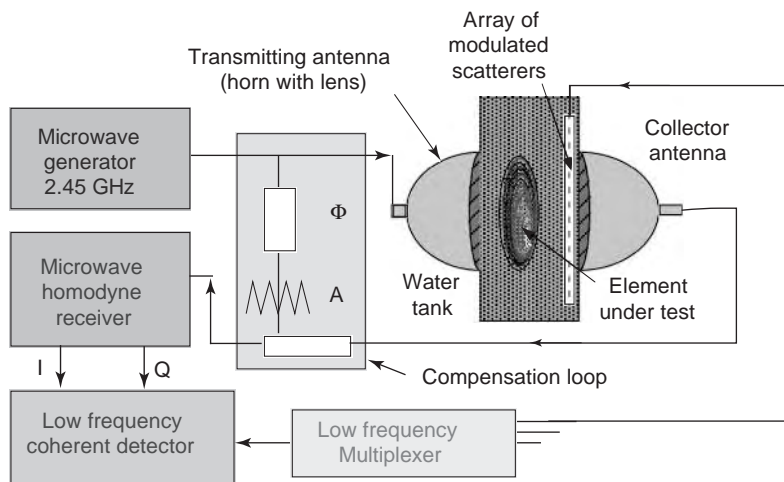


Figure 7. Schematic of the 2.45-GHz microwave camera developed at Supelec in France.

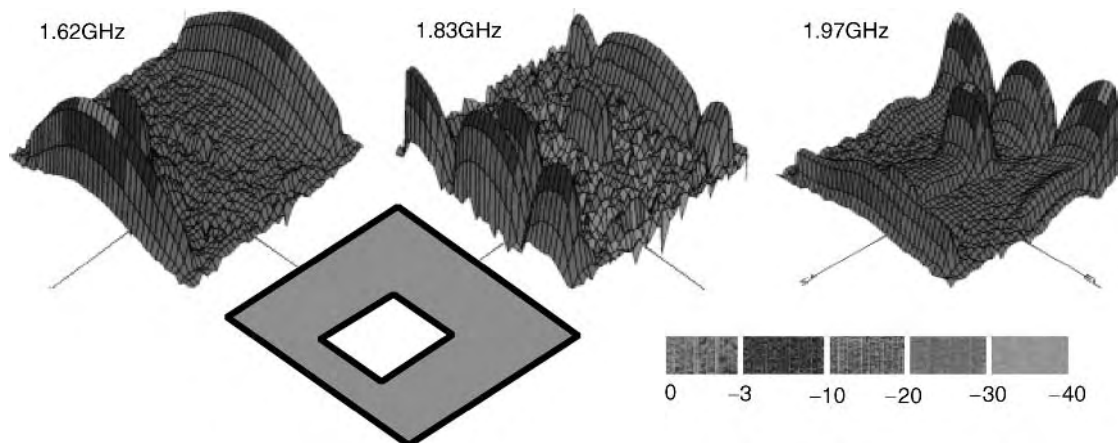


Figure 8. Amplitude of the longitudinal electric field over a rectangular patch antenna with a rectangular slot at three frequencies of resonance, showing how the field component is concentrated next to the edges of the patch and of the slot. (Courtesy of J.-F. Zürcher.)

4. SOME EXPERIMENTAL RESULTS

This section presents some results (For a few among many, see Ref. 3) obtained using the modulated scatterer technique.

At the Swiss Federal Institute of Technology, the test configuration shown in Fig. 5 was used to measure the electric and the magnetic fields over microstrip antennas and circuits. Figure 8 shows the amplitude of the tangential electric field slightly above a rectangular patch in which a rectangular slot was cut out. As can be expected, the field is concentrated mostly close to the edges of the patch and of the slot, whereas it vanishes on the metal surface. Distributions for three modes of resonance are

shown. At the lowest frequency, the antenna edges are active, while radiation at the edges of the slot becomes more important at the higher frequencies.

A planar inverted-F antenna (PIFA) was developed for dual-frequency operation in GSM cellular phones, at 900 MHz and 1.8 GHz (Fig. 9). The upper conductor strip is divided into two sections, which are connected by an LC filter. The lower frequency lies within the passband of the filter, and the currents then flow over the entire structure. On the other hand, the upper frequency is located in a stopband of the filter, so that only a part of the antenna is active in this case. Measured near fields show the distribution of the magnetic field component over the strip, illustrating the principle of operation.

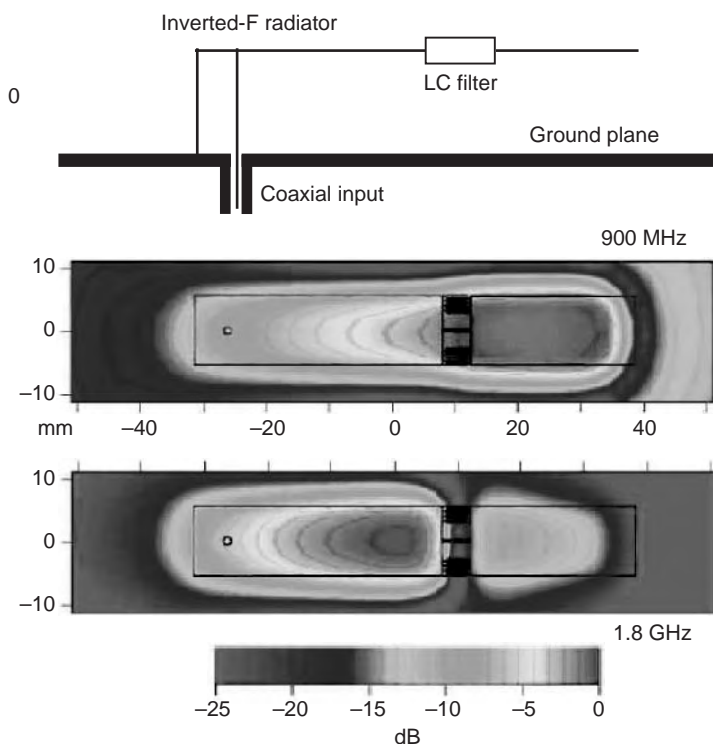


Figure 9. Amplitude of the normal magnetic field over a dual-frequency PIFA at the two frequencies of operation. (Courtesy of J.-F. Zürcher.) (This figure is available in full color at <http://www.mrw.interscience.wiley.com/erfme>.)

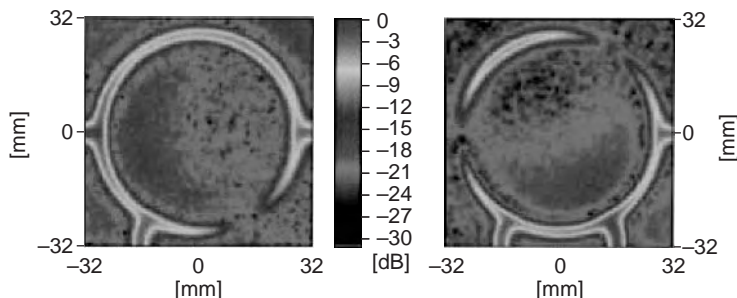


Figure 10. Amplitude of the normal electric field over a hybrid ring for two excitations. The port at the left on the left-hand figure is excited, while the port at the bottom right is excited on the right-hand figure. (Courtesy of J.-F. Zürcher.) (This figure is available in full color at <http://www.mrw.interscience.wiley.com/erfme>.)

The distribution of the normal electric field over a microstrip hybrid ring (ratrace) is shown in Fig. 10 for two excitations. The distance between successive ports in the lower part of the device is a quarter-wavelength, and 3 times that in the upper part. As a result, the signal fed at the input is evenly distributed among two output ports, while the fourth port lies in a trough of the standing wave, so that no signal comes out of it.

A similar behaviour appears in a directional coupler made of two coupled parallel transmission lines, as shown in Fig. 11 [9]. The signal propagates mostly on one transmission line (the mainline), while a small part of it is coupled to the second one. The coupled port is here the one located across from the input, while the fourth port is isolated.

A measurement setup, based on the reflecting configuration shown in Fig. 4a, was developed specifically to detect the presence of buried objects. Figure 12 shows several metal bars inside reinforced concrete, as detected by an array of 32 modulated scatterers with illuminating frequencies ranging from 7 to 13 GHz. Measurements were carried out at various frequencies within that range and then compared by a dedicated data processing software, which extracted the salient features [16]. The apparatus used was optimized for a spatial resolution smaller than 1 cm and an investigation depth of 10 cm.

Figure 13 shows the “microwave radiography” of a human hand as it appears in real time on the screen of

the microwave camera specifically developed for medical applications at the ISM frequency of 2.45 GHz (Fig. 7). The microwave beam propagates in a water tank, in which the object is immersed. Since water is highly lossy, it reduces spurious effects of waves propagating around the target and reflecting on the tank walls. The use of a water medium reduces surface reflections on many biological tissues, because these have a high water content. Finally, the use of a high-dielectric medium yields a much better spatial resolution—in this case, it is increased by a factor of 10 with respect to air.

5. EVALUATION

For many electrical engineering applications, it is useful, necessary, or at least interesting to know how electric and magnetic fields are distributed over some regions of space. One may indeed wish to dispose of some detailed information that the ubiquitous network analyzer simply cannot provide.

While one may directly measure near-field components with small antennas, the signals picked up must then be transmitted to a receiver, and the presence of connecting lines tends to disturb the field. In the modulated scatterer technique, one removes the high-frequency transmission lines entirely, replacing “wired” by “wireless” transmission; the probe antenna picks up the signal at the point of interest and reflects it, or radiates it toward some collector antenna located far enough not to perturb the measured field. Low-frequency modulation and coherent detection can detect very weak signals.

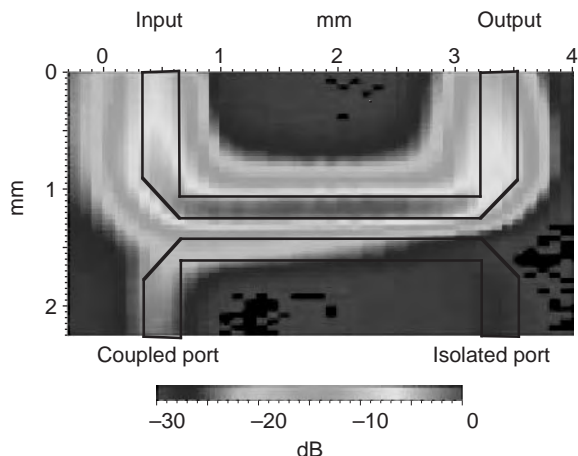


Figure 11. Amplitude of the normal electric field over an MMIC contradirectional coupler. (Courtesy of T. K. Budka.) (This figure is available in full color at <http://www.mrw.interscience.wiley.com/erfme>.)

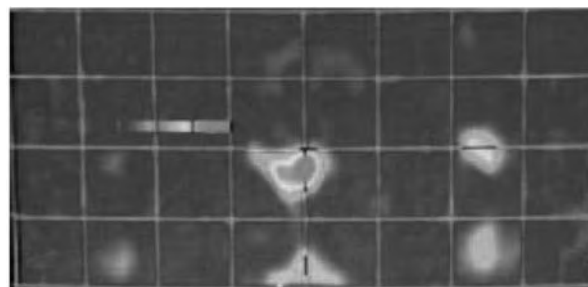


Figure 12. Metal bars buried in concrete, as detected by an array of 32 modulated scatterers operating over the 7–13 GHz frequency range. (Courtesy of Supelec/CNRS.) (This figure is available in full color at <http://www.mrw.interscience.wiley.com/erfme>.)



Figure 13. Microwave tomographic picture of a hand taken in the 2.45 GHz camera depicted in Fig. 7. (Courtesy of Supelec/CNRS.)

The modulated scatterer technique provides a broad spectrum of applications, offering a valuable way to carry out electromagnetic field measurements, some of them in difficult situations for which low perturbation, rapidity, or both, are required. In addition to being less perturbing for the fields, it is easier to implement than direct measurements, leading to many new possibilities.

The technique was already proposed in 1955, but it became interesting only with the advent of computer-controlled measurements and image processing—which yield detailed field plots in almost real time. The effects produced by changes in frequency, geometry, and other parameters can then be determined very rapidly, and this can be extremely valuable for the practical design of antennas and devices.

The first applications were in the field of antennas, proving useful for validation of theoretical assumptions and also for obtaining far-field antenna patterns. Diagnostics of printed circuits followed, together with many other applications in the EMC and ISM fields—but the large potential of the technique is not yet fully exploited.

Simple setups can be implemented using standard laboratory equipment, without need for large material investments. While a simple test setup will not provide a high accuracy, it may still prove an extremely valuable tool for design, demonstrations, and educational purposes.

Higher-grade applications use scatterer arrays, with electronic switching speeding up the measurement rate, sometimes by several orders of magnitude. A complete antenna pattern can be obtained within a matter of minutes. Near-field antenna ranges based on the modulated scatterer technique are now commercially available.

A number of applications were also found in the measurement of materials, in particular to control industrial manufacturing processes where the controlling system

must make rapid decisions. The field plots obtained with the modulated scatterers are basically similar to those provided by computer simulation, and thus permit easy comparison and mutual validation. The two approaches are complementary because each technique provides some information that is useful in checking and improving the validity and accuracy of the other.

BIBLIOGRAPHY

1. A. Cullen and D. Parr, A new perturbation method for measuring microwave fields in free space, *Proc. IEE.* **102**:836–844 (1955).
2. J. H. Richmond, A modulated scattering technique for the measurement of field distributions, *IRE Trans. Microwave Theory Tech.* **MTT-3**:13–15 (1955).
3. J. C. Bolomey and F. Gardiol, *Engineering Applications of the Modulated Scatterer Technique*, Artech House, Norwood, MA, 2001.
4. D. Picard, J. Ch. Bolomey, and A. Ziyat, Real-time analyzer of antenna near-field distribution, *Proc. 22nd European Microwave Conf.*, Espoo, Finland, Aug. 24–27, 1992, pp. 509–514.
5. R. King, On-line industrial applications of microwave moisture sensors, *Proc. Workshop on Electromagnetic Wave Interaction with Water and Moist Substances, IEEE-MTTS Int. Symp.*, San Francisco, 1996, pp. 75–78.
6. B. J. Cown and C. E. Ryan, Near-field scattering measurements for determining complex radar RCS, *IEEE Trans. Antenn. Propag.* (special issue on RCS of complex objects) **AP 37**:576–585 (1988).
7. G. Hygate and J. F. Nye, Measuring microwave fields directly with an optically modulated scatterer, *Meas. Sci. Technol.* **1**:703–709, (1990).
8. J.-F. Zürcher, A near-field measurement method applied to planar structures, *Microwave Engineering Europe*, June/July 1992, pp. 43–51.
9. T. P. Budka, S. D. Waclawik, and G. M. Rebeiz, A coaxial 0.5–18 GHz near electric field measurement system for planar microwave circuits using integrated probes, *IEEE Trans. Microwave Theory Tech.* **MTT-44**:2174–2184 (1996).
10. Ph. Garreau, K. van't Klooster, and J. Ch. Bolomey, Quasi real-time antenna testing by means of a 2D modulated scattering array in the focal plane of a compact range, *Proc. 14th AMTA Annual Meeting and Symp.*, Columbus, OH, Oct. 19–23, 1992, pp. 12/3–12/5.
11. G. Collignon, Y. Michel, F. Robin, J. Saint, and J. Ch. Bolomey, Quick microwave field mapping for large antennas, *Microwave J.* **25**(12): 129–132 (1982).
12. F. Volgyi and B. Zombori, A new application of WLAN concept: complex permittivity monitoring of large-sized composite boards, *Proc. Workshop on Electromagnetic Wave Interaction with Water and Moist Substances, IEEE MTT-S Symp.*, San Francisco, June 17–21, 1996, pp. 119–122.
13. R. Azaro and S. Caorsi, Enclosure shielding effectiveness evaluation by modulated scattering measurements, *Proc. 29th European Microwave Conf.*, Munich, Germany, Oct. 4–8, 1999, pp. 248–251.
14. L. Chommeloux, Ch. Pichot, and J. Ch. Bolomey, Electromagnetic modeling for microwave imaging of buried inhomogeneities, *IEEE Trans. Microwave Theory Tech.* **MTT-34**:1064–1076 (1986).

15. J. Ch. Bolomey, C. Pichot, and G. Gaboriaud, Planar microwave imaging camera for biomedical applications: Critical and prospective analysis of reconstruction algorithms, *Radio Sci.* **26**: pp. 541–549 (1991).
16. J. Ch. Bolomey and C. Pichot, Microwave tomography: From theory to practical imaging systems, *Int. J. Imag. Syst. Technol.* 144–156 (1990).

MEDICAL IMAGING WITH MICROWAVE: THERMOACOUSTIC TOMOGRAPHY

YUAN XU
LIHONG V. WANG
Texas A&M University
College Station, Texas

1. GENERAL REVIEW

Microwaves have two properties that are attractive for medical imaging applications: (1) they can penetrate deeply into biological tissues than can light waves and (2) the dielectric properties of biological tissues in the microwave frequency range are related to the tissues' physiological and pathological states. Imaging modalities that employ microwaves combine these two features to extract information about the physiological and pathological status of tissues that are deep in the body.

There are primarily two biomedical imaging modalities that utilize microwaves: thermoacoustic tomography [1] and pure microwave tomography [2]. Thermoacoustic tomography images the absorption of microwave energy in tissues, while pure microwave imaging images both the relative dielectric permittivity and the conductivity of tissues. In thermoacoustic tomography, a short-pulsed microwave is used to irradiate the tissues. When the electromagnetic radiation is absorbed in the biological tissues, the heating and subsequent expansion causes the emission of acoustic signals, which is called the *thermoacoustic effect*. In thermoacoustic tomography, the thermoacoustic signals are collected to map the distribution of radiative absorption within the tissues. In microwave tomography, tissues are irradiated by microwave pulses, and the scattered microwave signals from the tissues are collected to map the distribution of the dielectric properties of the tissues. Several two-dimensional (2D) and three-dimensional (3D) microwave tomography systems have been implemented experimentally with different numbers of antennas and different configurations, operation frequencies, and total acquisition times.

Thermoacoustic tomography combines the good imaging resolution of ultrasound with the good imaging contrast of microwave. Microwave tomography has the advantage of good imaging contrast but suffers from poor spatial resolution. On the other hand, purely ultrasonic imaging has good spatial resolution but poor contrast. Thermoacoustic tomography can bridge the gap between the two. Therefore, in this review, we will focus

primarily on thermoacoustic tomography in theoretical and experimental studies. Nevertheless, in vivo and in vitro results of both microwave tomography and thermoacoustic tomography will be presented in the applications section.

In the 1980s, several investigators employed microwave-induced thermoacoustic waves for imaging of biological tissues [3,4]; these early works, however, did not produce any tomographic or depth-resolved images. For example, in a study of the acoustic imaging of a model of a human hand using pulsed microwave irradiation [3], no tomographic reconstruction was utilized and, consequently, the produced image is a diffraction-propagated projection of the sample to the detection array. More recent progress realized tomographic imaging of biological tissues based on microwave-induced thermoacoustic waves. The microwave thermoacoustic tomography scanner reported in Ref. 5 was used to image a human breast in vivo and produced 3D maps of tissue absorption at 434 MHz with a spatial resolution of 1.5–4 mm throughout a $12.8 \times 12.8 \times 12.8$ cm cubical volume. Another research group achieved a spatial resolution of 0.5 mm in the 2D thermoacoustic tomography of phantoms [6].

The remainder of this article is composed as follows. First, we introduce the three mechanisms that are responsible for the dielectric properties of tissues over the microwave frequency range. Then we address some of the important theoretical issues surrounding thermoacoustic tomography, such as optimal microwave frequency, the effects of acoustical heterogeneity on breast thermoacoustic tomography, limited-view thermoacoustic tomography, the reconstruction algorithms, and spatial resolution. Then our experimental setups and results from applying thermoacoustic tomography to phantoms in planar and circular geometries are explained. Last, some in vivo and in vitro results of both pure microwave imaging and thermoacoustic tomography are presented.

2. MICROWAVE CONTRAST

There are primarily three mechanisms responsible for the dielectric properties of tissues over the microwave frequency range. The first one is the γ dispersion, in the gigahertz region, which is due to the dielectric relaxation of the free water in tissues. The second one, β dispersion, in the hundreds of kilohertz region, is due mainly to the polarization of cellular membranes that act as barriers to the flow of ions between intra- and extracellular media. Other contributions to the β dispersion come from the polarization of protein and other organic macromolecules. Last, the low-frequency α dispersion is associated with ionic diffusion processes at the site of the cellular membrane. In addition, tissues have finite ionic conductivities commensurate with the nature and extent of their ionic content and mobility [7]. For example, the contributions to the conductivity of barnacle muscle at 37°C from the α , β , and γ dispersions are 17, 7, and 1 mS/cm, respectively, at 1 GHz; 17, 16.5, and 6.5 mS/cm, respectively, at 2.5 GHz; and 17, 25.5, and 25.5 mS/cm, respectively, at 5 GHz [8]. Therefore, the dielectric properties of the tissues at the

microwave range are related to their ionic content and mobility, the membrane proteins, and the free water content.

3. THERMOACOUSTIC TOMOGRAPHY THEORY

In this section, some basic but important theoretical issues in thermoacoustic tomography are addressed to provide a comprehensive understanding of its technical side. The following topics are covered.

1. What is the optimal microwave frequency for a specific imaging application? Basically, two factors need to be considered here. The first one is imaging depth. Higher microwave frequency leads to more attenuation and, consequently, less imaging depth. The second factor is the contrast between different tissues or between malign and normal tissues. Usually, at higher frequencies, it is easier to distinguish different tissues. Balancing these two factors is essential in selecting the optimal microwave frequency for a specific application.
2. In a clinical environment, access to thermoacoustic signals is spatially limited. For example, in the thermoacoustic tomography of skin and breast, the thermoacoustic signals can be detected from only one side of the tissues. In these cases, do we have enough information to reconstruct the electromagnetic energy deposition in the tissues? This situation is referred to as *limited-view thermoacoustic tomography*.
3. Biological tissues are usually acoustically heterogeneous, which causes the distortion of thermoacoustic waves. Acoustic distortion has hindered the development of ultrasound tomography. Can thermoacoustic tomography overcome this obstacle? We use breast thermoacoustic tomography as an example to show that the acoustic distortion in the thermoacoustic tomography of soft tissues is not serious.
4. Other basic issues in thermoacoustic tomography, such as exact and approximate reconstruction algorithms and the point spread function of a thermoacoustic tomography system are also addressed here.

3.1. Optimal RF Frequencies for Thermoacoustic Tomography

Figure 1a shows the penetration depth of electromagnetic waves in various human tissues as a function of the frequency in the radiofrequency (RF) region, where the penetration depth is the inverse of the absorption coefficient [1]. The penetration depths of muscle and fat tissues are plotted in solid lines. At a frequency of 3 GHz, the penetration depths for fat and muscle are 9 and 1.2 cm, respectively. The penetration depths of normal and malignant human breast tissues are plotted in dashed lines [9]. At 3 GHz, the penetration depths for malignant and normal breast tissue are approximately 2.3 and 4.4 cm, respectively. Malignant breast tissue is more strongly absorbent to microwaves than the surrounding normal breast tissue. Muscle and fat tissues have very high and very low water contents, respectively; therefore, they represent the extreme microwave absorption properties. Most other soft tissues have an absorption coefficient between those of muscle and fat tissues. The wide range of values among various tissues is desirable for achieving high imaging contrast.

The dependence of the thermoacoustic signals on the electromagnetic frequency and the breast tumor location (the depth from the tissue surface) is shown in Fig. 1b [1]. If the detection system is instrument-noise-limited, the signal-to-noise ratio (SNR) of the system is different from this thermoacoustic signal by a constant factor. The SNR decreases as the tumor location is farther away because of the increasingly attenuated microwave intensity. When a tumor is located near the tissue surface, for example, at 1 cm depth, the SNR is better at higher RF frequencies. When the tumor is located more deeply, the choice of frequency for an optimal SNR is rather broad. This is because the decrease in thermoacoustic pressure that accompanies an increasing frequency is compensated for by the increasing difference of the RF absorption coefficients between the tumor and the normal breast tissues.

3.2. Limited-View Problem

Limited-view thermoacoustic tomography was investigated in Ref. 10 to determine what kind of boundary can be correctly reconstructed when some of the thermoacoustic signals are missed. A “detection region,” within which all points have sufficient detection views, was defined. It was explained analytically and shown numerically that the

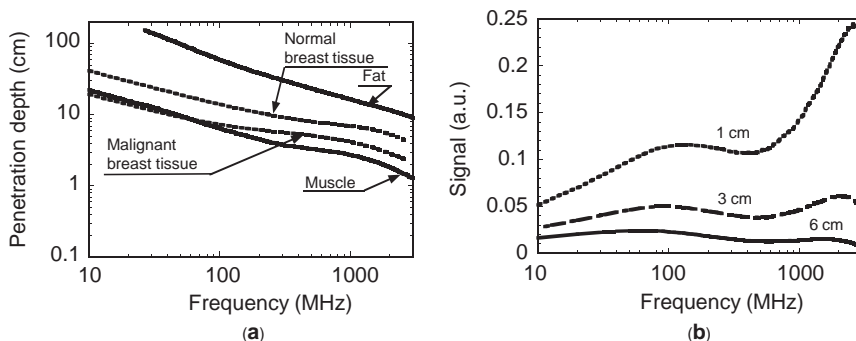


Figure 1. (a) Penetration depths of various biological tissues versus the microwave frequency; (b) a simulated piezoelectric signal in response to a thermoacoustic wave from a tissue sample containing a buried tumor versus the microwave frequency. (Reprinted with permission from Ref. 1. Copyright 2004, American Association of Physicists in Medicine.)

boundaries of any objects inside this region could be recovered stably. Outside of this region, some sharp details become blurred. One can identify in advance the parts of the boundaries that will be affected if the detection view is insufficient. In particular, a piece of the boundary of an object (i.e., interfaces between objects) can be stably reconstructed if, and only if, at least one of its two normal directions passes through a detector position. Otherwise the boundary piece cannot be reconstructed sharply no matter what reconstruction algorithms are used.

In order to support these theoretical conclusions, three types of reconstruction methods were utilized: a filtered backprojection (FBP) approximate inversion, which is shown to work well for limited-view data, a local-tomography-type reconstruction that emphasizes sharp details (e.g., boundaries of inclusions), and an iterative algebraic truncated conjugate gradient algorithm used in conjunction with FBP. Computations conducted for both numerically simulated and experimental data confirmed the theoretical predictions.

The following experimental results illustrate the abovementioned theoretical conclusions. The sample and the polar coordinate system describing the scanning orbit

in the experiment are shown in Fig. 2a. The sample consisted of a muscle cylinder of 4 mm in diameter and 5 mm in length embedded in a chunk of pork fat 1.2 cm in radius. There was a 10-mm fat layer below the muscle and another 7-mm one above it. An electromagnetic pulse was delivered to the sample from below (i.e., from behind the picture plane). Thermoacoustic data were collected around the sample over a 2π angular span with 161 steps, and a scanning radius of 71 mm. Figures 2b–2d show the reconstructed images using FBP with three sets of data. In the first of them, the data were collected along a circular detector arc of 92 degrees located at the top of the picture (Fig. 2a) and almost symmetric with respect to its vertical axis. One sees that the left and right boundaries of the muscle cylinder and of the pork chunk are blurred, because their normal lines do not touch the detector arc, while the rest of the boundary is sharp. The next figure shows a reconstruction obtained with the data collected from a 202° arc, which is the case when the whole phantom fits into the detection region. All boundaries are sharp now. Finally, the last figure shows the reconstruction with the full-view data. It can be seen that the image reconstructed from the partial-view data (Fig. 2c) has a

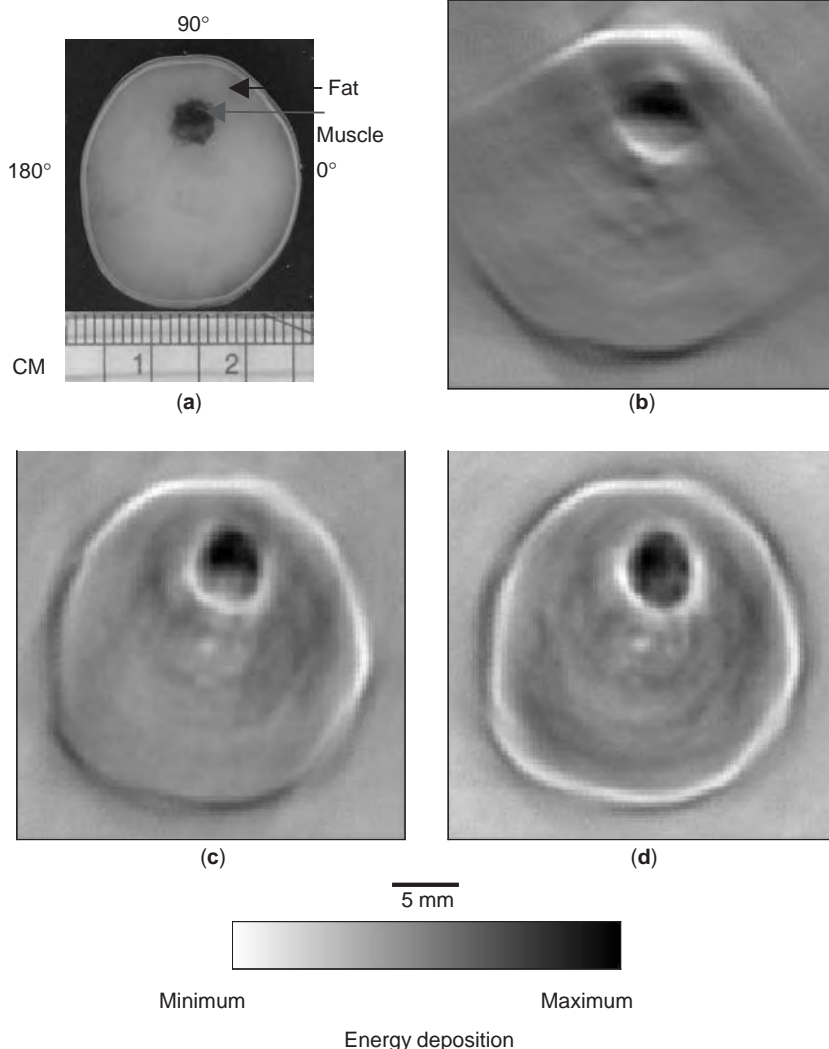


Figure 2. (a) Photograph of the experimental sample. (b–d) Thermoacoustic tomography reconstructions using detection arcs of 92° [from 50° to 142° in (a)], 202° (from -18° to 184°), and 360°, respectively. The blurred parts of the boundaries in (b), which are due to the limited view, agree with the theoretical predictions. In (c) all the boundaries are resolved, since the object fits into the “detection region”. (Reprinted with permission from Ref. 10. Copyright 2004, American Association of Physicists in Medicine.)

comparable quality with the image from the full-view data (Fig. 2d).

3.3. Effects of Acoustical Heterogeneity on Breast Thermoacoustic Tomography

Acoustic heterogeneities in breast thermoacoustic tomography can cause two types of wavefront distortion: amplitude distortion and phase distortion [11]. Amplitude distortion is due to refraction-induced multiple-path interference. When there is acoustic heterogeneity across a tissue interface, refraction occurs. Because of refraction, rays from a single source can reach the same receiver by different paths. The interference between these rays causes amplitude distortions. These amplitude distortions are strong in pure ultrasound tomography. However, the amplitude distortions are shown to be insignificant in thermoacoustic tomography because of the low-frequency nature of the thermoacoustic pulses [11]. The effects of phase distortions (errors in time of flight) were numerically studied. The numerical results on the spreads of the point sources and boundaries caused by phase distortions are in good agreement with the following formula

$$w(\mathbf{r}) = \int \alpha(\mathbf{r}'') dl_p \quad (1)$$

where $w(\mathbf{r})$ is the width of the point spread function at \mathbf{r} along line l_p and $\alpha(\mathbf{r}'') = 1 - v_{s0}/v_p(\mathbf{r}'')$ is the velocity deviation of $v_p(\mathbf{r}'')$, the acoustic speed at point \mathbf{r}'' , from the background speed v_{s0} .

Acoustic heterogeneity can result in blurring and artifacts. Nevertheless, it was demonstrated that the blurring of images can be compensated for by using the distribution of the acoustic velocity in reconstructions of weakly heterogeneous tissues. The effects of the errors in the acoustical velocities on this compensation were also investigated.

3.4. Reconstruction Algorithms

Reconstruction algorithms, including both exact and approximate ones, have been studied extensively in thermoacoustic tomography. It has been proved that exact reconstructions in thermoacoustic tomography are equivalent to time-reversing the pressure field across the detection surface back to the time when the thermoacoustic sources were excited. Exact reconstruction algorithms for thermoacoustic tomography have been derived for planar, cylindrical, and spherical geometries [6,12,13] using series expansion, and for an arbitrary geometry using time-reversal methods [14]. The reconstruction algorithms proposed in Refs. 12 and 13 are computationally efficient with the use of the fast Fourier transform. These formulas can also be used to evaluate the resolution of thermoacoustic tomography, as will be shown in Section 3.5, and to optimize the system design.

These exact thermoacoustic tomography reconstructions can also be implemented in a backprojection algorithm [14,15] after assuming that the distance between the objects and the detectors is much larger than the

typical acoustic wavelength

$$A(\mathbf{r}) = -\frac{1}{2\pi\eta v_{s0}^5} \oint_{\Sigma} dS_0 \frac{\mathbf{n} \cdot (\mathbf{r}_0 - \mathbf{r})}{t^2} \frac{\partial p(\mathbf{r}_0, t)}{\partial t} \Big|_{t=|\mathbf{r}_0-\mathbf{r}|/v_{s0}} \quad (2)$$

where $A(\mathbf{r})$ is the reconstructed value at \mathbf{r} , $p(\mathbf{r}_0, t)$ is the thermoacoustic signal at \mathbf{r}_0 and time t , \mathbf{n} is the outward normal to the detection surface Σ at \mathbf{r}_0 , and η is a constant. An important improvement of this backprojection algorithm over the usual backprojection (delay-and-sum) algorithms used in thermoacoustic tomography is that an orientation factor is included. Equation (2) can also be extended to derive quantitative reconstruction algorithms for limited-view thermoacoustic tomography [10].

3.5. Spatial Resolution

Spatial resolution is an important index of an imaging system. Spatial resolution in thermoacoustic tomography can be affected by various factors, such as the system bandwidth, the detector aperture, and the acoustic heterogeneity of the to-be-imaged object. The effects of acoustic heterogeneity on the resolution can be described by Eq. (1). In this subsection, we will first discuss the effects of the system bandwidth. The dependence of the spatial resolution on the system bandwidth, which is the combined bandwidth of the microwave bandwidth and the detector bandwidth, is presented in Ref. 16. Three special detection geometries, including spherical, planar, and cylindrical surface, as well as an arbitrary detection geometry, were investigated. Analytic expressions of the point spread function (PSF), as a function of the system bandwidth, were derived from rigorous reconstruction formulas. Extension of the results to an arbitrary geometry is also discussed. The analyses reveal that the PSF for an arbitrary detection geometry is space-invariant and depends only on the frequency response function of the thermoacoustic tomography system.

The effects of the finite size of the detector aperture on the system's resolution were also studied in the planar, spherical, and cylindrical detection geometries. In the planar geometry, the PSF is space-invariant and anisotropic; the lateral PSF (parallel to the detection plane) is just the profile of the detector and the axial PSF is a delta function. In the spherical geometry, the PSF is space-variant and anisotropic; the lateral PSF at \mathbf{r} (perpendicular to the radius) is just the profile of the detector scaled down by the ratio of the radius of point \mathbf{r} and the radius of the detection surface while the PSF along the radius is a delta function. In the cylindrical geometry, the PSF is space-variant and anisotropic and is a mix of the PSFs of planar and spherical geometries.

4. THERMOACOUSTIC TOMOGRAPHY EXPERIMENTS

In this section, the experimental setups and results of the thermoacoustic tomography of the phantoms are presented to demonstrate the principles and resolution capabilities of thermoacoustic tomography. Most of the thermoacoustic tomography setups are in either circular

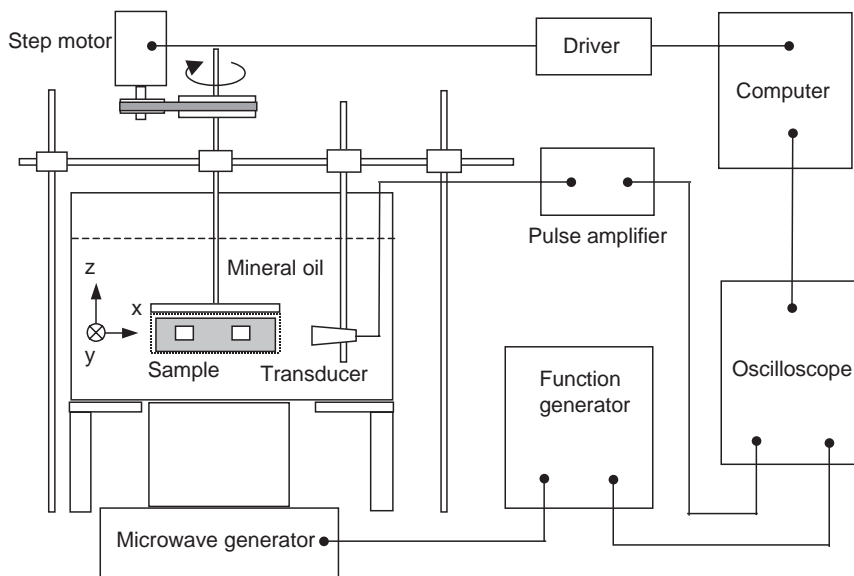


Figure 3. The experimental setup for circular thermoacoustic tomography. (Reprinted with permission from Ref. 6. Copyright 2002, IEEE.)

or planar geometry. In the circular geometry thermoacoustic tomography, the detector was scanned along a circle; while in the planar geometry thermoacoustic tomography, the detector was scanned along a line or a plane. The choice of the geometry depended mainly on the geometry of the tissues to be imaged.

4.1. Circular Geometry

Figure 3 shows the experimental setup for the circular thermoacoustic tomography [6]. The transducer was unfocused and had a central frequency of 2.25 MHz and a diameter of 6 mm. It pointed horizontally to the center of

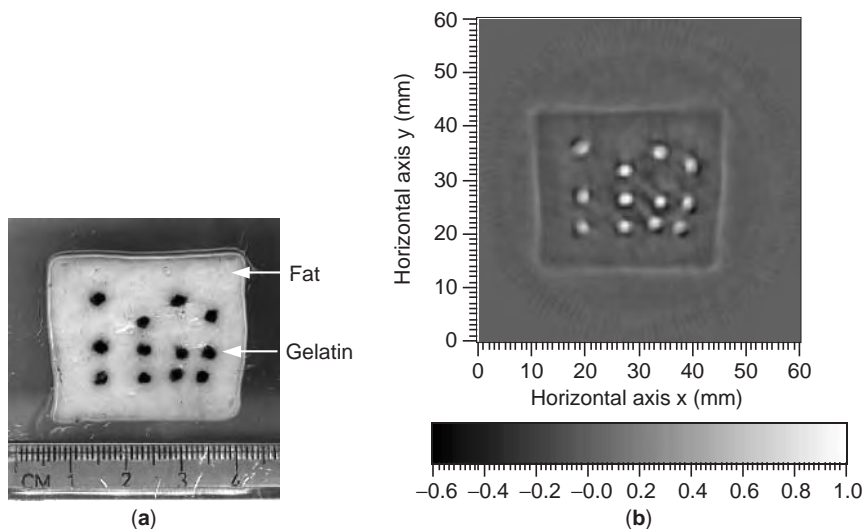
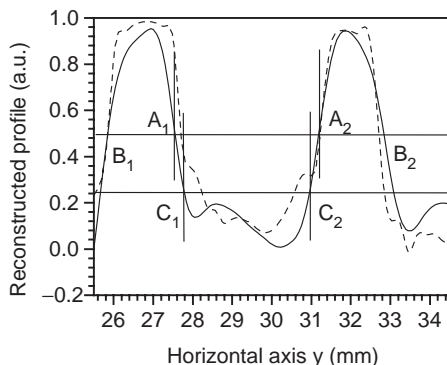


Figure 4. (a) Cross section of a tissue sample in circular thermoacoustic tomography; (b) reconstructed image; (c) comparison between a line profile (solid curve) of the reconstructed image (b) at $x = 27.45$ mm and the corresponding grayscale profile (dashed curve) of the original image (a). (Reprinted with permission from Ref. 6. Copyright 2002, IEEE.)



the rotation stage. For good coupling of the acoustic waves, both the transducer and the sample were immersed in mineral oil. The microwave pulses were transmitted from a 3-GHz microwave generator with a pulse energy of 10 mJ and a width of $0.5\ \mu\text{s}$, and then delivered to the sample from the bottom by a rectangular waveguide.

The sample shown in Fig. 4a was made of a thin piece of homogeneous pork fat tissue (5 mm thick and a maximum diameter of 4 cm) including a set of small gel cylinders (made from a solution of 5% gelatin, 0.8% salt, and a drop of dark ink to improve the photographic properties of the sample). During the experiment, the transducer rotationally scanned the sample from 0° to 360° with a stepsize of 2.25° . The detection radius was 43 mm.

The image reconstructed with the backprojection method is shown in Fig. 4b; it agrees well with the real sample. The relative locations and sizes of the gel cylinders are clearly resolved and perfectly match the original ones. Figure 4c shows the plot (solid curve) along the line at $x = 27.45\ \text{mm}$ in Fig. 4b. The reconstructed profile is in good agreement with the original profile (dashed curve), which is the corresponding grayscale profile in Fig. 4b. The half-amplitude line cuts across the reconstructed profile at points B_1 , A_1 , A_2 , and B_2 , respectively. The distances $|A_1B_1| = 1.72\ \text{mm}$ and $|A_2B_2| = 1.67\ \text{mm}$ in the image

are close to the measured real values of about 1.80 and 1.60 mm, respectively. Therefore, the width of the profile at the half-amplitude closely measures its physical size.

Figure 5 demonstrates the large penetration depth of microwave in soft tissues. The sample (Fig. 5a) is similar to the one used in Fig. 4 except that this one was much larger (the diameter of the fat is 70 mm), as shown. The reconstructed image (Fig. 5c) agrees well with the real sample (Fig. 5b).

4.2. Planar Geometry

In the planar thermoacoustic tomography, the detector was scanned over a plane or a line [12]. The experimental setup is reported in Ref. 17 and, for convenience, is only briefly described here (see also Fig. 6). The x axis points perpendicularly to the drawing plane, the y axis points to the right in the plane, and the z axis points downward along the acoustic axis. Microwave pulses were transmitted by a 9-GHz microwave generator. The pulsewidth is $0.5\ \mu\text{s}$. The imaged object shown in Fig. 7c is a cylinder of pork fat containing a thin layer of connective tissue, labeled as (7), and six yellow microstructures, labeled

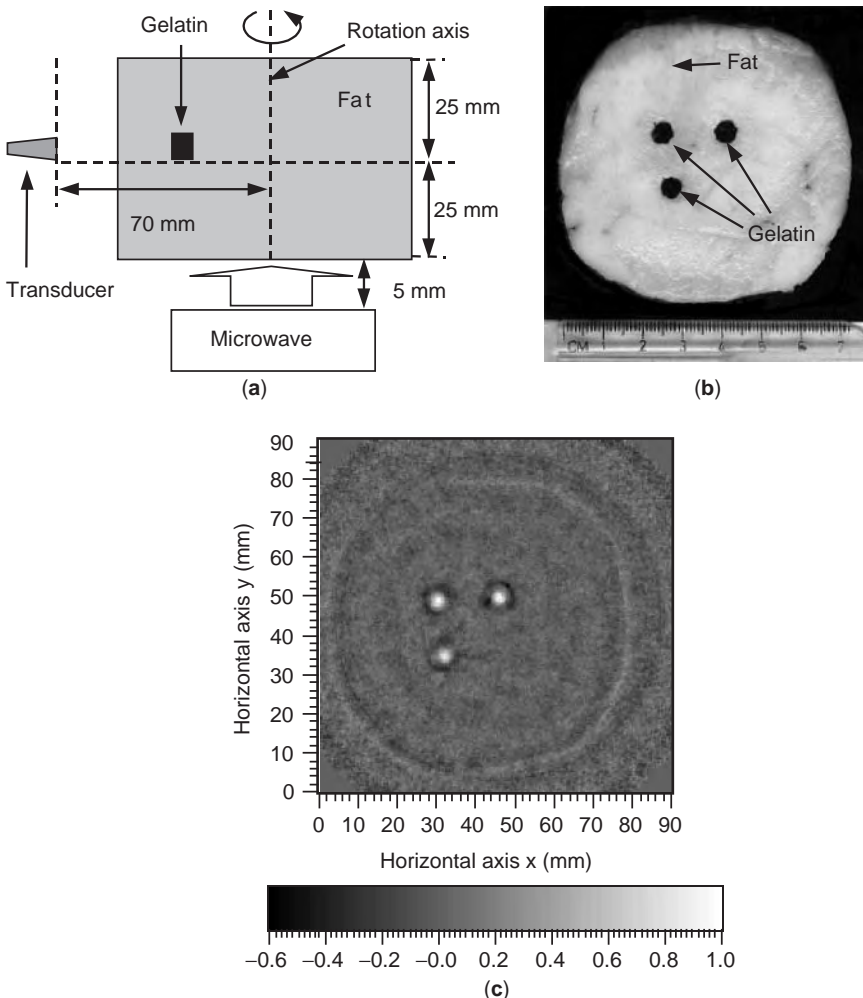


Figure 5. (a) Diagram of the sample structure and the measurement for circular thermoacoustic tomography; (b) cross-section of the tissue sample; and (c) reconstructed image. (Reprinted with permission from Ref. 6. Copyright 2002, IEEE.)

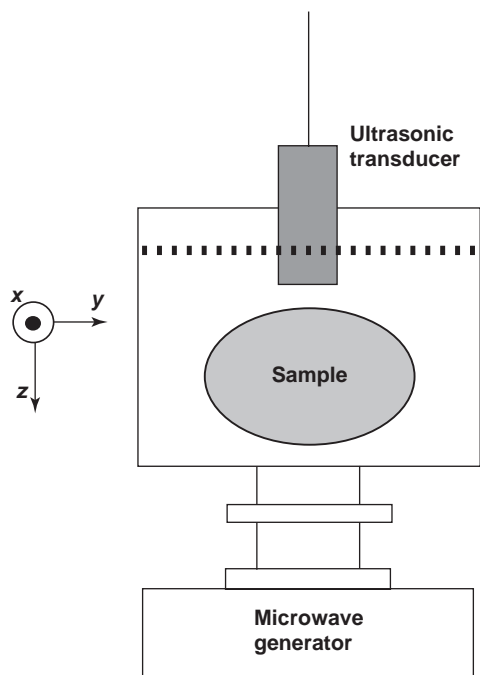


Figure 6. Experimental setup for planar thermoacoustic tomography. (Reprinted with permission from Ref. 12. Copyright 2002, IEEE.)

(1)–(6), respectively. The diameter of the cylinder fat was 14 mm and the length in the x direction 30 mm. The cylinder was immersed in mineral oil. The central frequency of the ultrasonic transducer was 2.25 MHz, the bandwidth was 1.8 MHz, and the diameter of the active element was 6 mm.

As shown in the discussion on resolution of thermoacoustic tomography in the last section, the finite size of the detector aperture can seriously blur the image. To improve the system resolution, deconvolution with respect to the finite size of the detector surface was applied to the reconstructed image [12]. In the reconstructed image before deconvolution (Fig. 7a), the connective tissue between the two parts of fat and the yellow microstructures is imaged clearly. The dimension of the image is 16.4 mm along the z direction and 19.2 mm along the y direction. However, it is obvious that the image before deconvolution is blurred along the y axis, which makes the lateral boundaries unclear and the yellow microstructures (1), (2) and (3), (4) merge into one object, respectively. The lateral resolution of the image after deconvolution (Fig. 7b) is greatly improved. The merged objects can be distinguished clearly, and the lateral boundaries of the cylinder become much clearer. The dimension of the fat cylinder in the image after deconvolution was 16.4 mm along the z direction and 16.7 mm along the y direction.

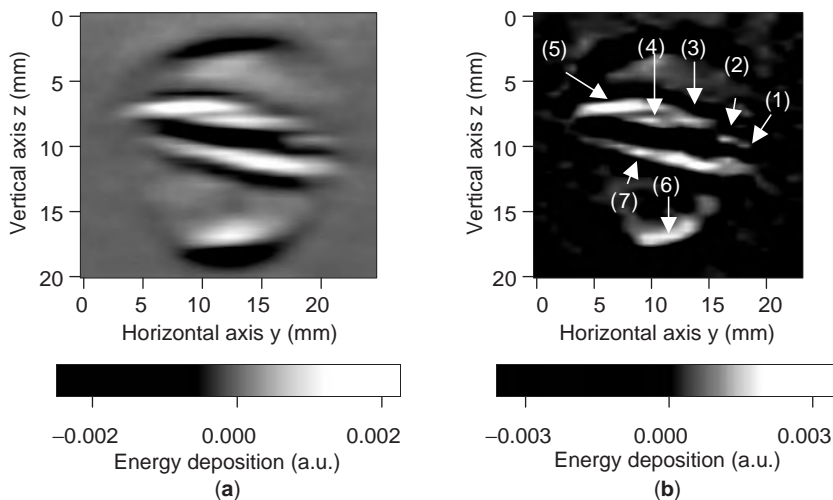
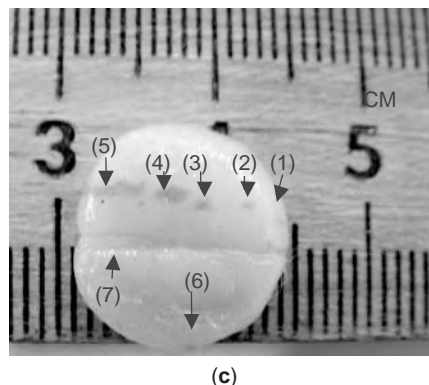


Figure 7. The reconstructed images from the experimental data in a planar thermoacoustic tomography (a) before and (b) after the deconvolution with respect to the detector surface; (c) cross section of a cylinder of fat sample containing six yellow microstructures labeled from (1) to (6) and a layer of connective tissue in the middle labeled as (7). (Reprinted from Ref. 12. Copyright 2002, IEEE.) (This figure is available in full color at <http://www.mrw.interscience.wiley.com/erfme>.)



5. APPLICATIONS OF THERMOACOUSTIC TOMOGRAPHY AND MICROWAVE TOMOGRAPHY

The feasibility of utilizing microwave tomography for biological imaging has been demonstrated on volunteers' forearms, a canine kidney, explanted static and beating canine hearts, and breast imaging. Figure 8 shows the results of imaging experiments and anatomical slices from a canine heart [18]. Both anatomical slices demonstrate an area of left ventricle myocardium with significant infarction. A longitudinal view (through the long axis base to apex) is presented on top in Fig. 8 for ϵ' (the real part of complex dielectric permittivity ϵ), and a transversal view (through an area with significant infarction injury) is presented at the bottom of Fig. 8 for ϵ'' (the imaginary part of ϵ). Areas of the images of the heart with dielectric properties similar to the dielectric properties of infarct myocardium are plotted in crimson and red for ϵ' and ϵ'' , respectively. As can be seen, the reconstructed images reveal the shape and intracardiac anatomy. Furthermore, suspected areas of infarction (in terms of the dielectric properties) are consistent with anatomical slices. Because of the imperfection of the procedure for image reconstruction, there are areas of the image of ϵ' with dielectric properties similar to those of the infarcted area (colored in crimson). However, correlation of suspected infarct areas of the images of ϵ' with corresponding areas of the images

of ϵ'' helps determine the location of the exact area of the infarction. This is supported by the next group of images presented in Fig. 9 for $|\epsilon|$.

The response of breast cancer to chemotherapy was also measured with thermoacoustic tomography [19]. Longitudinal changes in breast architecture during primary chemotherapy produce dramatic changes in RF absorption as revealed with thermoacoustic tomography. The tumor mass appears to have decreased markedly after 7 weeks of chemotherapy treatment, as indicated by the arrows, but there is little change thereafter (Fig. 10).

6. CONCLUSIONS AND FUTURE STUDIES

Microwaves can be used in medical imaging to extract the physiological and pathological status of tissues deep in the body. Thermoacoustic tomography has a higher resolution than does microwave tomography. Some preliminary results of studies on optimal microwave frequencies, the effects of acoustical heterogeneity on breast thermoacoustic tomography, limited-view thermoacoustic tomography, reconstruction algorithms, and spatial resolution are presented. The experimental results of circular thermoacoustic tomography show a spatial resolution of about 0.5 mm. We also present some in vivo and in vitro results that

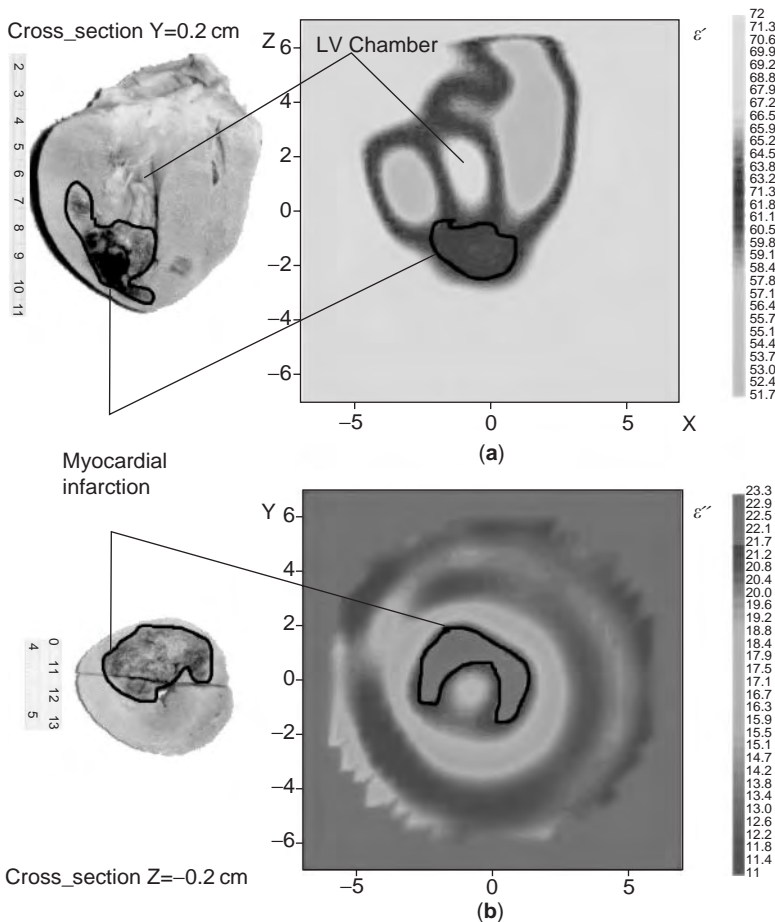


Figure 8. Reconstructed images of excised canine heart [(a) longitudinal view through the long axis base to apex and through the left ventricle (LV) chamber for ϵ' and (b) transversal view through an area with significant infarction injury for ϵ''] together with anatomical slices. Scales are in centimeters. (Reprinted from Ref. 18.) (This figure is available in full color at <http://www.mrw.interscience.wiley.com/erfme>.)

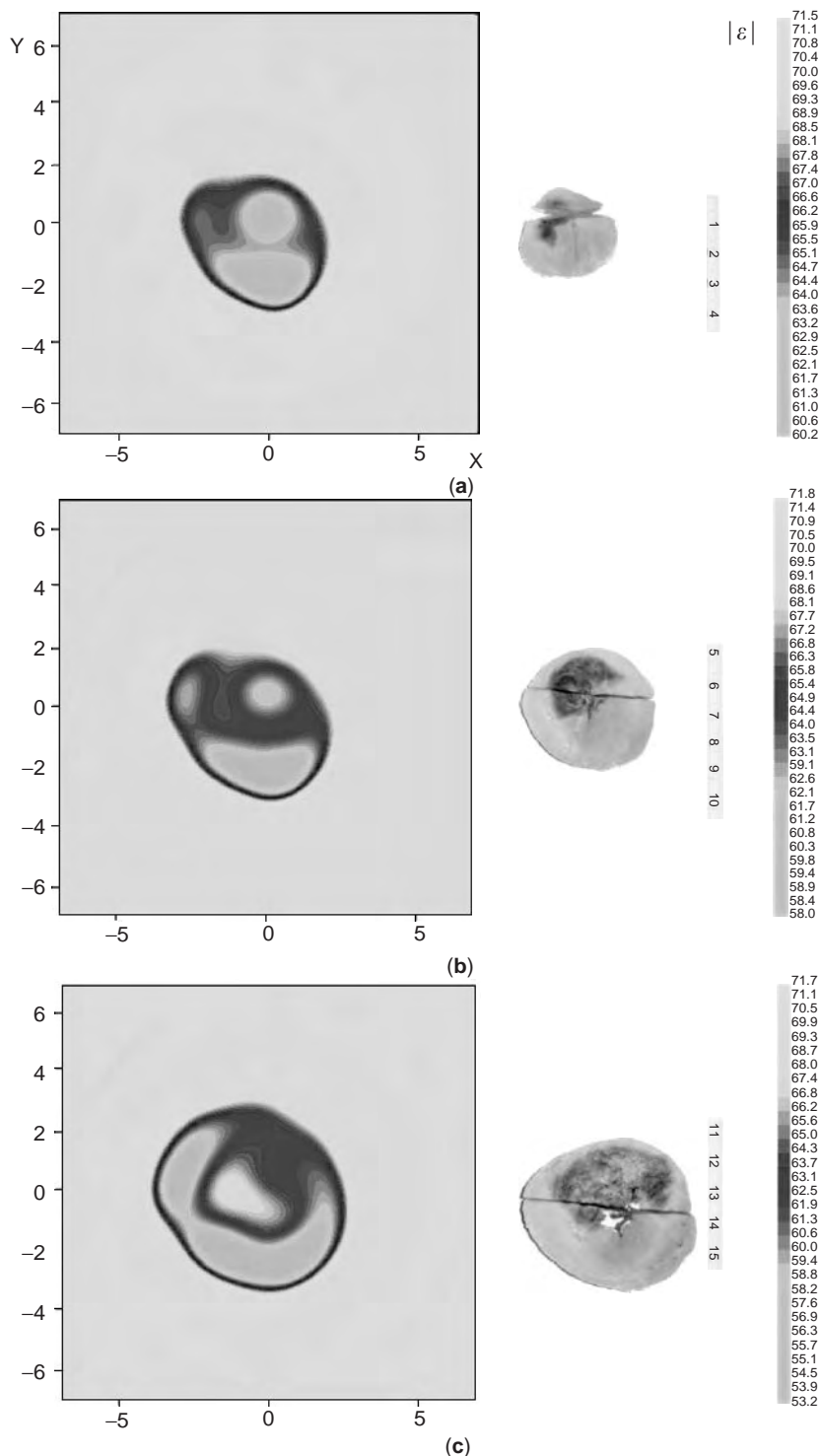


Figure 9. Reconstructed images of excised canine heart [(a–c) transversal view for $|\epsilon|$ with an increment of image position in the longitudinal direction of 1 cm] together with anatomical slices. Scales are in centimeters. (Reprinted with permission from Ref. 18.) (This figure is available in full color at <http://www.mrw.interscience.wiley.com/erfme>.)

demonstrate the feasibility of clinical applications of thermoacoustic tomography and microwave tomography.

Nevertheless, there are still questions about thermoacoustic tomography that deserve further investigation. For example, it has generally been assumed that with thermoacoustic tomography, microwaves are homogeneous in the tissues under study. However, microwave attenuation and the variation of microwave within one

wavelength can result in microwave heterogeneity. The effects of microwave heterogeneity on thermoacoustic tomography are still unknown. Another challenge for thermoacoustic tomography is brain imaging. In this case, the skull may cause distortion of the thermoacoustic waves. Consequently, the capability to obtain high-quality images from distorted signals is critical for the application of thermoacoustic tomography to brain imaging.

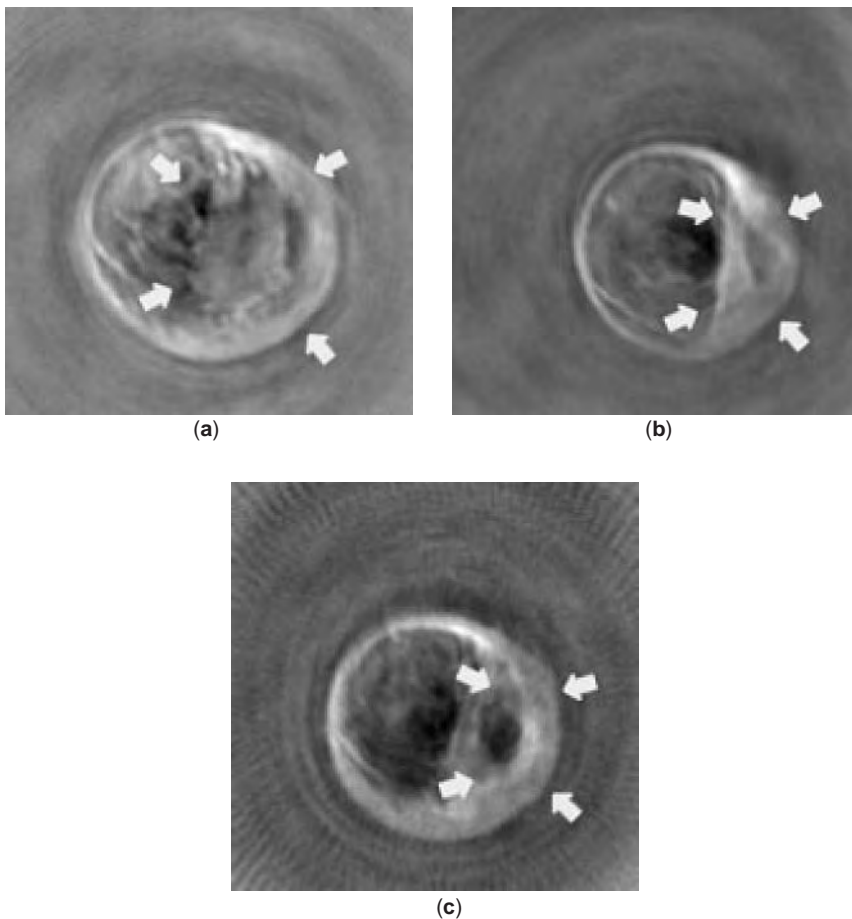


Figure 10. Thermoacoustic tomography breast images (a) before, (b) after 7 weeks in, and (c) after 13 weeks in chemotherapy. (Reprinted with permission from Ref. 19.)

BIBLIOGRAPHY

1. G. Ku and L.-H. V. Wang, Scanning microwave-induced thermoacoustic tomography: Signal, resolution, and contrast, *Med. Phys.* **28**:4–10 (2001).
2. P. M. Meaney, K. D. Paulsen, A. Hartov, and R. K. Crane, Microwave imaging for tissue assessment: Initial evaluation in multitarget tissue-equivalent phantoms, *IEEE Trans. Biomed Eng.* **43**:878–890 (1996).
3. T. Bowen, L. Nasoni, A. E. Pifer, and G. H. Sembrusk, Some experimental results on the thermoacoustic imaging of soft tissue-equivalent phantoms, *Proc. IEEE Ultrasonics Symp.*, 1981, Vol. 2, pp. 823–827.
4. R. Olsen and J. Lin, Acoustic imaging of a model of a human hand using pulsed microwave irradiation, *Bioelectromagnetics* **4**:397–400 (1983).
5. R. Kruger, W. Kiser, D. Reinecke, and G. Kruger, Application of thermoacoustic computerized tomography to breast imaging, *Proc. SPIE* **3659**:426–430 (1999).
6. M. Xu and L.-H. V. Wang, Time-domain reconstruction for thermoacoustic tomography in a spherical geometry, *IEEE Trans. Med. Imag.* **21**:814–822 (2002).
7. C. Gabriel, S. Gabriel, and E. Corthout, The dielectric properties of biological tissues: I. Literature survey, *Phys. Med. Biol.* **41**:2231–2249 (1996).
8. K. R. Foster and J. L. Schepps, Dielectric properties of tumor and normal tissues at radio through microwave frequencies, *J. Microwave Power* **16**:107–119 (1981).
9. S. Chaudhary, R. Mishra, A. Swarup, and J. Thomas, Dielectric properties of normal & malignant human breast tissues at radiowave and microwave frequencies, *Indian J. Biochem. Biophys.* **21**:76–79 (1984).
10. Y. Xu and L.-H. V. Wang, Reconstructions in limited-view thermoacoustic tomography, *Med. Phys.* **31**:724–733 (2004).
11. Y. Xu and L.-H. Wang, Effects of acoustic heterogeneity on thermoacoustic tomography in the breast, *IEEE Trans. Ultrason. Ferr. Freq. Control* **50**:1134–1146 (2003).
12. Y. Xu, D. Feng, and L.-H. V. Wang, Exact frequency-domain reconstruction for thermoacoustic tomography: I. Planar geometry, *IEEE Trans. Med. Imag.* **21**:823–828 (2002).
13. Y. Xu, M. Xu, and L.-H. V. Wang, Exact frequency-domain reconstruction for thermoacoustic tomography: II. Cylindrical geometry, *IEEE Trans. Med. Imag.* **21**:829–833 (2002).
14. Y. Xu and L.-H. V. Wang, Time reversal and its application to tomography with diffracting sources, *Phys. Rev. Lett.* **92**:033902 (2004).
15. M. Xu, Y. Xu, and L.-H. Wang, Time-domain reconstruction algorithms and numerical simulations for thermoacoustic tomography in various geometries, *IEEE Trans. Biomed. Eng.* **50**:1086–1099 (2003).
16. M. Xu and L.-H. Wang, Analytic explanation of spatial resolution related to bandwidth and detector aperture size in thermoacoustic or photoacoustic reconstruction, *Phys. Rev. E* **67**(056605):1–15 (2003).

17. D. Feng, Y. Xu, G. Ku, and L.-H. V. Wang, Microwave-induced thermoacoustic tomography: Reconstruction by synthetic aperture, *Med. Phys.* **28**:2427–2431 (2001).
18. S. Y. Semenov, A. E. Bulyshev, V. G. Posuk, Y. E. Sizov, T. C. Williams, and A. E. Souvorov, Microwave tomography for detection/imaging of myocardial infarction. I. Excised canine hearts, *Ann. of Biomed. Eng.* **31**:262–270 (2003).
19. R. A. Kruger, Homepage, Optosonics Inc. (Online), <http://www.optosonics.com/tct-human.html>(Jan. 15, 2004).

MEI METHOD

KENNETH K. MEI
City University of Hong Kong
Hong Kong

1. INTRODUCTION

The MEI (measured equation of invariance) method was originally developed as an absorbing boundary condition to terminate FD/FE (finite-difference/finite-element) equations at the mesh boundary. Later improvements, which have brought the MEI terminating equations to the boundary of the target surface, bypassing the need for the FD/FE mesh and equations, have advanced the MEI method to become a numerical method in its own right. The objective of this article is to present the theory on which the method is based, the latest developments in MEI technology, and a guide to numerous applications of the method.

Numerical solutions of Maxwell's equations use either integral equations or differential equations. The classical solution of a radiation problem by the differential equation approach requires a radiation condition, known as the *Sommerfeld's radiation condition*, applied at infinity, that is, at a distant location from the radiating object. Numerical solutions by the differential equation approach utilize the finite-difference or finite-element equations (FD/FE) also require radiation conditions, which are applied at the mesh boundary, preferably as close to the object boundary as possible. Such boundary equations are often known as absorbing boundary conditions (ABCs). An earlier absorbing boundary condition by Mei [1] is robust but is global in nature; that is, a full matrix of field values at all the boundary nodes is required. A representative local absorbing boundary condition, which produces equations of the fields only at a few neighboring nodes, is that by Enquist and Majda [2]; however, like most local absorbing boundary conditions, it is robust only when the mesh boundary is far from the object surface. An extensive list of references to local absorbing boundary conditions may be found in the Ref. 3. Almost all local absorption boundary conditions use plane waves as models for absorption. An absorption equation can usually absorb plane waves perfectly at a few angles of arrival. The latest addition to absorbing boundary condition is the perfectly matched layer (PML) by Berenger [4], which uses a special layer of

nonisotropic material capable of absorbing plane waves arriving at any angle.

Common to all absorbing boundary equations is that the equations are all derived from an assumption of a known incident wave. The MEI method of obtaining boundary equations is based on the observation that there is symmetry between the coefficients a_i and the field values ϕ_i in a linear equation:

$$a_1\phi_1 + a_2\phi_2 + a_3\phi_3 + a_4\phi_4 = 0 \quad (1)$$

Normally, the coefficients represent the equation, which are known, and the ϕ_i values represent the solutions to be found. The symmetry of the equation tells us that if the field values were known, we could also recover the coefficients or the equation at any point. In Eq. (1), for example, since the equation equals zero, one of the coefficients can be set to unity, and thus three sets of linearly independent solutions should give a 3×3 matrix, from which the coefficients can be calculated. This suggests that if Eq. (1) were a boundary equation of a radiation problem, the absorbing boundary equation would be contained in the solutions. We shall designate each linear equation of the a_i terms by substituting a set of solutions ϕ_i in Eq. (1) as a measure. This requires $n - 1$ measures to find the coefficients of a linear equation of n unknowns.

At first glance, the insight we have come up with does not seem to be useful because the solutions are unknowns, which are unavailable to us. Actually solutions to a radiation problem of a specific geometry are not difficult to obtain. Only the solution to a specific excitation and of a specific geometry is difficult to find. The procedures and justification for MEI are presented in the following sections.

2. THE POSTULATE OF INVARIANCE

Let us limit the present discussion to two-dimensional problems of wave scattering for pedagogical purposes. Figure 1 represents scattering of a plane wave, either TE or TM, by an infinite cylinder of arbitrary shape. A solution of the scattered field can be readily obtained by the following integral

$$\phi_k = \oint_C G(\mathbf{r}/\mathbf{r}') J_k(\mathbf{r}') dc' \quad (2)$$

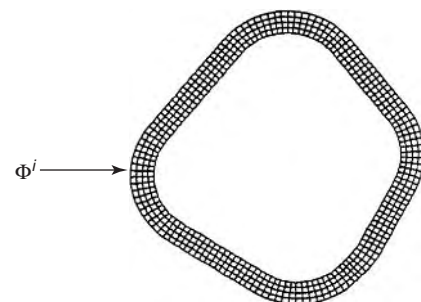


Figure 1. Schematics of a 2D scattering problem.

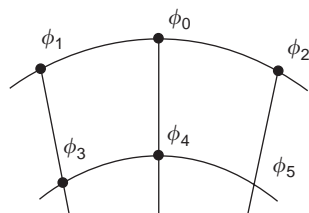


Figure 2. The six points for a boundary equation.

where $G(\mathbf{r}/\mathbf{r}')$ is the Green function of the 2D wave equation and J_k is a current we assign to the scatterer. We shall name each assigned current a “metron” and the resulting field ϕ_k , a measuring function. When $n - 1$ measuring functions are substituted into a boundary equation, we can calculate the coefficients of the boundary equations by solving an $(n - 1) \times (n - 1)$ matrix. In order for the method to work, it is necessary that the boundary equations be invariant with respect to the excitations or the incident fields. Mei [5] postulates that in order to bring the terminating boundary close to the scatterer, a terminating boundary equation should fit the following profile:

1. It must be different for different target geometry.
2. It must be different at different locations.
3. It must be invariant with respect to excitation so that the process of measure can work.

During the early development period of the MEI method, it was strictly used as a technique to terminate finite difference equations. The metrons

$$J_k(\mathbf{r}') = \cos\left\{2(k - 1)\pi \frac{l'}{L}\right\} \quad k = 1, 2, \dots \quad (3)$$

have been used, where L is the total circumferential length of the scatterer and l' is the circumferential distance from a reference. A two-dimensional scattering problem can normally be solved this way by only four layers of finite-difference equations. Each boundary equation is formulated at six adjacent nodal points on the outer two layers, as shown in Fig. 2. Figures 3 and 4 show

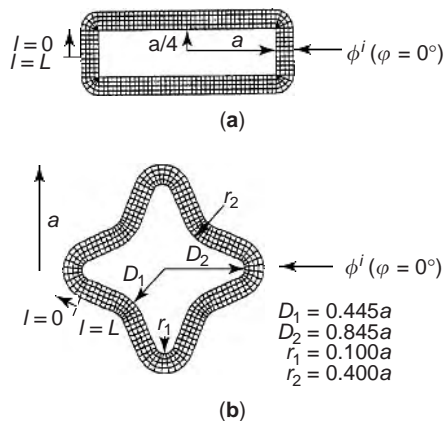


Figure 3. (a) The mesh around a rectangular cylinder; (b) the mesh around a star-shaped cylinder.

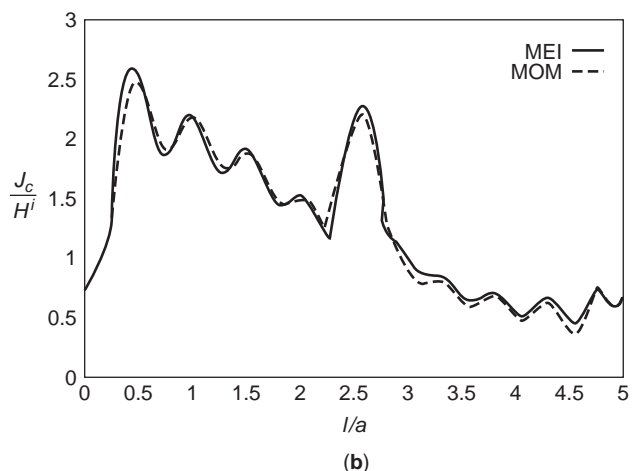
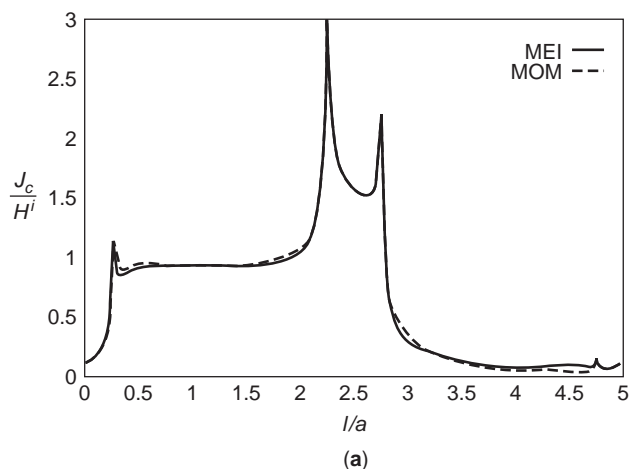


Figure 4. Induced current densities on a rectangular cylinder for $\lambda = a$ and angle of incidence of 30° as calculated by the MEI method and MoM for (a) E wave and (b) H wave.

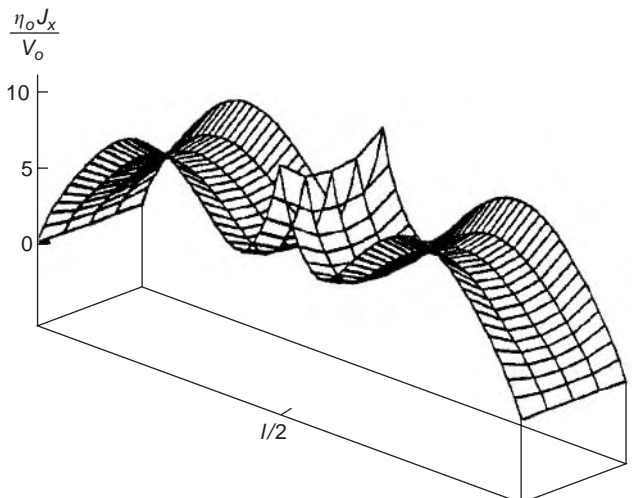


Figure 5. Currents on a center-fed thin-strip dipole antenna ($l = 18.5w$) for $l = 1.07\lambda$ (the scale in y has been enlarged by a factor of 4).

some of the surface current densities on two-dimensional scatterers found by the finite-difference method using MEI terminations, where the results by MoM are also

presented in the same figures for comparison. In addition to 2D problems, the MEI method has also been applied to ribbon antennas (see Figs. 5 and 6) and scattering of plane waves by rectangular patches and bodies of revolution [5].

3. ACCURACY OF MEI

Shortly after the appearance of the first paper on MEI [5], several papers appeared in the literature [6–9] debating the validity of the postulates of MEI, in particular the postulate of invariance. There are also papers [10] questioning the accuracy of the MEI. The postulate of invariance of the boundary equations to excitation (or incident fields) should be the least controversial one of the three postulates, because the terminating conditions are part of the system equations. In all linear systems, including the Maxwell equations, the equations should be independent of the excitations.

In fact, all absorbing boundary conditions in the published literature are obtained with no reference to excitation. This means that the same absorbing boundary equations are used regardless of the incident fields.

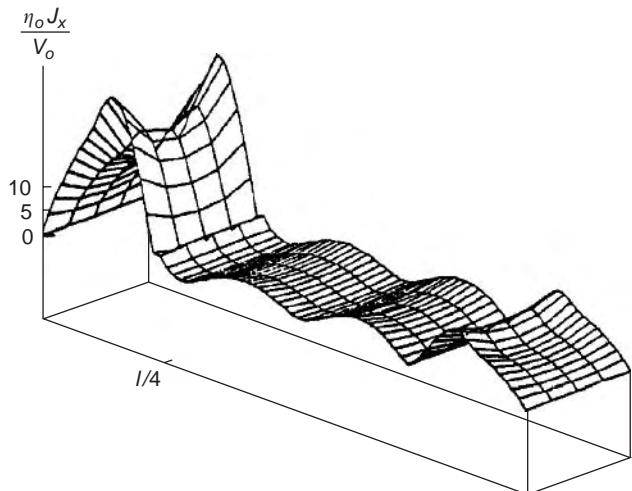


Figure 6. Current on an off-center-fed thin-strip dipole antenna ($l = 18.5w$) for $l = 2.12\lambda$ (the scale on y has been enlarged by a factor of 4).

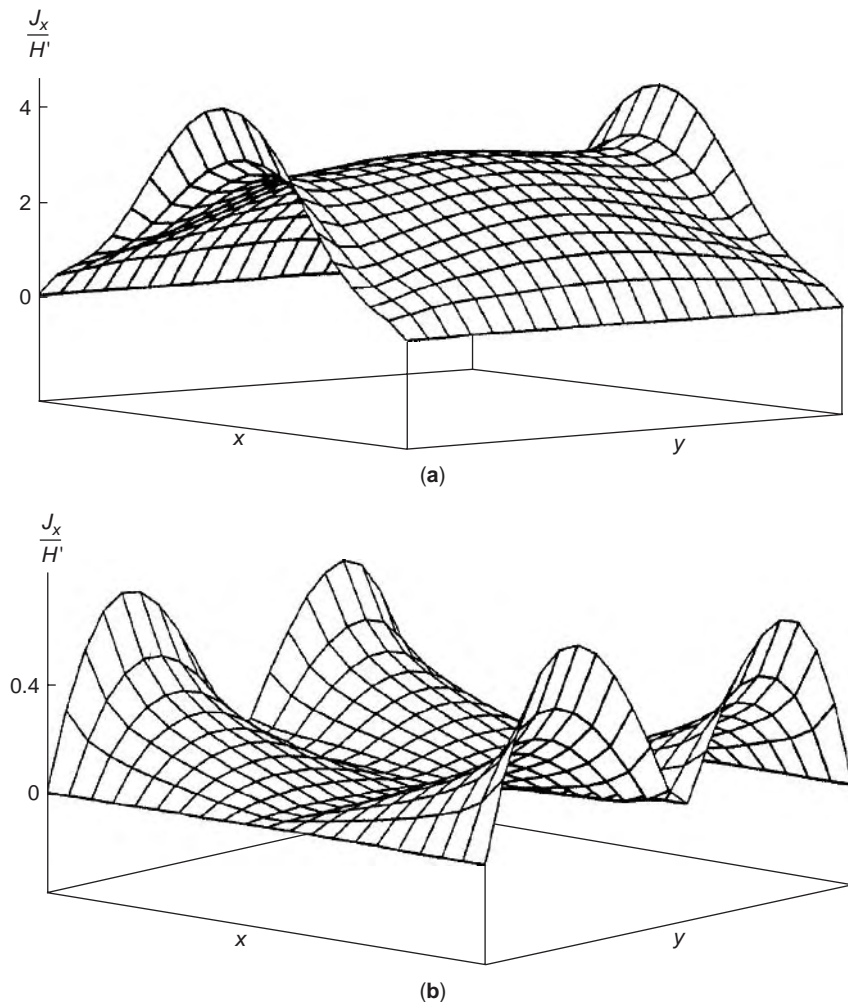


Figure 7. Current densities on a square plate when illuminated by a normally incident plane wave, with the E field polarized in the z direction, with $\lambda = a$: (a) J_x ; (b) J_y .

Mei and Liu [7] have shown that the criticism on the invariance arises from the misunderstandings, that the metrons were incident fields. And, the doubts on the accuracy arise from the misunderstanding that, the metrons were base functions. In the paper by Luo et al. [11], it is shown that the conclusions reached by Barkdoll and Lee

[10] that (1) MEI is not accurate for 3D as compared to 2D problems and (2) the distance between the target boundary and terminating boundary should be large for MEI to be accurate in 3D, are ill-founded because the authors have not properly applied the coupled finite difference equations for the body of revolution [10].

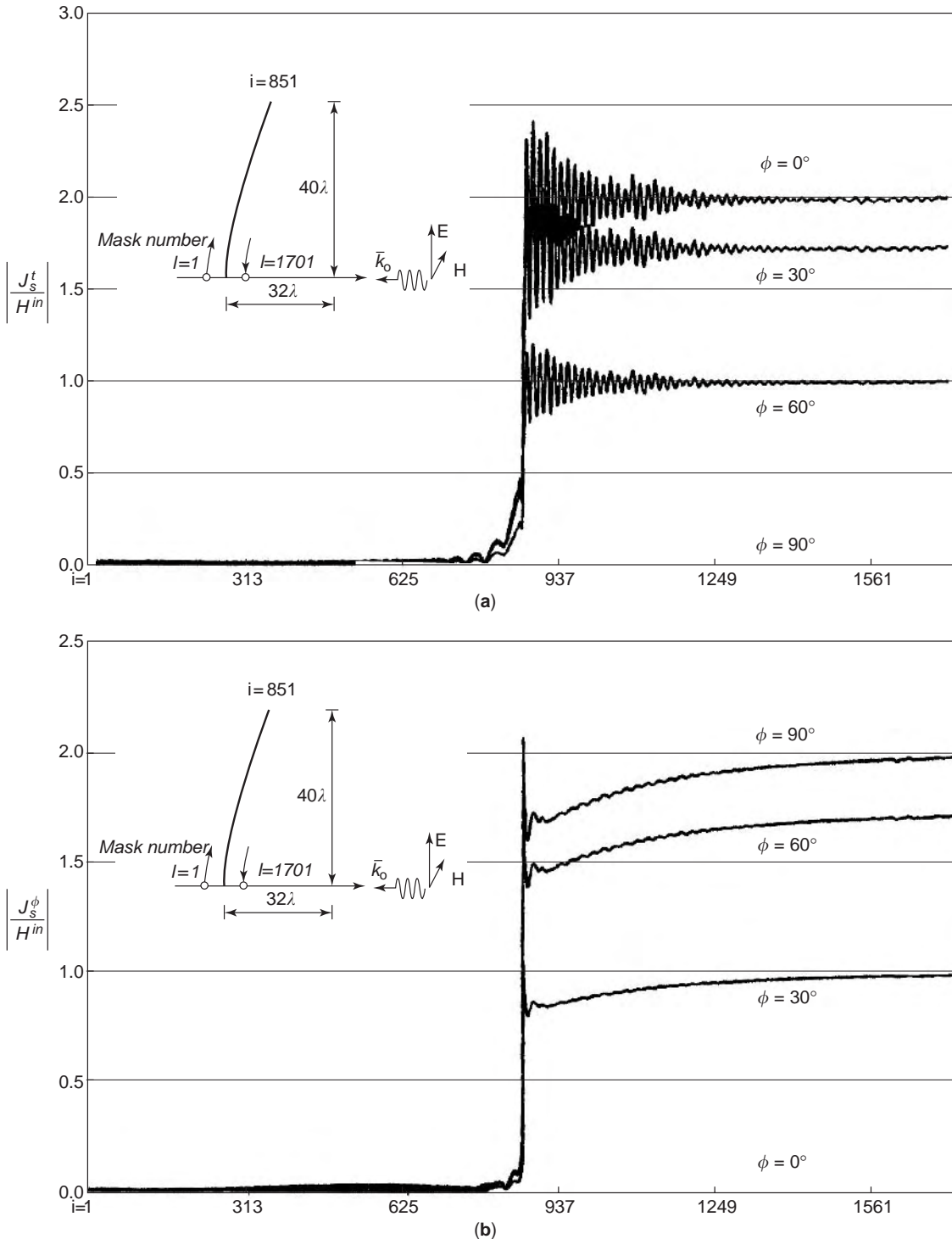


Figure 8. Solutions of electromagnetic scattering problem of axially symmetric parabolic reflector with parameters aperture = 80λ and $F_c = 32\lambda$: (a) J^t ; (b) J^ϕ .

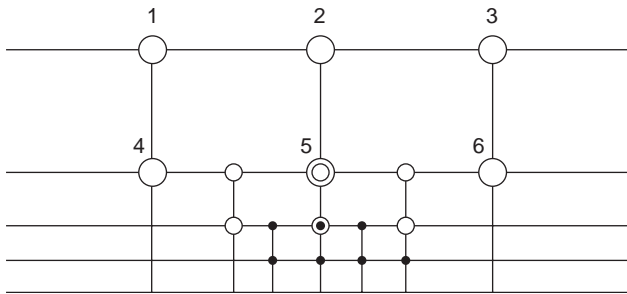


Figure 9. Schematics of doubling mesh density and doubling frequency.

4. APPLICATIONS OF MEI

4.1. Applications to Three-Dimensional Problems

The MEI method has been applied to scattering of plane waves by flat rectangular patches [12]. In this case, Maxwell’s equations are most conveniently formulated in terms of the vector potential, which has only two components. The scattered fields are

$$\mathbf{H}^s = \nabla \times \mathbf{A} \tag{4}$$

$$\mathbf{E}^s = \frac{1}{j\omega\epsilon} \nabla \times \mathbf{H}^s \tag{5}$$

The finite-difference mesh of the vector potentials A_x and A_y are structured around the patch for four layers. The measuring functions and the metrons are given by

$$\mathbf{A}_{m,n} = \int_0^a \int_0^b G(\mathbf{r}/\mathbf{r}') \mathbf{J}_{m,n}(\mathbf{r}') ds \tag{6}$$

where G is the free-space Green function and

$$J_{x/m,n}(x,y) = \frac{\sin \frac{m\pi x}{a} \bullet \cos \frac{(n-1)\pi y}{b}}{\sqrt{y(y-b)}} \tag{7}$$

$$1 \leq m \leq M, \quad 1 \leq n \leq N$$

$$J_{y/m,n}(x,y) = \frac{\cos \frac{(m-1)\pi x}{a} \bullet \sin \frac{n\pi y}{b}}{\sqrt{x(x-a)}} \tag{8}$$

$$1 \leq m \leq M, \quad 1 \leq n \leq N$$

where a, b are the width and length of the patch, respectively; and M, N are the total numbers of nodes along the width and length, respectively.

The surface current densities on a square plate of side dimension of 1.0λ are shown in Fig. 7. The applications to microstrip lines have been studied by Prouty [13].

4.2. Applications to Large Parabolic Reflectors

Parabolic reflectors are normally studied by physical optics, which assigns the current density as twice the tangential incident magnetic field in the illuminated surface and zero in the shadow region. It is well known that current behaviors are much more complicated than that, particularly near the edges. A detailed inspection of the current density cannot be realized unless we can solve the Maxwell equations associated with a parabolic reflector accurately. Such solutions can be realized nowadays by either MoM or FD/FE methods. MoM probably would be a preferable method for such a task over the FD/FE methods, when a large reflector is considered. However, with MEI, the situation is changed, in that the number of nodes

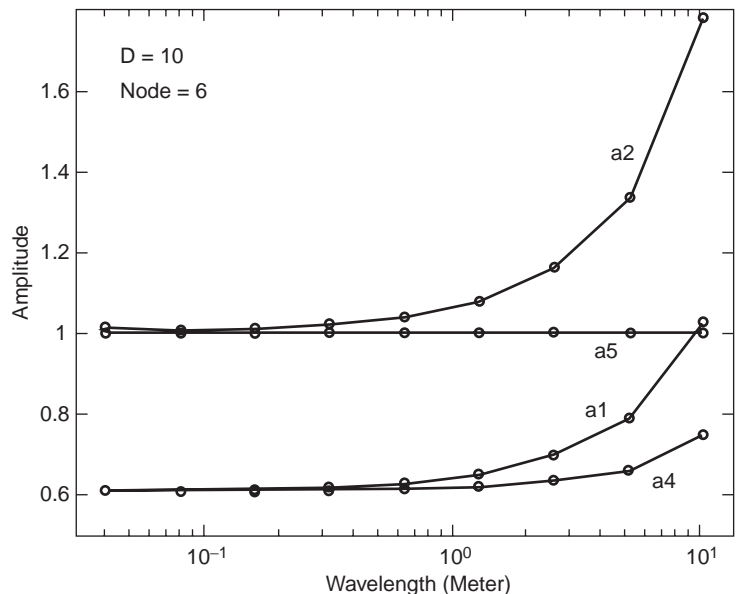


Figure 10. Variation of the MEI coefficients of a circular cylinder with respect to frequency.

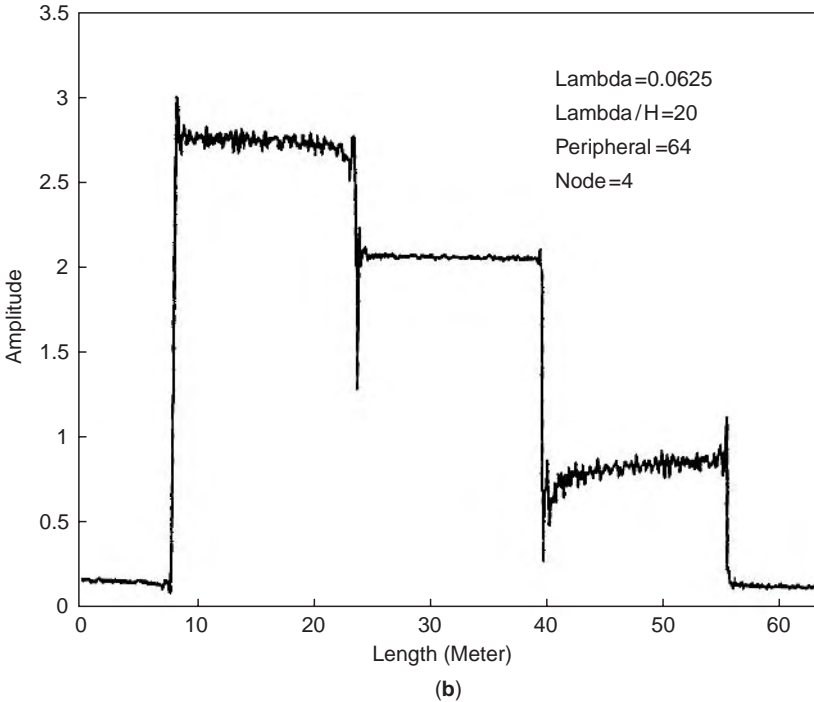
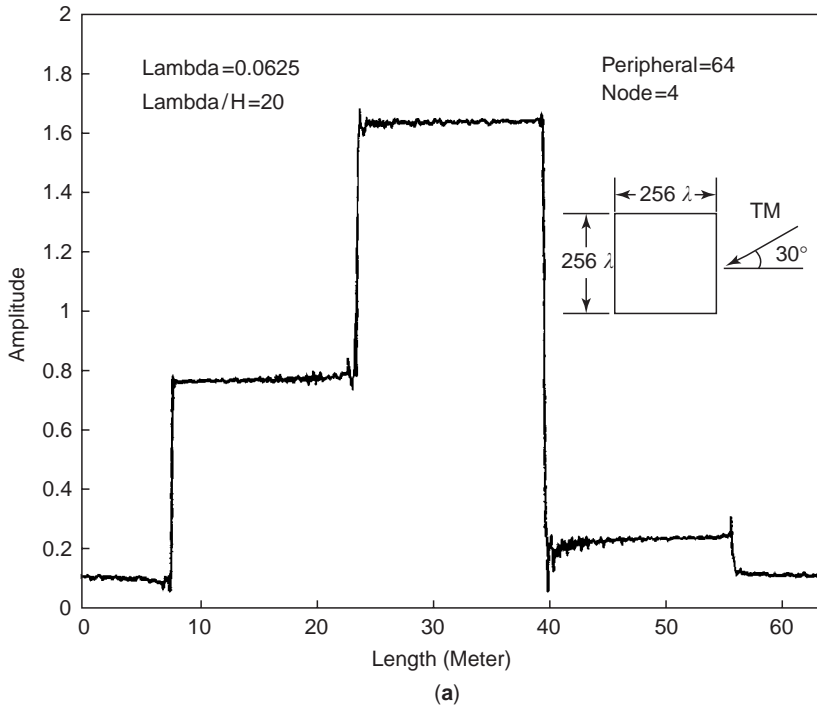


Figure 11. Current densities on a square cylinder of side dimension 256λ illuminated by 30° incidence as calculated by the MEI method as compared with those by MoM: (a) TM nodes; (b) TE nodes.

involved in the FD/FE is greatly reduced when MEI brings the mesh termination very close to the reflector surface and preserves the advantage of the sparse matrix of the FD/FE methods. The solutions of Maxwell's equations of parabolic reflectors of diameters up to 80λ have been obtained by Luo et al. [11] utilizing the MEI method. The current densities near the edge and shadow region have been presented in Fig. 8. The standing waves of the current densities are particularly pronounced for the radial

components, which are known to be the causes of high copper loss and high sidelobes.

4.3. Applications to Very Large Scatterers

When the FD/FE methods are used, the resulting matrices are very sparse. With the MEI method, which brings the mesh termination very close to the object boundary, the mesh region is also greatly reduced. So, the most time

consuming part of the computation is no longer the solution of the matrix. The task of finding the boundary equations, which involves the integrations around the target surface for the measuring functions, has become the most demanding part of the method. The integration time is proportional to N^2 , where N is the number of nodes on the object surface. When the object is very large, such as hundreds of wavelengths in dimension, the computational expense could be very large. To overcome such a predicament, one may consider the method of interpolation and extrapolation of the coefficients of MEI [14], instead of direct computation. Once the boundary equations are found for a specific mesh, it is possible to double, triple, or quadruple the density of the mesh, and obtain the boundary equations in between nodes, by interpolations of the coefficients. In effect, one can find the boundary equation at any location. Suppose that we solve a problem at a frequency f and double the mesh density to

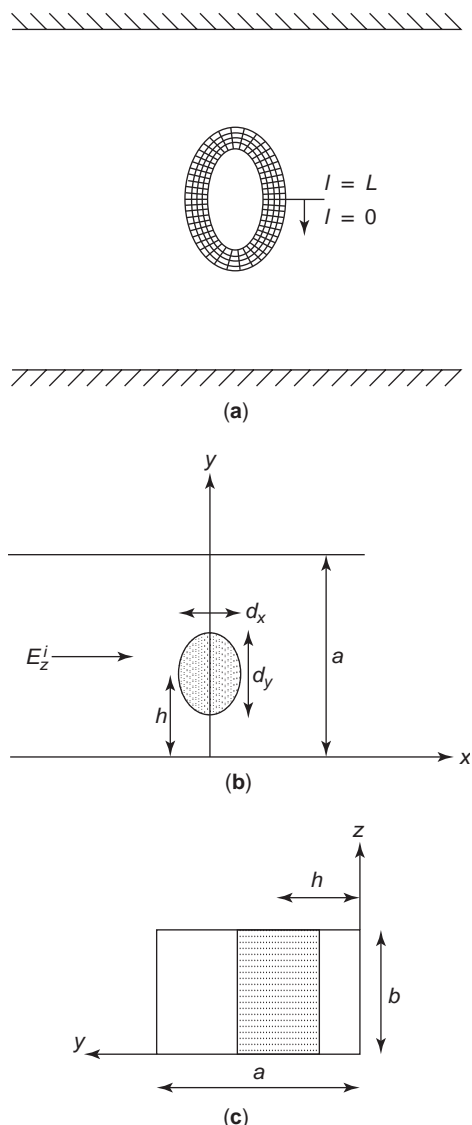


Figure 12. Mesh and schematics of a post in a rectangular waveguide: (a) mesh around a post; (b,c) schematics of scattering by a post in a rectangular waveguide.

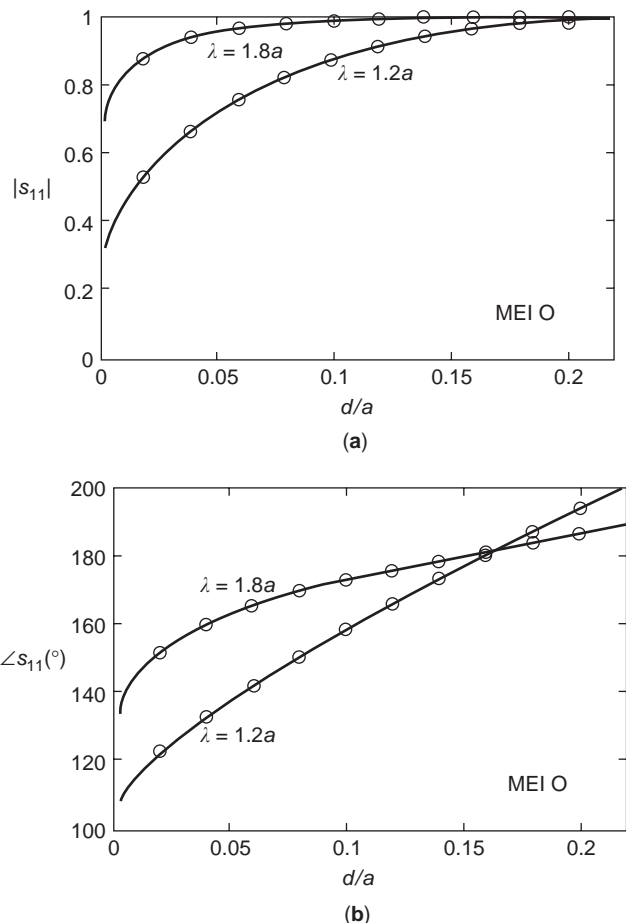


Figure 13. Results of MEI and those of variational principle for S_{11} of scattering inside a rectangular waveguide.

solve the problem at $2f$, and double it again to solve it at $4f$, and so on. As the boundary nodes get closer to the boundary surface as the frequency increases, the center node of the boundary equations approach normally toward the boundary. In that case, the coefficients of each boundary equation converge to their respective limits. Figure 9 shows the mesh configuration as the frequency is doubled, and Fig. 10 shows the extrapolation of the coefficients of MEI. Figure 11 shows the current densities on a rectangular cylinder of side dimension 256λ , calculated using the interpolation–extrapolation technique.

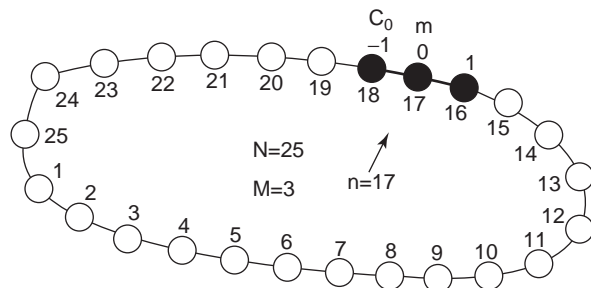


Figure 14. Boundary meshing of the scatterer for IE-MEI.

4.4. MEI and Absorbing Boundary Conditions

In an earlier paper by Ramahi et al. [15], multipole fields were used as measuring functions to find the absorbing boundary conditions for 2D scattering problems. They have termed such a boundary condition, the *numerical absorbing boundary condition* (NABC). The boundary equations, in that case, are independent of the geometry of the scatterer. They have also included MEI as part of the NABC [16]. We would like to point out here that MEI includes but is not limited to ABC. An ABC cannot account for reflections from an outer boundary; that is, it is applicable only if there is no incoming wave on the boundary surface. The MEI can still be applied when there are incoming waves on the terminating boundary. A case illustrating this point is the scattering by an inductive post in a rectangular waveguide. Figure 12 shows the FD mesh around an elliptical post inside a rectangular waveguide. The measuring functions are obtained by the integration of Eq. (2) using the Green function of the waveguide. In this case, ABC cannot be applied, but MEI is still valid. Figure 13 shows the MEI calculated S_{11} of the scattering configuration of Fig. 12 by the MEI method as compared with the same calculations by MoM.

5. ON-SURFACE MEI (OS-MEI) AND INTEGRAL EQUATION MEI (IE-MEI)

In the beginning of this article, we postulated that for a terminating boundary equation to work close to the object boundary, it should fit a profile of three characteristics. Of all terminating boundary conditions that we know of, only the MEI method offers boundary equations that fit all the characteristics of the profile. The immediate issue is how close one can move the MEI boundary toward the target surface. In the early development of the MEI, it was discovered that it was possible to have only one layer of nodal points around the target surface [12]. In that case, the nodes on the object boundary are directly connected to the terminating boundary. The number of unknowns is equal to that of MoM, but one needs to solve only a tridiagonal matrix instead of a full matrix. However, in order to bring the terminating boundary next to the target surface, one requires higher numerical accuracy, which involves double precision and singular integrals on the surface of the

object. To be on the safe side, to ensure that other researchers could easily duplicate the calculations, the earlier results were all obtained with four layers of finite-difference equations. Even with only one layer of nodes around the object surface, the method is still off-surface. One-sided finite differences are needed to find the surface current densities on the object surface, which contribute some extra errors to the calculations.

Instead of two layers of nodes, Rius et al. [17] derived the integral equation MEI (IE-MEI) utilizing the reciprocity theorem

$$\int_v (\mathbf{E}_1 \cdot \mathbf{J}_2 - \mathbf{H}_1 \cdot \mathbf{M}_2) dv = \int_v (\mathbf{E}_2 \cdot \mathbf{J}_1 - \mathbf{H}_2 \cdot \mathbf{M}_1) dv \quad (9)$$

and postulated the existence of local \mathbf{J}_2 and \mathbf{M}_2 on neighboring nodes on the surface of the object such that the right side of Eq. (9) will vanish for all testing sources \mathbf{J}_1 and \mathbf{M}_1 . For a two-dimensional problem, \mathbf{J}_2 and \mathbf{M}_2 will be on three adjacent nodes as shown in Fig. 14. For scattering by conducting cylinders, we may let $\mathbf{M}_1 = 0$, and designate appropriate metrons to find \mathbf{E}_1 and \mathbf{H}_1 to obtain the linear equations

$$\sum_{i=1}^n a_i \mathbf{H}_i^s + \sum_{i=1}^n b_i \mathbf{E}_i^s = \mathbf{0} \quad (10)$$

In Ref. 17 Rius et al. have calculated the radar scattering cross sections of an electrically large ogive as shown in Fig. 15. In a similar approach, Liu et al. [18] were able to arrive at Eq. (10) by replacing the off-surface layer of E nodes by the surface derivatives of the tangential H and named it *on-surface MEI* (OS-MEI). Hirose et al. have used the IE-MEI to solve scattering problems of impedance boundary conditions [19]. With IE-MEI, one is able to reformulate integral equations into sparse matrices, which enables us to solve large scattering problems. So, IE-MEI has been applied to solve 3D problems by Rius et al. [20] for electromagnetics and by Chowdhury et al. [21] for scalar fields.

6. CONCLUSION

It has been shown that despite some doubts expressed by some investigators of the MEI method, there have been many satisfactory applications of MEI reported by other

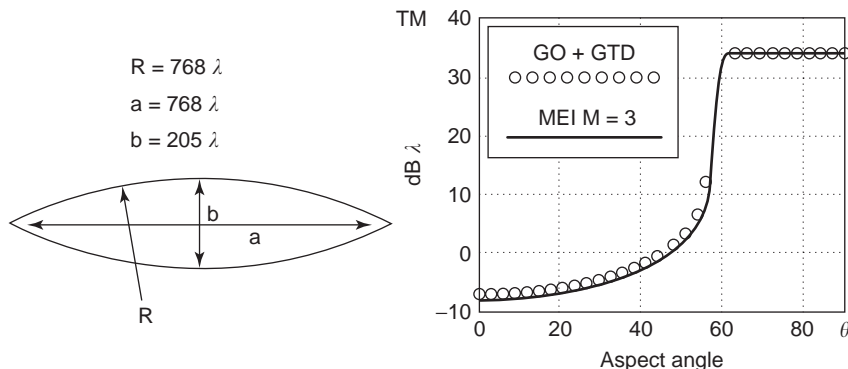


Figure 15. Radar cross section.

investigators. The most basic assumption of the MEI method is the existence of a local linear relation of the fields. Such an assumption is plausible for far fields, which is a differential relation of the fields, known as the *Sommerfeld radiation condition* in classical theory. One may question whether it can still be so assumed on the surface of the object. However, the success of IE-MEI suggests that it may be true that such local linear equations do exist on the object surface. If this were true, the on-surface Maxwell differential equations could be found. What an exciting discovery would that be! Mei has proved the existence of the differential equation of currents on thin wire structure. The readers may find the presentation in the MAXWELLIAN CIRCUITS article in this encyclopedia. Perhaps, it is not far away that someone will prove the existence of differential equations of the surface current density on conduction surfaces.

BIBLIOGRAPHY

1. K. K. Mei, Unimoment method of solving antenna and scattering problems, *IEEE Trans. Anten. Propag.* **AP-22**(6):760–766 (Nov. 1974).
2. B. Engquist and A. Majda, Absorbing boundary condition for the numerical simulation of waves, *Math. Comput.* **31**:629–651 (1977).
3. J. Fang, *Time Domain Finite Difference Computation for Maxwell's Equations*, Ph.D. dissertation, Univ. California, Berkeley, CA, 1989.
4. J. P. Berenger, A perfectly matched layer for absorption of electromagnetic waves, *J. Comput. Phys.* **114**:185–200 (Oct. 1994).
5. K. K. Mei, P. Pous, Z. Chen, Y. Liu, and M. Prouty, Measured equation of invariance—a new concept in field computations, *IEEE Trans. Anten. Propag.* **42**(3):320–328 (March 1994).
6. J. Jevtic and R. Lee, A theoretic and numerical analysis of the measured equation of invariance, *IEEE Trans. Anten. Propag.* **42**(8):1097–1105 (Aug. 1994).
7. K. K. Mei and Y. Liu, Comments on “A theoretic and numerical analysis of the measured equation of invariance,” *IEEE Trans. Anten. Propag.* **43**(10):1168–1171 (Oct. 1995).
8. J. Jevtic and R. Lee, How invariant the measured equation of invariance? *IEEE Microwave Guided Wave Lett.* **5**(2):45–47 (Feb. 1995).
9. K. K. Mei, Comments on “How invariant the measured equation of invariance?” *IEEE Microwave Guided Wave Lett.* **5**(11):417 (Nov. 1995).
10. T. L. Barkdoll and R. Lee, Finite element analysis of bodies of revolution using the measured equation of invariance, *Radio Sci.* **30**:803–815 (July–Aug. 1995).
11. Y. L. Luo, K. M. Luk, K. K. Mei, and E. K. N. Yung, Finite difference analysis of electrically large parabolic reflector antennas, *IEEE Trans. Anten. Propag.* **50**(3):266–276 (March 2002).
12. R. Pous, *Measured Equation of Invariance—a New Concept in Field Computations*, Ph.D. dissertation, Univ. California, Berkeley, CA, 1992.
13. M. Prouty, *Application of the Measured Equation of Invariance to Planar Microstrip Structures*, Ph.D. dissertation, Univ. California, Berkeley, CA, 1994.
14. Y. Liu, K. K. Mei, and E. K. N. Yung, Interpolation, extrapolation and application of the measured equation of invariance to scattering by very large cylinders, *IEEE Trans. Anten. Propag.* **45**(9) (Sept. 1997).
15. O. M. Ramahi, A. Khebir, and R. Mittra, Numerically derived absorbing boundary condition for solution of open region scattering problems, *IEEE Trans. Anten. Propag.* **39**:350–353 (March 1991).
16. B. Stupfel and R. Mittra, A theoretical study of numerical absorbing boundary conditions, *IEEE Trans. Anten. Propag.* **43**(5):478–486 (May 1995).
17. J. M. Rius, R. Pous, and A. Cardama, Integral formulation of the measured equation of invariance: A novel sparse matrix boundary element method, *IEEE Trans. Magn.* **32**(3):962–967 (May 1996).
18. Y. Liu, K. K. Mei, and E. K. N. Yung, Differential formulation of on-surface measured equation of invariance for 2-D conducting scatterings, *IEEE Microwave Guided Wave Lett.* **8**(2):99–101 (Feb. 1998).
19. M. Hirose, M. Miyake, J. Takada, and I. Arai, New integral equation formulation of the measured equation of invariance and the extension to analyze two dimensional cylinders with impedance boundary conditions, *Radio Sci.* **34**(1):65–82 (Jan.–Feb. 1999).
20. J. M. Rius, C. P. Carpintero, A. Cardama, and J. R. Mosig, Integral equation MEI applied to three dimensional arbitrary surfaces, *Electron. Lett.* **33**(24):2029–2031 (Nov. 1997).
21. N. M. A. Chowdhury, J. Takada, and M. Hirose, Novel formulation for scalar-field approach of IE-MEI method to solve three-dimensional scattering problem, *IEICE Trans. Fund. Electron. Commun. Comput. Sci.* **E86-A**(8):1905–1912 (Aug. 2002).

METHOD OF LINES

ALESSANDRO TOSCANO
LUCIO VEGNI
“Roma Tre” University
Rome, Italy

1. INTRODUCTION

Planar passive structures and planar transmission lines are widely used in microwave and millimeter-wave integrated circuits. Characterization and modeling of transmission lines and their discontinuities are of great importance in the development of integrated circuits. It is not economical, or in many cases not even feasible, to tune the circuits once they are fabricated. Therefore, accurate methods are needed to model the structures.

Quasistatic methods, equivalent waveguide models, and equivalent-circuit models have been used in the modeling of microstrip or slotlines, and discontinuities in the past [1,2]. A more rigorous approach, which takes into account all the physical effects including radiation and surface waves is the spectral-domain Galerkin method (SDGM) [3]. This method transforms an integral equation into a linear system of equations, where the solution (e.g., electric currents or fields) has to be computed numerically. The method is known to be efficient but is restricted, in

investigators. The most basic assumption of the MEI method is the existence of a local linear relation of the fields. Such an assumption is plausible for far fields, which is a differential relation of the fields, known as the *Sommerfeld radiation condition* in classical theory. One may question whether it can still be so assumed on the surface of the object. However, the success of IE-MEI suggests that it may be true that such local linear equations do exist on the object surface. If this were true, the on-surface Maxwell differential equations could be found. What an exciting discovery would that be! Mei has proved the existence of the differential equation of currents on thin wire structure. The readers may find the presentation in the MAXWELLIAN CIRCUITS article in this encyclopedia. Perhaps, it is not far away that someone will prove the existence of differential equations of the surface current density on conduction surfaces.

BIBLIOGRAPHY

1. K. K. Mei, Unimoment method of solving antenna and scattering problems, *IEEE Trans. Anten. Propag.* **AP-22**(6):760–766 (Nov. 1974).
2. B. Engquist and A. Majda, Absorbing boundary condition for the numerical simulation of waves, *Math. Comput.* **31**:629–651 (1977).
3. J. Fang, *Time Domain Finite Difference Computation for Maxwell's Equations*, Ph.D. dissertation, Univ. California, Berkeley, CA, 1989.
4. J. P. Berenger, A perfectly matched layer for absorption of electromagnetic waves, *J. Comput. Phys.* **114**:185–200 (Oct. 1994).
5. K. K. Mei, P. Pous, Z. Chen, Y. Liu, and M. Prouty, Measured equation of invariance—a new concept in field computations, *IEEE Trans. Anten. Propag.* **42**(3):320–328 (March 1994).
6. J. Jevtic and R. Lee, A theoretic and numerical analysis of the measured equation of invariance, *IEEE Trans. Anten. Propag.* **42**(8):1097–1105 (Aug. 1994).
7. K. K. Mei and Y. Liu, Comments on “A theoretic and numerical analysis of the measured equation of invariance,” *IEEE Trans. Anten. Propag.* **43**(10):1168–1171 (Oct. 1995).
8. J. Jevtic and R. Lee, How invariant the measured equation of invariance? *IEEE Microwave Guided Wave Lett.* **5**(2):45–47 (Feb. 1995).
9. K. K. Mei, Comments on “How invariant the measured equation of invariance?” *IEEE Microwave Guided Wave Lett.* **5**(11):417 (Nov. 1995).
10. T. L. Barkdoll and R. Lee, Finite element analysis of bodies of revolution using the measured equation of invariance, *Radio Sci.* **30**:803–815 (July–Aug. 1995).
11. Y. L. Luo, K. M. Luk, K. K. Mei, and E. K. N. Yung, Finite difference analysis of electrically large parabolic reflector antennas, *IEEE Trans. Anten. Propag.* **50**(3):266–276 (March 2002).
12. R. Pous, *Measured Equation of Invariance—a New Concept in Field Computations*, Ph.D. dissertation, Univ. California, Berkeley, CA, 1992.
13. M. Prouty, *Application of the Measured Equation of Invariance to Planar Microstrip Structures*, Ph.D. dissertation, Univ. California, Berkeley, CA, 1994.
14. Y. Liu, K. K. Mei, and E. K. N. Yung, Interpolation, extrapolation and application of the measured equation of invariance to scattering by very large cylinders, *IEEE Trans. Anten. Propag.* **45**(9) (Sept. 1997).
15. O. M. Ramahi, A. Khebir, and R. Mittra, Numerically derived absorbing boundary condition for solution of open region scattering problems, *IEEE Trans. Anten. Propag.* **39**:350–353 (March 1991).
16. B. Stupfel and R. Mittra, A theoretical study of numerical absorbing boundary conditions, *IEEE Trans. Anten. Propag.* **43**(5):478–486 (May 1995).
17. J. M. Rius, R. Pous, and A. Cardama, Integral formulation of the measured equation of invariance: A novel sparse matrix boundary element method, *IEEE Trans. Magn.* **32**(3):962–967 (May 1996).
18. Y. Liu, K. K. Mei, and E. K. N. Yung, Differential formulation of on-surface measured equation of invariance for 2-D conducting scatterings, *IEEE Microwave Guided Wave Lett.* **8**(2):99–101 (Feb. 1998).
19. M. Hirose, M. Miyake, J. Takada, and I. Arai, New integral equation formulation of the measured equation of invariance and the extension to analyze two dimensional cylinders with impedance boundary conditions, *Radio Sci.* **34**(1):65–82 (Jan.–Feb. 1999).
20. J. M. Rius, C. P. Carpintero, A. Cardama, and J. R. Mosig, Integral equation MEI applied to three dimensional arbitrary surfaces, *Electron. Lett.* **33**(24):2029–2031 (Nov. 1997).
21. N. M. A. Chowdhury, J. Takada, and M. Hirose, Novel formulation for scalar-field approach of IE-MEI method to solve three-dimensional scattering problem, *IEICE Trans. Fund. Electron. Commun. Comput. Sci.* **E86-A**(8):1905–1912 (Aug. 2002).

METHOD OF LINES

ALESSANDRO TOSCANO
LUCIO VEGNI
“Roma Tre” University
Rome, Italy

1. INTRODUCTION

Planar passive structures and planar transmission lines are widely used in microwave and millimeter-wave integrated circuits. Characterization and modeling of transmission lines and their discontinuities are of great importance in the development of integrated circuits. It is not economical, or in many cases not even feasible, to tune the circuits once they are fabricated. Therefore, accurate methods are needed to model the structures.

Quasistatic methods, equivalent waveguide models, and equivalent-circuit models have been used in the modeling of microstrip or slotlines, and discontinuities in the past [1,2]. A more rigorous approach, which takes into account all the physical effects including radiation and surface waves is the spectral-domain Galerkin method (SDGM) [3]. This method transforms an integral equation into a linear system of equations, where the solution (e.g., electric currents or fields) has to be computed numerically. The method is known to be efficient but is restricted, in

general, to well-shaped structures that involve infinitely thin conductors as ground planes. The main reason for the efficiency is that the SDGM allows significant analytical preprocessing in comparison to other numerical techniques such as the finite-difference method, finite-element methods, or the method of lines. The method of partial discretization or method of lines is a well-established technique for the analysis of different microwave structures.

The method of lines is regarded as a special finite-difference method but is more effective with respect to accuracy and computational time than is the regular finite-difference method. It basically involves discretizing a given differential equation in one or two dimensions while using an analytical solution in the remaining direction. The method of lines (MoL) has the merits of both the finite difference method and the analytical method; it does not yield spurious modes, nor does it have the problem of "relative convergence." Besides, the method of lines has the following properties that justify its use:

1. *Computational efficiency*—the semianalytical character of the formulation leads to a simple and compact algorithm, which yields accurate results with less computational effort than do other techniques.
2. *Numerical stability*—by separating discretization of space and time, it is easy to establish stability and convergence for a wide range of problems.
3. *Reduced programming effort*—by making use of the state-of-the-art well-documented and reliable ordinary differential equations (ODE) solvers, programming effort can be substantially reduced.
4. *Reduced computational time*—since only a small amount of discretization lines are necessary in the computation, there is no need to solve a large system of equations; hence computing time is small.

2. STEPS IN MoL APPLICATION

Application of MoL usually involves the following four basic steps:

1. Partitioning the solution region into lines
2. Discretization of the differential equation in one or two coordinate direction
3. Transformation to obtain decoupled ordinary differential equations
4. Introduction of the boundary conditions and solution of the equations.

2.1. Partitioning the Solution Region into Lines (Step 1)

The method of lines is particularly suitable for modeling a wide range of transmission lines and integrated structures with multiple layers [4–6]. This involves in the most general case discretizing the Helmholtz wave equation in two directions while the other direction is treated analytically. We will illustrate the method for planar integrated structures.

In this section we describe a formulation of the electromagnetic problem in an arbitrary general isotropic medium leading, besides, to the decoupling of the Maxwell's equations describing the electromagnetic field and to an equivalent-circuit representation of the layered medium.

The geometry of the problem and coordinate definitions of the structure are given in Fig. 1, where elementary current sources are shown and/or a plane wave is incident on a multilayer generalized planar structure. First, we consider the i th layer, which is not infinitely large in the planar direction (x - z plane) and the homogeneous material is characterized via the constitutive relation proper of the dielectric medium considered.

Starting from Maxwell's equations, the whole field may be obtained from the component in the \hat{z} -direction E_z and H_z . For these components the following wave equations hold

$$\frac{\partial^2 \psi}{\partial x^2} + \frac{\partial^2 \psi}{\partial y^2} + \frac{\partial^2 \psi}{\partial z^2} + k^2 \psi = 0 \quad (1)$$

where $\psi = E_z, H_z$, $k^2 = \omega^2 \mu \epsilon$ and μ and ϵ are the magnetic permeability and the electric permittivity, respectively.

The other four components can be expressed in terms of E_z and H_z as follows

$$\begin{pmatrix} \frac{\partial^2}{\partial z^2} + k^2 \end{pmatrix} \begin{bmatrix} E_x \\ E_y \end{bmatrix} = \begin{bmatrix} \frac{\partial^2}{\partial x \partial z} & -jk\eta \frac{\partial}{\partial y} \\ \frac{\partial^2}{\partial y \partial z} & jk\eta \frac{\partial}{\partial x} \end{bmatrix} \begin{bmatrix} E_z \\ H_z \end{bmatrix} \quad (2)$$

$$\begin{pmatrix} \frac{\partial^2}{\partial z^2} + k^2 \end{pmatrix} \begin{bmatrix} H_x \\ H_y \end{bmatrix} = \begin{bmatrix} j\eta \frac{\partial}{\partial y} & \frac{\partial^2}{\partial x \partial z} \\ -j\eta \frac{\partial}{\partial x} & \frac{\partial^2}{\partial y \partial z} \end{bmatrix} \begin{bmatrix} E_z \\ H_z \end{bmatrix} \quad (3)$$

where

$$\begin{cases} \eta = \sqrt{\mu_0/\epsilon} = \eta_0/\sqrt{\epsilon_r} \\ \eta_0 = \sqrt{\mu_0/\epsilon_0} \end{cases}$$

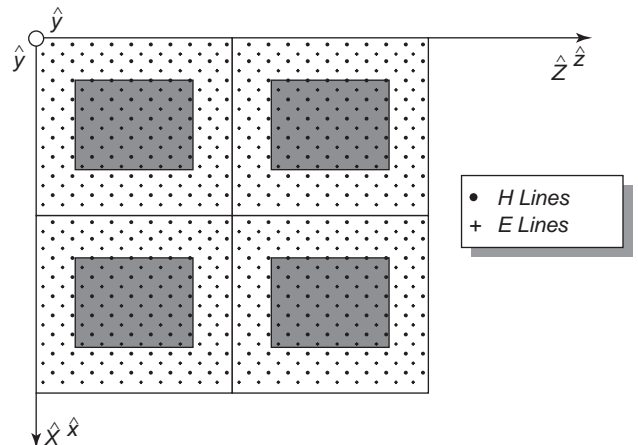


Figure 1. Geometry of the electromagnetic problem.

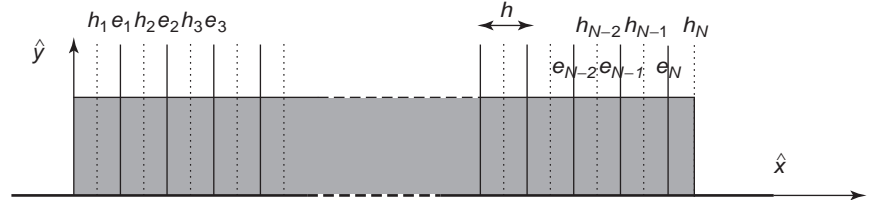


Figure 2. Transverse section of the generic layer of height d discretized along the \hat{x} direction (— e lines; - - - h lines).

It should be noted that the wave equation (1) and the field relations (2) and (3) are still valid also for inhomogenous isotropic media characterized by constitutive parameters $\mu = \mu_0$ and $\varepsilon = \varepsilon_0 \varepsilon_r(y)$.

Since we are considering the most general case of application of the method of line, here, for a solution of the wave equation (1) and for determination of the field components, a discretization along both the \hat{x} and the \hat{z} directions is performed. The discretization is performed using two different sets of lines: the so called e lines and h lines. The smallest separation between two e lines is s , while the smallest separation between an e and an h line is $s/2$. Different sets of boundary conditions at the two ends of the generic layer can be considered (e.g., Neumann and/or Dirichlet, periodic, absorbing boundary). In Fig. 2 we have depicted the transverse section of the generic discretized along the \hat{x} direction.

If N_x is the number of the e lines, N_x is also the number of the h lines and s is the separation between the lines. Once the transverse section of the generic layer is discretized, for the components of the electric field, we have

$$\begin{cases} E_x(x, y, z) \rightarrow \underline{E}_x(y) = [E_x^1(y), E_x^2(y), E_x^3(y) \cdots E_x^N(y)] \\ E_y(x, y, z) \rightarrow \underline{E}_y(y) = [E_y^1(y), E_y^2(y), E_y^3(y) \cdots E_y^N(y)] \\ E_z(x, y, z) \rightarrow \underline{E}_z(y) = [E_z^1(y), E_z^2(y), E_z^3(y) \cdots E_z^N(y)] \end{cases} \quad (4)$$

where, for instance, $\underline{E}_x(y)$ is the vector whose elements are the values of the \hat{x} component of the electric field sampled on the e lines. The discretization for the magnetic field is dual.

2.2. Discretization of Differential Equation in One or Two Coordinate Directions (Step 2)

The first-order derivative operators are replaced by difference operators that can be described by the Kröner products (\otimes) of the difference operators for the longitudinal ($\underline{\mathbf{d}}_z^m$) or azimuthal ($\underline{\mathbf{d}}_y^m$) line system and the unit matrices $\underline{\mathbf{I}}_x$ and $\underline{\mathbf{I}}_z$ of order $N_x \times N_x$ and $N_z \times N_z$, respectively:

$$\begin{cases} \underline{\mathbf{D}}_z^m = \underline{\mathbf{d}}_z^m \otimes \underline{\mathbf{I}}_x \\ \underline{\mathbf{D}}_x^m = \underline{\mathbf{I}}_z \otimes \underline{\mathbf{d}}_x^m \end{cases} \quad \text{with } m = e, h \quad (5)$$

The formal expression of the difference operators $\underline{\mathbf{d}}_z^m$ and $\underline{\mathbf{d}}_x^m$ depends on the boundary conditions used. In the case of Neumann and/or Dirichlet conditions they are given in Ref. 3, in the case of periodic boundary condition they are also given in Ref. 3, and for the case of absorbing boundary conditions they are given in Ref. 7.

For the second-order derivatives we directly have

$$\begin{cases} \underline{\mathbf{D}}\underline{\mathbf{D}}^m = -(\underline{\mathbf{d}}_z^m \otimes \underline{\mathbf{I}}_x) \cdot (\underline{\mathbf{d}}_z^m \otimes \underline{\mathbf{I}}_x)^t \\ = -(\underline{\mathbf{d}}_z^m \otimes \underline{\mathbf{I}}_x) \cdot (\underline{\mathbf{d}}_z^{m,t} \otimes \underline{\mathbf{I}}_x^t) = (\underline{\mathbf{d}}\underline{\mathbf{d}}_z^m \otimes \underline{\mathbf{I}}_x) \\ \underline{\mathbf{D}}\underline{\mathbf{D}}_x^m = -(\underline{\mathbf{I}}_z \otimes \underline{\mathbf{d}}_x^m) \cdot (\underline{\mathbf{I}}_z \otimes \underline{\mathbf{d}}_x^m)^t \\ = -(\underline{\mathbf{I}}_z \otimes \underline{\mathbf{d}}_x^m) \cdot (\underline{\mathbf{I}}_z^t \otimes \underline{\mathbf{d}}_x^{m,t}) = (\underline{\mathbf{I}}_z \otimes \underline{\mathbf{d}}\underline{\mathbf{d}}_x^m) \end{cases} \quad (6)$$

It can now be easily shown that the vector $\underline{\psi} = \underline{E}_z, \underline{H}_z$ satisfies the following set of coupled differential equations:

$$\frac{\partial^2 \underline{\psi}}{\partial y^2} + \underline{\mathbf{D}}\underline{\mathbf{D}}_x^{e,h} \cdot \underline{\psi} + \underline{\mathbf{D}}\underline{\mathbf{D}}_z^{e,h} \cdot \underline{\psi} + k^2 \underline{\psi} = 0 \quad (7)$$

2.3. Transformation to Obtain Decoupled Ordinary Differential Equations (Step 3)

The next step is to solve analytically the equations resulting along the y coordinate. To solve (7) analytically, we need to obtain a system of uncoupled ordinary differential equations from the coupled equation (7). To achieve this, we define the transformed vector $\underline{\psi}^*$ by letting

$$\underline{\psi} = \underline{\mathbf{T}}^{e,h} \cdot \underline{\psi}^* \quad (8)$$

and requiring

$$\begin{cases} (\underline{\mathbf{T}}^{e,h})^{-1} \cdot \underline{\mathbf{D}}\underline{\mathbf{D}}_x^{e,h} \cdot \underline{\mathbf{T}}^{e,h} = \underline{\Lambda}_x^2 \\ (\underline{\mathbf{T}}^{e,h})^{-1} \cdot \underline{\mathbf{D}}\underline{\mathbf{D}}_z^{e,h} \cdot \underline{\mathbf{T}}^{e,h} = \underline{\Lambda}_z^2 \end{cases} \quad (9)$$

where the elements of the diagonal matrices $\underline{\Lambda}_x^2, \underline{\Lambda}_z^2$ are the eigenvalues of $\underline{\mathbf{D}}\underline{\mathbf{D}}_x^{e,h}$ and $\underline{\mathbf{D}}\underline{\mathbf{D}}_z^{e,h}$, respectively.

In (8) we advanced the following position

$$\underline{\mathbf{T}}^{e,h} = \underline{\mathbf{t}}_z^{e,h} \otimes \underline{\mathbf{t}}_x^{e,h} \quad (10)$$

equaling $\underline{\mathbf{t}}_x^m$ and $\underline{\mathbf{t}}_z^m$, the eigenvector matrices belonging to second-order difference operators $\underline{\mathbf{d}}\underline{\mathbf{d}}_x^m$ and $\underline{\mathbf{d}}\underline{\mathbf{d}}_z^m$, respectively.

After some algebraic manipulations, it can be shown that, for homogeneous layers where μ and ε do not depend on y , the general solution for the k th component of the vector $\underline{\psi}^*$ can be expressed as

$$\psi_k^*(y) = A_k \cdot \cosh(k_{y,k}y) + B_k \cdot \sinh(k_{y,k}y) \quad (11)$$

where A_k and B_k are integration constants and depend on the proper boundary condition to be applied.

From the general solution (11) we can relate to each other the field solution at the interfaces in y_p and y_{p+1} of the generic p th layer as follows:

$$\begin{bmatrix} \underline{E}'_{zk}(y_{p+1}) \\ \underline{E}'_{zk}(y_p) \end{bmatrix} = \begin{bmatrix} \phi e_k^{(1,1)}(y_p, y_{p+1}) & \phi e_k^{(1,2)}(y_p, y_{p+1}) \\ \phi e_k^{(2,1)}(y_p, y_{p+1}) & \phi e_k^{(2,2)}(y_p, y_{p+1}) \end{bmatrix} \cdot \begin{bmatrix} \underline{E}^*_{zk}(y_{p+1}) \\ \underline{E}^*_{zk}(y_p) \end{bmatrix} \quad (12)$$

$$\begin{bmatrix} \underline{H}'_{zk}(y_{p+1}) \\ \underline{H}'_{zk}(y_p) \end{bmatrix} = \begin{bmatrix} \phi h_k^{(1,1)}(y_p, y_{p+1}) & \phi h_k^{(1,2)}(y_p, y_{p+1}) \\ \phi h_k^{(2,1)}(y_p, y_{p+1}) & \phi h_k^{(2,2)}(y_p, y_{p+1}) \end{bmatrix} \cdot \begin{bmatrix} \underline{H}^*_{zk}(y_{p+1}) \\ \underline{H}^*_{zk}(y_p) \end{bmatrix} \quad (13)$$

In (12) and (13) the apex prime stands for first derivative with respect the variable y and we have stated the following positions:

$$\begin{cases} \phi e_k^{(1,1)}(y_p, y_{p+1}) = -k_{y_k} \cdot \coth[(y_p - y_{p+1}) \cdot k_{y_k}] \\ \phi e_k^{(1,2)}(y_p, y_{p+1}) = k_{y_k} \cdot \operatorname{csch}[(y_p - y_{p+1}) \cdot k_{y_k}] \\ \phi e_k^{(2,1)}(y_p, y_{p+1}) = -k_{y_k} \cdot \operatorname{csch}[(y_p - y_{p+1}) \cdot k_{y_k}] \\ \phi e_k^{(2,2)}(y_p, y_{p+1}) = k_{y_k} \cdot \coth[(y_p - y_{p+1}) \cdot k_{y_k}] \end{cases} \quad (14)$$

$$\begin{cases} \phi h_k^{(1,1)}(y_p, y_{p+1}) = \frac{-k_{y_k} \cdot \coth[(y_p - y_{p+1}) \cdot k_{y_k}]}{k_{y_k}} \\ \phi h_k^{(1,2)}(y_p, y_{p+1}) = \frac{k_{y_k} \cdot \operatorname{csch}[(y_p - y_{p+1}) \cdot k_{y_k}]}{k_{y_k}} \\ \phi h_k^{(2,1)}(y_p, y_{p+1}) = \frac{-k_{y_k} \cdot \operatorname{csch}[(y_p - y_{p+1}) \cdot k_{y_k}]}{k_{y_k}} \\ \phi h_k^{(2,2)}(y_p, y_{p+1}) = \frac{k_{y_k} \cdot \coth[(y_p - y_{p+1}) \cdot k_{y_k}]}{k_{y_k}} \end{cases} \quad (15)$$

Now we derive from (12) and (13) the discretized transverse $\hat{\mathbf{x}}$ component of the electric and magnetic fields in terms of the E_z and H_z components as follows:

$$\begin{cases} \underline{E}_x(y) = \left[\underline{\mathbf{D}}_z^h \cdot \underline{\mathbf{D}}_z^e + \omega^2 \mu \underline{\mathbf{E}} \right]^{-1} \cdot \left[\underline{\mathbf{D}}_z^h \cdot \underline{\mathbf{D}}_x^e \cdot \underline{\mathbf{T}}^e \cdot \underline{E}_z^*(y) + j\omega\mu \cdot \underline{\mathbf{T}}^h \cdot \underline{H}_z^*(y) \right] \\ \underline{H}_x(y) = \left[\underline{\mathbf{D}}_z^e \cdot \underline{\mathbf{D}}_z^h + \omega^2 \mu \underline{\mathbf{E}} \right]^{-1} \cdot \left[\underline{\mathbf{D}}_z^e \cdot \underline{\mathbf{D}}_x^h \cdot \underline{\mathbf{T}}^h \cdot \underline{H}_z^*(y) - j\omega\epsilon \cdot \underline{\mathbf{T}}^e \cdot \underline{E}_z^*(y) \right] \end{cases} \quad (16)$$

It can now be shown that for the two interfaces A and B in y_p and y_{p+1} , respectively, of a generic layer the following

relation in matrix form holds:

$$\begin{bmatrix} \underline{\mathbf{H}}_B \\ \underline{\mathbf{H}}_A \end{bmatrix} = \begin{bmatrix} \underline{\mathbf{Y}}_{11}^{(a,b)} & \underline{\mathbf{Y}}_{12}^{(a,b)} \\ \underline{\mathbf{Y}}_{21}^{(a,b)} & \underline{\mathbf{Y}}_{22}^{(a,b)} \end{bmatrix} \cdot \begin{bmatrix} \underline{\mathbf{E}}_B \\ \underline{\mathbf{E}}_A \end{bmatrix} \quad (17)$$

where

$$\begin{cases} \underline{\mathbf{E}}_A = \begin{bmatrix} \underline{E}_x(a) \\ \underline{E}_z(a) \end{bmatrix} \\ \underline{\mathbf{E}}_B = \begin{bmatrix} \underline{E}_x(b) \\ \underline{E}_z(b) \end{bmatrix} \end{cases}, \quad \begin{cases} \underline{\mathbf{H}}_A = \begin{bmatrix} \underline{H}_x(a) \\ \underline{H}_z(a) \end{bmatrix} \\ \underline{\mathbf{H}}_B = \begin{bmatrix} \underline{H}_x(b) \\ \underline{H}_z(b) \end{bmatrix} \end{cases}$$

$$\begin{bmatrix} \underline{\mathbf{Y}}_{11}^{(a,b)} & \underline{\mathbf{Y}}_{12}^{(a,b)} \\ \underline{\mathbf{Y}}_{21}^{(a,b)} & \underline{\mathbf{Y}}_{22}^{(a,b)} \end{bmatrix} = \underline{\mathbf{B}} \cdot \underline{\mathbf{Z}} \cdot \underline{\mathbf{A}}^{-1}$$

$$\underline{\mathbf{A}} = \begin{bmatrix} \underline{\alpha} \cdot \underline{\mathbf{T}}^e & \underline{\gamma} \cdot \underline{\mathbf{T}}^h & \underline{\mathbf{0}} & \underline{\mathbf{0}} \\ \underline{\mathbf{T}}^e & \underline{\mathbf{0}} & \underline{\mathbf{0}} & \underline{\mathbf{0}} \\ \underline{\mathbf{0}} & \underline{\mathbf{0}} & \underline{\alpha} \cdot \underline{\mathbf{T}}^e & \underline{\gamma} \cdot \underline{\mathbf{T}}^h \\ \underline{\mathbf{0}} & \underline{\mathbf{0}} & \underline{\mathbf{T}}^e & \underline{\mathbf{0}} \end{bmatrix}$$

$$\underline{\mathbf{B}} = \begin{bmatrix} \underline{\beta} \cdot \underline{\mathbf{T}}^h & \underline{\delta} \cdot \underline{\mathbf{T}}^e & \underline{\mathbf{0}} & \underline{\mathbf{0}} \\ \underline{\mathbf{T}}^e & \underline{\mathbf{0}} & \underline{\mathbf{0}} & \underline{\mathbf{0}} \\ \underline{\mathbf{0}} & \underline{\mathbf{0}} & \underline{\beta} \cdot \underline{\mathbf{T}}^h & \underline{\delta} \cdot \underline{\mathbf{T}}^e \\ \underline{\mathbf{0}} & \underline{\mathbf{0}} & \underline{\mathbf{T}}^h & \underline{\mathbf{0}} \end{bmatrix}$$

$$\underline{\mathbf{Z}} = \begin{bmatrix} \underline{\mathbf{0}} & \underline{\phi h}^{(1,1)}(a, b) & \underline{\mathbf{0}} & \underline{\phi h}^{(1,2)}(a, b) \\ \underline{\phi e}^{(1,1)}(a, b) & \underline{\mathbf{0}} & \underline{\phi e}^{(1,2)}(a, b) & \underline{\mathbf{0}} \\ \underline{\mathbf{0}} & \underline{\phi h}^{(2,1)}(a, b) & \underline{\mathbf{0}} & \underline{\phi h}^{(2,2)}(a, b) \\ \underline{\phi e}^{(2,1)}(a, b) & \underline{\mathbf{0}} & \underline{\phi e}^{(2,2)}(a, b) & \underline{\mathbf{0}} \end{bmatrix}$$

$$\begin{cases} \underline{\alpha} = \left[\underline{\mathbf{D}}_z^h \cdot \underline{\mathbf{D}}_z^e + \omega^2 \mu \underline{\mathbf{E}} \right]^{-1} \cdot \underline{\mathbf{D}}_z^h \cdot \underline{\mathbf{D}}_x^e \\ \underline{\gamma} = j\omega\mu \left[\underline{\mathbf{D}}_z^h \cdot \underline{\mathbf{D}}_z^e + \omega^2 \mu \underline{\mathbf{E}} \right]^{-1} \\ \underline{\beta} = \left[\underline{\mathbf{D}}_z^e \cdot \underline{\mathbf{D}}_z^h + \omega^2 \mu \underline{\mathbf{E}} \right]^{-1} \cdot \underline{\mathbf{D}}_z^e \cdot \underline{\mathbf{D}}_x^h \\ \underline{\delta} = -j\omega\mu \left[\underline{\mathbf{D}}_z^e \cdot \underline{\mathbf{D}}_z^h + \omega^2 \mu \underline{\mathbf{E}} \right]^{-1} \end{cases}$$

Equation (17) gives the transfer equation for the generic layer. The transfer equation for a number of layers is obtained by multiplication of the transmission matrices proper of the single layers.

Special attention must be paid to the upper isotropic half-space. For the radiation condition, we have

$$\psi_k^*(y) = C_k \cdot e^{-k_{y_k} y} \quad (18)$$

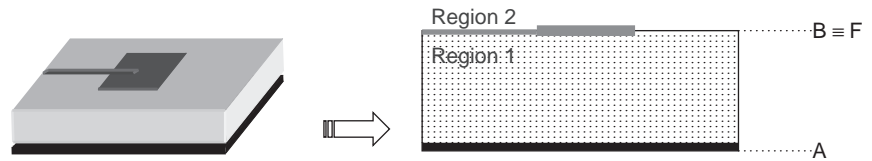


Figure 3. Geometry of the layered structure.

In this case we can write

$$\underline{\mathbf{H}}_F = \underline{\mathbf{Y}}_t^{(c)} \bullet \underline{\mathbf{E}}_F \tag{19}$$

where

$$\underline{\mathbf{Y}}_t^{(c)} = \underline{\mathbf{B}}^{(c)} \times \underline{\mathbf{Z}}^{(c)} \times (\underline{\mathbf{A}}^{(c)})^{-1}$$

$$\underline{\mathbf{A}}^{(c)} = \begin{bmatrix} \underline{\alpha} \times \underline{\mathbf{T}}^e & \underline{\gamma} \times \underline{\mathbf{T}}^h \\ \underline{\mathbf{T}}^e & \underline{\mathbf{0}} \end{bmatrix}$$

$$\underline{\mathbf{B}}^{(c)} = \begin{bmatrix} \underline{\beta} \times \underline{\mathbf{T}}^h & \underline{\delta} \times \underline{\mathbf{T}}^e \\ \underline{\mathbf{T}}^h & \underline{\mathbf{0}} \end{bmatrix}$$

$$\underline{\mathbf{Z}}^{(c)} = \begin{bmatrix} \underline{\mathbf{0}} & \underline{\zeta e}(y_N) \\ \underline{\zeta h}(y_N) & \underline{\mathbf{0}} \end{bmatrix}$$

$\underline{\zeta e}(y_N)$ and $\underline{\zeta h}(y_N)$ are diagonal matrices whose elements are given by $\overline{y}^{-1}(1/k_{y_k})$ and $-k_{y_k}$, respectively.

The method of lines can be used to analyze homogeneous and inhomogeneous cylindrical transmission structures [8–10] and circular and elliptic waveguides [11]. The principal steps involved in applying MoL in cylindrical coordinates are the same as in Cartesian coordinates.

2.4. Introduction of Boundary Conditions and Solution of Equations (Step 4)

Here, we illustrate with the use of MoL, an analysis of the electromagnetic characteristics of planar integrated structures.

In this section we apply the theory described in the previous sections to two practical geometries. The first one is a microstrip patch antenna fed by a coplanar microstrip line as shown in Fig. 3. The second one is a layered structure with three layers in the presence of an aperture between layers 2 and 3 (Fig. 4). We give two examples in Sections 2.4.1. and 2.4.2.

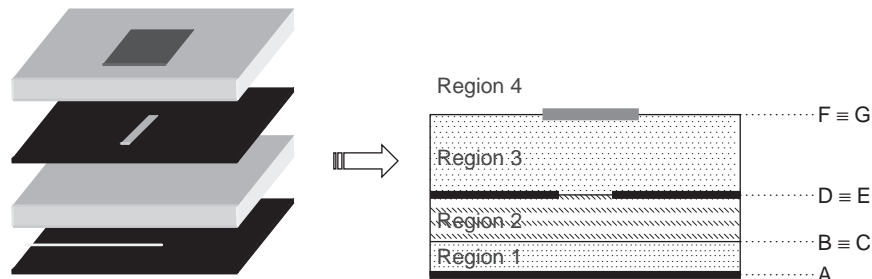


Figure 4. Geometry of the layered structure.

2.4.1. Coplanar Microstrip Line. Two different regions are described by the following transmission matrices:

Region 1 ($y_a \leq y \leq y_b$):

$$\begin{bmatrix} \underline{\mathbf{H}}_B \\ \underline{\mathbf{H}}_A \end{bmatrix} = \begin{bmatrix} \underline{\mathbf{Y}}_{11}^{(y_a, y_b)} & \underline{\mathbf{Y}}_{12}^{(y_a, y_b)} \\ \underline{\mathbf{Y}}_{21}^{(y_a, y_b)} & \underline{\mathbf{Y}}_{22}^{(y_a, y_b)} \end{bmatrix} \bullet \begin{bmatrix} \underline{\mathbf{E}}_B \\ \underline{\mathbf{E}}_A \end{bmatrix} \tag{20}$$

Region 2 ($y_b \leq y \leq \infty$):

$$\underline{\mathbf{H}}_F = \left[\underline{\mathbf{Y}}_t^{(y_b)} \right] \underline{\mathbf{E}}_F \tag{21}$$

On the ground plane we have

$$\vec{\mathbf{E}}_A = 0 \tag{22}$$

On the first in $y = y_b$ we must impose the continuity of the tangential components of the electric field. The magnetic field shows a discontinuity due to the presence of electric impressed sources ($\underline{\mathbf{J}}_{imp}$) on the feedline and of induced or scattered currents on the metallic path ($\underline{\mathbf{J}}_S$):

$$\begin{cases} \underline{\mathbf{H}}_F^{(patch)} - \underline{\mathbf{H}}_B^{(patch)} = \underline{\mathbf{J}}_S \\ \underline{\mathbf{H}}_F^{(feed)} - \underline{\mathbf{H}}_B^{(feed)} = \underline{\mathbf{J}}_{imp} \end{cases} \tag{23}$$

Moreover, on the metallic patches the tangential components of the electric field must vanish:

$$\vec{\mathbf{E}}_F \Big|_{patch} = 0 \tag{24}$$

From (20) and (22) we get

$$\vec{\mathbf{H}}_B = \underline{\mathbf{Y}}_{11}^{(y_a, y_b)} \bullet \vec{\mathbf{E}}_B \tag{25}$$

From the first equation of (23) and from (21) and (25), we can write

$$\begin{aligned} \begin{bmatrix} \underline{\mathbf{H}}_B^{(\text{patch})} \\ \underline{\mathbf{H}}_F^{(\text{feed})} \end{bmatrix} &= \begin{bmatrix} \underline{\mathbf{H}}_F^{(\text{patch})} \\ \underline{\mathbf{H}}_B^{(\text{feed})} \end{bmatrix} + \begin{bmatrix} -\underline{\mathbf{J}}_S \\ \underline{\mathbf{J}}_{\text{imp}} \end{bmatrix} \\ &= \begin{bmatrix} \underline{\mathbf{Y}}_t^{(y_b)} & \underline{\mathbf{0}} \\ \underline{\mathbf{0}} & \underline{\mathbf{Y}}_{11}^{(y_a, y_b)} \end{bmatrix} \times \begin{bmatrix} \underline{\mathbf{E}}_F^{(\text{patch})} \\ \underline{\mathbf{E}}_B^{(\text{feed})} \end{bmatrix} + \begin{bmatrix} -\underline{\mathbf{J}}_S \\ \underline{\mathbf{J}}_{\text{imp}} \end{bmatrix} \end{aligned} \quad (26)$$

and thus

$$\begin{aligned} \begin{bmatrix} \underline{\mathbf{Y}}_{11}^{(y_a, y_b)} & \underline{\mathbf{Y}}_{12}^{(y_a, y_b)} \\ \underline{\mathbf{Y}}_{21}^{(y_a, y_b)} & \underline{\mathbf{Y}}_{22}^{(y_a, y_b)} \end{bmatrix} \cdot \begin{bmatrix} \underline{\mathbf{E}}_F^{(\text{patch})} \\ \underline{\mathbf{E}}_B^{(\text{feed})} \end{bmatrix} \\ = \begin{bmatrix} \underline{\mathbf{Y}}_t^{(y_c)} & \underline{\mathbf{0}} \\ \underline{\mathbf{0}} & \underline{\mathbf{Y}}_{11}^{(y_a, y_b)} \end{bmatrix} \cdot \begin{bmatrix} \underline{\mathbf{E}}_F^{(\text{patch})} \\ \underline{\mathbf{E}}_B^{(\text{feed})} \end{bmatrix} + \begin{bmatrix} -\underline{\mathbf{J}}_S \\ \underline{\mathbf{J}}_{\text{imp}} \end{bmatrix} \end{aligned}$$

or, in a more compact form

$$\begin{aligned} (\underline{\mathbf{A}}_{11} - \underline{\mathbf{A}}_{12} \cdot \underline{\mathbf{A}}_{22}^{-1} \cdot \underline{\mathbf{A}}_{21}) \cdot \vec{\underline{\mathbf{E}}}_F + \vec{\underline{\mathbf{J}}}_S \\ = -\underline{\mathbf{A}}_{12} \cdot \underline{\mathbf{A}}_{22}^{-1} \cdot \vec{\underline{\mathbf{J}}}_{\text{imp}} \end{aligned} \quad (27)$$

with

$$\left\{ \begin{array}{l} \underline{\mathbf{A}}_{11} = \underline{\mathbf{Y}}_{11}^{(y_a, y_b)} - \underline{\mathbf{Y}}_t^{(y_b)} \\ \underline{\mathbf{A}}_{22} = \underline{\mathbf{Y}}_{22}^{(y_a, y_b)} - \underline{\mathbf{Y}}_{11}^{(y_a, y_b)} \end{array} \right\}, \quad \left\{ \begin{array}{l} \underline{\mathbf{A}}_{12} = \underline{\mathbf{Y}}_{12}^{(y_a, y_b)} \\ \underline{\mathbf{A}}_{21} = \underline{\mathbf{Y}}_{21}^{(y_a, y_b)} \end{array} \right\}$$

It is important to note that in Eq. (27) $\underline{\mathbf{E}}_F$ has to be set to zero in the metallic regions, where only $\underline{\mathbf{J}}_S$ and $\underline{\mathbf{J}}_{\text{imp}}$ have components and $\underline{\mathbf{J}}_S$ and $\underline{\mathbf{J}}_{\text{imp}}$ must be set to zero above the dielectric interface, where, on the contrary, only $\underline{\mathbf{E}}_F$ has components.

Thanks to this property, all those columns of the matrix $\underline{\mathbf{A}}_{11} - \underline{\mathbf{A}}_{12} \cdot \underline{\mathbf{A}}_{22}^{-1} \cdot \underline{\mathbf{A}}_{21}$ that multiply for column void values of $\underline{\mathbf{E}}_F$ can be replaced by columns of zeros. Therefore, to obtain a solution both for $\underline{\mathbf{E}}_F$ and $\underline{\mathbf{J}}_S$, it suffices to operate a sort of “fusion” of the two vectors in an only one (the vector $\underline{\mathbf{X}}$), and to rewrite Eq. (27) as the following linear, matrix equation:

$$\underline{\mathbf{A}} \cdot \underline{\mathbf{X}} = \underline{\mathbf{B}} \cdot \underline{\mathbf{J}}_{\text{imp}} \quad (28)$$

It is worth remarking that if we change the location and the dimensions of the radiating patches and the impressed source, we have only to compute again the vectors $\underline{\mathbf{X}}$ and $\underline{\mathbf{J}}_{\text{imp}}$ (which is not time-consuming) and numerically solve the same linear, matrix equation. So, the MoL analysis technique presented here is found to be sufficiently versatile to handle important practical configurations such as stacked patches, patches with superstrates, without

[unlike e.g., those for the moment method (MoM)] the expense of very long computer runtimes. We should also note that the computational efficiency is high, and thanks, to the reduced system (28), a smaller number of discretization lines is necessary.

2.4.2. Layered Structure with Three Layers in Presence of an Aperture. In this case four different regions are described by the following transmission matrices:

Region 1:

$$\begin{bmatrix} \underline{\mathbf{H}}_B \\ \underline{\mathbf{H}}_A \end{bmatrix} = \begin{bmatrix} \underline{\mathbf{Y}}_1^{(1,1)} & \underline{\mathbf{Y}}_1^{(1,2)} \\ \underline{\mathbf{Y}}_1^{(2,1)} & \underline{\mathbf{Y}}_1^{(2,2)} \end{bmatrix} \begin{bmatrix} \underline{\mathbf{E}}_B \\ \underline{\mathbf{E}}_A \end{bmatrix} \quad (29)$$

Region 2:

$$\begin{bmatrix} \underline{\mathbf{H}}_D \\ \underline{\mathbf{H}}_C \end{bmatrix} = \begin{bmatrix} \underline{\mathbf{Y}}_2^{(1,1)} & \underline{\mathbf{Y}}_2^{(1,2)} \\ \underline{\mathbf{Y}}_2^{(2,1)} & \underline{\mathbf{Y}}_2^{(2,2)} \end{bmatrix} \begin{bmatrix} \underline{\mathbf{E}}_D \\ \underline{\mathbf{E}}_C \end{bmatrix} \quad (30)$$

Region 3:

$$\begin{bmatrix} \underline{\mathbf{H}}_F \\ \underline{\mathbf{H}}_E \end{bmatrix} = \begin{bmatrix} \underline{\mathbf{Y}}_3^{(1,1)} & \underline{\mathbf{Y}}_3^{(1,2)} \\ \underline{\mathbf{Y}}_3^{(2,1)} & \underline{\mathbf{Y}}_3^{(2,2)} \end{bmatrix} \begin{bmatrix} \underline{\mathbf{E}}_F \\ \underline{\mathbf{E}}_E \end{bmatrix} \quad (31)$$

Region 4:

$$\underline{\mathbf{H}}_G = \underline{\mathbf{Y}}_G \cdot \underline{\mathbf{E}}_G \quad (32)$$

The boundary conditions are

Interface 1:

$$\underline{\mathbf{E}}_A = 0 \quad (33)$$

Interface 2:

$$\begin{cases} \underline{\mathbf{H}}_C - \underline{\mathbf{H}}_B = \underline{\mathbf{J}}_{\text{imp}} \\ \underline{\mathbf{H}}_C = \underline{\mathbf{H}}_B \end{cases} \quad (34)$$

Interface 3:

$$\begin{cases} \underline{\mathbf{H}}_E - \underline{\mathbf{H}}_D = \underline{\mathbf{J}}_{S1} \\ \underline{\mathbf{E}}_E|_{\text{slot}} = \underline{\mathbf{E}}_D|_{\text{slot}} \\ \underline{\mathbf{E}}_E|_{\text{ground}} = 0 \end{cases} \quad (35)$$

Interface 4:

$$\begin{cases} \underline{\mathbf{H}}_G - \underline{\mathbf{H}}_F = \underline{\mathbf{J}}_{S2} \\ \underline{\mathbf{E}}_G|_{\text{slot}} = \underline{\mathbf{E}}_F|_{\text{slot}} \\ \underline{\mathbf{E}}_G|_{\text{patch}} = 0 \end{cases} \quad (36)$$

From (29) and (33) we can write

$$\underline{\mathbf{H}}_B = \underline{\mathbf{Y}}_1^{(1,1)} \cdot \underline{\mathbf{E}}_B \quad (37)$$

From (35), (36), and (31) we have

$$\begin{bmatrix} \underline{\mathbf{H}}_F \\ \underline{\mathbf{H}}_E \end{bmatrix} = \begin{bmatrix} \underline{\mathbf{H}}_G \\ \underline{\mathbf{H}}_D \end{bmatrix} + \begin{bmatrix} -\underline{\mathbf{J}}_{S2} \\ \underline{\mathbf{J}}_{S1} \end{bmatrix} = \begin{bmatrix} \underline{\mathbf{Y}}_3^{(1,1)} & \underline{\mathbf{Y}}_3^{(1,2)} \\ \underline{\mathbf{Y}}_3^{(2,1)} & \underline{\mathbf{Y}}_3^{(2,2)} \end{bmatrix} \begin{bmatrix} \underline{\mathbf{E}}_G \\ \underline{\mathbf{E}}_D \end{bmatrix} \quad (38)$$

and then

$$\begin{bmatrix} \underline{\mathbf{Y}}_G \cdot \underline{\mathbf{E}}_F \\ \underline{\mathbf{H}}_D \end{bmatrix} + \begin{bmatrix} -\underline{\mathbf{J}}_{S2} \\ \underline{\mathbf{J}}_{S1} \end{bmatrix} = \begin{bmatrix} \underline{\mathbf{Y}}_3^{(1,1)} & \underline{\mathbf{Y}}_3^{(1,2)} \\ \underline{\mathbf{Y}}_3^{(2,1)} & \underline{\mathbf{Y}}_3^{(2,2)} \end{bmatrix} \begin{bmatrix} \underline{\mathbf{E}}_F \\ \underline{\mathbf{E}}_E \end{bmatrix} \quad (39)$$

From (34), (35), and (30) it follows that

$$\begin{bmatrix} \underline{\mathbf{H}}_D \\ \underline{\mathbf{H}}_C \end{bmatrix} = \begin{bmatrix} \underline{\mathbf{H}}_E \\ \underline{\mathbf{H}}_B \end{bmatrix} + \begin{bmatrix} -\underline{\mathbf{J}}_{S1} \\ \underline{\mathbf{J}}_{imp} \end{bmatrix} = \begin{bmatrix} \underline{\mathbf{Y}}_2^{(1,1)} & \underline{\mathbf{Y}}_2^{(1,2)} \\ \underline{\mathbf{Y}}_2^{(2,1)} & \underline{\mathbf{Y}}_2^{(2,2)} \end{bmatrix} \begin{bmatrix} \underline{\mathbf{E}}_D \\ \underline{\mathbf{E}}_C \end{bmatrix} \quad (40)$$

and then

$$\begin{bmatrix} \underline{\mathbf{H}}_E \\ \underline{\mathbf{Y}}_2^{(1,1)} \cdot \underline{\mathbf{E}}_B \end{bmatrix} + \begin{bmatrix} -\underline{\mathbf{J}}_{S1} \\ \underline{\mathbf{J}}_{imp} \end{bmatrix} = \begin{bmatrix} \underline{\mathbf{Y}}_2^{(1,1)} & \underline{\mathbf{Y}}_2^{(1,2)} \\ \underline{\mathbf{Y}}_2^{(2,1)} & \underline{\mathbf{Y}}_2^{(2,2)} \end{bmatrix} \begin{bmatrix} \underline{\mathbf{E}}_D \\ \underline{\mathbf{E}}_B \end{bmatrix} \quad (41)$$

Finally, from (39) and (41), after some algebraic manipulations, we derive the following linear system, which, when solved, gives the unknown electric field on the slot and the induced currents $\underline{\mathbf{J}}_{S1}$ and $\underline{\mathbf{J}}_{S2}$ on the metallizations at interfaces 3 and 4, respectively:

$$\begin{cases} \underline{\mathbf{P}}_1 \underline{\mathbf{E}}_F - \underline{\mathbf{P}}_2 \underline{\mathbf{E}}_E - \underline{\mathbf{J}}_{S1} = -\underline{\mathbf{P}}_3 \underline{\mathbf{J}}_{imp} \\ \underline{\mathbf{Q}}_1 \underline{\mathbf{E}}_F - \underline{\mathbf{Q}}_2 \underline{\mathbf{E}}_E - \underline{\mathbf{J}}_{S1} = 0 \end{cases} \quad (42)$$

Once we solve Eq. (42), the current distributions on the metallizations and the electric and magnetic fields can be computed in every region of the structure.

BIBLIOGRAPHY

1. K. G. Gupta, R. Garg, and I. J. Bahl, *Microstrip Lines and Slotlines*, Artech House, Dedham, MA, 1979.
2. R. K. Hoffmann, *Integrierte Mikrowellenschaltungen*, Springer-Verlag, Berlin, 1983.
3. T. Itoh, *Numerical Techniques for Microwave and Millimeter-Wave Passive Structures*, Wiley, New York, 1989.
4. R. Pregla, Analysis of planar microwave structures on magnetized ferrite substrate, *Arch. Elek. Ubertragung*, **40**: 270–273 (1986).
5. R. Pregla, About the nature of the method of lines, *Arch. Elek. Ubertragung*, **41**(6):368–370 (1987).
6. R. Pregla, Higher order approximation for the difference operators in the method of lines, *IEEE Microwave Guided Wave Lett.* **5**(2):53–55 (1995).
7. B. Engquist and A. Majda, Absorbing boundary conditions for the numerical simulations of waves, *Math. Comput.* **31**:629–651 (1977).
8. S. Xiao et al., Analysis of cylindrical transmission lines with the method of lines, *IEEE Trans. Microwave Theory Tech.* **44**(7):993–999 (1996).

9. R. Pregla, General formulas for method of lines in cylindrical coordinates, *IEEE Trans. Microwave Theory Tech.* **43**(7):1617–1619 (1995).
10. M. Thorburn et al., Application of the method of lines to cylindrical inhomogenous propagation structures, *Electron. Lett.* **26**(3):170–171 (1990).
11. K. Wu and R. Vahldieck, The method of lines applied to planar transmission lines in circular and elliptical waveguides, *IEEE Trans. Microwave Theory Tech.* **37**(12):1958–1963 (1989).

METHOD OF MOMENTS

AHMED A. KISHK
University of Mississippi
University, Mississippi

1. INTRODUCTION

A general electromagnetic problem of an object in unbounded media such as a scatterer or antenna is a complex mathematical boundary value problem, which so far has resisted exact analytical treatment, except in such special cases as circular cylinders [1], spheres [2], and spheroids [3]. In these cases the surface of the object coincides with one of the coordinate surfaces of an orthogonal coordinate system, in which the vector wave equation can be solved by the method of separation of variables. However, for an object of arbitrary shape, such an analytic solution is not feasible and an approximate or numerical solution must be obtained. The problem can, in general, be formulated using the integral equation method involving the surface field distributions or the differential equation method involving the field distribution throughout the volume. The equations describing the problem are exact and can generally be given as

$$L(f) = g \quad (1)$$

where L is an operator, f is the unknown response of the system to be determined, and g is the known source. If the solution to (1) satisfies the boundary conditions of the problem, then f is a unique solution to the problem due to the source g .

The process of solving (1) might require some approximations, and the accuracy of the solution will depend on the numerical technique and the number of samples used to describe the structure. Here we are interested in the method of moments as one of the most widely used numerical techniques. The method of moments, in general, reduces the linear operator equation (1) to a system of finite linear matrices that can be solved numerically to obtain the solution. The technique can be used in the frequency domain or the in the time domain. Here, we will consider the formulation of the problem using integral equations in the frequency domain.

The method of moment process is simple and straightforward. In electromagnetics, the physical problem is specified by Maxwell's equations and the boundary

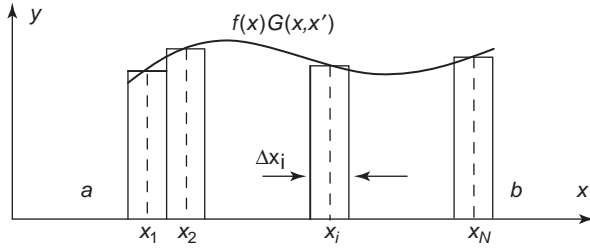


Figure 1. Representation of numerical integration using the rectangular rule.

conditions are reduced to integral equations. The unknowns (f) are under the integral, which is the operator (L). The unknowns are expanded as a series of known basis functions and unknown constant coefficients.

The method of moment can be understood easily if we draw an analogy with the numerical integration of a function. Let

$$F(x) = \int_a^b f(x')G(x, x')dx' \quad (2)$$

where $F(x)$ is unknown and the integrand $f(x')G(x, x')$ is known. If the integration is performed numerically using the simple rectangular rule, the interval $[a, b]$ can be divided to N segments of $\Delta x'_i$. For generality, the segments are considered unequal as shown in Fig. 1. Then (2) can be approximated as

$$F(x) = \sum_{i=1}^N f(x_i)G(x, x_i)\Delta x'_i \quad (3)$$

where x_i is the middle of the segment i and $f(x_i)$ is the value of the function at x_i . Equation (2) can be considered an integral equation when $F(x)$ is known as the source or the excitation and $f(x)$ is the unknown function. Then if the unknown function can be expanded as

$$f(x') = \sum_{i=1}^N a_i b_i(x') \quad (4)$$

where the b_i values denote known functions and the a_i values represent unknown constant coefficients. Substitute (4) in the integral equation (2) we obtain

$$\int_a^b \sum_{i=1}^N a_i b_i(x')G(x, x')dx' = F(x) \quad (5)$$

Because the a_i values are constants, we can write (5) as

$$\sum_{i=1}^N a_i \int_a^b b_i(x')G(x, x')dx' = F(x) \quad (6)$$

Now we have the completely known integrand, which can be integrated analytically or numerically. To make the analogy with the numerical integral using the rectangular

rule, let

$$b_i(x') = \begin{cases} 1 & x' = x_i \\ 0 & \text{elsewhere} \end{cases} \quad (7)$$

and thus (6) becomes

$$\sum_{i=1}^N a_i G(x, x_i)\Delta x_i = F(x) \quad (8)$$

which is similar to (3), and one can see that $a_i = f(x_i)$. However, Eq. (8) is one equation in N unknowns. If we evaluate (8) at each x_i , we obtain the following system of equations:

$$\begin{aligned} a_1 G(x_1, x_1)\Delta x_1 + a_2 G(x_1, x_2)\Delta x_2 + \cdots + a_N G(x_1, x_N)\Delta x_N &= F(x_1) \\ a_1 G(x_2, x_1)\Delta x_1 + a_2 G(x_2, x_2)\Delta x_2 + \cdots + a_N G(x_2, x_N)\Delta x_N &= F(x_2) \\ &\vdots \\ a_1 G(x_N, x_1)\Delta x_1 + a_2 G(x_N, x_2)\Delta x_2 + \cdots + a_N G(x_N, x_N)\Delta x_N &= F(x_N) \end{aligned} \quad (9)$$

Equation (9) can be expressed in matrix form as

$$\begin{bmatrix} G(x_1, x_1)\Delta x_1 & G(x_1, x_2)\Delta x_2 & \cdots & G(x_1, x_N)\Delta x_N \\ G(x_2, x_1)\Delta x_1 & G(x_2, x_2)\Delta x_2 & \cdots & G(x_2, x_N)\Delta x_N \\ \vdots & \vdots & \cdots & \vdots \\ G(x_N, x_1)\Delta x_1 & G(x_N, x_2)\Delta x_2 & \cdots & G(x_N, x_N)\Delta x_N \end{bmatrix} \begin{bmatrix} a_1 \\ a_2 \\ \vdots \\ a_N \end{bmatrix} = \begin{bmatrix} F(x_1) \\ F(x_2) \\ \vdots \\ F(x_N) \end{bmatrix} \quad (10)$$

or in a compact form as

$$[Z][I] = [V] \quad (11)$$

The Z is a square matrix, I is the unknown vector, and V is the known excitation vector. The solution of (11) will provide the unknown vector.

2. SIMPLE ELECTROMAGNETIC SCATTERING PROBLEM

To illustrate, how an electromagnetic problem can be formulated, consider an arbitrarily shaped conducting two-dimensional scatterer. A two-dimensional body is infinite in the axial direction (here considered to be the z direction) and has the same physical cross section in any

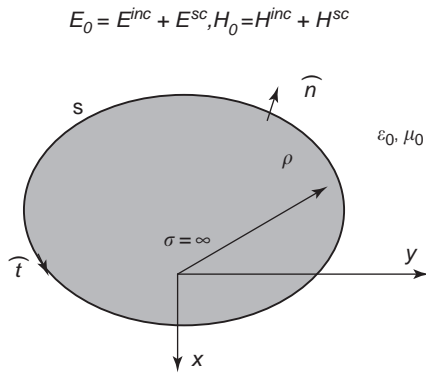


Figure 2. Original scattering problem.

plane cut, which is orthogonal to the axis (any plane cut parallel to the xy plane) as illustrated in Fig. 2. The scatterer is bounded by the surface S and surrounded by the free space, which is characterized by the permittivity and permeability of the free space (ϵ_0, μ_0). The excitation is an electromagnetic plane wave of the incident fields E^{inc} and H^{inc} . The total electric and magnetic fields in the exterior region are denoted by E_0 and H_0 , respectively. Inside the conducting object the fields are known and of zero value. The normal unit vector on the surface S is $\hat{n} = \hat{t} \times \hat{z}$ where \hat{z} and \hat{t} are the unit vectors in the direction of z and tangential to the surfaces S parallel to the xy plane. The time variation $e^{j\omega t}$ is implied and suppressed throughout.

The incoming wave in the 2D case always travels on a ray, which is orthogonal to the axis of the body. Because of this, an incoming wave of arbitrary polarization can always be written as the sum of waves, which are transverse electric (TE) and transverse magnetic (TM) to the axis of the body. A wave that is transverse magnetic has electric field components only in the z direction and a magnetic field with no z -directed components. The currents, which result from the arbitrarily polarized waves, can be obtained by summing the currents that result from the TE portion of the wave with those that result from the TM portion of the wave.

In order to use the free-space Green function in the solution of this problem, we have to have an unbounded homogeneous region. The surface equivalence principle is usually used to create an equivalent problem that converts the original problem from inhomogeneous region to a homogeneous region, but reserves the same boundary conditions of the original problem on the surface S . In the equivalent problem, the conducting object is removed and filled with the same materials of the exterior region of the original problem and forces the fields within the boundary of S to be zero and the fields outside S to be the same fields and materials of the original problem. Since the equivalent problem represents an unbounded homogeneous region, the fields must be continuous everywhere in the space, but by forcing the fields inside S to be zero, we have created discontinuity of the fields that must be compensated by inserting sources on the surface S . These sources are electric and magnetic surface currents that are proportional to the exterior tangential fields on S .

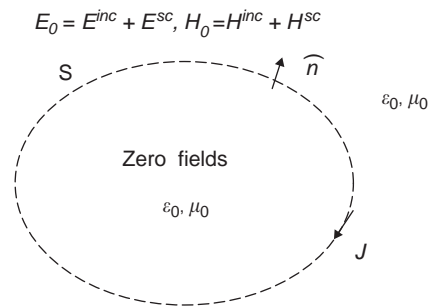


Figure 3. Surface equivalent problem.

The surface electric and magnetic currents are $\mathbf{J} = \hat{n} \times \mathbf{H}_0$ and $\mathbf{M} = -\hat{n} \times \mathbf{E}_0$. Since the surface of the original problem is a perfect conducting surface, the tangential electric fields to the surface are zero. Therefore, the equivalent surface magnetic current \mathbf{M} must be zero. Now, Fig. 3 illustrates the equivalent problem. The total fields in the exterior region are due to the equivalent electric current on the surface and the incident fields. The fields due to the equivalent electric current (E^{sc}, H^{sc}) are referred to as the *scattered fields*. It should be clear that the equivalent surface electric current is unknown and should be determined in order to compute the fields (E^{sc}, H^{sc}).

To formulate the integral equation, the boundary condition is applied on the surfaces S . The boundary condition is expressed as

$$E_{0|tan} = -\hat{n} \times (\hat{n} \times E_0) = 0 \text{ on } S \quad (12)$$

For simplicity, we consider the TM case. As mentioned above, for the TM case, only E_z exists and the magnetic field is transverse to z with no component in the z direction. Therefore, (12) can be written as

$$E_z^{sc} = -E_z^{inc} \text{ on } S \quad (13)$$

In an integral equation form, (13) can be written as

$$-j\omega\mu \int_C \mathbf{J}_z(\rho')g(\rho, \rho')d\ell = -E_z^{inc}(\rho) \text{ on } S \quad (14)$$

where C is the contour of the surface S along the tangential direction t and (ρ, ρ') are the position vectors in the xy plane that identify the field and source points, respectively. The contour integral proceeds in the direction of the tangential direction t . The function g is the Green function, which is given in terms of the Hankel function of zero order and second type as

$$g(\rho, \rho') = \frac{1}{4j} H_0^{(2)}(k_0|\rho - \rho'|) \quad (15)$$

where k_0 is the wavenumber. The plane-wave fields are given as

$$E_z^{inc} = A_0 e^{-jk_0 \hat{k} \cdot \rho} \text{ and } \mathbf{H}^{inc} = (\hat{k} \times \hat{z}) \frac{A_0}{\eta_0} e^{-jk_0 \hat{k} \cdot \rho} \quad (16)$$

where A_0 is the amplitude of the incident electric field and, $\hat{k} = -\hat{x} \cos \varphi^{\text{inc}} - \hat{y} \sin \varphi^{\text{inc}}$ is the unit vector in the direction of the plane-wave propagation, which is forming an angle φ^{inc} with the x axis. This integral equation is referred to as an *electric field integral equation* (EFIE).

To solve the surface integral equation (14), the contour of the scattering body is divided into a number of linear segments N with width ΔC . The end points of the segments lie on the actual contours of the body. The center of the segment i is located at ρ_i . The length of the zones is taken to be less than one-tenth of a wavelength. The currents are expanded in pulse basis functions multiplied by unknown coefficients as

$$\mathbf{J}_z = \sum_{i=1}^N I_i P_i \quad (17)$$

where I_i are the unknown constant current coefficients and P_i are the pulse basis functions, that defined as

$$P_i(\rho') = \begin{cases} 1 & \text{over the segment } i \\ 0 & \text{elsewhere} \end{cases} \quad (18)$$

Substitute (17) in (14). Then the point matching technique is employed to reduce the integral equations to a system of linear equations. Equation (14) reduces to a standard matrix element, which is placed in the proper location in the matrix. For each point matching j , equation (14) can be written as

$$\begin{aligned} & -\frac{\omega\mu_0}{4} \sum_{i=1}^N I_i \int_{\Delta C_i} H_0^2(k_0|\rho_j - \rho'|) d\ell \\ & = -A_0 e^{jk_0(x_j \cos \varphi^{\text{inc}} + y_j \sin \varphi^{\text{inc}})} \quad \text{on } \Delta C_j \end{aligned} \quad (19)$$

where (x_j, y_j) are the rectangular coordinates of the middle of the segment j and φ^{inc} is the angle of the incident plane wave measured from the x axis. Now, the matrix element Z_{ji} and the excitation vector element V_j can be written as

$$\begin{aligned} Z_{ji} &= -\frac{\omega\mu_0}{4} \int_{\Delta C_i} H_0^2(k_0|\rho_j - \rho'|) d\ell \quad \text{and} \\ V_j &= -A_0 e^{jk_0(x_j \cos \varphi^{\text{inc}} + y_j \sin \varphi^{\text{inc}})} \end{aligned} \quad (20)$$

In the method of moments, the diagonal elements of the matrix should always have special treatment because the integrand becomes singular at $\rho_j = \rho'$. The singular term can be subtracted and integrated analytically, or we may use the small-argument approximation for the Green function. When the argument of the Hankel function is very small, it can be approximated as

$$H_0^{(2)}(k_0\Delta\rho) \simeq 1 - j\frac{2}{\pi} \ln(1.7811k_0\Delta\rho/2) \quad (21)$$

Now the self-term ($i=j$) can be written as

$$Z_{jj} = -\frac{\omega\mu_0\Delta C_j}{4} \left[1 - j\frac{2}{\pi} \ln\left(\frac{1.781k_0\Delta C_j}{4e}\right) \right] \quad (22)$$

At this point, the MoM matrix is completely known. The solution of the matrix determines the current coefficients on the surface of the scattering body. Then these coefficients are used to obtain the near or the far scattered fields. For the far fields, far-field approximations can be considered, and the far scattered field after using the large-argument approximations of the Hankel function can be expressed as

$$E_z^{\text{sc}}(\rho, \varphi) = -\omega\mu_0 \sqrt{\frac{1}{2\pi\rho k_0}} e^{j\pi/4} e^{-jk_0\rho} \sum_{i=1}^N I_i \Delta C_i e^{jk_0\hat{\rho}\cdot\rho_i} \quad (23)$$

An important measure of the fields scattered by an object is the radar cross section (RCS). To determine the RCS, the scattering object is illuminated by a uniform plane wave. For the TM case the radar cross section σ is defined by the following equation:

$$\begin{aligned} \sigma(\phi) &= \lim_{\rho \rightarrow \infty} 2\pi\rho \frac{|E_z^{\text{sc}}(\rho, \phi)|^2}{|E_z^{\text{inc}}|^2} \\ &= \lim_{\rho \rightarrow \infty} 2\pi\rho \frac{|E_z^{\text{sc}}(\rho, \phi)|^2}{|A_0|^2} \end{aligned} \quad (24)$$

In Equation (23), $E_z^{\text{sc}}(\rho, \varphi)$ is the z component of the scattered electric field at the point (ρ, φ) .

The electric field integral equations (EFIE) suffer from the problem of internal resonance. If we are trying to solve a waveguide problem with a cross section similar to that of the scattering problem, the resulting integral equation will be exactly the same as the integral equation of the scattering problem. At the cutoff frequencies, the MoM matrix is singular and an infinite number of solutions exist for a source-free case. At these frequencies, the scattering problem doesn't provide a unique solution.

3. POSSIBLE INTEGRAL EQUATIONS

If we consider the equivalent problem in Fig. 3, another integral equation can be formulated. If we use the magnetic field integral equation in the same way that the tangential magnetic field on the surface S is discontinuous by the surface equivalent current \mathbf{J}_z , the integral equation can be written as

$$\hat{n} \times \mathbf{H}_0 = \mathbf{J} \Rightarrow H_t = J_z \quad \text{on } S \quad (25)$$

or in the form

$$J_z - H_t^{\text{sc}} = H_t^{\text{inc}} \quad \text{on } S \quad (26)$$

Equation (26) can be written in an operator form as

$$J_z - H_t(J_z) = H_t^{\text{inc}} \quad \text{on } S \quad (27)$$

which is referred to as the *magnetic field integral equation* (MFIE). The EFIE can be written as

$$-\frac{1}{\eta_0} E_z(J_z) = \frac{1}{\eta_0} E_z^{\text{inc}} \quad \text{on } S \quad (28)$$

where $H(J)$ and $E(J)$ are the magnetic field and electric field due to the surface electric current J . These operators will be defined later. The MFIE also suffer from the internal resonance problem. To avoid the internal resonance problem, the EFIE and MFIE are combined together to form the combined field integral equation (CFIE) as

$$\begin{aligned}
 J - H_t(J_z) - \frac{\alpha}{\eta_0} E_z(J) \\
 = H_t^{\text{inc}} + \frac{\alpha}{\eta_0} E_z^{\text{inc}} \text{ on } S
 \end{aligned}
 \tag{29}$$

The parameter α is a scalar combination factor less than or equal to 1. As can be seen, the EFIE is normalized to η_0 . This normalization adjusts the value level of the MoM matrix due to the EFIE part to values comparable to those of the MoM matrix element of the MFIE in order to obtain stable numerical inversion of the MM matrix. Note that all the expressions above are for the TM case of a two-dimensional infinitely extended conducting cylinder and all the expression are scalar equations. These expressions can be generalized and presented in vector form. After that, they should be reduced to scalar form, as will be described next.

4. GENERAL TWO-DIMENSIONAL PROBLEM

Consider a composite 2D object parallel to the z axis present with electric or magnetic harmonic current sources \mathbf{J} and \mathbf{M} , respectively. These current sources are of infinite extent and parallel to the z axis with harmonic variations in the z direction. Therefore, the total fields produced by these harmonic 2D sources must be harmonic in z as well in order to satisfy the boundary conditions on the objects [4]. The geometry and notations for such an object are given in Fig. 4. The whole space is divided into $N + 1$ homogeneous regions V_i , which may be either dielectric regions with permittivities ϵ_i and permeabilities μ_i , or closed conductor regions. These regions are numbered $i = 0, 1, 2, \dots, N$, where $i = 0$ corresponds to the exterior region, namely, free space. Lossy materials are

considered by allowing ϵ_i and μ_i , $i = 1, 2, \dots, N$, to be complex. Each region V_i is surrounded by a closed surface S_i and associated with an inward-directed normal unit vector \hat{n}_i . The surface interface between regions V_i and V_j is denoted as S_{ij} , $i \neq j$. Thus, S_i constitutes the set of all interface surfaces S_{ij} , where j represents all region numbers adjacent to region V_i . Note that S_{ij} is the same surface as S_{ji} ; however, the normal unit vectors \hat{n}_i and \hat{n}_j are in opposite directions to each other on the two surfaces. The concept of the equivalence principle is used to derive a surface integral equation (SIE) formulation for 2D objects with $N + 1$ homogeneous regions. The total fields in each homogeneous region are denoted by \mathbf{E}^i and \mathbf{H}^i $i = 0, 1, 2, \dots, N$ for the electric and magnetic fields, respectively. Any perfect conducting region need not be considered as a region because the fields are known to be equal to zero. In the free-space region V_0 , the total fields are denoted by $(\mathbf{E}^0, \mathbf{H}^0)$. From Maxwell's equations and the equivalence principle, one can express the fields in each region in terms of unknown electric and magnetic equivalent surface currents plus the fields due to the harmonic 2D sources present in the region.

According to the surface equivalence principle, we can break the original problem into a number of auxiliary problems that are equal to the number of the nonperfect conducting regions. To obtain the i th auxiliary problem, the boundaries of region V_i are replaced by equivalent surface currents radiating in a homogeneous medium with the constitutive parameters of region V_i using electric currents for the conductor boundaries and equivalent electric and magnetic currents for the dielectric boundaries. The electric and magnetic currents appearing on opposite sides of a dielectric interface in different auxiliary problems are taken equal in magnitude and opposite in direction to ensure the continuity of the tangential components of the fields on these boundaries, as in the original problem. In this procedure the fields produced by the equivalent currents within the region boundaries are the same as those in the original problem, while the zero field is produced outside these boundaries. The electric and magnetic surface currents along the boundaries are

$$\mathbf{J}^i = \hat{n}_i \times \mathbf{H}^i \text{ and } \mathbf{M}^i = -\hat{n}_i \times \mathbf{E}^i \text{ on } S_i \tag{30}$$

Both \mathbf{J}^i and \mathbf{M}^i have components in both the longitudinal \hat{z} and transverse \hat{t} directions

$$\begin{Bmatrix} \mathbf{J}^i \\ \mathbf{M}^i \end{Bmatrix} = \begin{Bmatrix} J_z^i \\ M_z^i \end{Bmatrix} \hat{z} + \begin{Bmatrix} J_t^i \\ M_t^i \end{Bmatrix} \hat{t} \text{ on } S_i \tag{31}$$

where \hat{n}_i is the unit normal to S_i . The currents on the surface S_i are the sum of the currents on all the boundaries S_{ij} , where $j \neq i$ and j represents the entire region numbers adjacent to the region V_i

$$\mathbf{J}^i = \sum_{vj} \mathbf{J}^{ij} \text{ on the boundaries of region } i \tag{32}$$

and similarly for \mathbf{M}^i . On the conductor boundaries the magnetic current is zero. We can now obtain the electric

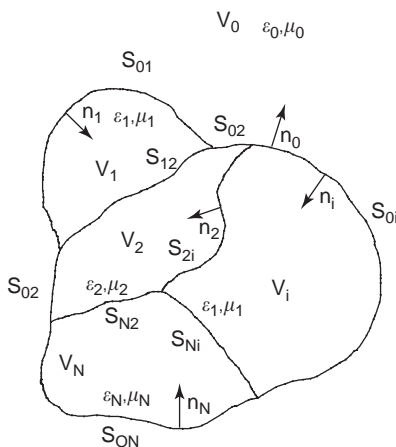


Figure 4. Cross section of multiregion cylindrical object.

and magnetic fields $E^i(\rho, k_z)$ and $H^i(\rho, k_z)$ due to the electric current $J^i(\rho', k_z)$ by using

$$\mathbf{E}^i(\rho, k_z) = -j\omega A^i(\rho, k_z) - j \frac{1}{\omega \epsilon_i \mu_i} \nabla \nabla \cdot \mathbf{A}^i(\rho, k_z) \quad (33)$$

$$\mathbf{H}^i(\rho, k_z) = \frac{1}{\mu_i} \nabla \times \mathbf{A}^i(\rho, k_z) \quad (34)$$

where the vector potential \mathbf{A} is

$$\mathbf{A}^i(\rho, k_z) = \frac{\mu_i}{j4} \int_{V'} \mathbf{J}^i(\rho', k_z) H_0^{(2)}(k_\rho |\rho - \rho'|) dl' \quad (35)$$

The ∇ operator is $\nabla = \nabla_t - jk_z \hat{z}$, $\nabla_t = (\partial/\partial x)\hat{x} + (\partial/\partial y)\hat{y}$ and $k_\rho = \sqrt{k^2 - k_z^2}$. For each value of $k_z \in [-k, k]$, the far field is radiating on a cone around the z axis with cone angle $\theta = \cos^{-1}(k_z/k)$ [4]. Equations (33) and (34) can be given in an operator form $\mathbf{E}^i(\mathbf{J}^i)$ and $\mathbf{H}^i(\mathbf{J}^i)$. The vector tangential operator can be presented in terms of their operator components as

$$\mathbf{E}_{\tan}^i(\mathbf{J}^i) = [E_t^i(J_t^i) + E_z^i(J_z^i)] \hat{t} + [E_z^i(J_t^i) + E_z^i(J_z^i)] \hat{z} \quad (36)$$

$$\mathbf{H}_{\tan}^i(\mathbf{J}^i) = [H_t^i(J_t^i) + H_z^i(J_z^i)] \hat{t} + H_z^i(J_t^i) \hat{z} \quad (37)$$

After some mathematical manipulations the electric and magnetic fields due to the electric currents can be expressed in operator form. Expressions are given for $E_t^i(J_t^i)$, $E_z^i(J_t^i)$, $E_z^i(J_z^i)$, and $E_z^i(J_z^i)$, which are the components of the vector operator $\mathbf{E}_{\tan}^i(\mathbf{J}^i)$ for the tangential E field at a point ρ on S_i , and in the same fashion we get $H_t^i(J_t^i)$, $H_z^i(J_t^i)$, and $H_z^i(J_z^i)$ for the tangential H -field vector operator $\mathbf{H}_{\tan}^i(\mathbf{J}^i)$. The electric and magnetic field operators due to the electric current components are expressed as

$$E_z(J_z) = \frac{-jk_z k_\rho}{4\omega \epsilon_0} e^{jk_z z} \int_C J_z H_1^{(2)}(k_\rho \Delta \rho) (\hat{t}' \bullet \Delta \hat{\rho}) dl' \quad (38)$$

$$E_t(J_z) = \frac{-jk_\rho k_z}{4\omega \epsilon_0} e^{jk_z z} \int_C J_z H_1^{(2)}(k_\rho \Delta \rho) (\hat{t} \bullet \Delta \hat{\rho}) dl' \quad (39)$$

$$E_z(J_z) = -\frac{k_\rho^2}{4\omega \epsilon_0} e^{jk_z z} \int_C J_z H_0^{(2)}(k_\rho \Delta \rho) dl' \quad (40)$$

$$E_t(J_t) = -\frac{e^{jk_z z}}{4\omega \epsilon_0} \int_C k_z^2 J_t \{(\hat{t}' \bullet \hat{t}) H_0^{(2)}(k_\rho \Delta \rho) - \frac{k_\rho}{\Delta \rho} H_1^{(2)}(k_\rho \Delta \rho) (\hat{t}' \bullet \hat{t}) - k_\rho [k_\rho H_0^{(2)}(k_\rho \Delta \rho) - \frac{2}{\Delta \rho} H_1^{(2)}(k_\rho \Delta \rho)] (\hat{t}' \bullet \Delta \hat{\rho}) (\hat{t} \bullet \Delta \hat{\rho})\} dl' \quad (41)$$

$$H_t(J_z) = -\frac{jk_\rho}{4} e^{jk_z z} \int_C J_z H_1^{(2)}(k_\rho \Delta \rho) (\hat{n} \bullet \Delta \hat{\rho}) dl' \quad (42)$$

$$H_z(J_z) = 0 \quad (43)$$

$$H_z(J_t) = -\frac{k_\rho}{4j} e^{jk_z z} \int_C J_t H_1^{(2)}(k_\rho \Delta \rho) (\hat{n}' \bullet \Delta \hat{\rho}) dl' \quad (44)$$

$$H_t(J_t) = -\frac{k_z}{4} e^{jk_z z} \int_C J_t H_0^{(2)}(k_\rho \Delta \rho) (\hat{t} \bullet \hat{n}') dl' \quad (45)$$

where $H_1^{(2)}(\cdot)$ is the Hankel function of the first order and second type and $\Delta \rho = |\rho - \rho'|$. The hat is used to indicate the unit vectors. In Eqs. (38)–(45) the prime is used to indicate the source coordinates. The fields due to the magnetic current $\mathbf{M}^i(\rho', k_z)$ can be obtained using duality [5, Chap. 3, Sect. 3-2]. Now the boundary conditions must be enforced on each boundary on the object, which can be used as surface integral equations after substituting the proper operators as follows

$$- [E_{\tan}^i(\mathbf{J}^i) + E_{\tan}^j(\mathbf{J}^j) + E_{\tan}^i(\mathbf{M}^i) + E_{\tan}^j(\mathbf{M}^j)] = [E_{\tan}^i(\mathbf{J}^{i,inc}) + E_{\tan}^i(\mathbf{M}^{i,inc}) - E_{\tan}^j(\mathbf{J}^{j,inc}) + E_{\tan}^j(\mathbf{M}^{j,inc})] \quad (46)$$

on S_{ij}

$$- \hat{n}_i \times [H^i(\mathbf{J}^i) + H^j(\mathbf{J}^j) + H^i(\mathbf{M}^i) + H^j(\mathbf{M}^j)] = \hat{n}_i \times [H^i(\mathbf{J}^{i,inc}) + H^i(\mathbf{M}^{i,inc}) - H^j(\mathbf{J}^{j,inc}) + H^j(\mathbf{M}^{j,inc})] \quad (47)$$

on S_{ij}

if the boundary S_{ij} is a perfect conducting boundary and the region V_j is a perfect conducting region, Eqs. (46) and (47) become

$$-E_{\tan}^i(\mathbf{J}^i) - E_{\tan}^i(\mathbf{M}^i) = E_{\tan}^i(\mathbf{J}^{i,inc}) + E_{\tan}^i(\mathbf{M}^{i,inc}) \text{ on } S_{ij} \quad (48)$$

$$- \hat{n}_i \times [H^i(\mathbf{J}^i) + H^i(\mathbf{M}^i)] = \hat{n}_i \times [H^i(\mathbf{J}^{i,inc}) + H^i(\mathbf{M}^{i,inc})] \quad (49)$$

on S_{ij} (just inside V_i)

Only one of the equations (48) and (49) can be used. If Eq. (48) is used on the perfect electric conductor (PEC) with (46) and (47) on the dielectric boundary, the formulation is called E-PMCHW formulation, and if Eq. (49) is used just inside the PEC boundary with (46) and (47) on the dielectric boundary, the formulation is referred to as H-PMCHW [6]. The combined field formulation on the conductor can be obtained if Eqs. (48) and (49) are combined together and used as one equation with (46) and (47) [6]. The combined field formulation is referred to as C-PMCHW.

Following the method of moments, the object contour C is divided into N linear segments with length ΔC^ℓ , $\ell = 1, 2, \dots, N$ as in Ref. 9, and each current component is expanded into N pulse basis function p^ℓ . In equation form, the unknown currents can be expressed as

$$\mathbf{J}^i = \sum_{\ell}^N (I_z^{\ell,i} \hat{t} + I_z^{\ell,i} \hat{z}) P^\ell \text{ on all } S_{ij} \quad (50)$$

and

$$M^i = \sum_{\ell=N+1}^{N+N_d} (M_t^{\ell,i} \hat{t} + M_z^{\ell,i} \hat{z}) P^\ell \quad (51)$$

only on the dielectric boundaries

where $I_{\alpha\beta}^{(\ell,i)}$ and $M_{\alpha\beta}^{(\ell,i)}$ are the unknown electric and magnetic current coefficients, respectively. The pulse function is $P^\ell = 1$ on the subdomain ΔC^ℓ and zero elsewhere. N_d is the number of segments on the dielectric boundaries. Substituting (50) and (51) into the operators defined in (38)–(45) and then satisfying (46) to (47) at the match point (middle of the segments), the integral equations reduce to a matrix of order $2(N + N_d)$, which can be written in the form

$$\begin{bmatrix} Z_{zz}^{ij,i} + Z_{zz}^{ij,j} & Z_{zt}^{ij,i} + Z_{zt}^{ij,j} & Y_{zz}^{ij,i} + Y_{zz}^{ij,j} & Y_{zt}^{ij,i} + Y_{zt}^{ij,j} \\ Z_{tz}^{ij,i} + Z_{tz}^{ij,j} & Z_{tt}^{ij,i} + Z_{tt}^{ij,j} & Y_{tz}^{ij,i} + Y_{tz}^{ij,j} & Y_{tt}^{ij,i} + Y_{tt}^{ij,j} \\ Y_{tz}^{ij,i} + Y_{tz}^{ij,j} & Y_{tt}^{ij,i} + Y_{tt}^{ij,j} & -\frac{1}{\eta_i} Z_{tz}^{ij,i} - \frac{1}{\eta_j} Z_{tz}^{ij,j} & -\frac{1}{\eta_i} Z_{tt}^{ij,i} - \frac{1}{\eta_j} Z_{tt}^{ij,j} \\ Y_{zz}^{ij,i} + Y_{zz}^{ij,j} & Y_{zt}^{ij,i} + Y_{zt}^{ij,j} & -\frac{1}{\eta_i} Z_{zz}^{ij,i} - \frac{1}{\eta_j} Z_{zz}^{ij,j} & -\frac{1}{\eta_i} Z_{zt}^{ij,i} - \frac{1}{\eta_j} Z_{zt}^{ij,j} \end{bmatrix} \begin{bmatrix} I_z^{ij} \\ I_t^{ij} \\ M_z^{ij} \\ M_t^{ij} \end{bmatrix} = \begin{bmatrix} V_z^{ij,i,\text{inc}} - V_z^{ij,j,\text{inc}} \\ V_t^{ij,i,\text{inc}} - V_t^{ij,j,\text{inc}} \\ I_t^{ij,i,\text{inc}} - I_t^{ij,j,\text{inc}} \\ I_z^{ij,i,\text{inc}} - I_z^{ij,j,\text{inc}} \end{bmatrix} \quad (52)$$

where $Z_{\alpha\beta}^{ij,i}$ and $Y_{\alpha\beta}^{ij,i}$ denote matrix elements obtained from the operators $E_{\alpha}^{ij}(J_{\beta})$ and $H_{\alpha}^{ij}(J_{\beta})$, respectively, on the surface S_{ij} from the region i . Therefore, the first suffix of the subscript refers to the field component, and the second suffix of the subscript refers to the current component. The first pair of the superscripts refers to the surface boundary ij and the second suffix, to the region number i or j . This matrix is built assuming that all the boundaries are dielectric boundaries, but on the perfect conducting parts the columns and the rows that correspond to the magnetic currents and the magnetic field, respectively, which are in the third and fourth columns and rows, respectively, must be removed, and in the first and second columns of (52) the parts that correspond to perfect conducting regions i or j must be forced to zero.

The quantities I_t^{ij} , I_z^{ij} , M_t^{ij} , and M_z^{ij} are the unknown expansion coefficients of the electric and magnetic currents, respectively. The right-hand-side (RHS) columns are the excitation vectors, where $V_t^{ij,i}$, $V_z^{ij,i}$, $I_t^{ij,i}$, and $I_z^{ij,i}$ denote the electric and magnetic fields, respectively, on the surface S_{ij} due to all electric and magnetic sources in the region i . The matrix elements can be written as

$$Z_{zz}^{ij} = \begin{cases} -\frac{k_\rho^2}{4k_0} \int_{\Delta C^j} H_0^{(2)}(k_\rho \Delta \rho^{ij}) dt' & i \neq j \\ -\frac{k_\rho^2}{4k_0} \Delta C^j \left[1 - \frac{2j}{\pi} \left(\ln \left(\frac{\Delta C^j \gamma k_\rho}{4} \right) + 1 \right) \right] & i = j \end{cases} \quad (53)$$

$$Z_{tz}^{ij} = \begin{cases} -\frac{jk_\rho k_z}{4\omega\epsilon_0} \int_{\Delta C^j} H_1^{(2)}(k_\rho \Delta \rho^{ij}) (\hat{t}_i \bullet \Delta \hat{\rho}^{ij}) dt' & i \neq j \\ 0 & i = j \end{cases} \quad (54)$$

$$Z_{zt}^{ij} = \begin{cases} -\frac{jk_z k_\rho}{4\omega\epsilon_0} \int_{\Delta C^j} H_1^{(2)}(k_\rho \Delta \rho^{ij}) (\hat{t}_j \bullet \Delta \hat{\rho}^{ij}) dt' & i \neq j \\ 0 & i = j \end{cases} \quad (55)$$

$$Y_{tt}^{ij} = \begin{cases} -\frac{k_z}{4} \int_{\Delta C^j} H_0^{(2)}(k_\rho \Delta \rho^{ij}) (\hat{t}_i \bullet \hat{n}_j) dt' & i \neq j \\ 0 & i = j \end{cases} \quad (56)$$

$$Z_{tt}^{ij} = \begin{cases} -\frac{1}{4k_0} \int_{\Delta C^j} \{k^2 (\hat{t}_j \bullet \hat{t}_i) H_0^{(2)}(k_\rho \Delta \rho^{ij}) \\ -\frac{k_\rho}{\Delta \rho^{ij}} H_1^{(2)}(k_\rho \Delta \rho^{ij}) (\hat{t}_j \bullet \hat{t}_i) \\ -k_\rho \left[k_\rho H_0^{(2)}(k_\rho \Delta \rho^{ij}) - \frac{2}{\Delta \rho^{ij}} H_1^{(2)}(k_\rho \Delta \rho^{ij}) \right] \\ (\hat{t}_j \bullet \Delta \hat{\rho}^{ij}) (\hat{t}_i \bullet \Delta \hat{\rho}^{ij}) dt' & i \neq j \\ \times \frac{2k_\rho H_1^{(2)} \left(\frac{k_\rho \Delta C^i}{2} \right) + \frac{k_0^2 \Delta C^i}{4k_0}}{4k_0} \\ \left[1 - \frac{2j}{\pi} \ln \left(\frac{\Delta C^i \gamma k_\rho}{4} \right) - 1 \right] & i = j \end{cases} \quad (57)$$

$$Y_{zz}^{ij} = 0 \quad (58)$$

$$Y_{zt}^{ij} = \begin{cases} -\frac{k_\rho}{4j} \int_{\Delta C^j} H_1^{(2)}(k_\rho \Delta \rho^{ij}) (\hat{n}_j \bullet \Delta \hat{\rho}^{ij}) dt' & i \neq j \\ -\frac{1}{2} & i = j \end{cases} \quad (59)$$

$$Y_{tz}^{ij} = \begin{cases} -\frac{jk_\rho}{4} \int_{\Delta C^j} H_1^{(2)}(k_\rho \Delta \rho^{ij}) (\hat{n}_i \bullet \Delta \hat{\rho}^{ij}) dt' & i \neq j \\ \frac{1}{2} & i = j \end{cases} \quad (60)$$

These integrals are performed numerically where $\Delta \rho^{ij} = |\rho^i - \rho^j|$ and ρ^j for the segment j . The excitation vector can be obtained in a manner similar to that for the matrix elements due to known electric and magnetic current sources. In the case of plane-wave incidence the excitation matrix elements are given as

$$H_t^{i,\text{inc}} = \frac{E_m}{\eta_0} \cos \theta_{\text{inc}} (E^p \sin \alpha_{\text{inc}} - E^n \cos \alpha_{\text{inc}}) \bullet \hat{t}_i e^{jk_\rho(\hat{\rho} \bullet \rho^i)} \quad (61)$$

$$H_z^{i,\text{inc}} = \frac{1}{\eta_0} \sin \theta_{\text{inc}} \sin \alpha_{\text{inc}} e^{jk_\rho(\hat{\rho} \bullet \rho^i)} \quad (62)$$

$$\mathbf{E}_z^{i,\text{inc}} = \frac{\mathbf{E}_m}{\eta_0} \sin \theta_{\text{inc}} \cos \alpha_{\text{inc}} e^{jk\rho(\hat{\rho} \cdot \hat{\rho}_i)} \quad (63)$$

$$\mathbf{E}_t^{i,\text{inc}} = \frac{\mathbf{E}_m}{\eta_0} (E^p \cos \alpha_{\text{inc}} + E^n \sin \alpha_{\text{inc}}) \bullet \hat{t} e^{jk\rho(\hat{\rho} \cdot \hat{\rho}^i)} \quad (64)$$

where the superscript i denotes the middle of segment i and α_{inc} is the angle between $\mathbf{E}^{i,\text{inc}}$ and the plane of incidence (k - z plane).

Once the MoM matrix equation is solved the far fields due to the currents on the outer surface boundary, and the current sources in the exterior region can be computed. The field will be along a cone of half-angle $\theta = \arcsin(k_z/k_0)$ around the structure [4].

5. SAMPLE RESULTS

Sample results are obtained using the formulations presented above to show the accuracy of the numerical method versus the exact solution for circular cylinder objects. Figure 5 shows the scattered field of a coated conducting cylinder with radii $ka = 2$ and $kb = 3$ and $\epsilon_r = 4$ for TM and TE polarization due to a plane wave incident by an angle of 45° from the z axis. The numerical solution is compared with the exact solution. Excellent agreement is observed.

In the preceding sections we have demonstrated the formulations of the integral equation for simple two-dimensional objects using the simplest possible basis function. This basis function is a slowly conversion function. Other basis functions can be used with better conversion rates. In the following section we will present literature review for the developments in the method of moments.

6. ADVANCED METHOD OF MOMENTS

Antennas, which usually consist of three-dimensional (3D) radiating elements (sources), can be present with two-dimensional (2D) structures (cylinders of infinite extent). Such problems can be analyzed by using a spectrum of two-dimensional solutions (S2DS), as described in Refs. 7

and 8. Generally, any antenna consisting of slots or dipoles in or in the vicinity of 2D structures of arbitrary cross-sectional shape and material combination can be analyzed by the S2DS technique.

The most significant part of an S2DS analysis is to solve repeatedly the special spectral-domain problem obtained by Fourier-transforming the sources in the z direction of the structure. This spectral-domain problem can be interpreted as a harmonic 2D spatial problem where the sources (and the resulting fields) have harmonic z variation of the form $\exp(-jk_z z)$, where $k_z = 0$ corresponds to the standard 2D problem. This general harmonic 2D problem must be solved for a large number of values of the spectral variable k_z in order to be able to inverse transform to 3D spatial domain. The radiation pattern, however, can normally be found directly without inverse transformation from the 2D harmonic solution [7].

The harmonic 2D problem is conveniently solved for each k_z by the method of moments (MoM). Plane-wave scattering from 2D composite objects [9,10] and scattering from an impedance cylinder with arbitrary cross section under oblique plane-wave incidence were analyzed, where the equivalent electric and magnetic currents were solved for by pulse expansion and point matching.

7. USE OF IMPEDANCE BOUNDARY CONDITIONS

The concept of the impedance boundary condition (IBC), which was first described by Leontovich in 1948 [11], has long been used in a variety of electromagnetic wave scattering problems. For closed bodies, it has been shown that the IBC is a valid approximation to the exact condition whenever (1) the refractive index is large compared with unity, (2) the total radii of curvature are much greater than the skin depth, (3) the body is much thicker than the skin depth, and (4) the spatial variation of the index of refraction is slow in comparison to the local wavelength [12–15]. Consequently, the IBC concept has long been utilized to solve many electromagnetic problems. Garbacz [16] investigated a special case of bistatic

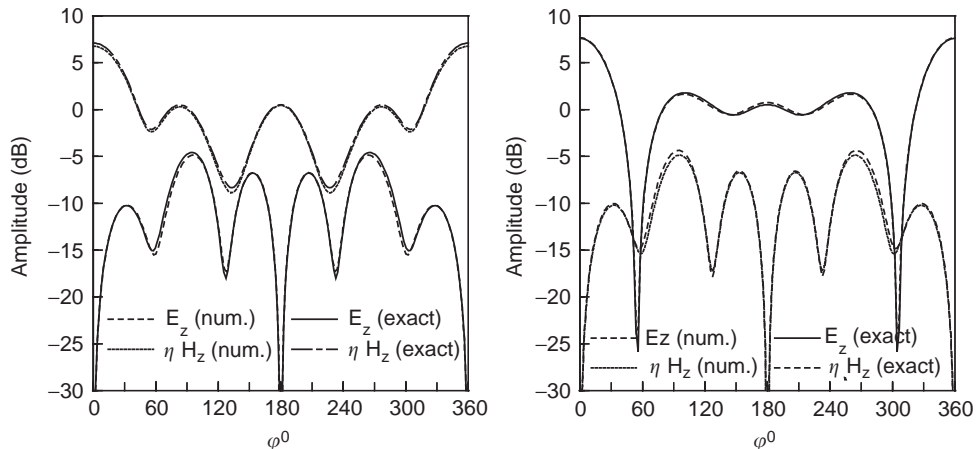


Figure 5. Far scattered field from a coated conducting cylinder with radii $ka = 2$, $kb = 3$, $\epsilon_r = 4$: (a) TM; (b) TE.

scattering from a class of lossy dielectric spheres subject to the impedance boundary condition, using the classical modal solution derived from Mie's series. Using the same approach, Wait and Jackson [17] presented many computed results for the scattering by an impedance sphere assuming various surface impedances. The usefulness of the IBC in determining the scattered fields has also been demonstrated by Cassedy and Fainberg [18] for finite cylinders.

The electromagnetic scattering from bodies made of electrically dissimilar materials has also been investigated using the IBC in conjunction with the method of moments (MoM). Different geometries have been considered, such as circular and elliptical cylinders [19,20] and spheroidal bodies [21]. The introduction of dissimilar materials has opened the door for more practical uses of the IBC in antenna problems. Iskander et al. [22] used the IBC to simulate transverse corrugations in a small conical horn. A modification of the IBC concept to treat the problem of homogeneous imperfectly conducting objects, with small radii of curvature, has been described by Mitzner [23].

Different integral equation formulations have been developed to treat the problem of scattering from impedance bodies of revolution. Iskander et al. [22] employed the electric field integral equation formulation (EFIE). Later, Graglia and Uslenghi [24] examined impedance-coated bodies of revolution using the generalized MFIE formulation. In these earlier studies the problem of internal resonances had not been addressed. However, the EFIE and MFIE formulations were shown to be ill-posed and lead to ill-conditioned matrices when solved by the MoM [25–28]. The internal resonance problem has been found to be similar to the one encountered with perfectly conducting bodies, which was reported in 1978 [29] and treated by the combined field integral equation (CFIE) formulation. The problem of the internal resonances with impedance bodies of revolution was reported and treated by many investigators using CFIE. Apparently, the internal resonance problem is not the only problem associated with impedance bodies. Rusch and Pogorzelski [30] reported another problem even when applying CFIE formulation with bodies having both thin and thick parts. Accordingly, a mixed-field solution that combines different integral equations on different parts of the scatterer must be employed. They [30] recommended that the EFIE be applied on the thin parts of the scatterer in order to provide a correct solution.

The calculation of scattering from bodies composed of lossless or low loss dielectric materials and surface impedance objects using a mix of exact and impedance boundary conditions is treated with different types of integral equations by Kishk [31,32].

Some complicated structures can be modeled approximately using the concept of surface impedance, such as corrugated objects or objects coated with lossy material or thin dielectric layers, which can even be loaded with metal strips. The surface impedance model deals with the outer boundary of the structure in terms of equivalent surface impedance, which can be obtained from the expected local relation between the tangential components of the electric and magnetic fields on the outer boundary. This relation

can be found approximately at any surface point from the solution of a canonical problem, which is similar to the local geometry around this point. The equivalent surface impedance is generally anisotropic, even if the coating is isotropic, in particular at an outer surface that has two different principal curvatures. Also, structures with periodic surface discontinuities such as corrugations or strip-loaded coatings can be modeled using the anisotropic surface impedance concept, if the periods of the corrugations or strips are smaller than half the wavelength. The advantage with the surface impedance concept is that the numerical analysis of the object becomes simpler and takes less time. This is because the exact geometry of the loads needs not to be modeled to facilitate description of the problem and so that the number of unknowns can be reduced dramatically.

The impedance boundary conditions (IBCs) are a valid approximation under certain conditions [15]; more references on IBC can be found in Kishk [32]. The use of IBC can simplify the analysis of many complex electromagnetic problems. However, in other problems the use of IBC is questionable [33]. In order to widen the applicability of the IBC, generalized impedance boundary conditions (GIBCs) was proposed [34] and later improved for coated 2D structures [35] at the expense, however, of considerable analytical complications, which requires specialized expertise to work with such problems. So far, GIBC has been used only with coated metallic surfaces without corrugations. On the other hand, IBC has been used successfully to analyze corrugated horns and waveguides [22]. Anisotropic surface impedances have also been used to define soft and hard surfaces [36].

Many papers have formulated the problem of electromagnetic scattering from 2D impedance structures due to a normally incident plane wave [37–39]. However, few have considered oblique incidence [40,41]. In [40], the finite element method was used to model arbitrarily shaped objects with isotropic impedance surfaces. Gordon and Kishk [41] used the finite-difference method in the frequency domain for elliptic isotropic impedance cylinders. The problem of scattering from a two-dimensional object of arbitrary cross section and anisotropic surface impedance due to an oblique plane wave incidence has been formulated [10]. The formulation is based on the surface integral equation and solved using the method of moment with pulse basis functions and point matching. With the proper implementation of this simple expansion and testing, accurate numerical solutions are obtained. The numerical solution is verified with the exact solution of a circular cylinder [42]. Different surface integral formulations are generated and found useful in the verification of the numerical solutions for arbitrary objects.

8. FULL-WAVE ANALYSIS OF MICROWAVE CIRCUITS

In conjunction with the widespread development of wireless information networks such as cellular, personal communication services (PCS), satellite communication systems, mobile computing, and other new systems and services, monolithic microwave integrated circuits

(MMICs) have advanced significantly. The primary motivation for developing MMIC in wireless communications such as PCS is to achieve higher quality, longer battery lifetime, lower cost, and lighter terminals [43]. Dielectric resonators (DRs) with high permittivity and low temperature coefficients are smaller than waveguide or coaxial resonators, are easily fabricated, and are compatible with MMIC implementation [44,45]. Using dielectric resonators, instead of metal cavities, in a multilayered medium coupled to a microstrip line or a slot aperture eliminates the need for microstrip to cavity adapters and provides greater flexibility to realize complicated bilateral and multilayered printed circuits, thus allowing very compact, high-density circuit integration.

With the advent of the high-dielectric-constant and low-temperature-coefficient ceramic materials, DR applications of the dielectric resonator in the design of passive and active microwave circuits [46,47] have spread toward low frequencies for mobile communications such as PCS at 1.8–2 GHz. An experimental study of a dielectric resonator, of relative dielectric constant 80 and of resonant frequency ~ 1.7 GHz, coupled to a microstrip line can be found in Ref. 48. The method of moments (MoM) has been used to calculate the characteristics of an isolated dielectric resonator that is of the revolution-type body [49,50]. This model includes both dielectric loss and radiation loss. Numerical analysis of in-circuit parameters of a dielectric resonator is more challenging. A study of the DR antennas excited by a coaxial probe or slot aperture has been conducted in both theory and measurement at the University of Mississippi [51–53], where theoretical investigations have considered mainly structures consisting of body-of-revolution dielectric resonators combined with wires or slots.

The MoM full-wave analysis procedure is developed to analyze the dielectric resonator of arbitrary shape in a multilayered medium coupled to a microstrip circuit. A new mixed potential integral equation (MPIE) formulation has been developed for the analysis of electromagnetic problems involving conducting or dielectric objects of arbitrary shape embedded in a planar stratified medium [54]. In the new MPIE formulation, the dyadic kernel of the vector potential is kept in the simplest form originally developed by Sommerfeld, yet the scalar potential, which is represented by a double dot product of a dyadic kernel with a dyadic charge density, remains compatible with the original implementation. The triangular patch model, originally developed for arbitrarily shaped objects in free space [55–59], is employed in conjunction with the new MPIE formulation to model the problem of a dielectric resonator excited by microstrip circuit. The numerical procedure has been modified to handle the potential dyadic kernels and the dyadic charge density. A matched-load simulation procedure has been used to extract the network S parameters of a DR microstrip circuit. The diameters (scattering) of the Q circles have been measured to determine the coupling coefficients and the Q factors of the dielectric resonator excited by a microstrip circuit. The validity of the new MPIE formulation and the numerical procedure has been verified by comparing the S parameters obtained and the available measurement data [54].

Ceramic materials of high dielectric constant and low loss can exhibit a very high Q factor. Therefore, they have been widely used as resonators in microwave filters and oscillators. To understand the behavior of these elements and to determine the best coupling mechanism, it is necessary to determine the electromagnetic field distribution inside the cavity. The resonant frequency and the Q factor have to be computed accurately before the electromagnetic fields in the vicinity of the resonators can be obtained. It is therefore important to be able to determine the resonant frequencies and Q factors of the desired modes.

Many different approaches to the analysis of dielectric resonators have been described in the literature [60–76]. Some of these methods are based on simplifications of the geometry, such as the perfect magnetic conducting (PMC) walls method [60–62]. Dielectric waveguide methods [63], as well as their perturbation corrections and the variation improvements [64] for cylindrical resonators, have also been developed. In 1975, Van Bladel reported a rigorous asymptotic method for evaluating the modes of dielectric resonators of arbitrary shape and high permittivity [65,66]. In addition, radial and axial mode-matching methods [67] for shielded resonators as well as asymptotic expansion methods [68] have been reported. Also, general mode-matching approaches using Green's dyadic functions or transverse modes in expanding the interior and exterior fields [69] have been successful approaches for this kind of problem. Glisson, Kajfez, and James introduced the use of the method of moments for the analysis of an open dielectric resonator [70–72]. The method was applied to dielectric bodies of revolution of arbitrary cross section and is useful for any azimuthal variation. Their results indicate that their method has yielded highly accurate values of resonant frequencies and Q factors for homogeneous dielectric resonators. The finite integration method was also used for axisymmetric shielded resonators [73]. Another approach to the electromagnetic resonance of open dielectric resonators is the null-field method [74,75] developed by Wenxin Zheng and Staffan Strom. In that approach, the resonance problem is solved by searching for zeros of the determinant of the so-called Q matrix for the dielectric resonators.

A previously developed numerical method [76] based on the method of moments is used to search for the complex resonant frequency, from which the resonant frequency and radiation Q factor can be computed, of both homogeneous and inhomogeneous dielectric resonators in free space. The geometries considered here are rotationally symmetric, so the body-of-revolution (BoR) approach is employed. The equivalence principle is used, and the surface integral equations are formulated for the problem. Then the method of moments is used to reduce the integral equations to a matrix equation. The "natural" resonant frequencies are defined as the frequencies at which the determinant of the moment matrix vanishes. Also, since the rotationally symmetric structure supports independent azimuthal modes, the azimuthal variation of the unknown equivalent currents is expanded in Fourier series. This allows one to search for the zeros of the moment matrix for modes having a particular azimuthal variation.

To compute the Q factor of nonradiating cavities, lossless structure and search for the resonant frequencies are considered. Once the resonant frequency is known, the surface currents are computed, which are then used to compute field distributions inside the cavity. Then, the perturbation method is employed to compute the stored energy and dissipated power from which we compute the Q factor [77].

For the solution of the EM modeling problems involving arbitrary geometries, the mixed potential surface integral equation (MPSIE) formulation and the method of moments (MoM) solution procedure are employed [55–58]. The E-PMCHW form [78] of the MPSIE formulation is used. EM scattering and radiation have been the subject of numerous studies covering the whole spectrum ranging from LF (low-frequency) to the optical frequencies. Although analytical solution methods are available for some canonical cases, they are limited to simple geometries, for example, an object with boundaries of constant coordinates. Such solutions can be a useful tool in EM modeling for validation and comparison of more general solutions, and for the development of approximate asymptotic techniques. Very often an analytically solvable object is either completely a conductor or purely a dielectric, but not a composite. For an arbitrarily shaped conducting or dielectric object, however, there is no analytic solution, and one must resort to numerical methods.

For EM problems there numerous numerical methods have been developed and can be classified in many ways [79,80]. The variety of the electromagnetic numerical methods is due to the extremely wide frequency range and diverse classes of EM problems that are of interest, such as multilayer, periodic, and frequency-selective structures, to name just a few. Needless to say, the variety of the methods testifies to the fact that no single method works for all problems, and that each numerical method is well suited for the analysis of particular types of problems. The MoM (method of moments) [81], FEM (finite-element method) [82], and FDTD (finite-difference time domain) [83–85] techniques are the most powerful full-wave methods used in this frequency range. The surface integral equations are derived from the equivalence principle [86] and appropriate boundary conditions.

Although the first reported dielectric resonator antenna was used in a millimeter-wave array [87], most of the research has focused on individual DRA elements of various common shapes [88–90]. More extensive references on DRAs are found in Ref. 91. Unlike other classes of antennas, a DRA has a minimum of metal parts and consists mainly of dielectric materials mounted over a metal ground plane. When compared with traditional metallic antennas, DRA's are small and low cost, and they have relatively small losses, especially in the millimeter-wave region, where the conductor losses become severe. Aperture-coupled DRAs provide compatibility with MMIC fabrication as well as isolation between the feeding and radiating structures. Possible advantages of DRAs over microstrip antennas of similar size are wider bandwidth and higher power-handling capabilities. Dielectric radiators also offer the freedom to choose a mode for broadside radiation or another for endfire radiation.

DRAs can be designed for wide bandwidth, desired field patterns, and a linear or circular polarization by choosing appropriate dielectric constants of the DR elements, element shapes, and feeding structures. One of the main disadvantages of DRAs, however, is the difficulty of their analysis. Although the early work on DRAs was based on experiments and simple models of a DR element [92–94], more rigorous and accurate numerical methods have been indispensable for better design of DRAs. One example of such a demand is a more compact and wideband handset antenna used in the wireless communication, for which the DRA is a good candidate.

At the University of Mississippi, the MPSIE/MoM procedure [56–58] and BoR (body of revolution)/MoM [95] developed for the analysis of general EM modeling has been applied to the study dielectric resonator antennas [96–102]. The MPSIE/MoM formulation has been further developed by D. R. Wilton et al. to become a standard procedure for SIE/MoM and VIE (volume integral equations)/MoM, and a package of standard subroutines has been available [59]. For problems with a finite number of homogeneous dielectric regions in combination with conducting bodies, SIE/MoM may be advantageous over VIE/MoM, FEM, or FDTD because it discretizes only the surface of the problem space rather than the whole volume. The wavelength within the dielectric may be much shorter than that of the free space, and thus girding the whole computational space uniformly with the resolution set by the critical geometry within the dielectric region results in a very inefficient situation. Therefore most numerical methods reported for DRAs have used SIE/MoM methods and taken further computational advantage of BoR models [96–102], by which their applications are limited to the problems of axially symmetric shapes.

However, the SIE/MoM can be quite tedious and difficult to implement when applied to arbitrary configurations with complex geometries or inhomogeneous dielectrics. By *arbitrary configurations*, we refer to an arbitrary number of dielectric regions, arbitrary compositions of conductors and dielectrics, general excitations, and other factors as well as arbitrary shapes. Although numerous MoM codes have been developed, when the arbitrariness of the geometries modeled is considered, the number dwindles down quickly, and the codes capable of handling the more general geometries often involve years of work and are expensive to obtain. A 3D surface of arbitrary shape is most suitably modeled by using the triangular patches or RWG (Rao–Wilton–Glisson) basis functions compared with many other approaches [102–107]. EM modeling of arbitrarily shaped conductors [58] or homogeneous dielectric [108] has been accomplished using the RWG basis functions.

Arbitrarily shaped composite bodies of conductors and dielectrics have often been treated with the constraint of a multilayer environment [109–113], where the dielectric layers are assumed to be of infinite extent. EM modeling of arbitrarily shaped 3D composite objects using RWG basis functions has been also reported in the literature [113–119]. However, the arbitrariness of the configurations treated by them is more or less confined and no systematic procedure for extension of the formulation has been provided. For example, for some cases the number of

dielectric regions is limited to two, including the free space, and arbitrary shape is allowed only for conductors in presence of axially symmetric dielectric bodies [120], or only junctions consisting of up to three intersecting surfaces are allowed. Moreover the procedures employed to deal with the composite objects of conducting and dielectric objects are more involved than the standard MPIE/MoM formulation.

9. TIME-DOMAIN INTEGRAL EQUATIONS

The method of moments is also applied in the time domain for conducting and dielectric bodies. Several formulations have been used for the solution of the time-domain integral equation to calculate the electromagnetic scattering from arbitrarily shaped 3D structures. For the 3D structures the triangular basis function is used [121]. The time derivative in EFIE formulation of the magnetic vector potential is implemented by differentiating all the terms in the EFIE with respect to time; this magnetic vector potential term is approximated by second-order finite differences [122]. However, the results become oscillatory for late times, which could be eliminated by approximating the average value of the current [123]. The incident field should be differentiated, but an impulse or step function for the incident field cannot be used as an excitation. In addition, to overcome this problem, a backward finite-difference approximation for the magnetic vector potential term has been used for the explicit technique [124]. Many numerical results using the explicit method with forward/backward-difference schemes have been shown in [121,124,125]. An implicit scheme has been proposed to solve scattering problems [126–130]. The explicit method requires a very small timestep, and the computed time-domain response becomes unstable. This is due to the accumulation of numerical error, and it consumes much computation time. This can be overcome using an implicit method. In the implicit method the timestep is larger than that for the explicit case. Therefore numerical error due to the approximation of a time derivative with the use of finite difference is increased. Jung and Sarkar used a central finite-difference methodology, which is more accurate and provides stable solutions [131]. In this work, the time domain CFIE formulation is used. The EFIE and MFIE are converted into matrix equations and are solved for CFIE solution. The goal is to find that the CFIE gives a unique solution of transient scattering problems when the incident wave includes resonant frequencies of the scatterer. The solution technique developed in this work is capable of handling either an explicit or implicit scheme of the EFIE, MFIE, and CFIE.

BIBLIOGRAPHY

1. J. J. Faran, Scattering of cylindrical waves by a cylinder, *J. Acoust. Soc. Am.* **25**:155–156 (1953).
2. S. B. Adler and R. S. Johnson, New back-scattering computation and tables for dielectric and metal spheres, *Appl. Opt.* **1**:655–660 (1962).
3. S. Asano and G. Yamamoto, Light scattering by spheroidal particle, *Appl. Opt.* **14**:29–49 (1975).
4. A. A. Kishk, P. Slattman, and P.-S. Kildal, Radiation from 3D sources in the presence of 2D objects of arbitrary cross-sectional shape, *Appl. Comput. Electromagn. Soc. (ACES) J.* **14**(1):17–24 (March 1999).
5. R. F. Harrington, *Field Computation by Moment Methods*, Macmillan, New York, 1968.
6. A. A. Kishk and L. Shafai, Different formulations for numerical solution of single or multibodies of revolution with mixed boundary conditions, *IEEE Trans. Anten. Propag.* **AP-34**:666–673 (May 1986).
7. P.-S. Kildal, S. Rengarajan, and A. Moldsvor, Analysis of nearly cylindrical antennas and scattering problems using a spectrum of two-dimensional solutions, *IEEE Trans. Anten. Propag.* **44**:1183–1192 (Aug.1996).
8. K. Forooghi and P.-S. Kildal, Transverse radiation pattern of a slotted waveguide array radiating between finite height baffles in terms of a spectrum of two-dimensional solutions, *IEE Proc. H* **140**:52–58 (1993).
9. A. A. Kishk and P. M. Goggans, Electromagnetic scattering from two-dimensional composite objects, *ACES J.* **9**:32–39 (1994).
10. A. A. Kishk and P.-S. Kildal, Electromagnetic scattering from two dimensional anisotropic impedance objects under oblique plane wave incidence, *ACES J.* **10**(3):81–92 (1995).
11. M. A. Leontovich, *Investigation of Propagation of Radio Waves*, Part II, Moscow, 1948.
12. T. B. A. Senior, Impedance boundary conditions for imperfectly conducting surfaces, *Appl. Sci. Res. B* **8**:418–436 (1961).
13. T. B. A. Senior, Impedance boundary conditions for statistically rough surfaces, *Appl. Sci. Res. B* **8**:437–462 (1961).
14. T. B. A. Senior, A note on impedance boundary conditions, *Can. J. Phys.* **40**:663–665 (1962).
15. T. B. A. Senior, Approximate boundary conditions, *IEEE Trans. Anten. Propag.* **AP-29**:826–829 (1981).
16. R. J. Garbacz, Bistatic scattering from a class of lossy dielectric spheres with surface impedance boundary conditions, *Phys. Rev.* **33**:A14–A16 (1964).
17. J. R. Wait and C. M. Jackson, Calculation of the bistatic scattering cross section of a sphere with an impedance boundary condition, *Radio Sci. J. Res.* **69D**:299–315 (1965).
18. E. S. Cassedy and J. Fainberg, Back scattering cross sections of cylindrical wires of finite conductivity, *IRE Trans. Anten.-Propag.* **AP-8**:1–7 (1960).
19. N. G. Alexopoulos and G. A. Tadler, Accuracy of the Leontovich boundary condition for continuous and discontinuous surface impedance, *J. Appl. Phys.* **46**:3326–3332 (1975).
20. N. G. Alexopoulos and G. A. Tadler, Electromagnetic scattering from an elliptic cylinder loaded by continuous and discontinuous surface impedance, *J. Appl. Phys.* **46**:1128–1134 (1975).
21. N. G. Alexopoulos, G. A. Tadler, and P. L. E. Uslenghi, Scattering from spheroidal composite objects, *J. Franklin Inst.* **309**:147–162 (1980).
22. K. A. Iskander, L. Shafai, A. Fransen, and J. E. Hansen, Application of impedance boundary conditions to numerical solution of corrugated circular horns, *IEEE Trans. Anten. Propag.* **AP-30**:366–372 (1982).
23. K. M. Mitzner, An Integral equation approach to scattering from a body of finite conductivity, *Radio Sci.* **2**:1459–1470 (1967).

24. R. D. Graglia and P. L. E. Uslenghi, Electromagnetic scattering by impedance bodies of revolution, *Proc. Natl. Radio Science Meeting, URSI/B-6-3*, Houston, 1983, p. 115.
25. A. A. Sebak and L. Shafai, E-field, H-field and combined field solutions for bodies of revolution with impedance boundary conditions, *Proc. Natl. Radio Science Meeting, URSI/B-16-5*, Boston, 1984, p. 211.
26. A. A. Sebak and L. Shafai, Performance of various integral equation formulations for numerical solution of scattering by impedance objects, *Can. J. Phys.* **62**:605–615 (1984).
27. J. R. Rogers, Numerical solutions of ill-posed impedance boundary condition integral equations, *1984 Int. Symp. Digest, APS-11-1*, 1984, pp. 347–350.
28. L. N. Medgyesi-Mitschang and J. M. Putnam, Integral equation formulation for imperfectly conducting scatterers, *IEEE Trans. Anten. Propag.* **AP-33**:206–214 (1985).
29. J. R. Mautz and R. F. Harrington, H-field, E-field, and combined-field solutions for conducting bodies of revolution, *Arch. Elektron. Übertragungstechn.* **32**:159–164 (1978).
30. W. V. T. Rusch and R. J. Pogorzelski, A mixed-field solution for scattering from composite bodies, *IEEE Trans. Anten. Propag.* **AP-34**:955–958 (1986).
31. A. A. Kishk, Formulation of impedance surfaces coated with dielectric materials, *Comput. Phys. Commun.* 145–156 (1991).
32. A. Kishk, Electromagnetic scattering from composite objects using a mixture of exact and impedance boundary conditions, *IEEE Trans. Anten. Propag.* **AP-39**(6):826–833 (June 1991).
33. J. R. Wait, Use and misuse of impedance boundary conditions in electromagnetics, *Proc. PIERS Symp.* Boston, July 1989, p. 358.
34. T. B. A. Senior and J. L. Volakis, Derivation and application of a class of generalized boundary conditions, *IEEE Trans. Anten. Propag.* **AP-37**:1566–1572 (1989).
35. D. J. Hoppe and Y. Rahmat-Sami, Scattering by superquadratic dielectric-coated cylinders using higher order impedance boundary conditions, *IEEE Trans. Anten. Propag.* **40**:1513–1523 (1992).
36. P.-S. Kildal, Artificially soft and hard surfaces in electromagnetics, *IEEE Trans. Anten. Propag.* **38**:1537–1544 (1990).
37. P.-S. Kildal, A. A. Kishk, and A. Tengs, Reduction of forward scattering from cylindrical objects using hard surfaces, *IEEE Trans. Anten. Propag.* **44**:1509–1520 (Nov. 1996).
38. P. M. Goggans, *A Combined Method-of-Moments and Approximate Boundary Condition Solution for Scattering from a Conducting Body with a Dielectric-Filled Cavity*, Ph.D. dissertation, Auburn Univ., 1990.
39. A. A. Kishk and P. M. Goggans, Electromagnetic scattering from two-dimensional composite objects, *ACES J.* **9**(1):32–39 (1994).
40. R. Gordon and A. A. Kishk, An efficient finite element method for determining the scattering from lossy cylinders using the impedance boundary condition and an absorbing boundary condition due to oblique incident, *Proc. 9th Annual Review of Progress in Applied Computational Electromagnetics Conf.* 1993, pp. 871–878.
41. J. Yan, R. K. Richard and A. A. Kishk, Electromagnetic scattering from impedance elliptic cylinders using finite difference method (oblique incidence), *J. Electromagn.* **15**:157–173 (1995).
42. A. W. Glisson, M. Orman, and D. Koppel, Electromagnetic scattering by a body of revolution with a general anisotropic impedance boundary condition, *IEEE Anten. Propagation Soc. Int. Symp. Digest*, 4:1997–2000 (June 1992).
43. P. Kaveh and A. H. Levesque, *Wireless Information Networks*, Wiley, New York, 1995.
44. D. Kajfez and P. Guillon, *Dielectric Resonators*, Vector Fields, Oxford, MS, 1990.
45. L. E. Larson, *RF and Microwave Circuit Design for Wireless Communications*, Artech House, Norwood, MA, 1996.
46. A. Podcameni and L. F. M. Conrado, Design of microwave oscillators and filters using transmission-mode dielectric resonators coupled to microstrip lines, *IEEE Trans. Microwave Theory Tech.* **MTT-33**:1329–1332 (Dec. 1985).
47. A. M. Pavio and M. A. Smith, A 20-40-GHz push-push dielectric resonator oscillator, *IEEE Trans. Microwave Theory Tech.* **MTT-33**:1346–1349 (Dec. 1985).
48. D. Kajfez and J. Guo, Precision measurement of coupling between microstrip and TE_{01} mode dielectric resonator, *Electron. Lett.* **30**:1772–1773 (Oct. 1994) (also, the data that were not published).
49. A. W. Glisson, D. Kajfez, and J. James, Evaluation of modes in dielectric resonators using a surface integral equation formulation, *IEEE Trans. Microwave Theory Tech.* **MTT-31**:1023–1029 (Dec. 1983).
50. D. Kajfez, A. W. Glisson, and J. James, Computed model field distributions for isolated dielectric resonators, *IEEE Trans. Microwave Theory Tech.* **MTT-32**:1609–1616 (Dec. 1984).
51. G. P. Junker, *Analysis of Dielectric Resonator Antennas Excited by a Coaxial Probe or Narrow Slot Aperture*, Ph.D. dissertation, Univ. Mississippi, Aug. 1994.
52. G. P. Junker, A. A. Kishk, and A. W. Glisson, Input impedance of dielectric resonator antennas excited by a coaxial probe, *IEEE Trans. Anten. Propag.* **AP-42**:960–966 (July 1994).
53. G. P. Junker, A. A. Kishk, D. Kajfez, A. W. Glisson, and J. Guo, Input impedance of microstrip-slot-coupled dielectric resonator antennas mounted on thin dielectric layers, *Int. J. Microwave Millimeter-wave Comput. Aided Eng.* **6**:174–182 (May 1996).
54. J. Y. Chen, A. A. Kishk, and A. W. Glisson, Application of new MPIE formulation to the analysis of a dielectric resonator embedded in a multilayered medium coupled to a microstrip circuit, *IEEE Trans. Microwave Theory Tech.* **49**:263–279 (Feb. 2001).
55. A. W. Glisson, *On the Development of Numerical Techniques for Treating Arbitrarily-Shaped Surfaces*, Ph.D. thesis, Univ. Mississippi, 1978.
56. S. M. Rao, *Electromagnetic Scattering and Radiation of Arbitrarily-Shaped Surfaces by Triangular Patch Modeling*, Ph.D. thesis, Univ. Mississippi, 1980.
57. S. M. Rao, D. R. Wilton, and A. Glisson, Electromagnetic scattering by surfaces of arbitrary shape, *IEEE Trans. Anten. Propag.* **AP-30**:409–418 (May 1982).
58. S. V. Yesantharao, *EMPACK: A Software Toolbox of Potential Integrals for Computational Electromagnetics*, master's thesis, Univ. Houston, 1989.
59. S. M. Rao, C. C. Cha, R. L. Cravey, and D. L. Wilkes, Electromagnetic scattering from arbitrary shaped conducting bodies coated with lossy materials of arbitrary thickness, *IEEE Trans. Anten. Propag.* **AP-39**:627–631 (May 1991).
60. H. Y. Yee, Natural resonant frequencies of microwave dielectric resonators, *IEEE Trans. Microwave Theory Tech.* **MTT-13**:256 (March 1965).
61. Y. Garault and P. Guillon, Best approximation for design of natural resonance frequencies of microwave

- dielectric disc resonants, *Electron. Lett.* **10**:505–507 (Nov. 1974).
62. Y. Konishi, N. Hosino, and Y. Utsumi, Resonant frequency of a TE₀₁ dielectric resonator, *IEEE Trans. Microwave Theory Tech.* **MTT-24**:112–114 (Feb. 1976).
 63. T. Itoh and R. Rudokas, New method for computing the resonant frequencies of dielectric resonator, *IEEE Trans. Microwave Theory Tech.* **MTT-25**:52–54 (Jan. 1977).
 64. D. Kajfez and P. Guillon, eds., *Dielectric Resonators* Noble Publishing, Atlanta, 1998.
 65. J. Van Bladel, On the resonances of a dielectric resonator of very high permittivity, *IEEE Trans. Microwave Theory Tech.* **MTT-23**:199–208 (Feb. 1975).
 66. J. Van Bladel, The excitation of dielectric resonators of very high permittivity, *IEEE Trans. Microwave Theory Tech.* **MTT-23**:208–217 (Feb. 1975).
 67. Y. Kobayashi, N. Fukuoka, and S. I. Yoshida, Resonant models for a shielded dielectric resonator, *Electron. Commun. Jpn.* **64-B**(11):44–51 (1981).
 68. K. A. Zaki and C. Chen, Coupling of non-axially symmetric hybrid modes in dielectric resonators, *IEEE Trans. Microwave Theory Tech.* **MTT-35**:1136–1142 (Dec. 1987).
 69. R. E. Collin and D. A. Ksienski, Boundary element method for dielectric resonators and waveguides, *Radio Sci.* **22**:1155–1167 (Dec. 1987).
 70. A. W. Glisson, D. Kajfez, and J. James, Evaluation of modes in dielectric resonators using a surface integral equation formulation, *IEEE Trans. Microwave Theory Tech.* **MTT-31**:1023–1029 (Dec. 1983).
 71. D. Kajfez, A. W. Glisson, and J. James, Computed model field distributions for isolated dielectric resonators, *IEEE Trans. Microwave Theory Tech.* **MTT-32**:1609–1616 (Dec. 1984).
 72. A. A. Kishk, A. W. Glisson, and D. Kajfez, Computed resonant frequency and far fields of isolated dielectric discs, *Proc. 1993 IEEE APS Int. Symp.* Ann Arbor, MI, June 1993, pp. 408–411.
 73. J. E. Lebaric and D. Kajfez, Analysis of dielectric resonator cavities using the finite integration technique, *IEEE Trans. Microwave Theory Tech.* **37**:1740–1748 (Nov. 1989).
 74. W. Zheng and S. Strom, The null-field approach to electromagnetic resonance of composite objects, *Comput. Phys. Commun.* 157–174 (March 1991).
 75. W. Zheng, Computation of complex resonance frequencies of isolated composite objects, *IEEE Trans. Microwave Theory Tech.* **MTT-37**:953–961 (June 1989).
 76. A. A. Kishk, Electromagnetic scattering from composite objects using a mixture of exact and impedance boundary conditions, *IEEE Trans. Anten. Propag.* **AP-39**(6):826–833 (June 1991).
 77. A. A. Kishk, D. Kajfez, and S. Chebolu, Resonant frequency and Q-factor of axisymmetric composite microwave cavities, *IEEE Trans. Microwave Theory Tech.* **50**(10):2287–2293 (Oct. 2002).
 78. A. A. Kishk and L. Shafai, Different formulations for numerical solution of single or multibodies of revolution with mixed boundary conditions, *IEEE Trans. Anten. Propag.* **AP-34**:666–673 (May 1986).
 79. E. K. Miller and G. J. Burke, Low-frequency computational electromagnetics for antenna analysis, *IEEE Proc.* **80**:24–43 (Jan. 1992).
 80. T. H. Hubing, *Survey of Numerical Electromagnetic Modeling Techniques*, Tech. Report TR91-001.3, Electromagnetic Compatibility Laboratory, Univ. Missouri—Rolla, 1991.
 81. R. F. Harrington, *Field Computation by Method of Moments*, Krieger, Malabar, FL, 1968.
 82. R. Coccioli, T. Itoh, G. Pelosi, and P. P. Silvester, Finite-element methods in microwaves: A selective bibliography, *IEEE Anten. Propag. Mag.* **38**:34–48 (Dec. 1996).
 83. K. S. Kunz and R. J. Luebbers, *The Finite Difference Time Domain Method for Electromagnetics*, CRC Press, 1993.
 84. A. Taove, *Computational Electromagnetics: The Finite-Difference Time-Domain Method*, Artech House, 1995.
 85. K. L. Shlager and J. B. Schneider, A selective survey of the finite-difference time-domain literature, *IEEE Anten. Propag. Mag.* **37**:39–57 New York, (Aug. 1995).
 86. R. F. Harrington, *Time Harmonic Electromagnetic Fields*, McGraw-Hill, 1963.
 87. M. T. Birand and R. V. Gelstrophe, Experimental millimetric array using dielectric radiators fed by means of dielectric waveguide, *Electron. Lett.* **17**:633–635 (Sept. 1981).
 88. M. W. McAllister and S. A. Long, Rectangular dielectric-resonator antenna, *Electron. Lett.* **19**:218–219 (March 1983).
 89. S. A. Long, M. W. McAllister, and L. C. Shen, The resonant cylindrical dielectric cavity antenna, *IEEE Trans. Anten. Propag.* **AP-31**:406–412 (May 1983).
 90. M. W. McAllister and S. A. Long, Resonant hemispherical dielectric antenna, *Electron. Lett.* **20**:657–658 (March 1984).
 91. A. Petosa, A. Ittipiboon, Y. M. M. Antar, and D. Roscoe, Recent advances in dielectric-resonator antenna technology, *IEEE Anten. Propag. Mag.* **40**:35–48 (June 1998).
 92. S. B. Cohn, Microwave bandpass filters containing high-Q dielectric resonators, *IEEE Trans. Microwave Theory Tech.* **MTT-16**:218–217 (April 1968).
 93. T. Itoh and R. S. Rudokas, New method for computing the resonant frequencies of dielectric resonators, *IEEE Trans. Microwave Theory Tech.* **MTT-25**:52–54 (Jan. 1977).
 94. D. Kajfez and P. Guillon, eds., *Dielectric Resonators*, Artech House, 1986.
 95. A. W. Glisson and C. M. Butler, Analysis of a wire antenna in the presence of a body of revolution, *IEEE Trans. Anten. Propag.* **AP-28**:604–609 (Sept. 1980).
 96. (a) A. A. Kishk, H. A. Auda, and B. C. Ahn, Radiation characteristics of cylindrical dielectric resonator antennas, *IEEE Anten. Propag. Soc. Newsl.* **31**:7–16 (1989); (b) A. A. Kishk, M. R. Zunoubi, and D. Kajfez, A numerical study of a dielectric disk antenna above a grounded dielectric substrate, *IEEE Trans. Anten. Propag.* **AP-41**:813–821 (June 1993).
 97. G. P. Junker, A. A. Kishk, A. W. Glisson, and D. Kajfez, Effect of an air gap around the coaxial probe exciting a cylindrical dielectric resonator antenna, *Electronics Letters*, vol. 30, pp. 177–178 (Feb. 1994).
 98. A. A. Kishk, G. Zhou, and A. W. Glisson, Analysis of dielectric-resonator antennas with emphasis on hemispherical structures, *IEEE AP-S Newsl.* **36**:20–31 (April 1994).
 99. G. Junker, A. Kishk, and A. Glisson, Input impedance of dielectric resonator antennas excited by a coaxial probe, *IEEE Trans. Anten. Propag.* **AP-42**:960–966 (July 1994).
 100. G. P. Junker, A. A. Kishk, and A. W. Glisson, Input impedance of an aperture coupled dielectric resonator antenna, *IEEE Trans. Anten. Propag.* **AP-44**:600–607 (May 1996).
 101. G. P. Junker, A. A. Kishk, and A. W. Glisson, Multiport network description and radiation characteristics of coupled dielectric resonator antennas, *IEEE Trans. Anten. Propag.* **AP-46**:425–433 (March 1998).

102. L. N. Medgyesi-Mitschang and J. M. Putnam, Electromagnetic scattering from axially inhomogeneous bodies of revolution, *IEEE Trans. Anten. Propag.* **AP-32**:797–806 (Aug. 1984).
103. N. N. Wang, J. H. Richmond, and M. C. Gilreath, Sinusoidal reaction formulation for radiation and scattering from conducting surfaces, *IEEE Trans. Anten. Propag.* **23**:376–382 (May 1975).
104. G. J. Burke and A. J. Poggio, *Numerical Electromagnetic Code (NEC): Method of Moments*, Naval Ocean Systems Center, San Diego, CA, Tech. Document 116, July 1977.
105. B. J. Rubin, General solution for propagation, radiation, and scattering in arbitrary 3D inhomogeneous structures, *IEEE Anten. Propag. Mag.* **34**:17–25 (Feb. 1992).
106. D. I. Kaklamani and N. K. Uzunoglu, Analysis of dielectrically loaded radiators using entire-domain Galerkin technique, *IEEE Anten. Propag. Mag.* **39**:30–54 (Oct. 1997).
107. B. M. Notaros and B. D. Popovic, General entire-domain method for analysis of dielectric scatters, *IEE Proc. Microwave Anten. Propag.* **143**:498–504 (Dec. 1996).
108. K. Umashanka, A. Taove, and S. M. Rao, Electromagnetic scattering by arbitrary shaped three-dimensional homogeneous lossy dielectric objects, *IEEE Trans. Anten. Propag.* **AP-34**:758–766 (June 1986).
109. K. A. Michalski and D. Zheng, Electromagnetic scattering and radiation by surfaces of arbitrary shape in layered media, Part I: Theory, *IEEE Trans. Anten. Propag.* **AP-38**:335–344 (March 1990).
110. K. A. Michalski and D. Zheng, Electromagnetic scattering and radiation by surfaces of arbitrary shape in layered media, Part II: Implementation and results for contiguous half-spaces, *IEEE Trans. Anten. Propag.* **AP-38**:345–352 (March 1990).
111. J. Y. Chen, *Full Wave Analysis of a Dielectric Resonator Embedded in a Uniaxial Multilayered Medium Coupled to a Microstrip Circuit*, Ph.D. thesis, Univ. Mississippi, 1996.
112. J. Chen, A. A. Kishk, and A. W. Glisson, Application of a new MPIE formulation to the analysis of a dielectric resonator embedded in a multilayered medium coupled to a microstrip circuit, *IEEE Trans. Microwave Theory Tech.* **MTT-49**:263–279 (Feb. 2001).
113. S. M. Rao, C. C. Cha, R. L. Cravey, and D. L. Wilkes, Electromagnetic scattering from arbitrary shaped conducting bodies coated with lossy materials of arbitrary thickness, *IEEE Trans. Anten. Propag.* **AP-39**:627–631 (May 1991).
114. T. K. Sarkar, S. M. Rao, and A. R. Djordevic, Electromagnetic scattering and radiation from finite microstrip structures, *IEEE Trans. Microwave Theory Tech.* **MTT-38**:1568–1575 (Nov. 1990).
115. S. M. Rao, T. K. Sarkar, P. Midya, and A. R. Djordevic, Electromagnetic radiation and scattering from finite conducting and dielectric structures: Surface/surface formulation, *IEEE Trans. Anten. Propag.* **AP-39**:1034–1037 (July 1991).
116. J. M. Putnam and L. N. Medgyesi-Mitschang, Generalized method of moments for three-dimensional penetrable scatterers, *J. Opt. Soc. Am. A* **11**:1384–1398 (April 1994).
117. J. M. Putnam and M. B. Gedera, CARLOS-3DTM: A general-purpose three-dimensional method-of-moments scattering code, *IEEE Anten. Propag. Mag.* **35**:69–71 (April 1993).
118. T. E. Durham and C. G. Christodoulou, Integral equation analysis of dielectric and conducting bodies of revolution in the presence of arbitrary surfaces, *IEEE Trans. Anten. Propag.* **AP-43**:674–680 (July 1995).
119. A. J. Movahedi, *Electromagnetic Radiation and Scattering by a Dielectric Loaded Conducting Body Coupled to an Arbitrary Wire*, Ph.D. thesis, Univ. Mississippi, 1995.
120. S. U. Hwu and D. R. Wilton, *Electromagnetic Scattering and Radiation by Arbitrary Configurations of Conducting Bodies and Wires*, Tech. Report TR87-17, Applied Electromagnetics Laboratory, Univ. Houston, 1989.
121. S. M. Rao, *Time Domain Electromagnetics*, Academic Press, Orlando, FL, 1999.
122. S. M. Rao and D. R. Wilton, Transient scattering by conducting surfaces of arbitrary shape, *IEEE Trans. Anten. Propag.* **AP-39**:56–61 (1991).
123. D. A. Vechinski and S. M. Rao, A stable procedure to calculate the transient scattering by conducting surfaces of arbitrary shape, *IEEE Trans. Anten. Propag.* **AP-40**:661–665 (1992).
124. S. M. Rao and T. K. Sarkar, An alternative version of the time-domain electric field integral equation for arbitrarily shaped conductors, *IEEE Trans. Anten. Propag.* **AP-41**:831–834 (1993).
125. P. J. Davies, On the stability of time-marching schemes for the general surface electric-field integral equation, *IEEE Trans. Anten. Propag.* **AP-44**:1467–1473 (1996).
126. S. M. Rao and T. K. Sarkar, Time-domain modeling of two-dimensional conducting cylinders utilizing an implicit scheme-TM incidence, *Microwave Opt. Technol. Lett.* **15**:342–347 (1997).
127. S. M. Rao and T. K. Sarkar, An efficient method to evaluate the time domain scattering from arbitrarily shaped conducting bodies, *Microwave Opt. Technol. Lett.* **17**:321–325 (1998).
128. S. M. Rao and T. K. Sarkar, Transient analysis of electromagnetic scattering from wire structures utilizing an implicit time-domain integral-equation technique, *Microwave Opt. Technol. Lett.* **17**:66–69 (1998).
129. S. M. Rao, D. A. Vechinski, and T. K. Sarkar, Transient scattering by conducting cylinders implicit solution for the transverse electric case, *Microwave Opt. Technol. Lett.* **21**:129–134 (1999).
130. T. K. Sarkar, W. Lee, and S. M. Rao, Analysis of transient scattering from composite arbitrarily shaped complex structures, *IEEE Trans. Anten. Propag.* **AP-48**:1625–1634 (2000).
131. B. H. Jung and T. K. Sarkar, Time-domain CFIE for the analysis of transient scattering from arbitrarily shaped 3D conducting objects, *Microwave Opt. Technol. Lett.* **34**(2):289–296 (2002).

MICROSTRIP ANTENNA ARRAYS

PETER S. HALL
The University of Birmingham
Edgbaston, Birmingham, UK

1. INTRODUCTION

Microstrip antenna arrays are formed from collections of microstrip antenna elements, which may then be interconnected and fed using microstrip transmission lines. For information on microstrip antenna elements, the reader is referred to other articles. In this article it is assumed that

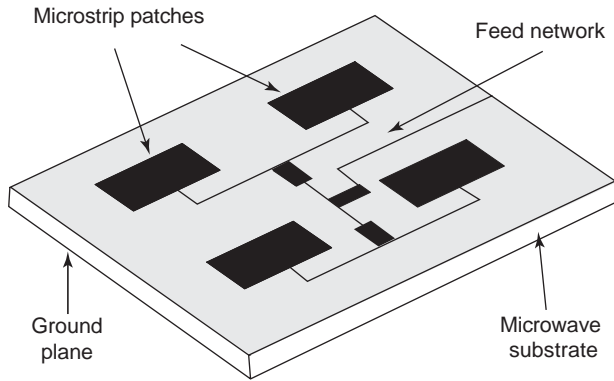


Figure 1. Microstrip patch array (typical dimensions for operation at 12 GHz, patch size = 9.7×7.2 mm, patch spacing = 17 mm, substrate height = 1.59 mm, $\epsilon_r = 2.32$, feedline width = 0.5 mm at patches, 2.5 mm at input) [57].

the elements may be a microstrip patch or a section of microstrip transmission line that radiates. This article is concerned with the architectures of microstrip arrays and some specific issues that arise in their design, such as surface waves and mutual coupling.

In using microstrip for both the radiating elements and the feed network, a low-profile planar structure results. The minimum thickness will be obtained when the feed is coplanar with the radiators (Fig. 1), which is to say that the array and the feed are manufactured by the process of photolithography on one side of a copper-clad microwave substrate. Improved performance and more functionality will be obtained if multilayer structures are used. For example, dual polarization, with separate output connectors for each, can be achieved using two feed networks in a multilayer configuration. It is the combination of a low-profile and simple manufacturing process that is the main attraction of microstrip antenna arrays. This results in low cost and ease of installation, which means that they have found application in many areas, including satellites, aircraft and ground-based systems for communications, navigation, and radar.

There is a large body of literature on microstrip arrays. Much of this is gathered together in several books that have been published [1–5].

2. DESCRIPTION OF ARRAY ARCHITECTURES

Good overviews of array architectures can be found in two other texts [2, Chaps. 1, 13, 14; 3, Chap. 6]. The primary classifications of microstrip arrays are parallel or series feeding. These are now discussed and other variants are described.

2.1. Parallel- or Corporate-Fed Arrays

A parallel, or corporate, feed network consists of a microstrip transmission line that splits successively from the input to the radiating elements so that all elements are connected [6,7]. Figure 1 illustrates a microstrip patch array with four elements and a parallel feed. The feed input is on the right-hand side of the substrate and splits into

two near the center. These two lines then split into two, and the four lines are then attached to the patches. An impedance match is maintained at each splitter by the use of quarter-wavelength matching sections, although short tapered sections have also been used. In this case, the splitters produce equal amplitudes at each of their outputs. This then results in an equal-amplitude excitation of each patch. If unequal splitters are used, then some control of the amplitude distribution can be obtained to allow the sidelobes to be controlled. Similarly, in the array of Fig. 1, the lengths from the input to each of the patches are equal, resulting in an equiphase excitation and a beam that points broadside, or normal, to the array plane. If the lengths of line between each splitter and the next or the patches are unequal, then control of the array excitation phase will be obtained, either allowing the beam to be shaped or causing it to point away from broadside.

The parallel-fed array produces a single pencil-shaped beam, with beamwidths inversely proportional to the array aperture dimensions. The radiation pattern is relatively insensitive to changes in frequency, in that, provided the feed is matched throughout, the array excitation does not change. In addition, for a broadside beam, the angle at which the beam points does not vary with frequency. The input impedance and gain bandwidth are controlled primarily by the bandwidth of the radiating elements.

2.2. Series-Fed Arrays

In a series-fed array, the radiating elements are arranged in a line and connected to a transmission line that runs close by them. Figure 2 shows an example of a four-patch series-fed array. The input connector is attached to the right-hand end of the line. The amplitude distribution along the array is controlled by the splitter ratios. In the case shown in which the splitters all have the same geometry, the amplitudes will have an exponentially reducing distribution. While each patch is fed with the same proportion of the feedline power, that power reduces at each splitter.

If a matched load is placed on the left-hand end of the feedline, a traveling-wave array is formed. In this case, as the patches are equispaced, the phase change between

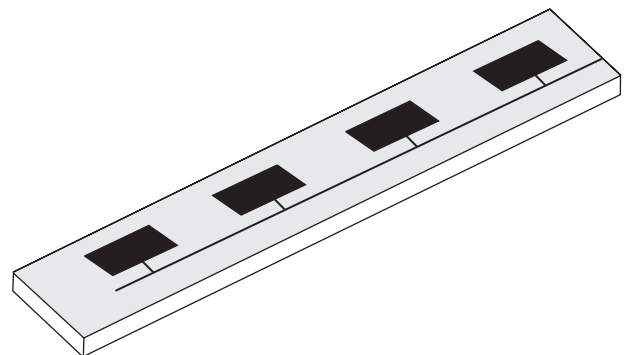


Figure 2. Series-fed patch array (typical dimensions same as those for Fig. 1).

elements down the array is constant. The relative element phase will then determine the beam pointing angle in the plane of the array. If the frequency is changed, then the relative phase will change and the beam angle will change. This type of array is thus called a *frequency scan array*.

If the feedline is not terminated in a matched load, then a resonant array is formed. The radiating elements should be placed a feedline wavelength apart. The array has a good input match albeit across a narrow beamwidth, and the beam points to broadside.

The beamshape of a single series-fed microstrip array is broad in the dimension across the array and narrow along the plane of the array. A pencil-shaped beam can be formed by placing many series arrays side by side. In this case, a one-dimensional corporate feed can be made coplanar with the array; or alternately, a series feed can be used to feed a set of series feeds. The cross-fed array [8] is a two-dimensional series array using equal-width feedlines that is center fed and automatically produces a tapered distribution with low sidelobes. Dual polarization can be obtained from a two-dimensional patch array [9] in which square patches are series-connected on all four sides, so that the horizontal connections produce horizontal polarization and the vertical connections, vertical polarization. The chain array structures give linear polarization and have rectangular [10] and triangular or honeycomb [11] shapes. The patches may be connected directly to the feedline to form a comblike array [12], coupled by a small airgap in the parasitically coupled patch array [13], or series-connected by a feedline connecting the centers of their sides [14].

As the feedline itself will radiate, the patches shown in Fig. 2 can be dispensed with and a meander array formed. There are many forms. Figure 3a shows a silhouette of the rampart line array [15] as an example. The function of radiation can be understood from the following description, which is based on an equivalent source model of microstrip radiation. Each of the four corners in each period radiates. The radiation has a polarization that is oriented 45° to the incoming line, as shown in Fig. 3b. If these four vectors, whose relative phase is determined by the intervening linelengths, are summed, then the total amount of

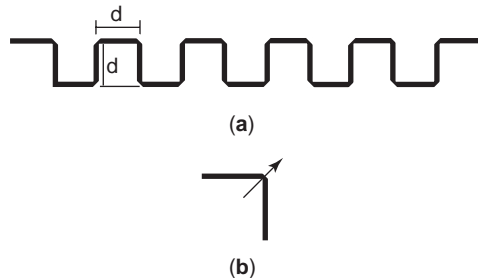


Figure 3. Rampart line series-fed microstrip array: (a) rampart line array (typical dimensions for operation at 15 GHz, linewidth = 1 mm, section length = $0.5\lambda_m$, substrate height = 0.793 mm, $\epsilon_r = 2.32$ [15]); (b) right-angle bend showing polarization of radiation (miter depth = $0.5 \times$ line width); λ_m = microstrip line wavelength.

radiation and its polarization can be determined. An array with uniform linewidth will result in an exponentially reducing amplitude distribution and a beam that is either broadside, if there is no matched load present on the line end; or a frequency-scanned beam, if there is a load. By varying the distance between the bends, longitudinal, transverse, or circular polarization can be obtained.

Many other forms of series array have been designed, including the serpent line [16,17], the rectangular loop line, [10], the Franklin line [18], and the circularly polarized chain antenna [19] (see Fig. 4). The dimensions can be determined from the Figure caption or the following. For the serpent line

$$\sin \theta = \frac{l_m}{s} \frac{\lambda_0}{\lambda_m} - \frac{\lambda_0}{2s} \tag{1}$$

where θ is the beam angle, λ_m and λ_0 are the line and free-space wavelengths, respectively; and l_m and s are as indicated in Fig. 4a. For the chain antenna

$$\sin \theta = \frac{2s + l_p + l_w - \lambda_0}{d} \tag{2}$$

where s, l_p, l_w and d are as indicated in Fig. 4d.

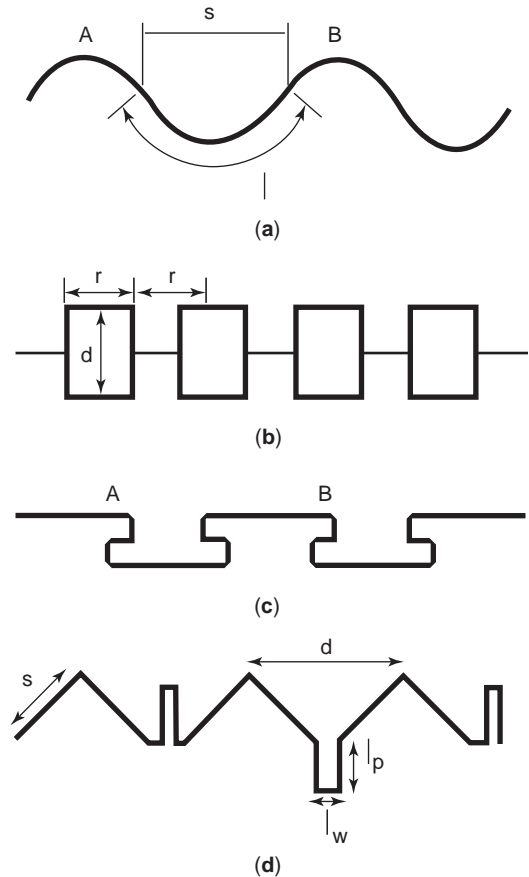


Figure 4. Microstrip series array: (a) serpent line [16,17], ($l = \lambda_m$); (b) rectangular loop line [10] ($d = \lambda_m, r = 0.4\lambda_m$); (c) Franklin line [18] (length along line A-B = $2\lambda_m$); (d) circularly polarized chain antenna [19] ($2l_p + l_w = 0.25\lambda_m$).

2.3. Leaky-Wave Arrays

A half-wavelength-wide microstrip line can also be made to radiate by feeding with an asymmetric step [20] to excite the first-order asymmetric mode, which then leaks to radiation down the array length. Synthesis of the radiation pattern is performed by modulating the line parameters, such as width or height, or by inserting radiating slots periodically down the length. A double-layer leaky-wave microstrip antenna has also been described [21].

2.4. Ultrawideband Arrays

Linear microstrip patch arrays can be made to operate over multioctave bandwidths using the log periodic principle [22] (Fig. 5 shows the architecture). A microstrip line is electromagnetically coupled to an array of patches whose dimensions and hence resonant frequency are scaled patch to patch by a constant factor τ , where

$$\tau = \frac{l_{m+1}}{l_m} = \frac{w_{m+1}}{w_m} = \frac{d_{m+1}}{d_m}$$

and l , w and d are the patch length, width, and spacing, respectively. The overall bandwidth is determined by the number of patches and the scale factor. For example, an array designed with $\tau = 1.05$ and 36 elements, achieved a 5:1 bandwidth and had a gain of around 10 dB and an input return loss of -10 dB over a 4–20 GHz range. Similar to the design of the log periodic dipole array, the element feeding arrangement is crucial. In the microstrip array, it is necessary to have electromagnetic coupling to prevent the formation of stopbands in the wanted frequency range due to the higher patch resonances. Reference 23 shows a log periodic array that consists of a feedline with directly connected patches. A useful, but limited, bandwidth of about 2:1 is achieved.

The array of Fig. 5 has a broadside beam. An endfire beam has also been demonstrated [24].

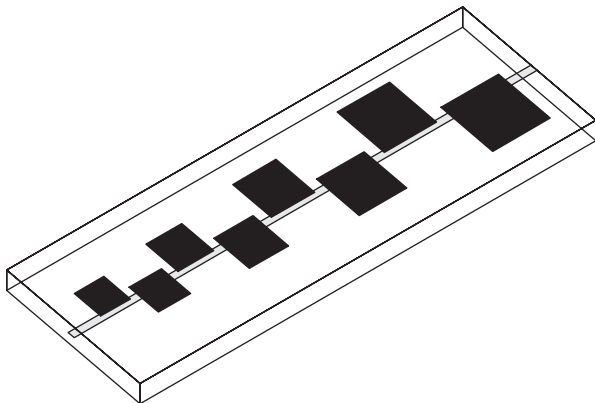


Figure 5. Log periodic microstrip patch array (typical dimensions for a 36-element array for operation at 4–18 GHz, smallest patch size 3.67×2.92 mm, smallest spacing = 3.67, $\tau = 1.05$, substrate height, feed = 0.793 mm, patch = 1.586 mm, $\epsilon_r = 2.32$) [22].

2.5. Multilayer Arrays

Multilayer arrays are designed to

- Reduce the perturbation to the pattern of radiation from the feed network in a coplanar form
- Allow multiple functions, such as dual polarization
- Prevent radiation from, and to protect active circuits in, active integrated antennas

Figure 6 shows an exploded diagram of a multilayer microstrip array. It can be seen that the front face contains only microstrip patch elements. The feed network is constructed in triplate stripline and located below the array substrate. The three layers are then glued together to form the integral array and feed. Zurcher [25] gives design techniques for high-efficiency multilayer arrays, by using foam-based low-permittivity dielectrics. An example in which multiple patch layers has been used to increase bandwidth is given by Legay and Shafai [26].

The connections from the ends of the feedline to the elements can be made either using vias or by aperture coupling. The via is a metallic rod or pin that is attached to the end of the feedline, at its lower point, and to a point on the patch that has the appropriate impedance, at its upper end. A clearance hole must be etched in the patch ground plane. The via can also be made using a plated through-hole. The aperture coupling is formed by having a (usually) rectangular aperture in the ground plane beneath the patch and above the feedline. Aperture coupling is now widely used as it is more reliable than a via connection. Examples of aperture-coupled arrays are given in Refs. 27 and 28.

2.6. Sequentially Fed Arrays

Multiple feeding of microstrip patch antennas has been shown to improve both the symmetry and the polarization

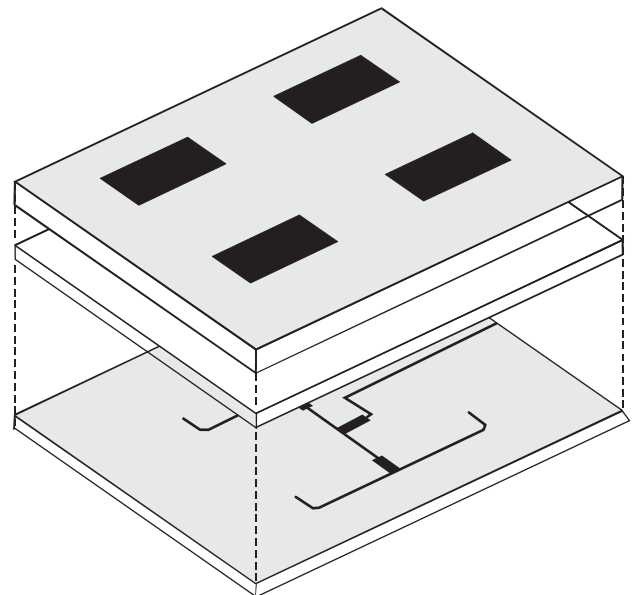


Figure 6. Multilayer microstrip array (patch and feed details same as those in Fig. 1).

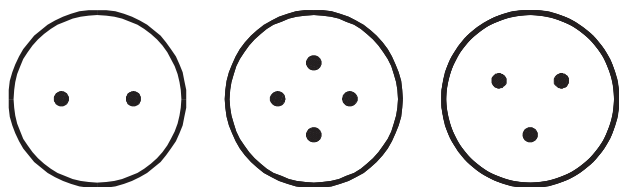


Figure 7. Multiple feeding of microstrip patches.

purity of the radiation pattern and the input impedance bandwidth [29,30], in addition to allowing the generation of circular and multiple polarizations. Figure 7 illustrates this principle. The circular patch shown on the left is fed at two points. This patch can, in principle, be fed at a single point. However, some asymmetry of the pattern results, due to the presence of higher-order modes in the patch. Provided that the two points shown in Fig. 7 are fed with signals that are of equal amplitude and in antiphase, that is, at 0° and 180° , respectively, then a symmetric radiation pattern is formed that is linearly polarized in the horizontal direction. The symmetry results from cancellation of the higher-order modes in the patch. If two further feeds are added as shown in the central patch example, and if these are fed with independent signals having equal amplitude and in antiphase, then a dual linearly polarized patch is formed. If these four points are fed with equal amplitude and in a phase sequence of 0° , 90° , 180° , and 270° , then circular polarization with highly symmetric patterns and low cross-polarization will result. It has also been shown that the three-point-fed element shown on the right of Fig. 7, when fed with equal amplitude and a phase sequence of 0° , 120° , and 240° , will also result in symmetric patterns but with a considerably wider input return loss bandwidth.

These multiple-fed patches can be used in arrays using the feed structures described earlier. However, a very simplified feed results if the multiple feedpoints are distributed among the elements in an array. Figure 8a shows four circular patches fed by a corporate feed. As the patches are fed diagonally, each will radiate with a diagonal polarization. The top left patch will have a polarization inclined to $+45^\circ$, while the top right one will have -45° , and so on. However, the feed is arranged to provide the top left patch with a phase of 0° and the top left with a phase of 90° , shifting the top power splitter to the left by a line-length equivalent to 45° . These two patches together thus generate circular polarization. The bottom pair is likewise arranged and generates circular polarization in the same hand as the top pair. However, it can be seen that these patches are fed from the top rather than the bottom, thus providing an inversion. By offsetting the central power splitter, the two pairs are fed to reinforce. The result is a feed that produces a phase sequence of 0° , 90° , 180° , and 270° , to feed patches that have a similar rotation sequence.

Although this illustrates the general polarization principle, it is usual when generating circular polarization to use circularly polarized elements as shown in Figs. 8b and 8c. There are slight pattern asymmetries induced by the displacements of the linearly polarized patches in Fig. 8a,

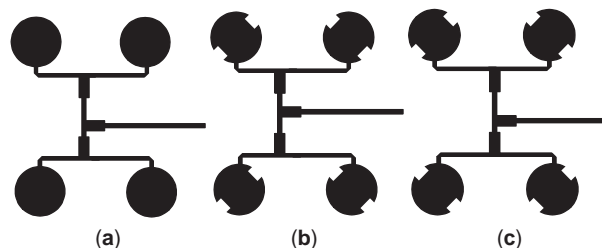


Figure 8. Sequentially rotated patch arrays (typical dimensions for operation at 8 GHz, patch diameter = 12.25 mm, patch spacing = 21.4 mm, patch notch size = 2×1 mm, substrate height, feed = 1.586 mm, $\epsilon_r = 2.32$) [32,33].

which can be removed in this way. Figure 8b shows an arrangement in which pairs of patches are rotated and Fig. 8c, one in which all four elements are rotated.

Figure 9 shows the performance improvement of sequential rotation applied to an eight-element array. Figure 9a shows that the boresight 3 dB axial ratio bandwidth has been increased by several factors and Fig. 9b, that the input return loss bandwidth has also significantly increased. Further information on the effects of sequential rotation of the array radiation pattern is provided in Refs. 31 and 32.

Dual polarization arrays can also benefit from sequential rotation [33]. Figure 10 shows two examples. Figure 10a shows a 2×2 -element array of square patches where dual linear polarization is achieved by feeding orthogonal edges of the patch. As noted above, this leads to poor cross-polarization in the radiation patterns and to isolation between the input ports. By arranging each successive patch to ensure rotated feeding, the isolation is improved, and the pattern problems are balanced out. For the array shown in Fig. 10a, improvements of nearly 10 dB in the isolation are noted. Figure 10b shows how a linear array can be similarly fed; in this case rotation is applied to the two groups of four patch elements.

Figure 11 shows how sequential rotation can be applied to dual circularly polarized arrays. Feed 1 has positive feed progression, while feed 2 is negative, with appropriate feedpoint rotation to offset the phasing. In this case, cross-polarization is reduced and input match is improved; however, isolation is unchanged from a conventionally fed array.

2.7. Phased Arrays

The microstrip array can be used to create phased arrays by the addition of phase shifters [34]. In general, due to the planar nature of the microstrip, this medium is ideal for integration of active devices, and there are examples where multilayer structures incorporate the phase shifting elements on layers below the radiating elements.

Many arrays have been built on low-dielectric-constant substrates, and this can lead to low costs, although the array cost will then be dependent primarily on the active device cost and hence on array size. Alternatively, more thought has been given to the integration of both the radiating patch and the phase shifter onto a semiconducting substrate. This has the potential to allow cost reduction

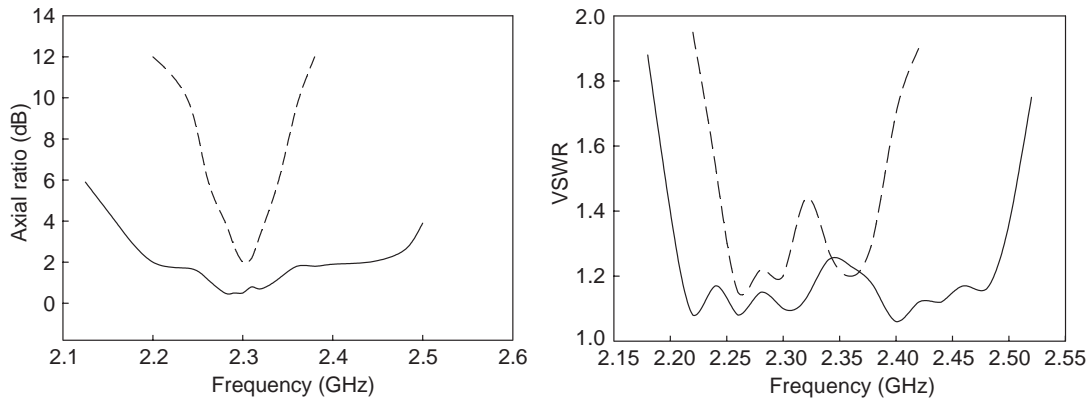


Figure 9. Performance of sequentially rotated arrays (----- conventional; - · - · - sequential); (eight elements, substrate height = 4 mm, $\epsilon_r = 2.26$).

through chip mass production or production of the complete array on a single wafer, which is possible at millimetric wavelengths. However to date no high-volume chips have been manufactured that adopt this approach. One of the reasons for this is the high dielectric constant of semiconducting substrates, which cause substantial wave trapping in the form of surface waves, which lead to the scan blindness phenomenon. This aspect of phased array design is discussed later in Section 3.3.

2.8. Conformal Arrays

Microstrip is an ideal medium in which to make conformal arrays as the radiating elements are relatively thin and the substrates can be formed in a variety of shapes [35–39]. Cylindrical arrays are relatively straightforward as the substrate can be easily bent around the cylinder. Conical arrays have also been made in this way.

Synthesis of the radiation pattern of conformal arrays is more difficult, and procedures vary with the geometry. More details are given in the Section 3.1.

2.9. Multiple-Beam Arrays

Many forms of beamformer lend themselves to printed circuit production methods and can thus be easily

integrated with microstrip arrays [40]. For example, Fig. 12 shows a Butler matrix designed to give four beams from the four-element patch array to which it is connected [41]. The Butler matrix is formed from a number of interconnected hybrid couplers, which present a set of excitations to the linear array that give rise to multiple beams; that is, the amplitudes are equal and the phase difference between elements is such to produce beams spaced in the plane of the array. The array in Fig. 11 consists of four microstrip patches. In principle, each element can assume any form, including linear arrays of patches of series-fed discontinuity arrays described earlier. This allows a two-dimensional array to be formed with a fan of pencil beams. Such a set of beams is ideal when coverage of a horizontal area in front of the array is needed; a radar antenna for collision avoidance is an example where the multiple beams deployed across the highway enable target discrimination to be achieved.

The Butler matrix forms, in general, a set of orthogonal beams, in which the beam spacing and sidelobe level are predetermined to minimize the coupling between the beams. The Blass matrix gives more flexibility and permits the shaping of beams and arbitrary sidelobe level and overlap to be obtained. However, power is lost in resistive terminations on the beamformer circuit.

Both of these beamformers are circuit-based and permit integration with a microstrip array in either coplanar (Fig. 12) or multilayer (Fig. 6) format. One configuration in which a Blass-like beamformer is integrated with a patch array is shown in Fig. 13 [42]. The radiating elements are series-connected patch arrays. Beneath each patch of each series array lies a feedline, and coupling between the feedlines is through the fringing fields. Between

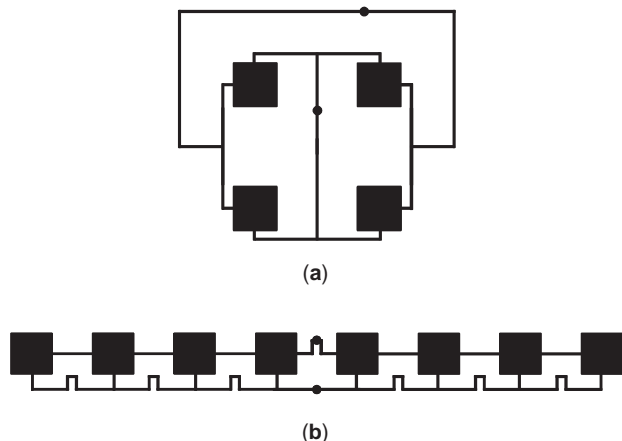


Figure 10. Examples of dual-polarized sequentially rotated arrays.

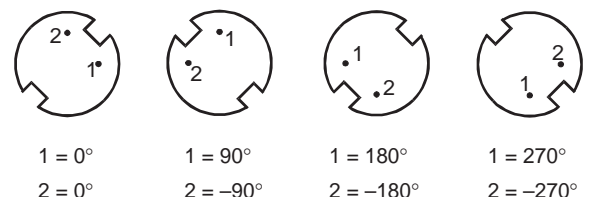


Figure 11. Sequential rotation for dual circularly polarized arrays.

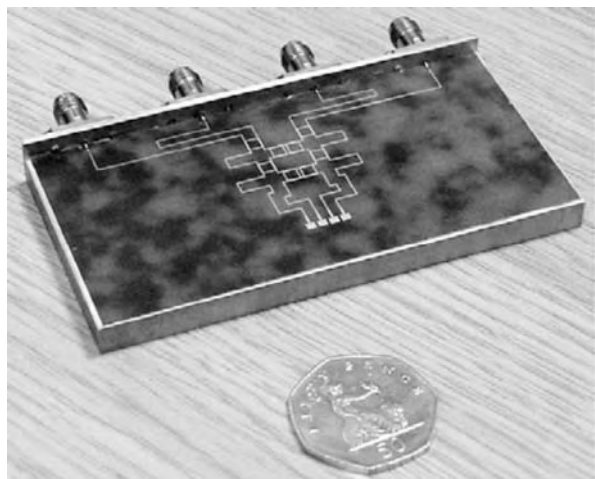


Figure 12. Printed circuit Butler matrix and patch array.

the coupling areas in the feedline are meandered line-lengths that set the phase shifts between elements. Each feed has a different meander length, and this excites a phase difference between the series-connected patch arrays proportional to the meander lengths of the other feeds. Each feed excites the whole array. A set of beams in the plane of the feedlines is created, with as many beams as there are feedlines. Coupling between the feedlines is minimized by the cancellation of the power coupled out of each series-connected array into the other feedlines, provided, of course, that an orthogonal beam set is excited. If the set is not orthogonal, then power will be absorbed in the matched terminations on the feedlines and the reflection coefficient seen at the input to the feedlines will be affected.

A circular conformal version of this multibeam array has been developed that is capable of creating a set of beams filling the azimuth plane of the array [43].

2.10. Reflectarrays

The microstrip reflectarray concept is illustrated in Fig. 14. It results in a reflector antenna whose reflector

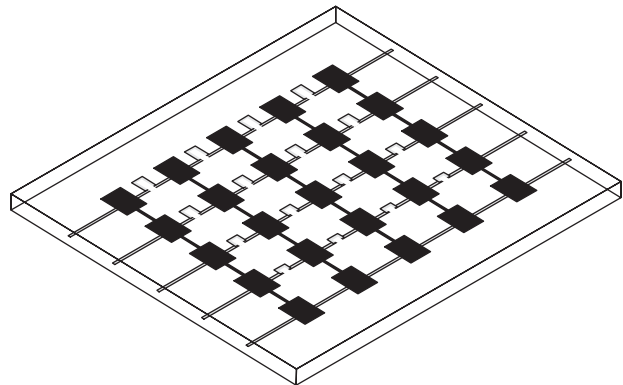


Figure 13. Microstrip multiple-beam array (typical dimensions for operation at 8.3 GHz with five beams, patch size = 11.8 × 5.9 mm, spacing along resonant arrays = 24.1 mm, spacing between resonant arrays = 18.75 mm, linewidths = 0.5 mm, substrate height, feed = 0.793 mm, patch = 1.586 mm, $\epsilon_r = 2.32$) [42].

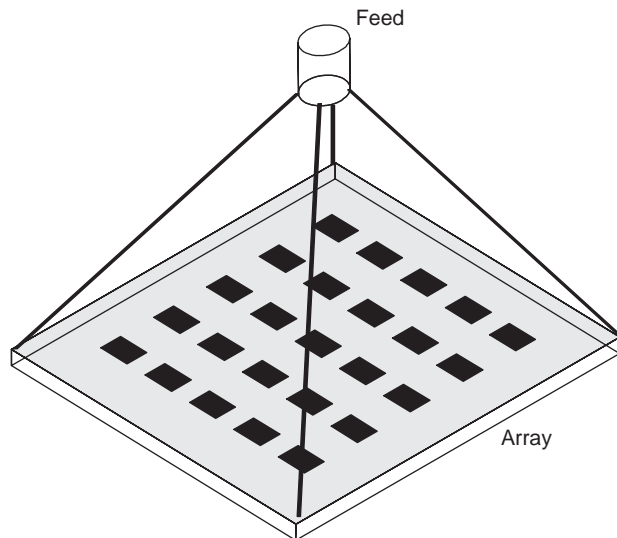


Figure 14. Microstrip reflectarray.

surface is flat and hence conformal, but whose bandwidth is much narrower than that of a conventional parabolic metal reflector [44,45].

The reflectarray works on the principle that the reflection phase of each element is appropriate for the production of a uniform phase front in the mainbeam direction. As the path length from the feed to the central element is different from the path length to the outer elements, the reflection phase of each element must vary from the center to the edge of the array. This reflection phase can be controlled in a number of ways [46,47]. Figure 15a shows how the patch size can be used. Figure 15b shows patches whose phase is controlled by a section of transmission line attached to the patch.

2.11. Active and Grid Arrays

The insertion of active devices into the radiating elements of microstrip arrays gives rise to a distinct class of array antennas known as *active integrated antennas*, with performance very different from that of conventional microstrip arrays. Several books and review papers have described design techniques and performance capabilities [5,48,49].

Microstrip antennas can be integrated either with an oscillating transistor or a power amplifier to form transmitting elements or with detecting diodes, downconversion mixers, or low-noise amplifiers to form receive

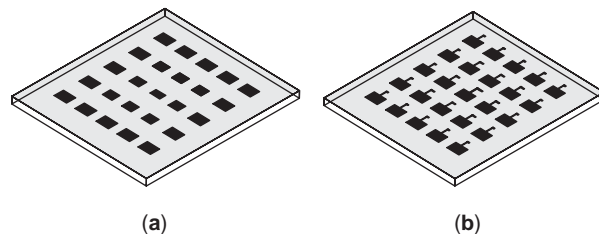


Figure 15. Microstrip reflectarray techniques: (a) size modulation; (b) tab length modulation.

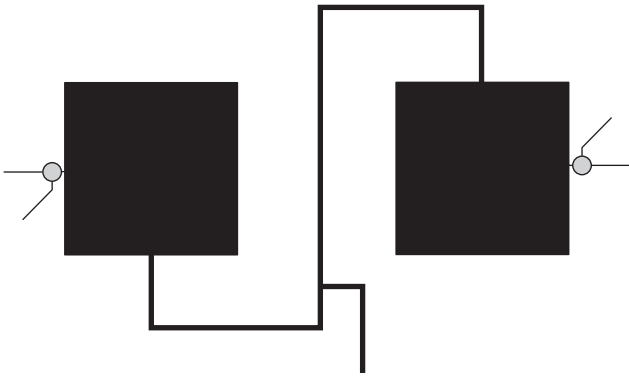


Figure 16. Microstrip duplex active integrated antenna array (typical dimensions for operation at 4.1 GHz, patch size = 24×24 mm, interconnecting linewidth = 1.55 mm, substrate height = 0.793 mm, $\epsilon_r = 2.32$, FET = atf26,884, FET stub width = 0.5 mm, lengths = 5, 19 mm) [50].

elements. Figure 15 shows examples of both classes. All of these can then be used to make active arrays.

Active arrays can be configured with conventional array spacing or very close spacing. Those with conventional spacing have been used to demonstrate the principles of such arrays, which include the integration of front-end functions with conventional beamforming. Close spacing has been used primarily in power combining arrays, where the motivation is to group together as many active elements as possible to create high powers.

Figure 16 shows an example of a conventionally spaced array that attempts to combine transmit and receive action with dual polarization [50]. The inclusion of active devices into antennas in general renders the resulting component nonreciprocal; that is, either transmit or receive. Most array examples are of one type or the other. In Fig. 16 a transmit power combining array is formed in the horizontal polarization by the use of two patch oscillators. The transistor and its source and gate loading lines can be seen attached to the outer edges of the two patches. Reception is in the vertical polarization where a low-noise amplifier and front end would normally be connected to the output port. The critical issue in duplex communication systems is the separation, or isolation, of the transmit and receive signals. This isolation determines the maximum transmit power and hence the range of the communication link. Isolation of around 25 dB is achieved by the use of orthogonal polarizations, and an additional 25 dB comes with sequential rotation in the receive-feed network. An 8×8 array of such elements could achieve a kilometer range. Active integrated transmit arrays also allow simple forms of beam scanning. The array of Fig. 16 can be phase-scanned if the free-running frequency of each patch oscillator is varied to form an appropriate phase front across the array. As the array is frequency-locked, each element continues to oscillate at a common frequency, while the radiated phase is determined by the difference between the (national) free-running frequency, controlled, for example, by the oscillator bias voltage, and the radiated frequency. Figure 17a shows this arrangement. Wide-angle scanning of a four-element array has been demonstrated using this technique [51].

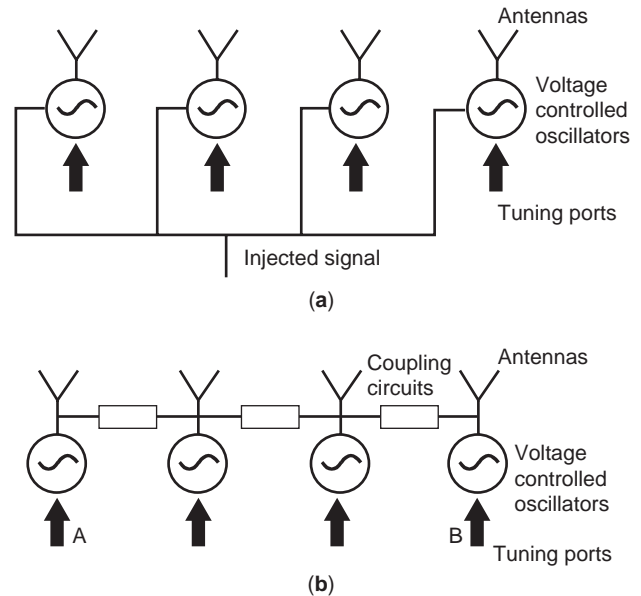


Figure 17. Active integrated antenna array configurations for beam scanning.

Figure 17b shows an arrangement of patch oscillators in which variation of the phase of the end elements gives rise to beam scanning [52]. The free-running frequencies of these elements can be controlled through their bias voltage, or by a varactor diode, through what is called the *tuning port*. All elements are locked to their neighbours through the mutual fringing fields, called *soft locking*, or through coupling circuits, called *hard locking*. A hard locking arrangement is shown. The end elements, A and B, are tuned in the opposite direction. This makes the phase of one increase while the other decreases. This phase difference is transmitted down the array and results in a linear phase front giving a well-controlled scanned beam. Scanning of two-dimensional arrays using this technique has proved harder to achieve.

Such scanning methods give rise to limitations in the maximum data rate that can be transmitted [53]. When data are applied by modulating the central element of a linear form of Fig. 17, the delays introduced by propagation of the locking signal along the array causes signal distortions. Frequency shift keying at rates of around 40 Mbps (million bits per second) have been shown to introduce significant amounts of amplitude modulation into the otherwise frequency modulation for a four-element array. Modulation of all array elements overcomes this problem, but increases the complexity of the array.

3. DESIGN ISSUES

3.1. Pattern Synthesis

Synthesis of the radiation pattern shape of microstrip linear arrays follows the fundamental methods defined for general arrays [54]. In principle, a uniform phase front is initially specified to produce a beam in the desired direction, and then beamwidth and sidelobe level are controlled by the array length and amplitude distribution.

For planar two-dimensional arrays, this technique is applied in each principal plane. For two-dimension conformal arrays, such as the cylinder or cone, such separation of the distributions in the principal planes is not possible, and more complicated synthesis procedure are necessary [35].

If the linear array is series-fed, then the synthesis procedure is modified to take account of the reducing power down the array as a proportion of it is coupled to radiation at each element [55]. While the techniques described above form the basis of synthesis, there are limits to the performance achievable. In particular, the sidelobe level is limited by manufacturing tolerances. While these have been quantified for general arrays [56], a specific study has shown that in patch arrays it is the precision with which the patch resonant frequency can be defined that sets the lower limit to sidelobe performance. Variations in the size of the patch, which affect the resonant frequency, are caused by variations in the photoetching process. The variations are the order of the thickness of the copper cladding on the substrate. These variations give rise to errors in the phase of the radiated signal, which degrade

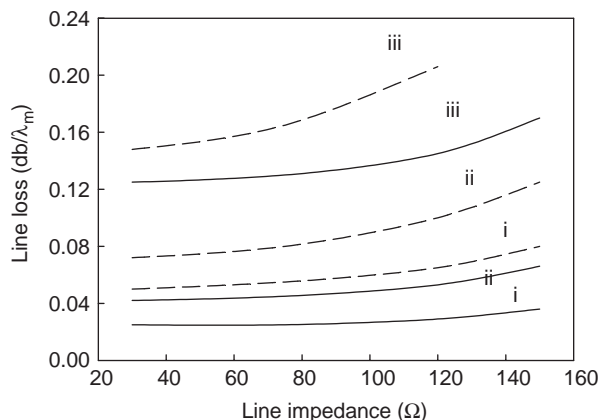
sidelobe level. This effect is more pronounced as the frequency increases but can be made more manageable by using thinner copper cladding. The study showed that a lower sidelobe level of around 30 dB could be achieved in practice without special measures.

3.2. Feed Loss and Radiation

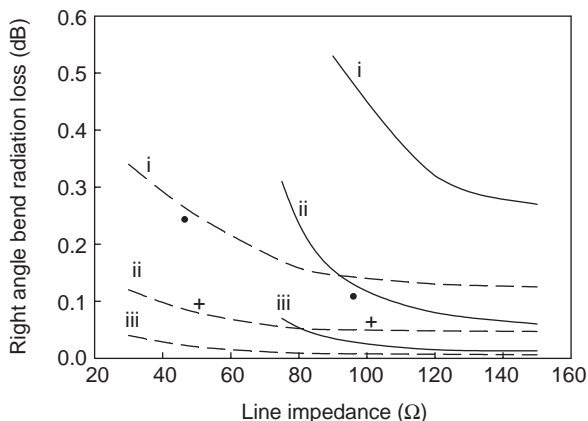
In large microstrip arrays, losses in the feed network limit the maximum achievable gain [57,58]. There are two sources of such loss: (1) the resistive losses in the dielectric substrate and metallic conductors give rise to loss; and (2) if a coplanar feed is used, then radiation loss can become significant, which can, in addition to limiting gain, significantly compromise the radiation pattern control.

Figure 18a shows calculated microstrip line loss for various substrates typically used in arrays and a variety of line impedances. It can be seen that line loss increases with increasing dielectric constant and impedance and reducing substrate thickness. Although typically less than 0.2 dB/line wavelength, this can be significant for arrays many wavelengths in size. Figure 18b illustrates typical radiation levels. Radiation loss from a right-angle bend is given and is seen to reduce with increasing dielectric constant and impedance and reducing substrate thickness. Again, while less than 0.5 dB per bend, a large corporate feed will have many bends, and splitters and radiation loss can be substantial.

For large microstrip arrays, these losses can become substantial. For example, for a substrate with thickness $h/\lambda = 0.06$ and $\epsilon_r = 2.32$, total losses of the order of 4 dB may occur for an array size of 16 elements and up to 10 dB for 256 elements. A similar situation occurs for $\epsilon_r = 1.06$ representing foam- or air-spaced substrates. These losses limit the array gain as shown in Fig. 19. As the array size is increased, two things happen: (1) the array gain increases because of the increasing aperture size; (2) however, for arrays of 10 wavelengths square and greater, this gain increase is offset by significant loss. Eventually this



(a)



(b)

Figure 18. Losses in microstrip arrays: (a) calculated line loss; (b) calculated radiation loss from right-angle bend (----- $\epsilon_r = 1.0$; --- $\epsilon_r = 2.32$); curves (i) $h/\lambda = 0.06$, (ii) $h/\lambda = 0.03$, (iii) $h/\lambda = 0.01$; smooth 90° bend, $\epsilon_r = 2.32$, $h/\lambda = 0.06$; bend radius, ● $\rho = 0.2\lambda_0$; + $\rho = 0.4\lambda_0$ [57].

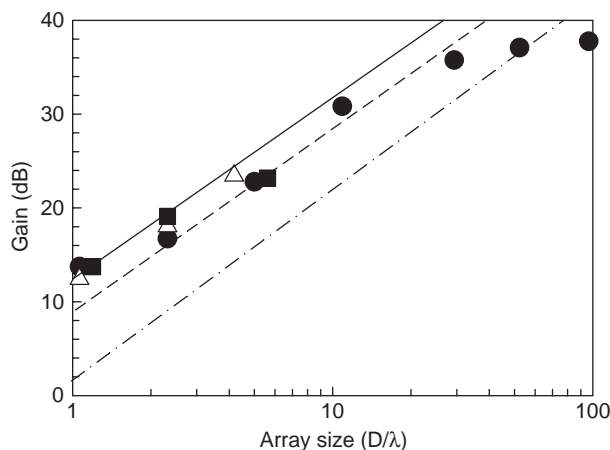
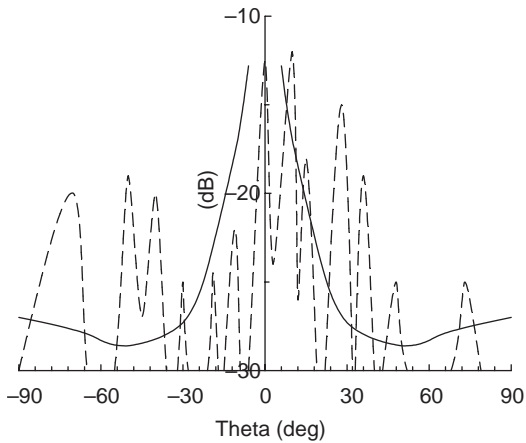
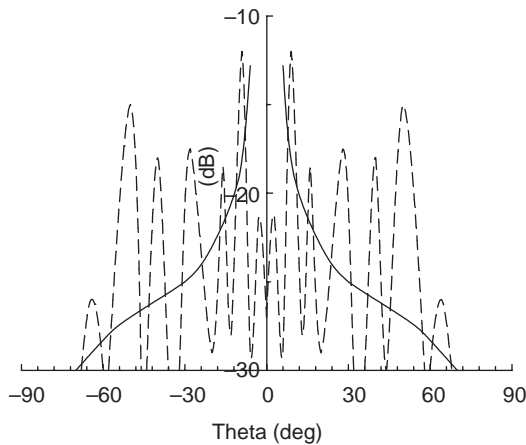


Figure 19. Microstrip array gain (efficiency—solid line = 100%, dotted line = 50%, dotted-dashed line = 10%); ● calculated, ■ measured, feed impedance 120 Ω, Δ measured feed impedance 200 Ω; $h/\lambda = 0.06$, $\epsilon_r = 2.1$) [57].



(a)



(b)

Figure 20. Calculated radiation pattern of 16×16 -element patch array (---- sidelobe envelope of patches): *E* plane—copolarized feed pattern; *H* plane—cross-polarized feed pattern [57].

increase in loss becomes greater than the increase in gain and a maximum of gain of around 35 dBi occurs.

Feed radiation also affects the radiation pattern. Figure 20 shows calculated radiation patterns for 16×16 patch arrays. The solid line is the envelope of sidelobe peaks from the patch radiators for a uniform amplitude and phase aperture distribution. The dotted lines show sidelobes, due to the feed radiation, that are significantly higher than those due to the patches.

3.3. Mutual Coupling

Mutual coupling between the radiating elements in arrays is a significant factor that both perturbs the aperture distribution and affects the input impedance of the elements. Figure 21 shows the mutual coupling between microstrip patch elements [59]. It is seen that a coupling in the *E* plane is stronger than in the *H* plane, and for $\epsilon_r = 2.55$ and spacing of $> 0.25\lambda_0$, as typically used in fixed-beam arrays, it is less than -20 dB.

In scanning arrays, the position is more complicated and in some cases, mutual coupling leads to undesirable

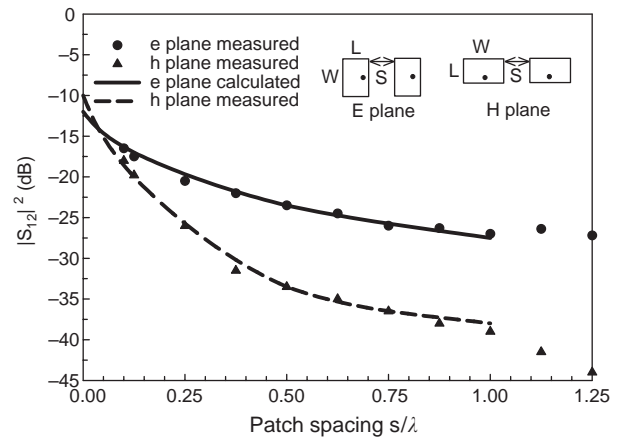
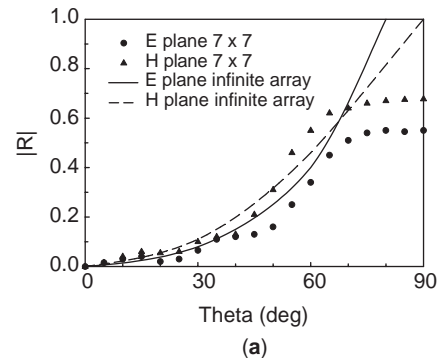
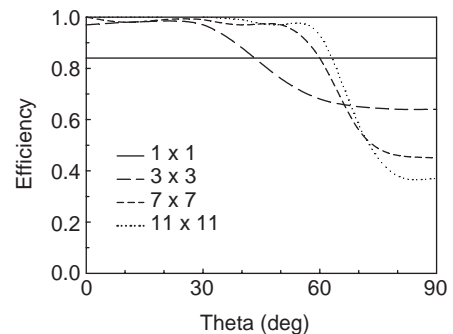


Figure 21. Mutual coupling between coaxially fed microstrip patches (---- calculated, ● measured; $W = 10.57$ cm, $L = 6.55$ cm, $d = 0.1588$ cm, $\epsilon_r = 2.55$, $f = 1.41$ GHz) [59].

blindness problems. Such effects are difficult to both measure and compute. The performance of patch elements in infinite arrays has been computed by the method of moments and Floquet mode theory and latterly by the finite-element method. Figures 22 and 23 show computed results for rectangular patches in finite arrays [60,61]. Figure 22a shows the input reflection coefficient of the center element of various size arrays or $\epsilon_r = 2.55$ substrate against scan angle. It can be seen that mutual coupling



(a)



(b)

Figure 22. Calculated performance of microstrip patches in arrays: (a) reflection coefficient magnitude versus scan angle; (b) efficiency of finite patch array versus *E*-plane scan angle ($\epsilon_r = 2.55$, substrate thickness $d = 0.04\lambda_0$, patch size $L = W = 0.3\lambda_0$, patch spacing $a = b = 0.5\lambda_0$, feed position $X = -L/2$, $Y = 0$) [61].

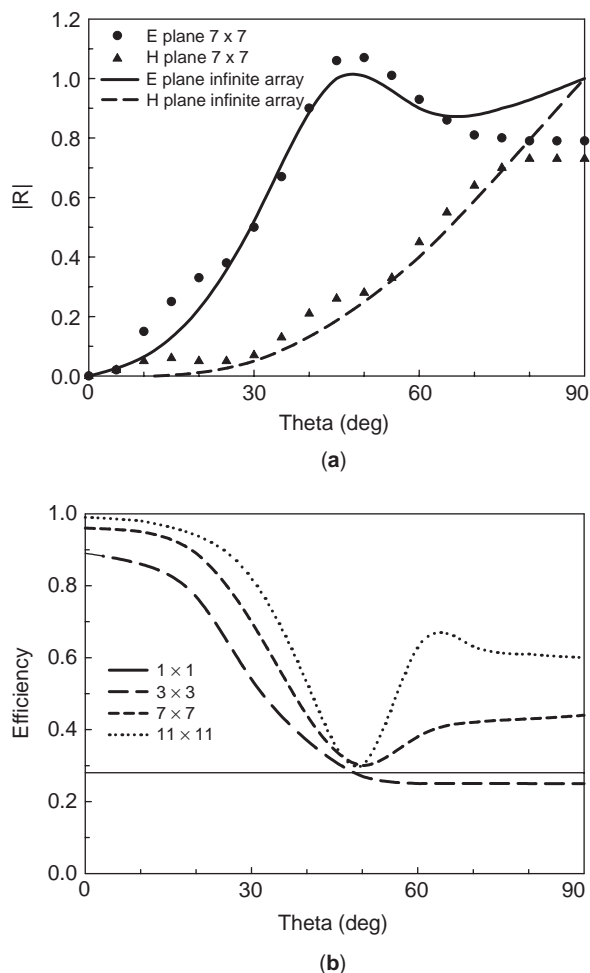


Figure 23. Calculated performance of microstrip patches in arrays: (a) reflection coefficient magnitude versus scan angle; (b) efficiency of finite patch array versus E -plane scan angle ($\epsilon_r = 12.8$, substrate thickness $d = 0.06\lambda_0$, patch size $L = 0.107\lambda_0$, $W = 0.15\lambda_0$, patch spacing $a = b = 0.5\lambda_0$, feed position $X = -L/2$, $Y = 0$) [61].

causes the reflection coefficient to increase with scan angle for both E - and H -plane scans. Results are similar to those for the infinite array case for scan angles ranging from 0° to 60° . The effect of this change in reflection coefficient is to reduce array efficiency at large scan angles, and this effect is worse for large arrays (Fig. 22b). In practice, some phased arrays incorporate circulators between the transmitter and the radiating element to absorb this reflected power. Others incorporate active matching, but this is a complicated and expensive solution.

Mutual coupling increases as the dielectric constant increases (Fig. 23). The attempts to integrate microstrip patch arrays onto semiconducting substrates led to similar computations for patch arrays on substrates with $\epsilon_r = 12.8$. While H -plane scanning performance (Fig. 23a) is similar to that on low-dielectric-constant substrates, E -plane scanning shows that the reflection coefficient becomes greater than 1.0 at scan angles near 40° . This is a classical scan blindness condition in which it is impossible to radiate power as the element is highly

mismatched. The fact that the reflection coefficient is greater than 1.0 does not violate the principle of energy conservation. The result is for one element of the array only. Other elements will have reflection coefficient less than 1.0 to achieve a power balance. At this blind angle, array efficiency is, of course, very low, as shown in Fig. 23b.

Similar computations have also been done for other types of patches, including circular patches [62], one- and two-probe-fed circular patches [63], and proximity coupled patches [64].

BIBLIOGRAPHY

1. J. R. James, P. S. Hall, and C. Wood, *Microstrip Antenna Theory and Design*, Peter Perigrinus, IEE, London, 1981.
2. J. R. James and P. S. Hall, eds., *Handbook of Microstrip Antennas*, Peter Perigrinus, IEE, London, 1989.
3. D. M. Pozar and D. H. Schaubert, eds., *Microstrip Antennas*, IEEE Press, selected reprint volume, New York, 1995.
4. K. F. Lee and W. Chen, eds., *Advances in Microstrip and Printed Antennas*, Wiley, New York, 1997.
5. K. C. Gupta and P. S. Hall, eds., *Analysis and Design of Integrated Circuit Antenna Modules*, Wiley Series in Microwave and Optical Engineering, Wiley, New York, 2000.
6. Ref. 1, pp. 116, 161.
7. P. S. Hall and J. R. James, Design of microstrip antenna feeds—Part 2: Design and performance limitations of triplate corporate feeds, *Proc. IEE* **128**(Part H):26–34 (1981).
8. J. C. Williams, Cross fed printed aerials, *Proc. 7th European Microwave Conf.*, Copenhagen, 1977, pp. 292–296.
9. A. G. Derneryd, Linearly polarised microstrip antennas, *IEEE Trans. Anten. Propag.* **AP-24**:846–851 (1976).
10. M. Tiuri, J. Henriksson, and S. Tallquist, Printed circuit radio link antenna, *Proc. 6th European Microwave Conf.*, Rome, 1976, pp. 280–282.
11. R. Hill, Printed planar resonant arrays, *Proc. IEE Int. Conf. Antennas and Propagation*, York, 1987, pp. 473–476.
12. J. R. James and P. S. Hall, Microstrip antennas and arrays; Part 2—new array design technique, *IEE J. Microwaves Optics Acoustics*, **1**(5):175–180 (Sept. 1977).
13. E. R. Cashen, R. Frost, and D. E. Young, *Improvement Relating to Aerial Arrangements*, British Provisional Patent (EMI Ltd.) Specification, 1294024.
14. T. Metzler, Microstrip series arrays, *IEEE Trans. Anten. Propag.* **AP-29**:174–178 (1981).
15. P. S. Hall, Microstrip linear array with polarisation control, *Proc. IEE* **103**(Part H):215–224 (1983).
16. G. von Trentini, Flachantenna mit periodisch gebogenem leiter, *Frequenz* **14**:230–243 (1960).
17. D. J. Skidmore and G. Morris, Design and performance of covered microstrip serpent antennas, *Proc. IEE Int. Conf. Antennas and Propagation*, Norwich, 1983, pp. 295–300.
18. S. Nishimura, K. Nakano, and T. Makimoto, Franklin type microstrip line antenna, *Proc. IEEE AP-S Symp.*, Seattle, 1979, pp. 134–137.
19. J. Henriksson, K. Markus, and M. Tiuri, Circularly polarised travelling wave chain antenna, *Proc. 9th European Microwave Conf.*, Brighton, 1979.
20. W. Menzel, New travelling wave antenna in microstrip, *Proc. 8th European Microwave Conf.*, Paris, 1978, pp. 302–306.

21. P. W. Chen, C. S. Lee, and V. Nalbandian, Planar double layer leaky wave microstrip antenna, *IEEE Trans.* **AP-50**(6):832–835 (June 2002).
22. P. S. Hall, Multi-octave bandwidth log periodic microstrip array antenna, *Proc. IEE* **133**(Part H) (2):127–137 (April 1986).
23. H. Pues, J. Bogaers, R. Pieck, and A. Van de Capelle, Wide-band quasi-log-periodic microstrip antenna, *Proc. IEE* **128**(Part H) (3):159–163 (1981).
24. P. S. Hall and A. Sparrow, Microstrip log periodic antenna array with end-ire beam, *Electron. Lett.* **23**(17):912–913 (Aug. 13, 1987).
25. J.-F. Zurcher, The SSFIP—a global concept for high performance broadband planar antennas, *Electron. Lett.* **24**(23):1433–1435 (Nov. 1988).
26. H. Legay and L. Shafai, New stacked microstrip antenna with large bandwidth and high gain, *IEE Proc. Microwave Anten. Propag.* **141**(3):199–204 (1994).
27. F. Croq and D. M. Pozar, Millimeter wave design of wide band aperture coupled stacked microstrip antennas, *IEEE Trans. Anten. Propag.* **AP-39**(12):1770–1776 (Dec. 1991).
28. J. C. MacKinchin, P. A. Miller, M. R. Straker, and J. S. Dahele, A wide bandwidth microstrip subarray for array applications using aperture coupling, *IEEE Antennas and Propagation Society Int. Symp. AP-S Digest*, 1989, pp. 878–881.
29. P. S. Hall, J. S. Dahele, and J. R. James, Design principles of sequentially fed wide bandwidth circularly polarised microstrip antennas, *Proc. IEE* **136**(Part H) (5):381–389 (Oct. 1989).
30. P. S. Hall, Application of sequential feeding to wide bandwidth circularly polarised microstrip patch arrays, *Proc. IEE* **136**(Part H)(5):390–398 (Oct. 1989).
31. P. S. Hall, Dual polarisation antenna arrays with sequentially rotated feeding, *Proc. IEE* **139**(Part H) (5):465–471 (Oct. 1992).
32. M. S. Smith and P. S. Hall, Analysis of radiation pattern effects in sequentially rotated arrays, *IEE Proc. Microwave Anten. Propag.* **141**(4):313–320 (Aug. 1994).
33. P. S. Hall and M. S. Smith, Sequentially rotated arrays with reduced sidelobe levels, *IEE Proc. Microwave Anten. Propag.* **141**(4):321–325 (Aug. 1994).
34. J. J. Schuss, et al., Design of the iridium phased array antennas, *Proc. IEEE AP-S Int. Symp., Ann Arbor*, 1993, pp. 218–221.
35. R. C. Hansen, *Conformal Antenna Array Design Handbook*, AD A110091, Jan, 1982.
36. R. E. Munson, Conformal microstrip antennas and microstrip phased arrays, *IEEE Trans. Anten. Propag.* **74**–79 (Jan. 1974).
37. K. R. Jacobsen, Radiation from microstrip antennas mounted on two dimensional objects, *IEEE Trans. Anten. Propag.* **AP-32**:1255–1259 (1984).
38. G. G. Sanford, Conformal microstrip phased array for aircraft tests with ATS-6, *IEEE Trans. Anten. Propag.* **AP-26**:642–646 (1978).
39. Ref. 2, pp. 1153–1191, 1227–1256.
40. A. R. Mishra, K. K. Sood, and A. Kumar, Cavity backed microstrip patch array feed for multiple beam applications, *Electron. Lett.* **34**(1):4–6 (Jan. 8, 1998).
41. B. P. Pirollo, E. Okon, R. A. Lewis, P. Gardner, G. Ma, L. Piel, L. Flamini, P. S. Hall, and K. Davies, Millimetric technologies for future vehicle communications, *Proc. Int. Conf. Microwaves and Millimeter-Wave Technology*, Beijing, Aug 2002, pp. 1–6.
42. P. S. Hall and S. J. Vetterlein, Integrated multiple beam microstrip array, *Microwave J.* **35**(1) (Jan. 1992).
43. P. S. Hall and S. J. Vetterlein, Advances in microstrip multiple beam arrays, *Proc. 7th IEE Conf. Antennas and Propagation*, York, April 1991, pp. 129–132.
44. J. Huang, Microstrip reflectarray, *Proc. IEEE AP-S Int. Symp.*, London, Ontario, June 1991, pp. 612–615.
45. Y. Zhuang, J. Litva, C. Wu, and K.-L. Wu, Modelling studies of microstrip reflectarrays, *IEE Proc. Microwaves Anten. Propag.* **142**(1) (Feb. 1995).
46. T. A. Metzler, Stub loaded microstrip reflectarrays, *IEEE Antennas and Propagation Society Int. Symp., AP-S Digest*, 1995, Vol. 1, pp. 18–23.
47. J. Huang and R. J. Pogorzelski, A Ka band reflectarray with elements having variable rotation angles, *IEEE Trans. Anten. Propag.* **AP-46**:650–656 (May 1998).
48. A. Mortazawi, T. Itoh, and J. Harvey, eds., *Active Antennas and Quasi-optical Arrays*, IEEE Press, 1999.
49. K. Chang, R. A. York, P. S. Hall, and T. Itoh, Active integrated antennas, *IEEE Trans. Microwave Theory Tech.* (50th anniversary issue) **50**(3):937–944 (March 2002) (invited paper).
50. M. J. Cryan, P. S. Hall, K. S. H. Tsang, and J. Sha, Integrated active antenna with full duplex operation, *IEEE Trans. Microwave Theory Tech.* **MTT-45**(10):1742–1748 (Oct. 1997).
51. I. L. Morrow, P. S. Hall, and J. R. James, Measurement and modelling of a microwave active patch phased array for wide angle scanning, *IEEE Trans. Anten. Propag.* **AP-45**(2):297–304 (Feb. 1997).
52. P. Liao and R. A. York, A new phase-shifterless beam scanning technique using arrays of coupled oscillators, *IEEE Trans. Microwave Theory Tech.* **MTT-41**(10):1810–1815 (Oct. 1993).
53. C. Kykkotis, P. S. Hall, and H. Ghafouri-Shiraz, Performance of active antenna oscillator arrays under modulation for communication systems, *IEE Proc. Microwaves Anten. Propag.* **145**(4):313–320 (Aug. 1998).
54. J. D. Kraus and R. J. Marhefka, *Antennas For All Applications*, 3rd ed., McGraw-Hill, 2002, pp. 90–164.
55. B. B. Jones, F. Y. M. Chow, and A. W. Seeto, The synthesis of shaped patterns with series-fed microstrip patch arrays, *IEEE Trans. Anten. Propag.* **AP-30**(6):1206–1212 (Nov. 1982).
56. D. M. Pozar and B. Kaufman, Design considerations for low sidelobe microstrip arrays, *IEEE Trans. Anten. Propag.* **AP-38**(8):1176–1185 (Aug. 1990).
57. P. S. Hall and C. M. Hall, Coplanar corporate feed effects in microstrip patch array design, *Proc. IEE* **135**(Part H) (3):180–186 (June 1988).
58. E. Levine, G. Malamud, S. Shtrikman, and D. Treves, A study of microstrip array antennas with the feed network, *IEEE Trans. Anten. Propag.* **AP-37**(4):426–434 (April 1989).
59. D. M. Pozar, Input impedance and mutual coupling of rectangular microstrip antennas, *IEEE Trans. Anten. Propag.* **AP-30**(6):1191–1196 (Nov. 1982).
60. D. M. Pozar, Finite phased arrays of rectangular microstrip patches, *IEEE Trans. Anten. Propag.* **AP-34**(5):658–665 (May 1986).
61. D. M. Pozar, Scanning characteristics of infinite arrays of printed antenna sub-arrays, *IEEE Trans. Anten. Propag.* **AP-40**(6):666–674 (June 1992).
62. K. Solbach, Phased array simulation using circular patch radiators, *IEEE Trans. Anten. Propag.* **AP-34**(8):1053–1058 (Aug. 1986).

63. J. T. Aberle and D. M. Pozar, Analysis of infinite arrays of one- and two-probe-fed circular patches, *IEEE Trans. Anten. Propag.* **AP-38**(4):421–432 (April 1990).
64. J. S. Herd, Modelling of wideband proximity coupled microstrip array elements, *Electron. Lett.* **26**:1282–1284 (Aug. 1990).

MICROSTRIP ANTENNAS

HOTON HOW
 Hotech, Inc.
 Belmont, Massachusetts

Microstrip circuitry consists of a metal strip or patch on a dielectric substrate backed by a metal ground plane. Microstrip antennas are finding increasing popularity owing to their advantages in size, cost, conformity to the supporting structure, low profile, and ease of fabrication. By using simple etching techniques it is possible to fabricate a wide variety of microstrip circuits including antenna arrays, feeding networks, and active devices such that preamps (preamplifiers) or distributed transmitters can be conveniently placed next to the antenna elements. In addition, diode phase shifter circuits can also be etched on the substrate to form single-board phased arrays. This article describes the microwave properties of patch antennas.

The lateral dimensions of microstrip patch antennas are large in comparison with the width of conventional microstrip lines. The main purpose of a patch antenna is to confine microwave energy within a compact region with a dimension compatible to the wavelength. Such confinement can be achieved via the resonant behavior of a finite guiding structure supporting propagation waves. As a consequence, electromagnetic energy radiates away from that part of the patch resonator that is open to free space, or the periphery of the patch antenna, in a manner similar to a slot opening cut along the side of a waveguide. In order to continuously radiate microwave energy, the patch needs to be electrically connected to a "feeder line." When the characteristic impedance of the feeder line matches the impedance of radiation waves, power is thus dumped into the confined space of the patch resonator without causing much reflection. This means that all the input microwave power delivered to the patch antenna is radiated away into free space.

At resonance electromagnetic excitations reinforce within the confined space of the patch antenna, attaining high intensity far exceeding than at the feeder-line region. Thus, radiation from the feeder line, or from a regular microstrip transmission line of the same length, is insignificant in comparison to a microstrip antenna driven at resonance. In microstrip circuitry power also radiates from open/short circuits and from discontinuities, such as corners. However, the radiated power is relatively small, since the radiation impedances there are normally very different from the characteristic impedance of the

microstrip transmission line encompassing these discontinuities.

This article introduces two calculational methods capable of quantitatively describing antenna performance. The first method, the so-called resonant cavity model, is less rigorous, but nevertheless has the advantage of being more analytical and, hence, can be applied with ease. For the cavity model perfect metal boundaries are assumed at the metal patch and at the ground-plane positions, and magnetic wall boundary conditions are assumed at the periphery, or at the sidewall position of the patch antenna. Due to fringe-field penetration, magnetic walls are located slightly beyond the boundary contour of the patch geometry. This fringe-field effect can thus be accounted for by considering the patch to fictitiously possess a boundary whose dimension extends outward by a distance consistent with the spatial extent of the fringe fields. Radiation and material imperfections are then considered as perturbations to a lossless cavity. In this manner, engineering parameters of the microstrip patch antenna, such as the resonant frequency, far-field radiation pattern, input impedance, radiation linewidth, directivity, and efficiency, are all calculable.

Although simple and straightforward, the drawback of the aforementioned analysis is that surface waves can hardly be accommodated by the cavity model, even if one is attempted in a perturbative manner. The reason for this limitation is that, unlike spatial waves, surface waves lack in closed-form expressions, and hence their existence is inconsistent with the nature of the cavity model, which requires calculations to be carried out analytically. Surface waves are identified as simple poles appearing in the integrand of a spectrum-domain analysis characteristic of the guiding structure of a microwave circuit supporting electromagnetic wave propagation along the lateral directions. Analogous to spatial radiation waves, while the asymptotic behaviors of surface waves can be readily deduced in analytic forms in the far-field zone, surface waves can hardly be accessed analytically in the near field, since the decomposition of currents into multipole expansions adopted by a conventional spatial-wave analysis is not available, rendering the failure for cavity-mode analysis. For this reason, the cavity model is considered inappropriate for a microstrip structure involving a thick substrate, or if the dielectric constant of the substrate is large, because it is known that under these conditions excitation of surface waves is significant.

The second calculational method concerns the Green function analysis. In general a Green function is defined as the solution of a (linear) differential/integral equation resulting from a (delta-function-like) point source satisfying the imposed (homogeneous) boundary conditions. Thus, under an arbitrary source excitation, the solution of the equation can be composed of a superposition of the Green functions, still satisfying the boundary conditions of the structure. In the presence of a point (dipole) current source in association with the geometry of a stratified structure consisting of dielectric/magnetic layers, the excited electromagnetic field is termed the *Green function dyad*, due to the vectorial nature of the source field and the observer field. The construction of dyadic Green

functions of a microstrip circuit is straightforward, and this article emphasizes its physical meanings and interpretations, as appearing in the original work by Sommerfeld [1].

Sommerfeld solved for the first time the Green functions associated with a horizontal point dipole and a vertical point dipole in the presence of a semiinfinite conductor half-space, our planet Earth [1]. Radiowaves are therefore radiated into free space either directly from the point dipole source or indirectly from the image dipole source induced by the (imperfect) ground plane, the Earth surface. They are called *spatial* (radiation) *waves*, because they exhibit a $1/r$ spatial dependence, where r denotes the distance from the original/image source point to the observer point. In addition, Sommerfeld also showed a second kind of radiation field that is tied to the air–Earth interface exhibiting a $1/\sqrt{\rho}$ dependence, where ρ denotes the 2D distance between the source point projected on the Earth surface to the observer point located also on the Earth surface [1]. These are called *surface waves* because they decay exponentially when departing away from the air–Earth interface. This article explains how the spatial-wave and the surface-wave solutions arrive in association with a (horizontal) point dipole source in the presence of a layered dielectric/magnetic structure.

By using the dyadic Green functions, one can then formulate the general field solution in a stratified structure excited by (external) current sources in terms of an integral equation, which is subsequently solved by applying the numerical (Galerkin) method. The external current sources are expressed in the form of surface conductor inhomogeneities appearing at the microstrip patch location. This article outlines procedures to calculate the engineering parameters of a microstrip antenna of an arbitrary geometry, and it illustrates calculational results on circular microstrip antennas, showing plots in radiation frequencies, bandwidths, far-field patterns, input impedances, effects in feeder-line positions, and interference between antennas. The dyadic Green functions involving anisotropic/gyromagnetic materials are introduced in Section 3, where the transfer matrix technique is explained. A transfer matrix translates the tangential components of the electromagnetic field over one layer of a stratified structure satisfying the boundary conditions therein. More recent developments on printed circuit antennas are reviewed in Section 4, including the important broadband techniques employing stacked parasitic elements to achieve high gain and low cross-polarization level. Fractal antennas involving a patch geometry exhibiting a fractional dimension are introduced in Section 5. More sophisticated treatments on microstrip antennas may be found in Ref. 2.

1. CAVITY MODEL

1.1. Introduction

A microstrip patch antenna is a narrowband device, and the bandwidth covers typically about 5% of the center radiation frequency. When the bandwidth Δf can be related

to the quality factor Q of a resonator, then

$$Q = 2\pi f \left(\frac{\text{maximum stored energy}}{\text{averaged power dissipation}} \right) = \frac{f}{\Delta f} \quad (1)$$

which implies that power dissipation is not significant and the circuit of a microstrip patch antenna can be approximated as a low-loss cavity resonator. This suggests that the performance of a microstrip patch antenna can be analyzed using a perturbation method; that is, the zeroth-order solution of the antenna is described in terms of the eigenmodes, or normal modes, of a lossless cavity. Losses are then added to the analysis as first-order perturbations, including conductor loss, dielectric loss, and radiation loss. Magnetic loss can also be included if ferrites are used as the substrate material.

Dissimilar to radiation loss, surface-wave loss can hardly be treated as perturbations in the cavity model. Radiation and surface waves represent leaky waves from the antenna; the former leaks directly from air and the latter, from the guided structure of the air–substrate interface. Surface waves lack analytic expressions and are not compatible with the closed-form representation of cavity modes. Surface-wave modes are identified as being associated with simple poles appearing in the integrand of a spectrum-domain analysis characteristic of the guiding structure of surface discontinuities in the circuit geometry. Surface-wave modes are readily included with a full-wave analysis, as discussed in the following section, introducing Green’s function formulation.

In contrast, the cavity model is easy to apply, allowing engineering parameters of a microstrip patch antenna to be calculated analytically, including bandwidth, input impedance, radiation efficiency, and near-field/far-field radiation patterns. Furthermore, the physical meaning of normal modes is evident in the cavity model. For example, the left/right-hand polarized radiations from a microstrip ferrite patch antenna can be readily calculated by using the cavity model. However, the cavity model will provide satisfactory calculations only if surface-wave loss is insignificant. Surface-wave loss is not important for a thin substrate exhibiting low dielectric constant, but not for a thick substrate with high dielectric constant. Also, the cavity model fails to describe the coupling effects between microstrip circuits placed close to each other. For these complex situations a full-wave analysis is needed, and the cavity model is too simple to be applicable. The full-wave analysis involving the use of dyadic Green’s functions is discussed in Section 2.

1.2. Resonant Frequency

Let a metal patch be deposited on top of a dielectric substrate backed by a ground plane. The patch geometry considered in this section is either rectangular or circular. Only dielectric substrates are considered in this section. Formulation of cavity normal modes for patch antennas fabricated on ferrite substrates can be found in Ref. 3. In the cavity model one assumes a lossless substrate in which the cavity is formed that is bounded by either electric or magnetic walls. The metal surfaces of the microstrip patch

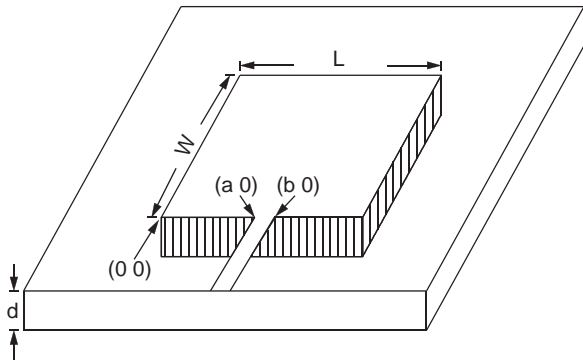


Figure 1. Feeding the rectangular patch antenna by a microstrip line. The resonant cavity is located directly under the patch bound by a magnetic wall shown shaded in the figure.

and the ground plane are approximated as perfect conductors, or electric walls, and the peripheral surface surrounding the antenna cavity directly under the patch boundary is a magnetic wall. This is illustrated in Fig. 1, in which a rectangular microstrip patch antenna is modeled as a resonator cavity with its periphery shown shaded as a magnetic wall. An electric wall is defined so that the tangential component of the electric field vanishes at the wall surface, and a magnetic wall is defined so that the tangential component of the magnetic field vanishes at the wall surface. Thus, a normal metal surface approaches an electrical wall if the value of conductivity goes to infinity. A magnetic wall imposes fictitious boundary conditions that insulate the inside of the cavity from the outside, allowing no electromagnetic energy to exchange across it.

The active volume of the cavity is slightly exceeds that implied by the physical dimension of the patch geometry, since fringe fields are excited at the periphery of the antenna. Therefore, the effective volume of the cavity consists of both regions directly under the patch pattern and its surrounding containing the fringe field. It is shown in Fig. 2 that the effective radius of the cavity is larger than that of the metal patch of the microstrip antenna. Thus,

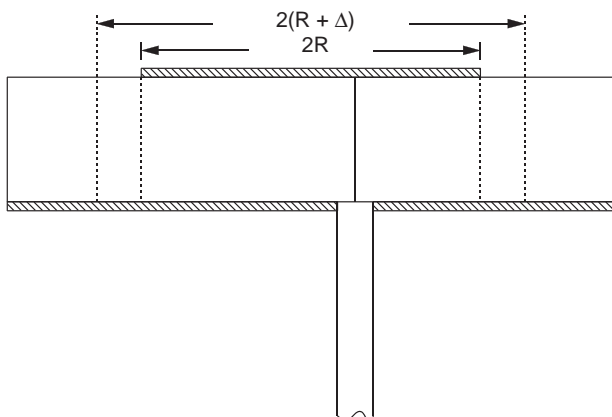


Figure 2. Feeding the circular patch antenna by a coaxial line. Because of the fringe-field effect, the effective radius of the resonator is larger than the resonator’s physical value.

the resonant length along the side of a rectangular patch antenna, denoted as $L' = L + 2\Delta$, is larger than the physical length L and the effective increment in length due to the fringe-field effect is 2Δ with [4]

$$\frac{\Delta}{d} = 0.412 \left(\frac{\epsilon_{\text{eff}} + 0.300}{\epsilon_{\text{eff}} - 0.258} \right) \left(\frac{L/d + 0.262}{L/d + 0.813} \right) \quad (2)$$

where d is the thickness of the substrate, ϵ_{eff} denotes the effective dielectric constant of the patch cavity given by [5]

$$\epsilon_{\text{eff}} = \frac{\epsilon_r + 1}{2} + \frac{\epsilon_r - 1}{2} \left(1 + \frac{10d}{L} \right)^{-1/2} \quad (3)$$

and ϵ_r is the dielectric constant of the substrate material. The rationale behind Eq. (3) is that, depending on the ratio of d/L , electromagnetic fields can extend into air directly above the metal patch, and so $\epsilon_{\text{eff}} < \epsilon_r$, and $\epsilon_{\text{eff}} \approx \epsilon_r$ if $d/L \ll 1$. The resonant frequency of the cavity resonator is therefore

$$f_n = \frac{cn}{2L'\sqrt{\epsilon_{\text{eff}}}} \quad (4)$$

where c denotes the speed of light in vacuum and n the order of the resonant mode ($n = 1$ for the fundamental mode).

On the basis of the same fringe-field consideration, we expect that for a circular patch antenna the effective resonant radius of the cavity, denoted as $R' = R + \Delta$, is larger than the physical radius of the metal patch, denoted as R , and [6]

$$\Delta = \frac{d}{\pi} \left[\ln \left(\frac{\pi R}{2d} \right) + 1.7726 \right] \quad (5)$$

as shown in Fig. 2. A similar expression for ϵ_{eff} , or Eq. (3), is expected for a circular microstrip cavity. However, such an expression is lacking in the present literature. We therefore use ϵ_r as ϵ_{eff} , bearing in mind that this approximation is true only if $R \gg d$. The resonant frequency of the cavity is therefore

$$f_{mn} = \frac{cX'_{mn}}{2\pi R'\sqrt{\epsilon_r}} \quad (6)$$

where X'_{mn} denotes the n th zero of the derivative of the Bessel function $J_m(x)$ of order m .

We note that the expressions given above for resonant frequencies for rectangular and circular microstrip patch antennas [Eqs. (4) and (6)] are derived from the cavity model assuming that standing modes are excited within the cavity. At high frequencies this quasistatic picture is no longer valid and surface waves of high orders are excited propagating away from the cavity region guided by the microstrip structure. As such, magneticwall boundary conditions are no longer adequate at the periphery of the antenna cavity. For these situations we must resort to a rigorous full-wave analysis to suitably address the leaky feature of the cavity generating surface waves, for example, by using the dyadic Green functions to be described in Section 2. To simplify notations in the following, we will

use ϵ_r for ϵ_{eff} and L and R for L' and R' , respectively, with the difference understood.

1.3. Normal Modes and Feeder-Line Excitations

The normal modes excited in a microstrip resonator cavity are normally TE waves exhibiting no nodal points along the z axis, the direction perpendicular to the substrate surface. Thus, the normal-mode solutions show no z dependence, and the electromagnetic components can be uniquely derived from E_z satisfying the following Helmholtz equation

$$(\nabla_t^2 + k_{mn}^2)E_z = 0 \quad (7)$$

where ∇_t denotes the transverse part of the del operator (with respect to the z axis), k_{mn} is given by

$$k_{mn} = \omega_{mn} \sqrt{\mu_0 \epsilon_0 \epsilon_r} \quad (8)$$

ω_{mn} is the angular frequency, and $\{m, n\}$ refers to the index of the normal mode. The boundary condition imposed on E_z is that the derivative of E_z along the normal direction of the boundary vanishes at the magnetic wall. Once E_z is solved from Eq. (7), the corresponding \mathbf{H} field is

$$\mathbf{H}_t = (j\omega\mu_0)^{-1} \mathbf{e}_z \times \nabla_t E_z \quad (9)$$

where \mathbf{e}_z denotes the unit vector along the z axis.

Let the rectangular patch be located at $0 \leq x \leq L$, and $0 \leq y \leq W$ (see Fig. 1). The normal modes are therefore

$$E_z^{mn}(x, y) = \cos \frac{m\pi x}{L} \cos \frac{n\pi y}{W} \quad (10)$$

with the corresponding modal wavenumber

$$k_{mn} = \left[\left(\frac{m\pi}{L} \right)^2 + \left(\frac{n\pi}{W} \right)^2 \right]^{1/2} \quad (11)$$

For a circular cavity of radius R the normal modes are (see Fig. 2)

$$E_z^{mn}(\rho, \phi) = J_m(k_{mn}\rho) \exp(jm\phi) \quad (12)$$

and the modal wavenumber is determined by the zeroing condition of the derivative of Bessel functions of order m

$$J'_m(k_{mn}R) = 0 \quad (13)$$

and (ρ, ϕ, z) denotes the cylindrical coordinate.

Let us consider the patch antenna be excited by either a microstrip line at the edge of the patch (Fig. 1) or by a coaxial feeder directly under the patch (Fig. 2). The angular frequency of the external driving field is $\omega = 2\pi f$. We expect that the cavity will be driven to attain the highest intensity when the excitation frequency approaches the normal-mode frequencies [Eq. (8)]. This phenomenon is generally known as the *forced oscillation* of a resonator, and it occurs commonly in many branches of physics.

Thus, at resonance, the cavity is driven by the external field undergoing the forced oscillation giving rise to a maximum efficiency in radiation. We first consider the excitation of the cavity by a microstrip feeder line. The boundary conditions for the cavity are that electric walls are located at metal boundaries and magnetic walls at the periphery not adjacent to the microstrip feeder line. At the input port of the feeder line adjacent to the cavity periphery we define a window where we assume that the excitation currents are uniformly distributed, inducing a uniform magnetic field there:

$$\mathbf{H} = \mathbf{n} \times \mathbf{e}_z h_0 \quad (14)$$

here \mathbf{n} denotes the unit vector pointing outward along the normal direction of the window and h_0 is a constant specifying the amplitude of the excitation current. The excitation field following Eqs. (7) and (9) can be uniquely solved subject to the boundary condition of Eq. (14).

For a rectangular patch depicted in Fig. 1, let the microstrip feeder be connected to the patch at the location defined by $a \leq x \leq b$, and $y = 0$. The excitation field is therefore

$$E_z(x, y) = jk\zeta h_0 \sum_{m=0}^{\infty} A_m \cos \frac{m\pi x}{L} \cos \beta_m(W - y) \quad (15)$$

$$H_x(x, y) = h_0 \sum_{m=0}^{\infty} A_m \beta_m \cos \frac{m\pi x}{L} \sin \beta_m(W - y) \quad (16)$$

$$H_y(x, y) = -h_0 \sum_{m=0}^{\infty} A_m \frac{m\pi}{L} \sin \frac{m\pi x}{L} \cos \beta_m(W - y) \quad (17)$$

where

$$\beta_m = \sqrt{k^2 - \left(\frac{m\pi}{L} \right)^2} \quad (18)$$

$$k = \omega \sqrt{\mu_0 \epsilon_0 \epsilon_r} \quad \zeta = \sqrt{\frac{\mu_0}{\epsilon_0 \epsilon_r}} \quad (19)$$

$$A_m = \frac{4}{m\pi} \frac{\sin \frac{m\pi(b-a)}{2L} \cos \frac{m\pi(b+a)}{2L}}{\beta_m \sin \beta_m W}, \quad (m \neq 0) \quad (20)$$

$$A_0 = \frac{b-a}{Lk \sin kW} \quad (21)$$

Note that when $\omega = \omega_{mn}$, then $A_m = \infty$, indicating that when the frequency of the external driving field equals one of the normal-mode frequencies, only that normal mode is excited in the cavity responsible for radiation. This statement is valid only if the cavity is lossless. However, when losses are included with the patch resonator, other normal modes can also be excited at resonance, but with much smaller amplitudes.

For a circular patch we consider the microstrip feeder line to be located at $-\alpha \leq \phi \leq \alpha$, and $\rho = R$. The excitation

field can then be written as

$$E_z(\rho, \phi) = j\zeta h_0 \sum_{n=0}^{\infty} C_n J_n(k\rho) \cos(n\phi) \quad (22)$$

$$H_\rho(\rho, \phi) = \frac{h_0}{k\rho} \sum_{n=1}^{\infty} C_n n J_n(k\rho) \sin(n\phi) \quad (23)$$

$$H_\phi(\rho, \phi) = h_0 \sum_{n=0}^{\infty} C_n J'_n(k\rho) \cos(n\phi) \quad (24)$$

$$C_n = \frac{2 \sin n\alpha}{n\pi J'_n(kR)}, \quad (n \neq 0) \quad (25)$$

where

$$C_0 = \frac{\alpha}{\pi J'_0(kR)} \quad (26)$$

and ζ and k are as given in Eq. (19). Again, from Eqs. (25) and (26) it is seen that the coefficient of C_n goes to infinity if the driving field frequency approaches the normal-mode frequencies, which are specified by Eq. (13), resulting in forced oscillation of a lossless cavity resonator.

Let us consider the excitation of the patch antenna by a coaxial line inserted directly under the patch. We assume that this line shows an inner filament of zero diameter ending in a point charge at the surface of the patch (see Fig. 2). The excitation current density is therefore

$$\mathbf{J}_e(x, y) = I_0 \delta(x - x_0) \delta(y - y_0) \mathbf{e}_z \quad (27)$$

for a rectangular patch

$$\mathbf{J}_e(\rho, \phi) = \frac{I_0 \delta(\rho - \rho_0) \delta(\phi - \phi_0)}{\rho \mathbf{e}_z} \quad \text{for a circular patch} \quad (28)$$

In the presence of a driving current, Eq. (7) is modified to include an inhomogeneous term, the source, on the right hand side:

$$(\nabla_t^2 + k_{mn}^2) E_z = j\omega\mu_0 \mathbf{J}_e \cdot \mathbf{e}_z \quad (29)$$

The boundary conditions are the same as before, leading to the normal-mode solutions, namely, electric walls at metal boundaries and magnetic walls at the periphery of the resonator cavity. Thus, Eq. (29) can be solved in terms of the normal-mode solutions:

$$E_z(x, y) = j\omega\mu_0 \sum_{m,n} \frac{E_z^{mn}(x, y)}{k^2 - k_{mn}^2} \times \frac{\int_0^L dx' \int_0^W dy' J_e(x', y') E_z^{mn}(x', y')^*}{\int_0^L dx' \int_0^W dy' |E_z^{mn}(x', y')|^2} \quad (30)$$

$$E_z(\rho, \phi) = j\omega\mu_0 \sum_{m,n} \frac{E_z^{mn}(\rho, \phi)}{k^2 - k_{mn}^2} \times \frac{\int_0^R d\rho' \int_0^{2\pi} \rho' d\phi' J_e(\rho', \phi') E_z^{mn}(\rho', \phi')^*}{\int_0^R d\rho' \int_0^{2\pi} \rho' d\phi' |E_z^{mn}(\rho', \phi')|^2} \quad (31)$$

These two equations apply for a rectangular patch and a circular patch, respectively, and the normal-mode solutions, $E_z^{mn}(x, y)$ and $E_z^{mn}(\rho, \phi)$, are as given in Eqs. (10) and

(12). We note that Eqs. (30) and (31) imply that when k approaches k_{mn} , the normal-mode $\{m, n\}$ acquires an infinite amplitude, as implied by a lossless cavity. The corresponding magnetic field can be derived using Eq. (9).

Thus, for the rectangular patch, we have

$$E_z(x, y) = \frac{4j\omega\mu_0 I_0}{LW} \sum_{m,n=1}^{\infty} \frac{\cos(m\pi x_0/L) \cos(m\pi x/L) \cos(n\pi y_0/W) \cos(n\pi y/W)}{k^2 - k_{mn}^2} \quad (32)$$

$$H_x(x, y) = \frac{4I_0}{LW} \sum_{m,n=1}^{\infty} \frac{n\pi}{W} \times \frac{\cos(m\pi x_0/L) \cos(m\pi x/L) \cos(n\pi y_0/W) \sin(n\pi y/W)}{k^2 - k_{mn}^2} \quad (33)$$

$$H_y(x, y) = \frac{-4I_0}{LW} \sum_{m,n=1}^{\infty} \frac{m\pi}{L} \times \frac{\cos(m\pi x_0/L) \sin(m\pi x/L) \cos(n\pi y_0/W) \cos(n\pi y/W)}{k^2 - k_{mn}^2} \quad (34)$$

For the circular patch, we have

$$E_z(\rho, \phi) = \frac{j\omega\mu_0 I_0}{\pi} \sum_{m=0}^{\infty} \sum_{n=1}^{\infty} \frac{(2 - \delta_{m0}) k_{mn}^2}{k^2 - k_{mn}^2} \times \frac{J_m(k_{mn}\rho) J_m(k_{mn}\rho_0) \cos[m(\phi - \phi_0)]}{(k_{mn}^2 R^2 - m^2) [J_m(k_{mn}^2 R^2)]^2} \quad (35)$$

$$H_\rho(\rho, \phi) = \frac{-I_0}{\pi\rho} \sum_{m=1}^{\infty} \sum_{n=1}^{\infty} \frac{m(2 - \delta_{m0}) k_{mn}^2}{k^2 - k_{mn}^2} \times \frac{J_m(k_{mn}\rho) J_m(k_{mn}\rho_0) \sin[m(\phi - \phi_0)]}{(k_{mn}^2 R^2 - m^2) [J_m(k_{mn}^2 R^2)]^2} \quad (36)$$

$$H_\phi(\rho, \phi) = \frac{I_0}{\pi} \sum_{m=0}^{\infty} \sum_{n=1}^{\infty} \frac{(2 - \delta_{m0}) k_{mn}^3}{k^2 - k_{mn}^2} \times \frac{J'_m(k_{mn}\rho) J_m(k_{mn}\rho_0) \cos[m(\phi - \phi_0)]}{(k_{mn}^2 R^2 - m^2) [J_m(k_{mn}^2 R^2)]^2} \quad (37)$$

where δ_{ij} denotes the Kröner delta function and $\delta_{m0} = 1$ if $m = 0$, and $\delta_{m0} = 0$, otherwise.

In Eqs. (32)–(34) and (35)–(37) the k_{mn} values are as given by Eqs. (11) and (13), respectively, and ζ and k are as defined in Eq. (19). Once the excitation fields are known [Eqs. (16, 17, 18, 22, 23, 24, 32, 33, 34, 35, 36, 37)], losses of various kinds, and hence the quality factor Q of the patch cavity can be calculated as discussed below.

1.4. Input Impedance

Having solved the electromagnetic fields inside a lossless cavity, we can relax the assumption of perfect electric and magnetic walls and allow electromagnetic waves to extend

beyond the wall boundaries. This results in ohmic loss and radiation (surface-wave) loss. Dielectric loss and magnetic loss occur in the interior of the patch cavity, which can be accounted for by assuming a lossy medium possessing a complex permittivity and a complex permeability, respectively. We consider first the radiation loss.

The Kirchhoff–Huygens principle, which is a vector analog of Green’s theorem, states that the electromagnetic field inside a closed volume V can be derived by the volume charge and current distributions inside V and the surface charges and currents distributed on the enclosing surface of V , denoted as S . The effective electric surface current density \mathbf{K}_e magnetic surface current density \mathbf{K}_m and electric surface charge density Σ are respectively [7]

$$\mathbf{K}_e = -\mathbf{n} \times \mathbf{H}, \mathbf{K}_m = \mathbf{n} \times \mathbf{E}, \Sigma = -\varepsilon \mathbf{n} \cdot \mathbf{E} \quad (38)$$

where \mathbf{n} denotes the unit outward vector normal to S and ε is the permittivity. Thus, if we consider the outside volume of the patch antenna cavity as the volume V , we conclude that the effective magnetic current density appearing on the magnetic wall is

$$\mathbf{K}_m = -2\mathbf{n} \times \mathbf{e}_z E_z \quad (39)$$

where \mathbf{n} denotes the unit outward vector normal to the magnetic wall whose sign changes as comparing to Eq. (38), and the factor of 2 in Eq. (39) accounts for the presence of the ground plane, \mathbf{K}_e and Σ do not show up on a magnetic wall.

The radiation field arising from the magnetic current density \mathbf{K}_m can be derived by using the same formula describing the electric current density \mathbf{K}_e but converted from the duality rule [7]. The duality rule states that the electromagnetic theory remains valid if one changes all the electric quantities into the corresponding magnetic quantities and the magnetic quantities into the negative of the corresponding electric quantities. Thus, the vector potential associated with \mathbf{K}_m can be expressed as [8]

$$\begin{aligned} \mathbf{A}_m(\mathbf{r}) &= \frac{\varepsilon_0 d}{4\pi} \oint_{C_m} d\ell' \frac{\mathbf{K}_m(\mathbf{r}')}{|\mathbf{r} - \mathbf{r}'|} e^{-jk_0|\mathbf{r} - \mathbf{r}'|} \\ &\approx \frac{\varepsilon_0 d}{4\pi} \frac{\exp(-jk_0 r)}{r} \oint_{C_m} d\ell' \mathbf{t}' E_z(\mathbf{r}') \exp(jk_0 \mathbf{e}_r \cdot \mathbf{r}') \end{aligned} \quad (40)$$

where d denotes the thickness of the substrate, C_m is the contour of the magnetic wall, \mathbf{t} is the unit vector along the contour C_m in the counterclockwise sense, \mathbf{e}_r is the unit vector pointing toward the observation point \mathbf{r} , and

$$k_0 = \omega(\mu_0 \varepsilon_0)^{1/2} \quad (41)$$

is the wavenumber in air. In Eq. (40) we denote “primed” symbols as referring to the source point, and have assumed $|\mathbf{r} - \mathbf{r}'| \gg d$.

In the far-field zone we have

$$\mathbf{H}(\mathbf{r}) = -j\omega \mathbf{A}_m(\mathbf{r}) \quad (42)$$

$$\mathbf{E}(\mathbf{r}) = -\zeta_0 \mathbf{e}_r \times \mathbf{H}(\mathbf{r}) \quad (43)$$

where

$$\zeta_0 = \left(\frac{\mu_0}{\varepsilon_0} \right)^{1/2} \quad (44)$$

is the wave impedance in air ($= 377 \Omega$). We derive, therefore

$$\begin{aligned} \mathbf{E}(\mathbf{r}) &\approx \frac{j\varepsilon_0 k_0 d}{4\pi} \frac{\exp(-jk_0 \mathbf{r})}{\mathbf{r}} \\ &\times \oint_{C_m} d\ell' (-\mathbf{t}' \cdot \mathbf{e}_\phi \mathbf{e}_\theta + \mathbf{t}' \cdot \mathbf{e}_\theta \mathbf{e}_\phi) E_z(\mathbf{r}') \exp(jk_0 \mathbf{e}_r \cdot \mathbf{r}') \end{aligned} \quad (45)$$

where \mathbf{e}_θ and \mathbf{e}_ϕ denote the unit vectors along the θ and ϕ directions at the observation point \mathbf{r} . By using Eq. (45) the far-field differential-power radiation from a circular patch antenna fed by a microstrip line [Eq. (22)] is, for example

$$\begin{aligned} \mathbf{E}(\mathbf{r}) &\approx \frac{\alpha \zeta_0 h_0 k_0 d}{\pi} \frac{R \exp(-jk_0 \mathbf{r})}{\mathbf{r}} \\ &\times \sum_{m=-\infty}^{\infty} j^{-m} \frac{J_m(kR)}{J'_m(kR)} \frac{\sin m\alpha}{m\alpha} \mathbf{e}^{-jm\phi} \\ &\cdot \left[\mathbf{e}_\theta J'_m(k_0 R \sin \theta) + j \mathbf{e}_\phi \cos \theta \frac{m J_m(k_0 R \sin \theta)}{k_0 R \sin \theta} \right] \end{aligned} \quad (46)$$

where it is understood that the ratio of $\sin m\alpha$ to $m\alpha$ is 1 when $m = 0$. Expressions of $\mathbf{E}(\mathbf{r})$ for the other rectangular patch geometry under both the microstrip and the coaxial-line feeder excitation configurations, or for the same circular patch geometry under the coaxial-line feeder excitation configuration, can be derived in a similar manner, but their explicit expressions are not given here.

The far-field differential-power radiation pattern can be calculated by using the following equation:

$$\frac{dP_r}{d\Omega} = \lim_{r \rightarrow \infty} \frac{r^2 |\mathbf{E}|^2}{2\zeta_0} \quad (47)$$

The total radiation power is then

$$P_r = \int_0^\pi \sin \theta d\theta \int_0^{2\pi} d\phi \frac{dP_r}{d\Omega} \quad (48)$$

Conductor loss and dielectric loss can also be derived from the zeroth-order normal-mode solutions of the cavity [7]. The conductor loss is given by

$$P_c = R_s \iint_{S_c} |\mathbf{H}|^2 ds \quad (49)$$

where S_c denotes the patch surface and R_s is the surface resistance

$$R_s = \sqrt{\frac{\omega \mu_0}{2\sigma}} \quad (50)$$

and σ is the conductivity of metal. The dielectric loss is given by

$$P_d = \frac{\omega \epsilon_r \epsilon_0 \tan \delta}{2} \iiint_{V_c} |E_z|^2 dv \quad (51)$$

where V_c denotes the volume of the cavity and $\tan \delta$ is the dielectric loss tangent.

The antenna efficiency or radiation efficiency is defined as the ratio of the radiated power to the input power

$$e = \frac{P_r}{P_r + P_c + P_d} \times 100\% \quad (52)$$

The total stored electric energy is

$$W_e = \frac{\epsilon_r \epsilon_0}{4} \iiint_{V_c} |E_z|^2 dv = \frac{P_d}{2\omega \tan \delta} \quad (53)$$

At resonance, because the stored magnetic energy W_m equals the stored electric energy W_e , we have thus the total stored electromagnetic energy

$$W_T = W_n + W_m = \frac{P_d}{\omega \tan \delta} \quad (54)$$

The Q factor of the cavity is, from the definition of Eq. (1)

$$Q = \frac{W_T}{P_T + P_c + P_d} \quad (55)$$

From which the VSWR bandwidth can be calculated. We define S_{\max} to be the maximum value of VSWR that can be tolerated in the radiation band. We then have [9]

$$\text{VSWR bandwidth (\%)} = \frac{100(S_{\max} - 1)}{Q\sqrt{S_{\max}}} \quad (56)$$

Typically, $S_{\max} = 2$.

The input susceptance of the antenna B can be calculated for a lossless patch cavity, which is thus a zeroth-order quantity. In contrast, the input conductance G must be calculated from the total loss of the cavity, which represents a first-order quantity. Thus

$$jB = \frac{-I}{V} \quad (57)$$

$$G = \frac{P_r + P_c + P_d}{|V|^2} \quad (58)$$

where I and V are the averaged input current and voltage at the input feeder position. For coaxial feeder with excitation current given by Eqs. (27) and (28), assuming a thin inner filament shown in Fig. 2, the current I is known and the voltage V can be calculated from E_z evaluated at the input position multiplied by the thickness of the substrate d . We have therefore

$$B^{-1} = \frac{4d\omega\mu_0}{LW} \sum_{m,n=1}^{\infty} \frac{\cos^2(m\pi x_0/L) \cos^2(n\pi y_0/W)}{k^2 - k_{mn}^2} \quad (59)$$

$$B^{-1} = \frac{d\omega\mu_0}{\pi} \sum_{m=0}^{\infty} \sum_{n=1}^{\infty} \frac{(2 - \delta_{m0})k_{mn}^2}{k^2 - k_{mn}^2} \times \frac{[J_m(k_{mn}\rho_0)]^2}{(k_{mn}^2 R^2 - m^2)[J_m(k_{mn}^2 R^2)]^2} \quad (60)$$

for rectangular and circular patch antennas, respectively. When excited by a microstrip feeder the input voltage is obtained by averaging E_z over the width of the feeder-line window joining the cavity multiplied by the thickness of the substrate d as dictated by Faraday's law. The input current can be derived by applying Ampère's law at the feeder-line window, and the result is h_0 times the transverse length of the window, specifically, $h_0(b-a)$ for the rectangular antenna, and $h_0(2\alpha R)$ for the circular antenna. We have therefore

$$B^{-1} = \frac{\zeta d}{L} \left[\text{ctn } kW + \sum_{m=1}^{\infty} \frac{8}{(m\pi)^2} \frac{L^2}{(b-a)^2} \frac{k}{\beta_m} \times \text{ctn } \beta_m W \left(\sin \frac{m\pi(b-a)}{2L} \cos \frac{m\pi(b+a)}{2L} \right)^2 \right] \quad (61)$$

$$B^{-1} = \frac{\zeta d}{2\pi R} \left(\frac{J_0(kR)}{J'_0(kR)} + \sum_{n=1}^{\infty} \frac{2 \sin^2 n\alpha J_n(kR)}{n^2 \alpha^2 J'_n(kR)} \right) \quad (62)$$

for rectangular and circular patch antennas, respectively. Here k_{mn} in Eq. (60) is as given by Eq. (13) and β_m in Eq. (61) is as given by Eq. (18).

From Eqs. (59)–(62) we note that when excited at the normal-mode frequencies, the input susceptance $B = 0$, and hence $B^{-1} = \infty$. These points are called *antiresonance points* when referred to in a Smith chart plot (e.g., see Fig. 4 in Section 2.3). In contrast, the resonant points are defined to be purely resistive so that at resonance the input resistance of the antenna is intended to match the

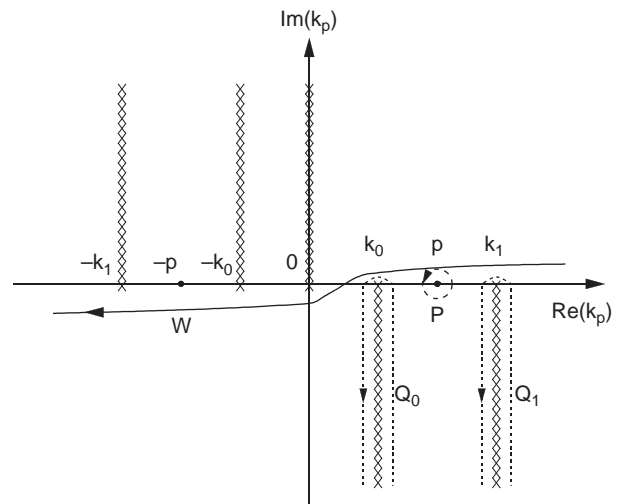


Figure 3. Integration contours for Sommerfeld integrals illustrating contribution from spatial-wave and surface-wave excitations.

feeder-line impedance, thereby resulting in zero reflection. Therefore, $B^{-1} = 0$ at resonance. The resonance frequency occurs slightly above the antiresonance frequency, which requires participation of normal modes of all orders, although one normal mode responsible for antiresonance is excited with the largest amplitude. Thus, by definition, at resonance the capacitive part of the stored energy equals the inductive part, rendering the overall input reactance to be zero. In calculating the susceptance, or the stored electromagnetic energy of the cavity, we should also include the capacitive contribution from the near-field excitation. However, this contribution has already been accounted for as the increment in the effective resonance length of the antenna cavity [Eqs. (2) and (5)]. The input impedance is

$$Z = (G + jB)^{-1} \quad (63)$$

We note that, in reality, at antiresonance B is finite because of the presence of losses occurring at the antenna patch cavity.

One severe drawback of the cavity model is that it is not able to address the surface-wave loss. James and Henderson [10] estimated that surface-wave excitation is not important if $d/\lambda_0 < 0.09$ for $\epsilon_r = 2.3$ and $d/\lambda_0 < 0.03$ for $\epsilon_r = 10$, where λ_0 is the free-space wavelength. The criterion given by Wood [11] is more quantitative: $d/\lambda_0 < 0.07$ for $\epsilon_r = 2.3$, and $d/\lambda_0 < 0.0023$ for $\epsilon_r = 10$, if the antenna is to launch no more than 25% of the total radiated power as surface waves. Work by Fonseca and Giarola showed that the size of the patch is also a parameter [12], as will be discussed in more detail in the next section. When ferrite material is used as the substrate, magnetic loss can be estimated using a formula similar to Eq. (51):

$$P_m = \frac{\omega\mu''}{2} \iint_{V_c} \int |\mathbf{H}|^2 dv \quad (64)$$

where μ'' denotes the imaginary part of the permeability. In concluding this section we note that the cavity model depicts a semiempirical picture where the parameters have been adjusted to fit experiments, for example, the effective dielectric constant ϵ_{eff} [Eq. (3)], and the increment in the resonant length of the patch Δ [Eqs. (2) and (5)]. Nevertheless, the calculated radiation pattern and input impedance compared very well with measurements [13].

2. DYADIC GREEN FUNCTION

2.1. Introduction

As we have mentioned in Section 1, the open structure of a microstrip patch antenna can be rigorously accounted for only in a full-wave analysis resorting to numerical solutions. Maxwell equations can be explicitly solved numerically in either the frequency or time domain using the generic 3D finite-element and finite-difference methods [14]. However, it is more informative to use the dyadic Green functions, since the electromagnetic fields generated by a point dipole current source has already been solved “analytically” in the same microstrip geometry, which is termed the *dyadic Green function*. The electromagnetic

fields excited by a patch antenna can then be composed as superposition of the point dipole solutions in the context of a conventional Green’s function method. The numerical technique comes in only when Galerkin method is called for to solve the resultant integral equations relating the unknown current variables to the local electric fields distributed across the metal patch boundaries.

The physical meaning of Green’s function is clear, and surface waves are treated with equal importance as spatial waves in the Green’s function formulation. Furthermore, the Green function solution usually requires 2D calculations, as in contrast to the generic 3D computational methods. This is true when the metal thickness compares much smaller than the thickness of the substrate, as is usually the case. Material losses can be readily included with the Green function if complex permittivity and permeability values are used. It turns out that efficient CAD tools can be constructed using the dyadic Green’s function solutions, which calculate engineering parameters of a microstrip antenna, including radiation frequency, far-field pattern, efficiency, and input impedance, and analyze the crosstalk problem inherent in common microstrip circuitries.

To illustrate the physics in the application of a Green function, we have decided not to regenerate many mathematical formulas in this section. Instead, we concentrate on Sommerfeld’s approach to Green function analysis [1], since it lends itself to more physical understanding of the problem. We wish to introduce the methodology leading to the formulation of the dyadic Green function for a general stratified structure, consisting of finite number of dielectric and magnetic layers as constituents. We assume this layered structure is infinite in both horizontal and vertical directions, although it is possible to include finite substrate and radiation space by employing periodic boundary conditions, for example. Also, we assume the current distribution is two-dimensional, resulting in 2D analysis of the Galerkin elements. The finite conductivity of the ground plane can be accounted for by invoking complex permittivity of the conductor layer [1]. Computational results are cited mainly from Ref. 15. Background material can be found in Ref. 16.

2.2. Point Dipole Solutions

We start by introducing the vector potential \mathbf{A} , and scalar potential V , in electrodynamics subject to a Lorentz gauge [17], which has been implicitly used by Sommerfeld [1]:

$$\mathbf{H} = \frac{1}{\mu_0} \nabla \times \mathbf{A} \quad (65)$$

$$\mathbf{E} = -j\omega\mathbf{A} - \nabla V \quad (66)$$

$$\nabla \cdot \mathbf{A} + j\omega\mu_0\epsilon V = 0 \quad (67)$$

This results in uncoupled equations for \mathbf{A} and V as follows

$$(\nabla^2 + k^2)\mathbf{A} = -\mu_0\mathbf{J} \quad (68)$$

$$(\nabla^2 + k^2)V = \frac{-1}{\epsilon_0} \rho \quad (69)$$

where \mathbf{J} and ρ are the current and charge densities, respectively, and normally $\rho=0$ (oscillating charges can hardly be realized physically). We note that Eq. (68) does not specify \mathbf{A} uniquely for a finite volume under consideration [17]. However, this gauge freedom is almost fixed for a system of infinite volume, since the only source-free radiation for the entire space is the incoming waves from infinity, which can be readily checked out and excluded from the solution of \mathbf{A} by performing proper gauge transformation. From Eq. (67) the scalar potential V is obtained from the divergence of \mathbf{A} , and hence only the vector potential \mathbf{A} needs to be solved.

We are now solving the vector potential, $\mathbf{A}(x, y, z)$ [Eq. (68)], induced by a point dipole current source, $\mathbf{J}_0(x, y, z)$, in the background of a dielectric/magnetic-layered structure. A point dipole is also called a Hertzian dipole, which can be approximated by a dipole antenna whose arms are much smaller than the wavelength of radiation [1]. Assume the point dipole to be located at $(0, 0, z_0)$. The current density associated with the point dipole is therefore

$$\mathbf{J}_0(x, y, z) = \mathbf{I}_0 d\ell \cdot \delta(x)\delta(y)\delta(z - z_0) \quad (70)$$

where $\mathbf{I}_0 d\ell$ (= finite) denotes the strength of the dipole. Without loss of generality, we assume that \mathbf{I}_0 is along the x direction. From Eq. (68) we know that A_x is nonzero, corresponding to the radiation field directly from the horizontal dipole. This is the field arising from the point dipole of Eq. (70) in empty space. However, in the presence of the layered structure, A_z is also nonzero, due to oblique reflection of A_x from the layer interfaces, corresponding to the radiation field from a vertical dipole in the absence of the stratified structure. Finally, A_y is identically zero as implied by the symmetry of the problem.

We require the tangential components of \mathbf{E} and \mathbf{H} to be continuous across the layer interfaces, and these boundary conditions need to be expressed in terms \mathbf{A} satisfying Eqs. (65) and (66). According to Sommerfeld [1], these boundary conditions can be deduced by integrating Eqs. (65) and (66) with respect to the transverse coordinates x and y , and the constants of integration are justified as zeros by letting x and y go to infinity. For example, suppose that one boundary condition requires the derivative of the function $f(x, y, z)$ with respect to x to be continuous across an interface. If $f(x, y, z)$ vanishes as x goes to infinity, either decreasing exponentially to zero as for a decaying wave or averaging to zero as for an oscillating wave, we can then integrate this boundary condition with respect to x to conclude that the function $f(x, y, z)$ itself must be continuous across the interface. As such, the boundary conditions imposed on the vector potential $\mathbf{A} = A_x \mathbf{e}_x + A_z \mathbf{e}_z$ as derived by Sommerfeld are the continuity conditions on the following four quantities [1],

$$\varepsilon\mu A_x, \quad \varepsilon\mu \left(\frac{\partial A_x}{\partial z} \right), \quad \varepsilon\mu A_z, \quad \frac{\partial A_x}{\partial x} + \frac{\partial A_z}{\partial z} \quad (71)$$

There are therefore four boundary conditions at each layer interface.

Recognizing the fact that the layered structure is homogeneous in the transverse directions, say, x and y , it implies that the Helmholtz equation, Eq. (68), can be conveniently solved in the transverse Fourier spectral domain. For a given transverse spectral vector, $\mathbf{k}_t = [k_x, k_y]$, we denote the corresponding spectral-domain vector potential components as $\tilde{A}_x(k_x, k_y, z)$ and $\tilde{A}_z(k_x, k_y, z)$, which relate to $A_x(x, y, z)$ and $A_z(x, y, z)$ via double Fourier integrals, respectively. For each layer, which does not contain the dipole source, we solve the Helmholtz equation, Eq. (68), to obtain the following solutions

$$\tilde{A}_x(k_x, k_y, z) = a \exp(+\gamma z) + b \exp(-\gamma z) \quad (72)$$

$$\tilde{A}_z(k_x, k_y, z) = c \exp(+\gamma z) + d \exp(-\gamma z) \quad (73)$$

where a, b, c, d are four unknowns to be determined by the boundary conditions and γ is given by

$$\gamma^2 = k_x^2 + k_y^2 - \varepsilon\mu\omega^2 \quad (74)$$

where ε and μ are respectively the permittivity and permeability of the layer under consideration. For the uppermost layer $a=0=c$, and for the lowermost layer $b=0=d$, as required by the boundary conditions at $z = \pm\infty$. For the layer that contains the dipole source, we integrate Eq. (68) from $z=z_0^-$ to $z=z_0^+$ and note that the double Fourier transform of the function $\delta(x)\delta(y)$ is $(2\pi)^{-1}$; we then derive the following discontinuity requirement on $\partial\tilde{A}_x(k_x, k_y, z)/\partial z$ on both sides of the plane $z=z_0$:

$$\frac{\partial\tilde{A}_x(k_x, k_y, z^-)}{\partial z} - \frac{\partial\tilde{A}_x(k_x, k_y, z^+)}{\partial z} = \frac{-I_0 d\ell}{2\pi} \quad (75)$$

We therefore insert a fictitious interface at $z=z_0$ assuming different a, b, c, d values for the two subregions above and below this interface [Eqs. (72) and (73)]; γ is the same across the fictitious interface [Eq. (74)]. Thus, the boundary conditions imposed on this fictitious interface are the same as before except that the requirement on the continuity of the quantity $\varepsilon\mu(\partial A_x/\partial z)$ is now being replaced by Eq. (75). If the z_0 plane occurs at one layer interface of the stratified structure, no fictitious interface is needed; we need only to replace the continuity requirement on $\varepsilon\mu(\partial A_x/\partial z)$ by Eq. (75) where γ differs across the interface.

Thus, we arrive at $4N$ unknowns with $4N$ boundary conditions for N interfaces, including the fictitious one, if there is one. We replace in the boundary conditions [Eq. (71)] the operator $\partial/\partial x$ by $-jk_x$, and $\partial/\partial z$ by $\pm\gamma$, whichever is applicable according to Eqs. (72) and (73). The $4N$ boundary conditions converts into algebraic equations, and hence the $4N$ unknowns can be solved. The amplitudes of these unknowns are all proportional to the dipole strength $I_0 d\ell$, which can be conveniently chosen to be 1, as defined by the Green function. The vector potentials $A_x(x, y, z)$ and $A_z(x, y, z)$ can then be solved from $\tilde{A}_x(k_x, k_y, z)$ and $\tilde{A}_z(k_x, k_y, z)$ by applying the inverse two-dimensional Fourier transforms. The electric and magnetic fields can finally be obtained by using Eqs. (65)–(67).

Material imperfection results in losses of various kinds whose effects can be analytically modeled by letting the permittivity and permeability be complex numbers. The dielectric loss is described by a loss tangent, $\tan \delta$, and the permittivity takes the form of $\epsilon_0 \epsilon_r (1 - j \tan \delta)$, where ϵ_r denotes the dielectric constant. For a partially magnetized magnetic substrate the permeability is $\mu_0(\mu' + j\mu'')$, and μ' and μ'' are the real and imaginary parts of the relative permeability [3]. For a metal conductor the permittivity contains both the displacement current and the conduction current, and hence the permittivity is modified as $\epsilon_0 - j\sigma/\omega$ where σ denotes the conductivity. This is the permittivity that was explicitly considered by Sommerfeld [1] solving the electromagnetic fields generated by a Hertzian dipole in response to Earth's surface.

If perfect metal is used as the ground plane, the electromagnetic field will not penetrate into it. Therefore, the boundary condition on the metal surface is that the tangential components of the electric field vanish, and it implies

$$A_x = 0, \quad \frac{\partial A_x}{\partial x} + \frac{\partial A_z}{\partial z} = 0 \quad (76)$$

Thus, we have $4N - 2$ unknowns and $4N - 2$ boundary conditions for a layered structure possessing a perfect metal ground plane.

Actually, the interface boundary conditions [Eq. (71)] specify the reflection and transmission of electromagnetic waves from one layer to another, and \tilde{A}_x is proportional to the magnetic field component and \tilde{A}_z is proportional to the electric field component. Oblique-angle reflection and transmission can be readily expressed by using Snell's law [18] and hence the coefficients of \tilde{A}_x and \tilde{A}_z [Eqs. (72) and (73)] are determined for each layer with relation to its preceding and succeeding layers. Thus, circumventing the need to solve the boundary conditions explicitly [Eq. (71)], all the a, b, c, d coefficients for the layers are correlated to each other and only four unknowns remain, corresponding to those at the outermost layers (top and bottom), which can then be solved by using the boundary conditions at the fictitious interface imposed by the point dipole [Eq. (75)]. Suppose the last layer is a perfect metal. For this case the a, b, c, d coefficients of the layer adjacent to the metal surface satisfy the following relationships

$$b = -a, \quad d = c \quad (77)$$

which are recognized as the total reflection condition. Equation (77) can also be derived from Eq. (76).

For completeness we list below the transverse spectral-domain vector potential induced by a horizontal point dipole located on top of a dielectric substrate backed by a perfect metal ground plane:

$$\tilde{A}_x(k_x, k_y, z) = \frac{\mu_0}{2\pi} \exp\left(\frac{-\gamma_0 z}{D_{TE}}\right)$$

$$\tilde{A}_z(k_x, k_y, z) = \frac{\mu_0}{2\pi} (\epsilon_r - 1) j k_x \exp(-\gamma_0 z) / (D_{TE} D_{TM}) \quad (78)$$

for $z > 0$

$$\tilde{A}_x(k_x, k_y, z) = \frac{\mu_0}{2\pi} \sinh \frac{\gamma(z+d)}{D_{TE} \sinh \gamma d}$$

$$\tilde{A}_z(k_x, k_y, z) = \frac{\mu_0}{2\pi} (\epsilon_r - 1) j k_x \cosh \frac{\gamma(z+d)}{D_{TE} D_{TM} \cosh \gamma d} \quad (79)$$

for $0z > -h$

and D_{TE} and D_{TM} are given by

$$D_{TE} = \gamma_0 + \gamma \coth \gamma d \quad (80)$$

$$D_{TM} = \epsilon_r \gamma_0 + \gamma \tanh \gamma d \quad (81)$$

Here the dipole is located at the plane $z = 0$, the dielectric substrate is of a thickness d and permittivity ϵ_r , and γ_0 and γ are given by Eq. (74) with the zero subscript (0) referring to air. The zeros of Eqs. (80) and (81) correspond to surface-wave TE and TM modes, respectively. While there exists at least one TM surface mode, it is not always the case that TE surface modes will be excited. The threshold for TE mode excitation is

$$k_0 d (\epsilon_r - 1)^{1/2} < \frac{\pi}{2}$$

or

$$f < \frac{75}{d \sqrt{\epsilon_r - 1}} \quad (82)$$

where f is expressed in unit of GHz, and d in unit of mm. Surface-wave modes will be further discussed in the following section.

2.3. Sommerfeld Integrals

Within each layer the dipole field solutions are obtained by performing inverse Fourier transform of $\tilde{A}_x(k_x, k_y, z)$ and $\tilde{A}_z(k_x, k_y, z)$ over the two-dimensional k_x - k_y plane, or, equivalently, k_ρ - k_ϕ plane. Here (k_ρ, k_ϕ) denotes the polar coordinate and (k_x, k_y) the Cartesian coordinate. For a layered structure consisting of isotropic materials, \tilde{A}_x and \tilde{A}_z can be expressed as the following functionals

$$\tilde{A}_x(k_x, k_y, z) = f(k_\rho, z) \quad (83)$$

and

$$\tilde{A}_z(k_x, k_y, z) = k_x g(k_\rho, z) = \cos k_\phi k_\rho g(k_\rho, z) \quad (84)$$

as can be checked from the boundary condition of Eq. (71). In other words, \tilde{A}_x is an even function of k_x and \tilde{A}_z is an odd function of k_x , as implied by the symmetry of the problem. Therefore, after integration over k_ϕ , we obtain

$$A_x(\rho, \phi, z) = \int_0^\infty J_0(k_\rho \rho) k_\rho f(k_\rho, z) dk_\rho \quad (85)$$

$$A_z(\rho, \phi, z) = j \cos \phi \int_0^\infty J_1(k_\rho \rho) k_\rho^2 g(k_\rho, z) dk_\rho \quad (86)$$

Although Eqs. (85) and (86) can be numerically integrated, as will be discussed below, it is informative to discuss the physical meanings implied by these integrals. Equations

(85) and (86) are called *Sommerfeld-type integrals* whose significance was first addressed by Sommerfeld [1]. Sommerfeld noticed that the seemingly real integration starting at the fixed point $k_\rho = 0$ can be converted into a complex k_ρ integration over a path W , which closes at infinity (see Fig. 3)

$$A_x(\rho, \phi, z) = \frac{1}{2} \int_W H_0^{(2)}(k_\rho \rho) k_\rho f(k_\rho, z) dk_\rho \quad (87)$$

$$A_z(\rho, \phi, z) = \frac{j \cos \phi}{2} \int_W H_1^{(2)}(k_\rho \rho) k_\rho^2 g(k_\rho, z) dk_\rho \quad (88)$$

where $H_0^{(2)}$ and $H_1^{(2)}$ are Hankel functions of the second kind of orders 0 and 1, respectively. In Fig. 3, the contour W is detoured slightly in the complex k_ρ plane not to run into branchcuts and poles such that the integrands remain finite and single-valued. In Fig. 3 we illustrate the case that the layered structure involves only two layer substances, the air, denoted by subscript 0 (zero), and a dielectric layer, denoted by subscript 1 (one). For example, the respective permittivities for air and the dielectric layer are denoted as ϵ_0 and ϵ_1 (the permeability of the dielectric layer is assumed to be the same as that of air, μ_0). In Fig. 3, k_0 and k_1 are the branch points given by

$$k_0 = (\epsilon_0 \mu_0)^{1/2}, \quad k_1 = (\epsilon_1 \mu_0)^{1/2} \quad (89)$$

and p is the smallest zero assumed by the function D_{TM} [Eq. (81)]. It is understood that more branchpoints, and hence more branchcuts, will appear in Fig. 3 if more layers are presented in the layered structure. Also, more simple poles will appear if D_{TE} and D_{TM} of Eqs. (80) and (81) admit more zeros. In Fig. 3 the branchpoint at $k_\rho = 0$ results from the Hankel functions $H_0^{(2)}$ [Eq. (87)]. However, for Eq. (88) this branchpoint, and hence its associated branchcut, is replaced by a simple pole due to the different singular behavior of $H_1^{(2)}$ at the origin.

According to Sommerfeld, the contour W shown in Fig. 3 can be analytically deformed into three components or more surrounding the respective branchcuts and simple pole, denoted as Q_0 , Q_1 , and P . Sommerfeld showed that [1] contour integrals of Q_0 and Q_1 give rise to spatial-wave radiation and for a large (spherical) distance r , they exhibit the following asymptotic dependence:

$$Q_0(Q_1) \propto \frac{\exp(-jk_0 r)}{r} \quad (90)$$

Actually, Q_0 gives rise to the free-space dipole radiation, and Q_1 is the radiation wave diffracted by the dielectric layer (or from the image dipole induced by that layer) [1]. Assuming that the air-dielectric interface is located at $z = 0$, then, for $z > 0$, contribution from contour P has the following asymptotic expressions:

$$P \propto H_0^{(2)}(p\rho) \exp[-\sqrt{p^2 - k_0^2} z], \quad \text{for } A_x, \quad [\text{Eq. (86)}] \quad (91)$$

$$P \propto \cos \phi H_1^{(2)}(p\rho) \exp[-\sqrt{p^2 - k_0^2} z], \quad \text{for } A_z, \quad [\text{Eq. (87)}] \quad (92)$$

These are surface waves tied to the interface and decrease in a rate proportional to $1/\sqrt{\rho}$ in the lateral directions, in contrast to the spatial-wave radiation, which exhibits a $1/r$ dependence [Eq. (90)].

The significance of Fig. 3 is that through Sommerfeld's interpretations [1], spatial and surface waves have been treated on an equal basis that for a given point dipole source in a layered structure the far-field solutions can be expressed explicitly by using Eq. (90) and Eqs. (91), (92), respectively, to show radiations either propagating away semispherically in free space, or guiding away concentrically on the surface of the layered structure. By using Sommerfeld's formulation, it is now possible to include a surface-wave analysis with the resonator cavity model discussed in Section 1, and the far-field surface wave radiation pattern and the total surface wave loss from the cavity can be calculated by using the perturbation theory in a manner similar to that for the spatial radiation waves. Specifically, when the zeroth-order solution is known for an isolated cavity, the far-field solution for surface waves can be expressed as the first-order perturbation by using Eq. (40) with the spatial dependence $\exp(-jk_0 r)/r$ for A_z by $H_0^{(2)}(p\rho) \exp[-\sqrt{p^2 - k_0^2} z]$, and for A_x by $\cos \phi H_1^{(2)}(p\rho) \exp[-\sqrt{p^2 - k_0^2} z]$ [see Eqs. (90)–(92)]. However, research in this direction is lacking in the current literature. Having discussed the analytic features of Sommerfeld-type integrals, in the following we discuss how Sommerfeld-type integrals are evaluated numerically.

In the presence of material losses, the branchpoints and simple pole(s) associated with spatial and surface waves, respectively, acquire imaginary components, which are then pushed off from the real axis toward the lower half of the complex k_ρ plane. As such, numerical integration of Eqs. (65) and (66) can be properly carried out. However, care needs to be taken in order to avoid large truncation errors. Integration of k_ρ along the real positive axis can be distinguished in three regions

$$\text{Region 1: } 0 < k_\rho < k_0$$

$$\text{Region 2: } k_0 < k_\rho < k_c$$

$$\text{Region 3: } k_c < k_\rho < \infty$$

where k_c denotes a cutoff wavenumber to be discussed below. In region 1 the integrands are well behaved. However, at the resonant frequencies of a metal patch dictated by the cavity model both the numerator and denominator of the integrand vanish, although their ratio remains finite. We call these geometric resonant points *quasisingularities* [15]. Near these quasisingular points the numerator and denominator need to be expanded in Taylor series on which their common zeros cancel out.

All the surface poles are contained in region 2, and conventionally, the upper bound of region 2, k_c , is defined to be 10 times the real part of the largest surface pole occurring at the integrand. In region 2 the integrand behaves wildly in the vicinity of a surface pole. When coming across a surface pole, the integrand transits from positive infinity to negative infinity, resulting in sharp cancellation during numerical integration. To circumvent this difficulty,

we expand the integrand in Laurent series in the vicinity of a surface pole $k_\rho = p$, and the quasisingular terms (with negative exponents) are then evaluated analytically (remember p is now a complex number). Equivalently, the singular part of integration is obtained via residual calculations. After subtracting the singular part from the integrand, the integrand becomes regular, which can then be numerically integrated in region 2.

In region 3 we are involved with integration of Bessel functions at infinity, which oscillate indefinitely as infinity is approached without exhibiting a strict period. This renders the conventional extrapolation scheme inaccurate. To perform integration in this region we consider asymptotic expansion of Bessel functions:

$$\begin{aligned}
 J_m(x) = & \sqrt{\frac{2}{\pi x}} \left[\cos\left(x - \frac{m\pi}{2} + \frac{\pi}{4}\right) \sum_{k=0}^{\infty} \frac{(-1)^k}{2^{2k}} \right. \\
 & \times \frac{\Gamma\left(m + 2k + \frac{1}{2}\right)}{(2k)! \Gamma\left(m - 2k + \frac{1}{2}\right)} x^{2k} - \sin\left(x - \frac{m\pi}{2} + \frac{\pi}{4}\right) \\
 & \left. \times \sum_{k=0}^{\infty} \frac{(-1)^k}{2^{2k+1}} \frac{\Gamma\left(m + 2k + \frac{3}{2}\right)}{(2k+1)! \Gamma\left(m - 2k - \frac{1}{2}\right)} x^{2k+1} \right] \quad (93)
 \end{aligned}$$

where the Γ terms denote gamma functions. As such, integrands are written in series containing terms of the form

$$\int_{k_c}^{\infty} \frac{A_p \sin(xx + \beta)}{x^p} dx \quad (94)$$

which can be readily evaluated by exploiting sine and cosine integrals and their derivatives if p is a positive integer, or error functions and their derivatives if p is a positive half-integer larger than 1 [15].

Having discussed the Green functions due to a point dipole source in a layered structure, we mention how these Green functions are modified in the presence of material losses. For a lossy material one may use complex permittivity $\varepsilon_0 \varepsilon_r (1 - j \tan \delta)$ and complex permeability $\mu_0 (\mu' + j \mu'')$ to describe its lossy characteristics, where ε_r denotes the dielectric constant, $\tan \delta$ represents the loss tangent, and μ' and μ'' are the real and imaginary parts of the relative permeability [3]. So far we have considered perfect metal boundary conditions on bounding a layered structure at the outermost surface [Eq. (77)]. For imperfect metal boundaries, for example, our Earth's surface, one may include the layer explicitly in the formulation, but using a complex permittivity $\varepsilon_0 - j\sigma/\omega$, where σ denotes the conductivity [1]. Alternatively, one can apply Snell law to specify the relationships between the a, b, c, d , coefficients resulting from reflections of incoming waves from the surface of an imperfect metal, in a manner similar to that deriving Eq. (77). Or, if the conductivity is large, say, a good metal such as copper, and the skin depth in penetration compares much smaller than the wavelength, one can even apply the perturbation theory. Thus, one first derives the Green's functions of the layered structure assuming

perfect metal boundaries followed by first-order modification that the metal boundary is withdrawn a distance δ into the interior of the imperfect metal bulk with the recessed volume to be filled by air [19]. Here δ_c denotes the (complex) skin depth

$$\delta_c = (1 + j) \sqrt{2/\omega \mu_0 \sigma} \quad (95)$$

This procedure is parallel to Wheeler's incremental impedance [20,21], since it is recognized that the definition of a Green's function is a transimpedance. To be explicit, in the presence of a good conductor ground plane Eq. (80) is modified to include its first-order Taylor expansion in d , or Wheeler's incremental impedance, and the result is [19]

$$D_{\text{TE}} = \gamma_0 + \gamma \coth \gamma d + \delta_c (1 - \tanh \gamma d) / (1 + \tanh \gamma d) \quad (96)$$

and D_{TM} is invariant under the first-order consideration. The construction of Green functions for a layered structure containing gyromagnetic materials will be discussed in Section 4.

2.4. Numerical Solutions

The dyadic Green function, $\underline{\mathbf{G}}(\mathbf{r}, \mathbf{r}')$, is defined as the electric field at location \mathbf{r} produced by a unit point dipole located at \mathbf{r}' . We are solving the current distribution over a microstrip metal patch of negligible thickness deposited on a layered structure backed by a ground plane. Therefore, \mathbf{r} and \mathbf{r}' are both located at the same metal patch (or located at different but mutually coupled metal patches), and essentially we are solving a two-dimensional problem with the third dimension, the z direction, being absorbed into the Green function. This results in the following integral equation

$$\mathbf{t}_e \left[\int_S \underline{\mathbf{G}}(\boldsymbol{\rho}, \boldsymbol{\rho}') \cdot \mathbf{J}(\boldsymbol{\rho}') d^2 \boldsymbol{\rho}' + R_s \mathbf{J}(\boldsymbol{\rho}) \right] = \mathbf{E}_e(\boldsymbol{\rho}) \quad (97)$$

where S denotes the metal patch with surface impedance $R_s = (1 + j) \sqrt{\omega \mu_0} / 2\sigma$. The first term in Eq. (97) is the electric field induced by the background layered structure, and the second term relates to ohm's current (induction and conduction), and \mathbf{E}_e is the electric field generated by external currents. Of special concern, in Eq. (97) \mathbf{t}_e results from integration along the z axis, and hence it defines the effective thickness of the metal patch, to be either the skin depth thickness, $\delta = (2/\mu_0 \omega \sigma)^{1/2}$, or the physical thickness of the metal patch t , whichever is smaller. For a perfect metal patch $\mathbf{t}_e = 0$. Thus, \mathbf{t}_e represents the singular behavior of the current distribution exhibiting a delta-function-like profile in the thickness direction. However, we expect that \mathbf{t}_e will not enter the final expressions when evaluating engineering parameters of the antenna, as is the case shown in Eqs. (98), (100), (101), and (105) below. In Eq. (97) we have used $\boldsymbol{\rho}$ and $\boldsymbol{\rho}'$ as the two-dimensional position vectors on the metal patch for which the z dependence is understood.

We denote $\{\mathbf{J}_{mn}(\boldsymbol{\rho})\}$ as a set of a complete orthonormal vector basis for currents on the metal patch. We define here $\{\mathbf{J}_{mn}(\boldsymbol{\rho})\}$ to be the regular part of the surface current density and the singular part has been factored out in

Eq. (99) as t_e^{-1} , characterizing, again, the delta-function-like distribution of surface current along the z direction. Thus, the dimension of \mathbf{J}_{mn} is amperes/meter. We apply the Galerkin's method to convert the integral equation [Eq. (97)], into the following matrix form

$$\sum_{m',n'} [B_{mnm'n'}][a_{m'n'}] = [b_{mn}], \quad (98)$$

where $[a_{mn}]$ are the unknown coefficients to be solved expressed in terms of the current basis $\{\mathbf{J}_{mn}(\rho)\}$:

$$\mathbf{J}(\rho) = t_e^{-1} \sum_{mn} a_{mn} \mathbf{J}_{mn}(\rho) \quad (99)$$

$[B_{mnm'n'}]$ are the matrix element derived from Eq. (97)

$$B_{mnm'n'} = \int_S d^2\rho \int_S d^2\rho' \mathbf{J}_{mn}^*(\rho) \cdot [\underline{\mathbf{G}}(\rho, \rho') + R_s \underline{\mathbf{I}}] \cdot \mathbf{J}_{m'n'}(\rho') \quad (100)$$

where $\underline{\mathbf{I}}$ denotes the identity dyad. The inhomogeneous term of Eq. (98), $[b_{mn}]$, is associated with current driving given by

$$b_{mn} = \int_S d^2\rho \mathbf{J}_{mn}^*(\rho) \cdot \mathbf{E}_e(\rho) = t_e^{-1} \int_V d^3\mathbf{r} \mathbf{E}_{mn}(\mathbf{r}) \cdot \mathbf{J}_e(\mathbf{r})^* \\ = \int_V d^3\mathbf{r} \int_S d^2\rho' \mathbf{J}_{mn}(\rho') \cdot \underline{\mathbf{G}}(\mathbf{r}, \rho') \cdot \mathbf{J}_e(\mathbf{r})^* \quad (101)$$

where \mathbf{E}_{mn} is the electric field generated by \mathbf{J}_{mn} , \mathbf{J}_e is the driving current density, and integration is over the whole volume, V . In Eq. (101) the reciprocity theorem has been used, which states that the response of a system to a source is unchanged if source and observer are interchanged [22]. The unit drive current density may be specified as

$$\mathbf{J}_e(\rho, z) = \underline{\mathbf{e}}_z \delta(x - x_0) \delta(y - y_0) [S(z) - S(z - d)] / 2 \\ \text{for rectangular patch} \\ = \underline{\mathbf{e}}_z \delta(\rho - \rho_0) \delta(\phi - \phi_0) [S(z) - S(z - d)] / (2\rho) \\ \text{for circular patch} \\ \mathbf{J}_e(\rho, z) = \underline{\mathbf{e}}_z [S(x - a) - S(x - b)] \delta(y) [S(z) \\ - S(z - d)] / [4(a + b)] \text{ for rectangular patch} \\ = \underline{\mathbf{e}}_z \delta(\rho - R) [S(\phi + \alpha) - S(\phi - \alpha)] [S(z) \\ - S(z - d)] / (8\alpha\rho) \text{ for circular patch} \quad (103)$$

These last two equations denote coaxial and microstrip feeders, respectively. We note that the current densities given in Eq. (103) are Huygens currents resulting from the external current fed at the microstrip input port [Eq. (38)]. By using Huygens principle the two feeder configurations, coax line and microstrip line, are cast in similar expres-

sions [Eqs. (102) and (103)] [23]. In Eqs. (102) and (103) $S(x)$ denotes the step function and

$$S(x) = 0 \quad \text{if } x < 0 \\ = 0.5 \quad \text{if } x = 0 \\ = 1 \quad \text{if } x > 0 \quad (104)$$

The input impedance is therefore, assuming unit excitation current

$$Z_{\text{in}} = -t_e \int_S d^2\rho \mathbf{E}_e^*(\rho) \cdot \mathbf{J}(\rho) \\ = - \sum_{m,n,m',n'} [b_{mn}]^* [B_{mnm'n'}]^{-1} [b_{m'n'}] \quad (105)$$

The radiation field associated with a point (Hertzian) dipole located at the air-dielectric interface of a microstrip structure is [16]

$$E_\theta = -j \frac{Z_0}{\lambda_0} \cos \phi g_\theta(\theta) \frac{e^{ik_0 r}}{r}, \quad (106)$$

$$E_\phi = j \frac{Z_0}{\lambda_0} \sin \phi g_\phi(\theta) \frac{e^{ik_0 r}}{r}$$

where

$$g_\theta(\theta) = \frac{T \cos \theta}{T - j \epsilon_r \cos \theta \cot(Tk_0 d)} \quad (107)$$

$$g_\phi(\theta) = \frac{\cos \theta}{\cos \theta - jT \cot(Tk_0 d)} \quad (108)$$

and

$$T = \sqrt{\epsilon_r - \sin^2 \theta} \quad (109)$$

The radiation pattern for a given patch current distribution $\mathbf{J}(\rho)$ [Eq. (106)] is therefore

$$\mathbf{E}^{\text{rad}}(\mathbf{r}) \\ = -j \frac{\zeta_0}{\lambda_0} \frac{\mathbf{e}^{-jk_0 r}}{r} \left[\int d^2\rho e^{i\mathbf{k} \cdot \rho} \mathbf{J}(\rho) \right] \cdot [g_\theta(\theta) \mathbf{e}_\theta \\ \times \mathbf{e}_z \mathbf{e}_\theta + g_\phi(\theta) \mathbf{e}_\phi \mathbf{e}_\phi] \quad (110)$$

where $\zeta_0 = (\mu_0/\epsilon_0)^{1/2}$ and $k_0 = 2\pi/\lambda_0 = \omega(\epsilon_0\mu_0)^{1/2}$ are, respectively, impedance and wavenumber in air.

Before performing numerical calculations, we must first determine which current basis is best suited for a given microstrip patch geometry implementing numerical calculations. For example, for a given microstrip of width expanded by interval $[-1, 1]$ one may use the triangular functions, Chebyshev polynomials, Legendre polynomials, and so on, as the functional basis to expand currents, but which one would provide the most advantages? The answer relies on the physical restriction imposed on current flow on a microstrip patch; the current basis needs to show zero (longitudinal) components when crossing the boundary of the patch; that is, the currents are not allow

to flow over metal boundaries. Under this restriction the freedom in choosing a current basis is largely fixed, which leads to the functional set of current potentials [24].

The simplest approach is to define a set of current potential $\{\psi_{mn}(\rho)\}$ satisfying the 2D Helmholtz equation

$$(\nabla_t^2 + k_{mn}^2)\psi_{mn}(\rho) = 0 \quad (111)$$

from which the current basis $\{\mathbf{J}_{mn}(\rho)\}$ is derived as

$$\mathbf{J}_{mn}(\rho) = \nabla_t \psi_{mn}(\rho) \quad (112)$$

The boundary condition imposed on $\{\mathbf{J}_{mn}(\rho)\}$ is that the current is not allowed to flow across the metal patch boundary, or, at the patch boundary

$$\mathbf{n} \cdot \mathbf{J}_{mn} = 0 \quad (113)$$

where \mathbf{n} denotes the unit outward normal at the metal patch boundary:

$$\mathbf{n} \cdot \nabla_t \psi_{mn} = 0 \text{ at patch boundary} \quad (114)$$

This equation determines the eigenvalues k_{mn} denoted in Eq. (111), and the current basis specified by Eq. (112) form a complete basis for vector fields on the metal patch.

Other advantages follow by deriving the current basis from current potentials:

1. The current potentials are intrinsic functions of the patch, so that the modal numbers $\{n,m\}$ reflect its symmetry. For example, for a rectangular microstrip antenna loaded with isotropic material the symmetry of the patch dictates currents with opposite parities do not couple. For a circular microstrip antenna loaded with isotropic materials currents with different angular modal numbers (monopole, dipole, quadrupole, etc.) do not couple. This results in largely reduced matrix size in Galerkin elements demanding numerical evaluation, thereby saving calculational efforts considerably.
2. Due to Green's theorem, in calculating a Galerkin element, most integrations required by (2D) Fourier and (2D) inverse Fourier transforms, for example [Eqs. (85) and (86)], can be performed analytically, leaving behind only onefold, or at most twofold, integrals that finally resort to numerical methods. This also saves calculational efforts.
3. By using current potentials Galerkin elements expressed by Eq. (100) reduce to scalar function multiplications rather than the originally proposed inner products between tensor and vector fields, thereby simplifying calculations.

On the basis of current potentials, we have solved the coupling problems between circular microstrip patch antennas, as introduced as follows.

For a rectangular patch located at $0 \leq x \leq L$, $0 \leq y \leq W$, the current potentials are

$$\psi_{mn}(x,y) = \frac{4}{LW} \cos \frac{m\pi x}{L} \cos \frac{n\pi y}{W}, \quad m, n = 1, 2, 3, \dots \quad (115)$$

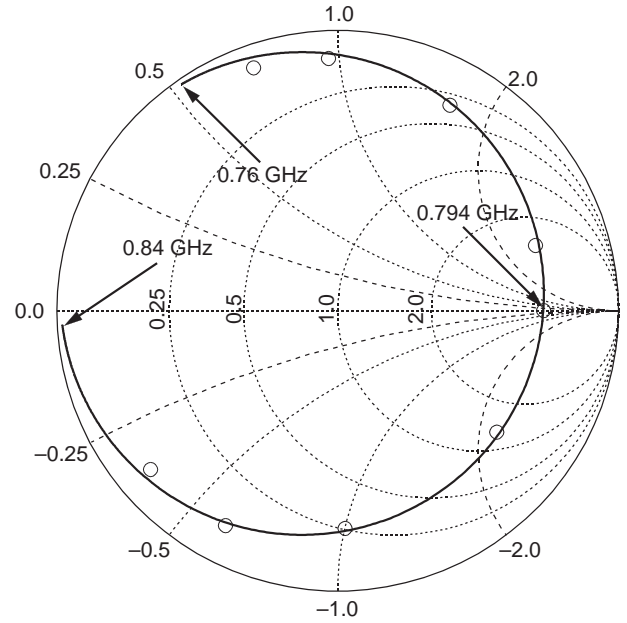


Figure 4. Input impedance loci of the antenna observed by Lo et al. The solid line is from calculation, and small circles represent measurements from Lo et al. [13].

and for a circular patch located at $0 \leq \rho \leq R$, they are

$$\psi_{mn}(\rho, \phi) = \left[\sqrt{\pi} \beta_{mn} R \left(1 - \frac{m^2}{\beta_{mn}^2 R^2} \right)^{1/2} J_m(\beta_{mn} R) \right]^{-1} \times J_m(\beta_{mn} \rho) \exp(jm\phi) \quad (116)$$

and β_{mn} denotes the root of the derivative of Bessel function, $J'_m(x)$:

$$J'_m(\beta_{mn} R) = 0 \quad (117)$$

In the following we present some calculational results for circular microstrip patch antennas [15]. For rectangular patch antennas, see Ref. 25. The first calculation applies to the published data of a circular antenna characterized by the following parameters [13]: $R = 6.75$ cm, $d = 0.1588$ cm, $\epsilon_r = 2.62$, and $\tan \delta = 0.001$. The

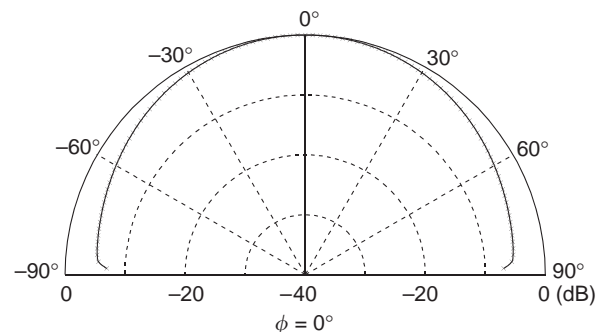


Figure 5. Radiation profile of the antenna observed by Lo et al. [13] in the $\phi = 0^\circ$ plane.

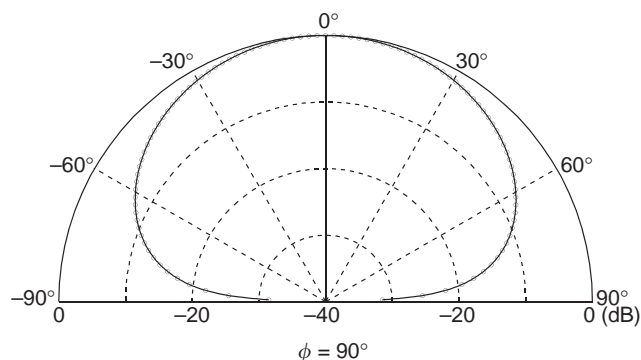


Figure 6. Radiation profile of the antenna observed by Lo et al. [13] in the $\phi = 90^\circ$ plane.

calculated resonance frequency of the fundamental mode is 0.7936 GHz [15], which compares exactly to the measured value of 0.794 GHz [13]. This is contrasted to the cavity model calculation presented in Section 1, which predicts a resonant frequency of 0.805 GHz [13]. The calculated input impedance of the antenna is shown in Ref. 15, which compares nicely with measurements shown as small circles in Fig. 4 [13]. Figures 5 and 6 show the calculated radiation pattern of the antenna in the $\phi = 0^\circ$ and $\phi = 90^\circ$ planes, respectively. We note that only the co-polarized radiations are generated from the fundamental mode excitation; the cross-polarized field cancels out for the two $m = 1$ and $m = -1$ modes at the fundamental resonant frequency.

The second patch antenna geometry considered is a microstrip disk of radius $R = 1$ cm, which is fed by either a coaxial or a microstrip line [15]. The substrate has dielectric constant, $\epsilon_r = 2.2$, loss tangent $\tan \delta = 0.001$, whose thickness d is subject to vary. Figures 7–9, assuming $\alpha = 0.2$ rad, show the calculated resonant frequency, input impedance, and radiation linewidth of the fundamental mode as a function of the substrate thickness, respectively.

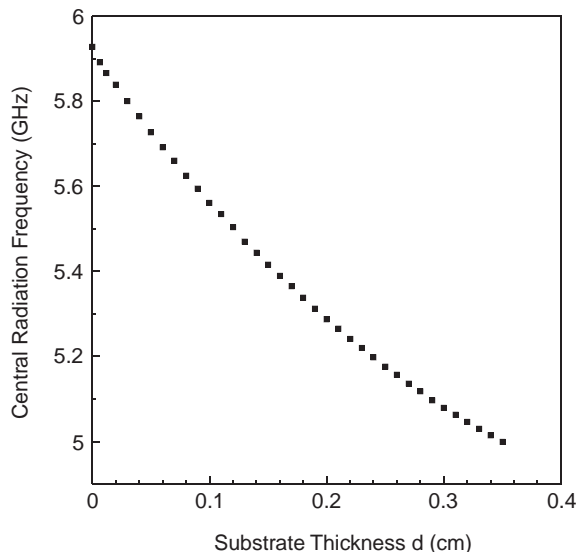


Figure 7. Calculated radiation frequency as a function of substrate thickness (fed by microstrip line).

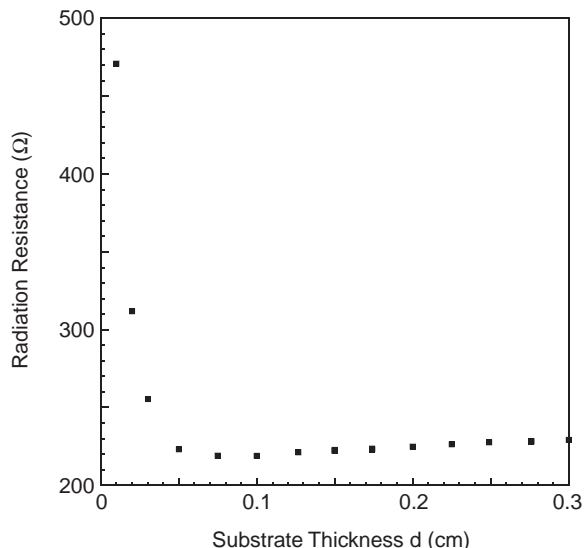


Figure 8. Calculated radiation resistance as a function of substrate thickness (fed by microstrip line).

In Fig. 7 the calculated resonant frequency of the antenna decreases monotonically with the substrate thickness d , indicating the effective dimension of the patch resonator increases with d , as expected for a leaky cavity. Figure 8 shows that the input impedance of the antenna is relatively a constant, unless d becomes very small, say, smaller than 0.05 cm. In Fig. 9 we see that the radiation bandwidth increases with d , and hence the Q factor of the antenna resonator decreases with d . This finding is consistent with that revealed from Fig. 7 exhibiting the leaky feature of the antenna patch cavity.

Figure 10 shows the calculated input impedance loci of the above circular antenna of substrate thickness $d = 0.1$ cm fed by a coaxial line located at $(\rho_0, 0)$. In Fig. 10 the parameter r_e is defined as $r_e = \rho_0/R$, and $r_e = 1.0, 0.8, 0.6,$ and 0.416 . For each feeder location the two resonant

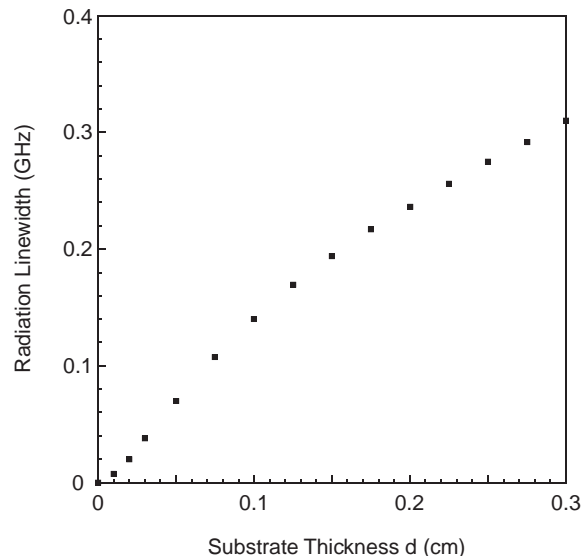


Figure 9. Calculated radiation linewidth as a function of substrate thickness (fed by microstrip line).

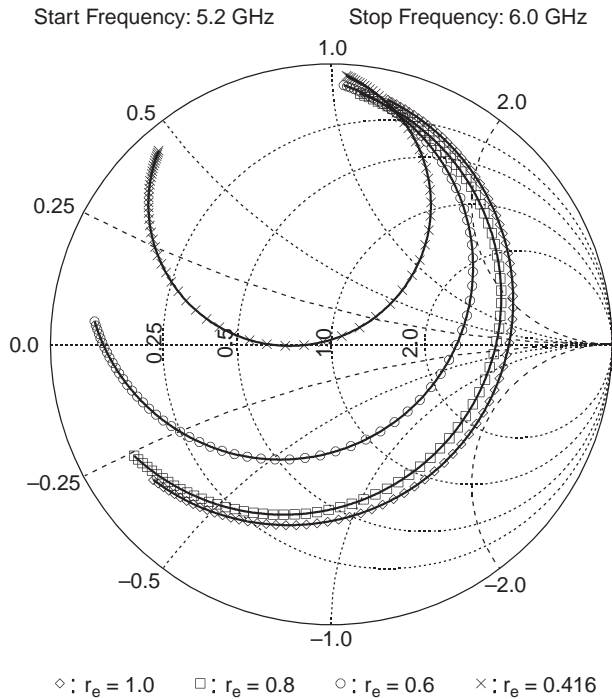


Figure 10. Input impedance loci of the antenna for several coaxial feeder positions.

frequencies shown in Fig. 10 are the resonance frequencies of the probe inductance in parallel with the detuned patch resonator forming a parallel-resonant circuit, and the resonance frequency of the probe inductance in series with the detuned patch resonator forming a series-resonant circuit. The field distribution of the patch at both frequencies shows very little difference, and the patch is operated at the same resonance mode, yet more or less detuned from its resonance frequency, which occurs between these two frequencies. It is seen in Fig. 10 that these resonant frequencies appear only if $0.416 \leq r_e \leq 1$.

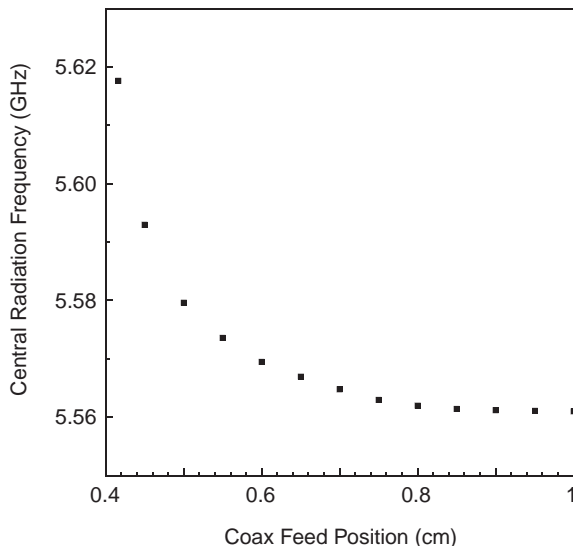


Figure 11. Calculated radiation frequency as a function of coaxial feeder position.

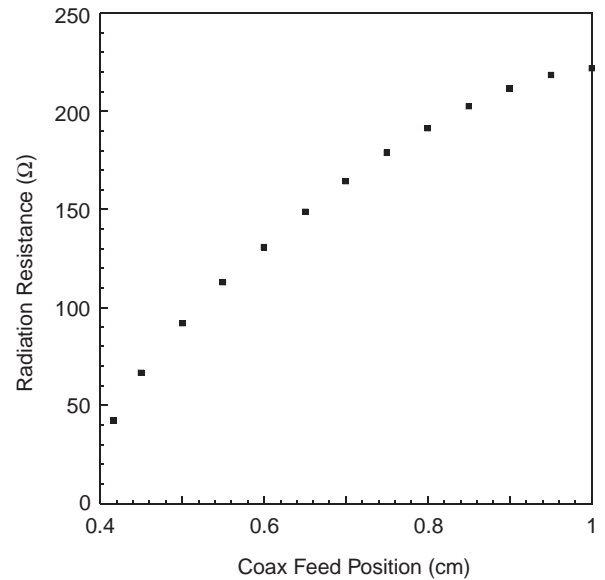


Figure 12. Calculated radiation resistance as a function of coaxial feeder position.

For $r_e \leq 0.416$ no patch resonance can be possibly excited. Figure 11 shows the calculated radiation frequency as a function of r_e , or ρ_0 . It is seen in Fig. 11 that radiation frequency remains roughly constant for $0.6 \leq r_e \leq 1$, which increases rapidly when r_e is further reduced. Figure 12 shows the calculated input resistance as a function of r_e , or ρ_0 . From Fig. 12 we see that the input impedance decreases with r_e , or ρ_0 , and hence it is possible to design 50 Ω input resistance of the antenna by feeding the antenna at $r_e = 0.442$ (or $r_e = 0.488$ for 75 Ω input impedance).

Finally, we consider the interaction between two identical circular microstrip patch antennas excited by microstrip feeders at equal amplitude and phase. Let the antennas be deployed in parallel exhibiting the same parameters considered before: $R = 1$ cm, $d = 0.1$ cm, $\epsilon_r = 2.2$, and the feeder lines possess 50 Ω resistance (width 0.312 cm). The separation between the antennas is designated as R_{12} measured between their respective centers. Figure 13 shows the calculated and measured input impedance for the coupled case, $R_{12} = 2$ cm (the patches are touching each other), and the uncoupled case, $R_{12} = 5$ cm (the patches are separated by 3 cm at their edges). Measurements were performed with respect to patch antennas fabricated using RT/duroid 5880 material (Rogers Co., Chandler, AZ). The measured resonant frequencies were 5.514 and 5.561 GHz for the coupled and uncoupled cases, respectively, which compare almost exactly to their calculated values of 5.5137 and 5.5642 GHz. The resonant frequencies of the patches and their input impedances have also been calculated as a function of the patch separation, R_{12} . These are shown in Figs. 14 and 15, respectively, with measurements shown as solid squares. From Fig. 14 it is seen that the resonant frequency changes most rapidly when R_{12} is small, say, when $2 \leq R_{12} \leq 3$ cm. Further increase in R_{12} does not significantly change the resonance frequency. However, the input impedance does show long-range interference between two patch antennas. As shown

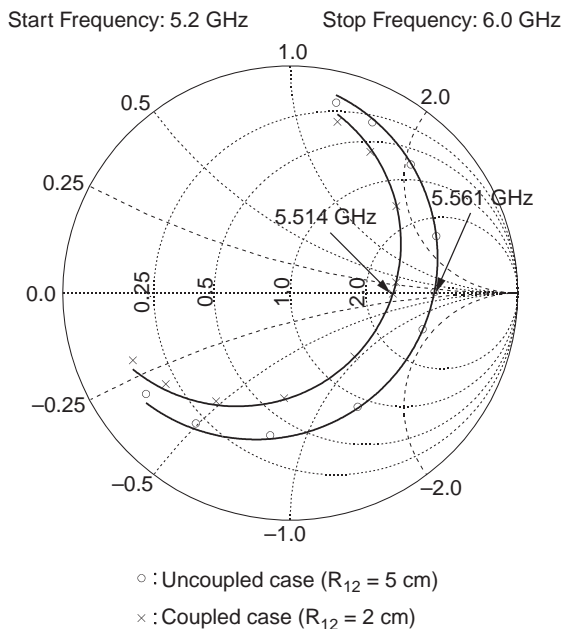


Figure 13. Calculated and measured input impedance loci of two coupled patch antennas.

in Fig. 15, the input impedance is still increasing when the two antennas are separated by 5 cm, although the rate of increase has slowed when compared with its initial rate at $R_{12} = 2$ cm.

We conclude that the leaky feature of an antenna cavity can be well characterized by using a full-wave analysis outlined in Section 2. Among many numerical methods, the dyadic Green function approach might prove to be the simplest one to apply, not only because the analysis is two-dimensional but also because the evaluation of the scalar Galerkin elements involves only one-fold Sommerfeld-type integrals. Surface-wave generation is significant for a thick dielectric substrate with large dielectric constant.

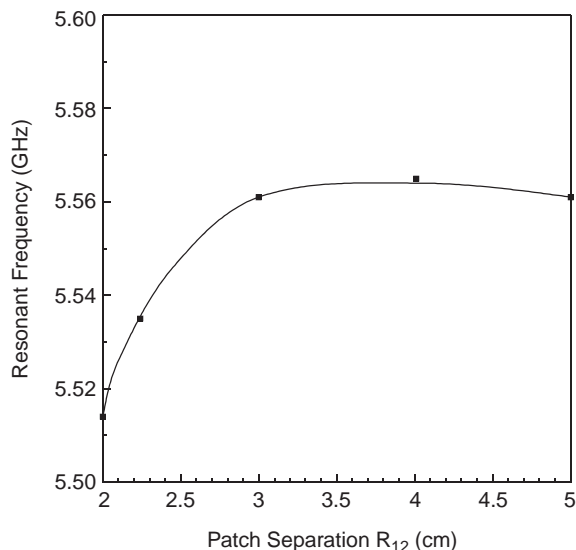


Figure 14. Calculated and measured resonant frequencies of two coupled patch antennas as a function of their separation distance.

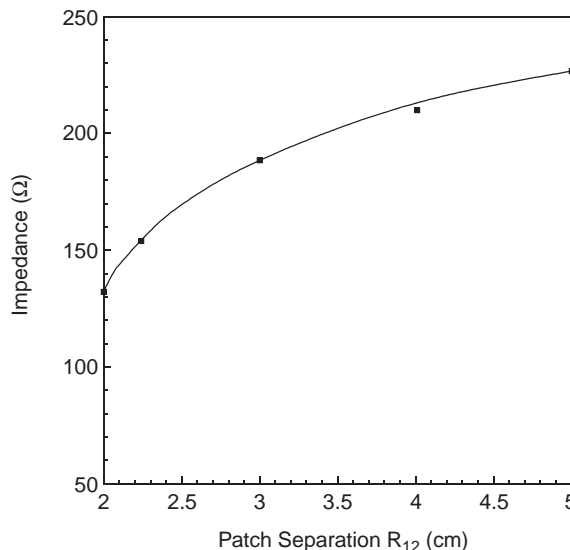


Figure 15. Calculated and measured input impedances at resonant of two coupled patch antennas as a function of their separation distance.

The coupling between microstrip elements is of long-range nature, although the radiation frequency of a patch is less influenced by its neighboring antenna elements.

3. ANISOTROPIC/GYROMAGNETIC LAYER

In Sections 1 and 2 we considered microstrip patch antennas fabricated on isotropic materials. Anisotropic substrates, due to either the process in material preparation or crystalline asymmetry, have been included in the fabrication of microwave integrated circuits (MICs). Also, electromagnetic wave propagation in a fully saturated ferrite substrate is anisotropic, called the *gyromagnetic effect*. For the former case the dielectric properties of the substrate can be described in terms of a permittivity tensor of rank 2, and for the latter case Polder permeability tensor results under the small-signal approximations [26]. While many authors have applied numerical calculations to microwave circuitries containing anisotropic substrates [27–31], in this section we consider wave propagation in a gyromagnetic substrate [32]. Specifically, we consider the electromagnetic wave propagation involving the microstrip geometry where the metal circuit is fabricated on top of a ferrite substrate for which the bias magnetic field is applied along an arbitrary direction that is not necessarily the symmetry axis. In order to minimize magnetic loss, the ferrite substrate needs to be fully saturated so that an external DC magnetic field is applied aligning magnetic domains achieving the single-domain configuration, thereby eliminating domain wall motion to be otherwise induced accompanying electromagnetic wave propagation [33]. This external magnetic bias field can be supplied by material anisotropy as occurring to a hexaferrite substrate considered in Ref. 32.

In contrast to the permittivity tensor, Polder tensor elements are highly frequency-dependent and exhibit the resonance response in frequency and in the bias magnetic

field [33]. For example, when ferrimagnetic resonance (FMR) is encountered, the effective permeability changes from a large positive number to a large negative number together with a nonzero imaginary part accounting for magnetic loss [26]. Magnetic loss at resonance is parametrized as FMR linewidth whose occurrence arises from magnetic relaxation processes accompanying the precessional motion of spins at resonance [33]. Most useful magnetic microwave devices are designed to operate near FMR so that the rapid change in magnetic permeability is exploited, either to obtain frequency tuning capability or to remove the degeneracy in electromagnetic modes, thereby inducing nonreciprocity in wave propagation [33]. For example, ferrite phase shifters [34], resonators [35], and filters [26] are operational according to the first principle [33] and circulators and isolators, according to the second [36].

Before solving the AC problem on wave propagation involving a ferrite substrate, one is required to first solve the DC problem to calculate the demagnetizing field arising from the finite dimensions of the ferrite geometry [33]. In a cubic ferrite sample material anisotropy is seldom important, since it is small in comparison to the external bias field. In a hexaferrite substrate the internal anisotropy field can be as large as 50 kOe, and hence it can no longer be neglected [37]. Actually, hexaferrites are purposely introduced with a microwave circuit to alleviate, or even eliminate [38], the external bias-field requirement at high frequencies. In a hexaferrite material magnetic anisotropy appears in the form of an easy axis or an easy plane. For an M-type hexaferrite the c axis is an easy axis, and the magnetization vector prefers to be aligned along the c axis so as to lower its free energy [33]. For a Y-type hexaferrite the ab plane is an easy plane, and the magnetization vector is energetically favorable to stay on the ab plane [38]. The total effective field inside a ferrite substrate can be calculated from the system Lagrangian, including magnetic anisotropy, FMR linewidth, exchange coupling, demagnetization, and magnetostriction [33].

In Section 2 we have considered the Green functions of a layered structure containing isotropic materials that were constructed using the vector potentials as introduced by Sommerfeld [1]. In this section we consider the Green function construction by using the plane-wave solutions for which the substrate/superstrate may contain anisotropic layers. While plane-wave solutions are trivial within an isotropic dielectric layer, plane-wave solutions for an unbounded ferrite bulk magnetized along an arbitrary direction are also available [26], whose properties can be found in Ref. 32. For a given frequency there are four independent electromagnetic modes in a substrate material that are all degenerate if the substrate shows isotropy for wave propagation. However, for an anisotropy substrate, say, a ferrite fully biased by a magnetic field (or, a gyromagnetic material), wave propagation for these four modes becomes nondegenerate, assuming different effective permeability values for different modes, resulting in different propagation speeds and polarizations. Similar to the isotropic case, the directions of electric field, magnetic induction, and wave propagation for each mode excited in an anisotropic substrate are mutually perpendicular to

each other, as dictated by Maxwell equations. For a gyromagnetic substrate, the magnetic field is no longer aligned with magnetic induction, although it is still required to be perpendicular to the direction of the electric field [32].

One may apply the transfer-matrix technique to construct the Green functions of a layered structure. A transfer matrix is formulated in the transverse spectrum domain, which translates the surface impedance, which is itself a 2×2 matrix, from one layer interface to another, assuming the tangential components of the electromagnetic fields to be continuous across the interfaces in the absence of circuit (conductor) inhomogeneities. The transfer matrices for a given layer can be constructed in terms of the four electromagnetic modes, or the plane-wave solutions in the spectral domain, in a manner similar to the a, b, c, d coefficients introduced by Eqs. (72) and (73) (except that the γ values differ for the four modes in an anisotropic layer). The *surface impedance matrix* is defined as the ratio of the tangential electric field to the tangential magnetic field at a given layer interface, and hence it is a 2×2 matrix. The outermost layers are either air or a metal surface of finite conductivity, giving rise to the (imperfect) open-circuited or short-circuited boundaries for the layered structure, respectively. The surface impedance matrices for the outmost two layers can thus be obtained, in a manner similar to that used to obtain Eq. (77). Via the transfer matrices defined for the layers, these two outermost surface impedance matrices are translated sequentially onto an interface containing a point source responsible for the Green function definition (a Green function is defined to be the response excited by the point source). After applying Ampère law the Green functions evaluated at this interface position can thus be obtained [32]. To be explicit, assuming the point source is located at the origin, the Green functions, or the Green dyads, are defined by

$$\begin{aligned} \underline{\mathbf{e}}_t(x, y) &= \frac{1}{4\pi^2} \int_{-\infty}^{\infty} dk_x \int_{-\infty}^{\infty} dk_y \int_{-\infty}^{\infty} dx' \int_{-\infty}^{\infty} dy' \exp[ik_x(x - x')] \\ &\quad \times \exp[ik_y(y - y')] \underline{\mathbf{G}}(k_x, k_y) \underline{\mathbf{j}}(x', y') \end{aligned} \quad (118)$$

and after applying Ampère law at the interface $z = 0$ the Green functions are obtained as

$$\begin{aligned} \underline{\mathbf{G}}(k_x, k_y) &= \{ \underline{\mathbf{Z}}(0^+; k_x, k_y) \}^{-1} \\ &\quad - \{ \underline{\mathbf{Z}}(0^-; k_x, k_y) \}^{-1} \begin{pmatrix} 0 & 1 \\ -1 & 0 \end{pmatrix} \end{aligned} \quad (119)$$

Here $\underline{\mathbf{j}}(x', y')$ denotes current density, $\underline{\mathbf{e}}_t(x, y)$ tangential electric field, and (k_x, k_y) the transverse spectral vector. In Eq. (119) $\underline{\mathbf{Z}}(0^+)$ denotes the impedance matrix that is transferred from the topmost layer, and $\underline{\mathbf{Z}}(0^-)$ from the bottommost layer, and $\underline{\mathbf{Z}}(0^+)$, $\underline{\mathbf{Z}}(0^-)$, and $\underline{\mathbf{G}}$ are all 2×2 matrices. Thus, once the Green function is known [Eq. (119)], the microstrip circuit involving a layered structure

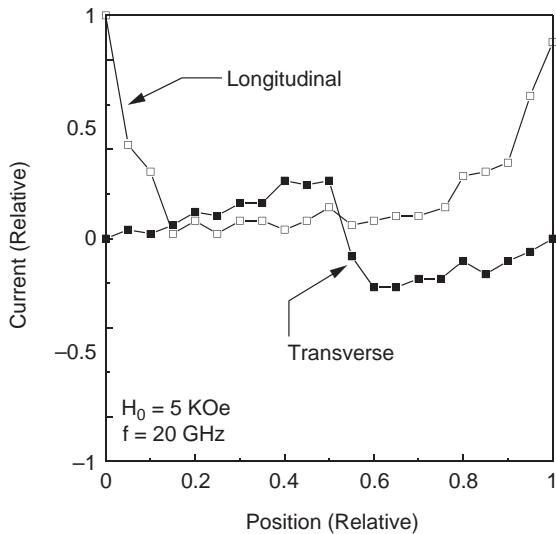


Figure 16. Calculated current profile for the longitudinal and the transverse components across the strip width of a microstrip line fabricated on top of a hexaferrite.

containing anisotropic materials can be solved in a manner identical to that shown in Section 2.

As we have just mentioned, wave propagation is anisotropic in an anisotropic medium, and in performing numerical calculations Galerkin elements need to be all evaluated in general, since symmetry of the system ceases to apply. This is illustrated in Fig. 16, where the induced current profiles along the width direction of a microstrip line fabricated on a hexaferrite substrate no longer show left–right symmetry, due to the gyromagnetic nature of a hexaferrite material [32]. In Fig. 16 the substrate was a single-crystal Y-type hexaferrite of composition $\text{Ba}_2\text{MgZnFe}_{12}\text{O}_{22}$, and the easy plane coincides with the substrate surfaces, the xy plane. The hexaferrite substrate was characterized by the following parameters: saturation magnetization $4\pi M_S = 2.86$ kG, anisotropy field $H_A = 7.94$ kOe, dielectric constant $\epsilon_f = 18$, dielectric loss tangent, $\tan \delta_f = 0.01$, and FMR linewidth $\Delta H = 100$ Oe. The width of the fabricated microstrip line was $w = 0.0051$ in. and length $\ell = 0.0157$ in. and the thickness of the hexaferrite substrate was $d = 0.010$ in. More calculations and measurements on this fabricated microstrip line can be found in Ref. 32.

4. FRACTAL ANTENNAS

Traditional approaches to the analysis and design of antenna systems are based on Euclidean geometry. More recently, however, there has been a considerable amount of interest in developing new types of antennas that employ fractal rather than Euclidean geometries. This new and rapidly growing field is referred to as *fractal antenna engineering*, and this topic is briefly introduced in this section.

A *fractal* is a recursive object that has a fractional dimension showing shape similarity in scale; that is, a fractal preserves its shape when viewed in different scales.

Many objects, including antennas, can be designed using the recursive nature of a fractal. The term *fractal*, which means broken or irregular fragments, was originally coined by Mandelbrot [39] to describe a family of complex shapes that possess an inherent self-similarity in their geometric structure. Since the pioneering work of Mandelbrot and others, a wide variety of applications for fractals have been found in many branches of science and engineering. One such area is fractal electrodynamics, in which fractal geometry is combined with electromagnetic theory for the purpose of investigating a new class of radiation, propagation, and scattering problems. One of the most promising areas of fractal electrodynamics is in its application to antenna theory and design.

In an Euclidean geometry, broadband and frequency-independent antennas were developed and analyzed in the early 1960s, and some convoluted shapes were developed whose performance indicated the dependence of the antenna radiation properties on its physical size relative to wavelength. Spirals and logperiodic structures are some examples of successful developments giving rise to frequency-independent radiations. Fractals might join some of those designs because of their self-scaling properties. Actually, fractal antennas have been shown to provide two advantages: to generate multiband radiations and to perform beamforming capabilities. As such, the current fractal antenna engineering is applied in two areas, and the fractal pattern is either used by an isolated antenna radiator or included as elements in an antenna array (a multipole configuration). As described in Section 1, since the radiation frequency is inversely proportional to the linear dimension of a radiator, a fractal antenna can thus emit multiband radiation [40]. Furthermore, a fractal antenna can also be viewed as arrays of arrays, and hence it possesses beamforming capability, if designed and operated properly [41]. It is these novel properties that make fractal antennas very attractive, allowing phased arrays to be fabricated with conformity and reduced sizes, resulting in convenience and flexibility.

Concerning these particular issues, Puente-Baliarda et al. described [40] the behavior of the first fractal multiband antenna—the Sierpinski monopole. Such a monopole displayed similar behavior at several bands in terms of both input return loss and radiation patterns. Some steps further in the field of multiband fractal antennas were reported by Cohen [43], who also discussed other interesting features regarding small and frequency-independent fractal antennas. In [40] the behavior of both the Sierpinski monopole and dipole have been investigated, and their performance has been compared with a conventional triangular (bowtie) antenna.

Figure 17 shows the original Sierpinski triangular pattern. The Sierpinski pattern is named after the Polish mathematician Sierpinski, who described some of the main properties of this fractal shape in 1916 [42]. The original pattern is constructed by subtracting a central inverted triangle from a main triangle shape (see Fig. 17). After the subtraction, three equal triangles remain on the structure, each one half the size of the original one. One can iterate this same subtraction procedure on the remaining triangles, and if the iteration is carried out an

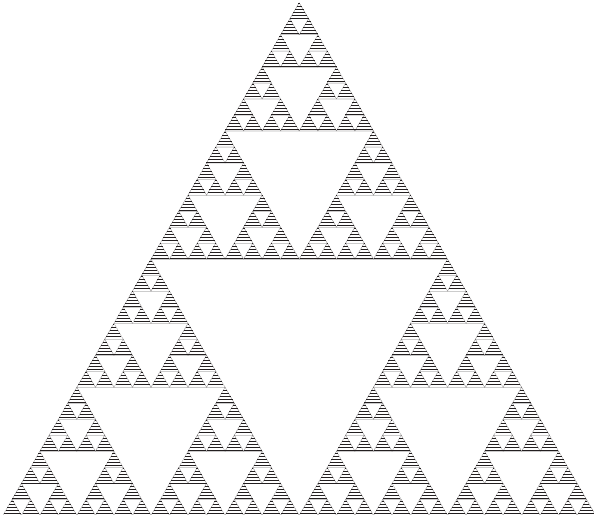


Figure 17. Fractal Sierpinski pattern.

infinite number of times, the ideal fraction Sierpinski pattern is obtained. In such an ideal structure, each of its three main parts is exactly equal to the whole object, but scaled by a factor of 2, and so are each of the three triangles that compose any of those parts. Because of these particular similarity properties, shared with many other fractal shapes, it is said that the Sierpinski pattern is a self-similar structure.

In Fig. 17 the Sierpinski pattern is shown with six levels in iterations, and the smallest scale is a single triangle shown shaded in Fig. 17. Sierpinski triangles constitutes the simplest geometry for a 2D fractal. In the monopole configuration, the feeder is located at the top vertex of the big (main) triangle. In this antenna geometry, if one neglects the contribution of the central holes to the antenna performance and admits that the current flowing from the feeder should concentrate over a region that is comparable in size to the wavelength, a behavior similar to six-scaled



Figure 18. A quadrupole fractal.

bowtie antennas (each one operating at its resonant frequency) could be expected. The scale factor among the six iterations is $\Delta = 2$; therefore, one should look for similarities at frequencies also spaced by a factor of 2. A Sierpinski dipole or quadrupole can be formed by joining two or four Sierpinski monopoles at the vertex points, respectively, showing improved frequency independency with reduced beamwidth in radiation. A Sierpinski quadrupole is shown in Fig. 18, which has been used as the company logo by Hotech, Inc. In conclusion, the most important features of a fractal array include the frequency-independent multiband characteristics, schemes for realizing low-sidelobe designs, systematic approach to thinning, and the ability to develop rapid beamforming algorithm, and fractal antennas are still active under current research and development.

5. RECENT DEVELOPMENTS

5.1. Wideband Techniques

A microstrip patch antenna is inherently narrowband, stemming from the cavity model, where an electromagnetic resonator confining energy locally in space with little dissipation is necessarily a high- Q , and hence narrowband, device. For a high- Q resonator the generation of surface waves is insignificant. For a thin substrate this condition amounts to $d/\lambda_0 < 0.07$ for $\epsilon_r = 2.3$ and $d/\lambda_0 < 0.023$ for $\epsilon_r = 10$, as stated at the end of Section 1 [10,11]. For a microstrip antenna fabricated on a thin substrate, the impedance bandwidth is typically 1–3%. This is contrasted with the bandwidth of 16% of a half-wave dipole with a radius:length ratio equal to 0.01, and 70% of a medium-length helix operating in the axial mode.

A number of techniques have been proposed to increase the bandwidth of a microstrip patch antenna. These techniques are generally classified into three categories: (1) a straightforward approach based on the use of a thick substrate whose dielectric constant is small, (2) an approach where a matching network is designed to enhance the bandwidth [44], and (3) a method using parasitically coupled elements in a variety of ways to produce closely spaced multiple resonances of the antenna [45,46].

By using a thick substrate whose dielectric constant is considerably different from that of air, surface waves will be generated and inevitably reduce the radiation efficiency and introduce interference between array elements. To resolve this problem, air cavities or holes may be introduced with the substrate to effectively reduce the dielectric constant of the patch. For example, Gauthier et al. [47] machined closely spaced holes in a Duroid substrate underneath a microstrip patch to lower the effective dielectric constant of the antenna. Using the micromachining technique, Zheng et al. measured a 12.8% impedance bandwidth on cavity-backed microstrip patch antennas fabricated on silicon wafers [48].

The bandwidth of the antenna is determined primarily by the rate of transition that the imaginary part of the impedance changes sign at resonance, as discussed at the end of Section 1. Thus, it is possible to introduce a cancellation mechanism on the input inductance so as to

smooth the impedance variation. For example, the inductance associated with the long wire lead of the coaxial probe will limit the bandwidth to $<10\%$ for a thick substrate. By etching a small circular slot around the probe on the patch, capacitance is thereby introduced, canceling the probe inductance to produce a bandwidth of 16% [49]. More recently, with the use of a U-shaped slot, a substantial increase in bandwidth (32%) has been demonstrated [50]. Alternatively, an L-shaped probe-wire has been shown to result a bandwidth of 28% [51].

The third method to achieving broadband operation is to couple the microstrip patch antenna parasitically with other dielectric resonators characterized by approximately the same resonant frequency of the patch. For an isolated patch the resonant frequency is determined by its lateral dimension. However, in the presence of fringe fields at the patch periphery the boundary of the antenna is neither sharply nor rigidly defined, leading to a slightly larger effective dimension of the patch, as described by Eqs. (2) and (5) for rectangular and circular microstrip patches, respectively. Thus, in contrast to a metal cavity, patch antennas have soft boundaries, which in turn give rise to finite bandwidth in radiation; the softer the boundary, the wider the bandwidth. For this reason a patch antenna fabricated on a thick substrate will show a wide bandwidth. Similarly, when coupled together many soft-boundary microstrip resonators/patches, the overall radiation bandwidth is consequently enlarged.

The disadvantage of using a thick substrate is that, besides its cost, surface waves may be generated in the substrate so as to reduce the antenna feeding efficiency. This disadvantage can be overcome by using multiple electromagnetically (EM) coupled patches. EM-coupled patches can be deployed either side-by-side (laterally coupled geometry) or layer-by-layer (vertically coupled geometry). For laterally coupled patches the antenna size will increase considerably, ultimately restricting its usage from large-array applications [52].

The two-layer EM coupled patch antenna consisting of a driven (feeder) patch in the bottom and a parasitic (radiating) patch on the top has been investigated by several authors. For circular [53], equitriangular [54], and rectangular [55] patches, experimental results have shown an enhanced gain and impedance bandwidth with low cross-polarization levels as compared to the conventional single-layer microstrip antenna. Actually, as analogous to Yagi antenna, the gain of a stacked antenna can be increased to above 20 dB at any scan angle if the thickness of the substrate and multiple superstrate layers is chosen properly [56]. Therefore, using stacked parasitic elements in microstrip arrays could improve the overall array performance, offering a higher gain and broader bandwidth, meeting with the same array design criteria of a conventional single-layer microstrip array but with fewer array elements.

5.2. Size Reduction

Microstrip antennas have a number of advantages over conventional antennas, namely, small size, light weight, low production cost, and natural conformal. However, for

many applications, for example, handheld mobile communication systems, half-wave microstrip antennas etched on a low-cost dielectric substrate are still too large to be accommodated on the portable phone. A well-known approach to reduce the size of a half-wave patch to a quarter-wave is to introduce an electrically short-circuiting wall at one of the radiating edges. Hiraswa and Haneishi [57] has shown that the length of the patch can be made sufficiently shorter than a quarter-wave by replacing the short-circuiting wall with a short-circuiting pin at the corner of the patch. Wang and Lin have shown that by replacing the short-circuiting pin with a chip resistor of low resistance, the antenna size can be further reduced in addition to an increase in bandwidth [58].

The other approach to reduce antenna size is to use a meandered geometry of the patch antenna [57]. By meandering the patch, the effective electrical length is greater than the physical length. Consequently, the resonant frequency of the meandered antenna can be much lower than that of a conventional design using the same physical length [59].

Finally, we note that it is not only possible to achieve high gain for printed circuit antennas, it is also feasible to shape the radiation pattern in some prescribed manner. Some very interesting phenomena, such as radiation into the horizon, radiation pattern monodirectionality, and azimuth-dependent radiation, have been found possible [60]. Furthermore, laterally coupled patches can serve as adaptive array antennas, because the phase of radiation from a parasitic element can be adjusted via a varactor diode inserted at some feeding position [61]. The important feature of an adaptive array antenna is that it can provide beamsteering as required by many communication and traffic control systems [62].

BIBLIOGRAPHY

1. A. Sommerfeld, *Partial Differential Equations*, Academic Press, New York, 1962.
2. J. R. James and P. S. Hall, eds., *Handbook of Microstrip Antennas*, Vols. 1, 2. Peter Peregrinus, London, 1989.
3. H. How, T.-M. Fang, and C. Vittoria, Intrinsic modes of radiation in ferrite patch antennas, *IEEE Trans. Microwave Theory Tech.* **MTT-42**(6):988 (1994).
4. E. O. Hammerstad, Equations for microstrip circuit design, *Proc. 5th European Microstrip Conf.*, Hamburg, Sept. 1975, pp. 268–272.
5. M. V. Schneider, Microstrip lines for microwave integrated circuits, *Bell Syst. Tech. J.* **48**:1421–1444 (1969).
6. L. C. Shen, Resonant frequency of circular disc, printed circuit antenna, *IEEE Trans. Anten. Propag.* **AP-25**:596 (1977).
7. J. A. Stratton, *Electromagnetic Theory*, McGraw-Hill, New York, 1941.
8. R. S. Elliott, *Antenna Theory and Design*, Prentice-Hall, Englewood Cliffs, NJ, 1981.
9. A. G. Derneryd, Microstrip array antenna, *Proc. 6th European Microwave Conf.*, 1976, pp. 339–343.
10. J. R. James and A. Henderson, High-frequency behavior of microstrip open-circuit terminations, *IEEE J. Microwaves Opt. Acoust.* **3**:205–218 (1979).

11. C. Wood, Analysis of microstrip circular patch antennas, *IEE Proc.* **128**(H):69–76 (1981).
12. S. B. A. Fonseca and A. J. Giarola, Microstrip disk antennas, Part I: efficiency of space wave launching, *IEEE Trans. Anten. Propag.* **AP-32**:561–567 (1984).
13. Y. T. Lo, D. Solomon, and W. F. Richards, Theory and experiment on microstrip antennas, *IEEE Trans. Anten. Propag.* **AP-27**:137–145 (1979).
14. R. C. Booton, Jr., *Computational Method for Electromagnetics and Microwaves*, Wiley, New York, 1992.
15. H. How and C. Vittoria, Computer aided design tools for microstrip circuitries, in N. K. Das and H. L. Bertoni, eds., *Directions for the Next Generation of MMIC Devices and Systems*, Plenum Press, New York, 1997, pp. 399–406.
16. J. R. Mosig, R. C. Hall, and F. E. Gardiol, Numerical analysis of microstrip patch antennas, in J. R. James and P. S. Hall, eds., *Handbook of Microstrip Antennas*, Peter Peregrinus, London, 1989, pp. 393–453.
17. J. D. Jackson, *Classical Electrodynamics*, Wiley, New York, 1975.
18. S. Y. Liao, *Microwave Devices and Circuits*, Prentice-Hall, Englewood, Cliffs, NJ, 1985.
19. H. How, C. Vittoria, and T. Fang, New formulation of dyadic Green's function: applied to a microstrip, *IEEE Trans. Microwave Theory Tech.* **MTT-41**(8):1580 (1994).
20. K. C. Gupta, R. Garg, and I. J. Bahl, *Microstrip Lines and Slotline*, Artech House, Norwood, MA, 1979.
21. H. How, R. Seed, C. Vittoria, D. B. Chrisey, and J. S. Horwitz, Microwave characteristics of superconducting coplanar waveguide resonator, *IEEE Trans. Microwave Theory Tech.* **MTT-41**(3):255 (1993).
22. R. F. Harrington, *Time Harmonic Electromagnetic Fields*, McGraw-Hill, New York, 1961.
23. H. How and C. Vittoria, Green's function calculations on circular microstrip patch antennas, *IEEE Trans. Anten. Propag.* **AP-49**:393 (1991).
24. H. How and C. Vittoria, Radiation modes in dielectric circular patch antennas, *IEEE Trans. Microwave Theory Tech.* **MTT-42**(10):1939 (1994).
25. D. M. Pozar, Input impedance and mutual coupling of rectangular microstrip antennas, *IEEE Trans. Anten. Propag.* **AP-30**:1191 (1982).
26. B. Lax and K. J. Button, *Microwave Ferrites and Ferrimagnetics*, McGraw-Hill, New York, 1962.
27. N. Alexópoulos, Integrated-circuit structures on anisotropic substrates, *IEEE Trans. Microwave Theory Tech.* **MTT-33**:847 (1985).
28. T. Q. Ho and B. Becker, Frequency-dependent characteristics of shielded broadside coupled microstrip lines on anisotropic substrates, *IEEE Trans. Microwave Theory Tech.* **MTT-39**:1021 (1991).
29. G. W. Hanson, A numerical formulation of dyadic Green's functions for planar bianisotropic media with application to printed transmission lines, *IEEE Trans. Microwave Theory Tech.* **MTT-44**:144 (1996).
30. M. R. Rosa, M. L. Albuquerque, A. G. D'Assumcio, R. G. Maia, and A. J. Giarola, Full wave analysis of microstrip lines on ferrite and anisotropic dielectric substrate, *IEEE Trans. Magn. Mag-25*:2944 (1989).
31. EL-B. El-Sharawy and R. W. Jackson, Coplanar waveguide and slot line on magnetic substrates: Analysis and experiment, *IEEE Trans. Microwave Theory Tech.* **MTT-36**:1071 (1988).
32. H. How, X. Zuo, E. Hokanson, and C. Vittoria, Calculated and measured characteristics of a microstrip line fabricated on a Y-type hexaferrite substrate, *IEEE Trans. Microwave Theory Tech.* **MTT-50**(5):1280–1288 (2002).
33. H. How, Magnetic microwave devices, in J. G. Webster, ed., *Encyclopedia of Electrical and Electronics Engineering*, Wiley, New York, 1999, Vol. 12, pp. 31–45.
34. H. How, P. Shi, C. Vittoria, E. Hokenson, M. H. Champion, L. C. Kempel, and K. D. Trott, Steerable phased array antennas using single-crystal YIG phase shifters—theory and experiments, *IEEE Trans. Microwave Theory Tech.* **MTT-48**:1544 (2000).
35. D. M. Pozar, Radiation and scattering characteristics of microstrip antennas on normally biased ferrite substrates, *IEEE Trans. Anten. Propag.* **AP-30**:1084 (1992).
36. H. How, S. A. Oliver, S. W. McKnight, P. M. Zavracky, N. E. McGruer, and C. Vittoria, Theory and experiment of thin-film junction circulator, *IEEE Trans. Microwave Theory Tech.* **MTT-46**:1645 (1998).
37. W. H. Von Aulock, ed., *Handbook of Microwave Ferrite Materials*, Academic Press, New York, 1965.
38. N. Zeina, H. How, and C. Vittoria, Self-biasing circulators operating at Ka band utilizing M-type hexagonal ferrites, *IEEE Trans. Magn. Mag-28*:3219 (1992).
39. B. B. Mandelbrot, *The Fractal Geometry of Nature*, Freeman, New York, 1983.
40. C. Puente-Baliarda, J. Romey, and R. Pous, On the behavior of the Sierpinski multiband fractal antenna, *IEEE Trans. Anten. Propag.* **AP-46**:517–524 (1998).
41. D. H. Werner, R. L. Haupt, and P. L. Werner, Fractal antenna engineering: The theory and design of fractal antenna arrays, *IEEE Trans. Anten. Propag.* **AP-41**:37–59 (1999).
42. H. O. Peitgen, H. Juergens, and D. Saupe, *Chaos and Fractals*, Springer-Verlag, New York, 1983.
43. N. Cohen, Fractal antennas, *Commun. Quart.* 53–66 (1996).
44. H. An, K. J. C. Nauwelaers, and A. R. Van de Capelle, Broadband microstrip antenna design with the simplified real frequency technique, *IEEE Trans. Anten. Propag.* **AP-42**(2):129–136 (Feb. 1994).
45. R. Q. Lee, K. F. Lee, and J. Bobinchak, Characteristics of a two layer electromagnetically coupled rectangular patch antenna, *Electron. Lett.* **23**:1070–1072 (Sept. 1987).
46. C. K. Aanandan, P. Mohanan, and K. G. Nair, Broadband gap-coupled microstrip antenna, *IEEE Trans. Anten. Propag.* **AP-38**(10):1581–1586 (Oct. 1990).
47. G. P. Gauthier, A. Courtay, and G. M. Rebeiz, Microstrip antenna on synthesized low-dielectric constant substrates, *IEEE Trans. Anten. Propag.* **AP-45**(8):1310–1314 (Aug. 1997).
48. M. Zheng, Q. Chen, P. S. Hall, and V. F. Fusco, Broadband microstrip patch antennas on micromachined silicon substrates, *Electron. Lett.* **34**(1):3–4 (1998).
49. P. S. Hall, Probe compensation in thick microstrip patches, *Electron. Lett.* **23**:606–607 (1987).
50. K. F. Lee, K. M. Luk, K. F. Tong, S. M. Shum, T. Huynh, and R. Q. Lee, Experimental and simulation studies of coaxially fed U-slot rectangular patch antenna, *IEE Proc. Microwave Anten. Propag.* **144**:354–358 (1997).
51. K. M. Luk, C. L. Mak, Y. L. Chow, and K. F. Lee, Broadband microstrip patch antenna, *Electron. Lett.* **34**(15):1442–1443 (1998).
52. S. Dey and R. Mittra, A compact broadband microstrip antenna, *Microwave Opt. Technol. Lett.* **11**(6):295–297 (1996).

53. A. Sabban, A new broadband stacked two-layer microstrip antenna, *IEEE AP-S Int. Symp. Digest*, 1983, pp. 63–66.
54. P. S. Bhatnagar, J. P. Daniel, K. Mahdjoube, and C. Terret, Experimental study on stacked triangular microstrip antennas, *Electron. Lett.* **22**:864–865 (1986).
55. R. Q. Lee and K. F. Lee, Experimental study of the two-layer electromagnetically coupled rectangular patch antenna, *IEEE Trans. Anten. Propag.* **AP-38**:1298–1302 (1990).
56. H. Y. Yang and G. N. Alexopoulos, Gain enhancement methods for printed circuit antennas through multiple superstrates, *IEEE Trans. Anten. Propag.* **AP-35**:860–863 (1987).
57. K. Hiraswa and M. Haneishi, *Analysis, Design, and Measurement of Small and Low-Profile Antennas*, Peter Peregrinus, London, 1992, Chap. 5.
58. K. Wang and Y. Lin, Small broadband rectangular microstrip antenna with chip-resistor loading, *Electron. Lett.* **33**(19):1593–1594 (1997).
59. S. Dey and R. Mittra, Compact microstrip patch antenna, *Microwave Opt. Technol. Lett.* **13**(1):12–14 (1996).
60. H. Y. Yang and N. G. Alexopoulos, Generation of nearly hemispherical and high gain azimuthal symmetric patterns with printed circuit antennas, *IEEE Trans. Anten. Propag.* **35**:972–977 (1987).
61. D. Cailleu, N. Haese, and P. A. Rolland, Microstrip adaptive array antenna, *Electron. Lett.* **32**(14):1246–1247 (1996).
62. R. J. Dinger, A planar version of a 4.0 GHz reactively steered adaptive array, *IEEE Trans. Anten. Propag.* **34**(3):427–431 (1986).

MICROSTRIP ANTENNAS, BROADBAND

K. M. LUK
 C. L. MAK
 City University of Hong Kong
 Kowloon, Hong Kong

R. CHAIR
 The University of Mississippi
 Oxford, Mississippi

H. WONG
 City University of Hong Kong
 Kowloon, Hong Kong

K. F. LEE
 The University of Mississippi
 Oxford, Mississippi

1. INTRODUCTION

The microstrip patch antenna offers many attractive features, including low profile, light weight, conformal structure, and inexpensive fabrication costs. The major drawback of this antenna is narrow bandwidth in its basic form. This article collects different approaches for bandwidth enhancement of linearly polarized microstrip antennas from conventional means to present-day methods, with emphasis on advanced techniques proposed by the authors (Section 2), particularly on the L-probe coupling technique. However, due to limited spacing, the

development of wideband elliptically polarized microstrip antennas will not be covered here. Interested readers can refer to some of the more recent designs reported in the literature [1–4].

The article also highlights wideband techniques for designing dual-polarized patch antennas (Section 3) and electrically small patch antennas (Section 4). In Section 3, the popular aperture coupling method for a dual-polarized patch antenna is described first. Emphasis is then placed on the wideband L-probe-coupled dual-polarized patch antenna. A technique for improving the isolation between the input ports is also presented in that section. Section 4 focuses on miniature patch antennas, including patches with shorting (short-circuiting) pins or shorting walls. Several wideband methods such as the use of stacked geometry, and the L-probe feed, are examined.

The wideband antennas discussed in Sections 3 and 4 are essential in today's wireless communication systems. For instance, the polarization diversity technique is found useful in cellular systems, and therefore most of the base station antennas require a $\pm 45^\circ$ dual-polarized feature as well as broadband characteristic. Modern mobile devices are getting smaller and smaller in size. Thus the dimensions of the antennas inside these devices have to be reduced accordingly. With the novel wideband techniques discussed, both dual-polarized patch antennas and miniature patch antennas can be operated with wide-bandwidth performance, which will be particularly useful in future high-speed wireless communications. The advanced wideband techniques proposed by the authors can also be applied to the design of dual-band and circular-polarized patch antennas.

2. LINEARLY POLARIZED WIDEBAND MICROSTRIP PATCH ANTENNAS

According to *The New IEEE Standard Dictionary of Electrical and Electronics Terms* [5], the bandwidth of an antenna is defined as “the range of frequencies within which its performance, in respect to some characteristics, conforms to a specified standard.” This characteristic can be selected as the input impedance or radiation pattern. For the former, which is more sensitive to frequency, a common standard is that the voltage standing-wave ratio VSWR, or simply SWR, should be less than a certain value, usually 1.5 ($|\Gamma(f)| = 0.2$) or 2 ($|\Gamma(f)| = \frac{1}{3}$), where Γ is the reflection coefficient. Equivalently, the return loss $S_{11}(f)$ should be less than -14 or -10 dB, respectively. Moreover, we usually express the impedance bandwidth in terms of percentage (BW), which is calculated by

$$BW = \frac{2(f_U - f_L)}{f_U + f_L} \times 100\%$$

where f_U and f_L are respectively the upper and lower cutoff frequencies of the operating bandwidth. Key methods developed to solve the inherently narrow bandwidth issue of linearly polarized microstrip patch antennas are discussed below.

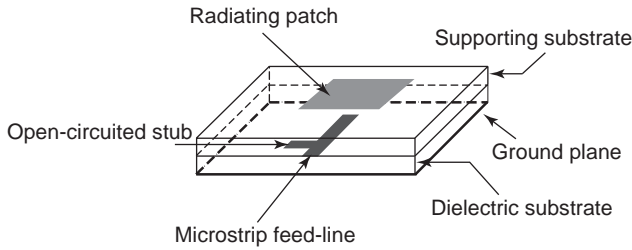


Figure 1. Proximity-coupled patch antenna. (From Pozar and Kaufman [10], reprinted with permission from IEEE.)

2.1. Utilization of Electrically Thick Substrate with Low Permittivity

The patch antenna works like a lossy dielectric-loaded cavity resonator bounded by two electric and four magnetic walls. Assuming that the only loss is due to radiation, we have the antenna quality factor $Q = 2\pi f_r U / P_{rad}$, where U is the total stored energy trapped inside the cavity between the patch and the ground plane at the resonant frequency f_r . P_{rad} is the total radiated power at f_r . This quality factor is similar to that of a parallel-resonant circuit having lumped circuit elements and can also be determined from the input resistance $R(f)$ and input reactance $X(f)$ at a frequency close to f_r . It is understood that a lower value of Q will result in a wider bandwidth. For a patch antenna employing a thin substrate, a higher value of Q [6] and a narrower bandwidth will be obtained. The quality factor can be lowered by simply increasing the substrate thickness; however, the surface wave introduced will

deteriorate the overall performance, including the bandwidth. Fortunately, a substrate with lower value of permittivity $\epsilon = \epsilon_r \epsilon_0$ can minimize the surface-wave power. It is known that the foam or air substrate has the lowest value of relative permittivity ϵ_r close to unity. Thus a patch antenna with electrically thick substrate could exhibit a wide bandwidth [7]. Examples are described in Refs. 8 and 9. In Ref. 8, the bandwidth of a patch antenna over a large ground plane with an air substrate thickness $0.14\text{--}0.27 \lambda_0$ was shown to be about 40% ($VSWR \leq 2$). In Ref. 9, a similar concept was implemented. The effective substrate thickness was increased by the use of a W-shaped ground plane. A 12% ($VSWR \leq 1.5$) bandwidth was reported.

2.2. Bandwidth Improvement by Related Impedance Matching in Different Feeding Mechanisms

2.2.1. Proximity or Electromagnetic Coupling. The proximity coupling technique for patch antennas was proposed by Pozar and Kaufman in 1987 [10]. Energy is electromagnetically coupled from the feedline through a substrate to the radiating element such as a patch [10] or a printed dipole [11]. It has the merit of being less sensitive to fabrication errors. For the proximity-coupled patch as described in Ref. 10 and shown in Fig. 1, there is a relatively small open-circuited tuning stub connected in parallel with the feedline, which provides related matching to the feedpoint; hence the bandwidth can be increased to 13% ($VSWR \leq 2$).

Another proximity-coupled patch with wider bandwidth was proposed in 1998 [12]. The geometry is shown in Fig. 2. Instead of adding a tuning stub, the feedline is

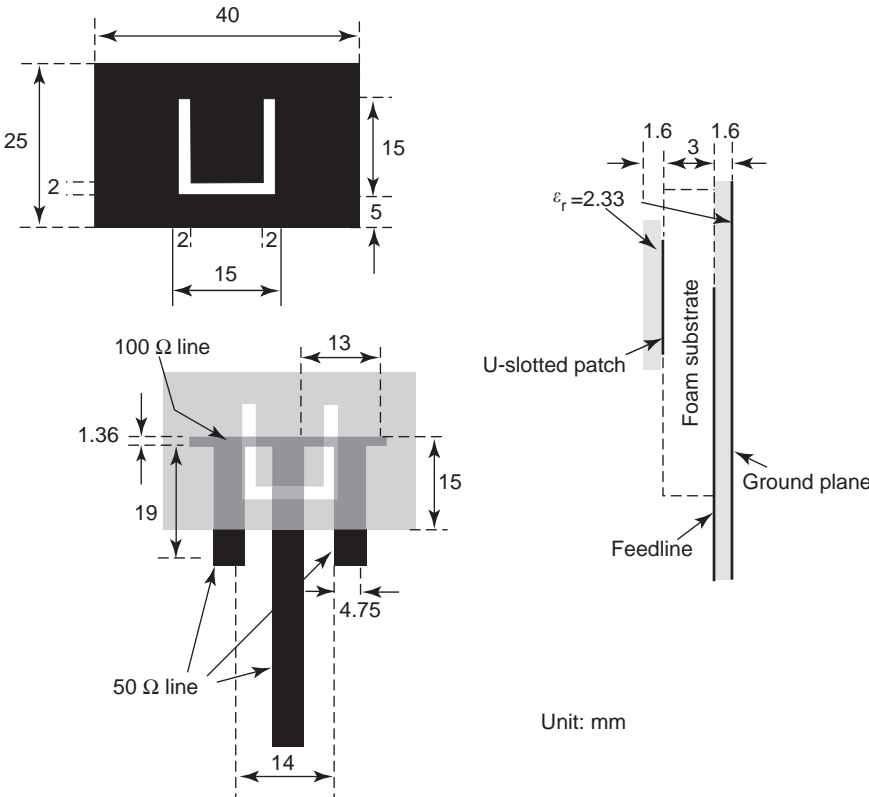


Figure 2. Geometry of proximity-coupled U-slot patch antenna. (From Mak et al. [12], reprinted with permission from IEEE.)

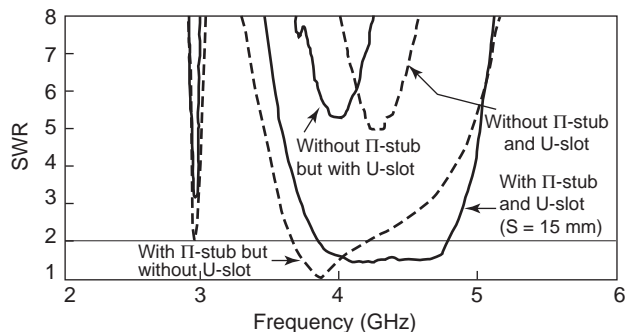


Figure 3. Variation of VSWR of the proximity-coupled patch antenna. (From Mak et al. [12], reprinted with permission from IEE.)

terminated by a Π -shaped stub, which is underneath the radiating patch. The patch is etched with a U-shaped slot, the function of which will be elaborated later. A bandwidth of 20% ($VSWR \leq 2$) and a gain of 7.5 dBi were achieved for this single-layer patch antenna. Figures 3 and 4 show the measured VSWR and gain of this antenna. Figure 5 shows the radiation patterns at 4.3 GHz. The antenna has a broadside radiation pattern with beamwidth of about 60° in both E plane and H plane. The cross-polar level is below -15 dB. This single-element antenna has been modified and employed for the design of wideband antenna array with excellent performance [13,14].

2.2.2. Aperture Coupling Method. The aperture coupling method was proposed 1985 by Pozar again [15]. The basic geometry is shown in Fig. 6. The microstrip feedline and the patch are located on different sides of the ground plane. Energy from the microstrip feedline is electromagnetically coupled to the patch through an aperture on the ground plane. The coupling aperture can be of different shapes, sizes, and locations with respect to the patch for different coupling characteristics [16,17]. An advantage of this feeding method is that the feedline is isolated from the radiating element by the ground plane. Thus radiation from the feedline in the broadside direction is insignificant. Also this method do not have the probe inductance problem arising in the coaxial probe feed case.

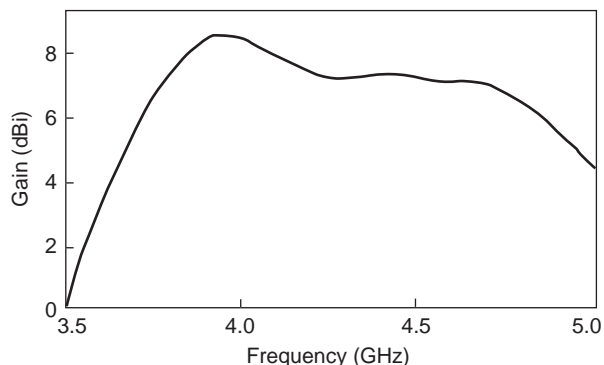


Figure 4. Gain of the proximity-coupled U-slot patch antenna. (From Mak et al. [12], reprinted with permission from IEE.)

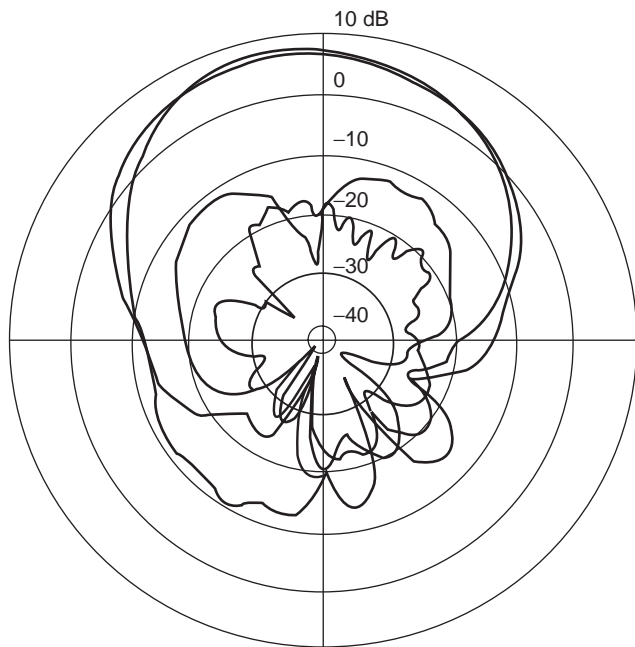


Figure 5. Radiation pattern at 4.3 GHz. (From Mak et al. [12], reprinted with permission from IEE.)

Disadvantages are comparative complexity in fabrication and relatively high level of backlobe radiation.

From Ref. 15, the bandwidth obtained was only 14%. There are two simple ways for tuning the antenna: the aperture shape and size and the stub length. So it is possible to obtain a better bandwidth if appropriate matching is achieved. One example was presented in 2002 [18], with the patch excited by an H-shaped aperture. An impedance bandwidth of 56.2% ($VSWR \leq 2$) and a 3 dB gain bandwidth of 24% were achieved.

2.2.3. Microstrip-Line Edge Feed and Coaxial Probe Feed. The microstrip-line edge feed and the coaxial probe feed are fundamental feeding methods for microstrip patch antennas, since they are the most direct way to transfer energy from the feedline to the patch and vice versa. Some methods have been proposed in the literature to improve the matching condition and the bandwidth as well. In Ref. 19, a patch is excited by a coupled linefeed. It was reported that the bandwidth can be increased by a

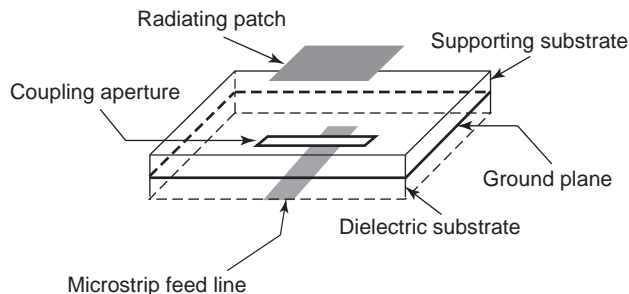


Figure 6. Basic geometry of aperture-coupled patch antenna.

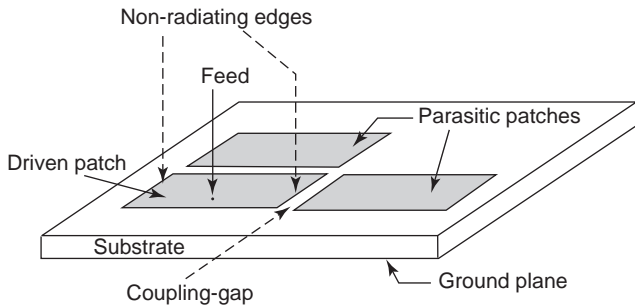


Figure 7. Examples of parasitic patches in coplanar configuration.

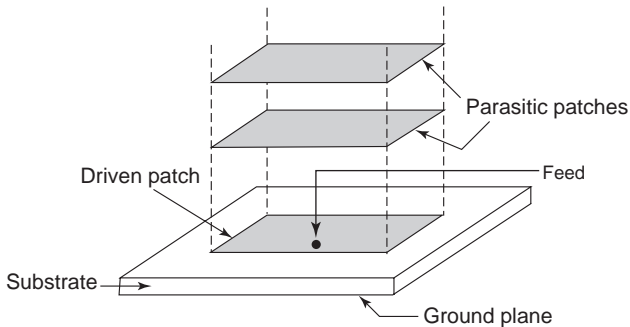


Figure 8. Examples of parasitic patches in stacked configuration.

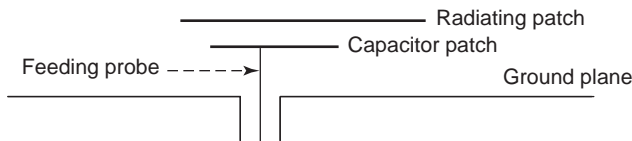
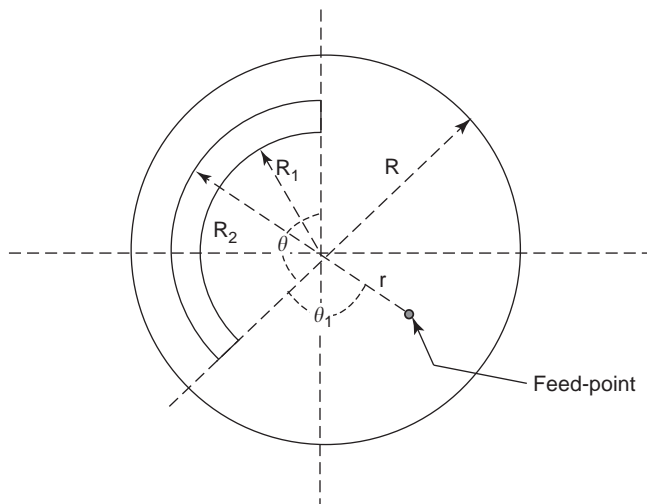


Figure 9. Capacitively fed patch antenna (side view).



R	r	R_1	R_2	θ	θ_1	Bandwidth (VSWR ≤ 2)
17 mm	10.5 mm	8.5 mm	12.5 mm	155°	80°	14%

Figure 10. Circular patch with an arc-shaped slot. (From Luk et al. [41], reprinted with permission from IEE.)

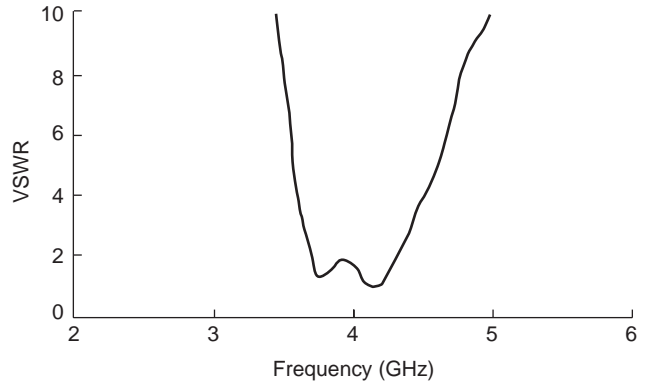


Figure 11. Measured VSWR of the offset feed circular patch with arc-shaped slot. (From Luk et al. [41], reprinted with permission from IEE.)

factor of > 2.5 as compared to the conventional edge feed method.

In using the coaxial probe feed, there are even more methods available to improve the matching condition of the single-patch configuration such as introducing a slot on the patch, adding a capacitor patch, or using the L-shaped probe. These techniques will be discussed in the following sections.

2.3. Bandwidth Widening Technique Using Parasitic Elements

The original geometry of a microstrip patch antenna consists of only one patch radiator, which is driven by the appropriate feeding techniques. The bandwidth of such a configuration can be very narrow. A significant improvement in bandwidth can be achieved by adding one or more parasitic patches next to or stacked above the

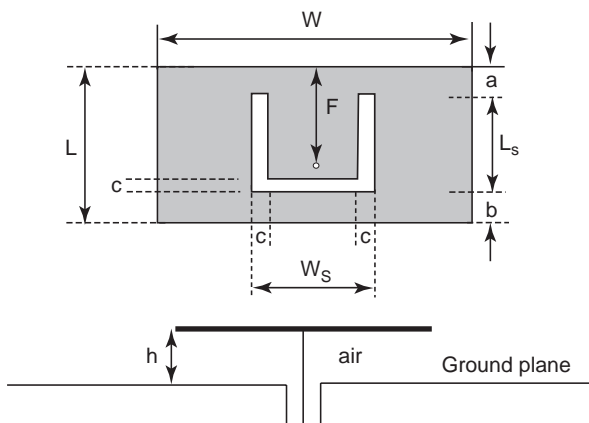


Figure 12. Wideband rectangular U-slot patch antenna. (From Lee et al. [47], reprinted with permission from IEE.)

Parameters	W	L	F	Ws	Ls	a	b	c	h	Bandwidth (VSWR ≤ 2)
Unit/mm	35.5	26	15	12	19.5	2.2	4.3	2.1	5	32.4%

driven patch. The parasitic elements can be of slightly different dimensions and are excited by electromagnetic coupling from the driven patch. By adding parasitic patches, the bandwidth can be improved because there are one or more resonant frequencies introduced by the parasitic patches. If these resonant frequencies are close to the original resonant frequency of the driven patch, they could combine together to yield a wider bandwidth. Obviously, the major drawback of using parasitic elements is the enlargement in volume of the antenna.

2.3.1. Coplanar Structure. In the coplanar geometry, the parasitic patches are placed on the same layer and adjacent to the driven patch as shown in Fig. 7. The coaxial probe feed [20–22] or the aperture-coupled feed [23] can be chosen to excite the driven patch. When using the coaxial probe feed method, 15% bandwidth (VSWR ≤ 2) can be yielded when two parasitic patches are placed next to the nonradiating edge of the driven patch [21]. In addition, if we add four parasitic patches gap-coupled to the four edges of the driven patch, around 25% bandwidth

(VSWR ≤ 2) can be obtained [21]. As for using the aperture-coupled feed, 23% bandwidth (VSWR ≤ 2) was achieved [23] when two parasitic elements were gap-coupled to the nonradiating edges of the fed patch.

2.3.2. Stacked Structure. In the stacked geometry, the parasitic patches are suspended above the driven patch and thus are placed in another upper layer with respect to the driven patch as shown in Fig. 8. Again, both coaxial probe feed [24,25] and aperture-coupled feed [26–31] methods for the driven patch are commonly used. Newer feed methods for the driven patch have been proposed: the co-planar waveguide feed (CPW) [32,33] and the L-shaped strip feed [34]. In using the coaxial probe feed method, more than 25% bandwidth (VSWR ≤ 2) can be achieved [25]. If the aperture-coupled feed is employed, around 40% bandwidth (VSWR ≤ 2) was obtained [28,29].

2.4. Wideband Patch Antenna with Probe Inductance Cancellation

As mentioned in Section 2.1, employing electrically thick substrate could increase the impedance bandwidth by about 20% (VSWR ≤ 2) [7] when the substrate thickness is around 0.15λ₀. However, in the probe feed case, the bandwidth is limited to about 10% (VSWR ≤ 2) because of

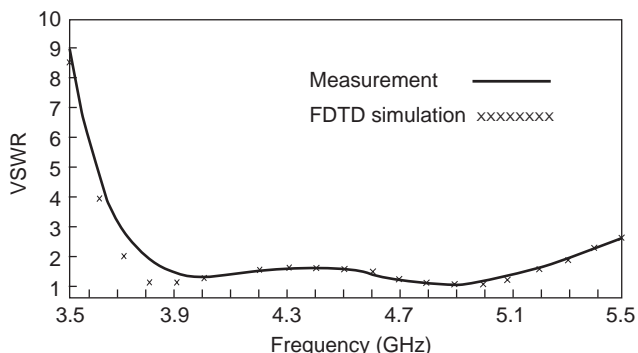


Figure 13. Measured and FDTD-simulated VSWR of rectangular U-slot patch antenna. (From Lee et al. [47], reprinted with permission from IEE.)

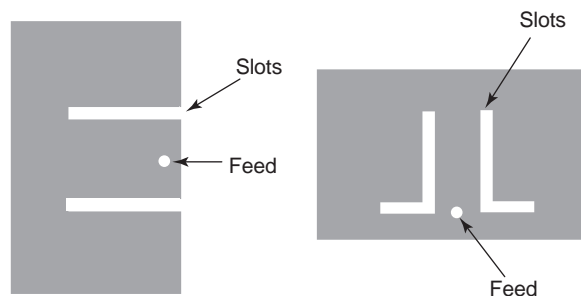
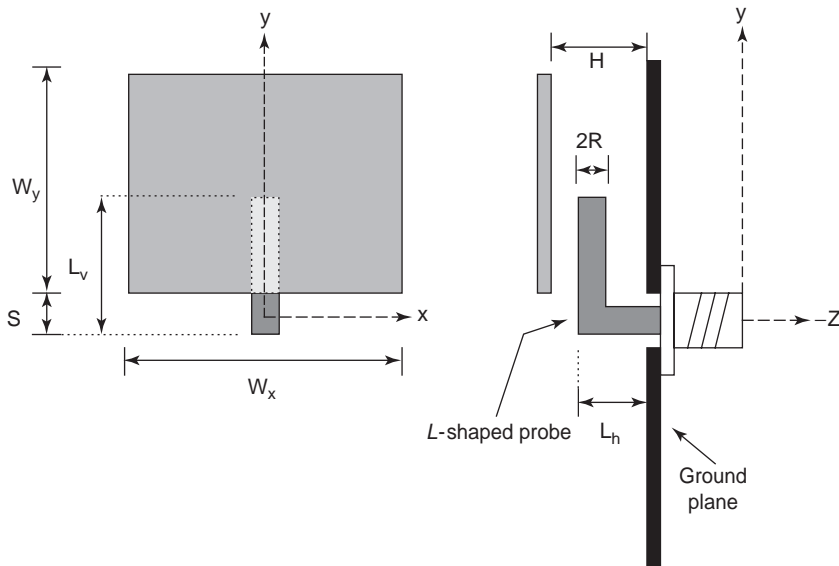


Figure 14. Examples of U-slot equivalent patches [52–54].



Parameters	W_x	W_y	H	L_h	L_v	S	R	Bandwidth (VSWR ≤ 2)
Unit/mm	30	25	6.6	5.5	10.5	2	0.5	36%

Figure 15. Basic geometry of L-shaped probe-fed patch antenna. (From Luk et al. [55], reprinted with permission from IEE.)

the larger probe inductance [35,36] introduced by the longer probe required. This undesired inductance results in antenna mismatch. Moreover, the unwanted radiation from the longer probe is a major source of high cross-polarization in the H plane and also causes an unsymmetric copolarization in the E plane. Thus a shorter probe and a thicker substrate are desired in designing wideband patch antennas. In one method, employing a W-shaped ground plane [9] to increase the (effective) substrate thickness without lengthening the feeding probe, a bandwidth of 15% (VSWR ≤ 1.5) can be achieved. Apart from retaining a short feeding probe, there are other effective methods to compensate the unwanted probe inductance in wideband patch antenna design.

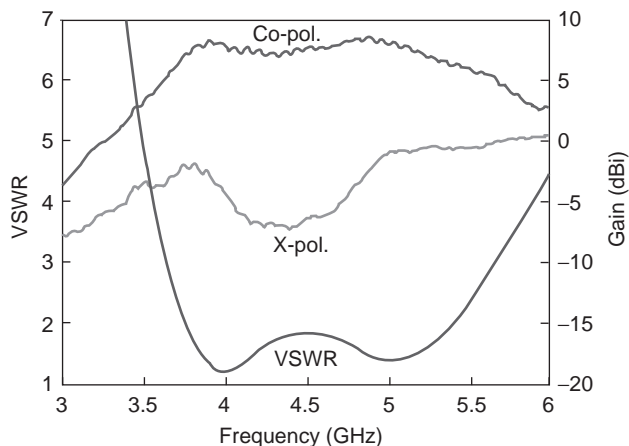


Figure 16. VSWR and gain of L-shaped probe-fed rectangular patch antenna. (From Luk et al. [55], reprinted with permission from IEE.)

2.4.1. Capacitive Coupling Patch Antenna. In the design of capacitively coupled patch antenna, a small patch, which is connected to the feeding probe, is introduced between the ground plane and the radiating patch as shown in Fig. 9 [37–39]. The structure is somewhat similar to the probe-fed stacked-patch antenna, but the small patch together with the radiating patch works as a capacitor that is used to cancel out the unwanted probe inductance within the antenna structure itself. Thus a simpler matching network can be used at the back of the ground plane. About 5% impedance bandwidth (VSWR ≤ 2) was reported [37].

2.4.2. Coaxial Probe-Fed Slotted Patch. Without using an additional capacitor patch between the ground and the radiating patch, the unwanted probe inductance can be canceled out by introducing appropriate slots, surrounding the feedpoint, on the patch [40]. The method can retain the advantage of a single-patch configuration. Not long ago, the authors introduced different-shaped slots on the patch, including an arc-shaped slot and a U-shaped slot, for wideband operation [41,42]. The latter case with U-shaped slot has received much attention in the literature [12,13,43–51]. Many similar designs have also been proposed such as the E-shaped patch [52,53], and the back-to-back L-shaped slotted patch [54].

2.4.2.1. Circular Patch with an Arc-Shaped Slot. In a procedure reported in 1997 [41], an arc-shaped slot was cut inside the circular patch as shown in Fig. 10. It is found that the offset feed ($r > 0$) will give a better bandwidth (VSWR ≤ 2) of 14% than the 11% of the center feed case ($r = 0$). Figure 11 shows the measured VSWR response.

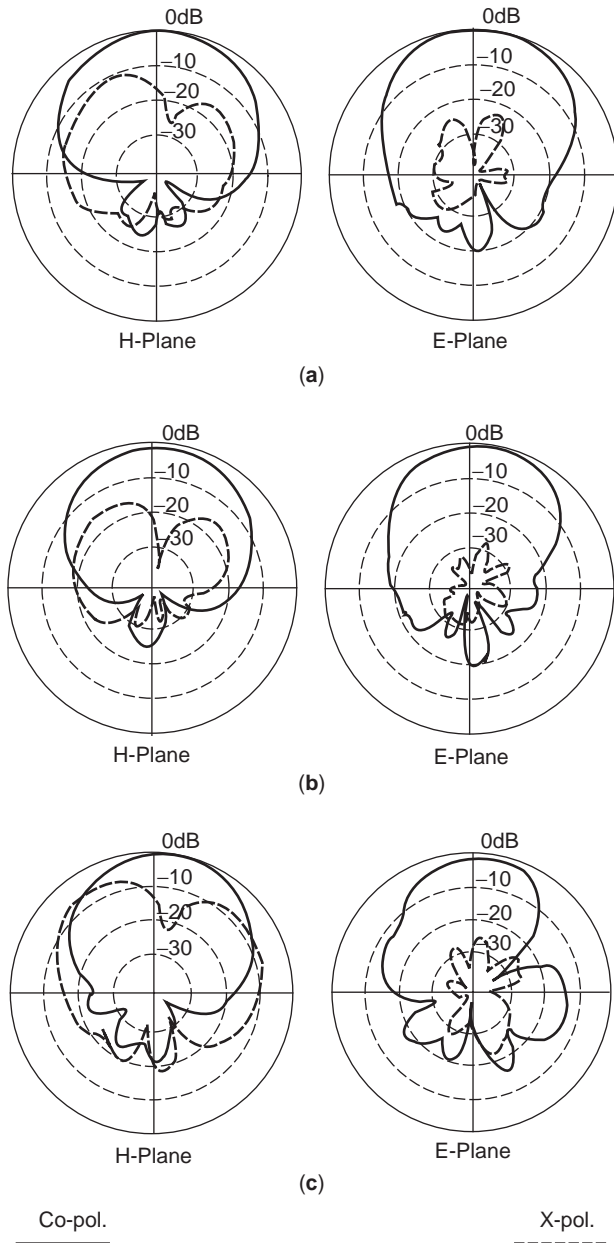


Figure 17. Far-field radiation patterns of L-shaped probe-fed patch antenna: (a) 4 GHz; (b) 4.53 GHz; (c) 5.34 GHz. (From Mak et al. [56], © 2000 IEEE.)

2.4.2.2. Rectangular Patch with a U-Shaped Slot. The design was first proposed in 1995 by Huynh and Lee [42]. An impedance bandwidth of around 30% ($VSWR \leq 2$) can be easily obtained [47]. A typical example is described below with the basic geometry shown in Fig. 12. Note that the thickness is around $0.08 \lambda_0$. Figure 13 shows the measured and simulated [finite-difference time-domain (FDTD)] results of VSWR of this wideband antenna.

The arc-shaped or U-shaped slot, surrounding the feed-point, on the patch provides a capacitive component in the input impedance of the antenna, compensating the strong inductive component from the long feeding probe. Therefore, appropriate matching can be obtained for wideband performance. Apart from the broadband characteristics,

the U-slotted patch preserves the single-patch low-profile feature in comparison to the geometry with parasitic patches. The thickness of such a wideband single-patch antenna is only $\leq 0.08 \lambda_0$. Due to such an attractive feature, many U-slot equivalent patch antennas have been designed for bandwidth enhancement. For examples, an E-shaped patch [52,53] and the back-to-back L-shaped slotted patch [54] were proposed, as shown in Fig. 14. Similar wide bandwidths of around 30% were reported.

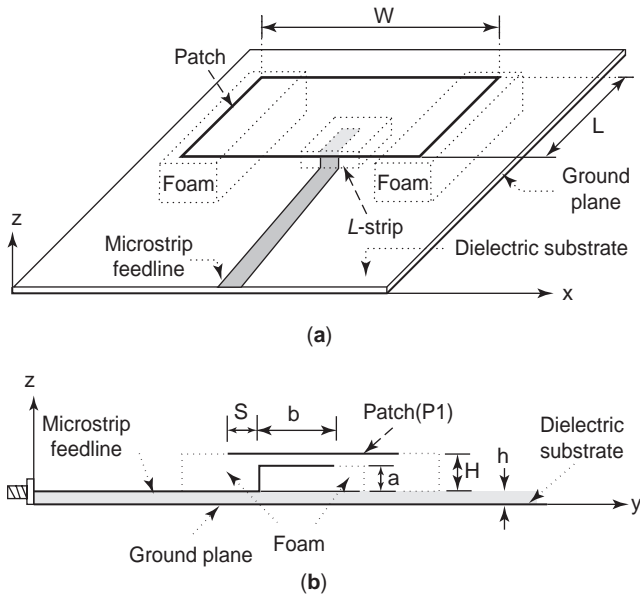
2.5. Wideband Patch Antenna with L-Shaped or T-Shaped Probe

It is believed that using slightly thicker substrate with low permittivity for patch antenna design is the most effective way to achieve wideband operation, at the same time retaining the attractive original low-profile characteristic. Of course, the probe-fed U-slotted patch can easily achieve such merit of wideband and low-profile structure. However, the fabrication process is not so convenient, and the fine-tuning process of the U-shaped slot is not an easy task. Such problems may increase the fabrication cost and time.

2.5.1. L-Probe-Coupled Patch Antenna. More recently, a novel L-probe coupling technique was invented, and awarded patents from the People's Republic of China and the United States. This design, first proposed in 1998 [55], preserves the original advantages of patch antennas with an improvement in impedance bandwidth without increasing the fabrication difficulties since no slot is needed on the patch and no soldering process is required. Many investigations have been undertaken on L-shaped probe coupling [49,50,56–66], including the circular polarization design and the dual-band design.

The basic geometry of the L-probe-coupled patch antenna is shown in Fig. 15. This is a single-layer patch antenna with a rectangular patch of width $W_x = 30$ mm ($0.45 \lambda_0$) and length $W_y = 25$ mm ($0.375 \lambda_0$). Note that the operating center frequency is $f_0 \approx 4.5$ GHz. The copper-made L-shaped probe is constructed by simply bending a straight copper wire of radius $R = 0.5$ mm ($0.0075 \lambda_0$) into an L shape. When this L-shaped probe is then connected to the inner conductor of a 50- Ω launcher without touching the patch, as shown in Fig. 15, it becomes an effective coupling probe for the radiating patch. The L-shaped probe has a vertical arm length $L_v = 10.5$ mm ($0.1575 \lambda_0$) and a horizontal arm length $L_h = 5.5$ mm ($0.0825 \lambda_0$), which are exciting the fundamental TM_{01} mode of the rectangular patch. A supporting foam layer ($\epsilon_r \approx 1$) is employed with thickness $H = 6.6$ mm ($0.099 \lambda_0$), which is about one-tenth of the operating wavelength. Moreover, from the top view, the distance between the lower edge of the patch and the horizontal arm of the L-shaped probe is $S \approx 2$ mm. The values of these parameters are chosen after a series of extensive appraisals, from $H \approx 3.3$ mm ($0.05 \lambda_0$) to $H \approx 16$ mm ($0.25 \lambda_0$) and are believed to provide an optimum performance of bandwidth and gain.

Both the measured VSWR and gain (copolarization gain at $\theta = 0^\circ$ and cross-polarization gain at $\theta \approx 45^\circ$ in

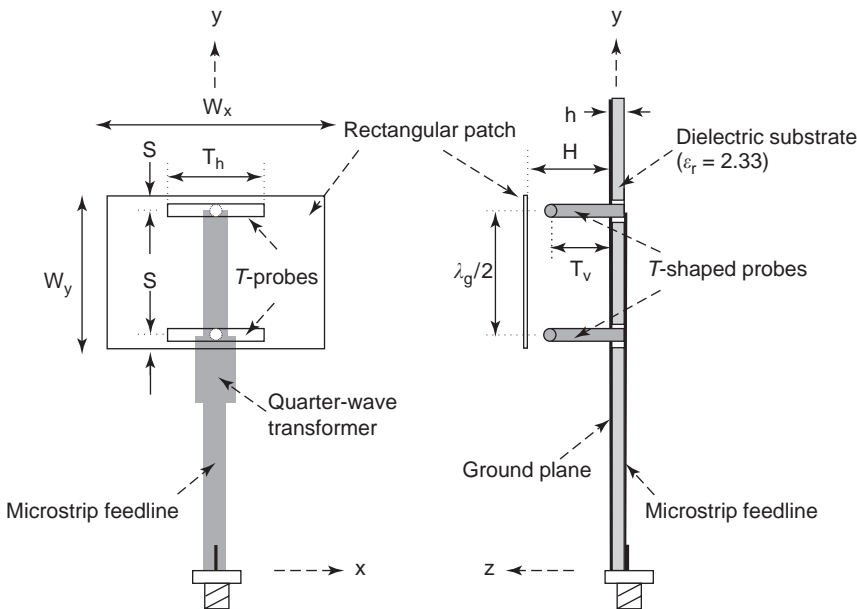


Parameters	W	L	H	a	b	S	h	Bandwidth (VSWR ≤ 2)
Unit/mm	30	25	8.3	5	10	1	1.6	49%

Figure 18. Geometry of L-shaped strip-fed rectangular patch antenna. (From Mak et al. [34], reprinted with permission from IEE.)

the *H* plane) are shown in Fig. 16, where θ is the azimuth angle. A wide bandwidth of up to 36% ($VSWR \leq 2$) with 7.5 dBi gain is obtained. The cross-polarization level in the *H* plane is slightly higher at the two ends of the band of

operation, and about 15 dB down from the copolarization level is attained at the center region of the band of operation. The far-field radiation patterns measured at 4, 4.53, and 5.34 GHz are shown in Fig. 17. It can be observed that



Parameters	W_x	W_y	H	T_h	T_v	h	Bandwidth (VSWR ≤ 2)
Unit/mm	30	25	6.6	9	5.6	1.6	41.6%

Figure 19. Geometry of the two-T-probe-coupled patch antenna. (From Mak et al. [67], reprinted with permission from IEE.)

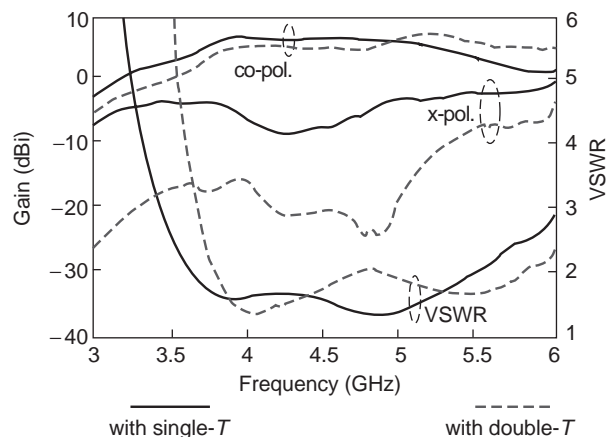


Figure 20. VSWR and gain of T-probe coupled patch antenna. (From Mak et al. [67], reprinted with permission from IEE.)

the copolarization patterns are stable across the band of operation, with the mainbeam toward the broadside direction.

Apart from the rectangular patch coupled by the L-shaped probe as described, circular and triangular patches are also investigated [57,58], which are also able to show the wideband characteristic. It is believed that the L-shaped probe coupling technique is also suitable for other common patch shapes such as elliptical patch, semidisk, and circular ring, as well as the bowtie patch and the notched patch for different requirements. The wideband performance of the L-probe-coupled patch antenna is achieved by two basic insights: (1) the use of an electrically thick substrate ($\approx 0.1\lambda$) [7], which provides a lower Q factor, thus potentially giving a wider bandwidth; and (2) probe inductance compensation [37–42], where, from the transmission-line perspective, the vertical arm between the patch and the ground forms an open circuit stub of length less than a quarter-wavelength; thus a capacitive reactance is provided. This is similar in concept to the capacitive coupled patch antenna [37–39]. Moreover, it is necessary to note that the total length of the L-shaped probe is less than a quarter-wavelength (i.e., $L_v +$

$L_h < 0.25\lambda$), thus maintaining the patch as the only radiating element. Experiments also show that the L probe itself without the patch does not act as an efficient radiator across the operation band.

In the process of finding an optimum configuration, it is found that the bandwidth generally increases with the value of H , the separation between the patch and ground. However, an optimum gain is obtained when H is around 0.1λ . Furthermore, the gain is highly sensitive to the value of H . Measurements also show that the gain is usually higher when part of the L probe is not under the patch, as shown in Fig. 15, than when the whole L probe is completely covered by the patch [56]. It is essential to mention that when varying the value of H , it is necessary to slightly alter the other parameters such as L_v , L_h , and S simultaneously in order to obtain a wideband performance again.

It has been shown that the L-shaped probe is effective for exciting linearly polarized patch antennas. For elliptical polarized patch antenna designs, some studies have been performed on the use of the L-probe coupling method [63–65]. For dual-band operation, an L-probe-coupled patch antenna operating at GSM/PCS band has also been investigated [59]. As for combining the L-probe coupling method with other bandwidth enhancement techniques, there are L-probe-coupled U-slotted patch antennas [49,50], together with a parasitic patch [60], or with a short-circuiting post [61].

2.5.2. Extensions of the L-Probe Coupling Technique.

Further development based on the original L-shaped probe design was made in order to provide more alternative coupling methods that maintain the fundamental features and enhance the flexibility of the design. One of these is an L-shaped strip coupling method [34]; the concept of the L-shaped probe is extended to accommodate a microstrip feedline without the process of drilling the substrate and soldering the L-shaped probe to the feedline. The use of a microstrip feedline can allow the array design using low-loss microwave substrates and inexpensive PCB substrates. The second design is based on the T-shaped probe coupling [67], which allows the vertical arm to point in a direction orthogonal to both arms of the original L-shaped probe. The feeding probe appears as a letter “T” when examined from the side view. Details of the two feeding techniques are discussed below.

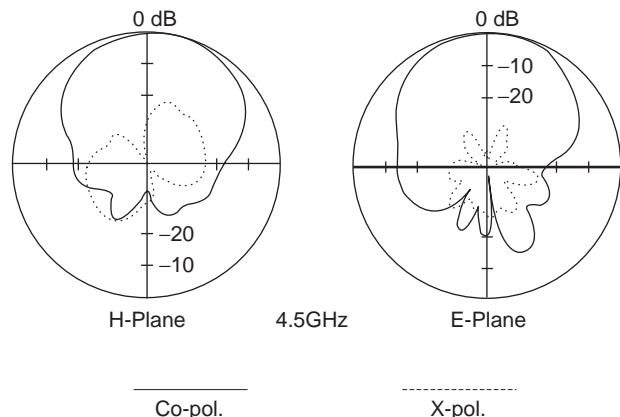


Figure 21. Far-pol radiation patterns of the two-T-probe-coupled patch antenna. (From Mak et al. [67], reprinted with permission from IEE.)

2.5.2.1. L-Strip-Coupled Patch Antenna.

A single-layer patch antenna coupled by an L-shaped strip is shown in Fig. 18. A rectangular patch, with $W \times L = 30 \times 25$ mm, is designed to operate at $f_0 = 4.5$ GHz. The air substrate has a thickness of $H = 8.3$ mm. A $50\text{-}\Omega$ microstrip feedline is etched on a microwave substrate ($\epsilon_r = 2.33$) of thickness $h = 1.6$ mm, which is located symmetrically with respect to the patch. A stepped feedline, referred to as an “L-shaped strip,” is introduced at the end of the $50\text{-}\Omega$ microstrip feedline. The width of the L-shaped strip is chosen to be the same as that of the feedline. Moreover, referring to Fig. 18b, the vertical and horizontal portions of this L-shaped strip, with dimensions $a = 5$ mm and $b = 10$ mm,

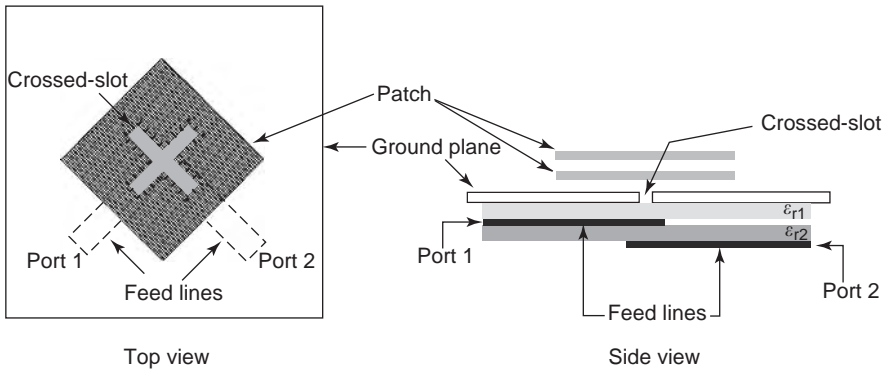


Figure 22. Configuration of a dual-polarized stacked-patch antenna with aperture-coupled feed. (From Edimo et al. [70], reprinted with permission from IEEE.)

respectively, excite the TM_{01} mode of the patch by electromagnetic coupling. Note that the horizontal portion of the L-shaped strip is supported by a foam material ($\epsilon_r \approx 1$) while the vertical portion is located under the patch at an inset distance $S = 1$ mm from the edge of the patch. The VSWR and gain (copolarization gain and cross-polarization gain) are measured. A wide bandwidth of up to 49% ($VSWR \leq 2$) and 7 dBi gain are achieved, details can be found in Ref. 34.

2.5.2.2. T-Shaped Probe-Coupled Patch Antenna. The second feeding method derived from the idea of the L-shaped probe is the T-shaped probe [67]. A single patch coupled by two identical T-shaped probes is discussed in this section. The geometry is shown in Fig. 19. The objective here is to improve the radiation performance by cancellation of unwanted probe radiation [68], caused by the vertical arm when using only one probe, without reducing the achievable bandwidth.

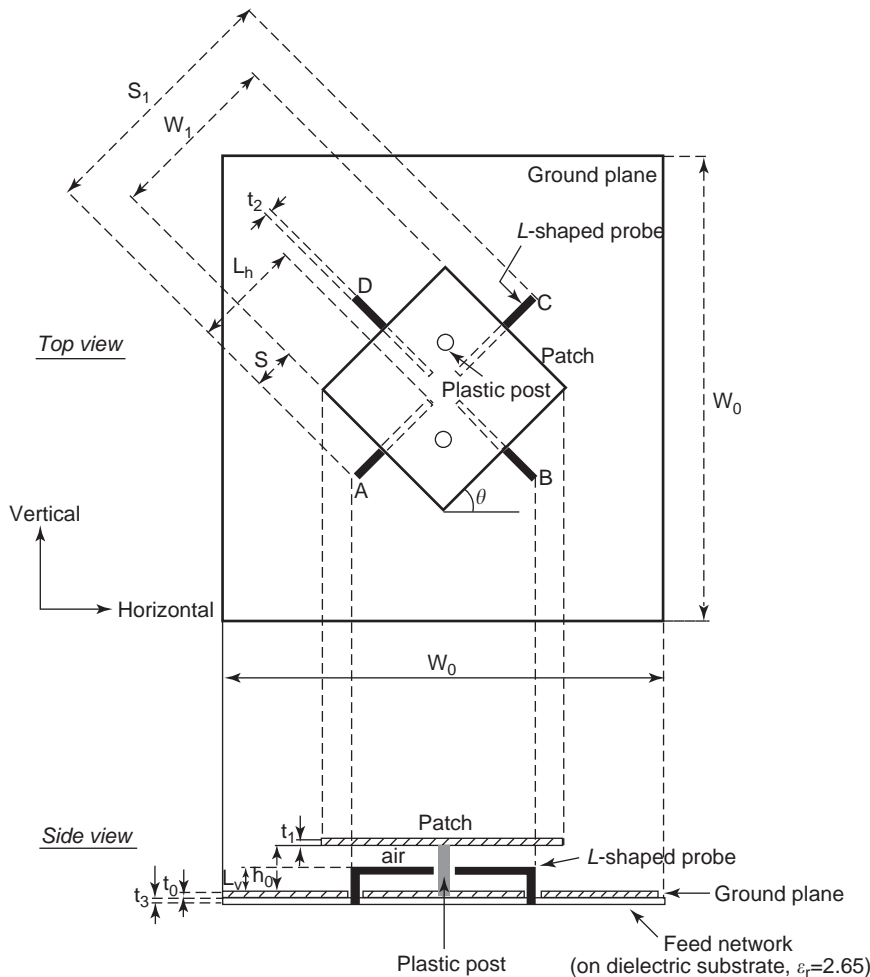


Figure 23. Geometry of a dual-polarized antenna with a dual feed. (From Wong et al. [71], © 2004 IEEE.)

(Unit: mm, $t_0=2$, $t_1=2$, $t_2=2$, $t_3=1.5$, $h_0=17$, $L_v=9$, $W_0=180$, $W_1=62$, $L_h=38$, $S=15$, $S_1=92$, $\theta=45^\circ$)

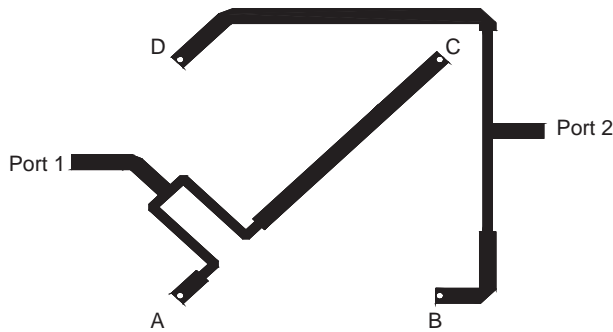


Figure 24. Outlook of feed network. (From Wong et al. [71], © 2004 IEEE.)

In Fig. 19, a microstrip feedline, with a quarter-wavelength transformer designed to operate at 4.5 GHz, is etched onto a dielectric substrate of thickness $h = 1.6$ mm and $\epsilon_r = 2.33$. Two identical T-shaped probes, $T_v = 5.6$ mm and $T_h = 9$ mm, are connected to the feedline below the ground plane and separated by $\lambda_g/2$, where λ_g is the guide wavelength at 4.5 GHz. A rectangular patch of dimensions 30×25 mm is located at a height of $H = 6.6$ mm. Also, the position of the patch is such that the two T-shaped probes are inset the same distance S from the patch edges and are symmetric with respect to the y axis, as shown in the top view. In addition, because of the $\lambda_g/2$ separation, the two T-shaped probes simultaneously excite the same TM_{01} mode of the patch.

Figure 20 shows the variations of VSWR with frequency, the broadside copolarization gain and the cross-polarization gain in the H plane with $\theta \approx 45^\circ$, together with that using one single T probe [67]. It is seen from the figure that both antennas have impedance bandwidth ($VSWR \leq 2$) of around 40%. Also both antennas have copolarization gain greater than 6.5 dBi across most of their bands of operation, and the patch with a single T probe has an average gain of 7 dBi. Most importantly, by using two T probes to excite a single patch, the cross-polarization in the H plane is significantly suppressed and is

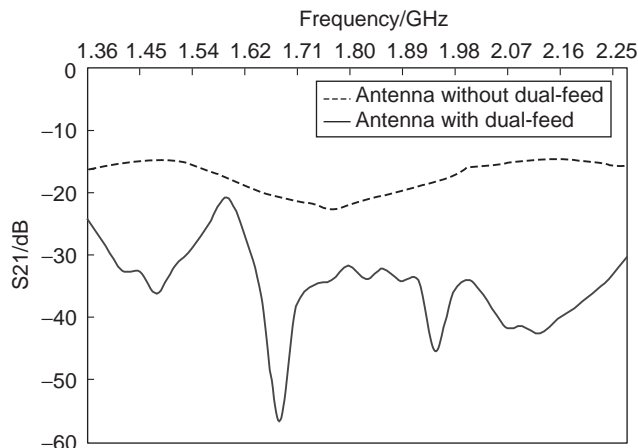


Figure 25. Isolation of dual-polarized L-probe-fed patch antenna with and without dual feed. (From Wong et al. [71], © 2004 IEEE.)

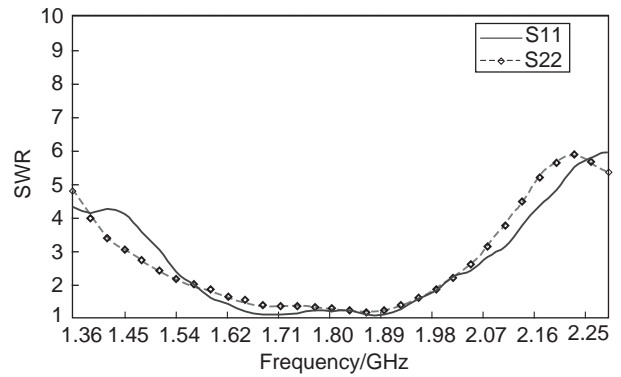


Figure 26. Measured SWR against frequency for dual-polarized L-probe-fed patch antenna with dual feed. (From Wong et al. [71], © 2004 IEEE.)

20 dB or more below the copolarization gain between 4.2 and 5.15 GHz.

The far-field radiation patterns at 4.5 GHz are shown in Fig. 21. It can be observed that the copolarization patterns in the H plane are symmetric about the broadside direction and have low backlobe radiation. Also, the cross-polarization patterns in the E plane are well below -25 dB. Moreover, with the use of the additional out-of-phase T-shaped probe, the dent in the E plane (when using a single T) disappears and the E -plane copolarized pattern becomes more symmetric. The H -plane cross-polarized pattern has also been effectively suppressed to less than -20 dB in all directions.

3. DUAL-POLARIZED WIDEBAND PATCH ANTENNA

3.1. Dual-Polarized Aperture-Coupled Stacked-Patch Antenna

A dual-polarized aperture-coupled stacked-patch antenna is shown in Fig. 22. Two square stacked patches are fed by two crossed and stacked microstrip lines through two crossed and nonresonate slots in the ground plane. A thin substrate is placed between the microstrip lines to enhance the port decoupling. The use of the stacked-patch design is to obtain a wideband operation [69]. By applying two orthogonal crossed slots located beneath the center of the patch, symmetric far-field copolarization patterns are achieved and high isolation can be obtained [70]. This structure of dual-polarized patch antenna yields about 30% impedance bandwidth (for $VSWR \leq 2$) and around 28 dB isolation across the operating bandwidth.

3.2. A Dual-Polarized L-Probe-Coupled Patch Antenna

A square patch antenna can be excited with $\pm 45^\circ$ polarizations by using only two orthogonal L-shaped probes. However, this antenna has poor input port isolation due to strong coupling between the two vertical arms of the L probes. To tackle this problem, a dual-feed concept is introduced here to improve the isolation.

A modified dual-polarized patch antenna coupled by two pair of L-shaped probes is shown in Fig. 23. The

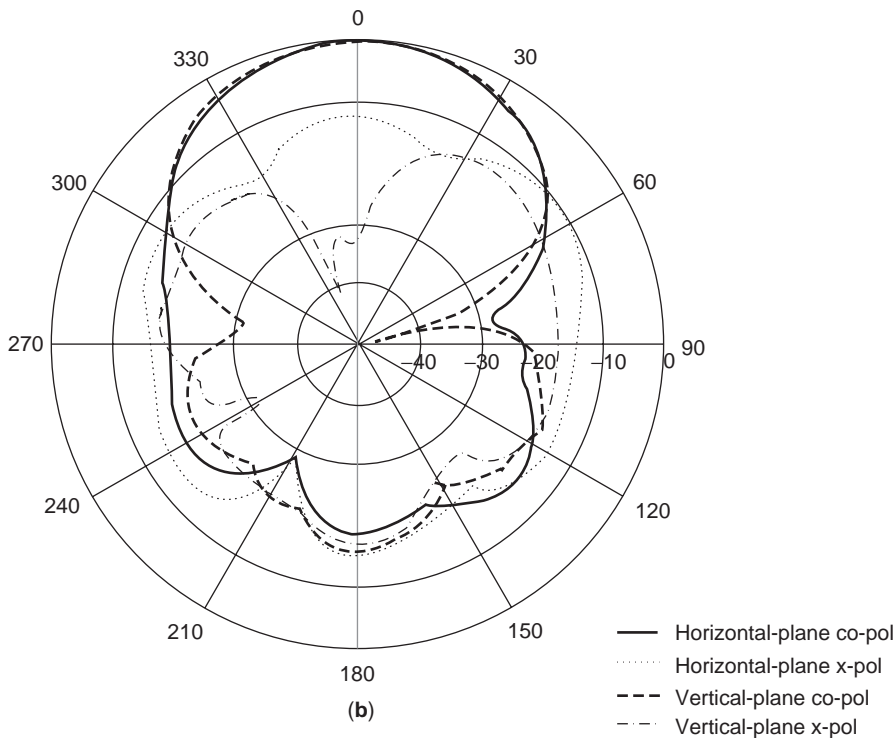
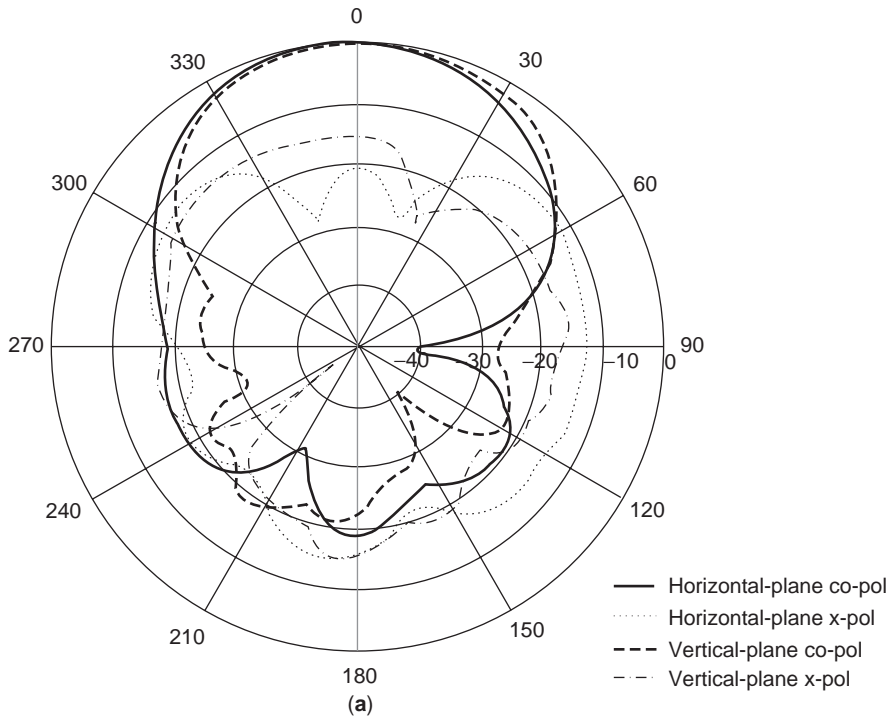


Figure 27. Measured far-field patterns at 1.8 GHz: (a) port 1; (b) port 2. (From Wong et al. [71], © 2004 IEEE.)

antenna employs a pair of L probes to excite one polarization, say, $+45^\circ$ polarization. Then, another pair excites the -45° polarization. The operating center frequency is $f_0 \approx 1.8$ GHz. The patch, which is made of aluminum with dimensions of $W_1 = 62$ mm ($0.37\lambda_0$) \times $W_1 = 62$ mm ($0.37\lambda_0$) \times $t_1 = 2$ mm ($0.012\lambda_0$), is supported by two plastic posts and is placed $h_0 = 17$ mm ($0.1\lambda_0$) above the ground plane.

Four copper L-shaped probe feeds with radius of 1 mm are located below the patch and are connected to a feed network. Each probe is designed to have an input impedance of $50\ \Omega$. The horizontal and vertical lengths of each probe are $L_h = 38$ mm ($0.22\lambda_0$) and $L_v = 9$ mm ($0.05\lambda_0$), respectively. As shown in the figure, the four L-shaped probes are located at points A , B , C , and D with $AB = BC = CD =$

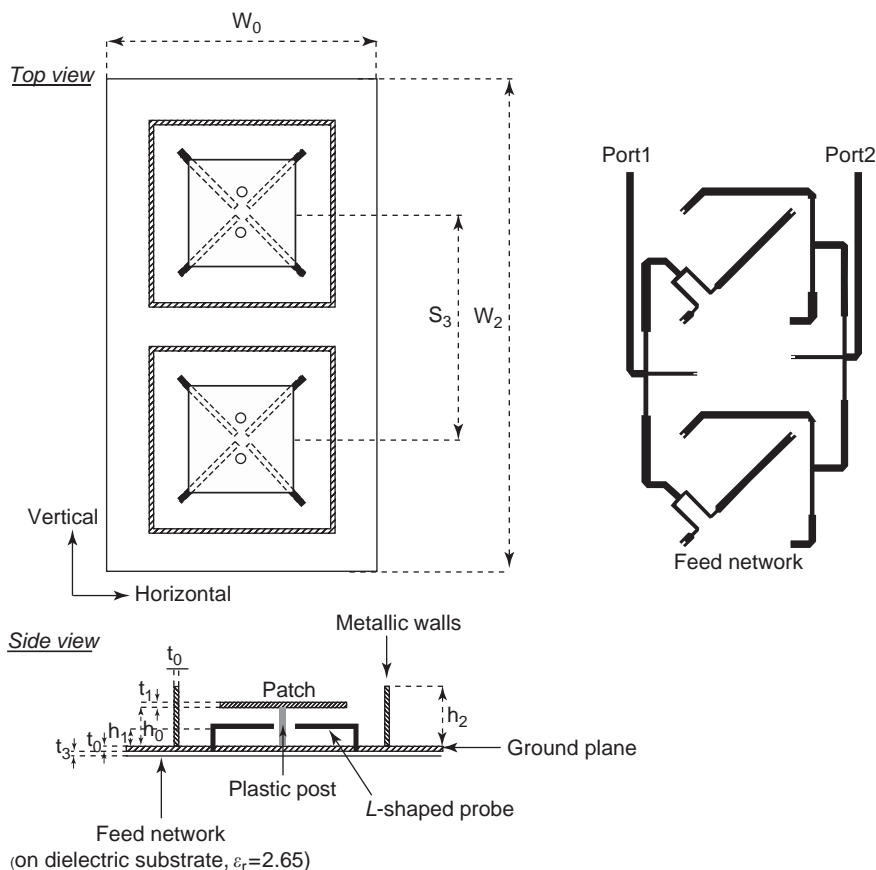


Figure 28. Configuration of a dual-polarized patch antenna array with surrounding metallic walls. (From Wong et al. [71], © 2004 IEEE.)

(Unit: mm, $t_0=2$, $t_1=2$, $t_3=1.5$, $h_0=22$, $h_1=9$, $h_2=30$, $W_0=180$, $W_2=300$, $S_3=133$)

DA. Probes A and C are excited with 180° phase difference, while probes B and D are also excited with antiphase. Probes A and C are used to excite the $+45^\circ$ polarization, while probes B and D are for the -45° polarization. Figure 24 shows the outlook of feed network that has a dielectric substrate of $\epsilon_r = 2.65$.

3.2.1. Experimental Results. Figure 25 shows measured results of S_{21} for both antennas with or without the dual-feed. It is observed that across the GSM1800 operating bandwidth from 1.71 to 1.88 GHz, the S_{21} of the antenna without the dual feed is about -19 dB and the corresponding value of the antenna with the dual feed is less than -30 dB. The 10 dB improvement is contributed by the dual feed suppression technique. The VSWR of the antenna with the dual feed (Fig. 26) is less than 2 in the frequency range from 1.56 to 1.99 GHz, and an impedance bandwidth of 23.8% is obtained. The VSWR is less than 1.5 from 1.66 to 1.94 GHz, and a 15% impedance bandwidth is obtained that is wide enough to cover the GSM1800 bandwidth.

The measured far-field patterns at 1.8 GHz for the antenna with dual feed are shown in Fig. 27. The 3 dB beamwidths are 61° and 62° in the vertical and horizontal planes, respectively, for the $+45^\circ$ polarization. The corresponding values for the -45° polarization are 62°

and 60° . The backlobe levels for both $+45^\circ$ and -45° polarizations are about -15 dB, which may be quite high. This is due to the use of a relatively smaller ground plane (180×180 mm) in the measurement. The antenna has the average gain of 8.5 dBi.

3.3. Dual-Polarized L-Probe Antenna Array

A basic element of a dual-polarized L-probe patch antenna has been presented in Section 3.2. Although the single element can have good self-isolation, in the array environment, the existence of coupling between array elements results in poor input port isolation. To solve this problem, we [71] also introduced techniques to enhance input ports isolation by reducing coupling between elements. To enhance the isolation of a dual-polarized patch antenna array, one solution is to use metallic walls surrounding each element [71]. The function of the walls is to act as a barrier, which avoids coupling between different elements. The configuration of a dual-polarized patch antenna array with surrounding metallic walls is shown in Fig. 28. The separation between two elements is 133 mm ($0.8\lambda_0$). For each element, a square aluminum patch with thickness of 1 mm and lengths of 58 mm is coupled by four identical L-shaped probes located at each corner of the patch. The patch is supported by plastic posts and placed 22 mm above the ground plane. Each probe with radius of 1 mm, vertical

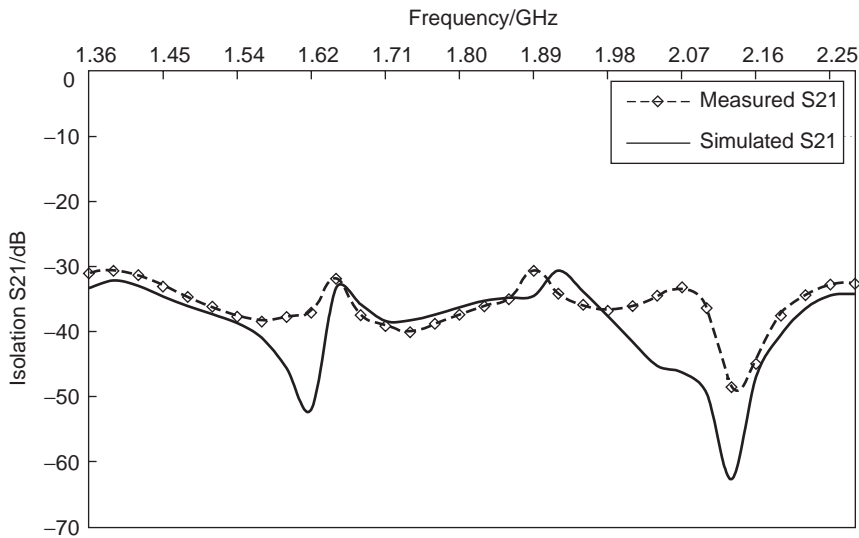


Figure 29. VSWR of antenna array with metallic walls surrounding elements. (From Wong et al. [71], © 2004 IEEE.)

length of 9 mm, and horizontal length of 38 mm is placed 13 mm below the patch. Each probe is designed to have a characteristic input impedance of $50\ \Omega$. Metallic walls with thickness of 2 mm surround the patch and act as an open-ended cavity with dimensions of $120 \times 120 \times 30$ mm. The size of ground plane is 180×300 mm. All L-shaped probes are connected to the feed network, and placed underneath the ground plane. Ports 1 and 2 are the input ports of the $+45^\circ$ and -45° polarizations, respectively.

3.3.1. Results. Measured results of S_{11} , S_{12} , and S_{22} for the antenna array are shown in Figs. 29 and 30. As seen in Fig. 29, the impedance bandwidth is 23.8% from 1.50 to 1.93 GHz, for $\text{VSWR} \leq 2$, and is 12% from 1.66 to 1.89 GHz for $\text{VSWR} \leq 1.5$. Across the frequency range from 1.71 to 1.88 GHz, the value of S_{12} is less than -30 dB as shown in Fig. 30. This indicates that the vertical metallic walls are able to reduce the coupling between different elements. The measured far-field patterns for the center frequency of 1.8 GHz are shown in Fig. 31. The 3 dB beamwidths are 31° and 64° in the vertical and horizontal planes, respectively,

for the -45° polarization. The corresponding values for the $+45^\circ$ polarization are 30° and 65° . The backlobe levels for both $+45^\circ$ and -45° polarizations are about -25 dB. The performance of this antenna array is suitable for using as base station antennas in mobile communication systems.

3.4. Dual-Polarized Patch Antenna with Hybrid Feeding Mechanism

A hybrid feeding mechanism for dual-polarized patch antennas have been proposed [72,73]. They combine an aperture coupling feed [15–17] and a capacitive coupling feed [37–39] to enhance the isolation between input ports. One of these hybrid dual-polarized patch antennas [72] is discussed here. The geometry of the antenna is shown in Fig. 32. The square patch, separated from the ground plane by a thick foam substrate, is fed by two perpendicular strip-lines etched on the feed layer, one through a small circular hole and the other through a near-resonance aperture formed in the upper ground plane. These two lines have

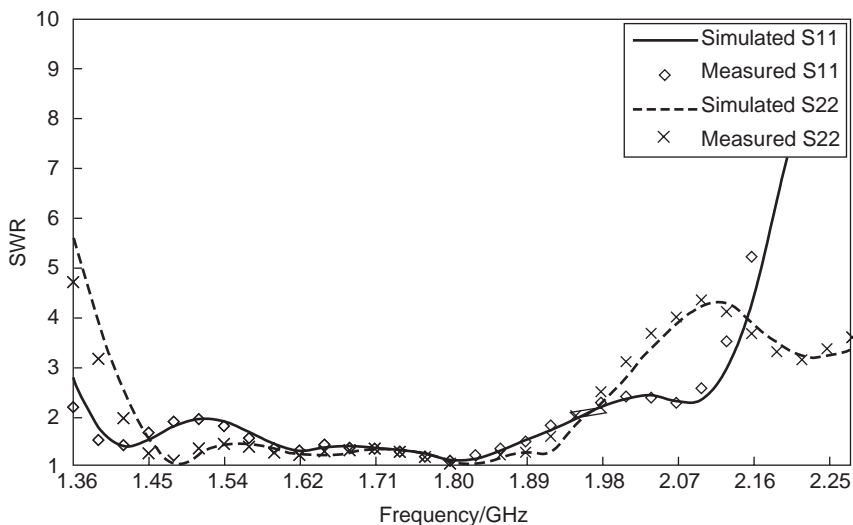


Figure 30. Isolation of antenna array with metallic walls surrounding elements. (From Wong et al. [71], © 2004 IEEE.)

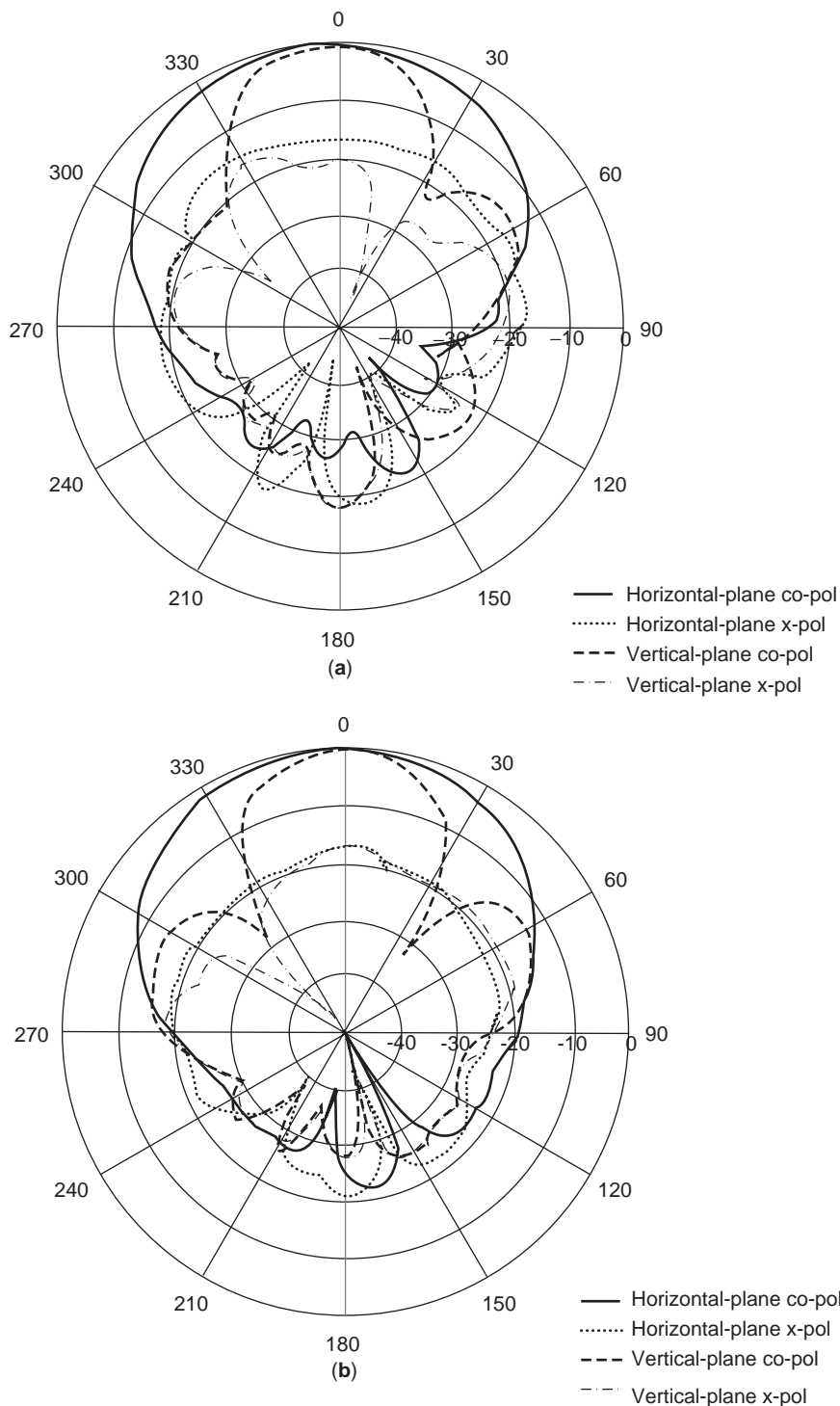
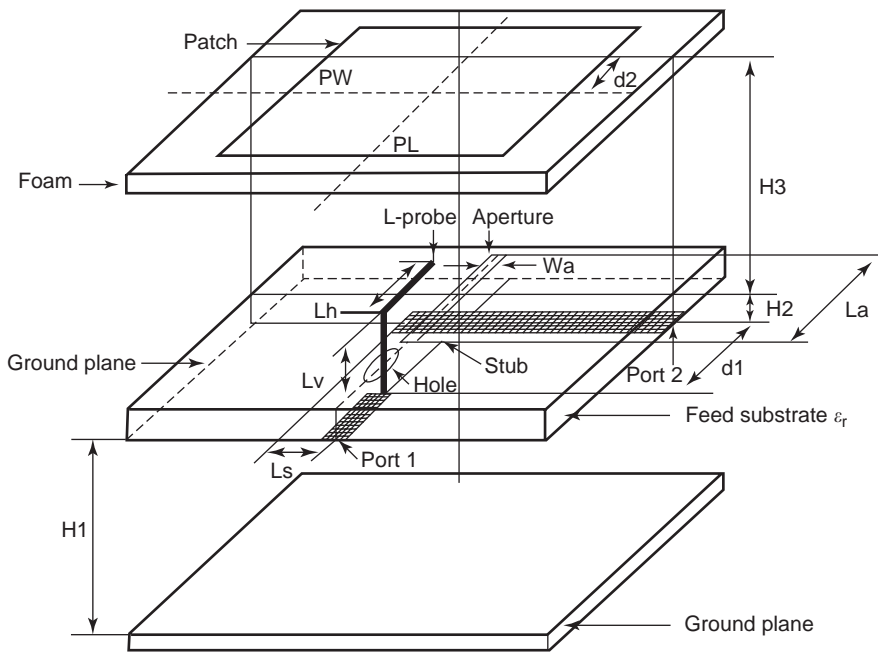


Figure 31. Measured far-field patterns at 1.8 GHz: (a) port 1; (b) port 2. (From Wong et al. [71], © 2004 IEEE.)

characteristic impedance $Z_c = 50 \Omega$. At port 1, an L-shaped probe is connected at the end of the line via the small circular hole to cancel the inductance introduced by the thick substrate. At port 2, an open-ended stub is needed to tune out the large inductive reactance delivered to the feedline by the aperture.

3.4.1. Measured Results. Figure 33 shows the measured VSWR and input port isolation of the antenna. It is ob-

served that, for $VSWR \leq 1.5$, the frequency range is 1.68–2.06 GHz, or $BW = 20.5\%$ for port 1 and 1.59–2.03 GHz, $BW = 24.9\%$ for port 2, respectively. Over the bandwidth, input port isolation is below -25 dB. The radiation patterns at 1.8 GHz for the two ports are shown in Fig. 34. The 3 dB beamwidths for the L-probe coupling case (port 1) are 70° and 71° in the E and H planes, respectively. The corresponding values for the aperture-fed case (port 2) are 60° and 72° , respectively. The measured gain at each of the



(Unit: mm, $H1 = 10$, $Lh = 34$, $Lv = 12$, $La = 48$, $Wa = 1$, $Ls = 10$, $d1 = 30$, $H2 = 1.6$, $H3 = 18$, $PL = PW = 59.5$, $d2 = 8$)

Figure 32. Antenna geometry. (From Guo et al. [72], © 2002 IEEE.)

two ports is greater than 6.0 dBi over the bandwidth. It can be observed that the level of backradiation is high, which is due to a relatively small ground plane used in the measurement and can be reduced through the use of a larger ground plane. The techniques described in Refs. 74 and 75 are also the efficient ways to reduce backradiation. The stripline feed structure can reduce backradiation considerably. On the other hand, backradiation from the aperture is trapped between the upper and lower metallic planes, resulting in the appearance of higher modes, which enhances the cross-polarization components. It is seen in Fig. 34 that the cross-polarization is quite high. The cross-polarization and efficiency can be improved with the use of shorting pins between the two ground planes

[76]. The high cross-polarization can also be overcome in the array design using a balanced feed mechanism [77].

4. MINIATURE WIDEBAND PATCH ANTENNAS

Extensive studies have been dedicated to size reduction techniques of microstrip patch antennas [78–81]. Several techniques have been proposed to reduce the size of the conventional half-wave patch. One approach involves the use of expensive high-dielectric-constant materials [82]. Other approaches are to use either a shorting (short-circuiting) wall [83,84] or a shorting pin [78–81,85–87] or various methods to increase the current pathlength flowing on the patch [88]. However, a narrow bandwidth of less than 6% ($VSWR \leq 2$) is achieved on these designs. In this section, we will summarize several designs of the miniature patch antenna with bandwidth enhancement. Bandwidth enhancements of small patch antennas with more than 10% ($VSWR \leq 2$) impedance bandwidth have been reported in a number of papers. The designs can be divided into two major categories, one based on the quarter-wave patch (shorting wall) structure and the other one based on the shorting pin structure.

4.1. Wideband Patch Antennas Design Based on Quarter-Wave Patch Structure

We know that placing a short circuit at the zero electric field line of a half-wave rectangular patch can reduce the size of the patch since half of the patch can be removed. The narrow bandwidth of only about 6% ($VSWR \leq 2$) is achieved on this quarter-wave patch antenna.

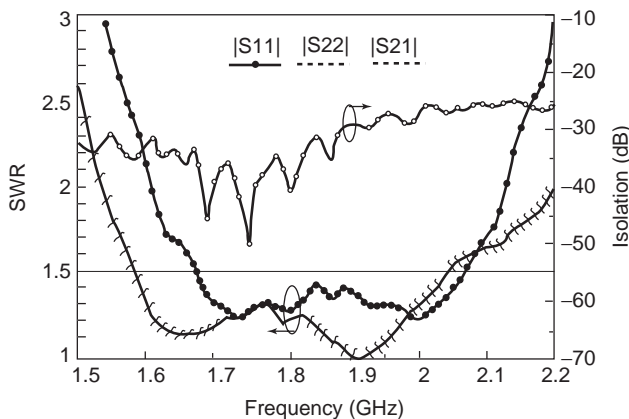


Figure 33. Measured reflection and coupling coefficients. (From Guo et al. [72], © 2002 IEEE.)

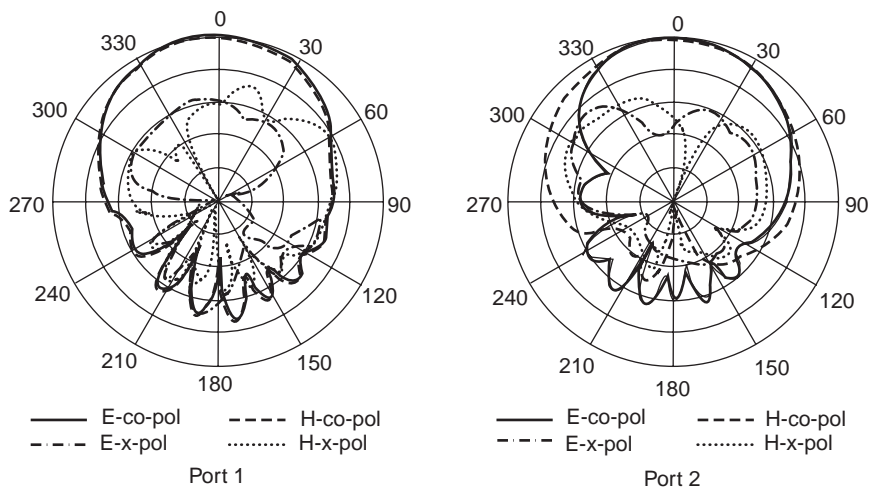


Figure 34. Measured patterns for ports 1 and 2 at 1.8 GHz, 10 dB/div. (From Guo et al. [72], © 2002 IEEE.)

4.1.1. Quarter-Wave Patch with Short-Circuiting Pin.

Figure 35 shows the conventional quarter-wave patch antenna and the quarter-wave patch antenna with shorting pin. By applying a shorting pin, as much as 20.7% bandwidth is achieved on the quarter-wave patch antenna [89]. The patch size is 30 mm (L) \times 20 mm (W), with one of the longer edge short-circuited to the ground via a short-circuiting wall. The feed position is $d_f = 5.5$ mm away from the shorting wall, and the feed radius is $r_f = 0.5$ mm. The shorting pin of radius $r_s = 0.5$ mm is placed $d_s = 11$ mm away from the open edge.

Figure 36 shows the VSWR of the quarter-wave patch antenna with shorting pin for different substrate thickness. The substrate thickness (h) varies from 3 mm ($0.375\lambda_0$) to 9 mm ($0.837\lambda_0$). The resonant frequency decreases when the substrate thickness increases. The bandwidth varies from 9% when $h = 3$ mm ($0.375\lambda_0$) at 3.76 GHz to 20.7% when $h = 9$ mm ($0.837\lambda_0$) at 2.79 GHz, where the feed location has varied in order to obtain the widest bandwidth. Table 1 summarizes the feedprobe location d_f , shorting pin location d_s , feedprobe radius r_f , and shorting pin radius r_s .

Figure 37 shows the measured radiation pattern when $h = 9$ mm. It is observed that the shorting wall leads to asymmetric radiation pattern and causes the $\phi = 0^\circ$ plane copolarized radiation pattern (E_θ) tilting away from the broadside direction, which is similar to the quarter-wave patch antenna. Also, the radiation of the shorting wall and

the shorting pin cause the cross-polarized field (E_ϕ) in the $\phi = 90^\circ$ plane to increase, and this becomes greater when the substrate thickness h is increased. This antenna achieves a gain of more than 3 dBi when the substrate thickness varies from $h = 3$ to 9 mm. Table 1 summarizes the performance of the antenna with different substrate thicknesses.

4.1.2. Shorted Two-Layer Patch Antennas.

The design of this type of antennas is based on the two-layer patch antenna. A shorting wall is placed at the line of symmetry of this two-layer patch antenna as shown in Fig. 38a. Figures 38b–38d show different configurations of the short-circuited two-layer patch antennas. The differences among the three antennas are the upper patch shape and the width of the shorting wall. The impedance bandwidth achieves more than 8% ($VSWR \leq 2$) in all designs [90–92].

The projection dimensions of the antenna are, width $W = 17.5$ mm and length $L = 17.5$ mm. The substrate between the upper patch and the lower patch has a thickness of $h_1 = 2$ mm. The antennas are excited in the TM_{10} mode by a coaxial feed, where the feed position is 13.5 mm away from the radiating edge. The lower patch is held by a foam substrate of thickness $h_2 = 6$ mm. The area of the shorted two-layer patch antenna has been reduced by 92% when compared with the conventional rectangular patch. The bandwidth has been enhanced to 8.3%. In cases with higher resonant frequency, the bandwidth can attain 11%.

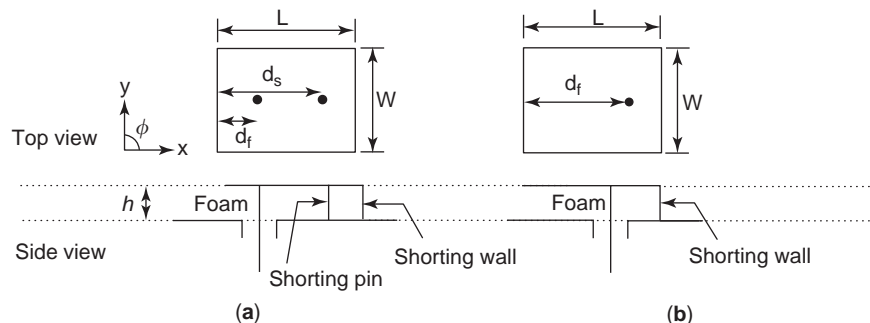


Figure 35. Geometry of quarter-wave patch antenna with short-circuiting pin. (From Mok et al. [89], reprinted with permission from IEE.)

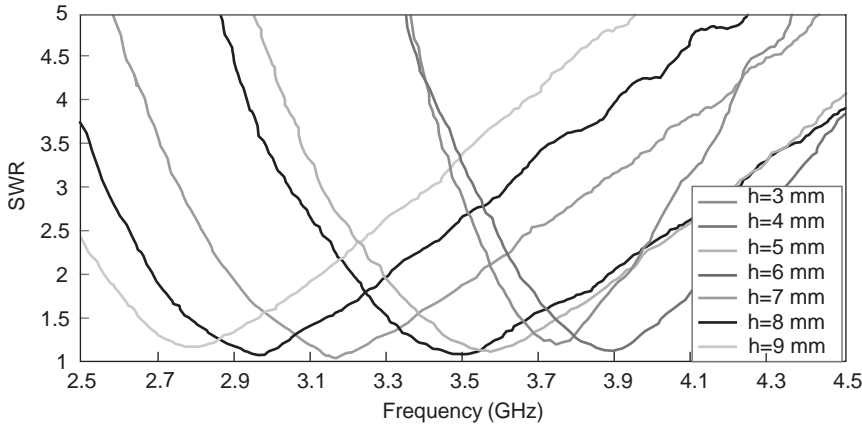


Figure 36. VSWR of quarter-wave patch antenna with short-circuiting pin. (From Mok et al. [89], reprinted with permission from IEE.) (This figure is available in full color at [http://www.mrw.interscience.wiley.com/erfme.](http://www.mrw.interscience.wiley.com/erfme))

Figure 39 shows the radiation pattern of the shorted two-layer patch antenna. Again, a relatively high cross-polarization level is measured as a result of the radiation of the coaxial feed. It is also observed that the shorting wall leads to the asymmetric radiation pattern. As the size has been greatly reduced, the average gain obtained is only 1.5 dBi for the configuration shown in Fig. 38d.

4.1.3. Other Structures with Shorting Walls

4.1.3.1. L-Probe Feed. The L-shaped probe coupling technique [55] has been demonstrated to enhance the bandwidth of the traditional patch antennas in Section 2.5. Here, the bandwidth is enhanced by applying the L-probe coupling techniques incorporated with the quarter-wave patch antenna [93], as shown in Fig. 40.

The patch is excited in the TM_{01} mode by the L-probe fed. The patch size has length $L=0.17\lambda_0$, width $W=0.46\lambda_0$, and height $H=0.1\lambda_0$. Figure 41 shows the impedance bandwidth and gain, where the impedance bandwidth achieves as much as 39% ($VSWR \leq 2$) with an average gain of 7 dBi. The radiation pattern is stable across the passband and is radiated in the broadside direction with a beam squint of $\sim 15^\circ$ due to the asymmetric structure of the antenna.

4.1.3.2. Capacitive Coupling. This is another feeding method introduced to enhance the bandwidth of regular patch antenna, as discussed in Section 2.4.1, and also for the miniature patch antenna. A circular disk is connected to the coaxial probe, which acts as a capacitor patch to

compensate the inductance introduced from the feeding probe [94]. The structure is shown in Fig. 42.

The capacitance from the capacitor patch and the inductance from the coaxial probe are in resonance near the patch resonance. As shown in Fig. 43, there are two resonances: one from the series resonance by the feed mechanism and the other one from the patch. Once the resonances are close to each other, a bandwidth of 35% ($VSWR \leq 2$) is achieved. The average gain obtained is 4 dBi across the passband. The cross polarization level is as high as the copolar value.

4.1.3.3. Stacked Patch. In the stacked-patch techniques (Section 2.3.2), where the parasitic patch has a close resonance to the driven patch, the bandwidth is enhanced because the two resonators have two closely packed resonant frequencies. Several designs have been reported on the bandwidth enhancement of the quarter-wave patch antenna using stacked structure [95–97]. Figures 44a and 44b show two different configurations. The structure shown in Fig. 44a consists of a driven lower patch with a parasitic element placed horizontally on top of it, and a common shorting wall is connected to both patches [95,96]. The driven patch is larger than the parasitic patch. Figure 44b shows another configuration with a tilted parasitic patch where the shorted edge is common to the shorted edge of the driven patch [97].

Table 1. Parameter Study of the Quarter-Wave Patch Antenna with Short-Circuiting Pin

h (mm)	d_f (mm)	d_s (mm)	f_0 (GHz)	Bandwidth (%)	Maximum Gain (dBi)
3	5	8	3.75	9.1	3.4
4	3	10	3.88	12.4	3.5
5	2	14	3.6	17.2	3.3
6	3	16	3.49	19.2	3.7
7	3	18	3.17	20.2	4
8	5	20	2.95	20.7	3
9	3	22	2.79	20	3.6

Source: From Mok et al. [89], reprinted with permission from IEE.

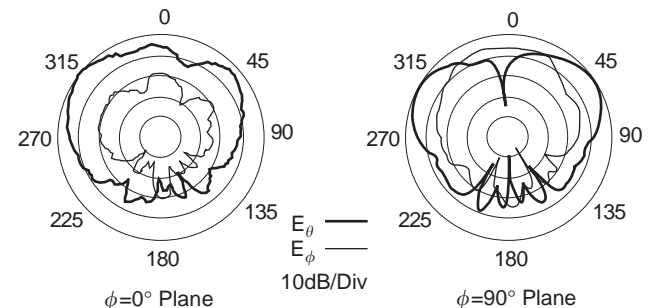


Figure 37. Radiation pattern of quarter-wave patch antenna with short-circuiting pin. (From Mok et al. [89], reprinted with permission from IEE.)

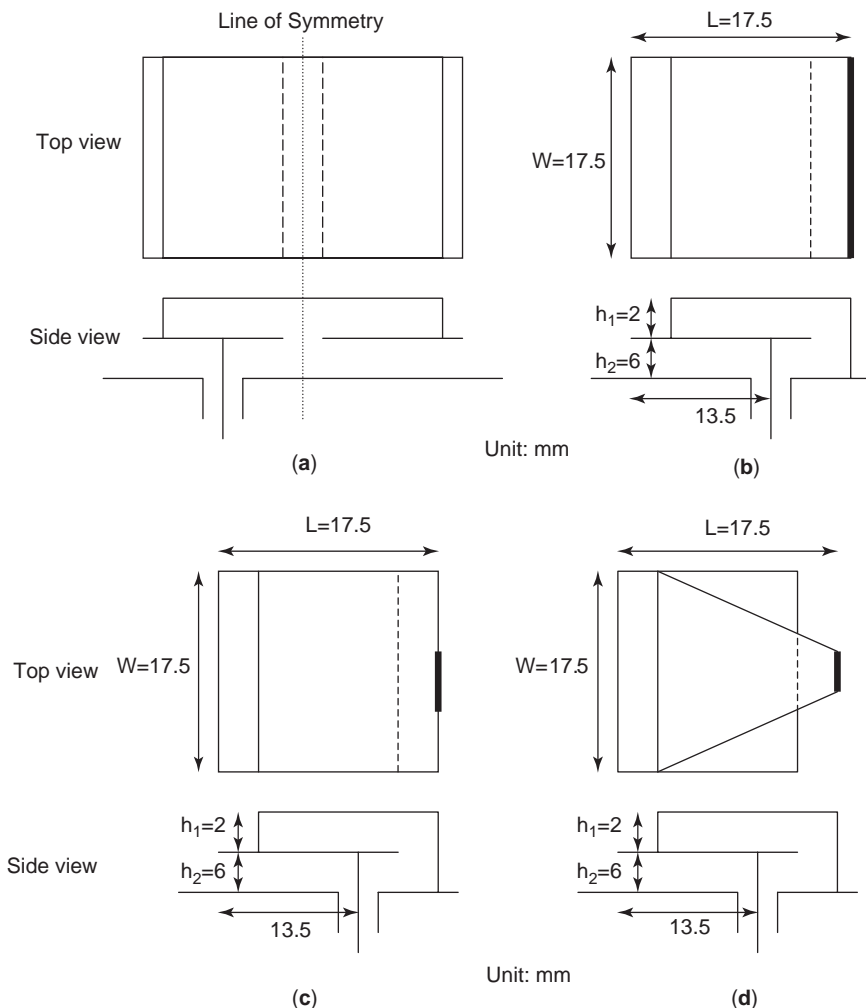


Figure 38. Geometry of short-circuited two-layer patch antennas. (From Chair et al. [90,91], reprinted with permission from IEE.)

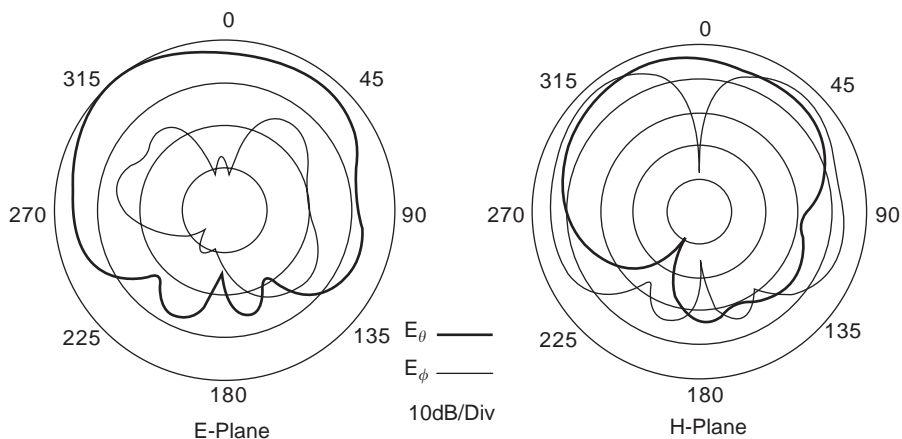


Figure 39. Radiation pattern of short-circuited two-layer patch antennas. (From Chair et al. [91], reprinted with permission from IEE.)

Figure 45 shows the VSWR of the quarter-wave patch antenna shown in Fig. 44a. Two resonances come from two stacked resonators. A maximum of 30% of impedance bandwidth is obtained when the antenna thickness is $0.082\lambda_0$. Table 2 summarizes the relationship between the antenna thickness and the impedance bandwidth.

In the second design, based on the stacked-patch structure, the upper patch is tilted by 13.6° and the impedance

bandwidth enhances to 44% ($VSWR \leq 2$). Both radiation patterns are stable across the passband with a shift of 45° in the *E*-plane copolarized field. This is due mainly to the asymmetric structure of the quarter-wave patch antenna. The cross-polarization levels in the *H*-plane are quite high, which is typical of the behavior of the quarter-wave patch antenna. Figure 46 shows the radiation pattern of the titled upper patch antenna.

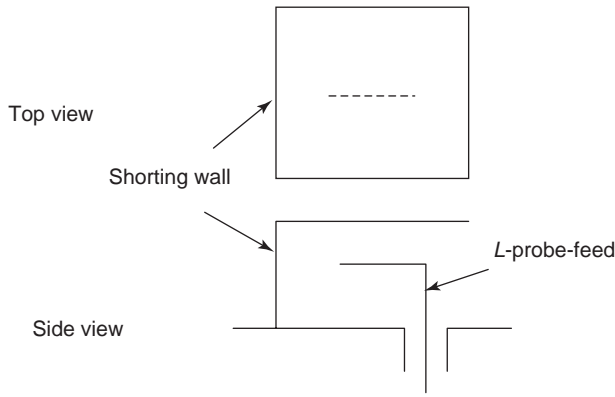


Figure 40. L-probe-fed patch antenna with short-circuiting wall. (From Guo et al. [93], reprinted with permission from IEE.)

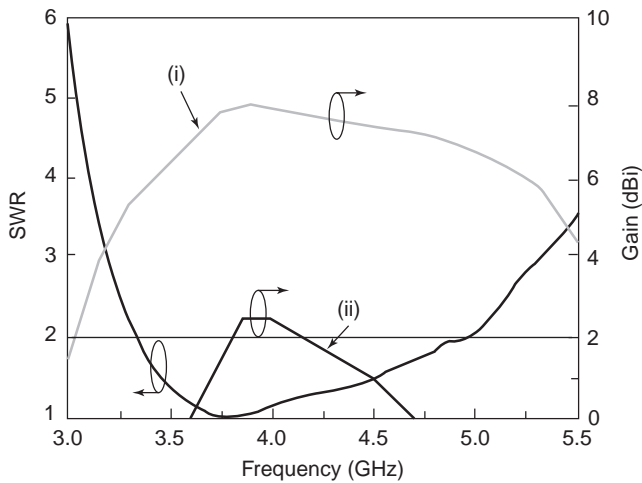


Figure 41. VSWR and gain of L-probe-fed patch antenna with short-circuited wall. (From Guo et al. [93], reprinted with permission from IEE.)

4.2. Wideband Patch Antenna Design Based on the Short-Circuiting Pin Structure

The use of a shorting pin to adjust the resonant frequency of a patch antenna is well known [98]. As the design is similar, but not identical, to the PIFA (planar inverted-F antenna) design, it was shown that the size of the traditional patch antenna can be reduced by adding a shorting pin near the feed location [81]. The size reduces by more than 80%; however, narrow impedance bandwidth is its drawback, and only 1.2% is achieved. With the use of a thicker substrate, around 0.06λ , the bandwidth can be improved to 6% [99].

4.2.1. Multiple Shorting Pins

4.2.1.1. Single-Layer Patch. In Ref. 99, by using more shorting pins, the bandwidth of the antenna can be increased. Figures 47a and 47b show the antennas structure with two and three shorting pins, respectively. The shape of the patch can be either circular or rectangular.

The bandwidth ($VSWR \leq 2$) with 7.9% and 9.4% is achieved when two and three shorting pins are used as shown in Figs. 47a and 47b, respectively. Unlike the single

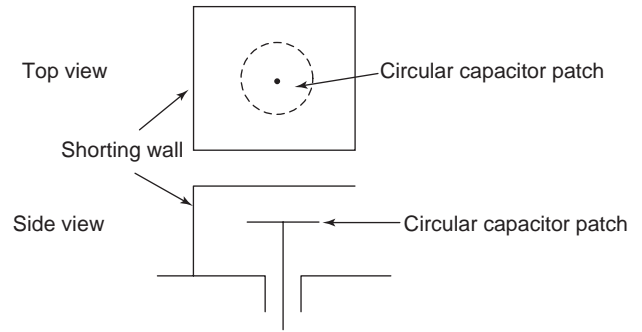


Figure 42. Capacitively fed patch antenna with short-circuiting wall. (From Voipio et al. [94], © 1998 IEEE.)

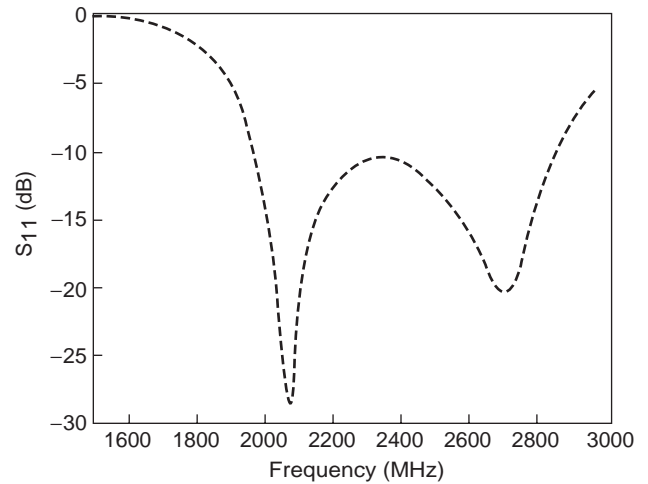


Figure 43. Measured return loss of capacitively fed patch antenna with short-circuiting wall. (From Voipio et al. [94], © 1998 IEEE.)

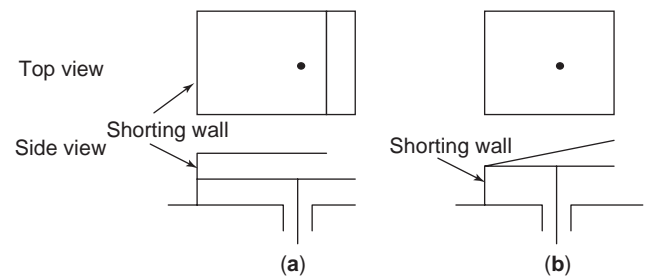


Figure 44. Stacked patch structures with short-circuiting wall. (From Zaid et al. [96], © 1999 IEEE and Bonefacic et al. [97], reprinted with permission from IEE.)

Table 2. Parameter Study on Patch Thickness and Impedance Bandwidth

Patch Thickness	Impedance Bandwidth ($VSWR \leq 2$) (%)
$0.039\lambda_0$	15.4
$0.043\lambda_0$	18.6
$0.055\lambda_0$	23
$0.082\lambda_0$	29.5

Source: From Zaid et al. [96], © 1999 IEEE.

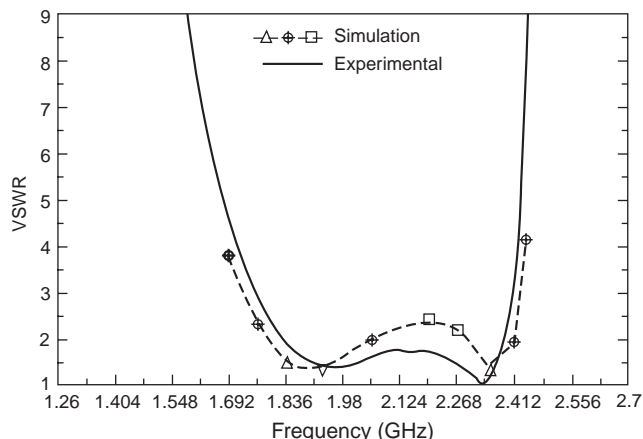


Figure 45. VSWR of stacked quarter-wave patch antenna. (From Zaid et al. [96], © 1999 IEEE.)

shorting pin, the multiple shorting pins should be positioned further apart. However, the tradeoff is the increase in patch size. Since the number of the shorting pins increases, the performance of the antenna tends toward a quarter-wave antenna behavior. The *H*-plane cross-polarization level is still relative high because the presence of the shorting pins.

4.2.2. Slot-Loaded Patch

4.2.2.1. U-Shaped Slot. Lee [42] proposed a U-shaped slot on the patch to enhance the bandwidth of the traditional probe feed patch, as discussed in Section 2.4.2.2. In Ref. 100, a design combining the U shaped slot and the shorting pin that can reduce the size and enhance the bandwidth of the antenna is presented. The structure is shown in Fig. 48.

This patch antenna can achieve an impedance bandwidth to 30% ($VSWR \leq 2$) with substrate thickness of $0.084\lambda_0$. The size of the proposed antenna is only 21% of the original half-wave patch antenna. As the size of this antenna has been greatly reduced, the average gain is

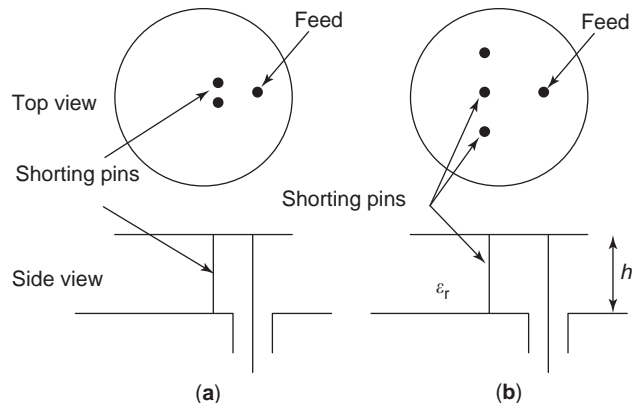


Figure 47. Structures with multiple short-circuiting pins. (From Waterhouse et al. [99], © 1998 IEEE.)

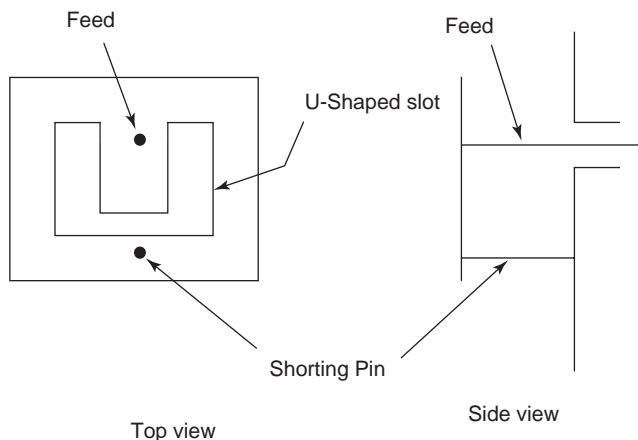


Figure 48. Structure of short-circuited U-slot patch antenna. (From Shackelford et al. [100], reprinted with permission from IEE.)

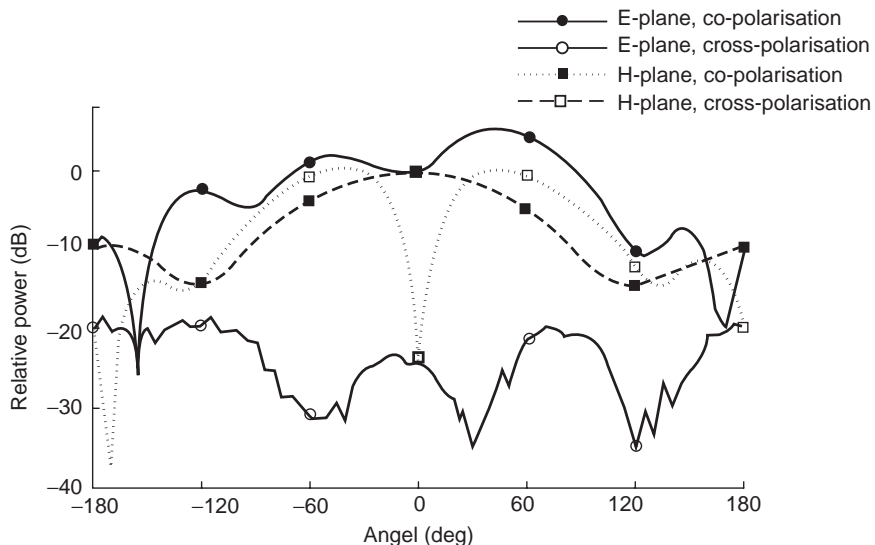


Figure 46. Radiation pattern of stacked quarter-wave patch antenna. (From Bonafacic et al. [97], reprinted with permission from IEE.)

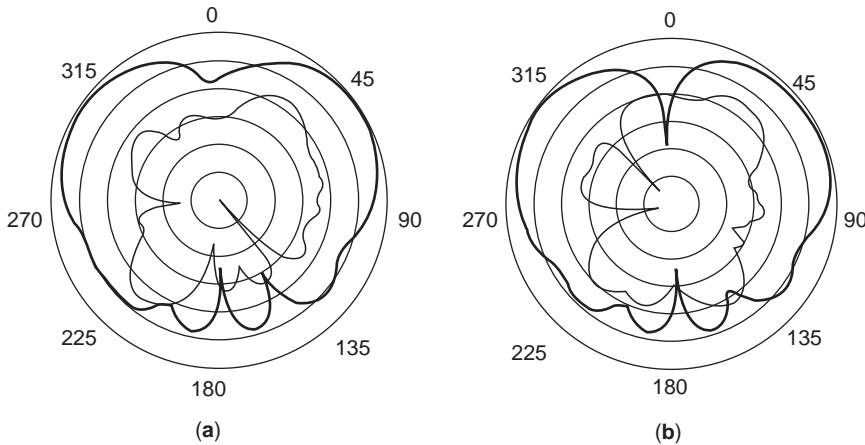


Figure 49. Radiation pattern of short-circuited U-slot patch antenna. (From Shackelford et al. [100], reprinted with permission from IEE.)

around 2 dBi. Figure 49 shows the radiation pattern of the antenna. The radiation pattern is stable across the band, whereas the strongest radiation has tilted 52° away from the broadside direction. The high cross-polarization level in the H -plane is obtained due to the radiation of the shorting pin and coaxial feed.

4.2.2.2. Rectangular Notch. Figure 50 shows the shorted rectangular shaped slot semidisk microstrip antenna [101]. The antenna is designed be used in the IMT2000 (1885–2200 MHz), DECT (1880–1900 MHz), and Bluetooth wireless communication (2400–2483.5 MHz) systems.

With an appropriate rectangular slot size and locations of the shorting pins, the impedance bandwidth achieves 32.4% ($VSWR \leq 2$), which covers the frequency range from 1.86 to 2.58 GHz. The size reduction is due mainly to the shorting pin, which acts as an inductive loading. Enhancement of the electric fields by the thin rectangular slot can further reduce the size of the antenna. With the thin rectangular slot, the shorted semidisk patch antenna excites dual-frequency resonance. Therefore, a broad bandwidth is obtained by optimizing the size of the rectangular slot in order to merge the two resonances closely packed. Figure 51 shows the return loss and input impedance of the antenna. The thickness of the antenna is about $0.07\lambda_1$, and the size is less than $0.35\lambda_1$, where λ_1 is the wavelength at the lowest frequency (1.86 GHz).

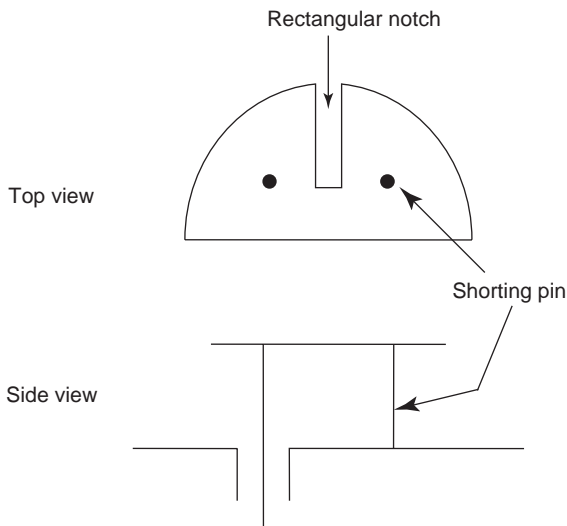


Figure 50. Structure of short-circuited notch patch antenna. (From Wang et al. [101], © 2002 John Wiley & Sons, Inc.)

5. CONCLUDING REMARKS

This article begins with the introduction of several common bandwidth-widening methods for microstrip antennas. Features of each method are discussed with

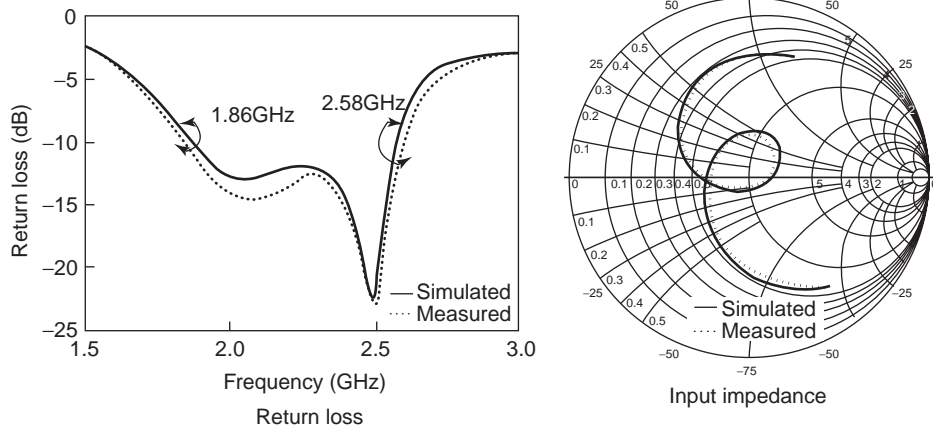


Figure 51. Return loss and input impedance of short-circuited notch patch. (From Wang et al. [101], © 2002 John Wiley & Sons, Inc.)

related illustrations and references. One of the basic means of increasing bandwidth is to employ electrically thick substrate with low dielectric constant, but the problem associated with increasing the substrate thickness is the increased reactance associated with the longer probe feed required. This limits the achievable bandwidth of microstrip antennas to only a few percent. Several wideband techniques designed by the authors are then discussed, including the advanced technique of employing the L-probe coupling technique. The article proceeds to discuss the wideband performance on two popular antenna designs: the wideband dual-polarized patch antennas designs and the wideband miniature patch antennas designs. Throughout the article, experimental results are presented and referenced.

BIBLIOGRAPHY

1. S. D. Targonski and D. M. Pozar, Design of wideband circularly polarized aperture-coupled microstrip antennas, *IEEE Trans. Anten. Propag.* **AP-41**(2):214–220 (Feb. 1993).
2. K. L. Wong and T. W. Chiou, Broad-band single-patch circularly polarized microstrip antenna with dual capacitively coupled feeds, *IEEE Trans. Anten. Propag.* **AP-49**(1):41–44 (Jan. 2001).
3. N. Herscovici, Z. Sipus, and D. Bonafacic, Circularly polarized single-fed wide-band microstrip patch, *IEEE Trans. Anten. Propag.* **AP-51**(6):1277–1280 (June 2003).
4. M. Sumi, K. Hirasawa, and S. Shi, Two rectangular loops fed in series for broadband circular polarization and impedance matching, *IEEE Trans. Anten. Propag.* **AP-52**(2):551–554 (Feb. 2004).
5. G. P. Kurpis and C. J. Booth, *The New IEEE Standard Dictionary of Electrical and Electronics Terms*, 5th ed., IEEE, Jan. 1993.
6. J. R. James and P. S. Hall, *Handbook of Microstrip Antennas*, Peter Peregrinus, 1989.
7. E. Chang, S. A. Long, and W. F. Richards, An experimental investigation of electrically thick rectangular microstrip antennas, *IEEE Trans. Anten. Propag.* **AP-34**(6):767–772 (June 1986).
8. N. Herscovici, A wide-band single-layer patch antenna, *IEEE Trans. Anten. Propag.* **AP-46**(4):471–474 (April 1998).
9. K. L. Wong, C. L. Tang, and J. Y. Chiou, Broad-band probe-fed patch antenna with a W-shaped ground plane, *IEEE Trans. Anten. Propag.* **AP-50**(6):827–831 (June 2002).
10. D. M. Pozar and B. Kaufman, Increasing the bandwidth of a microstrip antenna by proximity coupling, *Electron. Lett.* **23**(8):368–369 (April 1987).
11. H. G. Oltman and D. A. Huebner, Electromagnetically coupled microstrip dipoles, *IEEE Trans. Anten. Propag.* **AP-29**(1):151–157 (Jan. 1981).
12. C. L. Mak, K. M. Luk, and K. F. Lee, Proximity-coupled U-slot patch antenna, *Electron. Lett.* **34**(8):715–716 (April 1998).
13. K. L. Lau, K. M. Luk, and K. F. Lee, Wideband U-slot microstrip patch antenna array, *IEE Proc. Microwaves Anten. Propag.* **148**(1):41–44 (Feb. 2001).
14. C. Kidder, M. Li, and K. Chang, Broad-band U-slot patch antenna with a proximity-coupled double Π -shaped feed line for arrays, *IEEE Anten. Wireless Propag. Lett.* **1**:2–4 (2002).
15. D. M. Pozar, Microstrip antenna aperture-coupled to a microstripline, *Electron. Lett.* **21**(2):49–50 (Jan. 1985).
16. X. H. Yang and L. Shafai, Characteristics of aperture coupled microstrip antennas with various radiating patches and coupling apertures, *IEEE Trans. Anten. Propag.* **AP-43**(1):72–78 (Jan. 1995).
17. V. Rathi, G. Kumar, and K. P. Ray, Improved coupling for aperture coupled microstrip antennas, *IEEE Trans. Anten. Propag.* **AP-44**(8):1196–1198 (Aug. 1996).
18. H. S. Shin and N. Kim, Wideband and high-gain one-patch microstrip antenna coupled with H-shaped aperture, *Electron. Lett.* **38**(19):1072–1073 (Sept. 2002).
19. M. D. van Wyk and K. D. Palmer, Bandwidth enhancement of microstrip patch antennas using coupled lines, *Electron. Lett.* **37**(13):806–807 (June 2001).
20. C. Wood, Improved bandwidth of microstrip antennas using parasitic elements, *IEE Proc.-H: Microwaves Anten. Propag.* **127**(4):231–234 (Aug. 1980).
21. G. Kumar and K. C. Gupta, Nonradiating edges and four edges gap-coupled multiple resonator broad-band microstrip antennas, *IEEE Trans. Anten. Propag.* **AP-33**(2):173–178 (Feb. 1985).
22. C. K. Aanandan and K. G. Nair, Compact broadband microstrip antenna, *Electron. Lett.* **22**(20):1064–1065 (Sept. 1986).
23. T. M. Au, K. F. Tong, and K. M. Luk, Characteristics of aperture-coupled coplanar microstrip subarrays, *IEE Proc. Microwaves Anten. Propag.* **144**(2):137–140 (April 1997).
24. R. Q. Lee and K. F. Lee, Experimental study of the two-layer electromagnetically coupled rectangular patch antenna, *IEEE Trans. Anten. Propag.* **AP-38**(8):1298–1302 (Aug. 1990).
25. R. B. Waterhouse, Design of probe-fed stacked patches, *IEEE Trans. Anten. Propag.* **AP-47**(12):1780–1784 (Dec. 1999).
26. F. Croq and A. Papiernik, Stacked slot-coupled printed antenna, *IEEE Microwave Guided Wave Lett.* **1**(10):288–290 (Oct. 1991).
27. F. Croq and D. M. Pozar, Millimeter-wave design of wide-band aperture-coupled stacked microstrip antennas, *IEEE Trans. Anten. Propag.* **AP-39**(12):1770–1776 (Dec. 1991).
28. T. M. Au, K. F. Tong, and K. M. Luk, Analysis of offset dual-patch microstrip antenna, *IEE Proc. Microwaves Anten. Propag.* **141**(6):523–526 (Dec. 1994).
29. S. D. Targonski, R. B. Waterhouse, and D. M. Pozar, Design of wide-band aperture-stacked patch microstrip antennas, *IEEE Trans. Anten. Propag.* **AP-46**(9):1245–1251 (Sept. 1998).
30. H. Legay and L. Shafai, New stacked microstrip antenna with large bandwidth and high gain, *IEE Proc. Microwaves Anten. Propag.* **141**(3):199–204 (June 1994).
31. K. F. Tong, T. M. Au, K. M. Luk, and K. F. Lee, Two-layer five-patch broadband microstrip antennas, *Electron. Lett.* **31**(19):1621–1622 (Sept. 1995).
32. W. S. T. Rowe and R. B. Waterhouse, Broadband CPWfed stacked patch antenna, *Electron. Lett.* **35**(9):681–682 (April 1999).
33. C. H. Cheng, K. Li, and T. Matsui, Stacked patch antenna fed by a coplanar waveguide, *Electron. Lett.* **38**(25):1630–1631 (Dec. 2002).
34. C. L. Mak, K. M. Luk, and K. F. Lee, Microstrip line-fed L-strip patch antenna, *IEE Proc. Microwaves Anten. Propag.* **146**(4):282–284 (Aug. 1999).
35. F. Abboud, J. P. Damiano, and A. Papiernik, Simple model for the input impedance of coax-fed rectangular microstrip

- patch antenna for CAD, *IEE Proc.-H: Microwaves Anten. Propag.* **135**(5):323–326 (Oct. 1988).
36. B. M. Alarjani and J. S. Dahele, Feed reactance of rectangular microstrip patch antenna with probe feed, *Electron. Lett.* **36**(5):388–390 (March 2000).
 37. G. A. E. Vandenbosch and A. R. Van De Capelle, Study of the capacitively fed microstrip antenna element, *IEEE Trans. Anten. Propag.* **AP-42**(12):1648–1652 (Dec. 1994).
 38. G. A. E. Vandenbosch, Capacitive matching of microstrip antennas, *Electron. Lett.* **31**(18):1535–1536 (Aug. 1995).
 39. G. A. E. Vandenbosch, Network model for capacitively fed microstrip element, *Electron. Lett.* **35**(19):1597–1599 (Sept. 1999).
 40. P. S. Hall, Probe compensation in thick microstrip patches, *Electron. Lett.* **23**(11):606–607 (May 1987).
 41. K. M. Luk, Y. W. Lee, K. F. Tong, and K. F. Lee, Experimental studies of circular patch with slots, *IEE Proc. Microwaves Anten. Propag.* **144**(6):421–424 (Dec. 1997).
 42. T. Huynh and K. F. Lee, Single-layer single-patch wideband microstrip antenna, *Electron. Lett.* **31**(16):1310–1312 (Aug. 1995).
 43. K. L. Wong and W. H. Hsu, Broadband triangular microstrip antenna with U-shaped slot, *Electron. Lett.* **33**(25):2085–2086 (Dec. 1997).
 44. K. F. Tong, K. M. Luk, K. F. Lee, and R. Q. Lee, A broadband U-slot rectangular patch antenna on a microwave substrate, *IEEE Trans. Anten. Propag.* **AP-48**(6):954–960 (June 2000).
 45. K. M. Luk, K. F. Lee, and W. L. Tam, Circular U-slot patch with dielectric superstrate, *Electron. Lett.* **33**(12):1001–1002 (June 1997).
 46. Y. X. Guo, K. M. Luk, K. F. Lee, and Y. L. Chow, Double U-slot rectangular patch antenna, *Electron. Lett.* **34**(19):1805–1806 (Sept. 1998).
 47. K. F. Lee, K. M. Luk, K. F. Tong, S. M. Shum, T. Huynh, and R. Q. Lee, Experimental and simulation studies of the coaxially fed U-slot rectangular patch antenna, *IEE Proc. Microwaves Anten. Propag.* **144**(5):354–358 (Oct. 1997).
 48. M. Clenet and L. Shafai, Multiple resonances and polarisation of U-slot patch antenna, *Electron. Lett.* **35**(2):101–103 (Jan. 1999).
 49. K. M. Luk, Y. X. Guo, K. F. Lee, and Y. L. Chow, L-probe proximity fed U-slot patch antenna, *Electron. Lett.* **34**(19):1806–1807 (Sept. 1998).
 50. Y. X. Guo, K. M. Luk, and K. F. Lee, U-slot circular patch antennas with L-probe feeding, *Electron. Lett.* **35**(20):1694–1695 (Sept. 1999).
 51. W. X. Zhang, C. S. Pyo, S. I. Jeon, S. P. Lee, and N. H. Myung, A new type of wideband slot-fed U-slotted patch antenna, *Microwave Opt. Technol. Lett.* **22**(6):378–381 (Sept. 1999).
 52. F. Yang, X. X. Zhang, X. Ye, and Y. Rahmat-Samii, Wideband E-shaped patch antennas for wireless communications, *IEEE Trans. Anten. Propag.* **AP-49**(7):1094–1100 (July 2001).
 53. K. L. Wong and W. H. Hsu, A broad-band rectangular patch antenna with a pair of wide slits, *IEEE Trans. Anten. Propag.* **AP-49**(9):1345–1347 (Sept. 2001).
 54. Z. N. Chen, Experimental investigation of impedance characteristics of patch antennas with finite-size substrates, *Microwave Opt. Technol. Lett.* **25**(2):107–110 (April 2000).
 55. K. M. Luk, C. L. Mak, Y. L. Chow, and K. F. Lee, Broadband microstrip patch antenna, *Electron. Lett.* **34**(15):1442–1443 (July 1998).
 56. C. L. Mak, K. M. Luk, K. F. Lee, and Y. L. Chow, Experimental study of a microstrip patch antenna with an L-shaped probe, *IEEE Trans. Anten. Propag.* **AP-48**(5):777–783 (May 2000).
 57. K. M. Luk, L. K. Au Yeung, C. L. Mak, and K. F. Lee, Circular patch antenna with an L-shaped probe, *Microwave Opt. Technol. Lett.* **20**(4):256–257 (Feb. 1999).
 58. C. L. Mak, K. M. Luk, and K. F. Lee, Wideband triangular patch antenna, *IEE Proc. Microwaves Anten. Propag.* **146**(2):167–168 (April 1999).
 59. K. M. Luk, C. H. Lai, and K. F. Lee, Wideband L-probe-feed patch antenna with dual-band operation for GSM/PCS base stations, *Electron. Lett.* **35**(14):1123–1124 (July 1999).
 60. B. L. Ooi and C. L. Lee, Broadband air-filled stacked U-slot patch antenna, *Electron. Lett.* **35**(7):515–517 (April 1999).
 61. C. L. Mak, K. F. Lee, and K. M. Luk, Small-size wideband microstrip antenna: the shorted U-slot L-probe (SUL) patch, *Proc. Millennium Conf. Antennas and Propagation (AP2000)*, Davos, Switzerland, April 2000, Vol. 1, p. 361.
 62. Y. X. Guo, C. L. Mak, K. M. Luk, and K. F. Lee, Analysis and design of L-probe proximity fed patch antennas, *IEEE Trans. Anten. Propag.* **AP-49**(2):145–149 (Feb. 2001).
 63. W. K. Lo, J. L. Hu, C. H. Chan, and K. M. Luk, Circularly polarized patch antenna with an L-shaped probe fed by a microstrip line, *Microwave Opt. Technol. Lett.* **24**(6):412–414 (March 2000).
 64. W. K. Lo, J. L. Hu, C. H. Chan, and K. M. Luk, L-shaped probe-feed circularly polarized microstrip patch antenna with a cross slot, *Microwave Opt. Technol. Lett.* **25**(4):251–253 (May 2000).
 65. W. K. Lo, C. H. Chan, and K. M. Luk, Circularly polarized patch antenna array using proximity-coupled L-strip line feed, *Electron. Lett.* **36**(14):1174–1175 (July 2000).
 66. J. S. Jeon, Design of wideband patch antennas for PCS and IMT-2000 service (Technical Feature), *Microwave J.* (July 2002).
 67. C. L. Mak, K. F. Lee, and K. M. Luk, Broadband patch antenna with a T-shaped probe, *IEE Proc. Microwaves Anten. Propag.* **147**(2):73–76 (April 2000).
 68. A. Petosa, A. Ittipiboon, and N. Gagnon, Suppression of unwanted probe radiation in wideband probe-fed microstrip patches, *Electron. Lett.* **35**(5):355–357 (March 1999).
 69. F. Croq and A. Papiernik, Large bandwidth aperture-coupled microstrip antenna, *Electron. Lett.* **26**:1293–1294 (Aug. 1990).
 70. M. Edimo, A. Sharaiha, and C. Terret, Optimized feeding of dual polarized broadband aperture-coupled printed antenna, *Electron. Lett.* **28**:1785–1787 (Sept. 1992).
 71. H. Wong, K. L. Lau, and K. M. Luk, Design of dual-polarized L-probe patch antenna arrays with high isolation, *IEEE Trans. Anten. Propag.* **AP-52**:45–52 (Jan. 2004).
 72. Y. X. Guo, K. M. Luk, and K. F. Lee, Broadband dual polarization patch element for cellular-phone base station, *IEEE Trans. Anten. Propag.* **AP-50**:251–253 (Feb. 2002).
 73. T. W. Chiou and K. L. Wong, Broad-band dual-polarized single microstrip patch antenna with high isolation and low cross polarization, *IEEE Trans. Anten. Propag.* **AP-50**:399–401 (March 2002).
 74. S. D. Targonski, R. B. Waterhouse, D. M. Pozar, Wideband aperture coupled microstrip patch array with backlobe reduction, *Electron. Lett.* **33**(24):2005–2006 (Nov. 1997).
 75. D. Sievenpiper, L. Zhang, R. F. J. Broas, N. G. Alexopolous, and E. Yablonovitch, High-impedance electromagnetic sur-

- faces with a forbidden frequency band, *IEEE Trans. Microwave Theory Tech.* **MTT-47**:2059–2074 (Nov. 1999).
76. P. Brachat and J. M. Baracco, Dual-polarization slot-coupled printed antennas fed by stripline, *IEEE Trans. Anten. Propag.* **AP-43**:738–742 (July 1995).
 77. K. Levis, A. Ittipiboon, and A. Petosa, Probe radiation cancellation in wideband probe-fed microstrip arrays, *Electron. Lett.* **36**(7):606–607 (March 2000).
 78. T. K. Lo, C. O. Ho, Y. Hwang, K. K. W. Lam, and B. Lee, Miniature aperture-coupled microstrip antenna of very high permittivity, *Electron. Lett.* **33**:9–10 (Jan. 1997).
 79. S. Pinhas and S. Shtrikman, Comparison between computed and measured bandwidth of quarter-wave microstrip radiators, *IEEE Trans. Anten. Propag.* **AP-36**:1615–1616 (Nov. 1988).
 80. J. S. Kuo and K. L. Wong, A low-cost microstrip-line-fed shorted-patch antenna for a PCS base station, *Microwave Opt. Technol. Lett.* **29**(3):146–148 (May 2001).
 81. R. B. Waterhouse, Small microstrip patch antenna, *Electron. Lett.* **31**:604–605 (1995).
 82. C. L. Tang, H. T. Chen, and K. L. Wong, Small circular microstrip antenna with dual-frequency operation, *Electron. Lett.* **33**(13):1112–1113 (June 1997).
 83. T. Y. Wu and K. L. Wong, On the impedance bandwidth of a planar inverted-F antenna for mobile handsets, *Microwave Opt. Technol. Lett.* **32**(4):249–251 (Feb. 2002).
 84. F. R. Hslao, H. T. Chen, T. W. Chlou, G. Y. Lee, and K. L. Wong, A dual-band planar inverted-F patch antenna with a branch-line slit, *Microwave Opt. Technol. Lett.* **32**(4):310–312 (Feb. 2002).
 85. H. K. Kan and R. B. Waterhouse, Small printed-wing antenna suitable for wireless handset terminals, *Microwave Opt. Technol. Lett.* **30**(4):226–229 (June 1997).
 86. S. H. Yeh, S. T. Fang, and K. L. Wong, Dual-band shorted patch antenna for dual ISM-band application, *Microwave Opt. Technol. Lett.* **32**(1):79–80 (Jan. 2002).
 87. K. L. Wong, C. L. Tang, and H. T. Chen, Compact meandered circular microstrip antenna with a shorting pin, *Microwave Opt. Technol. Lett.* **15**(3):147–149 (June 1997).
 88. S. Dey and R. Mittra, Compact microstrip patch antenna, *Microwave Opt. Technol. Lett.* **13**(1):12–14 (Sept. 1996).
 89. W. C. Mok, R. Chair, K. M. Luk, and K. F. Lee, Wideband quarter-wave patch antenna with shorting pin, *IEE Proc. Microwaves Anten. Propag.* **150**(1):56–60 (Feb. 2003).
 90. R. Chair, K. M. Luk, and K. F. Lee, Miniature multi-layer shorted patch antenna, *Electron. Lett.* **36**:3–4 (Jan. 2000).
 91. R. Chair, K. M. Luk, and K. F. Lee, Miniature shorted dual-patch antenna, *IEE Proc. Microwaves Anten. Propag.* **147**(4):273–276 (Aug. 2000).
 92. R. Chair, K. M. Luk, and K. F. Lee, Radiation efficiency analysis on small antenna by Wheeler cap method, *Microwave Opt. Technol. Lett.* **33**(2):112–113 (April 2002).
 93. Y. X. Guo, K. M. Luk, and K. F. Lee, *L*-probe proximity-fed short-circuited patch antennas, *Electron. Lett.* **35**(24):2069–2070 (Nov. 1999).
 94. V. Voipio, J. Ollikainen, and P. Vainikainen, Quarter-wave patch antenna with 35% bandwidth, *Proc. 1998 IEEE AP-S Int. Symp.*, June 21–26, 1998, Vol. 2, pp. 790–793.
 95. J. Ollikainen, M. Fischer, and P. Vainikainen, Thin dual-resonant stacked shorted patch antenna for mobile communications, *Electron. Lett.* **35**(16):437–438 (March 1999).
 96. L. Zaid, G. Kossias, J.-Y. Dauvignac, J. Cazajous, and A. Papiemik, Dual-frequency and broad-band antennas with stacked quarter wavelength elements, *IEEE Trans. Anten. Propag.* **AP-47**(4):654–660 (April 1999).
 97. D. Bonafacic, J. Bartolic, and D. Kocen, Stacked shorted patch antenna with tilted parasitic radiator, *Electron. Lett.* **37**(18):1109–1110 (Aug. 2001).
 98. S. S. Zhong and Y. T. Lo, Single element rectangular microstrip antenna for dual frequency operation, *Electron. Lett.* **19**(8):298–300 (1983).
 99. R. B. Waterhouse, S. D. Targonski, and D. M. Kokotoff, Design and performance of small printed antennas, *IEEE Trans. Anten. Propag.* **AP-46**(11):1629–1633 (Nov. 1998).
 100. A. K. Shackelford, K. F. Lee, K. M. Luk, and R. Chair, U-slot patch antenna with shorting pin, *Electron. Lett.* **37**(12):729–730 (June 2001).
 101. Y. J. Wang, Y. B. Gan, and C. K. Lee, A broadband and compact microstrip antenna for IMT-2000, DECT, and Bluetooth integrated handsets, *Microwave Opt. Technol. Lett.* **32**(3):204–207 (Feb. 2002).

MICROSTRIP ANTENNAS, COMPACT

KIN-LU WONG
National Sun Yat-Sen
University
Kaohsiung, Taiwan

1. INTRODUCTION

Microstrip antennas are usually formed by printing a conducting patch on a grounded dielectric substrate, and show the attractive features of lightweight, low profile, easy fabrication, and conformability to mounting hosts [1]. In order to meet the miniaturization requirement of mobile communication equipment [2], researchers have devoted much attention to compact microstrip antennas. Many related compact designs with broadband, dual-frequency, dual-polarized, circularly polarized, and gain-enhanced operations have been reported since the late 1990s [3]. This article addresses these innovative designs for compact microstrip antennas.

In Section 2, promising design techniques for reducing the size of microstrip antennas at a fixed operating frequency are introduced. These techniques include the uses of a high-permittivity substrate, a short-circuited patch, a slotted or meandered patch, a slotted or meandered slotted ground plane, and chip capacitor loading. Some reported compact microstrip antenna designs are described and discussed in this section. Section 3 discusses compact broadband microstrip antenna designs. The design techniques for achieving broadband operation with reduced antenna size are described. The related design techniques include the use of a short-circuited patch with a thick air-layer substrate, stacked shorted patches, chip resistor loading, and slot loading in the radiating patch or ground plane. Some interesting designs are presented.

Sections 4 and 5 present the designs of compact dual-frequency and dual-polarized microstrip antennas, respectively. Compact microstrip antennas with dual-frequency operation have attracted much attention recently (as of 2004), and many related designs have been available in

the open literature. The advances in compact circularly polarized (CP) microstrip antennas are considered in Section 6. A variety of design examples of the compact CP microstrip antennas are presented. The designs for achieving gain-enhanced compact microstrip antennas are included in Section 7. Some design examples are demonstrated. Finally, in Section 8, concluding remarks are made, and some future studies of compact microstrip antennas are addressed.

2. DESIGN TECHNIQUES FOR COMPACT MICROSTRIP ANTENNAS

2.1. Use of a High-Permittivity Substrate

In general, microstrip antennas are a half-wavelength structure and are operated at the fundamental resonant mode of TM_{01} or TM_{10} , with a resonant frequency given by (valid for a rectangular microstrip antenna with a thin microwave substrate)

$$f_0 \cong \frac{c}{2L\sqrt{\epsilon_r}} \quad (1)$$

where c is the speed of light, L is the patch length of a rectangular microstrip antenna, and ϵ_r is the relative permittivity of the grounded microwave substrate. From (1), it is known that the radiating patch of the microstrip antenna has a resonant length approximately proportional to $1/\sqrt{\epsilon_r}$, and the use of a microwave substrate with a larger permittivity thus can result in a smaller physical antenna length required at a fixed operating frequency. For comparison, taking two microstrip antenna designs with substrates of different relative permittivities of 3 and 27 as an example, the required length of the microstrip patch of the latter design will be only about one-third of that of the former one, as predicted from (1); that is, the required patch size of the latter design is only about 10% that of the former one. This result suggests that an antenna size reduction as large as about 90% can be obtained, if the design with $\epsilon_r = 27$ is used instead of the case with $\epsilon_r = 3$ for a fixed operating frequency.

2.2. Use of a Short-Circuited Patch

Figure 1 shows the geometry of a short-circuited rectangular microstrip antenna with a short-circuiting (shorting) pin. For the case that the short-circuiting pin is absent, the rectangular microstrip antenna is usually operated as a half-wavelength antenna, and the fundamental resonant frequency is given in (1). When there is a short-circuiting (SC) pin placed at $x = L/2$, $y = 0$ (center of the patch edge) and the feed position is chosen from the centerline (x axis), the first resonant frequency occurs at about $0.38f_0$ [4] (When there is more than one SC pin at the edge or a SC wall is used, the first resonant frequency occurs close to or at about $0.5f_0$. In this case, the short-circuited microstrip antenna is operated as a quarter-wavelength antenna.). This behavior suggests that the SC-pin-loaded rectangular microstrip antenna is operated with a resonant length less than one quarter-wavelength, and a greater reduced antenna size than the case with a SC wall can be obtained.

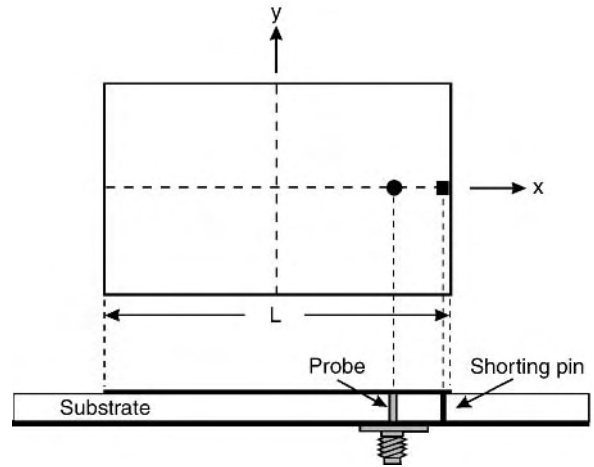


Figure 1. Geometry of a compact microstrip antenna with short-circuiting-pin loading.

With the SC-pin-loading technique, the antenna size reduction is due mainly to the shifting of the null voltage point at the center of the rectangular patch (excited at TM_{01} mode) and the circular patch (operated at TM_{11} mode) to their respective patch edges, which causes the short-circuited patches to resonate at a much lower frequency. Thus, at a given operating frequency, the required patch dimensions can be significantly reduced, and the reduction in the patch size is limited by the distance between the null voltage point in the patch and the patch edge. For this reason, compared to the case of SC-pin-loaded rectangular and circular patches, it is expected that an equilateral triangular microstrip patch excited at its fundamental mode (TM_{10} mode), where the null voltage point is at two-thirds of the distance from the triangle tip to the bottom edge of the triangle, will have a much larger reduction in the resonant frequency, when applying the SC-pin-loading technique. For comparison with the prediction, a compact triangular microstrip antenna with a SC pin loaded at the triangle tip was constructed and tested [5]. In this study, it is found that, for operating at about the same frequency, the side length of the compact (short-circuited) triangular microstrip antenna is only about 25% that of the conventional (regular-size) triangular microstrip antenna. This means a reduction of about 75% of the linear dimension of the antenna, or the size of the compact antenna is only about 7% of that of the conventional microstrip antenna. This reduction in antenna size is greater than those reported for the compact rectangular and circular microstrip antennas using the same technique.

2.3. Use of a Slotted or Meandered Patch

Compact operation of microstrip antennas can be obtained by embedding slots in the radiating patch or inserting slits at the boundary of the radiating patch. In this case, the effective surface current path in the radiating patch can be greatly lengthened or meandered, thereby leading to a large decrease in the antenna's fundamental resonant frequency. Figure 2 shows some slotted or meandered patches suitable for the design of compact microstrip antennas. In Fig. 2a, the embedded slot is a cross-slot, whose two

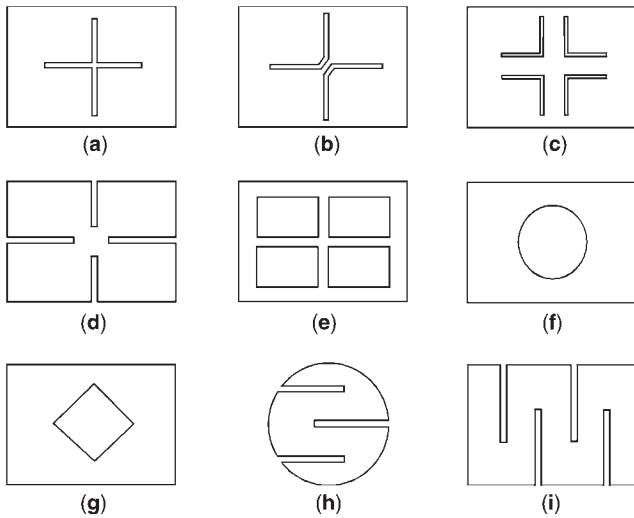


Figure 2. Some reported slotted or meandered patches suitable for the design of compact microstrip antennas.

orthogonal arms can be of unequal or equal lengths. This kind of slotted patch causes meandering of the patch surface current path in two orthogonal directions and is suitable for achieving compact circularly polarized radiation [6,7] or compact dual-frequency operation with orthogonal polarizations [8]. Similarly, the designs with a pair of bent slots [9] (Fig. 2b), a group of four bent slots [10] (Fig. 2c), four 90°-spaced inserted slits [11] (Fig. 2d), a perforated square patch or a square-ring patch with a cross-strip [12] (Fig. 2e), a circular slot [13] (Fig. 2f), a square slot [14] (Fig. 2g), and a group of meandering slits at the boundary of a circular patch [15] (Fig. 2h) or at the nonradiating edges of a rectangular patch [16] (Fig. 2i) have been successfully applied to achieve compact circularly polarized or compact dual-frequency microstrip antennas.

2.4. Use of a Slotted or Meandered Ground Plane

The technique shown in Section 2.3 for lengthening the excited patch surface current path to lower the antenna's fundamental resonant frequency can also be applied to the antenna's ground plane [17]. Figures 3a and 3b show, respectively, the geometries of compact microstrip antennas with a meandered ground plane and a slotted ground plane. The design in Fig. 3a is intended for achieving linearly polarized radiation for a compact microstrip antenna, while that in Fig. 3b can be used to generate dual linearly polarized waves for compact dual-polarized operation. In addition to a large decrease in the antenna's fundamental resonant frequency obtained, similar to the behavior described in Section 2.3, the impedance bandwidths of the compact microstrip antennas shown in Fig. 3 are all greater than that of the regular-size microstrip antenna. This behavior is due largely to the slots embedded in the antenna's ground plane, which effectively lowers the quality factor of the antenna. Moreover, an increase in the radiation efficiency of the antenna has also been obtained, and an enhanced antenna gain has been measured. From the results obtained in Ref. 17, for the case of using an FR4 substrate, the measured impedance bandwidth of the

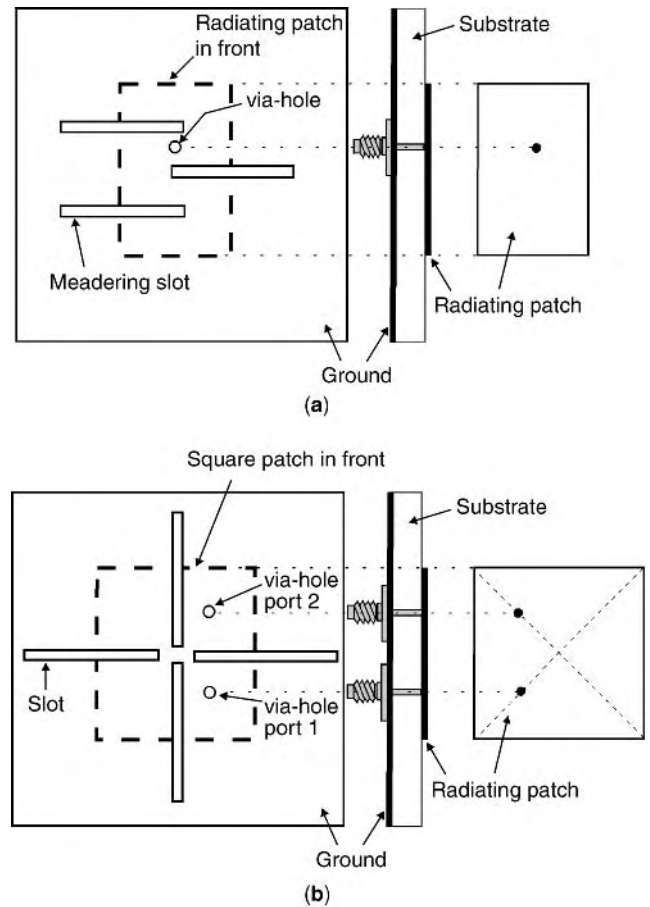


Figure 3. Geometries of compact microstrip antennas with (a) a meandered ground plane and (b) a slotted ground plane.

design shown in Fig. 3a is about 1.85 times that (3.7 vs. 2.0%) of a corresponding conventional (regular-size) microstrip antenna without embedded slots in the antenna's ground plane, and a gain enhancement of 1.6 dBi (4.6 vs. 3.0 dBi) is also obtained. However, a larger front-to-back ratio (F/B) was also measured. From the measured results, the backward radiation is increased by about 7 dBi, compared to the conventional microstrip antenna. This increase in the backward radiation is contributed by the embedded slots in the ground plane and the decreased ground-plane size in wavelength.

2.5. Use of a Chip Capacitor Loading Technique

With the use of one or more chip capacitors loaded into the microstrip antenna (see Fig. 4), compact microstrip antennas can be obtained [18,19]. For the construction of this kind of chip capacitor-loaded microstrip antenna, a via hole at a suitable position is first drilled through the substrate. Then, a chip capacitor of suitable capacitance is loaded into the via hole, with its two ends connected to the radiating patch and the ground plane. It has been reported that a large frequency reduction of about 65% can be obtained using the chip capacitor loading technique [19]. Moreover, with the large frequency reduction obtained, the radiated power from the antenna is almost the same. This suggests that no significant change in the antenna

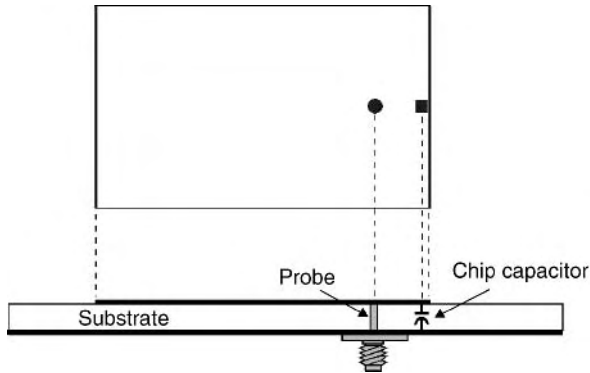


Figure 4. Geometry of a compact microstrip antenna with chip capacitor loading.

gain of such a compact microstrip antenna compared to a conventional microstrip antenna at a fixed operating frequency is expected.

3. COMPACT BROADBAND MICROSTRIP ANTENNAS

With the size reduction at a fixed operating frequency, the impedance bandwidth of a microstrip antenna is usually decreased. To obtain an enhanced impedance bandwidth, one can simply increase the antenna's dielectric substrate thickness to compensate the decreased electrical thickness of the substrate due to the lowered operating frequency or apply the compact broadband design techniques of using chip resistor loading, a short-circuited patch with a thick air-layer substrate, stacked short-circuited patches, and slot loading. These compact broadband design techniques are described in this section.

3.1. Use of a Chip Resistor Loading Technique

Figures 5a and 5b show two promising designs of chip-resistor-loaded microstrip antennas. Two different feed mechanisms using a probe feed and an inset microstrip-line feed have been implemented and analyzed [20]. This kind of microstrip antenna design is achieved by replacing the short-circuiting pin in a short-circuited microstrip antenna, as seen in Fig. 1, with a chip resistor of low resistance (generally $1\ \Omega$). In this case, with the same antenna parameters, the antenna size reduction obtained can be even greater for a design using SC-pin loading described in Section 2.2. Moreover, the obtained impedance bandwidth can be increased by a factor of six compared to a design using shorting-pin loading. For the case of using an FR4 substrate of thickness 1.6 mm and relative permittivity 4.4, the impedance bandwidth can reach 10% in the L-band operation [20]. However, as a result of the introduced ohmic loss of the chip resistor loading, the antenna gain is decreased, and is estimated to be about 2 dBi, compared to a shorted patch antenna with a SC pin.

3.2. Use of a Short-Circuited Patch with a Thick Air-Layer Substrate

Broadband short-circuited microstrip antennas fed by using a probe feed, a capacitively coupled feed [21] or an

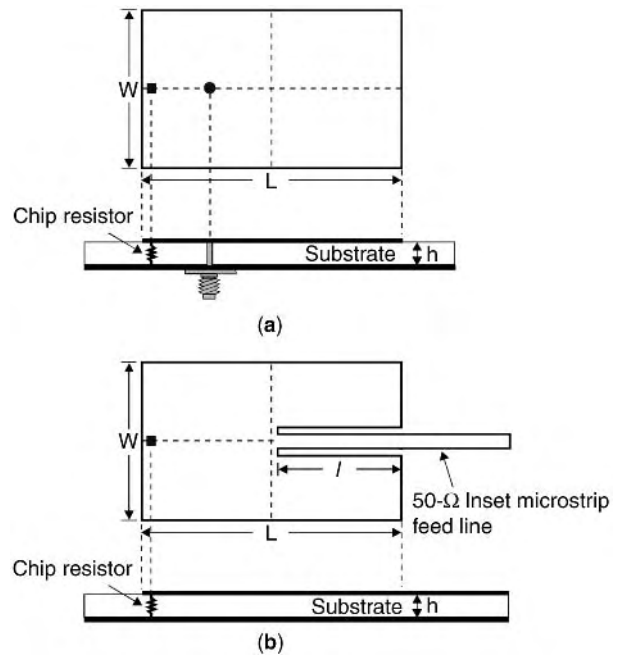


Figure 5. Geometries of chip-resistor-loaded microstrip antennas with (a) a probe feed and (b) an inset microstrip-line feed.

L-probe feed [22] have been reported. Figure 6 shows typical geometries of this kind of short-circuited microstrip antenna. The design shown in Fig. 6a uses a simple probe feed with a long probe pin, which may introduce a large inductance to the input impedance of the antenna, thus resulting in poor impedance matching for frequencies

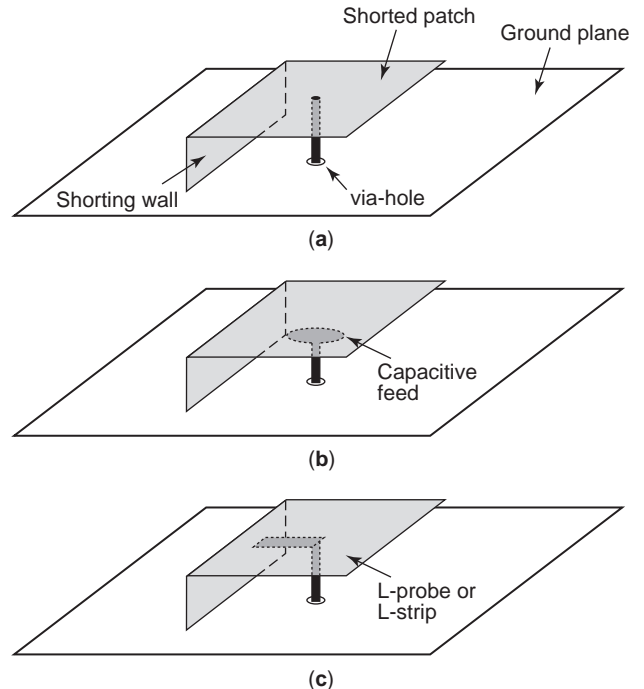


Figure 6. Geometries of short-circuited microstrip antennas with a thick air-layer substrate fed using (a) a probe feed, (b) a capacitively coupled feed, and (c) an L-probe or L-strip feed.

across the desired operating band. To solve the problem, the designs shown in Figs. 6b and 6c can be applied.

The design shown in Fig. 6b uses a capacitively coupled feed, which usually consists of either a circular or a rectangular metal plate to capacitively couple the electromagnetic energy from the source to the short-circuited radiating patch. By further incorporating a capacitive load to this short-circuited (SC) patch, it has been demonstrated that the overall length of the SC microstrip antenna with an air-layer substrate can be reduced from a quarter-wavelength to less than one-eighth wavelength [21]. Such a design with a volume of $20 \times 8 \times 4 \text{ mm}^3$ has been constructed, and an impedance bandwidth of 178 MHz centered at 1.8 GHz has been obtained, which meets the bandwidth requirement of the DCS (Digital Communication System) cellular communication system.

For the geometry shown in Fig. 6c, the capacitive coupling of the electromagnetic energy from the source to the SC patch is achieved by using an L probe or an L strip. It has been reported that, with the use of a foam substrate of thickness about $0.1\lambda_0$ (where λ_0 is the free-space wavelength of the center operating frequency), an impedance bandwidth of 39% can be obtained for an L-probe-fed SC microstrip antenna [22]. In this design, the L probe incorporated with the SC patch introduces a capacitance compensating some of the large inductance introduced by the long probe pin in the thick foam substrate, which makes it possible for achieving good impedance matching over a wide frequency range. However, a beam squint of about $15\text{--}60^\circ$ in the E -plane radiation pattern obtained has also been observed, which is probably attributed to the asymmetric current distribution of the shorted patch, due to the presence of the SC wall and the L probe.

3.3. Use of Stacked Short-Circuited Patches

The impedance bandwidth of a microstrip antenna is in general proportional to the antenna volume measured in wavelengths. However, by using two stacked short-circuited (SC) patches and making both patches radiate as equally as possible and have a radiation quality factor as low as possible, one can obtain enhanced impedance bandwidth for a fixed antenna volume [23]. Figure 7 shows two typical geometries of stacked SC microstrip antennas for broadband operation. In Fig. 7a, the two stacked SC patches have different short-circuiting (SC) walls. By selecting a proper distance between the two offset SC walls, one can achieve a wide impedance bandwidth for the antenna. For the geometry shown in Fig. 7b, a common SC wall is used for the two stacked SC patches. In this case, impedance matching is achieved mainly by selecting a proper feed position and a proper distance between the two SC patches. It should also be noted that, for the two geometries shown in Fig. 7, the upper SC patch can be considered to be a parasitic element coupled to the lower shorted patch, the driven element. In the design, the two SC patches are usually selected to have approximately the same, but unequal, dimensions. The substrates between the two SC patches and between the lower SC patch and the ground plane can be with air, foam or dielectric materials. Also, a partial SC wall or a SC pin can be used in

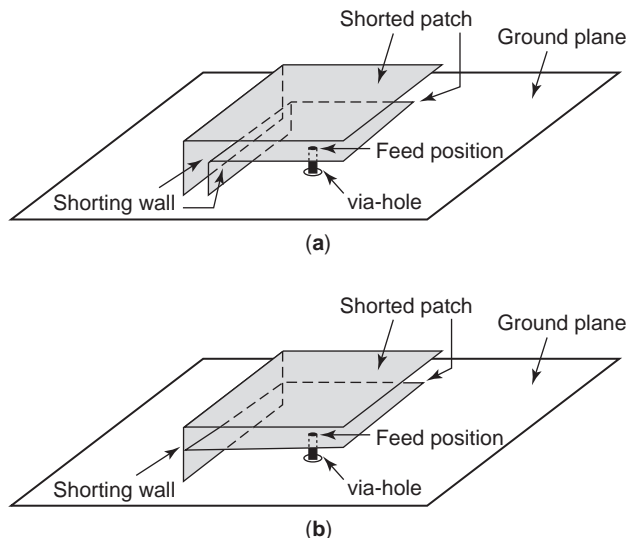


Figure 7. Geometries of stacked short-circuited microstrip antennas with (a) offset short-circuiting walls and (b) a common short-circuiting wall.

place of the offset SC walls or the common SC wall shown in Fig. 7.

3.4. Use of a Slot-Loading Technique

By embedding suitable slots in the radiating patch of a microstrip antenna, enhanced bandwidth with a reduced antenna size can be obtained [24]. A typical design with a slotted equilateral-triangular patch is shown in Fig. 8. It is found that, by embedding a pair of branchlike slots of proper dimensions, the first two broadside radiation modes of TM_{10} and TM_{20} of the equilateral-triangular microstrip antenna can be perturbed such that their resonant frequencies are both lowered and close to each other to form a wide-impedance bandwidth. In this design, the obtained impedance bandwidth is usually about equal to or less than 2.0 times that of a corresponding conventional microstrip antenna.

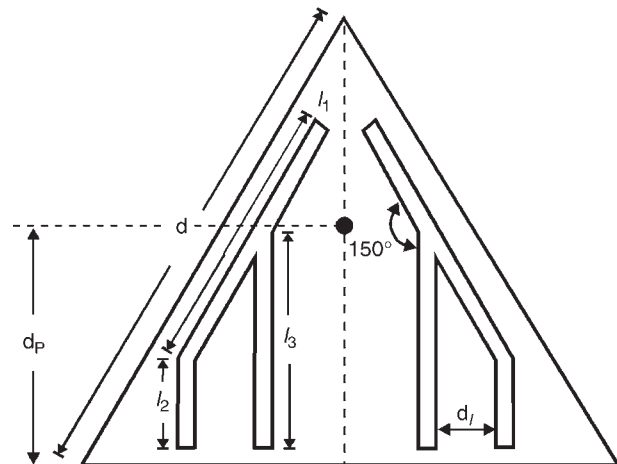


Figure 8. Geometry of a slotted equilateral triangular patch for the design of compact broadband microstrip antenna.

4. COMPACT DUAL-FREQUENCY MICROSTRIP ANTENNAS

Dual-frequency operation has been an important subject in microstrip antenna designs [25], and many such designs are known. To achieve dual-frequency operation for reduced-size or compact microstrip antennas, many promising designs have been reported [3]. Some typical compact dual-frequency designs are presented in this section. The two operating frequencies can have the same polarization planes [4,26–30] or orthogonal polarization planes [8,9]. In Section 4.1, two kinds of compact dual-frequency design techniques of using slot loading and SC-pin loading for the case with same polarization planes are introduced. In Section 4.2, the designs of compact dual-frequency microstrip antennas with orthogonal polarization planes are described.

4.1. With Same Polarization Planes

The design using a slot-loading technique is first described. Figures 9a and 9b show the promising geometries

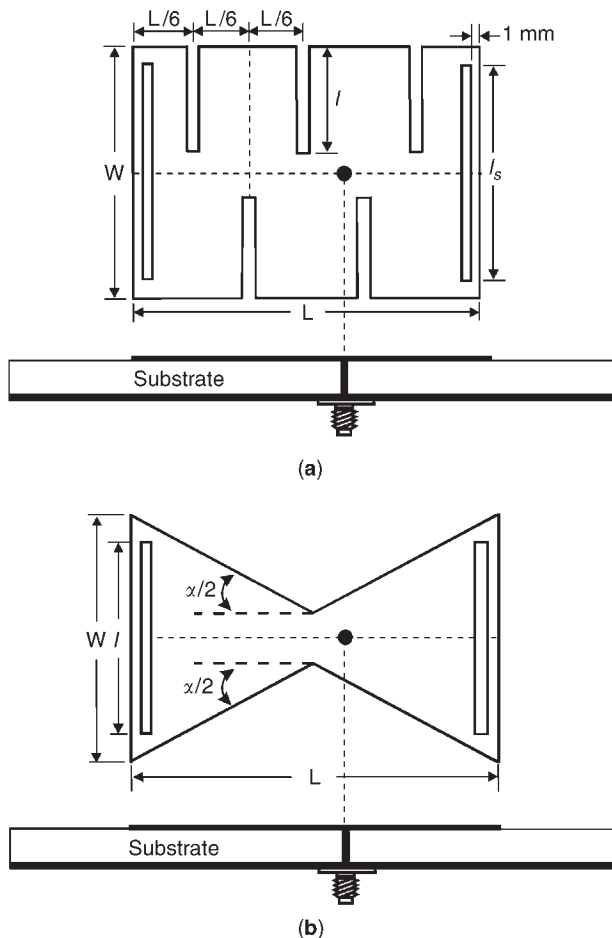


Figure 9. Geometries of (a) a slot-loaded, meandered rectangular microstrip antenna and (b) a slot-loaded, bowtie microstrip antenna for compact dual-frequency operation with same polarization planes.

of a slot-loaded, meandered rectangular microstrip antenna [26] and a slot-loaded, bowtie microstrip antenna [27] for compact dual-frequency operation with same polarization planes. In the design shown in Fig. 9a, the radiation characteristics of the antenna operated in the TM_{10} and TM_{30} modes are similar and have the same polarization planes. These two modes can be excited with good impedance matching using a single probe feed, and owing to the meandering of the rectangular patch with slits inserted at the patch's nonradiating edges, the resonant frequencies f_{10} and f_{30} of the two operating modes can be significantly lowered, with the radiation characteristics slightly affected. This indicates that a large antenna size reduction can be obtained by using the present design compared to the slot-loaded patch without slits for fixed dual-frequency operation.

Based on its compactness in antenna size for a fixed operating frequency and the fact that its radiation characteristics are similar to those of a regular-size rectangular microstrip antenna, the bowtie microstrip antenna is also a good candidate for achieving compact dual-frequency operation. A typical design obtained by using a slot-loading technique is shown in Fig. 9b. In this design, a pair of narrow slots is embedded close to the radiating edges of the bowtie patch. The bowtie patch has a flare angle of α and a patch width of W . The linear dimension of the bowtie patch in the resonant direction is fixed to be L . A pair of narrow slots having dimensions of $1\text{ mm} \times l$ are embedded in the bowtie patch and placed close to the radiating edges at a distance of 1 mm . A single probe feed is located along the centerline of the bowtie patch. It is found that both the TM_{10} and TM_{30} modes are strongly perturbed, and that their respective resonant frequencies decrease with increasing flare angle of the bowtie patch. In addition, there exists a feed position for good impedance matching of the two operating frequencies. In addition to the compact dual-frequency operation obtained, the two operating frequencies have the same polarization planes, and good cross-polarization radiation is observed, especially for the E -plane radiation [27].

In Fig. 10, the geometries of short-circuited microstrip antennas for compact dual-frequency operation with same polarization planes are presented. These designs are achieved by applying the SC-pin loading technique [4,28–30]. By incorporating a SC pin in the centerline of a rectangular microstrip patch and exciting the patch through a suitable feed position also chosen from the centerline (see Fig. 10a), a good matching condition for both the first two resonant frequencies of the microstrip antenna can be obtained, which makes possible the dual-frequency operation of such a compact microstrip antenna through a single coax feed. The obtained frequency ratios between the two operating frequencies have been reported to be about 2.0–3.2 [4]. For the case of using a circular microstrip antenna (Fig. 10b), the frequency ratio obtained for the compact dual-frequency operation is about 2.55–3.83 [28], while that for a triangular microstrip antenna is about 2.5–4.9 [29]. As for the case of using a bowtie microstrip antenna (see Fig. 10d), it is possible to obtain a frequency ratio of about 5.0 [30].

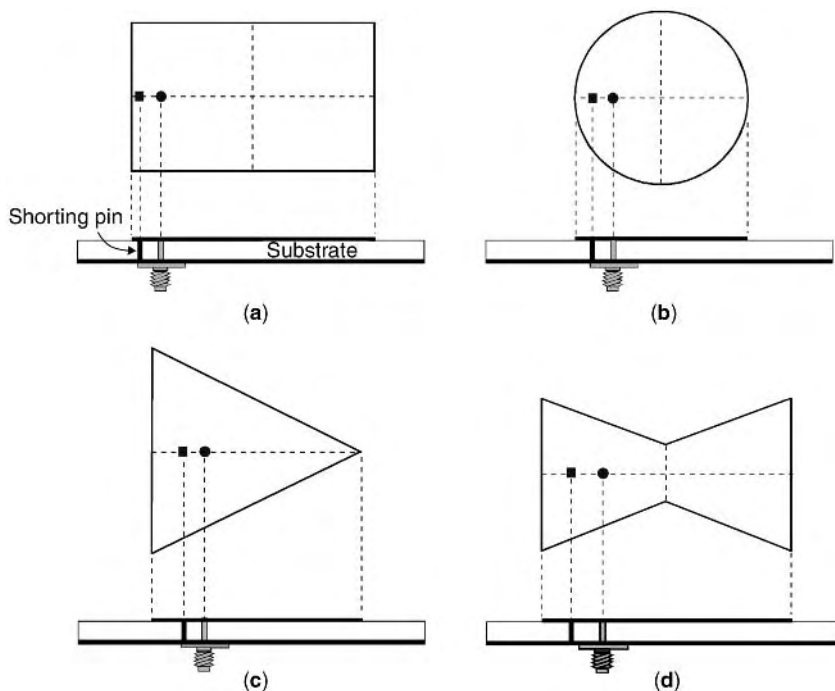


Figure 10. Geometries of short-circuited microstrip antennas for compact dual-frequency operation with same polarization planes.

4.2. With Orthogonal Polarization Planes

In this section, rectangular microstrip antennas with promising embedded slots or inserted slits for achieving compact dual-frequency operation with orthogonal polarization planes [8,9] are described. Figure 11 shows four promising designs of this kind of compact dual-frequency microstrip antenna. In the design shown in Fig. 11a, the embedded slot is a cross-slot of equal arm lengths. It is found that, by increasing the cross-slot length, both the antenna's first two excited resonant frequencies (f_{10} and f_{01}) can be lowered with the frequency ratio almost unchanged. Note that the frequency ratio obtained is close to the aspect ratio of the rectangular patch. It has also been found that the reduction in the two excited resonant frequencies results in a patch size reduction of about 23% for a given dual-frequency design [8].

With the loading of a pair of bent slots, compact dual-frequency operation for a rectangular microstrip antenna has been reported [9]. Figure 10b shows the antenna geometry studied. It has been determined that, for fixed dual-frequency operation, the required patch size is only about 68% that of the design using a simple patch without bent slots. This corresponds to a 32% patch size reduction. The measured radiation patterns of the two operating frequencies were also measured. Although the excited patch surface current paths are significantly altered to lower the desired resonant frequencies, no special distortion of the radiation patterns is observed and the cross-polarization radiation is at an acceptable level.

Figure 10c shows the design of using four inserted slits at the patch edges of a rectangular patch [3]. The four inserted slits are of the same length. When the slit length increases, the resonant frequencies of the first two resonant modes are lowered, similar to the cases with a cross-slot (Fig. 11a) or a pair of bent slots (Fig. 11b).

Experimental results have shown that, for fixed dual-frequency operation, the patch size of the present design can be reduced to 56% of that using a simple patch without inserted slits [3]. With the use of four T-shaped slots (Fig. 11d), a patch size reduction of about 38% has been obtained [3].

5. COMPACT DUAL-POLARIZED MICROSTRIP ANTENNAS

This section describes the dual linearly polarized operation of a compact square microstrip antenna with a slotted radiating patch. It is demonstrated that such a slotted microstrip antenna with a group of four symmetric bent slots can perform excellent dual-polarized radiation [31], while the antenna size is significantly reduced for operation at a fixed frequency. Figure 12 shows the geometries of two possible designs. In Fig. 12a, the design is with bent slots parallel to the patch's central lines (denoted design A), while the design in Fig. 12b is with bent slots parallel to the patch's diagonals (design B). The square patch has a side length of L , and the four bent slots are of the same dimensions and have a narrow width of 1 mm. The two arms of each bent slot have the same length ℓ , and are perpendicular to each other. The feed arrangement in design A excites 0° (\hat{x} -directed) and 90° (\hat{y} -directed) linearly polarized waves, while the feed arrangement in design B radiates $\pm 45^\circ$ slanted linearly polarized waves.

For design A, experimental results [31] indicate that the resonant frequency is lowered by about 25% compared to that of a simple square patch without bent slots. This lowering in the resonant frequency corresponds to an antenna size reduction of about 44%. Furthermore, the antenna shows an input isolation (S_{21}) of less than -39.2 dB across the obtained impedance bandwidth, which is better than that (-31.9 dB) of a simple square patch. This

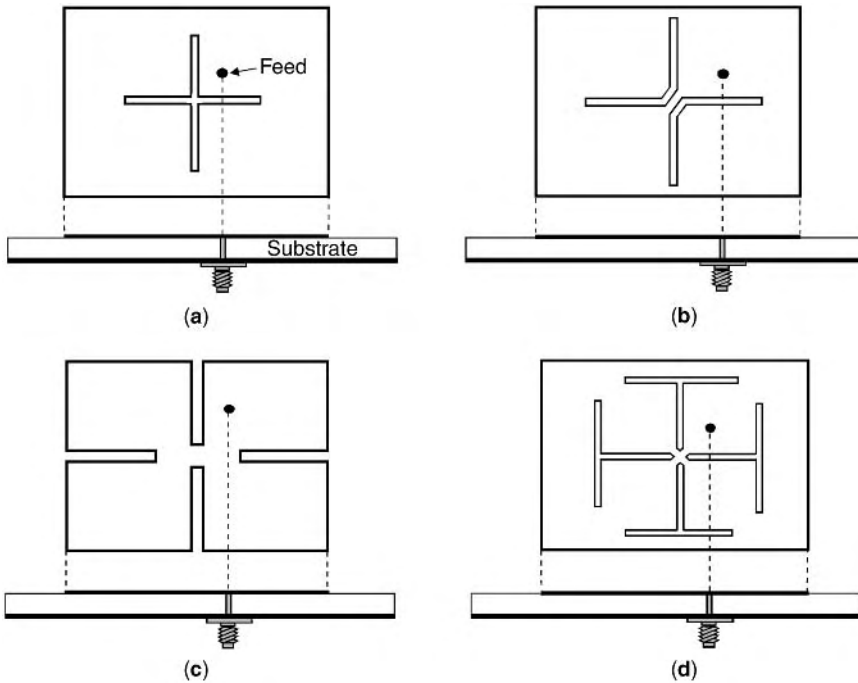


Figure 11. Geometries of slotted rectangular microstrip antennas for compact dual-frequency microstrip antennas with orthogonal polarization planes.

behavior suggests that improved input isolation can be obtained while resonant frequencies are significantly lowered for achieving compact operation.

For design B, an experimental study was also conducted. The side lengths of the square patch and microwave substrate used were the same as those in the study of design A. A reduction of about 16% compared to that of a simple square patch has been obtained [31]. This lowering in the resonant frequency corresponds to about 30% reduction in patch size for design B compared to the design with a simple square patch for fixed dual-polarized operation.

6. COMPACT CIRCULARLY POLARIZED MICROSTRIP ANTENNAS

Various CP designs with a compact patch size at a fixed operating frequency have been reported [3]. Figure 13 shows some reported patches suitable for the design of compact circularly polarized microstrip antennas. In Fig. 13a, the design is with a cross-slot of unequal arm lengths [32]. By incorporating a probe feed at 45° to the two arms of the cross-slot as shown in the figure, it has been found that CP radiation can be obtained at frequencies much lower than the fundamental resonant frequency of the antenna without a cross-slot. That is, for a fixed operating frequency, the antenna can perform CP radiation with a smaller antenna size than can a regular-size microstrip antenna without a cross-slot.

Figure 13b shows a square patch with four inserted slits for compact CP operation. Two pairs of the slits are cut in the centerlines of the square patch. Each pair of slits has equal lengths, but the total lengths of the two pairs of slits are unequal, which can split the resonant mode of interest into two orthogonal near-degenerate modes for CP radiation [11]. By embedding a group of four bent slots in a

corner-truncated square microstrip patch, a single-feed, compact circularly polarized microstrip antenna can easily be obtained. Figure 13c shows the geometry of the microstrip patch studied. The two arms of each bent slot are aligned parallel to the centerlines of the square patch. By increasing the arm length of the bent slots, the fundamental resonant frequency of the slotted square patch is significantly decreased. By further truncating a suitable size of the patch corners, the antenna can perform CP operation. Results show that, for a given CP operating frequency, the antenna can have a patch size reduction of more than 50% compared to the conventional CP design using a corner-truncated square patch without slots [10].

The method of producing single-feed CP operation of a square microstrip antenna by truncating a pair of patch corners used in Fig. 13c can also be applied to a modified square microstrip patch with four inserted slits of equal lengths to achieve compact CP operation with relaxed manufacturing tolerances. The geometry of such a microstrip patch is shown in Fig. 13d. The compactness of the proposed CP design is achieved because of the inserted slits at the patch corners of the square patch. These inserted slits result in meandering of the excited fundamental-mode patch surface current path, which effectively lowers the resonant frequency of the modified square patch, similar to the design using four inserted slits of different lengths at the boundary of a square patch (see Fig. 13b). Instead of using different slit lengths for CP excitation, which usually requires a very small slit length difference for the case of a large patch size reduction, the present design uses the perturbation of truncating a pair of patch corners, with the inserted slits to be of equal lengths. Experimental results show that the required size of the truncated corners for CP operation increases with increasing reduction in patch size [33]. This behavior gives the present design a relaxed manufacturing tolerance for

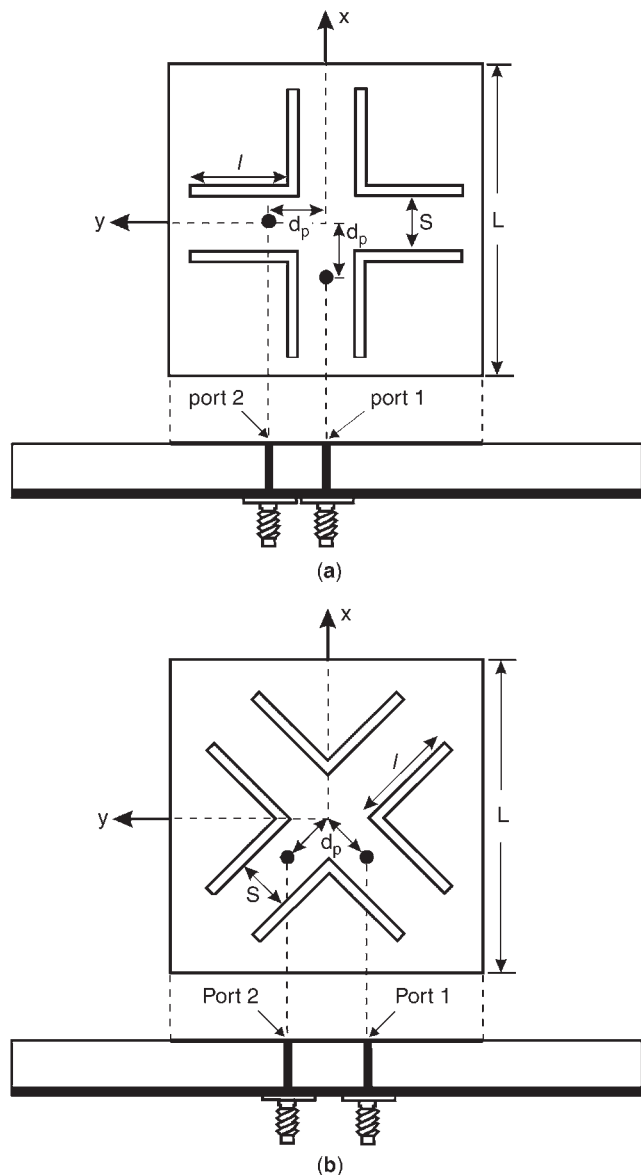


Figure 12. Geometries of compact dual-polarized square microstrip antennas: (a) design with bent slots in parallel with the patch's central lines (design A); (b) design with bent slots in parallel with the patch's diagonals (design B).

achieving a compact circularly polarized microstrip antenna.

Compact CP operation of the circular microstrip antenna with a cross-slot of equal arm lengths in the patch center and a pair of peripheral cuts at opposite sides of the patch boundary has been proposed and experimentally studied [6]. Figure 13e shows the geometry of the microstrip patch studied. Experimental results show that the present compact CP antenna has a center frequency about 10.4% lower than that of a corresponding regular-size antenna. This lowering of the center frequency corresponds to a patch size reduction of about 20% by using the present compact design in place of the regular-size design at a fixed operating frequency.

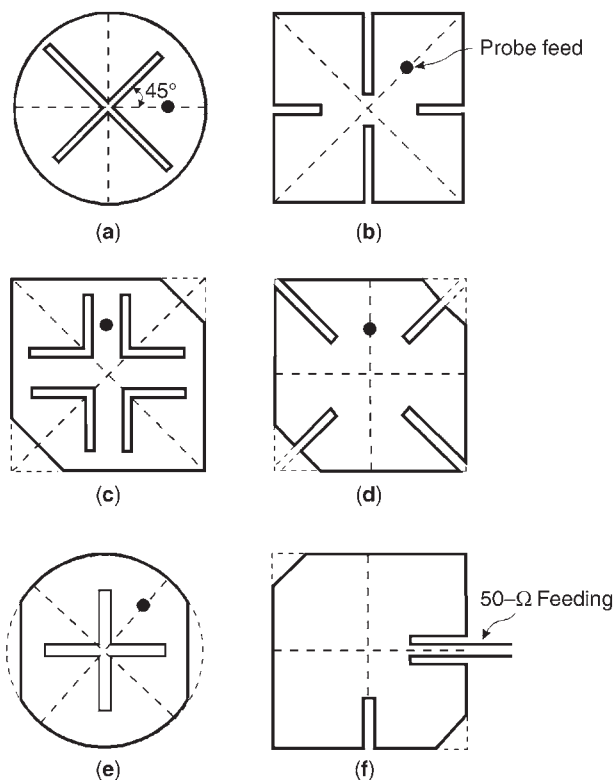


Figure 13. Some reported patches suitable for the design of compact circularly polarized microstrip antennas.

The CP design for exciting a circularly polarized microstrip antenna using a 50-Ω inset microstrip-line feed has been reported [34]. The proposed design is shown in Fig. 13f. In this design, a narrow slit is inserted at the patch edge. Because of the combined effects of the inset microstrip line and the inserted slit, two orthogonal near-degenerate modes for CP radiation can easily be excited. Also, the excited patch surface currents are meandered in the present design, and the CP operating frequency obtained is greatly lowered; thus, compact CP radiation can be achieved for the present design.

7. COMPACT MICROSTRIP ANTENNAS WITH ENHANCED GAIN

Most compact microstrip antenna designs show decreased antenna gain owing to the antenna size reduction. To overcome this disadvantage and obtain an enhanced antenna gain, several designs for gain-enhanced compact microstrip antennas with the loading of a high-permittivity dielectric superstrate have been demonstrated [35–37]. Figure 14 shows two promising designs of gain-enhanced compact broadband microstrip antenna. In Fig. 14a, a gain-enhanced compact broadband rectangular microstrip antenna is shown [35]. It has been demonstrated that, by adding a high-permittivity superstrate layer, the antenna gain of a chip-resistor-loaded microstrip antenna can be increased to about the same level of a conventional microstrip antenna. The radiating patch has

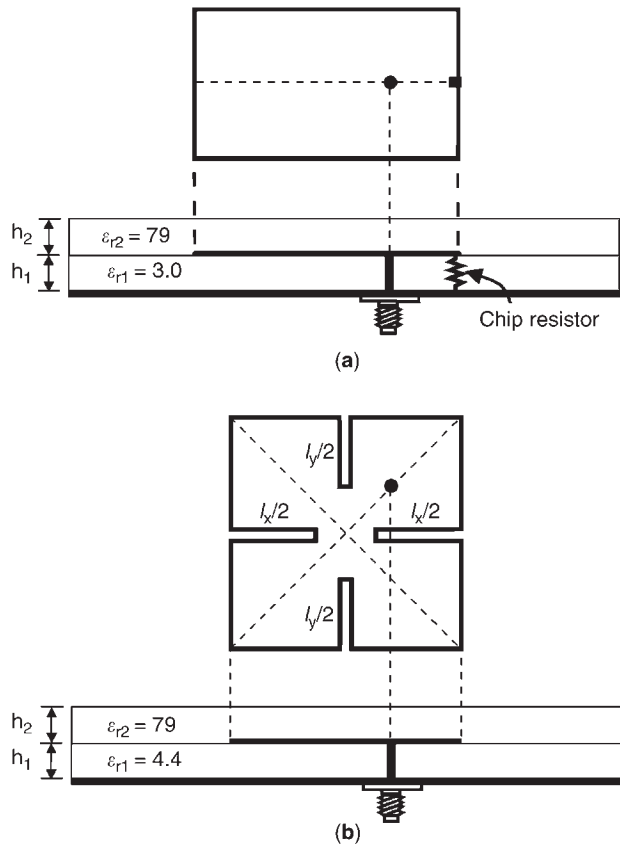


Figure 14. Geometries of gain-enhanced (a) compact broadband microstrip antenna and (b) compact circularly polarized microstrip antenna.

a 1-Ω chip resistor loaded at one of the patch edges. For operating at 1.84 GHz, a microwave substrate of $\epsilon_r = 3.0$ and $h_1 = 1.524$ mm is covered with a high-permittivity ceramic superstrate of $\epsilon_r = 79$ and $h_2 = 3.05$ mm. The superstrate thickness is determined by trying various thicknesses to optimize the enhanced gain with acceptable radiation patterns. Conventional and chip-resistor-loaded rectangular microstrip antennas were fabricated and measured for comparison. It is found that, at the fixed frequency $f = 1.84$ GHz, the patch size of the resistor and superstrate-loaded microstrip antenna can be reduced to 6.05% times that of a conventional microstrip antenna. The measured input impedance bandwidths (10 dB return-loss bandwidth) are 19.6 MHz (1.07%) for the conventional antenna, 145.6 MHz (7.91%) for the resistor-loaded antenna, and 120 MHz (6.52%) for the proposed resistor and superstrate-loaded antenna. The maximum relative received power for the proposed antenna is -46.9 dBm; that is, the proposed antenna has a net power increment of 10.4 dB compared with the resistor-loaded antenna (-57.3 dBm), and about 1.3 dB lower than that (-45.6 dBm) of the conventional antenna (Detailed results of the gain and radiation patterns can be found in Ref. 35.). A gain-enhanced compact microstrip antenna is thus achieved.

The design of a high-gain, compact microstrip antenna with CP radiation has been reported [36]. The small size of the microstrip antenna results from both the high-permit-

tivity superstrate loading and slits cut in the patch. In addition, the antenna gain is enhanced by choosing the superstrate thickness to be about one-quarter wavelength in the superstrate layer. A typical design of 30% lower antenna size (projection area) and 5.2 dB higher antenna gain compared to the conventional CP design has been obtained. Figure 14b shows the proposed compact circularly polarized microstrip antenna with an enhanced gain. The two pairs of unequal slits l_x and l_y ($l_x > l_y$) are cut in the patch to split the fundamental resonant mode into two orthogonal near-degenerate modes for CP operation. The case with $l_x > l_y$ and feed position shown in the figure is for right-hand CP operation. When the superstrates of various thicknesses are loaded onto the microstrip antenna, its resonant frequency is decreased, and the required slit lengths and 50-Ω feed position need to be readjusted to achieve good CP operation. High-permittivity ($\epsilon_{r2} = 79$) ceramic superstrates of various thicknesses were loaded onto a compact circularly polarized microstrip antenna. When no slits and superstrate are present, a square patch with dimensions 26.2×26.2 mm² has a fundamental resonant frequency of 2697 MHz. For antennas with various superstrate loadings, the slit length l_y is fixed and l_x is adjusted to achieve CP operation. For good impedance matching, the feed position is slightly varied along the patch diagonal. The results show that the microstrip antenna has a maximum relative received power when the superstrate thickness is about one-quarter of the wavelength of the wave propagating in the superstrate layer. Compared to a conventional CP design using a nearly square patch without slits and superstrate loading at the same operating frequency (2272 MHz), the proposed antenna has a 30% smaller patch size and a 5.21 dB greater antenna gain [36]. In addition, the results show that the CP bandwidth determined from 3-dB axial ratio is about 32 MHz or 1.4%, which is larger than that obtained for a conventional CP design.

8. CONCLUDING REMARKS

A variety of compact microstrip antennas with broadband, dual-frequency, dual-polarized, circularly polarized, and gain-enhanced operations have been presented. These compact microstrip antennas are attractive for applications in present-day wireless communication systems, in which portable communication products are becoming smaller and smaller. However, in order to be more competitive and attractive in practical applications, the reduction in the construction cost of compact microstrip antennas is yet an important topic for intensive studies.

To reduce the construction cost, it is most effective to use an inexpensive substrate such as the FR4 substrate for compact microstrip antennas. However, the FR4 substrate has a high loss, especially for higher operating frequencies, which usually leads to some degradation in antenna performance. Thus, some new dielectric materials with low cost and low loss for the substrate of compact microstrip antennas should be developed. Such substrate materials can make possible high-performance, low-cost compact microstrip antennas, which are very attractive for practical applications.

Another important topic for further studies is the ground-plane effects on compact microstrip antennas. Traditionally, compact or even regular-size microstrip antennas that have been studied are usually with the condition that the ground plane is symmetrically centered below the microstrip patch. However, for practical applications, the antenna may be required to be mounted on arbitrary positions on the ground plane of a wireless communication device, for example, along the edge of the ground plane of the system circuit board. In this condition, the effects of the ground plane on the performance of the compact microstrip antenna cannot be ignored. This is because the ground plane is an integral part of the compact microstrip antenna, and thus will greatly affect the impedance and radiation characteristics of the antenna. However, related studies on this issue are relatively scanty, and more efforts should be taken in this field of compact microstrip antenna designs.

BIBLIOGRAPHY

1. K. L. Wong, *Design of Nonplanar Microstrip Antennas and Transmission Lines*, Wiley, New York, 1999.
2. K. L. Wong, *Planar Antennas for Wireless Communications*, Wiley, New York, 2003.
3. K. L. Wong, *Compact and Broadband Microstrip Antennas*, Wiley, New York, 2002.
4. K. L. Wong and W. S. Chen, Compact microstrip antenna with dual-frequency operation, *Electron. Lett.* **33**:646–647 (April 10, 1997).
5. K. L. Wong and S. C. Pan, Compact triangular microstrip antenna, *Electron. Lett.* **33**: 433–434 (March 13, 1997).
6. W. S. Chen, C. K. Wu, and K. L. Wong, Compact circularly polarized circular microstrip antenna with cross slot and peripheral cuts, *Electron. Lett.* **34**:1040–1041 (May 28, 1998).
7. N. Ishitobi and N. Misawa, *Microstrip Antenna*, U.S. Patent 6,452,552 B1, (Sept. 17, 2002).
8. K. L. Wong and K. P. Yang, Small dual-frequency microstrip antenna with cross slot, *Electron. Lett.* **33**:1916–1917 (Nov. 6, 1997).
9. K. L. Wong and K. P. Yang, Compact dual-frequency microstrip antenna with a pair of bent slots, *Electron. Lett.* **34**:225–226 (Feb. 5, 1998).
10. W. S. Chen, C. K. Wu, and K. L. Wong, Compact circularly polarized microstrip antenna with bent slots, *Electron. Lett.* **34**:1278–1279 (June 25, 1998).
11. K. L. Wong and J. Y. Wu, Single-feed small circularly polarized square microstrip antenna, *Electron. Lett.* **33**:1833–1834 (Oct. 23, 1997).
12. W. S. Chen, C. K. Wu, and K. L. Wong, Square-ring microstrip antenna with a cross strip for compact circular polarization operation, *IEEE Trans. Anten. Propag.* **47**:1566–1568 (Oct. 1999).
13. H. D. Chen, A dual-frequency rectangular microstrip antenna with a circular slot, *Microwave Opt. Technol. Lett.* **18**:130–132 (June 5, 1998).
14. W. S. Chen, Single-feed dual-frequency rectangular microstrip antenna with square slot, *Electron. Lett.* **34**:231–232 (Feb. 5, 1998).
15. K. L. Wong, C. L. Tang, and H. T. Chen, A compact meandered circular microstrip antenna with a shorting pin, *Microwave Opt. Technol. Lett.* **15**:147–149 (Jun. 20, 1997).
16. J. H. Lu and K. L. Wong, Slot-loaded, meandered rectangular microstrip antenna with compact dual-frequency operation, *Electron. Lett.* **34**:1048–1050 (May 28, 1998).
17. J. S. Kuo and K. L. Wong, A compact microstrip antenna with meandering slots in the ground plane, *Microwave Opt. Technol. Lett.* **29**:95–97 (April 20, 2001).
18. M. C. Liang, *Frequency Tunable Patch Antenna Device*, U.S. Patent 6,462,712 B1 (Oct. 8, 2002).
19. M. C. Liang, Y. L. Kuo, Y. M. Yen, and W. C. Lai, Capacitor-loaded frequency control scheme for circular patch antenna, *Electron. Lett.* **36**:1757–1758 (Oct. 12, 2000).
20. K. L. Wong and Y. F. Lin, Small broadband rectangular microstrip antenna with chip-resistor loading, *Electron. Lett.* **33**:1593–1594 (Sept. 11, 1997).
21. C. R. Rowell and R. D. Murch, A capacitively loaded PIFA for compact mobile telephone handset, *IEEE Trans. Anten. Propag.* **45**:837–842 (May 1997).
22. Y. X. Guo, K. M. Luk, and K. F. Lee, L-probe proximity-fed short-circuited patch antenna, *Electron. Lett.* **35**:2069–2070 (Nov. 25, 1999).
23. J. Ollikainen, M. Fischer, and P. Vainikainen, Thin dual-resonant stacked shorted patch antenna for mobile communications, *Electron. Lett.* **35**:437–438 (March 18, 1999).
24. S. T. Fang and K. L. Wong, *Microstrip Antenna*, U.S. Patent 6,400,322 B2, (June 4, 2002).
25. S. Maci and G. Biffi Gentili, Dual-frequency patch antennas, *IEEE Anten. Propag. Mag.* **39**:13–20 (Dec. 1997).
26. J. H. Lu and K. L. Wong, Slot-loaded, meandered rectangular microstrip antenna with compact dual-frequency operation, *Electron. Lett.* **34**:1048–1050 (May 28, 1998).
27. K. L. Wong and W. S. Chen, Slot-loaded bow-tie microstrip antenna for dual-frequency operation, *Electron. Lett.* **34**(18):1713–1714 (Sep. 3, 1998).
28. C. L. Tang, H. T. Chen, and K. L. Wong, Small circular microstrip antenna with dual-frequency operation, *Electron. Lett.* **33**:1112–1113 (June 19, 1997).
29. S. C. Pan and K. L. Wong, Dual-frequency triangular microstrip antenna with a shorting pin, *IEEE Trans. Anten. Propag.* **45**:1889–1891 (Dec. 1997).
30. J. George, K. Vasudevan, P. Mohanan, and K. G. Nair, Dual frequency miniature microstrip antenna, *Electron. Lett.* **34**:1168–1170 (June 11, 1998).
31. G. S. Row, S. H. Yeh, and K. L. Wong, Compact dual-polarized microstrip antennas, *Microwave Opt. Technol. Lett.* **27**: 284–287 (Nov. 20, 2000).
32. H. Iwasaki, A circularly polarized small-size microstrip antenna with a cross slot, *IEEE Trans. Anten. Propag.* **44**: 1399–1401 (Oct. 1996).
33. W. S. Chen, C. K. Wu, and K. L. Wong, Novel compact circularly polarized square microstrip antenna, *IEEE Trans. Anten. Propag.* **49**:340–342 (March 2001).
34. W. S. Chen, K. L. Wong, and C. K. Wu, Inset microstripline-fed circularly polarized microstrip antennas, *IEEE Trans. Anten. Propag.* **48**:1253–1254 (Aug. 2000).
35. C. Y. Huang, J. Y. Wu, C. F. Yang, and K. L. Wong, Gain-enhanced compact broadband microstrip antenna, *Electron. Lett.* **34**:138–139 (Jan. 22, 1998).
36. C. Y. Huang, J. Y. Wu, and K. L. Wong, High-gain compact circularly polarized microstrip antenna, *Electron. Lett.* **34**:712–713 (April 16, 1998).
37. H. Nakano and Y. Hirachi, *Patch Antenna with Dielectric Separated from Patch Plane to Increase Gain*, U.S. Patent 6,492,950 B2 (Dec. 10, 2002).

MICROSTRIP CIRCUITS

TERRY C. EDWARDS
Engalco
Bridlington, East Yorkshire
United Kingdom

1. THE BASIC MICROSTRIP STRUCTURE

The general geometry of microstrip is shown in Fig. 1. Fundamentals and design equations for its manufacture are discussed in the article, where the basic advantages are also described in comparison with other types of MIC and MMIC transmission lines. The most important dimensional parameters are the microstrip width w and the height h (equal to the thickness of the substrate). Also of main importance is the relative permittivity of the substrate ϵ_r . In RF and microwave applications the thickness t of the metallic, top conducting strip is generally of much lesser importance and may quite often be neglected. However microstrip lines on chip and on MCMs are relatively thick as a result of the need to keep resistance down while still achieving a high wiring density by keeping the width down. We shall consistently refer to the xyz coordinate system as shown in Fig. 1.

Some of the particularly useful characteristics of microstrip include the following:

1. DC as well as AC signals may be transmitted.
2. Active devices, diodes, and transistors may readily be incorporated (shunt connections are also quite easily made).
3. In-circuit characterization of devices is straightforward to implement.
4. Line wavelength is reduced considerably (typically by one-third) from its free-space value, because of the substrate fields. Hence distributed component dimensions are relatively small.
5. The structure is quite rugged and can withstand moderately high voltages and power levels.

Most of the material presented here has been developed from Edwards and Steer [1].

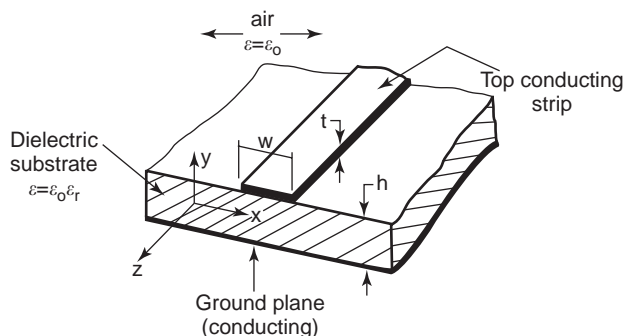


Figure 1. The general geometry of a microstrip line, including choice of coordinates.

2. QUASI-TEM MODE AND EFFECTIVE MICROSTRIP PERMITTIVITY

It is clear from Fig. 1 that microstrip involves an abrupt dielectric interface between the substrate and the air above it. Any transmission line that is filled with a uniform dielectric can support a single, well-defined mode of propagation, at least over a specified range of frequencies (TEM for coaxial lines, TE for waveguides, etc.).

Transmission lines that do not have such a uniform dielectric filling cannot support a single mode of propagation, and microstrip falls within this category. Although this is true, the bulk of the energy is transmitted along microstrip with a field distribution that quite closely resembles TEM; it is usually referred to as “quasi-TEM.” The detailed field distribution is quite complicated, but the main transverse electric field can be visualized as shown in Fig. 2.

Gupta et al. [2] have used Maxwell’s equations to convincingly demonstrate the necessity for longitudinal components of electric and magnetic fields. This is clearly inconsistent with a pure TEM or a TE propagating mode.

Representative views of the magnetic and electric field distributions are given in Fig. 3. (These are not precisely determined field contours, and they must be regarded only as diagrammatic illustrations of the situation.) The longitudinal components can be clearly seen, and these become increasingly significant as the frequency is raised.

From either of these diagrams, note the abrupt change in direction of the electric field line as it passes through the air–substrate interface. These fields have been analysed by a number of workers using various static techniques. We shall not study any of these techniques in detail here, but the results are powerful and significant for the circuit designer wishing to use microstrip. There are two reasons for this:

1. For the majority of microstrip lines suitable for MICs, the statically derived results are quite accurate where the frequency is below a few gigahertz.
2. At higher frequencies, up to the limits for the useful operation of microstrip, these “static” results can still be used in conjunction with frequency-dependent functions in closed formulas. This is developed in some detail later.

The earliest work concerning microstrip is generally accepted as that reported by Grieg and Engelmann [3]. Many other workers investigated basic characteristics of microstrip [4,5], but the major fundamental work on important and closely related parallel-strip transmission

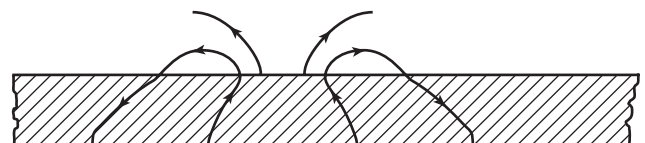


Figure 2. Transverse cross section of microstrip, showing electric field only.

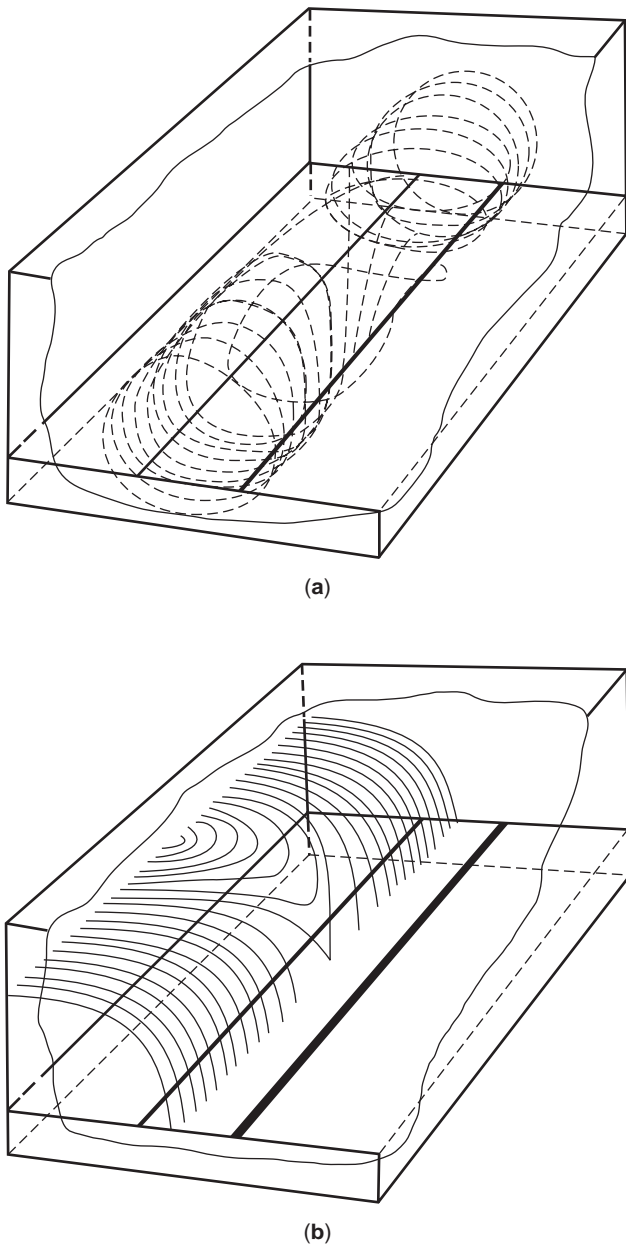


Figure 3. Three-dimensional views of approximate magnetic (a) and electric fields (partial view) (b) surrounding a shielded microstrip line. For simplicity here, only the electric field in the air is shown in (b).

lines was due to Wheeler [6]. This led to analysis and synthesis on the static TEM basis.

3. STATIC TEM PARAMETERS

The microstrip synthesis problem consists of finding the values of width w and length l corresponding to the characteristic impedance Z_0 , and electrical length θ (in degrees or radians) defined at the network design stage.

Initially a suitable substrate, of thickness h and relative permittivity ϵ_r , will have to be chosen. A wide range of substrates is available, suited to various types of

applications. Alumina is popular in many instances although LTCC (low-temperature cofired ceramic) tape is becoming increasingly important. Microstrip circuits are also designed on-chip (on-die) for MMICs and RFICs and then it is the relative permittivity and thickness of the semiconductor chip that form the starting data. A good example in this respect is semiinsulating GaAs. The choice of substrate, particularly “passive” substrates such as alumina, also depends on certain frequency limitations. The synthesis actually yields the normalized width-to-height ratio w/h initially, as well as an important quantity called the *effective microstrip permittivity* ϵ_{eff} . This quantity is unique to mixed-dielectric transmission-line systems and provides a useful link between various wavelengths, impedances, and propagating velocities. We shall shortly define the static TEM effective microstrip permittivity (ϵ_{eff}) precisely.

3.1. The Characteristic Impedance Z_0

For any TEM-type transmission line the characteristic impedance at high frequencies may be expressed in any one of three alternate forms:

$$Z_0 = \sqrt{\frac{L}{C}} \tag{1}$$

$$Z_0 = v_p L \tag{2}$$

$$Z_0 = \frac{1}{v_p C} \tag{3}$$

Note that both (2) and also (3) involve the phase velocity v_p of the wave traveling along the line. It is also recalled that this phase velocity is given by

$$v_p = \frac{1}{\sqrt{LC}} \tag{4}$$

When the substrate of the microstrip line is (effectively) removed, we have an air-filled line along which the wave will travel at c , the velocity of light in free space ($c = 2.99793 \times 10^8$ m/s). The characteristic impedance of this air-filled “microstrip” Z_{01} , is given by

$$Z_{01} = \sqrt{\frac{L}{C_1}} \tag{5}$$

where L remains unaltered by the change in dielectric constant and C_1 is the capacitance per unit length for this structure. Alternatively

$$Z_{01} = cL \tag{6}$$

$$Z_{01} = \frac{1}{cC_1} \tag{7}$$

Combining Equations (1), (6) and (7) yields the following very significant result:

$$Z_0 = \frac{1}{c\sqrt{CC_1}} \tag{8}$$

This means that we have the required characteristic impedance only if we can evaluate the capacitances per unit

length of the structure, with and without the presence of the dielectric substrate. One way in which this has been achieved will be outlined shortly.

3.2. The Effective Microstrip Permittivity ϵ_{eff}

For the air-spaced microstrip line, the propagation velocity is given by

$$c = \frac{1}{\sqrt{LC_1}} \tag{9}$$

and, dividing Eq. (9) by Eq. (4) and squaring, we obtain

$$\frac{C}{C_1} = \left(\frac{c}{v_p}\right)^2 \tag{10}$$

The capacitance ratio $C = C_1$ is termed the *effective microstrip permittivity* ϵ_{eff} , an important microstrip parameter. From (10), ϵ_{eff} is given by

$$\epsilon_{\text{eff}} = \left(\frac{c}{v_p}\right)^2 \tag{11}$$

Although this result has been derived on a static basis here, it is fundamentally important for microstrip and will be used again shortly, when v_p is taken to be frequency-dependent.

A useful relationship between Z_0 , Z_{01} , and ϵ_{eff} can be obtained by combining Eqs. (3), (7), (10), and (11). The result is

$$Z_0 = \frac{Z_{01}}{\sqrt{\epsilon_{\text{eff}}}} \tag{12}$$

that is

$$Z_{01} = Z_0 \sqrt{\epsilon_{\text{eff}}} \tag{13}$$

This expression is useful in several respects during microstrip circuit design procedures.

Upper and lower bounds can readily be found for ϵ_{eff} , in the static low-frequency limit, by considering the effects of very wide and very narrow lines as indicated in Fig. 4. For the very wide lines nearly all of the electric field is confined to the substrate dielectric, the structure resembles a parallel-plate capacitor, and therefore, at this extreme

$$\epsilon_{\text{eff}} \rightarrow \epsilon_r \tag{14}$$

In the case of very narrow lines the field is almost equally shared by the air ($\epsilon_r = 1$) and the substrate so

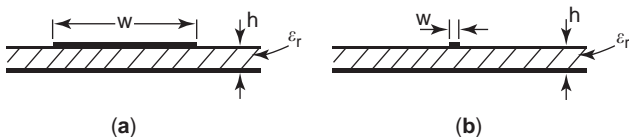


Figure 4. Microstrip lines: (a) extremely wide ($w \gg h$); (b) extremely narrow ($w \ll h$) lines.

that, at this extreme

$$\epsilon_{\text{eff}} \approx \frac{1}{2}(\epsilon_r + 1) \tag{15}$$

The range of ϵ_{eff} is therefore

$$\frac{1}{2}(\epsilon_r + 1) \leq \epsilon_{\text{eff}} \leq \epsilon_r \tag{16}$$

It may be convenient to express the effective microstrip permittivity as follows

$$\epsilon_{\text{eff}} = 1 + q(\epsilon_r - 1) \tag{17}$$

where the new quantity, the filling factor q , has the bounds

$$\frac{1}{2} \leq q \leq 1 \tag{18}$$

Wheeler [6,7] has evaluated this filling factor in detail.

3.3. Synthesis: The Width-to-Height Ratio w/h

The width-to-height ratio (w/h) is a strong function of Z_0 and of the substrate permittivity ϵ_r . Wheeler's results [7] are particularly useful in this respect, although it has been found that some modifications are necessary for high accuracy (within 1%) to be achieved [8]. Closed formulas for w/h are available [1].

3.4. Microstrip Wavelength and Physical Length

For any propagating wave, the velocity is given by the appropriate frequency-wavelength product. In free space we have $c = f\lambda_0$ and in microstrip the velocity is $v_p = f\lambda_g$. Substituting these products into (11), we obtain

$$\epsilon_{\text{eff}} = \left(\frac{\lambda_0}{\lambda_g}\right)^2 \tag{19}$$

or

$$\lambda_g = \frac{\lambda_0}{\sqrt{\epsilon_{\text{eff}}}} \tag{20}$$

where λ_0 is the free-space wavelength and λ_g is the wavelength of the dominant mode in the microstrip. More conveniently in practical design, where the frequency is given in gigahertz and denoted by F , the wavelength can be expressed directly in millimetres as follows:

$$\lambda_g = \frac{300}{F\sqrt{\epsilon_{\text{eff}}}} \text{ mm} \tag{21}$$

The physical length l of a microstrip line to yield a specified electrical length θ (in degrees) is easily determined. We begin with the well-known expression for the electrical length of a section of any transmission line of this physical length, as a function of the phase coefficient (in radians),

$$\beta l = \theta \tag{22}$$

and hence

$$\frac{2\pi l}{\lambda_g} = \theta \tag{23}$$

With θ in degrees this gives

$$l = \frac{\theta \lambda_g}{360} \tag{24}$$

Thus, with λ_g evaluated using (21), we can simply find l .

An important aspect to mention at this juncture is that all the way through we are specifically discussing open microstrip, whereas in practice the circuits will be shielded to some extent. Such shielding generally attracts more electric field into the airspace, above the substrate, and therefore a greater proportion of this field exists in air with relative permittivity 1. The effective permittivity is thereby decreased and the microstrip wavelength increases with the square root relationship (see equations above). So microstrip design lengths also increase. The closer the shielding gets to the microstrip lines, the greater this effect becomes.

4. DISPERSION AND ITS EFFECTS ON DESIGN

As we have seen in Section 3.2 above, because the electric and magnetic fields are in more than one medium (a non-homogeneous transmission line), as for the microstrip line shown in Fig. 1, the effective microstrip permittivity ϵ_{eff} is used. The characteristics of the nonhomogenous line are then more or less the same as for the same structure with a uniform dielectric of permittivity ϵ_{eff} .

Permittivity ϵ_{eff} changes with frequency as the proportion of energy stored in the different regions changes. This effect, called *dispersion*, causes a pulse to spread out as the different frequency components of the pulse travel at different speeds. Another way of looking at this situation is to observe that the phase coefficient is a nonlinear function of the phase (propagation) velocity. As a direct consequence, the microstrip wavelength λ_g is now a nonlinear function of frequency. Therefore, we must account for the dispersion effect if we are to design accurately at microwave frequencies.

Because of its importance in microstrip circuit design, over the years many researchers have analyzed and measured the basic microstrip structure and published dispersion results. Although intensive numerical analyses have been employed in several instances, using substantial computer power, currently much more convenient and useful closed-formulas are available that predict dispersion. All aim at determining the effective microstrip permittivity—but now as a nonlinear function of frequency $\epsilon_{\text{eff}}(f)$.

At DC there can be no dispersion, and all the static TEM expressions already given can be directly used. Theoretically, as the frequency approaches infinity (well into

sub-millimeter-wave region and beyond), $\epsilon_{\text{eff}}(f)$ approaches ϵ_r . This situation can be summarized as follows:

1. $\epsilon_{\text{eff}}(f)$ always increases with frequency.
2. $\epsilon_{\text{eff}}(f)(f \rightarrow 0) \Rightarrow \epsilon_{\text{eff}}$ (calculated using static TEM analysis)
3. $\epsilon_{\text{eff}}(f)(f \rightarrow \infty) \Rightarrow \epsilon_r$.

In addition to these three basic features, it is also noted that $\epsilon_{\text{eff}}(f)$ is asymptotic at both limits, and the fourth feature concerns phase velocity $v_p(f)$. This suffers inflection at some frequency close to the cutoff frequency f_c of the TE_1 surface wave. Therefore this fourth feature is $\partial^2 v_p / \partial f^2 = 0$ when $f = f_c$.

Several earlier researchers utilized all or most of these features to develop closed-form expressions for predicting microstrip dispersion. However, more recent work has resulted in more accurate formulas, notably from Kirschning and Jansen [9]. The approach adopted by these workers begins with a function used by most investigators in this area, as follows

$$\epsilon_{\text{eff}}(f) = \epsilon_r - \frac{\epsilon_r - \epsilon_{\text{eff}}}{1 + P(f)} \tag{25}$$

and the form of the denominator frequency function is

$$P(f) = P_1 P_2 \{ (0.1844 + P_3 P_4) 10 f h \}^{1.5763} \tag{26}$$

where

$$\left. \begin{aligned} P_1 &= 0.27488 + \left\{ \frac{0.6315 + 0.525}{(1 + 0.157 fh)^{20}} \right\} \frac{w}{h} \\ &\quad - 0.065683 \exp - \frac{8.7513w}{h} \\ P_2 &= 0.33622 \{ 1 - \exp(-0.03442 \epsilon_r) \} \\ P_3 &= 0.0363 \exp \left(- \frac{4.6w}{h} \right) \left[1 - \exp \left\{ - \left(\frac{fh}{3.87} \right)^{4.97} \right\} \right] \\ P_4 &= 1 + 2.751 \left[1 - \exp \left\{ - \left(\frac{\epsilon_r}{15.916} \right)^8 \right\} \right] \end{aligned} \right\} \tag{27}$$

These workers used computer-based matching in conjunction with the available hybrid-mode results (derived from full electromagnetic numerical computations) to force the correct asymptotic behavior of the function $P(f)$. An accuracy of better than 0.6% is claimed for all frequencies up to 60 GHz (although a full check appears to have been conducted up to only 30 GHz). The validity ranges are very wide:

$$\begin{aligned} 1 &\leq \epsilon_r \leq 20 \\ 0.1 &\leq \frac{w}{h} \leq 100 \\ 0 &\leq \frac{h}{\lambda_0} \leq 0.13 \end{aligned}$$

There are further formulations enabling the effects of dispersion in microstrip to be calculated at frequencies through millimeter waves. Although the last word has almost certainly not yet been stated in the literature on this subject, the position has been reached where reported accuracies are within 1% (of measurements and independent theoretical results over a wide range). Having said this, it must be recognized that care is always required in selecting an appropriate accurate dispersion expression.

5. OPERATING FREQUENCY LIMITATIONS FOR MICROSTRIP

As the signal frequency applied to an MIC (or an MMIC) is steadily increased, some characteristic frequency may be reached at which undesirable effects occur. Two possible spurious effects restrict the desirable operating frequencies: (1) the lowest-order TM mode and (2) the lowest-order transverse microstrip resonance. In practice, one of these modes will be experienced at some frequency lower than the other and will thus set the frequency limitation.

5.1. The TM-Mode Frequency Limitation

Vendelin [10] has indicated that the most significant modal limitations in microstrip are associated with strong coupling between the quasi-TEM mode and the lowest-order TM mode. In the cited paper Vendelin gives the main relationships quoted here (although the original analysis is due to Collin in Ref. 6 of Vendelin's paper).

We start with the substrate viewed as a dielectric slab, having the coordinate notation shown in Fig. 5. This slab is a fair approximation for the situation with narrow microstrip lines.

The analysis involves setting eigenvalues for air and substrate and solving these either graphically or using the computer. We will not pursue this analysis here, but the final result is given by Eq. (23) for the maximum "safe" frequency under these conditions:

$$f_{\text{TEM}1} = \frac{c \tan^{-1}(\epsilon_r)}{\sqrt{2\pi h} \sqrt{\epsilon_r - 1}} \quad (28)$$

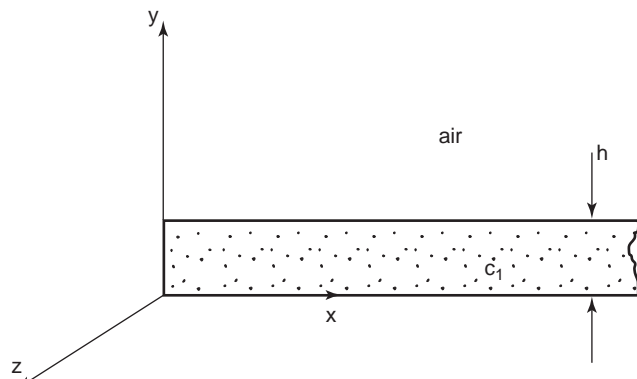


Figure 5. An (isotropic) substrate viewed as a dielectric slab, showing the nomenclature.

This is the frequency applying to strong coupling between the basic microstrip quasi-TEM mode and the TM mode.

In the important case of relatively narrow microstrip lines, where the relative permittivity is around 10 or greater, Eq. (28) tends toward

$$f_{\text{TEM}1} = \frac{106}{h\sqrt{\epsilon_r - 1}} \quad (29)$$

Using this equation, with thickness h directly substituted in millimeters, the frequency comes out directly in gigahertz.

The maximum restriction on usable substrate thickness is then easily obtained as

$$h = \frac{0.354\lambda_0}{\sqrt{\epsilon_r - 1}} \quad (30)$$

Care should be exercised in the use of these expressions, as Eq. (28) is more general and applicable to all types of substrates. Operating frequencies should be kept well below this maximum frequency. It is also recommended that substrates should be as thin as possible because Eq. (28) show that this makes the TM mode onset high. However, it should also be noted that thinner substrates result in lower Q factors, notably at lower frequencies.

5.2. The Lowest-Order Transverse Resonance in Microstrip

For a sufficiently wide microstrip line, a transverse resonant mode can exist that can also couple strongly to the quasi-TEM microstrip mode. At the cutoff frequency for this transverse resonant mode, the equivalent circuit is a resonant transmission line of length $(w + 2d)$, where d accounts for the microstrip side-fringing capacitance: $d = 0.2h$. In this situation a half-wavelength must be supported by the length $(w + 2d)$, stretching across the width of the microstrip. Setting down the simple equation for this transverse resonance and converting to the resonant frequency, we obtain

$$f_{\text{CT}} = \frac{c}{\sqrt{\epsilon_r}(2w + 0.8h)} \quad (31)$$

This is the maximum operating frequency under this limitation and it applies especially to relatively wide microstrips.

Vendelin [10] has indicated that slots, introduced into the metal strip, can suppress the transverse resonant mode. However, this may not always be practicable (e.g., when short stubs are involved), and it should be checked by calculating from Eq. (31), whether the transverse resonance might be excited. Sometimes a change in the circuit configuration will enable the offending wide lines to be avoided altogether.

In practice it is essential to check whether either the Eq. (28) or Eq. (31) frequency limitation will apply to every section of microstrip in a first-cut circuit design. The design must then be altered accordingly such that the operating frequencies remain below the set conditions as defined above.

5.3. Power Losses and Related Effects

Four separate mechanisms can be identified for power losses and parasitic effects associated with microstrip lines:

1. Conductor losses
2. Dissipation in the dielectric of the substrate
3. Radiation losses
4. Surface-wave propagation

The first two items are dissipative effects, whereas radiation loss and surface-wave propagation are essentially parasitic phenomena.

5.3.1. Conductor Losses. These losses occur as a result of the current conduction effects in the metal of the microstrip line and depend on several parameters associated with the microstrip and are probably best embodied in the expressions originally due to Hammerstad and Bekkadal [11]. The basic expression given by these workers is

$$\alpha_c = 0.072 \frac{\sqrt{f}}{wZ_0} \lambda_g \text{ dB/microstrip wavelength} \quad (32)$$

where the frequency f is in gigahertz and Z_0 is in ohms.

In practice, Eq. (32) yields somewhat low results, and surface roughness must be considered. Hammerstad and Bekkadal [11] gave the following curve-fitted formula to accommodate this problem:

$$\alpha'_c = \alpha_c \left[1 + \frac{2}{\pi} \tan^{-1} \left\{ 1.4 \left(\frac{\Delta}{\delta_s} \right)^2 \right\} \right] \quad (33)$$

where

Δ = RMS surface roughness

$\delta_s = 1/(R_s\sigma)$, the skin depth at the appropriate operating frequency, in which

R_s = surface resistance

σ = the conductivity of the metal

In order to observe the typical magnitudes involved, consider a copper microstrip, where the skin depth at a few gigahertz is $1 \mu\text{m}$. Also, assume the RMS surface roughness to be of similar magnitude, namely, $1 \mu\text{m}$ (this is fairly typical of rutile and some other hard substrates).

Equation (33) then shows that the attenuation coefficient becomes

$$\alpha'_c \approx 1.6\alpha_c \quad (34)$$

That is to say, the loss is approximately 60% increased when surface roughness is taken into account. The increase will be still greater for alumina and other substrates where the roughness can exceed $10 \mu\text{m}$.

5.3.2. Dielectric Loss. This type of loss has also been analyzed by several groups of workers, including again

Hammerstad and Bekkadal [11] and also Gupta et al. [12], who derived the following expression for the dielectric attenuation coefficient, α_d , per unit length

$$\alpha_d = 27.3 \frac{\epsilon_r(\epsilon_{\text{eff}} - 1) \tan \delta}{\sqrt{\epsilon_{\text{eff}}}(\epsilon_r - 1)\lambda_0} \text{ dB/unit length} \quad (35)$$

where $\tan \delta$ is the loss tangent for the substrate material and the microstrip wavelength λ_g given by

$$\lambda_g = \frac{\lambda_0}{\sqrt{\epsilon_{\text{eff}}}} \quad (36)$$

Equation (35) can also be written

$$\alpha_d = 27.3 \frac{\epsilon_r(\epsilon_{\text{eff}} - 1) \tan \delta}{\epsilon_{\text{eff}}(\epsilon_r - 1)} \text{ dB/microstrip wavelength} \quad (37)$$

which is the expression given by Hammerstad and Bekkadal [11].

For microstrip lines on alumina, $\epsilon_{\text{eff}} \rightarrow \epsilon_r$, at least very approximately, and the attenuation coefficient is, roughly, $\alpha_d = 27 \tan \delta$. In most cases $\tan \delta \sim 10^{-3}$ (or less) and therefore $\alpha_d \sim 0.027$ dB/microstrip wavelength. This is a factor of ≥ 5 smaller than the conductor loss that was calculated earlier. Conductor losses greatly exceed dielectric losses for most microstrip lines on alumina or sapphire substrates. However, where plastic substrates are used, this will by no means always be the case, and (especially) silicon or gallium arsenide substrates result in much larger dielectric losses (~ 0.04 dB/mm; i.e., 0.4 dB/microstrip wavelength at 10 GHz for silicon).

5.3.3. Loss Due to Radiation. This type of loss also represents a significant microstrip effect—again increasing as frequency rises. Microstrip is an asymmetric transmission line structure and is often used in unshielded or poorly shielded circuits where any radiation is either free to propagate away or to induce currents in the shielding. Further power loss is the net result.

In particular, discontinuities such as abruptly open-circuit microstrip (i.e., “open” ends), steps, and bends will all radiate to a certain extent. Such discontinuities form essential features of a microwave integrated circuit and radiation cannot therefore be avoided altogether. Efforts must be made to reduce such radiation and its undesirable effects. In circuits such as filters and amplifiers, this radiation is an acknowledged nuisance.

Both radiation and surface-wave propagation may be represented as a shunt admittance at the end of an open-circuit microstrip stub or at the plane location associated with some other abrupt discontinuity. This equivalent admittance is given by the following expression:

$$Y = G_r + G_s + jB \quad (38)$$

James and Henderson [13] show that, at frequencies where the surface wave is highly trapped in the substrate and with *thin substrates and narrow lines relative to the*

free-space wavelength, the radiation conductance G_r is approximated by

$$G_r Z_0 \approx \frac{4\pi h w_{\text{eff}}}{3\lambda_0^2 \sqrt{\epsilon_{\text{eff}}}} \quad (39)$$

in which w_{eff} is an effective microstrip width defined by the following expression:

$$w_{\text{eff}} = \frac{376.7h}{Z_0 \sqrt{\epsilon_{\text{eff}}}} \quad (40)$$

The remaining terms in Eq. (38), G_s and B , represent conductance due to surface-wave propagation and susceptance arising from the many field influences around the discontinuity.

Various techniques may be adopted to reduce radiation:

1. Metallic shielding or “screening”
2. Introduction of a small specimen of lossy (i.e., absorbent) material near any radiative discontinuity
3. Utilization of compact, planar inherently enclosed circuits (e.g., spurline filters or hairpin resonators)
4. Reduction of the current densities flowing in the outer edges of any metal sections so as to concentrate currents toward the center of the microstrip
5. Possibly shaping of the discontinuity in some way to reduce the radiative efficiency

5.3.4. Surface-Wave-Induced Loss. Surface waves also emanate from microstrip, and their undesirable effects have to be accounted for. Surface-wave propagation may be reduced by technique 2 listed above or by cutting slots into the substrate surface just in front of an open circuit. However, this is an expensive process and is usually unrealizable in MMICs. Parasitic coupling, where adjacent circuitry couples energy from nearby sources, is an undesirable consequence of surface-wave propagation. It is often necessary to minimize parasitic coupling (i.e., increase the isolation), and this requires attention to the following attributes:

1. Use relatively high permittivity substrates. Then ϵ_{eff} is relatively large (e.g., alumina is better than plastic, which should be anticipated on physical grounds).
2. Use fairly thin substrates (make the *free-space wavelength/thickness ratio* as large as possible).
3. Employ high-impedance (Z_0) stubs, for example, wherever this is feasible.

6. DISCONTINUITIES IN MICROSTRIP

All microstrip circuits must be designed with discontinuities fully accounted for. Several forms of discontinuity emerge from circuit requirements:

1. Foreshortened open circuits
2. Series coupling gaps

3. Short circuits through to the ground plane
4. Right-angled corners or “bends” (unmitered and mitered)
5. Step width changes
6. Transverse slit
7. T junction
8. Cross-junctions

An example of a microwave transistor amplifier layout is shown in Fig. 6, and at least three of the discontinuities can be readily identified. Some of these are numbered on the diagram, in accordance with the list above. Many other circuits, such as filters, mixers, and oscillators, involve several discontinuities. All technologies, whether hybrid MIC or MMIC, inherently involve such transmission discontinuities.

The various discontinuities are accommodated in the design process by approaches including extra line extensions and shifting the reference planes. In all cases the effects are strictly frequency-dependent, but in practice this results in only third-order adjustments at the most, so “quasi-TEM” (often DC) calculations are usually sufficient to quite accurately account for the effects of discontinuities. We will restrict the presentation here mainly to three types of discontinuity: the foreshortened open circuit, the right-angled bend, and the T junction.

With the *foreshortened open circuit*, the most common method of accommodating this is by supposing the line to be effectively longer than it is physically. We term this the *equivalent end-effect length*, and an empirical expression has been developed by Hammerstad and Bekkadal [11].

$$l_{\text{eo}} = 0.412h \left(\frac{\epsilon_{\text{eff}} + 0.3}{\epsilon_{\text{eff}} - 0.258} \right) \left(\frac{w/h + 0.262}{w/h + 0.813} \right) \quad (41)$$

It appears that, over a wide range of materials and microstrip width-to-height ratios, this expression can often give errors of $\geq 5\%$. In practice, however, this level of error

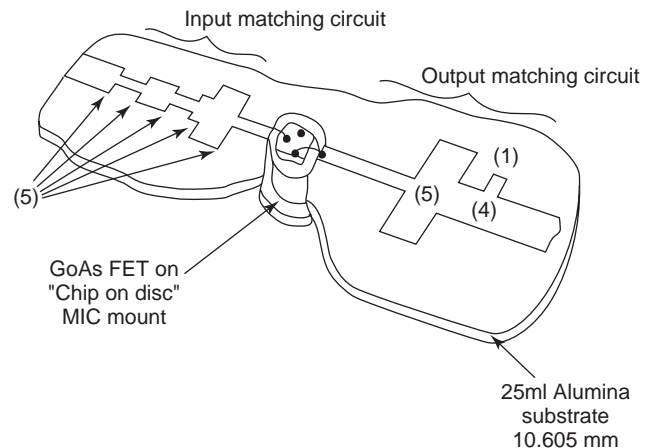


Figure 6. Layout of a simple, single-ended, hybrid MIC microwave amplifier using a GaAsFET device and showing several discontinuities in the microstrip lines (DC bias filters are not shown here).

almost always results in an acceptably small error in the overall microstrip-line design. For example, consider a microstrip line physically 3 mm in length and assume that the end-effect length extension calculates to 0.14 mm using Eq. (41). If this 0.14 mm is actually 6% high in error, then the corrected end-effect length will be just over 0.13 mm, giving a total effective length of 3.13 mm instead of 3.14 mm. The overall error is therefore about 0.3% and this is well within most acceptable design limits.

Series gaps represent a variation on the foreshortened open circuit, and the effective length extensions may be deduced by modifying Eq. (41). In general, because of the increased electric fields across such gaps compared to the foreshortened open circuit, the end-effect equivalent length extensions are somewhat greater. Series gaps are sometimes used in compact bandpass filters.

The *right-angled bend* (“corner”) is the second major form of microstrip discontinuity that we are considering here. Because the outer tip of the simple right-angled bend presents such a known and severe discontinuity (radiation and reflection), we shall restrict our attention to the *mitered right-angled bend*. Several techniques have been investigated for the compensation of microstrip bends, greatly reducing the effect of the capacitance and hence improving the VSWR and reducing the radiation. In particular, Anders and Arndt [14] have reported a moment method to calculate the appropriate capacitances and inductances for both curved and mitered bends.

Their results indicate that, at least up to a frequency of ~ 10 GHz, a mitered bend produces a performance as good as, or better than, that of curved bends. This applies to a wide range of bend angles, from 30° up to 120° . At least 70% mitering is recommended for an acute-angled bend of 120° , that is, one that acutely bends back on itself. Guidance for the design of such mitered bends, but for an angle of 90° , is also available for the structure shown in Fig. 7.

The equivalent circuit shown in Fig. 7b is for the region between planes P and P' , and the curves of Fig. 7c relate to measured results [15]. Although these curves apply to the specific instance defined, the considerable reduction of susceptance B (and therefore also capacitance C) would be expected in widely different substrates and structures. As can be seen, the equivalent linelength parameter l_c increases with enhanced mitering. Because of this and the substantial line narrowing in the center of the bend, the degree of miter is generally restricted to around the value calculated from the following expression:

$$1 - \frac{b}{\sqrt{2}w} \approx 0.6 \quad (42)$$

With this restriction the “extent of chamfer or miter parameter b ” becomes $b \approx 0.57w$, which means, for example, that the miter on a line that is 0.5 mm wide should optimally amount to $b \approx 0.28$ mm. It is instructive to observe that, whether unmitered or mitered, the effect of the discontinuity is that of a lowpass filter.

T junctions in microstrip are important in many circuits, notably amplifier-matching networks and stub-based filters. The basic, uncompensated, T junction and its equivalent circuit are shown in Fig. 8.

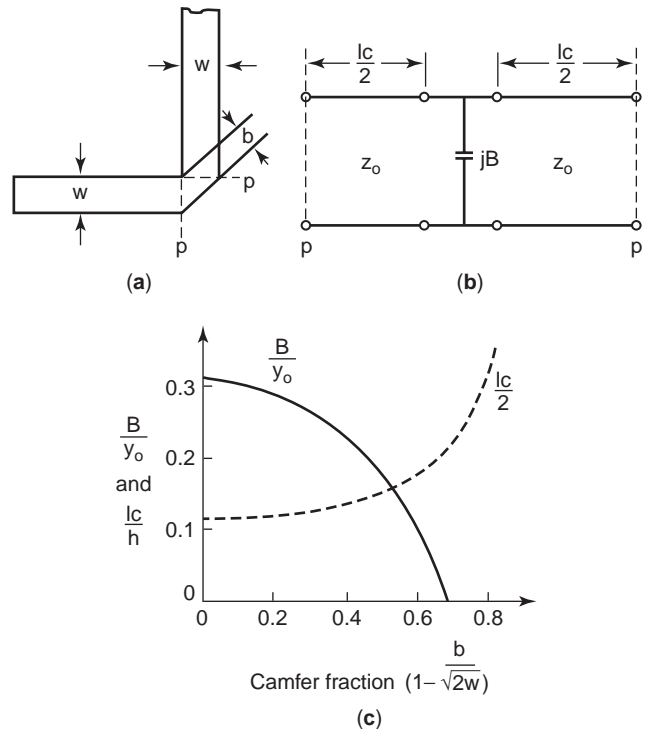


Figure 7. Mitered, right-angled bend together with its equivalent circuit and parameter variations (as a function of the amount of miter): (a) structure and nomenclature; (b) equivalent circuit; (c) parameter trends. (Reproduced by permission of the Institution of Electronic and Radio Engineers from Easter et al. [15].)

The immediate discontinuity effects, in the vicinity of the junction itself, are somewhat similar to those associated with the right-angled bend, represented as series inductance and shunt capacitance in the equivalent circuit. Note that the branchline of width w_2 (feeding out to what is termed a “secondary load” in Fig. 8a) is represented as a line coupled via an equivalent transformer of transformation ratio n in Fig. 8b.

Although rarely implemented (somewhat surprisingly), *compensated T junctions* are of considerable potential interest. One simple way to at least compensate the capacitance of a T junction is to introduce a slit across the width of the main through microstrip line, opposite the branch arm. Kompa [17] has shown further that a comparatively wide “slot” ($b \sim w_2$) in this position, specifically, a wide slit, strongly affects the transmission of higher-order modes in the mainline and leads to enhanced skirt sensitivity of filters composed of stubs with such modified T junctions. To the best of the present writers’ knowledge, this kind of approach has not yet been developed further, and more investigation could prove very fruitful.

Dydyk [18] has described a T-junction compensation technique that appears to work well in the case of a branch line microstrip coupler circuit. Dydyk’s aim was to modify the microstrip lines in the vicinity of the junction in order to compensate for reference plane shifts, at least over a specified range of frequencies. The analysis of such a junction can exclude any discussion of radiation loss with little error in circuit performance results, up to a frequency of

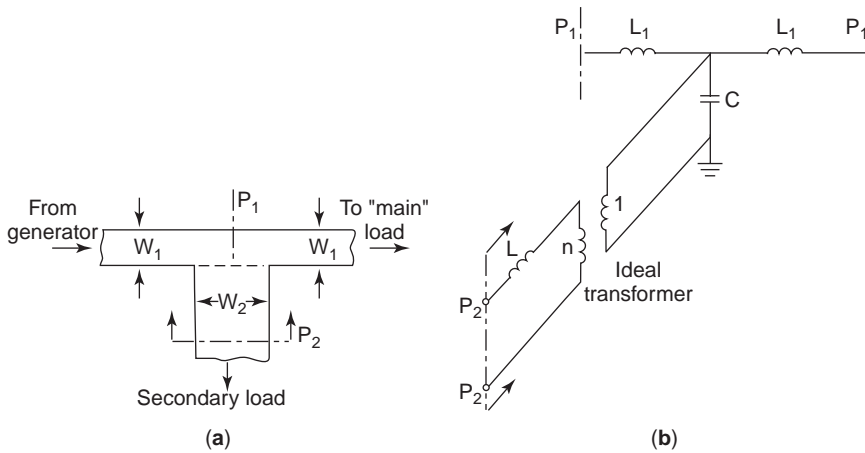


Figure 8. The T junction in microstrip: (a) structure and nomenclature; (b) equivalent circuit. (Copy right 1973 IEEE. Reprinted, with permission, from Silvester and Benedek [16]).

17 GHz at least. The compensated T junction takes on the form shown in Fig. 9.

A microstrip branch line coupler designed using these principles yielded the following performance over the frequency band 16–18 GHz:

- Insertion loss: 3.5–4.0 dB over the entire band
- Isolation: >20 dB over the entire band
- Return loss: 10 dB (at 17.5 GHz), otherwise 10 to –25 dB

The very “flat,” almost frequency-independent, insertion loss and isolation are attributed to the compensated junction design. Dydyk also describes an SPDT switch designed according to these principles.

7. PARALLEL-COUPLED MICROSTRIPS AND BANDPASS FILTERS

The arrangement shown in Fig. 10 illustrates the transverse cross-section basic structure under consideration here.

It will be assumed that both microstrip lines have the same widths, which is nearly always the case in practical applications. Some work has also been carried out on multiple arrays of such parallel, edge-coupled lines, but we can usefully restrict the considerations to just two lines in

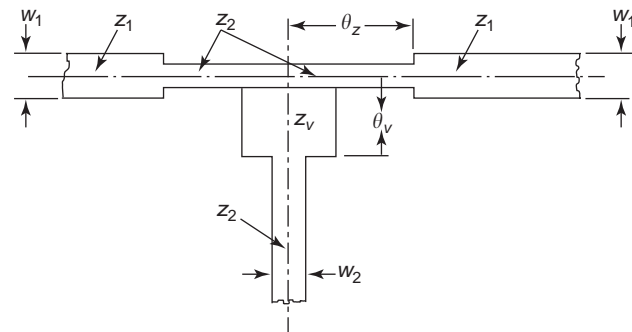


Figure 9. A compensated form of T junction. (Reproduced by permission of MicroWaves from Dydyk [18]).

this treatment. There are two general areas of application for these structures:

1. *Directional couplers*—for use in a variety of circuits including balanced mixers, balanced amplifiers, phase shifters, attenuators, modulators, discriminators, and measurement bridges
2. *Filters, delay lines, and matching networks*—often using arrays of parallel-coupled microstrips as resonant elements

In the first instance (1), a prescribed amount of the incident power is required to be coupled out of the system. Thus, for example, a “–3-dB coupler” is one in which half of the power input is coupled from one microstrip line into another and then on to separate circuitry. In practice, however, this simple structure is inadequate for such applications and special couplers are realized. This topic is outside the scope of the present discussion. Microstrip filters application (2) employing the parallel-coupled structure are usually of the bandpass or bandstop type. An outline example of a design approach employing resonators coupled in this manner is given later here.

For each half-cycle of the RF wave, the two coupled lines will have precisely opposite voltage polarities. In one half-cycle the opposing lines will be similarly polarized (e.g., equally positive), while in another half-cycle the lines will be oppositely polarized (i.e., one positive and one negative). In the first instance we term the situation even-mode; in the second instance, odd-mode. Each parameter associated with each polarisation has an extra

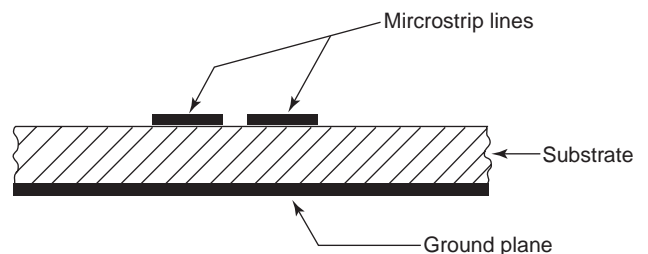


Figure 10. A pair of parallel, edge-coupled microstrip lines.

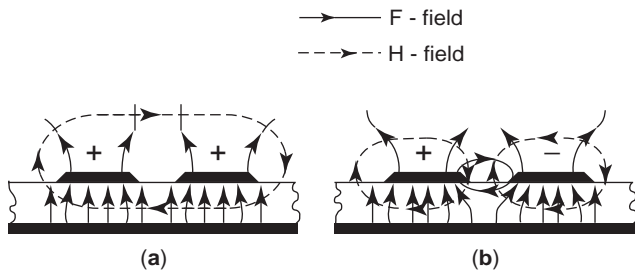


Figure 11. Field distributions resulting from (a) even-mode and (b) odd-mode excitation of parallel-coupled microstrip lines.

subscript attributed; “e” for even-mode and “o” for odd-mode.

The even- and odd-mode characteristic impedances ($Z_{0,e}$ and $Z_{0,o}$) are major design parameters for any parallel-coupled transmission-line configuration—whatever its application. These impedances are obtained at an early circuit/system design stage and are functions of the degree of coupling (C) and the single-line terminating characteristic impedance (Z_0). The relationships between $Z_{0,e}$ and $Z_{0,o}$ and the physical dimensions of the coupled structure (including the substrate permittivity) are therefore of prime significance to the designer. As with single microstrip lines, in this coupled situation as well we can determine $Z_{0,e}$ and $Z_{0,o}$ from known physical dimensions, which amounts to analysis. Alternatively, with greater difficulty, we may synthesize the physical structure from starting values of the impedances. Both of these procedures are useful in practice.

The electric (E) and magnetic (H) fields associated with each mode are indicated in Figs. 11.

In the design of filters or matching networks using parallel-coupled lines, we usually begin with either insertion loss as a function of frequency or VSWR requirements over some band. In either event we still arrive at desired values of $Z_{0,e}$ and $Z_{0,o}$ followed by a final synthesis aimed at the physical realization of the circuit. Input information required includes

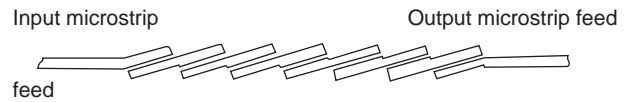


Figure 13. General top-view appearance of a practical parallel-coupled microstrip BPF.

- Bandwidth (B) and center frequency (f_0)
- In-band and attenuation-band insertion loss (both dB—for filters)
- Terminating characteristic impedance Z_0 (usually 50 Ω)
- Permittivity and thickness of the substrate

From this information the designer must ultimately determine the widths of the microstrip lines, the separation between them, the length of the coupled region, and hence ultimately the physical lengths of the microstrips.

For the present purposes we will not expound on the precise details of parallel-coupled microstrip design (this is covered in detail in Ref. 1). It should, however, be mentioned that dispersion is present in this structure, and this affects the even and odd modes differently. The single microstrip models covered in Section 1 can be modified to suit the parallel-coupled case.

With microstrip couplers, maximum coupling is obtained between physically parallel microstrips when the length of the coupled region is $\lambda_g/4$, or some odd multiple thereof. To achieve resonance, each resonator element has to be $\lambda_g/2$ in length, or many multiple thereof. Therefore the microstrip circuit must have the general layout shown in Fig. 12 where $l_1, \dots, l_4 \approx \lambda_g/4$.

We will assume, for the moment, that this fairly straightforward cascade of parallel-coupled (or edge-coupled) microstrip resonators can be designed on a basis of all-parallel resonator networks together with intervening circuits known as inverters.

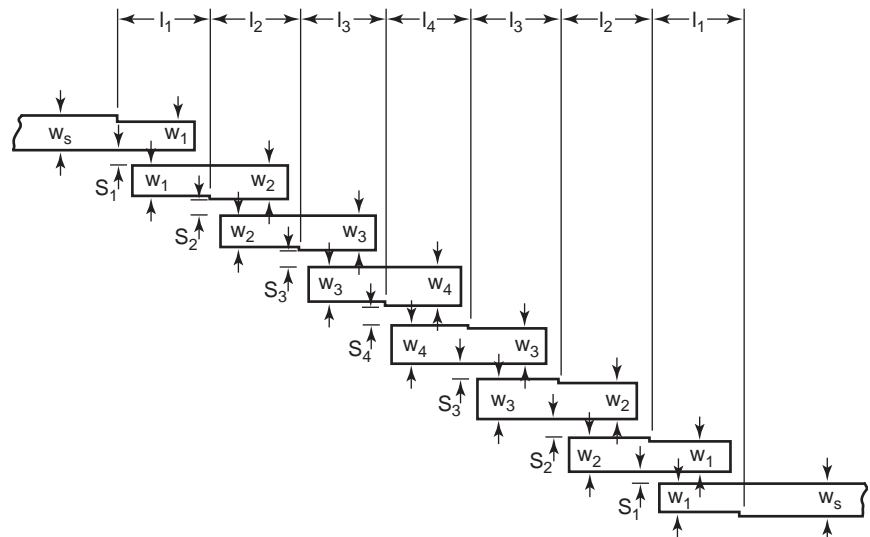


Figure 12. General microstrip configuration for a seven-section, parallel-coupled bandpass filter (BPF).

The four main design steps are outlined as follows:

1. Determine the one-type resonator network, to realize the specification, from the original prototype;
2. From the network parameters, evaluate the even- and odd-ordered characteristic impedances $Z_{0,e}$ and $Z_{0,o}$ applicable to the parallel-coupled microstrip (this is not discussed in detail here, but see ref. 1).
3. Relate the values of $Z_{0,e}$ and $Z_{0,o}$ to microstrip widths and separations (w,s) (detailed microstrip design).
4. Calculate the entire resonator length $2l'$, slightly less than $\lambda_g/2$ because of the semiopen end effects (see Section 6), and therefore of the coupled section length l' , which is slightly less than $\lambda_g/4$ for the end effect reason again (Fig. 12).

Here λ_g is the midband and average microstrip wavelength. Allowance must be made for the semi-open-circuit microstrip end effects that exist for all elements in this circuit.

In practice, most microstrip or related planar BPFs have their topologies rotated for spatial convenience (on chip or substrate) as shown in Fig. 13.

All the dense black features are microstrip lines, and Fig. 13 is not to scale since it is only meant to provide the concept of the layout.

BIBLIOGRAPHY

1. T. C. Edwards and M. B. Steer, *Foundations of Interconnect and Microstrip Design*, Wiley, Chichester, UK, 2000.
2. K. C. Gupta, R. Garg, and I. J. Bahl, *Microstrip Lines and Slotlines*, 2nd ed., Artech House, Dedham, MA, 1996.
3. D. D. Grieg and H. F. Engelmann, Microstrip—a new transmission technique for the kilomegacycle range, *Proc. Inst. Radio Eng.* **40**(12):1644–1650 (Dec. 1952).
4. W. E. Fromm and E. G. Fubini, Characteristics and some applications of stripline components, *Proc. Natl. Electronics Conf.*, 10, III., Oct. 4–6, 1954, 58–59.
5. J. M. C. Dukes, The application of printed circuit techniques to the design of microwave components, *Proc. Inst. Electric. Eng.* **105**(Part B):155–172 (March 1958).
6. H. A. Wheeler, Transmission-line properties of parallel wide strips by a conformal mapping approximation, *IEEE Trans. Microwave Theory Tech.* **12**:280–289 (May 1964).
7. H. A. Wheeler, Transmission-line properties of parallel strips separated by a dielectric sheet, *IEEE Trans. Microwave Theory Tech.* **13**:172–185 (March 1965).
8. R. P. Owens, Accurate analytical determination of quasi-static microstrip line parameters, *Radio Electron. Eng.* **46**(7):360–364 (July 1976).
9. M. Kirschning and R. H. Jansen, Accurate model for effective dielectric constant of microstrip with validity up to millimetre-wave frequencies, *Electron. Lett.* **27**:272–273 (March 18, 1982).
10. G. D. Vendelin, Limitations on stripline Q, *Microwave J.* **63**–69 (May 1970).
11. E. O. Hammerstad and F. Bekkadal, *A Microstrip Handbook*, ELAB Report, STF 44 A74169, Univ. Trondheim, Norway, 1975, pp. 98–110.

12. K. C. Gupta, R. Garg, I. J. Bahl, and P. Bhartia, *Microstrip Lines and Slotlines*, 2nd ed., Artech House, Norwood, MA, 1996, pp. 91–92.
13. J. R. James and A. Henderson, High-frequency behaviour of microstrip open-circuit terminations, *IEE J. Microwaves Opt. Acoust.* **3**(5):205–218 (Sept. 1979).
14. P. Anders and F. Arndt, Moment method of designing matched microstrip bends, *Proc. 9th European Microwave Conf.*, 1979, 430–434.
15. B. Easter et al., Theoretical and experimental methods for evaluating discontinuities in microstrip, *Radio Electron. Eng.* **48**(1/2):73–84 (Jan./Feb. 1978).
16. P. Silvester and P. Benedek, Microstrip discontinuity capacitances for right-angle bends, T-junction and crossings, *IEEE Trans. Microwave Theory Tech.* **21**(5):341–346 (May 1973).
17. G. Kompas, Reduced coupling aperture of microstrip stubs provides new aspects in stub filter design, *Proc. 6th European Microwave Conf.*, 1976, 39–43.
18. M. Dydyk, Master the T-junction and sharpen your MIC designs, *Microwaves*, 184–186 (May 1977).

MICROSTRIP LINES

ZHEWANG MA
EIKICHI YAMASHITA
KAZUHIKO ATSUKI
University of Electro-
Communications

1. TRANSVERSE ELECTROMAGNETIC TRANSMISSION LINES

One of the most familiar waveguiding structures is the conventional transmission line such as the two-wire line and the coaxial line. The fundamental mode of propagation on a transmission line is essentially a *transverse electromagnetic (TEM) wave*, which owns neither electric nor magnetic field in the direction of propagation [1].

An ideal lossless uniform TEM transmission line can be represented by a lumped circuit and consists of series inductance L and shunt capacitance C , all defined per unit length of the line, as shown in Fig. 1. The inductance L is proportional to the permeability μ of the surrounding medium, and the capacitance C proportional to the permittivity ϵ of the medium. Their values depend on the transverse geometry of the transmission line, and are determined from the electrostatic analysis [1] of the cross-section of the structure that solves a two-dimensional Laplace equation in the medium surrounding the conductors of the transmission line.

The voltage and current waves, expressed by $V = V_0 e^{\pm j\beta z}$ and $I = I_0 e^{\pm j\beta z}$, along the transmission line are solutions of the *telegraphists' or transmission-line equations* [1]

$$\frac{d^2 V}{dz^2} + \omega^2 L C V = 0 \quad (1)$$

$$\frac{d^2 I}{dz^2} + \omega^2 L C I = 0 \quad (2)$$

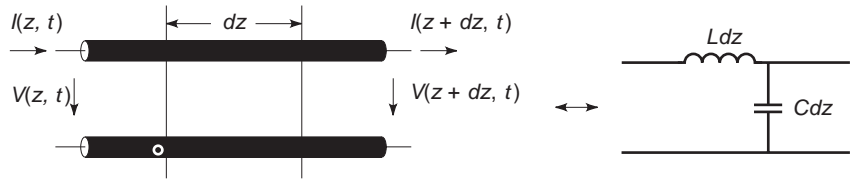


Figure 1. Lumped-circuit representation of an ideal TEM transmission line. L is the series inductance, C the shunt capacitance; both are defined per unit length of the line.

where $\omega = 2\pi f$ (frequency) is the radian frequency and β is the phase constant.

TEM transmission lines are characterized by line parameters such as phase constant, characteristic impedance, and attenuation constant. Formulas for line parameters of an ideal lossless transmission line are given in what follows [1,2]:

Phase constant

$$\beta = \omega\sqrt{LC} = \omega\sqrt{\mu\epsilon} = \omega/v \tag{3}$$

Characteristic impedance

$$Z_0 = \sqrt{\frac{L}{C}} = \frac{1}{vC} \tag{4}$$

Voltage and current along line

$$V(z) = V_0 e^{j\beta z} [1 + \Gamma(z)] \tag{5}$$

$$I(z) = \frac{V_0}{Z_0} e^{j\beta z} [1 - \Gamma(z)] \tag{6}$$

Input impedance

$$Z(z) = Z_0 \frac{Z_L \cos \beta z + jZ_0 \sin \beta z}{Z_0 \cos \beta z + jZ_L \sin \beta z} \tag{7}$$

In these expressions, v is the velocity of TEM waves in the dielectric of line, v_0 is the amplitude of the incident voltage, z_L is the value of the load impedance, and z is the distance along the line from the load end.

2. STRIPLINES

A stripline, also referred to as a *triplate line*, consists of a conducting strip lying between, and parallel to, two wide conducting ground planes, as shown in Fig. 2. The region between the strip and the planes is filled with a uniform dielectric. Stripline is one of the most commonly used transmission lines for passive *microwave integrated circuits* (MICs). The fundamental mode in a stripline is a TEM mode, and its field distribution is illustrated in Fig. 3.

The line parameters of a stripline can be obtained completely by electrostatic analysis such as the conformal mapping technique [1,3]. An approximate expression for the characteristic impedance of a stripline with zero-thickness strip is given by [2,3]

$$Z_0 = \frac{30\pi}{\sqrt{\epsilon_r}} \frac{K'(k)}{K(k)} \tag{8}$$

where ϵ_r is the relative permittivity of the dielectric filled in the stripline, $k = \tanh(\pi w/2h)$, K represents a complete

elliptic function of the first kind, and K' is its complementary function. The velocity of the TEM mode in a stripline is $v = 1/\sqrt{\mu_0\epsilon_0\epsilon_r}$. Both the wave velocity and characteristic impedance are independent of frequency.

An accurate but simple approximate expression for $K(k)/K'(k)$ is given by

$$\frac{K(k)}{K'(k)} = \begin{cases} \frac{\pi}{\ln[2(1 + \sqrt{k})/(1 - \sqrt{k})]} & \text{for } 0 \leq k \leq 0.707 \\ \frac{1}{\pi} \ln[2(1 + \sqrt{k})/(1 - \sqrt{k})] & \text{for } 0.707 \leq k \leq 1 \end{cases} \tag{9}$$

An approximate expression for the attenuation constant arising from the conductor surface resistance, $R_s = \sqrt{\omega\mu_0/2\sigma}$, is given by (1)

$$\alpha_c = \frac{R_s}{h\eta} \left[\frac{\pi w/h + \ln(4h/\pi t)}{\ln 2 + \pi w/2h} \right] \text{ Nps/m} \tag{10}$$

where $\eta = \sqrt{\mu_0/\epsilon_0\epsilon_r} = \eta_0/\sqrt{\epsilon_r}$, $\eta_0 = 120\pi$ is the wave impedance in free space and t is the thickness of the strip. Equation (10) is valid for $w > 2h$ and $t < h/10$.

The attenuation constant from lossy dielectric medium with $\epsilon = \epsilon' - j\epsilon''$ is expressed by

$$\begin{aligned} \alpha_d &= \text{Re}(j\omega\sqrt{\mu_0\epsilon}) = \text{Re}(j\omega\sqrt{\mu_0(\epsilon' - j\epsilon'')}) \\ &\approx \frac{\omega\sqrt{\mu_0\epsilon'}\epsilon''}{2\epsilon'} = \frac{\omega\sqrt{\mu_0\epsilon'}}{2} \tan \delta \text{ Nps/m} \end{aligned} \tag{11}$$

where $\tan \delta$ is the dielectric loss tangent.

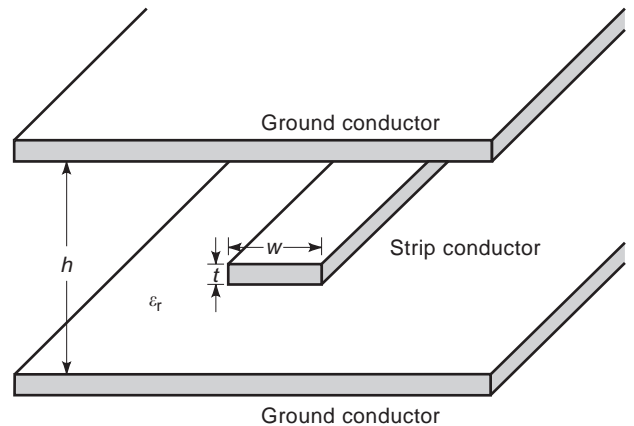


Figure 2. Geometry of a stripline. The strip conductor is sandwiched between two wide parallel conducting ground planes. The region between the strip and the ground planes is filled with a uniform dielectric.

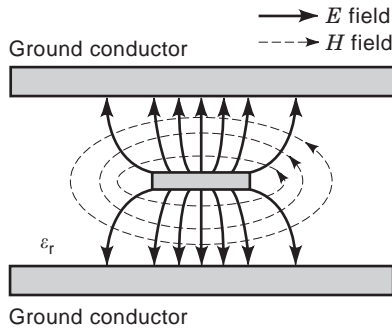


Figure 3. Electromagnetic field distribution in a stripline. The fundamental TEM mode is considered. The electric field goes from the conductor strip to the grounded planes. The magnetic field surrounds the conductor strip.

In addition to the dominant TEM mode, higher-order *transverse electric (TE) modes* and *transverse magnetic (TM) modes* can also propagate in a stripline. A TE mode owns magnetic field but no electric field in the direction of propagation. A TM mode contains electric field but no magnetic field in the direction of propagation. The cutoff frequency of the lowest order TE mode is [2]

$$f_c = \frac{15}{h\sqrt{\epsilon_r}} \frac{1}{w/h + \pi/4} \quad (12)$$

where f_c is given in gigahertz and w and h are in centimeters.

More detailed and accurate formulas for the stripline parameters, such as the characteristic impedance, and the attenuation constant, can be found in Ref. 2.

3. MICROSTRIP LINES

3.1. General Descriptions

3.1.1. Microstrip Geometry and Advantages. A microstrip line [4] is a type of open planar transmission line that consists of a dielectric substrate medium with a ground plane on the lower side and a conducting strip on the upper side. The geometry of a microstrip line is shown in Fig. 4. The substrate provides mechanical rigidity and permits the accurate positioning of the circuitry. The transmission-line characteristic parameters, like the

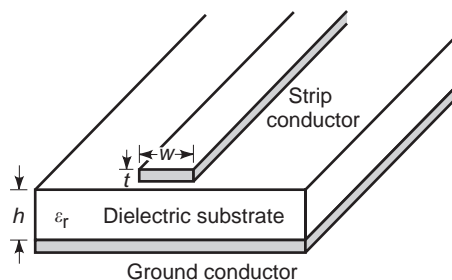


Figure 4. Geometry of a microstrip line. The conducting strip is placed above a dielectric substrate, which is supported on its bottom by a conducting plate.

phase constant and characteristic impedance, can be determined from the substrate permittivity (ϵ_r) and the geometrical dimensions (strip width w and thickness t , substrate thickness h) in the transverse plane. For this reason, various types of microstrip circuits can be fabricated conveniently with high precisions by employing the simple photolithographic and photoetching techniques. Use of these techniques at microwave and millimeter-wave frequencies has led to the development of hybrid and monolithic microwave integrated circuits (MICs) [5–11].

Microstrip line is now one of the most widely used transmission lines for MICs. Active devices (diodes and transistors), lumped circuit elements (capacitors, resistors, inductors), dielectric resonators, and antennas can be easily incorporated into the circuit. Compared with the traditional bulky and heavy metallic waveguides and coaxial lines, the planar microstrip structures are small-size, lightweight, easy for mass production, and inexpensive.

3.1.2. Dielectric Substrate. The properties of the dielectric substrate material affect the overall performance of the microstrip structures. Different substrate materials possess characteristics that may make them better suited for a given application. For instance, higher-dielectric-constant materials are preferred in order to achieve a very compact microwave circuit, while lower-dielectric-constant materials are required for antenna structures to ensure efficient radiation.

In general, the substrate material parameters, permittivity ϵ and permeability μ , should be homogeneous (independent of position), isotropic (independent of wave propagation direction), and should have low dispersion. The loss tangent should be small to reduce energy dissipation. Furthermore, these parameters should have very small variation with temperature to ensure circuit stability. The substrate thermal conductivity should be high enough to ensure efficient removal of heat from power transistors, attenuators, and loads in high-power applications. In high-power applications, a high breakdown voltage is also desirable. The thermal expansion coefficient of the material should be similar to that of the deposited conductors and housing to withstand temperature fluctuations and improve reliability. The material must allow drilling, cutting, machining, and etching for easy workability and lower production costs. Also important is a good surface finish to ensure good conductor adhesion and reduce conductor loss.

A wide variety of dielectric substrates are now commercially available. Characteristics, including mechanical and thermal as well as electronic facets, of a number of representative substrate materials, such as alumina, fused quartz, silicon, gallium arsenide, synthetic, and composite materials, are compared in Refs. 6–12.

Although the microstrip line appeared first in 1952 [4], the rapid increase of the use of microstrip circuits was seen during the 1960s when high permittivity and low-loss dielectric substrates became available. At the same time, microwave semiconductor devices appeared, and miniature lumped elements (capacitors, resistors, inductors)

became available for implantation on planar circuits. Coupled with steady advances in photolithographic technology, the combination of microstrips, lumped elements, and semiconductors led to the advent of microwave integrated circuits (MICs) [5–11].

3.1.3. Field Configuration and Analysis Methods. The microstrip line is an inhomogeneous transmission line, involving an abrupt dielectric interface between the substrate and the air above it. The electromagnetic fields extend over inhomogeneous regions, partly in the dielectric substrate, and partly in the air, as shown in Fig. 5. Waves propagating along the line cannot be purely TEM, TE, or TM modes, but *hybrid modes* containing both electric and magnetic fields in the transverse and longitudinal directions of propagation [6]. This may cause some complication in microstrip analysis and design. However, in many practical situations, the dominant mode of a microstrip line resembles closely a TEM mode. Therefore, it is usually referred to as quasi-TEM mode.

The microstrip line has been analyzed by numerous workers using various analytical and numerical techniques. As with many other transmission lines, the analysis methods for a microstrip line are aimed at determining the characteristic impedance and propagation constant (phase velocity and attenuation constant). The various methods of microstrip line analysis can be divided into two main groups [6–10]. In the first group, which comprises *quasistatic methods*, the nature of the mode of propagation is considered to be pure TEM and the microstrip characteristics are calculated from the electrostatic capacitance of the structure. The quasistatic methods commonly used include the conformal transformation method [13], the variational method [14,15], the finite-difference method, and the integral equation method [6–10]. It is found that this quasistatic analysis is adequate for designing circuits at lower frequencies where the strip width and the substrate thickness are much smaller than the wavelength in the dielectric material.

The methods in the second group are *full-wave approaches*, which take into account the hybrid nature of the mode of propagation. They include the integral equation method [16], the spectral-domain method [17], and the finite-difference time-domain (FDTD) method [6–10,17]. The full-wave analysis methods are more rigorous and

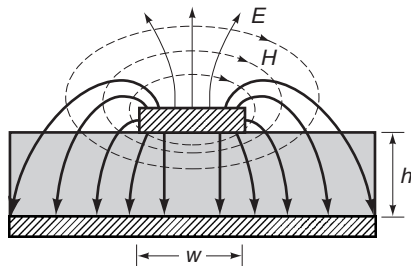


Figure 5. Electromagnetic field distribution in a microstrip line. The fundamental quasi-TEM mode is considered. The electromagnetic fields extend over inhomogeneous regions, partly in the dielectric substrate, and partly in the air.

can predict frequency-dependent variation of the microstrip characteristics. However, they are analytically complex, and usually require large computer memories and long computation time, which may become prohibitive when optimization process is demanded in the design of circuits.

3.1.4. High-Frequency Problems and Quasi-TEM Wave Results. Microstrip lines have been extensively used for MICs at frequencies ranging from hundreds of megahertz to tens of gigahertz. At high frequencies, particularly into the millimeter wavelength ranges, conductor ohmic and dielectric losses increase greatly. Surface waves of the dielectric substrate and higher-order modes excited at discontinuities start to propagate or to radiate [6–10]. The conductor and dielectric losses and radiation reduce the amplitude of a signal propagating along the line and may cause spurious coupling between neighbouring parts of a circuit. The simultaneous propagation of several modes, with different velocities, produces a distortion of the signal. The fabrication tolerances become very difficult to meet. These factors prohibit the extensive use of microstrip lines at high frequencies.

For the majority of microstrip lines suitable for MICs, the statically derived results are quite accurate when the frequency is below a few gigahertz. At higher frequencies, up to the limits for the useful operation of microstrip lines, these static results can still be used in conjunction with some quasiempirical functions in closed formulas to find the variations of microstrip characteristics with frequency. Therefore, results by the static techniques are powerful and significant in the design of microstrip circuits.

3.1.5. Quasi-TEM Wave Parameters. Under the quasi-TEM wave approximation, an ideal microstrip line can be represented by the lumped circuit for the TEM transmission line shown in Fig. 1. The characteristic impedance is expressed by

$$Z_0 = \sqrt{\frac{L}{C}} = \frac{1}{vC} \quad (13)$$

When the substrate of the microstrip line is replaced by air, we have an air-filled line along which the wave will travel at c , the velocity of light in free space. The characteristic impedance of this air-filled line, defined as Z_a , is given by

$$Z_a = \sqrt{\frac{L}{C_a}} = \frac{1}{c \cdot C_a} \quad (14)$$

Combining Eqs. (13) and (14), we get

$$Z_0 = \frac{1}{c\sqrt{C \cdot C_a}} \quad (15)$$

Phase constant

$$\beta = \frac{\omega}{v} = \omega\sqrt{LC} = \frac{\omega}{c} \sqrt{\frac{C}{C_a}} = \beta_0 \sqrt{\frac{C}{C_a}} \quad (16)$$

here β_0 is the wavenumber in free space. The normalized phase constant is written as

$$\frac{\beta}{\beta_0} = \frac{c}{v} = \frac{\lambda_0}{\lambda_g} = \sqrt{\frac{C}{C_a}} \quad (17)$$

here λ_0 and λ_g are the wavelengths in free space and along the microstrip line, respectively. Equations (15) and (17) indicate that the characteristic impedance and phase constant of a microstrip line can be obtained if we can evaluate the capacitance per unit length of the line, with and without the presence of the dielectric substrate.

The *effective permittivity* ε_e is defined as the capacitance ratio

$$\varepsilon_e = \frac{C}{C_a} \quad (18)$$

From Eq. (17) we immediately get

$$\varepsilon_e = \left(\frac{c}{v}\right)^2 \quad (19)$$

$$\beta = \sqrt{\varepsilon_e} \cdot \beta_0 \quad (20)$$

The effective permittivity has a physical meaning that the original inhomogeneous microstrip line is replaced by an equivalent homogeneous line with conductors having exactly the same geometry (w, h, t) , surrounded by a single homogeneous dielectric of effective permittivity ε_e .

From Eqs. (17) and (18), we also have the formula

$$\lambda_g = \frac{\lambda_0}{\sqrt{\varepsilon_e}} \quad (21)$$

3.1.6. Formulas for Quasi-TEM Wave Parameters. As stated previously, closed formulas are of significant importance in the design of microstrip-line circuits. Various workers have reported formulas for microstrip calculations [6–10]. These formulas may be classified into two types, one for the analysis purpose, and the other for the synthesis purpose. When the geometric and material parameters (w, h, t, ε_r) are known, we use the analysis formulas to evaluate the line's electrical characteristics ε_e , Z_0 , and λ_g . Conversely, when Z_0 and ε_r are given and we want to specify the width–height ratio w/h of the microstrip line, we employ the synthesis formulas.

3.1.7. Analysis Formulas (w/h and ε_r Given). Very accurate formulas derived by Hammerstad and Jensen [18] are provided below:

Effective permittivity ε_e .

$$\varepsilon_e = \frac{\varepsilon_r + 1}{2} + \frac{\varepsilon_r - 1}{2} \left(1 + 10 \frac{h}{w}\right)^{-a(w/h) \cdot b(\varepsilon_r)} \quad (22)$$

with

$$a\left(\frac{w}{h}\right) = 1 + \frac{1}{49} \ln \left\{ \frac{(w/h)^4 + [w/(52h)]^2}{(w/h)^4 + 0.432} \right\} \quad (23)$$

$$+ \frac{1}{18.7} \ln \left[1 + \left(\frac{w}{18.1h}\right)^3 \right]$$

$$b(\varepsilon_r) = 0.564 \left(\frac{\varepsilon_r - 0.9}{\varepsilon_r + 3}\right)^{0.053} \quad (24)$$

Characteristic impedance Z_0 .

$$Z_0 = \frac{\eta_0}{2\pi\sqrt{\varepsilon_e}} \cdot \ln \left[F_1 \left(\frac{w}{h}\right) \frac{h}{w} + \sqrt{1 + \left(\frac{2h}{w}\right)^2} \right] \quad (25)$$

with

$$F_1\left(\frac{w}{h}\right) = 6 + (2\pi - 6) \exp \left[-\left(30.666 \frac{h}{w}\right)^{0.7528} \right] \quad (26)$$

where $\eta_0 = 120\pi$ is the wave impedance in free space. The accuracy of these expressions is better than 0.01% for $w/h \leq 1$ and 0.03% for $w/h \leq 1000$.

3.1.8. Synthesis Formulas (Z_0 and ε_r Given) [7]. For narrow strips (when $Z_0 > (44 - 2\varepsilon_r) \Omega$)

$$\frac{w}{h} = \left(\frac{\exp(A)}{8} - \frac{1}{4 \exp(A)}\right)^{-1} \quad (27)$$

where

$$A = \frac{Z_0 \sqrt{2(\varepsilon_r + 1)}}{119.9} + \frac{1}{2} \left(\frac{\varepsilon_r - 1}{\varepsilon_r + 1}\right) \left(\ln \frac{\pi}{2} + \frac{1}{\varepsilon_r} \ln \frac{4}{\pi}\right)$$

For wide strips (when $Z_0 < (44 - 2\varepsilon_r) \Omega$)

$$\frac{w}{h} = \frac{2}{\pi} [(B - 1) - \ln(2B - 1)] \quad (28)$$

$$+ \frac{\varepsilon_r - 1}{\pi \varepsilon_r} \left[\ln(B - 1) + 0.293 - \frac{0.517}{\varepsilon_r} \right]$$

where

$$B = \frac{59.95\pi^2}{Z_0 \sqrt{\varepsilon_r}}$$

3.1.9. Strip Thickness Correction. In correcting the results above, ε_e and Z_0 given by Eqs. (22) and (25), for non-zero strip thickness t , a corrected strip width w_e/h is defined as follows [18]:

$$\frac{w_e}{h} = \frac{w}{h} + \frac{1}{2\pi} \frac{t}{h} \left[1 + \frac{1}{\cosh(\sqrt{\varepsilon_r - 1})} \right] \quad (29)$$

$$\cdot \ln \left[1 + \frac{4h \exp(1)}{t \coth^2(\sqrt{6.517}w/h)} \right]$$

With this corrected strip width, the effect of strip thickness on ε_e and Z_0 of microstrip lines can be included in the

Eqs. (22) and (25). We have therefore

$$\epsilon_e = \frac{\epsilon_r + 1}{2} + \frac{\epsilon_r - 1}{2} \left(1 + 10 \frac{h}{w_e}\right)^{-a(w_e/h) \cdot b(\epsilon_r)} \tag{30}$$

$$Z_0 = \frac{\eta_0}{2\pi\sqrt{\epsilon_e}} \cdot \ln \left[F_1 \left(\frac{w_e}{h} \right) \frac{h}{w_e} + \sqrt{1 + \left(\frac{2h}{w_e} \right)^2} \right] \tag{31}$$

where $\eta_0 = 120\pi$ is the wave impedance in free space. In these expressions, the functions $a(w_e/h)$, $b(\epsilon_r)$, and $F_1(w_e/h)$ are defined in Eqs. (23), (24), and (26), respectively, with the normalized strip width w/h replaced by the corrected normalized strip width w_e/h . It is observed that the effect of the strip thickness on ϵ_e and Z_0 is insignificant for small values of t/h . However, the effect of strip thickness is significant on conductor loss in the microstrip line.

3.1.10. Effect of Dispersion. The effect of frequency (dispersion) on ϵ_e and Z_0 has been described in a number of publications. The accurate expressions in Ref. 18 for $Z_0(f)$ and in Ref. 19 for $\epsilon_e(f)$ are

$$Z_0(f) = Z_0 \cdot \frac{\epsilon_e(f) - 1}{\epsilon_e - 1} \cdot \sqrt{\frac{\epsilon_e}{\epsilon_e(f)}} \tag{32}$$

$$\epsilon_e(f) = \epsilon_r - \frac{\epsilon_r - \epsilon_e}{1 + (f/f_{50})^m} \tag{33}$$

where

$$f_{50} = \frac{f_{k,TM_0}}{0.75 + [0.75 - (0.332/\epsilon_r^{1.73})]w/h}$$

$$f_{k,TM_0} = \frac{c \cdot \tan^{-1} \left(\epsilon_r \sqrt{\frac{\epsilon_e - 1}{\epsilon_r - \epsilon_e}} \right)}{2\pi h \sqrt{\epsilon_r - \epsilon_e}}$$

$$m = m_0 m_c$$

$$m_0 = 1 + \frac{1}{1 + \sqrt{w/h}} + 0.32 \left(\frac{1}{1 + \sqrt{w/h}} \right)^3$$

$$m_c = \begin{cases} 1 + \frac{1.4}{1 + w/h} \left[0.15 - 0.235 \exp \left(-\frac{0.45f}{f_{50}} \right) \right] & \text{for } w/h \leq 0.7 \\ 1 & \text{for } w/h > 0.7 \end{cases}$$

where Z_0 and ϵ_e are the quasi-TEM wave values obtained earlier, and c is the velocity of light in free space.

3.1.11. Effect of Enclosure. Most microstrip circuit applications require a metallic enclosure for hermetic sealing, mechanical strength, electromagnetic shielding, mounting connectors, and ease of handling. Because the fringing electromagnetic fields are prematurely terminated on the enclosure walls, both the top cover and side walls tend to lower impedance and effective dielectric constant.

Equations for evaluating the effect of the topcover and sidewalls on Z_0 and ϵ_e are provided in Refs. 6 and 7.

When the topcover and sidewalls are placed in close vicinity of the microstrip line, the line parameters may vary significantly. It is recommended to leave at least 10 times the substrate thickness between the circuit and the cover [11].

A metal box is actually a microwave cavity, which resonates at some particular frequencies corresponding to its resonant modes. The size of the box should be chosen in such a way that the signal frequency does not coincide with the resonant frequencies. When this cannot be done, the resonant modes can be damped by placing absorbing materials at carefully selected locations.

3.1.12. Attenuation. The attenuation constant of a transmission line is usually defined as

$$\alpha \approx \frac{P_{\text{loss}}}{2P(z)} = \frac{\text{power loss per unit length}}{2(\text{power transmitted})} \tag{34}$$

Attenuation in microstrip lines is caused by three loss components: conductor loss, dielectric loss, and radiation loss. They are discussed briefly next.

3.1.12.1. Ohmic Losses. Within the conductors, these result from the finite conductivity σ of the metal. The following approximate expression (9) is found sufficient in most situations

$$\alpha_c \approx 8.686 \frac{R_s}{wZ_0} \text{ dB/m} \tag{35}$$

where $R_s = \sqrt{\omega\mu/2\sigma}$ is the metal wall surface resistance.

3.1.12.2. Dielectric Losses. Produced by the energy dissipated within the substrate, these are proportional to its dielectric loss tangent $\tan \delta$ [9]

$$\alpha_d \approx 27.3 \cdot \frac{\epsilon_e - 1}{\epsilon_r - 1} \cdot \frac{\epsilon_r}{\sqrt{\epsilon_e}} \cdot \frac{f}{c} \cdot \tan \delta \text{ dB/m} \tag{36}$$

where c is the velocity of light in free space, and f is the frequency. The dielectric loss due to the substrate is normally very small compared with the conductor loss. However, the dielectric loss in silicon substrates (used for monolithic MICs) is usually of the same order as or even larger than the conductor loss because of the large loss tangent $\tan \delta$ of the silicon wafers.

3.1.12.3. Radiation Losses. An infinite straight microstrip line propagating the dominant quasi-TEM mode does not radiate. However, at every discontinuity, higher-order modes are excited, some of which will radiate part of the power.

3.2. Frequency Range of Operation

Like any other transmission line, microstrip lines cannot be utilized above a certain upper frequency limit. The maximum frequency of operation of a microstrip line is

limited because of several factors such as effects of dispersion, excitation of higher-order modes, and radiation losses.

The frequency at which significant coupling occurs between the quasi-TEM mode and the lowest-order TM surface wave is given by [20]

$$f_T = \frac{300 \tan^{-1}(\epsilon_r)}{\pi h \sqrt{2\epsilon_r - 2}} \quad (37)$$

where f_T is in gigahertz and h is in millimeters.

For a sufficiently wide microstrip line, a transverse resonant mode can exist that can also couple strongly to the quasi-TEM microstrip mode. By employing the transverse resonance equivalent circuit model, and taking into account the microstrip side-fringing effect, the cutoff frequency of the transverse resonant mode can be easily derived [20] as follows

$$f_c \approx \frac{300}{\sqrt{\epsilon_r}(2w + 0.8h)} \quad (38)$$

where f_c is in gigahertz and w and h are in millimeters.

For a microstrip line, radiation losses become significant at frequencies higher than [9]

$$f = 2.14 \cdot \frac{(\epsilon_r)^{0.25}}{h} \quad (39)$$

where f is in gigahertz and h is in millimeters.

3.3. Power-Handling Capability

Although microstrip lines are not as well suited for high-power application as are waveguides or coaxial lines of comparable cross section, they can be used for some medium-power applications. A 50- Ω microstrip on a 25-mil-thick alumina substrate can handle a few kilowatts of power [6].

The power-handling capacity of a microstrip line, like that of any other dielectric-filled transmission line, is limited by dielectric breakdown and by heating caused by ohmic and dielectric losses. An increase in the temperature due to conductor and dielectric losses limits the average power-handling capability of the microstrip line, while the breakdown between the strip conductor and ground plane limits the peak power-handling capability.

The average power-handling capability of microstrip lines is determined by the temperature rise of the conductor strip and the dielectric substrate. The transmission-line losses, the thermal conductivity of the substrate material, the surface area of the strip, and the temperature of the medium surrounding the microstrip line are the main factors determining the average power-handling capability of microstrip lines. Therefore, dielectric substrates with low-loss tangent and larger thermal conductivity will enhance the average power-handling capability of microstrip lines.

The peak voltage that can be applied without causing dielectric breakdown determines the peak power-handling capability of microstrip lines. Thick substrates can

support higher voltages. Therefore, low-impedance lines and lines on thick substrates have generally larger peak power-handling capability.

3.4. Other Types of Microstrip Lines

Several derivatives of microstrip lines are being used in MICs. These include inverted and suspended microstrip lines, a multilayered microstrip, a thin-film microstrip, and a valley microstrip line. These structures are briefly described in Refs. 6 and 7.

4. OTHER TOPICS

In actual microstrip circuits, various types of transmission line discontinuities, such as open ends, gaps, steps in width, bends, T junctions, and cross-junctions are frequently encountered. In the design of microstrip circuits, a complete understanding of the characteristics of microstrip discontinuities included in the circuits is necessary. At low frequencies, discontinuities can be represented by lumped-element equivalent circuits based on quasistatic models. However, at high frequencies, a more rigorous characterization of frequency-dependent parameters such as the scattering parameters is required. Various methods including quasistatic and full-wave analysis methods for characterizing microstrip discontinuities are described in Refs. 6–10 and 17.

Microstrip line is now the most widely used structure for microwave systems in radar and communication purposes. Examples of passive circuits include filters, impedance transformers, hybrids, couplers, power dividers/combiners, delay lines, baluns, and circulators. Amplifiers, oscillators, and mixers employing solid-state devices (diodes and transistors) constitute the other class. Microstrip-based antennas have also found wide applications [11,21,22]. Descriptions of the analysis and design of passive and active microstrip circuits and their applications in MICs and monolithic MICs (MMICs) are contained in numerous publications [6–10]. For further knowledge of the design and fabrication process of MICs and MMICs, see Refs. 23 and 24.

There have been a number of sophisticated microwave computer-aided design (CAD) packages available on the market. They can be used for analysis purpose (the user describes a structure and determines its electrical response) and synthesis purpose (the software determines a physical structure meeting a special electrical behavior). A survey of available CAD softwares for microwave circuits is given in Refs. 7 and 9.

In addition to the microstrip lines, two other types of planar transmission lines are also widely used today in various microwave systems. They are the *slotlines and coplanar lines* (coplanar waveguides and coplanar strips). Hybrid combination of these planer lines with microstrip lines allows flexibility of circuit design and improves the performance of some circuit functions. Coplanar lines have received particular attention because of their many appealing properties. These include low dispersion, high flexibility in the design of characteristic impedance, and ease of connecting shunt and series lumped elements, or

active devices without using via holes. Consequently, coplanar lines are used commonly in MMICs in conjunction with semiconductor devices, which are also coplanar in nature. Descriptions of the analysis and design of slotline and coplanar line circuits can be found in Ref. 6 for further study.

It is worth mentioning finally that the major portion of this article is devoted to the analysis and design aspects of the microstrip line with applications to the microwave integrated circuits. However, high-speed digital circuits include, as do microwave integrated circuits, active and passive circuit elements interconnected by sections of strip and other microstrip transmission lines having a wide range of characteristic impedances. The speed of digital circuits has steadily increased since the late 1980s; hence, the inductive effects on interconnect line performance due to line inductance that were previously assumed to be insignificant may be important. Moreover, the resulting junctions and discontinuities, and the electromagnetic coupling between the interconnects, contribute to reflections, signal delay and distortion, and crosstalk, which can degrade the circuit and system performance. The same problems are encountered in printed-circuit boards, single- and multichip modules, and other packages. Therefore, a high-speed circuit design and simulation must incorporate these interconnections. The analysis of the microstrip line in this article applies to the vast area of electrical interconnections for printed-circuit boards, single and multichip modules, and other packages. Examples of these additional applications can be found in Refs. 25–29, listed below.

BIBLIOGRAPHY

1. R. E. Collin, *Field Theory of Guided Waves*, 2nd ed., IEEE Press, New York, 1991.
2. I. J. Bahl, Transmission lines, in K. Chang, ed., *Handbook of Microwave and Optical Components*, Wiley, New York, 1989.
3. S. B. Cohn, Characteristic impedance of shielded strip transmission lines, *IRE Trans. Microwave Theory Tech.* **MTT-2**: 52–55 (1954).
4. D. D. Grieg, Microstrip—a new transmission technique for the kilomegacycle range, *IRE Proc.* **40**:1644–1650 (1952).
5. Microwave integrated circuits, special issue, *IEEE Trans. Microwave Theory Tech.* **MTT-19** (1971).
6. K. C. Gupta, R. Garg, I. Bahl, and P. Bhartia, *Microstrip Lines and Slotlines*, 2nd ed., Artech House, Norwood, MA, 1996.
7. T. Edwards, *Foundations for Microstrip Circuit Design*, 2nd ed., Wiley, Chichester, UK, 1992.
8. R. K. Hoffmann, *Handbook of Microwave Integrated Circuits*, Artech House, Boston, 1987.
9. F. E. Gardiol, Design and layout of microstrip structures, *IEE Proc. H* **135**:145–157 (1988).
10. F. E. Gardiol, *Microstrip Circuits*, Wiley, New York, 1994.
11. J.-F. Zürcher and F. E. Gardiol, *Broadband Patch Antennas*, Artech House, Norwood, MA, 1995.
12. J. A. Navarro and K. Chang, *Integrated Active Antennas and Spatial Power Combining*, Wiley, New York, 1996.
13. H. A. Wheeler, Transmission line properties of parallel strips separated by a dielectric sheet, *IEEE Trans. Microwave Theory Tech.* **MTT-13**:172–185 (1964).
14. E. Yamashita and R. Mittra, Variational method for the analysis of transmission lines, *IEEE Trans. Microwave Theory Tech.* **MTT-16**:251–256, 1968.
15. E. Yamashita, Variational method for the analysis of microstrip like transmission lines, *IEEE Trans. Microwave Theory Tech.* **MTT-16**:529–535 (1968).
16. E. Yamashita and K. Atsuki, Analysis of microstrip-like transmission lines by nonuniform discretization of integral equation, *IEEE Trans. Microwave Theory Tech.* **MTT-24**: 195–200 (1976).
17. T. Itoh (ed.), *Numerical Techniques for Microwave and Millimeter-Wave Passive Structures*, Wiley, New York, 1989.
18. E. Hammerstad and O. Jensen, Accurate models for microstrip computer-aided design, *IEEE MTT-S Int. Microwave Symp. Digest*, 1980, pp. 407–409.
19. M. Kobayashi, A dispersion formula satisfying recent requirements in microstrip CAD, *IEEE Trans. Microwave Theory Tech.* **MTT-36**:1246–1250 (1988).
20. G. D. Vendelin, Limitations on stripline Q, *Microwave J.* **5**: 63–69 (1970).
21. I. J. Bahl and P. Bhartia, *Microstrip Antennas*, Artech House, Dedham, MA, 1980.
22. J. R. James and P. S. Hall, eds. *Handbook of Microstrip Antennas*, Peter Peregrinus, London, 1989.
23. P. H. Ladbrooke, *MMIC Design: GaAsFETs and HEMTs*, Artech House, Boston, 1989.
24. A. Sweet, *MIC and MMIC Amplifier and Oscillator Design*, Artech House, Norwood, MA, 1990.
25. A. J. Rainal, Transmission properties of balanced interconnections, *IEEE Trans. Compon. Hybrids Manuf. Technol.* **16**:137–145 (1993).
26. A. J. Rainal, Impedance and crosstalk of stripline and microstrip transmission lines, *IEEE Trans. Compon. Pack. Manuf. Technol. Part B* **20**:217–224 (1997).
27. J. M. Jong, B. Janko, and V. Tripathi, Equivalent circuit modeling of interconnects from time-domain measurements, *IEEE Trans. Compon. Hybrids Manuf. Technol.* **16**:119–126 (1993).
28. S. Voranantakul, J. L. Prince, and P. Hsu, Crosstalk analysis for high-speed pulse propagation in lossy electrical interconnections, *IEEE Trans. Compon. Hybrids Manuf. Technol.* **16**:127–136 (1993).
29. S. Voranantakul, and J. L. Prince, Efficient computation of signal propagation delay with overshoot- and undershoot-control in VLSI interconnections, *IEEE Trans. Compon. Hybrids Manuf. Technol.* **16**:146–151 (1993).

MICROSTRIP TRANSITIONS

ERIC L. HOLZMAN
Northrop Grumman Corporation
Baltimore, Maryland

1. INTRODUCTION

Microstrip transmission lines are used widely in microwave and millimeter-wave printed electronic circuits for routing electromagnetic signals between components such

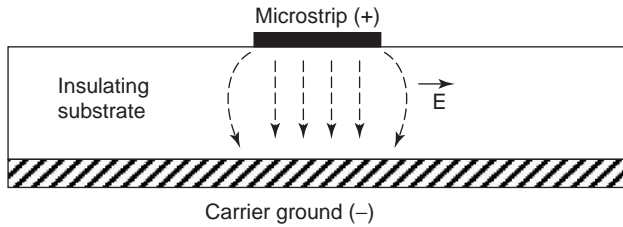


Figure 1. Microstrip transmission-line cross section.

as oscillators, amplifiers, and filters. As shown in Fig. 1, microstrip is a two-conductor transmission line. An insulating substrate separates the two conductors and supports a transverse field that is similar to the transverse electromagnetic (TEM) mode of a parallel-plate waveguide. A small portion of the transverse field permeates the air above the strip, thus making microstrip inhomogeneous. The dominant microstrip mode is a *quasi-TEM mode* that is slightly dispersive (the propagation constant is not a perfectly linear function of frequency). In general, this mode is broadband, with a cutoff frequency of 0 Hz. The first higher-order mode is a surface mode that propagates at a much higher frequency with a cutoff frequency that depends on the substrate's electrical thickness [1]. The TEM mode has two field components, both directed transversely. Figure 1 shows the electric field, oriented perpendicular to the conductors. The magnetic field is parallel to the conductors in the region between the strip and ground plane. Longitudinal current flows both in the strip and the ground plane. In the following discussion, we assume that only the quasi-TEM mode is propagating within the microstrip.

The *characteristic impedance* of a transmission-line mode is defined as the ratio of the mode's transverse electric and magnetic fields. Thus, two different transmission lines, such as microstrip and coaxial line, could have the same characteristic impedance but have very different field configurations. Typically, microstrip is dimensioned for a quasi-TEM mode characteristic impedance of 50 Ω . This impedance tends to decrease with frequency at a rate that depends on the substrate's electrical thickness. For substrates that are thin relative to a wavelength, the characteristic impedance is nearly constant over a wide frequency bandwidth.

One of microstrip's disadvantages is its lack of electrical isolation; the strip conductor is not completely surrounded by the ground plane. Consequently, microstrip circuits generally have to be housed in a conductive enclosure to prevent unwanted interference with other circuits in a microwave system. Coaxial or waveguide transmission lines provide the interconnections between different enclosed microstrip circuits. A *microstrip transition* is required to convert as efficiently as possible the microstrip electromagnetic properties to that of the interconnecting transmission line.

A well-designed microstrip transition converts the transverse field configuration and characteristic impedance of microstrip to that of the other transmission line over a desired frequency band of operation while maintaining low *insertion loss*, minimal radiation, and high

input *return loss*. Insertion loss, the amount of power exiting the transition, expressed as a fraction of the input level, should be less than 0.25 dB. Return loss, the amount of power reflected at the transition, expressed as a fraction of the input level, should exceed 15 dB. A good transition also is easy to fabricate, mechanically robust and insensitive to temperature variations.

Since the first microstrip circuits were constructed, a wide variety of transitions to other transmission lines have been developed. These transitions can be sorted into two main groups: (1) those that require a direct physical connection to the strip conductor and (2) those that use electromagnetic coupling to the strip conductor. Transitions to other TEM transmission lines such as coax most often use direct connections, which can provide very broadband performance. Transitions to waveguide tend to utilize electromagnetic coupling, which generally is more mechanically tolerant than a direct connection but is less broadband.

2. MICROSTRIP-TO-TEM TRANSMISSION LINES

Transitions between microstrip and other transmission lines propagating the TEM mode can have very wide *bandwidth* because the TEM-mode field configuration and characteristic impedance remain constant with frequency. In general, the upper frequency of these transitions is limited by the length of the electrical path connecting the ground conductors and by the tendency of the interconnections to radiate. In this section, we will study a number of microstrip transitions to other TEM structures.

2.1. Transitions to Coaxial Line

The coaxial transmission line provides an inexpensive and mechanically flexible means for making interconnections below 20 GHz. Figure 2 shows the cross section and electric field configuration of the dominant TEM mode in coax. At first glance, the field configuration of coax seems quite different than that of microstrip, but both have their primary field confined between two conductors. Unlike microstrip, the coaxial field is uniformly distributed around

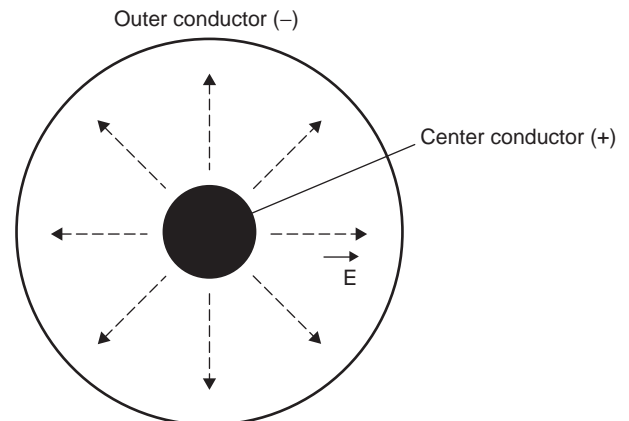


Figure 2. Coaxial transmission-line cross section.

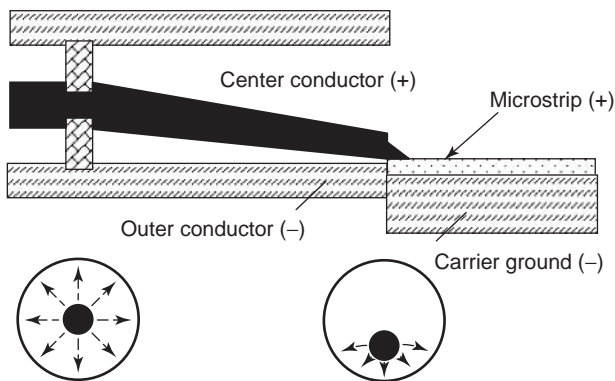


Figure 3. Microstrip-to-coax transition. (After Eisenhart [2].)

the center conductor. *Eisenhart's transition*, shown in Fig. 3, matches the two field configurations by offsetting the coaxial line center conductor in a controlled manner, forcing the coaxial-line field to concentrate below the center conductor much like that in the microstrip line [2]. The style of this transition is termed *inline or edge launch*, since the coaxial line and microstrip have their longitudinal or propagational axes in line. Eisenhart's transition attains very high performance: he has demonstrated greater than 25 dB return loss up to 18 GHz. Such a transition is ideal for testing prototype microstrip circuits. However, its significant length and relatively high cost make it undesirable as a transition for inexpensive microwave circuit boards.

Most microwave circuit interfaces require neither the bandwidth nor the return loss of the Eisenhart transition. Figure 4 shows a common *edge launch transition* between a microstrip on a multilayer circuit board and a sub-miniature-A (SMA) coax. The board-mount connector includes much of the transition. The center conductor of the coax line is extended out for solder attachment to the microstrip. The coax ground contact is made with coax ground pins attached to the connector. Commonly, two pins are placed below the circuit board also. Because the circuit board in Fig. 4 has multiple layers, and the

microstrip ground plane is not the bottom layer, this transition connects the ground pins to metalized pads on the plane of the microstrip. The pads have drilled and plated holes or *vias* that carry the ground currents through the circuit board to the microstrip ground plane. The length of the ground path, and in particular, the separation of the ground pins determines the upper frequency of operation for this transition. A tuning stub (see Fig. 4), printed on the circuit board, can provide additional bandwidth. Without the stub, the return loss of this transition is better than 15 dB past 5 GHz. With the stub, the bandwidth can be extended to 7 GHz. How much additional bandwidth a stub provides depends on whether the transition can be constructed in a consistent and repeatable manner. If the stub length has to be adjusted on each circuit board, the manufacturing process is not sufficiently consistent. Liang et al. have performed extensive analytical investigations of edge-launched SMA coax-to-microstrip transitions [3]. They compensated capacitively for the parasitic inductance of the soldered coax center pin by increasing the microstrip linewidth. The measured return loss of their transition exceeded 15 dB up to 13 GHz.

Occasionally, a connector like that in Fig. 4 may be inadequate. The connector ground pathlength limits the upper frequency of operation. A *connectorless transition* like that shown in Fig. 5 has a much shorter path between the coax and microstrip grounds. This transition has a return loss of 15 dB up to 12 GHz for a 0.047-in. coax cable attached to microstrip on a 0.008-in.-thick Rogers 4003 substrate. The insertion loss at 12 GHz is less than 0.25 dB, which indicates that the transition is not suffering significant radiation. However, assembling the transition can be more difficult when miniature coax cable is used.

Edge-launch transitions, as their name belies, are limited to placement at the edge of a circuit board. *Vertical mount or orthogonal launch transitions* can be placed almost anywhere on a circuit board. Figure 6 shows a vertical mounted SMA coax transition. As with the edge launch connector, the vertical mount connector comes with an extended center conductor probe and four ground

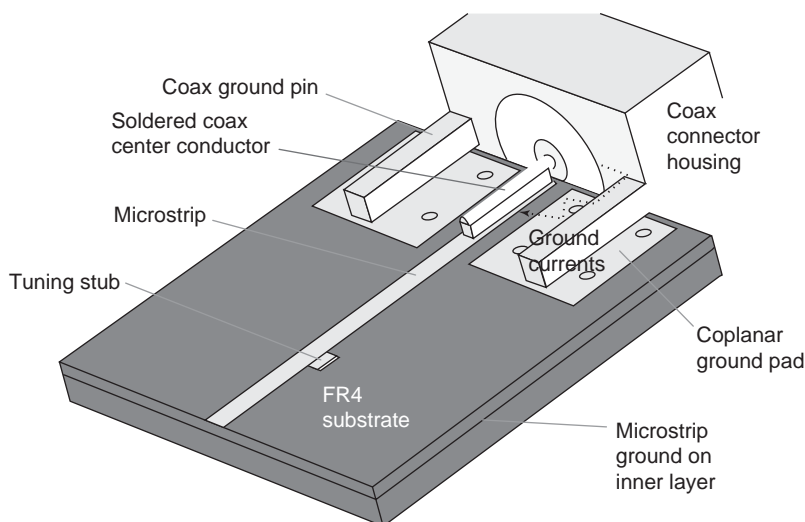


Figure 4. Multilayer circuit board mountable edge launch microstrip-to-coax transition.

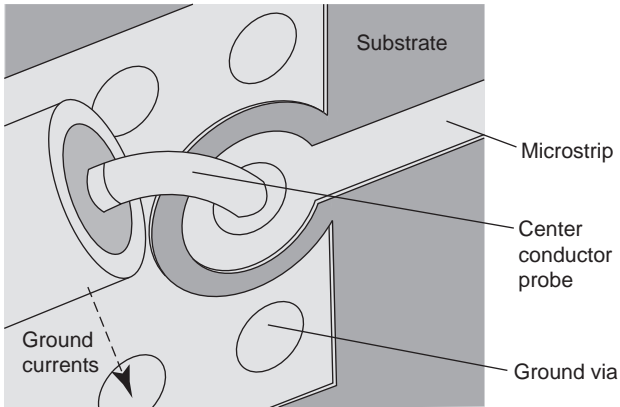


Figure 5. Inline, connectorless, microstrip-to-coax transition.

pins. The center conductor and ground pins pass through vias in the circuit board and are soldered to pads on the top layer. Within the circuit board, they propagate the electromagnetic wave as a five-wire transmission line. On all intervening conductor layers, it is important to clear metalization away so as not to short(-circuit) out the field. The transition shown in Fig. 6, with a 0.2-in. ground pin spacing, has a return loss greater than 25 dB to nearly 6 GHz. As with edge launch connectors, the pin-to-pin spacing establishes the maximum frequency of operation. An SMP connector, with 0.1-in. ground pin spacing, can be made to work up to 18 GHz. An indication that the spacing is too great or the circuit board too thick is excess insertion loss caused by radiation within the board. One can fix this problem and better confine the field by inserting circuit board vias close to the center conductor probe. The vias effectively replace the connector ground pins as carriers of the ground current within the circuit board.

2.2. Transitions to Other Planar Transmission Lines

Transitions from microstrip to other planar transmission lines are often required on multilayer circuit boards,

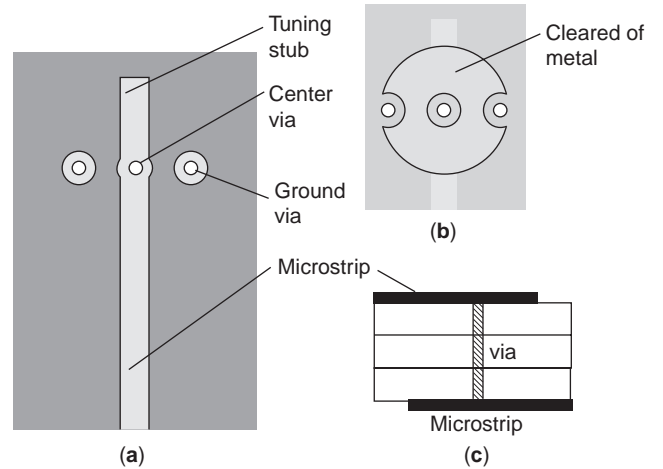


Figure 7. Microstrip-to-microstrip transition through a multi-layer circuit board: (a) top/bottom-layer metallization; (b) ground-layer metallization clearance; (c) circuit board cross section.

where it may be desirable to propagate the microwave energy within the circuit board. Figure 7 shows a *microstrip-to-microstrip transition* that passes vertically through a multilayer circuit board. Essentially, the transition comprises a pair of transitions from microstrip to three-via transmission line. The via separation and a microstrip open-circuited stub serve to tune the transition. The return loss of the transition on a circuit board made from three layers of FR4, 0.062 in. thick, exceeds 25 dB to nearly 5 GHz.

Transitions from *microstrip to coplanar waveguide* (CPW) are relatively common and straightforward to design. Via holes often are used to connect the microstrip ground to the coplanar waveguide ground as shown in Fig. 8. Such transitions are found on monolithic microwave integrated circuits (MMICs), which require wafer-probe-compatible CPW for their RF input and output [4]. Ellis et al. developed a CPW transition without vias for MMICs using a slotline to form a CPW as shown in Fig. 9

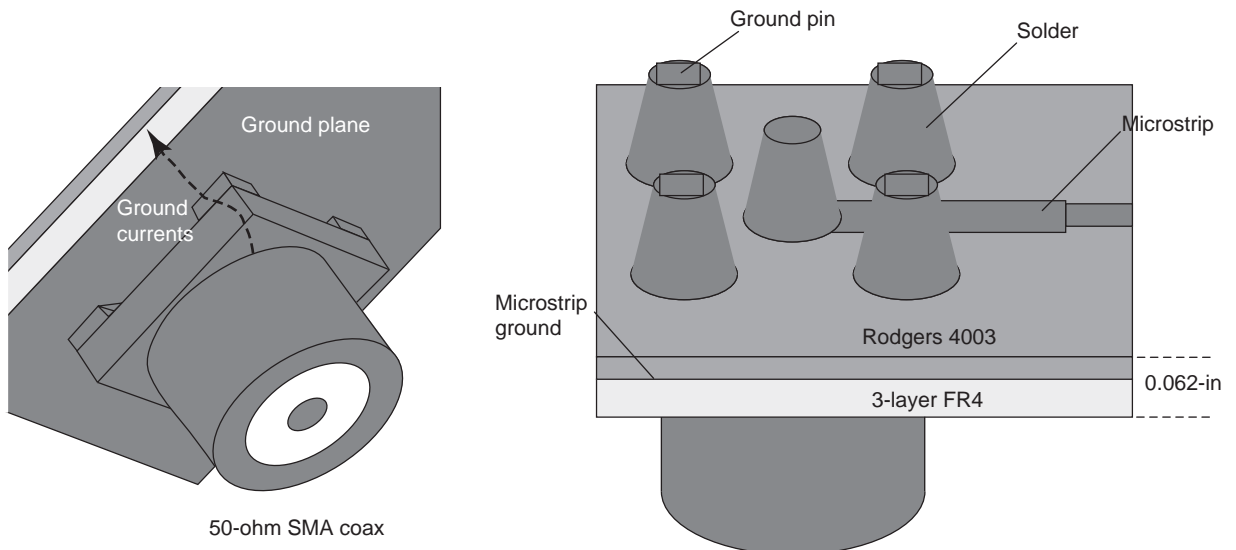


Figure 6. Vertical mount, microstrip-to-coax transition.

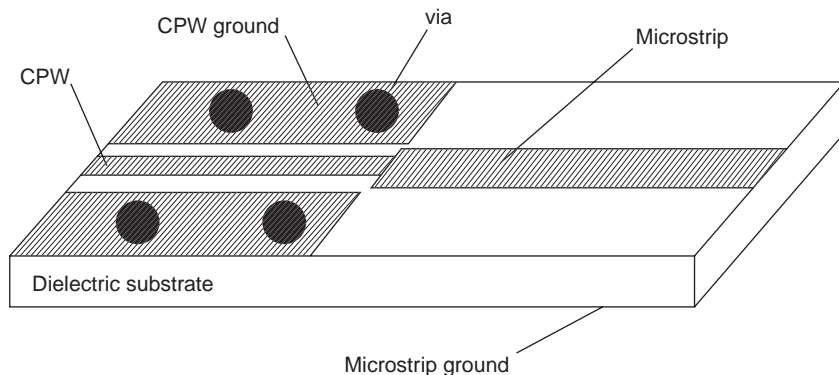


Figure 8. Microstrip-to-coplanar waveguide transition.

[5]. Their transition is unusual because it relies on coupling. The CPW is formed in the ground plane of the microstrip, and the microstrip conductor is coupled orthogonally to a single slotline that forms the pair of gaps in the CPW transmission line.

Transitions from microstrip to less commonly used planar transmission lines exist also. Drach and Koscica developed a transition between *microstrip and inverted microstrip* line for millimeter-wave applications [6].

3. MICROSTRIP TO WAVEGUIDE

Microstrip-to-waveguide transitions are used for the same reasons that transitions to coax are used—as interconnects between sealed modules or modules and antennas. However, unlike coaxial line, waveguides are used mostly above 20 GHz, often in the millimeter-wave bands, where their lower loss becomes a significant advantage.

Waveguide is formed from a single conductor, so its properties are markedly different than those of coax line.

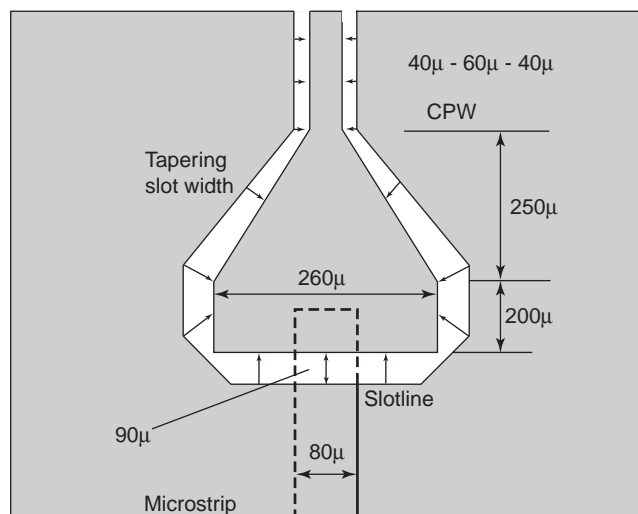


Figure 9. Microstrip-to-coplanar waveguide transition that operates at 75–110 GHz. (Source: T. J. Ellis, J. P. Raskin L. P. B. Katehi, and G. M. Rebeiz, A wideband CPW-to-microstrip transition for millimeter-wave packaging, 1999 *MTT-S International Microwave Symposium Digest*, Vol. 2, pp. 629–632. © 1999 IEEE. Reprinted with permission.)

The dominant propagating mode, typically of the transverse electric (TE) configuration, has a cutoff frequency below which the waveguide is highly attenuative to EM signals. Figure 10 shows rectangular and circular waveguides and their dominant-mode field configurations. Most transitions are designed to operate within the frequency band of dominant-mode propagation only, which is at most 2 : 1 for rectangular waveguide and 1.3 : 1 for circular waveguide.

The impedance characteristics of waveguide modes tend to make transitions more challenging to design. First, the *dispersive* behavior of waveguide means that the characteristic impedance of its modes change with frequency; moreover, the characteristic impedances of standard guides are much higher than 50Ω, typically a few hundred ohms for TE modes. Consequently, the bandwidth for most microstrip-to-waveguide transitions rarely equals the dominant mode bandwidth.

3.1. Orthogonal Transitions to Waveguide

A transition to rectangular waveguide is often used as the RF interface between a millimeter-wave transmitter or receiver and the antenna. Figure 11 shows an *orthogonal or right-angle transition*. The microstrip extends through a narrow channel into the waveguide. The channel dimensions are made sufficiently small so that only the microstrip mode can propagate over the band of operation. Within the waveguide, the microstrip ground is removed, so the microstrip or probe behaves like an antenna. Because the probe will radiate equally well both up and down

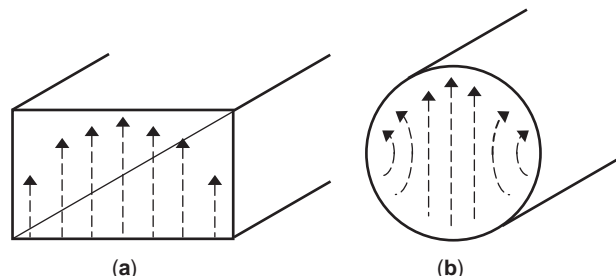


Figure 10. Commonly used waveguides with dominant-mode electric fields: (a) rectangular and TE₁₀ mode; (b) circular and TE₁₁ mode.

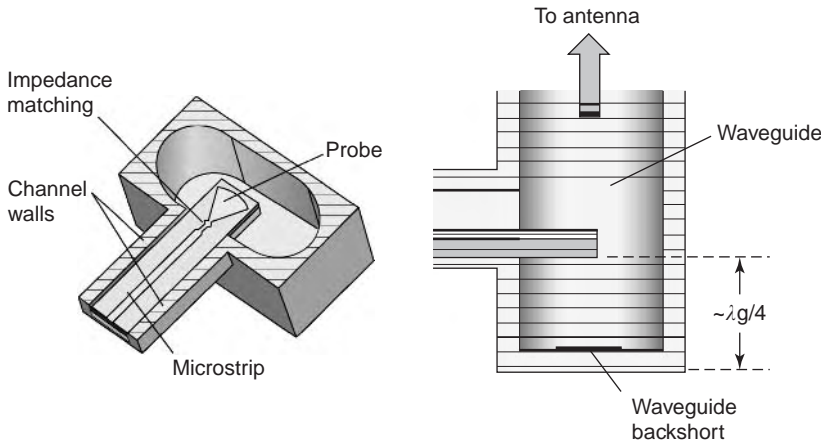


Figure 11. Transition from microstrip to full-radius rectangular waveguide.

the waveguide, a backshort (waveguide short circuit) is placed in the undesired direction approximately a quarter-wavelength away from the probe. An impedance tuning section on the probe circuit board, just at the input to the waveguide, and a fan-shaped probe increase the transition's bandwidth. This transition can be tuned to operate over a 40% bandwidth with better than 25 dB return loss.

In fabricating this type of transition, one must be sure that the microstrip ground plane makes electrical contact with the channel surface to avoid undesired radiative effects. The probe shown in Fig. 11 is fabricated on a multilayer substrate, and the microstrip ground plane is not the bottom layer. To guarantee contact between the microstrip ground and the channel floor, one can drill via holes on both sides of the microstrip. Also, to reduce the machining cost, the waveguide can be fully radiused as it is in the figure.

The orthogonal transition works well for *circular waveguide* also as shown in Fig. 12. Circular waveguide is easier to machine than rectangular waveguide, and one can use a commercially available, adjustable tuner, or simple dowel as the backshort. The primary disadvantage of circular waveguide is bandwidth related. Since the circular waveguide dominant (TE_{11})-mode and first higher-order (TM_{01})-mode cutoff frequencies are more closely spaced than those in the rectangular waveguide, the transition

bandwidth will be less. The transition illustrated in Fig. 12 can provide a return loss of more than 25 dB over a 20% bandwidth. Also, unlike rectangular waveguide, circular waveguide's polarization is arbitrary, so discontinuities will excite cross-polarized fields. A short section of straight waveguide to the antenna is best.

The transitions in Figs. 11 and 12 require *waveguide backshorts* spaced about one quarter-wavelength away from the probe. The position of the backshort must be controlled precisely to get the lowest insertion loss through the transition. Further, the backshort can be the tallest feature in an otherwise very thin module. Consequently, transitions that do not require backshorts or are insensitive to backshort position have been developed. Park and Holzman developed two transitions shown in Fig. 13 that use a slot printed in the microstrip ground plane to excite the rectangular waveguide [7,8]. Neither transition requires a precisely placed backshort, although both enclose the transition in a rectangular cavity to contain any unwanted radiation. The cavity dimensions are chosen so that no modes are resonant in the frequency band of operation. For standard rectangular waveguide sizes, the characteristic impedance of the TE_{10} mode is several hundred ohms, so one cannot expect a good match if a 50-Ω microstrip line is centered over the waveguide. Since the slot field amplitude varies sinusoidally across

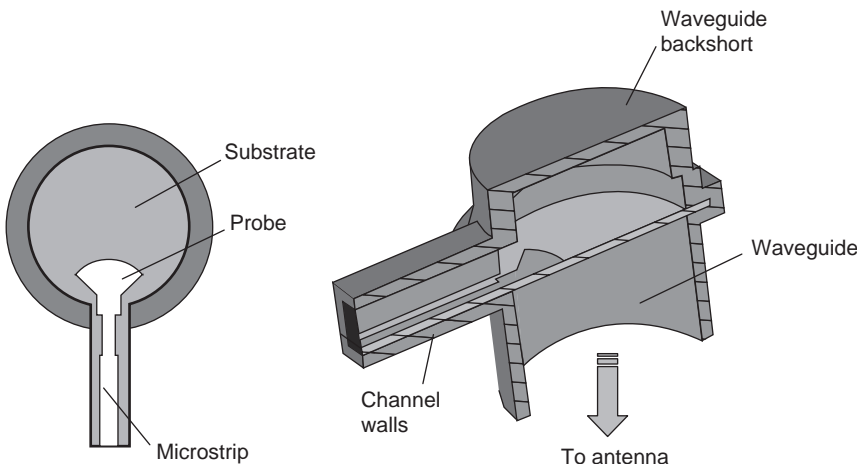


Figure 12. Microstrip-to-circular waveguide transition.

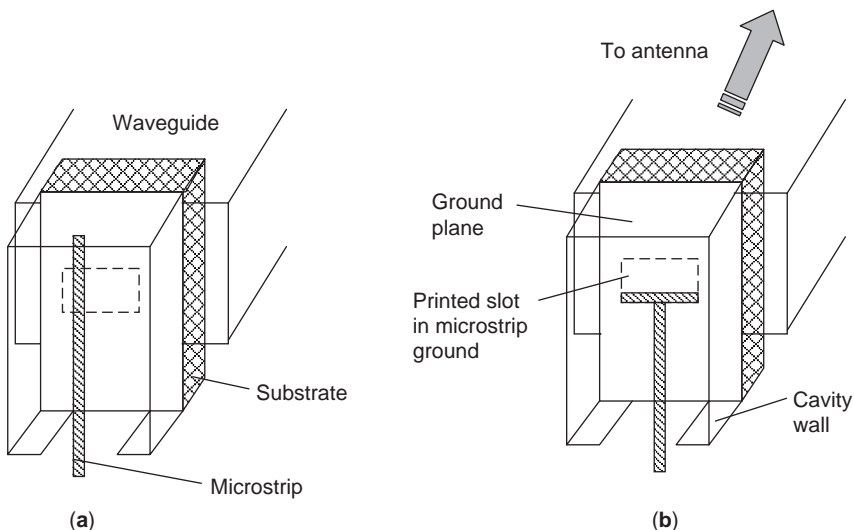


Figure 13. Microstrip-to-rectangular waveguide transitions using printed slot coupling: (a) offset strip; (b) tee strip. (After Park and Holzman [7,8].)

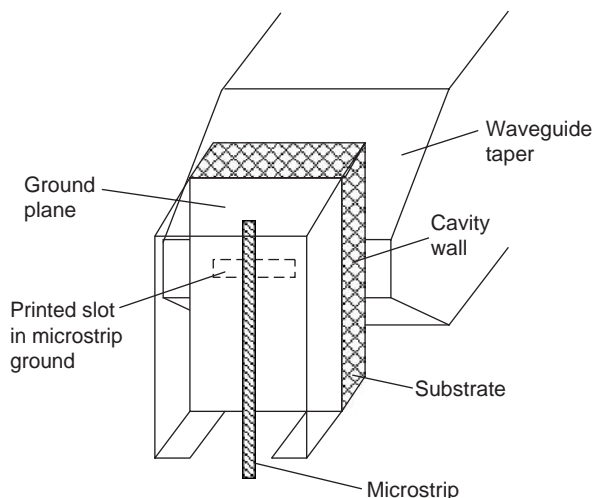


Figure 14. Microstrip-to-rectangular waveguide transition using printed slot coupling and waveguide taper. (After Davidovitz [10].)

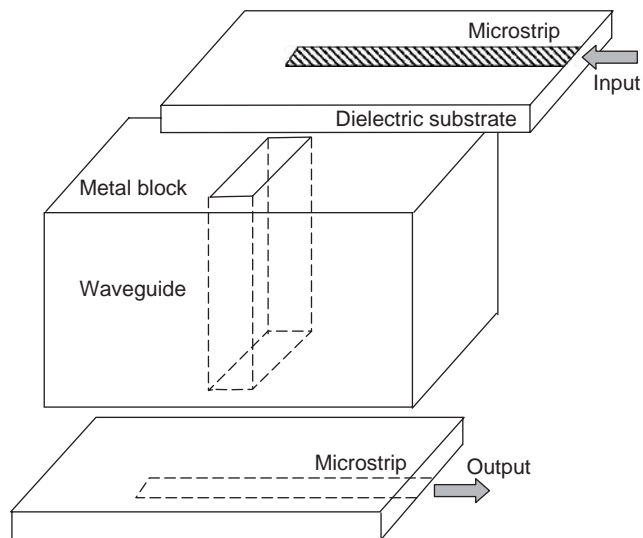


Figure 15. Microstrip-to-microstrip transition using waveguide. (After Davidovitz et al. [11].)

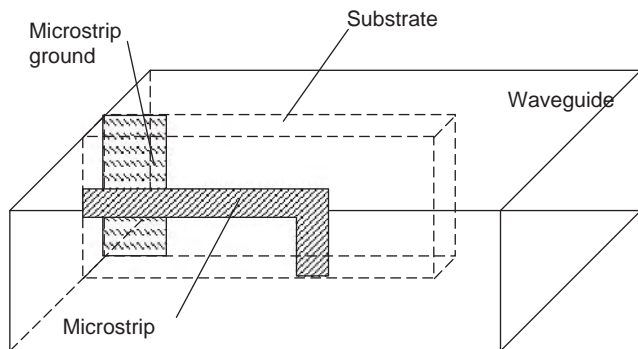


Figure 16. Inline, microstrip-to-waveguide transition. (After Ho and Shih [12].)

the length of the slot, while the magnetic field is essentially constant, one can offset the microstrip line as in Fig. 13a, and thereby lower the impedance presented to the strip. In Fig. 13b, a dipole-like structure terminates the microstrip line. Adjustment of the dipole position and arm-length matches the transition. In both transitions, all critical dimensions are photolithographically controlled with high accuracy. The transitions are extremely compact, but they also are narrowband, providing high return loss over less than a 10% bandwidth. Villegas et al. designed an end-launched transition that is much like Park and Holzman's and achieved a bandwidth of 10% centered around 45 GHz [9].

Davidovitz overcame the bandwidth limitation in the Park-Holzman transitions by adding a waveguide taper as shown in Fig. 14 [10]. Davidovitz reduced the waveguide height and mode impedance adjacent to the slot so that a centered microstrip could be matched. He flared the reduced height waveguide to the desired height using a tapered structure. His transition has a measured return loss exceeding 15 dB over a 50% bandwidth. Although Davidovitz' transition does not require a waveguide backshort, the length of his taper is about four TE_{10} mode wavelengths at the center of the band. To

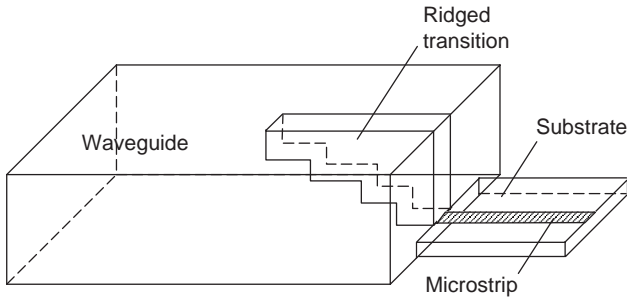


Figure 17. Inset, microstrip-to-waveguide transition using a ridged waveguide transition.

save space, one could use a waveguide quarter-wave transformer instead of a taper at the cost of reduced bandwidth.

Davidovitz has used a similar approach to create a microstrip-to-microstrip transition through a thick metal plate as shown in Fig. 15 [11]. A reduced-height waveguide provides strong coupling between two microstrip lines but the bandwidth is very narrow, only a couple of percent.

3.2. Inline Transitions to Waveguide

Another type of microstrip-to-waveguide transition is the *inline* topology shown in Fig. 16 [12]. This particular structure is constructed by inserting the microstrip substrate in line with the waveguide, and a printed circuit version of a current loop couples to the TE₁₀ waveguide mode. The end of the loop must make electrical contact with the floor of the waveguide. This transition has about a 30% bandwidth.

The transition illustrated in Fig. 17 uses a section of ridged waveguide to transition to standard rectangular waveguide [13]. The principle of operation is similar to that used by Eisenhart in his transition to coaxial line [2]. The electric field concentrates under the ridge, and as the ridge depth increases, the field begins to resemble that of the microstrip mode. Electrical contact is necessary between the microstrip line and the ridge.

Figure 18 shows another inline transition developed by Holzman, in this case, to a parallel-plate waveguide feeding a TEM horn radiator [14,15]. A microstrip and its substrate protrude through a hole in a metalized faceplate. The microstrip and its ground plane are shaped and flared such that the electric field is rotated 90°, from the microstrip mode into a parallel-plate TEM mode, which

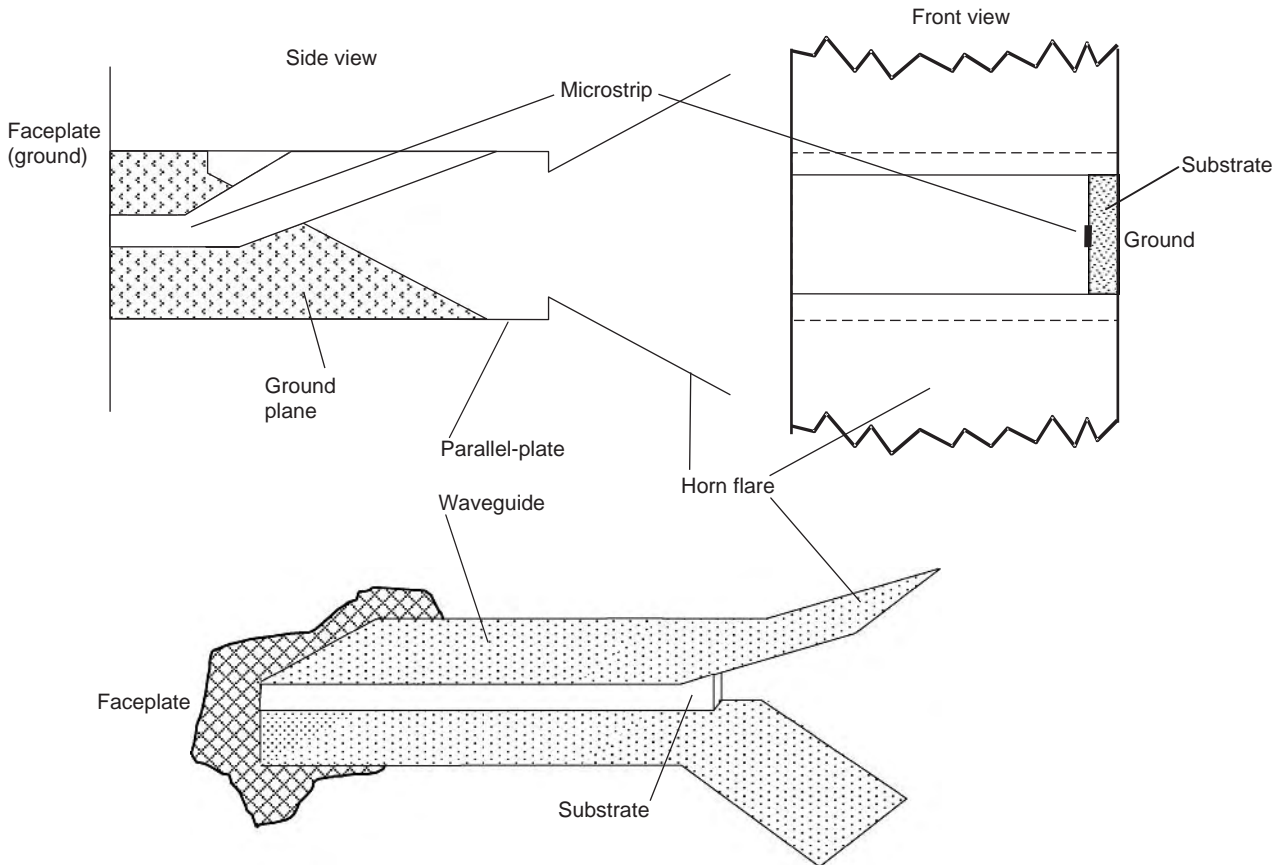


Figure 18. Inset, microstrip-to-parallel-plate waveguide transition feeding a TEM horn antenna. (Source: E. L. Holzman, A wide band TEM horn array radiator with a novel microstrip feed, *IEEE International Conference on Phased Array Systems and Technology Digest*, May 2000, pp. 441–444. © 2000 IEEE. Reprinted with permission.)

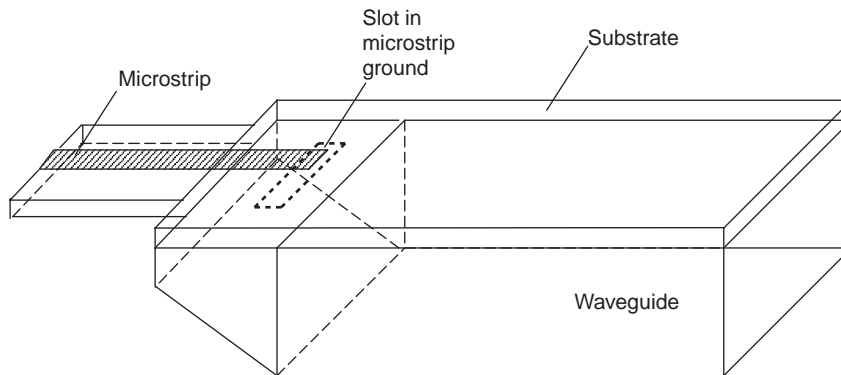


Figure 19. Inline, microstrip-to-waveguide transition using aperture coupling. (After Lynch [17].)

excites the flared horn. Because both the microstrip and parallel plate transmission lines propagate the TEM mode, this transition is very broadband, achieving a predicted bandwidth of 5 : 1. The transition's length must be at least a half-wavelength at the lowest frequency of operation. Because the field distribution is uniform in the parallel-plate waveguide, the transition works just as well whether the substrate is placed on the waveguide edge or centerline (see Fig. 18). Further, two or more substrates can be placed within a single parallel-plate waveguide, and the energy will be combined over the bandwidth of the transition. The inspiration for Holzman's transition was a similar transition to rectangular waveguide developed by van Heuven [16].

Figure 19 shows an inline transition that uses a printed slot in the microstrip ground plane to couple to a waveguide [17]. The substrate ground plane forms the upper surface of part of the rectangular waveguide.

4. CONCLUSION

Historically, transition design was an empirical effort, requiring time-consuming building, testing, tuning, and iteration of prototype circuits. Today, most transitions are designed with the aid of commercially available, highly accurate and fast three-dimensional, generalized electromagnetic software [18]. The first hardware prototype is built only after the transition design has been optimized on a computer. Further, the software affords those with new ideas the opportunity to evaluate them quickly. Thus, although many different microstrip transitions have been described in this article, one can expect to see new designs in the future.

BIBLIOGRAPHY

1. R. K. Hoffman, *Handbook of Microwave Integrated Circuits*, Artech House, Norwood, MA, 1987, pp. 181–187.
2. R. L. Eisenhart, A better microstrip connector, *IEEE MTT-S Int. Microwave Symp. Digest*, 1979, pp. 318–320.
3. H. Liang, K. Laskar, H. Barnes, and D. Estreich, Design and optimization for coaxial-to-microstrip transition on multi-layer substrates, *IEEE MTT-S Int. Microwave Symp. Digest*, 2001, Vol. 3, pp. 1915–1918.
4. A. M. E. Safwata, K. A. Saki, W. Johnson, and C. H. Lee, Novel design for coplanar waveguide to microstrip transition, *IEEE MTT-S Int. Microwave Symp. Digest*, 2001, Vol. 2, pp. 607–610.
5. T. J. Ellis, J. P. Raskin, L. P. B. Katehi, and G. M. Rebeiz, A wideband CPW-to-microstrip transition for millimeter-wave packaging, *IEEE MTT-S Int. Microwave Symp. Digest*, 1999, Vol. 2, pp. 629–632.
6. W. C. Drach and T. E. Kosciwa, Transitioning between microstrip and inverted microstrip, *IEEE Microwave Guided Wave Lett.* 1(3):49–50 (1991).
7. P. K. Park and E. L. Holzman, *End Launched Microstrip Line (or Stripline) to Waveguide Transition Using a Cavity Backed Slot Fed by an Offset Microstrip Line*, U.S. Patent 5, 724, 049 (1998).
8. P. K. Park and E. L. Holzman, *End Launched Microstrip Line (or Stripline) to Waveguide Transition Using a Cavity Backed Slot Fed by a T-Shaped Microstrip Line*, U.S. Patent 5, 726, 664 (1998).
9. F. J. Villegas, D. I. Stones, and H. A. Hung, A novel waveguide-to-microstrip transition for low-cost millimeter-wave and MMIC applications, *IEEE MTT-S Int. Microwave Symp. Digest*, 1997, pp. 739–742.
10. M. Davidovitz, Wide-band waveguide-to-microstrip transition and power divider, *IEEE Microwave Guided Wave Lett.* 6(1):13–15 (1996).
11. M. Davidovitz, R. A. Sainati, and S. J. Fraasch, A non-contact interconnection through an electrically thick ground plate common to two microstrip lines, *IEEE Trans. Microwave Theory Tech.* 43(4):753–759 (1995).
12. T. Q. Ho and Y. Shih, Analysis of microstrip line to waveguide end launchers, *IEEE Trans. Microwave Theory Tech.* 36(3):561–567 (1988).
13. M. V. Schneider, B. Gance, and W. F. Botman, Microwave and millimeter wave hybrid integrated circuits for radio systems, *Bell Syst. Tech. J.* 48:1703–1726 (1969).
14. E. L. Holzman, A wide band TEM horn array radiator with a novel microstrip feed, *IEEE Int. Conf. Phased Array Systems Technical Digest*, 2000, pp. 441–444.
15. E. L. Holzman, *Broadband Antenna Element, and Array Using Such Elements*, U.S. Patent 5,898,409 (1999).
16. J. H. C. van Heuven, A new integrated waveguide-microstrip transition, *IEEE Trans. Microwave Theory Tech.* 30(3):144–147 (1976).
17. J. J. Lynch, *Method and Apparatus for Coupling Strip Transmission Line to Waveguide Transmission Line*, U.S. Patent 6, 509, 809 B1 (2003).

18. D. G. Swanson and W. J. R. Hofer, *Microwave Circuit Modeling Using Electromagnetic Field Simulation*, Artech House, Norwood, MA, 2003.

FURTHER READING

- J. S. Izadian and S. M. Izadian, *Microwave Transition Design*, Artech House, Norwood, MA, 1988.

MICROWAVE AND RADIO FREQUENCY MULTIPLIERS

D.G. THOMAS Jr.
Panasonic
Atlanta, Georgia
G.R. BRANNER
University of California
Davis, California
B.P. KUMAR
Sacramento State University
Sacramento, California

Frequency multipliers are harmonic generators that produce various frequency multiples of an input (fundamental) frequency. These devices are employed in such diverse applications as electronic instruments, designing radar, communications, and electronic warfare systems. High-frequency signals are generated from lower-frequency signals by harmonic multiplication, as demonstrated in the simple representation depicted in Fig. 1. In the development of such a device, the circuit designer typically seeks to maximize the power delivered to the output load at the N th harmonic.

The capability of optimization of multiplier performance, in and of itself, can improve the overall performance of a system. Such potential for enhanced performance leads to the optimization process becoming a crucial consideration in the development of the system. Multiplier performance is dependent on the nonlinear device producing the required frequency harmonics and the design technique employed. The most important design considerations in frequency multipliers are conversion gain, harmonic suppression, output power, efficiency, DC bias requirements, and bandwidth. Frequency multipliers exhibiting high conversion gain, good harmonic suppression, wide bandwidth when required, and high efficiency are achieved from optimum designs. As will be discussed in this article, many authors give various, contradictory means of optimizing the performance of frequency multipliers.

One of the dominant operating parameters of a frequency multiplier is its conversion gain or conversion loss.

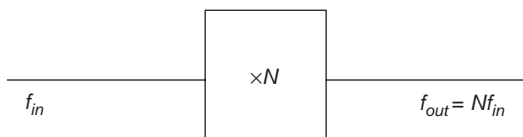


Figure 1. Simple harmonic multiplier.

The conversion gain is the ratio of the output power at the desired harmonic frequency to the input power at the fundamental frequency. It has been demonstrated that various parameters affecting the conversion gain include the bias level, the input power, the harmonic terminations, and the nonlinear device producing the frequency harmonics [1–7]. Techniques that maximize the conversion gain are necessary for the development of frequency multipliers.

With the advent of new active devices, such as the high-electron-mobility transistor (HEMT), the pseudomorphic high-electron-mobility transistor (PHEMT), and the heterojunction bipolar transistor (HBT), new multiplier designs incorporating these devices are desired. This has led to the emergence of new research areas where relatively little information has been reported in the literature. This presentation will address some of these areas. Some areas considered are the development of accurate nonlinear circuit models, identifying pertinent properties of the transistor, optimizing multiplier designs, and improving some of the existing design techniques.

1. APPLICATIONS OF FREQUENCY MULTIPLIERS

The extension of system operating frequencies into higher frequency bands has led to considerable interest in generating RF power at lower frequencies and using a nonlinear device to achieve RF power at a higher harmonic frequency. Harmonic generators provide a convenient source of signals at higher frequencies, where direct generation from an oscillator is difficult or inconvenient. The frequency multiplier produces an output signal at a harmonic frequency multiple of the fundamental input frequency and eliminates the requirement for a high-frequency oscillator. The ability to design frequency multipliers generating the higher harmonic frequencies has made frequency multipliers important circuits in RF and microwave components, and thus they find a wide range of use in the electronics arena. Applications include instrument design, radar systems, communication systems, subscriber radio systems, and low-phase-noise electronic warfare (EW) applications.

1.1. Communication Systems

As an illustration demonstrating the convenience of a frequency multiplier, consider a communication system requiring a 15 GHz local-oscillator (LO) source as shown in Fig. 2. The configuration shows a 15-GHz source driving the LO chain of the mixer. Alternatively, the 15 GHz source can be replaced by a 5-GHz local oscillator and frequency tripler to obtain the required 15 GHz signal. Advantages in using the 5-GHz source over the 15-GHz source lie in the cost associated with the two sources, because high-frequency components usually are more expensive than lower-frequency ones. Additionally, the 5-GHz source could possibly pose less of a design challenge than the 15-GHz source. With this change in the configuration, the final circuit is represented by Fig. 3.

Frequency multiplier applications have been extended to monolithic microwave integrated circuit (MMIC)

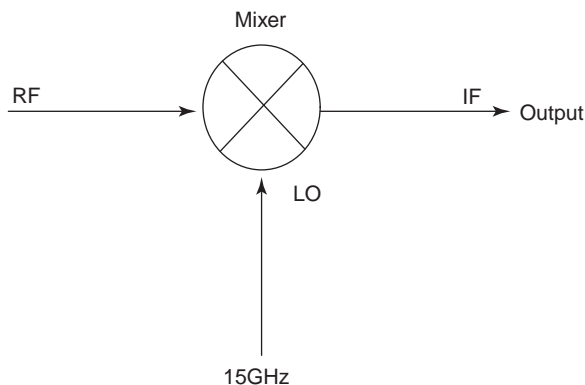


Figure 2. Configuration without frequency multiplier.

receivers in communication systems [8–11]. One such application is shown in Fig. 4 [9]. In this configuration, two doublers are used in series to supply the LO chain of the mixer. Using these doublers in the topology allows a 6.5 GHz voltage-controlled oscillation (VCO) to be implemented. The 6.5 GHz signal is led into the two frequency doubler circuits, which produce an output signal at 26 GHz. Without the use of the two doubler circuits in the block diagram, a 26-GHz VCO would have been required.

1.2. Cellular Applications

Wireless applications operating in the 900–2500 MHz range frequently use frequency multipliers in their design topologies. The systems include synthesizers, transmitters, receivers, and transceivers [12]. A transmitter topology demonstrating the use of frequency multipliers is shown in Fig. 5. The modulated signal at 450 MHz is multiplied by the doubler to produce a signal at 900 MHz for transmission.

The receiver topology using a frequency doubler is shown in Fig. 6. The doubler is placed in the LO chain of the downconverter. The downconverter produces an inter-

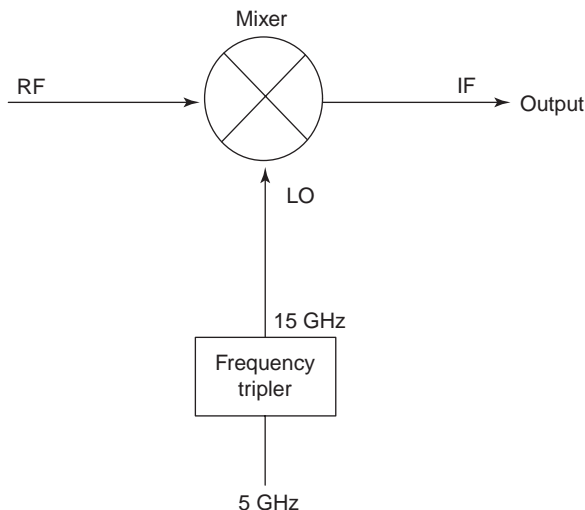


Figure 3. Configuration with frequency multiplier.

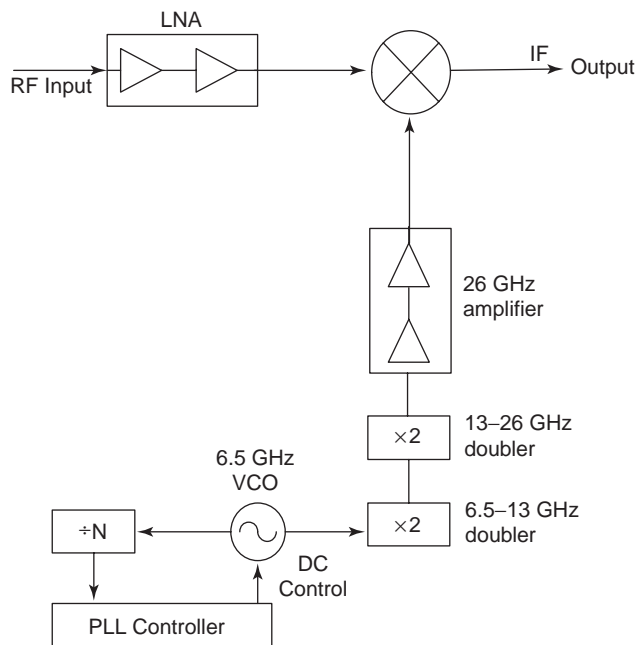


Figure 4. Block diagram of 26 GHz MMIC receiver Model.

mediate frequency (IF), which is signal-processed to obtain the desired information from the signal.

As a final example, a block diagram of a transceiver employing the use of a frequency doubler is shown in Fig. 7 [12]. This topology uses a single LO source. The doubler is used in the LO chain of the receiver and to produce the transmitting frequency in the transmitter.

2. PASSIVE FREQUENCY MULTIPLIERS

As mentioned previously, frequency multipliers are harmonic generators that produce frequency multiples of an input (fundamental) frequency. At radio- and microwave frequencies, frequency multipliers typically employ a nonlinear device to generate the desired harmonic spectrum. The choice of this nonlinear device divides multipliers into two categories: passive multipliers and active multipliers. In the case of the active multipliers, the nonlinear device includes any of the devices in the transistor classes (BJT, FET, MESFET, etc.), as will be discussed in the following section. This section will discuss the development of passive multipliers. The discussion will include the basic theory and operation of passive multipliers, various devices

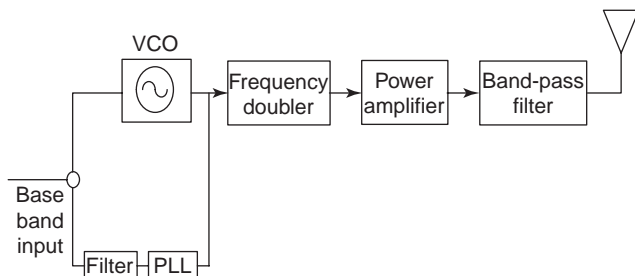


Figure 5. Block diagram of 26 GHz MMIC receiver model.

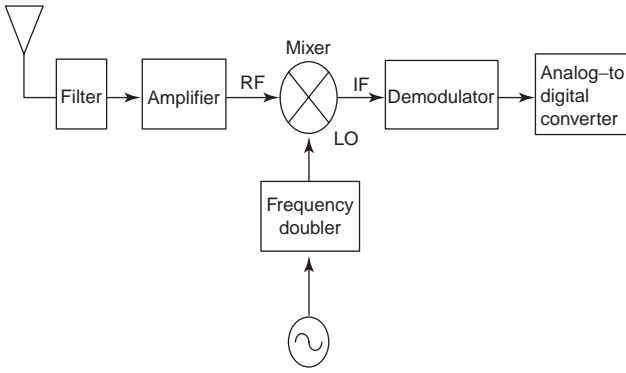


Figure 6. Receiver employing frequency multiplier.

that are typically used in the development of passive multipliers with their various advantages and disadvantages, the nonlinear mechanism responsible for harmonic production, power considerations, optimization of efficiency, realizations, and design topologies.

2.1. Background and Theory

As mentioned, frequency multipliers at radiofrequencies typically require a nonlinear element to produce the desired harmonic spectrum. For passive multipliers, this requirement is fulfilled by the exploitation of the nonlinear characteristics of nonlinear resistors, nonlinear inductors, or nonlinear capacitors. The excitation of these devices by an input fundamental frequency produces an output spectrum possessing the desired harmonic output of interest. Typical nonlinear devices providing the aforementioned properties in the development of passive frequency multipliers include rectifying metal–semiconductor junctions with their nonlinear current–voltage characteristics, reverse-biased metal–semiconductor or p-n junctions with their nonlinear capacitance, and nonlinear transmission lines having distributed nonlinear capacitance [13].

As mentioned, harmonic generation is produced in a passive frequency multiplier whenever a sinusoidal input signal drives a nonlinear impedance. A variable resistance, inductance, or capacitance whose magnitude varies instantaneously with the applied voltage or current characterizes this nonlinear impedance. Semiconductor diodes have been reported throughout the literature as

an efficient means of providing the necessary nonlinear characteristics for passive multiplier design [9,11,13–41]. The diodes have various characteristics, which produce, as expected, different performance.

Varactor diodes are commonly used by microwave designers in the development of passive multipliers with great success [14–17]. The varactor diode is a variable-reactance element where the diode junction capacitance changes nonlinearly as a function of the applied voltage, as will be discussed in the following section. Varactors are classified into two major categories: (1) p-n junction varactors, which are widely used at microwave frequencies, and (2) Schottky junction devices, typically used for millimeter-wavelength applications. It has been shown by Manley and Rowe [42], as will be discussed later, and it has been mentioned by other authors [19,43,44] that a nonlinear capacitance (reactance) harmonic generator, such as that developed with a junction varactor, can theoretically generate harmonics with efficiencies ($= P_{out}/P_{in}$) approaching 100%. On the other hand, passive frequency multipliers utilizing passive nonlinear resistors for harmonic generation have at most an efficiency of $1/N^2$, where N is the order of the harmonic, as shown by Page [45] and referenced by other authors [15,16,19]. Therefore, in the case of a frequency doubler, theoretically, the highest efficiency achievable is 25% ($N = 2$).

The step recovery diode is also used in passive frequency multiplier design for lower frequencies (30 GHz) [17]. The step recovery diode is another variable-reactance element, which is a variation of the varactor diode. Archer [26] states that the step recovery diode is a p-n junction diode explicitly designed to enhance the charge storage capacitance associated with minority carrier injection during forward conduction and that the charge storage capacitance supplies the nonlinearity necessary for harmonic generation. According to the available literature, step recovery diodes are not as popular as varactor diodes in the design of passive frequency multipliers because of the complexity in reproducible control of the forward injection of minority carriers. Therefore, the ensuing discussions will not focus on step recovery diodes.

2.2. Diode Model

As will be mentioned in the following section, one of the most important tools of microwave circuit designers is the

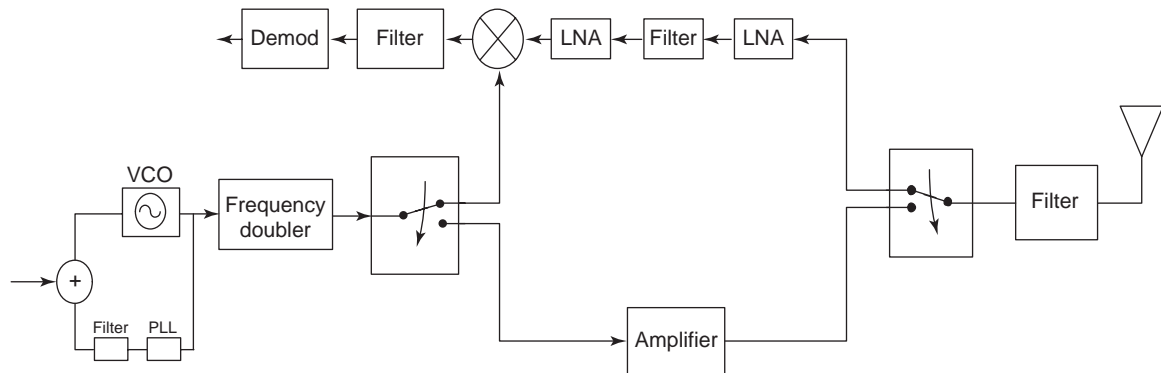


Figure 7. Transceiver employing frequency multiplier.

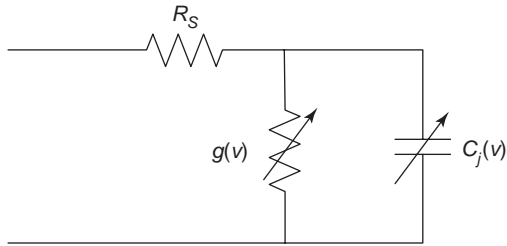


Figure 8. Varactor diode circuit model.

availability of device circuit models, which allows the performance of the device to be predicted before and after embedding with external networks. Since a diode model is essential in the understanding and development of passive frequency multipliers utilizing these devices as the source of nonlinearity, the following discussion will be devoted to the circuit model of the diode.

An equivalent-circuit model for the varactor model is shown in Fig. 8. This simple circuit model contains a frequency-dependent series resistance R_s and a voltage-dependent nonlinear conductance $g(v)$ in parallel with the voltage-dependent junction nonlinear capacitance $C_j(v)$, where v is the voltage over the junction [17,36]. The nonlinear conductance, which can produce resistive multiplication, is defined as [36]

$$g(v) = \frac{\partial i_g}{\partial v} \quad (1)$$

$$i_g = I_{\text{sat}} \left[\exp\left(\frac{qv}{\eta kT}\right) - 1 \right] \quad (2)$$

where I_{sat} is the diode saturation current, q is the magnitude of the electron charge, η is the ideality factor of the diode, k is the Boltzmann constant, and T is the diode temperature. The nonlinear capacitance $C_j(v)$, which is responsible for supplying the nonlinear reactance, is defined as [36]

$$C_j(v) = \frac{C_{j0}}{(1 - v/\phi_{\text{bi}})^2} \quad (3)$$

where C_{j0} is the zero-bias junction capacitance, “bi” is the built-in voltage potential, and is related to the doping profile in the epitaxial layer. Raisanen [36] indicates that typical values of these parameters for a varactor diode with radius of 1–5 m are as follows: the zero-bias junction capacitance $C_{j0} = 3\text{--}20$ fF, series resistance $R_s = 5\text{--}20$, built-in potential $\text{bi} = 0.6\text{--}1.0$ V, ranging from 0.4 to 0.5. The series resistance R_s arises from the undepleted materials in the diode and the contact resistance [14].

As shown in this model, suitable nonlinear elements exist for harmonic generation, namely, the nonlinear resistor $1/g(v)$ and the nonlinear capacitance $C_j(v)$. As was mentioned earlier and will be discussed later, harmonic generation due to the nonlinear reactance produced by $C_j(v)$ is theoretically more effective because it is possible to convert all the available power applied to a lossless nonlinear reactive element to output power at any higher harmonic frequency. An ideal resistive multiplier utilizing the nonlinear resistor $1/g(v)$ theoretically has a maximum efficiency of only $1/N_2$, where N is the harmonic frequency.

2.3. Nonlinear Mechanism

As mentioned previously, high-frequency signals can be generated from lower-frequency signals by harmonic multiplication. Frequency multipliers provide an efficient means of exploiting the nonlinear characteristics of various devices to provide the desired harmonic multiplication. The circuit designer of frequency multipliers seeks to accentuate the device nonlinearity in a particular way such that exciting the nonlinear device by a sinusoidal input signal at a fundamental frequency produces an output spectrum at harmonic frequencies of the input fundamental, which obviously includes the desired harmonic of interest. This section will identify and discuss the general nonlinear mechanisms responsible for harmonic production in passive frequency multipliers.

It was noted in the previous section that nonlinear resistors, nonlinear capacitors, and nonlinear inductors could be exploited for their nonlinear characteristics. Typical nonlinear devices providing these nonlinear characteristics essential for harmonic production include rectifying metal–semiconductor junctions with the nonlinear current–voltage characteristics, reverse-biased metal–semiconductor or p–n junctions with their nonlinear capacitance, and nonlinear transmission lines having distributed nonlinear capacitance [13]. As a simple example demonstrating harmonic generation, consider a nonlinear device whose nonlinear transfer function can be represented as a polynomial of the form

$$V_{\text{out}} = a_1 V_{\text{in}} + a_2 V_{\text{in}}^3 \quad (4)$$

where a_1 and a_2 are constants. Inserting a sinusoidal input ($V_{\text{in}} = \cos \omega t$) into Eq. (4) gives

$$\begin{aligned} V_{\text{out}} &= a_1 \cos \omega t + a_2 (\cos \omega t)^3 \\ &= a_1 \cos \omega t + a_2 \left(\frac{1}{4} \cos 3\omega t + \frac{3}{4} \cos \omega t \right) \\ &= \left(a_1 + \frac{3a_2}{4} \right) \cos \omega t + \frac{a_2}{4} \cos 3\omega t \end{aligned} \quad (5)$$

Equation (5) shows that an output harmonic is generated at the fundamental frequency (ω) and the third-harmonic frequency [3]. Therefore, for the specific application of a frequency tripler, this nonlinear device, as represented by the transfer function given in Eq. (4), theoretically provides the nonlinear characteristics for the design of a frequency tripler.

Throughout the literature, researchers and designers have developed passive multipliers, typically with nonlinear diodes. For this reason, the ensuing discussion focuses on the nonlinear mechanism associated with semiconductor diodes, which are used throughout the microwave industry.

As mentioned, semiconductor diodes have been reported throughout the literature as an efficient means of harmonic production. To demonstrate the nonlinear mechanism of the diode, consider an abrupt p–n junction diode, shown in Fig. 9, excited by an applied voltage V_a

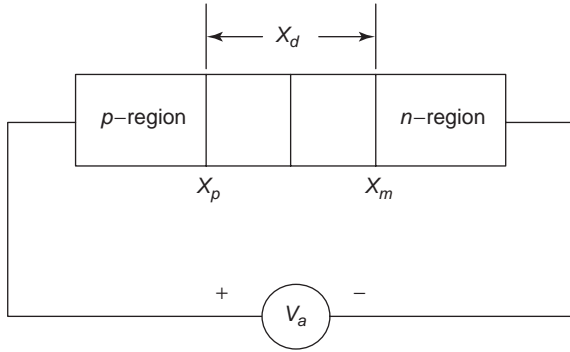


Figure 9. p-n junction diode structure.

[46]. Muller and Kamins [46] show that

$$X_d = X_p + X_n = \left[\frac{2\epsilon}{q} (\phi - V_a) \left(\frac{1}{N_a} + \frac{1}{N_d} \right) \right]^{1/2} \quad (6)$$

$$X_p = \left(\frac{2\epsilon(\phi - V_a)}{qN_a(1 + N_a/N_d)} \right)^{1/2} \quad (7)$$

$$X_n = \left(\frac{2\epsilon(\phi - V_a)}{qN_d(1 + N_d/N_a)} \right)^{1/2} \quad (8)$$

where

- X_p = reactance of depletion region extension into p-type semiconductor
- X_n = reactance of depletion region extending into the n-type semiconductor
- X_d = reactance of total depletion region
- ϕ = built-in potential
- V_a = applied voltage
- N_a, N_d = semiconductor dopant concentrations
- ϵ = permittivity

By charge neutrality, we obtain

$$N_a X_p = N_d X_n \quad (9)$$

$$Q = qN_d X_n = qN_a X_p \quad (10)$$

$$dQ = qN_d dX_n = qN_a dX_p \quad (11)$$

$$C_j(V_a) = \frac{dQ}{dV_a} = \frac{dQ}{dX_p} \frac{dX_p}{dV_a} \quad (12)$$

$$= qN_a \left(\frac{\epsilon}{2qN_a(1 + N_a/N_d)(\phi - V_a)} \right)^{1/2} \quad (13)$$

$$= \left(\frac{q\epsilon N_a N_d}{2(N_a + N_d)} \right)^{1/2} \frac{1}{\sqrt{\phi - V_a}} \quad (14)$$

$$= \frac{C_{j0}}{\sqrt{1 - V_a/\phi}} \quad (15)$$

where

$$C_{j0} = \left(\frac{q\epsilon N_a N_d}{2(N_a + N_d)} \right)^{1/2} \quad (16)$$

Equation (15) shows that the magnitude of the junction capacitance varies nonlinearly as a function of applied voltage V_a , which is essential for generating frequency harmonics when a sinusoidal voltage is added to V_a . Using a binomial series expansion on Eq. (15) yields

$$C_j(V_a) = C_{j0} \left(\frac{1 - V_a}{\phi} \right)^{-1/2} = C_{j0} \left[1 + \frac{1}{2} \left(\frac{V_a}{\phi} \right) + \frac{3}{8} \left(\frac{V_a}{\phi} \right)^2 - \frac{5}{16} \left(\frac{V_a}{\phi} \right)^3 + \dots \right] \quad (17)$$

$$= \alpha_0 + \alpha_1 V_a + \alpha_2 V_a^2 + \alpha_3 V_a^3 + \dots \quad (18)$$

$$= \sum_{i=0}^{\infty} \alpha_i V_a^i \quad (19)$$

where

$$\alpha_0 = C_{j0}$$

$$\alpha_1 = \frac{C_{j0}}{2\phi}$$

$$\alpha_3 = -\frac{5C_{j0}}{16\phi^3}$$

\vdots

From Eqs. (12) and (18), we obtain

$$dQ(V_a) = C_j(V_a) dV_a \quad (20)$$

$$Q(V_a) = \int C_j(V_a) dV_a \quad (21)$$

$$= \int (\alpha_0 + \alpha_1 V_a + \alpha_2 V_a^2 + \dots) dV_a \quad (22)$$

$$= \alpha_0 V_a + \frac{1}{2} \alpha_1 V_a^2 + \frac{1}{3} \alpha_2 V_a^3 + \frac{1}{4} \alpha_3 V_a^4 + \dots \quad (23)$$

$$= \sum_{i=0}^{\infty} \alpha'_i V_a^{i+1} \quad (24)$$

where

$$\alpha'_0 = \alpha_0$$

$$\alpha'_1 = \frac{1}{2} \alpha_1$$

$$\alpha'_2 = \frac{1}{3} \alpha_2$$

\vdots

Demonstrating the effect of applying a sinusoidal signal across the p-n junction, the current across the diode can be calculated from

$$I(t) = \frac{dQ}{dt} \quad (25)$$

Inserting Eq. (23) into Eq. (25) with the p-n junction excited by the sinusoidal signal $V_a = \cos \omega t$ gives

$$Q = \alpha_0 V_a + \frac{1}{2} \alpha_1 V_a^2 + \frac{1}{3} \alpha_2 V_a^3 + \dots \tag{26}$$

$$= C_{j0}(\cos \omega t) + \frac{C_{j0}}{4\phi} \cos^2 \omega t + \frac{C_{j0}}{8\phi^2} \cos^3 \omega t + \dots$$

$$= \frac{C_{j0}}{8\phi^2} + \left(C_{j0} + \frac{3C_{j0}}{32\phi^2} \right) \cos \omega t + \frac{C_{j0}}{8\phi} \cos 2\omega t$$

$$+ \frac{C_{j0}}{32\phi^2} \cos 3\omega t + \tag{27}$$

and inserting Eq. (27) and differentiating gives

$$I(t) = \frac{dQ}{dt}$$

$$= -\omega + \left(C_{j0} + \frac{C_{j0}}{32\phi^2} \right) \sin \omega t$$

$$- \frac{2\omega C_{j0}}{8\phi} \sin 2\omega t - \frac{3\omega C_{j0}}{32\phi^2} \sin 3\omega t + \tag{28}$$

This result illustrates the various frequency harmonics produced by the p-n junction when excited by a sinusoidal source and demonstrates the nonlinear mechanism by which the semiconductor diode produces harmonic generation. This variable capacitance has led semiconductor diodes, varactors, and the like to be vital components aiding microwave engineers in nonlinear circuit development.

2.3.1. Voltage–Capacitance and Charge–Capacitance Characteristics. As previously stated, harmonic generators utilizing the nonlinear capacitance characteristics of varactors are often employed throughout the microwave industry by researchers and designers. The voltage– and charge–capacitance characteristics of the varactor diode are important in analyzing and studying the behavior of diodes. This section will discuss the relationships between the voltage and the capacitance and between the charge and the capacitance, since they are often utilized in studying the performance and the design of passive frequency multipliers.

We refer to the diode example above along with Eqs. (12) and (15), which are restated below [18]:

$$C_j(v) = \frac{dQ}{dv} = \frac{C_{j0}}{1 - v/\phi^m} \tag{29}$$

where

- v = voltage across the junction in the absence of any applied bias
- ϕ = built-in potential
- C_{j0} = zero-bias junction capacitance
- m = index number ($\frac{1}{2}$ for abrupt junctions, and for linearly graded junctions)

Scanlan (18) indicates that the minimum capacitance (C_{\min}) occurs at the reverse breakdown voltage ($v = -V_R$)

and the junction capacitance at this bias is

$$C_{\min} = C_j(-V_R) = \frac{C_{j0}}{(1 + V_R/\phi)^m} \tag{30}$$

Letting $V_0 = V_R + \phi$ and rewriting Eq. (30) gives

$$C_{j0} = C_{\min} \left(1 + \frac{V_R}{\phi} \right)^m$$

$$= C_{\min} \left(1 + \frac{V_0 - \phi}{\phi} \right)^m \tag{31}$$

and inserting Eq. (31) in Eq. (29) gives

$$C_j(v) = \frac{C_{\min} \left(1 + \frac{V_0 - \phi}{\phi} \right)^m}{\left(1 - \frac{v}{\phi} \right)^m}$$

$$= C_{\min} \left(\frac{V_0}{\phi - v} \right)^m \tag{32}$$

From Eq. (29)

$$dQ = C_j(v)dv \tag{33}$$

and inserting Eq. (32), we obtain

$$Q(v) = \int C_j(v)dv$$

$$= -\frac{C_{\min} V_0^m}{1 - m} (\phi - v)^{1-m} + k \tag{34}$$

where k is the constant of integration. When $v = \phi$, the voltage across the junction is zero and the charge is zero, which indicates that $k = 0$ as well. This allows Eq. (34) to be rewritten as follows, where the charge is represented as a function of the voltage:

$$Q(v) = -\frac{C_{\min} V_0^m}{1 - m} (\phi - v)^{1-m} \tag{35}$$

The depletion region reactances X_p , X_n and the electric field across p-n junctions increase as the reverse bias increases [46]. Intuitively, there are physical limitations to these increases, as governed by the structure of the junction and the dopant concentrations. As the reverse bias increases, eventually a voltage is encountered where the barrier to current flow is broken, and current flow increases substantially. The voltage at which this occurs is defined as the breakdown voltage ($v = -V_R$). At the breakdown voltage, Eq. (35) gives

$$Q(-V_R) = Q_R = -\frac{C_{\min} V_0^m}{1 - m} (\phi + V_R)^{1-m} \tag{36}$$

and recalling that $V_0 = V_R + \phi$ gives

$$Q(-V_R) = Q_R = -\frac{C_{\min} V_0}{1 - m} \tag{37}$$

Now, dividing Eq. (35) by Eq. (37) gives

$$\begin{aligned} \frac{Q(v)}{Q_R} &= \frac{\frac{C_{\min} V_0^m}{1-m} (\phi - V_R)^{1-m}}{\frac{C_{\min} V_0^m}{1-m}} \\ &= \left(\frac{\phi - v}{V_0} \right)^{1-m} \end{aligned} \quad (38)$$

This expression relates the charge across the junction in terms of breakdown characteristics (V_R , Q_R) and the minimum capacitance (C_{\min}).

Historically, in the literature, the capacitance is used in defining the elastance [18,19]:

$$S(v) = \frac{1}{C(v)} \quad \text{and} \quad S_{\max} = \frac{1}{C_{\min}} \quad (39)$$

This allows Eq. (32) to be rewritten in terms of the elastance as shown below, where the elastance is written as a function of voltage:

$$\frac{C(v)}{C_{\min}} = \left(\frac{V_0}{\phi - v} \right)^m = \frac{S_{\max}}{S(v)} \quad (40)$$

or

$$\frac{S(v)}{S_{\max}} = \left(\frac{\phi - v}{V_0} \right)^m \quad (41)$$

Referring back to Eq. (38), the charge $Q(v)$ is expressed as a function of v . Alternatively, Eq. (38) can be rearranged to give the voltage as a function of the charge:

$$\begin{aligned} v(Q) &= \phi - V_0 \left(\frac{Q}{Q_R} \right)^{1/(1-m)} \\ &= V_0 - \phi - V_0 \left(\frac{Q}{Q_R} \right)^{1/(1-m)} \end{aligned} \quad (42)$$

and therefore

$$\begin{aligned} v + V_R &= V_0 \left[1 - \left(\frac{Q}{Q_R} \right)^{1/(1-m)} \right] \\ &= V_0 \left[1 - \left(\frac{Q}{Q_R} \right)^\gamma \right] \end{aligned} \quad (43)$$

where

$$\gamma = \frac{1}{1-m}$$

Equations (29)–(43) are mathematical expressions for the characteristics between the voltage, charge, capacitance, and elastance of p-n junction semiconductor diodes. Researchers and designers often use these expressions, among others, in analyzing diodes and incorporating diodes into multiplier designs.

2.4. Power Considerations

A discussion on power flow into and out of the nonlinear device is very useful in understanding the behavior of passive nonlinear devices and their usefulness in designing passive frequency multipliers, as it can be used to predict optimum power and conversion efficiency. Here we will discuss the power flow at the various harmonics and their relation to the performance of frequency multiplier designs, which leads to a fundamental understanding of the limitations imposed by diodes.

Manley and Rowe [42] have provided a general relation, which is commonly used throughout the microwave industry, for discussing the power flow of a particular class of nonlinear elements. They derive general power relations that govern single-valued nonlinear elements such as nonlinear inductors and capacitors. Their final derivations, independent of input power, give two independent equations characterizing the power content at various harmonics.

Manley and Rowe perform their derivation on an ideal nonlinear capacitor, but state that a similar analysis can be performed on a nonlinear inductor. Their analysis begins by evaluating the voltage across the nonlinear capacitor, which is defined as some arbitrary function of the charge. Then, they write an equation for the charge across the capacitor represented in a Fourier series. From the charge, they are able to calculate the current in Fourier series form. Next, the voltage across the nonlinear capacitor is given in a Fourier series, from which the Fourier coefficients for the voltage are calculated using orthogonality. After further substitutions and integrations, they conclude with the following equations

$$\sum_n \sum_m \frac{mP_{mn}}{mf_1 + nf_2} = 0 \quad (44)$$

$$\sum_n \sum_m \frac{nP_{mn}}{mf_1 + nf_2} = 0 \quad (45)$$

where m and n are integers representing various harmonics and P_{mn} is the average power flowing into the nonlinear reactances at the frequencies mf_1 and nf_2 . These equations are significant in that they indicate that for an ideal, lossless capacitance (with $R_s = 0$ in Fig. 8), the sum of all inward power flows at the different frequencies must be zero. This indicates, theoretically, that on exciting the nonlinear capacitor at a fundamental frequency, the output power at the desired harmonic has the same magnitude as the input power of the fundamental. This is achieved *provided* all power at the undesirable harmonics has been reactively terminated, which ensures that no power is dissipated at these undesirable harmonics.

As an example demonstrating this procedure, consider exciting a nonlinear capacitor at the fundamental frequency f_1 ($m = 1$, $n = 0$). Then Eq. (44) gives

$$\frac{P_{10}}{f_1} + \frac{mP_{m0}}{mf_1} = 0 \quad (46)$$

or

$$P_{10} = - \sum_{m=2}^{\infty} P_{m0} \quad (47)$$

or in general, the sum of all powers flowing at the various harmonic frequencies must be zero. Equation (47) indicates that the input power P_{10} at the fundamental is the sum of the output powers at all harmonics combined. Therefore, if external embedding circuitry to which the nonlinear capacitor is connected is developed such that the power at all undesirable harmonics is reactively terminated, then the power delivered to the load at the desired harmonic can, theoretically, represent conversion efficiencies of 100% (17). Practical diodes, however, exhibit nonzero series resistance ($R_s \neq 0$), so that practical conversion efficiencies are less than 100%.

2.5. Optimization of Efficiency

Achieving optimum efficiency is an essential goal in the design of any component. In the case of passive multipliers, proper techniques should be employed in efforts to maximize the conversion efficiency of the multiplier and maximize the power delivered to the load at the desired harmonic.

The Manly–Rowe equations given above indicate that, theoretically, an ideal nonlinear capacitor can achieve 100% conversion efficiency. In practical applications, nonlinear capacitors (varactors) are not ideal components but have some loss. Therefore, as a general example, the varactor utilized in passive multiplier design should exhibit low series resistance (R_s) at the frequency and power level of operation [18,36]. Impedance matching at the input of the nonlinear device is also required, to ensure that the input power is efficiently coupled to the diode. Similarly, output impedance matching at the desired harmonic of interest should be implemented so that power generated in the nonlinear device at the output harmonic is efficiently transferred to the load. Significant real power should exist in the diode at the fundamental and the output harmonic of interest and low-loss resonators should be utilized as idler circuits [13,42–44,47], which will be discussed later in the article.

Archer and Batchelor [17] note that an equivalent-circuit model of a varactor diode embedded in external circuitry can be utilized to predict and optimize the performance of a passive multiplier. They give an equivalent circuit for a varactor multiplier, showing the connection between the varactor and the embedding network, as in Fig. 10. There, the embedding network models the impedance presented to the diode at the fundamental frequency and other harmonics. The two networks (embedding and equivalent diode circuit model) are optimized to obtain maximum power transfer between the embedding network and the reactance of the diode at the input fundamental frequency and the output harmonics. This optimization can be performed manually using the mathematical equations governing the response of the networks or through an optimization routine provided by a commercial circuit simulator.

The conversion efficiency is dependent on the large-signal diode currents and voltages, which are determined by the impedances presented to the diode at the fundamental and higher harmonic frequencies [17,18]. Simulations can be performed to optimize the conversion efficiency,

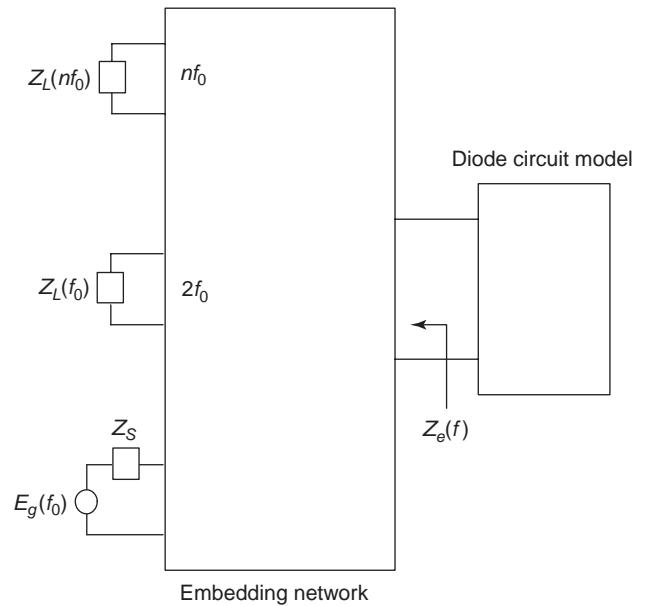


Figure 10. Equivalent network model of passive frequency multiplier.

utilizing the impedances presented to the diode in conjunction with the diode circuit model.

The steady-state large-signal voltage and current coefficients are V_k and I_k [17].

$$v_j(t) = \sum_k V_k e^{jk2\pi ft} \tag{48}$$

$$i_c(t) = \sum_k I_k e^{jk2\pi ft} \tag{49}$$

where f is the fundamental frequency. The predicted performance and thus the optimization of efficiency are determined after solving Eqs. (48) and (49) subject to the boundary conditions imposed by the diode and the embedding network [the embedding impedance $Z_c(f)$]. Such solutions have been calculated and presented by various authors [9,11,14–18,20–41], using idealized models, to obtain the nonlinear large-signal behavior of specific multipliers (doubblers, triplers, etc.). They present data on the efficiency, power handling, input and load resistances, and P_{max}/P_{in} , for example, versus frequency for various multipliers. Using such plots and data, theoretical optimization can be achieved for specific multiplier types.

In summary, it is important to optimize the performance of frequency multipliers. Chang et al. [29] state general guidelines for achieving this:

1. Good impedance matching should be provided at the input and output of the nonlinear device over the frequency range of interest, and all idler circuits terminated reactively with low loss.
2. At frequencies other than the fundamental, desired harmonic of interest, and idler harmonics, the nonlinear device should be mismatched to the embedding circuitry to minimize power loss.

3. The input and output networks should be isolated physically and electrically.

2.6. Idlers

An important concept in the fundamental development of passive frequency multipliers, as briefly mentioned in prior sections, is that of idler currents and idler circuits. Idler currents are currents flowing at frequencies other than the input fundamental frequency and output harmonic frequency, which are required for a particular class of passive multipliers [47]. This section will discuss the property of idlers and demonstrate the requirement of them for particular multiplier designs.

In Section 2.3.1, the voltage and charge relations of nonlinear varactors were discussed. Referring to Eq. (42), it is observed that a square-law characteristic is exhibited by an abrupt junction diode ($m = \frac{1}{2}$); the voltage is proportional to the square of the charge [43]. Consider the condition in which the charge across the junction of an abrupt junction diode is sinusoidal at the fundamental frequency ($\omega = 2\pi f$)

$$Q(t) = Q_0 + Q_1 \cos \omega t \quad (50)$$

where Q_0 is the DC biasing component. Inserting Eq. (50) into Eq. (42) and using the trigonometric identities gives

$$v(Q) = \phi - V_0 \left(\frac{Q}{Q_R} \right)^2 \quad (51)$$

$$\begin{aligned} v(t) &= \phi - V_0 \left(\frac{Q_0 + Q_1 \cos \omega t}{Q_R} \right)^2 \quad (52) \\ &= \phi - \frac{V_0}{Q_R^2} \left(Q_0^2 + \frac{Q_1^2}{2} \right) - \frac{2V_0 Q_0 Q_1}{Q_R^2} \cos \omega t \\ &\quad - \frac{V_0 Q_1^2}{2Q_R^2} \cos 2\omega t \quad (53) \end{aligned}$$

From Eq. (53) it is observed that the voltage produced by the charge across the abrupt junction diode has a DC component, a component at the fundamental frequency, and a component at the second-harmonic frequency, but no component at any harmonic higher than the second, such as required for frequency triplers, quadruplers, and so on. The component at the second-harmonic frequency indicates that this diode is suitable for a frequency doubler, however. This example indicates that except for the case of the doubler, if currents flow only at the input and output frequencies, it is impossible to generate harmonics higher than the second with an *abrupt* junction varactor. This is an expected result due to the square law behavior of the varactor. Thus, in order to achieve output harmonics for $n > 2$, it is necessary for intermediate currents (idler currents) to flow in the varactor at specific harmonic frequencies.

The abrupt junction varactor can be regarded as providing a mechanism for frequency doubling (due to the square-law relationship mentioned previously) and for frequency mixing when idler currents are utilized [19].

In the case of mixing, currents flowing at specific harmonic frequencies are mixed with the fundamental frequency and with each other (if more than one is introduced) to produce additional currents at various harmonics. Therefore, introducing an idler current into an abrupt junction varactor at the second-harmonic causes the second-harmonic to mix with the fundamental frequency to produce an output at the third harmonic. This additional idler produces the component necessary for frequency tripler design.

Introducing additional currents into an abrupt junction varactor provides a means for the device to generate higher harmonics. This extends the use of abrupt junction varactors from frequency doublers to higher-order multipliers.

2.7. Analysis Techniques

Passive frequency multipliers are nonlinear circuits requiring solutions from large-signal circuit analysis. As stated in preceding subsections, the efficiency of passive multipliers utilizing diodes is affected by the diode parameters: the embedding impedance $Z_e(nf_0)$ at the fundamental and harmonic frequencies, the input power level P_{in} , and the bias voltage. Various techniques are utilized by researchers and designers for analyzing and optimizing nonlinear circuits and, specifically, passive multipliers. In some simple cases, analytic closed-form solutions may be obtained for optimizing the efficiency; however, for most cases the most convenient method is through numerical analysis. Some of these techniques include power series analysis, Volterra series analysis, and harmonic balance techniques where time-domain current and voltage solutions are sought that satisfy the diode boundary conditions and frequency-domain solutions are sought that satisfy the external circuit equations. Using these analysis techniques along with an accurate equivalent circuit model of the passive nonlinear device, the predicted performance of the device embedded in external circuitry can be obtained.

Since the analysis techniques for passive and active frequency multipliers are similar, the author refers further discussion on this topic to a later section, where a detailed discussion is presented on the analysis techniques mentioned above. The final section of this article deals with active frequency multipliers, but the analysis techniques are applicable for passive nonlinear devices as well.

2.8. Pertinent Properties of Passive Devices

The RF performance of passive multipliers is governed by, among other things, the pertinent properties of the nonlinear device. These properties can be divided into two categories [41]: (1) those affecting the efficiency of the multiplier and (2) those affecting its power-handling capability. Tolmunen [41] notes that the efficiency of the nonlinear diode is affected mostly by the cutoff frequency, which will be defined below, the strength of the nonlinearity, and the type of multiplication (resistive or reactive, as discussed in Section 2.1). The power-handling capability is affected by the device area, the extent of the nonlin-

earity, and the breakdown voltage, which was discussed in Section 2.3.1).

Focusing on varactor frequency multipliers, for efficient varactor operation, it is necessary, as expected, for the reactance of the junction capacitance of the varactor to be much larger than the device series resistance (R_s in Fig. 8) [17]. Therefore, this necessitates an upper frequency limit (cutoff frequency) on the usefulness of a given varactor [18]. The dynamic cutoff frequency is defined as [41]

$$f_{cd} = \frac{1/C_{min} - 1/C_{max}}{2\pi R_s} \tag{54}$$

where C_{min} and C_{max} are the minimum and the maximum capacitance of the varactor and R_s is the diode series resistance. Therefore, for optimum performance, the cutoff frequency should be greater than the frequency of application.

A sharp nonlinearity in the C - V response of the varactor results in efficient harmonic generation, since the nonlinearity of the device is responsible for harmonic generation. The advantages of a sharp or steep nonlinearity depend on the extent of the voltage swing across the diode generated by the input power. Varactors have high input impedance, thus enabling large voltage swings to be generated across the device. A diode with high nonlinearity, even at low input power levels, produces significant voltage swings, and therefore is capable of achieving optimum performance. Typically, the optimum conditions occur in applications where the nonlinearity extends over voltages comparable to the voltage swing of the input power signal.

Tolmune [41] states that the power-handling capability is proportional to the average capacitance of the device area. As in the case of other high-power devices, diodes with large surface areas are able to handle larger input power levels and consequently produce larger RF current. In practical diode applications, however, this may result in matching problems, because matching the diode over a broad voltage range is quite challenging, and thus trade-offs have to be made. As will be shown in the discussion of design techniques in the last section, another approach commonly used to improve the power-handling capability is to stack devices in series or parallel. This configuration increases the total area of the diode, thus allowing it to sustain larger voltage swings. Large device arrays are useful in high-power applications.

2.9. Classical Realizations

The previous sections highlighted some of the basic properties of passive multipliers and the fundamental

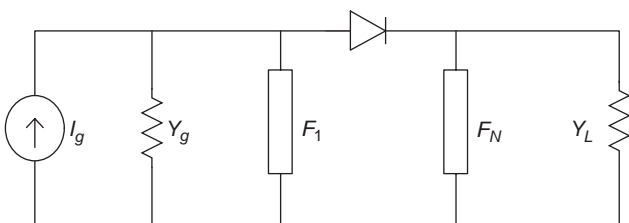


Figure 11. Series-mounted passive diode frequency multiplier.

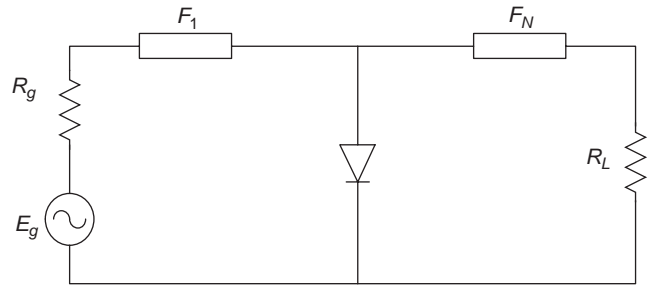


Figure 12. Shunt-mounted passive diode frequency multiplier.

characteristics of nonlinear components, which are utilized extensively in passive multiplier development. As mentioned, the nonlinear component is embedded in external circuitry to accentuate the desired harmonic. As seen throughout the literature, various topologies exist for realizing passive multipliers, revealing the interaction between the embedding circuitry and the nonlinear device. This section will highlight some of the classical realizations utilized extensively by microwave designers and researchers.

Scanlan [18] and Leeson and Weinreb [20] have presented some simple, classical realizations for passive multipliers, as shown in Figs. 11 and 12. Scanlan identifies the passive multiplier topology shown in Fig. 11 as a series model where the varactor diode is series-mounted with the embedding network. The input and output networks F_1 and F_N , respectively, represent ideal filters at the fundamental frequency and the N th harmonic, which permit voltages to exist at the fundamental frequency and the N th harmonic, respectively.

In other words, F_1 acts to short-circuit all frequencies other than the fundamental frequency, and F_N acts to short-circuit all frequencies other than the harmonic frequency of interest. Although more sophisticated filters may be required, parallel LC networks can be synthesized for F_1 and F_N at their respective frequencies, as shown by

$$\omega_0 = \frac{1}{\sqrt{LC}} \tag{55}$$

Figure 12, on the other hand, shows the shunt diode topology for passive frequency multiplier design using a nonlinear diode. Again, the input and output networks, F_1 and F_N , respectively, represent ideal filters at the

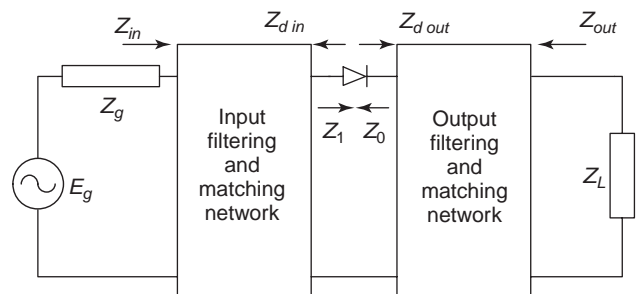


Figure 13. Block diagram of series-mounted diode frequency multiplier.

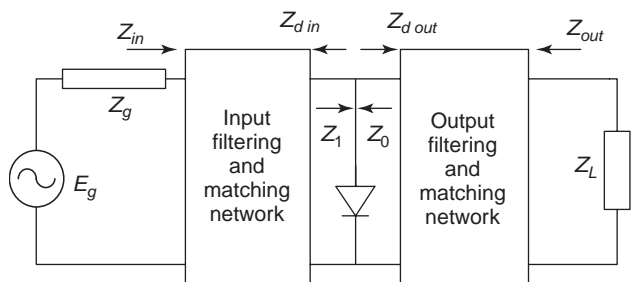


Figure 14. Block diagram of shunt-mounted diode frequency multiplier.

fundamental frequency and the N th harmonic, which permit currents to flow at the fundamental frequency and the N th harmonic, respectively. This indicates that F_1 acts to open-circuit all frequencies other than the fundamental frequency and F_N acts to open-circuit all frequencies other than the harmonic frequency of interest. Similarly, F_1 and F_N can be synthesized as series LC networks resonant at the fundamental frequency and the output harmonic frequency of interest.

Faber (13) has discussed the realizations presented by Scanlan, with emphasis on achieving optimum efficiency of the multiplier. Block diagrams of the realizations (series-mounted and shunt-mounted) shown by Faber are given in Figs. 13 and 14. Recall from the Section 2.4 that the Manly-Rowe power equations imply that it is theoretically possible to deliver all input power at the fundamental frequency to the output load at the desired harmonic of interest, thereby achieving 100% efficiency. Achieving optimum efficiency requires that should not be dissipated at any of the undesired harmonics in either the input network or the output network.

This indicates, with regard to Fig. 13, that

$$\text{Re } Z_{d, \text{out}}(f) \approx 0 \tag{56}$$

$$\text{Re } Z_{d, \text{in}}(nf) \approx 0 \tag{57}$$

when the input and output networks contribute to the device reactance compensation. If the conditions represented by Eqs. (56) and (57) are met, power is not dissipated at the fundamental frequency in the output network and power is not dissipated at any of the harmonic frequencies in the input network, respectively.

Similarly, for Fig. 14 the following conditions are sought:

$$\text{Re } Y_{d, \text{out}}(f) \approx 0 \tag{58}$$

$$\text{Re } Y_{d, \text{in}}(nf) \approx 0 \tag{59}$$

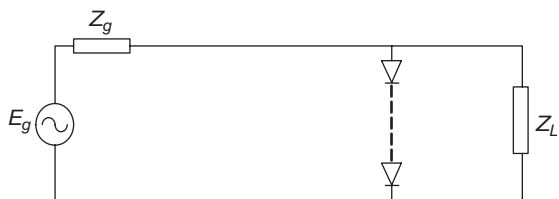


Figure 15. Series-connected diode multiplier topology.

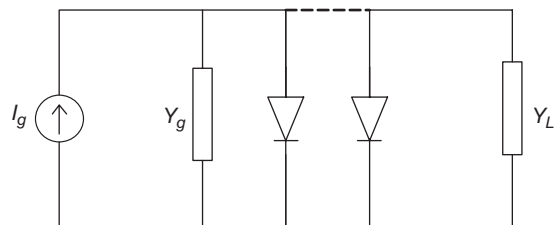


Figure 16. Parallel-connected diode multiplier topology.

Apart from the realizations mentioned previously, several variations of these topologies have been utilized as well. At RF and microwave frequencies several diodes connected in series or parallel have been utilized to handle cases where there was insufficient power, voltage, or current-handling capability of a single device or where the single-device impedance levels were inconvenient. Connecting m diodes in series (stacking) produces a breakdown voltage m times as high, and m diodes in parallel provide m times higher current [13]. Therefore, topologies such as those shown in Figs. 15 and 16 are commonly encountered.

The circuit complexity of passive multipliers can be increased even further. Some more complicated topologies are shown in Figs. 17–20 [13,17,18,30]. The antiparallel topology of Fig. 17 produces currents containing components at the fundamental frequency and higher odd-order harmonics. This can substantially simplify the design of input and output filters in the development of odd-order multipliers.

Figure 18 shows the antiseriess topology utilizing a transformer between the input signal and the diode circuit. The transformer provides a 180° phase shift between the input signal voltages feeding the two diodes. Therefore, the current components cancel in the load, producing no voltage across the load at the fundamental frequency. In contrast to the antiparallel topology, the antiseriess topology provides even-order harmonics and therefore leads to less stringent requirements on the input and output filters.

Figure 19 utilizes a transformer in the antiparallel series topology as well. Faber notes that the odd-order components are in phase, so that when the odd-order components flow through the transformer primary winding, they do not excite the load mesh. The even-order components, on the other hand, are of opposite phase, so they cancel in the input signal source branch but excite current in the load mesh. This action causes the antiparallel series topology to produce even-order harmonic multiplication.

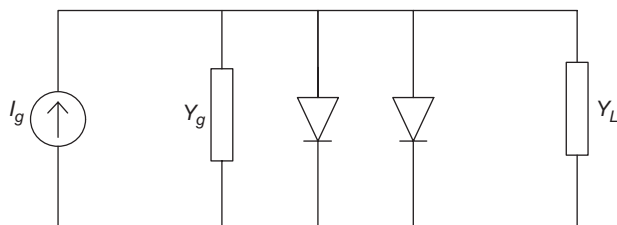


Figure 17. Antiparallel diode pairs.

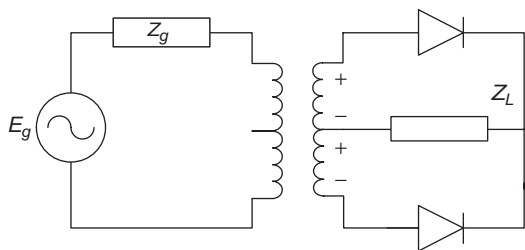


Figure 18. Antiseries diode pairs.

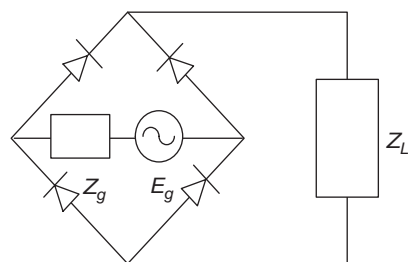


Figure 20. Bridge frequency multiplier.

Finally, Fig. 20 shows a bridge frequency multiplier. Similarly to full-wave rectifiers, bridge rectifiers can be used to produce even-order harmonic multiplication.

2.10. Passive Multiplier Design Techniques

2.10.1. Existing Design Techniques. Numerous techniques exist for the design of passive multipliers utilizing various topologies, many of which are presented in Section 2. This section presents, in perusal of the available literature, various existing design techniques, and in some cases details their performance.

A fundamental topological representation for realization of passive RF/microwave multiplier circuits is shown in Fig. 21, where networks N_1 and N_2 are on the input and output of the nonlinear device, respectively. As mentioned in a previous section, multiplier performance is governed by the embedding circuitry (networks N_1 and N_2) and the pertinent properties of the nonlinear device. Authors have used various networks in the synthesis of N_1 and N_2 . Traditional synthesis have included short-circuited and open-circuited stubs at the fundamental frequency and various harmonics [16,24,25], impedance matching and filter networks [15,26–29], and waveguides and filters [11,14,31–33,36–40].

As shown in Fig. 21, in the synthesis of N_1 and N_2 , several authors have utilized short-circuited and open-circuited stubs for low-frequency and high-frequency applications. Gavan and Peled [16], for example, use microstrip stubs in the development of a 1250–2500-MHz step recovery diode frequency doubler. They synthesize N_1 with a 0/8 stub (at $2f_0$) on the input network to provide a short circuit for the second-harmonic signal, and synthesize N_2 with a 0/4 microstrip stub (at f_0), which provides a short circuit to ground for the fundamental frequency. Using this design technique, they achieve conversion gain efficiency of 75%, but do not present any data on harmonic suppression. Chen et al. [24,25] perform a 47–94-GHz Schottky barrier

varactor diode frequency doubler design utilizing MMIC technology. They use a 0/2 short-circuited stub (at $2f_0$) on the input network to create an RF short circuit at 94 GHz, and a 0/4 short-circuited stub (at f_0) on the output to create an RF short circuit at the fundamental frequency. This high-frequency MMIC design provided a maximum conversion efficiency of 25% (6 dB conversion loss).

Several authors have developed passive frequency multipliers utilizing impedance-matching networks and filters in the input and output networks [15,26–29]. The impedance-matching networks are employed to match the input and output impedances of the nonlinear device, while the filters are used to attenuate specific harmonics. Gavan and Peled [15] designed a 1250–2500-MHz varactor frequency doubler utilizing the shunt varactor topology shown in Fig. 14 along with a lowpass filter in the input network and a two-section coupled bandpass filter at 2500 MHz in the output network. This design technique yields a maximum conversion gain efficiency of 71%. Chang et al. [29] developed a varactor 46–92-GHz frequency doubler utilizing a topology similar to that shown in Fig. 14. Input and output networks are synthesized with filters and additional matching networks to achieve optimum power transfer at the source and load. This design achieves a conversion loss of 8–9 dB over a 500 MHz bandwidth.

Furthermore, some authors have chosen to utilize a balanced topology for the design of frequency multipliers [30–33]. A block diagram of a balanced design topology is shown in Fig. 22. In typical balanced circuits, a 180° phase difference in the input signals feeding the nonlinear device produces fundamental signals and other odd-harmonic signals with opposite phase. By destructive interference, the fundamental and other odd harmonics cancel, giving good harmonic suppression, while the second-harmonic signals, on the other hand, interfere constructively, thereby enhancing the output signal at the second-harmonic. This design technique will be revisited in the discussion of active frequency multipliers.

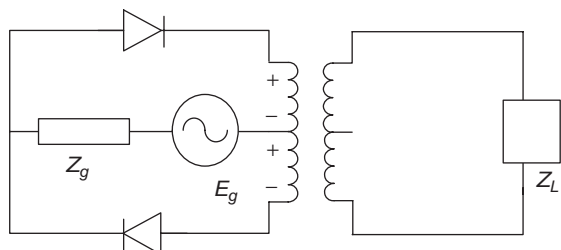


Figure 19. Antiparallel series-connected diodes.

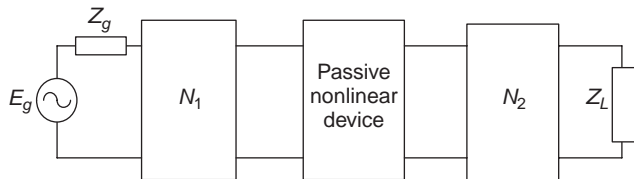


Figure 21. Passive frequency multiplier realization.

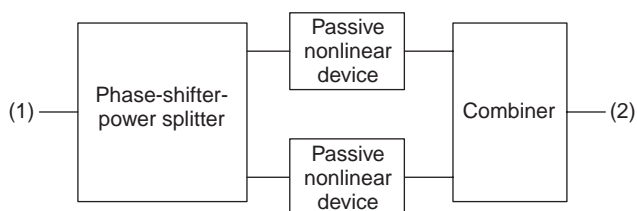


Figure 22. Block diagram of typical passive balanced frequency multiplier.

Bitzer [30] utilized a balanced topology similar to that shown in Fig. 19 and presented again in Fig. 23 to design a broadband Schottky barrier diode frequency doubler. In this structure, the input signal is fed antiphase to the diodes in order to switch on one diode patch every half-cycle. The rectified output signal is coupled to the load via a balun. As mentioned previously, the fundamental signals and other odd-harmonic signals from the diodes have opposite phase and therefore, by destructive interference, cancel, giving good harmonic suppression. The second-harmonic signals interfere constructively, thereby enhancing the output signal at the second-harmonic. Bitzer's data show that from 6–18 GHz, the conversion loss is 9.5 ± 1 dB and harmonic suppression > 15 dBc.

Archer [33] developed a balanced varactor diode 85–116-GHz frequency doubler similar to the typical topology shown in Fig. 22. Archer uses a waveguide T junction as a power divider on the input to feed two varactor diodes. On the output, a matched waveguide hybrid T junction combines the power at the output port. Using this design topology, a maximum conversion efficiency of 16.5% was achieved. Unfortunately, Archer does not present any data on harmonic suppression.

Waveguide circuitry provides an efficient means of realizing frequency multipliers [14]. Waveguides provide low loss, possess desirable highpass filter characteristics, and provide a good thermal path for dissipated power. Energy is typically coupled/decoupled from the input and output of the waveguide through a lowpass filter. Various authors have utilized waveguide circuitry in high-frequency multiplier designs [11,14,31–33,36–40]. Raisanen [36] notes that for frequencies from 100 ~ 500 GHz, for example, the highest efficiencies and highest output powers have been achieved with waveguide multipliers.

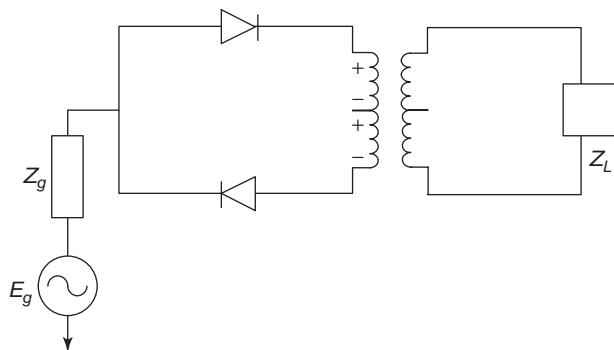


Figure 23. Antiparallel balanced diode configuration.

Archer [38] has developed a varactor frequency doubler at 260 GHz utilizing waveguides and filters. The input network consists of a lowpass filter and a waveguide. The lowpass filter is a seven-section design that passes the fundamental signal while attenuating higher-order harmonics. The output network consists of a $\lambda_0/4$ impedance transformer and a waveguide. Using this design technique, Archer achieves a conversion gain efficiency of 20% for narrowband applications (5% bandwidth) and conversion efficiencies of 10% for wider-band applications (8% bandwidth).

Mott [11] has developed a varactor frequency doubler design at a lower frequency (19–38 GHz), utilizing waveguides as well. Mott synthesized the input network with a waveguide, a $\lambda_0/4$ impedance transformer, and a lowpass filter and notes that the characteristic impedance of the filter is synthesized so that it equals the real part of the diode input impedance. The output network consists of an output waveguide impedance transformer synthesized to present the optimum load impedance to the output of the diode. Mott achieves a conversion efficiency of 60% (conversion loss of 2.2 dB) over a 1 dB output bandwidth of 640 MHz.

At higher frequencies, frequency multipliers are capable of achieving high conversion efficiency at low input powers, but the output power tends to saturate at rather low power levels [31]. The use of series arrays of diodes provides an attractive approach to overcoming this defect. Cascading multiple-diode junctions increases the breakdown voltage and provides greater power-handling capability [9]. A series array of n identical diodes can handle n^2 times as much power as a single diode [31]. For these reasons, various authors have utilized series- and parallel-stacked diodes in passive design, as shown in Figs. 15 and 16, to improve the power-handling capability of passive frequency multipliers [9,14,30,31,34,35]. Chu [34] developed an 18–36-GHz stacked-diode frequency doubler utilizing two series diodes. The input/output-matching circuits consist of $\lambda_0/4$ impedance transformer sections with open-circuited stubs resonant at the input and output frequencies. This design produced a maximum output power of 150 mW with a conversion efficiency of 24%, and a peak conversion efficiency of 35% at 95 mW of output power.

2.10.2. State of the Art. In the development of passive frequency multipliers as well as other technologies, researchers and designers are constantly pushing the leading edge in attempts to achieve better performance. In passive frequency multipliers, designers desire, among other things, greater power-handling capability and greater conversion gain efficiency. This section highlights state-of-the-art developments in passive frequency designs.

The available literature indicates that the leading edge of technology in passive designs is not focused so much on developing new design topologies as on new methods of fabricating new semiconductor diodes, particularly for millimeter and submillimeter-wavelength applications [25,36,39,41]. It has been demonstrated that the performance of passive frequency multipliers is highly dependent on the pertinent properties of the nonlinear device.

Therefore, it is reasonable to expect that efforts at improving the performance of passive frequency multipliers would begin with the nonlinear device.

Over the years, the GaAs Schottky varactor diode has served as one of the most important nonlinear elements for frequency multipliers [36,41]. Consequently, growing interest in novel diodes has brought to light new structures showing excellent theoretical performance comparable to or better than the conventional Schottky varactor. In comparison with the Schottky varactor, these new diodes have potential advantages, such as stronger nonlinearity or a special symmetry, which make them very attractive for millimeter and submillimeter-wave frequency multiplication. Stronger nonlinearities allow more efficient higher-order harmonic generation with smaller input signal levels [36]. These novel diodes include single-barrier varactors (SBVs), quantum barrier varactors (QBV), barrier-intrinsic- n^+ (BIN) diodes, and high-electron-mobility varactors (HEMVs).

The quantum well diode (QWD) has been studied since 1970 [41]. The QWD is a heterojunction diode in which a thin undoped layer between two thin barriers forms the quantum well. Its high speed and negative differential resistance make it attractive for millimeter-wave oscillators. Because of its symmetric structure, the highly nonlinear antisymmetric I - V curves and symmetric C - V characteristics result in odd-harmonic generation. Therefore, as expected, QWDs have been utilized in tripler designs, with some designs going up to 200 GHz. Raisanen [36] notes that the resulting output powers from these tripler designs are promising, but are lower than those achieved from the best Schottky multipliers. Replacing the quantum well with a single thicker barrier produces a QBV or a SBV, where the nonlinear current is suppressed but the nonlinear C - V characteristic remains. Because of its symmetric C - V characteristic, this diode is also attractive for tripler and quintupler design. SBV triplers have been developed up to 280 GHz, producing output powers of 2.5 mW [36].

The BIN diode has been proposed as an improved diode for harmonic generation [41]. Unlike QWDs or SBVs, which consist of a heterostructure and two ohmic contacts as terminals, the BIN diode is essentially a Schottky varactor with a unique doping profile that yields a sharper C - V characteristic than the Schottky varactor. The BIN diode consists of a Schottky contact, a barrier layer, and an intrinsic layer. Tolmunen [41] notes that connecting two BIN diodes back to back produces a symmetric C - V characteristic.

The HEMV is a modification of the planar Schottky varactor where a heterostructure is used. The electrons in this device have higher mobility, as in HEMTs (which are modeled and used in active multiplier designs in the final section), thus making it attractive for high-frequency applications. In a varactor, this structure produces a strongly nonlinear capacitance, but with an undesirable high parasitic capacitance associated with its structure.

Tolmunen [41] has designed several multipliers utilizing the abovementioned novel devices at 200 GHz. The conclusions from his study reveal that the sharp C - V characteristic of the BIN diodes improves the performance

at low input powers (10 mW) and makes them the most effective of all the devices. The SBV yields excellent theoretical performance, but is less efficient because of its high resistive losses. It does however, provide the best performance at high input power levels.

As researchers and designers continue to push the envelope of technology for higher-performance devices, these novel devices will be utilized extensively, particularly at submillimeter and millimeter frequencies.

3. ACTIVE FREQUENCY MULTIPLIERS

Another class of frequency multipliers encompasses those that are designed and constructed utilizing active nonlinear devices. As discussed earlier, multipliers require a nonlinear element for harmonic production [133–135]. Active frequency multipliers, as shown in the block diagram in Fig. 24, utilize the nonlinear characteristics of an active element properly biased to produce an output spectrum rich in harmonics when excited by a sinusoidal source. Typically, the active element consists of any of the transistor classes, which include the BJT, HBT, field-effect transistor (FET), MESFET, HEMT, and PHEMT.

Active multipliers offer various advantages over their passive counterparts. An example, which will be discussed in the following section, is in the conversion gain. Active multipliers are capable of producing conversion gains greater than 0 dB, whereas passive multipliers are not. This section will also discuss the development of active frequency multiplier technology, including the fundamental performance descriptions, and pertinent properties of the active device (which include modeling and quantification of the nonlinear properties). Design techniques of active frequency multipliers are discussed in Section 4.1.

In the systematic design of any *linear microwave amplifier*, an essential initial step in modern engineering practice, is the computer analysis of the proposed topology utilizing such tools as the HP/Agilent ADS simulator. An essential ingredient in this process is the use of realistic circuit models, some of which have required many worker-hours of development as exemplified by the microstripline models in that simulator. Simultaneously, realistic models of the transistor (FET, HEMT, HBT, etc.) are utilized. This model may be in the form of a physical model, measured S -parameter data, or an empirical model. In any case, some reasonable active device representation is used.

Such has *not* been the case for active microwave frequency multipliers until quite recently. These recent computer-based designs will be described in Section 4.2.

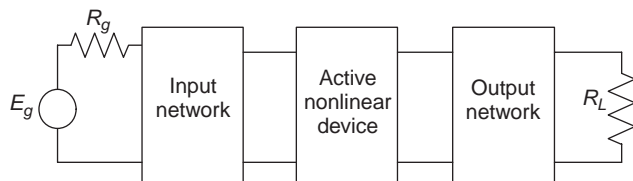


Figure 24. Block diagram of active frequency multiplier.

Numerous authors have presented discussions of active frequency multipliers that will be referenced throughout this presentation. A systematic design approach for development of active frequency multipliers, which is analogous to that for linear amplifiers, utilizes computer-based simulation. As a result, one of the primary concerns is the ability to accurately predict the linear and nonlinear performance of the active device before embedding it into other networks, which is typical in the development and design of frequency multipliers. Several authors [48–86,129,158–163] have presented details and techniques for modeling the active devices. Each author delineates the various advantages and disadvantage of their study. Techniques for modeling HEMTs are presented as an example in this discussion, since they are employed in the illustrative multiplier designs in later sections.

3.1. Fundamental Performance Descriptions

As discussed previously, frequency multipliers are nonlinear circuits that convert signals at an input fundamental frequency (f_0) into signals at a harmonic frequency multiple of the input frequency (nf_0). Several performance descriptions and parameters represent the effectiveness of frequency multipliers for frequency conversion. The objective of this section is to identify and discuss the prominent fundamental performance descriptions of active frequency multipliers.

Active frequency multipliers utilize the nonlinear characteristics possessed by any of the several properly biased transistor classes (BJT, FET, etc.). Exciting the nonlinear device with a fundamental frequency provides an output spectrum rich in frequency harmonics. One of the main advantages of active multipliers is their capability of producing positive conversion gains (conversion gains greater than 0 dB). The *conversion gain* of a frequency multiplier is defined as the ratio of the output power for a particular harmonic delivered to the load to the fundamental input power. Maximizing the conversion gain is crucial in the development and design of frequency multipliers. In the specific case of frequency doublers, an input signal at the fundamental frequency (f_0) is converted into a signal at the second-harmonic ($2f_0$). Mathematically, the conversion gain can be expressed as [87]

$$\text{Conversion gain} = \frac{P_{\text{out}}(2f_0)}{P_{\text{in}}(f_0)} \quad (60)$$

or

$$\text{Conversion gain (dB)} = P_{\text{out},2f_0}(\text{dBm}) - P_{\text{in},f_0}(\text{dBm}) \quad (61)$$

Frequency doublers, which will be presented in the next section, have been designed and developed exhibiting conversion gains approaching 12 dB. Alternatively, the conversion gain can be expressed as a percentage [88]. This percentage is defined as the ratio of the input power at the fundamental to the output power delivered to the load at the desired harmonic. Using the example of the frequency doubler, this can be represented as

$$\eta = \frac{P_{\text{in}}(f_0)}{P_{\text{out}}(2f_0)} \times 100\% \quad (62)$$

Similarly, as in the consideration of RF amplifiers, the effectiveness of the conversion of DC power into AC power is also a meaningful parameter in discussing frequency multipliers. In the case of frequency doublers, the consideration is focused on the effectiveness of converting DC power into AC power at the second-harmonic. A general expression for the DC-to-RF efficiency can be represented as [88]

$$\text{DC-to-RF} = \frac{P_{\text{out}}(\text{harmonic})}{P_{\text{DC}}} \times 100\% \quad (63)$$

From this equation, it is observed that optimum DC-to-RF efficiency performance is achieved when maximum RF power is produced from minimum DC power. For the class of frequency multipliers presented in the next subsection, DC-to-RF efficiencies of up to 24% have been obtained.

The transfer of power from the fundamental frequency at the generator to the desired harmonic at the load is dependent, amongst other things, on the return loss or voltage standing-wave ratio (VSWR) of the input port and the output port of the multiplier circuitry. The return loss is a measure of the impedance match of the input and output ports of the frequency multiplier to the source impedance and the load impedance. Computer simulations for HEMT frequency doublers are performed in Section 3.4.3. (see Tables 3 and 4) delineating the advantages of good impedance matching. In these simulations significant improvements in the conversion gain are achieved in the cases where the input and output ports are impedance-matched.

As discussed previously, frequency multipliers are harmonic generators that produce an output harmonic (nf_0) when excited by a fundamental frequency (f_0). In the generation of the desired harmonic, undesired harmonics are generated as well. As an example, in the case of a frequency doubler, the desired output harmonic is $2f_0$, but other harmonics at f_0 , $3f_0$, $4f_0$, are generated. The ability of the multiplier to suppress the undesired harmonics is another key performance factor. This property of the frequency multiplier is called *harmonic suppression*. It is defined mathematically as

$$\text{Suppression}_{(mf_0)}(\text{dBc}) = P_{0(nf_0)}(\text{dBm}) - P_{0(mf_0)}(\text{dBm}) \quad (64)$$

where nf_0 is the desired frequency harmonic and mf_0 is an undesired harmonic. In the case of the frequency doubler, $n = 2$ and $m = 1, 3, 4$, which indicates that the desired harmonic is $2f_0$ and harmonic suppression is calculated for the fundamental frequency (f_0), third-harmonic frequency ($3f_0$), and so on.

A previously discussed application of frequency multipliers is their use in communication systems in receivers and transmitters. A performance description of receivers in communication systems, and therefore of frequency multipliers used in receivers, is their *dynamic range*, defined as the range of input or output power levels where signals can be processed with high quality without signal distortion. At low power levels, the dynamic range is limited by the sensitivity to the noise floor or the minimum

detectable signal as governed by the noise floor. At higher powers, the dynamic range is limited by the acceptable level of signal distortion or, specifically, by the power level where the small-signal gain has been compressed by 1 dB [89,90].

Using these definitions for the dynamic range, the optimum dynamic range for frequency multipliers is achieved when the power range between the noise floor and signal distortion is maximized. It involves tradeoffs between the input signal drive level, the noise floor level, and the output signal distortion.

Another important multiplier performance parameter is the operational bandwidth. *Bandwidth* is defined as the frequency band where specific performance specifications are met; typically, one uses the conversion gain. Specifying a -3 dB bandwidth indicates the frequency band where the conversion gain decreases by 3 dB from its peak. Optimizing multiplier bandwidth is an important task to the designer. Typically, tradeoffs have to be made in the performance of the devices to achieve high bandwidths. As an example, higher conversion gains are achieved for narrow-bandwidth designs, and usually wide-bandwidth designs are accomplished at the expense of the conversion gain. One explanation for this is the difficulty of achieving impedance matching over broad ranges. Consequently, the conversion gain is reduced over the band to compensate for the extended bandwidth. Over narrow frequency bands impedance matching is less of a challenge and thus readily facilitates optimization of conversion gain.

3.2. Pertinent Properties of the Active Device

3.2.1. Nonlinear Modeling. As pointed out previously, accurate device models are an essential ingredient for the efficient design of active microwave multipliers. This section presents typical information on active devices necessary in active multiplier design. Since most of the effort on active multipliers employs FET-type devices, the remaining portions of this presentation will stress this class of active elements. Some multiplier realizations utilizing *Bipolar* devices are addressed in Ref. 95,155,156, and 164.

3.2.2. Classification of Device Models. Active-device circuit models are developed and categorized according to their specific applications. Depending on this classification, a specific model is typically employed, such as small-signal models and *S*-parameter data for small-signal amplifier applications.

Alternatively, for frequency multiplier applications, excellent nonlinear models are required to predict both the linear and nonlinear device performances.

The development of such models is a challenging undertaking that requires more depth in its exposition than space permits. The interested reader is referred to the literature [49–78] and [158–163] for in-depth treatment of this topic.

3.2.3. Development of Precision Models. Because of the necessity of precision nonlinear models for illustration of accurate multiplier designs, we will utilize a high-elec-

tron-mobility transistor manufactured by Fujitsu (FHX35LG) for that purpose.

Additionally, the frequency multiplier examples illustrated below are doublers, and thus, the highest frequency harmonic that will be modeled is the third harmonic. Furthermore, it has been pointed out in these applications, that the first three harmonics are of the greatest significance [99].

A number of authors [48–78] have developed nonlinear active-device models that are typically employable in active multiplier development. The interested reader is referred to Refs. 49 and 56 for in-depth discussion of most of these models.

For the purposes of our discussion, a general nonlinear FET/HEMT model is shown in Fig. 25. In this model, the nonlinear parameters include the following [49]:

D_{gs} = gate-to-source diode

D_{gd} = gate-to-drain diode

C_{gs} = gate-to-source capacitance

C_{gd} = gate-to-drain capacitance

C_{ds} = drain-to-source capacitance

I_{ds} = drain-to-source current

R_{ds} = output resistance = $\left(\frac{\partial I_{ds}}{\partial V_{gs}}\right)^{-1}$

g_m = transconductance (not shown in model but is represented by the equation: $g_m = \partial I_{ds} / \partial V_{gs}$)

In-depth discussions of these parameters and their device design implications are presented in Refs. 49 and 56.

3.3. Device Nonlinearities

It was discussed above that while the class of active devices available for multiplier applications includes BJT, MESFET, HEMT, and similar devices, this work will employ HEMT transistors as a vehicle for design illustrations.

The equivalent circuit for this device was shown in Fig. 25 with the nonlinear elements displayed that are exploited in the generation of frequency harmonics.

3.3.1. Analysis of Nonlinearities. In analyzing FET/HEMT performance, several authors have addressed the issue of identifying the elements that contribute to the nonlinear behavior of FET transistors [49,75,76,79,86,93,97,98,101]. Maas [86] has analyzed the nonlinear behavior of MESFET transistors. In his study, Maas provided the magnitude of all parasitic components (L_s , L_g , L_d , R_g , and R_d) and intrinsic components (R_i , R_{ds} , C_{gs} , C_{gd} , and g_m) in tabular form for various bias voltages. This provides insight into the nonlinear behavior of these components. R_i (not shown in Fig. 25) is the charging resistance in series with C_{gs} for a typical transistor. Maas' data for the parasitic inductors (L_s , L_g , and L_d) show that the magnitudes of these inductors are very small and are on the order of hundredths of nH. Their values vary from 0.03 to 0.08 nH for L_s , from 0.09 to 0.12 for L_g , and 0.06 to 0.07 nH for L_d or, in the worst case, their magnitudes vary by only 0.05 nH over the bias ranges. This

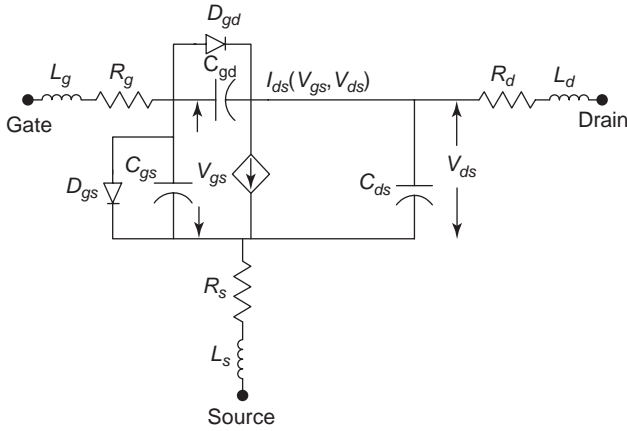


Figure 25. Nonlinear device equivalent circuit model.

indicates that at an arbitrary frequency of 1 GHz, the impedance of this inductance variation is approximately 0.25. This implies that the parasitic inductors can be approximated with fixed, constant values for all bias regions and, therefore, do not contribute as a source of nonlinearity to the MESFET. The magnitude of the parasitic resistors (R_g , R_s , and R_d) vary by only a few tenths of an ohm as functions of applied voltage. Therefore, similar to the parasitic inductors, their magnitudes can be fixed as constants in the device models.

Maas' data show that the output resistance of the MESFET varies nonlinearly over bias from approximately 10 to 283 [86].

This variation is significant and indicates that, as a result of this nonlinear characteristic, the output resistance of the transistor is one of the potential contributors to the nonlinear effects observed in the MESFET transistor. The gate-to-source and gate-to-drain capacitors (C_{gs} and C_{gd}) also vary nonlinearly as functions of applied voltage. C_{gs} is shown to vary from 0.415 to 0.636 pF, and C_{gd} varies from 0.049 to 0.266 pF. This nonlinear variation in C_{gs} and C_{gd} indicates that they are viable contributors to the harmonic production of the MESFET as well. The final element considered by Maas is the transconductance. The transconductance shows significant nonlinear variation over bias, particularly in the saturation region as it varies nonlinearly from 61.3 to 89.2 mS. This nonlinear variation indicates that it also contributes to the nonlinear behavior of the MESFET. In summary, Maas' study reveals that the elements significantly contributing to the nonlinear behavior of the MESFET are R_{ds} , C_{gs} , C_{gd} , and g_m . The remaining elements (L_s , L_g , L_d , R_i , R_g , R_s , and R_d) do not vary nonlinearly and can be considered to be constants in the models. Maas' study was performed on a MESFET; however, his results can be employed in identifying the nonlinear contributors to HEMT/PHEMT performance as well.

Gopinath and Rankin [79,119] have performed a study identifying the relative contributions of the various nonlinear elements of MESFETs valuable for harmonic generation. Their work emphasizes harmonic generation at the second-harmonic using computer simulations and

identifies the major contributors to the nonlinear behavior of the MESFET as (1) C_{gs} and C_{gd} ; (2) drain current nonlinearity, which results from the drain current clipping when V_{gs} swings below pinchoff or into forward conduction; (3) the nonlinearity of the drain current equation representing I_{ds} ; and (4) output resistance nonlinearity.

On the basis of computer analysis, Gopinath and Rankin conclude that, in the absence of other nonlinear contributions, the second-harmonic power level due to C_{gs} is on the order of 18–11 dB below the output power at the fundamental. In evaluating the effect of I_{ds} clipping, they neglect the transfer characteristic of I_{ds} and perform a Fourier analysis of the half-wave rectified waveform with $V_{gs} = 0$ V. They find that the second-harmonic output power level is 7.4 dB below the output power level at the fundamental. Gopinath and Rankin analyze the nonlinear contributions from the I_{ds} current equation nonlinearity and the output resistance by simulating the harmonic response of the FET with the drain current represented by Eqs. (65) and (66), respectively. The simulations show that the second-harmonic output power level is 16 dB below the output power level at the fundamental using Eq. (65) to represent I_{ds} , and that the second-harmonic output power level is 15 dB below the output power level at the fundamental when using Eq. (66) to represent I_{ds} :

$$I_{ds} = I_{dss} \left(1 - \frac{V_{gs}}{V_p} \right)^2 \quad (65)$$

$$I_{ds} = I_{dss} \left(1 - \frac{V_{gs}}{V_p} \right)^2 \left(1 + \frac{V_{ds}}{R_{do} I_{dss}} \right) \quad (66)$$

The conclusion is that the major contributor to the nonlinearity of the FET is the I_{ds} nonlinear clipping effect, which produced second-harmonic output power 7.4 dB below the output power at the fundamental. Slight contributions to the nonlinearity of the FET came from the C_{gs} nonlinearity, output conductance nonlinearity, and I_{ds} transfer nonlinearity. It should be noted, however, that the study uses approximations in the computer simulations. The computer model neglects the gate-to-drain branch of the circuit (C_{gd} and D_{gd}), the authors use a predetermined unknown resistive load (R_L), and they indicate that the results are valid only for $R_L \ll R_{do}$, where R_{do} is the output resistance. A final observation of this study is that measured data indicating the accuracy and practicality of the results are not presented.

With reference to the earlier work of Camargo [98], Dow [97] discusses the nonlinear contributions of the MESFET transistor using a graphical approach. He develops an equivalent-circuit model from measured S parameters to evaluate the bias-dependent nonlinear intrinsic circuit elements, and, afterward, presents curves representing g_m , C_{gs} , and G_{ds} versus V_{gs} and V_{ds} to show the nonlinear behavior of these parameters. Examining the curves, Dow identifies particular bias regions of V_{gs} and V_{ds} , where the nonlinear variation of g_m and G_{ds} is more prominent and significant for harmonic generation. With regard to the contribution from C_{gs} , Dow references the study performed by Gopinath and Rankin, as previously discussed,

in stating that second-harmonic generation is weakly dependent on C_{gs} nonlinearity. In summary, Dow's study concludes that harmonic generation is obtained from three sources of the MESFET: (1) nonlinearity of the intrinsic parameters C_{gs} , g_m , and G_{ds} ; (2) current rectification, which occurs when the gate voltage swings into forward conduction; and (3) current clipping occurring when the gate voltage swings below pinchoff.

The previous discussions have stressed the determination of the nonlinear elements responsible for harmonic generation in MESFETs. Focusing on the HEMT transistor, Golio [49] indicates that the major nonlinear elements of the HEMT device are (1) the drain-to-source current I_{ds} , from which the transconductance and output conductance are derived; (2) the gate-to-source and gate-to-drain capacitors (C_{gs} and C_{gd}); and (3) the gate-to-source and gate-to-drain diodes (D_{gs} and D_{gd}).

3.3.2. HEMT Characteristics. Modeled drain-to-source current, transconductance, and output conductance data for a Fujitsu FHX35LG HEMT are shown below to demonstrate the nonlinear characteristics of these types of active devices. Static I - V curves are shown in Figs. 26 and 27 for the transistor using the modeling techniques previously discussed and the equivalent nonlinear model shown in Fig. 28. From the static I - V curves, the transconductance and output conductance are derived and plotted against the drain-to-source (V_{ds}) and gate-to-source (V_{gs}) voltages as shown in Figs. 29–32. These plots graphically display the nonlinearity of the transconductance and output conductance of the HEMT transistor as functions of the DC bias voltages. As shown in these plots, these elements show varying degrees of nonlinearity, which are dependent on the drain-to-source (V_{ds}) and gate-to-source (V_{gs}) voltages bias. The exploitation of these nonlinearities with respect to the optimum bias conditions will be discussed in the following section.

3.4. Nonlinearities Utilized for Frequency Multiplication

The preceding sections presented a general synopsis of device nonlinearities. This section delineates the nonlinearities of specific importance for frequency multiplication applications, given certain optimum bias conditions. Additionally, the impact of terminating impedances on multiplier performance is detailed.

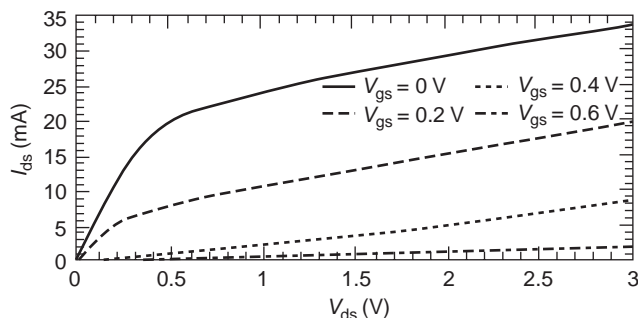


Figure 26. Modeled drain current of HEMT transistor versus drain-to-source voltage.

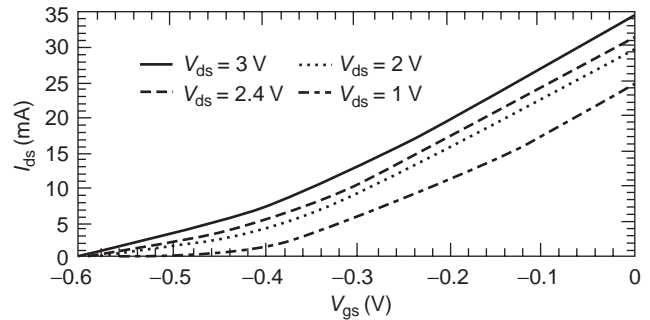


Figure 27. Modeled drain current of HEMT transistor versus gate-to-source voltage.

3.4.1. Optimum Bias Selection. Golio [49] has noted that the drain-to-source current (I_{ds}) contributes to the nonlinear behavior of the HEMT transistor. In this accord, static I - V curves representing the drain-to-source current are utilized to characterize two dominant nonlinear circuit elements previously identified: the transconductance (g_m) and the output conductance (g_{ds}). These parameters plotted versus the drain-to-source (V_{ds}) and gate-to-source (V_{gs}) voltages as shown in Figs. 26–32, show the nonlinearity of the elements displayed as a function of the DC bias voltages.

For the class of multipliers under consideration, the nonlinear behavior of the drain-to-source current (I_{ds}) produces harmonic generation through its clipping effect [79,98]. In the case of harmonic generation, the conclusion has been advanced that optimum harmonic generation occurs for either $V_{gs} = 0$ or $V_{gs} = V_p$ [97,98,102,127].

If the FET is biased at $V_{gs} = 0$, the input voltage waveform appearing across the gate-to-source capacitance (C_{gs}) is clipped and will be half-wave rectified because of the conduction cycles experienced by the gate-to-source diode. This rectified waveform is transferred to I_{ds} through the device's transfer properties as reflected by the analytical relation between I_{ds} and V_{gs} [55]. When the device is biased at the pinchoff voltage ($V_{gs} = V_p$), however, the input voltage at the gate causes the FET to turn on during the positive half-cycle of the input voltage, and the output voltage again becomes a half-wave rectified waveform.

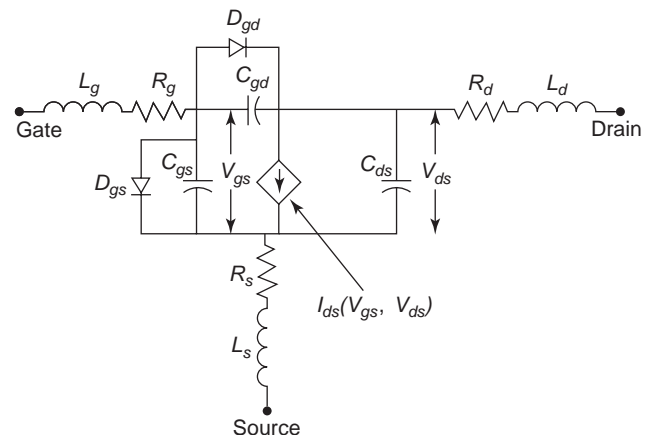


Figure 28. HEMT/PHEMT nonlinear equivalent model.

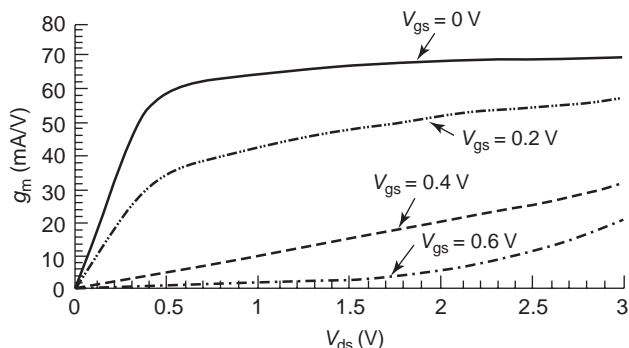


Figure 29. Modeled transconductance of HEMT transistor versus drain-to-source voltage.

When the gate voltage is biased between 0 V and pinchoff ($0 \geq V_{gs} \geq V_p$), and the input voltage swing is large enough to cause clipping on both ends, the output current at the drain will resemble a square wave. If the square wave is symmetric, the second-harmonic component will be small, but the third harmonic will be large, allowing frequency tripling [97].

It has been shown that rich harmonic generation will result for class A and class B operation of the transistor [96,97,98]. Class A operation occurs for $V_{gs} = 0$ V and causes drain current (I_{ds}) rectification when the gate diode swings into forward conduction. Class B operation occurs for $V_{gs} = V_p$, where V_p is the pinchoff voltage, and causes the drain current to clip when the gate voltage swings below pinchoff.

Dow [97] and Camargo [98] conclude that class A FET multipliers provide good multiplication gain and poor DC-to-RF efficiency, while class B FET multipliers have poor multiplication gain and good DC-to-RF efficiency.

Using the DC-to-RF efficiency expression [Eq. (63)], the efficiency for typical HEMT frequency doublers, which was simulated with $V_{gs} = V_p$ and $V_{gs} = 0$ V, respectively, can be computed. As an example, evaluating various simulation data for $V_{gs} = V_p$, the DC-to-RF efficiency is 23.5%, and for typical simulations for $V_{gs} = 0$ V, the DC-to-RF efficiency is 0.03%. In each simulation the DC supply voltage (V_{ds}) was 3 V, which causes the DC power for the simulation with $V_{gs} = 0$ V to be considerably higher and, subsequently, to reduce the DC-to-RF efficiency. Usually, for class A

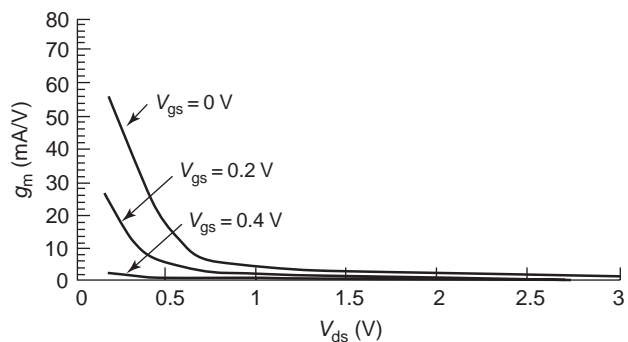


Figure 31. Modeled output conductance of HEMT transistor versus drain-to-source voltage.

operation the device is biased at a lower V_{ds} voltage than the case presented here, thus reducing the DC power and increasing the DC-to-RF efficiency.

More recent research has shown, however, that other V_{gs} values may provide better and more optimum results [166,172]. These results demonstrate that other biases provide improved performance from an output harmonic power perspective. This conclusion was based on the use of rather basic device models that contained no feedback, parasitic elements, or nonlinear G_d . Employing their analytical approach, which was a revision of Maas [44], O’Ciardha et al. [172] predict potentially realistic 8% improvement in output doubler power utilizing only modest changes in bias and input power. Theoretical improvements are shown to be up to 15%.

An investigation by Johnson [171] reveals that, while this is true, these new biases require greater input power and have inferior conversion gain.

Focusing on the Fujitsu FHX35LG HEMT device, measured and modeled measurements provide static I - V curves as shown in Fig. 33. From these data, measured and modeled transconductance and output conductance are derived.

Figures 34–37 show the transconductance and output conductances plotted as functions of the gate-to-source (V_{gs}) and drain-to-source (V_{ds}) voltages. Recalling that the optimum bias conditions are either $V_{gs} = 0$ or $V_{gs} = V_p$, the HEMT transconductance and output conductance plots of Figs. 34–37 show the nonlinear behavior of the

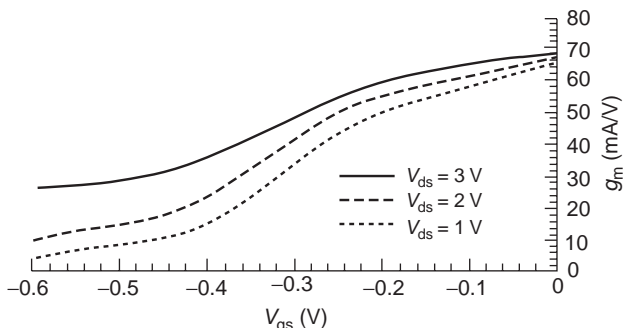


Figure 30. Modeled transconductance of HEMT transistor versus gate-to-source voltage.

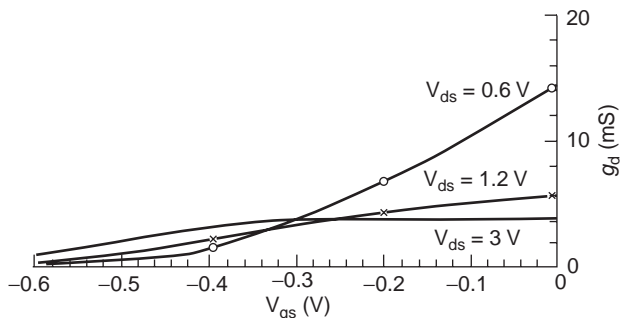


Figure 32. Modeled output conductance of HEMT transistor versus gate-to-source voltage.

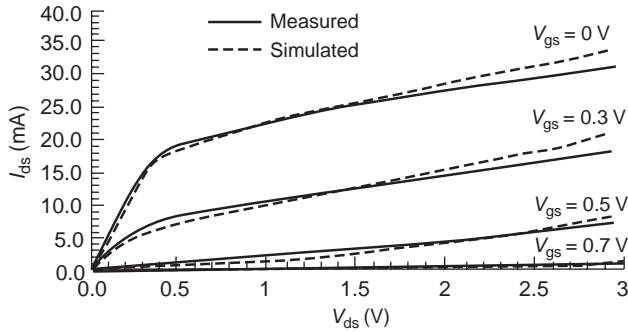


Figure 33. Modeled transconductance of HEMT transistor versus drain-to-source voltage.

transconductance and output conductance at the optimum bias regions.

In Figs. 34 and 36, oval circles representing the regions (region I) of optimum nonlinearity are indicated for $V_{gs} = 0$ V. These regions are identified as areas where the nonlinear variation in the transconductance and output conductance is greatest. In Fig. 34, the variation in the transconductance is actually greatest for $V_{ds} < 0.5$ V, but in this area of operation the transistor does not supply appreciable gain, thus limiting its usefulness at these bias levels for significant conversion gains. For $V_{ds} > 1$ V, the transconductance tends to flatten with no significant variation for $V_{gs} = 0$ V. This behavior is observed again in Fig. 36 with the output conductance.

In Figs. 35 and 37, regions (region II) for optimum nonlinearity are represented for $V_{gs} = V_p$. Again, areas where the nonlinear variation in the magnitudes of the transconductance and output conductance is greatest are indicated by oval circles. In Fig. 37, significant nonlinear variation in the transconductance is also seen in the vicinity of $V_{gs} = -0.3$ V. Operating in this vicinity is optimum for frequency multipliers, where the third harmonic (frequency tripler) is of interest [97]. Biasing in this vicinity with large voltage swings at the gate of the FET causes the I_{ds} waveform to clip at both pinchoff and forward conduction and causes I_{ds} to resemble a square wave, which enhances the third harmonic frequency [97]. In Fig. 37 significant variation in the output conductance also occurs for V_{gs} 0 to -0.1 V for lower V_{ds} values (V_{ds} 0.6 V). As mentioned previously, the gain of the transistor diminishes significantly in these bias areas, thus causing the

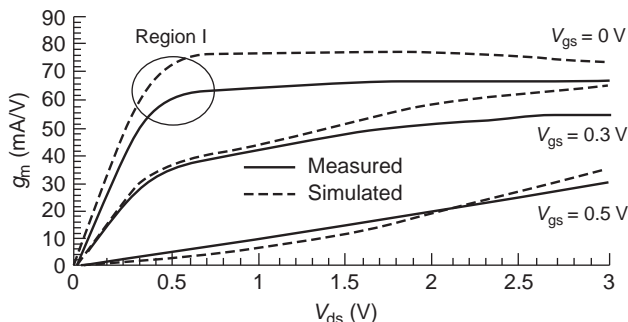


Figure 34. Measured and simulated transconductance of FHX35LG (region I).

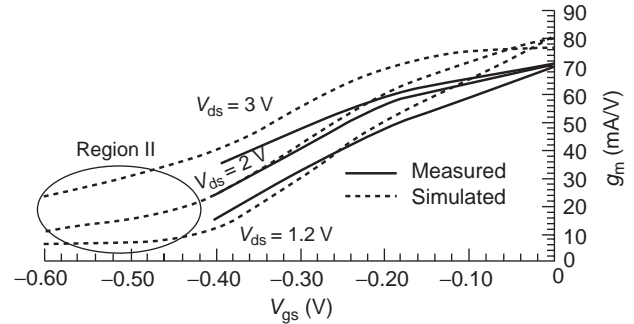


Figure 35. Measured and simulated transconductance of FHX35LG (region II).

conversion gain of the frequency multiplier to reduce as well. From these curves the prominent nonlinearity regions for $V_{gs} = 0$ is region I of Fig. 36, where g_{ds} is dominant and for $V_{gs} = V_p$, region II of Fig. 35, with g_m showing the dominant effect.

3.4.2. Detrimental Parasitics: Definition of the Parasitics. The equivalent-circuit topology for the nonlinear FET transistor as given in Fig. 25 includes the parasitic elements ($L_s, L_g, L_d, R_s, R_d,$ and R_g). These parasitics arise from the fabrication process in the development of semiconductor transistors and influence the performance of the transistor and thus warrant inclusion into the equivalent-circuit model. The parasitic inductors ($L_s, L_g,$ and L_d) primarily represent the inductance associated with the metal contact pads deposited on the active-channel layer of the FET. The source and drain parasitic resistors (R_s and R_d) represent the contact resistance of the ohmic contacts underneath the metal contact pads and any bulk resistance leading up to the active channel, and the gate parasitic resistance (R_g) represents the metallization resistance of the gate Schottky contact [49].

3.4.3. Optimum Bias Selection Referencing Harmonic Terminations. A primary factor affecting optimum performance of microwave multipliers employing nonlinear devices is the proper termination of the fundamental and other harmonic frequency components with regard to bias selection. This section presents a quantitative analysis leading to the assessment of optimum terminating impedances in the design of active frequency multipliers, with

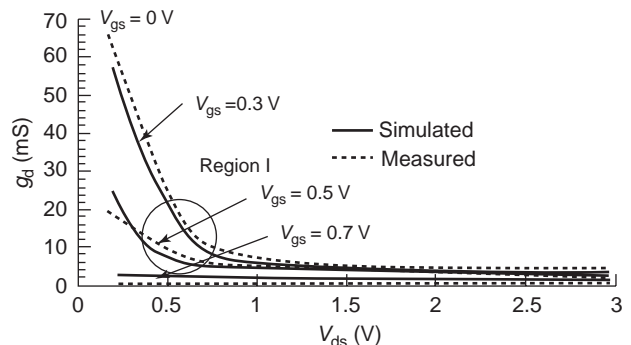


Figure 36. Measured and simulated output conductance of FHX35LG (region I).

special attention given to harmonics other than those desired. The analysis includes computer modeled HEMT data and supporting measured data for corresponding circuit realizations. Circuit designs are presented utilizing HEMT transistors as the active element to verify modeled results. From the available literature, the results demonstrate, for the first time, the quantitative effects of harmonic termination on active multiplier conversion gain and fundamental and higher-harmonic suppression. An experimental design, which will be discussed later, reveals an improvement in multiplier gain of 77% over the conventional approach, and data are presented that quantitatively illustrate the advantages of impedance termination considerations under optimal bias conditions.

3.5. Background and Motivation

Numerous techniques exist for the realization of frequency multipliers, as will be discussed below [87–88,91–128, 130–132,137–139]. At radiofrequencies, these techniques typically employ a nonlinear device to generate the desired frequency multiple. In the design of passive multipliers, the nonlinear element is typically a varactor diode. In the active case, the nonlinear element typically includes any of several transistor classes such as BJT and FET.

In many frequency multiplier design approaches, the operating performance is improved by the proper selection of input and output circuits terminating impedances at the fundamental and harmonic frequencies [91–95, 109,145].

This section presents a quantitative analysis of the optimization of active multiplier conversion gain and spectral purity, as governed by fundamental and harmonic terminating impedances and regions of nonlinearity. It is believed that access to this quantitative information will be of use for designers of future circuits. HEMT transistors are employed to represent the class of nonlinear elements to illustrate the approach. The optimum terminating impedances are determined for the input and output ports of the active device, utilizing a more recent nonlinear circuit model for HEMT transistors. This is in marked contrast with earlier studies, which used approximations in the simulated performance predictions [79,93,98]. The results presented in this section incorporate dependences between the input and output harmonic terminating impedances that are not found in previous studies. For the multipliers examined in this section, these impedances include terminations at the fundamental, second-harmonic, and third-harmonic frequencies. Measured data are presented that validate the practicality of the designs and the accuracy of the simulations.

3.5.1. Nonlinear Model. An accurate nonlinear circuit model is required for the quantitative assessment of optimum terminating impedances in the design of active frequency multipliers. Such an equivalent-circuit model permits supporting simulated data to accompany any measured data that further authenticate results. An accurate nonlinear model was presented earlier for the Fujitsu FHX35LG HEMT, which will be employed below for analyzing bias selection with regard to harmonic

terminations (case parasitics are included in the model but not shown in the figure).

Static I - V curves for this HEMT, obtained from the model of Fig. 25 and laboratory measurements, are employed to characterize two dominant circuit element nonlinearities: transconductance (g_m) and the output conductance (g_d). These parameters (modeled and measured), which were derived from the above mentioned sources, are plotted versus the drain-to-source (V_{ds}) and gate-to-source (V_{gs}) voltages shown in Figs. 33–37. These plots graphically display the nonlinearity of the corresponding HEMT elements as a function of the DC bias voltages. The conclusions for the HEMT multiplier are presented quantitatively below.

Utilizing the HEMT transconductance and output conductance plots of Figs. 33–37, the prominent nonlinear regions for the optimum DC bias points (either $V_{gs} = 0$ or $V_{gs} = V_p$) were identified in previous sections. Fundamental load-line analysis indicates that the optimum impedance for region I ($V_{gs} = 0$) is an open-circuit impedance that allows a maximum V_{ds} voltage swing, and for region II ($V_{gs} = V_p$) the optimum impedance is a short-circuit impedance that allows a maximum I_{ds} current swing [145]. These qualitative assertions will be substantiated quantitatively in the ensuing discussion.

3.5.2. Harmonic Terminations. The preceding analysis provides motivation for development of an optimal design approach. We employ the following multiplier design as an illustration. The basic topology of the frequency multiplier used is illustrated in Fig. 38. In this configuration, SC_i , $i = 1 \dots n$, and OC_j , $j = 1 \dots m$, represent short-circuit and open-circuit terminating impedances, respectively, for the multiplier input network at the respective frequencies. Similarly, SC_k , $k = 1 \dots o$, and OC_l , $l = 1 \dots p$, represent short- and open-circuit terminating impedances for the multiplier output network. An infinite number of circuit realizations exist that conform to the configuration of Fig. 38. This provides the motivation for development of a matrix of various circuit configurations as illustrated in Table 1, which displays various harmonic terminating impedances on the input and output ports of the multiplier realization depicted in Fig. 38. Tables have been constructed for multiplier operation (up to the third harmonic) utilizing the precision HEMT computer model with case

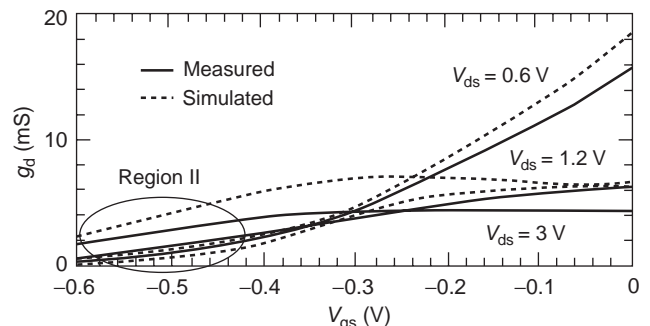


Figure 37. Measured and simulated output conductance of FHX35LG (region II).

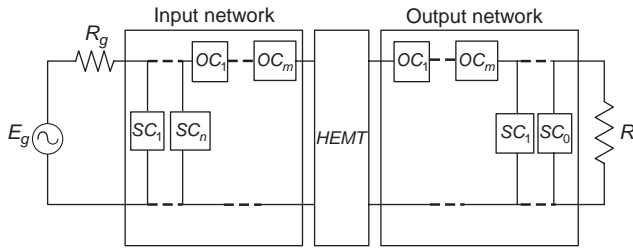


Figure 38. Frequency multiplier realization.

parasitics. In Table 1, the left-hand vertical column represents various impedance terminations of the input network at the fundamental, second-harmonic, and third-harmonic frequencies. The top horizontal row represents various impedances of the output network at the fundamental, second-harmonic, and third-harmonic frequencies.

To assess performance under various load terminations, several load configurations were analyzed. On the basis of previous discussions, fundamental and harmonic loads of interest may be short-circuited, open-circuited, matched, or 50.

As a first case, the options shown in Tables 1 and 2 were selected. Since only 50, short, and open loads are used, this choice of terminations would appear to provide a concrete basis for assessing the effects of a variety of other input and output harmonic load conditions. Table 1 illustrates the conversion gains obtained employing the FHX35LG HEMT utilizing a harmonic balance program with input and output networks synthesized with lumped elements to realize the indicated harmonic terminations with $f_0=3$ GHz. The HEMT in this table is biased at pinchoff $V_{gs}=V_p$ and driven with 0 dBm at the gate terminal (region II; Figs 35 and 37). This table is presented as a basis by which to measure the quantitative impact of a

Table 1. Doubler Simulations with Lumped Components ($V_{gs} = -0.7$ V, $P_{in} = 0$ dBm, $V_{ds} = 3$ V)

		Output Power (dBm) ^a								
		$\begin{pmatrix} 50 \\ 50 \\ 50 \end{pmatrix}$	$\begin{pmatrix} 0 \\ 50 \\ 50 \end{pmatrix}$	$\begin{pmatrix} \infty \\ 50 \\ 50 \end{pmatrix}$	$\begin{pmatrix} 0 \\ 50 \\ \infty \end{pmatrix}$	$\begin{pmatrix} \infty \\ 50 \\ \infty \end{pmatrix}$	$\begin{pmatrix} 50 \\ 50 \\ 0 \end{pmatrix}$	$\begin{pmatrix} 50 \\ 50 \\ \infty \end{pmatrix}$	$\begin{pmatrix} 0 \\ 50 \\ 0 \end{pmatrix}$	$\begin{pmatrix} \infty \\ 50 \\ 0 \end{pmatrix}$
Input Network (Ω) ^{a,b}	Output Network (Ω) ^{a,b}									
$\begin{pmatrix} 50 \\ 50 \\ 50 \end{pmatrix}$	$\begin{pmatrix} 50 \\ 50 \\ 50 \end{pmatrix}$	$\begin{pmatrix} 5.96 \\ -0.9 \\ -14.7 \end{pmatrix}$	$\begin{pmatrix} -73 \\ 0 \\ -14 \end{pmatrix}$	$\begin{pmatrix} -66.5 \\ -1 \\ -17.8 \end{pmatrix}$	$\begin{pmatrix} -73.2 \\ 0.3 \\ -72.5 \end{pmatrix}$	$\begin{pmatrix} -66.5 \\ 0.7 \\ -107 \end{pmatrix}$	$\begin{pmatrix} 5.9 \\ -1.3 \\ -94 \end{pmatrix}$	$\begin{pmatrix} 5.9 \\ -0.7 \\ -104 \end{pmatrix}$	$\begin{pmatrix} -73.2 \\ -0.2 \\ -94 \end{pmatrix}$	$\begin{pmatrix} -66.5 \\ -1.4 \\ -97.2 \end{pmatrix}$
$\begin{pmatrix} 50 \\ 0 \\ 50 \end{pmatrix}$	$\begin{pmatrix} 50 \\ 0 \\ 50 \end{pmatrix}$	$\begin{pmatrix} 6.2 \\ 0.3 \\ -11.8 \end{pmatrix}$	$\begin{pmatrix} -72.9 \\ 1.5 \\ -10.6 \end{pmatrix}$	$\begin{pmatrix} -66.3 \\ -0.1 \\ -17.2 \end{pmatrix}$	$\begin{pmatrix} -72.8 \\ 1.8 \\ -68.9 \end{pmatrix}$	$\begin{pmatrix} -66.3 \\ 0.2 \\ -106 \end{pmatrix}$	$\begin{pmatrix} 6.2 \\ 0 \\ -92 \end{pmatrix}$	$\begin{pmatrix} 6.3 \\ 0.7 \\ -100 \end{pmatrix}$	$\begin{pmatrix} -72.9 \\ 1.2 \\ -91.1 \end{pmatrix}$	$\begin{pmatrix} -66.3 \\ -0.5 \\ -97.7 \end{pmatrix}$
$\begin{pmatrix} 50 \\ 0 \\ 0 \end{pmatrix}$	$\begin{pmatrix} 50 \\ 0 \\ 50 \end{pmatrix}$	$\begin{pmatrix} 6 \\ 1.2 \\ -13.4 \end{pmatrix}$	$\begin{pmatrix} -72.9 \\ 1.5 \\ -10.6 \end{pmatrix}$	$\begin{pmatrix} -66.3 \\ -0.1 \\ -17.2 \end{pmatrix}$	$\begin{pmatrix} -72.8 \\ 1.8 \\ -99.1 \end{pmatrix}$	$\begin{pmatrix} -66.5 \\ 0.9 \\ -109.6 \end{pmatrix}$	$\begin{pmatrix} 6.2 \\ 0.3 \\ -11.8 \end{pmatrix}$	$\begin{pmatrix} 6.3 \\ 0.7 \\ -100.6 \end{pmatrix}$	$\begin{pmatrix} -72.9 \\ 1.2 \\ -91.1 \end{pmatrix}$	$\begin{pmatrix} -66.3 \\ -0.5 \\ -97.7 \end{pmatrix}$
$\begin{pmatrix} 50 \\ 50 \\ 0 \end{pmatrix}$	$\begin{pmatrix} 50 \\ 50 \\ 50 \end{pmatrix}$	$\begin{pmatrix} 5.9 \\ -2.2 \\ -17.1 \end{pmatrix}$	$\begin{pmatrix} -73.2 \\ 1.3 \\ -16.8 \end{pmatrix}$	$\begin{pmatrix} -66.5 \\ -2.3 \\ -15.8 \end{pmatrix}$	$\begin{pmatrix} -73.2 \\ -1.2 \\ -108.2 \end{pmatrix}$	$\begin{pmatrix} -66.5 \\ -1.7 \\ -106.6 \end{pmatrix}$	$\begin{pmatrix} 5.9 \\ -1.3 \\ -94.5 \end{pmatrix}$	$\begin{pmatrix} 5.9 \\ -2.1 \\ -108 \end{pmatrix}$	$\begin{pmatrix} -73.2 \\ -0.1 \\ -94.1 \end{pmatrix}$	$\begin{pmatrix} -66.7 \\ -2.7 \\ -90.5 \end{pmatrix}$
$\begin{pmatrix} 50 \\ \infty \\ 50 \end{pmatrix}$	$\begin{pmatrix} 50 \\ 50 \\ 50 \end{pmatrix}$	$\begin{pmatrix} 6.1 \\ -1 \\ -15.9 \end{pmatrix}$	$\begin{pmatrix} -73 \\ 0 \\ -15.3 \end{pmatrix}$	$\begin{pmatrix} -66.6 \\ -1.2 \\ -21.2 \end{pmatrix}$	$\begin{pmatrix} -73.1 \\ 0.1 \\ -104 \end{pmatrix}$	$\begin{pmatrix} -66.6 \\ -1 \\ -109 \end{pmatrix}$	$\begin{pmatrix} 6.1 \\ -1.1 \\ -96 \end{pmatrix}$	$\begin{pmatrix} 6.1 \\ -0.8 \\ -105 \end{pmatrix}$	$\begin{pmatrix} -73 \\ -0.2 \\ -96.1 \end{pmatrix}$	$\begin{pmatrix} -66.5 \\ -1.5 \\ -100.4 \end{pmatrix}$
$\begin{pmatrix} 50 \\ \infty \\ \infty \end{pmatrix}$	$\begin{pmatrix} 50 \\ 50 \\ 50 \end{pmatrix}$	$\begin{pmatrix} 6.1 \\ -0.9 \\ -15.7 \end{pmatrix}$	$\begin{pmatrix} -73 \\ 0 \\ -15.1 \end{pmatrix}$	$\begin{pmatrix} -66.5 \\ -1.1 \\ -20 \end{pmatrix}$	$\begin{pmatrix} -73 \\ 0.3 \\ -104 \end{pmatrix}$	$\begin{pmatrix} -66.5 \\ -0.9 \\ -108 \end{pmatrix}$	$\begin{pmatrix} 6.1 \\ -1.2 \\ 96.2 \end{pmatrix}$	$\begin{pmatrix} 6.1 \\ -0.7 \\ -105 \end{pmatrix}$	$\begin{pmatrix} -73 \\ -0.2 \\ -96 \end{pmatrix}$	$\begin{pmatrix} -66.5 \\ -1.4 \\ -99.8 \end{pmatrix}$
$\begin{pmatrix} 50 \\ 50 \\ \infty \end{pmatrix}$	$\begin{pmatrix} 50 \\ 50 \\ 50 \end{pmatrix}$	$\begin{pmatrix} 6 \\ -0.8 \\ 14.3 \end{pmatrix}$	$\begin{pmatrix} -73.1 \\ 0.1 \\ -13.6 \end{pmatrix}$	$\begin{pmatrix} -66.5 \\ -0.9 \\ -17 \end{pmatrix}$	$\begin{pmatrix} -73 \\ 0.4 \\ -102 \end{pmatrix}$	$\begin{pmatrix} -66.5 \\ -0.7 \\ -105 \end{pmatrix}$	$\begin{pmatrix} 6 \\ -1.3 \\ -94.4 \end{pmatrix}$	$\begin{pmatrix} 6 \\ -0.5 \\ -103 \end{pmatrix}$	$\begin{pmatrix} -73 \\ -0.2 \\ -93.9 \end{pmatrix}$	$\begin{pmatrix} -66.5 \\ -1.4 \\ -96.9 \end{pmatrix}$

^aAt $\begin{pmatrix} f_0 \\ 2f_0 \\ 3f_0 \end{pmatrix}$.

^b0 = short circuit; ∞ = open circuit.

Table 2. Doubler Simulations with Lumped Components ($V_{gs} = 0$ V, $P_{in} = 0$ dBm, $V_{ds} = 3$ V)

Input Network (Ω) ^{a,b}	Output Network (Ω) ^{a,b}	Output Power (dBm) ^a								
		$\begin{pmatrix} 50 \\ 50 \\ 50 \end{pmatrix}$	$\begin{pmatrix} 0 \\ 50 \\ 50 \end{pmatrix}$	$\begin{pmatrix} \infty \\ 50 \\ 50 \end{pmatrix}$	$\begin{pmatrix} 0 \\ 50 \\ \infty \end{pmatrix}$	$\begin{pmatrix} \infty \\ 50 \\ \infty \end{pmatrix}$	$\begin{pmatrix} 50 \\ 50 \\ 0 \end{pmatrix}$	$\begin{pmatrix} 50 \\ 50 \\ \infty \end{pmatrix}$	$\begin{pmatrix} 0 \\ 50 \\ 0 \end{pmatrix}$	$\begin{pmatrix} \infty \\ 50 \\ 0 \end{pmatrix}$
$\begin{pmatrix} 50 \\ 50 \\ 50 \end{pmatrix}$		$\begin{pmatrix} 12.5 \\ -10.1 \\ -13.9 \end{pmatrix}$	$\begin{pmatrix} -66.2 \\ -10.9 \\ -10.7 \end{pmatrix}$	$\begin{pmatrix} -62.1 \\ -2.4 \\ -7.1 \end{pmatrix}$	$\begin{pmatrix} -66.2 \\ -10.6 \\ -98 \end{pmatrix}$	$\begin{pmatrix} -62 \\ -2 \\ -92 \end{pmatrix}$	$\begin{pmatrix} 12.5 \\ -10.2 \\ -94.3 \end{pmatrix}$	$\begin{pmatrix} 12.5 \\ -10 \\ -101 \end{pmatrix}$	$\begin{pmatrix} -66.3 \\ -11.2 \\ -91.8 \end{pmatrix}$	$\begin{pmatrix} -62.1 \\ -2.2 \\ -89.5 \end{pmatrix}$
$\begin{pmatrix} 50 \\ 0 \\ 50 \end{pmatrix}$		$\begin{pmatrix} 12.4 \\ -11.1 \\ -14.1 \end{pmatrix}$	$\begin{pmatrix} -66 \\ -14.7 \\ -11.1 \end{pmatrix}$	$\begin{pmatrix} -62.2 \\ -2.6 \\ -7.3 \end{pmatrix}$	$\begin{pmatrix} -66 \\ -14.1 \\ -98.4 \end{pmatrix}$	$\begin{pmatrix} -62 \\ -2.1 \\ -92.7 \end{pmatrix}$	$\begin{pmatrix} 12.4 \\ -11.3 \\ -94.8 \end{pmatrix}$	$\begin{pmatrix} 12.5 \\ -10.8 \\ -101 \end{pmatrix}$	$\begin{pmatrix} -66.2 \\ -15.3 \\ -92.2 \end{pmatrix}$	$\begin{pmatrix} -62 \\ -2.7 \\ -89.8 \end{pmatrix}$
$\begin{pmatrix} 50 \\ 0 \\ 0 \end{pmatrix}$		$\begin{pmatrix} 12.4 \\ -11.2 \\ -18.6 \end{pmatrix}$	$\begin{pmatrix} -66 \\ -15.3 \\ -14.6 \end{pmatrix}$	$\begin{pmatrix} -62 \\ -3.2 \\ -5.9 \end{pmatrix}$	$\begin{pmatrix} -66 \\ -15.4 \\ -105 \end{pmatrix}$	$\begin{pmatrix} -62 \\ -2.2 \\ -94.2 \end{pmatrix}$	$\begin{pmatrix} 12.4 \\ -10.8 \\ -82.7 \end{pmatrix}$	$\begin{pmatrix} 12.4 \\ -11.1 \\ -109 \end{pmatrix}$	$\begin{pmatrix} -66.1 \\ -13.8 \\ -81.8 \end{pmatrix}$	$\begin{pmatrix} -62.4 \\ -2.8 \\ -78 \end{pmatrix}$
$\begin{pmatrix} 50 \\ 50 \\ 0 \end{pmatrix}$		$\begin{pmatrix} 12.4 \\ -10.2 \\ -18.3 \end{pmatrix}$	$\begin{pmatrix} -66.3 \\ -11.2 \\ -14.9 \end{pmatrix}$	$\begin{pmatrix} -62.1 \\ -3 \\ -5.7 \end{pmatrix}$	$\begin{pmatrix} -66 \\ -11.2 \\ -37.1 \end{pmatrix}$	$\begin{pmatrix} -62.1 \\ -2.1 \\ -93.9 \end{pmatrix}$	$\begin{pmatrix} 12.5 \\ -10.4 \\ -82.4 \end{pmatrix}$	$\begin{pmatrix} 12.4 \\ -10 \\ -109 \end{pmatrix}$	$\begin{pmatrix} -66 \\ -10.9 \\ -82.2 \end{pmatrix}$	$\begin{pmatrix} -62.3 \\ -2.4 \\ -78 \end{pmatrix}$
$\begin{pmatrix} 50 \\ \infty \\ 50 \end{pmatrix}$		$\begin{pmatrix} 12.6 \\ -9.3 \\ -13.7 \end{pmatrix}$	$\begin{pmatrix} -66.1 \\ -10.3 \\ -10.3 \end{pmatrix}$	$\begin{pmatrix} -62.1 \\ -2.1 \\ -7.1 \end{pmatrix}$	$\begin{pmatrix} -66.1 \\ -10.1 \\ -97.8 \end{pmatrix}$	$\begin{pmatrix} -62.1 \\ -1.7 \\ -92.4 \end{pmatrix}$	$\begin{pmatrix} 12.6 \\ -9.3 \\ -94.6 \end{pmatrix}$	$\begin{pmatrix} -12.6 \\ -9.2 \\ -101 \end{pmatrix}$	$\begin{pmatrix} -66.1 \\ -10.7 \\ -91.5 \end{pmatrix}$	$\begin{pmatrix} -62.1 \\ -1.9 \\ -89.6 \end{pmatrix}$
$\begin{pmatrix} 50 \\ \infty \\ \infty \end{pmatrix}$		$\begin{pmatrix} 12.6 \\ -9.3 \\ -13 \end{pmatrix}$	$\begin{pmatrix} -66 \\ -10.3 \\ -9.7 \end{pmatrix}$	$\begin{pmatrix} -62 \\ -1.9 \\ -7.3 \end{pmatrix}$	$\begin{pmatrix} -66 \\ -9.9 \\ -96.5 \end{pmatrix}$	$\begin{pmatrix} -62.1 \\ -1.7 \\ -91.6 \end{pmatrix}$	$\begin{pmatrix} 12.6 \\ -9.3 \\ -94.8 \end{pmatrix}$	$\begin{pmatrix} -12.6 \\ -9.2 \\ -100 \end{pmatrix}$	$\begin{pmatrix} -66 \\ -10.7 \\ -91.5 \end{pmatrix}$	$\begin{pmatrix} -62 \\ -1.8 \\ -90.7 \end{pmatrix}$
$\begin{pmatrix} 50 \\ 50 \\ \infty \end{pmatrix}$		$\begin{pmatrix} 12.5 \\ -10.1 \\ -13.3 \end{pmatrix}$	$\begin{pmatrix} -66.2 \\ -10.8 \\ -10.1 \end{pmatrix}$	$\begin{pmatrix} -62.1 \\ -2.2 \\ -7.3 \end{pmatrix}$	$\begin{pmatrix} -66.1 \\ -10.4 \\ -96.8 \end{pmatrix}$	$\begin{pmatrix} -62.1 \\ -2 \\ -91.6 \end{pmatrix}$	$\begin{pmatrix} 12.5 \\ -10.2 \\ -95.1 \end{pmatrix}$	$\begin{pmatrix} 12.5 \\ -9.9 \\ -100 \end{pmatrix}$	$\begin{pmatrix} -66.2 \\ -11.2 \\ -92 \end{pmatrix}$	$\begin{pmatrix} -62.1 \\ -2.1 \\ -90.7 \end{pmatrix}$

^aAt $\begin{pmatrix} f_0 \\ 2f_0 \\ 3f_0 \end{pmatrix}$.

^b0 = short circuit; ∞ = open circuit.

variety of terminations on multiplier conversion gain. The numbers to the right of each entry in the table represent the powers obtained at respective harmonics. It is instructive to consider a typical entry of interest in this table. The entry located in the second row and second column, for example, shows that a conversion gain of 1.5 dB is obtained if the input network terminates the fundamental f_0 and third harmonic $3f_0$ in 50, while the second-harmonic $2f_0$ is short-circuited. The output network for this entry terminates the fundamental in a short circuit and all other harmonics in 50. Several authors [93,98,99,102] have reported that the input network should terminate the second-harmonic in a short circuit. For lumped input circuit realizations, however, this table reveals that this provides a 1.5 dB improvement over a 50 or an open-circuit termination at $2f_0$ (row 1, column 2 and row 5, column 2, respectively). While the conversion gains represented in this table are not large and the dB values do not show great

variation, several trends are seen to emerge, and subsequent results will substantiate their implications. In particular, the impact of input network terminations from the data in rows 2 and 3 show, that for doubler operation, a short-circuit termination at $2f_0$ provides the best conversion gain in all cases considered.

Furthermore, a perusal of output network termination responses shows that a short circuit at f_0 provides the best performance using conversion gain as a basis.

Table 2 shows similar data when the HEMT is biased at $V_{gs} = 0$ (region I). This V_{gs} value was chosen in accordance with our previous discussion on optimum bias regions. While an important outcome of the $V_{gs} = 0$ table was typically lower conversion gains in comparison with Table 1, where $V_{gs} = V_p$, an even more significant observation is the dramatic improvement (~ 12 dB) obtained by employing an *open*-circuit termination at f_0 in the output network, in contrast with a short circuit, which was the

Table 3. Doubler Simulations Matched on Input with Microstrip Transmission Lines ($V_{gs} = -0.7\text{ V}$, $P_{in} = 0\text{ dBm}$, $V_{ds} = 3\text{ V}$)

		Output Power (dBm) ^a								
Input Network (Ω) ^{a,b}	Output Network (Ω) ^{a,b} :	$\begin{pmatrix} 50 \\ 50 \\ 50 \end{pmatrix}$	$\begin{pmatrix} 0 \\ 50 \\ 50 \end{pmatrix}$	$\begin{pmatrix} \infty \\ 50 \\ 50 \end{pmatrix}$	$\begin{pmatrix} 0 \\ 50 \\ \infty \end{pmatrix}$	$\begin{pmatrix} \infty \\ 50 \\ \infty \end{pmatrix}$	$\begin{pmatrix} 50 \\ 50 \\ 0 \end{pmatrix}$	$\begin{pmatrix} 50 \\ 50 \\ \infty \end{pmatrix}$	$\begin{pmatrix} 0 \\ 50 \\ 0 \end{pmatrix}$	$\begin{pmatrix} \infty \\ 50 \\ 0 \end{pmatrix}$
		$\begin{pmatrix} 50 \\ 50 \\ 50 \end{pmatrix}$		$\begin{pmatrix} 5.96 \\ -0.9 \\ -14.7 \end{pmatrix}$	$\begin{pmatrix} -217 \\ -0.3 \\ -221 \end{pmatrix}$	$\begin{pmatrix} -210 \\ -0.7 \\ -231 \end{pmatrix}$	$\begin{pmatrix} -215 \\ -0.2 \\ -270 \end{pmatrix}$	$\begin{pmatrix} -208 \\ 0.4 \\ -270 \end{pmatrix}$	$\begin{pmatrix} 5.5 \\ -3.9 \\ -232 \end{pmatrix}$	$\begin{pmatrix} 4.1 \\ 0.3 \\ -237 \end{pmatrix}$
$\begin{pmatrix} M \\ 0 \\ 54 \end{pmatrix}$		$\begin{pmatrix} 13 \\ 6.5 \\ -6.7 \end{pmatrix}$	$\begin{pmatrix} -65.7 \\ 8 \\ -4.1 \end{pmatrix}$	$\begin{pmatrix} -62.3 \\ 5 \\ -7.9 \end{pmatrix}$	$\begin{pmatrix} 65.7 \\ 8.6 \\ -92.1 \end{pmatrix}$	$\begin{pmatrix} -62.5 \\ 5.2 \\ -92.2 \end{pmatrix}$	$\begin{pmatrix} 13 \\ 6.1 \\ -87.6 \end{pmatrix}$	$\begin{pmatrix} 13 \\ 6.9 \\ -94.9 \end{pmatrix}$	$\begin{pmatrix} -65.6 \\ 7.4 \\ -84.7 \end{pmatrix}$	$\begin{pmatrix} -62.2 \\ 4.8 \\ -92.6 \end{pmatrix}$

^aAt $\begin{pmatrix} f_0 \\ 2f_0 \\ 3f_0 \end{pmatrix}$.

^b0 = short circuit; ∞ = open circuit; M = matched.

optimum case for region II. Note that Table 1 predicts only a 1.6 dB improvement for the analogous comparison.

On the basis of the observations above, we present results only for the specific case where the input network is short-circuited at $2f_0$ in the ensuing discussion.

Table 3 presents the results obtained for region II operation ($V_{gs} = V_p$) when the input network was synthesized to provide a matched load at the fundamental frequency f_0 and a short circuit at $2f_0$. In comparison with its counterpart in row 2 of Table 1, which had a 50 termination at f_0 , it is seen that, as expected, significant improvements occur in conversion gains for all output network impedance terminations. A perusal of the values indicates that significant increases in conversion gain of over 5 dB are typical in each case. Furthermore, the following quantitative results may be observed for various output network terminations: (1) 3.0 dB better conversion gains are obtained by short circuiting as compared with

open circuiting the fundamental (i.e., 8.0 dB vs. 5.0 dB), (2) 1.5 dB better conversion gain will be obtained for a short circuit at f_0 in comparison with a 50 ohm termination (notwithstanding the fact that the 50 ohm case would require some form of output circuit fundamental suppression), (3) 1.2 dB of additional conversion gain is obtained if the third harmonic is open-circuited in contrast with the frequently used short-circuited third harmonic (8.6 vs. 7.4 dB), and (4) 3.8 dB additional conversion gain is obtained over the case where an open-circuit fundamental and short-circuit third-harmonic output network are employed (i.e., 8.6 dB vs. 4.8 dB).

Table 4 presents the results obtained for region II operation when the output network is synthesized to provide a matched load at the second-harmonic ($2f_0$) versus the previous cases where a simple 50 ohm load was employed. On the basis of these results, it can be seen that for output network terminations, where the fundamental has been

Table 4. Doubler Simulations Matched on Input and Output with Microstrip Transmission Lines ($V_{gs} = -0.7\text{ V}$, $P_{in} = 0\text{ dBm}$, $V_{ds} = 3\text{ V}$)

		Output Power (dBm) ^a								
Input Network (Ω) ^{a,b}	Output Network (Ω) ^{a,b} :	$\begin{pmatrix} 50 \\ 50 \\ 50 \end{pmatrix}$	$\begin{pmatrix} 0 \\ M \\ 85 \end{pmatrix}$	$\begin{pmatrix} \infty \\ M \\ 85 \end{pmatrix}$	$\begin{pmatrix} 0 \\ M \\ \infty \end{pmatrix}$	$\begin{pmatrix} \infty \\ M \\ \infty \end{pmatrix}$	$\begin{pmatrix} 36 \\ M \\ 0 \end{pmatrix}$	$\begin{pmatrix} 37 \\ M \\ \infty \end{pmatrix}$	$\begin{pmatrix} 0 \\ M \\ 0 \end{pmatrix}$	$\begin{pmatrix} \infty \\ M \\ 0 \end{pmatrix}$
		$\begin{pmatrix} M \\ 0 \\ 54 \end{pmatrix}$		$\begin{pmatrix} 14.4 \\ 6.4 \\ -2.9 \end{pmatrix}$	$\begin{pmatrix} -70.2 \\ 10.1 \\ -8.1 \end{pmatrix}$	$\begin{pmatrix} -61.9 \\ -4.7 \\ -16.2 \end{pmatrix}$	$\begin{pmatrix} -70 \\ 10.4 \\ -89.5 \end{pmatrix}$	$\begin{pmatrix} -61.5 \\ 5 \\ -99.1 \end{pmatrix}$	$\begin{pmatrix} 12.8 \\ 9.1 \\ -95.8 \end{pmatrix}$	$\begin{pmatrix} 12.5 \\ 7.3 \\ -86.1 \end{pmatrix}$

^aAt $\begin{pmatrix} f_0 \\ 2f_0 \\ 3f_0 \end{pmatrix}$.

^b0 = short circuit; ∞ = open circuit; M = matched.

Table 5. Simulated Doubler Response with Microstrip Elements (Region II; ($V_{gs} = -0.7\text{ V}$, $P_{in} = 0\text{ dBm}$, $V_{ds} = 3\text{ V}$))

Input Network (Ω) ^{a,b}	Output Network (Ω) ^{a,b} :	Output Power (dBm) ^a					
		$\begin{pmatrix} 50 \\ 50 \\ 50 \end{pmatrix}$	$\begin{pmatrix} 0 \\ 50 \\ 0 \end{pmatrix}$	$\begin{pmatrix} \infty \\ 50 \\ 0 \end{pmatrix}$	$\begin{pmatrix} 0 \\ 62 \\ 0 \end{pmatrix}$	$\begin{pmatrix} \infty \\ 63 \\ \infty \end{pmatrix}$	$\begin{pmatrix} 27 \\ 49 \\ \infty \end{pmatrix}$
$\begin{pmatrix} 50 \\ 50 \\ 50 \end{pmatrix}$		$\begin{pmatrix} 5.96 \\ -0.9 \\ -14.7 \end{pmatrix}$	$\begin{pmatrix} -27.1 \\ -0.7 \\ -26.3 \end{pmatrix}$	$\begin{pmatrix} -10.4 \\ -0.9 \\ -36.2 \end{pmatrix}$	$\begin{pmatrix} -25 \\ 0.4 \\ -52.9 \end{pmatrix}$	$\begin{pmatrix} 17.3 \\ -0.8 \\ -60.1 \end{pmatrix}$	$\begin{pmatrix} 4 \\ 0.6 \\ -37.7 \end{pmatrix}$
$\begin{pmatrix} 50 \\ 0 \\ 50 \end{pmatrix}$		$\begin{pmatrix} 10.7 \\ 4.3 \\ -10.2 \end{pmatrix}$	$\begin{pmatrix} -27.4 \\ 5.4 \\ -22.6 \end{pmatrix}$	$\begin{pmatrix} -22 \\ 4.5 \\ -21 \end{pmatrix}$	$\begin{pmatrix} -19.9 \\ 7.7 \\ -46.9 \end{pmatrix}$	$\begin{pmatrix} -13.5 \\ 6.4 \\ -61 \end{pmatrix}$	$\begin{pmatrix} 9 \\ 7.2 \\ -32 \end{pmatrix}$

$$^a \text{At } \begin{pmatrix} f_0 \\ 2f_0 \\ 3f_0 \end{pmatrix}.$$

^b0 = short circuit; ∞ = open circuit.

short-circuited, an additional 2 dB has been obtained over the results in Table 3 and approximately 9 dB over Table 1 results.

Tables 5 and 6 display the results obtained utilizing microstrip-line circuits that were synthesized to provide short-circuited, open and 50 terminations at respective fundamental and harmonic frequencies as employed in many traditional designs [79,92,95,97,98,100–110].

With reference to Table 5 (region II, $V_{gs} = V_p$), a comparison of the effect of the distributed input network (row 2, column 1) with a 50 input network at f_0 , $2f_0$, and $3f_0$ (row 1, column 1) shows that 5.2 dB improvement in conversion gain performance may be obtained by employing the distributed structure with a short circuit at $2f_0$. Some additional conclusions obtained from a further perusal of this table are as follows: (1) 8.6 dB conversion gain improve-

ment may be obtained by providing a distributed output network that is short-circuited at f_0 and $3f_0$ as compared with 50 ohm input and output terminations (row 1, column 1 vs. row 2, column 4); (2) with the distributed input network terminated in a short circuit, 1.3 dB improvement in conversion gain may be obtained by short-circuiting the output network at f_0 and $3f_0$ (column 4) as compared with open circuits at f_0 and $3f_0$ (column 5); (3) the difference in termination in the output network between open and short circuits at f_0 is on the order of 1 dB; and (4) an additional 2.3 dB of conversion gain is obtained by introducing an additional short-circuited stub at $3f_0$.

Table 6 presents similar results for region I ($V_{gs} = 0$) operation. Several significant conclusions are evident from these results: (1) optimal performance is considerably less (2.8 vs. 7.7 dB) than that for region II operation,

Table 6. Simulated Doubler Response with Microstrip Elements (Region I; ($V_{gs} = -0\text{ V}$, $P_{in} = 0\text{ dBm}$, $V_{ds} = 3\text{ V}$))

Input Network (Ω) ^{a,b}	Output Network (Ω) ^{a,b} :	Output Power (dBm) ^a					
		$\begin{pmatrix} 50 \\ 50 \\ 50 \end{pmatrix}$	$\begin{pmatrix} 0 \\ 50 \\ 0 \end{pmatrix}$	$\begin{pmatrix} \infty \\ 50 \\ \infty \end{pmatrix}$	$\begin{pmatrix} 0 \\ 62 \\ 0 \end{pmatrix}$	$\begin{pmatrix} \infty \\ 63 \\ \infty \end{pmatrix}$	$\begin{pmatrix} 27 \\ 49 \\ \infty \end{pmatrix}$
$\begin{pmatrix} 50 \\ 50 \\ 50 \end{pmatrix}$		$\begin{pmatrix} 12.5 \\ -10.1 \\ -13.9 \end{pmatrix}$	$\begin{pmatrix} -20.2 \\ -11.4 \\ -26.3 \end{pmatrix}$	$\begin{pmatrix} -15.1 \\ -2.5 \\ -25.4 \end{pmatrix}$	$\begin{pmatrix} -22.9 \\ -10.9 \\ -49.3 \end{pmatrix}$	$\begin{pmatrix} -12.5 \\ -4 \\ -55.4 \end{pmatrix}$	$\begin{pmatrix} 11.1 \\ -10 \\ -33.9 \end{pmatrix}$
$\begin{pmatrix} 50 \\ 0 \\ 50 \end{pmatrix}$		$\begin{pmatrix} 14.7 \\ -12.5 \\ -8.4 \end{pmatrix}$	$\begin{pmatrix} -18.4 \\ -13.1 \\ -18.4 \end{pmatrix}$	$\begin{pmatrix} -14.4 \\ 1.8 \\ -25.6 \end{pmatrix}$	$\begin{pmatrix} -21.3 \\ -10.4 \\ -41 \end{pmatrix}$	$\begin{pmatrix} -11.1 \\ 2.8 \\ -52 \end{pmatrix}$	$\begin{pmatrix} 13.2 \\ -10.6 \\ -2.8 \end{pmatrix}$

$$^a \text{At } \begin{pmatrix} f_0 \\ 2f_0 \\ 3f_0 \end{pmatrix}.$$

^b0 = short circuit; ∞ = open circuit.

(2) significant conversion gain improvement is obtained when the output network is open circuited at f_0 in comparison with the short-circuited condition (1.8 vs. -13.1 to -15 dB, and (3) 1 dB of conversion gain performance improvement is achieved by introducing an additional open-circuited stub at the third harmonic.

This topic will be revisited in the next section in the discussion of active multiplier design. Specific multiplier designs are illustrated demonstrating the efficacy of harmonic terminations and optimum bias selection.

4. ACTIVE MULTIPLIER DESIGN TECHNIQUES

4.1. Existing Active Multiplier Design Techniques

Since the 1980s, numerous researchers have discussed numerous design approaches leading to various design procedures utilizing various active devices and topologies in different media and frequency ranges. This section presents various existing design techniques and other techniques implemented by the author.

A fundamental topological representation for realization of active microwave multiplier circuits is shown in Fig. 39. While this is not the most generalized topology, it is one of the most frequently used. The physical realization of an efficient frequency multiplier subject to design criteria utilizing this configuration is strongly reliant on the synthesis of networks N_1 , N_2 , and N_3 , which are typically, but not always, passive. The criteria for specification of N_1 , N_2 , and N_3 rely, heavily as usual, on fundamental active-device parameters. In the case of multipliers, this is heavily dependent upon bias conditions, input power level, and frequency.

Only very seldom have designers intentionally employed feedback (N_3) in multiplier designs in the realization of such circuits [165]. Synthesis of N_3 is typically avoided, due in part to potential stability problems [93,106,147]. This network, however, has the potential of providing useful improvement in conversion efficiency by proper combination of harmonics emerging from the active device with the input fundamental, for example, at the correct phase. The feedback network (N_3) combines a harmonic component from the drain (collector) of the transistor with the fundamental component on the gate (base).

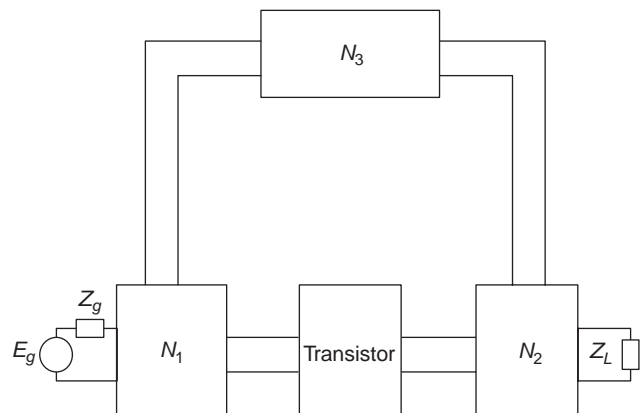


Figure 39. Frequency multiplier realization.

Theoretically, this produces an enhanced component at the desired output harmonic frequency on the drain (collector), assuming that in the ideal case the phase of the feedback is optimal [106,147].

Some designers have selected a balanced version of the topology given in Fig. 39 for doubler design, with expectations of superior doubler performance [91,109,111-113, 148,149]. These seem to have been inspired by the advantages actually realized in the design of diode doublers [150]. Developers of such balanced active multipliers state that these circuits are better because of the natural cancellation of the fundamental and all odd harmonics, thus providing a virtual ground at the output of the active devices and permitting the location of any matching networks closer to the drain (collector) of the devices [99]. Furthermore, they indicate that such designs have the advantage of high conversion efficiency, 3 dB better output power, better isolation, good harmonic suppression, and the elimination of the long ($\lambda/4$) stubs that are common in single-ended designs.

One of the design classes emphasizes the arrangement of two or more transistors in one of several topological configurations as shown in Figs. 40 and 41. The technique shown in Fig. 40 utilizes two identical fundamental frequency signals, which are fed 180° out of phase to transistors T_1 and T_2 . The circuit functions as a type of active full-wave rectifier in that when the voltage at port 1 is positive, T_1 conducts and T_2 is turned off and current flows through the emitter of T_1 to the load Z_L . When the polarity of the input signal $V(f_1)$ is reversed, T_2 conducts and T_1 is turned off and current flows through the collector of T_2 , providing an output to Z_L . This process effectively provides a rectified output at Z_L with the corresponding strong second-harmonic content. This approach has been demonstrated for doubler action over a broad frequency range (1-7 GHz) in MMIC topology. Conversion gains range from 0 to 12 dB, utilizing input and output amplification stages. Fundamental rejections of less than 10 dB appear to be realizable.

A block diagram of a typical balanced multiplier design is shown in Fig. 41. At the input, the input signal of the multiplier is fed through a powerdivider-phase shifter,

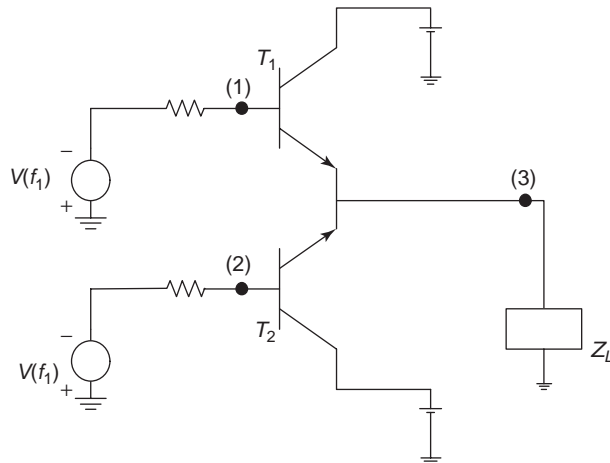


Figure 40. Block diagram of push-push topology of frequency multiplier.

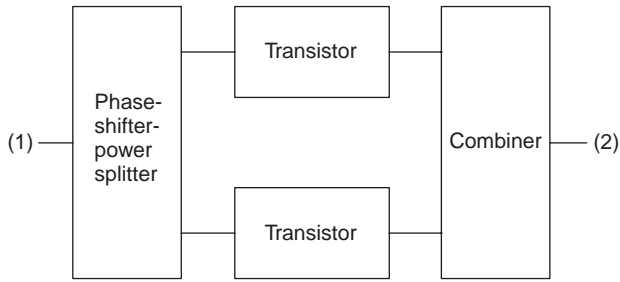


Figure 41. Block diagram of typical balanced frequency multiplier.

which divides the power between the two transistors with 180° phase difference between the input ports of the transistors. The drains (collectors) of the transistors are connected on the output by a combiner. At the output, the fundamental and odd harmonic signals have opposite phase, and, by destructive interference, cancel, giving good harmonic suppression. The second-harmonic signals from the transistors have the same phase and thus interfere constructively.

A perusal of the published literature on such balanced designs reveals, however, that they require complex components in their realization. In addition to two matched active devices (some designers use more in their active matching stages), balanced designs typically require large baluns or powersplitter–phase shifter combinations, T junctions, and in some cases airbridges. Some realizations also require complex transitions and additional lengths of transmission lines to rotate the active device outputs to achieve a pure reactance output. Finally, only frequency doubler designs are typically reported; however, Fudem and Niehenke [166] have realized a balanced tripler. It is found that, with due consideration of the importance of the particular active device characteristics and frequency bands, these designs in almost all cases are narrowband (10%) (Ref. 112, with -9 dB conversion gains, is one exception; it uses an additional active device), have modest conversion gain (-5 to $+5$ dB; 3 to 12 dB in one case), and frequently yield sparse data on fundamental suppression (typically between 12 and 30 dB).

Hiraoka [148], for example, developed a broadband MMIC balanced frequency doubler with a fundamental frequency of 5 GHz, consisting of a common-gate FET and a common-source FET directly connected in parallel, followed by an output-matching network. A phase shifter network precedes the common-gate FET to compensate for the phase error between the outputs from the common-gate FET and the common-source FET. A conversion loss of 8–10 dB was achieved for output frequencies between 6 and 16 GHz. Fundamental frequency isolation (suppression) better than 17 dB up to output frequencies of 20 GHz was obtained. Unfortunately, the author did not provide any data on the third-harmonic isolation (suppression).

Angelov [113] discusses a 20–40-GHz balanced doubler where two common-source PHEMTs are connected in parallel followed by sections of transmission lines on the gates before combining into a 3-dB coupler. The input signal to the doubler is fed to a power divider, which divides the power equally between the two input ports with 180°

phase difference between the input ports. Sections of transmission lines connect the power divider to the drain of the PHEMTs. The completed doubler circuit provides approximately -1 dB of conversion gain with a -3 dB bandwidth of approximately 5%. The author notes that the bandwidth is limited mainly by the 180° ratrace coupler. The author does not provide data on the fundamental and the third-harmonic suppression.

Takenaka and Ogawa [111,112] developed a wideband MMIC balanced frequency multiplier utilizing line-unified HEMT configurations. In line-unified HEMT configurations, coplanar lines such as slotlines and coplanar waveguides are used to connect the circuit electrically. A coplanar waveguide precedes a common-gate HEMT followed by a slotline series T junction, which acts as an out-of-phase divider to drive two parallel, common-drain HEMTs. The output of the two HEMTs is connected to a coplanar waveguide followed by the load resistance. This topology yields conversion loss of 8–10 dB in the 4–40 GHz output frequency range, and fundamental frequency signal isolation of better than 21 dB above the input frequency of 7 GHz. The authors do not provide any data on third-harmonic isolation.

One final observation on balanced designs is the almost universal disregard for the deleterious effects of channel imbalances. It has been reported that for phase imbalances of 10° , the output conversion gain at the second-harmonic will decrease by 1 dB in a 4-dB design, while an amplitude imbalance of 0.3 dB produces the same 1 dB decrease. A combination of imbalances of 10° and 0.3 dB together results in a 3 dB decrease in a 4-dB conversion gain design [113,151,167]. For these reasons, balanced realizations are not considered further in this article, although obviously some principles presented are directly transferable to balanced circuits.

Numerous investigators have reported designs for single-ended microwave multipliers. Referring to Figs. 25 and 39, these designs include networks N_1 and N_2 but exclude an external network N_3 . Thus, single-ended designs are based primarily on the realization of N_1 and N_2 . Traditional synthesis of N_1 and N_2 have followed the lines of the passive case where N_1 is traditionally composed of a bandpass or lowpass filter or matching network tuned to a fundamental frequency, and N_2 is similarly a matching network or bandpass or highpass filter tuned to the appropriate harmonic frequency of interest. Synthesis of these networks includes the use of cascades of filters and matching networks [87,88,97,99,108,110,116–123,124,125,128,147,152–154], and such methods have been realized utilizing transmission lines and stubs to open-circuit-, or short-circuit-specific harmonics [88,108,110,154], while some authors have additionally considered these networks as a cascade of matching and reflection networks [95,104,110,154]. Many of these techniques determine optimal networks by utilizing load-line analysis [91,92], intuitive reasoning based on previous results [92,124], computer optimization of generalized models [106,108], and experimental techniques based on stub tuner measurements [88,154].

The following paragraphs illustrate some specific examples of these classes of realizations. Dow [97]

developed a FET frequency doubler with a fundamental frequency of 20 GHz utilizing matching networks and tuners. Network N_1 includes a matching network at the gate designed to match the fundamental frequency and an output-matching network N_2 at the drain that was designed to match the second-harmonic. In addition to the matching networks, tuners were also included in both N_1 and N_2 to optimize the performance of the frequency doubler. A maximum conversion gain of -1.8 dB was achieved utilizing this topology.

Chen [87] developed a MESFET frequency doubler utilizing filters and matching networks. A lowpass filter was placed on the input of the circuit, which allows the fundamental frequency to pass through to the gate of the device, and a highpass filter was placed on the output of the device to allow the desired second harmonic to pass. A matching network designed to match the second-harmonic frequency was placed in series with the highpass filter. Utilizing this topology, Chen achieved 8 dB of conversion gain.

Borg [95] has developed BJT frequency doubler designs utilizing transmission lines and stubs. In one of these, a 50 transmission line is placed on the input of the circuit, and short-circuited stubs are employed on the output of the device. This design produces 2.5 dB of conversion gain. Rauscher [93] provides an FET frequency doubler utilizing transmission lines and stubs as well. On the input of the device, transmission lines are utilized to form impedance transformations and an open-circuited stub. On the output, they are utilized to provide an open-circuited stub at the fundamental frequency. Rauscher's data show that -0.5 dB of conversion gain was achieved in this design.

Stancliff [91] and Gilmore [92] determine optimal networks utilizing load-line analysis for their FET multiplier designs. Using the $I_{ds}-V_{ds}$ curves, they employ fundamental load-line analysis to demonstrate the output characteristics for a fundamental frequency open-circuited load line placed on the output of the FET. Stancliff utilizes this approach in a balanced configuration, whereas Gilmore uses it for the development of a single-ended multiplier.

Various authors have used computer optimization techniques for generalized large-signal device models to develop frequency multipliers [106,108]. El-Rabaie [108] uses a harmonic balance analysis technique to optimize a MESFET frequency doubler utilizing a large-signal MESFET device model. This technique determines the terminating impedance value that should be presented to the multiplier for optimum performance, while the approach utilized by Guo [106] determines optimum bias voltages and optimum load impedances.

Le [88] utilizes experimental techniques based on stub tuner measurements to design frequency multipliers. In this approach, load-pull measurements are performed to measure impedances at various harmonics at various bias voltages, and utilizing these data, frequency multipliers are designed optimizing conversion gain and efficiency.

Le uses this approach in the development of a frequency tripler, which provided a conversion gain of -2.4 dB.

Single-ended designs using the previously mentioned design techniques have exhibited excellent performance. Conversion gains approaching 9 dB, harmonic suppression exceeding 40 dBc, and bandwidths approaching 35% have

been reported [140,142,168]. A significant drawback of some single-ended designs is the potentially large size constraints required by matching networks and harmonic terminating stubs. Long stubs of lengths approaching $\lambda/4$ are commonly used. Even though the performance of frequency multipliers using these design techniques is excellent, they are unsuitable for applications where size constraints are specified. In certain cases, however, it has been shown that discrete networks are feasible for significant size reduction.

4.2. A Unified Design Technique

Existing frequency multiplier design techniques are presented in the previous sections. While these approaches suffice to produce multipliers that work, they are not necessarily efficient in that proper synthesis of N_1 and N_2 can yield significant improvements in performance as measured by conversion gain. In this section, a consistent design technique is proposed for the design of active frequency multipliers, using the topology shown in Fig. 42 stemming from research on terminating-impedance effects on active devices.

Because of the extraordinary complexity of nonlinear circuit problems, it is proposed that the technique, while heavily reliant on experimental measurements, be based on in-depth computer-aided design. From a perusal of the literature, there appears to be little discussion on this topic for active multipliers other than an occasional reference to power limitation in overdriving the drain in MESFET/HEMT realizations. As with any such active design, the first step requires the selection of an active device possessing the appropriate performance characteristics [113], and particularly, in this case, developing accurate nonlinear computer oriented device models. (In the present case, a particular device on hand has been selected for convenience.) Here, for example, we consider the effects of each devices nonlinearity (e.g., C_{gs} , C_{gd} , g_{ds} , I_{ds} , V_{gs} , V_{ds}) on augmenting a particular device harmonic [97]. At this point the nonlinear device model should be accurately developed, based on both DC and AC characteristics, to match the measured performance of the transistor [48,109,146].

The next step requires utilizing the device model and/or measured data to determine optimum bias points and input power levels, using both static and P_{in} versus P_{out} data. Examples of this process may be found in previous publications [97,147]. At this stage, it is important to develop the requirements on the termination networks N_1 and N_2 of Fig. 39 leading to optimum multiplier performance. This process requires the use of extensive

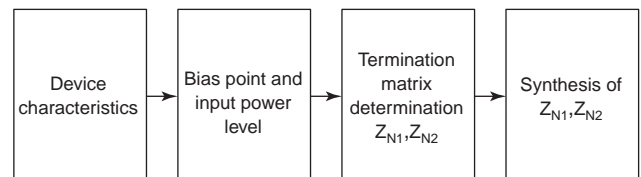


Figure 42. Topology of active microwave multiplier.

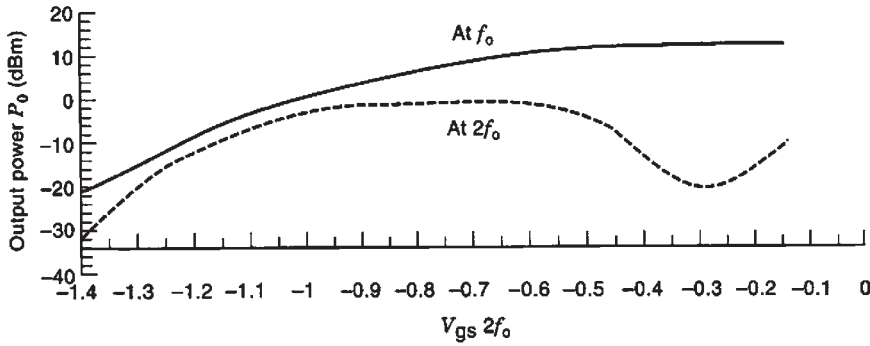


Figure 43. Simulated output power of FHX35LG HEMT versus V_{gs} ($P_{in} = 0$ dBm, $V_{ds} = 3$ V, $f = 3$ GHz).

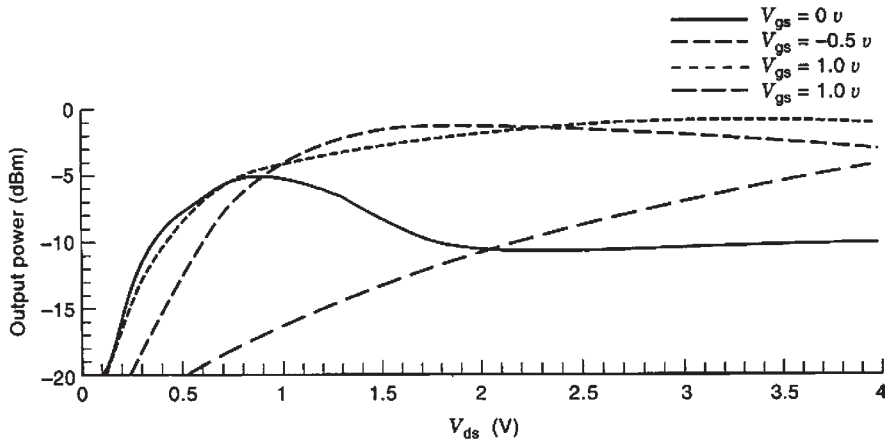


Figure 44. Simulated output of the second-harmonic versus V_{ds} for FHX35LG HEMT ($P_{in} = 0$ dBm, $f = 3$ GHz).

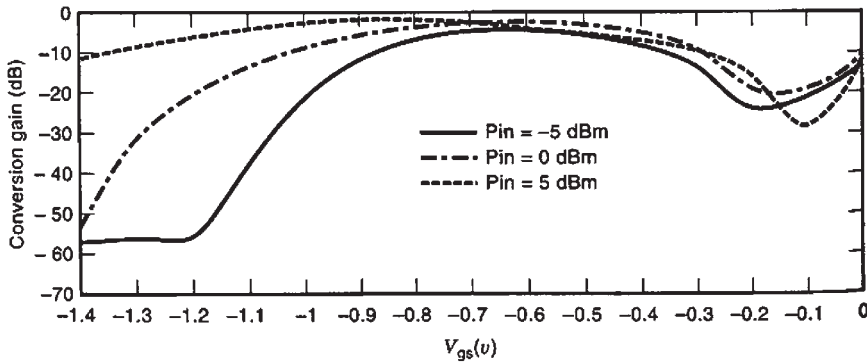


Figure 45. Simulated conversion gain of FHX35LG HEMT versus V_{gs} ($V_{ds} = 3$ V, $f = 3$ GHz).

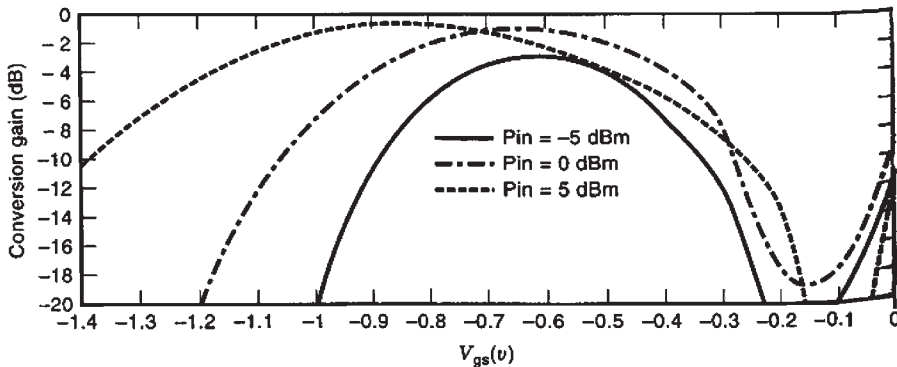


Figure 46. Simulated conversion gain of FHX35LG HEMT versus V_{gs} ($V_{ds} = 3$ V, $f = 3$ GHz).

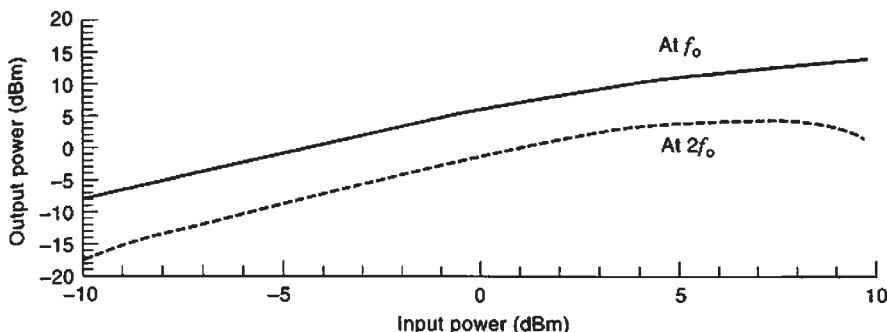


Figure 47. Simulated output power versus input power of FHX35LG ($V_{gs} = V_p = -0.7$ V, $V_{ds} = 3$ V, $f = 3$ GHz).

computer analysis to be efficient timewise, although, as has been done by several researchers [88,108], some limited results can be achieved by extensive time-consuming measurements. As mentioned previously, El-Rabaie [108] and Le [88] used computer optimization of generalized

nonlinear models to optimize frequency multipliers. The outcome of this process is the prescribed driving-point responses for networks N_1 and N_2 when terminated in R_g and R_L , respectively, where R_g is the source resistance and R_L is the load terminating impedance.

Table 7. Doubler Simulations with Ideal Transmission Lines ($V_{gs} = -0.7$ V, $P_{in} = 0$ dBm, $V_{ds} = 3$ V)

Input Network (Ω) ^{a,b}	Output Network (Ω) ^{a,b} :	Output Power (dBm) ^a									
		$\begin{pmatrix} 50 \\ 50 \\ 50 \end{pmatrix}$	$\begin{pmatrix} 0 \\ 50 \\ 50 \end{pmatrix}$	$\begin{pmatrix} \infty \\ 50 \\ 50 \end{pmatrix}$	$\begin{pmatrix} 0 \\ 50 \\ \infty \end{pmatrix}$	$\begin{pmatrix} \infty \\ 50 \\ \infty \end{pmatrix}$	$\begin{pmatrix} 50 \\ 50 \\ 0 \end{pmatrix}$	$\begin{pmatrix} 50 \\ 50 \\ \infty \end{pmatrix}$	$\begin{pmatrix} 0 \\ 50 \\ 0 \end{pmatrix}$	$\begin{pmatrix} \infty \\ 50 \\ 0 \end{pmatrix}$	
$\begin{pmatrix} 50 \\ 50 \\ 50 \end{pmatrix}$		$\begin{pmatrix} 5.96 \\ -0.9 \\ -14.7 \end{pmatrix}$	$\begin{pmatrix} -217 \\ -0.3 \\ -221 \end{pmatrix}$	$\begin{pmatrix} -210 \\ -0.7 \\ -231 \end{pmatrix}$	$\begin{pmatrix} -215 \\ 0.2 \\ -270 \end{pmatrix}$	$\begin{pmatrix} -208 \\ 0.4 \\ -270 \end{pmatrix}$	$\begin{pmatrix} 5.5 \\ -3.9 \\ -232 \end{pmatrix}$	$\begin{pmatrix} 4.1 \\ 0.3 \\ -237 \end{pmatrix}$	$\begin{pmatrix} -216 \\ -3.3 \\ -270 \end{pmatrix}$	$\begin{pmatrix} -209 \\ -4.2 \\ -270 \end{pmatrix}$	
$\begin{pmatrix} 50 \\ 0 \\ 50 \end{pmatrix}$		$\begin{pmatrix} 10.5 \\ 4.5 \\ -17.9 \end{pmatrix}$	$\begin{pmatrix} -213 \\ +5.4 \\ -215 \end{pmatrix}$	$\begin{pmatrix} -207 \\ 3.9 \\ -224 \end{pmatrix}$	$\begin{pmatrix} -211 \\ 6 \\ -270 \end{pmatrix}$	$\begin{pmatrix} -204 \\ 5.2 \\ -270 \end{pmatrix}$	$\begin{pmatrix} 10.2 \\ 1.8 \\ -225 \end{pmatrix}$	$\begin{pmatrix} 8.7 \\ 6.1 \\ -232 \end{pmatrix}$	$\begin{pmatrix} -212 \\ -2.5 \\ -270 \end{pmatrix}$	$\begin{pmatrix} -206 \\ 0.1 \\ -270 \end{pmatrix}$	
$\begin{pmatrix} 50 \\ 0 \\ 0 \end{pmatrix}$		$\begin{pmatrix} 8.7 \\ 2.5 \\ -12.6 \end{pmatrix}$	$\begin{pmatrix} -215 \\ 3.2 \\ -219 \end{pmatrix}$	$\begin{pmatrix} -208 \\ 2 \\ -232 \end{pmatrix}$	$\begin{pmatrix} -213 \\ 4.3 \\ -270 \end{pmatrix}$	$\begin{pmatrix} -205 \\ 2.8 \\ -270 \end{pmatrix}$	$\begin{pmatrix} 8.3 \\ -0.7 \\ -229 \end{pmatrix}$	$\begin{pmatrix} 6.9 \\ 4.3 \\ -235 \end{pmatrix}$	$\begin{pmatrix} -213 \\ 0.1 \\ -270 \end{pmatrix}$	$\begin{pmatrix} -207 \\ -0.9 \\ -270 \end{pmatrix}$	
$\begin{pmatrix} 50 \\ 50 \\ 0 \end{pmatrix}$		$\begin{pmatrix} 5.4 \\ -2 \\ -18.2 \end{pmatrix}$	$\begin{pmatrix} -218 \\ -1.4 \\ -213 \end{pmatrix}$	$\begin{pmatrix} -211 \\ -2.5 \\ -237 \end{pmatrix}$	$\begin{pmatrix} -216 \\ -2.3 \\ -270 \end{pmatrix}$	$\begin{pmatrix} -208 \\ -2.3 \\ -270 \end{pmatrix}$	$\begin{pmatrix} 3.4 \\ -4.1 \\ -220 \end{pmatrix}$	$\begin{pmatrix} 3.4 \\ -2.1 \\ -246 \end{pmatrix}$	$\begin{pmatrix} -217 \\ -3.6 \\ -270 \end{pmatrix}$	$\begin{pmatrix} -209 \\ -5.3 \\ -270 \end{pmatrix}$	
$\begin{pmatrix} 50 \\ \infty \\ 50 \end{pmatrix}$		$\begin{pmatrix} 2.7 \\ -4.4 \\ -19.8 \end{pmatrix}$	$\begin{pmatrix} -221 \\ -3.7 \\ -227 \end{pmatrix}$	$\begin{pmatrix} -213 \\ -4.1 \\ -239 \end{pmatrix}$	$\begin{pmatrix} -219 \\ -4.1 \\ -270 \end{pmatrix}$	$\begin{pmatrix} -211 \\ -3.8 \\ -270 \end{pmatrix}$	$\begin{pmatrix} 2.3 \\ -6.5 \\ -235 \end{pmatrix}$	$\begin{pmatrix} 0.6 \\ -4.2 \\ -246 \end{pmatrix}$	$\begin{pmatrix} -220 \\ -6 \\ -270 \end{pmatrix}$	$\begin{pmatrix} -212 \\ -7 \\ -270 \end{pmatrix}$	
$\begin{pmatrix} 50 \\ \infty \\ \infty \end{pmatrix}$		$\begin{pmatrix} 4.7 \\ -2.7 \\ -23.4 \end{pmatrix}$	$\begin{pmatrix} -219 \\ -3.2 \\ -219 \end{pmatrix}$	$\begin{pmatrix} -211 \\ -2.4 \\ -235 \end{pmatrix}$	$\begin{pmatrix} -217 \\ -5 \\ -270 \end{pmatrix}$	$\begin{pmatrix} -209 \\ -2.6 \\ -270 \end{pmatrix}$	$\begin{pmatrix} 4.3 \\ -4.9 \\ -237 \end{pmatrix}$	$\begin{pmatrix} 2.6 \\ -2.6 \\ -238 \end{pmatrix}$	$\begin{pmatrix} -217 \\ -4.8 \\ -270 \end{pmatrix}$	$\begin{pmatrix} -210 \\ -4.9 \\ -270 \end{pmatrix}$	
$\begin{pmatrix} 50 \\ 50 \\ \infty \end{pmatrix}$		$\begin{pmatrix} 3 \\ -4.3 \\ -15.9 \end{pmatrix}$	$\begin{pmatrix} -221 \\ -4 \\ -222 \end{pmatrix}$	$\begin{pmatrix} -212 \\ -4.2 \\ -235 \end{pmatrix}$	$\begin{pmatrix} -218 \\ -1.8 \\ -270 \end{pmatrix}$	$\begin{pmatrix} -210 \\ -2 \\ -270 \end{pmatrix}$	$\begin{pmatrix} 2.2 \\ -8.8 \\ -236 \end{pmatrix}$	$\begin{pmatrix} 1.2 \\ -1.6 \\ -232 \end{pmatrix}$	$\begin{pmatrix} -220 \\ -8.2 \\ -270 \end{pmatrix}$	$\begin{pmatrix} -212 \\ -8.5 \\ -270 \end{pmatrix}$	

^aAt $\begin{pmatrix} f_0 \\ 2f_0 \\ 3f_0 \end{pmatrix}$.

^b0 = short circuit; ∞ = open circuit.

Table 8. Doubler Simulations with Ideal Transmission Lines ($V_{gs} = 0\text{ V}$, $P_{in} = 0\text{ dBm}$, $V_{ds} = 3\text{ V}$)

Input Network (Ω) ^{a,b}	Output Network (Ω) ^{a,b}	Output Power (dBm) ^a								
		$\begin{pmatrix} 50 \\ 50 \\ 50 \end{pmatrix}$	$\begin{pmatrix} 0 \\ 50 \\ 50 \end{pmatrix}$	$\begin{pmatrix} \infty \\ 50 \\ 50 \end{pmatrix}$	$\begin{pmatrix} 0 \\ 50 \\ \infty \end{pmatrix}$	$\begin{pmatrix} \infty \\ 50 \\ \infty \end{pmatrix}$	$\begin{pmatrix} 50 \\ 50 \\ 0 \end{pmatrix}$	$\begin{pmatrix} 50 \\ 50 \\ \infty \end{pmatrix}$	$\begin{pmatrix} 0 \\ 50 \\ 0 \end{pmatrix}$	$\begin{pmatrix} \infty \\ 50 \\ 0 \end{pmatrix}$
$\begin{pmatrix} 50 \\ 50 \\ 50 \end{pmatrix}$		$\begin{pmatrix} 12.5 \\ -10.1 \\ -13.9 \end{pmatrix}$	$\begin{pmatrix} -211 \\ -11.3 \\ -219 \end{pmatrix}$	$\begin{pmatrix} -206 \\ -2 \\ -217 \end{pmatrix}$	$\begin{pmatrix} -208 \\ -11 \\ -270 \end{pmatrix}$	$\begin{pmatrix} -203 \\ -3.3 \\ -270 \end{pmatrix}$	$\begin{pmatrix} 11.9 \\ -13.2 \\ -232 \end{pmatrix}$	$\begin{pmatrix} 11.1 \\ -10.3 \\ -235 \end{pmatrix}$	$\begin{pmatrix} -209 \\ -14.2 \\ -270 \end{pmatrix}$	$\begin{pmatrix} -204 \\ -5 \\ -270 \end{pmatrix}$
$\begin{pmatrix} 50 \\ 0 \\ 50 \end{pmatrix}$		$\begin{pmatrix} 14.8 \\ -13.8 \\ -5.6 \end{pmatrix}$	$\begin{pmatrix} -209 \\ -11.8 \\ -211 \end{pmatrix}$	$\begin{pmatrix} -205 \\ 3.2 \\ -214 \end{pmatrix}$	$\begin{pmatrix} -207 \\ 11.2 \\ -270 \end{pmatrix}$	$\begin{pmatrix} -202 \\ 3 \\ -270 \end{pmatrix}$	$\begin{pmatrix} 14.2 \\ -18.7 \\ -223 \end{pmatrix}$	$\begin{pmatrix} 13.2 \\ -13.9 \\ -226 \end{pmatrix}$	$\begin{pmatrix} -208 \\ -14.7 \\ -270 \end{pmatrix}$	$\begin{pmatrix} -203 \\ 0.2 \\ -270 \end{pmatrix}$
$\begin{pmatrix} 50 \\ 0 \\ 0 \end{pmatrix}$		$\begin{pmatrix} 13.7 \\ -11.6 \\ -10.4 \end{pmatrix}$	$\begin{pmatrix} -210 \\ 19.8 \\ -216 \end{pmatrix}$	$\begin{pmatrix} -205 \\ 1.3 \\ -214 \end{pmatrix}$	$\begin{pmatrix} -207 \\ -19.5 \\ -270 \end{pmatrix}$	$\begin{pmatrix} -202 \\ 0.6 \\ -270 \end{pmatrix}$	$\begin{pmatrix} 13.2 \\ -15.7 \\ -228 \end{pmatrix}$	$\begin{pmatrix} 12.3 \\ -13.9 \\ -231 \end{pmatrix}$	$\begin{pmatrix} -208 \\ -22.4 \\ -270 \end{pmatrix}$	$\begin{pmatrix} -204 \\ -2 \\ -270 \end{pmatrix}$
$\begin{pmatrix} 50 \\ 50 \\ 0 \end{pmatrix}$		$\begin{pmatrix} 12.4 \\ -10 \\ -19.3 \end{pmatrix}$	$\begin{pmatrix} -211 \\ -9.3 \\ -213 \end{pmatrix}$	$\begin{pmatrix} -206 \\ -2.2 \\ -222 \end{pmatrix}$	$\begin{pmatrix} -208 \\ -10.3 \\ -270 \end{pmatrix}$	$\begin{pmatrix} -203 \\ -3.8 \\ -270 \end{pmatrix}$	$\begin{pmatrix} 11.9 \\ -12.6 \\ -224 \end{pmatrix}$	$\begin{pmatrix} 10.9 \\ -10.6 \\ -243 \end{pmatrix}$	$\begin{pmatrix} -210 \\ -12.8 \\ -270 \end{pmatrix}$	$\begin{pmatrix} -204 \\ -5 \\ -270 \end{pmatrix}$
$\begin{pmatrix} 50 \\ \infty \\ 50 \end{pmatrix}$		$\begin{pmatrix} 10.9 \\ -11.6 \\ -19.4 \end{pmatrix}$	$\begin{pmatrix} -212 \\ -11.6 \\ -226 \end{pmatrix}$	$\begin{pmatrix} -206 \\ -6.1 \\ -222 \end{pmatrix}$	$\begin{pmatrix} -210 \\ -12.4 \\ -270 \end{pmatrix}$	$\begin{pmatrix} -204 \\ -8.2 \\ -270 \end{pmatrix}$	$\begin{pmatrix} 10.3 \\ -14.4 \\ -236 \end{pmatrix}$	$\begin{pmatrix} 9.4 \\ -12.6 \\ -242 \end{pmatrix}$	$\begin{pmatrix} -211 \\ -14.1 \\ -270 \end{pmatrix}$	$\begin{pmatrix} -205 \\ -8.5 \\ -270 \end{pmatrix}$
$\begin{pmatrix} 50 \\ \infty \\ \infty \end{pmatrix}$		$\begin{pmatrix} 12.1 \\ -10.7 \\ -21.4 \end{pmatrix}$	$\begin{pmatrix} -211 \\ -13 \\ -215 \end{pmatrix}$	$\begin{pmatrix} -205 \\ -1.3 \\ -217 \end{pmatrix}$	$\begin{pmatrix} -209 \\ -13.9 \\ -270 \end{pmatrix}$	$\begin{pmatrix} -203 \\ -3.1 \\ -270 \end{pmatrix}$	$\begin{pmatrix} 11.6 \\ -15.8 \\ -226 \end{pmatrix}$	$\begin{pmatrix} 10.6 \\ -11.7 \\ -246 \end{pmatrix}$	$\begin{pmatrix} -210 \\ -15.7 \\ -270 \end{pmatrix}$	$\begin{pmatrix} -204 \\ -4.3 \\ -270 \end{pmatrix}$
$\begin{pmatrix} 50 \\ 50 \\ \infty \end{pmatrix}$		$\begin{pmatrix} 10.9 \\ -13.3 \\ -19.8 \end{pmatrix}$	$\begin{pmatrix} -212 \\ -10.4 \\ -228 \end{pmatrix}$	$\begin{pmatrix} -206 \\ -5.5 \\ -220 \end{pmatrix}$	$\begin{pmatrix} -210 \\ -9.5 \\ -270 \end{pmatrix}$	$\begin{pmatrix} -204 \\ -6.4 \\ -270 \end{pmatrix}$	$\begin{pmatrix} 10.3 \\ -16.8 \\ -239 \end{pmatrix}$	$\begin{pmatrix} 9.5 \\ -11.6 \\ -241 \end{pmatrix}$	$\begin{pmatrix} -211 \\ -14.5 \\ -270 \end{pmatrix}$	$\begin{pmatrix} -205 \\ -9.8 \\ -270 \end{pmatrix}$

^aAt $\begin{pmatrix} f_0 \\ 2f_0 \\ 3f_0 \end{pmatrix}$.

^b0 = short circuit; ∞ = open circuit.

The final step (Fig. 42) involves the synthesis of Z_{N_1} and Z_{N_2} to realize the prescribed impedances, where Z_{N_1} and Z_{N_2} are the respective driving point impedances of N_1 and N_2 .

4.2.1. Illustration of Unified Design Technique. Here we describe the design of an experimental frequency doubler based on the approach described above, utilizing a Fujitsu FHX35LG HEMT transistor. This transistor was modeled

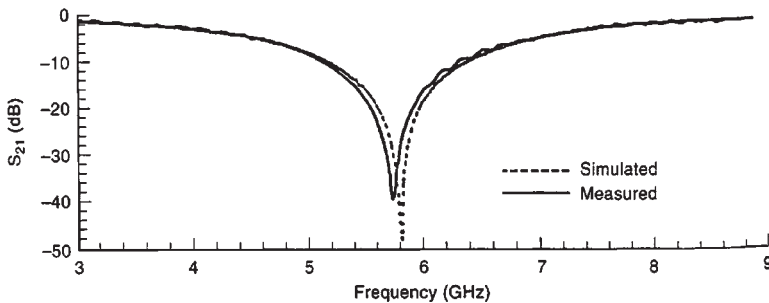


Figure 48. Transmission magnitude for input network (Z_{N_1}).

Table 9. Doubler Simulations with Microstrip Transmission Lines ($V_{gs} = 0\text{ V}$, $P_{in} = 0\text{ dBm}$, $V_{ds} = 3\text{ V}$)

Input Network (Ω) ^{a,b}	Output Network (Ω) ^{a,b}	Output Power (dBm) ^a								
		$\begin{pmatrix} 50 \\ 50 \\ 50 \end{pmatrix}$	$\begin{pmatrix} 0 \\ 50 \\ 50 \end{pmatrix}$	$\begin{pmatrix} \infty \\ 50 \\ 50 \end{pmatrix}$	$\begin{pmatrix} 0 \\ 50 \\ \infty \end{pmatrix}$	$\begin{pmatrix} \infty \\ 50 \\ \infty \end{pmatrix}$	$\begin{pmatrix} 50 \\ 50 \\ 0 \end{pmatrix}$	$\begin{pmatrix} 50 \\ 50 \\ \infty \end{pmatrix}$	$\begin{pmatrix} 0 \\ 50 \\ 0 \end{pmatrix}$	$\begin{pmatrix} \infty \\ 50 \\ 0 \end{pmatrix}$
$\begin{pmatrix} 50 \\ 50 \\ 50 \end{pmatrix}$		$\begin{pmatrix} 5.96 \\ -0.9 \\ -14.7 \end{pmatrix}$	$\begin{pmatrix} -27.1 \\ -0.7 \\ -26.3 \end{pmatrix}$	$\begin{pmatrix} -10.4 \\ -0.9 \\ -36.2 \end{pmatrix}$	$\begin{pmatrix} -25 \\ 0.4 \\ -52.9 \end{pmatrix}$	$\begin{pmatrix} -17.3 \\ 0.8 \\ -60.1 \end{pmatrix}$	$\begin{pmatrix} 5.6 \\ -5.1 \\ -26.9 \end{pmatrix}$	$\begin{pmatrix} 4 \\ 0.6 \\ -37.7 \end{pmatrix}$	$\begin{pmatrix} -26.1 \\ -4.3 \\ -41.8 \end{pmatrix}$	$\begin{pmatrix} -18.9 \\ -5.2 \\ -54.3 \end{pmatrix}$
$\begin{pmatrix} 50 \\ 0 \\ 50 \end{pmatrix}$		$\begin{pmatrix} 10.7 \\ 4.3 \\ -10.2 \end{pmatrix}$	$\begin{pmatrix} -27.4 \\ 5.4 \\ -22.6 \end{pmatrix}$	$\begin{pmatrix} -22 \\ 4.5 \\ -21 \end{pmatrix}$	$\begin{pmatrix} -20.5 \\ 8.6 \\ -42.8 \end{pmatrix}$	$\begin{pmatrix} -13.5 \\ 6.4 \\ -61 \end{pmatrix}$	$\begin{pmatrix} 10.5 \\ 0.3 \\ -24 \end{pmatrix}$	$\begin{pmatrix} 9 \\ 7.2 \\ -32 \end{pmatrix}$	$\begin{pmatrix} -21.2 \\ 1.3 \\ -37.3 \end{pmatrix}$	$\begin{pmatrix} -15.6 \\ -0.4 \\ -41.8 \end{pmatrix}$
$\begin{pmatrix} 50 \\ 0 \\ 0 \end{pmatrix}$		$\begin{pmatrix} 8.4 \\ 2.8 \\ -8.7 \end{pmatrix}$	$\begin{pmatrix} -24.5 \\ 3.2 \\ -22 \end{pmatrix}$	$\begin{pmatrix} -17.6 \\ 2.1 \\ -36.8 \end{pmatrix}$	$\begin{pmatrix} -22.2 \\ 5.5 \\ -46 \end{pmatrix}$	$\begin{pmatrix} -15 \\ 4.6 \\ -73.7 \end{pmatrix}$	$\begin{pmatrix} 8 \\ -2 \\ -21.3 \end{pmatrix}$	$\begin{pmatrix} 5.9 \\ 6.8 \\ -30.4 \end{pmatrix}$	$\begin{pmatrix} 23.6 \\ -0.9 \\ -35.6 \end{pmatrix}$	$\begin{pmatrix} -17 \\ -2.2 \\ -47 \end{pmatrix}$
$\begin{pmatrix} 50 \\ 50 \\ 0 \end{pmatrix}$		$\begin{pmatrix} 5.8 \\ -1.3 \\ -17 \end{pmatrix}$	$\begin{pmatrix} -27.4 \\ -0.2 \\ -29.1 \end{pmatrix}$	$\begin{pmatrix} -20 \\ -1.7 \\ -38.1 \end{pmatrix}$	$\begin{pmatrix} -23 \\ 1 \\ -55.2 \end{pmatrix}$	$\begin{pmatrix} -17.7 \\ -0.2 \\ -74 \end{pmatrix}$	$\begin{pmatrix} 5.5 \\ -5 \\ -27.6 \end{pmatrix}$	$\begin{pmatrix} 3.7 \\ 0.2 \\ -43.1 \end{pmatrix}$	$\begin{pmatrix} -18 \\ -5.6 \\ -33.5 \end{pmatrix}$	$\begin{pmatrix} -19.2 \\ -5.7 \\ -47.9 \end{pmatrix}$
$\begin{pmatrix} 50 \\ \infty \\ 50 \end{pmatrix}$		$\begin{pmatrix} 3.1 \\ -3.9 \\ -18.3 \end{pmatrix}$	$\begin{pmatrix} -28.4 \\ -3.6 \\ -43.8 \end{pmatrix}$	$\begin{pmatrix} -28.4 \\ -3.6 \\ -43.8 \end{pmatrix}$	$\begin{pmatrix} -28.2 \\ -3 \\ -64.3 \end{pmatrix}$	$\begin{pmatrix} -20.1 \\ -2.9 \\ -66.9 \end{pmatrix}$	$\begin{pmatrix} 2.9 \\ -7.1 \\ -28.1 \end{pmatrix}$	$\begin{pmatrix} 0.9 \\ -3.3 \\ -50.6 \end{pmatrix}$	$\begin{pmatrix} -30 \\ -6.4 \\ -43.2 \end{pmatrix}$	$\begin{pmatrix} -21.3 \\ -7.6 \\ -53 \end{pmatrix}$
$\begin{pmatrix} 50 \\ \infty \\ \infty \end{pmatrix}$		$\begin{pmatrix} 5.7 \\ -1.1 \\ -16.5 \end{pmatrix}$	$\begin{pmatrix} -27.6 \\ -1 \\ -30.2 \end{pmatrix}$	$\begin{pmatrix} -19.9 \\ -1 \\ -44.2 \end{pmatrix}$	$\begin{pmatrix} -25.7 \\ -0.5 \\ -55.4 \end{pmatrix}$	$\begin{pmatrix} -17.8 \\ -0.1 \\ -60.5 \end{pmatrix}$	$\begin{pmatrix} 5.5 \\ -5.1 \\ -29.2 \end{pmatrix}$	$\begin{pmatrix} 3.5 \\ 0 \\ -38.8 \end{pmatrix}$	$\begin{pmatrix} -26.4 \\ -4.5 \\ -43.8 \end{pmatrix}$	$\begin{pmatrix} -19 \\ -4.9 \\ -51.8 \end{pmatrix}$
$\begin{pmatrix} 50 \\ 50 \\ \infty \end{pmatrix}$		$\begin{pmatrix} 2.9 \\ -5.2 \\ -16.4 \end{pmatrix}$	$\begin{pmatrix} -35.5 \\ -5 \\ -29 \end{pmatrix}$	$\begin{pmatrix} -28.3 \\ -4.8 \\ -37.1 \end{pmatrix}$	$\begin{pmatrix} -28.3 \\ -4.2 \\ -50.3 \end{pmatrix}$	$\begin{pmatrix} -20.2 \\ -3.8 \\ -54.5 \end{pmatrix}$	$\begin{pmatrix} 2.3 \\ -10.1 \\ -35.4 \end{pmatrix}$	$\begin{pmatrix} 0.8 \\ -4.2 \\ -31.4 \end{pmatrix}$	$\begin{pmatrix} -29.5 \\ -9.7 \\ -47.5 \end{pmatrix}$	$\begin{pmatrix} -21.6 \\ -9.7 \\ -51.9 \end{pmatrix}$

^aAt $\begin{pmatrix} f_0 \\ 2f_0 \\ 3f_0 \end{pmatrix}$.

^b0 = short circuit; ∞ = open circuit.

in a previous section where measured and modeled data were presented showing the accuracy of the nonlinear model subsequent to performing the first step described above.

We need to determine the optimum bias points and input power levels from either measured or modeled data. Figures 43–47 show simulated data for various bias conditions and input power levels of the FHX35LG transistor. Figure 43 shows the simulated output power at 3 GHz versus the gate-to-source voltage V_{gs} at the fundamental frequency and the second-harmonic frequency, Fig. 44 shows the simulated output power at the second-harmonic frequency versus the drain-to-source voltage V_{ds} , Figs. 45 and 46 show the conversion gain at the second-harmonic versus V_{gs} for various input power levels, and Fig. 47 shows the simulated output power versus input power. Figures 43, 45, and 46 show that good second-harmonic generation occurs for $V_{gs} = 0\text{ V}$ and $V_{gs} = V_p = -0.7\text{ V}$. However, in the

present case, the conversion gain is greater by approximately 9 dB (–1 dB vs. –10 dB) when operating at $V_{gs} = V_p$ with $P_{in} = 0\text{ dBm}$ (Fig. 46) than when operating at $V_{gs} = 0\text{ V}$. The results indicate that the optimum bias and input power values for the doubler are $V_{gs} = V_p = -0.7\text{ V}$ and $P_{in} = 0\text{ dBm}$.

The next step requires the generation of matrix tables for the design of a frequency doubler operating at 3 GHz input. These matrix tables represent the simulated output powers of the HEMT frequency doubler for various combinations of the input and output impedances (Z_{N_1} and Z_{N_2}) presented to the HEMT. In this case extensive terminating tables were generated for both $V_{gs} = 0\text{ V}$ and $V_{gs} = V_p = -0.7\text{ V}$ [79]. Several matrix tables are shown in Tables 1–4.

Tables 1 and 2 show the output power simulations where lumped elements (not always practical values) were utilized to present the various impedances to the

Table 10. Doubler Simulations with Microstrip Transmission Lines ($V_{gs} = 0$ V, $P_{in} = 0$ dBm, $V_{ds} = 3$ V)

Input Network (Ω) ^{a,b}	Output Network (Ω) ^{a,b}	Output Power (dBm) ^a								
		$\begin{pmatrix} 50 \\ 50 \\ 50 \end{pmatrix}$	$\begin{pmatrix} 0 \\ 50 \\ 50 \end{pmatrix}$	$\begin{pmatrix} \infty \\ 50 \\ 50 \end{pmatrix}$	$\begin{pmatrix} 0 \\ 50 \\ \infty \end{pmatrix}$	$\begin{pmatrix} \infty \\ 50 \\ \infty \end{pmatrix}$	$\begin{pmatrix} 50 \\ 50 \\ 0 \end{pmatrix}$	$\begin{pmatrix} 50 \\ 50 \\ \infty \end{pmatrix}$	$\begin{pmatrix} 0 \\ 50 \\ 0 \end{pmatrix}$	$\begin{pmatrix} \infty \\ 50 \\ 0 \end{pmatrix}$
$\begin{pmatrix} 50 \\ 50 \\ 50 \end{pmatrix}$		$\begin{pmatrix} 12.5 \\ -10.1 \\ -13.9 \end{pmatrix}$	$\begin{pmatrix} -20.2 \\ -11.4 \\ -26.3 \end{pmatrix}$	$\begin{pmatrix} -15.1 \\ -2.5 \\ -25.4 \end{pmatrix}$	$\begin{pmatrix} -22.9 \\ -10.9 \\ -49.3 \end{pmatrix}$	$\begin{pmatrix} -12.5 \\ -4 \\ -55.4 \end{pmatrix}$	$\begin{pmatrix} 12 \\ -13.9 \\ -28.9 \end{pmatrix}$	$\begin{pmatrix} 11.1 \\ -10 \\ -33.9 \end{pmatrix}$	$\begin{pmatrix} -19.3 \\ -15.1 \\ -39.1 \end{pmatrix}$	$\begin{pmatrix} -14.3 \\ -6 \\ -36.3 \end{pmatrix}$
		$\begin{pmatrix} 14.7 \\ -12.5 \\ -8.4 \end{pmatrix}$	$\begin{pmatrix} -18.4 \\ -13.1 \\ -18.4 \end{pmatrix}$	$\begin{pmatrix} -14.4 \\ 1.8 \\ -25.6 \end{pmatrix}$	$\begin{pmatrix} -21.3 \\ -10.4 \\ -41 \end{pmatrix}$	$\begin{pmatrix} -11.1 \\ 2.8 \\ -52 \end{pmatrix}$	$\begin{pmatrix} 14.2 \\ -17.1 \\ -22 \end{pmatrix}$	$\begin{pmatrix} 13.2 \\ -10.6 \\ -2.8 \end{pmatrix}$	$\begin{pmatrix} -17.5 \\ -17 \\ -31.8 \end{pmatrix}$	$\begin{pmatrix} -13.6 \\ -2.5 \\ -34.5 \end{pmatrix}$
$\begin{pmatrix} 50 \\ 0 \\ 0 \end{pmatrix}$		$\begin{pmatrix} 13.6 \\ -11.5 \\ -9.3 \end{pmatrix}$	$\begin{pmatrix} -19.2 \\ -19 \\ -22.4 \end{pmatrix}$	$\begin{pmatrix} -14.6 \\ 0.5 \\ -21.8 \end{pmatrix}$	$\begin{pmatrix} -21.9 \\ -15.3 \\ -45 \end{pmatrix}$	$\begin{pmatrix} -11.7 \\ 0.4 \\ -59.6 \end{pmatrix}$	$\begin{pmatrix} 13.2 \\ -17.1 \\ -24.8 \end{pmatrix}$	$\begin{pmatrix} 12.3 \\ -11.2 \\ -28.8 \end{pmatrix}$	$\begin{pmatrix} -18.3 \\ -22.8 \\ -35.3 \end{pmatrix}$	$\begin{pmatrix} -13.9 \\ -3 \\ -32.3 \end{pmatrix}$
$\begin{pmatrix} 50 \\ 50 \\ 0 \end{pmatrix}$		$\begin{pmatrix} 12.6 \\ -10.3 \\ -17.5 \end{pmatrix}$	$\begin{pmatrix} -20.2 \\ -11.3 \\ -29.7 \end{pmatrix}$	$\begin{pmatrix} -15 \\ -2.6 \\ -29.5 \end{pmatrix}$	$\begin{pmatrix} -22.9 \\ -11.1 \\ -53 \end{pmatrix}$	$\begin{pmatrix} -12.3 \\ -4 \\ -53.4 \end{pmatrix}$	$\begin{pmatrix} 12.1 \\ -13.7 \\ -33.9 \end{pmatrix}$	$\begin{pmatrix} 11.1 \\ -10.4 \\ -36.5 \end{pmatrix}$	$\begin{pmatrix} -19.3 \\ -14.7 \\ -42.8 \end{pmatrix}$	$\begin{pmatrix} -14.2 \\ -5.9 \\ -41 \end{pmatrix}$
$\begin{pmatrix} 50 \\ \infty \\ 50 \end{pmatrix}$		$\begin{pmatrix} 11.2 \\ -11.4 \\ -18.9 \end{pmatrix}$	$\begin{pmatrix} -21.6 \\ -11.6 \\ -32.4 \end{pmatrix}$	$\begin{pmatrix} -15.6 \\ -6.8 \\ -32.3 \end{pmatrix}$	$\begin{pmatrix} -24.4 \\ -11.9 \\ -54.6 \end{pmatrix}$	$\begin{pmatrix} -13.1 \\ -8.5 \\ -60.4 \end{pmatrix}$	$\begin{pmatrix} 10.6 \\ -14.6 \\ -32.7 \end{pmatrix}$	$\begin{pmatrix} 9.7 \\ -12.1 \\ -39.8 \end{pmatrix}$	$\begin{pmatrix} -20.7 \\ -14.8 \\ -45.2 \end{pmatrix}$	$\begin{pmatrix} -14.7 \\ -9.6 \\ -42.6 \end{pmatrix}$
$\begin{pmatrix} 50 \\ \infty \\ \infty \end{pmatrix}$		$\begin{pmatrix} 12.7 \\ -9.4 \\ -13.5 \end{pmatrix}$	$\begin{pmatrix} -20.2 \\ -11.1 \\ -26.1 \end{pmatrix}$	$\begin{pmatrix} -14.8 \\ -1 \\ -23.2 \end{pmatrix}$	$\begin{pmatrix} -22.9 \\ -11.2 \\ -50.2 \end{pmatrix}$	$\begin{pmatrix} -12.1 \\ -2.9 \\ -52.2 \end{pmatrix}$	$\begin{pmatrix} 12.2 \\ -13.1 \\ -29.4 \end{pmatrix}$	$\begin{pmatrix} 11.2 \\ -10.5 \\ -33.1 \end{pmatrix}$	$\begin{pmatrix} -19.3 \\ -14.3 \\ -39.2 \end{pmatrix}$	$\begin{pmatrix} -13.9 \\ -4 \\ -34 \end{pmatrix}$
$\begin{pmatrix} 50 \\ 50 \\ \infty \end{pmatrix}$		$\begin{pmatrix} 11 \\ -12.1 \\ -18.8 \end{pmatrix}$	$\begin{pmatrix} -25 \\ -16.4 \\ -45.2 \end{pmatrix}$	$\begin{pmatrix} -15.8 \\ -6.1 \\ -27.7 \end{pmatrix}$	$\begin{pmatrix} -24.4 \\ -10.9 \\ -57 \end{pmatrix}$	$\begin{pmatrix} -13.3 \\ -8.3 \\ -55.1 \end{pmatrix}$	$\begin{pmatrix} 10.5 \\ -16.2 \\ -35.6 \end{pmatrix}$	$\begin{pmatrix} 9.6 \\ -11.9 \\ -38.4 \end{pmatrix}$	$\begin{pmatrix} -20.7 \\ -14.3 \\ -47.3 \end{pmatrix}$	$\begin{pmatrix} -15 \\ -10.2 \\ -39.5 \end{pmatrix}$

^aAt $\begin{pmatrix} f_0 \\ 2f_0 \\ 3f_0 \end{pmatrix}$.

^b0 = short circuit; ∞ = open circuit.

input and output ports of the HEMT for $V_{gs} = 0$ V and $V_{gs} = V_p$. As an example, Table 2 shows an analysis with the HEMT biased at $V_{gs} = 0$ V. The table illustrates the wide variation in the conversion gain based on resistive termination and pole-zero placement for both N_1 (Z_{N_1}) as the input network and N_2 (Z_{N_2}) as the output network. In particular, it is seen that if the device is driven from an N_1 that admits a real 50 ohm impedance presented to the gate and is terminated in a real 50 ohm impedance for N_2 seen from the drain, then the conversion gain will have a value of -10.1 dB for operation as a doubler or -13.9 dB as a tripler, with due consideration of unwanted harmonics. However, if N_1 presents an impedance to the gate of the HEMT of 50 at f_0 , a pole at $2f_0$, and 50 at $3f_0$, and N_2 presents a pole f_0 , 50 at $2f_0$, and a pole at $3f_0$, then the conversion gain increases 8.4 dB to a value of -1.7 dB.

In efforts to realize impedances with transmission lines, ideal transmission lines were used to present the

various ideal impedances to the HEMT, without considering losses, to obtain a best-case scenario before proceeding to practical microstrip lines. Tables 7 and 8 show the simulations of the output power of the doubler for $V_{gs} = 0$ V and $V_{gs} = V_p$, utilizing ideal transmission lines. Variations in the conversion gain, as observed in the previous matrix simulation tables, are observed in the simulations that utilize ideal transmission lines as well.

Doubler simulations utilizing practical microstrip lines are considered next. Figures 44–48 show simulations utilizing microstrip lines for $V_{gs} = 0$ V and $V_{gs} = V_p$ for input powers of 0 and -4 dBm.

A perusal of the matrix tables (specifically Tables 9–12) provides requirements for both input and output network impedances to provide optimal conversion gain performance for a frequency doubler. In Table 9, the optimum conversion gain is shown to be 8.6 dB (row 2, column 4), where the required input termination is a short circuit at

Table 11. Doubler Simulations with Microstrip Transmission Lines ($V_{gs} = 0.7\text{ V}$, $P_{in} = -4\text{ dBm}$, $V_{ds} = 3\text{ V}$)

Input Network (Ω) ^{a,b}	Output Network (Ω) ^{a,b}	Output Power (dBm) ^a								
		$\begin{pmatrix} 50 \\ 50 \\ 50 \end{pmatrix}$	$\begin{pmatrix} 0 \\ 50 \\ 50 \end{pmatrix}$	$\begin{pmatrix} 50 \\ 0 \\ 0 \end{pmatrix}$	$\begin{pmatrix} 0 \\ 50 \\ 0 \end{pmatrix}$	$\begin{pmatrix} 0 \\ 50 \\ 50 \end{pmatrix}$	$\begin{pmatrix} 50 \\ 50 \\ \infty \end{pmatrix}$	$\begin{pmatrix} \infty \\ 50 \\ \infty \end{pmatrix}$	$\begin{pmatrix} 0 \\ 50 \\ \infty \end{pmatrix}$	$\begin{pmatrix} \infty \\ 50 \\ 0 \end{pmatrix}$
$\begin{pmatrix} 50 \\ 50 \\ 50 \end{pmatrix}$		$\begin{pmatrix} 0.5 \\ -6.7 \\ -21.3 \end{pmatrix}$	$\begin{pmatrix} -32.7 \\ -6.1 \\ -34.3 \end{pmatrix}$	$\begin{pmatrix} -0 \\ -10.8 \\ -33.3 \end{pmatrix}$	$\begin{pmatrix} -31.6 \\ -10 \\ -48 \end{pmatrix}$	$\begin{pmatrix} -25.1 \\ -6.8 \\ -46.6 \end{pmatrix}$	$\begin{pmatrix} -1.5 \\ -4.9 \\ -43.4 \end{pmatrix}$	$\begin{pmatrix} -22.8 \\ -5.1 \\ -65.9 \end{pmatrix}$	$\begin{pmatrix} -35.9 \\ -4.8 \\ -60.6 \end{pmatrix}$	$\begin{pmatrix} -24.2 \\ -11.1 \\ -60.2 \end{pmatrix}$
$\begin{pmatrix} 50 \\ 0 \\ 50 \end{pmatrix}$		$\begin{pmatrix} 6 \\ 6 \\ -13.7 \end{pmatrix}$	$\begin{pmatrix} -26.9 \\ 1 \\ -26.6 \end{pmatrix}$	$\begin{pmatrix} 5.8 \\ -4.2 \\ -25.5 \end{pmatrix}$	$\begin{pmatrix} -25.9 \\ -3.2 \\ -39.4 \end{pmatrix}$	$\begin{pmatrix} -20.8 \\ -1 \\ -34.5 \end{pmatrix}$	$\begin{pmatrix} 4.5 \\ 3 \\ -36.2 \end{pmatrix}$	$\begin{pmatrix} -18.2 \\ 1.5 \\ -61.9 \end{pmatrix}$	$\begin{pmatrix} -29.5 \\ 4.3 \\ -49 \end{pmatrix}$	$\begin{pmatrix} -19.9 \\ -5.2 \\ -46.3 \end{pmatrix}$
$\begin{pmatrix} 50 \\ 0 \\ 0 \end{pmatrix}$		$\begin{pmatrix} -4 \\ -11.8 \\ -28.2 \end{pmatrix}$	$\begin{pmatrix} -29.9 \\ -2.2 \\ -28.6 \end{pmatrix}$	$\begin{pmatrix} 2.7 \\ -7.4 \\ -27.3 \end{pmatrix}$	$\begin{pmatrix} -28.9 \\ -41.6 \\ -6.4 \end{pmatrix}$	$\begin{pmatrix} -22.8 \\ -3.6 \\ -41.6 \end{pmatrix}$	$\begin{pmatrix} 1.5 \\ 0.3 \\ -37.3 \end{pmatrix}$	$\begin{pmatrix} -20.4 \\ -1 \\ -72 \end{pmatrix}$	$\begin{pmatrix} -32.7 \\ 0.8 \\ -50.2 \end{pmatrix}$	$\begin{pmatrix} -22 \\ -7.9 \\ -52.9 \end{pmatrix}$
$\begin{pmatrix} 50 \\ 50 \\ 0 \end{pmatrix}$		$\begin{pmatrix} 0.2 \\ -7.1 \\ -23.7 \end{pmatrix}$	$\begin{pmatrix} -33 \\ -6.1 \\ -34.9 \end{pmatrix}$	$\begin{pmatrix} -0.1 \\ -10.6 \\ -32.7 \end{pmatrix}$	$\begin{pmatrix} -31.9 \\ -9.5 \\ -45.8 \end{pmatrix}$	$\begin{pmatrix} -25.4 \\ -7.6 \\ -43.8 \end{pmatrix}$	$\begin{pmatrix} -1.9 \\ -5.6 \\ -53.8 \end{pmatrix}$	$\begin{pmatrix} -23.1 \\ -6.1 \\ -77.4 \end{pmatrix}$	$\begin{pmatrix} -36.3 \\ -4.4 \\ -65.1 \end{pmatrix}$	$\begin{pmatrix} -24.5 \\ -11.6 \\ -54 \end{pmatrix}$
$\begin{pmatrix} 50 \\ \infty \\ 50 \end{pmatrix}$		$\begin{pmatrix} -2.4 \\ -10.1 \\ -26.2 \end{pmatrix}$	$\begin{pmatrix} -35.8 \\ -9.4 \\ -39.7 \end{pmatrix}$	$\begin{pmatrix} -2.8 \\ -13.4 \\ -36 \end{pmatrix}$	$\begin{pmatrix} -34.7 \\ -12.8 \\ -50.7 \end{pmatrix}$	$\begin{pmatrix} -27.7 \\ -10.1 \\ -50.6 \end{pmatrix}$	$\begin{pmatrix} -4.6 \\ -9.1 \\ -57.5 \end{pmatrix}$	$\begin{pmatrix} -25.6 \\ -9 \\ -75.2 \end{pmatrix}$	$\begin{pmatrix} -39.1 \\ -8.2 \\ -69.5 \end{pmatrix}$	$\begin{pmatrix} -26.8 \\ -13.9 \\ -60 \end{pmatrix}$
$\begin{pmatrix} 50 \\ \infty \\ \infty \end{pmatrix}$		$\begin{pmatrix} 0.2 \\ -7 \\ -23.1 \end{pmatrix}$	$\begin{pmatrix} -33.1 \\ -6.7 \\ -37.2 \end{pmatrix}$	$\begin{pmatrix} 0 \\ -10.8 \\ -35.8 \end{pmatrix}$	$\begin{pmatrix} -32 \\ -10.1 \\ -50.2 \end{pmatrix}$	$\begin{pmatrix} -25.3 \\ -7.1 \\ -49.6 \end{pmatrix}$	$\begin{pmatrix} -2 \\ -5.7 \\ -46.2 \end{pmatrix}$	$\begin{pmatrix} -23.3 \\ -6 \\ -68.7 \end{pmatrix}$	$\begin{pmatrix} -36.5 \\ -5.4 \\ -66.1 \end{pmatrix}$	$\begin{pmatrix} -24.4 \\ -11 \\ -58 \end{pmatrix}$
$\begin{pmatrix} 50 \\ 50 \\ \infty \end{pmatrix}$		$\begin{pmatrix} -2.6 \\ -11.1 \\ -25.1 \end{pmatrix}$	$\begin{pmatrix} -35.9 \\ -10.9 \\ -38.5 \end{pmatrix}$	$\begin{pmatrix} -3.2 \\ -15.8 \\ -45.3 \end{pmatrix}$	$\begin{pmatrix} -35.1 \\ -15.3 \\ -57.6 \end{pmatrix}$	$\begin{pmatrix} -27.7 \\ -11.1 \\ -46.5 \end{pmatrix}$	$\begin{pmatrix} -4.7 \\ -9.7 \\ -39.3 \end{pmatrix}$	$\begin{pmatrix} -25.6 \\ -9.7 \\ -62.9 \end{pmatrix}$	$\begin{pmatrix} -39.2 \\ -10.4 \\ -58.3 \end{pmatrix}$	$\begin{pmatrix} -27 \\ -15.8 \\ -62.1 \end{pmatrix}$

$$^a \text{At } \begin{pmatrix} f_0 \\ 2f_0 \\ 3f_0 \end{pmatrix}.$$

^b0 = short circuit; ∞ = open circuit.

the second-harmonic frequency and the output network consists of an open-circuit termination at the third-harmonic frequency along with a short-circuit termination at the fundamental.

After the optimal impedances (Z_{N_1} and Z_{N_2}) have been determined, the impedances have to be synthesized in order to construct a physical frequency doubler to evaluate the efficacy of the results. In this analysis, the synthesis is performed using microstrip transmission lines. Figures 48 and 49 show the transmission response of the input network (short circuit at the second-harmonic) and the output network (short circuit at the fundamental and open circuit at the third harmonic), respectively. The measured and simulated responses for $|S_{21}|$ indicate that the desired short-circuit effect is established at the second-harmonic (6 GHz) for Z_{N_1} as shown in Fig. 48, and similarly for the measured and modeled response of Z_{N_2} in Fig. 49.

The complete experimental frequency doubler was realized on 50 m (20 mil) duroid, and its response is shown in Figs. 50 and 51. Figure 50 shows the conversion gain of the doubler using the technique outlined here, and Fig. 51 shows the harmonic suppression. Figure 50 shows that the maximum conversion gain is 8.5 dB with a -3 dB bandwidth of approximately 8% and with harmonic suppression greater than 20 dBc.

Conventional doubler designs have employed a short-circuit termination at the second-harmonic frequency on the input network along with a short-circuit termination at the fundamental on the output network. This conventional design approach (row 2, column 2 of Table 9) shows the simulated conversion gain as 3.2 dB less than the optimal case outlined by this new approach. For comparison, a frequency doubler utilizing the conventional approach mentioned is developed on 20 mil duroid as well. The

Table 12. Doubler Simulations with Microstrip Transmission Lines ($V_{gs} = 0.7\text{ V}$, $P_{in} = 4\text{ dBm}$, $V_{ds} = 3\text{ V}$)

Input Network (Ω) ^{a,b}	Output Network (Ω) ^{a,b}	Output Power (dBm) ^a								
		$\begin{pmatrix} 50 \\ 50 \\ 50 \end{pmatrix}$	$\begin{pmatrix} 0 \\ 50 \\ 50 \end{pmatrix}$	$\begin{pmatrix} \infty \\ 50 \\ 50 \end{pmatrix}$	$\begin{pmatrix} 0 \\ 50 \\ \infty \end{pmatrix}$	$\begin{pmatrix} \infty \\ 50 \\ \infty \end{pmatrix}$	$\begin{pmatrix} 50 \\ 50 \\ 0 \end{pmatrix}$	$\begin{pmatrix} 50 \\ 50 \\ \infty \end{pmatrix}$	$\begin{pmatrix} 0 \\ 50 \\ 0 \end{pmatrix}$	$\begin{pmatrix} \infty \\ 50 \\ 0 \end{pmatrix}$
$\begin{pmatrix} 50 \\ 50 \\ 50 \end{pmatrix}$		$\begin{pmatrix} 9.1 \\ -15.5 \\ -23.5 \end{pmatrix}$	$\begin{pmatrix} -23.3 \\ -14.5 \\ -38.7 \end{pmatrix}$	$\begin{pmatrix} -17.5 \\ -17.2 \\ -42.6 \end{pmatrix}$	$\begin{pmatrix} -26 \\ -14.2 \\ -61.3 \end{pmatrix}$	$\begin{pmatrix} -15 \\ -17.4 \\ -68.6 \end{pmatrix}$	$\begin{pmatrix} 8.7 \\ -18.8 \\ -38.8 \end{pmatrix}$	$\begin{pmatrix} 7.8 \\ -15.1 \\ -44 \end{pmatrix}$	$\begin{pmatrix} -22.3 \\ -18.2 \\ -51.7 \end{pmatrix}$	$\begin{pmatrix} -16.6 \\ -20.8 \\ -54 \end{pmatrix}$
$\begin{pmatrix} 50 \\ 0 \\ 50 \end{pmatrix}$		$\begin{pmatrix} 12.2 \\ -13.4 \\ -17.8 \end{pmatrix}$	$\begin{pmatrix} -20.2 \\ -16.9 \\ -29.5 \end{pmatrix}$	$\begin{pmatrix} -15.8 \\ -6.8 \\ -31 \end{pmatrix}$	$\begin{pmatrix} -22.9 \\ -14.2 \\ -51.8 \end{pmatrix}$	$\begin{pmatrix} -13.2 \\ -5.8 \\ -55.7 \end{pmatrix}$	$\begin{pmatrix} 12 \\ -16.7 \\ -32.5 \end{pmatrix}$	$\begin{pmatrix} 10.9 \\ -12.3 \\ -37.6 \end{pmatrix}$	$\begin{pmatrix} -19.3 \\ -20.7 \\ -42.5 \end{pmatrix}$	$\begin{pmatrix} -15 \\ -11.1 \\ -45.3 \end{pmatrix}$
$\begin{pmatrix} 50 \\ 0 \\ 0 \end{pmatrix}$		$\begin{pmatrix} 10.5 \\ -14 \\ -19.4 \end{pmatrix}$	$\begin{pmatrix} -21.9 \\ -16.1 \\ -34.5 \end{pmatrix}$	$\begin{pmatrix} -16.6 \\ -12.1 \\ -38.9 \end{pmatrix}$	$\begin{pmatrix} -24.7 \\ -13.3 \\ -57.5 \end{pmatrix}$	$\begin{pmatrix} -14.1 \\ -10.7 \\ -75.9 \end{pmatrix}$	$\begin{pmatrix} 10.1 \\ -17.7 \\ -35.7 \end{pmatrix}$	$\begin{pmatrix} 9.1 \\ -12.9 \\ -39 \end{pmatrix}$	$\begin{pmatrix} -21 \\ -20 \\ -47.5 \end{pmatrix}$	$\begin{pmatrix} -15.8 \\ -15.9 \\ -49.2 \end{pmatrix}$
$\begin{pmatrix} 50 \\ 50 \\ 0 \end{pmatrix}$		$\begin{pmatrix} 9.2 \\ -15.5 \\ -24.8 \end{pmatrix}$	$\begin{pmatrix} -23.3 \\ -14.7 \\ -39.1 \end{pmatrix}$	$\begin{pmatrix} -17.2 \\ -16.2 \\ -38.5 \end{pmatrix}$	$\begin{pmatrix} -26.1 \\ -14.8 \\ -61.8 \end{pmatrix}$	$\begin{pmatrix} -14.8 \\ -16.9 \\ -63 \end{pmatrix}$	$\begin{pmatrix} 8.8 \\ -18.5 \\ -40.9 \end{pmatrix}$	$\begin{pmatrix} 7.8 \\ -15.7 \\ -44.4 \end{pmatrix}$	$\begin{pmatrix} 22.4 \\ -17.9 \\ -52.7 \end{pmatrix}$	$\begin{pmatrix} -16.3 \\ -19.5 \\ -51.8 \end{pmatrix}$
$\begin{pmatrix} 50 \\ \infty \\ 50 \end{pmatrix}$		$\begin{pmatrix} 7.7 \\ -17.8 \\ -27.6 \end{pmatrix}$	$\begin{pmatrix} -25.1 \\ -17.4 \\ -43.3 \end{pmatrix}$	$\begin{pmatrix} -18.3 \\ -20.9 \\ -46.8 \end{pmatrix}$	$\begin{pmatrix} -27.8 \\ -17.9 \\ -65 \end{pmatrix}$	$\begin{pmatrix} -15.9 \\ -21.8 \\ -71.5 \end{pmatrix}$	$\begin{pmatrix} 7.1 \\ -20.9 \\ -41.4 \end{pmatrix}$	$\begin{pmatrix} 6.2 \\ -18.6 \\ -49.2 \end{pmatrix}$	$\begin{pmatrix} -24.2 \\ -20.4 \\ -56.4 \end{pmatrix}$	$\begin{pmatrix} -17.4 \\ -23.9 \\ -58.7 \end{pmatrix}$
$\begin{pmatrix} 50 \\ \infty \\ \infty \end{pmatrix}$		$\begin{pmatrix} 9.4 \\ -14.3 \\ -22.9 \end{pmatrix}$	$\begin{pmatrix} -23.3 \\ -14.3 \\ -38.2 \end{pmatrix}$	$\begin{pmatrix} -16.9 \\ -15.7 \\ -40.3 \end{pmatrix}$	$\begin{pmatrix} -26.1 \\ -14.6 \\ -61.8 \end{pmatrix}$	$\begin{pmatrix} -14.5 \\ -17 \\ -67 \end{pmatrix}$	$\begin{pmatrix} 9 \\ -17.5 \\ -39.3 \end{pmatrix}$	$\begin{pmatrix} 7.9 \\ -15.2 \\ -42.9 \end{pmatrix}$	$\begin{pmatrix} -22.4 \\ -17.3 \\ -51.8 \end{pmatrix}$	$\begin{pmatrix} -16.1 \\ -18.6 \\ -51.3 \end{pmatrix}$
$\begin{pmatrix} 50 \\ 50 \\ \infty \end{pmatrix}$		$\begin{pmatrix} 7.5 \\ -1.9 \\ -26.9 \end{pmatrix}$	$\begin{pmatrix} -30.3 \\ -16.4 \\ -45.2 \end{pmatrix}$	$\begin{pmatrix} -18.6 \\ -22.3 \\ -45.3 \end{pmatrix}$	$\begin{pmatrix} -27.8 \\ -17.5 \\ -67.4 \end{pmatrix}$	$\begin{pmatrix} -16.2 \\ -23 \\ -69.5 \end{pmatrix}$	$\begin{pmatrix} 7 \\ -22.9 \\ -43.8 \end{pmatrix}$	$\begin{pmatrix} 6.1 \\ -18.6 \\ -47 \end{pmatrix}$	$\begin{pmatrix} -24.1 \\ -20.8 \\ -58.1 \end{pmatrix}$	$\begin{pmatrix} -17.7 \\ -26.6 \\ -57.5 \end{pmatrix}$

^aAt $\begin{pmatrix} f_0 \\ 2f_0 \\ 3f_0 \end{pmatrix}$.

^b0 = short circuit; ∞ = open circuit.

measured and simulated conversion gain for the HEMT doubler utilizing this conventional approach is shown in Fig. 52. The circuit is seen to have a conversion gain of approximately 5 dB around the center frequency of 3 GHz,

rising to 6.7 dB at 3.08 GHz. As indicated previously, the conversion gain produced by the conventional design approach exhibits approximately 3 dB less conversion gain than doublers designed with the unified approach.

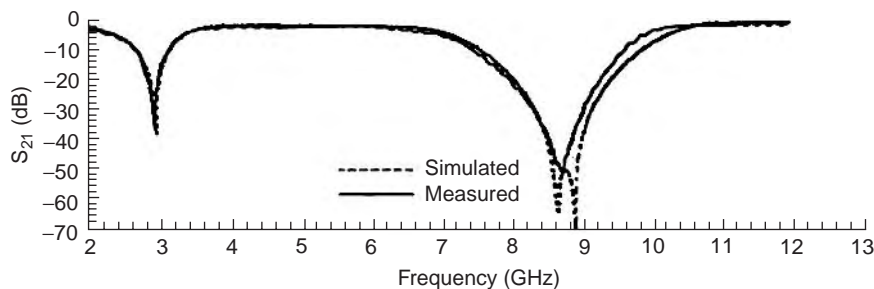


Figure 49. Transmission magnitude for output network (Z_{N_2}).

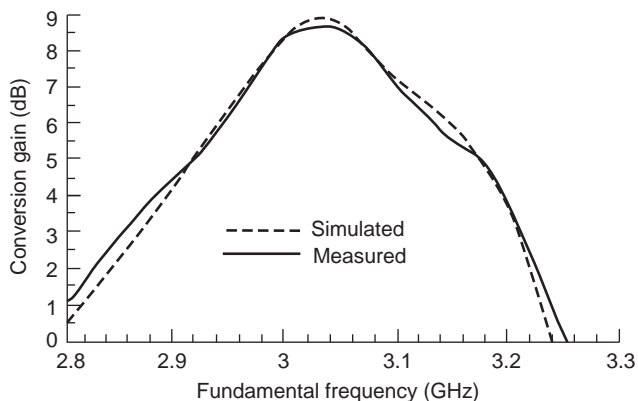


Figure 50. Conversion gain of HEMT doubler using the unified technique ($P_{in} = 0$ dBm, $V_{gs} = -0.7$ V, $V_{ds} = 3.0$ V).

4.3. Reflector Method

Another single-ended design technique [93,95,104,109, 141–145,168–171] is based on the use of reflector networks. This section presents examples of doubler designs operating in the S and C frequency bands incorporating such reflector networks to provide optimized performance. In this presentation, reflector networks are employed simultaneously on both the input and output of HEMT-based designs. In a common-source configuration, the input reflector network passes the fundamental frequency but reflects the desired higher-harmonic signal back into the gate of the device at an optimum phase. The output reflector network passes the desired harmonic while reflecting the fundamental frequency back into the drain of the device at the proper phase angle for maximizing the conversion gain. Measured and simulated results are given to strengthen this design philosophy.

Figure 51. Harmonic suppression of HEMT doubler using the unified technique ($P_{in} = 0$ dBm, $V_{gs} = -0.7$ V, $V_{ds} = 3.0$ V).

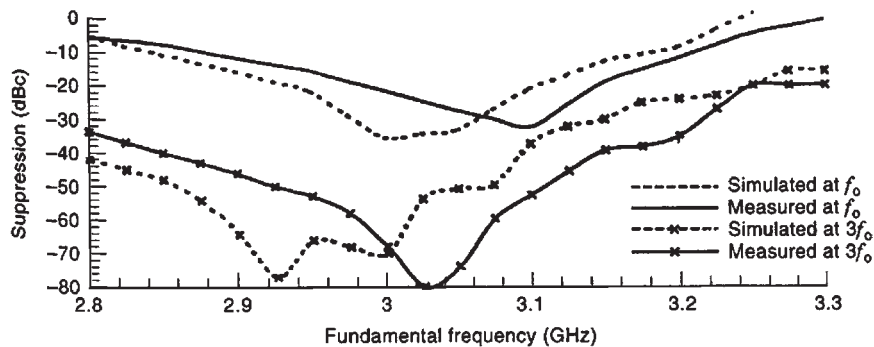


Figure 52. Conversion gain of HEMT doubler using conventional design ($P_{in} = 0$ dBm, $V_{gs} = -0.7$ V, $V_{ds} = 3.0$ V).

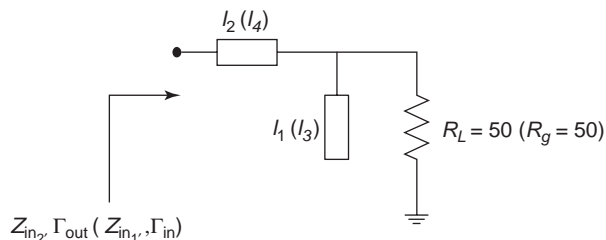
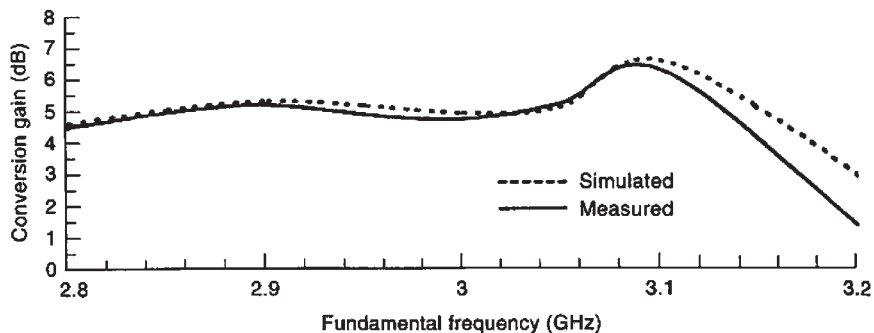


Figure 53. Fundamental output (input) reflector network.

4.3.1. Reflector Networks. Numerous techniques exist for the realization of frequency multipliers. All techniques at radiofrequencies employ a nonlinear device to generate the desired frequency multiple. The basic configuration of the single-ended frequency multiplier realization is illustrated in Fig. 24. As mentioned previously, the input network allows the fundamental frequency to pass through to the gate of the transistor, in a common-source configuration, while suppressing higher-harmonic frequencies. Similarly, the output network suppresses the fundamental and other unwanted harmonics, while allowing the desired harmonic to pass. The frequency multiplier reflector network design philosophy implemented in this section is applied to an HEMT (Fujitsu FHXLG) frequency doubler with a fundamental frequency of 3 GHz.

As stated above, a primary objective of the output and input networks is to suppress select harmonics. In the process of suppressing the undesired signals, it appears that relatively little attention is given to the possibility that the unwanted signals can be reflected back into the device from the input and output networks simultaneously. The nonlinearity of the device causes these harmonics and the fundamental to mix with other frequency

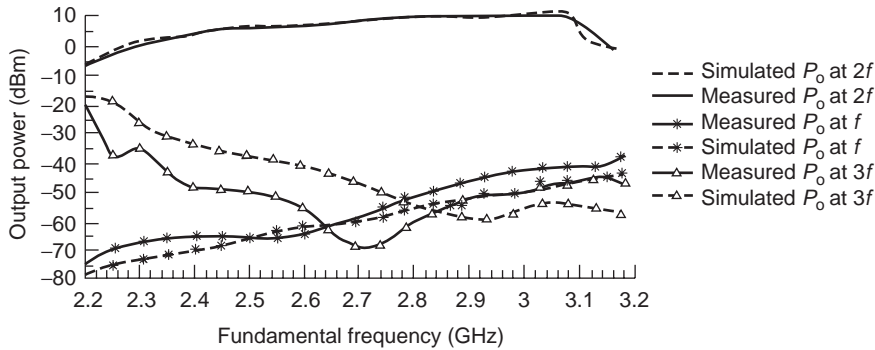


Figure 54. Wideband HEMT doubler design ($P_{in} = 0$ dBm, $V_{gs} = 0.6$ V).

components. This mixing process can either enhance or degrade the signal at the desired second harmonic. Therefore, it is important for the reflected signal to be properly phased, such that it interferes constructively with the desired harmonic (second harmonic in the case of the frequency doubler examples presented below). Thus, the input and output networks of Fig. 24 can be designed in such a way that in addition to their primary function of filtering, they are reflector networks meeting the above criteria. Owing to the complexity in calculating the actual effects of the reflector networks, there has not been a significant amount of analytical discussion on this topic until 2000 [157,168,169,171].

4.3.2. Consideration of Reflection Phase Angle. As stated, the input and output networks of Fig. 24 should be designed such that they are reflector networks, in addition to their primary function of filtering. The reflector networks developed in this section are analyzed on a frequency doubler with a fundamental frequency of 3 GHz. For a frequency doubler, the input network of Fig. 24 should be designed to reflect the second-harmonic back into the gate of the HEMT at the proper phase angle for constructive interference and optimum conversion gain. Similarly, the output network is designed such that it reflects the fundamental signal back into the drain of the HEMT at the optimum phase. The network of Fig. 53 is a logical choice for the output and input reflector functions described above, although it is not optimal in the input case. In this figure, Z_{in_2} , Γ_{out} , l_1 , l_2 , R_L and Z_{in_1} , l_3 , l_4 , R_g denote output and input reflector networks, respectively [157], and l_1 and l_3 are fixed at a quarter wavelength of the fundamental frequency and a quarter-wavelength of the second-harmonic frequency, respectively.

4.3.3. Effect of Reflection Angle on Conversion Gain. Optimization of the conversion gain of a HEMT (FHXLG) doubler can be obtained by varying the reflection angles on both input and output, using l_4 and l_2 , respectively. Computer analyses, substantiated by experimental measurements, show that conversion gain variation of over 20 and 27 dB result by changes of l_4 and l_2 , respectively. Maximum to minimum gain variations have been found to occur for l_4 , varying from 0 to 200° and l_2 varying from 0 to 180°.

4.4. Doubler Designs Based on Prior Analysis

It has been shown that optimum multiplier designs in terms of conversion gain can be developed. These designs are based on the proper synthesis of input and output networks with the requisite transfer, input magnitude $|Z_{in_2}|$, and phase $\angle Z_{in_2}$. Narrow, medium, and wideband designs have been demonstrated employing this approach [136,157]. Figure 54 shows a wideband design employing this technique.

4.5. Summary

This section has presented design techniques for single-ended frequency multiplier designs. These techniques incorporate reflector networks providing excellent performance characteristics, which includes effective conversion gain and harmonic suppression as demonstrated by the results. These results show the improvement in conversion gain using reflector networks with proper phase angles on the input and output networks simultaneously, which are useful for narrowband and wideband applications. Because of bandwidth constraints imposed by the use of single stubs, incorporating filters into the designs achieves bandwidth extension and improves harmonic suppression. This improvement in bandwidth and harmonic suppression, however, comes at the expense of conversion gain, as shown by the wideband designs. Another advantage of these designs is that they are single-ended, thus alleviating the requirement for complex baluns or transformers.

BIBLIOGRAPHY

1. M. Gupta et al., Performance and design of microwave FET harmonic generators, *IEEE Trans. Microwave Theory Tech.* **MTT-29**:261–263 (1983).
2. Y. Iyama et al., Second harmonic reflector type high-gain FET frequency doubler operating in K-band, *IEEE MTT-S Int. Symp. Digest*, 1989, Vol. 3, pp. 1291–1294.
3. R. Stancliff, Balanced dual gate GaAs FET frequency doublers, *IEEE MTT-S Int. Symp. Digest*, 1981, pp. 143–145.
4. R. Gilmore, Concepts in the design of frequency multipliers, *Microwave J.* **30**(3):129–139 (1987).
5. C. Rauscher, High-frequency doubler operation of GaAs field-effect transistors, *IEEE Trans. Microwave Theory Tech.* **MTT-31**:462–473 (1983).

6. E. Camargo and F. Corraera, A high gain GaAsMESFETfrequency quadrupler, *IEEE MTT-S Int. Symp. Digest*, 1987, pp. 177–180.
7. M. Borg and G. R. Branner, Novel MIC bipolar frequency doublers having high gain, wide bandwidth and good spectral performance, *IEEE Trans. Microwave Theory Tech.* **39**:1936–1946 (1991).
8. J. Lester et al., High performance HEMTMMIC's for low cost EHF satcom terminals, *Proc. IEEE Microwave Millimeter-Wave Circuits Symp.*, 1992, pp. 113–116.
9. P. Staecker, MM-wave transmitters using power frequency multipliers, *Microwave J.* **31**(2):175–181 (1988).
10. A. Chu et al., Monolithic analog phase shifters and frequency multipliers for mm-wave phased array applications, *Microwave J.* **29**(12):105–119 (1986).
11. R. Mott, High-performance frequency doublers for the COMSTAR beacon, *COMSAT Tech. Rev.* **7**(2):556–577 (1977).
12. A. Dao, personal conversation.
13. M. Faber, *Microwave and Millimeter-Wave Diode Frequency Multipliers*, Artech House, Norwood, MA, 1995.
14. D. Peterson, The varactor power frequency multiplier: A device for quietly extending the frequency range of microwave power sources, *Microwave J.* **33**(5):135–146 (1990).
15. J. Gavan and A. Peled, Low-power passive frequency doublers of high efficiency using varactor diodes, *Int. J. Electron.* **68**(6):1011–1019 (1990).
16. J. Gavan and A. Peled, Highly efficient passive frequency doublers in the L and S bands implemented by step recovery diodes, *Int. J. Electron.* **63**(3):401–408 (1987).
17. J. Archer and R. Batchelor, Multipliers and parametric devices, in K. Chang, ed., *Handbook of Microwave and Optical Components Microwave Solid-State Components*, Wiley, New York; 1989, Vol. 2, pp. 142–191.
18. J. Scanlan, Analysis of varactor harmonic generators, in L. Young, ed., *Advances in Microwaves*, Academic Press, New York, 1967, Vol. 2, pp. 165–236.
19. H. Watson, *Microwave Semiconductor Devices and Their Circuit Applications*, McGraw-Hill, New York, 1969, Chap. 8.
20. D. Leeson and S. Weinreb, Frequency multiplication with nonlinear capacitors—a circuit analysis, *Proc. IRE* 2076–2084 (Dec. 1959).
21. D. Roulston and A. Boothroyd, A large-signal analysis and design approach for frequency multipliers using varactor diodes, *IEEE Trans. Circ. Theory* 194–205 (June 1965).
22. P. Jounet and M. Fourrier, 20–40 GHz broadband frequency doubler with gallium arsenide varactor, *Rev. Sci. Instrum.*, **49**(1):124–125 (1978).
23. S. Nilssen et al., Single barrier varactors for submillimeter wave power generation, *IEEE Trans. Microwave Theory Tech.* **41**:572–579 (1993).
24. S. Chen et al., Rigorous design of a 94 GHz MMICdoubler, *Proc. IEEE Microwave Millimeter-Wave Monolithic Circuits Symp.*, 1993, pp. 89–92.
25. S. Chen et al., A high-performance 94 GHz MMICdoubler, *IEEE Microwave Guided Wave Lett.* **3**(6):167–169 (1993).
26. J. Archer, A novel quasi-optical frequency multiplier design for millimeter and submillimeter wavelengths, *IEEE Trans. Microwave Theory Tech.* **32**:421–426 (1984).
27. T. Takada et al., Hybrid integrated frequency doublers and triplers to 300 to 450 GHz, *IEEE Trans. Microwave Theory Tech.* **MTT-28**:966–973 (1980).
28. R. Hess, Low-power MIC diode doubler, *MSN & CT*, 58–67 (Dec. 1987).
29. K. Chang et al., W-band (75–110 GHz) microstrip components, *IEEE Trans. Microwave Theory Tech.* **MTT-33**:1375–1380 (1985).
30. R. Bitzer, Planar broadband MIC balanced frequency doublers, *Proc. IEEE Microwave Theory Tech. Symp.* 1991, pp. 273–276.
31. B. Rizzi et al., A high-power millimeter-wave frequency doubler using a planar diode array, *IEEE Microwave Guided Wave Lett.* **3**(6):188–190 (1993).
32. N. Erickson, High efficiency submillimeter frequency multipliers, *Proc. IEEE Microwave Theory Tech. Symp.* 1990, pp. 1301–1304.
33. J. Archer, High-output, single- and dual-diode, millimeter-wave frequency doublers, *IEEE Trans. Microwave Theory Tech.* **MTT-33**: 533–538, (1985).
34. A. Chu, Monolithic analog phase shifters and frequency multipliers for mm-wave phased array application, *Microwave J.* **29**(12):105–119 (1986).
35. J. Cushman et al., High power epitaxially stacked varactor diode multipliers: Performance and application at W-band, *Proc. IEEE Microwave Theory Tech. Symp.*, 1990, pp. 923–926.
36. A. Raisanen, Frequency multipliers for millimeter and submillimeter wavelengths, *Proc. IEEE* **80**:1842–1852 (1992).
37. P. Staecker and R. Chick, 10 to 40 GHz doubler-doubler chain for satcom applications, *Microwave J.* **28**(12):87–108 (1985).
38. J. Archer, Millimeter wavelength frequency multipliers, *IEEE Trans. Microwave Theory Tech.* **MTT-29**:552–557 (1981).
39. D. Choudhury et al., A 200 GHz tripler using a single barrier varactor, *IEEE Trans. Microwave Theory Tech.* **MTT-41**:595–599 (1993).
40. J. Archer, An efficient 200–290 GHz frequency tripler incorporating a novel stripline structure, *IEEE Trans. Microwave Theory Tech.* **MTT-32**:416–420 (1984).
41. T. Tolmunen, Theoretical performance of novel multipliers at millimeter and submillimeter wavelengths, *Int. J. Infrared Millim. Waves* **12**(10):1111–1133 (1991).
42. J. Manley and H. Rowe, Some general properties of nonlinear elements—Part I. General energy relations, *Proc. IRE* 904–913 (July 1956).
43. P. Penfield and R. Rafuse, *Varactor Applications*, MIT Press, Cambridge, MA, 1962.
44. S. Maas, *Nonlinear Microwave Circuits*, Artech House, Norwood, MA, 1988.
45. C. Page, Frequency conversion with positive nonlinear resistors, *J. Res. Natl. Bur. Stand.* **56**:179–182 (April 1956).
46. R. Muller and T. Kamins, *Device Electronics for Integrated Circuits*, 2nd ed., Wiley, New York; 1986.
47. B. Diamond, Idler circuits in varactor frequency multipliers, *IEEE Trans. Circ. Theory* 35–44 (March 1963).
48. M. Borg and G. R. Branner, Accurate modeling of high frequency composite transistors for nonlinear circuits, *IEEE Int. Circuits and Systems Conf. Record*, 1989.
49. J. Golio, *Microwave MESFETs and HEMTs*, Artech House, Norwood, MA; 1991.
50. S. Long and S. Butner, *Gallium Arsenide Digital Integrated Circuit Design*, McGraw-Hill, New York, 1990.

51. W. Curtice, A MESFET model for use in the design of GaAs integrated circuits, *IEEE Trans. Microwave Theory Tech.* **MTT-28**(5):448–456 (1980).
52. W. Curtice and M. Ettenberg, A nonlinear GaAs FET model for use in the design of output circuits for power amplifiers, *IEEE Trans. Microwave Theory Tech.* **MTT-33**(12):1383–1394 (1985).
53. A. Materka and T. Kacprzak, Computer calculation of large-signal GaAs FET amplifier characteristics, *IEEE Trans. Microwave Theory Tech.* **MTT-33**(2):129–135 (1985).
54. A. Materka and T. Kacprzak, Compact dc model of GaAs FETs for large-signal computer calculations, *IEEE J. Solid-State Circ.* **SC-18**:211–213 (April 1983).
55. H. Statz et al., GaAs device and circuit simulation in SPICE, *IEEE Trans. Electron. Dev.* **ED-34**(2):160–167 (1987).
56. R. Anholt, *Electrical and Thermal Characterization of MESFETs, HEMTs, and HBTs*, Artech House, Norwood, MA, 1995.
57. A. McCamant et al., An improved GaAs MESFET model for SPICE, *IEEE Trans. Microwave Theory Tech.* **MTT-38**(6):822–824 (1990).
58. R. Fair, Graphical design and iterative analysis of the DC parameters of GaAs FETs, *IEEE Trans. Electron. Dev.* **ED-21**(6):357–362 (1974).
59. H. Shichman and D. Hodges, Modeling and simulation of insulated-gate FET transistor switching circuits, *IEEE J. Solid-State Circ.* **SC-3**(3) (1968).
60. D. Root and S. Fan, Experimental evaluation of large-signal modeling assumptions based on vector analysis of bias-dependent S-parameter data from MESFETs and HEMTs, *MTT-S Digest* 1992, pp. 255–258.
61. D. Root et al., Measurement-based large-signal diode model, automated data acquisition system, and verification with on-wafer power and harmonic measurements, *MTT-S Digest* 1993, pp. 261–264.
62. D. Root et al., Technology independent large signal non quasi-static FET models by direct construction from automatically characterized device data, *Proc. 21st European Microwave Conf.* Sept. 1991, pp. 927–932.
63. K. Shirakawa et al., An approach to determining an equivalent circuit for HEMTs, *IEEE Trans. Microwave Theory Tech.* **MTT-43**(3):499–503 (1995).
64. C. Morton et al., A large-signal physical HEMT model, *MTT-S Digest*, 1996, pp. 1759–1762.
65. T. Tanimoto, Analytical nonlinear HEMT model for large signal circuit simulation, *IEEE Trans. Microwave Theory Tech.* **MTT-44**(9):1584–1586 (Sept. 1996).
66. HP-EEs of Libra Manual, Series IV, *Circuit Element Catalog*, 1994, Vol. 2, pp. 13-79–13-87.
67. I. Angelov and H. Zirath, New empirical nonlinear model for HEMT devices, *Electron. Lett.* **28**(2):140–143 (Jan. 1992).
68. I. Angelov et al., A new empirical nonlinear model for HEMT and MESFET devices, *IEEE Trans. Microwave Theory Tech.* **MTT-40**(12):2258–2266 (Dec. 1992).
69. I. Angelov et al., Validation of nonlinear HEMT model by power spectrum characteristics, *MTT-S Digest*, 1994, pp. 1571–1574.
70. I. Angelov et al., Temperature and dispersion effect extensions of Chalmers nonlinear HEMT and MESFET model, *MTT-S Digest*, 1995, pp. 1515–1518.
71. L. Bengtsson et al., An extraction program for nonlinear transistor model parameters for HEMTs and MESFETs, *Microwave J.* **38**(1):146–153 (Jan. 1995).
72. I. Angelov et al., Extensions of the Chalmers nonlinear HEMT and MESFET model, *IEEE Trans. Microwave Theory Tech.* **44**(10):1664–1674 (Oct. 1996).
73. S. Maas and D. Neilson, Modeling MESFETs for intermodulation analysis of mixers and amplifiers, *MTT-S Digest*, 1990, pp. 1291–1294.
74. W. Struble et al., A new small signal MESFET and HEMT model compatible with large signal modeling, *MTT-S Digest*, 1994, pp. 1567–1570.
75. H. Willing, C. Rauscher, and P. de Santis, A technique for predicting large-signal performance of a GaAs MESFET, *IEEE Trans. Microwave Theory Tech.* **26**(12):1017–1023 (Dec. 1978).
76. C. Rauscher and H. Willing, Simulation of nonlinear microwave FET performance using a quasi-static model, *IEEE Trans. Microwave Theory Tech.* **27**(10):834–840 (Oct. 1979).
77. M. Miller et al., Choosing an optimum large signal model for GaAs MESFETs and HEMTs, *MTT-S Digest*, 1990, pp. 1279–1282.
78. M. Novotny and G. Kompa, Unique and physically meaningful extraction of the bias-dependent series resistors of a 0.15 m PHEMT demands extremely broadband and highly accurate measurements, *MTT-S Digest*, 1996, pp. 1715–1718.
79. A. Gopinath and J. Rankin, Single-gate MESFET frequency doublers, *IEEE Trans. Microwave Theory Tech.* **30**(6):869–875 (June 1982).
80. J. Roux et al., Small-signal and noise model extraction technique for heterojunction bipolar transistor at microwave frequencies, *IEEE Trans. Microwave Theory Tech.* **43**(2):293–297 (Feb. 1995).
81. A. Abdipour and A. Pacaud, Temperature noise constants extraction of mm-wave FETs from measured s- and noise parameters, *MTT-S Digest*, 1996, pp. 1723–1726.
82. J. Leckey et al., Analysis of HEMT harmonic generation using a vector nonlinear measurement system, *MTT-S Digest*, 1996 pp. 1739–1742.
83. S. Peng et al., Simplified nonlinear model for the intermodulation analysis of MESFET mixers, *MTT-S Digest*, 1994, pp. 1575–1578.
84. R. Tucker, Third-order intermodulation distortion and gain compression in GaAs FETs, *IEEE Trans. Microwave Theory Tech.* **27**(5):400–408 (May 1979).
85. R. Minasian, Intermodulation distortion analysis of MESFET amplifiers using the Volterra series representation, *IEEE Trans. Microwave Theory Tech.* **28**(1):1–8 (Jan. 1980).
86. S. Maas, *Theory and Analysis of GaAs MESFET Mixers*, Ph.D. dissertation, Univ. California, Los Angeles, 1985.
87. P. Chen et al., Performance of a dual-gate GaAs MESFET as a frequency multiplier at Ku-band, *IEEE Trans. Microwave Theory Tech.* **27**(5):411–415 (May 1979).
88. D. L. Le et al., A novel approach for designing GaAs FET frequency multipliers with optimum conversion gain and power efficiency, *Microwave Opt. Technol. Lett.* **5**(9):403–408 (1992).
89. T. T. Ha, *Solid-State Microwave Amplifier Design*, Krieger Publishing, Malabar, FL; 1991.
90. G. Vendelin et al., *Microwave Circuit Design Using Linear and Nonlinear Techniques*, Wiley, New York; 1990.
91. R. Stancliff, Balanced dual gate GaAs FET frequency doublers, *IEEE MTT-S Int. Symp. Digest*, 1981, pp. 143–145.
92. R. Gilmore, Concepts in the design of frequency multipliers, *Microwave J.* 129–139 (March 1987).

93. C. Rauscher, High-frequency doubler operation of GaAs field-effect transistors, *IEEE Trans. Microwave Theory Tech.* **MTT-31**(6):462–473 (1983).
94. E. Camargo and F. Correria, A high gain GaAsMESFET frequency quadrupler, *IEEE MTT-S Int. Symp. Digest*, 1987, pp. 177–180.
95. M. Borg and G. R. Branner, Novel MIC bipolar frequency doublers having high gain, wide bandwidth and good spectral performance, *IEEE Trans. Microwave Theory Techn.* **39**(12): 1936–1946 (Dec. 1991).
96. M. Gupta et al., Performance and design of microwave FET harmonic generators, *IEEE Trans. Microwave Theory Tech.* **MTT-29**(3): 261–263 (1983).
97. G. Dow and L. Rosenheck, A new approach for mm-wave generation, *Microwave J.* 147–162 (Sept. 1983).
98. E. Camargo et al., Sources of non-linearity in GaAsMESFET frequency multipliers, *IEEE MTT-S Int. Symp. Digest*, 1983, pp. 343–345.
99. S. Maas, *Nonlinear Microwave Circuits*, Artech House, Norwood, MA; 1988, pp. 59–80.
100. M. Gupta, R. Laton and T. Lee, Frequency multiplication with high-power microwave field-effect transistors, *IEEE MTT-S Int. Symp. Digest*, April 1979, pp. 498–500.
101. E. Camargo, A study of single-gate GaAsMESFET doubler operation, *Proc. International Symposium on Circuits and Systems*, 1985, pp. 1591–1594.
102. E. Camargo, *Fenomenos Nao-lineares em Transistores de Feito de Campo de Microondas e Sua Aplicacao a Multiplicadores de Frequencia*, Ph.D. dissertation, Univ. Sao Paulo, 1985.
103. S. Meszaros et al., An integrated 18.75/37.5 GHz FET frequency doubler, *IEEE MTT-S Int. Symp. Digest*, 1988, pp. 815–818.
104. Y. Iyama et al., Second harmonic reflector type high-gain FET frequency doubler operating in K-band, *IEEE MTT-S Int. Symp. Digest*, 1989, pp. 1291–1294.
105. S.-W. Chen et al., A high performance 94-GHz MMIC doubler, *IEEE Microwave Guided Wave Lett.* **3**(6):167–169 (June 1993).
106. C. Guo et al., Optimal CAD of MESFET frequency multipliers with and without feedback, *IEEE MTT-S Int. Symp. Digest*, 1988, pp. 1115–1118.
107. T. Saito, A 45 GHz GaAsFET MIC oscillator-doubler, *IEEE MTT-S Int. Symp. Digest*, 1992, pp. 283–285.
108. S. El-Rabaie et al., A novel approach for the large signal analysis and optimization of microwave frequency doublers, *IEEE MTT-S Int. Symp. Digest*, 1988, pp. 1119–1122.
109. T. Hirota and H. Ogawa, Uniplanar monolithic frequency doublers, *IEEE Trans. Microwave Theory Tech.* **37**(8):1249–1254 (Aug. 1989).
110. C. Rauscher, Frequency doublers with GaAsFETs, *IEEE MTT-S Int. Symp. Digest*, 1982, pp. 280–282.
111. T. Takenaka et al., An ultra-wideband MMIC balanced frequency doubler using line-unified HEMTs, *IEEE Trans. Microwave Theory Tech.* **40**(10) (Oct. 1992).
112. H. Ogawa and A. Minagawa, Uniplanar MIC balanced multiplier—a proposed new structure for MIC's, *IEEE Trans. Microwave Theory Tech.* **35**(12) (1987).
113. I. Angelov et al., A balanced millimeter wave doubler based on pseudomorphic HEMTs, *IEEE MTT-S Int. Symp. Digest*, 1992, pp. 353–356.
114. A. Pavo et al., A distributed broadband monolithic frequency multiplier, *IEEE MTT-S Int. Symp. Digest*, 1988, pp. 503–505.
115. R. Bitzer, Planar broadband MIC Balanced frequency doublers, *IEEE MTT-S Int. Symp. Digest*, 1991, pp. 273–276.
116. C. Creamer, 43.5 to 45.5 GHz active times-4 frequency multiplier with 1.4 watt output power, *IEEE MTT-S Int. Symp. Digest*, 1991, pp. 939–942.
117. J. Lester et al., High performance HEMTMMICs for low cost EHF satcom terminals, *Proc. IEEE 1992 Microwave Millimeter-Wave Monolithic Circuits Symp*, 1992, pp. 113–116.
118. J. Henkus, A wideband tripler for X-band in microstrip, *Microwave J.* 106–111, March 1993.
119. A. Gopinath et al., Comparison of single- and dual-gate FET frequency doublers, *IEEE Trans. Microwave Theory Tech.* **30**(6):919–920 (June 1982).
120. G. Zhao et al., The effects of biasing and harmonic loading on MESFET tripler performance, *Microwave Opt. Technol. Lett.* **9**(4):189–194 (July 1995).
121. T. Hiraoka et al., A miniaturized broad-band MMIC frequency doubler, *IEEE Trans. Microwave Theory Tech.* **38**(12):1932–1937 (Dec. 1990).
122. J. Fikart and Y. Yuan, A new circuit structure for microwave frequency doublers, *Proc. IEEE 1992 Microwave Millimeter-Wave Monolithic Circuits Symp.* 1993, pp. 145–148.
123. K. Fricke et al., High-efficiency frequency doubling by GaAs traveling-wave MESFETs, *IEEE Trans. Electron. Dev.* **ED-34**(4):742–745 (April 1987).
124. P. Colantonio et al., On the optimum design of microwave active frequency doublers, *IEEE MTT-S Int. Symp. Digest*, 1995, pp. 1423–1426.
125. D. Filipovic, A MIC X7 DHBT frequency multiplier with low spurious harmonics, *IEEE MTT-S Int. Symp. Digest*, 1995, pp. 1325–1328.
126. M. Gupta, Frequency multiplication with high-power microwave field-effect transistors, *IEEE MTT-S Int. Symp. Digest*, 1979, pp. 498–500.
127. M. Gupta, Performance and design of microwave FET harmonic generators, *IEEE Trans. Microwave Theory Tech.* **29**(3):261–263 (March 1981).
128. J. Pan, Wideband MESFET microwave frequency multiplier, *IEEE MTT-S Int. Symp. Digest*, 1978, pp. 306–308.
129. G. Lambrianou and C. Aitchison, Optimization of third-order intermodulation product and output power from an X-band MESFET amplifier using Volterra series analysis, *IEEE Trans. Microwave Theory Tech.* **33**(12):1395–1403 (Dec. 1985).
130. J. Hinsaw, MMIC active multipliers, *RF Design* 64–68 (June 1988).
131. M. A. Tuko and I. Wolff, Novel 36 GHz GaAs frequency doublers using (M)MIC coplanar technology, *IEEE MTT-S Int. Symp. Digest*, 1992, pp. 1167–1170.
132. R. Konn and R. Genin, High performance aperiodic frequency multiplying, *Electron. Lett.* **15**(6): (March 1979).
133. M. Faber, *Microwave and Millimeter-Wave Diode Frequency Multipliers*, Artech House, Norwood, MA; 1995.
134. E. Carman et al., V-band and W-band broadband, monolithic distributed frequency multipliers, *IEEE MTT-S Int. Symp. Digest*, 1992, pp. 819–822.
135. P. Penfield and R. Rafuse, *Varactor Applications*, The MIT Press, Cambridge, MA; 1962, pp. 1–91.
136. B. Minnis, Printed circuit coupled line filters for bandwidths up to and greater than an octave, *IEEE Trans. Microwave Theory Tech.* **29**:215–222 (March 1981).
137. R. Gilmore, Octave-bandwidth microwave FET doubler, *Electron. Lett.* **21**(12):532–533 (June 1985).

138. T. Jerse, Nonlinear analysis of microwave circuits, *Class notes for EEC289N*, winter 1988, pp. 1–50.
139. HP-EEsof Libra Manual, Series IV, *Users Guide*, Vol. 1, 1993, pp. 10-1–10-44.
140. D. G. Thomas and G. R. Branner, Single-ended HEMTRF/microwave frequency doubler design using reflector networks, *Proc. 1995 Midwest Symp. Circuit Systems* 1995, Vol. 2, pp. 1014–1017.
141. D. G. Thomas, G. R. Branner, Optimization of active microwave frequency multiplier performance utilizing harmonic terminating impedances, *Proc. 1996 IEEE MTT-S Int. Microwave Symp.*, 1996, Vol. 2, pp. 659–662.
142. D. G. Thomas and G. R. Branner, New techniques for reflector network design in single-ended HEMTRF/microwave frequency multipliers, *Proc. 1996 Midwest Symp. Circuit System* 1996, pp. 1359–1362.
143. D. G. Thomas and G. R. Branner, Analysis of harmonic termination impedance on RF/microwave multiplier efficiency, *Proc. 1996 Midwest Symp. Circuit System*, 1996, pp. 1343–1346.
144. D. G. Thomas and G. R. Branner, Nonlinear properties of PHEMTtransistors exploited in the design of active RF/microwave frequency multipliers, *Proc. 1996 Midwest Symp. Circuit System*, 1996, pp. 245–248.
145. D. G. Thomas and G. R. Branner, Optimization of active microwave frequency multiplier performance utilizing harmonic terminating impedances, *Proc. 1996 IEEE Trans. Microwave Theory Tech.* **44**(12):2617–2624 (Dec. 1996).
146. (Online) 1998, available at <http://www.rfservices.com/networks.htm>.
147. E. Camargo and F. Corraera, A high gain GaAsMESFETfrequency quadrupler, *Proc. 1987 IEEE MTT-S Int. Microwave Symp.* 1996, pp. 177–180.
148. T. Hiraoka et al., A miniaturized broad-band MMICfrequency doubler, *IEEE Trans. Microwave Theory Tech.* **38**(12):1932–1937 (Dec. 1990).
149. M. Abdo-Tuko et al., A balanced Ka-band GaAsFETMMIC frequency doubler, *IEEE Microwave Guided Wave Lett.* **4**(7):217–219 (July 1994).
150. K. Katzebue and G. Matthaai, The design of broadband frequency doublers using charge storage diodes, *IEEE MTT-S Int. Microwave Symp.* **17**(12):1077–1086 (Dec., 1969).
151. W. Keese and G. R. Branner, Monolithic microwave integrated circuit research: Balanced active microwave frequency doublers for MMICapplications, *Proc. 1993 Symp. Circuit System*, 1993, pp. 562–565.
152. G. Zhang, R. D. Pollard, C. Snowden, A novel technique for HEMTtripler design, *1996 IEEE MTT-S Digest* 1996, pp. 663–666.
153. R. Gilmore, Design of a novel FETfrequency doubler using a harmonic balance algorithm, *Proc. 1986 IEEE MTT-S Int. Microwave Symp.* 1986, pp. 585–588.
154. O. Von Stein, J. Sherman, Odd order MESFETmultipliers with broadband, efficient, low spurious response, *Proc. 1996 IEEE MTT-S Int. Symp.* 1996, pp. 667–670.
155. X. Zhand and Y.-H. Yun, A DCto X band frequency doubler using GaAsHBTMMIC, *1997 IEEE MTT-S Digest*, 1997, pp. 1213–1216.
156. R. W. J. Barker, BJTfrequency doubling with sinusoidal output, *IEE Electron. Lett.* **11**(5):106–107 (March 1975).
157. D. G. Thomas, Jr. and G. R. Branner, Single-ended HEMTmultiplier design using reflector networks (in press).
158. I. Angelov, N. Rorsman, J. Stenarson, et al., An empirical table-based FETmodel, *IEEE Trans. Microwave Theory Tech.* **47**: 2350–2357 (Dec. 1999).
159. D. Schreurs, and J. Verspecht, Large-signal modeling and measuring *go hand-in-hand*: Accurate alternatives to indirect S-parameter methods, *Int. J. RF Microwave Comput.-Aided Eng.* **10**(1): 6–18 (Jan. 2000).
160. J.W. Bandler, R.M. Biernacki, S.H. Chen, J. Song, S. Ye, and Q.-J. Zhang, Analytically unified DC/small-signal/large-signal circuit design, *IEEE Trans. Microwave Theory Tech.* **39**(7):1076–1082 (July 1991).
161. A. Werthof, F. van Raay, and G. Kompa, Direct nonlinear power MESFETparameter extraction and consistent modeling, *IEEE. MTT -S Int. Microwave Symp. Digest*, New York, 1993, Vol. 2.
162. I. Angelov, L. Bengtsson, and M. Garcia, Extensions of the Chalmers nonlinear HEMTand MESFETmodel, *IEEE Trans. Microwave Theory Tech.* **44**:1664–1674 (Oct. 1996).
163. M. Fernandez-Barciela, P. J. Tasker, Y. Campos-Roca, M. Demmler, H. Massier, E. Sanchez, M. C. Curras-Francos, and M. Schlechtweg, A simplified broadband large-signal nonquasi-static table-based FETmodel, *IEEE Trans. Microwave Theory Tech.* **48**(3):395–405 (March 2000).
164. B. Thibaud, et al., CAD oriented design methods of frequency multipliers. Application to a millimeter wave MMIC, PHEMT tripler and a microwave HBT doubler, *IEEE MTT-S Digest*, 1999 pp. 733–736.
165. N. Siripon, M. Chongcheawchamnan, and I. D. Robertson, Novel frequency doubler using feedforward for fundamental frequency component suppression, *IEEE MTT -S, Int. Microwave Symp. Digest*, 2001, Vol. 2, pp. 1345–1348.
166. H. Fudem, and E. C. Niehenke, Novel millimeter wave active MMICtriplers, *IEEE MTT -S Int. Microwave Symp. Digest* 1998, Vol. 2, pp. 387–390.
167. I. Schmale, G. Kompa, Improving balanced frequency doublers through a design approach insensitive to residual asymmetries, *IEEE MTT -S Int. Microwave Symp. Digest*, 1999, Vol. 2, pp. 733–736.
168. B.Y. Huang, and G. R. Branner, Very high conversion gain microwave frequency doubler circuit design, *Proc. IEEE Midwest Symp. Circuits and Systems*, 2000, Vol. 1, pp. 24–26.
169. J.P. Mima and G. R. Branner, Synthesis of active microwave frequency triplers, *Proc. IEEE Midwest Symp. Circuits and Systems*, 2000, Vol. 1 pp. 20–22.
170. J. Johnson, G. R. Branner, and M. Chee, Quantitative analysis of microwave frequency multiplication in MESFET/HEMTdevices, *Proc. 44th IEEE Midwest Symp. Circuits and Systems*, 2001, Vol., 2, pp. 760–763.
171. J. Johnson, *Theory and Design of Active Frequency Multipliers*, Ph.D. dissertation, Univ. California, Davis, 2004.
172. E. O’Ciardha et al. Generic-device frequency-multiplier analysis—a unified approach, *IEEE Trans. Micro Theory Tech.* **48**(7) (July 2000).

FURTHER READING

- E. Carman, V-band and W-band broadband, monolithic distributed frequency multipliers, *Proc. IEEE Microwave Theory and Techniques Symp.*, 1992, pp. 819–822.
- R. Pantell, General power relationships for positive and negative nonlinear resistive elements, *Proc. IRE*, 1910–1913 (Dec. 1958).

MICROWAVE CIRCUITS

K. C. GUPTA
HAKI CEBI
CHOONSIK CHO
ZHIPING FENG
University of Colorado at
Boulder

The term “microwave circuits” is used to identify the electrical circuits used at microwave frequencies for performing signal processing functions like amplification, frequency conversion, mixing, detection, phase shifting, filtering, and power dividing. By “microwave frequencies,” we refer to electromagnetic signals whose wavelength is in centimeters, roughly from 30 cm to 1 mm with the corresponding frequencies ranging from 1 GHz ($\text{GHz} = 10^9 \text{ Hz}$) to 300 GHz. The frequency range from 30 to 300 GHz is also known as the *millimeter-wave band*. Microwave frequencies present several interesting and unusual features not found in other portions of the electromagnetic frequency spectrum. These features make microwaves uniquely suitable for several useful applications in telecommunications, radar, industrial heating and sensors, and so on. The most common consumer application of microwaves is the domestic microwave oven used for food processing.

Microwave circuits differ from lower-frequency electronic circuits for several reasons. Active devices (transistors, diodes, etc.) used at microwave frequencies are special designs and in several cases operate on entirely different physical principles. Parasitic reactances associated with passive and active circuit elements used at lower frequencies become significant and can cause disastrous effects on performance of circuits at microwave frequencies. Dimensions of lumped elements used in low-frequency electronics can become comparable to the wavelengths at microwave frequencies and cause what are known as distributed circuit effects. Transmission lines (and other structures) used for transmission of signals from one location to another inside a circuit need to be designed differently from those at lower frequencies. All these features make the design, technology, and operation of microwave circuits significantly different from their lower-frequency counterparts.

1. TYPES OF MICROWAVE CIRCUITS

Types of microwave circuits may be classified in several different ways. Depending on the type of active devices used, there are vacuum-tube circuits and solid-state circuits. Depending on the technology used, there are printed circuits, hybrid integrated circuits, monolithic circuits, and so on. Depending on the circuit functions, there are amplifier circuits, filter circuits, mixer circuits, power divider circuits, and so on. Depending on the special performance features, there are low-noise circuits, high-power circuits, and so on. Depending on the transmission structures whose sections form the basic building blocks for

circuit design, there are waveguide circuits, coaxial circuits, stripline circuits, microstrip circuits, coplanar waveguide (CPW) circuits, finline circuits, slotline circuits, dielectric waveguide circuits, and so on. Depending on the special material properties used, there are ferrite circuits, surface acoustic wave (SAW) circuits, and so on.

This article provides a brief overview of the important types of microwave circuits. Several specific types of microwave circuits are described in more detail in other articles in this encyclopedia. These include articles on frequency converters/mixers, microwave signal amplifiers, microwave couplers, microwave detectors, microwave filters and multiplexers, microwave oscillators, microwave phase shifters, microwave switches, power combiners/dividers, and stripline components.

2. LUMPED AND DISTRIBUTED CIRCUITS

All electronic circuits can be grouped into five classes depending on their physical dimensions compared to the wavelength at the frequency of operation. When all three physical dimensions of a component or a circuit are much smaller than the wavelength at the frequency of operation, we call it a “lumped circuit.” These are most extensively used components and circuits at lower frequencies. Lumped components are used at microwave frequencies also, but their dimensions have to be proportionately smaller. When one of the physical dimensions of a component is comparable to the wavelength (other two being still small), we refer to these as one-dimensional components, and the circuits using these components are called one-dimensional circuits. Circuits using sections of transmission lines as components, commonly known as transmission-line circuits, are one-dimensional. Transmission-line circuits are used extensively at microwave and millimeter-wave frequencies. Components and circuits with two of their dimensions comparable to the wavelength at the operating frequency are appropriately called “two-dimensional components.” Thin-film components, planar components and circuits fabricated on thin substrates, microstrip patch antennas, and reduced-height waveguide components belong to this class. These planar components are the important building blocks in microwave integrated circuits. The fourth class of electronic circuits have all three of their dimensions comparable to the wavelength at the operating frequency. These are known as three-dimensional components. Waveguides, hollow metallic cylindrical tubes used as transmission structures in place of conventional transmission lines, have both of their transverse dimensions comparable to the wavelength. Circuits using these waveguide sections and resonant cavities made out of these waveguides are examples of three-dimensional components and circuits used at microwave frequencies. Finally, the fifth class of electronic circuits (classified by their size) have at least one of their dimensions much larger than the wavelength at the operating frequency. These are known as quasioptical circuits. The term “quasioptical” is derived from their likeness to optical circuits that are orders of magnitude larger than the submicron wavelengths at optical frequencies.

3. EVOLUTION OF MICROWAVE CIRCUITS

For a long time the term “microwave circuits” was synonymous with “waveguide circuits.” A waveguide was recognized as a useful transmission structure for microwave frequencies in the early 1930s. The work of Southworth and others [1–3] at Bell Telephone Laboratories deserves mention in this respect. It was soon realized that a short length of waveguide, with suitable modifications, might function as a radiator and also as a reactive element. Resonant cavities and horn antennas are mentioned in a 1936 article by Southworth [1]. Modern waveguide circuitry had its beginning in the efforts to obtain both a more efficient transfer of microwave power from a source to a waveguide transmission line, thereby providing the elements of a transmitter, and again in the efficient recovery of microwave power at the receiving end, thereby providing the elements of a receiver. These efforts led to the development of several components like traveling detectors, wavemeters, terminations, and so on. Some idea of the techniques used in 1934 can be obtained by recalling that optical benches were commonly used to set up microwave experiments [4]. Several photographs of equipment of those days are available in an interesting article surveying the history of the progress of microwave arts published in the fiftieth anniversary issue of *Proceedings of the IRE* [4].

The principle of multiple reflections from discontinuities and the associated principle of cavity resonance played an important role in the development of microwave technology. In some cases, these principles were used to match a source of microwave power to a waveguide. In others, they served to match a waveguide to a receiver, such as a crystal detector. In still others, they served to pass freely a band of frequencies. Together, these principles formed the foundations of microwave circuits. One of the key features of microwave circuits has been the empirical adjustment or tuning of characteristics by screws and irises (and even by denting) in waveguides. In the beginning it was an art that was learned by trial and error. This came to be known as “plumbing” and had been for quite a long time a practical tool for microwave engineers.

Perhaps the greatest single contribution to the engineering analysis of microwave circuits was by Phillip H. Smith [5], who provided a graphical tool for solving otherwise complicated transmission-line problems. Not only were laborious calculations avoided, but, while solving the problems on a Smith chart, one could visualize the step-by-step processes underway. Few gadgets of microwave circuitry have been more useful than the Smith chart. Rapid developments in microwave circuits took place during World War II, when special laboratories were set up at the Massachusetts Institute of Technology and at Columbia University to apply microwave techniques to radar problems. Many significant developments in microwave circuits took place during these years, but were published later. A few of those deserve mention. Fox [6] developed devices by which phase could be added progressively to a waveguide. Another product was a hybrid tee (or magic tee) [7] and still another equally significant one was the

first directional coupler [8]. All these devices found practical uses immediately. Another direction of wartime evolution was the extension of filter techniques to higher frequencies, leading to transmission line filters. Simultaneously, analytical tools were also developed. The classical description of network performance in terms of voltages, currents, impedance, and admittance matrices was replaced by a description based on the transmitted and the reflected wave variables, leading to the concept of scattering matrix.

The scattering matrix formalism allows simpler representation of multiport microwave networks. At this stage in the development of microwave circuits, two basic transmission structures were employed frequently. These were the waveguide and the coaxial TEM-mode line. Waveguides provided higher power capability and low loss that lead to high- Q resonant cavities. Coaxial lines provided inherently wider bandwidth because of the absence of dispersion effects. Also, the concept of impedance could be easily interpreted in the case of coaxial lines. This simplified the design of components. These two transmission structures (waveguides and coaxial lines) grew as important components for microwave circuits. Often their roles have been complementary; sometimes they appear in the same module. It was at this stage that a very useful microwave technique emerged from a special adaptation of two-conductor transmission-line theory. Introduced by Barrett and Barnes [9] in 1951, this structure, as used presently, consists of a thin strip of conductor sandwiched between two dielectric plates metalized on the outside. This structure is known as a stripline. Early stripline work used razor blades and glue to cut the thin strips and paste them on dielectric sheets. With the availability of copper-clad laminates (first introduced for printed circuits) the stripline techniques have developed into a predictable and precise batch process technology. The first detailed account of stripline circuits was made available by the Sanders *Tri-plate* manual [10], published in 1956. A comprehensive account of stripline circuits was made available in a book by Harlan Howe, Jr. [11]. The most significant feature of a stripline transmission structure is that the characteristic impedance of the line is controlled by the width of the central strip, which is fabricated by photoetching a copper-clad dielectric substrate. The two-dimensional nature of the stripline circuit configuration permits the interconnection of many components without the need to break the outer conductor shielding. This also allows the placement of the input and output ports with a high degree of flexibility. Striplines were found to be very convenient for use in parallel-line couplers because of the natural coupling between two strips placed close to each other. The principles of the coupled-line directional coupler were introduced by Wheeler [12] in 1952. Even today a vast majority of directional couplers use a stripline configuration.

In the early 1950s, another type of transmission structure was conceived [13,14], consisting of a single dielectric laminate with a conducting strip on one side and a complete conducting coating on the other side. This structure is known as a microstrip line. Microstrip lines enjoyed a brief spell of popularity and intensive investigations in the

1950s, but were not readily accepted at that time for microwave use because of the high loss per unit length caused by radiation. This was largely a result of the low dielectric constant (about 2.5) of the substrate materials then in use. Further developments were prevented by the lack of availability of both the high-dielectric-constant, low-loss materials and suitable methods for processing and production.

Ever-increasing demands for miniaturized microwave circuitry for use in weapons, aerospace, and satellite applications led to renewed intense interest in microstrip circuits in the 1960s. An elegant analysis of microstrip structure based on conformal mapping transformation was presented by Wheeler [15,16]. The technology of high-dielectric-constant, low-loss dielectric materials and that of deposition of metallic films were perfected [17] and became easily available in the late 1960s. This led to rapid developments in the use of microstrip lines in microwave circuits. Today, microstrip line is the most common transmission structure used in hybrid and monolithic microwave integrated circuits.

The availability of a planar microwave transmission-line structure like microstrip line, coupled with the rapid developments in microwave semiconductor devices and the techniques of thin-film deposition and photolithography, eventually resulted in the technology of microwave integrated circuits [18–21]. Microwave integrated circuits (MICs) represent an extension of thin-film hybrid integrated circuit technology to microwave frequencies. These hybrid MICs consist mostly of passive components and circuits in the form of conducting patterns deposited on ceramic or dielectric substrates plus active devices mounted on these circuits in the form of chips or in specially designed packages. In addition to microstrip, other types of lines called slotline and coplanar lines [22,23] have been used in some MICs. Slotline consists of a slot in the conducting pattern on one side of a dielectric substrate. The other side of the substrate does not contain any metallization. Coplanar lines also involve a metallization pattern, but only on one side of the substrate.

Another trend in microwave circuits is the use of lumped elements. Previously, lumped elements could not be used because the size of available lumped elements was comparable to the wavelength at microwave frequencies. With the use of photolithography and thin-film techniques, the size of elements (capacitors, inductors, etc.) can be reduced so much that these elements can be used up to J-band (10–20 GHz) frequencies [24,25]. Use of lumped elements on dielectric substrates, along with semiconductor devices in chip form mounted thereon, is an attractive option for microwave integrated circuits. Cost reduction of the order of one-fiftieth or more has been predicted with the use of these types of circuits [24]. Apart from reduction in size, there is another advantage of lumped elements—circuit design and optimization techniques perfected at lower frequencies can now be directly used in the microwave frequency range. In addition to lumped elements and one-dimensional transmission-line components, two-dimensional planar components have also been proposed for use in microwave circuits [26]. These components are compatible with stripline and

microstrip line and provide a useful alternative in microwave circuit design.

The current generation of MICs is monolithic microwave integrated circuits (MMICs) using semiconductor substrates [27,28]. Semiconductor substrates used are high-resistivity gallium arsenide and, to a limited extent, high-resistivity silicon. Difficulties arise from the need to use a variety of microwave semiconductor devices that cannot be fabricated by a common process, as well as because of the requirement of large substrate areas when distributed elements (transmission-line sections) are used for passive functions. GaAs technology [29] and GaAs metal semiconductor field-effect transistors (MESFETs) [30] play the key role in microwave monolithic integrated circuits.

Microwave integrated circuits (hybrid or monolithic) exhibit almost the same advantages as those available in the case of integrated circuits at lower frequencies [31], namely: (1) improved system reliability, (2) reduced volume and weight, (3) batch production, and (4) eventual cost reduction when a large number of standardized items are required.

As in the case of low-frequency integrated circuits, the MICs are responsible for both the expansion of present markets and the opening of many new applications, including a host of nonmilitary uses.

There are some difficulties associated with the use of MICs [31]. Before MICs became popular, the microwave circuit designers and users had the flexibility to incorporate tuners and adjustment screws in circuits in order to optimize the performance of the circuit after fabrication. MICs, especially if they have to meet high reliability standards, lack these trimming arrangements. Consequently, devices used in MICs need to be characterized precisely and the circuits have to be designed more accurately. Computer-aided design, simulation, and optimization [32,33] techniques have therefore become a necessity.

The current state of the art in microwave circuits is summarized in several recent books [34–36].

4. WAVEGUIDE CIRCUITS

As pointed out in Section 3, hollow metallic single-conductor waveguides of rectangular and circular cross section were among the earliest forms of transmission structures used at microwave frequencies (see Fig. 1). A rectangular waveguide has been more popular and is still used today for many applications. A large variety of waveguide circuit components such as couplers, detectors, isolators, attenuators, and slotted lines are commercially available for various standard waveguide frequency bands ranging from 1 GHz to over 220 GHz [37,38,42]. Because of the more recent trend toward miniaturization and integration, more and more microwave circuits are currently fabricated using planar transmission lines (such as microstrip line and coplanar waveguides) discussed later in this article. However, there is still a need for waveguide circuits in many applications such as high-power systems, millimeter-wave systems, and some precision test/measurement applications [38,42]. Also waveguides can be

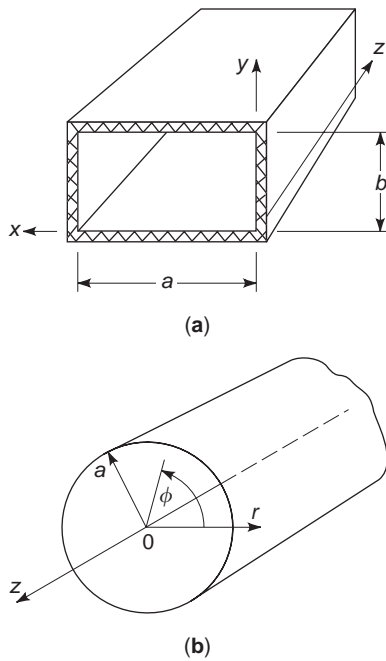


Figure 1. Hollow metallic single-conductor waveguides: (a) rectangular waveguide; (b) circular waveguide. Waveguides were the earliest form of transmission structures used at microwave frequencies and are still used today for special applications.

combined with other kinds of transmission lines [39] for some special applications.

4.1. Modes in a Waveguide

Unlike most of the other transmission structures discussed later in this article, waveguides do not support the transverse electromagnetic (TEM) mode of wave propagation. Waveguides support two other kinds of modes known as the transverse electric (TE) and transverse magnetic (TM) modes. TE modes have their electric field components only in a plane transverse to the direction of propagation along the waveguide, and for TM modes the magnetic field components are totally in the transverse plane. Both of these types of modes have cutoff frequencies below which wave propagation is not possible. For a rectangular waveguide the mode with the lowest cutoff frequency is the TE_{10} mode. Field patterns of the TE_{10} mode for a rectangular waveguide are shown in Fig. 2. Various field components for this mode can be expressed as [34, pp. 145–146]

$$\begin{aligned} E_y &= E_{y0} \sin(\pi x/a) e^{-j\beta z} \\ H_x &= H_{x0} \sin(\pi x/a) e^{-j\beta z} \\ H_z &= H_{z0} \cos(\pi x/a) e^{-j\beta z} \end{aligned} \quad (1)$$

where a is the waveguide width (in the x direction) and β is the phase constant of the wave along the z direction given by

$$\beta = \sqrt{\kappa^2 - \left(\frac{\pi}{a}\right)^2} \quad (2)$$

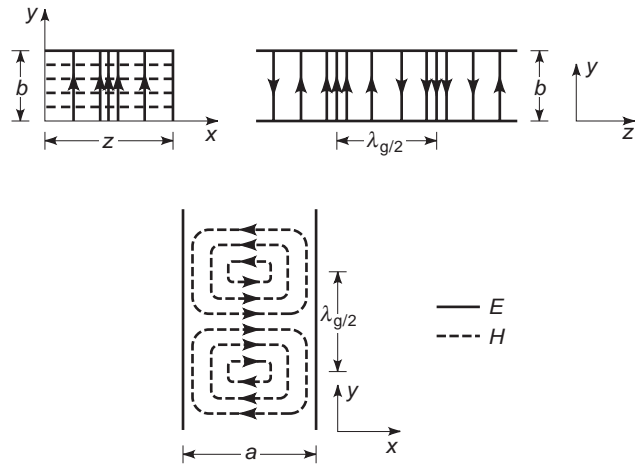


Figure 2. Field patterns of TE_{10} mode in a rectangular waveguide. Dashed lines show the H field, and solid lines show the E field. Note that there is no z component of electric field.

where κ is the wavenumber ($\kappa = \omega\sqrt{\mu\epsilon}$). The cutoff frequency for the dominant TE_{10} mode is given by

$$f_{c10} = \frac{1}{2a\sqrt{\mu\epsilon}} \quad (3)$$

4.1.1. Dispersion Characteristics. The fact that the propagation constant for individual waveguide modes is a nonlinear function of frequency, and that the different modes start to propagate at different frequencies, leads to wave dispersion in a waveguide [38, pp. 106–107].

4.1.2. Power-Handling Capability. The power-handling capability for a transmission medium needs to be characterized for high-power microwave circuits. Metallic waveguides can handle very high power because of their physical structure. In a rectangular waveguide operating in the fundamental mode, the maximum peak power that the waveguide can handle is given by [40]

$$P_{\max} = 416(ab) \text{ (kW/cm}^2\text{)} \quad (4)$$

where b is the waveguide dimension in the y direction.

4.2. Waveguide Circuit Components

Circuits for all kinds of signal processing functions have been designed using waveguides. A few of these are reviewed here.

4.2.1. Waveguide Phase Shifters. A phase shifter is a circuit that produces an adjustable shift in the phase angle of the wave transmitted through it. There are different types of waveguide phase shifters. Two of these, linear and rotary phase shifters, are described here:

Linear Phase Shifter. An example of linear phase shifters is the circuit consisting of three dielectric slabs placed in a rectangular waveguide [41] as shown in Fig. 3. The center slab is free to move longitudinally, and it is moved by a suitable drive mechanism to

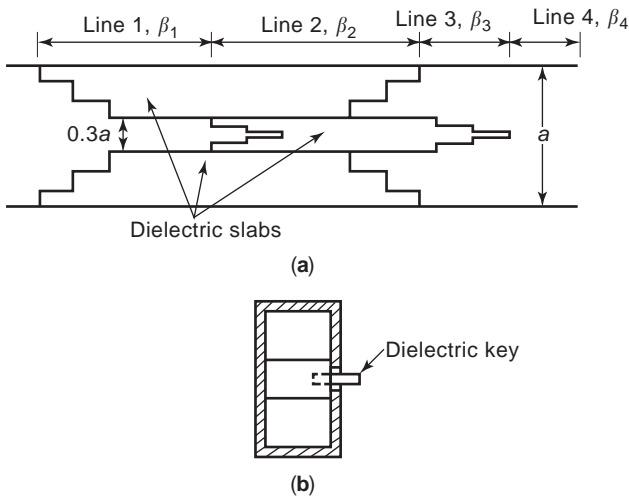


Figure 3. A linear phase shifter in a waveguide configuration. The dielectric key is used to move the central dielectric slab and thereby change the phase shift. (From Ref. 42, © Ellis Horwood Limited, reprinted with permission.)

which it is keyed by means of a dielectric key that protrudes through a long centered slot cut in one broad face of the guide. Each end of the dielectric slab is cut stepwise to provide a broadband multisection quarter-wave transformer to match the partially filled guide to the empty and completely filled guide. If the center slab is displaced a distance x to the right, the effect is to lengthen lines 1 and 3 by an amount x and to shorten lines 2 and 4 by the same amount x . Therefore, the phase shifter change undergone by a wave propagating through the structure is

$$\Delta\phi = [(\beta_1 + \beta_3) - (\beta_2 + \beta_4)]x \quad (5)$$

The phase shift $\Delta\phi$ is proportional to the displacement x . The amount of phase shift increases if the dielectric constant of the slab is increased. If a material whose ϵ_r equal to 2.56 is used in a 3-cm waveguide of dimensions $a = 2.25$ cm, the phase shift obtained is about 0.4 rad/cm of displacement. About 16 cm of displacement gives a phase shift of more than 360° .

Rotary Phase Shifter. The rotary phase shifter [42, pp. 262–266] is a better precision instrument than the linear phase shifter. It consists of a half-wave plate and two quarter-wave plates (see Fig. 4). The quarter-wave plate on the left converts a linearly polarized TE_{11} mode into a circularly polarized mode, and the quarter-wave plate on the right produces a linearly polarized wave when a circularly polarized wave is incident on it. Rotation of the half-wave plate through an angle θ changes the phase of the transmitted wave by an amount 2θ . This simple dependence of the phase change on mechanical rotation is the main feature of the rotary phase shifter.

4.2.2. Microwave Hybrid Junction. A rectangular waveguide hybrid, which is more popularly known as

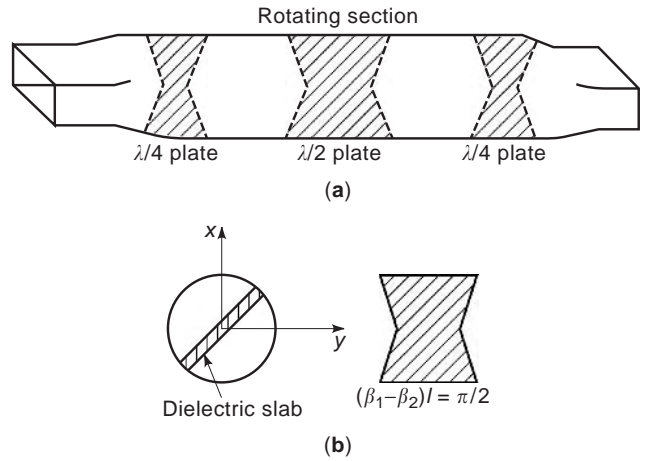


Figure 4. (a) A rotary phase shifter consists of a $\lambda/2$ plate and two $\lambda/4$ plates (rotation of the $\lambda/2$ plate changes the phase; $\lambda/4$ plates convert circular polarization into linear and vice versa); (b) details of the $\lambda/4$ plate. (From Ref. 53, © McGraw-Hill, 1992, reprinted with permission.)

“magic tee,” is shown in Fig. 5. If a wave in the dominant TE_{10} mode is incident at the port 4, the structure is symmetrical with respect to this wave, and hence equal powers are transmitted to port 1 and 3. If E_n^n represents the transmitted electric field in the n th port when the incident wave is in the m th port, then $E_4^1 = E_4^3$. Besides, it can be seen that no power is transmitted to port 2 from port 4, that is, $E_1^2 = 0$. On the other hand, if a TE_{10} wave is incident at port 2, the E field has an odd symmetry about the plane of symmetry and therefore excites fields in ports 1 and 3 which are 180° out of phase. Hence, $E_2^1 = -E_2^3$. Also, power incident at port 2 is not transmitted to port 4. Therefore, $E_2^4 = 0$. The power coupling factor may not be exactly one-half if ports 2 and 4 have reflections. To ensure a coupling of exactly one-half, which is desirable, the junction needs to be matched by irises or probes.

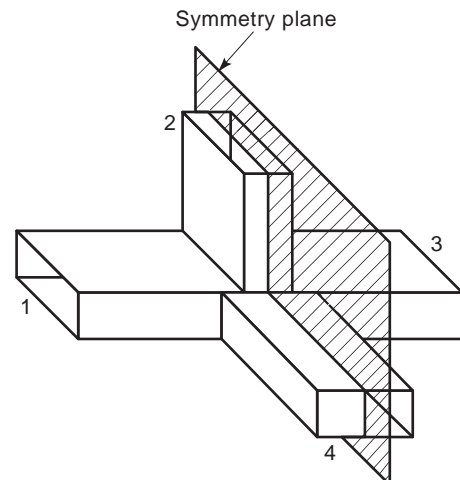


Figure 5. A microwave hybrid or magic tee in a rectangular waveguide configuration. The magic tee is a directional coupler with 3 dB coupling and is commonly used in balanced mixers.

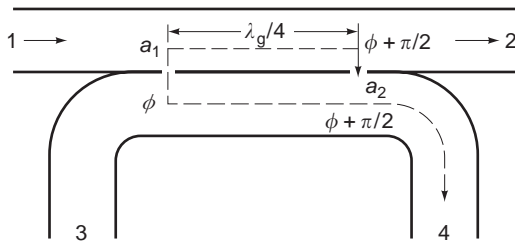


Figure 6. A waveguide directional coupler is a widely used circuit component used to sample the waves traveling in one particular direction (say, from 1 to 2) independent of the reflected wave traveling in the opposite direction (from 2 to 1).

4.2.3. Directional Couplers. A directional coupler is a four-port circuit. An example is shown in Fig. 6. A portion of the wave incident at port 1 couples into the bent waveguide through the hole a_1 . The remaining wave travels to the hole a_2 in the main waveguide (ports 1, 2), and a portion of it again couples into the bent waveguide. If the magnitudes of the energy coupled through holes a_1 and a_2 are equal, and if the distance between a_1 and a_2 is $\lambda_g/4$, then the two coupled signals are reinforced at port 4 because they arrive with equal phase. On the other hand, the two coupled signals cancel each other at port 3, because they are 180° out of phase. Similarly, a wave incident on the junction from port 2 travels to ports 1 and 3, but no signal travels to port 4. The ratios of signal flow between ports 1 and 4 and between ports 2 and 3 are known as the *coupling coefficient* of the directional coupler. In general, the leakage of energy through holes a_1 and a_2 is kept quite small. A directional coupler can be used as a standing-wave detector and forms an important component in microwave and millimeter-wave network analyzers. Some other designs [37, Sect. 7.2, 42, pp. 267–271] of typical waveguide directional couplers are shown in Fig. 7.

4.2.4. Waveguide Filters. Design procedures for filters using waveguides and other transmission structures have certain common features. These filters can be designed using the low-frequency prototype filter synthesis techniques. One such technique, called the *insertion-loss* method, begins with a complete specification of the attenuation characteristics of the filter and develops a basic prototype lowpass filter having the desired passband characteristics. Using suitable frequency transformations and element realizations, the required type of filter (lowpass, bandpass, highpass, or bandstop filters) is derived. The lumped element values of these filters are then realized in terms of the distributed circuit elements. Special features for implementing filters in waveguide configuration are reviewed in this section:

Waveguide Stub Filters. One of the simplest realizations of waveguide bandpass (or bandstop) filters is a waveguide stub filter [38, pp. 185–190] shown in Fig. 8. For bandpass filters, the short-circuited E -plane stubs are a half-wavelength long at the center frequency of the filter, and are connected in cascade with $\lambda/4$ separations. Band rejection filters use

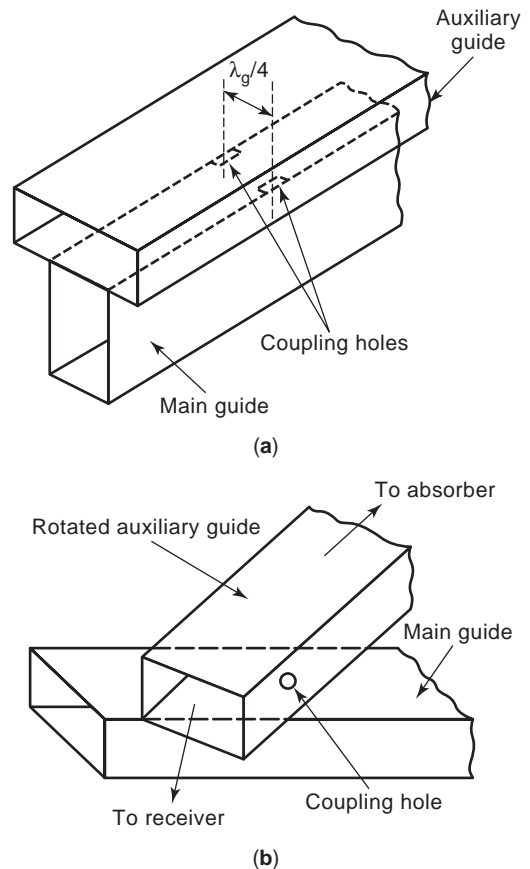


Figure 7. Two other designs of waveguide directional coupler circuits. In both of these cases, coupling takes place through holes in the common wall of the two waveguides.

stubs that are an odd multiple of quarter-wavelength, also separated by $\lambda/4$ distance. The stubs can be asymmetric or symmetric along the main waveguide and with or without steps. The selection of the stub configuration depends on the required bandwidth and power-handling capability. Filters with stepped stubs can be designed to yield narrower bandwidth. Filters with stubs on both sides of the waveguide broadwall have large power-handling capability.

E -Plane Filters. E -plane filters have been developed as compatible filtering structures for integrated millimeter-wave circuits [43,44] and are most often realized in finline techniques or as all-metal structures. Their common feature is that the filter metallization pattern is obtained using photolithographic techniques. Thus, the geometry of the component is realized with very small manufacturing errors, which is very important at millimeter-wave frequencies. Four different configurations of E -plane waveguide filters are shown in Fig. 9. All of types are designed as bandpass filters [43,45,46]. In Fig. 9, the shaded part is dielectric substrate to support the thin metallization structures; t_m is the thickness of the metal layer and t_d is the thickness of the dielectric substrate; and l_c is the length of the metal strip and l_r is the gap between metal strips.

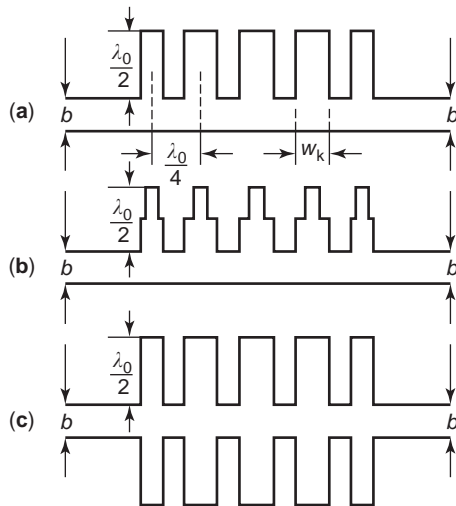


Figure 8. Waveguide stub filters: (a) asymmetric stubs without steps; (b) asymmetrical stubs with steps; (c) symmetric stubs without steps. Both bandpass and bandstop characteristics can be designed in these circuits.

Corrugated Waveguide Filters. Corrugated waveguide structures similar to that shown in Fig. 10 are used as lowpass filters in numerous antennas feed system to reject the spurious harmonics from transmitters [38, pp. 200–207; 49]. They can also be designed as bandpass filters, with a wide or narrow passband response [47,48].

Evanescent-Mode Waveguide Filters. Evanescent-mode waveguide filters (Fig. 11) can be designed [50–52] to provide a very wide stopband with low passband

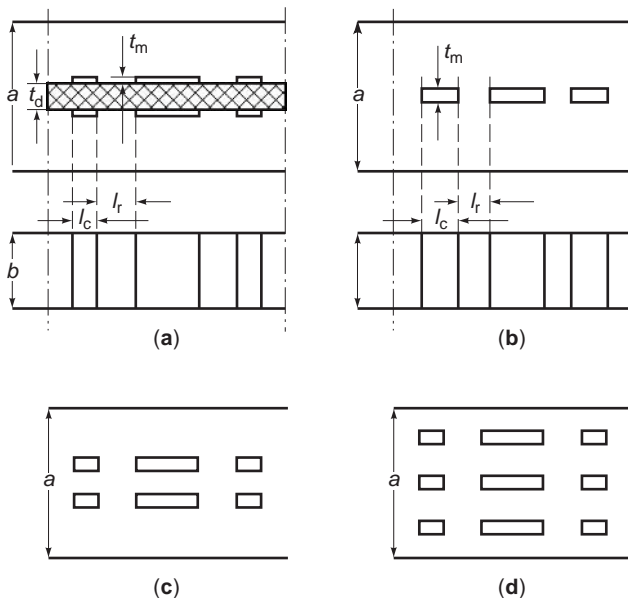


Figure 9. *E*-plane bandpass filters: (a) large gap finline filter; (b) single metal insert filter; (c) double metal insert filter; (d) triple metal insert filter. In these designs, fin dimensions and hence RF performance can be controlled accurately by photolithography techniques. (From Ref. 38, © Artech House, 1993, reprinted with permission.)

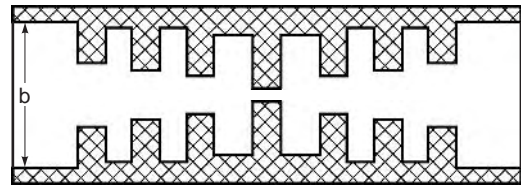


Figure 10. Longitudinal cross section of a corrugated waveguide filter.

insertion loss. Their size is compact, even when the passband is located in the lower microwave frequency region. For these reasons the evanescent-mode waveguide structures are often used as pseudolowpass filters, or as bandpass filters in a wide microwave spectrum. Because of the high skirt selectivity achievable in this filter type, they can also be used in duplexers and multiplexers.

4.3. Multiplexers

Multiplexer circuits are required for combination or separation of communication channels at different frequencies. The multiplexer for the antenna feed systems must provide separation of the receive and transmit bands and combination of the individual transmission channels that cover only a small portion of the frequency band. There are four different multiplexing methods that are applied in feed systems [38, pp. 252–307]: (1) the circulator/filter chain, (2) the directional filter approach, (3) the manifold multiplexing techniques, and (4) the branching filter concept. Each of these has its own particular properties and applications.

4.3.1. Waveguide Circuits Using Active Devices. Waveguide circuits using active devices can be designed for various applications, such as oscillator, mixer, detector, and so on [37, pp. 325–490]. A waveguide cavity Gunn oscillator [53] is shown in Fig. 12 as an example. In this design the high impedance of the waveguide is transformed into low impedance at the location of the Gunn device by means of quarter-wave transformers. The cavity resonant frequency can be adjusted by changing the location of the

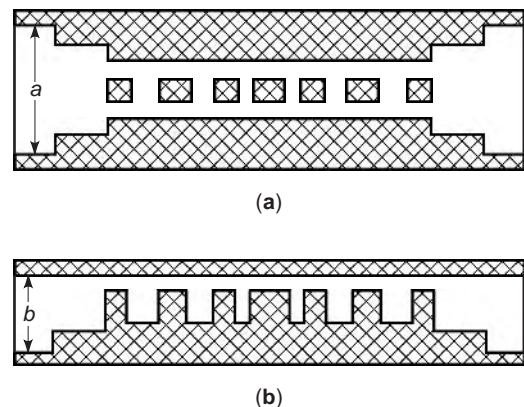


Figure 11. Ridged waveguide evanescent mode bandpass filter: (a) top view; (b) side view. These designs provide compact filters at lower microwave frequencies.

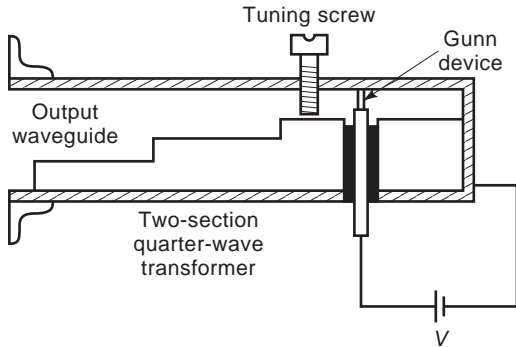


Figure 12. A Gunn oscillator waveguide circuit that uses two quarter-wave sections to transform the high impedance of the waveguide to a low impedance at the Gunn device. (From Ref. 53, © McGraw-Hill, 1992, reprinted with permission.)

short circuits. A tuning screw can be used for fine tuning of the cavity. More examples of active wave guide circuits can be found in Refs. 37 and 53.

4.4. Computer-Aided Design of Waveguide Circuits

Waveguide circuits require an approach for computer-aided design (CAD) different from that used for transmission-line circuits at microwave frequencies. The traditional CAD methods for waveguide circuit are usually based on the network analysis, with various discontinuities in the waveguide modeled separately by a combination of equivalent reactances [54]. This equivalent circuit approach has some drawbacks. The models are valid only for a specified geometry and only within a certain range of parameters. Another problem associated with using the equivalent circuit models is their inability to account for higher-order mode-coupling effects, which can occur if discontinuities are in close proximity. A field-theory-based approach [55] overcomes these limitations. Some features of this approach are a very accurate prediction of frequency responses, higher-order mode effects taken into account, no restrictions on the wavelength (or frequency range), and straightforward extension in millimeter-wave bands. Several numerical methods are used for field analysis of waveguide circuits; the most popular are the finite-different time-domain method (FDTD) [56] finite-element method (FEM) [57], transmission-line matrix method (TLM) [58], mode-matching techniques (MMT) [59], and the method of integral equations [60]. For automated design and yield analysis of waveguide circuits, modal analysis [61] has emerged as the most useful electromagnetic simulator, either in the generalized scattering matrix (GSM) formulation or in the generalized admittance matrix (GAM) form. It has been demonstrated [61] that for waveguide circuits the GAM approach requires only half the number of unknowns at the internal ports and hence is much more efficient than the GSM representation.

5. COAXIAL-LINE CIRCUITS

Coaxial line is the most commonly used transmission structure over a very wide range of frequencies from

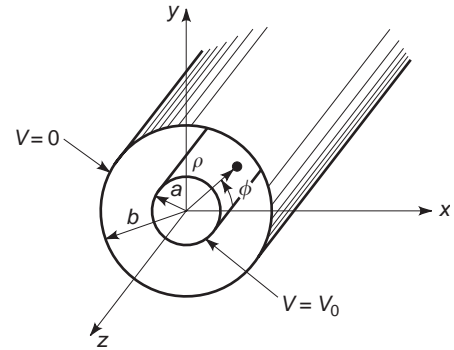


Figure 13. Geometry of a coaxial line. The ratio of the outer to inner conductor radii (b/a) determines the characteristic impedance Z_0 of the line.

very low frequencies through microwave frequencies and extending into the millimeter-wave frequency range. However, because of the convenience of physical size, coaxial line circuits are popular only in the microwave frequency range. They are too bulky at lower frequencies and very difficult to fabricate (as well as very lossy) at millimeter-wave frequencies.

The geometry of a coaxial line is shown in Fig. 13. One can derive the expressions for electromagnetic fields in this line solving Laplace equation for scalar potential. As shown in Fig. 13, the inner conductor is considered to be at V_0 volt potential and the outer conductor is at 0V. The electric and magnetic field vectors, can be derived as [34]

$$\bar{E}(\rho, \phi, z) = \frac{V_0 \hat{\rho} e^{-j\beta z}}{\rho \ln b/a} \quad (6)$$

$$\bar{H}(\rho, \phi, z) = \frac{V_0 \hat{\phi} e^{-j\beta z}}{\eta \rho \ln b/a} \quad (7)$$

where $\beta = \omega \sqrt{\mu\epsilon}$ and $\eta = \sqrt{\mu\epsilon}$ are the phase constant and the intrinsic impedance of the medium, respectively.

Coaxial lines possess general properties of TEM-mode transmission lines. Characteristic impedance Z_0 of a coaxial line filled with a dielectric material of relative dielectric constant ϵ_r as shown in Fig. 13, is

$$Z_0 = \frac{60}{\sqrt{\epsilon_r}} \ln \frac{b}{a} \Omega \quad (8)$$

In addition to TEM modes, coaxial lines can also support TE and TM waveguide modes. When coaxial line dimensions are selected appropriately for the operating frequency range; these modes are evanescent modes and they are excited only near discontinuities or sources. In practice, it is essential to know the cutoff frequencies of the lowest-order waveguide mode and use the coaxial line below this frequency. Various types of microwave circuits can be realized using coaxial lines [62,63]. However, with the more recent advances in planar circuit technology and because of their size and fabrication difficulties, they are not used commonly. In the past, coaxial lines have been widely used to design passive filter circuits. A common type of high-pass filters constructed by coaxial lines as shown in Fig. 14

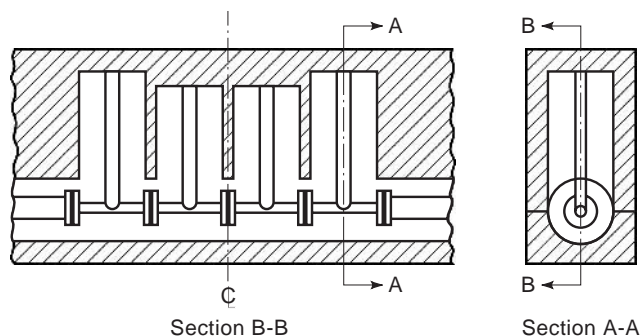


Figure 14. A highpass filter constructed by coaxial lines. Lumped series capacitors and shunt inductors provide the filter operation. (From Ref. 62, © Artech House, 1980, reprinted with permission.)

has been described in the classic book by Matthaei et al. [62]. In this configuration, coaxial stubs present shunt inductances, and disks spacers constitute series capacitors.

Another coaxial filter example described by Matthaei [62] is a series capacitance-coupled half-wave resonator circuit shown in Fig. 15. This filter is realized by breaking the inner conductor at several locations. The gap spacing needed to produce a desired coupling can be found either experimentally or theoretically.

Coaxial-line components are also used extensively as coaxial probes connectors in between various circuit assemblies and for connecting circuits to instrumentation, and so on. Most of the coaxial lines that are used as cables and connectors have a $50\ \Omega$ characteristic impedance except for $75\ \Omega$ coaxial cable used for television systems. Coaxial connectors must have low standing-wave ratio (SWR), no spurious higher-order modes, mechanical strength, and repeated usability. Some of the most common microwave coaxial connectors are popularly known as type N connector (originally named after P. Neill), (SMA) SubMiniature Amphenol connector, (SSMA) Scaled SubMiniature Amphenol connector, and (APC-7) Amphenol Precision Connector, 7-mm connector. These connector types are shown in Fig. 16. The type N connector is a relatively large connector with an outer diameter of 0.625 in. The recommended upper operating frequency ranges from 11 to 18 GHz. The SWR is typically less than 1.07. The SMA connector is small compared to the type N connector with an outer diameter of the female end of 0.210 in. and can be used up to 25 GHz. SMA connectors modified to work up to 40 GHz are known as K connectors. An SSMA connector is even smaller. The outer diameter of the female end is about 0.156 in. and the maximum operating frequency is about 38 GHz. The APC-7 connector is a precision connector which has an SWR less than 1.04 and an

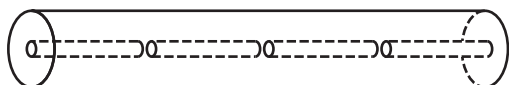


Figure 15. Series capacitance coupled half-wave resonators filter. Series coupling gaps are located in between cascaded straight resonator elements. The filter is realized by breaking the inner conductor at several locations.

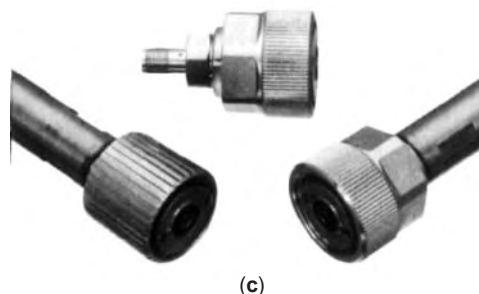
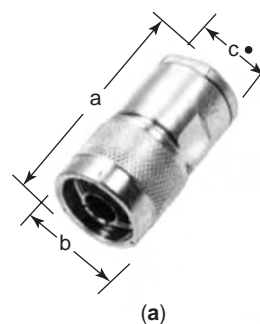


Figure 16. Some of the most common microwave coaxial connectors: (a) type N connector; (b) SMA connector; (c) APC-7 connector.

operating range of up to 18 GHz. Coaxial connectors are described in Refs. 34 (pp. 169–170) and 64.

6. STRIPLINE CIRCUITS

6.1. Striplines

A stripline [11,65] is a planar-type transmission line that lends itself well to microwave integrated circuitry and package feedthroughs. The geometry of a stripline is shown in Fig. 17a. A thin conducting strip of width W is centered between two wide conducting ground planes with a separation b . The entire region between the ground planes is filled with a dielectric.

Unlike microstrip lines and other open planar transmission lines described later in this article, a stripline can support a pure TEM mode because it has a homogeneous dielectric medium. The stripline, however, can also support higher-order TM and TE modes. These modes can be suppressed with shorting screws between the two ground planes and by restricting the ground planes spacing to less than one quarter wavelength. A sketch of the field lines for the TEM stripline mode is shown in Fig. 17b.

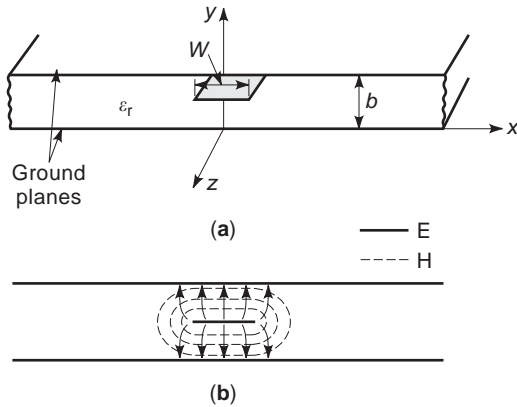


Figure 17. (a) Geometry of stripline—a thin strip of width W is inserted in a dielectric with ground planes on the top and the bottom; (b) electric and magnetic fields in a stripline. Striplines support a pure TEM mode.

6.2. Stripline Parameters

An exact solution of Laplace equation of electromagnetic fields in a stripline can be obtained by the conformal mapping approach [66]. However, closed-form expressions that give a good approximation of the exact results are used in circuit design [34].

The phase constant for a stripline is given (by the usual relation for homogeneously filled lines) as

$$\beta = \frac{\omega}{v_p} = \omega \sqrt{\mu_0 \epsilon_0 \epsilon_r} = \sqrt{\epsilon_r} k_0 \quad (9)$$

where ω is the angular frequency, v_p is the velocity of the wave along the line, μ_0 is the permeability of free space, ϵ_0 is the permittivity of free space, ϵ_r is the dielectric constant of the stripline dielectric, and k_0 is the phase constant of free space.

The characteristic impedance of a transmission line is given by

$$Z_0 = \sqrt{\frac{L}{C}} = \frac{1}{v_p C} \quad (10)$$

where L and C are inductance and capacitance per unit length of the line. An approximate expression for characteristic impedance [34] of striplines is

$$Z_0 = \frac{30\pi}{\sqrt{\epsilon_r}} \frac{b}{W_e + 0.441b} \quad (11)$$

where

$$\frac{W_e}{b} = \frac{W}{b} - \begin{cases} 0 & \text{for } W/b > 0.35 \\ (0.35 - W/b)^2 & \text{for } W/b < 0.35 \end{cases}$$

Since the stripline is a TEM-mode line, the attenuation due to the dielectric loss is obtained by the procedure commonly used for other TEM lines [67]. The attenuation due

to the conductor loss is approximated as

$$\alpha_c = \begin{cases} \frac{2.7 \times 10^{-3} R_s \epsilon_r Z_0}{30\pi(b-t)} A & \text{for } \sqrt{\epsilon_r} Z_0 < 120 \text{ Np/m} \\ \frac{0.16 R_s}{Z_0 b} B & \text{for } \sqrt{\epsilon_r} Z_0 > 120 \text{ Np/m} \end{cases} \quad (12)$$

with

$$A = 1 + \frac{2W}{b-t} + \frac{1}{\pi} \frac{b+t}{b-t} \ln \left(\frac{2b-t}{t} \right)$$

$$B = 1 + \frac{b}{0.5W + 0.7t} \left(0.5 + \frac{0.414t}{W} + \frac{1}{2\pi} \ln \frac{4\pi W}{t} \right)$$

where t is the thickness of the strip metallization.

6.3. Examples of Stripline Circuits

Design procedures for stripline circuits are identical to those for other TEM mode transmission line circuits. The main difficulty in transferring the design from one kind of transmission line (say, coaxial line) to another (say, stripline) arises from the fact that discontinuity and junction reactances are different for different kinds of transmission structures. Quite often, the first-order designs are carried out without considering the effect of discontinuity/junction reactances. Then the circuit performance is computed taking discontinuity/junction reactances into account, and designable parameters of the circuit are optimized to compensate for discontinuity/junction effects. This design methodology is common to microwave circuit design using any kind of transmission structure.

6.3.1. Branchline Directional Couplers. These couplers, similar to the one shown in Fig. 18 [68], are essentially power division networks with two important features—namely, the two ports are mutually isolated (ports 1 and 4 in Fig. 18 when the input signal is connected to port 1), and the output signals at the other two ports (ports 2 and 3 in Fig. 18) are out of phase by 90° . These circuits form building blocks of several other circuits such as balanced mixers, variable attenuators, pin-diode phase shifters, directional filters, diplexers, multiplexers, and transmit-receive (TR) switches. Branchline couplers are also used

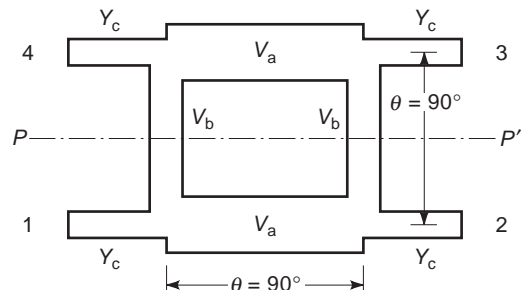


Figure 18. A branchline coupler using striplines. Port 1 is the input port, ports 2 and 3 are output ports, and port 4 is the isolated port. Output signals at ports 2 and 3 are 90° out of phase.

extensively in antenna array feed networks in preference to Y-junction-type power dividers and as impedance transformers. In active circuits, they provide the advantage of direct-current (DC) coupling for biasing. Branchline couplers are forward-wave couplers and hence can be cascaded without crossing lines.

6.3.2. Parallel-Coupled-Line Directional Couplers. Parallel-coupled-line directional couplers shown in Fig. 19 [69] offer much larger bandwidths as compared with the branchline couplers. They are mostly backward-wave couplers, although forward-wave couplers are also possible using an inhomogeneous medium. The most commonly used parallel-coupled directional coupler is the TEM-mode single-section backward-wave coupler. As the term “backward-wave coupler” implies, the electric and magnetic field interaction between the parallel-coupled conductors causes the coupled signal to travel in a direction opposite to that of the input signal. Maximum coupling occurs when the length of the coupling region is equal to one-quarter wavelength (or an odd multiple of quarter wavelength). Analysis of the couplers is carried out in terms of two normal modes of propagation known as *even* and *odd* modes for symmetrical couplers. Even and odd modes exhibit even and odd symmetry of fields with respect to the plane of symmetry. These couplers offer a perfect match and infinite directivity at all frequencies because of the inherent property that the even- and odd-mode phase velocities are equal when the propagating mode is a pure TEM.

6.3.3. Hybrid Rings. The branchline coupler as well as the coupled-line backward-wave coupler provides a phase difference of 90° between the two outputs. For hybrid ring couplers shown in Fig. 20 [70], the two output signals are either in-phase or 180° out of phase depending on the choice of the input port. The circumference of the ring is $3\lambda/2$, where λ is the wavelength in the stripline at mid-band frequency. For an input at port 1, outputs at ports 2 and 4 are 180° out of phase and the port 3 is isolated (with no output). When the input is at port 2, the two outputs at ports 1 and 3 are in phase and the port 4 is isolated.

6.3.4. Power Dividers. In several microwave applications (as, e.g., a feed for a phased-array antenna) the input signal is required to be divided into several

Figure 19. A parallel-coupled-line coupler realized in stripline structure. Equal widths are used for two strips. When a signal enters into port 1, port 2 is the direct output and port 3 is the coupled point. No signal comes out of port 4, which is called the “isolated port.”

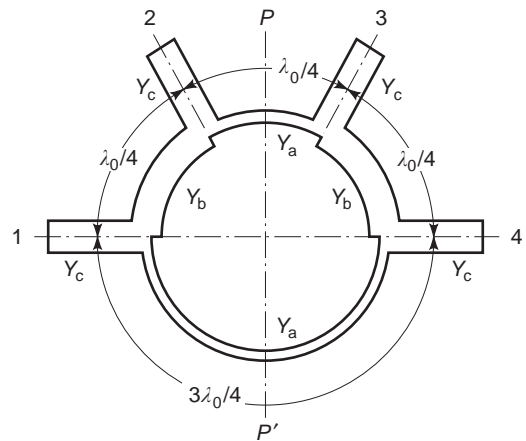
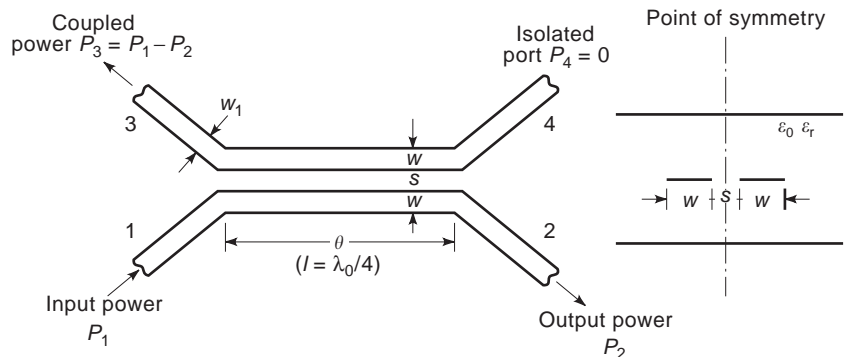


Figure 20. A stripline ring hybrid. The circumference is $3/2$ wavelengths. When a signal is fed to port 1, output signals at ports 2 and 4 are 180° out of phase, and port 3 is isolated. For an input signal fed to port 3, output signals at ports 2 and 4 are in phase and port 1 is isolated.

equiamplitude, equiphase output signals. A matched, symmetric n -way power divider has the advantage that it gives neither amplitude nor phase imbalance at any frequency. Such a power divider can also be used as an n -way power combiner by simply reversing the input and output ports. Using such combiners, output powers of a number of solid-state amplifiers and oscillators can be combined over a wide frequency range. A two-way power divider stripline circuit is shown in Fig. 21 [71]. The resistor R between the output port ensures input match at ports 2 and 3 when the circuit is used as a power combiner.

6.3.5. Filters. Stripline filters generally make use of a cascade of distributed circuit elements in the form of coupled resonators, stubs, and so on. As pointed out in the discussion for waveguide filters, stripline filters are also designed using low-frequency prototype filter synthesis techniques. A coupled-line bandpass filter is shown in Fig. 22 [72]. This configuration is also commonly used for other filters using planar lines such as microstrip lines and coplanar waveguides.

6.3.6. Pin-Diode Switches. A pin diode (which consists of an intrinsic layer sandwiched between p- and n-type

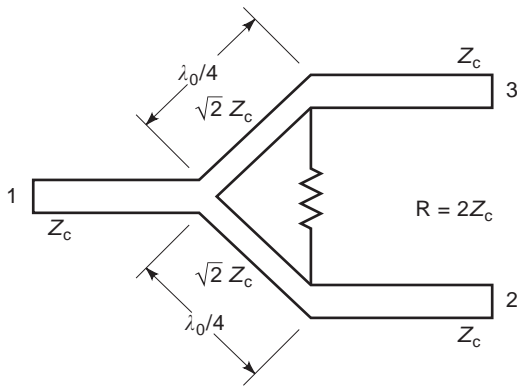


Figure 21. A matched stripline two-way power divider. Input power at port 1 splits equally into output ports 2 and 3. A resistor ($R = 2Z_c$) ensures that the circuit is matched at ports 2 and 3.

layers) acts as an electronic switch when operated at the forward and reverse bias states [73]. As a basic switching element, it is extensively used in the realization of multiple-throw switches, phase shifters, modulators, limiters, and duplexers. A single-pole single-throw switch using a pin diode is shown in Fig. 23 [65]. With a variable forward bias, the forward bias resistance of the pin diode can be varied over a wide range. This property is used in realizing electronically variable attenuators. Pin-diode circuits can also be used as attenuators by varying the forward bias current of the diodes. Pin-diode attenuators with constant input impedance characteristic can be built by incorporating a circulator or a hybrid coupler in the circuit. Figure 24 shows a hybrid-coupled pin-diode attenuator [65].

6.3.7. Phase Shifters. Phase shifters can be built using pin diodes, varactors, or GaAs field-effect transistors (FETs). Of these three semiconductor devices, pin diodes are the most commonly used because of reproducibility of their characteristics and high power-handling capability. Digital phase shifters are extensively employed in phased arrays to electronically scan the radiated beam. These phase shifters can be broadly classified as either the reflection type or the transmission type. The reflection-type phase shifters can be realized using a circulator or a hybrid coupler. Some common designs for transmission-

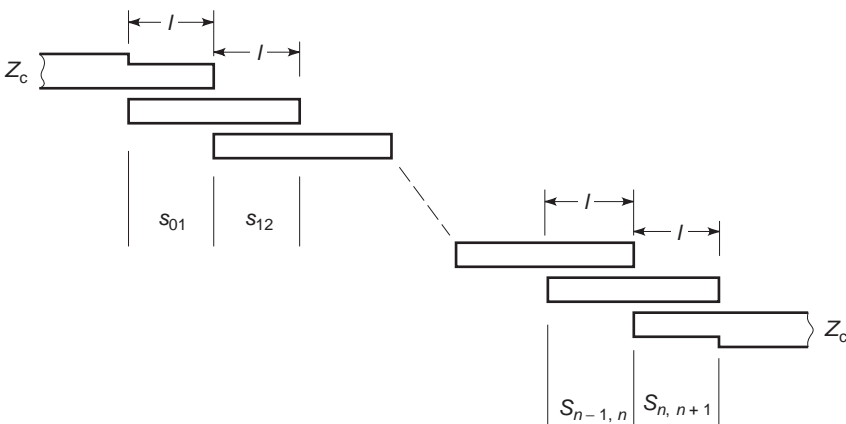


Figure 22. A stripline parallel-coupled band-pass filter. Each coupled section comprises one quarter-wavelength coupled lines ($l = \lambda/4$). Z_c is the characteristic impedance of input/output ports.

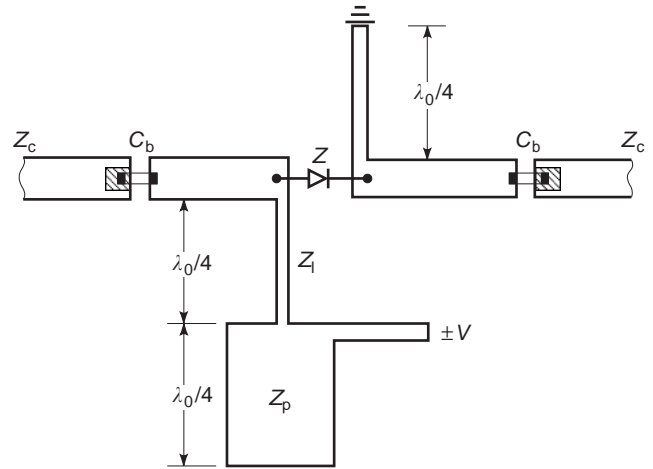


Figure 23. Layout of series SPST (single-pole single-throw) switch with the biasing circuit. dc blocking capacitors and dc return transmission inductor are used, and RF bypass transmission capacitor of a quarter-wavelength has low characteristic impedance ($Z_p < 25 \Omega$). (From Ref. 65, © New Age Int. Ltd., 1989, reprinted with permission.)

type phase shifters are the switched line, the loaded line, and the lowpass highpass. For phased array applications, several of these circuits are cascaded to form multibit phase shifters.

Microwave phase shifters can be designed using various different kinds of transmission lines. Figure 25 shows a switched-line phase shifter with series-mounted diodes [74].

6.3.8. Mixers. A mixer circuit is an essential component of almost all receivers used in communication, radar, and radioastronomy applications. Microwave mixers make use of nonlinear semiconductor devices, usually Schottky barrier diodes for mixing operation. A typical mixer consists of a nonlinear mixer diode together with coupling networks for feeding the signal [radiofrequency (RF)] and local-oscillator (LO) power and for extracting the (IF) signal. Practical mixer configurations can be broadly divided into three categories: single-ended mixers, balanced

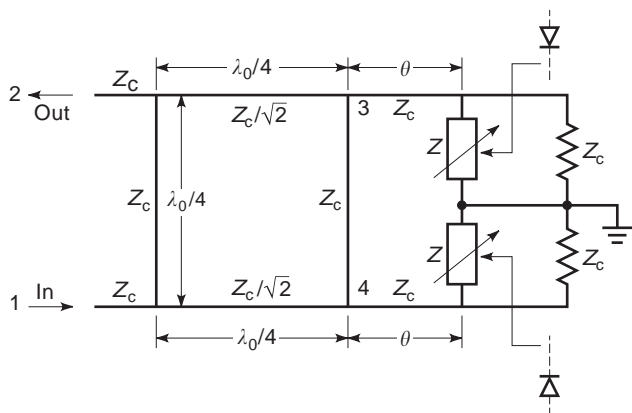


Figure 24. A hybrid-coupled pin-diode attenuator. The attenuation is controlled by varying the forward bias current of the diodes. Two identical diodes are mounted symmetrically in the two output arms of the 3 dB, 90° hybrid coupler and are shunted by matched loads. (From Ref. 65, © New Age Int. Ltd., 1989, reprinted with permission.)

mixers, and double-balanced mixers. Of the various types of mixers, the balanced mixer employing Schottky barrier diodes is the most commonly used configuration in practical application. Figure 26 shows a hybrid ring balanced mixer [65].

Several other types of stripline circuits have been reported in literature [11,34,65]. Microwave circuits described in this section can also be realized in microstrip configuration, described in the next section.

7. MICROSTRIP CIRCUITS

Microstrip line is the most frequently used planar transmission structure and forms the basic building block for almost all hybrid microwave integrated circuits (MICs) and monolithic microwave integrated circuits (MMICs). The physical geometry of a microstrip line is shown in Fig. 27a, and the approximate field distribution is depicted in Fig. 27b. Microstrip line consists of a single dielectric substrate with a complete conducting coating (ground plane) on one side and a conductor strip on the other side

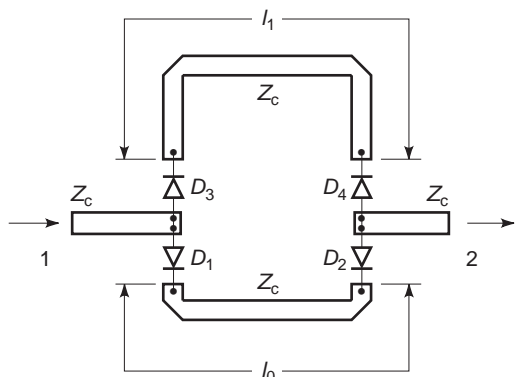


Figure 25. A switched-line phase shifter with series mounted diode to switch between two fixed transmission-line paths. The differential phase shift is $\beta(l_1 - l_0)$.

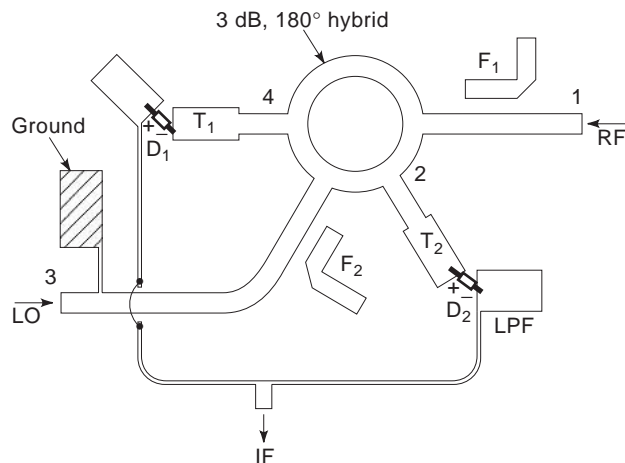


Figure 26. A hybrid ring balanced mixer where D_1, D_2 are mixer diodes; F_1, F_2 are image reject filters; and T_1, T_2 are matching transformers. The RF power fed to port 1 and the LO power fed to port 3 are split equally between the output ports 2 and 4. At the two mixer diodes, the RF signals appears 180° out of phase with each other whereas the LO signals appear in phase. (From Ref. 65, © New Age Int. Ltd., 1989, reprinted with permission.)

of the substrate. In contrast to a stripline, the top surface of the microstrip circuitry is open. Because of the nonhomogeneous dielectric medium surrounding the conductor strip (the substrate and the air above), the microstrip line cannot support a pure TEM mode. However, a quasi-TEM mode approximation is used for analysis of microstrip lines and is adequate for design of microstrip circuits [23].

Popularity of microstrip circuits is due to an increasing trend in miniaturization of, and cost considerations for, microwave circuits. Compared to waveguides, and coaxial lines, and striplines, it is easier to fabricate microstrip circuits and integrate them with other active and passive microwave devices. The open nature of the microstrip lines allows easy access to circuitry to mount active devices and lumped element components such as resistors,

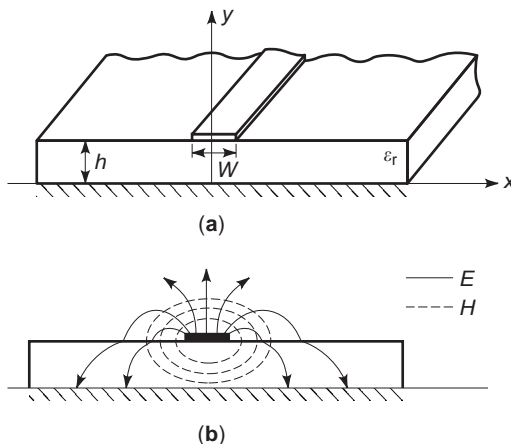


Figure 27. Geometry of a microstrip line: (a) geometry (h is substrate height, W is the width of the conducting strip, and ϵ_r is relative dielectric constant); (b) electric and magnetic field distribution in a microstrip-line quasi-TEM mode.

capacitors and inductors. However, microstrip line circuits have some disadvantages such as higher loss, radiation, dispersion, and spurious coupling among components when compared to coaxial-line circuits.

7.1. Design Formulas for Microstrip Lines

Analysis and design considerations for microstrip lines are very well documented in the literature [16,23,75,76].

7.1.1. Effective Dielectric Constant ϵ_{eff} . Because of the nonhomogeneous dielectric structure of microstrip lines, the concept of effective dielectric constant has been introduced [16] and is commonly used for calculating line wavelength and phase velocity as needed in microstrip circuit design. A formula that is commonly used for calculation of ϵ_{eff} is [75]

$$\epsilon_{\text{eff}} = \frac{\epsilon_r + 1}{2} + \frac{\epsilon_r - 1}{2} (1 + 10h/W)^{-1/2} \quad (13)$$

where h is height of the dielectric substrate, W is the width of the conducting strip, and ϵ_r is the dielectric constant of the substrate.

7.1.2. Characteristic Impedance (Z_0). As for any other transmission line, the characteristic impedance for the quasi-TEM mode is the most important parameter in microstrip circuit design. Given the dimensions h and W and the value of ϵ_r , the characteristic impedance of a microstrip line can be found by using the following formulas [35, pp. 52–53]:

For narrow strips ($W/h < 3.3$):

$$Z_0 = \frac{119.9}{\sqrt{2(\epsilon_r + 1)}} \left[\ln \left(4 \frac{h}{W} + \sqrt{16(h/W)^2 + 2} \right) - \frac{1}{2} \left(\frac{\epsilon_r - 1}{\epsilon_r + 1} \right) \left(\ln \frac{\pi}{2} + \frac{1}{\epsilon_r} \ln \frac{4}{\pi} \right) \right] \quad (14)$$

For wide strips ($W/h > 3.3$):

$$Z_0 = \frac{119.9\pi}{2\sqrt{\epsilon_r}} \left[\frac{W}{2h} + \frac{\ln 4}{\pi} + \frac{\ln(e\pi^2/16)}{2\pi} \left(\frac{\epsilon_r - 1}{\epsilon_r^2} \right) + \frac{\epsilon_r + 1}{2\pi\epsilon_r} \left(\ln \frac{\pi e}{2} + \ln \left(\frac{W}{2h} + 0.94 \right) \right) \right]^{-1} \quad (15)$$

where e is the exponential base; $e = 2.71828$. For given values of characteristic impedance and ϵ_r , the W/h ratio can be found by using the following expressions.

For narrow strips (when $Z_0 > 44 - 2\epsilon_r\Omega$):

$$\frac{W}{h} = \left\{ \frac{e^A}{8} - \frac{1}{4e^A} \right\}^{-1} \quad (16)$$

where

$$A = \frac{Z_0 \sqrt{2(\epsilon_r + 1)}}{119.9} + \frac{1}{2} \left(\frac{\epsilon_r - 1}{\epsilon_r + 1} \right) \left(\ln \frac{\pi}{2} + \frac{1}{\epsilon_r} \ln \frac{4}{\pi} \right)$$

For wide strips (when $Z_0 > 44 - 2\epsilon_r\Omega$):

$$\frac{W}{h} = \left(\frac{2}{\pi} \right) \{ (B - 1) - \ln(2B - 1) \} + \frac{\epsilon_r - 1}{\pi\epsilon_r} \times \left\{ \ln(B - 1) + 0.293 - \frac{0.517}{\epsilon_r} \right\} \quad (17)$$

where $B = 59.95\pi^2 / (Z_0 \sqrt{\epsilon_r})$.

7.2. Microstrip Discontinuities

Microstrip circuits, like other types of microwave circuits, contain transmission line discontinuities such as bends, width changes, gaps, and junctions. These discontinuities introduce parasitic reactances and cause a degradation in circuit performance. Various types of microstrip discontinuities which are encountered in microwave circuits are shown in Fig. 28. This figure also includes approximate lumped-element models for these discontinuities. At higher microwave frequencies, these discontinuity reactances become significant and need to be taken into account. Closed-form relations for discontinuity model elements

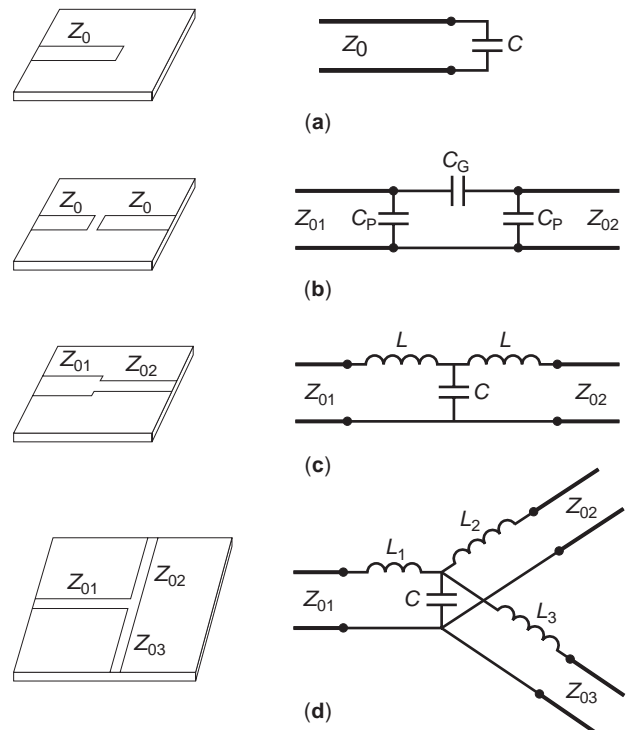


Figure 28. Some common types of microstrip discontinuities and their equivalent lumped-element models: (a) open-ended microstrip; (b) gap in microstrip; (c) change in width. (d) T junction.

and their values form a key part of any microwave circuit computer-aided design (CAD) software. However, equivalent lumped circuit models are not available for all types of discontinuities and substrate types. Another difficulty is that the accuracy for discontinuity models degrades at higher frequencies. Lack of accurate discontinuity models at millimeter-wave frequencies is still the main bottleneck in the CAD for millimeter-wave circuits [77].

In order to compensate for the discontinuity effects, one can construct the equivalent circuit for the discontinuity and take it into account in the design process. The second approach is to minimize the discontinuity effect by modifying the geometry of the discontinuity, such as chamfering or mitering the strip conductor in case of microstrip right-angle bends. Compensation techniques for discontinuities have been reported in the literature [35, pp. 140–165].

7.3. Passive Microstrip Circuits

Some commonly used microstrip passive circuits are couplers, power dividers, impedance matching circuits, and filters. Design process for these circuits is similar to that for stripline circuits.

7.3.1. Couplers. As in case of stripline circuits, the two common types of microstrip line couplers are also coupled line directional couplers and branchline directional couplers. Layouts of these couplers are similar to those of stripline couplers. Even and odd mode analysis technique is also applied in the design of microstrip couplers. For coupled line couplers in microstrip configuration, the phase velocities for even and odd modes are not equal. This factor limits the directivity of these couplers. Design of these couplers is well explained in Refs. 34 and 35 .

Branch line couplers are also similar to corresponding circuits in stripline configurations. They can be designed for different values of the coupling factor and may have more than two branches [34,35] in order to increase the circuit bandwidth.

7.3.2. Filters. Various types of filters [34,35] can be realized by using microstrip lines. Again, their design methodology is similar to those of stripline filters. Lowpass filters can be formed with cascaded sections of microstrip lines. One first designs the prototype filter using lumped elements and then substitutes these elements with their microstrip-line equivalents. A short ($< \lambda_g/4$) length of a high-impedance line behaves like a series inductance. Also a very short ($\ll \lambda_g/4$) length of low-impedance line behaves like a shunt capacitance. An example of a lowpass filter constructed by microstrip line elements is shown in Fig. 29.

Microstrip bandpass and bandstop filters can also be realized by using coupled sections of microstrip lines. Two popular types of microstrip bandpass filters are end-coupled and parallel (edge)-coupled bandpass filters. Figure 30 shows a general layout for an end-coupled microstrip bandpass filter. In this circuit, coupling gaps are located in between and couple the cascaded microstrip resonator elements. The gap width is usually much smaller than

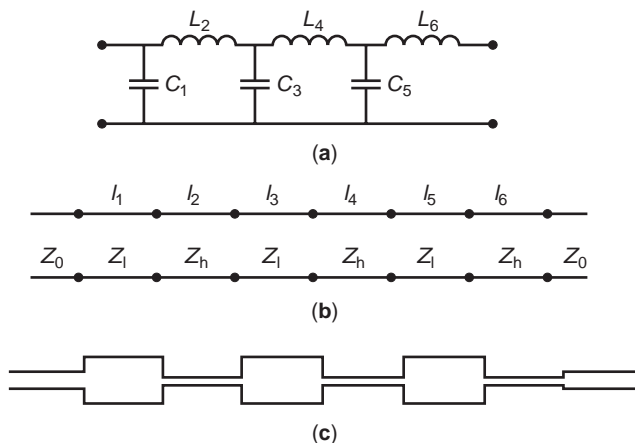


Figure 29. Filter design example: (a) lowpass filter prototype circuit using lumped elements; (b) stepped-impedance implementation; (c) microstrip layout of final filter; high-impedance lines (narrow lines) behave like inductances, and low-impedance lines (wide lines) behave like capacitances.

the substrate height to ensure the required coupling between the two adjacent resonators. Parallel-coupled bandpass microstrip filters are similar to the stripline filter shown in Fig. 22. Bandpass and bandstop filters [34,35] can also be realized using quarter-wave open-circuited or short-circuited microstrip line resonators.

7.4. Active Microstrip Circuits

Microstrip lines have been used in practically all possible types of active circuits used at microwave frequencies.

7.4.1. Microstrip Amplifiers. Microstrip lines are extensively used in various types of microwave amplifier circuits [34,78,79]. All microwave amplifier circuits require some type of matching circuits both at the input and output sides in order to obtain specified gain characteristics over a desired frequency range. Microstrip lines are used for realizing matching networks as well as for biasing networks for microwave amplifiers. Microstrip lines are also used in distributed amplifiers with multioctave bandwidths [78,79]. Various types of microstrip matching networks are: single-stub matching network, double-stub matching network, quarter-wave transformer, multisection transformer, and tapered line. Microstrip amplifier circuit design examples including matching and biasing network design considerations are available in Refs. 34, 78, and 79.

7.4.2. Microstrip Oscillators. There are numerous types of oscillator circuits. One of the most common types of

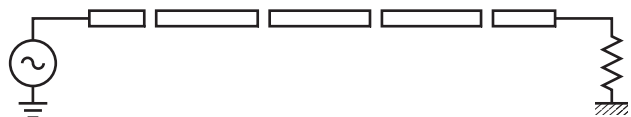


Figure 30. General microstrip layout for an end-coupled bandpass filter (series coupling gaps are located in between cascaded straight resonator elements).

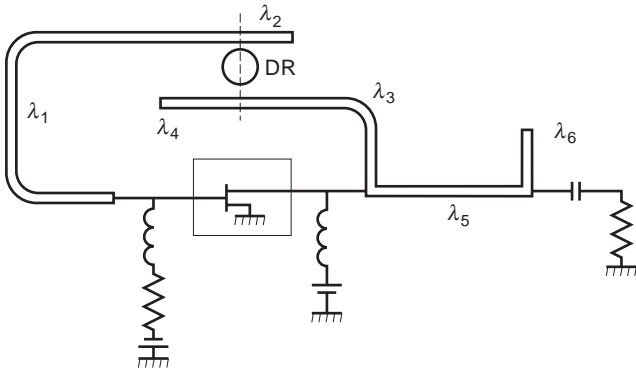


Figure 31. Microstrip implementation of the parallel feedback DRO. A dielectric resonator is coupled to two microstrip lines used to provide a feedback path from the drain to the gate of a MESFET [80].

microstrip oscillator circuits is the “dielectric resonator oscillator” (DRO). Layout of a microstrip DRO oscillator [35,80] is shown in Fig. 31. In this circuit, the dielectric resonator is coupled to two microstrip lines used to provide a feedback path from the drain to the gate of the MESFET. A microstrip single-stub matching circuit is used for the output matching.

7.4.3. Active Microwave Filters. Active microwave tunable filters have been reported in the literature [35,81]. Figure 32 shows a layout of a varactor-tuned, multipole active microwave bandpass filter described in Ref. 81.

7.4.4. Microstrip Circuits for High-Speed Digital Circuits. Microstrip lines are also used in ECL high-speed circuits or GaAs integrated circuits (ICs) for interconnection among the components and/or device chips. These

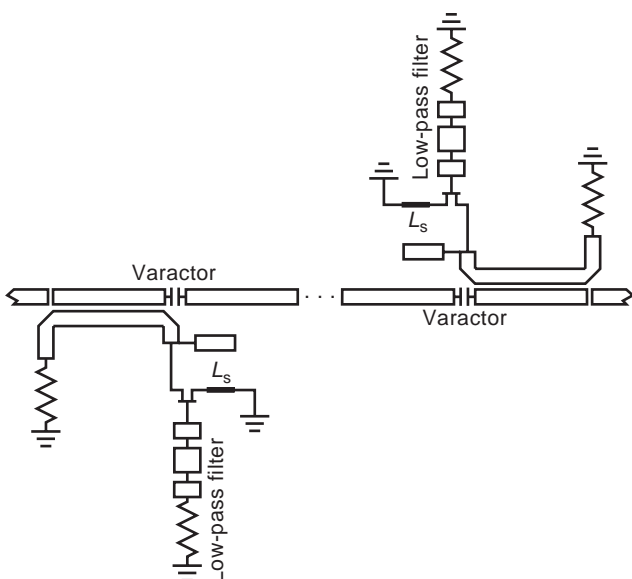


Figure 32. The multipole active tunable filter. The negative resistance is realized by the MESFET circuit. (From Ref. 81, © IEEE, 1990, reprinted with permission.)

microstrip lines are formed by the conductors of integrated circuits printed on a circuit board. At high frequencies or high speeds, it is essential to minimize reflection at the interconnections. Also, crosstalk between two parallel interconnects can become significant. Various design techniques for microstrip interconnections in high-speed digital circuits are described in the literature [35,82].

7.5. Monolithic Microstrip Circuits

Monolithic microwave integrated circuits (MMICs) are microwave circuits in which all circuit components (active and passive) are fabricated on the same semiconductor substrate [83]. MMIC circuits are used in many areas of microwave circuits with an increasing popularity because of their significant advantages over hybrid MICs in terms of lower cost, smaller size, better performance, and higher reliability. In the lower microwave frequency range, lumped elements are used for realizing microwave matching networks. However, in the higher frequency range (over 20 GHz), lumped elements become lossy and difficult to design, and distributed elements such as microstrip and coplanar waveguides are used.

Monolithic microwave circuits are described in a separate article in this encyclopedia.

8. COPLANAR WAVEGUIDE CIRCUITS

8.1. Coplanar Waveguides

Unlike microstrip lines, the ground plane in a coplanar waveguide (CPW) [84–86] is located on the same side of the substrate that contains the strip conductor. CPWs, coplanar strips, and slotlines are categorized as coplanar lines or uniplanar lines [85] because all the metallization is contained in a single layer. CPW configurations have been widely utilized to realize a variety of microwave circuits including capacitors, inductors, magic tees, mixers, filters, oscillators, resonators, distributed amplifiers, and so on. Configurations of coplanar strips, CPW, and slotlines are shown in Fig. 33.

8.1.1. Field Distribution in Coplanar Lines. Knowledge of field distribution in transmission lines is useful to microwave circuit designers because it helps in configuring location and orientation of lumped active and passive elements in transmission line circuits. Approximate electric field and magnetic field distributions in three coplanar transmission structures are shown in Fig. 34. The field distributions are different from those in a microstrip line, and they lead to some advantages these lines exhibit compared to microstrip lines.

8.2. Advantages of CPW Circuits

One of the advantages of CPW circuits over microstrip circuits arises from the fact that mounting of lumped components in shunt connection is easier in a CPW. In this case, drilling of holes through the substrate is not needed to reach the ground plane. Also, transition from a CPW to a slotline is easier to fabricate. This allows a great flexibility in the use of mixed transmission media.

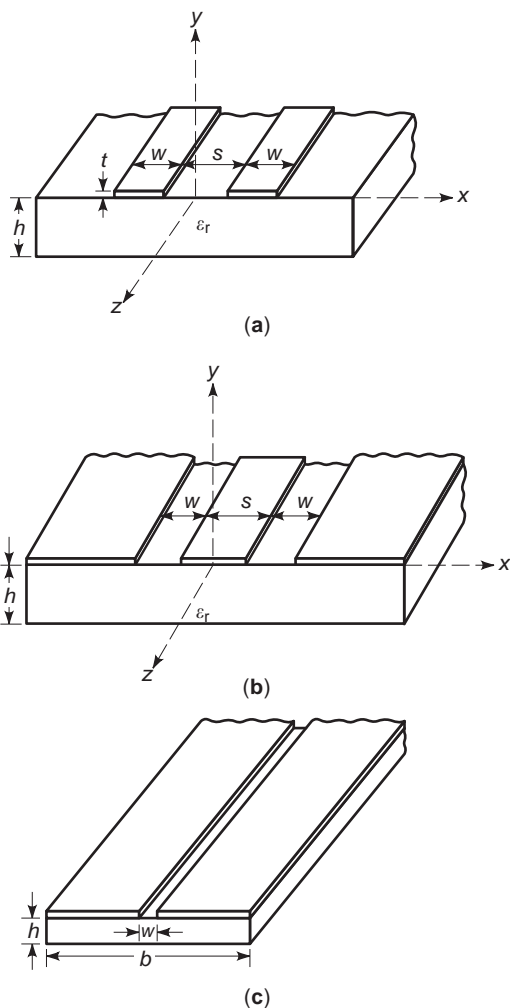


Figure 33. Various types of coplanar lines. (a) Coplanar strip. (b) Coplanar waveguide. (c) Slotline.

CPW circuit configurations can be designed to exhibit a lower sensitivity to substrate thickness, less dispersion effect, and lower losses than the corresponding microstrip circuits. Implementation of circuits in CPW configurations allows thick substrates to be used, thus avoiding the need to use fragile thin substrates at higher microwave and millimeter-wave frequencies, as occurs for microstrip circuits. Since active components can easily be inserted in CPW circuits also, CPW configurations are used increasingly in monolithic microwave and millimeter-wave integrated circuits. As strip width and gap dimensions in CPW can be reduced without changing the CPW characteristic impedance, CPW circuits can be designed to radiate much less energy than the corresponding microstrip circuits. In addition, dispersive effects in the CPW can be reduced by choosing smaller transverse dimensions.

The CPW configurations, however, have some disadvantages such as possible excitation of the slot mode, lower power-handling capability, and field nonconfinement. Slot mode is an alternative mode possible in a CPW when two ground planes are not at the same potential and E fields in two slots are oriented in the same direction. This

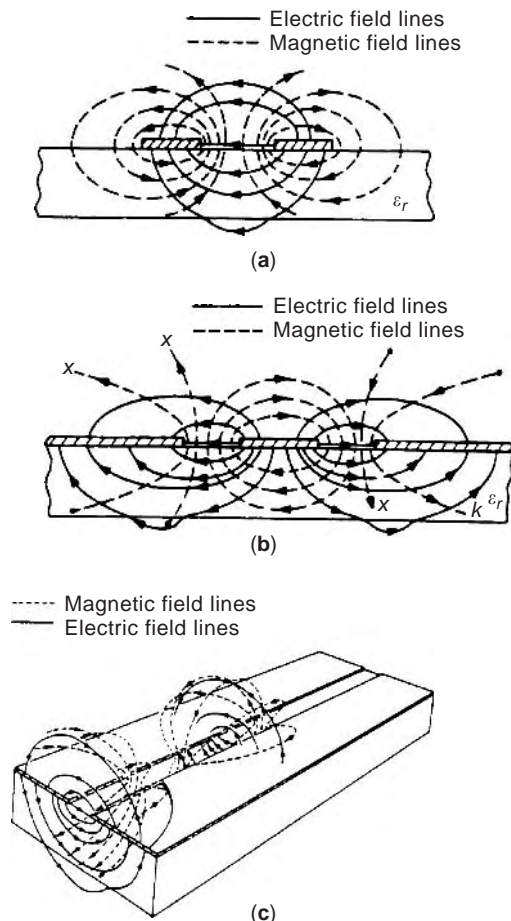


Figure 34. Electrical and magnetic field distributions in (a) coplanar strips, (b) a coplanar waveguide, and (c) a slotline.

mode can be excited by a nonsymmetric excitation (such as caused by a tee-junction discontinuity). Airbridges are needed to suppress excitation of the slot mode. The fields in a CPW are less confined than those in microstrip lines, and therefore they make the CPW circuits more sensitive to packaging covers or shields placed above the circuit.

8.3. CPW Circuit Design Considerations

The main difference in the design of CPW circuits as compared to microstrip circuits is the different characteristics of discontinuities occurring in CPW circuits. As the density of active and passive devices in CPW circuits increases, the population of discontinuities also increases. Thus, the slot mode can be excited more frequently because of asymmetric structure. When MMICs are composed of more than one kind of transmission lines, there is the need for appropriate transitions such as CPW to slotline or CPW to microstrip line. In the design of CPW circuits, characterization of these discontinuities and transitions needs to be taken into account for obtaining the desired performance. For the analysis and modeling of CPW discontinuities, several numerical methods like mode-matching method [87], finite-difference method [88], spectral domain analysis [89], transmission-line method [90],

integral equation method [91], and method of lines [92] have been used.

In addition to discontinuities, other factors such as dispersion, metallization thickness, dielectric loss, conductor loss, radiation, and surface wave loss also affect the performance of CPW circuits. All these factors need to be taken into account in the design of CPW circuits.

8.4. Examples of CPW Circuits

Most of microwave circuits developed using microstrip lines and other transmission lines can be realized in CPW configurations also. Some examples of CPW circuits are reviewed in this section.

8.4.1. Capacitors and Inductors. CPW circuits need the basic reactive elements, namely capacitors and inductors, to be realized in CPW configurations. Due to the flexibility provided by CPW configurations to accommodate lumped elements both in series and the shunt connections, capacitors and inductors may be implemented in many ways. Series or shunt circuits for capacitors or inductors are possible using CPW or CPW-slotline transitions, and some of these are shown in Fig. 35 [23].

8.4.2. Filters. Parallel-coupled-line filters and end-coupled bandpass filters can be realized in CPW configurations also [93,94]. Usually, the implementations of these filters utilize a single-layer configuration that is much easier to fabricate. Sometimes a double-layer geometry is used for a wide bandwidth [95]. Inductively coupled bandpass filters can also be realized using CPW. These filter configurations eliminate the need for via holes to the

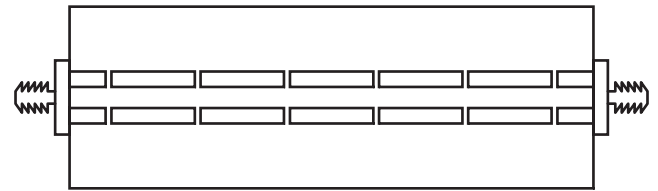


Figure 36. Layout of an inductively coupled multiresonator bandpass filter realized in a CPW configuration.

ground. The layout of an inductively end-coupled bandpass filter in a CPW configuration is shown in Fig. 36.

8.4.3. Hybrid Ring Couplers and Ring Resonators. The hybrid ring coupler can be realized in a CPW-slotline configuration [96] as shown in Fig. 37a. This circuit makes use of the properties of a slotline T junction and a CPW-slotline T junction together with the usual operation of a ratrace hybrid ring [97]. The circumference of the slot ring is one wavelength divided equally into four quarter-wave sections.

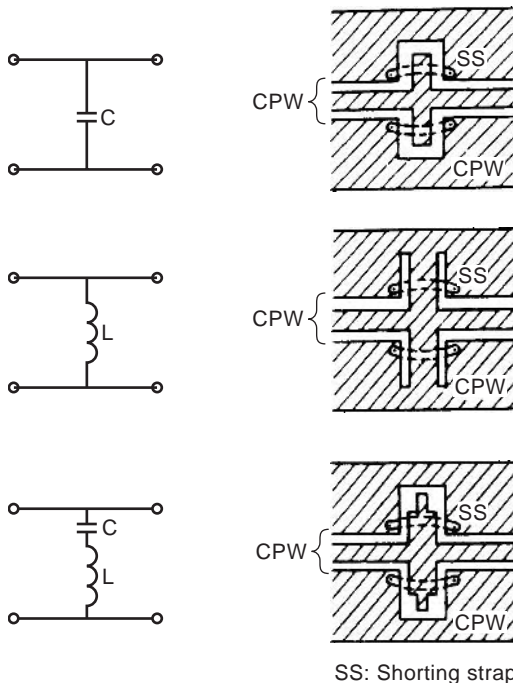


Figure 35. Capacitor and inductor elements realized in CPW configuration. *C* represents a capacitor and *L* represents an inductor.

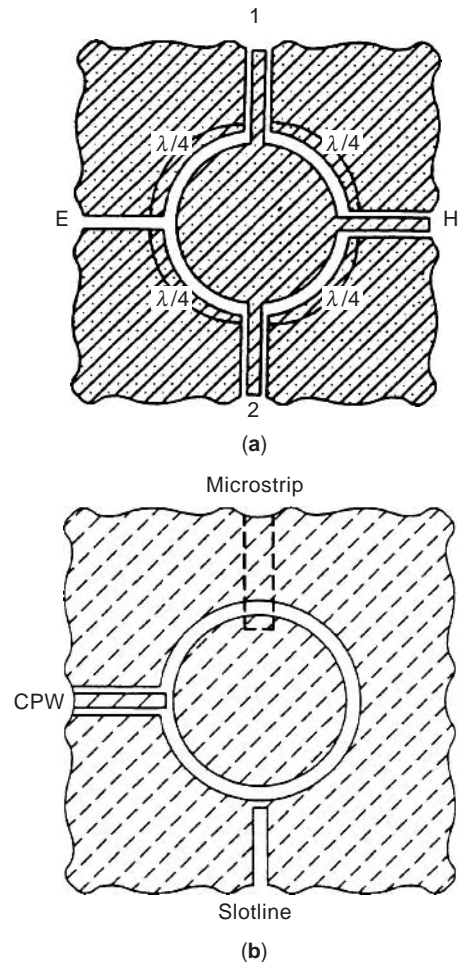


Figure 37. (a) Layout of a hybrid ring coupler in a CPW configuration where the slot ring is one wavelength (λ) and divided equally into four quarter-wave sections; (b) circuit configuration of a slotline ring resonator with different coupling schemes such as CPW, slotline, or microstrip line.

Ring resonators can also be realized using CPW or slot-line feed as shown in Fig. 37b [98]. The resonator can be easily integrated with shunt and series active devices and used for several applications [99,100]. The CPW-fed slot-line ring resonators show characteristics similar to those of microstrip-fed slotline ring resonators.

8.4.4. Mixers. Most of the microwave mixers use Schottky barrier diodes for mixing operation. A typical mixer circuit consists of a mixer diode together with coupling networks for feeding the RF signal and local oscillator (LO) power and for extracting the IF signal. One of the commonly used mixers is the balanced mixer.

Balanced mixers realized in a CPW configuration [101] use a balanced local oscillator input and an unbalanced signal input. One of the mixer configurations is shown in Fig. 38. Local-oscillator voltage is applied via the slotline, and the signal is fed through the coaxial line. Connection to the slotline is made by a small copper coaxial cable (not shown) at right angles to the slot, while a coaxial line connection to the CPW is made directly along as shown. The IF connecting wires are brought through holes in the substrate to mixer diodes.

8.4.5. Oscillators. A three-port MESFET oscillator designed in a CPW configuration [102] is shown in Fig. 39. The gate of the device is self-biased in order to minimize the number of bias points. The source and the drain are connected to 50Ω CPW transmission lines.

8.4.6. Distributed Amplifiers. A low-noise distributed CPW amplifier [103] is shown in Fig. 40. The distributed amplifier topology offers not only typically greater than octave bandwidth, but also an excellent phase linearity due to the transmission line characteristics inherent in its topology. A distributed amplifier is made up of a set of

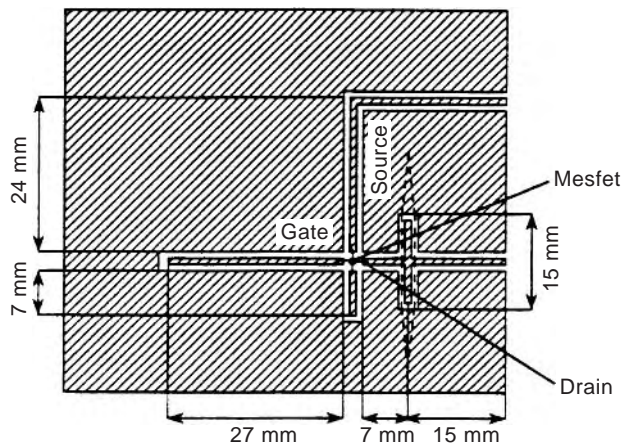


Figure 39. The circuit layout of an oscillator using CPW configurations where the gate of the MESFET is self-biased and is connected to a resonant section of open-circuited transmission line. The dashed line shows the possible position of optical waveguides in a Mach-Zehnde modulator. All CPW lines were designed to have an impedance of 50Ω. (From Ref. 102, © IEEE, 1993, reprinted with permission.)

cascaded devices, which act as shunt capacitances, connected together by high-impedance transmission lines that simulate inductances. The CPW configurations offer simplified fabrication processing and hence lower cost compared to similar microstrip amplifiers.

Various CPW circuit examples mentioned above provide a sampling of microwave circuits that can be designed in CPW configurations. Several other CPW circuit examples have been reported in the literature [104–107].

9. LUMPED-ELEMENT CIRCUITS

Circuits employing lumped elements, such as inductors and capacitors, are used extensively at lower frequencies. Lumped elements, by definition, are much smaller than the wavelength ($< \lambda/10$) at the operating frequency and exhibit small phase shift across any physical dimension. Thus, the frequency limit for lumped elements is dependent on the size of the element. With improving technology and with the development of monolithic microwave circuits, miniaturization of electronic elements becomes a possibility, and lumped-element circuits are used up to about 20 GHz. In millimeter wave monolithic circuits, lumped resistors and MIM capacitors are commonly used. Spiral inductors can be designed with self-resonance frequencies up to 40 GHz. There are several advantages of lumped-element circuits compared to distributed element transmission-line circuits [108, p. 118]. First, lumped elements have smaller frequency-dependence and are therefore good for wideband circuits. Second, the use of lumped elements affords a considerable size reduction (a factor of 10 in area) compared with distributed element circuits in microwave integrated circuits. Third, since the substrate area required is smaller and many lumped-element MICs can be processed simultaneously, the lumped elements are less costly.

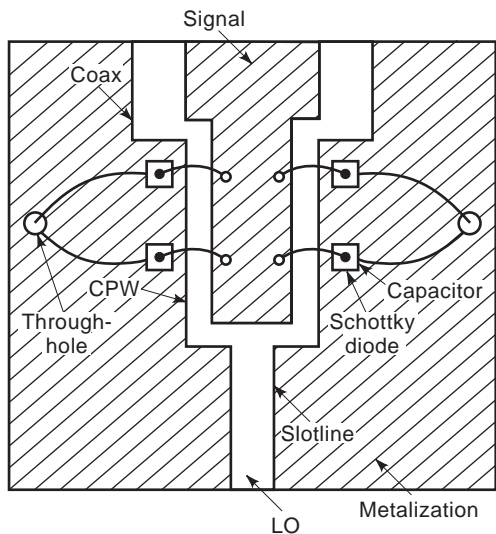


Figure 38. A circuit arrangement for a double balanced mixer using CPW where RF signal is fed through the coaxial line, LO voltage is applied via the slotline, and IF signal is brought out from the through-holes. (Based on Ref. 101.)

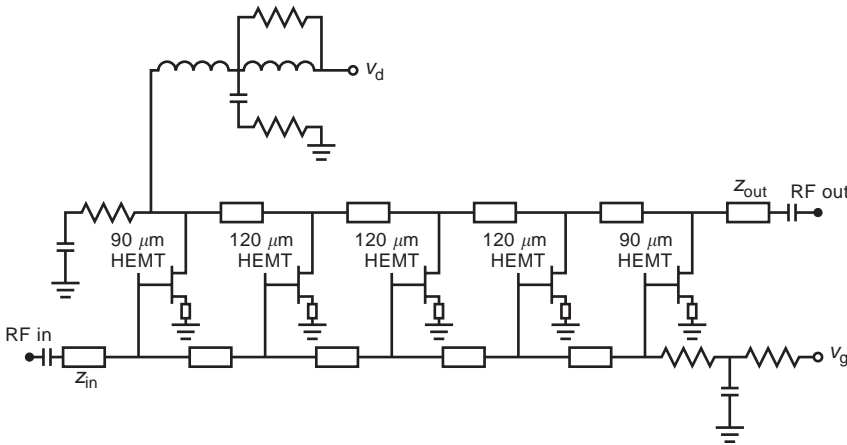


Figure 40. The circuit schematic of a 2–20-GHz CPW distributed amplifier using high-electron-mobility transistors (HEMTs) and CPW lines. (From Ref. 103, © IEEE, 1993, reprinted with permission.)

9.1. Lumped-Element Components

9.1.1. Inductors. Depending on the value of the inductance required, lumped inductors can be realized either as straight narrow strips (ribbon inductors), as single-loop inductors, or as multiturn spiral inductors:

Ribbon Inductors. A microstrip ribbon inductor and its equivalent circuit are shown in Fig. 41. For short lengths ($< \lambda_g/4$) the inductance L and shunt capacitances C at the two ends can be calculated [35]:

$$L = \frac{Z_0}{2\pi f} \sin\left(\frac{2\pi l}{\lambda_g}\right) \tag{18}$$

$$C = \frac{1}{2\pi f Z_0} \tan\left(\frac{\pi l}{\lambda_g}\right) \tag{19}$$

A narrow strip with high Z_0 is needed to achieve a high inductance value with low parasitic capacitance. However, in practice the choice of the strip width is determined by fabrication limits, by the direct-current-carrying capacity, and by the high resistance of very narrow strips. The strip length is limited simply by the need to ensure a realistic and economical chip size. The ribbon inductor is thus limited to values of less than 1 nH, but is a relatively “pure” inductor with low parasitic capacitances.

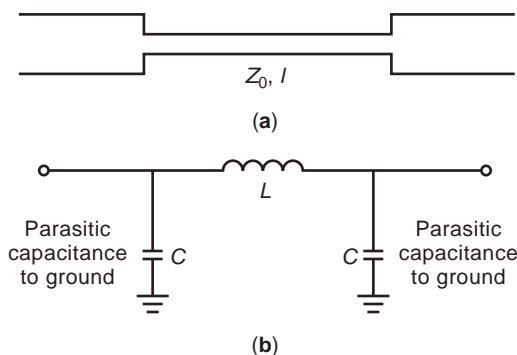


Figure 41. The ribbon inductor consisting of a high-impedance transmission line section: (a) physical layout; (b) equivalent circuit.

Loop Inductors. An example of a single-loop inductor is shown in Fig. 42. Because of their inefficient use of the chip area, loop inductors have been used very little in MMICs. However, design information can be found in a number of references [109–111].

Spiral Inductors. Spiral inductors with multiple turns are essential for inductance values above approximately 1 nH. There are two kinds of spiral inductors: circular spiral and square spiral (see Fig. 43). Circular (approximately) spirals have a slightly better quality factor at the cost of layout complexity and have a less convenient shape for integration with other components. So the square spirals are used more often in MMICs. Design equations can be found in Refs. 112–115. The drawback of the spiral inductors is that the need to connect the center turn back to the outside circuit dictates that either airbridge or dielectric crossovers must be used. There are a number of different solutions for this connection problem, and these are illustrated in Fig. 44.

Stacked Spirals. Stacked spiral inductors [83] comprise a pair of interwound spirals placed on separate metal layers. The major advantage is that the turns are much more tightly packed than what normal photolithography and metal patterning would allow for a single-layer spiral. Since the turns are separated vertically, there is less capacitance between adjacent turns than there would normally be with such small gaps. However, since the lower metal thickness is limited to 1 μm or less, stacked spirals have higher series resistances. They are generally used at frequencies below 5 GHz or so.

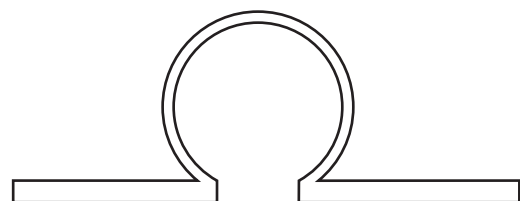


Figure 42. Layout of a single-loop inductor (not used much because of inefficient use of substrate area).

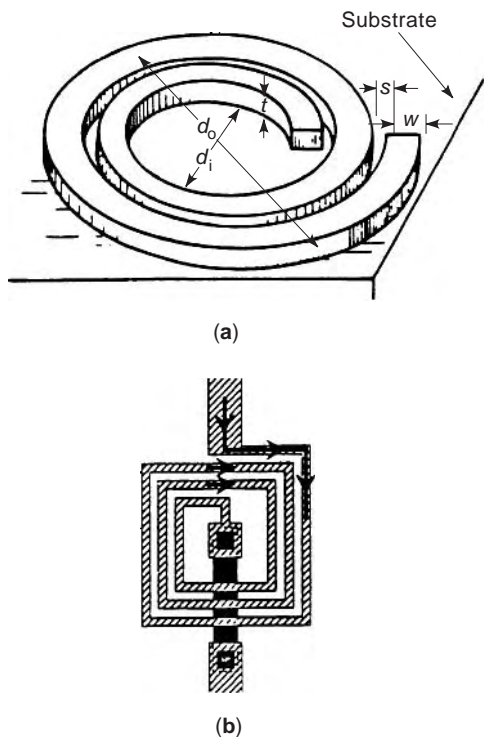


Figure 43. Spiral inductors: (a) circular spiral; (b) square spiral. Square spirals allow a more compact layout of components in MMICs.

9.1.2. Capacitors. Both overlay metal–insulator–metal (MIM) capacitors and interdigital capacitors are used in microwave circuits. Interdigital capacitors can be used for values up to approximately 1 pF, above which their size and the resulting distributed effects prevent their use. Overlay capacitors are therefore needed for most of applications, such as direct-current blocking and decoupling, where large capacitor values are required:

Overlay Capacitors. These consist of an MIM, with the most common insulators being silicon nitride, silicon

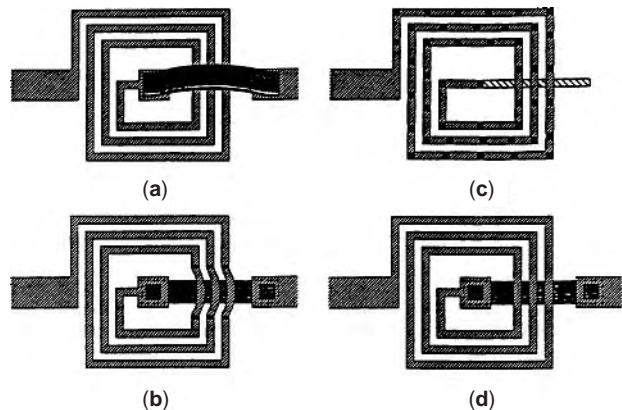


Figure 44. Different interconnection schemes for spiral inductors: (a) single airbridge; (b) airbridges over an underpass; (c) formed entirely of airbridges; (d) using two metal levels for an underpass. (From Ref. 83, © IEE, 1995, reprinted with permission.)

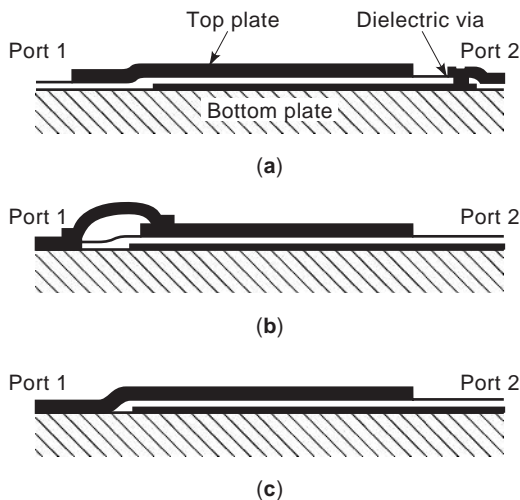


Figure 45. Overlay capacitors: (a) using a dielectric via; (b) with an airbridge; (c) without an airbridge or spacer dielectric.

dioxide, and polyimide. Silicon nitride is popular since it has a fairly higher ϵ_r compared to silicon dioxide and polyimide. The type of connection used from the capacitors to the rest of the circuit depends on whether an airbridge or a polyimide-based two-metal level process is used. Three types of overlay capacitors with connections are shown in Fig. 45. Design equations for C and capacitor quality factor Q can be found in Ref. 108, pp. 161–165.

Interdigital Capacitors. A capacitor, simpler than the MIM capacitors, is the single-layer interdigital capacitor. The interdigital capacitor consists of a number of interleaved microstrip fingers coupled together and is fabricated in a single-layer structure. Its structure and equivalent circuit are shown in Fig. 46. The maximum value of capacitance of an interdigital capacitor is limited by its physical size. It can be fabricated with values of 0.1 pF to 15 pF in a reasonable size. Because of the long length of gap between lines, large capacitors resonate at low frequency. Therefore only small value capacitors (less than 2 pF) are practical at higher frequencies. Since interdigital capacitors do not use a dielectric film, their capacitance tolerance is very good and is limited only by the accuracy of the metal pattern definition. Hence, they are ideal as tuning, coupling, and matching elements where small capacitor values are required but precise values are necessary. Design equations for these capacitors are available in Refs. 116 and 117.

9.1.3. Resistors. Because of the signal loss associated with resistances, the resistors are not used as much at microwave frequencies as in the low-frequency circuits. They are, however, irreplaceable in many cases such as for reflectionless terminations, for suppressing undesirable signals, for damping elements providing the isolation of circuits from each other, or for reducing the power level. Resistors can either use doped semiconductor layers (mesa resistors or implanted planar resistors) or sputtered thin-film resistive layers. Figure 47 shows the two

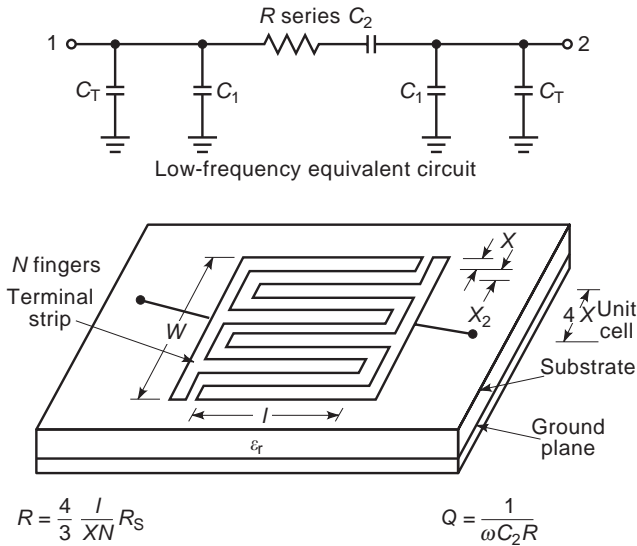


Figure 46. Interdigital capacitor layout and equivalent circuit. N is the number of fingers, $4X$ is the width of a unit cell. (From Ref. 116, © IEEE, 1970, reprinted with permission.)

resistor examples. In either case, since the layer or film thickness is fixed, it is very convenient to quote resistivity in terms of an ohm-per-square figure. Hence, the value of the resistor is chosen by selecting a suitable aspect ratio. A practical limit is imposed by the higher parasitic capacitance of large pads and the resistors physical size.

GaAs Mesa Resistors. The term “mesa” refers to the configuration where the whole wafer is doped and subsequently etched selectively so that active regions remain only where required. Figure 48 shows the details of a mesa resistor with passive and negative mesa edges [83, pp. 77–78]. The GaAs resistor relies on the linearity of the semiconductor’s current-field characteristic at low electric field values. Hence it is important to consider how much current is to be passed through the resistor. The maximum electric field allowed in the resistor is normally given as a

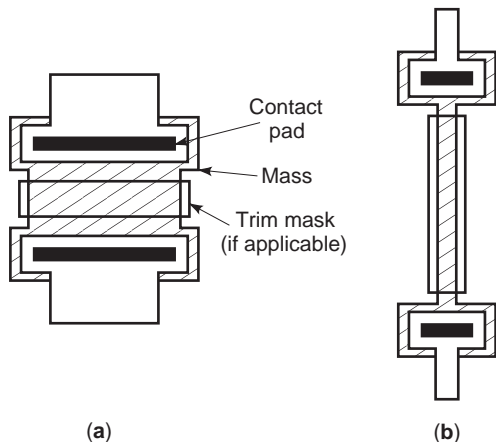


Figure 47. Lumped resistor examples: (a) small value ($= 50 \Omega$); (b) large value ($= 3000 \Omega$). (From Ref. 83, © IEE, 1995, reprinted with permission.)

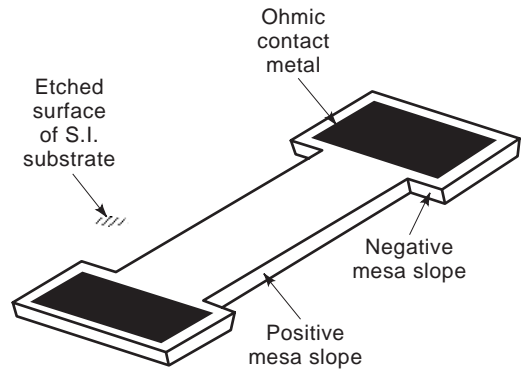


Figure 48. Mesa resistor view showing positive and negative mesa edges.

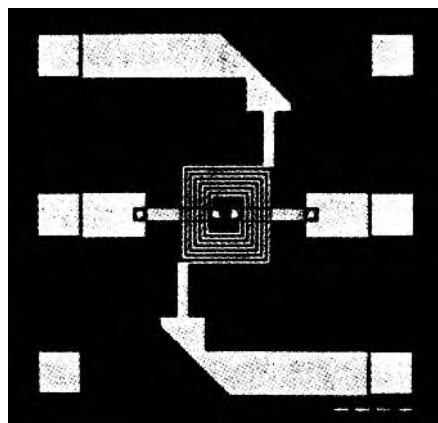
“volts per unit length” value for a certain permissible percentage deviation from perfect linearity.

Thin Film Resistors. Sputtered thin-film resistors offer improved linearity and lower temperature coefficients compared with the mesa types. In addition, the ohm-per-square figure can be optimized for the circuit designer without any limitations imposed by the requirements of the active devices. The most commonly used materials are tantalum nitride, cermet, and nickel chrome. Their temperature coefficients of resistance are less than one-tenth that of GaAs, and ohm-per-square figures of 50Ω can be produced, which is convenient for the circuit designers [118, pp. 158–159].

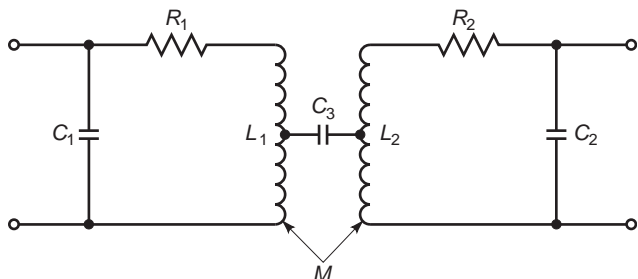
9.2. Examples of Lumped-Element Circuits

Planar Spiral Transformers. A lumped element transformer with spiral inductors offers direct-current (DC) blocking, matching, and DC bias injection functions in a very small size [120,121]. A planar spiral transformer, whose layout and equivalent circuit are shown in Fig. 49, is used as a lumped transformer up to 4 GHz or so [83, p. 73]. The two-coupled inductors have self-inductance and mutual inductance. There are series resistances in the conductors, interturn capacitance, and shunt capacitance to ground. The most serious parasitic is usually the capacitance between the two spirals since this makes the transformer resonant as the capacitive coupling becomes dominant at higher frequencies. To minimize this parasitic capacitance while achieving a high mutual inductance, the turns need to be very narrow and close together. Typically a transformer would have $5 \mu\text{m}$ conductor widths and $5 \mu\text{m}$ gaps.

Lumped-Element Matching Circuits for MMIC Amplifiers. A lumped-element amplifier circuit [83, p. 19] is shown in Fig. 50. Lumped-element matching networks (using spiral inductors or overlay capacitors) provide an appropriate arrangement at frequencies below 20 GHz. The chip is a 1–2 GHz single-stage amplifier. When operation frequency is higher than 20 GHz, the performance of spiral inductors degrades because of their self-resonances.



(a)



(b)

Figure 49. A lumped-element spiral transformer: (a) layout; (b) equivalent circuits. (From Ref. 83, © IEE, 1995, reprinted with permission.)

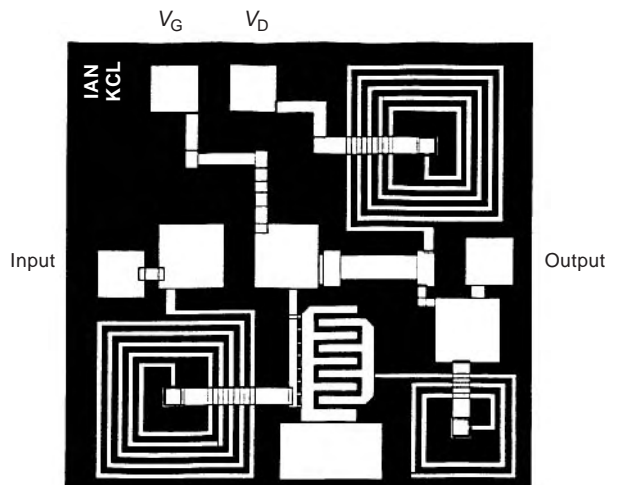
Lumped-Element Resonators. Series and parallel lumped-element resonators using interdigital capacitors are shown in Fig. 51 [117]. These kinds of resonators can be used at frequencies of 7 GHz and higher. A 0.3-pF capacitor with a 20 μm gap had a capacitance tolerance of less than 25% from sample to sample. These resonators are fabricated on one side of alumina or quartz substrate.

Filters. Figure 52 depicts a lumped element filter with bandstop loss of 30 dB at 9 GHz (117). The equivalent circuit is also shown. Interdigital capacitors are of practical use and allow the attainment of the few picofarad capacitor values required for the design of these filters at the higher microwave frequencies. Several other types of lumped element microwave circuits have been reported in the literature [83,118,119,121].

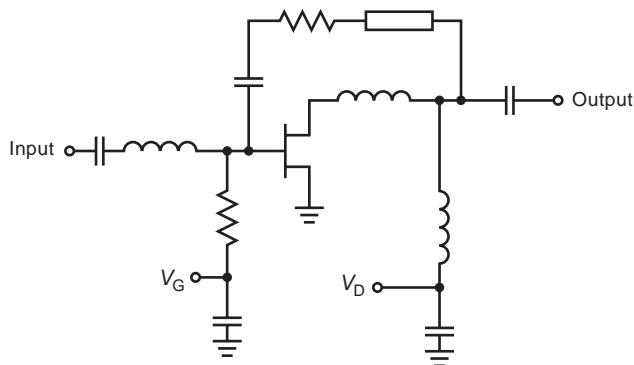
10. MULTILAYER MICROWAVE CIRCUITS

10.1. Multilayer Configurations

Portable microwave systems require circuits to be fabricated in smaller sizes and volumes. Multilayer configurations have begun to be adapted for microwave circuits to meet these size requirements [122–125]. Also, multilayer



(a)



(b)

Figure 50. A lumped-element 1–2-GHz MMIC amplifier: (a) layout; (b) circuit diagram. (From Ref. 83, © IEE, 1995, reprinted with permission.)

designs exhibit more flexibility and, in several cases, yield better performance than the corresponding designs in single-layer configurations [126]. A tight coupling is an outstanding characteristic that multilayer circuits can provide. Since a physical geometry with very narrow spacing is necessary to produce a tight coupling in single-layer directional couplers, directional couplers realized in two layers are well suitable for providing a tight coupling and high directivity [127]. This tight coupling also makes it possible to obtain wide bandwidth in filter circuits [123]. In addition, the circuits designed using symmetrical planar structures in traditional single-layer configurations can now be implemented in asymmetrical geometry. This asymmetry produces more design flexibility, leading to conveniently realizable physical geometries.

Multilayer configurations have also been utilized to integrate a number of passive components and active devices into a module to reduce the size and the volume of the whole system. This kind of use of multilayer structures has resulted in the development of multichip module (MCM) technology at microwave frequency [128,129]. However, multilayer configurations inherently require

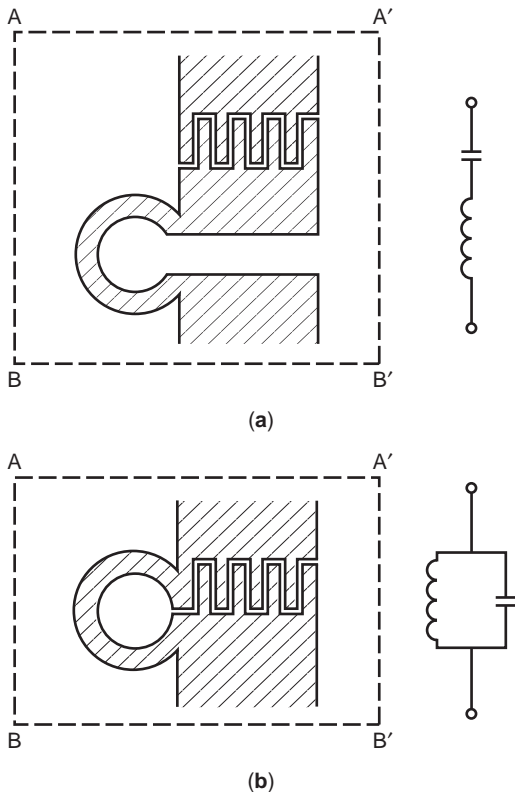


Figure 51. Series and parallel lumped-element resonator networks using interdigital capacitors: (a) series LC ; (b) parallel LC . The size $AA'BB'$ fits across a standard coaxial connector. (From Ref. 117, © IEEE, 1971, reprinted with permission.)

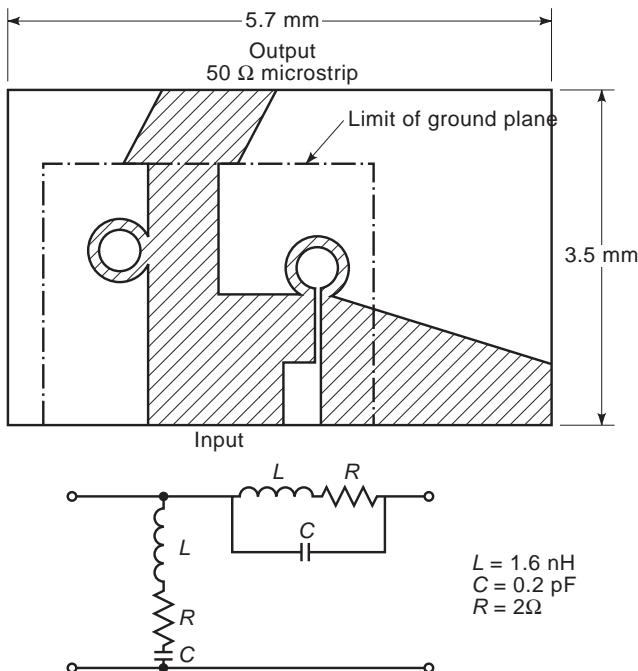


Figure 52. Bandstop filter and equivalent circuit. Bandstop loss at 9 GHz was 30 dB. (From Ref. 117, © IEEE, 1971, reprinted with permission.)

vertical interconnections between adjacent layers. Also, there is a possibility of air gap and misalignment between different dielectric layers, and these can affect the circuit performance.

10.2. Multilayer Microwave Circuit Technologies

10.2.1. Multilayer MMICs. Multilayer MMICs [130–132] are constructed using multilayer passive circuits integrated with active devices on the semiconductor substrate. Active devices, resistors, and MIM capacitors are formed on the surface of a semiconductor wafer. Dielectric films and conductors are stacked on the wafer, and transmission lines and the ground layers are connected through holes. This structure allows transmission lines with reduced linewidths, vertical interconnections with short signal delays, and miniaturized connections in a small area. In addition, this provides miniature but low-loss transmission lines and increased design flexibility.

For examples using this multilayer structure, several miniature passive circuits such as directional couplers, Wilkinson power dividers, transmission lines, and planar baluns have been designed and fabricated. Active circuits such as mixers, amplifiers, phase shifters, and upconverters are integrated with passive circuits in planar forms. Figure 53 [131] shows the typical configuration of a multilayer MMIC. In Fig. 53, a three-dimensional MMIC fabricated on a GaAs substrate integrates active devices, resistors, and MIM capacitors on the surface of a semiconductor wafer. A thin-film microstrip (TFMS) line offers a compact meanderline configuration while thin polyimide films and conductors are stacked on the wafer and ground metal is inserted between layers.

10.2.2. Multichip Modules. A multichip module (MCM) [129] is defined as multilayer sandwiches of dielectric and conducting layers, on which integrated circuits and passive components (if any) are mounted directly on (or inside of) the sandwich structure, without separate packaging for each of the active components. That is, the chips are mounted bare onto the MCMs, which then provide the

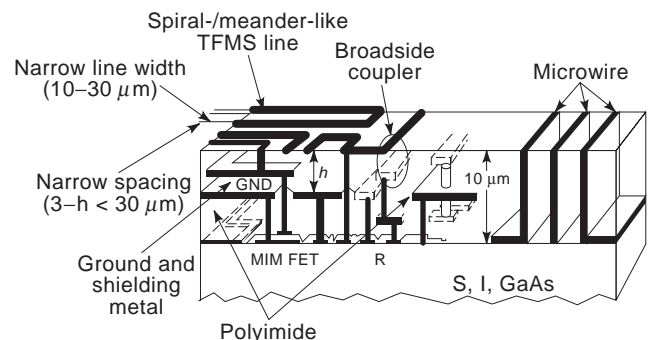


Figure 53. Structure of the three-dimensional multilayer MMIC fabricated on GaAs substrate. Active devices and an MIM capacitor are placed on the surface of a wafer, thin polyimide films and conductors are stacked on the wafer, and thin-film microstrip (TFMS) lines and ground layers are connected through via holes. (From Ref. 131, © IEEE, 1996, reprinted with permission.)

required power and ground, as well as all the signal interconnect and the electrical interface to the external environment. The entire MCM, including chips and passive components, may be placed in a hermetic package much like a large single-chip carrier, or it may be directly covered with a sealant material (such as epoxy or a glass passivation coating) to protect the components from physical damage.

Three general categories of MCMs are MCM-C (ceramic), MCM-L (laminated), and MCM-D (deposited). MCM-Cs are manufactured by stacking unfired layers of ceramic dielectric, onto which liquid metal lines are “silk-screened” using a metal ink process. The individual inked layers are then aligned, pressed together, and cofired into a solid planar structure, onto which integrated circuits can be installed. MCM-Ls are manufactured through the lamination of sheet layers of organic dielectric, and they are very similar to traditional printed circuit-board technology. MCM-Ds are manufactured through the deposition of organic or inorganic dielectrics onto a silicon or alumina support substrate. After each dielectric layer is deposited, one of several techniques is used to pattern metal lines as well as metal vias. The chips are then installed on the upper surface.

MCM-D technology can provide a versatile platform for the integration of GaAs MMICs and silicon devices for microwave circuits where performance, size, and weight are critical factors. Multilayer circuits such as spiral inductors, baluns, directional couplers, Lange couplers, transmission line transformers, filters, amplifiers, and voltage-controlled oscillators have been realized using this technology [129]. Figure 54 shows a typical configuration that can be fabricated by MCM-D technology suitable for design of multilayer microwave circuits.

10.3. Design of Multilayer Circuits

Multilayer microwave circuits can be divided into two groups, the first of which consists of planar components employing multilayer transmission structures, while in the second group, one integrates various circuits into a single multilayer module.

Multilayer couplers, filters, baluns, inductors, and so on, belong to the first group because these employ multilayer transmission structures to overcome difficulties occurring in single-layer designs. It is well known [62] that

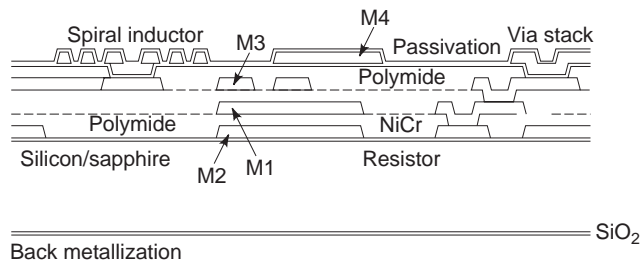


Figure 54. Multichip module (MCM-D) technology used for RF integration. Polymide dielectrics are deposited onto a silicon sapphire substrate; then the chips are installed on the upper surface, and transmission lines and vias are fabricated.

coupled lines realized in single-layer structures produce a weak coupling. Thus, when a tight coupling is required, coupled lines can be implemented in multilayer configurations because overlapping geometry between coupled lines is possible. Coupled-line couplers requiring a tight coupling and those requiring high directivity are designed [127] using this advantage. For the design of parallel coupled-line filters and end-coupled filters, a wide bandwidth is frequently required. For this purpose, multilayer structures used in coupled-line filters [133] and end-coupled filters [95] allow overlapping geometry in the design, which leads to a wide bandwidth and flexibility in selection of physical dimensions. Baluns using multilayer coupled lines [134] can also be designed for wideband operation and with compact dimensions because a tight coupling can easily be obtained in multilayer configurations. Apertures in the ground plane can be employed to achieve interconnection between different layers in multilayer circuits [135] such as aperture-coupled couplers and magic tees.

For the multilayer circuits in the second group, passive components and/or active devices are integrated into a single module for miniaturization and cost-effective production [131]. When these are integrated, vertical vias between different layers and apertures in the ground plane are placed appropriately considering miniaturization, crosstalk, and productivity.

10.4. Examples of Multilayer Circuits

Some examples of multilayer microwave circuits are discussed in this section.

10.4.1. Couplers. Since single-layer structure is not convenient for couplers requiring a tight coupling, multilayer configuration has been explored to overcome this difficulty. As a result, coupled-line directional couplers in two layers [136] and reentrant type couplers [137] designed for a tight coupling have been reported. Figure 55 shows a two-layer coupler [136]. Two conductors with unequal widths are placed on different layers to yield a tight coupling. Different port impedances can be used at the four external ports.

Figure 56 shows a reentrant-type coupler where two identical conductors placed on the top layer with a wider conductor on the bottom layer produce a tight coupling. The spacing between the two conductors on the top layer is wide, not leading to tight tolerance requirement of a narrow gap in fabrication.

10.4.2. Filters. Multilayer configurations have been used for wideband parallel coupled-line filters [138] and

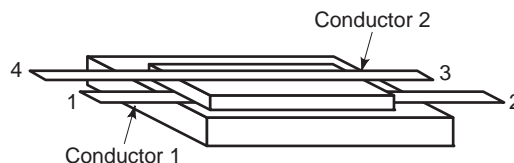


Figure 55. Two-layer coupled-line coupler. Conductors are placed on different levels. A tight coupling can be obtained.

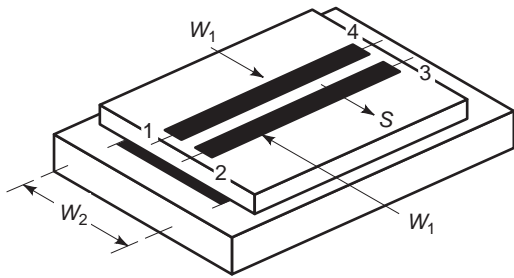


Figure 56. Reentrant-type coupler. Two identical conductors are placed on top layer with a wide spacing, a wide conductor is placed on the bottom layer. This coupler provides a tight coupling.

end-coupled bandpass filters [95] because filters in single-layer configurations cannot yield a wide bandwidth. Aside from the wide bandwidth, enhanced freedom in circuit layout in multilayer designs makes multilayer configurations more attractive. Parallel coupled-line filters and end-coupled bandpass filters have been developed in multilayer structure and also in multilayer coplanar waveguide structure. Examples of these filter circuits are shown in Figs. 57 and 58.

In Fig. 57, coupled lines, which can be placed on different layers, constitute a bandpass filter where each coupled line can have nonsymmetric geometry leading to flexibility in design. Due to these coupled lines offering tight coupling, multilayer coupled-line bandpass filters provide wide bandwidths which are not achievable in single-layer configurations. In Fig. 58, gap-coupled sections constitute a bandpass filter in two-layer configuration. Since this structure allows overlapping conductors in each gap-coupled section, this can also be used for obtaining a wide bandwidth.

10.4.3. Baluns. Due to the requirement for a wide bandwidth and compact design, planar Marchand baluns have been developed [134] using coupled lines in two-layer configurations. These baluns provide wide bandwidth (more than one octave) and compaction of physical dimensions. Figure 59 shows one such circuit reported in the literature. In Fig. 59, two kinds of coupled-line sections in two layers constitute a planar Marchand balun. An unbalanced signal entering port 1 is transformed into a balanced signal coming out of ports 2 and 3.

Three-line baluns using three-coupled lines have also been designed [139] in a two-layer structure, leading to compact design and good performance. Figure 60 shows one of such balun designs. In this design, one of the conductors is placed on one layer while two other conductors are placed on the second layer. With appropriate termi-



Figure 57. Multilayer parallel coupled-line filter. Various conductors can be placed on different levels; each coupled section produces tight coupling, leading to broad bandwidth for the filter.

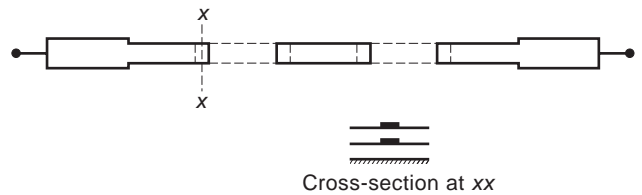


Figure 58. Two-layer end-coupled bandpass filter. Half-wave resonators shown in dotted lines are at lower layer. Each gap-coupled section can have overlapping geometry for tight coupling and therefore broad bandwidth of the filter.

nations at the ports, this balun transforms an unbalanced signal at port 1 to a balanced signal at ports 2 and 3.

10.4.4. Hybrids. Branchline couplers [140] and magic tees [135] have been developed using multilayer configurations to produce better performance than what can be obtained in single-layer configurations. Figure 61 [140] shows a multilayer branchline coupler where the two output ports are mutually isolated, and the signals at these two ports are out of phase by 90° . The distance between two microstrips or slotlines is one quarter-wavelength. It is possible to make 3 dB branchline couplers by suitably choosing the values of Z_m and Z_s .

Figure 62 shows [135] a multilayer magic tee where the microstrip line (difference arm) on the lower substrate is coupled to a slot-aperture and is terminated on the same layer by an open-circuit stub. The other three magic tee ports are located at the top layer. With the excitation at port 1 (difference port), signals at ports 2 and 3 are equal in magnitude and out of phase by 180° . When the sum port (port 4) is fed, signals at ports 2 and 3 are in phase and equal in magnitude. In addition to the circuits described above, there are many other multilayer circuits like transmission-line transformers [141], aperture-coupled multilayer circuits [142], and aperture-fed and microstrip patch antennas [143].

11. DESIGN OF MICROWAVE CIRCUITS

As is true also for design processes in other domains of engineering, the computer-aided design (CAD) approach [144–146] is being used extensively for the design of microwave circuits and is also being refined further. In order

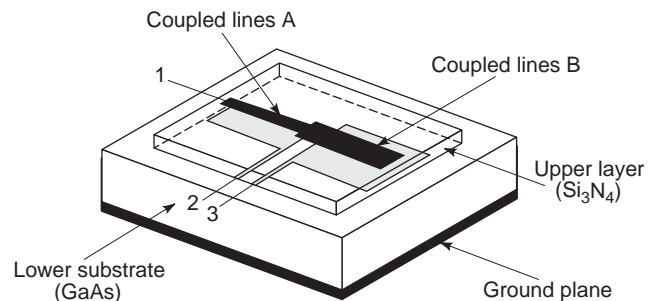


Figure 59. Planar Marchand balun. Two kinds of coupled lines constitute a balun transforming an unbalanced signal entering into port 1 to a balanced signal coming out of ports 2 and 3. (From Ref. 134, © IEEE, 1990, reprinted with permission.)

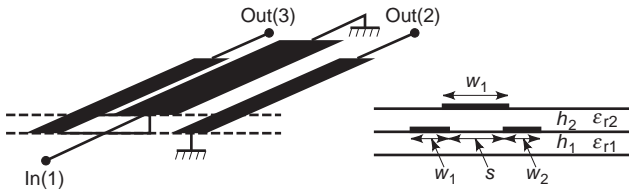


Figure 60. Two-layer three-line balun. One conductor is placed on one layer while two other conductors are placed on the other layer. With appropriate terminations at different ports, this circuit works as a balun.

to appreciate the CAD methodology, it is necessary to review the conventional design process that designers used before the CAD methods and software were developed.

11.1. Conventional Design Procedure

A flow diagram depicting the conventional design procedure is shown in Fig. 63. One starts with the desired circuit specifications and arrives at an initial circuit configuration. Available design data and previous experience are helpful in selecting this initial configuration. Analysis and synthesis procedures are used for deciding values of various parameters of the circuit. A laboratory model is constructed for the initial design, and measurements are carried out for evaluating its characteristics. Performance achieved is compared with the desired specifications; if the given specifications are not met, the circuit is modified. Adjustment, tuning, and trimming mechanisms incorporated in the circuit are used for carrying out these modifications. Measurements are carried out again and the results are compared with the desired specifications. The sequence of modifications, measurements, and comparison is carried out iteratively until the desired specifications are achieved. At times the specifications are compromised in view of the practically feasible performance of the circuit. The final circuit configuration thus obtained is sent for prototype fabrication.

The above procedure had been used for the design of microwave circuits for quite some time. However, it became increasingly difficult to use this iterative

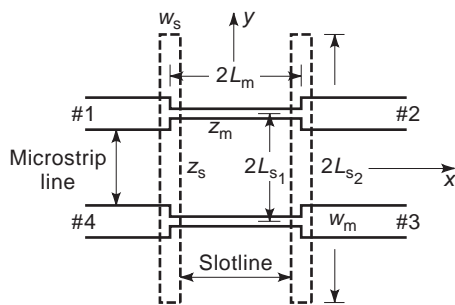


Figure 61. A branchline coupler in a two-layer structures. Slotlines are placed on the lower layer while two microstrip lines are located on the upper layer, and two outputs are (at ports 2 and 3) 90° out of phase and equal in magnitude. (From Ref. 140, © IEEE, 1995, reprinted with permission.)

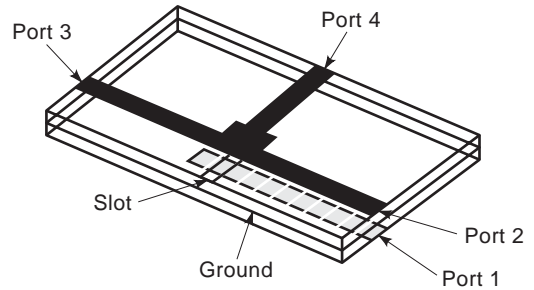


Figure 62. A two-layer microstrip magic-tee junction (ports 2, 3, and 4) coupled through a slot in the ground to a microstrip line (port 1) on the backside. (From Ref. 135, © IEEE, 1997, reprinted with permission.)

experimental method successfully because of the following considerations:

1. Increased complexity of modern systems demands more precise and accurate design of circuits and subsystems. Consequently, the effect of tolerances in the circuit design becomes increasingly important.
2. A larger variety of active and passive components, as described in previous sections, are now available for achieving a given circuit function. The choice of the appropriate device or transmission structure becomes difficult if the iterative experimental approach is used.

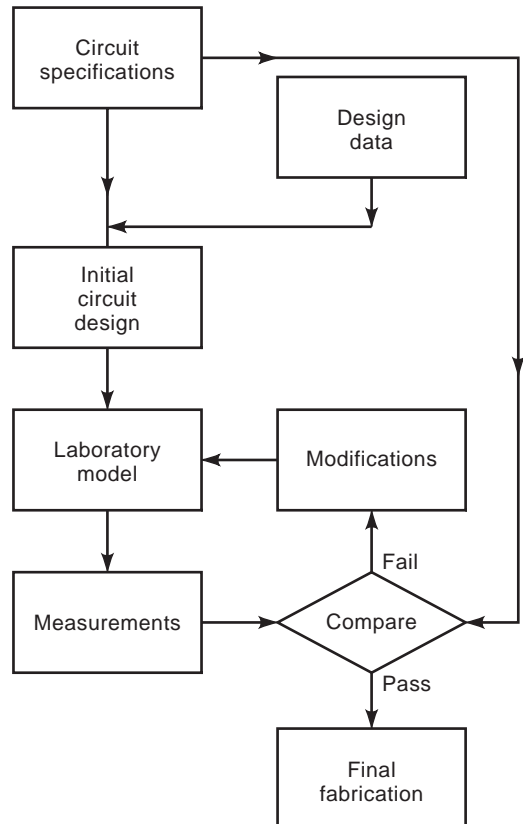


Figure 63. The conventional design procedure that was used for microwave circuits before CAD methods were developed.

- It is very difficult to incorporate any modifications in the circuits fabricated by MIC technology.

The method developed for dealing with this situation is known as “computer-aided design (CAD)”. Computer-aided design in its strict interpretation may be taken to mean any design process where the computer is used as a tool. However, usually the term CAD implies that without the computer as a tool, that particular design process would have been impossible or much more difficult, more expensive, more time-consuming, and less reliable and more than likely would have resulted in an inferior product.

11.2. CAD of Microwave Circuits

A typical flow diagram for the CAD procedure is shown in Fig. 64. As before, one starts with a given set of specifications. Synthesis methods and available design data (at times prestored in computer memory) help to arrive at the initial circuit design. The performance of this initial circuit is evaluated by a computer-aided circuit analysis. Numerical models for various components (passive and active) used in the circuit are needed for the analysis. These are called from the library of subroutines developed

for this purpose. Circuit characteristics obtained as results of the analysis are compared with the given specifications. If the results fail to satisfy the desired specifications, the designable parameters of the circuit are altered in a systematic manner. This constitutes the key step in the optimization. Several optimization strategies include sensitivity analysis of the circuit for calculating changes in the circuit parameters. The sequence of circuit analysis, comparison with the desired performance, and parameter modification is performed iteratively until the specifications are met or the optimum performance of the circuit (within the given constraints) is achieved. The circuit is now fabricated and the experimental measurements are carried out. Some modifications may still be required if the modeling and/or analysis are not accurate enough. However, these modifications, hopefully, are very small, and the aim of the CAD method is to minimize the experimental iterations as far as practicable.

The process of CAD, as outlined above, consists of three important segments:

- Modeling
- Analysis
- Optimization

Modeling involves characterization of various active and passive components to the extent of providing a numerical model that can be handled by the computer. In the case of microwave circuits, one comes across a variety of active and passive elements. Semiconductor devices used include bipolar and MESFET transistors, point contact and Schottky barrier detectors, varactor and pin diodes, and transferred electron and avalanche devices. Passive elements used in microwave circuits include sections of various transmission structures, lumped components, YIG and dielectric resonators, nonreciprocal components, and planar (two-dimensional) circuit elements. Transmission structures could be coaxial line, waveguide, stripline, microstrip line, coplanar line, slotline, or a combination of these. As mentioned earlier in article, not only do these transmission structures need to be characterized fully for impedance, phase velocity, and so on, it also becomes necessary to model the parasitic reactances caused by geometrical discontinuities in these densely packed transmission lines.

Modeling of components in microwave circuits had been the main difficulty in successful implementation of CAD techniques at microwave frequency. However, the development of electromagnetic (EM) simulation techniques developed since the late 1980s has helped to construct adequate models and bring microwave hybrid and monolithic circuit CAD software to level of maturity. Modeling still remains the major bottleneck for CAD of certain classes of microwave circuits [such as coplanar waveguide (CPW) circuits, multilayered circuits, and integrated circuit-antenna modules] and most of the millimeter-wave (above ~ 40 GHz) circuits. Current research in efficient use of EM simulation techniques and in use of artificial neural network models [77] will lead to further improvement in CAD tools for microwave and millimeter-wave circuits.

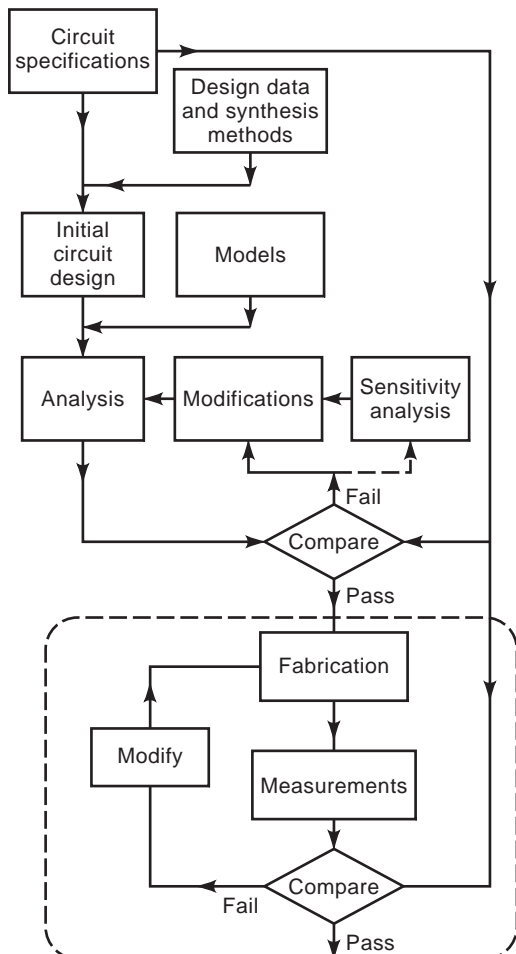


Figure 64. Computer-aided design methodology used for microwave circuits. Recent developments have brought microwave CAD tools to a level of maturity.

12. EMERGING TRENDS IN MICROWAVE CIRCUITS

Even after going through developments over almost a century, the field of microwave circuits continues to see developments in full swing even today; particularly in the areas of multilayered circuits, integrated circuit–antenna modules, quasioptical circuits and systems, and exotic methodologies for CAD.

12.1. Multilayered Circuits

Microwave multilayered circuits were described earlier in Section 10. Multilayered circuit technology is responsible for two novel innovations in monolithic microwave circuits. The first one of these is the development of three-dimensional passive circuit technology [147] as an evolution from the two-dimensional planar microwave circuit technology, which has been the cornerstone of integrated microwave circuit technology so far. Three-dimensional microwave circuits make use of multilayered configurations combined with vertical wall-like microwave structures. This technology can reduce the sizes of inductors and transmission lines to one-third or one-fourth of the size of two-dimensional configurations.

Another novel concept that has emerged from the application of multilayer circuit technique is that of master slice MMIC [148]. The basic idea is similar to that of gate arrays used for semiconductor application-specific integrated circuits (ASICs). In an MMIC master slice, many units that contain transistors, resistors, and lower electrodes for MIM capacitors are located repeatedly (nearly 6 units/mm²) on a GaAs or Si wafer to form a master array. Additional upper layers provide custom design interconnects and top conductor for capacitors to yield semi-custom-designed circuits.

12.2. Integrated Circuit-Antenna Modules

Another very interesting trend in microwave and millimeter-wave design is the integration of conventional circuit and antenna functions in single components. This integration has been made possible by common fabrication technology used for planar circuits and printed antennas. Various design approaches applicable to integrated circuit–antenna modules have been developed [149]. Quasioptical systems [150] designed to generate high power at millimeter-wave frequencies by employing a grid array of sources are important examples of integrated circuit–antenna modules.

12.3. Knowledge-Aided Design (KAD)

Emerging innovations in design techniques [77] for microwave circuits include use of artificial neural networks and development of knowledge-based design tools.

Artificial neural networks (ANNs) are neuroscience-inspired computational tools that learn from experience (training), generalize from previous examples to new ones, and abstract essential characteristics from inputs containing noise or irrelevant data. A significant application of ANN computing to microwave design has been for development of component models [151]. These models are

as accurate as results for EM simulators used for training them but are as efficient as network models. ANNs are expected to play a significant role in microwave design in areas of modeling and optimization and possibly as a means of embedding knowledge in design tools.

Any design process involves several steps starting from problem identification and going through specification generation, concept generation, initial analysis and evaluation, and initial design to a detailed optimized design. It is for the last of these steps (from initial design to detailed optimized design) that the current microwave CAD tools have been developed. The earlier steps in the design process are not at all trivial. We need a technology to aid the earlier stages of design where designers make important and expensive decisions. Knowledge-based system seems to be the most appropriate technology for this purpose.

BIBLIOGRAPHY

1. G. C. Southworth, Hyper-frequency waveguides—general considerations and experimental results, *Bell Syst. Tech. J.* **15**:284–309 (1936).
2. J. R. Carson, S. P. Meade, and S. A. Schelkunoff, Hyper-frequency waveguides—mathematical theory, *Bell Syst. Tech. J.* **15**:310–333 (1936).
3. G. C. Southworth, Some fundamental experiments with waveguides, *Proc. IRE* **25**:807–822 (1937).
4. G. C. Southworth, Survey and history of the progress of microwave arts, *Proc. IRE* **50**:1199–1206 (1962).
5. P. H. Smith, Transmission line calculator, *Electronics* **12**:29–31 (1939) An improved transmission line calculator, *ibid.*, **17**:130–133, 318, 320, 322, 324–325 (1994).
6. A. G. Fox, An adjustable waveguide phase changer, *Proc. IRE* **35**:1489–1498 (1947).
7. W. A. Tyrell, Hybrid circuits for microwaves, *Proc. IRE* **35**:1294–1306 (1947).
8. W. W. Mumford, Directional couplers, *Proc. IRE* **35**:160–165 (1947).
9. R. M. Barrett and M. H. Barnes, Microwave printed circuits, *Natl. Conf. Airborne Electronics, IRE*, Dayton, OH, 1951.
10. R. W. Peters et al., *Handbook of Tri-plate Microwave Components*, Sanders, Nashua, NH, 1956.
11. H. Howe, Jr., *Stripline Circuit Design*, Artech House, Dedham, MA, 1974.
12. H. A. Wheeler, *Directional Coupler*, U.S. Patent 1,606,974 (1952).
13. D. D. Greig and H. F. Engelmann, Microstrip—a new transmission technique for the kilomegacycle range, *Proc. IRE* **40**:1644–1650 (1952).
14. F. Assadourian and E. Rimai, Simplified theory of microstrip transmission systems, *Proc. IRE* **40**:1651–1657 (1952).
15. H. A. Wheeler, Transmission line properties of parallel wide strips by conformal mapping approximation, *IEEE Trans. Microwave Theory Tech.* **MTT-12**:280–289 (1964).
16. H. A. Wheeler, Transmission line properties of parallel strips separated by a dielectric sheet, *IEEE Trans. Microwave Theory Tech.* **MTT-13**:172–185 (1965).
17. S. W. Schilling and R. K. Durnwirth, The real world of microstrip substrates, Parts 1–5, *Microwave*, **7**(12):52–56 (1968); **8**(1):44–46 (1969); **8**(3):57–59 (1969); **8**(9):36–41 (1969); **8**(12):54–57 (1969).

18. Microwave integrated circuits (special issue), *IEEE Trans. Electron. Devices* **ED-15** (1968).
19. Microwave integrated circuits (special issue), *IEEE Trans. Microwave Theory Tech.* **MTT-19** (1971).
20. K. C. Gupta and A. Singh, eds., *Microwave Integrated Circuits*, Halsted Press, New York, 1974.
21. J. Frey, ed., *Microwave Integrated Circuits*, Artech House, Dedham, MA, 1974.
22. S. B. Cohn, Slot line on a dielectric substrate, *IEEE Trans. Microwave Theory Tech.* **MTT-17**:768–778 (1969).
23. K. C. Gupta et al., *Microstrip Lines and Slotlines*, 2nd ed., Artech House, Norwood, MA, 1996.
24. C. S. Aitchison et al., Lumped microwave circuits, Parts I–V, *Des. Electron.* **8**(11):23–28 (1971); **9**(1):30–39 (1971); **9**(2):42–51 (1971); **9**(3):47 (1971); **9**(4):41–48 (1972); also *Philips Tech. Rev.* **32**:305–314 (1971).
25. R. S. Pengelly and D. C. Rickard, Design, measurements and application of lumped elements up to J-band, *Proc. 7th Eur. Microwave Conf.*, Copenhagen, 1977, pp. 460–464.
26. T. Okoshi and T. Miyoshi, The planar circuit—an approach to microwave integrated circuitry, *IEEE Trans. Microwave Theory Tech.*, **MTT-20**:245–252, 1972.
27. E. W. Mehal and R. W. Wacker, GaAs integrated microwave circuits, *IEEE Trans. Electron. Devices* **ED-15**:513–516 (1968).
28. M. M. Hasan and S. K. Mullick, Monolithic MICs, in K. C. Gupta and A. Singh, eds., *Microwave Integrated Circuits*, Halsted Press, New York, 1974, pp. 259–277.
29. C. A. Liechti, Future of microwaves is monolithic, *Microwave Syst. News* **8**(11):60 (1978).
30. Microwave field-effect transistors (special issue), *IEEE Trans. Microwave Theory Tech.* **MTT-24** (1976).
31. K. C. Gupta, *Microwaves*, Halsted Press, New York, 1980, Chap. 10.
32. B. S. Perlman and V. G. Glenovatch, in L. Young and H. Sobol, eds., *Computer Aided Design, Simulation and Optimization in Advances in Microwaves*, Vol. 8, Academic Press, New York, 1974, pp. 321–399.
33. J. F. White, *Semiconductor Control*, Artech House, Dedham, MA, 1977, pp. 177–243.
34. D. M. Pozar, *Microwave Engineering*, Addison-Wesley, Reading, MA, 1990.
35. T. Edwards, *Foundations for Microstrip Circuit Design*, 2nd ed., Wiley, New York, 1992.
36. D. Fisher and I. Bahl, *Gallium Arsenide IC Applications Handbook*, Vol. 1, Academic Press, San Diego, 1995.
37. T. K. Ishii, *Handbook of Microwave Technology*, Vol. 1: *Components and Devices*, Academic Press, San Diego, 1995.
38. J. Uher, J. Bornemann, and U. Rosenberg, *Waveguide Components for Antenna Feed Systems: Theory and CAD*, Artech House, Dedham, MA, 1993.
39. J. J. Izadian and S. M. Izadian, *Microwave Transition Design*, Artech House, Dedham, MA, 1988, Chaps. 3 and 4.
40. H. M. Barlow, The relative power-carrying capacity of high-frequency waveguides, *IEE Proc.* **99**(Part III):21 (1952).
41. R. E. Collin, Waveguide phase changer, *Wireless Eng.* **32**:82–88 (1955).
42. R. Chatterjee, *Elements of Microwave Engineering*, Wiley, New York, 1986.
43. R. Vahldieck, Quasi-planar filters for millimeter-wave applications, *IEEE Trans. Microwave Theory Tech.* **37**:324–334 (1989).
44. P. J. Meier, Integrated finline millimeter-wave components, *IEEE Trans. Microwave Theory Tech.* **MTT-22**:1209–1219 (1974).
45. L. Q. Bui, D. Ball, and T. Itoh, Broad-band millimeter-wave E-plane bandpass filters, *IEEE Trans. Microwave Theory Tech.* **MTT-32**:1655–1658 (1984).
46. Y. Konishi and K. Uenakada, The design of bandpass filters with inductive strip-planar circuit mounted in waveguide, *IEEE Trans. Microwave Theory Tech.* **MTT-22**:869–873 (1974).
47. W. Hauth, R. Keller, and U. Rosenberg, The corrugated-waveguide band-pass filter—a new type of waveguide filter, *Proc. 18th European Microwave Conf.*, Stockholm, Sweden, 1988, pp. 945–949.
48. R. Levy, Synthesis of high power harmonic rejection waveguide filters, *IEEE MTT-S Int. Microwave Symp. Digest*, 1969, pp. 286–290.
49. R. Levy, Tapered corrugated waveguide low-pass filters, *IEEE Trans. Microwave Theory Tech.* **MTT-21**:526–532 (1973).
50. G. F. Craven and C. K. Mok, The design of evanescent mode waveguide bandpass filters for a prescribed insertion loss characteristics, *IEEE Trans. Microwave Theory Tech.* **MTT-19**:295–308 (1971).
51. R. V. Snyder, New application of evanescent mode waveguide to filter design, *IEEE Trans. Microwave Theory Tech.* **MTT-25**:1013–1021 (1977).
52. J. Bornemann and F. Arndt, Transverse resonance, standing wave, and resonator formulations of the ridge waveguide eigenvalue problem and its application to the design of E-plane finned waveguide filters, *IEEE Trans. Microwave Theory Tech.* **MTT-38**:1104–1113 (1990).
53. R. E. Collin, *Foundations for Microwave Engineering*, McGraw-Hill, New York, 1992.
54. N. Marcuvitz, *Waveguide Handbook*, Dover, New York, 1965.
55. A. Weisshaar, M. Mongiardo, and V. Tripathi, Full-wave computer-aided design of waveguide components by circuit simulation, *Int. J. RF Microwave Comput. Aided Eng.* **8**:236–247 (1998).
56. W. K. Gwarek, Analysis of an arbitrarily shaped planar circuit—a time domain approach, *IEEE Trans. Microwave Theory Tech.* **MTT-33**:1067–1072 (1985).
57. R. L. Ferrari, Finite element analysis of three-dimensional electromagnetic devices, *Proc. 15th European Microwave Conf.*, Paris, France, 1985, pp. 1064–1069.
58. W. J. R. Hofer, The transmission-line matrix method: Theory and applications, *IEEE Trans. Microwave Theory Tech.* **MTT-23**:882–893 (1985).
59. P. Clarricoats et al., Numerical solution of waveguide discontinuity problems, *IEE Proc.* **114**:878–886 (1967).
60. T. Vasilyeva et al., Computer-aided analysis of slant dielectric E-plane interface discontinuity in a rectangular waveguide, *Int. J. RF Microwave Comput. Aided Eng.* **8**:248–255 (1998).
61. F. Alessandri et al., Efficient full-wave automated design and yield analysis of waveguide components, *Int. J. RF Microwave Comput. Aided Eng.* **8**:200–207 (1998).
62. G. Matthaei, L. Young, and E. M. T. Jones, *Microwave Filters, Impedance-Matching Networks, and Coupling Structures*, Artech House, Dedham, MA, 1980.
63. G. L. Ragan, *Microwave Transmission Circuits*, Radiation Laboratory Series 9, Boston Tech., Lexington, MA, 1964.

64. J. H. Bryant, Coaxial transmission lines, related two-conductor transmission lines, connectors, and components: A U.S historical perspective, *IEEE Trans. Microwave Theory Tech.* **MTT-32**:970–983 (1984).
65. B. Bhat and S. K. Koul, *Stripline-Like Transmission Lines for Microwave Integrated Circuits*, Wiley, New York, 1989, pp. 566–687.
66. S. B. Cohn, Characteristic impedance of the shielded strip transmission line, *IEEE Trans. Microwave Theory Tech.* **MTT-2**:52–57 (1954).
67. B. E. Spielman, Dissipation loss effects in isolated and coupled transmission lines, *IEEE Trans. Microwave Theory Tech.* **MTT-25**:648–656 (1977).
68. R. Levy and L. F. Lind, Synthesis of symmetrical branch guide directional couplers, *IEEE Trans. Microwave Theory Tech.* **MTT-16**:80–89 (1968).
69. J. K. Shimizu and E. M. T. Jones, Coupled transmission line directional couplers, *IEEE Trans. Microwave Theory Tech.* **MTT-6**:403–410 (1958).
70. C. Y. Pon, Hybrid ring directional coupler for arbitrary power divisions, *IEEE Trans. Microwave Theory Tech.* **MTT-9**:529–535 (1961).
71. E. J. Wilkinson, An N-way hybrid power divider, *IEEE Trans. Microwave Theory Tech.* **MTT-8**:116–118 (1960).
72. S. B. Cohn, Parallel-coupled transmission line resonator filters, *IEEE Trans. Microwave Theory Tech.* **MTT-6**:223–231 (1958).
73. R. V. Garver, Diode switching, *Microwave Syst. News* **13**:194–204 (1983).
74. J. F. White, Diode phase shifters for array antennas, *IEEE Trans. Microwave Theory Tech.* **MTT-22**:658–674 (1974).
75. M. V. Schneider, Microstrip lines for microwave integrated circuits, *Bell Syst. Tech. J.* **48**:1421–1444 (1969).
76. R. K. Hoffmann, *Handbook of Microwave Integrated Circuits*, Artech House, Norwood, MA, 1987.
77. K. C. Gupta, Emerging trends in millimeter-wave CAD, *IEEE Trans. Microwave Theory Tech.* **46**:747–755 (1998).
78. G. Gonzales, *Microwave Transistor Amplifiers Analysis and Design*, 2nd ed., Prentice-Hall, Upper Saddle River, NJ, 1997.
79. A. Sweet, *MIC and MMIC Amplifier and Oscillator Circuit Design*, Artech House, Dedham, MA, 1990.
80. F. Filicori, V. A. Monaco, and G. Vannini, A design method for parallel feedback dielectric resonator oscillators, *Proc. 19th European Microwave Conf.*, London, 1989, pp. 412–417.
81. C. Y. Chang and T. Itoh, A varactor-tuned active microwave band-pass filter, *IEEE MTT-S Int. Microwave Symp.*, 1990, pp. 499–502.
82. J. A. Coekin, *High-Speed Pulse Techniques*, Pergamon, Oxford, UK, 1975.
83. I. D. Robertson, *MMIC Design*, Inst. Electr. Eng., London, 1995.
84. C. P. Wen, Coplanar waveguide: A surface strip transmission line suitable for non-reciprocal gyromagnetic device application, *IEEE Trans. Microwave Theory Tech.* **MTT-17**:1087–1090 (1969).
85. J. B. Knorr and K. D. Kuchler, Analysis of coupled slots and coplanar strips on dielectric substrate, *IEEE Trans. Microwave Theory Tech.* **MTT-23**:541–548 (1975).
86. R. W. Jackson, Considerations in the use of coplanar waveguide for millimeter-wave integrated circuits, *IEEE Trans. Microwave Theory Tech.* **MTT-34**:1450–1456 (1986).
87. A. Wexler, Solution of waveguide discontinuities by modal analysis, *IEEE Trans. Microwave Theory Tech.* **MTT-15**:508–517 (1967).
88. M. Naghed and I. Wolff, A three-dimensional finite-difference calculation of equivalent capacitors of coplanar waveguide discontinuities, *IEEE MTT-S Int. Microwave Symp.*, 1990, pp. 1143–1146.
89. T. W. Huang and T. Itoh, Full-wave analysis of cascaded junction discontinuities of shielded coplanar type transmission lines considering the finite metallization thickness effect, *IEEE MTT-S Int. Microwave Symp.*, 1992, pp. 995–998.
90. H. Jin and R. Vahldieck, Full-wave analysis of coplanar waveguide discontinuities using the frequency domain TLM method, *IEEE Trans. Microwave Theory Tech.* **41**:1538–1542 (1993).
91. R. W. Jackson, Mode conversion at discontinuities in finite-width conductor-backed coplanar waveguide, *IEEE Trans. Microwave Theory Tech.* **37**:1582–1589 (1989).
92. S. B. Worm, Full-wave analysis of discontinuities in planar waveguides by the method of lines using a source approach, *IEEE Trans. Microwave Theory Tech.* **MTT-38**:1510–1514 (1990).
93. F. Mernyei, I. Aoki, and H. Matsuura, MMIC bandpass filter using parallel coupled CPW lines, *Electron. Lett.* **30**:1862–1863 (1983).
94. D. F. Williams and S. E. Schwarz, Design and performance of coplanar waveguide bandpass filters, *IEEE Trans. Microwave Theory Tech.* **MTT-31**:558–566 (1983).
95. W. Schwab, F. Boegelsack, and W. Menzel, Multilayer suspended stripline and coplanar line filters, *IEEE Trans. Microwave Theory Tech.* **MTT-42**:1403–1407 (1994).
96. C.-H. Ho, L. Fan, and K. Chang, Broad-band uniplanar hybrid-ring and branch-line couplers, *IEEE Trans. Microwave Theory Tech.* **MTT-41**:2116–2125 (1993).
97. P. Troughten, High Q-factor resonator in microstrip, *Electron. Lett.* **4**:520–522 (1968).
98. C.-H. Ho, L. Fan, and K. Chang, Slotline annular ring elements and their applications to resonator, filter and coupler design, *IEEE Trans. Microwave Theory Tech.* **MTT-41**:1648–1653 (1993).
99. K. Chang et al., On the study of microstrip ring and varactor-turned ring circuits, *IEEE Trans. Microwave Theory Tech.* **MTT-35**:1288–1295 (1987).
100. J. A. Navarro, L. Fan, and K. Chang, The coplanar waveguide-fed electronically tunable slotline ring resonator, *IEEE MTT-S Int. Microwave Symp.*, 1992, pp. 951–954.
101. J. K. Hunton, A microwave integrated circuit balanced mixer with broad-bandwidth, *Proc. Microelectronics Symp.*, 1969, pp. A3.1–A3.2.
102. V. Radisic, V. Jevremovic, and Z. B. Popovic, CPW oscillator configuration for an electrooptic modulator, *IEEE Trans. Microwave Theory Tech.* **41**:1645–1647 (1993).
103. K. Minot, B. Nelson, and W. Jones, A low noise, phase linear distributed coplanar waveguide amplifier, *IEEE Trans. Microwave Theory Tech.* **41**:1650–1653 (1993).
104. L. Fan and K. Chang, Uniplanar power dividers using coupled CPW and asymmetrical CPS for MICs and MMICs, *IEEE Trans. Microwave Theory Tech.* **44**:2411–2420 (1996).
105. L. Giauffret, J.-M. Laheurte, and A. Papiernik, Study of various shapes of the coupling slot in CPW-fed microstrip antennas, *IEEE Trans. Anten. Propag. Soc.* **45**:642–647 (1997).
106. V. Trifunovic and B. Jokanovic, Review of printed Marchand and double Y baluns: Characteristics and application,

- IEEE Trans. Microwave Theory Tech.* **MTT-42**:1454–1462 (1994).
107. G. Forma and J. M. Laheurte, CPW-fed oscillating microstrip antennas, *IEEE Antennas Propag. Soc. Int. Symp.*, 1996, pp. 526–529.
 108. I. Kneppo and J. Fabian, *Microwave Integrated Circuits*, Chapman & Hall, London, 1994.
 109. R. S. Pengelly, *Microwave Field Effect Transistors: Theory, Design and Applications*, Research Studies Press, London, 1986.
 110. P. H. Ladbrooke, *MMIC Design GaAs FETs and HEMTs*, Artech House, London, 1989.
 111. F. Grover, *Inductance Calculations*, Van Nostrand, Princeton, NJ, 1946, reprinted by Dover, New York, 1962.
 112. F. J. Schumckle, The method of lines for the analysis of rectangular spiral inductors. *IEEE Trans. Microwave Theory Tech.* **MTT-41**:1183–1186 (1993).
 113. H. M. Greenhouse, Design of planar rectangular microelectronic inductors, *IEEE Trans. Parts Hybrids Pack.* **PHP-10**:101–109 (1974).
 114. F. H. Terman, *Radio Engineer Handbook*, McGraw-Hill, New York, 1943.
 115. M. Caulton and H. Sobol, Microwave integrated-circuit technology—a survey, *IEEE J. Solid-State Circ.* **SC-5**:292–303 (1970).
 116. G. D. Alley, Interdigital capacitors and their application to lumped-element microwave integrated circuits, *IEEE Trans. Microwave Theory Tech.* **MTT-18**:1028–1033 (1970).
 117. C. S. Aitchison et al., Lumped-circuit elements at microwave frequencies, *IEEE Trans. Microwave Theory Tech.* **MTT-19**:928–937 (1971).
 118. L. Young and H. Sobol, eds., *Advance in Microwaves*, Vol. 8, Academic Press, New York, 1974, pp. 158–159.
 119. S. A. Jamison et al., Inductively coupled push-pull amplifier for low cost monolithics microwave ICs, *IEEE GaAs IC Symp. Digest*, 1982, pp. 91–93.
 120. D. Ferguson et al., Transformer coupled high-density circuit technique for MMIC, *IEEE Microwave Millimeter-Wave Monolithic Circuits Symp. Digest*, 1984, pp. 34–36.
 121. L. Wiemer et al., Computer simulation and experimental investigation of square spiral transformers for MMIC applications, *IEE Colloq. Comput.-Aided Des. Microwave Circuits, Digest 99*, 1985, pp. V1-5.
 122. W. Menzel et al., Compact multilayer filter structures for coplanar MMIC's, *IEEE Microwave Guide Wave Lett.* **2**:497–498 (1992).
 123. W. Schwab and W. Menzel, On the design of planar microwave components using multilayer structures, *IEEE Trans. Microwave Theory Tech.* **MTT-40**:67–71 (1992).
 124. M. Engles and R. H. Jansen, Design of quasi-ideal couplers using multilayer MMIC technology, *IEEE MTT-S Int. Microwave Symp.*, 1996, pp. 1181–1184.
 125. C. Person et al., Wideband 3 dB/90° coupler in multilayer thick-film technology, *Electron. Lett.* **31**:812–813 (1995).
 126. F. Mernyei, I. Aoki, and H. Matsuura, A novel MMIC coupler—measured and simulated data, *IEEE MTT-S Int. Microwave Symp.*, 1994, pp. 229–232.
 127. S. Banba and H. Ogawa, Multilayer MMIC directional couplers using thin dielectric layers, *IEEE Trans. Microwave Theory Tech.* **MTT-43**:1270–1275 (1995).
 128. P. J. Zabinski et al., Example of a mixed-signal global positioning system (GPS) receiver using MCM-L packaging, *IEEE Trans. Compon. Pack. Manuf. Technol. Part B CPMT-18:13–17 (1995).*
 129. R. G. Arnold and D. J. Pedder, Microwave characterization of microstrip lines and spiral inductors in MCM-D technology, *IEEE Trans. Compon. Hybrids Manuf. Technol.* **CHMT-15**:1038–1045 (1992).
 130. M. Engels and R. H. Jansen, Modeling and design of novel passive MMIC components with three and more conductor levels, *IEEE MTT-S Int. Microwave Symp.*, San Diego, CA, 1994, pp. 1293–1296.
 131. T. Tokumitsu et al., Three-dimensional MMIC technology for multifunction integration and its possible application to masterslice MMIC, *IEEE Microwave Millimeter-wave Monolithic Circuits Symp.*, 1996, pp. 85–88.
 132. R. G. Arnold and D. J. Pedder, Microwave components in multichip module (MCM-D) technology, *Proc., Microwave RF*, Wembley, London, 1994, pp. 195–199.
 133. C. Cho and K. C. Gupta, Design methodology for multilayer coupled line filters, *IEEE MTT-S Int. Microwave Symp.*, Denver, CO, 1997, pp. 785–788.
 134. A. M. Pavio and A. Kikel, A monolithic or hybrid broadband compensated balun, *IEEE MTT-S Int. Microwave Symp.*, 1990, pp. 483–486.
 135. M. Davidovitz, A compact planar magic-T junction with aperture-coupled difference port, *IEEE Microwave Guided Wave Lett.* **7**:217–218 (1997).
 136. C. M. Tsai and K. C. Gupta, A generalized model for coupled lines and its applications to two-layer planar circuits, *IEEE Trans. Microwave Theory Tech.* **MTT-40**:2190–2198 (1992).
 137. C. M. Tsai and K. C. Gupta, CAD procedures for planar re-entrant type couplers and three-line baluns, *IEEE MTT-S Int. Microwave Symp.*, 1993, pp. 1013–1016.
 138. M. Tran and C. Nguyen, Modified broadside-coupled microstrip lines suitable for MIC and MMIC applications and a new class of broadside-coupled band-pass filters, *IEEE Trans. Microwave Theory Tech.* **41**:1336–1342 (1993).
 139. C. Cho and K. C. Gupta, A new design procedure for single-layer and two-layer 3-line baluns, *IEEE MTT-S Int. Microwave Symp.*, Baltimore, MD, 1998, pp. 777–780.
 140. C.-Y. Lee and T. Itoh, Full-wave analysis and design of a new double-sided branch-line coupler and its complementary structure, *IEEE Trans. Microwave Theory Tech.* **MTT-43**:1895–1901 (1995).
 141. M. Engels et al., Design methodology, measurement and application of MMIC transmission line transformers, *IEEE MTT-S Int. Symp.*, Orlando, FL, 1995, pp. 1635–1638.
 142. N. Herscovici and D. M. Pozar, Full-wave analysis of aperture-coupled microstrip lines, *IEEE Trans. Microwave Theory Tech.* **MTT-39**:1108–1114 (1991).
 143. P. R. Haddad and D. M. Pozar, Analysis of two aperture-coupled cavity-backed antennas, *IEEE Trans. Anten. Propag.* **AP-45**:1717–1726 (1997).
 144. K. C. Gupta, R. Garg, and R. Chadha, *CAD of Microwave Circuits*, Artech House, Dedham, MA, 1981.
 145. J. A. Dobrowolski, *Introduction to Computer Methods for Microwave Circuit Analysis and Design*, Artech House, Norwood, MA, 1991.
 146. J. A. Dobrowolski, *Computer-Aided Analysis, Modeling, and Design of Microwave Networks: The Wave Approach*, Artech House, Norwood, MA, 1996.
 147. M. Hirano, Three-dimensional passive circuit technology for ultra compact MMICs, *IEEE Trans. Microwave Theory Tech.* **MTT-43**:2845–2849 (1995).

148. I. Toyoda et al., Three-dimensional masterslice MMIC on Si substrate, *IEEE Trans. Microwave Theory Tech.* **MTT-45**:2524–2530 (1997).
149. J. A. Navarro and K. Chang, *Integrated Active Antennas and Spatial Power Combining*, Wiley, New York, 1996.
150. R. A. York and Z. B. Popovic, *Active and Quasi-Optical Arrays for Solid State Power Combining*, Wiley, New York, 1997.
151. P. M. Watson and K. C. Gupta, Design and optimization of CPW circuits using EM-ANN model for CPW components, *IEEE Trans. Microwave Theory Tech.* **MTT-45**:2515–2523 (1997).

MICROWAVE DETECTORS

RONALD E. HAM
Consultant

Microwave energy cannot be efficiently detected with equipment used for lower-frequency applications. Microwave-frequency voltage changes are too rapid to be captured on any but the fastest sampling oscilloscopes, and response time and parasitics of common test meters render them useless. Microwave detectors generally measure power in the controlled impedance environments afforded by transmission lines and waveguides. The system impedance is known, so voltage and current magnitudes can be derived. With the judicious application of other microwave components such as power splitters and quadrature couplers, phase information can be extracted from multiple power measurements; therefore, full characterization of a system or component is possible with only the microwave detector to convert microwave signal characteristics to the readily observable and measurable quantities of low-frequency voltages and currents.

Microwave detectors sense the amplitude or power of a signal, or the change in the amplitude or power of a signal. They are used for the determination of signal power level and for recovery of information placed upon the microwave signal amplitude. The microwave detector circuit (Fig. 1) consists of a matching circuit to match the impedance of the circuit being measured to the impedance of the detector itself, along with an output signal conditioning circuit to convert the detector output to a voltage or current that is proportional to the microwave signal input. Ideally, the detector impedance directly matches the system impedance, and the matching circuit is not required.

Microwave detectors can be separated into two categories: thermally dependent detectors and diode detectors.

Thermally dependent detectors absorb the incident microwave signal in a detector element, and the microwave energy is converted into heat energy. The increase in temperature of the detector element is directly detected, or a change in a physical parameter of the detector element due to the change in temperature, normally resistance, is detected. The diode detector rectifies the microwave signal, clipping either the positive or negative voltage of the alternating voltage waveform, and averages the resultant monopolar signal in a capacitive circuit to produce a DC signal with an amplitude related to the microwave signal amplitude.

The response time of the thermally dependent detector is a function of the thermal mass being heated by the incident energy and the thermal resistance of the detector to its surrounding environment. In general, the response time of a thermally dependent detector is slow compared to the response time of a diode detector and is on the order of milliseconds to seconds. Thermally dependent detectors are used primarily for the measurement of the power level of steady-state signals or to measure the average value of the power of a time-varying signal such as a pulsed radar transmitter output.

The response time of a diode detector can be within a few periods of the microwave signal being detected; hence, diode detectors can recover information placed in amplitude variations on a signal in addition to measuring the power of steady-state signals.

Small-signal thermally dependent detectors with a bandwidth of less than 100 Hz typically operate over a power range of +10 dBm to about –50 dBm, while diodes limited to the same bandwidth are useful from about +10 dBm to less than –80 dBm. Insertion of attenuators or couplers between the power source and the detector facilitates measuring much higher powers; however, measurement of very small amounts of power generally necessitates insertion of amplifiers or frequency conversion to lower frequencies where more sensitive techniques can be used to detect the signal.

1. THERMALLY DEPENDENT DETECTORS

Thermally dependent detectors depend on the heating of the detector element by the incident microwave energy. The heating is proportional to the electrical energy dissipated in the detector element. Bolometers and thermocouples are typical of thermally dependent microwave detectors. Because absorption of the available power in the incident signal depends on a proper impedance match between the transmission media and the absorbing detector circuit, the detector must have a well-established and controlled impedance.

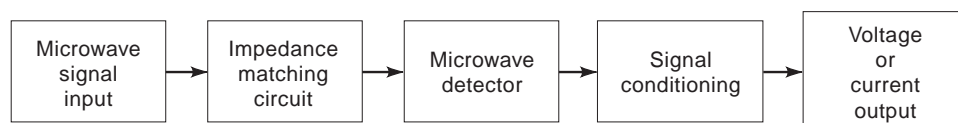


Figure 1. The impedance of the microwave detector should be matched to the impedance of the system being measured.

148. I. Toyoda et al., Three-dimensional masterslice MMIC on Si substrate, *IEEE Trans. Microwave Theory Tech.* **MTT-45**:2524–2530 (1997).
149. J. A. Navarro and K. Chang, *Integrated Active Antennas and Spatial Power Combining*, Wiley, New York, 1996.
150. R. A. York and Z. B. Popovic, *Active and Quasi-Optical Arrays for Solid State Power Combining*, Wiley, New York, 1997.
151. P. M. Watson and K. C. Gupta, Design and optimization of CPW circuits using EM-ANN model for CPW components, *IEEE Trans. Microwave Theory Tech.* **MTT-45**:2515–2523 (1997).

MICROWAVE DETECTORS

RONALD E. HAM
Consultant

Microwave energy cannot be efficiently detected with equipment used for lower-frequency applications. Microwave-frequency voltage changes are too rapid to be captured on any but the fastest sampling oscilloscopes, and response time and parasitics of common test meters render them useless. Microwave detectors generally measure power in the controlled impedance environments afforded by transmission lines and waveguides. The system impedance is known, so voltage and current magnitudes can be derived. With the judicious application of other microwave components such as power splitters and quadrature couplers, phase information can be extracted from multiple power measurements; therefore, full characterization of a system or component is possible with only the microwave detector to convert microwave signal characteristics to the readily observable and measurable quantities of low-frequency voltages and currents.

Microwave detectors sense the amplitude or power of a signal, or the change in the amplitude or power of a signal. They are used for the determination of signal power level and for recovery of information placed upon the microwave signal amplitude. The microwave detector circuit (Fig. 1) consists of a matching circuit to match the impedance of the circuit being measured to the impedance of the detector itself, along with an output signal conditioning circuit to convert the detector output to a voltage or current that is proportional to the microwave signal input. Ideally, the detector impedance directly matches the system impedance, and the matching circuit is not required.

Microwave detectors can be separated into two categories: thermally dependent detectors and diode detectors.

Thermally dependent detectors absorb the incident microwave signal in a detector element, and the microwave energy is converted into heat energy. The increase in temperature of the detector element is directly detected, or a change in a physical parameter of the detector element due to the change in temperature, normally resistance, is detected. The diode detector rectifies the microwave signal, clipping either the positive or negative voltage of the alternating voltage waveform, and averages the resultant monopolar signal in a capacitive circuit to produce a DC signal with an amplitude related to the microwave signal amplitude.

The response time of the thermally dependent detector is a function of the thermal mass being heated by the incident energy and the thermal resistance of the detector to its surrounding environment. In general, the response time of a thermally dependent detector is slow compared to the response time of a diode detector and is on the order of milliseconds to seconds. Thermally dependent detectors are used primarily for the measurement of the power level of steady-state signals or to measure the average value of the power of a time-varying signal such as a pulsed radar transmitter output.

The response time of a diode detector can be within a few periods of the microwave signal being detected; hence, diode detectors can recover information placed in amplitude variations on a signal in addition to measuring the power of steady-state signals.

Small-signal thermally dependent detectors with a bandwidth of less than 100 Hz typically operate over a power range of +10 dBm to about –50 dBm, while diodes limited to the same bandwidth are useful from about +10 dBm to less than –80 dBm. Insertion of attenuators or couplers between the power source and the detector facilitates measuring much higher powers; however, measurement of very small amounts of power generally necessitates insertion of amplifiers or frequency conversion to lower frequencies where more sensitive techniques can be used to detect the signal.

1. THERMALLY DEPENDENT DETECTORS

Thermally dependent detectors depend on the heating of the detector element by the incident microwave energy. The heating is proportional to the electrical energy dissipated in the detector element. Bolometers and thermocouples are typical of thermally dependent microwave detectors. Because absorption of the available power in the incident signal depends on a proper impedance match between the transmission media and the absorbing detector circuit, the detector must have a well-established and controlled impedance.

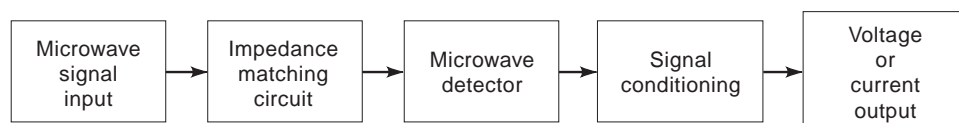


Figure 1. The impedance of the microwave detector should be matched to the impedance of the system being measured.

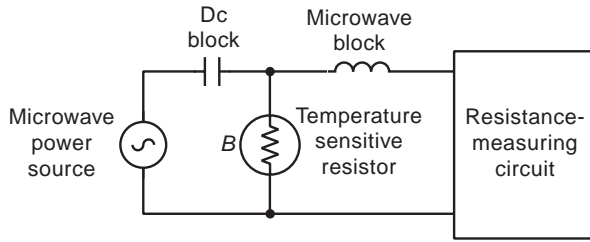


Figure 2. The bolometer *B* is a temperature-sensitive resistor.

The bolometer detects electromagnetic radiation by converting the energy in the transmission media to heat. It is placed across transmission line terminals, as shown in Fig. 2, or in the electric field of a waveguide. The nominal resistivity of the bolometer should be equal to the impedance of the transmission line or waveguide at the point of measurement, or the transmission media impedance should be matched to that of the bolometer. One method of making a detector that matches a 50 Ω coaxial system impedance while maintaining a relatively large 200 Ω DC resistance is to place two 100-Ω resistive elements in parallel for the microwave measurement but in series for the dc measurement, as shown in Fig. 3. Under matched conditions all the incident energy is dissipated and appears as heat in the bolometer. The change in the bolometer element resistivity is measured and equated to the magnitude of the incident electromagnetic radiation.

A significant change in the resistivity of a bolometer as power is absorbed can result in an impedance mismatch to the circuit being measured. This can result in unacceptable errors. A measurement circuit usually facilitates a method for accommodating the change in a bolometer element resistivity with the change in incident power. The most common is to use a power substitution technique. A bias current is passed through the bolometer as shown in Fig. 4. The bias current feeds more bias power to the element than the microwave energy that is to be measured. The bolometer element is designed to have an impedance equal to the characteristic impedance of the system being measured while the bias is at the quiescent level with no applied microwave energy. The resistance of the bolometer element becomes part of the resistive bridge. As microwave power is fed to the detector, its resistance changes;

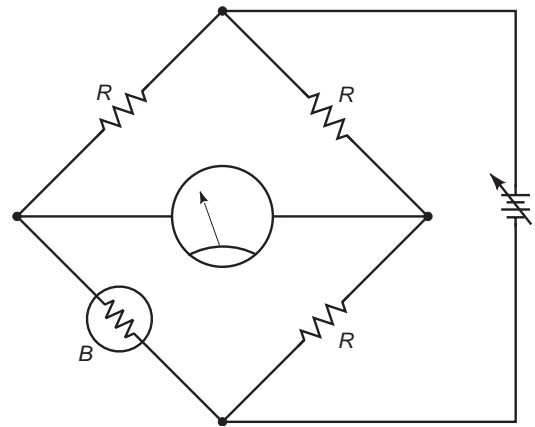


Figure 4. A bridge circuit is used to detect change in the bolometer resistance.

however, the bias power to the circuit must be reduced to balance the bridge. The reduction in bias power to the bolometer is equal to the applied microwave power; therefore, the external circuit measures this change in power, and the detector impedance remains matched to the system being measured. Numerous schemes for automatically balancing the bridge and deriving the change in bias power are used.

Bolometers are, by definition, temperature-sensitive. The more sensitive a bolometer detector is to incident microwave power, the more sensitive it will be to small ambient temperature variations; therefore, temperature compensation is virtually imperative for low-level power measurements. This is accomplished as shown in Fig. 5 by mounting two identical bolometer sets in the same detector package so that the thermal resistance path from each element is to the same heat sink. This forces changes in ambient temperature to cause identical temperature variations in both elements. Only one of the bolometer sets has microwave power applied. By effectively connecting the bolometers in a differential circuit, the common mode variations, introduced by ambient environmental temperature variations through the thermal resistance paths, are canceled.

The bolometer measures the power absorbed in its resistance. In many microwave circuits, unlike those at lower frequencies, current and voltage have little meaning because of the difficulty of their measurement. It is common in microwave applications to make power measurements in a controlled impedance environment; hence, the same circuit information is obtained but with different types of measurement.

A barretter is one form of bolometer. It is a small wire that increases its resistance because of the resultant heating when a microwave signal potential is placed across the ends of the wire. The wire is usually either platinum or tungsten. The response characteristic of a barretter is nominally

$$R - R_0 = JP^n \tag{1}$$

where R_0 is the room temperature resistance of the wire, R is the resistance of the wire with the power P being dissipated, and J and n are constants.

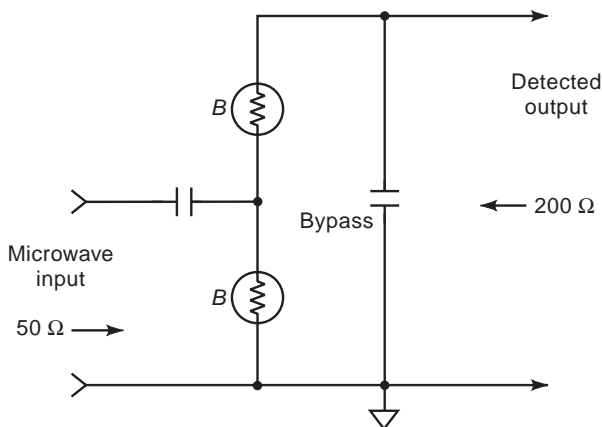


Figure 3. Using two bolometers increases detection sensitivity.

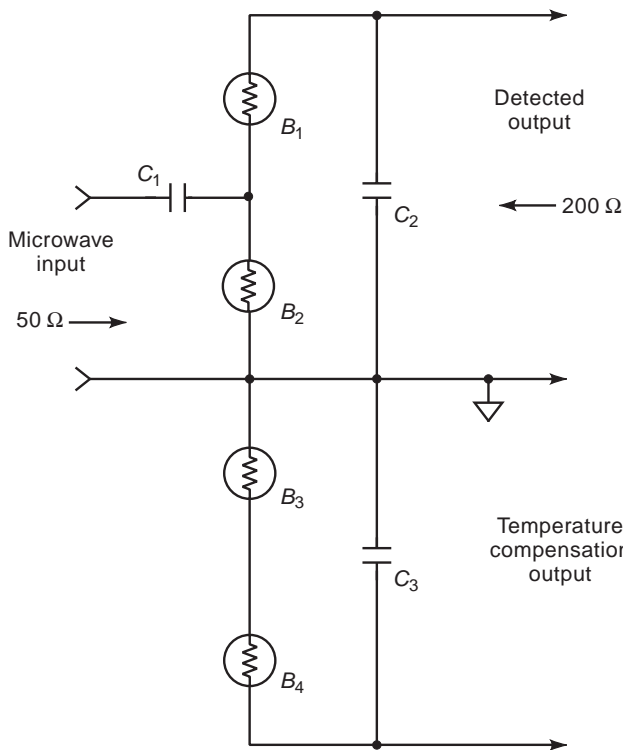


Figure 5. Bolometer set B_1, B_2 are detectors, and set B_3, B_4 are for temperature compensation.

For a specific commercial barretter intended for low-power measurements, $R_0 = 155 \Omega$, $n = 0.9$, and $J = 7.57$. The power sensitivity S is found by differentiating the resistance with respect to the absorbed power giving

$$S = \frac{dR}{dP} = \frac{n(R - R_0)}{P} \quad (2)$$

This unit has a recommended operating point of $R_{op} = 200 \Omega$ at an applied power of $P_{mW} = 15 \text{ mW}$, which is achieved at a bias current of 8.7 mA. Substituting this into the equation yields a sensitivity of 5 Ω/mW . The change e_{out} in the voltage across the unit with the applied power being much less than the bias power will be

$$e_{out} = \sqrt{\frac{P_{bias}}{R_{op}}} \cdot S \cdot P_{mW} \quad (3)$$

Applying 1 μW of power to this detector produces an output voltage of 44 μV . The kTB thermal noise in a 100 Hz bandwidth at the terminals of the unit is about $2.5 \times 10^{-8} \text{ V}$. This indicates that the smallest microwave signal that can be detected in the presence of the noise in the 100 Hz bandwidth is around 10 nW or -50 dBm . This is typical of low-power bolometers.

The thermistor is another form of bolometer. The thermistor consists of a small amount of resistive material with a high temperature sensitivity placed between two connecting wires as shown in Fig. 6. Typically, the material is a semiconductor with a large negative temperature coefficient of resistance; that is, the resistivity of the

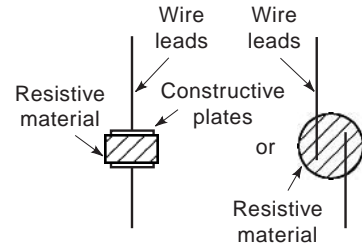


Figure 6. A thermistor is a resistor with a high temperature sensitivity.

material decreases with an increase in temperature. Placing a microwave signal potential across the thermistor results in a current that heats the temperature-sensitive material. With the semiconductor thermistor, this results in a reduction in the resistance between the terminals. The thermistor is used in the same bias substitution circuits as the bolometer with changes to allow for the negative change in resistance with increase in applied power. Because the magnitude of the negative temperature coefficient of the thermistor is typically much greater than the positive temperature coefficient of the barretter, the thermistor tends to be more sensitive than the barretter; however, the large volume of the thermistor leads to a larger thermal time constant, making its time response slower than that of the barretter.

Other variations in the construction of bolometers are possible, such as the deposition of thin metal resistive films on insulating substrates. These implementations readily lend themselves to varied microwave construction techniques such as monolithic and thin-film integrated circuits, stripline, slotline, coplanar waveguide, and microstrip. Note that such construction also facilitates thermal isolation, cooling, and miniaturization for sensitive millimeter-wave through infrared operation.

A thermocouple is formed by intimately joining two dissimilar pieces of wire, such as copper and constantan. A potential difference appears across the junction related to the temperature. Microwave energy can be detected by using the thermocouple to measure the change in temperature of a resistor that terminates the microwave circuit as shown in Fig. 7. Another method, resulting in a better form factor for microwave measurement, places a carbon resistor between the two dissimilar wires as in Fig. 8. This results in a smaller thermal mass and a resultant faster response time. In both examples, a standard thermocouple measurement system with a reference cold junction is required. Calibration of power into the detector as a function of thermocouple temperature must be experimentally derived.

Other calorimetric methods can be used for large-signal levels. For example, water pumped through an incident microwave energy-to-heat converter (a calorimetric load) increases in temperature. The energy required to change the temperature of the water is the energy in the incident microwave signal. This is illustrated in Fig. 9 and is a common method for measuring the average power output from large radar transmitters.

The ratio of the maximum power detected to the minimum detectable power with the thermal detector is

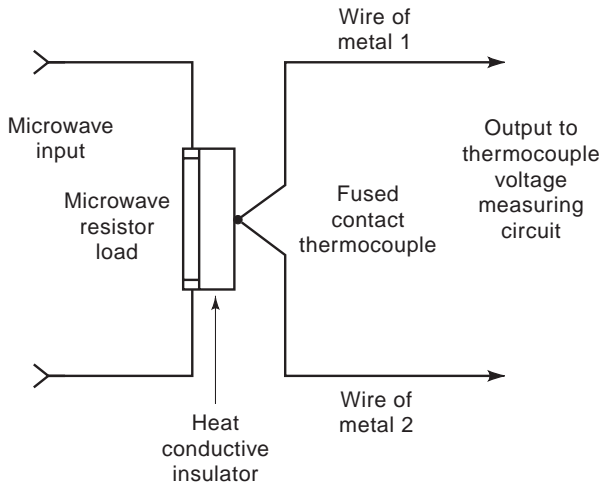


Figure 7. Microwave power is absorbed in the resistor, and the temperature increase is measured by the thermocouple.

relatively small; however, this is compensated for by measurement accuracy and repeatability. The time response of the thermal detector is a function of the thermal time response of the energy absorbing mass; therefore, barretters typically respond faster than a thermistor, and a thermistor is faster than a thermocouple. An advantage of the slowly responding detector is the ability to measure the average power of a pulsed signal, such as a radar.

Recent developments in temperature-dependent detectors is primarily focused in two areas. Increased miniaturization is intended to increase the frequency of operation up into the millimeter microwave range and to infrared. Arrays of these very small detectors can be used for imaging. There is also active research in cryogenic detectors because they produce less noise than heated detectors and hence yield improved small signal sensitivity.

2. DIODE DETECTORS

Semiconductor diode detectors respond rapidly to changes in the input signal. They rectify the voltage of the incident microwave signal, producing a direct current output that

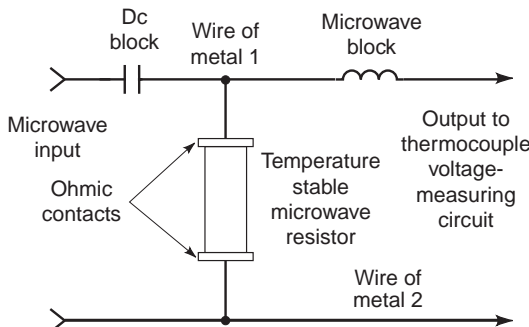


Figure 8. Direct series connection of the thermocouple to the resistor facilitates faster response because of the reduced thermal mass.

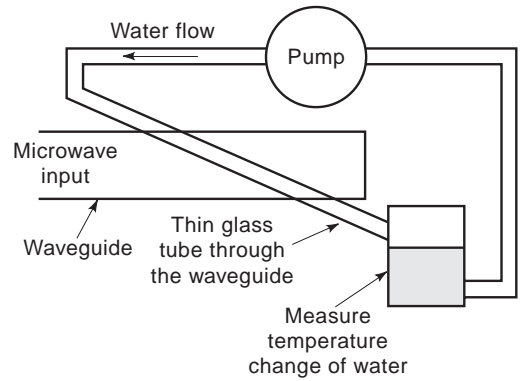


Figure 9. A water or calorimetric load can accurately measure large amounts of average power.

is related to the magnitude of the input. This process is illustrated in Fig. 10. The diode curve of current *I* through the diode versus the voltage *V* across the diode is roughly governed by the ideal diode equation

$$I = I_0(e^{qV/kT} - 1) \tag{4}$$

where

*I*₀ = is the diode leakage current with a reverse voltage applied

q = is the charge of an electron (1.60 × 10⁻¹⁹ C)

k = is Boltzmann's constant (8.62 × 10⁻⁵ eV/K) and

T = is the temperature in degrees Kelvin (degrees centigrade + 273)

At room temperature, *kT/q* = 26 mV. By applying a voltage across the diode, a corresponding current is forced through the diode. Using the circuit in Fig. 11, the current

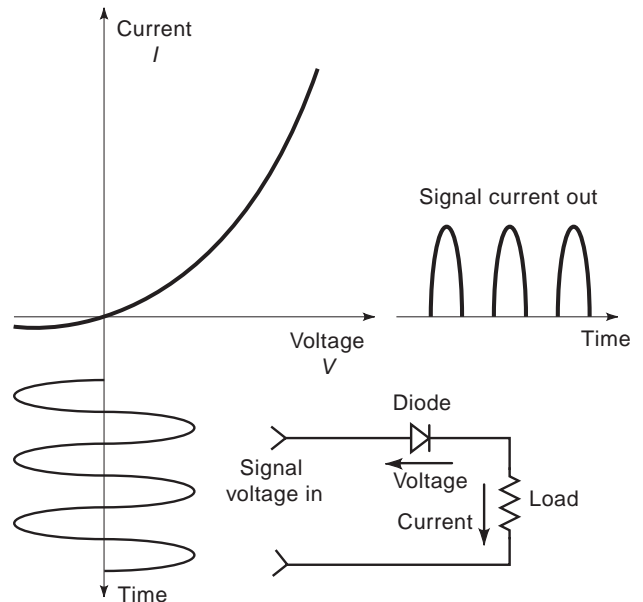


Figure 10. The diode detector rectifies the input signal.

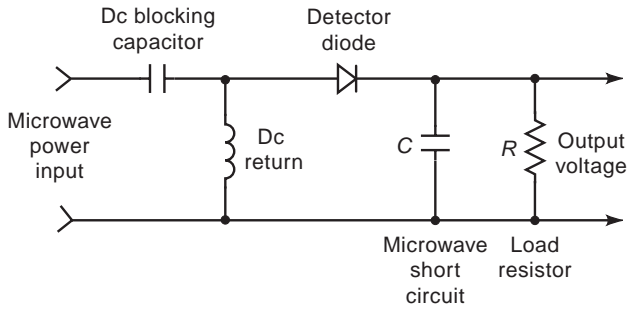


Figure 11. The rectified current through the series diode is averaged in the RC circuit to produce a DC or low-frequency output.

is averaged in a parallel resistor and capacitor to produce a DC output voltage that is related to the magnitude of the input voltage. Note that the microwave voltage component of the output voltage is shorted by the averaging capacitor. This AC short circuit also forces all of the applied high-frequency voltage to appear across the diode.

Two variations of the diode detector circuit are shown in Figs. 12 and 13. In the first, the applied voltage appears directly across the diode. On negative portions of the microwave cycle the voltage is shorted through the diode, resulting in a small negative voltage diode drop that is proportional to the current through the diode. On the positive portion of the cycle, all of the applied voltage appears across the diode. The RC circuit effectively integrates the voltage and produces a net positive output voltage that is proportional to the magnitude of the applied microwave signal. Figure 13 is a combination of the series and shunt connections. Each diode provides the necessary DC return path for the other, eliminating the necessity of the large biasing element.

Real semiconductor diode performance is more closely approximated by the equation

$$I = I_0(e^{qV/nkT} - 1) \tag{5}$$

where n is the ideality factor and is an indication of how close to ideal were the conditions under which the device was fabricated. It usually ranges from 1.0 to 1.06 for a silicon diode. The leakage current I_0 is a function of material, material doping, and various factors involved in the fabrication of the physical diode. The combination of all of these factors produces a distinct V - I curve for various

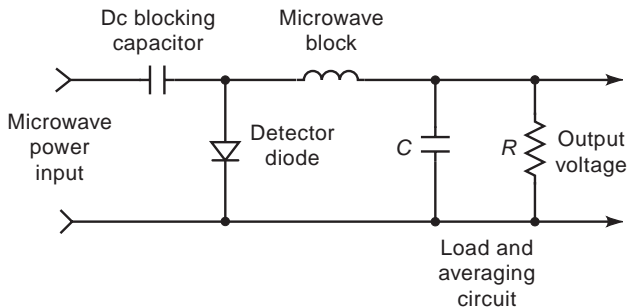


Figure 12. The rectified voltage waveform across the shunt diode is averaged in the RC circuit.

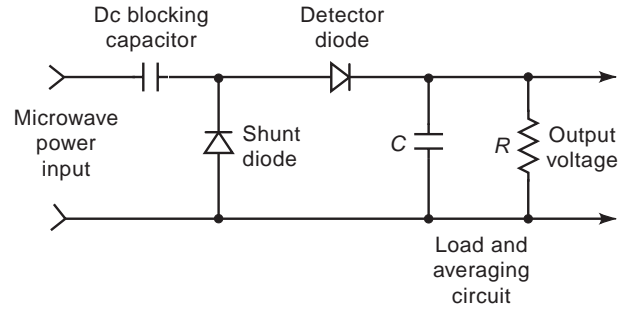


Figure 13. Combining the shunt and series diodes eliminates the inductors as the shunt diode provides the DC return path.

classes of diodes. The most significant physical parameter of these devices is the maximum voltage drop across the diode with a moderate amount of applied current. This is referred to as the *diode voltage*. For silicon pn junctions the diode voltage is nominally 0.7 V. For Germanium it is about 0.3 V. For metal semiconductor junctions, commonly called *Schottky barrier diodes*, the voltage drop can be tailored between nominally 0.2 and 0.6 V by material selection and processing technique variations.

The Schottky barrier is the most commonly used high-frequency detector diode because its relatively low forward voltage drop results in excellent sensitivity to small signals. It also can be switched from forward conduction to reverse isolation faster than a pn junction because there is no charge storage within the device due to diffusion capacitance. Figure 14 is a first-order equivalent circuit for a detector diode. The L , R , and C elements are commonly known as “parasitics.” The series resistance is primarily the bulk loss due to the substrate. The shunt capacitor across the diode proper is the junction capacitance and is a strong function of the diode area. The series inductance represents bondwires, beam leads, or any connections to the semiconductor die. The capacitor surrounding the circuit is plate capacitance between metallized areas and, for a packaged device, the packaging capacitance. Inserting the diode model into any of the diode detector circuits of Figs. 11–13, note that the parasitic capacitors can short out the diode at high frequencies. The smaller the parasitic capacitances, resistance, and inductance, the higher in frequency the diode detector can be made to operate.

Although the equations above roughly describe the transfer characteristic of the metal semiconductor diode, they do not properly define operation for very large input

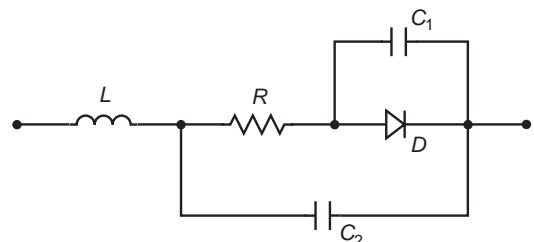


Figure 14. Parasitics limit the high-frequency performance of a diode detector.

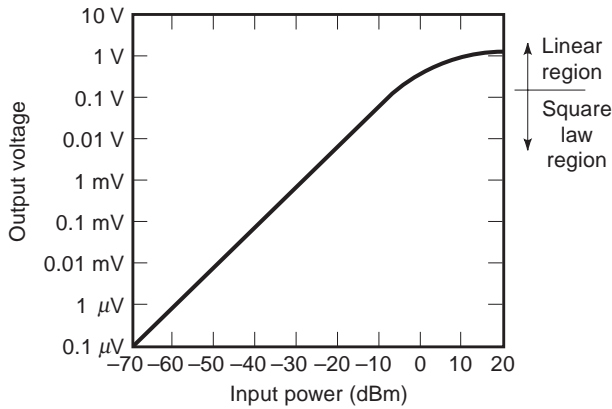


Figure 15. The diode detector follows a square law over most of its dynamic range.

signals. As shown in Fig. 15, the diode detector actually has two operating regions. From very low power until about 0 dBm input, the detector output voltage is proportional to the input power. This is the square-law region and is generally the desired region of operation. Further increasing the input results in an output proportional to the input voltage. This is the linear region.

Planar Schottky barrier diodes can be fabricated by evaporating a metal onto a wafer of doped semiconductor. Small dots or interdigitated patterns are photolithographically defined to establish the area and shape factor of the diodes to be made. The backside of the die is degenerately doped and metallized. Thermal activation of the metal semiconductor junctions results in a Schottky barrier diode on the topside and an ohmic contact on the backside of the semiconductor wafer.

The Schottky barrier diode, made by the deposition of thin metal films, represents an improvement in operational consistency and is a method of mass-producing a type of diode originally requiring considerable fabrication labor. The point contact diode, Fig. 16, was the first microwave metal semiconductor detector. It consists of a small die of semiconductor alloyed to a metal header to form an ohmic contact. A thin “cat whisker” of a stiff metal such as tungsten with a sharp point is brought into contact with the semiconductor. Although a thin layer of oxide contamination probably exists between the metal and the semiconductor, a rudimentary junction similar to a Mott diode is formed. The junction area is nominally increased or decreased by increasing or decreasing the pressure of the cat whisker on the semiconductor. Obviously, aging and

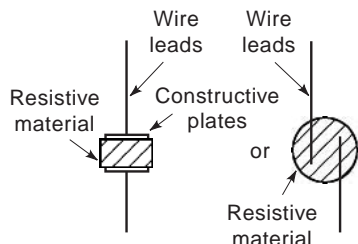


Figure 16. The point contact diode is a pressure contact between a stiff metal wire and a doped semiconductor die.

temperature cycling will change the junction characteristics, and vibration can be a definite hazard; however, there are many of these detectors, made in the early 1940s, still in service and doing an excellent job.

The diode parasitic capacitance is a function of the area of the junction; however, the power-handling capability is also a function of diode area. As the maximum useable frequency of a diode made with a particular fabrication process increases, the maximum power that can be fed to the diode decreases.

Diode detector sensitivity can, to some extent, be increased by supplying a small amount of DC bias current to the diode in addition to the microwave signal that is to be detected. This bias current moves the operating point to the right of the current axis and up the $I-V$ curve. Careful adjustment of this current can set the operating point at a region of maximum curvature, resulting in an increase in the output voltage from the detector for a given microwave power input; however, this does not necessarily indicate adjustment for maximum sensitivity because the diode generates $1/f$ noise due to the bias current. The increase in noise level from zero bias current kTB noise can exceed a factor of 10–1000 while significant amounts of the $1/f$ noise can extend well beyond 20 kHz. In general, maximum signal sensitivity with bias will occur somewhere between zero bias and the region of maximum curvature of the diode $I-V$ curve.

By heavily doping both sides of a pn junction, a diode producing a very small initial voltage drop is obtained. Carriers “tunnel” through the quantum mechanical potential barrier; hence, the diode, referencing Fig. 17, is called a *tunnel diode*. Although this diode, when used as a detector, can suffer from the same charge storage capacitance malady of other pn junctions, judicious matching of the diode area to the maximum applied power can result in a very sensitive zero-bias detector. As seen from the $I-V$ curve, if bias current is increased beyond the usable detector range, the impedance of the diode becomes negative. Biased in this region, the diode can be used as an oscillator or amplifier.

The ratio of the maximum power detectable to the minimum detectable power with the diode detector is

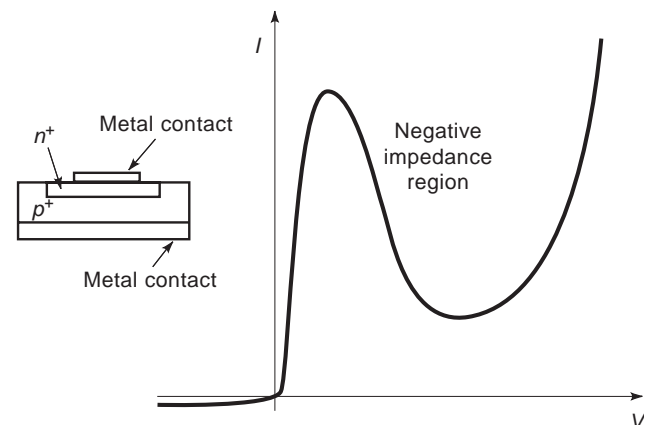


Figure 17. A tunnel diode is a highly doped pn junction with a very small low-current junction voltage.

relatively large; however, the difficulty of compensating thermal drift in the detector limits its use in accurate absolute power measurement applications.

BIBLIOGRAPHY

1. E. L. Ginzton, *Microwave Measurements*, McGraw-Hill, New York, 1957.
2. H. C. Torrey and C. A. Whitmer, *Massachusetts Institute of Technology Radiation Laboratory Series: Crystal Rectifiers*, McGraw-Hill, New York, 1948.
3. S. Y. Liao, *Microwave Devices and Circuits*, 2nd ed., Prentice-Hall, Englewood Cliffs, NJ, 1985.
4. B. G. Streetman, *Solid State Electronic Devices*, 2nd ed., Prentice-Hall, Englewood Cliffs, NJ, 1980.
5. T. Koryu Ishii, ed., *Handbook of Microwave Technology*, Academic Press, New York, 1995.
6. S. F. Adam, *Microwave Theory and Applications*, Prentice-Hall, Englewood Cliffs, NJ, 1969.

MICROWAVE FERROELECTRIC DEVICES

D. P. PATEL
J. M. POND
J. B. L. RAO
Naval Research Laboratory

Control of reactance in microwave circuits, devices, and systems is a common method by which the response of a microwave circuit such as a filter, resonator, or phase shifter can be tuned. Devices based on a class of voltage-dependent non-linear dielectrics known as ferroelectrics provide an alternative to semiconductor varactor diodes and ferrimagnetic components, which are the most common devices of this type.

After an overview of the relevant materials issues, this article describes microwave devices that exploit the variation of the ferroelectric's permittivity with applied DC electric field. The main feature of these "tunable" microwave devices is the change of their capacitance, impedance, or phase velocity. We will describe varactors, oscillators, tunable filters, and phase shifting devices.

1. FERROELECTRIC MATERIALS

Even though they do not contain iron, the name "ferroelectric" was selected because they possess a response to an electric field that, although not the dual, is analogous to a ferromagnetic material's response to a magnetic field. Ferroelectrics are a subgroup of nonlinear dielectrics. The complex permittivity of a ferroelectric material is a function of both the temperature and an applied DC electric field.

Ferroelectric materials possess spontaneous polarization below a temperature referred to as the "Curie temperature," at which point they undergo a phase transition.

Above the Curie temperature, they are in a paraelectric state where spontaneous polarization disappears, but they still retain a nonlinear dielectric constant with applied electric field. In this article, we will use the term ferroelectric to describe these materials even if they are being operated at temperatures where they are in the paraelectric phase. Unlike ferromagnetic materials, ferroelectric materials in either the ferroelectric or paraelectric state are reciprocal; that is, the transmission coefficient through these devices is the same for different directions of propagation. Until relatively, the dielectric losses in ferroelectric materials excluded them from being used at microwave frequencies. However, the continued improvement of ferroelectric materials suitable for use at microwave frequencies has resulted in the design of many microwave devices.

Tunability can be defined for a ferroelectric as the fractional change in the dielectric constant with applied dc bias voltage or

$$\text{Tunability} = \frac{\epsilon_{r,\max} - \epsilon_{r,\min}}{\epsilon_{r,\max}} \quad (1)$$

where $\epsilon_{r,\max}$ is the dielectric constant when no bias voltage is applied and $\epsilon_{r,\min}$ is the dielectric constant when maximum DC bias is applied. The dielectric constant of a ferroelectric decreases as the bias voltage is increased. Although larger tunability is a desirable feature for most microwave applications, a ferroelectric material with larger tunability usually has a relatively larger dielectric loss. Optimizing material tunability and loss to meet the needs of a particular microwave application remains a challenging task.

Ferroelectrics are inherently broadband; that is, they do not have a low frequency limit like ferrites. Switching time for these materials has been measured to be less than a nanosecond [1], which is sufficient for most microwave applications. Also, these materials are radiation-hardened. Ferroelectrics can be manufactured in bulk, thick-film, and thin-film form.

Like other ceramics, bulk ferroelectric ceramics can handle high peak powers. The limit on the average power is determined by the loss tangent ($\tan \delta$) of the ferroelectric. There are many known ferroelectrics, but the most widely used ferroelectric at microwave frequencies is barium strontium titanate, $\text{Ba}_{1-x}\text{Sr}_x\text{TiO}_3$ (BSTO). BSTO with $x = 0.5$ is frequently used for microwave applications since the Curie temperature is well below room temperature yet a reasonable tunability is retained. Bulk ceramics of this composition typically possess relative dielectric constants on the order of 1000 and loss tangents of 0.02 at 10 GHz [2,3]. BSTO's Curie temperature can be controlled by varying the barium-to-strontium ratio. A bulk composite material can be engineered by adding nonferroelectric oxides to BSTO to reduce the dielectric constant and the loss tangent [2,3]. For room-temperature operation of these composites in the paraelectric phase, tunability ϵ_r , and $\tan \delta$ decrease with decreasing barium content; they also decrease with increasing oxide content. Tunability increases linearly with an increase in bias

voltage. Bulk ceramics can be produced using usual ceramic processing techniques.

Thin films are compatible with integrated circuits, and they need lower bias voltages than does bulk material. Thin films can be manufactured by any of the common thin-film deposition techniques, pulsed-laser deposition, sputtering, metal organic chemical vapor deposition (MOCVD), and so on. In thin films, control of the ferroelectric composition and incorporation of doping is also possible to reduce losses at microwave frequencies [4]. Thin films can potentially be less costly and easier to manufacture, but they cannot handle high power levels. Thin films of the ferroelectric strontium titanate, SrTiO_3 (STO), are used at microwave frequencies because of their compatibility with the high-temperature superconductor (HTS) yttrium barium cuprate (YBCO).

Between bulk and thin-film ferroelectrics lies the realm of thick-film ferroelectrics, which can be produced via tape casting.

Throughout this article, it will be assumed that the ferroelectric is homogeneous and that it is linear with respect to a small, time-varying electric field. The dielectric strength of these ferroelectrics is relatively high. Large DC electric fields (in the range of a few MV/m) can be applied to STO and BSTO before dielectric breakdown occurs. Assuming that a particular ferroelectric composition meets the tunability, ϵ_r and $\tan \delta$ requirements of the application, the next two sections describe the various issues that need to be addressed before designing a microwave ferroelectric device.

2. MICROWAVE DEVICE CONSIDERATIONS

Most microwave devices can be categorized according to their physical size in relation to the wavelength at their upper frequency of operation. Those devices that are very small compared to their operational wavelength are called “electrically small” and can be modeled with discrete circuit components. The term “lumped-element” model is often employed. For devices whose dimensions are larger, it is usually necessary to take into account the frequency-dependent effects. Such devices are described by distributed networks of common circuit elements such as inductors and capacitors. The most common distributed device is the transmission line, which is modeled by a ladder network of series inductors and shunt capacitors. As a lumped element, a capacitor which uses ferroelectric material yields a tunable circuit reactance.

Transmission lines can usually be described by their phase velocity and characteristic impedance, which are given by

$$v_p = \frac{1}{\sqrt{LC}} \quad (2)$$

and

$$Z_c = \sqrt{\frac{L}{C}} \quad (3)$$

respectively, where L is the inductance per unit length and C is the capacitance per unit length. By introducing a

material whose dielectric constant ϵ_r is controlled (or tuned) by a direct-current (DC) bias voltage, the phase velocity and characteristic impedance can be varied by changing capacitance.

An issue to consider when choosing a microwave device topology is the power-handling requirements. For high-power applications, the number of device topologies that are appropriate is limited. Further discussion is offered in the next section.

In any nonlinear material, device, or system, another important practical consideration is the strength of signals generated at other than the desired frequency. Since most systems are bandwidth-limited, the most troublesome condition arises when two desired signals, f_1 and f_2 , both within the passband produce signal at frequencies $2f_1 - f_2$ and $2f_2 - f_1$, also within the passband. A plot of the signal strengths of f_1 , f_2 , $2f_1 - f_2$, and $2f_2 - f_1$ is often used to determine the third-order intercept point (IP3), which is an important figure of merit.

Since ferroelectrics have a high dielectric constant, the circuits that employ these materials tend to have very low impedance. Therefore, impedance matching is also another major issue to be addressed when using ferroelectrics. A consequence of a voltage-dependent capacitance being utilized to tune the phase velocity of a transmission line as given by Eq. (2) is that the characteristic impedance of the transmission line is also tuned per Eq. (3). This further complicates the impedance-matching problem.

3. MICROWAVE GUIDING STRUCTURES

At microwave frequencies, ferroelectrics can be introduced into many different types of rectilinear structures that are used to guide electromagnetic waves. These guiding structures include parallel-plate and rectangular waveguides, which can be loaded (or filled) with ferroelectric material. There are also many planar structures that use the ferroelectric material as a tunable substrate, like microstrip, slotline, coplanar strip, and coplanar waveguide. Each structure has a different set of advantages and disadvantages. For applications where ferroelectrics are used to provide bias-dependent propagation properties, it is convenient to divide the guiding structures into two categories: (1) geometries that can handle high microwave power but require large bias voltages (parallel plate and rectangular waveguide) and (2) those that are compatible with small microwave power levels and require only modest bias voltages (planar structures). Note that the ferroelectric permittivity is a function of the electric field. In a planar structure, the bias voltage is applied across a thinner ferroelectric, and so smaller bias voltage will produce the same variation of the permittivity as a larger bias voltage (which creates a similar electric field intensity) would produce in a parallel-plate or rectangular waveguide.

Planar waveguiding structures contain the metallization defining the waveguiding structure delineated on the one or more plane. Often this metallization layer is on the top surface of a dielectric substrate. Hence, these geometries are compatible with photolithographic processing. Since the metallization delineating the waveguide is at the

interface of two regions (usually dielectric), the guided wave is propagating such that a portion of the field is in each region. The choice of the correct planar transmission line is determined by many factors including (1) orientation of the bias field and microwave field with the ferroelectric region, (2) thickness of the ferroelectric material, and (3) compatibility with other circuit elements. Planar structures are compatible with ferroelectric thin films and with semiconductors for microwave monolithic integrated circuits. However, planar structures require a DC block to isolate the radio frequency (RF) from the high DC voltage that is used to tune the ferroelectric permittivity [5].

3.1. Microstrip

The most common planar transmission line is microstrip. As shown in Fig. 1, both the bias and the dominant-mode microwave electric field are oriented primarily normal to the interface. It should be noted that although microstrip is the most widely used planar transmission line, when using thin-film ferroelectrics deposited on a substrate with the delineated metal layer on top as shown in the Fig. 1b, the high dielectric constant of the ferroelectric results in decreased tuning efficiency. This can be seen by considering the capacitance per unit length to be a series combination of the ferroelectric capacitor and the substrate capacitor. The capacitance contribution from the thin-film ferroelectric is much smaller than that from the substrate, and the tunability of the phase velocity and the characteristic impedance of the dominant mode are reduced accordingly.

Tunable filters employing parallel-coupled microstrip resonators do not suffer from this inefficiency since the

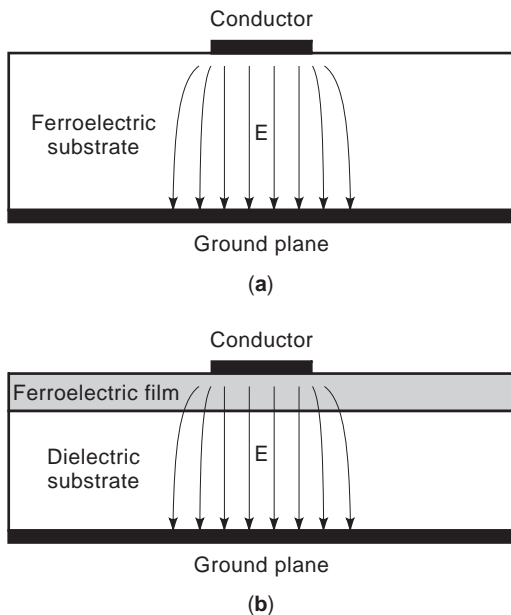


Figure 1. Microstrip planar transmission line cross section with (a) a homogeneous bulk substrate and (b) thin film on a bulk substrate. The electric field between the metal strip on the top surface and the metal ground plane is primarily normal to the surface.

coupled-line mode [6] possesses a significant electric field component parallel to the surface. This coupled-line mode is similar to the coplanar strip transmission line (discussed below) with a ground plane. Practical design equations for microstrip on layered dielectric substrates are based on a quasistatic analysis [7].

3.2. Coplanar Waveguide, Coplanar Strip, and Slotline

Other planar transmission lines such as coplanar waveguide, coplanar strip, and slotline have two or more conductors on the patterned surface. Hence the electric fields of both the dominant microwave mode and the bias are tangential to the substrate surface as shown in Fig. 2. The dominant mode of these planar transmission lines can be efficiently tuned with a bias field whether a bulk ferroelectric substrate or a thin-film ferroelectric on bulk dielectric substrate is employed. In the later case, good

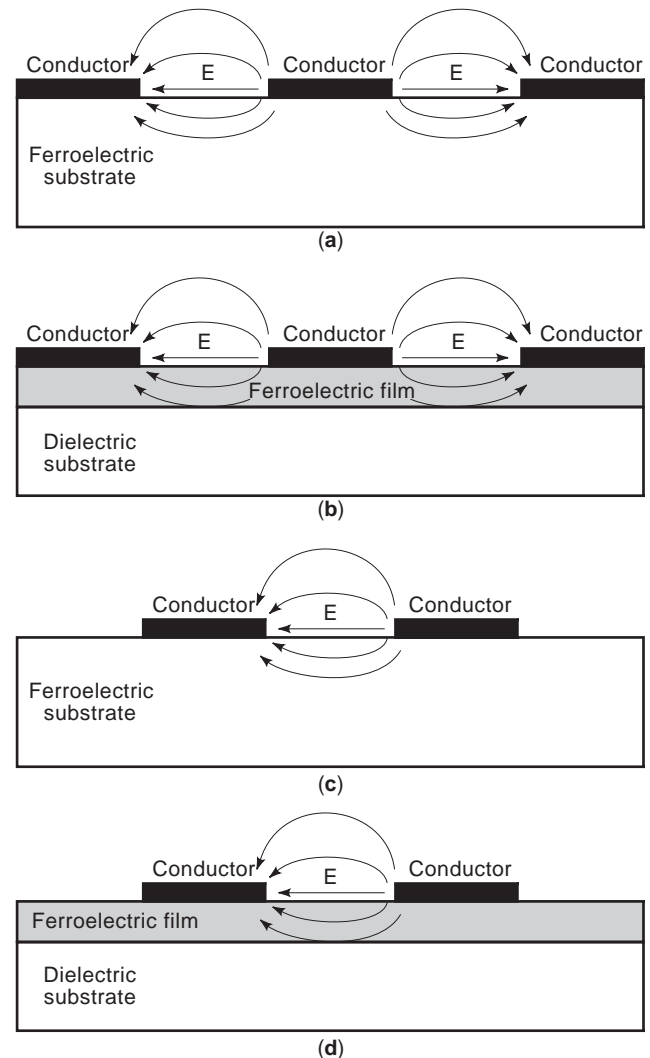


Figure 2. Coplanar waveguide (CPW) transmission line cross section with (a) a homogeneous bulk substrate and (b) a thin film on a bulk substrate and coplanar strip (CPS) transmission-line cross section with (c) a homogeneous bulk substrate and (d) a thin film on a bulk substrate. The electric field between the metal strips on the top surface is primarily parallel to the surface.

tunability is retained since the thin-film capacitance and substrate capacitance are in parallel. Design equations for a coplanar waveguide on multilayered dielectric substrates are available [7]. Similar analyses using a partial-capacitance conformal-mapping approach can be applied to other geometries to account for the ferroelectric thin film.

For the coplanar waveguide, the narrower the gaps between the center conductor and the ground planes, the higher the electric field intensity (and tunability) for a given bias voltage. Although coplanar waveguide is one of the simplest transmission lines, the microwave current density is sharply peaked at the edges of the strips causing large conductor losses. The problem is enhanced by the high dielectric constant and small thickness of the ferroelectric [8].

3.3. Parallel-Plate and Rectangular Waveguides

A parallel-plate waveguide is a two-conductor guiding structure that supports transverse electromagnetic (TEM) waves. Thus, the electric and magnetic field are orthogonal to each other and to the direction of propagation. Figure 3 shows how this type of waveguide can be loaded with a ferroelectric medium to provide a variable phase velocity, which is given by

$$v_p = \frac{1}{\sqrt{\mu\epsilon}} \quad (4)$$

where μ and ϵ are the permeability and permittivity of the ferroelectric. Both the DC and the RF electric field are vertical. The ferroelectric is bifurcated with an electrode that is used to apply the DC bias with respect to the grounded waveguide walls.

Rectangular waveguides are popular in the microwave region. They are single-conductor guiding structures that confine the electromagnetic wave in the interior of the waveguide. Typically, the waveguide is operated in the dominant TE₁₀ mode. Figure 4 shows how a ferroelectric can be used in this type of waveguide to provide a variable phase velocity, which is given by

$$v_p = \frac{1}{\sqrt{\mu\epsilon} \sqrt{1 - \left(\frac{\lambda}{\lambda_c}\right)^2}} \quad (5)$$

where λ_c is the cutoff wavelength. Again, both DC and RF electric field are vertical, and the ferroelectric is bifurcated by an electrode. Unlike the parallel-plate waveguide

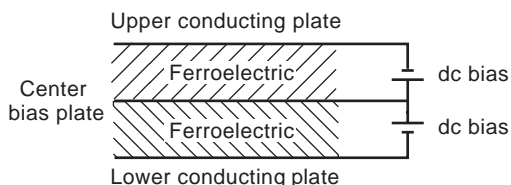


Figure 3. Parallel-plate waveguide phase shifter (propagation into or out of paper).

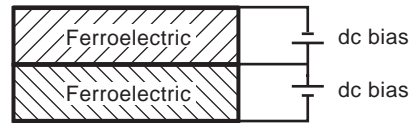


Figure 4. Rectangular waveguide phase shifter (propagation into or out of paper).

(which has no sidewalls), rectangular waveguide has sidewalls. Therefore, a slot needs to be cut into a sidewall to connect the electrode to a DC power supply. The area of the slot opening must be small to prevent the microwave energy from leaking out of the slot.

4. APPLICATIONS

In this section, we will describe several applications of ferroelectrics at microwave frequencies. These include varactors, voltage-controlled oscillators (VCOs), tunable filters, and phase shifting devices.

4.1. Varactor

Varactors are variable-reactance circuit elements. They are used in switching or modulation of a microwave signal, for the generation of harmonics in an applied microwave signal, and in the mixing of two microwave signals of different frequencies. As a discrete tunable capacitor, ferroelectric-based capacitors are applicable in a number of microwave circuits including VCOs, tunable filters, and oscillators. Parallel-plate configurations have not been successfully implemented (due to high required processing temperatures) in producing a high-quality ferroelectric thin film on a low-surface-resistance metal. Interdigitated capacitors [9], where the metal electrodes are deposited on top of the ferroelectric (either thin-film or thick-film) or bulk substrate, have proven to be a more practical option. A typical interdigitated capacitor is shown in Fig. 5. Although strongly dependent on the ferroelectric material involved, Figs. 6 and 7 show the level of performance available from thin-film ferroelectric interdigitated capacitor technology. Losses in ferroelectric interdigitated capacitors arise from the losses in the ferroelectric material as denoted by the dielectric loss tangent and from resistive losses in the metal electrodes. Using a low-surface-resistance metal such as silver or (in some cases) superconductors minimizes the electrode loss component, and in most cases the unloaded quality factor of the ferroelectric varactor is given by

$$Q_U = \frac{1}{\tan \delta} \quad (6)$$

Design and modeling of layered interdigitated lumped element capacitors is based on a conformal mapping approach [10].

4.2. Voltage-Controlled Oscillator

Resonant circuits are used in oscillators and tunable filters. An oscillator provides a sinusoidal signal, and it is

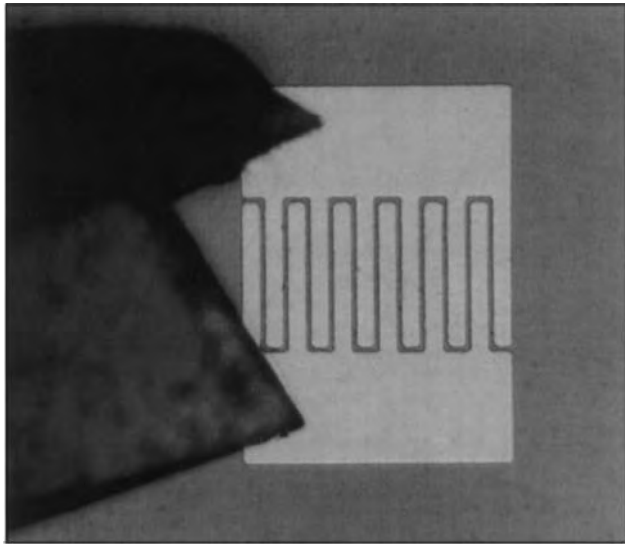


Figure 5. Photograph of a typical interdigitated capacitor on a thin-film ferroelectric covered substrate. The gap between fingers in the metal electrodes is $6\ \mu\text{m}$. A microwave probe is shown contacting the device from the left.

used as a source of microwave energy. The oscillator output should be clean (noiseless) and stable (frequency and power should not change with time). A high- Q resonator is used in an oscillator circuit to obtain good frequency stability and low noise. The tunable capacitance of a ferroelectric-based capacitor is particularly applicable to a class of devices called a voltage-controlled oscillator (VCO). The bias-controlled change in reactance varies the oscillation frequency of an active element such as a transistor. Although there are many different oscillator topologies the designer can choose from, to first order the oscillation frequency can be varied in proportion to the square root of the bias-dependent capacitance. In principle, there is no difference in the design of a VCO using a ferroelectric capacitor and a semiconductor varactor diode [11]. A VCO employing a ferroelectric tunable ring resonator has demonstrated 3% frequency tunability at 17 GHz [12]. Phase noise is one of the primary limitations

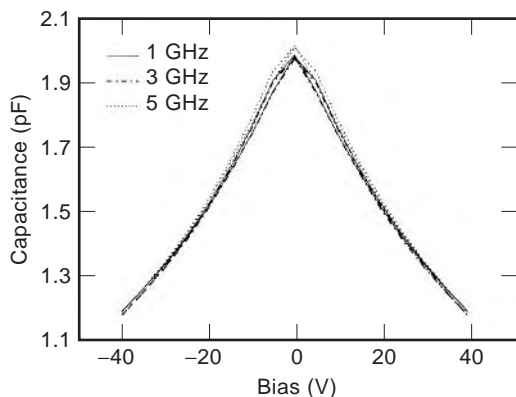


Figure 6. Capacitance versus bias voltage of a $\text{Sr}_{0.5}\text{Ba}_{0.5}\text{TiO}_3$ thin-film interdigitated capacitor on an MgO substrate for frequency values of 1, 3, and 5 GHz. The data represents bias swept from $-40\ \text{V}$ to $40\ \text{V}$ and back to $-40\ \text{V}$.

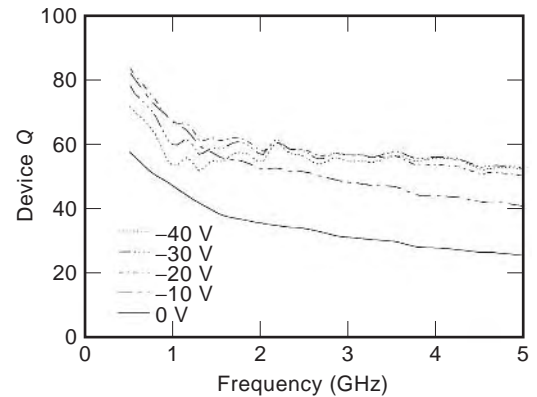


Figure 7. Interdigitated capacitor quality factor as a function of frequency for a $\text{Sr}_{0.5}\text{Ba}_{0.5}\text{TiO}_3$ thin film on an MgO substrate with bias voltages of $0\ \text{V}$, $-10\ \text{V}$, $-20\ \text{V}$, $-30\ \text{V}$, and $-40\ \text{V}$.

of any VCO application. Although several mechanisms contribute to phase noise, in many cases the Q factor of the tunable element is the limiting factor. As can be seen from Leeson's formula, we have [11]

$$\mathcal{L}(f_m) = \frac{1}{2} \left[1 + \frac{1}{f_m^2} \left(\frac{f}{2Q_L} \right)^2 \right] \frac{FkT}{P_{\text{avs}}} \left(1 + \frac{f_c}{f_m} \right) \quad (\text{dBc/Hz}) \quad (7)$$

where f_m is the offset frequency, f is the oscillation frequency, P_{avs} is the power level, F is the noise figure, f_c is the $1/f$ noise corner frequency, and Q_L is the loaded quality factor, which is related to the unloaded device quality factor Q_U by

$$Q_U = \frac{1}{\frac{1}{Q_L} - \frac{1}{Q_{\text{ext}}}} \quad (8)$$

where Q_{EXT} is the external quality factor. As can be seen in Leeson's formula, the quality factor of the variable capacitor, which is, to first order, the reciprocal of the dielectric loss tangent, has a major impact on the phase noise of the VCO.

4.3. Tunable Filter

A filter is any device or circuit that exhibits frequency selectivity; that is, the amplitude and phase of the output signal are functions of frequency. A simple example is a bandpass filter where, ideally, all frequencies in a certain range are passed without change to the signal, whereas at any other frequency no signal appears at the output. There are many different ways to realize a microwave filter [13]. Many of these rely on resonators that are coupled together in a carefully controlled fashion to realize the desired filter transfer function. Tunability of the filter transfer function can be achieved with ferroelectrics [14,15]. It has been demonstrated that the center frequency of a microwave filter can be tuned by approximately 10% using ferroelectrics. In practice, there are many filter topologies that lend themselves to tuning with ferroelectrics. Conceptually the simplest to envision is tuning the

center frequency of a bandpass filter composed of coupled half-wavelength resonators by varying the phase velocity of the resonant elements and hence their resonant frequency. From Eq. (2) it can be seen that the phase velocity is inversely proportional to the square root of the capacitance. Since many filter topologies rely on capacitive coupling of resonators, utilizing tunable coupling between resonators allows the design of tunable bandwidth filters.

4.4. Phased-Array Antenna

Phased-array antennas can steer transmitted and received signals without mechanically rotating the antenna. Each radiating element of a phased array is normally connected to a phase shifter and a driver, which determines the phase of the signal at each element to form a beam at the desired angle. The most commonly used phase shifters are ferrite and diode phase shifters. Ferrite phase shifters are preferred at microwave frequencies, but they are expensive. The cost of a phased array depends mainly on the cost of phase shifters and drivers, and thus lower-cost phase shifting devices need to be developed to make the phased array antenna affordable for more applications. In this section, three different applications of ferroelectrics to phased array antennas will be described.

4.4.1. Ferroelectric Lens Antenna. The cost of a phased array depends mainly on the cost of phase shifters and drivers. A typical array may have several thousand elements as well as several thousand phase shifters and drivers; hence, it is very expensive. Therefore, reducing the cost and complexity of the phase shifters, drivers, and controls is an important consideration in the design of phased arrays. The ferroelectric lens phased array uniquely incorporates bulk phase shifting [2,3,16,17]; the array does not contain individual phase shifters but rather uses ferroelectric material. This will reduce the number of phase shifters from $(n \times m)$ to $(n + m)$, where n is the number of columns and m is the number of rows in a phased array. The number of phase shifter drivers and

phase shifter controls is also significantly reduced by using row-column beam steering. The ferroelectric lens has the advantages of small lens thickness, high power-handling capability, and simple beamsteering controls, and it uses very low power to control the phase shift. Thus, it leads to low-cost phased arrays. However, it should be noted that the use of row-column steering may limit the level of sidelobes that can be achieved.

4.4.1.1. Description of Ferroelectric Lens and Its Operation.

The ferroelectric lens is shown in Fig. 8; each column of the lens is a set of conducting parallel plates that are loaded with bulk ferroelectric material. The material is bifurcated by a center conducting plate that is used to apply the DC bias voltage to the ferroelectric. The separation between the parallel plates at the input and output end is $\lambda_0/2$, where λ_0 is the free-space wavelength. Since only the TEM mode is desired, the separation between the parallel conducting plates is reduced to avoid higher-order mode propagation in the dielectric-loaded section of the waveguide. Specifically, the separation between the center bias plate and either conducting plate is less than $\lambda/2$, where λ is the wavelength in the ferroelectric. Quarter-wave dielectric impedance transformers are used to match the empty waveguide to the ferroelectric-loaded waveguide.

For scanning applications, a phase shifting device must provide 360° differential phase shift. The amount of the ferroelectric material needed (in the direction of propagation) to obtain 360° differential phase shift is [16]

$$t = \frac{\lambda_0}{\sqrt{\epsilon_{r,max}} - \sqrt{\epsilon_{r,min}}} = \frac{\lambda_0}{\sqrt{\epsilon_{r,max}} [1 - \sqrt{1 - \text{tunability}}]} \quad (9)$$

where $\epsilon_{r,max}$ is the dielectric constant when no bias voltage is applied, and $\epsilon_{r,min}$ is the dielectric constant when maximum DC bias is applied. Tunability is the fractional change in the dielectric constant as defined earlier. Thus, the thickness of the ferroelectric material needed is a function of the dielectric constant and the tunability of

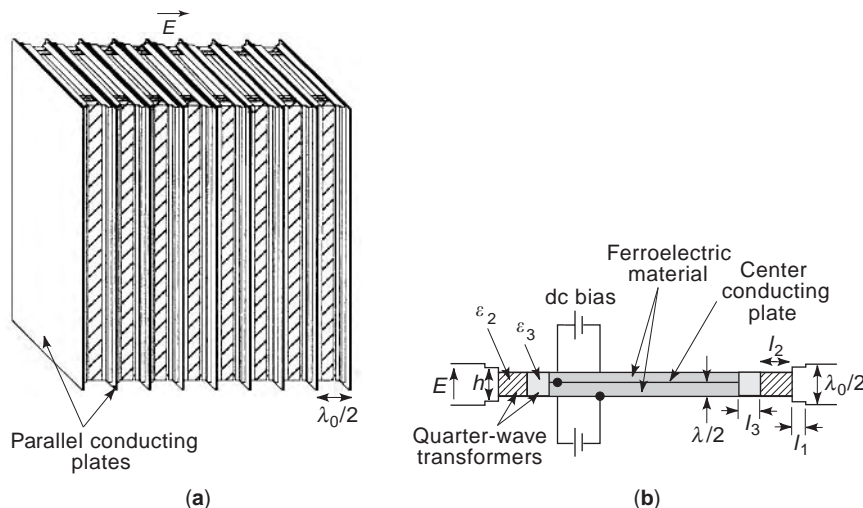


Figure 8. Ferroelectric lens.

the ferroelectric, and the wavelength. Also, it can be shown that in order to obtain 360° phase shift, the dielectric loss through the ferroelectric is [16]

$$\alpha(\text{dB}) = \frac{27.3 \tan \delta}{1 - \sqrt{1 - \text{tunability}}} \quad (10)$$

It may be noted that the lens loss is independent of the ferroelectric permittivity and depends only on its loss tangent and tunability.

In general, the ferroelectrics with higher dielectric constant offer higher tunability, which is desired to reduce the lens thickness. However, matching the lens to free space is easier for smaller ϵ_r . Therefore, a compromise is needed between reducing the lens thickness (to reduce overall lens size) and achieving reasonable impedance match to reduce reflections from the lens surface. For a typical value of $\epsilon_r \sim 100$, it is possible to obtain a tunability of 20%, which results in a reasonable lens thickness of $\sim \lambda_0$ (e.g., 3 cm at 10 GHz). From Eq. (10), it can be seen that the $\tan \delta$ must be less than 0.005 to limit the lens loss to less than 1 dB. The existing ferroelectric materials are a bit more lossy ($\tan \delta = 0.008$ at 10 GHz).

4.4.1.2. Phased-Array Configurations Using Ferroelectric Lens for Two-Dimensional Scanning. The ferroelectric lens offers electronic scanning in one plane. The lens proposed here can be fed by a non-scanning planar array, like a slotted waveguide array. A combination of slotted waveguide array with phase shifters and the lens proposed here can be used as a phased array that can scan in two planes. A space feed can be used with the combination of two lenses proposed here (with a polarization rotator in between) to scan the beam in two planes. The details of these alternatives are discussed elsewhere [16,17].

4.4.1.3. Theoretical and Experimental Results. For the theoretical analysis of the ferroelectric lens, an individual section between two conducting parallel plates of the lens can be considered as one column of a phased array.

The column can be analyzed as a two-dimensional (2D) parallel-plate waveguide with electric field of the TEM mode normal to the plates as shown in Fig. 8. A matching network was designed using mode matching technique assuming that the dielectric constant of the ferroelectric varies from 120 to 80 (33% tunability) over a frequency range of 8–12 GHz (40% bandwidth) and that $\lambda_0 = 0.8$ in. and $\lambda = 0.1$ in. The computed results are shown in Fig. 9. The matching network parameters are $l_1 = 0.2956$ in., $l_2 = 0.1860$ in., $l_3 = 0.0505$ in., $h = 0.2345$ in., $\epsilon_2 = 2.54$, and $\epsilon_3 = 35$ (see Fig. 8).

Experiments were performed with the ferroelectric composition $\text{Ba}_{0.55}\text{Sr}_{0.45}\text{TiO}_3$ with 60% oxide. This material offered a good compromise among ϵ_r , $\tan \delta$, and tunability. At 10 GHz, for this composition, $\epsilon_r = 100$ and $\tan \delta = 0.0079$. The ferroelectrics were 1 in. long (in the direction of propagation), 0.05 in. high and 5 in. ($\sim 4\lambda_0$ at 10 GHz) wide. Figure 10 shows the measured transmission and reflection coefficients at zero bias. The reflection coefficient is sufficiently small over a wide frequency band as the theory had predicted in Fig. 9. Figure 10 also shows that the loss increases with frequency; this is due to two reasons: (1) $\tan \delta$ increases with frequency, which is expected for ceramics; and (2) the electrical length (in terms of wavelengths) of the ferroelectric in the direction of propagation increases with frequency since the physical length is kept constant (1 in.).

Figure 11 shows the measured phase shift as a function of the bias voltage for various frequencies. As expected, the phase shift increases linearly with frequency because the electrical length of the material increases with frequency. Since ferroelectrics are good insulators, the DC current requirements are very low. For example, at 10 kV bias voltage, the DC current drawn was 0.05 mA, and thus the dc power dissipated is only 0.5 W. The bias voltage can be reduced by further bifurcating the ferroelectrics (using interdigital electrodes).

Figure 12 shows the reflection coefficients as a function of frequency for various bias voltages. The standing-wave ratio (SWR) is less than 2 for frequency range of 8–12 GHz as theoretically predicted earlier (see Fig. 9).

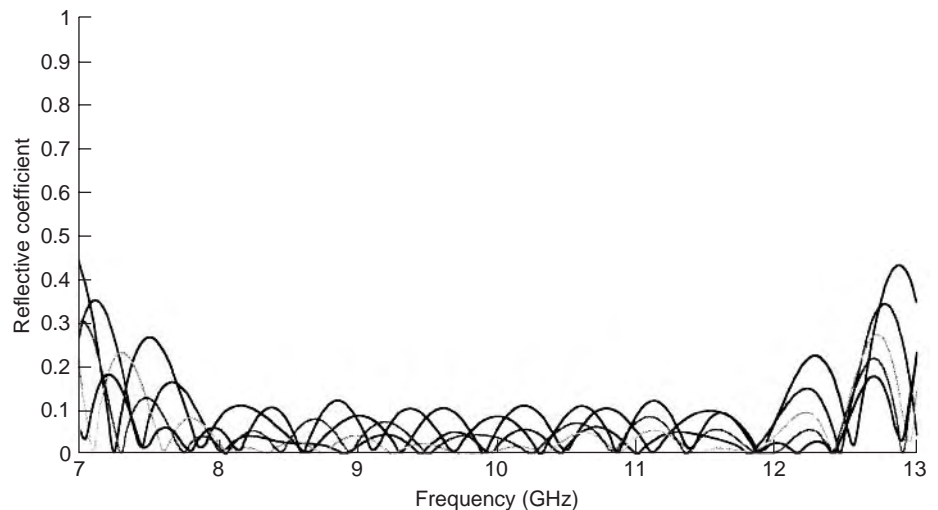


Figure 9. Theoretical reflection coefficient for ϵ_r to 80–120.

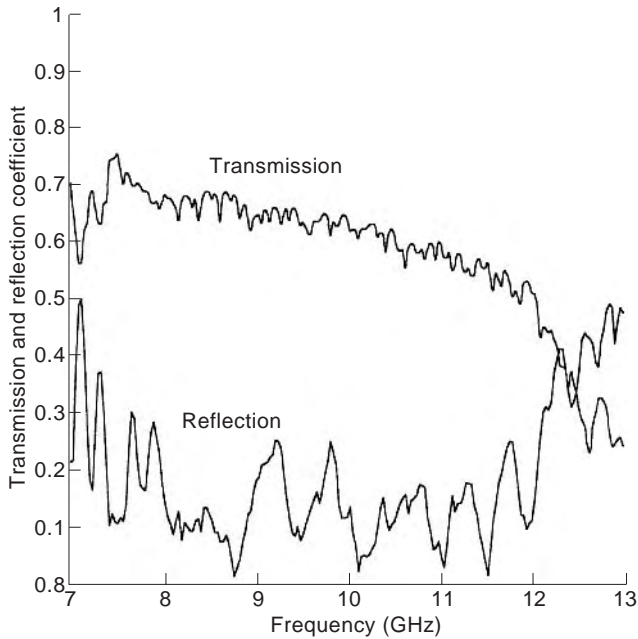


Figure 10. Measured reflection and transmission coefficient at zero bias voltage.

4.4.2. Traveling-Wave Antenna. Another type of phased-array antenna that also uses bulk phase shifting is a traveling-wave antenna, as shown in Fig. 13. The antenna is a slab of ferroelectric material with conducting strips on the topside of the slab and a ground plane on the bottom. This type of antenna is well suited for millimeter-wave applications when a low-loss dielectric (not a ferroelectric) is used as a substrate, and frequency variation is used to scan the antenna beam electronically. Instead of changing the frequency, the dielectric constant of the ferroelectric substrate can be changed to electronically scan the antenna beam in the E plane [17–19]. It can be shown [18] that the radiation angle of the antenna beam is given by

$$\theta = \sin^{-1} \lambda_0 \left(\frac{1}{\lambda_g} - \frac{1}{d} \right) \quad (11)$$

where λ_0 and λ_g are the free space and guide wavelength, respectively, and d is the spacing between the conducting

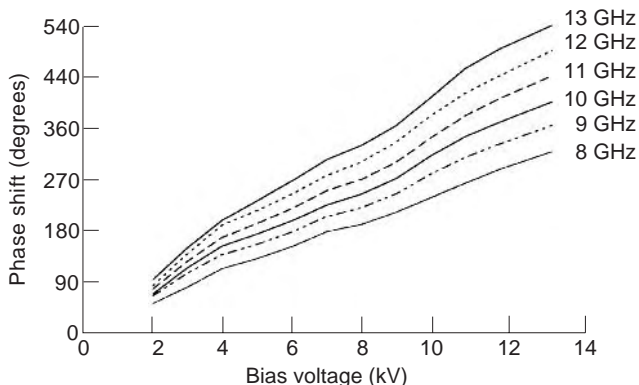


Figure 11. Measured differential phase shift.

strips. The guide wavelength and thus the scan angle change as the dielectric constant of the substrate changes. The main advantage of this type of antenna is that only a single DC power supply is needed to scan the beam, and it is a very simple structure. However, this antenna has a major disadvantage that makes it quite impractical. Since the physical size of most microwave antennas is at least a few wavelengths (if not a few tens of wavelengths), the loss that the electromagnetic wave would suffer as it travels down the antenna is enormous. Also, the instantaneous bandwidth of this antenna is very small because it is a frequency scan antenna; that is, the beam pointing direction changes as the frequency changes. Like the ferroelectric lens, the traveling-wave antenna offers electronic beam scanning in one plane. Electronic scanning in the other plane (azimuth plane in Fig. 13) can be achieved with phase shifters in the linear array feed for this antenna.

4.4.3. Discrete Phase Shifter. Ferroelectrics have also been proposed for discrete phase shifter applications at microwave frequencies. There are several advantages of using ferroelectrics over ferrites in phase shifters. First, since ferroelectrics are voltage-driven devices, the dc control power requirements are small. However, unlike latching ferrite phase shifters that only require current pulses, the bias voltage needs to be applied to the ferroelectrics during the entire transmit and/or receive cycle. Second, ferroelectrics provide reciprocal phase shift. Third, the high dielectric constant of the ferroelectric has the effect of decreasing the overall size of the phase shifter. At the present time, however, the dielectric loss in ferroelectrics is higher than that in ferrites at microwave frequencies.

The basic design equations for a discrete phase shifter are the same as those for the ferroelectric lens. For the same electric field applied in the lens, the discrete phase shifter should provide similar phase shift using the same ferroelectric. Phase shifters have been designed using ferroelectric-loaded rectangular waveguides as well as planar transmission lines, like microstrip and coplanar waveguide, on a ferroelectric substrate [5,20,21].

For the rectangular waveguide, impedance matching techniques similar to the ones used in the ferroelectric lens can be applied. For the microstrip line, several impedance-matching techniques have been tried [5] including quarterwave transformers, open-circuit stubs, and radial stubs. For the coplanar waveguide, usually the lines are tapered to provide a 50Ω impedance [21].

4.5. High-Temperature Superconductors and Ferroelectrics

The discovery of high-temperature superconductors (HTSs) has generated many tunable device designs [22] using both thin films and bulk ferroelectrics. One of the main incentives is the promise of the low conductor loss associated with HTS. In addition, both STO and BSTO are closely lattice matched with the HTS yttrium barium cuprate, $\text{YBa}_2\text{Cu}_3\text{O}_{7-\delta}$ (YBCO), meaning that the ferroelectric and YBCO can be epitaxially grown on top of each other to form multilayer thin film structures. This has been done with STO and YBCO. To take advantage of the

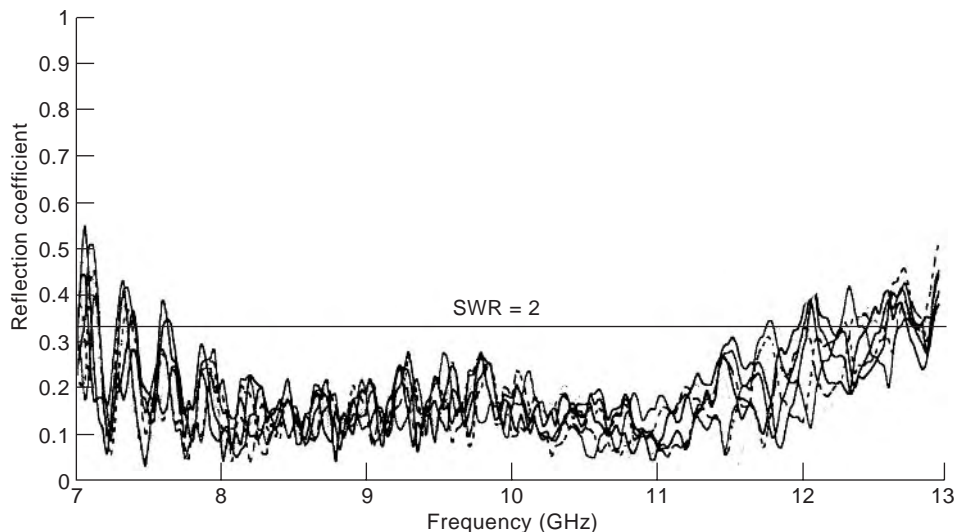


Figure 12. Measured reflection coefficient for various bias voltages (0–13.5 kV).

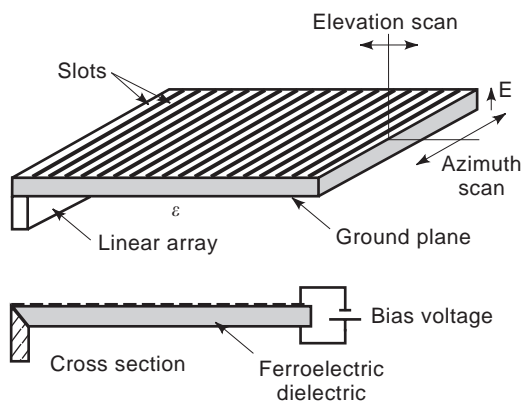


Figure 13. Ferroelectric traveling-wave antenna.

low microwave losses, operation must be below the critical temperature for YBCO. Most of the research has been done at 77 K, the liquid nitrogen boiling temperature. In BSTO, the barium to strontium ratio can be adjusted so that BSTO can be operated in the paraelectric phase at 77 K, and STO remains paraelectric down to the lowest temperatures.

BIBLIOGRAPHY

- P. K. Larsen et al., Nanosecond switching of thin ferroelectric films, *Appl. Phys. Lett.* **59**(5):611–613 (1991).
- J. B. L. Rao, D. P. Patel, and L. C. Sengupta, Phased array antennas based on bulk phase shifting with ferroelectrics, *Integr. Ferroelectric.* **22**:307–316 (1998).
- J. B. L. Rao et al., Ferroelectric materials for phased array applications, *IEEE Antennas Propag. Soc. Int. Symp. Digest*, 1997, Vol. 4, pp. 2284–2287.
- J. S. Horwitz et al., Structure/property relationships in ferroelectric thin films for frequency agile microwave electronics, *Integr. Ferroelectric.* **22**:279–289 (1998).
- R. W. Babbitt, T. E. Kosciwa, and W. C. Drach, Planar microwave electro-optic phase shifters, *Microwave J.* **35**(6):63–79 (1992).
- K. C. Gupta, R. Garg, and I. Bahl, *Microstrip Lines and Slot Lines*, 2nd ed., Artech House, Boston, MA, 1996.
- J. Svacina, A simple quasi-static determination of basic parameters of multilayer microstrip and coplanar waveguide, *IEEE Microwave Guided Wave Lett.* **MGWL-2**:385–387 (1992).
- S. S. Gevorgian et al., HTS/ferroelectric devices for microwave applications, *IEEE Trans. Appl. Superconduct.* **ASC-7**(2):2458–2461 (1997).
- J. M. Pond et al., Microwave properties of ferroelectric thin films, *Integr. Ferroelectric.* **22**:317–328 (1998).
- S. S. Gevorgian et al., CAD models for multilayered substrate interdigital capacitors, *IEEE Trans. Microwave Theory Tech.* **MTT-44**(6):896–904 (1996).
- G. D. Vendelin, A. M. Pavio, and U. L. Rohde, *Microwave Circuit Design*, Wiley, New York, 1990.
- R. R. Romanofsky, F. W. Van Kuels, and F. A. Miranda, A cryogenic GaAs PHEMT/ferroelectric Ku-band tunable oscillator, *3rd European Workshop on Low Temperature Electronics*, San Miniato, Italy, June 24–26, 1998.
- G. Matthaei, L. Young, and E. M. T. Jones, *Microwave Filters, Impedance-Matching Networks, and Coupling Structures*, Artech House, Norwood, MA, 1980.
- S. S. Gevorgian et al., Tunable superconducting band-stop filters, *IEEE MTT-S 1998 Int. Microwave Symp. Digest*, 1998, Vol. 2, pp. 1027–1030.
- G. Subramanyam, F. Van Keuls, and F. A. Miranda, A novel K-band tunable microstrip bandpass filter using a thin film HTS/ferroelectric/dielectric multilayer configuration, *IEEE MTT-S 1998 Int. Microwave Symp. Digest*, 1998, Vol. 2, pp. 1011–1014.
- J. B. L. Rao, D. P. Patel, and V. Krichevsky, Voltage controlled ferroelectric lens phased arrays, *IEEE Trans. Anten. Propag.* (in press).
- J. B. L. Rao, G. V. Trunk, and D. P. Patel, Two low-cost phased arrays, *Proc. 1996 IEEE Int. Symp. Phased Array Systems and Technology*, 1997, pp. 119–124.

18. V. K. Varadan et al., Electronically steerable leaky wave antenna using a tunable ferroelectric material, *Smart Mater. Struct.* **3**:470–475 (1994).
19. T. W. Bradely et al., Development of a voltage variable dielectric (VVD), electronic scan antenna, *Proc. Radar 97, IEE Pub.* **449**:383–385 (1997).
20. V. K. Varadan et al., Ceramic phase shifters for electronically steerable antenna systems, *Microwave J.* **35**(1):116–127 (1992).
21. C. M. Jackson, New phase shifters for smart systems, in V. K. Varadan, ed., *Smart Structures and Materials 1995: Smart Electronics, Proc. SPIE* **2448**:218–225 (1995).
22. O. Vendik, I. Mironenko, and L. Ter-Martirosyan, Superconductors spur applications of ferroelectric films, *Microwaves RF* **33**(7):67–70 (1994).

MICROWAVE FILTERS

LEI ZHU
Nanyang Technological
University
Singapore

1. INTRODUCTION

Microwave filters [1,2] are the basic building blocks with frequency-selective or filtering functionality in the development of various wireless systems that operate at frequency ranges above 300 MHz. Filter blocks play a key role in effectively transmitting the desired signals in certain passband regions while attenuating all the undesired signals in the remaining bandstop regions. The latter types are caused predominantly by the interference signals and unanticipated nonlinearity of many microwave active devices, and they have to be highly rejected by different types of filter blocks in order to transmit the desired signals, without receiving any distortion in amplitude and phase, which usually cover a certain frequency region. Basically, microwave filters can be classified into four distinct categories: lowpass, highpass, bandpass, and bandstop filter blocks [1]. The first two types of blocks realize effective transmission in the entire frequency region below or above a cutoff frequency while the third and fourth types transmit or attenuate signals within a certain frequency region that is terminated by the lower and upper cutoff frequencies.

At low frequencies, lumped-element capacitors and inductors can be reasonably constructed to make up all the filter blocks classified above on the basis of the efficient synthesis approach [1]. However, as the operating frequency increases to the microwave region of interest here, the reactance or susceptance of all the microwave circuit elements, including the so-called lumped elements, varies as a nonlinear function of frequency. Strictly speaking, the exact design of microwave filters should account for the distributed parameters of a variety of microwave circuit elements; thus it becomes very complicated in the design procedure to account for complex frequency behavior. But these elements can still be reasonably considered as

quasilumped elements in the low- or narrowband frequency region. As a result, the early developed synthesis procedure still can be effectively executed in the microwave range to efficiently design the microwave filters with acceptable accuracy in the frequency region of interest. In addition to the frequently cited classical handbook [1], many textbooks and reference books have been published so far so as to provide the beginners with a fundamental understanding of microwave filters as well as their relevant design approaches and practical implementation [3–6], or concentrate on the design of planar transmission-line filters [7,8] and waveguide filters [9]. In the following, we will start with the fundamental theorem for the microwave filters and then present a variety of practical microwave filters that have been widely used in the today's communication systems.

2. LOWPASS PROTOTYPE FILTERS

Figure 1 depicts the schematic of a generalized two-port filter block that is driven by a voltage source (V_s) with the internal impedance (Z_s) and terminated by the load impedance (Z_L). Under the assumption that the incident wave has the unity amplitude, the amplitudes of the reflected and transmitted waves are referred to as the *reflection* and *transmission coefficients*, namely, $R(\omega)$ and $T(\omega)$ (ω = angular frequency), which are frequency-dependent in a complex manner in conjunction with the varied passband–stopband characteristics. Figure 2 illustrates the frequency responses of the four categories of ideal filters with perfect transmission in the passband and infinite attenuation in the stopband, $T(\omega) = 1$ and $T(\omega) = 0$, respectively. As seen in Figs. 2a and 2b, lowpass filters transmit all signals below the cutoff frequency (ω_c) and reject those above ω_c , while the highpass filters attenuate all signals below ω_c and pass those above ω_c . On the other hand, the ideal bandpass and bandstop filters perfectly pass and attenuate all frequencies in the range of lower and upper cutoff frequencies, ω_{c1} and ω_{c2} , as designated in Figs. 2c and 2d, respectively. The frequency responses plotted there allow one to briefly grasp the basic frequency characteristics of various filter blocks via idealized frequency responses, but the actual microwave filters operate in a much more complex frequency-distributed function of frequency with finite-extent passband transmission and stopband attenuation, as will be discussed below.

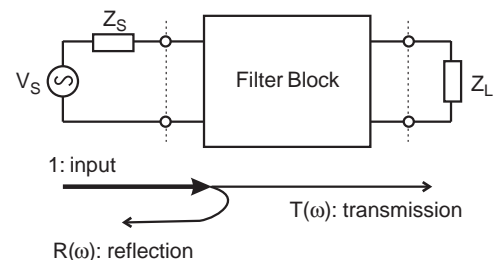


Figure 1. Schematic of a two-port filter block that is characterized via frequency-dependent reflection and transmission coefficients: $R(\omega)$ and $T(\omega)$.

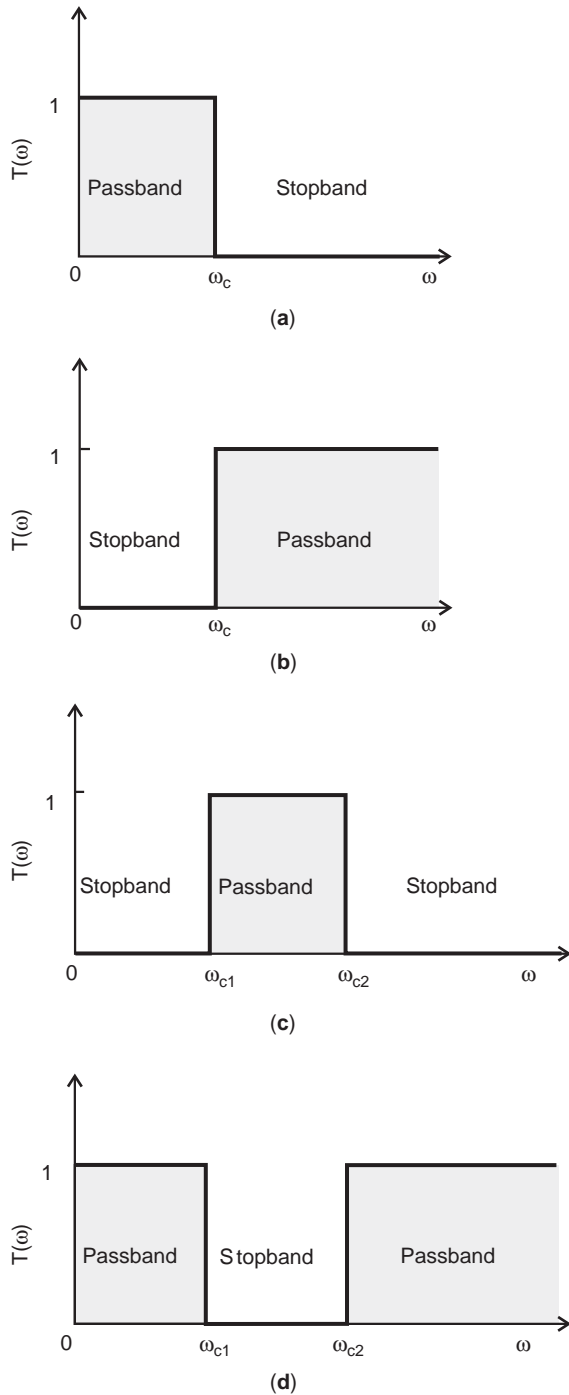


Figure 2. Graphical description of the four categories of idealized frequency-filtering/selective characteristics to be targeted in the filter design: (a) lowpass filter; (b) highpass filter; (c) bandpass filter; (d) bandstop filter.

Regardless of varied frequency responses described above, almost all microwave filters with lowpass, high-pass, bandpass, and bandstop performances can be realized and designed on a basis of the well-developed synthesis approach for a lowpass prototype filter network [1] via frequency transformation. This lowpass prototype filter is characterized in the normalized frequency $\Omega = \omega /$

ω_c , where ω_c is the cutoff frequency, and its frequency response is specified under the power insertion loss parameter: $L(\Omega) = 1/|T(\Omega)|^2$. Furthermore, $L(\Omega)$ is readily expressed in terms of a generalized polynomial function $F_N(\Omega)$, where N is the order of the lowpass filter, such that

$$L(\Omega) = 1 + k^2 F_N(\Omega) \tag{1}$$

where k is the constant related to the ripple or tolerance within the passband. Selection of $F_N(\Omega)$ should be based on the condition that the network topology can be physically constructed. In this context, two essential forms can be specified in the practical implementation: maximally flat or Butterworth filters and Chebyshev or equal-ripple filters. Equations (2) and (3) indicate their insertion loss parameters as a function of Ω , respectively, in which $T_N(\Omega)$ is the N th-order Chebyshev function.

$$L(\Omega) = 1 + k^2 \Omega^{2N} \tag{2a}$$

$$L(\Omega) = 1 + k^2 T_N^2(\Omega) \tag{2b}$$

Figures 3a and 3b depict the frequency responses of the decibel insertion losses L (dB) of the third-order lowpass prototype filters with $N = 3$. In order to quantitatively evaluate their lowpass characteristics, the insertion loss at the cutoff frequency ($\Omega_c = 1$) is readily specified as L_c . Meanwhile, an additional one (L_s) at a particular frequency (Ω_s) may be needed to characterize the upper stopband behavior beyond Ω_c . Looking at these two curves together, one can easily find that the Chebyshev filter increases much more rapidly beyond Ω_c in comparison to its Butterworth counterpart. In other words, the Chebyshev one has a much sharper cutoff frequency region separating the lower and higher stopbands, which is preferably desired to approach the ideal frequency response as shown in Fig. 2a.

Figures 4a and 4b depict the ladder networks of the two possible lowpass prototype filters, in which the element g_k is the k th normalized inductance or capacitance while g_0 and g_{N+1} are the normalized source and load resistance or conductance at the input and output ports, respectively. Their input impedances are first derived and then converted to their relevant insertion loss. As such, the values of each elements g_k ($k = 1, 2, \dots, N$) for the load $g_{N+1} = 1$ can be analytically calculated under the exact equality of the two sets of insertion loss, given in Eq. (2) and derived from the ladder networks in Fig. 4, respectively. For the Butterworth lowpass prototype filter with $L_c = 3$ dB at $\Omega_c = 1$ in which $k = 1$, the element values (g_k) may be calculated in the following closed-form equation and the values of each element are further listed in Table 1 up to $N = 8$:

$$g_0 = g_{N+1} = 1 \tag{3a}$$

$$g_k = 2 \sin\left(\frac{2k-1}{2N} \pi\right) \quad k = 1, 2, \dots, N \tag{3b}$$

For the Chebyshev prototype filter with the required insertion loss L_c at $\Omega_c = 1$, one can at first determine the constant k via Eq. (2b): $L_c = 10 \log_{10}(1 + k^2)$. For instance, if $L_c = 0.1$ dB, which is the equal ripple in the low

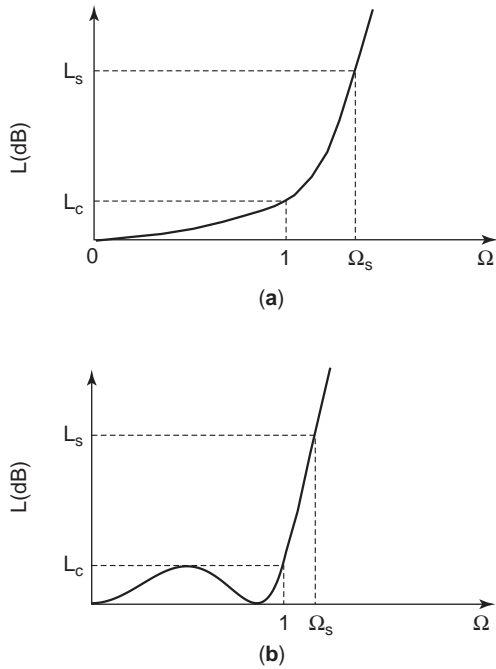


Figure 3. Frequency-dependent attenuation responses of the two types of the third-order lowpass prototype filters: (a) Butterworth type; (b) Chebyshev type.

passband, one can obtain $k=0.153$. Next, the values of each element g_k can be derived for the given N using Eq. (4). Table 2 lists the values of each element g_k for $L_c = 0.1$ dB. Considering the fact that the rising rate of insertion loss L (dB) beyond $\Omega_c = 1$ is gradually incremented with N for both prototype filters, selection of the integer number of N should be based on the required stopband performance that can be specified by the insertion loss (L_s) at the frequency Ω_s with reference to Figs. 3a and 3b

$$g_1 = \frac{2a_1}{\sinh(\beta/2N)} \quad (4a)$$

$$g_k = \frac{4a_{k-1}a_k}{b_{k-1}g_{k-1}} \quad k = 2, 3, \dots, N \quad (4b)$$

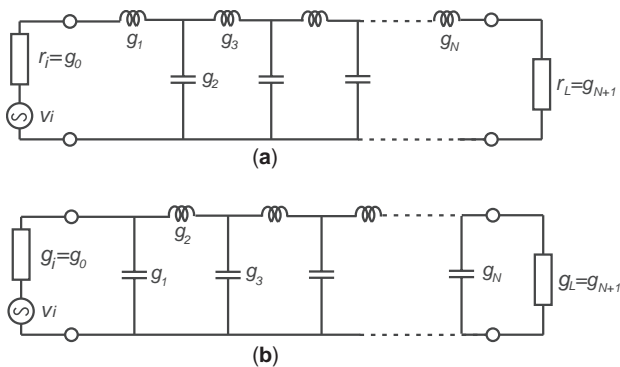


Figure 4. Lumped-element ladder networks of the two types of lowpass prototype filters: (a) inductive type; (b) capacitive type.

$$g_{N+1} = \begin{cases} 1 & N \text{ odd} \\ 2k^2 + 1 - 2k\sqrt{1+k^2} & N \text{ even} \end{cases} \quad (4c)$$

where

$$\beta = \ln\left(\frac{\sqrt{1+k^2}+1}{\sqrt{1+k^2}-1}\right), \quad a_k = \sin\left(\frac{2k-1}{2N}\pi\right),$$

$$b_k = \sinh^2\left(\frac{\beta}{2N}\right) + \sin^2\left(\frac{k\pi}{N}\right)$$

3. LUMPED-ELEMENT PRACTICAL FILTERS

The lowpass prototype filter is characterized above using the normalized source/load resistance or conductance (g_0 and g_{N+1}) as well as the normalized susceptance or reactance (g_k) of a N th-order ladder network in the normalized frequency domain ($\Omega = \omega/\omega_c$). In order to apply this approach to design of the lumped-element practical lowpass, highpass, bandpass, and bandstop filters that operate in the real frequency domain (ω), the so-called frequency transformation is required to map a frequency response in the Ω domain to that in the ω domain. Meanwhile, the impedance scaling procedure should be executed to guarantee the identical insertion loss responses of the lowpass prototype filter and its transformed practical filter. Under this restriction, the normalized prototype elements can be readily scaled to their relevant resistance/conductance elements at the source and load sides as well as the reactive/susceptive elements of various practical filter networks. In the following, the four typical frequency and element transformations are summarized with reference to the different network topologies in Figs. 5b–5e and different frequency responses in Figs. 6b–6e. Regardless of varied frequency transformations as denoted in Fig. 5, the source and load resistances can be commonly assumed ($g_0R_i = g_{N+1}R_L$) for simplification of theoretical description.

3.1. Lowpass-to-Lowpass Transformation

Figure 5b depicts the ladder network of a lumped-element lowpass filter with the source resistance (R_i), load resistance (R_L), as well as a number of series inductance (L_k) and shunt capacitance (C_k). In order to transform the Ω -domain frequency response of a lowpass prototype filter to its ω -domain counterpart (Figs. 6a and 6b), the frequency should be mapped to change the cutoff frequency from unity ($\Omega_c = 1$) to ω_c under the same insertion loss (L_c), and the normalized prototype elements also must be properly scaled to their corresponding lumped elements as expressed in Fig. 6b in such a way that

$$\Omega = \frac{\omega}{\omega_c} \quad (5a)$$

$$L_k = \frac{g_k R_L}{\omega_c} \quad (5b)$$

$$C_k = \frac{g_k}{\omega_c R_L} \quad (5c)$$

Table 1. Values of g_k for Butterworth Lowpass Prototype Filters ($g_0 = 1, L_c = 3.0$ dB)

N	g_1	g_2	g_3	g_4	g_5	g_6	g_7	g_8	g_9
1	2.0000	1.0000							
2	1.4142	1.4142	1.0000						
3	1.0000	2.0000	1.0000	1.0000					
4	0.7654	1.8478	1.8478	0.7654	1.0000				
5	0.6180	1.6180	2.0000	1.6180	0.6180	1.0000			
6	0.5176	1.4142	1.9318	1.9318	1.4142	0.5176	1.0000		
7	0.4450	1.2470	1.8019	2.0000	1.8019	1.2470	0.4450	1.0000	
8	0.3902	1.1111	1.6629	1.9616	1.9616	1.6629	1.1111	0.3902	1.0000

3.2. Lowpass-to-Highpass Transformation

For the highpass filter network in Fig. 5c, one needs to transform the prototype lowpass band to the highpass band covering from the cutoff frequency ω_c to infinity, as illustrated in Fig. 6c. As such, the frequency and element transformations should be inversely undergone so as to swap over the frequency stopband and passband, such that

$$\Omega = -\frac{\omega_c}{\omega} \tag{6a}$$

$$L_k = \frac{R_L}{g_k \omega_c} \tag{6b}$$

$$C_k = \frac{1}{g_k \omega_c R_L} \tag{6c}$$

3.3. Lowpass-to-Bandpass Transformation

To make up the bandpass filter in Fig. 5d, the frequency transformation should be selected to realize a bandpass response with the passband via Eq. (7a). Figure 5d also implies us that the inductive and capacitive prototype elements should be simultaneously transformed to the series and parallel LC resonators in the bandpass filters. Under the restriction that the insertion losses (L_c) at the lower/higher cutoff frequencies (i.e., ω_{c1} and ω_{c2} in Fig. 6d), must be equal to that (L_c) at $\Omega_c = 1$ of its related lowpass prototype filter, the inductance and capacitance, L_k and C_k , of each LC resonator are derived by

$$\Omega = \frac{\omega_0}{\omega_{c2} - \omega_{c1}} \left(\frac{\omega}{\omega_0} - \frac{\omega_0}{\omega} \right) \text{ where } \omega_0 = \sqrt{\omega_1 \omega_2} \tag{7a}$$

$$L_k = \frac{g_k R_L}{\omega_{c2} - \omega_{c1}}, \quad C_k = \frac{\omega_{c2} - \omega_{c1}}{\omega_0^2 g_k R_L} \text{ for series } LC \tag{7b}$$

$$L_k = \frac{R_L(\omega_{c2} - \omega_{c1})}{\omega_0^2 g_k}, \quad C_k = \frac{g_k}{R_L(\omega_{c2} - \omega_{c1})} \tag{7c}$$

for parallel LC

3.4. Lowpass-to-Bandstop Transformation

The bandstop frequency response can be achieved via frequency transformation as indicated in Eq. (8a) so as to formulate the bandstop region between ω_{c1} and ω_{c2} as depicted in Fig. 6e. In this way, the elements of each LC resonator in the bandstop filter network in Fig. 5e can be derived in terms of the lowpass prototype elements by

$$\frac{1}{\Omega} = \frac{\omega_0}{\omega_{c2} - \omega_{c1}} \left(\frac{\omega}{\omega_0} - \frac{\omega_0}{\omega} \right) \text{ where } \omega_0 = \sqrt{\omega_1 \omega_2} \tag{8a}$$

$$L_k = \frac{\omega_0^2 R_L}{g_k(\omega_{c2} - \omega_{c1})}, \quad C_k = \frac{g_k(\omega_{c2} - \omega_{c1})}{\omega_0^2 R_L} \tag{8b}$$

for series LC

$$L_k = \frac{g_k R_L(\omega_{c2} - \omega_{c1})}{\omega_0^2}, \quad C_k = \frac{1}{g_k R_L(\omega_{c2} - \omega_{c1})} \tag{8c}$$

for parallel LC

4. PRACTICAL FILTERS WITH IMMITTANCE INVERTERS

Looking at Figs. 5a–5e closely, one can see that all the filter ladder networks definitely require the occurrence of series and shunt elements that may be the inductance,

Table 2. Values of g_k for Chebyshev Lowpass Prototype Filters ($g_0 = 1, L_c = 0.1$ dB)

N	g_1	g_2	g_3	g_4	g_5	g_6	g_7	g_8	g_9
1	0.3052	1.0000							
2	0.8430	0.6220	1.3554						
3	1.0315	1.1474	1.0315	1.0000					
4	1.1088	1.3061	1.7703	0.8180	1.3554				
5	1.1468	1.3712	1.9750	1.3712	1.1468	1.0000			
6	1.1681	1.4039	2.0562	1.5170	1.9029	0.8618	1.3554		
7	1.1811	1.4228	2.0966	1.5733	2.0966	1.4228	1.1811	1.0000	
8	1.1897	1.4346	2.1199	1.6010	2.1699	1.5640	1.9444	0.8778	1.3554

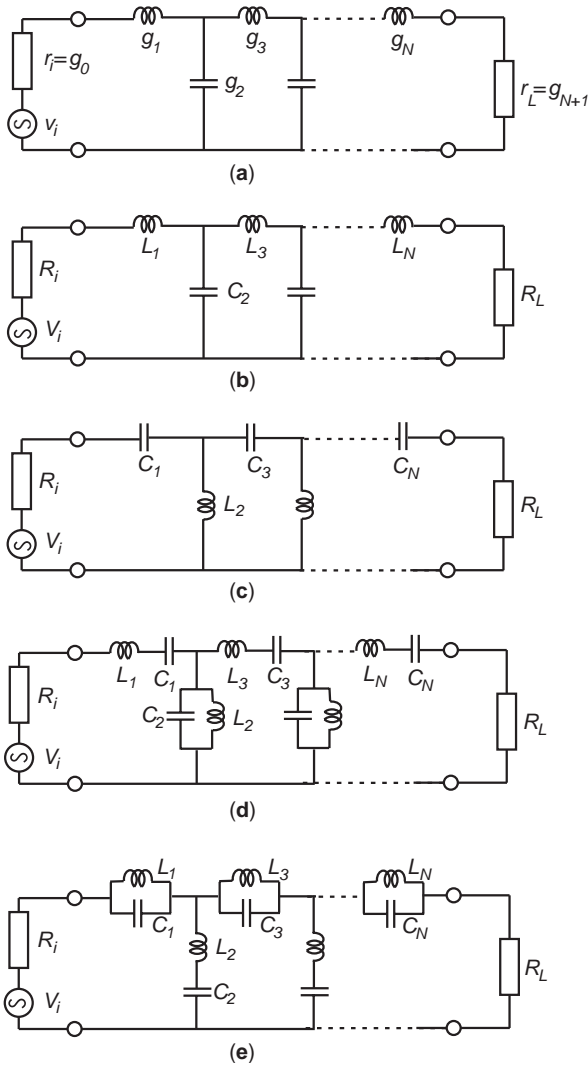


Figure 5. Ladder networks of the lowpass prototype filter and its relevant microwave filters: (a) lowpass prototype filter; (b) lowpass microwave filter; (c) highpass microwave filter; (d) bandpass microwave filter; (e) bandstop microwave filter.

capacitance, or series/parallel LC resonators. In the practical implementation, it sometimes seems so difficult, especially in the microwave frequency range, to simultaneously make up both series and parallel LC resonators. As such, the immittance inverter, which is either an impedance or admittance inverter, is utilized to build up an alternative class of filter networks containing only series elements or only parallel elements. Figures 7a and 7b depict the two-port impedance and admittance inverters that invert the load impedance Z_b or admittance Y_b at one port to the input Z_a or Y_a at the other port with respect to the squared characteristic impedance and admittance, namely, K and J , respectively:

$$Z_a = \frac{K^2}{Z_b}, \quad Y_a = \frac{J^2}{Y_b} \quad (9)$$

Consider the parallel admittance element $Y_p(\omega)$ sandwiched by the two identical impedance inverters (K) at its two sides as shown in Fig. 8a. If the two output ports

are simultaneously terminated by the short circuits, the entire two-port network can be simplified as $Y_p(\omega)$ in parallel with the two open circuits at the two sides. Thus, the input impedance, looking into this network from both left and rightsides, can be derived as $K^2 Y_p(\omega)$, that is, the series impedance $Z_s(\omega)$. So, the shunt admittance $Z_p(\omega)$ can be inverted to the series impedance $Z_s(\omega)$. Similarly, the series impedance $Z_s(\omega)$ with the admittance inverters (J) at its two sides is the equivalence of a parallel admittance $Z_p(\omega)$ as denoted in Fig. 8b. The unique feature of these immittance inverters enables us to convert the practical filter blocks in Fig. 5 to those with either series or parallel elements. Most importantly, it provides us with much more convenience in the design of microwave bandpass filters with only series or parallel lumped/distributed resonators.

Figures 9a and 9b describe the two types of bandpass filter networks using the impedance and admittance inverters, respectively. In the former case, only series resonators with the reactance $X_k(\omega)$ are involved, and the two adjacent ones with $X_k(\omega)$ and $X_{k+1}(\omega)$ are cascaded across the impedance inverter, $K_{k,k+1}$, which is assumed frequency-independent. In the latter case, only parallel resonators with the susceptance $B_k(\omega)$ exist and the admittance inverter $J_{k,k+1}$ is utilized to link the two adjacent resonance susceptances $B_k(\omega)$ and $B_{k+1}(\omega)$. As will be discussed later on, the series or shunt resonators are usually the distributed circuits that are equivalently formulated by various transmission-line and waveguide cavity resonators. In order to factor in these distributed circuits in the synthesis approach, the two quantities, called *reactance slope* and *susceptance slope* parameters, x and b , respectively, are defined at the resonant frequency ω_0 , where $X(\omega_0) = 0$ or $B(\omega_0) = 0$, by

$$x = \frac{\omega_0}{2} \left. \frac{dX(\omega)}{d\omega} \right|_{\omega=\omega_0}, \quad b = \frac{\omega_0}{2} \left. \frac{dB(\omega)}{d\omega} \right|_{\omega=\omega_0} \quad (10)$$

which demonstrates that the slope parameter x becomes $\omega_0 L$ for the series lumped LC resonator, whereas b is equal to $\omega_0 C$ for a parallel lumped LC resonator. With the use of these two slope parameters, the bandpass filter with immittance inverters as shown in Fig. 9 can be transformed from their lumped-element counterparts. For the filter with impedance inverters in Fig. 9a, the source/load resistances are given as R_i and R_L , respectively. Thus, the characteristic impedances of all the impedance inverters can be derived in terms of the normalized prototype elements as denoted in Figs. 4a and 4b under the specified fractional bandwidth of $w = (\omega_{e2} - \omega_{e1})/\omega_0$:

$$K_{01} = \sqrt{\frac{R_i x_1 w}{g_0 g_1}} \quad (11a)$$

$$K_{k,k+1} = w \sqrt{\frac{x_k x_{k+1}}{g_k g_{k+1}}} \quad (k = 1, 2, \dots, N-1) \quad (11b)$$

$$K_{N,N+1} = \sqrt{\frac{R_L x_N w}{g_N g_{N+1}}} \quad (11c)$$

For the filter with admittance inverters terminated by the source/load conductances, G_i and G_L , as denoted in Fig. 9b,

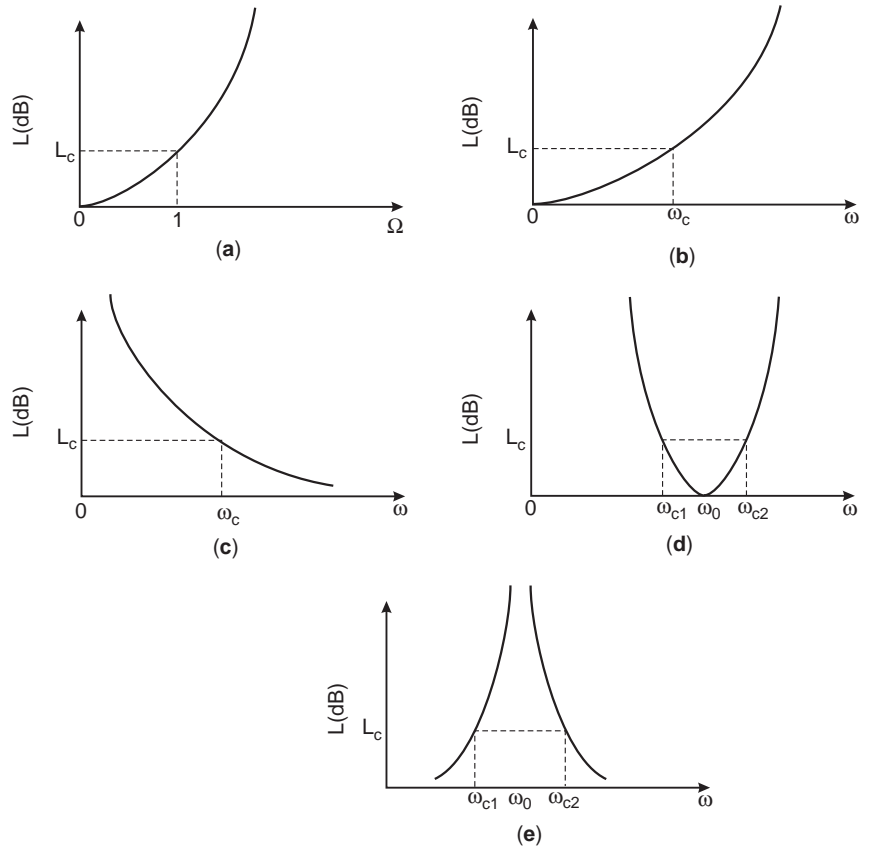


Figure 6. Frequency-dependent attenuation responses of the lowpass prototype filter and its relevant microwave filters: (a) lowpass prototype filter; (b) lowpass microwave filter; (c) highpass microwave filter; (d) bandpass microwave filter; (e) bandstop microwave filter.

the relevant expressions can be accordingly obtained by

$$J_{01} = \sqrt{\frac{G_i b_1 w}{g_0 g_1}} \quad (12a)$$

$$J_{k,k+1} = w \sqrt{\frac{b_k b_{k+1}}{g_k g_{k+1}}} \quad (k = 1, 2, \dots, N - 1) \quad (12b)$$

$$J_{N,N+1} = \sqrt{\frac{G_L b_N w}{g_N g_{N+1}}} \quad (12c)$$

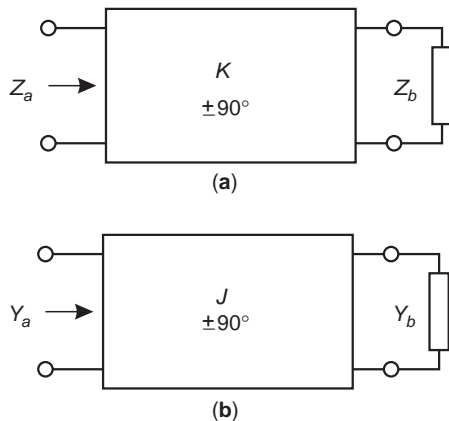


Figure 7. Definition and block diagram of (a) impedance inverter and (b) admittance inverter.

In these filters, the impedance and admittance inverters are the two indispensable circuit elements that could be in practice constructed via quasilumped inductors/capacitors at low frequencies, distributed quarter-wavelength transmission lines with lower/higher characteristic impedances, and so on. As shown in Figs. 10a and 10b, the lumped T network with the positive inductance/capacitance, L or C , in shunt and two identical negative ones, $-L$ or $-C$, in series can make up a simple impedance inverter with the characteristic impedance $K = \omega L$ or $K = 1/\omega C$. Similarly, the admittance inverter can be formulated via the lumped π network and its characteristic admittance can be expressed as $J = 1/\omega L$ or $J = \omega C$, as also denoted in Figs. 10c and 10d. The negative L or C may be absorbed into adjacent series or parallel resonators so as to eliminate them from the overall filter network in practical design.

5. MICROWAVE LOWPASS FILTERS

As discussed in Section 3, the lumped-element lowpass filters consist of a number of series capacitances and shunt inductances in cascade as illustrated in Fig. 5b. These lumped elements are realized in the microwave range by an electrically short section of guided-wave structures, such as transmission line and waveguide, with high or low characteristic/wave impedance [1,3–8]. Figure 11a indicates a high-impedance transmission-line section with the length l_L much shorter than one

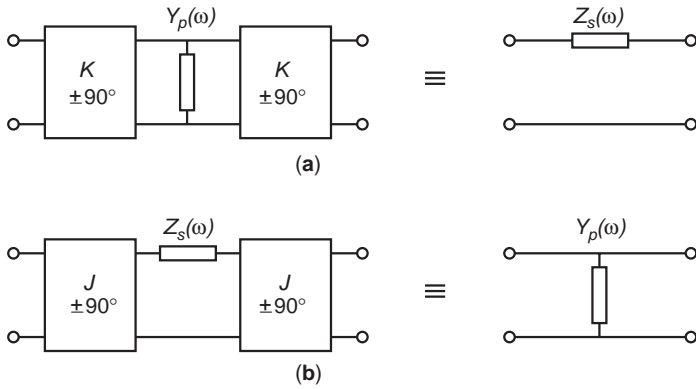


Figure 8. Illustration of equivalent transformation between the shunt susceptance and series reactance via inverter elements: (a) impedance inverter; (b) admittance inverter.

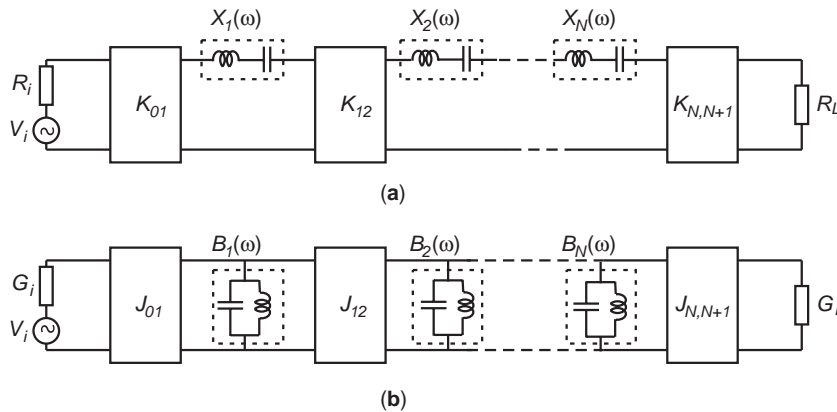


Figure 9. Equivalent networks of lumped-element microwave bandpass filters using (a) impedance inverter and (b) admittance inverter.

guided-wave length λ_g , in which Z_{0L} is much higher than Z_0 of the two feeding lines. This high-impedance line operates as a quasilumped series inductance, and its equivalent T network is depicted in Fig. 11b. Under the assumption that $Z_{0L} \gg Z_0$ and $l_L \ll \lambda_g$, series L and shunt

C can be obtained by [5]

$$L = \frac{Z_{0L}l_L}{c} \sqrt{\epsilon_{reL}} \tag{13a}$$

$$C = \frac{l_L}{2cZ_{0L}} \sqrt{\epsilon_{reL}} \tag{13b}$$

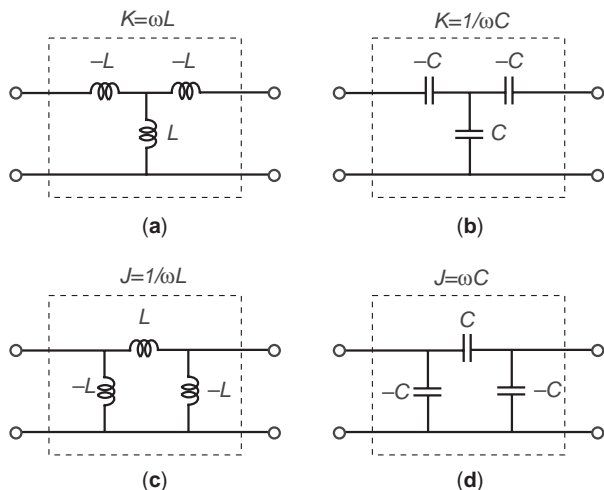
where c is the speed of light in free space and ϵ_{reL} is the effective dielectric constant of this transmission line in an inhomogeneous medium. For the microstrip line, the high impedance can be easily achieved by narrowing the strip conductor, as demonstrated in Fig. 11c. Similarly, the high-impedance coaxial line can be realized by reducing the diameter of its inner conductor with cylindrical configuration, and its cross-sectional view is shown in Fig. 11d.

On the other hand, the shunt quasilumped capacitance can be reasonably formed via an electrically short transmission line with the low impedance Z_{0C} , as depicted in Fig. 12a. As such, an equivalent π network with one major shunt capacitance (C) and the two minor series inductances (L) can be deduced as shown in Fig. 12b. The relevant equations are given as below to calculate these elements [5]

$$C = \frac{l_C}{cZ_{0C}} \sqrt{\epsilon_{reC}} \tag{14a}$$

$$L = \frac{Z_{0C}l_C}{2c} \sqrt{\epsilon_{reC}} \tag{14b}$$

Figure 10. Lumped-element impedance and admittance inverters to be constructed: (a) inductance T network; (b) capacitance T network; (c) inductance π network; (d) capacitance π network.



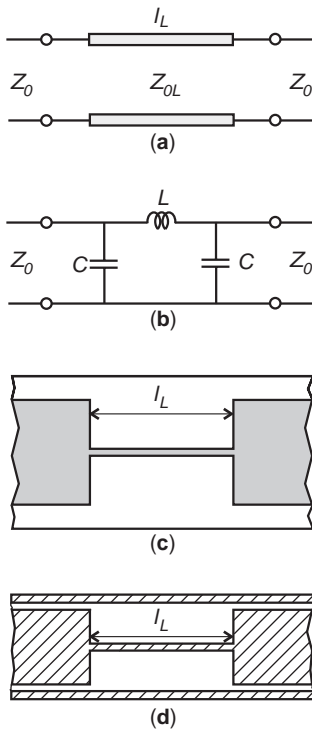


Figure 11. Schematic, equivalent network, and implementation of a high-impedance transmission-line section with finite length: (a) schematic; (b) T network; (c) microstrip-line configuration; (d) coaxial-line configuration.

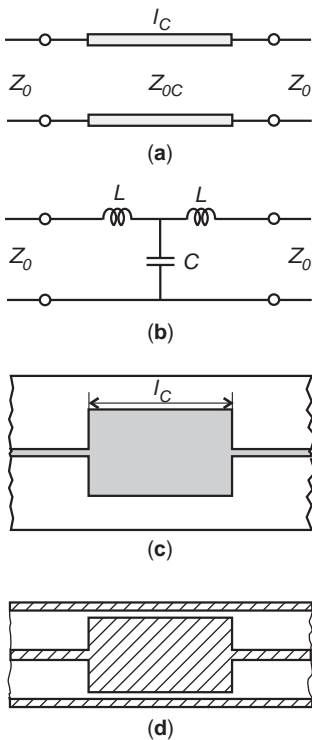


Figure 12. Schematic, equivalent network, and implementation of a low-impedance transmission-line section with finite length: (a) schematic; (b) π network; (c) microstrip-line configuration; (d) coaxial-line configuration.

where l_C and ϵ_{reC} are the physical length and the effective dielectric constant of this low-impedance transmission line. Figure 12c indicates the top view of a low-impedance microstrip line with increased strip width, whereas Fig. 12d is the cross-sectional view of a low-impedance coaxial line with enlarged diameter of the inner conductor. With these equivalent quas lumped elements in mind, various microwave lowpass filters can be accordingly designed on the basis of the synthesis approach discussed above.

Figure 13a describes a fifth-order microstrip lowpass filter, and its equivalent lumped ladder network is illustrated in Fig. 13b. At low frequencies in which each microstrip section is extremely shorter than λ_g , the wide- and narrow-stripline sections can be equivalently considered as quas lumped shunt capacitances (C_1, C_3, C_5) and series inductances (L_2, L_4). As usual, the source and load impedances are assumed as the standard 50Ω . The specifications for the microwave lowpass filter include the cutoff frequency (ω_c), passband ripple (L_c) at ω_c , and insertion loss (L_s) at the defined ω_s in the stopband. On the selection of Butterworth or Chebyshev lowpass prototype, the value of L_s is utilized to determine the order of this filter under the desired L_c ; thus the relevant normalized prototype elements are found from Table 1 or 2. Next, the lumped L_k and C_k in Fig. 13b are calculated via Eqs. (5b) and (5c), thereby

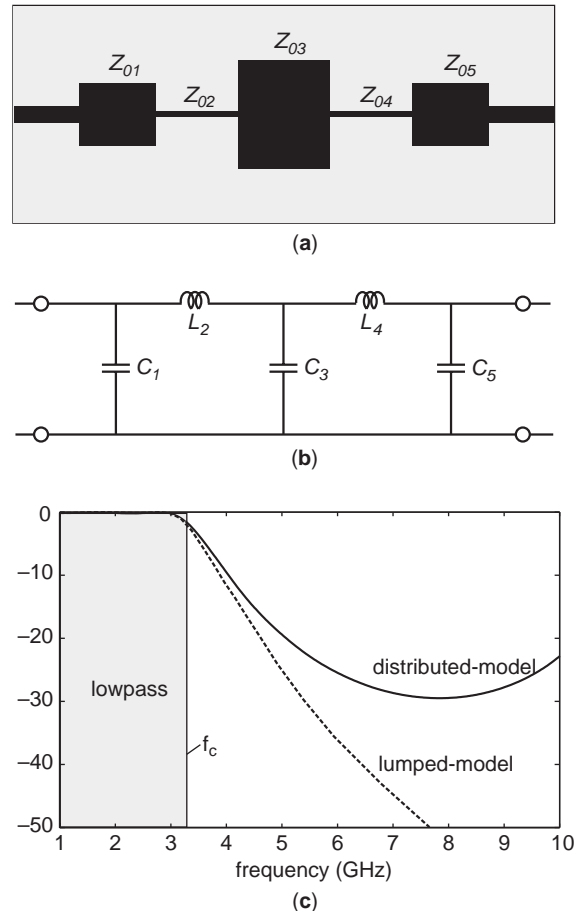


Figure 13. Front view and equivalent lumped-element representation of a fifth-order microstrip-line lowpass filter: (a) front view; (b) equivalent network; (c) attenuation response.

allowing us to obtain the width/length of each microstrip-line section using the closed-form formulas [10] under the selected dielectric substrate via Eqs. (13) and (14).

After filter layout is designed, the frequency response can be derived via a lumped network in Fig. 13b and full-wave simulation over its physical layout, as illustrated in Fig. 13c. Both results seem to closely match each other at low frequencies, but become increasingly different as the frequency rises. This is attributed to the approximation in the lumped model, which fully ignores the frequency distribution of each finitely extended microstrip line section. In fact, each line section is no longer electrically short at high frequencies, and it may operate as a distributed transmission-line section with the length comparable to or even exceeding one guided wavelength (λ_g).

6. MICROWAVE BANDPASS FILTERS

Two basic types of circuit elements are involved in the design of microwave bandpass filters: lumped resonators and immittance inverters. The resonator elements are equivalently made up by the uniform transmission-line sections or waveguide cavities with the length of one-quarter, half- or full wavelength at the center of the concerned passband. In addition to the uniformly shaped resonators, extensive work has been done so far to formulate a number of modified nonuniform resonator configurations toward realizing the compact size, harmonic suppression, and so on, as discussed widely in the literature [e.g., 8]. The inverter elements are basically constructed by various quasi-lumped and distributed capacitive and/or inductive coupling structures. In the following paragraphs, several typical inverter structures will be described in terms of their physical structures and equivalent-circuit networks.

Figure 14a depicts the front view of a microstrip gap element [10] that is formulated by closely spacing the two microstrip open ends via a gap or space of width (S). Its equivalent-circuit network is illustrated in Fig. 14b with a lumped T network, where the coupling effect between the two open ends is modeled as a mutual capacitance (C_g) and the two open ends themselves are perceived as the two identical shunt capacitances (C_p) due to the fringing field distribution. The relevant formulas are given in Ref. 11. This lumped network, driven by the two microstrip lines with the characteristic admittance of Y_0 , can be further converted to an alternative one with a distributed J inverter at the center and the two equivalent electrical lengths ($\phi/2$) at the two sides, as indicated in Fig. 14c. Under the exact equivalence of these two networks, we can obtain [1]

$$\frac{J}{Y_0} = \tan \left[\frac{\phi}{2} + \tan^{-1} \left(\frac{B_p}{Y_0} \right) \right] \quad (15a)$$

$$\phi = \tan^{-1} \left(\frac{2B_g}{Y_0} + \frac{B_p}{Y_0} \right) + \tan^{-1} \left(\frac{B_p}{Y_0} \right) \quad (15b)$$

where $B_p = \omega C_p$ and $B_g = \omega C_g$. To satisfy the requirement of widening the passband, various microstrip gap elements with unequal or offset microstrip feeding lines are

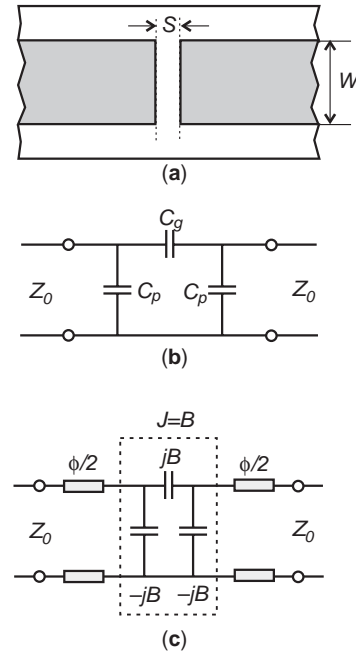


Figure 14. Microstrip series-capacitive coupling element for constructing an admittance inverter: (a) layout; (b) capacitance π network; (c) J -inverter network.

comprehensively discussed in Ref. 12 in terms of their equivalent lumped networks. To further raise the passband width, a microstrip interdigital capacitor with enhanced coupling degree is characterized as a more general J -inverter network with the two unequal electrical line lengths [13], allows the success in designing a compact wideband filter.

The parallel-coupled microstrip line [10] is realized by spacing the two open-end microstrip lines in parallel via longitudinal slot. Figure 15a illustrates such a coupled microstrip-line J -inverter element with the overlapped length of about one quarter-wavelength (i.e., $\phi = \pi/2$) for the filter design [14]. Here, the parameters of Z_{0e} and Z_{0o} are the characteristic impedances of the even and odd modes propagating along the coupled microstrip line. Because of its overlapped configuration and tightened coupling degree, this structure has gained wide application in the design of the compact and wideband microstrip bandpass filters. Figure 15b illustrates its related J -inverter network. Strictly speaking, the inverter admittance (J) appears to be frequency-dependent, but, it is usually considered as a constant value near the frequency in which $\phi = \pi/2$ if the relative narrow passband is considered. Under this restriction, J can be approximately derived by

$$Z_{0e} = Z_0 [1 + JZ_0 + (JZ_0)^2] \quad (16a)$$

$$Z_{0o} = Z_0 [1 - JZ_0 + (JZ_0)^2] \quad (16b)$$

Because of the essential difference between the phase constants of even and odd modes in the inhomogeneous coupled microstrip line, the first harmonic passband appears at the frequency twice that of the dominant passband. This problematic issue is addressed by loading the two

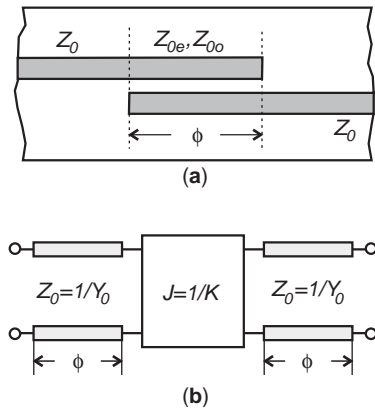


Figure 15. Parallel-coupled microstrip line with about one quarter-wavelength coupled length: (a) layout; (b) J -inverter network.

lumped capacitors at the two terminals [15]. In addition, a stepped-impedance resonator technique [16] has been developed to effectively suppress the concerned parasitic passbands in parallel-coupled line bandpass filters.

Coplanar waveguide (CPW) bandpass filters [17,18] with half- or quarter-wavelength resonators are constituted and explored in terms of CPW open-end gaps and/or short-end stubs, circuit models of which are described in Ref. 19. Similar to the microstrip gap, the CPW open-end structure operates as a series capacitive coupling element; thus its equivalent J -inverter network is the exactly same as those in Figs. 14b and 14c. Figure 16a indicates the CPW short-end stub, in which a pair of strip stubs with the width (S) electrically links the central conductor together and the two-side ground planes. In this way, such

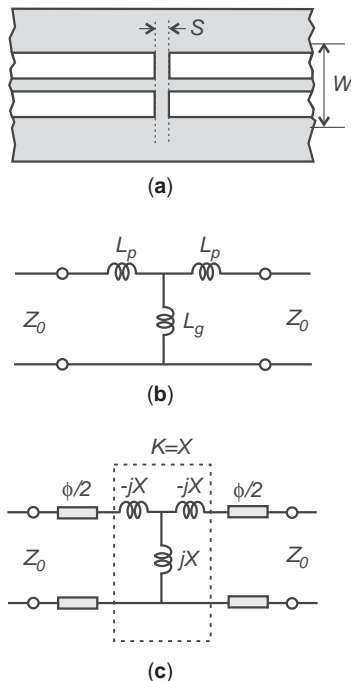


Figure 16. Coplanar waveguide shunt inductive coupling element for constructing an impedance inverter: (a) layout; (b) inductance T network; (c) K -inverter network.

the paired stubs can be equivalently considered as a shunt inductance (L_g) and the two-side CPW short ends are modeled as the two series inductances (L_p), thus forming a quasilumped T network as seen in Fig. 16b. Furthermore, such a lumped network can be converted into its corresponding K -inverter impedance (K) with the two equivalent electrical lengths ($\phi/2$) at the two sides. The complete network is depicted in Fig. 16c, and the relevant network parameters can be obtained by

$$\frac{K}{Z_0} = \tan \left[\frac{\phi}{2} + \tan^{-1} \left(\frac{X_p}{Z_0} \right) \right] \quad (17a)$$

$$\phi = \tan^{-1} \left(\frac{2Z_g}{Z_0} + \frac{X_p}{Z_0} \right) + \tan^{-1} \left(\frac{X_p}{Z_0} \right) \quad (17b)$$

where $X_p = \omega L_p$ and $X_g = \omega L_g$.

In parallel, various waveguide-based coupling structures [1,9] have also been widely investigated to design advanced waveguide bandpass filters with extremely small insertion loss and narrow bandwidth by making effective use of the very high quality factor (Q -factor) of an enclosed waveguide cavity. For instance, Figs. 17a and 17b illustrate the geometry of the two shunt inductive coupling waveguide structures, namely, inductive window/iris and inductive post. Their relevant equivalent-circuit networks can be commonly expressed as a π network, as shown in Fig. 17c, with the major shunt reactance (X_g) at the center, as investigated by Marcuvitz [20]. In the former, the metallic iris thickness is, as usual, extremely thin; thus the two series reactances (X_p) can be ignored and only shunt X_g remains. In the latter, the metallic post

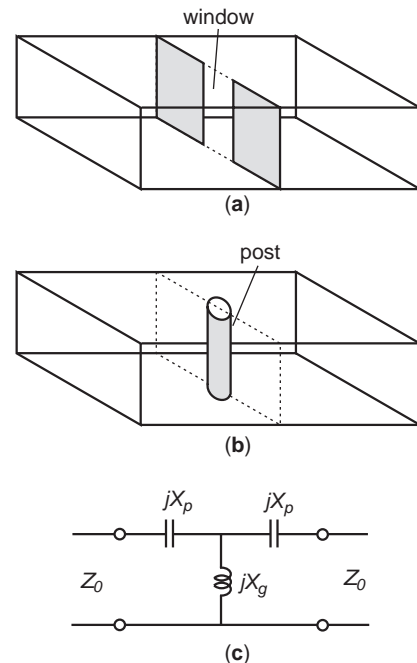


Figure 17. Metallic waveguide shunt inductive coupling elements: (a) inductive window; (b) inductive post; (c) equivalent T network.

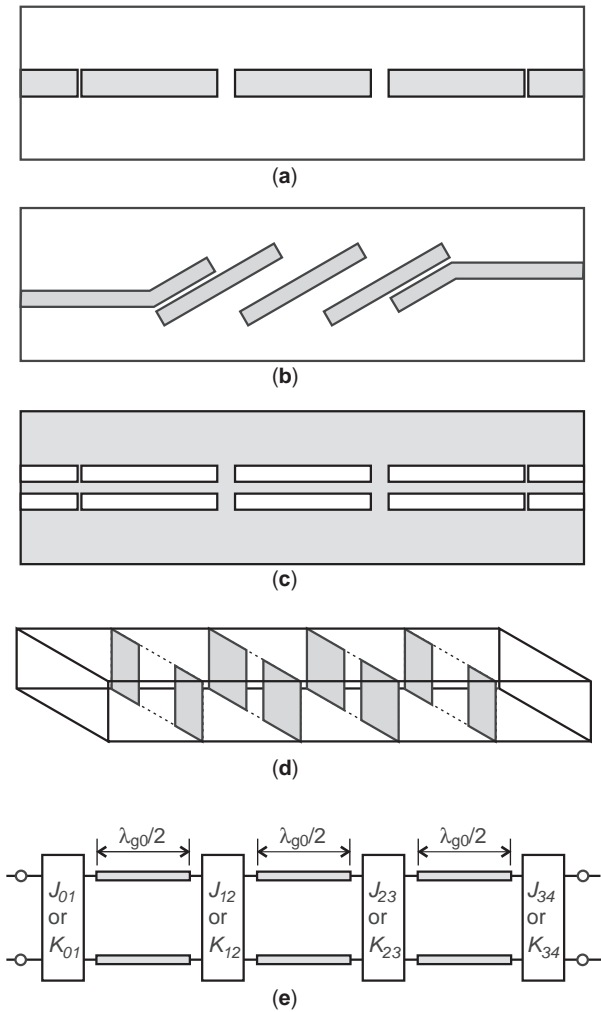


Figure 18. Examples of various planar transmission-line and waveguide bandpass filters (BPFs): (a) direct-coupled microstrip BPF; (b) parallel-coupled microstrip BPF; (c) coplanar waveguide BPF; (d) direct-coupled waveguide resonator BPF; (e) unified equivalent network.

has to be modeled in terms of the complete network in Fig. 17c because of its electrically finite diameter.

Using the above-described coupling structures together with transmission-line or waveguide resonators, various microwave bandpass filters can be constructed and then designed with the Butterworth or Chebyshev frequency response on a basis of the efficient synthesis approach discussed above. For instance, Figs. 18a and 18b demonstrate the layouts of the end-coupled and parallel-coupled microstrip-line bandpass filters [1,3,7], respectively, in which the two adjacent half-wavelength microstrip resonators are connected via equivalent J -inverter networks given in Figs. 14c and 15b. Figure 18c describes a CPW bandpass filter [18] via shunt inductive K -inverter network as shown in Fig. 16c. In addition, a waveguide bandpass filter [1] is demonstrated in Fig. 18d, in which the thin iris serves as the K inverter to link the metallic cavities together [20]. Regardless of different physical configurations as studied above, all these bandpass filters can be equivalently

expressed as a simple cascaded network with J or K inverters as well as several transmission-line resonators, whose lengths should be approximately equal to the half-wavelength (λ_{g0}) at the center of the frequency passband.

7. MICROWAVE HIGHPASS FILTERS

As the reciprocal structure of a lowpass filter, the highpass filter [1,21] can be constructed by cascading the series capacitances and shunt inductances in a ladder configuration as illustrated in Fig. 5c. It suffers from high insertion loss at low frequency because of very small series susceptances and shunt reactances. As the increases become sharper, these frequency-dependent parameters appear to be enhanced in a linear function, thus bringing out the almost perfect transmission beyond the cutoff frequency (ω_c). In order to achieve the specified small ripples in the highpass band, the values of each capacitance and inductance should be properly selected on the basis of lowpass-to-highpass transformations, as described in Section 3.

Figure 19a shows the ladder network of a fifth-order lumped-element highpass filter. The critical point here is how to produce the two types of lumped series capacitance and shunt inductances to a high degree, as usually requested in practical design. Figure 19b depicts the cross-sectional view of a coaxial-line filter [1]. Herein, the series capacitances are realized by closely spacing the two metallic disks of the two inner conductors, and the shunt inductances are formulated by the short-end stub line with small diameter and electrically short length. In addition, a microstrip highpass filter [8] is described in Fig. 19c that consists of microstrip interdigital capacitors and short-end

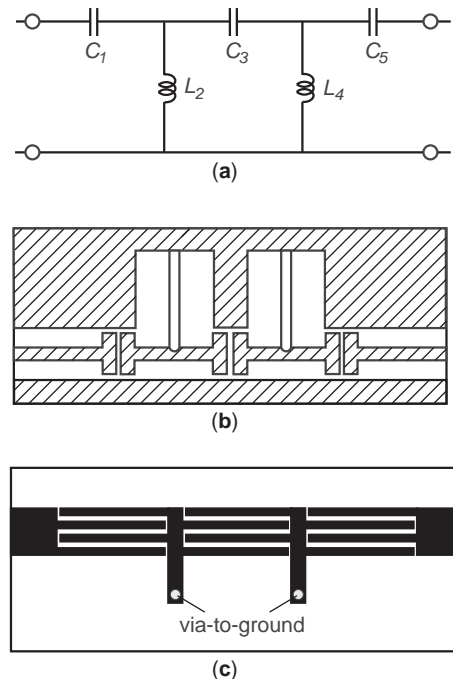


Figure 19. Equivalent-circuit diagram and implementation of highpass microwave filters: (a) lumped-element diagram; (b) coaxial-line configuration; (c) microstrip-line configuration.

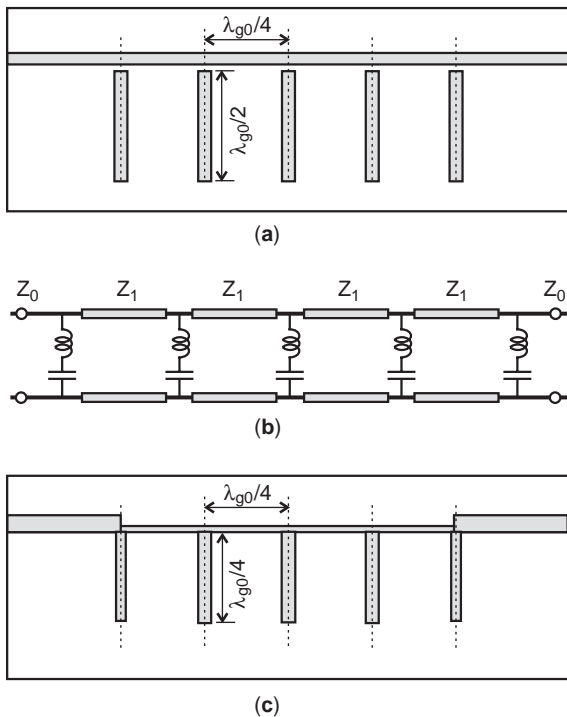


Figure 20. Narrow- and wideband microstrip bandstop filters (BSFs): (a) layout of narrowband BSF; (b) equivalent network of a narrowband BSF; (c) layout of a wideband BSF.

microstrip stubs. These two elements operate as enhanced quasilumped series capacitances and shunt inductances at low frequencies, where their electrical lengths are negligibly short. At high frequencies, however, they no longer behave as lumped elements because their lengths become comparable with the wavelength, thereby degrading the desired highpass behaviors and restricting the highpass bandwidth.

8. MICROWAVE BANDSTOP FILTERS

There exist two essential types of microwave bandstop filters [1] with narrow and wide stopbands. The narrowband filter can be produced in such a way that a uniform transmission line or waveguide is either electrically or magnetically coupled to multiple resonators in periodic intervals with the periodicity of one quarter-wavelength or its odd integer numbers [1,8]. For instance, Fig. 20a shows the layout of such a fifth-order microstrip bandstop filter with a bandwidth of $<20\%$. In this case, a main microstrip line is periodically coupled to the five half-wavelength ($\lambda_{g0}/2$) microstrip-line resonators at the space of a quarter-wavelength ($\lambda_{g0}/4$) near the resonance. Figure 20b indicates its equivalent-circuit network, in which the line resonator and capacitive coupling gap are combined so as to constitute a shunt-series LC resonator. The reactance slope of each LC resonator needs to be properly adjusted by slightly differentiating the coupling gap and/or line resonator dimensions so as to achieve the requested values of each normalized element in the lowpass prototype filter. Furthermore, each $\lambda_{g0}/4$ -length line operates as an immit-

tance inverter in order to utilize the only shunt-series LC resonators. Its impedance may be equal to the source/load impedance (i.e., $Z_1 = Z_0$) for the Butterworth filter, but should be selected as below for the Chebyshev bandstop filter with the N th order:

$$\frac{Z_1}{Z_0} = \frac{1}{\sqrt{g_0 g_{N+1}}} \quad (18)$$

Figure 20c depicts an alternative microstrip bandstop filter [22] in which the main microstrip line is directly connected with the five quarter-wavelength open-end stubs at the space of a quarter-wavelength. This type of bandstop filter may be designed with any stopband width. However, for the narrow-stopband case, the characteristic impedances of these microstrip-line stubs, especially those located close to the input/output feeding lines, must achieve an impractically large width. Thus, this type of filter is found more suitable for design of wideband bandstop filters.

9. CONCLUSIONS

This article systematically describes the fundamental theorem, design approach, and practical implementation of various microwave filters. In the synthesis design of these filters, a lowpass prototype filter is first modeled as a ladder network and its frequency response is specified by preselected polynomial functions, thus determining the order and elements involved in this network per the specifications of concern. With the use of frequency transformation, the frequency response and ladder network of this prototype filter can be easily converted to those of microwave filters with lowpass, bandpass, highpass, and stopband frequency-selective characteristics. Moreover, a variety of representative planar transmission line and waveguide filters are investigated and discussed, allowing the reader to understand the practical implementation of microwave filters.

BIBLIOGRAPHY

1. G. L. Matthaei, L. Young, and E. M. T. Jones, *Microwave Filters, Impedance-Matching Networks, and Coupling Structures*, Artech House, Dedham, MA, 1980.
2. R. Levy and S. B. Cohn, A history of microwave filter research, design, and development, *IEEE Trans. Microwave Theory Tech.* **32**(9):1055–1067 (1984).
3. R. E. Collin, *Foundations for Microwave Engineering*, McGraw-Hill, New York, 1992.
4. R. S. Elliott, *An Introduction to Guided Waves and Microwave Circuits*, Prentice-Hall, Englewood, NJ, 1993.
5. T. Edwards, *Foundations for Microstrip Circuit Design*, Wiley, New York, 1992.
6. K. Chang, I. Bahl, and V. Nair, *RF and Microwave Circuit and Component Design for Wireless Systems*, Wiley, New York, 2002.
7. J. A. G. Malherbe, *Microwave Transmission Line Filters*, Artech House, Dedham, MA, 1979.
8. J. -S. Hong and M. J. Lancaster, *Microstrip Filters for RF/Microwave Applications*, Wiley, New York, 2001.

9. J. Uher, J. Bornemann, and U. Rosenberg, *Waveguide Components for Antenna Feed Systems: Theory and CAD*, Artech House, Norwood, MA, 1993.
10. K. C. Gupta, R. Garg, I. Bahl, and P. Bhartia, *Microstrip Lines and Slotlines*, Artech House, Norwood, MA, 1996.
11. P. Benedek and P. Silvester, Equivalent capacitance for microstrip gaps and steps, *IEEE Trans. Microwave Theory Tech.* **20**(11):729–733 (1972).
12. L. Zhu and K. Wu, Unified equivalent-circuit model of planar discontinuities suitable for field theory-based CAD and optimization of M(H)MIC's, *IEEE Trans. Microwave Theory Tech.* **47**(9):1589–1602 (1999).
13. L. Zhu and K. Wu, Accurate circuit model of interdigital capacitor and its application to design of new quasilumped miniaturized filters with suppression of harmonic resonance, *IEEE Trans. Microwave Theory Tech.* **48**(3):347–356 (2000).
14. S. B. Cohn, Parallel-coupled transmission-line-resonator filters, *IRE Trans. Microwave Theory Tech.* **6**(2):223–231 (1958).
15. I. J. Bahl, Capacitively compensated high performance parallel-coupled microstrip filters, *IEEE MTT-S Int. Microwave Symp. Digest*, 1989, pp. 679–681.
16. M. Makimoto and S. Yamashita, Bandpass filters using parallel coupled stripline stepped impedance resonators, *IEEE Trans. Microwave Theory Tech.* **28**(12):1423–1427 (1980).
17. D. F. Williams and E. Schwarz, Design and performance of coplanar waveguide bandpass filters, *IEEE Trans. Microwave Theory Tech.* **31**(7):558–566 (1983).
18. J. K. A. Everard and K. K. M. Cheng, High performance direct coupled bandpass filters on coplanar waveguide, *IEEE Trans. Microwave Theory Tech.* **41**(9):1568–1573 (1993).
19. L. Zhu and T. Yakabe, Fullwave MoM-SOC technique for extraction of equivalent circuit models of coplanar waveguide discontinuities: CPW- and CSL-mode cases, *IEICE Trans. Electron.* **86**(11):2292–2299 (2003).
20. N. Marcuvitz, *Waveguide Handbook*, McGraw-Hill, New York, 1951.
21. R. Levy, A new class of distributed prototype filters with applications to mixed lumped/distributed component design, *IEEE Trans. Microwave Theory Tech.* **18**(12):1064–1071 (1970).
22. B. M. Schiffman and G. L. Matthaei, Exact design of band-stop microwave filters, *IEEE Trans. Microwave Theory Tech.* **8**(1):6–15 (1964).

MICROWAVE HEATING

JOHN M. OSEPCHUK
Full Spectrum Consulting

Microwave heating is only part of the noncommunications applications of electromagnetic energy and only part of the range of electromagnetic heating [1,2]. The *microwave* range of the spectrum is variously defined. One prefers to think it is characterized by the fact that the dimension of the object to be heated is of the order of the wavelength. In practical terms this means heating at either 915 or 2450 MHz, two of the industrial, scientific, and medical (ISM) frequency assignments (in the United States) for

power or noncommunication applications. There are some medical heating applications (hyperthermia) at non-ISM frequencies where the expense of reducing leakage radiation to meet FCC (Federal Communications Commission) or CISPR (Special International Committee on Radio Interference) limits can be tolerated.

Industrial heating applications of microwaves exist at both 915 and 2450 MHz, but the higher power applications tend to use 915 MHz for meat tempering, bacon cooking, curing of rubber tires, and many other applications. Power levels of such systems range from 5 to 500 kW. At 915 MHz the dominant source of power is the magnetron, providing power from 25 to 75 kW protected by a circulator. By far the most dominant heating application is the microwave oven, which today operates at only 2450 MHz. There are roughly 200 million ovens in the world and roughly 20–25 million ovens are manufactured each year. Most of these are for the consumer market, although a small but significant number are produced for commercial and professional use. The widespread microwave oven market is made possible only because of the unique properties of the *cooker magnetron*. These include high efficiency (~70%) at power on the order of 1 kW, compatibility with simple unfiltered power supplies and arbitrary loads, and above all, low cost (~\$10 per tube in large quantities). An unavoidable (so far) concomitant to efficiency is high noise and other anomalous phenomena. A basic text on the microwave oven [3] and a broader treatment of industrial heating [4] have been published.

Most applications, whether for the microwave oven or industrial machine, correspond to the simple schematic depicted in Fig. 1. The basic objective is to deliver microwave power efficiently to the load. Thus, the system must be designed to minimize the reflected power. A practical microwave oven will not have a circulator or directional coupler, but in the design stage these tools or their equivalents will be present.

The absorption of microwave power depends on the dielectric properties of the load, which are temperature-dependent, its size and shape. Given these parameters, the extensive literature on dosimetry permits one to calculate or estimate the power absorbed by the load when it is exposed to a plane wave of given flux density. A convenient reference is the *Radiofrequency Radiation Dosimetry Handbook* [5] published by the U.S. Air Force. Most non-medical applications must be carried out in an enclosure. Thus, the modal and quasioptical properties of that enclosure will influence the equivalent plane waves that irradiate the object. The task of efficiently coupling energy from the power source waveguide to the enclosure is the function of the *feed*, which may be an antenna, aperture, or other coupling device. To achieve reasonable uniformity of heating, there must be some randomizing element in the system, for example, a rotating stirrer or scatterer or rotating feed antenna. Alternatively, there could be a rotating turntable on which the load is placed or a load-bearing belt that moves through a conveyerized oven of one or more cavities.

Because the magnetron is a key component of practical systems, knowledge of its properties is necessary. Frequency pushing, as the tube anode current varies, as well

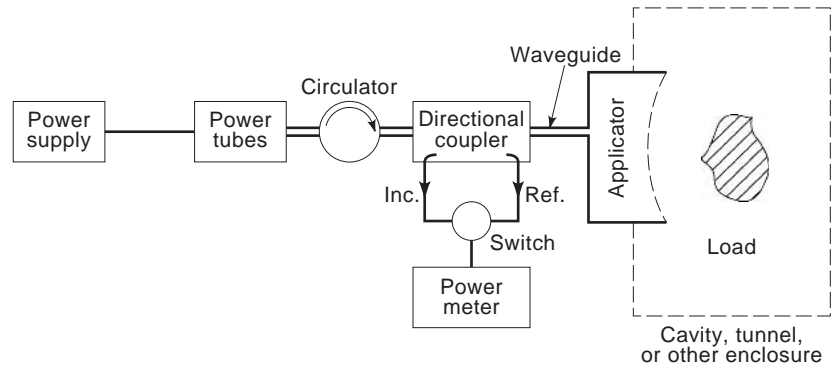


Figure 1. Basic elements of a microwave power system for processing of materials.

as frequency pulling as the load varies per stirrer rotation and load temperature increase, both spread out the power spectrum and average out or smear modal properties of the field pattern around the load. These variations also produce a complex pattern of electromagnetic noise both at microwave frequencies and at baseband frequencies. This information influences the design of the door seal and other parts of a practical system to meet limits imposed by the FCC or CISPR as well as the Food and Drug Administration (Center for Devices and Radiological Health).

At present, design procedures are basically empirical, in view of the complex dependence of the heating pattern on many variables, making prediction, and even experimental replication, impractical if accuracy (a few percent) is required. There are some pilot studies on computer codes for microwave heating, but they are useful only for the simplest systems, for example, a uniform rod in a waveguide. In the future, as tube sources are improved in noise, efficiency, and available frequencies coupled with improvements in applicators (e.g., multiple feeds), one can expect significant advances in microwave heating. Still further ahead are more exotic heating applications where the pulse or modulation characteristics of the source are important (e.g., in the stimulation of chemical catalysts).

1. BASIC PRINCIPLES OF MICROWAVE HEATING

The principles of microwave heating are well-established [1-5]. It is generally assumed that the material to be heated is adequately specified in terms of the macroscopic complex dielectric permittivity ϵ defined by

$$\epsilon = \epsilon_0(\epsilon_r + j\epsilon_i) = \epsilon_0 \left(\epsilon_r + \frac{j\sigma}{\omega\epsilon_0} \right) \quad (1)$$

where $\epsilon_0 = 8.86 \times 10^{-12}$ F/m, the permittivity of free space, ϵ_r is the real part of the relative dielectric constant, and σ is the conductivity in S/m (mho/m) which is equivalent to the following

$$\epsilon_i = \frac{\sigma}{\omega\epsilon_0} \quad (2)$$

where ω is the assumed radian frequency of the fields. It is convenient to define auxiliary terms like the loss

tangent, $\tan \delta$:

$$\tan \delta = \frac{\epsilon_i}{\epsilon_r} = \frac{\sigma}{\omega\epsilon_r\epsilon_0} \quad (3)$$

The rate of internal density of absorbed energy, or power P , is derived from the real part of the product of current density, from Maxwell's equations, and the internal electric field E_i , yielding

$$P = \sigma |E_i|^2 = \omega\epsilon_r\epsilon_0 \tan \delta |E_i|^2 \quad (4)$$

where P is in terms of watts per cubic meter. Equation (4) is the practical formula for computing power dissipation in materials and objects of uniform composition when adequately described by the simple dielectric parameters.

Given the values of the dielectric parameters, one can then calculate the penetration depth D , at which, for plane-wave irradiation of a material, the fields are reduced by a factor of $1/e$. The result is

$$D = \frac{0.225\lambda}{\epsilon_r^{1/2}} \cdot [(1 + \tan^2 \delta)^{1/2} - 1]^{1/2} \quad (5)$$

or for low-loss materials where $\tan \delta < 1$

$$D \cong \frac{0.318\lambda}{\epsilon_r^{1/2}(\tan \delta)} \quad (6)$$

where λ is the free-space wavelength of the microwave radiation.

For low frequencies or small objects, the components of electrical fields normal to a material boundary are related by the following equation

$$\left| \frac{E_i}{E_o} \right| \cong \frac{\omega\epsilon_0}{\sigma} \quad (7)$$

where E_i and E_o are the internal and external fields, respectively. The material is characterized by σ , and the outside volume is free space. If the applied field E_o is parallel to the surface, then the internal field is equal to E_o . Thus, if the applied field is parallel to the long axis of a body, the internal field is approximately equal to the external field. Otherwise, if the applied field is perpendicular

Table 1. Dielectric Properties of Foods and Other Materials at 2450 MHz and 20°C

Material	ϵ	$\tan \delta$
Distilled water	78	0.16
Raw beef	49	0.33
Paper	2–3	0.05–0.1
Wood	1.2–5	0.01–0.1
Alumina	7.8	0.001
Borosilicate glass	4.5	0.004–0.007
Neoceram	6.2	0.003
Plastics		
ABS	2.85	0.006
Ultem	3.0	0.001–0.004
Polysulfone	2.1	0.006
Polypropylene	2.2	0.0005
Teflon	2.0	0.0004
Liquid crystal polymer	3.9	0.007

to the long axis, the internal field, according to Eq. (7), is much less than the external field even for moderate conductivity of the order of 1 S/m.

The principal task in microwave heating problems is the determination of internal fields in an object that permit through Eq. (4) the determination of the heating distribution over time. The dielectric parameters are key data for such a calculation, particularly the dependence on temperature. Standard methods for measurement of these parameters are readily available [6]. The simplest technique, and often the preferred method, is that in which rods or long slender samples of the material of interest are placed in the central vertical plane of a rectangular waveguide through small access holes centrally located on top and bottom walls [7]. This is also a method for uniform heating of such a small sample, except for small volumes near the top and bottom access holes. Classical perturbation theory [7] permits the determination of ϵ and $\tan \delta$. Considerable data for a wide range of materials at room temperature and at various microwave frequencies are found in the literature [8].

Table 1 lists such data for a few important materials at 2450 MHz, the most commonly used frequency for microwave heating. Values of $\tan \delta$ well below 0.01 signify negligible absorption and heating, whereas values above

0.1 are considered good absorbers. Data on temperature dependence of dielectric parameters are not widely available in the literature. The classic data from Bengtsson and Risman [9] on temperature dependence for foods are reproduced in Fig. 2. They illustrate some general properties for heating of foods. The high value of ϵ , in the range of 40–80, signifies substantial reflection at the boundary of large food volumes of the order of 50%. For most foods, the value of $\tan \delta$ decreases with temperature, following that of water. This dependence is the basis for stabilization of heating, which aids a trend to uniformity of heating. On the other hand, a few foods such as ham that have significant salt content (ionic conductivity) show an increase in $\tan \delta$ with temperature. This tends to trigger thermal runaway at hot spots and nonuniform heating. When this happens in a glass or even ceramic tray in an empty oven, this can lead to dramatic melting at one spot. Although data for foods are generally limited to below 100°C, the temperatures of interest are much higher for oils and nonfood objects. Interest in ferrite materials as browning aids at a stable Curie temperature has been replaced by the development of the *susceptor* [10], in which a very thin (less than 100 Å) film of aluminum that is deposited on suitable insulating dielectrics highly absorbs impinging microwave radiation.

The calculation of absorption distributions in simple geometries (e.g., spheroids) is amply described in the literature [5]. Only for very small spheres is heating uniform and approximately uniform in long thin rods aligned with the E field. At very high frequencies penetration and heating is superficial. In general, heating is nonuniform. For frequencies in the resonance range and for some materials and certain frequencies, dramatic hot spots are possible in the center of objects. Figure 3 shows the visualization of such a hotspot in a sphere of glue with a cloud point near 50°C. This can lead to superheating and explosive phenomena associated with such spherical objects. This is an example where the geometry of the sample is the prime factor determining temperature distribution in an object rather than external field patterns or modal properties of the applicators. Another such factor is the concentration of field and heating at corners and cusps of objects to be heated.

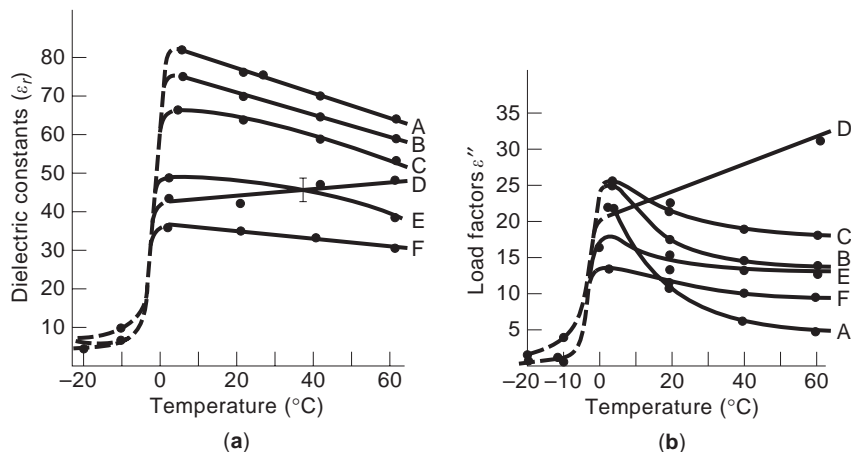


Figure 2. Properties of foods near 2.45 GHz as a function of temperature, where A represents distilled water; B, cooked carrots; C, mashed potatoes; D, cooked ham; E, raw beef; F, cooked beef; and G, corn oil: (a) dielectric constants and (b) load factors, $\epsilon'' = \epsilon \tan \delta$ [9]. (From Ref. 9 with permission. © International Microwave Power Institute).

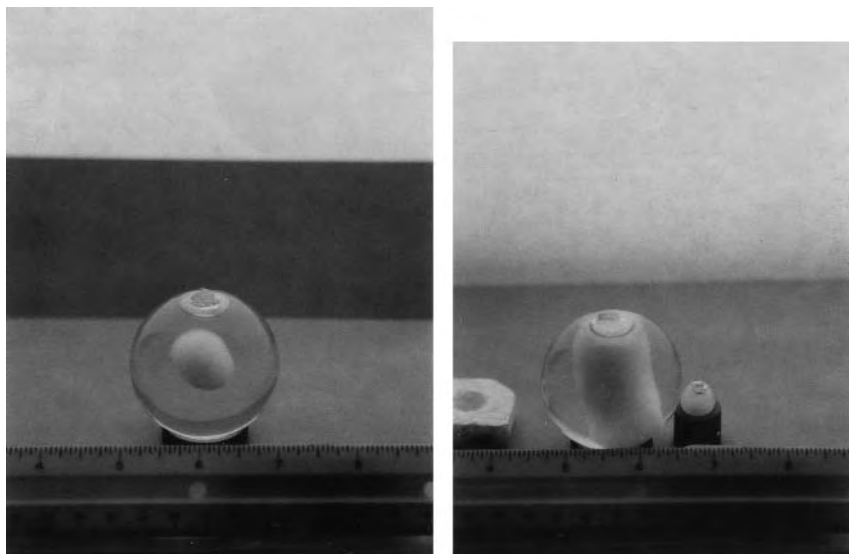


Figure 3. Samples of phantom material heated in a microwave oven, Sekusui Glue—R-500 (water and polyvinyl alcohol), cloud temperature of 51°C.

2. MICROWAVE APPLICATORS

Figure 1 depicts an *applicator* acting as a transducer or coupling agent between the feed waveguide and the load object. The simplest applicator may be a rectangular guide with access holes on top and bottom walls [7] allowing thin rods or tubes of flowing liquid to be heated. More specialized applicators include helices and slow-wave applicators. These have been described by Metaxas and Meredith [4]. Antennas and other applicators for heating limited parts of the human body for diathermy or hyperthermia are reviewed by Guy [11], who restricts the reader’s attention to the multi-mode cavity because it is the basis of most ovens and industrial machines that must handle large quantities of material or a large variety of objects. The engineering literature on waveguides is dominated by papers on properties at low frequencies where one or only a few modes can propagate. Considerable literature also exists for the high-frequency limit where optical

properties come into the forefront. Little exists on the properties of waveguides that influence the performance of microwave heating systems.

A series of tests were conducted by the author on a machined aluminum cavity of dimensions 7 ft long by 2 ft². The cavity was excited by various antennas at one end and the transmitted signal was received at the other end with the same or a different antenna. Measurements were made of the incident, reflected, and transmitted signals over a broad range of frequencies from 0 to 8 GHz. The upper frequency limit corresponds to a factor of over 32 times the lowest cutoff frequency of the 2 × 2-ft waveguide or a transverse dimension of 16 free-space wavelengths. It may be noted that the transverse dimension of most microwave ovens and industrial machines is approximately three wavelengths.

Figure 4 shows transmission data when a 4-in. axially aligned monopole is used at both ends of the 7-ft-long wave-guide, over the frequency range of 0–1.8 GHz.

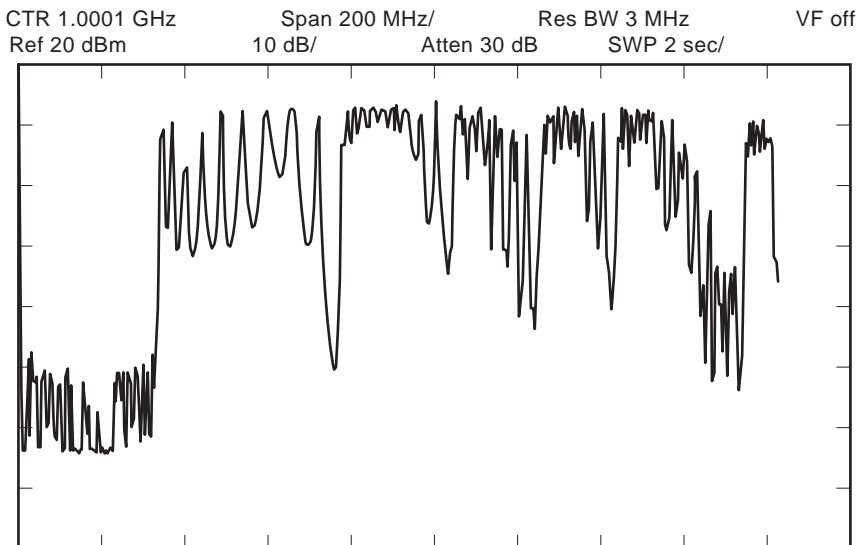


Figure 4. Transmission of microwaves through a 7-ft-long section of waveguide (2 × 2 ft), 0.0–1.8 GHz with axially aligned 4-in. monopole antennas at each end. This antenna preferably excites TM modes.

Although the maximum transmission peaks reflect an insertion loss of only 2–3 dB, there are occasional severe dips in transmission. It can be shown that these occur at or near the cutoff frequencies of transverse magnetic (TM) modes, which tend to be excited by an axial monopole. Reflection measurements show that the low transmission is associated not only with dissipative losses at cutoff resonances, but also severe reflection losses just below cutoff. One can see that according to the relation above for $D \sim 3\lambda$, the typical microwave oven might correspond to about 1.5 GHz. One can see a large dip near that frequency that can be related to mode indices of three and five. In fact, in practical microwave oven work, it has been found that when an antenna exciting TM modes is used in an oven with transverse dimensions near such a cutoff relation, an input impedance match cannot be achieved with ordinary tuning elements. Quine [12] has shown that properties near such TM mode cutoff resonances are related to the blindspot phenomenon found in the radiation properties of phased-array antennas. He shows that the application of the image theorem for an antenna near a ground plane clarifies the connection between a waveguide and a phased array.

If a shielded loop antenna is substituted at the ends of the cavity in place of the monopoles, the transmission data shown in Fig. 5 are obtained. Absent are the severe transmission dips at cutoff frequencies. The effects at cutoff frequencies are greatly diminished when present. Data taken above 2 GHz with this waveguide show the diminishing effect of cutoff resonances as frequency increases, and the increasing density of modes as a cavity with three mode indices. Furthermore, although absorption by an object in the guide is affected by its size-dependent cross section, there is some suggestion that higher frequencies yield more consistent absorption. One might speculate that this results from the lesser prevalence of sizable *coldspots* in field patterns at higher frequencies.

One can see that studies of such a waveguide can yield valuable insights for understanding practical microwave heating cavities. Location of the load object is an

important parameter. One can intuitively judge that the location of objects near a conducting wall is not desirable. In this case, if the space between the object and the wall is less than a freespace wavelength, it can be shown [13] that the only modal propagation in that interspace is of the slow-wave or bound-wave variety that exhibits a large propagation attenuation constant, α .

It is of interest to review the mode density of such cavities as a function of frequency. A review of such mode-counting exercises by Voss [14] shows that although the increase of density with frequency will on the average follow simple formulas, there are discrete regions where the mode density is quite low and other regions where it is much greater, for example, a factor of ≥ 5 when considering a bandwidth of 50 MHz or more at 2.45 GHz. A typical microwave oven cavity may be expected to show an average mode separation of approximately 4 MHz. Therefore, in the ISM band of 2.4–2.5 GHz, one could conceivably benefit from the mixing of up to 25 modes. In practice, any such benefit is not exploited because a much smaller frequency variation of the practical magnetrons is used. There is enough frequency variation, however, to prevent simple single frequency calculations to be of any direct relevance to practical performance.

3. PRACTICAL MICROWAVE HEATING SYSTEMS

Most practical microwave heating systems employ a heating space confined by metal walls, that is, a cavity or waveguide. The basic reason is related to efficiency, although limitation of radiated leakage and out-of-band noise is also a determining factor. Today all microwave ovens operate at 2450 MHz.

Figure 6 shows an exploded view of a typical microwave oven. Shown are the main features or components that relate to power and efficiency. Not shown are the electronic timer and control circuitry or the door interlock system. The basic elements are the microwave power generator, the magnetron, driven by an AC high-voltage power

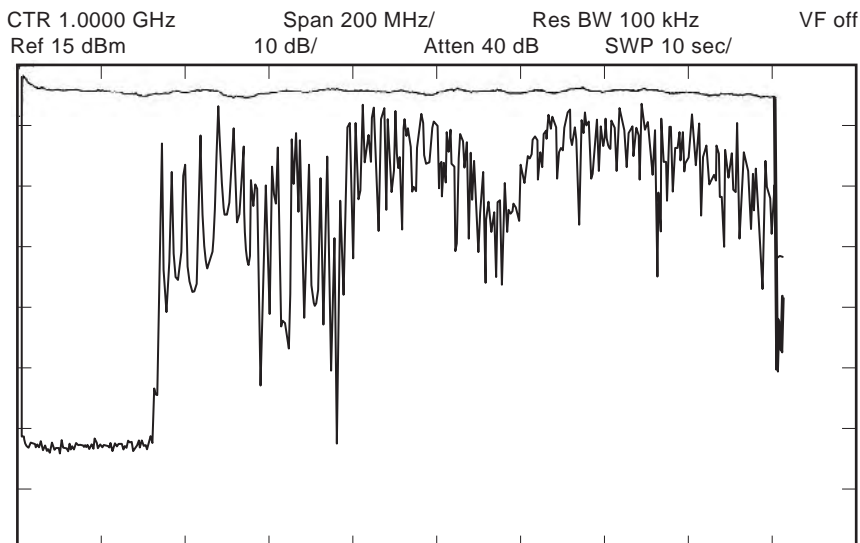


Figure 5. Transmission of microwaves through a 7-ft-long section of waveguide (2×2 ft), 0–18 GHz with shielded-loop antennas at each end. This antenna preferably excites TE modes.

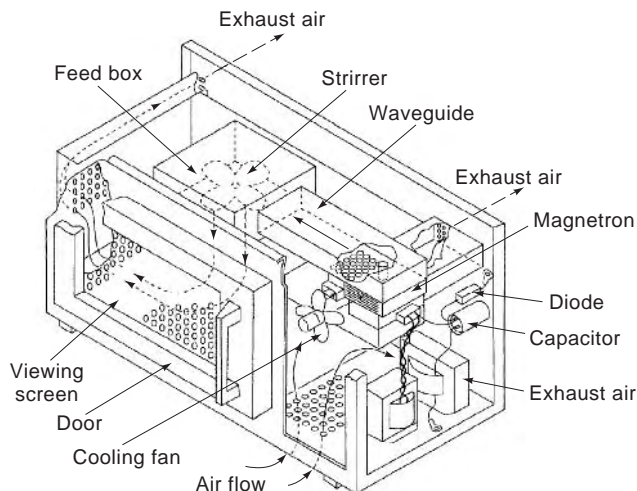
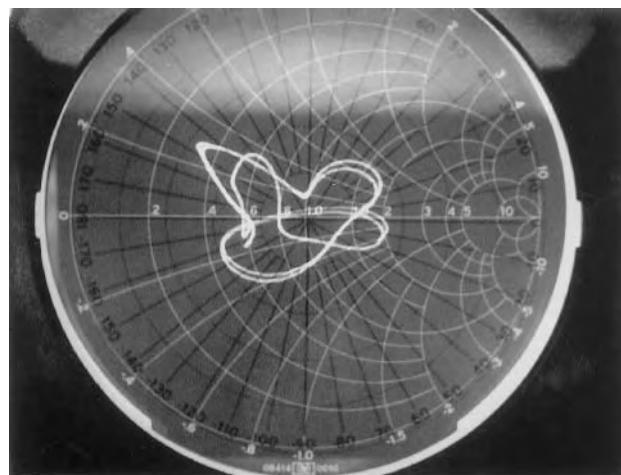


Figure 6. Exploded view of a microwave oven showing power components, microwave components, and cooling system; electronic control circuits are not shown.

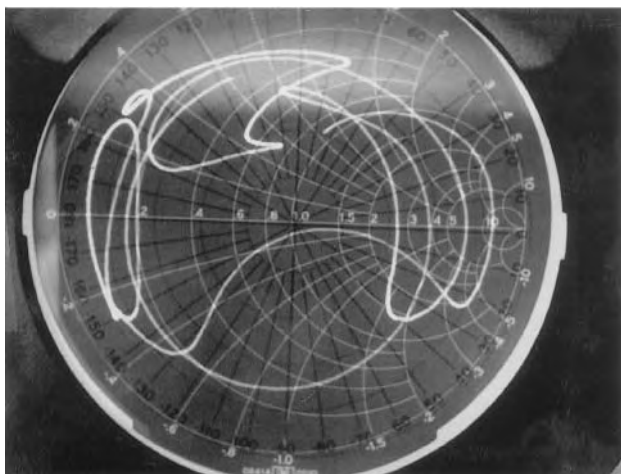
supply connected to the electricity source. The magnetron is connected to a short section of low waveguide, which, in turn, couples energy into the oven cavity either through an antenna similar to a monopole, strip, or patch antenna or through a simple waveguide aperture. Most ovens employ a randomizing element such as the rotation of an antenna or a rotating *stirrer* (a scatterer) in the case of an aperture coupling. Contemporary oven designs also include a rotating turntable for the load placement in addition to (or in a few cases the substitution for) the stirrer. Moving conveyor belts also help smooth out heating patterns, but they are employed almost exclusively in industrial systems.

Practical microwave ovens dispense with a circulator and means of monitoring reflection (Fig. 1). These elements, however, are almost mandatory in high-power industrial systems, which operate at powers of many tens of kilowatts. Because the magnetron is not isolated from the variable load by a circulator, it will exhibit significant pulling, on the order of 10–20 MHz. The effect of the changing load on the power and frequency of the magnetron is shown in the Rieke diagram supplied by the tube manufacturer. For maximum efficiency, this diagram points the oven designer to the selection of a load impedance of a matched load or somewhat into the sink region of the diagram.

Because of the complexity of the situation, including the need for accommodating any food load, the feed design is optimized by empirical techniques. With water loads or even actual food loads, the input impedance is determined with a suitable reflectometer circuit [3,4]. Data obtained are a Smith chart representation similar to that shown in Fig. 7, where at a fixed frequency (e.g., 2450 MHz) the recurring path of the impedance locus is shown as the oven stirrer goes through its cycle. Figure 7a shows the impedance pattern for a large load of 2000 mL. It is desirable that the pattern be located close to the center match point or slightly into the sink phase of the magnetron (determined by appropriate techniques, [3,4]). This is done by



(a)



(b)

Figure 7. Input impedance contour of a microwave oven at a constant frequency as the variable element (stirrer) goes through its cycle: (a) for 2000 mL water load; (b) for an empty cavity.

appropriate tuning techniques, for example, by adjusting the length of the waveguide or adding a tuning post. Of course, all of this was done at a single frequency, hopefully to approximate the dominant frequency emitted by the magnetron at full power. But the oven impedance is a rapid function of frequency as well. For example, Fig. 8 shows a typical recorded impedance at a fixed position of an antenna (or stirrer) over the frequency range of 2.4–2.5 GHz. Thus, the designer must examine a two-dimensional array of datasets or plots such as those of either Fig. 7 or Fig. 8 and adjust for an optimum feed match over the anticipated range of frequency and stirrer position. Figure 7b shows the impedance plot at one frequency for an empty oven as the stirrer rotates. The wildly gyrating pattern is not susceptible to matching, of course; but its importance lies in signifying that when an oven operates with no load or light load (like popcorn), it will subject the magnetron to an extreme of impedance variations. This in turn leads to a wider range of frequency and noise emissions, including frequency skips.

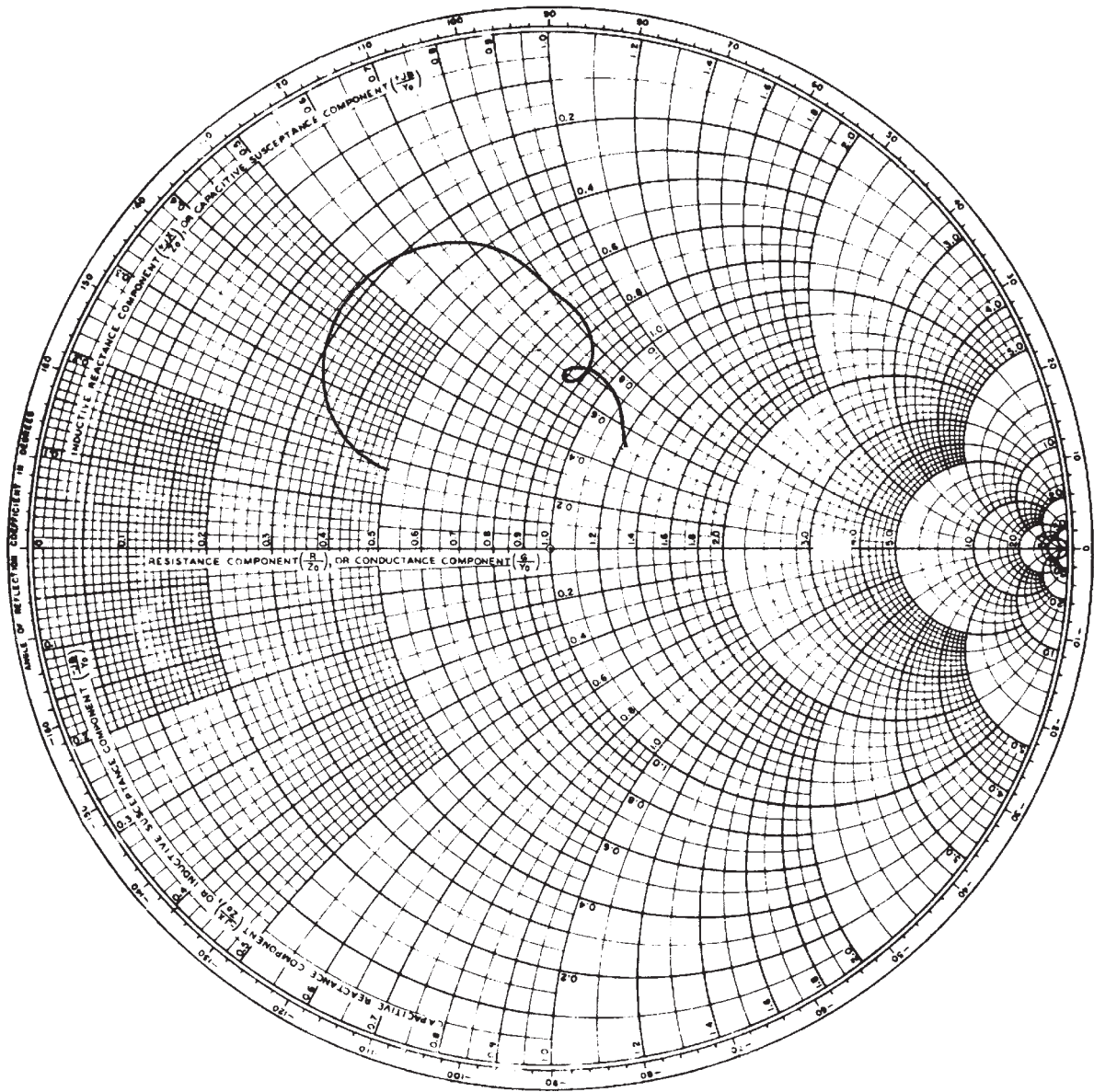


Figure 8. Input impedance contour of a microwave oven at a constant position of the variable element (stirrer) as frequency is swept from 2.4 to 2.5 GHz.

Current magnetrons at 2.45 GHz may exhibit an efficiency of 70%. Because of losses in the power supply and losses in the feed and cavity, the net efficiency for a large load may be of the order of only 50%. For smaller loads down to 50 mL, there will be a further significant reduction of efficiency as shown in Table 2 taken from a typical set of data for several current ovens. The dominant causes for low efficiency at small loads are reduced magnetron efficiency at unfavorable load phases and reduced microwave circuit efficiency with significant heating of metal walls and dielectric parts, such as a tray.

Heating patterns, especially at 2.45 GHz, are notoriously difficult to replicate and optimize. An acceptable variation in array tests is a 10–20% variation in temper-

ature rise values. The prediction of an even measurement of heating patterns is a complex problem and no ideal solution has been found. For very thin sheets, frequency diversity as provided by a traveling-wave tube (TWT) (e.g., 2–4 GHz) yields dramatically improved uniformity [15]. For most applications however, TWTs remain unacceptably high in cost.

Conveyor systems, by virtue of varying load position, measurably and usually acceptably improve heating uniformity. Most high-power systems at 915 MHz utilize conveyors. On the other hand, circulators are used so that the magnetron frequency is not pulled. There remains only a few megahertz of frequency pushing, which is not a large contribution to frequency diversity as an element in improving uniformity.

Table 2. Effective Power Levels for Various-Size Water Loads in a Typical Microwave Oven (Three Different Models): 1–2 Min Operation

Water Load (mL)	Measured Power Relative to Power at 1000 mL		
	Oven A ^a	Oven B ^b	Oven C ^c
100	0.61	0.52	0.59
250	0.44	0.88	0.74
500	0.83	0.96	0.80
1000	1.00	1.00	1.00

^aOven A power at 1000 mL: 673 W.
^bOven B power at 1000 mL: 705 W.
^cOven C power at 1000 mL: 754 W.

4. POWER SOURCE PROPERTIES

Because the magnetron is almost exclusively the microwave generator of choice for microwave heating systems, it is important to focus on the properties of that tube and its associated power supplies. These determine the operating power spectrum from pushing and pulling characteristics. Furthermore, the noise and moding characteristics of the magnetron impacts on interference phenomena and the ability to meet increasingly stringent radiated and conducted noise limits imposed by regulatory authorities. Figure 9 is a schematic depicting the main electronic circuits and elements in a microwave oven. A half-wave high-voltage power supply is indicated with both filament and high-voltage secondary on the same transformer. This reflects the fact that most microwave ovens are cold-start. Thus, the magnetron current is a rectified pulse of roughly half-sinusoidal shape with a repetition frequency of 60 Hz and a pulsewidth of roughly 8 ms. The peak current is about 1 A for an average current of 0.3 A for a 700–800-W oven.

The magnetron is known to exhibit high noise at currents below 0.3 A, occasional discrete spurious sideband signals for currents between 0.3 and 0.6 A, and is typically quiet above 0.6 A [16]. The result is that the typical magnetron radiates spurious noise and signals in 1 ms pulses during the rise and fall of each pulse. Figure 10 depicts a full-wave power supply that yields a current waveform of two rectified half-waves per 60 Hz period and, therefore, lower peak current for the same average current. This does little to reduce magnetron noise. Note that in this supply there is a separate filament transformer. This supply may be used in commercial ovens. Figure 11 is a photo of several modern magnetrons. Note the small size (approximately 4 in. maximum dimension) and the *filter box* that reduces baseband radiation and emissions conducted to the powerline.

Figure 12 is an example of the radiated noise (peak signals) a few feet from a microwave oven when operating with a light load. Peak levels approaching 100 dB/pW effective radiated power are not uncommon in the range between 2.3 and 2.4 GHz. Because of the potential interference with various wireless communications systems, there is activity within CISPR (Special International Committee on Radio Interference) to apply more stringent limits on noise radiated from magnetron-powered systems [17].

Magnetrons can mode and produce spurious signals in the 4–5 GHz range that have interfered with satellite

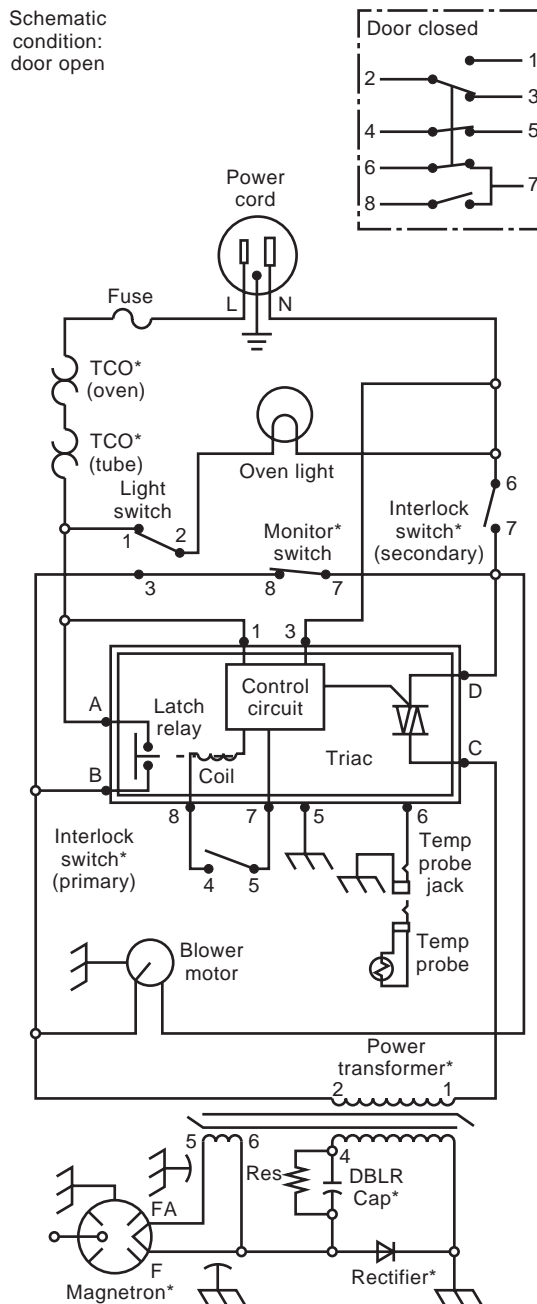


Figure 9. Schematic diagram of a microwave oven showing half-wave doubler power supply, interlock system, and electronic controls. (Courtesy of Amana Appliances.)

communication links. This can occur when there is insufficient cathode emission (as at the end of life) or even when there is too much emission. This occurs because high emission may strengthen spurious sideband oscillations that can also cause moding. Figure 13 shows an example of a recorded magnetron voltage-current trace during such a moding event. Magnetrons in microwave ovens will exhibit as much as 4–5 MHz pushing and up to 20 MHz of frequency pulling.

In the higher power systems at 915 MHz for industrial use, the magnetrons are always protected by a circulator. Therefore, there is no pulling by load variations.

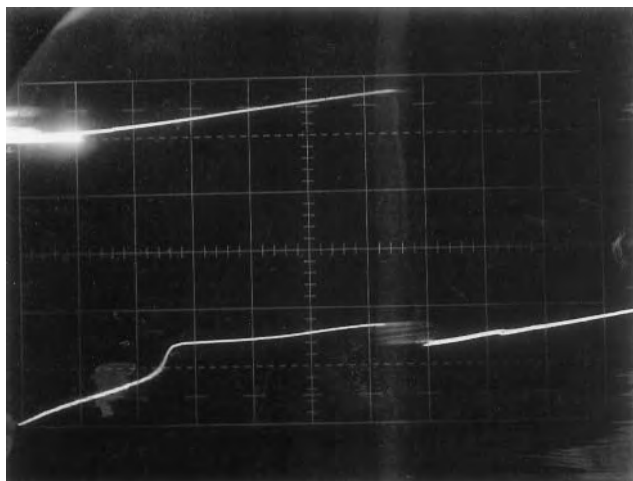


Figure 13. Voltage–current trace of a magnetron depicting moding at a spurious oscillation discontinuity; vertical—250 V/div; horizontal—0.1 A/div.

is that more emphasis should be placed on food standards without relying on the heating of foodstuffs for food safety.

6. FUTURE ADVANCES IN MICROWAVE HEATING

Microwave heating is in its infancy as pointed out by Kapitza [21]. Future expansion in large part awaits the development of efficient and low-cost power sources at various frequencies and power levels beyond what is now available. Thus, in the future one expects such power sources at 5.8 GHz, 24.125 GHz, and the millimeter-wave ISM frequencies. In addition, the availability at power levels down to 100 W, as well as high powers of many kilowatts, will spur many new applications. At present, many such applications are being explored [22] in the fields of chemistry, ceramics, and materials processing. In addition, there are applications to agriculture, pharmaceuticals, and various medical procedures.

In parallel with heating applications are important nonheating power applications, such as microwave-powered lighting [23]. The list of research needs includes: (1) a resolution of the efficiency versus noise tradeoff inherent in magnetrons, (2) the achievement of successful computer models [24] for characterizing real-life microwave heating systems, (3) improved applicators of various types, (4) improved door seals and suppression tunnels to meet noise limits, and (5) the exploitation of pulse modulation techniques for special interactions as in chemistry [25].

BIBLIOGRAPHY

1. J. M. Osepchuk, Microwave technology, in *Kirk-Othmer Encyclopedia of Chemical Technology*, 4th ed., Vol. 16, Wiley, New York, 1995.
2. J. M. Osepchuk, A history of microwave heating applications, *IEEE Trans. Microwave Theory Tech.* **MTT-32**:1200–1224 (1984).
3. C. R. Buffer, *Microwave Cooking and Processing*, Van Nostrand Reinhold, New York, 1992.
4. A. C. Metaxas and R. J. Meredith, *Industrial Microwave Heating*, Peter Peregrinus, London, 1983.
5. C. H. Durney, H. Massoudi, and M. F. Iskander, *Radiofrequency Radiation Dosimetry Handbook*, 4th ed., USAF School of Aerospace Medicine, Brooks AF Base, TX, 1986.
6. ASTM, *Standard Methods of Test for Complex Permittivity (Dielectric Constant) of Solid Electrical Insulating Materials at Microwave Frequencies and Temperatures to 1650C*, Document D2520-86 (reapproved 1990), American Society for Testing and Materials, Philadelphia; 1986.
7. M. A. Rzepecka and M. A. K. Hamid, Modified perturbation method for permittivity measurements at microwave frequencies, *J. Microwave Power* **9**(4):317–328 (1974).
8. W. Tinga and S. Nelson, Dielectric properties of materials for microwave processing—tabulated, *J. Microwave Power* **8**(1):23–65 (1973).
9. N. Bengtsson and P. Risman, Dielectric properties of foods at 3 GHz as determined by a cavity perturbation technique. Measurement on food materials, *J. Microwave Power* **6**(2):107–123 (1971).
10. C. Turpin, Browning and crisping: The functions, design and operation of susceptors, *Microwave World* **10**(6):8–13 (1989).
11. A. W. Guy and C. K. Chou, Electromagnetic heating for therapy, in E. Adair, ed., *Microwave and Thermoregulation*, Academic Press, New York, 1983.
12. J. P. Quine and S. M. Bakanowski, Impedance and heating characteristics of microwave ovens, in *Industrial Applications of Microwaves Workshop Digest*, Int. Microwave Power Inst., Manassas, VA, 1984.
13. P. O. Risman, T. Ohlsson, and B. Wass, Principles and models of power distribution in microwave oven loads, *J. Microwave Power* **22**:173–181 (1987).
14. R. F. B. Turner et al., On the counting of modes in rectangular cavities, *J. Microwave Power* **19**(3):199–208 (1984).
15. R. J. Lauf et al., A 2 to 18 GHz broadband microwave heating system, *Microwave J.* **36**(11):24–28 (1993).
16. J. M. Osepchuk, The cooker magnetron as a standard in crossed-field research, *Proc. 1st Int. Workshop Crossed-field Devices*, Univ. Michigan, Ann Arbor, 1995.
17. P. E. Gawthrop et al., *Radio Spectrum Measurements of Individual Microwave Ovens*, NTIA Report 94-303-1, US Dept. Commerce, Washington, DC, 1994.
18. IEEE, *IEEE Standard for Safety Levels with Respect to Human Exposure to Radio Frequency Electromagnetic Fields, 3 kHz to 300 GHz*, C95.1-1991, IEEE, Piscataway, NJ, 1991 (adopted by ANSI, 1992).
19. J. M. Osepchuk, A review of microwave oven safety, *J. Microwave Power* **13**(1):13–26 (1978).
20. J. M. Osepchuk, Radiofrequency safety issues in industrial heating systems, in D. E. Clark et al., eds., *Microwaves: Theory and Application in Materials Processing*, Ceramics Transactions, Vol. 21, American Ceramics Soc., Cincinnati, OH, 1991, pp. 125–137.
21. V. A. Vanke, V. M. Lopukhin, and V. L. Savvin, Satellite solar power systems, *Sov. Phys. Usp.* **20**:989–1001 (1977).
22. *Proc. 1st World Congr. Microw. Process.*, Cincinnati, OH: American Ceramics Soc., (in press).
23. M. G. Ury et al., High pressure microwave plasma light sources, in Ref. 22.
24. M. Sundberg, Microwave modeling—from analysis to synthesis, *Microwave World* **17**(1):19–22 (1996).
25. T. A. Treado, High-power-pulsed-microwave catalysis of chemical reactions, in Ref. 22.

MICROWAVE INTEGRATED CIRCUITS

NIROD K. DAS
DONALD M. BOLLE
Polytechnic University

In this article a general overview and basic principles of operation of a class of highly integrated analog devices and circuits, used for applications in the microwave and millimeter-wave frequency range, are presented. Although there are subgroups of sister technologies that evolved over the years, having different acronyms such as MIC (microwave integrated circuits in hybrid form), MMIC (monolithic microwave integrated circuits), and MCMs (multichip modules), their basic principles of operation are similar, with their objectives and scopes rapidly overlapping. The discussions in this article may be directed to a broad class of such integrated circuits, referred to in general as microwave and millimeter-wave integrated circuits, with "MMIC" as a generic acronym. Essential building blocks of MMICs, such as the substrate material and parameters, transmission line geometries, passive and active devices, integrated antennas, integration architectures, and packaging concepts, are explained at a fundamental level for readers new to the subject. Fundamental design considerations and modern analytical and computer-aided design tools for the design of MMICs are introduced. Current trends and future directions of the technology are also discussed. More knowledgeable readers are referred to a selection of significant technical articles for further reading.

As indicated, *microwave and millimeter-wave integrated circuits* refer to a special group of highly integrated analog circuits, operating in the microwave and millimeter-wave frequency range. In this frequency range the various circuit functions that were usually implemented in the past using bulky metal waveguides and coaxial lines, can now be implemented using printed microstrip lines or other forms of planar transmission lines. These planar circuits can also be fabricated together with semiconductor active devices on a single chip, employing a technology similar to that used in microelectronic circuits. As a result, quite complex microwave and millimeter-wave circuits and systems have been realized in a compact, reliable, and cost-effective manner. In many ways, this class of modern integrated circuits has opened the promise and potential for microwave and millimeter-wave communication, much like what silicon digital integrated circuit technology has done for computers.

From a historical perspective, after the experimental demonstration of electromagnetic waves by Heinrich Hertz in 1888, and then the successful achievement of transatlantic communication by Guglielmo Marconi in 1901, signal distribution and circuit components in the microwave frequency range were implemented using rectangular metal waveguides. These waveguides were essentially hollow rectangular metal pipes capable of guiding microwave signals, and are sometimes referred to as "uniconductor waveguides." They are so named because the rectangular hollow waveguides use only one conductor,

which is fundamentally different from conventional signal transmission in the very-low-frequency range using two conductor transmission lines. Although the uniconductor waveguides had the advantages of low-loss propagation compared to two-conductor lines, due to their limited bandwidth of operation, dispersion and, above all, their bulky physical size, interest later shifted to "two-conductor lines," such as coaxial lines, for microwave circuits. However, due to the inconvenience of fabricating circuit components in coaxial form, flattened versions of coaxial lines were then introduced. Soon after, attempts were made to implement two-conductor lines by laminating metal strips on a hard dielectric surface in order to greatly simplify the fabrication process. The stripline and the microstrip line were the candidates of choice. The geometries of various waveguiding media used for microwave applications leading up to the printed microstrip line are shown in Fig. 1. A good discussion of the historical developments leading to MMICs is presented in Ref. 1.

Sometime in the 1960s, the concept of microwave integrated circuits was introduced. Instead of building individual microwave components separately and then connecting them on a piece-by-piece basis, it was thought cost effective to laminate or print an entire circuit on a single dielectric substrate with individual components (filter, coupler, etc.), connected to each other in a continuous

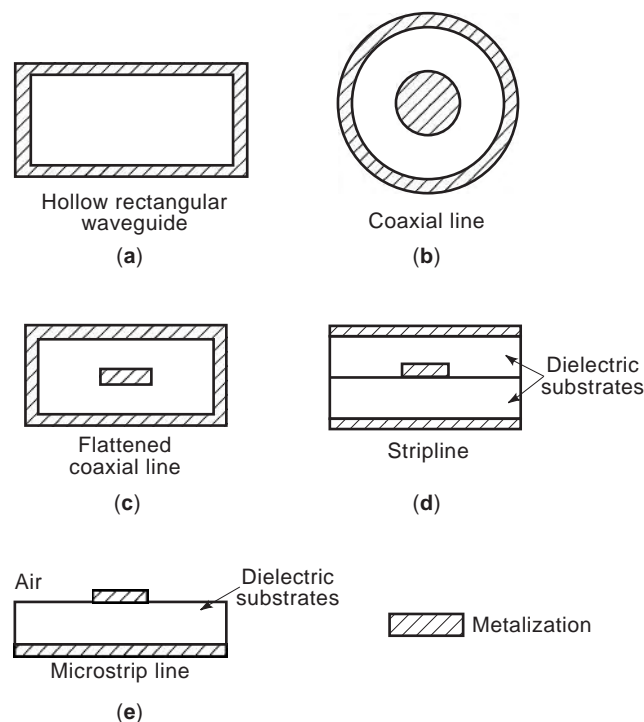


Figure 1. Evolution of waveguide geometries (cross sections) used for microwave circuits, from (a) hollow (uniconductor) metal waveguide, to (b) coaxial line, to (c) flattened coaxial line, to (d) stripline, and currently to (e) microstrip line. Microstrip line is now the most commonly used transmission line for MMICs. Interest in other forms of transmission lines, such as slotline and coplanar waveguides, came later in order to meet specialized needs.

integrated fashion. Miniaturization of the circuit was possible by meandering the connecting microstrip lines. Also by using high dielectric-constant substrates, the same electrical size could be achieved while maintaining smaller physical dimensions. The transmission-line components were printed on a hard dielectric substrate by photolithographic processes, and they constituted a major portion of the circuit. Other passive components, such as chip capacitors or chip resistors, and any active components, such as diodes or transistors, were discretely mounted on the circuit board. In this sense the MICs are really “hybrid” integrated circuits. The substrate materials commonly used include alumina, sapphire, low-loss plastics (fiber-reinforced), and ceramics. Although such MICs are much more cost-effective and compact, compared with bulky waveguide circuits, the density of circuits that can be implemented is strictly limited by the precision required in the manual placement of discrete components. Small to moderately complex circuits are implemented in this manner. Complexities could be increased, however, by using double-sided or multilayered circuit boards.

It was natural, then, to try direct integration of microwave semiconductor devices together with the printed transmission line components on the same substrate (i.e., in a “monolithic fashion”), in order to implement active as well as passive circuit functions. This generation of integrated circuits was called MMIC (monolithic microwave integrated circuits) [2]. The result was a dramatic reduction in size, allowed increased circuit complexity, and reduced cost. The substrate material needed for MMICs must be a semiconducting material, such as GaAs or Si, on which both active and passive components can be printed. As a result, the fabrication cost is increased, while allowing batch processing of significantly more complex and compact circuits, compared to the hybrid MIC. A comprehensive discussion of monolithic microwave integrated circuits, specifically those based on GaAs material, is available in Refs. 3 and 4.

As the acronyms suggest, the MIC and MMIC are meant for applications in the microwave range. The basic concepts of the technology are similar for applications in the millimeter-wave range, except for the need to maintain tighter dimensional tolerance in the fabrication process due to smaller wavelengths at these frequencies. A more specialized category of monolithic integrated circuits was then developed specifically for applications in a broader frequency band covering the millimeter-wave range. Though MMICs may generically refer to the microwave as well as the millimeter-wave range, a different acronym, MIMIC (microwave and millimeter wave monolithic integrated circuits) is sometimes used to cover millimeter-wave applications.

MICs, MMICs, and MIMICs are now rapidly taking on new meanings and employing new materials, 3D integration, integration of antennas, optical and optoelectronic components, high-speed digital circuits, and other specialized functions. Circuits and systems of greater complexity may be implemented on a single chip or module, consisting of multiple MMIC or MIMIC chips interconnected and packaged together in a hybrid MIC form [called a *multi-chip module* (MCM)] [1]. The entire circuit or system may

also be integrated through a batch process using multi-level processing technology. With the objective merging of these sister technologies, all related technologies for large-scale integration of circuits and systems operating in the microwave to millimeter-wave range are generally referred to as “microwave and millimeter-wave integrated circuits”—generically called by the common acronym MMIC. The applications may even cover the lower radio frequency (RF) range.

In the following sections the essential building blocks of MMIC, such as the substrate material and parameters, transmission-line geometries, passive and active components, integrated antennas, integration architectures, and packaging concepts are discussed.

1. THE SUBSTRATE

The choice of a proper substrate for MMICs is conditioned by several factors, including dielectric constant, resistivity, thermal characteristics, mechanical strength, and fabrication tolerance. For hybrid MICs the required characteristics are low-loss, low-cost, and mechanically rigid insulating materials, such as alumina or soft-plastic substrates. Alumina is a ceramic-type material with relative dielectric constant, $\epsilon_r = 9.7$. Teflon and similar types of soft-plastic materials can provide ϵ_r values ranging from 2 to 11. Usually the higher dielectric-constant substrates are preferred because they reduce the wavelength of propagation, which results in smaller-size circuits. However, for higher-frequency applications (20 GHz or higher), where the wavelength is already small and fabrication of very small-sized circuit components is a problem, a high-dielectric-constant substrate may not be desirable. Substrates of lower dielectric constant may be more useful in this high-frequency range. This results in increased wavelength allowing the design of larger-size circuit components, so that inaccuracies in dimensions during the fabrication process can be better tolerated.

For monolithic microwave circuits, where active devices have to be fabricated together with passive components, the substrate will have to be a semiconductor. Si and GaAs are the most common types of substrate materials in use. Two factors become important in the selection of a semiconductor substrate for MMICs: (1) higher substrate resistivity, in order to achieve low propagation loss and (2) higher carrier mobility, in order for the active devices to operate at higher frequencies. Si and GaAs, in their semiconducting states, cannot maintain high resistivity. Therefore, the base substrate must be in an insulating (or semiinsulating) state with higher resistivity levels, on which the passive microwave circuits can be printed. Then active devices are grown on the same base substrate in isolated regions, using ion implantation or epitaxial techniques. Table 1 lists the material parameters of various substrates pertinent to MMICs. It is seen that the electron mobility of GaAs is more than 5 times that of Si, and that the semiinsulating GaAs has a much higher (100 times or more) resistivity compared with that of Si, thus making GaAs a better choice for MMICs [3,4]. However, compared with GaAs, Si fabrication technology is much more ma-

Table 1. Properties of Semiconductors and Insulators Used in Microwave and Millimeter-Wave Integrated Circuits

Type of Substrate	Relative Dielectric Constant (ϵ_r)	Resistivity (ρ , Ω cm)	Electron Mobility μ_n , cm^2/V	Thermal Conductivity k , $\text{W/cm } ^\circ\text{K}$
Semiconductor				
Si	11.7	—	800 ^a	1.45
SemiinsulatingSi	11.7	10^3 – 10^5	—	1.45
GaAs	12.9	—	4300 ^a	0.45
SemiinsulatingGaAs	12.9	10^7 – 10^9	—	0.45
InP	12.6	—	—	—
Insulator				
Alumina	9.7	10^{11} – 10^{14}	—	0.37
Sapphire	11.6	$>10^{14}$	—	0.46
Soft-plastic PTFE/glass	2–10	$>10^{13}$	—	0.002–0.004

^aAt $10^{17}/\text{cm}^3$ doping.

ture, owing to its extensive use in digital electronics. Also, as discussed earlier, in modern MMICs it is desirable to fabricate digital circuits for peripheral processing and control functions together with microwave circuits. The above situation makes it more compelling to try to use Si for MMICs. In this pursuit, the higher propagation loss due to lower values of resistivity of semiinsulating Si is a major hurdle. This problem is overcome by using silicon-on-sapphire (SoS) technology, where the base substrate is made out of low-loss sapphire, instead of the lossy semiinsulating Si. Even then, the SoS technology, due to lower carrier mobility of Si, usually finds application at lower frequencies (several gigahertz), leaving GaAs as the principal choice for the millimeter-wave range.

Assuming a printed microstrip line as the transmission line-of-choice for signal distribution in a MMIC, Fig. 2 shows the signal attenuation constant α for different

substrates as a function of frequency. A set of parameters of practical interest to MMICs were chosen for these data, assuming copper to be the conducting medium. As seen in Fig. 2, the semiinsulating Si is the most lossy, SOS and GaAs are comparable in their loss performance, whereas alumina substrate provides the lowest loss. It turns out that for SOS, GaAs, and alumina substrates, the loss is dominated by the metal loss, not by loss in the substrate material. For semiinsulating Si, however, the loss in the substrate material contributes significantly to the total loss.

Besides material loss in the substrate, the substrate parameters influence the power lost to radiation in the form of “surface waves” generated at various transmission-line junctions and circuits. The substrate thickness and the dielectric constant are the governing parameters. Figure 3 shows the effective dielectric constant, $\epsilon_e = (\lambda_0/\lambda)^2$, of the fundamental and the first higher-order surface-wave modes, where λ_0 is the wavelength in free space, and λ is the wavelength of the surface-wave mode [5]. The fundamental mode propagates for all frequencies, whereas the higher-order mode has a cutoff frequency. In order to avoid excessive surface-wave loss, the cutoff thickness ($d = d_c$) of the substrate at which the second higher-order mode is excited is often used as a reference value for design of the substrate thickness. As a general rule, up to one-third of the critical value d_c can be safely used and will yield reasonable levels of surface-wave loss. This amounts to maximum practical thicknesses of about $725 \mu\text{m}$ at 10 GHz, and $244 \mu\text{m}$ at 30 GHz, for GaAs, and somewhat higher thicknesses for Si and alumina. These thicknesses do not usually pose a manufacturing problem for monolithic circuits, but can be an important consideration for mechanical strength in hybrid MICs.

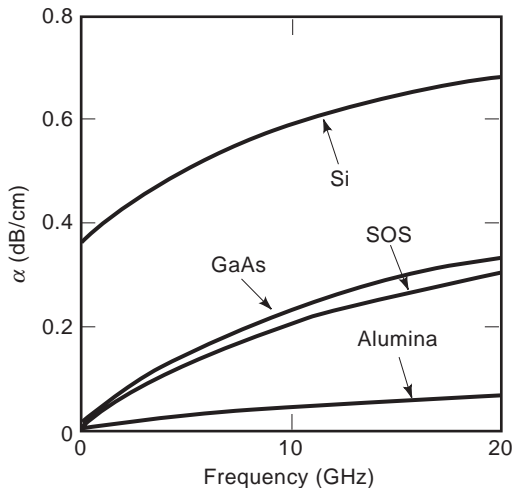


Figure 2. Attenuation (α) in a microstrip line with different substrate materials [semiinsulating Si and GaAs, indicated simply as Si and GaAs, SOS (silicon-on-sapphire), and alumina] as a function of frequency. All lines have approximately 50Ω characteristic impedance. Alumina substrate thickness $H = 500 \mu$ (for hybrid circuits), and for all other substrates $H = 100 \mu$. Resistivity of SOS = $10^{14} \Omega$ cm; for semiinsulating GaAs = $10^7 \Omega$ cm; for semiinsulating Si = $10^3 \Omega$ cm; and for alumina = $10^{11} \Omega$ cm. Line width W : SOS and semiinsulating Si, 80μ ; semiinsulating GaAs, 70μ ; alumina, 500μ . Conducting medium is assumed to be copper.

2. CHIP SIZE AND CIRCUIT COMPLEXITY

An estimate for the circuit complexity that one can achieve in a MMIC of a certain size, at two selected frequencies—3 GHz for lower-frequency and 30 GHz for higher-frequency applications—is presented here. A Si substrate is assumed for calculations, but the estimates should be close for GaAs and alumina, since these materials have similar dielectric constants. At 3 GHz, a

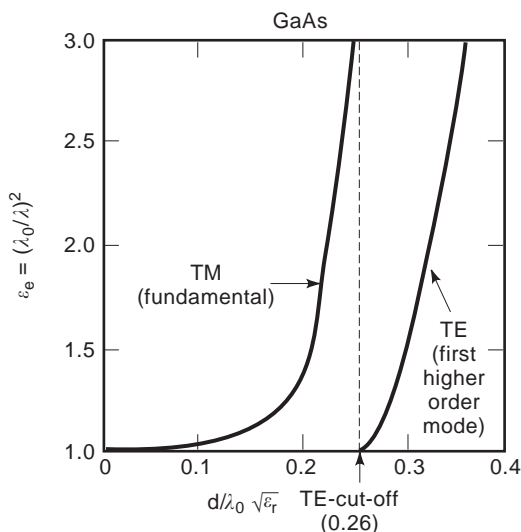


Figure 3. Dispersion characteristics for the fundamental (TM) and the first higher-order (TE) mode of a GaAs substrate with a metallized ground plane on one side, used in MMICs. The cutoff value of $\sqrt{\epsilon_r}d/\lambda_0$ for the first higher-order TE mode is 0.26. The dispersion characteristics for Si and alumina substrates are very similar to that of GaAs, with the corresponding cut-off numbers for the first TE modes equal to 0.261 and 0.264, respectively.

microstrip transmission line on Si has a guide wavelength $\lambda \simeq 4$ cm. The distributed “subcircuits” are assumed to be $\lambda/4 \times \lambda/4 \simeq 1 \text{ cm} \times 1 \text{ cm}$ in size (these are typical dimensions for distributed circuits) and therefore occupy most of the substrate area. If a mixture of 20% distributed functions and 80% lumped-circuit functions (of size $1 \times 1 \text{ mm}$) are used, a 2×2 -in. substrate can accommodate about 120 circuits or, equivalently, about 60 circuit functions if a factor of 2 is used to account for additional space required between components, to avoid intercomponent coupling. At 30 GHz, on the other hand, the distributed and lumped circuits are comparable in size: $\lambda/4 \times \lambda/4 \simeq 1 \text{ mm} \times 1 \text{ mm}$. This will yield about 1300 circuit functions on a 2×2 -in. substrate, taking into account a factor of 2 for additional intercomponent spacing. These figures are indicative of a low level of integration density in MMICs, compared with that achievable in digital integrated circuits. This fact strongly motivates the use of multilevel integration by stacking circuit layers with proper electrical isolation between layers. Although this stacked integration leads to other constraints, it can potentially increase the effective circuit density several times, while also allowing convenient integration as well of other functions (digital, optical, antennas, etc.) on independent layers.

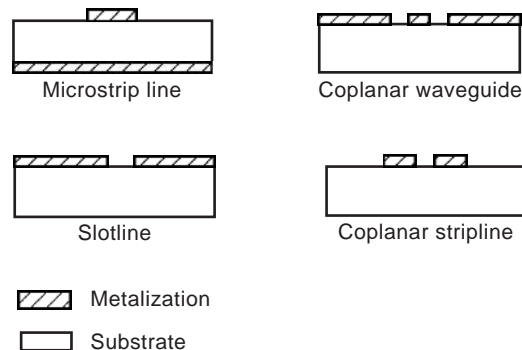


Figure 4. Different configurations of printed transmission lines (cross sections) currently used in MMICs. The slotline and coplanar waveguides may sometimes use a conductor backing under the dielectric substrate for added mechanical support, but require careful design [8,9,30]. Other variations of these transmission lines with multilayer substrates are also useful.

3. TRANSMISSION MEDIA

Figure 4 shows various configurations of printed transmission lines that are used in MMICs [6,7]. Other variations of these transmission lines with different arrangements of the dielectric substrates or metal planes are also useful. For example, the slotline or coplanar waveguide may be used with a conductor backplane for added mechanical support and increased signal isolation [8,9]. Among the geometries in Fig. 4, the microstrip line is the most commonly used transmission line for MMICs. However, under certain situations other geometries may be more suitable. Table 2 compares the practical features of various transmission lines. Specific technical details of the transmission lines can be obtained for microstrip [10,11], coplanar waveguide [12,13], and slotline [14].

In the following, basic design data are provided, and important design considerations for MMICs are discussed, based on requirements for the transmission line used. Microstrip line is assumed as the transmission line of choice. Figures 5a–e present data for various useful transmission-line characteristics for GaAs, Si, and alumina substrates.

Figure 5a shows variation of the characteristic impedance Z_c of a microstrip line as a function of W/H , while keeping the substrate thickness H fixed, for different substrate materials. Data are plotted for values of W/H around 1, where the characteristic impedance is nominally 50 Ω . The characteristic impedance reduces for larger values of W/H , owing to an increase in the effective capacitance between the line and the ground plane. Figure 5b shows the attenuation constant owing to material loss for

Table 2. Characteristic Features of Common Printed Transmission Lines

Type of Line	Z_c (Ω)	Loss	Dispersion	Connect Series Element	Connect Shunt Element	Discontinuity Radiation
Microstrip line	10–100	Low	Low	Easy	Difficult	Low
Coplanar waveguide (CPW)	20–150	Medium	Medium	Easy	Easy	Low
Coplanar stripline (CPS)	40–250	Medium	Medium	Easy	Easy	High
Slotline	60–250	High	High	Difficult	Easy	High

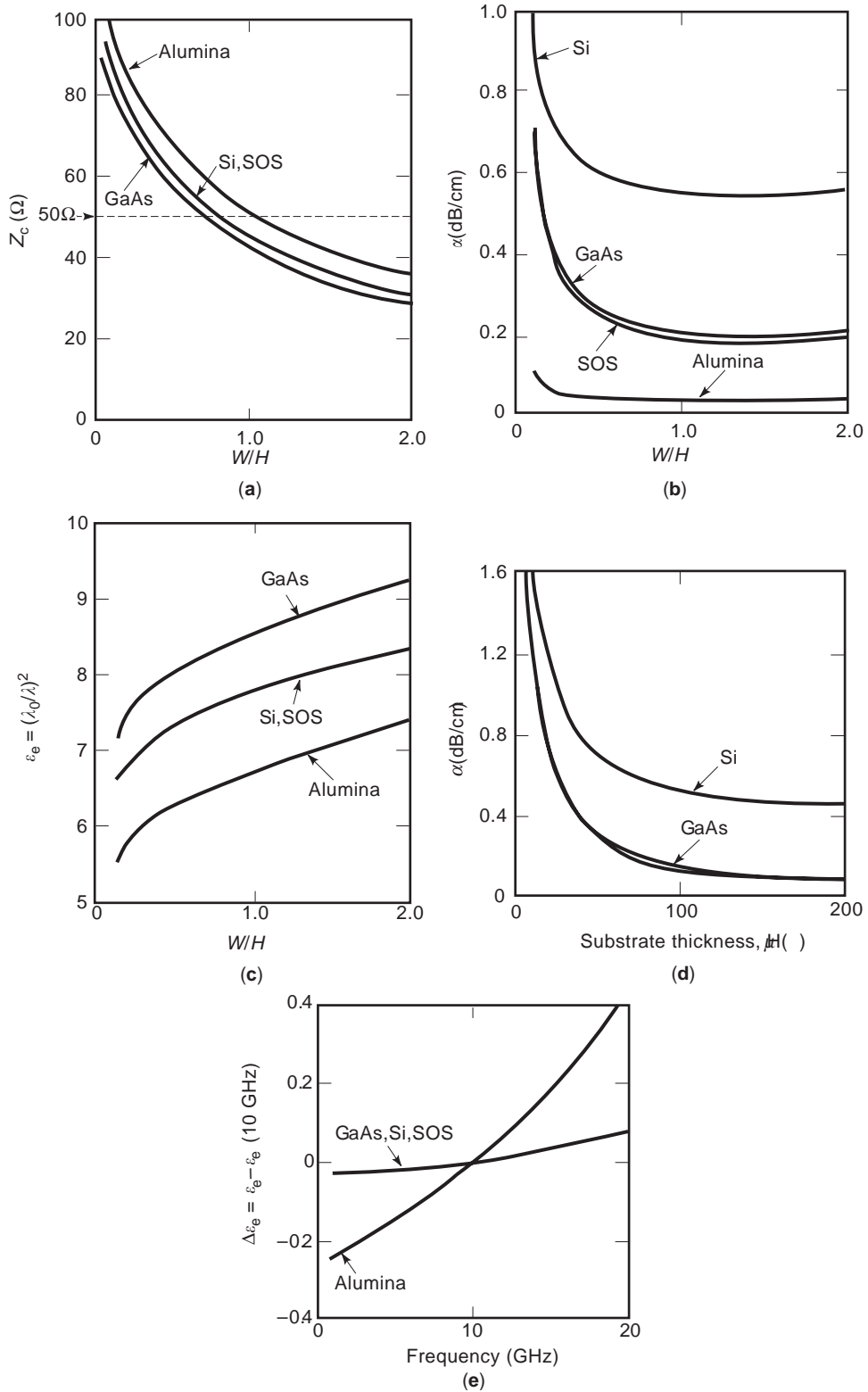


Figure 5. Variation of (a) characteristic impedance Z_c ; (b) attenuation constant α ; and (c) effective dielectric constant $\epsilon_e = (\lambda_0/\lambda)^2$, as a function of W/H for the substrates of Fig. 2, but with frequency = 10 GHz. Variation of α for semiinsulating Si and GaAs substrates (characteristics for SOS and alumina are close to that of GaAs) as a function of substrate thickness H (with W selected for different H to have $Z_c = 50 \Omega$) at 10 GHz is plotted in (d). Frequency variation for the ϵ_e of (c) is plotted in (e), in order to show dispersion behavior.

the same parameters of Fig. 5a. As can be seen from Fig. 5b, the loss increases sharply for smaller values of W/H , making small values of W/H undesirable. In order to maintain compactness of integration the upper limit of W/H is restricted—a reasonable upper limit for W/H is 4. The aforementioned constraints in W/H limit the range of Z_c values that can be practically attained to about 10–100 Ω .

Figure 5d shows the variation of attenuation constant for different values of substrate thickness H , while maintaining a 50- Ω line (with properly adjusted linewidth W). These data show that material loss sharply increases as the substrate thickness is reduced. Therefore, the choice of substrate thickness H below a certain limit is not desirable. It may be recalled that the upper limit for H is restricted, in order to minimize excitation of substrate modes.

The microstrip line, like other printed transmission lines used in MMICs, does not support the TEM (transverse electromagnetic) mode. This is so because the material medium around the transmission line is not uniform—it is partly air and partly the substrate material. As a result, the transmission line is dispersive. The effective dielectric constants ϵ_e of microstrip lines on different MMIC substrates are shown in Fig. 5c. As should be expected, the effective dielectric constant lies between 1.0 and ϵ_r of the substrate material. The actual value depends on the electrical “filling factor” of the substrate. This filling factor increases with increased W/H . This is because as W/H increases, the fraction of the total electric field confined in the dielectric material increases, allowing only a small fraction to fringe out into the air medium. Figure 5e shows the dispersion behavior of ϵ_e for the same parameters of Fig. 5c, but keeping the linewidth W fixed. Notice that the dispersion is stronger for the line on an alumina substrate. This is because the alumina substrate chosen for the data in Fig. 5e is much thicker than is the case for Si or GaAs. Dispersion worsens for thicker substrates. This is also a consideration that limits the substrate thickness to smaller values.

Besides the restriction on the linewidth and substrate thickness, it is important to consider the constraint on the spacing between two adjacent lines. The lower limit of the line-to-line separation determines the minimum level of isolation that can be maintained between nearby circuits. This consequently restricts the compactness of integration. Figure 6a plots the electric field of a 50- Ω transmission line on a GaAs substrate as a function of distance Δ (normalized with respect to the linewidth W) from the center of the transmission line in the transverse direction. The field rapidly drops beyond the region below the line. At a distance 4 times the linewidth W the field strength drops to about 3% of its peak value. In order to achieve this high level of isolation, one must, therefore, maintain a center-to-center separation S between two lines of about 8 times the linewidth W ($7W$ for edge-to-edge separation). For a 10% field isolation the corresponding value for center-to-center separation is about $4W$. Figure 6b illustrates how this field coupling translates to coupling of signal power, as a function of edge-to-edge separation S between lines. For $S/W=3$ one can achieve better than about 25 dB isolation, which can be increased to about 30 dB

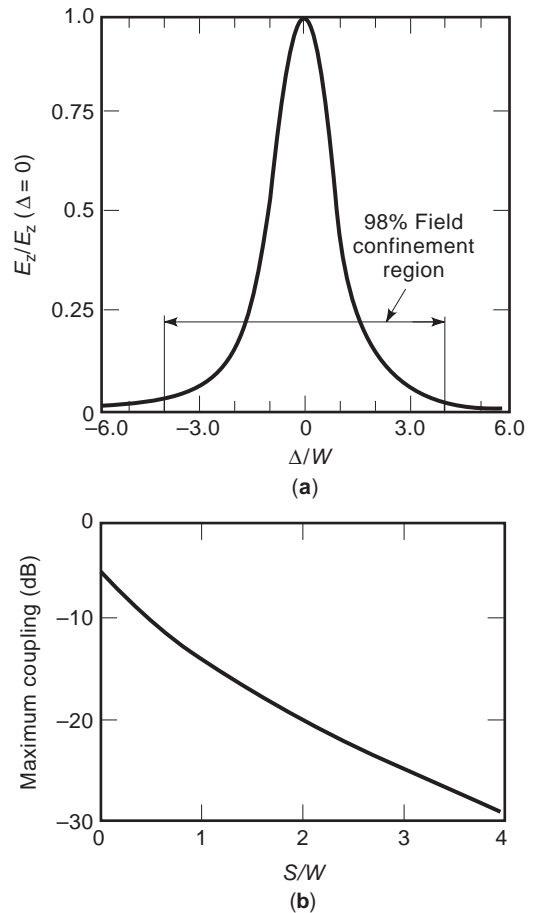


Figure 6. (a) Variation of the field strength of normal (to the substrate) component of electric field of a 50- Ω microstrip line on a 100- μ -thick GaAs substrate, sampled at the bottom ground plane, plotted as a function of the distance Δ from the center of the line. Width W of the line is 70 μ , and frequency = 10 GHz. (b) Level of power that can be coupled from a signal line to a nearby line as a function of edge-to-edge separation S between the lines. It is assumed here that the signal line is matched to the source and terminated by the characteristic impedance of the line. The coupled line is also match terminated at both ends. Here the maximum level of power that can be coupled between the lines, which occurs when the line lengths are odd multiples of $\lambda/4$, is plotted. Such characteristics also generally apply to other substrates and frequency, and are useful to determine the minimum separation one must maintain between lines in an MMIC in order to maintain a minimum level of isolation.

for $S/W=4$. In most practical applications an S/W ratio greater than 3 provides reasonable isolation.

4. PASSIVE COMPONENTS

Some of the passive components commonly used in MMICs include (1) resistors, (2) capacitors, and (3) inductors. These components can be implemented in lumped form if their physical size can be maintained sufficiently small ($< \lambda/10$) compared to the operating wavelength λ . Otherwise, “distributed” behavior becomes more pronounced, and therefore the components no longer operate as normally expected. The lumped condition is more easily

satisfied at lower microwave frequencies (where λ is larger), making the use of such lumped components more practical in this range. Except for resistances, the inductive and capacitive elements can also be realized in distributed form, using a transmission-line stub of a certain length. As a basic principle, however, the lengths of such distributed components are proportional to the operating λ . At a low operating frequency, where the operating wavelength may be too large, the required large length of the distributed components can make it difficult to implement in an MMIC. Therefore, the use of the distributed elements in MMICs is limited only to the higher-frequency range (where the wavelength is sufficiently small). In the intermediate frequency range (around 10–20 GHz) a mixture of lumped and distributed components may prove useful.

Besides implementing simply inductances and capacitances in distributed form, a variety of other circuit functions, such as delay lines, couplers, resonators, and filters can be implemented only in distributed form. Transmission-line segments are interconnected in a variety of ar-

rangements to achieve circuit functions that are useful in many microwave applications. However, all such distributed-circuit elements are essentially transmission-line metallizations, which can be fabricated in a MMIC similar to other metal interconnections. The various lengths and widths of transmission-line segments required can be designed using distributed-circuit theory [15,16].

In the following only lumped-circuit elements as used in MMICs will be discussed. Figure 7 shows various configurations of MMIC lumped components, some of which may be relevant to hybrid-type integration, and others to monolithic integration.

4.1. Capacitors

Figure 7a shows useful configurations of capacitance components used in MMICs: (1) edge-coupled, (2) end-coupled, (3) interdigitated, (4) end-coupled overlay, (5) overlay, and (6) chip capacitor. Of these, (4) and (5) are relevant only to monolithic integration, (6) only to hybrid MIC configuration, and the others can be implemented in either

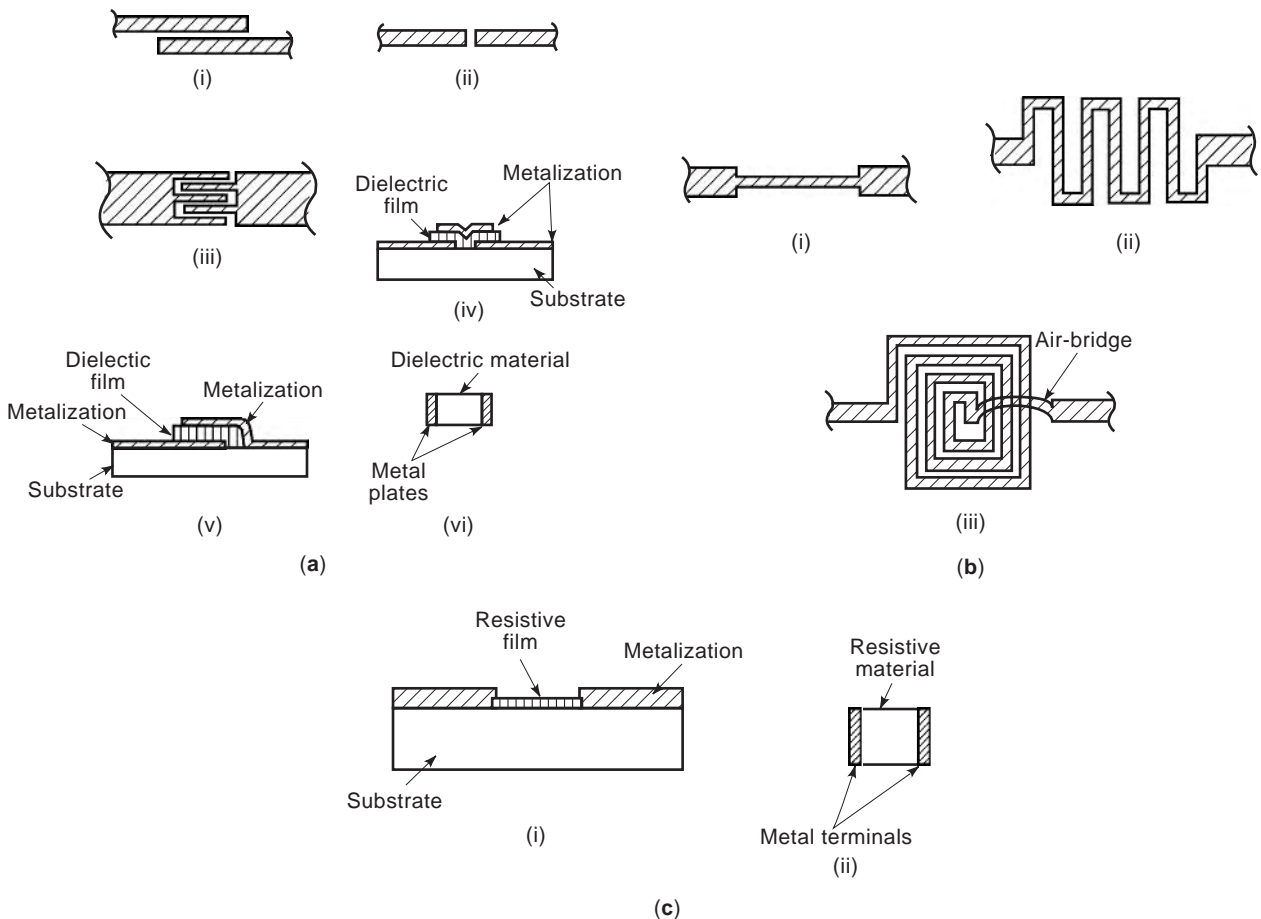


Figure 7. Various configurations of lumped passive components used in MMICs. (a) Capacitors in different forms: (i) edge-coupled, (ii) end-coupled, (iii) interdigitated, (iv) end overlay, (v) overlay, and (vi) chip capacitor. (i)–(iii) are planar forms showing the top view of the metallizations, whereas (iv)–(vi) are nonplanar components showing their side views. (b) Planar inductors in different forms: (i) using a straight section of a high-impedance transmission line, (ii) meander-type line, and (iii) spiral inductor with an overbridge connection. (c) Resistances in two forms: (i) film resistance and (ii) chip resistance.

monolithic or hybrid form. All capacitances shown in Fig. 7a are essentially series-type circuit elements, but a shunt-type capacitance can be realized by connecting a via hole to one of the terminals. Up to about 1 pF capacitance can be achieved using an edge-coupled or end-coupled design, with some higher values possible from an interdigitated configuration. Capacitance values in the range of 10–30 pF can be realized by overlay-type designs, which are useful for RF-bypass or dc-blocking applications. Much higher values can be implemented only in discrete chip form, which can be used in hybrid MICs, but not in monolithic form.

The edge-coupled, end-coupled, and interdigitated capacitors are implemented in MMICs as two metallized lines with a suitable gap(s) maintained between them. No additional dielectric film is required. In all other designs in Fig. 7a an additional dielectric film is needed. In a monolithic fabrication process such film capacitances are realized by controlled deposition of dielectric films of required thickness. Some important considerations for the dielectric films to be used include (1) dielectric constant of the material (and hence the capacitance values that can be achieved per unit area), (2) compatibility with monolithic fabrication process, (3) microwave losses, and (4) breakdown field. The capacitance would exhibit some resistive behavior in the microwave frequencies, due to (1) losses in metal and dielectric film, and (2) radiation into the free-space and/or substrate medium. Q factors of the order of 50–100 can be achievable in the X band (10 GHz). Distributed effects are always present, to some extent, resulting in deviations from lumped behavior of the device. These effects may be taken into account through the use of computer-aided modeling and design.

4.2. Inductors

Figure 7b shows different configurations of MMIC inductors: (1) using a high-impedance line, (2) a meanderline type, and (3) a spiral type, among which the spiral type allows a higher range of inductance that can be achieved. All such inductors are implemented in a planar metallized form, and, thus, can be used in hybrid or monolithic integration. In the spiral-type inductor one would need an airbridge to connect to the center of the spiral. This would require an additional fabrication step in monolithic form, or could be manually established in a hybrid MIC. The operation of all inductance elements is based on the production of strong magnetic stored energy in the vicinity of the device (equivalent to the operation of a coil in audio or RF circuits). The goal here is to achieve high inductance within a small physical space.

Unavoidable capacitive effects are also present in the planar inductor design, due to edge coupling between lines and the presence of the ground plane under the metal lines. This is in addition to resistive effects owing to material loss (metal and dielectric), as well as radiation. Therefore, the planar inductor does not behave like an ideal inductance, but needs to be treated as an $R-L-C$ resonant circuit, with a dominant inductive effect in the operating frequency range. All the nonideal factors must be carefully accounted for, requiring the use of accurate

computer-aided modeling tools. Inductance values on the order of 10 nH can be achieved using planar spiral inductors, with Q factors on the order of 50 in the X band. These values are useful for RF isolation/bypass purposes. The use of inductors requiring higher inductance values should be avoided in MMICs.

4.3. Resistors

Figure 7c shows two general classes of MMIC resistors: (1) the resistive film element and (2) the chip resistor. Chip resistors find application only in hybrid circuits, while the film resistors are convenient to implement in monolithic circuits. The resistors are useful in resistive loading and match termination elements. Resistances requiring high power dissipation (e.g., in DC biasing) should be avoided in MMICs.

The resistive film used in a film-type resistor can be realized by the deposition of a lossy metal film or a semiconductor film. A lossy metal film of an appropriate material can be deposited in the MMIC fabrication process, in a manner similar to the fabrication of a film capacitance. Important considerations for the choice of the lossy metal film are: (1) sheet resistivity (which determines the resistance per unit length), (2) thermal variation of resistivity, and (3) compatibility with MMIC fabrication. The resistive film may also be realized in an MMIC using a semiconductor process, similar to that used for active devices. The doping level in the semiconductor controls the resistance value, which can be realized using an epitaxial or implantation technique. The use of metal films for resistors is usually preferred over semiconductor films, owing to nonlinearity behavior of the latter at high current values and poor thermal stability. Nonideal effects common to both types of film resistors include additional capacitive effects between the film and the ground plane, inductive effects of the metal connection, and some radiative effects. This results in frequency dependence of the performance, which must be properly accounted for in the design process.

4.4. Other Passive Elements

Besides the aforementioned passive circuit components, other passive circuit configurations such as (1) junctions between transmission lines, (2) transmission line bends, (3) vias, and (4) open ends, which are frequently used in MMICs, need to be considered. These are generally called “discontinuity” elements, whose presence is not desirable but inevitable in MMICs. The discontinuity elements can be modeled as $R-L-C$ equivalent circuits, using a computer simulation or some approximate theoretical approach. Whenever possible, their unwanted effects should be minimized by proper design of the discontinuity itself, or through compensation within the design of the rest of the circuit.

It is desirable to integrate antenna elements together with other microwave circuits in an MMIC. This approach is particularly attractive in large integrated phased-array radars, in order to avoid the complexity of fabricating the circuits and antenna elements separately and then manually connecting them. Although current applications of

MMICs in the wireless communication industry are growing, large phased-array radars are still the major driving force behind MMIC technology. The microstrip antenna [17] is the most suitable candidate for such integration. This is mainly because of the planar nature of microstrip antennas, which can be fabricated with an MMIC process in a manner similar to other metallizations. The basic geometry of the metallization structure of a microstrip antenna, which can be connected to the rest of the MMIC by a microstrip line, is shown in Fig. 8a. The radiation from this microstrip antenna is along the broadside direction (outward, perpendicular to the substrate). Sometimes it may be preferable to have the antenna element radiate

along the endfire direction (along the substrate plane). Figure 8b shows one such printed antenna configuration, called a tapered-slot antenna [18]. The tapered-slot antenna shown in Fig. 8b is fed by a slotline, and radiates to the right along the plane of the substrate.

One of the drawbacks of integrating antennas with MMICs is that it often occupies significant space on the valuable semiconductor substrate. Another problem is that since the MMIC substrate is normally optimized for circuit functions in order to minimize radiation from the circuit components, the same substrate cannot at the same time be optimal for antenna radiation. Certain techniques may sometimes be used to provide a compromise between

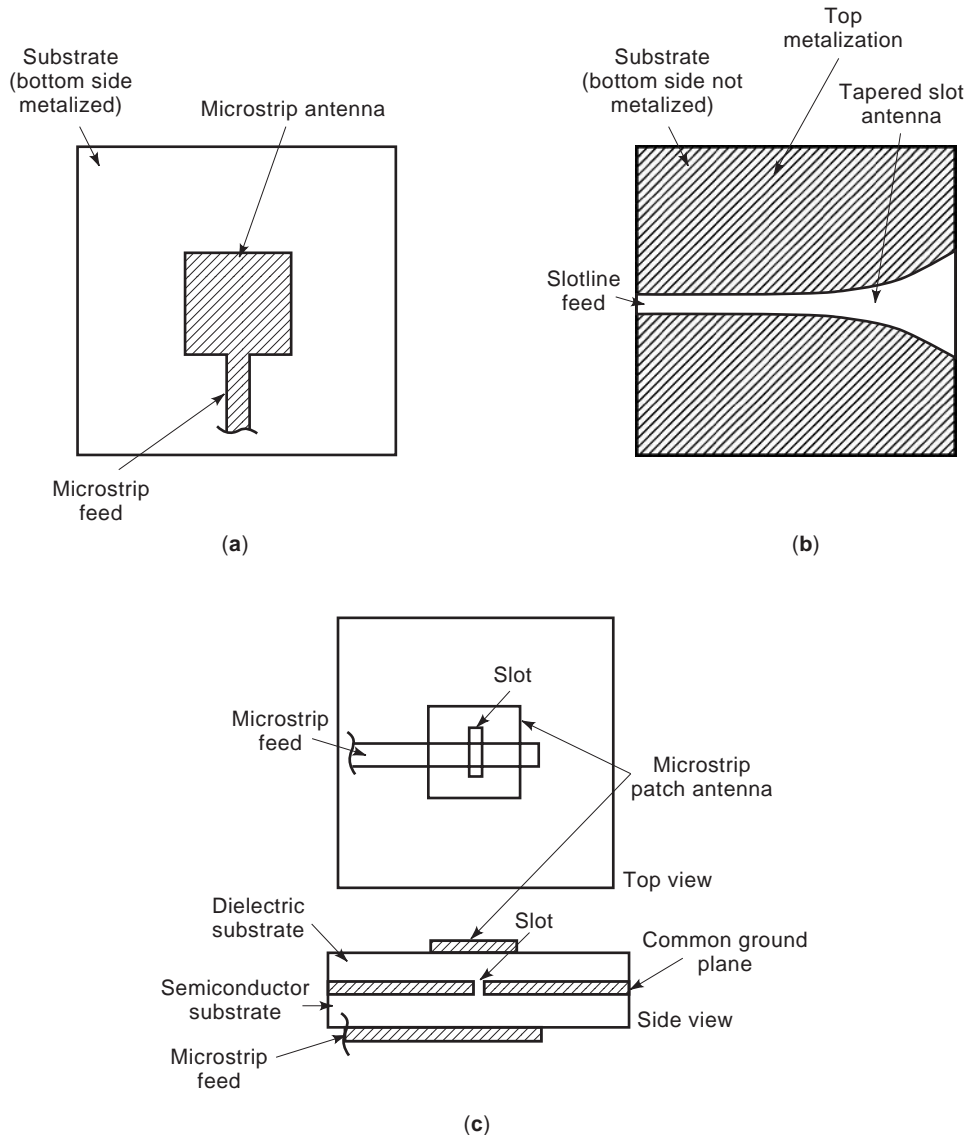


Figure 8. Geometries of printed antennas that can be integrated together with MMICs: (a) a microstrip-line-fed printed antenna (shows top surface) for radiation normal to the substrate; (b) a coplanar stripline-fed printed tapered-slot antenna (shows top surface), which radiates along endfire direction, (toward the right side along the substrate plane). In (a) and (b) the antenna and microwave circuitry are printed on the same substrate, whereas (c) shows an aperture-coupled microstrip antenna, where the antenna is printed on a different substrate layer, coupled to the microwave circuit layer through an aperture on a common ground plane.

both functions. In such a situation, a multilevel integration, as shown in Fig. 8c is desirable, where the antenna is fabricated on a cheaper dielectric substrate, independently optimized for antenna radiation, retaining the valuable semiconductor substrate only for circuit integration. The common metal plane between the antenna and circuit layers serves as the ground plane for both. It may be noticed in Fig 8c that the antenna and circuit layers are electrically isolated from each other by the common ground plane, while they are “electromagnetically” connected between each other only through a small slot etched on the ground plane [19]. This idea can be naturally extended to more layers, with possibly more than one antenna layer, or an additional dielectric layer for distributed feeding circuitry, thus reserving the bottom semiconductor layer mostly for active functions.

5. ACTIVE DEVICES AND PROCESSING

For hybrid-type integration there is flexibility gained in using heterogeneous active components such as bipolar or field-effect devices, and two- or three-terminal devices. However, uniformity must be maintained in the type of active device one might use in monolithic integration. In the following the active device and fabrication process used in monolithic MMICs will be discussed. Some early forms of MMICs used two-terminal active devices, such as Schottky and Gunn diodes. Modern MMICs use MESFETs (metal semiconductor field-effect transistor) as a versatile active component (20). MESFETs are convenient to fabricate in an MMIC process, and are known to provide good performance in implementing a large class of active circuits, including specialized amplifiers with low-noise, high-gain, and broadband features, as well as mixers, switches, oscillators, and phase shifters. The power levels that can be achieved from a single MESFET amplifier or oscillator are low to moderate. Power may be increased by use of on-chip power combiners. However, operation of MMICs should be limited to moderate power levels, to avoid problems associated with heat dissipation. Power outputs on the order of 10 W can be realized from a single chip using power-combining techniques. For a detailed theory of MESFETs one may refer to texts on semiconductor devices [20–22]. Theoretical work and practical techniques for the design of microwave active circuits can be found elsewhere [15,23–25].

The MMIC fabrication process starts with a good-quality substrate wafer, followed by more than 30–40 individual processing steps. For GaAs MMIC, the substrate material is semiinsulating GaAs, whereas in SoS (silicon-on-sapphire) MMIC the base material is sapphire. The specific processing steps for the two cases are different, though they more or less share a major set of common processing techniques. Only the major processing techniques will be briefly discussed. First, an active semiconducting layer, which is needed for active device fabrication, is formed on the substrate. There are two techniques commonly used in forming the active layer: (1) epitaxy and (2) ion implantation, which may be used independently or in combination. In the epitaxial technique,

a doped single-crystal semiconducting layer can be deposited on top of a crystalline base substrate. An intermediate high-resistivity buffer layer is used in the epitaxy process, in order to screen out any diffusion of impurity atoms from the substrate into the active layer. There are different types of epitaxial growth processes: VPE (vapor-phase epitaxy), MBE (molecular-beam epitaxy), and LPE (liquid-phase epitaxy), each having different basic advantages and drawbacks. In the ion implantation technique, on the other hand, the dopant atoms can be implanted directly onto a semiinsulating semiconductor substrate, using high-energy impurity ions. This process is quite versatile, and even selective doping profiles at different locations on the substrate may be possible. However, this process requires a base semiconductor substrate with a high state of purity. Therefore, if direct implantation is not practical, an epitaxially grown “buffer” layer on top of the primary substrate may be used as the implantation medium.

Once the active layers are formed using one or a combination of the above techniques, the active device areas are isolated from the surrounding regions, leaving “mesas.” This is important for microwave circuits, in order to reduce parasitic coupling to the active components. Mesa isolation may be achieved by deep etching of the substrate around the active area. The mesa-etching process may be substituted by implantation of oxygen onto the epitaxial layer surrounding the active device region. The oxygen implantation creates the required high-resistivity barriers. This process is called isolation implant, which essentially uses the epitaxial deposition in combination with selective ion implantation.

Next, ohmic contacts to the active areas are made to provide source and drain contacts for the MESFET. The standard approach involves alloying of Au (gold) or AuGe (gold–germanium) onto the substrate. This results in a heavily doped region under the contact, which facilitates establishing the ohmic junction. The gate regions of the MESFET are then processed. The gates are Schottky-type contacts, which are formed by depositing Ti-Pt-Au (titanium–platinum–gold compound). Because the gate regions are usually small ($\leq 1 \mu\text{m}$), this calls for high alignment accuracy in the lithographic patterning process. Some form of lithography (optical or electron-beam) is needed here, as well as in other fabrication steps, for accurate definition of devices and the interconnection layout.

At this stage the active device processing is essentially completed. The active devices are now subjected to on-wafer DC and microwave tests. Wafers that do not meet process control specifications are rejected, in order to avoid any subsequent processing costs. Following this, the first layer of metallization is deposited for external contacts, transmission line interconnections, spiral inductors, and distributed circuits. Then, thin films of appropriate resistive or dielectric materials are deposited to form thin-film resistors and capacitors. Resistors may also be realized using semiconductor material in the initial epitaxial or implantation process. Then a second layer of metallization is deposited to connect thin-film capacitors, and to form crossovers or other miscellaneous connections. The two-level metallization process allows topological flexibility in

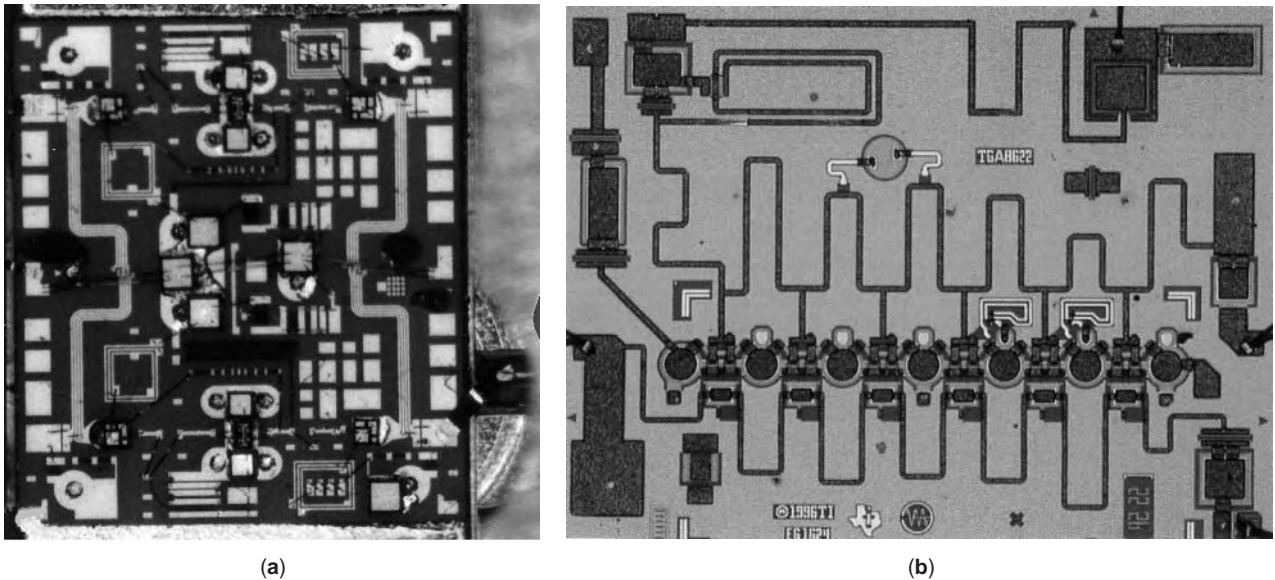


Figure 9. Photographs of commercially used hybrid and monolithic microwave/millimeter wave integrated circuits: (a) A balanced amplifier operating in the 2–8 GHz frequency range, consisting of printed Lange coupler, FETs and associated power supply and biasing circuits (film/chip resistance, chip capacitance, and printed inductance) integrated in a hybrid MIC form. Actual size is $\frac{3}{8}$ in. \times $\frac{1}{8}$ in. (Picture courtesy of Mini-Circuits, Brooklyn, NY.) (b) A GaAs traveling-wave MMIC amplifier (7 dB gain, 18 dBm output power level) operating over a broad bandwidth of 2 GHz to 18 GHz, consisting of six stages of GaAs FETs, printed transmission lines, biasing film resistance, capacitance and printed inductance, integrated in a monolithic MMIC form. Actual size 0.11 in. \times 0.086 in. (Picture courtesy of MITEQ Inc., Hauppauge, NY.)

the circuit layout. Some of the functionalities of the first- and second-level metallizations may be interchanged as needed.

The final steps in the MMIC fabrication involve backplating of the substrate, in order to provide the ground plane for the circuit. The thickness of the substrate is critical for maintaining correct values of characteristic impedance of the transmission-line components. Therefore, the back side of the wafer must be “thinned” in a controlled manner. The entire backside is then metallized. Ground connections from the bottom metal plane to the circuits on the top surface are provided through “via holes.” This is possible by the etching of through-holes at required locations and then metallizing the inner surface of the hole. Wet-chemical etching, reactive-ion etching (RIE), or combinations thereof are used.

It may be mentioned that much of the technologies used for MMIC fabrication have been adapted from well-established techniques used in the silicon digital IC industry. Each processing step needs to be optimized for MMIC application, however—particularly for GaAs MMIC [4]. Figure 9 shows photographs of two integrated circuits fabricated in hybrid and monolithic processes.

6. COMPUTER-AIDED DESIGN

It is virtually impossible to design complex MMICs through an experimental trial-and-error procedure. Except for a few simple MMIC components, analytical

formulas are not available for accurate design. This is owing to the complexity of electromagnetic interactions in and between different MMIC components. Because of the nature of MMIC fabrication, any “tuning” after fabrication would also be quite difficult or impossible. From the above considerations, computer-aided simulation and design [26] play a critical role in the successful design of MMICs.

The computer-aided simulation tools for MMICs that are currently available may be classified into four broad categories: (1) purely circuit-based tools, (2) circuit 2D tools, (3) circuit 2.5D tools, and (4) full EM-based tools or 3D EM tools. Purely circuit-based tools perform simulations employing simple circuit theory, which requires the user to provide an equivalent-circuit model for individual components, valid for the microwave frequency range of operation. As a result of the relative simplicity of the circuit theory used in simulation, such tools are computationally fast (particularly for linear circuits), but electromagnetic interactions cannot be properly modeled. This approach has only limited use, because accurate equivalent-circuit models for MMIC components are often not available. On the other hand, purely EM-based tools can rigorously model all electromagnetic interactions in an MMIC, and can handle arbitrary geometries of components, package structures, and microstrip antennas. This is accomplished by treating the entire chip as a 3D (three-dimensional) electromagnetic system and, therefore, such tools may be called “3D EM” tools. However, compared with purely circuit-based tools, the 3D EM tools are often computationally quite time-consuming. A suitable

compromise between the purely circuit-based and purely EM-based (or 3D EM) tools is provided by the circuit 2D and circuit 2.5D tools, which are based on hybrid circuit EM models. Compromise between speed and rigor is also achieved, having subgroups among the 3D EM tools, depending on the level of rigor, type, and size of geometries the software tools can handle.

In the circuit 2D tools the parameters of the transmission lines are calculated by treating them as infinite-length lines, which simplifies the problem to a 2D structure. An approximate "quasistatic" or a more accurate "full wave" approach may be used to this effect [6,15]. Coupling between nearby transmission lines can also be incorporated via coupled-line analysis. However, electromagnetic effects of transmission line discontinuities, such as junctions, bends, and open/short circuits, coupling among lumped/distributed components, and the effect of

the surrounding package structure, are ignored. The circuit 2.5D tools, on the other hand, model the electromagnetic effects of the discontinuities, in addition to the transmission line parameters, but still fail to model the electromagnetic interactions among components and package. The term "2.5D" in circuit 2.5D tools appropriately suggests that the rigor of EM modeling used here lies somewhere between the circuit 2D and 3D EM tools.

The various commercial CAD tools that are currently available mainly provide simulation capability, where the operator needs to manually iterate the simulation procedure to arrive at a final design. In addition to the simulation, limited design capability may also be available in some cases, where a final design with user-defined parameters can be reached, starting with an approximate design specified by the user. However, owing to the excessive computation needed in design algorithms, such design-oriented tools are mostly circuit-based, with very limited EM-modeling.

The EM-modeling required for different types of MMIC CAD tools can be performed using a variety of numerical techniques. The major techniques include (1) moment method (MM), (2) finite-element method (FEM), (3) transmission line matrix method (TLM), and (4) finite-difference method (FDM). The individual techniques have their own advantages and drawbacks, and have specific strength in being able to handle specific classes of problems. For example, the moment method may be suitable for planar geometries, whereas FEM can be useful for nonplanar components, such as film capacitors, via holes, and so on. A comprehensive review of commercial EM simulation tools currently available, their modeling techniques, and scope of application, is presented in Ref. 27. Major suppliers of product lines for MMIC CAD include Hewlett-Packard Co. (HP-EESOF), Westlake Village, CA; Ansoft Corporation, Pittsburg, PA; and Sonnet Software Inc., Liverpool, NY.

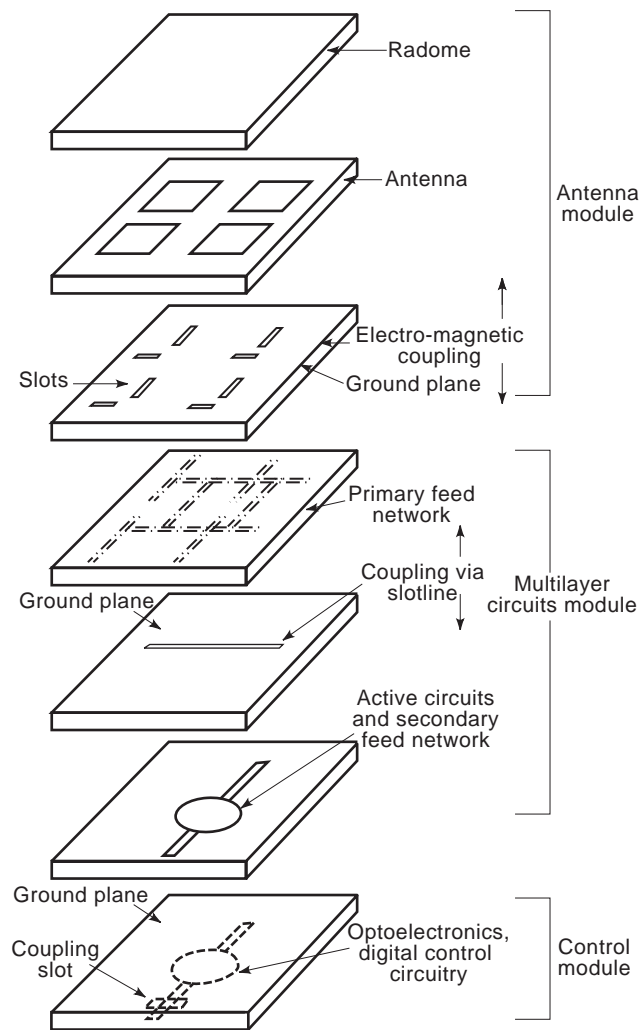


Figure 10. Conceptual sketch of a multifunctional MMIC configuration with microwave/millimeter wave active and passive circuits integrated together with printed antennas, optoelectronics, digital circuits, and possibly other specialized functions, in multiple levels. The next generations of MMICs may take such forms in order to realize high-density, reliable, and multifunctional integration on a single package.

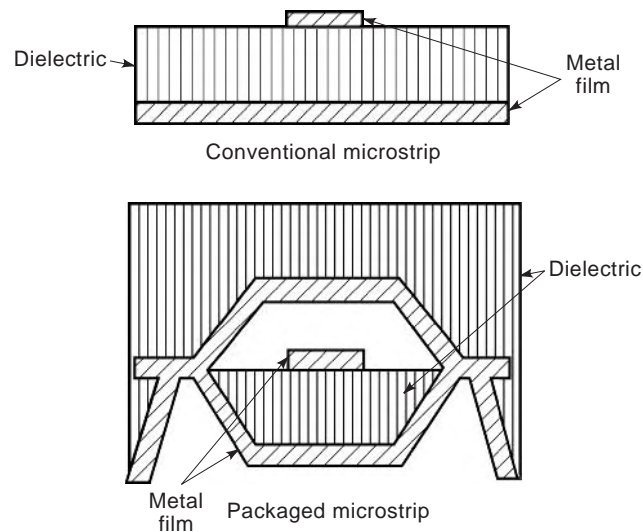


Figure 11. Geometry of a packaged microstrip line, in contrast to a conventional microstrip line, which can be useful for avoiding parasitic coupling between nearby components. Similar packaged configurations for other types of printed lines are also possible.

7. CURRENT TRENDS AND FUTURE DIRECTIONS

In current MMIC technology there is greater emphasis on advanced interconnects and packaging of MMICs in the form of multichip modules (MCM). In addition to compact, highly integrated chips, future system applications will require greater packaging density and increased functionality at the MCM level. The effect of the packaging structure is recognized to have a critical role in the overall performance of MMICs. Packaging of multichip modules in a “tile” architecture, interconnected in multiple levels using layer-to-layer transitions, and between chip to substrate or chip to chip using “solderless” connections, is an attractive approach to achieve the high-density, low-cost, and multifunctionality demands of the future. A sketch of one such architecture is shown in Fig. 10. The multichip modules may be fabricated similarly to the chip itself on a larger substrate, using a common semiconductor processing technique. The functional and fabrication concepts of chips and MCM will therefore merge, expanding the scope of MMICs to also include digital, optoelectronic, and other functionalities. A review of current trends and future directions of MMIC research and technology can be found in Ref. 1.

In a multilevel architecture, particularly for applications in higher frequencies, there may be fundamental problems owing to a nonconventional “power leakage” phenomenon. Under certain conditions power can leak or couple from the printed transmission lines to the surrounding substrate structure [28]. This can cause attenuation of the signal along the transmission line, and also result in undesired coupling to the surrounding structure. Such problems should be carefully considered in advanced MMIC designs. The undesired effects can be minimized or eliminated by using shorting pins, properly designed multilayer substrate arrangement, or new types of transmission media [8].

Besides the nonconventional leakage problem, conventional parasitic coupling between various planar trans-

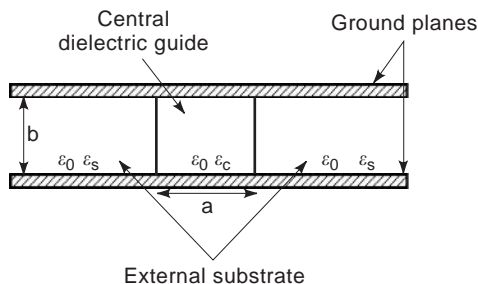


Figure 12. The geometry of a dielectric guide that exhibits low-loss characteristics, compared with metal lines for millimeter and submillimeter applications. The guide is not truly a dielectric guide, because it has metal planes on top and bottom (sometimes called NRD guide [31], H-guide [32], or PPDW [33], operating in different preferred modes). The metal planes are useful for isolation from top and bottom, permitting integration of circuits in multiple levels on top of one another. Most of the signal is contained in the dielectric medium between the metal planes, resulting in lower attenuation, compared with commonly used metal lines (e.g., microstrip line or coplanar waveguide).

Top layer	Active devices and/or passive devices
Heat dissipation	
PPDW layer	Passive devices, power distribution, interconnects
Low-loss	
Bottom layer	Active devices and/or passive devices
Heat dissipation	

Figure 13. Schematic of a hybrid-integration architecture in multiple levels, with parallel-plate dielectric waveguide (PPDW) in the middle level(s) for signal distribution, and printed metal lines in the top and bottom levels for connection to active components. Such architectures will be attractive for millimeter and submillimeter ranges for low-loss signal distribution. Conventional circuits with metal lines (e.g., microstrip line) will prove to be too lossy at high frequencies.

mission line discontinuities may also be prohibitive at higher millimeter and submillimeter frequencies, requiring new techniques to achieve greater isolation between components. Approaches to minimizing the parasitic coupling, by placing components physically farther apart, will not be desirable due to space limitations. Lines fabricated in a “boxed” manner, with metal walls surrounding the central line (see Fig. 11) may be useful. This can be achieved in semiconductor processing using “micromachining” technology [29]. Ironically, this concept is equivalent to a “flattened coaxial line,” which in the past was rejected for use in MMICs because of perceived inconvenience in fabrication.

Another concern is the metallic loss experienced by printed lines at higher frequencies. This loss can be significantly reduced by using dielectric-type guides (see Fig. 12), where a significant fraction of the field is confined to a dielectric medium (which will have lower loss than metals). However, the dielectric waveguides will not be suitable for connecting to active devices that require metal connections for their operation. A hybrid architecture with combinations of metal lines and dielectric guides, as schematically shown in Fig. 13, can solve this problem. Designs combining the dielectric waveguide concept, together with other ideas discussed above, may allow us to meet diverse and fundamental challenges.

BIBLIOGRAPHY

1. N. K. Das and H. L. Bertoni, eds., *Directions for the Next Generation of MMIC Devices and Systems*, Plenum, New York, 1997.
2. C. Mahle, MMIC’s in communications, *IEEE Commun. Mag.* **23**(9):8–15 (1985).
3. R. A. Pucel, Design considerations for monolithic microwave circuits, *IEEE Trans. Microwave Theory Tech.* **MTT-29**(6):513–534 (1981).
4. R. A. Pucel, ed., *Monolithic Microwave Integrated Circuits*, IEEE Press, New York, 1985.
5. R. F. Harrington, *Time Harmonic Electromagnetic Fields*, McGraw-Hill, New York, 1984.
6. K. C. Gupta, R. Garg, and I. J. Bahl, *Microstrip Lines and Slotlines*, Artech House, Norwood, MA, 1979.
7. T. Itoh, ed., *Planar Transmission Line Structures*, IEEE Press, New York, 1987.

8. N. K. Das, Methods of suppression or avoidance of parallel-plate leakage from conductor-backed transmission lines, *IEEE Trans. Microwave Theory Tech.* **MTT-44**(2):169–181 (1996).
9. Y. Liu and T. Itoh, Leakage phenomena in multilayered conductor-backed coplanar waveguides, *IEEE Microwave Guided Wave Lett.* **MTT-39**(11):426–427 (1993).
10. H. A. Wheeler, Transmission-line properties of a strip on a dielectric sheet on a metal plane, *IEEE Trans. Microwave Theory Tech.* **MTT-25**(8):631–647 (1977).
11. E. J. Denlinger, A frequency dependent solution for microstrip transmission lines, *IEEE Trans. Microwave Theory Tech.* **MTT-19**(1):30–39 (1971).
12. C. P. Wen, Coplanar waveguide: A surface strip transmission line suitable for nonreciprocal gyromagnetic device applications, *IEEE Trans. Microwave Theory Tech.* **MTT-17**(12):1087–1090 (1969).
13. R. W. Jackson, Considerations in the use of coplanar-waveguide for millimeter-wave integrated circuits, *IEEE Trans. Microwave Theory Tech.* **MTT-34**(12):1021–1027 (1986).
14. S. B. Cohen, Slotline on a dielectric substrate, *IEEE Trans. Microwave Theory Tech.* **MTT-17**(10):768–778 (1969).
15. D. M. Pozar, *Microwave Engineering*, Addison-Wesley, Reading, MA, 1990.
16. R. E. Collin, *Foundations for Microwave Engineering*, McGraw-Hill, New York, 1992.
17. D. M. Pozar, Microstrip antennas, *IEEE Proc.* **80**:79–91 (1992).
18. K. S. Yngvesson et al., Tapered slot antenna—a new integrated element for millimeter wave applications, *IEEE Trans. Microwave Theory Tech.* **MTT-37**(2):365–374 (1989).
19. D. M. Pozar, A reciprocity method of analysis of printed slots and slot-coupled microstrip antennas, *IEEE Trans. Anten. Propag.* **AP-34**(12):1439–1446 (1986).
20. S. M. Sze, *Physics of Semiconductor Devices*, Wiley, New York, 1981.
21. S. Y. Yngvesson, *Microwave Semiconductor Devices*, Kluwer Academic Publishers, Boston, 1991.
22. S. Y. Liao, *Microwave Devices and Circuits*, Prentice-Hall, Englewood Cliffs, NJ, 1990.
23. G. Gonzalez, *Microwave Transistor Amplifiers, Analysis and Design*, Prentice-Hall, Englewood Cliffs, NJ, 1984.
24. T. T. Ha, *Solid-State Microwave Amplifier Design*, Wiley, New York, 1981.
25. G. D. Vandelin, *Design of Amplifiers and Oscillators by the S-Parameter Method*, Wiley, New York, 1982.
26. K. C. Gupta, R. Garg, and R. Chadha, *Computer-Aided Design of Microwave Circuits*, Artech House, Norwood, MA, 1980.
27. M. S. Mirotznik and D. Prather, How to choose EM software, *IEEE Spectrum Mag.* (Dec. 53–58, 1997).
28. N. K. Das, Power leakage, characteristic impedance and mode-coupling behavior of finite-length leaky printed transmission lines, *IEEE Trans. Microwave Theory Tech.* **MTT-44**(4):526–536 (1996).
29. R. F. Drayton and L. P. B. Katehi, Development of self-packaged high frequency circuits using micromachining techniques, *IEEE Trans. Microwave Theory Tech.* **MTT-43**(9):2073–2080 (1995).
30. N. K. Das, Characteristics of modified slotline configurations, *IEEE Microwave Theory Tech. Symp. Digest*, 1991, pp. 777–780.
31. T. Yoneyama and S. Nishida, Nonradiative dielectric waveguide for millimeter-wave integrated circuits, *IEEE*

Trans. Microwave Theory Tech. **MTT-29**(11):1188–1192 (1981).

32. F. J. Risher, H guide with laminated dielectric slab, *IEEE Trans. Microwave Theory Tech.* **MTT-18**(1):5–9 (1970).
33. N. K. Das et al., Multilayer integration of microwave and millimeter-wave circuits: New interconnect methods and design considerations, in N. K. Das and H. L. Bertoni, eds., *Directions for the Next Generation of MMIC Devices and Systems*, Plenum, New York, 1996, pp. 83–96.

MICROWAVE ISOLATORS

VERNON E. DUNN
Space Systems/Loral

Isolators are used extensively in microwave equipment to prevent interaction between other components of the system. This article describes the principles of operation of the most common types of microwave isolators and typical operating characteristics of these isolators. In addition, references are provided for further information on the theory of operation and design details.

An isolator is a two-port device that has low insertion loss from port 1 to port 2 and high insertion loss from port 2 to port 1, as shown schematically in Fig. 1. An ideal isolator is represented by the following scattering matrix, which indicates that ideally the device is also perfectly matched at the input and output ports:

$$S = \begin{bmatrix} 0 & 0 \\ S_{21} & 0 \end{bmatrix} \text{ where } |S_{21}| = 1 \quad (1)$$

Isolators find wide application in microwave systems eliminating interactions between components, for instance, as in Fig. 2a, between a transmitter's power amplifier and an antenna. The output from the amplifier is transmitted with low loss to the antenna, but energy reflected from the antenna is absorbed by the isolator. Other typical applications are to reduce interaction between stages of amplification (Fig. 2b) or between a local oscillator and a mixer (Fig. 2c).

An ideal isolator would have no insertion loss in the forward direction, infinite loss in the reverse direction, and a perfect match at the input and output. It would maintain these characteristics over a wide frequency range and would be able to handle high-power signals in both the forward and reverse directions without limiting or distorting the signal by generating nonlinear intermodulation products. Practical, commercially available isolators typically are expected to have less than 0.5 dB



Figure 1. Schematic representation of an isolator.

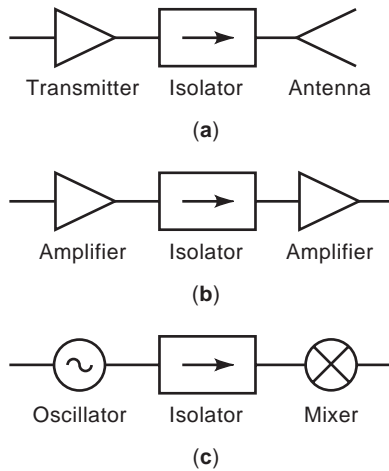


Figure 2. Typical isolator applications: (a) isolating transmitter from antenna; (b) isolating two stages of an amplifier; (c) isolating local oscillator from mixer.

insertion loss in the forward direction, greater than 20 dB loss in the reverse direction, and return loss of the input and output ports greater than 20 dB over frequency bandwidths up to an octave. If the isolator must operate over a wider frequency range, some sacrifice in insertion loss and isolation performance must be expected. Conversely, better performance may be required for some applications and is obtainable over narrow bands.

In a typical application illustrated in Fig. 3, the effect of the less-than-ideal characteristics of the actual isolator would be analyzed by considering the reflection at port *b* resulting from the mismatch between the load and the output impedance of the isolator. This reflected signal is then attenuated by the isolation of the isolator, and the resulting signal at port *a* is added vectorily to the reflection resulting from the mismatch between the source impedance and the input impedance of the perfectly terminated isolator. For example, if the isolator has an insertion loss of 0.5 dB, isolation of 20 dB, and an input and output return loss of 20 dB and the signal at port *b* is totally reflected back to the isolator, the reflected signal returning to the input port will be 20.5 dB below the incident signal and will be added vectorily to the reflection resulting from the input port mismatch, which is 20 dB down from the incident signal. The resulting total return loss will be between 14.2 and 45 dB depending on the relative phases.

Microwave isolators make use of the nonreciprocal microwave properties of a ferrite material biased by an applied direct-current (DC) magnetic field. Of the many different approaches that have been devised to use these

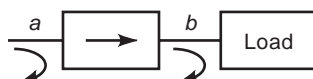


Figure 3. The total reflected signal at *a* is the vectorial sum of the reflection resulting from the mismatch of port *a* plus the signal reflected at *b* reduced by the isolation of the isolator.

properties to form practical devices, most are included in the following general categories:

1. Terminated circulators
2. Faraday rotation isolators
3. Resonance isolators
4. Field displacement isolators

All these isolators differ from the ideal. In evaluating these different types of isolators, important characteristics that must be considered are forward and reverse insertion loss and the frequency bandwidth over which those values are obtained as well as the power handling capability. Some approaches are more applicable to some frequency ranges than others, and they differ in their applicability to different transmission media such as waveguide, coaxial line, or microstrip.

The following discussions describe the operation of these different types of isolators and compare their characteristics.

1. TERMINATED CIRCULATORS

Microwave circulators are described in detail in another article of this encyclopedia and are devices with three or more ports with low loss, for example, from ports 1 to 2, 2 to 3, and 3 to 1 as illustrated in Fig. 4a. Ideally they are lossless and are described by

$$S = \begin{bmatrix} 0 & 0 & S_{13} \\ S_{21} & 0 & 0 \\ 0 & S_{32} & 0 \end{bmatrix} \text{ where } |S_{13}| = |S_{21}| = |S_{32}| = 1 \quad (2)$$

Terminating port 3 of a three-port circulator (Fig. 4b) in a matched load results in an isolator between ports 1 and 2.

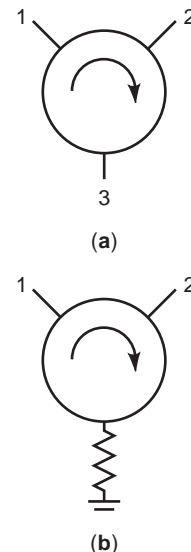


Figure 4. Connecting a matched load to port 3 of a three-port circulator forms a two-port isolator.

The isolation depends on the match between the termination and port 3 of the circulator.

The circulator may be constructed in any of the many forms described elsewhere, such as waveguide, stripline, microstrip, or lumped constant, and at frequencies from UHF to millimeter wavelengths. In addition to being compatible with the wide variety of transmission media, the terminated circulator approach has a significant advantage over other types of isolators in that the nonreciprocal function performed by the circulator is entirely separated from the problem of dissipating the energy of the signal propagating in the reverse direction. Thus, in applications where a large amount of reverse power must be dissipated, a high-power load, with external cooling if necessary, can be provided; or in low-power applications, a miniature termination such as a chip resistor can be integrated with the circulator to form a compact device.

The successful development of junction circulators in many forms and over a wide frequency range has resulted in the terminated circulator being the most common type of ferrite isolator.

2. FARADAY ROTATION ISOLATOR

The Faraday rotation isolator (1) was one of the first types of microwave ferrite devices. Its operation can be described with reference to Fig. 5. The Faraday rotator section consists of a ferrite rod at the center of a circular waveguide with its axis parallel to that of the waveguide. A DC magnetic bias field is applied along the axis of the ferrite rod. It is a property of the Faraday rotator that, if the input to the rotator section is a signal in the TE_{11} mode of circular waveguide, the orientation of the E field will rotate as the signal propagates through the rotator as shown. This Faraday rotation can be demonstrated theoretically by considering the linearly polarized field in the circular waveguide section to be composed of two counterrotating circularly polarized modes. The magnetized ferrite can be shown to present a different microwave permeability to the two counterrotating modes, which therefore propagate with different velocities, resulting in the rotation of the total field pattern [2].

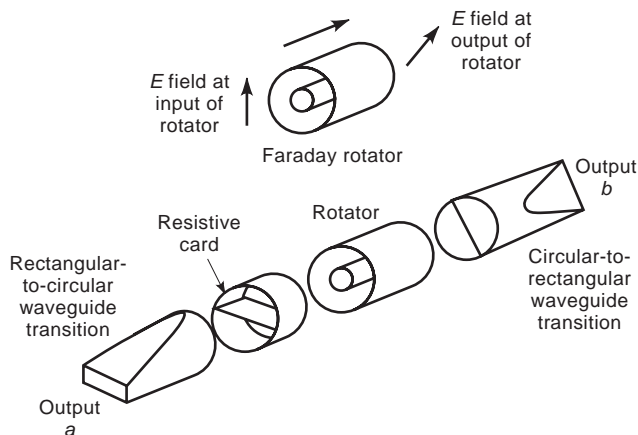


Figure 5. A Faraday rotation isolator.

To make an isolator from this Faraday rotator, rectangular-to-circular waveguide transitions are placed at the input and output with matching provided to the ferrite-loaded section. Resistive cards are placed across the circular sections of the guide at both the input and output. An incoming signal from port a will go through the rectangular-to-circular waveguide transition transforming to the TE_{11} mode in the circular guide with the E field perpendicular to the resistive absorber. Thus the signal is transformed with low loss to the ferrite-loaded section. The ferrite-loaded portion of the guide is terminated at the point where the E field has been rotated by 45° , where it passes another resistive absorber oriented perpendicular to the E field and enters the transition back to the rectangular guide. Thus, the signal passes with low loss to the output port b .

On the other hand, if a signal is applied to port b , it again passes with low loss to the ferrite-loaded section, where it is rotated so that at port a it is oriented with the E field parallel to the resistive absorber. The signal is then attenuated by the absorber.

The Faraday rotation isolator was one of the first microwave ferrite devices to be introduced, but it suffers from several performance limitations. The rotation in the basic device of Fig. 5 is frequency-dependent, so the isolator is narrowband. In addition, the rotator is inherently a low-power device because of its geometry. The ferrite and the absorber are thermally isolated so that the power that can be handled, especially in the reverse direction, is limited. Techniques have been developed to increase the bandwidth over that of the basic device [2,3]. For example, dielectric loading, ridged waveguide, and cascading of stagger-tuned sections have been used to produce acceptable performance over bandwidths of several gigahertz at X band, but because of its limitations the Faraday rotator has largely been superseded by the other isolator approaches discussed here.

One version of the Faraday rotation isolator that still finds application was described by Barnes [4]. In this approach, instead of using a circular waveguide loaded by a ferrite rod, the conducting waveguide walls are eliminated, and the ferrite rod is increased in diameter so that the ferrite becomes a dielectric waveguide. The high dielectric constant (typically between 12 and 15) of the relatively large ferrite rod confines most of the energy to the ferrite.

The details of this type of isolator are described in detail by Barnes [4]. The rotator consists of a short length of ferrite rod suspended in a nonconducting housing by plastic supports and is coupled to the input and output rectangular waveguides by dielectric tapers that protrude into the waveguides. The attenuator films that provide the reverse loss are deposited metal films sandwiched into the tapered dielectric waveguides.

Barnes shows that, because the dielectric rod guide with approximately 95% of the energy confined to the ferrite behaves much like an infinite ferrite medium, the Faraday rotation is less dependent on frequency than in a ferrite-loaded metal waveguide. Figure 6 shows the performance reported by Barnes for a 50–60-GHz isolator, along with the performance of a “conventional” Faraday rotation isolator. Because of its broadband performance

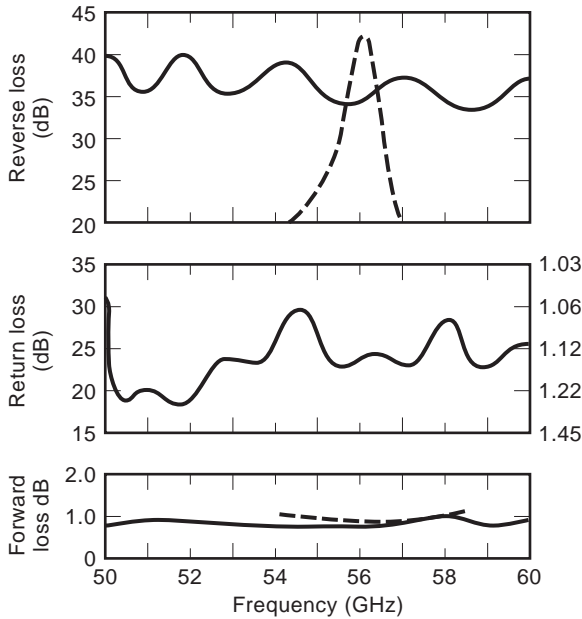


Figure 6. Performance of the broadband isolator of Barnes (solid curves) compared with a “conventional” Faraday rotation isolator (dashed curves) [4]. (Copyright © 1961 IEEE.)

and low magnetic bias field requirement, this approach has proved to be useful for broadband millimeter wavelength isolators.

3. RESONANCE ISOLATORS

The resonance isolator makes direct use of the phenomenon of ferromagnetic resonance, characterized by the precession of the magnetization vector in a ferrite about the direction of an applied DC bias field [2]. In an unperturbed state, the direction of the magnetization vector of the ferrite is aligned with an applied bias field. Any disturbance, such as a momentary magnetic field applied perpendicular to the bias field, will cause the magnetization to precess about the direction of the bias field, as illustrated in Fig. 7. After the perturbation is removed, the precession will decay at a rate that depends on the magnetic losses of the material, until the magnetization is again aligned with the DC field.

The frequency of the precession, the ferromagnetic resonance frequency, is proportional to the DC field. In an

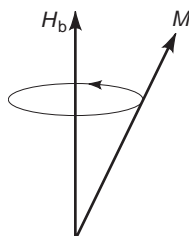


Figure 7. When perturbed from the steady state, the magnetization M will precess about the bias field H_b at the ferromagnetic resonant frequency.

infinite ferrite medium

$$f_0 = \gamma H_{dc} \tag{3}$$

where, in the commonly used units, γ is 2.8 MHz/oersted. In the case of a finite ferrite element such as a plate or rod, the demagnetizing factor of the sample must be taken into account to relate the applied bias field to the internal field that determines the resonant frequency. For readily achievable magnetic fields, this resonant frequency is in the microwave region. Microwave signals near the resonant frequency with magnetic fields perpendicular to the bias field will interact strongly with the ferrite magnetization. In particular, circularly polarized fields in the plane perpendicular to the bias field will interact strongly if the sense of polarization corresponds to the direction of the resonant precession but only weakly if the sense of circular polarization is opposite to the direction of the precession.

Now consider a rectangular waveguide operating in the fundamental TE_{10} mode. Figure 8 shows the magnetic field of this mode, looking down on the broad face of the guide. At point A in the guide, the magnetic field will be circularly polarized in the counterclockwise direction for a signal traveling from left to right and in a clockwise direction for a signal traveling from right to left. If a ferrite is placed in the waveguide at this point and biased by a DC field, as shown in Fig. 9, the ferrite will interact strongly with a signal in the waveguide with a frequency near the ferromagnetic resonant frequency when the direction of propagation is such that the sense of circular polarization corresponds to direction of the ferromagnetic precession. The interaction will be weak for a signal traveling in the opposite direction. By proper design, the parameters such as the dimension and location of the ferrite, ferrite material properties, and bias field can be chosen so that, at frequencies near the ferromagnetic resonance frequency, excellent isolator performance can be achieved.

In principal resonance isolators can be constructed in any transmission line where circularly polarized radiofrequency (RF) magnetic fields exist. For example, they have been built with various degrees of success in dielectric-loaded coaxial line, finline, dielectric waveguide, and image line; however, by far the largest application of the resonance isolator approach is in rectangular and ridged waveguide where extensive analysis and optimization has resulted in devices with very attractive properties.

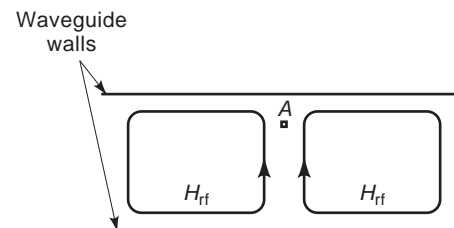


Figure 8. At point A the RF magnetic field for a signal traveling from left to right in the fundamental mode of the rectangular waveguide will be circularly polarized in the counterclockwise direction.

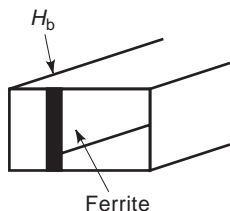


Figure 9. In this basic resonance isolator, the ferrite will interact strongly with a signal in one direction but not with one in the opposite direction.

Of the possible geometries illustrated in Fig. 10, Fig. 10b has demonstrated advantages over Fig. 10a. Placing the ferrite in a thin strip along the broad waveguide wall allows efficient dissipation of the heat produced in high-power operation. In addition, the magnetic fields are more nearly circularly polarized in the configuration of Fig. 10b than in Fig. 10a, and experiments of Weiss [5] have shown Fig. 10b to have a superior ratio of isolation to forward insertion loss. This ratio of isolation to forward insertion loss is a figure of merit used to compare different isolator configurations. The figure of merit for Fig. 10b was determined by Weiss to be 75 compared with 14 for Fig. 10a. Further improvement can be achieved with dielectric loading as illustrated in Fig. 10c. The dielectric concentrates the energy in the vicinity of the ferrite and increases the figure of merit to 150.

Resonance isolators in rectangular waveguide have been developed to give good performance over a full waveguide bandwidth (e.g., 30 dB isolation, 1 dB forward loss, and 1.15 VSWR over 8.2–12.4 GHz, or 12.4–18 GHz).

Such resonance isolators are large and heavy because of the permanent magnets required to bias the ferrite to ferromagnetic resonance at microwave frequencies (approximately 1.5 kg in the case of the previously mentioned 8.2–12.4-GHz and 12.4–18-GHz isolators). This becomes a serious problem at higher frequencies. Because the DC field required to bias the ferrite to resonance is proportional to frequency, at millimeter wavelengths this field becomes quite large, on the order of 1.5–3.5 T or more. In order to minimize the size and weight of millimeter

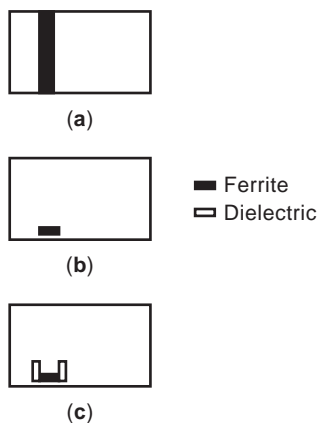


Figure 10. Three different configurations for a resonance isolator in rectangular waveguide.

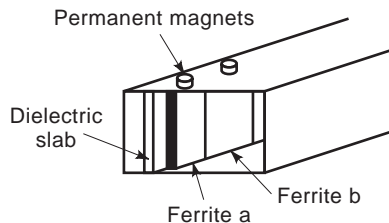


Figure 11. A resonance isolator using hexagonal ferrites.

wavelength resonance isolators, devices have been developed making use of magnetoplumbites, often called *hexagonal ferrites* [6]. Such materials have a strong anisotropy field. All ferrite materials exhibit a certain amount of magnetic anisotropy because, in the individual crystallites that make up the material, the crystalline structure produces a preferred direction for the orientation of the magnetic moment vector. In a typical polycrystalline ferrite, however, these microscopic crystallites are randomly oriented with respect to each other, so that in the bulk material the effect of the anisotropy of the individual crystallites averages out, resulting in an isotropic material.

The materials most useful for resonance isolators are the so-called uniaxial compounds that possess a large anisotropy field along the *C* axis of the hexagonal crystals. By special processing used to produce the ferrite material, for instance by pressing the slurry of the appropriate material in the presence of a large magnetic field before firing, it is possible to produce a material in which the individual crystallites are oriented in a particular direction. This results in a large anisotropy field that in some ways is indistinguishable from an externally applied bias field. In this way, it is possible to make self-biased materials, or materials that require very little applied field to bias them to resonance at millimeter wavelengths.

Such an isolator is illustrated in Fig. 11. Thin slices of the hexagonal ferrite material are bonded to the dielectric slab, which serves to concentrate circularly polarized magnetic fields in the ferrite. In order to achieve wide bandwidth, the isolator may consist of a cascade of several sections of ferrite materials with different anisotropy fields and dielectric characteristics. Additional small permanent magnets can be used to achieve the correct resonant frequencies for the different sections. Figure 12 shows the performance of an isolator of this type weighing only 160 g. Materials have been developed enabling such isolators to be built at frequencies to 110 GHz.

4. FIELD DISPLACEMENT ISOLATORS

Field displacement isolators can be of many types but are all based on the fact that, in a transmission line loaded by a magnetically biased ferrite, the field pattern may exhibit nonreciprocal behavior by being distinctly different for the two directions of propagation. An isolator can then be built by judiciously locating dissipative material in an area where the fields are intense for one direction of propagation but weak for the other.

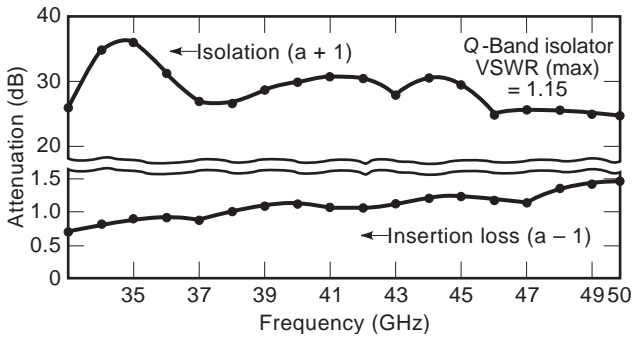


Figure 12. Performance of a 33–50 GHz isolator using hexagonal ferrites [6]. (Copyright © 1963 IEEE.)

Figure 13 illustrates an early type of isolator based on this principle [7]. As in the resonance isolator, a ferrite slab is introduced into the rectangular waveguide, and a DC magnetic field is applied across the narrow dimension of the waveguide; however, in this case the bias field is less than that required for ferromagnetic resonance. With an appropriate choice of dimensions, ferrite properties, and magnetic bias, the resulting field pattern for the two directions of propagation can be as shown with a concentration of electric fields at one surface of the ferrite in one direction and minimal electric field at that surface for the other direction of propagation. If a sheet of resistive material is placed at this surface of the ferrite, it will dissipate energy for one direction and have very little effect on the other. An isolator of this type can produce, for example, isolation of greater than 30 dB over the 5.9–6.4 GHz band with a forward loss of less than 0.25 dB [8]. The isolator of Fig. 13 was one of the earliest types of microwave ferrite devices, but it has largely been supplanted by the other types of isolators.

One more recent type of field displacement isolator that has significant unique advantages, particularly in regard to broadband operation, is the peripheral mode, or edge-guided, isolator. This device uses the edge-guided mode analyzed by Hines [9]. Circulators and isolators using this mode of propagation were patented by Anderson [10].

The analysis by Hines revealed that in a stripline, or microstrip transmission line, with a wide center conductor and ferrite as the dielectric medium, and with a magnetic bias field perpendicular to the ground plane(s), a mode of

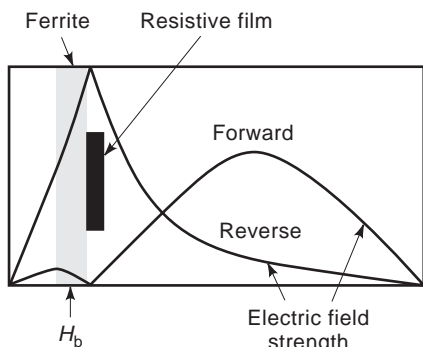


Figure 13. A field displacement isolator in a rectangular waveguide.

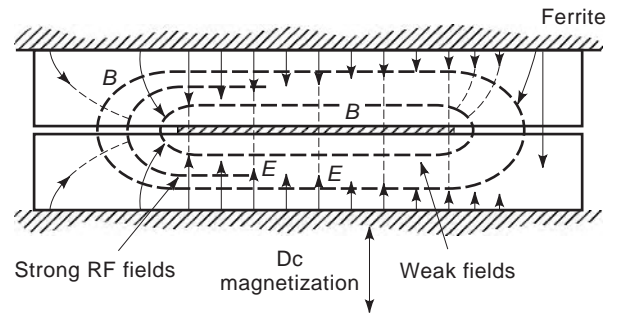


Figure 14. Fields in a ferrite-filled stripline as analyzed by Hines [9]. (Copyright © 1971 IEEE.)

propagation exists in which the energy concentrates toward one edge of the center conductor. The fields of this mode in stripline are illustrated in Fig. 14. The fields are similar to transverse electromagnetic (TEM) modes except for their displacement to one side or the other of the center conductor, depending on the direction of the bias field with respect to the direction of propagation. Hines has shown that for a very wide center conductor in comparison to the ground-plane spacing, with a weak bias field, sufficient only to saturate the ferrite, this mode of propagation is free of dispersion and has a constant characteristic impedance over all frequencies.

Because the energy is concentrated at one edge of the center conductor, an isolator can be constructed by placing lossy material along one edge of this conductor. One direction of propagation will be unperturbed by this material, while a signal in the opposite direction can be strongly absorbed. Such an isolator is illustrated in Fig. 15. In the idealized case, this isolator would have infinite bandwidth. In practice, the bandwidth is limited by low field losses at low frequencies, by higher-order modes at high frequencies, and by the difficulties in matching at the input and output to or from a conventional stripline or coaxial line. Nevertheless, very broadband isolators can be achieved using this approach. Hines reported the results shown in Fig. 16 for a basic microstrip configuration and in Fig. 17 for the case of added capacitive loading along the low-loss edge. Thus the approach yields performance acceptable for some applications over a multioctave band.

The isolators described in this article are those that have found significant application in microwave systems.

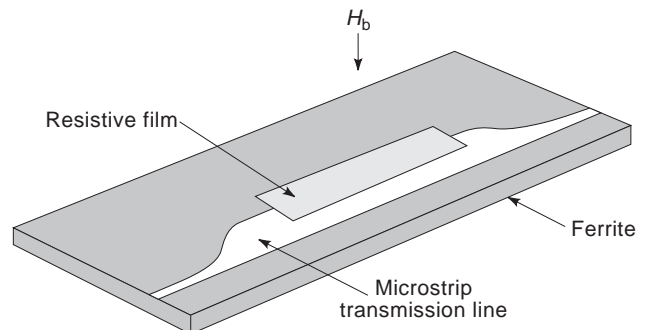


Figure 15. A broadband isolator using the edge-guided mode of a microstrip transmission line on a ferrite substrate.

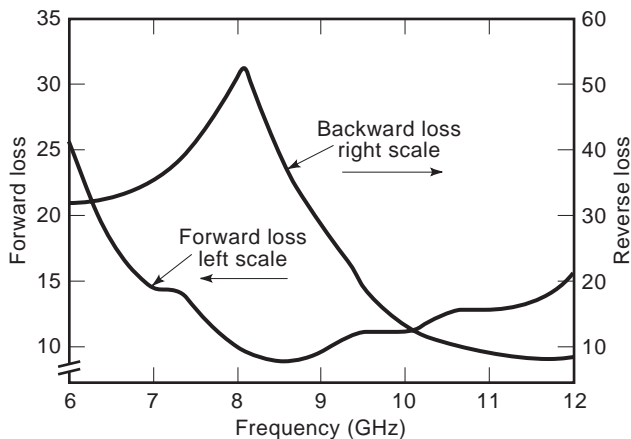


Figure 16. Measured performance of a microstrip isolator similar to that of Fig. 15 [9]. (Copyright © 1971 IEEE.)

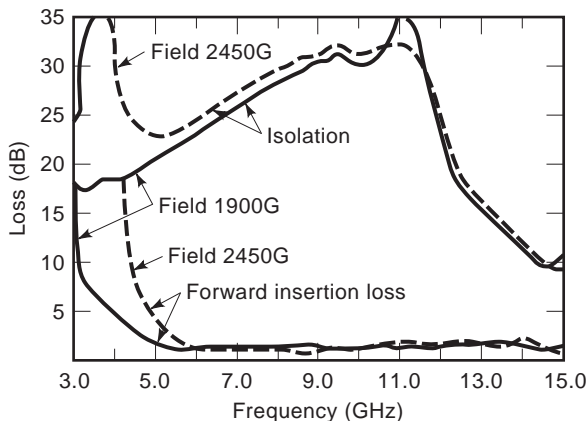


Figure 17. Measured performance of a microstrip isolator similar to that of Fig. 15, but with added capacitive compensation along the low-loss edge [9]. (Copyright © 1971 IEEE.)

In recent years development of microwave isolators has continued with most effort being devoted toward development of isolators compatible with newer types of transmission lines, particularly for application at millimeter wavelengths. For example isolators have been developed for use with finlines [11,12], image lines [13], and quasi-optical transmission lines [14]. These isolators will become important as these transmission media find application.

BIBLIOGRAPHY

1. C. L. Hogan, The microwave gyrator, *Bell Syst. Tech. J.* **31**:1 (1952).
2. B. Lax and K. J. Button, *Microwave Ferrites and Ferrimagnetics*, McGraw-Hill, New York, 1962.
3. P. H. Vartanian, J. L. Melchor, and W. P. Ayres, Broadbanding ferrite microwave isolators, *IRE National Convention Record*, 1956, Part 5, p. 79.
4. C. E. Barnes, Broad-band isolators and variable attenuators for millimeter wavelengths, *IRE Trans. Microwave Theory Tech.* **9**:519 (1961).
5. M. T. Weiss, Improved rectangular waveguide resonance isolators, *IRE Trans. Microwave Theory Tech.* **4**:240 (1956).

6. D. R. Taft, G. R. Harrison, and L. R. Hodges, Millimeter resonance isolators utilizing hexagonal ferrites, *IEEE Trans. Microwave Theory Tech.* **11**:346 (1963).
7. S. Weisbaum and H. Seidel, The field displacement isolator, *Bell Syst. Tech. J.* **35**:877 (1956).
8. R. L. Comstock and C. E. Fay, Operation of the field displacement isolator in rectangular waveguide, *IRE Trans. Microwave Theory Tech.* **8**:605 (1960).
9. M. E. Hines, Reciprocal and nonreciprocal modes of propagation in ferrite stripline and microstrip devices, *IEEE Trans. Microwave Theory Tech.* **MTT-19**:442-451 (1971).
10. R. Anderson, *Gyromagnetic Device Having a Plurality of Outwardly Tapering Members*, U.S. Patent 3,555,459 (Jan. 12, 1971).
11. L. E. Davis and D. B. Sillars, Millimetric nonreciprocal coupled-slot finline components, *IEEE Trans. Microwave Theory Tech.* **MTT-34**(7) (1986).
12. A. Beyer and K. Solbach, A new fin-line ferrite isolator for integrated millimeter-wave circuits, *IEEE Trans. Microwave Theory Tech.* **MTT-29**(12) (1981).
13. J. M. Owens et al., W-band ferrite-dielectric image-line field displacement isolators, *1989 IEEE MTT-S Int. Microwave Symp. Digest*, 1989.
14. G. M. Smith et al., Design, analysis and application of high performance permanently magnetised, quasi-optical, Faraday rotators, *1994 IEEE MTT-S Int. Microwave Symp. Digest*, 1994.

MICROWAVE LIMITERS

ROGER KAUL
U.S. Army Research Laboratory

A microwave limiter is designed to allow low-power signals to pass through it, while attenuating high-power signals. Stated another way, microwave limiters are power-dependent attenuators that prevent intense microwave energy from interfering with susceptible microwave components in the latter stages of a cascade.

Most limiters operate by reducing the impedance of a transmission line when the incident power is above the threshold power level, reflecting or absorbing the incident power. Although, in most cases, a limiter reflects the majority of the intense incident power back toward the power source on the transmission line, where a circulator, an isolator, or a hybrid coupler may divert or absorb it, a microwave limiter may also be designed to absorb the incident power in the same manner as a microwave switch.

In most applications, microwave limiters (sometimes referred to as *receiver protectors* and *terminal protection devices*) are located near the antenna port. However, limiters have also been used in intermediate-frequency channels, where signals from a number of channels are combined to create an intense signal (e.g., the intermediate frequency circuit of a phased-array radar). In radar applications, the term "duplexer" is sometimes used to refer to the front-end receiver protection circuitry.

Table 1. Common Microwave Limiter Technologies

Technology	Common Implementations
Solid-state	p-i-n diode MESFET
Gaseous	Waveguide Stripline
Ferrite	Filter Stripline

Many microwave limiter technologies have been investigated since the midtwentieth century. The common technologies are identified in Table 1. The solid-state limiter, which was first designed using the varactor diode, today employs the Si p-i-n (or PIN) diode, because of the p-i-n's lower capacitance per unit area resulting in better thermal characteristics, in addition to the fact that it requires no external power supply. Also shown in the table is the fact that a MESFET-based, MMIC-compatible microwave limiter is being developed for integration with the low-noise amplifiers common in MMIC designs. Furthermore, although gaseous limiters are widely used in high-power radars as receiver protectors, ferrite limiters have not found the same wide use.

1. SOLID-STATE LIMITERS

At radiofrequencies, it is common to place back-to-back signal diodes (e.g., 1N914) shunted to ground across the input transmission line of a radio receiver, as shown in Fig. 1a. When the peak voltage on the line exceeds the forward conduction voltage (typically, 0.7 V) the transmission line voltage is clipped. Below the threshold voltage, the diodes appear as shunt capacitors across the line. The high capacitance of the 1N914 prevents the extension of this design to microwave frequencies, where the capacitive reactance becomes very low, yielding an undesirable impedance discontinuity, shunting the transmission line that must be tuned out to retain a small voltage standing-wave ratio (VSWR) at low line voltages. The additional reactance narrows the bandwidth of the transmission line, which may be unacceptable.

1.1. p-i-n Diode Limiter

The p-i-n diode has a lower capacitance for a given cross-sectional area than other diode designs, because the distance between the p⁺ and n⁺ regions is separated with the i (intrinsic) region, whereas in other signal diodes, only the depletion region separates the two highly doped regions. The i-region thickness of a p-i-n diode is typically in the 1–200 μm range, whereas other diode depletion regions are typically less than 2 μm. A good measure of the i-region thickness (h) is the reverse breakdown voltage (V_b) at a few microamperes. Several relations are used, including $V_b = 36h^{0.81}$ [1] and the simpler rule of thumb $V_b = 20h$ for $h \geq 5$, where V_b is in volts and h is in micrometers.

Since the capacitance of a parallel-plate capacitor is inversely proportional to the separation distance of the charged plates (represented by p⁺ and n⁺ charge

regions), the p-i-n diode has significantly lower capacitance per unit area at zero bias than a signal diode. This feature allows the p-i-n diode to be a high reactance connected in shunt across a transmission line even at microwave frequencies, yielding low insertion loss. The feature also provides more volume than a signal diode for dissipating heat from intense incident pulses.

The i region changes the terminal current-voltage relationship, as compared to other minority-carrier (e.g., signal) or majority-carrier (Schottky) diodes. Varactor diodes have carrier distributions similar to thin i-region p-i-n diodes. For this reason, varactor diodes were used as limiter diodes until the special doping profile of the p-i-n was developed. Leenov [2] studied the p-i-n diode configuration and determined that, at frequencies lower than the inverse transit time of the i region, the diode rectifies with a low series resistance. At very high frequencies, the charge distributions at the edges of the i region oscillate with the applied terminal voltage; however, since carriers do not have time to transit the i region, the current is primarily a displacement current and the diode impedance remains high. Leenov found that, when excited with a sine wave, the diode resistance is

$$R = \frac{10^{-4}kT}{q(D/2\pi f)^{1/2}} \left(\frac{Z_0}{P_i} \right) h \quad \Omega \quad (1)$$

where k is Boltzmann's constant ($1.38 \times 10^{-23} \text{ W} \cdot \text{s/K}$), T is the absolute temperature (K), q is the electron charge ($1.6 \times 10^{-19} \text{ C}$), D is the diffusion coefficient ($15.6 \text{ cm}^2/\text{s}$ for Si), Z_0 is the impedance of the transmission line in ohms, and P_i is the incident power in watts. Garver [3] uses Eq. (1) to show that the attenuation α provided by a single diode across a transmission line is

$$\alpha = 10 \times \log \frac{(q/kT)^2 D Z_0 P_i}{8 \times 10^{-8} \pi f h^2} \quad \text{dB}$$

The attenuation is proportional to the $\log(1/fh^2)$ for a given impedance and p-i-n device material. At higher frequencies, the h must be reduced, resulting in a higher shunt capacitance per unit area for the diode and increased low-power level attenuation or bandwidth limiting. To compensate for this effect, the cross-sectional area of the diode is reduced. Brown [4] showed that the device thickness should be less than about 25 μm at 0.1 GHz to 2.5 μm at 10 GHz in order to avoid high spike leakage, high power absorption during the transition from the high-impedance diode state to the low-impedance diode state, and low insertion loss at low signal levels. Spike leakage is the momentary power that passes through the limiter before the diode's impedance reduces, thus reflecting the incident power back toward the source. Fast-risetime, incident pulses will appear to have a "spike" of leakage power at the output of the limiter.

Since the performance of the p-i-n diode depends on the ability of carriers to transit the i region, transient effects occur that are dependent on frequency and other parameters (e.g., i-region doping density). For example, Fig. 2 shows the voltage-time waveform of a limiter consisting of

20- μm Si p-i-n diodes closely spaced in shunt with a 50- Ω transmission line as shown in Fig. 1a with $l \cong 0$ at four incident voltage amplitudes. Note that this circuit is shown only to present the concept; actual limiters might use thinner i-region diodes arranged in another configuration (see Figs. 1b-1f). All these circuits allow rectified current to flow through both diodes. Leenov [2] showed that a DC current is much more efficient in lowering the p-i-n diode's impedance than an RF current. Unless this

rectified current is allowed to flow in a low-impedance circuit (typically less than 5 Ω), the p-i-n diode resistance may not be reduced to a few ohms (typical). The voltage-time waveforms on the left in Fig. 2 are the incident voltage at 1.1 GHz, and the waveforms on the right are the voltage following the dual-diode limiter. The p-i-n diodes do not clip the incident wave as would a high-speed signal diode; rather, their impedance is reduced by injection of carriers into the i region. At the lowest incident voltage V_i ,

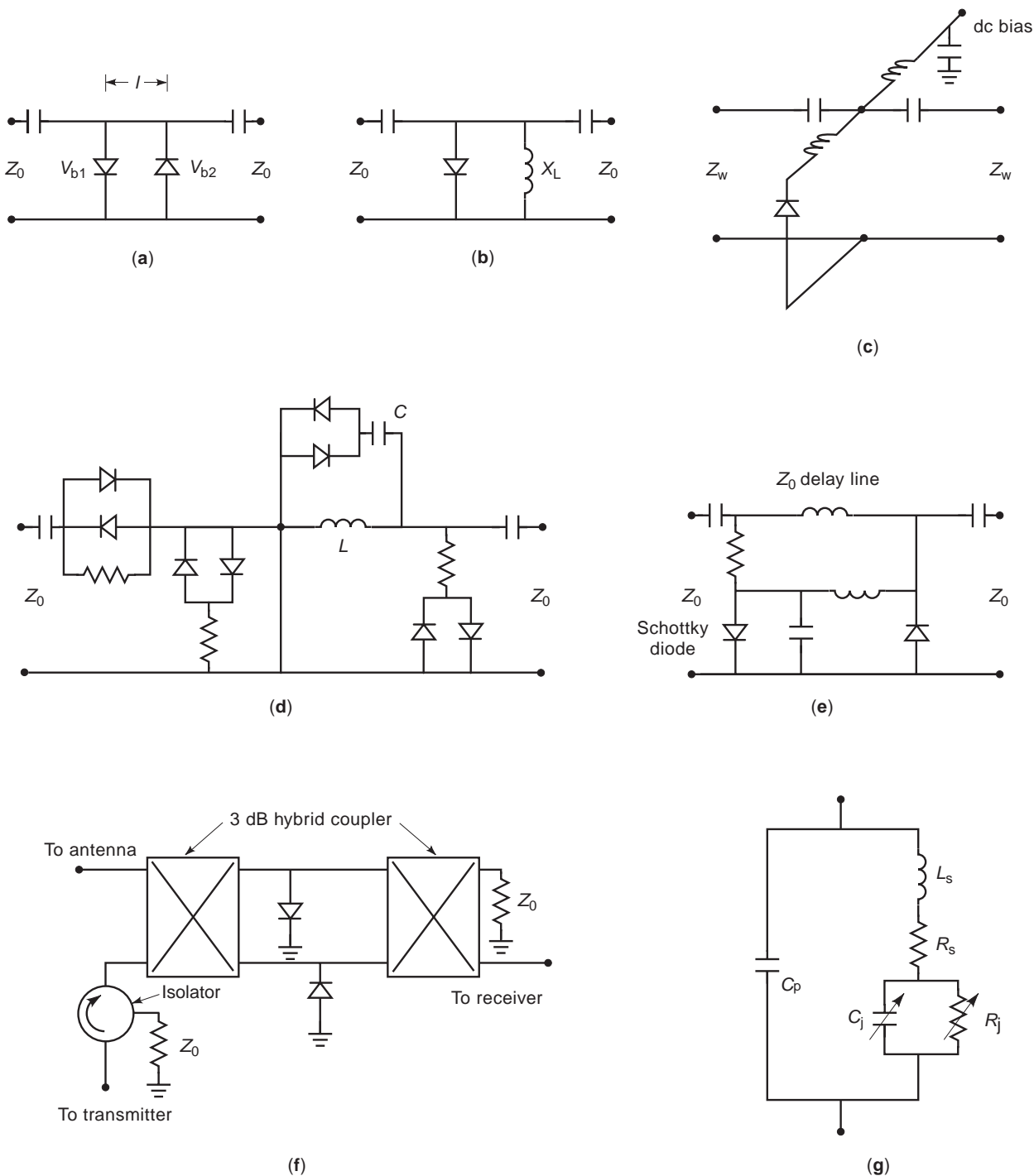


Figure 1. Diode limiter equivalent circuits.

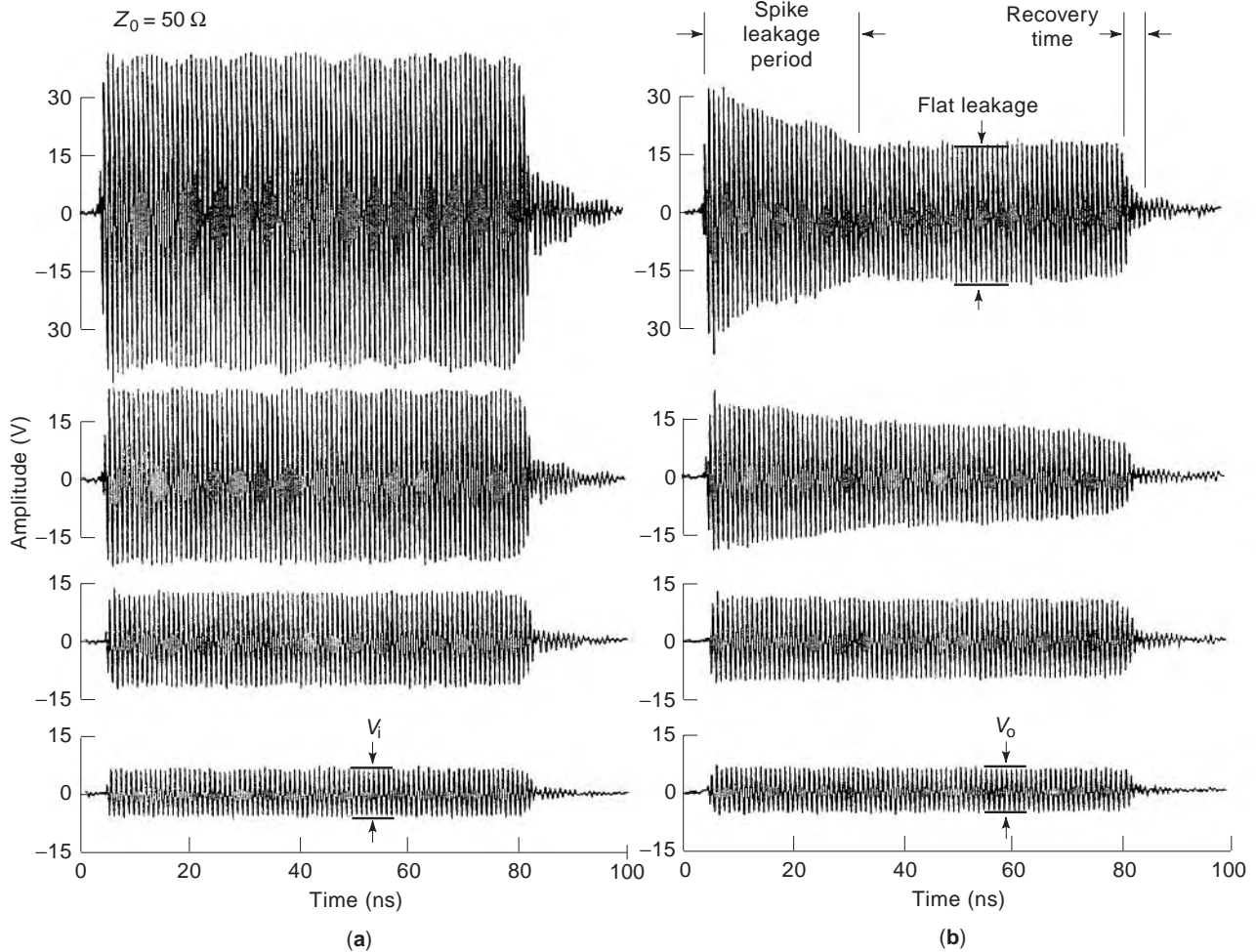


Figure 2. Incident and output voltage-time waveforms for a p-i-n diode limiter.

the attenuation (insertion loss) of the limiter is $20 \log_{10}(V_o/V_i) \approx -1$ dB, where V_o is the output voltage. As the V_i is doubled, the V_o tends to show an initial transmission transient (termed “spike leakage”), followed by a relatively constant output voltage (termed “flat leakage”). It requires tens of nanoseconds for the two diodes to lower their impedance below the Z_o of the transmission line. However, the spike leakage period would be much more rapid if the *i* region were thinner or the 20- μm diodes were excited at a lower frequency. The amount of energy in this period (i.e., the integral of the power-time profile) is the spike energy that may destroy susceptible microwave devices in cascade with the limiter. As a rule of thumb, low-noise, microwave amplifiers will be destroyed if the spike energy exceeds 1 μJ , and destruction of microwave mixers will occur at the 10 μJ level. If the spike energy must be reduced, the second limiter diode with a thinner *i* region is located with a quarter-wavelength behind the first limiter diode as shown in Fig. 1a with $l = \frac{1}{4}$ wavelength.

A commercial limiter using three p-i-n diodes shunting a soft-substrate, 50- Ω transmission line is shown in Fig. 3. The thinnest p-i-n diode is located near the output receiver port, of the limiter and activates first, setting the threshold for limiting. The 10-turn coil allows the rectified

current to flow through the diode(s). The standing wave reflected from the thinnest diode excites the middle diode, and the thickest diode is activated at higher incident power levels. At signal levels below threshold, the bandwidth (defined by $\text{VSWR} \leq 1.6 : 1$) of this limiter design is 2–8 GHz, with an insertion loss less than 1.3 dB. The limiter is specified to sustain a 3 W continuous incident power, with 0.1 W output level. The input-output curve measured at 2 GHz for the commercial limiter (shown in Fig. 4) confirms the flat leakage level at 0.1 W, and the insertion loss at less than 1 dB at the low end of the operating band. The input 1 dB compression point was measured to be 11 dBm, and the input third-order intercept was 18 dBm at 3 GHz and was 15 dBm at 7 GHz. During pulsed operation, the unit will sustain a 1000 W pulsetrain, with a 1 μs length and a 1% duty cycle. The recovery time (defined as the time to return to low insertion loss after the high incident power is removed) is specified as less than 1 μs .

1.2. Spike Leakage

The data in Fig. 2 show that the peak spike leakage power increased and the duration of the spike decreased with increasing incident voltage. The measured spike energy

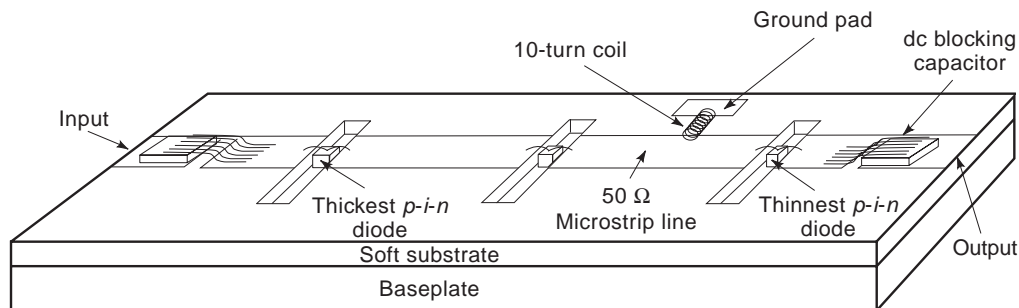


Figure 3. Sketch of a multistage p-i-n diode limiter.

for 1.5 and 5- μm i-region diodes is shown in Fig. 5. Calculations supporting these results (1) show that a slightly p-doped (10^{15} cm^{-3}) intrinsic region would exhibit less spike leakage than does the usual n-doped (10^{14} cm^{-3} or less) intrinsic region. This result arises because a higher density of the lower mobility holes yields a lower impedance i region than in the usual case with the n-doped i region

1.3. Diode Limiter Circuits

Figure 1 shows many configurations of diode limiter circuits. Figure 1a has been discussed previously. Figure 1b is a single-diode circuit in which the rectified current flows through the inductor. Note that since the diode's impedance is lowered at high signal levels throughout the cycle, the single diode does not rectify the positive or negative peak voltages on the transmission line; if that were the case, the maximum isolation would be only 3 dB. The inductor's reactance X_L should be high at the operating frequency, but have a low inductance at frequencies associated with buildup of the rectified current to allow the rectified current to build up rapidly, thereby reducing spike leakage.

In waveguides, the p-i-n diode is mounted parallel to the electric field lines in the lowest-order mode on an inductive post. The equivalent circuit in Fig. 1c shows the reactances of the post in shunt with the waveguide impedance Z_w . For self-activated limiter operation, the low-pass filter for inserting the DC bias is not needed. The

limiters shown in Figs. 1a-1c reflect most of the incident power back toward the source. If this reflected power is undesirable (e.g., an application in which a limiter is used for stealth purposes), a nonreflective limiter (i.e., a power-dependent attenuator, as shown in Fig. 1d) may be required. A nonreflective design developed by Glenn et al. [5] is self-activating but does not provide the same amount of isolation that reflective limiters provide. The nonreflective design is parallel-resonated by the L and C at high signal levels, for added isolation. Nonresonant, nonreflective circuits using resistors are possible; however, resistors provide only moderate levels (10-15 dB) of isolation.

Where spike leakage is a significant problem at high power levels, the delay-line limiter (Fig. 1e) rectifies a sample of the large signal and applies a DC bias to the p-i-n diode, lowering its impedance before the intense signal arrives. The delay line may be implemented in a low-loss coaxial cable yielding an approximate 3 ns delay per meter.

Figure 1f shows the duplexer application for a pulsed, monostatic radar receiver protector. At normal receive signal levels, the balanced duplexer design employs two 3 dB, 90° , hybrid couplers to split the input signal between two diode limiters. Since the limiters are in their high-impedance state, the signals are recombined at the output into the receiver input. If an intense receive signal is present, the p-i-n diodes conduct, and the signal is reflected back into the transmitter's circulator stage, where

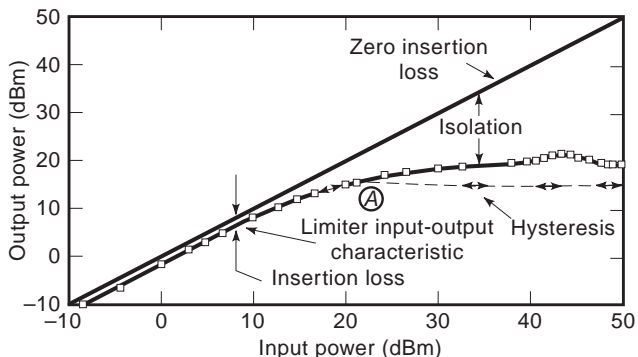


Figure 4. Input-output power characteristic of a p-i-n diode limiter.

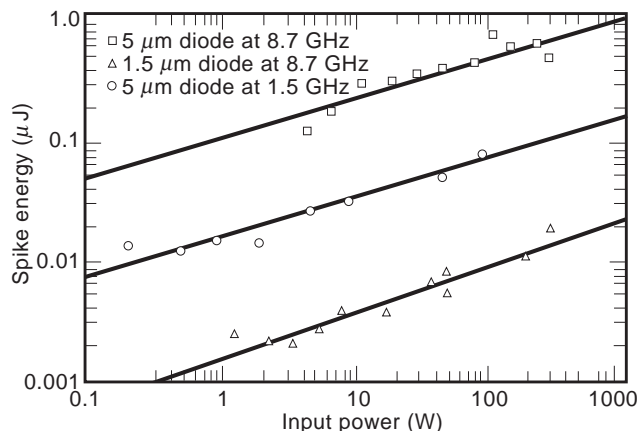


Figure 5. Spike energy for 1.5 and 5- μm -thick i-region p-i-n diodes.

it is absorbed in the matched load. During transmit, the p-i-n diodes are low impedance and reflect the power out of the antenna port. If the antenna VSWR is high, the transmitter power is rereflected by the diodes and is absorbed in the load of the three-port circulator. This duplexer circuit uses all passive components. If desired, the p-i-n diodes can be externally biased during the transmitter's pulse. If a DC path for the rectified p-i-n diode current is not available through the 3-dB hybrids, one must be provided via shunt inductors or other bias circuitry.

In Fig. 1, all diodes assume no package parasitics. These package parasitics (see Fig. 1g) can have a significant effect at microwave frequencies. The p-i-n diode is represented by the variables C_j and R_j , where C_j is small (typically less than 1 pF) and R_j is large at low signal levels. At high signal levels, R_j is small (typically 1–2 Ω), thereby shunting C_j . R_s represents the series contact resistance of the diode and the resistance of the inductive bondwire L_s to the diode chip. C_p is the package capacitance. Additional details of limiter design in microstrip and waveguide configurations are found in White [6] and Garver [3].

1.4. Unexpected Effects

Some limiters exhibit a hysteresis effect when operated CW, or with long pulses, as sketched in Fig. 4. The sudden increase in the isolation above an input power threshold is retained as the input power is reduced, until the input power equals the value marked A in Fig. 4. If the power is increased again, the original input-output curve is retraced and the threshold can be observed. However, if the input power is not reduced to point A, the lower input-output curve is followed, and a threshold cannot be observed. A plausible explanation, based on space-charge effects, is given in Ward et al. [1]; however, the hysteresis effect needs further experimental investigation.

When connected to high- Q circuits (e.g., filters), limiters may exhibit the nonlinear dynamic effects (chaos) of period doubling and noisy behavior. This behavior was first observed with a limiting filter that utilized a p-i-n diode as a capacitive reactance at the output of a microwave filter structure developed by Tan [7]. Unexpected signal generation by a limiter appears to be avoidable above 1 GHz by using i-region thickness exceeding 3 μm and a circuit Q less than 100. Further experiments and analyses are needed to fully understand and alleviate this device-circuit interaction.

1.5. Limiter Burnout Levels

The CW burnout level of a commercial p-i-n diode limiter is usually only a few watts. It is recommended that the CW power specification not be exceeded since the diode may be operating above its maximum junction temperature or the mounting solder could melt. The same power limitation applies to pulse lengths long compared to the thermal response time of the diode.

Most limiters are also specified for pulsed operation with 1 μs pulselength at 0.1% duty cycle (1000 pps). In general, these ratings are conservative and can usually be exceeded by 3 dB.

Table 2 shows the burnout level results of a limited number of experiments in 50- Ω coaxial circuits for p-i-n diode limiters with varied-thickness i regions. Damage was observed in three stages: (1) reverse current increases causing reduced reverse breakdown voltage, (2) as the diode impedance became lower the insertion loss increased, and (3) eventually fusing occurred and the diode became an open circuit, ceasing its limiting action.

GaAs p-i-n diode limiters have been fabricated and their performance has been measured. There appears to be little advantage to using GaAs, since its lower thermal conductivity cannot transfer the heat generated in the diode to the heatsink as effectively as Si can. However, for GaAs monolithic microwave integrated circuit (MMIC) devices, where high volumes make the specialized assembly of Si technology expensive, GaAs p-i-n devices may be a viable alternative. Fabrication of the GaAs i region is usually an additional process in manufacturing GaAs MMIC devices, incurring higher cost and possibly leading to lower MMIC yields. The reliability of GaAs p-i-n diode limiters have been questioned. GaAs limiters designed for high-power, high-duty-cycle, pulsed operation have degraded and become lossy after a few thousand hours of operation. However, majority-carrier GaAs devices (e.g., MESFETs) do not appear to exhibit this form of degradation.

1.6. MESFET Limiters

MMICs are finding increasing application in today's designs when uniform performance and high quantities can justify the relatively high nonrecurring design engineering costs. Use in applications such as phased-array radars and high-volume consumer products is typical. In these applications, low-noise devices with relatively small physical dimensions are used, resulting in a susceptibility to burnout due to incident short single- or multiple-pulse

Table 2. Single-Pulse Damage Levels for p-i-n Diode Limiters

i-Region Thickness	Pulselength	Frequency (GHz)	Damage Level (kW)	Damage Observed
0.5	10 ns	2.7	30	V_b reduced 1 V
1	1 μs	9.4	0.2	V_b reduced to 12 V
1	1 μs	3.3	1.1	V_b reduced to 25 V
2	10 ns	2.7	135	V_b reduced to 10.5 V
5	10 ns	2.7	> 330	No damage up to 300 kW
10	1 μs	9.4	10	V_b reduced to 9 V

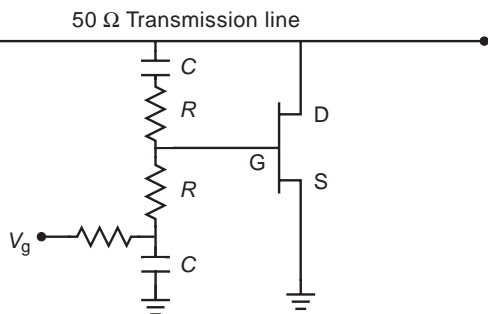


Figure 6. Schematic of a simple MESFET limiter.

energies from 0.1 μJ to 10 μJ . (Most devices can sustain a CW incident power up to 0.1 W without degradation.) A MESFET limiter that operates as a switch has been built using standard MMIC technology, to allow its fabrication along with the circuit that it must protect. This cost-effective approach avoids the requirement for employing mixed technologies (e.g., using an Si limiter with a GaAs MMIC, or adding an i-region fabrication step to the GaAs fabrication process).

The GaAs MESFET limiter circuit in Fig. 6 shunts the transmission line to ground when the gate voltage allows current from drain to source. Note that the location of the drain and source change each half-cycle, based on the instantaneous polarity at the limiter's terminal connected to the transmission line. The MESFET is operated in a bidirectional mode, since no dc bias is required on the transmission line. The R - C voltage divider network that biases the gate is high impedance (typically, $40Z_0 \Omega$), thereby shunting the line. This bias port (V_g) may be used as a switch in applications for which the presence of the high-power incident pulse is known a priori (e.g., the transmitter's pulse in a phased-array radar). When V_g is grounded, a depletion-mode MESFET exhibits low impedance across the transmission line, protecting the front end when not in use. An enhancement-mode version of the MESFET limiter has been developed [8]. It operates in a similar fashion to the p-i-n diode limiter and requires no external bias in the low-loss state.

When the gate is backward-biased (backbiased) at small signal levels, the MESFET represents a small capacitance, consisting of the drain-to-gate and gate-to-source capacitances in series, in parallel with the drain-to-source capacitance. These capacitances are proportional to the gate width for a given MESFET technology. When the gate is not backbiased, the saturated drain-to-source current (I_{dss}) and the drain-to-source resistance are also proportional to the gate width. As a result, the designer performs a tradeoff of the amount of shunt MESFET capacitance allowed across the transmission line, to the peak current that the MESFET can pass (which, in turn, sets the power limit rating) in order to determine the gate width of the MESFET. A typical design (e.g., using a 1 mm gate width) will have an insertion loss less than 1 dB at 10 GHz and sink 0.2 A peak. The insertion loss decreases at lower frequencies because the MESFET's capacitive reactance shunting the transmission line increases. Larger

MESFET widths allow more current with increased insertion loss.

Simple limiter circuits have been refined for specific applications by Vasile [9] and Podell and Stoneham [10].

2. GASEOUS LIMITERS

Gaseous limiters are able to operate over a wide range of incident power levels from a few watts to megawatts. For this reason, gaseous limiters are the technology of choice for the highest-power applications throughout the microwave spectrum. Most gaseous limiter designs have a few percent bandwidth and are suitable for radar receiver protector applications. However, a new TEM design has low insertion loss over several octaves of bandwidth.

Gaseous limiters use the breakdown of a gas in a high electric field to change the impedance across a transmission line. The typical high-power waveguide design shown in Fig. 7 places a quartz tube filled with a noble gas (typically Ar) across the waveguide gap at the point of the highest electric field. The capacitance of the posts is canceled by the inductance of the iris in the waveguide. These two reactances limit the bandwidth to a few percent. Other designs use waveguide windows to contain the gas in the post region. The window design has a lower lifetime because of the increased absorption cross section of the gas (or gas cleanup) with the metal (typically Ni) walls, resulting in reduced gas pressure and performance. Because the quartz absorption cross sections are several orders of magnitude smaller than those made of metals, gaseous limiters using quartz gas reservoirs have useful lifetimes usually exceeding 20 years.

At electric field intensities below the arc threshold, the posts and iris appear to be a resonant circuit across the waveguide. The gaseous pressure, mixture, and electric field intensity in the presence of "seed" electrons set the threshold for the arc. When the arc occurs, the increased conductance across the posts presents a severe mismatch to the waveguide impedance, resulting in significant

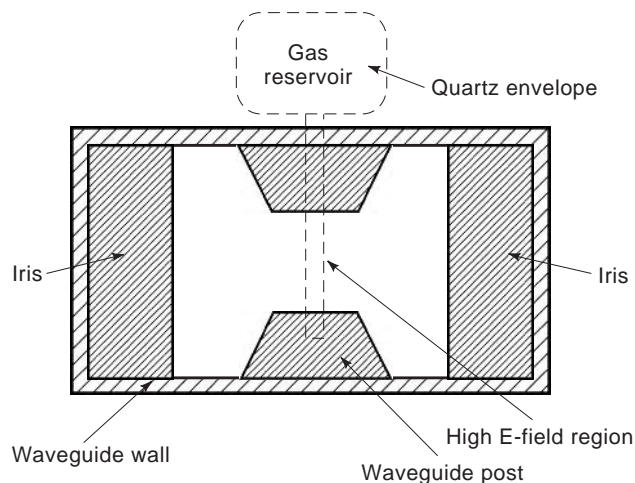


Figure 7. Cross section of a gaseous limiter in waveguide.

reflected power. The arc absorbs about 7% (10%, worst case) of the incident power, resulting in heat that must be conducted through the quartz tube to the walls of the waveguide posts. Because quartz has a high melting point, pulsed operation with hundreds of kilowatts incident is possible. The gas pressure and mixture is adjusted according to the Paschen curve (see discussion of gas-discharge tubes) for the desired arc threshold. The seed electrons are provided by a radioactive source or a small microwave oscillator. The tritium source (typically 100 mCu) emits electrons with a half-life of 12.6 years. Since only a few electrons are needed to initiate the arc, the tritium is useful for three half-lives. The tritium is positioned to irradiate the gas between the posts. Goldie and Patel [11] used a small microwave oscillator that continually excite enough gas molecules to provide the “seed” electrons. When Ar is used for the gas the threshold is several watts, with a recovery time of several milliseconds. If the Ar recovery time is too long, a chlorine–oxygen mixture may be used in which the electrons and ions recombine faster (typically within 100 ns), and the arc loss is lower, but the arc threshold is higher (10 W to 20 W). If the flat leakage of the gaseous limiter is too great, p–i–n limiters may be cascaded to remove the spike leakage and lower the flat leakage to an acceptable level.

The wideband gaseous limiter operates on the same principle as the narrowband device. Patel et al. [12] configured a suspended, 50 Ω , stripline with the gas mixture surrounding the transmission line. Units with 6–8 W threshold and 50 W of average power have been built. The device operates over a 30% bandwidth primarily limited by coax-to-stripline transitions at the ports.

3. FERRITE LIMITERS

Ferrites [e.g., yttrium iron garnet (YIG)] are used for tunable filters and other applications. These filters are narrowband devices in which the magnetic spin vectors (magnetic dipoles) of the ferrite are oriented by an externally applied magnetic field (typically, 100 Oe) that can be varied to change the resonant frequency of the filter. The spins on the lattice sites are also coupled to the magnetic field of a microwave signal. If the strength of the signal’s magnetic field exceeds a threshold, energy from the signal’s magnetic field is coupled to the spin vectors of the fixed lattice ions, thereby creating spin waves. These spin waves are able to transfer energy to heat the lattice, removing energy from the incident microwave signal. The process is nonlinear, with respect to incident microwave magnetic field strength, and yields substantially different performance as a microwave limiter. Lax and Button [13] stated that limiting thresholds vary from –25 dBm to 50 dBm.

Carter and McGowan [14] developed a limiter consisting of a ferrite slab mounted against the narrow wall of a waveguide with a 1500 Oe externally applied magnetic field. This ferrite limiter was able to dissipate 10 kW incident pulses. The insertion loss over the 8.9–9.5 GHz range was less than 1 dB. The threshold power and flat leakage power levels were 28 W. At 10 kW incident power, the spike energy was 3 μ J with a spike power level of

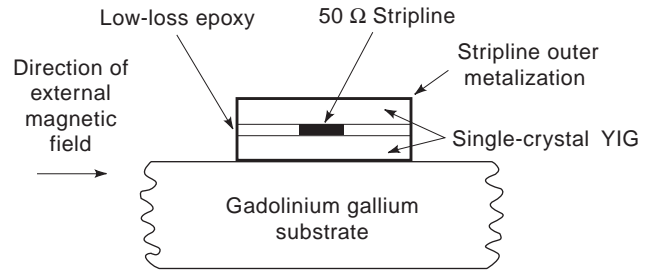


Figure 8. Cross section of a frequency-selective limiter.

2.9 kW. The recovery time was less than 20 ns, which is much shorter than that of a gaseous limiter. The threshold and flat-leakage power levels were reduced to <30 mW with the addition of a varactor (thin i-region p–i–n diode) limiter behind the ferrite limiter.

Because of their tunability by varying the externally applied magnetic field by at least an octave, ferrite filters can be used as frequency-selective limiters. They have the ability to attenuate a signal at a frequency selected by the magnitude of the external field, while providing minimal attenuation at nearby frequencies. Adam and Stitzer [15] determined that the bandwidth of the limiting frequencies (typically 50 MHz) is related to the linewidth of the spin-wave coupling. A frequency-selective limiter will attenuate an intentional jamming signal, while an electronic warfare receiver is able to listen to signals on nearby frequencies.

A stripline configuration of the frequency-selective limiter was developed by Adam and Stitzer [15] using single-crystal YIG in place of the usual microwave dielectric material, as shown in Fig. 8. The limiting threshold was about 20 dBm. The ultimate limiting capability of this technique appears to be in the 15–20 dB range. By cascading limiter, amplifier, limiter, and so on, they demonstrated that an incident power range of 60 dB could be compressed to a dynamic range of less than 5 dB.

Ferrite limiters require a significant amount of peripheral support, since they require an external magnetizing field; their insertion losses are usually high (except in the waveguide configuration), necessitating an external amplifier; they are sensitive to temperature variations; and they are large and heavy, when compared to other technologies. For these reasons, they have been used only in applications that require tunability.

4. OTHER LIMITER TECHNOLOGIES

4.1. Multipactor

Experimentation has been taken place using numerous other technologies, with mixed success. A summary of some of the technologies appears in Table 3.

The multipactor takes advantage of secondary electron resonance (multipacting) to provide low impedance across a waveguide. The multipactor is usually configured as the first stage of a two-stage limiter, since it limits the power to only several watts. The second stage is a p–i–n diode limiter, with a flat leakage of less than 100 mW.

Table 3. Other Limiter Technologies

Technology	Performance	Status
Multipactor	Excellent, requires external biases	Implemented in waveguide configurations
Bulk Window switch array	Excellent millimeter wave switch	Limiter performance untested, difficulty making thin <i>i</i> region
Electrooptic	Fair, requires laser and optics	Relatively high insertion loss
Superconductor	Fair, 50 ns turnon	Demonstrated at 10 GHz
Field emitter array limiter	Unknown	Needs fabrication on low-loss substrate
Varistor paint	Unknown	Initial attempts failed
Temperature-dependent resistor	Fair	Only analyzed to date

Multipacting is an electron avalanche phenomenon operating in a vacuum. The multipacting region allows electrons in an alternating electric field to flow across a gap in less than a one-half cycle of the field. Both surfaces of the gap are coated, so that the secondary electron emission coefficient δ is greater than 1. The incident electric field accelerates the electrons toward one of the gap surfaces. As these initial electrons N_i strike the surface, the RF field changes sign, and the secondary electrons δN_i are accelerated toward the opposite surface. The speed at which the multipactor ignites is $N = N_i \delta^{2if}$, where t is the time and f is the frequency (in hertz) of the electric field. Electron multiplication continues until a space charge in the gap inhibits additional electrons from being emitted from the gap's surfaces. At 10 GHz, the saturated electron density of 3×10^{10} electrons/cm³ is achieved in 0.6 ns. The impinging RF field is reflected by the lower impedance in the gap region and is absorbed by conversion to heat in the electron cloud.

The multipactor gap consists of low- Q resonators in a combline filter configuration. An electron source emits enough electrons (N_i) into the gaps to cause the multiplication to begin on the first few cycles of RF. A supply of oxygen is leaked into the gap region so that the metal oxides continue to have a coefficient δ , since prolonged electron bombardment of the surface reduces the oxides to the metal with low δ . To counter this leak of oxygen, a small ion pump is required. The pump maintains a vacuum pressure suitable to enable the electrons to be accelerated across the gap without colliding with the oxygen molecules. Clearly, the multipactor is a more complex limiter than the others discussed here. Therefore, it has found only limited application where biases for the ion pump are already available. The multipactor operates within the bandpass of the combline filter, while the filter protects the receiver's front end from intense signals out of band. Measured performance of a 9.6-GHz multipactor had a 12% bandwidth (VSWR < 1.6:1), would attenuate a 50 kW pulse to a 50 mW flat leakage with a 2 μ J spike energy, and had a recovery time of less than 15 ns. Below threshold, the insertion loss was 1.5 dB, due to the combline filter [16].

4.2. Bulk Window Waveguide Switch Array

This switch array (or the monolithic diode array) was developed by M/A-COM Semiconductor Products, Burlington, MA, as a low-loss millimeter-wave switch for use in waveguide applications. The switch consists of a matrix of Si p-i-n diodes grown monolithically onto an insulating Si

substrate. The substrate acts as a carrier, which is attached to a waveguide flange with suitable contacts to apply bias to the switch. The few attempts to operate the switch array as a self-activated limiter have not been successful, apparently because the *i* region could not be designed thin enough at millimeter-wave frequencies to allow the microwave energy to lower the impedance of the p-i-n diodes. However, with external bias, the switch array has sustained operation at 1 kW pulse and 20 W levels at 94 GHz, with a low signal-level insertion loss of only 1 dB [17].

4.3. Electrooptic

The electrooptic limiter uses a coplanar waveguide transmission-line configuration on an electrooptically active, semiinsulating semiconductor as the switched medium. When illuminated with photons that have sufficient energy to excite electron-hole pairs, the coplanar transmission line becomes lossy and absorbs most of the incident power. This limiter design is complicated because it requires an intense light source (e. g., a laser) to create enough electron-hole pairs to provide the level of conductivity modulation of the substrate. The light source is activated above a threshold established by external circuitry coupled to the coplanar line, similar to the delay-line limiter shown in Fig. 1e. An implementation of this limiter design in semiinsulating Si yielded more than 30 dB isolation at 1.7 GHz, with over 100 mW of optical power. The isolation bandwidth was 25%. With no optical illumination, the same limiter had a high insertion loss of 6.5 dB, which was probably due to the high series resistance of the center conductor of the coplanar transmission line.

4.4. Superconductor

High- T_c superconductor (HTSC) films with a superconducting-to-normal transition at 86 K have been fabricated that show a surface resistivity change of 10^5 . Gaidukov et al. [18] fabricated a two-element filter in a 8.0–12.4-GHz rectangular waveguide. The filter used resonant irises spaced a quarter-wavelength apart, fabricated with HTSC film strips across the opening of each iris. In the superconducting state, the film strip appears as a resonant inductor across the iris, with an insertion loss of ≈ 1 dB. The 3 dB bandwidth is ≈ 1 GHz. In the normal state, the film strip is resistive, reducing both the Q and the resonant frequency of the iris, and yielding over 20 dB of isolation. When operated at 65 K with 0.8 μ s pulses, the limiting began at 50 mW, and the pulse shape was unaffected by the limiter up to 0.5 W. With increased power

levels, the pulse shape showed more attenuation later in the pulse, due to the heating of the HTSC film with a time constant ranging from 0.1 to 0.5 μ s. The insertion loss increased about 5 dB during a pulse. If the HTSC film strips are heated with an external current, the dual iris assembly can be used as a switch.

4.5. Field Emitter Array

Field emission from a cathode incorporating a matrix of TaSi₂ rods with final tip radii of curvature in the range of 1–10 nm has been measured at DC. Kirkpatrick et al. [19] showed that the parameters of the Fowler–Nordheim relation depend on the magnitude of the electric field at the tip. The emission is fast enough to be useful at microwave frequencies, when configured as a suspended 50- Ω microstrip (cathode) above a ground plane (anode). The TaSi₂ rods are mounted in an insulating Si substrate. For the limiter application, Glenn et al. [20] used a configuration similar to that shown in Fig. 8, with a vacuum replacing the YIG and a microstrip-to-ground plane spacing of 40 μ m. When the electric field at the tips exceeded a threshold, electrons were emitted that shunted the transmission line, thereby operating as a limiter. As expected, the device worked with a DC threshold voltage of \approx 200 V, providing limiting above 400 W on a 50- Ω transmission line. The device showed a high insertion loss at 1 GHz, which was attributed to losses in the Si substrate.

Two other limiter circuit technologies have been proposed, but have not been demonstrated to date: varistor paint and temperature-dependent resistor. The first technology uses the coplanar waveguide configuration with a varistor paint, shunting the center conductor to the coplanar ground planes. Initial attempts to build this device failed because the fringing electric field from the coplanar line was too low to activate the varistor paint.

The second technology is a highly temperature-dependent resistor (e.g., tungsten) with a small thermal mass, in series with a transmission line. The limiter could be used in series with, or in place of, the bondwire of a susceptible microwave component. However, experimental results indicated that the shunt capacitance of the temperature-dependent resistor was too high, reducing the current heating in the resistor.

5. FUTURE ACTIVITIES

While p–i–n diode limiter technology is rather well developed, several investigations still remain to be conducted. These investigations include: determining why input–output power hysteresis occurs for continuous and long-pulse operation; experiments to determine whether a slightly p-doped i-region diode will have lower spike leakage than do present designs; and determining why GaAs p–i–n devices appear to degrade with intense pulses.

MESFET limiters must be designed to carry higher pulsed currents to enable operation above 100 W, without the requirement for a large gate width. Also, limiters must be developed using the low-noise PHEMT technology, to make them compatible with the amplifiers they must protect.

Although self-activated, high-power, millimeter-wave limiters are not presently available, the monolithic diode array concept appears to be the most likely to have low insertion loss, if the thickness of the i region can be reduced. Furthermore, the monolithic diode array does not increase the loss at low signal levels, due to the distribution of the carriers at the p⁺–i and the n⁺–i transitions.

BIBLIOGRAPHY

1. A. L. Ward, R. J. Tan, and R. Kaul, Spike leakage of thin Si PIN limiters, *IEEE Trans. Microwave Theory Tech.* **42**:1879–1885 (1994).
2. D. Leenov, The silicon PIN diode as a microwave radar protector at megawatt levels, *IEEE Trans. Electron. Devices* **ED-11**:53–61 (1964).
3. R. V. Garver, *Microwave Diode Control Devices*, Artech House, Norwood, MA, 1978, Chap. 9.
4. N. J. Brown, Design concepts for high-power PIN diode limiting, *IEEE Trans. Microwave Theory Tech.* **MTT-1**:732–742 (1967).
5. C. M. Glenn et al., *Nonreflective Limiter*, U.S. Patent 5,345,199 (1994).
6. J. F. White, *Semiconductor Control*, Artech House, Norwood, MA, 1977, Chap. 7.
7. R. J. Tan, *Limiting Filter*, U.S. Patent 5,280,256 (1994).
8. C. Trantanella, M. Pollman, and M. Shifrin, An investigation of GaAs MMIC high power limiters for circuit protection, *IEEE MTT-S Int. Microwave Symp. Digest*, Denver, CO, June 8–13, 1997, pp. 535–538.
9. C. F. Vasile, *FET Adaptive Limiter with High Current FET Detector*, U.S. Patent 5,157,289 (1992).
10. A. F. Podell and E. B. Stoneham, *Input Protection Circuit*, U.S. Patent 5,301,081 (1994).
11. H. Goldie and S. Patel, An rf-primed all-halogen gas plasma microwave high-power receiver protector, *IEEE Trans. Microwave Theory Tech.* **MTT-30**:2177–2183 (1982).
12. S. D. Patel et al., Microstrip plasma limiter, *IEEE MTT-S Int. Microwave Symp. Digest*, Long Beach, CA, June 13–15, 1989, pp. 879–882.
13. B. Lax and K. J. Button, *Microwave Ferrites and Ferrimagnetics*, McGraw-Hill, New York, 1962.
14. J. L. Carter and J. W. McGowan, X-band ferrite-varactor limiter, *IEEE Trans. Microwave Theory Tech.* **MTT-17**:231–232 (1969).
15. J. D. Adam and S. N. Stitzer, Frequency selective limiters for high dynamic range microwave receivers, *IEEE Trans. Microwave Theory Tech.* **41**:2227–2231 (1993).
16. T. P. Carlisle, X-band high-power multipactor receiver protector, *IEEE Trans. Microwave Theory Tech.* **26**:345–347 (1978).
17. A. L. Armstrong and Y. Anand, A limiter for high-power millimeter-wave systems, *IEEE Trans. Microwave Theory Tech.* **31**:238–241 (1983).
18. M. M. Gaidukov et al., Microwave power limiter based on high- T_c superconductive film, *Electron. Lett.* **26**:1229–1231 (1990).
19. D. A. Kirkpatrick, A Mankofsky, and K. T. Tsang, Analysis of field emission from three-dimensional structures, *Appl. Phys. Lett.* **60**:2065–2067 (1992).
20. C. M. Glenn et al., *Microwave field emitter array limiter*, U.S. Patent applied for March 6, 1996.

MICROWAVE MEASUREMENTS

ANDREA FERRERO
 VALERIA TEPPATI
 UMBERTO PISANI
 Politecnico di Torino
 Torino, Italy

1. INTRODUCTION

During World War II, intense research and effort in the radar development program brought about the radiofrequency (RF) spectrum extension beyond the usual applications in radiocommunications. Shorter wavelengths induced specific design of reduced dimension laboratory equipment, in order to generate, convey, transmit, and detect higher-frequency signals. By convention, the RF/microwave region ranges between 30 MHz and 300 GHz, since shorter than 1 mm wavelengths require equipment too small to be easily realized.

Voltage, current, and impedance concepts lose their conventional meanings when operating wavelength is approximately equal to the dimensions of the structures under test, and the behavior of propagating electromagnetic waves must be analyzed in terms of electric and magnetic fields. However, as there is no simple and direct way to measure these quantities, it is necessary to resort to indirect methods.

Until the 1960s, microwave measurements were carried out by instruments such as

- *microwave cavities*, for wavelength measurements
- *power sensors*, for power measurements
- *standing-wave-ratio meters* (slotted lines) and waveguide bridges, for impedance measurement

All the techniques were based on scalar measurements combined with precision mechanical measurements (e.g., probe displacement in a slotted line). Vector quantity, such as impedance measurements, were indirectly carried out by making different scalar measurements along a slotted line.

In the 1960s, another type of microwave power measuring instrument was introduced, based on the principle of superheterodyne conversion: the *spectrum analyzer*. This instrument, which has evolved to have wider bands and dynamic ranges and to perform math and calibration, exploits the principle of converting each microwave signal frequency component to an intermediate frequency (IF), where the signal can be more easily detected.

At the same time, the first scattering parameter measurements were performed with the most popular microwave instrument: the *vector network analyzer* (VNA); this instrument is based on subsampling or mixing techniques, to downconvert the microwave signals to an IF frequency, where they can be detected in both magnitude and phase. From the first scalar versions, the instrument evolved into vector measurements, with faster acquisition times and higher (up to 130 dB) dynamic ranges. Up-to-date instrumentation can include a PC microprocessor plus operating

system and perform automatic measurements as well as the required calibrations.

In the following sections, power, spectral, and network analyzer measurements are described. A final section is dedicated to advanced microwave measurements.

2. POWER, SPECTRAL AND NOISE MEASUREMENTS

Since the beginning of the microwave years, the main techniques for microwave measurements were based on *power meters*. Those instruments evolved from traditional bolometer-based systems to diode-based power sensors for peak power measurements; furthermore, the dynamic range increased to 70 dB, from the initial 40–45 dB. Power measurements are also used as primary microwave standards with calorimeters, to correlate microwave power to basic standard units [4,17].

A power meter is typically based on a main unit and one or more power heads; the heads are generally specified with respect to the bandwidth and the power range, while the main unit contains the interface circuits, the head bias control, and, more recently, math and calibration functionalities.

The core of a power head can be a thermistor, placed on a low-frequency resistive bridge, as shown in Fig. 1. The system measures the RF power through a DC substitution technique by keeping constant the total dissipated power (RF + DC), on the thermistor. Since the value of the thermistor resistance changes with the temperature (i.e., the dissipated power), the bridge becomes unbalanced as more RF is injected. The feedback network acts on the bridge DC voltage supply arm to reduce the amount of DC dissipated power and to keep the bridge balanced. In this way, the change of DC voltage corresponds to the amount of RF power injected, and its measurement, usually done with a digital conversion system, provides an accurate measurement of the RF power. Since a change of external temperature may induce the same effect as an RF signal, an identical (and within the same environment) bridge is used, so that a temperature compensation is also applied.

Ordinary power heads are calibrated through a reference chain to the National Power Reference Standard, generally based on a microcalorimeter [61]. An alternative way to measure microwave power is given by the *spectrum analyzer*, which measures the power of each frequency component of an input signal and is based on a superheterodyne conversion.

A simplified scheme is shown in Fig. 2; the local voltage-controlled oscillator (VCO) sweeps over frequency, so that the portion of the input signal which has $f_{in} = f_{VCO} - f_{IF}$ is converted to the IF frequency, then detected and passed to elaboration or display. The sweep of the local oscillator is chosen to cover the desired spectrum of the input signal, while the band of the IF filter determines the frequency resolution of the spectral measurement and is thus called *resolution bandwidth* (RBW). If two adjacent frequency components of the input signal are within the RBW, they are combined together at the filter output and their measurement becomes misleading, as shown in Fig. 3. A large RBW may introduce unacceptable error

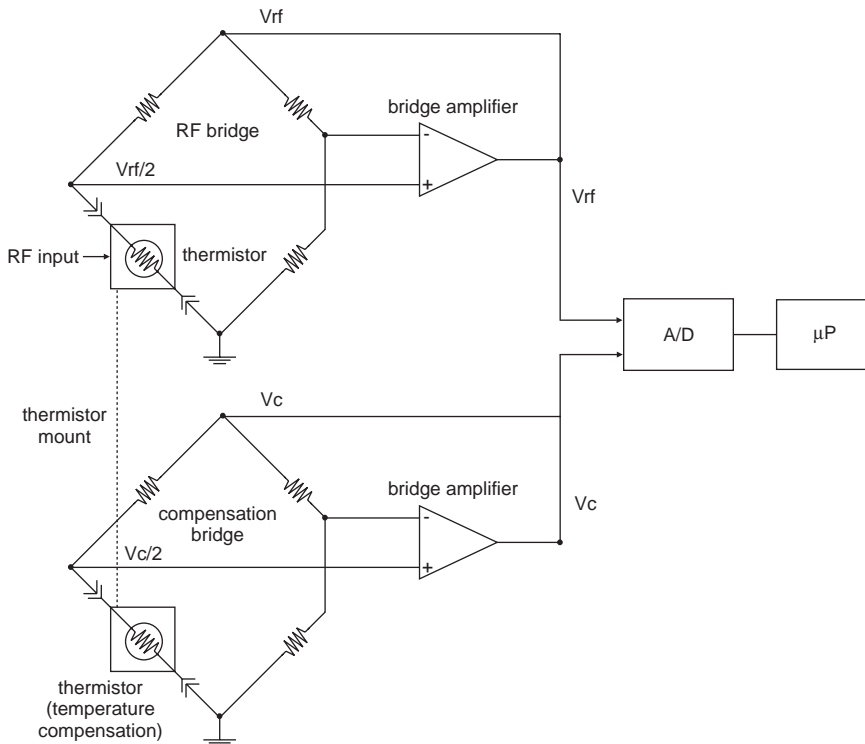


Figure 1. Simplified diagram of a power meter thermistor-based power head.

especially in measurements such as intermodulation distortion.

The RBW is also linked with the measurement speed, since the filter settling time fixes the minimum time required to have a stable output, and thus the maximum change rate of the mixer output. For this reason if a better resolution is required, specifically, a narrow IF band, a slower VCO speed is set.

Another effect of RBW is linked to noise floor. Thermal noise generally prevails over other noise sources, and its contribution is constant versus frequency (white noise). The revealed noise power is thus proportional to RBW. A reduction of a factor 10 on RBW implies a reduction of 10 dB in noise floor.

Unfortunately, noise floor cannot be reduced by rising the value of the input attenuator, since noise main contri-

butions are introduced right after the first converter. Furthermore the RF attenuator reduces the signal-to-noise ratio (SNR) of the measured signal. Thus, in order to maximize the SNR, it's preferable to work with the minimum RF attenuation that gives the minimum distortion of the mixers.

Spectrum analyzers are widely used for noise measurements. The measurement of network properties in terms of noise is especially felt in receiving systems, when noise becomes comparable to signal. To increase the SNR, a reduction of the noise introduced by the receiver components is required. For this purpose, reliable noise measurements are necessary, to characterize the receiver components.

The most popular quality factor for noise performance is the noise figure. It is defined for two port devices [34] as

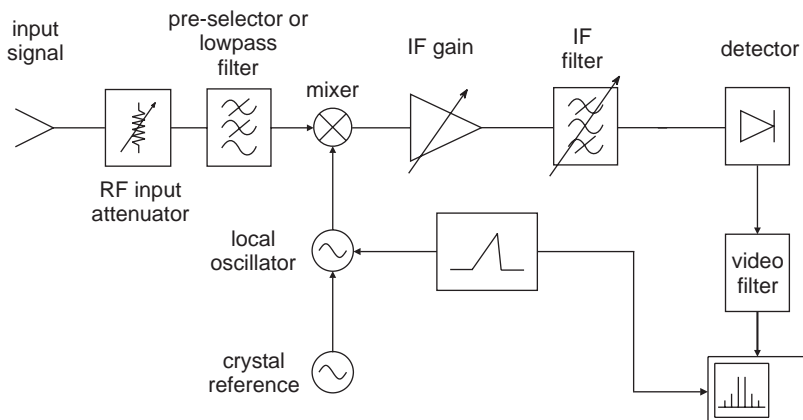


Figure 2. Simplified diagram of a spectrum analyzer with superheterodyne detection.

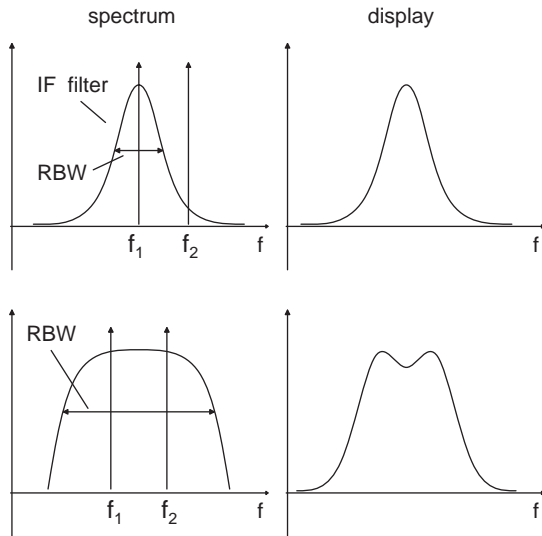


Figure 3. Errors introduced by large RBW in intermodulation distortion measurements. On the left side of the figure, the input signals f_1, f_2 and RBW filter spectra are sketched, while on the right side the corresponding spectrum analyzer displays are shown for a correct RBW configuration (top) and in an erroneous configuration (bottom).

the ratio of SNR input to SNR output

$$F = \frac{S_i/N_i}{S_o/N_o} \tag{1}$$

where S_i, N_i and S_o, N_o are the input and output signal and noise powers.

Any receiver component, such as an amplifier, adds its own noise to the output. Thus noise figure becomes

$$F = \frac{S_i/N_i}{S_o/N_o} = \frac{N_a + G_a N_i}{G_a N_i} \tag{2}$$

where G_a is the amplifier gain ($S_o = G_a S_i$) and N_a is the noise power added by the amplifier, and the overall output noise power becomes $N_o = N_a + G_a N_i$. If the noise can be represented as thermal noise, then the noise output power is:

$$N_o = N_a + G_a k_b B T_i \tag{3}$$

where k_b is Boltzmann's constant, B is the equivalent bandwidth, and T_i is the temperature of the noise source at the input of the amplifier. The noise figure is then

$$F = \frac{N_a + G_a k_b B T_i}{G_a k_b B T_i} \tag{4}$$

Noise figure meters determine the noise added by a DUT (device or design under test) by comparing it to the noise present at the input. Generally, they switch a solid-state noise source on and off to generate two equivalent noise temperature points (T_c and T_h) and measure the corresponding two noise power outputs with a tuned receiver with a fixed RBW. As shown in Fig. 4, N_a is

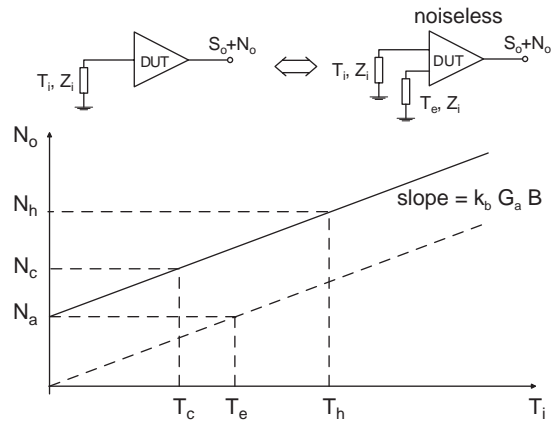


Figure 4. Noise introduced by an amplifier (N_a) is measured extrapolating two measurement points corresponding to T_c and T_h . The situation can be modeled with a noiseless amplifier plus an additional noise source, with equivalent temperature T_e .

computed by extrapolating the straight line to the $T_i = 0$ point. The added noise can be then transformed in an equivalent input noise temperature (see Fig. 4) T_e with $N_a = G_a k_b B T_e$. Finally, with Eq. (4) or

$$F = 1 + \frac{T_e}{T_i} \tag{5}$$

the noise figure F is presented to the user.

3. NETWORK ANALYZER MEASUREMENTS

In the 1960s, the basic principle for network analysis was introduced in an innovative instrument called a *vector voltmeter* [15], which is able to measure a microwave signal in both magnitude and phase.

The idea was the conversion to an intermediate frequency (IF), where the use of ordinary AC voltmeter and phasemeter is possible, of a test and a reference microwave signal, with a synchronous conversion. This is achieved through a subsampling process [7], where a strobe signal, formed by a series of very narrow pulses spaced by the sampling period t_s , samples an input signal, having period $T(t_s \gg T)$, as shown in Fig. 5a. In the frequency domain the strobe signal is again a series of pulses, spaced by $f_s = 1/t_s$, while the input signal is generally a sinusoidal one. The process is called *subsampling* since the sampling frequency is well below the Nyquist one, and the technique can be applied if the input is sinusoidal or with a periodic pattern; thus the microwave signal has an effective bandwidth well below the sampling frequency.

The microwave signal is acquired when the equation $f_{IF} = f_{in} - n f_s$ is satisfied for a certain n value, where $n f_s$ is the strobe signal n th harmonic. By a proper choice of f_s through a PLL (phase-locked loop) technique, the IF frequency can track any change of the input frequency.

By subsampling two microwave signals at the same frequency with two identical sampling pulses, the IF signals keep the same magnitude and phase relationships

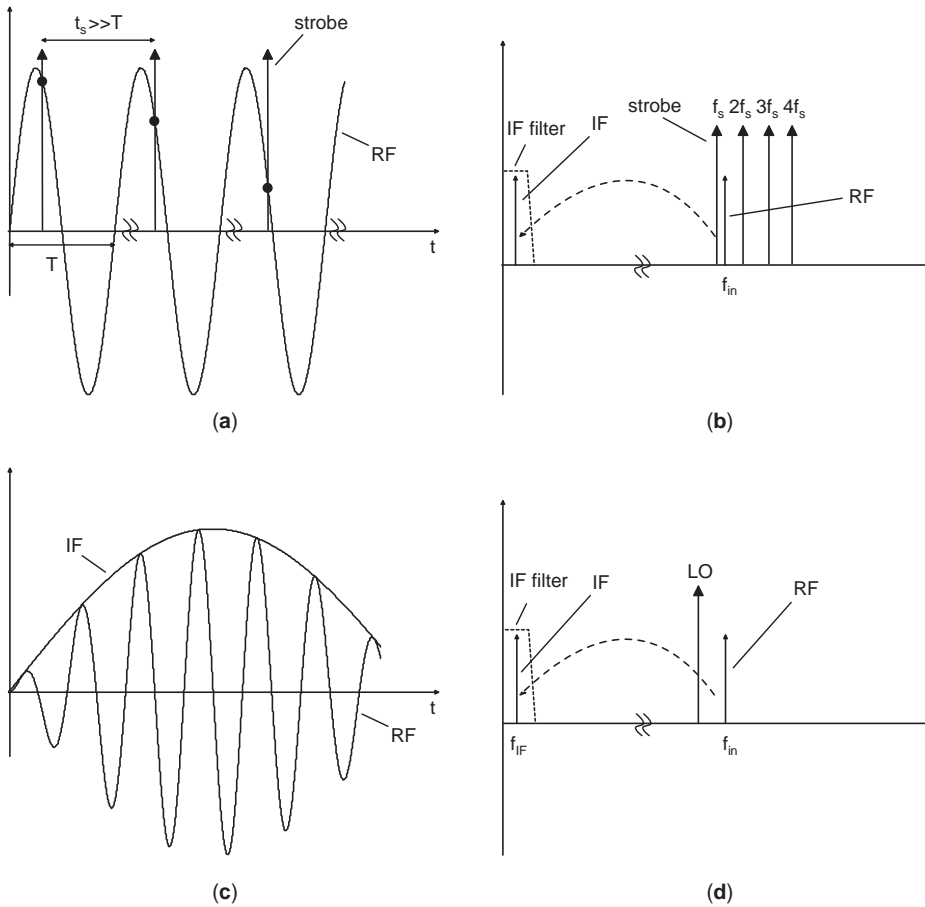


Figure 5. Comparison between sub-sampling process in time domain (a) and frequency domain (b) and mixing process in time domain (c) and frequency domain (d).

existing between the original waves, but at a much lower frequency, so that they can be easily measured in amplitude and phase with ordinary instrumentation [7].

The block scheme of the vector voltmeter is shown in Fig. 6. A PLL technique adjusts the frequency of a voltage-tuned local oscillator (VTLO) that triggers the samplers as explained above. The frequencies out of IF band are rejected by the narrowband IF filter. Therefore, the system becomes frequency-selective and reaches great perfor-

mance in terms of dynamic range, reduction of noise, and resolution. Finally, the two sampled signals are measured with low-frequency A.C. voltmeter and phasemeter, or digitally acquired through S/H (sample-and-hold) and A/D (analog-to-digital) converting circuits.

The phase-locked sampling process is equivalent to a heterodyne conversion with mixers, but with a basic advantage—it does not require a microwave frequency local oscillator to downconvert the input signal, but it only

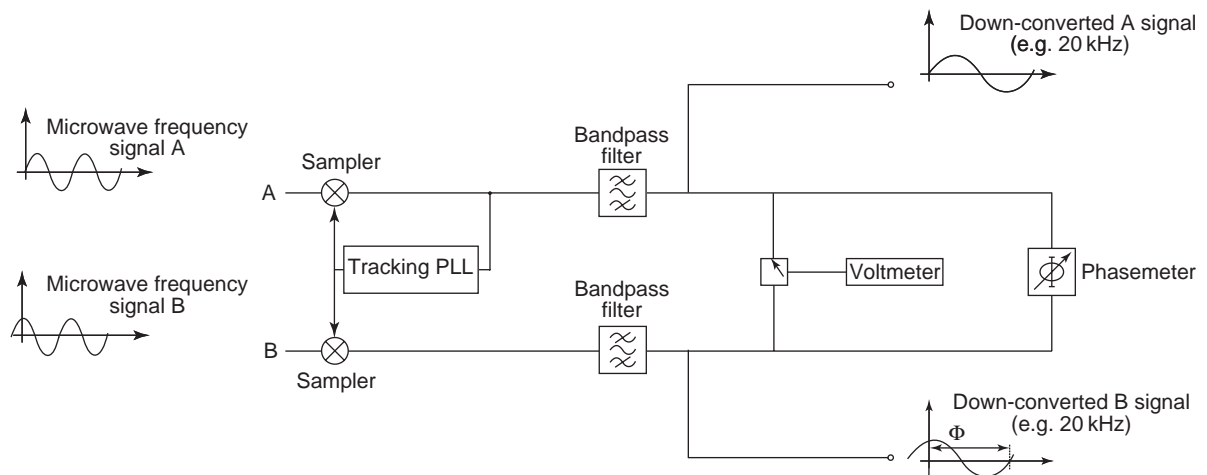


Figure 6. Block scheme of a vector voltmeter based on sub-sampling techniques.

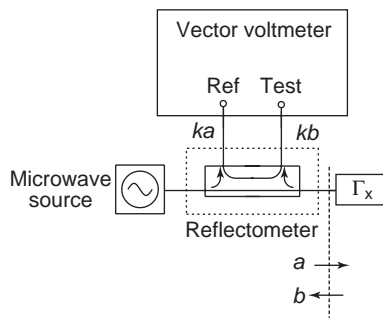


Figure 7. Reflectometer system.

needs a low-frequency pulsed VTLO. As a drawback, the sampler philosophy requires a PLL to tune the VTLO; thus the phase lock is reached after a finite amount of time and it requires a stable reference signal, or it can be lost.

This measurement principle, joined with the introduction of high-directivity, low-loss broadband directional couplers, which separate the forward and reverse traveling waves along a transmission line, formed an alternative system to a direct measurement of reflection coefficients (in amplitude and phase) rather than the classic slotted-line standing-wave ratio meter. As shown in Fig. 7, a directional coupler is used to pick up the forward and reverse traveling waves from the mainline through its coupled arm where the reference and test inputs of a vector receiver are connected. In this way a direct reading of the reflection coefficient is easily obtained.

From the basic reflectometer, an extension of the *S*-parameter measurement system, termed a *vector network analyzer* (VNA), follows immediately.

The VNAs were introduced in the late 1960's [5,38,53] for one-port and two-port device characterization in coaxial environment and since the mid-1970s they became a fundamental testset for all microwave laboratories. While the lower frequency ranges span from 30 kHz to 100 MHz, the upper frequency of commercial systems extended, at the beginning, up to 12 GHz, afterward to 18 GHz, and today it reaches 110 GHz.

A complete VNA is a very complex system, which usually includes

- A microwave synthesized source
- Dual reflectometer testset based on directional couplers or directional bridges and switches to separate and select incident and reflected waves at the device ports
- A multichannel microwave receiver where the separated signals are downconverted
- A central unit for intermediate frequency (IF) detection, A/D conversion, data processing, and presentation [18].

A simplified block scheme of a two-port network analyzer is shown in Fig. 8.

This system allows very broadband measurements with hundreds of frequency points or limited measurement bands with extremely high-frequency resolution (useful for testing high selectivity devices).

Normally, VNAs have coaxial (for very broadband applications) or waveguide measurement ports while DUTs can have leads on microstrip, on-chip contacts, on-wafer ports, and so on. Such mechanical and/or electrical

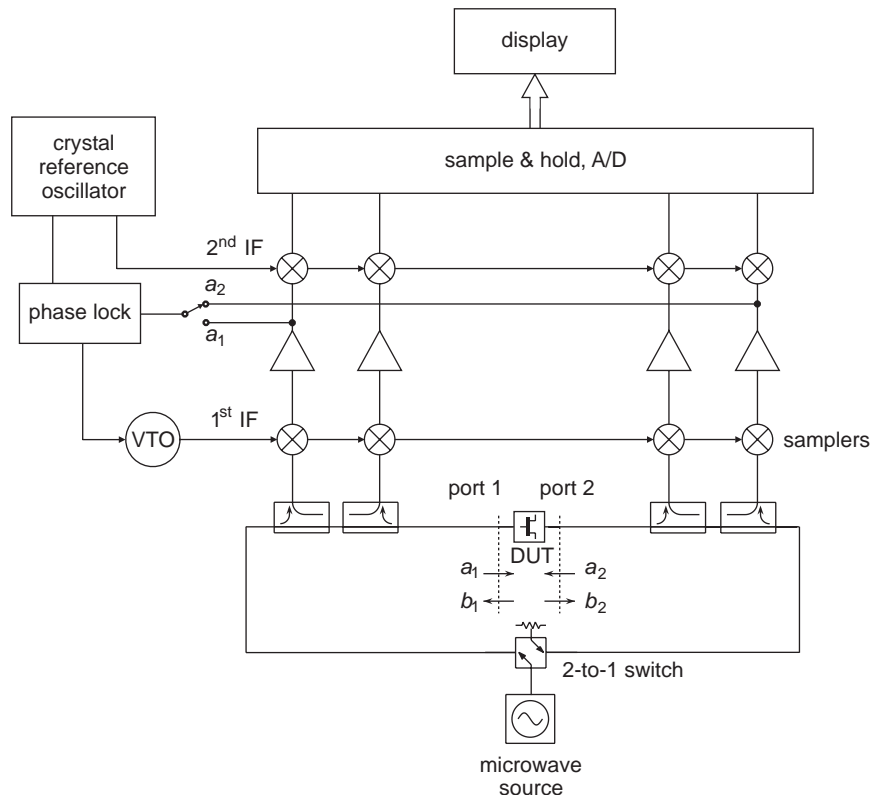


Figure 8. Block scheme of two-port network analyzer [18].

discontinuities from one transmission line to the other require accurate studies of the interface between the measurement equipment and the device to reduce the measurement errors, since they can be only partially corrected by a calibration procedure.

3.1. Calibration of Network-Analyzer-Based Systems

Network analyzer measurements are affected by different kinds of errors and uncertainties, generally classified as

- Random uncertainties
- Drifts
- Systematic errors

Random uncertainties are due mainly to noise and connector repeatability effects, while drifts are typically due to temperature, but the effects of systematic errors overwhelm all the others by at least an order of magnitude. For such reasons the use of an appropriate calibration technique is mandatory for useful VNA based measurements. Typical causes of systematic errors are

- Directional couplers imperfections (directivity, port mismatch, frequency variation of the coupling coefficient)
- Mismatch errors due to adapters and cables
- Coaxial configuration switches losses and mismatch
- Crosstalk

The traditional way to handle such errors was to develop different models based on flowgraph representation of each error effect. The first studies in this field began right after the introduction of vector network analyzers in the 1960s [5,15,63], but it was only with the introduction of microprocessor controlled VNA, like the HP8510, that the so-called *calibration procedures* became common and widely used. Here, a brief overview of how an error removal procedure is organized and the limitations of the today available techniques will be given.

Modern calibration procedures are based on a systematic model of errors that overcomes the traditional approach. The actual VNA is viewed as an ideal system without systematic error followed by a linear network, called *error box*, which models the influence of the systematic errors altogether, as shown in Fig. 9.

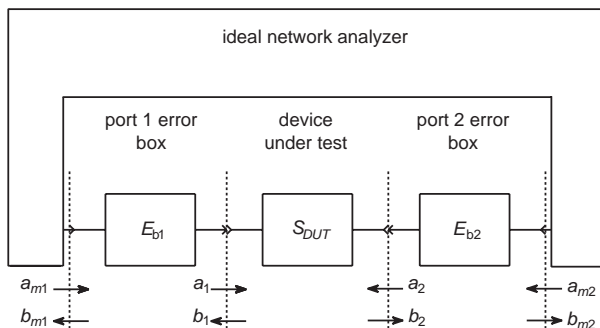


Figure 9. Error box model of VNA systematic errors.

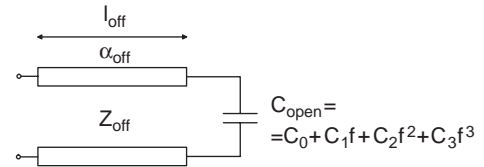


Figure 10. Typical model of coaxial open standards. The nonlinear capacitance depends on frequency. The line parameters (length l_{off} , characteristic impedance Z_{off} , and losses α_{off}) are evidenced in the scheme.

This error model is the basis of all calibration techniques available today, where the various solutions vary according to how they handle identification of the error box parameter. However, the whole approach works if, and only if, the actual VNA can be seen as a perfect linear receiver; otherwise the entire process of error coefficient computation and correction fails, since the error box is everywhere assumed as a linear network (i.e., the relationships between raw and corrected parameters are linear equations). This is a typical case for the current systems with >100 dB of dynamic range, but for accurate measurements of a highly isolated device, it is mandatory to check for proper power levels at each port, in order to quantify the amount of nonlinearity errors [50].

To compute the error box parameters, calibration techniques use a set of precise components called *standards*. Each standard is modeled through electromagnetic simulation or through low-frequency measurement of scaled devices. A typical model for an open standard is given in Fig. 10.

The model parameters are stored inside the VNA and their electrical responses computed during the calibration procedure. The error box parameters are obtained from comparison of the modeled responses and the actual standard measurements.

Different calibrations are normally classified respect to the degree of the standard knowledge they require:

- Calibrations based on well-known standards such as
 - Short (circuit)/open (circuit) load thru (through) (SOLT)
 - Offset shorts (short circuits)
- Self-calibrations such as
 - Thru reflect line (TRL)
 - Line reflect match (LRM)
 - Short (circuit)/open (circuit) load reciprocal (SOLR)

These techniques are only few of the various calibration algorithms available today; furthermore, although originally obtained separately, [2,26–28,31,32,39–41,45,52,64], they are all special cases of a more general theory derived for one- and two-port VNAs [56]. Description of the algorithm is beyond the scope of this section; instead, the focus will be on the differences in terms of accuracy, required standards, and applicability.

The most widely adopted calibration for the two-port VNA is the SOLT, an acronym obtained from the required standards: a short (circuit), an open (circuit), a load, and a

direct port connection, called a “thru.” This technique has been applied since the early years of automatic VNAs, and the corresponding standards are available in almost every environment (e.g., waveguide, coaxial, on-wafer). All VNA manufacturers as well as other independent companies have these standards in their catalogs; this procedure is also available in every VNA firmware. The main drawbacks of SOLT are

- Perfect knowledge of all standards is required.
- A large number of standard connection and measurements are needed.
- A direct port connection (i.e., the thru) is mandatory.

The degree of measurement accuracy following the calibration procedure is strongly contingent on the

- Number of standards implied during the calibration,
- Degree of their knowledge,
- Quality of the interconnections.

The SOLT ideally requires a perfect knowledge of all the standards used, and this condition obviously cannot be achieved.

Other calibration techniques, as TRL or LRM, do not require a complete set of fully known calibration standards, and for this reason they are called “self-calibrations.” In particular, the TRL technique is based on the use of one direct connection (i.e., the *thru*), one reference transmission line of unknown length (i.e., the *line*), and an unknown *reflection*, measured at both VNA ports. Since the direct port connection cannot be considered standard and the reflection is unknown, this technique requires only the knowledge of the line reference impedance.

Furthermore, it has been proved [44] that TRL allows an accurate definition of the scattering parameters in terms of traveling waves referred to the line reference impedance, which is easy to correlate to the line mechanical properties. For this reason, TRL is commonly used as a reference calibration technique at metrology laboratories.

The only significant drawback of TRL is the working bandwidth, which is limited below the resonant frequency of the line. At this frequency, the line does not introduce any phase shift and is undistinguishable from the thru connection (zero length, for definition), thus invalidating the calibration. To overcome this problem, a set of lines of varying lengths is normally used, and their measurements combine to achieve a broad frequency coverage [45].

Another very popular self-calibration method is the line reflect match (LRM) technique. It uses a fully known one-port matched load to substitute the line of the TRL algorithm and is particularly useful for on wafer applications, where probe movement is difficult. Very high-precision laser trimmed resistors are normally used as match standards, offering constant resistance and low parasitic effects up to 50 GHz.

To close this brief overview on the most recent calibration techniques, it’s worth noting the short/open load reciprocal (SOLR) [31], which requires three fully known one-port standards and an unknown, but reciprocal, two-port device. This technique avoids the use of a fully known

two-port device, such as the thru, which is compulsory in all other calibrations. Thus SOLR is very useful in many situations where the direct port connection cannot be achieved or substituted with an accurate two-port device, such as when the DUT ports have the same gender or when they are too far apart.

More recently, rather than describing the standards through electrical models, a precharacterization technique has been used. The standards are measured in a certified laboratory with TRL-calibrated VNAs, and data files substitute the standard electrical models.

This approach is widely used for the so called *electronic calibrator* module, generally a pin (positive–intrinsic–negative) diode network that presents a precharacterized series of electrical states that simulate the different standard insertions. The user connects only the electronic calibrator to the VNA, while a computer changes the impedance shown by the module at its ports and measures them through the VNA, as they would be different standard connections. The error boxes are computed using a SOLT-adapted algorithm [25,60,66], where the standard parameters are substituted by the previously measured data files.

3.2. Time-Domain Reflectometry

The technique of time-domain reflectometry (TDR) was introduced in the early 1960s as a simple way to characterize the position and type of a reflection along a line, using an oscilloscope. In particular, using a step generator and sampling the reflected waveform with an oscilloscope, the impedance of simple discontinuities could be calculated [58].

While the traditional TDR was useful as a qualitative tool, it has some limitations affecting its accuracy and utility:

- Limited risetime
- Sampling scope jitter
- Poor dynamic range
- DC path needed

Common TDR systems based on sampling scope and step or pulse generator, such as the one sketched in Fig. 11, are still commonly used, especially for digital bus characterization. After the introduction of VNA and digital signal processing, it was clear that the reflection coefficient as a function of time could be easily obtained by the inverse Fourier transform of the network reflection coefficient as a function of frequency, which is normally measured by the VNA. This technique, called *synthetic TDR*, is now widely adopted in every VNA and is used in many fields, from cable discontinuity detection to parasitic interconnection modeling.

The use of frequency-domain data, followed by data processing, has several advantages over the traditional TDR, in particular

- Exact knowledge of the step or pulseshape and equivalent bandwidth

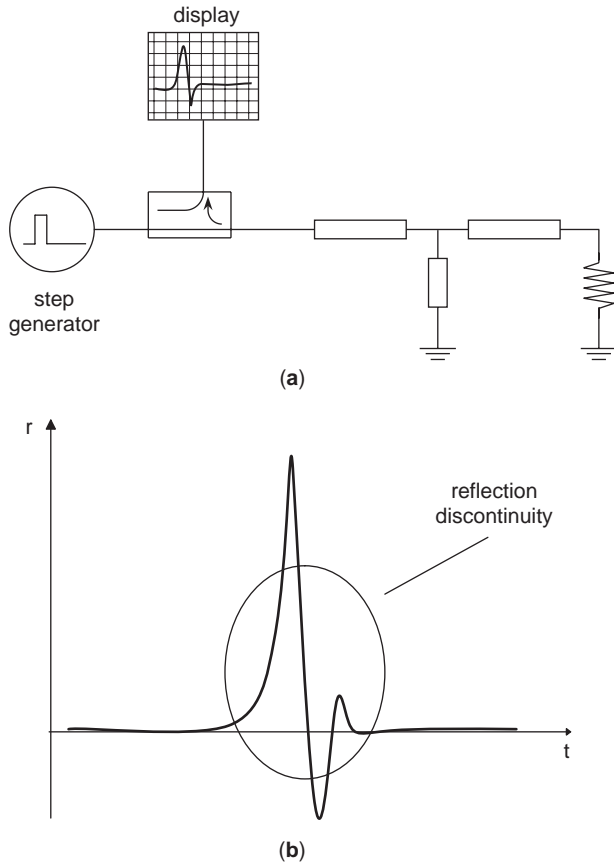


Figure 11. TDR system based on sampling scope and pulse generator (a) and typical time-domain pulse response (b).

- Vectorial error corrected data that avoid spurious reflections from cables and interconnections
- High dynamic range

Different types of excitation can be easily computed, and the time-domain network response is normally shown on the VNA screen; furthermore, the use of sophisticated signal processing tools, such as time-domain gate function and frequency-domain windows, allow one to greatly increase the technique capabilities. For example, by gating the time-domain response of a particular discontinuity and retransforming the data into the frequency domain, accurate modeling of interconnections and launchers can be obtained [11,12,58].

3.3. Multiport and Differential Measurements

The VNA is currently evolving from the basic two-port instrument toward a more sophisticated multiport system. Typical currently available multiport VNA has 4 ports, while 8 or even 12 ports are available at low-frequency bands. Applications of such VNAs span from the television distribution systems up to bus characterization of differential digital circuits.

In this latter case the traditional definition of scattering parameters has been extended to the *differential S parameters* [14], which are obtained as the difference between the traditional single-ended lines and allow one

to better highlight the behavior of microwave systems where the signal flows on coupled lines rather than on a single-ended ones. This technique is very promising in the digital marketplace, where the bus speed is reaching the microwave field and the crosstalk effects need to be precisely controlled and simulated.

4. ADVANCED MICROWAVE MEASUREMENTS

The more recent technological advances require the evolution of microwave measurements to very complex setups that can perform different types of characterization simultaneously and can extract more and more information for the new modeling and designing needs. Nonlinear techniques for active devices will be briefly described in the following text.

4.1. Nonlinear and Load-Pull Measurements

When the devices work under a strong nonlinear state, the models and best operating conditions cannot be often predicted by linear analysis or measurements, since input and output matching networks (as well as bias point) influence the performance of any transistor or power amplifier. Therefore, a traditional way to characterize a transistor for power amplifier applications consists in effectively trimming the load (Γ_L) and the source (Γ_S) reflection coefficients seen by the device under nonlinear conditions, to meet the required amplifier specifications [21]. In this case of power amplifiers, transistor nonlinearities play a fundamental role and the optimum loading conditions may be significantly different from the linear case, where *S* parameters are used to compute the best loading conditions.

Measurement setups that allow one to change the loading conditions are often referred as *load-* and *source-pull systems* [21,24]. Load-pull application examples are high power amplifier, mixer [43], and oscillator design [36], while source-pull systems have important applications in low-noise amplifier design, where the best noise figure and, in general, the transistor noise parameters are found by applying different source impedance values [3,16,22,42].

A simplified scheme of a generic real-time load source-pull system is shown in Fig. 12. To obtain a variable load, passive networks with manual or automatic variable elements can be used (slug tuners, solid state tuners, etc.)

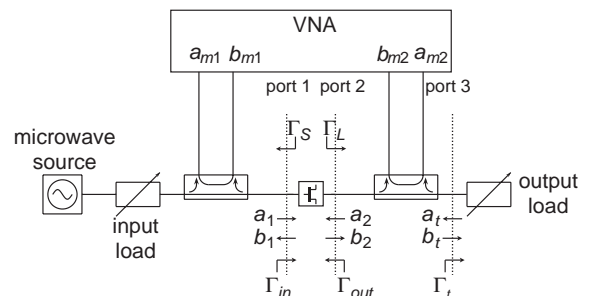


Figure 12. Real-time load/source-pull setup.

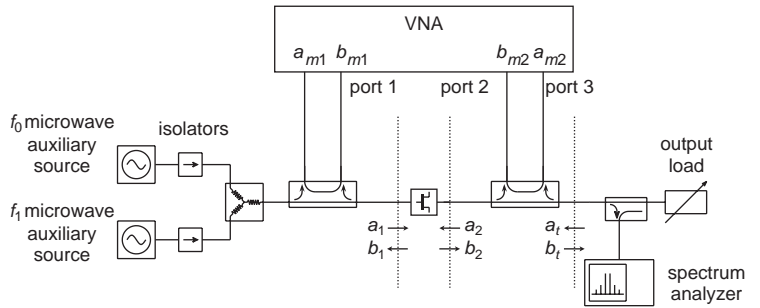


Figure 13. Load-pull system for intermodulation measurements [23].

[1,46,55,62]. The alternatives are active loads, which electronically synthesize the required reflection coefficients by properly amplifying, phase shifting, and combining microwave signals [10,59].

In the simplest load-pull implementation, the device is driven by the microwave source at a single frequency, and its performance is measured while physically changing Γ_L or Γ_S . Vector measurement techniques with VNA allow real-time determination of the load and source reflection coefficients, as well as input and output power, through the dual directional couplers, shown in Fig. 12.

A very popular and less expensive technique exploits power meters, connected to the system through directional couplers, at the input and output of the DUT. Since no vectorial real-time correction is possible in this case, the measurements rely on the accuracy of directional coupler and tuner precalibration. For this reason, VNA-based systems are faster and have lower uncertainties than do power-meter-based systems, as has been demonstrated in Ref. 33.

4.1.1. Harmonic Measurements. Load-pull measurements are inherently for single-frequency or small-bandwidth applications; nevertheless, nonlinear devices produce harmonics, and the loading conditions at harmonic frequencies may significantly affect device performance, as proved by theory [57] and experiments [30]. Harmonic source- and load-pull systems allow one to change Γ_S and Γ_L values at a discrete set of frequencies (typically two or three), while measuring device performance over the entire spectrum of interest. A typical application is the design of high-efficiency solid-state amplifiers and transceiver output stages [6,54]. The introduction of harmonic tuners [47,48] has provided a compact and economic solution for harmonic source load-pull testsets. However, like any other passive tuner, harmonic tuners cannot offer highly reflective terminations at higher frequencies, due

to losses; a good solution is, again, the active load, realized by combining, with power splitters and combiners, more single-frequency active loads [37,48,51].

4.1.2. Intermodulation Set-ups. By driving the device with two tones or with digitally modulated signals, intermodulation or adjacent-channel power ratio (ACPR) are traditionally measured to evaluate the linearity characteristics of the transistor. A typical application is the power amplifier design for CDMA- and WCDMA-based telecommunication systems, where the phone and base station performance is more sensitive by amplitude distortion than in previous access technologies based on constant-envelope modulation schemes.

Like all the other device characteristics, intermodulation distortion depends on the loading conditions; therefore, load-pull systems have evolved to integrated load-pull and intermodulation measurement capabilities, as shown in Fig. 13 [23].

4.2. Time-Domain Waveform Measurements

The growth of strongly nonlinear devices for wireless applications (mobile units and base stations), has compelled the development of another measurement philosophy: time-domain waveform measurements. This technique can provide important information for both device modeling [35,49] and design [9,13]. For example, if the waveforms at the input and output of the device are directly accessible, the effects of the harmonic terminations [8] or of the envelope impedance [65] can be studied directly in the time domain.

Time-domain waveforms are commonly measured by *sampling oscilloscopes*, which are based on microwave signal subsampling, as sketched in Fig. 5. The IF filter is not a narrow-, bandpass filter one as in the VNA, but a low-pass filter, and IF signal spectra become exact copies of the microwave signals. The magnitude and phase

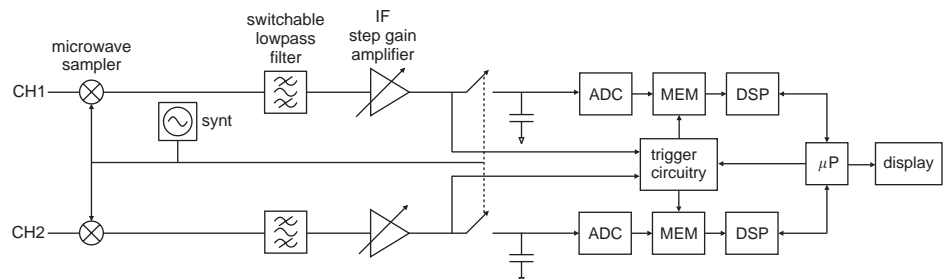


Figure 14. Simplified block scheme of a time-domain waveform receiver.

relationships between the spectral components are maintained and are measured by A/D conversion and FFT of the IF signals, as shown in Fig. 14 [19,20].

Calibrations can be performed in the frequency domain, after fast Fourier transform (FFT); then, corrected measurements are displayed again in the time domain, after an inverse fast Fourier transform (IFFT) [29]. The main drawbacks of waveform measurements is the low dynamic range and speed.

BIBLIOGRAPHY

- V. Adamian, 2-26.5 GHz on-wafer noise and S-parameter measurements using a solid state tuner, *34th ARFTG Conf. Digest*, Dec. 1989, pp. 33–40.
- V. Adamian, A novel procedure for network analyzer calibration and verification, *41st ARFTG Conf. Digest*, June 1993, pp. 8–17.
- V. Adamian and A. Uhlir, A novel procedure for receiver noise characterization, *IEEE Trans. Instrum. Meas.* **IM-22**:181–182 (June 1973).
- J. W. Allen, F. R. Clague, N. T. Larsen, and M. P. Weidman, *NIST Microwave Power Standards in Waveguide*, NIST Technical Note 1511, Boulder, CO, 1999.
- R. Anderson and O. Dennison, An advanced new network analyzer for sweep-measuring amplitude and phase from 0.1 to 12.4 GHz, *Hewlett-Packard J.* **18**:2–9 (Feb. 1967).
- I. Bahl, E. Griffin, A. Geissberger, C. Andricos, and T. Brukiewa, Class-B power MMIC amplifiers with 70 percent power-added efficiency, *IEEE Trans. Microwave Theory Tech.* **MTT-37**:1315–1320 (Sept. 1989).
- A. Bailey, *Microwave Measurements*, 2nd ed., Peter Peregrinus, London, 1989, Chaps. 15–16.
- D. Barataud, C. Arnaud, B. Thibaud, M. Campovecchio, J. M. Nebus, and J. P. Villotte, Measurements of time-domain voltage/current waveforms at RF and microwave frequencies based on the use of a vector network analyzer for characterization of nonlinear devices—application to high-efficiency power amplifiers and frequency-multipliers optimization, *IEEE Trans. Instrum. Meas.* **IM-47**:1259–1264 (Oct. 1998).
- D. Barataud, M. Campovecchio, and J.-M. Nebus, Optimum design of very high-efficiency microwave power amplifiers based on time-domain harmonic load-pull measurements, *IEEE Trans. Microwave Theory Tech.* **49**(6):1107–1112 (June 2001).
- G. P. Bava, U. Pisani, and V. Pozzolo, Active load technique for load-pull characterization at microwave frequencies, *Electron. Lett.* **18**(4):178–179 (Feb. 1982).
- C. Beccari, A. Ferrero, and U. Pisani, In-fixture calibration of an s-parameter measuring system by means of time domain reflectometry, *32nd ARFTG Conf. Digest*, Phoenix, AZ, Dec. 1988, pp. 89–97.
- C. Beccari, A. Ferrero, and U. Pisani, Time domain reflectometry applied to mmic passive component modeling, *33rd ARFTG Conf. Digest*, Long Beach, CA, June 1989, pp. 1–10.
- J. Benedikt, R. Gaddi, P. J. Tasker, and M. Goss, High-power time-domain measurement system with active harmonic load-pull for high-efficiency base-station amplifier design, *IEEE Trans. Microwave Theory Tech.* **48**(12):2617–2624 (Dec. 2000).
- D. Bockelman and W. Eisenstadt, Combined differential and common-mode scattering parameters: Theory and simulation, *IEEE Microwave Theory Tech.* **MTT-43**:1530–1539 (July 1995).
- R. Carlson and F. Weinert, The RF vector voltmeter—an important new instrument for amplitude and phase measurements from 1 MHz to 1000 MHz, *Hewlett-Packard J.* **17**:2–12 (May 1966).
- G. Caruso and M. Sannino, Determination of microwave two-port noise parameters through computer-aided frequency-conversion techniques, *IEEE Trans. Microwave Theory Tech.* **MTT-27**:779–783 (Sept. 1979).
- F. R. Clague, *A Calibration Service for Coaxial Reference Standards for Microwave Power*, NIST Technical Note 1374, Boulder, CO, 1995.
- Hewlett-Packard Co., *HP8510 Network Analyzer System Operating and Programming Manual*, HP 08510-90005, Santa Rosa, CA, 1985.
- Hewlett-Packard Co., *The Microwave Transition Analyzer: A Versatile Measurement Set for Bench and Test*, HP Product Note 70820-1, Rohnert Park, CA, 1991.
- Hewlett-Packard Co., *The Microwave Transition Analyzer: Measure 25 ps Transitions in Switched and Pulsed Microwave Components*, HP Product Note 70820-2, Rohnert Park, CA, 1991.
- S. C. Cripps, *RF Power Amplifiers for Wireless Communications*, Artech House, Boston, 1999.
- A. Davidson, B. Leake, and E. Strid, Accuracy improvements in microwave noise parameter measurements, *IEEE Trans. Microwave Theory Tech.* **MTT-37**:1973–1978 (Dec. 1979).
- M. Demmler, B. Hughes, and A. Cognata, A 0.5–50 GHz on-wafer, intermodulation, load-pull and power measurement system, *IEEE MTT-S Int. Microwave Symp. Digest*, Orlando, FL, May 1995, pp. 1041–1044.
- R. Soares, ed., *GaAs MESFET Circuit Design*, Artech House, Norwood, MA, 1988, Chap. 6.3.
- G. Engen, R. Judish, and J. Juroshek, The multistate two port: An alternative transfer standard, *41st ARFTG Conf. Digest*, June 1994, pp. 11–18.
- H. J. Eul and B. Schieck, Thru-match-reflect: One result of a rigorous theory for de-embedding and network analyzer calibration, *Proc. 18th European Microwave Conf.*, Stockholm, 1988, pp. 909–914.
- H. J. Eul and B. Schieck, A generalized theory and new calibration procedures for network analyzer self-calibration, *IEEE Trans. Microwave Theory Tech.* **MTT-39**:724–731 (April 1991).
- H. J. Eul and B. Schieck, Reducing the number of calibration standards for network analyzer calibration, *IEEE Trans. Instrum. Meas.* **IM-40**:732–735 (Aug. 1991).
- P. Ferrari, G. Angenieux, and B. Flechet, A complete calibration procedure for time domain network analyzers, *IEEE MTT-S Int. Microwave Symp. Digest*, Albuquerque, NM, June 1992, pp. 1451–1454.
- A. Ferrero and U. Pisani, Large signal 2nd harmonic on wafer MESFET characterization, *36th ARFTG Conf. Digest*, Monterey, CA, Dec. 1990, pp. 101–106.
- A. Ferrero and U. Pisani, Two-port network analyzer calibration using an unknown “thru,” *IEEE Microwave Guided Waves Lett.* **MGWL-2**:505–507 (Dec. 1992).
- A. Ferrero and F. Sanpietro, A simplified algorithm for leaky network analyzer calibration, *IEEE Microwave Guided Wave Lett.* **MGWL-5**:119–121 (April 1995).
- A. Ferrero, V. Teppati, and A. Carullo, Accuracy evaluation of on-wafer load-pull measurements, *IEEE Trans. Microwave Theory Tech.* **MTT-49**(1):39–43 (Jan. 2001).

34. H. T. Friis, Noise figures of radio receivers, *Proc. IRE*, July 1944, pp. 419–422.
35. R. Gaddi, J. A. Pla, J. Benedikt, and P. J. Tasker, Ldmos electro-thermal model validation from large-signal time-domain measurements, *IEEE MTT-S Symp. Digest*, 2001, Vol. 1, pp. 399–402.
36. F. M. Ghannouchi and R. Bosisio, Source-pull/load-pull oscillator measurements at microwave/mm wave frequencies, *IEEE Trans. Microwave Theory Tech.* **MTT-41**:32–35 (Feb. 1992).
37. F. M. Ghannouchi, R. Larose, and R. Bosisio, A new multi-harmonic loading method for large-signal microwave transistor characterization, *IEEE Trans. Microwave Theory Tech.* **MTT-39**:986–992 (June 1991).
38. R. A. Hackborn, An automatic network analyzer system, *Microwave J.* **11**:45–52 (May 1968).
39. H. Van Hamme and M. Van Den Bossche, Flexible vector network analyzer calibration with accuracy bounds using an 8-term or a 16-term error correction model, *IEEE Microwave Theory Tech.* **MTT-42**:976–987 (Aug. 1991).
40. J. Helton and R. Speciale, A complete and unambiguous solution to the super-TSD multiport-calibration problem, *IEEE MTT-S Int. Microwave Symp. Digest*, Boston, May 1983, pp. 251–252.
41. J. Jargon, R. Marks, and D. Rytting, Robust SOLT and alternative calibrations for four-sampler vector network analyzers, *IEEE Trans. Microwave Theory Tech.* **MTT-47**:2008–2013 (Oct. 1999).
42. D. Le and F. Ghannouchi, Noise measurements of microwave transistor using and uncalibrated mechanical stub tuner and a built-in reverse six-port reflectometer, *IEEE Trans. Instrum. Meas.* **IM-44**:847–852 (Aug. 1995).
43. D. Le and F. Ghannouchi, Multitone characterization and design of FET resistive mixers based on combined active source-pull/load-pull techniques, *IEEE Trans. Microwave Theory Tech.* **MTT-46**:1201–1208 (Sept. 1998).
44. R. Marks and D. Williams, A general waveguide circuit theory, *J. Res. NIST* **97**:533–561 (Sept. 1992).
45. R. B. Marks, A multiline method of network analyzer calibration, *IEEE Trans. Microwave Theory Tech.* **MTT-39**:1205–1215 (July 1991).
46. C. McIntosh, R. Pollard, and R. Miles, Novel MMIC source-impedance tuners for on-wafer microwave noise-parameter measurements, *IEEE Trans. Microwave Theory Tech.* **MTT-47**:125–131 (Feb. 1999).
47. ATN Microwaves, A load-pull system with harmonic tuning, *Microwave J.* 128–132 (March 1996).
48. Focus Microwaves, An affordable harmonic load pull setup, *Microwave J.* 180–182 (Oct. 1998).
49. D. G. Morgan, G. D. Edwards, A. Phillips, and P. J. Tasker, Full extraction of pHEMT state functions using time domain measurements, *IEEE MTT-S Symp. Digest*, 2001, Vol. 2, pp. 823–826.
50. *HP8510C Network Analyzer System Specification and Performance Verification Program Manual*. HP8510 Software Supplement.
51. D. B. Poulin and R. B. Stancliff, Harmonic load-pull. *IEEE MTT-S Int. Microwave Symp. Digest*, **79**(1):185–187 (April 1979).
52. M. Roos and V. Sotoudeh, A measurement and calibration technique for accurate measurement of amplifier S parameters, *IEEE MTT-S Int. Microwave Symp. Digest*, Las Vegas, NV, June 1987, pp. 449–451.
53. D. Rytting and S. Sanders, A system for automatic network analysis, *Hewlett-Packard J.* **21**:2–10 (Feb. 1970).
54. F. Sechi, High efficiency microwave FET power amplifier, *Microwave J.* 59–63 (Nov. 1981).
55. F. Sechi, R. Paglione, B. Perlman, and J. Brown, A computer controlled microwave tuner for automated load pull, *RCA Rev.* **44**:566–572 (Dec. 1983).
56. K. J. Silvonon, A general approach to network analyzer calibration, *IEEE Microwave Theory Tech.* **MTT-40**:754–759 (April 1992).
57. D. Snider, A theoretical analysis and experimental confirmation of the optimally loaded and overdriven rf power amplifier, *IEEE Trans. Electron. Dev.* **ED-14**:851–857 (Dec. 1967).
58. H. E. Stinehelfer, Sr., Discussion of de-embedding techniques using time-domain analysis, *IEEE Proc.* **74**(1):90–94 (Jan. 1986).
59. Y. Takayama, A new load-pull characterization method for microwave power transistor, *IEEE MTT-S Int. Microwave Symp. Digest*, Cherry Hill, NJ, June 1976, pp. 218–220.
60. Agilent Technologies, *Agilent Electronic Calibration (ECal) Modules for Vector Network Analyzers*, 5963-3743E, Santa Rosa, CA, 2003.
61. Agilent Technologies, *Fundamental of RF and Microwave Power Measurements*, 5988-9213/6E, Santa Rosa, CA, 2003.
62. C. Tsironis, A novel design method of wideband power amplifier, *Microwave J.* 303–304 (May 1992).
63. V. Pozzolo and U. Pisani, Errors caused by directional couplers and impedance mismatches in a test set for s-parameter measurements, *Alta Frequenza* **37**(10):911–915 (April 1968).
64. R. L. Vaitkus, Wide-band de-embedding with a short, an open and a through line, *Proc. IEEE* **74**:71–74 (Jan. 1986).
65. D. J. Williams, J. Leckey, and P. J. Tasker, A study of the effect of envelope impedance on intermodulation asymmetry using a two-tone time domain measurement system, *IEEE MTT-S Int. Microwave Symp. Digest*, Seattle, WA, June 2002, pp. 1841–1844.
66. K. Wong and R. Grewal, Microwave electronic calibration: Transferring standards lab accuracy to the production floor, *Microwave J.* 94–105 (Sept. 1994).

MICROWAVE MIXERS

R. S. TAHIM
RST Scientific Research, Inc.
New York

1. INTRODUCTION

Mixer as a component is found in almost all kinds of microwave and millimeter-wave systems that include various communication systems, interferometer systems, phased arrays, sensors, and radar systems. Microwave mixers form a highly mature technology [1]. However, there are still interesting and new circuits that continue to be developed in order to make the microwave/millimeter-wave systems more efficient. A number of microwave systems are extremely vital to the defense applications involving the collection and distribution of information

both to and from the forward-deployed troops and between the command centers and the troops in the field. Wideband radar systems that incorporate wideband mixers are needed in large-scale surveillance, tracking targets, identification, and reconnaissance applications. Therefore, the U.S. military has placed significant emphasis on the development of wideband microwave and millimeter-wave transceiver systems for both radar and data transmission systems at high frequencies. Such wideband systems are needed for transferring high-value data such as videos, high-resolution images, and radar, optical, and computer data that military personnel need to carry out the military operations more efficiently and effectively.

Radar and the wireless telecommunications industry have also established itself as one of the strongest growth areas in the commercial sector side. Although vigorous expansion is expected to continue in the established wireless applications, the next major growth areas in the wireless revolution have already begun to emerge. As a result, variety of new applications are envisioned in such areas as homeland security, intelligent highway systems, autonomous landing systems, mobile satellite communications, intersatellite links, tracking and data relay, direct conversion receivers, ultra-wide-band (UWB) systems, advanced security systems, and local multipoint distribution systems. In most of these applications, low-noise receivers that include high-performance microwave mixers are desirable.

In all RF, microwave, and millimeter-wave systems there are two major parts: the transmitter and the receiver. In a microwave communication system, the transmitter and receiver systems are installed at different locations. The message is sent from the transmitter to the receiver using the antennas. In a radar system, the transmitter and the receiver are located very close together. The transmitted signal is reflected by a target or the targets to the receiver; thus the information about the target (range and velocity) is obtained by the radar. Along with the development of communication and radar systems for military applications, another highly interesting area called *electronic warfare* (EW) has also emerged over the years. In EW applications, the receivers are used to intercept signals of limited information from a hostile transmitter, while a jamming transmitter is used to generate false information or noise to mask the true signal received by the possible hostile radar receiver.

2. MIXER OPERATION

In the microwave systems for both radar and communications, the incoming signal at microwave frequency (f_s) is downconverted in a mixer to generate a low intermediate frequency (f_{IF}), which is further processed to generate the baseband signal in order to retrieve the required information or data. Frequency down-conversion is accomplished by utilizing the properties of a nonlinear impedance element of the mixer, which is simultaneously interacting with the receive signal (f_s) and a usually a much stronger signal at f_{LO} generated by a local oscillator. In the mixer conversion process, information about the frequency,

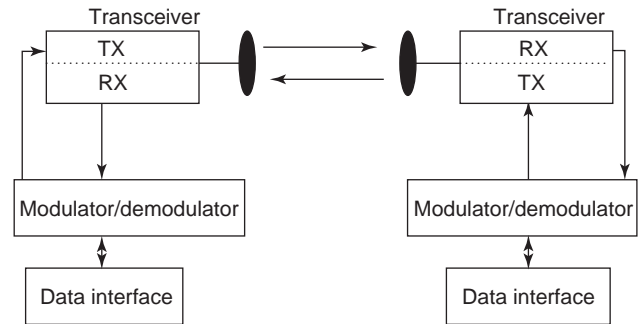


Figure 1. Schematic of a microwave communication system.

amplitude, and phase of the original signal is preserved. Therefore, we find the mixer as a component in almost all kinds of microwave systems that include various communication systems, interferometer systems, phased arrays, radars, and all kinds of instruments such as frequency upconverters, modulators, frequency synthesizers, spectrum analyzers, and network analyzers.

3. MIXERS IN MICROWAVE/MM-WAVE SYSTEMS

Microwave mixers in a communication receiver and radar system play a critical role in the data transfer and the identification of the targets. Figure 1 is a basic block diagram of a wireless communication system, which generally consists of two transceivers, each transmitting and receiving the microwave signals. In the modern telecommunication systems, a receiver consists of a low-noise-amplifier (LNA) followed by a mixer circuit.

A monopulse receiver topology consisting of low-noise amplifier and microwave/millimeter-wave mixers is shown in Fig. 2 [2]. In the receiver system, the signal f_s from the antennas is first amplified in the low-noise amplifier before being downconverted using a balanced

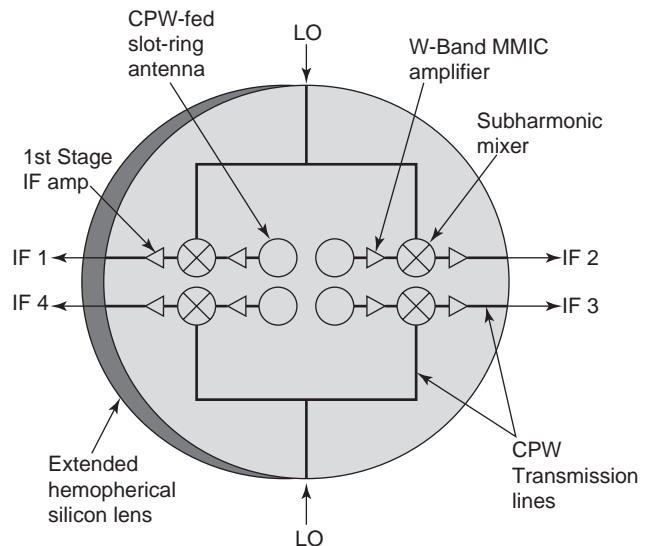


Figure 2. A monopulse receiver topology with four slot-ring antennas.

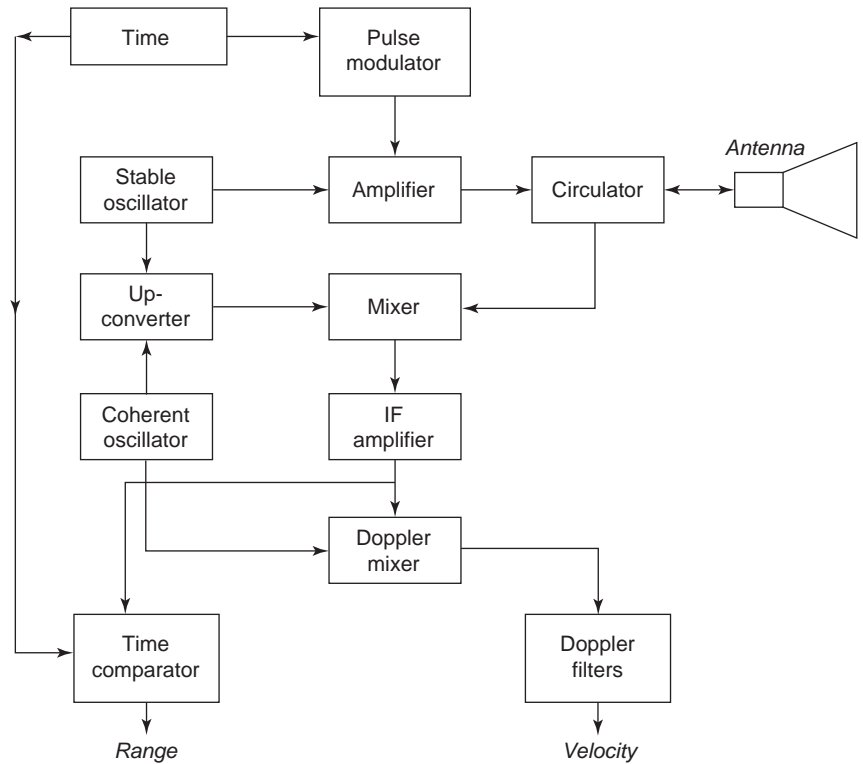


Figure 3. Microwave mixer in Doppler radar system.

mixer to the IF frequency band. A low noise and a highly stable local oscillator source or a dielectric resonator oscillator (DRO) is generally used as the local-oscillator (LO) source to drive the mixer (frequency downconverter).

A system block diagram of a typical radar system illustrating the use of a microwave mixer in the system is shown in Fig. 3. In the radar receiver, the returned echo is mixed with the stable oscillator frequency to obtain the Doppler shift frequency [3]. The Doppler frequency is passed through a set of Doppler filters to determine the target velocity. The return signal is also compared with the reference time in a time comparator to determine the target range. In the system, the exciter provides the local oscillator power to the downconverter (mixer) to generate the desired intermediate frequency (IF).

In the receiver, as long as the amplifier gain before the mixer is sufficiently high to mask the contribution of the mixer noise figure, the overall noise figure of the receiver is determined mainly by the amplifier noise figure. However, at millimeter-wave range, the way to obtain high gain for the amplifier is to cascade several amplifiers. In such a case, either the cost or the complexity of the circuit is increased. In order to achieve a low receiver noise figure in the system, it is more desirable to use the mixer in the receiver front end as a first element and to minimize the mixer conversion loss to achieve the low receiver noise figure.

The receiver and mixer parameters in the microwave communication system, are related as [4]

$$S/N = (G_T P_T)(G_R/T_S)(\epsilon_p/k\Delta f)(\lambda^2/[4\pi R]^2) \quad (1)$$

where

- G_T = transmit antenna gain
- P_T = input power to antenna
- G_R = receive antenna gain
- T_S = effective noise temperature at receiver input
- k = Boltzmann constant = $1.379 \times 10^{-23} = -228.6$ dB (W/Hz · K)
- $\Delta f = B$ = bandwidth of receiver

The receiver noise figure in the system in which mixer is used in the front end is given by [5]

$$F = L_c(N_r + F_{IF} - 1) \quad (2)$$

where L_c is the total conversion loss (including frequency conversion loss, diode series resistance loss, and the mismatch losses) in the mixer, then F_{IF} is the noise figure of the IF amplifier followed by the mixer and N_r is the diode noise ratio.

4. MIXER CONFIGURATIONS

Seven basic types of mixers have been developed for various applications:

1. Single-ended mixers
2. Single-balanced mixers
3. Double-balanced mixers
4. Subharmonically pumped mixers

5. Image-rejection mixers
6. Image-enhanced mixers
7. Quadrature mixers

The single-ended mixer is the simplest mixer configuration using one mixer diode. However, microwave mixer configurations using two or more Schottky diodes are quite common and have proved to provide substantial advantages in terms of operating bandwidth, intermodulation, spurs, LO noise cancellation, high dynamic range, low intermodulation, and so on [6,7]. At high microwave and millimeter-wave frequency bands, subharmonically pumped mixer designs are preferred because the LO frequency requirement in subharmonic mixers is roughly half that required in the fundamental mixer design. The two-diode mixer also provides substantial AM local oscillator noise suppression [7]. The noise associated with the LO sources (used in the frequency downconverter), when translated at the IF frequency band during the conversion process, can be a source of problems in the receiver. Another important property of subharmonically pumped mixer is the strong attenuation of downconverted local oscillator noise available at the IF output.

5. MIXER PARAMETERS

High-performance mixers in the microwave and millimeter-wave receivers form an important part in the current telecommunications, meteorology, and electronic warfare systems. Important mixer parameters that determine its usefulness in such microwave and millimeter-wave systems are

- Conversion loss
- Operating bandwidth
- Local-oscillator power requirements
- Isolation between the RF, LO, and IF ports
- RF and IF impedance match
- Intermodulation
- LO noise cancellation
- Dynamic range

The *conversion loss* of a microwave mixer is defined as the ratio of the IF output power to the signal input power. Conversion loss measures the efficiency with which mixer converts RF energy to the IF energy and is one of the most important mixer parameters. Conversion loss L_c is expressed in the form

$$L_c = L_o L_p \quad (3)$$

where L_o includes the intrinsic conversion loss arising from the conversion process within the nonlinear resistance of the diode plus the signal loss associated with the impedance mismatch losses at the RF and IF ports. L_p is the parasitic loss associated with the parasitic elements of the diode, such as junction capacitance C_j , the spreading resistance R_s , and series inductance L_s .

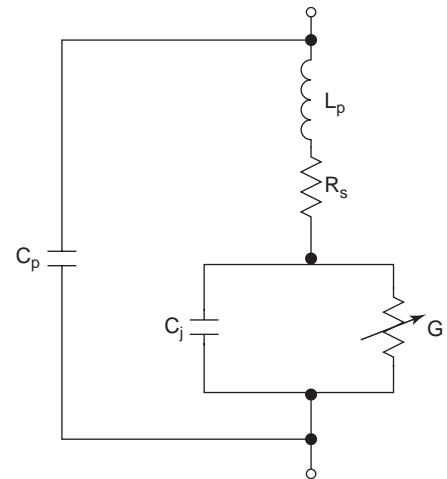


Figure 4. Equivalent circuit of a mixer diode.

The junction capacitance C_j , series resistance R_s , and other parasitic reactance L_s are shown in Fig. 4 for the diode equivalent circuit, and they are frequency-dependent. Their effect on controlling the mixer performance such as operating bandwidth and the conversion efficiency becomes much stronger at high microwave and millimeter-wave frequencies [8].

Since $C_j \propto d^2$ and $R_s \propto d^{-1}$, where d is the diameter of the junction, d should be reduced as the operating frequency is increased. Reducing the size of the junction area of the diode increases the current density through the diode and consequently may increase the intrinsic conversion loss of the mixer [9].

In addition to the parasitic losses, the conversion loss depends on the losses in the RF circuitry surrounding the mixer, the quality of the nonlinear device, the mismatch between the RF circuit and the diodes and the bias level to the diodes. When no energy is dissipated at the idler frequencies, the fundamental limit on the conversion loss of a mixer is 3 dB [10]. The discrepancy between the measured mixer loss and the predicted loss is shown to have three main causes and is generally divided into the following three parts:

L_1 mismatch loss due to impedance mismatch at RF and IF ports

L_2 diode parasitic losses due to junction capacitance and series resistance

L_3 intrinsic junction loss of the diode

The overall conversion loss L is the sum of three losses:

$$L = L_1 + L_2 + L_3 \quad (\text{all in dB}) \quad (4)$$

The conversion loss is a very important mixer parameter, especially in the receivers without RF amplifier in front of the mixer, since the first component at the input of a receiver has the most influence on the noise figure of the receiver. In a mixer circuit, in which the $2f_{LO} - f_s$ frequency product lies close to the RF signal, the conversion loss can be further improved by extracting the power associated with $2f_{LO} - f_s$ signal [11] by remixing this signal with LO to generate more IF power.

When the signal power approaches the same power level as the local oscillator, the mixer becomes saturated; specifically, the output IF power no longer increases linearly with the input power. Since the mixer is a three-port device, isolation between RF and LO ports, isolation between RF and IF ports, and isolation between LO and IF ports is very important. Isolation is the measure of circuit balance within the mixer. Poor isolation between the RF and LO means that a LO signal can reach the RF port and power can radiate through the receiving antenna [12]. In receivers, where LNA forms the front end, the poor isolation between the LO and RF can result in signal distortion because the FET devices in the amplifier also exhibit nonlinear characteristics. Isolation between the mixer ports becomes a problem in a multichannel receiver in which a single LO is used to feed a number of mixers [13].

In the resistive mixer operation, the signal level in a mixer is significantly lower than that of LO power and does not therefore perturb the LO-pumped conductance waveform. Under such conditions, no harmonics of signal are generated. However, if the RF and LO signal powers are at sufficiently high level, the harmonics and inter-modulation products are generated according to $\pm mf_{\text{RF}} \pm nf_{\text{LO}}$, where $m = 0, 1, 2, \dots$ and $n = 0, 1, 2, \dots$, although a filter is used at the mixer output to allow only f_{IF} to pass. In case the intermodulation frequency product falls within the IF frequency range, it must be -40 dBc below the actual IF signal level.

In a wireless system, which must operate in severe interference environments, microwave receivers are especially susceptible to intermodulation frequency products generated in mixers. Spurious signals or distortion in mixers continue to be problems in virtually all microwave systems. Mixers are frequently the dominant components in establishing the system's distortion performance. Inter-modulation (IM) products are undesirable mixer generated output products exiting the mixer from any port. Any RF frequency that satisfies the following equation can generate spurious responses, spurs, in a mixer

$$mf_{\text{RF}} - nf_{\text{LO}} = \pm f_{\text{IF}} \quad (5)$$

where f_{IF} is the desired IF frequency.

6. MIXER DESIGN TOPOLOGIES

Although single-ended mixers occasionally are used, most practical mixers are balanced mixers incorporating more than one Schottky mixer diode. Balanced mixers require baluns or hybrids, which largely determine the bandwidth and overall performance of the mixer. Thus, they have been the subject of considerable research interest. As a result, a number of balanced mixer configurations have been developed for various applications. A few of these design configurations are:

- Planar balanced mixer
- Crossbar balanced mixer
- Inline balanced mixer
- Subharmonically pumped mixer

In spite of the maturity of FET circuits, diode mixers are still widely used in microwave circuits, because diode mixers have an important advantage over FETs and bipolar devices. The Schottky barrier diode is inherently a resistive device and as such has very wide bandwidth. The bandwidths of diode mixers are generally limited primarily by the bandwidths of baluns, not the diodes [14]. FETs have high- Q gate input impedance, causing difficulties in achieving flat wide bandwidth as compared to the mixer designs using Schottky mixer diodes. Diode mixers usually have 5–8 dB conversion loss, while active mixers usually can achieve at least a few decibels of gain. More recently, a number of design topologies for the balanced mixers have been developed for various applications. Many of these design topologies provide state-of-the-art performance in terms of bandwidth, conversion loss, and other parameters.

Marchand baluns have been found to be quite useful for planar mixer designs and can achieve a 10–1 bandwidth. Figure 5 shows the mixer design topology using Marchand balun [14]. Planar mixers using microstrip transmission-line couplers operating up to W-band frequency ranges have also been developed [15].

Figure 6 shows the configuration of broadband microwave integrated circuit crossbar mixer. In the crossbar mixer RF and LO signals are coupled (using waveguides) to two Schottky mixer diodes orthogonally. Such configuration provides the necessary isolation between the RF and LO ports. Such design configurations also provide very broadband performance. Crossbar mixers have been developed in high-microwave and millimeter-wave frequency spectra [16,17].

The two-diode subharmonically pumped mixer design topology on suspended substrate strip transmission line is shown in Fig. 7. Two Schottky mixer diodes are shunt-mounted with opposite polarities. Two lowpass filters are used to separate the signal frequency at $\omega_s = 2\omega_p \pm \omega_{\text{IF}}$, the LO frequency ω_p , and the IF frequency ω_{IF} .

Quadrature mixers are important in many communication systems and in direct-conversion receivers. A quadrature mixer typically consists of a pair of balanced mixers with the input signal split into in phase and quadrature

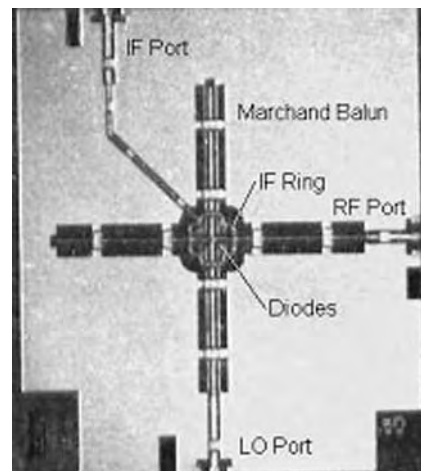


Figure 5. Planar mixer using Marchand balun.

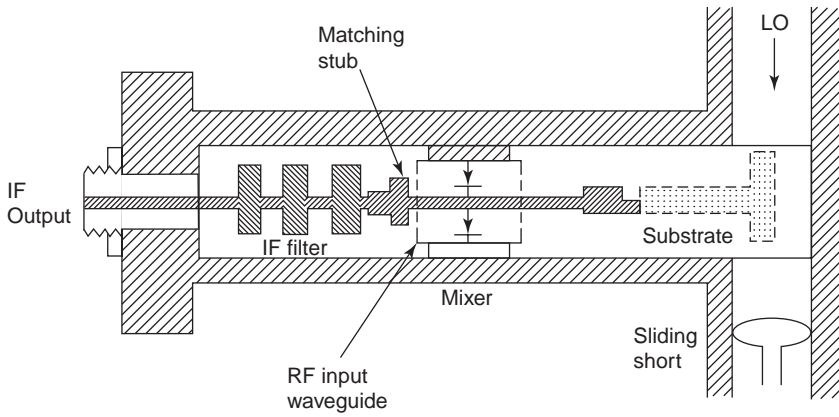


Figure 6. Crossbar mixer design using suspended stripline configuration.

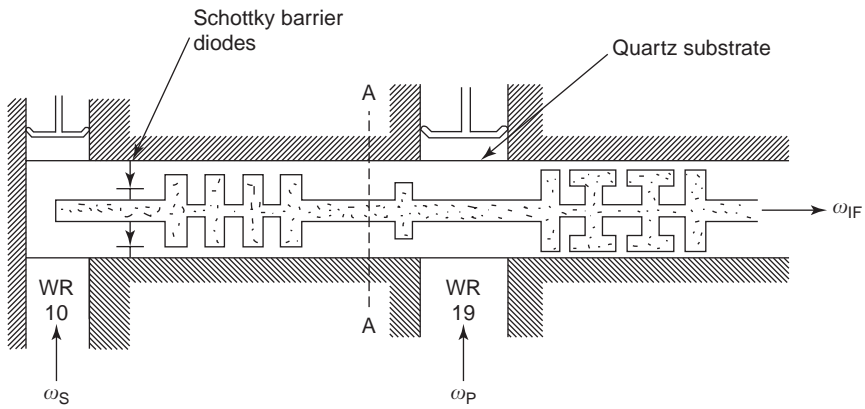


Figure 7. Millimeter-wave subharmonically pumped mixer.

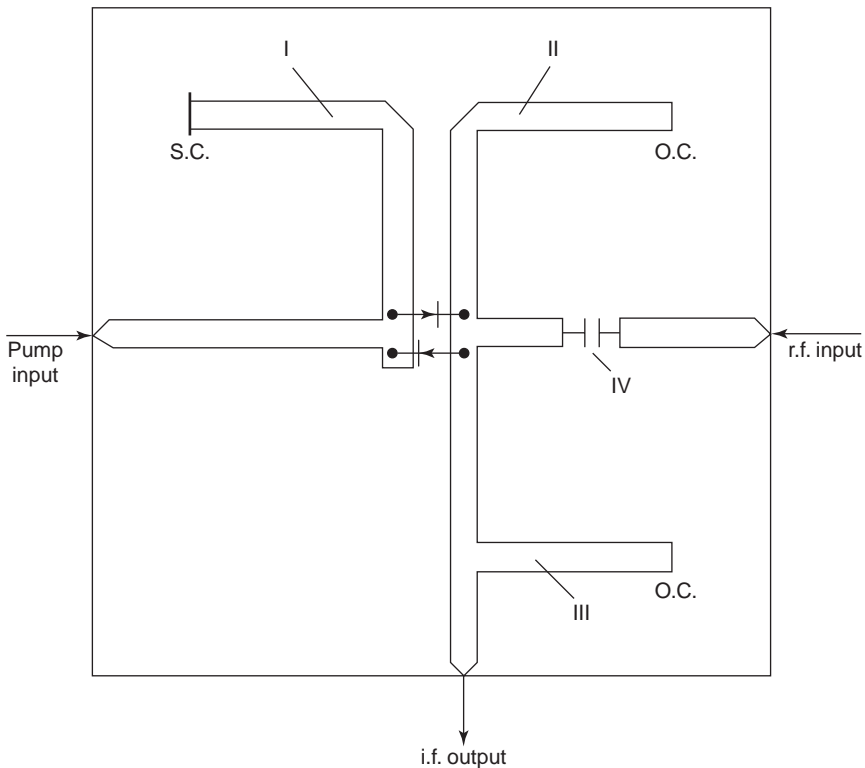


Figure 8. Microstrip layout of subharmonically pumped mixer.

parts, resulting in the in-phase and quadrature signals translated to the intermediate frequency.

A planar microstrip subharmonically pumped mixer circuit layout is shown in Fig. 8 [18]. In this design, the short-circuited stub (SC) I does not impede the pump signal but shorts the RF signal to the ground. The open stub (OC) II, on the other hand, short circuits the pump signal without affecting the RF signal. The SC stub and OC stubs are $\lambda/4$ in length at LO frequency. Two antiparallel pair of Schottky mixer diodes are connected between the LO and RF ports as shown in Fig. 8. The conversion loss of harmonic mixers is about 0.5–1 dB higher than that of a conventional balanced mixer [18].

7. CONCLUSIONS

Although mixer design is often viewed as a mature technology, there seems to be no end to the supply of new ideas for mixer circuits. Mixer parameters are generally determined by the system designers who are constantly researching for high performance, low-cost, manufacturability and integratable designs. This is particularly true of mixers for wireless and other modern communication systems and radar systems where distortion is a major concern. As a result, there are continual developments in mixer technology. These include new circuits, new devices and device technologies.

BIBLIOGRAPHY

1. S. A. Mass, *Microwave Mixers*.
2. S. Raman, S. Barker, and G. M. Rebeiz, A W-band dielectric-lens-based integrated monopulse radar receiver, *IEEE Trans. Microwave Theory Tech.* **46**:2283–2288 (Dec. 1998).
3. G. W. Stimson, *Introduction to Airborne Radar*, 2nd ed., Mendham, NJ, 1998.
4. R. J. Mailloux, *Phased Array Antenna Handbook*, Artech House, Boston, 1994.
5. B. L. Sharma, *Metal-Semiconductor Schottky Barrier Junctions and Their Applications*, Plenum Press, New York, 1984.
6. E. R. Carlson, M. V. Schneider, and T. F. McMaster, Sub-harmonically pumped millimeter-wave mixers, *IEEE Trans. Microwave Theory Tech.* **MTT-26**:706–715 (Oct. 1978).
7. P. S. Henry, B. S. Glance, and M. V. Schneider, Local-oscillator noise cancellation in sub-harmonically pumped down-converter, *IEEE Trans. Microwave Theory Tech.* **MTT-24**:254–257 (May 1976).
8. L. Mania and G. B. Stracca, Effects of the diode junction capacitance on the conversion loss of microwave mixers, *IEEE Trans. Commun.* **COM-22**:1428–1435 (Sept. 1974).
9. M. McColl, Conversion loss limitations on Schottky-barrier mixers, *IEEE Trans. Microwave Theory Tech.* **MTT-25**:54–59 (Jan. 1977).
10. A. J. Kelly, Fundamental limits on conversion loss of double side-band resistive mixers, *IEEE Trans. Microwave Theory Tech.* **MTT-25**:867–869 (Nov. 1977).
11. T. H. Oxley et al., Image recovery mixers, Paper presented at European Microwave Conf., Sweden, 1971.
12. K. Chang, *RF and Microwave Wireless Systems*, Wiley-Interscience, New York, 2000.
13. J. B. Tsui, *Microwave Receivers and Related Components*, Avionics Laboratory, U.S. Air Force, Wright Aeronautical Laboratories, 1983.
14. S. A. Maas and K. W. Chang, Broadband, planar, doubly balanced monolithic Ka-band diode mixer, *IEEE Microwave and Millimeter-wave Monolithic Circuits Symp. Digest*, 1993, p. 53.
15. K. Chang, D. M. English, R. S. Tahim, A. J. Grote, T. Pham, C. Sun, G. M. Hayashiabara, P. Yen, and W. Piotrowski, W-band (75–110 GHz) microstrip components, *IEEE Trans. Microwave Theory Tech.* **MTT-31**:1375–1382 (Dec. 1985).
16. L. T. Yuan, Design and performance analysis of an octave bandwidth waveguide mixer, *IEEE Trans. Microwave Theory Tech.* **MTT-25**:1048–1054 (Dec. 1977).
17. R. S. Tahim, G. M. Hayashibara, and K. Chang, Design and performance of W-band broad-band integrated circuit mixers, *IEEE Trans. Microwave Theory Tech.* **MTT-31**:277–283 (March 1983).
18. J. D. Buchs and G. Begemann, Frequency conversion using harmonic mixers with resistive diodes, *IEEE J. Microwave Opt. Acoust.* **2**:71–76 (May 1978).

MICROWAVE OSCILLATORS

JONGHOON CHOI
AMIR MORTAZAWI
University of Michigan
Ann Arbor, Michigan

Oscillators are an integral part of receiving and transmitting systems used for communication, radar, and other applications. Any oscillator circuit consists of an active device and a resonant circuit that determines the frequency of oscillation. The active device can be either a two-terminal negative-resistance device such as Gunn diode, IMPATT (impact avalanche transit time) diode, resonant tunneling diode (RTD), and so on, or a transistor with appropriate feedback to cause instability. In general, an oscillator can operate at a fixed frequency, or its frequency of operation can be tunable. The frequency tuning can be achieved either mechanically or electronically. An oscillator is usually characterized by its frequency of operation, output power, noise, long-term frequency stability, and DC-to-RF efficiency.

1. MODELING OF MICROWAVE OSCILLATORS

An oscillator consists of linear circuits and active devices, and its operation relies on the nonlinear behavior of the active devices. In order to accurately characterize an oscillator, it has to be analyzed using linear and nonlinear circuit analysis techniques. An oscillator can be analyzed using either the feedback model or the negative-resistance model. These two analysis models are identical; however, the negative-resistance model is the most commonly used approach in the design of microwave oscillators. The popularity of the negative-resistance model is due to its simplicity and the fact that it can be related to device and

circuit reflection coefficients since they can be measured accurately at microwave frequencies. In the negative-resistance model, the oscillator is divided into two parts, the active device and the embedding passive circuit. In a simplified oscillator analysis, the active device is assumed to operate under small-signal conditions. This type of analysis can provide some information about startup conditions for oscillation and predict the approximate frequency of oscillation. In order to accurately determine the oscillation frequency, output power, stability, and spectral purity of an oscillator, large-signal analysis of the oscillator circuit must be performed. Usually simplified large-signal models for active devices can provide valuable insight into the operation of oscillators.

1.1. Oscillator Design Using One-Port Negative-Resistance Devices

Figure 1 shows the simplified block diagram of an one port oscillator circuit. The small-signal impedance of the negative-resistance device and the embedding circuit impedance can be denoted as $Z_d = -R_d + jX_d$ and $Z_c = R_c + jX_c$. For a series-resonant circuit, assuming that current I is flowing through the circuit, we obtain

$$I[Z_d + Z_c] = 0 \quad (1)$$

which results in

$$Z_d + Z_c = 0 \quad (2)$$

The startup conditions for oscillation for a series resonant circuit are given as follows:

$$-R_d + R_c < 0 \quad (3)$$

$$X_d + X_c = 0 \quad (4)$$

This means that the magnitude of the device negative resistance must be larger than the overall circuit losses in order for oscillation to build up. The startup of oscillation is initiated either from noise present in the circuit or from

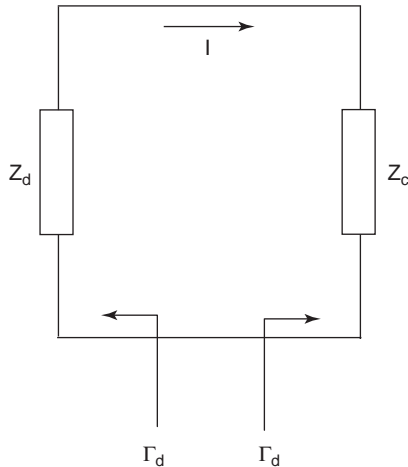


Figure 1. Simplified block diagram of a one-port oscillator.

transient introduced during power turnon. As the oscillation amplitude builds up, the device enters into its non-linear region, where the device negative resistance drops and eventually becomes equal to the overall circuit losses. At this point the oscillation amplitude reaches its steady state.

For a parallel-resonant circuit, the steady-state oscillation condition is given in terms of active device and circuit admittances Y_d and Y_c , respectively as

$$Y_d + Y_c = 0 \quad (5)$$

The startup conditions for a parallel-resonant circuit are given by

$$-G_d + G_c < 0 \quad (6)$$

$$B_d + B_c = 0 \quad (7)$$

where $Y_d = -G_d + jB_d$ and $Y_c = G_c + jB_c$.

The steady-state oscillation condition can be written in terms of device and circuit reflection coefficients Γ_d and Γ_c as

$$\Gamma_d \cdot \Gamma_c = 1 \quad (8)$$

Voltage-controlled devices such as the Gunn diode should be connected to a parallel-resonant circuit, and the appropriate startup conditions for oscillation should be satisfied. Current-controlled devices such as IMPATT diode are placed in a series-resonant circuit for proper operation. In this case startup conditions for oscillation for a series-resonant circuit should be met. The startup oscillation frequency can be different than the steady-state oscillation frequency. This is because the large-signal device impedance is a function of the voltage (or current) amplitude across (through) the device. As the oscillation amplitude builds up, the device impedance varies until it reaches its final value. However, for high- Q circuits, the steady-state oscillation frequencies are very close to the startup frequency of oscillation. It should also be mentioned that the startup condition for oscillation is a necessary but not sufficient condition for having an unstable circuit [1–3]. (Nyquist or root locus analysis can always be used to determine the circuit instability.)

1.2. Oscillator Design Using Two-Port Devices

The block diagram of a two-port oscillator circuit is shown in Fig. 2. Most microwave transistors are conditionally stable within a limited range of frequencies. By plotting the input and output stability circles on a Smith chart, one can graphically determine the range of impedances for unstable operation. When designing microwave oscillators, the input port of the two-terminal device can be terminated with a purely reactive load that lies in the unstable region of the Smith chart. This is shown in Fig. 2 as Z_T . This will result in the output impedance (Z_{out}) looking into the device to render negative real parts ($|\Gamma_{out}| > 1$). The load impedance Z_L must be chosen to satisfy the startup conditions for oscillation. In practice,

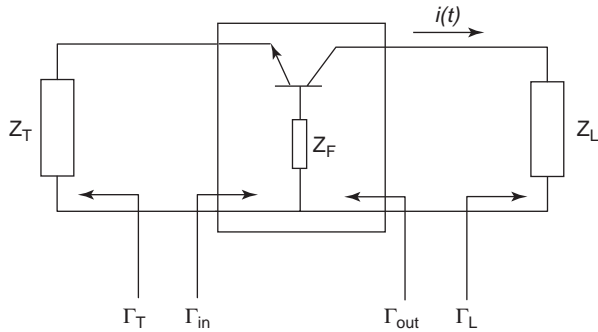


Figure 2. Block diagram of a transistor oscillator.

the load impedance is determined by Eqs. (9) and (10) in order to achieve maximum power

$$X_L(\omega_o) = -X_{out}(\omega_o) \tag{9}$$

$$R_L(\omega_o) = \frac{|R_{out}(A, \omega_o)|_{A=0}}{3} \tag{10}$$

where A is the amplitude of $i(t)$, ω_o is the oscillation frequency, R_L and X_L are the real and imaginary parts of the load impedance (Z_L), and R_{out} and X_{out} are the real and imaginary parts of the output impedance (Z_{out}).

When a microwave oscillator is designed according to this procedure, the measured oscillation frequency will usually deviate from the design frequency by several percentages. This is because the design procedure is based on the small-signal, linear S parameters that do not consider the fact that R_{out} and X_{out} are functions of the oscillation amplitude.

The steady-state oscillation condition for a two-port oscillator in terms of the transistor's S -parameter load and

source reflection coefficients is given by

$$\frac{1}{\Gamma_T} = S_{11} + \frac{S_{12}S_{21}\Gamma_L}{1 - S_{22}\Gamma_L} \tag{11}$$

$$\frac{1}{\Gamma_L} = S_{22} + \frac{S_{12}S_{21}\Gamma_T}{1 - S_{11}\Gamma_T} \tag{12}$$

If the oscillation conditions are satisfied at one port, they are satisfied at all other ports [4,5]. If the oscillator is stable at the desired frequency of operation, it can be made unstable by using series (Z_F in Fig. 2) or shunt feedback. There are a total of six configurations: three for series feedback and three for shunt feedback as shown in Fig. 3 [6].

1.3. Oscillator Design Using Large-Signal Analysis

The large-signal design approach, called *device-line measurement*, can be applied to one-port oscillator design in order to achieve better accuracy compared to the oscillator design using small-signal S parameter [7]. For the large-signal oscillator design, a nonlinear model for the active device and a nonlinear simulation technique such as the harmonic balance are needed to predict the large-signal S parameters and the output power.

Starting with a two-port network (Fig. 2), one first terminates one of the ports with a proper impedance (Z_T) such that the impedance of the resulting one-port network (Z_{out}) has a negative real part, or equivalently, the magnitude of its reflection coefficient (Γ_{out}) is larger than unity. A test source is then connected to the aforementioned one-port negative-resistance network, as shown in Fig. 4, to determine its large-signal reflection coefficient. It should be mentioned that the device-line measurement system requires the internal impedance (Z_s) to prevent the measurement circuit from oscillating. Therefore, R_s , which has a larger value than the magnitude of the real

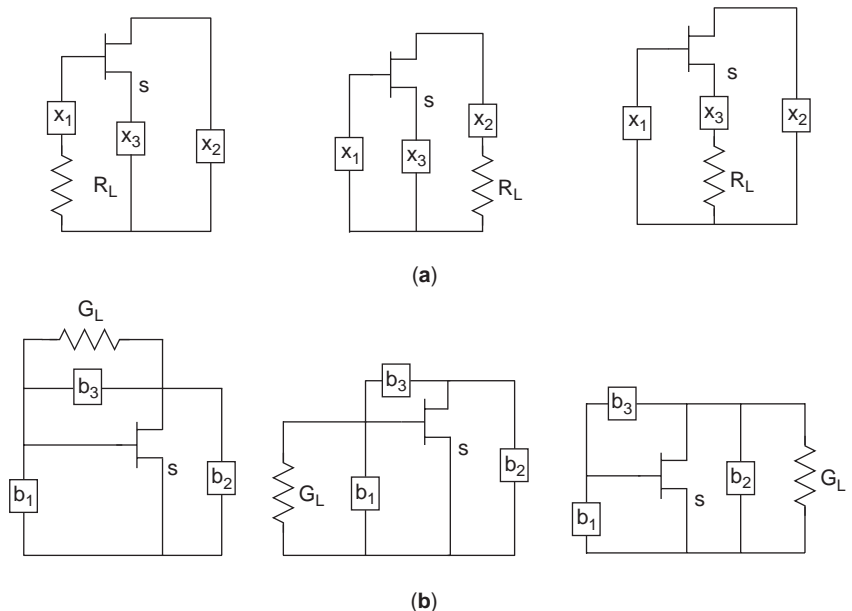


Figure 3. Circuit configurations for (a) series feedback oscillators and (b) shunt feedback oscillators.

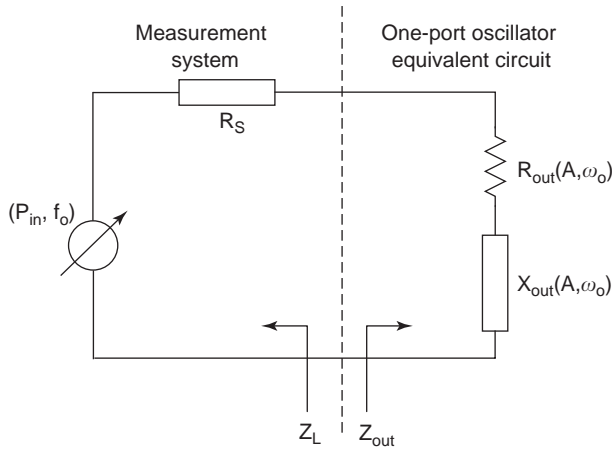


Figure 4. Device-line measurement setup.

part of the output impedance ($|R_{out}|$), should be inserted next to the test source. By varying the amplitude of the RF signal at the design frequency, the large-signal dependence of Γ_{out} can be measured. Since $|\Gamma_{out}|$ is larger than unity, due to the negative resistance $R_{out}(A, \omega_o)$, the added power (P_{add}), as given in the following equation, is therefore positive

$$P_{add} = P_{av}(|\Gamma_{out}|^2 - 1) \quad (13)$$

where P_{av} is the available power of the source.

When the load impedance (Z_L) is selected to satisfy the steady-state oscillation condition, specifically, $\Gamma_{out}\Gamma_L = 1$, the designed oscillator can generate the same power as the added power (P_{add}) that the one-port negative resistance device generated as determined by Eq. (13). On the basis of the large-signal output reflection coefficient, the load impedance Z_L is determined as follows:

$$X_L(\omega_o) = -X_{out}(A_o, \omega_o) \quad (14)$$

$$R_L(\omega_o) = -R_{out}(A_o, \omega_o) \quad (15)$$

The device-line measurement technique can be used to maximize the output power of an oscillator. By varying RF source power at the design frequency, the point where the added power is maximized can be found. At this power level, one can measure the large-signal output reflection coefficient and design the load impedance on the basis of Eqs. (14) and (15). Furthermore, a more accurate estimate of oscillator frequency is obtained using this technique.

1.4. Injection Locking of Microwave Oscillators

Injection locking of a microwave oscillator is accomplished by applying a small signal to the free-running microwave oscillator, provided the frequency of the small signal is close enough to the free-running frequency of the oscillator. Through injection-locking a free-running microwave oscillator to a low-noise low-power source, the free-running frequency is locked to the injection signal frequency, thereby improving its frequency stability and phase noise. It has been shown that the phase noise of the

injection-locked oscillator is reduced to that of the external locking source near the carrier frequency; however, it approaches that of the free-running oscillator far from the carrier frequency [12].

The effect of the injection signal can be studied by adding a small current source in parallel with the equivalent circuit for a free-running microwave oscillator as shown in Fig. 5. Suppose that the injected and the free-running oscillator signals are represented by $i_i(t) = I_i(t) \exp j[\omega_i t + \phi_i(t)]$ and $v(t) = V(t) \exp j[\omega_o t + \phi(t)]$, respectively.

The circuit equation for this injection-locked oscillator is given by

$$C \frac{dv(t)}{dt} + [G - G_d]v(t) + \frac{1}{L} \int v(t) dt = i_i(t) \quad (16)$$

where $-G_d$ is the negative conductance of a nonlinear active device. Using the assumption that the amplitudes of $v(t)$ and $i_i(t)$ are very slowly time-varying signals, and dividing the real and imaginary parts of Eq. (16), the amplitude and phase equations for the injection-locked oscillator can be obtained by

$$\frac{dV(t)}{dt} + \frac{G - G_d}{2C} V(t) = \frac{1}{2C} I_i(t) \cos[\phi(t) - \phi_i(t)] \quad (17)$$

$$\frac{d\phi(t)}{dt} + \omega_i - \omega_o = -\frac{1}{2C} \frac{I_i(t)}{V(t)} \sin[\phi(t) - \phi_i(t)] \quad (18)$$

When this system reaches the steady state, the first term in Eq. (17) with the time derivative goes to zero and can be further simplified:

$$G - G_d = \frac{I_i(t)}{V(t)} \cos[\phi(t) - \phi_i(t)] \quad (19)$$

Assuming that the device negative conductance is not a function of frequency, the left side of Eq. (19) goes to zero because $G - G_d \approx 0$. Also, the right side of Eq. (19) is close to zero because the amplitude of the injected signal is negligibly small compared to the amplitude of the free-running oscillator ($|I_i(t)| \ll |V(t)|$). Ultimately, the left and right sides of the amplitude equation [Eq. (17)] become balanced in the steady state. On the other hand, the phase equation [Eq. (18)] has a more significant meaning in the injection-locking process. In the steady-state

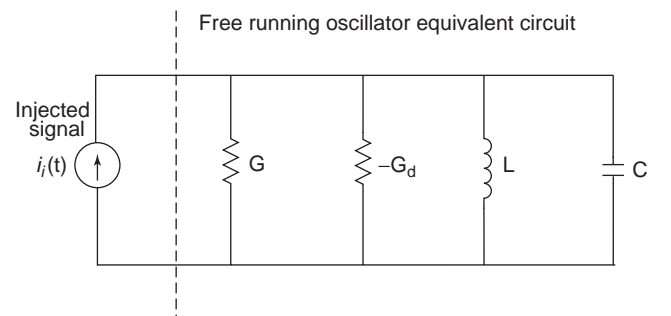


Figure 5. Equivalent circuit of an injection-locked oscillator.

condition, Eq. (18) can be simplified to

$$\omega_i - \omega_o = \frac{\omega_o I_i(t)}{2Q I(t)} \sin[\phi(t) - \phi_i(t)] = -\omega_m \sin \phi \quad (20)$$

where Q is the external quality factor ($Q = \omega_o C/G$).

The following condition must be satisfied for the phase difference ϕ in Eq. (20) to be real:

$$-\omega_m \leq \omega_i - \omega_o \leq \omega_m \quad (21)$$

This condition indicates that when the injection signal frequency remains within the locking range, the steady-state solution for the phase equation can be obtained and the injection-locking behavior is realized.

The locking bandwidth can be expressed as

$$\Delta\omega_{\text{lock}} = 2\omega_m = \frac{\omega_o}{2Q} \sqrt{\frac{P_i}{P_o}} \quad (22)$$

where P_i and P_o are the injection signal power and the free-running oscillator output power, respectively. Equation (22) shows that one can decrease the oscillator circuit Q and increase the injection signal power in order to increase the locking bandwidth.

Through injection locking, the oscillator's free-running frequency is locked to the injection frequency and the phase difference between the free-running signal and the injection signal is determined by Eq. (20).

2. NOISE IN OSCILLATORS

The spectral purity of an oscillator is degraded by the random fluctuations of its amplitude, frequency, and phase. Noise generated in the active device and passive components modulates the signal produced by the oscillator. The sources of random sideband noise in an oscillator include thermal noise, shot noise, and flicker ($1/f$) noise. These noise sources result in amplitude and phase noise in oscillators. In general, the output of a noisy oscillator can be represented by

$$v(t) = (A + a(t)) \cdot \cos(\omega_o t + \phi(t)) \quad (23)$$

where A and ω_o are deterministic amplitude and frequency and $a(t)$ and $\phi(t)$ are random amplitude and phase noise, respectively. In practice, amplitude noise can be dramatically attenuated by an amplitude-limiting mechanism of oscillators. In case an oscillator has large amplitude noise, amplitude noise can be easily eliminated by placing a limiter at the output of the oscillator. Therefore phase noise plays a dominant role in the spectral purity performance of oscillators. As shown in Fig. 6b, the existence of phase noise broadens the frequency spectrum of a noisy oscillator output around the carrier frequency, whereas the frequency spectrum of an ideal oscillator output is represented by a delta function (Fig. 6a).

Phase noise of the oscillators in radio receivers and transmitters limits the performance of the communication system. Phase noise of the local oscillator in a radio receiver downconverts the adjacent channels into intermediate frequency (IF), thereby limiting the receiver's immunity to nearby interference. In a radio transmitter phase noise can overwhelm the nearby weak channels.

Normally, phase noise is measured as the ratio of noise power (P_n) in one sideband contained in a specified bandwidth (B) at an offset frequency ($\Delta\omega$) compared to the carrier output power, referred to here as P_s . Such a power ratio is usually expressed as decibels below carrier per hertz (dBc/Hz).

To explain the behavior of phase noise, several models for phase noise can be considered. The most general model for phase noise in oscillators was described by Leeson [13]. This model is constructed using an oscillator consisting of a feedback amplifier and a resonator, under the assumption that the oscillator is a linear and time-invariant (LTI) system. When we consider only white noises such as thermal and shot noise, the noises decrease with frequency offset as a result of the filtering effect of the resonator in the oscillator. Therefore, phase noise is given by

$$L(\Delta\omega) = 10 \log \left[\frac{2kT}{P_s} \left(\frac{\omega_o}{2Q_L \Delta\omega} \right)^2 \right] \quad (24)$$

where k is Boltzmann's constant, T is the absolute temperature, and Q_L is the loaded quality factor of the resonator. However, since flicker ($1/f$) noise in active devices is upconverted to the oscillation frequency by means of

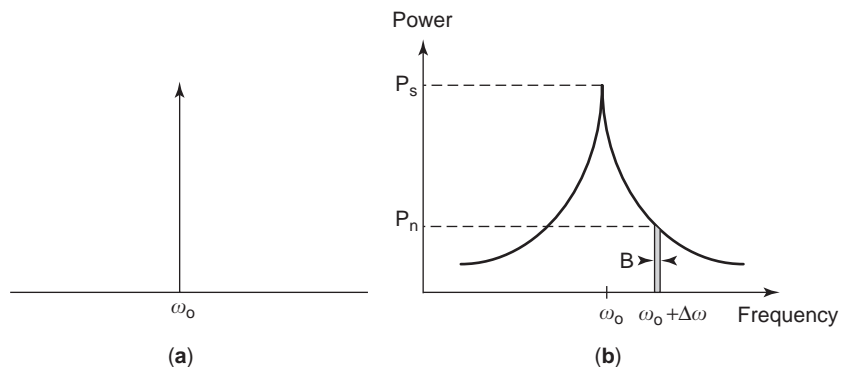


Figure 6. Output spectrum in (a) noiseless and (b) noisy oscillators.

nonlinear modulation mechanism in practical oscillators, Eq. (24) is modified into the final form of Leeson's formula as

$$L(\Delta\omega) = 10 \log \left[\frac{2kTF}{P_s} \left\{ 1 + \left(\frac{\omega_o}{2Q_L\Delta\omega} \right)^2 \right\} \left(1 + \frac{\Delta\omega_{1/f^3}}{|\Delta\omega|} \right) \right] \quad (25)$$

where F is the excess noise measure (empirical constant) and $\Delta\omega_{1/f^3}$ is the corner frequency between $1/f^2$ and $1/f^3$ regions. Leeson's formula [Eq. (25)] can be graphically depicted as seen in Fig. 7. The effect of flicker noise is dominant near the carrier frequency, leading to the decrease of phase noise with offset frequency at 9 dB/octave up to the $1/f^3$ corner frequency. From the $1/f^3$ corner frequency to $\omega_o/2Q_L$, phase noise shows a decreasing slope of 6 dB/octave. Also, Leeson's model suggests the following methods to reduce phase noise of an oscillator:

1. Use a high- Q resonator because phase noise is inversely proportional to Q^2 .
2. Increase the signal output power.
3. Select an active device with low flicker noise and low noise figure.

Even though Leeson's LTI model provides valuable insights into microwave oscillator designs in an engineering perspective, it cannot explain several phase noise phenomena such as flicker noise upconversion. To overcome this limitation, many approaches based on linear time-varying (LTV) models have been investigated. More recently a LTV model in conjunction with the concept of impulse-sensitive function based on the fact that phase fluctuation varies according to where the impulse noise is injected into a free-running oscillator has been introduced [14]. For microwave oscillators with distributed components, a perturbation theory for phase noise behavior was proposed, based on the solution of the Langevin equations describing the stochastic behavior [15]. A unifying theory for phase noise derived an exact nonlinear equation for oscillators in the presence of deterministic and random perturbations, which led to a general mathematical solution for phase noise representation [16].

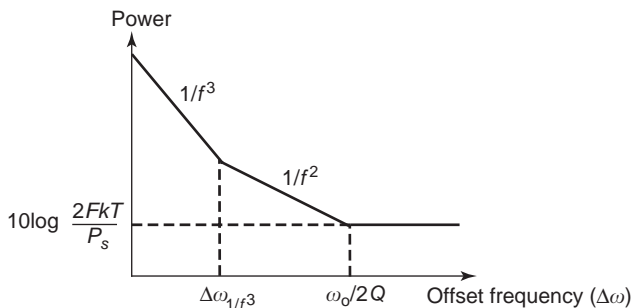


Figure 7. Phase noise spectrum of Leeson's model.

3. OSCILLATOR TYPES

3.1. Gunn Oscillators

The Gunn diode [17] is a negative-resistance device that operates on the basis of transfer of electrons between two valleys in the conduction band of a semiconductor material. For this reason it is also referred to as a *transferred-electron device* (TED). A Gunn device may be described as a bulk of GaAs that exhibits negative resistance when DC bias is applied. In this respect the Gunn diode is not precisely a diode since it does not contain any junctions. Gunn diodes are capable of producing from a few milliwatts to a few watts with efficiencies up to 15–20%. The operation frequency of Gunn diodes reaches 100 GHz. Gunn diodes have a good phase noise performance. The equivalent of the Gunn diode chip can be described by a parallel RC circuit where the value of R is negative. Gunn diodes exhibit a negative resistance at low frequencies as well as RF frequencies. Precautions must be taken in order to avoid parasitic oscillations due to resonances introduced by the bias circuit. This can be achieved by rendering the bias circuit lossy at low frequencies in order to stabilize it.

The Gunn diode oscillator can be made in waveguide, coaxial, and microstrip lines. The most widely used Gunn oscillator circuit is an iris-coupled waveguide cavity oscillator. This circuit has high stability and low phase noise because of its high Q . Furthermore one can mechanically or electronically tune the oscillation frequency. Figure 8 shows the iris-coupled waveguide cavity Gunn oscillator. The resonance frequency of the waveguide cavity is determined by the distance between the iris to the effective back wall and should be a half-wavelength. The effective back wall is in between the diode's post and the physical back wall. If the diode's post is near the cavity's sidewall, then the effective back wall is very close to the physical back wall. By adjusting the diameter and the position of the diode's post with respect to sidewalls, optimum impedance match to the cavity resonator can be achieved. In order to mechanically tune the frequency of the cavity, a dielectric rod can be inserted into the cavity resonator. The electronic tuning of oscillation frequency can be accomplished by mounting a varactor diode inside the cavity using another post. By adjusting the varactor bias, the

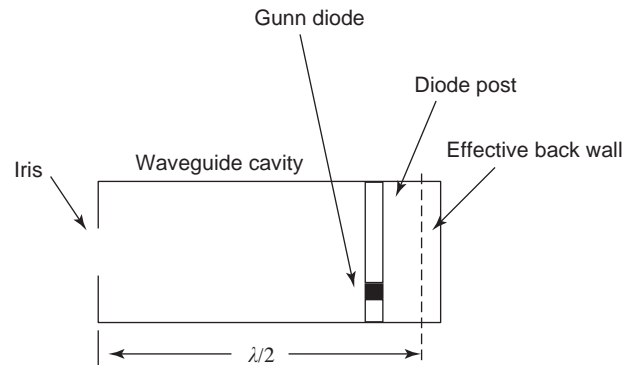


Figure 8. An iris-coupled waveguide cavity Gunn diode oscillator.

oscillation frequency is tuned. This is a simple method for frequency-modulating such an oscillator.

3.2. IMPATT Oscillators

The term *IMPATT* is an acronym for *impact avalanche transit time*. IMPATT diode is used in the design of solid-state microwave and millimeter-wave oscillators with an operating range of frequencies from several gigahertz to >200 GHz. The IMPATT diode exhibits negative resistance due to 180° phase delay of the current with respect to the voltage. This phase delay is due to (1) the finite delay between the applied RF voltage and the current due to avalanche breakdown and (2) the subsequent transit of carriers through a drift region. One version of IMPATT operation was first proposed by Read in 1958 [18]. The first demonstration of an IMPATT oscillator was reported by DeLoach [19]. The two most commonly used versions of IMPATT diodes are the single-drift region and double-drift region. IMPATT diodes produce from 0.5–4 W with efficiencies usually greater than 10% (≤ 30 GHz) and 4% (≤ 100 GHz). IMPATT diodes differ from Gunn diodes in several respects: (1) the output powers of IMPATTs are up to 10 times higher than Gunn diodes, (2) IMPATT diodes are more efficient than Gunn diodes, (3) the operating voltage for the IMPATT is higher than that of the Gunn diode (20–100 V for an X-band IMPATT as compared to ≤ 10 V for an X-band Gunn), (4) IMPATT diodes are noisier than Gunn diodes, and (5) the circuit design using IMPATT diodes is more difficult because their negative resistance is about one order of magnitude lower than that of Gunn diodes.

The IMPATT diode is a current-controlled device and therefore requires a current source for bias. The IMPATT diode equivalent circuit consists of a series *RC* circuit, where *R* is a negative number. Since IMPATT diode is a current-controlled device, it is usually placed in a series-resonant circuit for stable oscillations. Usually a radial line (Fig. 9a) or a coaxial line (Fig. 9b) quarter-wave transformer is used to match the low negative resistance of the IMPATT to a waveguide cavity.

3.3. Dielectric Resonator Oscillators

Microstrip resonators have a limited *Q* on the order of 100. In order to reduce the phase noise of oscillators, it is necessary to increase the resonant circuit's *Q*. A low-cost technique to increase the resonator's *Q* is to couple a dielectric resonator to a microstrip circuit. Typical dielectric resonators have a cylindrical geometry with a dielectric constant between 10 and 100. The $TE_{01\delta}$ of the cylindrical dielectric resonator can be coupled to a microstrip line by placing it on top of the substrate close to the microstrip line. The distance between the resonator and the microstrip line determines the coupling factor. The *Q* of dielectric resonators is on the order of several thousand. The resonance frequency of a dielectric resonator can be adjusted by placing a movable metal plate on top of the dielectric resonator. Figure 10 shows different configurations of dielectric resonator oscillators.

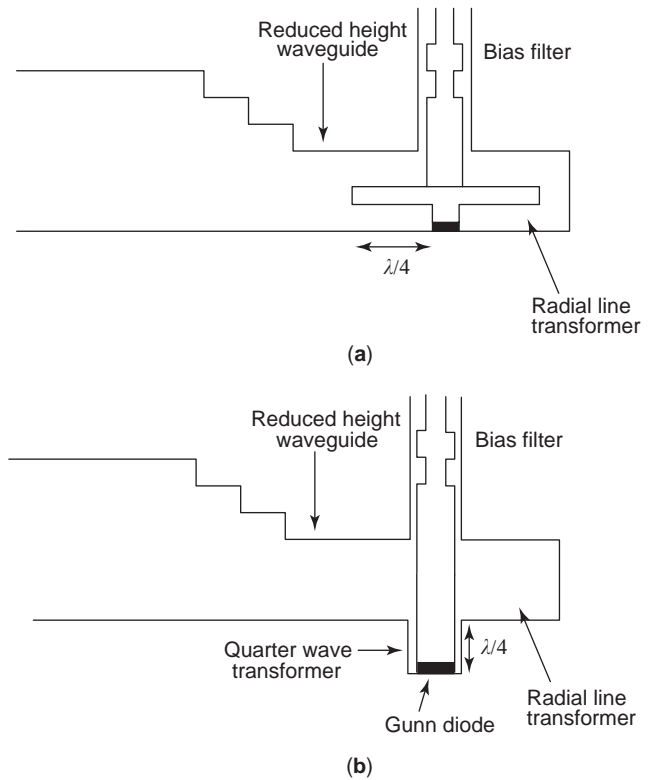


Figure 9. IMPATT diode oscillators in waveguide using (a) a radial-line transformer and (b) a coaxial-line transformer.

3.4. Electronically Tunable Oscillators

In order to construct electronically tunable oscillators, either a varactor diode is connected to the resonator, or an yttrium iron garnet (YIG) sphere is used to construct the

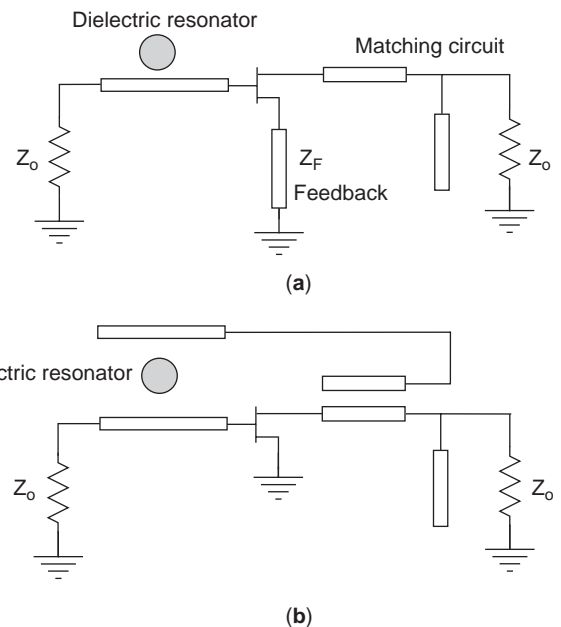


Figure 10. Dielectric resonator oscillator circuits using (a) series feedback and (b) shunt feedback.

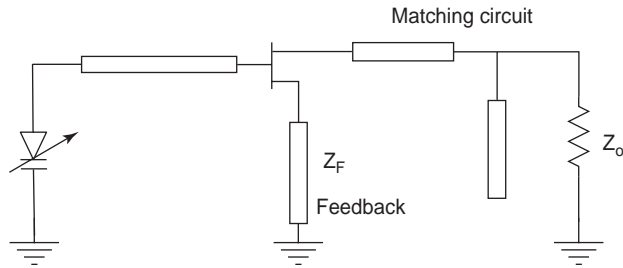


Figure 11. A varactor-tuned oscillator.

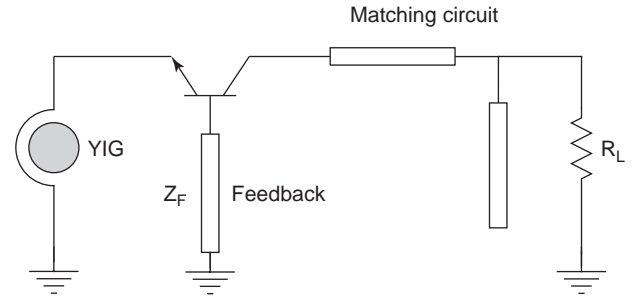


Figure 12. Diagram of a YIG-tuned oscillator.

resonator. In varactor-tuned oscillators, by changing the reverse bias voltage across the varactor, the varactor capacitance and thereby the resonance frequency can be tuned. The tuning range is dependent on the varactor's capacitance ratio C_{\max}/C_{\min} . This ratio is largest for hyperabrupt varactor diodes. The frequency tuning limit of a varactor tuned oscillator is determined by [4].

$$\frac{\omega_{\max}}{\omega_{\min}} = \sqrt{\frac{C_{\max}}{C_{\min}}} \quad (26)$$

A typical varactor-tuned oscillator circuit is shown in Fig. 11.

Another technique for construction of an electronically tunable oscillator is to make the resonator by using a magnetic material. Single-crystal yttrium iron garnet is a magnetic material that resonates at microwave frequencies when subjected to a DC magnetic field. The resonance frequency is directly proportional to the applied magnetic field; hence a linear frequency tuning over wideband can be achieved by adjusting its biasing DC magnetic field. The YIG resonator consists of a RF coupling loop, an electromagnet, and a YIG sphere. YIG is a low-loss material, and YIG resonators can provide Q factors as high as several thousand. YIG tuned oscillators are commonly used in sweep generators. The frequency tuning range of the YIG oscillators is determined by the bandwidth over which the active device provides negative resistance. Figure 12 shows a diagram of a YIG tuned oscillator. YIG tuned oscillators with oscillation frequencies as high as 60 GHz have been reported [20].

3.5. MMIC Oscillators

Because of their low cost, improved reproducibility, and small size, many oscillators have been implemented using

monolithic microwave integrated circuit (MMIC) technique. Table 1 compares the different types of RF/microwave oscillators reported in more recently published scientific papers in terms of active device, resonator type, operation frequency, output power, and phase noise. In the design of MMIC oscillators, important figures of merit are phase noise, DC-to-RF efficiency, and the tuning range for phase-locked loop applications. To satisfy these goals, the choice of active devices is crucial. Each device has different characteristics such as the $1/f$ corner frequency, forward gain, and cutoff frequency (f_T), which can produce oscillators with varying degrees of performance.

In most cases, practical MMIC oscillators have been implemented with GaAs MESFET or silicon bipolar transistor. The GaAs MESFET can operate at high frequencies (up to millimeter-wave frequency) because of its high cutoff frequency. In addition, it has higher gain and higher output power than does the silicon bipolar transistor. However, the high $1/f$ noise corner frequency of the GaAs MESFET (around 10–100 MHz) degrades the noise performance of oscillators significantly. Therefore, many designs for low-noise oscillators are based on the silicon bipolar transistor because of its low $1/f$ noise corner.

Since the high-electron-mobility transistor (HEMT) has the advantages of high electron mobility and high f_T , it presents high power capability at high frequencies and low-noise characteristics. Therefore, HEMT MMIC oscillators show good performance at extremely high frequencies of 70–200 GHz.

The heterojunction bipolar transistor (HBT) is a bipolar transistor with a structure similar to that of a silicon bipolar transistor; however, HBT consists of different semiconductor materials, while the BJT contains only silicon. The heterojunction structure enables the HBT to operate at higher frequencies than the silicon BJT. In addition, the

Table 1. Recently Reported Integrated Microwave Oscillators

Year [Ref.]	Active Device	Resonator Type	Frequency (GHz)	Output Power (dBm)	Phase Noise (dBc/Hz)
2000 32	SiGe HBT	LC	4.63–4.90	–13	–100 at 100 kHz
2000 32	Si BJT	LC	5.59–5.94	–9	–90 at 100 kHz
2000 33	GaAs MESFET	LC	11.25–11.8	11.5	–91 at 100 kHz
2000 34	CMOS	LC	1.1–1.45	4	–119 at 600 kHz
2002 35	SiGe HBT	Sapphire resonator	4.85	–	–133 at 1 kHz
2002 36	SiGe BJT	LC	43.6–47.3	5.6	–108 at 1 MHz
2003 37	CMOS	LC	5.86–6.02	–4	–110 at 1 MHz
2004 38	InGaP-GaAs HBT	LC	12.71–13.54	0	–113.8 at 1 MHz

HBT presents intrinsic characteristics of low $1/f$ noise corner, which makes it a good candidate for low-noise oscillators at microwave frequencies. Additionally, the capability of generating high negative resistances over a wide frequency range makes this device suitable for the VCO design. Currently, SiGe HBTs have been actively researched because of reduced fabrication costs, higher integration levels, and the compatibility with lower frequency circuits on the same chip.

The advances in CMOS processing technology begin to challenge GaAs devices and bipolar transistors in commercial circuits with the benefit of cost-effective mass production. Reducing the minimum channel length leads to the increase in f_T , which makes CMOS an attractive candidate for microwave oscillators. However, the major challenges in the oscillator design using silicon technology including silicon BJT, SiGe HBTs, and CMOS, lie in the difficulty in implementing good passive elements, such as on-chip inductors and high- Q resonators. This is due to the fact that silicon substrates exhibit frequency-dependent losses. Therefore, the development of high- Q on-chip inductors is one of the active research topics in the oscillator design. Many topologies such as the optimized one-layer inductor, the series-parallel stacked inductor, the differential inductor, and the 3D micromachined solenoid inductor have been proposed in order to increase circuit Q .

BIBLIOGRAPHY

- N. M. Nguyen and R. G. Meyer, Start-up and frequency stability in high-frequency oscillators, *IEEE J. Solid-State Circ.* **27**(5):810–8120 (May 1992).
- R. W. Jackson, Criteria for onset of oscillations in microwave circuits, *IEEE Trans. Microwave Theory Tech.* **40**(3):566–569 (March 1992).
- R. D. Martinez and R. C. Compton, A general approach for the S-parameter design of oscillators with 1 and 2-port devices, *IEEE Trans. Microwave Theory Tech.* **40**(3): 569–574 (March 1992).
- I. Bahl and P. Bhartia, *Microwave Solid State Circuit Design*, Wiley-Interscience, New York, 1988, Chap. 9.
- G. D. Vandelin, A. M. Pavio, and U. L. Rohde, *Microwave Circuit Design Using Linear and Nonlinear Techniques*, Wiley-Interscience, New York, 1990, Chap. 6.
- K. L. Kotzebue and W. J. Parrish, The use of large signal S-parameters in microwave oscillator design, *Proc. Int. IEEE Microwave Symp.*, 1975.
- W. Wagner, Oscillator design by device line measurement, *Microwave J.* (Feb. 1979).
- S. A. Maas, *Nonlinear Microwave and RF Circuits*, 2nd ed., Artech House, Norwood, MA, 2003.
- G. Gonzalez, *Microwave Transistor Amplifiers: Analysis and Design*, Englewood Cliffs, NJ, Prentice-Hall, 1997.
- A. E. Siegman, *Lasers*, Univ. Scientific Books, Mill Valley, CA, 1986.
- R. A. York and T. Itoh, Injection- and phase-locking techniques for beam control, *IEEE Trans. Microwave Theory Tech.* **46**:1920–1929 (Nov. 1998).
- H. Chang, X. Cao, M. J. Vaughan, U. K. Mishra, and R. A. York, Phase noise in externally injection-locked oscillator arrays, *IEEE Trans. Microwave Theory Tech.* **45**:2035–2042 (Nov. 1997).
- D. B. Leeson, A simple model of feedback oscillator noise spectrum, *Proc. IEEE* **54**(2):329 (Feb. 1966).
- A. Hajimiri and T. H. Lee, A general theory of phase noise in electrical oscillators, *IEEE J. Solid-State Circ.* **33**:179–194 (Feb. 1998).
- F. X. Kaertner, Determination of the correlation spectrum of oscillators with low noise, *IEEE Trans. Microwave Theory Tech.* **37**:90–101 (Jan. 1989).
- A. Demir, A. Mehrota, and J. Roychowdhury, Phase noise in oscillators: A unifying theory and numerical methods for characterization, *IEEE Trans. Circ. Syst.* **47**:655–674 (May 2000).
- J. B. Gunn, Microwave oscillation in III–V semiconductors, *Solid State Commun.* **1**:88 (1963).
- W. T. Read, A proposed high efficiency negative resistance diode, *Bell Syst. Tech. J.* **37**:401 (1958).
- B. C. DeLoach, Jr., The IMPATT story, *IEEE Trans. Electron. Devices* **ED-23**:657 (1976).
- D. Zenous et al., GaAs FET YIG oscillator tunes from 26 to 40 GHz, *Microwaves RF* **22**:120–139 (Oct. 1983).
- S. Yngvesson, *Microwave Semiconductor Devices*, Kluwer Academic Publishers, 1991, Chap. 6.
- K. K. Kurokawa, Some basic characteristics of broad band negative resistance oscillator circuit, *Bell Syst. Tech. J.* **48**(6):1937–1955 (July 1969).
- M. E. Hines, J. R. Collinet, and J. G. Ondria, FM noise reduction of an phase locked oscillator, *IEEE Trans. Microwave Theory Tech.* **16**(9):738–742 (Sept. 1968).
- K. Kurokawa, *An Introduction to the Theory of Microwave Circuits*, Academic Press, New York, 1969, Chap. 9.
- F. Schwiertz and J. J. Liou, *Modern Microwave Transistors—Theory, Design, and Performance*, Wiley, Hoboken, NJ, 2003.
- I. D. Robertson and S. Lucyszyn, *RFIC and MMIC Design and Technology*, IEE, London, 2001.
- K. Chang, *Microwave Solid-State Circuits and Applications*, Wiley, New York, 1994.
- E. C. Niehenke, R. A. Pucel, and I. J. Bahl, Microwave and millimeter-wave integrated circuits, *IEEE Trans. Microwave Theory Tech.* **50**(3):846–857 (2002).
- L. M. Burns, Application for GaAs and silicon integrated circuits in next generation wireless communication systems, *IEEE Trans. Microwave Theory Tech.* **30**(10):1088–1095 (1995).
- R. Götzfried, F. Beisswanger, and S. Gerlach, Design of RF integrated circuits using SiGe bipolar technology, *IEEE J. Solid-State Circ.* **33**(9):1417–1422 (1998).
- V. Radisic et al., 80 GHz MMIC HEMT VCO, *IEEE Microwave Wireless Compon. Lett.* **11**(8):325–327 (2001).
- H. Jacobsson et al., Low-phase-noise low-power IC VCOs for 5-8-GHz wireless applications, *IEEE Trans. Microwave Theory Tech.* **48**(12):2533–2539 (2000).
- C. H. Lee, S. Han, B. Matinpour, and J. Laskar, A low phase noise X-band MMIC GaAs MESFET VCO, *IEEE Microwave Guided Wave Lett.* **10**(8):325–327 (2000).
- F. Svelto, S. Deantoni, and R. Castello, A 1.3 GHz low-phase noise fully tunable CMOS LC VCO, *IEEE J. Solid-State Circ.* **35**(3):356–361 (2000).
- O. Llopis, G. Cibiel, Y. Kersale, M. Regis, M. Chaubet, and V. Giordano, Ultra low phase noise sapphire-SiGe HBT

- oscillator, *IEEE Microwave Wireless Compon. Lett.* **12**(5):157–159 (2002).
36. H. Li, H.-M. Rein, R. Kreienkamp, and W. Klein, 47 GHz VCO with low phase noise fabricated in a SiGe bipolar production technology, *IEEE Microwave Wireless Compon. Lett.* **12**(3):79–81 (2002).
37. Y. Chu and H. Chuang, A fully integrated 5.8 GHz U-NII Band 0.18- μm CMOS VCO, *IEEE Microwave Wireless Compon. Lett.* **13**(7):287–289 (2003).
38. D. Baek, S. Ko, J. Kim, D. Kim, and S. Hong, Ku-Band InGaP-GaAs HBT MMIC VCOs with balanced and differential topologies, *IEEE Trans. Microwave Theory Tech.* **52**(4):1353–1359 (2004).

MICROWAVE PARAMETRIC AMPLIFIERS

MAREK T. FABER
Warsaw University of
Technology
Warsaw, Poland

1. INTRODUCTION

It has been known since nineteenth century that a mechanical system or an electric circuit in which there is a parameter that varies periodically with time may oscillate under certain conditions. The first use of this periodic variation to amplification, frequency changing, or harmonic generation was investigated in the 1940s, but real progress in the parametric amplification dated from the development in the mid-1950s of semiconductor diodes in which the barrier capacitance could be modulated at microwave frequencies. Since then, there has been a continual and tremendous increase in the amount of theoretical and experimental work devoted to parametric amplifiers [1–11]. This is because of their ability to maintain a low level of noise that is inevitably introduced at each stage of analog signal processing. A typical microwave receiver of the early 1960s consisted of a silicon point-contact diode mixer followed by a vacuum-tube amplifier. The addition of a parametric amplifier (or *paramp*, as it was popularly called) ahead of the mixer gave an order of magnitude improvement in sensitivity of the receiver.

The question arose at that time as to why the parametric amplification allows noise levels lower than with the usual type of amplifier. To answer this fundamental question, it should be remembered that an amplifier consists of both passive elements and active energy sources and that the whole is terminated by two ports, one receiving the signal to be amplified and the other delivering the amplified signal. In the ordinary type of amplifier, the energy sources consist of DC sources that are incorporated into a network of passive elements that may be linear or nonlinear. The essential condition for such a system to act efficiently as an amplifier is the inclusion of a nonlinear and/or electrically controlled resistive element to provide an energy transfer from the source to the signal [11].

Unfortunately, its operation is accompanied by a background noise that is an inevitable result of its dissipative character. In order to obtain an amplifier with a low noise level, the energy must no longer be supplied to the network directly from DC sources, and so other methods of energy transfer must be envisioned. One of these methods is to employ AC sources. It has been shown [1,4,6,8] that if a nonlinear reactance is incorporated in the network, a system of this kind may be used efficiently as an amplifier. In such a parametric amplifier a nonlinear reactance does not generate any noise, provided it is free from loss.

The first practical realization of the principle of transferring energy from a “pump” source at a high frequency to a signal at a lower frequency was based on a nonlinear inductance [2,3,7], with the nonlinearity depending on the properties of ferrite materials. Unfortunately, large levels of pump power were required to provide the necessary nonlinearity. With pump levels in the kilowatt region and relatively high loss in the reactance, this type of amplifiers had only very limited applications.

Capacitive parametric amplifiers depend on the nonlinear capacitance–voltage characteristic of semiconductor diodes. The diodes, which are specially made for the purpose, are called *varactor diodes* or more simply *varactors*. When used in a parametric amplifier, the varactor junction is biased in the reverse direction to prevent current flow across the junction and thus suppress “shot” noise associated with the current, leaving only thermal noise present in series resistance of a real diode. The effective noise level of the amplifier depends on both the signal and pump frequencies as well as on the properties of the diode, and, as it is thermal in origin, the noise level also depends on the temperature of the diode. Thus, it can be lowered by cooling the amplifier.

Varactor parametric amplifiers could be operated at convenient temperatures from room temperature, through liquid nitrogen temperature, down to liquid helium temperature, and offered versatility of system design. These amplifiers gained popularity because the improvement in sensitivity they offered outweighed the complications they introduced (the requirement for a low-loss ferrite circulator and a high-power, high-frequency pump oscillator—coupled with a reputation for being touchy to operate) [12]. Among uncooled amplifiers, the parametric amplifier was the most sensitive amplifier in existence in the 1960s. The noise level of a cooled paramp was not as low as that of a maser, but the paramp was much smaller and much less costly and did not require a liquid helium cryostat to operate. The wideband ultra-low-noise paramps [5,6,9] had been the key devices that had brought commercial and military communication satellite systems into existence. They also dominated in radio astronomy receivers throughout the world, opening new horizons in exploration of our universe. The growth in technology of the wideband paramps in the late 1960s had been exceptionally rapid. The microwave parametric amplifier evolved from a relatively high noise temperature device (250–300 K) with narrow bandwidth of 25–50 MHz to one capable of operational noise temperature as low as 12 K in cryogenically cooled mode and as low as 50–120 K in an uncooled mode and 1 dB bandwidth in excess of 500 MHz. In the early

1970s, Peltier cooled paramps were the configuration of the day.

In the early 1980s parametric amplifiers were challenged by gallium arsenide field-effect transistor (MESFET) amplifiers. With their simplicity and cost advantages, the MESFETs were encroaching on the previously exclusive property of the paramps, eroding their monopoly. Rapid improvement in GaAs MESFET technology and development of the high-electron-mobility transistor (HEMT) resulted in lower intrinsic noise, and thus less noisy amplifiers, leaving paramps behind in the race for the highest sensitivity [13] and finally displacing them at microwave frequencies. But the elegance and refinement of the parametric amplification are still fascinating, and the technique might emerge in its classical form at the terahertz region of the electromagnetic spectrum where there are no active semiconductor devices but there are many powerful far-infrared lasers to pump contemporary submillimeter-wave varactors [14]. More recently optical control in optoelectronic devices and nonlinear interaction between optical and microwave signals in semiconductor devices have gained much interest because of potential application in signal switching, mixing, and frequency modulation. Parametric amplification plays an important role in increasing sensitivity of such devices employing semiconductor photodetectors [15,16].

2. PRINCIPLE OF OPERATION

In a parametric amplifier, the energy at one (signal) frequency is increased by supplying energy at a second (pump) frequency. The basic idea is illustrated in Fig. 1. Considering the simple resonant circuit of Fig. 1, it is assumed for the purpose of illustration that the plates of the capacitor can be separated mechanically [2,17]. Let us assume that prior to a time $t=0$, the circuit has been induced to oscillate at its resonant frequency. Suppose that when the charge in the capacitor is reaching its first maximum after $t=0$, separation of the plates is suddenly increased, thereby decreasing the capacitance. Because of the electric field, this separation requires mechanical work to be supplied. The relation between charge q , capacitance c , and voltage v on a capacitor is, of course, $q=cv$. Thus, if the plate separation is increased and the capacitance thereby decreased, in a time short enough for q to be considered essentially constant, the voltage and also the stored energy $qv/2$ must both be suddenly increased. If, at the next zero of voltage across the plates, the original separation is suddenly restored, this does not change the stored energy of the circuit since the field is then zero. If the whole sequence is then repeated every half-cycle, the voltage and energy may also be increased every half-cycle, giving a buildup of the voltage across the capacitor and the energy stored in the circuit (thus also the charge in the capacitor). This buildup will continue until the energy added by separation of the plates exactly equals the energy dissipated in the circuit. It should be noted that the plates are moved (or "pumped") at twice the resonant frequency and that the phase of the pumping is important. A variable-capacitance amplifier operating

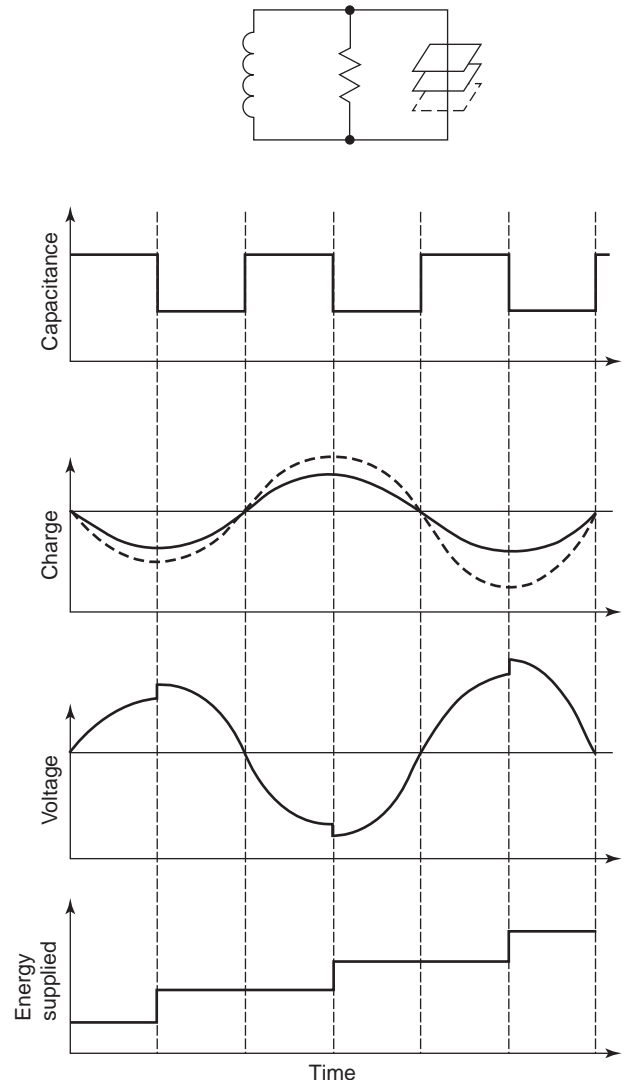


Figure 1. Illustration of basic parametric amplifier principle. The separation of the plates forming the capacitor is increased (thus the capacitance is decreased) so fast that the charge q remains constant, giving buildup in voltage $v=q/c$ and stored energy $qv/2$. Original separation is then restored at the moment when $q=0$. The whole sequence is repeated every half-cycle.

exactly on this principle, in which a signal is supplied at the resonant frequency f_s with the pump frequency $f_p = 2f_s$, is called a *degenerate amplifier*.

Nondegenerate parametric amplifiers, which do not impose this restriction on pump frequency or phase, can be constructed by connecting a second tuned circuit across the variable capacitance. This circuit is known as the *idler*, and its frequency f_i is tuned to $f_p - f_s$. Operation of such an amplifier can be explained in much the same way as above for the single resonant circuit; interested readers may refer to Ref. 17.

In practical circuits a semiconductor junction is used as an electronically variable capacitance instead of a mechanically controlled parallel-plate capacitor. The waveform changing such a capacitance is sinusoidal (rather than rectangular) and is produced by a special generator

(called a *pump*) pumping energy to the nonlinear capacitance. The theoretical power flow into and out of an idealized lossless nonlinear reactance is described in terms of two generalized equations known as the Manley–Rowe relations, which can be written as

$$\begin{aligned} \sum_{m=0}^{\infty} \sum_{n=-\infty}^{\infty} \frac{mP_{mn}}{mf_1 + nf_2} &= 0 \\ \sum_{n=0}^{\infty} \sum_{m=-\infty}^{\infty} \frac{nP_{mn}}{mf_1 + nf_2} &= 0 \end{aligned} \quad (1)$$

where P_{mn} represents, algebraically, the power flow into the nonlinear reactance at the frequencies $mf_1 + nf_2$. These equations are a result of only the nonlinear variation of the reactance and are independent of the shape of its characteristic and of the driving power levels. The spectrum of signals at the nonlinear reactance is illustrated at Fig. 2. If we consider a typical case of three-frequency amplifiers (however, more frequencies may be used in some specific applications)— f_1 , f_2 , f_3 , where $f_3 = f_1 + f_2$ —then, provided $f_1 \ll f_1 + f_2$, the general Manley–Rowe equations can be simplified to

$$\frac{P_1}{f_1} + \frac{P_3}{f_3} = \frac{P_2}{f_2} + \frac{P_3}{f_3} = 0 \quad (2)$$

This equation and Fig. 2 can be used to understand the operation of some of the different types of parametric amplifiers (nonlinear capacitance is assumed here to be lossless).

Let $f_1 = f_s$ be the signal frequency and power be supplied from an external source at frequency $f_2 = f_p$. Since pump power $P_2 = P_p$ is supplied to the capacitor ($P_p > 0$), then $P_3 < 0$ represents power leaving the reactance at the frequency $f_3 = f_p + f_s$; hence $P_1 = P_s > 0$. It follows that the device is absolutely stable and has the maximum power gain equal to $f_3/f_1 = 1 + f_p/f_s$. This type of amplifier is called an *upper-sideband (noninverting) upconverter*.

Now, let $f_1 = f_s$ be the signal frequency but let power be supplied from the pump at the frequency $f_3 = f_p$. Hence, $P_3 = P_p > 0$ and both $P_1 = P_s < 0$ and $P_2 < 0$; so the reactance can deliver energy at frequencies $f_1 = f_s$ and $f_2 = f_p - f_s$. If the power is extracted at the frequency f_2 , the device is called a *lower-sideband (inverting) upconverter*. The term *inverting* is used because the input signal spectrum is inverted at the output in this mode of operation.

If, as stated, the nonlinear capacitance is pumped at the frequency $f_3 = f_p$, that is, $P_3 = P_p > 0$ and $P_1 = P_s < 0$

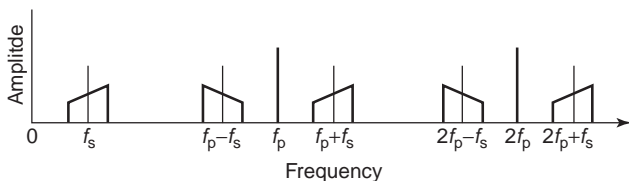


Figure 2. Spectrum of signals at a nonlinear reactance. Input signal spectrum (f_s and its vicinity) appears at both sides of the harmonics nf_p of the pumping signal.

and $P_2 < 0$, but the output is at the frequency $f_1 = f_s$, then the negative sign of P_1 indicates that the capacitor emits more power than that fed from the generator at $f_1 = f_s$. It should be noted that the power supplied from the varactor to the signal source is independent of that supplied by the source itself; thus infinite gain is possible and the device is able to oscillate. It indicates that the pumped varactor presents a negative resistance to the signal source. Hence, with this frequency arrangement the signal power can be amplified at the same frequency, in contrast to the previous cases. The powers P_1 and P_2 are strongly dependent on the pump power and the external impedances. When the input and output frequencies are the same at $f_1 = f_s$, power at $f_2 = f_p - f_s$ is simply dissipated in the circuit and is unused. It justifies the name *idler* used traditionally for this frequency. The idler signal is an inevitable byproduct of this type of amplification, and suppressing it would also suppress the desired amplification of the signal. The separation of the idler and signal frequency is an important factor determining design and properties of this single-port (or *reflection* type) amplifier—the closer the idler to the signal, the more difficult it is to separate them by filtering. If the signal and idler frequencies are separated far enough so that the signal circuit does not pass the idler, the amplifier is called a *nondegenerate* amplifier. In the opposite case, if the signal circuit passes both the signal and idler bands and the input termination is common to both, that is, $f_i = f_p - f_s \approx f_s$, the amplifier is said to be *degenerate*.

3. VARACTOR DIODES

The most convenient nonlinear reactance element is a semiconductor diode specially designed to provide large variation of diode junction capacitance as a function of the applied (reverse) pumping voltage. Varactors may be classified into two broad groups, depending on the method of fabrication: the junction varactors, widely used at microwave frequencies, and the Schottky barrier varactors, generally used at millimeter waves and in high-performance amplifiers. Both groups are extensively discussed elsewhere in this encyclopedia, so only brief descriptions are given here and only problems specific for parametric amplifiers applications are discussed.

A typical junction varactor is made on an n-type silicon or gallium arsenide wafer, with a highly doped conducting substrate on which is grown a lower doped epitaxial layer. A suitable p-type dopant is then diffused into the epilayer to the obtain p^+ region and to form the p^+ -n junction. Ohmic contacts are made to a small circular area on the top of the wafer for the anode and to the bottom of the wafer for the cathode. Most of the epitaxial layer is then etched away, except the portion that is under the top contact. In this way a mesa of the desired diameter is formed. Diodes fabricated in this manner are called *diffused epitaxial varactors*.

A Schottky barrier varactor diode consists of a circular metallic contact pad (usually platinum) deposited on a lightly doped n-type layer epitaxially grown on a heavily doped GaAs substrate. The epitaxial layer is conductive

except in the vicinity of the metal–semiconductor interface, where an insulating depletion zone is formed. Depletion-layer thickness, and thus the capacitance, varies with the biasing voltage applied to the metal–semiconductor junction.

Simple, but justified by relatively low operating frequencies, varactor models are used in the analysis and design of parametric amplifiers; the reader is referred to Ref. 14 for advanced modeling of varactor diodes. A typical equivalent circuit of a microwave varactor is shown in Fig. 3. The reverse-bias junction is modeled in this simple circuit by a voltage dependent capacitor $C_j(v)$ and series resistance R_s . The terms L_p , C_p , and C_s are linear parasitic inductance, capacitance, and stray capacitance, respectively. The dependence of the junction capacitance on the applied reverse voltage v is given by

$$C_j(v) = C_{j0} \left(1 - \frac{v}{\phi} \right)^{-\vartheta} \quad (3)$$

where ϕ is the barrier potential and C_{j0} is the zero-bias capacitance. The exponent ϑ depends on the doping profile of the epitaxial layer of the varactor. For Schottky diode varactors with uniform epitaxial layer doping, it is close to $\frac{1}{2}$. For p^+ - n -junction varactors the ϑ factor varies from $\frac{1}{3}$ for a linearly graded diffused junction up to $\frac{1}{2}$ for an ideal abrupt junction. Other doping profiles (e.g., hyperbolic) have also been used in *hyperabrupt varactors* to obtain larger capacitance variation and thus higher values of the ϑ factor (ϑ in excess of 1 have been reported). However, the performance of the parametric amplifier depends not only on the capacitance change ΔC_j but also on the series resistance R_s of the varactor. Unfortunately, hyperabrupt varactors have high series resistance ($\Delta C_j/R_s$ is lower than for other varactors), which excludes their use in high-performance amplifiers.

In Schottky barrier varactors the series resistance is dominated by the contribution from the undepleted epitaxial layer. For parametric amplifiers, a breakdown voltage of a few volts is sufficient and this allows relatively high doping and a thin epitaxial layer, thereby reducing the series resistance. In diffused epitaxial varactors there are additional sources of parasitic resistance, namely, the resistance of the diffused p^+ -region and the resistance of the ohmic top contact. The p^+ -region resistance becomes large at cryogenic temperatures, causing serious degradation of diode performance. Similarly, silicon diodes cannot be used in cooled amplifiers because of series resistance

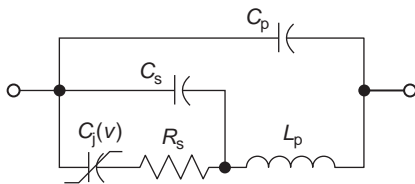


Figure 3. Equivalent circuit of a varactor. The reversed-bias junction is represented by a voltage-dependent capacitor $C_j(v)$ and a series resistance R_s . L_p , C_p , and C_s are parasitic inductance, capacitance, and stray capacitance, respectively.

increase and carrier freezeout below 40 K [14]. Hence gallium arsenide Schottky varactors have been the best choice for cooled parametric amplifier applications because of their low, relatively temperature-insensitive resistance.

3.1. Varactor Figures of Merit

Efficient varactor operations require the reactance of the junction capacitance to be much larger than the diode series resistance. It places an upper frequency limit on the usefulness of a given varactor, and figures of merit quantify this limit.

The static *cutoff frequency* f_c gives an indication of loss and is defined as that frequency at which the capacitive reactance of the junction at zero bias becomes equal to the series resistance:

$$f_c = \frac{1}{2\pi R_s C_{j0}} \quad (4)$$

For varactor applications the diode is characterized by the *dynamic cutoff frequency* defined as

$$f_{cd} = \frac{1}{2\pi R_s} \left(\frac{1}{C_{j,\min}} - \frac{1}{C_{j,\max}} \right) \quad (5)$$

where $C_{j,\min}$ and $C_{j,\max}$ are the values of C_j at the reverse breakdown voltage and at the zero bias voltage (or at $1 \mu\text{A}$ forward current), respectively.

Correspondingly, the quality factors at a specified frequency f_0 are given as $Q = f_c/f_0$ and for a pumped abrupt junction as $Q_d = 0.25 f_{cd}/f_0$.

In an amplifier, the capacitance is modulated by the application of microwave power at the pump frequency f_p and thus varies periodically in time. Hence $C_j(t)$ can be expanded into Fourier series

$$C_j(t) = C_0 \left(1 + \sum_{n=1}^{\infty} 2\gamma_n \cos 2\pi n f_p t \right) \quad (6)$$

where C_0 and γ_n are the Fourier coefficients. The values of γ_n , in particular that of γ_1 , determine parametric amplifier performance. In most practical cases higher terms may be ignored and only C_0 (the average value of the pumped capacitance) and γ_1 need to be considered. The diode capacitance *modulation coefficient* γ_1 is, of course, a function of the voltage developed across the diode at pump frequency, but will have a maximum attainable value, termed *nonlinearity factor*, given by

$$\gamma = \frac{C_{j,\max} - C_{j,\min}}{2(C_{j,\max} + C_{j,\min})} \quad (7)$$

When γ is referred to, it is usually this maximum value that is intended.

For parametric amplifier applications the most useful quantity to characterize the diode is the *pumped figure of merit*, defined as

$$M = \gamma f_{c0} \quad (8)$$

where

$$f_{c0} = \frac{1}{2\pi R_s C_0} \tag{9}$$

is the *pumped cutoff frequency*. A high pumped figure of merit indicates a low attainable noise of the amplifier.

4. NONDEGENERATE PARAMETRIC AMPLIFIER

As mentioned above, several three-frequency amplifier configurations are feasible. Of these, the negative-resistance nondegenerate parametric amplifier with a varactor diode providing a suitable nonlinear capacitance has achieved the most success as a practical low-noise paramp. A lumped-circuit analog of the microwave amplifier is used to obtain some insight into the operation of this type of amplifier. The model, shown in Fig. 4, consists of three resonant circuits coupled by a varactor that may be represented by the equivalent circuit of Fig. 3. So that the properties of the nonlinear element, rather than these of the resonant circuits, can be emphasized, it is assumed that the resonant circuits are ideal, and this is taken to mean that at certain frequencies they are pure resistances, while at all other frequencies they are very high impedances and, therefore, virtually open circuits.

With these assumptions, the behavior of the amplifier at the frequency $f_1 = f_s$ can be described in terms of a negative resistance \Re (voltage developed across \Re is out of phase of the current flowing through it), which appears in the equivalent circuit of the amplifier at this frequency. Its value is given by [1,8]

$$\Re = -\frac{\gamma^2}{\omega_s \omega_i R_{Ti} C_0^2} \tag{10}$$

where $R_{Ti} = R_s + R_2$ is the total series resistance at the idler frequency $f_i = f_2$.

The transducer power gain is taken as the ratio of power dissipated in the load resistance R_L to the available power from the signal source (internal resistance R_g) and

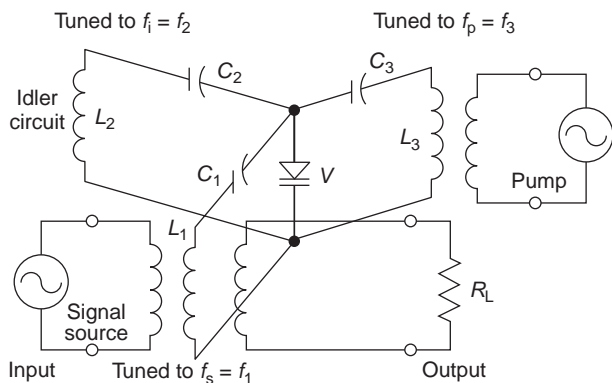


Figure 4. Lumped-element model of a microwave nondegenerate parametric amplifier. Three ideal resonant circuits tuned to signal, $f_s = f_1$, idler, $f_i = f_2$, and pump, $f_p = f_3$, frequencies are coupled by a varactor represented by the equivalent circuit of Fig. 3.

is given by

$$G_p = \frac{4R_g R_L}{(R_g + R_L + R_s + \Re)^2} \tag{11}$$

clearly, for high gain $R_g + R_L + R_s \approx |\Re|$.

In common with all other negative-resistance amplifiers, the negative-resistance parametric amplifier is extremely sensitive to small changes in the value of \Re and changes in source and/or load resistance when it is operated under high-gain conditions. In practice \Re may change as a result of fluctuations in the pump power and frequency, and control circuits have often been employed in conjunction with klystron pump sources in an effort to minimize such fluctuations. The popular approach was to control the attenuator in the pump line to maintain a constant varactor bias. Frequency fluctuations were handled in critical applications by locking the pump to a stable reference. The introduction of Gunn oscillators as pump sources resulted in a considerable improvement in stability, making stabilization schemes unnecessary in most cases [12].

4.1. Operation with a Circulator

Nonreciprocal devices such as circulators are used to separate the amplified output from the input and to protect the amplifier against changes in impedance at the input or at the following stage of the receiver. An ideal circulator is a circuit element that directs energy from one port to the next port without loss and prevents transmission in the opposite direction. This passive component obtains its nonreciprocity from the presence of a central ferrite structure placed in a DC magnetic field.

Early paramps used three-port circulators, but most recent designs incorporated five-port circulators to increase immunity from the effect of source impedance variation and to provide greater isolation between adjacent stages in multistage amplifiers. (For stability, the gain was usually limited to 20–25 dB for a single-stage device. If higher gain was required, a number of 10–15-dB stages were connected in cascade.)

Knowing that the variation of the varactor’s junction capacitance is completely controlled by the pump, it is then possible to concentrate entirely on that variation, and omit details of the source that produced it. The circuit of Fig. 4 can therefore be redrawn as in Fig. 5, leaving out the pump circuit; the capacitance is then specified as $C_j(t)$, emphasizing in this way the time variation. The signal source and the load are connected to the amplifier via a three-port circulator.

4.1.1. Power Gain. The power gain of the amplifier-circulator combination can be seen to depend on the ratio of the powers entering and leaving the amplifier. Since the circulator has a characteristic impedance Z_0 to which it should be matched, source and load resistances will have the same value, and the circuit available gain will equal the transducer gain. The required power gain is therefore equal to the square of the magnitude of the voltage reflection coefficient Γ and, since $R_g = R_L = Z_0$, is

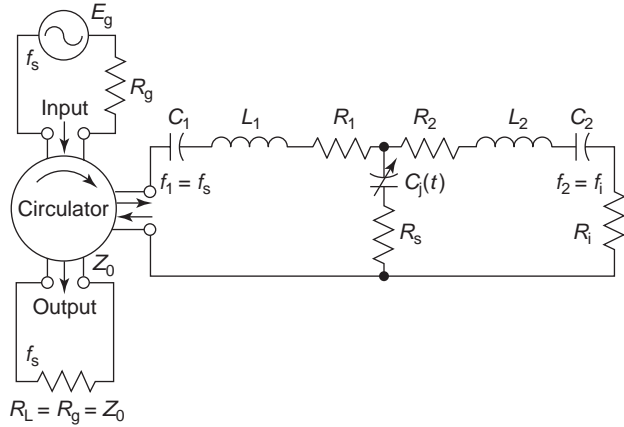


Figure 5. Equivalent circuit of the nondegenerate parametric amplifier employing a circulator to separate the amplified output from the input. The pumped varactor is represented by a capacitance $C_j(t)$ periodically varying in time and series resistance R_s .

given by

$$G_p = \Gamma\Gamma^* = \left| \frac{R_s + R_L - \Re}{R_s + R_L + \Re} \right|^2 \quad (12)$$

With the use of a circulator, the input loop of the amplifier effectively contains only one of two resistors, R_g or R_L . For high gain, that is, $R_L + R_s \approx |\Re|$, Eq. (12) can be rewritten as

$$G_p = \frac{4R_L^2}{(R_L + R_s + \Re)^2} \quad (13)$$

Comparing the expressions for power gain with and without the circulator (setting $R_g = R_L$ and remembering that $R_s \ll R_L$), it can be seen that the use of a circulator has increased the power gain 4 times for the same gain stability, where instability of gain results from changes in \Re .

4.1.2. Noise Temperature. In low-noise amplifiers, it is more convenient to express noise performance in terms of *effective noise temperature* (or, in short, *noise temperature*), which is related to the noise figure F by the equation

$$T_e = T_0(F - 1) \quad (14)$$

where $T_0 = 290$ K is a standard temperature.

The effective noise temperature of the parametric amplifier depends on the thermal noise contributions from all the resistances in the circuit (shot noise is not present in the reverse-biased junction). Neglecting contributions other than that from the varactor itself, the noise temperature of a negative-resistance reflection-type parametric amplifier can be calculated in this limiting case from the following equation [5,7,8]

$$T_{ea} = T \left(1 - \frac{1}{G_p} \right) \frac{\left(\frac{f_{c0}}{f_i} \right)^2 \gamma^2 + 1}{\frac{f_{c0}^2}{f_s f_i} \gamma^2 - 1} \quad (15)$$

where T is the diode physical temperature and G_p is the amplifier power gain. It is possible to calculate the pump frequency $f_{p,opt}$ at which the parametric amplifier noise temperature has its minimum value. This is given by

$$f_{p,opt} = f_s \left[1 + \left(\frac{f_{c0}}{f_s} \right)^2 \gamma^2 \right]^{1/2} \approx \gamma f_{c0} = M \quad (16)$$

and the optimum noise temperature for large gain becomes

$$T_{ea,opt} = T \frac{2f_s}{\gamma f_{c0}} = \frac{2f_s T}{M} \quad (17)$$

Thus, it is apparent that for good amplifier performance a diode should combine high cutoff frequency with a marked capacitance variation, even at low temperatures, in order to achieve low noise temperature.

If we now add contributions from losses in the signal and idler circuits, the circuit behavior of the circulator-type amplifier (where $R_L = R_g$), is then described by the noise temperature

$$T_{ea} = \frac{T_1 R_1}{R_g} + \frac{T_d R_s}{R_g} + \frac{f_s |\Re|}{f_i R_g} \left[\frac{T_d R_s + T_2 R_2}{R_2 + R_s} \right] \quad (18)$$

where \Re is the negative resistance given by Eq. (10), R_g is the generator resistance in the signal circuit and R_1 and R_2 represent losses (other than R_s) in signal, $f_1 = f_s$, and idler, $f_i = f_2$, circuits. T_1 , T_2 , and T_d are the temperatures of R_1 , R_2 , and R_s , respectively. In practical amplifiers temperatures are usually equal, that is, $T_1 = T_2 = T_d = T$ and the amplifier is designed to have, as far as possible, R_1 and R_2 negligibly small in comparison with R_s . Then, at high gain, that is, $|\Re| \approx R_g + R_s$, the noise temperature is given by

$$T_{ea} = T \left(\frac{R_g + R_s}{R_g} \frac{f_p}{f_i} - 1 \right) \quad (19)$$

For many applications cooling is not necessary. Adequate low-noise performance can be achieved using simple circuits with diode of moderate cutoff frequency. If lower noise temperatures are required, it is necessary to use higher idler frequencies, and this is possible only if a diode of sufficiently high cutoff frequency is used. When cooling is necessary to lower the noise temperature, it must be remembered that any loss in the path between the signal source, such as an antenna, and the parametric amplifier may considerably degrade the overall noise temperature. If the loss of the circulator is $A = 10 \log(L)$, then the noise temperature of the circulator-amplifier cascade is calculated from

$$T_{e,c-a} = T_{e1} + \frac{T_{e2}}{G_1} = (L - 1)T + LT_{ea} \quad (20)$$

If, for example, a circulator with $A = 0.41$ dB transmission loss is ahead of a low-noise, $T_e = 100$ -K amplifier, then at room temperature, $T = 290$ K, the receiver has noise

temperature $T_{e,c-a} = 0.1T + 1.1T_{ea} = 139$ K. When the amplifier is cooled down to temperature 20 K, its noise temperature lowers to, say, $T_{ea} = 10$ K. Leaving the circulator uncooled will increase the overall noise temperature 4 times to $T_{e,c-a} = 40$ K. It is thus obvious that both the circulator and the amplifier must be cooled down to obtain low-noise performance of the receiver ($T_{e,c-a} = 13$ K in this illustrative example).

4.1.3. Bandwidth. Much effort has been spent in devising ways of obtaining the broad bandwidth essential in some applications—see Ref. 9 for a thorough review of advanced techniques used for the purpose. Because the bandwidth of an amplifier depends on its gain (decreases with increase of gain), the gain–bandwidth product is used to characterize the amplifier performance. It can be shown [8] that for a negative-resistance amplifier operated in conjunction with a circulator, the gain–bandwidth product may be derived as

$$G_p^{1/2}B = 2 \left(\frac{1}{B_s} + \frac{1}{B_i} \right)^{-1} \quad (21)$$

where B_s and B_i are the unpumped signal and idler circuit bandwidths, respectively. Both signal and idler circuits should therefore be as broadband as possible to give the amplifier a good gain–bandwidth product.

Since the signal circuit is loaded externally by the source resistance, whereas the idler has no external loading, the latter will tend to be a high- Q circuit limiting the bandwidth. The resistance present in the idler has already been fixed at the diode resistance R_s , and any increase in this will degrade the amplifier performance. Therefore, in order to optimize the bandwidth of the idler circuit, it is necessary to keep the reactance of the idler circuit as low as possible. (The bandwidth of a series-tuned circuit is given by the R/L ratio.) This can be achieved by confining the idler power to the varactor encapsulation. From Fig. 3 it can be seen that there is the possibility of a series resonance, associated with L_p , C_0 (the average value of the pumped junction's capacitance), C_s , and R_s at the frequency given by

$$\omega_{si}^2 \approx \frac{1}{L_p(C_0 + C_s)} \quad (22)$$

neglecting the effect of R_s . The resonant frequency f_{si} can be arranged to be the idler frequency of the amplifier, but in order to use the series resonance in this way, a return path for the current must be provided (e.g., by a lumped circuit or a length of transmission line). An elegant solution to this problem uses two antiparallel connected diodes. When sufficiently excited, the idler current will circulate around this structure and will not propagate to any other part of the amplifier. A further development of this idea has seen the production of suitable diodes in one encapsulation. Another approach is to mount the diodes back to back across the pump waveguide with signal line entering through the sidewall and contacting the junction between them (crossbar configuration).

For parametric amplifiers with a high idler frequency it is more convenient to use the parallel resonance of the encapsulated diode (which is actually a series resonance for the idler currents) to form the idler circuit. Such an amplifier uses a single diode and can be further refined by modifying the series resonance to support the signal frequency.

Careful attention to the design of the idler circuit leaves the bandwidth of the signal circuit as the main limitation on the overall bandwidth of the parametric amplifier. An estimate of the maximum attainable bandwidth under these conditions may be made putting $B_i \ll B_s$ in Eq. (21) to yield

$$G_p^{1/2}B \simeq 2B_s \quad (23)$$

If the signal circuit is now designed for the minimum possible Q -factor associated with the source resistance, then the added inductance must just resonate the diode capacitance at the signal frequency (i.e., single-tuned circuit). Then under the high-gain condition, it is found that

$$G_p^{1/2}B \simeq 2\gamma f_s \left(\frac{\gamma f_{c0}}{f_p - f_s} \right) = 2\gamma^2 f_{c0} \frac{f_s}{f_i} \quad (24)$$

The result suggests that high-quality diodes are important in securing large gain–bandwidth products, and that there must be a tradeoff between effective noise temperature and bandwidth in selecting the pump and, therefore, the idler frequency.

Considerable improvement in the overall gain–bandwidth product can be achieved by introducing a filter structure in place of a simple single resonant circuit. Improvements of over 5 times have been reported with little increase of noise temperature. For a maximally flat design, the limiting bandwidth should be given by $B \log(G_p) = \text{const}$, but in practice the use of more than two or three compensating elements leads to practical difficulties in tuning the device.

5. OTHER PARAMETRIC AMPLIFIER CONFIGURATIONS

5.1. Degenerate Parametric Amplifiers

In the degenerate parametric amplifier, the pump frequency is approximately twice the signal frequency. The signal and idler passbands overlap, and instead of idler circuit being terminated inside the amplifier, it is effectively terminated in the input of the amplifier. The absence of a separate idler circuit makes construction of such an amplifier much simpler than the corresponding non-degenerate version. The additional advantages are a low pump frequency and a wider bandwidth. Therefore, degenerate amplifiers were finding applications in some early broadband radiometers and more recently in millimeter-wave paramps.

The phase-coherent degenerate amplifier in which the pump frequency is exactly twice the signal frequency is by its nature a single-frequency device since no departure from coherence with the pump is allowed [1,4,8]. To

achieve the required frequency relationship, in practice it would be necessary to synchronize the pump frequency to the second harmonic of the signal frequency with special phase-locked loop (PLL) circuitry. It can be shown [1] that the gain of the amplifier changes with changes in phase of the pump signal, rendering the use of this amplifier impracticable in the majority of potential applications.

Even if phase relations are loosened and the signal frequency is only approximately equal to the idler frequency, care must be taken in using the amplifier. It should be noted that the degenerate amplifier is not suitable for direct use with frequency-modulated signals, since when f_s increases in frequency, then $f_i = f_p - f_s$, which is present at the same terminals, decreases in frequency. The signal fed into a degenerate amplifier may be amplitude-modulated, although if the amplifier has the idler frequency only approximately equal to the signal frequency, beats between the two waveforms can cause interference. A cascade of the degenerate paramp followed by a parametric converter pumped synchronously at $0.5f_p$ was used to overcome both difficulties (1).

The major disadvantage of degenerate amplifiers becomes apparent when we consider that a signal entering receiver appears in both idler and signal responses of the amplifier and the output contains both the signal and its image (also noise from both responses adds at the amplifier output). When coherent communication signals are involved, this double response is unacceptable. In radiometer applications, where the signal takes the form of broadband noise, this type of amplifier has good sensitivity, since the signal is received equally in both the signal and idler bands. In general, the use of degenerate amplifier must be judged carefully considering the nature of the signal, single- or double-sideband operation at the input and the output of the amplifier, and the nature of the detector employed in the receiver. A detailed discussion of this subject can be found in Refs. 4, 10, and 11.

5.2. Multiple-Idler Parametric Amplifiers

To circumvent some of the disadvantages of the three-frequency paramps, many other frequency combinations had been proposed for parametric amplifiers in the hope that an improved performance would outweigh the disadvantages of (usually) increased complexity. If more than one idler frequency is used, it is possible to use a pump frequency lower than the signal frequency. In the 2-idler case (the so called four-frequency paramp), the usual restriction

$$f_i = f_p - f_s > 0 \quad (25)$$

is replaced by

$$f_{i1} = f_s - f_p > 0 \quad (26)$$

for the first idler, and

$$f_{i2} = (f_p - f_{i1}) = 2f_p - f_s > 0 \quad (27)$$

for the second idler. Therefore $\frac{1}{2}f_s < f_p < f_s$ is required for efficient operation (negative resistance at signal frequencies $f_p < f_s < 2f_p$). Note that if f_p is chosen as $\frac{2}{3}f_s$,

then the two idler frequencies will both be equal to $\frac{1}{3}f_s$. The lack of adequate pump generators was the main reason to use four-frequency paramps at millimeter waves. However, more complex microwave construction usually resulted in higher losses and hence poor noise performance and, therefore, multiple-idler paramps found only limited applications [9].

5.3. Traveling-Wave Parametric Amplifier

Up to now parametric devices utilizing essentially resonant structures have been considered. Such circuits suffer from previously discussed drawbacks; some of them can be minimized by resorting to nonresonant propagating circuits. A variety of configurations are possible, each with its own characteristics. Perhaps the simplest is the case where all the three traveling waves—signal, idler, and pump—have positive phase and group velocities. This was exploited in amplifiers taking the form of a transmission line periodically loaded with varactor diodes. It was difficult in practice to satisfy phase requirements for all the signals, and some experimental amplifiers provided separate pump feeds for each diode [10]. For frequencies below 1.5 GHz, experimental amplifiers had usually the form of stripline with diodes between the central and outer conductors [1,7]. For higher frequencies, the diodes were mounted across rectangular waveguide or a series of coupled cavities [10].

In practice, because of the difficulties of providing a considerable number of identical diodes and the experimental difficulties of providing the correct phase characteristics at the three frequencies, the performance of traveling-wave amplifiers was worse than that achieved with much more simple and requiring much less pump power single-diode devices. Therefore, traveling-wave parametric amplifiers have never been developed beyond the experimental stage and have never left the laboratory. A distributed varactor was needed for success in this field. However, it appeared at the end of the 1970s in a form of nonlinear transmission line employing distributed Schottky barrier varactors [14]. It was too late—parametric amplifiers were just giving way to new technology of GaAs field-effect transistor amplifiers.

6. ILLUSTRATIVE EXAMPLE

There were many species of microwave parametric amplifiers, and a wide range of amplifiers design were available (see Refs. 4–6, and 9–11 for detailed and complete design theories and practical considerations). The choice was dependent on the particular application. In many applications, the lower limit of background noise in the system was determined by thermal noise entering the antenna from the terrestrial surroundings, and for such applications relatively simple uncooled parametric amplifiers were commercially available. For reception of the weak signals from communication satellites or interplanetary probes, however, extremely low system noise temperature was essential and a whole range of specialized cooled amplifiers was developed offering noise temperatures as low as 12–15 K (comparable with masers).

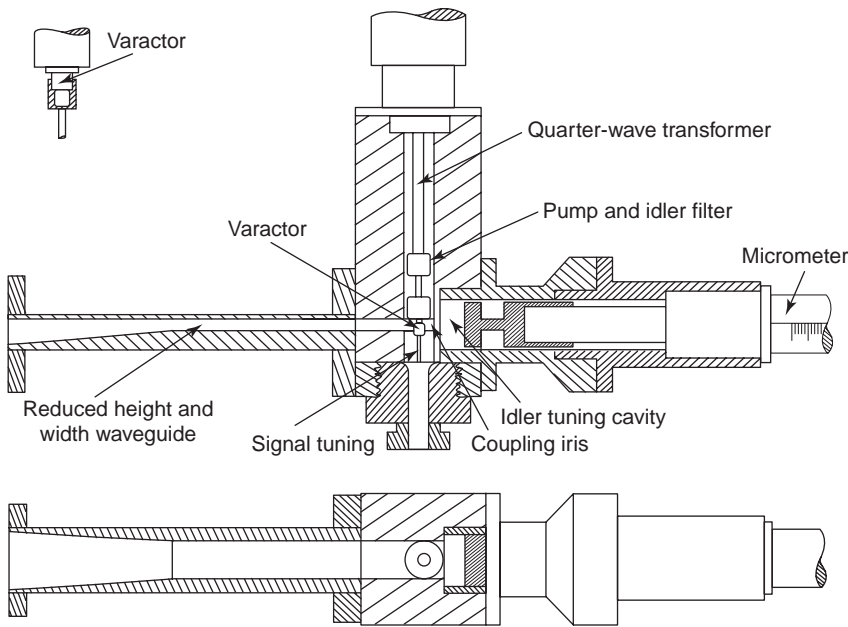


Figure 6. Representative example of the microwave construction of a parametric amplifier: section diagram of a 3.25-GHz nondegenerate parametric amplifier. (Source: J. W. Archer and R. Batchelor, Multipliers and parametric devices, in K. Chang, ed., *Handbook of Microwave and Optical Components*, Vol. 2, p. 187. ©1990 John Wiley & Sons. Reprinted by permission of John Wiley & Sons, Inc.)

Bandwidth and operating frequency requirements were widely diversified. Paramps were made to amplify signals up to the millimeter-wave frequencies (60-GHz paramps are reported in Ref. 9). For some terrestrial communication and radar requirements, with several MHz bandwidth were routinely manufactured. Satellite communication systems required 500 MHz bandwidth, and specially designed paramps were developed for such systems.

A 3.25-MHz nondegenerate parametric amplifier [12] has been selected as a representative example to illustrate the elegant design and refinement of microwave construction. The amplifier designed for spectral line radio astronomy covers the frequency range 3.1–3.4 GHz with an instantaneous bandwidth of 40 MHz. A section drawing of the amplifier is shown in Fig. 6. Description of the amplifier is rewritten here with permission of John Wiley & Sons, Inc.:

The varactor diode is mounted in the E -plane of a reduced-height waveguide which couples pump power from a 22 GHz reflex klystron to the varactor. A short length of high-impedance coaxial line series resonates the diode mean capacitance at the signal frequency. A three-element low-pass filter isolates the pump and idler from the input line while the pump waveguide is cut off at the idler frequency, confining the idler to the vicinity of the varactor and the idler cavity. The idler circuit contains a tunable cavity coupled to the varactor by an iris. The position of this iris was chosen to optimize the pump coupling to the varactor. The idler frequency is determined by the combination of the package parasitic reactances, the coupling, and the tunable cavity, which consists of a micrometer-adjustable noncontacting short circuit in a cylindrical tube. The pump and idler blocking filter forms part of a quarter-

wave transformer in the input coaxial line, which is used to transform the characteristic impedance of an external cir-

culator to the value required to obtain a desired gain [R_L in Eq. (13)].

No external bias is provided, the varactor being pumped until self-bias is developed.

The amplifier gain was set to 20 dB and, from noise measurements of uncooled receiver, its effective noise temperature was estimated to be 60 K.

BIBLIOGRAPHY

1. L. A. Blackwell and K. L. Kotzebue, *Semiconductor-Diode Parametric Amplifiers*, Prentice-Hall, Englewood Cliffs, NJ, 1961.
2. B. W. Siergowancew, *Microwave Parametric Amplifiers* (in Russian), Sowietskoje Radio, Moscow, 1961.
3. A. P. Bielousow, *Parametric Amplifiers with Varactor Diodes* (in Russian), Oborongiz, Moscow, 1961.
4. P. Penfield, Jr. and R. P. Rafuse, *Varactor Applications*, MIT Press, Cambridge, MA, 1962.
5. M. Uenohara, Cooled varactor parametric amplifiers, in L. Young, ed., *Advances in Microwaves*, Academic Press, New York, 1967, Vol. 2.
6. M. Uenohara and J. W. Gewartowski, Varactor applications, in H. A. Watson, ed., *Microwave Semiconductor Devices and Their Circuit Applications*, McGraw-Hill, New York, 1969.
7. H. N. Daghish, J. G. Armstrong, J. C. Walling, and C. A. P. Foxell, *Low-Noise Microwave Amplifiers*, Cambridge Univ. Press, Cambridge, UK, 1968.
8. D. P. Howson and R. B. Smith, *Parametric Amplifiers*, McGraw-Hill, London, 1970.
9. C. L. Cuccia, Ultralow-noise parametric amplifiers in communication satellite earth terminals, in L. Young, ed., *Advances in Microwaves*, Academic Press, New York, 1971, Vol. 7.

transformer in the input coaxial line, which is used to transform the characteristic impedance of an external cir-

10. K. St. Grabowski, *Parametric Amplifiers and Mixers with Varactor Diodes* (in Polish), Wydawnictwa Naukowo-Techniczne, Warsaw, 1968.
11. J. C. Decroly, L. Laurent, J. C. Lienard, G. Marechal, and J. Vorobeitchik, *Parametric Amplifiers*, Macmillan, London, 1973.
12. J. W. Archer and R. A. Batchelor, Multipliers and parametric devices, in K. Chang, ed., *Handbook of Microwave and Optical Components*, Wiley, New York, 1990, Vol. 2.
13. S. Weinreb, M. W. Pospieszalski, and R. Norrod, Cryogenic, HEMT, low-noise receivers for 1.3 to 43 GHz range, *IEEE MTT-S Int. Microwave Symp. Digest*, 1988, pp. 945–948.
14. M. T. Faber, J. Chramiec, and M. E. Adamski, *Microwave and Millimeter-Wave Diode Frequency Multipliers*, Artech House, Boston–London, 1995.
15. A. Khanifar, R. J. Green, A. Khosrowbeygi, N. T. Ali, and M. Milovanovic, The analysis of photoparametric amplifying devices and characteristics, *IEEE MTT-S Int. Microwave Symp. Digest*, 1995, pp. 1503–1506.
16. J. -C. Lee, H. F. Taylor, and K. Chang, Degenerate parametric amplification in an optoelectronic GaAs CPW-to-slotline ring resonator, *IEEE Microwave Guided Wave Lett.* **7**(9):267–269 (1997).
17. H. V. Shurmer, *Microwave Semiconductor Devices*, Pitman Publishing, London, 1971.

FURTHER READING

- S. Okwit, An historical view of the evolution of low-noise concepts and techniques, *IEEE Trans. Microwave Theory Tech.* **MTT-32**(9):1068–1082 (1984).
- M. E. Hines, The virtues of nonlinearity—detection, frequency conversion, parametric amplification and harmonic generation, *IEEE Trans. Microwave Theory Tech.* **MTT-32**(9):1097–1104 (1984).
- D. G. Tucker, *Circuits with Periodically-Varying Parameters*, Macdonald, London, 1964.
- S. A. Maas, *Nonlinear Microwave and RF Circuits*, 2nd ed., Artech House, Boston–London, 2003.
- S. Yngvesson, *Microwave Semiconductor Devices*, Kluwer, Boston, 1991.
- S. A. Maas, *Microwave Mixers*. 2nd ed., Artech House, Boston–London, 1993.

MICROWAVE PHASE SHIFTERS

JOSEPH F. WHITE
JFW Technology, Inc.

1. SCANNING ARRAY ANTENNA APPLICATIONS

Mechanical motion necessary for antenna scanning was perceived to be slow and unreliable. For this reason the microwave industry developed an intense interest in phased-array antennas, primarily for military but also

for commercial applications. The antenna's radiated wavefront would be steered by thousands of individual radiators, roughly one for each half-wavelength square area of the radiating aperture. Each radiator would be controlled by a solid-state (either semiconductor or ferrite) phase shifter, having low insertion loss and 0–360° of phase shift. For computer control the phase shift would be accomplished in binary bits. Thus a 3-bit phase shifter would have a 180°, a 90°, and a 45° section and these could be used to provide 0–315° control in 45° steps (the last step to 360° is not needed, being equivalent to 0° in the steady state). The antennas would be more expensive, both because of their need for numerous control elements (a circular aperture 30 wavelengths in diameter requires about 2500 elements) and the fact that, since a phased array provides only about $\pm 45^\circ$ of steering, four separate apertures are needed for 360° azimuthal coverage. But they would be fast and nearly failsafe, since a failure of a few elements would result in but “graceful degradation” of the system.

Ideally time delay (Fig. 1) is used to steer an array of antenna elements, and a two-dimensional array uses total time delay equal to that required for both azimuth and elevation steering. When time delay is used, the steering is frequency-independent, very desirable for a broadband antenna. However, the time delay required, equivalent to 70% of the antenna width for 45° beam steering along either of the antenna's steering axes, can amount to thousands of degrees of control. Instead, phase control is used. The requisite time delay is first calculated by the beam-steering computer and then all integer wavelengths dropped. The residue in degrees is then provided (to within one-half of the least significant bit) as a command to the binary bit phase shifter. In some cases, groups of adjacent phase shifters (subarrays) may employ time-delay steering to enhance antenna bandwidth performance.

Over the last four decades there has been a keen competition between the rival technologies, semiconductor and ferrite, to achieve the phase control. The semiconductor devices and their circuitry are generally faster switching and inherently reciprocal (having the same phase shift on transmit as receive), a useful antenna property. Being switches, their phase control is essentially temperature invariant, and the circuits more easily reproduced. Driver circuits, which interface the microwave control circuit to the array antenna beam steering computer, are very simple for the semiconductor phase shifter. However, semiconductors are discrete and small switching elements, and thereby limited in their peak power-handling

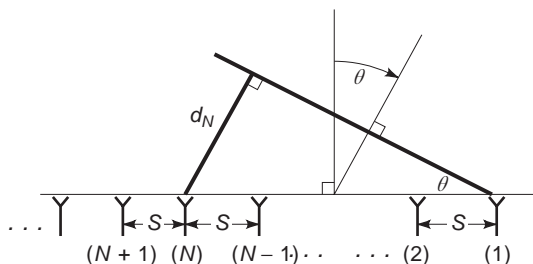


Figure 1. A linear phased array steered with time delay.

capacity. Furthermore, their insertion losses increase with frequency.

Ferrites are a controllable propagation medium for microwaves and thus have more volume and a higher power-handling capacity. Properly designed, they have low losses at higher microwave frequencies and, for certain circuit configurations, can be made reciprocal, even though propagation through the medium itself is nonreciprocal. Considerable attention must be given to the ferrite's flux driver circuitry to achieve reproducible binary phase control from unit to unit and over temperature and bias supply voltage changes. In fact, taking its driver circuit into account, a ferrite phase shifter typically includes more semiconductors than does a semiconductor phase shifter.

This section treats the semiconductor phase shifter. While they could be built using a variety of semiconductors, diodes, and bipolar and field-effect transistors, the principal development was with silicon pin diodes because of their relatively low cost, high microwave Q , and inherent inertia to changes in characteristics with applied microwave (RF) excitation. To appreciate this requires some description of the pin diode.

2. THE PIN DIODE

Generally, semiconductor pn junctions have rapid response to an applied voltage and even can be used to rectify an RF signal for detection purposes. However the pin has a high resistivity (intrinsic), undoped region between its p and n zones. The result is that holes and electrons which are injected from the p and n zones under forward bias move by diffusion into the i region, where they serve as mobile charge not unlike electrons in copper, rendering the i region conductive to an applied RF signal. Electrons and holes can combine with one another, resulting in carrier death, but to do so they must give up energy equal to the energy difference between the valence and conduction bands (the bandgap). For silicon this is 1.1 electronvolts, and such a drop in energy requires an energy emission, if performed in one step, of a photon of visible light. We do not observe silicon to be glowing with such light emission, because such a transition is very unlikely. Put another way, the lifetime of an electron-hole pair is long, tens of microseconds for the resistivities obtained in practical diodes. The "staircase" of energy steps resulting from impurities and stresses in an otherwise ideal silicon crystal produce a far more likely energy transition between bands, consequently lower carrier lifetime.

The charge storage in a pin's i region is equal to the product of the lifetime and the forward bias (Fig. 2). Thus, for example, a 1000 V breakdown pin diode might have a $5 \mu\text{s}$ lifetime and be biased with a current of 100 mA, resulting in a stored charge of $0.5 \mu\text{C}$. When a 1 GHz sinusoid having a peak current of 50 A is applied to the diode, it causes a peak-to-peak charge movement of less than $0.025 \mu\text{C}$, less than 5% of the charge stored by the bias. The result is that the diode appears to be a low value of resistance throughout the entire RF sinusoid.

The same diode, when operated at a reverse bias of -100 V , is able to sustain, without conduction, an applied

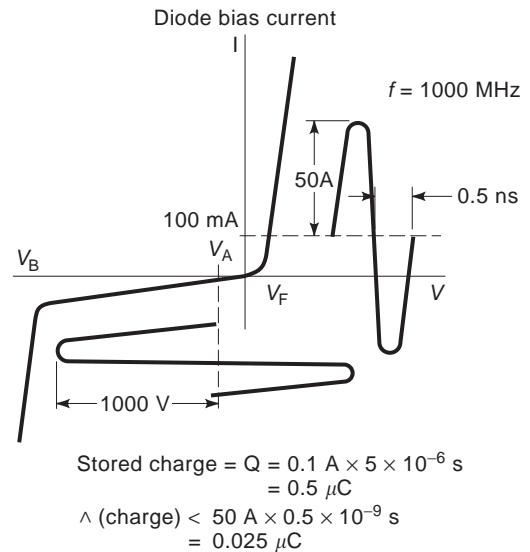


Figure 2. Example comparing charge stored in a pin diode by the bias to the charge movement due to a high-level RF signal.

RF sinusoid of 1000 V peak. This is because the diode requires a microsecond or more to establish a conducting state in the i region, much longer than the 0.5 ns forward-going voltage duration of a 1 GHz sinusoid.

Well-made pin diodes enjoy a bulk breakdown voltage of about $10 \text{ V}/\mu\text{m}$ ($250 \text{ V}/\text{mil}$) of i-region width. It is this bulk breakdown that determines the pin's ability to sustain RF voltage. Conduction due to impact ionization in the i region can occur rapidly, even within an RF half-cycle.

Ryder [1] has likened the bias on a pin diode to the "large signal" and the RF as the "small ac component," the truth of which is evident from the relative magnitudes of the charges related to each. The result of this remarkable behavior is that the pin can control tens of kilowatts of RF power, using only fractions of a watt of bias power.

Using the charge control approach for determining the RF properties the RF resistance, R_i , of the pin under forward bias is found to be [2, p. 62]

$$R_i = W^2 / (2\mu_{AP}\tau i_0) \quad (1)$$

where, in the pin diode's i region, W = the i region thickness; μ_{AP} = the ambipolar mobility (the effective average velocity per unit applied electric field of the holes and electrons); τ = the average lifetime of holes and electrons; and i_0 = the forward bias current.

For the pin used in the example of Fig. 1, $W = 100 \mu\text{m}$ (4 mils), $\mu_{AP} = 610 \text{ cm}^2/\text{V}$ (in silicon), $\tau = 5 \mu\text{s}$, and a suitable bias current is 0.1 A, resulting in an RF resistance of only 0.16Ω . To R_i must be added the ohmic contributions of the p and n regions of the diode, as well as the contact resistances of the diode package. Even so, the total forward-biased resistance R_F is usually 0.5Ω or less. Interestingly, R_i is not dependent on i-region diameter D , directly. However, indirectly it is, since smaller diameter diodes have lower τ , because carriers, on average, are

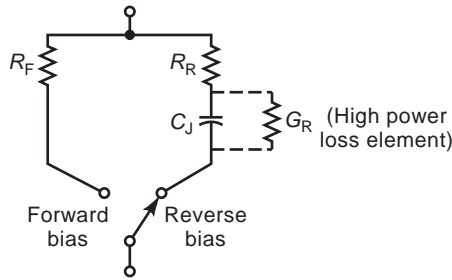


Figure 3. pin-diode chip equivalent circuit.

closer to the i-region boundaries at which recombination can more readily take place.

PIN diode area A does relate to the junction capacitance, C_J , which follows the parallel plate formula fairly closely.

$$C_J = \epsilon_R \epsilon_0 A / W \tag{2}$$

At low frequencies, say, 1 MHz, a C change between zero and reverse bias voltage is observable; however, at RF, it is the minimum capacitance that is experienced due to the dielectric relaxation of the i region [2]. With the high dielectric constant of silicon ($\epsilon_R = 11.8$), there is little fringing of the electric field.

In series with this capacitance is a resistance R_R (not necessarily equal to R_F), which is determined by measurement. An RF figure of merit for the pin is the switching cutoff frequency F_{CS} , given by

$$F_{CS} = 1 / (2\pi C_J \sqrt{R_F R_R}) \tag{3}$$

As will be described later, the F_{CS} value permits a prediction of the minimum insertion loss to be obtained in a phase shifter, switch, or duplexer circuit, even before the circuit configuration has been specified [2, Chap. 5]. The RF equivalent circuit of the pin chip in its two bias states is shown in Fig. 3. Package capacitance and inductance must be added for a complete packaged diode. For our sample diode, having a junction diameter of 0.49 mm (19 mils), $C_J = 0.2$ pF.

When suitably soldered either into a package or onto a good heat sink, it is found that the junction temperature rise of our sample diode is about 15°C per watt of power dissipated in the junction. Equivalently stated, its thermal resistance, $\theta = 15^\circ\text{C}/\text{W}$. In pulsed RF power applications there may be insufficient time during the pulse for thermal equilibrium to be reached. The junction temperature may rise linearly and the diode i region, small as it may seem, must sink the heat dissipated until it can flow out through the thermal resistance path (Fig. 4). The heat capacity HC of the i region is given by

$$\text{HC} = (\text{specific heat}) \times (\text{density}) \times (\text{volume}) \tag{4}$$

which, for a silicon $pin = (0.74 \text{ J/g}\cdot^\circ\text{C}) \times (2.43 \text{ g/cm}^3) \times (\pi D^2 W / 4)$.

For our sample diode, having $D = 49 \mu\text{m}$ (19 mils) and $W = 100 \mu\text{m}$ (100 mils), $\text{HC} = 34 \mu\text{J}/^\circ\text{C}$. This is indeed a small heat capacity, yet it implies that, for a given

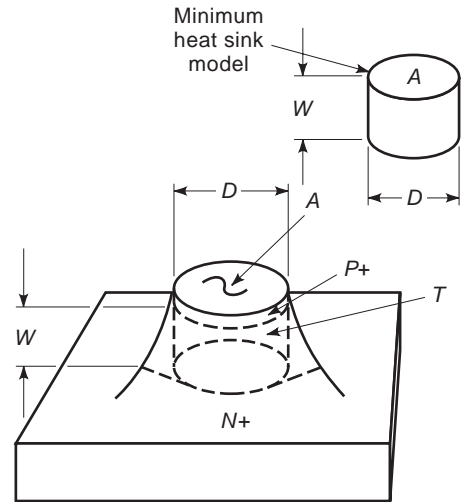


Figure 4. pin model used for heatsinking calculation.

temperature rise, the pin could dissipate nearly 7 times as much power for 1 μs as it could sustain with continuous dissipation. Furthermore, this HC calculation is conservative, because it ignores the heatsinking capacity of the bondwires and the p and n portions of the diode that are in intimate contact with the i region. The product of HC and θ gives the thermal time constant, τ_T , from which the temperature rise, ΔT_J of the i region can be estimated for any pulse length, t , of power dissipation, P_D . Thus

$$\tau_T = (\text{HC})(\theta) \tag{5}$$

$$\Delta T_J = P_D \theta (1 - e^{-t/\tau_T}) \tag{6}$$

The temperature rise is shown graphically in Fig. 5. For the sample diode the minimum τ_T is 500 μs . If a safe temperature rise is considered to be 100°C, then the diode could dissipate 6.6 W continuously, 16 W for 500 μs , 66 W for 50 μs , and so forth. Following the pulse, the diode cools during the interpulse periods with the same thermal time constant (Fig. 6).

This same reasoning could be applied to develop a more complete thermal model of the diode, which includes its thermal surroundings. Figure 7 shows a more representative model of the diode, with its thermal elements and

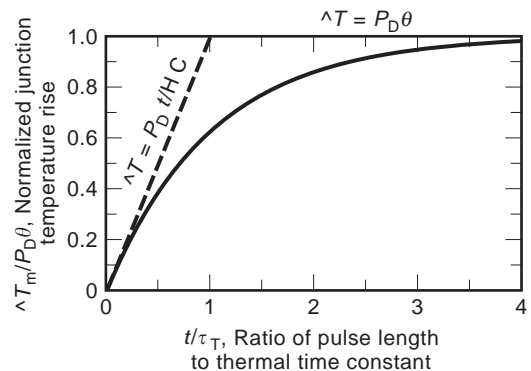


Figure 5. General pulsed temperature-rise profile of a pin diode, using the minimum-time-constant model.

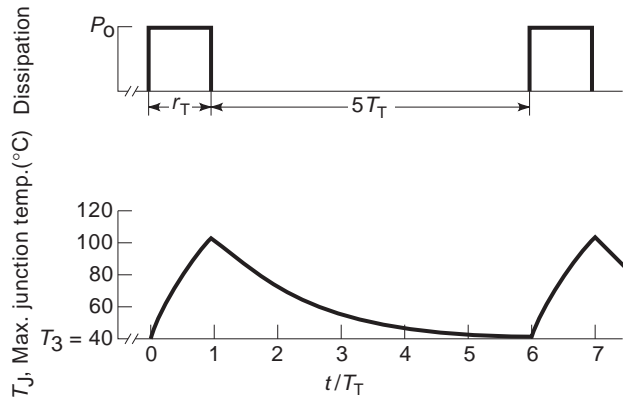


Figure 6. Sample estimate of pin junction temperature during a train of power dissipating pulses.

that of the packaging materials. Generally, however, the simple conservative model is sufficient to estimate the maximum temperature rise to be expected from a given pulsed power dissipation.

A representative listing of a wide range of pin diodes is shown in Table 1. Given these parameters, it is possible to estimate most of the performance of a variety of RF phase shifter, switch, and duplexer circuits, even before the circuits themselves are specified.

3. LOADED LINE PHASE SHIFTER

A diode phase shifter is a device whose primary function is to change, by means of a control bias, the propagation

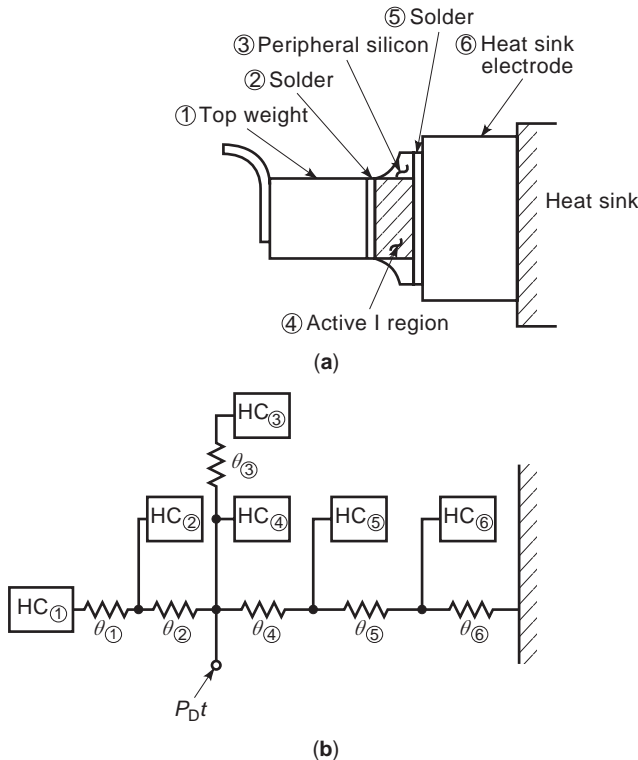


Figure 7. Construction pin detail and its thermal model.

phase of a microwave signal. Most switches, attenuators, limiters, and duplexers introduce phase shift, although seldom by design. Moreover, since any reactance placed in series or shunt with a transmission line introduces phase shift, the possibilities for phase shift networks are unlimited. However, adding the requirement that the device has minimum insertion and reflective losses reduces the selection of practical circuits.

Most think of switching between circuit paths as a direct means of phase shift (Fig. 8). Actually this is a switched time-delay circuit, producing phase shift that is linearly proportional to frequency. This might seem all the more desirable, since it could lead to broadband array antenna steering. However, in practice, the switching between paths is accomplished with limited isolation of the nonselected path. Figure 9 shows how the loss can increase dramatically when the OFF arm resonates.

While time delay circuits have a place, they are not efficient. All the RF power must be switched between paths and four diodes minimally are required to do this. The insertion loss is the same for all bits, whereas in a phase shifter circuit, only two diodes are required per bit and the diode loss is much less for small phase shift bits. Accordingly, we shall omit further discussion of time-delay circuits and proceed to phase shifters (which, generally, do not have linearly increasing phase change with frequency).

Initially it was thought that very high power phase shifters would be required. In fact, the author conducted a Navy-sponsored project, whose objective was a 100 kW peak power phase shifter—an objective that was met and applied to a high power array! The key to the development was the recognition that, since numerous diodes would be required for very high power, each contributing a small amount of the total phase shift required, a circuit lightly coupling the diodes to the propagating wave was needed.

The solution was the transmission phase shifter (Fig. 10), in which pairs of diode-switched susceptances load the transmission line. The spacing of the susceptances, about 90°, is selected to cause mutual cancellation of their reflections. The magnitude of the susceptances is made small (less than 0.4 Y₀), and so the diodes are subjected to relatively small RF currents and voltages, producing low dissipation in each diode. This enhances both power-handling and insertion-loss performance.

This loaded line section has an equivalent circuit [2, p. 410] consisting of a uniform line section of new characteristic admittance Y_E and electrical length θ_E, related to the loaded line's admittance Y₀ and electrical length θ by

$$\cos \theta_E = \cos \theta - (B/Y_0) \sin \theta \tag{7}$$

$$Y_E = Y_0 [1 - (B/Y_0)^2 + 2(B/Y_0) \cot \theta]^{1/2} \tag{8}$$

Consider Eq. (7) first. If the line loading susceptance is somehow switched by the pin diode between equal-magnitude and opposite-sign susceptors, B₁ and B₂, then the electrical length of the loaded line is described by the vector diagram in Fig. 11.

Notice from Fig. 11 that when θ = 90° the sine of the phase shift Δφ/2, produced by each of the equal susceptances B_i, is equal to the normalized susceptance term

Table 1. Typical Parameters of Available PIN Diodes

Symbol	Electrical and Physical Parameters	Units	<div style="display: flex; justify-content: space-between; font-size: small;"> M/A-47889 M/A-47891 M/A-47892 M/A-47893 M/A-47894 M/A-47895 M/A-47896 M/A-47897 M/A-47898 M/A-47899 M/A-47152 M/A-47154 M/A-47156 </div>															
			150(6)				100 (4)				50 (2)				25 (1)		12 (0.5)	6 (0.25)
(1) W	i region width	μm (mils)	150(6)	100 (4)				50 (2)				25 (1)		12 (0.5)	6 (0.25)	2 (0.1)		
(2) V_{BB}	Bulk breakdown voltage	kV	1.8	1.2				0.6				0.3		0.15	0.07	0.03		
(3) D	i region effective diameter	Mm (mils)	2.3 (92)	1.56 (61)	1.10 (43)	0.49 (19)	0.35 (14)	0.65 (26)	0.35 (14)	0.25 (10)	0.25 (10)	0.18 (7)	0.12 (5)	0.09 (3)	0.05 (2)			
(4) C_j	Junction capacitance	PF	3	2	1	0.2	0.1	0.7	0.2	0.1	0.2	0.1	0.1	0.1	0.1			
(5) T_w	Average carrier transit time	ns	8500	3800				950				250		55	14	1.5		
(6) I_F	Forward	mA	250	150	100			50			25		25	25	25			
(7) V_R	Reverse	V	200	100				50				25		10	10	10		
(8) R_F	Forward resistance at 1 GHz at i_F	Ω	0.2	0.3	0.4	0.8	1	0.4	0.7	1	0.9	1	1	1	1			
(9) R_R	Reverse resistance at 1 GHz at V_R	Ω	0.2	0.3	0.5	3	6	0.6	3	4	2	4	4	4	3			
(10) f_C	Cutoff frequency (reverse bias)	GHz	250	250	300	250	250	350	250	400	400	400	400	400	550			
(11) f_{CS}	Switching cutoff frequency	GHz	250	250	350	500	600	350	550	700	600	800	800	800	800			
(12) τ	Carrier lifetime at 10 mA	μs	15	8	5	4	3	2	1.5	1	0.8	0.5	0.2	0.1	0.02			
(13) θ	Thermal Resistance	$^{\circ}\text{C}/\text{W}$	1.5	3	4	15	25	7	12	15	15	25	30	35	40			
(14) HC	i region heat capacity	$\mu\text{J}/^{\circ}\text{C}$	1100	340	170	34	17	30	8	4	2	1	0.2	0.06	0.007			
(15) τ_t	Minimum thermal time constant	μs	1650	1000	680	500	425	210	96	60	30	25	6	2	0.3			

Offered by the M/A-COM Division of AMP Inc. in Burlington, MA.

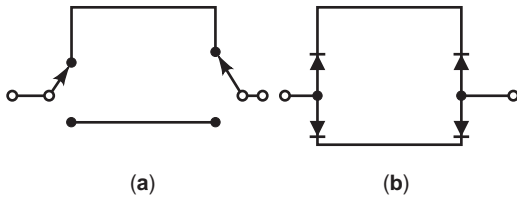


Figure 8. Schematic for switched delay line phase shifter.

$BZ_0 (Z_0 = 1/Y_0)$. Then, approximating the sine by its angle, the total phase shift in radians obtained by switching between B_1 and B_2 is given by

$$\Delta\phi \cong (B_2 - B_1)Z_0 \tag{9}$$

For example, if the normalized susceptances switch between plus and minus 0.2, then the phase shift is 0.4 radians, near 22.5° , a 16th of a wavelength. The respective 4 bits of a phase shifter can be made up of one, two, four, and eight such sections in cascade.

But, the reader may ask, suppose that the individual reflections from each section, although small in themselves, combine when 15 such sections are cascaded to produce very large reflection and with it high mismatch loss.

Such is not the case. Referring to Eq. (8) and applying the values $\theta = 90^\circ$ and $|B_i Z_0| = 0.2$, gives $Y_E = 0.98Y_0$. This is true for either positive (capacitive) or negative (inductive) line loading. Thus, even as the phase length of

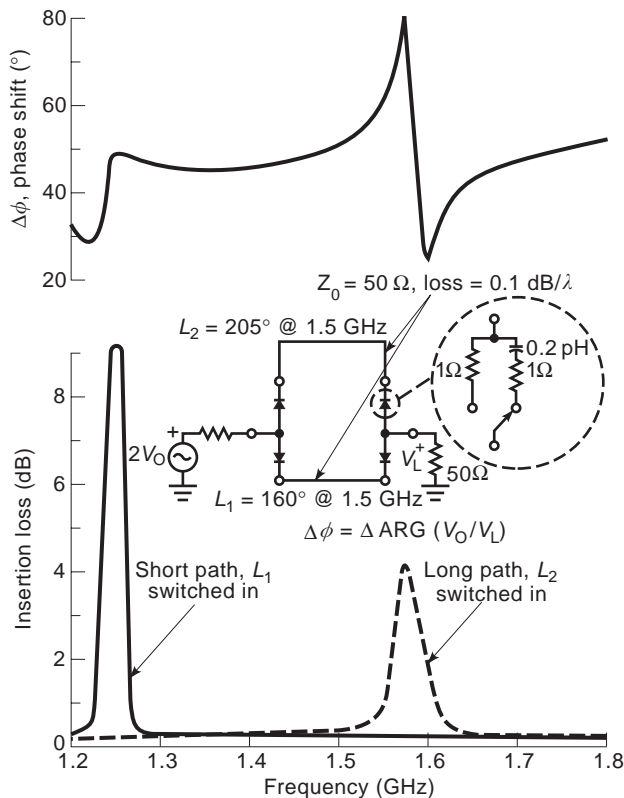


Figure 9. Switched path circuit example demonstrating loss resonances.

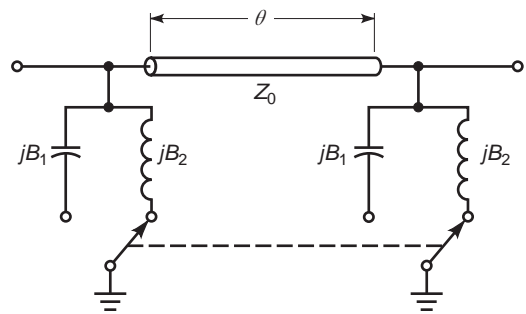


Figure 10. Switched transmission phase shifter section, also called the loaded line phase shifter.

the section changes, its characteristic admittance does not. Nor is its value very different from Y_0 . Accordingly, an arbitrarily long cascade combinations of such sections would not result in a VSWR larger than 1.04, provided that there are no line sections intervening between the phase shift sections. Even this small mismatch could be further compensated by installing a quarter-wave line of admittance $1.02Y_0$ at each end of the phase shifter cascade. This inherent match of the loaded line phase shifter is one of its most useful attributes.

It now remains to design the line loading circuits, such that a two-state diode can yield the ± 0.2 normalized susceptance switching. The first circuit approach used shunt stubs, whose length was varied by pin-diode switches (Fig. 12). The diodes were similar to the 0.2-pF, 4-mil I region model described in Table 1. The line lengths α_1 and α_2 were adjustable. The phase shift was proportional to α_1 while the average of the two lengths was adjusted to control the transmission match. With 5° of phase shift per stub pair, a level of 140 kW peak power was sustained with 0.001 duty cycle, 5- μ -sec-long pulses at 1300 MHz. There were eight sections in the experimental model and the results are shown in Fig. 13.

The maximum powers listed are those that cause or nearly cause burnout, usually occasioned by voltage breakdown of the pin diodes in the reverse biased state. For pins, as well as all semiconductors, reliable operation requires a rating that impose only 50% of this maximum voltage stress on the semiconductor. Since power is related

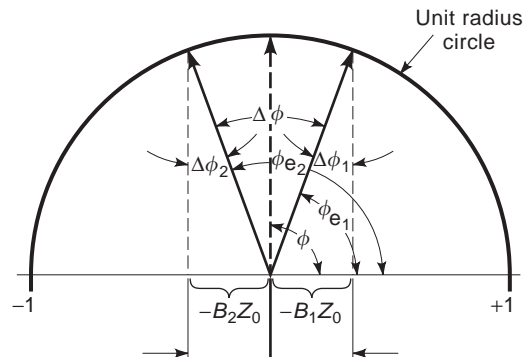


Figure 11. Graphical representation of the loaded line phase shifter's change in electrical length caused by switching the loading susceptances.

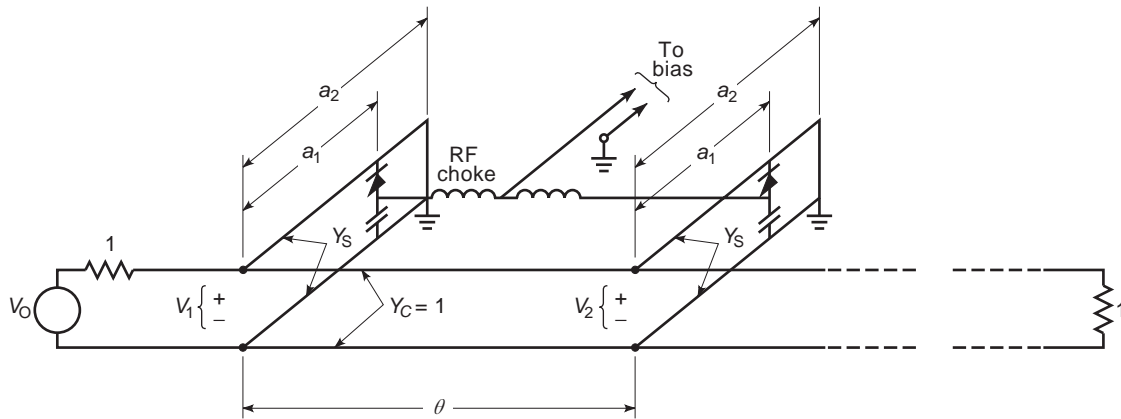


Figure 12. Equivalent circuit for one section of the switched stub, loaded line phase shifter tested at 1300 MHz under high peak power.

to the square of voltage, this means devices need be rated at one-fourth the power level, which would cause immediate failure.

For microwave phase shifters this is especially useful in the event of a short-circuited output, which could nearly double the voltage stress on its diodes. Such a short can result from an arc over or damaged radiating element, even a disconnected output. Indeed, a customary acceptance test for a high-power-control device is operation into a short-circuited load, which is varied through all phases. Given this derating, very high reliability of pin phase shifters is experienced, as is necessary in an array antenna.

While it is true that no practical phased array could radiate such levels (a 2500-element array using 35 kW

phase shifters would radiate 87 MW peak power), this result is significant, because single-pole double-throw switches can be constructed by installing such phase shifters between 3 dB hybrid couplers, allowing, for example, the full output power of a radar to be switched between alternate antennas.

The loaded line approach was extended to 3 GHz in a circuit in which the diode's own capacitance terminates the quarterwave shunt stub. Switching between forward and reverse bias changed between $-j50 \Omega$ (the diode has about 3 pF capacitance) and its forward resistance of 0.5Ω . Adjusting the shunt stub impedance produced as much as 45° phase shift per pair and a maximum RF peak power of 70 kW [2, p. 429]. This phaser was used in the U.S. Safeguard system, of which only a prototype system was built.

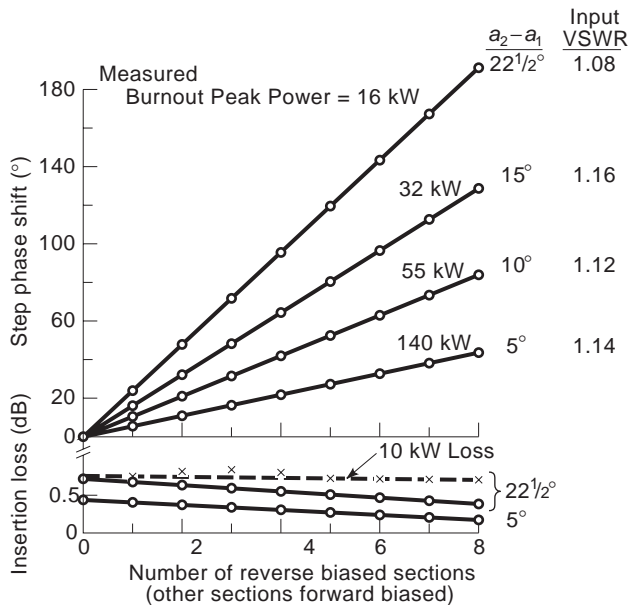
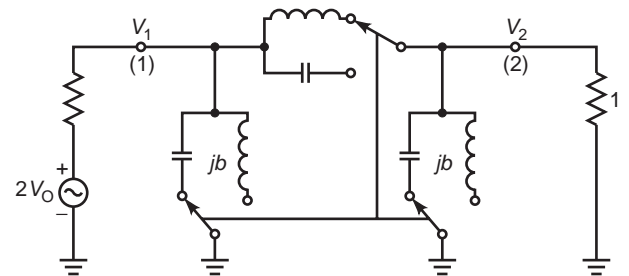


Figure 13. L-band measurements of phase shift, insertion loss, and ultimate peak power capability of the switched stub, loaded line phase shifter. Varying switched stub lengths (a_2 and a_1) produced the different phase shift values and adjusted transmission match.



$$\begin{bmatrix} A & B \\ C & D \end{bmatrix}_{1,2} = \begin{bmatrix} 1 & 0 \\ jb & 1 \end{bmatrix} \cdot \begin{bmatrix} 1 & jx \\ 0 & 1 \end{bmatrix} \cdot \begin{bmatrix} 1 & 0 \\ jb & 1 \end{bmatrix}$$

$$= \begin{bmatrix} (1 - bx) & jx \\ jb(2 - bx) & (1 - bx) \end{bmatrix}$$

For a match, $|A + B|^2 = 1$
 $x = \frac{2b}{1 + b^2}$

and under this condition,
 $\phi = \arg(V_2/V_0) = -\arg(A + B)$

$$\phi = \tan^{-1}\left(\frac{2b}{b^2 - 1}\right)$$

Figure 14. The lumped-element π -configuration phase shifter.

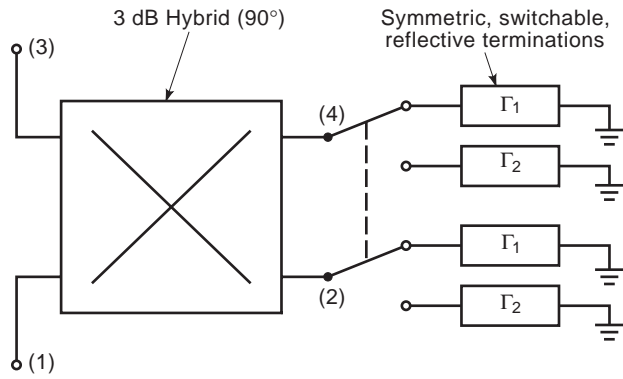


Figure 15. The reflection phase shifter circuit employing a coupler to achieve matched two-port transmission.

4. LUMPED-ELEMENT PHASE SHIFTERS

If the quarterwave section of line in the loaded line section is replaced with a diode switchable reactance (Fig. 14), the lumped-element, *highpass-lowpass* π circuit is obtained, which can yield up to 180° of phase shift. A similar tee configuration [2] is also practical. These circuits are advantageous in integrated circuit applications, because they employ a minimum of switching elements and no space-consuming distributed elements.

For modest power levels, the most common diode phase shifter configuration is the reflection circuit, employing a 3-dB, 90° coupler (Fig. 15). The coupler can be realized in numerous ways, three of which are shown in Fig. 16. The operation of the coupler is to convert the pair of variable phase reflection circuits containing pin diodes into a matched two-port network, having the reflection angle change of the terminations.

This operation can be explained based on the coupler's operation. Consider the backward-wave (hybrid coupler) circuit at the bottom of Fig. 16. Power enters the coupler at port 1 and divides evenly to exit at ports 2 and 4. The wave exiting port 4 has an additional 90° . On encountering the reflective circuits at ports 2 and 4, all energy reenters the

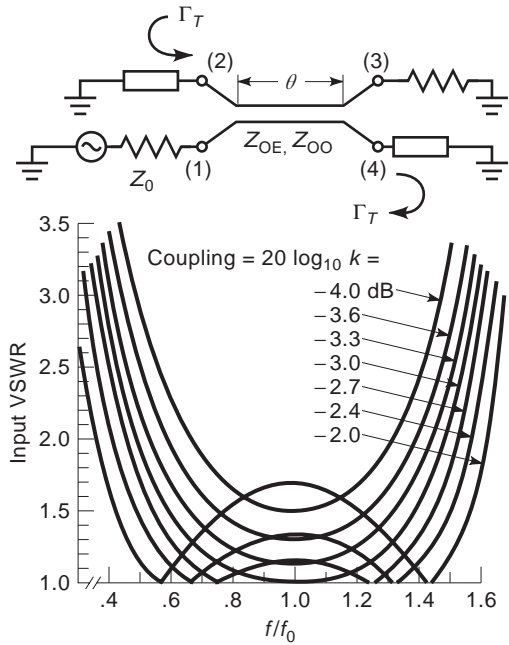


Figure 17. VSWR performance with frequency for a coupled-line hybrid coupler terminated in symmetric reflections for various coupling values. Note that the -2.4 -dB coupler would operate with a maximum VSWR of 1.35 over a band of 0.5 – $1.5 f_0$, a 3–1 frequency range (f_0 is the frequency at which the coupling section is 90° long).

coupler, but due to the second 90° phase difference in the signals on this second pass, they cancel at the input (port 1), but add perfectly at the normally decoupled port 3.

This operation requires perfectly even power split and 90° phase difference. The backward coupler (but not the other types shown) has the remarkable property that the 90° phase difference prevails at all frequencies [2, p. 194]. Of course, the power split varies with frequency, being equal at only one frequency (or two frequencies if the design is overcoupled at the center frequency). Nevertheless, more than octave bandwidth (Fig. 17) with modest VSWR

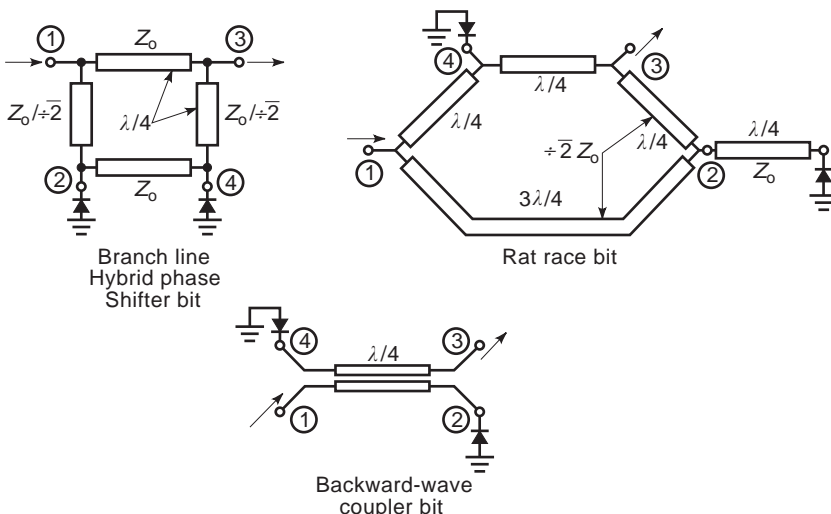


Figure 16. Methods of realizing 3-dB, 90° couplers.

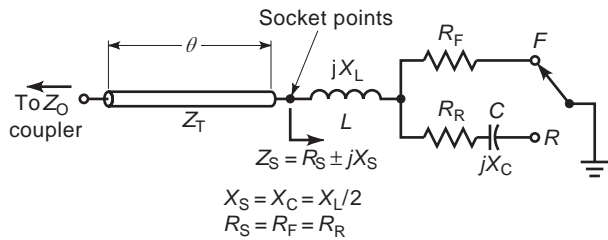


Figure 18. The loss-equalized phase shifter termination with series inductor and quarter-wave transformer to adjust phase shift value.

can be obtained with a single coupled line section, even more bandwidth with multistage couplers.

As was true of the loaded line circuit, there are numerous ways to configure the pin in a reflection circuit to yield any desired phase shift. However, regardless of what configuration is used, if the circuit is designed to present to the pin its maximum sustainable RF voltage V_M in the reverse biased state and the maximum sustainable RF current I_M in the forward-biased state, Hines [3] showed that the maximum power P_M sustainable when the circuit yields a phase shift $\Delta\phi$ is as shown in Table 2. Similarly, if the circuit is designed such that the fraction of incident power dissipated (P_D/P_A) is the same in both forward bias and reverse bias, then the minimum for this ratio is that shown in Table 2.

Generally, the choice of circuit that would provide the maximum power stresses to the diode is not the same

choice that would produce equal power dissipation in its two states, but the two limits are very useful for estimating what performance limits a practical circuit might incur. Furthermore, since phase shifter bits are usually designed for low loss, the average of the losses in the two bias states is about equal to the minimum value specified in Table 2. The loss so calculated is for pin dissipation only. Circuit losses add to this value; but, as will be shown, a practical 3-bit, L-band phase shifter can be made with less than 1 dB of total insertion loss.

If the series resistance of the pin is about the same in both bias states ($R_F = R_R$), an equal loss phase shifter can be made by installing the pin at the 3 dB outputs of the coupler with a series inductance whose reactance magnitude is half that of the pin's capacitive reactance. By installing a quarterwave transformer between coupler and diode termination (Fig. 18), the phase shift can be adjusted to any desired value, allowing use of the same pin and series inductance for all bits (Fig. 19).

The method for constructing the backward-wave coupler [2] reflection phase shifter is shown in Figs. 20 and 21. A three-layer dielectric stripline sandwich is employed, wherein the center dielectric is used for the coupled lines. Using this approach, a 3-bit phase shifter was designed for use in the Cobra Dane radar built for the U.S. Air Force by the Raytheon Company on Shemya Island, near the western tip of the Aleutian Island chain. To minimize losses, the outer dielectrics were removed, resulting in air stripline in the transformer and diode regions. The operating bandwidth was approximately 1200–1400 MHz,

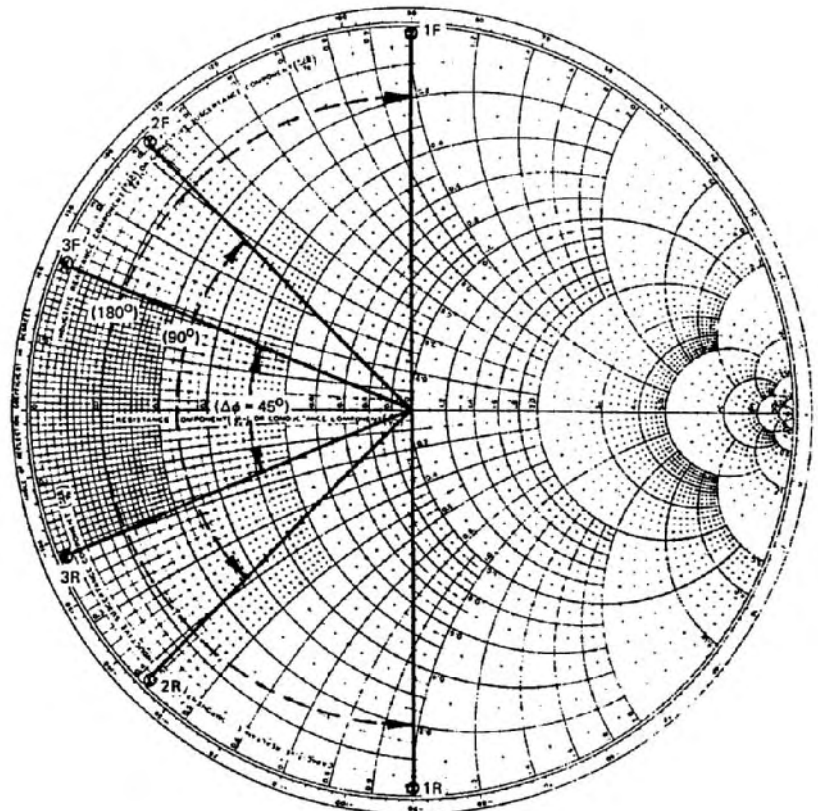


Figure 19. The reflection coefficients seen at the coupler for loss-equalized 180°, 90°, and 45° phase shift bits.

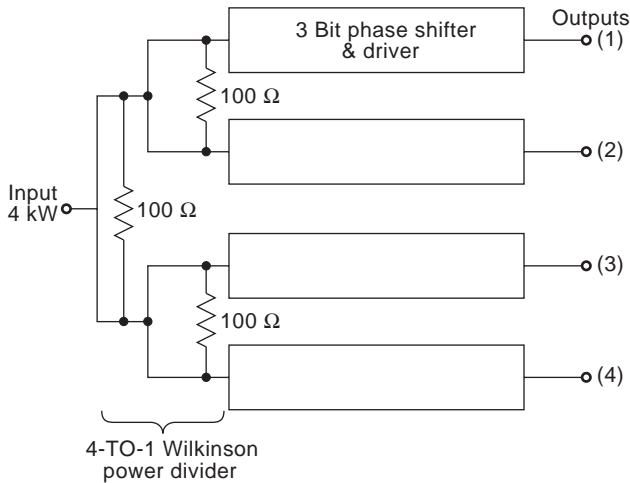


Figure 20. The 4-to-1 power divider and phaser assembly.

and the required power-handling capacity was to be 1 kW peak, with evenly spaced pulses of up to 2000 μs and 0.05 duty cycle.

The schematic diagram for the unit is shown in Fig. 20. Four separate phase shifters and a Wilkinson equal-phase power divider were housed in a single assembly to reduce costs and interface connections. Figure 21 shows the diode mount detail, and measured performance is shown in Fig. 22. A photograph of the completed assembly is shown in Fig. 23.

The diode used for all bits was the 3-pF, 1800-V bulk breakdown pin listed in the first column of Table 1. The individual phase shifter section, tested with -200 V bias on all diodes, sustained 4.1–4.8 kW peak power before burnout, and therefore could be rated for 1 kW operating level. The insertion loss of each phase shifter, including both pin diode and circuit losses, was 0.7 dB. About 16,000 phase shifters were installed in the Cobra Dane antenna array, which radiates approximately 16 MW peak and 1 MW of average power. At the time of installation the array was operated 20 h per day, resulting in nearly 2 million device hours daily.

In separate projects, pin phase shifters of 3- and 4-bit designs were implemented at S, C, and X bands [2, Chap. 6]. C-band phasers find use in the scanning-beam microwave landing system (MLS), for which a worldwide standard exists. Generally, higher-frequency diode phasers have progressively higher insertion loss and lower peak

Table 2. Limits of Power Handling and Insertion Loss (P_D/P_A) for Transmission and Reflection Phase Shifters

	Power	Loss
Reflection circuit	$P_M = \frac{V_M I_M}{4 \sin(\Delta\phi/2)}$	$\frac{P_D}{P_A} \approx f \left(\frac{f}{f_{cs}} \right) \sin \left(\frac{\Delta\phi}{2} \right)$
Transmission circuit	$P_M = \frac{V_M I_M}{2 \tan(\Delta\phi)}$	$\frac{P_D}{P_A} \approx 2 \left(\frac{f}{f_{cs}} \right) \tan(\Delta\phi)$
		$10f < f_{cs}$

$$f_{cs} = \frac{1}{2\pi c_j \sqrt{R_F R_R}}$$

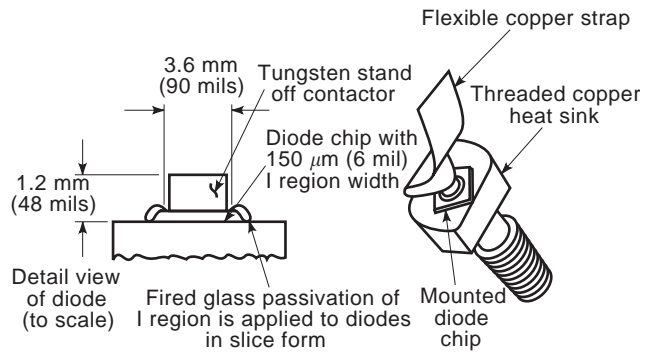


Figure 21. The high-voltage pin chip mounted on a copper heat-sink.

power capacity. At X band, the 4-bit design had 2 dB of insertion loss and a burnout power of about 1000 W with 1 μs pulselengths and 0.001 duty cycle.

5. CONSTANT PHASE SHIFT WITH FREQUENCY

Frequently there is a need for a phaser whose phase shift is constant over a considerable bandwidth. Schiffman [2,4] observed that when the backward wave coupler has ports 2 and 4 connected to each other (Fig. 24), an allpass network results, having a dispersion characteristic (an electrical length that does not increase linearly with frequency) that can be adjusted with the coupling coefficient (Fig. 25).

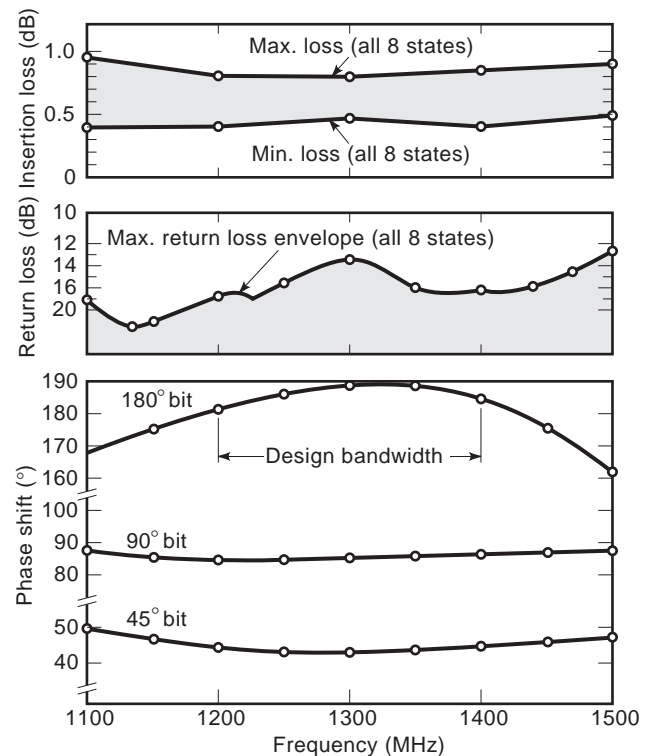


Figure 22. Measured performance for the L-band, 3-bit stripline phase shifter.

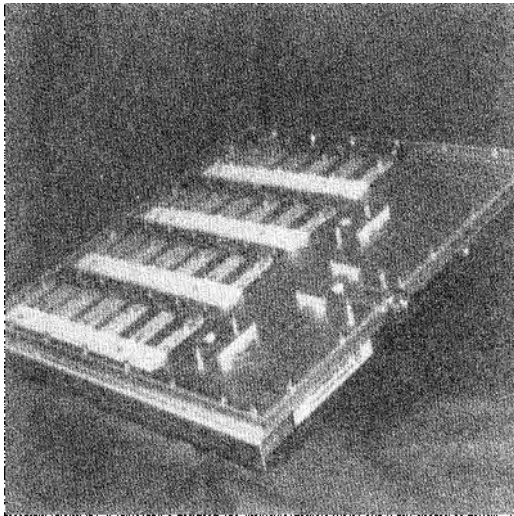


Figure 23. Photograph of the Cobra Dane 4-to-1 divider and highpower phase shifter assembly.

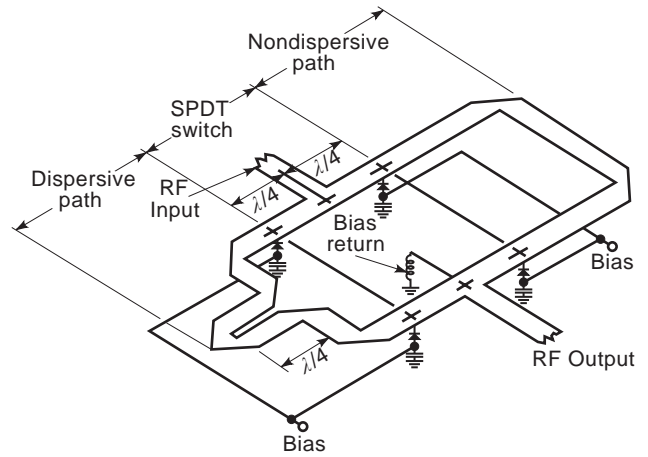


Figure 26. A stripline Schiffman phase shifter using diode path switching (after Grauling and Geller [5]).

variable over a 5–1 or wider range with the application of a reverse bias. Such a variable reactance can be used in place of the pin in the reflection phase shifter circuit, to provide phase control that varies continuously with applied bias voltage. Of necessity, the continuous phase

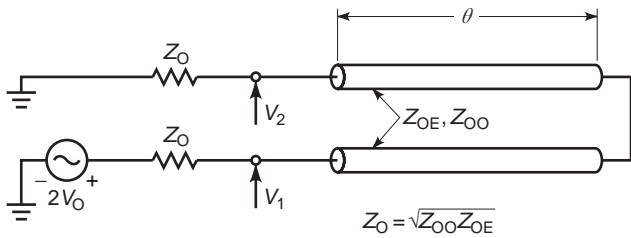


Figure 24. Schiffman phase shift section.

A switched-path phase shifter (Fig. 26), which alternates between a Schiffman section and a uniform transmission line of appropriate length, can be made to have a nearly constant phase shift over an octave bandwidth (Fig. 27).

6. VARACTOR DIODE, CONTINUOUS PHASE SHIFTER

The varactor diode, lacking a wide I region, consists only of a pn junction, whose capacitance at RF frequencies is

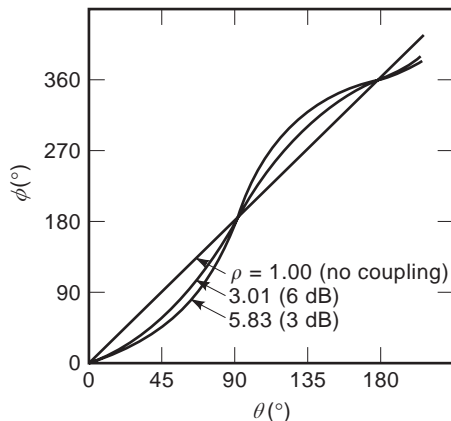


Figure 25. Dispersion characteristic of the Schiffman section.

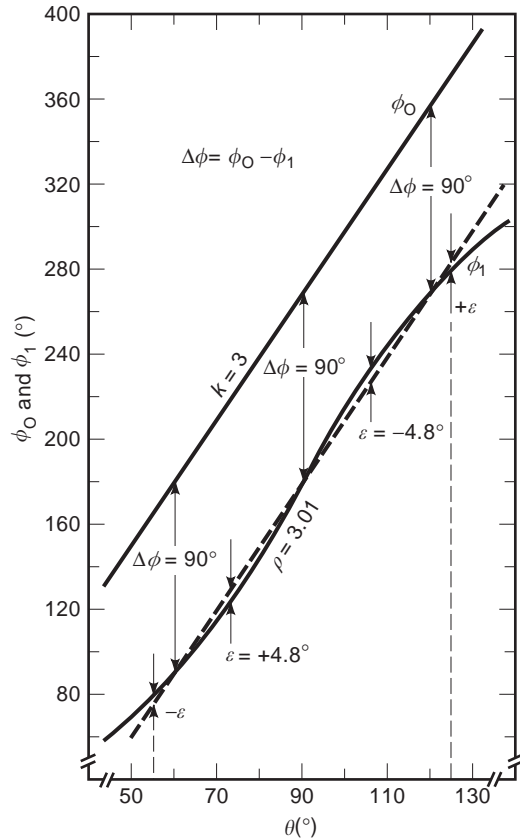


Figure 27. The octave bandwidth Schiffman phase shifter formed by a $\rho = 3.01$ [2] coupled line pair θ long a uniform line path 3θ long. Phase shift is $90^\circ \pm 4.8^\circ$ for $55^\circ \leq \theta \leq 125^\circ$, a 2.24:1 frequency ratio.

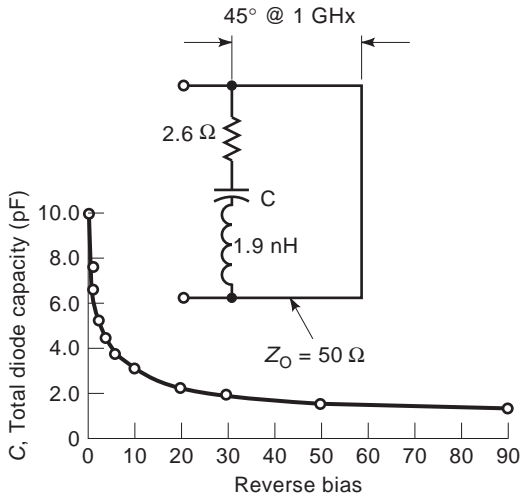


Figure 28. Representative varactor diode capacitance and circuit termination for a varactor continuous phase shifter.

shifter is limited to low power, below 1 W, since the varactor capacitance can change at the RF rate. In fact, varactors are used as the nonlinear element in frequency multipliers.

For varactor phase shifters, a figure of merit F applies [2, p. 486], relating the number of degrees of phase shift per decibel of loss to the cutoff frequency of the varactor, $f_c = 1/2\pi RC_{MIN}$, where C_{MIN} is the minimum capacitance obtained at a reverse bias just before the breakdown voltage, V_B ; M is the ratio of the capacitance at zero volts to

that at V_B ; and f is the frequency of operation.

$$F = (fc/f)(1 - 1/M)(6.6^\circ/\text{dB}) \tag{10}$$

This equation applies when the loss is small, below 1 dB. Thus a varactor having a junction capacitance which varies from 10 to 2 pF in series with a 2.6 Ω resistance (Fig. 28) has a cutoff frequency of 159 GHz and could yield 323°/dB at 1 GHz. Circuit losses must be added to this value.

Generally, higher loss is obtained as a result of the tuning effect of the varactor’s series inductance and the circuit reactance employed to transform the reflection coefficient into a range which covers both the upper (inductive) and lower (capacitive) halves of the Smith chart (Figs. 29 and 30).

The varactor phase shifter experiences little variation with temperature, typically only a 1% change in total phase shift over a 50°C temperature change. Even this small change may be attributable to circuit changes and possibly could be reduced further. However, variations in RF power beyond one watt produce significant changes, particularly near zero bias, at which the applied RF voltage swings into the forward conducting region (Fig. 31).

7. THE FET AS A SWITCHING DEVICE

Actually, any electronically switched device can be used as the control element in a phase shifter as long as it has sufficient Q to provide acceptably low insertion loss. The considerable strides made in the development of field effect

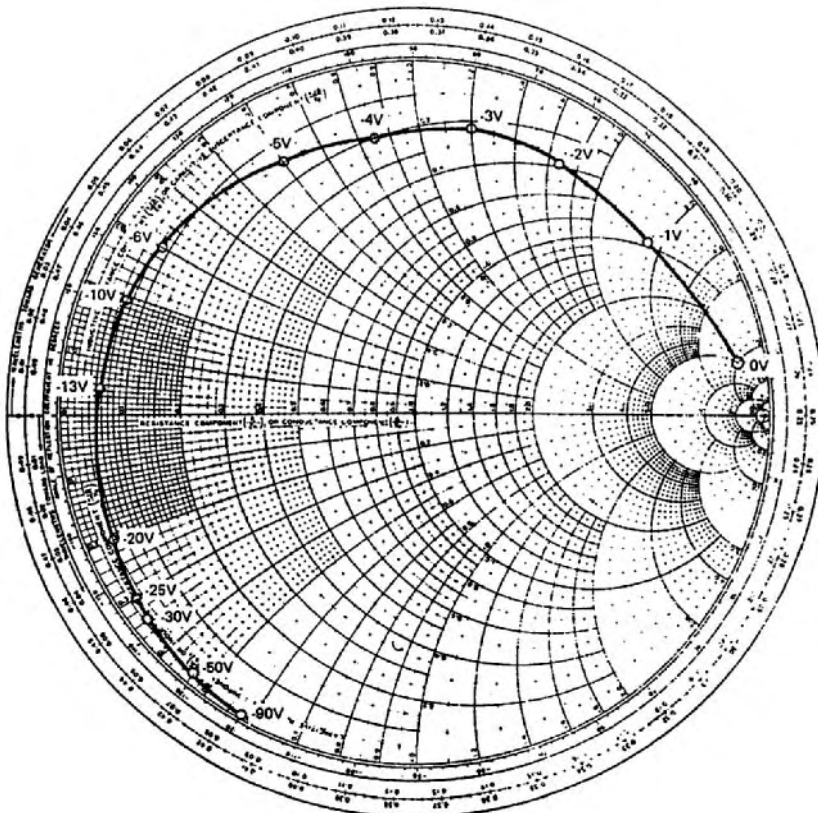


Figure 29. Phase shift (change in reflection coefficient angle) and loss (departure from unity reflection coefficient magnitude) of varactor circuit in Fig. 28.

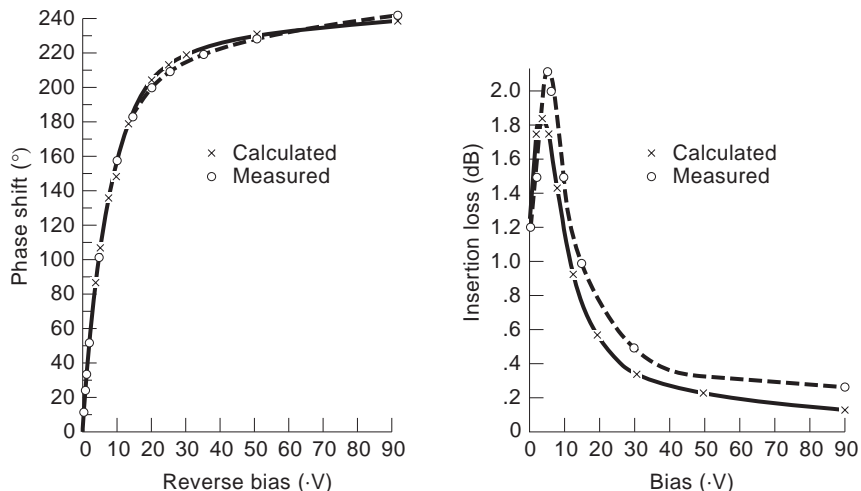


Figure 30. Calculated and measured phase shift and insertion loss at 1 GHz for the varactor termination of Fig. 27.

transistors (FETs) both for microwave power generation and switching [12–18] have two important implications for semi-conductor phase shifting.

First, phase shifting for array antennas can be performed at low power levels with subsequent amplification by FETs and other solid-state devices to the required output level at the array antenna radiating element. With this approach the achievement of lowest insertion loss is less critical. Of course, the amplification generally will be nonreciprocal, requiring that switching be performed between transmission and reception modes.

Second, the phase shifter can be realized using FET elements for switching instead of pin diodes. FET switches have an inherent advantage when compared to pin diodes in that the FET has a third (gate) terminal to which bias is applied, simplifying the design of the microwave circuitry in which bias blocking otherwise is needed for two terminal control elements.

FETs can be modeled as a lossy capacitor in the non-conducting state and a resistor in the conducting state,

essentially the same equivalent circuit format used for the PIN diode. As a result, most of the formation developed for the pin can be used directly with FETs. The FET switched phase shifter can be reciprocal, as is the pin phase shifter.

Acknowledgment

The contents of this article have been excerpted, with permission, from the author’s text, *Microwave Semiconductor Engineering* [2]. The author thanks Randy Rhea and Gary Breed for this opportunity. The phase shifter development described took place at M/A-COM, formerly Microwave Associates, and now a division of AMP, Inc., located in Burlington, Massachusetts. Much of the development of both the pin and varactor diodes, as well as the circuits to exploit them, was sponsored by the U.S. Government through its Air Force, Navy and Army research agencies.

BIBLIOGRAPHY

1. R. Ryder, Bell Telephone Labs, Murray Hill, NJ, in a talk given at the NEREM Conference in Boston, MA, circa 1970.
2. J. F. White, *Microwave Semiconductor Engineering*, Noble Publishing, Tucker, GA (originally published under the title *Semiconductor Control*, Artech House, Norwood, MA, 1977; later republished under the current title by Van Nostrand Reinhold Co., New York, 1982, and translated with permission into Japanese).
3. M. E. Hines, Fundamental limitations in RF switching and phase shifting using semiconductor diodes, *Proc. IEEE* **52**:697–708 (1964).
4. B. M. Schiffman, A new class of broadband microwave 90° phase shifters, *IEEE Trans. Microwave Theory Tech.* **MTT-6**:232–237 (1958).
5. C. H. Grauling and B. D. Geller, A broadband frequency translator with 30 dB suppression of spurious sidebands, *IEEE Trans. Microwave Theory Tech.* **MTT-18**:651–652 (1970).
6. W. J. Ince and D. H. Temme, Phasers and time delay elements, in L. Young, ed., *Advances in Microwaves*, Vol. 4, Academic Press, 1969, pp. 1–189.

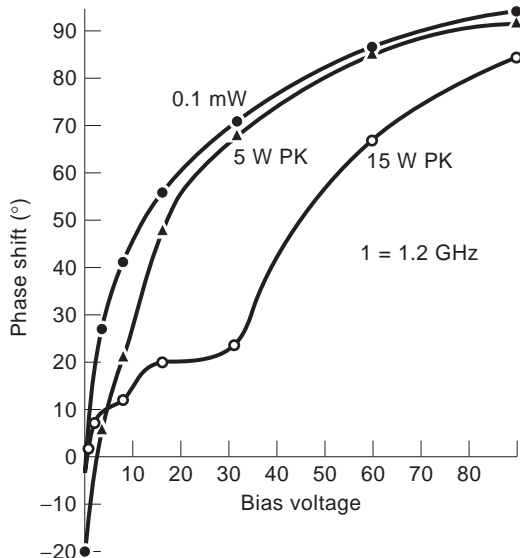


Figure 31. Typical variation of phase shift with RF input power.

7. I. Bahl and P. Bhartia, *Microwave Solid State Circuit Design*, Wiley, New York, 1988, Chaps. 8, 13.
8. J. F. White, Semiconductor Control Devices: PIN Diodes, in K. Chang, ed., *Handbook of Microwave and Optical Components*, Vol. 2, Wiley, New York, 1990, Chap. 4.
9. A. I. Sreenivas and R. Stockton, Semiconductor control devices: Phase shifters and switches, in K. Chang, ed., *Handbook of Microwave and Optical Components*, Vol. 2, Wiley, New York, 1990, Chap. 5.
10. S. Yngvensson, *Microwave Semiconductor Devices*, Kluwer, Norwell, MA, 1991, Chap. 9.
11. K. Chang, *Microwave Solid State Circuits and Applications*, Wiley, New York, 1994, Chap. 8.
12. A. Mallet-Guy et al., Modeling and performance of a sub-nanosecond high isolation DC-18 GHz monolithic SPST with driver, *IEEE MTT-S Int. Microwave Symp. Digest*, 1991, Vol. 1, pp. 193–196.
13. H. Takasu et al., GaAs FET switch model for X-band MMIC phase shifter design, *1994 IEEE MTT-S Int. Microwave Symp. Digest*, 1994, Vol. 3, pp. 1413–1416.
14. M. J. Schindler and T. E. Kazior, High power 2–18 GHz MMIC TR switch, *Appl. Microwave Mag.* 90–94 (summer 1991).
15. F. McGrath et al., Multi gate FET power switches, *Appl. Microwave Mag.* 77–86 (summer 1991).
16. T. Tokumitsu, I. Toyoda, and M. Aikawa, Low voltage, high power T/R switch MMIC using LC resonators, *IEEE Microwave Millimeter-Wave Monolithic Circuits Symp. Digest*, June 1993, pp. 27–30.
17. A. Ehoud et al., Extraction techniques for FET switch modeling, *IEEE MTT-S Trans.* Aug. 1995, pp. 1863–1867.
18. K. Purnell et al., GaAs MESFET, passive element, MMIC phase shifter, *IEEE Int. Microwave Symp. Digest*, 1996, Vol. 2, pp. 1197–1200.

MICROWAVE PHOTONICS: TECHNOLOGICAL EVOLUTION AND ITS APPLICATIONS

AFSHIN S. DARYOUSH
Drexel University
Philadelphia, Pennsylvania

1. INTRODUCTION

The last two decades of the twentieth century witnessed significant advances in IC technologies and proliferation of commercial fiberoptic communication techniques, and microwave photonics has emerged as a new discipline. It is envisioned that microwave photonics systems will be employed in many civilian and military systems. Although optical control of microwave devices and circuits was initially considered as one of the most promising applications of microwave photonics, now its most widely used applications are for optical distribution and processing of information in telecommunication systems, such as radio-over-fiber, as shown for a wireless local-area network in an office environment. In this figure, personal computers (PCs) are networked together through this hybrid wireless–fiberoptic networks in applications such as radio-over-fiber (ROF). The digital data from the PC is upconverted by a millimeter-wave (MMW) stable carrier and are then radiated by an omnidirectional antenna. The modulated received RF signal is then downconverted to the coded digital signals using the same stabilized MMW local oscillator (LO). The coded digital signal is then networked to other users through a high-speed fiberoptic network at data rates well above 100 Mbps (megabits per second).

An important component of a personal communication services (PCS) for the portable PC or PDA is the use of the low-power-consuming frequency translation circuits, which up- and downconverts the information without any degradation in its spectral purity. Frequency stability of the local oscillators used in the MMW wireless communication, and the clock recovery circuits used in the decision circuits, are critical in accurate data retrieval Fig. 1.

This evolution could not be realized without technological advances in optical sources/amplifiers, passive components, modulators, and detectors. The presentation in this article follows the assumption that the reader has a general understanding of these technologies (please review for fundamentals of optics and device physics aspects of photonics the books by Saleh and Tiejch [1] and Bhattacharya [2] respectively) and discussions in here are primarily on subsystem-level implementations of analog fiberoptic links for distribution of data and local oscillator, RF signal processing, analog-to-digital conversion, and medical imaging.

2. LIGHT INTERACTION WITH DEVICES AND CIRCUITS

From the early beginning of optical control of TRAPPAT (trapped plasma avalanche triggered transit) and IMPATT (impact avalanche transit time) in 1970, optical control of semiconductor devices has provided the promise of remote control along with isolation of optical source other electrical sources. Over time a number of techniques have been developed to control performance of a number of devices and circuits using optical interactions. Various optically controlled microwave subsystems have been demonstrated

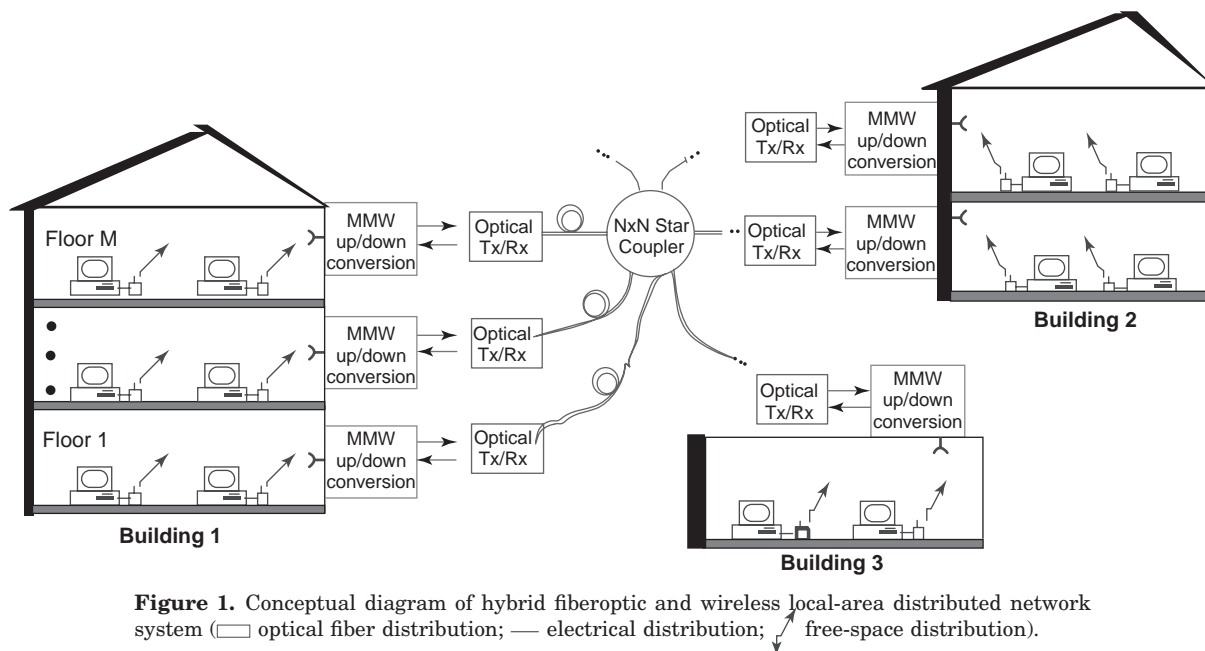


Figure 1. Conceptual diagram of hybrid fiberoptic and wireless local-area distributed network system (□ optical fiber distribution; — electrical distribution; ↗ free-space distribution).

Table 1. Sources of Photodetection Mechanisms in Popular Microwave Semiconductor Transistors and Comparison to PIN Photodiode as Baseline

	I_{pvi}		I_{pvx}		I_{pc}		I_{pci}		I_{pd}	
	Gain	Speed	Gain	Speed	Gain	Speed	Gain	Speed	Gain	Speed
PIN	—	—	—	—	—	—	—	—	None	Very fast
HBT	—	—	—	—	—	—	Moderate (linear)	Fast	None	Very fast
FET	Large (log)	Slow	Large (log)	Very slow	Small	Fast	—	—	—	—
HEMT	Large (log)	Slow	Large (log)	Very slow	Small	Fast	—	—	—	—

since the early 1980s, such as optically tuned antennas [3], phase shifters [4], oscillators and filters [5], switches [6], and amplifiers [7]. Although these techniques are intriguing, they have not yet found significant applications. More recently, spurred by rapid developments in fiberoptic-based networks (MAN and LAN), the chip-level integration of photonic and microwave components for high-performance optical receivers have attracted attention. PIN-amplifier configurations, such as PIN-HEMT [8], have been reported, and more recently high-performance PIN-HBT combinations have been realized by Gutierrez-Aitken et al. [9]. The three-terminal microwave devices are preferred to perform photodetection and control functions in the receiver front end [10,11]. This configuration enhances receiver performance by reducing parasitics, requires less pre-amplification due to intrinsic gain of transistors, and has lower power consumption and less costly fabrication.

Key to these developments and related applications in communications and control of microwave systems is understanding of the optical properties of microwave devices [12] in transistors. In particular, photoresponse of HBT, MESFET, and HEMT could be unified and a comparison is made in terms of inherent photodetection mechanism, gain, sensitivity, and bandwidth.

2.1. Static Analysis

Table 1 summarizes various effects that contribute to the photoresponse of the HBT, MESFET, HEMT, and comparison of these devices to the PIN photodiode. (The performance of the PIN photodiode is considered as the baseline.) For the PIN photodiode, the photoresponse current is determined by the photogenerated electron-hole pairs in the intrinsic region and no current gain is experienced. The light level directly controls the photocurrent in a linear fashion. On the other hand, in HBT, in addition to photogenerated electrons at the collector depletion region, there is an increase in the effective base current due to the drift of photogenerated holes from the collector depletion region to the base. This source of this term is a change in the current injection rate due to change in base voltage and hence it is termed the *internal photoconductive effect*; since this increase occurs under constant bias current, it results in current gain. The photoresponse of the HBT is linear with optical power. On the other hand, the photoresponse in both field-effect transistors (MESFET and HEMT) is attributed to three mechanisms [13]. The photogenerated carries collected at the gate yield a photovoltage V_{phx} , when passing through an external resistor. Thus the *external photovoltaic* increases in gate

bias, which opens the channel and results in a photocurrent of $I_{pvx} = g_m V_{phx}$. The *internal photovoltaic effect* results in $I_{pvi} = g_m V_{ph}$, where for MESFET [14] V_{ph} is a light-induced modulation of the channel height and in the case of the HEMT, V_{ph} represents a shift in the quasi-Fermi level [15]. The *photoconductive effects* I_{pc} are very small and are neglected. The optical responsivity of microwave semiconductor transistors is compared in Fig. 2. At low illumination the logarithmic response of FET devices provides large gain. However, photoresponse saturates rapidly, which limits their dynamic range. The HBT, which has relatively large dark current but low noise [16], performs best at moderate and high illuminations.

2.2. Dynamic Response

The frequency response of a PIN is limited by the carrier transit time, where a shorter intrinsic region yields a faster response, but this behavior is at the expense of quantum efficiency for vertical devices. (Traveling-wave photodiodes are designed to simultaneously meet high power-handling, speed, and efficiency requirements.) The speed of the HBT is governed by sum of different time constants associated with the charging time of the base-emitter junction, the base transit time, the charging time of the base-collector junction, and the transit time across the collector depletion region. The optical response of the HBT is fast since these time constants are the same as those that determine the HBT ultra-high-speed response, whereas for FET devices the external photovoltaic effect is very slow because of the long charging time of the gate external circuit. The MESFET's dynamic response is dominated by the

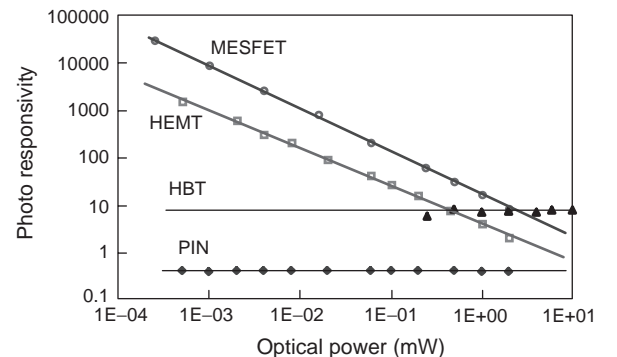


Figure 2. Comparison of the static light responsivity for microwave transistors and performance comparison to PIN photodiode as a baseline.

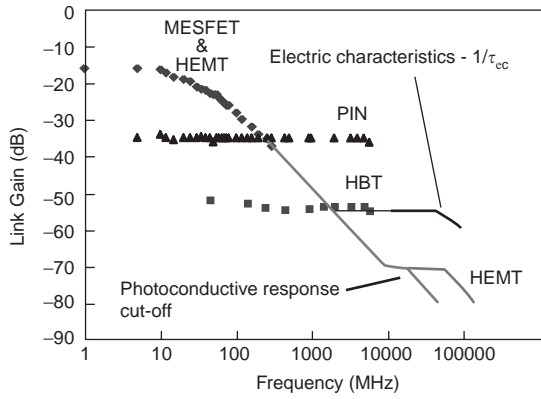


Figure 3. Frequency response of microwave devices. Measured data are represented by discrete points and theory by solid lines. The optical coupling efficiencies were calculated to be less than 1% for the HBT, 4% for the MESFET and HEMT, and 60% for the PIN diode.

dynamics of the internal photovoltaic effect, which is defined by the RC time constant of substrate resistance and the epitaxial layer–substrate junction capacitance [16]. For the HEMT, on the other hand, the RC time constant, determined by the buffer resistance and the change in electron concentration in the 2DEG (two-dimensional electron gas) channel [14], defines the speed. It is important to note that the speed of the photoresponse of the FETs is independent of their microwave speed.

The measured and calculated frequency response for these devices is depicted in Fig. 3. At low frequencies FETs perform well, but the intrinsically slow photovoltaic effect yields a small gain–bandwidth product. The speeds of the HBT and the PIN are comparable. Note that increasing the coupling efficiency of the HBT from 1% to 10%, which is a feasible task, will reduce the link insertion loss by 20 dB, thus superseding that of the PIN. Using devices with larger β (e.g., 250 instead of 25) will also give additional advantage to the HBT.

A publication by Madjedi et al. on the nonlinear behavior of high-temperature superconducting film as photomixer has provided an opportunity to generate terahertz signals using the kinetic inductive photoresponse [17]. These new applications maintain interest in interactions between light and microwave circuits.

3. FIBEROPTIC LINK DEVELOPMENT

Fiberoptic (FO) links are employed for distribution of frequency reference as well as data communications in dis-

tributed systems, where these links need to provide RF signals with high dynamic range and low phase noise degradation. The information is distributed by intensity modulation of light using an either directly or externally modulated laser (see Fig. 4) and is detected primarily directly since the evolution of optical amplifiers. The FO link gain and noise performance will impact signal-to-noise performance, while the nonlinearity of various elements in the optical system will contribute to a limited dynamic range. The nonlinear phase and amplitude variation with input RF power will result in AM-AM and AM-PM conversion. Moreover, in dense wavelength-division multiplexed systems, where channel capacity increases by multiplexing various colors of light, stimulated Raman scattering in optical fiber could introduce distortion and channel interference.

First, analytical expressions are presented for gain, noise figure, and dynamic range, and sources of phase noise degradation in directly and externally modulated FO links are presented. Next, fiber nonlinearity is introduced in a dense WDM system. Finally, the performance of a multifunction circuit, realized on the basis of a long Fabry–Perot laser structure that is monolithically integrated with an electroabsorption modulator, where efficient transmission of data and carrier signals with high SFDR (spurious-free dynamic range) and low phase noise degradation are achieved, is reviewed.

3.1. Directly Modulated FO Link

The gain of a fiberoptic link can be calculated in terms of microwave scattering parameters using the signal flow diagram (SFD) technique [18]. The transducer gains of the optical transmitter and optical receiver are derived separately and then combined to yield the gain of the complete link. The link gain is expressed as

$$G = \frac{P_{\text{out,Tx}}}{P_{\text{av,Rx}}} = G_{\text{TX}} \times |H_L|^2 \times G_{\text{RX}}$$

$$= \frac{|S_{21D}|^2 |S_{21L}|^2 (1 - |\Gamma_{\text{las}}|^2) (\eta_L K_L L K_D \eta_D)^2}{|1 - \Gamma_{\text{las}} S_{22L}|^2 |1 - \Gamma_{\text{SD}} S_{11D}|^2}$$

When a directly modulated semiconductor laser diode is employed in the optical transmitter, the SFD is obtained by considering the forward-bias junction resistance of the laser diode to be the port 2 termination of a two-port network consisting of the microwave impedance-matching circuit and driving circuit combined with the other device parameters of the laser. Whereas a reverse-biased p-i-n

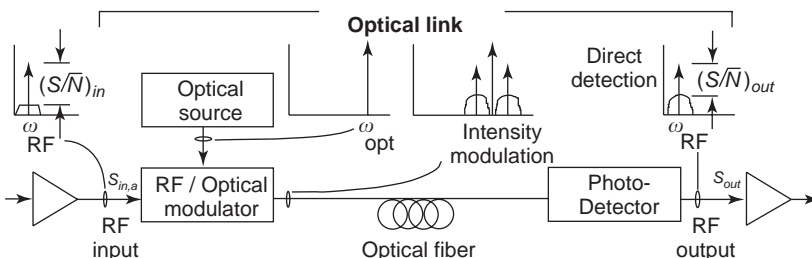


Figure 4. Overall structure of a fiberoptic link. Note that for the directly modulated system the optical source is internally modulated whereas in the externally modulated link the electrooptic property is used to perform intensity modulation in a Mach–Zehnder modulator.

photodiode is employed in the optical receiver, the SFD is obtained by considering the junction resistance of the diode to be the port 1 terminating load to a two-port network consisting of the microwave impedance-matching circuit and the other device parameters of the detector. The link current transfer function H_L is defined as the ratio of detector current to RF current across the laser. This is a measurable quantity that is a function of the electrooptic device quantum efficiencies as well as optical attenuation and coupling efficiency, where η_L is the laser diode external quantum efficiency, η_D is the detector responsivity, L is the optical attenuation in the fiber, and K_L , K_D are the laser-to-fiber and fiber-to-detector coupling efficiencies, respectively. Nonlinear fiber performance due to stimulated Brillouin and Raman scattering processes for long-fiber-length L is ignored for the moment, but this issue will be discussed later.

The four contributions to the noise power of the directly modulated fiberoptic link. The total noise power at the output of the detector is the sum of all these individual noise powers:

$$\begin{aligned} N_{\text{out}} &= N_{\text{RIN}} + N_{\text{shot}} + N_{\text{th,Tx}} + N_{\text{th,Rx}} \\ &= N_{\text{RIN}} + N_{\text{shot}} + N_{\text{th}} \end{aligned}$$

The dominant term is the laser RIN (relative intensity noise) noise power, which is expressed as

$$\begin{aligned} N_{\text{RIN}} &= \text{RIN}(f)(I_b - I_{\text{th}})^2 (\eta_L K_L L K_D \eta_D)^2 \\ &\times \frac{|S_{21D}|^2}{|(1 - \Gamma_{\text{SD}} S_{11D})|^2} B Z_0 \end{aligned}$$

The next dominant noise source is shot noise of the detector, including dark current noise

$$\begin{aligned} N_{\text{shot}} &= 2e[(I_b - I_{\text{th}})(\eta_L K_L L K_D \eta_D) + I_d] \\ &\times B \frac{|S_{21D}|^2}{|(1 - \Gamma_{\text{SD}} S_{11D})|^2} Z_0 \end{aligned}$$

followed with the thermal noise of the transmitter:

$$\begin{aligned} N_{\text{th,Tx}} &= 4kT_a B (\eta_L K_L L K_D \eta_D)^2 \text{Re}\{Y_{\text{th1}}\} \\ &\times \frac{|S_{21D}|^2}{|(1 - \Gamma_{\text{SD}} S_{11D})|^2} Z_0 \end{aligned}$$

Finally we obtain the thermal noise of the detector:

$$N_{\text{th,Rx}} = 2kT_a B (1 - |\Gamma_{\text{in}}|^2)$$

The only noise source at the input of the link is the thermal noise in the transmitter circuitry: $N_{\text{in}} = kT_a B$. The noise figure of the fiberoptic link is defined as

$$\text{NF}_{\text{link}} = \frac{(\text{SNR})_i}{(\text{SNR})_o} = \frac{P_{\text{in}} * N_{\text{out}}}{P_{\text{out}} * N_{\text{in}}} = \frac{1}{G_{\text{link}}} * \frac{N_{\text{out}}}{N_{\text{in}}} \quad (1)$$

3.2. Externally Modulated FO Link

The small-signal gain of an externally modulated fiberoptic link is derived using the SFD technique as was applied to direct modulation. When a Mach-Zehnder interferometric modulator is employed in the optical transmitter to impress a microwave signal on the optical carrier in a single-mode fiber, the transmitter SFD is obtained by considering the capacitance C_M across the modulator terminals to be the port 2 termination of a two-port network consisting of the microwave impedance-matching circuit and other device parameters in the equivalent circuit of the modulator. The output power of a fiberoptic link depends on the amplitude of photocurrent I_{det} generated in the detector, which is in turn proportional to the RF voltage V_M across the capacitor C_M . This gain is represented as

$$\begin{aligned} G &= \left(\frac{\pi L K_D \eta_D P_{\text{in,op}} Z_0}{2V_\pi} \right)^2 \\ &\times \frac{|S_{21M}|^2 |S_{21D}|^2 |1 + \Gamma_M|^2}{|1 - S_{22m} \Gamma_M|^2 |1 - S_{11D} \Gamma_{\text{SD}}|^2} \end{aligned}$$

where V_π is bias voltage required for 100% optical modulation and $P_{\text{in,op}}$ is the optical output of the modulator. Figure 3 compares the achievable gain of directly and externally modulated fiberoptic links. Note that a higher gain is achieved when optical source and detector with efficient light coupling and responsivity are employed. Finally, gain of the externally modulated FO link monotonically increases as the optical power squared. Four noise sources contribute to the output noise power of the link. The dominant term in the case of large input optical power is the shot noise followed by excess RIN noise of the laser. The shot noise of the detector, including dark current, is expressed as

$$\begin{aligned} N_{\text{shot}} &= 2e \left[\left(\frac{\eta_{\text{op}} \eta_D P_{\text{in,op}}}{2} \right) + I_d \right] \\ &\times B \frac{|S_{21D}|^2}{|1 - \Gamma_{\text{SD}} S_{11D}|^2} Z_0 \end{aligned}$$

The excess noise of the laser is related to optical source RIN noise, which could be significantly lower than that for the semiconductor laser diode:

$$\begin{aligned} N_{\text{excess}} &= \left[\text{RIN} \left(\frac{\eta_{\text{op}} \eta_D P_{\text{in,op}}}{2} \right) - 2e \right] \\ &\times \left(\frac{\eta_{\text{op}} \eta_D P_{\text{in,op}}}{2} \right) B \frac{|S_{21D}|^2}{|1 - \Gamma_{\text{SD}} S_{11D}|^2} Z_0 \end{aligned}$$

The thermal noise sources of the transmitter and of the detector are presented respectively as

$$\begin{aligned} N_{\text{th,Tx}} &= kT_a B \left(\frac{\pi \eta_{\text{op}} \eta_D P_{\text{in,op}} Z_0}{2V_\pi} \right)^2 \\ &\times \frac{|S_{21m}|^2 |S_{21D}|^2 |1 + \Gamma_M|^2}{|1 - \Gamma_M S_{22m}|^2 |1 - \Gamma_{\text{SD}} S_{11D}|^2} \end{aligned}$$

$$N_{\text{th,Rx}} = 2kT_a B (1 - |\Gamma_{\text{in}}|^2)$$

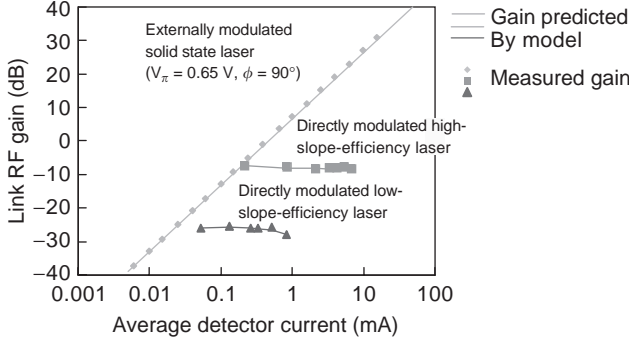


Figure 5. Comparison of experimental and simulation results of directly and externally modulated fiber optic links at HF [17]. (Courtesy of Ed Ackerman of Photonics Inc.)

The total noise power at the output of the detector is the sum of all these individual noise powers. As in the direct-modulation case, the noise power at the input to the external modulation link is simply $kT_a B$. Therefore the noise figure is given by Eq. (1). Note that the total shot noise increases as optical power; therefore the signal-to-noise ratio increases as optical power increases in the externally modulated links. However, the challenge is to develop high-speed high-power-handling-capability photodetectors.

Figure 5 depicts comparison measured and analytical calculated gain results of directly and externally modulated fiber optic links. The optical power can be high in externally modulated fiber optic links when a solid-state laser is employed as an optical source. A low- V_π Mach-Zehnder (MZ) modulator and operation in the quadrature point of $V_b = V_\pi/2$ (i.e., $\phi = 90^\circ$) along with a high-power-handling-capability photodiode allows for the highest reported gain for FO links. Naturally a higher responsivity (i.e., η_L and η_D) laser diode and photodiode result in a lower insertion loss.

3.3. Dynamic Range

Spurious-free and compression dynamic range are directly related to linearity of the optical modulator (i.e., laser diode in the case of directly, and MZ modulator in the externally modulated FO links). The third-order intercept point and 1 dB compression point for the directly modulated are calculated [18] on the basis of the optical modulation index m :

$$P_{in,int} = \frac{m_{int}^2 (I_b - I_{th})^2 |1 - S_{22L} \Gamma_{Las}|^2 Z_0}{|S_{21L}|^2 (1 - |\Gamma_{Las}|^2)}$$

$$P_{in,1dB CP} = \frac{m_{1dB CP}^2 (I_b - I_{th})^2 |1 - S_{22L} \Gamma_{Las}|^2 Z_0}{|S_{21L}|^2 (1 - |\Gamma_{Las}|^2)}$$

In a similar fashion, the third-order intercept point and 1 dB compression point are derived for externally modu-

lated fiberoptic links as follows:

$$P_{in,int} = \frac{8V_\pi^2 |1 - S_{22m} \Gamma_M|^2}{\pi^2 Z_0 |S_{21m}|^2 |1 + \Gamma_M|^2}$$

$$P_{in,1dB CP} = \frac{0.950454^2 V_\pi^2 |1 - S_{22m} \Gamma_M|^2}{\pi^2 Z_0 |S_{21m}|^2 |1 + \Gamma_M|^2}$$

Using the derived relationship for intercept and compression points, spurious-free and compression dynamic range are calculated using the following expressions:

$$SFDR = \frac{2}{3} \times 10 \log_{10} \left[\frac{P_{out,int}}{kT_a GNF} \right] \text{ dB} \cdot \text{Hz}^{2/3}$$

$$CFDR = 10 \log_{10} \left[\frac{P_{out,1dB CP}}{kT_a GNF} \right] \text{ dB} \cdot \text{Hz}$$

3.4. Fiber Nonlinearity

WDM optical systems are employed in radio-over-fiber and optically controlled phased-array antenna architectures. In pushing these systems to the limits of transmission capability, aspects such as fiber nonlinearities need to be understood. These aspects include the nonlinear fiber phenomena of SRS (stimulated Raman scattering) [20], SBS (stimulated Brillouin scattering) [21], and XPM (cross-phase modulation) [22]. These nonlinear effects become noticeable particularly in WDM subcarrier-multiplexed (SCM) systems that may cover many closely packed video channels cover long distances. These nonlinearities result in optical power transfer to higher and lower optical frequencies. Each nonlinear effect creates a distortion level that becomes intolerable above the acceptable threshold level. Threshold requirements are based on electrical nonlinear distortion requirements, composite second-order (CSO) and composite triple (or third-order) beat (CTB) (particularly CTB), which have been determined in published works such as Refs. 23 and 24.

Figure 6 shows the SRS crosstalk level for a two-channel WDM system, while the fiber length is varied and for

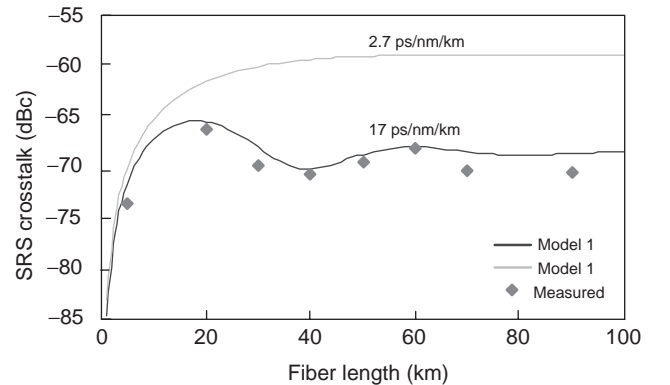


Figure 6. Measured and simulated SRS-induced crosstalk versus fiber length for an input optical power level of 4 dBm, fiber dispersion of $17 \text{ ps mm}^{-1} \text{ km}^{-1}$ RF frequency of 151.85 MHz, and a channel spacing of 9.4 nm.

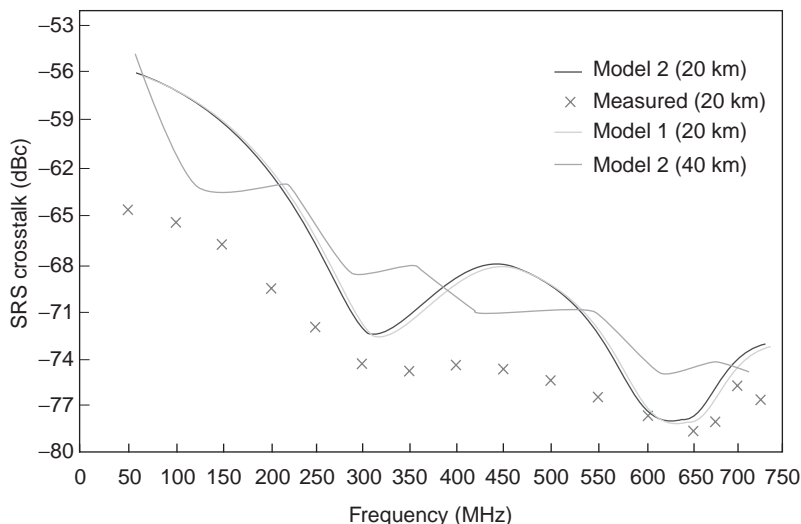


Figure 7. Measured and simulated SRS crosstalk versus RF frequency with a fiber length of 20 km, fiber dispersion of $17 \text{ ps nm}^{-1} \text{ km}^{-1}$, channel spacing of 9.4 nm, and a 4 dBm (2.5 mW) input power per channel; also, a simulation of 40 km using only the Phillips–Ott model [25].

9.4 nm channel spacing, and input power of 4 dBm, a dispersion of $17 \text{ ps nm}^{-1} \text{ km}^{-1}$, and a subcarrier frequency of 152 MHz. The two curves in the figure represent the high- and low-dispersion fibers. The more dispersive fiber generates lower XT due to the walkoff effect. As is expected, the crosstalk level begins to increase as the fiber length increases. However, the XT level reaches a peak value and then decreases as the length is increased further. As the length is increased beyond 70 km, eventually the SRS level reaches a steady-state value. This behavior shows a sinusoidal dependence of crosstalk on fiber length for dispersive fiber but a monotonic increase for the dispersion-shifted fiber. The importance of this result is that, due to the walkoff effect, the crosstalk level for a length of fiber may not increase as the fiber length increases. Hence, the crosstalk level can be reduced or increased depending on the fiber length. In comparison of the measurement and simulation (Model 1: Wang et al. model [24] and Model 2: Phillips–Ott model [25]), the maximum error is less than 5%. Measurement results of the SRS crosstalk while increasing the RF frequency from 50 to 725 MHz in steps of 50 MHz is depicted in Fig. 7. Also included in the figure is a simulation of Phillips–Ott model [25]. As depicted in Fig. 7, the SRS crosstalk level changes as the

frequency is increased, following a behavior similar to a sinc function (i.e., $\sin x/x$) squared fashion.

3.5. Phase Noise Degradation

The FO distribution link contributes residual phase noise to the reference signal, which is a function of operation frequency. This impact is significant mostly in the directly modulated fiberoptic links where the RIN of the optical source is far stronger than the externally modulated FO links. Moreover, directly modulated fiberoptic links are preferable to externally modulated links because of their lower cost than. The phase noise of the reference signal could be degraded if residual phase noise were too close to the signal noise floor level. Therefore, an appropriate selection of reference frequency is necessary to avoid significant degradation after passing through the FO link. For example, as shown in Fig. 8, to generate a 12-GHz local oscillator (LO) at front end, a reference signal at frequency of 100 MHz (UHF), 4 GHz (C band), and 12 GHz (X band) can be sent through FO link. Since the phase noise contributions for FO links are different at these frequencies, an optimum frequency for reference signal can be found to have the least phase noise degradation due to the FO link.

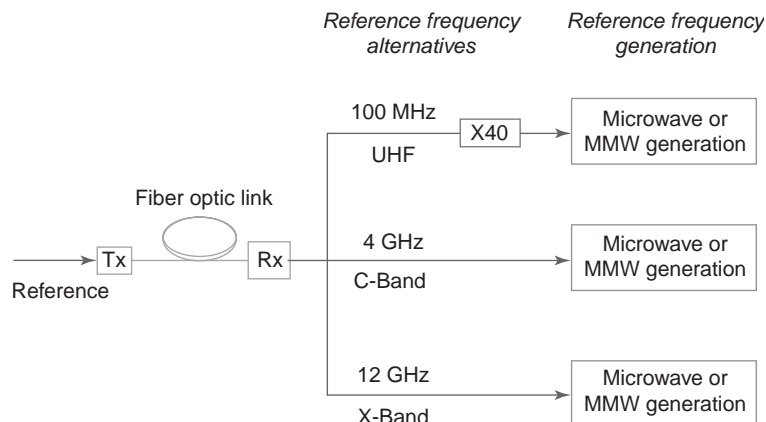


Figure 8. Distribution of frequency reference and generation of MMW signal using various frequency references used in a FO-based local-oscillator (LO) synchronization network.

The optical spectra of a modulated optical signal are expressed as $P_{\text{opt}}(1 + m \cos(\omega_m t + \delta\phi_m(t)) + n_{\text{RIN}}(t)) \cos(\omega_{\text{opt}} t + \phi_{\text{opt}}(t) + \delta\phi_{\text{opt}}(t))$, where P_{opt} is the averaged optical power and m is the optical modulation index at modulating microwave carrier ω_m . The focus of present work is $\delta\phi_m$, the residual phase noise added to the microwave carrier from the laser diode noise source. n_{RIN} is the relative intensity noise; ω_{opt} is the optical frequency; ϕ_{opt} is the optical phase signal due to side modes and modulation, and $\delta\phi_{\text{opt}}$ is the phase noise of the optical signal. Since most fiberoptic links for antenna remoting applications use intensity detection, only the noise signals in optical intensity affect the microwave carrier signal, namely, $\delta\phi_m$ and n_{RIN} . The n_{RIN} could contribute to the FM noise of the reference signal through nonlinear AM/PM conversion [27].

The laser diode SSB phase noise of the n th harmonic of the modulating signal \mathcal{L}_{out} has contributions from three noise terms: (1) the input reference signal phase noise, \mathcal{L}_{in} , (2) the low-frequency noise of the laser diode upconverted to the carrier frequency \mathcal{L}_{up} ; and (3) the RIN noise at the offset microwave carrier \mathcal{L}_{RIN} . This behavior is quite analogous to microwave systems [28]. Therefore at angular offset carrier frequency of Ω , \mathcal{L}_{out} can be approximately expressed as [29]:

$$\mathcal{L}_{\text{out},n\omega}(\Omega) = n^2 \mathcal{L}_{\text{in},\omega}(\Omega) + n^2 \mathcal{L}_{\text{up},\omega}(\Omega) + \mathcal{L}_{\text{RIN},n\omega}(\Omega) \quad (2)$$

The factor of n is the harmonic order of the modulation signal, if any nonlinearity of the laser diode is exploited to generate the n th harmonic [28]. (If the fundamental frequency is employed, then $n = 1$.) The subscript ω indicates the modulation frequency. The upconversion factor of low-frequency RIN to phase noise is the dominant noise source. Calculation of this upconversion factor depends on the derivative of the RF phase with respect to the RF derive amplitude and is $C_{\text{up},\omega} = \frac{1}{2} (\partial\theta(\omega)/\partial P_o)^2 P_o^2$, which θ is phase of optical signal at the modulating frequency ω . The dependence of phase on the optical output power in a directly modulated system is a bit more complicated than in an externally modulated system since the nonlinear be-

havior is dependent on modulation index of laser diode and the relationship of its operation frequency compared to the relaxation oscillation frequency. This process is nonlinear and at certain frequencies results in AM-PM compression. The results are related to modulation index through the a parameter, which is a function of modulation frequency and averaged optical power [18].

Since RIN noise in semiconductor laser diodes is strong up to 100 MHz because of mode partition noise, it is predicted that the spectral purity of the UHF reference signal is greatly degraded, resulting in a higher FM noise. Moreover, the X-band modulating signal is close to the relaxation oscillation frequency where RIN is peaked. The best frequency for reference signal distribution through DMFO link is the C-band signal as depicted in Fig. 9, where the phase noise of the 12-GHz LO signal is generated from the reference signal through the abovementioned DMFO link. Clearly, the signal generated from a C-band signal has the best phase noise performance. The signal from UHF reference degrades greatly because the residual phase noise of the FO link is higher than the reference phase noise at offset frequency higher than 100 Hz.

3.6. Monolithically Integrated Mode-Locked Laser

A monolithic version of a laser with external cavity is realizable using semiconductor fabrication process and reported by a number of researchers. Figure 10a shows a schematic drawing of the monolithic laser with an integrated EA (electroabsorption) modulator. Stacked structure consisting of two MQW layers, a MQW (multi-quantum well) for laser diode (MQW-LD) and a MQW for EA modulator (MQW-MD) are employed. The Fabry-Perot (FP) cavity length for our experiment is cleaved approximately for a length of 2170 μm . This total length is composed of a 1970- μm -long gain section, a 150- μm -long modulator, and a 50- μm -long separation region. The facet of the modulator section is coated with high-reflectivity film ($R \approx 85\%$). The facet of the gain section is as cleaved. The laser is mounted in a high-frequency package. The schematic diagram of the long FP laser with integrated EA modulator is shown in Fig. 10b.

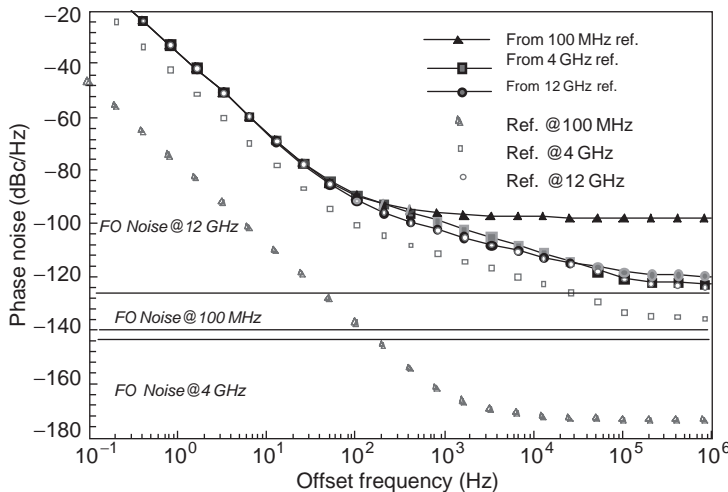


Figure 9. The simulated phase noise of a LO signal at 12 GHz, is generated from different reference signals through a directly modulated FO link as depicted in Fig. 8.

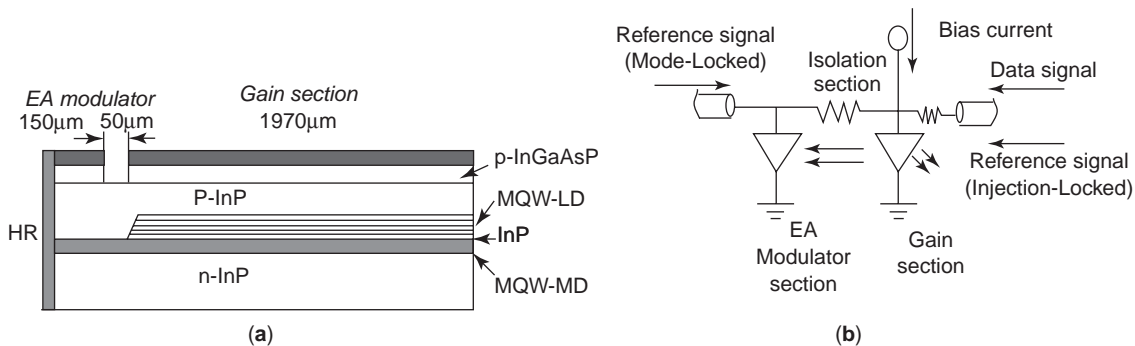


Figure 10. (a) Conceptual representation of the long FP laser integrated with an electroabsorption modulator; (b) mechanical fixture used for mounting of the laser diode for injection-locking, mode-locking, and optoelectronic conversion evaluations.

The gain section of the laser diode is forward-biased at different bias currents, and the EA section is reverse-biased by different voltage levels. A resonance peak is observed that is associated with the longitudinal mode separation in the long FP laser. The longitudinal-mode separation is calculated as $\Delta f = c/2nL \approx 19.3$ GHz, where $c = 300$ mm · GHz is the speed of light in free space, $n \approx 3.5$ is the index of refraction of the waveguide, and $L \approx 2.17$ mm is the FP cavity length. This resonant frequency has a frequency tuning sensitivity of ≈ 1 MHz/mA. The optical oscillations are stabilized using an injection-locking process [27], where a single oscillation peak that appears as the gain section is modulated by a frequency reference of $P_m \geq -1$ dBm at $f_m = 19.258$ GHz. The familiar one-sided injection-locking spectra are observed outside the injection-locking range and the close-in to carrier phase noise is significantly reduced within the locking range. The measured close-in to carrier phase noise degradation at 100 Hz offset carrier is depicted in Fig. 11, where 31 and 6 dB degradation are measured for the injected power of $P_m = +0.5$ dBm in the resistively and reactively-matched modules respectively. However for

injected power level of +4.5 dBm, a close-in to carrier phase noise identical to the reference source is measured for the reactively matched case Fig. 11.

The resonance frequency could also be stabilized using fundamental mode locking by modulating the EA section by a synthesized source. The close-in to carrier phase noise are measured and comparison is made against the reference signal from an HP83640A source. The results are summarized in Table 2 for different laser operation points. As indicated, a very small phase noise degradation is observed; however, the results for $V_m = -1$ V are better

Table 2. Phase Noise Degradation of LO Signal as Function of Various Offset Frequencies and Laser Operation Points

f_m (GHz)	V_m (V)	$\mathcal{L}(\Omega)$ (dBc/Hz)		Δ (dB)	
		$\Omega = 100$ Hz	$\Omega = 1$ kHz	$\Omega = 100$ Hz	$\Omega = 1$ kHz
19.13400	-4.5	-75.4	-81	2.6	2.4
19.29469	-2.5	-77.0	-82	1.0	1.1
19.29406	-1.0	-77.6	-82	0.4	0.4

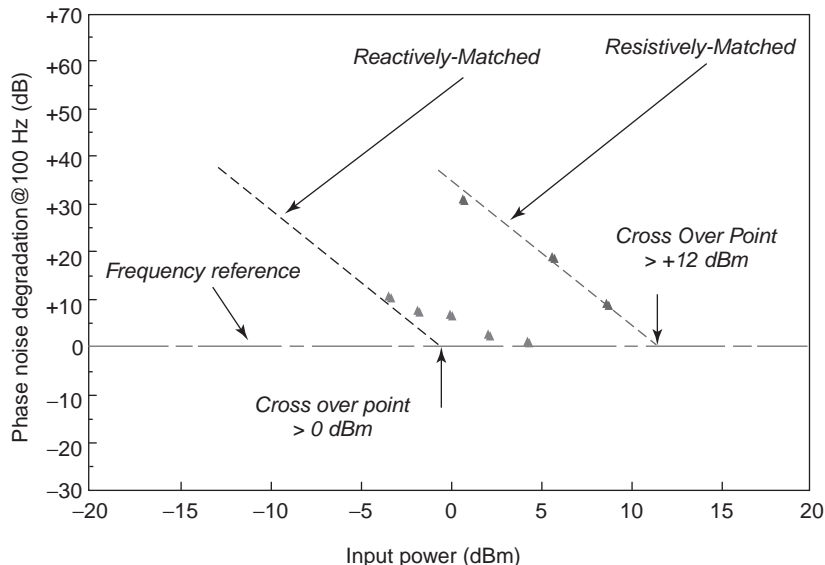


Figure 11. Measured FM noise degradation at 100-Hz-offset carrier for the injection locked inter-modal oscillation. The measured injection-locking power of the long FP laser diode is also depicted at the crossover point for the resistively (\blacktriangle) and reactively matched (\blacktriangle) lasers.

than the results for $V_m = -4.5$ V for the same laser current of $I_b = 140$ mA.

Since this stabilized signal has much cleaner close-in to carrier phase noise than does the free-running oscillation, it could be employed as the LO signal. The laser diode's gain section is forward-biased ($I_b = 140$ mA), and the EA modulator section is reverse-biased ($V_m = -1$ V). This operating point is selected because of the efficient mode-locking process while maintaining the least amount of phase noise degradation of the carrier signal. The laser diode optical output is collimated to a single-mode optical fiber using a polarizing collimator with an overall fiber coupling efficiency of 12%. The optical fiber output is connected to an optical receiver integrated with RF analyzer, which automatically dis-embeds the calibrated optical receiver response from the measurement and displays it in the optical domain. The electrical domain power levels, in dBm, are easily calculated by multiplying the depicted optical domain results, displayed in dBm, by a factor of 2.

Next the gain section of this laser is modulated by S-band signals (2.2 GHz \pm 50 MHz). Strong nonlinearity of the mode-locked laser at the LO signal of 19.3 GHz upconverts the S-band signals to 17.1 and 22.5 GHz as shown in Fig. 12. The data modulation power level is changed over a wide range. An optical conversion loss is defined as the ratio of the generated mixed RF signal (19.3 ± 2.2 GHz) to the IF signal (2.2 GHz). The optical conversion loss is as low as 1.4 dB, resulting in an electrical conversion loss of 2.8 dB. The optoelectronic conversion loss for the lower sideband (LSB) at 17.1 GHz is higher than the upper sideband (USB) of 22.5 GHz by 1.3 dB (i.e., 2.6 dB electrical) [31].

On the other hand, a modulation loss greater than 51 dB is measured when the gain section is directly modulated by the RF signal at 17.1 GHz. The spurious-free dynamic range (SFDR) of this optoelectronic mixer is also evaluated. The intermodulation distortion (IMD) measurements are conducted for two modulating tones that are 5 MHz apart (e.g., $f_1 = 2.200$ GHz and

$f_2 = 2.205$ GHz). Both tones are upconverted by a stable LO signal of 19.360 GHz and IMDs of the upconverted RF signals are measured at LSB and USB frequencies. Based on the mode-locked laser IMD and RIN noise measurement results for the upconverted RF tones, SFDR LSB and USB RF signals are ≈ 88 dB \cdot Hz^{2/3} and 89 dB \cdot Hz^{2/3}, respectively.

4. FIBEROPTIC DISTRIBUTION FOR PHASED-ARRAY ANTENNAS

One of the simplest methods antenna remoting is based on the concept of direct replacement of the electrical interconnects by FO links. However, there are challenges associated with reliability of optical components, cost of system integration, and the architecture employed for achieving the best attributes possible.

4.1. Device Innovations and Reliability

A vast number of research work reported in the literature have focused on the device improvements to meet the performance requirement of commercial fiberoptic communication. Performance of sampled directly and externally modulated fiberoptic links operating at S band is rendered in Table 3 (circa 1995), where the best performance is achieved for DFB laser monolithically integrated with the EA modulator. The performance of the mode-locked laser is quite acceptable for many telecommunication systems. (The results of the MZ modulator may appear worse than what is reported in the literature, but in this case a semiconductor laser with optical power of only a few mW is used as a source.) Monolithically integrated EA modulator with sampled grating DBR laser (SGDBR) [32] has been developed where SFDR of 120 dB \cdot Hz^{2/3} is achieved over a large tuning bandwidth. However, the harsh military and space environment imposes additional burdens on the performance of lightwave technology components.

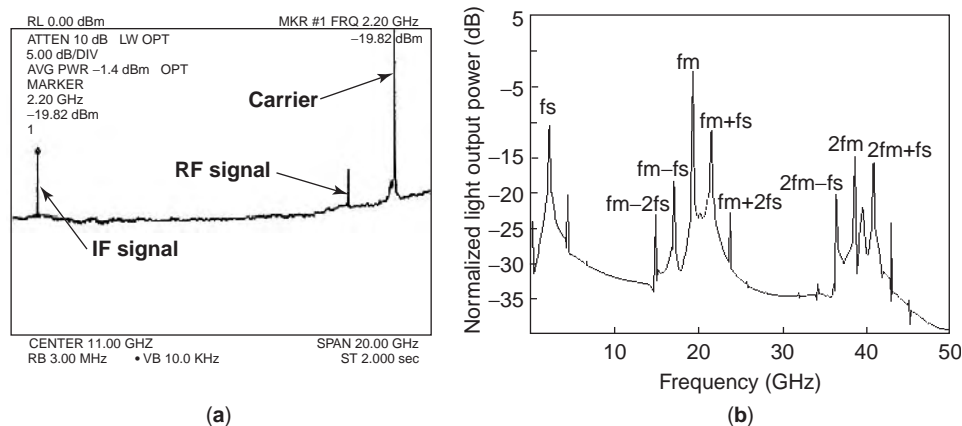


Figure 12. Optoelectronic mixing of data signal with local-oscillator signal in the mode-locked long FP laser diode: (a) experimental results for operation conditions $I_b = 140$ mA, $V_m = -1$ V, $f_m = 19.360$ GHz, $P_m = +15$ dBm, $f_{\text{data}} = 2.200$ GHz, and $P_{\text{data}} = -25$ dBm—data, lower sideband RF, and local-oscillator signals (center frequency 11.0 GHz and frequency span 20.0 GHz); (b) simulation results based on traveling-wave equation [30].

Table 3. Comparison of Various Components Off the Shelf (COTS) Fiberoptic Links at S-Band^a

	Directly Modulated FO Links		Externally Modulated FO Links	
	Mode-Locked Laser	Ortel DFB Laser	DFB/EA Modulator	Sumitomo MZ Modulator
Frequency	2.2 GHz	2.5 GHz	2.2 GHz	2.5 GHz
Gain(dB)	-8	-44	-12	-40
IP3 (dBm)	+17	+27	+14	+23
Noise floor (dBm/Hz)	-142	-151	-151	-151
SFDR (dB · Hz ^{2/3})	101	86	103	90

^aNote the MZ modulator is based on DFB laser as optical source.

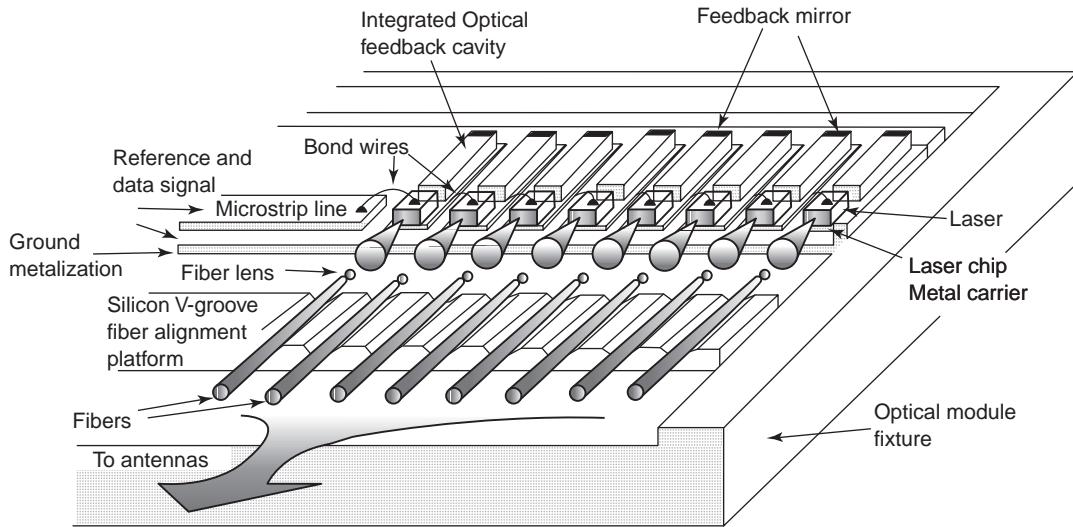


Figure 13. Conceptual representation of an optimized optical transmitter using eight series-mounted laser diodes with monolithically integrated external optical cavity coupled to the lensed fibers using a Si V-groove fiber alignment system.

4.2. Packaging Requirements

As indicated in the gain expressions of directly and externally modulated fiberoptic links, a dB improvement in the optical coupling improves insertion gain by 2 dB. However, mechanical tolerances of optical fibers and sources are in submicrometer range, hence making the low-cost integration of optical components with optical fibers challenging at the least. Moreover, this process has to be done in a cost-effective manner. Another important aspect of the light coupling is that reflection has to be minimized since any optical feedback introduces modulation of the dynamic response, which resembles the transmission characteristics of FP resonators. Therefore, optical isolators combined with angle polished fibers are required to reduce the light feedback level below 50 dB in certain applications. Another important aspect is temperature control of semiconductor devices to avoid any sensitivity to temperature in harsh environments of space. Finally, directly modulated fiberoptic links or externally modulated systems using EA modulators experience input impedance that corresponds to high-reflectivity coefficients (i.e., approximately short for a laser diode and open for an EA modulator). To avoid high reflection loss, impedance matching circuits are needed to be developed, which is not easy to accomplish over a large fractional bandwidth. Figure 13 depicts a designed structure of monolithically integrated optical

source with an EA modulator [33], which is used for distribution of both LO signal and data signal. This structure is also based on cascading a number of lasers with a monolithically long FP cavity in series, hence increasing the forward PN junction resistance, while maintaining the same RF current modulating all the gain sections. In essence, since the input impedance of laser diode (i.e., a forward-biased p-n junction) is about 4Ω , by series combination of the impedances, a level closer to 50Ω is achieved.¹ Moreover, a lower Q_{ex} factor is obtained, which simplifies the matching circuit design. Finally, the fiber coupling is achieved cost-effectively by combining a number of lensed fibers mounted on a silicon V groove. This process will enable packaging of a large number of laser diode sources.

4.3. Architecture Innovations

In large-aperture phased-array antennas or ROF systems, the RF signal could be downconverted to the IF signals for further processing at the centralized receiver. This architecture, shown in Fig. 14, is the conventional one. The challenges for implementation of optically controlled

¹A similar approach is currently pursued in quantum cascade lasers, although the latter is a unipolar device. For more information, see, for example, the paper by Faist et al. [34].

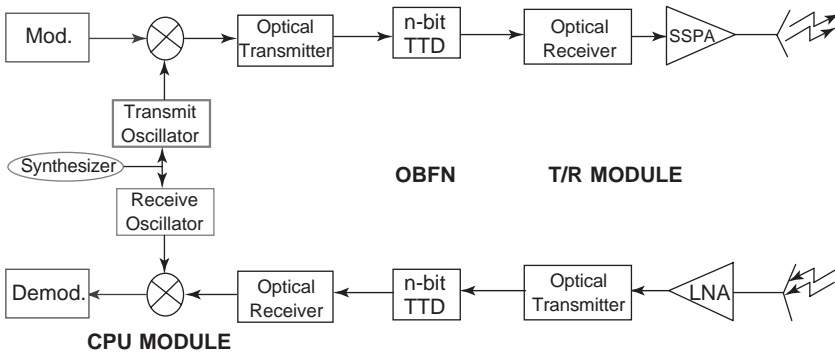


Figure 14. CPU-level data mixing architecture for transmit/receive-mode operation. Note that real-time-delay are required for broadband operation without beam squint.

phased array using this architecture are (1) a high-dynamic-range fiberoptic links are required at ultrahigh frequencies, (2) phase and frequency control must be maintained in the distribution network all the way to the central processor, and (3) as will be shown later, a higher resolution for a true time-delay device is required. On the other hand, the T/R-level data mixing architecture, shown in Fig. 15, provides a great opportunity to perform downconversion of the RF signals to IF and avoid the limitations encountered in the CPU-level data mixing. Additional requirements are: (1) the need for stabilized LO at each element to coherently down-or upconvert the received RF or IF signals, (2) increase in the number of optical links, and (3) the requirement of phase control in addition to TTD to obtain a squint-free radiated beam. Nonetheless, experimental comparison of a 2×4 MMIC-based C-band phased-array antenna was conducted, where a superior dynamic range was measured for T/R-level data mixing architecture over CPU level 1 [35]. These apparent limitations were avoided using a cascaded ILPLL oscillator [36], a self-oscillating mixer [37], and an optoelectronic mixer using MLL [38]. The most important advantage of T/R-level data mixing is its reduction in the number of resolution bits required in real-time-delay devices to generate a squint-free-beam. This issue is highlighted next.

Figure 16 depicts radiation pattern of a 25-element linear phased array (with $\lambda/2$ separation) designed for operation at center frequency of 33 GHz with bandwidth of 3 GHz (i.e., each graph is composite of three simulated graphs at frequencies of 31.5, 33, and 34.5 GHz). The simulation results are for CPU-level data mixing. The re-

quired time delay is achieved using a switched delay line TTD (real-time-delay device) with minimum time resolution of 10 ps. As this simulation result indicates as the beam is pointed away from broadside, sidelobe levels increase to only -6 dBc, and the mainbeam decreases by 2 dB. On the other hand, Fig. 17 depicts the simulated performance of the same phased array when it is constructed on the basis of T/R-level data mixing. This structure employs a 2π analog phase shifter based on the concept of cascaded oscillators [36] along with a TTD with a time resolution of 30 ps (i.e., decreasing the time delay number of bits by factor of ~ 4). As this figure clearly indicates, no reduction in mainbeam peak level or increase in sidelobe levels is observed for any scan angles. In fact, the sidelobe levels are compatible with the expected theoretical level of 13.6 dB for a uniform array.

5. MICROWAVE PHOTONIC SIGNAL PROCESSORS

One of the most significant advantages of microwave photonics is not the antenna remoting concepts, but rather the opportunity to perform signal processing in the optical domain. The primary figure of merit is the time-bandwidth product, which could exceed 10^4 , hence leading to significant rejection and filtering using various delay lines. A few realizations of signal processors using microwave photonic techniques are discussed next.

5.1. Memory Loop

Fiberoptic-based memory loops are used for recirculation of the incoming RF pulses. The simplified schematic dia-

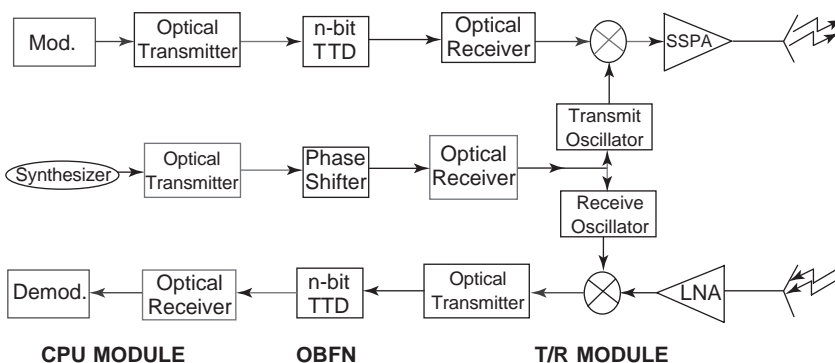


Figure 15. T/R-level data mixing architecture for transmit/receive-mode operation, where distributed local oscillators need to be synchronized to a frequency reference. Note that both real-time-delay and phase shifter devices are required for beam-squint-free operation in broadband systems.

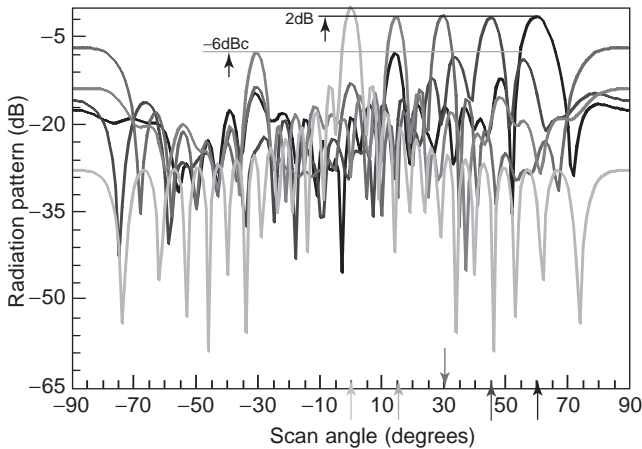


Figure 16. Simulated radiation pattern of 25-radiating-element linear multibeam phased-array antenna based on a CPU-level data mixing architecture where a real-time-delay line with 10 ps resolution is employed to generate beams at different angles ($f_{LO} = 24$ GHz, $f_{data} = 7.5\text{--}10.5$ GHz, $f_{RF} = 31.5\text{--}34.5$ GHz).

gram of a fiberoptic-based recirculating memory loop is shown conceptually in Fig. 18. This system consists of four basic elements: a switch, an electrical amplifier, a fiberoptic time-delay element, and a gain equalizer. The gain equalizer is composed of a YIG tunable filter and an attenuator. The RF input pulse is routed through the switch to the time-delay device. The switch closes the loop and thus controls the recirculation. As the signal reenters the microwave circuit, it is amplified and rerouted through the fiber. As a result, a pulsetrain is obtained that has a pulse repetition interval corresponding to one recirculation time through the loop.

The number of recirculations is not limited by dispersion, and for higher recirculation the following steps are established (1) reducing the insertion loss and noise figure of the fiberoptic link and (2) flattening the frequency response of the closed-loop system. Using a 1-km optical

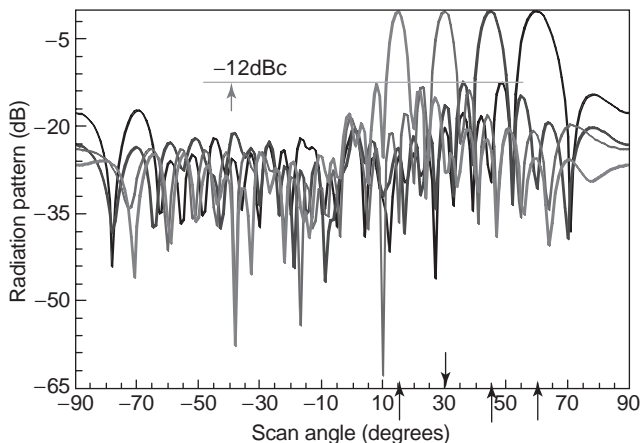


Figure 17. Simulated radiation pattern of 25-radiating-element linear multibeam phased-array antenna based on a T/R-level data mixing architecture where a real-time-delay line with 30 ps resolution along with analog phase shifter for LO is employed to generate beams at different angles ($f_{LO} = 24$ GHz, $f_{data} = 7.5\text{--}10.5$ GHz, $f_{RF} = 31.5\text{--}34.5$ GHz).

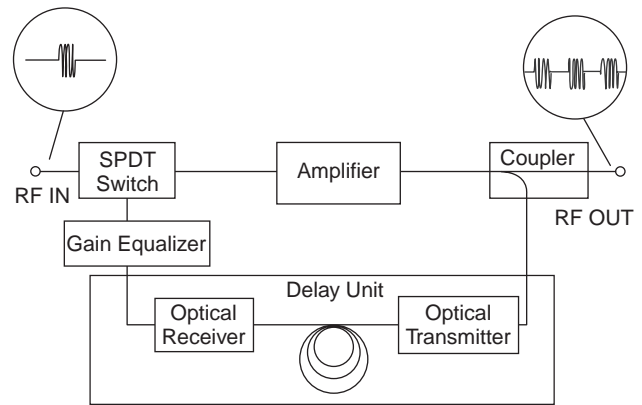


Figure 18. Conceptual drawing of a fiberoptic-based recirculating delay line. It is composed of a SPDT switch, electronic amplifier, coupler, optical delay element, and gain equalizer.

delay line over 2–4 GHz with an insertion loss of -11 dB (flatness of 4 dB) and a spurious-free dynamic range of $87 \text{ dB} \cdot \text{Hz}^{2/3}$, a short electrical pulse has recirculated for as long as a millisecond. The spectral purity of the recirculated signal is evaluated, and the spectral purity of the output pulses is as shown in Fig. 19 after 10, 20, and 35 recirculations. The phase noise degradation is measured for offset carrier frequencies of 10, 50 and 100 Hz.

Since the frequency response of the open loop is not, in practice, flat over the bandwidth, to enhance the performance of the memory loop, a gain equalizer is required. The amplification of the recirculating signal can be realized in either the electrical [39] or the optical domain. For broadband microwave signal processing, however, where the incoming signals in the frequency range of 2–18 GHz are analyzed, pulse recirculation in the optical domain is preferable to that in the electrical domain.

The maximum number of recirculations in the loop in terms of the characteristics of the system components can then be numerically evaluated as a function of gain flatness C . In particular, the maximum number of recirculations n_{max} is limited to the maximum number allowable by NF_{Tmax} and the open-loop noise figure NF_B as follows [39]:

$$NF_{Tmax} \approx \frac{1}{2} (NF_B - 1) \left[\frac{1}{C^n} \frac{1 - C^n}{1 - C} + n \right]$$

The implication of nonflat frequency response of the delay unit is that the noise will increase at a faster rate at frequencies where open-loop gain is greater than unity. Therefore, the nonflat frequency response and high noise figure of the delay element will restrict the maximum time delay attainable by the memory loop. Naturally, to overcome the n_{max} limitation, while achieving long total time delays of $n\tau$, one could increase the unit time delay τ , but the long unit delay will produce a void in the time domain for the short input pulses.

5.2. Advanced Optical Signal Processing Techniques

The use of passive optical components such as optical isolators, array waveguide grating, superposed array

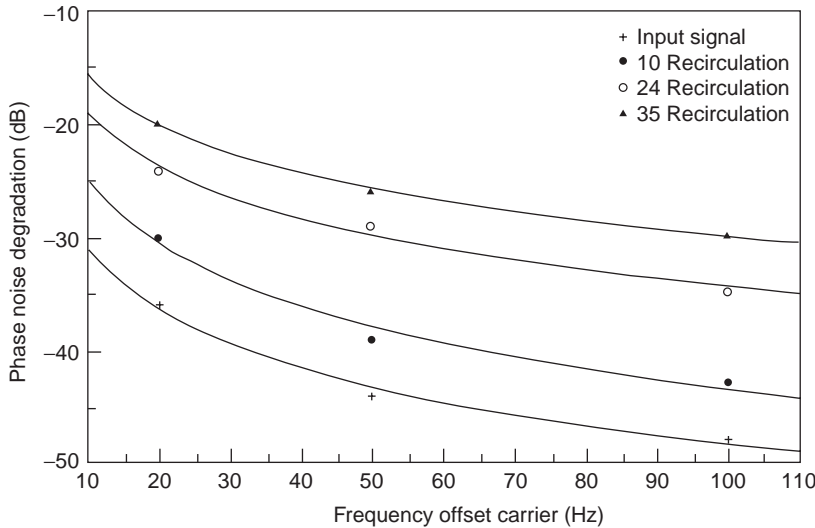


Figure 19. Spectral purity and phase noise degradation compared to the input electrical pulse at various offset carriers as a function of number of recirculations.

grating, and spatial light modulators provides for a number of signal processing techniques, such as interference mitigation [40–42] and adaptive waveform generation [43]. The basic principle of these techniques is based on translating spectrum to time using dispersive fibers or delay lines. As the number of taps increases, increased resolution in frequency domain can be observed. On the other hand, using mode-locked pulses with short sampling periods will increase the time resolution. As the tap weights and unit time delay are adjusted, an arbitrary waveform in time domain is generated that corresponds to the desired transfer function. Figure 20 depicts the structure of a tunable filter, where a tunable filter with a Q as high as 800 is demonstrated [44]. Although discrete grating arrays are simpler for design implementation, but superposed arrays are quite practical for sampling bandwidth in the terahertz range [44].

Moreover, tapped delay lines are employed in combination with positive and negative optical amplitude to adjust transfer function and shape of the transversal filter. High-birefringence materials combined with a polarizer are employed to create all-optical transversal filters. Figure 21 depicts the shape of filter impulse response. The desired impulse response is converted to the desired bandpass filter. Moreover, notch filters could be developed using RF interference in the optical fiber while the other frequencies are transmitted through without much attenuation. Interference mitigation by 50 dB is experimentally demonstrated at 75 MHz [44].

6. OPTICAL ADC TECHNIQUES

Another application of microwave photonics is in the development of the analog-to-digital converter (ADC). Opto-electronic devices have demonstrated ultrafast switching speed, and mode-locked solid-state lasers have achieved high-speed and accurate optical pulses as low as 10 fs. With capability of sampling electrical signals of resolutions of subpicoseconds, implementation of optical ADC has long intrigued many researchers because of the

following advantages: (1) optical sampling has time jitter that is about two orders of magnitude lower than that of an electronic clock, (2) optical sampling decouples the electrical clock signal used for optical sampling from the sampled electrical signal, and (3) an optical sampled or quantized signal is easy to distribute by fiber and to remotely control. Also, many photonic ADC approaches also produce output as Gray codes directly, eliminating the need for additional encoding circuits. However optical

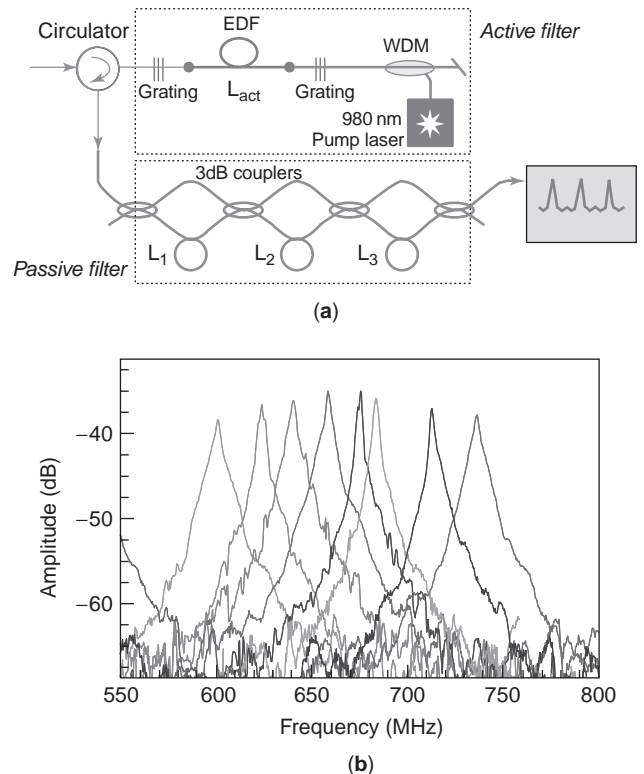


Figure 20. Optical signal processing using a tunable filter: (a) experimental setup; (b) transfer function in terms of modulated frequency. (Courtesy of Prof. Robert Minasian of University of Sydney.)

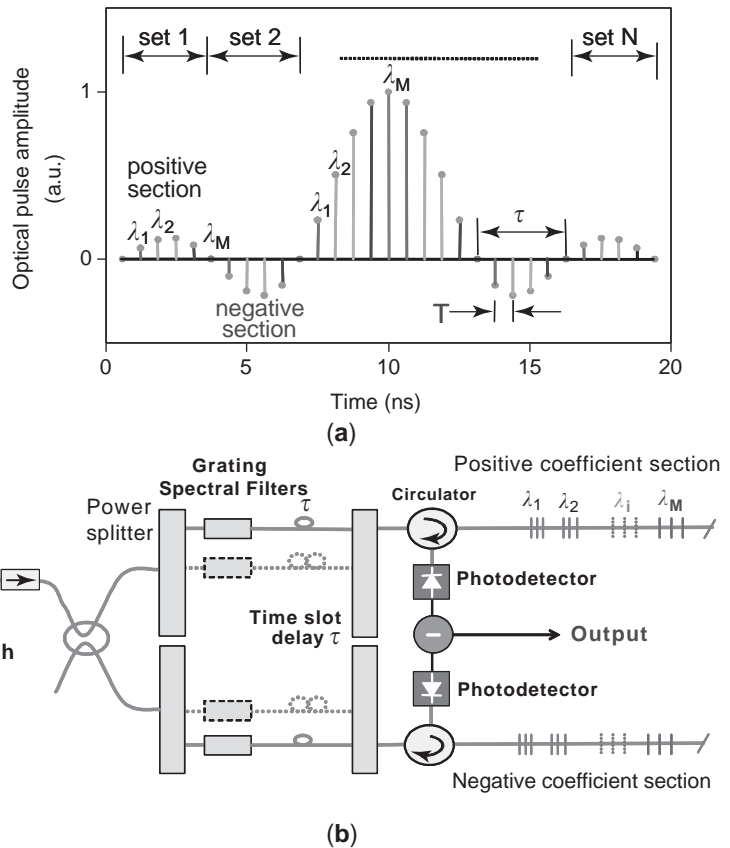


Figure 21. Filter impulse response (FIR) using spectral time mapping: (a) desired signal in the domain; (b) experimental set-up. (Courtesy of Prof. Robert Minasian of University of Sydney.)

quantization is generally limited to resolution of a few bits, and this remains a major challenge. There are two approaches to quantize the information after sampling by optical signal: (1) hybrid optoelectronic ADC, where electrical quantizers are employed; and (2) all-optical ADC, where optical quantization is implemented.

6.1. Hybrid Optoelectronic ADC

Hybrid Optoelectronic ADC, also called “optically assistant ADC”, employs optical sampling followed by electronic quantization. It attempts to combine advantages of both optical and electronic ADC technologies: high-speed rate of optical sampling and high resolution of electronic quantization. But the speed of electronic devices is much lower than the optical sampling rate. So the sampled optical signal has to be downconverted to a lower speed and channeled to parallel electronic quantizers. For example, 100 Gsps sampled pulses can be split into eight channels in time domain, and the pulse rate in every channel is 12.5 Gsps. Most optical sampling transducers are implemented with Mach-Zehnder modulators [45], where the output intensity of the MZ interferometer is a function of the applied voltage

$$I_{out} = I_i \cos^2 \left[\left(\frac{\varphi_0}{2} \right) - \left(\frac{\pi V}{2V_\pi} \right) \right]$$

where $\varphi_0 = 2\pi nL/\lambda_0$, the optical distance of a branch, and V_π is the half-wave voltage, defined as the applied voltage

at which the phase shift changes by π . Optical sampling operates in a small range around V_π , the output is approximately linearly proportional to applied voltage V . To extend the linear range of MZ modulator, a number of linearization approaches were demonstrated. In photonic ADC, the linearization can be implemented in digital domain by directly inverting the transfer function in DSP.

The key issue in hybrid optoelectronic ADC is to channelize high-speed sampled optical pulses and ensure that channels match in both amplitude and time. Based on approaches of channelization, three major schemes are proposed: (1) time interleaving [46], (2) WDM channelization [47], and (3) time stretching [48]. The optical sampling and time interleaving is employed by Juodawlkis et al. [46] to implement an ADC with bandwidth up to 505 Msps by using 1–8 optical demultiplexers and 14-bit electrical quantizers. A dual-output LiNbO₃ MZ modulator is used for linearization processing and a 65 dB SFDR and 47 dB SNR, corresponding to an effective resolution of 7.5 bits. The sampled optical pulses are split into eight channels by optical time-division demultiplexers, which are composed of three stages of 1×2 switches controlled by 505-MHz driving signals. Therefore the 16 parallel high-resolution electronic quantizers are operating at 63 Msps [47]. To achieve an interleaving SFDR of 80 dB, the converter-to-converter gains must be matched to $\sim 0.01\%$, the offset must be matched to $\sim 0.01\%$ of the signal amplitude, and the converter-to-converter crosstalk must be less than one part in 10^4 .

On the other hand, using optical dispersive components, a multiwavelength optical wave is smeared (for continuous spectrum) or split (for discrete wavelengths) in time, and borrowing a concept from WDM communication, the sampled optical signal can be channelized in both wavelength and time domains. The RF signal is sampled by the WDM pulses and then channelized by a WDM demultiplexer. Clark et al. demonstrated a 100-Gsps photonic ADC based on the time- and wavelength-interleaved scheme [47] using a mode-locked fiber laser (MLFL) that generates 12.5 GHz pulsetrain, and a 100-GHz sampling optical pulse is obtained by $8 \times$ multiplexer. The pulses propagate through different fiber delays and attenuators, which then are recombined in the WDM. The delay fibers and attenuators can be adjusted for time matching and amplitude equalizing, respectively. The time-interweaved pulsetrain is then demultiplexed into eight channels according to wavelengths. The resulting parallel pulses are then quantized by >12.5 -Gsps quantizers, but an 8-bit ADC operating at only 781 Msps has been achieved with SNR 22–26 dB, which corresponds to about 4 bits. The resolution of wavelength-channelized ADC is still limited since it faces difficulties similar to those encountered by the time interleaving ADC. The time uncertainty and amplitude uniformity between channels are difficult to control.

Bhushan et al. demonstrated a record ultrafast sampling rate of 130 Gsps using the time stretching approach [48]. The idea behind this ADC is similar to wavelength-channelized ADC, but in the time-stretched approach an RF input signal modulates a broadband optical continuous wave (CW) other than that sampled by optical pulses with discrete wavelengths. The detected analog optical signal is sampled and quantized by electronic ADC. Figure 22 shows a limited time application of time-stretch pre-processing, where a passively mode-locked fiber laser with 20 MHz repetition rate followed by a 17-nm filter is used to generate broadband short pulses. The optical pulse propagates through a dispersive fiber of length L_1 and is dispersed in time to yield a time aperture of 0.8 ns. The wave is then modulated by the RF signal to be converted. The modulated wave is sent to another piece of dispersive fiber of L_2 to be stretched in time domain. The ADC obtains a stretch ratio of $M = 16.2$ by correct choice of either L_1 or L_2 , where the stretched signal is detected and digitized by a single 8-Gsps electronic ADC of an oscilloscope. So the

effective sampling rate is about 130 Gsps ($8 \text{ Gsps} \times 16.2$) with SNR ~ 45 dB, corresponding to 7.5 bits of resolution.

On the other hand, for continuous signals in time, a parallel architecture must be used in order to preserve the information. In this process an arrayed waveguide grating (AWG) is employed to sample a portion of the optical spectrum, and since each optical wavelength corresponds to a different propagation time delay, the filter performs sampling in time. Then each segment is time-stretched by the same factor M prior to entering a slow electronic ADC; however, both time alignment and amplitude in balance between various arms of are crucial importance.

6.2. All-Optical ADC

There are quite a few ways to implement optical quantization, but probably the best-known photonic ADC is based on a patent from 1977 [49]; a revised design called “optical folding-flash” ADC was patented in 1995 [50]. Figure 23 shows a block diagram of a 4-bit optical folding-flash ADC. The geometric scaling of V_π or electrode length is eliminated by a parallel–serial combined configuration. This scheme uses identical electrode length but sets DC bias at different points on the interferometer transfer characteristic curve. The resulting transfer function of MSB-2 and LSB branch is obtained by multiplying the functions of all stages at different bias, showing doubled frequency compared to the previous bit. However, this scheme also presents some additional challenges: (1) the MSB is susceptible to high noise levels because of the slowly changing slope at the digital edges, and (2) the transit-time limitation is still not eliminated; moreover, the hardware complexity increases exponentially in terms of interferometer number as $2^{(b-1)} + 1$ and strongly relies on accurate bias.

Another way to quantize an optical signal is to exploit variable electroabsorption semiconductor modulators demonstrated by Hayduk [51]. The quantization is achieved using an architecture that relates the received analog voltage to an optical intensity, which is based on the same concept as the electronic flash ADC, in which $2^N - 1$ comparators with different threshold values are used. The use of passive materials in this flash photonic ADC architecture with no external voltage requirement gives this module very low power dissipation. The authors claim that the ADC has the potential to operate at more

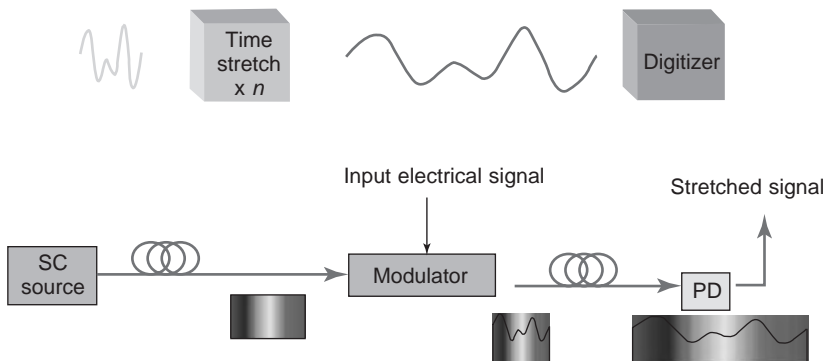


Figure 22. Time-limited signal converted by time stretching ADC [45]. (Courtesy of Prof. B. Jalali from UCLA.)

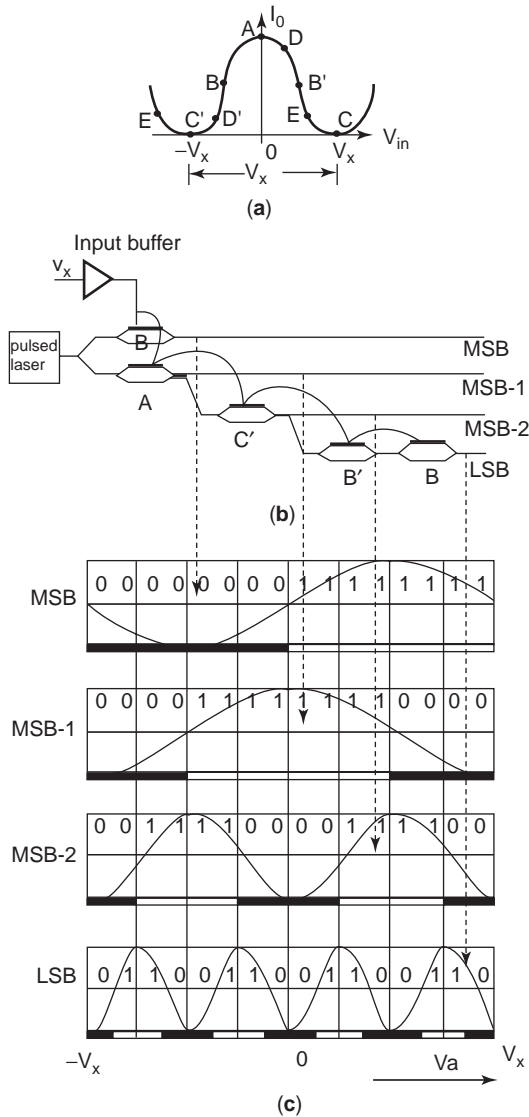


Figure 23. Optical folding-flash ADC [47]. a) various bias points of all optical ADC, b) realization of MZ modulators for quantization, c) the received signal.

than 100 Gbps combined with a resolution as high as 12–14 bits. But this scheme is susceptible to amplitude fluctuation and unbalanced energy splitting. A similar idea is also employed in all-optical ADC quantization using photodetectors with different sensitivities [52].

In the two ADC schemes mentioned above, the RF signal is sampled and quantized by optical amplitude. However, the amplitude errors strongly depend on source fluctuation, device linearity, and loss along the optical link. So it is difficult to build a construct high-resolution all-optical ADC based on optical amplitude. An all-optical ADC operating in spectrum domain is demonstrated by Zmuda et al. [53], as shown in Fig. 24. The input signal is sampled by a tunable laser and quantized by processor filters with binary behavior. The output wavelength of the tunable laser is modulated by the applied electrical field, so the electrical amplitude is represented as wavelength in spectrum domain. The postsampled light is processed by a parallel optical filter array. If the spectrum line falls into the passband, the output is represented as “1”; otherwise a “0” will be read. Each filter has periodic equally spaced passband and stopband and organized in a Gray code manner.

The major challenges for this scheme are the filter design of sharp transition and tunable laser. A 4-bit optical ADC using Bragg grating filters and a ring cavity tunable laser is proposed and analyzed. Because of the convergence time limitation of the Fabry–Perot cavity, only 4 bits of resolution can be achieved at 10 Gbps. Moreover, the performance of Bragg grating filters (see Fig. 25) show limited resolution. The authors proposed a folding circuit to enhance its resolution, where a Mach–Zehnder interferometer performs the optical folding circuit and a first-order linearization circuit corrects the nonlinear folded signal. Thus, two low-resolution ADCs are coupled with the folding circuit to achieve $M + N$ bits of resolution. The author claimed that the ADC would be able to operate at conversion speeds in excess of 10 GHz with up to 10–12 bits of resolution. However, it is not clear how the upper M -bit ADC achieved the additional 6–8 bits. But it indicates a promising way to perform analog-to-digital conversion in spectrum domain.

7. NEAR-IR OPTICAL SPECTROSCOPY

Near-infrared (NIR) spectroscopy is a new, noninvasive technique employed to analyze living tissue. In NIR spectroscopy, the main aim is to extract the optical properties (absorption and scattering) of the living tissue. Absorption information is used to characterize the concentration of biological chromophores, such as hemoglobin (in oxy and deoxy forms), which in turn indicates the physiological changes in blood. Scattering data provide information on

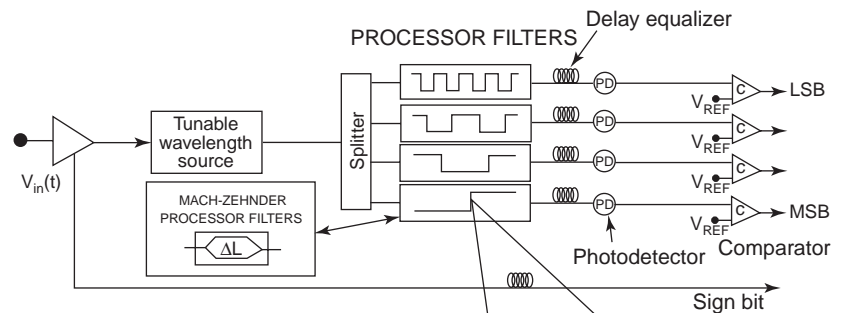


Figure 24. Optical ADC using tunable laser and filters [53].

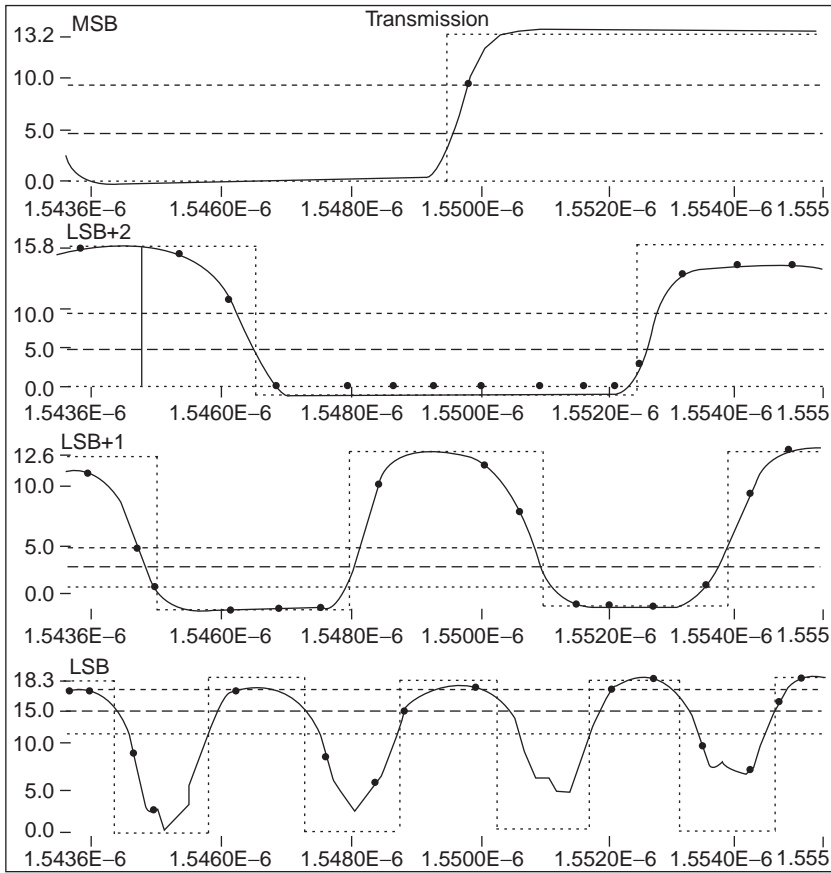


Figure 25. Performance of Bragg grating filters.

composition, density, and organization of tissue structures, such as cells and subcellular organelles [54,55]. Therefore, NIR techniques provide information about disease-related functional and structural changes. More specifically, it has been shown that physiological changes such as ischemia, necrosis, and malignant transformation can produce important perturbations in tissue optical properties [55]. The importance of the NIR spectrum lies in the fact that in this region tissue absorption is much lower than in other parts of the spectra (see Fig. 26). Apart from tissue information content, this region is attractive since NIR instruments are inexpensive to construct and are easily portable. These features render NIR instruments as an attractive alternative to other techniques, such as MRI (magnetic resonance imaging). Moreover, NIR light is not an ionizing radiation; therefore, it can be used as a usual clinical monitoring of patients in radiation therapy.

The modulated NIR could be employed for greater spatial and temporal information and could be explained on the basis of the following physical principle. When photons enter a turbid (multiply scattering) medium, the photons scatter randomly in all directions, diffuse through the medium, and are absorbed during this diffusion process. When source detector separation is large enough and scattering dominates the absorption, the diffusion theory provides a very suitable approximation for photon transport

$$\frac{1}{c} \frac{\partial \Phi(r, t)}{\partial t} - D \nabla^2 \Phi(r, t) + \mu_a \Phi(r, t) = S(r, t)$$

where Φ is the fluence rate (W/cm^2), c is the speed of light in the tissue, S is the source term, μ_a is the absorption, and D is the diffusion constant, which is related to the reduced scattering constant μ'_s by $D = 1/(3\mu'_s)$. In an infinite medium for a point source, the photon diffusion wave (PDW) can be

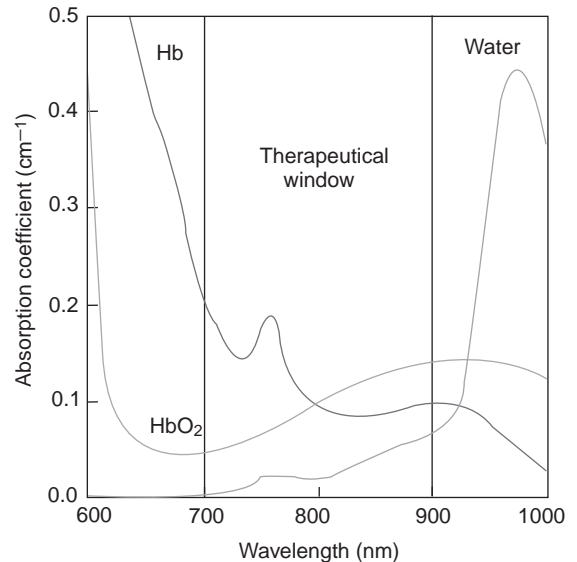


Figure 26. Absorption spectrum of Hb (deoxy-hemoglobin), HbO2 (oxy-hemoglobin), and water in the NIR region.

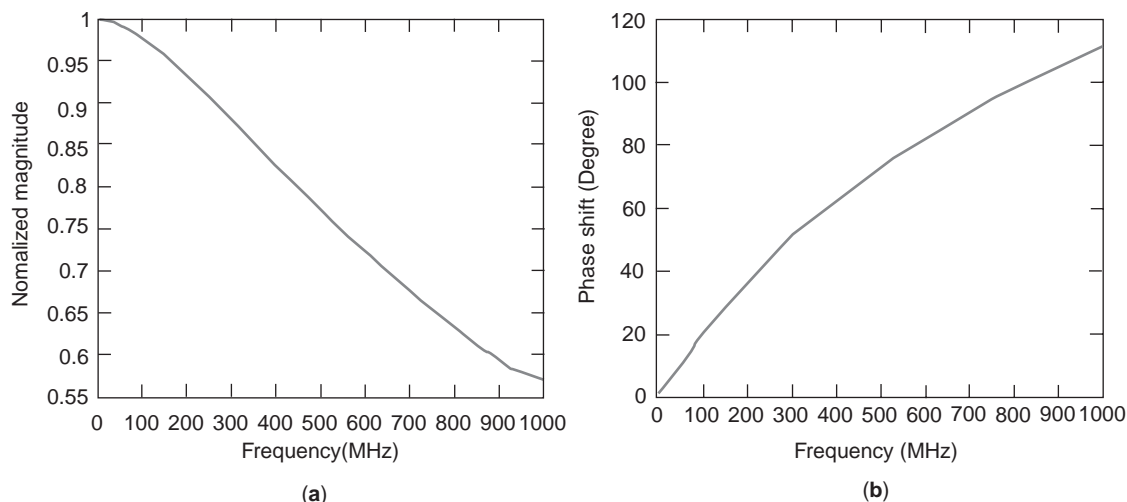


Figure 27. Normalized amplitude attenuation (a) and phase shift (b) of photon diffuse waves as a function of frequency.

expressed analytically as

$$\Phi(r, t) = \frac{S}{4\pi D} \frac{\exp(ikr)}{r}$$

where k is the complex wavevector (i.e., $k = k_{\text{real}} + ik_{\text{imag}}$) and is described as combination of modulating frequency, diffusion, and absorption coefficients as $k = \sqrt{-\mu_a/D + i\omega/(c \cdot D)}$. The backscattered PDW has phase lag and amplitude attenuation relative to the source as

$$\Theta_{\text{lag}}(r, \omega) = k_{\text{imag}} \cdot r$$

$$A_{\text{att}}(r, \omega) = \exp(-k_{\text{real}}r)/(4\pi Dr)$$

Figure 27 shows the solution of amplitude attenuation and phase shift of photon diffuse waves with respect to frequency (up to 1 GHz) for breast tissue with optical absorption and scattering coefficients properties of $\mu_a = 0.05 \text{ cm}^{-1}$, $\mu_s = 10 \text{ cm}^{-1}$. NIR techniques are also being used for brain imaging as seen in Fig. 28 [57,58]. The

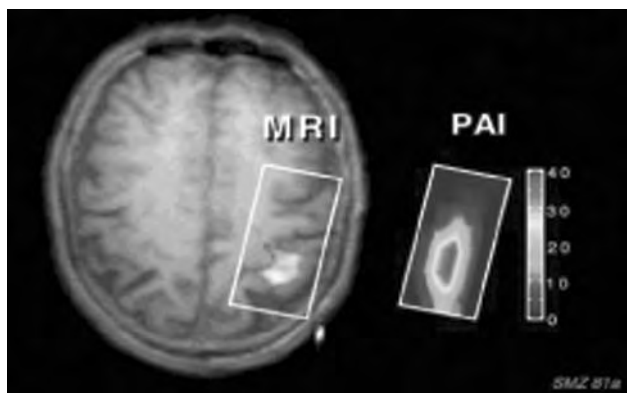


Figure 28. Brain activation image: MRI image is shown on the left, and the image from diffuse optical tomography is depicted on right. (Courtesy of Prof. Britton Chance of University of Pennsylvania.)

image on the left is obtained from MRI. The image on the right is obtained from diffuse optical tomography.

The NIR technique uses continuous-wave (CW), time-domain, and frequency-domain instruments according to their applications and information content. CW systems are very inexpensive but suffer from limited resolution. Frequency-domain (FD) instruments are more compact and cheaper, and FD algorithms are easier to handle than those of the time-domain techniques; hence FD instruments are more attractive. In FD photon migration concept is also easier. When light is modulated by frequencies in the megahertz region, diffuse photon density waves (PDW) are generated, propagating with a wavelength of several centimeters [59–62]. At the detector one measures the amplitude decay and phase shift data of these waves (see Fig. 27). Amplitude and phase data are used to map the optical absorption and scattering properties of the medium. Optical constants in turn are used to obtain hemoglobin concentration, blood volume, and oxygen saturation. Greater accuracy of the extracted results is achieved when a frequency-swept mode is employed, and as the modulation frequency increases to the microwave region, a higher spatial resolution is attained.

8. CONCLUSIONS

This article provides a personal perspective of microwave photonics and its evolution toward a mature field. From its fundamental beginning of light interaction with semiconductor devices and circuits, the goal has been to take advantage of isolation between optical and electrical systems. Moreover, the injection photogenerated electron–hole pair influences the dynamics of microwave devices, leading to the development of novel devices. Light interaction with microwave devices and circuits has seen a new resurgence, particularly in applications dealing with integrated optical detectors with microwave functions. HBT (heterojunction phototransistor)-based devices seem to provide high gain and speed performance.

Fiber-fed phased-array antennas and wireless communications have been the second driver for the microwave photonics. The performance of analog fiberoptic links is analyzed in terms of link gain and dynamic range for data signal distribution; performance of FO links are also analyzed in terms of AM/PM conversion employed in remoting of the frequency reference to stabilize the distributed local oscillators. Moreover, distortion induced by SRS in dense WDM systems is discussed. Fiberoptic links based on direct modulation could meet cost-performance requirements for many applications, even though monolithically integrated EA modulators are becoming very attractive. Another innovation is in the design of multi-function circuits, such as the monolithically, integrated FP laser with EA modulator, where simultaneous transmission of frequency reference of data signals is accomplished. The optical oscillation in this novel device could be stabilized as a LO signal using either injection locking or mode locking. The achieved close-in to carrier phase noise of the stabilized LO signal is lower in the case of injection locking than mode locking for the same modulating power level. However, the nonlinear behavior of the mode-locked laser provides opportunity for efficient optoelectronic mixing of LO and data signals, while maintaining a very high SFDR. This multifunction circuit creates the possibility of generating a RF signal from the frequency reference and data signals, thus bypassing the need for integration with electrical mixers in up/downconversion.

Among the technologies that are unique to microwave photonics is the issue of optical signal processing, which could lead to very large time-bandwidth products, hence resulting in high frequency selectivity. Memory loop devices, transversal filters, and tapped delay lines are attractive solutions that command unique advantages over the electrical signal processing techniques. Moreover, the optical ADC is considered another important advantage over electrical systems because of its lower timing jitter, hence achieving a high resolution ADC at the Gbps level. This technology is critical in the development of digital receivers for software radiocommunication systems. Finally, new applications for microwave photonics are emerging in the medical imaging using the photon density wave. The RF modulated light at microwave frequency at wavelengths associated with absorption peaks of oxy- and deoxyhemoglobin provides a higher spatial resolution with function imaging of the biological tissues. This technique is currently being pushed for clinical applications to medical imaging of brain, breast, and skin tissues.

There many innovations in the field of microwave photonics that, because of space limitations in this article, impossible to cover here. However, the author wishes to recommend as further reading a number of special issues of *IEEE Transactions on Microwave Theory and Techniques* that are dedicated to reviews of the latest innovations in microwave photonics as further reading.

Acknowledgment

The author wishes to acknowledge the contribution of many of his students, particularly Dr. Murilo Romero, Dr. Edward Ackerman, Dr. Reza Saedi, Mr. Adam McIn-

vale, Dr. Tsang-der Ni, Dr. Xiang-dong Zhang, Dr. Manouchehr Ghanevati, Dr. Joong-Hee Lee, and Dr. Xiaobo Hou. Moreover, technical discussions with his colleagues Prof. Asher Madjar, Technion, Tel Aviv, Israel; Dr. Kenji Sato, NTT, Yokosuka, Japan; Dr. Hiroyo Ogawa, CRL, Yokosuka, Japan; Prof. Robert Minasian, University of Sydney, Australia; Prof. Peter Herczfeld, Drexel University, Philadelphia; Prof. Bahram Jalali, UCLA, Los Angeles; Prof. Britton Chance, University of Pennsylvania, Philadelphia; and Prof. Tibor Berceli, Budapest University of Science and Technology, Budapest, Hungary are greatly appreciated.

BIBLIOGRAPHY

1. B. Saleh and M. Tiech, *Fundamentals of Optics*, Wiley, New York, 1991.
2. P. Bhattacharya, *Semiconductor Optoelectronic Devices*, Prentice-Hall, Englewood Cliffs, NJ, 1994.
3. A. S. Daryoush, K. Bontzos, and P. R. Herczfeld, Optically tuned patch antenna for phased array applications, *IEEE Int. APS Symp. Digest*, Philadelphia, PA, 1986.
4. P. Cheung, D. P. Neikirk, and T. Itoh, Optically controlled coplanar waveguide phase shifters, *IEEE Trans. Microwave Theory Tech.* **38**(5):586-595 (1990).
5. M. Belaga, *Application of an Optically Controlled PIN Diode in Microwave Circuits*, M.S. thesis, Drexel Univ., Philadelphia, PA, 1987.
6. A. Rosen and F. Zutavern, *High-Power Optically Activated Solid-state Switches*, Artech House, 1994.
7. R. Simons, Microwave performance of an optically controlled AlGaAs/GaAs high electron mobility transistor and GaAs MESFET, *IEEE Trans. Microwave Theory Tech.* **35**(12):1444-1455 (1987).
8. Y. Akatsu, High-speed monolithically integrated pin-HEMT photoreceivers, *Proc. 1995 IEEE/LEOS Summer Topical Meeting, ICs for New Age Lightwave Communications*, pp. 33-34.
9. A. L. Guiterrez-Aitken, K. Yang, X. Zhang, G. I. Haddad, P. Bhattacharya, and L. M. Lunardi, 16-GHz bandwidth In-AlAs-InGaAg monolithically integrated p-i-n/HBT photoreceiver, *IEEE Photon. Technol. Lett.* **7**(11):1339-1341 (Nov. 1995).
10. S. Chandrasekhar, L. Lunardi, A. H. Ganuck, R. A. Hamm, and G. J. Qua, High-speed monolithic p-i-n/HBT and HPT/HBT photoreceivers implemented with simple phototransistor structure, *IEEE Photon Technol. Lett.* **5**(11):1316-1318 (1993).
11. J. Lasri, D. Dahan, A. Bilenca, G. Eisenstein, and D. Ritter, Clock recovery at multiple bit rates using direct optical injection locking of self oscillating InGaAs/InP heterojunction bipolar photo-transistor, *IEEE Photon. Technol. Lett.* **13**:1355-1357 (2001).
12. A. J. Seeds and A. A. de Salles, Optical control of microwave semiconductor devices, *IEEE Trans. Microwave Theory Tech.* **38**(5):577-585 (1990).
13. A. Madjar, P. Herczfeld, and A. Paoletta, A novel analytical model for optically generated currents in GaAs MESFETs, *IEEE Trans. Microwave Theory Tech.* **40**(8) (1992).
14. M. A. Romero, *Modulation Doped Field Effect Photodetectors*, Ph.D. thesis, Drexel Univ., Philadelphia, PA, 1995.

15. H. Ogawa, S. Banba, E. Suematsu, H. Kamitsuna, and D. Polifko, A comparison of noise performance between a pin diode and MMIC HEMT and HBT optical receivers, *IEEE Int. Microwave Symp. Digest*, Atlanta, GA, 1993, pp. 225–228.
16. A. Paoletta, A. Madjar, and P. Herczfeld, Modeling the GaAs MESFET's response to modulated light at radio and microwave frequencies, *IEEE Trans. Microwave Theory Tech.* **42**(7):1122–1130 (1994).
17. A. H. Madjedi, S. K. Chaudhuri, and S. Safavi-Naeini, Optical-microwave interaction modeling in high-temperature superconducting film, *IEEE Trans. Microwave Theory Tech.* **49**(10):1873–1881 (2001).
18. A. S. Daryoush, E. Ackerman, N. Samant, D. Kasemsat, and S. Wanuga, Interfaces for high-speed fiber optic links: Analysis and experiment, *IEEE Trans. Microwave Theory Tech.* **39**(12) (Dec. 1991).
19. E. Ackerman, Photonics Inc., private communications.
20. A. R. Chraplyvy and P. S. Henry, Performance degradation due to stimulated Raman scattering in wavelength-division-multiplexed optical-fiber systems, *Electron. Lett.* **19**(16) (Aug. 1983).
21. A. R. Chraplyvy, Limitations on lightwave communications imposed by optical-fiber nonlinearities, *J. Lightwave Technol.* **8**(10) (Oct. 1990).
22. Z. Wang et al., Effects of cross phase modulation in wavelength SCM video transmission systems, *Electron. Lett.* **31**(18) (Aug. 1995).
23. T. E. Darcie et al., Lightwave multi-channel analog AM video distribution systems, *IEEE Int. Conf. Communications*, Boston, MA, June 1989.
24. Z. Wang, A. Li, C. Mahon, G. Jacobsen, and E. Bodtker Performance limitations imposed by stimulated Raman scattering in optical WDM SCM video distribution systems, *IEEE Photon. Technol. Lett.* **7**(12) (Dec. 1995).
25. M. R. Phillips and D. M. Ott, Crosstalk due to optical fiber nonlinearities in WDM CATV lightwave systems, *J. Lightwave Technol.* **17**(10) (Oct. 1999).
26. X. Zhang, and T. D. Ni, and A. S. Daryoush, Laser induced phase noise in optically injection locked oscillator, *IEEE MTT Symp. Digest*, 1992, pp. 765–768.
27. X. Zhang and A. S. Daryoush, Bias dependent low frequency noise up-conversion in HBT oscillators, *IEEE Microwave Guided Wave Lett.* **4**(12):423–425 (Dec. 1994).
28. T. D. Ni, X. Zhang, and A. S. Daryoush, Experimental study on close-in carrier phase noise of laser diode with coherent feedback, *IEEE Trans. Microwave Theory Tech.* **43**(9):2277–2283 (Sept. 1995).
29. A. S. Daryoush, K. Sato, K. Horikawa, and H. Ogawa, Efficient opto-electronic mixing at Ka-band using a mode-locked laser, *IEEE Microwave Guided Wave Lett.* **9**(8):317–319 (Aug. 1999).
30. A. S. Daryoush et al., Applications of opto-electronic mixing in distributed systems, *2001 Topical Symp. Millimeter Wave Digest*, (TSMMW2001), Yokosuka, Japan, March 2001, pp. 175–178.
31. A. S. Daryoush, K. Sato, K. Horikawa, and H. Ogawa, Efficient optoelectronic mixing at Ka-band using a mode-locked laser, *IEEE Microwave Guided Wave Lett.* **9**(8):317–319 (Aug. 1999).
32. H. X. Shi, D. A. Cohen, J. Barton, M. Majewski, L. A. Coldren, M. C. Larson, and G. A. Fish, Dynamics range of widely tunable sampled grating DBR lasers, *Electron. Lett.* **38**:180–181 (Feb. 2002).
33. A. S. Daryoush, K. Sato, K. Horikawa, and H. Ogawa, Dynamic response of long optical cavity laser diode for Ka-band communication satellites, *IEEE Trans. Microwave Theory Tech.* **45**(8):1288–1295 (Aug. 1997).
34. J. Faist, F. Capasso, D.L. Sivco, C. Sirtori, A.L. Hutchinson, and A.Y. Cho, *Science* **264**: 553 (1994).
35. R. Saedi, W. Jen, N. Samant, A. S. Daryoush, D. Sturzebecher, and P. Herczfeld, Comparison of CPU level data mixing to T/R level data mixing architectures in optically controlled phased arrays, *Proc. 1993 Int. Microwave Symp.*, Atlanta, GA, June 1993.
36. X. Zhang and A. S. Daryoush, Full 360° phase shifting of injection locked oscillators, *IEEE Microwave Guided Wave Lett.* **3**(1):14–16 (1993).
37. X. Zhou and A. S. Daryoush, An efficient self-oscillating mixer for communications, *IEEE Trans. Microwave Theory Tech.* **42**(10):1858–1862 (Oct. 1994).
38. A. S. Daryoush, K. Sato, K. Horikawa, and H. Ogawa, Efficient optoelectronic mixing at Ka-band using a mode-locked laser, *IEEE Microwave Guided Wave Lett.* **9**(8):317–319 (Aug. 1999).
39. R. Saedi, A. S. Daryoush, and P. Herczfeld, Fiberoptic based recirculating memory loop, *IEEE Int. Microwave MTT-S Symp. Digest*, Albuquerque, NM, June 1992, Vol. II, pp. 677–680.
40. D. B. Hunter, R. A. Minasian, and P. A. Krug, Tunable optical transversal filter based on chirped gratings, *Electron. Lett.* **31**:2205–2207 (1995).
41. J. Campany, D. Pastor, and B. Ortega, New and flexible fiber-optic delay line filters using chirped Bragg gratings and laser arrays, *IEEE Trans. Microwave Theory Tech.* **47**:1321–1326 (1999).
42. X. Wang and K. T. Chan, Tunable all-optical incoherent bipolar delay-line filter using injection-locked FP laser and fiber Bragg gratings, *Electron. Lett.* **36**(24) (2000).
43. A. M. Weiner et al., *IEEE J. Quantum Electron.* **28**:908 (1992).
44. R. A. Minasian, K. E. Alameh, and E. H. W. Cahan, Photonics-based interference mitigation filters, *IEEE Trans. Microwave Theory Tech.* (special issue on microwave and millimeter-wave photonics) **49**(10):1894–1899 (2001).
45. B. L. Shoop, *Photonic Analog-to-Digital Conversion*, Springer, 2001.
46. P. W. Juodawlkis, J. C. Twichell, G. E. Betts, J. J. Hargreaves, R. D. Younger, J. L. Wasserman, F. J. O'Donnell, K. G. Ray, and R. C. Williamson, Optically sampled analog-to-digital converters, *IEEE Trans. Microwave Theory Tech.* **49**(10): 1840–1853 (Oct. 2001).
47. T. R. Clark, J. U. Kang, and R. D. Esman, Performance of a time- and wavelength-interleaved photonic sampler for analog-digital conversion, *IEEE Photon. Technol. Lett.* **11**(9):1168–1170 (Sept. 1999).
48. A. S. Bhushan, P. V. Kelkar, B. Jalali, O. Boyraz, and M. Islam, 130-Gsa/s photonic analog-to-digital converter with time stretch preprocessor, *IEEE Photon. Technol. Lett.* **14**(5):684–686 (May 2002).
49. H. F. Taylor, *Electro-Optic A/D Converter*, U.S. Patent 4,058,722 (1957).
50. B. Jalali and Y. M. Xie, Optical folding-flash analog-to-digital converter with analog encoding, *Opt. Lett.* **20**(18):1901–1903 (1995).
51. M. J. Hayduk, *Photonic Analog-to-Digital Conversion Using Light Absorption*, U.S. Patent 6,326,910.
52. J. T. Gallo, *Photonic A/D Converter Using Parallel Synchronous Quantization of Optical Signals*, U.S. Patent 6,188,342.

53. H. Zmuda, E. N. Toughlian, G. Li, and P. Li Kam Wa, A photonic wideband analog-to digital converter, *Proc. 2001 IEEE Aerospace Conf.*, 2001, Vol. 3, pp. 1461–1472.
54. B. Chance, M. Cope, E. Gratton, N. Ramanujam, and B. Tromberg, Phase measurement of light absorption and scatter in human tissue, *Rev. Sci. Instrum.* **69**:3457–3481 (1998).
55. B. Tromberg, N. Shah, R. Lanning, A. Cerussi, J. Espionza, T. Pham, L. Svaasand, and J. Butler, Non-Invasive in vivo characterization of breast tumors using photon migration spectroscopy, *Neoplasia* **2**:26–40 (2000).
56. J. B. Fishkin, O. Coquoz, E. Anderson, M. Brenner, and B. Tromberg, Frequency-domain photon migration measurements of normal and malignant tissue optical properties in a human subject, *Appl. Opt.* **36**:10–20 (1997).
57. B. Chance, E. Anday, S. Nioka, S. Zhou, L. Hong, K. Worden, C. Li, T. Murray, Y. Ovetsky, D. Pidikiti, and R. Thomas, A novel method for fast imaging a brain function, non-invasively, with light, *Opt. Express* **2**:411–423 (1998).
58. V. Ntziachristos, A. G. Yodh, M. Schnall, and B. Chance, MRI-guided diffuse optical spectroscopy of malignant and benign breast lesions, *Neoplasia* **4**(4):347–354 (2002).
59. J. B. Fishkin and E. Gratton, Propagation of photon density waves in strongly scattering media containing an absorbing semi-infinite plane bounded by a straight edge, *J. Opt. Soc. Am. A* **10**:127–140 (1993).
60. S. Fantini, M. Franceshini, and E. Gratton, Semi-infinite-geometry boundary problem for light migration in highly scattering media: A frequency-domain study in the diffusion approximation, *J. Opt. Soc. Am. B* **11**:2128–2138 (1994).
61. J. B. Fishkin, S. Fantini, M. J. vandeVen, and E. Gratton, Gigahertz photon density waves in a turbid medium: Theory and experiments, *Phys. Rev. E* **53**:2307 (1996).
62. T. H. Pham, O. Coquoz, J. B. Fishkin, E. Anderson, and B. Tromberg, Broad bandwidth frequency domain instrument for quantitative tissue optical spectroscopy, *Rev. Sci. Instrum.* **71**:2500–2513 (2000).

MICROWAVE POWER AMPLIFIERS

PAOLO COLANTONIO
FRANCO GIANNINI
ERNESTO LIMITI
Università degli Studi di Roma
Tor Vergata
Rome, Italy

1. INTRODUCTION

A power amplifier (PA) is a system component whose main task is to increase the power level of the signal at its input up to a predefined level. As contrasted to low-level amplifiers, often specified in terms of small-signal gain, the absolute output power level is the PA main feature. This characteristic on one hand forces the selection of the active devices composing the PA on the basis of their output power capabilities; on the other hand, in order to fully exploit such capabilities, the devices are typically operated under large-signal regimes, forcing the exploration of nonlinear operating regions. A PA is therefore an intrinsically non-

linear system component, whose large-signal operating conditions often lead to detrimental effects on the output signal, resulting in a distorted replica of the input. Moreover, the linear approximation underlying small-signal amplifier design techniques is no longer strictly valid and hence does not allow their direct application to PA design. Dedicated methodologies therefore have to be adopted, even if preliminary and first-guess simplified approaches are often employed. The present contribution is aimed at addressing the microwave power amplifier design and performance. Radiofrequency (RF) or other approaches at lower operating frequencies (below 1 GHz) are therefore not covered in detail, except where explicitly stated.

Microwave PA system applications span a broad range of areas [1], including telecommunications, radar [2–4], electronic warfare, heating [5,6], and medical microwave imaging [7–12], which represent only a few examples. Given such extremely diversified fields, PA specifications differ greatly on operating, technological, and design requirements. Examples of such differences range from traveling-wave-tube (TWT) amplifiers in satellite payloads to solid-state amplifiers for personal wireless communication handsets, from microwave heating tubes to amplifiers composing hyperthermia apparatuses.

The large differences in system applications are reflected back into the technologies adopted for realization of the PA active module. The early days of the microwave era were characterized by an extensive, widespread use of vacuum-tube devices [13–16] for both generation and amplification of microwave signals. If microwave electronics may be dated back to the pioneering work of H. Hertz and J. C. Bose [17–20], a major push toward high-power microwave generation and use came from the World War II military application in the radar field, with the introduction and use of the cavity magnetron by British researchers and the klystron as a high-power source in 1939/40. The klystron evolved in Stanford University toward a high average power amplifier, leading to modern applications involving clustered cavity klystron and traveling-wave tubes [21–23].

In such a scenario, solid-state devices and related amplifiers are relatively recent players, being the first GaAs MESFET, with good performance at X band, commercially available since the early 1970s, despite the device introduction in the early work of Stuetzer and Shockley [24,25]. The technology rapidly advanced and, in the 1970s, the development of techniques for semiconductor crystal growth such as molecular-beam epitaxy (MBE) permitted optimized p-n-junction structures to be realized, allowing a series of two- and three-terminal devices to be fabricated with frequency operation ranging from a few gigahertz well into the millimeter-wave region [26–28]. To the two-terminal device category can be assigned IMPATT transit-time and Gunn transferred electron devices, which have been and are still used for both frequency generation and amplification, as negative-resistance amplifiers, in the millimeter-wave frequency region. The broader and much more frequently adopted category of three-terminal active devices includes the already mentioned metal semiconductor field-effect device (MESFET), the high-electron-mobility transistor (HEMT; demonstrated by Mimura in

1980 [26]) with its pseudomorphic (PHEMT) and metamorphic (MHEMT) variants, the heterojunction bipolar transistor (HBT; introduced by Kroemer in 1957 [29]), and finally, due to the more recent major advances of high-frequency silicon technology, MOS and bipolar silicon transistors, including laterally diffused MOS structures (LDMOS, [30,31]) and silicon-germanium (SiGe) HBTs [32,33] as key representatives. Nevertheless, the “work horse” technology for microwave power amplification is indeed based on III-V technologies, mainly of the GaAs type. The latter technology is capable of providing, as the output of a single device, output power levels close to 50 dBm [34] with operating frequencies approaching W band. In the upper frequency range, InP solutions are more appropriate, even if they provide very limited output power levels.

Even if “combined device” concepts utilizing both solid-state and vacuum-tube devices have been proposed, the former are generally utilized for low-moderate power output while the latter is indeed necessary whenever high power and high frequency of operation are addressed as schematically indicated in Fig. 1.

Performance of the given device type may be readily demonstrated to exhibit a well-known behavior if considered in their frequency limit region, i.e. following the law:

$$P \cdot f^2 \approx \text{const} \tag{1}$$

where P and f represent output power and the operating (narrowband) frequency, respectively.

The single solid-state device output can be combined utilizing a series of different techniques, and therefore solid-state power amplifiers with output powers compara-

ble to the ones of a vacuum-tube source (i.e., in the kilowatt region) may be obtained in the microwave frequency region (up to X band). On the other hand, practical limitations arise from the systematic application of combining techniques as operating frequency increases, thus imposing the use of vacuum-tube sources.

The increase in solid-state single-device performances will therefore lead to new device concepts and new developing technologies. Among the latter ones, SiC [35] and GaN wide-bandgap semiconductor technologies are actually being explored; whereas SiC MESFET and HEMT have demonstrated 4–5 W/mm output power density throughout X band [36], nitride-based components are extremely promising, setting a new upper limit to device performance in the range of 20 W per millimeter of device periphery, as compared to the 1–2 W limit of GaAs FET-based technologies and the 2–4 W of the HBT ones [37–39]. Even if experimentally demonstrated in the microwave range, such performances are expected to be exported to higher operating frequencies, well into the millimeter-wave spectrum.

The more recent trends toward increasingly high power densities, pushed mainly by radar and electronic warfare applications, is the latest development of the tremendous growth experienced by the high-frequency semiconductor industry. In fact, since the early 1990s, mobile and personal communications systems, ranging from cellular telephony to wireless LAN, with the corresponding demand for high-quality radiolinks, is posing a major challenge to high-frequency technologies and subsystem performances, especially in the microwave frequency region.

The demand for portable apparatuses, whose main characteristic is battery duration and overall size, logically

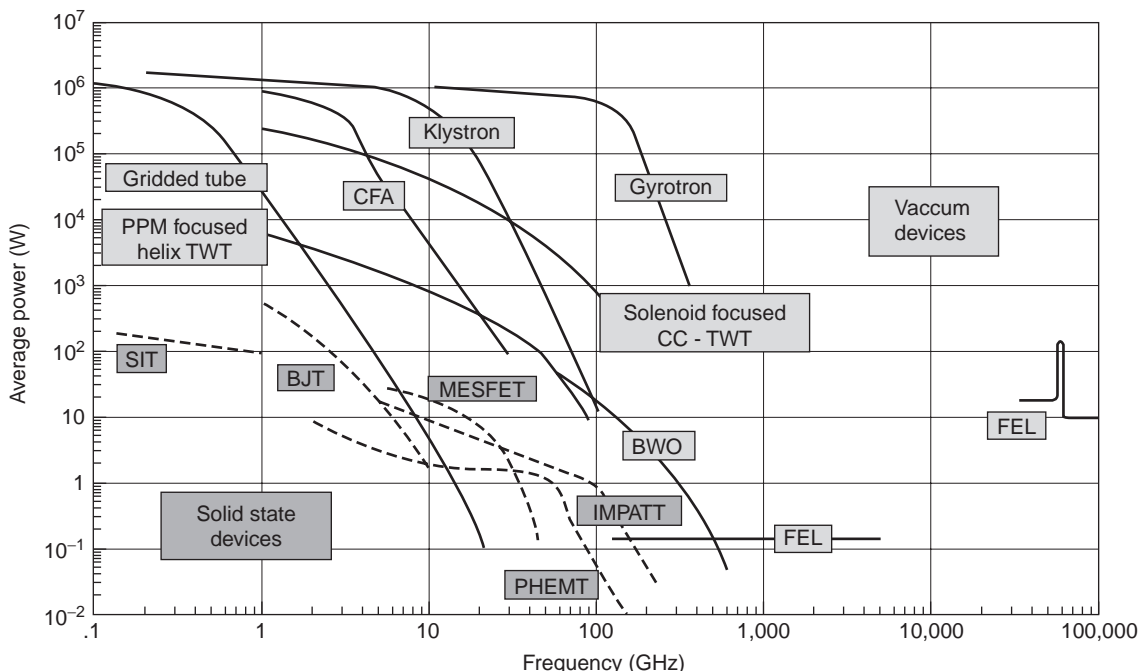


Figure 1. Single-device output power as a function of frequency for solid-state and vacuum devices. [From V. L. Granatstein et al., Vacuum electronics at the dawn of the twenty-first century, *Proc. IEEE* 87(5):702–716 (May 1999).]

translates into a low-power electronic system. Since the PA in the transmitter section clearly represents the main source of supply power consumption, such feature is directly transferred to its specifications. A difficult tradeoff is therefore demanded of the PA designer, balancing among the contrasting goals of high transmitted power, low power consumption, and, for many telecommunication systems, linear operation. Given the widespread diffusion of many telecom applications, all of the abovementioned specifications have to be fulfilled keeping unit cost to a minimum. Such goals and the resulting compromise may vary depending on the type of radiolink to be established and overall system specifications, but their challenge has heavily influenced industrial, technical, and research directions in the PA field since early 1990s.

As a consequence, the high-frequency semiconductor industry has finally moved toward high-volume production. In particular, the search for an high output power is pushing, from the technological point of view, toward the design of active devices with high power densities, simultaneously exhibiting high reliability, and reproducibility, and at a reasonable cost. Six-inch wafers are currently adopted for high-volume production in GaAs, as compared with the former prototyping 3- or 4-in. low-volume productions, with a corresponding increase in reproducibility, wafer uniformity, and yield, at a lower cost. As a consequence, many beneficial effects on PA performance in terms of process maturity and stage performance have been realized. From the device side, GaAs FET discrete packaged power devices are actually produced and commercialized, allowing high output power (≤ 40 W in S bands in partially matched conditions or > 100 W directly in push-pull configuration for base-station applications [34]) even in X or Ku band (> 20 W in internally matched configuration in 14–14.5 GHz range [34]).

Where intrinsic difficulties of material growth and resulting quality are encountered, metamorphic solutions have been proposed, allowing the growth of high-quality materials on a solid and reliable bulk substrate; this is the case for high-indium-content devices and structures utilizing GaAs wafers. The inherent volume and cost advantages are evident, with minor performance degradation; the latter is due mainly to quality of the transition between materials, gradually accommodating the lattice mismatch, which can be appropriately optimized.

2. BASIC DEFINITIONS AND PERFORMANCE PARAMETERS

Regardless of the specific application, a PA may be ultimately considered, from the energy perspective, as a component converting DC power from supplies (P_{DC}) into microwave power (P_{out}), driven by an input power (P_{in}). This process is schematically depicted in Fig. 2.

The effectiveness of this conversion process is usually described in terms of the amplifier's efficiency η , or conversion efficiency, defined as the ratio between output RF and supplied DC power:

$$\eta \equiv \frac{P_{out}}{P_{DC}} \cdot 100 \quad (\%) \quad (2)$$

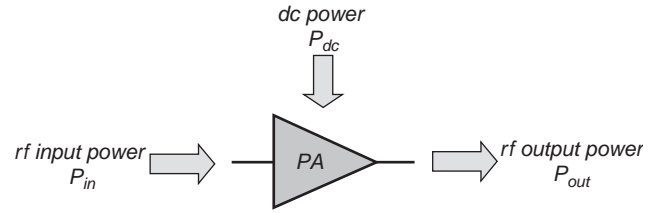


Figure 2. Energetic schematic representation of PA operation.

Efficiency is often further specified as “drain efficiency” or “collector efficiency,” in the case of a solid-state PA based on field-effect or bipolar transistor respectively.

Amplifier efficiency is in one of the key parameters in specifying overall system performances; as noted above, for a given amount of output power required by system specification for the PA, the efficiency actually fixes the DC power budget and hence the supply power. A reduced supply power resulting from high-efficiency performance is a key goal of mobile apparatuses, typically battery-operated, whose operating time depends strictly on the transmitting section power requests.

Moreover, since practical and physical constraints impose an actual efficiency lower than the theoretical maximum of 100%, high-efficiency performances imply in turn a low power dissipated on the power-amplifying device, therefore reducing actual size and weight of the eventually required heatsinks. On the other hand, for a given available DC power, high-efficiency performance allows higher transmitted power with a corresponding increase in overall system capabilities.

As frequency increases, however, the PA gain decreases, as a result of its active constituents gain rolloff behavior. Considering the input-output transfer characteristics of the PA, its power gain is defined as

$$G \equiv \frac{P_{out}}{P_{in}} \quad (3)$$

and usually expressed in logarithmic units [decibels(dB)]. The contribution to the output power coming directly from the input drive cannot be neglected since it constitutes, at microwave frequencies and beyond, a significant portion of the total amount. As a consequence, defining the *added power* P_{add} , that is, the net increase in the signal power from the PA input to its output, we obtain

$$P_{add} \equiv P_{out} - P_{in} = P_{out} \cdot \left(1 - \frac{1}{G}\right) \quad (4)$$

Power-added efficiency (PAE or η_{add}) is defined as the ratio between the added power and the supplied DC power:

$$\eta_{add} \equiv \frac{P_{add}}{P_{DC}} = \frac{P_{out} - P_{in}}{P_{DC}} = \frac{P_{out} \cdot \left(1 - \frac{1}{G}\right)}{P_{DC}} \quad (5)$$

$$= \eta \cdot \left(1 - \frac{1}{G}\right)$$

An alternative definition of η_{add} , less frequently used in common practice, is [40]

$$\eta_{\text{add}} \equiv \frac{P_{\text{out}}}{P_{\text{DC}} + P_{\text{in}}} = \eta \cdot \frac{1}{1 + \frac{\eta}{G}} \quad (6)$$

i.e. the ratio of output power to the total input power fed into the amplifier (RF plus DC; see Fig. 2). The two definitions (5) and (6) practically converge for high-gain amplifiers, while giving substantially different results for low-gain amplifiers, especially when hardly driven into compression (note that the conventional η_{add} definition may lead to negative results). If nonconstant envelope signals have to be treated by the PA, an average efficiency can be introduced [40,41], defined as in (2), where the quantities in the expression are replaced by input and output powers averaged over an envelope period and weighted by the envelope probability density function.

The conversion from DC to RF power implies that a fraction of the supplied power is actually dissipated on the active power device. The main contribution to the latter is spent at the active device output, and is given by

$$P_{\text{diss,out}} \equiv \frac{1}{T} \cdot \int_T v(t) \cdot i(t) \cdot dt \quad (7)$$

where $v(t)$ and $i(t)$ are the device output voltage and current, integrated over a period (T) of the RF signal. To increase the conversion efficiency, as will be discussed later, a possible strategy consists in the minimization of such dissipated power, namely, in the proper shaping of device output voltage and current waveforms.

For cascaded (matched) PAs, as depicted in Fig. 3, the overall efficiency η_{tot} is easily computed by

$$\eta_{\text{tot}} = \frac{P_{\text{out}}}{P_{\text{DC},1} + P_{\text{DC},2}} = \frac{\eta_2}{1 + \frac{P_{\text{DC},1}}{P_{\text{DC},2}}} = \frac{\eta_2}{1 + \frac{\eta_2}{\eta_1 \cdot G_2}} \quad (8)$$

Since the DC supply power for the final stages ($P_{\text{DC},2}$) is usually much higher than the driver supply ($P_{\text{DC},1}$), overall efficiency is dominated from the former amplifier. On the contrary, for a low-gain final amplifier, the driver’s effect also becomes crucial for overall conversion efficiency.

Regardless of the definition adopted for η_{add} , its maximization is to be achieved at the nominal drive level for the PA, that is, while the latter is delivering the specified output power. In such operating conditions, the amplifier is typically driven into compression, thus leaving its almost linear region and exploring the nonlinear active-device physical limitations, as depicted in Fig. 4, where a typical $P_{\text{in}}-P_{\text{out}}$ power sweep is plotted.

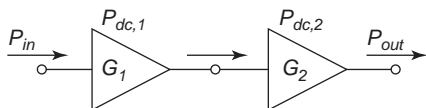


Figure 3. Cascade connection of two PAs.

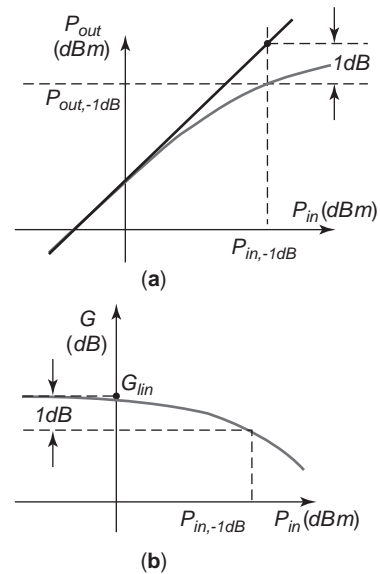


Figure 4. Sample $P_{\text{in}}-P_{\text{out}}$ power sweep (a) and corresponding amplifier gain (b); $P_{-1\text{dB}}$ can be derived from both.

From the power sweep in Fig. 4, a commonly used compression level figure of merit, $P_{\text{out},-1\text{dB}}$, can be derived, defined as the output power corresponding to a deviation of 1 dB from the ideal linear behaviour. The corresponding input power level, $P_{\text{in},-1\text{dB}}$, usually marks the border between “highly nonlinear” and “almost linear” operating conditions.

The peak drain/collector or power-added efficiency usually occur at higher drive levels, corresponding to 2–4 dB PA gain compression (Fig. 5). In such a region the active-device behavior is therefore highly nonlinear, and correspondingly design methodologies for high efficiency operation must cope with such intrinsic deviation from linearity.

PAs are normally classified into “operating classes” where the device output current conduction angle α (i.e., the fraction of the RF signal period where a nonzero current is flowing) is considered in detail, and where the classification in Table 1 holds.

The classification above is typically adopted regardless of the PA drive level, in order to simply indicate the biasing region of the active device, as determined by its quiescent supply conditions (Fig. 6).

Even for class A or B PAs, for which the conduction angle is fixed by definition, if the drive level is increased

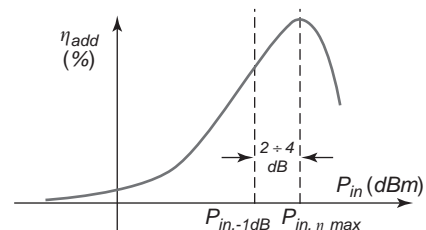


Figure 5. Typical power-added efficiency in a PA as a function of input drive.

Table 1. Classification of PAs in Terms of Output Current Conduction Angle α

Operating Class	Current Conduction Angle (α)	Dependence on Drive Level	Bias
A	$\alpha = 2\pi$	No	Midway between Device Pinchoff and Saturation Regions
AB	$\pi < \alpha < 2\pi$	Yes	Above pinchoff
B	$\alpha = \pi$	No	Device pinchoff
C	$\alpha < \pi$	Yes	Below pinchoff

up to compression regions (i.e., if the amplifiers are *overdriven* or *saturated*), a variation of current conduction angles occurs. It is clear that the two definitions may lead to misleading interpretations. Nevertheless, above all in communication systems characterized by non-constant-envelope transmitted signals (as in the case of QAM or in digital cellular communications with GSM and NADC standards), the transmitter has to satisfy tight requirements, not only in terms of efficiency but also linearity and signal spectral purity.

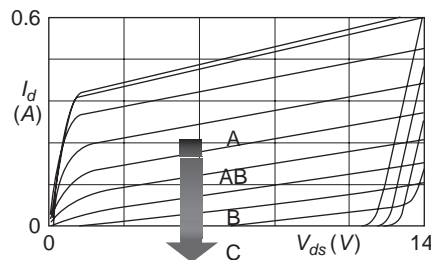
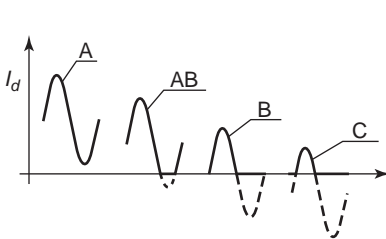
Several indicators of PA linearity are used, depending on the system specifications and modulation schemes that are adopted. In order to introduce and define them, a simple third-order approximation of the PA transfer characteristic is usually assumed

$$y(t) = A \cdot [x(t) + k_2 \cdot x^2(t) + k_3 \cdot x^3(t)] \quad (9)$$

where $x(t)$ and $y(t)$ are the input and output signals to the amplifier, respectively (they may be regarded as normalized voltages or currents), A is the small-signal voltage (or current) gain, and k_2, k_3 are the first two coefficients of a McLaurin expansion of the PA transfer characteristic, truncated to the third order. Please note that the approximation above, relating the output signal to the instantaneous input value, actually describes a memoryless system, and therefore memory effects cannot be accounted for using this description.

If a single-tone excitation is assumed for the input signal, with amplitude X and frequency f

$$x(t) = X \cdot \cos(2 \cdot \pi \cdot f \cdot t) = X \cdot \cos(\omega \cdot t) \quad (10)$$


Figure 6. Class of operation defined as output current conduction angle (left) or simply by the device quiescent bias point (right).

the corresponding input power P_x (on a unitary normalizing resistor) is

$$P_x = \frac{X^2}{2} \quad (11)$$

Output power at frequency $f(P_y)$ and large-signal gain G are easily obtained as

$$\begin{aligned} P_{y,f} &= A^2 \cdot \left(1 + \frac{3}{2} \cdot k_3 \cdot P_x\right)^2 \cdot P_x \\ &= G_{\text{lin}} \cdot \left(1 + \frac{3}{2} \cdot k_3 \cdot P_x\right)^2 \cdot P_x \end{aligned} \quad (12)$$

$$G = \frac{P_{y,f}}{P_x} = G_{\text{lin}} \cdot \left(1 + \frac{3}{2} \cdot k_3 \cdot P_x\right)^2 \quad (13)$$

where $G_{\text{lin}} = A^2$. Since usually k_3 is negative, the previous derivation accounts for large-signal gain compression, namely, decrease from the ideal linear constant value (G_{lin} above).

In the same way, from the single-tone excitation, harmonic generation at $2f$ and $3f$ arise, leading to a corresponding output power at harmonic frequencies $P_{y,2f}$ and $P_{y,3f}$ given by

$$P_{y,2f} = \frac{G_{\text{lin}} \cdot k_2^2}{2} \cdot P_x^2 \quad P_{y,3f} = \frac{G_{\text{lin}} \cdot k_3^2}{4} \cdot P_x^3 \quad (14)$$

therefore justifying the increase in harmonic power by n dB per dB of input power increase, where n is the order of the harmonic under consideration, as in Fig. 7.

The harmonic distortion (HD) due to the n th output harmonic component is therefore easily defined by

$$\text{HD}_{nf} \equiv \frac{P_{y,nf}}{P_{y,f}} \quad (15)$$

resulting in the approximated expressions for second- and third-harmonic distortion (HD_{2f} , HD_{3f}) in the simple cubic memoryless model [9]:

$$\text{HD}_{y,2f} = \frac{G_{\text{lin}} \cdot k_2^2}{2} \cdot P_x \quad \text{HD}_{y,3f} = \frac{G_{\text{lin}} \cdot k_3^2}{4} \cdot P_x^2 \quad (16)$$

Similarly, a total harmonic distortion (THD) is defined summing up all harmonic distortion components in the

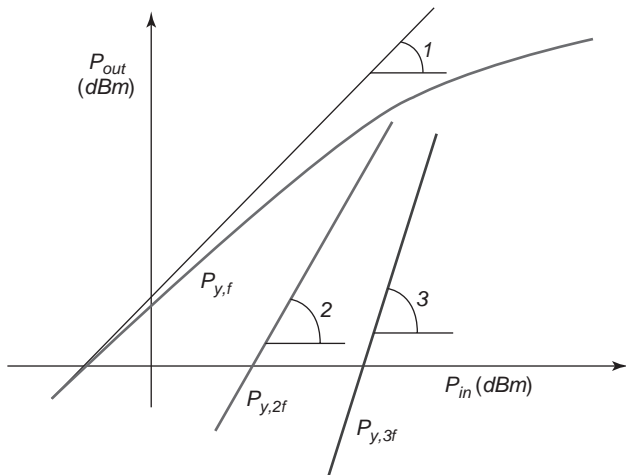


Figure 7. Output power in a single-tone test at fundamental frequency (red), second- (green) and third- (blue) harmonic components.

output signal:

$$THD \equiv \sum_{n \geq 2} \frac{P_{y,nf}}{P_{y,f}} \quad (17)$$

The quantities above are typically measured in decibel over the carrier power (dBc).

The model (9) is indeed an instantaneous model, that is, a memoryless description of the PA input–output characteristics. Real-world amplifiers are dynamic systems with memory, whose nonlinear behavior affects not only the amplitude but also the phase of the output signal. In fact, if the input signal to the PA is assumed to be

$$x(t) = X(t) \cdot \cos[2 \cdot \pi \cdot f \cdot t + \varphi(t)] \quad (18)$$

the output signal may exhibit nonlinear phenomena in both amplitude and phase

$$y(t) = G[X(t)] \cdot \cos\{2 \cdot \pi \cdot f \cdot t + \varphi(t) + \Phi[X(t)]\} \quad (19)$$

giving rise to the AM/AM compression and AM/PM conversion effects (Fig. 8), described by a nonlinear relationship between input and output amplitudes (which actually represents the amplifier’s output power compression) and a phase that depends on the input signal drive level:

$$G[X(t)] \neq A \cdot X(t) \quad \Phi[X(t)] \neq \text{const} \quad (20)$$

In particular, the AM/PM conversion effect represents a change in the phase of the output that depends on the input drive level; this effect is potentially dangerous not only in communication systems, giving rise for instance to distorted QAM constellations, but also in phased-array applications where the phase of each signal exiting the respective PA actually determines the active antenna pointing characteristics. Nevertheless, the PA description in terms of its AM/AM and AM/PM characteristics leads to a narrowband model; it is valid until the amplitude and

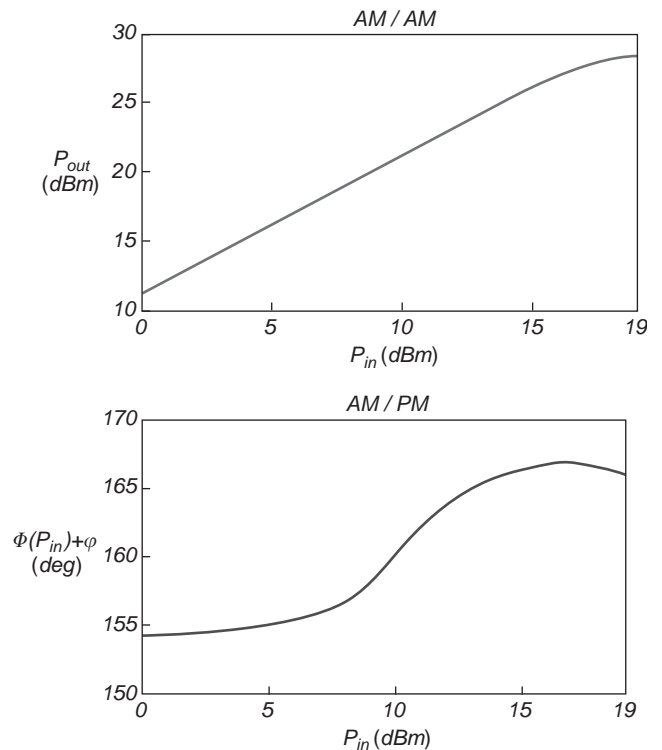


Figure 8. Typical AM/AM compression and AM/PM conversion curves for a PA.

phase modulating signal frequencies are much lower than the carrier one. Regardless of its applicability to narrow-band operation of PA, the AM/AM compression–AM/PM conversion model has been widely adopted, also forming the base for blackbox (or behavioral) modeling of PA operation. Such a behavioral model may be derived from Volterra analysis [42,43] or directly from experimental data [44]. The Volterra series approach may also be generalized to extend the model validity to broadband operation of the PA [45].

Resorting to the memoryless PA model (9), a two-tone test may be performed, attempting in this way to simulate the simultaneous treatment of two different signals and therefore their mutual interaction caused by the nonlinear PA. Much in the same way, this test may give insight on a narrowband signal, whose components (the tones in the test) may interfere, leading to a distorted output. This is clearly an approximation since the two signals are in reality much more complex than a simple sinusoid; on the other hand, the two-tone test is simple enough to be easily carried out experimentally. The input signal in this case is given by two closely spaced tones at frequencies f_1 and f_2 ($f_1 < f_2$) with amplitudes X_1 and X_2 , respectively:

$$\begin{aligned} x(t) &= X_1 \cdot \cos(2 \cdot \pi \cdot f_1 \cdot t) + X_2 \cdot \cos(2 \cdot \pi \cdot f_2 \cdot t) \\ &= X_1 \cdot \cos(\omega_1 \cdot t) + X_2 \cdot \cos(\omega_2 \cdot t) \end{aligned} \quad (21)$$

In such a two-tone test, the frequency spacing ($f_2 - f_1$) is much lower than the single frequencies, to replicate a narrowband excitation. By inserting an input drive such

Table 2. Output Components in a Two-Tone Test Grouped by Originating Term in Truncated Series Expansion

Originating Term	Output Frequencies	Corresponding Amplitude	
$x(t)$	f_1, f_2	X_1, X_2	Linear term
$x^2(t)$	$2f_1, 2f_2$	X_1^2, X_2^2	Second harmonic
	DC	X_1^2, X_2^2	Rectified component
	$f_1 - f_2$	$X_1 \cdot X_2$	Second-order intermodulation
$x^3(t)$	$f_1 + f_2$	$X_1 \cdot X_2$	Second-order intermodulation
	f_1, f_2	X_1^3, X_2^3	Compression
	f_1, f_2	$X_1 \cdot X_2^2, X_1^2 \cdot X_2$	Capture
	$3f_1, 3f_2$	X_1^3, X_2^3	Third harmonic
	$2f_1 - f_2, 2f_2 - f_1$	$X_1^2 \cdot X_2, X_1 \cdot X_2^2$	Third-order intermodulation
	$2f_1 + f_2, 2f_2 + f_1$	$X_1^2 \cdot X_2, X_1 \cdot X_2^2$	Third-order intermodulation

as that described above into the PA truncated expansion, a series of output frequency components results, which are grouped in Table 2, by the term in the expansion (linear, quadratic, or cubic) from which they originated.

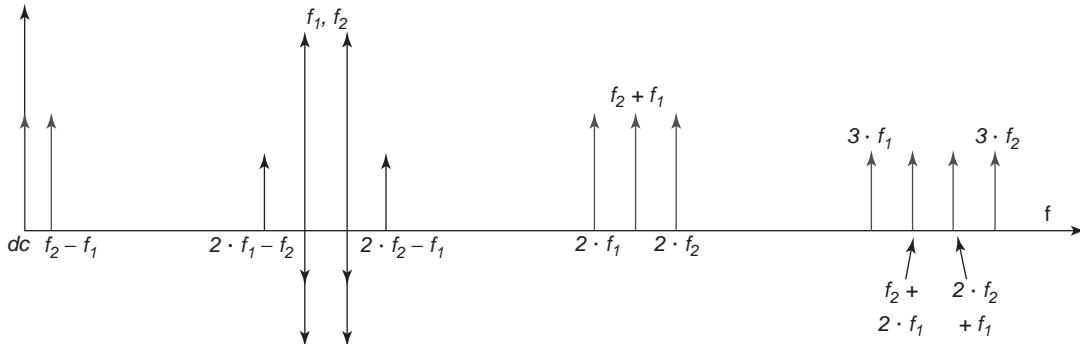
The terms in Table 2 are plotted as a function of frequency in Fig. 9. From Table 2 and Fig. 9, a series of conclusions can be drawn. Firstly, the interaction between the two input frequencies does create, in the nonlinear PA, a series of frequency components that are not present if the PA is separately excited by the single frequencies. In fact, while DC, harmonic components, and compression terms are already generated from the single-tone excitation, intermodulation frequencies and “capture” terms arise from the interaction between the two tones. The latter contributions, giving rise to *out-of-band* and *in-band* components, actually have a power rising as 3 dB per dB increase of the single tone’s power (Table 2). In particular, the capture term (often referred to as “suppression” term) tends to decrease power output at a given fundamental frequency (say, f_1) proportionally to the square of the power of the other (f_2) fundamental frequency; this phenomenon is particularly effective for high drive levels, and may eventually lead to the cancellation of one of the signal components at the PA output, thus justifying the “suppression” denomination.

Moreover, if signal purity is concerned, harmonic contributions (at DC, second, and third harmonic of each input excitation) together with second-order intermodulation and the terms at $2f_2 + f_1$ and $2f_2 + f_1$ (all in blue in Fig. 9) are far away from the useful part of the output signal (at f_1 and f_2 , in green in Fig. 9), and are therefore

easily eliminated by simple filtering. Other contributions, much closer to the desired input replica, cannot be filtered out; from the simple derivation above, they consist in frequency terms located at $2f_2 - f_1$ and $2f_1 - f_2$ (commonly referred to as *third-order intermodulation components*, giving rise to *intermodulation distortion*, (IMD) and at the input signal frequencies f_1 and f_2 (in-band distortion, given by the compression and suppression/capture terms).

Considering one of the two third-order intermodulation components and sweeping the input tone’s power, the *third-order intercept point* (IP3) is defined as the output (IP3_{out}, or input, IP3_{in}) power level at which the third-order IMD component level equals the ideal linear output power of the PA. Such definition is graphically depicted in Fig. 10. Even if both useful output signal power and IMD power tend to saturate for some input drive level, the IP3 definition consists in the ideal extrapolation of both output signal components (black and blue lines, respectively, in Fig. 10), ideally rising by 1 and 3 dB per dB increase in input drive respectively, and in the search for their intercept (the IP3). On the basis of such construction, it is clear that the resulting input drive level (IP3_{in} in Fig. 10) is well into the PA nonlinear operating region and is by far beyond typical PA operating drives. Similar intercept points can be defined (even if seldom used) by extension for higher-order intermodulation products, such as IP5 (for fifth-order distortion, located at $3f_2 - 2f_1$) or IP7 (for seventh-order distortion, located at $4f_2 - 3f_1$).

Resorting to the power-series expansion (9), it can be demonstrated that the IP3 output power level (IP3_{out}) can

**Figure 9.** Frequency allocation of the output components originating in a two-tone test.

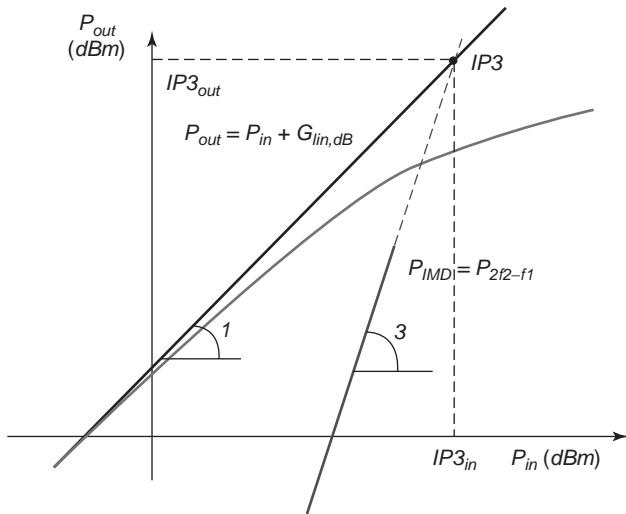


Figure 10. Third-order intercept point definition.

be related to the 1-dB compression point ($P_{-1\text{dB,out}}$) by

$$IP3_{\text{out}} \approx P_{-1\text{dB,out}} + 10.6\text{ dB (dBm)} \quad (22)$$

In real-world PAs, this expression typically overestimates $IP3_{\text{out}}$ by 2–3 dB. The approximations inherent to the truncated expansion adopted are in fact valid in a limited range for input drive level, which is typically violated for the IP3 region. For such large drive levels, fifth- and higher-order contributions arise and significantly modify the results of the simplified approach. In any case, once the PA $IP3_{\text{out}}$ is known, actual IMD level relative to the output signal level may be estimated from

$$P_{\text{IMD}} = 3P_{\text{out,dBm}} - 2IP3_{\text{out}} \quad (23)$$

Another frequently adopted indicator of the PA nonlinear behavior is the C/I or *carrier-to-intermodulation ratio*,

defined as the ratio between useful output power and IMD output power, usually measured in dB below the carrier (dBc):

$$C/I \equiv \frac{P_{\text{out}}}{P_{\text{IMD}}} \quad (24)$$

where $P_{\text{IMD}} = P_{2f_2-f_1}$ (or $P_{\text{IMD}} = P_{2f_1-f_2}$). Such C/I is clearly dependent on the input power to the PA, decreasing by 2 dB per dB increase of the input drive. Combining the two relationships (23) and (24):

$$C/I = 2(IP3_{\text{out}} - P_{\text{out,dBm}}) \text{ (dBc)} \quad (25)$$

For moderate drive levels (say, up to 10 dB below $P_{-1\text{dB,out}}$), the third-order intermodulation component is the dominant distortion. It is therefore possible to define a linearity range for the PA as the range of input drive levels for which the P_{IMD} stays below the noise floor of the amplifier, usually specified as thermal noise at ambient temperature; such linearity range, whose lower bound is determined by the useful output power emerging from the noise floor, is usually indicated as the *spurious-free dynamic range* (SFDR; Fig. 11).

From knowledge of the PA noise figure (NF), its bandwidth B and (available) gain G , the SFDR is given, at room temperature, by

$$SFDR_{\text{dB}} = \frac{2}{3} \cdot [IP3_{\text{out,dBm}} - NF_{\text{dB}} - G_{\text{dB}} - \left(\frac{B}{1\text{ Hz}}\right)_{\text{dB}} + 174\text{ dBm}] \text{ (dB)} \quad (26)$$

The quality factors defined above for linearity evaluation are related to single- or two-tone tests, in an attempt to mimic in this way the behavior of the PA in response to a narrowband or multicarrier input. Real-world input signals to a PA may deviate substantially from the

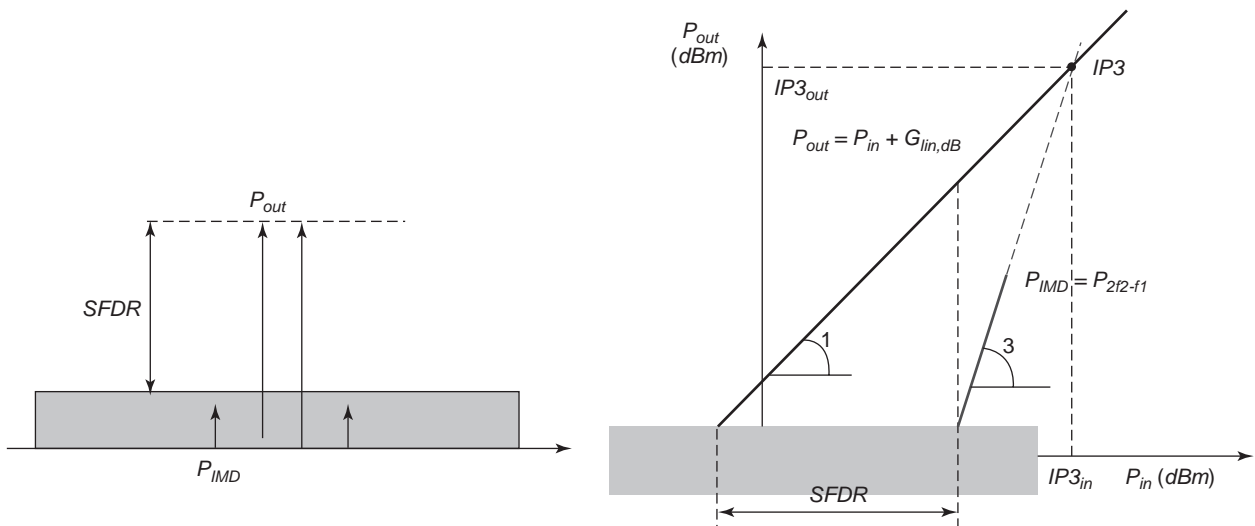


Figure 11. Definition of the spurious-free dynamic range; shaded area represents thermal output noise power at ambient temperature.

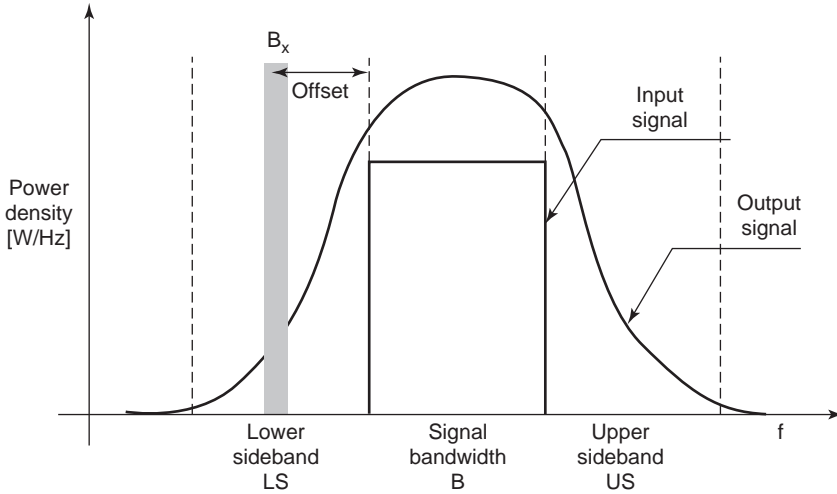


Figure 12. Input and output power densities for adjacent-channel power ratio definitions.

single-tone approximation, since modulation formats and bandwidth occupation may differ to a great extent. In order to account for signal distortion and the related spectral regrowth in the case of bandlimited input signals, an *adjacent-channel power ratio* (ACPR) is introduced. With reference to Fig. 12, several definitions are adopted in this respect; the most commonly used refers to the *total ACPR* (ACPR_{TOT}), the ratio between the total output power in the signal bandwidth to the total output power in adjacent channels:

$$ACPR_{TOT} \equiv \frac{\int_B P_{out}(f) \cdot df}{\int_{LS} P_{out}(f) \cdot df + \int_{US} P_{out}(f) \cdot df} \quad (27)$$

Clearly, if a single sideband is concerned, a *lower-sideband ACPR* (ACPR_{LS}) or *upper-sideband ACPR* (ACPR_{US}) can be defined, using the proper adjacent-channel power in the definition

$$ACPR_{LS} \equiv \frac{\int_B P_{out}(f) \cdot df}{\int_{LS} P_{out}(f) \cdot df} \quad (28)$$

$$ACPR_{US} \equiv \frac{\int_B P_{out}(f) \cdot df}{\int_{US} P_{out}(f) \cdot df}$$

Moreover, a *spot ACPR* (ACPR_{SPOT}) can be introduced, utilizing the adjacent-channel power contained in a predefined bandwidth (B_x) at a given offset (see Fig. 12), defined by

$$ACPR_{SPOT} \equiv \frac{\int_B P_{out}(f) \cdot df}{\int_{B_x, offset} P_{out}(f) \cdot df} \quad (29)$$

The various ACPR figures clearly give a deeper insight into the distortion properties of a PA than do their single- or two-tone counterparts, as they are related to a specific bandlimited input signal. Nevertheless, if the input signal is approximated by a number of equally spaced equal-amplitude tones, closed-form relationships may be found between the figures [46,48].

Other indicators of PA linearity and appropriate tests are the noise power ratio and cochannel power ratio [47,48].

3. BASIC CONCEPTS IN PA DESIGN

Power limiting mechanisms in active devices reside in their inherent physical constraints. For a FET device (but also for a bipolar one, with different physical effects taking place), such constraints are both on output current and voltage: for the former, current saturation related to input junction forward conduction and device channel pinchoff; for the latter, device ohmic behavior and breakdown (related to both channel and gate-drain junction). Such physical limitations are graphically depicted in Fig. 13, where sample output device characteristics are shown.

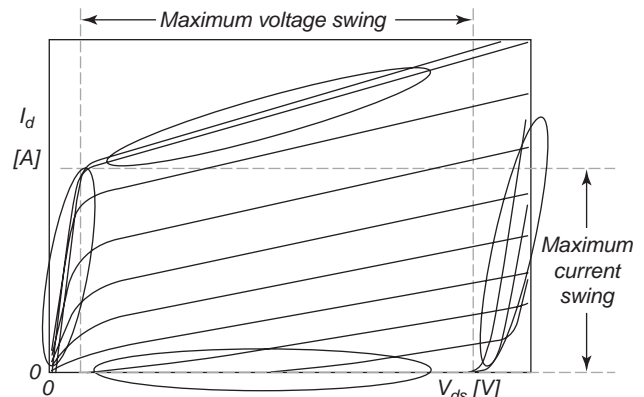


Figure 13. Sample device output characteristics and physical limitations on output current and voltage.

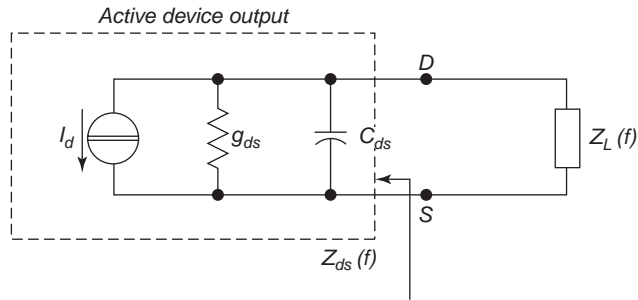


Figure 14. Schematic representation of the active-device output connected to an external load Z_L .

Collectively, such limitations pose an upper limit to the maximum swings that output current and voltage may experience, reflecting in a limit corresponding to the device output power.

Small-signal amplifier design is based on well-established techniques. After the active device to be employed is selected together with its operating (bias) point, from knowledge of the device scattering parameters and depending on the amplifier specifications, input and output matching network characteristics (i.e., the impedances to be presented at the device input and output ports) are readily obtained via closed-form expressions [49–51].

If a simplified device model is considered, as depicted in Fig. 14, composed of a controlled current source (controlled by the input voltage if a FET is considered) shunted by its output small-signal admittance (represented by an output conductance g_{ds} and capacitance C_{ds}), the condition that is imposed, compatibly with device stability, for maximum power transfer from the device output to the external load is the well-known conjugate matching

$$Z_L(f) = Z_{ds}^*(f) \leftrightarrow \begin{cases} G_L(f) = g_{ds} \\ B_L(f) = -j \cdot 2\pi f \cdot C_{ds} \end{cases} \quad (30)$$

where

$$Z_L(f) = G_L(f) + j \cdot B_L(f) \quad (31)$$

$$Z_{ds}(f) = G_{ds}(f) + j \cdot B_{ds}(f) = g_{ds} + j \cdot 2\pi f \cdot C_{ds} \quad (32)$$

The conjugate matching condition therefore implies the compensation of the active-device output reactive part and a match in its small-signal output conductance, ensuring at the same time the maximization of the amplifier small-signal gain. If the active-device output characteristics are now considered, the load line dictated by the small-signal matching condition (curve A) can be superimposed, as depicted in Fig. 15. If the same condition is adopted, driving the amplifier to operate into large-signal regime, a reduced current swing results, producing in turn an earlier compression of the device output power (current-limited operation). On the other hand, if the external load is selected in order to fully exploit the maximum current swing, (as in B, Fig. 15), a reduced voltage swing is produced (voltage-limited operation), again driving active device output into compression. The optimum situation is in

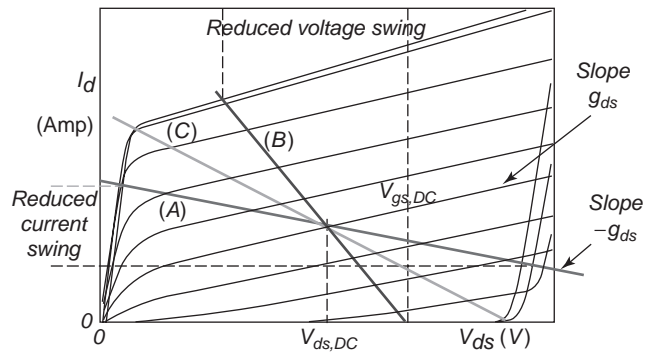


Figure 15. Active-device output characteristics with superimposed the conjugate-matched load line (A); with voltage-limited (B), and optimum loading (C). (This figure is available in full color at <http://www.mrw.interscience.wiley.com/erfme>.)

the simultaneous maximization of current and voltage swings (as in C, Fig. 15), often referred to as *load-line matching* condition. The typical output power behavior corresponding to the three situations described in Fig. 15 is shown in Fig. 16 as a function of the input drive level.

Nevertheless, PAs that are load-line-matched exhibit poor output VSWR in the system in which they are employed. If necessary, this problem can be solved through the use of output isolators (clearly decreasing output power and efficiency by their losses) or resorting to balanced configurations if possible; also in this case the insertion loss of the combining structure actually affects overall power performance.

In order to have some quantitative indication of the optimum loading in the simplified conditions described above, the device output characteristics are often substituted by their piecewise linear approximation, leading to a “box model” for the active-device current source. Such a model is depicted in Fig. 17 for the case of a constant transconductance (g_m) device (equally spaced output characteristics, left) and linear transconductance (linearly increasing transconductance, right). The case of a linear variation, introduced by Kushner [52,53], tries to mimic the decrease in transconductance typically observed while

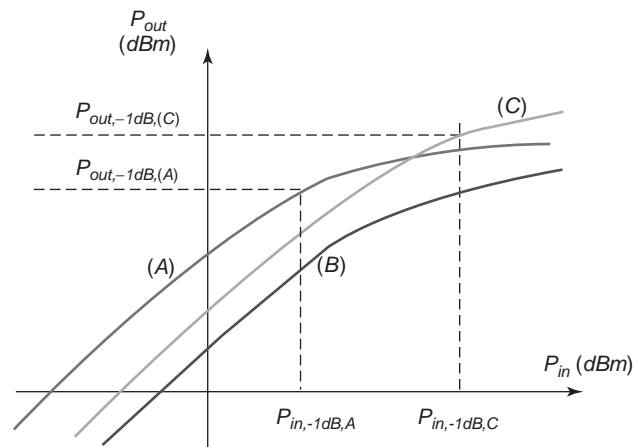


Figure 16. Output power for three loading conditions: current-limited (A), voltage-limited (B), and optimum loading (C).

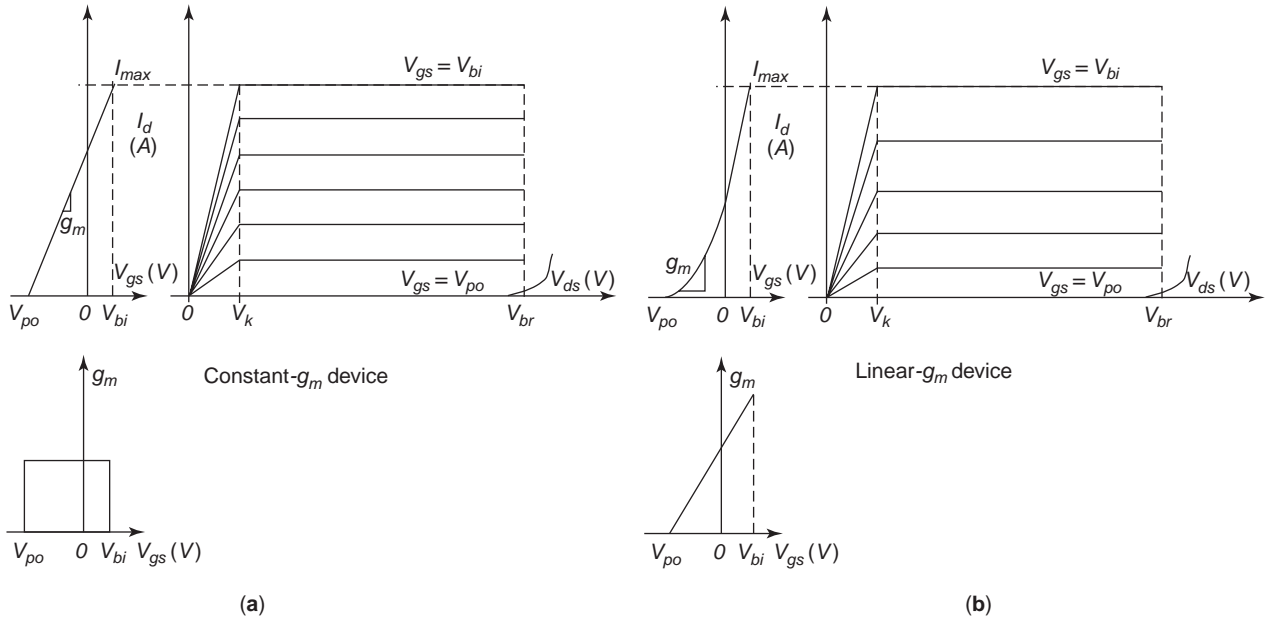


Figure 17. Piecewise linear approximation of the device output characteristics in the case of constant (a) and linear (b) transconductance.

decreasing the device gate bias toward pinchoff. On the other hand, such approximation actually generates artificial distortion components even with low driving signals, while requiring, for its actual implementation, a nonuniform doping profile.

In Fig. 17 V_k is the device “knee” voltage, marking the transition between the device ohmic and saturation regions, V_{br} the breakdown voltage (drain–gate junction breakdown), I_{max} the maximum drain current (occurring for fully opened channel, that is, for $V_{gs} = V_{bi}$ where V_{bi} is the input junction built-in voltage) and V_{po} the device pinchoff voltage. We now assume a purely resistive loading of the active device at fundamental and all harmonic frequencies, and we drive the device up to its limit linear behavior (i.e., without overdriving it into highly nonlinear regimes). In both cases, if the device is biased at $V_{ds,DC}$ for class A and class B operation as in Fig. 18, and the minimum drain voltage is assumed to be $V_{ds,min} = V_k$, defining

$$\gamma = \frac{V_k}{V_{ds,DC}}, \quad R_A = 2 \cdot \frac{V_{ds,DC} - V_k}{I_{max}} \quad (33)$$

the optimum resistive loads $R_{L,opt}$ for class A and B bias conditions (i.e., for the device biased at $I_{d,DC} = I_{max}/2$ and $I_{d,DC} = 0$ respectively) are reported in Table 3, together with maximum drain–source voltage ($V_{ds,max}$), dissipated power (P_{diss}), drain efficiency (η), and output power at fundamental frequency (P_{out}). Several observations may be performed on the results in Table 3.

Clearly, the output power directly depends on the maximum currents and voltages sustained by the active device, namely, I_{max} and V_{br} (implicitly in Table 3 through the limit it imposes on the maximum voltage $V_{ds,max}$ and hence on $V_{ds,DC}$). The limit imposed by the device maximum current may be overcome by increasing device gate periphery and/or through the use of device power combining tech-

niques. The former approach, often used in monolithic design, can be carried out by increasing device finger width and/or increasing the number of device fingers (if a interdigitated device structure is considered, as in the case of power transistors), as schematically depicted in Fig. 19.

Such device scaling actually enables one to increase power output capabilities. Nevertheless, such an option is related to the availability of an affordable monolithic technology (it is clearly not applicable to hybrid design approaches). Moreover, the scaling properties of a given technology are strictly valid for moderate scaling only. For the same total gate periphery, in fact, while output power is almost constant (at a given frequency), large-signal gain decreases with unit gate width, thus affecting efficiency performances as demonstrated experimentally in Fig. 20.

Moreover, an increase in device periphery actually increases device parasitic effects, thus leading to a further reduction in gain and frequency of operation. From the thermal management point of view, scaling up device periphery induces an increase in dissipated power; the resulting increase in device junction operating temperature has detrimental effects on device performance in terms of both actual performance and reliability, especially if high-reliability applications such as satellite payload transmitters are concerned. The commonly adopted solution to this effect consists in device substrate thinning, thus decreasing thermal resistance and the temperature difference between the device channel and its backside. Clearly, from the design point of view, a viable solution is in the exploitation of “cold” biasing regions (i.e., decrease in bias toward class B), accurately accounting for the consequences both on output power and linearity.

A second possibility for increasing output power performances consists in an increase of the drain voltage swing. This task can be accomplished mainly by increasing the

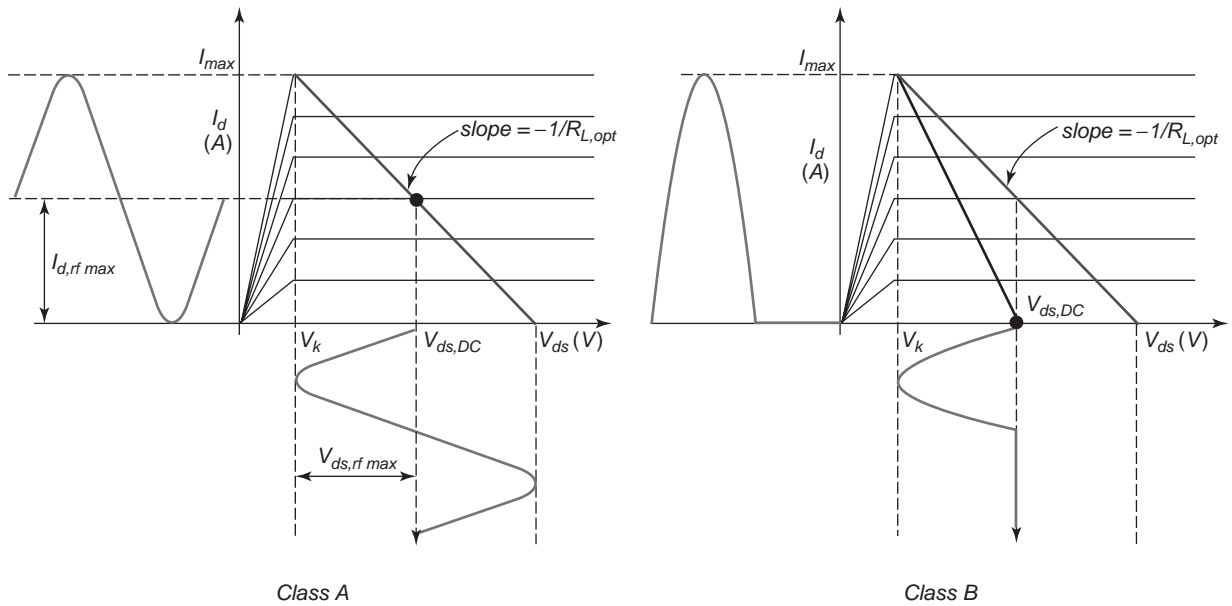


Figure 18. Class A and B operating conditions for purely resistive loading.

device breakdown voltage. Unfortunately the latter is an intensive quantity, depending mainly on material properties and device fabrication process. The more recent increasing interest in wide-bandgap materials [viz., gallium nitride (GaN) and silicon carbide (SiC)] is in fact motivated from the intrinsic high breakdown field that devices based on such alloys exhibit, with typical values in the range of 100 V, as contrasted to the few tens of the traditional GaAs-based FET devices. On the other hand, as shown in Table 3, PA drain efficiency and output power are limited by the presence of a nonnegligible “knee” voltage. The effect of such low-voltage limit is especially important if a low-voltage PA has to be designed; this is the case in mobile handsets and in general in every portable battery-operated transmitter, in which the actual size and weight of the overall apparatus are dictated by the choice of a lightweight and small battery pack. In this case a few volts are available for the PA bias, and any lower limit in the device voltage swing is very important. As an example, assuming a 3 V supply and a 0.9 V knee voltage for the active device, a PA operating in class A decreases its efficiency from the ideal textbook 50% down to a modest 35% (as per Table 3, class A, constant transconductance, with $\gamma=0.7$). The problem becomes even harder to deal with if high-perfor-

mance deep-submicrometer CMOS devices are employed, with knee voltages that can be 2–3 times higher than the ones of typical power transistors.

Up to this point, the two simple cases of class A and B PAs under the maximum linear operation have been considered. The output power and efficiency performances can, however, be greatly improved by making use of harmonic tuning strategies or switching-mode operating classes. To this goal, a first step resides in the use of the tuned-load (TL [52,53]) operating mode of the power stage. With reference to Fig. 21, TL operation consists in loading the active device output with short-circuit terminations (idlers) at harmonic frequencies, maximizing at the same time the fundamental frequency voltage and current swing.

The device output is assumed to operate as a voltage-controlled current source (controlled by the input gate-source voltage) and therefore its time-domain waveform can be expressed as a truncated sinusoid

$$i_d(t) = \begin{cases} \frac{I_{\max}}{1 - \cos\left(\frac{\alpha}{2}\right)} \cdot \left[\cos(\omega \cdot t) - \cos\left(\frac{\alpha}{2}\right) \right] & \text{if } |\omega \cdot t| \leq \frac{\alpha}{2} \\ 0 & \text{otherwise} \end{cases} \quad (34)$$

Table 3. Single-Device PA Performance with Resistive Loading for Classes A and B Bias and Constant and Linear Transconductance

Biasing Class	g_m	$R_{L,\text{opt}} (\Omega)$	$V_{\text{ds,max}} (\text{V})$	$P_{\text{diss}} (\text{W})$	$\eta (\%)$	$P_{\text{out}} (\text{W})$
A	Constant	R_A	$V_{\text{ds,DC}} + (V_{\text{ds,DC}} - V_k)$	$\frac{(V_{\text{ds,DC}} - V_k) \cdot I_{\max}}{4}$	$50 \cdot (1 - \gamma)$	$\frac{(V_{\text{ds,DC}} - V_k) \cdot I_{\max}}{4}$
A	Linear	$\frac{4}{5} \cdot R_A$	$V_{\text{ds,DC}} + \frac{3}{5}(V_{\text{ds,DC}} - V_k)$	$\frac{(0.65 V_{\text{ds,DC}} + 0.85 V_k) \cdot I_{\max}}{4}$	$53 \cdot (1 - \gamma)$	$\frac{(V_{\text{ds,DC}} - V_k) \cdot I_{\max}}{5}$
B	Constant	$\frac{\pi}{\pi - 1} \cdot \frac{R_A}{2}$	$V_{\text{ds,DC}} + \frac{V_{\text{ds,DC}} - V_k}{\pi - 1}$	$\frac{(0.4 V_{\text{ds,DC}} + 0.87 V_k) \cdot I_{\max}}{4}$	$58 \cdot (1 - \gamma)$	$\frac{\pi(V_{\text{ds,DC}} - V_k) \cdot I_{\max}}{8 \cdot (\pi - 1)}$
B	Linear	$\frac{2}{3} \cdot R_A$	$V_{\text{ds,DC}} + \frac{V_{\text{ds,DC}} - V_k}{3}$	$\frac{(0.33 V_{\text{ds,DC}} + 0.66 V_k) \cdot I_{\max}}{4}$	$48 \cdot (1 - \gamma)$	$\frac{32(V_{\text{ds,DC}} - V_k) \cdot I_{\max}}{27 \cdot \pi^2}$

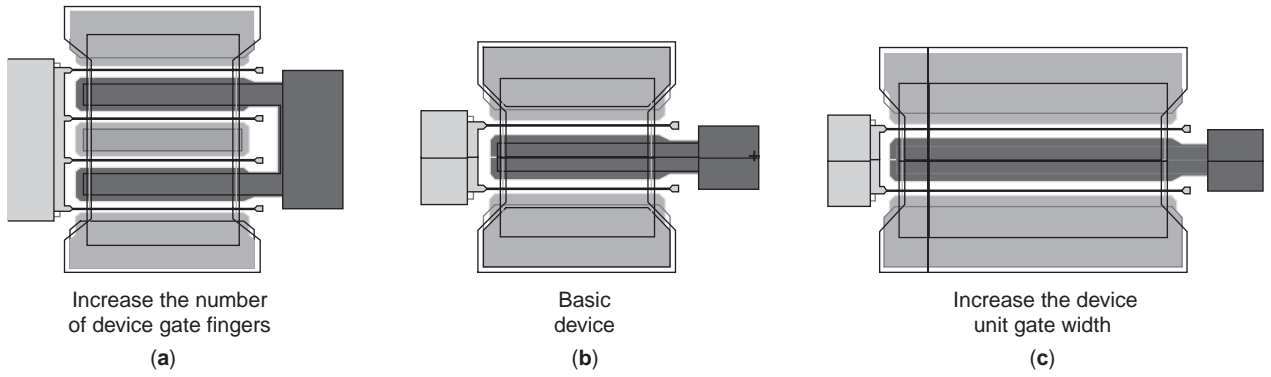


Figure 19. Increasing device maximum current by scaling the number of gate fingers (a) or device unit gate width (c) from a basic device (b).

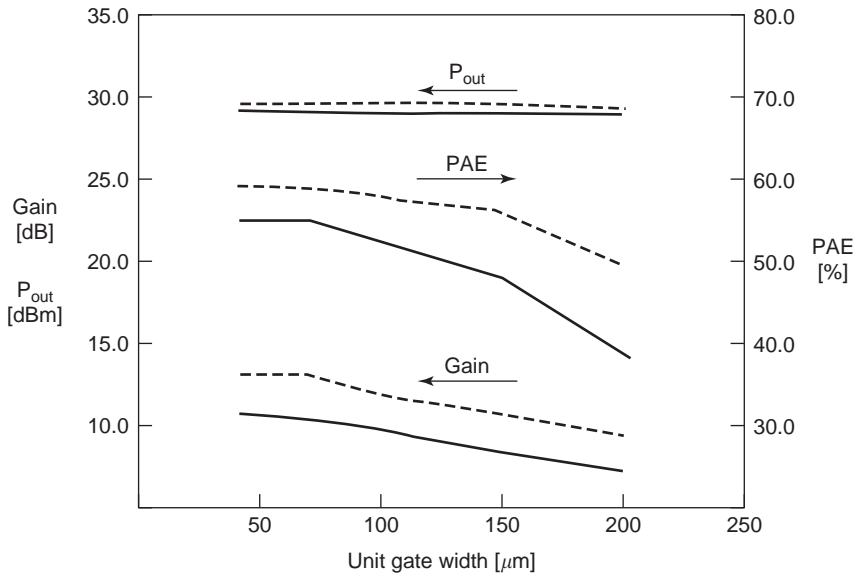


Figure 20. Effect of device unit gate width scaling for a fixed total periphery (1.2 mm). Solid and dashed lines indicate 18 and 14 GHz, respectively. (Data from Raytheon, 1998 IEEE MTT-S Symposium, Workshop WFF.)

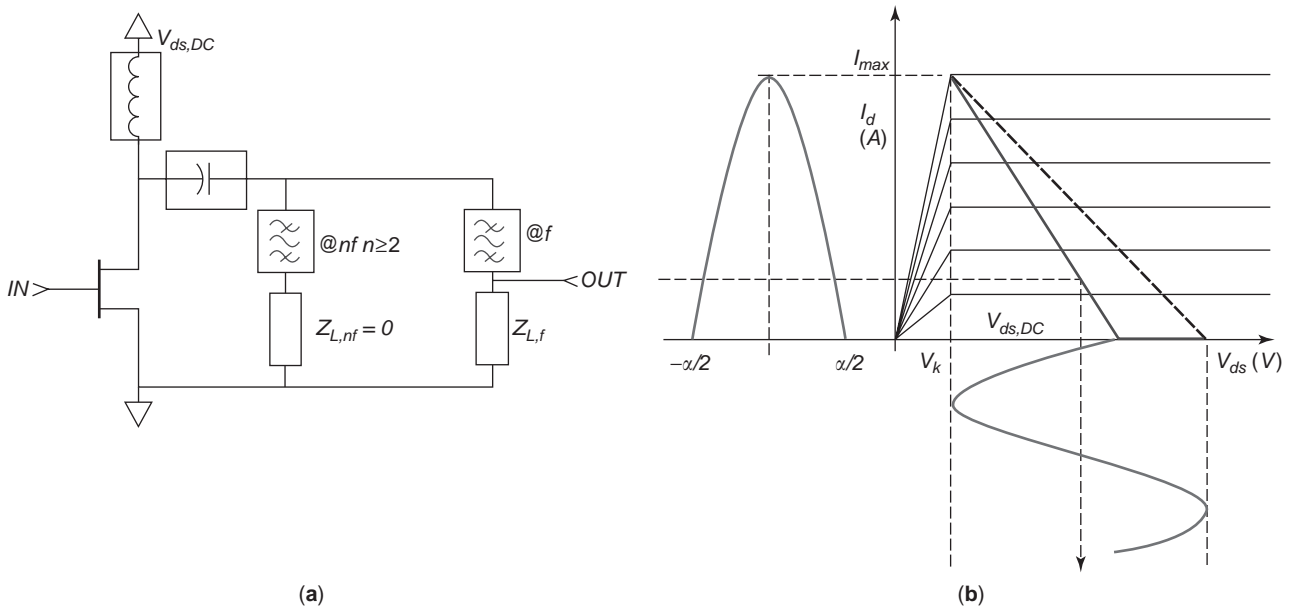


Figure 21. Tuned load loading conditions (a) together with typical voltage and current waveforms superimposed on piecewise linear output characteristics (b).

where $\omega = 2\pi \cdot f$ and α is the drain current conduction angle (Fig. 21), while the output drain voltage, thanks to the short-circuit terminations, is a purely sinusoidal waveform:

$$v_{ds}(t) = V_{ds,DC} - V_1 \cdot \cos(\omega \cdot t) \quad (35)$$

Treatment of the actual device output admittance will be omitted in the following in order to simplify the approach. Nevertheless, the hypothesis of short-circuit output terminations actually help in this assumption (if a real short circuit could be imposed at the device intrinsic terminals, not accounting for device parasitic effects), together with the device output capacitive behavior, effectively short-circuiting very-high-frequency output components. Drain current can be expressed in terms of its Fourier series expansion with coefficients I_n graphically depicted in Fig. 22 as a function of the current conduction angle α .

The fundamental frequency current component is, under the assumptions performed, a function of the current conduction angle only. The drain voltage fundamental component is related to the current one via the fundamental frequency output load $Z_{L,f}$. The latter is to be selected as a purely resistive termination in order to maximize active power generation together with output voltage swing. To this goal, if the device is biased at $V_{ds,DC}$, maximum output voltage fundamental frequency amplitude is given by $V_{1,max} = V_{ds,DC} - V_k$, thus obtaining, for the optimum load at fundamental R_{TL} ,

$$R_{TL}(\alpha) = \frac{V_{1,max}}{I_1(\alpha)} = R_A \cdot \pi \cdot \frac{1 - \cos(\frac{\alpha}{2})}{\alpha - \sin(\alpha)} \quad (36)$$

where the optimum value is expressed evidencing the R_A value (optimum resistance in the case of resistive loading, or *load-line match* for the case of a class A PA; see Table 3). Moreover, in the same way, DC supply power $P_{DC,TL}$, output power at fundamental $P_{out,TL}$, and drain efficiency η_{TL}

can be easily obtained, again normalized to the class A reference values in Table 3:

$$P_{DC,TL} = I_0 \cdot V_{ds,DC} = \frac{P_{DC,A}}{\pi} \cdot \frac{2 \cdot \sin(\frac{\alpha}{2}) - \alpha \cdot \cos(\frac{\alpha}{2})}{1 - \cos(\frac{\alpha}{2})} \quad (37)$$

$$P_{out,TL} = \frac{I_1 \cdot V_1}{2} = \frac{P_{RF,A}}{\pi} \cdot \frac{\alpha - \sin(\alpha)}{1 - \cos(\frac{\alpha}{2})} \quad (38)$$

$$\eta_{TL} = \frac{P_{out,TL}}{P_{DC,TL}} = \eta_A \cdot \frac{\alpha - \sin(\alpha)}{2 \cdot \sin(\frac{\alpha}{2}) - \alpha \cdot \cos(\frac{\alpha}{2})} \quad (39)$$

The quantities described above are presented in graphical form as functions of α in Fig. 23.

The results attainable via a TL approach are briefly discussed:

1. An increase in output power over the reference class A design is possible utilizing a class AB bias with the TL output loading. Such increase in power performance is maintained even moving toward class B bias, where a simple resistive loading implies a decrease in output power with respect to a class A bias. Clearly, such a result does not account for the gain performance, since a maximum swing is assumed, independently on the necessary drive level. In particular, for class A and B biases, the same output power is obtained, but utilizing, for the class B drive, twice the input drive signal (i.e., 6 dB higher input power is necessary).
2. The optimum load exhibit a weak dependence on the current conduction angle, thus allowing almost the same resistive loading from class A to class B bias.

Efficiency performances exhibit a constant increase moving toward low-bias regions, with a limiting value that doubles the class A performance (thus toward the theoretical limit of 100% efficiency). This is true, however, only to a first approximation, since the simplifying assumptions performed on the device characteristics impose a constant breakdown voltage, regardless of the device gate bias; real-world devices have an almost constant gate-drain breakdown, and therefore biasing the device below pinchoff actually decreases the drain-source maximum voltage ($V_{br,ds} = V_{br,gd} - V_{gs}$). Finally, the power dissipated on the active device, $P_{diss,TL}$, shown in Fig. 24, is

$$P_{diss,TL} = \frac{P_{DC,A}}{\pi} \cdot \frac{\sin(\frac{\alpha}{2}) \cdot [2 + \cos(\frac{\alpha}{2})] - \frac{\alpha}{2} \cdot [1 + 2 \cdot \cos(\frac{\alpha}{2})]}{1 - \cos(\frac{\alpha}{2})} \quad (40)$$

As expected, moving from class C bias toward class A operation actually increases the power dissipated on the active device, therefore decreasing the efficiency correspondingly.

A final consideration can be drawn regarding device input terminations. Input loading at fundamental frequency

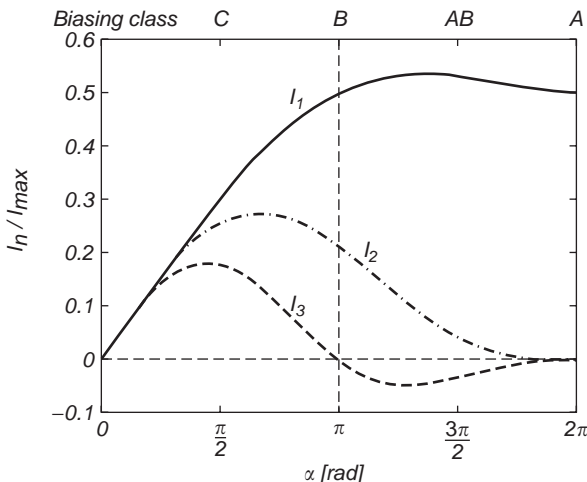


Figure 22. Fourier components I_1, I_2, I_3 normalized to the device maximum current I_{max} as functions of the drain current conduction angle α .

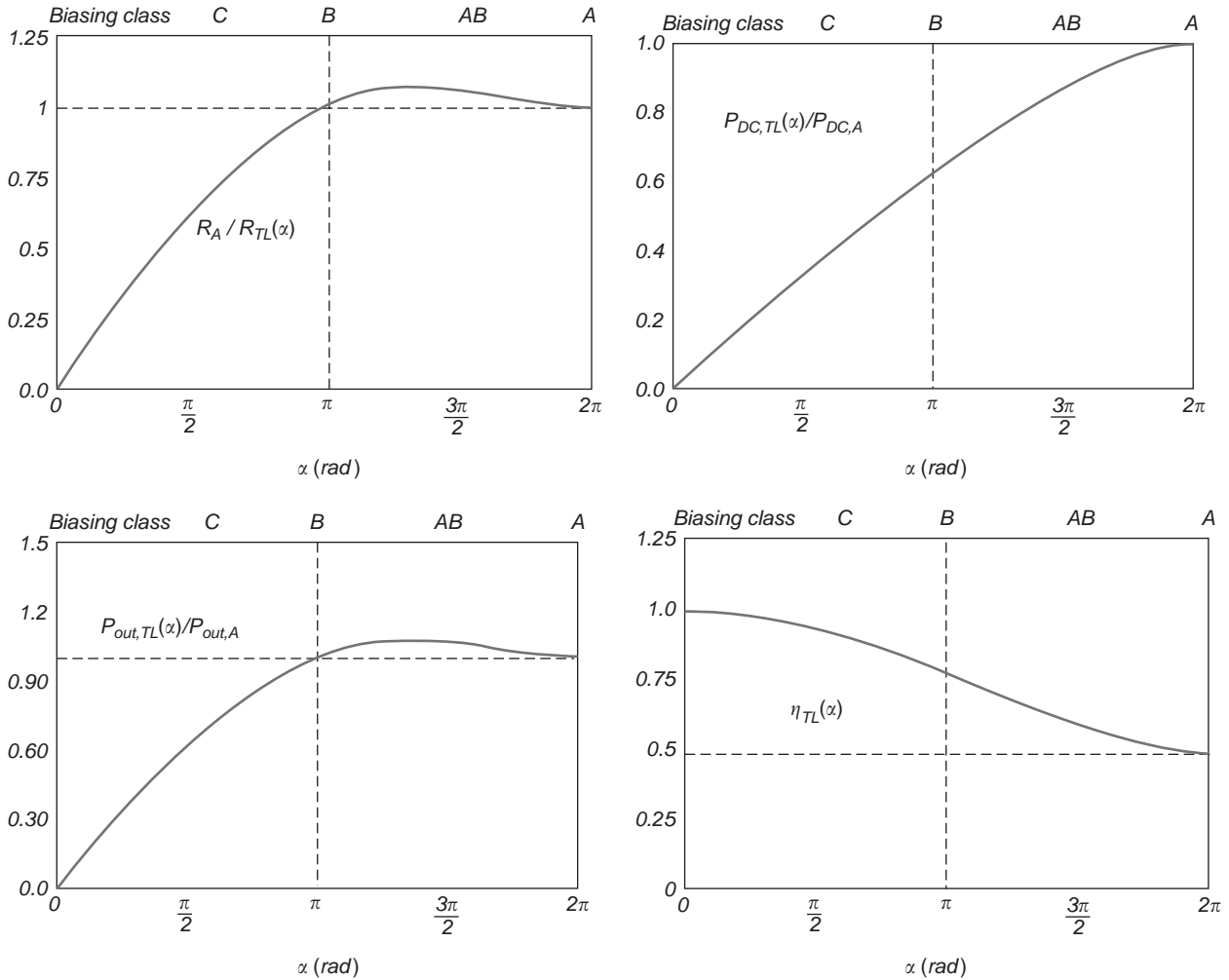


Figure 23. Optimum load R_{TL} , DC power $P_{DC,TL}$, output power $P_{out,TL}$, and drain efficiency η_{TL} for the tuned load operating condition normalized to the corresponding class A (resistive load) quantities.

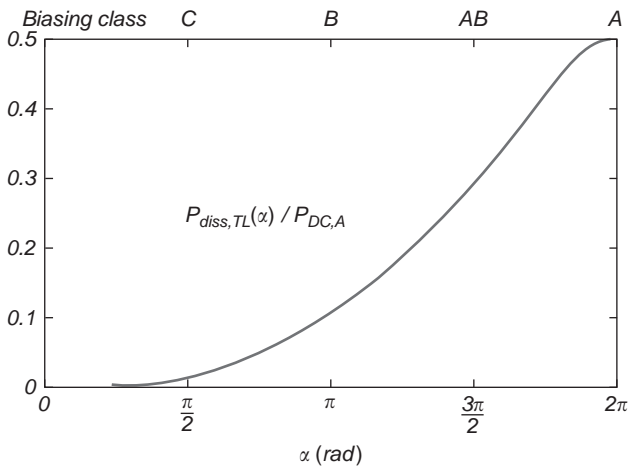


Figure 24. Power dissipated on the active device $P_{diss,TL}$ for the tuned load operating condition normalized to the class A (resistive load) DC power as a function of the drain current–drain conduction angle.

is to be performed in order to fulfill maximum power transfer to the active device; this is the well-known conjugate matching condition. This condition ensures maximum gain for a given output loading, while ensuring optimum input VSWR. Clearly the device input is, for moderate drive levels, mildly nonlinear and therefore the conjugate matching must be attained under large-signal operating conditions (i.e., the maximum power transfer condition depends on the drive level). Harmonic input loading is seldom investigated, leaving this task to harmonic tuning strategies.

4. POWER BALANCE AND DIFFERENT DESIGN APPROACHES

In order to generalise the approach outlined for the TL operating condition and the approach outlined in Refs. 54 and 55 for switched-mode stages (see Section 6s), with the aim to introduce high-efficiency operating classes, let us consider the power balance in a PA, distinguishing, in the

output power, the two contributions to fundamental ($P_{\text{out},f}$) and harmonic terminations ($P_{\text{out},nf}$, $n \geq 2$). In greater detail, the power balance of a PA system can be stated as

$$P_{\text{DC}} + P_{\text{in}} = P_{\text{diss},\text{in}} + P_{\text{diss},\text{out}} + P_{\text{out},f} + P_{\text{out},nf} \quad (41)$$

where $P_{\text{diss},\text{in}}$ and $P_{\text{diss},\text{out}}$ are the two contributions to the dissipated power (i.e., converted to heat) in the input and output sections of the PA stage, respectively. In this equation, the input power can be thought to be entirely dissipated in the device input (i.e., $P_{\text{diss},\text{in}} \approx P_{\text{in}}$), therefore leading to

$$P_{\text{DC}} = P_{\text{diss},\text{out}} + P_{\text{out},f} + P_{\text{out},nf} \quad (42)$$

which represents a power balance equation related to the output circuit only. The result in (42) is valid at the lower microwave frequencies and, in general, if the active device internal feedback can be neglected. In the output circuit, device current and voltage may be expressed by their Fourier series expansion

$$i_{\text{D}}(t) = I_0 + \sum_{n=1}^{\infty} I_n \cdot \cos(n \cdot \omega \cdot t + \xi_n) \quad (43)$$

$$v_{\text{DS}}(t) = V_{\text{ds,DC}} - \sum_{n=1}^{\infty} V_n \cdot \cos(n \cdot \omega \cdot t + \psi_n) \quad (44)$$

where ξ_n and ψ_n are the phases of the n th output current (I_n) and voltage (V_n) harmonic components, respectively.

On the basis of such assumptions, harmonic terminations to the output of the active device can be defined as the ratio of the respective voltage and current harmonic components:

$$Z_{\text{L},nf} = \frac{V_n \cdot e^{j\psi_n}}{I_n \cdot e^{j\xi_n}} = \frac{V_n}{I_n} \cdot e^{j(\psi_n - \xi_n)} = \frac{V_n}{I_n} \cdot e^{j\varphi_n} \quad (45)$$

obtaining, for the bias DC power, the power dissipated on the device and the power delivered to fundamental and harmonic frequencies:

$$P_{\text{DC}} = V_{\text{ds,DC}} \cdot I_0 \quad (46)$$

$$P_{\text{diss}} = \frac{1}{T} \cdot \int_T i_{\text{D}}(t) \cdot v_{\text{ds}}(t) \cdot dt = P_{\text{DC}} - P_{\text{out},f} - \sum_{n=2}^{\infty} P_{\text{out},nf} \quad (47)$$

$$P_{\text{out},nf} = \frac{1}{2} \cdot V_n \cdot I_n \cdot \cos(\varphi_n) \quad n = 1, 2 \dots \quad (48)$$

Utilising these expressions in the definition of drain efficiency, it follows that

$$\eta = \frac{P_{\text{out},f}}{P_{\text{DC}}} = \frac{P_{\text{out},f}}{P_{\text{diss}} + P_{\text{out},f} + \sum_{n=2}^{\infty} P_{\text{out},nf}} \quad (49)$$

From this expression, the necessary and sufficient condition needed to reach a complete conversion of DC power into useful fundamental power (i.e., 100% efficiency) is that both the following conditions be fulfilled *simultaneously*:

$$P_{\text{diss}} = 0 \quad (50)$$

$$\sum_{n=2}^{\infty} P_{\text{out},nf} = \frac{1}{2} \cdot \sum_{n=2}^{\infty} V_n \cdot I_n \cdot \cos(\varphi_n) = 0 \quad (51)$$

More explicitly, on one hand dissipated power on the active device has to be nulled, and this can be accomplished by correctly shaping voltage and current waveforms in order to ensure a null overlapping; thus the current on the device must vanish for a nonzero voltage and vice versa. Moreover, harmonic *active* power has to be nulled, thus implying either the zeroing of current/voltage harmonic components ($V_n = 0$ or $I_n = 0$ or both) or their proper phasing ($\varphi_n = \pi/2$). Therefore, in low-frequency applications, assuming an infinite number of controllable harmonic terminations, two possibilities are available to ensure the fulfillment of the latter condition:

- *Class F* [56–58] or *inverse class F* [59] strategies, in which $V_n I_n = 0$ for $n > 1$. Note that these are idealized approaches since voltage and current harmonic components, which in a real device are related by load impedances as in Eq. (45), and are considered separately. The class F strategy has been successfully applied in class AB [61,62] amplifier stages. Nevertheless, its application may lead to poor efficiency performances if class C or deep-AB (near-B) biasing classes are adopted [60].
- *Class E* or *switched-mode strategies*, in which $\varphi_n = \pi/2$ for $n > 1$. The active device is operated as a switch, and closed-form design expressions are available [63]. In such conditions, the stage acts more as a DC/RF converter rather than an amplifier. In this case, the power gain of the stage is not controlled and specified during the design phase; it is a specification to be fulfilled by a separately designed driver circuit, using information about the input port characteristics of the power transistor to be driven. Moreover, nothing is said about the input network, except that the input voltage waveform must properly drive the device to operate as a switch (i.e., be deeply pinched off and saturated). In any case, an inspection of expression (49) suggests two possible directions for the efficiency optimization: (1) either the maximization of device output power (for the same DC supply) or (2) the minimization of the dissipated power (considered as the sum of internally dissipated power $P_{\text{diss},\text{out}}$ and harmonic active power $P_{\text{out},nf}$).

The designer's task is therefore in the appropriate shaping of current and voltage waveforms, consisting in the selection of appropriate harmonic terminations leading to the fulfillment of the conditions described above.

5. HARMONIC TUNING APPROACHES

Harmonic tuning approaches for microwave PA design represent indeed a hot discussion topic for both the academic and the industrial communities given the beneficial effect on stage efficiency that can be obtained by a proper selection of harmonic terminations. Contributions in this field range from experimental observation of performance levels [66–68] to introduction of novel topologies as in the case of harmonic reaction amplifiers [64,65], from systematic investigations of experimental performances [70] to design methods for special harmonic tuning configurations [69].

In fact, however, if the operating frequency enters the microwave region, both approaches cited in the previous section (viz., the standard class F and the switching-mode class E) exhibit a degradation in performance. For instance, actual class F amplifiers are usually designed making use of two or three idlers only to control second and third output harmonic impedances. As frequency increases (e.g., >20 GHz), the control of both the second and third harmonic output impedances becomes troublesome, since the active-device output capacitive behavior practically short-circuits higher components, not allowing the desired waveshaping. Moreover, for low-voltage applications, a class F strategy is not the best solution, since different methodologies (based on second-harmonic output impedance tuning) have demonstrated better performance [71]. On the other hand, the switching mode operation of the active device, necessary to implement class E strategy, is not feasible in microwave communication systems, since it requires that the PA operate in saturated conditions, thus often increasing IMD levels and potentially affecting active-device reliability.

Circuit complexity issues and effectiveness of the harmonic control therefore suggest the control of the first two harmonic terminations for a PA stage, leaving higher terminations dominated by the shunting effect of the output device capacitive behavior. Assuming purely resistive terminations for the sake of simplicity, the drain voltage waveform can be expressed as [72]

$$v_{DS}(t) = V_{ds,DC} - V_1 \cdot [\cos(\omega \cdot t) + k_2 \cdot \cos(2 \cdot \omega \cdot t) + k_3 \cdot \cos(3 \cdot \omega \cdot t)] \quad (52)$$

where

$$k_2 \equiv \frac{V_2}{V_1} \quad k_3 \equiv \frac{V_3}{V_1} \quad (53)$$

and

$$V_1 = R_1 \cdot I_1 \quad V_2 = R_2 \cdot I_2 \quad V_3 = R_3 \cdot I_3 \quad (54)$$

Hence, for a given device drive and bias, that is, for given current source harmonic components (I_n), the designer's task is in the selection of proper terminations at fundamental (R_1) and harmonic frequencies (R_2, R_3) maximizing the fundamental component (V_1) of the swing experienced by $v_{DS}(t)$, with the constraints dictated by the device

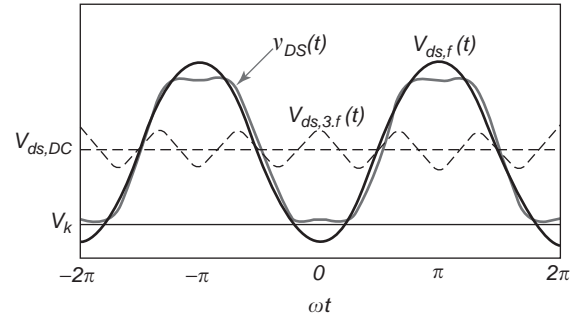


Figure 25. Voltage waveform $v_{DS}(t)$ (red curve) obtained via the introduction of a third-harmonic component (dashed line) summed to a fundamental frequency component (continuous line) exceeding the physical limitation (V_k). (This figure is available in full color at <http://www.mrw.interscience.wiley.com/erfme>.)

physical limitations (knee and breakdown voltages). This is equivalent to the determination of the values of the pair (k_2, k_3), which, for given physical limits and therefore for a given voltage swing, allows maximization of the V_1 component. An example of this effect is reported in Fig. 25, utilising, for simplicity, a third-harmonic component only summed to the fundamental one. In this scenario, for a fixed swing, dictated in this case by the bias voltage $V_{ds,DC}$ and V_k physical limitation, the introduction of a third-harmonic component actually increases the fundamental frequency amplitude beyond the value of the TL case (viz., $V_{ds,DC} - V_k$ in this case).

Analytically, this is accomplished defining the *voltage gain function* δ by the ratio of the resulting fundamental voltage component normalized to the unmanipulated case (the tuned load value, numerically coincident with the distance between the drain bias and the closer physical limit):

$$\delta(k_2, k_3) \equiv \frac{V_1}{V_{1,TL}} \quad (55)$$

The voltage gain δ is plotted in Figs. 26 and 27 as a function of (k_2, k_3) in a three-dimensional and contour plot format.

As it is possible to note, the δ function exhibits a clear maximum for (k_2, k_3) = (−0.55, 0.17) whose value is

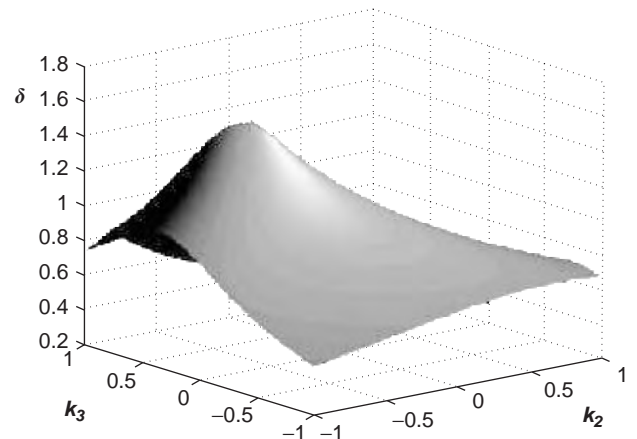


Figure 26. Voltage gain function δ versus k_2 and k_3 .

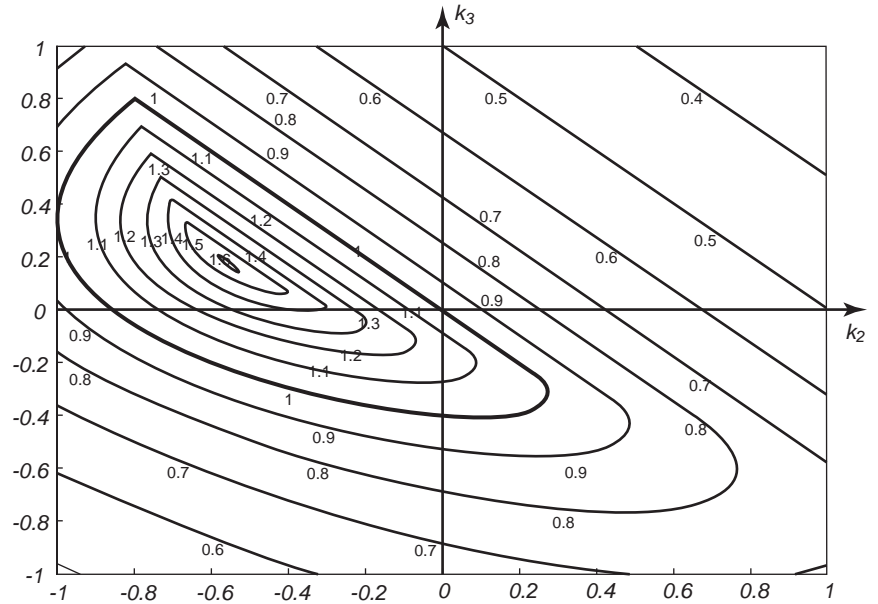


Figure 27. Constant voltage gain function δ contours in the (k_2, k_3) plane.

approximately 1.62. The function is higher than unity (i.e., use of the second and third harmonics effectively increases fundamental drain voltage harmonic component) within the marked region in Fig. 26.

The increase in fundamental frequency output voltage component obtained via a proper selection of the (k_2, k_3) pair, is directly reflected in a corresponding increase in power performances of the PA stage. In fact, under the hypothesis that the controlled source is not affected by the device harmonic terminations (i.e., its harmonics components I_n remain unchanged), the output power, large-signal gain, drain, and power-added efficiency of the stage become

$$P_{out}(k_2, k_3) = P_{out,TL} \cdot \delta(k_2, k_3) \tag{56}$$

$$G(k_2, k_3) = G_{TL} \cdot \delta(k_2, k_3) \tag{57}$$

$$\eta(k_2, k_3) = \eta_{TL} \cdot \delta(k_2, k_3) \tag{58}$$

$$\eta_{add}(k_2, k_3) = \eta_{add,TL} \cdot \delta(k_2, k_3) \cdot \left(\frac{G_{TL} - 1/\delta(k_2, k_3)}{G_{TL} - 1} \right) \tag{59}$$

The harmonic terminations that actually shape output voltage with a given selection of the (k_2, k_3) pair are therefore

$$R_1 = \delta(k_2, k_3) \cdot R_{TL} \tag{60}$$

$$R_2 = \delta(k_2, k_3) \cdot k_2 \cdot \frac{I_1}{I_2} \cdot R_{TL} \tag{61}$$

$$R_3 = \delta(k_2, k_3) \cdot k_3 \cdot \frac{I_1}{I_3} \cdot R_{TL} \tag{62}$$

In the derivations above, clearly the role of the device output conductance (g_{ds}) is not evidenced; the latter clearly poses an upper limit to the impedance values that can

effectively be presented to the active-device internal current source. The effect of actual device output conductance leads to a modification of the approach presented here [60].

Furthermore, the use of even-harmonic components (the second one in this case) actually breaks the natural symmetry of the voltage waveform; the desired flattening while approaching the physical limitation is accompanied by a peaking in the remaining part of the RF cycle, which can actually reach the opposite physical limitation. This effect has to be carefully controlled and is quantitatively evaluated via a voltage overshoot function [72].

However, several important cases can be extracted from Fig. 26. The first one consists in the previously discussed TL condition, corresponding to the origin of the (k_2, k_3) plane, where $\delta(0,0) = 1$. If a single voltage harmonic is controlled at a time, terminating the remaining one on a short-circuit termination, two possibilities arise. The first one is obtained for $k_2 = 0$, consisting in the control of third harmonic only: this situation corresponds to the high-frequency class F design approach [60,73], which is represented in Fig. 26 by the k_3 axis. In this harmonic control scheme the maximum value for the voltage gain function is obtained for $\delta(0, -0.167) \approx 1.15$. In this case, therefore, the use of a high-frequency class F approach results in an increase of 15% in output power, efficiency, and large-signal gain over the tuned-load condition. Maximally flat waveforms are a special case of such design approach [73].

The second possibility consists in setting $k_3 = 0$, therefore controlling the second-harmonic component only [71]. Moving along the k_2 axis in Fig. 26 results in a maximum value for $\delta(-0.35, 0) \approx 1.41$ and in the corresponding increase in power performances. The results attainable via harmonic tuning of the second and third output harmonic components are summarized in Table 4.

It should be noted, however, that the potential increases in the PA power performances are obtained only if the proper loading is imposed on the active-device output.

Table 4. Maximum Theoretical Improvements in Drain Efficiency over the Tuned Load Approach Attainable with Tuning Second-, Third-, and Second/Third-Harmonic Output Terminations

Controlled Frequencies		k_2	k_3	δ	η Improvement (%)
F	Tuned load	0	0	1	0
$f, 3f$	High-frequency class F	0	-0.17	1.15	15
$f, 2f$	2nd-harmonic tuning	-0.35	0	1.41	41
$f, 2f, 3f$	2nd/3 rd -harmonic tuning	-0.55	0.17	1.62	62

This is not always possible. In fact, with reference to Fig. 22, output current harmonic components, generated via the clipping effect of the device pinchoff on a sinusoidal input drive, show a different behavior as a function of the current conduction angle. In particular, focusing on the region $\alpha \in [\pi, 2\pi]$ (i.e., from class B to class A bias), the second harmonic current component is always positive, while the third one is negative (clearly taking the fundamental one as a reference). Since actual terminations are passive (i.e., $R_i \geq 0, i = 1, \dots, 3$), this consideration implies that positive k_2 and negative k_3 are feasible:

$$k_2 = \frac{V_2}{V_1} = \frac{R_2 \cdot I_2}{R_1 \cdot I_1} \geq 0 \quad k_3 = \frac{V_3}{V_1} = \frac{R_3 \cdot I_3}{R_1 \cdot I_1} \leq 0 \quad (63)$$

Therefore, if current clipping effects only are exploited, only third-harmonic (high-frequency class F) tuning is directly possible; the simultaneous use of second- and third-harmonic components implies, in fact, from Fig. 26, that $k_2 < 0$ and $k_3 > 0$. An improper use of harmonic tuning may, on the other hand, bring detrimental results on overall power performances, as exemplified in Fig. 28, where the case in Fig. 25 has been repeated with an incorrect phasing of the third-harmonic component.

Clearly the possibility to generate the properly phased current harmonic components is related to the driving waveform, up to now assumed to be purely sinusoidal. In fact, even if a perfectly sinusoidal drive is assumed, the drain current waveform actually reflects not only the hardlimiting clipping phenomena due to the device pinch-off but also the effect of local mild nonlinearities, slightly modifying the “truncated sinusoid” assumption adopted up to now [74]. On the other hand, the driving waveform

can be properly selected, eventually leading to quartic or rectangular input signals [75], allowing in this way the application of harmonic tuning strategies in limited ranges for the drain current conduction angle. The alternative approach (i.e., the exploitation of the device input nonlinearities and therefore the input terminations to the active device) has been the subject of a series of investigations, leading to experimental and theoretical studies, with frequently contrasting results [76–80]; the input nonlinearities of the device itself can be used to generate the harmonic of interest [81], with effects that can be effectively predicted using Volterra-like approaches [82], leading to an harmonic control scheme including input and output terminations, schematically depicted in Fig. 29.

The possibility of effectively controlling input and output harmonic control has been experimentally verified by several authors. In Fig. 30 the measured results are reported for the power performances of four single-device PA stages, designed utilizing TL, second-harmonic tuning, third-harmonic tuning, and second/third-tuning combined. The PA stages, realized in this case using hybrid technology, operate with a 5 GHz fundamental frequency, with a 5% operating bandwidth, and adopt a power 1-mm MESFET device from Alenia Marconi Systems.

A final consideration regarding the linearity performances of harmonic-controlled power amplifiers has to be drawn. The high-efficiency tuning of PA stages designed according to a harmonic control scheme leaves in fact some open questions on the resulting linearity. The proper tradeoff among such requirements is not clearly evidenced to date, even if experimental results demonstrate that a high-efficiency tuning does not necessarily imply detrimental linearity effects [83]. Moreover, harmonic injection techniques have been proposed to optimize linearity performance [84]. In any case however, proper subsystem linearization techniques can be adopted in the case of harmonic tuned PA stages, regardless of the adopted modulation scheme, using predistortion [85], feedback [86], or feedforward [87] approaches. Clearly a system-level linearization approach implies a decrease in efficiency performance and often a major increase in subsystem complexity.

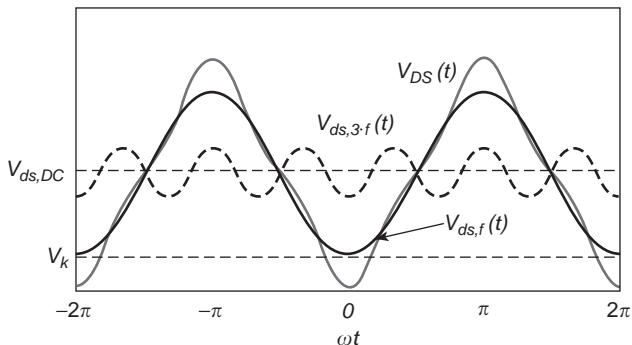


Figure 28. Voltage waveform $v_{DS}(t)$ (red curve) exceeding the physical limitation (V_k) obtained via the introduction of a third-harmonic component (dashed line) summed to a fundamental frequency component (continuous line). (This figure is available in full color at <http://www.mrw.interscience.wiley.com/erfme>.)

6. SWITCHING-MODE POWER AMPLIFIERS

In this category, a number of different approaches can be grouped, all characterized by the assumption that the active device (or devices) utilized in the power stage is (are) operated as switches, commuted between the two “completely ON” (i.e., short-circuit-like) and “completely OFF”

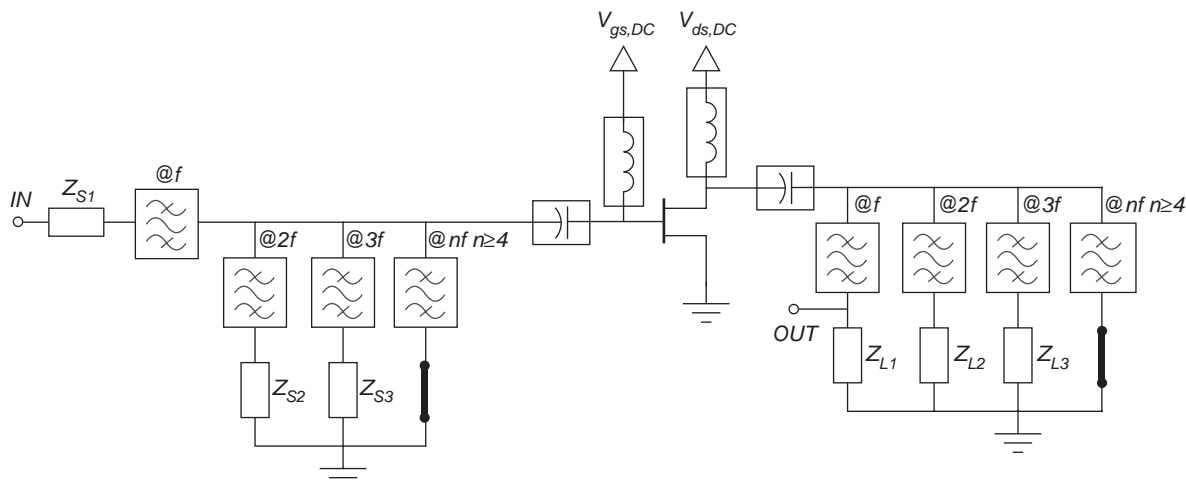


Figure 29. Harmonic control scheme including input and output terminations.

(i.e., open-circuit-like) states. As compared to the approaches described previously, in which the active device is basically represented as a controlled current source replicating with good fidelity the input driving stimulus, switching-mode PAs, ideally driving the active device in the ON and OFF states, indeed exhibit highly nonlinear characteristics. Such inherent lack of linearity is not a problem for constant-envelope modulations, for which a switched-mode operation may infer the great benefit of high-efficiency operation of the transmitter, while preventing their use if amplitude-modulated signals are fed into the amplifier. On the other hand, techniques consisting in the envelope elimination and restoration [88,89], outphasing [90,91], or other high linearity modulating schemes may alleviate the linearity drawback.

A further consideration applies to the large majority of switched-mode PA strategies. As they are based on the assumption of an active device operated as a switch, their effective implementation and resulting performance levels rely largely on the validity of such an assumption. It is

clear that the switching behavior of the device is strictly possible only when the effect of device parasitics is negligible, up to moderately high frequencies, including the low microwave range. The class D and class E amplifiers will be briefly addressed in the following text. For a more complete listing of switched-mode PAs and the relevant references, see Chap. 14 in Ref. 92. The class D amplifier, introduced by Baxandall [93], is composed, in its basic form, of a pair of active devices whose output is fed to an output tuning circuit, as depicted in Fig. 31.

In such a basic configuration, referred to as “complementary voltage switching,” the two devices act as a two-pole switch, whose output voltage tends to be an ideal square waveform, whose harmonic components are effectively filtered by the series-tuned resonator formed by L and C in Fig. 31, therefore delivering a sinusoidal signal to the output load R . The two transistors are driven, in fact, via the transformer, to deliver two output (drain) 180° out-of-phase currents T_1 and T_2 , which pass alternately between ON and OFF states. Assuming a 50% duty

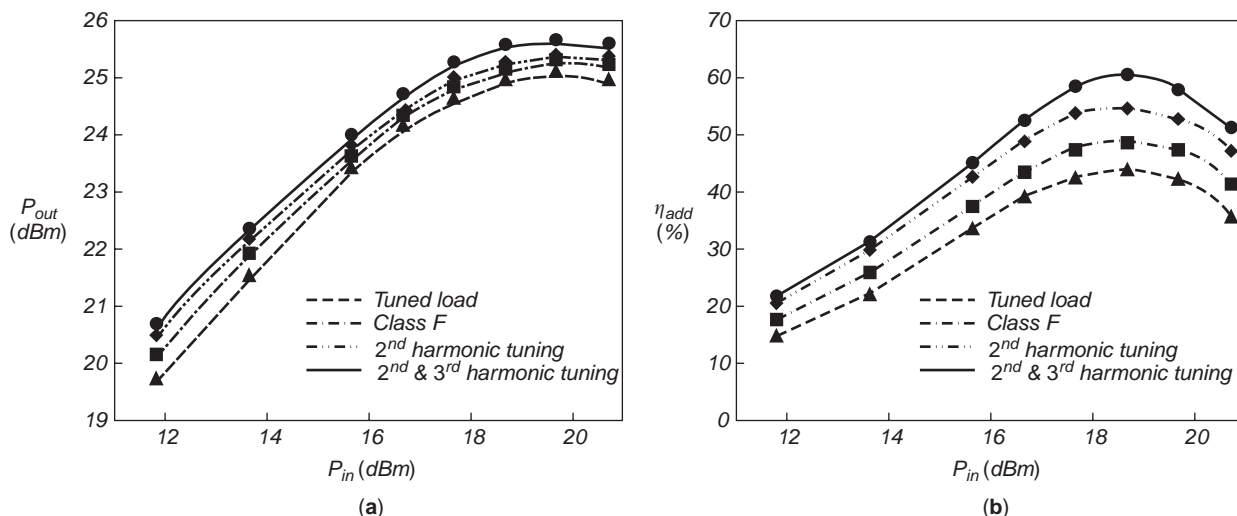


Figure 30. Output power (a) and power-added efficiency (b) measured performances of four single-device PA stages designed utilizing different harmonic tuning strategies.

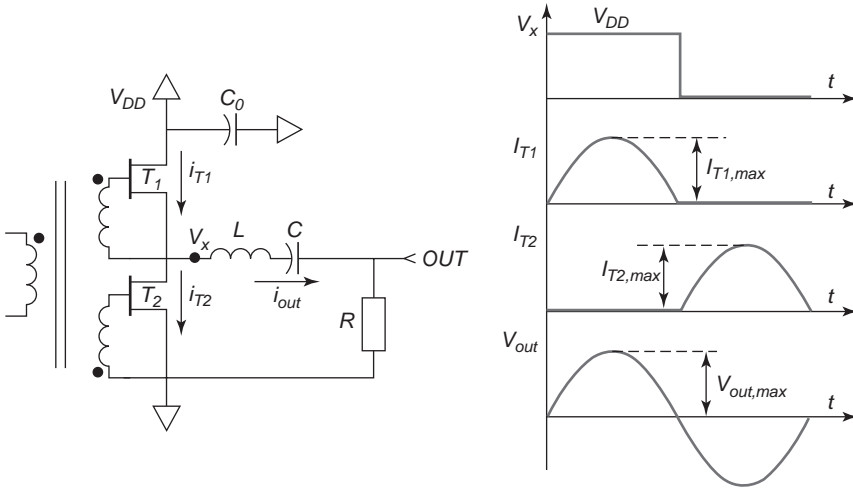


Figure 31. Schematic representation of a basic class D amplifier and basic waveforms.

cycle, the voltage V_x in Fig. 31 may be represented by a square waveform, whose Fourier expansion is given by

$$V_x(t) = \frac{V_{DD}}{2} \cdot \left(1 + \frac{4}{\pi} \cdot \sin(2\pi f \cdot t) + \frac{4}{3\pi} \cdot \sin(3 \cdot 2\pi f \cdot t) + \frac{4}{5\pi} \cdot \sin(5 \cdot 2\pi f \cdot t) + \dots \right) \quad (64)$$

This voltage waveform is applied to the series output R - L - C network. If the L - C series-resonant circuit is tuned to the fundamental switching frequency of operation f and exhibits an acceptable quality factor, the fundamental frequency component of V_x is directly obtained at the output load R , thus obtaining a purely sinusoidal output current:

$$i_{out}(t) = \frac{2 \cdot V_{DD}}{\pi \cdot R} \cdot \sin(2\pi f \cdot t) \quad (65)$$

Under the hypothesis described above, the drain currents in the two transistors (i_{T1} and i_{T2}) are therefore two half-sinusoids, as in Fig. 31, and, from inspection of the previous expression, the peak drain current value for both transistors is therefore

$$i_{T1,max} = i_{T2,max} = \frac{2 \cdot V_{DD}}{\pi \cdot R} \quad (66)$$

while the output power delivered to the load is

$$P_{out} = \frac{1}{2} \cdot \frac{2 \cdot V_{DD}}{\pi} \cdot \frac{2 \cdot V_{DD}}{\pi \cdot R} = \frac{2 \cdot V_{DD}^2}{\pi^2 \cdot R} \quad (67)$$

and the DC input power (i.e., from the power supply) is given by the product of the applied voltage V_{DD} times the mean value of the current through T_1

$$P_{DC} = V_{DD} \cdot \frac{2 \cdot V_{DD}}{\pi^2 \cdot R} = \frac{2 \cdot V_{DD}^2}{\pi^2 \cdot R} \quad (68)$$

thus obtaining a theoretical 100% drain efficiency:

$$\eta_{class D} = \frac{P_{out}}{P_{DC}} = 1 \quad (69)$$

The series-resonant L - C circuit actually provides the adequate harmonic filtering, which can be further improved if the circuit quality factor is not adequate by a subsequent lowpass filter. The bypass capacitor C_0 actually has a DC filtering purpose, which can be further improved by a series choke inductor directly connected to the bias supply V_{DD} .

Maintaining the same operating principle, transformer coupling configurations may be applied, introducing center-tapped output transformers. The dual configuration, that is, the current-switching one, can be implemented as well [92]. The idealized operation of the class D amplifier, however, has to be complemented by some practical constraints arising from actual device operation. In fact, the device ON-state resistance is in series with the output load (regardless of the specific complementary or transformer-coupled voltage switching configuration), thus decreasing the effective output voltage and efficiency. The T_1 transistor is, on the other hand, ungrounded, posing serious problems for the actual implementation of the scheme at high frequencies, for both driver requirements and connection parasitics [94]. Moreover, since actual transistors exhibit a parasitic output capacitance that sums up to the circuit stray capacitances, the result is that, for each RF cycle, the stored energy in such reactance is dissipated during the ON state in the transistor itself. Such energy, whose amount is approximately proportional to the susceptance associated with this parasitic [95], actually produces an increase in the input (DC) power required to the proper operation of the stage for the same output power, with the resulting decrease in stage efficiency.

The abovementioned parasitic output capacitance is one of the major factors responsible for finite transistor switching times, which up to now have been assumed as vanishingly small. As a result, finite transitions between ON and OFF states produce a net decrease in stage drain efficiency [92].

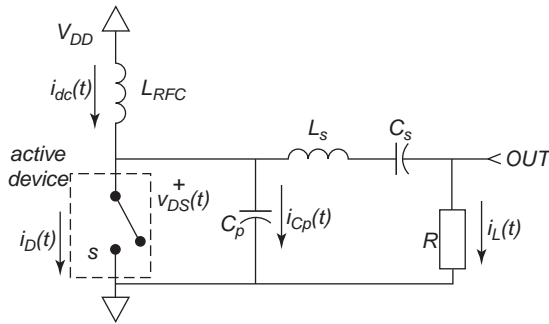


Figure 32. Circuit schematic of a class E power amplifier.

A very popular and effective switching mode PA configuration is the class E amplifier. Introduced and patented by Sokal in 1975 [96,97], the class E configuration has been extensively studied [54,98], receiving, with expiration of the issued patent, renewed interest [63,99–102]. The basic circuit configuration of a class E PA is depicted in Fig. 32, where the active device is represented by a switch.

The capacitor C_p includes both device output parasitic reactance and circuit stray capacitances and is eventually increased by an external capacitor. Its value is not such, however, to short-circuit all voltage harmonics. Ideal current and voltages on the active device, represented in Fig. 33, are such that dissipated power is nulled. If a Fourier analysis is further performed on such waveforms, the phase difference between each current and voltage harmonic component is equal to $\pi/2$, therefore fulfilling both conditions indicated by (50) and (51) for efficiency maximization.

Analysis of the circuit in Fig. 32 can be carried out considering a 50% duty cycle, together with an ideal switch operation (i.e., assuming a null ON-state switch resistance and an infinite OFF-state one). Furthermore, the RF choke is assumed ideal, and no losses are accounted for the external elements in the circuit, the active power is dissipated in the external load R only. The current flowing in the external load may be assumed to be a purely sinusoidal one thanks to the series resonator formed by the L_s – C_s pair, tuned to operate at the circuit fundamental frequency and with an infinite quality factor.

The two currents $i_L(t)$ and $i_{DC}(t)$ are therefore always a sinusoidal one and a constant one, respectively, regardless

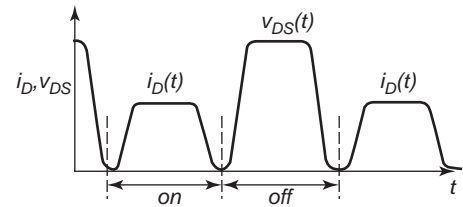


Figure 33. Idealized current (i_D) and voltage (v_{DS}) waveforms.

of the switch position. The current flowing through the parallel combination of the active device (switch) and the capacitor C_p is therefore always a DC-offset sinusoid. Clearly, when the switch is ON, all such current flows through it, and when the switch is OFF, the offset sinusoidal current passes through the capacitor only:

$$\begin{aligned}
 i_{DC}(t) &= i_{DC} \\
 &\Rightarrow i_d(t) + i_{C_p}(t) = i_{DC} + i_L \cdot \cos(\omega \cdot t) \\
 i_L(t) &= i_L \cdot \cos(\omega \cdot t)
 \end{aligned}
 \tag{70}$$

The onset of the switch ON state will be determined therefore from the zero crossing of such DC-offset current. An example of the resulting switch current is shown in Fig. 34. The corresponding voltage $v_{ds}(t)$ will be obtained by the integration, over the OFF state of the switch period, of the capacitor charge

$$v_{DS}(t) = v_{C_p}(t) = \frac{1}{C_p} \cdot \int i_{C_p}(t) \cdot dt
 \tag{71}$$

obtaining the corresponding voltage waveform depicted in Fig. 34.

Closed-form design expressions may be derived for the circuit components in Fig. 32. The latter may be found in Ref. 63, and the step-by-step derivation of voltages and currents may be found in Refs. 92 and 94 following a time-domain approach.

With reference to Fig. 32, current and voltage in the “ON state” of the switch are expressed as

$$\begin{aligned}
 i_D(t) &= i_{DC} \cdot [1 - a \cdot \sin(\omega t + \phi)] \\
 v_{DS}(t) &= 0
 \end{aligned}
 \tag{72}$$

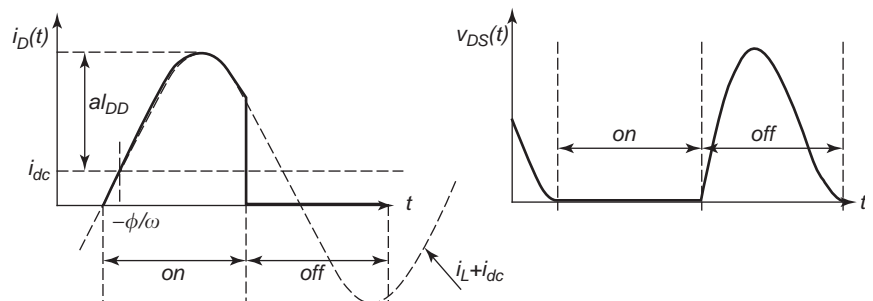


Figure 34. Switch current and voltage.

while in the “OFF state” as

$$\begin{aligned} i_D(t) &= 0 \\ v_{DS}(t) &= \frac{1}{C_p} \cdot \int_0^t i_D(\tau) d\tau \\ &= \frac{i_{DC}}{\omega \cdot C_p} [\omega \cdot t + a \cdot \cos(\omega \cdot t + \phi) - \cos(\phi)] \end{aligned} \quad (73)$$

Imposing a null switch (capacitor) voltage at the onset of the ON state, together with its first derivative (optimum operation)

$$v_{ds}(t)|_{t=(T/2)} = 0; \quad \left. \frac{dv_{ds}(t)}{dt} \right|_{t=(T/2)} = 0 \quad (74)$$

it is possible to obtain

$$a = \sqrt{1 + \frac{\pi^2}{4}}; \quad \phi = -\tan^{-1}\left(\frac{2}{\pi}\right); \quad V_{DD} = \frac{i_{DC}}{\pi \cdot \omega \cdot C_p} \quad (75)$$

From the expression derived, noting that the dissipated power is null on the active device (neglecting the switch ON-state resistance), the output power P_{out} equals the input supply power P_{DC} , given by

$$P_{DC} = P_{out} = V_{DD} \cdot i_{DC} = \pi \cdot \omega \cdot C_p \cdot V_{DD}^2 \quad (76)$$

bringing the efficiency of the class E PA stage to unity. If a nonzero ON resistance for the switch (R_{on}) is considered, the stage efficiency becomes

$$\eta = \frac{1 + \frac{\pi}{2} + \omega \cdot C_p \cdot R_{on}}{\left(1 + \frac{\pi^2}{4}\right) \cdot (1 + \pi \cdot \omega \cdot C_p \cdot R_{on})^2} \quad (77)$$

An alternative derivation, based on a phasor-based frequency-domain approach, can be found in Ref. 101. In this case the result can be expressed in terms of harmonic load impedances Z_L , namely, the total impedance loading the active device, given by

$$Z_L = \begin{cases} \frac{0.28015}{\omega C_p} e^{j49.0524^\circ} & \text{at } f \\ \infty & \text{at } nf, n > 1 \end{cases} \quad (78)$$

where the parallel capacitance C_p is related to the rf output power P_{out} by

$$C_p = \frac{P_{out}}{\pi \cdot \omega \cdot V_{DD}^2} \quad (79)$$

This expression implicitly poses an upper limit to the maximum operating frequency of the class E amplifier. In fact, once the capacitor value is determined from optimum circuit conditions, the maximum operating

frequency can be obtained as

$$f_{max} = 0.0177 \cdot \frac{I_{max}}{V_{DD} \cdot C_p} \quad (80)$$

where

$$I_{max} = a \cdot I_{DD} + i_{DC} \quad (81)$$

is the maximum value of the current flowing into the active device. Furthermore, the maximum voltage across the switching device obtained by expression (71) may rise well beyond the DC supply, being given by

$$v_{ds,max} \approx 3.562 \cdot V_{DD} \quad (82)$$

For safe and reliable operation, a value such as this must be kept well below the device breakdown region. On the other hand, the limitation imposed by (82) actually decreases the maximum output power that can be achieved utilizing the class E approach if compared to conventional class AB linear PA design, forcing a much lower bias. Indeed, the class E scheme exhibits several advantages, including the evident scheme simplicity, together with the high efficiency attainable.

Constraint imposed on the output circuit high- Q operation may be severe, however, if high-frequency operation is concerned. The result of a low quality factor for the output series resonant circuit will be a nonzero harmonic current flowing into the output, implying a nonoptimum drain voltage waveform, with possible ringing phenomena. Nevertheless, since the class E amplifier has to be over driven by a driver stage well into device compression regions, its large-signal gain may be well below the level that can be attained by a comparable linear power amplifier (say, 3–5 dB [94]). Given the typical frequency rolloff of power devices, this poses an intrinsic frequency limitation to the applicability of the class E scheme. The frequency limit is further decreased by the intrinsic reactive behavior of the device output (dominated by the device output capacitance) that actually restrict the possible values for the capacitance C_p in the class E scheme, as suggested from (80).

7. LOAD-PULL TECHNIQUES

As widely noted previously, PA performance is determined mainly by the terminations imposed to the active device, mainly at its output but also considering its input nonlinearities. This consideration naturally leads us to consider the possibility of experimentally characterizing the device power performance by means of a setup that actually modifies device terminations and records the related performance [106]. The loads are therefore “pulled” to test device power performance levels at both the device output (*load-pull*) and input (*source-pull*) ports. Such investigation is carried out at fundamental frequency (*fundamental load pull*, i.e., controlling the loading conditions at fundamental frequency) or even at harmonic frequencies

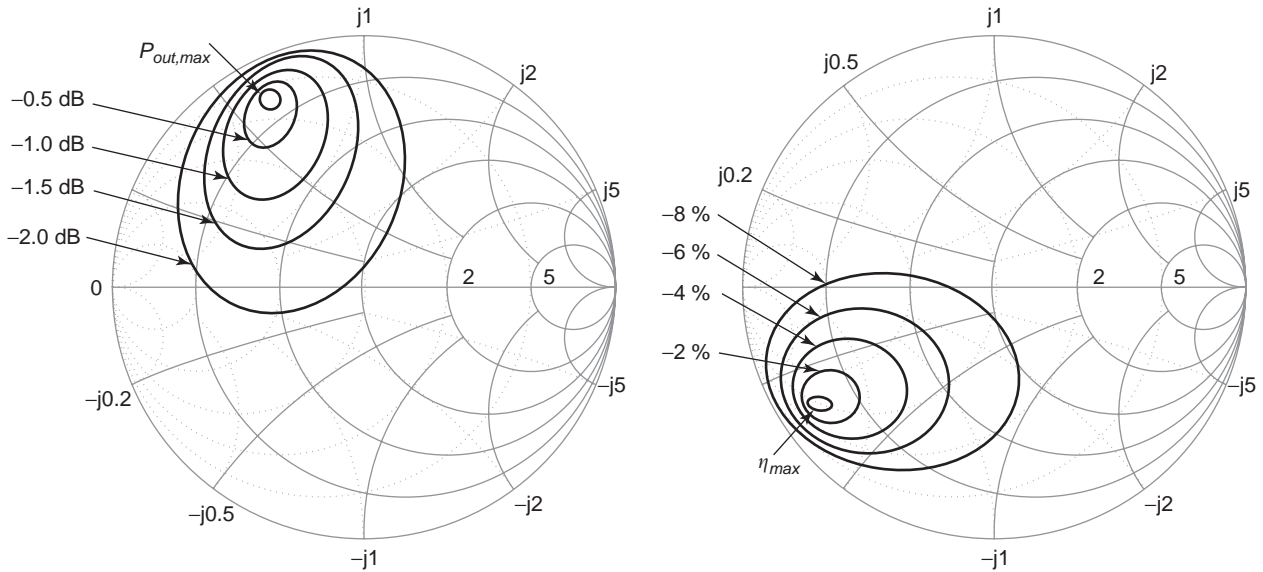


Figure 35. Typical load-pull contours for constant output power and drain efficiency at -1 and -2 dB gain compression, respectively.

(harmonic load pull, i.e. controlling the loading conditions at one or more harmonic frequencies [107–110]).

The result of such a measurement campaign, creating a database of power performances corresponding to a given combination of terminations, driving power, biases, and frequency is typically organized in graphical form. Usually constant-parameter curves are drawn on the corresponding load Smith chart, in order to immediately detect optimality condition. For example, in Fig. 35 the constant output power and drain efficiency curves at -1 dB and -2 dB gain compression respectively are shown in the load reflection coefficient plane.

The load pull therefore gives directly all that is necessary for optimum load selection, as the result of a tradeoff between the performance behaviors of interest. The PA designer therefore needs an automated load-pull measurement bench and physically the selected device, that must be available in the appropriate form, to avoid tedious and risky deembedding procedures. It should be noted, however, that load-pull systems may be fruitfully employed not only as a design tool but also for active-device nonlinear model extraction/verification setup, where the model can be compared and tested using data that have not been used for its extraction.

Before describing the details of the load-pull characterization setup, we present a technique due to Cripps

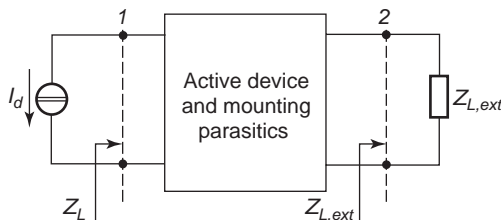


Figure 36. Simplified scheme of the active-device output and parasitics for application of the techniques in Ref. 103.

[103,104] and further refined by Kondoh [105], allowing determination of load-pull output power contours for a class A biased active device. The technique, based on a series of approximations performed on both the active device and the external circuit, is widely adopted and typically forms the basis for successive investigation (for both load-pull characterization and actual PA design). The active-device output is represented through its voltage-controlled current source I_d , assuming the remaining components and parasitic elements grouped together in the network between Sections 1 and 2 in Fig. 36, eventually constituting device mounting parasitics.

A piecewise linear description of the controlled source is adopted, as outlined in Section 3, and a class A bias is selected (corresponding to $I_{ds,DC} = I_{max}/2$, $V_{ds,DC} = V_{DD}$) as in Fig. 37.

The optimum load $Z_{L,opt}$ imposed at the current source terminals in Fig. 36, simultaneously maximizing current and voltage swings, already determined in Section 3 (see

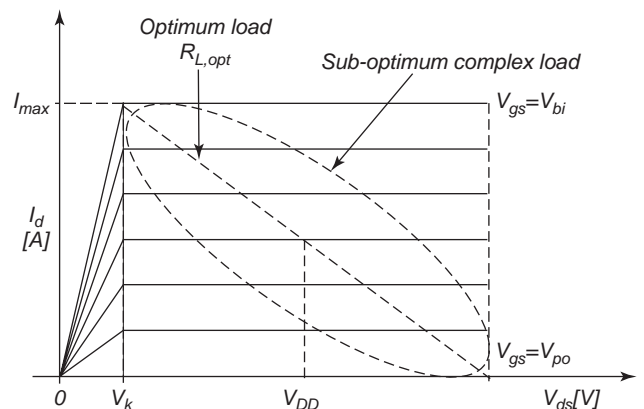


Figure 37. Piecewise linear representation of the device controlled current source, with superimposed optimum and suboptimum load curves corresponding to a resistive and complex load.

Table 3) as R_A , is a purely resistive one. Its value and the corresponding power delivered by the source are given by

$$\begin{aligned} Z_{L,opt} &= R_{L,opt} \\ &= 2 \cdot \frac{V_{ds,DC} - V_k}{I_{max}} = R_A; \\ P_{L,opt} &= \frac{(V_{ds,DC} - V_k) \cdot I_{max}}{4} \end{aligned} \quad (83)$$

If the source is loaded by a complex termination with the same magnitude $|Z_{L,opt}|$, a lower active output power results as a consequence of the phase difference between voltage and current waveforms. The resulting load curve, that is, the instantaneous plot of current and voltage at the source terminals, is an ellipse, as indicated in Fig. 38.

A lower resistance load ($R_{L,I} < R_{L,opt}$) will cause the device current hard limitations (viz., pinchoff and fully opened channel) to limit the current swing, occurring for a reduced voltage swing and resulting in a reduced output power. The same applies for a higher resistive loading ($R_{L,V} > R_{L,opt}$) in which the voltage limiting mechanism (viz., the device ohmic region) will occur for a reduced current swing. The resulting output power for the current- ($P_{L,I}$) and voltage- ($P_{L,V}$) limited operation are easily computed as follows:

$$P_{L,I} = \frac{R_{L,I}}{R_{L,opt}} \cdot P_{L,opt}; \quad P_{L,V} = \frac{R_{L,opt}}{R_{L,V}} \cdot P_{L,opt} \quad (84)$$

If a reactive part is added in series to the lower-resistance load $R_{L,I}$, the active output power will remain at same level, causing, on the other hand, the load curve to transform into an ellipse, as depicted in Fig. 38. The same applies to the voltage-limited case if a susceptance is added in parallel to the selected load $R_{L,V}$. Clearly in both cases, the output power will be constant until the resulting load curve will incur the voltage (for the current-limited case) or current (for the voltage-limited case) physical limit.

In order to draw a X -dB contour plot (i.e., the locus, on the Smith chart, characterized by an output power given by $P_{L,opt} - X$ dB), the resistive values in the current- and

voltage-limited cases ($R_{L,I}$, and $R_{L,V}$ respectively) are found from (84):

$$R_{L,I} = R_{L,opt} \cdot 10^{-(X/10)}; \quad R_{L,V} = R_{L,opt} \cdot 10^{(X/10)} \quad (85)$$

The X -dB contour can be drawn therefore following constant-resistance (with a value $R_{L,I}$ in the current-limited case) and constant-conductance (with a value $R_{L,V}$ in the voltage-limited case) loci on the Smith chart. The procedure can be repeated for a number of constant-output power loci, resulting in the typical contour plot in Fig. 39, where a 1 dB step has been adopted.

The load at the current source terminals must now be transformed into an external load, thus including device reactive elements and parasitics, together with mounting ones. To this purpose, standard Smith chart transformations apply, moving the reference plane from Section 1 to Section 2 in Fig. 36, and resulting in the final plot on the right side of Fig. 39.

Clearly a series of strong approximations have been applied to get the final result. Nevertheless, the results of the procedure are often in very good agreement with measured load-pull contours, justifying the popularity and widespread use of the Cripps technique. However, if a complete characterization and design charts involving the actual nonlinear nature of the active device are necessary, a load-pull measurement setup has to be used. The measurement systems adopted for load-pull setup may differ greatly. They range from relatively simple scalar setups, based on power meters and/or scalar network analysers, up to vector receivers. In the former case scalar information is available only on the device power performance, but their cost and relative simplicity is indeed a strong point.

Alternatively, vector information can be gained from the use of vector network analyzers (VNA, or from six-port approaches [111]) or by means of time-domain measurement systems [adopting, e.g., a microwave transition analyzer (MTA)]; in this case more complete vector information on the device can be extracted, together with higher accuracy on the results, due to the vector calibrations that can be adopted in the case of VNA (e.g., [112–117]) or with time-domain waveform capabilities in the case of a

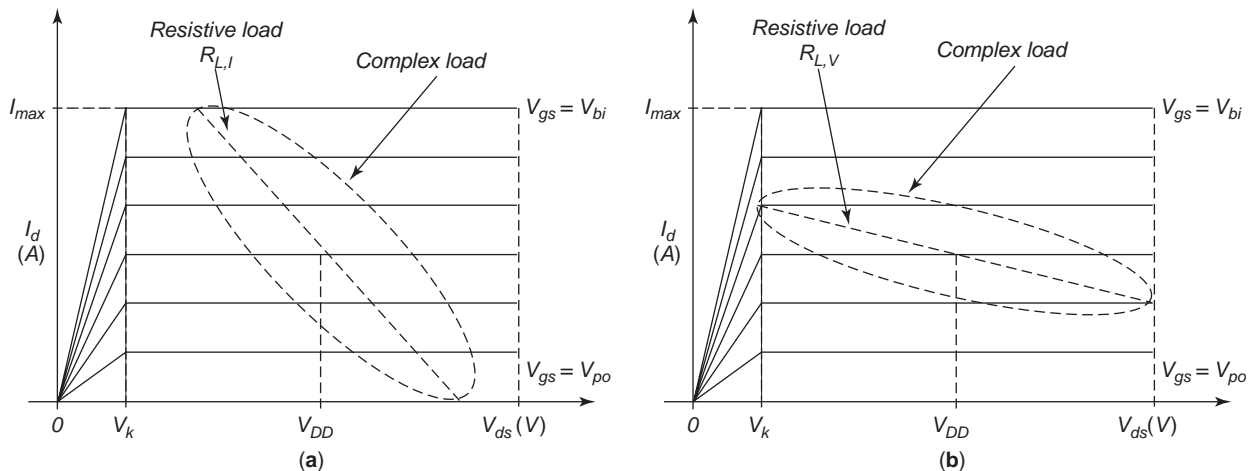


Figure 38. Current- (a) or voltage-limited (b) load lines.

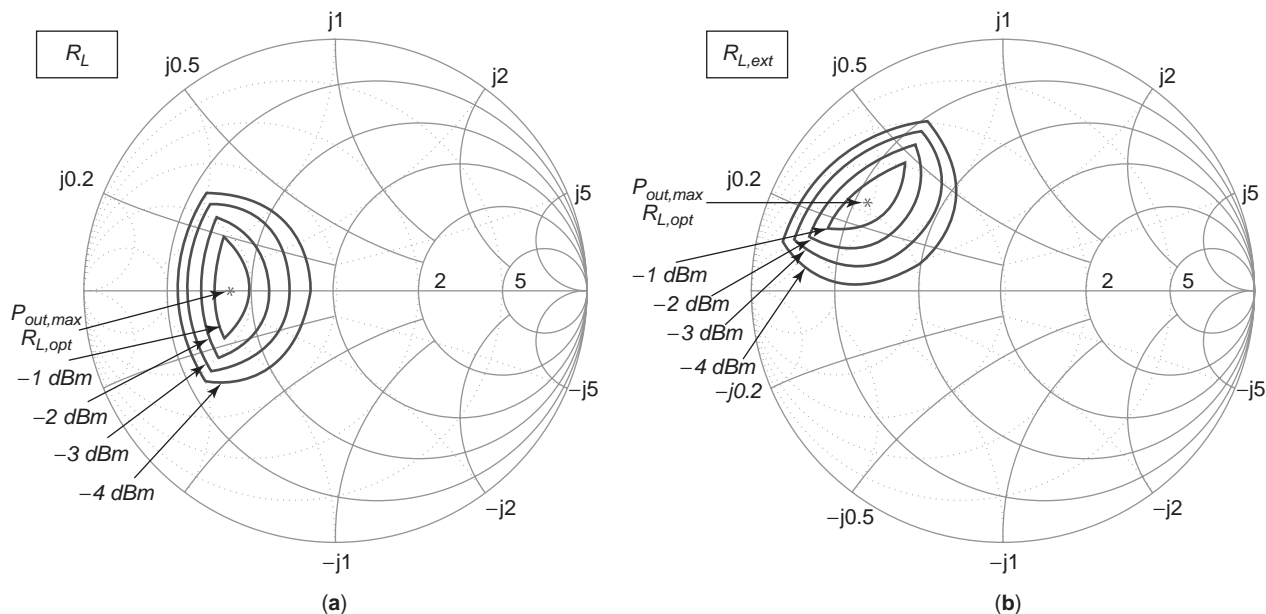


Figure 39. Derivation of constant output power contours, at the device intrinsic terminals (a) and at the extrinsic ones (b). (This figure is available in full color at <http://www.mrw.interscience.wiley.com/erfme>.)

MTA [118,119]. In both cases, however, such improved capabilities are obtained at the expense of an higher bench complexity and cost.

The load to be synthesized can be realized by means of passive systems (*passive load*, resulting in *passive load-pull* systems); the latter consist in mechanical (typically realized via a slotted transmission line with slugs) or electrical (i.e., PIN-diode-based) tuners [120–122]. A typical passive scalar load-pull system is schematically depicted in Fig. 40.

The adopted single- or double-slug tuners have to be accurately precharacterized by means of a VNA, or alternatively the scheme can be extended to include a series of electromechanical switches connecting alternatively the tuners to the DUT or to the VNA input for on-site impedance measurements. Tuners are generally GP-IB-controlled, and tuner position repeatability is guaranteed by precision stepped motors. Moreover, above all for mechanical tuners, the power-handling capability suffices for most power applications.

On the other hand, the synthesized reflection coefficient is limited in magnitude by the unavoidable tuner

and setup (cables, on-wafer probes, etc.) losses. Such limitation implies that highly reflective loads cannot be realized and presented to the active device. Especially for high-power devices this precludes the investigation of maximum power regions for the output fundamental load, since the optimum termination (approximately) results from the ratio of the bias voltage to device maximum current [explicitly for the class A, PA (33)]. This effect is clearly amplified if higher and higher frequencies (and hence higher losses) are explored. Moreover, if an harmonic load pull has to be performed, where optimum harmonic terminations may be typically close to purely reactive ones (see Section 5), a further drawback arises.

In order to overcome the problem, several solutions have been proposed [123], based on the use of either tuner prematching networks (at the device level) or pre-matching tuners (at the measurement system level; see Fig. 41).

In this way, higher reflection coefficient magnitudes are attainable. Nevertheless, especially in the case of pre-matching tuners, precharacterization is indeed a problem,

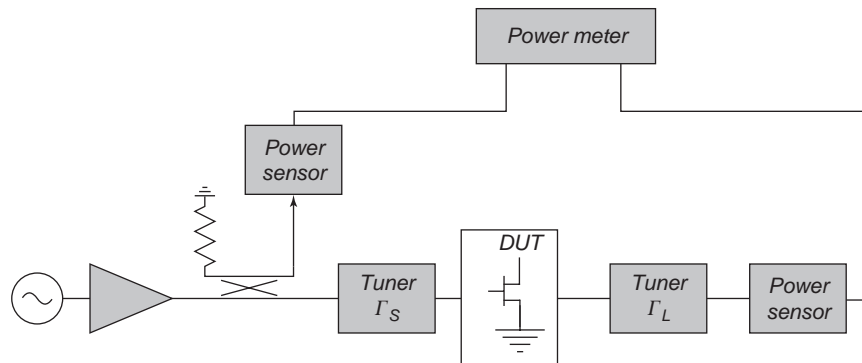


Figure 40. Schematic representation of a passive scalar load-pull setup.

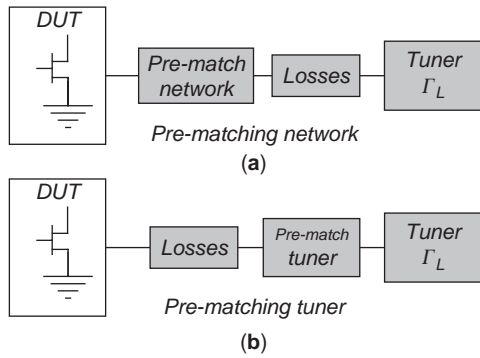


Figure 41. Overcoming setup losses with prematching networks (a) or prematching tuners (b).

since it implies the use of a five-dimensional variables space; moreover, harmonic terminations are not controlled (even if they can be monitored). In the latter case, in order to control harmonic terminations, more than a single tuner can be used or a combination of harmonic resonators, one for each harmonic to be controlled (Fig. 42).

Clearly the first solution increases the bench complexity and losses, but at the same time exhibits a greater flexibility for frequency control and variation, as contrasted with harmonic resonators, whose resonant frequency actually fixes the measurement frequency.

An alternative solution to the use of passive loads consist in the synthesis of the load to be presented at the active-device terminals with active techniques (*active load*, leading to *active load-pull* systems). Basically the active

load is synthesized reflecting back to the device port a power wave whose amplitude and phase are in an externally controlled magnitude–phase relationship with the emitted wave emerging from the device.

Two basic schemes are usually adopted to this goal, following the “two-signal path” and “active loop” techniques, both schematically depicted in Fig. 43.

In further detail, in the two-signal path technique, the device output is fed by a fundamental frequency signal directly generated by the same signal source feeding the device input, while in the active loop technique the reflected power to the device output is the device output signal itself, appropriately amplified and shifted in phase. In the former, technique however, the synthesized output reflection coefficient does vary in magnitude and phase while the source power is swept. Hence, for each input power a different load is presented to the active-device output, and therefore attenuation and phase shift must be controlled to keep the load constant. The same problem holds when the device heats up. On the other hand, such a technique is inherently stable, since no oscillation loop is created in the measurement setup. The latter problem does exist in the active loop scheme, which must be carefully dimensioned in order to avoid spurious oscillations (even at harmonics of the fundamental frequency). The active loop technique exhibits, on the other hand, a stable load termination with input power to the active device. Both techniques allow great flexibility in load control and selection, if compared to the passive approaches. In particular, setup losses are easily compensated by the loop amplifier, in most cases a TWT power amplifier, given the

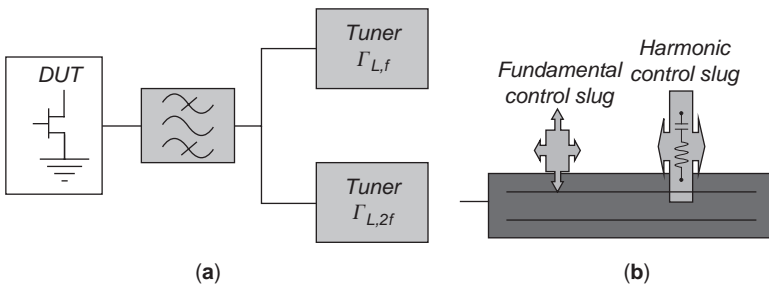


Figure 42. Harmonic control in passive load-pull systems by means of harmonic tuners (a) or resonators (b).

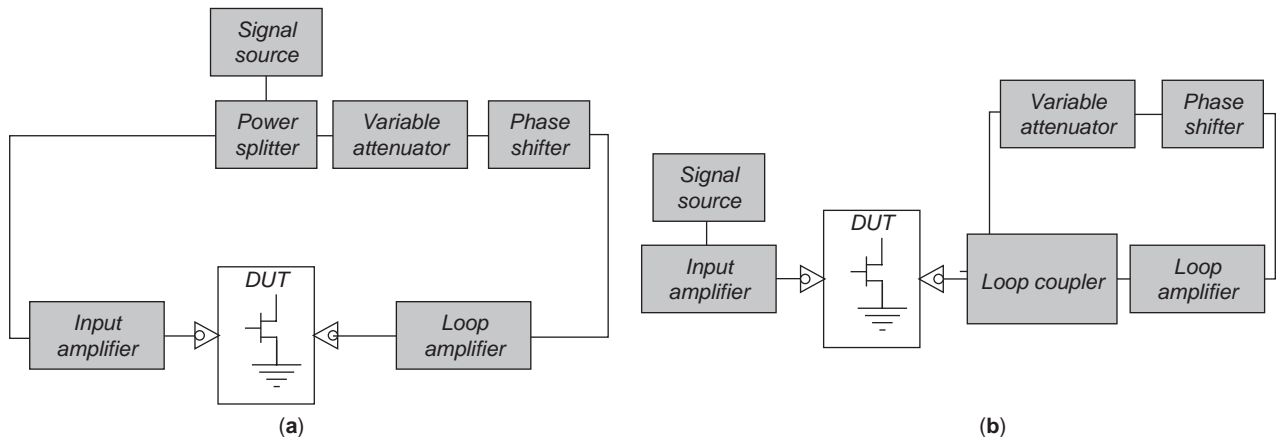


Figure 43. Two-signal path (a) and active loop (b) active load-pull techniques.

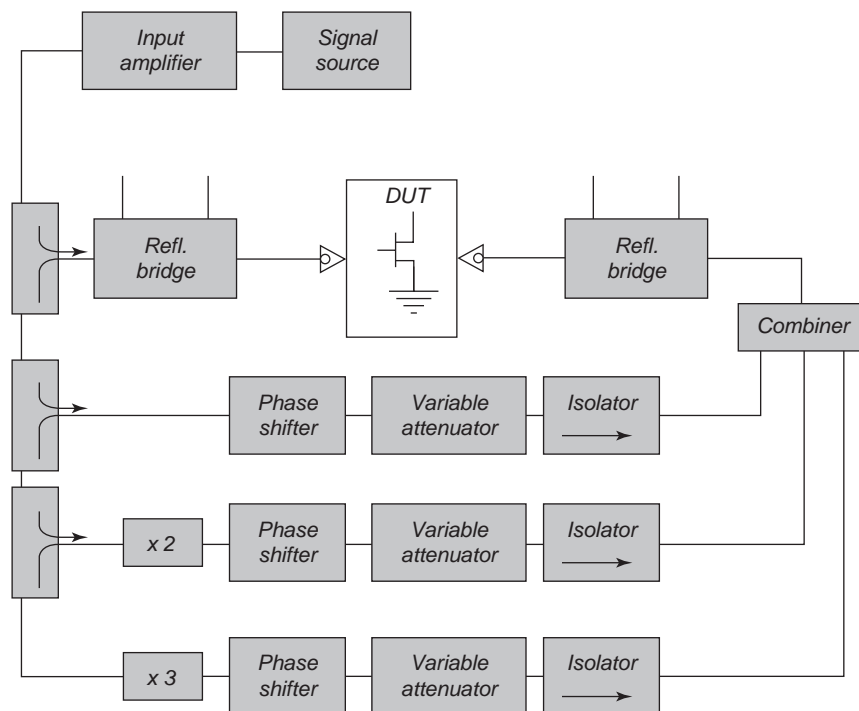


Figure 44. Extension for harmonic load pull of the two-signal path active load-pull technique.

power and linearity requirements. Highly mismatched (or even active) terminations are therefore easily synthesized with an active load-pull approach, clearly with an increased test bench complexity and overall cost.

If accuracy is a concern, in passive load-pull systems it depends mainly on tuner position repeatability, residual S-parameter measurement uncertainty, and power measurement uncertainty. For active systems [124], the main uncertainty source is in power calibration coefficients, which are strongly dependent on the presence of an input power amplifier (TWTA) before the active device under test. Such uncertainty is a strong function of the load reflection coefficient magnitude, rapidly increasing with it. The result is that for low to moderate reflection coefficient magnitudes the output power uncertainty performances of active systems are better than those for passive ones, but

rapidly degrade while approaching highly mismatched load regions.

If an active harmonic load pull has to be performed, the previous schemes can be extended for harmonic control, leading to the setups schematically depicted in Figs. 44 and 45, respectively.

The load-pull techniques can be adopted to test a series of device output performances, not restricted to classical output power, large-signal gain, drain, or power-added efficiency. In particular, depending on the measurement setup, time-domain waveform capabilities can be tested, together with linearity indicators: ACPR or two-tone tests can be performed as well [125,126], thus providing in situ information on the device linearity and allowing the designer to trade off between often contrasting goals directly by means of load-pull charts. As an example, in Fig. 46 a

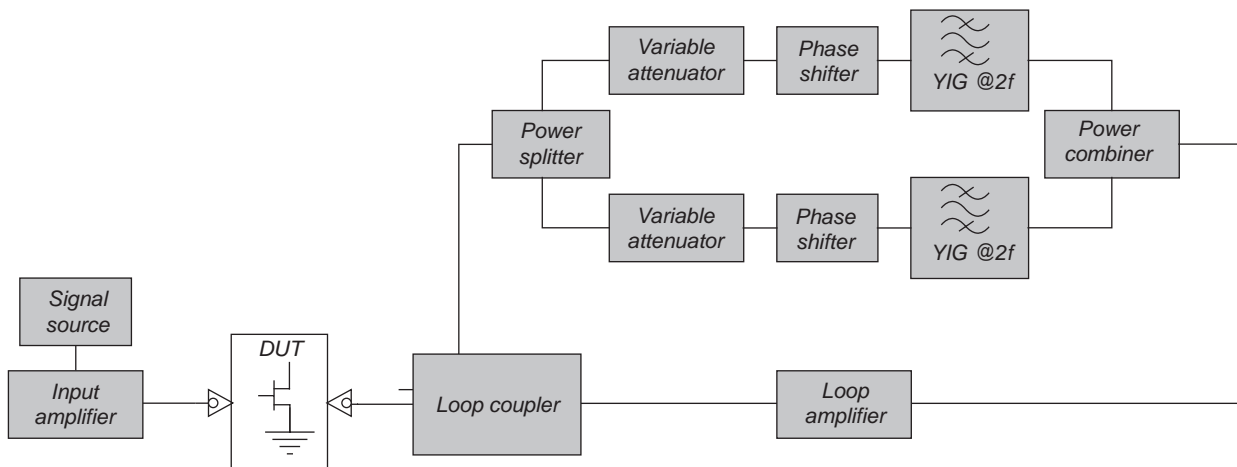


Figure 45. Extension for harmonic load pull of the active loop active load-pull technique.

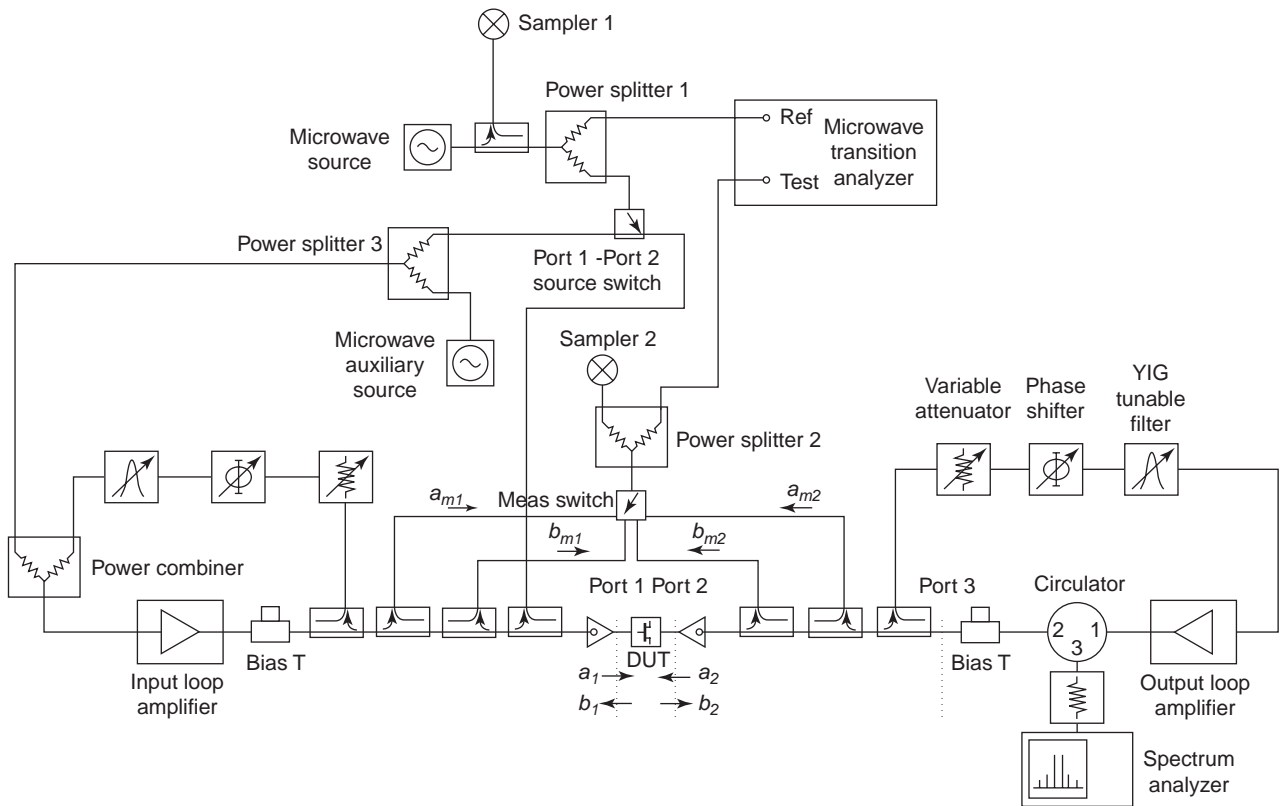


Figure 46. Schematic active load-pull bench with time-domain waveform and spectrum capabilities [127].

harmonic measurement setup [127] is shown, which combines S -parameter capability, real-time load and source-pull (single tone or harmonic) and intermodulation measurements with time-domain waveform measurements.

Any linear vector network analyzer with at least two samplers can be used as linear receiver, while a microwave transition analyzer is used as a nonlinear receiver, measuring the phase relationships between harmonics of the signals at the device under test (DUT) ports. The setup is completed with two active loops (but more loops could be added), controlled independently. The loops can be set at the input or output of the device, and tuned for both single-tone and harmonic measurements.

A final and general consideration regarding load-pull-based PA design has to be stressed. A complete power characterization of a given device is indeed a heavy task, especially if harmonic terminations have to be investigated. If frequencies up to the third harmonic are considered at both device input and output, this easily brings in the control of a six-variable state space, to which a further variable (drive level) is necessarily added. This formidable task is further complicated if fundamental frequency variation and device bias are varied. It is clear, therefore, that load pull has to be matched with some physical insight gained on the power generating mechanisms in the device by means of the harmonic tuning strategies and design procedures described before. Furthermore, an approach consisting in the control and consequent variation of a termination at a time is risky and may lead to suboptimum conditions [128].

8. CAD-BASED TECHNIQUES

Computer-aided design (CAD) tools have experienced a dramatic improvement both in performances and simulation capabilities. Such improvement is due to both increase in computing speed and hardware progress (workstations and PCs), and in the assessment of appropriate analysis techniques.

Modern CAD tools include linear and nonlinear simulation capabilities, coupled with electromagnetic field solvers, layout generation, and system simulation capabilities [129–135]. For the analysis and design of PA circuits obviously the nonlinear simulation capabilities are indeed necessary; the latter may be based on time-domain techniques (derived from widely diffused SPICE-like approaches [136], adapted to deal with microwave problems), adopted mainly for transient analysis, mixed time–frequency-domain techniques [of the harmonic-balance (HB) type, [138]] for steady-state analysis, fully frequency-domain algorithms [137], and finally Volterra series approaches [82]. While Volterra-based approaches find their intended application to circuits exhibiting mild nonlinearities and specifically to the analysis of PA linearity [48], the work horse of all commercial nonlinear CAD software is indeed the HB technique [140,141]. This approach has been extended from the piecewise formulation to include nasty nonlinear problems, such as nonlinear noise analysis, forced autonomous circuits, and input signals with complex modulation schemes. In the latter case, especially important for the analysis of PA

performance in actual operating conditions in communication systems, envelope-based approaches and multitone ones are adopted ([139,142,143]), demonstrating excellent simulation capabilities and numerical efficiency.

The availability, in commercial CAD software packages, of powerful HB simulation engines, together with 2D or 2.5D EM simulators efficiently modeling passive structures and interconnects, is a valuable support for microwave integrated circuit design. Nevertheless, the fidelity of simulated results to measured data is not completely achieved yet; whereas the accuracy of the analysis tool is in fact far beyond the process parameter variations, this is not true if active-device models are considered. Indeed, the effectiveness of a simulated result is to a great extent based on the availability of an accurate device model, especially if nonlinear operation is concerned.

Without entering the wide field of nonlinear device modeling, well beyond the scope of this contribution, a few key points have to be addressed. The active-device nonlinear models currently adopted in CAD tools may be basically classified into two main categories: empirical blackbox models [144–146] and equivalent-circuit based models [147,148]. The former are generally built on a large database of measured data and appropriate expressions to model the active device in the region of interest, while the latter consist in fitting predefined expression for the elements of a given model topology to model parameter data extracted from selected bias and operating conditions.

As a general consideration, the blackbox modeling approach does exhibit a better agreement with measured data, while the equivalent-circuit approach is more compact, is easier to hardwire into commercial CAD tools, and gives a deeper insight into device physical behavior, since its equivalent-circuit elements are directly related to physical mechanisms inside the device.

Nevertheless, equivalent-circuit approaches may suffer from physical inconsistencies [149,150] that may arise from either an improperly selected topology on fitting functions. Moreover, frequency dispersion, temperature, and trapping effects are not easily incorporated into a nonlinear equivalent-circuit device model [151,152]. Pulsed (DC and RF) measurements are utilized to evidence the abovementioned effects, but the resulting model may account for them in a limited range of parameter values (e.g., in a range of biases). Intermodulation prediction is a typical test where most nonlinear general-purpose active-device models may deviate substantially from their corresponding measured behavior. The commonly adopted solution is therefore in the development of a special-purpose model, valid in a limited parameter range that fits well within the desired application. Clearly such special-purpose models are not always available, nor they can be easily extracted. Scaling dimensions of the active device and the properties of the respective model further complicate the picture.

In any case, the adoption of a given device model in the design process is a key point, and the available one (if any) must be investigated in depth in both its field of validity and extraction methods. As previously noted, the outcomes of a design by a nonlinear CAD tool are strongly linked to the accuracy of the device model adopted, and

the adequacy of the latter to the specific design to be performed has to be carefully evaluated beforehand. For example, suppose that a large-signal model for a given device is available, extracted from DC and multibias small-signal S -parameter measured data. If such a model has to be used for optimization of the device output power performance (even in class A operation) and therefore for optimum load impedance determination, the designer cannot expect a high degree of accuracy versus measured power data; DC output curves do not represent actual large-signal RF operating conditions, due to temperature and trapping effects. Only an estimate can therefore be obtained, even with a powerful CAD tool. Similarly, a model optimized for the active-device (i.e., class A) operating region does not represent the same device biased in class C, and the model adopted for tradeoff purposes between class A and B performances should average between the two situations.

Nevertheless, with the precautions stated above, nonlinear CAD tools and active-device models are frequently and effectively utilized for the design of PA stages. After the operating mode of the PA stage is appropriately selected (i.e., a harmonic tuning strategy or a switching mode operating class) on the basis of a preliminary evaluation of attainable performances as compared to the desired specification, together with a preliminary device bias, commonly adopted nonlinear CAD strategies are essentially based on a series of repeated analyses. In particular, a possibility resides in the implementation of a “simulated load pull,” in which the measurement bench is replaced by the nonlinear simulator and its analysis capabilities and the active device is replaced by its model. With reference to Fig. 47, a simulated load pull may be performed in subsequent steps. First, a series of power sweep analyses are performed, each obtained by varying the fundamental frequency load (Z_{L1} in Fig. 47) and adjusting the input termination (Z_{S1}) in order to conjugately match the subcircuit input at fundamental frequency. In such power sweeps, harmonic terminations are kept fixed at a reference value (typically short-circuit termination, so as to simulate a TL scheme or 50Ω). The data gathered are then organized in order to obtain, for each load terminating value, the relevant performances at a given compression level (e.g., -1 dB gain compression or maximum efficiency). The resulting data are organized and plotted as shown in Fig. 35. If the tradeoff attainable with the generated charts fulfills the imposed design goals, the next step is in the actual synthesis of the resulting fundamental and harmonic terminations, that is, in a linear synthesis problem, which can be solved in classical fashion. Otherwise, keeping the fundamental frequency terminations at their optimum values, harmonic terminations may be varied and contour plots of power performances as functions of harmonic terminations are drawn, as in Fig. 48, where constant-power-added-efficiency loci are plotted as a function of the output reflection coefficient at second harmonic.

Applying the information presented above, a new design choice is performed regarding second-harmonic termination. The procedure is then repeated. Clearly the limit is in the number of harmonic terminations that can

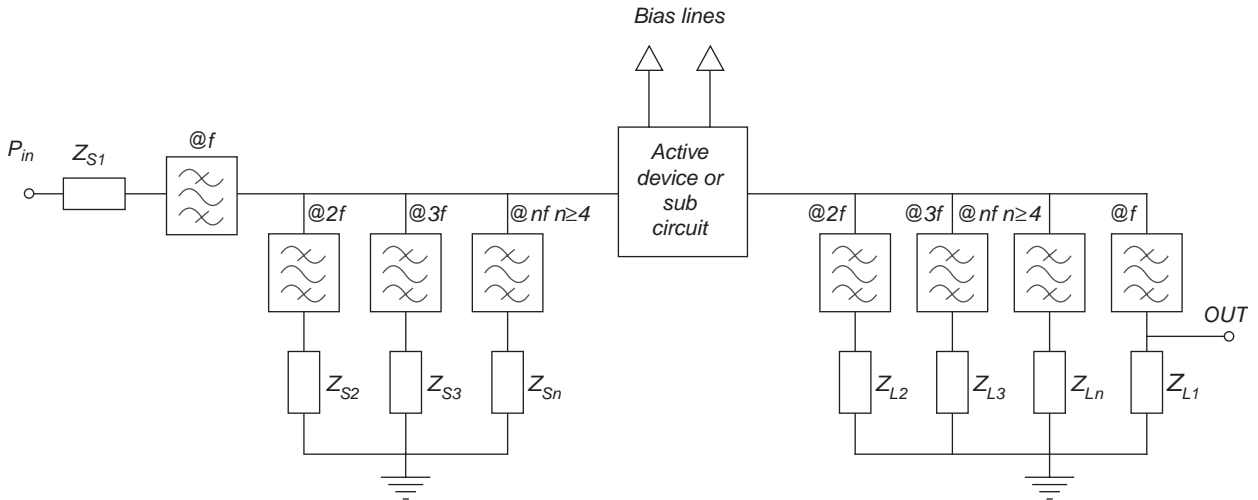


Figure 47. Simulated load-pull scheme.

be effectively controlled and implemented, without sacrificing circuit complexity, size, and clarity. The simulated load pull can be applied as well to the determination of optimum bias levels; the technique is extremely versatile and much faster than the corresponding real load pull. In fact, if a series of operating frequencies have to be investigated, an experimental load-pull characterization may be impractical and time-consuming.

An alternative technique may be implemented, however. Since any iterative analysis technique for a nonlinear microwave circuit (such as the harmonic-balance one) is

based on the actual linearization at each analysis step of the nonlinear part of the circuit, the latter can be used, during the analysis, for external linear circuit optimization [154–156]. In other words, simultaneously and consistently with the nonlinear analysis, a circuit optimization may be carried out, consisting in the fulfillment of optimum design conditions. The latter, for a microwave PA stage, may consist in the imposition of a purely resistive termination at the intrinsic current source terminals of the active-device model (thereby maximizing the stage efficiency) or in the attainment of maximum large-signal

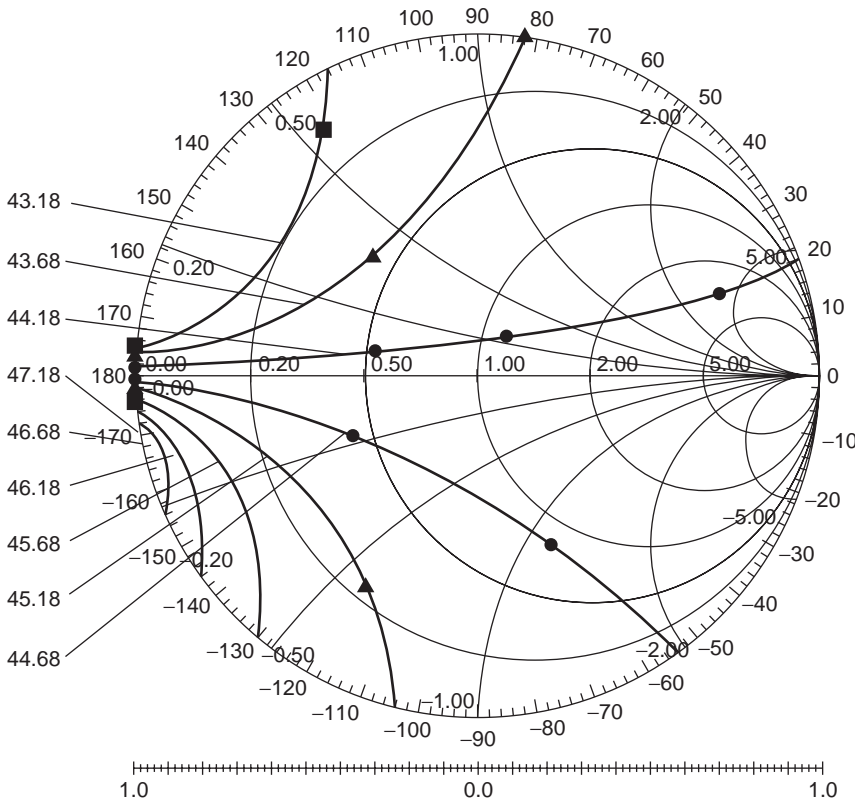


Figure 48. Power-added efficiency on the second-harmonic load plane (from Rohde and Newkirk [153]).

power transfer (i.e., conjugate matching) at the device input terminals.

However, both direct synthesis and simulated load-pull techniques are inevitably based on a proper device model and the difficulties reside in its extraction apply for both validity range and accuracy of the latter.

BIBLIOGRAPHY

1. H. Sobol and K. Tomiyasu, Milestones of microwaves, *IEEE Trans. Microwave Theory Tech.* **50**(3):594–611 (March 2002).
2. M. Skolnik, Role of radar in microwaves, *IEEE Trans. Microwave Theory Tech.* **50**(3):625–632 (March 2002).
3. W. Keydel, Perspectives and visions for future SAR systems, *IEE Proc. Radar Sonar Nav.* **150**(3):97–103 (June 2003).
4. B. A. Kopp, M. Borkowski, and G. Jerinic, Transmit/receive modules, *IEEE Trans. Microwave Theory Tech.* **50**(3):827–834 (March 2002).
5. J. M. Osepchuk, Microwave power applications, *IEEE Trans. Microwave Theory Tech.* **50**(3):975–985 (March 2002).
6. J. M. Osepchuk, A history of microwave heating applications, *IEEE Trans. Microwave Theory Tech.* **32**(9):1200–1224 (Sept. 1984).
7. A. Rosen, M. A. Stuchly, and A. Vander Vorst, Applications of RF/microwaves in medicine, *IEEE Trans. Microwave Theory Tech.* **50**(3):963–974 (March 2002).
8. G. C. Giakos, M. Pastorino, F. Russo, S. Chowdhury, N. Shah, and W. Davros, Noninvasive imaging for the new century, *IEEE Instrum. Meas. Mag.* **2**(2):32–35, 49 (June 1999).
9. E. C. Fear, X. Li, S. C. Hagness, and M. A. Stuchly, Confocal microwave imaging for breast cancer detection: Localization of tumors in three dimensions, *IEEE Trans. Biomed. Eng.* **49**(8):812–822 (Aug. 2002).
10. I. T. Rekanos and A. Raisanen, Microwave imaging in the time domain of buried multiple scatterers by using an FDTD-based optimization technique, *IEEE Trans. Magn.* **39**(3):1381–1384 (May 2003).
11. L. Q. Huo, W. Zhong, T. T. Qing Zhang, J. A. Bryan, G. A. Ybarra, L. W. Nolte, and W. T. Joines, Active microwave imaging. I. 2-D forward and inverse scattering methods, *IEEE Trans. Microwave Theory Tech.* **50**(1):123–133 (Jan. 2002).
12. E. C. Fear, P. M. Meaney, and M. A. Stuchly, Microwaves for breast cancer detection? *IEEE Potentials* **22**(1):12–18 (Feb.–March 2003).
13. R. S. Symons, Modern microwave power sources, *IEEE Aerospace Electron. Syst. Mag.* **17**(1):19–26 (Jan. 2002).
14. F. Murgadella, F. Payen, and P. Coulon, SSPAs & TWTAs: An evolutive situation for electronic warfare applications, *23rd Annual Gallium Arsenide Integrated Circuit (GaAs IC) Symp. Tech. Digest*, Oct. 21–24, 2001, pp. 149–152.
15. F. Murgadella, P. Coulon, and C. Moreau, Comparisons of technologies and MMICS results for military needs, *23rd Annual Gallium Arsenide Integrated circuit (GaAs IC) Symp. Tech. Digest*, Oct. 21–24, 2001, pp. 223–227.
16. R. K. Parker, R. H. Abrams, B. G. Danly, and B. Levush, Vacuum electronics, *IEEE Trans. Microwave Theory Tech.* **50**(3):835–845 (March 2002).
17. J. M. Anderson, Irving Langmuir and the origins of electronics, *IEEE Power Engg. Rev.* **22**(3):38–39 (March 2002).
18. J. F. Ramsay, Microwave antenna and waveguide techniques before 1900, *Proc. IRE* **46**:405–414 (Feb. 1958).
19. H. Hertz, *Electric Waves*, Macmillan, New York, 1893, Chap. XI.
20. T. K. Sarkar and D. L. Sengupta, An appreciation of J. C. Bose's pioneering work in millimeter waves, *IEEE Anten. Propag. Mag.* **39**(5):55–62 (Oct. 1997).
21. R. H. Varian and S. F. Varian, A high frequency oscillator and amplifier, *J. Appl. Phys.* **10**:321–327 (May 1939).
22. S. Nakajima, The history of Japanese radar development to 1945, in R. Burns, ed., *Radar Development to 1945*, Peter Peregrinus, Stevenage, UK, 1988, Chap. 18, pp. 243–258.
23. M. Chodorow, E. L. Ginzton, I. R. Nielson, and S. Sonkin, Design and performance of a high-power pulsed klystron, *Proc. IRE* **41**:1584–1602 (Nov. 1953).
24. O. M. Stuetzer, A crystal amplifier with high input impedance, *Proc. IRE* **38**:868 (Aug. 1950).
25. W. Shockley, A unipolar "field-effect" transistor, *Proc. IRE* **40**:365 (Nov. 1952).
26. T. Mimura, S. Hiyamizuk, T. Fujii, and K. Nanbu, A new field effect transistor with selectively doped GaAs/n-AlGaAs heterostructures, *Jpn. J. Appl. Phys.* **19**:L225–L227 (1980).
27. W. P. Dumke, J. M. Woodall, and V. L. Rideout, GaAs–GaAlAs heterojunction transistor for high frequency operation, *Solid State Electron.* **15**:1339–1334 (Dec. 1972).
28. P. M. Asbeck, D. L. Miller, W. C. Petersen, and C. G. Kirkpatrick, GaAs/GaAlAs heterojunction bipolar transistors with cutoff frequencies above 10 GHz, *IEEE Electron. Device Lett.* **EDL-3**:366–368 (Dec. 1982).
29. H. Kroemer, Theory of a wide-gap emitter for transistors, *Proc. IRE* **45**:1535–1537 (Nov. 1957).
30. E. Gebara, N. Rorsman, J. Olsson, H. Zirath, K. Eklund, and J. Laskar, Power characteristics of high-voltage LDMOS transistors, *Proc. 30th European Microwave Conf.*, 2000, Vol. 3, pp. 8–11.
31. S. Nuttinck, E. Gebara, J. Laskar, N. Rorsman, J. Olsson, H. Zirath, K. Eklund, and M. Harris, Comparison between Si-LDMOS and GaN-based microwave power transistors, *Proc. IEEE Lester Eastman Conf. High Performance Devices*, Aug. 2002, pp. 149–154.
32. R. Strong, A. Agarwal, T. Smith, R. Messham, S. Mani, V. Hegde, M. Hanes, H. Nathanson, P. Potyraj, K. Petrosky, T. Knight, and P. Brabant, X-band SiGe power HBT's, *1998 Topical Meeting on Silicon Monolithic Integrated Circuits in RF Systems, Digest of Papers*, Sept. 1998, pp. 57–60.
33. J.-S. Rieh, L.-H. Lu, Z. Ma, X. Liu, P. B. Katehi, P. Bhattacharya, and E. T. Croke, Small- and large-signal operation of X-band CE and CB SiGe/Si power HBT's, *IEEE MTT-S Int. Microwave Symp. Digest*, June 1999, Vol. 3, pp. 1191–1194.
34. <http://www.fesi.fujitsu.com>.
35. R. J. Trew, J.-B. Yan, and P. M. Mock, The potential of diamond and SiC electronic devices for microwave and millimeter-wave power applications, *Proc. IEEE* **79**(5):598–620 (May 1991).
36. C. M. Johnson, N. G. Wright, M. J. Uren, K. P. Hilton, M. Rahimo, D. A. Hinchley, A. P. Knights, D. J. Morrison, A. B. Horsfall, S. Ortolland, and A. G. O'Neill, Recent progress and current issues in SiC semiconductor devices for power applications, *IEE Proc. Circ. Devices Syst.* **148**(2):101–108 (April 2001).
37. C. Lee, P. Saunier, and Y. Jinwei, and M. A. Khan, AlGaIn-GaN HEMTs on SiC with CW power performance of >4 W/mm and 23% PAE at 35 GHz, *IEEE Electron. Device Lett.* **24**(10):616–618 (Oct. 2003).

38. C. Lee, Y. Jinwei, M. A. Khan, and P. Saunier, Ka-band CW power performance by AlGaIn/GaN HEMTs on SiC, *Proc. 2003 Device Research Conf.*, June 23–25, 2003, pp. 17–18.
39. U. K. Mishra, P. Parikh, Y.-F. Wu, AlGaIn/GaN HEMTs—an overview of device operation and applications, *Proc. IEEE* **90**(6):1022–1031 (June 2002).
40. F. H. Raab, P. Asbeck, S. Cripps, P. B. Kenington, Z. B. Popovic, N. Potheary, J. F. Sevic, and N. O. Sokal, Power amplifiers and transmitters for RF and microwave, *IEEE Trans. Microwave Theory Tech.* **50**(3):814–826 (March 2002).
41. F. H. Raab, Average efficiency of power amplifiers, *Proc. RF Technology Expo*, Anaheim, CA, Jan.–Feb. 1986, pp. 474–486.
42. A. Leke and J. S. Kenney, Behavioral modeling of narrow-band microwave power amplifiers with applications in simulating spectral regrowth, *IEEE MTT-S Int. Microwave Symp. Digest*, June 1996, Vol. 3, pp. 1385–1388.
43. H. Ku and J. S. Kenney, Behavioral modeling of nonlinear RF power amplifiers considering memory effects, *IEEE Trans. Microwave Theory Tech.* **51**(12):2495–2504 (Dec. 2003).
44. H. Ku, M. D. Mckinley, and J. S. Kenney, Extraction of accurate behavioral models for power amplifiers with memory effects using two-tone measurements, *IEEE MTT-S Int. Microwave Symp. Digest*, June 2002, Vol. 1, pp. 139–142.
45. A. Zhu, M. Wren, and T. J. Brazil, An efficient Volterra-based behavioral model for wideband RF power amplifiers, *IEEE MTT-S Int. Microwave Symp. Digest*, June 2003, Vol. 2, pp. 787–790.
46. J. C. Pedro and N. B. Carvalho, On the use of multi-tone techniques for assessing RF components' intermodulation properties, *IEEE Trans. Microwave Theory Tech.* **MTT-47**(12):2393–2402 (Dec. 1999).
47. P. Kenington, *High Linearity RF Amplifier Design*, Artech House, Norwood, MA, 2000.
48. J. C. Pedro and N. B. Carvalho, *Intermodulation Distortion in Microwave and Wireless Circuits*, Artech House, Norwood, MA, 2003.
49. T. T. Ha, *Solid-State Microwave Amplifier Design*, Wiley, New York, 1981.
50. I. Bahl and P. Bhartia, *Microwave Solid State Circuit Design*, Wiley, New York, 1988.
51. R. J. Weber, *Introduction to Microwave Circuits*, IEEE Press, Piscataway, NJ, 2001.
52. L. J. Kushner, Output performances of idealised microwave power amplifiers, *Microwave J.* 103–110 (Oct. 1989).
53. L. J. Kushner, Estimating power amplifier large signal gain, *Microwave J.* 87–102 (June 1990).
54. B. Molnar, Basic limitations on waveforms achievable in single-ended switching mode tuned (class-E) power amplifiers, *IEEE J. Solid-State Circ.* **SC-19**(2):144–146 (Feb. 1984).
55. M. K. Kazimierczuk, Generalization of conditions for 100-percent efficiency and nonzero output power in power amplifiers and frequency multipliers, *IEEE Trans. Circ. Syst.* **CAS-33**(8):805–807 (Aug. 1986).
56. V. J. Tyler, A new high efficiency high power amplifier, *Marconi Rev.* **21**(130):96–109 (fall 1958).
57. D. M. Snider, A theoretical analysis and experimental confirmation of the optimally loaded and overdriven RF power amplifiers, *IEEE Trans. Electron. Devices* **ED-14**(6):851–857 (June 1967).
58. F. H. Raab, Introduction to class-F power amplifiers, *RF Design* **19**(5):79–84 (May 1996).
59. A. Inoue, T. Heima, A. Ohta, R. Hattori, and Y. Mitsui, Analysis of class-F and inverse class-F amplifiers, *IEEE MTT-S Symp. Digest*, 2000, pp. 775–778.
60. P. Colantonio, F. Giannini, G. Leuzzi, and E. Limiti, On the class-F power amplifier design, *Int. J. RF Microwave Comput. Aided Eng.* **9**(2):129–149 (March 1999).
61. C. Duvanaud, S. Dietsche, G. Pataut, and J. Obregon, High-efficient class F GaAs FET amplifiers operating with very low bias voltages for use in mobile telephones at 1.75 GHz, *IEEE Microwave Guided Wave Lett.* **3**(8):268–270 (Aug. 1993).
62. P. Colantonio, F. Giannini, E. Limiti, and G. Saggio, Experimental performances of 5 GHz harmonic-manipulated high efficiency microwave power amplifiers, *Electron. Lett.* **36**(9):800–801 (April 2000).
63. N. O. Sokal, Class-E switching-mode high-efficiency tuned RF/microwave power amplifier: Improved design equations, *IEEE MTT-S Symp. Digest*, 2000, pp. 779–782.
64. S. Nishiki and T. Nojima, High efficiency microwave harmonic reaction amplifier, *IEEE MTT-S Symp. Digest*, 1988, pp. 1007–1010.
65. T. Nojima and S. Nishiki, Harmonic reaction amplifier—a novel high-efficiency and high-power microwave amplifier, *IEEE MTT-S Symp. Digest*, 1987, pp. 963–966.
66. B. Kopp and D. D. Heston, High-efficiency 5-Watt power amplifier with harmonic tuning, *IEEE MTT-S Int. Microwave Symp. Digest*, 1988, pp. 839–842.
67. M. A. Khatibzadeh and H. Q. Tserng, Harmonic tuning of power FETs at X-band, *IEEE MTT-S Int. Microwave Symp. Digest*, 1990, pp. 989–992.
68. S. Toyoda, High efficiency amplifiers, *IEEE MTT-S Symp. Digest*, San Diego, CA, May 1994, pp. 253–256.
69. A. Mallet, T. Peyretailade, R. Sommet, D. Floriot, S. Delage, J. M. Nebus, and J. Obregon, A design method for high efficiency class-F HBT amplifiers, *IEEE MTT-S Symp. Digest*, San Francisco, CA, May 1996, pp. 855–858.
70. J. Staudinger, Multiharmonic load termination effects on GaAs power amplifiers, *Microwave J.* 60–77 (April 1996).
71. P. Colantonio, F. Giannini, G. Leuzzi, and E. Limiti, Class G approach for high efficiency PA design, *Int. J. RF Microwave Comput. Aided Eng.* **10**(6):366–378 (Nov. 2000).
72. P. Colantonio, F. Giannini, G. Leuzzi, E. Limiti, Multi harmonic manipulation for highly efficient microwave power amplifiers, *Int. J. RF Microwave Comput. Aided Eng.* **11**(6):366–384 (Nov. 2001).
73. F. H. Raab, Class-F power amplifiers with maximally flat waveforms, *IEEE Trans. Microwave Theory Tech.* **MTT-45**(11):2007–2012 (Nov. 1997).
74. P. Colantonio, F. Giannini, G. Leuzzi, and E. Limiti, Input/output optimum 2nd harmonic terminations in low-voltage high-efficiency power amplifiers, *Proc. 10th MICROCROLL*, Budapest, Hungary, March 1999, pp. 401–406.
75. T. M. Scott, Tuned power amplifiers, *IEEE Trans. Circ. Theory* 385–389 (Sept. 1964).
76. M. Maeda et al., Source second-harmonic control for high efficiency power amplifiers, *IEEE Trans. Microwave Theory Tech.* **MTT-43**(12):2952–2958 (Dec. 1995).
77. P. M. White, Effect of input harmonic terminations on high efficiency class-B and class-F operation of PHEMT devices, *IEEE MTT-S Symp. Digest*, 1998, pp. 1611–1614.
78. K. Jeon, Y. Kwon, and S. Hong, Input harmonics control using nonlinear capacitor in GaAs FET power amplifier, *IEEE-MTT-S Symp. Digest*, 1997, pp. 817–820.

79. S. Watanabe, S. Takatuka, K. Takagi, H. Works, and Y. Oda, Simulation and experimental results of source harmonic tuning on linearity of power GaAs FET under class AB operation, *IEEE MTT-S Symp. Digest*, 1996, pp. 1771–1774.
80. S. R. Mazumder, A. Azizi, F. E. Gardiol, Improvement of a class-C transistor power amplifier by second-harmonic tuning, *IEEE Trans. Microwave Theory Tech.* **MTT-27**(5):430–433 (May 1979).
81. P. Colantonio, F. Giannini, G. Leuzzi, and E. Limiti, High efficiency low-voltage power amplifier design by second harmonic manipulation, *Int. J. RF Microwave Comput. Aided Eng.* **10**(1):19–32 (Jan. 2000).
82. S. L. Bussgang, L. Ehrman, and J. W. Graham, Analysis of non-linear systems with multiple inputs, *Proc. IEEE* **62**:1088–1119 (Aug. 1974).
83. P. Colantonio, F. Giannini, G. Leuzzi, and E. Limiti, High-efficiency low-IM microwave PA design, *IEEE MTT-S Symp. Digest*, Phoenix, AZ, May 2001, Vol. 1, pp. 511–514.
84. M. R. Moazzam and C. S. Aitchison, A low third order intermodulation amplifier with harmonic feedback circuitry, *IEEE MTT-S Int. Microwave Symp. Digest*, 1996, pp. 827–830.
85. C. G. Rey, Predistorter linearizes CDMA power amplifiers, *Microwave RF J.* 114–123 (Oct. 1998).
86. E. Ballestreros, Analysis and design of microwave linearised amplifiers using active feedback, *IEEE Trans. Microwave Theory Tech.* **MTT-36**(3) (March 1988).
87. N. Potechary, *Feedforward Linear Amplifiers*, Artech House, 1999.
88. L. R. Kahn, Single sideband transmission by envelope elimination and restoration, *Proc. IRE* **40**:803–806 (July 1952).
89. F. H. Raab and D. J. Rupp, High efficiency SSB transmitter based upon envelope elimination and restoration, *Proc. 6th Int. Conf. HF Radio Systems and Techniques*, York, UK, July 1994, pp. 21–25.
90. H. Chireix, High power outphasing modulation, *Proc. IRE* **23**(11):1370–1392 (Nov. 1935).
91. P. H. Raab, Efficiency of outphasing power amplifier systems, *IEEE Trans. Commun.* **33**:1094–1099 (Oct. 1983).
92. H. L. Krauss, C. W. Bostian, and F. H. Raab, *Solid State Radio Engineering*, Wiley, New York, 1980.
93. P. J. Baxandall, Transistor sinewave oscillators, *IEE Proc. B* **106**(Suppl. 16):748–758 (May 1959).
94. S. C. Cripps, *RF Power Amplifiers for Wireless Communications*, Artech House, Norwood, MA, 1999.
95. W. J. Chudobiak and D. F. Page, Frequency and power limitations of class D transistor amplifiers, *IEEE J. Solid-State Circ.* **4**:25–37 (Feb. 1969).
96. N. O. Sokal and A. D. Sokal, Class E—a new class of high-efficiency tuned single-ended switching power amplifiers, *IEEE J. Solid State Circ.* **SC-10**(3):168–176 (June 1975).
97. N. O. Sokal, A. D. Sokal, High Efficiency tuned Switching Power Amplifier, U.S. Patent 3,919,656 (Nov. 11, 1975) (expired).
98. F. H. Raab, Idealised operation of the class E tuned power amplifier, *IEEE Trans. Circ. Syst.* **CAS-24**(12):725–735 (Dec. 1977).
99. T. Mader and Z. Popovic, The transmission-line high efficiency class-E amplifiers, *IEEE Trans. Microwave Theory Tech.* **MTT-9**(5):290–292 (Sept. 1995).
100. T. Sowlati, C. A. T. Salama, J. Sitch, G. Rabjohn, and D. Smith, Low voltage, high efficiency GaAs class E power amplifiers for wireless transmitters, *IEEE J. Solid State Circ.* **30**(10):1074–1079 (Oct. 1995).
101. T. Mader, E. Bryerton, M. Markovic, M. Forman, and Z. Popovic, Switched-mode high-efficiency microwave power amplifiers in a free-space power-combiner array, *IEEE Trans. Microwave Theory Tech.* **MTT-46**(10):1391–1398 (Oct. 1998).
102. N. O. Sokal, *Class-E RF power amplifiers*, QEX (published by American Radio Relay League, 225 Main St., Newington, CT 06111-1494, USA (204):9–20 (Jan./Feb. 2001).
103. S. C. Cripps, A theory for the prediction of GaAs FET Load-Pull power contours, *IEEE MTT-S Symp. Digest*, Boston, MA, May 1983, pp. 221–223.
104. S. C. Cripps, Old-fashioned remedies for GaAs FET power amplifier designers, *IEEE MTT-S Newsl.* 13–17 (Summer 1991).
105. H. Kondoh, FET power performance prediction using a linearized device model, *IEEE MTT-S Symp. Digest*, 1989, pp. 569–572.
106. J. M. Cusak et al., Automatic load-pull contour mapping for microwave power transistors, *IEEE Trans. Microwave Theory Tech.* 1146–1152 (Dec. 1974).
107. F. Larose, F. Ghannouchi, and R. Bosisio, A new multi-harmonic load-pull method for non-linear device characterization and modeling, *IEEE Int. Microwave Symp. Digest*, June 1990, pp. 443–446.
108. R. Hajji, F. Beaugard, F. Ghannouchi, and R. G. Bosisio, Multitone power and intermodulation load-pull characterization of microwave transistors suitable for linear SSPA design, *IEEE Trans. Microwave Theory Tech.* **MTT-45**:1093–1099 (1997).
109. P. Berini, M. Desgagn, F. Ghannouchi, and R. G. Bosisio, An experimental study of the effects of harmonic loading on microwave MESFET oscillators and amplifiers, *IEEE Trans. Microwave Theory Tech.* **MTT-42**:943–950 (1994).
110. F. Blache, J. Nebus, P. Bouysse, and J. Villotte, A novel computerized multi-harmonic load-pull system for the optimization of high-efficiency operating classes in power transistors, *IEEE Int. Microwave Symp. Digest*, Orlando, FL, June 1995, pp. 1037–1040.
111. G. Berghoff, E. Bergeault, B. Huyart, and L. Jallet, Automated characterization of HF power transistor by source-pull and multiharmonic load-pull measurements based on six-port techniques, *IEEE Trans. Microwave Theory Tech.* **MTT-46**:2068–2073 (Dec. 1998).
112. D. Rytting, ARFTG Short-Course: Network Analyzer Calibration Theory, 1997.
113. R. Marks, Formulation of the basic vector network analyzer error model including switch terms, *Proc. 50th ARFTG Conf.*, Dec. 1997, pp. 115–126.
114. A. Ferrero and U. Pisani, An improved calibration technique for on-wafer large-signal transistor characterization, *IEEE Trans. Instrum. Meas.* **IM-47**:360–364 (April 1993).
115. G. Engen and C. Hoer, Thru-reflect-line: An improved technique for calibrating the dual six-port automatic network analyzer, *IEEE Trans. Microwave Theory Tech.* 987–993 (Dec. 1979).
116. R. Marks, A multi-line method of network analyzer calibration, *IEEE Trans. Microwave Theory Tech.* 1205–1215 (July 1990).
117. *MultiCal™ User's Manual*, v. 1.0, National Institute of Standards and Technology, 1997.

118. J. Benedikt, R. Gaddi, P.J. Tasker, and M. Goss, High-power time-domain measurement system with active harmonic load-pull for high-efficiency base-station amplifier design, *IEEE Trans. Microwave Theory Tech.* **MTT-48**(12):2617–2624 (Dec. 2000).
119. G. Kompa and F. van Raay, Error-corrected large-signal waveform measurement system combining network analyzer and sampling oscilloscope capabilities, *IEEE Trans. Microwave Theory Tech.* **MTT-38**(4):358–365 (April 1990).
120. *Automated Tuner System User's Manual*, v. 1.9, Maury Microwave Corp., 1998.
121. *Computer Controlled Tuner System User's Manual*, v.6.0, Focus Microwave Corp., 1998.
122. *LP2 Automated Load Pull System User's Manual*, ATN Microwave Corp., 1997.
123. J. Sevic, A sub 1Ω load-pull quarter-wave pre-matching network based on a two-tier TRL calibration, *Proc. 52nd ARFTG Conf.*, Dec. 1998, pp. 73–81.
124. A. Ferrero, V. Teppati, A. Carullo, Accuracy evaluation of on-wafer load-pull measurements, *IEEE Trans. Microwave Theory Tech.* **MTT-49**(1):39–43 (Jan. 2001).
125. J. Sevic, R. Baeten, G. Simpson, and M. Steer, Automated large-signal load-pull characterization of adjacent-channel power ratio for digital wireless communication system, *Proc. 45th ARFTG Conf.* Nov. 1995, pp. 64–70.
126. J. Sevic, K. Burger, and M. Steer, A novel envelope-termination load-pull method for the ACPR optimization of RF/microwave power amplifiers, *IEEE Int. Microwave Symp. Digest*, June 1998, pp. 723–726.
127. A. Ferrero and V. Teppati, A complete measurement test-set for non-linear device characterization, *58th ARFTG Conf. Digest*, San Diego, CA, Nov. 2001.
128. P. Colantonio, F. Giannini, E. Limiti, and V. Teppati, An approach to harmonic load- and source-pull measurements for high-efficiency PA design, *IEEE Trans. Microwave Theory Tech.* **52**(1):191–198 (Jan. 2004).
129. *Advanced Design System, ADS Users' Manual*, Agilent EEsof EDA, Palo Alto, CA.
130. *Microwave Office Users' Manual*, Applied Wave Research Inc., El Segundo, CA.
131. *Ansoft Designer Users' Manual*, Ansoft Corp., Pittsburgh, PA.
132. *APLAC 7.91 Users' Manual*, APLAC Solutions Corp., Espoo, Finland.
133. *LINMIC 6.2 Users' Manual*, AC Microwave GmbH, Aachen, Germany.
134. *MIMICAD Users' Manual*, Optotek Ltd., Ottawa, Ontario, Canada.
135. *WaveMaker*, Barnard Microsystems Ltd., London, United Kingdom.
136. L. W. Nagel, *SPICE, 2, a Computer Program to Simulate Semiconductor Circuits*, Ph.D. thesis, Univ. California, Berkeley, 1975.
137. M. B. Steer, C.-R. Chang, and G. W. Rhyne, Computer-aided analysis of non-linear microwave circuits using frequency-domain non-linear analysis techniques: The state of the art, *Int. J. Microwave Millimeter-Wave Comput. Aided Eng.* **1**(2):181–200 (Feb. 1991).
138. V. Rizzoli, A. Lippardini, and E. Marazzi, A general-purpose program for nonlinear microwave circuit design, *IEEE Trans. Microwave Theory Tech.* **33**(9):762–770 (Sept. 1983).
139. E. Ngoya and R. Larcheveque, Envelop transient analysis: a new method for the transient and steady state analysis of microwave communication circuits and systems, *IEEE MTT-S Int. Microwave Symp. Digest*, June 1996, pp. 1365–1368.
140. V. Rizzoli and A. Neri, State of the art and present trends in nonlinear microwave CAD techniques, *IEEE Trans. Microwave Theory Tech.* **MTT-36**:343–365 (1988).
141. V. Rizzoli et al., State-of-the-art harmonic-balance simulation of forced non-linear microwave circuits by the piecewise technique, *IEEE Trans. Microwave Theory Tech.* **MTT-40**(1):12–28 (Jan. 1992).
142. V. Rizzoli, A. Neri, and F. Mastri, A modulation-oriented piecewise harmonic balance technique suitable for transient analysis and digitally modulated signals, *Proc. 26th European Microwave Conf.* Prague, Sept. 1996, pp. 546–550.
143. D. Sharrit, New circuit simulation analysis methods for communication systems, *IEEE MTT-S Workshop WMFA: Nonlinear CAD, Digest*, San Francisco, June 1996, pp. 29–41.
144. F. Filicori and G. Vannini, Mathematical approach to large-signal modelling of electron devices, *Electron. Lett.* **27**(4):357–359 (Feb. 14, 1991).
145. F. Filicori, G. Vannini, V.A. Monaco, A nonlinear integral model of electron devices for HB circuit analysis, *IEEE Trans. Microwave Theory Tech.* **40**(7):1456–1465 (July 1992).
146. D. E. Root, S. Fan, and J. Meyer, Technology independent non quasi-static FET models by direct construction from automatically characterized device data, *Proc. 21th European Microwave Conf.* Stuttgart, Germany, Sept. 1991, pp. 927–932.
147. I. Angelov, H. Zirath, and N. Rosman, A new empirical nonlinear model for HEMT and MESFET devices, *IEEE Trans. Microwave Theory Tech.* **40**(12):2258–2266 (Dec. 1992).
148. T. Kacprzak and A. Materka, Compact DC model of GaAs FETs for large-signal computer calculation, *IEEE J. Solid-State Circ.* **18**(2):211–213 (April 1983).
149. V. Rizzoli, A. Costanzo, C. Cecchetti, and A. Chiarini, A nonlinear model of the power MESFET including temperature and breakdown effects, *IEEE MTT-S Int. Microwave Symp. Digest*, June 7–12, 1998, Vol. 3, pp. 1603–1606.
150. V. Rizzoli and A. Costanzo, A fully conservative non-linear empirical model of the microwave FET, *Proc. 24th European Microwave Conf.* Cannes, Sept. 1994, pp. 1307–1312.
151. Non-linear measurement and modelling, Paper presented at IEEE MTT-S '97 Int. Symp. Workshop, Denver, CO, June 1997.
152. A. K. Jastrzebski, Characterisation and modelling of temperature and dispersion effects in power MESFETs, *Proc. 24th European Microwave Conf.*, Cannes, Sept. 1994, pp. 1319–1324.
153. U. L. Rohde and D. P. Newkirk, *RF/Microwave Circuit Design for Wireless Applications*, Wiley, New York, 2000, App. B.
154. F. Giannini, G. Leuzzi, E. Limiti, and L. Scucchia, Harmonic-loaded microwave power amplifiers: Non-linear design procedure, *Int. J. Microwave Millimeter-Wave Comput. Aided Eng.* **5**(1):20–25 (Jan. 1995).
155. P. Colantonio, F. Giannini, G. Leuzzi, and E. Limiti, Direct-synthesis design technique for non-linear microwave circuits, *IEEE Trans. Microwave Theory Tech.* **MTT-43**(12):2851–2855 (Dec. 1995).

156. P. Colantonio, F. Giannini, G. Leuzzi, and E. Limiti, A fast tool for high-efficiency microwave power amplifier design, *Microwave Engineering Europe*, May 1997, pp. 33–41.

MICROWAVE POWER TRANSMISSION

BERNDIE H. STRASSNER
 Sandia National Laboratories
 Albuquerque, NM
 KAI CHANG
 Texas A & M University
 College Station, TX

1. INTRODUCTION

Microwave power transmission (MPT) is the wireless transfer of large amounts of power at microwave frequencies from one location to another. MPT is often referred to in the literature as wireless power transmission (WPT) at microwave frequencies. MPT research has been driven primarily by the desire to remotely power unmanned aerial vehicles (UAVs) and by the concept of space solar power first conceived by Dr. Peter Glaser of the Arthur D. Little Company in 1968 [1]. Figure 1 shows a block diagram for the specific application of MPT pertaining to space solar power (SSP). SSP is an MPT system with the addition of solar cells and magnetrons for microwave power generation.

The SSP idea calls for a constellation of solar power satellites (SPSs) to be placed in geosynchronous orbit (“geo”; 36,800 km above Earth) in order to capture the sun’s energy using arrays of solar cells. The satellites each measuring several miles across, would be located in geo to keep them in view of the sun 99% of the time, marking a double improvement over terrestrial solar cells. In addition, the closer the satellites are placed to the sun, the larger their effective collection area since light intensity decreases by the inverse-square of distance. The solar cell

panels output large DC voltages to awaiting cavity magnetrons positioned on various subarrays within each of the SPS’s phased-array apertures. These magnetrons convert the high-voltage DC outputs of the solar panel arrays to microwave power. The microwave energy is then beamed to Earth to “farms” of rectifying antenna (rectenna) arrays that convert the incoming microwave energy back to DC power [3].

Since its inception, SSP has gained considerable attention since it has the potential of providing clean, renewable, and continuous power for generations to come. With the widespread belief that fossil fuel supplies cannot support the projected energy demand based on population growth and increased development, SSP is seen as a possible remedy. In addition, SSP is seen as circumventing pollution problems associated with currently used energy enablers such as nuclear energy and coal. SSP is also seen as meeting future energy demands where other limited clean resources such as hydroelectric power and wind fall short. As an added incentive, SSP can be delivered to the most remote locations without connective infrastructure such as pipes or powerlines. By making SSP an available technology, developed nations will no longer be at the mercy of OPEC, which includes many unstable and/or unfriendly nations [4].

Both the fruition of SSP and the present-day desire to remotely power unmanned aerial vehicles (UAVs) serve as the main driving forces behind current advancements being made in MPT. The use of UAVs for communication and surveillance is seen as an essential capability, especially for the U.S. military. MPT has been shown experimentally as a way for people on Earth to remotely power unmanned high-altitude platforms such as UAVs. Additional uses for MPT include powering space probes from future space stations into deep space and powering robots to enter dangerous environments such as nuclear contaminated areas.

2. MPT SYSTEM ARCHITECTURE

2.1. Traditional Transmitting Aperture

In order to achieve maximum transfer of the microwave energy from the source to the receiver, the transmitting antenna must be designed such that its sidelobes are

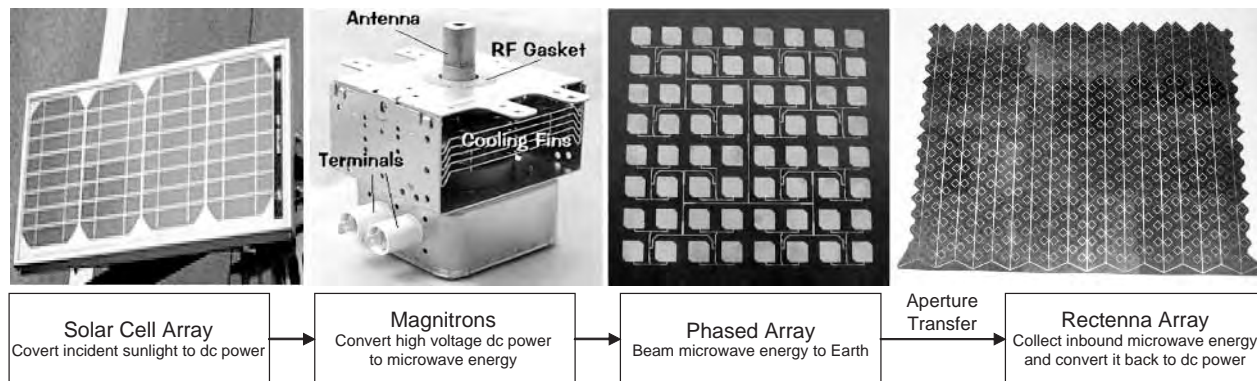


Figure 1. Block diagram of an SSP MPT system, including a BP solar cell array, magnetron, a circularly polarized (CP) phased array [2], and CP rectenna array [2].

reduced to the lowest possible levels and that its proper beamwidth keeps spillover losses to a minimum. In the past, high-gain reflectors and horns antennas have been used to transmit large amounts of power; however, modern systems call for electronically steered phased arrays for greater flexibility in keeping the microwave beam on target. Figure 2 illustrates the geometry of a typical array.

The $m \times n$ array of Fig. 1 contains $m = 2M$ columns and $n = 2N$ rows. One way to achieve low sidelobes is to apply a tapered weighting to the array's aperture. Such tapered weightings include Taylor and Hamming distributions. For its simplicity, Hamming weighting is analyzed in the following. Each u, v element in the array receives power based on the amplitude weighting given by

$$A_{u,v} = \left[\frac{27}{50} + \frac{23}{50} \cos \left(\frac{\left(\frac{2u - (2M + 1)}{2} \right) - \frac{1}{2}}{M + 1} \pi \right) \right] \times \left[\frac{27}{50} + \frac{23}{50} \cos \left(\frac{\left(\frac{2v - (2N + 1)}{2} \right) - \frac{1}{2}}{N + 1} \pi \right) \right] \quad (1)$$

$u = 1, 2, \dots, m$

$v = 1, 2, \dots, n$

where the subscript u pertains to the u th element in \hat{x} and v identifies the v th element in \hat{y} . This applied aperture taper will lower the sidelobes to more than 30 dB below the mainbeam peak so that power is not radiated in undesirable directions. This becomes a serious concern in SSP because of the large amount of power being transmitted. If no taper is applied to the transmitting aperture, that is, if the array has uniform weighting, the worst-case sidelobes will be around -12.5 dB, or 12.5 dB below the peak gain of the radiation pattern.

The array factor (AF) of the transmitting antenna array is defined as

$$\text{AF} = \sum_{u=1}^m \sum_{v=1}^n A_{u,v} \exp j \left(\left(\frac{2u - (2M - 1)}{2} \right) - 1 \right) \times (k\Delta x \sin \theta_t \cos \phi_t + \beta_x) \times \exp j \left(\left(\frac{2v - (2N - 1)}{2} \right) - 1 \right) (k\Delta y \sin \theta_t \sin \phi_t + \beta_y) \quad (2)$$

where $k = 2\pi/\lambda_0$, and Δx and Δy are the element spacings in the \hat{x} and \hat{y} directions. The elevation angle θ_t is the angle measured from the \hat{z} axis toward the \hat{x} - \hat{y} plane, and the azimuth angle ϕ_t is measured from the \hat{x} axis toward the \hat{y} axis. β_x and β_y represent the progressive phase shift in the \hat{x} and \hat{y} directions, respectively, for steering the beam. The array elements should be spaced approximately $\lambda_0/2$ from each other in both \hat{x} and \hat{y} directions to avoid harmful gradient lobes. It is important to be aware that aperture tapering for sidelobe reduction lowers antenna radiation efficiency and broadens the mainbeam of the array's radiation pattern. The efficiency reduction is caused simply by the fact that the outer elements of the array are contributing little to the radiated power. Some of the antenna array's elements positioned farthest from the array's center radiate very little, especially in large arrays, but these remotely positioned elements are still vital for sidelobe reduction.

In the proposed SSP system, a magnetron will be located on a subarray with each antenna element in the subarray having equal power. A graphical representation of multiple subarrays within an array aperture is shown in Fig. 3a. Figure 3a shows a particular array aperture composed of 9×9 subarrays, each having 8×8 elements of equal weight. Thus, the transmitting aperture consists of 72×72 antenna elements. The Hamming taper is applied at the subarray level. If the 72×72 antenna elements are spaced $\lambda_0/2$ in both \hat{x} and \hat{y} directions with no progressive

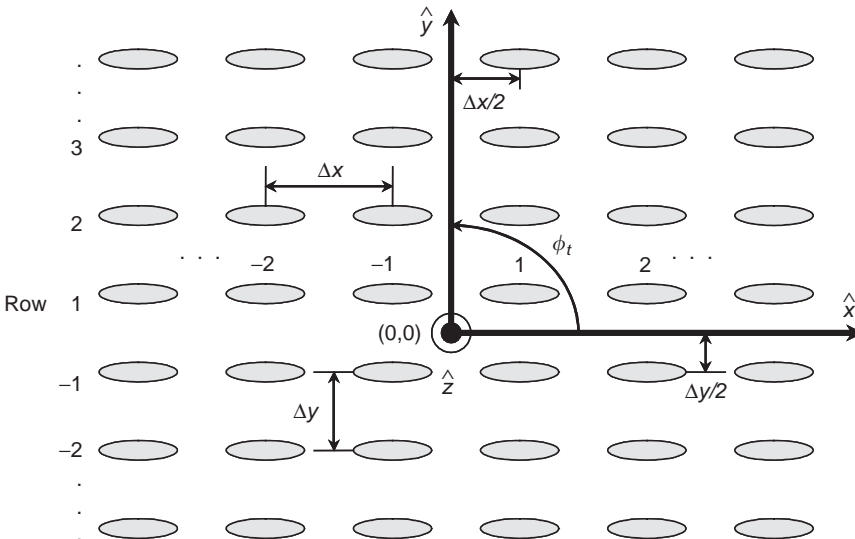


Figure 2. Two-dimensional even array geometry containing m columns and n rows. In this analysis the number of elements is considered even, and the number of rows is even.

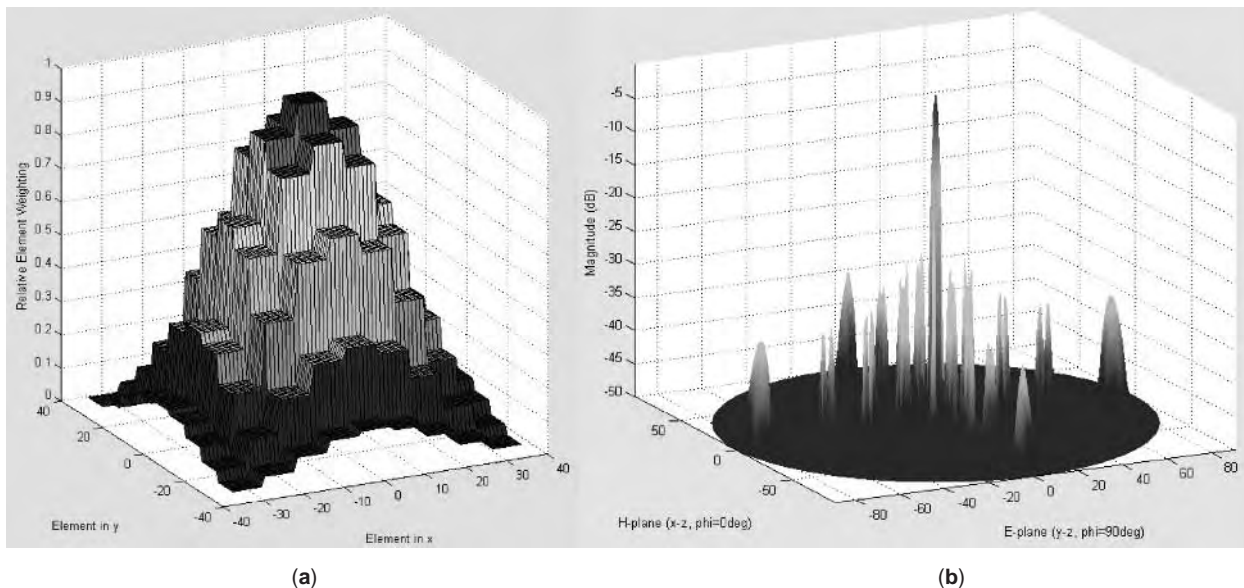


Figure 3. SSP array: (a) amplitude taper for an array containing 9×9 Hamming weighted sub-arrays with each subarray consisting of 8×8 equal-power antenna elements denoting an aperture of 72×72 antennas; (b) corresponding array factor for elements spaced $\lambda_0/2$ in both \hat{x} and \hat{y} directions and no progressive phase shift between the elements.

phase shift, the resultant array factor shown in Fig. 3b is generated. This array factor has worst-case sidelobes of -25 dB at $\pm 13.5^\circ$. The sidelobe suppression can be improved by reducing the subarray size, by increasing the overall size of the array or by applying a monotonic Taylor \bar{n} -bar distribution over the array's aperture. In addition, the size of a subarray is chosen according to the amount of microwave power released by the magnetron into the subarray input port. The overall size of the transmitting aperture is based on the desired transmitting gain and the beamwidth necessary to avoid unnecessary spillover losses.

2.2. Split Gaussian Transmitting Aperture

The temperature of the transmitting aperture becomes an issue in SSP and other MPT applications where the generated power fed to the transmitting array is significantly large. Any array inefficiencies will result in heat being propagated through the transmitting aperture. This heat can destroy sensitive electronics such as phase shifters and could potentially melt the array elements. The array radiation pattern discussed in the previous section is formed using an aperture taper with maximum current weighting delivered to the centermost antenna elements. Consequently, the centermost elements are more susceptible to melting than those moving away from the center.

Two solutions to reducing the temperature at the center of the transmit array are the split Gaussian and the Gaussian with an attenuated center region [5]. These two distributions are illustrated in Fig. 4. These novel weighting schemes distribute power throughout the aperture more uniformly than in the aforementioned traditional transmitting aperture case. As a result, the heat caused by losses in the transmitter is distributed more evenly in the aperture lowering the chance of failure. The split Gaussian has a center weighting equal to the outermost edges. The distribution in Fig. 4b has a center level that can vary.

Both tapers shown in Fig. 4 are radially symmetric for all ϕ_t . If we consider changing the coefficients c_a and c_b of the more versatile Gaussian with the center attenuation region depicted in Fig. 4b, the aperture tapers shown in Fig. 5 result.

These tapers were analyzed by P. Zepeda [5] to a transmit array 250 m in diameter with an operating frequency of 5.8 GHz. The power density of the array's aperture versus center power reduction based on the varying coefficients of Fig. 5 is shown in Fig. 6a. The coefficients also affect the sidelobe performance of the array as illustrated in Fig. 6b. Surprisingly, sidelobe levels below 20 dB are possible with this unconventional aperture distribution. This split Gaussian taper produces sidelobes in the range of the example weighting given in the aforementioned conventional

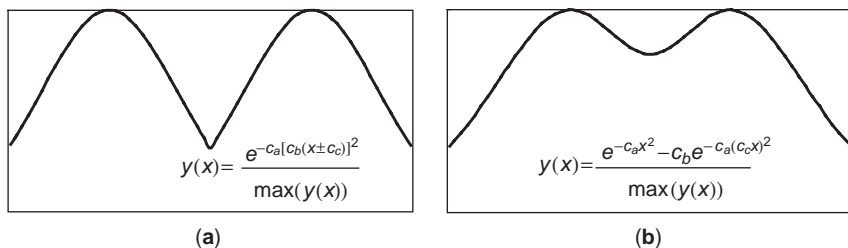


Figure 4. (a) Normalized split Gaussian taper; (b) normalized Gaussian taper with an attenuated center region.

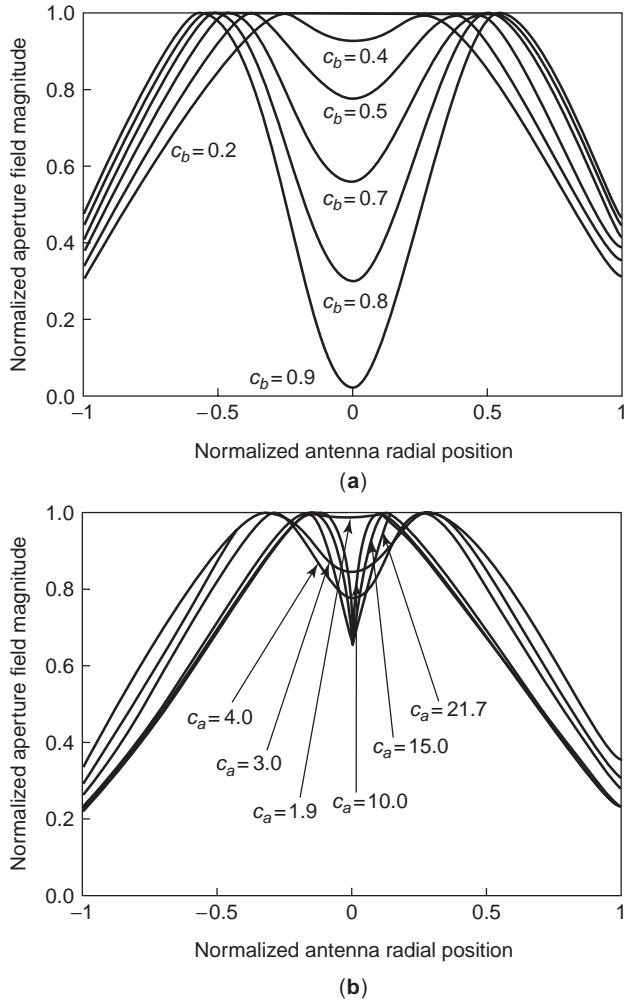


Figure 5. Aperture tapers: (a) Varying C_b for the normalized Gaussian taper with an attenuated center region; (b) varying C_a for the normalized Gaussian taper with an attenuated center region.

“Hamming” case with great heat reduction, which is vital to the reliability of the SPS transmitting array.

2.3. Aperture-to-Aperture Transfer

For MPT systems, the transmitting antenna is normally either a high-gain reflecting antenna, a horn antenna, or a large array consisting of many individual elements. Historically, the receiving unit in MPT systems has been a rectenna array made up of cascaded rectennas. Each of these rectennas is a combination receiving antenna and rectifying circuit consisting of a rectifying semiconductor diode. A typical MPT setup is shown in Fig. 7.

The power in watts received at the receiving antenna based on Friis free-space transmission equation is

$$\begin{aligned}
 P_r = & P_t e_{\text{cdt}} e_{\text{cdr}} (1 - |\Gamma_t|^2) (1 - |\Gamma_r|^2) \left(\frac{\lambda_0}{4\pi R} \right)^2 \\
 & \times D_t(\theta_t, \phi_t) D_r(\theta_r, \phi_r) |\hat{\rho}_t \cdot \hat{\rho}_r^*|^2 \\
 & \times (10^{(L_a(z)/10)}) (10^{(L_{ra}(t)/10)})
 \end{aligned} \quad (3)$$

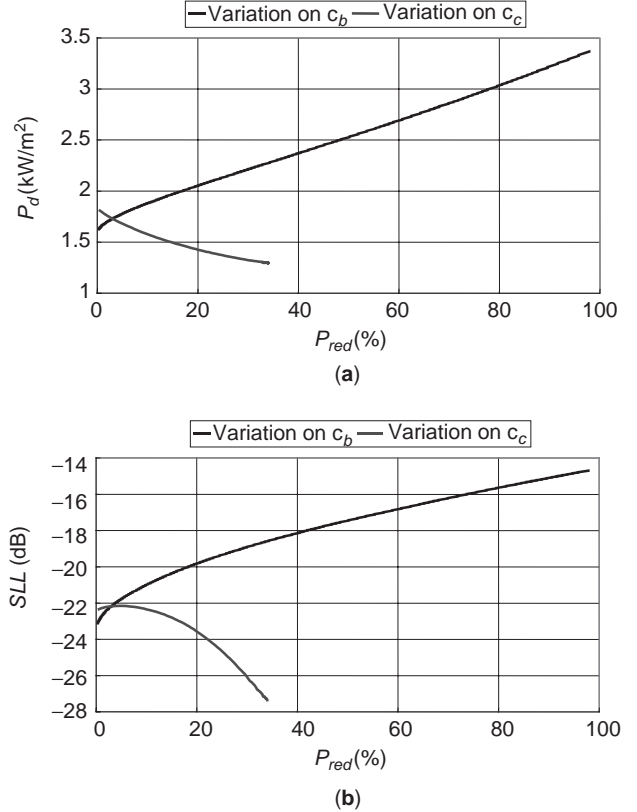


Figure 6. (a) Power density of the transmit array as a function of the center power reduction in percent; (b) sidelobe levels in dB as a function of the center power reduction in percent.

where P_t is the source power transmitted, e_{cdt} and e_{cdr} are the cumulative conductor and dielectric losses of the transmitter and receiver antennas, λ_0 is the free-space wavelength of the energy at the frequency of operation f , and R is the distance separating the midpoints of the transmitting and receiving antenna apertures. The quantity $(\lambda/4\pi R)^2$ is declarative of the path loss L_p between the two antennas.

The quantities $(1 - |\Gamma_t|^2)$ and $(1 - |\Gamma_r|^2)$ represent the mismatch losses at the inputs of the transmitting and receiving antennas. For any fielded MPT system, these mismatch losses should be mitigated to less than 1% reflected power relating to a return loss better than 20 dB. Any reflected power at the receiver port could cause large amounts of reradiated or reflected energy back into free space. This could affect electronic devices in the vicinity of the receiver, especially for an SSP system where large amounts of power could be reradiated. Since large power levels are supplied to the transmitting antenna, any reflected power could damage the transmitter through collective heating. The efficiency of the transmitter falls rapidly as temperature increases.

The variables D_t and D_r are the directive gains (directivities) of the antennas in the oriented direction (θ_t, ϕ_t) and (θ_r, ϕ_r) , respectively. θ_t and θ_r represent the elevation angles and ϕ_t and ϕ_r are the azimuth angles of the transmitting and receiving antennas, respectively. The directive gains of the antenna are related to the antenna

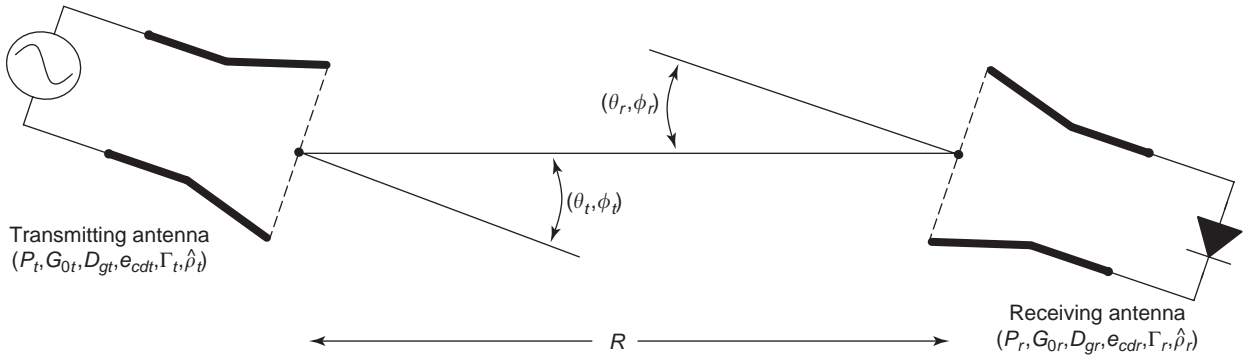


Figure 7. Geometric depiction of a typical MPT setup [6].

measurable gains by

$$G_t(\theta_t, \phi_t) = e_{cdt}(1 - |\Gamma_t|^2)D_t(\theta_t, \phi_t) \quad (4)$$

$$G_r(\theta_r, \phi_r) = e_{cdr}(1 - |\Gamma_r|^2)D_r(\theta_r, \phi_r) \quad (5)$$

If the antennas both have peak directivity broadside of the array's aperture (normal to the aperture plane), maximum power transfer will occur if $\theta_t = \theta_r = 0^\circ$.

The polarization mismatch is calculated by $|\hat{\rho}_t \cdot \hat{\rho}_r^*| = |\cos \psi_p|^2$, where $\hat{\rho}_t$ and $\hat{\rho}_r$ are the polarizations of the transmitting and receiving antennas, respectively, and ψ_p is the angle between their corresponding ϕ -unit polarization vectors. To avoid polarization mismatch using linearly polarized antennas, ϕ_t and ϕ_r must be such that the time-harmonic electric field vectors of each antenna lie in the same ϕ -plane. This polarization mismatch problem can be avoided by making both antennas circularly polarized. Circular polarization also avoids "depolarization" caused by polarization rotation of the electric field vector of the microwave energy as it propagates through the atmosphere. Depolarization is primarily caused by water present in the propagation path and becomes a serious problem during rainfall.

2.4. Atmospheric Absorption

Another important consideration in MPT design is atmospheric attenuation. This attenuation is caused by the presence of oxygen and water in the atmosphere during normal calm conditions and increases as the vertical distance z from the Earth increases. Attenuation is greatest near sea level since oxygen and water levels decrease moving away from the Earth. The atmospheric attenuation is denoted $L_a(z)$ to reflect the height dependence and can be deduced from Fig. 8. Other gases such as carbon dioxide can contribute attenuation, but oxygen and water dominate because of their prevalence.

The choice of operating frequency for an MPT system is governed by atmospheric absorption. The industrial, scientific, and medical (ISM) bands at 2.45 and 5.8 GHz have been chosen for MPT in the past because there attenuation is low relative to higher frequencies and the sizes of the transmitting and receiving antennas are of reasonable size. More importantly, the ISM bands are permissible for

individual use by the Federal Communications Commission (FCC). For this reason, consumer microwave ovens have been designed at 2.45 GHz, and the technology behind their microwave source magnetrons has matured to the point of providing efficiencies over 80% DC-to-RF conversion efficiency at 2.45 GHz. Similar source performance at 5.8 GHz still needs some work, but 5.8 GHz appears to be the frequency of choice for future MPT SSP since it allows smaller antenna apertures. An MPT system designed at 22 GHz would see large amounts of attenuation due to water vapor, especially in humid climates near sea level. Similarly, oxygen would hamper MPT at 60 GHz.

Inclement weather further complicates the problem by adding variable amounts of attenuation. The attenuation loss in dB due to rainfall is [8]

$$L_{ra}(t) = \int_0^{R(t)} a[A(z, t)]^b dz \quad (6)$$

where

$$a = \begin{cases} 4.21 \times 10^{-5} f^{2.42}, & 2.9 \leq f \leq 54 \text{ GHz} \\ 4.09 \times 10^{-2} f^{0.699}, & 54 \leq f \leq 180 \text{ GHz} \end{cases} \quad (7)$$

$$b = \begin{cases} 1.41 f^{-0.0779}, & 8.5 \leq f \leq 25 \text{ GHz} \\ 2.63 f^{-0.272}, & 25 \leq f \leq 164 \text{ GHz} \end{cases} \quad (8)$$

and $R(t)$ is the time-dependent portion of the path between the transmitting and receiving antennas that contains the rain. $A(z, t)$ is the amount of rainfall in mm/h at time t at a distance z km measured from the ground along the path. These atmospheric attenuation problems are well known to satellite communication designers and have the potential of greatly undermining an MPT system. In a dry laboratory environment where R is just within the far field of the transmitter, both $L_a(z)$ and $L_{ra}(t)$ from Eq. (3) can be neglected.

2.5. Rectenna Array

The rectenna array serves as both the absorber of the microwave energy from the transmitter and the rectifier of the microwave energy to DC power [9]. A diagram of a typical rectenna array is shown in Fig. 9.

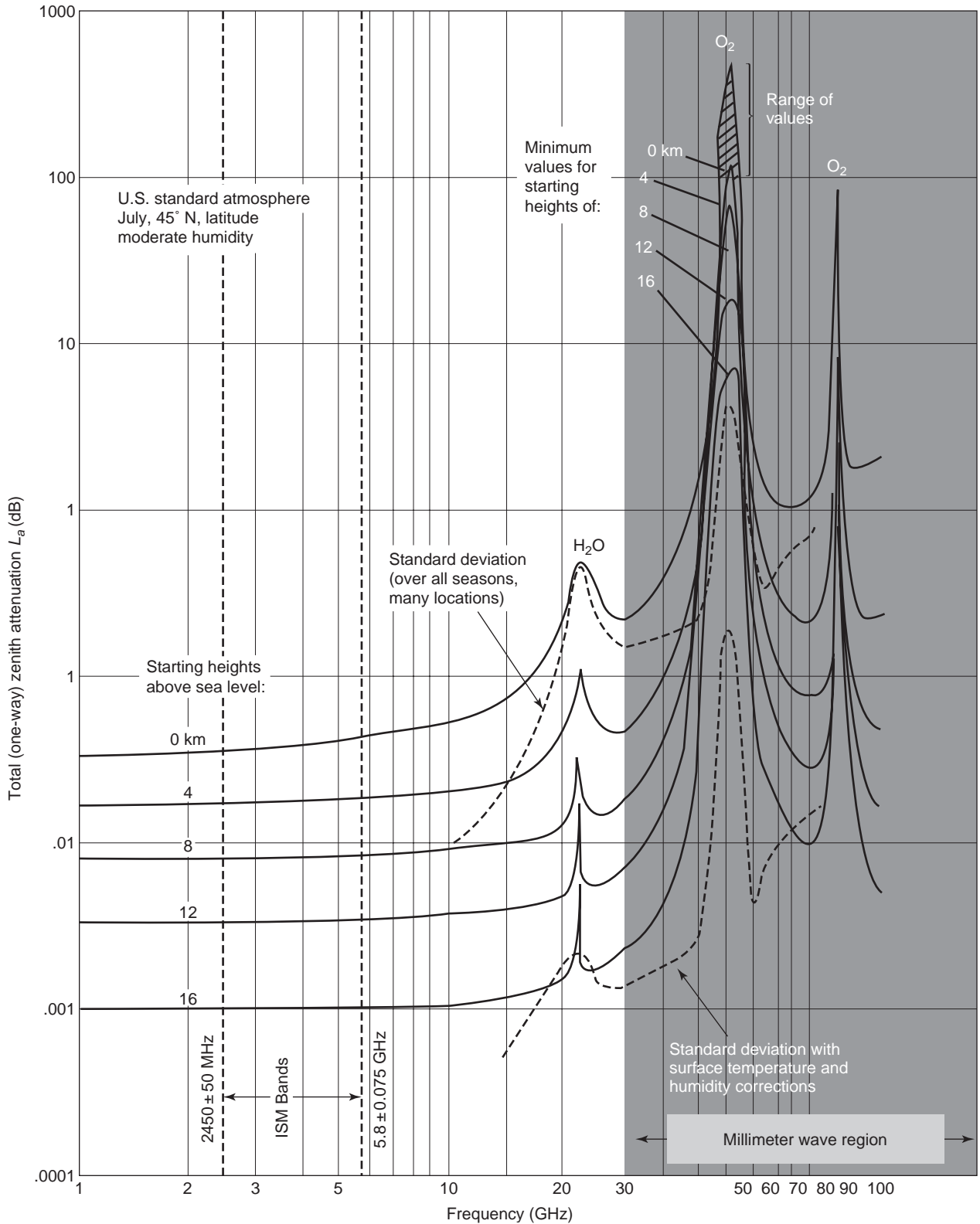
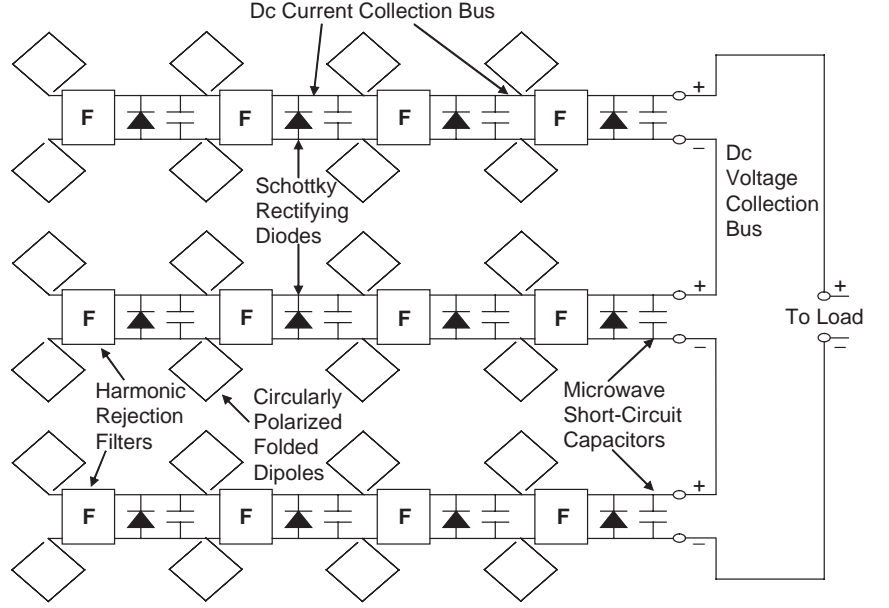


Figure 8. Atmospheric absorption under normal calm conditions [7].

Each rectenna is isolated RF-wise from the next adjacent rectenna by the capacitors that appear as short circuits to the incident microwave energy that strikes them. The antennas in this case are circularly polarized

folded dipoles that send captured microwave energy at frequency f through the harmonic rejection filters (Fs) to the Schottky rectifying semiconductor diodes. The diodes' mixing processes create power at DC (f , $2f$, $3f$, etc.). In

Figure 9. Rectenna array consisting of 12 individual rectennas. Currents add along each row on the current collection bus, and the three row voltage outputs are summed on the voltage collection bus to result in a collective power delivered to the load. The rectenna array is positioned approximately $\lambda_0/4$ above a reflecting metal plane to enhance the gain of each circularly polarized antenna by 3 dB in the desired direction of radiation coming out of the page.



each rectenna, these energies are then led to both the filter F and the capacitor. The DC power is passed through the capacitors along the current collection bus to the peripheral voltage collection bus. Each capacitor appears as a short circuit to the microwave energy returning the microwaves to the diode for further mixing. The capacitors also tune out the imaginary part of the diode impedance to avoid mismatch losses at the diode terminals. Similarly, all microwave circuit components should be matched to each other. Much of the matching of the various components is done experimentally. The filter F rejects harmonic energy at $2f$ and higher back to the diodes for further mixing. F keeps these higher order harmonic frequencies from reradiating, which could interfere with electronic devices in the vicinity of the rectenna array. This additional mixing produces more DC power, increasing the RF-to-DC conversion efficiency η_A of the rectenna array. Some fundamental f energy is lost to the antenna for reradiation, but has been shown to be minimal since the Schottky diodes used currently have very high RF-to-DC conversion efficiencies on the order of 80%.

If the power density on the rectenna array is uniform, the maximum η_A will occur when the rectenna array is loaded with a real resistance equal to [10]

$$R_A = R_L \frac{N_x}{N_y} \quad (9)$$

where N_x is the number of rows in the array and N_y is the number of rows connected by the voltage collection bus. R_L is the optimal load resistance for each individual rectenna, which needs to be calculated or experimentally determined. The diodes are connected in parallel in each row, and the rows are connected in series. The setup for determining the η_A is depicted in Fig. 10.

The RF-to-DC conversion efficiency η_A is defined in terms of the rectenna array's aperture area A_A^{eff} as

$$\eta_A = \frac{P_{\text{DC}}}{P_r} = \frac{4\pi R^2 \left(\frac{V_A^2}{R_A} \right)}{P_t G_t(\theta_t, \phi_t) A_A^{\text{eff}} |\hat{\rho}_t \cdot \hat{\rho}_r^*|^2 (10^{L_a(z)/10}) (10^{L_{ra}(t)/10})} \quad (10)$$

where $A_A^{\text{eff}} = 4ab$. It is important to make sure the rectenna's aperture is positioned such that each of its antennas point toward the transmitter: $\theta_r = 0^\circ$. The rectenna array is composed of numerous elements, each corresponding to a particular transmit gain distribution $G_{xy}(x, y, R)$. The average transmit gain seen across the rectenna array's aperture is [10]

$$G_{\text{avg}}(a, b, R) = \frac{1}{4ab} \int_{-b}^b \int_{-a}^a G_{xy}(x, y, R) dx dy \quad (11)$$

This takes into account the fact that the power striking the rectenna array aperture is normally not a plane wave. In other words, the transmit power density is greatest at (0,0) and decreases toward the rectenna array's edges. The RF-to-DC conversion efficiency can now be expressed as [10]

$$\eta_A = \frac{\pi R^2 \left(\frac{V_A^2}{R_A} \right)}{ab P_t G_{\text{avg}}(a, b, R) |\hat{\rho}_t \cdot \hat{\rho}_r^*|^2 (10^{L_a(z)/10}) (10^{L_{ra}(t)/10})} \quad (12)$$

Some previous designs compensated for the tapered power density present at the rectenna array's surface to increase η_A . One way this compensation is accomplished is by tuning the load resistance or by changing the lengths between

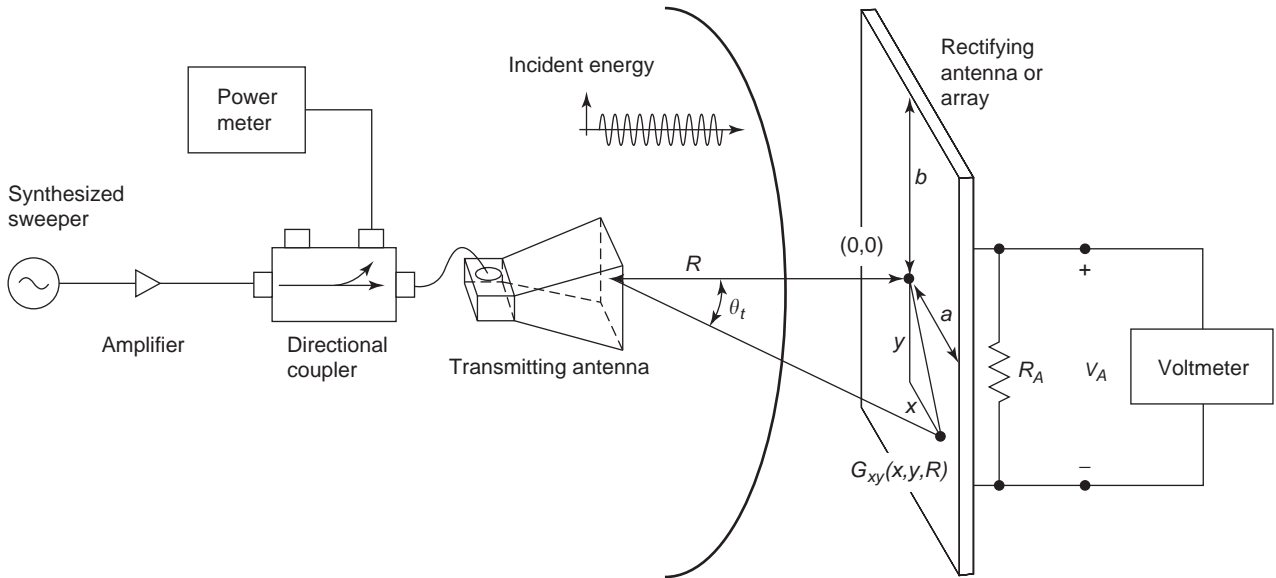


Figure 10. Typical laboratory setup for measuring the RF-to-DC conversion efficiency of a rectenna array. The rectenna array output power is defined by the square of the voltage V_A divided by the load resistance R_A [9].

various components within each rectenna. Typical curves for rectenna performance are shown in Fig. 11.

2.6. Retrodirectivity

The final thing to consider in an MPT design is retrodirectivity. For the SSP example, the rectenna array such as the one illustrated in Fig. 9 is fixed, although some thought has been given to mechanically steering the rectenna panels to vary θ_r . The SPS is proposed to be in geostationary orbit, but if phase errors occur in the phased array or the SPS, which is extremely large in size, undergoes some inertial structural bending even in the slightest amount, the microwave beam can veer off of the rectenna array. To avoid this problem, a feedback loop is established by a pilot beam sent from the rectenna array back to the transmitting phased array in order to determine the proper angle θ_t and set the proper aperture phase taper to keep the beam on the rectenna array [11]. In the case of SSP, a microwave beam rampaging through the countryside could cause some public alarm even if the power density at Earth’s surface is at acceptable safe levels. The pilot beam can also send information about air traffic in the vicinity overhead of the rectenna array so that the microwave beam coming from the SPS can be turned off.

2.7. Other Applications of MPT

Apart from SSP, MPT can be applied to numerous other applications. One such application is in radiofrequency identification or (RFID). In RFID systems, power is transmitted from a reader to a tag device that identifies that which it is mounted to. In some applications the tags are passive, meaning that they contain no battery to drive the tag’s onboard electronics. Some environments such as ones with extreme heat can render batteries useless.

Passive tags rectify a majority of the incident RF power to DC with the use of a rectifying diode in order to drive the electronics. In essence, each of these tags is a rectenna combined with identifying digital electronics. The use of MPT has even been associated with such ideas as remotely powering airplanes, tanks, and naval ships. The main problem is that the required power to move such objects is immense and the rectenna arrays would need to be of ridiculous size such that they become impractical. However, MPT applied to lightweight mobile craft is feasible and has been done in the past. Such craft include high-altitude platforms such as UAVs and blimp airships in which helium is used in conjunction with MPT to move the airships. The main thing for MPT to be applicable is how much power on the receiving end is needed to perform a particular task. For space-to-space applications, MPT is seen as a realizable technology since gravitational effects are minimized. MPT could be a real asset in the future with regard to powering space probes from space stations or even other planets. Some plans have called for making the moon both an MPT transmission site and/or a rectenna array site.

3. HISTORICAL MILESTONES FOR MPT

3.1. Early Years

The earliest example of power transmission by radiowaves was carried out by Heinrich Hertz [12]. Hertz used a spark-gap to generate high-frequency power and to detect the same power on the receiving end. Reflecting antennas were used for transmitting and receiving the energy. In essence, Hertz created a complete system for energy transfer.

Most of the early advances in WPT were achieved at the turn of the twentieth century by Nikola Tesla [13]. Using

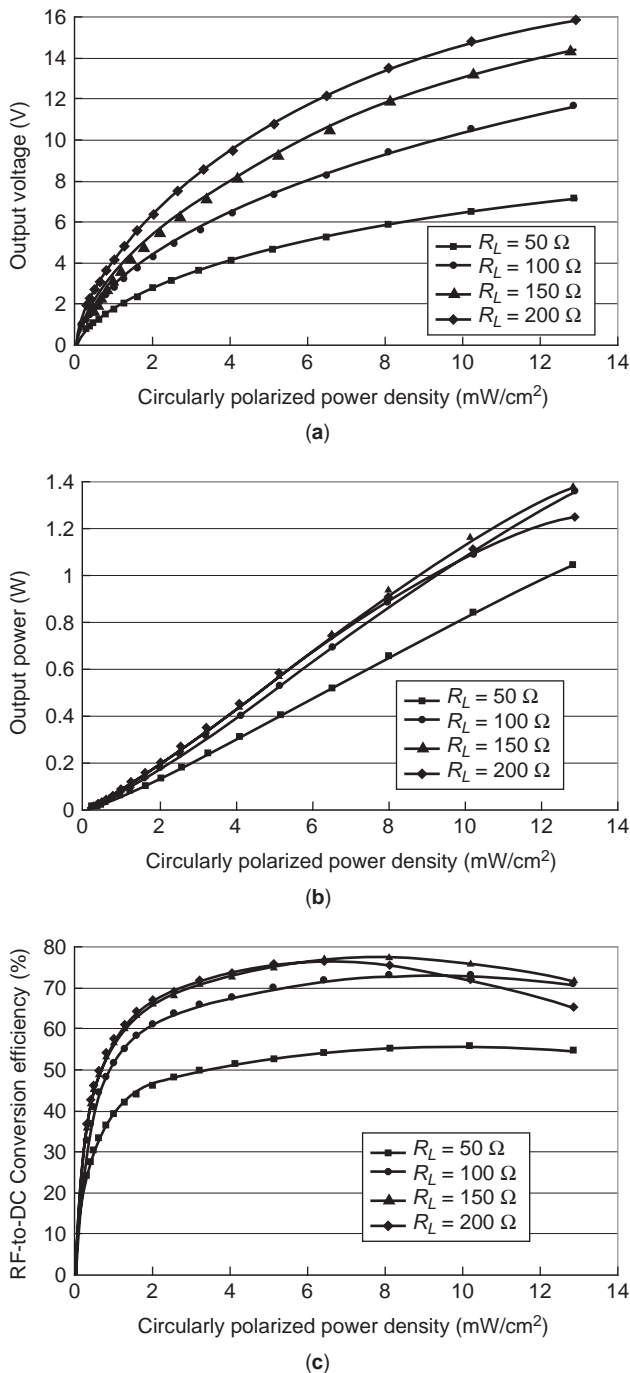


Figure 11. Rectenna array circularly polarized measured performance: (a) rectified voltage; (b) output power; (c) RF-to-DC conversion efficiency for various resistive loading values.

the concepts of resonance first displayed by Hertz, Nikola Tesla demonstrated the transmission of low-frequency electrical power using wires over long distances. Tesla built several alternating current (AC) power grids and proved their numerous advantages over the then commonly used direct current (DC) systems backed by Thomas Edison. Much to the dismay of Edison, Tesla proved that AC had much lower conductor losses than did DC and therefore could be transferred over much greater

distances. Tesla continued to carry out experiments in his New York City laboratory and turned his attention to MPT or the transfer of high power wirelessly. While at his laboratory, Tesla drew up plans to apply alternating surges of current running up and down a metallic mast in order to set up oscillations of electrical energy that would propagate over large areas on Earth. These oscillations would create a standing wave around Earth into which receiving antennas could be positioned at the standing-wave maximum amplitude locations. In other words, Tesla wanted to connect the world without wires. This would become Tesla's obsession.

Tesla's first attempt to transmit power without wires at Colorado Springs in 1899. Under a \$30000 grant from Colonel John Jacob Astor, owner of the Waldorf-Astoria Hotel in New York City, Tesla built the huge "Tesla coil" shown in Fig. 12a in a square building over which rose a 200-ft metallic mast with a 3-ft-diameter ball positioned at the top. The Tesla coil resonated 300 kW of low-frequency electric energy at 150 kHz. According to Tesla, when the RF output of the Tesla coil was unleashed into the mast, 100 MV of RF potential was produced on the sphere. Very large discharges of electrical energy were seen by people living in and around Colorado Springs. Unfortunately, no data were collected on whether any significant amount of power would be collected at any distant point.

With the self-heralded success of the Colorado Springs experiment, Tesla obtained financial backing from J. P. Morgan to construct a setup similar to the one in Colorado Springs on 2000 acres of land 60 mi east of New York City at Shoreham, in Suffolk County, Long Island. The building plans called for a wooden tower, namely, the Wardencliff Tower shown in Fig. 12b, 154 ft high that would support a giant copper electrode 100 ft in diameter shaped like a donut at its top. The structure was nearly completed when the financial resources ran dry, and Tesla was forced to halt construction. The installation was eventually torn down, during World War I, by the U.S. government because of its belief that the structure could constitute a possible target. Tesla continued to pursue his dream of connected the world without wires, but his efforts went unnoticed, and, with little outside interest and no financial supporters, Tesla took a step backwards into seclusion. The first radio transmission was achieved not by Tesla but instead by Guglielmo Marconi in 1901. After Tesla's death, the U.S. government seized Tesla's documented works on WPT. The U.S. government saw the technology as the scientific bases for their proposed "death ray" weapon in which WPT would be used to destroy enemy weapon systems. Many of these concealed records were later released to the general public.

From a historical point of view, Tesla was decades ahead of his time. Not until the 1930s was another attempt on WPT carried out. This experiment, performed by H. V. Noble at the Westinghouse Laboratory, consisted of identical transmitting and receiving 100-MHz dipoles separated by 25 ft. No attempts to focus the energy were made, but several hundred watts of power were transferred between the two dipoles. This experiment was demonstrated again to the general public at the Chicago's World Fair of 1933/34.



Figure 12. Tesla's MPT experiments: (a) Colorado Springs; (b) Wardencllyffe tower.

The primary reason why WPT received little interest in the first part of the twentieth century was that knowledgeable engineers and scientists knew that, in order to achieve efficient point-to-point transmission of power, the electromagnetic energy had to be concentrated into a narrow beam, reducing what is commonly referred to today as “spillover loss”. It was theorized at this time that the only way to obtain such confined energy would be to utilize energy at high frequencies and use radiating elements of reasonable size. The other problem was that the existing sources that created high-frequency energy outputted only a few milliwatts of energy—not enough for a feasible WPT system.

In the late 1930s, two inventions were made that solved the high-frequency source problem. The first was the velocity-modulated beam tube first described by O. Heil which after a few modifications became the well-known klystron tube. The second invention was the microwave cavity magnetron developed by Randall and Boot in Great Britain in 1940 and passed to the United States under great secrecy during World War II [14]. These developments allowed the transition of WPT from lower frequencies to microwave frequencies or MPT.

During World War II, with the advent of radar made possible by the introduction of both the klystron and magnetron, antenna development and microwave generation technologies so basic to MPT improved greatly. The U.S. government took notice of the emerging technologies and started proposing applications for the new capabilities.

3.2. Modern U.S. Contributions

In the late 1950s, a number of developments occurred that revealed that WPT approaching 100% was possible. Calculations and experimental results gathered by Goubau and Schwering demonstrated that microwave power could be transmitted with close to 100% efficiency by a beam waveguide consisting of lenses and/or reflecting mirrors [15]. These findings dispelled the previously held assumption that power density always decays by the square of the distance. Another vital development was the high-powered microwave tube amplifier or Amplitron. The last development propelling MPT was the realization of the growing need to communicate by line of sight over long distances, which a platform placed at high altitudes in Earth's atmosphere could afford. Later satellites would be used for this purpose.

The combination of the aforementioned developments motivated the Raytheon Company to propose the Raytheon airborne microwave platform (RAMP) concept in 1959 to the U.S. Department of Defense as a solution to surveillance and communication problems. The proposed platform was a large helicopter positioned at 50,000 ft in a region above the jetstream, where the atmospheric winds are almost nonexistent. To fly at this altitude, the helicopter needed to be powered from Earth by an Amplitron having an output of 400 kW of energy at 3 GHz with an efficiency over 80%. This high-powered Amplitron was developed at Raytheon's Spencer Laboratory in 1960 by William Brown, who is largely regarded as the principal pioneer of practical MPT [16]. The only capability missing was the ability to convert microwave energy to DC power in order to drive motors attached to the rotor blades. The U.S. Air Force awarded several contracts to study this rectification problem. One of the studies, carried out by R. George and E. Sabbagh at Purdue University, showed that a semiconductor diode could be used as an effective rectifier [17]. At the same time, W. Brown at Raytheon carried out research on the use of a thermionic diode rectifier [18]. Now that both high-powered sources on the transmitting side and efficient rectifiers on the receiving side were obtainable, MPT for the first time became both a feasible and possibly useful technology.

The Air Force continued to partner with W. Brown and Raytheon during the early 1960s in order to pursue the emerging MPT technological possibilities. One of the best-known examples of MPT occurred on July 1, 1964 inside Raytheon's Spencer Laboratory. There, a microwave-powered helicopter much smaller than the one proposed in RAMP was flown a few inches off the ground. It was the first heavier-than-air vehicle to be flown and was sustained solely by a 2.45-GHz microwave beam. This helicopter experiment was demonstrated again to the mass media on October 28, 1964. The helicopter shown in Fig. 13 was flown for 10 h at an altitude of 50 ft [19]. The presentation was covered by Walter Cronkite's CBS news program and displayed to the world the real possibilities of MPT. Dipole antennas were used to collect the incoming microwave energy, and the DC energy that powered the propeller was obtained using 4480 semiconductor diodes. This rectifying circuit was built and tested by R. George at Purdue University. It was the first demonstration of a rectifying antenna array in which each antenna element and its corresponding semiconductor rectifying diode

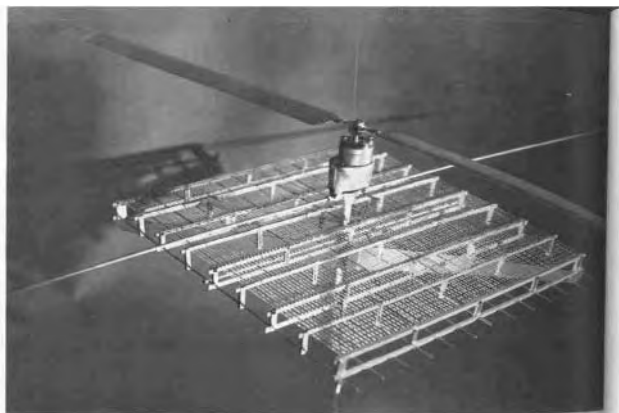


Figure 13. This U.S. Air Force–Raytheon-sponsored demonstration of a microwave-powered helicopter was made to public media in October 1964.

circuit are integrated together. Today such integrated circuits are known as “rectennas”.

After the helicopter flight, the U.S. Air Force elected to discontinue their MPT endeavors. In 1967 W. Brown began to court Dr. Werner von Braun and his staff at NASA’s Marshall Space Flight Center (MSFC) on MPT possibilities in space. In 1970 MSFC awarded Raytheon a contract to improve the overall DC-to-DC efficiency of the MPT system. This DC-to-DC efficiency includes the conversion from DC to RF in the magnetron, the aperture transfer efficiency, and the RF-to-DC conversion of the rectenna array. By multiplying these three efficiencies, an overall system efficiency can be determined.

Raytheon continued to improve various rectenna designs throughout the 1970s under the MSFC contract. Another vital improvement to the MPT system was the design of a dual-mode horn by P. D. Potter of the Jet Propulsion Laboratory (JPL) [20]. The modified horn launched a Gaussian beam with negligible sidelobes to improve the aperture transfer efficiency. Advances to solid-state rectifying diodes in the 1970s improved the RF-to-DC conversion significantly. The MSFC program resulted in drastic improvements in MPT system efficiency.

In 1971, Brown of Raytheon and Glaser, the SPS mastermind, along with members of Northrop Grumman and the solar photovoltaic company Textron, carried out a 6-month study on the SPS concept and concluded that the idea was sound. A letter was then sent to the director

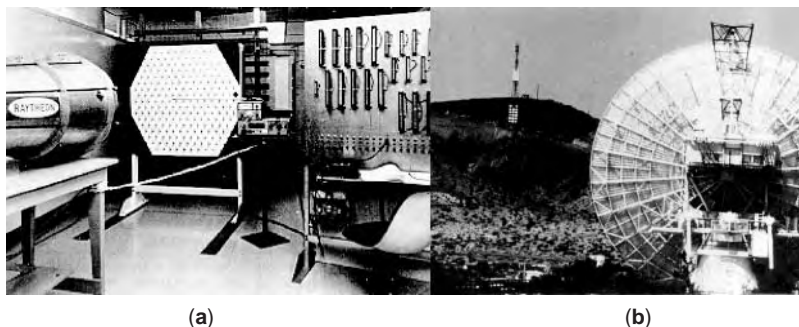
of NASA requesting funding [21]. As a result, NASA’s Lewis Research Center (LeRC) awarded a small contract to Brown and his Raytheon colleagues to improve the overall efficiency of existing MPT systems in order to meet the stringent requirements necessary for a fielded SPS. During the early 1970’s NASA began to shift more and more focus to SSP with JPL, under the guidance of Richard Dickinson, playing a major role in the process. The culmination of efforts occurred in 1974 with the MPT setup shown in Fig. 14a having an overall DC-to-DC conversion efficiency of $54 \pm 1\%$. The operating frequency was 2.446 GHz, and the rectenna’s output power level was 600 W. This efficiency was certified by JPL’s Quality Assurance organization and to this day stands as the highest MPT end-to-end efficiency. The breakdown of the 54.18% overall efficiency is 68.9% for the DC-to-microwave power conversion, 95% for the aperture-to-aperture transfer, and 82.4% for the beam collection and rectification [22,23].

In 1975, another important milestone was shown at the Venus Site of JPL’s Goldstone Facility. In this demonstration shown in Fig. 14b, microwave energy at 2.388 GHz was sent over a 1 mi distance to an awaiting 288 ft² rectenna array. The rectenna array was designed by W. Brown at Raytheon and outputted 30 kW [24]. Both the JPL certified and Goldstone experiments gave NASA the confidence it needed into the viability of MPT and its possible use in Glaser’s SPS concept.

Even with the success of Goldstone, LeRC continued to push for improvements to the transmitting antenna array as well as the rectenna. In 1977, Brown improved the design of rectenna arrays by introducing thin-film etched rectennas in which the DC bussing is achieved in the plane of the antennas [25]. Before etched rectennas, the DC networks were attached behind the antennas, making previous rectenna arrays more complex, much heavier, and more costly. Almost all currently designed rectennas are etched.

Between the years of 1977 to 1980, NASA worked jointly with the U.S. Department of Energy (DoE) to further evaluate SSP possibilities in providing affordable energy to consumers on Earth. The study concluded in a 670-page document that determined that SSP was a feasible technology and should be pursued in the future [26]. One idea coming out of the study was the idea of retrodirectivity or the ability to keep the microwave beam on target. Unfortunately, the NASA sponsored program ended in 1980, and the U.S. lead in SSP came to an end.

Figure 14. Raytheon/JPL MPT experiments: (a) an overall system efficiency of $54.18\% \pm 0.94\%$ was obtained at the Raytheon Company with the demonstration setup shown—the DC power output was 495 W, and the frequency was 2.446 GHz; (b) demonstration of beamed power over one mile distance at the JPL Goldstone facility in the Mojave Desert, CA.



3.3. International Involvement

During the 1980s and early 1990s, the center of MPT research and development shifted to Japan and to a lesser extent Europe and Canada. Since Japan was and remains a large energy consumer with little natural energy resources, the promise of SPS warranted investigation. As a result of the investigation into SPS, Japan carried out in-space experiments. The first of Japan's in-space experiments was the Microwave Ionosphere Nonlinear Interaction eXperiment (MINIX) conducted by Matsumoto and colleagues in 1983. MINIX focused on how the plasma wave dynamic spectrum changes when high-powered microwave energy is transmitted into ionospheric plasma [27,28]. The second in-space experiment was the International Space Year–Microwave Energy Transmission in Space (ISY-METS) in 1993. In ISY-METS microwave energy was transferred from one rocket to a second rocket that carried two different rectenna arrays. ISY-METS represented the first example of MPT in space [29].

In 1980, a program to develop a long-endurance high-altitude platform called the Stationary High Altitude Relay Program (SHARP) was proposed in Canada [30]. The platform was to be the first unmanned, fuel-less, lightweight airplane powered remotely by microwaves, which enabled it to stay afloat for long periods of time. On September 17, 1987, the $\frac{1}{8}$ -scale prototype SHARP with a wingspan of 4.5 m seen in Fig. 15a flew on beamed microwave power for 20 min at an altitude of 150 m. A 2.45-GHz microwave beam was transmitted by a parabolic dish antenna, providing a power density at the airplane of 400 W/m^2 . The dual-polarized rectenna array received enough microwave energy to generate 150 W of DC power to the electric motor in order to lift and fly the 4.1-kg airplane.

Another example of driving a model airplane using microwave power was the MICrowave Lifted Airplane eXperiment (MILAX) conducted by Japan in 1992. The experiment was the first to use an electronic scanned phased array to keep the 2.411-GHz microwave beam on the moving target or, in this case, the airplane shown in Fig. 15b. Two charge-coupled device (CCD) cameras recognized the airplane's pattern feeding the location to a computer that scanned the array to the appropriate location. The transmitting array was located on a sports utility vehicle that was also in motion during the tests. MILAX received nationwide media coverage in Japan and impressed SSP favorably on the Japanese public [31].

3.4. Recent MPT Focus

NASA took notice of the Japanese successes and in 1995 undertook the “Fresh Look Study” to reconsider the challenges of large-scale SSP systems. The study emphasized the most recent technological advancements, which rendered SSP more viable than it was in the late 1980s [32]. In 1998, NASA conducted the “SSP Concept Definition Study”, in which experts within NASA and outside the agency were engaged. The second study backed up findings from the “Fresh Look Study”, but it also narrowed the SSP concepts by invalidating some of the earlier ideas. In 2000, NASA MSFC conducted the SSP Scientific Exploratory Research and Technology (SERT) program. The program broadened the scientific community's involvement and resulted in successful demonstrations on a variety of system-level components.

The SERT program addressed numerous concerns previously outlined by Glaser. Some of these issues relate to economic and societal assessment, environmental effects, resource requirements, and legal issues. The economic assessment studies provided a cost-effectiveness analysis of the SSP system. The societal assessment included the understanding that SSP is for everyone even in the most remote locations where SSP has an obvious advantage. This avoids the situation where a country monopolizes the technology. The environment issues focused on human exposure to the microwave energy, especially with regard to the people working at or near the rectenna array. Studies have shown that the rectenna arrays can be designed to accept power densities within human exposure limits. Questions still remain on how birds would be affected when flying through the microwave beam, and how birds could be convinced not to roost on the warm rectenna arrays. Some focus was also given to possible climate change, although studies have shown negligible effect even in heavy rainstorms when the absorption of microwave power in the troposphere is expected to increase. A concern resonated during SERT meetings was the impact of reradiated energy from the rectenna arrays. This energy could interfere with other electronic devices operating in the same frequency bands, especially since the SPS is radiating large amounts of power with some spillover loss. Research in this area is ongoing, but it has been shown that rectennas can be designed to minimize harmonic energy reradiation with the use of harmonic filtering. The land that a rectenna may need is also a concern. The rectenna would most likely be placed in an



Figure 15. MPT applied to unmanned remotely powered model aircraft: (a) SHARP; (b) MILAX.

arid environment since rain can reduce rectenna efficiency. This would hopefully mitigate the number of birds and people since both reside for the most part along the coasts and waterways. Another concern is that the astronomers will be upset that a large object that reflects sunlight is appearing in the night sky. This is a viable concern, especially since an SSP system will call for a myriad of satellites. Finally, the transport of materials to space to construct the SSPs, is a daunting task. How to use the Space Shuttle's payload bay more efficiently and the elevator to space concept are being studied for transporting the necessary supplies. With the recent nanotube technological breakthroughs, the elevator idea is not as far-fetched as it might seem.

With the renewed U.S. involvement and continuing efforts by Japanese researchers and others, SSP is progressing steadily. Much of the research since 1990 has focused on producing extremely efficient rectenna arrays. One such etched rectenna design funded by the SSP SERT program and demonstrated at the 2002 World Space Congress in Houston, Texas, accepts circularly polarized energy at 5.8 GHz and outputs DC at 82% efficiency [2]. This efficiency was made possible by the recent advances made in reducing the parasitic losses of flip-chip Schottky diodes. The frequency 5.8 GHz was used for its ability to propagate through the atmosphere with relatively low loss and because the receiving and transmitting antennas become reasonably small in terms of SPS construction feasibility. Circular polarization was chosen because of depolarization. Consequently, linearly polarized systems used for SSP would most likely see degradations in efficiency.

Currently, the part of the SSP system that warrants the greatest focus is the photovoltaic solar cells. The state of the art for solar cell sunlight to DC efficiency has remained around 30% since the mid-1990s. The other 70% is predominately heat loss, which can heat the transmitting aperture, lowering the radiated power. Improvements in solar cell efficiency are essential before fielding a functioning SSP system.

4. CONCLUSIONS

Future applications of MPT may apply to SSP, but in the near term MPT will probably be applied to unmanned aerial vehicles (UAVs). UAVs are capable of delivering services such as communications and remote sensing and are finding increasing use for synergistic military applications. The idea of powering space probes from transmitters positioned in outer space also is seen as a realizable and sensible technology. However the "holy grail" for MPT is SSP. SSP is seen by some experts as a way of meeting energy demands for all future generations. The reality is that MPT SSP-associated systems will have relevance until the sun stops emitting light, and by that time, presumably billions of years from now, all life will have ceased to exist, anyway.

BIBLIOGRAPHY

1. P. Glaser, Power from the sun: Its future, *Sci. Mag.* **162**(3856):857–861 (Nov. 1968).
2. B. Strassner, S. Kokel, and K. Chang, 5.8 GHz circularly polarized low incident power density rectenna design and array implementation, *Proc. IEEE AP-S Symp.*, June 22, 2003, pp. 950–953.
3. P. E. Glaser, F. P. Davidson, and K. I. Csigi, *Solar Power Satellites*, Wiley, New York, 1994.
4. R. Nansen, *Sun Power*, Ocean Press, Ocean Shores, WA, 1995.
5. P. Zepeda, Modeling of a sandwich transmitting array satellite, *World Space Congress*, Houston, TX, 2002.
6. C. Balanis, *Antenna Theory*, Wiley, New York, 1982.
7. L. J. Ippolito, R. D. Kaul, and R. G. Wallace, *Propagation Effects Handbook for Satellite Systems Design* [NASA Reference Publication 1082(03)], NASA, Washington, DC, June 1983.
8. R. L. Olsen, D. V. Rogers, and D. B. Hodge, The aR^b Relation in the culmination of rain attenuation, *IEEE Trans. Anten. Propag.* **AP-26**:318–329 (March 1978).
9. W. C. Brown and E. E. Eves, Beamed microwave power transmission and its application to space, *IEEE Trans. Microwave Theory Tech.*, **40**(6) (June 1992).
10. B. Strassner and K. Chang, Highly efficient C-band circularly polarized rectifying antenna array for wireless microwave power transmission, *IEEE Trans. Anten. Propag.* **51**(5):1548–1553 (May 2003).
11. L. H. Hsieh, B. H. Strassner, S. L. Kokel, C. T. Rodenbeck, M. Y. Li, and K. Chang, Development of a retrodirective wireless microwave power transmission system, *Proc. IEEE AP-S Symp.*, June 22, 2003, pp. 393–396.
12. H. Hertz, *Dictionary of Scientific Biography*, Vol. VI, Scriber, New York; 1998, pp. 340–349.
13. M. Cheney, *Tesla, Man Out of Time*, Prentice-Hall, Englewood Cliffs, NJ, 1981.
14. H. Boot and J. Randall, Historical notes on the cavity magnetron, *IEEE Trans. Electron. Devices* **ED-23**(7), (July 1976).
15. G. Goubau and F. Schwerng, On the guided propagation of electromagnetic wave beams, *IRE Trans. Anten. Propag.* **AP-9**:248–256 (May 1961).
16. J. F. Showron, G. H. MacMaster, and W. C. Brown, The super power CW amplitron, *Microwave J.* (Oct. 1964).
17. R. H. George and E. M. Sabbagh, An efficient means of converting microwave energy to dc using semiconductor diodes, *IEEE Microwave Theory Tech.* **11**(part 3):132–141 (March 1963).
18. W. C. Brown, Thermionic diode rectifier, in E. C. Okress, ed., *Microwave Power Engineering*, Academic Press, New York, 1968, Vol. I, pp. 295–298.
19. W. C. Brown, *Experimental Airborne Microwave Supported Platform*, Tech. Report RADC-TR-65-188, Contract AF30 (602) 3481, Dec. 1965.
20. W. C. Brown, *Free-Space Microwave Power Transmission Study*, Combined Phase III and Final Report, Raytheon Report PT-4601, NASA Contract NAS-8-25374, Sept. 1975.
21. W. C. Brown, Satellite power stations—a new source of energy? *IEEE Spectrum*, **10**(3):38–47 (March 1973).
22. R. M. Dickinson and W. C. Brown, *Radiated Microwave Power Transmission System Efficiency Measurements*, Tech. Memo 33-727, Jet Propulsion Lab., California Inst. Technology, Pasadena (JPL/cal Tech) March 15, 1975.
23. R. M. Dickinson, *Evaluation of a Microwave High-Power Reception-Conversion Array for Wireless Power Transmission*, Tech. Memo 33-741, JPL/Cal Tech, Pasadena, CA, Sept. 1, 1975.
24. R. M. Dickinson, *Reception-Conversion Subsystem (RXCV) Transmission System*, Raytheon Final Report Microwave

- Power, ER75-4386, JPL Contract 953968, NASA Contract NAS 7-100, Sept. 1975.
25. W. C. Brown, *Electronic and Mechanical Improvement of the Receiving Terminal of a Free-Space Microwave Power Transmission System*, Raytheon Contract Report PT-4964, NASA CR-135194, Aug. 1977.
 26. *Final Proc. Solar Power Satellite Program Rev. ODOE/NASA Satellite Power System Concept Development Evaluation Program*, Conf.-800491, July 1980.
 27. H. Matsumoto, N. Kaya, I. Kimura, S. Miyatake, M. Nagatomo, and T. Obayashi, MINIX project toward the solar power satellite-rocket experiment of microwave energy transmission and associated nonlinear plasma physics in the ionosphere, *Proc. ISAS Space Energy Symp.*, 1982, pp. 69–76.
 28. M. Nagatomo, N. Kaya, and H. Matsumoto, Engineering aspect of the microwave ionosphere nonlinear interaction experiment (MINIX) with a sounding rocket, *Acta Astronaut.* **13**(1):23–29 (1986).
 29. R. Akiba, K. Miura, M. Hinada, H. Matsumoto, and N. Kaya, ISY-METS rocket experiment, *Inst. Space Astronaut. Sci.* **65**:2:1–13 (1993).
 30. J. Schlesak, A. Alden, and T. Ohno, SHARP rectenna and low altitude flight trials, *Proc. IEEE Global Telecommunications Conf.*, New Orleans, Dec. 2–5, 1985.
 31. Y. Fujino, T. Ito, N. Kaya, H. Matsumoto, K. Kawabata, H. Sawada, and T. Onodera, A rectenna for MILAX, *Proc. Wireless Power Transmission Conf.*, Texas, Feb. 1993, pp. 273–277.
 32. J. M. Mcspadden and J. C. Mankins, Summary of recent results from NASA's space solar power (SSP) programs and the current capabilities of microwave WPT technology, *IEEE Microwave Mag.* **3**:46–57 (Dec. 2002).

MICROWAVE RECEIVERS

JAMES BAO-YEN TSUI
Wright-Patterson Air Force Base
Ohio

A microwave receiver is used to receive information transmitted at microwave frequencies (from 1 to 220 GHz). Most microwave receivers are integral parts of a system, that is, communication or radar, and they are designed together with the transmitter. In other words, the receiver is designed to receive a specific signal with maximum efficiency. For example, the video bandwidth of a pulsed radar receiver matches the bandwidth of the transmitted pulse so as to receive maximum energy in the signal while at the same time limit its noise bandwidth to a minimum value. The receiver of a frequency modulation (FM) radar has a dispersive delay line matching the transmitted signal and compresses it into a short pulse to increase the processing gain. In the global positioning system (GPS) the coarse acquisition (C/A) signals are code-division multiple access (CDMA). In a GPS receiver locally generated C/A codes are used to correlate with an input signal to perform acquisition and signal tracking. In an FM receiver, the frequency variation information is converted into amplitude information through a frequency discriminator. From these examples one can see that each receiver is uniquely designed.

Another type of microwave receiver detects uncooperative signals. This type of receiver is usually referred to as an *intercept receiver*. This type of receiver has some designs in common, because each subtype is designed to detect signals with very limited information. For example, there are police radar receivers and police radar detectors. The police radar receiver, designed to match the transmitted signal to achieve the highest sensitivity, is an integral part of a radar system. The police radar detector used in automobiles is an intercept receiver. The purpose of the radar detector is to detect whether police traffic radar is being used. An intercept receiver does not have the detailed information of the radar signal; instead, it uses coarse information, that is, the frequency range over which the radar operates. Although the intercept receiver has less sensitivity than the radar receiver, the intercepted signal is much stronger than the signal returned to the radar. The signal strength received by a radar receiver is proportional to $1/R^4$, where R is the distance between the radar and the target (or intercept receiver). The intercepted signal strength is proportional to $1/R^2$, which is stronger than the returned signal.

In this article, intercept microwave receivers will be the main subject because of their similarities in design goals. Intercept receivers are very useful in military applications. Used in electronic warfare (EW), they are often referred to as EW receivers. These receivers are used to intercept hostile communication as well as radar signals. It is a more challenging task to design military intercept receivers, because it is a common military practice to design signals that cannot be detected by an intercept receiver and cannot be jammed.

Receivers can sometimes be used to detect unintentional radiation. For example, one can use a microwave receiver to check the microwave power leakage level of a microwave oven. This type of receiver is also useful in military applications. For example, the detection of sparkplug radiation from automobiles can help locate enemy vehicles.

In the past, most microwave receivers were built using analog techniques. Because of recent advances in digital circuits, that is, with today's high-speed analog-to-digital converters (ADC) with their large number of bits and recent high-speed digital signal processing (DSP) techniques, it appears that the trend is to build digital receivers. Some narrowband receivers have already been built using digital techniques. Wideband digital microwave receivers are in the research stage. Digital receivers should be more reliable because they require less maintenance and adjustment.

This article includes descriptions of a generic receiver, followed by a discussion of the important terminology and definitions used in receiver design. A classification of receivers is then presented, with a discussion of analog and digital receivers to follow in subsequent sections. A comparison of different types of receivers concludes the article.

1. GENERIC RECEIVERS

In general, the signals received by an antenna are very weak. It is difficult to process the signals or even to detect

their presence directly. A common approach is to amplify the signals to a higher power level before further processing or detection. This amplification is accomplished through a radiofrequency (RF) chain.

The RF chain usually contains the following components: RF amplifiers, filters, mixers, local oscillators, intermediate-frequency (IF) amplifiers, IF filters, and attenuators. Amplifiers are used to raise the signal power level. Filters are used to limit out-of-band noise as well as spurious responses (undesired frequencies) generated from some components. The mixer and local oscillator are used in combination to shift the input frequency to another frequency, often referred to as the IF. At IF, additional filters and amplification can be provided. In many receivers the input signals are not converted to a different frequency and, therefore, the mixer and local oscillator are not needed. Attenuators are used to adjust the overall gain of the RF chain. The overall gain in the RF chain must be of a specific value. Often commercial amplifiers with specific gain values are used in receiver design and it is difficult to implement the desired value. A common practice is to use amplifiers to provide more gain than the desired value and attenuators to lower the gain to the correct value.

In communication receivers, automatic gain control (AGC) is sometimes used. The AGC changes the gain of the RF chain according to the input signal strength: lower gain for strong signal and higher gain for weak signal. The AGC is seldom used in receivers intercepting pulsed signals, because it is difficult to build an AGC with very fast response time.

After the RF chain in an analog receiver, the signal is detected by a crystal video detector. The detector filters out the RF but retains the information of the signal, often referred to as the *video signal*. Further processing is needed to obtain the necessary information, which includes digitizing the video signal. A basic analog receiver is shown in Fig. 1a. In some analog receivers, there are no RF amplifiers and a crystal video detector is used to detect signals directly. These receivers usually have low sensitivity and can detect only very strong signals.

After the RF chain in a digital microwave receiver, an ADC is used to convert the input into digital data as shown in Fig. 1b. Because the output of the ADC is digital, digital signal processing (DSP) can be used to obtain the necessary information.

2. DEFINITIONS USED IN RECEIVERS

The two most important specifications to describe a receiver are sensitivity and dynamic range. These two parameters can be used to specify all kinds of receivers whether they are intercept receivers or receivers designed for a specific signal. *Sensitivity* can be briefly defined as the capability to receive the weakest possible signal. *Dynamic range* is the maximum signal amplitude range that a receiver can process without distortion. A strong signal above the upper limit of the dynamic range can produce distortion or generate spurious responses. It is desirable to have high sensitivity to receive weak signals and high

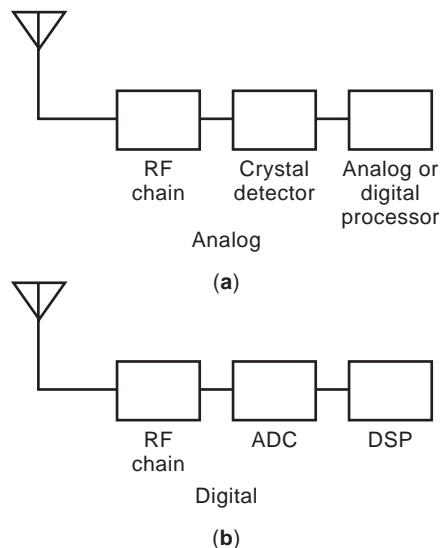


Figure 1. (a) A basic analog receiver with RF amplifier chain, crystal detector, and analog/digital processor. The RF amplifier chain is used to amplify the input signal. The crystal detector changes the RF signal into a video signal. The processor takes the video signal and generates the desired digital information. (b) A basic digital receiver with RF amplifier chain, ADC, and DSP. The ADC digitizes the analog input signals. The DSP processes the digitized data and generates the desired digital information.

dynamic range to receive a broad range of signals. However, high sensitivity often causes lower dynamic range and vice versa. Therefore, in designing a receiver, the tradeoff between sensitivity and dynamic range becomes an important issue.

Sensitivity is closely related to noise floor, the noise figure of the receiver, and the gain in the RF chain. In an analog receiver, the sensitivity depends on the video bandwidth after the detector. In a digital receiver, the DSP algorithm used after the ADC affects the overall bandwidth of the receiver and determines receiver sensitivity. When a receiver can process only one signal, there is only one definition of dynamic range. If a receiver can process simultaneous signals, there are usually three definitions of dynamic range. They are denoted as the single signal, two-signal spur-free, and two-signal instantaneous dynamic range. The lower limit of the dynamic range is always the sensitivity level. The upper limit depends on the definition of the dynamic range. These definitions, terminology and calculations to obtain some of the values, will be discussed in the following paragraphs. Most equations can be found in Ref. 1.

2.1. Receiver Input Bandwidth and Instantaneous Bandwidth

The *input bandwidth* of a receiver refers to the frequency range in which the receiver can detect an input signal. This is also referred to as the *operational bandwidth* or the *overall bandwidth* of the receiver. The *instantaneous bandwidth* means that any signals with sufficient amplitude in the bandwidth will be detected immediately. Usually, the input bandwidth is wider than the instantaneous bandwidth, but in some receivers they are the same. The

instantaneous bandwidth can be assigned to different portions of the input bandwidth. For example, a receiver may have a 16 GHz (2–18 GHz) input bandwidth but a 1 GHz instantaneous bandwidth. This 1 GHz bandwidth can be placed in any one of the bands in the 2–18 GHz range to receive signals in that band. The input bandwidth and the instantaneous bandwidth are not used to determine the sensitivity. They are mentioned here only to distinguish them from the RF bandwidth.

2.2. RF Bandwidth

The RF bandwidth is used to determine the sensitivity of a receiver. In an analog receiver, the filter with the narrowest bandwidth in the RF chain is the RF bandwidth. In some receivers, the input and the instantaneous and RF bandwidths may be the same. In a digital receiver, usually the inverse of the DSP length will be used as the RF bandwidth. For example, if the input is digitized at 1000 MHz, each sample is separated by 1 ns. If 256 samples will be processed through the fast Fourier transform (FFT), the RF bandwidth will be approximately 3.9 MHz ($1/256 \times 10^{-9}$ s).

2.3. Video Bandwidth

The video bandwidth of a receiver is determined by the video circuit following the crystal detector. The desired bandwidth is determined by the input signals. For an electronic warfare (EW) receiver, the video bandwidth is determined by the shortest pulse anticipated. In a digital receiver, it is determined by the processing scheme and is sometimes assumed to have the same as the RF bandwidth.

2.4. Noise

Noise generated by a resistor R can be represented by a noise generator in series with the resistor. Maximum power transfer from a generator to a load occurs when the load impedance is matched to the generator impedance. *Available power* refers to the power that would be delivered to a matched load. The available thermal noise power N_i in watts at the input of a receiver can be expressed as

$$N_i = kTB \quad (1)$$

where k is Boltzmann's constant ($= 1.38 \times 10^{-23}$ J/K), T is the temperature of resistor R , and B is the bandwidth of the receiver in hertz. The power level in a typical receiver system is very low and is usually expressed in milliwatts or in dBm, which is defined as

$$P(\text{dBm}) = 10 \log(P) \quad (2)$$

where the P on the right-hand side is power in milliwatts and the base of the log is 10. The thermal noise at room temperature where $T = 290$ K can be expressed in dBm as

$$P(\text{dBm}) = -174 \text{ dBm/Hz} \quad (3)$$

or

$$P(\text{dBm}) = -114 \text{ dBm/MHz}$$

These two values are commonly used in receiver designs. It should be noted that with an antenna aimed skyward, the noise temperature can be very low.

2.5. Gain

The *gain* of an amplifier is defined as

$$G = \frac{S_o}{S_i} \quad (4)$$

where S_o and S_i are the available output and input signal powers, respectively. The gain is often defined in decibels as

$$G(\text{dB}) = 10 \log(G) \quad (5)$$

When N amplifiers are connected in cascade, the overall gain can be expressed as

$$G = G_1 G_2 \cdots G_N \quad (6)$$

or

$$G(\text{dB}) = G_1(\text{dB}) + G_2(\text{dB}) + \cdots + G_N(\text{dB})$$

where G_1, G_2, \dots, G_N are the gain of each individual amplifier.

2.6. Noise Figure

The noise figure is defined as

$$\begin{aligned} F &= \frac{N_o}{GN_i} \\ &= \frac{\text{noise output of practical receiver}}{\text{noise output of an ideal receiver at temperature } T} \end{aligned} \quad (7)$$

where N_o is the noise at the output of the receiver, G is the gain of the RF chain in the ratio form, and N_i is the input thermal noise ($= kTB$). Substituting Eq. (4) into Eq. (7), the result is

$$F = \frac{S_i/N_i}{S_o/S_o} = \frac{\text{signal-to-noise ratio at input of receiver}}{\text{signal-to-noise ratio at output of receiver}} \quad (8)$$

The noise figure is often defined in decibels as

$$F(\text{dB}) = 10 \log(F) \quad (9)$$

If there are N amplifiers connected in cascade, the noise figure ratio form can be expressed as

$$F = F_1 + \frac{F_2 - 1}{G_1} + \frac{F_3 - 1}{G_1 G_2} + \cdots + \frac{F_N - 1}{G_1 G_2 \cdots G_{N-1}} \quad (10)$$

where G_1, G_2, \dots and F_1, F_2, \dots are the gain and noise figure of the first, second, ... amplifiers, respectively, and are expressed in power ratio rather than in decibels. From Eq. (10) it can be shown that if the first component in the RF chain is a high-gain amplifier, the overall noise figure can be approximately equal to the noise figure of the first amplifier.

2.7. Sensitivity

The sensitivity of a receiver depends on the noise power at the input of the receiver, which is related to the bandwidth of the RF chain, gain, and video bandwidth for an analog receiver and the DSP algorithm used for a digital receiver. It is often specified along with false-alarm rate and probability of detection. The false-alarm rate is defined as the number of false measurements when there is no input signal. In some cases more restrictions can be added to the definition of sensitivity; that is, the parameters measured by the receiver must be within certain limits. In designing a receiver, the sensitivity can be determined from curves generated based on the RF bandwidth, the video bandwidth, the probability of detection, and the probability of false alarm from this author’s work [1]. Once a receiver is built, one can apply specific requirements to evaluate its sensitivity. The sensitivity is usually frequency-dependent, which means that its value varies across the frequency range of the receiver.

2.8. Tangential Sensitivity

As the sensitivity of a receiver with given false alarm and probability of detection is tedious to calculate and measure, an easily calculable and measurable sensitivity is defined. For an analog receiver, the tangential sensitivity is measured through visual display on an oscilloscope that monitors the output of a video amplifier following the detector. The input must be a pulse signal. On the scope display, when the bottom of the noise trace in the pulse region is roughly tangential to the top of the noise trace between pulses, as shown in Fig. 2a, the receiver is at tangential sensitivity. At tangential sensitivity, the signal-to-noise ratio is 8 dB at the output of the detector with a standard deviation of 0.4 dB. Based on these values, the tangential sensitivity of a digital receiver can be illustrated from the signal-to-noise ratio of 8 dB as shown in Fig. 2b. When there is sufficient gain in the RF chain, the tangential sensitivity is independent of the characteristics of the video detector. This case is referred to as the *noise-limited case*. If there is insufficient gain, the tangential sensitivity depends on the characteristics of the detector and is referred to as the *gain-limited case*. The minimum gain required for the noise-limited case is to raise the noise floor to the tangential sensitivity of the crystal detector (approximately -35 to -45 dBm). Above this gain value, the sensitivity is gain-independent. Most modern microwave receivers fulfill this condition. The tangential sensitivity (TSS) for

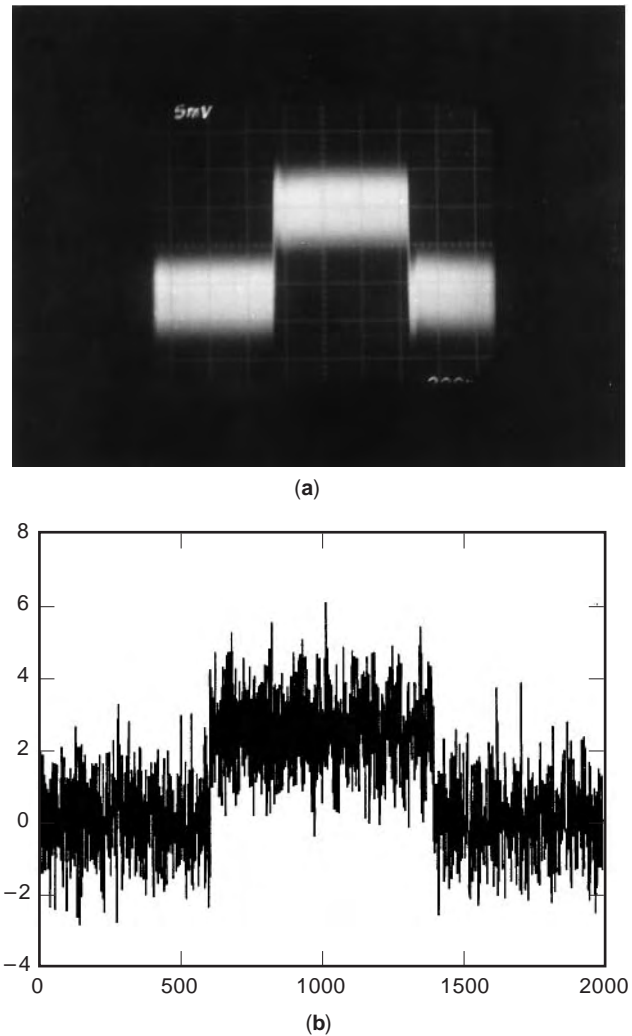


Figure 2. (a) Tangential sensitivity of an analog signal from an oscilloscope display. The output signal-to-noise ratio = 8 dB. (b) Tangential sensitivity of a digital signal where the signal-to-noise ratio = 8 dB.

the noise-limited case is

$$TSS = -114 + 10 \log(F) + 10 \log(3.15B_v + 2.5\sqrt{2B_R B_v - B_v^2}) \text{ dBm for } B_v \leq B_R < 2B_v \tag{11}$$

$$B_v \leq B_R < 2B_v$$

$$TSS = -114 + 10 \log(F) + 10 \log(6.31B_v + 2.5\sqrt{2B_R B_v - B_v^2}) \text{ dBm for } B_R \geq B_v$$

$$(6.31B_v + 2.5\sqrt{2B_R B_v - B_v^2}) \text{ dBm for } B_R \geq B_v$$

where -114 is the noise floor of 1 MHz bandwidth, F is the overall noise figure of the receiver, and B_v and B_R are the video and RF bandwidths, respectively.

The tangential sensitivity is usually too low to be used as the operating sensitivity level, because at this level the

false-alarm rate is very high. The rule of thumb is that the operating sensitivity is approximately 6 dB higher than the tangential sensitivity level.

2.9. Single-Signal Dynamic Range

This dynamic range is applicable to all receivers. The lower limit is the sensitivity level. When an input signal is very strong, it may cause some components in the RF chain or the ADC in a digital receiver to become saturated. Under this condition, the output signal will be distorted or spurious signals will occasionally be generated. Depending on the specifications of a certain receiver, the upper limit is determined accordingly.

2.10. Two-Tone Third-Order Intermodulation Products and Third-Order Intercept Point

If the passband of a receiver is less than an octave, the third-order intermodulation products are the lowest-order intermodulation products that can fall within the passband. That is why they are used as the upper limit of the two-tone spur-free dynamic range. The third-order intermodulation is measured with two input signals of equal amplitude. When the input signals f_1 , and f_2 , are strong enough to drive the RF chain into saturation, spurs will be produced at frequencies $2f_1 - f_2$ and $2f_2 - f_1$ as shown in Fig. 3. The outputs at these two frequencies are referred to as *third-order intermodulation*. The amplitude of the third-order intermodulation can be experimentally measured.

Another quantity related to third-order intermodulation is referred to as the *third-order intercept point*. The third-order intercept point can be obtained from the third-order intermodulation in Fig. 4. The straight line with a 1:1 slope represents the gain of an amplifier. Another straight line is drawn that passes the measured third-order intermodulation point with a 3:1 slope that represents the anticipated amplitude change of the third-order intermodulation as a function of input signal. The intercept point between these two lines is the third-order intercept point and the value is often read from the output axis. It should be kept in mind that these two straight lines are projected results. They cannot actually

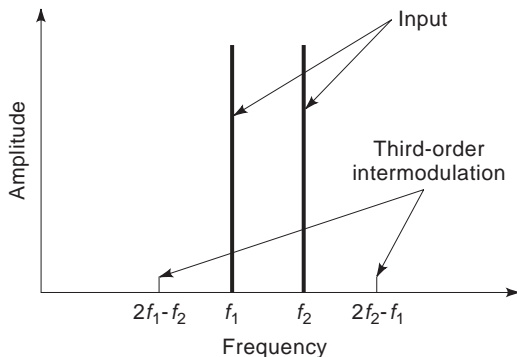


Figure 3. Third-order intermodulation products. The input signals are at f_1 and f_2 with equal amplitude and the third-order intermodulations are at $2f_1 - f_2$ and $2f_2 - f_1$.

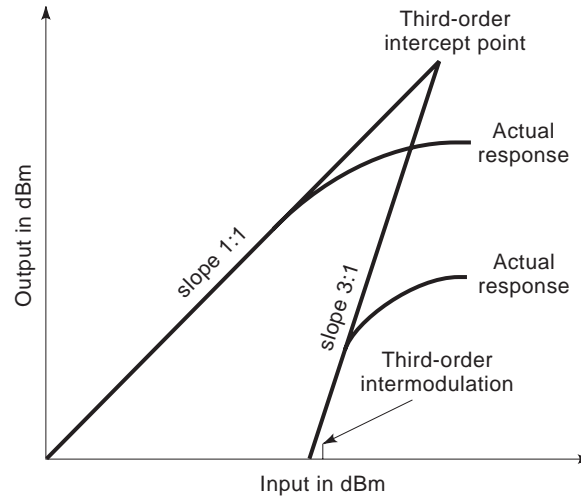


Figure 4. Third-order intercept point. The fundamental output has a slope of 1:1, and the third-order output has a slope of 3:1. The third-order intercept point is where the extrapolated fundamental and third-order outputs intercept. The third-order intermodulation is also shown.

be measured because, when a component is approaching saturation, the actual measured lines will bend downward. This quantity is used to determine the spur-free dynamic range. The third-order intercept point of many microwave components is provided by the manufacturers.

2.11. Third-Order Intercept Point of Cascade Components

The overall third-order intercept Q_i of N components connected in cascade is given by

$$Q = \frac{G_1 G_2 \cdots G_N}{\frac{G_1}{Q_1} + \frac{G_1 G_2}{Q_2} + \cdots + \frac{G_1 G_2 \cdots G_N}{Q_N}} \quad (12)$$

where Q_1, Q_2, \dots are the third-order intercept point of the first, second, ... components. If a component is passive, for example, as with an attenuator, a high third-order intercept value can be assigned to the device and its effect will be negligible from that seen in Eq. (12).

2.12. Two-Signal Spur-Free Dynamic Range

This dynamic range (DR) is usually applied to receivers that can process simultaneous signals. The lower limit is the sensitivity level. The upper limit is reached when two strong signals of equal amplitude begin to generate a detectable third-order intermodulation. For convenience, the detectable level is often chosen to be the noise floor. With this assumption, the two-signal spur-free dynamic range can be written as

$$DR = \frac{2}{3}(Q - G - N_o) \text{ dB} \quad (13)$$

where Q is the third-order intercept point, G is the gain of the RF chain, and N_o is the noise power at the output of

the RF chain and can be expressed as

$$N_o = -114 + F + 10 \log(B_R) \text{ dBm} \quad (14)$$

where -114 is the noise floor of 1 MHz bandwidth, F is the overall noise figure of the receiver, and B_R is the RF bandwidth. To achieve a certain sensitivity and dynamic range in a receiver, the gain of the RF chain must be of a specific value. Although higher gain may improve sensitivity, it degrades the dynamic range. However, a third-order intercept point higher than the designed value will not produce any adverse effect.

2.13. Two-Signal Instantaneous Dynamic Range

This dynamic range is applicable to receivers that can process simultaneous signals. It represents the capability of the receiver to receive a strong as well as a weak signal simultaneously. The *instantaneous dynamic range* is defined as the maximum amplitude separation between two simultaneous signals such that the receiver can measure both correctly. Generally speaking, this dynamic range depends on the frequency separation of the two signals. When two signals are close in frequency, the instantaneous dynamic range is low. When the frequencies of two signals are widely separated, the instantaneous dynamic range is high.

If a microwave receiver is used to intercept radar signals, two additional parameters are important: the throughput time (throughput rate) and delay time.

2.14. Throughput Time (Throughput Rate)

If a receiver can process only one signal at a time, the throughput time is the shortest time between two pulses the receiver can process. If the receiver can process N simultaneous signals, the throughput time is the shortest time between two groups of N simultaneous pulses the receiver can process. The information of a pulsed signal, that is, RF and pulse amplitude, can be obtained from the front of the pulse, but the pulsewidth must be measured at the end of the pulse. Therefore, the throughput time is pulsewidth-dependent. To keep the throughput time an intrinsic characteristic of the receiver, it should be measured with signals of minimum pulsewidth. The inverse of the throughput time is called the *throughput rate*.

2.15. Delay Time

The delay time is measured from the time a pulse reaches the input of a receiver to the time it is completely encoded. If delay lines are used in the receiver to store information temporarily, the delay time can be only a few microseconds. Delay time is important for intercept receivers used to generate information to respond on the same signal. If delay time is too long, the information cannot be used by a jammer to respond on the same signal.

3. CLASSIFICATION OF RECEIVERS

There are many ways to classify microwave receivers. One popular classification uses operating frequency range,

that is, Ku band, X band, or extremely high-frequency (EHF) receivers. Another way of classifying them is by application, for example, satellite receiver, or global positioning system (GPS) receiver. Even the intercept receivers can be subdivided by application, such as warning or electronic intelligent (ELINT) receivers. Although these classifications can reveal some specific information about the receiver, they do not reveal the technology on which the receiver is based.

In this article receivers are classified by their structure and only intercept receivers will be discussed. These receivers are designed to receive different kinds of signals, and all receivers have similar input. Different techniques can be used to build intercept receivers. These techniques, fundamental to receiver designs, are adopted in many other types of receivers. For example, the superheterodyne technique is used in most receiver designs. Almost all communication receivers irrespective of their operating frequency and applications often use superheterodyne techniques.

A very important factor in a receiver is whether the receiver can process multiple simultaneous signals. Since it is usually easy to isolate one desired signal, it is relatively easy to build a receiver that can process only one signal at a time. Most commercial communication receivers belong to this category. A scanning receiver can listen to many stations in a sequential manner, but it can process only one signal at a time. It is relatively difficult to build a receiver that processes more than one signal, especially when high instantaneous dynamic range is required. High instantaneous dynamic range requires the receiver to distinguish a weak signal from a spurious response, which is difficult to achieve. For low instantaneous dynamic range requirement, the problem is not as severe. For example, a GPS receiver must receive simultaneous signals from many satellites. As the signals from different satellites have about the same amplitude, the required instantaneous dynamic range is low and it is relatively easy to build such a receiver. If a large number of simultaneous signals need to be processed, considerable hardware will be required and the receiver can become rather complicated.

The receivers are divided by structure into two major groups: analog and digital. Comparatively speaking, analog receivers are technologically more mature. In fact, most commercial and military receivers are analog. Therefore, several techniques are used in designing analog intercept receivers that will be discussed here. Although the digital receiver is in its infancy, it is anticipated that this kind of receiver will become popular because advances in digital hardware and software can be applied to receiver design and processing.

4. ANALOG INTERCEPT RECEIVERS

This discussion is limited to radar intercept receivers. The receivers will be divided into six types depending on their structures. The first three types, which process only one signal at a time, are the crystal video, superheterodyne, and instantaneous frequency measurement (IFM) receivers. The next three types, which can process simultaneous

signals, are the channelized, Bragg cell, and compressive receivers.

In a radar intercept receiver five parameters will be measured. These parameters are RF, angle of arrival (AoA), pulse amplitude, pulsewidth, and time of arrival (ToA). Pulse amplitude is measured from the amplitude of the detected video pulse. Pulsewidth is measured from the width of the video pulse. The ToA is measured from the leading edge of the video pulse. These three parameters are measured similarly for different receivers. The AoA is measured from several antennas and receivers combined together and will not be included in this article. A digital EW receiver must also be able to generate these five parameters as output.

4.1. Crystal Video Receiver

This is the simplest analog receiver and has existed for many years. The receiver consists of an RF chain and a crystal video detector. In the RF chain there is a wide bandpass filter and RF amplifiers. Along with the detector there is a video filter, a video amplifier, and a comparator as shown in Fig. 5. Sometimes, the RF amplifiers are not available to cover the desired bandwidth or they do not have sufficient gain. Under this condition, the sensitivity of the receiver depends on the sensitivity of the detector and the tangential sensitivity cannot be calculated from Eq. (11). As a result, sensitivity will be poor. To improve sensitivity, the detector is occasionally biased in the forward direction as shown in Fig. 5. However, improving the sensitivity of the detector may decrease bandwidth. At the output of the detector a video filter will be used to limit the output bandwidth. The video filter bandwidth should match the shortest pulsed signal anticipated. For example, if the shortest pulse anticipated is 100 ns, the video filter will be approximately 10 MHz ($1/100 \times 10^{-9}$). The video amplifier is used to amplify the video level to a level that can be properly processed. Sometimes a logarithmic (log) video amplifier is used instead of a video amplifier. A

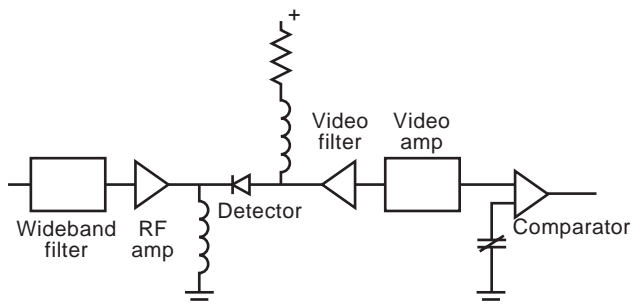


Figure 5. A basic crystal video receiver. This receiver consists of a wideband filter, an RF amplifier chain, a biased detector, a video amplifier, and a comparator. The wideband filter is used to limit out-of-band signals. The RF amplifier is used to amplify the input signal. The detector is used to change the RF signal to a video signal. The bias applied to the detector is to increase the detector sensitivity. The video filter is designed to match the anticipated minimum pulsewidth to maximize the detection efficiency. The video amplifier is used to amplify the video signal. The comparator is used to detect signals crossing a certain threshold.

log video amplifier takes a video signal as input and generates a video output that is proportional to the logarithm of the input signal. Finally, a comparator is used to determine whether a signal is crossing a certain threshold.

A crystal video receiver usually has a very wide input bandwidth and often covers a bandwidth of an octave or more. A crystal video receiver does not provide frequency information. The only frequency information is the detected signal within the input band of the receiver. The receiver can measure pulse amplitude, pulsewidth, and ToA. When simultaneous signals arrive at the input of the receiver, the receiver can receive and process all of them. However, the receiver does not have the capability to indicate the existence of simultaneous signals. The pulse amplitude measured will be the sum of the amplitudes of the simultaneous signals if the frequency separation of the signals is much greater than the video bandwidth. However, when this condition is not met, the pulse amplitude measured will be the vector sum of the signals. The pulsewidth measured will be from the first leading edge to the last trailing edge of the pulses in the group. The ToA measured will be the first leading edge of the group.

Because of its relatively low sensitivity and poor frequency accuracy, this type of receiver is no longer widely used. However, due to simplicity of the receiver, sometimes it is used to provide AoA information. The AoA information is often obtained through amplitude comparison from four directional antennas and four crystal receivers. In this application, log video amplifiers are used after the detectors. The difference between two adjacent channels is equal to the amplitude ratio due to the logarithmic relationship. The amplitude ratio can be converted into AoA information.

4.2. Superheterodyne Receiver

In the superheterodyne concept, the input signal is changed from one frequency to a different frequency while also maintaining all the signal information. This is very important to the technology, with most of today's communication receivers using superheterodyne techniques. Almost all receiver systems use this methodology at one stage or another. For example, an intercept receiver may have an instantaneous bandwidth of 1 GHz and an input bandwidth of 18 GHz. One common approach is to divide the input bandwidth into eighteen 1-GHz bands and convert each band to a common frequency range through the superheterodyne technique. The intercept receiver is timeshared among these bands to measure the input signals.

A generic superheterodyne receiver is shown in Fig. 6. In this design, the first element is a tunable filter and an RF amplifier. If higher sensitivity is desirable, an RF amplifier can be placed in front of the filter. A combination mixer/oscillator is used to change the input frequency to a different frequency, usually referred to as the IF. The IF can be either higher or lower than the input signal. If the IF is higher than the input frequency, it is called *upconversion*. If the IF is lower than the input, it is referred to as *downconversion*. The IF signal is further amplified and filtered before reaching the crystal detector. Sometimes an

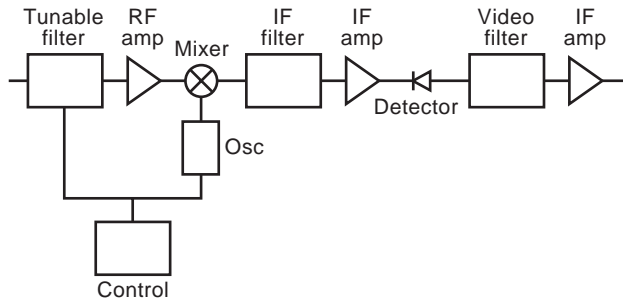


Figure 6. A basic superheterodyne receiver. This receiver consists of a tunable filter, an RF amplifier chain, a mixer and local oscillator, an IF filter, IF amplifiers, a detector, and a video amplifier. The tunable filter and the local oscillator are controlled by the same control circuit, and their frequencies are tracked to filter out unwanted input signals. The RF amplifier is used to amplify the input signal. The mixer and local oscillator combined changes the input frequency to the IF. The IF filter is used to limit spurious signals generated by the mixer. The IF amplifiers are used to amplify the IF signal. The detector changes the RF signal into a video signal, and the video amplifier is used to amplify the video signal.

IF logarithmic (log) video amplifier is used. An IF log video amplifier takes IF as input and generates a video signal proportional to the logarithm of the input. In an IF log video amplifier, many IF amplifiers and detectors are used. Each detector covers approximately 10–15 dB of dynamic range. Therefore, the amplifier can cover a wide dynamic range and provide high accuracy. Along with the detector there are video amplifiers and video filters to shape the video signal.

A mixer is a nonlinear device that converts a signal from one frequency to another. In order to change frequency the device must be nonlinear. However, in receiver design, a mixer is considered to be a linear component with a negative gain (loss) and a third-order intercept point. The desired output IF frequency f_{IF} of a mixer is

$$f_{IF} = f_i \pm f_o \quad \text{or} \quad f_{IF} = f_o \pm f_i \quad (15)$$

where f_i is the input frequency and f_o is the oscillatory frequency. The plus sign is used for upconversion; the minus sign, for downconversion. If $f_i > f_o$, the first part of the equation is used; when $f_o > f_i$, the second part is used. The input frequency is usually downconverted to a lower IF, because amplifiers and narrowband filters are more available at lower frequencies. The IF is fixed at a certain value, and the frequency of the oscillator is tuned across the input bandwidth of the receiver to find signals. Once the input signal is converted to the IF, the signal will be detected and the video signal will be processed. The frequency of the input signal can be measured from the preceding equation, because f_{IF} and f_o are known.

When the input frequency is higher or lower by f_{IF} than the local oscillator frequency, they will be detected by the receiver; these are images of each other. If the input bandwidth is not properly limited, both the signal and its image can be received by the receiver. An image rejection mixer

can be used to separate signals above the local oscillator frequency from signals below it. However, it is often desirable to limit the input band of the receiver either above or below the local oscillator frequency. Limiting the bandwidth to one side of the local oscillator frequency also reduces the noise by 3 dB.

As a mixer is a nonlinear device, many other frequencies will be generated in addition to the desired frequency. These extraneous frequencies are referred to as “spurs.” The frequencies f_i of the spurs, including the desired IF, can be determined by

$$f_i = Mf_1 + Nf_2 \quad (16)$$

where f_1 and f_2 are used to represent the input and oscillator frequencies; M and N are integers (either positive or negative) and the output frequency f_i must be a positive value. In order to limit the spurious outputs, two filters are often used in a superheterodyne receiver. An IF filter with a fixed center frequency f_{IF} is used to reject spurs at the output of the mixer. Because the input bandwidth is much wider than the IF filter, several signals present at the input of a mixer will cause it to generate spurs. A tunable filter with bandwidth comparable to that of the IF filter can be placed at the input of the receiver to limit the instantaneous bandwidth and reduce spur generation. The tunable filter and the local oscillator must be synchronized, and the difference frequency between them must equal f_{IF} . Thus, one control unit is often used to tune the tunable filter as well as the oscillator. The frequency range of the input filter and the oscillator must be wide enough to cover the input bandwidth of the receiver.

Because the filter bandwidth of a superheterodyne receiver is very narrow, the sensitivity is high. The spurious responses generated by the mixer are carefully filtered, so the dynamic range is usually high. It is relatively easy to build superheterodyne receivers with matched performance, that is, amplitude and phase, because of the narrow bandwidth. The probability of intercept of a superheterodyne receiver is low and it cannot process simultaneous signals. Therefore, a superheterodyne receiver alone is seldom used as an intercept receiver. It is often used as part of an intercept system such as one that measures AoA information through multiple antenna and receiver combinations.

4.3. IFM Receiver

An IFM receiver uses the autocorrelations function to measure the input frequency. A signal is correlated with its delayed version. The outputs are lowpass filtered to generate the desired video signals, which in turn can be used to produce the frequency information. There are many different ways to build a correlator by using different RF components such as 90° hybrids and in-phase power dividers. One common approach is shown in Fig. 7.

The input signal is divided into two paths, and in one of the paths a known delay time τ is added. Four hybrids are used to obtain the desired phase relations. The detectors are used to perform multiplication. If the input frequency is f , the outputs of the detectors consist basically of two

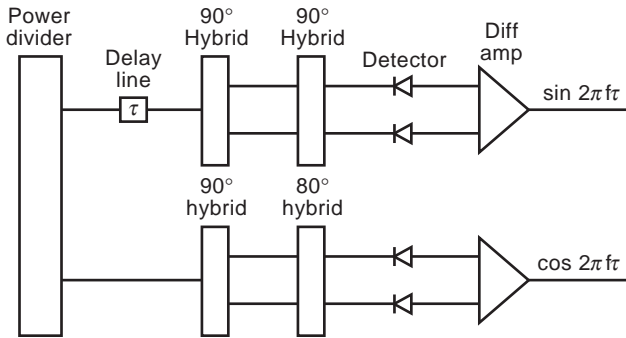


Figure 7. A correlator for the IFM receiver. The correlator consists of a power divider, a delay line of known delay time, three 90° and one 180° hybrids, four detectors, and two differential amplifiers. The power divider divides the input signal into two parallel paths, and the signal in one path is delayed by a known time. The four hybrids are used to provide the necessary phase shifts. The detectors are used to convert RF signals into video signals as well as to perform multiplication of two signals. The two differential amplifiers are used to cancel a DC bias term. The outputs from the correlator are $\sin(2\pi f\tau)$ and $\cos(2\pi f\tau)$.

terms—a double frequency term and a DC term. The outputs of the detectors are lowpass-filtered to stop the high frequency and pass the DC components. They represent the autocorrelation functions of the input signal. The differential amplifiers are used to remove a constant term in the DC components, and the outputs are $\sin(2\pi f\tau)$ and $\cos(2\pi f\tau)$. As the delay time is known, the frequency of the input signal can be found as

$$f = \frac{\theta}{2\pi\tau} \quad (17)$$

where

$$\theta = \tan^{-1}\left(\frac{\sin(2\pi f\tau)}{\cos(2\pi f\tau)}\right) = 2\pi f\tau$$

By measuring the $\sin(2\pi f\tau)$ and $\cos(2\pi f\tau)$, the angle θ can be found and the frequency can be calculated.

As the angle θ calculated from the sine and cosine is less than 2π , this relation limits $f\tau < 1$. If the desired input bandwidth is 2 GHz, the delay time must be less than 0.5 ns. Using this τ value to measure frequency, the accuracy is rather poor because of the poor angle resolution. In order to cover a wide instantaneous bandwidth and at the same time produce fine frequency accuracy, several correlators are needed. Correlators with short delay times are used to resolve ambiguity; correlators with the longest delay line provide frequency accuracy. The longer the delay line, the better the frequency accuracy a correlator can provide. The longest delay line must be shorter than the shortest pulse anticipated and must allow the pulse and its delayed version to have sufficient overlap. The delay-line lengths are commonly selected to be multiples of each other. The two common delay-line ratios are 1 : 2 and 1 : 4. Two examples will be used to illustrate these two design ideas.

To cover a 2 GHz bandwidth, it is common practice to select the unambiguous bandwidth wider than the desired value, that is, 2.56 GHz, and the corresponding shortest delay time is 0.390625 ns ($1/2.56$ GHz). In the 1 : 2 ratio case, the delay-line lengths are 1, 2, 4, 8, 16, 32, and 64, and the shortest delay line is considered as unit length. There are seven correlators in this design. In the 1 : 4 ratio case, the delay-line lengths are 1, 4, 16, and 64, and there are only four correlators. The correlators with the longest delay line have the same design in both cases and they provide the frequency accuracy (usually about 1 MHz). Decoding schemes for the other correlators are slightly different. The decoding scheme of the correlators with a 1 : 2 ratio is simpler than the ones with a 1 : 4 ratio because the former one is required to generate only 1 bit and the latter one must generate 2 bits of information. Therefore, both approaches are popularly adopted in IFM receiver designs.

An IFM receiver uses a very unique RF front-end design. The RF chain of most receivers uses linear components to avoid generating spurs and retain the amplitude information of the input signals. In an IFM receiver it is common practice to use a limiting amplifier in the RF chain. This kind of amplifier raises all signals above a certain threshold to a constant level. Therefore, amplitude information is lost with the limiting amplifier. A separate circuit must be used to measure pulse amplitude. As the limiting amplifier is a nonlinear device, it generates strong spurious responses. When two signals are present in the amplifier, the strong one will suppress the weak one. This is referred to as the *capture effect*. Because an IFM receiver can process only one signal at a time, the capture effect will enhance the receiver performance to measure the strong signal under simultaneous signal conditions.

An IFM receiver has many advantages over other types of intercept receivers. The receiver can cover a very wide instantaneous bandwidth [possibly 16 GHz (2–18 GHz)] and provide fine frequency accuracy on short pulses, for example, 1 MHz accuracy on a 100 ns pulse. As the structure of the receiver is very simple, the receiver can be very compact, low cost, and reliable. The only deficiency is that the receiver cannot process simultaneous signals. Not only is it unable to process simultaneous signals, but simultaneous signals with amplitude within about 5 dB may cause the receiver to produce an erroneous frequency report without reporting the mistake. This is considered a major problem with the IFM receiver and limits its usage. However, the concept of the IFM receiver is very important and can be adopted in many receiver designs, including digital receivers.

4.4. Channelized Receiver

A channelized receiver can intercept simultaneous signals. The basic concept is very simple. It uses a bank of filters with adjacent frequencies to separate signals. Signals with different frequencies will exit from different filters. By measuring the outputs of the filters one can determine the frequencies of the input signals. A basic channelized receiver, shown in Fig. 8, consists of four

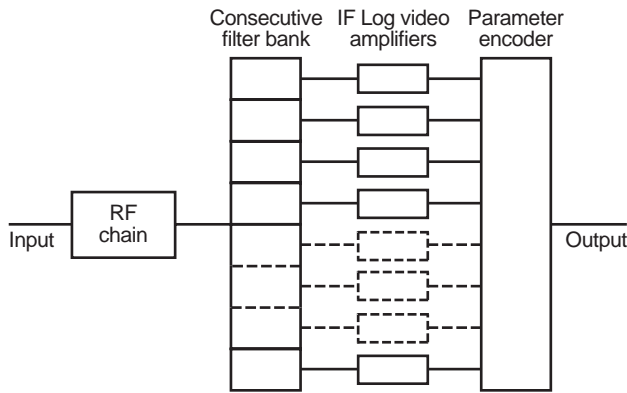


Figure 8. A basic channelized receiver. The receiver consists of an RF amplifier chain, a filterbank with contiguous filters, IF log video amplifiers, and a parameter encoder. The RF amplifier is used to amplify the input signal. The filterbank is used to separate signals with different frequencies into different output ports. The IF log video amplifiers amplify the IF signals and convert them into video signals. The parameter encoder generates the desired digital information from the input video signals.

major components. The first one is the RF chain. The second component is a filterbank with consecutive center frequencies. In order to retain the amplitude information, IF log video amplifiers are used after the filters. The last component is a parameter encoder, which takes the outputs from the filters and converts them into the desired information. These components are discussed here.

The RF chain usually consists of amplifiers, filters, and mixers to shift the input frequency. The RF chain must operate in the linear region to avoid generation of spurs. As the bandwidth of a channelized receiver is wide, some spurs generated from mixers will not be filtered out but be present in the output.

The output of the RF chain is fed to the input of the filterbank. A common way to feed the filterbank is through a power divider. Using a power divider can improve impedance matching to the filters, but they cause insertion loss. Every time a signal is divided into two paths there is a 3 dB loss. These losses must be recovered by placing additional amplifiers in the receiver. Although a frequency multiplexer is a better approach to feed the input of the filter, it is usually difficult to achieve the desired filter requirements. In each filter usually only one signal can be processed. If more than one signal is in one filter, they will be processed as one signal and may produce erroneous results. Depending on the center frequency of the filters and their bandwidth, different techniques can be used to build the filters, for example, surface acoustic wave (SAW) technology and lumped *LC* elements. The two general requirements of these filters are low insertion loss and small size. The filter must also have low sidelobes in the frequency and time domains. The required shape of the filter is usually based on the encoding circuit design.

The outputs of the filters are further amplified by IF log video amplifiers. If the amplitude information after a filter is not of interest, a limiting amplifier followed by a crystal detector can be used to convert the IF into a video signal. With only one signal processed within a filter,

intermodulation and spurs are not of concern. Therefore, in designing a receiver, the third-order intercept point in the IF channel is not of concern. If amplitude is not retained after the IF amplifiers, pulse amplitude information must be obtained from another part of the receiver.

A parameter encoder takes the video signals from all of the filters as input and produces the desired information. Most of the effort in encoder design is directed toward obtaining frequency information. There are usually two ways to obtain frequency information. One is to compare amplitudes from adjacent filter outputs. In this approach, IF log video amplifiers must be used to generate amplitude information at the filter outputs. One problem with this approach is that it is difficult to balance the gain in all the channels. If the gain from one channel changes slightly, that is, due to temperature drift, the encoder must be adjusted accordingly. Sometimes it can be a major problem in a receiver with many channels. Another approach is to detect the transient response of a filter output. If a pulsed signal passes the center of a filter, the transient effect is not significant, which means that the pulseshape is slightly distorted. On the other hand, if a pulsed signal passes the skirt of a filter, the transient effect is very significant, which means that the pulseshape is drastically distorted. By measuring the transient on the output pulse, one can determine whether a signal is in the middle or on the skirt of a filter. In this design, both limiting amplifiers and IF log amplifiers can be used after the filters. The problem with this approach is that the variation on the leading edge of the pulse can change the transient response and the performance of the encoding circuits. In some receiver designs both the amplitude comparison and transient phenomenon are used to obtain better results. The filter shape, which controls the amplitude and the transient of the video signal, is often determined from the encoding circuit design. The encoder design is the most critical element in building a channelized receiver.

In a receiver that can process simultaneous signals, there are two quantities related to frequency measurement. One is frequency resolution, which tells the receiver to separate two simultaneous signals that are close in frequency. The other one is frequency accuracy, which is related to the error in the frequency measurement. The minimum pulsewidth determines the minimum filter bandwidth, which determines the frequency resolution of the receiver. Frequency measurement must be carried out after the transient dies off. The transient is approximately equal to the inverse of the filter bandwidth. During the transient period both the shape and the RF of the pulse change. If the desired minimum pulsewidth is 100 ns, the minimum bandwidth of the filter is approximately 10 MHz and the frequency resolution is close to 10 MHz. However, the receiver can be designed with a filter bandwidth that is much wider than the minimum filter bandwidth. A wideband filter has a shorter transient time. If additional processing, that is, the concept of an IFM receiver is used, better frequency accuracy can be obtained. It is difficult to design a receiver with both high-frequency resolution and frequency accuracy on short pulses because it takes a longer time to generate a fine frequency reading. In general, the anticipated minimum pulsewidth deter-

the minimum filter bandwidth and thus the minimum frequency resolution. This design rule applies to all receivers with simultaneous signal capability.

Because the concept of channelized receivers is very simple, a general misunderstanding is that it is very easy to build. As a result, the design goals might be set too high to achieve. In general, a receiver has fewer problems when the filter bandwidth is wide because the receiver has fewer parallel channels. However, wider bandwidth means poor frequency resolution and lower sensitivity. When a high instantaneous dynamic range is desired, the receiver must detect a weak signal in the presence of strong signals. Sometimes it is difficult to distinguish a spurious response from a weak signal. Therefore, a high-dynamic-range receiver may produce a spurious signal report. When the instantaneous dynamic range requirement is low, the receiver can be designed to produce fewer spurious responses.

The input bandwidth of a channelized receiver is proportional to the number of channels and their bandwidth. When a large number of channels are built, a channelized receiver can be bulky and expensive but have better frequency resolution. If the channel bandwidth is wide, a small number of channels can cover a wide frequency range. Because the encoding circuit also has fewer inputs, the receiver can be relatively small.

4.5. Bragg Cell Receiver

A Bragg cell receiver can be considered another type of channelized receiver where channelization is accomplished by optical means. The term *Bragg cell receiver*

derives from the concept of the Bragg angle of optical diffraction. A basic Bragg cell is shown in Fig. 9. The optical arrangement will be discussed first. A laser is used as a coherent light source. A diode laser is often preferred to a gas laser because of its small size. The beam expander and the collimator are used to form the lightbeam into the desired shape to shine on the Bragg cell. A Bragg cell is used to diffract input light. A Bragg cell is made of a crystal transparent to the laser light. At one end of the crystal is a transducer to change the input electric signals into acoustic signals. At the other end of the Bragg cell is absorption material used to eliminate acoustic wave reflection to avoid the generation of standing waves. The acoustic wave produces variations in the refractive index of the crystal. This refractive index modulation causes the laser beam to deflect. The *time-bandwidth product* (TBP) of a Bragg cell is defined as the time of the acoustic wave traveling through the window of the Bragg cell multiplied by the bandwidth. The laser beam is incident on the Bragg cell at the Bragg angle where the desired diffracted light is at maximum intensity. The light output from the Bragg cell passes through a Fourier transform lens and focuses on a photodetector array. The photodetector changes the optical signal back into a video signal.

The input signal to the receiver is applied to the transducer of the Bragg cell through an RF chain containing amplifiers and filters. There is an impedance matching network to match the output of the RF chain to the input impedance of the Bragg cell. The output power from the RF chain should keep the Bragg cell operating in its linear region. High input power can drive the Bragg cell into the nonlinear region and generate spurious responses.

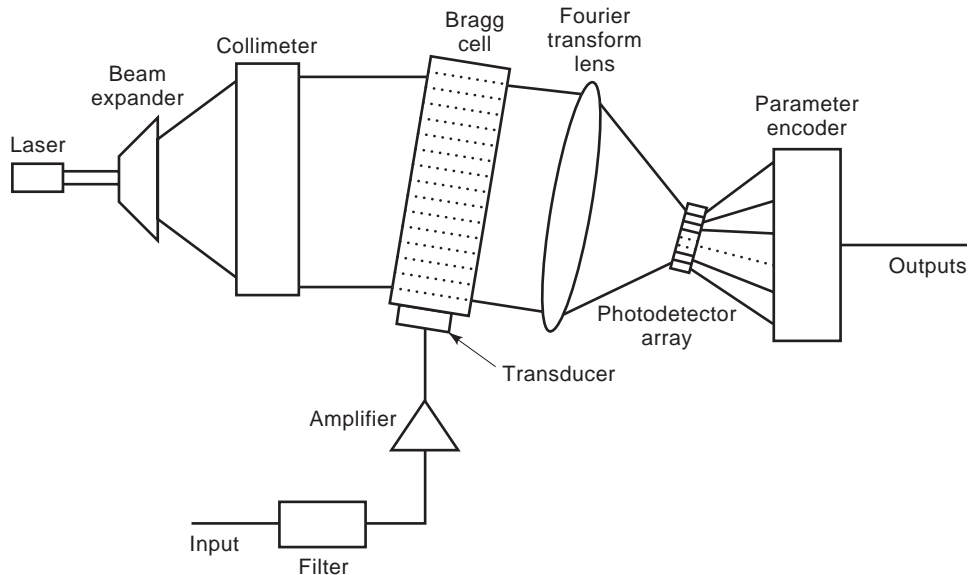


Figure 9. A basic Bragg cell receiver. The receiver consists of an RF chain, a laser, a beam expander, a collimator, a Bragg cell, a Fourier transform lens, a photodetector array, and a parameter encoder. The RF amplifier is used to amplify the input signal. The beam expander and the collimator shape the laser light into the desired shape. The input signal is converted into an acoustic wave in the Bragg cell to form a grating and diffract the light from the laser. The Fourier transform lens focuses the light on the photodetector array, which converts the light into video signals. The light position on the photodetector array determines the frequency of the input signal. The parameter encoder generates the desired digital information from the input video signals.

The input signal is converted into a traveling acoustic wave in the Bragg cell. The position of the diffracted light-beam on the detector array is related to the frequency of the input signal. If more than one signal is present in the Bragg cell, there will be multiple outputs on the detector array. The maximum number of outputs is equal to the time-bandwidth product of the Bragg cell. The amplitude of the output is related to the power of the input signal.

The video outputs from the photodetector array can be considered as outputs from a filterbank with adjacent frequencies. The parameter encoder takes these outputs and generates the desired information. In a channelized receiver, IF log video amplifiers or limiting amplifiers are used after the filters to provide more RF gain. To provide the same gain in a Bragg cell receiver, a light amplifier must be used in each output channel, however, such a device is not available with today's technology. Thus, the sensitivity of the receiver depends on the laser power and the characteristics of the photodetectors. A laser with higher power can be used to improve sensitivity. As the outputs from the photodetectors are video signals, some of the encoding schemes applicable to a channelized receiver may not be adopted for Bragg cell receivers. Another difference between the photodetector and the crystal detector is that the output from a photodetector is proportional to the input light power and, therefore, proportional to the input power. The output from a crystal detector is proportional to the voltage of the input signal, which is related to the square root of the input power. Therefore, a crystal detector covers more dynamic range.

Compared to a channelized receiver, a Bragg cell receiver has less dynamic range. The major advantage of a Bragg cell receiver is its simplicity and compactness. A Bragg cell receiver including the optical bench (consisting of beamforming lenses and Bragg cell), laser and detector array, but excluding the RF chain, is only a few cubic inches in size. Such a small receiver can provide over 100 parallel outputs. The size of the optical bench can be further reduced using integrated optics. In the integrated optical approach, the entire optical bench can be fabricated on a single chip. The light is transmitted through a light waveguide and the Bragg cell uses SAW technology. All optical components can be made on the chip, and the laser and detector array can be attached from the ends of the chip. Thus, the size can be a few cubic centimeters.

The Bragg cell receiver already discussed here is often referred to as the *power Bragg cell receiver*, because the detector output is proportional to the power of the input signal. In order to improve the dynamic range of a Bragg cell receiver, an interferometric approach can be used. The main goal of this approach is to make the photodetector proportional to the voltage of the input signal rather than the power. In this arrangement, the laser beam is split into two paths through a beamsplitter with a Bragg cell in each path. The input to one Bragg cell is a locally generated spread-spectrum signal covering the entire bandwidth of the Bragg cell. The input signal is applied to the other Bragg cell. The outputs of the two Bragg cells are focused on a photodetector array, and the location represents the input frequency. Each photodetector is used as an optical mixer and the output is an IF signal rather than

a video signal. Thus, IF amplifiers and filters can be used to improve the performance of the receiver. After the IF chain, crystal detectors are used to convert the IF signals into video signals. Although this approach has the potential to improve the dynamic range of the receiver, it sacrifices the simplicity of the Bragg cell receiver. Individual IF channels have to be built separately and the optical bench is equivalent to the filterbank in a channelized receiver.

As in designing channelized receivers, the parameter encoder of a Bragg cell receiver is a major portion of the effort.

4.6. Compressive Receiver

A compressive receiver can also process simultaneous signals. As opposed to a channelized receiver where all outputs are in parallel, the outputs from a compressive receiver are in series. A basic compressive receiver is shown in Fig. 10. In this figure the RF chain is not included. The two major components in a compressive receiver are the local oscillator and the dispersive delay line. The output from the local oscillator is a repetitive FM signal. The frequency range of the FM signal can be very wide and the period very short, such as 1 GHz/200 ns. This receiver is also called a *microscan receiver* because the scan time is short. The input signal after mixing with the local oscillator output is converted into an FM signal. This FM signal passes through the dispersive delay line (often referred to as *compressive line*) and is compressed into a pulse. The position of the pulse relative to the beginning of the scan represents the frequency of the input signal. The amplitude of the compressed pulse represents the amplitude of the input signal.

The instantaneous bandwidth of the compressive line is generally equal to the IF bandwidth of the receiver. The input bandwidth can be either wider or narrower than the IF bandwidth. In one common design, the local oscillator scans the sum of the IF bandwidth and the receiver input bandwidth. In order to compress the FM signal from the output of the mixer into a short pulse, the frequency-time slope of the local oscillator and the slope of the compressive line must be properly matched. In most designs, the compressive line is made from SAW technology with bandwidths of up to 1 GHz and dispersive delays of a few hundred nanoseconds. The local oscillator is often implemented from a dispersive delay line because a short pulse applied to the input of a dispersive delay line generates an FM signal at the output. This signal can be amplified and used as the local oscillator output. Because the frequency of the local oscillator is wider than the compressive line bandwidth, the requirements on the dispersive delay line to generate the local oscillator signal are more stringent. An oscillator built from a dispersive delay line is easier to match the frequency-time slope of the compressive line. The time-bandwidth product of the compressive line is defined as the dispersive delay time multiplied by the bandwidth. The maximum number of compressed pulses generated per scan is approximately equal to the time-bandwidth product of the compressive line. The maximum number of compressed pulses can be

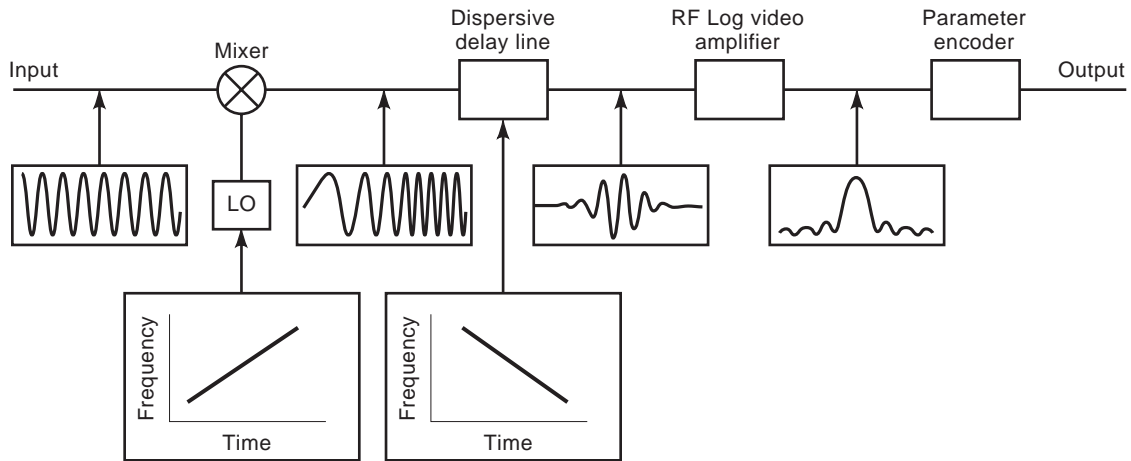


Figure 10. A basic compressive receiver. The receiver consists of a local oscillator, a mixer, a dispersive delay line, an RF log video amplifier, and a parameter encoder. The local oscillator generates a linear FM signal that changes the input to a linear FM signal through the mixer. The dispersive delay line compresses the FM signal into a short pulse. The RF log video amplifier is used to generate the logarithm from the compressed pulses. By measuring the output time of the pulse with respect to the beginning of the scan, the signal frequency can be determined. The parameter encoder converts the scan to scan information to a pulse-by-pulse information.

considered equivalent to the total number of parallel channels in a channelized receiver.

The compressed pulse is very short and is inversely proportional to the bandwidth of the compressive line. The pulse output rate equals approximately the bandwidth of the compressive line. If the bandwidth of the compressive line is 1 GHz, the pulsewidth is close to 1 ns (1/1 GHz) and the output rate is about 1 GHz. The center frequency of the pulse equals the center frequency of the compressive line. The compressed pulse has a main peak and many sidelobes. The sidelobes should be reduced to simplify the frequency encoding circuit design. The sidelobes can be reduced by adding a weighting (window) function to the compressive line. An IF log video amplifier is used to convert the compressed pulse into video pulses for further processing. The video bandwidth of the IF log video amplifier must be wide enough to accommodate the compressed pulsewidth.

A compressive receiver usually intercepts a pulsed signal in many consecutive scans. It is desirable to report the information on the intercepted signal on a pulse-by-pulse basis rather than a scan-by-scan basis. The parameter encoder will sort and combine the scan-by-scan information into pulse-by-pulse information. The outputs from each scan are the number of simultaneous signals intercepted during the scan time. From this operation, it is easily seen that the time resolution in generating pulsewidth and ToA equals the scan time. Thus, it is usually coarser than the time resolution in other types of receivers.

The main function of the parameter encoder is to find the frequency of the input signal. Because the compressed pulse output rate is usually rather high, the encoder must be able to process the signals at the same rate. Although the parameter encoder is quite different from a

channelized receiver, they face the same basic challenges: detecting the signal and avoiding the sidelobes and spurious responses. The bandwidth of a compressive receiver is limited by the technology used in the compressive line as well as the speed of the logic circuit in the parameter encoder.

There are several different ways to design a compressive receiver. One of the most common designs is to make the receiver bandwidth equal to the IF bandwidth. Under this condition, the outputs of the compressive line are present only 50% of the time. This affects the probability of intercept. If a short pulse (less than half the scan time) falls in the silent half, the receiver will miss the pulse. To improve the probability of intercept, another mixer and local oscillator can be added in parallel. The beginning of the FM signal from this local oscillator is shifted to the middle of the original one. For example, if the scan time is 200 ns, the original scan is from 0 to 200 ns and the additional scan is from 100 to 300 ns. Outputs from both channels are combined and fed into the compressive line. With this arrangement, the compressive line can have output 100% of the time. This technique is called the interlace scan. The outputs from the IF log video amplifier are in series, so less hardware is required in the parameter encoder as compared with a channelized receiver; however, operational speed is very high and matches the bandwidth of the compressive line.

The minimum pulsewidth that a compressive receiver can process is approximately equal to the scan time or half the scan time if the interlace scan is used. The frequency resolution is close to the inverse of the minimum pulsewidth. Compared with a channelized receiver, it shows that the same laws of physics govern the performance of both receivers; that is, the frequency resolution is inversely proportional to the pulsewidth.

5. DIGITAL RECEIVERS

A digital receiver consists of three building blocks: the RF chain, the ADCs, and the DSP. Once a signal is digitized the data are less affected by ambient conditions such as temperature changes. In an analog receiver, the performance of the components may change because of temperature variation and aging, while digital circuits do not have these problems. The digitized data can be processed with many different DSP approaches. Although most of the DSP are still hardwired for receiver applications, increasing the processing speed may permit changing receiver functions through software switching. Thus, the software receiver concept is becoming popular. With this concept many different receivers can be implemented using the same hardware. The software receiver idea is particularly popular for military communication receivers because of its potential versatility.

Strictly speaking, an ADC is a nonlinear device. It can be considered as a linear device for a large number of quantization levels. The discussion in the following sections is based on the linear model of an ADC. Nonlinear operation still exists if strong signals drive the ADC into saturation. Under this condition, the output of the receiver may produce many spurious responses. Special procedures must be considered to deal with this phenomenon.

To cover a wide bandwidth, the ADC must operate at high speed. The Nyquist sampling theorem requires that the minimum sampling speed be twice the information bandwidth. To cover a wide dynamic range, the ADC must have a large number of bits. The number of quantization levels is related to the number of bits b as 2^b . If the dynamic range is defined from a signal at the highest level to a signal at the lowest level, it can be readily expressed as

$$DR = 20 \log(2^b) \approx 6b \quad (18)$$

In this equation, the ADC is assumed ideal, that is, the quantization levels are uniform and there is no jitter in the sampling window. In a typical ADC, there are noise, nonuniform quantization level and sampling window jitter. An effective bit is often used to characterize a nonideal ADC. The number of effective bits is less than the actual number of bits and is defined as [2]

$$b_{\text{eff}} = b - \log_2 \left\{ \frac{\text{RMS error (actual)}}{\text{RMS error (ideal)}} \right\} \quad (19)$$

The effective bits change with frequency and have fewer bits at higher frequency. The number of effective bits should be used in Eq. (18) to determine the dynamic range. If the highest spurious response is used as the lower limit of a receiver, the dynamic range varies. However, Eq. (18) provides a simple estimation.

Digital receivers can be divided into two generic groups: narrowband and wideband receivers. Usually, one can consider a narrowband receiver to receive only one kind of signal and the receiver is not required to process simultaneous signals. For each type of signal a

narrowband receiver will be designed individually. There are exceptions to this definition. For example, a GPS C/A (coarse acquisition) code receiver has a narrow bandwidth, because the input signals have the same frequency. However, this receiver can receive multiple signals with different code. A wideband receiver can receive simultaneous signals over a wide frequency range. The input signals can be either known or unknown. For a wideband communication receiver the signals are known. For an intercept receiver the signals are unknown.

Another way of differentiating narrowband and wideband digital receivers is by the frequency tuning schemes. In a narrowband receiver, the frequency tuning is accomplished through analog means by changing the frequency of the local oscillator and selecting the proper filters. For this type of tuning, input to the ADC is usually an isolated signal rather than the full input bandwidth of the receiver. Thus, the ADC and the DSP following it can operate at a lower frequency.

In a wideband digital receiver the frequency tuning method is implemented digitally. The sampling frequency of the ADC and the following DSP must be high enough to accommodate the input bandwidth of the receiver. For example, one can build an FM radio through either a narrowband or a wideband approach. The input bandwidth of an FM radio is 20 MHz (88–108 MHz). If a single FM station is selected by analog tuning, the signal bandwidth is 200 kHz. If the sampling rate is 2.5 the signal bandwidth, an ADC with a sampling speed of 500 (2.5×200) kHz is required. If the frequency will be tuned digitally, the sampling speed must be 50 (2.5×20) MHz. Although the signal information bandwidth is only 200 kHz, the following DSP must match this operational speed of 50 MHz. The potential advantages of digital tuning are superior filter shape and flexible tuning ability.

In the following sections, a narrowband receiver with a band folding concept and a wideband channelized receiver will be presented.

5.1. Narrowband Digital Receiver

The Nyquist sampling theory requires that the minimum sampling speed be twice the signal bandwidth, not twice the highest frequency of signals. For example, the C/A code of the GPS signal is at L_1 band (1575.42 MHz) with a bandwidth of 2 MHz from null to null. The minimum sampling frequency to acquire this signal is 4 MHz, although the signal is at 1575.42 MHz. If the input bandwidth of the ADC can accommodate the 1575.42 MHz frequency, the signal can be sampled directly at slightly higher than 4 MHz. Sampling will alias the input signal to a baseband as shown in Fig. 11. In this figure the sampling frequency is f_s ; thus, the maximum unambiguous bandwidth is $f_s/2$. All the input bandwidth from 0 to $(n+1)f_s$ will fold into the bandwidth $f_s/2$. From this frequency folding property, the RF chain of the receiver should be designed with at least two bandpass filters. The first one should be placed near the front of the RF chain to reject out-of-band signals as in an analog receiver. The second filter should be placed in front of the ADC to limit the out-of-band noise generated from the amplifiers in the RF chain.

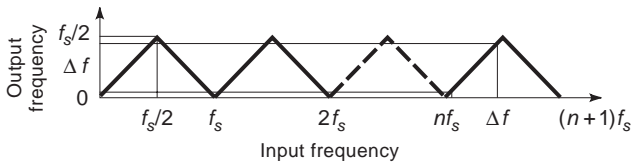


Figure 11. A sampling scheme transferring the input to baseband. The sampling frequency is f_s ; the maximum unambiguous bandwidth is $f_s/2$. A signal with bandwidth of $\Delta f < f_s/2$ in the frequency range of nf_s to $(n + 1/2)f_s$ can be transferred to the baseband of 0 to $f_s/2$ through sampling.

One can design a receiver to receive several narrowband signals separated in frequency through sampling at a proper frequency. An example will be used to illustrate this approach. The Y code of the GPS signal at L_2 band has a bandwidth of 20 MHz centered at 1227.6 MHz. If one desires to receive the C/A code at L_1 and the Y code at L_2 of the GPS signals, the total bandwidth is 22 MHz ($2 + 20$). The minimum required sampling frequency should be 44 MHz (2×22). Some specific sampling frequencies can be used to fold the two signals into the baseband. One sampling frequency is 51.6 MHz. Under this condition, the Y code is aliased to 5–25 MHz and the C/A code is aliased to 0.62–2.62 MHz. These two frequency bands are not overlapped in the baseband. In general, it is desirable to fold the two signals into separate regions of the baseband to avoid interference. If interference is not a problem, it is possible to overlap the two signals to save bandwidth. However, overlapping two signals into one frequency range also folds the noise together. The noise floor will increase at the overlap region. This concept can be extended to more than two signal bands.

5.2. Wideband Digital Receiver

The most popular wideband digital receiver is a digital channelized receiver. The basic idea is the same as it is for an analog channelized receiver—to separate the input into many parallel consecutive frequency channels. In a digital channelized receiver, the filterbank is implemented digitally. To cover a wide bandwidth and high dynamic range, the ADC must operate at very high speed and have many output bits.

The simplest way to build a channelized digital receiver is to use discrete Fourier transform (DFT) implemented using the fast Fourier transform (FFT). The FFT should operate on the input data on a continuous manner. The FFT outputs from different time intervals can be considered as the outputs of each individual filter. This technique requires the FFT to operate at high speed. If a receiver covers a 1 GHz bandwidth, the sampling speed must be above 2 GHz. Suppose that the sampling speed is 2560 MHz and a 256-point FFT can produce 256 parallel channels. However, only 128 channels provide useful information, and the other 128 outputs are the complex conjugate of the first ones. It takes 100 ns to accumulate 256 data points and the output channel bandwidth is 10 MHz ($1/100 \times 10^{-9}$ s). As the bandwidth of the receiver is 1 GHz, only the center 100 outputs will be used and the remaining 28 end channels will not be monitored. To pre-

vent missing data, the FFT must perform 256 point FFT at least every 100 ns. If any overlap of the FFT is desired, the processor must operate at a faster speed.

In general, it is difficult to match the digital processing speed to the speed of the ADCs. One common way to solve this problem is to reduce the total number of output channels, but keep the input at 256 data points. This approach reduces the frequency resolution of the receiver. For example, one can perform a 32-point FFT to reduce the output to sixteen 80-MHz channels. Under this condition, a bandpass filter will be used to limit the input bandwidth to 1 GHz, which will partially block the input of the two end channels. The input data are decimated 32 times, then each of the 8 data points will convolve with an 8-point filter as shown in Fig. 12. The coefficients of the 32 filters are obtained from decimating a 256-point filter, which is designed to shape the frequency response of the 16 filters. The 32 outputs from the filters become the input to the 32-point FFT. In order not to miss data, a 32-point FFT must be performed every 100 ns, which is a less stringent requirement than the previous case. If the FFT can operate at a higher speed, the input data can be processed in an overlap mode, that is, performing FFT every 50, 25, or 12.5 ns. This overlap mode is a common practice in channelized receiver design. Finally, the outputs from the FFT must be correctly decoded to generate the desired information. If the receiver is used to intercept radar signals, the encoder will provide the five parameters: frequency, AoA, ToA, pulse amplitude, and pulsewidth.

5.3. Hybrid Receivers

One common hybrid receiver design is to build a wideband receiver such as channelized or compressive receiver with a coarse frequency resolution. For example, one can divide the input bandwidth of 1 GHz into 10–20 uniform bands with a frequency resolution of 100–50 MHz. Once a signal is detected and its coarse frequency is measured, a narrowband receiver or receivers can be used to obtain fine-grain information on the signal. One approach is to rapidly tune a narrowband IFM receiver to measure the

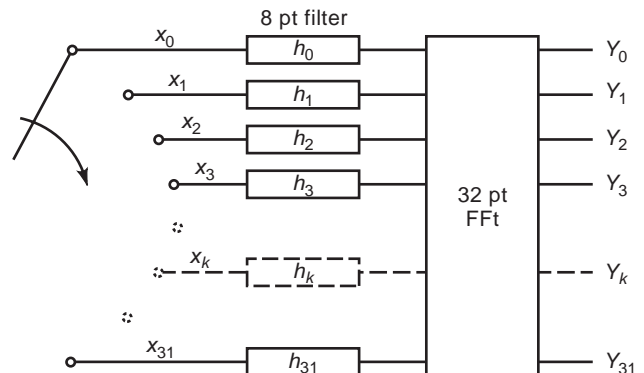


Figure 12. A 32-output filterbank using decimation scheme. The main goal is to perform a 32-point FFT with 256 input data points. The input is decimated into 32 parallel channels. In each channel, there is an 8-point filter. The output from each filter contains 8 input data points. These outputs are used as the input to the 32-point FFT.

Table 1. Receiver Performance

	Crystal Video	Superheterodyne	IFM	Channelized	Bragg ^a Cell	Compressive	Digital ^b Channel
Instantaneous BW	Very wide	Narrow	Very wide	Wide	Wide	Wide	Wide
Simultaneous signal capability	None	None	None	Good	Good	Good	Good
Frequency accuracy	Poor	Excellent	Excellent	Good	Good	Good	Good
Sensitivity	Poor–fair	Excellent	Good	Good	Fair–Good	Good	Good
Single-signal DR	Fair	Excellent	Excellent	Good	Fair–Good	Good	Good
Two-signal instant DR	N/A	N/A	N/A	Good	Fair	Good	Good
Two-signal spur-free DR	N/A	N/A	N/A	Good	Fair	Good	Good
Structure	Simple	Moderate	Simple	Complex	Moderately complex	Complex	Complex
Size	Small	Small/moderate	Small	Bulky	Small–moderate	Moderate	Bulky

^aThis represents the power Bragg cell receiver. The interferometric Bragg cell receiver performance should be comparable to a channelized receiver, but the structure is more complicated.

^bThe digital receiver is in the development stage, and performance should improve in the near future.

frequency of the input signal, because the IFM receiver can provide improved frequency resolution. Another design is to rapidly tune several narrowband receivers that are connected to different antennas to measure the AoA of the input signal. In this design, it is easier to match the amplitude and phase of narrowband receivers. It is a common practice to combine these two approaches in one hybrid receiver design. These approaches can be implemented in both analog and digital receivers. In an analog hybrid receiver design, RF delay lines must be used to temporarily store the input signal while the narrowband receiver or receivers can be tuned to the desired frequency. Wideband low-loss RF delay lines are not available and this is one of the major problems in analog hybrid receiver design. In digital design, since the digitized data can be stored easily, delay lines are no longer required. Once the basic properties of a receiver are understood, they can be combined in various ways to solve specific problems.

6. COMPARISON OF DIFFERENT TYPES OF RECEIVERS

It is difficult to compare the performance of different types of receivers. For example, one can consider a channelized receiver to be complicated if there are a large number of channels. If there are only a few channels, the receiver can be rather simple. The same argument holds for Bragg cell and compressive receivers. To make the assessment meaningful, it is assumed that the four types of receivers—channelized, Bragg cell, compressive, and digital channelized—all have the same number of output channels. The other three types of receivers—crystal video, superheterodyne, and IFM—cannot process simultaneous signals. It is also difficult to put quantitative measures on the performance. For one specific receiver this should be the correct way to present its performance. However, for one type of receiver it may be difficult to do so. For example, one channelized receiver is designed for higher sensitivity and lower dynamic range, and another one is designed for higher dynamic range and lower sensitivity. If the best performance of each receiver is reported, the results can be misleading because they cannot be achieved in one

receiver design. Therefore, the performance is listed in a qualitative manner as in Table 1.

BIBLIOGRAPHY

1. J. B. Y. Tsui, *Microwave Receivers with Electronic Warfare Applications*, Wiley, New York, 1986.
2. J. Keffel, T. R. McComb, and R. Malewski, Comparative evaluation of computer methods for calculating the best fit sinusoid to the high purity sine wave, *IEEE Trans. Instrum. Meas.* **IM-36**:418–422 (June 1987).

MICROWAVE RESONANCE PLASMA SOURCE

ALEXANDER L. TAUBE
GREGORY M. DEMYASHEV
Swinburne University of
Technology
Melbourne, Australia

1. INTRODUCTION

Low-temperature thermal plasmas operating at atmospheric pressure are used for a variety of contemporary plasma-enhanced technologies, such as plasma chemistry, materials processing, coating deposition, surface treatment, and waste treatment. Conventional plasma spray sources running at atmospheric pressure are based on electric arc [1] or radiofrequency (RF) [2–6]. The currently employed industrial plasma spray sources have a number of disadvantages [7], including low efficiency of energy consumption, plasma contamination, and low efficiency of precursor consumption.

Generally a microwave plasma electrodeless concept is based on using microwave electromagnetic energy in order to form and sustain a plasma discharge. There are various ways to supply the microwave energy for plasma generation [8].

Ionization of feed gases and precursors by electric field is defined by the ratio of “electric field strength to gas

pressure" [9]. Depending on a working pressure in a chamber, conventional microwave plasma discharges can be classified as follows:

- High-vacuum electron cyclotron resonance plasma
- Low-pressure microwave plasma
- Atmospheric-pressure waveguide-based setup microwave plasma

The electron cyclotron resonance (ECR) plasma is based on the cyclotron phenomenon of electrons in a static magnetic field, which allows transfer of the microwave energy to plasma. The ECR plasma operates in fairly high vacuum (10^{-1} – 10^{-3} Pa) [10–13]. The ECR can be realized through the proper combination of a microwave frequency and strength of magnetic field. The frequency of the alternating electric field is made to match the natural frequency of the electrons orbiting magnetic lines of the magnetic field. For 2.45 GHz the required strength of magnetic field is ~ 875 G. The ECR plasma has the electron density of 10^{10} – 10^{12} cm $^{-3}$ and a high degree of ionization (10%). The disadvantages of ECR plasma sources include

- Difficult process control
- Costly equipment due to the added variable magnetic field and due to high vacuum
- Low rate of deposition (~ 2 nm/min)

For example, ECR has been used for deposition of AlN [14], SiO $_2$ [15], SiN $_x$ O $_y$ [12], microwave plasma heating [16], tungsten incorporated carbon films (W-C:H) [17], and other applications.

Low-pressure microwave plasma discharge (LPMPD) runs at relatively low pressure (133 Pa–13 kPa) [13,18–22]. *Low pressure* implies more collisions between electrons and neutral molecules.

The LPMPD can be realized in either a waveguide setup, where a dielectric tube evacuated to low pressure is put through a *waveguide* [23], or a dielectric jar (or discharge chamber [24,25] evacuated to low pressure, where the dielectric jar is located inside a vessel supplied with microwave power. Quartz (or alumina) is commonly used as materials for the dielectric tube/jar.

The *waveguide* setup utilizes the standing-wave mode of TE $_{01}$. A movable plunger is used to tune the electric field maximum of the standing wave so that the maximum coincidences with quartz tube location.

The LPMPD has a few peculiarities. The electrons have a temperature of 10^3 – 10^4 K and a plasma electron density of 10^9 – 10^{14} cm $^{-3}$. The temperature of heavy particles (ions, radicals, species, etc.) in LPMPD is approximately 500 K. The LPMPD is commonly used for deposition of diamond like carbon [23,26–28], low-pressure plasma cleaning [29], and other procedures.

The *waveguide* setup of atmospheric pressure microwave plasma source is similar to that for the LPMPD. A *waveguide* plasma applicator contains quartz tube at the end of a *rectangular waveguide*. A movable short-circuiting plunger allows the adjustment of a maximum electric

field at the plasma-containing quartz tube. A trigger (tungsten rod) is an integral part of this type of plasma source in order to sustain a plasma discharge. The waveguide setup of atmospheric-pressure microwave plasma source commonly operates with 2.45 GHz *magnetrons* [30–33], but other frequencies, such as 896 MHz [34] and 915 MHz [35], are employed as well. The *waveguide*-based plasma applicator is an inherent part of fluidized-bed microwave plasma reactors operating at atmospheric pressure [36]. The ion density of the waveguide setup of atmospheric-pressure microwave plasma varies within 10^{11} – 10^{12} cm $^{-3}$ [30], $\sim 10^{16}$ cm $^{-3}$ [32,34].

From time to time other microwave plasma sources operating at atmospheric pressure are mentioned in the literature. All of them are difficult to classify in scientific terms because the basic information provided in the industry is very limited. For example, Ecotec (Taiwan) Co. Ltd. enounced a new construction of a microwave plasma surface operating at atmospheric pressure [37]. This microwave plasma burner allows one to obtain a plasma temperature near the nozzle in the range of 3000–4500 K. Plasma is produced just near the end of the central electrode (tube), then drifts outward, and microwave energy is released the gas apart from the nozzle.

2. BACKGROUND

2.1. Single Resonance Mode for Microwave Resonance Plasma Source (MRPS)

To create a required E field and ignite plasma, a high-efficiency resonance cavity with high Q factor should be designed. A *high-efficiency microwave resonance cavity* is defined as a resonant circuit element in a microwave network, where the resonance frequency of the resonant circuit element is a function of its characteristic complex impedance [38,39].

The Q factor of a high-efficiency microwave resonance cavity at the resonance frequency is described by

$$Q = \omega(\text{energy}_{\text{max stored}} / \text{power}_{\text{average dissipated}})_{\text{over a cycle}}$$

When a high-efficiency microwave resonance cavity runs and a load in the form of a plasma slab is present in the cavity, the Q factor is defined by the total energy absorbed by both the resonance cavity and the plasma slab. The plasma slab absorbs all microwave power, and the microwave energy stored by the resonance cavity is negligible small. However, when the plasma slab disappears, the microwave energy stored by the resonance cavity is maximised.

The microwave resonance cavity in question generally employs a TM $_{01n}$ mode since this mode creates a displacement current associated with longitudinal electric field E_z along the axis of the cylindrical guide. In particular, the TM $_{013}$ mode is widely used to increase the Q factor. A schematic representation of this is shown in Fig. 1, where E represents the lines of electric field and H , the magnetic lines.

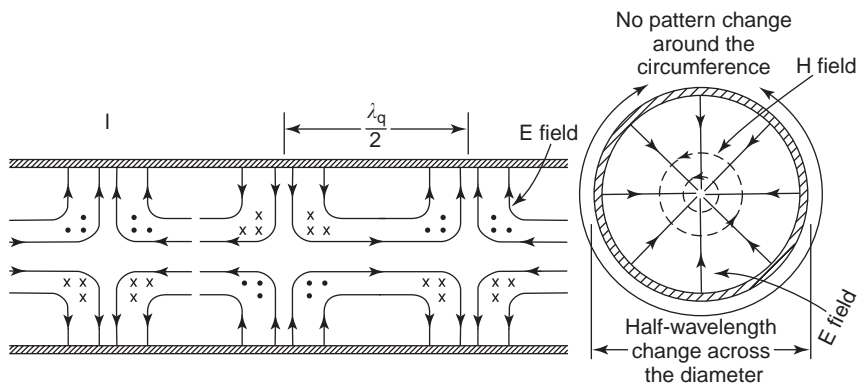


Figure 1. The field configuration of the TM_{013} mode in the cylindrical resonant cavity: longitudinal section (above) and cross section (on the left).

3. MRPS DESIGN AND OPERATION

3.1. Design

The geometry of a resonant cavity is the key element in the design of the MRPS [40]. Cavity geometry will identify the resonant mode of the microwave electric field and, therefore, ensure that only the required mode oscillates the cavity's length, and the diameter should be carefully calculated. As the radius of the resonant cylindrical cavity is difficult to modify in order to optimize and tune the microwave resonance, the length (L) of the resonant cavity can be tuned with a threaded plug (6) moving it in or out during operation of the resonant cavity (numbers in parentheses refer to points in diagrams).

A block diagram of the instrumentation employed in this research is shown in Fig. 2. The actual design of the cylindrical resonance cavity is displayed in Fig. 3. The

resonant cavity is constructed of a highly conductive material, such as brass and, to reduce ohmic losses (R_s), is covered with silver. Genuine setup of the MRPS, which consists of the TM_{013} cylindrical resonance cavity, waveguide, and a magnetron (1.3 KW, 2.45 GHz), is displayed in Fig. 4. The six-port analyzer is inserted in the scheme for measurement purposes.

In order to maintain two separate chambers of the resonant cavity, a dielectric partition has been built in and hermetically sealed in order to provide vacuum evacuation of chamber 1 (Ch1). The dielectric partition allows for plasma to form only in the Ch1, limited by length l (Fig. 2). The dielectric plate is made of hexagonal boron nitride (hBN), which is transparent for microwave radiation. The hBN plate acts as a pressure-dividing baffle between the Ch1 and the chamber 2 (Ch2), which is always under atmospheric pressure. It allows a lets plasma well to form in Ch1. After evacuation of Ch1 up to 20 kPa, plasma

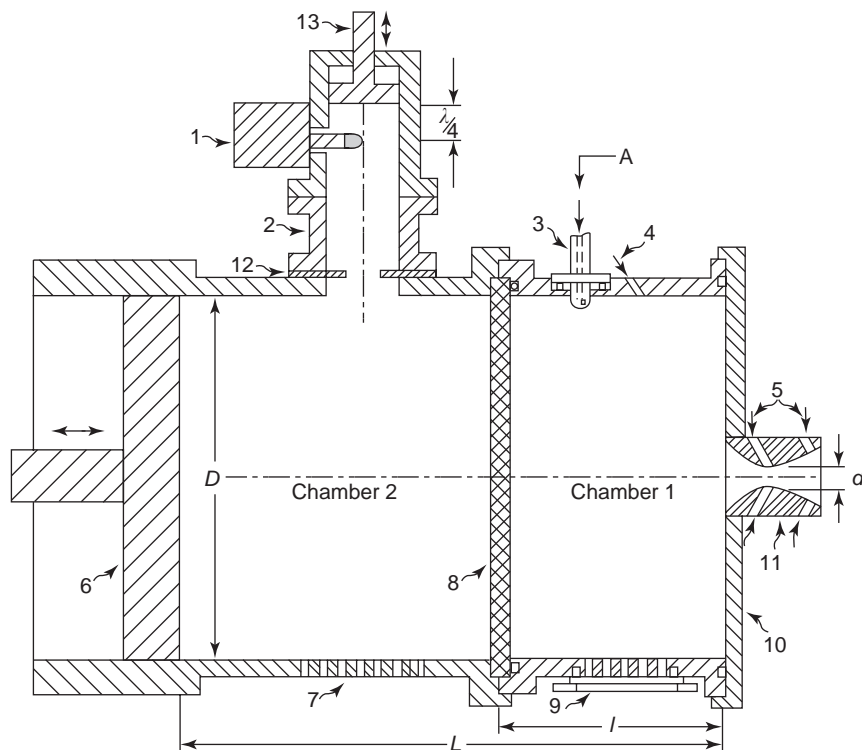


Figure 2. Sketch of the cylindrical resonant cavity: 1—magnetron, 1.3 kW, 2.45 GHz; 2—waveguide (WR-340); 3—inlet nozzles; 4,5—channels for precursors; 6,13—adjusted pistons; 7,9—watching windows; 8—hBN partition; 10—face lead; 11—convergent-divergent (Laval-type) nozzle; 12—rectangular aperture.



Figure 3. General view of the microwave resonant cavity.

begins to form under microwave radiation only in the low-pressure area (i.e., in Ch1). Once started, plasma is sustained with microwave energy only in Ch1.

The outlet nozzle was manufactured from stainless steel. It was found that the inlet geometry of the outlet nozzle is crucial because the plasma can concentrate at the sharp edges of the outlet nozzle. Stabilization of the plasma in the center was achieved by rounding the inlet profile of the outlet nozzle.

To introduce microwave energy, a magnetron launcher on the base of a standard section of WR-340 waveguide was attached to the cylindrical wall of Ch2. The aperture (12)—a symmetric iris, which can be an elliptical, circular, or rectangular slot—was used for coupling between a cylindrical cavity and a rectangular WR-340 waveguide operating in the dominant TE_{10} mode. The aperture ensures the maximum amount of microwave energy absorbed within the resonant cavity, instead of being reflected

back toward the magnetron. The optimal shape of the aperture is determined experimentally.

As in TE_{10} mode, a magnetic field component, which is parallel to the long dimensions of the slot, will be coupled through aperture. For the slot orientation perpendicular to the longitudinal z axis of cylinder, the TE_{10} magnetic field couples into the cavity, creating a magnetic field pattern within the cavity, which allows any of the TM_{01n} resonance modes to excite. When the waveguide and aperture is centrally located along the z dimension, the n mode must be even, but for odd values ($n=3$ for TM_{013}) the magnetic field is zero at that point in the cavity. Thus, the axis of the aperture should be approximately $\lambda/4$ from the ends of the cavity [38].

In order to maintain a stable plasma stream at the Laval nozzle, the gas flow should rotate within Ch1 (Fig. 5). Chamber 1 has three inlet nozzles (IN). The IN (3) are symmetrically placed close to the dividing BN plate. The diameter of the calibrated orifices must be optimized with a flowrate of gases, with power of microwave supply, plasma parameters (ion concentration, ionization ratio, etc.) for different atomic (Ar, He, etc.) or molecular (O_2 , N_2 , CH_4 , etc.) gases, and with the throat of the Laval nozzle. The IN should be directed tangentially to the wall and at a small angle of $10\text{--}20^\circ$ to the hBN plate. The plasma torch is formed from the Laval nozzle (5), which can have channels (5) for supplying powders/precursors into the plasma torch. Chamber 1 can have channels (4) for introduction of precursors directly into plasma slab.

The inlet and outlet can be optimized. The gases used are considered to be ideal, and the gas flow through the nozzles is isotropic. For a standard converging-diverging nozzle, the plasma flow is optimized when the plasma velocity at the throat is at the speed of sound. This condition is known as “shocked flow.” For shocked plasma flow, the velocity of the plasma after the throat in the diverging section of the nozzle will continue to increase until the pressure is equal to the ambient outlet pressure. For optimized or shocked flow, the point at which the diverging section of the nozzle ceases to accelerate the flow is dependent on the half-angle of the outlet nozzle and the length of the nozzle. The actual values of the length of the exhaust nozzle can be found only by experiment. The flow may also fluctuate due in proportion to the temperature fluctuations within the resonant cavity and the ambient outlet conditions.

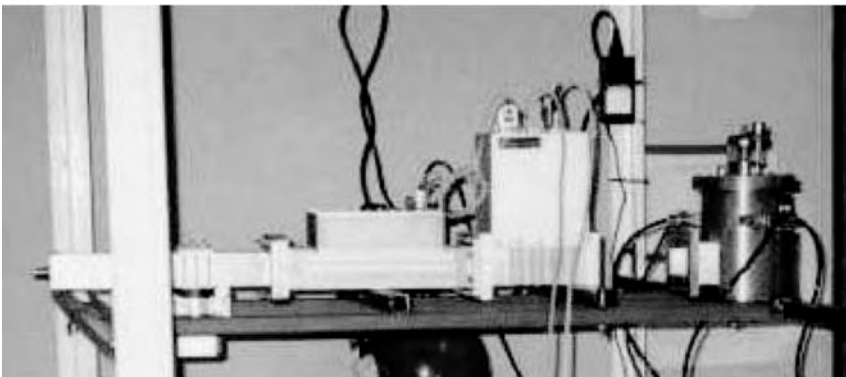


Figure 4. Experimental setup of the microwave resonance plasma source.

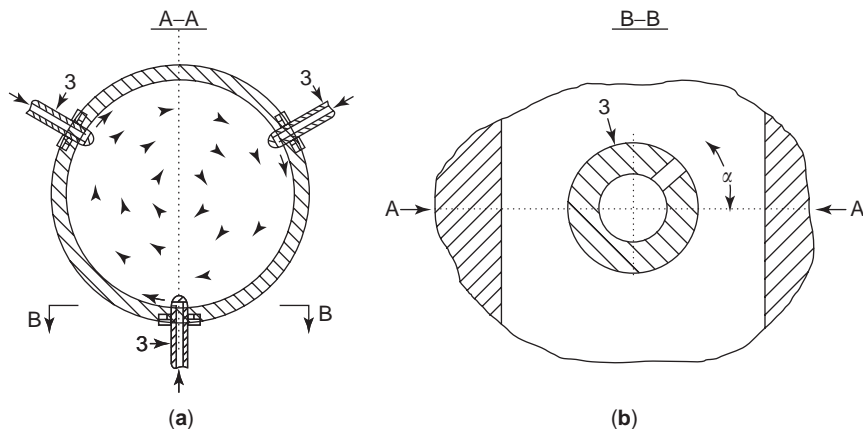


Figure 5. A cross-sectional view (A-A) of the plasma outlet chamber in place of connection of three calibrated orifices (see A-A cross section positioned in Fig. 2).

The MRPS makes available a required ionizing electric field density for plasma discharge and uses microwave energy to produce expanding plasma, which is directed through the convergent-divergent nozzle. Plasma acts as a resistive load that absorbs the incident microwave energy and dissipates it as thermal energy, which is transferred to a flowing gas. It is common to refer to this type of plasma as a “free-floating plasma” since it is located at regions of maximum electric field density within the interior of the cavity and does not have to be attached to an interior solid surface of the resonance cavity.

The MRPS design with the rectangular waveguide for transmission of microwave energy in Ch1 has a number of major advantages:

- It is easy to adjust during MRPS operation.
- Less manufacturing is required.
- It has higher power-handling capability.
- It is more efficient (lower loss per unit length of microwave transmitter).

3.2. Operation

The microwave plasma torch is a flamelike discharge and has a central plume (Fig. 6a). The plasma torch shown in

Fig. 6b is formed from the Laval nozzle (Fig. 6a). The microwave energy is coupled into the resonant cavity via a *rectangular waveguide* and a carefully designed aperture for the best coupling. Tuning can be accomplished by adjusting the position of the fine-tuned piston (6) (Fig. 2). With the piston set near its optimal position, the plasma can be ignited easily with a short burst inside the cylindrical resonance cavity (Fig. 6c).

In maximum region of electric field density, ionization of a carrier gas occurs, producing a microwave resonance-induced plasma discharge. Ionization of a carrier gas by electric field is dependent on the ratio of “electric field strength to pressure (i.e., the E/p ratio). The MRPS discharge will be maintained when the production of newly ionized species scarcely is equal to the rate of losses, namely, recombination and formation of torch.

For ignition of plasma, the exhaust nozzle is capped (Fig. 3) and the air is evacuated from the chamber 1, and then microwave power is introduced to the resonant cavity. After the formation of plasma in Ch1, a fore-vacuum pump is disconnected and the carrier gas begins to flow into Ch1. On the commencement of flow into Ch1, the plasma coalesces and moves toward the outlet nozzle. Once atmospheric pressure is achieved in Ch1, the nozzle cap is removed. From this moment, the microwave

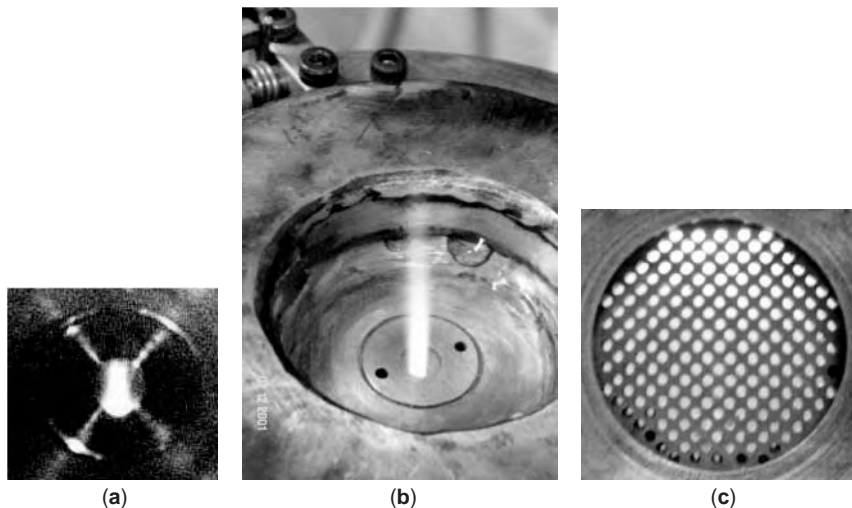


Figure 6. (a) Top view of the plasma torch at atmospheric pressure; (b) side view of the plasma torch at atmospheric pressure; (c) a plasma slab of MRPS operating at atmospheric pressure in plasma-forming chamber.

resonance plasma torch begins to run. Adjustment of the length (L) of the resonant cavity would also occur to maximize the microwave power absorption.

A typical position of the MRIPS is stabilization of the plasma slab at the center of the Ch1 touching the Laval nozzle. The plasma would concentrate at the edge of the outlet nozzle, and swirl in the same direction as the inlet swirl.

4. COMPARISON OF MICROWAVE PLASMA SOURCES

4.1. Equivalent Circuits of Microwave Plasma Sources

4.1.1. Waveguide Setup Plasma Source. An equivalent scheme of *waveguide*-type plasma reactor is shown in Fig. 7. In this equivalent circuit the distributed-circuit parameters are given in the form of equivalent lumped impedances.

Typically, the impedance of the plasma column can be represented by two parallel inductive and active resistances as a central part of a T-shape equivalent scheme in which the symmetric lumped complex impedances Z_1 and Z_2 depend on the geometric dimensions of the *waveguide* and discharge tubes. It is important that the impedance of plasma torch depend on the temperature, pressure, gas flow, and absorbed microwave power. A lossless shorting plunge is represented by shortcut transmitted line with impedance:

$$Z_s = jZ_0 \tan(2\pi d / \lambda_g)$$

where

- Z_s = impedance of the shortcut line
- Z_0 = characteristic of the shortcut line
- d = length o the line
- λ_g = wavelength

To get the maximum value of electric field in the required plasma location ($\leq 20,000$ V/m in the standard WR-340 waveguide at 2.45 GHz), l is usually equal to $(2n + 1)\lambda_g/4$, where n is an integer, so $Z_s \rightarrow \infty$, which is approximately analogous to the open-circuit line. Analysis of this equivalent circuit shows that before plasma have been generated, the input impedance of this system Z_{in} approaches to infinity, as it equals to the series connection of lumped complex impedances Z_2 and Z_s .

The starting plasma is rather difficult because there are no free electrons that act in response to the E field. Incident microwave power is not absorbed by cold gases and is almost completely reflected. The corresponding reflection coefficient rises to $|\Gamma| = 0.95$. Consequently, at atmospheric pressure the microwave discharge in this type of plasma source can be generated and sustained only by a trigger (such as tungsten rod), which is an inherent part of this type of plasma source. Moving off the tungsten trigger leads to sparking of the plasma discharge; therefore, this plasma discharge is classified as a trigger-sustaining plasma. After plasma was generated, the incident power begins to be partially absorbed by the plasma column; however for this type of plasma source, the reflection coefficient still remains high up to $|\Gamma| = 0.5$, so almost 25% of the power is reflected [5]. The Q factor of this type of plasma source is evaluated at ~ 100 – 500 for 2.45 GHz.

4.1.2. Waveguide-to-Coaxial Setup Plasma Source. Generally, this form of plasma generator is used as a coaxial line which has a characteristic impedance lower than that of waveguides. As a result, it is more easy to transform the coaxial plasma apparatus impedance and to match it with the characteristic impedance of a waveguide without much reflection. In this type of plasma source, the waveguide-to-coaxial transformer is loaded by the plasma chamber at the end of the coaxial line. The *coaxial line* is connected to the broadwall of the *waveguide* with its outer conductor terminating on the wall. Another end of coaxial line is connected with various kinds of the plasma discharge chamber. One end of waveguide is connected to power source and another to the lossless shorting plunge. One such configuration of the waveguide-to-coaxial type of plasma source together with an equivalent lumped circuit and an equivalent circuit with distributed circuit elements is shown in Fig. 8.

Equivalent circuits for coaxial line loaded with plasma chamber to *waveguide* junction connected to microwave generator is composed of complex impedances Z_1 , Z_2 and Z_3 and, which are characterize electromagnetic field behaviour and power losses due to evanescent higher-order modes that are exited at each of discontinuity, and power losses due to active losses in waveguide-to-coaxial junction. The equivalent scheme also comprises the lumped impedance of coaxial plasma structure Z_p , and Z_s —the impedance of the waveguide transmitted line with shorting plunge [41].

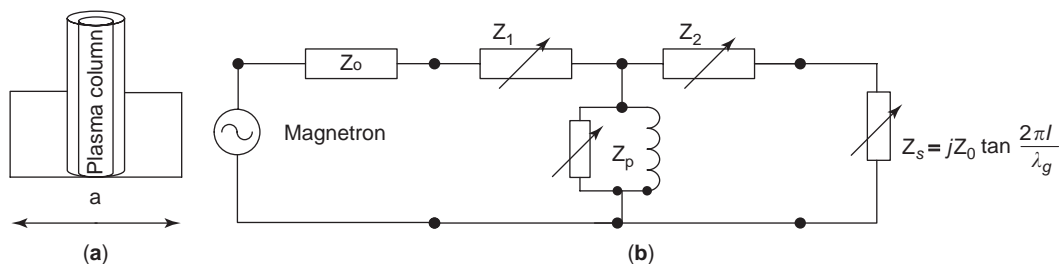


Figure 7. Equivalent scheme of waveguide array plasma source: (a) sketch of plasma slab; (b) equivalent circuit.

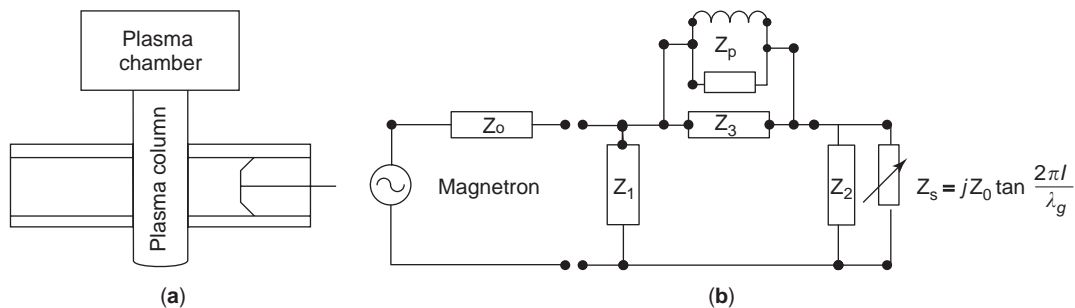


Figure 8. Equivalent circuit with distributed circuit elements.

Figure 8b shows that lumped plasma formation impedance is included in series in the transmitted waveguide; thus there is a very narrow band of impedance matching in order to ignite the plasma. Furthermore, any random destabilizing processes exert influence on absorption of microwave energy by plasma and cause reflection of microwave power. Thus, this kind of microwave plasma design also requires constant sparking ignition.

4.1.3. Microwave Resonance Plasma Source. There is a different scenario when plasma starts inside the high-*Q*-factor resonance cavity [42]. The equivalent scheme comprises the lumped complex impedances Z_1 , Z_2 related to impedances of iris and impedances of high-*Q*-factor resonance cavity X_r , L_r , R_r and the lumped complex impedance of plasma column Z_p , which depend on various factors such as temperature of plasma, gas flow, pressure, and absorbed power, (Fig. 9).

This MRPS uses microwave energy to generate self-sustaining plasma within the resonance cavity that is directed as a plasma torch through a convergent-divergent nozzle. A cold gas passes through the cavity, is ionized and heated by microwave power, and passes out of the cavity through a nozzle to produce the plasma torch.

4.1.4. Equivalent-Circuit Parameters. There are two major theoretical techniques for obtaining the equivalent circuits constants: the energy methods and the admittance methods. The first method analyses energy stored by the circuit's elements followed by a description of equivalent "intrinsic" inductance, capacitance, and resistance. Admittance/impedance method considers voltage and current across the microwave circuit elements and conse-

quently computes the characteristics of the equivalent-circuit elements. The equivalent circuits of stable, passive, and geometrically simple elements can be obtained relatively easily by integrating the electromagnetic field inside the microwave system, using the energy methods or admittance method [43]. But obtaining the equivalent microwave plasma circuit parameters with non-regular-shaped microwave elements and with randomly changing reflected and absorbed by plasma microwave power is usually complicated.

Some researchers applied method of "geometric similarity," when the equivalent complex impedance of part of the plasma column within the waveguide can be found by analogy with the ideally conducting metal rod. In the same approach the equivalent parameters of holes in the wider walls of waveguide, capacitance between plasma column and waveguide walls, and impedance of other elements of scheme were calculated [5]. However, in real discharge systems, width and temperature of the plasma column differ from point to point and can be represented as a lossy dielectric rather than ideal conducting metal rod; therefore, it seems inappropriate to use the method of "geometric similarity" in the GHz frequency range because the wavelength becomes comparable to the waveguide system dimensions, and what geometrically appears to be inductance can possess strong resonance properties in real system.

The most accurate methods used to obtain characteristics of the equivalent scheme is waveguide/cavity perturbation technique, which is one of the most important and widely used techniques to study the microwave impedance of materials and devices and offers both qualitative and fairly accurate quantitative information for engineering purposes [44]. However, even this highly

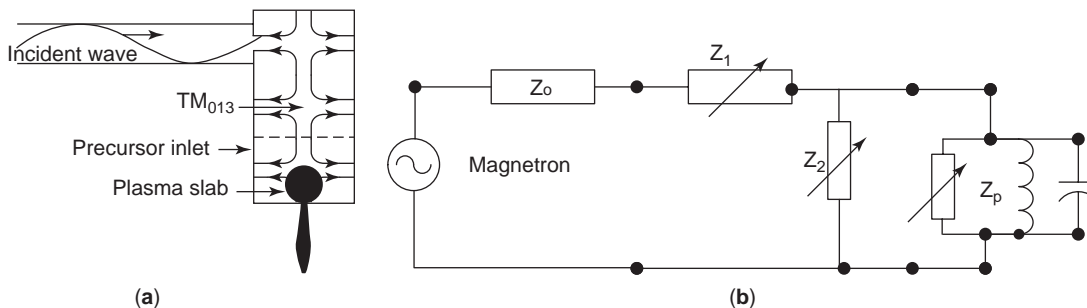


Figure 9. Equivalent scheme of resonance plasma source.

sensitive and relatively simple technique cannot be applied to nonstable, irregular, and fluctuating plasma when most of or all parameters of the equivalent scheme of plasma sources are interdependent and are similar with respect to absorbed power, temperature, type of gas, flow-rate, and so on.

4.2. Incident/Reflected Microwave Power

Because of high rate of electron collisions with neutrals and ions, the plasma in the MRPS is resistive and inherently absorptive. Since the plasma occupies the region where most of the electric field energy is stored in the cavity, the resistive plasma discharge exerts a strong damping on the cavity by absorbing approximately 98% of the incident microwave power (Fig. 10) and transforms the microwave energy into thermal plasma, which is transferred to the flowing gas. Thus, the plasma transforms the cavity from a high-*Q* to a low-*Q* cavity, and any disturbing factors that render the plasma unstable will again increase the *Q* factor of the resonance cavity. Therefore, increasing the electric field sufficiently reignites the plasma. As evaluated [5,45], the coefficient of microwave power

absorption for the nonresonance plasma sources very seldom surpasses 50%.

4.3. Smith Chart

The *Smith Chart* (Fig. 11) illustrates the differences of microwave plasma discharges generated in the resonance microwave plasma source (Fig. 9) and in the nonresonance plasma source (Figs. 7 and 8). In resonance design, the impedance point shifts to the center of the Smith chart (Fig. 11a) after the plasma is ignited and the operation spot is located predominantly, around “1.” In the waveguide, coaxial-to-waveguide, or coaxial design, the operating conditions are randomly distributed throughout Smith chart (Fig. 11b).

4.4. Stability of Microwave Plasma Sources

The most significant feature of these microwave plasma sources is their stability [42]. Therefore it is very important to analyze an influence of disturbing factors, such as gas flow instability, pressure, and absorbed power, doping mass and flow variations, on the main types of microwave plasma sources.

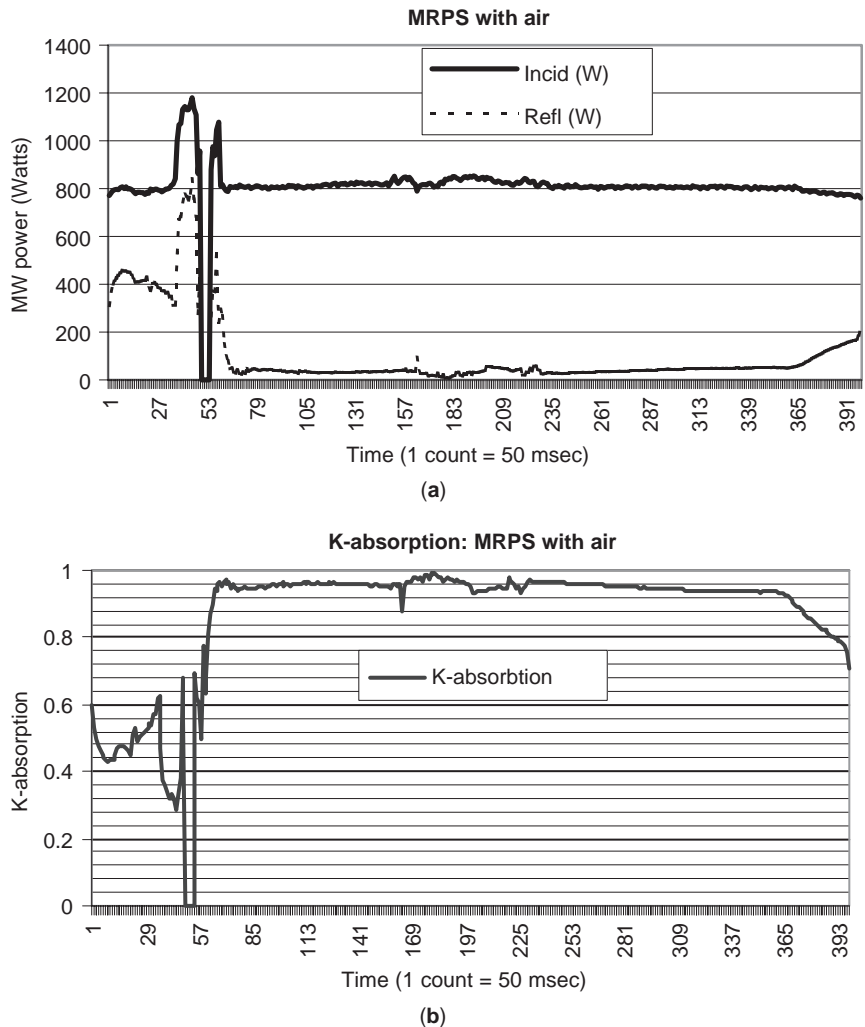


Figure 10. Incident/absorbed microwave power (a) and coefficient of absorption (b) as a function of time for the MRPS.

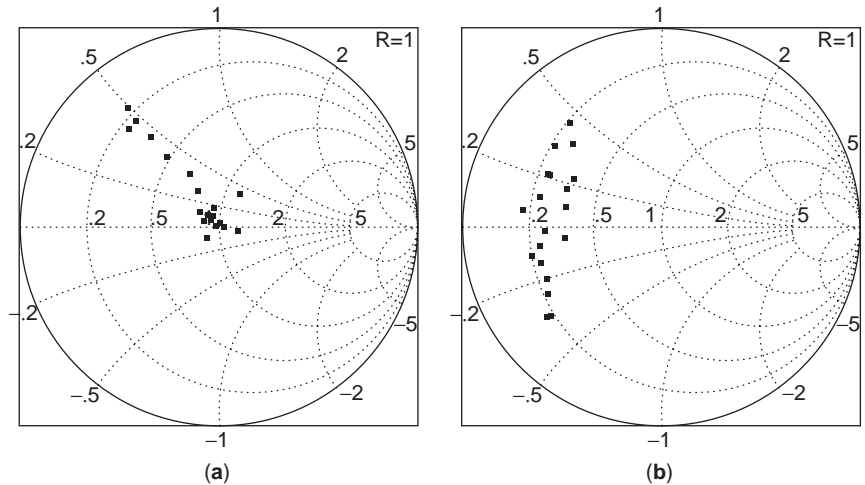


Figure 11. Operational points of resonance (a) and nonresonance (b) plasma sources on Smith chart.

The problem with plasma discharge stability can be solved by analysis of current–voltage characteristics [5]. As a result, the stability criterion was formulated as a rising current–voltage characteristic of the load or by considering the gradient of functional dependence of the required power and the plasma column admittance. But analysis of plasma source performance by considering the plasma source’s equivalent scheme is unreliable as there are uncertainties in parameter calculations and in definition of voltage and current in microwave schemes.

To analyze the instability effect of any of the perturbation factors (temperature of plasma, gas flowrate, pressure, etc.) on plasma sources performance the *Q*-factor method was proposed and applied [42]. If we describe perturbation injurious effect of any of the influencing quantities as *P*, so any change in perturbation factors will represent the absolute value $|\Delta P|$. Now the criterion for stability (*S*) of plasma design can be expressed as

$$S = \delta Q / (\delta |\Delta P|) > 0$$

Thus, when energy stored in the system is increased with a change of any of the influencing quantities, the microwave plasma source will be stable and self-sustained. Therefore, if the stability factor $S > 0$, any injurious effects of the influencing conditions, which cause the plasma to become unstable, will again increases the *Q* factor of the resonance cavity, thus increasing the electric field sufficiently to reignite the plasma.

For illustration, let us consider the conventional low *Q*-factor waveguide setup plasma source (Fig. 7). It is useful

to represent a plasma slab as a “quasidielectric rod” integrated in the microwave system with absorbed microwave power depending on type, pressure, flowrate of gases, and other parameters.

For this type of design, there is a very narrow interval of parameters in which plasma can exist and be stable. Any interchange in condition will result in changes in impedance matches and power balance. For example, when the plasma temperature increases as a result of any destabilizing factors, the concentration of charged particles in plasma increases so that the active component of the plasma column impedance changes. This in turn increases the reflection from the plasma slab. As a result, the *Q* factor of the system and, therefore, the absorbed power decrease, stability factor $S < 0$, that renders plasma generation unstable. When the plasma temperature decreases under the influence of fluctuating factors, the local electric field as well as absorbed microwave power decreases and the plasma extinguishes, and the stability factor $S < 0$. This kind of plasma source requires high stability of the external parameters or a constant “ignition” such as the tungsten trigger.

The microwave plasma stability in the MRPS and in the waveguide setup plasma source can be compared with equilibrium between a ball in a valley and on a hill. Like the MRPS, any destabilizing factors (ΔD) return the ball to equilibrium position (Fig. 12a). In case of the MWTPS, the destabilizing factors (ΔD) move the ball away from the equilibrium state (Fig. 12b).

Stability of MRPS, intensity of microwave power absorption, and the size of a plasma slab have been

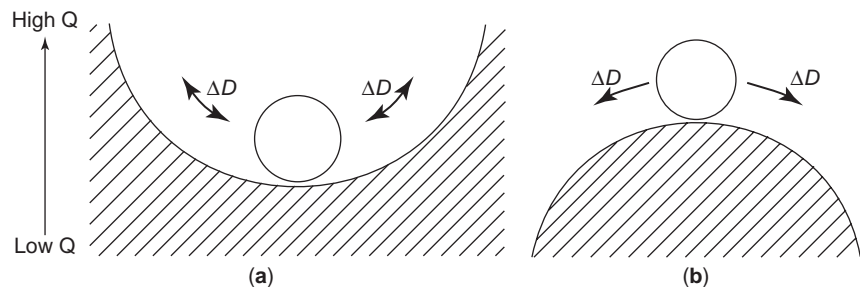


Figure 12. Mechanical analogy of plasma stability in the MRPS (a) and the waveguide array plasma source (b).

investigated, depending on type and flowrate of the gases (air, CO₂, N₂, He, etc.) [46]. It was revealed that the volume of microwave plasma slab for given applied microwave power is inversely proportional to ionization potential of applied gases and their flowrate. Because of peculiarities in MRPS design, a precursor mixture totally passes through the plasma stage, significantly enhancing the efficiency of the MRPS in comparison with microwave waveguide-type plasma sources.

5. SOME PLASMA CHARACTERISTICS OF MRPS

A chemical kinetic modeling of the MRPS action on CO₂ reduction was realized [47] on the basis of experimental data published earlier [46]. The software CHEMKIN [48] was employed for modeling the chemical kinetics. The plasma model was built up. It was shown [47] that the predicted electron (T_e) and ion (T_i) temperatures are very close at ~ 7000 K for this case [46]: $T_e \approx 7500$ K and $T_i \approx 6500$ K when the gas mixture flow is around 2 L/min. Therefore, this plasma can be classified as thermal plasma with a temperature of approximately 7000 K. These calculations predicted that the nonthermal effect (i.e., $T_e \approx 7500$ K and $T_i \approx 2500$ K) becomes remarkable when the gas flowrate is > 10 L/min. At a flowrate of 100 L/min, the predicted temperatures electrons and ions were $T_e \approx 6500$ K and $T_i \approx 500$ K respectively, which corresponds to the nonequilibrium plasma state.

6. ADVANTAGES OF MRPS

The MRPS has a number of advantages over a conventional thermal plasma sources (arc plasma, RF plasma, etc.) in that no electrodes are necessary. No electrodes are needed for the generation of the microwave resonance plasma that eliminates a potential source of the plasma contamination. The absence of a cathodic sheath with high potentials leads to a very-low-energy ion bombardment of a given surface, minimizing surface damage. The MRPS provides a downstream plasma torch unidirectional-acting on surfaces that allows surface engineering of 3D-shaped workpieces, which have to be rotated.

Incorporation of waveguide for introduction of the microwave energy into the resonant cavity has a number of advantages over the design using the coupling probe connected to a coaxial cable, namely:

- Noncontaminating plasma source
- Easy to adjust during MRPS operation;
- Simpler and cheaper design (coaxial is more expensive than waveguide)
- Less manufacturing required
- Higher power-handling capability;
- Higher efficiency (lower loss per unit length of microwave transmitter).

The novel MRPS described is a synergy of microwave technique and a technique intended for materials processing, plasma chemistry, plasma surface treatment, plasma

sterilization, and other applications. Microwave technology, together with materials science, promises research opportunities with great potential in areas such as nanotechnology, composite materials, and biomaterials. Potential benefits include enhanced performance, extended life, cheap lifecycle costs, reduced environmental impact, improved cost-effectiveness and value-added use of materials through advanced manufacturing.

7. POTENTIAL APPLICATIONS OF MRPS

7.1. Surface Treatment

The microwave resonance plasma technique proposed in this research of both deposition of coatings and surface treatment at atmospheric pressure has great potential in surface engineering. It is common to use a conventional plasma spray technology for coating at atmospheric pressure [7]. A plasma surface treatment (nitriding, oxinitriding, nitrocarburizing, etc.) is applied mostly by vacuum-based methods such as direct-current glow discharge (DCGD), and plasma immersion ion implantation (PI³).

In order to demonstrate the possibility of the novel MRPS for surface treatment by nitriding and oxinitriding, typical materials such as titanium with a microhardness of 300–350 VH₅₀ and its alloys, stainless steels 304 and 316 and mild steel 5140, were chosen for nitriding by MRPS at atmospheric pressure [40,49]. Operational MRPS parameters for nitriding/oxinitriding were incident power 800–1000 W and gas flow 1–5 L/min. The gas flowrates of nitrogen and air were controlled by flowmeters accurate to approximately 5% of the maximum flowrate. The MRPS creates a stable plasma torch of 3–6 cm long.

The steel 5140 of chemical composition [(0.38–0.45)C, (0.15–0.35)Si, (0.7–0.9)Cr] and stainless steels, 305 and 316 were nitrided by the MRPS. X-ray and metallographic investigations of the nitrided layer on the steel surface showed the formation of the amorphous layer (Fig. 13a). Nitriding of steel 5140 in pure nitrogen plasma starts at $\sim 50^\circ\text{C}$ of the substrate. Temperature increase of the substrate up to 100°C leads to transformation of nitriding to oxinitriding. This transformation is accompanied by changing of color from light orange to dark pink. Above 100°C of steel 5140 substrate, the surface nitriding transformed to oxidization and the color of the oxidized surface became violet. Stainless-steel 304/316 substrates

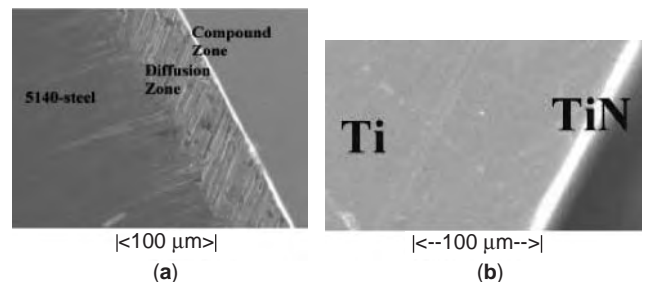


Figure 13. Scanning electron microscopic cross sections of 5140-steel (a) and Ti (b) after microwave plasma nitriding at atmospheric pressure.

commenced nitriding at $\sim 60^\circ\text{C}$. Above 150°C , the stainless steels started to oxidise, and the surface acquired a violet color.

The MRPS nitriding demonstrated that the Ti surface exhibits a somewhat distinct “golden” color that is characteristic of titanium nitride. Diffusion of implanted nitrogen seldom occurs in the operative temperature range of the DCGD and the PI^3 , because of the affinity of Ti for nitrogen. In case of the MRPS nitriding, the proper layer of TiN_x with a hardness of $\sim 1500 \text{ VH}_{200}$ is formed on the Ti surface (Fig. 13b). It was observed that a thin surface layer (5–10 μm) of X-ray amorphous TiN was formed immediately. The introduction of (21 vol% of O_2 and 79 vol% of N_2) into the MRPS had no significant effect on the performance of the nitrided layers for the given air plasma.

Titanium begin to nitride at $\sim 100^\circ\text{C}$ of substrate. This Ti nitriding transformed to oxidization and the treated Ti surface became violet above $\sim 200^\circ\text{C}$. Addition of oxygen (up to 21 vol% of O_2) to the pure nitrogen plasma shifted the starting temperature of nitriding ($\sim 60^\circ\text{C}$) for steel 5140 and at $\sim 100^\circ\text{C}$ for stainless steels 304/316. In the case of Ti, nitriding started at $> 120^\circ\text{C}$. Transitional temperatures, from which oxinitriding passes to oxidizing, became lower, such as $\sim 75^\circ\text{C}$ for steel 5140, $\sim 115^\circ\text{C}$ for stainless steel (SS) 304/316, and $\sim 175^\circ\text{C}$ for Ti.

Reflectance Fourier transform infrared (FTIR) spectroscopy was employed to study the changes in chemical composition of the nitrided layers. In particular, the reflectance FTIR spectra of steel 5140 nitrided by the MRPS are displayed in Fig. 14. The maximum absorption (~ 0.7) of the nitrided layer is reached at $\sim 1400\text{--}1600 \text{ cm}^{-1}$. The band, where absorption is more than 0.5, is between 1700 and 1000 cm^{-1} .

FTIR spectroscopy of conventionally plasma (ion) nitride steel 5140 by direct-current glow discharge (DCGD) detected the strong absorption (> 0.5) within the range of $800\text{--}2000 \text{ cm}^{-1}$. Absorption (~ 0.85) peaked

at $\sim 1150 \text{ cm}^{-1}$. Comparing these spectra, one can note the significant differences between plasma–material interaction for MRPS and that for the conventional DCGD, creating an equilibrium nitrided layer consisting of microcrystalline nitrides on surface.

Titanium surface nitrided by MRPS radically differs from that for steel 5140. An intense absorption peak was detected at approximately 850 cm^{-1} . The MRPS nitriding forms a sharp band of nitrogen–titanium bonding.

7.2. Amorphization and Nanostructuring of Surface

The MRPS operating at atmospheric pressure [50] allows the modification of a microcrystalline surface structure, which becomes amorphous to X-rays [51]. In particular, the X-ray amorphous nitride layers were formed on the surfaces of Ti, SS 304, SS 316, and plain steel 5140 [50–52], using a nitrogen-based mixture for the MRPS. Generally, it is possible to alloy the amorphous layers by boron, carbon, chromium, and other elements by employing appropriate precursors in both gaseous and solid state.

This ability of novel MRPS to amorphize a surface microcrystalline layer up to $\sim 10 \mu\text{m}$ thick, combined with alloying, was used in this study to transform an original microcrystalline surface layer into a nanocrystalline state via an amorphous state. The novelty of this research is to amorphize a microcrystalline surface by MRPS. The subsequent heat treatment in order to transform the metastable amorphous phase to a nanocrystalline state is described in Ref. 53.

7.3. Nanostructured Biomaterials

A feasibility study of plasma nitriding/oxinitriding has demonstrated that a novel low-cost plasma torch developed on the basis of the microwave resonance phenomenon can be practical for nanotechnology [45,54], in particular for bioengineering coatings such a nanostructured

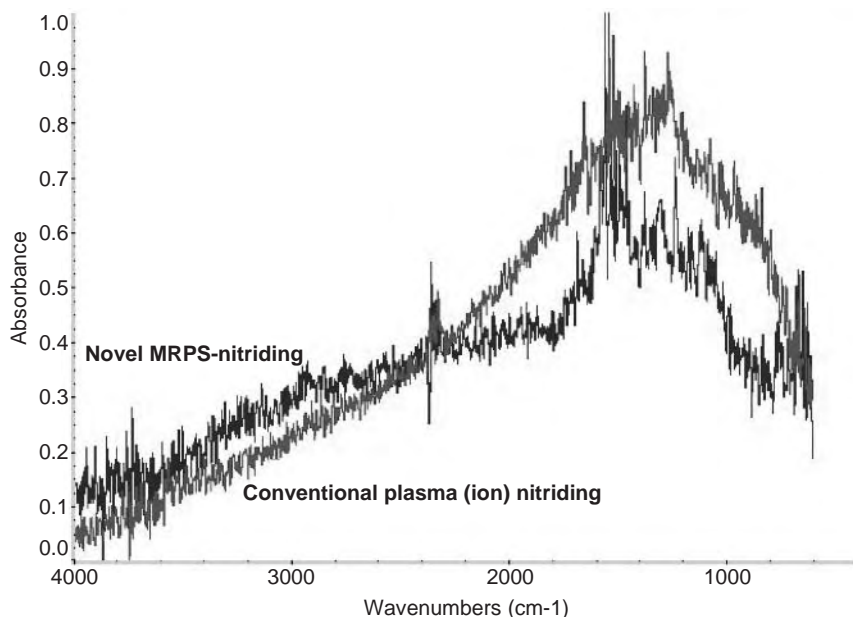


Figure 14. FTIR spectra of 5140 steel treated by the novel MRPS nitriding and the conventional DCGD nitriding. (This figure is available in full color at <http://www.mrw.interscience.wiley.com/erfme>.)

zirconium/titanium oxide, carbyne-containing nanocomposites [55–58], diamondlike carbon, and carbon nitride.

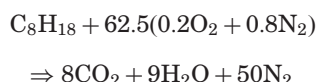
Novel materials are required for cardiovascular therapies, such as replacement of blood vessels and heart valves and the provision of devices that intimately contact components of the cardiovascular system, for example, dialysis and oxygenation membranes, interventional catheters, and cardiovascular stents. Improved biocompatibility of these implants could result in patients requiring lower doses of medication to prevent blood clotting.

MRPS allows the deposition of nanostructured biomaterials and coatings on metal/nonmetal surfaces using a variety of carrier gases and the precursor materials, which can be powders, liquids, or gases. This technology is also capable of surface engineering of complex 3D shapes that might be required for artificial implants. Advantages of the proposed method overall include an enhancement of biocompatibility and extended service life of artificial implants.

One current trend in biomedical applications is to use novel carbon-based biomaterials. Carbynes, which possess a higher degree of biocompatibility and low litho- and thrombogenic activity [59], have shown promise in modifying coating on a surface of biocompatible material for use in reconstructive surgery. For example [55,57,58], nanocomposite coatings (nc-W₃C/nc-carbynes) containing carbynes as a binder demonstrated a high hardness (35–40 GPa), chemical inertness, a low friction coefficient (0.1–0.12), and excellent biocompatibility.

7.4. Plasma Chemistry

Environmental pollution by exhaust/flue gases is a topical subject of the greenhouse effect. For example, a petrol engine, which consumes of ~14 L of liquid petrol per 100 km, throws ~38 L/s of exhaust gases. Currently, an incredible amount of effort has been undertaken to reduce such emissions and has been responsible for the longstanding interest in the theoretical and experimental research of plasma exhaust/flue gas treatment. Currently it is suggested that microwave plasma treatment of exhaust/flue gases is able to solve the problem of exhaust/flue gas environmental pollution. Exhaust gases represent a multicomponent gaseous system. After, the combustion of petrol, which consists of ~96% of octane [CH₃·(CH₂)₆·CH₃], exhaust gases correspond predominantly to a mixture of vapor (H₂O), carbon dioxide (CO₂), and nitrogen (N₂):



Nitrogen is the ballast gas component because air, which is used for combustion, is a mixture of oxygen (~20 vol% O₂ vol%) and nitrogen (~80 vol% N₂). Nitrogen amounts to 75% of total volumetric portion of exhaust gases: CO₂-H₂O-N₂ ≈ 1–1–6. These three gaseous components define microwave plasma chemistry treatment of exhaust gases. Small additions of oxygen (2–5 vol%) and carbon monoxide (~0.15 vol%) play a minor role.

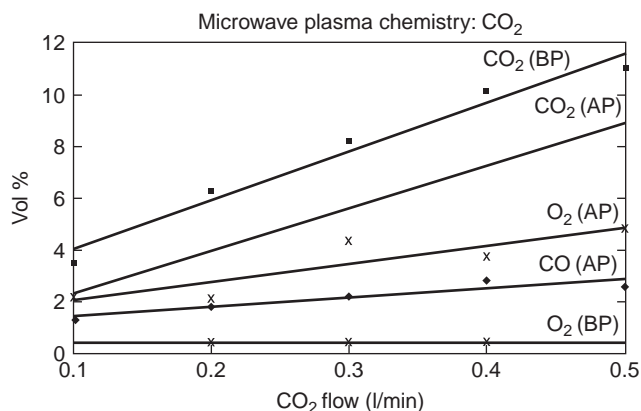


Figure 15. Volumetric portion of gases before (BP) and after (AP) plasma treatment of carbon dioxide as a function of CO₂ flowrate.

The microwave plasma chemistry of the CO₂-H₂O-N₂ gas system is important for technical application. In particular [46], an attempt was made to investigate the plasma chemistry of the gas mixture of CO₂-N₂ and CO₂-H₂O as potential precursors for a coating deposition of superhard carbon nitride, diamondlike carbon, carbyne-based nanocomposites, and other compounds.

The results of the microwave plasma chemistry experiment are shown in Figs. 15–17. As can be seen in Figs. 15 and 16, carbon dioxide decomposes on carbon monoxide and oxygen. According to the formula CO₂ ⇒ CO + 0.5O₂ (ΔH = 29.78 kJ/mol), two decayed molecules of CO₂ create two molecules of CO and one molecule of O₂. Comparison of the experimental volumetric portions of the gases after microwave plasma treatment (Fig. 15) reveals good agreement between these experiments with the equation given above. Visible traces of solid carbon isolated in any form have not been detected.

This scenario changed radically when nitrogen was added on a ratio of CO₂-N₂ = 6. Yield of CO increased significantly. Every alternate CO₂ molecule was dissociated. Visible traces of solid carbon were not detected. The most unexpected result was that the addition of nitrogen

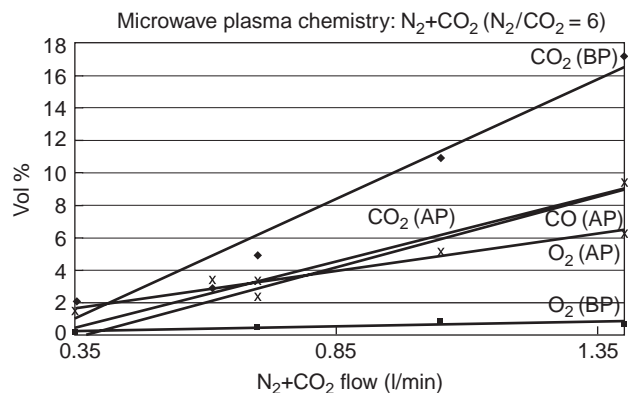


Figure 16. Volumetric portion of gases before (BP) and after (AP) plasma treatment of (N₂ + CO₂) mixture as a function of (N₂ + CO₂) flowrate where N₂/CO₂ ≈ 6.

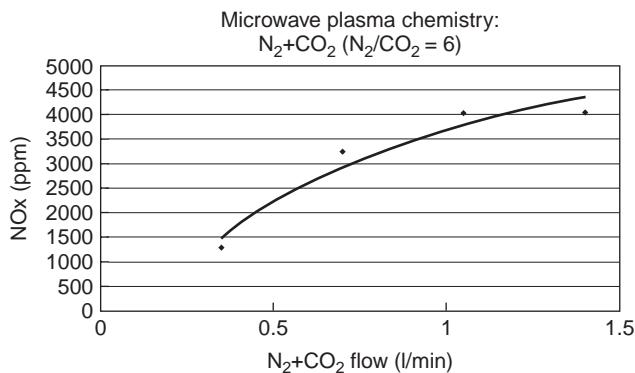


Figure 17. Concentration of nitrogen oxides after plasma treatment of N₂ + CO₂ mixture as a function of (N₂ + CO₂) flowrate where N₂/CO₂ ≈ 6.

initiated an extra yield of carbon monoxide. As stated earlier [5], a small addition of nitrogen does not affect the yield of carbon monoxide. In this case, the CO yield increases in by a factor of 1.5.

Nitrogen oxides are inherent byproducts of microwave resonance plasma treatment when a gaseous mixture contains nitrogen and oxygen in any combination. Nitrogen oxides are usually formed in plasma at temperatures exceeding 2000°C. In the course of the experiments (Fig. 17), the concentration of nitrogen oxides increased in proportion to the volumetric portion of nitrogen and carbon dioxide beyond the upper limit of 4000 ppm (particles per million) when NO_x was measured using a gas analyzer [46].

The experiments showed a very rapid decomposition of carbon dioxide into the main stable species CO and O₂. Comparison of the decomposition of carbon dioxide without and with nitrogen addition revealed that the ratio between carbon monoxide and oxygen is altered by a factor of 1.5 at steady state.

The characteristics of atmospheric pressure microwave resonance plasma chemistry of carbon dioxide are

- No visible dissociation of carbon dioxide up to solid carbon in any form when using the gas mixture of CO₂ + He
- Effect of increasing the yield of CO by a factor of 1.5 when using nitrogen addition to gas mixture of CO₂ + He

8. EVALUATION

The design of the novel MRPS source based on the TM₀₁₃ mode has a number of advantages over the conventional plasma spray sources, including

- High (~98%) efficiency of microwave energy consumption
- High efficiency of precursor consumption
- Simple and reliable design
- Noncontaminating thermal plasma source

- Ease of operation
- Variety of carrier gases for thermal plasma
- Selective surface treatment/coating
- Operating at atmospheric pressure
- Stability of the plasma torch
- Reliability of the MRIP source
- No inherent problem of erosion (no electrodes)
- Low capital and running costs
- Retrofittable design
- Compactness
- Low maintenance requirements
- Simple surface preparation for modification.

It is believed that the MRPS could find interesting applications in plasma thermal spray technology for deposition of coatings and in plasma chemistry for materials processing. The novel MRPS is innovative for deposition and coating of bionanomaterials.

The research and development have demonstrated the commercial potential of the MRPS [40,60]. The MRPS can be a commercial processing tool for the solid-state amorphization of a surface layer, which is a transitional stage for nanocrystallisation under an appropriate thermal annealing.

Acknowledgments

The authors would like to thank Prof. Kai Chang (Texas A&M University) for this opportunity to contribute to the *Wiley Encyclopedia of RF and Microwave Engineering* by preparing this article, and Kris Parrish and Cassandra Craig (John Wiley & Sons, Inc., Hoboken, NJ) for their assistance in preparation of this article, Mrs. Fiona O'Donnell (Hawthorn library of Swinburne University of Technology, Melbourne, Australia) for inestimable information support, as well as Mrs. Andrea Meyer (IRIS, Swinburne University of Technology, Melbourne, Australia) for their assistance in polishing the manuscript.

BIBLIOGRAPHY

1. M. Rahmane, G. Soucy, M. I. Boulos, and R. Henne, Fluid dynamic study of direct current plasma jets for plasma spraying applications, *J. Thermal Spray Technol.* **7**:349–356 (1998).
2. S. V. Dresvin, A. V. Donskoi, V. M. Goldfarb, and V. S. Klubnikin, *Physics and Technology of Low-Temperature Plasmas*, Iowa State Univ. Press, Ames, 1997.
3. A. Garscadden, PECVD RF discharge models review, in *Proc. Materials Research Soc. Symp. on Characterization of Plasma-Enhanced CVD Processes*, Nov. 27–28, 1989, Boston, MA, Materials Research Society, Pittsburgh, 1990, Vol. 165, pp. 3–15.
4. J. L. Cecchi, Introduction to plasma concepts and discharge configuration, in S. M. Rosnagel, J. J. Cuomo, and W. D. Westwood, eds., *Handbook of Plasma Processing Technology. Fundamentals, Etching, Deposition and Surface Interactions*, Noyes Publications, Park Ridge, IL, 1990, pp. 14–69.

5. V. M. Batenin, I. I. Klimovskii, G. V. Lysov, and V. N. Troitskii, *Superhigh Frequency Generators of Plasma*, CRC Press, Boca Raton, FL, 1994, p. 175.
6. M. I. Boulou, RF induction plasma spraying: State-of-the-art review, *J. Thermal Spray Technol.* **1**:33–40 (1992).
7. C. C. Berndt, W. Brindley, A. N. Goland et al., Current problems in plasma spray processing, *J. Thermal Spray Technol.* **1**:341–356 (1992).
8. C. M. Ferreira, M. Moisan, and Z. Zakrzewski, in M. Moisan and J. Pelletier, eds., *Microwave Excited Plasmas*, Elsevier, Amsterdam, 1992, pp. 11–52.
9. J. Feinman, *Plasma Technology in Metallurgical Processing*, Iron & Steel Society, Warrendale, PA, 1987, p. 27.
10. J. Pelletier, Distributed ECR: Concept, performance and perspectives, in C. M. Ferreira and M. Moisan, eds., *Microwave Discharges: Fundamentals and Applications*, Plenum Press, New York, 1992, pp. 181–204.
11. R. Willhelm, ECR plasma sources, in C. M. Ferreira and M. Moisan, eds., *Microwave Discharges: Fundamentals and Applications*, Plenum Press, New York, 1992, pp. 161–180.
12. A. A. Chtcherbakov and P. L. Swart, Automatic microwave tuner for plasma deposition applications using a gradient search method, *J. Microwave Power Electromagn. Energy*, **32**:28–33 (1997).
13. H. Conrads and M. Schmidt, Plasma generation and plasma sources, *Plasma Sources Sci. Technol.* **9**:441–454 (2000).
14. G. Eecke, G. Eichhorn, J. Pezpldt, C. Reinhold, T. Stauden, and F. Supplith, Deposition of aluminium nitride films by electron cyclotron resonance plasma-enhanced chemical vapour deposition, *Surf. Coat. Technol.* **98**:1503–1509 (1998).
15. P. Bulkin, N. Bertrand, and Drevillon, Deposition of SiO₂ in integrated distributed electron cyclotron resonance microwave reactor, *Thin Solid Film* **296**:66–68 (1997).
16. A. J. Chacon Velasco and V. D. Dougar-Jabon, Physical principles of microwave plasma heating and its technological applications, *Proc. 7th Int. Conf. Microwave and High Frequency Heating*, Valencia, Spain, Sept. 13–17 1999, pp. 99–102.
17. M. Rusli, S. F. Yoon, H. Yang, J. Ahn, Q. F. Huang, Q. Zhang, Y. P. Guo, C. Y. Yang, E. J. Teo, A. T. S. Wee, A. C. H. Huan, and F. Watt, Tungsten-carbon thin films deposited using screen grid technique in an electron Cyclotron resonance chemical vapour deposition system, *Surf. Coat. Technol.* **123**:134–139 (2000).
18. M. L. Passow, M. L. Brake, P. Lopez, W. B. McColl, and T. E. Repetti, Microwave resonant-cavity-produced air discharge, *IEEE Trans. Plasma Sci.* **19**:219–228 (1991).
19. Z. Zakrzewski, M. Moisan, and G. Sauve, Surface-wave plasma sources, in C. M. Ferreira and M. Moisan, eds., *Microwave Discharges: Fundamentals and Applications*, Plenum Press, New York, 1992, pp. 117–140.
20. G. Bohm, Fabry-Perot-type microwave resonator, in C. M. Ferreira and M. Moisan, eds., *Microwave Discharges: Fundamentals and Applications*, Plenum Press, New York, 1992, pp. 215–224.
21. M. Moisan, J. Hubert, J. Margot, G. Sauve, and Z. Zakrzewski, The contribution of surface-wave-sustained plasmas to HF plasma generation. Modelling and applications: Status and perspectives, in C. M. Ferreira and M. Moisan, eds., *Microwave Discharges: Fundamentals and Applications*, Plenum Press, New York, 1992, pp. 1–24.
22. M. Moisan, Z. Zakrzewski, R. Grenier, and G. Sauve, Large diameter plasma generation using a waveguide-based field application at 2.45 GHz, *J. Microwave Power Electromagn. Energy* **30**:58–65 (1995).
23. J. Laimer and S. Matsumoto, Pulsed microwave plasma-assisted chemical vapour deposition of diamond, *Int. J. Refractory Metals Hard Mater.* **14**:179–184 (1996).
24. P. K. Bachmann and H. Lydtin, Diamond forming discharges, in *Proc. Materials Research Society Symp. on Characterization of Plasma-Enhanced CVD Processes*, Boston, Nov. 27–28, 1989, Materials Research Society, Pittsburgh, 1990, Vol. 165, pp. 181–197.
25. M. Baeva, X. Luo, B. Pfler, T. Repsilber, and J. Uhlenbusch, Experimental investigation and modelling of a low-pressure pulsed microwave discharge in oxygen, *Plasma Source Sci. Technol.* **9**:128–145 (2000).
26. Y. Mitsuda, Y. Kojima, T. Yoshida, and K. Akashi, The growth of diamond in microwave plasma under low pressure, *J. Mater. Sci.* **22**:1557–1562 (1987).
27. M. A. Cappelli, T. G. Owano, A. Gicquel, and X. Duten, Methyl concentration measurements during microwave plasma-assisted diamond deposition, *Plasma Chem. Plasma Process.* **20**:1–12 (2000).
28. K. Donnelly, D. P. Dowling, R. V. Flood, M. L. McConnell, O. Berkefeld, and J. Svennebrink, Diamond deposition using a novel microwave applicator, *Surf. Coat. Technol.* **124**:248–252 (2000).
29. W. Perasch, B. Kegel, H. Schmid, K. Lendenmann, and H. U. Keller, Low-pressure plasma cleaning: A process for precision cleaning applications, *Surf. Coat. Technol.* **97**:176–181 (1997).
30. A. Muller, M. Emme, D. Korzec, and J. Engemann, Direct power coupling into a waveguide cavity plasma source, *Surf. Coat. Technol.* **116–119**:674–678 (1999).
31. A. I. Al-Shamma'a, S. R. Wylie, J. Lucas, and C. F. Pau, Design and Construction of a 2.45 GHz waveguide-based microwave plasma jet at atmospheric pressure for material processing, *J. Phys. D: Appl. Phys.* **34**:2734–2741 (2001).
32. A. I. Al-Shamma'a, S. R. Wylie, J. Lucas, and R. A. Stuart, Microwave plasma jet for material processing at 2.45 GHz, *J. Mater. Process. Technol.* **121**:143–147 (2002).
33. M. Moisan, Z. Zakrzewski, and J. C. Rostaing, Waveguide-based single and multiple nozzle plasma torches: The TIAGO concept, *Plasma Sources Sci. Technol.* **10**:387–394 (2001).
34. J. D. Yan, C. F. Pau, S. R. Wylie, and M. T. Fang, Experimental characterization of an atmospheric argon plasma jet generated by an 896 MHz microwave system, *J. Phys. D: Appl. Phys.* **35**:2594–2604 (2002).
35. J. B. Salsman, Microwave plasma process for the accelerated synthesis of nanostructured carbides, in K. Upadhy, eds., *Plasma Synthesis and Processing of Materials*, TMS, Denver, 1993, pp. 155–162.
36. M. Karches and P. R. von Rohr, Microwave plasma characteristics of a circulating fluidized bed plasma reactor for coating of powders, *Surf. Coat. Technol.* **142–144**:28–33 (2001).
37. http://www.abba.com.tw/html/microwave_burner.htm.
38. P. A. Rizzi, Microwave resonators and filters, in *Microwave Engineering*, Prentice-Hall, Englewood, NJ, 1988, p. 412.
39. J. F. Gerling, Techniques to improve the performance of microwave process systems which utilize a high Q-cavities, in D. E. Clark, F. D. Gac, and W. H. Sutton, eds., *Ceramic Transactions, Vol. 21, Microwaves: Theory and Application in Materials Processing*, American Ceramic Society, Waterville, 1991, pp. 667–674.
40. A. L. Taube, G. M. Demyashev, and E. Siores, Microwave resonance-induced plasma technologies at atmospheric pressure:

- a commercial reality in Australia, in *Microwave Technologies in National Economy: Introduction, Problems, Prospects*, Ukraine Science Technology Centre, Kiev–Odessa, 2002, Part 5, pp. 60–68.
41. R. Chatterjee, *Advance Microwave engineering*, Ellis Horwood Ltd., UK, 1988, p. 125.
 42. A. L. Taube and G. M. Demyashev, Comparative analysis of atmospheric pressure microwave plasma sources: TM₀₁₃ resonance cavity and waveguide-type, *Proc. 2002 Asia-Pacific Microwave Conference (APMC-2002)*, Kyoto, Japan, Nov. 2002, Vol. 2, pp. 811–814.
 43. T. Koryulishii, *Microwave Engineering*, Harcourt Brace Jovanovich, Orlando, FL, 1989, p. 136.
 44. J. L. Altman, *Microwave Circuits*, Van Nostrand, Princeton, NJ, 1964, p. 173.
 45. G. M. Demyashev, A. L. Taube, and E. Siores, Superhard nanocomposite coatings, in H. S. Nalwa, ed., *Handbook of Organic-Inorganic Hybrid Materials and Nanocomposites*, Vol. 2, *Nanocomposites*, American Scientific Publishers, Los Angeles, 2003, Chap. 1, pp. 1–61.
 46. A. L. Taube and G. M. Demyashev, Peculiarities of plasma formation in the microwave resonance system for plasma chemistry applications, *Proc. IMPI 37th Annual Int. Microwave Symp.* Atlantic City, NJ, July 2002, pp. 12–15.
 47. R. T. Deam, Reduction of CO₂ by microwave induced plasma, *Proc. 9th Int. Conf. Microwave and High Frequency Heating*, Loughborough Univ., UK, Sept. 2003, 1–5, pp. 417–420.
 48. CHEMKIN Collection Release 3.6. September 2000, <http://www.reactiondesign.com/>.
 49. G. M. Demyashev, A. L. Taube, and E. Siores, Feasibility of plasma nitriding by atmospheric pressure microwave resonance-induced plasma source, in D. Tonchich, ed. *Profiles in Industrial Research: Knowledge & Innovation-2001*, IRIS (Swinburne Univ. Technology), Melbourne, Australia, 2001, pp. 274–299.
 50. E. Siores, A. L. Taube, and G. M. Demyashev, TM₀₁₃ resonance cavity microwave plasma torch, *Proc. IMPI 36th Annual Int. Microwave Symp.*, San Francisco, April 2001, pp. 75–78.
 51. A. L. Taube, G. M. Demyashev, and E. Siores, Microwave resonance-induced plasma source for surface modification technologies at atmospheric pressure, *Proc. 2001 Asia-Pacific Microwave Conf. (APMC-2001)*, Taipei, Taiwan, Dec. 2001, Vol. 2, pp. 733–736.
 52. A. L. Taube, G. M. Demyashev, and E. Siores, Microwave resonance-induced plasma source for surface treatment at atmospheric pressure, *Abstracts 8th Int. Conf. Microwave and High Frequency Heating*, Bayreuth, Germany, Sept. 2001, pp. 49–51.
 53. K. Lu, Thermodynamics and kinetics of the amorphous-to-nanocrystalline transformation, in C. Suryanarayana, J. Singh, and F. H. Froes, eds., *Processing and Properties of Nanocrystalline Materials*, TMS, Warrendale, 1996, pp. 23–33.
 54. G. M. Demyashev, A. L. Taube, and E. Siores, Superhard nanocomposites, in H. S. Nalwa, ed., *Encyclopedia of Nanoscience and Nanotechnology*, American Scientific Publishers, Los Angeles, 2004, Vol. 10, pp. 191–236.
 55. G. M. Demyashev, A. L. Taube, and E. Siores, Nanostructured tungsten-based composite coatings and their applications, *NANO Lett.* 1:183–187 (2001).
 56. G. M. Demyashev, A. L. Taube, and E. Siores, Surface modification of titanium carbide with carbyne-containing nano-coatings, *J. Nanosci. Nanotechnol.* 2:133–137 (2002).
 57. G. M. Demyashev and A. L. Taube, Carbyne-containing nano-structured coatings for bioapplications: Synthesis and structure, in A. Dorner-Reisel and C. Schurer, eds., *Surface Engineering of Biomaterials—Properties, Processing and Potentials of Carbon Coatings*, Wiley Verlag, Freiberg, 2003.
 58. G. M. Demyashev and A. L. Taube, Carbyne-containing biomaterials, in M. Akay ed., *Wiley Encyclopedia of Biomedical Engineering*, Wiley, New York, (in press).
 59. V. I. Kirpatovsky, Medical applications of carbynoid materials, in R. B. Heimann, S. E. Evsyukov, and L. Kavan, eds., *Carbynes and Carbynoid Structures*, Kluwer, Dordrecht, 1999, pp. 427–435.
 60. A. L. Taube and G. M. Demyashev, *Microwave Resonance Plasma Source Operating at Atmospheric Pressure: Method and Apparatus*, Australian Provisional Patent (2003).

MICROWAVE SCATTERING MODELS FOR EARTH TERRAIN

ADRIAN K. FUNG

University of Texas at Arlington
Arlington, Texas

1. INTRODUCTION

The scattering properties of a terrain generated by an impinging electromagnetic wave are generally represented by a quantity proportional to the average scattered power called the *scattering coefficient*. This quantity is dependent on the exploring frequency, view angle, polarization, and the geometric and electric properties of the terrain. Hence, it is a quantity that relates the geometric and electric properties of the terrain and the sensing system parameters to the scattering phenomenon. Its precise definition will be given in the next section.

The scattering of waves that takes place at a surface boundary between two homogeneous media is called *surface scattering*. For natural ground surfaces where the roughness can be described only statistically, the scattered field will vary from location to location. Such a variation in the received signal is called *fading*, and the associated field amplitude and power distributions are its *fading statistics*. A meaningful signature of the rough surface is the statistically averaged, received power. It follows that this average power must be a function of the statistical parameters of the surface such as the standard deviation of the surface height (RMS height) and its height correlation function. In remote sensing it is the scattered field that is received by the observing antenna. Thus, scattering is the key mechanism. However, in the presence of an inhomogeneous medium such as a vegetation layer, sea ice, or a snow layer, the propagating fields within the medium are equally important, since they are part of the sources of the scattered field. For an inhomogeneous layer with irregular boundaries, an incident wave will generate

- a commercial reality in Australia, in *Microwave Technologies in National Economy: Introduction, Problems, Prospects*, Ukraine Science Technology Centre, Kiev–Odessa, 2002, Part 5, pp. 60–68.
41. R. Chatterjee, *Advance Microwave engineering*, Ellis Horwood Ltd., UK, 1988, p. 125.
 42. A. L. Taube and G. M. Demyashev, Comparative analysis of atmospheric pressure microwave plasma sources: TM₀₁₃ resonance cavity and waveguide-type, *Proc. 2002 Asia-Pacific Microwave Conference (APMC-2002)*, Kyoto, Japan, Nov. 2002, Vol. 2, pp. 811–814.
 43. T. Koryulishii, *Microwave Engineering*, Harcourt Brace Jovanovich, Orlando, FL, 1989, p. 136.
 44. J. L. Altman, *Microwave Circuits*, Van Nostrand, Princeton, NJ, 1964, p. 173.
 45. G. M. Demyashev, A. L. Taube, and E. Siores, Superhard nanocomposite coatings, in H. S. Nalwa, ed., *Handbook of Organic-Inorganic Hybrid Materials and Nanocomposites*, Vol. 2, *Nanocomposites*, American Scientific Publishers, Los Angeles, 2003, Chap. 1, pp. 1–61.
 46. A. L. Taube and G. M. Demyashev, Peculiarities of plasma formation in the microwave resonance system for plasma chemistry applications, *Proc. IMPI 37th Annual Int. Microwave Symp.* Atlantic City, NJ, July 2002, pp. 12–15.
 47. R. T. Deam, Reduction of CO₂ by microwave induced plasma, *Proc. 9th Int. Conf. Microwave and High Frequency Heating*, Loughborough Univ., UK, Sept. 2003, 1–5, pp. 417–420.
 48. CHEMKIN Collection Release 3.6. September 2000, <http://www.reactiondesign.com/>.
 49. G. M. Demyashev, A. L. Taube, and E. Siores, Feasibility of plasma nitriding by atmospheric pressure microwave resonance-induced plasma source, in D. Tonchich, ed. *Profiles in Industrial Research: Knowledge & Innovation-2001*, IRIS (Swinburne Univ. Technology), Melbourne, Australia, 2001, pp. 274–299.
 50. E. Siores, A. L. Taube, and G. M. Demyashev, TM₀₁₃ resonance cavity microwave plasma torch, *Proc. IMPI 36th Annual Int. Microwave Symp.*, San Francisco, April 2001, pp. 75–78.
 51. A. L. Taube, G. M. Demyashev, and E. Siores, Microwave resonance-induced plasma source for surface modification technologies at atmospheric pressure, *Proc. 2001 Asia-Pacific Microwave Conf. (APMC-2001)*, Taipei, Taiwan, Dec. 2001, Vol. 2, pp. 733–736.
 52. A. L. Taube, G. M. Demyashev, and E. Siores, Microwave resonance-induced plasma source for surface treatment at atmospheric pressure, *Abstracts 8th Int. Conf. Microwave and High Frequency Heating*, Bayreuth, Germany, Sept. 2001, pp. 49–51.
 53. K. Lu, Thermodynamics and kinetics of the amorphous-to-nanocrystalline transformation, in C. Suryanarayana, J. Singh, and F. H. Froes, eds., *Processing and Properties of Nanocrystalline Materials*, TMS, Warrendale, 1996, pp. 23–33.
 54. G. M. Demyashev, A. L. Taube, and E. Siores, Superhard nanocomposites, in H. S. Nalwa, ed., *Encyclopedia of Nanoscience and Nanotechnology*, American Scientific Publishers, Los Angeles, 2004, Vol. 10, pp. 191–236.
 55. G. M. Demyashev, A. L. Taube, and E. Siores, Nanostructured tungsten-based composite coatings and their applications, *NANO Lett.* 1:183–187 (2001).
 56. G. M. Demyashev, A. L. Taube, and E. Siores, Surface modification of titanium carbide with carbyne-containing nano-coatings, *J. Nanosci. Nanotechnol.* 2:133–137 (2002).
 57. G. M. Demyashev and A. L. Taube, Carbyne-containing nano-structured coatings for bioapplications: Synthesis and structure, in A. Dorner-Reisel and C. Schurer, eds., *Surface Engineering of Biomaterials—Properties, Processing and Potentials of Carbon Coatings*, Wiley Verlag, Freiberg, 2003.
 58. G. M. Demyashev and A. L. Taube, Carbyne-containing biomaterials, in M. Akay ed., *Wiley Encyclopedia of Biomedical Engineering*, Wiley, New York, (in press).
 59. V. I. Kirpatovsky, Medical applications of carbynoid materials, in R. B. Heimann, S. E. Evsyukov, and L. Kavan, eds., *Carbynes and Carbynoid Structures*, Kluwer, Dordrecht, 1999, pp. 427–435.
 60. A. L. Taube and G. M. Demyashev, *Microwave Resonance Plasma Source Operating at Atmospheric Pressure: Method and Apparatus*, Australian Provisional Patent (2003).

MICROWAVE SCATTERING MODELS FOR EARTH TERRAIN

ADRIAN K. FUNG

University of Texas at Arlington
Arlington, Texas

1. INTRODUCTION

The scattering properties of a terrain generated by an impinging electromagnetic wave are generally represented by a quantity proportional to the average scattered power called the *scattering coefficient*. This quantity is dependent on the exploring frequency, view angle, polarization, and the geometric and electric properties of the terrain. Hence, it is a quantity that relates the geometric and electric properties of the terrain and the sensing system parameters to the scattering phenomenon. Its precise definition will be given in the next section.

The scattering of waves that takes place at a surface boundary between two homogeneous media is called *surface scattering*. For natural ground surfaces where the roughness can be described only statistically, the scattered field will vary from location to location. Such a variation in the received signal is called *fading*, and the associated field amplitude and power distributions are its *fading statistics*. A meaningful signature of the rough surface is the statistically averaged, received power. It follows that this average power must be a function of the statistical parameters of the surface such as the standard deviation of the surface height (RMS height) and its height correlation function. In remote sensing it is the scattered field that is received by the observing antenna. Thus, scattering is the key mechanism. However, in the presence of an inhomogeneous medium such as a vegetation layer, sea ice, or a snow layer, the propagating fields within the medium are equally important, since they are part of the sources of the scattered field. For an inhomogeneous layer with irregular boundaries, an incident wave will generate

scattering throughout the volume of the layer. Such a scattering mechanism is called *volume scattering*. In general, there will also be surface scattering at the boundaries and hence surface–volume interaction, multiple volume scattering, and surface scattering are also present within the inhomogeneous layer. When the phase relationship between scatterers is needed in volume scattering calculation, the type of scattering is said to be *coherent*. Otherwise, the total scattered power can be calculated by adding the scattered power from individual scatterers, and the associated scattering is said to be *incoherent* or independent. In the radiative transfer formulation [1] coherent calculation is used to derive the *scattering phase function*, which describes single scattering by a single scatterer in a sparse medium or a group of scatterers in a dense medium.

A region with vegetation cover can be viewed as a vegetation layer above an irregular ground surface. The volume occupied by the vegetation biomass relative to the total volume of a vegetation layer is generally less than 1%. For this reason a vegetation medium is taken to be a sparse medium where multiple scattering beyond the second order is assumed to be negligible. A more precise definition of a *sparse medium* is a situation in which the scatterers are in the far field of one another. The usual condition for *far field* is that the range between scatterers is greater than $2D^2/\lambda$, where D is the largest dimension of the scatterer and λ is the operating wavelength in the medium in which the wave is propagating. Under this condition the phase of the propagating wave is a linear function of the range. In such a medium it is possible to ignore phase relations (or coherency) between scatterers in scattering calculations. A vegetated medium does not really satisfy this far-field condition. However, estimates of scattering using far-field calculations have been shown to give results that compare well with measurements [2].

A snow-covered region consists of an inhomogeneous layer of ice particles sitting above an irregular ground surface. The volume fraction of ice particles in snow generally ranges from about 10 to 40%, while the ice particle size is in the range of 0.03–0.3 cm. Two scenarios are possible:

1. Within the distance of a wavelength there are two or more scatterers. Such a medium is called an *electrically dense medium*. In this case two or more scatterers scatter as a group and a scattering phase function for the group is needed in the scattering calculation.
2. The adjacent scatterers are not in the far field of each other, but the average spacing between them is more than a wavelength. In this case the scattering phase function is for a single scatterer, but the far-field approximation is not applicable. Such a medium is a *spatially dense medium*.

A general dense medium may be spatially and electrically dense. Hence, the general scattering phase function for snow must include both of these effects [3–5]. In a dense medium scattered fields from scatterers interact at all range values. They are said to interact in the *near field*,

when the range between scatterers is small compared to the operating wavelength.

2. BASIC TERMS IN SCATTERING

In radar remote sensing the quantity measured is the radar cross section for an isolated target or the scattering coefficient for an area extensive target. To measure the radar cross section of a target, the size of the target must be smaller than the coverage of the radar beam; the converse is true in measuring the scattering coefficient. Intuitively, an object can scatter an incident wave into all possible directions with varying strength, and this scattering pattern should vary with the incident direction. To compare between the scattering strengths of objects in a given direction, some common reference is needed. For the radar cross section of an object, the common reference is an idealized isotropic scatterer. Thus, the radar cross section of an object observed in a given direction is the cross section of an equivalent *isotropic scatterer* that generates the same scattered power density as the object in the observed direction. Mathematically the *radar cross section* σ_r of an object observed in a given direction is the ratio of the total power scattered by an equivalent isotropic scatterer to the incident power density on the object

$$\sigma_r = \frac{4\pi R^2 |E^s|^2}{|E^i|^2} \equiv 4\pi |S|^2 \quad (1)$$

where R is the range between target and the radar receiver; E^i is the incident field; E^s is the scattered field along the direction under consideration, and S is the *scattering amplitude* of the object defined by $(R|E^s|)/|E^i|$. For an area extensive target such as a randomly rough soil surface, the scattered field comes from the area illuminated by the radar antenna. To avoid dependence on the size of the illuminated area A_0 , we want to define a per unit area quantity, the *scattering coefficient* of the surface σ^0 , which is the statistically averaged radar cross section of A_0 divided by A_0 . Let $\langle \rangle$ be the symbol for *statistical* or *ensemble average*. Then, σ^0 can be written as

$$\sigma^0 = \frac{\langle \sigma_r \rangle}{A_0} = \frac{4\pi R^2 \langle |E^s|^2 \rangle}{A_0 |E^i|^2} \equiv \frac{4\pi \langle |S|^2 \rangle}{A_0} \quad (2)$$

When the transmitting and receiving antennas of the radar are collocated, the radar is said to operate in the *monostatic mode*. If the locations of these antennas are separated, it is said to operate in a *bistatic mode*. The scattering coefficient corresponding to the bistatic operation is referred to as a *bistatic scattering coefficient*.

2.1. Wave Polarization Consideration

In remote sensing of the Earth environment we generally encounter plane-wave reflection from and transmission through a weakly finitely conducting medium. This problem has been extensively treated in Ref. 6. As shown in Fig. 1, a plane wave incident at a plane boundary is said to be *horizontally polarized* or a TE wave, if its electric field

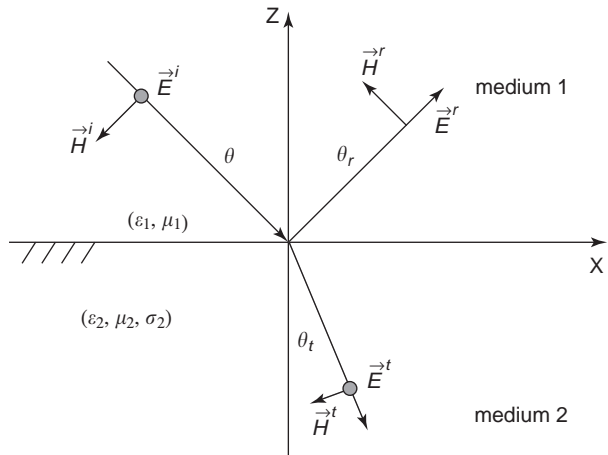


Figure 1. Reflection and transmission at a plane boundary between a dielectric upper medium and a finitely conducting lower medium.

vector is perpendicular to the *plane of incidence*, which is the plane parallel to the wave propagation direction and the normal vector to the boundary, the xz plane in Fig. 1. In this case the magnetic field vector is parallel to the plane of incidence. The incident wave is said to be *parallel* or *vertically polarized* or a TM wave, if the direction of the electric field vector is parallel to the plane of incidence. The law of reflection requires the incident and reflected angles to be the same, $\theta_r = \theta$, and *Snell's law* for dielectric media shows that the angle of transmission can be computed from

$$\theta_t = \sin^{-1} \left[\frac{(\mu_1 \epsilon_1)^{1/2} \sin \theta}{(\mu_2 \epsilon_2)^{1/2}} \right] \quad (3)$$

where μ and ϵ denote, respectively, the permeability and permittivity of a medium. When the lower medium is finitely conducting but the conductivity is small, Eq. (3) still gives a good estimate of the transmission angle, and the attenuation of the transmitted field in medium 2 may be estimated by the loss factor, $\exp[-0.5\sigma_2\eta_2|z|]$, where σ_2 is the conductivity, z is the distance into medium 2, and $\eta_2 = (\mu_2/\epsilon_2)^{1/2}$ is the intrinsic impedance of medium 2. The reader is referred to Ulaby et al. [6] for θ_t and attenuation calculations, when the loss is not small.

For most naturally occurring media, $\mu_1 \approx \mu_2 \approx \mu_0$. From Eq. (3) we see that if $\epsilon_1 > \epsilon_2$ the sine of θ_t may exceed unity for some range of θ . The θ for which $\sin \theta_t = 1$ is called the *critical angle* θ_c . When $\theta > \theta_c$, $\sin \theta_t > 1$, and there is no real angle of transmission. Physically, the incident field is totally reflected.

The *Fresnel reflection and transmission coefficients* for horizontal polarization with $\mu_1 \approx \mu_2 \approx \mu_0$ may be written for the electric fields as [6]

$$R_h = \frac{E^r}{E^i} = \frac{k_1 \cos \theta - k_2 \cos \theta_t}{k_1 \cos \theta + k_2 \cos \theta_t} = \frac{\eta_2 \cos \theta - \eta_1 \cos \theta_t}{\eta_2 \cos \theta + \eta_1 \cos \theta_t} \quad (4)$$

and

$$T_h = \frac{E^t}{E^i} = 1 + R_h \quad (5)$$

where $k_{1,2} = \omega(\mu_0\epsilon_{1,2})^{1/2}$ is the wavenumber of the medium. For finitely conducting lower media, $k_2 \cos \theta_t$ is actually a complex quantity. Its exact representation may be found in Ref. 6. For media with a small conductivity, it is possible to approximate R_h, T_h by replacing ϵ_2 by $\epsilon_2 - j\sigma_2/\omega$ and use (3) to calculate θ_t . For example,

$$k_2 \cos \theta_t \approx \omega \left[\mu_0 \left(\epsilon_2 - j \frac{\sigma_2}{\omega} \right) \right]^{1/2} \cos \theta_t \quad \text{and} \quad (6)$$

$$\frac{\eta_2}{\cos \theta_t} \approx \left[\frac{\mu_0}{\epsilon_2 - j \frac{\sigma_2}{\omega}} \right]^{1/2} \frac{1}{\cos \theta_t}$$

Analogous relations for the Fresnel reflection and transmission coefficients of vertically polarized waves for the magnetic fields can be obtained by interchanging the positions of k_1, η_1 with those of k_2, η_2 as

$$R_v = \frac{H^r}{H^i} = \frac{k_2 \cos \theta - k_1 \cos \theta_t}{k_2 \cos \theta + k_1 \cos \theta_t} = \frac{\eta_1 \cos \theta - \eta_2 \cos \theta_t}{\eta_1 \cos \theta + \eta_2 \cos \theta_t} \quad (7)$$

and

$$T_v = \frac{H^t}{H^i} = 1 + R_v \quad (8)$$

Although it is not possible for R_h to be zero with $\epsilon_1 \neq \epsilon_2$ between dielectric media for some incident angle, it is possible for R_v to be zero. This particular incident angle is called the *Brewster angle* θ_B . At this incident angle $T_v = 1$, $R_v = 0$ for dielectric media. The Brewster angle can be found from

$$\theta_B = \tan^{-1} \left(\frac{\epsilon_2}{\epsilon_1} \right)^{1/2} \quad (9)$$

To extend the scattering coefficient σ^0 to include polarization dependence, let p denote the incident polarization and q the scattered polarization. The symbols p and q may represent either vertical or horizontal polarization. Then, we can add "q" and "p" as subscripts to the scattering coefficient as σ_{qp}^0 .

2.1.1. Like and Cross Polarizations. Radar measurements are generally acquired in both like (or copolarized) and cross polarizations. The polarization of an antenna used for measurement is defined to be the same as that of the wave that it transmits, and the polarization of the wave is the direction of its electric field vector. The term, *like polarization*, means transmitting and receiving with matched antennas

$$|\mathbf{a}_r \cdot \mathbf{a}_t| = 1 \quad (10)$$

where $\mathbf{a}_t, \mathbf{a}_r$ are the polarizations of the transmitting and receiving antennas, respectively. The *cross or orthogonal polarization* is defined to be with zero reception:

$$|\mathbf{a}_r \cdot \mathbf{a}_t| = 0 \quad (11)$$

To illustrate the meaning of Eq. (10), consider the transmitting antenna with polarization defined by Eq. (12), which represents a left-hand *elliptically polarized* plane wave from a transmitting antenna. The term *left-hand* means that when the thumb of the left hand is in the direction of propagation, the fingers are pointing in the direction of rotation of the electric field vector as time increases (Fig. 2):

$$\mathbf{E}_t = \mathbf{x} \cos \tau_t \cos(\omega t - kz) - \mathbf{y} \sin \tau_t \sin(\omega t - kz) \quad (12)$$

The angle τ_t defines the relative magnitudes of the semi-axes of the ellipse and is known as the *ellipticity angle*. A sign change in τ_t or z would make the wave right-handed. If the receiving antenna is chosen to have the same polarization, its radiated field will have the same mathematical form but expressed in coordinates for the receiving antenna (the primed coordinates in Fig. 2). As illustrated in Fig. 2, transmitting and receiving antenna systems must point in opposite directions. This means that when the radiated field of the receiving antenna is expressed in the coordinates of the transmitting antenna, its propagation phase must take the form $\omega t + kz$. The coordinate system for the receiving antenna may be related to that of the transmitting antenna as follows:

$$\begin{aligned} \mathbf{x}' &= \mathbf{x} \\ \mathbf{y}' &= -\mathbf{y} \end{aligned} \quad (13)$$

Thus, the radiating field from the receiving antenna expressed in the coordinates of the transmitting antenna is

$$\mathbf{E}_r = \mathbf{x} \cos \tau_r \cos(\omega t + kz) + \mathbf{y} \sin \tau_r \sin(\omega t + kz) \quad (14)$$

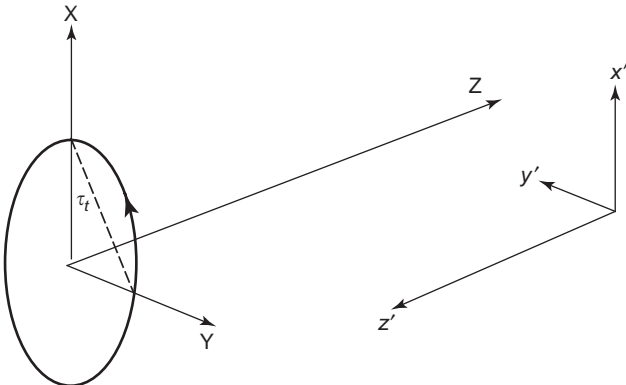


Figure 2. Illustration of the polarizations of transmitting and receiving antenna systems. A left-hand elliptically polarized transmitted field is shown.

When we convert it to phasor form, it becomes

$$\mathbf{E}_r = (\mathbf{x} \cos \tau_r - j\mathbf{y} \sin \tau_r) \exp[j(\omega t + kz)] \equiv \mathbf{a}_r e^{j(\omega t + kz)} \quad (15)$$

Similarly, from Eq. (12) the polarization unit vector in phasor form for the transmitting antenna is

$$\mathbf{a}_t = \mathbf{x} \cos \tau + j\mathbf{y} \sin \tau$$

when we set $\tau_t = \tau_r = \tau$. Clearly it is the complex conjugate of \mathbf{a}_r and $|\mathbf{a}_r \cdot \mathbf{a}_t| = 1$. The polarization states of both antennas are *left-hand elliptic*. Hence this case is referred to as *like polarization*. The special case, where τ is zero, yields linear polarization in \mathbf{x} direction for both the transmitting and receiving antennas.

To illustrate cross- or orthogonal polarization, consider the receiving antenna defined by Eq. (14) and set $\tau_r = \tau_t - \pi/2$. Thus, the polarization vector of the receiving antenna expressed in the transmitting coordinates after setting $\tau_t = \tau$ becomes

$$\hat{\mathbf{a}}_r = \mathbf{x} \sin \tau + j\mathbf{y} \cos \tau \quad (16)$$

If we take the dot product according to Eq. (11), we find that $\mathbf{a}_r \cdot \mathbf{a}_t = 0$. When we check the polarization state of the receiving antenna, it is *right-hand elliptic*. Thus, left-hand elliptic and right-hand elliptic polarizations are mutually orthogonal. The special case, when τ is zero, yields linear polarization with \mathbf{x} direction for the transmitting antenna and \mathbf{y} direction for the receiving antenna. These directions are clearly orthogonal.

3. RADIATIVE TRANSFER FORMULATION

In this section we present the basic development of the radiative transfer theory and its formulation for scattering from and propagation through an inhomogeneous layer with irregular boundaries. In the classical formulation of the radiative transfer equation [7] the fundamental quantity used is the *specific intensity* I_ν . It is defined in terms of the amount of power dP (watts) flowing along the \mathbf{r} direction within a solid angle $d\Omega$ through an elementary area dS in a frequency interval $(\nu, \nu + d\nu)$ as follows:

$$dP = I_\nu \cos \alpha dS d\Omega d\nu \quad (17)$$

where α is the angle between the outward normal \mathbf{s} to dS and the unit vector \mathbf{r} . The dimension of I_ν is expressed in $\text{W m}^{-2} \text{sr}^{-1} \text{Hz}^{-1}$. In most remote-sensing applications, the radiation at a single frequency is considered. Thus, it is more convenient to consider the intensity I at a frequency ν , which is defined as the integral of I_ν over the frequency interval $(\nu - d\nu/2, \nu + d\nu/2)$. In terms of intensity, the amount of power at a single frequency can be written as

$$dP = I \cos \alpha dS d\Omega \quad (18)$$

The *equation of transfer* governs the variation of intensities in a medium that absorbs, emits, and scatters radia-

tion. Within the medium, consider a cylindrical volume of unit cross section and length dl . The change in intensity may be a gain or a loss. The loss in intensity I propagating through the cylindrical volume along the distance dl is due to absorption and scattering away from the direction of propagation, and the gain is from thermal emission and scattering into the direction of propagation

$$dI = -\kappa_a Idl - \kappa_s Idl + \kappa_a J_a dl + \kappa_s J_s dl \quad (19)$$

where κ_a, κ_s are the *volume absorption* and *volume-scattering coefficients*. In Eq. (19) J_a and J_s are the *absorption source function* (or emission source function) and the *scattering source function*. Equation (19) is the radiative transfer equation in which the definition of J_s is

$$J_s(\theta_s, \phi_s) = \frac{1}{4\pi} \int_0^{2\pi} \int_0^\pi P(\theta_s, \phi_s; \theta, \phi) I(\theta, \phi) \sin \theta d\theta d\phi \quad (20)$$

where $P(\theta_s, \phi_s; \theta, \phi)$ is the phase function accounting for scattering within the medium to be defined in the next subsection. It is clear from Eq. (20) that J_s is not an independent source of the medium but is itself a function of the propagating intensity. On the other hand, J_a is an independent source function proportional to the temperature profile of the medium; namely, it is the source function in passive remote sensing problems. As such, it should be dropped in active remote sensing problems in which the source is an incident wave from the radar transmitter outside the scattering medium.

For the active sensing problem to be considered in this section, we will treat partially polarized waves by introducing the *Stokes parameters*. Then, we will generalize the scalar radiative transfer equation to a matrix equation. In so doing, it is helpful first to establish the relation between the scattered intensity and the incident intensity and then to relate these intensities to the corresponding electric fields.

3.1. Stokes Parameters, Phase Matrices, and Radiative Transfer Equations

For an elliptically polarized monochromatic plane wave, $\mathbf{E} = (\mathbf{E}_v \mathbf{v} + \mathbf{E}_h \mathbf{h}) \exp(j\mathbf{k} \cdot \mathbf{r})$, propagating through a differential solid angle $d\Omega$ in a medium with intrinsic impedance η , where \mathbf{v} and \mathbf{h} are the unit vectors denoting vertical and horizontal polarization, respectively, the *modified Stokes parameters* I_v, I_h, U , and V in the dimension of intensity can be defined in terms of the electric fields as

$$I_v d\Omega = 0.5 \operatorname{Re} \left\langle \frac{|\mathbf{E}_v|^2}{\eta^*} \right\rangle \quad (21)$$

$$I_h d\Omega = 0.5 \operatorname{Re} \left\langle \frac{|\mathbf{E}_h|^2}{\eta^*} \right\rangle \quad (22)$$

$$U d\Omega = \operatorname{Re} \left\langle \frac{\mathbf{E}_v \mathbf{E}_h^*}{\eta^*} \right\rangle \quad (23)$$

$$V d\Omega = \operatorname{Im} \left\langle \frac{\mathbf{E}_v \mathbf{E}_h^*}{\eta^*} \right\rangle \quad (24)$$

where $*$ is the symbol for complex conjugate, $\eta = [\mu/(\epsilon - j\sigma/\omega)]^{1/2}$ for finitely conducting medium and the right-hand side of Eq. (21) or (22) is the *average Poynting vector* representing power density in units of watts per meter squared. These four parameters have the same dimension and hence are more convenient to use than amplitude and phase, which have different dimensions. It has been shown that the amplitude, phase, and polarization state of any elliptically polarized wave can be completely characterized by these parameters [8].

3.1.1. Phase Matrix for Rough Surfaces. To relate the scattered intensity to the incident intensity, consider a plane wave illuminating a rough surface area A_0 . The relation between the vertically and horizontally polarized scattered field components E_v^s, E_h^s and those of the incident field components E_v^i, E_h^i is

$$\begin{bmatrix} E_v^s \\ E_h^s \end{bmatrix} = \frac{e^{jkR}}{R} \begin{bmatrix} S_{vv} & S_{vh} \\ S_{hv} & S_{hh} \end{bmatrix} \begin{bmatrix} E_v^i \\ E_h^i \end{bmatrix} \quad (25)$$

where S_{pq} (where subscripts ‘‘p, q’’ = vertical or horizontal) is the *scattering amplitude* in meters, R is the distance from the center of the illuminated area to the point of observation, and k is the wavenumber. Consider $|E_v^s|^2/\eta^*$

$$\frac{|E_v^s|^2}{\eta^*} = \frac{1}{R^2} \left(\frac{|S_{vv}|^2 |E_v^i|^2}{\eta^*} + \frac{|S_{vh}|^2 |E_h^i|^2}{\eta^*} + 2 \operatorname{Re} \frac{S_{vv} S_{vh}^* E_v^i E_h^{i*}}{\eta^*} \right)$$

where

$$\begin{aligned} & 2 \operatorname{Re} \frac{S_{vv} S_{vh}^* E_v^i E_h^{i*}}{\eta^*} \\ &= 2 \operatorname{Re} \left[\operatorname{Re}(S_{vv} S_{vh}^*) + j \operatorname{Im}(S_{vv} S_{vh}^*) \right] \\ & \times \left[\frac{\operatorname{Re} E_v^i E_h^{i*}}{\eta^*} + j \operatorname{Im} \frac{E_v^i E_h^{i*}}{\eta^*} \right] \} \\ &= 2 \operatorname{Re}(S_{vv} S_{vh}^*) \operatorname{Re} \frac{E_v^i E_h^{i*}}{\eta^*} - 2 \operatorname{Im}(S_{vv} S_{vh}^*) \operatorname{Im} \frac{E_v^i E_h^{i*}}{\eta^*} \end{aligned}$$

Recognizing the relation above, we can obtain the following quantities using Eqs. (25) and (21) through (24):

$$\begin{aligned} & 0.5 \operatorname{Re} \frac{\langle |E_v^s|^2 \rangle}{\eta^*} \\ &= \frac{\langle |S_{vv}|^2 I_v + |S_{vh}|^2 I_h + \operatorname{Re}(S_{vv} S_{vh}^*) U - \operatorname{Im}(S_{vv} S_{vh}^*) V \rangle d\Omega}{R^2} \end{aligned} \quad (26)$$

$$\begin{aligned} & 0.5 \operatorname{Re} \frac{\langle |E_h^s|^2 \rangle}{\eta^*} \\ &= \frac{\langle |S_{hv}|^2 I_v + |S_{hh}|^2 I_h + \operatorname{Re}(S_{hv} S_{hh}^*) U - \operatorname{Im}(S_{hv} S_{hh}^*) V \rangle d\Omega}{R^2} \end{aligned} \quad (27)$$

$$\begin{aligned} & \text{Re} \left\langle \frac{E_v^s E_h^{s*}}{\eta^*} \right\rangle \\ &= \frac{\langle [2 \text{Re}(S_{vv} S_{hv}^*) I_v + 2 \text{Re}(S_{hh}^* S_{vh}) I_h] \rangle d\Omega}{R^2} \\ &+ \frac{\langle [\text{Re}(S_{vv} S_{hh}^* + S_{vh} S_{hv}^*) U - \text{Im}(S_{vv} S_{hh}^* - S_{vh} S_{hv}^*) V] \rangle d\Omega}{R^2} \end{aligned} \quad (28)$$

$$\begin{aligned} & \text{Im} \left\langle \frac{E_v^s E_h^{s*}}{\eta^*} \right\rangle \\ &= \frac{\langle [2 \text{Im}(S_{vv} S_{hv}^*) I_v + 2 \text{Im}(S_{hh}^* S_{vh}) I_h] \rangle d\Omega}{R^2} \\ &+ \frac{\langle [\text{Im}(S_{vv} S_{hh}^* + S_{vh} S_{hv}^*) U - \text{Re}(S_{vv} S_{hh}^* - S_{vh} S_{hv}^*) V] \rangle d\Omega}{R^2} \end{aligned} \quad (29)$$

The left-hand sides of these equations are in watts per square meter. To convert them to intensity, we need to divide both sides of the equation by the solid angle subtended by

but are defined for spherical waves. They differ from the plane wave definition in the normalizing solid angle $(A_0 \cos \theta_s)/R^2$. The element of the phase matrix relating I_v^s to I_v^i is $\sigma_{vv}^0/\cos \theta_s$. To summarize, all possible incident intensities from all directions contributing to \mathbf{I}^s along a given direction, we integrate over all solid angles:

$$\mathbf{I}^s = \frac{1}{4\pi} \int_{4\pi} \mathbf{P} \mathbf{I}^i d\Omega \quad (33)$$

This equation is the generalized version of Eq. (20), for partially polarized waves. Here \mathbf{I}^s , \mathbf{I}^i are column vectors whose components are the Stokes parameters. The detailed contents of the phase matrix written in terms of scattering amplitudes are summarized below

$$\mathbf{P} = \frac{4\pi \langle \mathbf{M} \rangle}{A \cos \theta_s} \quad (34)$$

where the *Stokes matrix* \mathbf{M} is

$$\begin{bmatrix} |S_{vv}|^2 & |S_{vh}|^2 & \text{Re}(S_{vv} S_{vh}^*) & -\text{Im}(S_{vv} S_{vh}^*) \\ |S_{hv}|^2 & |S_{hh}|^2 & \text{Re}(S_{hv} S_{hh}^*) & -\text{Im}(S_{hv} S_{hh}^*) \\ 2\text{Re}(S_{vv} S_{hv}^*) & 2\text{Re}(S_{vh} S_{hh}^*) & \text{Re}(S_{vv} S_{hh}^* + S_{vh} S_{hv}^*) & -\text{Im}(S_{vv} S_{hh}^* - S_{vh} S_{hv}^*) \\ 2\text{Im}(S_{vv} S_{hv}^*) & 2\text{Im}(S_{vh} S_{hh}^*) & \text{Im}(S_{vv} S_{hh}^* + S_{vh} S_{hv}^*) & \text{Re}(S_{vv} S_{hh}^* - S_{vh} S_{hv}^*) \end{bmatrix}$$

the illuminated area A_0 at the point of observation, $(A_0 \cos \theta_s)/R^2$, where θ_s is the angle between the scattered direction and the direction normal to A_0 . Eq. (26) becomes

$$\begin{aligned} \frac{0.5R^2 \text{Re}(|E_v^s|^2)}{(\eta^* A_0 \cos \theta_s)} &= \frac{\langle |S_{vv}|^2 I_v + |S_{vh}|^2 I_h + \text{Re}(S_{vv} S_{vh}^*) U \rangle d\Omega}{A_0 \cos \theta_s} \\ &- \frac{\langle \text{Im}(S_{hv} S_{hh}^*) V \rangle d\Omega}{A_0 \cos \theta_s} \end{aligned} \quad (30)$$

The term on the left-hand side of this equation is the intensity of the scattered field. In view of Eq. (2), we can rewrite the equation in terms of the scattering coefficients as

$$I_v^s = \frac{(\sigma_{vv}^0 I_v + \sigma_{vh}^0 I_h + \sigma_{vvvh}^0 U + \sigma_{hvhv}^0 V) d\Omega}{4\pi \cos \theta_s} \quad (31)$$

Similarly, we can convert the left-hand sides of Eqs. (27)–(29) into intensities and rewrite all four resulting equations into a matrix equation. This matrix equation relates the scattered intensities \mathbf{I}^s to the incident intensities \mathbf{I}^i through a dimensionless quantity known as the *phase matrix* \mathbf{P} :

$$\mathbf{I}^s = \frac{1}{4\pi} \mathbf{P} \mathbf{I}^i d\Omega \quad (32)$$

The components of \mathbf{I}^i are the Stokes parameters as defined by Eqs. (21)–(24) for the incident plane wave. The components of the scattered intensity \mathbf{I}^s are also *Stokes parameters*

3.1.2. Phase Matrix for an Inhomogeneous Medium. Consider a homogeneous medium embedded randomly with scatterers. Each scatterer is characterized by a *bistatic radar cross section* σ_p due to a p -polarized [$p=v$ or h (vertical or horizontal)] incident intensity. The *scattering cross section* of the scatterer Q_{sp} is defined as the cross section that would produce the total scattered power surrounding the scatterer due to a unit incident Poynting vector of polarization p

$$Q_{sp}(\theta, \phi) = \frac{1}{4\pi} \int_{4\pi} \sigma_p d\Omega_s = \int_{4\pi} (|S_{vp}|^2 + |S_{hp}|^2) d\Omega_s \quad (35)$$

where θ, ϕ indicate the incident direction and integration is over the scattered solid angle. The *volume scattering coefficient* for the inhomogeneous medium and polarization p is

$$\kappa_{sp} = N_v Q_{sp} \quad (36)$$

where N_v is the number of scatterers per unit volume [8] or the *number density*. The *volume scattering coefficient* κ_{sp} represents the scattering loss per unit length and has the units of Np/m (nepers per meter). In the case of a continuous, inhomogeneous medium defined by a spatially varying permittivity function, the scattering amplitudes S_{vp}, S_{hp} are for an effective volume V . The

volume scattering coefficient is defined as [9]

$$\kappa_{\text{sp}} = \frac{1}{V} \mathbf{Q}_{\text{sp}} \quad (37)$$

Another important parameter for characterizing an inhomogeneous medium is its absorption loss, represented by the *volume absorption coefficient*, κ_{ap} . This quantity may be defined in terms of the average relative permittivity ϵ_{ap} of the medium, where p denotes the incident polarization. Letting k_0 be the free-space wavenumber, we define the absorption coefficient for p polarization as

$$\kappa_{\text{ap}} = 2k_0 |\text{Im} \sqrt{\epsilon_{\text{ap}}}| \quad (38)$$

This equation may be used for either a continuous inhomogeneous medium or a discrete inhomogeneous medium. In the latter case the *absorption cross section* \mathbf{Q}_{ap} for one particle and p polarization can be defined as

$$\mathbf{Q}_{\text{ap}} = \frac{\kappa_{\text{ap}}}{N_{\text{v}}} \quad (39)$$

From Eqs. (36) and (39) the total cross section, also known as the *extinction cross section*, for a scatterer is

$$\mathbf{Q}_{\text{ep}} = \mathbf{Q}_{\text{ap}} + \mathbf{Q}_{\text{sp}} \quad (40)$$

and the *extinction coefficient* is $\kappa_{\text{ep}} = N_{\text{v}} \mathbf{Q}_{\text{ep}}$. In Eq. (40), \mathbf{Q}_{ep} is the effective area that generates the total scattered and absorbed power due to a unit incident Poynting vector of polarization p . The ratio of κ_{sp} to κ_{ep} is the *albedo* of the random medium. Conceptually, either \mathbf{Q}_{ep} or \mathbf{Q}_{sp} may be used in place of $\text{Acos} \theta_s$ in Eq. (34) to define the phase matrix of a single scatterer. However, unlike $\text{Acos} \theta_s$, \mathbf{Q}_{ep} and \mathbf{Q}_{sp} have polarization dependence in general [10] and hence are matrices. Let us denote them as \mathbf{Q}_{e} and \mathbf{Q}_{s} . The choice of the definition for the *phase matrix* depends on the assumed form of the scattering source term in Eq. (19). When the term is written as $\kappa_{\text{s}} \mathbf{J}_{\text{s}}$, the definition is [11]

$$\mathbf{P}_{\text{s}} = 4\pi \mathbf{Q}_{\text{s}}^{-1} \langle \mathbf{M} \rangle \quad (41)$$

If the term is written as $\kappa_{\text{e}} \mathbf{J}'_{\text{s}}$, then the definition should be [8]

$$\mathbf{P}_{\text{e}} = 4\pi \mathbf{Q}_{\text{e}}^{-1} \langle \mathbf{M} \rangle \quad (42)$$

Both definitions have appeared in the literature. Clearly, the phase matrix is a term created for convenience; the scattering source term is the fundamental quantity. Thus, while Eq. (41) is not the same as Eq. (42), the source terms are the same in both cases, as they should be:

$$\kappa_{\text{s}} \mathbf{J}_{\text{s}} = \kappa_{\text{e}} \mathbf{J}'_{\text{s}} = \int_{4\pi} N_{\text{v}} \langle \mathbf{M} \rangle \mathbf{I} d\Omega \quad (43)$$

In view of Eqs. (43) and (19), the radiative transfer equation for *partially polarized waves* in a discrete

inhomogeneous medium is

$$\begin{aligned} \frac{d\mathbf{I}}{dl} &= -\kappa_{\text{e}} \mathbf{I} + \frac{\kappa_{\text{e}}}{4\pi} \int_{4\pi} \mathbf{P}_{\text{e}} \mathbf{I} d\Omega + \kappa_{\text{a}} \mathbf{J}_{\text{a}} \\ &= -\kappa_{\text{e}} \mathbf{I} + \frac{\kappa_{\text{s}}}{4\pi} \int_{4\pi} \mathbf{P}_{\text{s}} \mathbf{I} d\Omega + \kappa_{\text{a}} \mathbf{J}_{\text{a}} \end{aligned} \quad (44)$$

or

$$\frac{d\mathbf{I}}{dl} = -\kappa_{\text{e}} \mathbf{I} + \int_{4\pi} N_{\text{v}} \langle \mathbf{M} \rangle \mathbf{I} d\Omega + \kappa_{\text{a}} \mathbf{J}_{\text{a}} \quad (45)$$

In a continuous, inhomogeneous medium, it is more convenient to use the *Stokes matrix* instead of the phase matrix. Making use of Eq. (37), we have

$$\frac{d\mathbf{I}}{dl} = -\kappa_{\text{e}} \mathbf{I} + \int_{4\pi} \frac{\langle \mathbf{M} \rangle}{V} \mathbf{I} d\Omega + \kappa_{\text{a}} \mathbf{J}_{\text{a}} \quad (46)$$

In Eq. (46), V is the effective illuminated volume as given in Eq. (37) and will cancel out upon evaluating $\langle \mathbf{M} \rangle$. It is clear from Eqs. (45) and (46) that the fundamental quantity in scattering is the *scattering amplitude*, while phase function is an artificially created quantity.

The radiative transfer equation is formulated on the basis of energy balance. The phase changes of the scattered wave and its cross-correlation terms are ignored in the solution of the transfer equation. For a sparsely populated random medium it is not necessary to track the phase change between scatterers. In a *dense medium* a group of scatterers may scatter coherently. Thus phase relation among scatterers must be taken into account in the derivation of the phase function. However, phase effects in multiple scattering calculations can still be ignored because the mechanism of multiple scattering tends to destroy phase relation between scatterers. To date, the radiative transfer formulation is still the most practical approach to compute multiple scattering from an inhomogeneous medium. Furthermore, it provides a natural way to combine surface boundary scattering with volume scattering from within an inhomogeneous layer, as we shall see in the next section.

4. SCATTERING FROM AN INHOMOGENEOUS LAYER WITH IRREGULAR BOUNDARIES

For bounded media, scattering or reflection may occur at the boundary. Both incident and scattered intensities are needed in the boundary conditions. Therefore, it is necessary to split the intensity matrix into upward \mathbf{I}^+ and downward \mathbf{I}^- components and rewrite Eq. (45) as two equations. For active sensing applications, the thermal source term is not needed. It is also a standard practice to express the slant range in terms of the vertical distance, that is, let $l = z/\cos \theta$ (Fig. 3)

Consider the problem of a plane wave in air incident on an inhomogeneous layer above a ground surface. The geometry of the scattering problem is depicted in Fig. 3. The inhomogeneous layer is assumed to have such

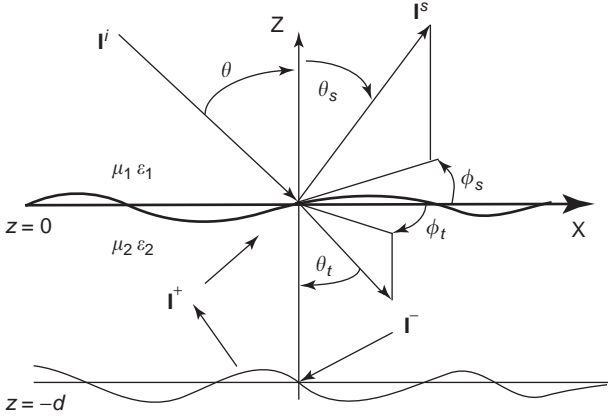


Figure 3. Scattering geometry for an inhomogeneous layer above a homogeneous half-space.

characteristics that the *upward intensity* \mathbf{I}^+ and the *downward intensity* \mathbf{I}^- satisfy the radiative transfer equation. On rewriting (45) in terms of these intensities we obtain [1]

$$\begin{aligned} \mu_s \frac{d}{dz} \mathbf{I}^+(z, \mu_s, \phi_s) &= -\kappa_e \mathbf{I}^+(z, \mu_s, \phi_s) \\ &+ \frac{1}{4\pi} \int_0^{2\pi} \int_0^1 \kappa_s \mathbf{P}_s(\mu_s, \mu, \phi_s - \phi) \mathbf{I}^+(z, \mu, \phi) d\mu d\phi \quad (47) \\ &+ \frac{1}{4\pi} \int_0^{2\pi} \int_0^1 \kappa_s \mathbf{P}_s(\mu_s, -\mu, \phi_s - \phi) \mathbf{I}^-(z, \mu, \phi) d\mu d\phi \end{aligned}$$

$$\begin{aligned} \mu_s \frac{d}{dz} \mathbf{I}^-(z, \mu_s, \phi_s) &= \kappa_e \mathbf{I}^-(z, \mu_s, \phi_s) \\ &- \frac{1}{4\pi} \int_0^{2\pi} \int_0^1 \kappa_s \mathbf{P}_s(-\mu_s, \mu, \phi_s - \phi) \mathbf{I}^+(z, \mu, \phi) d\mu d\phi \quad (48) \\ &- \frac{1}{4\pi} \int_0^{2\pi} \int_0^1 \kappa_s \mathbf{P}_s(-\mu_s, \mu, \phi_s - \phi) \mathbf{I}^-(z, \mu, \phi) d\mu d\phi \end{aligned}$$

where $\mu_s = \cos \theta_s$; $\mu = \cos \theta$, \mathbf{I}^+ , \mathbf{I}^- are column vectors containing the four *modified Stokes parameters* and \mathbf{P}_s is the *phase matrix*.

To find the upward intensity due to an incident intensity \mathbf{I}^i , where $\mathbf{I}^i = \mathbf{I}_0 \delta(\mu - \mu_i) \delta(\phi - \phi_i)$, $\delta(\cdot)$ is the *Dirac delta function* and (θ_i, ϕ_i) denotes the direction of propagation of the incident wave, we need to solve Eqs. (47) and (48), subject to the following boundary conditions. At $z = -d$ the upward and downward intensities are related through the ground-scattering phase matrix \mathbf{G} as

$$\begin{aligned} \mathbf{I}^+(-d, \mu_s, \phi_s) &= \frac{1}{4\pi} \int_0^{2\pi} \int_0^1 \mathbf{G}(\mu_s, -\mu, \phi_s - \phi) \\ &\times \mathbf{I}^-(-d, \mu, \phi) d\mu d\phi \quad (49) \end{aligned}$$

If the ground surface is flat, \mathbf{G} may be written in terms of the reflectivity matrix \mathbf{R}_g as

$$\mathbf{G} = 4\pi \mathbf{R}_g \delta(\mu_s - \mu) \delta(\phi_s - \phi) \quad (50)$$

At the top boundary $z = 0$, the upward and downward intensities are related through the surface-scattering and transmission *phase matrices* \mathbf{S}_R and \mathbf{S}_T [12]

$$\begin{aligned} \mathbf{I}^-(0, \mu_s, \phi_s) &= \frac{1}{4\pi} \int_0^{2\pi} \int_0^1 \mathbf{S}_R(-\mu_s, \mu, \phi_s - \phi) \mathbf{I}^+(0, \mu, \phi) d\mu d\phi \\ &+ \frac{1}{4\pi} \int_0^{2\pi} \int_0^1 \mathbf{S}_T(-\mu_s, -\mu, \phi_s - \phi) \mathbf{I}^i(0, \mu, \phi) d\mu d\phi \quad (51) \end{aligned}$$

Once $\mathbf{I}^+(0, \mu_s, \phi_s)$ is determined within the inhomogeneous layer, the upward intensity transmitted from the layer into air can be found using the transmission scattering matrix of the surface, \mathbf{S}_T as

$$\begin{aligned} \mathbf{I}^+(\mu_s, \phi_s) &= \frac{1}{4\pi} \int_0^{2\pi} \int_0^1 \mathbf{S}_T(\mu_s, \mu, \phi_s - \phi) \\ &\times \mathbf{I}^+(0, \mu, \phi) d\mu d\phi \quad (52) \end{aligned}$$

The total scattered intensity in air is given by the sum of $\mathbf{I}^+(\mu_s, \phi_s)$ and \mathbf{I}_s , where \mathbf{I}_s is the intensity due to random surface scattering by the top layer boundary:

$$\mathbf{I}_s = \frac{1}{4\pi} \int_0^{2\pi} \int_0^1 \mathbf{S}_R(-\mu_s, -\mu, \phi_s - \phi) \mathbf{I}^i(0, \mu, \phi) d\mu d\phi \quad (53)$$

The explicit forms of the matrices \mathbf{R}_g , \mathbf{S}_R , and \mathbf{S}_T are available in Fung [1]. The expressions for \mathbf{S}_R and \mathbf{S}_T are for an irregular boundary. The \mathbf{G} matrix is assumed to have the same mathematical form as \mathbf{S}_R . Once the total scattered intensity for a p -polarized component I_p^s of the intensity matrix is found, the scattering coefficient for this component is defined relative to the incident intensity $I_q^i = I_{q0} \delta(\mu - \mu_i) \delta(\phi - \phi_i)$ of polarization q along (μ_i, ϕ_i) direction as

$$\sigma_{pq}^0 = \frac{4\pi I_p^s \cos \theta_s}{I_{q0}} \quad (54)$$

The transfer equations given by Eqs. (47) and (48) can be solved exactly by using numerical techniques [13,14]. Analytic solutions by iteration are available to the first order in *albedo* [1, Chapter 2], which is also known as the *Born approximation*. Generally, it is practical to carry the iterative solution process to the second order in albedo. This additional complexity is justified only for cross-polarization in the plane of incidence, because its first-order solution is zero. For like polarization the difference between the first- and second-order results is generally within experimental error.

4.1. First-Order Solution of the Layer Problem

In many practical applications the volume scattering from an inhomogeneous layer can be approximated by using a first-order solution whenever the albedo of the medium is smaller than about 0.3. Furthermore, because volume

scattering has a slow varying angular behavior over incident angles in the range between 0° and 70° , we can approximate the transmission across an irregular boundary by a plane boundary. Under these conditions the first-order solution to the radiative transfer equations consists of four major terms: (1) *volume scattering* by the inhomogeneous layer transmitted across the top boundary, (2) scattering by the bottom layer boundary passing through the layer into the upper medium, (3) scattering between layer volume and lower boundary passing through the layer into the upper medium, and (4) *surface scattering* by the top boundary. Note that only the last term represents pure surface scattering and does not involve propagation through the layer volume. The second and third terms are dependent on contributions from the lower boundary and can be ignored in dealing with half-space or very thick layer.

The volume backscattering term for p polarized scattering has the form [1]

$$\begin{aligned} \sigma_{\text{vpp}}^0(\theta) &= 0.5 \cos \theta_t \frac{\kappa_s}{\kappa_e} T_p(\theta, \theta_t) T_p(\theta_t, \theta) \left(1 - \exp\left(\frac{-2\kappa_e d}{\cos \theta_t}\right) \right) \\ &\quad \times P_{\text{spp}}(\theta_t, \pi; \pi - \theta_t, 0) \\ &= 2\pi \cos \theta_t T_p(\theta, \theta_t) 1 - \exp\left(\frac{-2\kappa_e d}{\cos \theta_t}\right) \\ &\quad \times \frac{\langle |S_{\text{pp}}(\theta_t, \pi; \pi - \theta_t, 0)|^2 \rangle}{\sigma_e} T_p(\theta_t, \theta) \end{aligned} \quad (55)$$

where θ_t is the angle of transmission, $T_p(\theta_t, \theta)$ is the Fresnel power transmission coefficient for p polarization, d is the depth of the layer, $S_{\text{pp}}(\theta_t, \pi; \pi - \theta_t, 0)$ is the scattering amplitude and the *ensemble average* is over the distribution of the orientation of the scatterer, and $\kappa_e = N_v \sigma_e$; N_v is the number density of scatterers and the extinction cross section is given by

$$\sigma_e = - \left(\frac{4\pi}{k} \right) \text{Im}[\langle S_{\text{pp}}(\pi - \theta_t, 0; \pi - \theta_t, 0) \rangle] \quad (56)$$

The *extinction coefficient* κ_e is the controlling factor for propagation through the layer. Both the scattering and the extinction coefficients are dependent on the scattering amplitude of the scatterer. In Eq. (55) we provide two forms of the scattering coefficient because for some problems such as *Rayleigh scattering* the phase function P_{spp} is known, and for others only the scattering amplitude is available.

Surface backscattering from the lower boundary is given by the *surface scattering coefficient* from the lower boundary, $\sigma_{\text{spp}}^0(\theta)$, modified by propagation loss through the layer and transmission across the top boundary as

$$\sigma_{\text{lpp}}^0(\theta) = \cos \theta T_p(\theta, \theta_t) \frac{\sigma_{\text{spp}}^0(\theta_t)}{\cos \theta_t} T_p(\theta_t, \theta) \exp\left(\frac{-2\kappa_e d}{\cos \theta_t}\right) \quad (57)$$

The explicit form of the surface scattering coefficient $\sigma_{\text{spp}}^0(\theta)$ is given in the next section. Finally, we give the expression for the volume–surface interaction term

resulting from the incident wave transmitted through the layer, reflected by the lower boundary, and then scattered by layer inhomogeneities back into the direction of the receiver. By reciprocity, the wave that traverses the same path in the reverse direction makes the same contribution to the receiver. This term has the form

$$\begin{aligned} \sigma_{\text{lpp}}^0(\theta) &= \cos \theta T_p(\theta, \theta_t) \frac{\kappa_s d |R_p(\theta_t)|^2}{\cos \theta_t} T_p(\theta_t, \theta) \exp\left(\frac{-2\kappa_e d}{\cos \theta_t}\right) \\ &\quad \times \{P_{\text{spp}}(\pi - \theta_t, \pi; \pi - \theta_t, 0) + P_{\text{spp}}(\theta_t, \pi; \theta_t, 0)\} \\ &= \cos \theta T_p(\theta, \theta_t) \frac{N_v d |R_p(\theta_t)|^2}{\cos \theta_t} T_p(\theta_t, \theta) \exp\left(\frac{-2\kappa_e d}{\cos \theta_t}\right) \\ &\quad \times (4\pi) \{ \langle |S_{\text{spp}}(\pi - \theta_t, \pi; \pi - \theta_t, 0)|^2 \rangle \\ &\quad + \langle |S_{\text{spp}}(\theta_t, \pi; \theta_t, 0)|^2 \rangle \} \end{aligned} \quad (58)$$

In Eq. (58), $|R_p(\theta_t)|^2$ is the p -polarized *Fresnel reflectivity* and N_v is the *number density*.

The relative importance of each of the four terms and the actual contents of the phase function or scattering amplitude are dependent on applications. This is illustrated in the subsequent sections.

5. SCATTERING FROM SOIL SURFACES

When an incident electromagnetic wave impinges on an irregular surface, it induces a current on it. The waves radiated by this current is called the *scattered wave*. To calculate surface scattering, one needs to solve the integral equation that governs this induced current on the surface. In general, there is no closed-form, analytic solution for this integral equation. An approximate solution to it is available in Chapter 4 of Ref. 1 and in Ref. 15. It is shown in Chapter 5 of Ref. 1 that the classical backscattering coefficients under high and low frequency conditions for rough surfaces, that is, those based on the Kirchhoff and the small perturbation approximations, are special cases of this scattering coefficient. Hence, we can examine rough surface scattering properties over the entire frequency band with this coefficient. Only single-scatter, backscattering from a randomly rough soil surface is considered here. Readers interested in bistatic scattering and multiple surface scattering are referred to Fung [1,15] and Hsieh et al. [16], respectively.

5.1. Backscattering from a Randomly Rough Soil Surface

To compute backscattering from a soil surface, we need to know both the electric and geometric properties of the surface. In general, the permeability of the soil can be taken to be the same as air, and only the complex dielectric constant is needed. An empirical formula for the relative complex dielectric constant of soil is available from Ulaby et al. [17]. It has the form

$$\epsilon_r = \left[1 + \frac{\text{SBD}(4.7^{0.65} - 1)}{2.65} + m v^b (\epsilon_w^{0.65} - 1) \right]^{1/0.65} \quad (59)$$

where SBD stands for soil bulk density in g/cm^3 , mv is the volumetric soil moisture, and ϵ_w is the permittivity of water given by

$$\epsilon_w = 4.9 + \frac{(\epsilon_{w0} - 4.9)}{1 + jfT_\tau}$$

$$T_\tau = \frac{1.1109}{10} - \frac{3.824T}{10^3} + \frac{6.938T^2}{10^5} - \frac{5.096T^3}{10^7}$$

$$\epsilon_{w0} = 88.045 - 0.4147T + \frac{6.295T^2}{10^4} + \frac{1.075T^3}{10^5}$$

f = frequency in GHz

T = Temperature in degree centigrade and

$b = 1.09 - 0.11S + 0.18C$ is the parameter accounting for the percent of clay C and the percent of sand S in the soil

For a randomly rough surface not skewed by natural forces such as the wind, it is sufficient to describe the geometry of the surface by its first- and second-order statistics. They are the surface *root mean squared* (RMS) height σ and its *autocorrelation function* $\rho(\xi)$, normalized to its height variance σ^2 . The general forms of the back-scattering coefficients for vertically σ_{vv}^0 , horizontally σ_{hh} , and cross- σ_{vh} polarized scattering based on an improved integral equation method (IIEM) [15,16] are given below by Eqs. (60) and (64).

$$\begin{aligned} \sigma_{pp}^0 &= \frac{k^2}{4\pi} \exp[-4k_z^2 \sigma^2] \left\{ \left| (2k_z \sigma) f_{pp} + \frac{\sigma}{4} (F_{pp1} + F_{pp2}) \right|^2 \right. \\ &\quad \left. w(2k \sin \theta, 0) + \sum_{n=2}^{\infty} \left| (2k_z \sigma)^n f_{pp} \right. \right. \\ &\quad \left. \left. + \frac{\sigma}{4} F_{pp1} (2k_z \sigma)^{n-1} \left| \frac{2w^{(n)}(2k \sin \theta, 0)}{n!} \right| \right\} \end{aligned} \quad (60)$$

where $p = v, h$, $f_{vv} = 2R_v / \cos \theta$, $f_{hh} = -2R_h / \cos \theta$, and

$$\begin{aligned} F_{vv1} &= \frac{4k}{\sqrt{\epsilon_r - \sin^2 \theta}} \left\{ (1 - R_v)^2 \epsilon_r \cos \theta + (1 - R_v)(1 + R_v) \right. \\ &\quad \times \sin^2 \theta \left(\sqrt{\epsilon_r - \sin^2 \theta} - \cos \theta \right) \\ &\quad \left. - (1 + R_v)^2 \left[\cos \theta + \frac{\sin^2 \theta}{2\epsilon_r} \left(\sqrt{\epsilon_r - \sin^2 \theta} - \cos \theta \right) \right] \right\} \end{aligned}$$

$$\begin{aligned} F_{vv2} &= 4k \sin^2 \theta \left[(1 - R_v)^2 \left(1 + \frac{\epsilon_r \cos \theta}{\sqrt{\epsilon_r - \sin^2 \theta}} \right) \right. \\ &\quad - (1 - R_v)(1 + R_v) \left(3 + \frac{\cos \theta}{\sqrt{\epsilon_r - \sin^2 \theta}} \right) \\ &\quad \left. + (1 + R_v)^2 \left(1 + \frac{1}{2\epsilon_r} + \frac{\epsilon_r \cos \theta}{2\sqrt{\epsilon_r - \sin^2 \theta}} \right) \right] \end{aligned}$$

$$\begin{aligned} F_{hh1} &= \frac{-4k}{\sqrt{\epsilon_r - \sin^2 \theta}} \left\{ (1 - R_h)^2 \cos \theta + (1 - R_h)(1 + R_h) \right. \\ &\quad \times \sin^2 \theta \left(\sqrt{\epsilon_r - \sin^2 \theta} - \cos \theta \right) \\ &\quad \left. - (1 + R_h)^2 \left[\epsilon_r \cos \theta + \frac{\sin^2 \theta}{2} \left(\sqrt{\epsilon_r - \sin^2 \theta} - \cos \theta \right) \right] \right\} \\ F_{hh2} &= -4k \sin^2 \theta \left[(1 - R_h)^2 \left(1 + \frac{\cos \theta}{\sqrt{\epsilon_r - \sin^2 \theta}} \right) \right. \\ &\quad - (1 - R_h)(1 + R_h) \left(3 + \frac{\cos \theta}{\sqrt{\epsilon_r - \sin^2 \theta}} \right) \\ &\quad \left. + (1 + R_h)^2 \left(1 + \frac{1}{2} + \frac{\cos \theta}{2\sqrt{\epsilon_r - \sin^2 \theta}} \right) \right] \end{aligned}$$

The quantities $w, w^{(n)}$ are the surface spectra corresponding to the two-dimensional *Fourier transforms* of the surface correlation coefficient $\rho(x, y)$ and its n th power, $\rho^n(x, y)$, defined as follows in polar forms:

$$w(\kappa, \varphi) = \int_0^{2\pi} \int_0^{\infty} \rho(r, \phi) e^{-j\kappa r \cos(\varphi - \phi)} r dr d\phi \quad (61)$$

$$w^{(n)}(\kappa, \varphi) = \int_0^{2\pi} \int_0^{\infty} \rho^n(r, \phi) e^{-j\kappa r \cos(\varphi - \phi)} r dr d\phi$$

If the surface roughness is independent of the view direction, the correlation coefficient is isotropic depending only on r . In this case Eq. (61) becomes

$$w(\kappa) = 2\pi \int_0^{\infty} \rho(r) J_0(\kappa r) r dr, \quad (62)$$

$$w^{(n)}(\kappa) = 2\pi \int_0^{\infty} \rho^n(r) J_0(\kappa r) r dr$$

where $J_0(\kappa r)$ is the zeroth-order Bessel function. It is worth noting that the first term in (60) reduces to the first-order perturbation model when $h\sigma$ is small.

In Eq. (60) R_v, R_h are the Fresnel reflection coefficients, which can be generalized by replacing them with a reflection transition function [18] that allows the argument of the *Fresnel reflection coefficients* to change from the incident angle to the specular angle as the operating frequency changes from low to high or roughness from small to large. They are defined as follows

$$R_{vt} = R_v(\theta) + [R_{v0} - R_v(\theta)] \left(1 - \frac{S_t}{S_{t0}} \right) \quad (63)$$

$$R_{ht} = R_h(\theta) + [R_{h0} - R_h(\theta)] \left(1 - \frac{S_t}{S_{t0}} \right)$$

where R_{v0}, R_{h0} are the Fresnel reflection coefficients evaluated at the specular angle, which means normal

incidence for backscattering:

$$S_t = \frac{|F_t|^2 \sum_{n=1}^{\infty} \frac{(k\sigma \cos \theta)^{2n}}{n!} w^{(n)}(2k \sin \theta)}{\sum_{n=1}^{\infty} \frac{(k\sigma \cos \theta)^{2n}}{n!} \left| F_t + \frac{2^{n+2} R_{v0}}{e^{(k\sigma \cos \theta)^2} \cos \theta} \right|^2 w^{(n)}(2k \sin \theta)},$$

$$F_t = 8R_{v0}^2 \sin^2 \theta \left(\frac{\cos \theta + \sqrt{\epsilon_r - \sin^2 \theta}}{\cos \theta \sqrt{\epsilon_r - \sin^2 \theta}} \right)$$

$$S_{t0} = \left| 1 + \frac{8R_{v0}}{F_t \cos \theta} \right|^{-2} \text{ is the limit of } S_t \text{ as } k\sigma \rightarrow 0.$$

The functional form of this transition function indicates that $1 - S_t/S_{t0} \rightarrow 1$ as frequency or surface RMS height becomes large and goes to zero as frequency or surface RMS height is small. For very large dielectric values the magnitudes of R_{vt} , R_{ht} approach unity. Thus, the reflection coefficients with transitional properties R_{vt} , R_{ht} provide a desired change when either frequency or roughness changes.

In a practical application, it is not realistic to expect that a ground surface can always be represented as a continuous surface at all frequencies. In many cases, there are isolated vegetation, pebbles, rocks, and other material sitting above a ground surface. They may be negligible at low frequencies but not at higher frequencies when their physical size is comparable to the incident wavelength, λ .

For cross-polarized backscattering the single-scattering contribution is zero. Its backscattering coefficient based on multiple surface scattering with a chosen shadowing function is

$$\sigma_{vh}^0 = \frac{S(\theta)k^4}{64\pi^3} \int_0^1 \int_0^{2\pi} \left(\sum_{m=1}^{\infty} \sum_{n=1}^{\infty} \exp[-2(k_z\sigma)^2] \right. \\ \left. \times \frac{(k_z\sigma)^{2(m+n)}}{m!n!} S(v) |F_{vh}(v, \varphi)|^2 W^{(m)} W^{(n)} \right) d\varphi dv \tag{64}$$

where $S(\theta)$, $S(v)$ are the shadowing functions, $W^{(m)} = W^{(m)}[k(v \cos \varphi - \sin \theta), k v \sin \varphi]$, $W^{(n)} = W^{(n)}[k(v \cos \varphi + \sin \theta), k v \sin \varphi]$,

$$F_{vh} = \frac{v^2 \cos \varphi \sin \varphi}{\cos \theta} \left\{ \left(\frac{1-R}{q} - \frac{1+R}{q_t} \right) \times (1-3R) \right. \\ \left. - \left(\frac{1-R}{q} - \frac{1+R}{\epsilon_r q_t} \right) (1+R) + \left(\frac{1+R}{q} - \frac{1-R}{q_t} \right) (1+3R) \right. \\ \left. - \left(\frac{1+R}{q} - \epsilon_r \frac{1-R}{q_t} \right) (1-R) \right\}$$

The reflection coefficient in Eq. (64) is defined as the difference between the vertically and horizontally polarized Fresnel reflection coefficients divided by 2, $(R_v - R_h)/2$. In F_{vh} , $q = (1 - v^2)^{0.5}$ and $q_t = (\epsilon_r - v^2)^{0.5}$.

The integration variable v has been normalized to the wavenumber k so that to cover all propagating modes, we only need to integrate to a value less than one as denoted by 1^- .

5.2. Theoretical Model Behaviors

In this section we illustrate the surface backscattering coefficient given by Eq. (60) on the type of correlation function, roughness scales, and the dielectric constant.

5.2.1. Effects of Surface Correlation. To show the effect of the surface correlation function on surface scattering, the backscattering coefficients based on correlation coefficients (1) exponential-like, $\exp[-(r/L)(1 - \exp[-r/x])]$, $x > 0$; (2) x -power, $(1 + r^2/L^2)^{-x}$, $x > 1$; and (3) Gaussian, $\exp[-r^2/L^2]$ are shown in Figs. 4 and 5 for several values of x for the first two correlations with the Gaussian correlation serving as a reference. In Fig. 4 we see that the exponential-like correlation generally causes the backscattering function to appear exponential over small angles of incidence ($0^\circ < \theta < 30^\circ$) and the amount of dropoff over large angles is dependent on the choice of the x value.

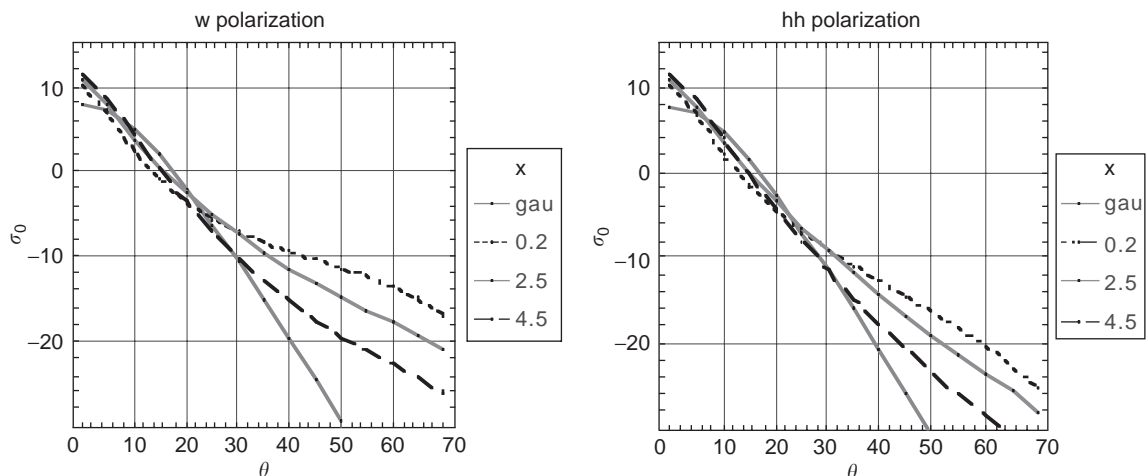


Figure 4. Effects of exponential-like correlation on backscattering with $k\sigma = 0.52$, $kL = 5.2$, and dielectric constant = $25 - j2.5$. Backscattering based on the exponential-like correlation function with several values of x are shown relative to the backscattering curve with Gaussian correlation. (This figure is available in full color at <http://www.mrw.interscience.wiley.com/erfme>.)

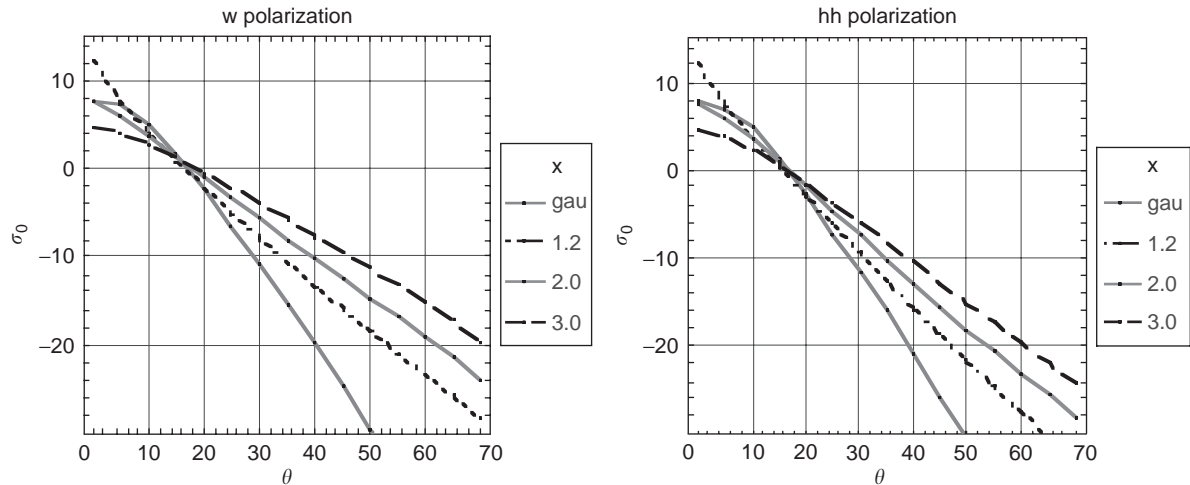


Figure 5. Effects of x -power correlation on backscattering with $k\sigma = 0.52$, $kL = 5.2$, and dielectric constant $= 25 - j2.5$. Backscattering based on the exponential-like correlation function with several values of x are shown relative to the backscattering curve with Gaussian correlation. (This figure is available in full color at <http://www.mrw.interscience.wiley.com/erfme>.)

A larger value of x makes the dropoff closer to the Gaussian. This is because a larger x will cause a wider range of the correlation function to be Gaussian-like. However, the angular trends remain exponential over all angles. In Fig. 5 we use the x -power correlation to calculate the backscattering coefficient. Over small angles of incidence there is a significant change in the angular trends from exponential to Gaussian as x increases. Beyond 30° , the angular trends are nearly linear. Similar to the exponential-like function, the dropoff over large angles of incidence is greater for larger x .

5.2.2. Effects of σ and L . Next we show the effect of the surface RMS height σ . This is illustrated in Fig. 6. Here the exponential-like correlation function is used. The parameter kL is chosen to be 5.2 in Fig. 6. The backscattering coefficient is seen to rise in level as σ increases from 0.2 to 0.8 except near vertical incidence. Intuitively,

as RMS height increases, we have a rougher surface and more backscattering at larger angles of incidence. The overall effect is that scattering tends to be more isotropic. This is why scattering near vertical incidence rises initially and then decreases. Now we consider the effects of the surface correlation length L on the backscattering coefficient in Fig. 7, when $k\sigma$ is fixed at 0.42. An increase in L is seen to cause a significant rise in backscattering near vertical and a faster dropoff at large angles of incidence in both vertical and horizontal polarizations. The nearly parallel angular curves over large angles of incidence is due to the use of the exponential-like correlation function.

5.2.3. Dependence on Dielectric Constant. Generally, a larger dielectric constant for the surface represents a greater discontinuity and hence should lead to a stronger backscattering over all angles of incidence. In backscattering, cross-polarized scattering is due to multiple scattering.

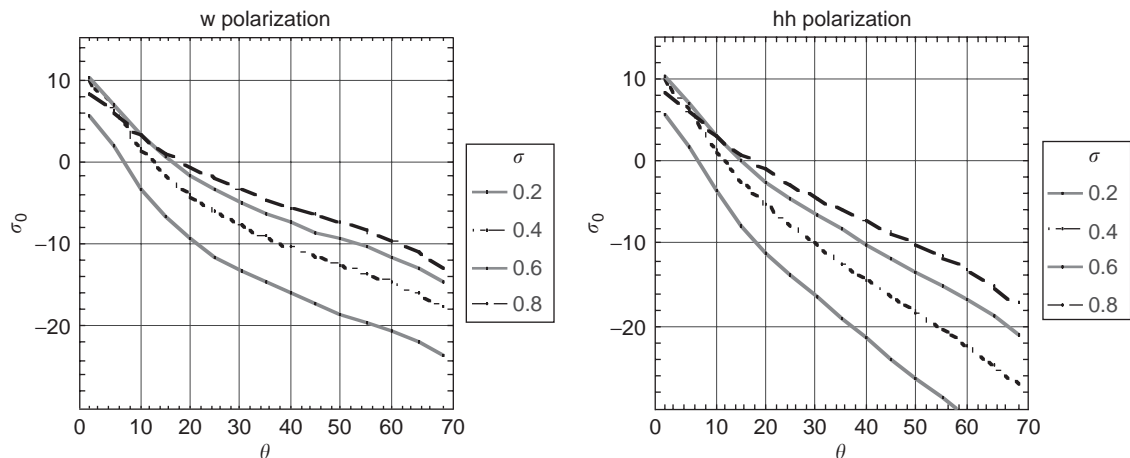


Figure 6. Backscattering curves are shown for vv and hh using exponential-like correlation at 5 GHz, $kL = 5.2$, $\epsilon_r = 25 - j2.5$, when the RMS height, σ , varies from 0.2 to 0.8 cm. There is an initial rise with a subsequent drop near vertical, when σ is greater than 0.6 cm. (This figure is available in full color at <http://www.mrw.interscience.wiley.com/erfme>.)

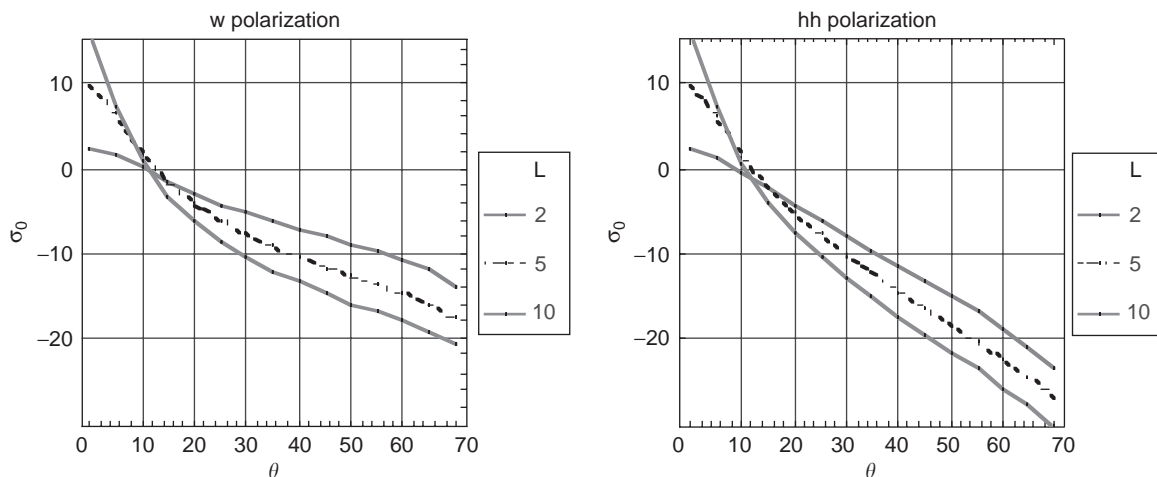


Figure 7. Backscattering curves are shown for vv and hh using exponential-like correlation at 5 GHz, $k\sigma = 0.42$, $\epsilon_r = 25 - j2.5$, when the correlation length L varies from 2 to 10 cm. There is continued rise near vertical as L increases along with a faster dropoff indicating an effectively smoother surface. (This figure is available in full color at <http://www.mrw.interscience.wiley.com/erfme>.)

Thus, a change in the dielectric constant has a greater influence on cross polarization in the backscattering direction. This point is illustrated in Fig. 8 with the x -power and Gaussian correlation functions. There is a large rise in the level of the backscattering curve as the dielectric constant increases. The general shape of the angular curves are similar but the overall angular dropoff is larger for Gaussian correlation.

5.3. Comparisons with Soil Measurements

In making comparisons with measurements it is important to realize that different scales of roughness could be responsible for scattering at two different frequencies. If so, a single parameter correlation function cannot be used for both frequencies without changing the value of its correlation length. This is why for multifrequency measurements it is generally not possible to use the same

surface parameter for all frequencies. On the other hand, when the same roughness scale is responsible for scattering at two frequencies, only one correlation parameter needs to be used.

In Fig. 9, we show a comparison between the surface model given by Eq. (60) and measurements from a rough soil surface in Ref. 23, where ground truth data were acquired by researchers. The roughness parameters are known to be $\sigma = 1.12$ cm and $L = 8.4$ cm. Dielectric values are fixed at $\epsilon_r = 15.34 - j3.7$ and $\epsilon_r = 15.23 - j2.1$ for 1.5 and 4.74 GHz, respectively. Except for the 50° point at 1.5 GHz, a very good agreement is realized in levels and trends between the model predictions using an exponential-like correlation with $x = 0.8$ cm and data at 1.5 GHz. At 4.75 GHz, an x value of 0.25 is used. A good agreement is realized in VV except at 20° and 60° . For HH polarization, the agreement is good except at 20° and 70° . In Fig. 10 we show another comparison with data collected by

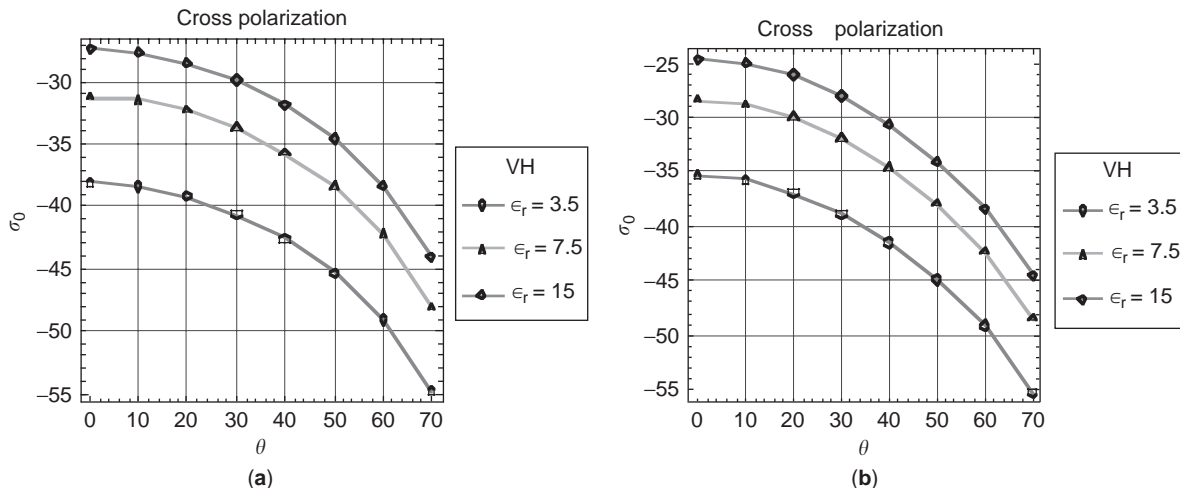


Figure 8. Cross-polarized backscattering coefficient with $k\sigma = 0.315$, $kL = 2.1$ for (a) x -power correlation with $x = 1.5$ and (b) Gaussian correlation. (This figure is available in full color at <http://www.mrw.interscience.wiley.com/erfme>.)

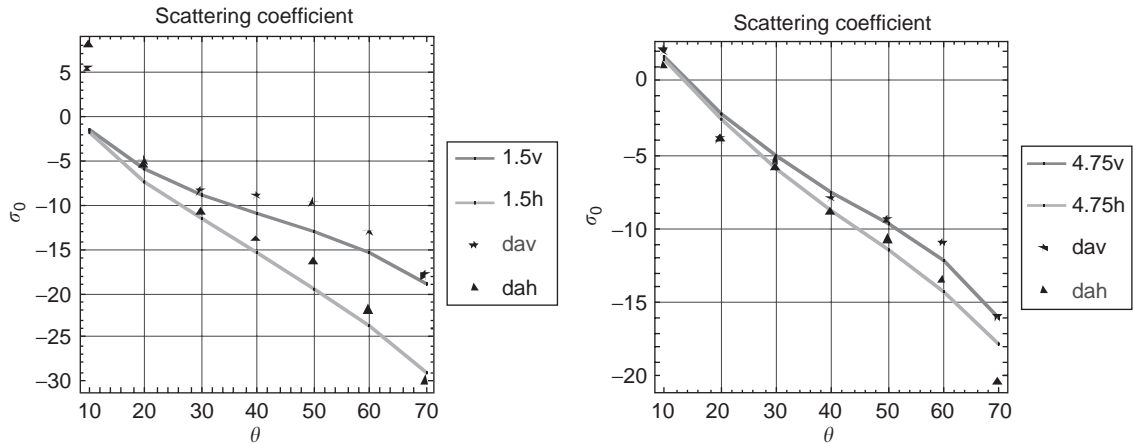


Figure 9. A comparison with measurements from Ref. 24 using surface parameters provided: $\sigma = 1.12$ cm, $L = 8.4$ cm with $\epsilon_r = 15.34 - j3.7$ for 1.5 GHz and with $\epsilon_r = 15.23 - j2.1$ for 4.75 GHz. The correlations selected are $\exp[-(r/L)(1 - \exp[-1.25r])]$ and $\exp[-(r/L)(1 - \exp[-4r])]$. (This figure is available in full color at <http://www.mrw.interscience.wiley.com/erfme>.)

Ulaby et al. [17] over an asphalt surface at 17 and 35.6 GHz from 10° to 70° incidence. At both frequencies the RMS height and correlation length are chosen to be 0.12 and 0.6 cm. The dielectric values are 16 and 12 using the exponential-like correlation with x equals 0.25 and 0.05, respectively. The overall agreements for both fields are good and some finer adjustments have been made of the exponential-like correlation function through the choice of x . This effect has been shown in Fig. 4.

6. SCATTERING FROM A VEGETATED AREA

A vegetation layer may be viewed as an inhomogeneous layer without a top boundary. In general, the scatterers within the layer are collections of leaves, stems, branches, and trunks. At frequencies around 8.6 GHz or more leaves are usually the dominant scatterer and attenuator beyond 20° off the vertical in the backscattering direction. To

illustrate volume scattering by leaves, we consider only backscattering from a half-space of disk- and needle-shaped leaves in this section. Readers are referred to Chapter 11 of Fung [1] for scattering by combinations of leaves, branches, and trunks.

To use Eq. (55) for volume scattering calculation from leaves, we need the scattering amplitude of disk- and needle-shaped leaves. A basic approach to this problem is to use the scattered field formulation based on the volume equivalence theorem

$$E^s(\mathbf{r}) = \frac{k^2(\epsilon_r - 1)}{4\pi} \int_V \frac{\exp(-jk|\mathbf{r} - \mathbf{r}'|)}{|\mathbf{r} - \mathbf{r}'|} \mathbf{E}_{in} dV' \quad (65)$$

where k is the wavenumber in air, ϵ_r is the relative permittivity of the scatterer (leaf), \mathbf{E}_{in} is the field inside the scatterer, and integration is over the volume V of the scatterer defined in terms of the prime variables. Clearly,

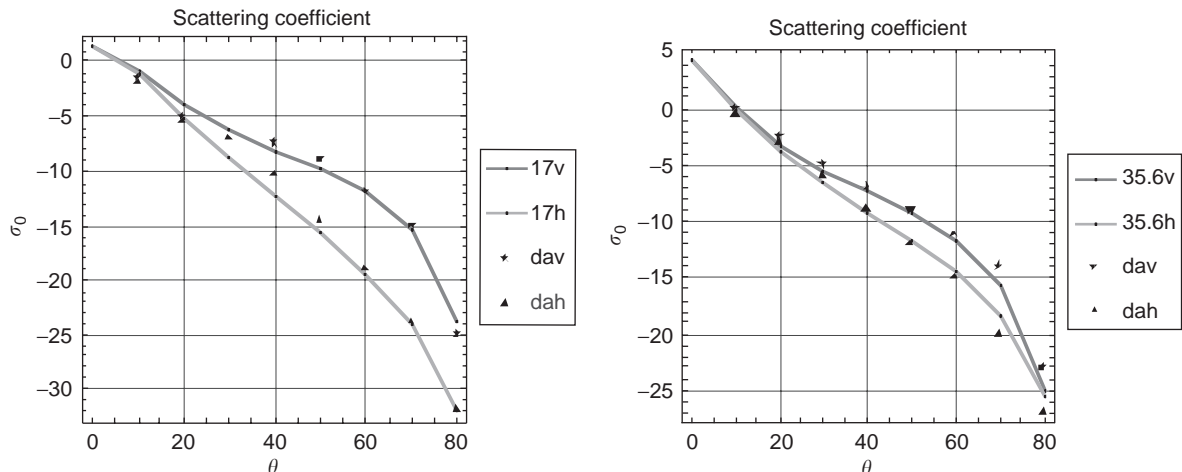


Figure 10. Comparison with measurements from asphalt road from Ref. 17. The exponential-like correlation function with $x = 0.25, 0.05$ is used with $\sigma = 0.12$ cm, $L = 0.6$ cm, and dielectric values of 16 and 12 at 17 and 35.6 GHz, respectively. (This figure is available in full color at <http://www.mrw.interscience.wiley.com/erfme>.)

the scattered field can be found, if the field inside the scatterer is known. To facilitate integration we need to express the integration variables in the local frame (principal frame of the scatterer) and then relate the local frame to the reference frame. This setup will also allow arbitrary orientation of the scatterer relative to the reference frame, since the angular separations between the two frames can be varied. Furthermore, the leaves of a given species will have an orientation distribution and we need to average over this distribution in order to find the scattering coefficient.

6.1. Scattering Amplitudes of Scatterers

To derive the scattering amplitudes for leaf-type scatterers, we need to allow the leaves to be arbitrarily oriented and obtain an estimate of the fields inside the leaf. Three types of leaf shape are considered: elliptic disk, circular disk, and needle. Because of a lack of symmetry, the orientation of an elliptic disk is specified by three

$$\begin{bmatrix} x'' \\ y'' \\ z'' \end{bmatrix} = \begin{bmatrix} (\cos \alpha \cos \beta \cos \gamma - \sin \gamma \sin \alpha) & (\sin \alpha \cos \beta \cos \gamma + \cos \alpha \sin \gamma) & -\sin \beta \cos \gamma \\ -\cos \alpha \cos \beta \sin \gamma - \sin \alpha \cos \gamma & -\sin \alpha \cos \beta \sin \gamma + \cos \alpha \cos \gamma & \sin \beta \sin \gamma \\ \cos \alpha \sin \beta & \sin \alpha \sin \beta & \cos \beta \end{bmatrix} \begin{bmatrix} x \\ y \\ z \end{bmatrix} \equiv \mathbf{U}_e \begin{bmatrix} x \\ y \\ z \end{bmatrix} \quad (68)$$

angles, while the circular and needle-shaped leaves are specified by only two.

6.1.1. Relation between Reference and Local Frames. To relate a reference frame (x, y, z) , to a local frame that is the principal frame of the scatterer (x'', y'', z'') for a symmetric scatterer such as a needle or a circular disk, we need to specify a polar angle β and an azimuthal angle α of rotation between the coordinates. Let z'' correspond to the normal vector to the disk or needle axial axis. From Fig. 11, the two angles between the coordinate systems are defined by first rotating around z'' by α and then around y''

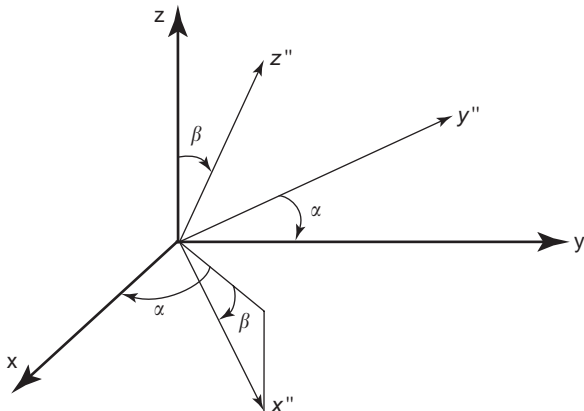


Figure 11. Principal frame of the scatterer relative to the reference frame.

by β , yielding

$$\begin{bmatrix} x'' \\ y'' \\ z'' \end{bmatrix} = \begin{bmatrix} \cos \beta \cos \alpha & \cos \beta \sin \alpha & -\sin \beta \\ -\sin \alpha & \cos \alpha & 0 \\ \cos \alpha \sin \beta & \sin \alpha \sin \beta & \cos \beta \end{bmatrix} \begin{bmatrix} x \\ y \\ z \end{bmatrix} \equiv \mathbf{U} \begin{bmatrix} x \\ y \\ z \end{bmatrix} \quad (66)$$

For an elliptic disk another rotation with respect to the z'' axis by an angle γ defined by

$$\begin{bmatrix} x' \\ y' \\ z' \end{bmatrix} = \begin{bmatrix} \cos \gamma & \sin \gamma & 0 \\ -\sin \gamma & \cos \gamma & 0 \\ 0 & 0 & 1 \end{bmatrix} \begin{bmatrix} x'' \\ y'' \\ z'' \end{bmatrix} \equiv \mathbf{U} \begin{bmatrix} x'' \\ y'' \\ z'' \end{bmatrix} \quad (67)$$

is needed, yielding the final relation after redefining the coordinates as

where \mathbf{U} and \mathbf{U}_e are unitary matrices. Their inverses are equal to their transposes. Clearly, \mathbf{U} is a special case of \mathbf{U}_e when $\gamma=0$.

6.1.2. Estimate of the Field Inside a Scatterer. For an elliptic disk the field inside the scatterer in the local frame is related to the incident field, $\mathbf{E}_i = \mathbf{E}_0 \exp(-j\mathbf{k} \cdot \mathbf{r})$ (where $\mathbf{k} = ik\mathbf{i}$; \mathbf{i} is the unit vector in the incident direction and \mathbf{r} is the displacement vector in the reference frame), by Stratton [19]

$$\mathbf{E}_{\text{local}} = \begin{bmatrix} \frac{1}{a_1} & 0 & 0 \\ 0 & \frac{1}{a_2} & 0 \\ 0 & 0 & \frac{1}{a_3} \end{bmatrix} \mathbf{U}_e \cdot \mathbf{E}_i \quad (69)$$

Converting it to the reference frame, we have

$$\mathbf{E}_{\text{in}} = \mathbf{U}_e^{-1} \cdot \mathbf{E}_{\text{local}} \equiv \mathbf{A}_e \cdot \mathbf{E}_i \quad (70)$$

where \mathbf{A}_e is the matrix of transformation relating the incident field in the reference frame to the inner field in the same frame. In Eq. (69) a vector that appears with a matrix is understood to be a column matrix and

$$\begin{aligned} a_1 &= 1 + (\epsilon_r - 1)g_1 \\ a_2 &= 1 + (\epsilon_r - 1)g_2 \\ a_3 &= 1 + (\epsilon_r - 1)g_3 \end{aligned} \quad (71)$$

where the g_i values are the demagnetizing factors that vary depending on the shape of the scatterer. For an elliptic disk-shaped leaf, we have [20]

$$\begin{aligned} g_1 &= \frac{c}{a}(1-e^2)^{0.5} + \frac{K(e, \pi/2) - E(e, \pi/2)}{e^2} \\ g_2 &= \frac{c}{a} \frac{E(e, \pi/2) - (1-e^2)K(e, \pi/2)}{e^2(1-e^2)^{0.5}} \\ g_3 &= 1 - \frac{c}{a} \frac{E(e, \pi/2)}{(1-e^2)^{0.5}} \end{aligned} \quad (72)$$

where $a > b \gg c$ are the semiaxes of the elliptic disk, $e = [1 - (b/a)^2]^{0.5}$, and the elliptic integrals of the first and second kinds are given by

$$\begin{aligned} K\left(e, \frac{\pi}{2}\right) &= \int_0^{\pi/2} \frac{1}{\sqrt{1-e\sin^2\xi}} d\xi \\ E\left(e, \frac{\pi}{2}\right) &= \int_0^{\pi/2} \sqrt{1-e\sin^2\xi} d\xi \end{aligned} \quad (73)$$

For a circular disk-shaped leaf ($a = b \gg c$), we should replace \mathbf{A}_e by \mathbf{A}_c , which is equal to \mathbf{A}_e with $\gamma = 0$ and the demagnetizing factors given by

$$\begin{aligned} g_1 = g_2 &= \frac{1}{2(m^2-1)} \left[\frac{m^2}{\sqrt{m^2-1}} \sin^{-1}\left(\frac{\sqrt{m^2-1}}{m}\right) - 1 \right] \\ g_3 &= \frac{m^2}{m^2-1} \left[1 - \frac{1}{\sqrt{m^2-1}} \sin^{-1}\left(\frac{\sqrt{m^2-1}}{m}\right) \right], \\ m &= \frac{a}{c} \end{aligned} \quad (74)$$

For a needle-shaped leaf ($a = b \ll c$), we should replace \mathbf{A}_e by \mathbf{A}_n , which is equal to \mathbf{A}_e with $\gamma = 0$, and another set of demagnetizing factors given by

$$\begin{aligned} g_1 = g_2 &= \frac{m'(m'^2-1)}{2} \left[\frac{m'}{m'^2-1} + \frac{1}{2} \ln\left(\frac{m'-1}{m'+1}\right) \right] \\ g_3 &= -(m'^2-1) \left[\frac{m'}{2} \ln\left(\frac{m'-1}{m'+1}\right) + 1 \right], \\ m' &= \sqrt{1 - \frac{a^2}{c^2}} \end{aligned} \quad (75)$$

The use of Eq. (71) in (65) with the phase of the incident field $\mathbf{k} \cdot \mathbf{r}$ replaced by $(\mathbf{U}_e \cdot \mathbf{k}) \cdot \mathbf{r}'$ allows the integration variables to be expressed in the local frame to facilitate integration.

6.1.3. Scattering Amplitude of an Elliptic Disk. In this section we show the expression for the scattering amplitude with \mathbf{s}, \mathbf{i} denoting the unit vectors in the scattered and incident directions, respectively. For a \mathbf{p}_s polarized scattered field the amplitude portion of $\mathbf{p}_s \cdot \mathbf{E}_{in}$ is $\mathbf{p}_s \cdot \mathbf{E}_{in} = \mathbf{p}_s \cdot \mathbf{A}_e \cdot \mathbf{E}_0$. From Eq. (65) we can write the \mathbf{p}_s polarized scattered field component for an elliptic disk in

the far field by letting $|\mathbf{r} - \mathbf{r}'|$ equal to $r - \mathbf{s} \cdot \mathbf{r}'$ in the phase and equal to $|\mathbf{r}| = r$ in the amplitude. Then, Eq. (65) reduces to

$$\begin{aligned} \mathbf{p}_s \cdot \mathbf{E}^s(r) &= \frac{k^2(\epsilon_r - 1)}{4\pi} \int_V \frac{\exp[-jk(r - \mathbf{s} \cdot \mathbf{r}')] }{|\mathbf{r}|} (\mathbf{p}_s \cdot \mathbf{E}_{in}) dV' \\ &\approx \frac{k^2(\epsilon_r - 1)}{4\pi r} (\mathbf{p}_s \cdot \mathbf{A}_e \cdot \mathbf{E}_0) \exp(-jkr) \int_V \exp[jk(\mathbf{s} - \mathbf{i}) \cdot \mathbf{r}'] dV' \\ &\equiv \frac{k^2(\epsilon_r - 1)}{4\pi r} (\mathbf{p}_s \cdot \mathbf{A}_e \cdot \mathbf{E}_0) \exp(-jkr) I_e \\ &= \mathbf{p}_s \cdot \left[k^2(\epsilon_r - 1) \frac{\mathbf{A}_e}{4\pi} I_e \right] \cdot \mathbf{E}_0 \frac{\exp(-jkr)}{r} \\ &\equiv \mathbf{p}_s \cdot \mathbf{f}_e(\mathbf{k}_s, \mathbf{k}_i) \cdot \mathbf{p}_i E_0 \frac{\exp(-jkr)}{r} \end{aligned} \quad (76)$$

where $\mathbf{f}_e(\mathbf{k}_s, \mathbf{k}_i)$ is the scattering amplitude matrix for an elliptic disk; $\mathbf{k}_s = k\mathbf{s}$; $\mathbf{k}_i = k\mathbf{i}$. The elements of this matrix defined in accordance with vertical and horizontal polarizations can be written as

$$\begin{aligned} \mathbf{p}_s \cdot \mathbf{f}_e(\mathbf{k}_s, \mathbf{k}_i) \cdot \mathbf{p}_i &= \frac{k^2(\epsilon_r - 1) I_e}{4\pi} \begin{bmatrix} (\mathbf{v}_s \cdot \mathbf{A}_e \cdot \mathbf{v}_i) & (\mathbf{v}_s \cdot \mathbf{A}_e \cdot \mathbf{h}_i) \\ (\mathbf{h}_s \cdot \mathbf{A}_e \cdot \mathbf{v}_i) & (\mathbf{h}_s \cdot \mathbf{A}_e \cdot \mathbf{h}_i) \end{bmatrix} \\ &\equiv \begin{bmatrix} f_{vv} & f_{hv} \\ f_{vh} & f_{vh} \end{bmatrix} \end{aligned} \quad (77)$$

where the vertical and horizontal polarization unit vectors in Eq. (77) are chosen to agree with θ and ϕ unit vectors of a standard spherical coordinate system and form an orthogonal set with \mathbf{s} as

$$\begin{aligned} \mathbf{s} &= \mathbf{x} \sin \theta_s \cos \phi_s + \mathbf{y} \sin \theta_s \sin \phi_s + \mathbf{z} \cos \theta_s \\ \mathbf{v}_s &= \mathbf{x} \cos \theta_s \cos \phi_s + \mathbf{y} \cos \theta_s \sin \phi_s - \mathbf{z} \sin \theta_s \\ \mathbf{h}_s &= -\mathbf{x} \sin \phi_s + \mathbf{y} \cos \phi_s \end{aligned} \quad (78)$$

Similarly, the unit polarization vectors associated with the incident direction form another orthogonal system as

$$\begin{aligned} \mathbf{i} &= \mathbf{x} \sin \theta_i \cos \phi_i + \mathbf{y} \sin \theta_i \sin \phi_i + \mathbf{z} \cos \theta_i \\ \mathbf{v}_i &= \mathbf{x} \cos \theta_i \cos \phi_i + \mathbf{y} \cos \theta_i \sin \phi_i - \mathbf{z} \sin \theta_i \\ \mathbf{h}_i &= -\mathbf{x} \sin \phi_i + \mathbf{y} \cos \phi_i \end{aligned} \quad (79)$$

$$I_e = \int_V \exp[jk(\mathbf{s} - \mathbf{i}) \cdot \mathbf{r}'] dV' = 4\pi abc \frac{J_1(\bar{q})}{\bar{q}} \quad (80)$$

where $\bar{q} = k \sqrt{\{a[\mathbf{U}_e \cdot (\mathbf{s} - \mathbf{i})_x]^2 + \{b[\mathbf{U}_e \cdot (\mathbf{s} - \mathbf{i})_y]^2\}}$.

6.1.4. Scattering Amplitude of a Circular Disk. For a circular disk-shaped leaf, the forms of Eqs. (76), (77), and (80) are valid, but we need to replace \mathbf{A}_e by \mathbf{A}_c because the definitions for the demagnetizing factors g_1, g_2, g_3 are different and we need to set $a = b$ in Eq. (80).

6.1.5. Scattering Amplitude of a Needle. For a needle-shaped leaf, the forms of Eqs. (76) and (77) are valid, but we need to replace \mathbf{A}_e by \mathbf{A}_n because the definitions for the demagnetizing factors g_1, g_2, g_3 are different. The corresponding expression for I_e will be called I_n . Its integral form is the same as Eq. (80), except we have to evaluate it differently. Letting its length be $L = 2c$, we have

$$\begin{aligned}
 I_n &= (\pi a^2) \int_{-L/2}^{L/2} \exp(jz''q_z'') dz'' \\
 &= \frac{\pi a^2 [\exp(jq_z''L/2) - \exp(-jq_z''L/2)]}{jq_z''} \quad (81) \\
 &= \frac{2\pi a^2}{q_z''} \sin \frac{q_z''L}{2}
 \end{aligned}$$

6.2. Theoretical Model Behaviors

We consider the frequency, size, and moisture dependence of the backscattering coefficients σ^0 of a circular- and needle-shaped leaf in this section. To do so, we need an estimate for the dielectric constant for leaves as a function of frequency and moisture content. The empirical formula we use here is from Ref. 21.

6.2.1. Permittivity of Vegetation Given GMC. When the gravimetric moisture content (GMC) is given and denoted by M_g , the nondispersive residual component of the dielectric constant is

$$\epsilon_n = 1.7 - 0.74M_g + 6.16M_g^2$$

The free-water volume fraction is

$$vf_f = M_g(0.55M_g - 0.076)$$

while the volume fraction for the bound water is

$$vf_b = \frac{(4.64M_g^2)}{1 + 7.36M_g^2}$$

With these quantities known, the permittivity of vegetation is given as a function of frequency in gigahertz by

$$\begin{aligned}
 \epsilon(M_g) &= \epsilon_n + vf_f \left\{ 4.9 + \frac{75}{\left[1 + j\left(\frac{f}{18}\right)\right]} - j\frac{22.86}{f} \right\} \\
 &+ vf_b \left\{ 2.9 + \frac{55}{\left[1 + j\left(\frac{f}{0.18}\right)^{0.5}\right]} \right\} \quad (82)
 \end{aligned}$$

6.2.2. Dependence on Moisture Content, Size, and Frequency. In Fig. 12 we see that σ^0 increases over all incident angles as the moisture content of the circular

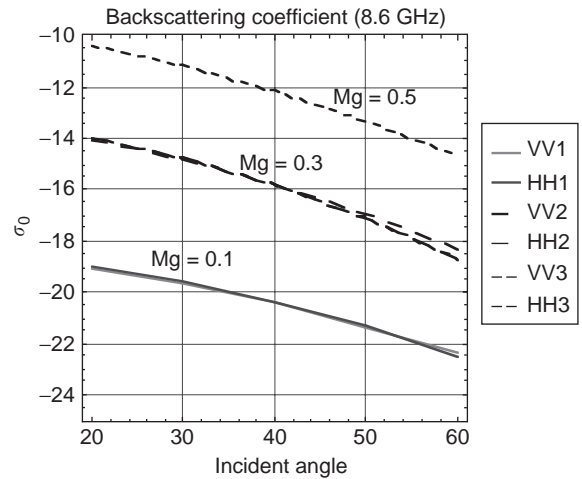


Figure 12. Dependence of backscattering coefficient on the gravimetric moisture content of a circular disk-shaped leaf ($M_g = 0.1, 0.3, 0.5$). Thickness of the leaf = 0.01 cm and radius = 1.5 cm. Results indicate negligible difference between vertical and horizontal polarizations and a monotonic increase of σ^0 with moisture. (This figure is available in full color at <http://www.mrw.interscience.wiley.com/erfme>.)

leaves increases from 0.1 to 0.5 for both vertical and horizontal polarization. In general, there is very little differences between horizontal and vertical polarization because we assumed random orientation distribution for the leaves. Similar results in trend are expected for needle-shaped leaves. In Fig. 13a we show circular leaf size dependence (radius) at 8.6 GHz, 40° incidence at a dielectric constant of $14.9 - j2.5$. There is a steep rise over small-size values reminiscent of the Rayleigh region followed by an oscillatory behavior indicating the resonant region. Finally, it shows saturation where the length or radius of the scatterer exceeds a wavelength. In the Rayleigh region vertical polarization is smaller than horizontal, while the reverse is true in the larger region. A similar plot versus the length of the needle-shaped leaf is shown in Fig. 13b, where we see a similar trend without oscillations and a higher horizontal than vertical polarization in level for length exceeding 2 cm. Similar plots of the extinction cross sections give a monotonic increase with the size of the disk in Fig. 14a and the length of the needle in Fig. 14b. The increase is much faster for the disk than the needle. For the disk-shaped leaf, horizontal polarization is seen to experience more attenuation than the vertical and the role of the polarizations reverses for the needle-shaped leaf. In Fig. 15 we show the frequency dependence of the backscattering coefficient for the two types of leaf. Both horizontal and vertical polarization increase with frequency and the increase is faster for the needle-shaped leaf.

6.3. Comparisons with Vegetation Measurements

The first volume scattering medium considered is a soybean canopy. It is modeled as a half-space of randomly oriented, disk-shaped leaves. Figure 16 shows the comparisons between Eq. (55) and the data from Ref. 22. The agreement between model and data is very good. Then, in

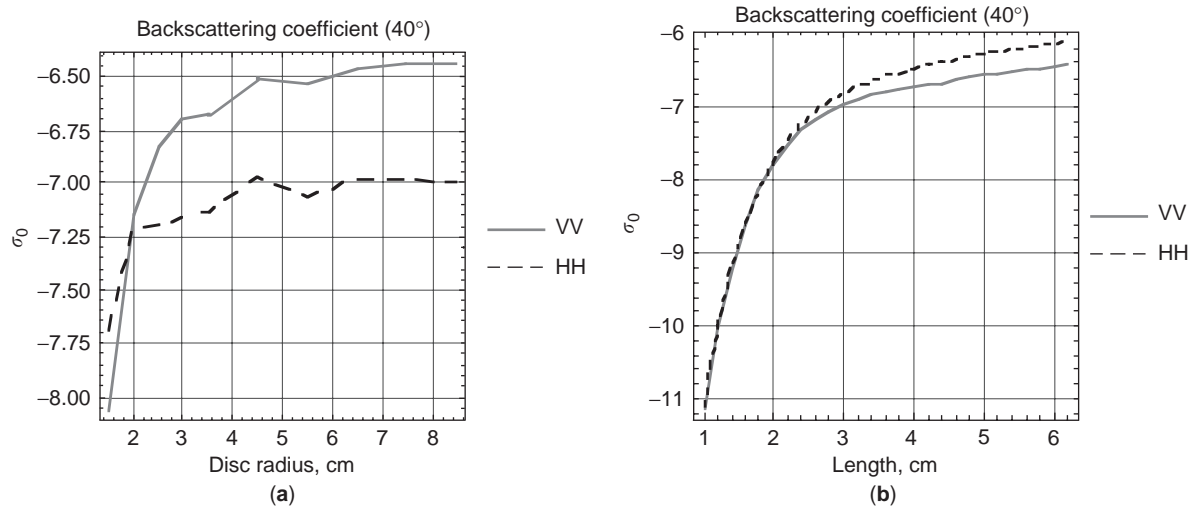


Figure 13. Dependence of backscattering coefficient at 8.6 GHz with (a) the radius of a randomly oriented circular disk-shaped leaf of thickness 0.01 cm and $\epsilon_r = 14.9 - j2.5$; (b) a randomly oriented needle with radius 0.12 cm and $\epsilon_r = 8.36 - j3.12$. There is a Rayleigh region for small size and a saturation behavior when the length or radius of the scatterer exceeds a wavelength. (This figure is available in full color at <http://www.mrw.interscience.wiley.com/erfme>.)

Fig. 17 we show another comparison of Eq. (55) with data from deciduous trees. Again very good agreement is obtained. Since the leaves of soybeans and trees are clearly different in shape, it follows that while shape should make a difference in scattering, its effect becomes negligible when we consider random distributions. Thus, the volume scattering model is applicable to disk-shaped leaves regardless of their shape whenever the leaf distribution is very wide.

For needle-shaped vegetation, in Fig. 18 we show a comparison with coniferous vegetation. Very good agreement is obtained between Eq. (55) and the data reported in Ref. 23.

7. SCATTERING FROM SNOW-COVERED SURFACE

A snow medium is a densely populated concentration of wet or dry ice particles in air with a volume fraction usually between 0.1 and 0.4. Within the distance of a centimeter there are several needle-like ice particles that are randomly oriented. Because of their random orientation, spherical particles have been used to model snow with a radius of ~ 0.5 mm. As a result of metamorphism, actual snow layer may have a grain size that increases with depth. It is clear that snow is a *dense medium* both spatially and electrically in the microwave region. Recall that the classical radiative transfer formulation is for

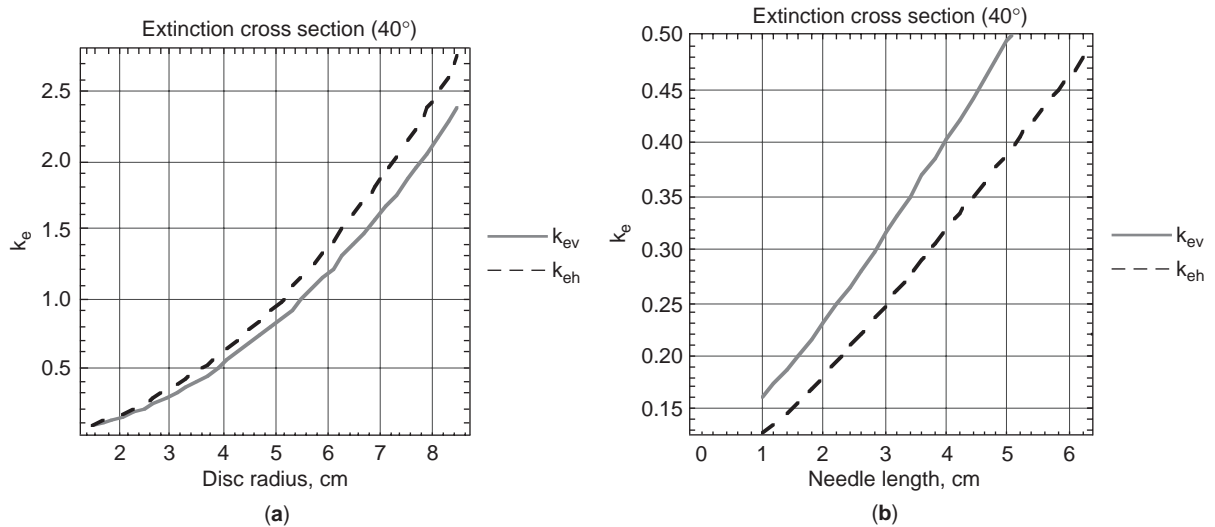


Figure 14. Variation of the extinction cross section at 8.6 GHz with (a) the radius of a randomly oriented circular disk-shaped leaf of thickness 0.01 cm and $\epsilon_r = 14.9 - j2.5$; (b) a randomly oriented needle with radius 0.12 cm and $\epsilon_r = 8.36 - j3.12$. For circular leaves extinction cross section is higher for horizontal polarization and for needle-shaped leaves, vertical polarization is higher. (This figure is available in full color at <http://www.mrw.interscience.wiley.com/erfme>.)

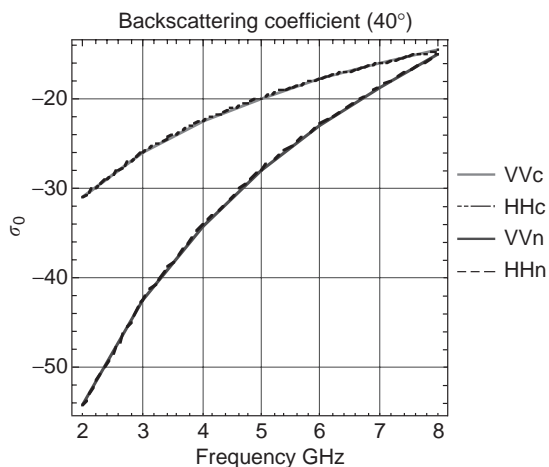


Figure 15. Vertically and horizontally polarized backscattering coefficients from a volume of randomly oriented circular disks, VVc,HHc and needles, VVn,HHn, plotted as a function of frequency at a moisture content of 0.4. Disk thickness = 0.01 cm, radius = 1.5 cm. Needle radius = 0.17 cm, length = 1.67 cm. The level of backscattering is higher for circular disk-shaped leaves, but backscattering increases more rapidly with frequency for needle-shaped leaves. (This figure is available in full color at <http://www.mrw.interscience.wiley.com/erfme>.)

sparse media and that the phase function is the product between the average of the magnitude squared of the scattering amplitude $\langle |S|^2 \rangle$ of a single scatterer multiplied by the number density n_0 . This definition of the phase function is applicable to sparse media where independent scattering occurs. For snow the scatterers may scatter as a group in some correlated manner, and near-field interaction may have to be included. For this reason we need an effective number density for correlated scatterers to account for phase coherency and a modified scattering amplitude to include near-field interaction [5]. The effective number density of scatterers is smaller than the actual number because several scatterers are acting

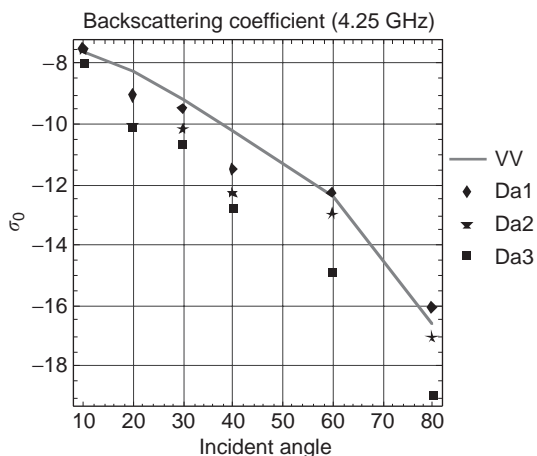


Figure 16. Comparison between volume scattering model and measurements from a soybean canopy shows very good agreement. Leaf thickness = 0.02 cm; radius = 1.5 cm, $\epsilon_r = 29.1 - j6.1$. (From Ref. 22). (This figure is available in full color at <http://www.mrw.interscience.wiley.com/erfme>.)

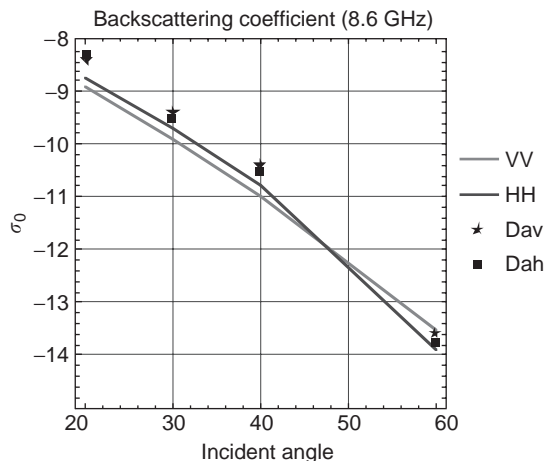


Figure 17. Comparison between volume scattering model given by Eq. (55) with measurements from deciduous trees in Kansas. Leaf thickness = 0.01 cm; radius = 1.5 cm, $\epsilon_r = 14.9 - j4.9$. Both data and model indicate negligible difference between horizontal and vertical polarizations in backscattering from trees. (This figure is available in full color at <http://www.mrw.interscience.wiley.com/erfme>.)

coherently as one scatterer. This effect can be very significant under large-volume-fraction conditions or when only a few scatterers are within the distance of a wavelength. Because of random orientation when there are too many scatterers lying within a wavelength, the coherence among scatterers can be destroyed. Thus, the most significant correction for dense media is the replacement of the number density by the effective number density.

7.1. An Effective Number Density

From Ref. 4 an effective number density n_{eff} was derived for spherical scatterers. It is assumed that the positions of

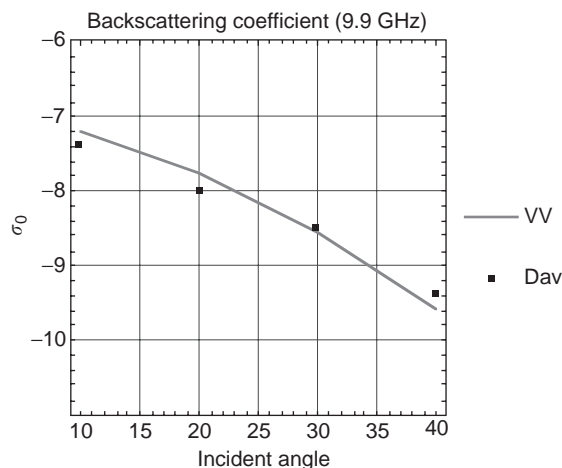


Figure 18. Comparison of model given by Eq. (55) with coniferous tree data from Ref. 21. Length = 1.67 cm, radius = 0.17 cm, $\epsilon_r = 8.36 - j3.12$, $f = 9.9$ GHz. The agreement validates the model for coniferous vegetation. (This figure is available in full color at <http://www.mrw.interscience.wiley.com/erfme>.)

these scatterers are Gaussian correlated. It has the form

$$n_{\text{eff}} = \frac{1 - e^{-k_{\text{si}}^2 \sigma^2}}{d^3} + \frac{e^{-k_{\text{si}}^2 \sigma^2}}{d^3} \sum_{m=1}^{\infty} \frac{(k_{\text{si}}^2 \sigma^2)^m}{m!} \left[\left(\sqrt{\frac{\pi}{m}} \frac{L}{d} \right)^3 \right. \\ \left. \times \exp\left(\frac{-k_{\text{si}}^2 \sigma^2}{4m}\right) - a(k_x)a(k_y)a(k_z) \right] \quad (83)$$

where

$$a(k_r) = \sqrt{\frac{\pi}{m}} \frac{L}{d} \exp\left(\frac{-k_r^2 L^2}{4m}\right) \text{Re} \left\{ \text{erf} \left(\frac{(md/L) + jk_r L}{2\sqrt{m}} \right) \right\}$$

$$\mathbf{k}_s = k(\mathbf{x} \sin \theta_s \cos \phi_s + \mathbf{y} \sin \theta_s \sin \phi_s + \mathbf{z} \cos \theta_s)$$

$$\mathbf{k}_i = k(\mathbf{x} \sin \theta_i \cos \phi_i + \mathbf{y} \sin \theta_i \sin \phi_i + \mathbf{z} \cos \theta_i)$$

$$\mathbf{k}_s - \mathbf{k}_i = \mathbf{x}k_x + \mathbf{y}k_y + \mathbf{z}k_z \equiv \mathbf{k}_{\text{si}}$$

and σ^2 is the variance of a scatterer from its mean position, L is the correlation length among scatterer positions, and d is the average spacing between adjacent scatterers. For spherical scatterers Ref. 4 has extended the *Mie phase function* to include the near-field interaction by not invoking the far-field approximation. Since the contents of the Mie phase function is complex but well documented in the literature, the reader is referred to Refs. 4 and 16 for its content.

7.2. Comparison with Measurements

In this section we want to show an application of the layer model defined by Eqs. (55), (57), (58), and (61) and the relative contributions of the surface and volume scattering

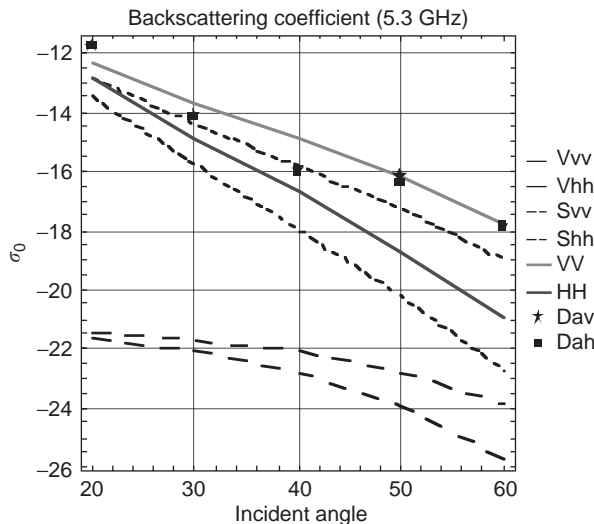


Figure 19. Comparison between the layer model defined by Eqs. (55), (57), (58), and (60) and snow data reported by Kendra et al. [24]. The notations Vvv,Vvh stand for total volume scattering; Svv,Shh, for total surface scattering; and VV,HH, for total scattering by the layer for vertical and horizontal polarizations, respectively. Dav,Dah denote data. Relative importance between surface and volume scattering is shown. (This figure is available in full color at <http://www.mrw.interscience.wiley.com/erfme>.)

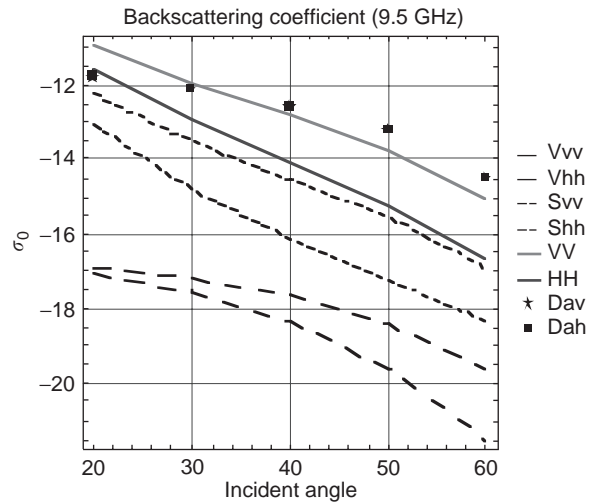


Figure 20. Comparison between the layer model defined by Eqs. (55), (57), (58), and (60) and snow data reported by Kendra et al. [24]. The notations Vvv,Vvh stand for volume scattering; Svv,Shh, for surface scattering; and VV,HH, for total scattering by the layer for vertical and horizontal polarizations, respectively. Dav,Dah denote data. Relative importance between surface and volume scattering is shown. (This figure is available in full color at <http://www.mrw.interscience.wiley.com/erfme>.)

terms to the total backscattering from a snow-covered irregular ground surface. Most of the model parameters have been estimated by Ref. 25, so very little selection is needed. The RMS heights of the snow-air boundary and snow-ground boundary are 0.45 and 0.32 cm; correlation lengths of snow and ground surface are chosen to be 0.7 cm and 1.1 cm, and the snow and ground permittivities are $1.97 - j0.007$ and 4.7. We use exponential correlation function for both surfaces. Within the snow medium, the ice particle radius and permittivity are respectively 0.014 cm and 3.15, snow density is 0.48 g/cm^3 , and snow depth is 60 cm. Using these values, we compute backscattering at 5.3 GHz in Fig. 19 and at 9.5 GHz in Fig. 20. The results are in very good agreement with the dry-snow data, which are available only for vertical polarization. Figure 19 indicates that surface scattering contribution is dominating but that volume scattering from snow also makes significant contribution to total scattering. The volume scattering contribution is larger at 9.5 GHz, where it accounts for about 2 dB of difference.

BIBLIOGRAPHY

1. A. K. Fung, *Microwave Scattering and Emission Models and Their Applications*, Artech House, Norwood, MA, 1994
2. M. A. Karam, A. K. Fung, R. H. Lang, and N. S. Chauhan, Microwave scattering model for layered vegetation, *IEEE Trans. Geosci. Remote Sens.* **30**(4):767-784 (1992).
3. A. K. Fung, S. Tjuatja, J. W. Bredow, and H. T. Chuah, Dense medium phase and amplitude correction theory for spatially and electrically dense media, *Proc. IGARSS'95*, 1995, Vol. 2, pp. 1336-1338.
4. H. T. Chuah, S. Tjuatja, A. K. Fung, and J. W. Bredow, A phase matrix for a dense discrete random medium: Evaluation of

- volume scattering coefficient, *IEEE Trans. GRS* **34**(5):1137–1143 (1996).
5. H. T. Chuah, S. Tjuatja, A. K. Fung, and J. W. Bredow, Radar backscatter from a dense discrete random medium, *IEEE Trans. Geosci. Remote Sens.* **35**(4):892–900 (July 1997).
 6. F. T. Ulaby, R. K. Moore, and A. K. Fung, *Microwave Remote Sensing*, Vol. 1, Chapter 2, Artech House, Norwood, MA, 1981; reissued by IEEE Press and Oxford Univ. Press, 1997.
 7. S. Chandrasekhar, *Radiative Transfer*, Dover Publications, New York, 1960.
 8. A. Ishimaru, *Wave Propagation and Scattering in Random Media*, Vol. 1, Academic Press, New York, 1978, pp. 30–33, 157–165.
 9. L. Tsang and J. A. Kong, Thermal microwave emission from half space random media, *Radio Sci.* **11**:599–609 (1976).
 10. A. Ishimaru and R. L. Cheung, Multiple scattering effects on wave propagation due to rain, *Ann. Telecommun.* **35**:373–378 (1980).
 11. H. C. Van de Hulst, *Light Scattering by Small Particles*, Wiley, New York, 1957.
 12. A. K. Fung and H. J. Eom, Multiple scattering and depolarization by a randomly rough Kirchhoff surface, *IEEE Trans. Anten. Propag.* **29**:463–471 (1981).
 13. A. K. Fung and M. F. Chen, Scattering from a Rayleigh layer with an irregular interface, *Radio Sci.* **16**:1337–1347 (1981).
 14. A. K. Fung and H. J. Eom, A theory of wave scattering from an inhomogeneous layer with an irregular interface, *IEEE Trans. Anten. Propag.* **29**:899–910 (1981).
 15. A. K. Fung, W. Y. Liu, K. S. Chen, and M. K. Tsay, An improved IEM model for bistatic scattering from rough surfaces, *J. Electromagnetic Waves and Applications* **16**(5):689–702 (2002).
 16. C. Y. Hsieh, A. K. Fung, G. Nesti, A. J. Sieber, and P. Coppo, A further study of the IEM surface scattering model, *IEEE Trans. Geosci. Remote Sens.* **35**(4):901–909 (July 1997).
 17. F. T. Ulaby, R. K. Moore, and A. K. Fung, *Microwave Remote Sensing: Active and Passive*, Vol. 3, Artech House, Dedham, MA, Appendix E8, p. 2103, 1986.
 18. T. D. Wu, K. S. Chen, J. Shi, and A. K. Fung, A transition model for the reflection coefficient in surface scattering, *IEEE Trans. Geosci. Remote Sens.* **39**(9):2040–2050 (Sept. 2001).
 19. J. A. Stratton, *Electromagnetic Theory*, McGraw-Hill, New York, 1941.
 20. M. A. Karam and A. K. Fung, Leaf-shape effects in electromagnetic wave scattering from vegetation, *IEEE Trans. Geosci. Remote Sens.* **27**(6):687–697 (Nov. 1989).
 21. F. T. Ulaby and M. A. El-Rayes, Microwave dielectric spectrum of vegetation Part II: Dual dispersion model, *IEEE Trans. GRS* **25**(5):550–557 (1987).
 22. A. K. Fung and H. J. Eom, A scatter model for vegetation up to Ku-band, *Remote Sens. Environ.* **15**:185–200 (1984).
 23. H. Hirose, H. Ishida, T. Ochi, and Y. Matsuzaka, Measurement of microwave backscatter from trees, Paper Presented at Int. Colloquium on Special Signature of Objects in Remote Sensing, Les Arcs, France, Dec. 16–20, 1985.
 24. Q. Li, J. Shi, and K. S. Chen, A generalized power law spectrum and its applications to the backscattering of soil surfaces based on the integral equation method, *IEEE Trans. GRS*, **40**(2):271–279 (2002).
 25. J. R. Kendra, K. Sarabandi, and F. T. Ulaby, Radar measurements of snow: Experiment and analysis, *IEEE Trans. GRS*, **36**(3):864–879 (1998).

MICROWAVE SOLID-STATE DEVICES

DOMINIQUE M. M.-P.
SCHREURS
K.U.Leuven
Leuven-Heverlee, Belgium

1. INTRODUCTION

Microwave and millimeter-wave solid-state devices are used in applications in the 3–300 GHz frequency range. These devices can be divided into two large groups: (1) two-terminal devices or diodes and (2) three-terminal devices or transistors. The diodes can be subdivided into passive and active devices, referring to the real part of the impedance as positive and negative, respectively. The active diodes can further be classified to the origin of the negative resistance. The three-terminal active devices are divided into minority and majority carrier devices. The classification is summarized as follows:

1. Two-terminal devices

- a. Passive diodes
 - i. Schottky barrier diode
 - ii. pin (positive–intrinsic–negative) diode
- b. Active diodes
 - i. Transit-time effect based on
 - (1) Avalanche injection: IMPATT (impact avalanche transit time) diode, TRAPATT (Trapped Plasma Avalanche-Triggered Transit) diode
 - (2) Forward injection: BARITT (barrier injection transit time) diode
 - (3) Tunnel injection: TUNNETT (tunnel injection transit time) diode
 - ii. Bulk effect: Gunn diode
 - iii. Tunnel effect: tunnel diode

2. Three-terminal devices

- a. Minority-carrier devices: BJT, HBT (bipolar junction transistor, heterojunction bipolar transistor)
- b. Majority-carrier devices: FET, MOSFET, MESFET, HEMT (field-effect transistor, metal oxide semiconductor FET, metal semiconductor FET, high-electron-mobility transistor)

In this article, we focus on the most frequently used microwave and millimeter-wave devices: the Schottky barrier diode, pin diode, IMPATT diode, BARITT diode, Gunn diode, tunnel diode, MESFET, HEMT, and HBT. Nowadays, there is also an increasing interest in the use of MOS-type transistors for applications in the lower microwave frequency range. For each of these devices, we first briefly explain their physical operation. For a more detailed analysis of the device's solid-state physics, we however refer to the books listed in the Further Reading List. Subsequently, we discuss the devices' properties and frequency limitations, and finally we outline their main application areas.

2. MICROWAVE AND MILLIMETER-WAVE DIODES

2.1. Schottky Barrier Diode

2.1.1. Description. We first mention the p-n junction diode [1], because this component serves as the foundation of many solid-state devices. A p-n junction is formed at the metallurgical interface of two regions in a semiconductor where one region contains impurity elements that create equivalent positive (p-type) charges and the other semiconductor region contains impurities that create negative (n-type) charges.

A Schottky barrier diode is formed by placing a metal layer directly onto a unipolar semiconductor substrate. When the metal and the semiconductor materials are brought into contact, electrons in the material having higher Fermi energy diffuse into the other material that has lower Fermi energy. This process proceeds rapidly until the Fermi energies of the two materials are balanced. In case the semiconductor is n-type (p-type) and the work-function of the semiconductor is smaller (larger) than that of the metal, a potential barrier is formed at the metal-semiconductor boundary, exhibiting rectifying current-voltage characteristics. When reverse-biased, the diode behaves as a voltage-dependent capacitance with low losses since the reverse current is small. Diodes operated under this condition are called *varactors*.

2.1.2. Properties and Frequency Limitations. The small-signal equivalent circuit of the Schottky diode is presented in Fig. 1. It consists of an extrinsic part and an intrinsic part. The extrinsic part consists of the parasitic elements that are inherent to the geometry of the device and hence depends on the way that the device is inserted in the circuit. The parasitic capacitance C_{pg} and the inductance L_s are determined by the metallisations of the access lines to the device. The resistance R_s is the sum of the resistance of the anode metal and the ohmic cathode resistance. The intrinsic part is within the dashed rectangle. The resistance R_{gsf} models the current through the Schottky diode. The capacitance C_{gs} models the change in the depletion

charge with respect to the voltage across the Schottky diode. R_{gs} models the charging resistance of the Schottky junction. The extrinsic elements are independent of the applied voltage, while the intrinsic elements are bias-dependent.

Important figures of merit are the cut-off frequency $f_c(V)$ and the dynamic cutoff frequency f_{cd} . For a given voltage V (typically 0 V) applied across the Schottky diode, the cutoff frequency $f_c(V)$ is defined as follows:

$$f_c(V) = \frac{1}{2\pi R_s C_{gs}(V)} \quad (1)$$

The dynamic cutoff frequency f_{cd} , defined for varactors, gives an indication of the nonlinear variation of the capacitance. It is defined as

$$f_{cd} = \frac{1}{2\pi R_s} \left(\frac{1}{C_{gs,\min}} - \frac{1}{C_{gs,\max}} \right) \quad (2)$$

where R_s is the series resistance and $C_{gs,\min}$ and $C_{gs,\max}$ are the minimum and maximum capacitance values. The cutoff frequency $f_c(V)$ can be maximized by decreasing the series resistance and the capacitance. The ohmic cathode resistance is inversely proportional to the width, while the resistance of the anode metal is proportional to the width and inversely proportional to the square of the number of fingers. The capacitance is proportional to the width. This implies that there exists an optimal width to maximise the figures of merit.

Schottky diodes that have to be compatible with a standard monolithic microwave integrated circuit (MMIC) technology are often realized by connecting the drain and source of a MESFET or HEMT device. Those Schottky diodes typically have cutoff frequencies up to a few hundred gigahertz. The f_c can be increased up to terahertz frequencies by modifying the layer structure and the layout [2]. Schottky diodes aimed for submillimeter-wave applications are typically circular with an anode diameter of less than 2.5 μm .

2.1.3. Applications. Schottky diodes have been used extensively in nonlinear circuit applications. At microwave and also at millimeter-wave frequencies, Schottky diodes are now often replaced by transistors. The reason is the potential conversion gain when employing transistors. Schottky diodes are, however, still the basic nonlinear elements in microwave broadband mixers and in millimeter- and submillimeter-wave nonlinear applications. We can distinguish two modes of operation for Schottky diodes: the varistor and the varactor type.

In the first case, the diode is operated by utilizing the nonlinear characteristics in the forward-biased I - V curve. Varistors have potential very large bandwidths. An important application is the mixer diode. This is a device that converts the input RF signal to a lower- or higher-frequency signal. As mentioned above, the technology can be optimized for a certain application. In the case of mixer diodes, the noise is an important specification. To reduce the noise, the conversion loss should be decreased. This

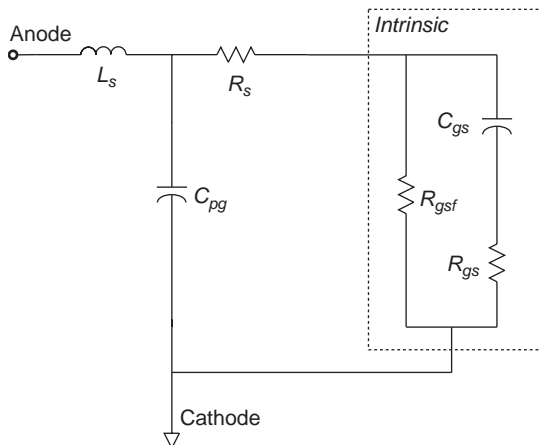


Figure 1. Small-signal equivalent circuit of the Schottky diode in parallel configuration.

can be obtained by a high carrier concentration and high-mobility material. From this point of view, GaAs, which has higher mobility than Si, is currently used for high-sensitivity (low-noise) and high-frequency-operation mixer diodes. In addition to the noise performance, we have to take account of the local oscillator drive level as a performance parameter of mixer diodes. Silicon is superior to GaAs from this point of view. The reason is that the barrier height of the Schottky barrier contact on GaAs is fixed at 0.7–0.8 eV. Therefore, a GaAs mixer diode usually requires a local oscillator drive level of 0 to 10 dBm. On the other hand, a silicon mixer diode can be operated even at a local-oscillator drive level of -10 dBm, because the barrier height can be varied by choosing the Schottky metal.

The second Schottky barrier diode type is the varactor. The term “varactor” originates from the term “variable reactor,” which means that the diode capacitance is variable with the external, reverse bias. Since the power consumption is theoretically zero, the potential power-added efficiency is high, but varactors exhibit a narrow fixed-tuned bandwidth. A first application area of varactors is voltage-variable tuning. Such a varactor has to possess high-capacitance change ratios, high values of the quality factor Q (defined as the ratio of energy stored to energy dissipated), and a wide voltage dynamic range. Since these values are related and generally involve tradeoffs, elaborate design criteria should be established to determine the material and geometric parameters of the diodes. A second application is harmonic generation, such as frequency multipliers. By changing the layer structure, for example, by using hyperabrupt junctions, the series resistance can be decreased and the characteristic of the capacitance as a function of the voltage can be optimized for particular designs. For example for frequency triplers, a symmetric profile around a DC bias of 0 V is preferred, since it suppresses the even order harmonics. This can be realized by means of a multi-quantum-well heterostructure varactor diode. Other varactor applications are nonlinear transmission lines, which require an abrupt $C(V)$ profile, MMIC phase shifters, and mixing detection.

2.2. pin Diodes

2.2.1. Description. In a pin diode, an intrinsic (i) layer is sandwiched between the p^+ and n^+ layers (Fig. 2). When the diode is forward-biased, its impedance goes low with the injection of carriers into the highly resistive intrinsic layer, and the diode acts as a resistance. On the other hand, when the diode is reverse-biased, the impedance becomes very high with spread of the depletion layer in the intrinsic layer and the diode acts as a capacitance.

2.2.2. Properties and Frequency Limitations. The intrinsic small-signal equivalent circuit of the pin diode at forward and reverse bias is shown in Fig. 3. As mentioned above, this scheme needs to be completed by the appro-

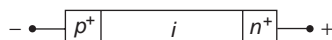


Figure 2. Layer structure of the pin diode.

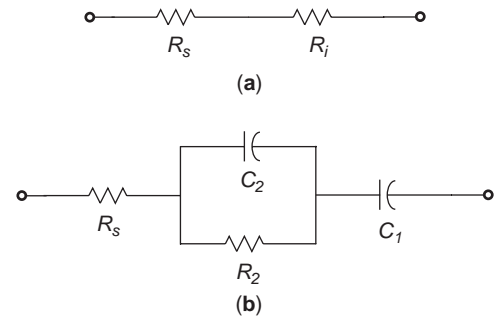


Figure 3. Intrinsic small-signal equivalent circuit of the pin diode in forward (a) and reverse (b) mode.

appropriate extrinsic elements that strongly depend on the device configuration within the microwave or millimeter-wave circuit and possible package. The resistance R_i is the intrinsic-layer resistance, R_s is the series resistance of the p^+ and n^+ layers, C_1 is the reverse-biased depleted capacitance, and C_2 and R_2 are the reverse-biased undepleted capacitance and resistance, respectively.

Important specifications of pin diodes are low insertion loss, high power-handling capability, and fast switching time. In the ideal case, the lowest switching time is determined by the time to sweep away the stored charge in the intrinsic layer and is expressed by the transit time τ

$$\tau = \frac{V_b}{E_{\max} v_s} \quad (3)$$

where v_s is the saturation velocity of electrons, V_b is the breakdown voltage, and E_{\max} is the electric field where breakdown occurs. Therefore, V_b needs to be kept low for faster switching. However, in actual diodes, the switching time is almost entirely governed by the parasitics of the diode. For microwave applications, GaAs pin diodes are often used instead of Si. The reason is that the resistance is lower for GaAs, reflecting the higher mobility.

2.2.3. Applications. pin diodes are used as phase shifters for phased-array radars, switches for pulsed radars, limiters to protect the receiver circuit against overload, and attenuators. In microwave integrated circuit (MIC) design, pin diodes are preferred to Schottky diodes because of their lower series resistance and capacitance, which leads to superior performance. The layer structure of pin diodes is, however, not straightforwardly compatible with standard MMIC technology. Therefore, monolithic integrated phase shifter circuits are realized with Schottky diodes, “cold” FETs, (i.e., with no DC current), or dual-gate FETs.

2.3. IMPATT Diodes

2.3.1. Description. The IMPATT (*impact avalanche transit time*) diode employs the impact ionisation and transit properties of a semiconductor p-n junction to produce negative resistance at microwave frequencies. The diode type was first proposed by Read [3] in 1958. The p^+ -i-p- n^+ layer structure is represented in Fig. 4. In

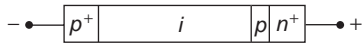


Figure 4. Layer structure of the IMPATT diode.

operation the diode is reverse-biased into avalanche breakdown. The p layer is the avalanche region, followed by a “drift region,” the i layer, for the generated charge carriers to drift. The electric field in this drift region should be high enough to enable the generated carriers to travel at their saturation velocity.

When the diode is placed in a microwave resonant circuit, RF voltage fluctuations in the bias circuit grow and are forced into a narrow frequency range determined by the impedance characteristics of the resonant circuit. As a result of the avalanche process, the RF current across the avalanche region lags the RF voltage by 90°. This inductive delay is by itself not sufficient to produce an active characteristic. However, when the 90° phase shift is added to that arising from an additional inductive delay caused by the transit time of the carriers drifting through the remainder of the diode external to the avalanche region, a phase shift between the RF voltage and current greater than 90° is obtained. A Fourier analysis of the resulting waveforms reveals a device impedance with a negative real part. That means that the device is active and can be used to generate or amplify RF signals.

2.3.2. Properties and Frequency Limitations. The intrinsic small-signal equivalent circuit of the IMPATT diode is shown in Fig. 5. It consists of the ohmic resistance R_s ; the negative resistance R_d in series with the inductor L_d , which models the inductive delay; and the p-n junction capacitance C_j .

For optimum performance, the drift region is designed such that the electric field throughout the RF cycle is sufficiently high to produce velocity saturation for the charge carriers. In order to achieve this, it is common to design complex structures consisting of alternating layers of highly doped and lightly doped semiconductor regions. They can also be fabricated in a back-to-back arrangement to form double-drift structures. IMPATT diodes can be fabricated from most semiconductors, but are generally fabricated from Si or GaAs.

2.3.3. Applications. IMPATT diodes are particularly attractive for millimeter-wave applications and have been operated as high as a few hundred gigahertz. The devices are capable of good RF output power (mW to W) and good DC-to-RF conversion efficiency ($\approx 10\text{--}20\%$). They have

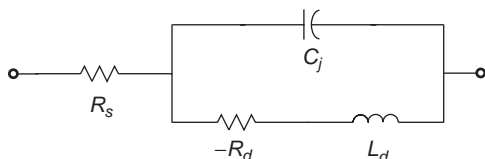


Figure 5. Intrinsic small-signal equivalent circuit of the IMPATT diode.

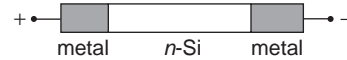


Figure 6. Layer structure of the BARITT diode.

moderate bandwidth capability, but relatively poor noise performance due to the impact ionisation process.

2.4. BARITT Diodes

2.4.1. Description. Another diode belonging to the transit-time diode family is the BARITT (*barrier injection transit time*) diode. The mechanisms responsible for the microwave oscillation are the thermoionic injection and diffusion of minority carriers across a forward-biased barrier and a transit-time delay of the injected carriers traversing the drift region. Several structures can be operated as BARITT diode, such as metal-n-metal and p-n-p, p-n-metal.

The first BARITT operation was obtained from a metal-n-metal reach-through diode [4], shown in Fig. 6. It is basically two Schottky diodes connected back to back. When a sufficiently large bias is applied to the device, the electric field will reach through the entire device. Under this condition, thermoionic injection of holes across the barrier, located at the left-side metal–semiconductor interface, occurs. The injected holes traverse the drift region from this barrier to the right-side metal contact.

2.4.2. Properties and Frequency Limitations. The BARITT diode has no avalanche delay because the thermoionically injected carriers are in phase with the AC voltage swings. The consequence is that the efficiency of a BARITT diode is substantially lower than that of an IMPATT diode. This is because during a part of the period, both the AC voltage and current are positive. This implies that AC power is dissipated in the device. This power will cancel some of the AC power generated by the device during the other part of the period. Therefore, the net AC power generated is smaller than the AC power of the IMPATT diode.

2.4.3. Applications. BARITT diodes are used in low-noise millimeter-wave applications, since they are much less noisy than IMPATT diodes. The reason is that the noise associated with carrier injection across the barrier is much smaller than the avalanche noise in an IMPATT diode. Disadvantages are the low efficiency and relatively narrow bandwidth.

2.5. Gunn Diodes

2.5.1. Description. The Gunn diode was developed by Gunn [5] in 1963. The name Gunn diode is given to all two-terminal devices whose operation depends on the transferred-electron effect. Gunn diodes are a type of active diodes. The negative conduction derives from the complex conduction band structure of certain compound semiconductor devices, such as GaAs and InP. In these direct-bandgap materials the central (or Γ) conduction band is in close energy-momentum proximity to secondary, higher-order conduction bands: the X and L valleys.

The electron effective mass is determined by the shape of the conduction bands. The electron effective mass is “light” in the Γ valley, but “heavy” in the higher-order X and L valleys. When the crystal is biased, the current flow is initially due to electrons in the light effective mass Γ valley and hence the conduction is ohmic. However, as the bias field is increased, an increasing proportion of the free electrons are transferred into the X and L valleys, where the electrons have heavier effective mass. The increased effective mass slows down the electrons, with a corresponding decrease in conduction current through the crystal. The net result is that the crystal displays a region of applied bias voltages where current decreases with increasing voltage. This means that a negative conductance is generated. The device is unstable and, when placed in an RF circuit or resonant cavity, oscillators or amplifiers can be fabricated. It is important to note that this device is not a diode in the strict sense, since no p-n or Schottky junction is used. The phenomenon is a characteristic of the bulk material and the special structure of the conduction bands in certain compound semiconductors. Few semiconductors have the conduction band structure necessary for the transferred electron effect.

2.5.2. Properties and Frequency Limitations. The intrinsic small-signal equivalent circuit of the Gunn diode is represented in Fig. 7. The Gunn diode can be modeled as a negative conductance $1/R_d$ in parallel with a capacitance C_j . The bandwidth of the Gunn effect is limited by the speed with which the electrons can transfer from one valley to another and back. This is a scattering process characterized by a time constant. It turns out to be shorter in InP than in GaAs. In GaAs the Gunn effect can be used up to ~ 80 GHz, while in InP frequencies about twice as high can be reached.

2.5.3. Applications. Transferred electron devices are widely used in oscillators from the microwave through high-millimeter-wave frequency bands. They have good RF output power capability (milliwatts to watts level), moderate efficiency ($< 20\%$), and excellent noise and bandwidth capability. Octave band tunable oscillators are easily fabricated using devices such as YIG (yttrium iron garnet) resonators or varactors as the tuning element. Most commercially available solid-state sources for the 60–100 GHz operation generally use InP transferred electron devices. Compared to the IMPATT diode, the Gunn diode produces less output power, but can exhibit lower noise performance.

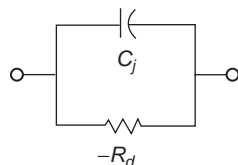


Figure 7. Intrinsic small-signal equivalent circuit of the Gunn diode and the tunnel diode.

2.6. Tunnel Diodes

2.6.1. Description. Tunnel diodes [6] generate active characteristics by a mechanism involving the physical tunneling of electrons between energy bands in highly doped semiconductors. For example, if a p-n junction diode is heavily doped, the conduction and valence bands will be located in close proximity and charge carriers can tunnel through the electrostatic barrier separating the p- and n-type regions, rather than be thermoionically emitted over the barrier as generally occurs in this type of diode. When the diode is (forward or reverse)-biased, current immediately flows and the junction conduction is basically ohmic. In the forward-bias direction, conduction occurs until the applied bias forces the conduction and valence bands to separate. The tunnel current then decreases, and normal junction conduction occurs. In the forward-bias region where the tunnel current is decreasing with increasing bias voltage, a negative immittance characteristic is generated.

2.6.2. Properties and Frequency Limitations. Tunnel diodes are described by a negative conductance $1/R_d$ in shunt with a capacitance C_j (Fig. 7). Tunnel diodes are limited in operation frequency by the time it takes for charge carriers to tunnel through the junction. Since this time is very short (on the order of 1 ps), the operation frequency can be very high, approaching 1 THz. They have been operated at hundreds of gigahertz, limited by practical packaging and parasitic impedance considerations. The RF power available from a tunnel diode is limited (hundreds of milliwatts level), since the maximum RF voltage swing that can be applied across the junction is limited by the forward turnon characteristic of the device (typically 0.6–0.9 V). Increased RF power can be obtained only by increasing device area to increase RF current, but device area is limited by operation frequency according to an inverse law.

2.6.3. Applications. Tunnel diodes have moderate DC-to-RF conversion efficiency ($< 10\%$), and very low noise figures and are hence useful in low-noise applications, such as microwave and millimeter-wave receivers.

3. MICROWAVE AND MILLIMETER-WAVE TRANSISTORS

3.1. FETs

3.1.1. Description. The fundamental structure of the field-effect transistor (FET) has been proposed by Shockley in 1952 [7]. A FET consists of an n-type semiconductor layer, sandwiched by p-type layers, and ohmic contacts, formed at the edges of the n-type layer. The ohmic contacts are called *source* and *drain*. The p-n junctions serve as a control element and are called the *gate*. When reverse bias is applied across the p-n junctions, space charge regions form. Consequently, current flows from the drain to the source through a channel of the n-type layer bounded by the controlled space charge regions.

Other types of FETs utilize different ideas for the gate from that of the p-n junction type. These types include the

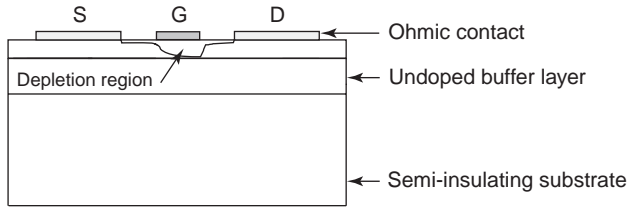


Figure 8. Layer structure of the MESFET.

metal-insulator-semiconductor (MIS), in which a gate electrode is formed on the semiconductor via an insulator, and the metal-semiconductor (MES), in which a Schottky barrier is used as the gate. The best-known MIS transistor type is the MOSFET with an oxide as insulator. The cross section of the MESFET is represented in Fig. 8. Possible operation modes are the common-source configuration and the less frequently used common-gate configuration. The former means that the drain contact is biased at a specified potential (positive drain potential for an n-channel device) and the source is grounded. The flow of current through the conducting channel is controlled by negative DC and superimposed RF potentials applied to the gate, which modulate the channel current and provide RF gain. The current flow is composed of only one type of charge carrier (generally electrons), and the device is hence termed unipolar.

3.1.2. Properties and Frequency Limitations. The small-signal equivalent circuit and the definitions of the typical figures of merit are identical to those of HEMT devices. Therefore, we refer to the corresponding part of the subsequent HEMT section.

3.1.3. Applications. There is an increasing interest in using several types of Si MOSFETs [CMOS (complementary MOS), SOI (silicon on insulator), LDMOS (Laterally Diffused MOSFET) (MOS), etc.] in analog RF applications in the lower microwave frequency band [8,9]. For microwave applications, however, compound semiconductor materials, and in particular gallium arsenide (GaAs) are preferred. The reason is that the electrode mobility and the peak drift velocity of GaAs are 6 times and twice as high, respectively, as those of Si. These properties result in larger transconductance, shorter electron transit times, and lower parasitic resistances. In addition, unlike Si, semiinsulating GaAs substrates can be formed. This contributes to the simple structure of FETs and to an important reduction of parasitics. p-n junctions with fine patterns are difficult to realize in GaAs because of the enhanced lateral diffusion at the surface. MIS structures with a low interface state density, such as SiO_2/Si , are very difficult to obtain. On the other hand, GaAs MESFETs, fabricated for the first time by Mead in 1966 [10], have been widely successful. GaAs MESFETs are the most important active devices used in microwave applications, while the high-performant HEMTs are typically employed at millimeter-wave frequencies. MESFETs can be optimized for small-signal, low-noise operation or for large-signal, RF power applications. Generally, low-noise

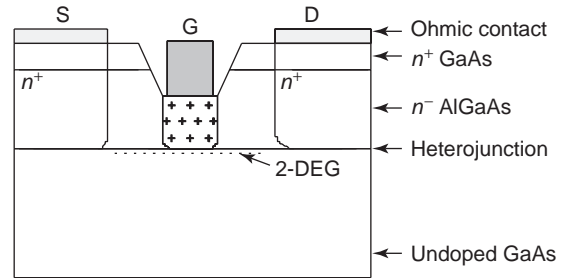


Figure 9. Layer structure of the conventional AlGaAs/GaAs HEMT.

operation requires short gate lengths, small gate widths, and highly doped channels. Power devices generally have longer gate lengths, much wider gate widths, and lower doped channels.

3.2. HEMTs

3.2.1. Description. The high-electron-mobility transistor (HEMT), first demonstrated by Dingle et al. in 1978 [11], derives its name from the high low-field mobility of its channel electrons that are captured at the interface between two semiconductor materials with a different bandgap energy and with a similar lattice constant. This type of interface is called a *heterojunction*.

A schematic cross section of the conventional HEMT, based on the AlGaAs/GaAs heterojunction, is shown in Fig. 9. Free electrons provided by the n-doped AlGaAs layer diffuse across the heterojunction into the narrow bandgap GaAs and become captured in the quasitriangular potential well at the interface caused by the conduction band discontinuity (ΔE_c). This leads to a two-dimensional electron gas (2DEG) consisting of electrons that are confined in the direction perpendicular to the heterojunction interface, but free to move in parallel directions. Because of the spatial separation between carriers and dopants, electrons in the channel obtain a very high low-field mobility, especially at low temperatures. The flow of electrons between the source and drain ohmic contact regions is modulated using an external gate voltage applied on a Schottky gate contact. While for a MESFET the bias on the Schottky gate contact controls the depth of the undepleted channel, for HEMTs the gate bias directly controls the carrier density in the channel.

The conventional lattice-matched AlGaAs/GaAs layer structure is now widely replaced by other combinations of compounds leading to improved HEMT characteristics. The main reason is that the conventional HEMT suffers from a small conduction band discontinuity ΔE_c . By incorporating indium in the channel, the conduction band discontinuity can be enhanced leading to three additional types of HEMTs, which are indicated on the energy band-gap versus lattice constant diagram of Fig. 10:

- The pseudomorphic HEMT (PHEMT) grown on a GaAs substrate and based on the $\text{Al}_x\text{Ga}_{1-x}\text{As}/\text{In}_y\text{Ga}_{1-y}\text{As}$ heterojunction

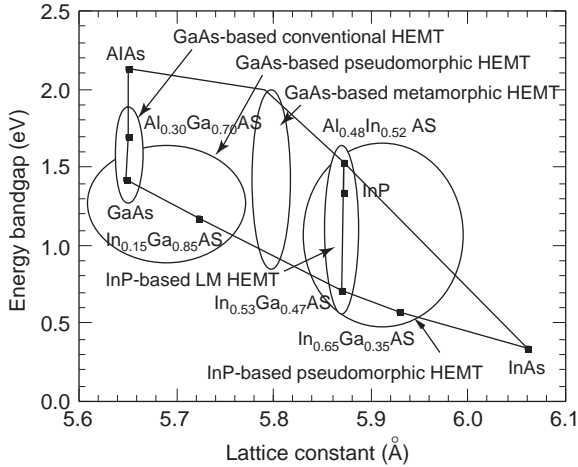


Figure 10. Energy bandgap–lattice constant diagram indicating the four different HEMT families.

- The InP lattice-matched HEMT (LMHEMT) grown on an InP substrate and based on the $\text{Al}_{0.48}\text{In}_{0.52}\text{As}/\text{In}_{0.53}\text{Ga}_{0.47}\text{As}$ heterojunction
- The InP pseudomorphic HEMT (InP PHEMT) grown on an InP substrate and based on the $\text{Al}_{0.48}\text{In}_{0.52}\text{As}/\text{In}_x\text{Ga}_{1-x}\text{As}$ ($0.53 > x > 0.80$) heterojunction

For completeness, the relatively new GaAs-based metamorphic HEMT (MMHEMT) is also shown in Fig. 10. This HEMT is grown strain-relaxed on GaAs and is based on the $\text{Al}_{1-y}\text{In}_y\text{As}/\text{In}_x\text{Ga}_{1-x}\text{As}$ ($0.3 > x > 0.5$) heterojunction [12]. Another development is the wide-bandgap device, such as AlGaN/GaN HEMTs [13].

3.2.2. Properties and Frequency Limitations. The small-signal equivalent circuit of the MESFET and HEMT devices is shown in Fig. 11. As has already been indicated above, the small-signal equivalent circuit consists of an extrinsic, bias-independent part and an intrinsic, bias-dependent part. The parasitic capacitances C_{pg} , C_{pd} , and C_{pgd} and the inductances L_s , L_d , and L_g are determined by the metallizations of the access lines to the device. It has to be noted that in case of on-wafer devices, the measure-

ments are typically de-embedded up to the reference plane of the device, which is the device as it will be inserted in the actual circuit design. The effect of the probe pads is hence not included in this small-signal equivalent scheme. The resistances R_d and R_s are caused mainly by the drain and source ohmic contacts, while the gate resistance R_g is determined primarily by the gate Schottky contact. The intrinsic part is within the dashed rectangle. The resistances R_{gsf} and R_{gdf} model the current through the gate–source and gate–drain Schottky diodes. The capacitances C_{gs} and C_{gd} model the change in the depletion charge with respect to the gate–source V_{gs} and gate–drain V_{gd} voltages, respectively. The drain–source capacitance C_{ds} is included in the equivalent circuit to account for geometric capacitance effects between the source and the drain electrodes. The intrinsic gain mechanism of the HEMT is provided by the transconductance g_m , which is a measure of the incremental change in the drain–source output current I_{ds} for a given change in gate–source input voltage V_{gs} . Mathematically, it is defined as $g_m = \partial I_{ds} / \partial V_{gs}$. The output conductance g_{ds} is a measure of the incremental change in drain–source output current I_{ds} with the drain–source output voltage V_{ds} . It is defined mathematically as $g_{ds} = \partial I_{ds} / \partial V_{ds}$. R_{gs} and R_{gd} model the charging resistances in the channel. The transconductance cannot respond instantaneously to changes in the gate–source voltage V_{gs} . The delay inherent to this process is described by the transconductance delay τ . Physically, it represents the time it takes for the charge in the channel to redistribute itself after a fluctuation of V_{gs} .

Important figures of merit for MESFETs and HEMTs [14] are the transition frequency f_T and the maximum oscillation frequency f_{max} . The transition or cutoff frequency f_T is defined as the frequency at which the short-circuit current gain (h_{21}) becomes unity. The h_{21} can be derived from the S parameters as

$$h_{21} = \frac{-2S_{21}}{(1 - S_{11})(1 + S_{22}) + S_{12}S_{21}} \quad (4)$$

In order to get a better physical understanding of the f_T , we express the intrinsic h_{21} in terms of the intrinsic

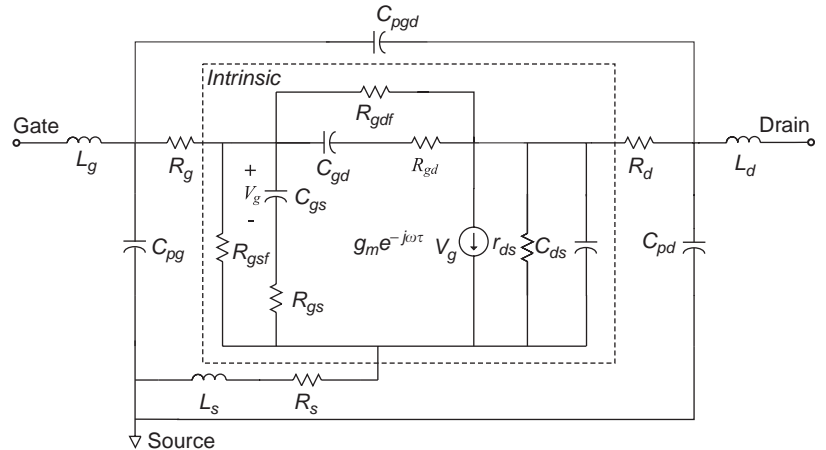


Figure 11. Small-signal equivalent circuit of the MESFET and the HEMT.

small-signal elements

$$h_{21} = \frac{g_m}{2\pi(C_{gs} + C_{gd})f} \quad (5)$$

where f is the frequency. This equation indicates a -20 -dB/decade rolloff for h_{21} and yields the usual approximate expression for the intrinsic f_T :

$$f_{T,i} = \frac{g_m}{2\pi(C_{gs} + C_{gd})} \quad (6)$$

When taking the influence of the extrinsic resistances R_s and R_d [15] and the gate pad capacitance, defined as $C_{pad} = C_{pg} + C_{pgd}$, into account, the expression for the transition frequency can be further refined to

$$\begin{aligned} f_T &= \frac{1}{2\pi\tau_T} \\ &= \frac{1}{2\pi} \left\{ \frac{g_m}{(C_{gs} + C_{gd})[1 + g_{ds}(R_s + R_d)] + C_{gd}g_m(R_s + R_d)} \right. \\ &\quad \left. + \frac{g_{m,ext}}{C_{pad}} \right\} \end{aligned} \quad (7)$$

where $g_{m,ext}$ is the extrinsic transconductance and g_m represents the intrinsic transconductance. The additional terms in this equation can be explained by a resistive divider effect at the output causing a current flow in the output resistance and thus reducing the short-circuit current with a factor $1 + g_{ds}(R_s + R_d)$, and by a Miller effect increasing the effective C_{gd} with a factor $1 + g_m(R_s + R_d)$. The influence of C_{pad} results in an extra charging time of the pad capacitance by the extrinsic transconductance $g_{m,ext}$.

For the derivation of the previous equations only the influence of the capacitances, resistances, and transconductance was taken into account, leading to a -20 -dB/decade rolloff for h_{21} . This fixed slope makes it possible to derive f_T by extrapolation from low-frequency measurements. When also taking the influence of the inductances L_s and L_d into account, a h_{21} deviating from the -20 -dB/decade slope is observed with at high frequencies a resonance behavior. Neglecting C_{gd} , the resonance frequency of the circuit can be, approximated by

$$f_0 = \frac{1}{2\pi} \sqrt{\frac{1}{L_{in}C_{gs}} + \frac{1}{L_{in}C_{gs}} \left[1 - \frac{(R_{in}C_{gs} + g_m L_s)^2}{L_{in}C_{gs}} \right]} \quad (8)$$

with $L_{in} = L_g + L_s$ and $R_{in} = R_g + R_{gs} + R_s$. As a result of this behavior, the use of the original definition for f_T yields a cutoff frequency that is much higher than the extrapolated one. Still, as this artificially high f_T is not related with the physical device operation, the f_T value is generally determined by an extrapolation with a -20 -dB/decade slope of the h_{21} measured at lower frequencies. As the resonance behavior leads to a lower slope for h_{21} at high frequencies, while gate leakage can lead to a flattening

and thus a lower slope of h_{21} at low frequencies, it is important not to rely on an extrapolation with an arbitrary slope as is sometimes found in literature.

To obtain a high extrinsic f_T , it is necessary to have a small transit time of the electrons from the source to drain contact [16] and thus short gates, low access resistances R_s and R_d , a low output conductance g_{ds} , feedback capacitance C_{gd} , and pad capacitance C_{pad} .

The maximum oscillation frequency f_{max} is defined as the frequency for which the two-port becomes passive or the maximum power gain is unity. The derivation of f_{max} is more complicated than that of f_T as there is no standard two-port parameter representing the maximum power gain. While the f_T can be derived directly from the short-circuit current gain h_{21} , the power gain is strongly dependent on the input and output matching networks.

In general, the transducer power gain G_T , which is the ratio of the power delivered to the load and the power available from the source, can be written as a function of the source and load reflection coefficients Γ_S and Γ_L :

$$G_T = \frac{(1 - |\Gamma_S|^2)|S_{21}|^2(1 - |\Gamma_L|^2)}{|(1 - S_{11}\Gamma_S)(1 - S_{22}\Gamma_L) - S_{12}S_{21}\Gamma_S\Gamma_L|} \quad (9)$$

For an unconditionally stable two-port, the maximum transducer gain $G_{T,max}$ is obtained for a simultaneous conjugate match at both ports. For these conditions, $G_{T,max}$ is equal to the maximum available gain (MAG) and is given by [17]

$$G_{T,max} = \text{MAG} = \frac{|S_{21}|}{|S_{12}|} \left(K - \sqrt{K^2 - 1} \right) \quad (10)$$

with K defined by Eq. (15).

The necessary and sufficient conditions for unconditional stability of a two-port network at a given frequency are [18,19]

$$|\Gamma_S| < 1 \quad (11)$$

$$|\Gamma_L| < 1 \quad (12)$$

$$|\Gamma_{IN}| = \left| S_{11} + \frac{S_{12}S_{21}\Gamma_L}{1 - S_{22}\Gamma_L} \right| < 1 \quad (13)$$

$$|\Gamma_{OUT}| = \left| S_{22} + \frac{S_{12}S_{21}\Gamma_S}{1 - S_{11}\Gamma_S} \right| < 1 \quad (14)$$

where Γ_{IN} is the input reflection coefficient and Γ_{OUT} is the output reflection coefficient of the two-port network. These equations state that for all passive load impedances, the real part of the input impedance must be positive and that for all passive source impedances, the real part of the output impedance must be positive.

The following derived formulation [Eqs. (15) and (16)] often used. Unconditional stability requires that the

two-port meets the two inequalities:

$$K = \frac{1 - |S_{11}|^2 - |S_{22}|^2 + |\Delta|^2}{2|S_{12}S_{21}|} > 1 \quad (15)$$

$$|\Delta| = |S_{11}S_{22} - S_{12}S_{21}| < 1 \quad (16)$$

For high-performance HEMTs, however, the relation $K < 1$ holds up to very high frequencies such that in the normal measurement range the quantity MAG is not defined. For this range in which the transistor is potentially unstable, the maximum stable gain (MSG) can be used as a measure to calculate the potential gain of the device when inserted in an amplifier after being stabilized with a lossless network, such as an inductive negative feedback network at the source, making $K = 1$:

$$\text{MSG} = \frac{|S_{21}|}{|S_{12}|} = \frac{g_{m,\text{ext}}}{2\pi f(C_{\text{gd}} + C_{\text{pgd}})} \quad (17)$$

Unfortunately, the MSG and MAG have different slopes of -10 and -20 -dB/decade, respectively. This makes an extrapolation with a fixed slope, as is done for the f_T , impossible. Therefore the extrapolation of the f_{max} normally relies on the unilateral power gain U or Mason's gain [20]. This figure allows to derive a MAG for an unstable two-port as it is defined as the maximum available power gain when the two-port is simultaneously conjugately matched while the feedback parameter Y_{12} is compensated by an external lossless network. As shown by Rollett [21], this type of neutralization is possible for any two-port. U is expressed by

$$U = \frac{1}{2K} \frac{|S_{21}/S_{12} - 1|^2}{|S_{21}/S_{12} - \text{Re}(S_{21}/S_{12})|} = \frac{1}{4} \left(\frac{f_T}{f} \right)^2 \frac{R_{\text{ds}}}{R_g} \quad (18)$$

A second figure delivering an approximately -20 -dB/decade slope over the whole region is the maximum unilateral transducer gain $G_{\text{TU,max}}$ which is the maximum available gain in the assumption that the device is unilateral ($S_{12} = 0$). For a unilateral device, the maximum gain is reached for $\Gamma_S = S_{11}^*$ and $\Gamma_L = S_{22}^*$, and is given by

$$G_{\text{TU,max}} = \frac{1}{1 - |S_{11}|^2} |S_{21}|^2 \frac{1}{1 - |S_{22}|^2} \quad (19)$$

The error made when setting S_{12} equal to zero can be estimated from the unilateral figure of merit F_U [17]:

$$F_U = \frac{|S_{12}||S_{21}||S_{11}||S_{22}|}{(1 - |S_{11}|^2)(1 - |S_{22}|^2)} \quad (20)$$

The maximum error introduced by using G_{TU} instead of G_T is bounded by

$$\frac{1}{(1 + F_U)^2} < \frac{G_T}{G_{\text{TU}}} < \frac{1}{(1 - F_U)^2} \quad (21)$$

Consistent with the theoretical derivation of the unilateral gain U , the modeled extrapolation to unity of both the

$G_{\text{T,max}}$ and U yield an identical f_{max} . It has to be noted that in practice the slopes of U , $G_{\text{TU,max}}$, and MAG deviate from their respective ideal slopes. Therefore, as measurements only at lower frequencies are usually available, the f_{max} is in practice determined using an extrapolation with a fixed -20 -dB/decade slope.

An alternative way to determine f_{max} is to use the extracted small-signal model. However, as the analytical derivation of f_{max} is rather complicated, a large number of different approximate expressions for f_{max} can be found in literature, such as [22]

$$f_{\text{max}} = \frac{f_{\text{T,i}}}{2\sqrt{g_{\text{ds}}R_{\text{in}} + \pi f_{\text{T,i}}C_{\text{gd}}(R_{\text{in}} + R_g)}} \quad (22)$$

whereby the influence of R_{gd} , C_{ds} , R_{d} and of the transconductance delay have been neglected. From this equation, one can see that to obtain a high f_{max} , it is important to have a high intrinsic f_T or a small transit time, a small gate resistance R_g , source resistance R_s and channel charging resistance R_{gs} , a low output conductance g_{ds} , and a small parasitic C_{gd} associated with gate fringing.

3.2.3. Applications. HEMTs are and will be employed in microwave and especially millimeter-wave (wireless) telecommunication systems, automotive applications, and radio astronomy. Their main application is high-gain and low-noise amplifiers at frequencies ranging to beyond 100 GHz. According to the particular circuit specifications, the circuit designer selects the most appropriate HEMT technology (InP/GaAs-based, lattice-matched or pseudomorphic, etc.). The wide-bandgap devices [13] are applied in high-power applications, such as base-station terminals.

An attractive configuration of the HEMT is the dual-gate HEMT. The dual-gate FET introduced in 1971 [23] is a MESFET with two parallel gate electrodes between drain and source. There are two main topologies for the dual-gate HEMT. In the first topology, an RF signal can be applied to the second gate. The second topology is the cascode configuration, which means that the second gate is RF-grounded. This is equivalent to the cascade connection of a common-source HEMT and a common-gate HEMT. The RF input is the gate of the common-source HEMT and the RF output is the drain of the common-gate HEMT. Figure 12 presents the (non)linear model of the dual-gate (cascode) HEMT. It consists of the cascode connection of the (non)linear models of two equivalent intrinsic single-gate HEMTs, supplemented with appropriate extrinsic elements [24]. The parasitic elements consist of those of the equivalent single-gate HEMT and three additional elements: the feedback capacitance C_{pgd} , the substrate leakage resistance R_{sub} , and the resistance between the two gates R_{int} . The capacitance C_{pg2} represents the extrinsic pad capacitance in case of the dual-gate device, and it represents the large capacitance to RF ground the second gate in case of the dual-gate cascode device. Because of its topology, the cutoff frequency of the current gain f_T is smaller and the MSG is theoretically higher than the figures of merit of the single-gate HEMT [25]. It is important to note that the dual-gate HEMT has suppressed kink and

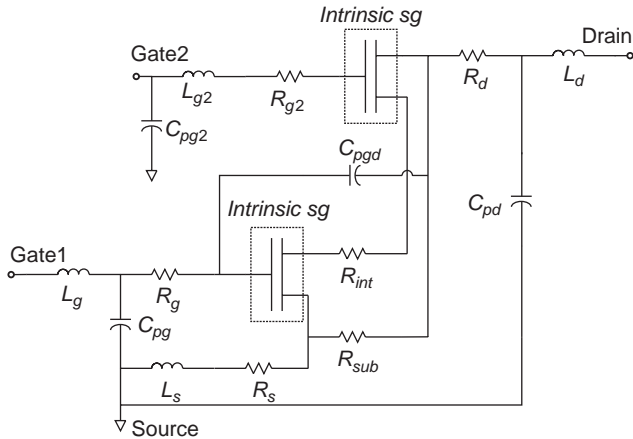


Figure 12. Small-signal equivalent circuit of the dual-gate MESFET and HEMT.

hence impact ionization [26], but the noise is slightly degraded compared to that of single-gate devices. Circuit applications for dual-gate (cascode) HEMTs are multiple [27,28]. The dual-gate cascode configuration is applicable in broadband distributed and variable-gain amplifiers, active phase shifters, oscipliers, and self-oscillating mixers. The dual-gate HEMT is especially encountered in mixers, due to the inherent isolation between the local-oscillator signal and the RF signal.

3.3. HBTs

3.3.1. Description. The bipolar junction transistor (BJT) was invented by Bardeen and Brattain [29] in 1948. It consists of two back-to-back p-n junctions arranged in a sandwich structure. The three regions are designated the emitter, base, and collector. This type of device differs from the field-effect transistors in that both electrons and holes are involved in the current transport process, which explains the term “bipolar.” Two structures are possible: pnp or npn, depending upon the conductivity type common to both p-n junctions. For microwave applications the npn structure is preferred since device operation is controlled by electron flow. Electron transport is faster than that for holes, and hence npn transistors are capable of superior high-frequency performance compared to comparable pnp transistors.

In operation, the base-emitter p-n junction is forward-biased and the collector-base p-n junction is reverse-biased. When an RF signal is applied to the base-emitter junction, the junction allows a current to be injected into the base region. The current in the base region consists of minority charge carriers, namely, carriers with the opposite polarity compared to the base material, such as electrons for an npn transistor. These charge carriers then diffuse across the base region to the base-collector junction, where they are swept across the junction by the large reverse-bias electric field. The reverse-bias electric field in the base-collector region is generally made sufficiently large that the carriers can travel at their saturation velocity. The transit time of the charge carriers across this region is small, except in millimeter-wave transistors,

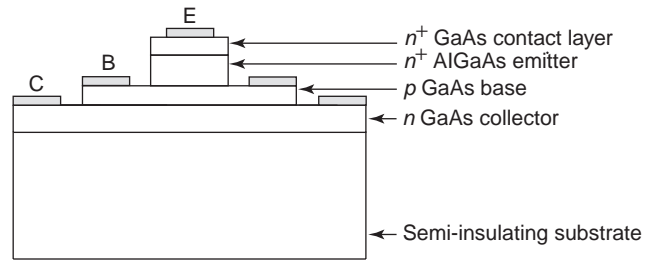


Figure 13. Layer structure of the HBT.

where the base-collector region transit time can be a significant fraction of the total time required for a charge carrier to travel from the emitter through the collector.

The heterojunction bipolar transistor (HBT) is an improved high-frequency bipolar transistor that is fabricated using heterostructures of compound semiconductors. These devices have their emitters fabricated from a wide-bandgap semiconductor, and the remainder of the device is fabricated from a lower-bandgap semiconductor, such as AlGaAs (emitter)/GaAs (base) (Fig. 13). This basic concept was proposed in 1957 by Kroemer [30]. In an npn HBT, the hole current flowing from base to emitter is suppressed by the potential barrier originating from the bandgap difference between the emitter and the base, which implies that a higher current injection efficiency is obtained compared with that of the homojunction bipolar transistor [31]. This allows the base to be more heavily doped than the emitter, leading to a low base resistance and emitter-base capacitance, in contrast with the homojunction bipolar transistor, where the heavily doped base degrades the emitter injection efficiency. These three features—high emitter injection efficiency, low base resistance, and low emitter-base capacitance—are the essential points in obtaining high current gain at high frequencies.

The AlGaAs/GaAs heterojunction has been studied most intensively. More recently, the heterostructure concept has been applied in Si-based devices using SiGe/Si heterostructures. The SiGe base has a lower bandgap than does the Ge emitter, allowing the resistivity to be decreased with respect to homojunction bipolar transistors. AlGaAs/GaAs HBTs generally exhibit performance superior to that of SiGe HBTs, but they require increased processing sophistication, [i.e., MBE (molecular-beam epitaxy) vs. standard epilayer processing] [32]. The SiGe HBT technology has the great advantage of being compatible with standard Si technology.

3.3.2. Properties and Frequency Limitations. The small-signal equivalent scheme of the HBT is presented in Fig. 14. This scheme consists also of a number of extrinsic, bias-independent and intrinsic, bias-dependent components. The parasitics associated with the access lines are represented by the shunt capacitances C_{bcp} , C_{bep} , and C_{cep} , and the series inductances L_b , L_e , and L_c . The distributed base-collector capacitance is modeled as a combination of the effective intrinsic capacitance C_c and the effective extrinsic capacitance C_{bc} [33]. R_e , R_b , and R_c are the emitter, base, and collector series, resistances, respectively. The

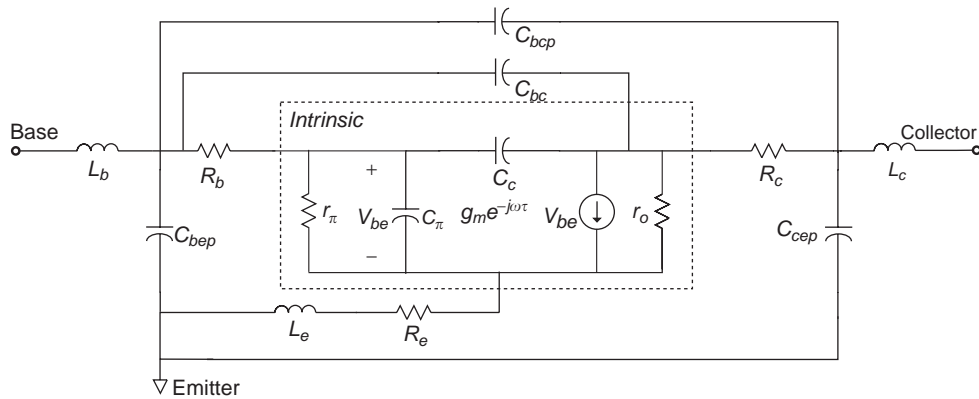


Figure 14. Small-signal equivalent circuit of the HBT.

intrinsic hybrid π network consists of the small-signal input resistance r_π , the collector output resistance r_o , the complex intrinsic transconductance g_m , and the sum of the base-emitter depletion capacitance and the base charging capacitance, denoted by C_π .

The operation of the transistor is primarily controlled by the ability of the minority charge carriers to diffuse across the base region. For this reason microwave transistors are designed with narrow base regions in order to minimize the time required for the carriers to travel through this region. The base region transit time is generally the limiting factor in determining the high-frequency capability of the transistor. The gain of the transistor is also significantly affected by minority-carrier behavior in the base region. The density of minority carriers is significantly smaller than the density of majority carriers for typical operating conditions, and the probability that the minority charge will recombine with a majority carrier is high. If recombination occurs, the minority charge cannot reach the base-collector junction but appears as base current. This, in turn, reduces the current gain capability of the transistor. Narrow base regions reduce the semiconductor volume where recombination can occur and, therefore, result in increased gain. Typical base regions are on the order of 0.1–0.25 μm . The frequency response of a BJT can be determined by an analysis of the total time it takes for a charge carrier to travel from the emitter through the collector. The total time can be expressed as

$$\tau_{ec} = \tau_e + \tau_b + \tau_c + \tau'_c \quad (23)$$

where τ_{ec} is the total emitter-collector transit time, τ_e is the base-emitter junction capacitance charging time, τ_b is the base region transit time, τ_c is the base-collector junction capacitance charging time, and τ'_c is the base-collector region transit time. The total emitter-base time is related to the gain-bandwidth capability of the transistor according to the relation

$$f_T = \frac{1}{2\pi\tau_{ec}} \quad (24)$$

Since the BJT has three terminals, it can be operated in various configurations, depending on the electrode

selected as the common terminal. The two most commonly employed are the common-emitter (CE) and the common-base (CB) configurations. The current gains of the transistor operated in the CE and CB configurations are β of h_{fe} and α , respectively. The CE current gain β is much larger than the CB current gain α , which is limited to values less than unity.

The static common-emitter current gain h_{FE} , which is the ratio of the collector current to the base current, is expressed by [34]:

$$h_{FE} = \frac{\alpha_0}{1 - \alpha_0} \quad (25)$$

where α_0 is the DC current gain with common-base configuration. The AC common-emitter current gain h_{fe} is expressed as:

$$h_{fe} = \frac{h_{FE}}{1 + jh_{FE}\omega/2\pi f_T} \quad (26)$$

Microwave power transistors are usually operated under a common-base configuration [34] since the power gain when operated under that configuration is higher than the gain obtained under a common-emitter configuration. A measure of the RF power gain for the transistor is indicated by the unilateral power gain U , which can be expressed as

$$U = \frac{\alpha_0}{16\pi^2 R_b C_c \left(\tau_{ec} + \frac{R_e C_c}{\alpha_0} \right)} \quad (27)$$

The frequency at which U is reduced to unity, f_{max} , is the maximum frequency at which the device will have active characteristics. This frequency is [35]

$$f_{max} = \sqrt{\frac{f_T}{8\pi R_b C_c}} \quad (28)$$

In order to maximise the high-frequency performance of a BJT, it is necessary to design the device so that it has high current gain f_T , low base resistance R_b , and low collector

capacitance C_c . As R_b and C_c have an influence on f_T , optimization is needed.

Other important specifications for power transistors are the maximum available current density and the breakdown voltage.

3.3.3. Applications. BJTs operating to about 20 GHz are generally fabricated from Si. They are useful in moderate gain, low-noise and low-high-RF power applications. HBTs are employed in both low-noise and high-RF power applications in the microwave frequency range. BJTs and HBTs exhibit better phase-noise performance than do FET devices, but FETs generally have a better noise figure.

BIBLIOGRAPHY

- W. Shockley, The theory of p - n junctions in semiconductors and p - n junction transistors, *Bell Syst. Tech. J.* **28**:435 (1949).
- T. W. Crowe, T. C. Grein, R. Zimmermann, and P. Zimmermann, Progress toward solid-state local oscillators at 1 THz, *IEEE Microwave Guid. Wave Lett.* **6**:207–208 (1996).
- W. T. Read, A proposed high-frequency negative-resistance diode, *Bell Syst. Tech. J.* **37**:401–466 (1958).
- D. J. Coleman and S. M. Sze, A low-noise metal-semiconductor-metal (MSM) microwave oscillator, *Bell Syst. Tech. J.* **50**:1695 (1971).
- J. B. Gunn, Microwave oscillation of current in III-V semiconductors, *Solid-State Commun.* **1**:88 (1963).
- S. M. Sze, *Physics of Semiconductor Devices*, Wiley-Interscience, 1981.
- W. Shockley, A unipolar ‘field-effect’ transistor, *Proc. IRE* **40**:1365–1376 (1952).
- N. Camilleri, J. Costa, D. Lovelace, and D. Ngo, Silicon MOSFETs, the microwave device technology for the 90s, *IEEE MTT-S Int. Microwave Symp. Digest*, 1993, pp. 545–548.
- G. Ma, W. Burger, C. Dragon, and T. Gillenwater, High efficiency LDMOS power FET for low voltage wireless communications, *IEEE IEDM Digest*, 1996, pp. 91–94.
- C. A. Mead, Schottky barrier gate field-effect transistor, *Proc. IEEE* **54**:307–308 (1966).
- R. Dingle, H. Stormer, A. C. Gossard, and W. Wiegmann, Electron mobilities in modulation doped semiconductor heterojunction superlattices, *Appl. Phys. Lett.* **33**:665–667 (1978).
- A. Cappy, Metamorphic InGaAs/AlInAs heterostructure field effect transistors: Layer growth, device processing and performance, *Proc. 8th Int. Conf. Indium Phosphide and Related Materials (IPRM)*, 1996, pp. 3–6.
- R. J. Trew, SiC and GaN transistors — is there one winner for microwave power applications? *Proc. IEEE* **90**:1032–1047 (2002).
- L. Nguyen, L. Larson, and U. Mishra, Ultra-high-speed modulation-doped field-effect transistors: A tutorial review, *Proc. IEEE* **80**:494–518 (1992).
- P. J. Tasker and B. Hughes, Importance of source and drain resistance to the maximum f_T of millimeter-wave MODFETs, *IEEE Electron. Dev. Lett.* **10**:291–293 (1989).
- N. Moll, M. R. Hueschen, and A. Fischer-Colbrie, Pulsed doped AlGaAs/InGaAs pseudomorphic MODFETs, *IEEE Trans. Electron. Dev.* **35**:878–886 (1988).
- G. Gonzalez, *Microwave Transistors Amplifiers — Analysis and Design*, Prentice-Hall, Englewood, Cliffs, NJ, 1984.
- K. Kurokawa, Power waves and the scattering matrix, *IEEE Trans. Microwave Theory Tech.* Vol.13, No.2, pp. 194–202, (March 1965).
- T. T. Ha, *Solid State Microwave Amplifier Design*, Wiley-Interscience, 1981.
- S. J. Mason, Power gain in feedback amplifiers, *IRE Trans. Circuit Theory* **1**:20–25 (1954).
- J. M. Rollett, The measurement of the transistor unilateral gain, *IEEE Trans. Circuit Theory* **12**:91–97 (1965).
- R. Soares, *GaAs MESFET Circuit Design*, Artech House, 1988.
- J. A. Turner, A. J. Waller, E. Kelly, and D. Parker, Dual-gate gallium-arsenide microwave field effect transistor, *Electron. Lett.* **7**:661–662 (1971).
- D. Schreurs, Y. Baeyens, J. Verspecht, K. van der Zanden, B. Nauwelaers, W. De Raedt, M. Van Hove, and M. Van Rossum, Non-linear table-based model for GaAs and InP dual-gate cascode HEMTs, *Proc. 4th Int. Workshop on Integrated Nonlinear Microwave and Millimeterwave Circuits (INMMC’96)*, 1996, pp. 83–88.
- Y. K. Chen, G. W. Wang, D. C. Radulescu, and L. F. Eastman, Comparisons of microwave performance between single-gate and dual-gate MODFETs, *IEEE Electron. Dev. Lett.* **9**:59–61 (1988).
- W. Daumann, P. Ellrodt, W. Brockerhoff, R. Bertenburg, R. Reuter, U. Auer, W. Molls, F.-J. Tegude, InAlAs/InGaAs/InP HFET with suppressed impact ionization using dual-gate cascode-devices, *IEEE Electron. Dev. Lett.* **17**:488–490 (1996).
- C. Tsironis, GaAs dual gate MESFETs and their applications in microwave circuits, *Acta Electron.* **23**:317–324 (1980).
- S. A. Maas, *Microwave Mixers*, 2nd ed., Artech House, 1993.
- J. Bardeen and W. H. Brattain, The transistor, a semiconductor triode, *Phys. Rev.* **74**:230–231 (1948).
- H. Kroemer, Theory of a wide-gap emitter for transistors, *Proc. IRE* **45**:1535–1537 (1957).
- H. Kroemer, Heterostructure bipolar transistors and integrated circuits, *Proc. IEEE* **70**:13–25 (1982).
- A. Chantre, M. Marty, J. L. Regolini, M. Mouis, J. de Pontcharra, D. Dutartre, S. Jouan, F. Chaudier, M. Assous, C. Morin, and M. Roche, A highly manufacturable 0.35 μm SiGe HBT technology with 70 GHz f_{max} , *Proc. 28th European Solid-State Device Research Conf.* 1998, pp. 448–451.
- M. B. Das, High-frequency performance limitations of millimeter-wave heterojunction bipolar transistors, *IEEE Trans. Electron. Dev.* **35**:604–614 (1988).
- R. J. Chaffin, *Microwave Semiconductor Devices*, Wiley, 1973.
- R. Aliison, Silicon bipolar microwave power transistors, *IEEE Trans. Microwave Theory Tech.* **27**:415–422 (1979).

FURTHER READING

- S. Y. Liao, *Microwave Solid-State Devices*, Prentice-Hall, 1985.
- S. M. Sze, *Semiconductor Devices — Physics and Technology*, J Wiley, 1985.
- E. A. Wolff and R. Kaul, *Microwave Engineering and Systems Applications*, J Wiley, 1988.
- R. Goyal, *Monolithic Microwave Integrated Circuits: Technology and Design*, Artech House, 1989.
- P. H. Ladbrooke, *MMIC Design GaAs FETs and HEMTs*, Artech House, 1989.
- F. Ali and A. Gupta, *HEMTs and HBTs: Devices, Fabrication and Circuits*, Artech House, 1991.

- M. J. Golio, *Microwave MESFETs and HEMTs*, Artech House, 1991.
- Y. Konishi, *Microwave Integrated Circuits*, Marcel Dekker, 1991.
- T. G. van de Roer, *Microwave Electronic Devices*, Chapman & Hall, 1994.
- R. Anholt, *Electrical and Thermal Characterization of MESFETs, HEMTs and HBTs*, Artech House, 1995.
- M. T. Faber, J. Chramiec, and M. E. Adamski, *Microwave and Millimeter-Wave Diode Frequency Multipliers*, Artech House, 1995.
- M. Golio, *The RF and microwave handbook*, CRC Press, 2001.

MICROWAVE SUPERCONDUCTOR DEVICES

CARLES SANS
 Pompeu Fabra University
 Spain
 GENICHI TSUZUKI
 Superconductor Technologies,
 Inc.
 Santa Barbara, California

1. INTRODUCTION

At microwave frequencies, superconductor materials conduct electric current with a level of resistance that is two or three orders of magnitude lower than that of copper. This property of superconductors can be exploited to produce electronic components and systems with increased efficiency and reduced levels of electronic interference and noise. Microwave superconductor devices provide superior sensitivity and speed while dramatically reducing power consumption, size, and weight. Since 1990, many passive microwave superconductor devices, including delay lines, antennas, matching networks, resonators, and filters, have been fabricated and tested.

In delay-line devices, superconductors provide very high bandwidth and very low loss and dispersion. The best performance can be obtained with stripline designs. These high-performance superconducting delay lines can be used to build finite impulse response filters for signal processing applications. There are a number of systems where superconducting delay lines or finite impulse response filters could be employed but competing technologies; for example, surface acoustic waves (SAWs) show much lower technological risk and are smaller and much cheaper. SAW technology was developed in the 1970s and is today a mature technology and an excellent choice in the range 10 MHz–1 GHz, although they also work at higher frequencies. Superconducting delay-line filters offer a much lower loss and a higher bandwidth than do SAW filters but still have not gained market acceptance for commercial systems.

The extremely low loss of superconductors is the most important benefit for antenna devices. Electrically small antennas have low radiation resistance, and their efficiency can be greatly improved by using superconductors. However, the high Q of the superconducting resonator that forms the antenna also reduces its bandwidth, and a

broadband impedance matching network is needed. To keep the noise figure down, both antenna and matching network can be made superconducting. In fact, antenna miniaturization is an interesting application for superconductors, because it can lead to fully integrated microwave receivers with antenna, matching network and preselect filters within the same package. The technical challenge with superconducting antennas is how to provide the cryogenic environment for operation.

1.1. Superconducting Filters

So far, the most promising device application for superconductors is the resonator-based filter. High Q factors of planar superconducting resonators in the range of 10^4 – 10^5 and higher allow for the fabrication of miniaturized multipole microwave filters with very low insertion loss and very sharp skirts. Generally, a size reduction of the filter leads to reduced performance due to higher insertion loss. However, when using superconductors, the size can be reduced while maintaining or even improving the filter performance. Miniaturization of the filters can be achieved in a number of ways such as using substrates with higher dielectric constant, more compact resonator geometries, or thinner substrates. Many different types of filters have been demonstrated since the 1990s, ranging from conventional designs to completely novel ones that become practical only when using superconductors.

The very low insertion loss of superconducting filters allows for the fabrication of filters with very large number of poles and extremely high out-of-band rejection, approaching the shape of an ideal filter response. The filter response in Fig. 1 corresponds to a 22-pole filter that provides out-of-band rejection of almost 100 dB with an insertion loss at midband of only 0.22 dB [1].

Planar superconducting filters do not perform well at high power levels. The effects in the frequency response can be seen as an increase in insertion loss and a distortion of the shape. In addition to these, the filter generates unwanted harmonics due to its nonlinear behavior. This fact limits the practical use of superconducting filters to low-power applications. As of today, superconducting filters have been included in receiver front-end systems for wireless base stations, where they provide excellent rejection performance to filter out any unwanted interferers.

2. SUPERCONDUCTING FILTER DESIGN

The filter design process follows three steps: design of the filter response, synthesis of the coupling coefficients, and physical realization of the synthesized couplings in a layout. The final layout needs fine adjustments through a few iterations until a good filter is obtained.

2.1. Filter Response

Three basic filter responses are normally used for planar superconducting filters: Chebyshev, Butterworth, and quasielliptic. Those are shown in Fig. 2.

2.1.1. Chebyshev Response. Chebyshev response is widely used because of its relatively high rejection perfor-

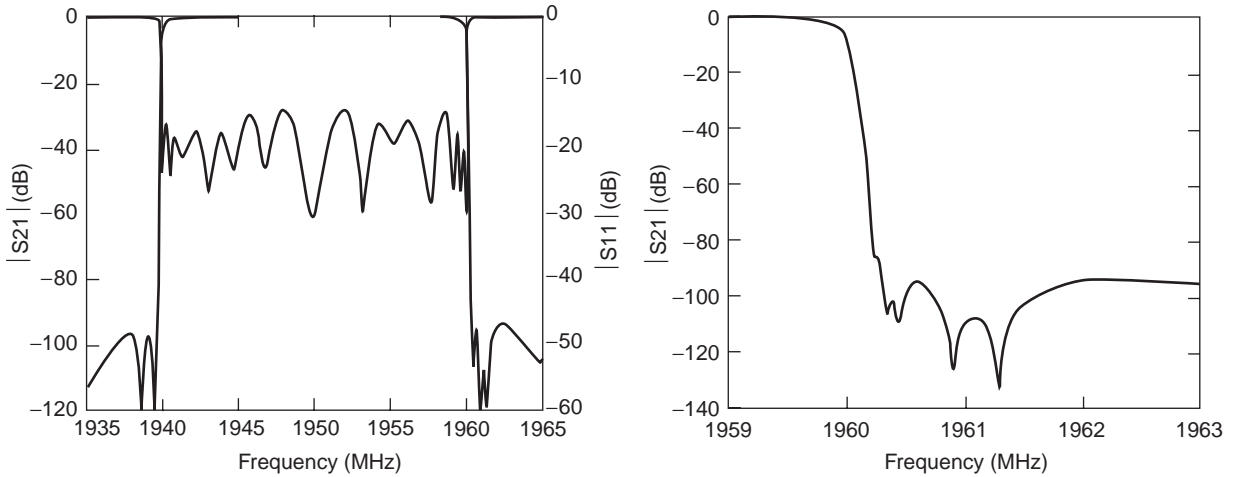


Figure 1. Filter response of the 22-pole filter.

mance with a simple design and realization. This filter renders rejection steeper by having ripple in the pass-band. The transfer function of an N -pole filter is given as

$$|S_{21}| = \frac{1}{\sqrt{1 + \epsilon^2 C_N^2}}, \quad C_N = \cosh[N \cosh^{-1}(\omega)]$$

2.1.2. Butterworth Response. Butterworth response is also known as a *maximally flat filter* because it does not have ripple. The transfer function is given as

$$|S_{21}| = \frac{1}{\sqrt{1 + \omega^{2N}}}$$

In terms of filter realization, Butterworth and Chebyshev filters are similar but with slightly different coupling values between resonators.

2.1.3. Elliptic Response. The elliptic response has transmission zeros at finite frequencies ω_i , thus improving rejection performance. The transfer function is given as

$$|S_{21}| = \frac{1}{\sqrt{1 + \epsilon^2 C_N^2}}$$

$$C_N = \cosh \left[N \sum_{i=1}^N \cosh^{-1} \left(\frac{\omega - 1/\omega_i}{1 - \omega/\omega_i} \right) \right]$$

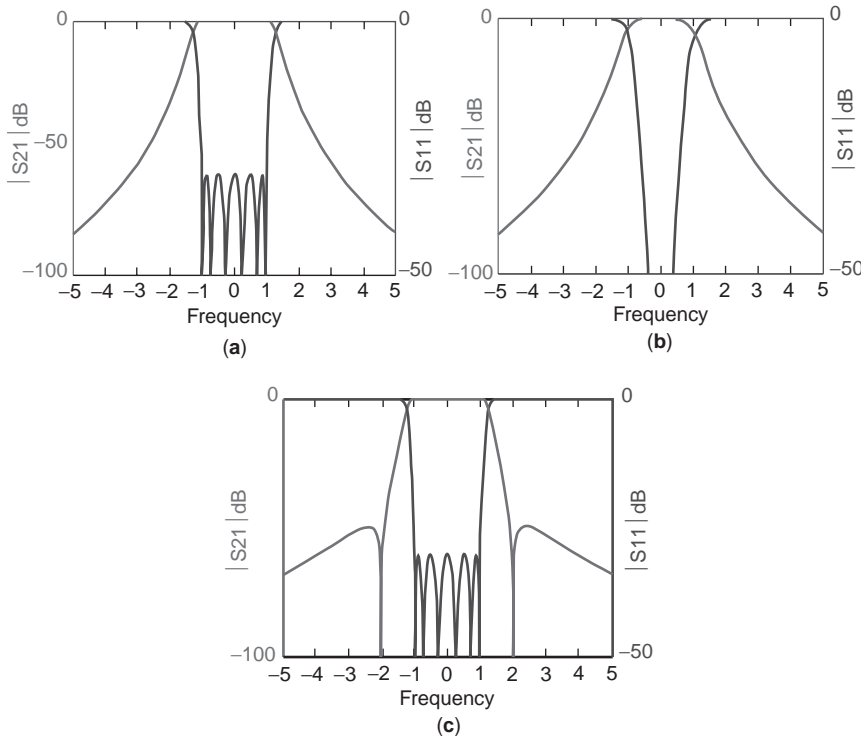


Figure 2. Typically used filter responses: (a) Chebyshev; (b) Butterworth; (c) elliptic. (This figure is available in full color at <http://www.mrw.interscience.wiley.com/erfme>.)

Transmission zeros make filter realization more difficult because additional cross-couplings between nonadjacent resonators are necessary. Details on how to realize the required cross-couplings are discussed in the following section.

2.2. Cross-Coupling Structures

The cross coupling technique was originally developed for cavity filters [2,3]. When applied to planar superconducting filters [4], steeper rejection slopes can be obtained without increasing the number of resonators. *Cross-coupling* is coupling that is intentionally introduced between nonadjacent resonators in addition to the main coupling between adjacent resonators. The cross-coupling structure creates two signal paths that can cancel each other out at some frequency near the band edge, creating a transmission zero. To achieve the cancellation, the signs of main coupling and cross-coupling have to be opposite. Different cross-coupling structures are described below.

2.2.1. Trisection Cross-Coupling. A trisection cross-coupling structure is realized by introducing an additional coupling path between the first and last resonator in the three-resonator structure shown in Fig. 3a. It is the shortest possible cross-coupling path and the simplest way to implement a transmission zero. The transmission zero can be realized either at the low side or at the high side of the

passband depending on the cross-coupling sign. If the sign is the same as the main coupling sign, the transmission zero appears at the high side of the passband and vice versa. Since every transmission zero is controlled by its corresponding trisection, the filter realization and tuning are straightforward.

Trisection structures can produce both symmetric or asymmetric rejection responses. An asymmetric response like the one shown in Fig. 3b is needed, for example, when transmit and receive bands are next to each other and the rejection slope near the boundary between the two bands is required to be very steep.

2.2.2. Quadruplet Cross-Coupling. This cross-coupling technique is the most commonly used for planar superconducting filters because it realizes a symmetric pair of transmission zeros more efficiently at both sides of the passband using the cascaded four-resonator sections shown in Fig. 4a. The cross-coupling sign has to be opposite the main couplings sign in order to produce transmission zeros. Instead, if the sign of the cross-coupling is the same, the structure is used to obtain linear phase filters for wideband applications such as CDMA systems.

As with trisections, quadruplets can be cascaded when multiple transmission zeros are necessary to achieve the required rejection performance. By cascading multiple quadruplets, multiple pairs of symmetric transmission zeros can be realized. Since every quadruplet controls

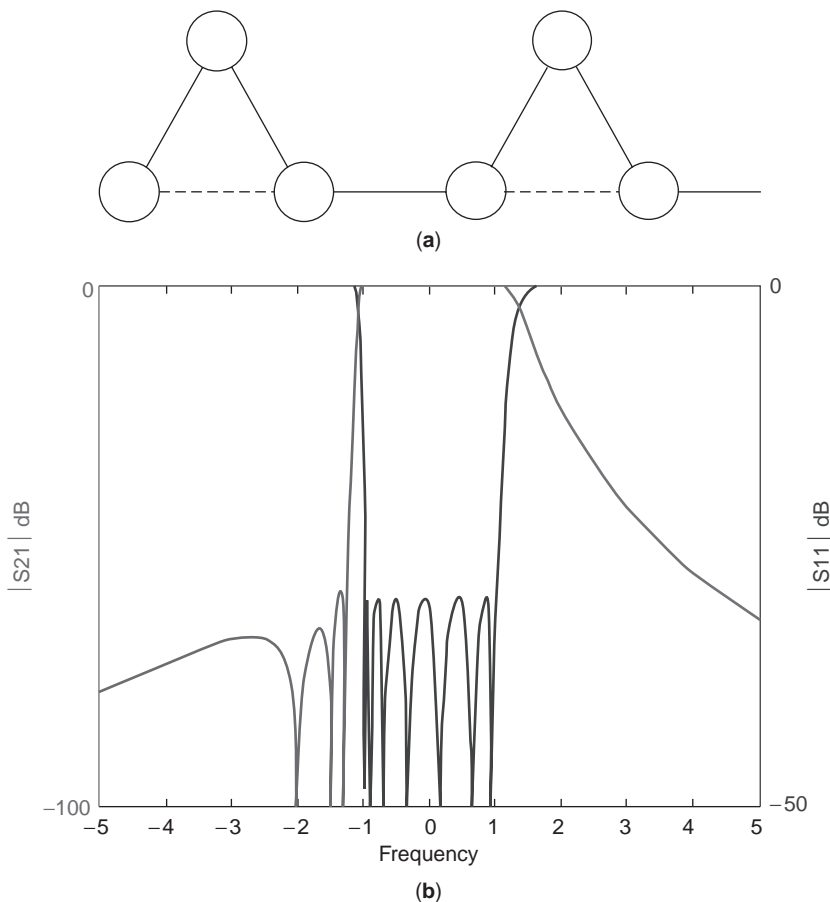


Figure 3. Trisection cross coupling: (a) cross-coupling structure — circles denote resonators, and solid lines and dashed lines denote main coupling paths and cross-coupling paths, respectively; (b) example of asymmetric response — three transmission zeros are produced only on the low side of its passband asymmetrically. (This figure is available in full color at <http://www.mrw.interscience.wiley.com/erfme>.)

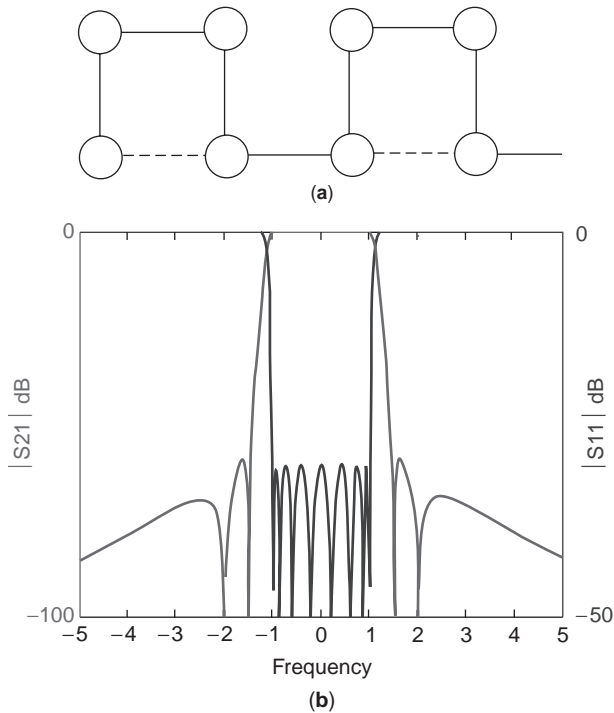


Figure 4. Quadruplet cross-coupling: (a) cross coupling structure — circles denote resonators, and solid and dashed lines denote main coupling paths and cross-coupling paths, respectively; (b) example of response — two pairs of transmission zeros are produced symmetrically on both sides of the passband. (This figure is available in full color at <http://www.mrw.interscience.wiley.com/erfme>.)

one corresponding symmetric pair of transmission zeros, the filter realization and tuning is straightforward as in the trisection case.

2.2.3. Other Cross-Coupling Structures. The folded cross-coupling structure shown in Fig. 5 is widely used in conventional cavity filters. It can realize more transmission zeros with the same number of resonators than can the previously discussed cross-coupling structures. However, it is not suitable for planar filters because of the unwanted parasitic coupling between physically close resonators.

2.3. Coupling Synthesis

There is a well-known simple formula for Chebyshev and Butterworth filter synthesis [5]. From this formula, a set of coupling values is obtained and hence the synthesis procedure is very simple. On the contrary, the synthesis of filters with cross-coupling coefficients is not that simple.

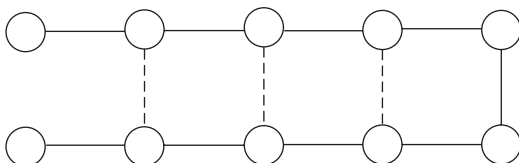


Figure 5. Folded cross-coupling: circles denote resonators, and solid and dashed lines denote main coupling paths and cross-coupling paths, respectively.

Many approaches have been reported for the synthesis, but all of them can be divided into two main streams: coupling matrix rotation [6] and curve fitting [7].

A coupling matrix is constructed from the coupling coefficients between resonators, the external loads, and the resonant frequencies of each resonator. The coupling matrix rotation approach starts from a full coupling matrix where every resonator can be coupled to any other one. That full matrix, although it realizes the intended filter response, is not convenient because it requires a complicated filter layout. Therefore, the next task is to obtain an equivalent matrix that realizes the same filter response with a lot fewer coupling components between the filter resonators. Using a matrix rotation technique, the number of nonzero elements of the coupling matrix can be greatly reduced and a much simpler layout obtained. This simpler layout can be realized, for example, by a cascaded quadruplet cross-coupling structure.

The curve fitting approach for the synthesis is based on, first, choosing the preferred cross-coupling structure that is able to realize the target filter response. Then, main couplings and intended cross-couplings are adjusted through optimization until the synthesized filter curve ideally fits the defined filter curve along with the prescribed transmission zero locations. During the optimization process, the remaining couplings, that is, all nonadjacent couplings excluding the cross-couplings, are set to zero. Therefore, the preferred cross-coupling structure is enforced and a filter realization obtained only if a solution exists. This second approach is also useful for the analysis of measured filter data [8]. The actual realized coupling values of a particular filter can be extracted by applying the curve fitting process to measured data of the filter. A curve fitting example with measured data is shown in Fig. 6.

2.4. Filter Realization

Once a coupling structure is defined and a coupling matrix or a set of coupling coefficients is obtained through a synthesis process, the next step is the filter realization. For planar superconducting filter design, the resonators can be either lumped-element or distributed. A serious concern with planar superconducting filters is parasitic couplings because the resonators are physically very close. This parasitic coupling is unwanted coupling between nonadjacent resonators, which has a visible effect on the measured filter response by canceling, adding, or displacing the transmission zeros. The higher the frequency or the narrower the bandwidth of the filter, the more important these parasitic coupling effects become.

2.4.1. Lumped-Element Filters. Lumped-element filters are based on resonators that are much smaller in size relative to the filter operating wavelength. Hence, at high frequencies where the wavelength is short, these filters are very small. Of course, the smaller the filter, the higher the insertion loss, and here comes the advantage of using superconductors. Lumped-element filter technology can be used as long as the required linewidths can be realized by the patterning process. This condition typically means

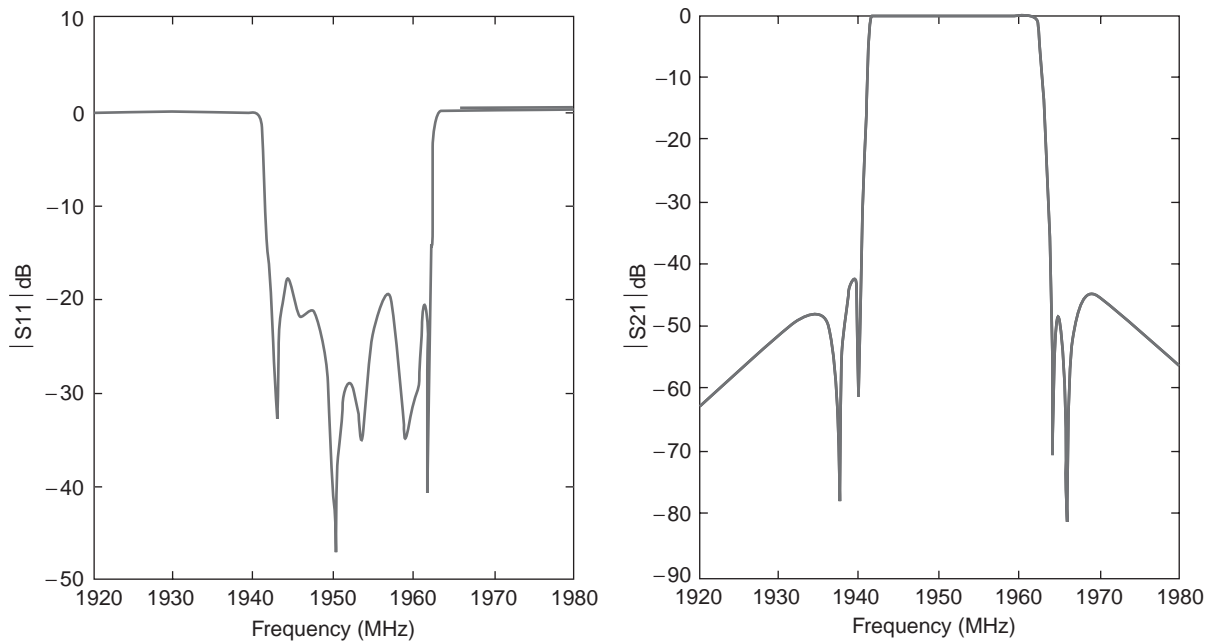


Figure 6. Measurement analysis; blue curve represents measured data and red curve, fitted data. (This figure is available in full color at <http://www.mrw.interscience.wiley.com/erfme>.)

that lumped-element filters can be used up to a few tens of gigahertz, a broad frequency range where superconductors clearly outperform normal conductors.

Since the available surface of superconducting films is rather small, lumped-element filters are very desirable especially when many poles are required or at low frequencies where the filter becomes too large. A pair of 800-MHz multipole pole filters can be fabricated on a



Figure 7. Miniature lumped element filter.

2-in.-diameter wafer (Fig. 7). Obviously, since the filters are smaller, the insertion loss is slightly higher because of the locally high current densities, especially in the inductors of the filter. However, if the superconducting film is of high quality, miniature lumped-element resonators achieve quality factors on the order of 50,000 and higher, depending on the frequency of operation.

Figure 8 shows an example of a lumped-element superconductor filter [9]. Since the center frequency of the filter is quite low, a lumped-element design is a good choice to keep it small enough to fit in a typical 2-in.-diameter wafer. The transmission zero appearing at the high stopband is due to parasitic coupling.

2.5. Distributed Resonator Filters

Distributed resonators provide higher Q factors than do lumped-element resonators. In general, the Q factor is determined by the linewidth of the resonator at locations where the current distribution is high. In lumped-element resonators, the linewidth is typically narrower in order to obtain high inductance values and reduce the resonator size. This size reduction limits the Q factor that can be achieved.

There are two ways to physically realize the cross-coupling in planar superconducting filters. The filter structure in Fig. 9a realizes a cross-coupling between the third resonator and the sixth resonator by laying out the resonators' direction properly [10]. All the couplings are inductive except for the cross-coupling between third and sixth resonators, where the resonators are placed with their respective ends facing each other. Thus, the coupling takes place in a region where the electric field is maximum, unlike the case for the remaining resonators, which couple each other magnetically. By doing this, the sign of the cross-coupling is set opposite the main couplings

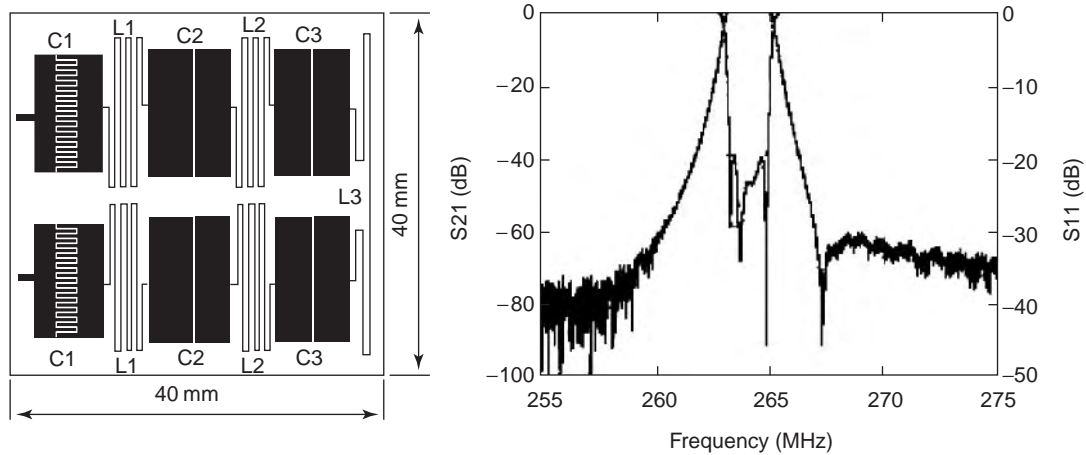


Figure 8. An example of a lumped-element filter and its response.

or negative, and a pair of transmission zeros can be obtained.

The filter in Fig. 9b shows an alternative way to realize the cross coupling [11]. In this case, additional transmission lines are introduced between first and fourth, fourth and seventh, and seventh and tenth resonators. These transmission lines produce coupling between those resonators through capacitors at both ends of the line. The coupling transmission lines have to be designed short enough so that they do not resonate themselves. The magnitude of the cross-coupling is controlled by adjusting both the length of the line and the coupling capacitance to the resonators.

The filter layout in Fig. 10a shows a refinement of this second cross-coupling technique, where primary and secondary couplings between a pair of resonators have been used [12]. Applying such a concept, large or small bandwidth filters can be made without very small or very large resonator spacing. In addition, the same cross-coupling layout configuration may be designed to achieve either positive or negative coupling results.

2.6. Filter Tuning

Due to the fabrication variation in the production line, the filter usually needs tuning to adjust its response. Filter tuning may be done by either mechanical tuning or process tuning. Two different mechanical tuning approaches are known. One of these approaches uses a high-dielectric-constant material in order to locally modify the electric field of the resonators. Usually a dielectric rod is used, and the distance to the resonator is adjusted by turning a screw that holds the dielectric rod in the bottom. The other

approach modifies the magnetic field by placing a conductor material close to the resonators. Usually a small superconductor-coated substrate tip is used and tuning is adjusted by changing the distance to the resonator. Both tuning elements should be placed to effectively produce a frequency shift of the resonator and at the same time minimize any change in the coupling values.

The second category of tuning does not use any mechanical actuator, but the resonator itself is modified in the filter fabrication process. One of those approaches is laser trimming. Laser trimmed filters are tuned by scribing a part of the resonators to produce the desired frequency shift. Another process tuning approach is dielectric layer deposition [13]. After the normal filter fabrication process, a dielectric layer is deposited on the resonators. The thickness of this layer and the coverage over the resonator can be adjusted for every individual resonator so that the required frequency shift is obtained. The amount of tuning has to be determined previously by measuring the filter and adjusting the resonant frequencies of the resonators.

2.7. High-Order Filters

The high Q factor of superconducting distributed resonators allows the fabrication of very-high-order filters with very small insertion loss. A first example of a high-order filter is the 32-pole Chebyshev filter shown in Fig. 11 [13]. The basic resonator design is based on a conventional hairpin structure but formed as a letter 'J' shape in order to minimize the coupling ratio between both adjacent and nonadjacent resonators. By adjusting the shape, parasitic couplings between nonadjacent resonators can be reduced and at the same time passband return loss maintained. The circular layout of the resonators along the wafer shape also helps reduce the parasitic couplings and any undesired housing propagation effect.

A second example of a high-order filter is the 22-pole quasielliptic filter shown in Fig. 1 [1]. The basic resonator of this filters, shown in Fig. 12, is also a distributed type. The high current region in the center of the half-wavelength resonator has been opened to facilitate the tuning

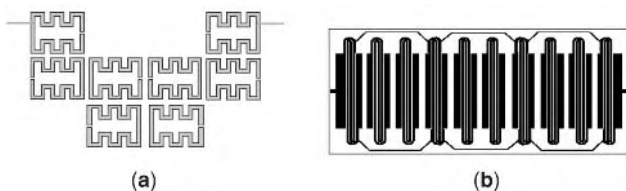


Figure 9. Cross-coupling realizations.

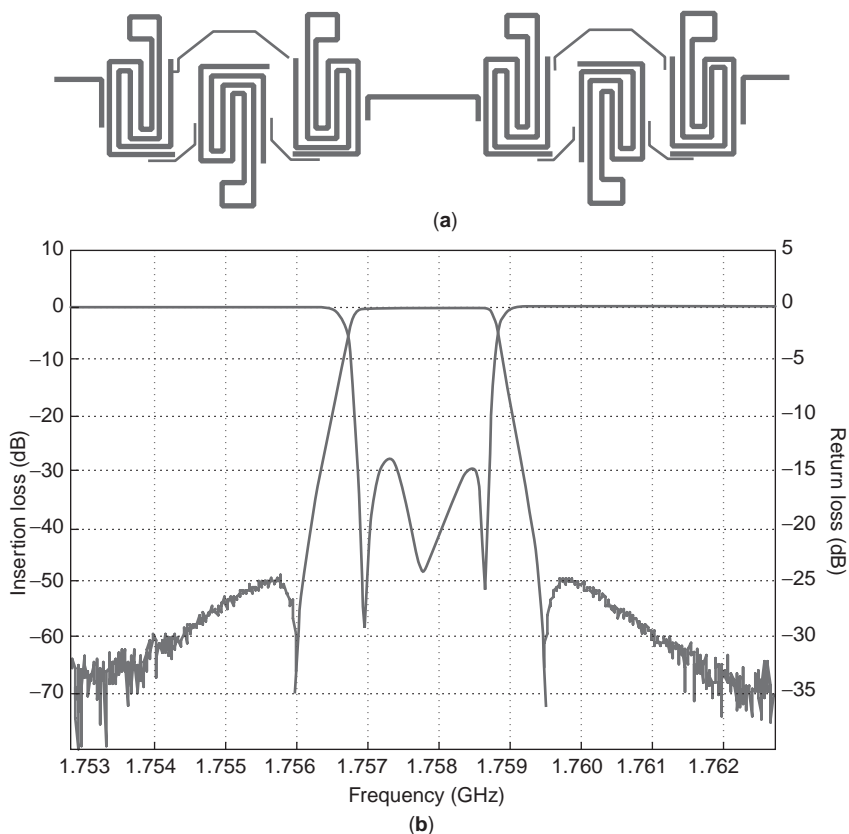


Figure 10. A six-pole thin-film superconductor filter layout and its response. Both trisections use primary and secondary couplings. (This figure is available in full color at <http://www.mrw.interscience.wiley.com/erfme>.)

process. This filter contains five quadruplet cross-couplings and is able to produce five transmission zeros at each side as shown in Fig. 1. As a result, the rejection slope can be extremely sharp.

3. WIRELESS APPLICATION

The most important application today of microwave superconductor devices is in the wireless communications industry. Due to the spectacular growth of cellular subscribers, this industry has undergone an important deregulation leading to many providers in most countries. Superconducting front-end filters may play an important role in both existing and future wireless base stations by

increasing the overall system capacity and interference suppression capability. This will allow wireless providers to deploy and improve their networks rapidly as they follow the market directions.

3.1. Superconducting Front Ends

So far, mostly receiver front-end preselect filters have been successfully introduced. A wireless receiver front end is the analog circuitry at the base station that performs the signal processing after the antenna and low-loss cable. A typical superconducting front end consists of one or more preselected superconducting filters and a low-noise amplifier (LNA) for every sector of the base station. Both devices are cooled to an operating temperature

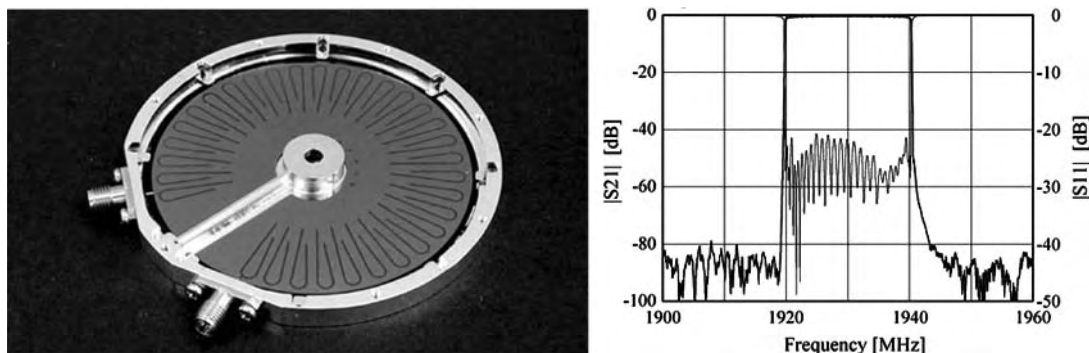


Figure 11. Photograph and measurement data of a 32-pole filter.

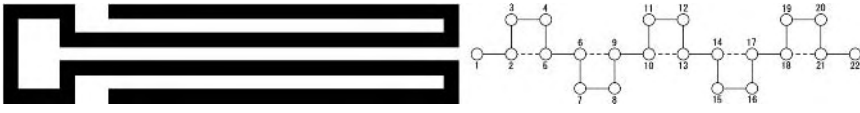


Figure 12. Resonator shape and cross-coupling structure of a 22-pole filter.

around 60–70 K inside a cryogenic vessel, so that the LNA also improves its noise figure. The system usually incorporates a bypass that would switch to conventional technology filters and LNAs in case of cooler or vacuum failure (Fig. 13). In principle, superconductors could be used in all the components that form the receiver front end. However, a combination of a superconducting filter and a conventional LNA, typically a one- or two-stage high-performance GaAs HEMT or FET circuit, provides the best performance. The front end is followed by a resistive splitter and a bank of parallel receiver chains, each one composed of a conventional mixer, a conventional IF bandpass filter to select different frequency channels, an IF amplifier, and an analog-to-digital converter (ADC) with bandpass sampling.

The main interference challenge for the receiver front end is the intermodulation products (IMPs) that result from frequency mixing of two or more strong out-of-band signals in the nonlinear LNA and mixer. When an IMP falls on the radio channel being received, the result may be a noisy or dropped call. Particularly strong signals can also cause LNA saturation, which greatly diminishes sensitivity. To eliminate interfering IMPs and potential LNA saturation, the causal out-of-band signals must be attenuated and the linear dynamic range of the LNA must be increased. However, conventional filters with very sharp skirts might have unacceptable insertion loss for in-band signals, and LNAs with wide dynamic range and sufficiently low noise are difficult to design. Hence, for this engineering challenge the cryogenic superconducting front end appears to be the perfect solution, providing both extremely high selectivity and great sensitivity.

A limitation, however, arises as a result of the intrinsic compromise between frequency resolution and integration time. The high selectivity of the superconducting filter is accompanied by a large group delay, especially at the passband edges. This strong frequency dependence in the transition region causes intersymbol interference and, therefore, should be compensated by either an

additional analog allpass equalizer in the RF or IF part. Future software radio architectures will employ a wideband receiver followed by a wideband ADC with high sampling rate and resolution. Separation of frequency channels or group delay equalization will be accomplished in a software-controlled manner in digital signal processing (DSP). This approach will allow the realization of reconfigurable transceivers, increasing the flexibility of base-station equipment. However, the realization of these architectures requires a sufficiently high dynamic range in the RF front end, which is limited by the nonlinearities in the mixer and LNA. Adaptive analog prefiltering with superconducting tunable filters could be a solution to overcome this limitation if sufficient progress is made to achieve enough tuning range without excessive loss.

At the system level, cryogenic front ends with superconducting filters provide broader coverage and lower interference levels, resulting in superior quality of service. The broader coverage is a direct consequence of the improved sensitivity of the receiver, thanks to the low insertion loss of superconducting filters and the low physical temperature of both the filter and the LNA (see, e.g., the Front-end apparatus in Fig. 14). The cooled LNA reduces the overall noise figure of the RF front end to about 0.5 dB (typically 0.8–1 dB at room temperature and 0.4 dB at 70 K). The total improvement in insertion loss is in the order of 2–2.5 dB. Even more impressive is the capability to reduce interference. The sharp skirts and high rejection of superconducting filters help to attenuate adjacent channels easily more than 60 dB with a more than acceptable noise figure. Typically, the filter reduces any out-of-band signals to levels where the IMPs generated are negligible compared to thermal noise levels.

3.2. Cooling Requirements

The superconducting wireless application requires 3–10 W of cooling power in the temperature range from 60 to 80 K. In order to achieve these temperatures, the cryocooler has

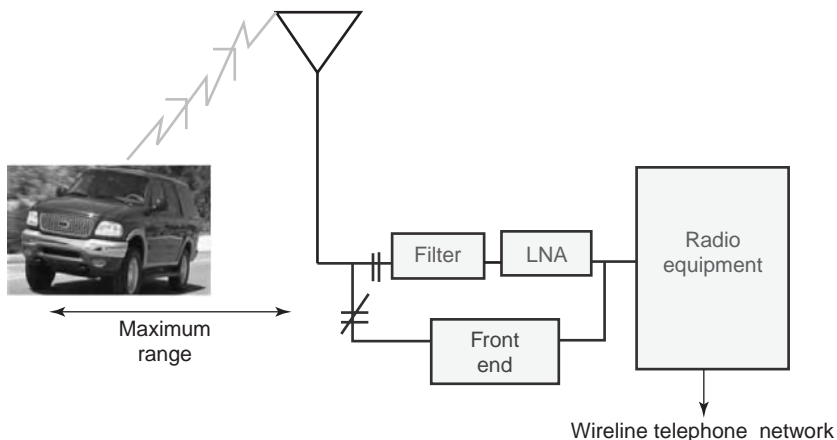


Figure 13. Superconducting front end and bypass with conventional technology, between antenna and base-station radio equipment.



Figure 14. Rack-mountable superconducting receiver front end that incorporates superconducting filters and cooled low-noise amplifiers inside a cryogenic vacuum vessel.

to remove not only the heat that is stored and generated within the RF components and surrounding packaging but also the heat that comes in from the warmer environment that surrounds the cryogenic assembly (see Fig. 15). This parasitic heat is transmitted through conduction and

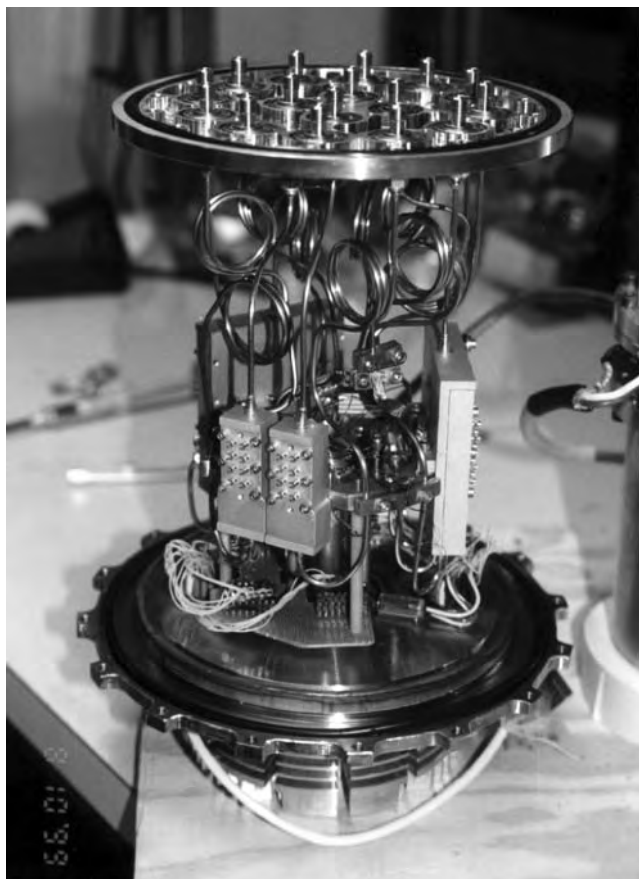


Figure 15. Detail of superconducting filters mounted inside a cryogenic vacuum vessel.

radiation and must be constantly removed along with the dissipated heat generated by the cryogenically cooled LNAs to maintain the HTS filters at some stable temperature between 60 and 80 K.

The thermal loads from all of these sources are on the order of 3–5 W depending on the system configuration (omnidirectional with two channels or three-sector with six channels.) More complex 6-sector (twelve channel) configurations are expected to require as much as 8 W of cooling power within this temperature range. For a wireless front-end application, the ideal cooler should be capable of a coefficient of performance (CoP) of at least 5%, with CoP understood as net cooling power: input power ratio. Furthermore, it has to be low-cost (\sim \$1000), be small ($<$ 5 kg), and have a maintenance-free life of more than 40,000 h (5 years). Nowadays, the cooler and cryopackage represents the most important part of the total cost of the system, and remains the main challenge in the establishment of a viable business model for commercial wireless products.

Manufacturers of superconductor filter systems are faced with a series of tradeoffs in the features and characteristics of various cryocoolers. The compelling reliability advantage of GM designs is an important consideration but is not the only one. Stirling cryocoolers are smaller, lighter, and less noisy, and hence, a good choice in applications where operating lifetime is less important. Very promising data on the reliability of Stirling cryocoolers has been reported [14] showing no infant mortality and an accumulated lifetime of more than 17,250 h to date.

3.3. Benefits in Wireless Networks

The overall improvement to the wireless network can be measured in a number of different ways depending on the environment (rural, suburban, or urban) and the type of access protocol in the RF link. The characteristics that can be measured are (1) reduced number of dropped and blocked calls, (2) improved voice quality, (3) increased channel availability, (4) increased base-station coverage or reduced number of base stations, (5) reduced mobile transmit power, (6) increased network capacity and minutes of use (MoU), and (7) reduced bit error rate (BER) in digital systems.

Customer field trials have been taking place since 1996 in the United States for the analog cellular spectrum advanced mobile phone service (AMPS), with 824–849 MHz receive and 869–894 MHz transmit bands. Data from multiple trial reports are already available for 1G and 2G wireless networks. In 1G networks the basic benefits are range extension, coverage improvement, voice quality enhancement, and a reduced number of dropped calls. From the viewpoint of the service providers, these benefits have translated into increased minutes of use of their base stations, which is the economic variable of interest. However, major deployment of superconductor subsystems in 1G networks has not yet taken place for a combination of reasons. First, the technology has only relatively recently gained the confidence of the industry and second and most importantly, the main focus of service providers has been the deployment of 2G digital networks in urban and suburban environments where most of their revenues are derived.

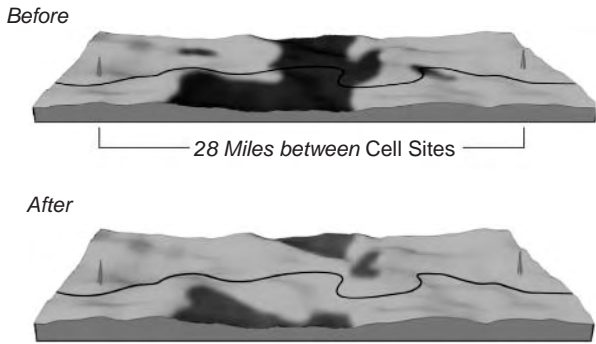


Figure 16. Increased coverage with superconducting front end.

However, the benefit of superconducting front ends in 1G networks is clear especially in the rural case. A necessary condition to transform a reduced noise figure of the receiver front end into a system benefit is a low antenna noise figure. This is the case for rural environments where the antenna is exposed to low noise and low interfering signals. Hence, in rural networks the lower noise figure of superconducting filters translates into increased coverage, allowing less base stations for a given area or higher quality of service in shadowed areas. Figure 16 shows a coverage problem that would require an additional base station for the shadowed area that intercepts the road. The coverage can be improved in just a few hours by replacing the conventional front end with a superconducting one. The benefit is clear, since another base station would cost more than \$400,000 plus a few months of work.

On the other hand, in urban areas with a lot of traffic and human-generated noise, the antenna noise temperature can be as high as 2000 K. To maintain the antenna signal-to-noise ratio (SNR), the handset power has to be higher and the receiver must be exposed to high-energy out-of-band signals that might limit the sensitivity with IMPs. Such is the case of the TDMA A-band operator interfered with by high-power Special Mobile Radio (SMR) signals (Fig. 17). By replacing the conventional front end with a superconducting one, all interferers are almost suppressed, greatly reducing the possibility of significant IMPs.

Digital networks have become the dominant technology in the wireless industry. Many analog cellular networks have been converted to digital technology. However, there is mounting evidence that digital technology has unexpected capacity and service limitations as well as significant coverage problems. The coexistence of different digital protocols creates unique interference mechanisms that need to be accounted for. TDMA transmitters are likely to cause interference to CDMA receivers because CDMA systems are designed to operate at the minimum possible power, whereas TDMA systems raise the power level in order to increase coverage and capacity. These limitations represent a significant market opportunity for superconducting front ends. In 2G TDMA networks significant benefits have already been demonstrated in coverage, capacity, and interference suppression, and even better benefits are expected in 2G CDMA networks. The most significant benefit of superconductor technology in 2G base stations is the ability to provide superior interference rejection, which allows service providers to utilize their available spectrum without introducing guardbands

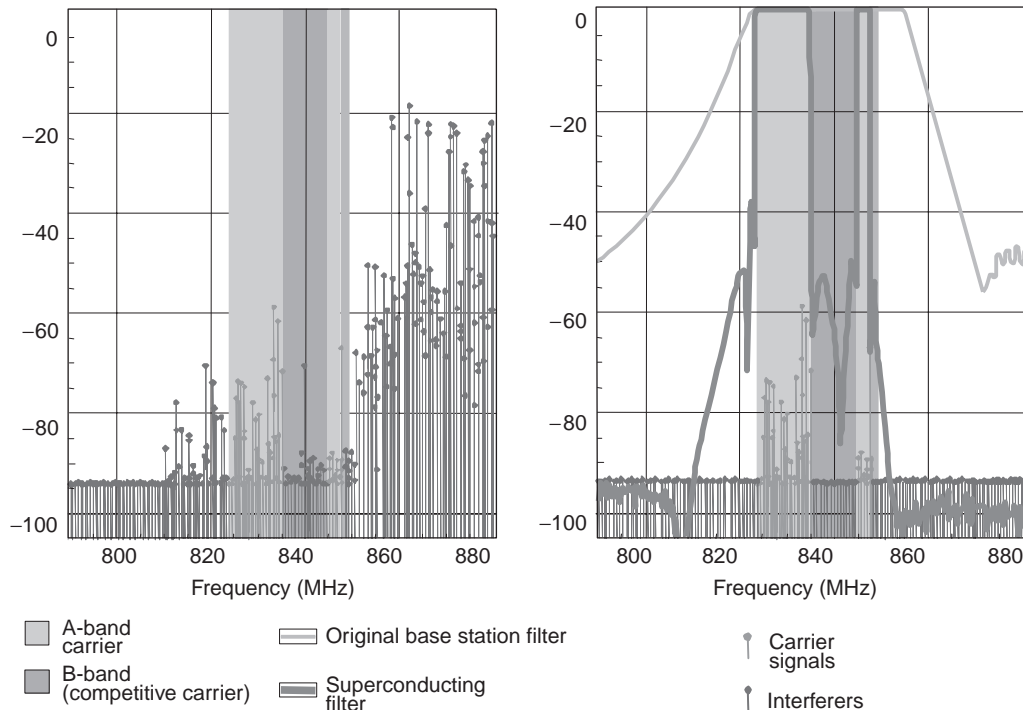


Figure 17. Out-of-band interference suppression with superconducting front end. (Data taken in Half Moon Bay, CA.). (This figure is available in full color at <http://www.mrw.interscience.wiley.com/erfme>.)

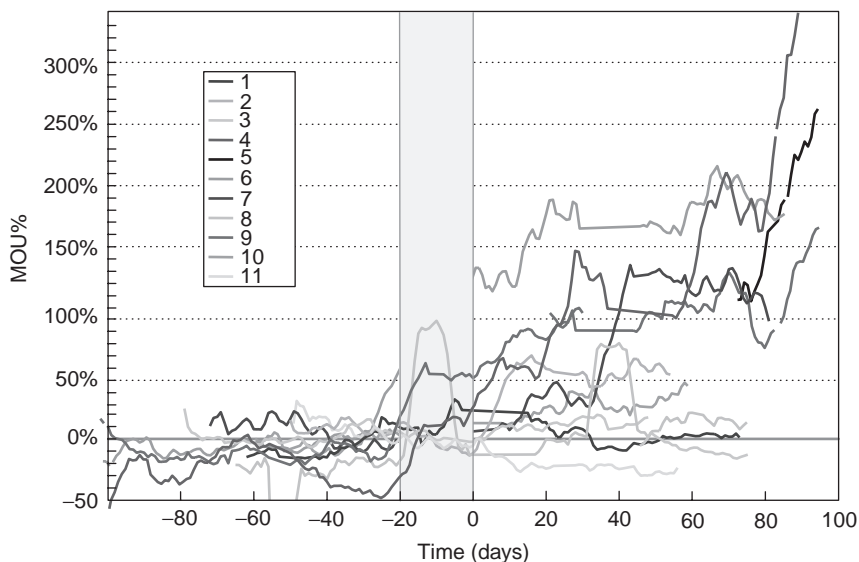


Figure 18. Percentage change in minutes of use (MoU) for 11 CDMA cell sites before and after a conventional front end was replaced by a superconducting one. Average increase in MoU is 43%. (This figure is available in full color at <http://www.mrw.interscience.wiley.com/erfme>.)

or blocked channels. CDMA systems operate in an interference-limited scenario, where the maximum cell radius is determined by capacity considerations. A reduction of receiver noise can be translated into increased capacity and MoU. The replacement of conventional front ends with superconducting ones in 11 CDMA cell sites has, resulted in an impressive average MoU increase of 43% (Fig. 18).

Third-generation (3G) systems will offer high-burst-rate packet communications in addition to high-quality voice and medium-rate data. IMT-2000, the standard for 3G systems adopted by the International Telecommunication Union (ITU), identifies two frequency bands, 1885–2025 MHz and 2110–2200 MHz, which will operate with wideband CDMA (WCDMA) protocol. Currently, portions of these bands are being used by 2G systems, and it is expected that the coexistence of 2G and 3G systems will become a new interference problem.

For example, Japanese 2G Personal Handyphone System (PHS) base stations employ a frequency band that is only 0.55 MHz away from the lowest 20-MHz IMT-2000 block. PHS cell sites are present every 300 m in cities and suburbs in Japan. This situation results in increased BER, increased mobile transmit power and reduced coverage, capacity, and bandwidth. Since the signal quality is degraded, cellphones end users tend to speak loud increasing the transmit power. As a result, the signal-to-interference ratio (SIR) at the base station drops and the cell collapses. When the superconducting front end is introduced, the interference is filtered out and the cell normal operation can be restored (19).

There are other examples where superconducting front ends offer clear advantages over conventional ones. In Europe, the Universal Mobile Telecommunications System (UMTS) must accommodate high-power-level transmit signals adjacent to receive-only bands in WCDMA. In

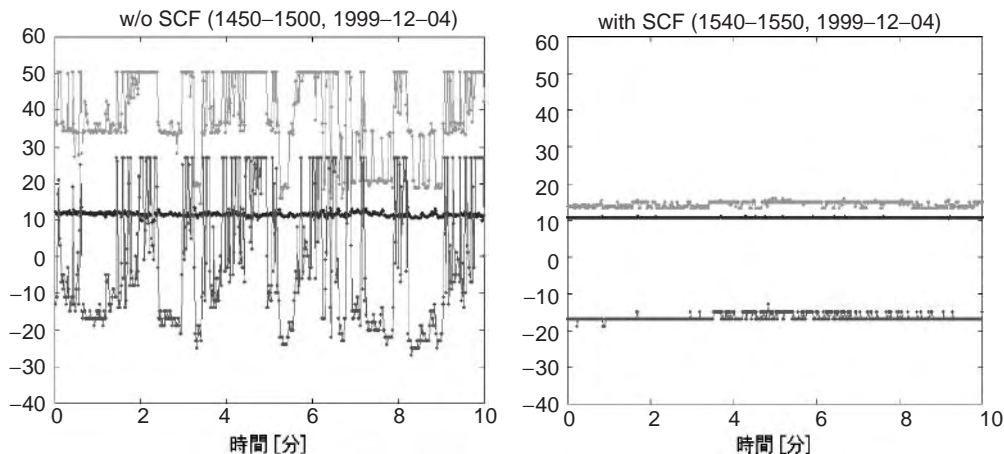


Figure 19. A 3G WCDMA cell site is completely restored to its normal levels of operation after the superconducting front end is introduced. The plotted signals as a function of time in minutes are base-station interference [dBμ] (green), base-station signal: interference ratio (SIR) [dB] (yellow), and mobile transmit power [dBm] (red). (This figure is available in full color at <http://www.mrw.interscience.wiley.com/erfme>.)

some regions, new WCDMA bands will be located as close as 2 MHz to the band edge of existing PCS bands. Another example is hierarchical cell structures where uplink signals of nearby microcells arrive at the macrocell (umbrella cell) at a much higher power level than do the uplink signals of remote users in the macrocell. Acceptable wireless transmission of data requires at least four orders of magnitude lower BER than what is needed for voice transmission. Superconducting front ends can provide this enhanced BER without raising the power level in the wireless network, which is a significant benefit in 3G WCDMA.

BIBLIOGRAPHY

1. G. Tsuzuki, S. Berkowitz and S. Ye, Ultra-selective 22-pole 10-transmission zero superconducting bandpass filter surpasses 50-pole Chebyshev filter, *IEEE Trans. Microwave Theory Tech.* **50**: 2924–2929 (Dec. 2002).
2. A. E. Atia, and A. E. William, Narrow bandpass waveguide filters, *IEEE Trans. Microwave Theory Tech.* **MTT-20**: 258–265 (April 1972).
3. H. C. Bell, Jr., Canonical asymmetric coupled resonator filter, *IEEE Trans. Microwave Theory Tech.* **MTT-30**: 1335–1340 (Sept. 1982).
4. J. F. Liang, C. F. Shin, Q. Huang, D. Zhang, and G. C. Liang, HTS microstrip filters with multiple symmetric and asymmetric prescribed transmission zeros, *IEEE MTT-S Int. Microwave Symp. Digest*, June 1999, Vol. 4, 1551–1554.
5. G. L. Matthaei, L. Young, and E. M. T. Jones, *Microwave Filters, Impedance-Matching Networks, and Coupling Structures*, Artech House, Norwood, MA, 1987.
6. R. J. Cameron, General coupling matrix synthesis methods for Chebyshev filtering functions, *IEEE Trans. Microwave Theory Tech.* **MTT-47**:433–442 (April 1999).
7. S. Amari, Synthesis of cross-coupled resonator filters using an analytical gradient-based optimization technique, *IEEE Trans. Microwave Theory Tech.* **MTT-48**:1559–1564 (Sept. 2000).
8. H. -T. Hsu, H. -W. Yao, K. A. Zaki, and A. E. Atia, Computer-aided diagnosis and tuning of cascaded coupled resonators filters, *IEEE Trans. Microwave Theory Tech.* **MTT-50**:1137–1145 (April 2002).
9. K. Saito, N. Sakakibara, Y. Ueno, Y. Kobayashi, D. Yamaguchi, K. Sato, and T. Mimura, 264 MHz HTS lumped element bandpass filter, *IEICE Trans. Electron.* **E83-C**(1):15–19 (Jan. 2000).
10. J. Hong, and J. Lancaster, 8-pole superconducting quasi-elliptic function filter for mobile communication application, *Proc. 1998 IEEE Int. Microwave Symp.* TU4E, Baltimore, June, 1998.
11. K. F. Raihn, R. Alvarez, J. Costa, and G. L. Hey-Shipton, *IEEE MTT-S Int. Microwave Symp. Digest*, WE1C-3, June 2000.
12. S. Ye, and C. Sans, New advances in HTS microstrip filter design, *IEEE MTT-S Int. Microwave Symp. Digest*, June 2003.
13. G. Tsuzuki, M. Suzuki, and N. Sakakibara, Superconducting filter for IMT-2000 band, *IEEE Trans. Microwave Theory Tech.* **48**:2519–2525 (Dec. 2000).
14. R. B. Hammond, Cryogenic subsystems for wireless base stations, Superconductor Technologies, Inc. IMS2002 Workshop, June 7, 2002, Seattle, WA; available online at www.suptech.com.

MICROWAVE SWITCHES

ROBERT H. CAVERLY
Villanova University
Villanova, Pennsylvania

1. INTRODUCTION

Modern microwave systems often require the routing of microwave signals to different locations or subsystems. This signal routing is frequently controlled electronically, and strict system requirements often require rapid signal routing. The system component used to control this flow of microwave energy is the *microwave switch*. Depending on the application, these devices must be able to rapidly switch microwave signals whose power levels range from the microwatt range in receiver applications to hundreds of kilowatts in high-power radar applications.

A common use of a microwave switch is to connect a single antenna to either a receiver or a transmitter. Figure 1 is a schematic diagram of a transmit/receive switch or *TR switch*. When switch SW_A is closed (connected) and switch SW_B is open (disconnected), the receiver is directly connected to the antenna. The transmitter is connected to antenna when SW_B is closed and SW_A is open.

2. MICROWAVE SWITCH TERMINOLOGY AND TYPES

An ideal microwave switch in the connected or ON state should exhibit no losses. These losses will absorb the microwave energy as it flows through the switch. The ideal microwave switch in the disconnected or OFF state will not allow transmission of energy. In reality, losses do occur in the ON-state switch, and these losses must be minimized through careful selection and design of the switch element. The term that microwave engineers use to describe these ON-state switch losses is switch *insertion loss*. In the OFF-state switch, some transmission of energy does occur, but can be minimized by careful selection and design. For the OFF-state switch, the measure of the level of signal transmission is termed switch *isolation*. The microwave engineer attempts to design microwave switches with low insertion loss and high isolation over the entire frequency and power range of operation. Often the engineer finds that by improving one switch property, another one is adversely affected, so engineering tradeoffs are always a part of the design process. Several design passes using computer-aided design tools and construction of actual switch prototype circuits are usually needed before the optimum microwave switch configuration is determined.

Modern microwave switch applications require the actual switching action be done electronically rather than mechanically (as in a light switch), allowing a digital computer system, for example, to control the switching operation. The utility of electronically controlled microwave switches can be shown by an example based on the TR switch shown in Fig. 1. Consider a radar transmitter sending out pulses of energy that will be reflected back to the receiver if an object is encountered. If the object is

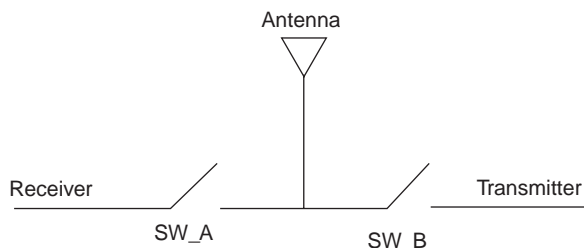


Figure 1. Schematic diagram of a microwave TR switch.

25 km away from the radar site, the travel time for a single radar pulse to go from the transmitter to the object and back to the receiver is approximately $130\ \mu\text{s}$. The microwave switch must switch the radar antenna between the high-power radar transmitter and the receiver in this short time period (or shorter if the object is closer), and the switch must be capable of repeating this action hundreds of times each second.

Two classes of electronically controllable microwave switching elements are widely used: *solid-state switch* elements based on specialized diode and transistor elements and *ferrite switch* elements based on magnetic material that controls the direction of microwave energy flow. Solid-state devices are used in applications such as battery-operated radio systems, nuclear magnetic resonance imaging systems, and electronically steered antenna arrays. Ferrite switches are usually found only in applications such as high-power radar systems where hundreds of kilowatts of power must be controlled. A third class of electronically controllable microwave switching element is the solid-state MEMS (microelectromechanical system) switch. Although this type of switch is fabricated using processes similar to those for diode and transistor-based solid-state switches, its operation is significantly different from these other switch elements to be warrant separate discussion.

Solid-state switching devices are further divided into two types: those based on two terminal switch elements such as p-i-n diodes (fabricated using silicon or gallium arsenide semiconductors) or three-terminal switch elements such as gallium arsenide metal semiconductor field-effect transistors (MESFETs). Both types of solid-state switching elements are physically small. Microwave p-i-n diodes that are used for low power but very high frequency may be as small as $10\ \mu\text{m}$ in diameter and $25\ \mu\text{m}$ in length. Higher-power diodes can be $100\ \mu\text{m}$ in diameter and $250\ \mu\text{m}$ thick to aid in handling the additional power requirements. FET switch elements may reside on a square of semiconductor material no larger than $1000\ \mu\text{m}$ on a side. A large RF MEMS switch matrix array can be placed on a single semiconductor die since the physical size of the individual switch elements can be as small as $25\ \mu\text{m}$ on a side. The bulk of a microwave switch module can be taken up by the package used to contain the solid-state switch element, allowing the switch module to be handled by skilled circuit fabrication technicians or automated electronic fabrication machines. Ferrite switches are physically larger than their solid-state counterparts because of both the physical operation of the switch and the high power that the switch must handle.

Table 1. Characteristics of Common Microwave Switch Elements

Switch Type	Switching Energy	Switching Time	Power-Handling Range
Ferrite switch	High	Very slow ($\geq 100\ \mu\text{s}$)	Megawatts
FET elements	Very low	Very fast (10 ns)	Watts
MEMS	Very low	Slow (2–20 μs)	Watts
p-i-n diodes	Medium	Fast (10–50 ns)	Kilowatts

The amount of energy used to activate the microwave switch is also an important design specification. Ferrite and some p-i-n diode switch elements can control much higher powers than can FET and MEMS-based switches, but FET and MEMS switches require very little energy to activate, although MEMS switches require somewhat higher switching voltages than do the diode and transistor-based solid-state switching elements. The switching energy is unusually high in some ferrite switches because of the relatively high current required to generate the necessary magnetic field that governs ferrite operation. Table 1 summarizes some important microwave switch characteristics and table shows that selection of switch type is strongly dependent on the application. The designer must balance these specifications with other design specifications such as physical size, insertion loss, isolation, and cost.

3. MICROWAVE SWITCH MODELING

The primary design specification that a microwave switch designer considers is the switch circuit's insertion loss and isolation. Insertion loss (IL) and isolation (ISO) are defined as the level of microwave power present at the load after the switch is installed with respect to that present at the load before the switch is installed. This definition can be written mathematically as [1]:

$$\frac{\text{IL}}{\text{ISO}} = 10 \log \frac{P_{\text{La}}}{P_{\text{Lb}}} \text{ dB} \quad (1)$$

where $P_{\text{La(Lb)}}$ is the power available at the load after (before) the switch module is inserted into the system. Typical values of switch insertion loss range from 0.2 to 1.0 dB, with the higher values of insertion loss typical for microwave switch elements used at X band (8–12 GHz) and above. A good microwave switch will exhibit isolation greater than 20 dB. At low frequencies, microwave switch isolation can be greater than 80 dB depending on the actual switch configuration. Because of the nature of microwave switch elements, isolation and insertion loss often exhibit marked variations with frequency.

The microwave switch designer's task is simplified by use of *lumped-element switch modeling*. These switch models replace the actual switch with simple circuit elements that can be quickly and easily analyzed. Insertion loss and isolation for the various switch elements is computed by modeling each individual switch element as a

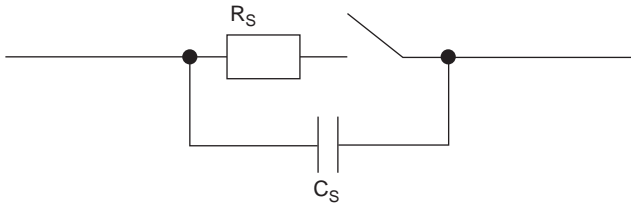


Figure 2. Simplified model for a microwave switch element, showing the ON-state resistance R_S and the OFF-state capacitance C_S .

parallel combination of an ideal switch and resistance R_S and capacitance C_S . This simple microwave switch element model is shown in Fig. 2. The utility of this model can be seen by studying the simplest microwave switch topology, the single-pole single-throw (SPST) switch. The switching elements in the SPST circuit can be placed either in series or shunt. Figure 3 shows a series connected switch element (with switch model in place), and Fig. 4 shows the shunt connected switch element. Z_0 is the source and load impedance (the so-called matched-load condition). Using the circuit diagrams shown in Figs. 3 and 4, relationships for insertion loss and isolation can be developed. For the series switch, insertion loss and isolation can be written in terms of R_S , C_S , and the operating radian frequency ω as

$$IL = 20 \log \left[1 + \frac{R_S}{2Z_0} \right] \tag{2}$$

and

$$ISO = 10 \log \left[1 + \left(\frac{1}{2\omega C_S Z_0} \right)^2 \right] \tag{3}$$

whereas for the shunt switch, insertion loss and isolation can be written as

$$IL = 10 \log [1 + (0.5\omega C_S Z_0)^2] \tag{4}$$

and

$$ISO = 20 \log \left[1 + \frac{Z_0}{2R_S} \right] \tag{5}$$

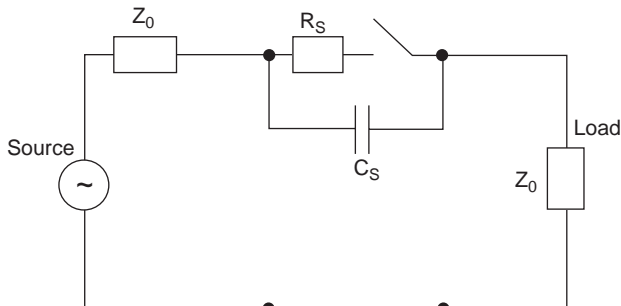


Figure 3. Series-connected SPST microwave switch showing source, load, and equivalent circuit for the switch element.

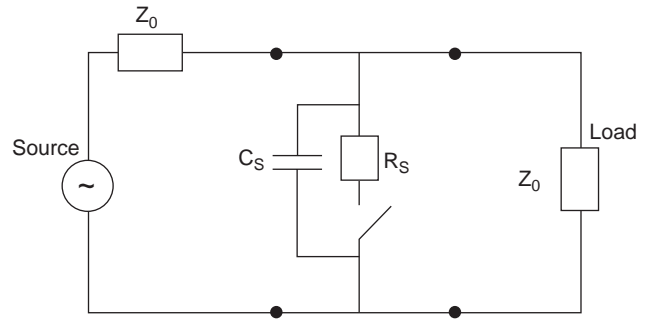


Figure 4. Shunt-connected SPST microwave switch showing source, load, and equivalent circuit for the switch element.

Insertion loss for the shunt switch is frequency-dependent because of the reactance of the shunt capacitance, whereas isolation for the series switch is the frequency-dependent parameter. Figure 5 shows the insertion loss (isolation) for the series (shunt) SPST switch as a function of resistance R_S . The data shown in Fig. 5 indicate that low insertion loss (less than 0.5 dB) occurs for resistance values of less than approximately 5Ω for the series switch. Isolation greater than 20 dB occurs for resistance values of approximately 2Ω or less for the shunt switch. Figures 6 and 7 illustrate the isolation (insertion loss) for the shunt (series) SPST 50- Ω switch as a function of frequency using the switch capacitance C_S as a parameter. Figure 6 shows that isolation of the series switch is greater than 25 dB at 1000 MHz using capacitance values less than 0.1 pF. Figure 7 indicates that a shunt switch with capacitance of 1.0 pF or less exhibits less than 0.5 dB insertion loss at 1000 MHz.

Multithrow microwave switches are designed using combinations of series and shunt elements to implement the desired switching function. The operation of a single-pole double-throw (SPDT) TR switch illustrated in Fig. 1, for example, can be predicted by replacing the two switches SW_A and SW_B by the switch element model in Fig. 2. Various applications often require more complex switch topologies, but the insertion loss and isolation of these circuits can still be estimated using the lumped-element switch model in Fig. 2. It should be noted that Fig. 2 represents

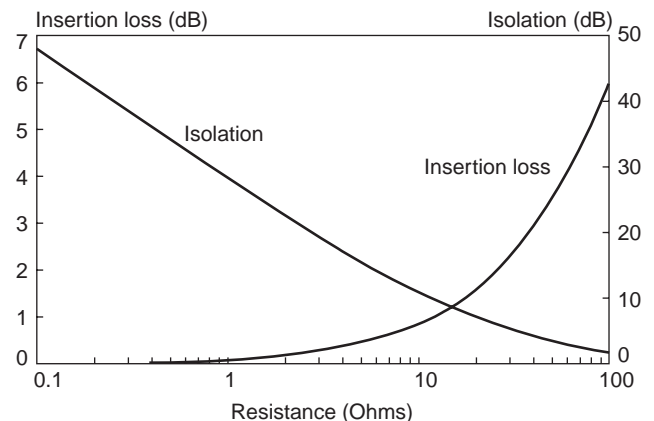


Figure 5. Insertion loss and isolation for the series and shunt SPST 50- Ω switch as a function of series resistance R_S .

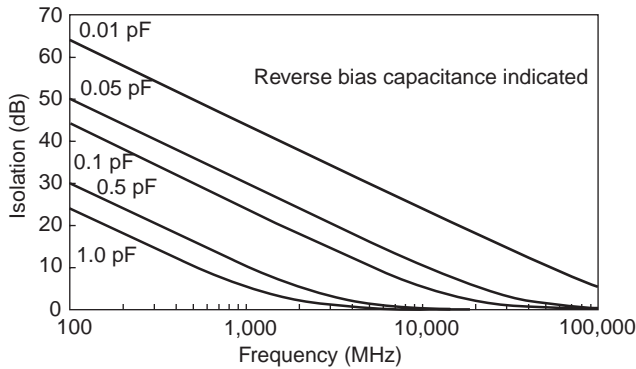


Figure 6. Isolation for the series SPST 50- Ω switch as a function of frequency using the switch capacitance C_S as a parameter.

the simplest of switch element models. Switch packaging and circuit connections introduce their own undesired properties that must be included by the microwave engineer as part of the design process. Some of these undesired or *parasitic elements* are package capacitance, contact resistance, and bond wire inductance. The parasitic elements influence both microwave switch insertion loss and isolation.

When a microwave switch is in its high-impedance state, the majority of the signal voltage is dropped across the switching element. In the low-impedance state, the current flow through the switch element can be large. These maximum voltages and currents, and the corresponding peak power, must be known at the time of the design so that suitable switch elements can be selected. These specifications can vary widely depending on the application, from low-power low-voltage requirements for receive-only applications to high-voltage high-power switching devices for radar or other transmitter applications. A wide variety of switching elements have been developed over the decades in response to these differing system requirements. The choices facing the microwave switch designer are detailed in the next section.

4. MICROWAVE SWITCH ELEMENTS

Both p-i-n diodes and FETs are the primary solid-state switch elements used in modern microwave switches. p-i-n

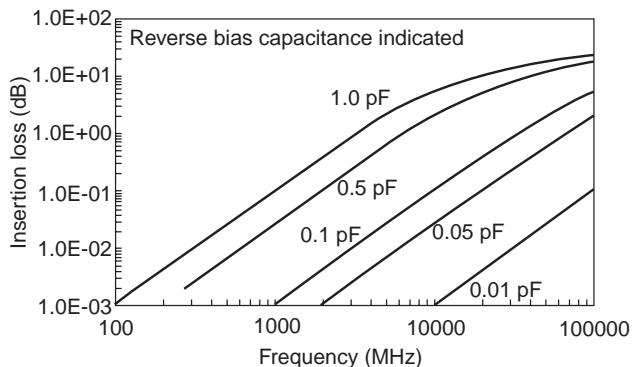


Figure 7. Insertion loss for the shunt SPST 50- Ω switch as a function of frequency using the switch capacitance C_S as a parameter.

diodes fabricated using either silicon or gallium arsenide are used in switching applications from frequencies below 1 MHz to 50 GHz and beyond, and can switch peak microwave power into the tens of kilowatts range. p-i-n diode switching elements exhibit ON- and OFF-state characteristics that are modeled using parameters illustrated in Fig. 2.

A p-i-n diode consists of a nearly intrinsic or pure semiconductor region (i region) sandwiched between heavily doped n/p-type regions. The ON-state or forward-bias resistance R_S of the p-i-n diode is a function of the i-region width W as well as the i-region carrier lifetime τ and the DC bias current flowing through the device I_0 . In its simplest form, the ON-state resistance can be written as [2]

$$R_S = \frac{W^2}{2\mu I_0 \tau} \quad (6)$$

where μ is the ambipolar carrier mobility. The i-region carrier lifetime τ is the average time a carrier exists in the i region of the device, and can vary from 1 ns in thin gallium arsenide p-i-n diodes to 10 μ s or longer in thick silicon diodes. The i-region thickness W can vary from 1 μ m or less in low-power p-i-n diodes to 200 μ m and higher in p-i-n diodes designed for high-power high-voltage applications. Under reverse-bias conditions, a capacitance is developed across the p-i-n diode's i region. Beyond a certain reverse bias voltage, termed the *punch-through voltage*, the OFF-state or *punch-through capacitance* is constant and is modeled as C_S . Gallium arsenide p-i-n diodes and some thin silicon p-i-n diodes typically exhibit punch-through with no voltage applied (*zero-bias punch-through*).

p-i-n diode switch elements are available as either discrete devices or multithrow switching modules. Switch modules provide the microwave switch designer ease of design, whereas discrete devices provide more design flexibility. Discrete devices are usually used in very high-power operation. A wide variety of discrete p-i-n switching diodes of different electrical and physical properties are commercially available. Manufacturer's data-sheets often specify their p-i-n diode products in terms of W , τ , R_S at certain bias currents (1 or 10 mA) and frequencies (usually 100 MHz), C_S at a certain reverse bias voltage (typically -6 V) and a frequency of 1 MHz, and the diode's maximum voltage rating. p-i-n diode switching modules are specified by their multithrow switch operation, operating frequency range, minimum isolation, maximum insertion loss, diode voltage rating, and maximum power handling.

A common misconception involved in specifying p-i-n diodes is the relationship between carrier lifetime τ and p-i-n diode *switching time*. These two parameters are only weakly related, with the switching time more a function of the external driver circuitry. This driver circuit must remove the i-region *stored charge* ($Q = I_0 \tau$) to completely turn the diode off or inject the necessary charge to turn the diode on. The p-i-n diode driver circuit is seldom included in switch circuit diagrams, but is fundamental to proper switch operation. Silicon p-i-n diodes cannot be driven

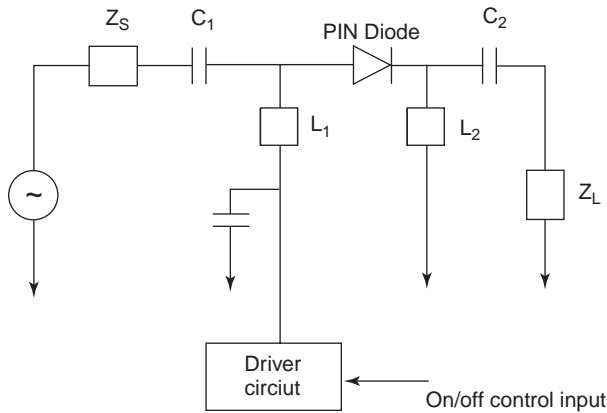


Figure 8. SPST p-i-n diode switch with driver circuit DC decoupling elements shown.

directly from digital TTL (transistor–transistor logic)-compatible signals, so a driver circuit is used to translate these digital signals into voltages and currents needed to turn the p-i-n diode on and off quickly. The driver circuit must also be AC-decoupled from the microwave switch circuit. Zero-bias punch-through diodes such as gallium arsenide p-i-n diodes can be driven directly by digital TTL-compatible signals without the need for complex driver circuitry, although AC decoupling is still required. The circuit elements used in this decoupling circuit frequently limit the usable bandwidth and switching speed of the p-i-n diode switch. Figure 8 shows an example of an SPST p-i-n diode switch circuit with driver circuit and AC decoupling elements included. Capacitors C_1 and C_2 act as DC blocks, preventing DC from reaching either the source or the load. Inductor L_1 isolates the driver circuit from the AC signal path, and inductor L_2 provides a DC return path. L_2 and C_2 may be eliminated if the load Z_L can act as the DC return path.

To improve isolation or insertion loss in p-i-n diode switch circuits, multiple diodes may be placed in series or parallel. If two shunt connected p-i-n diodes replace the one diode illustrated in Fig. 4, the effective series resistance R_S is halved, increasing the isolation by 6 dB. When two or more p-i-n diodes are used in shunt, improved switch performance can frequently be obtained by spacing the diodes a quarter-wavelength ($\lambda/4$) apart. This spacing can be obtained physically by the use of transmission lines or a lumped-element equivalent. This technique, however, can restrict the overall bandwidth of the switching module.

A significant achievement in switch module and monolithic microwave integrated circuit (MMIC) technology occurred with the development of metal semiconductor FET (MESFET) switch elements in gallium arsenide. This technology not only provides switch elements in modular form but also allows entire systems, switching included, to be fully integrated onto a single gallium arsenide integrated circuit. Modern microwave FET switches can be directly connected to their driver circuitry without the need for complex driver or decoupling circuitry since the control port of the FET, a three-terminal device, is inherently isolated from the signal ports. FETs switch faster than do p-i-n diodes since the amount of charge that must

be added or removed during switching is much less. Switching energy is lower for FET switches since only a few microamperes flow into the control line versus milliamperes in p-i-n diodes. The disadvantages of FET switches are that they are only available in switch modules and can handle power levels only in the tens of watts. Another disadvantage of FET over p-i-n diode switch modules occurs in unipolar power supply applications. Gallium arsenide FET switches require negative voltages to turn them off, so the microwave switch designer must float or DC-isolate the switch to obtain the proper voltage polarity. These DC decoupling elements complicate the switch design and can limit the switch bandwidth.

FET switch modules can operate over wider bandwidths than p-i-n diode switches. Packaged FET modules exhibit good switch performance from DC to 2 GHz. Wider bandwidths of DC to 18 GHz can be obtained using unpackaged switch chips that are directly connected (e.g., by wire bonding) to the circuit to be controlled. Gallium arsenide MESFET switch modules are specified by their multi-throw switch operation, packaging (packaged or chip form), operating frequency range, minimum isolation, maximum insertion loss, diode voltage rating, and maximum power handling. Insertion loss is usually higher and isolation usually lower for the wider-bandwidth switch modules because of engineering tradeoffs that are needed to extend the bandwidth in these devices. Gallium arsenide FET switch insertion loss typically ranges from 0.2 to 1.0 dB, with the higher values of insertion loss typical for operation at 8 GHz and above. A good MESFET switch will exhibit isolation greater than 20 dB, although isolation at lower frequencies can be greater than 80 dB.

Microwave MEMS switches utilize moving parts at the microscopic level to create the switching action. The two main MEMS switch structures are the cantilever beam and the capacitive membrane switch; the capacitive membrane switch is more widely used at microwave frequencies (Fig. 9), frequently using coplanar waveguide. Both of these switch structures rely on the application of an electrostatic force (the switch voltage, usually in the tens of volts) to overcome the force due to the spring constant of the un-deformed structure. For the capacitive membrane MEMS switch (the most common structure at microwave frequencies), the actuation voltage is a function of the switch area (A), the spring constant (k), and the gap above the actuation electrode (g) [3]:

$$V_P = \sqrt{\frac{8kg^3}{27\epsilon A}} \quad (7)$$

Using typical values of $k = 10 \text{ N/m}$, $A = 10^4 \mu\text{m}^2$, and a $2.5\text{-}\mu\text{m}$ gap yields a switch actuation voltage of approximately 23 V. Once the switch has been activated, g is reduced and the holding voltage is correspondingly less.

MEMS switches exhibit better insertion loss and isolation performance at high microwave frequencies than do their solid-state counterparts, but tend to switch at slower rates [3]. Using the typical MEMS switch values above, the membrane switch exhibits an OFF-state capacitance of approximately 35 fF (10^{-15} farads), which yields less than

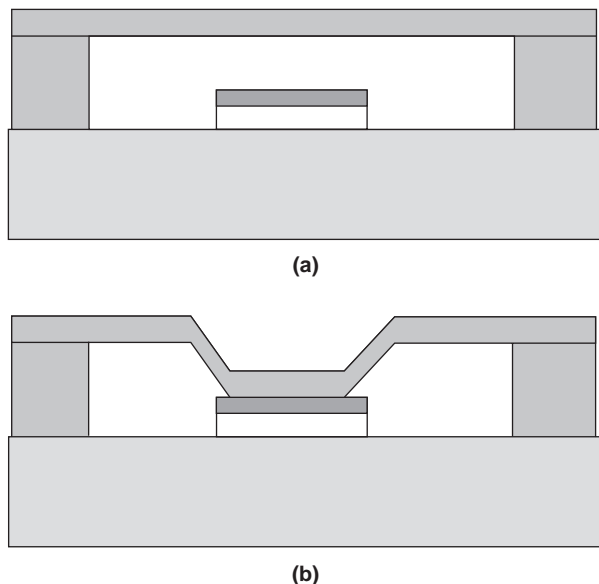


Figure 9. RF MEMS capacitive membrane switch over coplanar waveguide in its open (a) and closed (b) positions.

0.1 dB insertion loss at 10 GHz when used in a shunt configuration (Fig. 9a). When the switch is activated (Fig. 9b), the gap g is substantially reduced, increasing the capacitance by a factor of 10 or more. This increases the loss of the switch, providing the isolation between the source and the load. For a gap reduction of 50 (1.7 pF), an isolation of 10 dB can be achieved.

Ferrite switch modules have been largely replaced by semiconductor switches for all except high-power applications. Ferrite switch modules are physically large and bulky. However, they provide the only method of controlling microwave power into the megawatt levels. Peak powers of more than a megawatt can be easily switched at frequencies below 8 GHz with ferrite switches with low loss (less than 0.5 dB) and isolation greater than 20 dB. Ferrite switches based on switching circulators have been used as high as 220 GHz [4].

A common ferrite switch uses a switched *ferrite circulator* as the basic switching module. The arrow in Fig. 10 shows the direction of microwave energy flow. With one magnetic field orientation, microwave energy entering port 1 leaves port 2, and energy entering port 2 leaves port 3. By reversing the magnetic field orientation, the circulation pattern (1→2→3→1) changes to (1→3→2→1), and the circulator acts as a nonreciprocal SPDT switch. Because of the nonreciprocity of the switch, energy entering port 1 leaves port 2 but energy entering port 2 leaves port 3. A reciprocal version of this SPDT switch requires one nonreciprocal switching module and two fixed circulators [5]. Ferrite switch modules are inherently narrow band. Figure 11 shows insertion loss, isolation, and VSWR of a 35-GHz latching ferrite switch module [6], illustrating the relatively narrowband properties of the module. Ferrite switches exhibit insertion losses of less than 0.5 dB at frequencies below 12 GHz, although higher losses (up to 1.0 dB) occur at higher operating frequencies. Isolation of 20 dB or greater is typical at frequencies of 94 GHz and

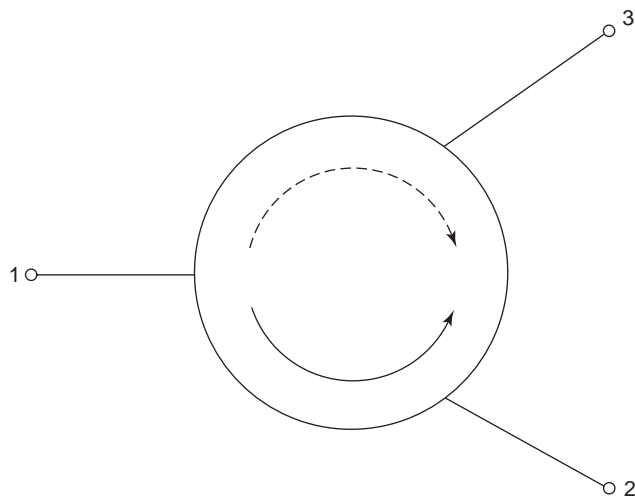


Figure 10. Microwave energy flow in a switching ferrite circulator [7] (copyright 1989, John Wiley and Sons, reprinted by permission of John Wiley & Sons, Inc.).

beyond. The bandwidth of a ferrite switch can be extended using special matching techniques [7].

Another drawback for the ferrite switch compared to the solid-state microwave switch is the ferrite switch's relatively slow switching speed. To change switch states, the magnetic field in the ferrite must be reversed, and phenomena such as material demagnetization and switching eddy currents combine to slow the switching speed. Switching speeds of several hundred nanoseconds have been achieved in some ferrite switch modules [6]. Relatively large currents are needed to induce the ferrite switch action, making them unsuitable for most battery or portable applications.

5. NONIDEAL MICROWAVE SWITCH ELEMENT OPERATION

The insertion loss and isolation are measures of the microwave switch's impact on the fundamental microwave signal. A side effect of using active microwave switch elements is their generation of unwanted signals based on the level of microwave signal energy. These so called

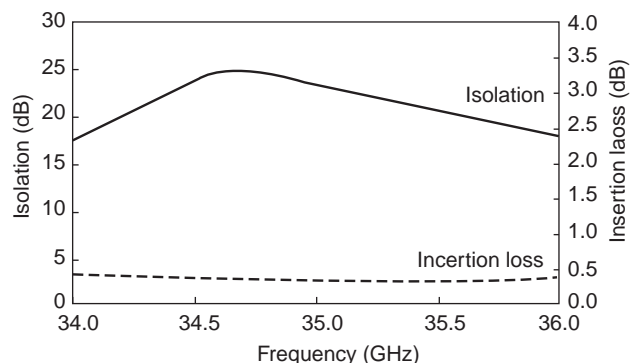


Figure 11. Insertion loss, isolation, and VSWR for a 35-GHz latching ferrite switch [6] (copyright 1966 IEEE).

nonlinear effects produce spurious signals that are harmonically related to the fundamental microwave signal, introducing *distortion* into the system. The two most widely specified microwave switch distortion products are second- and third-order *intermodulation distortion*. These distortion products are measured using the *two-tone test*, where two signals of equal amplitude but slightly different frequency (F_1 and F_2) are incident on the microwave switch. The second-order nonlinear effects in the microwave switch generate spurious signals at frequencies $2F_1$ and $2F_2$ (*harmonic distortion*) and at frequencies $F_1 \pm F_2$ (*intermodulation distortion*). The third-order nonlinear effect generates signals at frequencies $3F_1$ and $3F_2$ (*harmonic distortion*), and $2F_1 \pm F_2$ and $2F_2 \pm F_1$ (*intermodulation distortion*). The most difficult distortion terms to manage are the third-order intermodulation products ($2F_1 - F_2$ and $2F_2 - F_1$) because these frequency components can be close to the fundamental frequencies F_1 and F_2 , and hence are difficult to remove by filtering. Second- and third-order microwave switch intermodulation distortion is frequently specified using distortion intercept points IP2 and IP3. The intercept point is determined by measuring the distortion power with respect to the power in the fundamental [8]:

$$\text{IP2} = P_F + R_{ab/a} \quad (8)$$

$$\text{IP3} = P_F + 0.5R_{2ab/a} \quad (9)$$

where P_F is the fundamental power (in dBm), and $R_{ab/a}$ and $R_{2ab/a}$ are the relative second- and third-order distortion powers (in dBc), respectively. Equations (8) and (9) also show that the distortion power can be computed given the distortion intercept point and fundamental power level. Less distortion is introduced into the system by using high intercept point switches or switching elements.

For a single-series p-i-n diode switch, the ON-state (forward-biased p-i-n diode) IP2 and IP3 have been found to be a function of QF/R_S , where Q ($I_0\tau$) is the i-region stored charge, F is the operating frequency, and R_S is the series resistance. For a series connected p-i-n diode switch, IP2 and IP3 have been computed as [8]

$$\text{IP2} = 34 + 20 \log \left(\frac{Q_{nc} F_{\text{MHz}}}{R_S} \right) \text{dBm} \quad (10)$$

$$\text{IP3} = 24 + 15 \log \left(\frac{Q_{nc} F_{\text{MHz}}}{R_S} \right) \text{dBm} \quad (11)$$

where Q_{nc} is the i-region stored charge in nanocoulombs, F is the frequency in MHz, and R_S is the series resistance in ohms. This ratio can be increased by increasing the i-region stored charge (high DC bias current or large carrier lifetime) and/or lowering the series resistance. Distortion also improves as the frequency of operation increases. The underlying cause of forward-biased p-i-n diode distortion is modulation of the i-region DC stored charge by the microwave signal.

The p-i-n diode also introduces distortion in its OFF state (reverse bias) due to modulation of the reverse bias capacitance C_S by the microwave signal. Second- and

third-order distortion for the series-connected p-i-n diode switch can be estimated from the reverse-bias capacitance-voltage characteristic, specifically the first and second derivative (C'_S and C''_S , respectively) [9]:

$$\text{IP2} = \frac{1}{32(C'_S)^2 Z_0^3 (\omega_1 + \omega_2)^2} \quad (12)$$

$$\text{IP3} = \frac{1}{12(C''_S) Z_0^2 (2\omega_1 + \omega_2)} \quad (13)$$

Since multithrow switch circuits have combinations of ON- and OFF-state p-i-n diodes for each switch state, all diode distortion contributions must be included for an accurate microwave switch distortion prediction. The ON-state p-i-n diode usually contributes more distortion than do p-i-n diodes in the OFF state.

Gallium arsenide MESFET switches also introduce distortion [10]. ON-state MESFET switch distortion is caused by modulation of the conducting channel region by the applied microwave signal. In the OFF state, distortion is generated by variations in the gate-drain and gate-source capacitance (C_{GD} and C_{GS} , respectively) by the applied signal. Figure 12 shows ON-state IP2 and IP3 versus frequency for a typical $1000 \times 1\text{-}\mu\text{m}$ series-connected MESFET switch. The transition region for the distortion occurs in the vicinity of $R_B(C_{GS} + C_{GD})$, where R_B is the gate bias resistor. In the OFF state, MESFET switch distortion increases with increasing frequency. Figure 13 shows IP2 and IP3 for a gallium arsenide MESFET SPST switch. Typical IP2 (IP3) values range from 80 dBm (50 dBm) for 2-GHz SPDT gallium arsenide MESFET switch modules to 65 dBm (40 dBm) for 18-GHz switch modules. Similar to p-i-n diodes, MESFET switch ON-state distortion is usually much larger than distortion in the OFF state. Since gallium arsenide MESFET switches are typically available only in module form, IP2 and IP3 are specified only for the ON state.

The ferrite circulator will generate intermodulation distortion as well. The two main sources of nonlinearity in the ferrite circulator are due to uniform precession of the ferrite magnetization and by the presence of spin

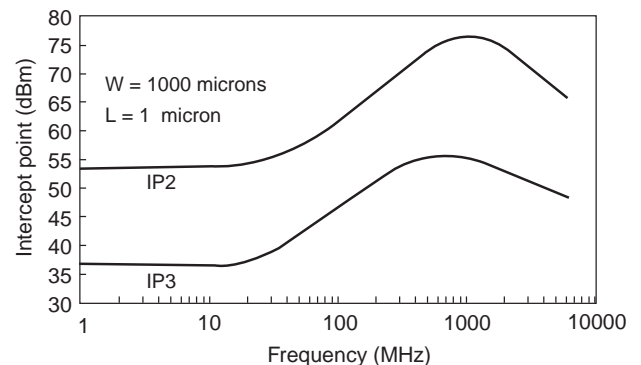


Figure 12. Simulated second- and third-order distortion intercept points (IP2 and IP3, respectively) for the ON-state series-connected GaAs MESFET SPST switch (reprinted with permission from *Microwave Journal*, Sept. 1994).

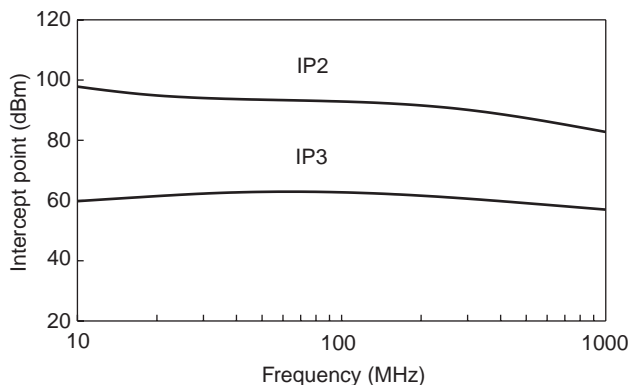


Figure 13. Simulated second- and third-order distortion intercept points (IP2 and IP3, respectively) for the OFF-state series-connected GaAs MESFET SPST switch (reprinted with permission from *Microwave Journal*, Sept. 1994).

waves [11]. Third-order intermodulation distortion has been shown to improve with increasing frequency, similar to the behavior of the p-i-n diode. However, the amount of distortion introduced by the ferrite is significantly lower than that introduced by either the p-i-n diode or MESFET switch element. Since the switching ferrite circulator is used at high power levels, the low distortion behavior of the ferrite device is an asset.

6. OTHER MICROWAVE SWITCH ELEMENTS

Semiconductor and ferrite microwave switches require direct-wired connections to control their switch state. Optical control of microwave switches has been investigated by a number of workers. The two most common types of optically controlled switches use bulk semiconductor [12] and p-i-n diodes [13,14]. Bulk semiconductor switches, or photoconductive semiconductor switches, use light energy (usually from a high-power laser) to modulate the conductivity of the material. The most common optically controlled microwave switch circuit topology has a transmission-line gap with the bulk semiconductor within the gap (Fig. 14). The transmission-line gap can range from a few micrometers in low-power applications to millimeters in high-power or high-voltage applications. During the OFF (dark) state, the high resistivity of the bulk semiconductor effectively isolates the two transmission

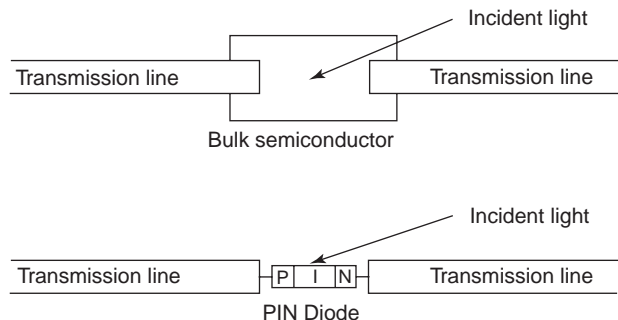


Figure 14. Optically controlled microwave switches: bulk semiconductor and reverse-biased p-i-n diode physical layouts.

lines. The switch is activated by an intense beam of photons directed on the semiconductor material, which quickly generates electron-hole pairs in the material, increasing the semiconductor’s conductivity, and providing a low loss connection between the two transmission lines. When the light source is removed, the electron-hole pairs recombine, returning the switch to its OFF state. This turnoff process is dependent on the carrier lifetime of the electron-hole pairs in the semiconductor material. Various semiconductor processing techniques such as introducing a high density of recombination centers have been developed to lower the carrier lifetime to speed the switching action.

Optically controlled p-i-n diode switches also rely on electron-hole pair generation by an incident beam of photons as well. The OFF state (high isolation) is accomplished with a reverse-biased p-i-n diode bridging the transmission line gap instead of the bulk semiconductor material (Fig. 14). The switch is turned on with a beam of photons focused on the i region, causing the generation of electron-hole pairs. The i-region conductivity dramatically increases, thereby creating a low-loss connection across the gap. Carriers swept out of the i region by the electric field are continually replenished by the optically generated carriers. This same field quickly sweeps all the electron-hole pairs out of the i region when the light source is removed, rapidly returning the microwave switch to its OFF state. These switches can be activated in less than 100 ps and turned off in several nanoseconds [13,14].

Considerable research and development has been done in developing entire microwave communications systems on a single integrated circuit [called *system on a chip* (SOC) or *single-chip radio* (SCR)]. The recent technologies of interest have been silicon because of the integrability of the high-frequency section with digital control and signal processing components. The microwave switch elements of interest in SOC research are primarily based on MOS, BiCMOS, and MEMS silicon technologies. Silicon MOSFET RF circuit topologies mimic those of their gallium arsenide counterparts, but since the current-carrying characteristics of silicon MOSFETs are poorer than gallium arsenide MESFETs, the resulting transistor sizes are larger and therefore the frequency response of these RF control elements is poorer. The silicon MOSFET also does not handle as much power as the gallium arsenide MESFET without creating large signal distortion. However, with silicon technologies approaching 100 nm (10^{-7} m) gate widths, these devices are being used in applications up to several gigahertz [15].

Microwave-switching FETs based on other technologies such as silicon germanium (SiGe) have shown promise up to 5 GHz in switching applications [16]. Higher-power microwave switch technologies based on so-called wide-band-gap semiconductors (silicon carbide and gallium nitride) have been proposed and studied and show promise in this area [17].

REFERENCES

1. P. Rizzi, *Microwave Engineering: Passive circuits*, Prentice-Hall, Englewood Cliffs, NJ, 1988.

2. J. White, *Semiconductor Control*, Artech House, Dedham, MA, 1977.
3. G. M. Rebeiz and J. B. Muldavin, RF MEMS switches and switch circuits, *IEEE Microwave Mag.* **2**(4):59–71 (2001).
4. J. A. Rabel, S. W. Schell, and D. Davidson, 140 and 220 GHz ferrite components, *IEEE 1985 Int. Microwave Symp. Digest*, June 1985, pp. 233–236.
5. A. Calvin, Reciprocal and nonreciprocal switches utilizing ferrite junction circulators, *IEEE Trans. Microwave Theory Tech.* **11**(5):217–218 (May 1963).
6. W. C. Passaro and J. McManus, A 35 GHz latching switch, *IEEE Trans. Microwave Theory Tech.* **14**(12):669–672 (Dec. 1966).
7. E. Schwarz, Broadband matching of resonant circuits and circulators, *IEEE Trans. Microwave Theory Tech.* **16**(3):158–165 (March 1968).
8. R. Caverly and G. Hiller, Distortion in p-i-n diode control circuits, *IEEE Trans. Microwave Theory Tech.* **MTT-35**(5):492 (May 1987).
9. R. Caverly and G. Hiller, Distortion in microwave and RF switches by reverse biased PIN diodes, *IEEE 1989 Int. Microwave Symp. Digest*, Vol. III, June 1989, pp. 1073–1076.
10. R. Caverly, Distortion in GaAs MESFET switches, *Microwave J.* (Sept. 1994).
11. Y. Wu, W. Ku, and J. Erickson, A study of nonlinearities and intermodulation characteristics of 3-port distributed circulators, *IEEE Trans. Microwave Theory Tech.* **24**(2):69–77 (Feb. 1976).
12. C. H. Lee, Picosecond optics and microwave technology, *IEEE Trans. Microwave Theory Tech.* **MTT-38**(5):597–607 (May 1990).
13. P. Stabile, A. Rosen, and P. Herczfeld, Optically controlled lateral PIN diodes and microwave control circuits, *RCA Rev.* **47**:443–456 (Dec. 1986).
14. A. Kim, L. Domenico, R. Youmans, A. Balekdjian, M. Weiner, and L. Jasper, Monolithic photoconductive ultra-wideband RF devices, *1993 IEEE Int. Microwave Symp. Digest*, 1993, pp. 1221–1224.
15. R. H. Caverly, Linear and nonlinear characteristics of the silicon CMOS monolithic 50-ohm microwave and RF control element, *IEEE J. Solid-State Circuits* **34**(1):124–126 (1999).
16. R. Tayrani, M. Teshiba, and G. Sakamoto, A broadband (1–20 GHz) SiGe monolithic SPDT switch, *Proc. 2002 IEEE GaAs IC Symp.*, 2002, pp. 255–258.
17. R. H. Caverly, N. V. Drozdovski, C. Joye, and M. Quinn, Gallium nitride: Use in high power control applications, *Proc. IEEE 2002 GaAs IC Symp.*, Oct. 2002, pp. 131–134.
18. Y. Ayasli, Microwave switching with GaAs FETs, *Microwave J.* **25**:61–74 (Nov. 1982).
19. A. Gopinath and J. B. Rankin, GaAs FET RF switches, *IEEE Trans. Electron. Devices* **ED-22**:1272–1278 (July 1985).
20. D. Fryklund and R. Walline, Low cost, low drain, high speed, wideband GaAs MMIC switches, *Microwave J.* **28** (1985).
21. Cumulative index: 1953–1980, *IEEE Trans. Microwave Theory Tech.* **MTT-29**(6) (June 1981).
22. Cumulative index: 1981–1988, *IEEE Trans. Microwave Theory Tech.* **MTT-37**(6) (June 1981).
23. Microwave Digital Archive: 1953–1998, with supplemental updates, IEEE Microwave Theory and Techniques Society, available online from the IEEE at <http://www.ieee.org>.

FURTHER READING

Several excellent publications on microwave switches are available for further reading. The classic treatment of p-i-n diode switches can be found in Ref. [2]. For gallium arsenide MESFET switches, the classic papers in the field are in Refs. [18, 19, 20]. Since ferrite switches are usually based on circulator technology, the reader is encouraged to read the sections on ferrite devices elsewhere in the encyclopedia. A good overview of the use of MEMS for microwave switches can be found in Ref. [3]. The most widely used research publications containing information on microwave switches are the *IEEE Transactions on Microwave Theory and Techniques* and the *Microwave Journal*. The *Transactions on Microwave Theory and Techniques* has cumulative indices listing the *Transactions'* publications from 1950 to 1988 [21, 22]. A digital archive of all publications from the IEEE Microwave Theory and Techniques Society from 1953 to the present is also available [23]. Application notes from suppliers of microwave switch elements and modules are also good sources of design information.

MICROWAVE TUBES

VICTOR L. GRANATSTEIN
University of Maryland
College Park, Maryland
ROBERT K. PARKER
Naval Research Laboratory
Washington, D.C.

Microwave tubes are devices that generate or amplify electromagnetic radiation in the frequency range of 0.3–300 GHz (microwave frequencies); they are based on the interaction between the electromagnetic radiation and a stream of electrons inside a vacuum envelope (the tube). Compared with solid-state microwave devices, microwave tubes operate at much higher power levels. Average output power ratings for state-of-the-art, single microwave tubes or solid-state devices are plotted versus frequency in Fig. 1 for the decades from 1950 to 1990. It can be seen that in 1990 microwave tubes were 1000 times more powerful than the most powerful solid-state devices at a frequency of 1 GHz, and 100,000 times more powerful at a frequency of 100 GHz.

Because of their compactness, solid-state devices are usually the preferred choice for low-power systems, with microwave tubes preferred in high-power systems. The breakpoint comes for system average output power of approximately 100 W. There, the greater efficiency of microwave tubes (typically, 50% vs. 25% for solid-state devices) results in a more compact overall system when a microwave tube output stage is combined with a smaller power supply.

The superior efficiency of microwaves may be understood from the fact that in vacuum the electrons do not pass through a background material that would impeded

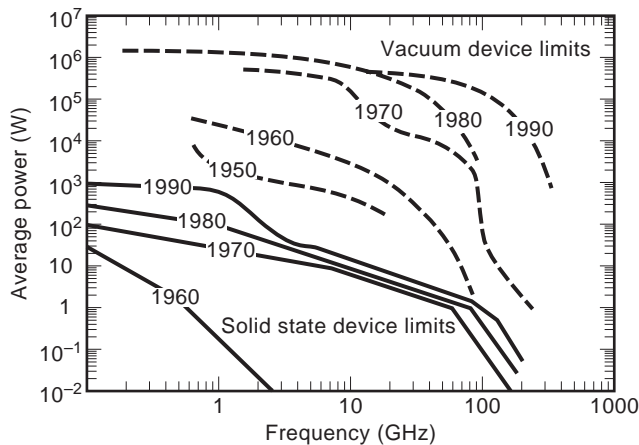


Figure 1. Histogram of power available from a single microwave oscillator or amplifier as a function of frequency. The solid lines represent solid-state device limits. The dashed lines represent vacuum electronic device limits.

their movement. Thus, the heating of a background material is not a limiting factor of high-power operation. Also, the electron trajectories are not randomized by collisions with a background material so that after passing through the microwave generation region the energy spectrum of the spent electrons is concentrated in a relatively narrow energy range; this facilitates energy recovery from the spent electrons and high overall device efficiency.

1. PRINCIPLES OF OPERATION

Electrons that are accelerated (or decelerated) emit electromagnetic radiation. However, unless the positions of the electrons form an ordered pattern (bunching), the emitted radiation will be incoherent; that is, the phase of the electromagnetic wave emitted by an electron will be random compared with the phases of the waves emitted by the other electrons. To achieve powerful radiation the emitted waves must add up in phase (coherent radiation), and this requires bunching.

The microwave tube contains a structure (the circuit) that supports electromagnetic waves that can interact with the electronbeam to form microbunches of electrons. An unbunched electronbeam passing through the vacuum tube with axial velocity v_z is shown in Fig. 2a. The periodic axial electric field component of an electromagnetic wave (transverse magnetic mode) is also shown in this figure, and this field will exert a force on the electrons that will concentrate them into bunches as shown in Fig. 2b.

When the phase of the bunches is arranged with respect to the wave electric field as shown in Fig. 2, the electrons are decelerated. The decrease in electron energy is accompanied by an equal increase in the energy of the electromagnetic wave. This can be regarded as coherent radiation of microwaves by the electrons; the bunching is required for coherence. In order for the wave to keep extracting energy from the beam, its axial phase velocity must match the electron axial velocity; this condition is called *beam/wave synchronism*.

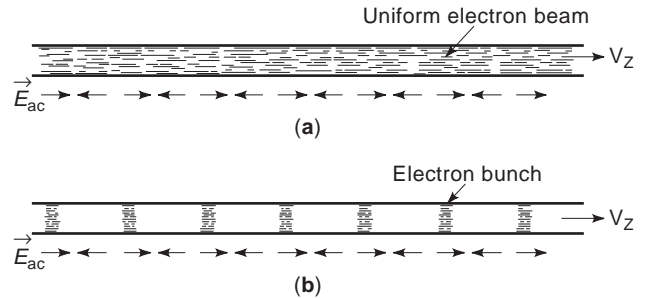


Figure 2. (a) An unbunched beam of electrons passing through a vacuum tube together with the periodic axial electric field of an electromagnetic wave; (b) a bunched electron beam with the bunches arranged to be decelerated by the wave field.

The bunching process results from excitation of the natural modes of an electronbeam with charge density ρ streaming with axial velocity v_z in the presence of a constant, externally applied, axial magnetic field B_0 . These modes of oscillation are of two types:

1. Space charge waves that involve the plasma frequency

$$\omega_p = \sqrt{\frac{e\rho}{m\epsilon_0}}$$

where e and m are, respectively, the charge and mass of an electron and ϵ_0 is the permittivity of free space

2. Cyclotron waves that involve the electron cyclotron frequency

$$\omega_c = \frac{eB_0}{m}$$

The propagation of a particular wave is described by its dispersion equation, which is a relationship between its frequency ω and its axial wavenumber β . The space charge waves on an electronbeam obey the dispersion equation

$$\omega = \beta v_z \pm \omega_p F \quad (1)$$

where F , the space charge reduction factor, depends on the finite transverse geometry of the waveguide; for an electronbeam filling a hollow cylindrical waveguide with conducting walls of radius a , we obtain

$$F = \left[1 + \left(\frac{2.405}{\beta a} \right)^2 \right]^{-1/2}$$

Thus, F approaches unity as βa becomes large. In Eq. (1), the plus sign refers to the fast space charge wave while the minus sign is for the slow space charge wave.

If the electrons also have a velocity component transverse to the axis v_\perp , then cyclotron waves may exist in addition to the space charge waves. The dispersion equation for the cyclotron waves is

$$\omega = \beta v_z \pm \omega_c \quad (2)$$

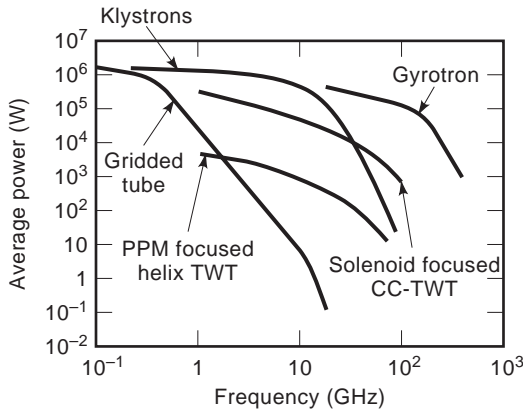


Figure 3. The average power capability of a single microwave tube versus frequency shown for some major types of microwave tube.

where the plus sign refers to the fast cyclotron wave and the minus sign refers to the slow cyclotron wave.

Finally in this section, we note that the microwave tube can be either an oscillator or an amplifier. Oscillators have no microwave input signal and effectively amplify noise; they are most commonly used in heating applications such as domestic cooking, industrial processing of materials, and heating of the ionized gas (plasma) in a controlled fusion reactor to the temperature required for thermonuclear ignition. Amplifiers do have a microwave input signal that is strengthened by its interaction with the electronbeam to produce an output signal that is much stronger than the input; the output signal tracks the frequency and phase of

the input signal. Amplifiers are used in communications and radar systems and in other systems that require phase control, such as high-energy particle accelerators.

2. TYPES OF MICROWAVE TUBES

A number of important types of microwave tubes differ with regard to the configuration of the circuit inside the vacuum envelope and/or with regard to the electrode configuration used for generating the electronbeam. These differing configurations lead to a variety of combinations of performance characteristics (e.g., operating frequency, power, bandwidth, oscillator or amplifier operation). The average power capability of some of the more important types of microwave tubes are plotted in Fig. 3 as a function of frequency.

In Table 1 the important features and applications of each of the major types of microwave tubes is indicated. Each tube type is identified as either an oscillator or amplifier, depending on its most usual deployment; however, we have also indicated the complementary tubes that use similar configurations. We will now describe the circuit configuration, the electronbeam configuration, the process of electron bunching, and the process of microwave amplification in each of the major tube types.

2.1. Traveling-Wave Tube (TWT) Amplifiers

The configuration of a helix TWT amplifier is sketched in Fig. 4. The Pierce electron gun ideally produces a solid cylindrical electronbeam that streams through the circuit

Table 1. Major Types of Microwave Tubes

Tube Type	Circuit	Electron Beam	Advantages	Most Common Applications	Complimentary Tube
Traveling wave tube (TWT) amplifier	Periodic waveguide; helix or coupled cavity (CC)	Solid cylindrical beam produced by Pierce electron gun	Wide bandwidth	Communications; jammers	Backward wave oscillator (BWO); wide tunability; used for spectroscopy
Klystron amplifier	Resonant, small-gap cavities separated by cutoff drift tubes	Solid cylindrical beam produced by Pierce electron gun	High gain; ^a high efficiency ^b	Radar; electron accelerators for medical applications and high-energy physics research	Reflex klystron oscillator
Magnetron oscillator	Coaxial configuration of inner cathode cylinder and outer anode that contains periodic arrangement of resonant cavities	Rotating electron-beam in annular space between cathode and anode	Rugged; low-cost	Domestic cooking; industrial heating of materials	Cross-field amplifier (CFA); used in radar
Gyrotron oscillator	Resonant cavity employing high-order transverse electric mode (e.g., TE _{15,2})	Annular beam of spiraling electrons produced by magnetron injection gun (MIG)	High average power at millimeter wavelengths (30–300 GHz)	Plasma heating in controlled thermonuclear fusion research (CTFR)	Gyroklystron amplifier; used in millimeter-wave radar (35 GHz, 94 GHz)

^aGain is the ratio of power in the output microwave signal to power in the input microwave signal.

^bEfficiency is the fraction of electron beam power that is converted to microwave output power.

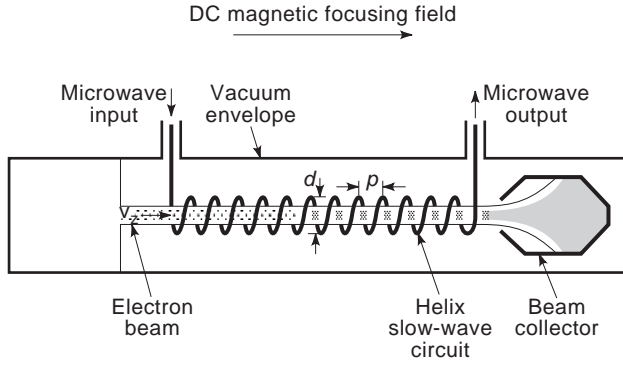


Figure 4. Configuration of a helix traveling-wave tube amplifier.

along the lines of the externally applied axial magnetic field with velocity v_z and without appreciable transverse velocity. The circuit is a helix that supports the propagation of slow electromagnetic waves; that is, the phase velocity of the wave in the axial direction is less than the speed of light, c . For a helix of period p and diameter d , the axial phase velocity is

$$v_p = c \frac{p}{\sqrt{p^2 + (\pi d)^2}}$$

and if v_p is made equal to the initial value of electron velocity, v_z , beam/wave synchronism will be achieved. Bunching and deceleration of the electrons can then occur as depicted in Fig. 2; the process can be regarded as an interaction between the slow electromagnetic wave of the helix circuit and the slow space charge wave of the electronbeam. In Fig. 5, the dispersion curves of the circuit wave and of the slow space charge wave are sketched. They are seen to be approximately in synchronism (i.e., almost touching) over a wide range of frequencies (one to three octaves) with maximum value of frequency just a little smaller than $2\pi v_z \omega / a$.

Amplification may then occur over this wide range of frequencies. The amplifier linear gain in dB is given by

$$G(\text{dB}) = -9.54 + 3.75 \frac{\omega L}{v_z} \left(\frac{\omega_p}{\omega} \right)^{3/2} \quad (3)$$

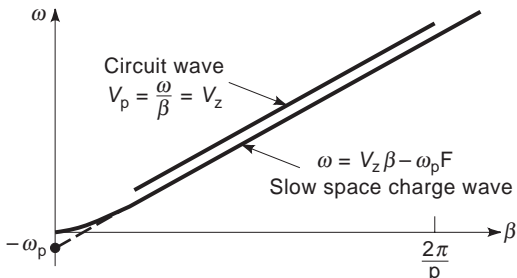


Figure 5. Dispersion curves of the helix circuit wave and the slow space charge wave.

where L is the length of the helix circuit and the first term on the right-hand side is the insertion loss caused by excitation of beam modes that do not grow.

The amplification process saturates when v_z is decreased from its initial value by deceleration to such an extent that the synchronism $v_z = v_p$ is no longer maintained to an adequate degree. Single-pass efficiency is on the order of only 10%, but this may be increased to approximately 50% by the use of techniques to recover energy in the spent electronbeam, such as depressed collectors.

The helix circuit is especially capable of wide bandwidth, but it is rather delicate and will not support a very large power rating, especially as frequency rises (see Fig. 3). The coupled-cavity periodic circuit, which also supports slow waves, is much more robust and is capable of supporting larger powers; however, its bandwidth is more limited.

A miniaturized helix TWT is used as the output power stage of the 100 W continuous-wave (CW) microwave power module (MPM). The MPM is more compact overall than a system with a solid-state output stage because of the 50% efficiency of the TWT. This tube also achieves a gain of 50 dB in a length of 22 cm and covers a frequency of range of 4.5–18 GHz. Coupled cavity TWTs have a much smaller bandwidth of only a few percent, but they have achieved 700 W average power at 94 GHz.

2.2. Magnetron

Magnetrons are the most ubiquitous of microwave tubes, used by the tens of millions in domestic microwave ovens. They also have a celebrated history, enabling high-power radar in World War II and credited for the victory of the Allies in the Battle of Britain and perhaps the entire war. The primary reason for the magnetron being the earliest radar power tube and its present widescale domestic application is the simplicity of its structure. In contrast to the TWT amplifier sketched in Fig. 4, the magnetron has no electron gun. Instead, the anode and cathode are coaxial with the annular space between them functioning as the region in which the electron stream and the electromagnetic waves interact.

A cross section of the coaxial magnetron geometry is sketched in Fig. 6. There is a DC voltage V_0 applied between the anode and cathode that produces a radial DC electric field

$$E_0 = \frac{V_0}{r \ln(b/a)} \approx \frac{V_0}{2r} \frac{b+a}{b-a} \quad (4)$$

where r is the radial coordinate and a and b are the cathode and anode radii, respectively. A DC magnetic field B_0 is applied in the axial direction. Under the influence of the crossed electric and magnetic fields, the electrons execute a cycloidal motion that can usually be decomposed into small orbit Larmor rotations at the electron cyclotron frequency and a lower azimuthal motion around the annulus with velocity

$$\vec{v}_\phi = \frac{\vec{E}_0 \times \vec{B}_0}{B_0^2} \quad (5)$$

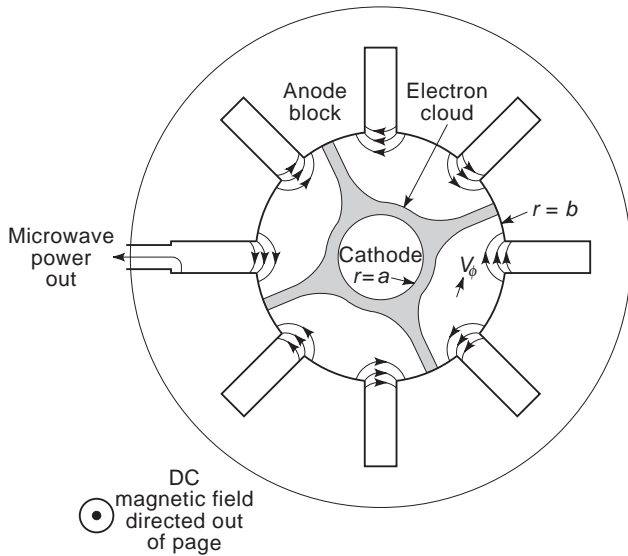


Figure 6. Configuration of a coaxial magnetron oscillator.

Cavities that are resonant at the operating frequency are cut into the anode block and arranged periodically around the azimuth. For the π mode in which the field in adjacent cavities are 180° out of phase as shown in Fig. 6, the fringing fields at radius r in the annular space appear to rotate with phase velocity

$$v_p = \frac{2\omega r}{N} \tag{6}$$

where N is the number of cavities.

An interaction between the rotating electron cloud and the electromagnetic fields can then lead to a growing electromagnetic wave in a manner related to the process in the TWT. This requires synchronism between the electron azimuthal velocity given by Eq. (5) and the phase velocity given by Eq. (6). For electrons at the center of the annular space, that is, $r = (b + a)/2$ and with E_0 related to V_0 by Eq. (4), the synchronism condition gives

$$V_0 = B_0 \omega \frac{b^2 - a^2}{N} \tag{7}$$

This type of synchronism relationship between V_0 and B_0 is known as a *Buneman–Hartree equation*.

There is also an inequality that V_0 must satisfy to ensure that the DC electron trajectories will not strike the anode. This is known as the *Hull cutoff condition* and is

$$V_0 < \frac{1}{8} \frac{e}{m} B_0^2 \frac{(b^2 - a^2)^2}{b^2} \tag{8}$$

As the electromagnetic wave grows, energy is extracted from the rotating electron cloud. The electrons in the process are forced outward to new radial positions where their potential energy is lower. The magnetron process may therefore be viewed as converting electron potential energy to electromagnetic wave energy. The electron kinetic energy, however, remains sufficient to maintain the synchronism between v_ϕ and v_p until the electron eventually reads the anode. Because of this mechanism for maintaining a synchronous interaction, magnetrons have relatively large efficiency compared with the single-pass efficiency of TWT amplifiers.

The 2.45 GHz magnetrons used in ovens for domestic cooking typically operate at better than 50% efficiency with average output power of 600 W. Other magnetrons have been developed with efficiency as great as 85% and with average power of hundreds of kilowatts.

2.3. Klystrons

Although magnetrons are high-power and efficient microwave oscillators, they are not suitable for applications that require high-gain amplifiers; for such applications klystrons have been the devices of choice. The layout of a two-cavity klystron is sketched in Fig. 7. Interaction between the electronbeam and electromagnetic waves occurs only while the electrons are passing through narrow gaps that form the capacitive regions of the resonant cavities; the drift tube between the cavities is cut off for electromagnetic waves.

Each resonant cavity has a coaxial outer region that is inductive with inductance

$$\mathcal{L} = \frac{1}{\pi} \sqrt{\frac{\mu_0}{\epsilon_0}} \ln\left(\frac{b}{a}\right) \frac{1}{\omega} \tan\left(\frac{\omega L}{2c}\right)$$

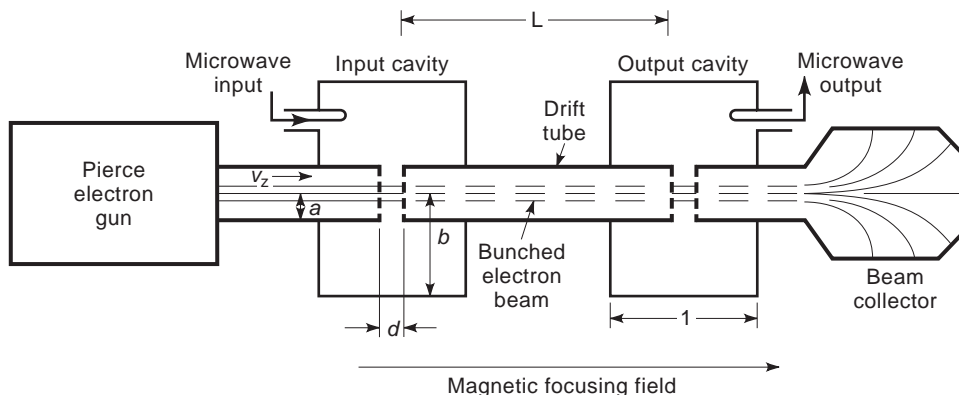


Figure 7. Configuration of a two-cavity klystron amplifier.

where μ_0 is the permeability of free space. This inductance may be considered to be in parallel with the narrow-gap region that has capacitance

$$\mathcal{C} = \frac{\epsilon_0 \pi a^2}{d}$$

The resonant frequency of the cavity will be $\omega_r = 1/\mathcal{L}\mathcal{C}$. Each cavity will also be characterized by its unloaded quality factor

$$Q_0 = \frac{\omega_r \mathcal{C}}{G_W}$$

where G_W is the wall conductance whose nonzero value is a measure of the microwave power that is lost in heating the cavity walls.

When the electron beam passes through the gap in the first cavity, it is modulated in velocity by the microwave field in the gap. This leads to excitation of both the slow space charge wave and the fast space charge wave that grow and phase interfere in the drift tube. The interference leads to axial bunching of the electron as shown in Fig. 7, and when such a bunched beam streams through the gap in the output cavity, it excites microwave fields there that may be much stronger than the fields in the input cavity.

In the regime of small signal linear operation, gain is optimum when the distance between the gaps in the two cavities is chosen to be

$$L = \frac{\pi v_z}{2 \omega_p F}$$

Then, the linear gain is

$$G = \frac{1}{\pi^2} \left(\frac{I_0}{V_0} \right)^2 \left(\frac{\omega L}{v_z} \right)^2 \frac{G_L}{G_i(G_o + G_L)^2} \tag{9}$$

where we have assumed that the gap width d is much less than the wavelength; G_i and G_o are the G_W conductances representing wall losses in the input cavity and output cavity, respectively; G_L is the conductance representing power coupled from the output cavity into the load. The electron beam voltage and current are given by V_0 and I_0 , respectively.

While it is in general much more difficult to analyze nonlinear behavior, a nonlinear analysis of the two-cavity klystron has been carried out in the limit of small space charge effects:

$$\omega_p F \ll \frac{v_z}{L}$$

In this limit the efficiency of converting electron kinetic energy to microwave energy in the output cavity has been shown to be given by

$$\eta_E = J_1(X) \tag{10}$$

where η_E is called the electronic efficiency, J_1 is the Bessel function of the first kind of order 1, and the beam

bunching parameter is given by

$$X = \frac{1 E_i d \omega L}{\pi V_0 v_z}$$

where E_i is the magnitude of the microwave electric field developed across the gap in the input cavity. The electronic efficiency as given by Eq. (10) has a maximum value of $\eta_E = 58.2\%$ when the beam bunching parameter $X = 1.841$.

Even higher efficiency, and certainly much higher gain than is indicated by Eq. (9), is attainable in klystron amplifiers with more than two cavities. A five-cavity, 11.4 GHz klystron amplifier has been developed at the Stanford Linear Accelerator Center for driving the next generation of electron/positron accelerators for high-energy physics research. It has a gain of 50 dB with peak output power of 56 MW in 1.5 μ s-long pulses. The pulse repetition frequency is 180 pps (pulses per second), the electron beam in the klystron is focused with permanent magnets, and klystron output efficiency is 60%.

2.4. Gyrotrons

As capable as klystrons are, they do become limited in power rating as frequency rises to the millimeter-wave regime (≥ 30 GHz). This is true because their cutoff drift tubes and their resonant cavities shrink in size with the wavelength. A relatively new vacuum electronics device that has operated successfully using a highly overmoded circuit is the gyrotron. The configuration of a gyrotron oscillator is sketched in Fig. 8.

The magnetron injection gun produces an annulus of electrons that travel along the circuit spiraling around the lines of the axial DC magnetic field. An important parameter of such an electron beam is the ratio of perpendicular velocity v_\perp to axial velocity v_z . Usually v_\perp/v_z is in the range of 1.0–2.0. The low value gives greater stability against spurious oscillation, while the high value gives greater efficiency.

A cross section of the electron beam is shown schematically in Fig. 9, where the electrons are initially seen to have random phase in their electron orbits. Also shown in Fig. 9 is E_θ , the azimuthal electric field of a TE_{0n} mode of the cylindrical gyrotron cavity. An electron such as 1 (in Fig. 9) will be decelerated by the electron beam, and its mass will decrease (this is a relativistic effect) leading to an increase in its cyclotron frequency as

$$\omega_c = \frac{eB_0}{m} = \frac{eB_0}{m_0} \sqrt{1 - (v_z^2 + v_\perp^2)/c^2}$$

where m_0 is the electron rest mass. Similarly, an electron with phase like electron 2 will be accelerated by E_θ , and its cyclotron frequency will decrease.

This modulation of the cyclotron frequencies can lead to phase bunching in the cyclotron orbits as shown in Fig. 10. If the electromagnetic wave is propagating axially at the same speed as the electrons and switching its polarity at the cyclotron frequency in the beam frame ($v_z = 0$), it can continuously decelerate the electrons and extract energy from their decrease in transverse velocity.

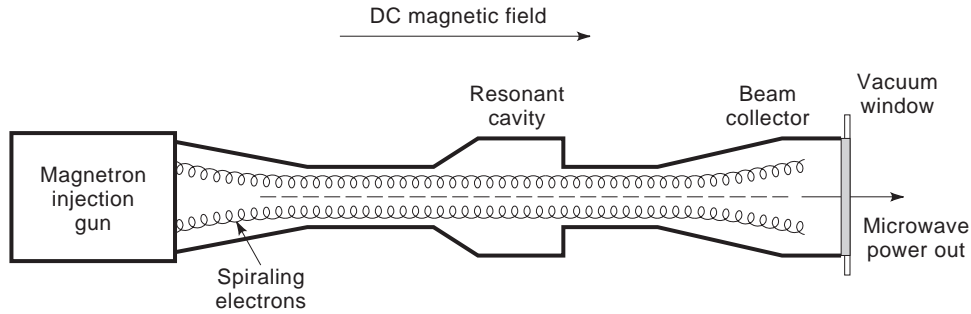


Figure 8. Configuration of a gyrotron oscillator. The strong DC magnetic field which is required is usually provided by a superconducting solenoid.

The process of phase bunching and energy extraction may be regarded as an interaction between a fast ($v_p > c$), transverse electric (TE), electromagnetic wave, and the fast cyclotron wave of the electron beam. The dispersion curves of these two waves is plotted in Fig. 11. The point of grazing intersection, where the two curves just touch, is the usual point of operation. Simultaneous solution of the two dispersion equations plotted in Fig. 11 for the case of grazing intersection gives the following equation, which may be used to design a gyrotron oscillator. The cutoff frequency of the operative TE mode is given by

$$\omega_n^2 = \omega_c^2 \frac{c^2}{c^2 - v_z^2} \quad (11)$$

Also, the axial wavenumber is given by

$$\beta = \frac{\omega_c v_z}{c^2 - v_z^2} \quad (12)$$

For example, if the electron energy, the ratio v_\perp/v_z , and the DC magnetic field were specified, then for a given $TE_{m,n,p}$ mode, Eq. (11) could be used to determine the

cavity radius and Eq. (12) could be used to determine the cavity length.

We also note that there is a threshold value that v_\perp must exceed in order to turn on the gyrotron. This is given approximately by the inequality

$$v_\perp > \left(0.1 \frac{\bar{\omega}_p^2 \omega_c^3 v_z c^2}{\beta \omega_n^4} \right)^{1/4}$$

where $\bar{\omega}_p$ is the plasma frequency averaged over the cavity cross section.

Gyrotron oscillators are quite efficient in converting the transverse kinetic energy of the spiraling electrons into microwave energy; however, the axial electron energy is not utilized. Overall, the output efficiency of a gyrotron oscillator is typically in the range of 30–40%. This is also subject to improvement by techniques for recovering energy from the spent electron beam.

Gyrotron oscillators developed for the plasma heating application have had peak output power of 1038 kW and average output power of 198 kW at a frequency of 140 GHz. There is also an active gyrotron amplifier research-and-development program; a 94-GHz gyrokystron has been produced with an average power of 2.5 kW and a bandwidth of 0.35%; the average power rating is several

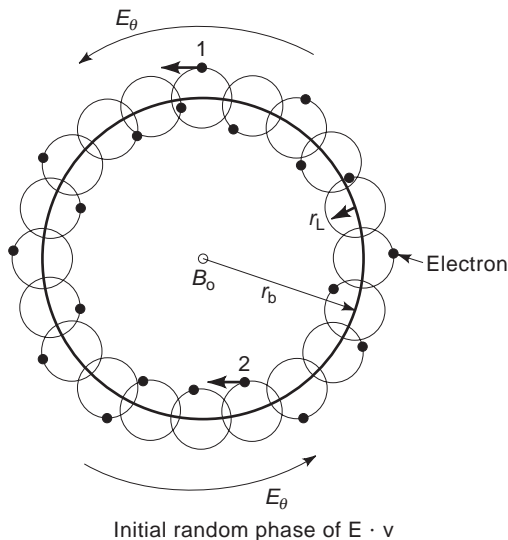


Figure 9. Cross section of the annulus of spiraling electrons in a gyrotron circuit showing the initial random phases.

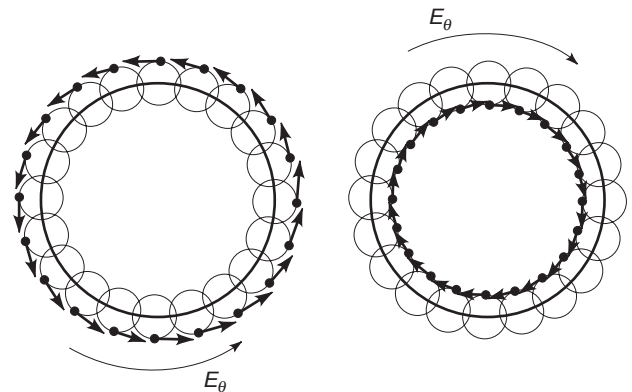


Figure 10. Electrons in a gyrotron that are phase-bunched in their cyclotron orbits. The relationship between the phase of the electrons and the phase of the azimuthal field of a TE_{0n} electromagnetic wave is shown on alternating half-cycles of the cyclotron frequency.

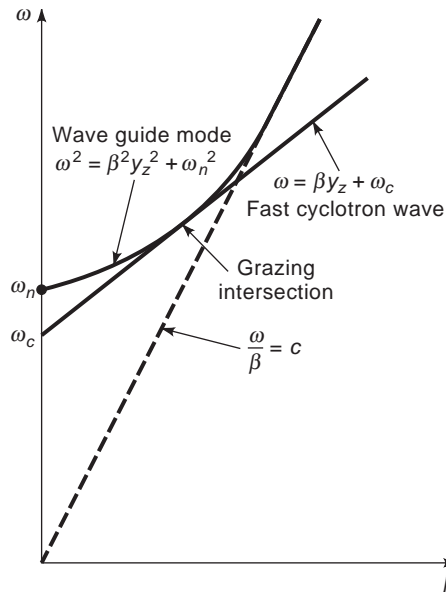


Figure 11. Dispersion curves for the TE electromagnetic wave with cutoff frequency ω_n and for the fast cyclotron wave.

times larger than the most capable 94-GHz coupled-cavity TWT amplifier. Finally, gyroklystrons are being evaluated as drivers for high-energy electron accelerators, especially if these are operated at microwave frequency much larger than at present (say, ≥ 20 GHz); a 20-GHz gyroklystron amplifier has been demonstrated with pulsed output power of 30 MW.

3. FUTURE DIRECTIONS

There is a continuing and vigorous program of research and development of microwave tubes to meet the needs of advanced applications. The microwave power module (MPM) combines three elements: (1) a low-noise, high-gain, solid-state input amplifier; (2) a compact, high efficiency, vacuum traveling-wave tube functioning as output power booster; and (3) an integrated electronic power supply. The MPM, as mentioned previously, achieves 100 W average power levels over an extended frequency range in a package that is more compact and lighter than an all solid-state system, and it is especially attractive for deployment on platforms where weight and prime power are at a premium. Current thrusts in MPM research aim at developing a 3 octave bandwidth capability that will cover the frequency range of 2–18 GHz in a single module. Work is also under way on developing a high-frequency MPM that will cover the range of 18–40 GHz; this push to millimeter wavelengths is of special interest for satellite communications. There has also been preliminary consideration of developing an MPM-like system with 100 W CW capability in the frequency range 84–104 GHz; this module would involve a serpentine folded waveguide circuit rather than a helix circuit in order to realize the 100 W average power rating at such a short wavelength (~ 3 mm).

For applications that require higher power than TWTs but do not need such an extended bandwidth, gyrotron amplifiers are being developed. For 94-GHz radar, a four-cavity, TE₀₁ mode gyroklystron is under construction that will have 40 dB gain, 0.8% bandwidth, peak power of 80 kW, and average power of 10 kW. Gyrotron amplifier circuits with wider bandwidth capabilities (e.g., gyro-TWTs and gyrotwistrons) are being considered for future development. Also, the use of higher-order modes is being considered to increase the amplifier average power.

Klystron amplifiers at 11.4 GHz for driving electron-positron colliders in high-energy physics research are also under development. The aim is to extend the 56 MW output power already achieved to 75 MW. Improvements in efficiency are also sought since the 7000 klystrons that will be required to drive the 1-TeV NeXT collider that is being planned at the Stanford Linear Accelerator Center will represent consumption of large amounts of average power.

For electron-positron colliders at 3–10 TeV energy, a higher microwave frequency will likely be chosen. Gyro-klystrons may then be the optimum choice of amplifier. Current experimental studies at 17.1 GHz are aimed at demonstrating an output peak power of 100 MW. Efficiency could be enhanced to the 50% level by using depressed collectors in this device. Design studies have indicated that similar performance might be achievable at 34 GHz with the use of a superconducting solenoid to provide the gyroklystron magnetic field. Typically, such amplifiers for driving colliders operate with a duty factor of 3×10^{-4} so that 100 MW peak power would correspond to about 30 kW average power.

Higher average power has already been achieved in gyrotron oscillators, which have operated at 200 kW average power out to frequencies of 140 GHz. These oscillators, which are intended for plasma heating in controlled thermonuclear fusion research, are currently being developed with a goal of 1 MW average output power. Lower-power (10 kW average) gyrotron oscillators are being developed at millimeter wavelengths with an emphasis on minimizing system cost so that they may be widely adopted by industry for material processing applications.

Finally, we note that progress in materials research and in computer science are enabling rapid advances in microwave tube performance. Producing vacuum output windows that would allow for the passage of very high average power microwave and fabricating focusing magnets that are compact and lightweight are among the major technological challenges in high-power microwave electronics. Diamond windows are very promising for high-power devices. High-temperature superconductors promise to make microwave tubes that require high magnetic fields (e.g., gyrotrons) practical for an increased number of applications.

Time-dependent, multimode computer codes have been developed that have effectively been applied to modeling the operation of a variety of microwave generators and have led to improving their design. The creation of an integrated computational framework for microwave tubes for initial design to production has been initiated. Extensive software tools are incorporated including thermomechanical analysis codes and electromagnetic

computational codes. This will allow for interactive study of the performance of the microwave tube being designed.

These advances will allow not only for higher power ratings of microwave tubes at higher frequencies but also for production of microwave power systems that are less costly, lighter in weight, more compact, and more efficient. The enhanced capabilities of microwave tubes will be exploited to improve the performance of radar and communication systems, to enable new industrial processing techniques and to extend the reach of basic and applied research.

FURTHER READING

- J. Benford and J. Swegle, *High Power Microwaves*, Artech House, Boston, 1992.
- R. E. Collin, *Foundations for Microwave Engineering*, 2nd ed., McGraw-Hill, New York, 1992.
- A. V. Gaponov-Grekhov and V. L. Granatstein, *Applications of High Power Microwaves*, Artech House, Boston, 1994.
- A. S. Gilmour, Jr., *Microwave Tubes*, Artech House, Boston, 1986.
- A. S. Gilmour, Jr., *Principles of Traveling Wave Tubes*, Artech House, Boston, 1994.
- V. L. Granatstein and I. Alexeff, eds., *High-Power Microwave Sources*, Artech House, Boston, 1987.
- V. L. Granatstein and C. Armstrong, eds., New vistas for microwave vacuum electronics, special issue of *Proc. IEEE*, 1998.

MILITARY COMMUNICATION

CHARLES C. WANG
TIEN M. NGUYEN
GARY W. GOO
The Aerospace Corporation

In general, military communication systems are different from ordinary systems in various specific security requirements, namely, robustness in hostile environments, shielding from adversaries, and immunity from unfriendly eaves-dropping.

Hostile environments to communications are radiofrequency interference (RFI), spoofing, jamming, and fading, either natural or human-made. RFI is unintentional but can significantly degrade performance. Spoofing is intentional and can cause a great deal of confusion. Jamming is also intentional and can completely shut down the entire communication. Fading can severely disrupt communications. A conventional communication system is not able to survive in such hostile environments. All spread-spectrum schemes can be utilized for counterattacking the measurements from spoofer and jammer. A good military communication system generally requires the addition of an antenna nulling technique that can isolate the effect of an intentional jammer or spoofer. Techniques such as channel interleaving can be employed to "whiten" the channel in the presence of fading to reduce their efficacy. Other schemes such as channel coding, diversity, or equal-

ization are also important to make a system robust under a jamming or a fading environment.

The requirement of shielding from adversaries refers to the ability of not being detected by enemies. In modern warfare, using electronic equipment for communication, position location, and so on, is crucial for tactical movement, combat, evasion, and rescue. However, an adversary can detect the signal that is intended for the friendly party. Consequently, the location of a soldier or a command post can be identified and life can be jeopardized. Therefore, low probability of detect (LPD) or low probability of intercept (LPI) becomes critical for designing military systems.

Eavesdropping is a technique used to surreptitiously intercept intelligence information from an enemy. This can always change the outcome of a battle or a war. Unlike detecting the existence of a signal, which can usually be achieved by using a radiometer, eavesdropping requires the right demodulator, decoder, and so on. In order to be immune to eavesdropping, in addition to sophisticated spread-spectrum techniques, such as direct sequence, frequency hopping and time hopping, a system needs a cryptography technique to ensure the secrecy of communications.

Other important areas in military communications include target recognition (classification) and navigation. Target recognition involves a great deal of data collection and processing. Optical remote sensing methods, such as optical lenses, laser or infrared light, is always a way of collecting target images. However, in poor weather conditions, it can be difficult if not impossible to obtain any image using optical equipment. In recent years, synthetic aperture radar (SAR) has been extensively utilized for remote sensing. Besides providing better quality and resolution of the image, the SAR system can be operated regardless of the weather condition.

The global positioning system (GPS) is a satellite-based navigation system with global coverage. In view of four GPS satellites, a GPS receiver can determine its three-dimensional position to an accuracy of better than 16 m. Greater accuracy of less than 1 meter can be achieved by using correction information from another GPS receiver at a known location. The Persian Gulf region, with its wide expanses of featureless desert, is the ideal combat environment in which to prove the value of GPS. Without a reliable navigation system like GPS, the U.S. forces could not have performed the maneuvers that contributed to the success of Operation Desert Storm in 1991.

1. UNINTENTIONAL INTERFERENCE

The radiofrequency interference (RFI) from another unintentional interferer can be substantial in a multiuser, multiservice communication system. RFI can penetrate the receiver from main-, side-, or backlobes of the receiving antenna, resulting in significant performance degradation. From the spectral point of view, the RFI can be located within the intended receiving bandwidth, referred to as the cochannel interference (CCI), or leaked from the

adjacent channels, referred to as the adjacent-channel interference (ACI).

The CCI can be initiated from intermodulations, leakage from spatial discriminated cochannel signals, and code-division multiple-access (CDMA) scenarios, such as direct-sequence spreading and frequency hopping (to be discussed later). In general, making use of channel coding to enhance the power efficiency of the desired signal can mitigate the CCI problem.

The ACI is caused by leakage of the signal power from adjacent channels next to the desired signal bandwidth. This leakage exists because no ideal brick-wall filter, which passes 100% of the signal power within a certain range of frequencies and also completely cuts off the power beyond this range, can be realized. Thus, portions of the power spectra of adjacent channels overlap each other, resulting in leakage. In addition to the channel coding, the mitigation technique for the ACI rejection includes the adoption of a bandwidth-efficient modulation scheme, such as Gaussian minimum shift keying (GMSK) or filtered phase shift keying (FPSK), which basically has a confined power spectrum with no sidelobes.

2. SPOOFING

Spoofing is defined as the purposeful degradation, denial, or deception to a receiver by an external source using a “look-alike” signal. Spoofing can cause greater damage than other intentional interference, such as jamming, because armed forces personnel may make a costly or deadly mistake in response to a deceived command without knowing it.

3. JAMMING

A jammer is a device that seeks to nullify a communication system by inserting energy into the target spectrum. The jammer power at the target antenna system can be represented by

$$J = P_j G_j / (4\pi R_j^2) B_{s/j} / L_j \tag{1}$$

where

- J = jammer power at target antenna
- P_j = RF power delivered to jammer antenna
- G_j = gain of jammer antenna
- R_j = range from jammer to target antenna
- $B_{s/j}$ = ratio between bandwidth overlap between energy inserted into the target spectrum and jammer’s transmitted spectrum
- L_j = losses in propagation between jammer and target antenna

To be effective, the jammer must act to lower the SNR, and hence the E_b/N_{total} , to raise the bit error rate (BER) of the communication system beyond acceptable levels:

$$E_b/N_{total} = E_b / (N_0 + J_0) = [(1/E_b/N_0) + (1/E_b/J_0)]^{-1} \tag{2}$$

where E_b is the signal energy per bit, J_0 is the jamming energy per bit, and N_0 is the one-sided power spectral density of the received additive white Gaussian noise (AWGN).

A measure of jammer power versus signal power is

$$J/S = (P_j G_j) / (P_t G_t) (B_{s/j}) (R_t / R_j)^2 (L_a / L_j) \tag{3}$$

where

- S = signal power at antenna
- P_t = power delivered to transmit antenna
- G_t = gain of the transmit antenna
- R_t = range from transmit to receive antenna
- L_a = losses in propagation between transmit and receive antenna

If there are differences in range between the communications transmitter and jammer from the receive antenna, a standoff distance can be computed for a known J/S value where the jammer becomes ineffective:

$$\begin{aligned} \text{Standoff distance} &= R_t [(P_j G_j) / (P_t G_t) \\ &\times (S/J) (B_{s/j}) (L_a / L_j)]^{1/2} \end{aligned} \tag{4}$$

The jammer nominally attempts to disrupt communications with minimal resource use; that is, for a given total power it will maximize jamming energy at the detector. The jammer can use several waveform strategies to maximize its effectiveness and reduce E_b/J_0 .

3.1. Broadband Noise Jamming

A broadband noise jammer, as shown in Fig. 1, employs a noise source of bandwidth B_j that covers the entire allocated spectrum B_s of the communication system under attack. The noise density is

$$\text{Noise density} = J/B_j = J_0 \quad (B_j = B_s) \tag{5}$$

3.2. Partial-Band Noise Jamming

A partial-band noise jammer (PBNJ), as shown in Fig. 2, employs a noise source that covers some fraction α of the allocated spectrum of the communication systems under attack. For given jammer power J , this raises the noise density over that part of the band:

$$\text{Noise density} = J/B_j = J / (\alpha B_s) = J_0 \quad (B_j < B_s) \tag{6}$$

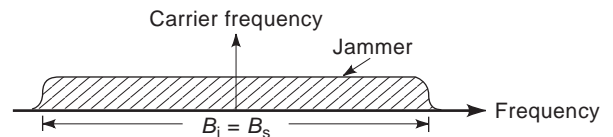


Figure 1. Spectrum of a broadband noise jammer.

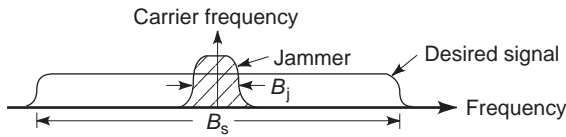


Figure 2. Spectrum of a partial-band jammer.

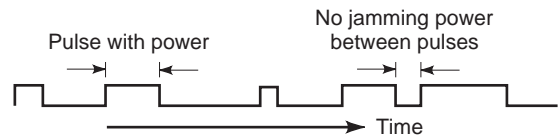


Figure 4. A pulsed jammer in time domain.

3.3. Worst-Case Partial-Band Jamming

A worst-case partial band jammer (WCPBJ) is employed against a system whose instantaneous bandwidth is less than allocated spectrum, $B_j = \beta B_s$. One must compute the joint probability of likely coincidence, ρ_0 , with the waveform and noncoincidence, $(1 - \rho_0)$, to obtain statistics of BER. The WCPBJ would attempt to vary the value of ρ_0 , the fraction of bandwidth occupied, to maximize BER in the joint probability computation.

3.4. Multitone Jamming

A multitone jammer, as shown in Fig. 3, employs sets of sinusoids instead of noise sources to cover the jamming band. Generally these are generated by a harmonic source, resulting in frequency spacings that are equidistant. The power per tone for the equal-amplitude amplitude case is

$$P_j = J/N \tag{7}$$

where N is the number of tones. For the case of equidistant frequency tones, the total jamming bandwidth occupied is

$$B_j = f_s(N - 1) \tag{8}$$

where f_s is the frequency spacing.

3.5. Pulsed Jamming

A pulsed jammer, as shown in Fig. 4, seeks to obtain a high instantaneous power output by reducing its duty cycle; that is, the power production is for a fraction of time. Some microwave tubes have the ability to produce large amounts of instantaneous but not continuous power. The source waveform for small duty cycles is generally rectangular—that is, a pulse, which is rich in harmonics and can cover a wide instantaneous bandwidth.

3.6. Smart Jammers

The category of smart jammers includes the frequency follower, the store and forward, and frequency chirp jammers. The frequency follower and the store-and-forward class of jammers is nominally frequency-agile and captures or senses the victim signal and mimics the carrier frequency and perhaps the modulated waveform. These

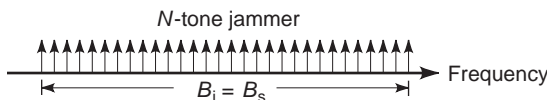


Figure 3. Spectrum of a multitone jammer.

jammers are effective against stationary or slow frequency hoppers where the signal stays at frequency long enough for the jammer to copy and transmit to the victim in one frequency hop period.

The frequency chirp jammer, as its name implies, frequency sweeps or chirps the intended jamming band to put energy into the victim receiving system. These jammers would be employed if certain aspects of the victim system are known and can be exploited by a nonstationary signal.

4. ANTISPOOFING AND ANTIJAMMING TECHNIQUES

To make a system robust in hostile environments, antispoofting and antijamming techniques need to be implemented. Different techniques should be adopted to counterattack different types of jamming. They can be based on the concepts of power, frequency, time, and spatial discriminations. In most cases, a hybrid system that includes more than one antijamming technique is implemented. All techniques described here can be used for antispoofting purposes as well without being particularly specified in the context.

4.1. Direct Sequence

Direct sequence (DS) is a spread-spectrum technique that is usually used with the phase shift keying (PSK) signaling. A pseudorandom number (PN) binary sequence whose elements have values of $+1$ or -1 are generated by a PN sequence generator N_c times faster than the data rate. Conventionally, the unit of each element of a PN sequence is called a “chip.” Therefore, the chip time T_c equals T_d/N_c , where T_d is the data bit duration. Practically, the N can be between 100 and 10^6 or higher, depending on the capability of antijamming (antispoofting) and/or the spread bandwidth of the system. Let $d(t)$ and $c(t)$ be denoted as the original data and PN sequence, respectively. Then

$$d(t) = \sum_{k=-\infty}^{\infty} d_k p_d(t) \tag{9}$$

and

$$c(t) = \sum_{k=-\infty}^{\infty} c_k p_c(t) \tag{10}$$

where d_k and c_k are either $+1$ or -1 , and $p_d(t)$ and $p_c(t)$ are unit pulse functions with duration T_d and T_c , respectively. In the DS spread PSK system, the modulating signal is the multiplication of $d(t)$ and $c(t)$. Figure 5 illustrates the waveforms of $d(t)$, $c(t)$ and $d(t)c(t)$.

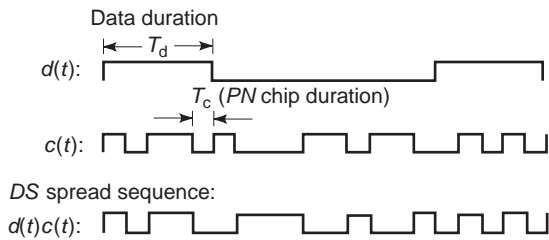


Figure 5. Waveforms of data $d(t)$, PN sequence $c(t)$, and modulating signal $d(t)c(t)$.

The DS spread binary PSK (DS/BPSK) signal can be expressed as

$$x(t) = \sqrt{2S}d(t)c(t) \cos \omega_c t = c(t)s(t) \quad (11)$$

where

$$s(t) = \sqrt{2S}d(t) \cos \omega_c t \quad (12)$$

is the ordinary BPSK signaling. Since $c(t)$ changes its polarity N_c times faster than $d(t)$, the bandwidth of $x(t)$, denoted by W_{DS} , is N_c times wider than that of $d(t)$, which is $R_d (= 1/T_d)$. The processing gain of this DS/BPSK system is simply

$$PG = \frac{W_{DS}}{R_d} = N_c \quad (13)$$

In the presence of jamming signal $J(t)$, the received signal at the receiver can be represented by

$$r(t) = x(t) + J(t) \quad (14)$$

The receiver multiplies the received signal $r(t)$ by a duplicate of the PN signal $c(t)$ to obtain

$$z(t) = c(t)(x(t) + J(t)) = s(t) + c(t)J(t) \quad (15)$$

since $c^2(t) = 1$. Therefore, the effective noise component at the input to the BPSK demodulator becomes $n(t) = c(t)J(t)$. Again, for the case that jammer's bandwidth B_J is much smaller than $R_c = 1/T_c$, the bandwidth of $n(t)$ will be approximately $N_J (= R_c/B_J)$ times wider than that of $J(t)$. For a fixed amount of jammer power J , the value of the power spectrum density function of $n(t)$ at the carrier frequency ω_0 is approximately $1/N_J$ that of $J(t)$. As a result of this, after the signal $z(t)$ passes through the front-end filter of the BPSK demodulator, which is approximately R_d , the effective noise component contributed to the decision rule is significantly reduced. Hence, this technique essentially enhances the effective SNR input to the demodulator. This implies that the direct-sequence spread-spectrum approach is based on the concept of power discrimination.

It has been shown [1] that the BPSK data modulation with QPSK direct sequence spreading is a robust antijamming system to combat either continuous-wave (tone) or random (partial-band) jammer.

It is worthwhile to mention that the DS technique can be also used for the purpose of multiple access. The multiple access scheme that adopts the DS technique is called code division multiple access (CDMA). Other types of multiple access include frequency division multiple access (FDMA) and time division multiple access (TDMA). In a CDMA system, users each have their own unique code ID. The same idea of using process gain stated early in this section is the concept used to discriminate the unwanted user from the desired one.

4.2. Frequency Hopping

A frequency hopping (FH) system is driven by a frequency synthesizer that responds to a PN sequence from a PN code generator. The most commonly used modulation schemes when the FH technique is adopted are M -ary frequency shift keying (MFSK) modulations. Based on the output sequence from a PN code generator, the frequency hopper outputs a continuous sinusoidal waveform that frequency jumps from one value to another. These frequencies are, in turn, used as the carrier frequencies of a MFSK signal.

Depending on the hopping rate that the frequency changes, the FH system can be categorized into slow frequency hopping (SFH) and fast frequency hopping (FFH).

- *Slow Frequency Hop.* The hopping rate is slower than or equal to the data rate, which implies that there are one or more data bits in each hop, as shown in Fig. 6a.

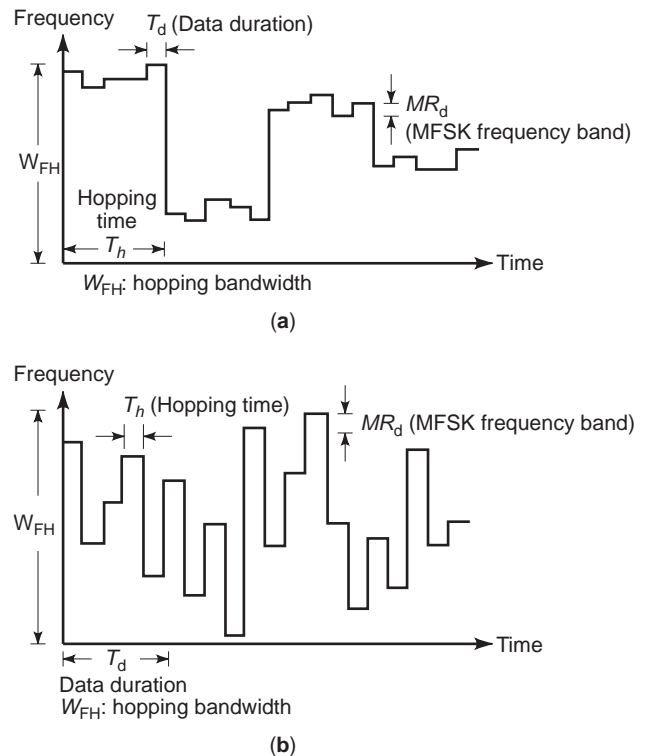


Figure 6. (a) Slow frequency hopping; (b) fast frequency hopping.

- *Fast Frequency Hop.* The hopping rate is faster than the data rate, which implies that there are multiple hops within each data bit duration, as shown in Fig. 6b.

Note that the FH/MFSK system has a much wider range of frequencies than the ordinary MFSK system. For a fixed jammer power J , the broadband jammer needs to spread its power over the entire FH bandwidth W_{FH} . Hence, the effective corrupting power fallen into a single MFSK band is J/PG , where PG is the processing gain of the FH/MFSK system and is defined as

$$PG = \frac{W_{FH}}{MR_d} \quad (16)$$

Because the PG is usually very large, the FH/MFSK is very effective in counterattacking broadband jamming.

For a stationary partial-band or multitone jammer, an FH system is also considered to be robust. This is due to the fact that the signal is lost for only a small portion of time when the hopping frequency falls into the fixed jamming band. For a majority of time, the signal is free of jamming. This implies that the FH is based on the concept of frequency discrimination.

Unfortunately, the partial-band or multitone jammer is intelligent enough to be able to detect the transmitted FH/MFSK signal, follow the hopping pattern, and concentrate its total power J to jam the full band of M MFSK carriers. Therefore, the FH/MFSK system becomes vulnerable to the intelligent partial-band and multitone jammers. To solve this problem, an FFH must be adopted so that the jammer is not able to follow the hopping pattern. In addition, the coding and time diversity becomes desirable in this scenario.

4.3. Time Hopping

Like FH, time hopping (TH) is also driven by a PN sequence generated by a PN code generator. Instead of hopping the carrier frequencies in a much wider frequency band, the time hopper controls the time stamps for turning on and off the signal transmission in the time domain. This technique is effective only to the pulsed jamming. A TH system can force a jammer to stay on at all times in order to be effective. Under the constraint of a fixed energy, the jammer needs to reduce its transmitting power, resulting in less interference. Obviously, the TH system is based on the concept of time discrimination [2].

4.4. Time Diversity

Time diversity is a technique in which each information bit is subdivided into multiple equally spaced subbits before entering the modulator. It is usually implemented in the FFH system to counterattack the partial-band or multitone jamming. To make the counterattack more effective, the hop duration has to be equal to or less than the subbit duration. Therefore, if one subbit is jammed, other subbits of the same bit may be hopped to a frequency outside the jamming band and detected without errors. This

antijamming technique is also based on the concept of time discrimination.

4.5. Antenna Nulling

A spatial discriminating technique for antispoofing and antijamming is antenna nulling or sidelobe cancellation [3]. In order to provide a nulling capability, the antenna system needs to be equipped with an array of element antennas and associated electronics for beamforming. At least two spot beam element antennas, each of which can be pointed and controlled independently, are needed. The received signals from all element antennas are phase-shifted and amplitude-attenuated independently and individually, and then combined to form a single signal. The combination of this array of element antennas is called *phased-array antenna*.

First, the antenna system tries to sense the presence of a spoofer or jammer within the antenna field of view by sampling the received signal from each element antenna and determining whether there is significant energy outside the expected bandwidth. After the spoofer or jammer is detected, a nuller algorithm processor decides and adjusts accordingly to the phases and attenuation weights of all element antennas. As a result, a null is generated at the direction to the spoofer or jammer so that the interference attack becomes completely ineffective. Figure 7 illustrates a conceptual diagram of forming an antenna null. In most military communications systems, such as the military satellite communications (MILSATCOM) systems, the antenna nulling scheme is required to be implemented on spacecraft.

4.6. Forward Error Correcting Code

In general, using a forward error correcting (FEC) code to improve the power efficiency can be also considered as an anti-spoofing or antijamming technique. Various coding schemes have been included in various systems for this purpose. The $(7, \frac{1}{2})$ convolutional code with Viterbi decoding has been widely used because of its good FEC capability [4]. The Reed–Solomon code has been shown to be powerful for correcting burst errors [5]. Concatenated code structure with $(7, \frac{1}{2})$ convolutional code as the inner code and Reed–Solomon code as the outer code has been known

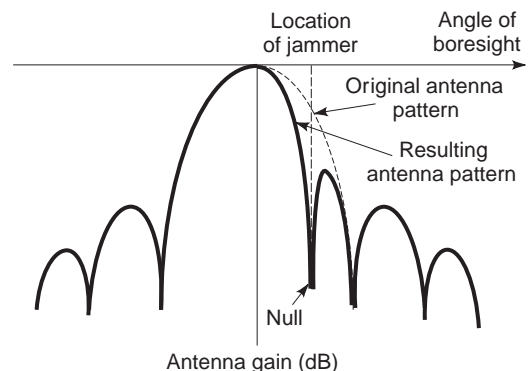


Figure 7. A conceptual antenna pattern of nulling.

to have a significant anti-corruption capability [6]. Recently, a newly invented turbo code has demonstrated its ability to provide a near-Shannon-limit coding gain [7].

5. PROPAGATION CHANNEL CHARACTERISTICS

The term *fading channel* is used when the physical medium affects radiowave propagation such that the received signal appears to have amplitude fading and/or phase jitter. Three principal fading phenomena are (1) multipath, (2) ionospheric effects, and (3) nuclear-blast-induced plasma.

5.1. Multipath Fading

Multipath fading is usually associated with terrestrial communications or low-elevation-angle satellite communications where the transmit and receive signals are subject to reflection from terrain and objects, fixed or moving. Measurement data have been provided from NASA missions [8,9], and Brayer of MITRE also performed several investigations in this area [10,11]. In multipath fading, the signal is a composite of the line-of-sight wave and reflections, from the earth's surface, that occur along the propagation channel. Fade condition is dependent on the terrain encountered, such as mountainous, smooth, lake, or oceanic. The received signal is a composite of constructive and destructive interference of the primary and coherent reflections to induce the scintillation behavior. It is convenient to define the single-frequency case after Bullington [12] for the primary and echo without modulation:

$$v = 1 + Re^{i(\theta + (n-1)\pi)} = Le^{-i\gamma} \tag{17}$$

with

$$\tan \gamma = \frac{R \sin \theta}{1 - R \cos \theta} \tag{18}$$

where R is the instantaneous amplitude and θ is the instantaneous phase of the "composite echo." Experiments have shown that both fades and their duration would be proportional to the combined amplitude L as

$$\text{Prob}[(L_{\min}/L) \leq X] = X, \quad \text{where } 0 \leq X \leq 1 \tag{19}$$

Figure 8 illustrates a relationship between fade duration and percent of fades for an example of multipath fading at 4 GHz.

5.2. Ionospheric Effects

Fading or scintillation occurs in the ionosphere because of the influence of electron densities in the propagation medium. Ionospheric scintillation can be a major factor for satellite communications depending on carrier frequency, satellite to terminal locations, time of day, season, and magnetic activity. Figure 9 indicates the change of ionospheric scintillation as the frequency changes [13].

Equatorial scintillation is caused by electron gradients at altitudes of several hundred kilometers. High-latitude

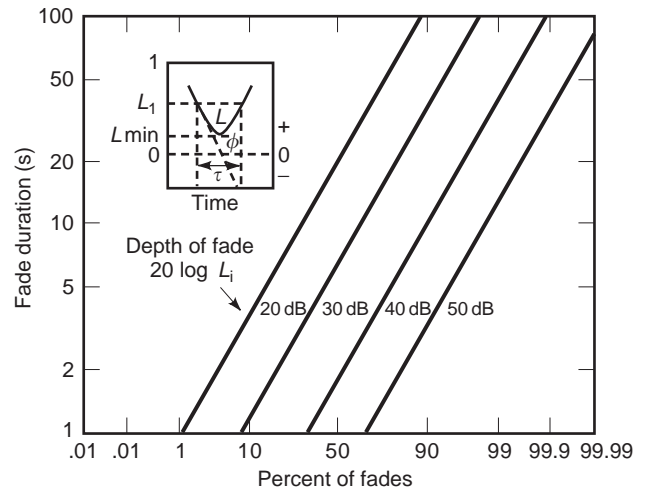


Figure 8. Duration of fading at 4 GHz on a 30-mi path.

scintillation occurs from the visible aurora region (regions D and E) and from the polar cap to the aurora [14]. The electron densities in the ionosphere tend to align with the earth's magnetic field lines. This causes the fading characteristics to be highly geometry-dependent, particularly at high latitudes and at the poles. Figure 10 shows the geographic distribution of the ionospheric scintillation [15], in which the darker the region, the severer the fade.

5.3. Nuclear-Blast-Induced Plasma

Nuclear-induced scintillation is postulated when such ordinance is detonated in the upper atmosphere to cut off communications, particularly via satellite. Corroboration of such characteristics were conducted by the "Starfish" experiments in the 1950s and by the STRESS test, in which barium clouds were set up in the upper atmosphere through which radiowave propagation was studied.

The generalized power spectrum $\Gamma(f, \tau)$ of the scintillation fading can be characterized by the scintillation

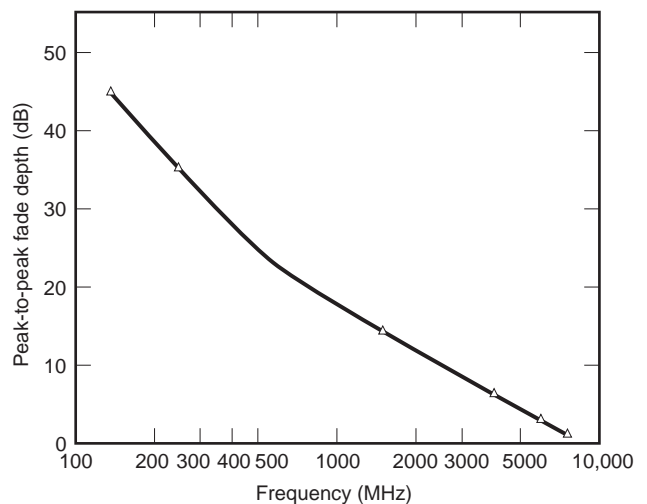


Figure 9. Frequency dependence of ionospheric scintillation fading.

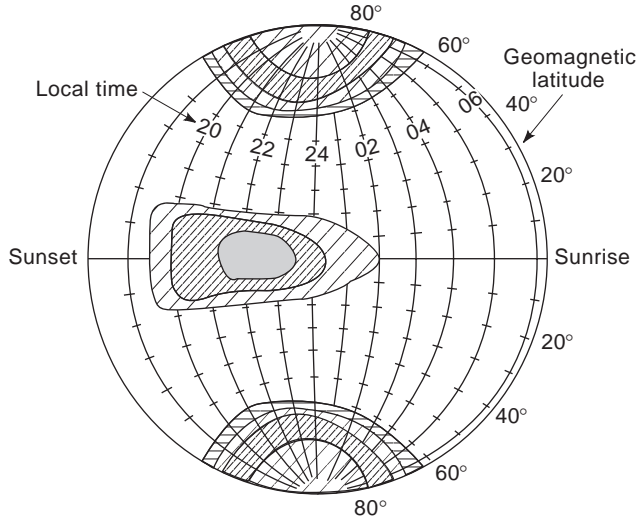


Figure 10. Geographic distribution ionospheric scintillation. The depth of scintillation fading is proportional to the density of cross-hatching.

decorrelation time τ_0 and the frequency-selective bandwidth f_0 [16]

$$\Gamma(f, \tau) = \frac{1.864\tau_0\delta(\tau)}{[1 + 8.572(\tau_0f)^2]^2} \quad (20)$$

for $f_0 \cdot T > 1$, where T is the minimum symbol time, and δ is the Dirac delta function. For frequency-selective fades ($f_0T < 1$), we have

$$\begin{aligned} \Gamma(f, \tau) &= 2.981 \frac{f'\tau_0}{C_1^{1/2}} \exp \\ &\times \left\{ -\frac{1}{2C_1^2} [(\pi\tau_0f)^2 - 2\pi f'\tau]^2 - (\pi\tau_0f)^2 \right\} \\ &\times \int_{-\infty}^{\infty} \exp\{-x^4 - 2x^2 \\ &\times \left[\frac{C_1}{2^{1/2}} \left(1 + \frac{1}{C_1^2} ((\pi\tau_0f)^2 - 2\pi f'\tau) \right) \right]\} dx \end{aligned} \quad (21)$$

where

$$\begin{aligned} f' &= f_0(1 + C_1^2)^{1/2} \\ C_1 &= \text{delay parameter } (\approx 0.25) \end{aligned} \quad (22)$$

For both Eqs. (20) and (21), we have

$$\int_{-\infty}^{\infty} \int_{-\infty}^{\infty} \Gamma(f, \tau) df d\tau = 1 \quad (23)$$

In scintillation, there are random time-varying components of the electron density. If the random component is zero mean and normally distributed, Wittwer [16] has

given the variance of this component $g(f)$ as

$$\begin{aligned} &\overline{g * (f)g(f')} \\ &= \begin{cases} \delta(f - f') \frac{\tau_0(f_c/r_0c)^2}{[a^2 + (2\pi f\tau_0)^2]^{3/2}} & \text{for } f \leq f_r \\ 0 & \text{for } f > f_r \end{cases} \end{aligned} \quad (24)$$

where

$$\begin{aligned} g(-f) &= g^*(f) \\ a^2 &= (r_0 \cdot c \cdot N_L(t)/f_c)^{-2} \\ r_0 &= \text{classical electron radius } (2.82 \times 10^{-5} \text{ m}) \\ c &= \text{light speed } (3 \times 10^8 \text{ m/s}) \\ N_L(t) &= \text{large scale (slow component of electron density)} \\ f_c &= \text{carrier frequency} \\ f_r &= 1/(2\pi\sigma\tau_0) \\ \sigma &= \text{Rayleigh phase variance, Rayleigh scintillations} \\ &= 0 \text{ phase-only scintillation} \end{aligned}$$

6. FADING MITIGATION TECHNIQUES

There are five major techniques that can be employed to specifically combat the effects of fading: (1) frequency band selection and diversity, (2) spatial diversity, (3) time diversity (interleaving), (4) polarization, and (5) equalization. In addition, coding and frequency hopping (with or without chirp combined), where the hop rate is faster than the data rate, also mitigate fading.

6.1. Frequency Band Selection and Diversity

Scattering and scintillation are two major factors that cause fading in communication systems. As was shown in the previous section, the effectiveness of these two factors depends on the operating frequency. Therefore, properly selecting a frequency band for a satellite system to operate becomes very important. Furthermore, transmitting the signal on multiple carriers and employing a diversity combiner is also an effective way to combat the fading loss.

6.2. Spatial Diversity

Due to link geometry, the effects of the fading phenomena are spatially selective as well. Fading is more sensitive to spacing with vertical than with horizontal distance by about an order of magnitude. Spacing the transmit/receive apertures to decorrelate fading provides immunity. Providing multiple receptions by utilizing more than one ground station and then combining the received signals can build up a robust system in fading environments.

6.3. Polarization

Polarization is the orientation of the plane on which the electric field vibrates when an electromagnetic wave propagates through the medium. The wave can be linearly, elliptically, or circularly polarized. Jordan suggested that multipath effects can be limited by use of circular rather

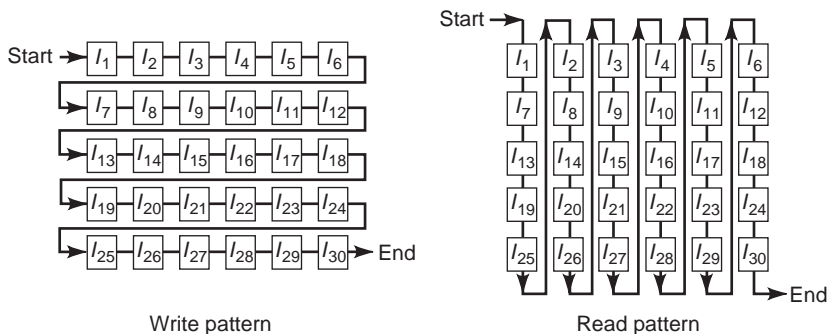


Figure 11. A 5 × 6 block interleaver.

than linear polarization [17]. This is due to the nature of the wave propagation and multipath reflections. Therefore, in a fading environment, circular polarization is preferable.

6.4. Equalization

Equalization attempts to compensate for the time dispersion effect in the fading channel. The effects of the multipath channel has the effect of time smearing the signal introducing intersymbol interference (ISI). A common equalizer structure is the mean-square error (MSE), where the sum of the squares of ISI and noise power is minimized. Lee and Messerschitt [18], Widrow and Stearns [19], and Orfanidis [20] discussed the concept of equalization and adaptive signal processing. A synchronization sequence must be transmitted to aid the adaptation process.

6.5. Coding

Using an effective FEC code is an important antifading scheme. Because fading is usually on and off so that the received signal is corrupted only in a small portion of a duty cycle, the errors generally come in bursts. Reed–Solomon code is known to be good for burst error correction. However, in a severe fading environment where the fade duration is long, the concatenated code structure, with a convolutional or turbo code as the inner code and a Reed–Solomon code as the outer code, incorporated with interleaving is required.

6.6. Interleaving/Deinterleaving

Interleaving is essentially a permutation among the transmitted channel symbols. Thus, when an interleaving technique is adopted, the continuous data need to be subdivided into blocks. In addition, it generally comes with an FEC code. In the transmitter, the modulated symbols at the output of modulator are permuted before entering the channel. The channel symbols are corrupted in bursts in a fading environment. At the receiver, a deinterleaver re-scrambles channel symbols using a reverse permutation pattern so that the order of the originally modulated symbols is preserved. Due to the process of deinterleaving, the burst channel symbol errors are broken into scattered random errors that will be, in turn, easily corrected by an FEC decoder. In order to ensure the randomness of the channel symbol errors after deinterleaving, the inter-

leaving depth should be linearly increased as the fade duration increases.

It should be pointed out that interleaving/deinterleaving results in a delay that depends on the interleaving depth and type. Theoretically, the interleaving pattern can be any format of permutation. Block and convolutional interleavings are the two most commonly used patterns.

- *Block Interleaver.* As shown in Fig. 11, a block interleaver is a regular interleaver in that the input symbols are written in rows and read in columns. For a 5 × 6 block interleaver, if $I_1, I_2, I_3, I_4, \dots$ are the input symbols, the outputs are $I_1, I_7, I_{13}, I_{19}, I_{25}, I_2, I_8, I_{14}, \dots$. It can be seen that the permutation cannot take place until the entire block is filled up with the input symbols. Therefore, a block interleaver of size N suffers a delay of N symbol intervals.
- *Convolutional Interleaver.* Figure 12 illustrates the structure of a convolutional interleaver. For the same input symbols $I_1, I_2, I_3, I_4, \dots$, the outputs become $I_1, X, X, X, X, X, I_7, I_2, X, X, X, X, I_{13}, I_8, I_3, X, X, X, I_{19}, I_{14}, I_9, I_4, X, X, I_{25}, I_{20}, I_{15}, I_{10}, I_5, X, \dots$, where X is a dummy symbol. It can be seen that the convolutional interleaver reads out the symbols on diagonals. So, the convolutional interleaver can start its output without having the entire block filled up. As a result, the delay is one-half of the interleaver depth.

7. LOW PROBABILITY OF DETECT/LOW PROBABILITY OF INTERCEPT (LPD/LPI)

In electronic warfare, radio signals from transmitters can be detected by adversaries. As a result, the location of soldiers and command posts can be identified, jeopardizing human lives and success of operations. In order to prevent signals from being intercepted, receivers are designed

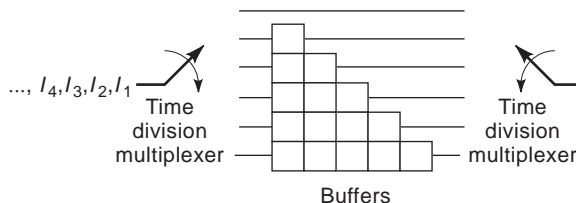


Figure 12. A convolutional interleaver of depth 6.

with good capability of low probability of detect (LPD) or low probability of intercept (LPI).

7.1. Detection of Signals in the Presence of Noise

In communication systems, the most commonly used theory is the detection theory. This refers to the technique of making a decision as to whether a radio signal is received in the presence of noise. It is possible that the receiver misdetects a radio signal when it thinks that only the noise is received. On the other hand, the receiver may present a false alarm by declaring that a radio signal is present when no signal actually exists. Hypothesis testing is one of the most important statistical tools for making such decisions [21]. The hypotheses are statements of the possible decisions that are being considered. For example, in a radar detection problem we might select two hypotheses—a target is present (H_1) or no target is present (H_0).

The total power radiometer is a commonly used device that detects the existence of a radio signal in the presence of noise. It operates as a square-law device that outputs the average power of the input signal within a certain bandwidth and over a certain period of time T_0 . Figure 13 shows the block diagram of a total power radiometer.

The input $x(t)$ to the radiometer includes the signal component $s(t)$ of power P_s and the noise component $n(t)$, which is white with power spectrum N_0 . The test statistic z out of the radiometer can be expressed as

$$z = \frac{1}{T_0} \int_{t_0}^{t_0+T_0} (s(t) + n^*(t))^2 dt \quad (25)$$

where t_0 is a particular time instant for starting the observation, T_0 is the observation period, and $n^*(t)$ is the band-limited noise component. Let the likelihood function, $p_0(z)$ and $p_1(z)$, be defined as the probability of observable being at z given conditions of H_0 and H_1 , respectively. It can be shown [22] that $p_0(z)$ and $p_1(z)$ can be approximated by Gaussian probability density functions with mean values, m_0 and m_1 , and variances, σ_0^2 and σ_1^2 , respectively, given by

$$\begin{aligned} m_0 &= P_s + N_0 B \\ m_1 &= N_0 B \\ \sigma_0^2 &= (2P_s + N_0 B)N_0/T_0 \\ \sigma_1^2 &= N_0^2 B/T_0 \end{aligned} \quad (26)$$

where B is the bandwidth of the input filter of the radiometer, assuming that an ideal filter is used.

It should be pointed out that the design of the front-end filter bandwidth of a receiver is based on the requirement of adjacent-channel interference (ACI). For example, a system may require the ACI at the edge of the input filter bandwidth to be at least -20 dB of the center carrier

power so that the system can provide a good link quality to the customer. In this case, the bandwidth of the input filter, assuming to be ideal, has to be at least 1.8 times the R_s for QPSK signaling [23], where R_s is the channel symbol rate. On the other hand, if the receiver is used simply to detect the presence of a radio signal, the bandwidth of the input filter can merely match the 3 dB bandwidth of the power spectrum of the signal. In this section, we assume that the input filter bandwidth of the radiometer is equal to R_s of the $s(t)$, which is close to the 3 dB bandwidth.

When a single fixed-length packet is transmitted with a packet duration less than the observation time T_0 , we will replace the above P_s by μP_s , where μ is the duty cycle of the packet within T_0 , assuming that the entire packet is to be observed within the observation period T_0 . This is a practical assumption as long as T_0 is much larger than the packet duration.

To decide whether it is H_0 or H_1 , the observable z is compared against a threshold. The signal is declared to be present if z is above or equal to the threshold, and absent if z is below the threshold. Let us define the probability of detection P_d as the probability that the signal is declared to be present (z is above or equal to the threshold) when the signal indeed exists, while the probability of false alarm P_{fa} is defined as the probability that the signal is declared to be present when no signal is actually transmitted. It can be seen that the sensitivity of the detection (interception) depends on the threshold set. If it is set too low, although the signal will not likely be missed, the P_{fa} will be high, which is not desirable. To the contrary, if the threshold is set too high, the radiometer will not be able to effectively detect the presence of a signal. Therefore, for any specified values of P_{fa} and P_d there is a corresponding threshold. In this type of detection problem, the Neyman-Pearson criterion [21], which maximizes the likelihood ratio $p_1(z)/p_0(z)$ for a given P_{fa} is generally adopted for setting up the threshold.

In order to be effective, a channelized total power radiometer is used, in that a bank of filters and integrate-and-dump circuits are implemented, each of which matches with the frequency band of each channel so that the radiometer can detect the entire transmitted frequency band. Because different communication systems may allocate different bandwidths for the entire system, for the sake of fairness, the LPD/LPI capabilities for different systems should be compared based on the same length of observation period T_0 and the same specification of false-alarm rate (FAR). FAR is defined as the number of false-alarm declarations within a unit of time and for a unit of bandwidth. Hence, P_{fa} (for each channel) = T_0 [FAR] [channel bandwidth]. For example, for a FAR = 1/h/MHz and $T_0 = 1$ s, P_{fa} (for each channel) = (channel bandwidth in MHz)/3600.

Let us consider a case where the threshold of the radiometer is set such that the probability of correctly detecting a radio signal P_d exceeds 50% (with FAR = 1/h/MHz). Based on the Neyman-Pearson criterion, the normalized threshold, defined as

$$\eta = \frac{\text{mean difference}}{\text{standard deviation}} \quad (27)$$

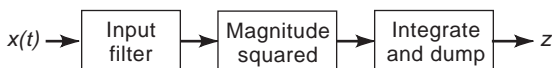


Figure 13. Block diagram of a total power radiometer.

is such that

$$P_{fa} = \frac{1}{\sqrt{2\pi}} \int_{\eta}^{\infty} \exp\left(-\frac{x^2}{2}\right) dx \quad (28)$$

Thus, the threshold η depends on only P_{fa} , which may vary for different systems. From Eq. (26), it can be seen that

$$\eta = \frac{\mu P_s}{N_0} \sqrt{\frac{T_0}{B}} \quad (29)$$

Using this threshold and the fact that $B = R_s$, the received signal-to-noise ratio (SNR), defined as P_s/N_0B , required for this detection is

$$\text{SNR}_{\text{detection}} = \frac{\eta}{\mu \sqrt{R_s T_0}} \quad (30)$$

When a very sensitive detection device is implemented so that the radiometer can detect the signal given a very small amount of energy, a much finer integration time can be used for detection. As a result, this so-called intelligent radiometer is able to pinpoint the time at which each received packet starts and ends. In this case, the total observation time can essentially match with the actual packet duration. Therefore, the duty cycle is always 1. Accordingly, the $\text{SNR}_{\text{detection}}$ used in the intelligent radiometer will be different under the same specifications of P_d and P_{fa} .

7.2. Range of Vulnerability

The range of vulnerability, which is defined as the range from the adversary within which a radio can be detected, is used to quantify the capability of the LPI/LPD of a system. From above, it was shown that the sensitivity of detect (intercept) of a radiometer depends on the threshold set. This implies that the range of vulnerability is dependent on the level of threshold. The lower the threshold, the longer the range for a radio not being detected. Thus, the range of vulnerability is meaningful only under specified values of P_{fa} and P_d .

It is well known [24] that the received power of a radio signal at the receiver can be represented by

$$P_r = P_t G_t G_r / L \quad (31)$$

where P_t is the transmitting power, G_t is the transmit antenna gain, G_r is the receive antenna gain, and L is the loss during propagation. The received noise power can be represented by

$$N = N_0 B = kTB \quad (32)$$

where k is Boltzmann's constant ($= 1.379 \times 10^{-23}$ J/K), T is the receiver system temperature in kelvin, and B is the bandwidth of the input filter in hertz. Combining Eqs. (31)

and (32), the receiving SNR at the radiometer can be expressed as

$$\text{SNR} = (\text{EIRP})(G_r/T)/(LkB) \quad (33)$$

where $\text{EIRP} (= P_t G_t)$ is the transmitted equivalent isotropic radiated power from a radio and G_r/T is defined as the figure of merit of the receiving antenna.

The range of vulnerability can be studied under two categories, ground collection and airborne collection. The ground vulnerability range is associated with an adversarial radiometer, which is on or near the ground. In this case, the dominant loss of the radiowave power is due to the reflection from the terrain. The airborne vulnerability range is associated with radiometer placed on the aircraft, in which case the free space loss is only considered in determining the received radio power.

7.2.1. Ground Collection. Blake showed that when a radiowave is reflected from the ground, the received signal is subject to a loss of $L = R^4/(h_t^2 h_r^2)$, where R is the distance between a radio and the radiometer, h_t is the radio's transmit antenna height (from ground), and h_r is the radiometer antenna height [24]. Therefore, from Eq. (33), the vulnerability range for the ground collection can be expressed as

$$R = [(\text{EIRP})(h_t^2 h_r^2)(G_r/T)/(kR_s)/\text{SNR}_{\text{detection}}]^{1/4} \quad (34)$$

7.2.2. Airborne Collection. For airborne collection, L is simply the free-space loss that is equal to $(4\pi R/\lambda)^2$, where λ is the wavelength of the carrier. Therefore, the vulnerability range becomes

$$R = [(\text{EIRP})(\lambda/4\pi)^2(G_r/T)/(kR_s)/\text{SNR}_{\text{detection}}]^{1/2} \quad (35)$$

Plugging Eq. (30) into both Eq. (34) and Eq. (35), it can be illustrated that

$$R \propto \left(\frac{\text{EIRP} \cdot \mu}{\eta} \sqrt{\frac{T_0}{R_s}} \right)^e \quad (36)$$

where $e = 1/4$ for ground collection and $1/2$ for air collection.

From Eq. (36), it can be seen that a radio with higher channel symbol rate R_s is less vulnerable to the radiometer detection. That is why the LPI/LPD capability is significantly improved when a CDMA system is utilized. Note that adopting TDMA in a system will reduce the duty cycle μ and increase the R_s by the same factor of γ , resulting in a reduction of range of vulnerability by a factor of $\gamma^{3/2}$. This implies that a TDMA system also has a good LPI/LPD property. Furthermore, Eq. (36) also explains why the radio is more vulnerable to an intelligent radiometer than a basic radiometer. This is due to the fact that when an intelligent radiometer is used, the observation time is reduced by a factor of $1/\mu$ (T_0 becomes μT_0 ; $\mu < 1$) and the μ in Eq. (36) is replaced by 1, resulting in an

increase of vulnerability range R by a factor of $\sqrt{1/\mu}$. Thus, a TDMA system becomes vulnerable when an intelligent radiometer is utilized.

8. CRYPTOGRAPHY

One of the more important elements that differentiates military communications from commercial communications is secrecy. Without appropriate safeguards, the transmitted data are susceptible to unauthorized interception, deletion, addition, and modification. Such unwanted exposure of data may jeopardize national security. Cryptography is a practical method of protecting transmitted information from being intercepted.

8.1. Classical Cryptology

When a transmitter generates a plaintext or unenciphered message to be communicated over an insecure channel to a legitimate receiver, an eavesdropper can easily intercept it. In order to prevent the eavesdropper from learning it, in the classic cryptography system, the transmitter operates on the plaintext with an invertible transformation to produce a ciphertext or cryptogram. The inverse transformation (or called "key") is either already known by or transmitted via a secure channel to the legitimate receiver. Therefore, the receiver can decipher the received ciphertext by applying the key and recover the original plaintext. This system requires exchanges of the secret keys among communicators.

8.2. Public Key Cryptosystems

The public key cryptosystem is the first secrecy system that does not rely on exchanges of secret keys to obtain its security from cryptanalysis [25]. This system employs a public directory in that each subscriber places a key to be used by other subscribers for encrypting their transmitted messages addressed to each recipient. All subscribers keep secret their corresponding decryption keys for decrypting their received messages.

8.3. Methods of Encryption

In any cryptosystem, the most important thing is to design a means of encryption so that it is practically impossible for cryptanalysis to break it. Wang developed an algorithm of generating a significantly long pseudo-random number (PN) sequence using exponentiation in finite fields [26]. This PN sequence can be used as an encryption/decryption code that is applied to the plaintext by the same way as in the direct-sequence (DS) spread-spectrum system. Diffie and Hellman used the finite field exponentiation as the operation for encipher or decipher [25]. Merkle and Hellman designed a so-called trapdoor knapsack n -vector as the public encryption key [27]. McEliece suggested using a linear error correcting code, Goppa code, for the encryption algorithm [28].

9. TARGET RECOGNITION OR CLASSIFICATION

Identifying a target in a sense with object distortions and background clutter present is a challenging problem for military applications. Two basic mechanisms, optics and electronics, can be adopted for target image collection. Lens, laser, and infrared light are commonly used for optical sensing, while the classic radar and synthetic aperture radar (SAR) [29] are used for electronic sensing.

After the image is collected, an extensive amount of processing is required. In general, there are five levels of processing required to complete a target recognition: (1) detection, (2) image enhancement, (3) segmentation, (4) feature extraction, and (5) identification.

9.1. Detection

Detection is the most computationally demanding stage. It must handle every pixel in the input scene, accommodate target distortions, reject clutter, and locate all candidate regions of interest (RoIs). It does not attempt to recognize the object from the background; it merely attempts to locate RoIs. Because it conceivably must process every pixel in every image, it must contain simple and fast algorithms to avoid long processing time. Various types of correlator (detection filter), such as hit/miss (H/M) and rank order H/M, were developed [30].

9.2. Image Enhancement

Once RoIs have been located, each RoI must be further enhanced to reduce background noises, and fill in holes and sharp edges. These processes will help remove false alarms and achieve identification. Optical morphology [31] is a technique used to enhance the optically collected images.

9.3. Segmentation

Segmentation refers to the inference about objects within each RoI and includes rejection of clutter, omission of false alarms, and identification of macroclass (large-sized) target. Early rule-based inference systems such as MYCIN used certainty factors and developed a simple calculus to compute an overall certainty factor for a hypothesis [32]. More recently the Dempster-Shafer theory of evidence was developed and refined to address the evidence accumulation issue in target recognition [33,34]. Currently, a popular approach to evidence accumulation is via Bayes nets [35]. Bayes nets are graphs, primarily tree-structured but not necessarily so, that use Bayes' rule to lay out all of the conditional probability relationships in assessing the probability that a given hypothesis is true.

9.4. Feature Extraction

The next step for target recognition is to examine the RoI and extract features that would support the inference. In optical sensing systems, computer generated hologram filters can be used [36]. In SAR, the extracted features might be the locations of scattering centers, the shape of the diffuse return of the object, or the location of shadows. The concept is that appropriate features be detected, located,

and characterized so that they can be matched against predicted features in the final stage, identification.

9.5. Identification

The K nearest neighbor (K -NN) is a classic algorithm for target identification or classification [37]. The problems of this method are selecting the threshold and requiring the number of classes that were known a priori. This process is also slow since it uses a feedforward unsupervised learning method [38]. More recently, feedforward neural networks have been used for target identification [39]. This algorithm is fast, less noisy, and more accurate. It can also classify multitarget and multibackground images [40].

10. GLOBAL POSITIONING SYSTEM

In military applications, ranging and navigation are essential. To achieve them, a space-based navigation system, global positioning system (GPS), has been developed and launched [41]. The objective of GPS is to provide accurate, continuous position location information in three dimensions anywhere on or near Earth in all weather conditions. The concept involves measuring the times of arrival of radio signals transmitted from satellites whose positions are precisely known. This gives the ranges to the known satellites, which, in turn, establishes the user's position. To be effective, atomic clocks are installed onboard each satellite, which must be synchronized with a master system clock. Transmission frequencies are selected to minimize timing errors caused by Earth's ionosphere and to be unaffected by rain and weather. By measuring the distance to four GPS satellites, it is possible to establish the three coordinates of a user's position (latitude, longitude, and altitude), as well as GPS time.

10.1. Space Segment

The complete GPS space segment consists of 24 satellites. The satellites travel in 12 h circular orbits 11,000 nautical miles above Earth. They occupy six orbital planes, inclined 55° , with four operational satellites in each plane. The satellites are positioned so that six are observable nearly 100% of the time from any point on the earth. Each is equipped with a combination of rubidium or cesium atomic clocks, which are accurate to within 10 ns. By 1994, the GPS had already completed its full 24-satellite constellation.

10.2. Control Segment

The worldwide GPS ground control segment includes monitor stations, ground antennas, and a master control station. Receivers at the monitor stations track the GPS satellites, record their positions and status, and relay information to the master control station. There the data are processed to establish the satellites' clock correction factors and current orbital elements for transmission back to the satellites via the ground antennas. Currently, the master station is at Falcon Air Force Base, Colorado. The GPS monitor stations are located in Kwajalein,

Hawaii, Diego Garcia, Ascension Island, and Colorado. Ground antennas are located at Kwajalein, Diego Garcia, Ascension Island, and Cape Canaveral.

10.3. User Segment

GPS receiver equipment, unique to each application, can be placed onboard aircraft, ships, submarines, trains, cars, trucks, or other vehicles, or it can be hand-carried. The receivers detect, decode, and process the GPS satellite signals. GPS can determine a user's position with an accuracy of better than 16 m. Greater accuracy, less than 1 m, can be obtained by using corrections sent from another GPS receiver at a known location, and used as a reference.

Today, there are more than 100 different receiver models in use for a wide variety of military and civilian applications. The typical handheld receiver is about the size of a cellular phone, and is getting smaller. The hand-held units distributed to U.S. armed forces personnel during the Persian Gulf war weighed only 28 ounces.

11. MILITARY SATELLITE COMMUNICATION SYSTEMS

Military satellite communication systems of the United States have been developed to support communication beyond line of sight and to provide global dispersed forces and global power protection [42–44]. The system can also support polar regions and oceans. The systems have been designed to have both interoperability and compatibility features so that they can support users of all types of platforms such as land, ship, shore, submarine, air, transportable, and mobile. The choice of frequency bands is critical in designing the MILSATCOM systems. Three basic frequency bands, namely, ultrahigh frequency (UHF), superhigh frequency (SHF), and extremely high frequency (EHF), are available and each provides different advantages. UHF with frequency ranging from 300 to 3000 MHz is suitable for mobile systems, which can work in bad weather conditions and dense foliage. Moreover, UHF systems are inexpensive. Since the operating frequencies for SHF systems range from 3 to 30 GHz, they can support higher data rates and hence provide more jam resistance than UHF (because we spread the signals wider than UHF). EHF frequency bands provide the highest data rates and are the most jam-resistant of the three bands because the operating frequencies are allocated in the range of 30–300 GHz. Designed systems are also required to provide maximum flexibility for situations such as unpredictable conflicts in location, time, and operation duration and intensity. The systems are able to support voice, text, data, imagery, and video. Figure 14 shows a typical MILSATCOM system.

In the following section we will briefly describe the current MILSATCOM systems and Milstar architecture.

11.1. Current MILSATCOM Systems

Based on the frequency bands allocated to the MILSATCOM systems, one can classify the current systems into three categories, namely UHF, SHF, and EHF systems.

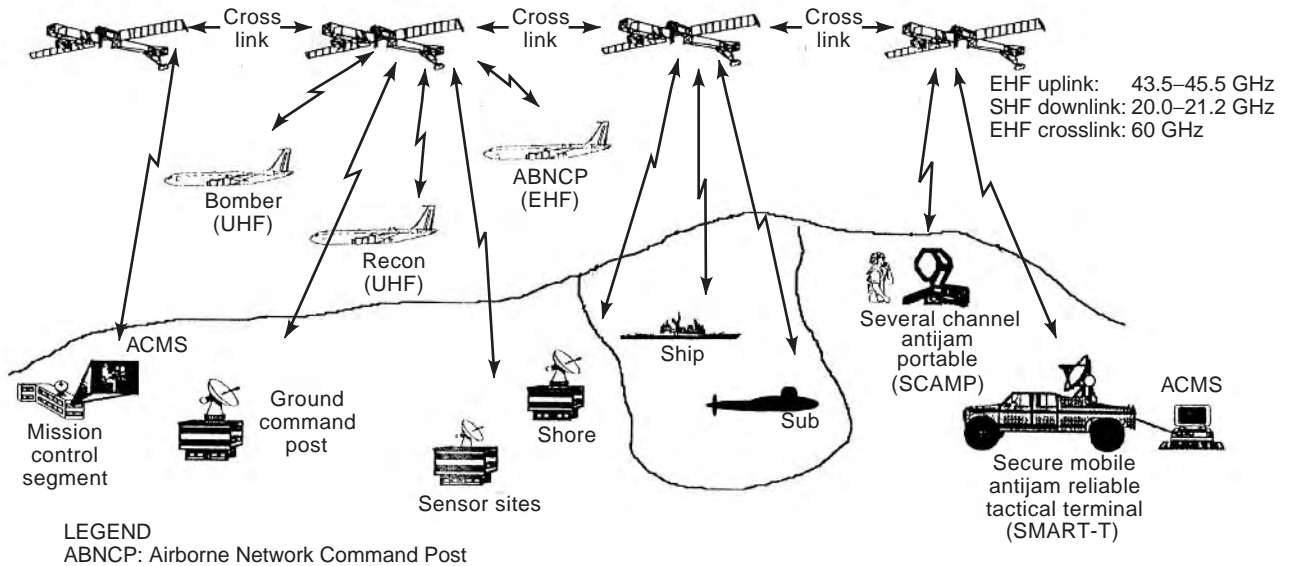


Figure 14. MILSATCOM system.

11.1.1. UHF Systems. UHF systems consist of two types of satellites:

- *FLTSATCOM and AFSATCOM.* The FLTSAT serves Navy surface ships, submarines, aircraft, and shore stations. The AFSAT serves Air Force strategic aircraft, airborne command posts, and ground terminals. The two systems share a set of eight satellites in synchronous equatorial orbits. The Air Force also has communications payload on several satellites in high inclination orbits to provide coverage of the north polar region, which is not visible from the equatorial satellites. These satellites were built by TRW with a design life of 5 years and a weight of 1860 kg at launch. The satellites operate in the frequency ranges of 240–400 MHz with onboard signal processing for SHF uplink. The FLTSATs 7 and 8 have fleet EHF packages.
- *UFO.* UFO stands for UHF follow-on satellites, which are built to replace the FLTSAT. The program is managed by the Navy as a lead service with a plan for 10 satellites, with two satellites in each of five coverage areas. These satellites are built by Hughes Aircraft Company with a 14-year design life. These satellites also have EHF onboard signal processing packages.

11.1.2. SHF Systems. The Defense Satellite Communication System (DSCS) has been developed to provide the Department of Defense (DoD), other government agencies, and U.S. allies with global communications services. DSCS provides required national security and maintains thorough communications during crisis and conflict. The DSCS provides services that cannot be provided by other media. The services are provided for both stressed and unstressed environments. Stressed environments contain jamming, nuclear scintillation, and tactical antijam (AJ).

Unstressed environments include ATM, dedicated voice and data, high-speed computer to computer, wideband and high capacity during peace and precrisis. These satellites are built by TRW for Air Force Space Systems Division with a design life of 5 years and operating frequency ranging from 7200 to 8400 MHz.

11.1.3. EHF Systems. EHF systems can be classified into two systems:

- *Milstar.* This system, which is the latest addition to and the most advanced in the MILSATCOM architecture, provides service for mobile users for both strategic and tactical missions. The tactical missions are command and control using a low-data-rate (LDR) communication mode, tactical intelligence dissemination using both LDR and medium-data-rate (MDR) modes, Army mobile subscriber equipment using an MDR mode, and Navy task force connectivity also using an MDR mode. The strategic missions include strategic intelligence relay, tactical warning/attack assessment data relay, force management, and force report back.

The Milstar system and satellites are built to be survivable throughout all levels of conflict. The satellites are hardened to resist the effects of nuclear radiation. The Milstar communication links have high threat mitigation features such as LPI, LPD, exploitation, antijam, and antiscintillation capabilities. Other salient features associated with Milstar include LDR and MDR communication services using robust signal waveform, flexible network configuration, and interoperable terminal base.

Milstar is a joint MILSATCOM program consisting of a six-satellite constellation operating at UHF (225–400 MHz), SHF (20.2–21.2 GHz), and EHF (43.5–45.5 GHz). Milstar satellites can provide

narrow coverage spot beams and MDR nulling antenna capabilities.

- *UFO/E*. This is the ultrahigh frequency follow-on/EHF with operating frequencies in the range of 43.5–45.5 GHz for the uplink and 20.2–21.2 GHz for the downlink. The UFO/E does not support the cross-links, and it provides LDR capability only. However, UFO/E provides high-speed fleet broadcast capability.

11.2. Milstar Architecture

The Milstar system consists of three segments and the support facilities. The three segments are space, mission control, and terminal segments.

11.2.1. Space Segment. The space segment includes orbiting satellites with satellite bus, LDR and MDR payloads, and cross links. Milstar satellites are placed in geosynchronous orbits that can provide coverage up to $\pm 65^\circ$ latitude. Satellites use EHF and SHF for the uplink and downlink, respectively. There are two Milstar I satellites in orbit today with the LDR payload only. The first Milstar II was expected to be launched in early 1999.

- *LDR Payload*. This provides UHF uplink with 2 GHz bandwidth and SHF downlink with 1 GHz bandwidth. It also provides fleet broadcast services. The payload has onboard signal processing, and routing provides interconnections from EHF/SHF links to UHF uplinks and downlinks. The following are some of the features associated with the LDR payload:
 - Data rate: 75–2400 bps.
 - Frequency hopping with either low hop rate (LHR) or high hop rate (HHR).
 - Multiplexing: TDM/FDM on the uplink and TDM on the downlink.
 - Modulation: FSK on the uplink and DPSK/FSK on the downlink.
- *MDR Payload*. This supports EHF uplink with 2 GHz bandwidth and SHF downlink with 1 GHz bandwidth. It provides crosslink processing of MDR data. The payload has onboard signal processing and resource control. The following are some of the features associated with the MDR payload:
 - Data rate: 4.8 kbps–1.544 Mbps.
 - Multiplexing: TDM (up to 70 channels)/FDM (32 channels) on the uplink and single TDM on the downlink.
 - Modulation: Filter symmetric DPSK on the uplink and DPSK on the downlink.
 - Capacity: Maximum throughput of about 45 Mbps.
- *Crosslink Payload*. This simultaneously allows LDR and MDR communication data transmissions and reception between satellites. The crosslink payload also allows for command and telemetry to and from all satellites from a single ground station.

11.2.2. Mission Control Segment. The mission control segment consists of satellite control subsystem and three mission elements, namely, mission support, mission development, and mission planning elements.

- *Satellite Control Subsystem*. This provides distributed command and control via multiple satellite mission control subsystems (SMCS) and preplanned response to satellite. This subsystem uses LDR terminal EHF/SHF communications to control Milstar satellites.
- *Mission Support Element (MSE)*. This provides software and databases to control Milstar satellites. This element also supports launch, satellite initialization, and resolution of complex satellite anomalies.
- *Mission Development Element*. This provides a software tool for building SMCS and MSE database, and system simulation supports training and software/database validation.
- *Mission Planning Element*. This provides communications planning software and generates satellite and terminal database information. This element also supports communication resource apportionment, conflict resolution, contingency planning, and detailed communications network planning.

11.2.3. Terminal Segment. The terminal designs and communications protocols are required to provide for interoperable communications among Army-, Navy-, and Air Force–developed terminals. LDR terminals provide survivable tactical and strategic user communications, voice, teletype, and data. LDR terminals also provide force direction/report back, tactical command and control, and emergency message dissemination. MDR terminals can provide all of the features that LDR can provide, including imagery, targeting updates, and mobile subscriber equipment range extension. There are three basic types of terminals: Air Force Milstar, Navy, and Army terminals.

- *Air Force Milstar Terminals*. This include EHF/UHF command post-ground and transportable, as well as UHF force element (also referred to as AFSATCOM dual modem upgrade II).
- *Navy Terminals*. These include ship, shore, submarine, and MDR upgrade program.
- *Army Terminals*. These include secure mobile anti-jam reliable tactical terminal (SMART-T) and single/multiple channel anti-jam portable terminal (SCAMP) Block I and II.

11.2.4. Support Facilities. The two basic support facilities are Milstar auxiliary support center and on-orbit test facility.

BIBLIOGRAPHY

1. M. K. Simon et al., *Spread Spectrum Communications*, Vol. I, Computer Science Press, Rockville, MD, 1985.
2. R. C. Dixon, *Spread Spectrum Systems*, Wiley, New York, 1975.

3. R. Nitzberg, *Adaptive Signal Processing for Radar*, Artech House, Norwood, MA, 1991.
4. A. J. Viterbi and J. K. Omura, *Principles of Digital Communication and Coding*, McGraw-Hill, New York, 1979.
5. W. W. Peterson and E. J. Weldon, Jr., *Error-Correcting Codes*, MIT Press, Cambridge, MA, 1971.
6. R. F. Rice, *Channel Coding and Data Compression System Consideration for Efficient Communication of Planetary Imaging Data*, Tech. Memo 33-695, Jet Propulsion Laboratory, Pasadena, CA, 1974.
7. C. Berrou, A. Glavieux, and P. Thitimajshima, Near Shannon limit error-correcting code: Turbo code, *Proc. 1993 IEEE Int. Conf. Commun.*, Geneva, Switzerland, 1993, pp. 1064–1070.
8. J. J. Lemmon and R. W. Hubbard, *Multipath Measurements for the Land Mobile Satellite Radio Channel*, MSAT-X Report, **126**, Jet Propulsion Laboratory, California, 1985.
9. V. Jamnejad, *A Study of Multipath Propagation in Land Mobile Satellite Systems*, MSAT-X Report **135**, Jet Propulsion Laboratory, Pasadena, CA, 1986.
10. K. Brayer, Error patterns measured on transequatorial HF communications links, *IEEE Trans. Commun.* **COM-16**:215–221 (1968).
11. K. Brayer, Error correction code performance on HF, troposcatter and satellite channels, *IEEE Trans. Commun.* **COM-19**:781–789 (1971).
12. K. Bullington, Phase and amplitude variation in multipath fading on microwave signal, *Bell Syst. Tech. J.* **50**:2039–2053 (1971).
13. A. Johnson, *The Effect of Ionospheric Scintillation on Aircraft-to-Satellite Communications*, AFAL Report AFAL-TR-78-171, U.S. Air Force Wright Aeronautical Laboratories.
14. A. Johnson, Advisory Group for Aerospace Research and Development, AGARD Conf. 1980.
15. J. Aaros, Global morphology of ionospheric scintillations, *Proc. IEEE* **70**:360–378 (1982).
16. L. A. Wittwer, *A Trans-Ionospheric Signal Specification for Satellite C³ Applications Robust Communication Links*, 1980 Wescon Professional Program, Anaheim, CA, 1980.
17. K. L. Jordan, Jr., *Multipath Characteristics in a Satellite-Aircraft Link at 230 MHz*, Lincoln Laboratory, **MS-2605**, MA, MIT: 1969.
18. E. A. Lee and D. G. Messerschitt, *Digital Communications*, Kluwer Academic Publishers, Boston, MA, 1988.
19. B. Widrow and S. D. Stearns, in A. V. Oppenheimer, ed., *Adaptive Signal Processing*, Prentice-Hill, Englewood Cliffs, NJ, 1985.
20. S. J. Orfanidis, *Optimum Signal Processing—an Introduction*, 2nd ed., Macmillan, New York, 1985.
21. A. Whalen, *Detection of Signals in Noise*, Academic Press, New York, 1971.
22. H. Urkowitz, Energy detection of unknown deterministic signals, *Proc. IEEE* **55**:523–531 (1967).
23. J. Omura and M. Simon, *Modulation/Demodulation Techniques for Satellite Communications; Part I: Background*, JPL Publication 81–73, 1981.
24. L. V. Blake, *Radar Range-Performance Analysis*, Artech House, Norwood, MA, 1986.
25. W. Diffie and M. Hellman, New directions in cryptography, *IEEE Trans. Inform. Theory* **IT-22**:644–654 (1976).
26. C. C. Wang, *Exponentiation in Finite Fields*, Ph.D. dissertation, Univ. California, Los Angeles, 1985.
27. R. Merkle and M. Hellman, Hiding Information and Receipts in Trapdoor Knapsacks, *IEEE Trans. Inform. Theory* **IT-24**:525–530 (1978).
28. R. J. McEliece, *A Public Key Cryptosystem Based on Algebraic Coding*, DSN Progress Report **42–44**, Jet Propulsion Laboratory, 1978.
29. R. O. Harger, *Synthetic Aperture Radar Systems Theory and Design*, Academic Press, New York, 1976.
30. D. Casasent, R. Schaefer, and R. Sturgill, Optical hit-miss morphological transform, *Appl. Opt.* **31**(29):6255–6263 (1992).
31. D. Casasent, Optical morphological processors, *Proc. SPIE—Int. Soc. Opt. Eng.* **1350**:380–394 (1990).
32. J. B. Adams, Probabilistic reasoning and certainty factors, in B. G. Buchanan and E. H. Shortliffe, eds., *Rule-Based Expert Systems*, Addison-Wesley, Reading, MA, 1988, pp. 263–271.
33. G. Shafer, *A Mathematical Theory of Evidence*, Princeton Univ. Press, Princeton, NJ, 1976.
34. J. Gordon and E. H. Shortliffe, The Dempster–Shafer theory of evidence, in B. G. Buchanan and E. H. Shortliffe, eds., *Rule Based Expert Systems*, Addison-Wesley, Reading, MA, 1988, pp. 272–292.
35. J. Pearl, *Probabilistic Reasoning in Intelligent Systems: Networks of Plausible Inference*, Morgan Kaufmann, San Mateo, CA, 1988.
36. D. Casasent, Computer generated holograms in pattern recognition: A review, *Opt. Eng.* **24**:724–730 (1985).
37. R. D. Scott et al., Sensor fusion using K-nearest neighbor concepts, *Proc. SPIE—Int. Soc. Opt. Eng.* **1383**:367–378 (1991).
38. G. Parthasarathy and B. N. Chatterji, Class of new KNN method for low sample problems, *IEEE Trans. Syst., Man Cybern.* **20**:715–718 (1990).
39. S. K. Rogers et al., Artificial Neural for Automatic Target Recognition, *Proc. SPIE—Int. Soc. Opt. Eng.* **1294**:2–12, (1990).
40. R. Mamlook and W. E. Thompson, A multi-target and multi-background classification algorithm using neural networks, *Proc. SPIE—Int. Soc. Opt. Eng.* **1955**:218–225 (1993).
41. The Institute of Navigation, *Global Positioning System*, Vol. I and II, Washington DC, 1984.
42. D. H. Martin, *Communication Satellites, 1958–1992, 1991*, The Aerospace Corporation, El Segundo, CA.
43. MILSATECOM, JETO, Milstar Training, Part I, Milsatcom Joint Terminal Eng. Office.
44. MILSATECOM, JETO, Milstar Training, Part II, Milsatcom Joint Terminal Eng. Office.

MILLIMETER-WAVE INTEGRATED CIRCUITS

HUEI WANG
 KUN-YOU LIN
 REN-CHIEH LIU
 HONG-YEH CHANG
 National Taiwan University
 Taipei, Taiwan

Millimeter-wave (MMW) components are becoming more available and affordable because of advances in the design, processing, testing, and packaging technology. MMW circuits have become smaller, highly integrated, and low-cost, and are being applied in instrumentation, electronic

warfare, satellite communications, and other applications. As a result, many MMW systems are being developed and deployed that provide new and unique capabilities such as more information transfer (wider bandwidth), enhanced precision (higher resolution), and all-weather operation (through fog, dust, and smoke), for both military and commercial applications. Monolithic MMW integrated circuits (MMICs¹) are crucial to meet the requirements for the MMW systems and play an important role in the MMW components. This article describes the current status of MMW monolithic integrated circuits, including the MMIC technologies, representative designs, and performance for various integrated circuits.

1. MMIC TECHNOLOGIES IN MMW REGIME

For MMW electronics, a large number of different semiconductor materials such as Si, SiGe, GaAs, InP, and other III–V compounds, as well as wide-bandgap materials, have been employed [1]. Various types of microwave transistors exist, including metal semiconductor field-effect transistors (MESFETs), metal-oxide-semiconductor field-effect transistors (MOSFETs), high-electron-mobility transistors (HEMTs), and heterojunction bipolar transistors (HBTs). MMW transistors are the backbone of all the MMW systems. They have also undergone an impressive evolution. Continuous efforts in research of traditional GaAs FETs and HBTs have been improved. New classes of microwave transistors, such as wide-bandgap FETs and metamorphic GaAs HEMTs, have been introduced. Furthermore, Si saw a renaissance in microwave electronics. SiGe HBTs are now available commercially [2]. In addition, Si MOSFETs, which formerly were considered slow devices not suited for MMW operation, have progressed rapidly and demonstrated the applications in MMW MMICs.

1.1. High-Electron-Mobility Transistor (HEMT)

HEMT is a field-effect transistor whose conduction carriers are separated from the donor impurities that supply the electrons. Other names include two-dimensional electron gas FET (TEGFET), modulation-doped FET (MODFET), heterostructure FET (HFET), and selectively doped heterostructure transistor (SDHT), which focus on different aspects of the device. Since no impurities are present in the channel as scatterers, the electron mobility increases, which means that HEMT has higher operating frequency, and lower noise figure than do those of the MESFET counterparts [3]. A typical layer structure of a HEMT device is shown in Fig. 1. MESFET, on the other hand, has a structure similar to that of MOSFET, except that in a MESFET, the gate is isolated from the drain and source by the Schottky junction instead of an actual oxide layer.

Several families of HEMTs currently exist, categorized by their substrate and composition of their channels. The

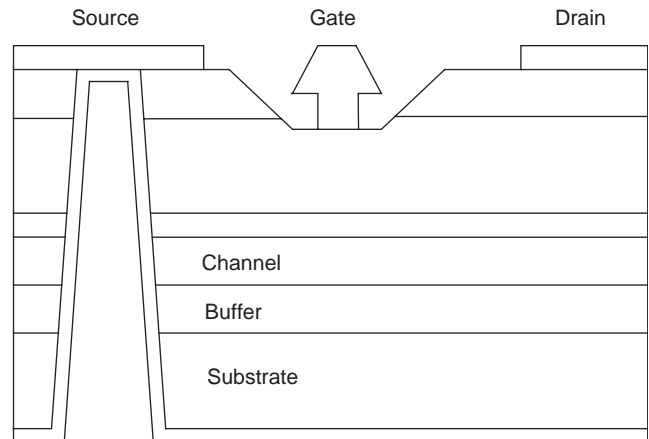


Figure 1. Cross section of a HEMT structure. Electrons travel in the undoped channel layer, which are provided by the layers adjacent to the channel; in MESFETs, the channel is n-doped GaAs, and the doping reduces the electron mobility of the material and therefore yields a poorer performance compared to that of HEMT.

earliest HEMT devices were lattice-matched HEMTs [4]. In lattice-matched HEMT, the electron gas is located on the undoped GaAs in the AlGaAs/GaAs junction. With addition of indium to the channel, the electron mobility can be increased. Pseudomorphic HEMTs (PHEMT), InP HEMT, and metamorphic HEMTs (MHEMT) were developed by adding different concentrations of indium in the electron gas channel. The performance of these devices has superseded that of lattice-matched HEMTs; therefore lattice-matched HEMTs on GaAs are rarely seen nowadays. PHEMT on GaAs substrate is currently the most popular type of HEMT available; a thin-strained $\text{In}_x\text{Ga}_{1-x}\text{As}$ ($x = 0.15\text{--}0.35$) layer is grown at the site where the two-dimensional electron gas is located, and this strained layer, while maintaining lattice integrity, is responsible for the term “pseudomorphic” for this device. InP HEMTs use InP as the substrate, and $\text{In}_x\text{Ga}_{1-x}\text{As}$ ($x = 0.53$) as a channel, which is lattice-matched to the InP substrate. InP PHEMT consists of $\text{InAlAs}/\text{In}_x\text{Ga}_{1-x}\text{As}$ ($x > 0.53$) on InP substrate. InP PHEMTs have exhibited the best performance in noise and operating frequency to date, but the substrate is very brittle and difficult to fabricate. To circumvent the disadvantages of InP substrate and still retain the performance of InP HEMTs, MHEMT grown on GaAs substrate has been developed. In MHEMTs, a buffer layer is grown to provide good lattice match between the GaAs substrate and the GaInAs channel. Another HEMT device, namely, GaN HEMT, which has wide bandgap (3.4 eV) and moderate electron mobility, is extremely attractive for power amplifier designs. Presently, the lack of a GaN substrate poses a disadvantage for mass production, but its electrical properties still make GaN HEMT a potential contender in power applications at microwave frequency. The characteristics and performance of each type of HEMT will be introduced in the following text.

1.1.1. GaAs pseudomorphic HEMT. GaAs PHEMT is currently most popular because of its early development and mature fabrication. Many commercial MMIC foundries are

¹The acronym MMIC usually stands for monolithic microwave and/or MMW integrated circuit. In this article, we use it for monolithic MMW integrated circuit in particular.

available, including the most advanced 6-in. GaAs wafer processes. A lot of information can be found in the literature on the subject of GaAs PHEMTs, such as a brief summary and comparison of various PHEMT devices and InP HEMT devices [5]. Depending on gate length and periphery, GaAs PHEMTs can operate from 2 to 120 GHz, with output RF power up to 1 W at 44 GHz [6].

Traditional PHEMTs are AlGaAs/InGaAs/GaAs structures. However, this structure has several disadvantages, mostly in the area of fabrication control and thermal stress. More recent research on GaAs PHEMT has focused on InGaP/InGaAs/GaAs structure. InGaP has several advantages over AlGaAs: higher bandgap (1.92 eV), higher valence band discontinuity, no deep-complex center, excellent etching selectivity between InGaAs, and good thermal stability [7]. InGaP contains no aluminum, which makes the device more inert in atmosphere, adding to the stability of the device. These advantages translate to lower noise, higher associated gain, constant threshold voltage, and lower $1/f$ noise. Huang et al. have shown a 0.25- μm InGaP/InGaAs/GaAs HEMT with an f_T of 85 GHz, f_{max} of 160 GHz, and a minimum noise figure of 0.46 dB at 12 GHz [7].

1.1.2. InP HEMT. In GaAs PHEMTs, the two-dimensional electron gas is at the strained $\text{In}_x\text{Ga}_{1-x}\text{As}$ ($x = 0.15\text{--}0.35$) layer. It is possible to increase the speed of the electrons in the channel by increasing the mole fraction of indium. However, higher indium composition will excessively distort the lattice making the device incapable of being manufactured on GaAs substrate. Because InP has a lattice constant closer to that of InGaAs, channels that are InGaAs (where indium has the higher mole fraction) are fabricated on InP substrates. HEMTs on InP substrate can also be fabricated into pseudomorphic HEMTs, but the distinction between InP lattice-matched HEMT and PHEMT is seldom emphasized.

InP HEMTs have a significantly better speed/frequency response ratio compared to that of GaAs PHEMTs. Several reports demonstrated f_T over 300 GHz [8–10], and a device with 400-GHz f_T has been reported [11]. An f_{max} of >600 GHz has also been reported [12,13]. InP HEMTs also have the lowest noise figure of any room-temperature receiver technology, and are often further exploited by cryogenic freezing to achieve ultra-low-noise amplifications. Grundbacher et al. demonstrated a W-band cryogenic MMIC LNA operating at 20 K that shows over 23 dB gain with a noise temperature of 30–40 K (0.45–0.6 dB noise figure) over the band of 80–105 GHz [14].

1.1.3. GaAs metamorphic HEMT. MHEMT combines the affordability of GaAs process and the performance of InP HEMTs by growing the active layers on a strain-relaxed, compositionally graded metamorphic buffer layer. This buffer layer can be adjusted to accommodate any indium content channel desired (30–80%), which allows device designers an additional degree of freedom to optimize the transistor performance. GaAs MHEMTs outperform GaAs PHEMTs in terms of noise and efficiency, and rival InP HEMTs.

The indium content of MHEMTs can be adjusted over a wide range. MHEMTs with intermediate indium content

(25–45%) can offer high breakdown voltages, large power densities, and better noise performance than PHEMTs. Whelan et al. [15] demonstrated the performance of MHEMT at 25 GHz with an NF_{min} (minimum noise figure) of 1.18 dB and associated gain of 10.7 dB; a GaAs PHEMTs with the same periphery has 0.4 dB higher NF_{min} and 3 dB less associated gain. The power density of MHEMT at 35 GHz is 830 mW/mm and a PAE (Power-added efficiency) of over 40%, which beats (outperforms) the same PHEMT by 130 mW/mm. A V-band MHEMT MMIC power amplifier with high efficiency has also been demonstrated with an output power of 23 dBm and PAE of 39–43% from 56 to 63 GHz [16].

1.1.4. GaN HEMT. Most power devices have a low input impedance (under 10 Ω), which makes matching network design very difficult. The higher power density of GaN HEMT translates to a smaller device periphery, which offers an input impedance much higher than that of other power devices. High operation voltages make GaN HEMTs compatible with 28-V systems (standard wireless base stations), which offer higher efficiency and simplified cooling [17]. Because of the lack of native substrates, GaN HEMTs are usually fabricated on SiC or sapphire. GaN HEMTs on Si substrate were also demonstrated, but suffered a loss of power density.

The highest power density of GaN HEMTs reported to date has been fabricated on SiC substrate [18]. At a frequency of 10 GHz, a 1.5-mm device has an output power of 13.8 W (power density of 9.2 W/mm), and PAE of 33%. At a frequency of 20 GHz, a power density of 6.4 W/mm and PAE of 16% was demonstrated [19]. The noise performance of GaN HEMTs on SiC substrate was also reported with a minimum noise figure of 1.5 dB at 26 GHz [20]. GaN HEMTs on sapphire substrates demonstrate a power density of 3.6–4.2 W/mm at 8–10 GHz [21,22]. GaN HEMTs on Si substrate usually has a power density of under 2 W/mm, but a GaN HEMT on resistive Si has demonstrated a power density of 6.6 W/mm at 2 GHz [23].

Several commercial HEMT processes are available. Lattice-matched HEMTs are virtually nonexistent nowadays. Velocium provides several GaAs PHEMT and InP HEMT processes [204], and its performance is recognized as state of the art. Their 0.15- μm GaAs PHEMT process has an f_T of 80 GHz and f_{max} of 200 GHz and 0.10- μm GaAs PHEMT process has an f_T of 120 GHz and f_{max} of 250 GHz; the 0.10- μm InP HEMT process has an f_T of 180 GHz and f_{max} of 350 GHz. Raytheon RF Components (now part of Fairchild RF) offers the best commercial MHEMT process; their standard low noise 0.10- μm MHEMT process has an f_{max} of over 260 GHz [204] and ultralow noise of 0.24 dB NF_{min} at 12 GHz [205]. There has been no commercial GaN HEMT process until now; most reports have been in academia or R&D; however, many online resources give up-to-date news on the latest developments of GaN technology [206,207].

1.2. Heterojunction Bipolar Transistor (HBT)

The heterojunction bipolar transistor (HBT) is an improved type of conventional bipolar transistor (BJT).

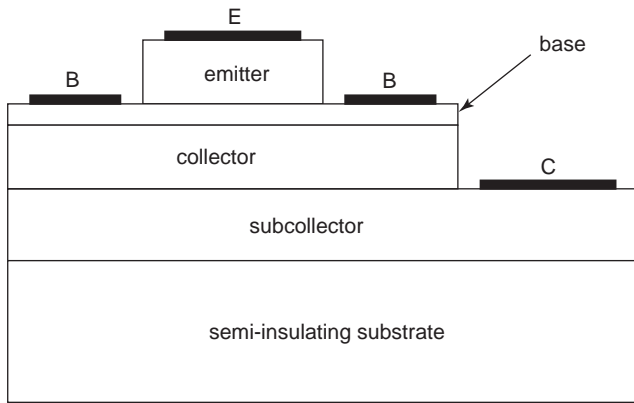


Figure 2. Cross section of HBT structure.

HBT has the same vertical structure as that of BJT, as shown in Fig. 2. This emitter material has a wider energy bandgap than does base material, and therefore the term “heterojunction” applies for this device. With wider bandgap, the base doping density can be increased without decreasing the current gain. Increasing base doping thus reduces base resistance and improves the maximum oscillating frequency (f_{max}). This significantly improves the operating frequency of the HBT [1].

In comparison to bipolar transistors, HBT can be optimized for a higher f_T , a higher Early voltage (high output resistance), a lower base-emitter capacitance, a reduced base resistance, or a higher voltage-handling capability. Compared with GaAs- or InP-based HEMT, HBT offers a higher transconductance, a higher current density, a lower flicker noise ($1/f$ noise), and better threshold voltage uniformity.

Several families of HBTs currently exist, which can be categorized by their substrates and layer materials. HBT on GaAs substrate is most popular now. In GaAs-based HBT, GaAs and AlAs both have the zincblende structure with a lattice constant of about 5.65 Å. Since GaAs and AlAs have similar lattice constants, one can choose the composition x of the ternary compound $Al_xGa_{1-x}As$ as the layer material to fit the particular device requirement. InP HBTs use InP as substrate and InGaAs as layer material. Because GaAs and InAs do not have the same lattice constant with InP, the ratio of In and Ga in InGaAs should be selected carefully. One can choose $In_{0.53}Ga_{0.47}As$ to grow a lattice-matched layer to InP substrate. SiGe HBTs use Si as the substrate and SiGe as the layer material. The materials used to produce HBTs can be classified according to substrate materials, as shown in Table 1.

Table 1. Range of HBT Materials Currently in Use

Substrate	Emitter	Base	Collector
GaAs	AlGaAs	GaAs orAlGaAs	GaAs orAlGaAs
	GaInP	GaAs orAlGaAs	GaAs orGaInP
InP	InP	InGaAs	GaAs orGaInP
	AllnAs	InGaAs	InGaAs orGaInP
Si	Si/poly-Si	SiGe	Si
Sapphire	AlGaN	GaN	GaN

Source: Ref. 24.

1.2.1. GaAs HBT. AlGaAs was the first material used for emitter material of GaAs HBT. Because GaAs and AlAs have similar lattice constants and AlGaAs has a wider bandgap than does GaAs, one can arbitrarily choose the concentration of Al in AlGaAs to produce the emitter, or even a grading emitter. However, Al suffers from the incorporation with oxygen; that is, Al_2O_3 will increase the recombination current and thus decrease the current gain. InGaP is found to be more appropriate for manufacturing because of the selective etching solution. To etch GaAs using H_2O_2 to adjust with NH_4OH automatically stops at InGaP, while using HCl to etch InGaP also stops at GaAs [25]. In addition, InGaP will not suffer from the oxidation as the AlGaAs does. However, it is difficult to use InGaP to produce grading emitter because the lattice constant is different from that of GaAs. The f_T and f_{max} of GaAs HBT are generally higher than 100 GHz. In 2001, an InGaP/GaAs HBT with an f_T of 156 GHz and f_{max} of 255 GHz, with a collector-emitter breakdown voltage of 9.6 V was reported [26]. This means that GaAs HBTs have the potential to operate at frequencies higher than 200 GHz.

Several commercial foundries provide GaAs HBT processes. WIN Semiconductors provides 2- μm HBT with 35-GHz f_T and 100-GHz f_{max} , together with 1- μm HBT of 65-GHz f_T and 80-GHz f_{max} [208]. Velocium has GaAs HBT with 42-GHz f_T and 72-GHz f_{max} [209]. TriQuint Semiconductor provides 3- μm InGaP HBT with 28-GHz f_T and 46-GHz f_{max} [210]. Global Communication Technology Corporation (GCTC) provides 2- μm HBT with 35-GHz f_T and 60-GHz f_{max} [211]. GCS provides high-power process with 45-GHz f_T and 55-GHz f_{max} , while a high-speed process is available with 65-GHz f_T and 70-GHz f_{max} [212].

1.2.2. InP HBT. InP has higher electron mobility than does GaAs, and thus it can operate at higher frequency. It has the best potential for high-speed operation, with f_T and f_{max} usually higher than 150 GHz. InP HBT is also suitable for very high speed applications. The f_T and f_{max} of InP-based HBT have also been demonstrated to exceed 300 GHz [27,28], with the DHBT (double heterojunction bipolar transistor) structure, which means that the base-emitter and base-collector junctions are all heterojunctions. This makes InP HBT the highest-speed transistor at present.

There are a couple of commercial InP HBT foundry services. Velocium provides InP HBT with 150-GHz f_T and 180-GHz f_{max} [209]. Global Communication Semiconductors, Inc. (GCS) also has InP HBT with 150-GHz f_T and 180-GHz f_{max} [212].

1.2.3. SiGe HBT. SiGe HBT has received a much attention lately because it can be easily adopted to the highly matured Si-based CMOS process and thus is potentially lower cost compared with the III-V material-based HBTs (GaAs- or InP-based HBTs). SiGe HBT technology is rapidly advancing at present. Besides the potential of low cost, since SiGe HBT is also fabricated on silicon substrate, it can easily be integrated with CMOS technology. However, it has the disadvantage of lower breakdown

voltage and poorer power handling than the GaAs- and InP-based HBTs.

At present, SiGe HBTs with f_T and f_{max} greater than 150 GHz were reported. In 2001, a 0.18- μm -emitter-width HBT with 180-GHz f_{max} and 210-GHz f_T was reported [29]. The breakdown voltages of collector-emitter and collector-base are 3.3 and 5.5 V, respectively. Although the operating frequency of the SiGe HBT is comparable to that of GaAs HBT, the breakdown voltage is usually lower. There are still some challenges to improve the breakdown voltage and thus enhance the power performance.

The companies that provide SiGe HBT foundry service are as follows. Taiwan Semiconductor Manufacturing Company Ltd. (TSMC) provides 0.35- μm SiGe HBT with 62-GHz f_T and 70-GHz f_{max} [213]. IBM has provided 0.18- μm SiGe HBT with 120-GHz f_T and 100-GHz f_{max} , together with 0.25- μm , 0.35- μm , and 0.5- μm HBT [214]. Atmel provides 0.3- μm SiGe HBT with 50-GHz f_T and 90-GHz f_{max} , as well as 0.5- μm HBT with 30-GHz f_T and 50-GHz f_{max} [215].

1.2.4. Applications. In digital applications, high-speed digital circuits using emitter-coupled logic (ECL) or current-mode logic (CML) are implemented by HBTs. With high operating frequency of HBT, ECL of up to several tens of GHz can be designed. For example, a 47–48-GHz frequency divider was reported using GaAs HBT ECL and CML [30]. On the other hand, for analog applications, HBTs cover a range of applications, including linear amplifiers, wideband amplifiers, power amplifiers, low-phase-noise oscillators, and mixers. Among these, the power amplifier is most important for current wireless communication applications. HBTs have advantages for power amplifier design due to their high breakdown voltage and high current density. Many commercial power amplifier products are fabricated using HBTs. Another important application for HBT is low-phase-noise oscillators due to the low flicker noise characteristics of the HBT. HBTs were also used to design wideband amplifiers. Using the Darlington pair, a compact wideband InP HBT amplifier operating up to 85 GHz was reported in 2000 [31]. The device has an f_T of 120 GHz and f_{max} of 150 GHz.

1.3. CMOS/BiCMOS

Since the late 1970s, the metal oxide semiconductor field-effect transistor (MOSFET) has been extremely popular. Most very-large-scale integrated circuits (VLSI), such as digital logic, memory, and analog functions, are fabricated using MOS technology at the present time. RF integrated circuits (RFICs) are also preferably designed using complementary MOS (CMOS) transistors, due to the low cost of Si process and integration capability with baseband circuits. Owing to the rapid development of the deep-submicrometer CMOS technologies, many CMOS MMW circuits have been demonstrated [32–36].

In most MOSFETs, the gate is one plate of a capacitor separated by a thin dielectric from the bulk. With no voltage applied to the gate, the transistor is essentially non-conductive between the source and drain terminals. When a voltage of sufficient magnitude is applied to the gate,

charge of opposite polarity is induced in the semiconductor, thereby enhancing the conductivity.

1.3.1. CMOS. A p-channel enhancement-type MOSFET (PMOS) is fabricated on an n-type substrate with p^+ regions for the drain and source, with holes as charge carriers. In contrast, an NMOS is formed on a p-type substrate with n^+ regions for the drain and source, and electrons as charge carriers. PMOS was originally the dominant technology. However, since the electron mobility is higher than the hole mobility, the speed and the current-driving capability of NMOS devices are much better than those of the PMOS devices. NMOS technology has eventually replaced PMOS. Complementary MOS (CMOS) RF ICs are designed using complementary MOS (CMOS) technology employs both PMOS and NMOS transistors and enables various aspects of circuit design. Therefore, CMOS is most popular among all the MOS IC technologies at the present time.

A cutoff frequency of 125 GHz for a 70-nm gate bulk Si MOSFET [37] and 245 GHz f_T [38] for an 80-nm CMOS were reported in 1997 and 2001, respectively. For a long time, MOSFETs suffered from relatively low power gains at high frequencies and low f_{max} . The main reasons for this were the high specific resistance of the gate material (polysilicon) and the fact that the mushroom gates generally used in HEMT were not yet available in standard Si CMOS processes. A lot of efforts have been spent to reduce the gate resistance by depositing silicides or metal on top of the polysilicon and by employing metal gates. These effects finally led to improved power gain and f_{max} behavior. A 0.18- μm gate bulk MOSFET with an f_{max} of 150 GHz has been reported [39]. A standard commercial process featuring 0.25-, 0.18-, 0.13- and 90-nm CMOS mixed-signal (MS) and RF technologies has been reported [2]. The traditionally limited f_T and f_{max} in CMOS have been improved through the shrinkage of gate oxide thickness and device dimension. The f_T increases from 33 GHz in 0.25- μm technology with 50 Å of gate oxide to 110 GHz in 90-nm technology with 17 Å of gate oxide. Meanwhile, f_{max} of the 90-nm technology is improved to approximately 90 GHz from the f_{max} of 30 GHz for 0.25- μm technology.

1.3.2. SoI/SoS technologies. SoI (Silicon on Insulator) CMOS devices are placed on the insulator, namely, the silicon dioxide. Each SoI CMOS device is completely separated from the silicon substrate. The SoI CMOS is advantageous over bulk CMOS because of the elimination of area junction capacitance, the lack of reverse body effect in stacked circuits, and the fact that the SoI body is slightly forward-biased under most operating conditions. A 0.13- μm SoI CMOS has been used to implement a 40-GHz VCO with 9–15% tuning range [40]. A 40-nm gate SoI MOSFET with a record f_{max} of 193 GHz [41] and a 80-nm gate SoI MOSFET with a record f_{max} of 185 GHz [42] have been reported. Silicon-on-sapphire (SoS) CMOS technology is also attractive for RF applications because of its reduced parasitic capacitance and reduced minimal capacitive substrate loss. Fabricated 250-nm T-gated devices can achieve 105-GHz f_T and 50-GHz f_{max} for n-channel operation [43]. However, both

Table 2. State-of-the-Art LNA above 30 GHz

Technology	Frequency (GHz)	Gain (dB)	NF (dB)	Ref.
GaAs PHEMT	43	22	1.8	48
InP HEMT	60	22.8	2.2	49
InP HEMT	93	20	3.7	50
GaAs PHEMT	94	30.8	4	51
GaAs PHEMT	113	10	5.5	52
InP HEMT	142	9	—	53
InP HEMT	155	12	5.1	54
InP HEMT	170	6	6	55
InP HEMT	205	17	—	56
InP HEMT	215	17	—	57

SoI and SoS CMOS technologies are mostly in the R&D phase and are not widely being used for production.

1.3.3. SiGe HBT and BiCMOS. There is clear trend to shift the research efforts to HBTs for higher frequencies, especially for MMW applications. SiGe HBT can be fabricated with the existing Si CMOS technology with only a few more steps added [2]. A 60-GHz SiGe bipolar transceiver circuit including an LNA, a direct downconverter, a PA, and a VCO has been reported [219]. On the other hand, BiCMOS technology development began in the early 1980s as a way of significantly enhancing digital performance. This technology combines bipolar and CMOS transistors on the same IC chip and therefore is attractive for high-level integrations, and even system-on-chip (SoC) applications. The low frequency and broadband noise characteristics of SiGe HBT are superior to those of CMOS. The high transconductance of the BJT and HBT leads to lower optimum source reflection coefficient and noise resistance, simplifying lower-power noise matching. The resulting circuits retain the characteristics of low power, high input impedance, and wide noise margin of CMOS and the high current-driving capability and high speed of operation of bipolar transistor [44].

2. MILLIMETER-WAVE MMICs

2.1. Amplifiers

2.1.1. Low-Noise Amplifiers. A low-noise amplifier (LNA) is usually the first component in a receiver, due to the signal-to-noise ratio (SNR) consideration. The gain and noise figure are the two most important parameters in the design. For a MMW LNA, although the design principle is similar to that in the microwave range, as documented in many textbooks [17], there are some special

considerations. The appropriate technology must be selected before the circuit design. GaAs PHEMT and InP-based HEMT are typically the choices for low noise and high gain. MHEMT has received attention and demonstrated comparable performance as InP HEMT. The device size needs to be carefully selected to fulfill the design goals based on an accurate device model or measured small-signal scattering (S) parameters and noise-parameters. Both microstrip-line and coplanar waveguide (CPW) designs were found in the literature. Either way, the layout design tends to be simple, especially for those designs above 100 GHz in order to avoid the uncertainties of the passive-element models. The substrate thickness is also a concern in the microstrip-line design for single-mode operation, such as 3-mil or thinner is typically used for circuits above 100 GHz. EM simulation, nevertheless, is critical in high-frequency LNA design. The layout, EM, and circuit simulation will need to be performed iteratively to attain the desired targets. The stability issue also requires thorough investigations; one needs to ensure that the circuit is free of oscillation from very low frequency until it has no gain.

The state-of-the-art LNAs above 40 GHz are listed in Table 2. It is observed that the HEMT technology still demonstrates low noise and high gain performance in MMW regime and InP HEMT produces best results above 100 GHz. The highest-frequency LNA to be reported as of 1999 [45] had 17 dB gain at 215 GHz with six stages, and the layout is shown in Fig. 3.

Regarding silicon-based devices, CMOS and SiGe HBT have also evolved rapidly. The unity-gain frequency (f_T) values of CMOS and SiGe HBT have been reported to be about 95 and 90 GHz, respectively [46,47], indicating the potential for high-frequency application of silicon technology. Currently there are MMIC LNAs above 20 GHz using CMOS and SiGe HBT [47,48]. It is expected that MMW LNA using Si-based device will be reported in the near future.

2.1.2. Power Amplifiers. A power amplifier (PA) is typically used at the front end in a transmitter and is required to provide sufficient gain and output power to transmit the signal. In the MMW regime, traveling-wave tube amplifiers (TWTAs) have been used for very-high-power applications up to 140 kW level [58]. More recently, solid-state power amplifiers (SSPAs) and MMIC PAs for medium-power-level applications of several watts have been developed [59]. In addition to the output power, linearity is usually another important design consideration in many communication systems.

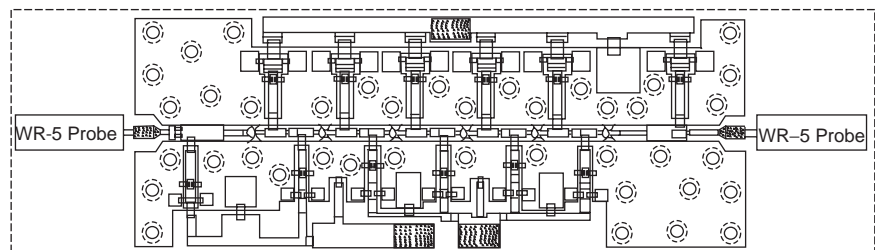


Figure 3. Layout of the six-stage amplifier including WR-5 coupling probes (© 1999 IEEE) [45].

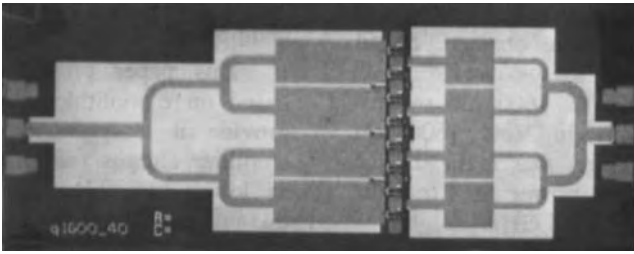


Figure 4. The Ka-band prematch structure (©1993 IEEE) [60].

The design principle of a MMW PA is also similar to that in the microwave regime. However, it is still not easy to obtain accurate optimal load impedance of a power transistor from load-pull testing since such a transistor usually has a large size and thus very low input and output impedances. Instead, the prematch approach was proposed, and an example can be found in Ref. 60. The combined transistors with a total gate periphery of $1600\ \mu\text{m}$ were used to form a pre-matched structure as shown in Fig. 4, and thus the very low input/output impedances were transformed to desired values that can be measured and characterized. A two-stage Ka-band 1.6-W amplifier was developed using a single prematched structure to drive four prematched structures [60]. The MMIC PAs with higher power and gain requirements can then be designed on the basis of a similar structure in the next iteration. On the other hand, the more recent advancement of nonlinear modeling techniques and CAD tools is no doubt beneficial to predict the power contour of a transistor, even at high frequencies.

The MMW MMIC PAs are currently dominated by III-V compound HEMT (GaAs- or InP-based) devices, due to high gain characteristics at high frequencies. A few low-medium-power amplifiers designed for high linearity using HBTs were also reported at Q band [61]. For thermal concerns of PA design, the thin-substrate (≤ 2 mil) MMIC technology has been emphasized [62]. The thin substrate not only enhances the thermal conductivity but also benefits the PA design with a number of features: (1) the ground via holes can be made smaller so that they can be placed under the HEMTs for a more compact device layout; (2) the via hole inductance, which directly translates to the source inductance of the common source HEMT, is drastically reduced and thus enhances the gain performance at MMW frequencies; and (3) the low impedance microstrip lines on a thinner substrate are narrower and thus make the whole PA layout more compact. All these

features will improve the output power, power gain, and power-added efficiency (PAE) of a PA. In fact, most of state-of-the-art MMW MMIC PA results to date were obtained using 2-mil technologies. A Q-band 3-W PA is realized with 2-mil $0.15\text{-}\mu\text{m}$ GaAs PHEMT process [63], and a 62.5-GHz PA using the same technology has demonstrated 564 mW and achieved 21% PAE [64]. A set of PA MMIC chips reported by Wang et al. [65] covers 70–113 GHz using 2-mil, $0.1\text{-}\mu\text{m}$ GaAs PHEMTs.

The power-combining technique is often used to build a high-power module with multiple MMIC PA chips. Since the combining structures usually occupy large areas, they can be implemented using low loss and less expensive substrates, such as Al_2O_3 , or quartz. A Ka-band power module demonstrated 6-W output power, 24% PAE, and 21.5 dB associated power gain using an eight-way binary Wilkinson combiner realized on Al_2O_3 substrate, as illustrated in Fig. 5 [59]. A V-band power module design utilizing an eight-way radial combiner consisting of eight basic units, with each basic unit containing three-way planar combiners and three power amplifiers, has been reported [66]. It achieved 3.8 W output power and 31 dB power gain. A 0.35-W, 94-GHz PA module was also reported [67].

A number of amplifiers with medium output power and/or wide bandwidth were also reported using InP-based devices, such as a 85-GHz 16.2-dBm common-base amplifier and a 90-GHz 14 dBm cascode amplifier, fabricated using InP DHBT [68], and also a 60–145-GHz amplifier with 24 mW output power using $0.1\text{-}\mu\text{m}$ InP HEMTs [69].

2.1.3. Broadband Amplifiers

2.1.3.1. Distributed Amplifiers. Distributed amplifiers (DAs), also commonly referred to as *traveling-wave amplifiers* (TWAs), are broadband circuits whose gain-bandwidth product substantially exceeds the transistor unity-gain frequency f_T because the input and output capacitances of the active devices can be absorbed in the distributed structures. Figure 6 shows the schematic of a conventional DA designed with FETs. It consists of input and output transmission lines coupled by the transconductances of the FETs. The transmission lines are formed by using lumped inductors and are referred to as the *gate* and *drain lines*. The gate line is periodically loaded by the FET gate-source capacitance and is terminated in its characteristic impedance at the end. As the RF signal travels on the gate line, each transistor is excited by the traveling voltage wave and transfers the signal to the

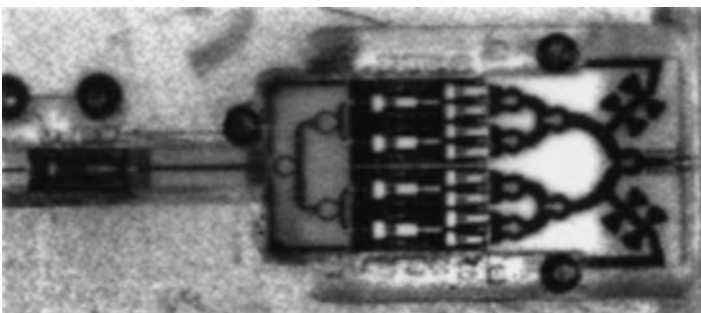


Figure 5. Photograph of a 6-W power module (© 1997 IEEE) [59].

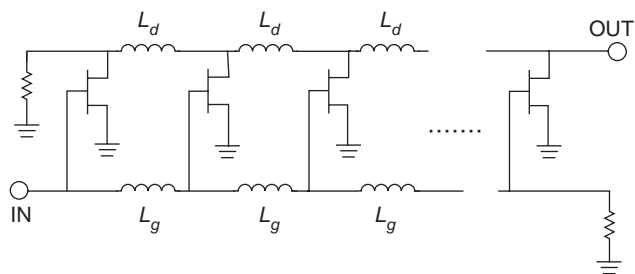


Figure 6. Schematic of the conventional distributed amplifier designed using FETs.

drain line through its transconductance. If the phase velocities on the gate line and drain line are identical, the in-phase signals on the drain line will add up along the forward direction as they arrive at the output. The out-of-phase wave traveling in the reverse direction will be absorbed by the drain-line termination.

A GaAs HEMT distributed amplifier, shown in Fig. 7, demonstrated 20 dBm output power at 1–50 GHz [70]. To improve the output power, a cascade broadband driver distributed PHEMT amplifier with a high-output-power output stage and a bandwidth of 17–40 GHz with an output power of 22.5 dBm has been proposed [71].

2.1.3.2. Cascode Distributed Amplifier. In addition to the common-source topology DAs [72,73], the cascode configuration is generally used to improve the gain-bandwidth product of MMW DAs. The cascode configuration, known for its high maximum available gain, wide bandwidth, improved input-output isolation, and variable gain control capability, has been utilized in many applications such as mixers, frequency multipliers, and distributed amplifiers. The DAs using InP-based HEMTs demonstrated 1–112 GHz bandwidth with 7 dB gain and 1–157 GHz bandwidth with 5 dB gain, and Fig. 8 shows the schematic and chip photo [74]. These amplifiers were designed using cascode cell and gate-line capacitive division to achieve high cutoff frequency.

2.1.3.3. Matrix Distributed Amplifier. The matrix DA has the advantages of additive and multiplicative amplification and provides higher gain as well as better reverse isolation over a wide frequency range. The matrix DA was

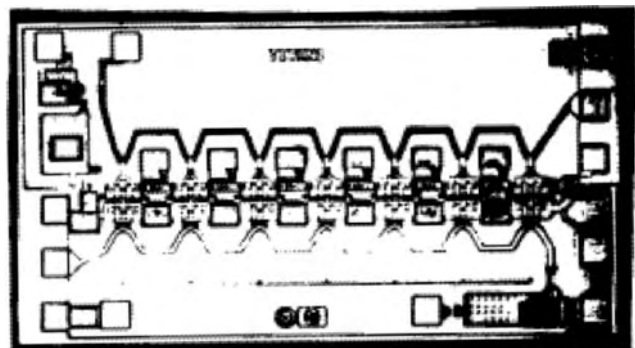
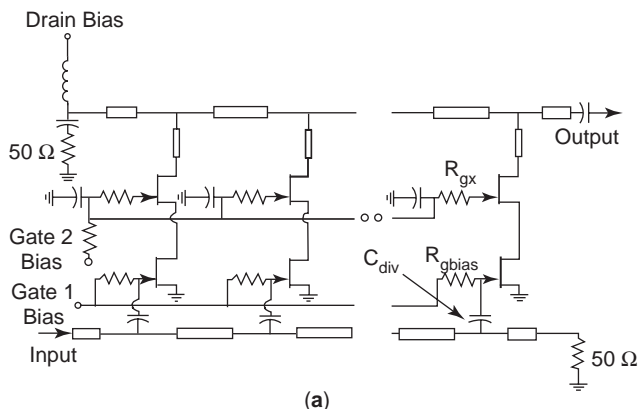
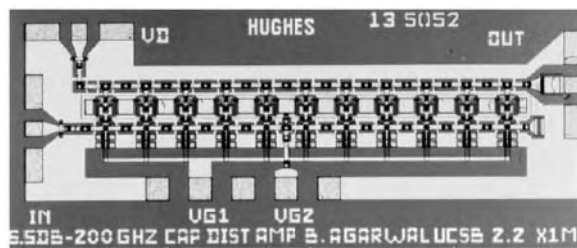


Figure 7. Photograph of the 1–50-GHz power amplifier [70].



(a)



(b)

Figure 8. (a) Schematic, and (b) chip photo of the cascode capacitive-division distributed amplifier (© 1998 IEEE) [74].

formed by adding a new dimension to the distributed amplifier with one or more rows of transistors [75], as shown in the schematic of Fig. 9. A matrix DA using GaAs HEMT technology demonstrated 9 dB gain at 2–52 GHz [76].

2.1.3.4. Cascaded Single-Stage Distributed Amplifier. The cascaded single-stage DA CSSDA shows excellent performance with high gain, good gain flatness, lower input/output VSWRs, flat group delays, and a low noise figure. Using the concept as for traveling-wave gain stages to maintain the DA broadband performance, the cascaded single-stage distributed amplifiers (CSSDA) [76,77] can be

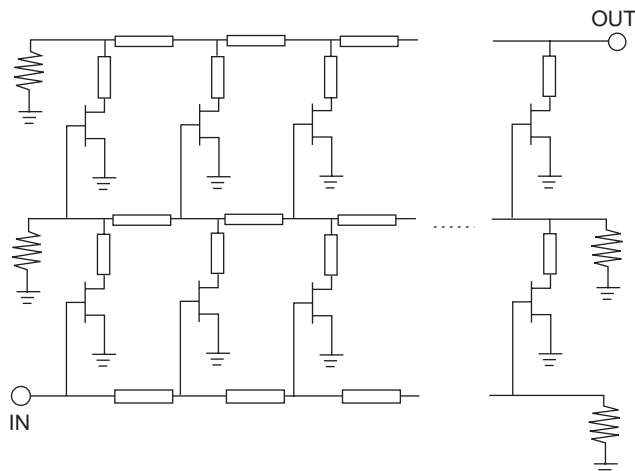


Figure 9. Schematic of a matrix distributed amplifier.

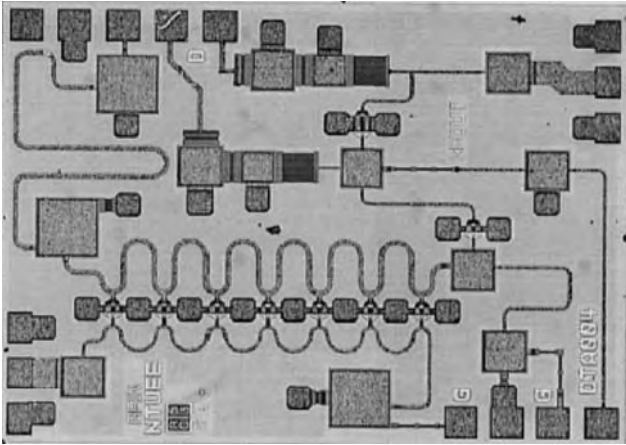


Figure 10. Chip photo of the amplifier combines a conventional DA and a CSSDA (© 2003 IEEE) [78].

used for broadband gain stages. By adopting this topology in the DA design, the high gain and wide bandwidth could be obtained simultaneously. With the combination of a conventional DA and a CSSDA, an amplifier demonstrated 22-dB small-signal gain from 0.1 to 40 GHz with a chip size of $1.5 \times 2 \text{ mm}^2$, as shown in Fig. 10 [78].

2.1.3.5. DA Using Si-Based Transistors. DAs using CMOS and SiGe HBT processes also evolve rapidly. The reported unity-gain frequency (f_T) values of CMOS and SiGe HBT were 95 and 90 GHz, respectively [75,79], indicating the potential of the high-frequency application of silicon technology. In fact, a MMIC DA using SiGe HBT demonstrated 50 GHz bandwidth with a gain of 5–9 dB [80]; another SiGe differential distributed amplifier has a single-ended gain of 7 dB with a 3 dB bandwidth of 81 GHz [218]. There is also a MMIC DA reported to operate from 0.6 to 22 GHz using the CMOS process [81]. It is expected that MMW DAs using CMOS processes will appear in the near future.

2.1.3.6. Transimpedance Amplifiers. Transimpedance amplifiers (TIAs) are also typical broadband amplifiers covering the MMW regime. TIAs are most widely used as preamplifiers in the receivers of optical communication systems because of high dynamic range, wide bandwidth, and relatively high output voltage (high transimpedance gain). TIAs convert and amplify the current from the photodiode to voltage. The *gain* is defined as the output

voltage over the input current ($\delta V_{\text{out}}/\delta I_{\text{in}}$), which has the same unit (Ω), as that of a resistor, and thus is called “transimpedance gain.”

Table 3 summarizes the most recently reported TIAs with operation frequencies up to the MMW regime [82–88]. A TIA using InP HBT demonstrated a transimpedance gain of $3.6 \text{ k}\Omega$ (71 dB· Ω) with a bandwidth of 60 GHz. This TIA benchmarks the best gain–bandwidth product (GBP) of 1.9 THz, which is the highest transimpedance–bandwidth product (TZBWP) of $216\Omega \cdot \text{THz}$ and the highest TZ-BWP per DC power efficiency of 797 $\Omega \cdot \text{GHz/mW}$ for a 40-Gbps transimpedance amplifier [82].

2.2. Mixers

Mixers play the role of frequency conversion in a wireless communication system and directly affect the integrity of the signal transmitted or received [89]. A mixer in a receiver (downconverting mixer) is often placed after the LNA because of the system noise consideration. On the other hand, an upconverting mixer is used in a transmitter and usually feeds the output signal to a PA and then to the antenna.

MMIC mixers can be classified as active mixers and passive mixers, depending on the bias conditions of mixing devices. Passive mixers use diodes or transistors in passive mode. An active mixer utilizes transistors or diodes operated in active region to perform frequency mixing, and has the advantage of conversion gain or low conversion loss, with a lower local oscillator (LO) power requirement. Mixers with special functions, such as for modulation applications and broad bandwidth, are also described in this section.

2.2.1. Passive Mixers

2.2.1.1. Diode mixers. The diode mixer is the most common MMW mixer, and a Schottky diode is usually used for its fast switching speed.

The most primitive mixer is the single-device mixer. Although it is simple and easy to implement, it requires filters at each I/O port to separate different frequencies and thus attain good port-to-port isolation. Balanced configurations are most frequently adopted to achieve port-to-port isolations, which use a coupler (or hybrid) to split one input signal into two with different phase (90° or 180°), and then perform frequency mixing at the devices, finally combining the mixed signals at the output port. Take the downconverting mixer, for example; the preprocessed

Table 3. TIAs with Operation Frequency to MMW Regime

Technology	Bandwidth (GHz)	Gain dB· Ω	Input Noise ^a (pA/ $\sqrt{\text{Hz}}$)	P_{DC} (mW)	Ref.
InP HBT	60	71	20	797	82
InP HBT	40	62.3	—	165	83
SiGeBiCMOS	46	47	24	300	84
SiGe HBT	50	49	30	~150	85
SiGe HBT	30	47.6	—	230	86
MHEMT	43	48.4	—	180	87
InP HEMT	52	52	—	520	88

^aEquivalent input noise current spectral density.

input (RF or LO) signals with opposite phases will cancel out at the output terminal (IF), and thus a satisfactory isolation will be achieved. The isolation between the RF and LO ports is determined by the hybrid under matched conditions. Another advantage of the balanced mixer is the suppression of certain spurious signals.

2.2.1.2. Singly Balanced Diode Mixers. The singly balanced mixer can be implemented with a 90° or 180° hybrid. A 90° hybrid singly balanced mixer is seldom adopted, since the LO-to-RF isolation is poor. The 180° hybrid singly balanced mixer is more frequently used, where one signal (either RF or LO) is applied at the devices in phase and the other is applied out of phase. If LO is applied out of phase, the LO power, along with AM noise and spurious signals on the LO, would cancel out. For a balanced diode mixer, the conversion loss is determined by the diode ON-state resistance, while the bandwidth is determined by the hybrid. A diode mixer with a wideband hybrid could have octave bandwidth. A CPW rat-race mixer using $0.18\text{-}\mu\text{m}$ GaAs MESFET process achieves a conversion loss of 14.7 dB at 3.5 dBm LO power [90].

2.2.1.3. Doubly Balanced Diode Mixers. For a doubly balanced mixer, both RF and LO signals are applied in opposite phase and would cancel out at IF. They possess numerous advantages, such as good isolation between all terminals and low-order spurious signal rejection. Nevertheless, they suffer low conversion gain (high conversion loss) and high LO power requirement. There exist “ring” and “star” configurations for doubly balanced mixers. The schematic of a ring mixer is shown in Fig. 11. Four diodes are connected as a ring, and LO, RF are applied at each node between diodes through a balance to unbalance transformer, or simply denoted as “balun,” which is indeed an 180° hybrid. Figure 12 shows the schematic of a star mixer. As the star mixer has no IF return inductors, it has lower series inductance at IF port and can demonstrate wider IF bandwidth [91].

2.2.1.4. Subharmonically Pumped (SHP) Mixers. In the MMW regime, it is sometimes expensive to use a fundamental frequency LO for a mixer. Furthermore, monolithic signal sources at such high frequencies may suffer from high phase noises and limited power level. A mixer using the harmonic signals of LO source in mixing is called a

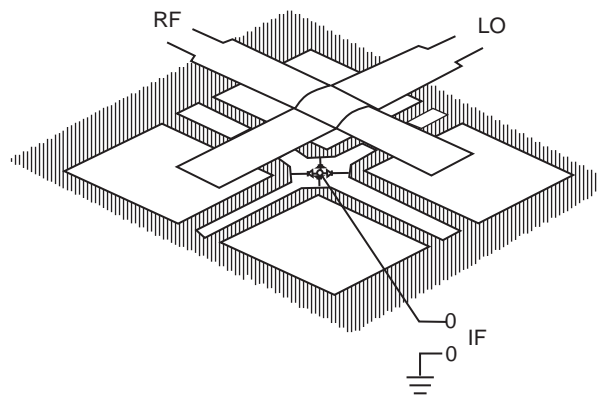


Figure 12. Schematic of a doubly balanced star diode mixer (© 1993 IEEE) [91].

subharmonically pumped (SHP) mixer. For a SHP mixer, all the mixing frequencies are usually distant from each other and can be separated easily so that good isolation can be achieved. Balanced and subharmonically pumped configurations can be applied simultaneously to enhance performance. The output signal of a SHP mixer is produced by mixing the RF signal and high-order harmonics of a LO signal. A 94-GHz SHP mixer using antiparallel diode pair (APDP) has been reported. This mixer demonstrated a minimum conversion loss of 11.4 dB at a RF frequency of 94 GHz and a LO frequency of 23.5 GHz [92].

2.2.1.5. Resistive FET mixers. The resistive mixer is popular in the MMW regime [93]. The transistor is operated in passive mode as a variable resistor. Compared with the diode mixer, a resistive mixer demonstrates a compatible noise figure, conversion loss, and similar LO power requirement, with higher linearity and lower distortion [94,95]. Besides, no drain DC current is present, so less $1/f$ noise is generated and thus the noise performance is usually better than that of its active counterparts [96]. Singly balanced resistive mixers in different frequency bands have been reported [93]. RF signal is fed in the devices through two coupled-line filters to achieve low insertion loss and IF rejection. The capacitors and the transmission lines form a lowpass filter to ensure LO-to-IF and RF-to-IF rejection. The resistive mixers attained wide bandwidth with moderate conversion loss for a high-IF system, as summarized in Table 4 and Table 5.

2.2.2. Active FET (HEMT) mixers

2.2.2.1. Gate Mixer. The LO power is applied at gate to achieve a time-varying transconductance (g_m) at LO frequency. The RF signal is applied as small-signal voltage input at gate, and the resulting IF signal can be derived at drain. A W-band GaAs HEMT gate mixer has been reported [8]. The device is biased near pinchoff so that g_m can be maximized. Radial stubs are inserted as short circuits at RF/LO frequencies. With careful design, this method has achieved conversion gain with 2 dBm LO power.

2.2.2.2. Drain Mixer. The transistor is biased at the knee region of the DC IV curves, and a LO signal is

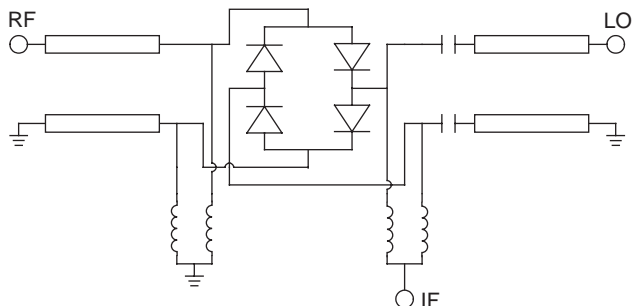


Figure 11. Schematic of a doubly balanced ring diode mixer (© 1993 IEEE) [91].

Table 4. Comparisons of Balanced Diode Mixers

	LO-to-RF Isolation	LO Power Requirement	IP3	Spur. Rejection
Single device	Filter dependent	Low	Low	None
Single balanced (180° hybrid)	Good	Moderate	Moderate	Good
Single balanced (90° hybrid)	Poor	Moderate	Moderate	Moderate
Doubly balanced	Good	High	High	Great

Source: Ref. 89.

applied at drain. A 60-GHz drain mixer using InGaP/InGaAs HEMT demonstrated a good noise performance of 3.16 dB at 58.5 GHz [103]. The mixer implemented the image rejection function with a 90° hybrid and a Wilkinson in-phase power divider. The complete downconverter, which consists of a four-stage LNA and the drain mixer, achieved a maximum conversion gain of 22.9 dB at RF of 61 GHz, and a minimum noise figure of 3.16 dB at RF of 58.5 GHz, with an LO power of 5 dBm.

2.2.2.3. Dual-Gate Mixer. A dual-gate mixer can be considered as a special gate mixer. The dual-gate device has two separate gates, and thus good LO-to-RF isolation can be achieved without extra couplers compared with the single-gate mixers [104,105]. Design of a dual-gate mixer beyond microwave frequency is rarely considered because of this mixer's notorious noise figure and the difficulty of device modeling. However, a MMW dual-gate mixer utilizing a GaAs HEMT process was reported [105]. The LO power is applied at the first gate (G1) so that the transconductance and output impedance of the second gate (G2) are modulated. The upper gate also operates as an IF amplifier. Since RF and LO are separated properly, the matching for each end (RF and LO) is easier. A compact die size can be achieved without the requirement of a coupler. This circuit showed a conversion gain of 3 dB with 5 dBm LO power and good RF return loss of better than 10 dB from 87 to 100 GHz. The RF-to-LO isolation is better than 17 dB.

2.2.3. Mixer for Modulator Application. The balanced mixers can be used for amplitude modulation (AM), binary phase shift keying (BPSK) modulation, and IQ modulation, due to their superior spur performance, linearity, and port-to-port isolation [97,98]. Most of them are composed of doubly balanced mixers or singly balanced mixers due to the isolation between LO and RF ports. This is important since an unwanted (spurious) carrier signal could

degrade modulation quality at high-level amplification, and also increase difficulty in demodulation.

Modulators based on the Gilbert cell or resistive ring architectures have been reported in the literature [99,100]. They featured good amplitude/phase match and LO rejection; however, most of them operated below 10 GHz. For MMW applications, the modulators can be based on a double-balanced diode mixer structure and show good amplitude/phase balance. However, they usually need a high LO drive power [97,98]. On the other hand, a balanced reflection-type phase shifter [9] can be used for the BPSK modulator, which utilized a Lange coupler as a 90° hybrid and two shunt cold-mode devices for switching. The cold-mode devices can be either HEMT [101] or HBT [102] devices, and can be operated to 110 GHz with good amplitude/phase match.

2.2.4. Wideband mixers

2.2.4.1. Gilbert Cell Mixer. Gilbert-cell active mixers basically consist of the RF differential transconductance pair and four-quadrant switching devices. An RF signal is transferred by the transconductance pair into switching devices and mixed via switching devices driven by the LO signal. Filters and/or matching networks could lead to the IF output port to enhance the mixer performance. Because of the differential LO/RF input and symmetry of transconductance pair, the Gilbert cell mixer has excellent LO/RF, LO/IF, and RF/IF isolation. Besides, owing to the RF transconductance amplification and IF restrengthening property, Gilbert cell mixers can achieve conversion gain in some frequency range. These advantages and compact chip size make Gilbert cell mixers very popular in wireless communication applications [106,107].

Gilbert cell mixers (Fig. 13) were not popular at high frequencies because of transistor parasitic capacitance and gain degradation. With the advanced device technologies and design techniques, there are a few examples have been reported in the MMW regime. A Gilbert cell mixer could have good conversion efficiency in the MMW

Table 5. Summary of the Reported Resistive Mixer

RF Frequency (GHz)	Conversion Loss (dB)	IF Frequency (GHz)	Spurious Signal Rejection	$P_{1\text{ dB}}$ (dBm)
Q band (42–56 GHz)	11.7	11	–35	4 (RF = 50 GHz)
V band (56–72 GHz)	12.8	18	–35	2 (RF = 60 GHz)
W band (72–84 GHz)	10.6	30	–30	–2 (RF = 77 GHz)

Source: Ref. 15. (©2000 IEEE.)

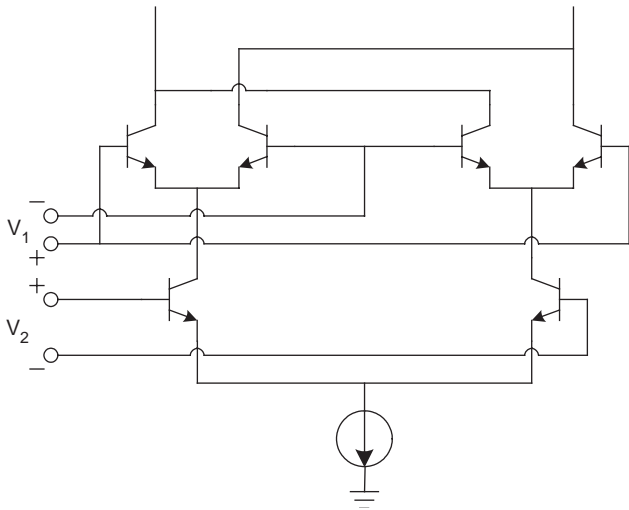


Figure 13. Basic Gilbert cell mixer structure.

range with proper RF matching, and it can also achieve very wide bandwidth (from DC to millimeter wave) with a lossy matching technique. The Gilbert cell configuration can also be used to design an analog multiplier; a 1–17-GHz Gilbert cell mixer and a multiplier have achieved a conversion gain of 9.3 dB [108]. Another distributed Gilbert cell analog multiplier using InP HEMT has –5 dB conversion gain from DC to 38 GHz [106].

2.2.4.2. Distributed Mixer. Wideband mixers can also be implemented using distributed configurations [109–111]. A 3–33-GHz distributed mixer using GaAs HEMT has been reported [109]. The RF and LO signals are applied at the gate and drain lines, respectively, and the IF signal is extracted via a lowpass filter. The mixer demonstrated a conversion loss of better than 4 dB from 3 to 33 GHz.

2.3. MMW Oscillators and Frequency Sources

A millimeter-wave (MMW) source is a key component in a transceiver system, especially for the applications of communication, radar, image, and remote sensing [112]. The typical requirements of a MMW oscillator are high reliability, low phase noise, and low cost. The frequency sources can be implemented via either simply designing fundamental oscillators or using lower-frequency oscillators with frequency multipliers. Applying the multiple-push approach is also an alternative for MMW frequency sources.

2.3.1. Design Considerations

2.3.1.1. Noise in Oscillators. There are three sources of noise in an oscillator: AM noise due to amplitude modulation, FM noise due to frequency modulation, and PM noise due to phase modulation by the noise sources. These noise modulations cause spectrum spread and degrade the phase noise performance of an oscillator. The primary noise sources in a MMIC oscillator are the $1/f$ noise and thermal noise.

Phase noise theory has been investigated [113,114]. In order to minimize the phase noise of an oscillator, the following should be considered in the design:

1. Maximize the unloaded Q factor of the resonator.
2. Select an active device with low noise figure and low flicker noise.
3. Use a low LC ratio and maximize the reactive energy.
4. Minimize the phase perturbation for the circuit design.

Off-chip high- Q components are usually applied to enhance phase noise performance, such as dielectric resonators (DRs) and varactors. Dielectric resonator oscillators (DROs) in the MMW regime exhibit excellent phase noise performance and temperature stability because of the extremely high Q factor and good temperature coefficient of DR.

2.3.1.2. Fundamental Oscillators. The fundamental frequency oscillator is the simplest approach for the MMW frequency source, but has drawbacks of low Q factor and insufficient device gain at the MMW regime. The oscillation frequency is limited by the figure of merit f_{max} of the transistor.

2.3.1.3. Oscillator and Frequency Multiplier Chain. An MMW source can be composed of a lower-frequency oscillator and frequency multipliers to obtain desired frequencies. There are several advantages to this approach. It is easier to achieve low phase noise for an oscillator operating at lower frequency. Also, a wider bandwidth can be achieved because of the frequency multiplication. Several MMW frequency sources have been reported using MMIC technology, including lower-frequency fundamental oscillators and frequency multipliers [115,116]. Figure 14

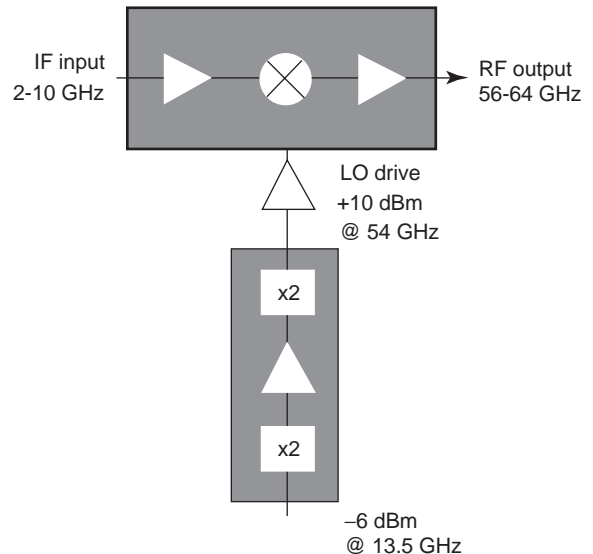


Figure 14. Block diagram of the V-band up-converter with the LO chain consisting of lower-frequency fundamental oscillator and frequency multipliers (© 1994 IEEE) [115].

shows a block diagram of the V-band up-converter with the LO chain consisting of lower-frequency fundamental oscillator and frequency multipliers.

2.3.1.4. Multiple-Push Oscillator. A push–push (or double-push) oscillator design consists of two fundamental frequency oscillators operating at half of the desired output frequency. Also, the higher- Q -factor resonator and sufficient device gain are easily obtained at half of the output frequency. The push–push oscillators have been reported in MMW range [117,118], with phase noises of -88 and -109 dBc/Hz achieved at 1- and 10-MHz offsets, respectively. A novel coupling method for push–push DRO, although it is a hybrid circuit, demonstrated excellent spectral purity at 40 GHz, output power, and phase noise of about -100 dBc/Hz at 100-kHz offset [119].

The triple-push oscillator approach, extending from the push–push oscillator, has been proposed [121]. Figure 15 shows the chip photo of a 28.4-GHz HBT MMIC triple-push oscillator. It consists of three identical fundamental oscillators with a phase shift of 120° among three odd-mode fundamental signals. The fundamental and the second-harmonic signals cancel out altogether, and the desired third harmonic signals combine in phase. Consequently, a triple-push oscillator can extend the usable frequency range and obtain high- Q -factor resonance more easily than can a push–push oscillator. Multiple-push ($n > 3$) oscillators can operate with a similar principle [120]. Ka- and Q-band MMIC triple- and quadruple-push oscillators have also been reported [121–124].

2.3.2. Device Technologies for Oscillators. HEMT has dominated the MMW MMIC designs because of its high f_T and f_{max} , as well as superior low noise figure. The MMIC fundamental frequency oscillator implemented using GaAs-based PHEMTs demonstrated W-band (~ 90 GHz) oscillations with phase noise of -90 dBc/Hz at 1-MHz offset [125]. Monolithic oscillators using InP-based HEMTs were also reported above 100 GHz [126,127].

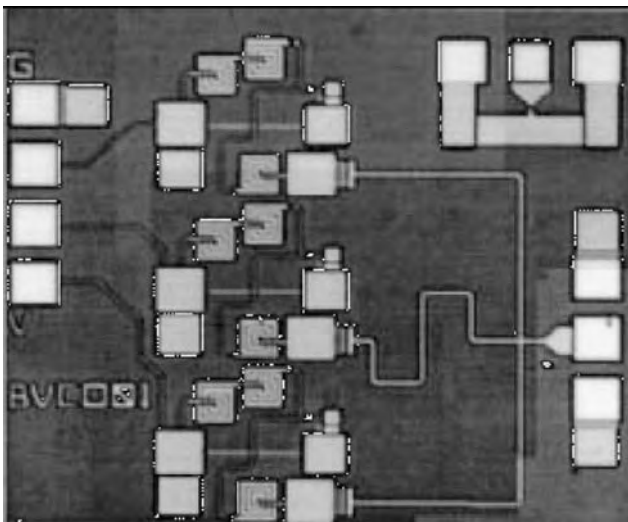


Figure 15. Chip photo of the 28.4-GHz HBT MMIC triple-push oscillator (© 2001 IEEE) [121].

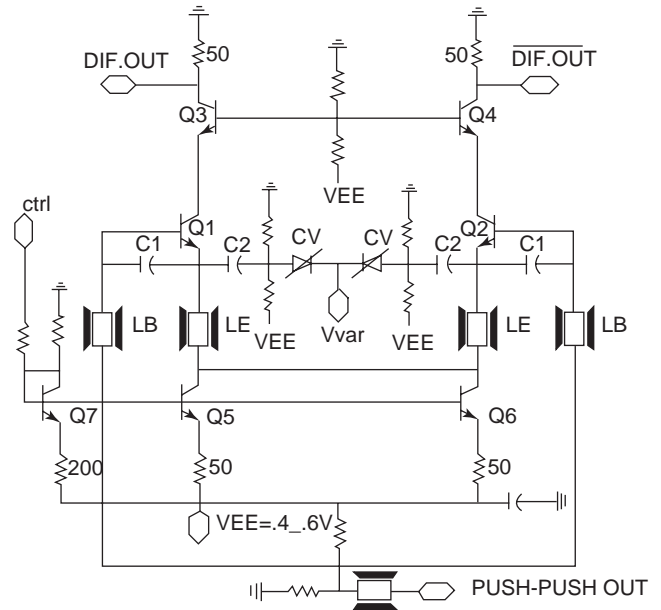


Figure 16. Schematic of the 150-GHz SiGe HBT push–push oscillator (© 2003 IEEE) [135].

For low-phase-noise applications, HBT is the preferred because of its superior $1/f$ noise characteristics. To date, the highest-frequency oscillator using GaAs HBT was reported by Uchida et al. [128] with 106 GHz output and -88 dBc/Hz phase noise at 1-MHz offset. On the other hand, InP-based HBTs exhibit even lower $1/f$ noise than do GaAs HBTs because of the lower surface recombination velocity in InP-based materials and the absence of DX center in the emitter. InP-based HBT VCOs demonstrated impressive high-frequency performance [116,129], with -65 dBc/Hz phase noise at 1-MHz offset of 150 GHz operation frequency [116]. Also, a superior phase noise of -95 dBc/Hz for 1-MHz offset at 104 GHz oscillation has been reported [130].

As for silicon-based (CMOS and SiGe HBT) technologies, the fundamental frequency CMOS VCOs were achieved to 50 GHz with a phase noise of -85 dBc/Hz at 1-MHz offset [131,132]. Using push–push topology, a CMOS VCO achieved a measured output power of -4 dBm, a tuning range of 2.5 GHz, and a phase noise of -85 dBc/Hz at 1-MHz offset without any output amplifier in a commercial $0.25\text{-}\mu\text{m}$ CMOS process [216]. Fully integrated MMW MMIC oscillators using SiGe HBTs were also reported operated at 50 GHz with phase noise between -103 and -110 dBc/Hz at 1-MHz offset [133,134]. A SiGe push–push VCO with a phase noise of -85 dBc/Hz at 1-MHz offset and operating up to 150 GHz has been reported [135]. The schematic is shown in Fig. 16.

2.4. Frequency Multipliers

A frequency multiplier is a component used to generate the harmonic signal of the input signal. The conversion loss, which is the power ratio of the desired output harmonic signal to the input fundamental signal, reveals the efficiency of the multiplier. Beside the conversion loss, the

Table 6. Features and Performance of Reported Passive and Active Multipliers

Ref.	Multiplier ^a	Frequency (GHz)	Process	Device	Conversion Gain (dB)
140	Doubler (P)	16–40	GaAs	Diode	~ -12
141	Tripler (P)	75–110	GaAs	Diode	-20.6 to -17.3
142	Tripler (P)	87–102	GaAs	Diode	-20 to -18
143	Doubler (A)	54	InP	HEMT	5
144	Doubler (A)	76.5	InGaAs	HEMT	1

^aA—active mode; P—passive mode.

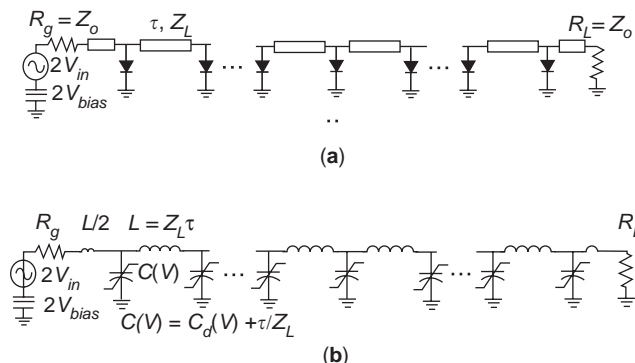


Figure 17. (a) Schematic and (b) LC ladder network equivalent circuit of the nonlinear transmission line (© 1996 IEEE) [145].

port return losses and harmonic rejections are also important design considerations. All the frequency multipliers degrade the phase noise by at least $20 \log(n)$ dB, where n is the multiple number [136].

Doublers and triplers are mostly used. Higher-harmonic multipliers are seldom found because of the low power level of harmonic signals. Although there exist quadruplers and higher-order multipliers using single transistor, the multipliers are often composed of two cascaded doublers or triplers with buffer amplifiers [137–139].

In designing multipliers, the type of device determines the performance of the multiplier. Basically, active multipliers feature better conversion loss and even better ability to achieve conversion gain, while passive multipliers, although lossy, can be made very broadband, such as the multipliers using Schottky barrier diodes. As shown in Table 6, while passive multipliers achieve broadband performance, active ones yield conversion gains within narrowband frequency.

Passive multipliers are probably the most practical in modern microwave and RF systems because of their bandwidth [140–142]. Popular structures for passive doublers are single-ended and balanced configurations. The passive triplers are usually implemented by using an antiparallel

diode pair (APDP) due to the odd harmonics, which are combined in phase while the even harmonics are canceled out [141,142].

Multipliers utilizing nonlinear transmission lines (NLTLs) and distributed varactors feature broad bandwidth. Figure 17 shows the schematic and LC ladder network equivalent circuit of the nonlinear transmission line. The NLTL doubler demonstrates 6.6 dB conversion loss in the 3 dB bandwidth 52–63.1 GHz, and a NLTL tripler with 11.2 dB conversion loss in the 3 dB bandwidth at 81–109 GHz [145].

As mentioned, active multipliers can yield conversion gain within a narrow band. Most of them have the conversion loss of better than 5 dB [143,144,146–150]. Broad bandwidth can also be achieved with the tradeoff of conversion gain. Table 7 lists the features and performance of reported active broadband multipliers.

The most practical way to design an active multiplier is with the balanced structure, providing good fundamental and odd-harmonic rejections. It contains two FETs and an input balun or a 180° hybrid. Basically, it can be used only for even-harmonic multipliers and is most suitable for doublers. However, a modified balanced structure using Lange couplers for the tripler as shown in Fig. 18 has been reported [154]. The third-harmonic signal will add in phase at the output port with suppression of the unwanted harmonics. Also, broadband active multipliers can be implemented using distributed configurations [155]. Single-device structure is generally used for a compact chip size and features good efficiencies, although fundamental-frequency leakage can be a problem [143,144].

2.5. RF Switches

Switches are important components that control the signal flow in communication systems. Transmit/receive (TR) switches are components directly connected the low-noise amplifiers and power amplifiers in the TR modules. Two major design parameters for a switch are minimum insertion loss in the ON state and maximum isolation in the OFF

Table 7. Features and Performance of Reported Active Broadband Multipliers

Multiplier	Frequency (GHz)	Process	Approach	Conversion Loss (dB)	Ref.
Doubler	V band	GaAs	Balanced	8.5–11.38	151
Doubler	2–40	—	Balanced	10 ± 1.5	152
Doubler	50–68	GaAs	Balanced	5.5 ± 2.5	153
Tripler	42–51	GaAs	Balanced	11.1–17.6	154

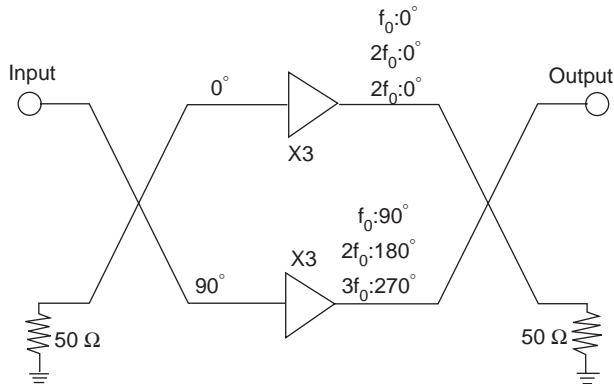


Figure 18. Schematic of a balanced tripler using Lange couplers.

state. Power-handling capability is another important design consideration.

2.5.1. MEMS switch. Microelectromechanical system (MEMS) switches are operated by using mechanical movement to achieve a short circuit or an open circuit. The force required for mechanical movement is obtained by electrostatic means. MEMS switches have demonstrated excellent switching performance in MMW frequency range due to very small parasitic effect [156–159]. The DC power consumption of the MEMS switch is almost zero, but a high drive voltage (20–80 V) is required. Few MEMS switches can handle power more than 20–50 mW. MEMS switches need to be packaged in inert atmospheres (nitrogen, argon) and low humidity, so the packaging costs are very high [160]. Most of the reported MEMS switches are of single-pole single-throw (SPST) configuration and have demonstrated isolation of better than 30 dB [157–159].

2.5.2. Pin Diode Switch. The p-type-insulator-n type (pin) diode is widely used for MMW switch design because of its low insertion loss, high isolation, and high power-handling capability [161–165]. Because pin diodes will consume DC current when the diodes are in the ON state, pin diode switches require DC blocking capacitors and biased network, such as RF choke or quarter-wavelength short stub. Compared with MEMS switches and passive FET switches, pin diode switches have demonstrated the best power-handling capability. For example, the SPDT (single-pole double-throw) switch provided by Skyworks Inc. achieves watt-level power-handling capability [165].

2.5.3. Passive HEMT Switch. Since the pin diode and MEMS processes are not compatible with the HEMT MMIC process, the passive HEMT (or FET) switches are still very popular because of their integrability with other major building blocks in a MMW TR module, which are fabricated mostly using the HEMT MMIC process. For frequencies of 20 GHz or lower, series and/or shunt configurations of passive FET can readily serve as very good switches with excellent isolation and insertion loss results demonstrated in two studies [166,167]. However, at higher frequencies, the parasitic capacitor will significantly

degrade the isolation performance of a series switch and the insertion loss of a shunt switch. Several methods to improve switching characteristics of the passive FET switches were reported [168–173].

2.5.3.1. Parallel Resonant Technique. Because the parasitic drain-to-source capacitor degrades the switch performance significantly in the high-frequency range, the parallel-inductor resonant technique is widely used to compensate the parasitic capacitor of OFF-state FET. Because the impedance of OFF-state capacitors become low in high frequency, a small inductor is placed between the drain and the source of the transistor to resonate out the OFF-state capacitor. In general, the small inductor is implemented by a high-impedance transmission line. The OFF-state FET and the parallel inductor are used to form a parallel resonator, and this resonator represents high impedance around the resonant frequency. The ON-state FET with a parallel inductor still represents low impedance. The parallel resonant technique can improve the isolation of the series switches and insertion loss of the shunt switches. A W-band SPST series switch employing the parallel resonant inductor demonstrated 1.6 dB insertion loss and 22.5 dB isolation at 94 GHz [168].

2.5.3.2. Impedance Transformation. This method utilizes impedance transformation to compensate the drain-to-source capacitance of the OFF-state passive HEMT switches. As shown in Fig. 19, the ON- and OFF-state impedances of the passive HEMT are transformed to near open circuit and near short circuit simultaneously by an impedance transformation. By using this concept, a Q-band SPDT switch demonstrated a measured isolation better than 30 dB and 2 dB insertion loss from 38 to 45 GHz, while a V-band switch has a measured isolation better than 30 dB and 4 dB insertion loss from 53 to 61 GHz [169].

2.5.3.3. Traveling-Wave (Distributed) Concept. The traveling-wave concept was also proposed for wide band

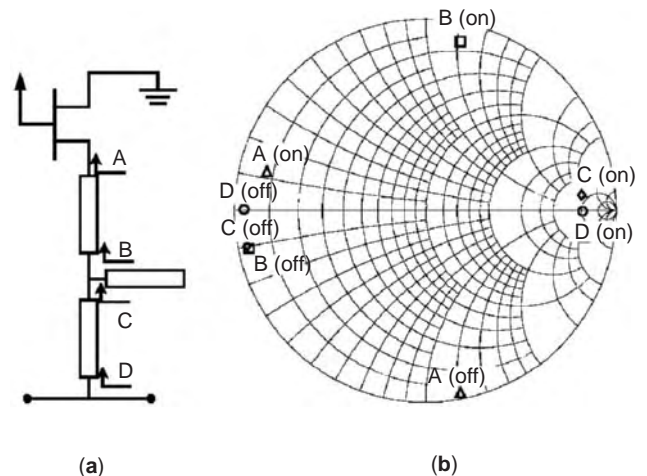


Figure 19. (a) Schematic of a FET connected in series with the impedance transformation network; (b) input impedances looking into points A, B, C, D of the passive switch with impedance transformation network.

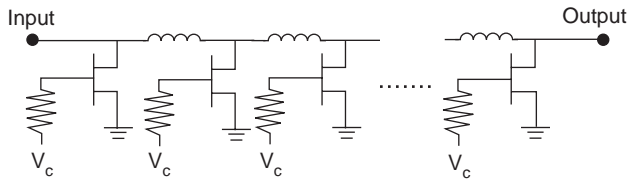


Figure 20. Schematic of the SPST traveling-wave switch.

switch design. A traveling-wave switch consists of a finite numbers of series inductors and shunt FETs as shown in Fig. 20. The series inductors are usually implemented with high-impedance transmission lines, and the OFF-state transistors can be simplified as a small capacitor. The complete traveling-wave switch represents as a 50- Ω artificial transmission line while the FETs are at OFF state. The switches using the traveling-wave concept manifest broadband characteristics. A DC–40-GHz SPDT switch demonstrated 3 dB insertion loss and 23 dB isolation [170], and a 15–80-GHz SPDT switch using a quarter-wavelength transformer has an insertion of lower than 3.6 dB and an isolation of better than 25 dB [171].

2.5.3.4. Special Process. By employing the ohmic electrode-sharing technology (OEST), no interconnect lines are needed between the FETs because an ohmic electrode is shared by the source of one FET and the drain of another FET. The DC–40 GHz SPDT switches demonstrated 3.5 dB insertion loss and 25.5 dB isolation at 40 GHz, while the SPST switch has an insertion loss of better than 1.64 dB and an isolation of better than 20.6 dB from DC to 60 GHz [172].

The distributed FET has a single gate, with input/output ports connected to the drain electrode of the FET, and the source terminal connected to several via holes. The structure of an SPST switch using distributed FET is shown in Fig. 21. The small-signal characteristics of this switch were expressed by a lossless transmission-line model while the FET is pinched off, and a lossy transmission-line model while the FET is in ON state. A DC–110-GHz SPST switch using the distributed FET has shown an insertion loss of lower than 2.55 dB and an isolation of better than 22.2 dB [173].

2.6. Phase Shifter

A phase shifter is a device that changes the phase of a signal. Classified by the type of phase control, phase shifters can be divided into groups of analog and digital phase

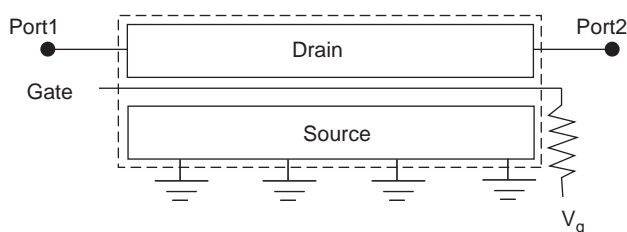


Figure 21. Structure of SPST switch using distributed FET (© 2000 IEEE) [173].

shifters, in which the phase shifts are, respectively, continuous and discrete. The most essential design parameter of a phase shifter is the shift of the phase, that is, the difference between the phases of the output signal and the input signal. Insertion loss is also important for passive shifters. For a digital phase shifter, limits must also be imposed on its phase error, which is a measure of the extent to which the actual phase shift deviates from the desired or ideal phase shift.

The analog phase shifter has the advantage of continuous phase shift and thus can be adjusted to achieve precise phase shift. The reflective-type phase shifter (RTPS), which contains a 3-dB 90° coupler and varactor diodes (or MEMS capacitors), often has low insertion loss and low sensitivity on temperature and process variation [174]. Another kind of phase shifter employs the concept of vector sum as shown in Fig. 22 [175], which does not depend on varactor diodes in its phase shift mechanism and therefore its shift range will not be limited by the tuning range of the varactor diodes. A vector sum phase shifter may utilize either variable attenuators or variable-gain amplifiers for its gain control. The distributed phase shifter utilizing a varactor-tuned transmission line is also a popular approach. The phase shift is achieved by changing the phase velocity of the varactor-tuned transmission line. The varactor can be implemented by either diodes [176] or MEMS capacitors [177], and thus the phase shift is achieved. There still exist other design concepts such as tunable phase shifter [178], but they are rarely found.

Digital phase shifters use binary-represented control signals. An n -bit digitally controlled phase shifter has n phase shift blocks and 2^n states; thus the phase shift precision is $360^\circ/2^n$. There are two paths in a phase shift unit. A switching mechanism is applied to determine the direction in which the way the signal will pass, while the relative phase difference between the two paths is the phase shift of that phase shift unit. The phase-shifting path may be implemented with either filters [179] or delay lines [180], depending on the operating frequency of the circuits. The vector sum concept has also been applied to the design of a digitally controlled phase shifter [181]. There is also a digital RTPS, in which the termination is discretely tuned. Figure 23 shows a schematic and chip photo [182].

Combination of analog-controlled and digitally controlled phase shifters has been attempted [181]. The phase shift is first roughly achieved by a digitally controlled phase shifter and then fine-tuned by an analog-controlled phase shifter. This architecture alleviates the difficulty of designing analog phase shifter with a large phase shift. It has been shown to significantly reduce the required phase shift of an analog-controlled phase shifter while still achieving 360° of phase control. The drawback is large chip size when all the components are integrated into a single chip.

In the MMW regime, a DC–60-GHz distributed MEMS phase shifter has demonstrated a capability of a 360° phase shifter with an insertion loss of 5.1 dB at 40 GHz and 4 dB at 60 GHz, respectively [183]. Also, a 60–110-GHz MEMS phase shifter features a figure of merit of the ratio for tuning phase range over an insertion loss of 70°/dB

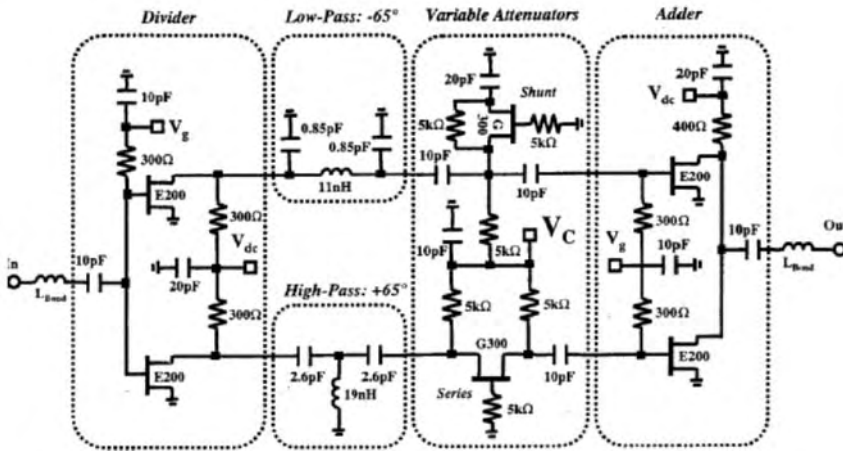


Figure 22. Schematic of the vector modulator-based phase shifter (© 2002 IEEE) [175].

from 60 to 110 GHz [184]. Monolithic phase shifters have been operated up to 100 GHz with switching times well under 1 μs [185]. The RTPS can also be implemented in the MMW regime with broadband couplers. The HEMT-based monolithic RTPS were reported in Ref. 186, while the HBT-based can be found in Ref. 187.

2.7. Multifunction MMICs and System Applications

The advancement of MMIC technology not only improves the existing system performance but also enables new system applications. A multifunction MMIC incorporates several single-function circuits onto a single chip. Although many individual components can be integrated onto a single chip, the level of integration heavily depends on the maturity of MMIC process and circuit design. A typical example is a transceiver chip, which usually includes a LNA and a downconverting mixer for the receiving end and an upconverting mixer, and a PA for the transmitting end. Sometimes the VCO and frequency multipliers could also be included as the LO chain. Since there are too many configurations for multifunction MMICs, we introduce only a few examples for MMW applications in this article.

2.7.1. Single-Chip Radar Transceiver for Automotive Radar Application.

The forward collision warning (FCW) and autonomous intelligent cruise control (AICC) radars are forward-looking automotive radars (FLARs) that require a sensor range of about 100 m. The FCW radar will detect potential forward collision situations and provide a warning to the driver, while the AICC will operate in an autonomous control loop to maintain a continuous safe following distance.

Cost and hardware size are two dominant factors, in addition to the performance requirement for all-weather conditions that drive the technology for automotive radars. MMW radars have the advantages of small hardware size and high range resolution over the microwave radars. They can also be operated in the so-called all-weather conditions, such as in rains and fogs, thus outperforming the infrared systems. Low cost is the key factor for consumers in accepting the radar as an affordable safety component of their vehicles. The size constraint is also essential for integration of the radar onto the vehicle without major impact on vehicle design and performance. Several W-band TR MMICs, including single multifunction chips and chipsets, were developed for FLAR and/or other automotive applications [188–192].

As an example, the block diagram of the single-chip W-band FMCW transceiver is shown in Fig. 24 [188]. This transceiver chip consists of a VCO, a PA, a mixer, and an LNA. Transmit and receive channels used separate

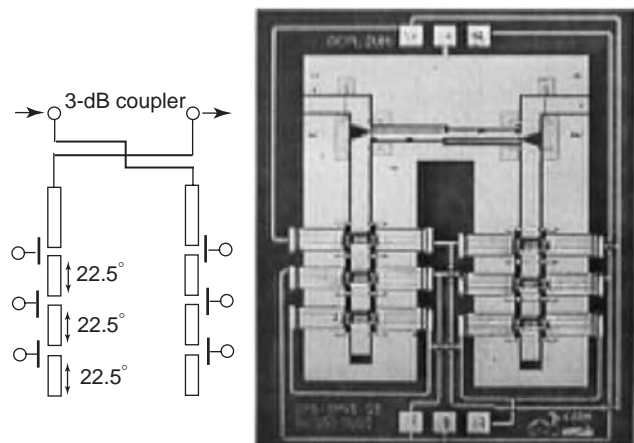


Figure 23. Schematic and photograph of 2-bit reflection-type MEMS phase shifter (© 2002 IEEE) [182].

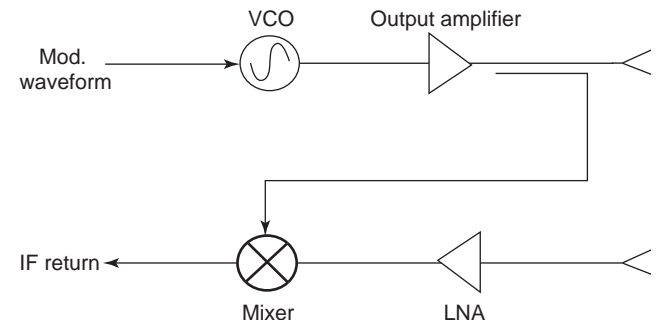


Figure 24. Block diagram of the single chip W-band FMCW transceiver (© 1995 IEEE) [188].

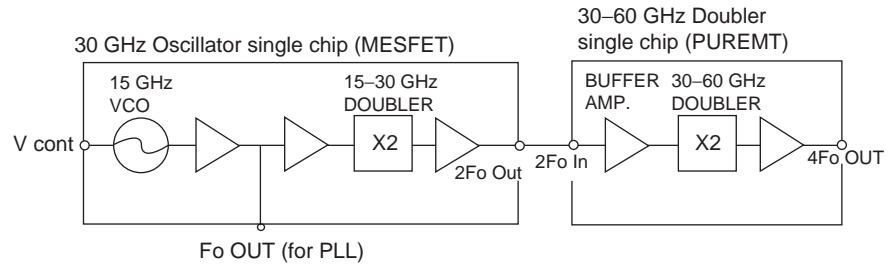


Figure 25. Block diagram of the MMIC LO chipset [196].

antennas for better isolation. An FCW signal was generated from the VCO and fed to the transmit amplifiers. A portion of the transmit power was coupled back to the receiving channel and used as an LO source for the mixer. The transmitter had more than 10 dBm output power with a tuning range of 500 MHz around 92.5 GHz. The receiving chain had a conversion gain of 9 dB. However, the receiving noise figure was higher than 20 dB for IF less than 10 MHz because of the flicker noise of the gate-HEMT diode mixer. This might impact the system sensitivity for the homodyne FCW operation for an object at a long range. A number of W-band transceiver architectures have been investigated to improve the sensitivity [191,192].

2.7.2. Passive Imaging Application. The interest in MMW imaging is due primarily to its capability of imaging through fog, cloud, smoke, sandstorms, and darkness. Owing to lack of MMW components, MMW imaging arrays typically were previously based on the heterodyne approach and relied on a front-end mixer to convert an incoming signal to low frequency for signal processing. This approach not only suffers from high conversion loss and high noise figure but also requires complicated LO signal generation and distribution. The LO problem is aggravated as imaging array size increases. An alternative approach is to employ a direct-detection architecture, which requires a high gain LNA and a detector circuit. This approach has the advantages of no LO requirement, low DC power consumption, fewer parts, and low cost. These advantages become even more pronounced in focal plane staring array systems. Owing to advances in MMW MMIC technology, the direct-detection imaging receiver was developed because of the enabling MMIC components, in particular, the high-gain LNA, and thus the simple direct-detection approach became feasible. A W-band monolithic integrated seven-stage LNA and detector on a single chip was developed [193]. The LNA has a linear gain of 34 dB from 92 to 96 GHz with a noise figure of 4 dB. The complete monolithic chip was tested via on-wafer probing with a W-band noise source as the input signal and showed a net output of 10 mV between the noise source in ON and OFF states. This chip has been successfully implemented in a real-time MMW imaging system to facilitate aircraft landing in inclement weather [194,195].

2.7.3. MMIC Chipset for a V-Band Phase-Locked Local Oscillator. A local oscillator is essential in all microwave and MMW communication systems for frequency conversion. Many systems also require a voltage-controlled oscillator for precise and fast frequency synthesis. As

demand increases for higher data transmission speeds, the radiofrequency must be increased and the MMW local oscillator will be more important.

A V-band fully monolithic voltage controlled LO chipset has been developed to realize a MMW synthesizer [196]. The chipset is composed of a highly integrated multifunction MMIC for 15 GHz voltage-controlled oscillation and 15–30-GHz frequency doubling, and a 30–60-GHz frequency doubler. A block diagram of the MMIC LO chipset is shown in Fig. 25. The 30-GHz oscillator chip was fabricated with a 0.3- μm ion-planted MESFET process. The chip includes a 15-GHz VCO, a 15–30-GHz balanced frequency doubler, and an output amplifier. Output of the 15-GHz VCO is amplified by a dual-output amplifier. One of the two amplifier outputs is for a phase-locked loop (PLL), and the other is fed to a 15–30-GHz frequency doubler. The other chip, a 30–60-GHz doubler, was fabricated with the 0.1- μm pseudomorphic AlGaAs/InGaAs/GaAs HEMT process. It includes a buffer amplifier, a 30–60-GHz frequency doubler, and a 60-GHz amplifier. The buffer amplifier is essential since the output impedance of the frequency doubler changes significantly with the frequency of the input signal. Each circuit is greatly reduced in size by using the uniplanar structure. Output power of 3.5 ± 1.5 dBm and tuning performance of 55.6–60.3 GHz with SSB phase noise of less than -80 dBc/Hz at 1-MHz offset were achieved. The chip set allows a small and simple MMW synthesizer to be realized.

2.7.4. Ka-Band Transceiver for BCIS System. The objective of the battlefield combat identification system (BCIS) is to provide quick and positive target identification, either friendly or unknown, without any additional impact to the platform operators [197]. The shooter platforms would be equipped with an interrogator/transponder set, while the armored personnel carrier would only have the transponder unit. The BCIS is initiated by the shooter platform by simply pointing the interrogator antenna and transmitting a Ka-band spread-spectrum signal to the potential target. If the potential target is also equipped with the BCIS set, it would then receive the interrogation signal and respond to the query with the requester's and its own identification through the transponder unit. The shooter platform validates the returned transponder message and determines whether it is friendly or unknown. The entire query-response process takes less than one second.

The Ka-band transceiver unit is the key unit in the BCIS equipment set. The transceiver module was developed using a total of 13 GaAs MMIC chips [197]. Later

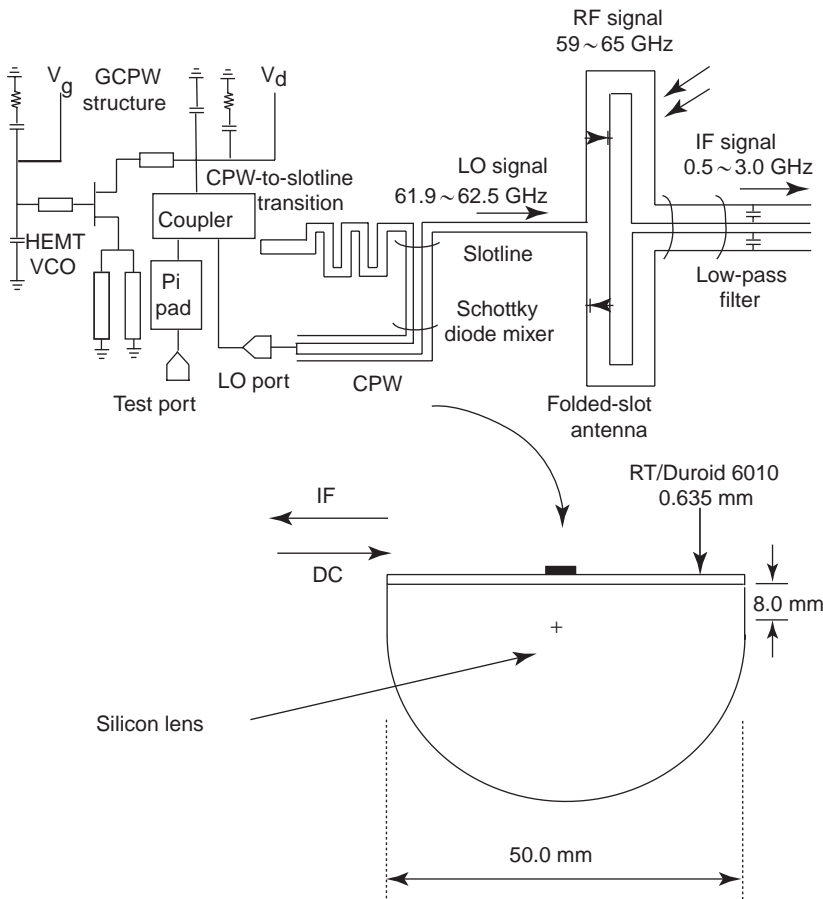


Figure 26. Schematic of the quasioptical integrated antenna-receiver front end (© 2003 IEEE) [217].

most of the HEMT chips were replaced by multifunction transceiver chips [198,199].

2.7.5. HEMT and HBT MMIC Integration. Monolithic integration of HEMT and HBT is attractive since it allows circuit designers to take the advantages of the features of each device. Both GaAs- and InP-based HEMT-HBT integration using selective regrowth of HEMT islands on patterned and etched HBT materials have been reported [200,201]. A few examples of MMW multifunction MMICs based on the InP HEMT-HBT integration process have been demonstrated. One of them is a single-chip 94-GHz frequency source, which includes a 23.5-GHz HBT VCO and a buffer amplifier, followed by a 23.5–94-GHz HEMT quadrupler composed of a 23.5–47-GHz doubler, a 47-GHz buffer amplifier, and a 47–94-GHz doubler [202]. The other is a 94-GHz HEMT low-noise amplifier with HBT bias regulation [203].

2.7.6. V-Band Integrated Antenna-Receiver Front End. A V-band GaAs HEMT monolithic integrated antenna-receiver front end has been developed [217]. This chip consists of a folded-slot antenna integrated with a singly balanced diode mixer, a voltage-controlled oscillator, a CPW-to-slotline transition, and a lowpass filter. Figure 26 shows the complete schematic of the quasioptical integrated antenna-receiver front end. It demonstrates a 15 dB single-sideband isotropic conversion loss.

Acknowledgement

The authors would like to thank Chia-Chi Chang, Shih-Fone Chao, Po-An Chen, Kuo-Liang Deng, Jia-Shiang Fu, Ping-Chen Huang, Ming-Fong Lei, Chin-Shen Lin, Chong-Liang Lin, Zhi-Wei Ling, Shih-Chieh Shin, Zou-Min Tsai, Chi-Hsueh Wang, and Mei-Chao Yeh of National Taiwan University for their help in the literature survey. Thanks also go to Professors Liang-Hung Lu, Shey-Shi Lu, Tian-Wei Huang of the Department of Electrical Engineering, National Taiwan University for their discussions and suggestions.

BIBLIOGRAPHY

1. F. Schwierz and J. J. Liou, *Modern Microwave Transistors: Theory, Design, and Performance*, Wiley, Hoboken, NJ, 2003.
2. J. C. H. Lin, T. H. Yeh, C. Y. Lee, C. H. Chen, J. L. Tsay, S. H. Chen, H. M. Hsu, C. W. Chen, C. F. Huang, J. M. Chiang, A. Chang, R. Y. Chang, C. L. Chang, S. H. Wang, C. C. Wu, C. Y. Lin, Y. L. Chu, S. M. Chen, C. K. Hsu, R. S. Liou, S. C. Wong, D. Tang, and J. Y. C. Sun, State-of-the-art RF/analog foundry technology, *IEEE Proc. Bipolar/BiCMOS Circuits and Technology Meeting 4.1*, 2001, pp. 73–79.
3. F. Ali and A. Gupta, *HEMTs & HBTs: Devices, Fabrication and Circuits*, Artech House, Norwood, MA, 1991.
4. T. Mimura, The early history of the high electron mobility transistor (HEMT), *IEEE Trans. Microwave Theory Tech.* **50**(3):780–782 (March 2002).

5. J. A. del Alamo and M. H. Somerville, Breakdown in millimeter-wave power InP HEMTs: A comparison with GaAs PHEMTs, *IEEE J. Solid State Circ.* **34**(9):1204–1211 (Sept. 1999).
6. Y. Kwon, K. Kim, E. A. Sovero, and D. S. Deakin, Watt-level Ka- and Q-band MMIC power amplifiers operating at low voltages, *IEEE Trans. Microwave Theory Tech.* **48**(6):891–897 (June 2000).
7. H. K. Huang, Y. H. Wang, C. L. Wu, C. Wang, and C. S. Chang, Super low noise InGaP gated PHEMT, *IEEE Electron. Device Lett.* **23**(2):70–72 (Feb. 2002).
8. L. D. Nguyen, A. S. Brown, M. A. Thompson, and L. M. Jelloian, 50-nm self-aligned-gate pseudomorphic AlInAs/GaNAs high electron mobility transistors, *IEEE Trans. Electron. Devices* **39**(9):2007–2014 (Sept. 1992).
9. M. Wojtowicz, R. Lai, D. C. Streit, G. I. Ng, T. R. Block, K. L. Tan, P. H. Liu, A. K. Freudenthal, and R. M. Dia, 0.1 μm graded InGaAs channel InP HEMT with 305 GHz f_T and 240 GHz f_{max} , *IEEE Electron. Device Lett.* **15**(11):477–479 (Nov. 1994).
10. T. Suemitsu, T. Ishii, H. Yokoyama, Y. Umeda, T. Enoki, Y. Ishii, and T. Tamamura, 30-nm-gate InAlAs/InGaAs HEMTs lattice-matched to InP substrates, *1998 IEDM Tech. Digest*, 1998, pp. 223–226.
11. K. Shinohara, Y. Yamashita, A. Endoh, K. Hikosaka, T. Matsui, T. Mimura, and S. Hiyamizu, Ultrahigh-speed pseudomorphic InGaAs/InAlAs HEMTs with 400-GHz cutoff frequency, *IEEE Electron Device Lett.* **22**(11):507–509 (Nov. 2001).
12. P. M. Smith, S.-M. J. Liu, M.-Y. Kao, P. Ho, S. C. Wang, K. H. G. Duh, S. T. Fu, and P. C. Chao, W-band high efficiency InP-based power HEMT with 600 GHz f_{max} , *IEEE Microwave Guided Wave Lett.* **5**(7):230–232 (July 1995).
13. C. Pobanz, M. Matloubian, V. Radisic, G. Raghavan, M. Case, M. Micovic, M. Hu, C. Nguyen, S. Weinreb, and L. Samoska, High performance MMICs with submillimeter wave InP-based HEMTs, *Proc. 2000 Int. Conf. Indium Phosphide and Related Materials*, 2000, pp. 67–70.
14. R. Grundbacher, R. Lai, M. Barsky, R. Tsai, T. Gaier, S. Weinreb, D. Dawson, J. J. Bautista, J. F. Davis, N. Erickson, T. Block, and A. Oki, 0.1 μm InP HEMT devices and MMICs for cryogenic low noise amplifiers from X-band to W-band, *Proc. 2002 Int. Conf. Indium Phosphide and Related Materials*, 2002, pp. 455–458.
15. C. S. Whelan, W. F. Hoke, R. A. McTaggart, M. Lardizabal, P. S. Lyman, P. F. Marsh, and T. E. Kazior, Low noise $\text{In}_{0.32}(\text{AlGa})_{0.68}\text{As}/\text{In}_{0.43}\text{Ga}_{0.57}\text{As}$ metamorphic HEMT on GaAs substrate with 850 mW/mm output power density, *IEEE Electron. Device Lett.* **21**(1):5–8 (Jan. 2000).
16. O. S. A. Tang, S. M. J. Liu, P. C. Chao, W. M. T. Kong, K. C. Hwang, K. Nichols, and J. Heaton, Design and fabrication of a wideband 56- to 63-GHz monolithic power amplifier with very high power-added efficiency, *IEEE J. Solid State Circ.* **35**(9):1298–1306 (Sept. 2000).
17. U. K. Mishra, P. Parikh, and Y. Wu, AlGaIn/GaN HEMTs—an overview of device operation and applications, *Proc. IEEE* **90**(6):1022–1031 (June 2002).
18. A. P. Zhang, L. B. Rowland, E. B. Kaminsky, J. B. Tucker, J. W. Kretchmer, A. F. Allen, J. Cook, and B. J. Edward, 9.2 W/mm (13.8 W) AlGaIn/GaN HEMTs at 10 GHz and 55 V drain bias, *Electron. Lett.* **39**(2):245–247 (Jan. 2003).
19. R. S. Schwindt, V. Kumar, A. Kuliev, G. Simin, J. W. Yang, M. A. Khan, M. E. Muir, and I. Adesida, Millimeter-wave high-power 0.25- μm gate-length AlGaIn/GaN HEMTs on SiC substrates, *IEEE Microwave Wireless Compon. Lett.* **13**(3):93–95 (March 2003).
20. I. P. Smorchkova, M. Wojtowicz, R. Tsai, M. Barsky, C. Namba, P.-S. Liu, R. Dia, M. Truong, D. Ko, J. Wang, H. Wang, and A. Khan, AlGaIn/GaN HEMTs—operation in the K-Band and above, *IEEE Trans. Microwave Theory Tech.* **51**(2):665–668 (Feb. 2003).
21. D. H. Youn, V. Kumar, J. H. Lee, R. Schwindt, W. J. Chang, J. Y. Hong, C. M. Jeon, S. B. Bae, M. R. Park, K. S. Lee, J. L. Lee, and I. Adesida, High power 0.25 μm gate GaN HEMTs on sapphire with power density 4.2 W/mm at 10 GHz, *Electron. Lett.* **39**(6):566–567 (March 2003).
22. A. Chini, R. Coffie, G. Meneghesso, E. Zanoni, D. Buttari, S. Heikman, S. Keller, and U. K. Mishra, 2.1 A/mm current density AlGaIn/GaN HEMT, *Electron. Lett.* **39**(7):625–626 (April 2003).
23. R. Behtash, H. Tobler, M. Neuburger, A. Schurr, H. Leier, Y. Cordier, F. Semond, F. Natali, and J. Massies, AlGaIn/GaN HEMTs on Si(111) with 6.6 W/mm output power density, *Electron. Lett.* **39**(7):626–627 (April 2003).
24. P. A. Houston, High-frequency heterojunction bipolar transistor device design and technology, *Electron. Commun. Eng. J.* **12**:220–228 (Oct. 2000).
25. S. S. Lu, C. C. Wu, C. C. Huang, F. Williamson, and M. I. Nathan, DC characterization of GaInP/GaAs tunneling emitter bipolar transistors, *Proc. 4th Int. Conf. Indium Phosphide and Related Materials*, April 1992, pp. 445–448.
26. T. Oka, K. Hirata, H. Suzuki, K. Ouchi, H. Uchiyama, T. Taniguchi, K. Mochizuki, and T. Nakamura, High-speed small-scale InGaP/GaAs HBT technology and its application to integrated circuits, *IEEE Trans. Electron. Devices* **48**:2625–2630 (Nov. 2001).
27. M. W. Dvorak, C. R. Bolognesi, O. J. Pitts, and S. P. Watkins, 300 GHz InP/GaAsSb/InP double HBTs with high current capability and $\text{BVCEO} > 6\text{V}$, *IEEE Electron. Device Lett.* **22**:361–363 (Aug. 2001).
28. M. Ida, K. Kurishima, N. Watanabe, and T. Enoki, InP/InGaAs DHBTs with 341-GHz f_T at high current density of over 800 kA/cm², *2001 Intl. IEDM Techn. Digest*, Dec. 2001, pp. 35.4.1–35.4.4.
29. S. J. Jeng, B. Jagannathan, J. S. Rieh, J. Johnson, K. T. Schonenberg, D. Greenberg, A. Stricker, H. Chen, M. Khater, D. Ahlgren, G. Freeman, K. Stein, and S. Subbanna, A 210-GHz f_T SiGe HBT with a non-self-aligned structure, *IEEE Electron. Device Lett.* **22**:542–544 (Nov. 2001).
30. D. Mensa, R. Pallela, Q. Lee, J. Guthrie, S. C. Martin, R. P. Smith, S. Jaganathan, T. Mathew, B. Agarwal, S. I. Long, and M. Rodwell, 48-GHz digital ICs and 85-GHz baseband amplifiers using transferred-substrate HBTs, *IEEE J. Solid State Circ.* **34**:1196–1203 (Sept. 1999).
31. H. S. Tsai, R. Kopf, R. Melendes, M. Melendes, A. Tate, R. Ryan, R. Hamm, and Y. K. Chen, 90 GHz baseband lumped amplifier, *Electron. Lett.* **36**:1833–1834 (Oct. 2000).
32. D. Kehler, H. D. Wohlmut, H. Knapp, M. Wurzer, and A. Scholtz, 40-Gb/s 2:1 multiplexer and 1:2 demultiplexer in 120 nm standard CMOS, *IEEE ISSCC Digest Tech. Papers*, 2003, pp. 344–345.
33. J. Lee and B. Razavi, A 40-Gb/s clock recovery circuit in 0.18 μm CMOS technology, *IEEE ISSCC Digest Tech. Papers*, 2003, pp. 242–243.
34. A. Ryllyakov, S. Rylov, H. Ainspan, and S. Gowda, A 30-Gb/s 1:4 demultiplexer in 0.12 μm CMOS, *IEEE ISSCC Digest Tech. Papers*, 2003, pp. 176–177.

35. M. Tiebout, H.-D. Wohlmuth, and W. Simburger, A 1 V 51 GHz fully integrated VCO in 0.12 μm CMOS, *IEEE IS-SCC Digest Tech. Papers*, 2002, pp. 300–301.
36. H. Wang, A 50 GHz VCO in 0.25 μm CMOS, *IEEE ISSCC Digest Tech. Papers*, 2001, pp. 372–373.
37. C. Wann, F. Assaderaghi, L. Shi, K. Chan, S. Cohen, H. Hovel, K. Jenkins, Y. Lee, D. Sadana, R. Viswanathan, S. Wind, and Y. Taur, High-performance 0.07- μm CMOS with 9.5-ps gate delay and 150 GHz f_T , *IEEE Electron. Device Lett.* **18**(12):625–627 (Dec. 1997).
38. H. S. Momose, E. Morifuji, T. Yoshimoto, T. Ohguro, M. Saito, and H. Iwai, Cutoff frequency and propagation delay time of 1.5-nm gate oxide CMOS, *IEEE Trans. Electron. Devices*, **48**(6):1165–1174 (June 2001).
39. F. Tiemeijer, H. M. J. Boots, R. J. Havens, A. J. Scholten, P. H. W. de Vreede, P. H. Woerlee, A. Heringa, and D. B. M. Klaassen, A record high 150 GHz f_{max} realized at 0.18 μm gate length in an industrial RF-CMOS technology, *IEEE IEDM Tech. Digest*, 2001, pp. 223–226.
40. N. Fong, J.-O. Plouchart, N. Zamdmer, D. Liu, L. Wagner, C. Plett, and G. Tarr, A 40 GHz VCO with 9 to 15% tuning range in 0.13 μm SOI CMOS, *IEEE Very Large Scale Integration Symp.* 2002, pp. 186–189.
41. S. Narasimha, A. Ajmera, R. J. Park, D. Schepis, N. Zamdmer, K. A. Jenkins, J.-O. Plouchart, W.-H. Lee, J. Mezzapelle, J. Bruley, B. Doris, J. W. Sleight, S. K. Fung, S. H. Ku, A. C. Mocuta, I. Yang, P. V. Gilbert, K. P. Muller, P. Agnello, and J. Welsler, High-performance sub-40 nm CMOS devices on SOI for the 70 nm technology node, *IEEE IEDM Tech. Digest*, 2001, pp. 625–628.
42. T. Hirose, Y. Momiya, M. Kosugi, H. Kano, Y. Watanabe, and T. Sugii, A 185 GHz f_{max} SOI DTMOS with a new metallic overlay-gate for low-power RF applications, *IEEE IEDM Tech. Digest*, 2001, pp. 943–945.
43. I. Lagnado, P. R. de la Houssaye, and W. B. Dubbelday, Silicon-on-sapphire for RF Si system 2000, *IEEE SMIC in RF Systems Tech. Digest*, 2000, pp. 79–82.
44. A. S. Sedra and K. C. Smith, *Microelectronic Circuits*, 3rd ed., Saunders College Publishing, 1990.
45. S. Weinreb, T. Gaier, M. Barsky, Y. C. Leong, and L. Samoska, High-gain 150–215 GHz MMIC amplifier with integral waveguide transitions, *IEEE Microwave Guided Wave Lett.* **9**:282–284 (July 1999).
46. G. Schuppender, T. Harada, and Y. Li, A 23-GHz low-noise amplifier in SiGe heterojunction bipolar technology, *2001 IEEE Radio Frequency Integrated Circuits Symp.*, 2001, pp. 177–180.
47. Brian A. Floyd, L. Shi, Y. Taur, I. Lagnado, and K. K. O, A 23.8 GHz SOI CMOS tuned amplifier, *IEEE Trans. Microwave Theory Tech.* **50**(9):2193–2196 (Sept. 2002).
48. T. Kashiwa, M. Komaru, T. Katoh, N. Yoshida, N. Tanino, T. Takagi, and O. Ishihara, A Q-band gigh gain and low noise variable gain amplifier using dual gate HEMTs, *Proc. IEEE GaAs IC Symp.* 1995, pp. 210–213.
49. A. Fujihara, E. Mizuki, H. Miyamoto, Y. Makino, K. Yamano-guchi, and N. Samoto, High performance 60 GHz coplanar MMIC LNA using InP heterojunction FETS with AlAs/InAs superlattice layer, *2000 IEEE Int. Microwave Symp. Digest*, 2000, pp. 21–24.
50. V. Radisic, C. Pobanz, M. Hu, M. Micovic, M. Wetzel, P. Janke, M. Yu, C. Ngo, D. Dawson, and M. Matloubian, A high-performance 85–119 GHz GCPW MMIC low noise amplifier, *Proc. 2000 IEEE Radio Frequency Integrated Circuits Symp.* 2000, pp. 43–46.
51. D.-W. Tu, W. P. Berk, S. E. Brown, N. E. Byer, S. W. Duncan, A. Eskandarian, E. Fischer, D. M. Gill, B. Golja, B. C. Kane, S. P. Svensson, and S. Weinreb, High gain monolithic PHEMT W-band four-stage low noise amplifiers, *Proc. 1994 IEEE Microwave and Millimeter-Wave Monolithic Circuits Symp.* 1994, pp. 29–32.
52. H. Wang, T. N. Ton, K. L. Tan, D. Garske, G. S. Dow, J. Berenz, M. W. Pospieszalski, and S. K. Pan, A D-band monolithic low noise amplifier, *Proc 1992 Gallium Arsenide Integrated Circuit (GaAs IC) Symp.* 1992, pp. 23–26.
53. H. Wang, R. Lai, D. C. W. Lo, D. C. Streit, P. H. Liu, R. M. Dia, M. W. Pospieszalski, and J. Berenz, A 140-GHz monolithic low noise amplifier, *IEEE Microwave Guided Wave Lett.* **5**:150–152 (May 1995).
54. H. Wang, R. Lai, Y. L. Kok, T. W. Huang, M. V. Aust, Y. C. Chen, P. H. Siegel, T. Gaier, R. J. Dengler, and B. R. Allen, A 155-GHz monolithic low-noise amplifier, *IEEE Trans. Microwave Theory Tech.* **46**:1660–1666 (Nov. 1998).
55. Y. L. Kok, H. Wang, T. W. Huang, R. Lai, M. Barsky, Y. C. Chen, M. Sholley, T. Block, D. C. Streit, B. R. Allen, L. Samoska, and T. Gaier, 160–190 GHz monolithic low-noise amplifiers, *IEEE Microwave Guided Wave Lett.* **9**:311–313 (Aug. 1999).
56. C. Pobanz, M. Matloubian, V. Radisic, G. Raghavan, M. Case, M. Micovic, M. Hu, C. Nguyen, S. Weinreb, and L. Samoska, High performance MMICs with submillimeter wave InP-based HEMTs, *Proc. 2000 Int. Conf. Indium Phosphide and Related Materials*, 2000, pp. 67–70.
57. S. Weinreb, T. Gaier, M. Barsky, Y. C. Leong, and L. Samoska, High-gain 150–215 GHz MMIC amplifier with integral waveguide transitions, *IEEE Microwave Guided Wave Lett.* **9**:282–284 (July 1999).
58. D. B. McDermott, H. H. Song, L. R. Barnett, Y. Hirata, A. T. Lin, H. L. Hsu, P. S. Marandos, J. S. Lee, T. H. Chang, K. R. Chu, and N. C. Luhmann, Jr., High power broadband W-band gyrotron traveling wave amplifier, *2002 Infrared and Millimeter-Waves Conf. Digest*, 2002, pp. 201–202.
59. D. L. Ingram, D. I. Stones, T. W. Huang, M. Nishimoto, H. Wang, M. Siddiqui, D. Tamura, J. Elliott, R. Lai, M. Biedenbender, H. C. Yen, and B. Allen, A 6 watt Ka-band MMIC power module using MMIC power amplifiers *1997 IEEE Int. Microwave Symp. Digest*, June 1999, Vol. 3, pp. 1183–1186.
60. A. K. Sharma, G. S. Dow, M. Aust, J. Canyon, B. Allen, S. Pak, D. Yang, Y. Hwang, and K. Tan, Ka-band power PHEMT on-wafer characterization using prematched structures, *1993 IEEE Int. Microwave Symp. Digest*, June 1993, Vol. 3, pp. 1343–1346.
61. K. W. Kobayashi, M. Nishimoto, L. T. Tran, H. Wang, J. C. Cowles, T. R. Block, J. H. Elliott, B. R. Allen, A. K. Oki and D. C. Streit, A 44-GHz high IP3 InP-HBT amplifier with practical current reuse biasing, *IEEE Trans. Microwave Theory Tech.* **46**(12):2541–2552 (Dec. 1998).
62. R. Lai, M. Nishimoto, Y. Hwang, M. Biedenbender, B. Kasody, C. Geiger, Y. C. Chen, and G. Zell, A high efficiency 0.15 μm 2-mil thick InGaAs/AlGaAs/GaAs V-band power HEMT MMIC, *1996 Gallium Arsenide Integrated Circuit (GaAs IC) Symp.* 1996, pp. 225–227.
63. J. A. Lester, J. Chi, R. Lai, M. Biedenbender, D. Garske, R. Rordan, and P. D. Chow, 3-watt Q-band waveguide PHEMT MMIC power amplifier module, *1997 IEEE Int. Microwave Symp. Digest*, May 1997, Vol. 2, pp. 539–542.
64. O. S. A. Tang, K. H. G. Duh, S. M. J. Liu, P. M. Smith, W. F. Kopp, T. J. Rogers, and D. J. Pritchard, Design of high-power, high-efficiency 60-GHz MMICs using an improved

- nonlinear PHEMT model, *IEEE J. Solid State Circ.* **32**(9):1326–1333 (Sept. 1997).
65. H. Wang, L. Samoska, T. Gaier, A. Peralta, H. H. Liao, Y. C. Leong, S. Weinreb, Y. C. Chen, M. Nishimoto, and R. Lai, Power-amplifier modules covering 70–113 GHz using MMICs, *IEEE Trans. Microwave Theory Tech.* **49**(1):9–16 (Jan. 2001).
 66. J. Goel, G. Onak, D. I. Stones, D. Yamauchi, A. Sharma, K. Tan, and J. Mancini, High power V-band power amplifier using PHEMT technology, *1996 IEEE Int. Microwave Symp. Digest*, June 1996, Vol. 1, pp. 17–21.
 67. P. P. Huang, T. W. Huang, H. Wang, E. Lin, Y. H. Shu, G. S. Dow, R. Lai, M. Biedenbender, and J. Elliot, A 94-GHz 0.35-W power amplifier module, *IEEE Trans. Microwave Theory Tech.* **45**(12) (Part 2):2418–2423 (Dec. 1997).
 68. Y. Wei, S. Lee, K. Sundararajan, M. Dahlstrom, M. Urteaga, and M. Rodwell, W-band InP/InGaAs/InP DHBT MMIC power amplifiers, *1995 IEEE Int. Microwave Symp. Digest*, June 2002, Vol. 2, pp. 917–920.
 69. L. Samoska and Y. C. Leong, 65–145 GHz InP MMIC HEMT medium power amplifiers, *2001 IEEE Int. Microwave Symp. Digest*, May 2001, Vol. 3, pp. 1805–1808.
 70. J. Perdomo, B. Hughes, H. Kondoh, L. Studebaker, G. Zhou, T. Taylor, C. Li, and T. Ma, A monolithic 1 to 50 GHz distributed amplifier with 20 dBm output power, *Proc. 1992 Gallium Arsenide Integrated Circuit (GaAs IC) Symp.* 1992, pp. 203–206.
 71. K. M. Simon, R. M. Wohlert, J. P. Wendler, L. M. Aucoin, and D. W. Vye, K through Ka-band driver and power amplifiers, *1996 Microwave and Millimeter-Wave Monolithic Circuits Symp. Digest*, June 1996, pp. 29–32.
 72. J. B. Beyer, S. N. Prasad, R. C. Becker, J. E. Nordman, and G. K. Hohenwarter, MESFET distributed amplifier design guidelines, *IEEE Trans. Microwave Theory Tech.* **32**(3):268–275 (March 1984).
 73. Y. Avasio, R. L. Mozzi, J. L. Vorhaus, L. D. Reynolds, and R. A. Pucel, A monolithic GaAs 1–13-GHz traveling-wave amplifier, *IEEE Trans. Microwave Theory Tech.* **30**(7):976–981 (July 1982).
 74. B. Agarwal, A. E. Schmitz, J. J. Brown, M. Matloubian, M. G. Case, M. Le, and M. Lui, 112-GHz, 157-GHz and 180-GHz InP HEMT traveling-wave amplifiers, *IEEE Trans. Microwave Theory Tech.* **46**(12):2553–2559 (Dec. 1998).
 75. K. B. Niclas and R. R. Pereira, The matrix amplifier: a high-gain module for multioctave frequency bands, *IEEE Trans. Microwave Theory Tech.* **35**(3):296–306 (March 1987).
 76. B. Y. Banyamin and M. Berwick, Analysis of the performance of four-cascaded single-stage distributed amplifiers, *IEEE Trans. Microwave Theory Tech.* **48**(12):2657–2663 (Dec. 2000).
 77. J. Y. Liang and C. S. Aitchison, A proposal of a broadband high gain block using cascaded single stage distributed amplifiers, *Proc. High Performance Electron Devices for Microwave and Optoelectronic Applications, 1995, (EDMO)* Nov. 1995, pp. 173–178.
 78. K. L. Deng, T. W. Huang, and H. Wang, Design and analysis of novel high-gain and broadband GaAs PHEMT MMIC distributed amplifiers with traveling-wave gain stage, *IEEE Trans. Microwave Theory Tech.* **51**(11):2188–2196 (Nov. 2003).
 79. R. Heilig, D. Hollmann, and G. Baumann, A monolithic 2–52 GHz matrix distributed amplifier in coplanar waveguide technology, *1994 Microwave and Millimeter-wave Monolithic Circuit Symp. Digest*, May 1994, pp. 191–194.
 80. J. Aguirre and C. Plett, A 0.1–50 GHz SiGe HBT distributed amplifier employing constant-k m-derived sections, *2003 IEEE Int. Microwave Symp. Digest*, June 2003, Vol. 2, pp. 923–926.
 81. R. C. Liu, K. L. Deng, and H. Wang, A 0.6–22-GHz broadband CMOS distributed amplifier, *2003 IEEE Radio Engineering Integrated Circuits (RFIC) Symp. Digest*, 2003, pp. 103–106.
 82. K. W. Kobayashi, State-of-the-art 60 GHz, 3.6 K-ohm transimpedance amplifier for 40 Gb/s and beyond, *Proc. 2003 IEEE RFIC Symp. Digest*, 2003, pp. 55–58.
 83. K. W. Kobayashi, An InP HBT common-base amplifier with tunable transimpedance for 40 Gb/s applications, *Proc. 2002 Gallium Arsenide Integrated Circuit (GaAs IC) Symp.* 2002, pp. 155–158.
 84. S. Kudzusz, A. Shahani, S. Pavan, D. Shaeffer, and M. Tarsia, A 46-GHz distributed transimpedance amplifier using SiGe bipolar technology, *2003 IEEE Int. Microwave Symp. Digest*, June 2003, Vol. 3, pp. 1387–1390.
 85. J. S. Weiner, A. Leven, V. Houtsma, and P. Paschke, SiGe differential transimpedance amplifier with 50 GHz bandwidth, *Proc. 2002 Gallium Arsenide Integrated Circuit (GaAs IC) Symp.* 2002, pp. 67–69.
 86. S. A. Steidl, D. Rowe, T. W. Krawczyk, P. Wong, A. Tam, and C. Hornbuckle, A transimpedance amplifier for OC-768 applications designed using a SiGe HBT BiCMOS technology, *IEEE Optical Fiber Communication Conference and Exhibit Digest*: 2002, pp. 276–277.
 87. C. F. Campbell, M. S. Heins, M. Y. Kao, M. E. Muir, and J. M. Carroll, A 0.15- μm GaAs MHEMT transimpedance amplifier IC for 40-Gb/s applications, *2002 IEEE Int. Microwave Symp. Digest*, June 2002, Vol. 1, pp. 79–82.
 88. H. Shigematsu, M. Sato, T. Suzuki, T. Takahashi, K. Imanishi, N. Hara, H. Ohnishi, and Y. Watanabe, 49-GHz Pre-amplifier with transimpedance gain of 52 dB Ω using InP HEMTs, *Proc. 2000 Gallium Arsenide Integrated Circuit (GaAs IC) Symp.* 2000, pp. 197–200.
 89. S. A. Maas, *Microwave Mixers*, 2nd ed., Artech House, Boston, 1993.
 90. R. Shimon, D. Caruth, J. Middleton, H. Hsia, and M. Feng, Low cost coplanar 77 GHz single-balanced mixer using ion-implanted GaAs Schottky diodes, *1998 Int. Microwave Symp. Digest*, June 1998, Vol. 3, pp. 1439–1442.
 91. S. A. Maas and K. W. Chang, A broadband, planar, doubly balanced monolithic Ka-band diode mixer, *IEEE Trans. Microwave Theory Tech.* **41**(12):2330–2335 (Nov. 1993).
 92. K. Kanaya, K. Kawakami, T. Hisaka, T. Ishikawa, and S. Sakamoto, A 94 GHz high performance quadruple subharmonic mixer MMIC, *2002 Int. Microwave Symp. Digest*, June 2002, Vol. 2, pp. 1249–1252.
 93. M. Kimishima, T. Ataka, and H. Okabe, A family of Q, V and W-band monolithic resistive mixers, *2001 IEEE Int. Microwave Symp. Digest*, May 2001, Vol. 1, pp. 115–118.
 94. T. H. Chen, T. N. Ton, G. S. Dow, K. Nakano, L. C. T. Liu, and J. Berenz, A Q-band monolithic balance resistive HEMT mixer using CPW/slotline balun, *IEEE J. Solid State Circ.* **26**(10):1389–1394 (Oct. 1991).
 95. K. Won and K. Youngwoo, Analytical analysis of noise figures in FET resistive mixers, *Electron. Lett.* **35**:1169–1170 (July 1999).
 96. U. Schaper, A. Schafer, A. Werthof, H. J. Siweris, H. Tischer, L. Klapproth, G. Bock, and W. Kellner, 70–90 GHz balanced resistive PHFET mixer MMIC, *Electron. Lett.* **34**:1377–1379 (July 1998).

97. R. Desrosiers, J. Cowles, C. Hornbuckle, A. Gutierrez-Aitken, and J. Becker, Monolithic 14 GHz widerband InP HBT BPSK modulator, *Proc. 1998 Gallium Arsenide Integrated Circuit Symp.* 1998, pp. 135–138.
98. I. Telliez, A. M. Couturier, C. Rumelhard, C. Versnaeyen, P. Champion, and D. Fayol, A compact monolithic microwave demodulator-modulator for 64-QAM digital radio links, *IEEE Trans. Microwave Theory Tech.* **39**(12):1947–1954 (Dec. 1991).
99. A. Alexanian, M. Wu, A. Burgess, Y. Wei, and X. Xhang, A SiGe transceiver chipset for 100 Mbps/1 Gbps digital communication over cable system, *2002 IEEE Radio Frequency Integrated Circuits Symp.*, 2002, pp. 119–122.
100. A. Weetzel, A stable 250 to 4000 MHz GaAs IQ modulator IC, *1997 IEEE Int. Solid-State Circuits Conf. Digest*, 1997, pp. 364–365.
101. H. Y. Chang, T. W. Huang, and H. Wang, Vector signal characterization for a HEMT IQ modulator MMIC at 94 GHz, *2003 Asia Pacific Microwave Conf. Digest*, Nov. 2003.
102. H. Y. Chang, T. W. Huang, H. Wang, Y. C. Wang, P. C. Chao, and C. H. Chen, A broadband HBT MMIC IQ modulator and millimeter-wave vector signal char SiGe acterization, *2003 IEEE Int. Microwave Symp.* June 2003, Vol. 1, pp. 99–102.
103. T. Saito, N. Hidaka, K. Ono, Y. Ohashi, and T. Shimura, 60-GHz MMIC image-rejection downconverter using InGaP/InGaAs HEMT, *Proc. 1995 Gallium Arsenide Integrated Circuit (GaAs IC) Symp.*, 1995, pp. 222–225.
104. C. Tsirois, R. Stahlmann, and R. Meierer, Modelling and evaluation of dual gate MESFETs as low-noise, self-oscillating and image-rejection mixers, *1983 IEEE Int. Microwave Symp. Digest*, May 1983, pp. 443–445.
105. Y. Kwon, D. Pavlidis, P. Marsh, G. T. Ng, T. Brock, and D. Streit, A miniaturized W-band monolithic dual-gate InAlAs/InGaAs HEMT mixer, *1993 Gallium Arsenide Integrated Circuit (GaAs IC) Symp.* 1993, pp. 215–218.
106. Y. Imai, S. Kimura, Y. Umeda, and T. Enoki, DC to 38-GHz distributed analog multiplier using InP HEMT's, *IEEE Microwave Guided Wave Lett.* **4**:399–401 (Dec. 1994).
107. K. W. Kobayashi, R. M. Desrosiers, A. Gutierrez-Aitken, J. C. Cowles, B. Tang, L. T. Tran, T. R. Block, A. K. Oki, and D. C. Streit, A DC-20-GHz InP HBT balanced analog multiplier for high-data-rate direct-digital modulation and fiber-optic receiver applications, *IEEE Trans. Microwave Theory Tech.* **48**:194–202 (Feb. 2000).
108. B. Tzeng, C. H. Lien, H. Wang, Y. C. Wang, P. C. Chao, and C. H. Chen, A 1-17-GHz InGaP-GaAs HBT MMIC analog multiplier and mixer with broad-band input-matching networks, *IEEE Trans. Microwave Theory Tech.* **50**:2564–2568 (Nov. 2002).
109. K. L. Deng and H. Wang, A 3-33 GHz PHEMT MMIC distributed drain mixer, *Proc. 2002 IEEE Radio Frequency Integrated Circuits Symp.*, 2002, pp. 151–154.
110. D. Hollmann, R. Heilig, and G. Baumann, A monolithic broadband 10-50 GHz distributed HEMT mixer including active LO-RF combiner, *Proc. 1994 Gallium Arsenide Integrated Circuit (GaAs IC) Symp.* 1994, pp. 100–103.
111. R. Majidi-Ahy, C. Nishimoto, J. Russel, W. Ou, S. Bandy, and G. Zdasik, 23-40 GHz InP HEMT MMIC distributed mixer, *1992 IEEE Int. Microwave Symp. Digest*, June 1992, Vol. 2, pp. 1063–1066.
112. K. W. Chang, H. Wang, T. N. Ton, T. H. Chen, K. L. Tan, G. S. Dow, G. Hayashibara, B. Allen, J. Berenz, P. H. Liu, D. C. Streit, and L. C. T. Liu, A W-band image-rejection downconverter, *IEEE Trans. Microwave Theory Tech.* **40**(12):2332–2336 (Dec. 1992).
113. G. D. Vendelin, A. M. Pavio, and U. L. Rohde, *Microwave Circuit Design Using Linear and Nonlinear Techniques*, Wiley-Interscience, New York, 1990.
114. A. A. Sweet, *MIC and MMIC Amplifier and Oscillator Circuit Design*, Artech House, Norwood, MA, 1990.
115. H. Wang, Y. Huang, L. Shaw, M. Amadi, M. Siddiqui, B. L. Nelson, D. L. Tait, B. Martin, R. E. Asody, W. L. Jones, D. Brnone, and M. Sholey, Monolithic V-band frequency converter chip set development using 0.2 μm AlGaAs/InGaAs/GaAs pseudomorphic HEMT technology, *IEEE Trans. Microwave Theory Tech.* **42**:11–17 (Jan. 1994).
116. H. Wang, K. W. Chang, L. Tran, J. Cowles, T. Block, E. W. Lin, G. S. Dow, A. Oki, D. Streit, and B. R. Allen, Low phase noise millimeter-wave frequency sources using InP-based HBT MMIC technology, *IEEE J. Solid-State Circ.* **31**(10):1419–1425 (Oct. 1996).
117. Y. Baeyen, C. Dorschky, N. Weimann, Q. Lee, R. Kopf, G. Georgiou, J. P. Mattia, R. Hamm, and Y. K. Chen, Compact InP-Based HBT VCOs with a wide tuning range at W- and D- band, *IEEE Trans. Microwave Theory Tech.* **48**(12):2403–2408 (Dec. 2000).
118. K. W. Kobayashi, J. Cowles, L. T. Tran, A. Gutierrez-Aitken, T. Block, F. Yamada, A. K. Oki, and D. C. Streit, A low phase noise W-band InP-HBT monolithic push–push VCO, *Proc. 1998 Gallium Arsenide Integrated Circuit (GaAs IC) Symp.* 1998, pp. 237–240.
119. A. M. Pavio and M. A. Smith, A 20–40 GHz push-push dielectric resonator oscillator, *IEEE Trans. Microwave Theory Tech.* **33**(12):1346–1349 (Dec. 1985).
120. Y. L. Tang, *A Triple-Push Oscillator Approach*, Master's Thesis, National Taiwan Univ., 2000.
121. Y. L. Tang and H. Wang, Triple-push oscillator approach: Theory and experiments, *IEEE J. Solid-State Circ.* **36**(10):1472–1479 (Oct. 2001).
122. P.-Y. Chen, Y.-L. Tang, H. Wang, et al., A 39-46 GHz MMIC HBT triple-push VCO using cascode configuration, *Proc. 2002 IEEE Asia-Pacific Conf. Application-Specific Integrated Circuit* 2002, pp. 61–64.
123. H. Xiao, T. Tanaka, and M. Aikawa, A Ka-band quadruple-push oscillator, *2003 IEEE Int. Microwave Symp. Digest*, June 2003, Vol. 2, pp. 889–892.
124. S. C. Yen and T. H. Chu, An Nth-harmonic oscillator using an N-push coupled oscillator array with voltage-clamping circuits, *2003 IEEE Int. Microwave Symp. Digest* 2003, Vol. 3, pp. 2169–2172.
125. P. Y. Chen, Z. M. Tsai, S. S. Lu, and H. Wang, An ultra low phase noise W-Band GaAs-based PHEMT MMIC CPW VCO, *33rd European Microwave Conf. Proc.*, Munich, Germany, Oct. 2003, pp. 503–506.
126. Y. Kwon, D. Pavlidis, T. Brock, and D. C. Streit, A D-band monolithic fundamental oscillator using InP-Based HEMTs, *1993 IEEE Microwave and Millimeter-Wave Monolithic Circuits Symp. Digest*, June 1993, pp. 49–52.
127. S. E. Rosenbaum, L. M. Jelloian, A. S. Brown, M. A. Thompson, M. Matloubian, L. E. Larson, R. F. Lohr, B. K. Kormanyos, G. M. Rebeiz, and L. P. B. Katchi, A 213 GHz AlInAs/GaInAs/InP HEMT MMIC oscillator, *Proc. 1993 Int. Electron Devices Meeting* Dec. 1993, pp. 924–926.
128. K. Uchida, H. Matsuura, T. Yakihara, S. Kobayashi, S. Oka, T. Fujita, and A. Miura, A power combined W-band HBT

- oscillator, *2000 IEEE Int. Microwave Symp. Digest*, June 2000, Vol. 1, pp. 51–54.
129. H. Wang, L. Tran, J. Cowles, E. Lin, P. Huang, T. Block, D. Streit, and A. Oki, Monolithic 77- and 94-GHz InP-based HBT MMIC VCOs, *Proc. 1997 IEEE Radio Frequency Integrated Circuits Symp.* 1997, pp. 91–94.
 130. K. Uchida, I. Aoki, H. Matsuura, T. Yakihara, S. Kobayashi, S. Oka, T. Fujita, and A. Miura, 104 and 134 GHz InGaP/InGaAs HBT oscillators, *Proc. 1999 Gallium Arsenide Integrated Circuit (GaAs IC) Symp.* 1999, pp. 237–240.
 131. H. Wang, A 50 GHz VCO in 0.25 μm CMOS, *Proc. 2001 Proc. IEEE Int. Solid-State Circuits Conf.*, 2001, pp. 372–373.
 132. M. Tiebout, H.-D. Wohlmuth, and W. Simbürger, A 1 V 51 GHz fully integrated VCO in 0.12 μm CMOS, *Proc. 2002 IEEE Int. Solid-State Circuits Conf.* 2002, pp. 85–88.
 133. H. Li, H. M. Rein, R. Kreienkamp, and W. Klein, 47-GHz VCO with low phase noise fabricated in a SiGe bipolar production technology, *IEEE Microwave Wireless Compon. Lett.* **12**:79–81 (March 2002).
 134. H. Li and H. M. Rein, Millimeter-wave VCOs with wide tuning range and low phase noise, fully integrated in a SiGe bipolar production technology, *IEEE J. Solid State Circ.* **38**(2):184–191 (Feb. 2003).
 135. Y. Baeyens and Y. K. Chen, A monolithic integrated 150 GHz SiGe HBT push-push VCO with simultaneous differential V-band output, *2003 IEEE Int. Microwave Symp. Digest*, June 2003, Vol. 2, pp. 877–880.
 136. K. V. Puglia, Phase noise analysis of component cascades, *IEEE Microwave Mag.* **3**(4):71–75 (Dec. 2002).
 137. H. Wang, K. W. Chang, D. C. W. Lo, K. L. Tan, D. Streit, G. S. Dow, and B. R. Allen, Monolithic 23.5 to 94 GHz frequency quadrupler using 0.1 μm pseudomorphic AlGaAs/InGaAs/GaAs HEMT technology, *IEEE Microwave Guided Wave Lett.* **4** (March 1994).
 138. M. Schefer, Integrated quadrupler circuit in coplanar technology for 60 GHz wireless applications, *2002 IEEE Int. Microwave Symp. Digest*, June 2002, Vol. 1, pp. 355–358.
 139. M. Morgan, S. Weinreb, N. Wadefalk, and L. Samoska, A MMIC-based 75–110 GHz signal source, *2002 IEEE Int. Microwave Symp. Digest*, June 2002, Vol. 3, pp. 1859–1862.
 140. S. A. Maas and Y. Ryu, A broadband, planar, monolithic resistive frequency doubler, *1994 IEEE Microwave and Millimeter-Wave Monolithic Circuits Symp. Digest*, May 1994, pp. 175–178.
 141. M. Morgan and S. Weinreb, A full waveguide band MMIC tripler for 75–110 GHz, *2001 IEEE Int. Microwave Symp. Digest* June 2001, Vol. 1, pp. 103–106.
 142. K. Y. Lin, H. Wang, M. Morgan, T. Gaier, and S. Weinreb, A W-band GCPW MMIC diode tripler, *32nd European Microwave Conf. Proc.*, Sept. 2002, Vol. 1, pp. 441–444.
 143. L. Tran, M. Delaney, R. Isobe, D. Jang, and J. Brown, Frequency translation MMICs using InP HEMT technology, *1996 Microwave and Millimeter-Wave Monolithic Circuits Symp. Digest*, 1996, pp. 193–196.
 144. A. Werthof, H. Tischer, and T. Grave, High gain PHEMT frequency doubler for 76 GHz automotive radar, *2001 IEEE Int. Microwave Symp. Digest*, May 2001, Vol. 1, pp. 107–109.
 145. E. Carman, M. Case, M. Kamegawa, R. Yu, K. Giboney, and M. J. W. Rodwell, V-band and W-band broad-band, monolithic distributed frequency multipliers, *IEEE Microwave Guided Wave Lett.* **2**:253–254 (June 1996).
 146. Y. Campos-Roca, L. Verweyen, M. Fernández-Barciela, W. Bischof, M. C. Currás-Francos, E. Sánchez, A. Hülsmann, and M. Schlechtweg, 38/76 GHz PHEMT MMIC balanced frequency doublers in coplanar technology, *IEEE Microwave Guided Wave Lett.* **10**:484–486 (Nov. 2000).
 147. H. Wang, R. Lai, L. Tran, J. Cowles, Y. C. Chen, E. W. Lin, H. H. Liao, M. K. Ke, T. Block, and Y. C. Yen, A single-chip 94 GHz frequency source using InP-based HEMT-HBT integrated technology, *Proc. 1998 IEEE Radio Frequency Integrated Circuits Symp.* 1997, pp. 275–278.
 148. Y. Campos-Roca, L. Verweyen, M. Neumann, M. Fernandez-Barciela, M. C. Currás-Francos, E. Sanchez-Sanchez, A. Hülsmann, and M. Schlechtweg, Coplanar pHEMT MMIC frequency multipliers for 76-GHz automotive radar, *IEEE Microwave Guided Wave Lett.* **9**:242–244 (June 1999).
 149. A. Boudiaf, D. Bachelet, and C. Rumelhard, A high-efficiency and low-phase-noise 38-GHz pHEMT MMIC tripler, *IEEE Trans. Microwave Theory Tech.* **48**(12):2546–2553 (Dec. 2000).
 150. Y. Campos-Roca, L. Verweyen, M. Fernandez-Barciela, E. Sanchez, M. C. Currás-Francos, W. Bronner, A. Hülsmann, and M. Schlechtweg, An optimized 25.5–76.5 GHz PHEMT-based coplanar frequency tripler, *IEEE Microwave Guided Wave Lett.* **10**:242–244 (June 2000).
 151. B. Piernas, H. Hayashi, K. Nishikawa, K. Kamogawa, and T. Nakagawa, A broadband and miniaturized V-band PHEMT frequency doubler, *IEEE Microwave Guided Wave Lett.* **10**:276–278 (July 2000).
 152. F. van Ray and G. Kompa, Design and stability test of a 2–40 GHz frequency doubler with active balun, *2000 IEEE Int. Microwave Symp. Digest*, June 2000, Vol. 3, pp. 1573–1576.
 153. K. Nishikawa, B. Piernas, T. Nakagawa, and K. Araki, Miniaturized and broadband V-band balanced frequency doubler for highly integrated 3-D MMIC, *2002 IEEE Int. Microwave Symp. Digest*, June 2002, Vol. 1, pp. 351–354.
 154. H. Fudem and E. C. Niehenke, Novel millimeter wave active MMIC tripler, *1998 IEEE Int. Microwave Symp. Digest*, June 1998, Vol. 2, pp. 387–390.
 155. K. L. Deng and H. Wang, A miniature broad-band PHEMT MMIC balanced distributed doubler, *IEEE Trans. Microwave Theory Tech.* **51**(4):1257–1261 (April 2003).
 156. N. S. Barker and G. M. Rebeiz, Distributed MEMS true-time delay phase shifters and wide-band switches, *IEEE Trans. Microwave Theory Tech.* **46**(11):1881–1890 (Nov. 1998).
 157. J. B. Muldavin and G. M. Rebeiz, High-isolation CPW MEMS shunt switches-part 2: Design, *IEEE Trans. Microwave Theory Tech.* **48**(6):1053–1056 (June 2000).
 158. J. B. Muldavin and G. M. Rebeiz, All-metal high-isolation series and series/shunt MEMS switches, *IEEE Microwave Wireless Compon. Lett.* **11**:373–375 (Sept. 2001).
 159. M. Ulm, J. Schobel, M. Reimann, T. Buck, J. Dechow, R. Moller-Firdler, H.-P. Trah, and E. Kasper, Millimeter-wave microelectromechanical (MEMS) switches for automotive surround sensing systems, *Topic Meeting on Silicon Monolithic Integrated Circuits in RF Systems Digest*, 2003, pp. 142–149.
 160. G. M. Rebeiz and J. B. Muldavin, RF MEMS switches and switch circuits, *IEEE Microwave Mag.* 59–71 (Dec. 2001).
 161. E. Alekseev and D. Pavlidis, 77 GHz high-isolation coplanar transmit-receive switch using InGaAs/InP PIN diodes, *Proc. 1998 Gallium Arsenide Integrated Circuit (GaAs IC) Symp.* 1998, pp. 177–180.
 162. A. Klaassen and J. M. Dieudonne, 77 GHz monolithic MMIC Schottky- and PIN-diode switches based on GaAs MESFET and silicon SIMMWIC technology, *1995 IEEE Int. Microwave Symp. Digest*, May 1995, Vol. 3, pp. 1631–1634.

163. K. W. Kobayashi, L. Tran, A. K. Oki, and D. C. Streit, A 50 MHz–30 GHz broadband co-planar waveguide SPDT PIN diode switch with 45-dB isolation, *IEEE Microwave Guided Wave Lett.* **5**:56–58 (Feb. 1995).
164. M. Case, M. Matloubian, and H. C. Sun, High-performance W-band GaAs PIN diode single-pole-triple-throw switch CPW MMIC, *1997 IEEE Int. Microwave Symp. Digest*, June 1997, Vol. 2, pp. 1047–1051.
165. AP640R7-00, Product Data Sheet, Skyworks Inc.
166. S. G. Hounq, T. Tsukii, and M. J. Schindler, 60–70 dB isolation 2–19 GHz MMIC switches, *Proc. 1989 Gallium Arsenide Integrated Circuit (GaAs IC) Symp.* 1989, pp. 173–176.
167. N. Imai, A. Minakawa, and H. Okazaki, Novel high isolation FET switches, *IEEE Trans. Microwave Theory Tech.* **MTT-44**(5):685–691 (May 1996).
168. H. Takasu, F. Sasaki, H. Kawasaki, H. Tokuda, and S. Kamihashi, W-band SPST transistor switches, *IEEE Microwave Guided Wave Lett.* **6**:315–316 (Sept. 1996).
169. K. Y. Lin, Y. J. Wang, D. C. Niu, and H. Wang, Millimeter-wave MMIC single-pole-double-throw passive HEMT switches using impedance-transformation networks, *IEEE Trans. Microwave Theory Tech.* **51**:1076–1085 (April, 2003).
170. M. J. Schindler and A. Morris, DC-40 GHz and 20–40 GHz MMIC SPDT switches, *IEEE Trans. Microwave Theory Tech.* **35**(12):1486–1493 (Dec. 1987).
171. W. H. Tu, P. Y. Chen, K. Y. Lin, H. Wang, and R. B. Wu, A 15–80 GHz MMIC SPDT switch using traveling wave concept, *2002 Asia-Pacific Microwave Conf. Technical Digest*, Nov. 2002, pp. 57–59.
172. H. Mizutani, N. Funabashi, M. Kuzuhara, and Y. Takayama, Compact DC-60-GHz HJFET MMIC switches using ohmic electrode-sharing technology, *IEEE Trans. Microwave Theory Tech.* **46**(11):1597–1603 (Nov. 1998).
173. H. Mizutani and Y. Takayama, DC-110-GHz MMIC traveling-wave switch, *IEEE Trans. Microwave Theory Tech.* **48**(5):840–845 (May 2000).
174. F. Ellinger, R. Vogt, and W. Bachtold, Compact reflective-type phase-shifter MMIC for C-band using a lumped-element coupler, *IEEE Trans. Microwave Theory Tech.* **49**:913–917 (May 2001).
175. F. Ellinger and W. Bachtold, Novel principle for vector-modulator-based phase shifters operating with only one control voltage, *IEEE J. Solid State Circ.* **37**(10):1256–1259 (Oct. 2002).
176. A. S. Nagra, J. Xu, E. Erker, and R. A. York, Monolithic GaAs phase shifter circuit with low insertion loss and continuous 0–360 phase shift at 20 GHz, *IEEE Microwave Guided Wave Lett.* **9**:31–33 (Feb. 1999).
177. J. S. Hayden and G. M. Rebeiz, Low-loss cascaded MEMS distributed X-band phase shifters, *IEEE Microwave Guided Wave Lett.* **10**:142–144 (April 2000).
178. D. Jr. Viveiros, D. Consonni, and A. K. Jastrzebski, A tunable all-pass MMIC active phase shifter, *IEEE Trans. Microwave Theory Tech.* **50**(8):1885–1890 (Aug. 2002).
179. C. F. Campbell and S. A. Brown, A compact 5-bit phase-shifter MMIC for K-band satellite communication systems, *IEEE Trans. Microwave Theory Tech.* **48**(12):2652–2656 (Dec. 2003).
180. M. Aust, H. Wang, R. Carandang, K. Tan, C. H. Chen, T. Trinh, R. Esfandiari, and H. C. Yen, GaAs monolithic components development for Q-band phased array application, *1992 IEEE Int. Microwave Symp. Digest*, May 1992, Vol. 2, pp. 703–706.
181. P. Y. Chen, *Design of MMIC Active Phase Shifter*, Master's Thesis, National Taiwan Univ. (2002).
182. H. T. Kim, J. H. Park, J. Yim, Y. K. Kim, and Y. Kwon, A compact V-band 2-bit reflection-type MEMS phase shifter, *IEEE Microwave Wireless Compon. Lett.* **12**:324–326 (Sept. 2002).
183. N. S. Barker and G. M. Rebeiz, Optimization of distributed MEMS phase shifters, *1999 IEEE Int. Microwave Symp. Digest*, June 1999, Vol. 1, pp. 299–302.
184. N. S. Barker and G. M. Rebeiz, Optimization of distributed MEMS transmission-line phase shifters U-band and W-band designs, *IEEE Trans. Microwave Theory Tech.* **48**(11):1957–1966 (Nov. 2001).
185. S. Weinreb, W. Berk, S. Duncan, and N. Byer, Monolithic varactor 360 degree phase shifters for 75–110 GHz, *Int. Semi-Device Conf. Digest*, Charalottesville, VA, Dec. 1993.
186. D. C. W. Lo, H. Wang, B. R. Allen, G. S. Dow, K. W. Chang, M. Biedenbender, R. La, S. Chen, and D. Yang, Novel monolithic multifunctional balanced switching low-noise amplifiers, *IEEE Trans. Microwave Theory Tech.* **42**(12):2629–2634 (Dec. 1994).
187. S. Nam, N. Shala, K. S. Ang, A. E. Ashtiani, T. Gokdemir, I. D. Robertson, and S. P. Marsh, Monolithic millimeter-wave balanced bi-phase amplitude modulator in GaAs/InGaP HBT technology, *1999 IEEE Int. Microwave Symp. Digest*, June 1999, Vol. 1, pp. 243–246.
188. K. W. Chang, H. Wang, G. Shreve, J. Harrison, M. Core, A. Paxton, M. Yu, C. H. Chen, and G. S. Dow, Forward looking automotive radar using a W-Band single-chip transceiver, *IEEE Trans. Microwave Theory Tech.*, **43**(7):1659–1668 (July 1995).
189. Y. Mimino, K. Nakamura, K. Sakamoto, Y. Aoki, S. Kuroda, and T. Tokumitsu, Design techniques of reducing chip area and highly integrated MMIC for W-band application, *2001 IEEE Int. Microwave Symp. Digest*, May 2001, Vol. 3, pp. 2167–2170.
190. J. Udomoto, T. Matsuzuka, S. Chaki, K. Kanaya, T. Katoh, Y. Notani, T. Hisaka, T. Oku, T. Ishikawa, M. Komaru, and Y. Matsuda, A 38/77 GHz MMIC transmitter chip set for automotive applications, *2003 IEEE Int. Microwave Symp. Digest*, June 2003, Vol. 3, pp. 2229–2232.
191. K. W. Chang, H. Wang, G. S. Dow, T. H. Chen, D. C. W. Lo, M. Biedenbender, and B. Allen, W-band monolithic single side-band transceiver for automotive radar applications, *Proc. 1994 Gallium Arsenide Integrated Circuit (GaAs IC) Symp.* 1994, pp. 84–87.
192. D. C. W. Lo, G. S. Dow, E. Lin, K. W. Chang, H. Wang, M. Biedenbender, and B. Allen, A single-chip W-band transceiver with front-end switching receiver for FMCW radar applications, *1995 IEEE Int. Microwave Symp. Digest*, May 1995, Vol. 2, pp. 873–876.
193. D. C. W. Lo, G. S. Dow, L. Yujiri, S. Chen, M. Biedenbender, H. Wang, M. Mussetto, and B. R. Allen, A monolithic W-band seven-stage LNA/detector for radiometric imaging applications, *1995 IEEE Int. Microwave Symp. Digest*, May 1995, Vol. 3, pp. 1117–1120.
194. D. C. W. Lo, L. Yujiri, G. S. Dow, T. N. Ton, M. Mussetto, and B. R. Allen, A W-band direct-detection radiometric imaging array, *1994 IEEE Microwave and Millimeter-wave Monolithic Circuits Symp. Digest*, May 1994, pp. 41–44.
195. G. S. Dow, D. C. W. Lo, Y. Guo, E. W. Lin, T. T. Chung, M. D. Biedenbender, O. Miromontes, A. Marashi, L. Yujiri, P. S. C. Lee, M. M. Shoucri, and B. R. Allen, Large scale W-band focal plane array for passive radiometric imaging, *1996*

- IEEE Int. Microwave Symp. Digest*, June 1996, Vol. 1, pp. 369–372.
196. A. Kanda, T. Hirota, H. Okazaki, and M. Nakamae, An MMIC chip set for V-band phase-locked local oscillator, *Proc. 1995 Gallium Arsenide Integrated Circuit (GaAs IC) Symp.* 1995, pp. 259–262.
 197. G. Nesbit, T. Dere, D. English, V. Purdy, and B. Parrish, Ka-band MMIC-based transceiver for battlefield combat identification system, *1995 Microwave and Millimeter-Wave Circuit Symp. Digest* 1995, pp. 53–57.
 198. E. W. Lin, Y. L. Kok, G. S. Dow, H. Wang, T. T. Chung, S. Lau, D. Okamuro, and B. R. Allen, An advanced single-chip Ka-band transceiver, *1996 IEEE Int. Microwave Symp. Digest*, June 1996, Vol. 2, pp. 513–515.
 199. Y. L. Kok, M. Ahmadi, H. Wang, B. Allen, and T. S. Lin, A Ka-band monolithic single-chip transceiver using sub-harmonic mixer, *1998 IEEE Int. Microwave Symp. Digest*, June 1998, Vol. 1, 309–311.
 200. D. C. Streit, D. K. Umemoto, K. W. Kobayashi, and A. K. Oki, Monolithic HEMT-HBT integration by selective MBE, *IEEE Trans. Electron. Devices* **42**(4):618–623 (April 1995).
 201. L. Tran, J. Cowles, R. Lai, T. Block, P. Liu, A. Oki, and D. Streit, Monolithic integration of InP HBT and HEMT by selective molecular beam epitaxy, *Proc. 1996 Int. Conf. Indium Phosphide and Related Materials (IPRM)*, April 1996, pp. 76–78.
 202. H. Wang, R. Lai, L. Tran, J. Cowles, Y. C. Chen, E. Lin, H. H. Liao, M. K. Ke, T. Block, and H. C. Yen, A single-chip 94-GHz frequency source using InP-based HEMT-HBT integration technology, *1998 IEEE Int. Microwave Symp. Digest*, Vol. 1, June 1998, pp. 219–222.
 203. K. W. Kobayashi, H. Wang, R. Lai, L. T. Tran, T. R. Block, P. H. Liu, J. Cowles, Y. C. Chen, T. W. Huang, A. K. Oki, H. C. Yen, and D. C. Streit, An InP HEMT W-band amplifier with monolithically integrated HBT bias regulation, *IEEE Microwave Guided Wave Lett.* **7**:222–224 (Aug. 1997).
 204. K. J. Herrick et al; 95 GHz metamorphic HEMT power amplifiers on GaAs, *2003 IEEE MTT-S Digest*, 2003, pp. 137–140.
 205. C. S. Whelan et al; GaAs metamorphic HEMT: An attractive alternative to InP HEMTs for high performance low noise and power applications, *IPRM2000 Conf. Proc.* 2000, pp. 337–340.
 206. www.compoundsemiconductor.net.
 207. www.semireporter.com.
 208. <http://www.winfoundry.com>.
 209. <http://www.velocium.com>.
 210. <http://www.triquint.com>.
 211. <http://www.gct.com.tw>.
 212. <http://www.gcsincorp.com>.
 213. <http://www.tsmc.com>.
 214. <http://www-306.ibm.com>.
 215. <http://www.atmel.com>.
 216. R. C. Liu, H. Y. Chang, C. H. Wang, and H. Wang, A 63-GHz VCO using a standard 0.25- μ m CMOS process, *IEEE ISSCC Digest Tech. Papers*, 2004 (24.7).
 217. I. J. Chen, H. Wang, and P. Hsu, AV-band quasi-optical GaAs HEMT monolithic integrated antenna and receiver front end, *IEEE Trans. Microwave Theory Tech.* **51**(12):2461–2468 (Dec. 2003).
 218. O. Wohlgenuth, P. Paschke, and Y. Baeyens, SiGe broadband amplifiers with up to 80 GHz bandwidth for optical applications at 43 Gbit/s and beyond, *33rd European Microwave Conf. Proc.*, Munich, Germany, Oct. 2003, pp. 1087–1090.
 219. S. Reynolds, B. Floyd, U. Pfeiffer, and T. Zwick, 60 GHz transceiver circuits in SiGe bipolar technology, *IEEE IS-SCC Digest Tech. Papers*, 2004 (24.5).

MILLIMETER-WAVE MEASUREMENT

GUY VERNET
 Université Paris—Sud
 GERARD BEAUDIN
 Observatoire de Paris—Meudon
 DOMINIQUE CROS
 Université de Limoges
 PAUL CROZAT
 Université Paris—Sud
 GILLES DAMBRINE
 Institut d'Electronique et
 Microélectronique du Nord
 (IEMN)
 BERNARD HUYART
 Ecole Nationale Supérieure des
 Télécommunications (ENST)
 JEAN-MICHEL NEBUS
 Université de Limoges

The millimeter-wavelength spectral band covers the frequency range 30 GHz ($\lambda = 10$ mm) to 300 GHz ($\lambda = 1$ mm). In the larger view, it can include a part of the submillimeter band: the extended range up to 1 THz ($\lambda = 0.3$ mm), which represents one of the least explored portions of the electromagnetic spectrum. The frontier between the millimeter–submillimeter region and the far-infrared region is arbitrary and variable. The distinction comes mainly from the detection techniques employed (coherent or incoherent detection). The millimeter spectrum is presented in Fig. 1.

In the microwave domain, the atmosphere is transparent to frequencies up to 40 GHz except for a weak water vapor absorption line at 22 GHz. However, in the millimeter domain, there are several strong absorption lines: (1) a large and complex set of oxygen lines around 55–60 GHz, (2) a single oxygen line around 119 GHz, and (3) a water vapor line around 183 GHz. Above 300 GHz, several absorption lines exist, mainly due to the water vapor. The spectral region located in between these lines, currently called “windows,” is decreasingly transparent when the frequency increases.

Millimeter waves offer a solution to the increasing demand in frequency allocation due to the low-frequency-band saturation and the requirement for higher data rates. Moreover, a high directivity can be obtained with small antennas associated with small-sized circuits that become more easily integrable. Applications are numerous, ranging from mobile communications, local-area

- IEEE Int. Microwave Symp. Digest*, June 1996, Vol. 1, pp. 369–372.
196. A. Kanda, T. Hirota, H. Okazaki, and M. Nakamae, An MMIC chip set for V-band phase-locked local oscillator, *Proc. 1995 Gallium Arsenide Integrated Circuit (GaAs IC) Symp.* 1995, pp. 259–262.
 197. G. Nesbit, T. Dere, D. English, V. Purdy, and B. Parrish, Ka-band MMIC-based transceiver for battlefield combat identification system, *1995 Microwave and Millimeter-Wave Circuit Symp. Digest* 1995, pp. 53–57.
 198. E. W. Lin, Y. L. Kok, G. S. Dow, H. Wang, T. T. Chung, S. Lau, D. Okamuro, and B. R. Allen, An advanced single-chip Ka-band transceiver, *1996 IEEE Int. Microwave Symp. Digest*, June 1996, Vol. 2, pp. 513–515.
 199. Y. L. Kok, M. Ahmadi, H. Wang, B. Allen, and T. S. Lin, A Ka-band monolithic single-chip transceiver using sub-harmonic mixer, *1998 IEEE Int. Microwave Symp. Digest*, June 1998, Vol. 1, 309–311.
 200. D. C. Streit, D. K. Umemoto, K. W. Kobayashi, and A. K. Oki, Monolithic HEMT-HBT integration by selective MBE, *IEEE Trans. Electron. Devices* **42**(4):618–623 (April 1995).
 201. L. Tran, J. Cowles, R. Lai, T. Block, P. Liu, A. Oki, and D. Streit, Monolithic integration of InP HBT and HEMT by selective molecular beam epitaxy, *Proc. 1996 Int. Conf. Indium Phosphide and Related Materials (IPRM)*, April 1996, pp. 76–78.
 202. H. Wang, R. Lai, L. Tran, J. Cowles, Y. C. Chen, E. Lin, H. H. Liao, M. K. Ke, T. Block, and H. C. Yen, A single-chip 94-GHz frequency source using InP-based HEMT-HBT integration technology, *1998 IEEE Int. Microwave Symp. Digest*, Vol. 1, June 1998, pp. 219–222.
 203. K. W. Kobayashi, H. Wang, R. Lai, L. T. Tran, T. R. Block, P. H. Liu, J. Cowles, Y. C. Chen, T. W. Huang, A. K. Oki, H. C. Yen, and D. C. Streit, An InP HEMT W-band amplifier with monolithically integrated HBT bias regulation, *IEEE Microwave Guided Wave Lett.* **7**:222–224 (Aug. 1997).
 204. K. J. Herrick et al; 95 GHz metamorphic HEMT power amplifiers on GaAs, *2003 IEEE MTT-S Digest*, 2003, pp. 137–140.
 205. C. S. Whelan et al; GaAs metamorphic HEMT: An attractive alternative to InP HEMTs for high performance low noise and power applications, *IPRM2000 Conf. Proc.* 2000, pp. 337–340.
 206. www.compoundsemiconductor.net.
 207. www.semireporter.com.
 208. <http://www.winfoundry.com>.
 209. <http://www.velocium.com>.
 210. <http://www.triquint.com>.
 211. <http://www.gct.com.tw>.
 212. <http://www.gcsincorp.com>.
 213. <http://www.tsmc.com>.
 214. <http://www-306.ibm.com>.
 215. <http://www.atmel.com>.
 216. R. C. Liu, H. Y. Chang, C. H. Wang, and H. Wang, A 63-GHz VCO using a standard 0.25- μ m CMOS process, *IEEE ISSCC Digest Tech. Papers*, 2004 (24.7).
 217. I. J. Chen, H. Wang, and P. Hsu, AV-band quasi-optical GaAs HEMT monolithic integrated antenna and receiver front end, *IEEE Trans. Microwave Theory Tech.* **51**(12):2461–2468 (Dec. 2003).
 218. O. Wohlgenuth, P. Paschke, and Y. Baeyens, SiGe broadband amplifiers with up to 80 GHz bandwidth for optical applications at 43 Gbit/s and beyond, *33rd European Microwave Conf. Proc.*, Munich, Germany, Oct. 2003, pp. 1087–1090.
 219. S. Reynolds, B. Floyd, U. Pfeiffer, and T. Zwick, 60 GHz transceiver circuits in SiGe bipolar technology, *IEEE IS-SCC Digest Tech. Papers*, 2004 (24.5).

MILLIMETER-WAVE MEASUREMENT

GUY VERNET
 Université Paris—Sud
 GERARD BEAUDIN
 Observatoire de Paris—Meudon
 DOMINIQUE CROS
 Université de Limoges
 PAUL CROZAT
 Université Paris—Sud
 GILLES DAMBRINE
 Institut d'Electronique et
 Microélectronique du Nord
 (IEMN)
 BERNARD HUYART
 Ecole Nationale Supérieure des
 Télécommunications (ENST)
 JEAN-MICHEL NEBUS
 Université de Limoges

The millimeter-wavelength spectral band covers the frequency range 30 GHz ($\lambda = 10$ mm) to 300 GHz ($\lambda = 1$ mm). In the larger view, it can include a part of the submillimeter band: the extended range up to 1 THz ($\lambda = 0.3$ mm), which represents one of the least explored portions of the electromagnetic spectrum. The frontier between the millimeter–submillimeter region and the far-infrared region is arbitrary and variable. The distinction comes mainly from the detection techniques employed (coherent or incoherent detection). The millimeter spectrum is presented in Fig. 1.

In the microwave domain, the atmosphere is transparent to frequencies up to 40 GHz except for a weak water vapor absorption line at 22 GHz. However, in the millimeter domain, there are several strong absorption lines: (1) a large and complex set of oxygen lines around 55–60 GHz, (2) a single oxygen line around 119 GHz, and (3) a water vapor line around 183 GHz. Above 300 GHz, several absorption lines exist, mainly due to the water vapor. The spectral region located in between these lines, currently called “windows,” is decreasingly transparent when the frequency increases.

Millimeter waves offer a solution to the increasing demand in frequency allocation due to the low-frequency-band saturation and the requirement for higher data rates. Moreover, a high directivity can be obtained with small antennas associated with small-sized circuits that become more easily integrable. Applications are numerous, ranging from mobile communications, local-area

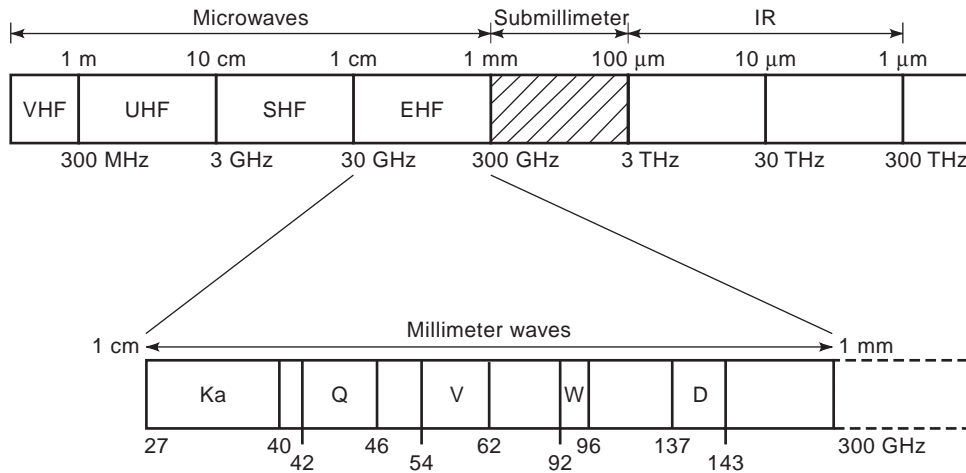


Figure 1. Atmospheric transmission in the millimeter domain.

networks, and collision avoidance radars to satellite communications, radio astronomy, radio altimetry, and robotics.

In the millimeter-wave range up to 100 GHz, the equipment and methods of measurement have been extended from the microwave domain. The major problems in the millimeter field are due to the small size of the devices and the transmission line losses. Above 100 GHz, as an alternative, other equipment and methods of measurement, using a quasi-optic setup, have been developed or adapted from far-infrared techniques (dielectric waveguide cavity resonator, free-space methods).

1. MILLIMETER-WAVE AUTOMATIC NETWORK ANALYZER

As all other types of automatic network analyzer (ANA), the millimeter-wave automatic network analyzer (MWANA) measures magnitudes and phases of scattering parameters (S parameters) of the device under test (DUT).

1.1. Main Types of MWANA

1.1.1. Broadband Coaxial Systems. In this group, single or multiple synthesized sweeper network analyzers are commercially available [1]. The single synthesized source systems perform S -parameter measurements up to 50 GHz using 2.4 mm coaxial accessories, and up to 67 GHz using 1.85 mm coaxial elements (V connectors). The multiple synthesized sources system may cover the 40 MHz to 110 GHz frequency range using 1 mm coaxial elements (W connectors).

1.1.2. Rectangular Waveguide Systems. These network analyzers perform S -parameter measurements in Q (33–50 GHz), U (40–60 GHz), V (50–75 GHz), and W (75 “to” 110 GHz) frequency ranges; the rectangular waveguide standards are WR-22, WR-19, WR-15, and WR-10, respectively.

In the multiple-source network analyzer, one synthesized source provides the radiofrequency (RF) (stimulus) signal and the second provides the local-oscillator (LO) signal. Figure 2 shows a simplified block diagram of this system common to all waveguide bands. This system consists of a conventional network analyzer, two microwave sources (RF and LO), and a pair of band-dependent millimeter-wave test set modules covering the frequency bands given above. The RF signal after amplification is routed to the port 1 test set module for forward measurements (S_{11} and S_{21}) or to the port 2 test set module for reverse measurements (S_{22} and S_{12}). Components in the millimeter-wave test set module provide frequency multiplication, signal separation to sample incident, reflected and transmitted signals, and the harmonic mixers to accomplish the intermediate frequency (IF) conversion (generally first IF) to some MHz (e.g., 20 MHz). The second source provides the LO for the four harmonic mixers. This LO source is set such that the millimeter-wave RF test signal frequency and the appropriate LO harmonic are offset by exactly the IF (e.g., 20 MHz). For instance, in the case of the HP8510C MWANA [1] with V-band millimeter-wave test set modules, the frequency of the two microwave sources (RF and LO) can be expressed as follows

$$\text{RF} = \frac{F_{\text{op}}}{4} \quad \text{and} \quad \text{LO} = \frac{(F_{\text{op}} + 20 \text{ MHz})}{14}$$

where F_{op} is the operating frequency.

As compared with a single-source network analyzer (coaxial), the rectangular waveguide system has inherent drawbacks. Indeed the power of the RF signal injected to the DUT cannot be controlled due to the frequency multiplication. This power may be close to 0 dBm (1 mW on 50-W system) and may be more dependent on the frequency band. This feature may induce nonlinear phenomena (compression, distortion) when the DUT is an active device (transistor, amplifier, etc.). Moreover, reactive impedance of a rectangular waveguide below its cutoff frequency may allow instability of the active DUT.

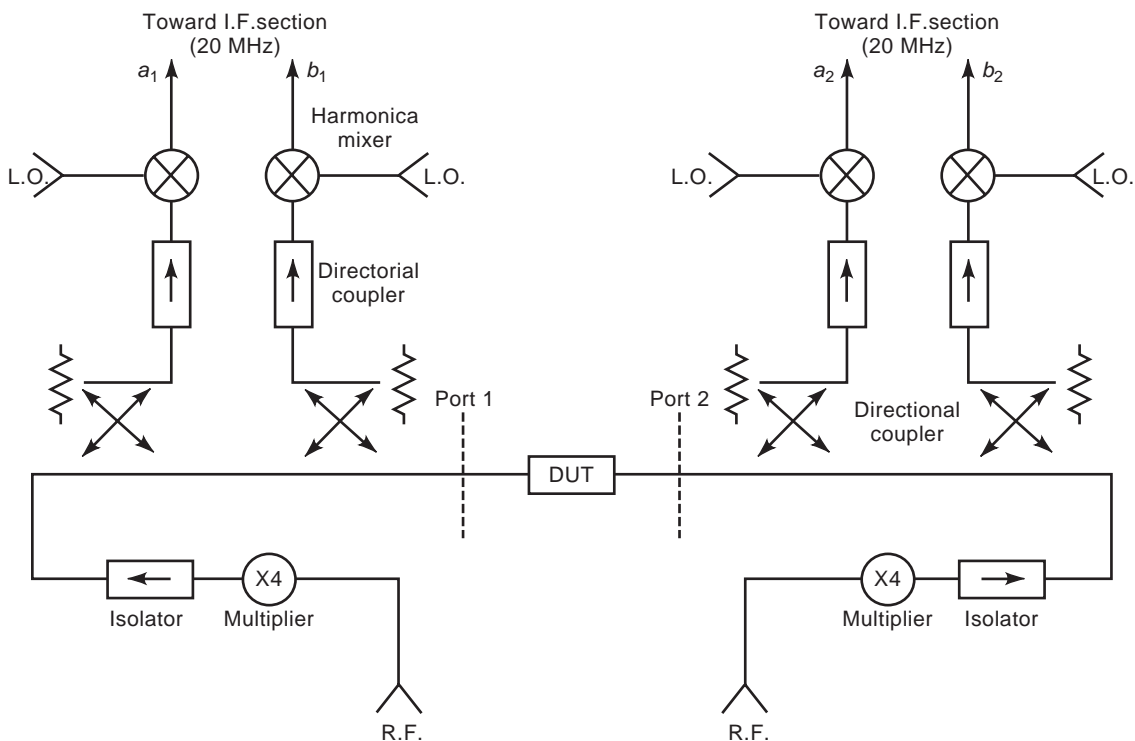


Figure 2. Simplified synopsis of a MWANA test set, for an HP85106D V-band system (50–75 GHz).

1.2. Dynamic Range of Millimeter-Wave Automatic Network Analyzer

Dynamic range, which is the key consideration in most measurement systems, relates to the ability of a receiver to accurately detect a signal over a large amplitude range. The largest input signal is usually limited by compression in the input receiver, while the smallest ones that can be detected are limited by the noise floor and other undesirable signals. Dynamic range can be improved by increasing the number of measurement averages and changing video IF bandwidth. Table 1 summarizes the dynamic range of HP8510C for transmission measurements as function of the frequency band.

1.3. On-Wafer Probing System

Commercially available coplanar probes cover the full millimeter-wave band [2]. On-wafer probing in millimeter-wave measurement is by far the most precise technique, due to (1) better positioning and (2) better contact

repeatability. For millimeter-wave measurement, only ground–signal–ground (G–S–G) topology is useful, since fundamental modes must only be excited at the probe tip. There are mainly two types of coplanar probes: coaxial-to-coplanar probe tips and wave-guide-to-coplanar probe tips. The former one uses the internal MWANA test set bias tee, while the latter one may include a direct-current (DC) bias tee inside the probe (Fig. 3). Typical values for return loss and insertion loss are, respectively, within 10–15 dB and 1–2 dB [2]. The connection between the probe and the test set port must be kept as short as possible, and the millimeter-wave coaxial cable may easily add several decibels to the insertion loss.

1.4. Specific On-Wafer Calibration Technique

High-precision measurement relies on careful reference plane definition and on-chip parasitic access determination [4]. Reference plane definition strongly correlates with the calibration used. For SOLT (short, open, load, and through standards) calibration, the reference plane is

Table 1. Dynamic Range of HP8510C for Transmission Measurements as a Function of the Frequency Band

Frequency range (GHz)	38–50	40–60	50–75	75–110
Maximum power measured at port 2, nominal value	+12 dBm	+10 dBm	+10 dBm	0 dBm
Reference power at port 1, nominal value	0 dBm	0 dBm	0 dBm	–3 dBm
Minimum power measured at port 2	–87 dBm	–87 dBm	–75 dBm	–79 dBm
Receiver dynamic range ^a	99 dB	97 dB	85 dB	79 dB
System dynamic range ^b	87 dB	87 dB	75 dB	75 dB

^a“Receiver dynamic range” is defined as the ratio of the maximum signal level at port 2 for 0.1 dB compression to the system noise floor.

^b“System dynamic range” is defined to the ratio of the maximum signal at port 1 and the system noise floor.

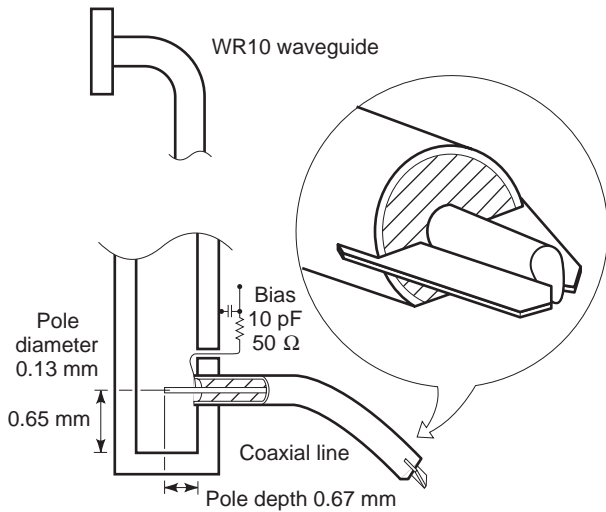


Figure 3. Mechanical structure of the waveguide-coaxial transition and the coaxial probe. (From Ref. 3.)

defined by the coherent values declared for “short” and “open.” Through losses must be kept low, and delay declaration must be coherent with reference plane positioning. Any inconsistency will lead to poor measurement. For TRL (through, reflect, line standards) or LRM (line, reflects, match standards) calibration, the reference plane is always located in the center of the through, but may be moved to some other convenient place after calibration. When using on-chip standards, some or all of the on-chip access parasitics may be included in the calibration, while use of specific standards (on alumina substrate) implies subsequent determination (deembedding) of the access parasitics. In the latter case, the reference plane is usually located under the probe tip. The main error sources are (1) bad calibration and (2) bad access parasitic determination. Advanced calibration techniques have been devised for improving calibration while use of specific on-wafer elements may improve deembedding of the access parasitic.

1.4.1. Advanced Calibration Technique. This technique uses more standards in order to (1) obtain better standards definition (SOLT calibration) and (2) perform vector errors correction (LRM calibration and TRL calibration). None of these techniques are implemented in ANA hardware, so specific computer programs are needed.

1.4.1.1. SOLT Enhancement. The reference plane is solely determined by the short declaration (usually 0 pF). An open-ended long line measurement is performed with an incorrect open declaration and an error model to allow finding for each frequency the open declaration error, thus leading to a better frequency dependent open declaration [5]. This allows precise measurement with SOLT up to 110 GHz.

1.4.1.2. LRRM Calibration. A standard LRM calibration is performed, a new reflect is measured (a short if the calibration reflect was an open), and a new set of error vectors is calculated [6]. This allows us to correct for

a small probe misplacement in addition to true load deviation.

1.4.1.3. NIST Multiline Calibration. The TRL calibration technique is based only on the accurate knowledge of the characteristic impedance of transmission line standards. One of the main drawbacks of TRL is its relatively narrow operating frequency range. To perform a very broadband (up to 110 GHz) TRL calibration, a multiline calibration technique has been proposed by the National Institute of Standards and Technology (NIST) [7].

1.5. Deembedding of the Access Parasitic

The use of an on-chip-specific design may allow precise determination of all access parasitics between a reference plane and a DUT port. This is an alternative to techniques based on frequency dependence of Y and Z parameters, which allow parasitic determination for transistor measurement [8]. The deembedding uses direct S -parameter correction or correction through precise parasitic modeling using a specially designed on-chip test device.

1.5.1. Direct S -Parameter Correction. The measurement of open and short placed at the DUT port position allows direct S -parameter correction, using S -to- Y transformation:

$$Y_{\text{device}} = ((Y_{\text{meas}} - Y_{\text{open}})^{-1} - (Y_{\text{short}} - Y_{\text{open}})^{-1})^{-1}$$

This technique is frequently used for microwave measurement on silicon devices but is also interesting in millimeter-wave measurement. However, extreme care must be taken to compensate for open capacitance (fringing field) and short inductance (ground access) when designing the specific open and short device.

1.5.2. Precise Parasitic Modeling. This usually uses several short, open, and through devices. A careful modeling of all these elements allows us to find out the true access parasitic and the intrinsic device parasitic. Once the access parasitic models are known, correction of the DUT measurement are obtained through the use of a linear simulator.

1.6. Specific Characterizations of Transistors in Millimeter Wave

In view of the increasing number of applications in the centimeter-wave range, the millimeter-wave range is now largely used. MVDS (40.5–42.5 GHz), wireless local area networks (60 GHz WLAN), and automotive radar (77 GHz) are among the most focused millimeter-wave applications today. In addition, advanced technologies are now available for manufacturing integrated circuits used in this range. The main challenge is to design this integrated circuit accurately. To this end, reliable broadband transistor models are needed for designing a millimeter-wave integrated circuit. Linear models (or equivalent circuit) including high-frequency noise sources are usually deduced from S parameter and noise parameter on-wafer

measurements. The accuracy of each element of such models depends on the measurement accuracy. The determination of equivalent circuit elements may be difficult and inaccurate in the millimeter-wave range. The key considerations in designing a reliable equivalent circuit of transistors in the millimeter-wave range are as follows:

1. The choice of calibration technique as a function of the topology of the transistor and the nature of the substrate,
2. The choice of the equivalent circuit topology including parasitic elements.

Another solution consists in establishing an equivalent circuit of transistors from S parameters and noise parameters performed in a relatively lower frequency range (for instance, up to 50 GHz). The main advantage is that the accuracy of measurement in this frequency range is better controlled than that in the millimeter-wave range. To validate the reliability of such an equivalent circuit, we calculate the S parameters and noise parameters from the elements of the equivalent circuit and we compare these calculated data with measured ones in the millimeter-wave range.

1.7. Millimeter-Wave Cryogenic On-Wafer Measurement

There are basically two different solutions depending on the temperature range. For measurements down to 200 K, the setup is similar to that of the system used for high temperature measurement. The system works at ambient pressure, only the chuck is cold, and a local overpressure of drier air or nitrogen is used to prevent icing of wafer or probe tips. In this case, the temperature gradient is mainly located on the probe itself, so cable length at low temperatures is kept minimal. The calibration substrate may be kept at room temperature.

For measurements down to a few kelvin, the device and probes are kept under vacuum in a nitrogen or helium flow cryostat. Probe displacement under vacuum is obtained through the use of a bellow, cable length is significant, and calibration and measurement must be made at the same temperature.

2. VOLTAGE AND POWER RATIO TECHNIQUES: SIX-PORT NETWORK ANALYZER

The voltage and power ratio techniques and the six-port network analyzer (SPNA) are based on direct detection of the millimeter-wave. The hardware configuration of these measurement systems is simple because it is composed of diode or thermal detectors and of directional couplers or probes. In contrast, heterodyne detection systems involve multiple frequency conversions requiring local oscillators. The complexity of the measurement system makes random and systematic errors more difficult to estimate. That is why direct detection techniques provide much of the basis for precision microwave metrology. This article deals with the measurement of the scattering parameters S_{ij} of n -port millimeter devices using a slotted line, a (tuned) reflectometer, and an SPNA.

2.1. Slotted Line

This is the oldest method for measuring the reflection coefficient S_{11} of an impedance. In the millimeter frequency range, the slotted line is realized using a piece of metallic rectangular waveguide with a slot located at the center of the broad wall of the guide. The electric field inside the guide is sampled with a wire antenna connected to a Schottky diode detector. The magnitude of S_{11} is given by the voltage standing-wave ratio (VSWR). The phase of S_{11} is given by the position of the antenna for which the detected voltage is minimum. This technique has been largely replaced by an automated method.

2.2. The Tuned Reflectometer

A simple reflectometer requires one or two directional couplers and power detectors in order to measure the magnitude of S_{11} . These techniques suffer from low directivity of the couplers and from the mismatches of the source and the measurement port Γ_0 . A tuned reflectometer includes tuners in order to overcome these difficulties. The measurement system is composed of a millimeter-wave source, one coupler of directivity D , one power detector, and two tuners. The detected power P may be written as follows:

$$P = K \left| \frac{S_{11} + D}{1 - S_{11}\Gamma_0} \right|^2$$

where K is a constant characterizing the measurement system.

The measurement procedure consists of successively connecting a sliding load and a sliding short in order to null D and Γ_0 using the tuners. Thereafter, the magnitude of S_{11} is given by the power ratio

$$|S_{11}| = \frac{P}{P_{cc}}$$

where P_{cc} is the power measurement when a short circuit takes place at the DUT. For a frequency equal to 110 GHz, the uncertainty measurement (defined at 2σ) of $|S_{11}|$ using the tuned reflectometer is in the range of 0.005–0.06 when $|S_{11}|$ varies from 0.01 to 0.5. In metrological labs, transmission measurements (S_{21}) are performed using an IF attenuator (IF substitution method).

2.3. Six-Port Network Analyzer

The term “six-port” is due to the six-port millimeter-wave junction (Fig. 4). At its four output ports it provides power readings P_3 to P_6 , which are a weighted addition of the incident a_2 and reflected b_2 waves. The complex value of S_{11} (b_2/a_2) derives from the six-port equations:

$$\frac{P_i}{P_3} = K_i \left| \frac{\alpha_i a_2 + \beta_i b_2}{\alpha_3 a_2} \right|^2, \quad i = 4, 5, 6$$

where α_i and β_i are the weighted factor of the waves a_2 and b_2 at the i th port and K_i is a constant of the power detector.

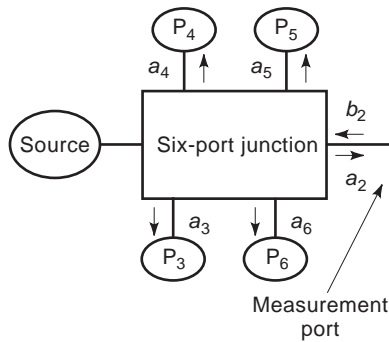


Figure 4. Six-port measurement system. It provides the complex value of the reflection coefficient S_{11} of the load connected at the measurement port. The power detector, connected at each output port, measures the power of b_i , where $i = 3-6$.

The four scattering parameters may be obtained by the connection of two SPNAs at the two ports of the DUT or one SPNA in the reflection or transmission mode.

2.4. Practical SPNA Junctions

Six-port theory is, in principle, applicable to arbitrary design. However, for better accuracy assessment, design objectives should be obtained:

- At one output port, the wave is proportional (α_3) to the incident wave a_2
- At the three remaining ports we have $|q_i| = 1.5$ and $\arg(q_i - q_j) = 120^\circ$, where $q_i = -\alpha_i / \beta_i$ for $i, j = 4, 5, 6$.

A simple six-port junction consists of one directional coupler and three voltage probes (as used in the slotted line) separated by about $\lambda/6$. A similar junction replaces the probes by a waveguide coupling structure [9]. This structure contains two *E*-plane T junctions at the upper broad wall of the main R320 (26.5–40 GHz) waveguide and

one *E*-plane T junction at the lower broadwall. The distances between the T junctions are about $\lambda/6$.

Figure 5 shows a six-port junction using techniques [10] at submillimeter wave (300 GHz). Similar quasioptical techniques have been applied in optic domains for a wavelength of $0.633 \mu\text{m}$ [11]. The beamsplitter may be replaced by directional couplers using a metallic waveguide or dielectric waveguide structure (94 GHz) [12].

A more wideband system [13] (75–110 GHz) has been realized by means of connecting five 3-dB 90° hybrid couplers. It can be shown that the q_i points are frequency-independent and are equal to $(-j, 1+j, -1+j)$ assuming identical and symmetrical couplers with a coupling factor of 3 dB. This feature is interesting in the millimeter-wave range because the phase property of commercial couplers are usually unknown.

Another technique is the multistate reflectometer. It consists of two directional couplers. The internal matched termination on the fourth arm of one coupler has been replaced by a phase shifter. Three states of the phase shifter provide the three equivalent power ratios of the six-port technique. Currently, this system permits on-wafer measurement at a frequency of 140 GHz [14].

2.5. Experimental Results

Table 2 shows S_{11} measurement results obtained with different systems. The measurement results labeled “SPNA,” “HP8510,” or “AB millimeter” can be compared with the values labeled “LCIE” given by the calibration center of LCIE (Laboratoire Central des Industries Electriques en France), which are considered arbitrarily to be the references. In this case, the magnitude of S_{11} was determined with a tuned reflectometer while the phase is obtained with a slotted line. The mean standard deviation is equal to 0.01 for the magnitude and 4° for the phase. The small differences may be due to temperature effects or the non-repeatability of the connections.

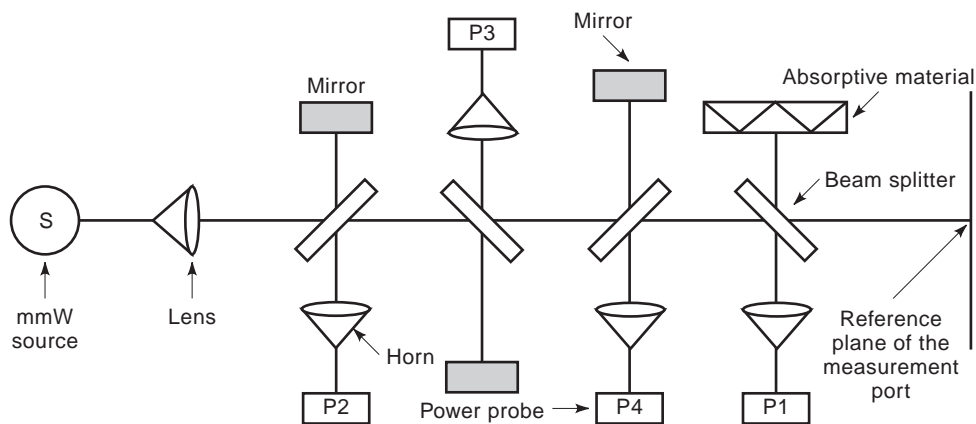


Figure 5. Six-port millimeter-wave junction using quasioptical techniques. It comprises five horns and four dielectric sheets. Each of the dielectric sheets is a beamsplitter. A metallic mirror is placed on the fourth branch of each beamsplitter except the one which involves the measurement of the source signal. The distance between the mirror and the dielectric sheet gives the weight of the added signals.

Table 2. Measurement Comparison Among Network Analyzers

Network Analyzer	93 GHz	94 GHz	95 GHz	96 GHz
LCIE	0.415 −100.8°	0.447 174.8°	0.479 91.4°	0.515 13°
SPNA	0.01 −0.1°	−0.013 +0.2°	0.012 −0.8°	−0.013 7°
HP8510	0.005 5°	0.002 3°	0.01 5°	0.002 3°
AB millimeter	0.006 0.1°	−0.007 −4°	0.02 −3°	0.01 −1°

2.6. Future Trends

The six-port junction may be realized using a microwave monolithic integrated circuit (MMIC). The MMIC chips can be used as a sensor in an antenna array or integrated inside the tips of a probe station. In the latter case, the series of losses of the probe tips and the line connection do not decrease the measurement accuracy of the wafer probe station.

3. SOURCE-PULL AND LOAD-PULL TECHNIQUES

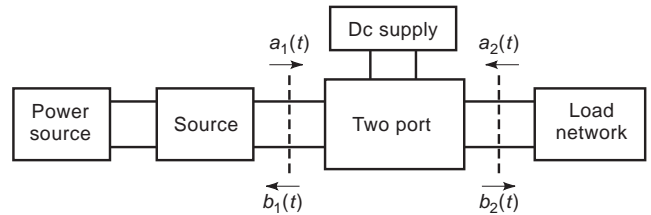
Large-signal millimeter-wave measurements of representative samples of semiconductor devices are of prime importance for two main reasons: (1) accuracy and consistency check of nonlinear transistor models for CAD and (2) experimental optimization of transistor optimum operating conditions without the use of any model.

Nonlinear devices demonstrate different aspects of their behavior depending on the source and load match. Therefore, large-signal measurement systems use either computer-controlled tuners or active loads to change source and load impedances of the DUT to reach the optimum matching conditions under large-signal operation (load-pull system).

Tuner systems operating up to the W band are commercially available. They are widely used for the design of low-noise amplifiers [15], power amplifiers and oscillators [16], and mixers [17]. However, such systems do not allow synthesis of impedances close to the edge of the Smith chart. This main drawback becomes more and more crucial if the operating frequency increases (millimeter wave) or if on-wafer measurements are performed. For these reasons the active source and load-pull technique has emerged. Going further in the large-signal characterization, novel measurement systems allowing the extraction of voltage/current waveforms at the DUT's ports have been developed.

3.1. Basic Considerations on the Source and Load-Pull Techniques

The principle of the large-signal characterization of any non-linear two-port is sketched in Fig. 6. If a single-tone power source is used, the four power waves are expressed

**Figure 6.** Source- and load-pull techniques: principle.

as follows:

$$a_1(t) = \sum_n A_{1n} \cos(n\omega t + \varphi_{1n}),$$

$$b_1(t) = \sum_n B_{1n} \cos(n\omega t + \theta_{1n})$$

$$a_2(t) = \sum_n A_{2n} \cos(n\omega t + \varphi_{2n}),$$

$$b_2(t) = \sum_n B_{2n} \cos(n\omega t + \theta_{2n})$$

A vector network analyzer (VNA) or six-port reflectometer provides the measurements of the magnitudes $|A_{in}|$, $|B_{jn}|$ ($i, j = 1, 2$) and the power wave ratios at the same frequency. From this information, powers, impedances and gains can be calculated. Unfortunately, classical VNAs do not allow the measurements of absolute phases φ_{in} and θ_{in} . As a consequence, time-domain waveforms cannot be extracted. A novel system allowing the measurements of time-domain waveforms will be described later.

First a conventional source and load-pull system (measurements of impedances and powers) is considered. Referring to Fig. 6, a systematic approach for performing large-signal characterization of a DUT is as follows:

1. Impose desired DC voltages or currents.
2. Tune the source and load networks.
3. Sweep the power level of the input source and measure powers, efficiency, and gain.

Then the same procedure can be repeated for different operating conditions. This implies the use of a fully automated measurement system.

3.2. Multiharmonic Active Source and Load-Pull System

Multiharmonic source and load-pull systems are very useful in designing optimized nonlinear microwave circuits. Both source and load impedances have a great influence on the performances of DUTs in terms of efficiency and linearity. The load-pull characterization has also become a key step in the whole modeling process of semiconductor devices.

3.2.1. Load Pull [18]. The block diagram of a multiharmonic load-pull system is shown in Fig. 7. The measurements of absolute powers and power wave ratios are performed by using a VNA (receiver operation mode) calibrated with a TRL procedure. The synthesis of load

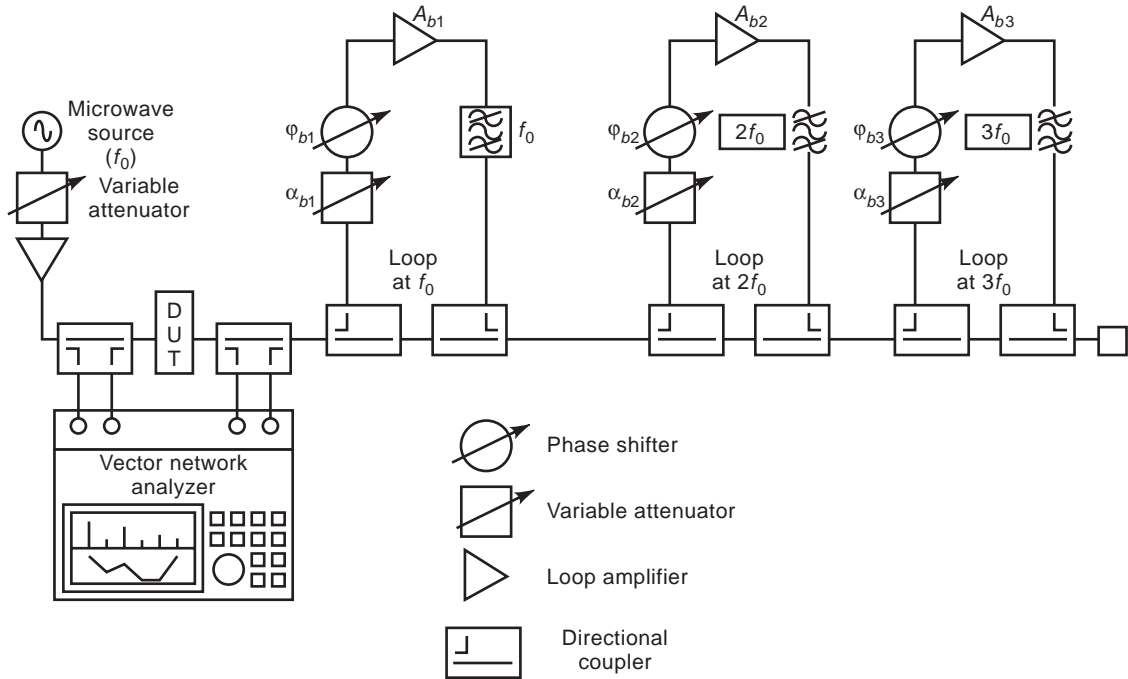


Figure 7. Multiharmonic load-pull system block diagram.

impedances at the first three harmonics coming out of the DUT is performed by using active loops and monitoring the complex gain of each loop with attenuators and phase shifters. Once the gains are fixed, a power sweep at the input of the DUT is performed and input/output power characteristics of the DUT are measured.

3.2.2. Source Pull [19]. Figure 8 shows a measurement system based on the use of six-port reflectometers. This system integrates both input and output active loops to perform source and load-pull measurements. Depending

on the position of switch 1, the input six-port measures either the input reflection coefficient of the DUT or the reflection coefficient of the source load presented to the DUT. For both cases the error terms found by a classical calibration procedure are valid.

3.3. Time-Domain Waveform Measurement System [20]

As mentioned previously, conventional VNAs do not allow the measurements of absolute phases of harmonically related signals. As a consequence, time-domain waveforms cannot be extracted. Therefore, different institutes have

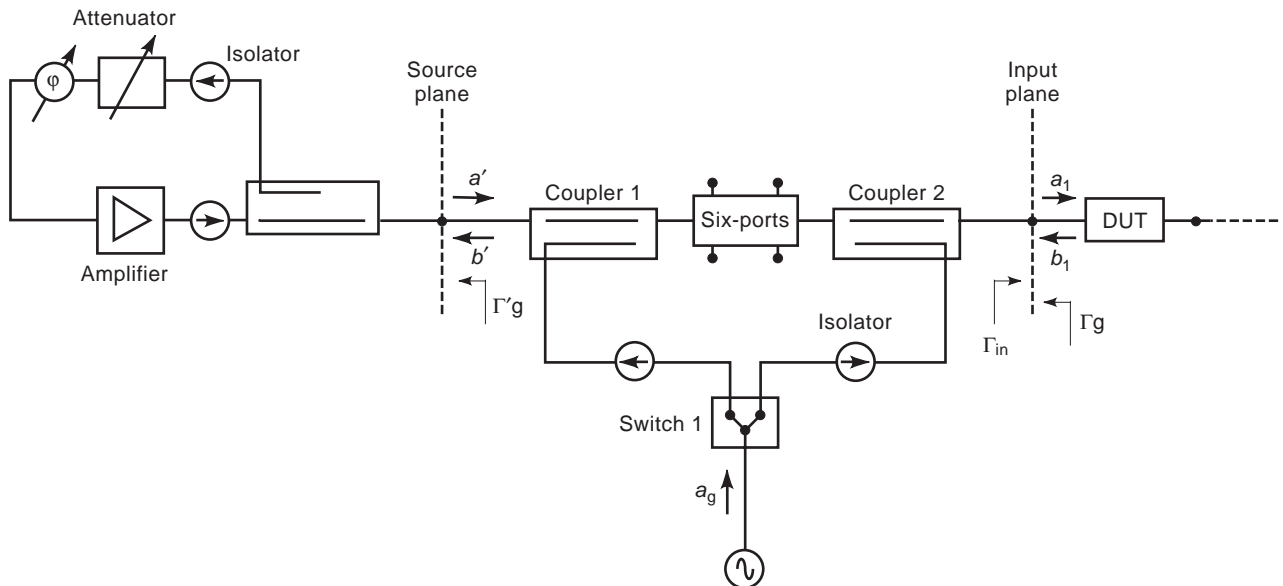


Figure 8. Source-pull implementation with a millimeter-wave six-port junction.

developed measurement systems to extract time waveforms in one or another way usually based on the HP microwave transition analyzer. The potential of the combination of the nonlinear network measurement system (NNMS) with active source and load-pull techniques is under study.

This NNMS is mainly composed of a four-channel broadband downconverter followed by digitizers. It uses the harmonic mixing principle to convert RF fundamental and harmonics into IF fundamental and harmonics. This instrument takes the place of the VNA in the system previously presented.

The calibration of the system is performed in three main steps:

1. Classical TRL calibration
2. Power calibration calibration
3. Phase calibration

During the last step, a reference generator (step recovery diode) is connected instead of the DUT [21]. The reference generator is calibrated using the nose-to-nose calibration procedure [22].

4. DIELECTRIC WAVEGUIDE CAVITY RESONATOR

As millimeter waves, resonators are useful for a large number of applications in communication systems and measurements of dielectric properties. In the millimeter-wave and submillimeter-wave ranges, difficulties arise from wavelengths which are very short, and devices are difficult to machine with a large degree of accuracy. So the problem is to achieve high circuit Q for volumic or hybrid millimeter-wave integrated circuits.

Different resonator structures are used. Some of them are derived from low-frequency application, like a cylindrical metallic cavity, but other devices have been developed specially for millimeter-wave measurement. In the following subsections we present mainly the devices given in Fig. 9, which are often used.

4.1. Cylindrical Metallic Cavity

This structure presented in Fig. 9a is composed of a cylindrical metallic waveguide closed at the top and the bottom by a metallic plane. The resonant frequency depends on the dimensions of the cavity (diameter and height) and

the mode that is excited in the structures. These modes are chosen to be TE_{01n} or TM_{01n} modes and depend on excitation line position. The unloaded Q factor of these resonators increases with the axial number n . But it is difficult to use axial numbers greater than five, because a lot of modes are excited in a frequency band and it is difficult to obtain good frequency isolation. Typically, at room temperature and with copper to realize the cavity, values of unloaded Q factor are equal to 12,000 at 30 GHz and 7000 at 100 GHz on the TE_{013} modes.

4.2. Open Resonators

The most popular of this type of resonator is the Fabry–Perot, which is presented in Fig. 9b [23,24]. These resonators are used from the short microwave to the optical domains [25]. The basic device is composed of two reflectors of arbitrary radius of curvature separated by a length d . At low frequencies, the dimensions of the mirror will be very large, so for this reason these devices are used essentially at very high frequencies. TEM_{plq} mode is excited in these structures, where p , l , and q are, respectively, radial, azimuthal, and axial variations of the energy which is localized in the center between the two mirrors. In a great number of applications, the TEM_{00q} mode is used and resonant frequency of these modes are periodic along the q parameter. As in metallic cavities, the unloaded Q factor increases with the number of axial variations, and values of the Q factor greater than 10^6 are possible in millimeter-wave measurement.

4.3. Dielectric Resonators

For high frequencies the dimension of resonators excited on conventional modes becomes impractically small. A solution consists of using dielectric resonators excited on whispering-gallery modes (WGMs), which are higher-order modes. The first advantage of this solution is the dimension of the resonators, which is approximately 10 times bigger than resonator excited on conventional modes. The geometry of the resonators is a disk with a diameter greater than thickness, as shown in Fig. 9c [26,27]. So these resonators are easy to integrate in planar circuits.

Moreover, acting on these modes, energy is confined at the periphery of the dielectric resonator, and radiation losses are negligible. Thus, unloaded Q factors are very large and only limited by dielectric losses of the material used to realize the resonators.

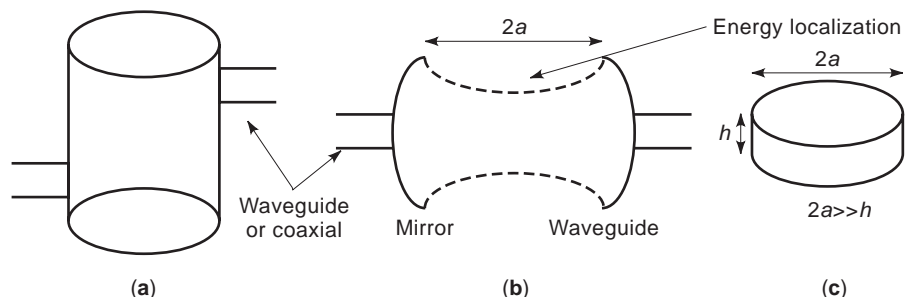


Figure 9. Example of millimeter-wave resonators: (a) cylindrical metallic cavity; (b) open resonators; (c) whispering-gallery dielectric resonators.

At room temperature and using quartz material, a measured Q factor of 30,000 has been obtained at 100 GHz. Placed in a metallic cavity and at 77 K, a Q factor of 30,000,000 has been measured at 7 GHz with sapphire.

4.4. Applications to Millimeter Devices

In millimeter-wave devices, a large number of applications use resonator circuits. These elements are used in devices such as filters or oscillators, or for material measurements to determine complex permittivity and permeability. In both cases, it is very interesting to have a high Q factor of the resonance modes.

4.4.1. Filtering. Insertion losses and rejection depend on Q factor of the resonators. To realize these circuits, cylindrical metallic cavity or WGM dielectric resonators are suitable because association of several resonators is possible. At high frequencies, topologies of these structures are the same as for low-frequency devices.

4.4.2. Oscillator. Frequency stabilization and phase noise need a high Q value of the resonant device. For millimeter-waves, dielectric resonators excited on WGM give good results and are easy to integrate in the devices. With these modes, the original topology of oscillators can be realized by using the wave propagation effect at the periphery of the resonators, which is another property of these modes.

4.4.3. Dielectric Material Measurement. These resonator devices are currently used because they permit good accuracy with regard to the complex permittivity of the material. For metallic cavities or open resonators, the method consists of comparing the resonant frequency and the unloaded Q factor of the empty and loaded resonators. This method is convenient if the thickness of the material under test is smaller than the wavelength. For material with a large thickness, methods using WGM are suitable. In this case, measurements of resonance frequency and Q factor are compared with results obtained by electromagnetic simulator. These methods can be used for anisotropic dielectric or magnetic material [28].

4.5. Future Trends

The performance of millimeter-wave resonator devices is limited by the difficulty of integration of resonators in devices (in particular, for cavity or open resonators) or by losses of metallic or dielectric materials. Since the late 1980s, with the development of new dielectric materials like sapphire in the microwave domain, performances have been improved with regard to the unloaded Q factors. Unfortunately, characteristics of these materials change with temperature, and frequency stabilization is difficult to obtain without using regulating temperature devices. In the future, with technology development, we can hope to obtain material with optimum characteristics.

5. FREE-SPACE METHODS: INTERFEROMETRY

Waveguide loss becomes important for millimeter waves; free-space transmission has lower loss and is good for low-noise applications as well as for high-power applications (in addition, larger area of beams spread produces a lower power density). Free-space measurement is required when contact is not possible. Such is the case in radiometry for measurement of temperature and chemical composition, as well as in interferometry and in radar detection for measurement of distance, velocity, and position.

Very often for millimeter waves, the beam diameter is a relatively small number of wavelengths; thus, diffraction must be considered. A wide variety of components and systems have been developed using quasioptical techniques, either similar to waveguide devices or derived from infrared and optical techniques [29,30].

5.1. Quasioptical Techniques

5.1.1. Gaussian Beams. Paraxial propagation of a beam in free space is relatively simple to analyze if the transverse electric field amplitude variation has a Gaussian form

$$E(r)/E(0) = \exp[-(r/w)^2]$$

where r is the distance from the axis of propagation and w is called a "beam radius." A Gaussian beam is produced with, or focused to, a minimum size; this minimum beam radius w_0 called a "beam waist."

The feedhorn is the best coupling device between the Gaussian beam and the guided wave (Fig. 10). The best coupling (98%) is obtained with a scalar feedhorn pattern. Several types of planar antennas (patch, bowtie, traveling-wave slot) can also be used. An associated lens is used to obtain reasonable coupling efficiency. Several types of planar antennas (patch, bowtie, traveling-wave slot) can be used. An associated lens allows us to reduce the beam size and increase the coupling efficiency.

5.1.2. Quasioptical Components Used in Millimeter-Wave Measurement. Quasioptical components provide a wide variety of functions used for millimeter measurements:

- Beam transformations require focusing elements such as parabolic or ellipsoidal mirrors and lenses. To minimize the absorptive loss of lenses, low-loss dielectrics must be selected (PTEE, alumina, fused silica, etc.); and to obtain low reflection loss, a matching layer or grooves are essential, except for low-index materials.
- High- Q -factor ($\gg 10,000$) resonant cavities can be formed with two spherical mirrors or one spherical and one plane mirror.
- Signal filtering can be achieved by interferometers (see below) and by plate filters: Perforated conductive plates or arrays of resonant patterns are printed on a dielectric substrate.
- Polarizing grids are usual in quasioptical systems, often used as beamsplitters for a polarized signal.

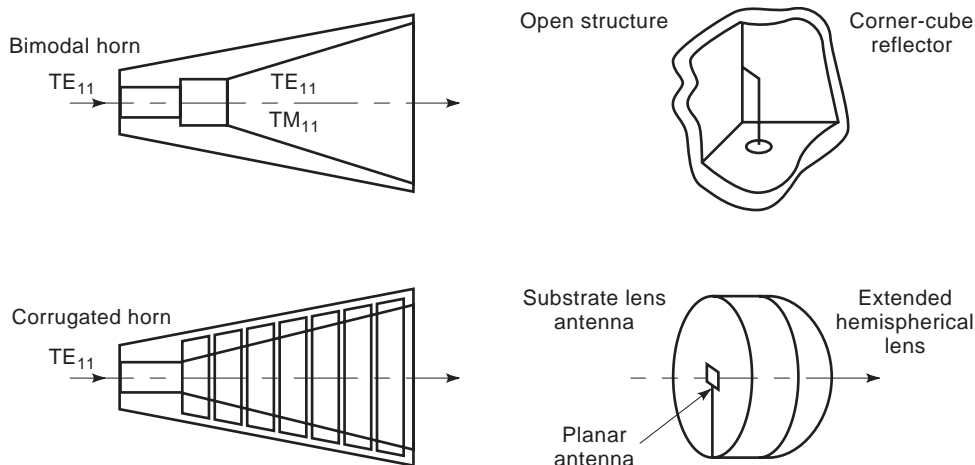


Figure 10. Devices for millimeter-wave and sub-millimeter-wave beam production (horn and open-structure examples).

These grids can be formed with freestanding wires or with dielectric-supported conducting strips. Dielectric plates are also used as beamsplitters and can function as hybrids (90° phase shift between reflected and transmitted beams).

- Different types of interferometers are developed from beamsplitters and reflective devices: dual-beam interferometers or Fabry-Perot interferometers.

5.1.3. Quasioptical Bench. The purpose of the quasioptical bench is to create a “beam waveguide” including a sufficient measurement area. Figure 11 shows a basic bench, in which the measurement area is located between a signal generator and a detector equipped with free-space coupling devices (horns and lenses). The relative positions must be finely adjustable (in three rectangular directions and two or three rotating angles) while staying extremely

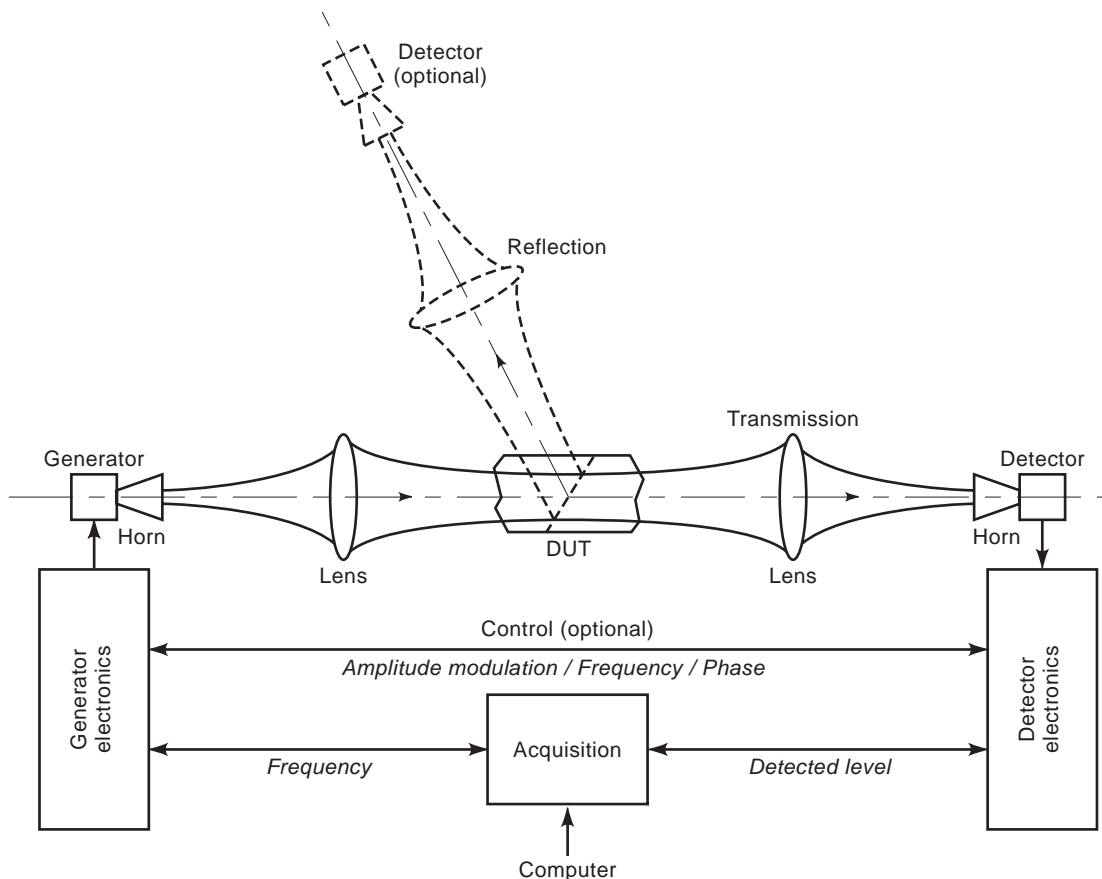


Figure 11. Quasioptical bench.

stable. As in coaxial or waveguide measurements, generators and detectors can use frequency multipliers and heterodyne and phase-locked systems to increase the sensitivity and stability.

Free-space measurements may use a device for analog-to-coaxial calibration set parts. The methods are identical, but special care is required to (1) decrease the multiple reflections by using absorbing shields and anechoic rooms, (2) take VSWR into account, and (3) manage external (or internal, electromagnetic interferences. Another source of error and instability is atmospheric absorption, when the measuring frequency band comes over the absorption bands of an atmospheric molecule.

5.2. Free-Space Antenna Measurement

The antenna characteristics that have to be measured in the millimetric range are mainly radiation patterns in co- and cross-polarization. Phase center measurements of primary feeds, as well as beam efficiency, also have a great importance for reflector antenna design. Measurement techniques are much the same as at lower frequencies, but with specific difficulties and requirements [31]. (See also RADIOMETRY, ELECTROMAGNETIC FIELD MEASUREMENT.)

5.2.1. Radiation Pattern Measurements. Far-field measurements must be performed outdoors if antenna dimensions are large compared with the wavelength, which generally is the case for reflector antennas at millimetric frequencies. However, atmospheric attenuation and geographic implementation become prohibitive when the far field exceeds 1 km. Compact antenna test ranges (CATRs) remedy this problem for medium-to-large reflector antennas in the millimetric range.

For antennas of moderate (cm) dimensions, far-field measurements can be performed indoors. Horns and printed antennas are tested in anechoic chambers. In CATRs, a local plane wave is created in a zone called the “quiet zone,” by way of one or several reflectors used to collimate the beam of a smaller source. Various designs exist, ranging from the basic one with a single offset reflector to triple reflector systems, according to the required cross-polarization and spillover levels and the size of the antennas under test. Diffraction at the edges of the reflectors is less critical than in the microwave range, but reflector surfaces requirements are more stringent because the root-mean-square (rms) surface error should be better than $\frac{1}{100}$ wavelength to obtain good precision on the plane wave phase. Corrugated or special multimode horns are used as sources.

Hologram CATRs are being developed. Reflectors are replaced by a hologram, with a surface accuracy requirement divided by 10. This technique is thus less expensive, but it is still very new and faces problems concerning the size of the required holograms as well as frequency bandwidth limitations (20–30%) and polarization difficulties.

In the near-field scanning technique, fields are measured close to the antenna under test, on either a planar, cylindrical, or spherical surface. This technique requires both amplitude and phase measurements,

because the sampled fields are used to calculate the radiated far-field through a near-field to far-field transformation. In the millimeter-wave domain, this technique encounters problems of time consumption and precision phase measurement.

5.2.2. Other Antenna Performance Measurement. The “beam efficiency measurement” is performed by measuring the power radiated within the mainbeam of the antenna. It is especially important for radiometer antennas, which must have very low sidelobes. It requires both radiation pattern measurements, although not with wide-angle scanning, and absolute power measurements. The “phase center position measurement” is useful only for horns used as primary sources in reflector antennas. It is performed by positioning the center of phase patterns in different planes along the axis of the horn. It requires precise phase measurements and mechanical positioners.

5.3. Quasioptical Measurement

5.3.1. Power Measurement. Most of the power detectors used in the microwave measurement (Schottky diodes for instance) still work in the millimeter-wave frequency range. Moreover, bolometers and the calorimeters also operate in this range. These devices mounted in a waveguide structure can be associated with a horn to make up a beam detector. To increase the sensitivity, synchronous detection and heterodyne conversion may be used. Absolute calibration must be performed with photoacoustic detectors (used at Brewster angle and through amplitude modulation).

5.3.2. Quasioptical Device Characteristics Measurement. A basic quasioptical bench allows us to measure the main of millimeter-wave characteristics of a DUT inserted in the optical path: transmittance, loss and scattering by insertion, and reflection by comparison with a good reflector. Much attention must be paid to (1) the radial size of the DUT compared with the usable beam size, (2) the compensation for phase differences, and (3) the VSWR (which can be reduced by choosing an incidence angle other than zero).

For low losses, noise measurements provide a better accuracy. The equivalent noise temperature T_1 is increased to T_2 by the insertion of a DUT at the front of a low noise receiver. Giving the DUT physical temperature T_d , the loss factor L is obtained from

$$T_2 = T_d(L - 1) + LT_1(1 + \Gamma^2)$$

with $\Gamma^2 = [(VSWR - 1)/(VSWR + 1)]^2$.

5.3.3. Noise Measurement. In addition to classic noise measurement using a noise source (diode, gas tube) associated in this case with a horn, the common noise measurement uses two absorbing targets with two different radiant temperatures. The target with the higher temperature T_h , the “hot load,” takes the place of the target with the lower temperature T_c , the “cold load,” in front of the

DUT. The respective output powers are P_h and P_c . With ideal targets the equivalent noise temperature of the DUT is

$$T_x = (T_h \cdot P_c - T_c \cdot P_h) / (P_h - P_c)$$

Radiometer systems must be extremely stable over long periods and linear over the whole level range. The target size must be enough to cover the whole beam. Temperature and absorption coefficients must be homogeneous over the target surface. At millimeter wavelengths, $h\nu < kT$, the brightness temperature is very near the physical temperature. Measurement uncertainties come from variations of the effective emissivity of the target and from the mismatch with the receiver. In addition, as a result of the standing-wave effect, the total noise entering the receiver becomes frequency-dependent.

The standard ferrite-loaded foam absorbers may be used as calibration targets in the lower frequency range, but for higher frequencies the reflected power unfortunately reaches -20 dB, depending on the polarization angle. For a single polarization and when the configuration is fixed, a specially developed ridged absorber or dielectric surface at the Brewster angle acts as a quasi-perfect absorber.

To achieve good precision ($<1\%$), a lot of specific targets have been developed from the principle of a conical hole with an angle of $<10^\circ$ to increase the number of reflections.

5.3.4. Other Quasioptical Measurements. The frequency measurement may use a downconversion by means of a millimeter mixer coupled with a local oscillator by a quasioptical coupler (an interferometer or a simple dielectric plate). The local oscillator and the low frequency counter are phase/frequency locked on a reference ultrastable oscillator. On the other hand, wavemeters may use very-high- Q -factor cavities in quasioptical techniques.

The measurement of the polarization of a signal usually takes advantage of the sensitivity of the detector for one electromagnetic field direction (detection diodes and rectangular waveguide mounts). To increase the accuracy or to use a non-polarized detector, a polarized plate (grid) may be inserted (with an incident angle to decrease a possible VSWR effect). This method requires us to rotate the whole receiver or to insert a waveguide twist behind the horn (causing a calibration problem). The other solution is to use a quasioptical polarization rotator on the optical path. This device uses three grids in transmission [32] or one grid and one reflector [33]. In this way the mechanical rotation is limited to one light device, and the transition time may be very short (<10 ms). Circular polarization may be measured with a particular disposition of Martin-Puplett interferometer.

The knowledge of the insertion effects (loss and phase variations) allows us to compute the complex dielectric constant of a material. Other methods for material characteristics measurement use modifications of a cavity resonator's Q factor.

5.4. Interferometry

The resolution of an antenna has a diffraction limit of $\approx \lambda/D$, and an interferometer increases the resolution according to the area covered by two or several connected antennas. More generally, an interferometer can be used to measure the Fourier components of a brightness distribution. Since Ryle and Hewish [34] have formulated the principle of aperture synthesis, many interferometers have been built or are in progress (mainly for radio astronomy). The aperture may be synthesized by multiplication, physically moving of elements, or by using the rotation of the earth. As baselines are increased, the major problem in millimeter-wave measurement is the maintenance of phase stability of local oscillators; for very-long-baseline interferometry (VLBI), the local oscillators are independent and need very accurate frequency standards.

BIBLIOGRAPHY

1. Technical information available from Hewlett-Packard (online) at www.hp.com Anritzu.
2. Technical information available from Cascade Microtech Inc. (online) at www.cmicro.com. and Picoprobe, a GGB Industries Inc. (Online). Available [www:WWW.picoprobe.com](http://www.WWW.picoprobe.com)
3. S. M. J. Liu and G. G. Boll, A new probe for W-band on-wafer measurements, *IEEE MTT-S Digest*, 1993.
4. See application note from Cascade Microtech Inc., Hp, and Picoprobe.
5. P. Crozat, J. C. Henaux, and G. Vernet, Precise determination of the open circuit capacitance of coplanar probes for on-wafer automatic network analyzer measurements, *Electron. Lett.* **27**:1476-1478 (1991).
6. A. Davidson, K. Jones, and E. Strid, LRM and LRRM calibrations with automatic determination of load inductance, *36th ARFTG Conf. Digest*, 1990, pp. 57-63.
7. R. B. Marks, A multiline method of network analyzer calibration, *IEEE Trans. Microwave Theory Tech.* **39**:1205-1215 (1991).
8. G. Dambrine et al., A new method for determining the F.E.T. small signal equivalent circuit, *IEEE Trans. Microwave Theory Tech.* **36**:1151-1159 (1988).
9. U. Stumper, Experimental investigation of mm W Six port incorporating simple waveguide structure, *IEEE Trans. Instrum. Meas.* 469-472 (1991).
10. U. Stumper, A six port reflectometer operating at submillimeter wavelengths, *Proc. 15th European Conf.*, 1985.
11. N. C. Wolker and J. E. Carrol, Simultaneous phase and amplitude measurements on optical signals using a multiport junction, *Electron. Lett.* **20**:981-983 (1984).
12. G. Hjiiperis, R. J. Collier, and J. Griffin, A mm W six port using dielectric waveguide, *IEEE Trans. Microwave Theory Tech.* **38**:54-61 (1990)
13. S. A. Chahine et al., A six-port reflectometer calibration using Schottky diodes operating in AC detection mode, *IEEE Trans. Instrum. Meas.* **42**:505-510 (1993).
14. R. J. Collier and I. M. Boese, Impedance measurements using a multistate reflectometer from 110-170 GHz, *BEMC*, 3-1, 3-4, 1996.
15. Focus Microwave Inc., An ultra wideband tuner system for load pull and noise characterization, *Microwave J.* **38**(6):90-94 (1995).

MIMO SYSTEMS FOR WIRELESS COMMUNICATIONS

AHMED IYANDA SULYMAN
 MOHAMED IBNKAHLA
 Queen's University
 Kingston, Ontario, Canada

1. INTRODUCTION

Wireless data services have grown rapidly both for micro- and macrocellular systems,¹ and high- and low-mobility applications. This is due to the various technological breakthroughs recorded in wireless applications such as: mobile computing, mobile and high-speed internet access, mobile multimedia, and a host of personal communications (PC) services. The demands for ubiquitous access to these services are ever increasing, and necessitating continued additions of new techniques to provide more services.

Wireless channels suffer from severe distortions caused mainly by multipath² fading. The severity of these distortions often makes it impossible for the mobile receiver to make a correct detection of the transmitted symbols, unless some less attenuated replicas of the transmitted signal are provided to the receiver. This is referred to as *diversity*. Diversity techniques are based on the notion that errors occur in reception when the channel is in deep fade—a phenomenon that is more pronounced in mobile communications, due to the mobility of the transmitter, the receiver, or both of them. Therefore, if the receiver is supplied with several replicas, say, L , of the same information signal transmitted over independently fading channels, the probability that all the L independently fading replicas fade below a critical value is P^L (where P is the probability that any one signal will fade below the critical value). The error rate performance of the system is thus improved without increasing the transmitted power. Most of these diversity solutions, however, have traditionally focused on the receiver diversity considerations. Examples of diversity technique for wireless applications can be found in Refs. 1–4.

Another powerful fading combatant that has been used for wireless channels is the *coding technique*. While diversity system introduces spatial redundancies in the received signals, coding technique on the other hand introduces the redundancies in the temporal sense. In the coding technique, an encoder takes as input n information bits at any time instant and adds error correcting bits (or redundancies) to produce at its output m bits ($m > n$) of information bearing code, known as *codeword*, and this is transmitted over the wireless channel. The

¹In mobile cellular system, cell sizes (range within which a user can be served by a nearby base station before being transferred to another base station) may vary from large macrocells to small microcells. Macrocells provide services to high speed mobiles, while microcells provide services to low-mobility applications.

²Signals emanating from the transmitter arrive at the receiver via different paths, with different delays and phase. These are referred to as multipaths (see Section 1.1).

16. F. M. Ghannouchi and R. G. Bosisio, Source pull/load pull oscillators measurements at microwave/MM wave frequencies, *IEEE Trans. Instrum. Meas.* **41**:32–35 (1992).
17. D. L. Le and F. M. Ghannouchi, Source-pull measurements using reverse six-port reflectometers with application to MESFET mixer design, *IEEE Trans. Microwave Theory Tech.* **42**:1589–1595 (1994).
18. F. Blache et al., A novel computerized multiharmonic active load pull system for the optimization of high efficiency operating classes in power transistors, *IEEE MTT Symp.*, Orlando, FL, 1995, pp. 1037–1040.
19. G. Berghoff et al., Automated characterization of HF power transistors by source pull and multiharmonic load pull, *IEEE Trans. Microwave Theory Tech.* (in press).
20. D. Barataud et al., A novel time domain characterization technique of intermodulation in microwave transistors. Application to the visualization of the distortion of high efficiency power amplifiers, *IEEE MTT Symp.*, Denver, 1997, pp. 1687–1690.
21. J. Verspecht et al., Accurate on wafer measurement of phase and amplitude of the spectral components on incident and scattered voltage waves at the signal ports of a nonlinear microwave device, *IEEE MTT Symp.*, Orlando, 1995, pp. 1029–1032.
22. J. Verspecht and K. Rush, individual characterization of broadband sampling scopes with a nose to nose calibration procedure, *IEEE Trans. Instrum. Meas.* **43**:347–354 (1994).
23. J. C. McCleavy and K. Chang, Low-loss quasioptical open resonators filters, *IEEE MTT Symp. Digest*, 1991, pp. 313–316.
24. D. Steup, Quasioptical SMMW resonator with extremely high Q factor, *Microwave Opt. Technol. Lett.* **8**(6):275–279 (1995).
25. D. Cros and P. Guillon, Whispering gallery dielectric resonator modes for W-band devices, *IEEE Trans. Microwave Theory Tech.* **38**:1667–1674 (1990).
26. O. Di Monaco et al., Mode selection for a whispering gallery mode resonator, *Electron. Lett.* **32**(7):669–670 (1996).
27. J. Krupka et al., Study of whispering gallery modes in anisotropic single-crystal dielectric resonators, *IEEE Trans. Microwave Theory Tech.* **42**:56–61 (1994).
28. A. Parash. J. K. Vaid, and A. Mansinch, Measurement of dielectric parameters at microwave frequencies by cavity perturbation technique, *IEEE Trans. Microwave Theory Tech.* **27**:791–795 (1979).
29. P. F. Goldsmith, Quasioptical techniques at millimeter and submillimeter wave-lengths, in K. J. Button, ed., *Infrared and Millimeter Waves*, Vol. 6, Academic Press, New York, 1982, pp. 277–343.
30. J. C. G. Lesurf, *Millimeter-wave Optics, Devices & Systems*, Adam Hilger, Bristol, UK, 1990.
31. A. D. Olver and C. G. Parini, Millimetre wave compact antenna test ranges, *Proc. JINA 92*, Nice, 1992, pp. 121–128.
32. R. K. Garg and M. M. Pradhan, Far-infrared characteristics of multielement interference filters using different grids, *Infrared Phys.* **18**:292–298 (1978).
33. C. Prigent, P. Abba, and M. Cheudin, A quasioptical polarization rotator, *Int. J. Infrared Millimeter Waves* **9**(5):447–490 (1988).
34. M. Ryle and A. Hewish, *Monthly Notices Roy. Astron. Soc.* **120**–220 (1960).

ratio of the input–output bitlength of the encoder, n/m is known as the code rate and is a measure of the amount of information contained in one data bit after the encoding operation. At the receiving end, an event of error due to corruption in the wireless channel will be detected and corrected by the decoder using its knowledge of the valid codewords for the coding techniques employed, as long as the numbers of bits in error are not greater than the error correcting capability of the code. This process is known traditionally as *channel coding*. Thus the temporal redundancies added to the transmitted bits by the encoder are used to achieve link quality improvement. Examples of coding techniques for wireless applications can be found in Refs. 5 and 6.

A combined coding–diversity scheme, known as *space-time codes*, promising dramatically high data rates as well as reliable communication over the wireless channels was proposed in [7]. This scheme employs coding techniques appropriate to multiple transmit antennas to achieve a combined coding and diversity gains that enables higher data rates, without prejudice to error rate performance. Age-long approach to achieve higher data rates is to expand the signal constellation and use powerful coding and modulation techniques. However, this approach falls short of the goal of achieving truly high-speed data services because of the substantial SNR penalty paid for increasing the signal constellation size. In addressing this problem, the deployment of wireless systems employing multiple transmit antenna (transmit diversity) were first proposed in the context of signal processing in several publications [4,8–10] using the concept of delay transmit diversity. In the delay transmit diversity scheme, replicas of the information signal are transmitted through multiple antennas at different times, and necessary signal processing techniques are employed at the receiver to retrieve the original information signal. The delay transmit diversity scheme was shown to achieve significant performance boost to the wireless channel compared to the conventional system with single transmit antenna.

Tarokh et al. [7] then adapted a coding perspective to this scheme, and proposed the spacetime coding employing multiple transmit–multiple receive antennas. The multiple transmit antennas are used to send different encoded signals in parallel at the transmitter, and multiple antennas are employed at the receiver for signal detection. An appropriate code is employed such that the number of codewords at the output of the encoder matches the number of the transmit antennas. Spacetime codes achieve much more significant performance improvement over the conventional wireless system than does the delay diversity transmission [7]. This celebrated result has therefore spurred a host of research works aimed at increasing the

wireless channel capacity through the spacetime processing [11–18].

Alamouti [15] designed a simple but elegant MIMO system exploiting transmitter diversity to obtain system performance similar to a maximum ratio combining (MRC) receiver diversity. In his scheme, a pair of symbol is transmitted using two antennas at first, and the transformed version of the same pair is transmitted in the next time slot, to obtain the MRC-like diversity gain. Space-time block codes were later designed, using orthogonal structure, and were shown to generalize the Alamouti scheme for various MIMO configurations [13]. Several variants of the MIMO signal processing techniques have since been exploited. These include the spatial multiplexing system [19] and MIMO maximum ratio combining (MIMO-MRC) [14], among others. System performance and information capacity of the wireless communication system employing these MIMO technologies have been demonstrated to increase dramatically over those of the conventional wireless systems [16,19–23].

1.1. Basic Baseband MIMO Channel Model

This section illustrates a basic baseband model for the MIMO wireless communication system. Throughout the article, we assume a MIMO system with N transmitting antennas at the transmitter, and L receiving antennas at the receiver. We use the notation h_{ij} to denote the sampled complex channel gain from transmit antenna j to receive antenna i at discrete time k , where $i = 1, 2, \dots, L$ and $j = 1, 2, \dots, N$. Therefore, we express the $L \times N$ complex MIMO channel matrix at time k as

$$\mathbf{H}(k) = \begin{bmatrix} h_{11}(k) & h_{12}(k) & \cdots & h_{1N}(k) \\ h_{21}(k) & h_{22}(k) & \cdots & h_{2N}(k) \\ \vdots & \vdots & \ddots & \vdots \\ h_{L1}(k) & h_{L2}(k) & \cdots & h_{LN}(k) \end{bmatrix}$$

Figure 1 illustrates a general block diagram for MIMO communication systems. The system equation describing the input–output behavior of the MIMO system can be expressed, for a flat fading channel as

$$\mathbf{y}(k) = \mathbf{H}(k) \mathbf{c}(k) + \mathbf{n}(k) \quad (1)$$

where $\mathbf{y}(k) = [y_1(k), y_2(k), \dots, y_L(k)]^T$ denotes the $L \times 1$ complex received signal vector, $\mathbf{c}(k) = [c_1(k), c_2(k), \dots, c_N(k)]^T$ denotes the $N \times 1$ complex signal vector transmitted from the N transmit antennas, and k is the time index. $\mathbf{n}(k) = [n_1(k), n_2(k), \dots, n_L(k)]^T$ is the $L \times 1$ complex channel noise [additive white Gaussian noise (AWGN)] vector.

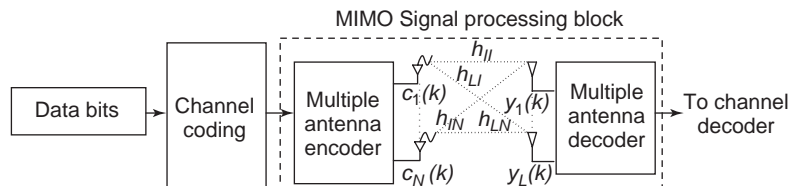


Figure 1. MIMO communication systems.

Here it is assumed that the AWGN is spatially and temporally white [i.e., $\mathbf{n}(k)$ is a zero-mean complex Gaussian vector with covariance matrix $\sigma_n^2 \mathbf{I}$].

1.2. Channel Effect in Mobile Wireless Communications

Channel effects in mobile wireless communication systems arise from multipath propagation and user mobility, besides the regular propagation loss and fading (attenuation) on wireless links. The multipath effect is a feature associated with the fact that the signal transmitted from a mobile unit undergoes scattering, reflections, or diffraction before reaching the base station, where it arrives from different paths, each with its own fading, propagation delay, and angle of arrival. Multipath scattering may arise from scatterers local to the mobile unit, remote scatterers, or scatterers local to the base station, or all of them. The signal received at the base station is a summation of these multipaths signals. Figure 2 displays a typical mobile wireless propagation environment.

The combined effect of these features leads to the characterization of mobile wireless channels as time-varying fading channels, as well as frequency-selective fading channels.

The equation describing the input–output behavior of the MIMO system can be expressed for frequency-selective fading channel as

$$\tilde{\mathbf{y}}(k) = \sum_{l=0}^{m-1} \mathbf{H}(k; l) \mathbf{c}(k-l) + \mathbf{n}(k) \quad (2)$$

where $\mathbf{H}(k; l) (l=0, 1, 2, \dots, m-1)$ is the $L \times N$ MIMO channel matrix representing the l th tap of the mobile channel matrix response with $\mathbf{c}(k)$ as the input and $\mathbf{y}(k)$ as the output at time instant k . The parameter m denotes the memory length of the impulse response of the mobile channel. To simplify the exposition hereafter, we drop the time index k in the system equations where necessary.

1.3. Capacity of MIMO Systems

For a given channel and a given transmitter input power P_T , Shannon definition of capacity for the single transmit–single receive antenna, or single input–single output

(SISO), system can be expressed as

$$C = \log_2 \left(1 + \frac{P_T}{\sigma_n^2} \right) \text{ bps/Hz} \quad (3)$$

where σ_n^2 is the noise variance and bps is bits per second.

For the case of MIMO transmission, assuming that the channel state information (CSI) is unknown at the transmitter, and that the transmitted power is divided equally among the transmit antennas, then the capacity formula can be written for a deterministic MIMO channel as [24–27]

$$C_{L < N} = \log_2 \det \left(\mathbf{I}_L + \frac{P_T}{N\sigma_n^2} \mathbf{H} \mathbf{H}^H \right) \text{ bps/Hz} \quad (4)$$

and

$$C_{L \geq N} = \log_2 \det \left(\mathbf{I}_N + \frac{P_T}{N\sigma_n^2} \mathbf{H}^H \mathbf{H} \right) \text{ bps/Hz} \quad (5)$$

where $C_{L < N}$ denotes the capacity for the case when the number of receive antennas L is less than the number of transmit antennas N , while $C_{L \geq N}$ denotes the capacity for the case when the number of receive antennas is greater than or equal to the number of transmit antennas.

The ergodic capacity for fading MIMO channel is obtained by taking the expectation of the capacity expression above with respect to the random channel. Assuming that the MIMO channel is spatially white (i.e., uncorrelated), and consider that $N=L=K$, then for arbitrarily large number of transmit and receive antennas, it can be shown using the strong law of large numbers that the MIMO channel capacity in the absence of channel knowledge at the transmitter approaches [28–31]

$$C \rightarrow K \log_2 \left(1 + \frac{P_T}{\sigma_n^2} \right) \text{ bps/Hz} \quad (6)$$

Comparing Eq. (3) and (6), we can observed that the capacity of MIMO channel increases linearly with the number of antennas K , when K is very large. Therefore, the bandwidth efficiency growth for MIMO transmission is linear with the number of antennas. Figure 3 illustrates the MIMO capacity presented by Paulraj et al. [28] for various MIMO configurations. In this figure, the number

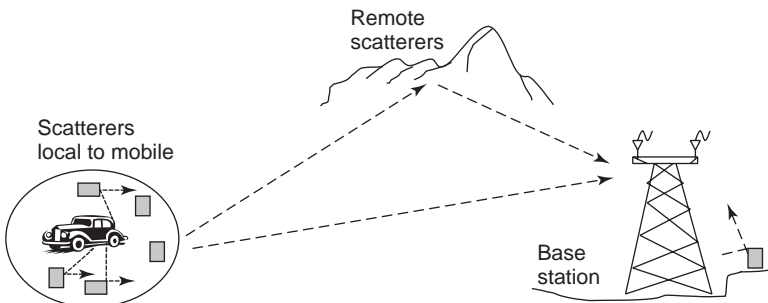


Figure 2. Mobile radio propagation environment.

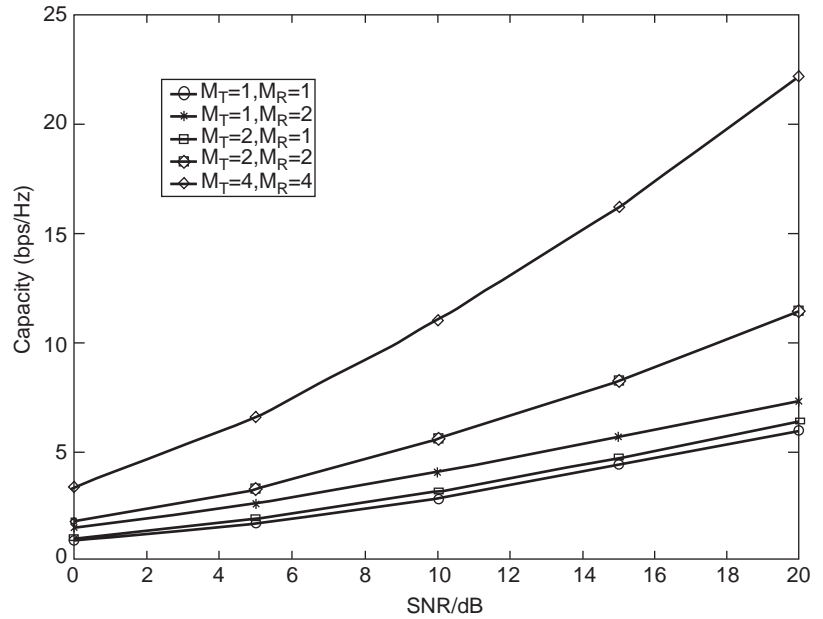


Figure 3. Ergodic capacity for various MIMO antenna configurations.

of transmit antennas is denoted as $N = M_T$ and the number of receive antennas is denoted as $N = M_R$. The capacity increase of the MIMO system over the SISO system (the case $N = 1, L = 1$) is clearly depicted in the figure.

2. MIMO COMMUNICATION SYSTEM DESIGNS

MIMO communication system design can be broadly categorized into two groups:

1. *Spatial multiplexing (SM)* methods exploiting capacity increase from the multiple antenna system
2. *Diversity* methods exploiting link quality improvements from the multiple antenna system

Figure 1 displays a general block diagram for both methods. In the former, incoming data bits are partitioned into multiple substreams and each substream is transmitted, simultaneously, on a different antenna, thereby increasing the link capacity [19]. The multiple antennas at the receiver are then expended in separating these substreams and therefore diversity against fading is rarely provided in SM—at least in the initial design known as V-BLAST (vertical Bell Labs layered spacetime codes).

In the diversity method, approaches include those exploiting both diversity and coding gains from the MIMO

processing block shown in Fig. 1, known as *spacetime coding systems* [7], and those exploiting only the diversity gain, known as *MIMO-MRC systems* [14]. In spacetime codes, coding techniques appropriate to multiple transmit antennas are incorporated in the MIMO signal processing block, in addition to the external channel codes, thereby achieving combined coding and diversity gains from this block. In the MIMO-MRC system, only channel codes external to the MIMO signal processing block are employed. The transmit–receive multiple antennas are utilized purely for diversity gains, with each transmit antenna allocated a weighted fraction of the total transmitted power. The transmit weighting vector is usually matched to the channel in a way to maximize the postprocessing SNR at the output of the channel [14]. MIMO-MRC systems have specific advantage of simplicity of implementations because the scheme employs MRC-like detection at the receiver—which is typically less complex than maximum-likelihood detection (MLD) used in spacetime coding. A detailed comparison among the performances of these methods can be found in Ref. 21.

2.1. MIMO-MRC

Figure 4 displays the model for a MIMO-MRC system consisting of N antennas at the transmitting station and L antennas at the receiving station. The symbol c to be

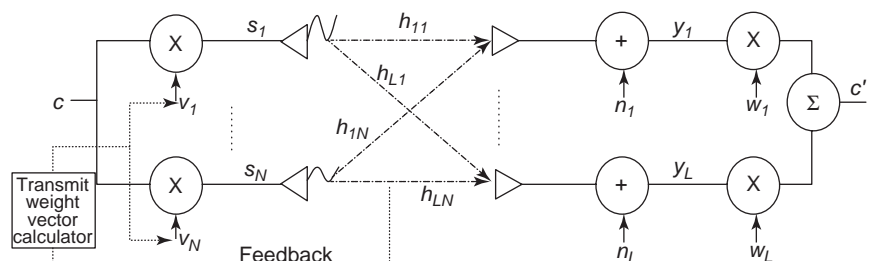


Figure 4. MIMO-MRC model.

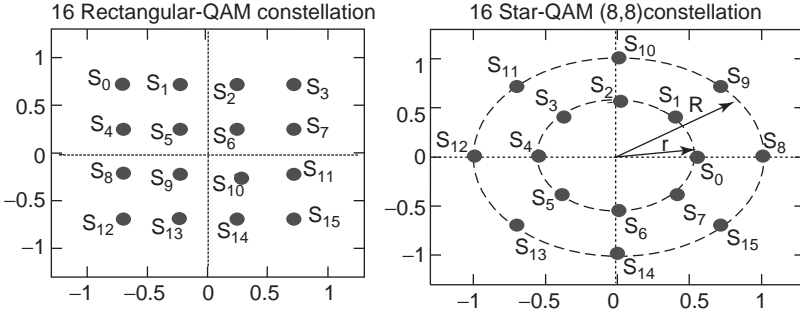


Figure 5. 16 rectangular QAM signal constellations and 16 star-QAM (8,8) signal constellations.

transmitted is weighted with a transmit weighting vector $\mathbf{v} = [v_1 \dots v_N]^T$ to obtain the transmitted signal vector:

$$\mathbf{s} = [s_1 \dots s_N]^T = c \sqrt{E_{av}} [v_1 \dots v_N]^T \quad (7)$$

where E_{av} is the average signal energy at each antenna. The transmit weight vector \mathbf{v} is chosen as [14,32–34]:

$$\mathbf{v} = [v_1 \dots v_N]^T = \mathbf{H}^H \mathbf{w} / \|\mathbf{H}^H \mathbf{w}\| \quad (8)$$

where $\mathbf{w} = [w_1 \dots w_L]^T$ is the weight vector at the receiver. For i.i.d. (independent, identically distributed) channel coefficients, the condition on \mathbf{w} to achieve maximum post-processing SNR is $|w_1| = |w_2| = \dots = |w_L|$ [14]. Without loss of generality, \mathbf{w} can be a unit vector. The received signal vector is therefore characterized as

$$\mathbf{y} = \mathbf{H}\mathbf{s} + \mathbf{n} \quad (9)$$

where \mathbf{H} is the $L \times N$ MIMO channel matrix and \mathbf{n} is the additive white Gaussian noise (AWGN) vector. The decision variable for detecting the transmitted symbol c is obtained in an MRC-like processing by taking the dot product of \mathbf{w} and \mathbf{y} , which can be expressed from Eqs. (7)–(9) as:

$$\mathbf{w}^H \mathbf{y} = c \sqrt{E_{av}} \|\mathbf{H}^H \mathbf{w}\| + \mathbf{w}^H \mathbf{n} \quad (10)$$

The output SNR from the MIMO-MRC receiver γ_{MIMO} is therefore given by

$$\gamma_{\text{MIMO}} = \frac{E_{av}}{N_0} \|\mathbf{H}^H \mathbf{w}\|^2 / \|\mathbf{w}\|^2 \quad (11)$$

where N_0 is the noise power.

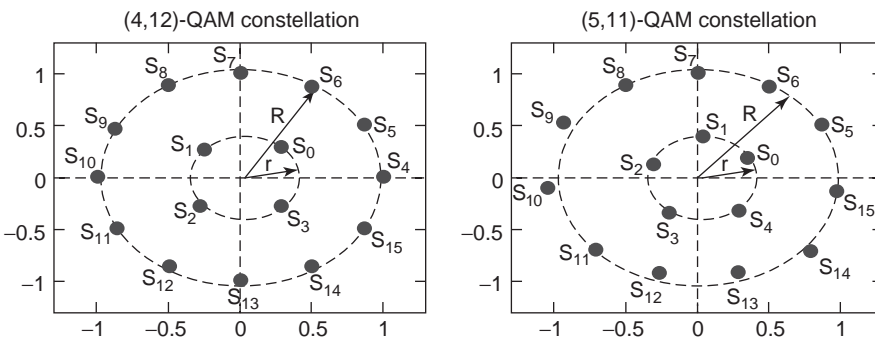


Figure 6. (4,12)-QAM signal constellations and (5,11)-QAM signal constellations.

2.1.1. Performance Results. In this section, we present some results to illustrate the performance of MIMO-MRC system for several quadrature amplitude modulation (QAM) constellations, both circular and rectangular formats. Four QAM constellations have been considered in this illustration: rectangular 16-QAM, star-QAM (8,8), (4,12), and (5,11) constellations (Figs. 5 and 6). For the circular QAM formats [star-QAM, (4,12)-QAM, and (5,11)-QAM], note that the signals in the constellations are arranged on inner and outer circles. The ratio between the radius of the outer and inner circles of a constellation is known as the *ring ratio*, $\alpha = R/r$.

Figure 7 compares the symbol error probability (SEP) of rectangular 16-QAM, star-QAM, (4,12), and (5,11) QAM constellations in MIMO channels, for various fading scenarios and various MIMO configurations. All the results presented in this figure for the circular constellations have been computed using the respective asymptotic optimum value of the ring ratio [35]. It is observed from the results that rectangular 16-QAM has similar performance with (5,11) format, with the latter having slightly better SEP performance at high MIMO order. Similarly, star-QAM and (4,12) have close SEP performance, with (4,12) having better SEP performance than star-QAM. Rectangular and (5,11) constellations both have better SEP performance than (4,12) and star-QAM constellations in all the MIMO configurations considered. For all these constellations however, dramatic improvements in the SEP performance of the MIMO system is observed as the MIMO dimension is increased (from $N=2, L=2$ to $N=4, L=4$ in this figure). This is an illustration of the link quality improvement achieved through the multiple antenna transmission.

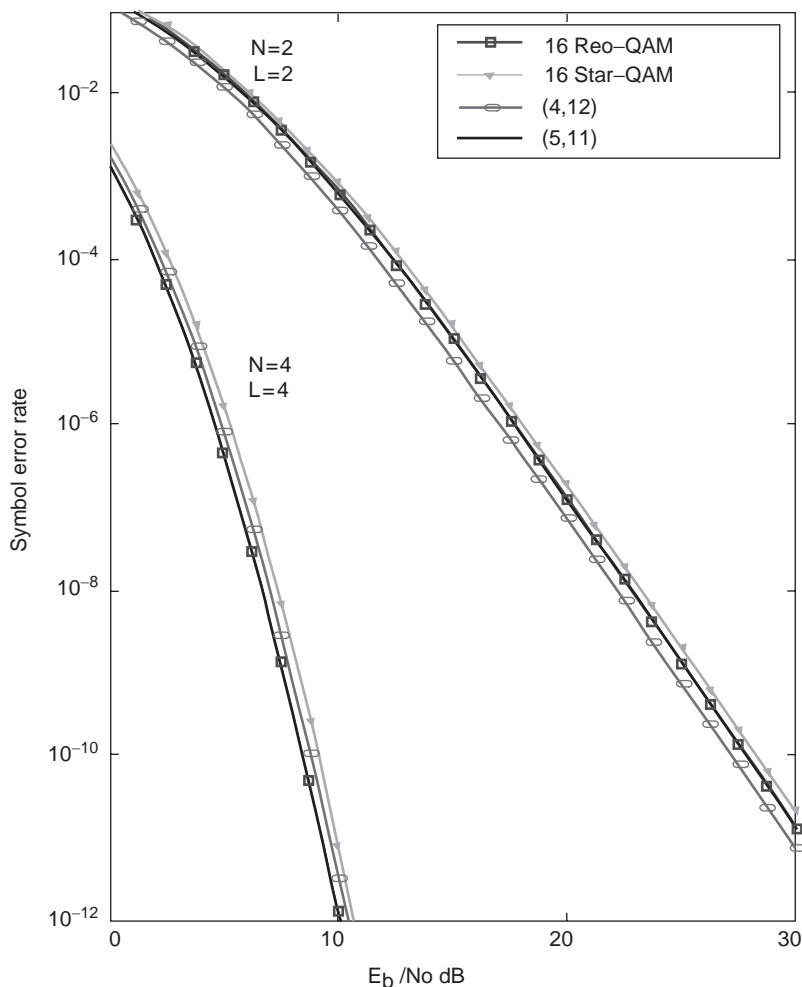


Figure 7. SEP of rectangular and circular 16-QAM signals in MIMO channels. (This figure is available in full color at <http://www.mrw.interscience.wiley.com/erfme>.)

2.2. Spacetime Coding

Spacetime codes make smart use of the multiple antenna system by combining modulation, coding, and diversity transmission in one function and then use the multiple transmit antennas to transmit different codewords simultaneously at each time instant. The system utilizes both coding and diversity gains to realize significant performance improvements (higher capacity) over the single antenna system. The code construction is done in a way to ensure that both the coding and diversity gains at the receiver are maximized. A celebrated pioneer work on spacetime codes [7] presents the details of the system design criteria and code constructions.

Consider a spacetime coding system, with N transmitting and L receiving antennas, over a wireless communication channel illustrated in Fig. 8. At any time instant k , let the information-bearing signals, $d(k)$, be encoded by the spacetime encoder as $N \times 1$ code vector $\mathbf{c}(k) = [c_1(k) \ c_2(k) \ \dots \ c_N(k)]^T$, and each code symbol is transmitted simultaneously from a different antenna. All N transmitted signals have the same transmission period. At the receiver side, signals arriving at the different receive antennas undergo independent fading. The received signal is a linear combination of the transmitted signal and the MIMO channel coefficients h_{ij} , ($i = 1, \dots, N$), ($j = 1, \dots, L$), corrupted by additive noise. The received signal vector at the k th transmission period is therefore given by Eq. (1).

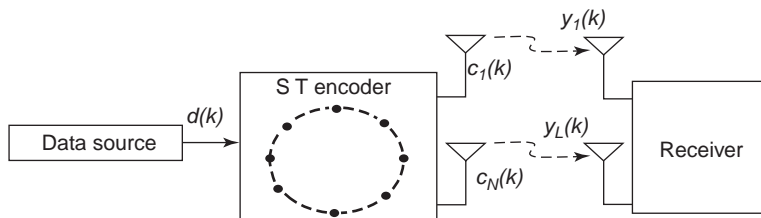


Figure 8. Spacetime coding system.

An appropriate signal processing operation is used to extract an estimate of the information stream from the noisy superposition of the faded version of the N transmitted signals, received by each of the antennas, which is then passed on to the detector. The main techniques proposed for this purpose include and minimum mean square error (MMSE), maximum-likelihood detection (MLD), and singular value decomposition (SVD). While some of these techniques (e.g., MLD) perform MIMO signal processing only at the receiver, others (e.g., SVD) perform MIMO processing both at the transmitter and receiver [36]. Among these detection techniques, MLD is optimum in terms of minimizing the overall error probability [37]. In the following therefore, we focus only on MLD. Assuming that maximum likelihood decoding of the transmitted data $\mathbf{c}(k)$ from the received signal sequences is carried out at the receiver, and assuming that l consecutive code vectors, $\{\mathbf{c}(k)\}_{k=1}^l$, have been transmitted. The maximum likelihood (ML) decoder can be realized using the Viterbi algorithm with the ML metric given, in the form of minimum Euclidian distance, as

$$\begin{aligned} \hat{\mathbf{c}} &= \arg \min_{\{\hat{\mathbf{c}}(1), \hat{\mathbf{c}}(2), \dots, \hat{\mathbf{c}}(l)\}} \|\mathbf{y}(1), \mathbf{y}(2), \dots, \mathbf{y}(l) \\ &\quad - (\hat{\mathbf{H}}(1) \mathbf{c}(1), \hat{\mathbf{H}}(2) \mathbf{c}(2), \dots, \hat{\mathbf{H}}(l) \mathbf{c}(l))\|^2 \quad (12) \\ &= \arg \min_{\{\hat{\mathbf{c}}(1), \hat{\mathbf{c}}(2), \dots, \hat{\mathbf{c}}(l)\}} \sum_{k=1}^l \|\mathbf{y}(k) - \hat{\mathbf{H}}(k) \hat{\mathbf{c}}(k)\|^2 \end{aligned}$$

where $\hat{\mathbf{H}}(k)$ is the MIMO channel estimate at the receiver at time instant k .

2.2.1. Spacetime Trellis Codes. For the case when the underlying code is trellis-coded modulation, an expression for upper bound on the pairwise error probability (PWE) of the resulting spacetime trellis code (STTC) is given [7] as

$$P(\mathbf{c} \rightarrow \hat{\mathbf{c}}) \leq \left(\prod_{i=1}^r \lambda_i \right)^{-L} \cdot \left(\frac{E_s}{4N_0} \right)^{-rL} \quad (13)$$

where r is the rank of the error matrix between the transmitted (true) codeword and the received (possibly erroneous) codeword [7]. $\lambda_i, i = 1, \dots, r$ are the nonzero eigenvalues of this error matrix, while E_s/N_0 is the average signal-to-noise power ratio (SNR). The first term $\delta_r = \prod_{i=1}^r \lambda_i$ represents the coding gain achieved by the spacetime code, and the second term $(E_s/4N_0)^{-rL}$ represents a diversity gain of rL achieved from the use of multiple antennas. Hence, in designing a spacetime trellis code, the rank of the error matrix r should be maximized (thereby maximizing the diversity gain) and at the same time, δ_r should be also maximized (thereby maximizing the coding gain).

An example of a four-state STTC code constructed for 4-PSK signal [7] is shown in Fig. 9. This code is designed for systems with two transmit antennas. The label ij refers to the transition between the states i and j in the trellis, and each symbol pairs in a given row labels the transition out of a given state.

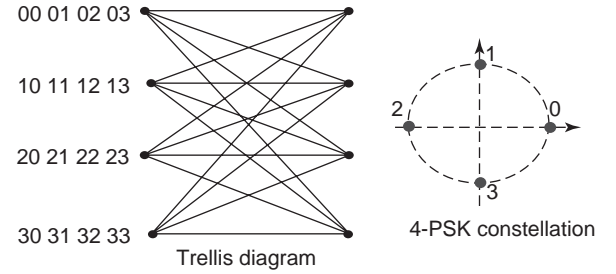


Figure 9. Trellis diagram for four-state spacetime code for 4-PSK signals. (This figure is available in full color at <http://www.mrw.interscience.wiley.com/erfme>.)

2.2.2. Spacetime Block Codes. Alamouti [15] proposed an ingenious spacetime block coding scheme for transmission with two antennas. In this scheme, input symbols are grouped in pairs and transmitted at time instant k , and a transformed version of the symbols is transmitted at time $k + 1$. Let the symbols c_1 and c_2 be transmitted at time k from the first and second antennas, respectively. Then at time $k + 1$, symbol $-c_2^*$ is transmitted from the first antenna and symbol c_1^* is transmitted from the second antenna, where $(\cdot)^*$ denotes the complex conjugate. The received signals at the j th receive antenna are therefore given by

$$\begin{aligned} y_j^1 &= h_{j1}c_1 + h_{j2}c_2 + n_1 \quad j = 1, \dots, L \\ y_j^2 &= -h_{j1}c_2^* + h_{j2}c_1^* + n_2 \quad j = 1, \dots, L \end{aligned} \quad (14)$$

where we have assumed that the channel is fixed for the two transmission periods.

Alamouti's spacetime block codes have been adopted in several wireless standards such as wideband code-division multiple access (W-CDMA) and CDMA 2000 [38]. The code has the following attractive features: (1) it achieves full diversity at full transmission rate for any real or complex signal constellation and (2) the code does not require knowledge of CSI at the transmitter. Third, maximum likelihood decoding of the code involves only linear processing at the receiver, which reduces the decoding complexity significantly. The Alamouti code has been extended to the case of more than two transmit antennas [13] using the theory of orthogonal designs.

2.3. Spatial Multiplexing

Figure 10 illustrates the principle of spatial multiplexing. As shown in the figure, the input (information bearing) bitstream is first demultiplexed into p substreams and each substream is mapped to a predetermined digital modulation [e.g., phase shift keying (PSK) or QAM]. The p substreams are then transmitted simultaneously over the channel using N ($N \geq p$) independent transmit antennas [19]. The same modulation constellation with size Q is used for each substream. Therefore, $\log_2(Q)$ information bits are mapped into one Q -ary symbol. At the receiving end, the signals received by L ($L \geq p$) antennas are processed (using any of the techniques mentioned in Section 2.2) to recover the original bit-stream. Spatial

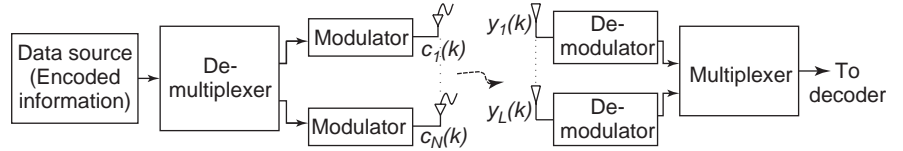


Figure 10. Spatial multiplexing.

multiplexing achieves high data rate through the transmission of parallel bitstreams.

3. RECEIVER SIGNAL PROCESSING FOR MIMO TRANSMISSIONS OVER MOBILE CHANNELS

The combined effect of the features of mobile radio propagation environment (discussed in Section 1.1) leads to the characterization of mobile wireless channels as time-varying fading channels, as well as frequency-selective fading channels. For the time-varying fading problem, the channel strengths may have significant variation within a transmission block (rapid fading) or from one block to another (quasistatic fading). In either case, channel tracking can be employed [39,40] to estimate the amount of attenuation in the wireless link, and this information [or channel state information (CSI)] is then used in the detection of the transmitted signals. The frequency selectivity problem on the other hand, results in the introduction of intersymbol interference (ISI) among successive symbols transmitted over mobile radio channels, causing severe performance degradation unless corrective measure known as *equalization* is employed.

3.1. MIMO Channel Equalization

For MIMO transmission over frequency-selective (mobile radio) channels, the channel output is given by the expression in Eq. (2) and has the Z transform given by

$$\mathbf{y}(z) = \tilde{\mathbf{H}}(z)\mathbf{c}(z) + \mathbf{n}(z) \tag{15}$$

where $\tilde{\mathbf{H}}(z) = \sum_{l=0}^{m-1} \mathbf{H}(k; l)z^{-l}$

The function of an adaptive equalizer employed at the MIMO receiver is to carry out a reverse operation of the frequency-selective MIMO channel actions in Eq. (15) in order to recover the original information bits from the noisy observation $\mathbf{y}(z)$.

If we assume perfect knowledge of the MIMO channel coefficients at the receiver, then the optimum receiver is a maximum-likelihood sequence estimator (MLSE). For transmission over frequency-selective MIMO channel, therefore, the best performance in terms of error rate, can be achieved through trellis equalization of the space-time codes based on MLSE or symbol-by-symbol maximum a posteriori probability (MAP) estimation [41]. However, it is well known that the complexity of these methods is proportional to the number of states of the trellis, which grows exponentially with the product of the channel memory and the number of transmit antennas. The complexity of the algorithm therefore becomes somewhat impractical when the channel memory becomes large and high-order constellations are used. In address-

ing this problem, some suboptimum, reduced-complexity, equalization methods have been developed. In the next section, we review two families of such suboptimum equalizers achieving a good performance-complexity tradeoff, which have been employed in MIMO channels. The first of these is the family of the block linear and Decision-Feedback equalizers, and the second is the family of the list-type equalizers.

3.2. Block Linear and Decision Feedback Equalizers

Block linear and decision feedback equalizers are by nature optimized for block transmission systems [42]; therefore these equalizers are easily adapted for MIMO systems.

3.2.1. Block Linear Equalizers. The expression for the signal estimate at the output of ZF-BLE can be written in the form

$$\hat{\mathbf{d}}_{\text{ZF-BLE}} = \mathbf{d} + \mathfrak{N}\mathbf{n} \tag{16}$$

where \mathbf{d} is the $Nl \times 1$ vector that stacks the transmitted symbols (from the N transmit antennas) during the transmission of a block of length l . The matrix \mathfrak{N} is an amplification factor that represents noise enhancements due to the zero-forcing operation, and \mathbf{n} is the noise vector.

A similar expression for the MMSE-BLE can be written as

$$\hat{\mathbf{d}}_{\text{MMSE-BLE}} = \mathbf{W}\hat{\mathbf{d}}_{\text{ZF-BLE}} \tag{17}$$

where the elements of \mathbf{W} can be seen as coefficients of a Wiener filter. The estimate from an MMSE-BLE can then be interpreted as the output of the ZF-BLE followed by a Wiener filter. The Wiener filter reduces the performance degradation caused by noise enhancement in ZF-BLE. Therefore, the SNR at the output of the MMSE-BLE per symbol is, in general, larger than that of the ZF-BLE.

3.2.2. Block Decision Feedback Equalizers. Figure 11 shows the block diagram of a block decision feedback equalizer employed in a MIMO setup. At any time instant, k , the received signal vector $\mathbf{y}(k)$ is filtered by the equalizer's feedforward filter (FFF), with coefficients $\mathbf{W}(k)$, to obtain the filtered signal vector $\mathbf{y}'(k)$. Previously obtained data estimates are processed through a feedback filter (FBF), with coefficients $\mathbf{B}(k)$, and subtracted from $\mathbf{y}'(k)$. The resultant signals are then fed into threshold detectors from where estimates of the transmitted data $\hat{\mathbf{c}}(k - \Delta)$, are obtained, where Δ is the delay in the equalizer, and $\hat{\mathbf{c}}(k - \Delta)$ corresponds to the input signals at time $k - \Delta$.

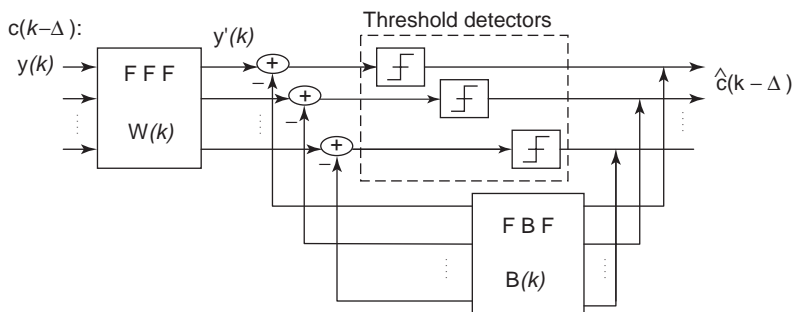


Figure 11. MIMO DFE block diagram.

Similar comparative analysis for the MMSE-BDFE and ZF-BDFE [41] shows that the SNR at the output of MMSE-BDFE is in general larger than the SNR at the output of the counterpart ZF-BDFE. Therefore, both block linear and block decision feedback equalization of MIMO channel based on MMSE criterion will yield better performance than will their counterpart zero-forcing schemes. This conclusion is consistent with what is known for the SISO channel case.

3.3. List-Type Equalizers

The list-type equalizer is another reduced complexity suboptimum equalization method. It employs a state reduction algorithm in the Viterbi or MAP equalizer, using the concept of per survivor processing (PSP) [43], to achieve a reduced complexity. The equalizers consider a reduced number of taps of the channel to construct the trellis, leading to a reduced number of states, and an adaptive equalization of the channel is carried out on the basis of the reduced states. To ensure that the best suboptimum performance is achieved, a receiver filter that concentrates the channel energy on the first few taps chosen for the trellis construction is used. This ensures that the chosen taps have the strongest energy. In the MIMO channel case, this is achieved using a multidimensional whitened matched filter (WMF) as a prefilter for the equalizer.

Comparing the performances of the block equalizers and the prefiltered list-type MAP equalizers in MIMO channel [41], it is observed that the prefiltered list-type MAP equalizer achieves better performance than the block equalizer. However, the list-type MAP equalizer is much more complex to implement. Hence, the regular tradeoff between performance and complexity has to be part of the criteria for selecting any of these structures for MIMO applications.

4. CONCLUSION

This article has presented a survey of the most popular MIMO signal processing techniques used in wireless communications. We have discussed in particular the spatial multiplexing, spacetime code, and MIMO-MRC systems. The capacity increase achieved through the spacetime MIMO transmission is also illustrated and shown to improve dramatically over the conventional wireless communication system as the number of transmit–receive antennas increase. Equalization techniques employed in

MIMO receivers for transmissions over frequency-selective, mobile communication, channels are then reviewed.

Acknowledgments

This work has been supported in part by the Natural Sciences and Engineering Research Council of Canada (NSERC), Communications and Information Technology Ontario (CITO), and the Ontario Premier’s Research Excellence Award (PREA)

BIBLIOGRAPHY

1. N. Kong and L. B. Milstein, Combined average SNR of a generalized diversity selection combining scheme, *Proc. IEEE Int. Conf. Commun.*, June 1998, Vol. 3, pp. 1556–1560.
2. A. I. Sulyman and M. Kousa, Bit error rate performance of a generalized selection diversity combining scheme in Nakagami fading channels, *Proc. IEEE-WCNC2000*, Sept. 2000.
3. M. K. Simon and M.-S. Alouini, Performance analysis of generalized selection combining with threshold test per branch (T-GSC), *IEEE Trans. Vehic. Technol.* **51**(5):1018–1029 (Sept. 2002).
4. A. Wittneben, A new bandwidth efficient transmit antenna modulation diversity scheme for linear digital modulation, *Proc. IEEE ICC '93*, 1993, pp. 1630–1634.
5. S. Al-Semari and T. Fuja, Performance analysis of coherent TCM systems with diversity reception in slow Rayleigh fading, *IEEE Trans. Vehic. Technol.* (Jan. 1999).
6. G. Ungerboeck, Channel coding with multilevel/phase signals, *IEEE Trans. Inform. Theory* **28**:55–67 (Jan. 1982).
7. V. Tarokh, N. Seshadri, and A. R. Calderbank, Space-time codes for high data rate wireless communication: performance criterion and code construction, *IEEE Trans. Inform. Theory* **44**:744–765 (March 1998).
8. A. Wittneben, Base station modulation diversity for digital SIMULCAST, *Proc. IEEE VTC*, May 1993, pp. 505–511.
9. N. Seshadri and J. Winters, Two signaling schemes for improving the error performance of FDD transmission systems using transmit antenna diversity, *Proc. IEEE VTC*, May 1993, pp. 508–511.
10. J. Winters, The diversity gain of transmit diversity in wireless systems in Rayleigh fading, *Proc. ICC/Supercomm*, New Orleans, LA, May 1994, Vol. 2, pp. 1121–1125.
11. V. Tarokh, A. Naguib, N. Seshadri, and A. R. Calderbank, Space-time codes for high data rate wireless communication: performance criteria in the presence of channel estimation errors, mobility and multiple paths, *IEEE Trans. Commun.* (Feb. 1999).

12. V. Tarokh, H. Jafarkhani, and A. R. Calderbank, Space-time block coding for wireless communications: Performance results, *IEEE J. Select. Areas Commun.* **17**:451–459 (March 1999).
13. V. Tarokh, H. Jafarkhani, and A. R. Calderbank, Space-time block codes from orthogonal designs, *IEEE Trans. Inform. Theory* **45**:1456–1467 (July 1999).
14. T. K. Y. Lo, Maximum ratio transmission, *IEEE Trans. Commun.* **47**:1458–1461 (Oct. 1999).
15. S. M. Alamouti, A simple transmit diversity technique for wireless communications, *IEEE J. Select. Areas Commun.* **16**(8):1451–1458 (Oct. 1998).
16. P. W. Wolniansky, G. J. Foschini, G. D. Golden, and R. A. Valenzuela, V-BLAST: An architecture for realizing very high data rates over rich scattering wireless channels, *Proc. ISSSE-98*, Sept. 1998, pp. 295–300.
17. A. Naguib, V. Tarokh, N. Seshadri, and A. R. Calderbank, A space-time coding for high-data-rate wireless communications, *IEEE JSAC*, Oct. 1998.
18. A. Naguib, N. Seshadri, and A. R. Calderbank, Increasing data rate over wireless channels, *IEEE Signal Process. Mag.* **77**–92 (May 2000).
19. H. Sampath and A. J. Paulraj, Joint transmit and receive optimization for high data rate wireless communication using multiple antennas, *Proc. 33rd IEEE Asilomar Conf. Signals, Systems, and Computers*, Oct. 1999, Vol. 1, pp. 215–219.
20. C.-N. Chuah, D. N. C. Tse, J. M. Kahn, and R. A. Valenzuela, Capacity scaling in MIMO wireless systems under correlated fading, *IEEE Trans. Inform. Theory* **48**(3):637–650 (March 2002).
21. S. Catreux, L. J. Greenstein, and V. Erceg, Some results and insights on the performance gains of MIMO systems, *IEEE J. Select. Areas Commun.* **21**(5):839–847 (June 2003).
22. A. Jemmali and A. Kouki, Investigation of MIMO channel correlation and capacity based on partial embedded RF measurements, *Proc. IEEE-CCECE'04*, Niagara Falls, Canada, May 2004, pp. 531–534.
23. G. Levin and S. Loyka, Statistical analysis of a measured MIMO channel, *Proc. IEEE-CCECE'04*, Niagara Falls, Canada, May 2004, pp. 875–878.
24. S. Haykin and M. Moher, *Modern Wireless Communications*, Prentice-Hall 2005.
25. G. D. Durgin, *Space-Time Wireless Channels*, Prentice-Hall, 2003.
26. A. J. Paulraj, R. U. Nabar, and D. Gore, *Introduction to Space-Time Wireless Communications*, Cambridge Univ. Press, 2003.
27. S. N. Diggavi, N. Al-Dhahir, A. Stamoulis, and A. R. Calderbank, Great expectations: The value of spatial diversity in wireless networks, *Proc. IEEE* **92**(2):219–246 (Feb. 2004).
28. A. J. Paulraj, D. A. Gore, R. U. Nabar, and H. Bolcskei, An overview of MIMO systems—a key to Gigabit wireless, *Proc. IEEE* (special issue on Gigabit wireless communications: technologies and challenges) **198**–218 (Feb. 2004).
29. O. Oyman, R. U. Nabar, H. Bolcskei, and A. J. Paulraj, Characterizing the statistical properties of mutual information in MIMO channels, *IEEE Trans. Signal Process.* **51**(11):2784–2795 (Nov. 2003).
30. L. Zheng and D. N. C. Tse, Communication on the grassmann manifold: A geometric approach to the noncoherent multiple antenna channels, *IEEE Trans. Inform. Theory* **48**:359–383 (Feb. 2002).
31. I. E. Telatar, Capacity of multi-antenna Gaussian channels, *Eur. Trans. Telecommun.* **10**(6):585–595 (Nov./Dec. 1999).
32. M. Kang and M.-S. Alouini, Performance analysis of MIMO MRC systems over Rician fading channels, *Proc. IEEE VTC'02*, 2002, Vol. 2, pp. 869–873.
33. V. Tarokh and T. K. Y. Lo, Principal ratio combining for fixed wireless applications when transmitter diversity is employed, *IEEE Commun. Lett.* **2**(8):223–225 (Aug. 1998).
34. P. A. Dighe, R. K. Mallik, and S. S. Jamuar, Analysis of transmit-receive diversity in Rayleigh fading, *IEEE Trans. Commun.* **51**(4):694–703 (April 2003).
35. A. I. Sulyman and M. Ibnkahla, Performance analysis of non-linearly amplified M-QAM signals in MIMO channels, *Proc. IEEE Int. Conf. Acoustics, Speech, and Signal Processing, ICASSP'04*, May 2004.
36. R. Choi and R. Murch, MIMO transmit optimization for wireless communication systems, *Proc. IEEE Int. Workshop Electron. Design, Test, and Applications, (DELTA '02)*, 2002.
37. X. Zhu and R. D. Murch, Performance analysis of maximum likelihood detection in a MIMO antenna system, *IEEE Trans. Commun.* **50**(2) (Feb. 2002).
38. N. Al-Dhahir, Space-time coding and signal processing for broadband wireless communications, in M. Ibnkahla, ed., *Signal Processing for Mobile Communications Handbook*, CRC Press, 2004, Chap. 13.
39. M. Ibnkahla et al., Adaptive signal processing for mobile communication, in R. Dorf, ed., *Electrical Engineering Handbook*, (in press).
40. S. Haykin, Adaptive tracking of linear time-variant systems by extended RLS algorithm, *IEEE Trans. Signal Process.* **45**(5):1118–1128 (May 1997).
41. N. Sellami, I. Fijalkow, and M. Siala, Overview of equalization techniques for MIMO fading channels, in M. Ibnkahla, ed., *Signal Processing for Mobile Communications Handbook*, CRC Press, 2004, Chap. 18.
42. G. Kaleb, Channel equalization for block transmission systems, *IEEE J. Select. Areas Commun.* **13**(1):110–121 (1995).
43. T. Hashimoto, A list-type reduced-constraint generalization of the Viterbi algorithm, *IEEE Trans. Inform. Theory* **IT-33**:866–876 (1987).

MINIATURIZED PACKAGED (EMBEDDED) ANTENNAS FOR PORTABLE WIRELESS DEVICES

M. ALI
University of South Carolina
Columbia, South Carolina

1. INTRODUCTION

With the rapid growth of wireless communications there has been an ever-increasing demand for small, wideband/multiband packaged or embedded antennas for mobile phones, wireless PDAs, pagers, GPS receivers, implantable wireless devices, and RFID tags [1–3]. The application list is not exhaustive and may also include many other scenarios, such as “man-pack” devices for the land-warrior and smart multifunctional wireless device for law enforcement personnel. When an embedded antenna is concerned one thing is common, the antenna is packaged within the housing of the device. In some cases the antenna is

printed directly on the device PCB, its housing, or an onboard chip.

This problem, however, is not very easy to solve. Depending on the specific application, there is always a set of requirements that must be fulfilled before a useful antenna can be designed. These requirements can vary widely from mobile phone application to Bluetooth to GPS. Nevertheless, the key challenges that we need to confront are bandwidth, gain, radiation pattern, polarization, and SAR (specific absorption rate). When an antenna is packaged or embedded within a device it suffers degradation in some or all of these performance characteristics. This happens because the antenna (1) needs to be miniaturized to be accommodated within a device and (2) operates in close proximity to other metallic and/or dielectric objects in its vicinity. Thus a careful evaluation of antenna performance is required. Unfortunately, since the antenna is very platform-dependent, any change in the platform or embedding medium requires full characterization and optimization. Albeit phenomenal progress has been made in electromagnetic analysis using the finite-element method or method of moments (MoM) or the finite-difference time-domain method the results obtained there from can serve as guidelines only. The actual performance predictor is an antenna prototype built and tested in the laboratory. Thus simulations must be conducted to get a broad knowledge and an overall understanding of the antenna design. In circumstances where the simulation model can replicate the exact CAD environment of the wireless device, very realistic results are obtainable. The efficacy of the simulation tools lies in their rapid prediction capabilities, which save a significant amount of time from the concept to production phase of an embedded antenna. Thus modeling and measurement must proceed hand in hand to get a functioning antenna in an embedded environment.

Note that as the development phase of the product progresses more and more variables start to add up. Thus a significant number of measurements need to be conducted to ascertain that performance criteria are met. As a simple example, consider a mobile phone antenna. It starts with a simple model of the antenna on a blank printed circuit board. Then the board gets populated with components, the mechanical components begin to add, the radio starts functioning, the audio works, and so on. Thus the antenna needs to be measured and tuned accordingly in free space, in the presence of a phantom in various talk positions, and for SAR every step of the way.

2. ANTENNAS FOR MOBILE PHONES

Before discussing antennas for mobile phones, it is worthwhile to mention the frequency bands of interest. For instance, for the AMPS (Advanced Mobile Phone Systems) system the frequency bands are 824–859 MHz for transmit (Tx) and 869–894 MHz (Rx) for receive (see Table 1). From an antenna design perspective, the two frequency bands are fairly close to each other. Thus usually a single antenna is designed to support the entire 824–894-MHz band. Respective transmit and receive frequency bands for the GSM, DCS, and PCS systems are listed in Table 1 [4].

Table 1. Frequency Bands of Different Mobile Telephone Systems

System	Transmit Frequency Band (Tx) (MHz)	Receive Frequency Band (Rx) (MHz)	Antenna Operational Band (MHz)
AMPS	824–859	869–894	824–894
GSM	880–915	925–960	880–960
DCS	1,710–1,785	1,805–1,880	1,710–1,880
PCS/GSM 1900	1,850–1,910	1,930–1,990	1,850–1,990

Lately almost all phones are at least dual-band (one low-frequency band and the other high-frequency band). Interest is growing to develop triple or quad-band phones also which will enable a user to use the same phone in different geographic locations with different air interface standards. One example is a dual-mode AMPS/GSM phone that can be easily triple band. Clearly it is greatly desirable to support all three bands by just one antenna. Thus there is demand for triple- and quad-band antennas.

A mobile phone antenna has to satisfy various performance and regulatory requirements. Among these are bandwidth, gain, radiation pattern, and SAR (specific absorption rate). The antenna must have good VSWR bandwidth (usually within a maximum VSWR of 2.5–1). Even though a VSWR limit of 2–1 is preferred, it is difficult to achieve that with a small embedded antenna. The antenna must also have reasonable peak and average gain in free space and in talk position. The gain in the talk position is extremely critical to ensure proper operation. The peak gain provides a good basis point to determine the EIRP (effective isotropic radiated power). While there are near-field chambers to measure complete three-dimensional patterns and the antenna efficiency thereof, a generally acceptable representation is obtainable by measuring the principal plane cuts. If average gain data is required it can be obtained from the total three-dimensional field distribution. The amount of head blockage (pattern shadowed by or energy absorbed by the user head) varies from antenna to antenna and from phone to phone. Thus proper electromagnetic modeling or measurement is necessary to predict the antenna average gain for each design. Antenna gain in talk position is generally measured with the aid of a phantom head consisting of brain simulating fluid.

After the phone is manufactured, radiated live tests are conducted and EIRP and receiver sensitivity are measured at different channels to obtain a complete picture of the phone performance. This is done before the product and test data are sent to the respective regulatory agencies for compliance. In the United States the Federal Communications Commission (FCC) has a set of requirements that must be met before a mobile phone can be sold in the market. These include the EIRP, out-of-band emission, and most importantly, SAR (specific absorption rate).

2.1. External Antennas

Until around 2000 most mobile phone antennas were external. In the earlier days end-fed sleeve dipoles were used

to achieve a figure-eight radiation pattern [1]. Such patterns are most common with half-wave dipole antennas. Albeit a dipole antenna works better than a monopole (ground plane independent and suffers from less head blockage) its larger size, and the requirement for a balun (when coaxial line feed is used) forced design engineers to explore and utilize the monopole geometry. In the latter case the cellular phone PCB (printed-circuit board) along with its housing (if metallic) acts as the monopole ground plane (counterpoise).

For example, at 900 MHz a resonant thin-wire monopole antenna should be about 78 mm long. This length will vary to some extent based on the wire radius and the position of the antenna with respect to the device housing. Since a conventional monopole operates on a large ground plane (several wavelengths in diameter for a circular ground plane) its radiation pattern is restricted to the upper hemisphere only with the peak of the beam directed toward the horizon. The directivity in such a case is 5.1 dBi, which is 3 dB higher than the directivity of a half-wave dipole [5]. Such a large ground plane is completely impractical for a mobile phone. Because the mobile phone ground plane is much smaller, there is a significant amount of current flow on it and the ground plane generally dominates the radiation pattern. If a phone measures $110 \times 40 \times 25$ mm, the 78-mm-long antenna and the phone housing ensemble represents an asymmetric dipole where the longer and wider ground plane dominates over the small monopole antenna. Thus the radiation pattern has a butterfly shape and is directed to Earth for a vertically oriented phone [6]. The maximum field strength is not directed toward the horizon.

External antennas have also evolved a great deal over the years primarily due to the need for miniaturization. Engineers have focused on reducing the antenna size by inductive loading. This is achieved either by employing a helical, meander, or zigzag geometry. Such an antenna can, in general, have a three-dimensional shape. In case of a meander or zigzag configuration it can also be planar. Examples of small helical or meander stub antennas as small as 35–40 mm are everywhere. Some phones come with a retractable geometry where ordinarily the antenna is a small stub which when extended can be much longer in size. As apparent a small stub will be more susceptible to performance degradation when placed close to a user's head than a 78-mm-long monopole antenna. The smaller stub is simply shadowed much more than a longer antenna. However, experience has shown that a small stub still provides reasonable performance for most cases. For dual- or triple-band operation branches are created to excite separate current flow paths. Usually the branch having a longer current flow path is responsible for the low-frequency band of operation while the shorter current flow path is responsible for the high-frequency band of operation.

2.2. Packaged (Embedded) Planar Inverted-F Antennas

2.2.1. Background. There has been a surge of interest in planar inverted-F antennas (PIFAs) for mobile phone applications [7–19]. Such antennas are smaller than

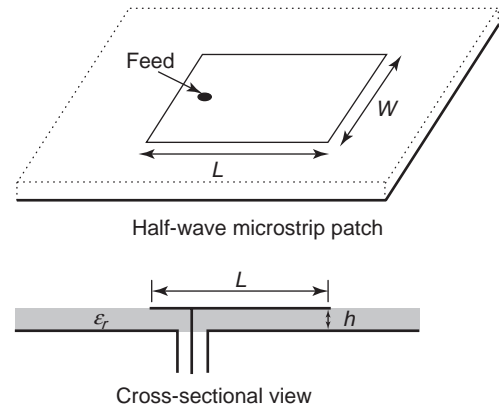


Figure 1. Half-wave microstrip patch.

resonant half-wavelength-long microstrip patches and can be easily placed internally within the housing of a mobile phone. For mobile phone applications the PIFA is usually placed under the back cover of the phone right above the battery line.

The PIFA evolved from a shorted quarter-wave microstrip patch antenna. A conventional microstrip patch is a half-wavelength (0.5λ) long (guided wavelength), including the edge effects and dielectric loading (see Fig. 1). A quarter-wave patch has a short circuit along one of its edges (Fig. 2). The short circuit is positioned along one of the patch edge and has a width of W and depth of h as indicated in Fig. 2. Thus the length L determines the operating frequency (0.25λ minus the effect of dielectric and the edge effect).

In contrast, a PIFA (see Fig. 3) consists of a shorting pin instead of a large plate as it is for a quarter-wave patch. The shorting pin diameter can be the same as the probe feed or can be different. Since only one shorting pin is present the antenna resonant length is approximately determined by $L + W$, which is about a quarter-wavelength ($\sim 0.25\lambda$) at the operating frequency. However, for mobile phone applications the positioning of the PIFA is generally at one of the edges of the PCB for convenience and better utilization of space. The PIFA performance is determined largely by the antenna parameters L, W, h and the spacing between the feed and shorting pin S . The size of the PCB also plays a dominant role in antenna performance, particularly at the low-900-MHz frequency band. As an example, if $L = 50$ mm, $W = 23$ mm, $h = 6$ mm, and the feed–shorting pin spacing is 6 mm, the PIFA will operate at 890 MHz with a bandwidth of 100 MHz within 2.5–1 VSWR. Ground-plane size is 110×50 mm.

In designing a PIFA the primary challenge is to achieve the necessary operating bandwidth, which requires that the PIFA height be about 8–12 mm from the ground plane. This large antenna height makes the phone thicker even

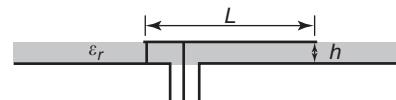


Figure 2. Quarter-wave microstrip patch.

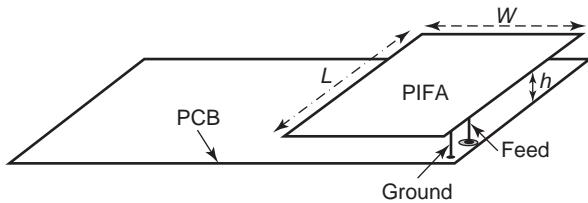


Figure 3. PIFA on a mobile phone PCB.

though the battery is very thin. It will be greatly advantageous if PIFAs with much smaller heights can be designed. However, bandwidth becomes extremely narrow as antenna height is reduced.

It has been reported [20–22] that the bandwidth of a PIFA also depends on the size of the ground plane. For instance, for optimal bandwidth in the 900-MHz band the combined dimensions of the length and width of the ground plane should be 0.5λ [21]. Ground planes that are smaller than that provide much narrower bandwidth. As an example, a PIFA ($h = 4$ mm) on a 90×35 mm ground plane has 2.5% bandwidth while that on a 130×35 mm ground plane has 9.5% bandwidth. Conversely, it can be inferred that for a fixed bandwidth, a much thinner antenna can be designed if a larger ground plane is utilized.

Based on this concept, a slotted meandered ground plane was proposed in [16] that can effectively reduce the heights of PIFAs by more than 50%. The meander-line configuration proposed in [16] can be viewed as a slow-wave structure where the phase velocity of the propagating wave is smaller than the velocity of light. This makes a slotted meandered ground plane appear electrically longer, even though its physical size is unchanged, and hence helps achieve much thinner PIFA design.

2.2.2. Dual-band PIFA on Conventional and Modified Ground Planes. An example of a dual-band PIFA is shown in Fig. 4. The antenna consists of two radiating elements joined near the feedpoint. The larger element has a longer current flow path from the feed and hence is responsible for low band while the smaller element, which is close to the feed, is responsible for the high band. However, the two elements are not completely independent from each other as it pertains to overall performance characteristics. Both elements are at a height h from the PCB and the

feed–shorting pin (ground) spacing is s . All antenna parameters can be adjusted to vary the resonant frequency, bandwidth, and pattern. Typically, a design will start with a full-wave three-dimensional electromagnetic model development using the method of moments (MoM) or finite-element method (FEM), or finite-difference time-domain (FDTD) method. Concurrently or afterward antenna prototypes must be developed and tested. The prototype development and testing continues for each phase of the phone development and each degree of complexity and sophistication in the phone may require the engineer to evaluate and redesign the antenna over time.

As mentioned earlier, the typical dual-band PIFA shown in Fig. 4 depends heavily on the antenna height from the ground plane. Larger heights are usually required to satisfy the bandwidth requirements. To alleviate this problem, an alternative scheme has been proposed [16]. This scheme is shown in Fig. 5. Using this slotted meandered ground plane, PIFA heights can be reduced by more than 50%. The meanderline configuration proposed in Ref. 16 can be viewed as a slow-wave structure where the phase velocity of the propagating wave is smaller than the velocity of light. This makes a slotted meandered ground plane appear electrically longer, even though its physical size is unchanged, and hence helps achieve much thinner PIFA design.

Figure 6 shows the computed and measured VSWR data for the dual-band designs. As apparent, a significant improvement in bandwidth can be achieved with the proposed new ground plane for both the low- and high-frequency bands. In the low-frequency band, computed bandwidth for antennas on conventional and modified ground planes are 2.1% and 7.8%, respectively. Measured bandwidth for the PIFA on the modified ground plane is 7.6%.

In the high-frequency band, bandwidth of antennas on conventional and modified ground planes are 3.1% and 8.8%, respectively, whereas measured bandwidth on the modified ground plane is 7.1%.

2.3. Packaged (Embedded) Monopole-Type Antennas

Apart from PIFAs monopole-type radiators are also of interest for embedded applications. In that case the antenna can be considered as a volume lying at a height adjacent to

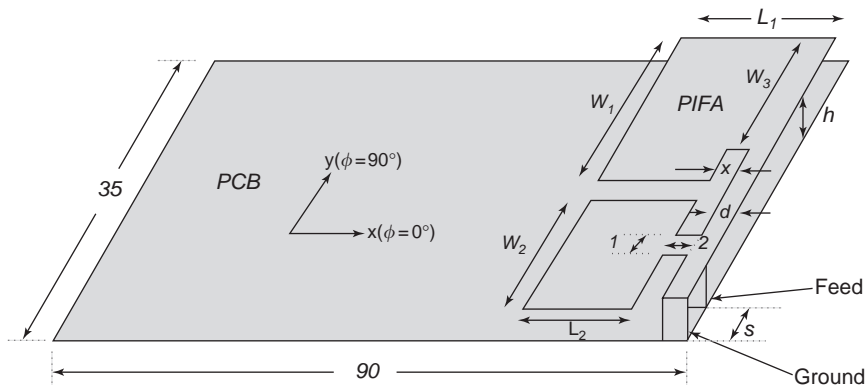
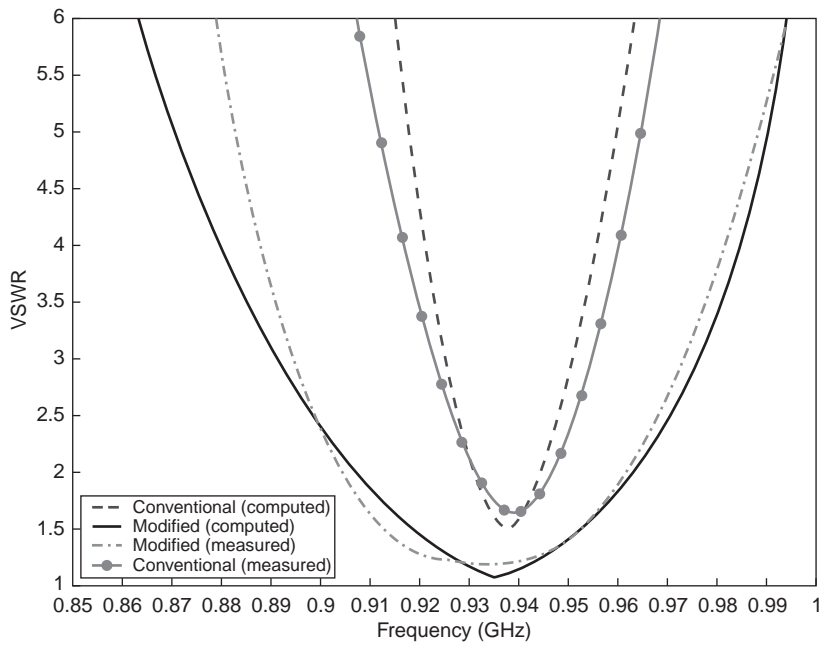
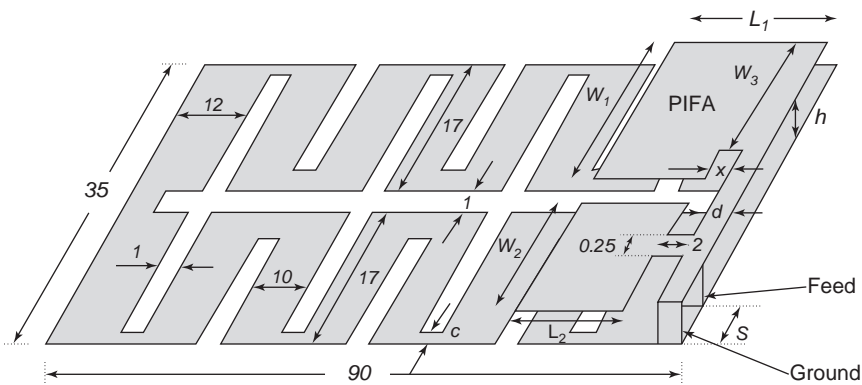
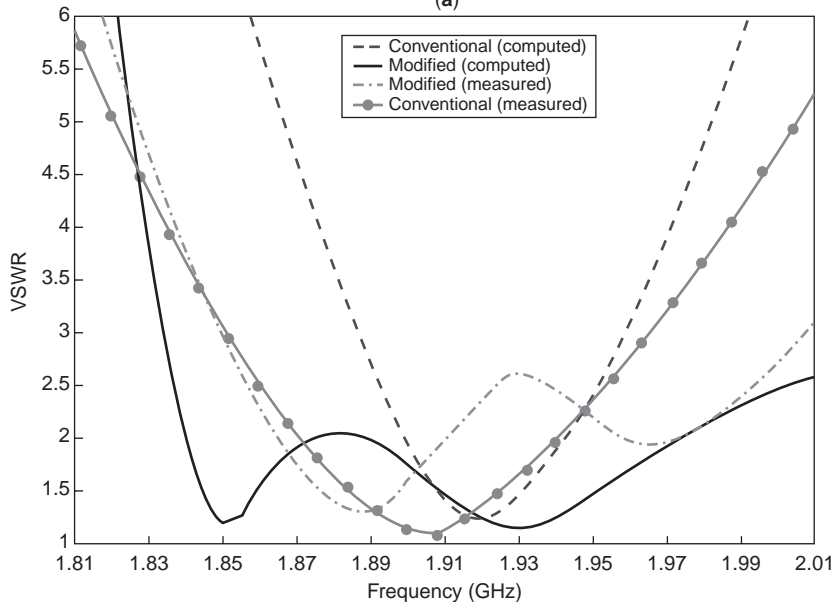


Figure 4. Dual-band PIFA on a conventional PCB. [© 2004 IEEE. Reprinted, with permission, from M. F. Abedin and M. Ali, Modifying the ground plane and its effect on planar inverted-F antennas (PIFAs) for mobile phone handsets, *IEEE Anten. Wireless Propag. Lett.* 2(15):226–229 (2003).]

Figure 5. Dual-band PIFA on a meandered PCB. [© 2004 IEEE. Reprinted, with permission, from M. F. Abedin and M. Ali, Modifying the ground plane and its effect on planar inverted-F antennas (PIFAs) for mobile phone handsets, *IEEE Anten. Wireless Propag. Lett.* 2(15):226–229 (2003).]



(a)



(b)

Figure 6. VSWR characteristics of dual-band PIFAs. [© 2004 IEEE. Reprinted, with permission, from M. F. Abedin and M. Ali, Modifying the ground plane and its effect on planar inverted-F antennas (PIFAs) for mobile phone handsets, *IEEE Anten. Wireless Propag. Lett.* 2(15):226–229 (2003).] (This figure is available in full color at <http://www.mrw.interscience.wiley.com/erfme>.)

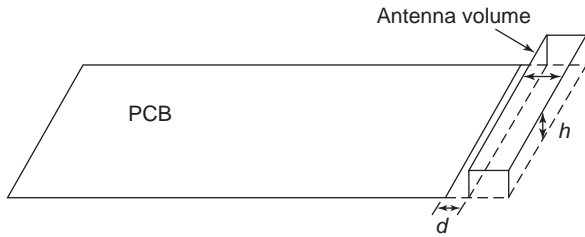


Figure 7. A monopole-type embedded antenna.

the ground plane. In general there cannot be any metal below the antenna. In addition, there should be additional clearance area kept in between the antenna and the ground plane (d in Fig. 7). The antenna should have a specific height h from the ground plane.

By developing antenna geometries of various different shapes and sizes, operation in single or multiple frequency bands can be achieved. Such an antenna has been described in [23,24], consisting of a driven meanderline element and two parasitic coupled elements. The geometric configuration, size, and proximity of the driven and parasitic elements help materialize the desired multiband operation. The complete antenna assembly is internal to the handset. The antenna can be tuned to operate in either the (1) 824–894-, 880–960-, and 1850–1990-MHz bands or (2) 824–894-, 880–960-, and 1710–1880-MHz bands. The size of the antenna is $50 \times 10 \times 6$ mm (3 cm^3) or less.

The geometry of the antenna and its associated printed-circuit board (PCB) is shown in Fig. 8. As can be seen, there are two metal layers. The bottom layer (layer 2) consists of a PCB and two parasitic metallic strips. The meanderline element is on the top layer at a height h from the PCB. The antenna volume is $50 \times 10 \times h$ mm. The distance d is a small separation between one of the parasite

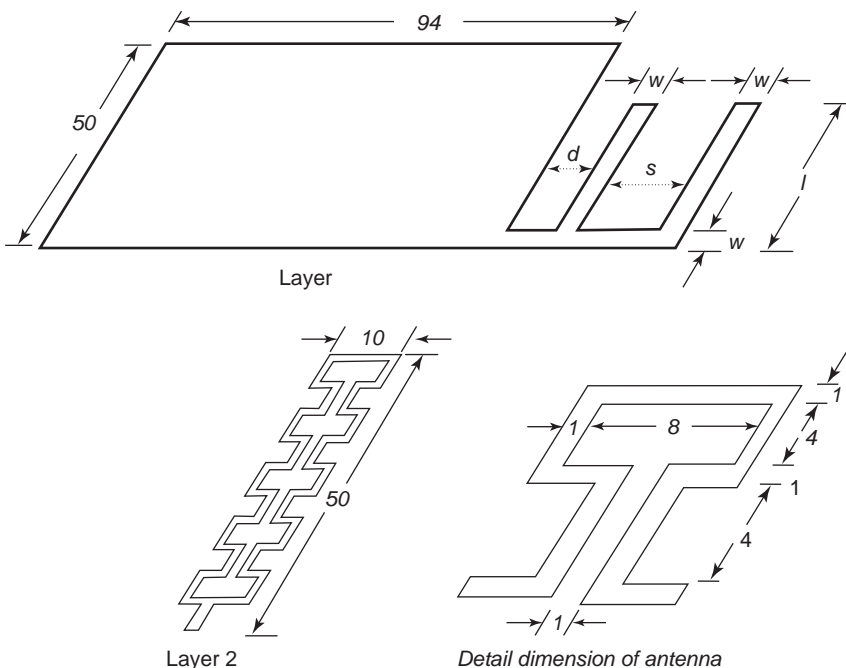


Figure 8. Antenna and PCB geometry with associated parameters (dimensions in mm). [© 2004 IEEE. Reprinted, with permission, from M. Ali, G. J. Hayes, H.-S. Hwang, and R. A. Sadler, Design of a multi-band internal antenna for third generation mobile phone handsets, *IEEE Trans. Anten. Propag.* **51**(7):1452–1461 (July 2003).]

and the PCB that can be minimized when PCB space is critical. The parasites are directly connected to the PCB ground. The antenna is on the upper layer at a height h from the PCB. The antenna is fed using a connector pin from a RF signal pad on the PCB (not shown).

The double-meander geometry for the antenna has been chosen for two reasons: (1) to shorten the length of the antenna and make it the same size as the width of the PCB (50 mm) and (2) to achieve wideband characteristics [25]. The length of the antenna can be further reduced (current length = 50 mm) by increasing the width (antenna width = 10 mm). Note that the length of a resonant quarter-wave monopole operating at 900 MHz is about 78 mm. The double meandering reduces the antenna length to 50 mm, so that it can be enclosed within the device housing.

Computed VSWR as function of antenna height h is shown in Fig. 9, where $l = 26.5$ mm, $S = 6$ mm, $d = 4$ mm, and $w = 2$ mm. It is apparent that the antenna has two resonances at around 900 and 1920 MHz. The first resonance is due to the meander antenna, while the second is due to the parasites attached to the PCB [25,26]. The antenna VSWR changes as h varies, which has two effects: (1) a shift in the resonance frequency (as h is reduced, the resonant frequencies move higher as expected) and (2) the overall level of the minimum VSWR. It is also clear that for $h = 6$ mm, the antenna is well suited for triple-band operation. In the low-band the bandwidth is 250 MHz (27.8%) within a VSWR of 2.5–1. This is far greater than the required bandwidth for AMPS 800 and GSM 900 combined (15.25%). In the high-band the antenna bandwidth is 9.4%. The bandwidth required for TDMA/GSM 1900 is 1850–1990 MHz or 7.3%. For practical purposes VSWR of 2.5–1 as an upper limit has been generally found to be acceptable for mobile handsets, which creates only ~ 0.4 dB of loss as the VSWR changes from 2–1 to 2.5–1.

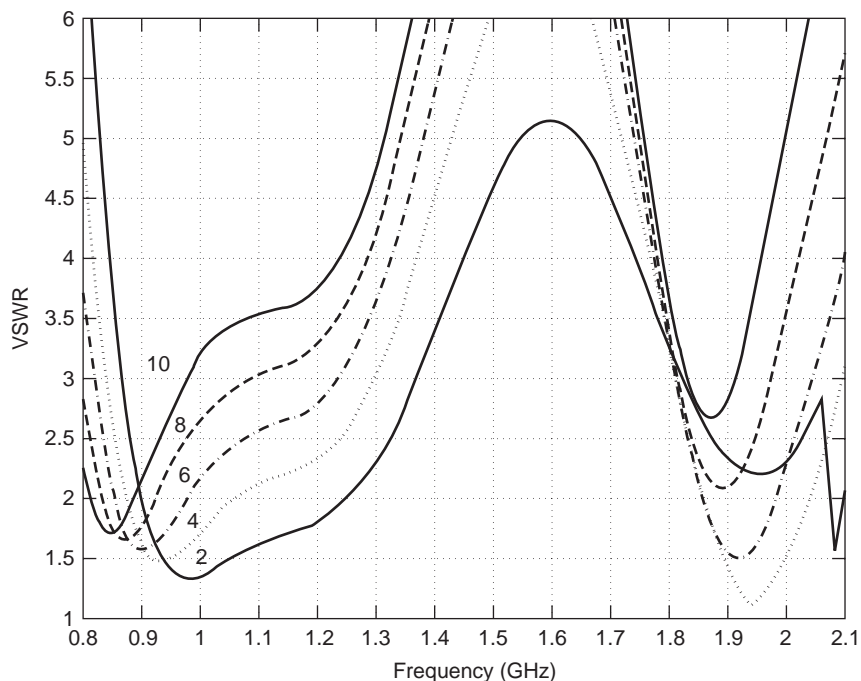


Figure 9. Computed VSWR versus frequency with antenna height h (mm) as parameter $d = 4$ mm, $l = 26.5$ mm. [© 2004 IEEE. Reprinted, with permission, from M. Ali, G. J. Hayes, H.-S. Hwang, and R. A. Sadler, Design of a multi-band internal antenna for third generation mobile phone handsets, *IEEE Trans. Anten. Propag.* **51**(7):1452–1461 (July 2003).]

A prototype antenna was fabricated and tested (see Fig. 10). Computed and measured VSWR data are compared in Fig. 11. The resonant frequencies of the antenna for both the computed and measured cases are about the same. The measured bandwidths in each band (low and high) are also in good agreement with the computed bandwidths within 2.5–1 VSWR. It is clear from Fig. 11 that the antenna operates in the AMPS 800 and GSM 900 band within 2–1 VSWR and the GSM 1900 band within VSWR of 2.3–1. Antenna radiation patterns and gain were measured with reference to two standard gain antennas (the gain values of which were known from the manufacturer's

datasheet). A logperiodic dipole antenna and a rectangular horn antenna were used for the 900 and 1900 MHz bands, respectively. Measured gain for the two principal plane patterns are listed in Table 2. The free-space peak gain at 900 MHz is between 0 and -0.5 dBi, while that at 1900 MHz is between 2.3 and 2.5 dBi. This is expected since the antenna is more directional in the high band.

Measured normalized radiation patterns for the proposed antenna are shown in Fig. 12. The azimuth (xy -plane) patterns at 900 and 1900 MHz are shown in Figs. 12a and 12b. At 900 MHz the vertical component is the dominant one and its variation is nearly uniform. The front-to-back ratio is about 3 dB. At 1900 MHz the vertical field component is fairly directional, front-to-back ratio is about 8 dB. Although the vertical component is not uniform, fairly good angular coverage can still be obtained when both vertical and horizontal components are combined.

The angular region where coverage is between -8 and -10 dB is limited between the angular region of 60 – 120° . This region will be blocked by the operator head. The directionality in the high band can be considered as an advantage since less energy is being deposited in the operator head. Also to note is the significance of total field rather than just one component. In a mobile environment polarization purity is absent. Thus when both components exist and are comparable they need to be combined to get the total field.

3. ANTENNAS FOR BLUETOOTH/WLAN APPLICATIONS

Bluetooth [27] is a consortium pioneered by Ericsson in the late 1990s and later on adopted by a large number of companies. This is an air interface standard proposed to support short-distance communication between devices,

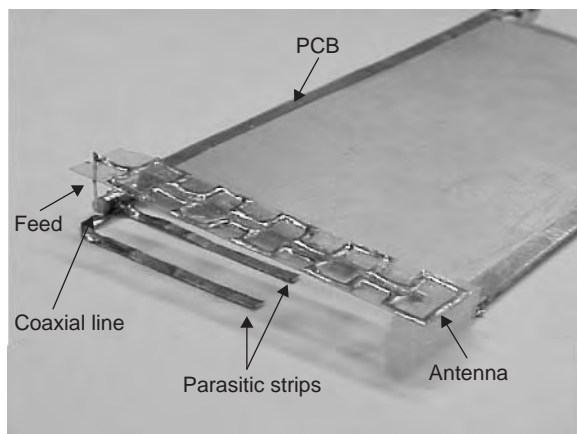


Figure 10. Laboratory prototype of the proposed antenna. The antenna is placed on a thin transparency film to show all parameters in one picture. In actual measurement a foam ($\epsilon_r \approx 1.0$) substrate 6 mm thick was used to support the antenna. [© 2004 IEEE. Reprinted, with permission, from M. Ali, G. J. Hayes, H.-S. Hwang, and R. A. Sadler, Design of a multi-band internal antenna for third generation mobile phone handsets, *IEEE Trans. Anten. Propag.* **51**(7):1452–1461 (July 2003).]

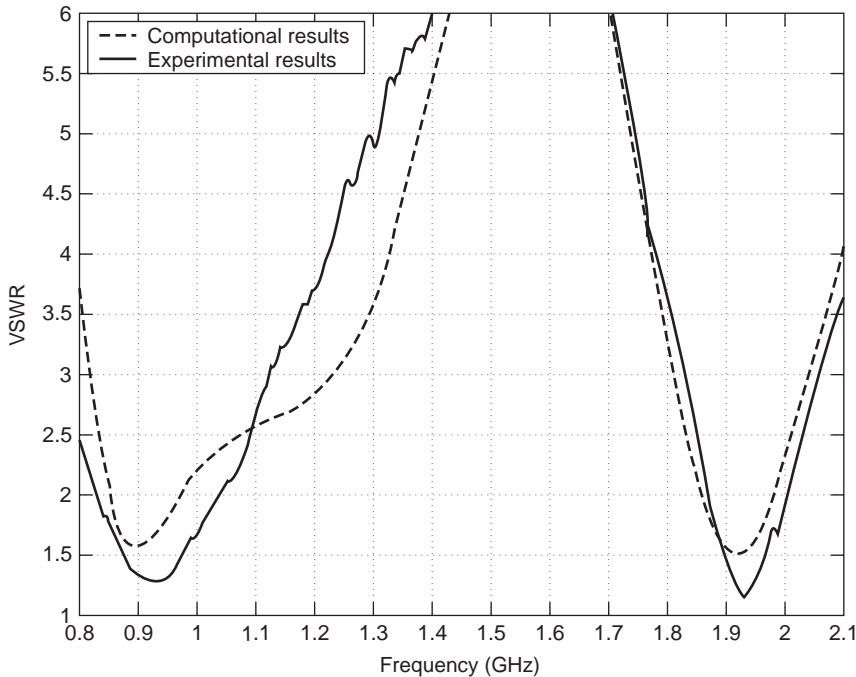


Figure 11. Computed and measured VSWR versus frequency; $d = 4$ mm, $s = 6$ mm, and $l = 26.5$ mm. [© 2004 IEEE. Reprinted, with permission, from M. Ali, G. J. Hayes, H.-S. Hwang, and R.A. Sadler, Design of a multi-band internal antenna for third generation mobile phone handsets, *IEEE Trans. Anten. Propag.* **51**(7):1452–1461 (July 2003).]

such as mobile phones, laptops, desktops, and PDAs. The frequency band of operation in the United States is 2.4–2.485 GHz. This band also coincides with the IEEE 802.11b standard. For more detailed information on Bluetooth, please see Ref. 27. Typically the transmitter has 0 dBm of output power, which can provide a link of up to 10 m, which can be extended to up to 100 m by increasing the output power to 20 dBm. In addition to Bluetooth, there are the WLAN protocols based on several IEEE standards, such as the IEEE 802.11a,b,e,g. There is also Hyperlan in Europe. For high-speed directional WLAN links, one must resort to directional high-gain antennas, which are not practical for embedding within the device. Thus most if not all embedded Bluetooth and WLAN antennas are essentially nondirectional.

3.1. Surface Mount PIFAs

The most popular among embedded antennas for these types of applications is the surface mount PIFA as depicted in Fig. 13. This antenna is essentially a planar inverted-F antenna (PIFA) fabricated on a dielectric

Table 2. Measured Peak Gain Data for Proposed Antenna (Free-Space) at 5.25 and 5.78 GHz^a

Frequency (GHz)	Peak Gain (dBi), yz Plane	Peak Gain (dBi), xy Plane
5.25	1.8 at $\theta = 0^\circ$	-0.5 at $\theta = 210^\circ$
5.78	0.8 dBi at $\theta = 140^\circ$	0.6 dBi at $\theta = 190^\circ$

^aFor pattern characteristics and beam peak locations for yz and xy planes, see Fig. 6.

Source: © 2004 IEEE. Reprinted, with permission, from M. Ali, T. Sittironnarit, H.-S. Hwang, R. A. Sadler, and G. J. Hayes, Wideband/dual-band packaged antenna for 5–6 GHz WLAN application, *IEEE Trans. Anten. Propag.* **52**(2):610–615 (Feb. 2004).

substrate, such as FR4. Typical antenna size can be about $25 \times 4 \times 4$ mm (length, width, height). As indicated, the antenna has a feed and shorting pin that are connected to the respective pads on the PCB when surface-mounted. The antenna size can be further reduced by either modifying the geometry or using higher dielectric constant substrates (ceramics). Geometry modification usually occurs in the form of employing a meanderline configuration. This can be utilized either on the top surface or on the top as well as the side surfaces. Whether it is geometry modification or high dielectric substrate antenna size reduction will result in bandwidth and gain degradation. Thus clearly one must focus on the required bandwidth (e.g., for Bluetooth it is 2.4–2.485 GHz). Once a surface mount PIFA is fabricated it must be embedded within the device PCB and housing and its characteristics evaluated. Since in most circumstances the PIFA has to reside on the same PCB as the mobile phone antenna adequate isolation between them must be ensured (typically 10 dB or better). Usually this is achieved by employing spatial separation between the two antennas.

3.2. Integrated IFAs

3.2.1. Board-Mounted IFA. As indicated, surface mount PIFAs are fabricated separately from the wireless device PCB and hence they need to be assembled on the PCB later on. After the placement of the antenna its characteristics is then evaluated and if performance deficiency is noted the design is changed accordingly. A superior and alternative solution was proposed by Ali et al. [11,15]. In their proposal the Bluetooth/WLAN antenna is an integrated inverted-F antenna (IFA) rather than a PIFA. The IFA is directly printed on the wireless device PCB, and hence no assembly is required. Testing is conducted as soon as the board is released. The antenna requires that

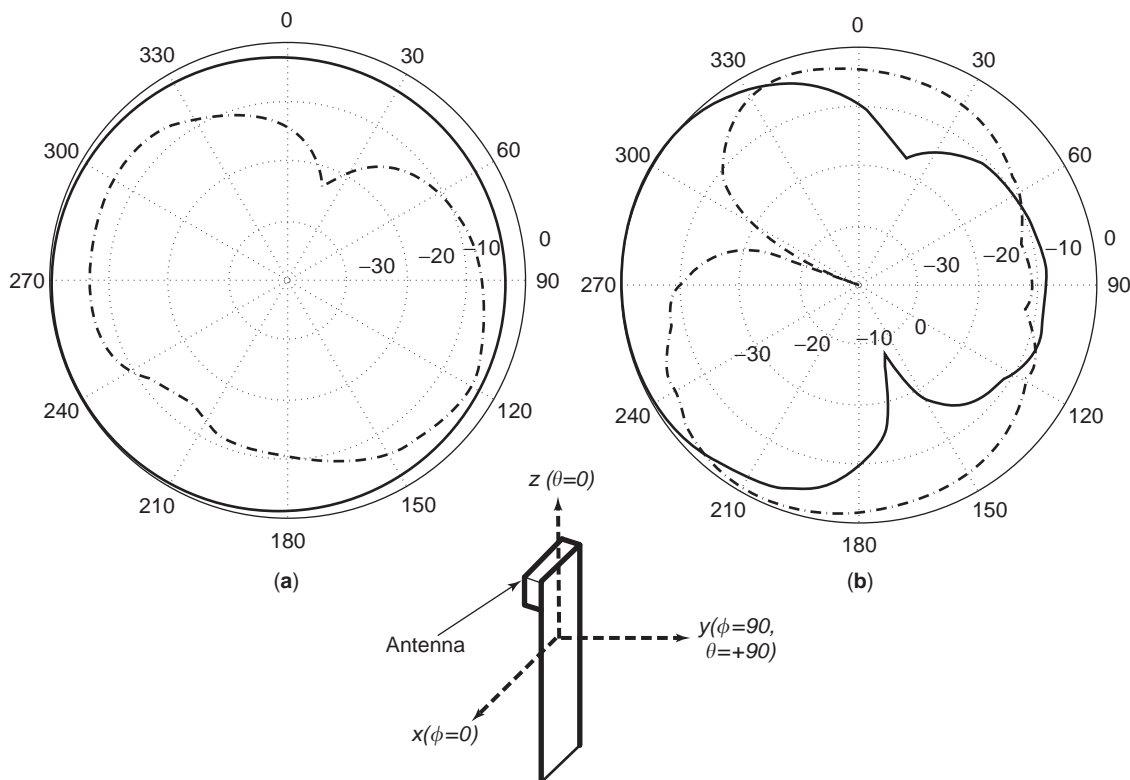


Figure 12. Measured normalized azimuth plane patterns: (a) xy plane (900 MHz); (b) xy plane (1900 MHz). Solid line—vertical component; dashed line—horizontal component; $d = 4$ mm, $s = 6$ mm, and $l = 26.5$ mm. [© 2004 IEEE. Reprinted, with permission, from M. Ali, G. J. Hayes, H.-S. Hwang, and R. A. Sadler, Design of a multi-band internal antenna for third generation mobile phone handsets, *IEEE Trans. Anten. Propag.* **51**(7):1452–1461 (July 2003).]

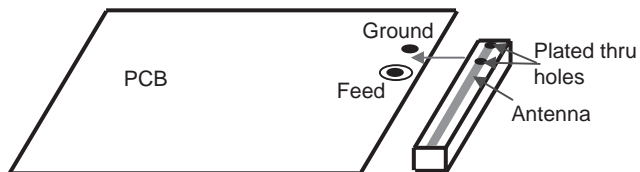


Figure 13. Surface-mount PIFA.

there be an opening on both sides of the PCB so that it can radiate (see Fig. 14). The antenna is directly printed on the substrate material. In Fig. 14, dielectric material has been shown as removed from the region to help visualize the antenna. In reality, dielectric material will be present

and the antenna will be printed on it. Note that the antenna consists of a trace, a feed (that brings the signal through a transmission line, usually a microstrip or strip-line), a via (through hole), and a shorting pin just adjacent to the feed. The transmission line and via are not shown in the figure. In the window where the antenna is located there is no metal on the top or bottom part of the PCB except the antenna, its feed, and the shorting pin. In addition, when the PCB is placed inside a device housing, there cannot be any metal shadowing the antenna.

In Fig. 15 measured VSWR is plotted against the frequency response for the proposed antenna. Note that the antenna works under 2–1 VSWR throughout the entire Bluetooth band. Finally, we show measured elevation

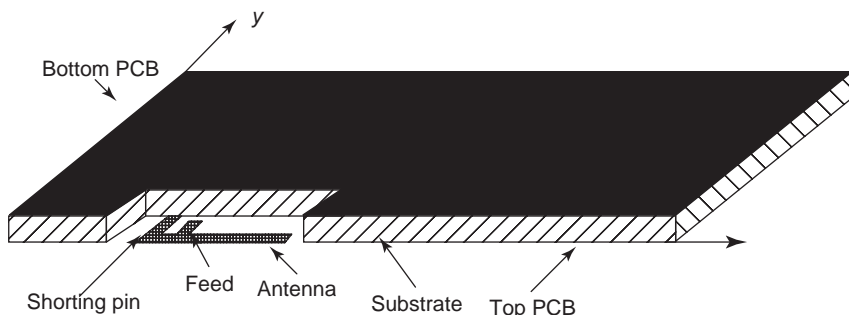


Figure 14. Integrated inverted-F antenna (IFA) [15].

plane pattern data for a typical Bluetooth PIFA on a PC board (Fig. 15). For comparison the pattern of a half-wave dipole on a PC board is also shown. The dipole is twice as long as the PIFA. Note that the peak gain of the PIFA is slightly smaller. The PIFA pattern is much broader and does not have sharp nulls as the dipole. Patterns in other orthogonal planes also show comparable performance.

3.2.2. Flexible Film-Type Antenna. Ali et al. [14] presented a small internal inverted-F antenna printed on the

inside surface of the stylus holder of a PDA (Fig. 16). The antenna can be printed on a flexible film substrate and bonded to the plastic with an adhesive. The proposed antenna operated with or without the stylus considering that the stylus and the stylus holder both were made of plastic material.

Input impedance data for the proposed antenna with and without a dielectric insert are shown in Fig. 17. It is evident that the impedance locus for each case is very close to the center of the Smith chart, especially within the

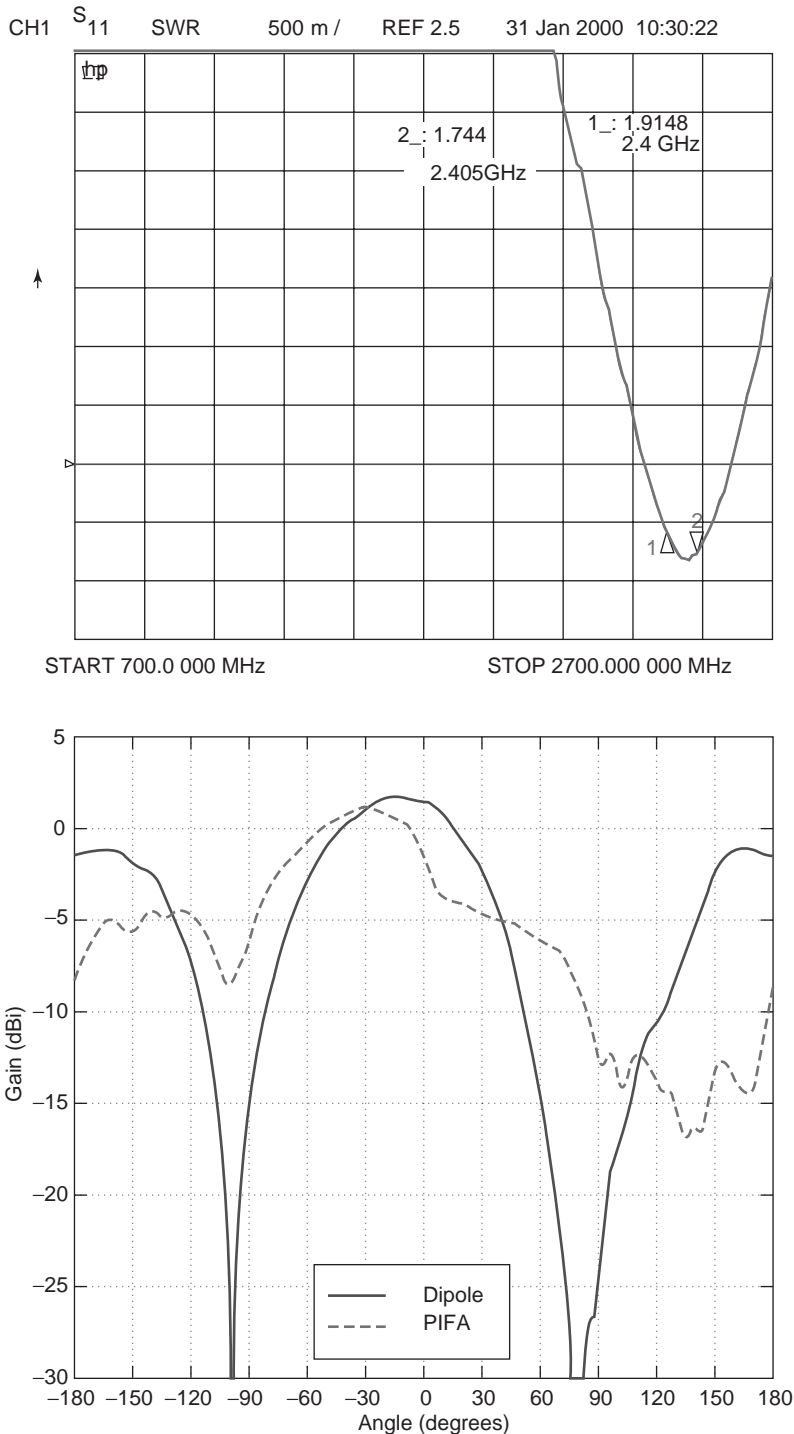


Figure 15. Measured VSWR and radiation patterns [15].

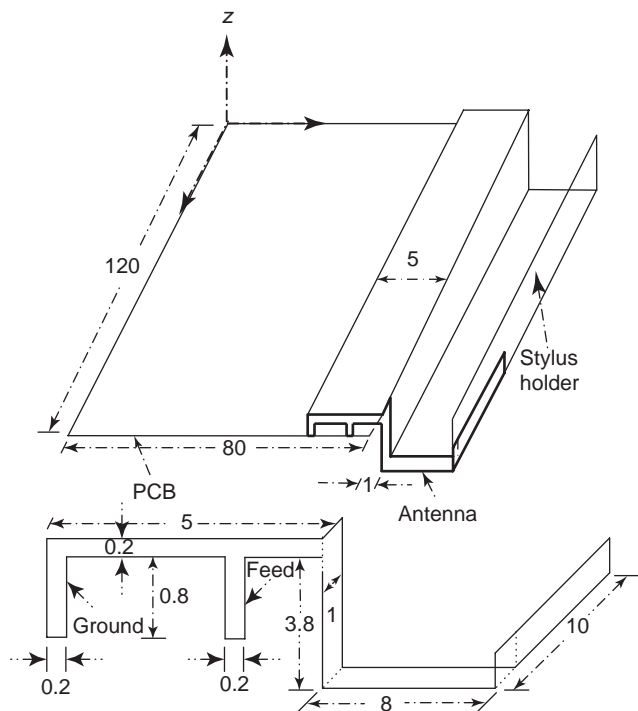


Figure 16. A uniquely packaged inverted-F antenna for Bluetooth or WLAN. [© 2004 IEEE. Reprinted, with permission, from M. Ali, R. A. Sadler, and G. J. Hayes, A uniquely packaged internal inverted-F antenna for Bluetooth or wireless LAN application, *IEEE Anten. Wireless Propag. Lett.* 1(1):5-7 (2002).]

frequency range of 2.4–2.485 GHz. The center frequency is 2.45 GHz, and the bandwidth is 11%. The antenna operates within 1.5–1 VSWR throughout the entire Bluetooth band (2.4–2.485 GHz).

The yz-plane pattern is shown in Fig. 18. This is the most important pattern that provides clear understanding about the angular coverage that the antenna can provide.

3.3. Monopole-Type Radiators

In Fig. 19 a monopole type embedded antenna is shown for wideband WLAN application in the 5–6-GHz bands [28,29]. This antenna can support the IEEE 802.11a wireless local-area network bands (5.15–5.35 GHz and 5.725–5.825 GHz). The configuration is similar to the ones presented in Refs. 30 and 31. In Ref. 30, only a single-band folded design was presented for Bluetooth application (2.4–2.485 GHz, 3.5% bandwidth). No method of wideband/dual-band operation was described. The proposed packaged design can either be used as a wideband antenna, which can provide bandwidths in excess of 10% within 2–1 VSWR, or it can be used for dual-band operation, where the bands are separated by 500–700 MHz in the 5–6 GHz band. This latter property has been exploited to present a design that satisfies the IEEE 802.11a WLAN 5.15–5.35-GHz and 5.725–5.825-GHz bands. The antenna design presented here is packaged within the housing of a personal digital assistant (PDA) and has the maximum dimensions of $28 \times 9 \times 3$ mm. The wideband/dual-band operation has been achieved through proximity parasitic

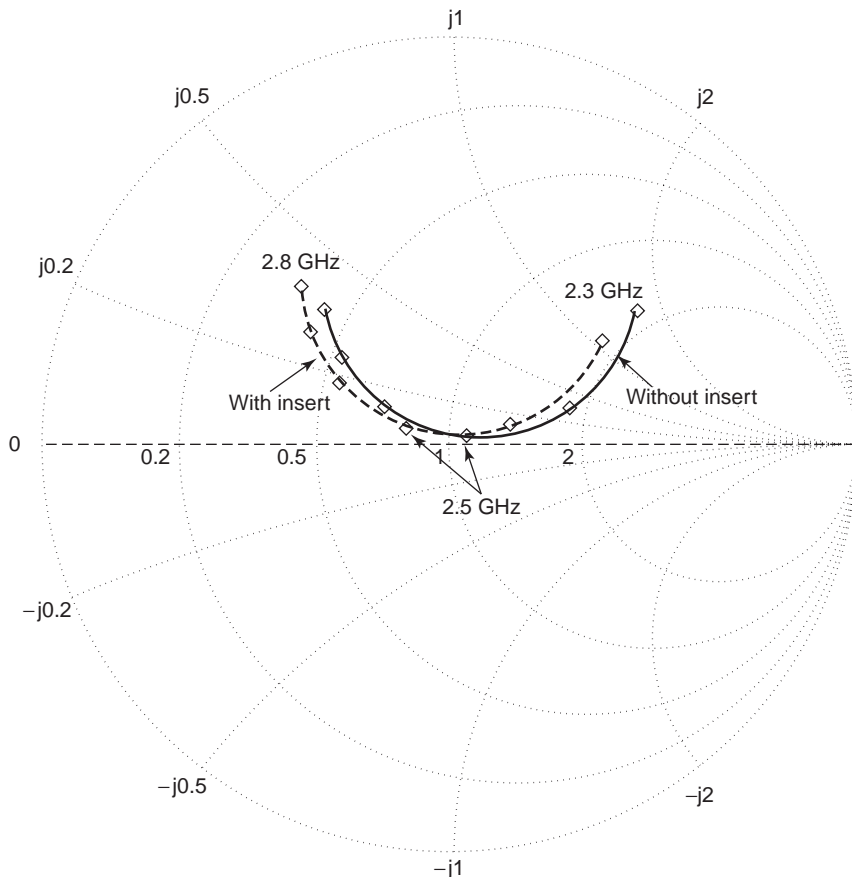


Figure 17. Input impedance of proposed antenna. [© 2004 IEEE. Reprinted, with permission, from M. Ali, R. A. Sadler, and G. J. Hayes, A uniquely packaged internal inverted-F antenna for Bluetooth or wireless LAN application, *IEEE Anten. Wireless Propag. Lett.* 1(1): 5-7 (2002).]

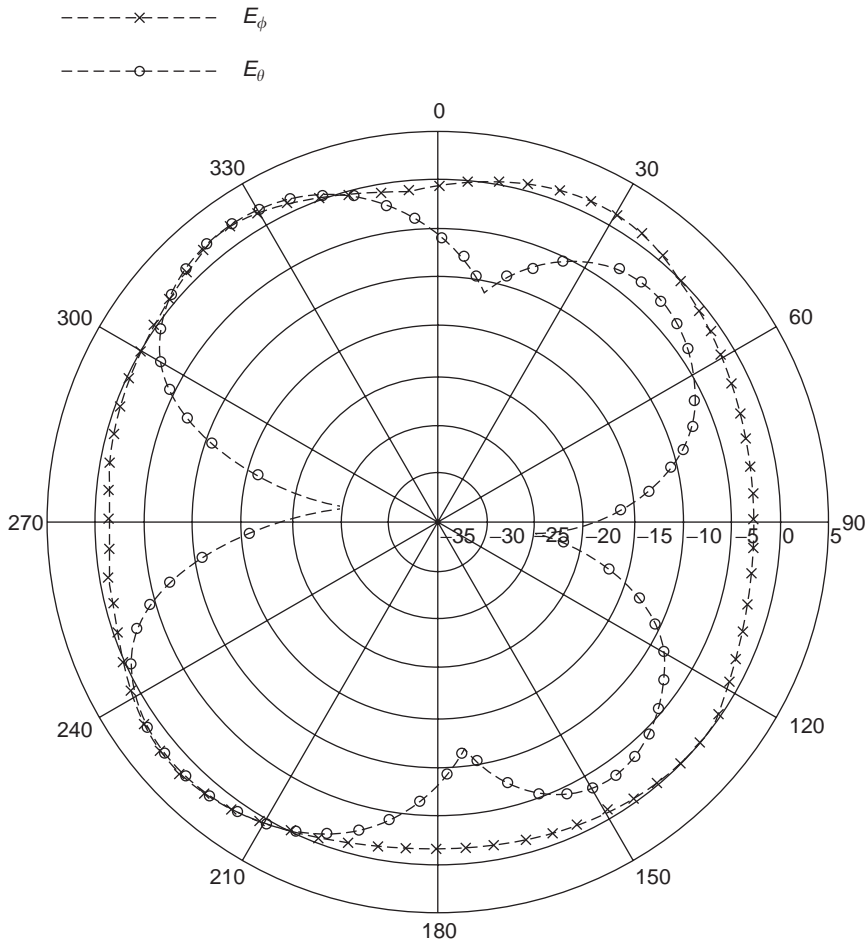


Figure 18. yz -plane pattern. [© 2004 IEEE. Reprinted, with permission, from M. Ali, R. A. Sadler, and G. J. Hayes, A uniquely packaged internal inverted-F antenna for Bluetooth or wireless LAN application, *IEEE Anten. Wireless Propag. Lett.* 1(1):5–7 (2002).]

coupling between a folded radiator and an extended PCB ground plane. The dimensions of the extended PCB ground plane have been appropriately adjusted to ensure the desired coupling.

The proposed antenna can also be manufactured to operate in air. In such a case manufacturing the antenna should be much simpler and easier. Computed VSWR data for antenna on FR4 and in air are shown in Fig. 20.

Bandwidth obtained is 15.5% with 3 mm antenna height and 18.0% with 4 mm antenna height (within VSWR of 2–1). In contrast bandwidth obtained with FR4 was 10% with 3 mm antenna height (within VSWR of 2–1). Thus wider bandwidth can be obtained by replacing FR4 with air. However, the dimensions of the antenna in air are about $50 \times 22 \times 3$ mm, while that on FR4 are $28 \times 9 \times 3$ mm. A laboratory prototype of the proposed antenna

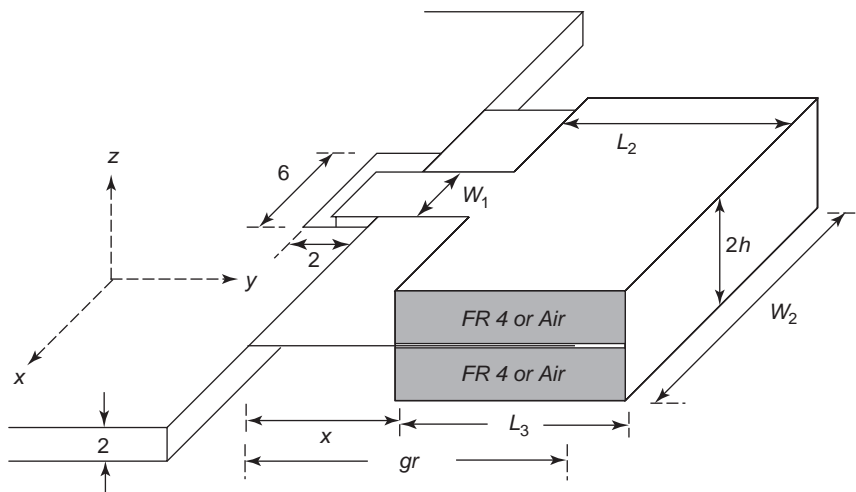


Figure 19. Antenna and PCB geometry. [© 2004 IEEE. Reprinted, with permission, from M. Ali, T. Sittironnarit, H.-S. Hwang, R. A. Sadler, and G. J. Hayes, Wideband/dual-band packaged antenna for 5–6 GHz WLAN application, *IEEE Trans. Anten. Propag.* 52(2): 610–615 (Feb. 2004).]

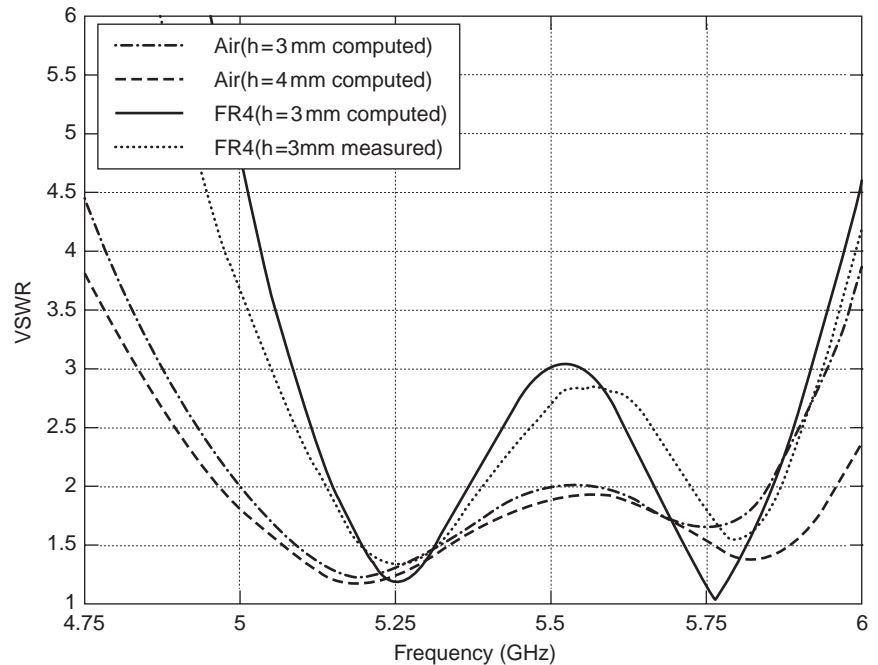


Figure 20. VSWR characteristics. [© 2004 IEEE. Reprinted, with permission, from M. Ali, T. Sittironnarit, H.-S. Hwang, R. A. Sadler, and G. J. Hayes, Wideband/dual-band packaged antenna for 5–6 GHz WLAN application, *IEEE Trans. Anten. Propag.* **52**(2): 610–615 (Feb. 2004).]

(on FR4) was built and tested for VSWR. Measured and computed VSWR data are compared in Fig. 20. The agreement between the measured and computed data is quite good. Computed and measured resonant frequencies are about the same. The measured bandwidths in both bands are also in good agreement with the computed bandwidths within 2–1 VSWR. It is clear that the antenna satisfies the bandwidth requirements for the IEEE 802.11a LAN (5.15–5.35 GHz and 5.725–5.825 GHz). The midband VSWR is only as high as 2.7–1. Antenna radiation pattern and gain were measured inside an anechoic chamber. Measured gain for the two principal plane patterns are listed in Table 2. The free-space peak gain at 5.25 GHz is 1.8 dBi, while that at 5.78 GHz is 0.8 dBi.

4. ELECTRICALLY SMALL ANTENNAS, DIELECTRIC LOADING, AND BANDWIDTH

As defined by Wheller [32], an electrically small antenna has its maximum dimension contained within a sphere with radius $\lambda/2\pi$. Thus, clearly, if a linear antenna such as a straight thin-wire dipole is constructed, it needs to be λ/π or smaller to fall within this category. A comprehensive study on the minimum achievable antenna quality factor (Q) is available in the literature [32–36]. These references are extremely useful if one intends to explore the fundamental limits on small antennas. Since most embedded or packaged antennas for mobile phones utilize these platforms, it is unlikely that these antennas will fall within the category of electrically small antennas. However, antennas for wireless radios or small antennas for VHF and other UHF applications may belong to the class of electrically small antennas. Primarily the antenna bandwidth diminishes with extreme miniaturization, and specifically for an electrically small antenna, the spherical volume

needs to be utilized properly to achieve the lowest possible Q . A thin-wire dipole represents a rather poor utilization of the radian sphere, a normal-mode helical antenna, most commonly used in police radios (scanners) and mobile phones, represents a better utilization of the same axial dimension, while the disk-loaded monopole or the Gobou antenna represents even better utilization of the small antenna volume. There has been some effort in terms of genetically optimizing electrically small antennas [37].

Apart from geometric modification, electrically small antennas can also be developed using dielectric loading. This invariably results in narrower antenna bandwidth and lower antenna gain. For instance, a small GPS patch using ceramic dielectric can be easily fabricated. Also since for GPS, bandwidth required is extremely small (only to satisfy tolerance), a small antenna size can be readily achieved. However, comparing a 25-mm² patch with a 12-mm² patch shows that the peak right-hand circularly polarized gain can fall from 6.5 to –2 dBi. A good discussion on dielectric loading of antennas can be found in Ref. 38. A more recent example of a dielectric loaded antenna can be found in Ref. 39.

5. DISCUSSION AND FUTURE TRENDS

Research will continue on antenna miniaturization and broadbanding. Miniaturization will be achieved primarily by utilizing the available antenna volume rather than a planar surface. Thus designers will increasingly utilize a three-dimensional space. Antenna geometric modification will also occur in the form of employing meander, zigzag, and fractal-type elements.

While electromagnetic bandgap (EBG) materials have shown tremendous progress in improving the gain of microstrip patch antennas by reducing the surface waves,

such structures have not been very useful for small mobile antenna applications. This is due partly to the fact that mobile antennas are so dependent on their counterpoise. There have already been some research activities in terms of small, low-profile antenna development using novel materials [40–46]. Nevertheless, in future negative reflection coefficient materials, negative transmission-line materials and EBG materials may find some useful role in packaged (embedded) antenna development.

Fractal geometries have been considered to design small resonant antennas because of their unique space filling properties. The usefulness of a Hilbert wire antenna in order to lower the antenna resonant frequency has been studied [47–49]. Zhu et al. [48] conducted a parametric study on a matched Hilbert antenna to understand its bandwidth and cross-polarization level. A printed Hilbert antenna was proposed [49] for operation in the UHF band. More recently we have proposed a miniaturized Hilbert shaped PIFA for dual-band applications (900 and 1900 MHz) [50]. The proposed antenna occupied a volume of only $40 \times 10.65 \times 10$ mm (4.3 cm^3). In contrast, a conventional dual-band PIFA made of polygonal plates occupies a volume of $40 \times 22.6 \times 10$ mm (8.4 cm^3). Thus, a 50% saving in antenna volume was readily achieved with our proposed design.

Apart from wire or printed dipole/monopole type antennas, miniaturized slot antennas are also drawing interests. Some examples can be found in Refs. 51–54. As wireless devices shrink in size and more and more functionalities are added (phone, WLAN, GPS for E-911), the need for reconfigurable/multifunctional antennas will also grow. Such antennas must be researched and developed within the embedding platform. MEMs switches can play a dominant role in that area.

As evidenced from numerous publications, smart antennas are becoming increasingly popular to increase system capacity in a mobile communication system. Currently researchers are focusing mostly on arrays for base-station application that can scan the beam in space in an adaptive fashion and track the mobile user. This way a much larger antenna gain can be achieved with little or no interference in any other angular direction. Introducing smart antennas in mobile portable or handheld terminals will require significant progress since array elements have to be placed in very close proximity to each other.

Acknowledgment

This work was supported in part by the National Science Foundation (NSF) Career Award ECS-0237783.

BIBLIOGRAPHY

1. K. Fujimoto and J. R. James, ed., *Mobile Antennas Systems Handbook*, Artech House, 1994.
2. K.-L. Wong, *Design of Non-Planar Microstrip Antennas and Transmission Lines*, Wiley, 1999.
3. K.-L. Wong, *Compact and Broadband Microstrip Antennas*, Wiley, 2002.
4. T. S. Rappaport, *Wireless Communications, Principles and Practice*, Prentice-Hall, 1996.
5. C. A. Balanis, *Antenna Theory Analysis and Design*, 2nd ed., Wiley, 1997.
6. M. Ali, Antenna design for mobile hand held devices, *Recent Research Development in Microwave Theory and Techniques*, Vol. 2, Trans-world Research Network, 2002, pp. 261–278.
7. M. A. Jensen and Y. Rahmat-Samii, Performance analysis of antennas for hand-held transceivers using FDTD, *IEEE Trans. Anten. Propag.* **42**:1106–1113 (Aug. 1994).
8. K. L. Virga and Y. Rahmat-Samii, Low-profile enhanced-bandwidth PIFA antennas for wireless communications packaging, *IEEE Trans. Microwave Theory Tech.* **45**:1879–1888 (Oct. 1997).
9. L. Z. Dong, P. S. Hall, and D. Wake, Dual-frequency planar inverted-F antennas, *IEEE Trans. Anten. Propag.* **45**:1451–1458 (Oct. 1997).
10. C. R. Rowel and R. D. Murch, A capacitively loaded PIFA for compact mobile telephone handsets, *IEEE Trans. Anten. Propag.* **45**:837–884 (May 1997).
11. M. Ali and G. J. Hayes, Analysis of integrated inverted-F antennas for Bluetooth applications, *IEEE Antennas and Propagation Conf. Wireless Communication Digest*, Waltham, MA, Nov. 2000, pp. 21–24.
12. M.-S. Tong, M. Yang, Y. Chen, and R. Mittra, Finite difference time domain analysis of a stacked dual-frequency microstrip planar inverted-F antenna for mobile telephone handsets, *IEEE Trans. Anten. Propag.* **49**:367–376 (March 2001).
13. G. K. H. Lui and R. D. Murch, Compact dual-frequency PIFA designs using LC resonators, *IEEE Trans. Anten. Propag.* **49**(7):1016–1019 (July 2001).
14. M. Ali, R. A. Sadler, and G. J. Hayes, A uniquely packaged internal inverted-F antenna for Bluetooth or wireless LAN application, *IEEE Anten. Wireless Propag. Lett.* **1**(1):5–7 (2002).
15. M. Ali and G. J. Hayes, A small printed integrated inverted-F antenna for Bluetooth application, *Microwave Opt. Technol. Lett.* **33**(5):347–349 (June 5, 2002).
16. M. F. Abedin and M. Ali, Modifying the ground plane and its effect on planar inverted-F antennas (PIFAs) for mobile phone handsets, *IEEE Anten. Wireless Propag. Lett.* **2**(15):226–229 (2003).
17. M. Ali, G. Yang, H. S. Hwang, and T. Sittironnarit, Design and analysis of an R-shaped dual-band planar inverted-F antenna for vehicular applications, *IEEE Trans. Vehic. Technol.* **53**(1):29–37 (Jan. 2004).
18. R. Sadler, G. Hayes, and M. Ali, *Compact, Broadband Inverted-F Antennas with Conductive Elements and Wireless Communicators Incorporating Same*, U.S. Patent 6,218,992 (April 17, 2001).
19. R. Sadler, M. Ali, and G. J. Hayes, *Multi-Frequency Band Inverted-F Antennas with Coupled Branches and Wireless Communicators Incorporating Same*, U.S. Patent 6,563,466 (May 13, 2003).
20. M. C. Huynh and W. L. Stutzman, Ground plane effects on PIFA antennas, *USNC/URSI Radio Science Meeting Digest*, 2000, p. 223.
21. M. C. Huynh, *A Numerical and Experimental Investigation of Planar Inverted-F Antennas for Wireless Communication Applications*, M.S. thesis, Virginia Tech., 2000.
22. http://www.nokia.com/downloads/aboutnokia/research/library/communication_systems/CS20.pdf.
23. M. Ali, G. J. Hayes, H.-S. Hwang, and R. A. Sadler, Design of a multi-band internal antenna for third generation mobile

- phone handsets, *IEEE Trans. Anten. Propag.* **51**(7):1452–1461 (July 2003).
24. M. Ali, *Dual-Band Antenna Having Mirror Image Meandering Segments and Wireless Communicators Incorporating Same*, U.S. Patent 6,184,836 (Feb. 6, 2001).
 25. M. Ali, S. S. Stuchly, and K. Caputa, A wide-band dual meander-sleeve antenna, *J. Electromagn. Waves Appl.* **10**(9):1223–1236 (1996).
 26. M. Ali, M. Okoniewski, M. A. Stuchly, and S. S. Stuchly, Dual-frequency strip-sleeve monopole for laptop computers, *IEEE Trans. Anten. Propag.* **47**(2):317–323 (Feb. 1999).
 27. *www.bluetooth.com*.
 28. M. Ali, T. Sittironnarit, H.-S. Hwang, R. A. Sadler, and G. J. Hayes, Wideband/dual-band packaged antenna for 5–6 GHz WLAN application, *IEEE Trans. Anten. Propag.* **52**(2):610–615 (Feb. 2004).
 29. K. V. Kumar, M. Ali, H. S. Hwang, and T. Sittironnarit, Study of a dual-band packaged patch antenna on a PC card for 5–6 GHz wireless LAN applications, *Microwave Opt. Technol. Lett.* **37**:423–428 (June 2003).
 30. A. Faraone and D. O. McCoy, The folded patch omnidirectional antenna, *IEEE AP-S Int. Symp. Digest*, 2001, Vol. 2, pp. 712–715.
 31. G. Christodoulou, P. F. Wahid, M. R. Mahbub, and M. C. Bailey, Design of a minimum-loss series-fed foldable microstrip, *IEEE Trans. Anten. Propag.* 1264–1267 (Aug. 2000).
 32. H. A. Wheller, Small antennas, *IEEE Trans. Anten. Propag.* **AP-23**:462–469 (July 1975).
 33. L. J. Chu, Physical limitations on omni-directional antennas, *J. Appl. Phys.* **19**:1163–1175 (Dec. 1948).
 34. R. C. Hansen, Fundamental limitations in antennas, *Proc. IEEE* **69**:170–182 (Feb. 1981).
 35. J. S. McLean, A re-examination of the fundamental limits on the radiation Q of electrically small antennas, *IEEE Trans. Anten. Propag.* **44**:672–676 (May 1996).
 36. G. A. Thiele, P. L. Detweiler, and R. P. Peno, On the lower bound of the radiation Q for electrically small antennas, *IEEE Trans. Anten. Propag.* **51**:1263–1269 (June 2003).
 37. E. E. Altshuler, Electrically small self-resonant wire antennas optimized using a genetic algorithm, *IEEE Trans. Anten. Propag.* **50**:297–300 (March 2002).
 38. K. Fujimoto et al., *Small Antennas*, Wiley, New York, 1987.
 39. J.-I. Moon and S.-O. Park, Small chip antenna for 2.4/5.8-GHz dual ISM-band applications, *IEEE Anten. Wireless Propag. Lett.* **2**(21):313–315 (2002).
 40. R. F. J. Broas, D. F. Sievenpiper, and E. Yablonovitch, A high-impedance ground plane applied to a cell-phone handset geometry, *IEEE Trans. Microwave Theory Tech.* **49**(7):1262–1265 (July 2001).
 41. Z. Du, K. Gong, J. S. Fu, B. Gao, and Z. Feng, A compact planar inverted-F antenna with a PBG-type ground plane for mobile communications, *IEEE Trans. Vehic. Technol.* **52**(3):483–489 (May 2003).
 42. D. Pavlickovski and R. B. Waterhouse, Shorted microstrip antenna on a photonic bandgap substrate, *IEEE Trans. Anten. Propag.* **51**(9):2472–2475 (Sept. 2003).
 43. S. Clavijo, R. E. Diaz, and W. E. Mckinzie III, Design methodology for Sievenpiper high-impedance surfaces: an artificial magnetic conductor for positive gain electrically small antennas, *IEEE Trans. Anten. Propag.* **51**:2678–2690 (Oct. 2003).
 44. M. F. Abedin and M. Ali, Application of EBG substrates to design ultra-thin wideband directional dipoles, *IEEE Antennas and Propagation Society Int. Symp. and URSI/USNC Meeting*, Monterey, CA, June 2004.
 45. F. Auzanneau and R. W. Ziolkowski, Artificial composite materials consisting of nonlinearly loaded electrically small antennas: Operational-amplifier-based circuits with applications to smart skins, *IEEE Trans. Anten. Propag.* **47**:1330–1339 (Aug. 1999).
 46. R. W. Ziolkowski and A. D. Kipple, Application of double negative materials to increase the power radiated by electrically small antennas, *IEEE Trans. Anten. Propag.* **51**:2626–2640 (Oct. 2003).
 47. S. R. Best and J. D. Morrow, The effectiveness of space-filling fractal geometry in lowering resonant frequency, *IEEE Anten. Wireless Propag. Lett.* **1**(5):112–115 (2002).
 48. J. Zhu, A. J. Hoorfar, and N. Engheta, Bandwidth, cross-polarization and feed point characteristics of matched Hilbert antennas, *IEEE Anten. Wireless Propag. Lett.* **2**(1):2–5 (2003).
 49. X. Chen, S. S. Naeini, and Y. Liu, A down sized printed Hilbert antenna for UHF band, *Proc. IEEE Antennas and Propagation Society Int. Symp.*, Columbus, OH, June 2003, Vol. 2, pp. 581–584.
 50. M. Z. Azad and M. Ali, A miniature Hilbert planar inverted-F antenna (PIFA) for dual-band mobile phone applications, *IEEE Antennas and Propagation Society Int. Symp. and URSI/USNC Meeting*, Monterey, CA, June 2004.
 51. R. Azadegan and K. Sarabandi, A novel approach for miniaturization of slot antennas, *IEEE Trans. Anten. Propag.* **51**(3):421–429 (March 2003).
 52. J. M. Kim, J. G. Yook, W. Y. Song, Y. J. Yoon, and J. Y. Park, Compact meander type slot antennas, *IEEE AP-S Symp. Digest*, 2001.
 53. H. Y. Wang, J. Simkin, C. Emason, and M. J. Lancaster, Compact meander slot antennas, *Microwave Opt. Technol. Lett.* **24**:377–380 (2000).
 54. A. T. M Sayem, M. Ali, and H. S. Hwang, A miniature Hilbert slot antenna for dual-band wireless application, *IEEE Antennas and Propagation Society Int. Symp. and URSI/USNC Meeting*, Monterey, CA, June 2004.

MISSILE GUIDANCE

ARMANDO A. RODRIGUEZ
Arizona State University
Tempe, Arizona

1. A BRIEF HISTORY: FROM 1944 TO THE PRESENT

1.1. The Missile Age

Even prior to World War I—when powered flight was in its first decade—forward-thinking individuals from several countries advocated the use of unmanned vehicles to deliver high-explosive weapons from afar. Although the earliest efforts to develop a practical flying bomb were undertaken in the United States and Great Britain, it was in Germany that a workable concept finally emerged. After 14 years of intense research, the Germans ushered in the missile age during World War II with their Vengeance

weapons: the Luftwaffe-developed V-1 buzz bomb, and the Army-developed V-2 rocket [1].

1.1.1. Lark Guided Missile. Because of the lack of success of anti-aircraft artillery in stopping Kamikaze aircraft attacks against naval vessels, the U.S. Navy initiated the development of the Lark guided missile in 1944. The first successful intercept of an unmanned aircraft occurred 6 years later on December 2, 1950. An account of this, as well as the development of other missiles (e.g. Sparrow, Hawk), is provided in Ref. 2.

1.1.2. The First Ballistic Missiles. The first long-range ballistic missile, deployed in 1944, was the German V-2. After World War II, significant improvements in inertial guidance system technology led to the Redstone missile—the first short-range U.S. ballistic missile with a highly accurate inertial guidance system. Additional progress was made with the medium-range U.S. Jupiter missile [3].

1.1.3. Intercontinental Ballistic Missiles (ICBMs). Further advancements in the area of nuclear warhead design, inertial guidance system, and booster engine technology led to the development of the intercontinental ballistic missile (ICBM). The first U.S. ICBM—the Atlas—was tested in 1959. The Atlas would be used to launch satellites into orbit, launch probes to the (Earth's) Moon and other planets, and to launch the Mercury spacecraft into orbit around Earth. The Atlas was followed by the Titan one year later. Both Atlas and Titan were liquid-fueled multistage rockets that required fueling immediately prior to launch. In 1961, the Minuteman ICBM was put into service. Located within dispersed hardened silos, the Minuteman used a solid propellant stored within the missile. The LGM-30 Minuteman III was deployed in 1970. This system was designed such that specially configured EC-135 airborne launch control aircraft could automatically assume command and control of an isolated missile or missiles in the event that command capability is lost between the launch control center and the remote missile launch facilities. In 1986, the LGM-118A Peacekeeper was deployed. This three-stage solid propellant system permits 10 warheads to be carried via multiple independent (independently targeted) reentry vehicles (MIRVs). At the peak of the cold war, the Soviet Union possessed nearly 8000 nuclear warheads on ICBMs. During the cold war, the United States built up its strategic defense arsenal, focusing on a nuclear triad consisting of (1) long-range bombers (B-52 bombers and KC-135 tankers) with nuclear air-to-surface missiles, (2) USA-based ICBMs, and (3) submarine-launched ballistic missiles (SLBMs) launched from nuclear-powered submarines (<http://www.chinfo.navy.mil/navpalib/factfile/ships/ship-ssbn.html>). To complement the ground-based leg of the triad, the U.S. Navy would develop the submarine-launched Polaris, Poseidon, and Trident ICBMs (<http://www.chinfo.navy.mil/navpalib/factfile/missiles/wep-d5.html>). Trident I and II were deployed in 1979 and 1990, respectively. Both accommodate nuclear MIRVs and are deployed in Ohio-class

(Trident) submarines, each carrying 24 missiles (eight 100 kiloton warheads per missile).

1.2. Treaties and Programs

1.2.1. Nuclear Proliferation Treaties: SALT and MAD. Because of the large number of Soviet nuclear warheads during the cold war, some felt that U.S. ICBM fields were threatened. On March 14, 1969, President Nixon announced his decision to deploy a missile defense system (called *Safeguard*) to protect U.S. ICBM fields from attack by Soviet missiles. This initiated intense strategic arms negotiations between the United States and the Soviet Union. The Strategic Arms Limitation Talks (SALT), between the United States and the Soviet Union led to a 1971 agreement fixing the number of ICBMs that could be deployed by the two nations. The Anti-ballistic Missile (ABM) Treaty—signed by the United States and the Soviet Union on May 26, 1972—was designed to implement the doctrine of *mutually assured destruction* (MAD). MAD was intended to discourage the launching of a first strike by the certainty of being destroyed by retaliation. The treaty prohibits deployment of sea-, air-, and space-based missiles and limits deployment of sea-, air-, and space-based sensors. The impetus behind these arguments was to perpetuate the existing balance of power and avoid the economic chaos that would result from a full-scale arms race. In 1976, the U.S. Congress ordered the closing of Safeguard—only 4 months after it was operational. In 2001, the ABM treaty came under attack in the U.S. Congress as the United States and Russia (the former Soviet Union) discussed how to differentiate between theater and strategic missile defenses.

1.2.2. BMD and SDI. In 1983, President Reagan initiated the Ballistic Missile Defense (BMD) program under the Strategic Defense Initiative (SDI). SDI would focus on space-based defense research. Because SDI deployment would contravene the ABM treaty, many critics felt SDI, with its potential offensive use, would escalate the arms race. In 1984, the Strategic Defense Initiative Organization (SDIO) was formed. In 1987, Judge Abraham D. Sofaer, State Department Legal Advisor, concluded that the ABM treaty did not preclude testing of space-based missile defense systems, including directed energy weapons; SDI research would continue. With the breakup of the Soviet Union in 1991, the need for great nuclear arsenals came into question. In 1993, the Ballistic Missile Defense Organization (BMDO) was formed, replacing the SDIO, and SDI was abandoned for ground-based anti-missile systems.

1.2.3. Strategic Arms Reduction Treaties. In November 1994, the Strategic Arms Reduction Treaty I (START I) became effective, with the United States, Russia, Belarus, Kazakhstan, and Ukraine agreeing to reduce nuclear warheads by 25%. In appreciation for the ratification, the United States appropriated \$1.5 billion for assistance in dismantling nuclear weapons, properly storing weapons grade materials, and turning military factories into civilian buildings. The 2004 Treaty of Moscow promises to reduce the number of warheads from 6000 to 2200 by 2012.

1.3. Missile Warning Systems

Although the United States has no active ABM defense system in place, an extensive warning system has been in place for many years. Air and space defense is delegated to the North American Aerospace Defense Command (NORAD)—a joint U.S.-Canadian organization. A Ballistic Missile Early Warning System (BMEWS) consisting of warning and tracking radars in Alaska, Greenland, and the United Kingdom can detect missiles 4800 km (~3000 mi) away and provides a 15-min warning of an attack on North America. The Perimeter Acquisition Radar Characterization System (PARCS), operating within the United States interior, tracks incoming warheads and determines impact areas. Phased-array radar antennas along the U.S. Atlantic, Pacific, Alaskan, and Gulf coasts provide warning of SLBM launches.

1.4. Persian Gulf War

In January 1991, the role of air power in modern warfare was dramatically demonstrated during the Persian Gulf War. Initial attacks by the United States–led multinational coalition were designed to suppress Iraqi air defenses. These attacks included Tomahawk cruise missiles launched from warships in the Persian Gulf, F-117A Stealth fighter-bombers armed with laser-guided smart bombs, and F-4G Wild Weasel aircraft carrying high-speed antiradiation missiles (HARMs). These attacks permitted F-14, F-15, F-16, and F/A-18 fighter bombers to achieve air superiority and to drop TV- and laser-guided precision bombs. During the ground war, A-10 Thunderbolts with armor-piercing heat-seeking or optically guided AGM-65 Maverick missiles, provided support for ground units. The AH-64 Apache and AH-1 Cobra helicopters fired laser-guided Hellfire missiles, guided to tanks by ground observers or scout helicopters. The E-3A airborne warning and control system (AWACS), a flying radar system, provided targeting information to coalition members.

1.5. Missile Defense

While most weapon systems performed superbly during the Gulf War, little could be done to stop the Iraqi Scuds launched against Saudi Arabia and Israel. However, a Patriot surface-to-air missile (SAM) system was brought in to repel Scud attacks. Although the Patriot system had been used in 1987 to destroy another Patriot during a demonstration flight, the system was originally designed as an anti-aircraft defense system. Thus, its effectiveness against the Scuds was limited, because intercepts often did not take place at sufficiently high altitudes. Part of the problem was attributed to the fact that the Patriot relied on proximity detonation rather than a “hit to kill”. This would often cause the incoming Scud to break up, leaving a free-falling warhead to detonate on the civilian population below. The many Patriot–Scud engagements were televised to a world audience and demonstrated the need for a high altitude air defense system that could intercept (tactical) ballistic missiles far from critical military assets and civilian population centers. For this reason much research shifted toward the development of hit-to-kill thea-

ter high-altitude air defense (THAAD) systems. In his January 1991 State of the Union address, President George H.W. Bush formally announced a shift in SDI to a concept of global protection against limited strikes (GPALS), and by December, he signed into law the Missile Defense Act of 1991. On January 24, 1997, a Standard Missile 2 (SM-2) Block IVA successfully intercepted and destroyed a Lance missile at the White Sands Missile Range in New Mexico. During the test, the SM-2 successfully transitioned from radar midcourse guidance to its heat-seeking endgame/terminal guidance system prior to destroying the target with its blast fragmentation warhead. On February 7, 1997, BMDO carried out a test in which a Patriot Advanced Capability-2 (PAC-2) missile successfully intercepted a theater ballistic target missile over the Pacific Ocean. In April 1997, BMDO established the Joint Program Office (JPO) for the National Missile Defense (NMD). On June 24, 1997, the first NMD flight test was successfully completed. During this test an exo-atmospheric kill vehicle (EKV) sensor was used to identify and track objects in space. To appreciate the formidable problems associated with developing a THAAD system, it is necessary to understand issues associated with the design of missile guidance systems.

2. MISSILE GUIDANCE, NAVIGATION, AND CONTROL SUBSYSTEMS

We begin our technical discussion by describing the subsystems that make up a missile system. In addition to a warhead, a missile contains several key supporting subsystems. These subsystems may include a target-sensing system, a missile-navigation system, a guidance system, an autopilot or control system, and the physical missile (including airframe and actuation subsystem) (see Fig. 1).

2.1. Target Sensing System

The target sensing system provides target “information” to the missile guidance system, including relative position, velocity, line-of-sight (LOS) angle and rate. Target sensing systems may be based on a number of sensors, such as radar, laser, heat, acoustic, or optical sensors. Optical sensors, for example, may be as simple as a camera for a weapons systems officer (WSO) to visualize the target from a remote location. They may be a sophisticated imaging system (see text below). For some applications, target coordinates are known a priori (e.g., via satellite intelligence) and a target sensor becomes irrelevant. In

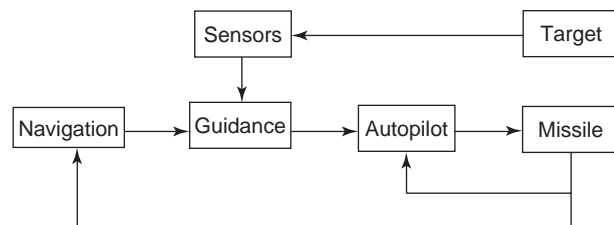


Figure 1. Information flow for missile–target engagements.

such a case, the navigation system provides the required information.

2.2. Navigation System

A navigation system provides information to the missile guidance system about the missile position in space relative to some inertial frame of reference, such as a flat-Earth constant-gravity model for short-range flights and a rotating Earth variable-gravity model for long-range flights. To do so, it may use information obtained from a variety of sensors. These may include simple sensors such as accelerometers or a radar altimeter. It may include more sophisticated sensors such as a global positioning system (GPS) receiver or an optical terrain sensor that relies on comparisons between an image of the terrain below with a stored image and a stored desired trajectory. Optical stellar sensors rely on comparisons between an image of the stars above with a stored image and a stored desired trajectory.

2.3. Guidance System

Target and missile information is used by the guidance system to compute updated guidance commands, which, when issued to the missile autopilot, should ideally guide (or steer) the missile toward the target [4,5]. When target coordinates are known a priori, missile coordinates provided by the navigation system (e.g., GPS-based) are periodically compared with the (preprogrammed) target coordinates to compute appropriate guidance corrections. In general, the quality of the computed guidance commands depends on the quality of the sensor data gathered and the fidelity of the models used for the missile and target. Targets may be stationary, mobile, or highly maneuverable (e.g., silo, ship, fighter aircraft). Physically, guidance commands may represent quantities such as desired thrust, desired (pitch/yaw) acceleration, desired speed, desired flight path or roll angle, and desired altitude. Guidance commands issued by the guidance system to the missile autopilot are analogous to the speed commands issued by automobile drivers to the cruise control systems in their cars. In this sense, the missile guidance system is like the automobile driver and the missile autopilot is like the automobile cruise control system. Missile guidance commands are computed in accordance with a guidance algorithm. Guidance algorithms and navigational aids will be discussed below.

2.4. Autopilot

The primary function of the autopilot—sometimes referred to as the *flight control system* (FCS) or attitude control system (ACS)—is to ensure (1) missile attitude stability and (2) that commands issued by the guidance system are followed as closely as possible [4]. The autopilot accomplishes this command-following objective by computing and issuing appropriate control commands to the missile's actuators. These actuators may include, for example, rocket thrusters, ramjets, or servomotors that

move aerodynamic control surfaces. More specifically, the autopilot compares commands issued by the guidance system with real-time measurements (e.g., acceleration, attitude and attitude rate, altitude) obtained from on-board sensors (e.g., accelerometers, gyroscopes, radar altimeters) and/or external tracking systems. This comparison, essentially a subtraction of signals, produces a feedback error signal, which is then used to compute control commands for the missile actuators. This computation may be based on a very complex mathematical model that captures the following: missile airframe, aerodynamics (depending on speed, dynamic pressure, angle of attack, side-slip angle, etc.), actuators, sensors, flexible modes, and uncertainty descriptions (e.g., dynamic uncertainty, parametric uncertainty [6,7], disturbance/noise bounds). It should be noted that commands that are issued by the guidance system to the autopilot cannot always be followed exactly because of the presence of multiple sources of uncertainty. Sources of uncertainty may include disturbances acting on the missile, sensor noise, unmodeled or uncertain missile airframe, actuator, and sensor dynamics.

2.5. Flight Phases

The flight of a missile can be broken into three phases: (1) a launch, separation, or boost phase; (2) a midcourse or cruise phase; and (3) an endgame or terminal phase. During each phase, a missile may use distinct guidance, navigation, and control systems, specifically designed to accommodate the requirements during that phase of the flight. During each phase, the missile may very well use different sets of sensors, actuators, and power sources.

2.6. Guidance System Performance Terminology

To describe the function and performance of a guidance system, some terminology is essential. The imaginary line that connects a missile center of gravity (c.g.) to the target c.g. is referred to as the *line of sight* (LOS) [8]. The length of this line is called the *range*. The associated vector from missile to target is referred to as the *range vector*. The time derivative of the range vector is called the *closing velocity*. The most important measure of performance for any missile guidance system is the so-called miss distance. "Miss distance" is defined to be the missile-target range at that instant when the two are closest to one another [8, p. 27]. The objective of most guidance systems is to minimize the miss distance within an allotted time period. For some applications (e.g., hit to kill), zero miss distance is essential. For some applications (e.g., to minimize collateral damage), it is essential to impact the target at a specific angle. Because miss distance is sensitive to many variables and small variations from missile to missile, other quantities are used to measure performance. One of the most common measures used is circular error probability (CEP). The CEP for a missile attempts to provide an average miss distance for a class of missile-target engagements. If a missile has a CEP of 10 m, then most of the time, say, 68% of the time, it will detonate within 10 m of the target.

3. CLASSIFICATION OF MISSILES, TARGETS, GUIDANCE SYSTEMS, NAVIGATION METHODS, AND TARGET SENSING METHODS

The guidance system used by a missile depends on the intended use of the missile. Missiles are classified according to many categories. The most commonly used classifications are as follows: strategic, tactical, exoatmospheric, endoatmospheric, aerodynamic, ballistic, surface-to-surface, surface-to-air, air-to-surface, air-to-air, inertially guided, terrain guided, stellar guided, satellite guided, passive; active, homing, command-guided, radar-guided, laser-guided, heat seeking, fire-and-forget, line-of-sight guided, radar terrain-guided, TV guided, cruise, skid-to-turn (STD), and bank-to-turn (BTT). Each category is now briefly discussed.

3.1. Missile Types

3.1.1. Strategic Missiles. Strategic missiles are used primarily against strategic targets, that is, resources that permit an enemy to conduct large-scale military operations (e.g., battle management/command, control, and communication centers, industrial/weapons manufacturing centers). Such targets are usually located far behind the battle line. As such, strategic missiles are typically designed for long-range missions. While such missiles are usually launched from naval vessels or from missile silos situated below ground, they are sometimes launched from aircraft (e.g., strategic bombers). Because such missiles are intended to eliminate the most significant military targets, they typically carry nuclear warheads rather than conventional warheads. Strategic missiles typically operate at orbital speeds (~ 5 mi/s), outside the atmosphere, over intercontinental distances. They use rockets/thrusters/fuel and require very precise instrumentation for critical midcourse guidance. GPS has made such systems very accurate.

3.1.2. Tactical Missiles. Tactical missiles are used primarily against tactical targets, that is, resources that permit an enemy to conduct small-scale military operations (a ship, an airfield, a munitions bunker, etc.). Such targets are usually located near the battle line. As such, tactical missiles are typically designed for short- or medium-range missions. Such missiles carry conventional explosive warheads, the size of which depends on the designated target. Tactical missiles sometimes carry nuclear warheads in an effort to deter the use of tactical nuclear/chemical/biological weapons and to engage the most hardened targets (e.g., enemy nuclear strategic missile silos). Tactical missiles typically operate at lower speeds (< 1 mi/s), inside the atmosphere, and over short to medium distances (e.g., 150 mi). They typically use aerodynamic control surfaces (discussed below) and require adequate instrumentation for midcourse and terminal guidance. A target sensor (e.g., radar seeker) permits such missiles to engage mobile and highly maneuverable targets.

3.1.3. Exoatmospheric Missiles. Exoatmospheric missiles fly their missions mostly outside Earth's atmosphere.

Such missiles are used against long-range strategic targets. Because they fly outside the atmosphere, thrusters are required to change direction. Such thrusters use onboard fuel. In order to maximize warhead size, and because missile weight grows exponentially with fuel weight, it is important that guidance and control systems for long-range missiles (e.g., strategic, exoatmospheric) provide for minimum fuel consumption.

3.1.4. Endoatmospheric Missiles. Endoatmospheric missiles fly their missions inside Earth's atmosphere. Such missiles are used against strategic and tactical targets. In contrast to exoatmospheric missiles, endoatmospheric missiles may use movable control surfaces such as fins (called *aerodynamic control surfaces*), which deflect airflow in order to alter the missile flight path. In such a case, the missile is called an *aerodynamic missile*. Endoatmospheric missiles may, in some cases, rely entirely on rocket power. In such a case, they are not aerodynamic. Exoatmospheric missiles that fly outside Earth's atmosphere rely on rocket power and thrusters. These are not aerodynamic. Examples of aerodynamic missiles are the Sidewinder and Patriot.

3.1.5. Ballistic Missiles. Ballistic missiles assume a free-falling (unpowered) trajectory after an internally guided, self-powered (boost and midcourse) ascent. Such missiles are usually used against long-range strategic targets. ICBMs, for example, are usually exoatmospheric strategic missiles that were developed for use against strategic targets, and are typically launched from underground missile silos and submarines. Modern ICBMs contain multiple independently targeted nuclear warheads deployed via MIRVs. Examples of ICBMs are the Atlas, Titan, Minuteman, and Polaris. The Iraqi Scud, used in the Persian Gulf War, is another ballistic missile.

3.1.6. Surface-to-Surface Missiles (SSMs). SSMs are typically launched from the ground, beneath the ground (e.g., from a missile silo), or from naval platforms against ground targets (e.g., tank, munitions depot, missile silo) or naval targets (e.g., battleship, submarine). ICBMs are typically SSMs. SSMs may carry nuclear, biological, chemical, or conventional warheads. Examples of SSMs are the antiship Silkworm and the Tomahawk.

3.1.7. Surface-to-Air Missiles (SAMs). SAMs are typically launched from the ground, beneath the ground (e.g., from a missile silo), or from naval platforms against aircraft and missiles. SAMs were developed to defend surface targets from air attacks, especially from high-altitude bombers flying well above the range of conventional anti-aircraft artillery (AAA). Most air defense SAMs employ separate radars to acquire (detect) and track enemy air threats. The separate radar is also used to guide the SAM toward the hostile target; endgame guidance may be accomplished by the missile's onboard guidance system. SSMs are typically heavier and carry larger warheads than SAMs because they are usually intended to penetrate hardened targets. Shoulder-launched SAMs (e.g., Stinger)

have become a major concern given increased terrorist activities.

3.1.8. Air-to-Surface Missiles (ASMs). ASMs are launched from aircraft against ground targets (e.g., a bridge, airfield) or naval targets. While ASMs are typically intended for tactical targets, they are used by both strategic and tactical bombers. Equipping strategic bombers with long-range ASMs extends their range, significantly reducing the range that they need to travel toward the intended target. Examples of ASMs are the antitank Hawk and Hellfire, the antiradar AGM-88 HARM, the antiship Exocet and AGM-84D Harpoon, and the antiarmored vehicle AGM-65 Maverick (<http://www.af.mil/factsheets/>). Other ASM systems include the advanced medium-range air-to-air missile (AIM-120 AMRAAM) and the airborne laser (ABL) system being developed by several defense contractors. The ABL system has been considered for boost-phase intercepts during which the launched missile has the largest signature and is traveling at its slowest speed.

3.1.9. Air-to-Air Missiles (AAMs). AAMs are launched from aircraft against aircraft, ballistic missiles, and most recently against tactical missiles. Such missiles are typically light, highly maneuverable, tactical weapons. AAMs are generally smaller, lighter, and faster than ASMs since ASMs are typically directed at hardened, less mobile, targets. Some SAMs and ASMs are used as AAMs and vice versa. Examples of AAMs are the AIM-7 Sparrow, AIM-9 Sidewinder, AIM-54 Phoenix, and the AIM-120A AMRAAM.

3.2. Guidance Methods: Fixed Targets with Known Fixed Positions

A missile may be guided toward a target, having a known fixed position, using a variety of guidance methods and/or navigational aids, such as inertial, terrain, stellar, and satellite guidance and navigation.

3.2.1. Inertially Guided Missiles. Inertially guided missiles use missile spatial navigation information relative to some inertial frame of reference to guide a missile to its designated target. For short-range missions, one may use a flat-Earth constant-gravity inertial frame of reference. This is not appropriate for long-range missions, approaching intercontinental distances, for which Earth may not be treated as flat. For such missions, the sun or stars provide an inertial frame of reference. One can also use an Earth-centered variable-gravity frame. Position information is typically obtained by integrating acceleration information obtained from accelerometers or by pattern matching algorithms exploiting imaging systems. Because accelerometers are sensitive to gravity, they must be mounted in a fixed position with respect to gravity. Typically, accelerometers are mounted on platforms that are stabilized by gyroscopes or star tracking telescopes. Terrain and stellar navigation systems are examples of imaging systems. Satellite navigated missiles use satellites for navigation. Some satellite guided missiles use the Navstar

Global Positioning System (GPS)—a constellation of orbiting navigation satellites—to navigate and guide the missile to its target. GPS has increased precision significantly.

3.3. Guidance Methods: Mobile Targets with Unknown Positions

If the target position is not known a priori, the forementioned methods and aids may be used in part but other real-time target acquisition, tracking, navigation, and guidance mechanisms are required. The most commonly used classifications for the guidance system in such cases are as follows: passive, active, and semiactive. These are now discussed.

3.3.1. Passive Missiles. Passive missiles are missiles that have a target sensor sensitive to target energy emissions (e.g., radar and thermal energy) and a guidance system that uses received target emission signals to guide the missile toward the target. Such missiles are said to have a passive guidance system. While such systems are, in principle, simple to implement, it should be noted that they rely on a “cooperative target”: targets that radiate energy at appreciable (detectable) power levels. Such systems are also susceptible to decoys.

3.3.2. Active Missiles. Active missiles use an energy-emitting transmitter combined with a reflection-detection receiver (e.g., an active seeker) to acquire targets and guide the missile toward the target. Such missiles are said to have an active guidance system. For such systems, great care is taken to ensure that transmitted and received signals are isolated from one another. Stealthy targets are those that absorb or scatter (misdirect) the transmitted energy. Receivers can consist of a gimballed (movable) seeker antenna. Such mechanically directed antennas are slow and have a limited field of view. Fixed phase array antennas—operating on interferometric principles—offer rapid electronic scanning capability as well as a broad field of view.

3.3.3. Semiactive Missiles. Semiactive missiles use a reflection-sensitive receiver to guide the missile to the target. The reflected energy may be provided by a ground-based, ship-based, or aircraft-based energy emission (e.g., radar or laser) system or by such a system aboard the launching platform. In either case, a human operator (e.g., WSO) illuminates the target with a radar or laser beacon and the missile automatically steers toward the source of the reflected energy. Such missiles are said to possess semiactive guidance systems. For such implementations, the illuminating power can be large.

Passive systems, of course, are stealthier than semiactive or active systems as they do not intentionally emit energy toward the target. Anti-radar missiles typically use passive guidance systems since radars are constantly emitting energy. As an antiradar missile approaches the intended radar, radar operators typically shut down the radar. This causes the missile to lose its critical guidance signal. In such a case, an active guidance system must

take over. Active systems require more instrumentation than passive systems and hence are heavier and more expensive.

Guidance system performance is limited by various noise sources. For active systems, there is range dependent noise that is proportional to the square of the distance from the missile to the target. For semiactive systems, there is range dependent noise that is proportional to the distance from the missile to the target. For either system, the noise is wideband, may be modeled as white, and goes to zero at intercept. For either system, there are random fluctuations due to the target radar return. This source of noise is referred to as glint noise. It depends directly on the physical dimensions of the target and is typically highly correlated [8].

3.4. Other Guidance Methods and Missile Types

3.4.1. Homing Missiles. Homing missiles, like homing pigeons, home in on a target by steering toward energy emitted by or reflected from the target. If the missile homes in on energy emitted by the target, then it uses a passive guidance system. If the missile transmits a signal and homes in on the reflected energy, its guidance system is active. In principle, sensor information and homing improve as the missile gets closer to the target.

3.4.2. Command-Guided Missiles. A command guided missile is a remotely controlled missile. A cooperating (ground-, ship-, or aircraft-based) control station uses a radar (or two) to acquire the target, track the target, and track the missile. Available computers are used to compute guidance commands (on the basis of ranges, elevations, and bearings) that are transmitted via radio uplink to the missile autopilot. Powerful computers, capable of exploiting complex target models and performance criteria, can provide precision guidance updates in real time. Such systems are limited by the distance from the tracking station to the missile and target. Noise increases, and guidance degrades, as the engagement moves further from the tracking station. Such systems are also more susceptible to electronic countermeasures (ECMs). While command-guided missiles do not require a seeker, one can be included for terminal guidance to maximize the probability of interception at long distances from the tracking station. The Patriot is a command-guided SAM. To significantly increase ECM immunity, some short-range command guided missiles have a wire that unspools at launch, keeping the missile connected to the command station, e.g., the all-weather optically guided antitank Tow missile.

3.4.3. Beam Rider Guidance (BRG). BRG is a specific form of command guidance in which the missile flies along a beam (e.g., radar or laser), which, in principle, points continuously toward the target. If the missile stays within the beam, an intercept will occur. Guidance commands steer the missile back into the beam when it deviates.

BRG causes problems at large ranges because of beam spreading issues.

3.4.4. Command-to-LOS Guidance. Command-to-LOS guidance—used by the Tow missile—is another command guidance method that improves on beam rider guidance by taking beam motion into account.

3.4.5. Energy-Guided Missiles. Radar-guided missiles are guided to the target on the basis of radar energy. Laser-guided missiles are guided on the basis of laser energy. The Hellfire is a laser-guided antitank missile. Heat-seeking missiles are guided on the basis of infrared (IR, heat, or thermal) energy. The AIM-9 Sidewinder is a heat-seeking AAM. Most AAMs employ radar homing or heat-seeking devices and have replaced automatic gunfire as the main armament for fighter aircraft. The shoulder-operated Stinger is a heat-guided fire-and-forget SAM. Such a missile is called a “fire-and-forget missile” because it allows the user to fire, take evasive action, forget, and engage other hostile targets.

3.4.6. Degradation of Electromagnetic Energy-Based Sensors. The performance of many electromagnetic energy-based sensors (e.g., millimeter-wave radars, electrooptical thermal imagers, and laser radar) degrades under adverse weather conditions such as rain, fog, dust, or smoke. This occurs when the size of the weather particles are on the same order as the wavelength of the energy return from the target. Under adverse conditions, microwave radars with wavelengths in centimeters (10 GHz) are not degraded, millimeter radars with millimeter wavelengths (100 GHz) are slightly degraded, and electrooptical systems with micrometer wavelengths (10^5 GHz) are severely degraded. The AIM-120A AMRAAM is a fighter-launched fire-and-forget AAM that uses infrared (IR) sensors to acquire (detect) targets at long range. It uses inertial mid-course guidance without the need for the fighter to illuminate the target. A small active seeker is used for endgame homing.

3.4.7. LOS Guidance. When a missile is near the target, the guidance system may use line-of-sight (LOS) guidance. The guidance system of a LOS guided missile uses target range and LOS information obtained from the target sensor (e.g., a seeker) to generate guidance commands to the missile autopilot.

3.4.8. Radar Terrain Guidance. A radar terrain guided missile uses a radar altimeter, an a priori stored path and terrain profile to navigate and guide the missile over the terrain during the midcourse phase of a flight (typically). The stored path represents a desired path over the terrain. The down-looking radar altimeter is used to measure the altitude with respect to the terrain below. This is used to determine where the missile is with respect to the desired path. Deviations from the path are corrected by adjusting guidance commands to the autopilot. The Tomahawk is an all-weather cruise missile

that uses radar terrain guidance called *terrain contour matching* (TERCOM) [9]. TERCOM terrain profiles—obtained by reconnaissance satellites and other intelligence sources—become finer as the missile approaches the target. Such navigational/guidance systems permit terrain hugging. Terrain echoes (referred to as clutter) then confuse observing radars.

3.4.9. TV Guidance. TV guided missiles use imaging systems that permit a WSO to see the target and remotely guide the missile to the target.

3.4.10. Cruise Missiles. Cruise missiles are typically SSMs that use inertial and terrain following navigation/guidance systems while cruising toward the target. When near the target, endgame guidance is accomplished by either (1) homing in on target emitted/reflected energy, (2) focusing on a target feature by exploiting a forward-looking imaging system and an onboard stored image, or (3) using a more detailed terrain contour with a more accurate downward-looking sensor. Cruise missiles offer the ability to destroy heavily defended targets without risking air crew. Because they are small, they are difficult to detect on radar, particularly when they hug the terrain. Examples of cruise missiles are the AGM-86, Tomahawk [9], and Harpoon. The Tomahawk uses a TERCOM guidance during the cruise phase. For terminal guidance, a conventionally armed Tomahawk uses an electrooptical digital scene matching area correlator (DSMAC) guidance system, which compares measured images with stored images. This technique is often referred to as an *offset navigation or guidance technique*. At no time during the terminal scene matching process does the missile look at the target. Its sensor always looks down. DSMAC makes Tomahawk one of the most accurate weapon systems in service around the world.

3.4.11. Skid-to-Turn and Bank-to-Turn Missiles. Skid-to-turn (STT) missiles, like speedboats, skid to turn. Bank-to-turn (BTT) missiles, like airplanes, bank to turn [5,10–16]. BTT airframe designs offer higher maneuverability than conventional STT designs by use of an asymmetric shape and/or the addition of a wing. BTT missile autopilots are more difficult to design than STT autopilots because of cross-coupling issues. STT missiles achieve velocity vector control by permitting the missile to develop angle-of-attack and side-slip angles [5]. The presence of side-slip imparts a skidding motion to the missile. BTT missiles ideally should have no side-slip. To achieve the desired orientation, a BTT missile is rolled (banked) so that the plane of maximum aerodynamic normal force is oriented to the desired direction. The magnitude of the force is controlled by adjusting the attitude (i.e., angle of attack) in that plane. BTT missile control is made more difficult by the high roll rates required for high performance (i.e., short response time) [4, p. 285]. STT missiles typically require pitch-yaw acceleration guidance commands, whereas BTT missiles require pitch-roll acceleration commands. An overview of tactical missile control design issues and approaches is provided in Ref. 44.

4. GUIDANCE ALGORITHMS

In practice, many guidance algorithms are used [4,8,17–19]. The purpose of a guidance algorithm is to update missile guidance commands that will be issued to the autopilot. This update is to be performed on the basis of missile and target information. The goal of any guidance algorithm is to steer the missile toward the target, resulting in an intercept within an allotted time period (i.e., until the fuel runs out or the target is out of range). The most common algorithms are characterized by the following terms: proportional navigation, augmented proportional navigation, and optimal [8,19]. To simplify the mathematical details of the exposition to follow, suppose that the missile–target engagement is restricted to the two-dimensional pitch plane of the missile. Given this, the engagement dynamics take the following simplified form [20]

$$\dot{R}(t) = V_t \cos(\lambda(t) - \gamma_t(t)) - V_m \cos(\lambda(t) - \gamma_m(t)) \quad (1)$$

$$\dot{\lambda}(t) = \frac{1}{R(t)} [-V_t \sin(\lambda(t) - \gamma_t(t)) + V_m \sin(\lambda(t) - \gamma_m(t))] \quad (2)$$

where (V_m, V_t) , (γ_m, γ_t) denote missile–target speeds (assumed constant) and flight path angles.

4.1. Proportional Navigation Guidance (PNG)

For proportional navigation guidance (PNG) [8,19], the missile is commanded to turn at a rate proportional to the closing velocity V_c (i.e., range rate) and to the angular velocity of the LoS $\dot{\lambda}$. The constant of proportionality N is referred to as the *PNG gain or constant*. For a PNG law, the pitch plane acceleration command $a_{c,\text{PNG}}(t)$ takes the form

$$a_{c,\text{PNG}}(t) = NV_c(t)\dot{\lambda}(t) \quad (3)$$

Typically, N takes on values in the range [3,5].

PNG is relatively easy to implement. For tactical radar homing missiles using PNG, an active seeker provides LOS rate while a Doppler radar provides closing velocity. Traditionally, LOS rate has been obtained by filtering the output of a 2-degree-of-freedom rate gyro mounted to the inner gimbal of the seeker [21]. More recently, ring laser gyros (RLGs) have been used. Unlike conventional spinning gyros, the RLG has no moving parts, no friction, and hence negligible drift. For IR missiles using PNG, the IR system provides LOS rate information, but V_c must be estimated. The Lark was the first missile to use PNG [8].

4.1.1. PNG Optimality and Performance Issues. It can be shown that PNG minimizes the square integral criterion $\int_0^{t_f} a_c^2(\tau) d\tau$ subject to a zero-miss distance at t_f , linearized (small angle) missile–target dynamics, and constant missile–target speeds [22], where t_f denotes the flight time. A missile using PNG is fired not at the target, but at the expected intercept point if the target were to move at constant velocity in a straight line; thus, the missile is fired so that, at least initially, it is on a collision triangle with the

target. The initial angle between the missile velocity vector and the LOS is the missile lead angle. If the missile is not on a collision triangle with the target, then there exists a heading error (HE). It is instructive to understand how PNG missile acceleration requirements vary with (1) initial heading error when the target is not maneuvering, and (2) a constant acceleration target maneuver. These cases are now briefly discussed assuming linearized (small-angle) 2D dynamics with constant missile and target speeds (V_m, V_t), missile autopilot responds instantaneously to guidance acceleration commands (i.e., no lag), and ideal sensor dynamics [8]. We note that the Stinger is an example of a fire-and-forget supersonic SAM that uses PNG with passive IR/UV homing.

4.1.2. PNG Performance: Nonmaneuvering Target, Heading Error. First, consider the impact of a heading error on PNG missile acceleration requirements when the target moves at a constant speed in a straight line. Under the simplifying assumptions given above, the resulting commanded acceleration is as follows:

$$a_{c,PNG}(t) = \frac{-V_m N \text{HE}}{t_f} \left[1 - \frac{t}{t_f} \right]^{N-2} \quad (4)$$

This expression shows that PNG immediately begins removing any heading error (HE) and continues doing so throughout the engagement. The acceleration requirement decreases monotonically to zero as the flight progresses. A larger N results in a larger initial missile acceleration requirement, but a lesser final missile acceleration requirement. The larger the N , the faster the heading error is removed.

4.1.3. PNG Performance: Target Undergoing Constant Acceleration. Now, consider the impact of a constant target acceleration a_t on PNG missile acceleration requirements. Under the simplifying assumptions given above, the resulting commanded acceleration is as follows:

$$a_{c,PNG}(t) = \frac{N}{N-2} \left[1 - \left(1 - \frac{t}{t_f} \right)^{N-2} \right] a_t \quad (5)$$

In sharp contrast to the heading error case examined above, this expression shows that the PNG missile acceleration requirement for a constant target maneuver increases monotonically throughout the flight. As in the heading error case, a higher N results in a greater initial acceleration requirement and a relaxed acceleration requirement near the end of the flight [$a_{c,PNG,max} = a_{c,PNG}(t_f) = (N/(N-2))a_t \leq a_t$].

4.1.4. Zero-Effort Miss (ZEM) Distance. An important concept in guidance law design is that of zero-effort miss distance, denoted $ZEM(t)$ and defined as the miss distance that would result if the target would continue at a constant speed in a straight line and the missile made no further corrective maneuvers. Given this, if one defines the time to go as $t_{go} \stackrel{\text{def}}{=} t_f - t$ and the ZEM distance perpendicular to the LOS as $ZEM_{PLOS}(t)$, then for PNG it can

be shown that

$$a_{c,PNG}(t) = N \left(\frac{ZEM_{PLOS}(t)}{t_{go}^2} \right) \quad (6)$$

where $ZEM_{PLOS}(t) = y + \dot{y}t_{go}$, $y \approx R\lambda$ denotes the relative (small angle) vertical displacement between the missile and target, and $R \approx V_c t_{go}$. The concept of ZEM distance is used to derive more advanced guidance laws [8]. The concept is very powerful since ZEM can be approximated in so many different ways.

4.1.5. PNG Miss Distance Performance: Impact of System Dynamics. For the two cases considered above, the associated relative displacement $y \approx R\lambda$ satisfies

$$\ddot{y} + \frac{N}{t_f - t} \dot{y} + \frac{N}{(t_f - t)^2} y = a_t, \quad y(t_f) = 0$$

and we have zero-miss distance. The preceding discussion on PNG assumes that guidance-control-seeker dynamics are negligible. In practice, this assumption is not satisfied and the inherent lag degrades miss distance performance. When a first order lag with time constant τ is assumed for the combined guidance-control-seeker dynamics, one obtains small miss distances so long as τ is much smaller than t_f (e.g., $t_f > 10\tau$). In practice, of course, high-frequency dynamics impose bandwidth constraints that limit how small τ can be. Despite the above (general) rule of thumb, it is essential that high-frequency system dynamics be carefully modeled or analyzed to obtain reliable performance predictions. Such dynamics include those associated with: control system, computational delays, A/D and D/A conversion, actuators (e.g., thrusters, canards, tailfins), missile structure (e.g., flexible modes), guidance system (e.g., lead-lag compensation), and sensors (e.g., seeker radome, accelerometers, gyros). As one might expect, noise and parasitic effects place a practical upper bound on the achievable guidance system bandwidth. In practice, statistical Monte Carlo simulations (exploiting adjoint methods [8]) are used to evaluate performance prior to flight testing. Such simulations consider the above as well as acceleration/control saturation effects [14,15], typical target maneuvers, and worst-case target maneuvers.

4.1.6. TPNG and PPNG. Shukla and Mahapatra [23] distinguish between true PNG (TPNG) and pure PNG (PPNG). For missile's using TPNG, acceleration commands are issued perpendicular to the LOS (as above). For PPNG, acceleration commands are issued perpendicular to the missile velocity vector. The advantages of PPNG over traditional TPNG are highlighted [23]. In contrast to PPNG, TPNG requires (1) a forward acceleration and deceleration capability (because acceleration command is perpendicular to LOS; not missile velocity), (2) unnecessarily large acceleration requirements, and (3) restrictions on the initial conditions to ensure intercept.

4.2. Tactical Missile Maneuverability

Tactical radar guided missiles use a seeker with a radome. The radome causes a refraction or bending of the incoming radar wave, which in turn, gives a false indication of target location. This phenomenon can cause problems if the missile is highly maneuverable. One parameter that measures maneuverability is the so-called missile (pitch) turning rate frequency (or bandwidth) defined by [2]

$$\omega_x \stackrel{\text{def}}{=} \frac{\dot{\gamma}}{\alpha} \quad (7)$$

where $\dot{\gamma}$ denotes the time rate of change of flight path angle and α denotes angle of attack (AOA). ω_x measures the rate at which the missile rotates (changes flight path) by an equivalent AOA. Assuming that the missile is modeled as a “flying cylinder” [8] with length L and diameter D , it has a lift coefficient

$$C_L = 2\alpha[1 + 0.75(S_{\text{plan}}/S_{\text{ref}})\alpha] \quad (8)$$

where $S_{\text{plan}} \approx LD$, $S_{\text{ref}} = \pi D^2/4$. Noting that $a_m = V_m \dot{\gamma}$ is the missile acceleration, $Q = \frac{1}{2}\rho V_m^2$ the dynamic pressure, $W = mg$ the missile weight, and ρ the density of air, it follows that

$$\omega_x \stackrel{\text{def}}{=} \frac{\dot{\gamma}}{\alpha} = \frac{a_m}{V_m} = \frac{gQS_{\text{ref}}C_L}{W\alpha V_m} = \frac{\rho g V_m S_{\text{ref}} \left[1 + 0.75 \frac{S_{\text{plan}}}{S_{\text{ref}}} \alpha \right]}{W} \quad (9)$$

From this, it follows that ω_x decreases with increasing missile altitude and with decreasing missile speed, i.e., when aerodynamic effectiveness is low.

4.3. Radome Effects: Homing–Robustness Tradeoffs

Let ω denote the guidance–control–seeker bandwidth. If ω is too small, homing is poor and large miss distances result. Typically, we desire $\omega_x < \omega$ so that the closed-loop system “accommodates” the capabilities of the missile. As expected, problems can occur if ω is too large. This, in part, is because of radome–aerodynamic feedback of the missile acceleration a_m into $\dot{\lambda}$. Assuming n -pole dynamics, it can be shown that the missile acceleration a_m takes the form

$$\begin{aligned} a_m &= FG[\dot{\lambda} - R\dot{\theta}] \\ &= FG[\dot{\lambda} - RAa_m] \\ &= [FG/(1 + FGRA)]\dot{\lambda}, \end{aligned} \quad (10)$$

where $G = NV_c$ represents the guidance system, $F = [\omega/(s + \omega)]^n$ represents the flight control system, R is the radome slope (can be positive or negative), and $A = (s + \omega_x)/(\omega_x V_m)$ denotes the missile transfer function from a_m to pitch rate $\dot{\theta}$. For stability robustness, we require the

associated open-loop transfer function

$$L \stackrel{\text{def}}{=} FGRA = NV_c \left(\frac{\omega}{s + \omega} \right)^n R \left(\frac{s + \omega_x}{\omega_x V_m} \right)$$

to satisfy an attenuation specification such as $|L(j\omega)| = NV_c |R| [\omega/\omega_x V_m] < \varepsilon$ for some sufficiently small constant $\varepsilon > 0$. This, however, requires

$$\omega < \varepsilon \left(\frac{V_m}{|R|NV_c} \right) \omega_x \quad (11)$$

for stability robustness. This implies that the bandwidth ω must be small when V_m is small, ($|R|$, N , V_c) are large, or ω_x is small (high altitude and low missile speed). In general, therefore, designers must tradeoff homing performance (bandwidth) and stability robustness properties. Missiles using thrust vectoring (e.g., exoatmospheric missiles) experience similar performance–stability robustness tradeoffs.

4.4. Augmented Proportional Guidance (APNG)

Advanced guidance laws reduce acceleration requirements and miss distance but require more information (time to go, missile–target range, etc.) [18]. In an attempt to take into account a constant target acceleration maneuver a_t , guidance engineers developed augmented proportional guidance (APNG). For APNG, the commanded acceleration is given by

$$a_{c,\text{APNG}}(t) = NV_c \dot{\lambda}(t) + \frac{1}{2} Na_t = a_{c,\text{PNG}}(t) + \frac{1}{2} Na_t \quad (12)$$

or $a_{c,\text{APNG}}(t) = N(ZEM/t_{\text{go}}^2)$, where $ZEM = y + \dot{y}t_{\text{go}} + \frac{1}{2}a_t t_{\text{go}}^2$ is the associated zero-effort miss distance. Equation (10) shows that APNG is essentially PNG with an extra term to account for the maneuvering target. For this guidance law, it can be shown (under the simplifying assumptions given earlier) that

$$a_{c,\text{APNG}}(t) = \frac{1}{2} N \left[1 - \frac{t}{t_f} \right]^{N-2} a_t \quad (13)$$

In contrast with PNG, this expression shows that the resulting APNG acceleration requirements decrease rather than increase with time. From the expression, it follows that increasing N increases the initial acceleration requirement but also reduces the time required for the acceleration requirements to decrease to negligible levels. For $N = 4$, the maximum acceleration requirement for APNG, $a_{c,\text{APNG,max}} = \frac{1}{2} Na_t$, is equal to that for PNG, $a_{c,\text{PNG,max}} = [N/(N - 2)]a_t$. For large $N = 5$, APNG requires a larger maximum acceleration but less acceleration than PNG for $t \geq 0.2632t_f$. Therefore, APNG is more fuel-efficient for exoatmospheric applications than PNG. Finally, it should be noted that APNG minimizes $\int_0^{t_f} a_c^2(\tau) d\tau$ subject to zero-miss distance, linear dynamics, and constant target acceleration [8].

4.5. PNG Command Guidance Implementation

To implement PNG in a command guidance setting (i.e., no seeker), a differentiating filter must be used to estimate the LOS rate. As a result, command guidance is more susceptible to noise than homing guidance. This issue is exacerbated as the engagement takes place further from the tracking station, noise increases, and guidance degrades. Within [24], the authors address command guided SAMs by spreading the acceleration requirements over t_{go} . The method requires estimates for target position, velocity, acceleration, and t_{go} , but takes into account nonlinear engagement geometry.

4.6. Advanced Guidance Algorithms

Classical PNG and APNG were initially based on intuition. Modern or advanced guidance algorithms exploit optimal control theory: optimizing a performance measure subject to dynamic constraints. Even simple optimal control formulations of a missile–target engagement (e.g., quadratic acceleration measures) lead to a nonlinear two-point boundary value problem requiring creative solution techniques, such as, approximate solutions to the associated Hamilton–Jacobi–Bellman equation—a formidable nonlinear partial-differential equation [22]. Such a formulation remains somewhat intractable given today’s computing power—even for command guidance implementations that can exploit powerful remotely situated computers. Given this, researchers have sought alternative approaches to design advanced (near-optimal) guidance laws. Within [19], Nesline and Zarchan present a PNG-like control law that optimizes square-integral acceleration subject to zero-miss distance in the presence of a one-pole guidance–control–seeker system.

Even for advanced guidance algorithms (e.g., optimal guidance methods), the effects of guidance and control system parasitics must be carefully evaluated to ensure nominal performance and robustness [19]. Advanced (optimal) guidance methods typically require additional information such as time-to-go, target acceleration, and target model parameters (e.g., ballistic coefficient). Given this, Kalman filter and extended Kalman filter (EKF) techniques are often used to estimate the required information. For optimal guidance (OG) algorithms to work well, the estimates must be reliable [19]. Cloutier et al. [17] give an overview of guidance and control techniques, including a comprehensive set of references. Other approaches to guidance law design are discussed below.

4.7. Variants of PNG

Nesline and Zarchan [19] compare PNG, APNG, and optimal guidance (OG). The zero-miss distance (stability) properties of PPNG are discussed by Oh [25]. A nonlinear PPNG formulation for maneuvering targets is provided by Yang and Yang [26]. Closed-form expressions for PPNG are presented by Becker [27]. A more complex version of PNG that is “quasi-optimal” for large maneuvers (but requires t_{go} estimates) is discussed by Axelband and Hardy [28]. Park and Kabamba [20] conducted 2D miss distance analysis [20] for a guidance law that combines PNG and

pursuit guidance. White et al. extend PNG by using an outer LOS rate loop to control the terminal geometry of the engagement (e.g. approach angle) [29]. Generalized PNG, in which acceleration commands are issued normal to the LOS with a bias angle, is addressed by Yuan and Hsu [30]. Yang and Yang address 3D generalized PNG [31] using a spherical coordinate system fixed to the missile to better accommodate the spherical nature of seeker measurements. Analytical solutions are presented without linearization. Yang et al. present generalized guidance schemes [32] that result in missile acceleration commands rotating the missile perpendicular to a chosen (generalized) direction. When this direction is appropriately selected, standard laws result. Time–energy performance criteria are also examined. Capturability issues for variants of PNG are addressed in Ref. 33 and the references cited therein. Yang and Yang [34] present a 2D framework showing that many developed guidance laws are special cases of a general law. The 3D case, utilizing polar coordinates, is considered by Tyan [35].

4.8. Optimal Guidance (OG) Laws

Kalman filtering techniques are often combined with OG laws. Such is the case when weaving targets are under consideration. Weaving targets can cause large miss distances when classical and “standard” OG laws are used. Tactical ballistic missiles, for example, can spiral or weave into resonances as they enter the atmosphere as a result of mass or configurational asymmetries. An OG law, based on weaving (variable amplitude) sinusoidal target maneuvers, is developed by Aggarwal [36]. An EKF is used to estimate the target maneuver weave frequency. Methods for intercepting spiraling weaving tactical ballistic targets are also presented in [37]. This includes an optimal weave guidance law incorporating an EKF to estimate relative position, relative velocity, target acceleration, target jerk information, and weave frequency information.

4.9. Differential Game Guidance

Differential game-theoretic concepts have been addressed [22]. In such formulations, a disturbance (e.g., target maneuver) “competes” with a control (e.g., missile acceleration command). The disturbance attempts to maximize a performance index (e.g., miss distance) while the control attempts to minimize the index. Shima and Golan [38] provide an analytical study using a zero-sum pursuit–evade differential game formulation to develop endgame guidance laws assuming that the interceptor has two controls. Linear biproper transfer functions are used to represent the missile’s control systems—a minimum phase transfer function for the canard system and a non-minimum-phase (NMP) transfer function for the tail control system. A first-order strictly proper transfer function is used for the target dynamics. Bounds are assumed for each of the abovementioned transfer function inputs (i.e., reference commands). The optimal strategy is bang-bang in portions of the game space. A switching time exists prior to interception because of the NMP nature of the tail control system. This feature requires good estimates of t_{go} . \mathcal{H}^∞ theory [7] provides a natural differential

game-theoretic framework for developing guidance laws as well as control laws.

4.10. Lyapunov-Based and Other Guidance Laws

Lyapunov methods have been very useful for deriving stabilizing control laws for nonlinear systems [39]. Such methods have been used to obtain guidance laws that require target aspect angle (relative to LOS) rather than LOS rate [40] and that address maneuvering targets in 3D [41]. A new guidance law—referred to as *circular navigation guidance* (CNG)—steers the missile along a circular arc toward the target [42]. Traditionally, the guidance and control systems are designed separately. While this approach has worked well for years, increasing performance requirements affirm the value of an integrated guidance and control system design methodology. Integrated guidance and control issues have been addressed within a polar coordinate framework [43]. New advanced guidance laws may benefit from linear parameter varying (LPV) [44] and state-dependent Riccati equation (SDRE) [45] concepts.

4.11. Nonlinear State Estimation: Extended Kalman Filter

As discussed earlier, OG laws often require missile–target model state/parameter estimates, such as relative position, velocity of target, and acceleration of target t_{go} . An extended Kalman filter (EKF) is often used to obtain the required estimates. This involves using quasilinearized dynamics to solve the associated matrix Riccati differential equation for a covariance matrix that is used with a model based estimator—mimicking the original nonlinear dynamics—to generate quasioptimal estimates. It is well known that poor estimates for t_{go} , for example, can result in large miss distances and significant capture region reduction [19]. Estimating t_{go} as R/V_c is valid only if V_c is nearly constant. A recursive (noniterative) algorithm for t_{go} estimates, which can be used with OG laws, is provided by Tahk et al. [46].

To develop useful estimation techniques, much attention has been placed on modeling the target. Initially, researchers used simple uncorrelated target acceleration models that yielded misleading results. This led to the use of simple dynamical models—point mass and more complex. Both Cartesian and spherical coordinate formulations have been investigated [47]; the latter better reflect the radial nature of an engagement. Single- and multiple-modeled EKFs have been used [48] to address the fact that no single model captures the dynamics that may arise. Low-observability LOS measurements make the problem particularly challenging [48]. Target observability is explored [49] under PNG and noise-free angle-only measurements in 2D. Williams and Friedland present a method for obtaining required estimates for APNG (e.g. y, \dot{y}, a_t, t_{go}) [50]. Since no single (tractable) model and statistics can be used to accurately capture the large set of possible maneuvers by today's modern tactical fighters, adaptive filtering techniques have been employed. Such filters attempt to adjust the filter bandwidth to reflect the target maneuver. Some researchers have used classical Neyman–Pearson hypothesis testing to detect bias in the

innovations to appropriately reinitialize the filter. Threshold levels must be judiciously selected to avoid false detections that result in switching to an inappropriate estimator.

4.12. Long-Range Exoatmospheric Missions: Weight Considerations

For long-range exoatmospheric missions approaching intercontinental ranges, orbital speeds are required (e.g., $\sim 20,000$ ft/s or 13,600 mi/h or 4 mi/s). To study such interceptors, two new concepts are essential. Fuel-specific impulse, denoted I_{sp} , is defined as the ratio of thrust to the time rate of change of total missile weight. It corresponds to the time required to generate a weight equivalent amount of thrust. Fuel-efficient missiles have higher fuel-specific impulses. Typical tactical missile fuel-specific impulses lie in the range of 200–300 s. Fuel mass fraction, denoted mf, is defined as the ratio of propellant weight W_{prop} to total weight $W_T = W_{prop} + W_{structure} + W_{payload}$. SAMs, for example, have a larger fuel mass fraction than do AAMs because SAMs must travel through the denser air at lower altitudes. For fuel-specific impulses less than 300 s, large fuel mass fractions (approaching 0.9) are required for exoatmospheric applications. A consequence of this is that it takes considerable total booster weight to propel even small payloads to near-orbital speeds. More precisely, it can be shown [8, pp. 265–267] that the weight of the propellant required for a single-stage booster to impart a speed change ΔV to a payload weighing $W_{payload}$ is given by

$$W_{prop} = W_{payload} \overline{\text{mf}} \left[\frac{\exp\left(\frac{\Delta V}{g I_{sp}}\right) - 1}{1 - (1 - \overline{\text{mf}}) \exp\left(\frac{\Delta V}{g I_{sp}}\right)} \right] \quad (14)$$

where g denotes the acceleration due to gravity near Earth's surface and $\overline{\text{mf}} \stackrel{\text{def}}{=} W_{prop}/(W_{prop} + W_{structure})$ denotes an (approximate) fuel mass fraction that neglects the weight of the payload $W_{payload}$. Staging can be used to reduce total booster weight for a given fuel-specific impulse I_{sp} and (approximate) fuel mass fraction mf. Efficient propellant expenditure for exoatmospheric intercepts has been addressed [51]. 3D midcourse guidance for SAMs intercepting nonmaneuvering high-altitude ballistic targets has also been addressed [52]. Neural networks are used to approximate (store) optimal vertical guidance commands and estimate t_{go} . Feedback linearization [39] is used for lateral guidance commands.

4.13. Acceleration Limitations

Endoatmospheric missile acceleration is limited by altitude, speed, structural, stall AOAAOA, and drag constraints—stall AOA at high altitudes and structural limitations at low altitudes [see Eq. (8)]. Exoatmospheric interceptor acceleration is limited by thrust-to-weight ratios and flight time; the latter is due to the fact that when the fuel is exhausted, exoatmospheric missiles cannot maneuver.

4.14. THAAD Systems

More recent research efforts have focused on the development of THAAD systems. Calculations show that high-altitude ballistic intercepts are best made head-on so that there is little target deceleration perpendicular to the LOS [8]. This is because such decelerations appears as a target maneuver to the interceptor. EKF methods have been suggested for estimating target ballistic coefficients and state information to be used in OG laws. Estimating ballistic coefficients

$$\beta \stackrel{\text{def}}{=} (W/S_{\text{ref}} C_{D,0}), \quad (15)$$

where $C_{D,0}$ is the zero-lift drag coefficient] is particularly difficult at high altitudes where there is little drag ($\alpha_{\text{drag}} = (1/2\beta)\rho g V_m^2$). Also, the high closing velocity of a ballistic target engagement significantly decreases the maximum permitted guidance system bandwidth for radome slope stability. Noise issues significantly exacerbate the ballistic intercept problem.

5. FUTURE DEVELOPMENTS

Future developments will focus on theater-class ballistic missiles, guided projectiles, miniature kill vehicles, space-based sensors for missile defense, and boost-phase interceptors. The future of missile guidance depends to a large extent on the ongoing reinterpretation of the ABM treaty between the United States and the former Soviet Union. After September 11, 2001, work was initiated on the development of mininukes for underground bunkers. The need for guided missiles that permit precision strikes with minimal collateral damage was also reaffirmed.

Acknowledgment

This research has been supported, in part, by a 1998 White House Presidential Excellence Award from President Clinton, by National Science Foundation (NSF) Grants 0231440 and 9851422, by the Western Alliance to Expand Student Opportunities (WAESO), Center for Research on Education in Science, Mathematics, Engineering and Technology (CRESMET), Boeing A.D. Welliver Faculty Fellowship, Intel, and Microsoft. For additional information, please contact aar@asu.edu.

BIBLIOGRAPHY

1. M. J. Neufeld, *The Rocket and the Reich*, Harvard Univ. Press, Cambridge, MA, 1995.
2. M. W. Fossier, The development of radar homing missiles, *J. Guid. Control Dynam.* **7**:641–651 (Nov.–Dec. 1984).
3. W. Haeussermann, Developments in the field of automatic guidance and control of rockets, *J. Guid. Control Dynam.* **4**(3):225–239 (May–June 1981).
4. J. H. Blakelock, *Automatic Control of Aircraft and Missiles*, McGraw-Hill, New York, 1992, p. 229.
5. D. E. Williams, B. Friedland, and A. N. Madiwale, Modern control theory for design of autopilots for bank-to-turn missiles, *J. Guid. Control* **10**(4):378–386 (July–Aug. 1987).
6. C. F. Lin, *Modern Navigation, Guidance, and Control Processing*, Prentice-Hall, Englewood Cliffs, NJ, 1991, pp. 14, 184.
7. K. Zhou and J. C. Doyle, *Essentials of Robust Control*, Prentice-Hall, Upper Saddle River, NJ, 1998.
8. P. Zarchan, *Tactical and Strategic Missile Guidance*, AIAA Inc., 1990.
9. N. Macknight, *Tomahawk Cruise Missile*, Motorbooks International, 1995.
10. A. Arrow, *An Analysis of Aerodynamic Requirements for Coordinated Bank-to-Turn Missiles*, NASA CR 3544, 1982.
11. J. J. Feeley and M. E. Wallis, *Bank-to-Turn Missile/Target Simulation on a Desk Top Computer*, The Society for Computer Simulation International, 1989, pp. 79–84.
12. F. W. Reidel, *Bank-to-Turn Control Technology Survey for Homing Missiles*, NASA R 3325, 1980.
13. M. J. Kovach, T. R. Stevens, and A. Arrow, A bank-to-turn autopilot design for an advanced air-to-air interceptor, *Proc. AIAA GNC Conf.*, Monterey, CA, Aug. 1987, pp. 1346–1353.
14. A. A. Rodriguez and J. R. Cloutier, Performance enhancement for a missile in the presence of saturating actuators, *AIAA J. Guid. Control Dynam.* **19**:38–46 (Jan.–Feb. 1996).
15. A. A. Rodriguez and Y. Wang, Performance enhancement for unstable bank-to-turn (BTT) missiles with saturating actuators, *Int. J. Control* **63**(4):641–678 (1996).
16. A. A. Rodriguez and M. Sonne, Evaluation of missile guidance and control systems on a personal computer, *SIMULATION, J. Soc. Comput Simul.* **68**(6):363–376 (1997).
17. J. R. Cloutier, J. H. Evers and J. J. Feeley, Assessment of air-to-air missile guidance and control technology, *IEEE Control Syst. Mag.* 27–34 (Oct. 1989).
18. T. L. Riggs and P. L. Vergaz, *Advanced Air-to-Air Missile Guidance Using Optimal Control and Estimation*, AFATL-TR-81-56, Air Force Armament Laboratory, Eglin AFB, Florida.
19. F. W. Nesline and P. Zarchan, A new look at classical versus modern homing guidance, *J. Guid. Control* **4**(1):78–85 (Jan.–Feb. 1981).
20. J. Park and P. T. Kabamba, Miss distance analysis in a new guidance law, *Proc. 1999 American Control Conf.* June 2–4, 1999, Vol. 4, pp. 2945–2949.
21. J. Waldmann, Line-of-sight rate estimation and linearizing control of an imaging seeker in a tactical missile guided by proportional navigation, *IEEE Trans. Control Syst. Technol.* **10**(4):556–567 (July 2002).
22. A. E. Bryson and Y. C. Ho, *Applied Optimal Control: Optimization, Estimation, and Control*, Hemisphere Publishing Co., 1975.
23. U. S. Shukla and P. R. Mahapatra, The proportional navigation dilemma—pure or true? *IEEE Trans. Aerospace Electron. Syst.* **26**(2):382–392 (March 1990).
24. D. Ghose, B. Dam, and U. R. Prasad, A spreader acceleration guidance scheme for command guided surface-to-air missiles, *Proc. IEEE 1989 Nat. Aerospace and Electronics Conf.*, NAECON 1989, May 22–26, 1989, Vol. 1, pp. 202–208.
25. J. H. Oh, Solving a nonlinear output regulation problem: Zero miss distance of pure PNG, *IEEE Trans. Automatic Control* **47**(1):169–173 (Jan. 2002).
26. C. D. Yang and C. C. Yang, Optimal pure proportional navigation for maneuvering targets, *IEEE Trans. Aerospace Electron. Syst.* **33**(3):949–957 (July 1997).

27. K. Becker, Closed form solution of pure proportional navigation, *IEEE Trans. Aerospace Electron. Syst.* **26**(3):526–533 (1990).
28. E. Axelband and F. Hardy, Quasi-optimum proportional navigation, *IEEE Trans. Automatic Control* **15**(6):620–626 (Dec. 1970).
29. B. A. White, R. Zbikowski, and A. Tsourdos, Aim point guidance: An extension of proportional navigation to the control of terminal guidance, *Proc. 2003 American Control Conf.*, June 4–6, 2003, Vol. 1, pp. 384–389.
30. P. J. Yuan and S. C. Hsu, Solutions of generalized proportional navigation with maneuvering and nonmaneuvering targets, *IEEE Trans. Aerospace Electron. Syst.* **31**(1):469–474 (Jan. 1995).
31. C. D. Yang and C. C. Yang, Analytical solution of generalized 3D proportional navigation, *Proc. 34th IEEE Conf. Decision and Control*, Dec. 13–15, 1995, Vol. 4, pp. 3974–3979.
32. C. D. Yang, F. B. Hsiao, and F. B. Yeh, Generalized guidance law for homing missiles, *IEEE Trans. Aerospace Electron. Syst.* **25**(2):197–212 (March 1989).
33. A. Chakravarthy and D. Ghose, Capturability of realistic generalized true proportional navigation, *IEEE Trans. Aerospace Electron. Syst.*, **32**(1):407–418 (Jan. 1996).
34. C. D. Yang and C. C. Yang, A unified approach to proportional navigation, *IEEE Trans. Aerospace Electron. Syst.* **33**(2):557–567 (April 1997).
35. F. Tyan, An unified approach to missile guidance laws: A 3D extension, *Proc. 2002 American Control Conf.* May 8–10, 2002, Vol. 2, pp. 1711–1716.
36. R. K. Aggarwal, Optimal missile guidance for weaving targets, *Proc. 35th IEEE Decision and Control* Dec. 11–13, 1996, Vol. 3, pp. 2775–2779.
37. P. Zarchan, Tracking and intercepting spiraling ballistic missiles, *Proc. IEEE Position Location and Navigation Symp.* March 13–16, 2000, pp. 277–284.
38. T. Shima and O. M. Golan, Bounded differential games guidance law for a dual controlled missile, *Proc. 2003 American Control Conf.*, June 4–6, 2003, Vol. 1, pp. 390–395.
39. H. Khalil, *Nonlinear Systems*, 2nd ed., Prentice-Hall, S Englewood Cliffs, NJ, 1996.
40. T. L. Vincent and R. W. Morgan, Guidance against maneuvering targets using Lyapunov optimization feedback control, *Proc. American Control Conf.* May 8–10, 2002, pp. 215–220.
41. Z. Youan, H. Yunan and G. Wenjin, Lyapunov stability based three-dimensional guidance for missiles against maneuvering targets, *Proc. 4th World Congress on Intelligent Control and Automation*, June 10–14, 2002, Vol. 4, pp. 2836–2840.
42. I. R. Manchester and A. V. Savkin, Circular navigation guidance law for precision missile/target engagements, *Proc. 41st IEEE Conf. Decision and Control*, Dec. 10–13, 2002, Vol. 2, pp. 1287–1292.
43. S. N. Balakrishnan, D. T. Stansbery, J. H. Evers, and J. R. Cloutier, Analytical guidance laws and integrated guidance/autopilot for homing missiles, *Proc. 2nd IEEE Conf. Control Applications*, Sept. 13–16, 1993, Vol. 1, pp. 27–32.
44. D. B. Ridgely and M. B. McFarland, Tailoring theory to practice in tactical missile control, *IEEE Control Syst. Mag.* **19**(6):49–55 (Dec. 1999).
45. J. S. Shamma and J. R. Cloutier, Existence of SDRE stabilizing feedback, *IEEE Trans. Automatic Control* **48**(3):513–517 (March 2003).
46. M. J. Tahk, C. K. Ryoo and H. Cho, Recursive time-to-go estimation for homing guidance missiles, *IEEE Trans. Aerospace Electron. Syst.* **38**(1):13–24 (Jan. 2002).
47. C. N. D'Souza, M. A. McClure, and J. R. Cloutier, Spherical target state estimators, *Proc. American Control Conf.*, June 29–July 1, 1994, Vol. 2, pp. 1675–1679.
48. C. Rago and R. K. Mehra, Robust adaptive target state estimation for missile guidance using the interacting multiple model Kalman filter, *Proc. IEEE 2000 Position Location and Navigation Symp.*, March 13–16, 2000, pp. 355–362.
49. M. J. Tahk, H. Ryu, and E. J. Song, Observability characteristics of angle-only measurement under proportional navigation, *Proc. 34th SICE Annual Conf. Int. Session Papers*, July 26–28, 1995, pp. 1509–1514.
50. D. E. Williams and B. Friedland, Target maneuver detection and estimation [missile guidance], *Proc. 27th IEEE Conf. Decision and Control*, Dec. 7–9, 1988, Vol. 1, pp. 851–855.
51. S. Brainin and R. McGhee, Optimal biased proportional navigation, *IEEE Trans. Automatic Control* **13**(4):440–442 (Aug. 1968).
52. E. J. Song and M. J. Tahk, Three-dimensional midcourse guidance using neural networks for interception of ballistic targets, *IEEE Trans. Aerospace and Electron. Syst.*, **38**(2):404–414 (April 2002).

MIXED-SIGNAL CMOS RF INTEGRATED CIRCUITS

MICHEL STEYAERT
 PATRICK REYNAERT
 KULeuven ESAT-MICAS
 Leuven, Belgium

1. INTRODUCTION

The world of wireless communication and its applications have begun to grow rapidly. The driving force behind this lies in the introduction of digital coding and digital signal processing in wireless communications. This digital revolution is driven by the development of high-performance, low-cost CMOS technologies that allow for the integration of an enormous amount of digital functions on a single die. As CMOS is mainly a digital technology, placing all digital functions on a single die is merely a matter of handling the system complexity. To achieve a truly single-chip solution, the analog part also has to be integrated in CMOS.

The telecommunication market is generally considered to be a business where a single-chip solution in a cheap (CMOS) technology results in a huge cost benefit; the main reason is the high volume of user equipment. Furthermore, in these systems, small size, low board area, low power consumption, and high talktime are crucial, and therefore it is of utmost importance to achieve a high level of integration. This trend toward single-chip, fully integrated systems can clearly be seen in the development of RF systems such as GSM, EDGE, Bluetooth, and wireless LAN. In all these systems, the analog part mainly consists of an RF front end.

Deep submicrometer technologies allow for the operation frequency of CMOS circuits above 1 GHz, which opens the way to fully integrated RF systems. Several research groups have developed high-performance downconverters,

low-phase-noise voltage-controlled oscillators, and dual-modulus prescalers in standard CMOS technologies. The research has already demonstrated fully integrated receivers and synthesizers with no external components, nor tuning or trimming. Further research on low-noise amplifiers, power amplifiers, and synthesizers has resulted in fully integrated CMOS RF transceivers for DCS1800, Bluetooth, and wireless LAN [1–3].

In this article, we will focus on the evolution from the well-known heterodyne receiver topology to the zero- and low-IF topology used in modern receivers. We will also discuss the interaction between the analog part and the digital part regarding substrate noise and decoupling.

2. TECHNOLOGICAL ASPECTS OF MIXED-SIGNAL DESIGN

2.1. Deep Submicrometer MOS Transistors

Because of the never-ending progress in technology down-scaling and the requirement to achieve a higher degree of integration for DSP circuits, deep submicrometer technologies are now considered as standard CMOS technologies. Transistors with f_T values near 100 GHz have been demonstrated in 0.1- μm technologies [4,5]. However, the speed increase of deep submicrometer technologies is reduced by the parasitic capacitance of the transistor, meaning the gate–drain overlap capacitance and the drain–bulk junction capacitance. This can clearly be seen in Fig. 1 in the comparison for different technologies between f_T and the $f_{3\text{dB}}$, the latter is defined as the 3 dB point of a diode connected transistor [6]. The $f_{3\text{dB}}$ is more important for analog design because it reflects the speed limitation of a transistor in a practical configuration, namely, a simple two-stage common-source amplifier. As can be seen in Fig. 1, the f_T rapidly increases, but for real circuit designs ($f_{3\text{dB}}$) the speed improvement is only moderate.

2.2. Integration of Passive Components

In integrated CMOS RF circuits [7,8] it becomes clear that the transistor will not be the limiting factor but rather the passive components and packaging will be. Since the RF signals have to come off the chip sooner or later, and since the RF antenna signal has to get into the chip, any

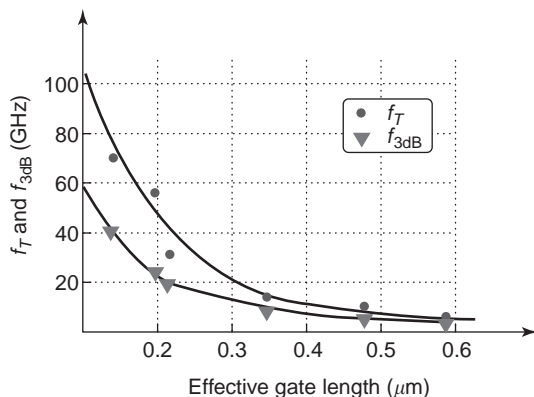


Figure 1. Comparison between f_T and $f_{3\text{dB}}$.

parasitic PCB, packaging, or bondwire in combination with the ESD (electrostatic discharge) protection network and packaging pin capacitances will strongly affect and degrade the RF signal. Another important aspect in mixed-signal design is the quality factor of the passive elements. High-quality metal–insulator–metal capacitors and low-resistance top-metal layers for inductors are process options that add to the total mask count, and a high amount of passive elements will increase the total die area. An alternative is to separate the processing of the active devices from the processing of the passive components. An example is given in Ref. 9, where a low-cost passive integration and packaging technology is combined with a high-performance CMOS technology. These solutions are feasible as long as the parasitics due to the interconnection of the two dies are small.

3. ARCHITECTURAL ASPECTS

In mixed-signal design, the aim is to integrate both the digital and the analog parts on one single die. However, many analog front-end architectures are not well suited for integration. Therefore, new architectures have been (re)invented that allow a fully integrated solution. The heterodyne receiver, for example, is the best-known and most frequently used receiver topology. In this receiver the desired signal is downconverted to a relatively high intermediate frequency. Very high performances can be achieved with the heterodyne topology. However, the main problem is the poor degree of integration that can be achieved as every stage requires going off chip and requires the use of a discrete bandpass filter.

The zero-IF receiver (see Fig. 2) has been introduced as an alternative that can achieve a much higher degree of integration because this topology uses a direct quadrature downconversion of the desired signal. Theoretically, no discrete high-frequency bandpass filter is required, allowing for the realization of a fully integrated receiver [10]. However the zero-IF receiver is intrinsically very sensitive to parasitic baseband signals such as DC-offset voltages and self-mixing. These drawbacks have kept the zero-IF receiver from being used on large scale in new wireless applications. It has, however, been shown that with the use of dynamic nonlinear correction algorithms,

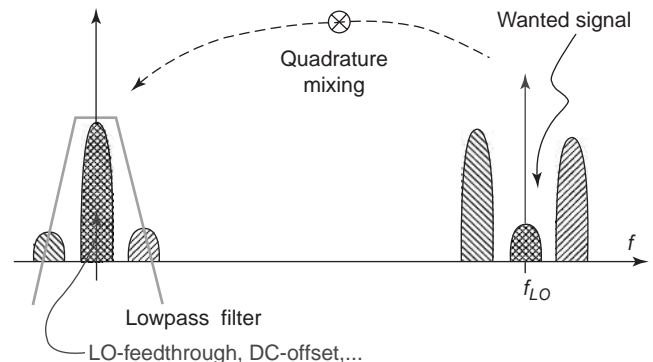


Figure 2. Zero-IF receiver principle.

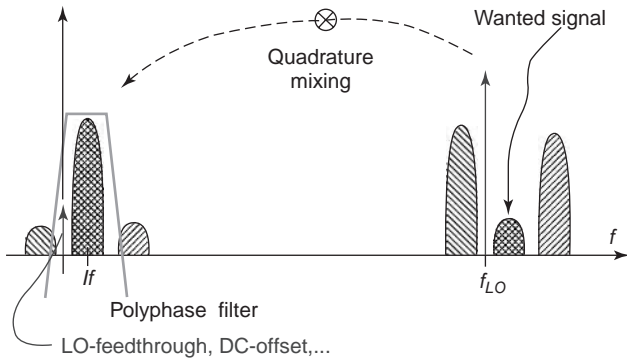


Figure 3. Low-IF receiver principle.

implemented in the DSP, the zero-IF topology can be used for high-performance applications such as GSM and DECT [11,12]. In such a system, the performance of the analog architecture is improved by the use of digital algorithms, which clearly demonstrates another benefit of a single-chip mixed-signal approach.

New receiver topologies such as the low-IF receiver [3,13,28] have been introduced. The low-IF receiver performs a downconversion from the antenna frequency directly to—as the term already indicates—a low IF (i.e., in the range of a few 100 kHz; see Fig. 3). Downconversion is done in quadrature and the mirror signal suppression is performed at low frequency, after downconversion, by a polyphase filter. This polyphase filter is a complex filter, consisting of two signal paths: an in-phase path and a quadrature path. This allows for an asymmetric filter characteristic: a passband filter for positive frequencies and a suppression at the same negative frequencies. The polyphase filter can be implemented either as an analog filter [13] or in the DSP, together with the other digital functions. This again demonstrates how the interaction between the analog architecture and the digital part improves the performance of the system. The low-IF receiver is closely related to the zero-IF receiver since it can also be fully integrated and uses a single-stage direct downcon-

version. The difference is that the low-IF receiver does not use baseband operation, resulting in a total immunity to parasitic baseband signals, resolving in this way the main disadvantage of the zero-IF receiver. By the use of a double-quadrature structure, converters requiring neither any external components nor any tuning or trimming have been demonstrated [28].

4. ANALOG CIRCUIT DESIGN IN A DIGITAL CMOS TECHNOLOGY

The general transceiver architecture, depicted in Fig. 4, requires analog functions implemented in a digital technology. As mentioned before, due to the high f_T and $f_{3\text{dB}}$ of current technologies, operating frequencies of 5 GHz and above become possible. The low-noise amplifier, the power amplifier, and the synthesizer are the most critical analog functions since the overall performance of the transceiver will depend mainly on the performance of these analog building blocks.

4.1. The Low-Noise Amplifier

The low-noise amplifier is a very critical building block, since mainly this block will determine the overall noise figure and linearity of the receiver. Furthermore, in deep submicrometer technologies, ESD issues are becoming very important, and this will have a great influence on the LNA design. Most RF CMOS LNA topologies use single-stage inductive degeneration techniques [14,15] to provide resistive input impedance to the antenna. The input of the LNA is usually protected against ESD by two reverse-biased diodes. Care has to be taken since those protection networks increase the noise, capacitive input load, and as such the power drain of the circuit. In Fig. 5, an example of a 0.8-dB noise figure LNA is presented [15]. The LNA has been measured in its nominal 9-mW regime, drawing 6 mA from a 1.5-V power supply. The forward gain (S_{21}) reaches more than 20 dB at 1.23 GHz. At the same time, the reverse isolation is better than 31 dB. The

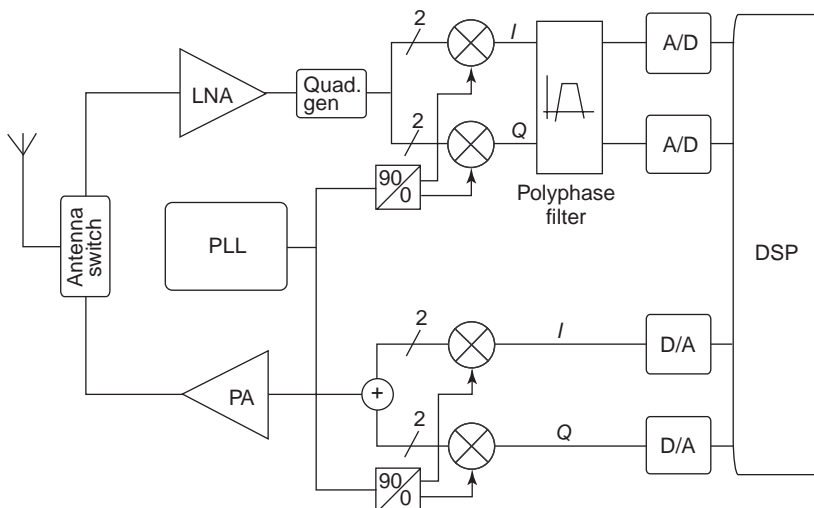


Figure 4. General transceiver architecture.

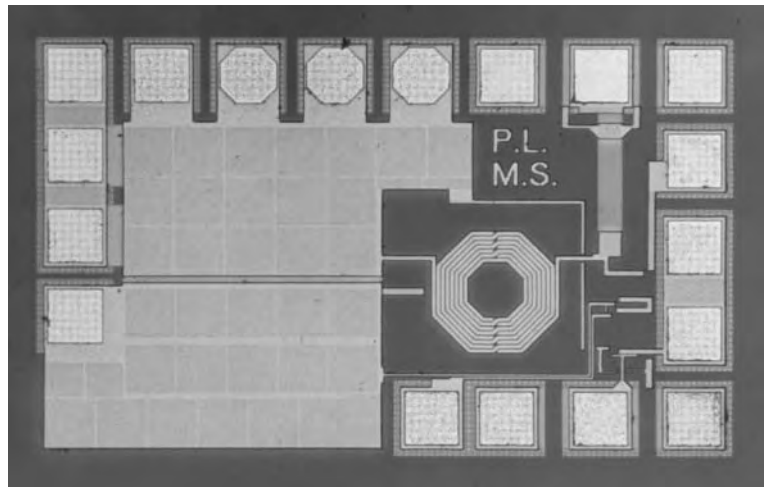


Figure 5. A 0.8-dB noise figure LNA in 0.25- μm CMOS.

noise figure of the LNA, in nominal operation, reaches a minimum of 0.79 dB at 1.24 GHz. An HBM (human body model) test has shown that the LNA is able to withstand positive ESD pulses up to 0.6 kV and negative ESD pulses up to -1.4 kV, surpassing the 0.5 kV specification.

4.2. The Voltage-Controlled Oscillator

The local oscillator is responsible for the correct frequency selection in up- and downconverters. The signal level of the desired receive channel can be very small, whereas adjacent channels can have very large power levels. Therefore the phase noise specifications for the local-oscillator signal are very critical. Usually, the local oscillator is realized as a phase-locked loop. The very rigid specifications are reflected in the design of the voltage-controlled oscillator (VCO). For the realization of a gigahertz VCO in a submicrometer CMOS technology, two options exist: either ringoscillators or oscillators based on the resonance frequency of an LC tank. The inductor in this LC tank can be implemented as an active inductor or a passive one. It has been shown that for ring oscillators as well as active LC oscillators [16], the phase-noise is inversely related to the power consumption. Therefore, the only viable solution to a low-power, low-phase-noise VCO is an LC oscillator with a passive inductor. As could be expected, the limitation in this oscillator is the integrated passive inductor. For extremely low phase noise requirements, the concept of bondwire inductors has been investigated [16,17]. Since a bondwire has a parasitic inductance of approximately 1 nH/mm and a very low series resistance, very-high- Q inductors can be created. The most elegant solution is the use of a spiral coil on a standard silicon substrate, without any modifications. In combination with fractional- N techniques, low-phase-noise PLL circuits can be obtained. For example, in Fig. 6 a fully integrated synthesizer in a 0.25- μm CMOS technology is presented [18]. The measured phase noise is less than 120 dBc/Hz at 600 kHz, while the reference and fractional spurious signals are respectively 70 dB and 100 dB below the carrier signal.

4.3. A/D Conversion

After downconversion, an analog-to-digital converter is the interface to the DSP. Once the signal is downconverted to DC or low IF, there is the desired signal, along with unwanted blockers that are significantly higher than the signal itself. Digitizing that combination of signals requires a high-dynamic range analog-to-digital converter with excellent noise and spurious-free dynamic range performance. As an example, in the case of Global System for Mobile Communications (GSM), the blocker at 3 MHz offset from the carrier can be 76 dB above the signal, while the blocker at 600 kHz offset is 56 dB above the signal. This sets the upper limit of the A/D converter. Furthermore, at reference sensitivity level, the desired signal at the A/D input would be 1 mV (-60 dBV). Since the quantization noise floor must be low enough not to degrade the noise figure performance, the noise floor required would be -80 dBV. On the other hand, CDMA and wideband code-division multiple access have much lower signal-to-noise requirements, so the tolerable quantization noise floor is relaxed for these application. A trend can be observed to shift the A/D conversion more toward the antenna. This clearly enables the use of multiple standard radio and reduces the chip area of the analog interface. The cost however, is a higher power consumption of the A/D converter.

4.4. The Power Amplifier

In the transmitter path, the power amplifier is the most challenging block for integration in a CMOS technology. Most of the CMOS transceivers reported in open literature deliver power levels in the range of 0 dBm. To achieve a fully integrated CMOS system, the power amplifier also has to be realized in a CMOS technology, on the same die. An alternative is to place the 0-dBm transceiver and the power amplifier in the same package. In this case, one can still benefit from implementing the PA in CMOS, because of the cost reduction and the advantage of a single-technology solution. Another alternative is to use a low-cost technology to integrate the passives [9] and to combine this substrate with the CMOS die.

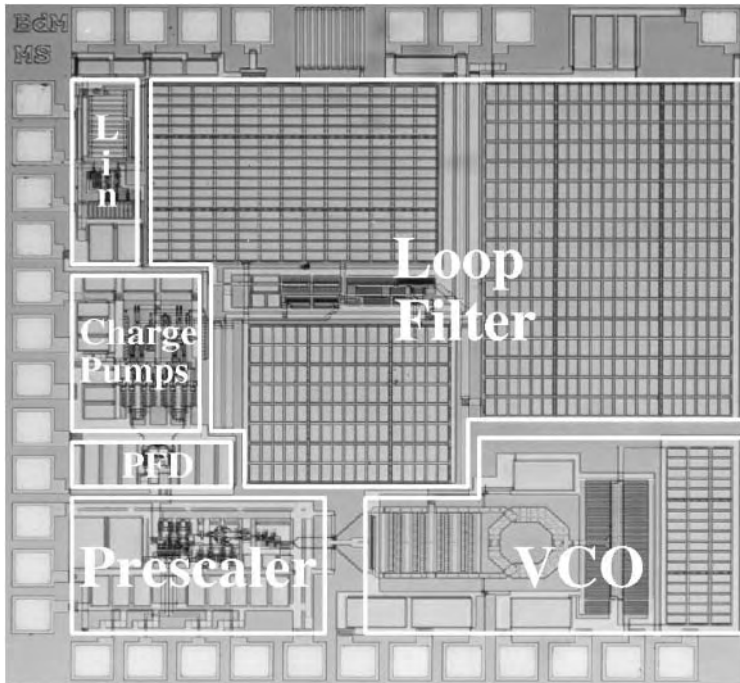


Figure 6. A fully integrated 0.25- μm CMOS Phase-locked loop.

In a digital CMOS technology, switching-mode power amplifiers are the favored candidates for wireless communications, due to their excellent high efficiency. A simplified presentation of a switching amplifier is an NMOS transistor loaded with a parallel tank, consisting of a power supply inductor, a shunt capacitor, and a load resistor (Fig. 7). Because of the switching LC structure, the maximum voltage at the drain will be higher than the power supply, hence making the transistor sensitive to several failure mechanisms, such as oxide breakdown and hot electrons. The major advantage of a switching topology is that the maximum voltage is present only when the NMOS transistor is switched off. As a consequence, the hot-electron issue is simplified and the main cause of destruction is oxide breakdown, a failure mechanism that is easy to characterize. An important aspect is the integration of the passive components in a CMOS technology. It

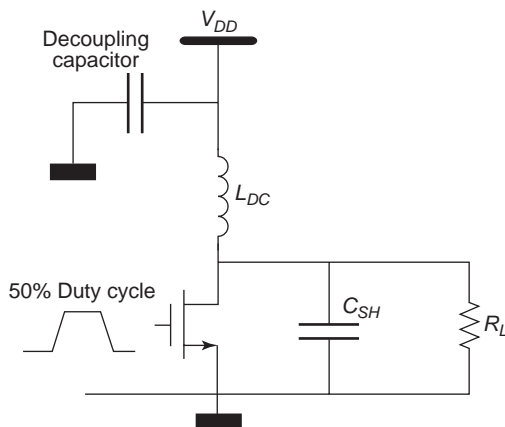


Figure 7. Basic CMOS switching amplifier.

can be shown that a fixed relationship exists between the required inductor L_{DC} , the output power, the operating frequency, and the breakdown voltage [19]. When moving toward GHz frequencies and deep-submicrometer technologies, the value of the inductor L_{DC} becomes very small, as can be seen in Fig. 8. The only way to realize such a small inductance is to integrate it on the same die as the CMOS transistors, since the parasitic inductance and capacitance of bondwires will be too large relative to the required inductance. The decoupling capacitance required for the PA also needs to be integrated on the same die as the power amplifier itself. The resonance frequency of an off-chip decoupling capacitor typically lies around 1 GHz for a 10 pF of decoupling. In order to achieve either more decoupling or a higher frequency, the decoupling has to be

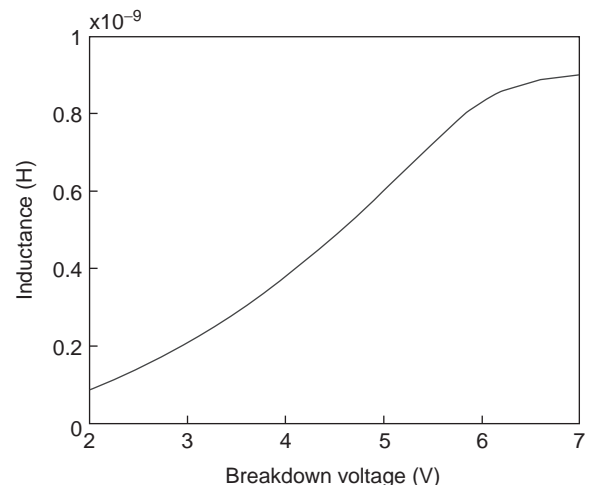


Figure 8. Value of L_{DC} for a lossless Bluetooth power amplifier.

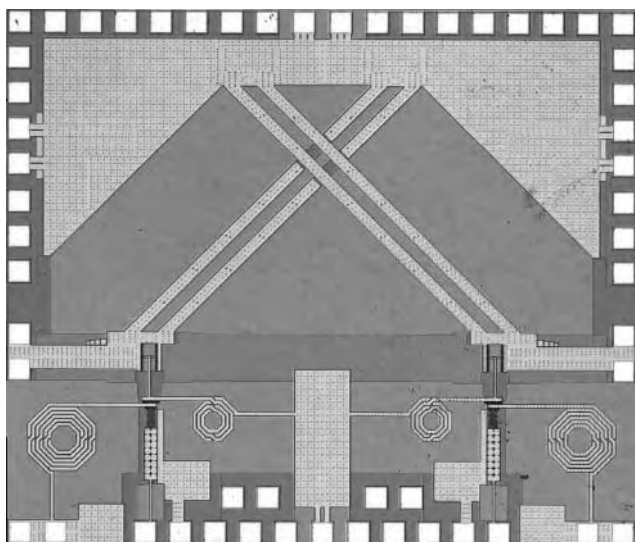


Figure 9. Fully integrated 0.25- μm CMOS Bluetooth power amplifier.

integrated on the same die as the power amplifier, hence justifying the trend toward full integration. Finally, as can be seen in Fig. 4, the power amplifier needs to be driven by the upconversion mixer. Therefore, it is of utmost importance to achieve sufficient power gain in the amplifier. On the other hand, a high power gain will require more driver stages, hence lowering the overall efficiency of the transceiver. Therefore, many tradeoffs are involved in the design of a power amplifier and overall optimization is required [20,21]. In Fig. 9 a fully integrated power amplifier in a 0.25- μm CMOS technology is presented [8]. It can deliver up to +21 dBm, the required input power is only -10 dBm, and the measured power-added efficiency (PAE) is 25.8%.

5. SUBSTRATE COUPLING BETWEEN THE DIGITAL AND ANALOG PARTS

In mixed-signal design, substrate coupling between the analog and the digital parts is an important aspect that needs special attention during design and layout. The issue of substrate coupling is still under research, since a simple and straightforward method is lacking. However, the designer can take some precautions to minimize the influence of the digital switching noise on the sensitive analog blocks [29].

It is a common practice to define the ultimate voltage reference, the ground, off chip. In high-speed applications, various techniques such as separated digital and analog powerlines are used to make an on-chip ground close to the external reference. In this approach all voltages are artificially referred to the external ground, with the on chip ground tied as close to this external reference as possible. As integrated circuits are on chip, however, they are naturally related to the on-chip ground, which will never be exactly equal to the off-chip reference. It is therefore more suitable to define the reference for a circuit on chip. An adequate decoupling will keep the local circuit power constant relative to this local reference. Signal distortion due to limited power supply rejection ratio (PSRR) is thus minimized. As a result of fast current variations in power pads, two analog subcircuits may have a different local reference, even when they share the same analog ground pad [22,23]. Eventually, several local references may be defined for various subsystems and decoupled locally. The transmission of the signal to another subcircuit or to the outside world can be regarded as a separate problem when using a differential approach even for voltages that are single-ended at first sight. A voltage is not an absolute entity, but a difference in electric potential relative to a predetermined reference. For example, the input of a transistor is the voltage difference and the unwanted bulk to

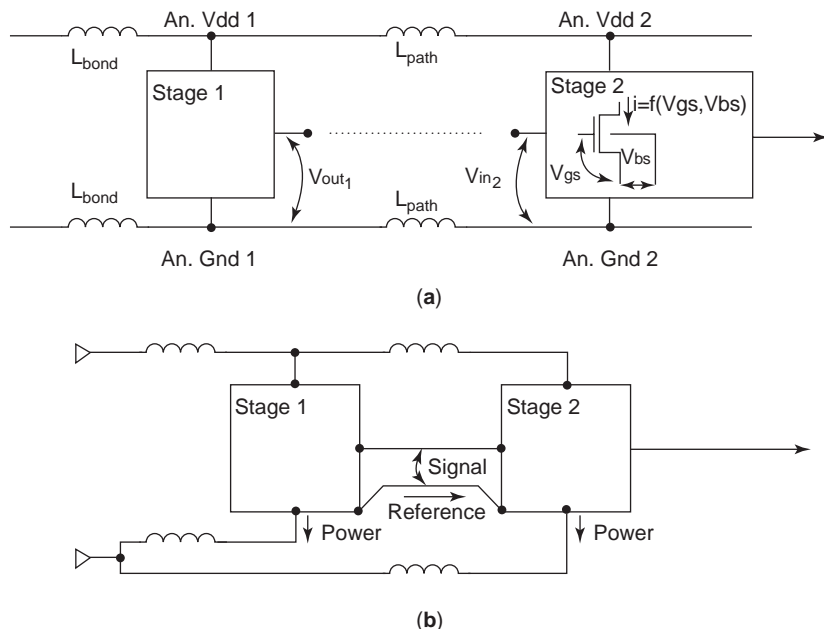


Figure 10. The use of differential circuits in mixed-mode ICs.

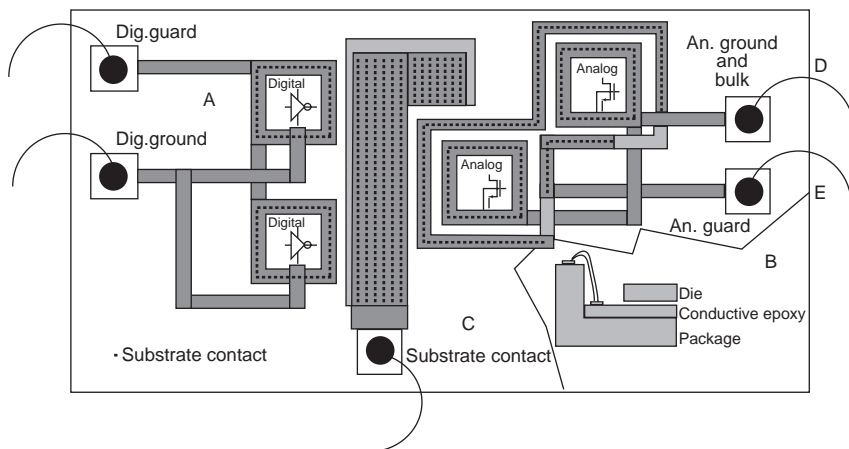


Figure 11. Placement and biasing of guard rings.

source voltage (Fig. 10a). To avoid signal disturbance due to reference variations from one place to another, voltages should be transferred concurrently with their reference through a dedicated path (Fig. 10b) rather than rely on a common ground. Similarly, to get the signal off chip, dedicated pins are used for the references.

The relative bondwires' placement requires some attention too. Although coupling between the wires is relatively small [24], it can be sufficient to transfer noise from a noisy path to an adjacent node. Sensitive inputs' bondwires should therefore never be close to noisy wires. Eventually they can be shielded by enclosing them with extra bondwires connected to a quiet ground. Even an optimally decoupled analog circuit can be disturbed by substrate noise injected on some other place on the chip [25]. Guard rings can limit this effect when used correctly. Figure 11 summarizes the correct placement and biasing of the rings. The first step in reducing substrate coupling is the limitation of the injected noise. A guard ring close to the digital transistors and biased with a dedicated pin will provide a return path for injected currents (Fig. 11A). This ring may not be biased with either of the on-chip grounds. Biasing with the digital ground would inject extra noise into the substrate, while using the analog ground would couple substrate noise directly into it. To reduce the effect of the current that reaches the bulk, a low-impedance return path is of utmost importance [26,27]. For heavily doped substrates, the best result is obtained by mounting the die with conductive epoxy to the leadframe using several bondwires to connect it to the external ground (Fig. 11B). Eventually, large substrate contacts with a dedicated pin filling spare places on the chip can be an alternative (Fig. 11C). In lightly doped substrates, where most currents flow just underneath the chip surface, a guard ring with dedicated pin surrounding the digital block is an effective return pad. In these substrates, physical separation of noise source and sensitive circuit is also very effective as the resistance in the noise path continuously increases with the distance. For heavily doped material, a separation of more than 4 times the epilayer thickness is useless as most of the disturbing current then just passes through the low ohmic bulk [26]. Substrate noise disturbs the analog circuits through their bulk to source voltage. To reduce this bulk effect, bulk source

voltage variations of analog MOS transistors should be minimized. The bulk must thus be tied locally to the analog reference rather than to the (slightly different) external one. This is achieved with bulk contacts close to the analog transistors and biased with the local analog ground (Fig. 11D), which results in an optimal output voltage relative to the local on-chip analog reference. A guard ring with dedicated pin around the analog circuits eventually enhances the noise immunity even further (Fig. 11E) [26], but does not eliminate the need of the good bulk contacts to the local analog ground.

6. CONCLUSIONS

The trend toward deep-submicrometer technologies has enabled the use of CMOS for the integration of high-performance analog functions. First, the analog architecture needs to be adjusted to allow a fully integrated solution. The next step is to place both the digital and the analog functions on a single die, which allows. For an interaction between the analog architecture and the digital DSP, which enables one to achieve a higher performance of the analog part. This results in highly reconfigurable mixed-circuit systems in the cheapest technology available. The trend toward deep-submicrometer technologies will allow achieving those goals as long as the short-channel effects will not limit the performance concerning linearity and intermodulation problems. Furthermore, substrate noise coupling between the digital part of the system and the sensitive analog blocks can degrade the analog performance, hence demanding some precautions regarding bulk contacts, guard rings, and packaging.

BIBLIOGRAPHY

1. A. Rofougaran et al., A 5-GHz direct-conversion CMOS transceiver utilizing automatic frequency control for the IEEE 802.11a Wireless LAN Standard, *IEEE J. Solid-State Circ.* **38**(12):2209–2220 (Dec. 2003).
2. J. Rudell et al., A single-chip digitally calibrated 5.15-5.825-GHz 0.18 μm CMOS transceiver for 802.11a Wireless LAN, *IEEE J. Solid-State Circ.* **38**(12):2221–2231 (Dec. 2003).

3. M. Steyaert et al., A single chip CMOS transceiver for DCS1800 wireless communications, *Proc. IEEE-ISSCC*, Feb. 1998.
4. R. Yan et al., High performance 0.1 micron room temperature Si mosfets, *Digest of Technical Papers, 1992 Symp. VLSI Technology*, June 2–4, 1992.
5. J. Chen et al., A high speed SOI technology with 12 ps/18 ps gate delay operation at 1.5 V, *Proc. IEEE Int. Electron Devices Meeting*, San Francisco, CA, Dec. 13–16, 1992.
6. M. Steyaert and W. Sansen, Opamp design towards maximum gain-bandwidth, *Proc. AACD workshop*, The Netherlands, Delft, March 1993, pp.63–85.
7. I. Aoki et al., Fully integrated CMOS power amplifier design using the distributed active transformer architecture, *IEEE J. Solid-State Circ.* **37**(3):371–383 (March 2002).
8. K. Mertens and M. Steyaert, A fully integrated class 1 Bluetooth 0.25 μm CMOS PA, *Proc. ESSCIRC*, Sept. 2002, pp. 219–222.
9. P. Lok, RF power amplifiers, *Proc. GiRaFe Workshop*, ISSCC, Feb. 2004.
10. C. H. Hull, R. R. Chu, and J. L. Tham, A direct-conversion receiver for 900 MHz (ISM band) spread-spectrum digital cordless telephone, *Proc. ISSCC*, San Francisco, Feb. 1996, pp. 344–345.
11. J. Sevenhans, A. Vanwelsenaers, J. Wenin, and J. Baro, An integrated Si bipolar transceiver for a zero IF 900 MHz GSM digital mobile radio front-end of a hand portable phone, *Proc. CICC*, May 1991, pp.771–774.
12. J. Sevenhans et al., An analog radio front-end chip set for a 1.9 GHz mobile radio telephone application, *Proc. ISSCC*, San Francisco, Feb. 1994, pp. 44–45.
13. J. Crols and M. Steyaert, A single-chip 900 MHz CMOS receiver front-end with a high performance low-IF topology, *IEEE J. Solid-State Circ.* **30**(12):1483–1492 (Dec. 1995).
14. J. Janssens and M. Steyaert, CMOS noise performance under impedance matching constraints, *Electron. Lett.* **35**(15):1278–1280 (July 1999).
15. P. Leroux, J. Janssens, and M. Steyaert, A 0,8 dB NF ESD-protected 9 mW CMOS LNA, *Proc. ISSCC 2001*, San Francisco, 2001, pp. 410–411.
16. J. Craninckx and M. Steyaert, Low-noise voltage controlled oscillators using enhanced LC-tanks, *IEEE Trans. Circ. Syst.—II: Analog Digital Signal Process.* **42**(12):794–804 (Dec. 1995).
17. A. Rofougaran, J. Rael, M. Rofougaran, and A. Abidi, A 900 MHz CMOS LC-oscillator with quadrature outputs, *Proc. ISSCC*, Feb. 1996, pp. 392–393.
18. B. De Muer and M. Steyaert, A 1.8 GHz CMOS sigma-delta fractional-N synthesizer, *Proc. European Solid-State Circuits Conf.*, Villach, Austria, Sept. 17–21, 2001, pp. 44–47.
19. P. Reynaert, K. Mertens, and M. Steyaert, A state-space behavioral model for CMOS class E power amplifiers, *IEEE Trans. Comput. Aided Design Integr. Circ. Syst.* **22**(2):132–138 (Feb. 2003).
20. K. Mertens, P. Reynaert, and M. Steyaert, Performance study of CMOS power amplifiers, *Proc. European Solid-State Circuits Conf.*, Villach, Austria, Sept. 17–21, 2001, pp. 440–443.
21. P. Reynaert, K. Mertens, and M. Steyaert, Optimizing the dimensions of driver and power transistor in switching CMOS RF amplifiers, *Analog Integr. Circ. Signal Process.* **32**(2): 171–182 (Aug. 2002).
22. A. J. Rainal, Eliminating inductive noise of external chip interconnections, *IEEE J. Solid-State Circ.* **29**:126–129 (Feb. 1994).
23. Y.-I. S. Shin, Maintain signal integrity at high digital speeds, *Electron. Design*, 77–90 (May 14, 1992).
24. L. J. Giacoletto, *Electronics Designers' Handbook*, McGraw-Hill, New York, 1977, pp. 3.42–3.49.
25. L. Gal, On-chip cross talk—the new signal integrity challenge, *Proc. CICC*, 1995, pp. 251–254.
26. D. K. Su, M. J. Loinaz, S. Masui, and B. A. Wooley, Experimental results and modeling techniques for substrate noise in mixed-signal integrated circuits, *IEEE J. Solid-State Circ.* **28**:420–428 (April 1993).
27. R. Gharpurey and R. G. Meyer, Modeling and analysis of substrate coupling in integrated circuits, *IEEE J. Solid-State Circ.* **31**:344–353 (March 1996).
28. M. Steyaert, J. Janssens, B. De Muer, M. Borremans, and N. Itoh, A 2-V CMOS cellular transceiver front-end, *IEEE J. Solid-State Circ.* **35**(12):1895–1907 (Dec. 2000).
29. M. Ingels and M. Steyaert, Design strategies and decoupling techniques for reducing the effects of electrical interference in mixed-mode IC's, *IEEE J. Solid-State Circ.* **32**(7):1136–1141 (July 1997).

MIXER CIRCUITS

KATSUJI KIMURA
NEC Corporation

A frequency mixer inputs two frequencies—a radiofrequency (RF) and a local-oscillator (LO) frequency—mixes them, and produces their difference frequency and sum frequency. The output signal is tuned by a filter, and one of the two output frequencies is selected: the difference or the sum. When the output difference frequency is an intermediate frequency (IF), the mixer is usually called a down-conversion frequency mixer, and when the output sum frequency is a high frequency, it is usually called an up-conversion frequency mixer.

A frequency mixer is fundamentally a multiplier, because the analog multiplier outputs a signal proportional to the product of the two input signals. Therefore, a frequency mixer is represented by the symbol for the multiplier, as shown in Fig. 1.

The transfer function of a nonlinear element is expressed as

$$f(u) = a_0 + a_1u + a_2u^2 + a_3u^3 + \dots + a_nu^n + \dots \quad (1)$$

The product xy of the two input signals x and y can be derived from only the second-order term: a_2u^2 , where $u = x + y$,

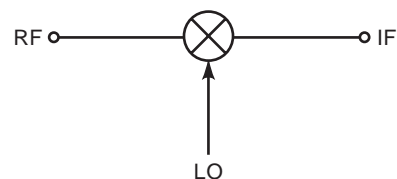


Figure 1. A symbol for a frequency mixer. The symbol for a multiplier is used.

and x and y are the two input signals. The product of the two input signals is produced by a nonlinear element, such as a diode or transistor. For example, single-diode mixers, singly balanced diode mixers, doubly balanced diode mixers, single-transistor mixers, singly balanced transistor mixers, and doubly balanced transistor mixers are usually used as frequency mixers.

1. APPLICATION TO RECEIVERS

Mixers are used to shift the received signal to an intermediate frequency, where it can be amplified with good selectivity, high gain, and low noise, and finally demodulated in a receiver. Mixers have important applications in ordinary low-frequency and microwave receivers, where they are used to shift signals to frequencies where they can be amplified and demodulated most efficiently. Mixers can also be used as phase detectors and in demodulators, and must perform these functions while adding minimal noise and distortion.

Figure 2 shows, for example, the block diagram of a VHF or UHF communication receiver. The receiver has a single stage input amplifier; this preamp, which is usually called an RF amplifier, increases the strength of the received signal so that it exceeds the noise level of the following stage; therefore, this preamp is also called a low-noise amplifier (LNA). The first IF is relatively high (in a VHF or UHF receiver, the widely accepted standard has been 10.7 MHz); this high IF moves the image frequency well away from the RF, thus allowing the image to be rejected effectively by the input filter. The second conversion occurs after considerable amplification, and is used to select some particular signal within the input band and to shift it to the second IF. Because narrow bandwidths are generally easier to achieve at this lower frequency, the selectivity of the filter used before the detector is much better than that of the first IF. The frequency synthesizer generates the variable-frequency LO signal for the first mixer, and the fixed-frequency LO for the second mixer.

Figure 3 illustrates an ideal analog multiplier with two sinusoids applied to it. The signal applied to the RF port has a carrier frequency ω_s and a modulation waveform $A(t)$. The other, the LO, is a pure, unmodulated sinusoid at frequency ω_p .

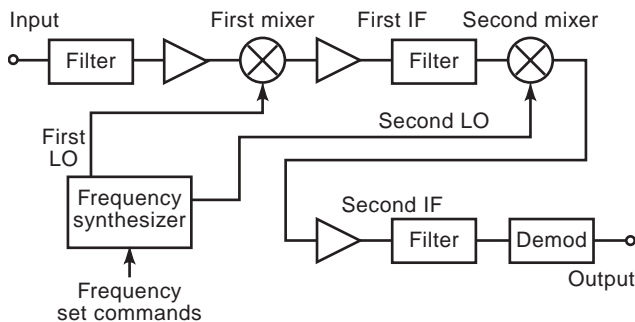


Figure 2. Double-superheterodyne VHF or UHF communication receiver.

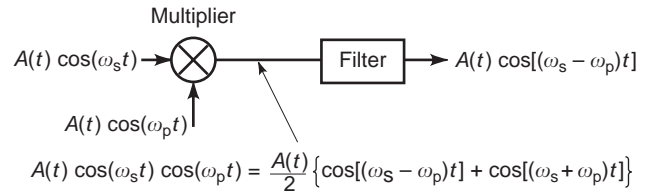


Figure 3. A mixer is fundamentally a multiplier. The difference frequency in the IF results from the product of sinusoids.

Applying some basic trigonometry to the output is found to consist of modulated components at the sum and difference frequencies. The sum frequency is rejected by the IF filter, leaving only the difference.

Fortunately, an ideal multiplier is not the only device that can realize a mixer. Any nonlinear device can perform the multiplying function. The use of a nonideal multiplier results in the generation of LO harmonics and in mixing products other than the desired one. The desired output frequency component must be filtered from the resulting chaos.

Another way to view the operation of a mixer is as a switch. Indeed, in the past, diodes used in mixers have been idealized as switches operated at the LO frequency. Figure 4a shows a mixer modeled as a switch; the switch interrupts the RF voltage waveform periodically at the LO frequency. The IF voltage is the product of the RF voltage and the switching waveform.

Another switching mixer is shown in Fig. 4b. Instead of simply interrupting the current between the RF and IF ports, the switch changes the polarity of the RF voltage periodically. The advantage of this mixer over the one in Fig. 4a is that the LO waveform has no DC component, so the product of the RF voltage and switching waveform does not include any voltage at the RF frequency. Thus,

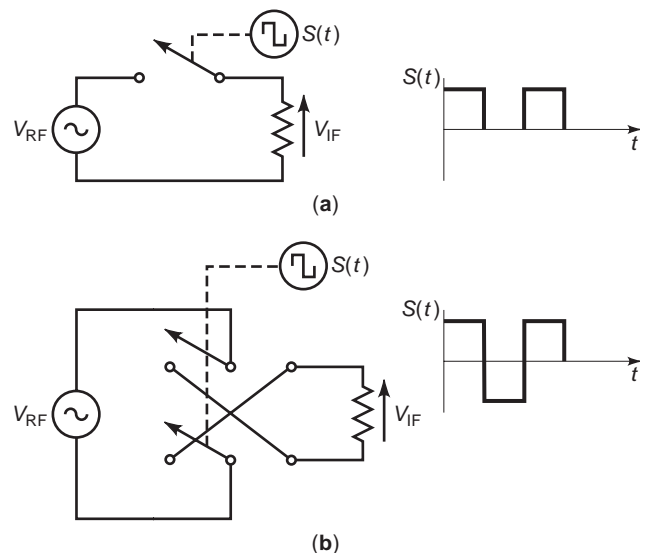


Figure 4. Two switching mixers: (a) a simple switching mixer; (b) a polarity-switching mixer. The IF is the product of the switching waveform $s(t)$ and the RF input, making these mixers a type of multiplier.

even though no filters are used, the RF and LO ports of this mixer are inherently isolated. Doubly balanced mixers are realizations of the polarity-switching mixer.

2. SEMICONDUCTOR DEVICES FOR MIXERS

Only a few devices satisfy the practical requirements of mixer operation. Any device used as a mixer must have strong nonlinearity, electrical properties that are uniform between individual devices, low noise, low distortion, and adequate frequency response. The primary devices used for mixers are Schottky barrier diodes and field-effect transistors (FETs). Bipolar junction transistors (BJT) are also used occasionally, primarily in Gilbert cell multiplier circuits (see Fig. 6d), but because of their superior large-signal-handling ability, higher frequency range, and low noise, FET devices such as metal-oxide-semiconductor FETs (MOSFET), gallium arsenide (GaAs) metal-semiconductor FETs (MESFET), and high-electron-mobility transistors (HEMTs) have been usually preferred.

The Schottky barrier diode is the dominant device used in mixers. Because Schottky barrier diodes are inherently capable of fast switching, have very small reactive parasitics, and do not need DC bias, they can be used in very broadband mixers. Schottky barrier diode mixers usually do not require matching circuits, so no tuning or adjustment is needed.

Although mixers using Schottky barrier diodes always exhibit conversion loss, transistor mixers are capable of conversion gain. This helps simplify the architecture of a system, often allowing the use of fewer amplifier stages than necessary in diode mixer receivers.

Since the 1950s, bipolar transistors have dominated mixer applications as single-transistor mixers in AM radio and communication receivers. In particular, an analog multiplier consisting of a doubly balanced differential amplifier, called the *Gilbert cell*, was invented in the 1960s. Since then, the Gilbert cell mixer has been used as a monolithic integrated circuit (IC) for AM radio receivers and communication equipment. Silicon BJTs are used in mixers because of their low cost and ease of implementation with monolithic ICs. These bipolar devices are used as mixers when necessary for process compatibility, although FETs generally provide better overall performance. Silicon BJTs are usually used in conventional single-device or singly and doubly balanced mixers. Progress in the development of heterojunction bipolar transistors (HBT), which use a heterojunction for the emitter-to-base junction, may bring about a resurgence in the use of bipolar devices as mixers. HBTs are often used as analog multipliers operating at frequencies approaching the microwave range; the most common form is a Gilbert cell. Silicon-germanium (Si-Ge) HBTs are a new technology that offers high performance at costs close to that of silicon BJTs.

A variety of types of FETs are used in mixers. Since the 1960s, silicon MOSFETs (often dual-gate devices) have dominated mixer applications in communication receivers up to approximately 1 GHz. At higher frequency, GaAs MESFETs are often used. The LO and RF signals can be applied to separate gates of dual-gate FETs, allowing good

RF-to-LO isolation to be achieved in a single-device mixer. Dual-gate devices can be used to realize self-oscillating mixers, in which a single device provides both the LO and mixer functions.

Although silicon devices have distinctly lower transconductance than GaAs, they are useful up to at least the lower microwave frequencies. In spite of the inherent inferiority of silicon to GaAs, silicon MOSFETs do have some advantages. The primary one is low cost, and the performance of silicon MOSFET mixers is not significantly worse than GaAs in the VHF and UHF range. The high drain-to-source resistance of silicon MOSFETs gives them higher voltage gain than GaAs devices; in many applications this is a distinct advantage. Additionally, the positive threshold voltage (in an n-channel enhancement MOSFET), in comparison with the negative threshold voltage of a GaAs FET, is very helpful in realizing low-voltage circuits and circuits requiring only a single DC supply. Mixers using enhancement-mode silicon MOSFETs often do not require gate bias, and dual-gate MOSFETs offer convenient LO-to-RF isolation when the LO and RF are applied to different gates.

A MESFET is a junction FET having a Schottky barrier gate. Although silicon MESFETs have been made, they are now obsolete, and all modern MESFETs are fabricated on GaAs. GaAs is decidedly superior to silicon for high-frequency mixers because of its higher electron mobility and saturation velocity. The gate length is usually less than 0.5 μm , and may be as short as 0.1 μm ; this short gate length, in conjunction with the high electron mobility and saturation velocity of GaAs, results in a high-frequency, low-noise device.

HEMTs are used for mixers in the same way as conventional GaAs FETs. Because the gate I - V characteristic of a HEMT is generally more strongly nonlinear than that of a MESFET, HEMT mixers usually have greater intermodulation (IM) distortion than FETs. However the noise figure (NF) of an HEMT mixer usually is not significantly lower than that of a GaAs FET. An HEMT is a junction FET that uses a heterojunction (a junction between two dissimilar semiconductors), instead of a simple epitaxial layer, for the channel. The discontinuity of the bandgaps of the materials used for the heterojunction creates a layer of charge at the surface of the junction; the charge density can be controlled by the gate voltage. Because the charge in this layer has very high mobility, high-frequency operation and very low noise are possible. It is not unusual for HEMTs to operate successfully as low-noise amplifiers above 100 GHz. HEMTs require specialized fabrication techniques, such as molecular beam epitaxy, and thus are very expensive to manufacture. HEMT heterojunctions are invariably realized with III-V semiconductors; AlGaAs and InGaAs are common.

2.1. Passive Diode Mixers

Figure 5 shows the most common form of the three diode mixer types: a single-device diode mixer, a singly balanced diode mixer, and a doubly balanced diode mixer. Conversion loss of 6–8 dB is usually accepted in these passive mixers.

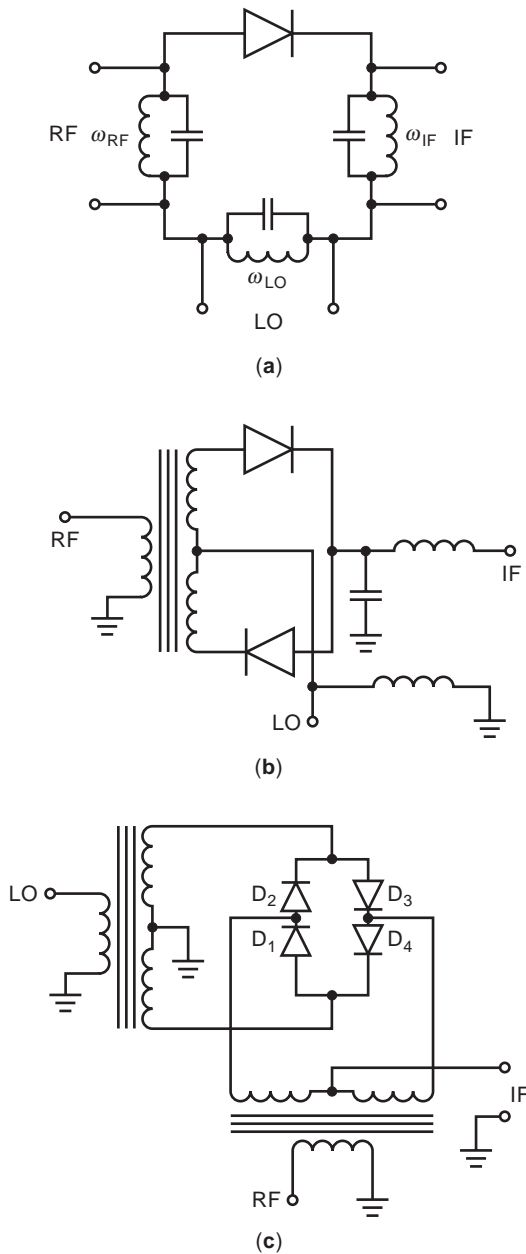


Figure 5. The three most common diode mixer types: (a) single-device; (b) singly balanced; (c) doubly balanced.

2.2. Active Transistor Mixers

Active transistor mixers have several advantages, and some disadvantages, in comparison with diode mixers. Most significantly, an active mixer can achieve conversion gain, while diode and other passive mixers always exhibit loss. This allows a system using an active mixer to have one or two fewer stages of amplification; the resulting simplification is especially valuable in circuits where small size and low cost are vital. A precise comparison of distortion in diode and active transistor mixers is difficult to make because the comparison depends on the details of the system. Generally, however, it is fair to say that distortion levels of well-designed active mixers are usually comparable to those of diode mixers.

It is usually easy to achieve good conversion efficiency in active mixers. Thus, active transistor mixers have gained a reputation for low performance. Nevertheless, achieving good overall performance in active transistor mixers is not difficult.

Because transistors cannot be reversed, as can diodes, balanced transistor mixers invariably require an extra hybrid at the IF. This can be avoided only by using a p-channel device instead of an n-channel device, or vice versa, however, this is possible only in silicon circuits, and even then the characteristics of p- and n-channel devices are likely to be significantly different.

2.2.1. Bipolar Junction Transistor Mixers. Figure 6 shows BJT mixers, a single-device BJT mixer, a singly balanced BJT mixer, a differential BJT mixer, and a doubly balanced BJT mixer.

In a single-device BJT mixer (Fig. 6a), the input signals are introduced into the device through the RF and LO diplexer, which consists of an RF bandpass filter, an LO bandpass filter, and two strips, $\lambda/4$ long at the center of the RF and LO frequency ranges; the square-law term of the device's characteristic provides the multiplication action. A single-device BJT mixer achieves a conversion gain of typically 20–24 dB, a noise figure of typically 4–5 dB (which is about 3 dB more than that of the device in the amplifier at the RF), and a third intercept point near 0 dBm. The IM product from this type of single-device BJT mixer usually depends on its collector current, but when the supplied collector-to-emitter voltage V_{CE} is not enough (typically below 1.2 V), the IM product increases as V_{CE} decreases.

A singly balanced BJT upconversion mixer (Fig. 6b) consists of two BJTs interconnected by a balun or hybrid. The two collectors are connected through a strip, $\lambda/2$ long at the center of the LO frequency range, for reducing the LO leakage. This upconversion mixer exhibits 16 dB conversion gain and 12 dB LO leakage suppression versus the wanted RF output level at 900 MHz.

A singly balanced BJT differential mixer (Fig. 6c) consists of an emitter-coupled differential pair. The RF is superposed on the tail current by AC coupling through capacitor C_2 , and the LO is applied to the upper transistor pair, where capacitive degeneration and AC coupling substantially reduce the gain at low frequencies. Note that the circuit following C_2 is differential and hence much less susceptible to even order distortion.

A multiplier circuit (Fig. 6d) conceived in 1967 by Barrie Gilbert and widely known as the Gilbert cell (although Gilbert himself was not responsible for his eponym; indeed, he has noted that a prior art search at the time found that essentially the same idea—used as a “synchronous detector” and not as true mixer—had already been patented by H. Jones) is usually used as an RF mixer and sometimes as a microwave mixer.

Ignoring the basewidth modulation, the relationship between the collector current I_C and the base-to-emitter voltage V_{BE} for a BJT is

$$I_C = I_S \exp\left(\frac{V_{BE}}{V_T}\right) \quad (2)$$

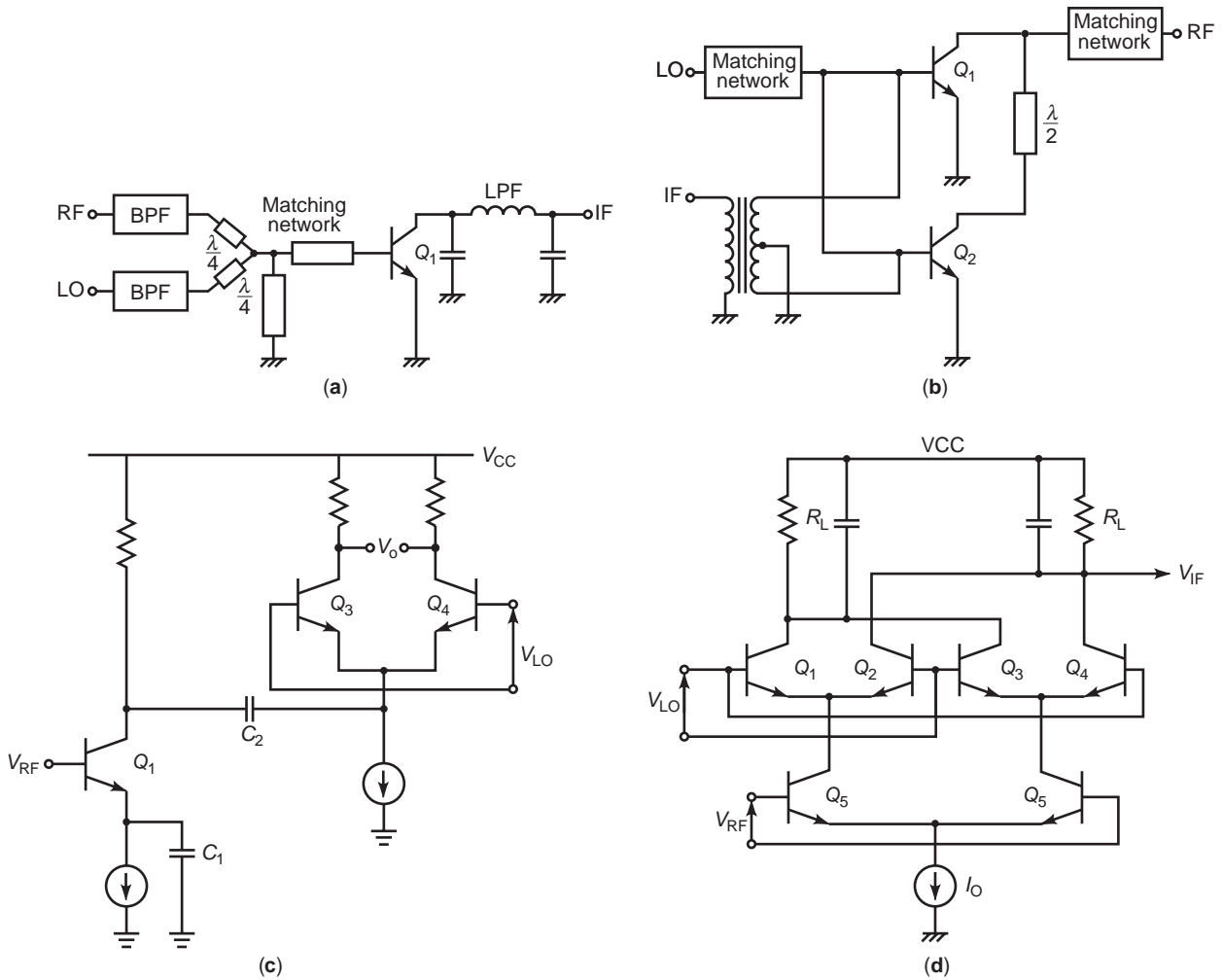


Figure 6. BJT mixers: (a) a single-device BJT mixer; (b) a singly balanced BJT upconversion mixer; (c) a singly balanced BJT differential mixer; (d) a doubly balanced BJT mixer consisting of a Gilbert cell.

where $V_T = kT/q$ is the thermal voltage, k is Boltzmann’s constant, T is absolute temperature in Kelvin, and q is the charge of an electron. I_S is the saturation current for a graded-base transistor.

Assuming matched devices, the differential output voltage of the Gilbert cell is

$$V_{IF} = -R_L I_{EE} \tanh\left(\frac{V_{RF}}{2V_T}\right) \tanh\left(\frac{V_{LO}}{2V_T}\right) \quad (3)$$

For small inputs

$$V_{IF} \approx -\frac{R_L I_{EE}}{4V_T^2} V_{RF} V_{LO} \quad (4)$$

The product $V_{RF} V_{LO}$ is obtained by the Gilbert cell at small signals.

2.2.2. FET Mixers. Figure 7 shows FET mixers: a single-device FET mixer, a dual-gate FET mixer, a singly

balanced FET mixer, a differential FET mixer, and a doubly balanced FET mixer.

In a single-device FET mixer (Fig. 7a), the RF–LO diplexer must combine the RF and LO and also provide matching between the FET’s gate and both ports. The IF filter must provide an appropriate impedance to the drain of the FET at the IF and must short-circuit the drain at the RVF and especially at the LO frequency and its harmonics.

The configuration of a dual-gate mixer (Fig. 7b) provides the best performance in most receiver applications. In this circuit, the LO is connected to the gate closest to the drain (gate 2), while the RF is connected to the gate closest to the source (gate 1). An IF bypass filter is used at gate 2, and an LO–RF filter is used at the drain. A dual-gate mixer is usually realized as two single-gate FETs in a cascade connection.

A singly balanced FET mixer (Fig. 7c) uses a transformer hybrid for the LO and RF; any appropriate type of hybrid can be used. A matching circuit is needed at the gates of both FETs. The IF filters provide the requisite short circuits to the drains at the LO and RF frequencies, and additionally provide IF load impedance transformations.

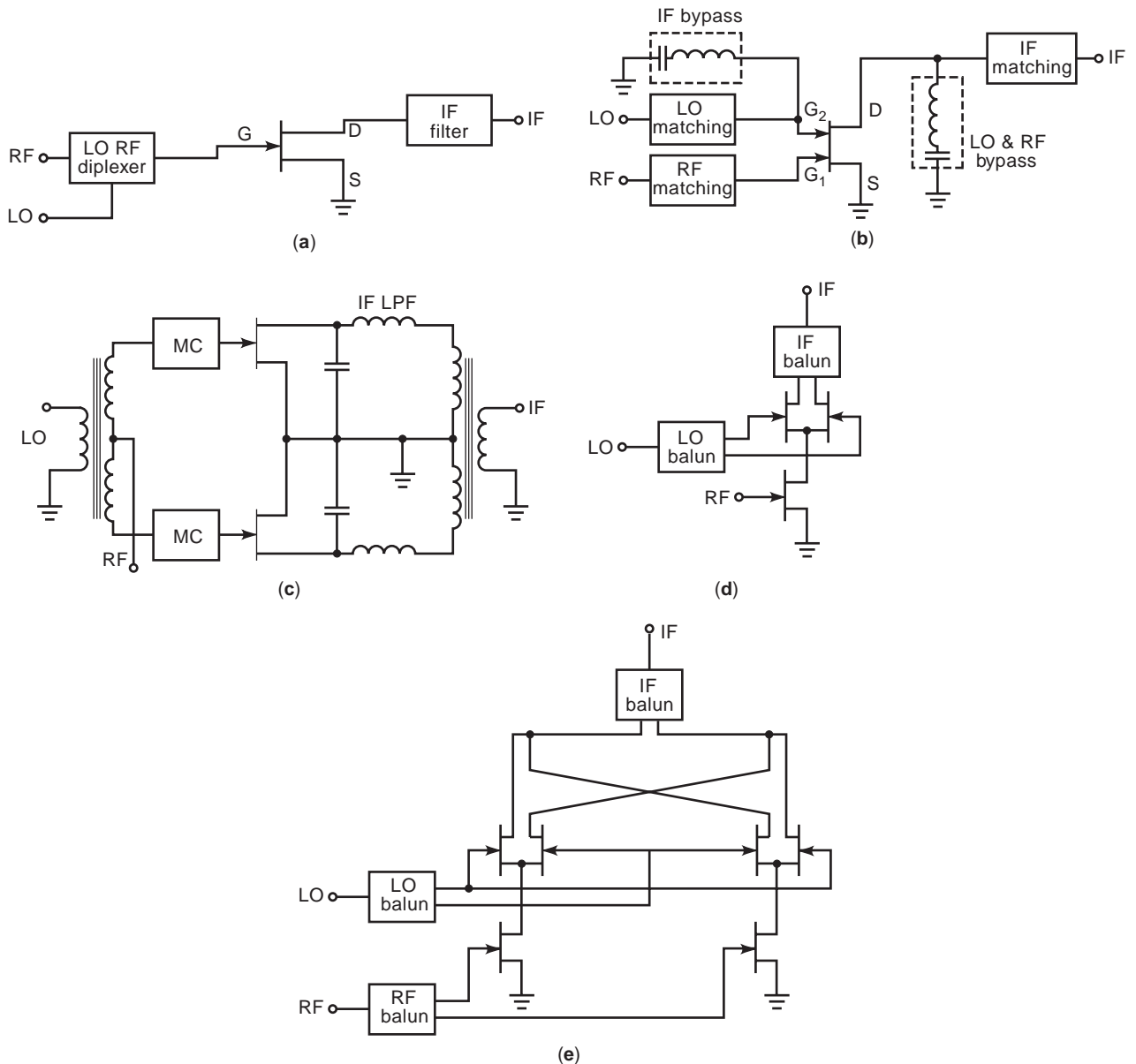


Figure 7. FET mixers: (a) a single-device FET mixer; (b) a dual-gate FET mixer; (c) a singly balanced FET mixer; (d) a differential mixer; (e) a doubly balanced mixer.

The singly balanced mixer of Fig. 7c is effectively two single-device mixers interconnected by hybrids.

In a differential FET mixer (Fig. 7d), the RF is applied to the lower FET, and the LO is applied through a balun or hybrid to the upper FETs. This mixer operates as an alternating switch, connecting the drain of the lower FET alternately to the inputs of the IF balun. An LO matching circuit may be needed. Because the RF and LO circuits are separate, the gates of the upper FETs can be matched at the LO frequency, and there is no tradeoff between effective LO and RF matching. Similarly, the lower FET can be matched effectively at the RF. An IF filter is necessary to reject LO current.

A doubly balanced FET mixer (Fig. 7e) is frequently used as an RF or microwave mixer. Like many doubly balanced mixers, this mixer consists of two of the singly

balanced mixers shown in Fig. 7d. Each half of the mixer operates in the same manner as that of Fig. 7d. The interconnection of the outputs, however, causes the drains of the upper four FETs to be virtual grounds for both LO and RF, as well as for even order spurious responses and IM products.

3. IMAGE-REJECTION MIXERS

The image-rejection mixer (Fig. 8) is realized as the interconnection of a pair of balanced mixers. It is especially useful for applications where the image and RF bands overlap, or the image is too close to the RF to be rejected by a filter. The LO ports of the balanced mixers are driven in phase, but the signals applied to the RF ports have 90°

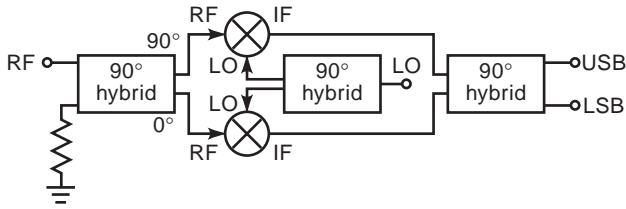


Figure 8. Image-rejection mixer.

phase difference. A 90° IF hybrid is used to separate the RF and image bands. A full discussion of the operation of such mixers is a little complicated.

The most difficult part of the design of an image-rejection mixer is the IF hybrid. If the IF is fairly high, a conventional RF or microwave hybrid can be used. However, if the mixer requires a baseband IF, the designer is placed in the problematical position of trying to create a Hilbert transforming filter, a theoretical impossibility. Fortunately, it is possible to approximate the operation of such a filter over a limited bandwidth.

4. MIXING

A mixer is fundamentally a multiplier. An ideal mixer multiplies a signal by a sinusoid, shifting it to both a higher and a lower frequency, and selects one of the resulting sidebands. A modulated narrowband signal, usually called the RF signal, represented by

$$S_{RF}(t) = a(t) \sin(\omega_s t) + b(t) \cos(\omega_s t) \tag{5}$$

is multiplied by the LO signal function

$$f_{LO}(t) = \cos(\omega_p t) \tag{6}$$

to obtain the IF signal

$$S_{IF}(t) = \frac{1}{2} a(t) \sin[(\omega_s + \omega_p)t] + \sin[(\omega_s - \omega_p)t] + \frac{1}{2} b(t) \cos[(\omega_s + \omega_p)t] + \cos[(\omega_s - \omega_p)t] \tag{7}$$

In the ideal mixer, two sinusoidal IF components, called *mixing products*, result from each sinusoid in $s(t)$. In receivers, the difference-frequency component is usually desired, and the sum-frequency component is rejected by filters.

Even if the LO voltage applied to the mixer’s LO port is a clean sinusoid, the nonlinearities of the mixing device distort it, causing the LO function to have harmonics. Those nonlinearities can also distort the RF signal, resulting in RF harmonics. The IF is, in general, the combination of all possible mixing products of the RF and LO harmonics. Filters are usually used to select the appropriate response and eliminate the other (so-called spurious) responses.

Every mixer, even an ideal one, has a second RF that can create a response at the IF. This is a type of spurious response, and is called the image; it occurs at the

frequency $2f_{LO} - f_{RF}$. For example, if a mixer is designed to convert 10 GHz to 1 GHz with a 9-GHz LO, the mixer will also convert 8 GHz to 1 GHz at the same LO frequency. Although none of the types of mixers we shall examine inherently reject images, it is possible to create combinations of mixers and hybrids that do reject the image response.

It is important to note that the process of frequency shifting, which is the fundamental purpose of a mixer, is a linear phenomenon. Although nonlinear devices are invariably used for realizing mixers, there is nothing in the process of frequency shifting that requires nonlinearity. Distortion and spurious response other than the sum and difference frequency, though often severe in mixers, are not fundamentally required by the frequency-shifting operation that a mixer performs.

4.1. Conversion Efficiency

Mixers using Schottky barrier diodes are passive components and consequently exhibit conversion loss. This loss has a number of consequences: the greater the loss, the higher the noise of the system and the more amplification is needed. High loss contributes indirectly to distortion because of high signal levels that result from the additional preamplifier gain required to compensate for this loss. It also contributes to the cost of the system, since the necessary low-noise amplifier stages are usually expensive.

Mixers using active devices often (but not always) exhibit conversion gain. The conversion gain (CG) is defined as

$$CG = \frac{\text{IF power available at mixer output}}{\text{RF power available to mixer input}} \tag{8}$$

High mixer gain is not necessarily desirable, because it reduces stability margins and can increase distortion. Usually, a mixer gain of unity, or at most a few decibels, is best.

4.2. Noise

In a passive mixer whose image response has been eliminated by filters, the noise figure is usually equal to, or only a few tenths of a decibel above, the conversion loss. In this sense, the mixer behaves as if it were an attenuator having a temperature equal to or slightly above the ambient.

In active mixers, the noise figure cannot be related easily to the conversion efficiency; in general, it cannot even be related qualitatively to the device’s noise figure when used as an amplifier. The noise figure (NF) is defined by the equation

$$NF = \frac{\text{input signal-to-noise power ratio}}{\text{output signal-to-noise power ratio}} \tag{9}$$

The sensitivity of a receiver is usually limited by its internally generated noise. However, other phenomena sometimes affect the performance of a mixer front end

more severely than does noise. One of these is the AM noise, or *amplitude noise*, from the LO source, which is injected into the mixer along with the LO signal. This noise may be especially severe in a single-ended mixer (balanced mixers reject AM LO noise to some degree) or when the LO signal is generated at a low level and amplified.

Phase noise is also a concern in systems using mixers. LO sources always have a certain amount of phase jitter, or phase noise, which is transferred degree for degree via the mixer to the received signal. This noise may be very serious in communications systems using either digital or analog phase modulation. Spurious signals may also be present, along with the desired LO signal, especially if a phase-locked-loop frequency synthesizer is used in the LO source. Spurious signals are usually phase modulation sidebands of the LO signal, and, like phase noise, are transferred to the received signal. Finally, the mixer may generate a wide variety of intermodulation products, which allow input signals—even if they are not within the input passband—to generate spurious output at the IF. These problems must be circumvented if a successful receiver design is to be achieved.

An ideal amplifier would amplify the incoming signal and incoming noise equally and would introduce no additional noise. From Eq. (9) such an amplifier would have a noise figure equal to unity (0 dB).

The noise figure of several cascaded amplifier stages is

$$NF = NF_1 + \frac{NG_2 - 1}{G_1} + \frac{NF_3 - 1}{G_1 G_2} + \dots + \frac{NF_n - 1}{\prod_1^n G_n} \quad (10)$$

where NF is the total noise figure, NF_n is the noise figure of the n th stage, and G_n is the available gain of the n th stage.

From Eq. (10), the gain and noise figure of the first stage of a cascaded chain will largely determine the total noise figure. For example, the system noise figure (on a linear scale) for the downconverter shown in Fig. 9 is

$$NF = \frac{1}{L_{RF}} + \frac{NF_{LNA} - 1}{L_{RF}} + \frac{1}{L_{RF} G_{LNA}} \left(\frac{1}{L_{IM}} - 1 \right) + \frac{NF_M - 1}{L_{RF} G_{LNA} L_I} + \dots = \frac{1}{L_{RF}} \left(NF_{LNA} + \frac{NF_M - L_I}{G_{LNA} L_I} + \dots \right) \quad (11)$$

where L_{RF} and L_I are the insertion losses of the RF filter and the image-rejection filter, respectively, NF_{LNA} and NF_M are the noise figures of the LNA and the mixer, respectively, and G_{LNA} is the power gain of the LNA. This equation assumes that the noise figures of the filters are the same as their insertion losses.

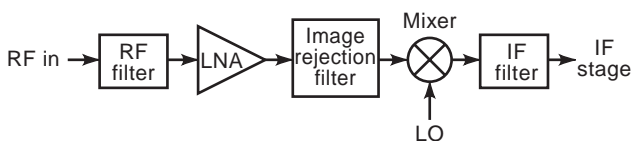


Figure 9. RF front end.

4.3. Bandwidth

The bandwidth of a diode mixer is limited by the external circuit, especially by the hybrids or baluns used to couple the RF and LO signals to the diodes. In active mixers, bandwidth can be limited either by the device or by hybrids or matching circuits that constitute the external circuit; much the same factors are involved in establishing active mixers' bandwidths as amplifiers' bandwidths.

4.4. Distortion

It is a truism that everything is nonlinear to some degree and generates distortion. Unlike amplifiers or passive components, however, mixers often employ strongly nonlinear devices to provide mixing. Because of these strong nonlinearities, mixers generate high levels of distortion. A mixer is usually the dominant distortion-generating component in a receiver.

Distortion in mixers, as with other components, is manifested as IM distortion (IMD), which involves mixing between multiple RF tones and harmonics of those tones. If two RF excitations f_1 and f_2 are applied to a mixer, the nonlinearities in the mixer will generate a number of new frequencies, resulting in the IF spectrum shown in Fig. 10. Figure 10 shows all intermodulation products up to third order; by n th order, we mean all n -fold combinations of the excitation tones (not including the LO frequency). In general, an n th-order nonlinearity gives rise to distortion products of n th (and lower) order.

An important property of IMD is that the level of the n th order IM product changes by n decibels for every decibel of change in the levels of the RF excitations. The extrapolated point at which the excitation and IMD levels are equal is called the n th-order IM intercept point, abbreviated IP_n . This dependence is illustrated in Fig. 11. In most components, the intercept point is defined as an output power; in mixers it is traditionally an input power.

Given the intercept point IP_n and input power level in decibels, the IM input level P_1 in decibels can be found from

$$P_1 = \frac{1}{n} P_1 + \left(1 - \frac{1}{n} \right) IP_n \quad (12)$$

where P_1 is the input level of each of the linear RF tones (which are assumed to be equal) in decibels. By convention, P_1 and P_1 are the input powers of a single frequency component where the linear output level and the level of the n th order IM product are equal; They are not the total

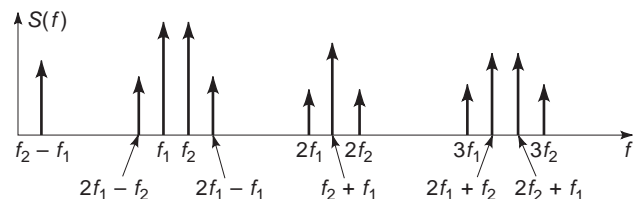


Figure 10. IF spectrum of intermodulation products up to third order. The frequencies f_1 and f_2 are the excitation.

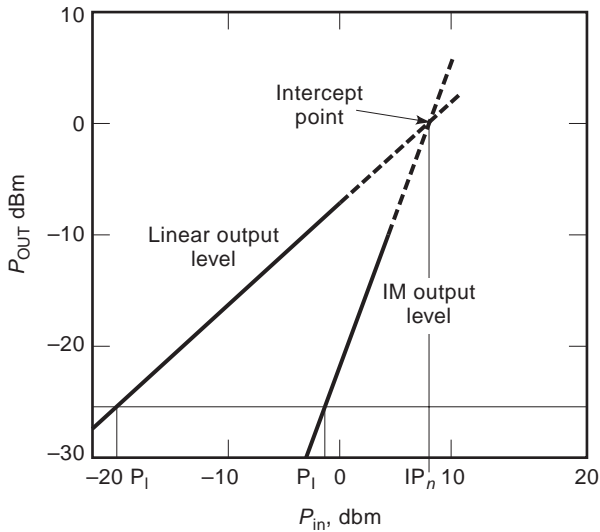


Figure 11. The output level of each n th-order IM product varies n decibels for every decibel change in input level. The intercept point is the extrapolated point at which the curves intersect.

power of all components. For example, P_1 is the threshold level for the receiver. The fluctuation of the IMD level is rather small in spite of the fluctuations of P_1 and IP_n .

4.5. Spurious Responses

A mixer converts an RF signal to an IF signal. The most common transformation is

$$f_{IF} = f_{RF} - f_{LO} \tag{13}$$

although others are frequently used. The discussion of frequency mixing indicated that harmonics of both the RF and LO could mix. The resulting set of frequencies is

$$f_{IF} = mf_{RF} - nf_{LO} \tag{14}$$

where m and n are integers. If an RF signal creates an in-band IF response other than the desired one, it is called a *spurious response*. Usually the RF, IF, and LO frequency ranges are selected carefully to avoid spurious responses, and filters are used to reject out-of-band RF signals that may cause in-band IF responses. IF filters are used to select only the desired response.

Many types of balanced mixers reject certain spurious responses where m or n is even. Most singly balanced mixers reject some, but not all, products where m or n (or both) are even.

4.6. Harmonic Mixer

A mixer is sensitive to many frequencies besides those at which it is designed to operate. The best known of these is the image frequency, which is found at the LO sideband opposite the input, of the RF frequency. The mixer is also sensitive to similar sidebands on either side of each LO harmonic. These responses are usually undesired; the

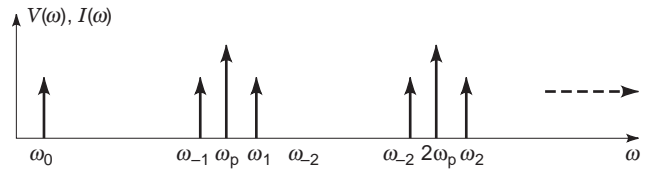


Figure 12. Small-signal mixing frequencies ω_n and LO harmonics $n\omega_p$. Voltage and current components exist in the diode at these frequencies.

exception is the harmonic mixer, which is designed to operate at one or more of these sidebands.

When a small-signal voltage is applied to the pumped diode at any one of these frequencies, currents and voltages are generated in the junction at all other sideband frequencies. These frequencies are called the small-signal mixing frequencies ω_n and are given by the relation

$$\omega_n = \omega_0 + n\omega_p \tag{15}$$

where ω_p is the LO frequency and

$$n = \dots, -3, -2, -1, 0, 1, 2, 3, \dots \tag{16}$$

These frequencies are shown in Fig. 12. The frequencies are separated from each LO harmonic by ω_0 , the difference between the LO frequency and the RF.

5. MODULATION AND FREQUENCY TRANSLATION

5.1. Modulation

Modulation is the process by which the information content of an audio, video, or data signal is transferred to an RF carrier before transmission. Commonly, the signal being modulated is a sine wave of constant amplitude and is referred to as the carrier. The signal that varies some parameter of the carrier is known as the modulation signal. The parameters of a sine wave that may be varied are the amplitude, the frequency, and the phase. Other types of modulation may be applied to special signals, such as pulsewidth and pulse position modulation of recurrent pulses. The inverse process—recovering the information from an RF signal—is called *demodulation* or *detection*. In its simpler forms a modulator may cause some characteristic of an RF signal to vary in direct proportion to the modulating waveform: this is termed analog modulation. More complex modulators digitize and encode the modulating signal before modulation. For many applications digital modulation is preferred to analog modulation.

A complete communication system (Fig. 13) consists of an information source, an RF source, a modulator, an RF channel (including both transmitter and receiver RF stages, the antennas, the transmission path, etc.), a demodulator, and an information user. The system works if the information user receives the source information with acceptable reliability. The designer’s goal is to create a low-cost working system that complies with the legal restrictions on such things as transmitter power, antenna

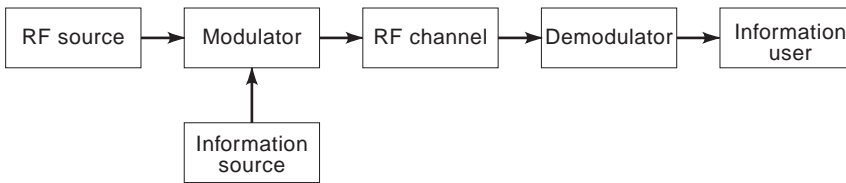


Figure 13. Conceptual diagram of a communication system.

height, and signal bandwidth. Since modulation demodulation schemes differ in cost, bandwidth, interference rejection, power consumption, and so forth, the choice of the modulation type is an important part of communication system design.

Modulation, demodulation (detection), and heterodyne action are very closely related processes. Each process involves generating the sum and/or difference frequencies of two or more sinusoids by causing one signal to vary as a direct function (product) of the other signal or signals. The multiplication of one signal by another can only be accomplished in a nonlinear device. This is readily seen by considering any network where the output signal is some function of the input signal e_1 , for example

$$e_0 = f(e_1) \quad (17)$$

In any perfectly linear network, this requires that

$$e_0 = ke_1 \quad (18)$$

and, assuming two different input signals

$$e_0 = k(E_a \cos \omega_a t + E_b \cos \omega_b t) \quad (19)$$

where k is a constant. In this case the output signal contains only the two input-signal frequencies. However, if the output is a nonlinear function of the input, it can, in general, be represented by a series expansion of the input signal. For example, let

$$e_0 = k_1 e_1 + k_2 e_1^2 + k_3 e_1^3 + \cdots + k_n e_1^n \quad (20)$$

When e_1 contains two frequencies, e_0 will contain the input frequencies and their harmonics plus the products of these frequencies. These frequency products can be expressed as sum and difference frequencies. Thus, all modulators, detectors, and mixers are of necessity nonlinear devices. The principal distinction between these devices is the frequency differences between the input signals and the desired output signal or signals. For example, amplitude modulation in general involves the multiplication of a high-frequency carrier by low-frequency modulation signals to produce sideband signals near the carrier frequency. In a mixer, two high-frequency signals are multiplied to produce an output signal at a frequency that is the difference between the input-signal frequencies. In a detector for amplitude modulation, the carrier is multiplied by the sideband signals to produce their different frequencies at the output.

To understand the modulation process, it is helpful to visualize a modulator as a blackbox (Fig. 14) with two

inputs and one output connected to a carrier oscillator producing a sinusoidal voltage with constant amplitude and frequency f_{RF} . The output is a modulated waveform

$$F(t) = A(t) \cos[\omega_s t + \Theta(t)] = A(t) \cos \Phi(t) \quad (21)$$

whose amplitude $A(t)$ or angle $\Phi(t)$, or both, are controlled by $v_m(t)$. In amplitude modulation (AM) the carrier envelope $A(t)$ is varied while $\Theta(t)$ remains constant; in angle modulation $A(t)$ is fixed and the modulating signal controls $\Phi(t)$. Angle modulation may be either frequency modulation (FM) or phase modulation (PM), depending upon the relationship between the angle $\Phi(t)$ and the modulation signal.

Although the waveform [21] might be called a modulated cosine wave, it is not a single-frequency sinusoid when modulation is present. If either $A(t)$ or $\Theta(t)$ varies with time, the spectrum of $F(t)$ will occupy a bandwidth determined by both the modulating signal and the type of modulation used.

5.1.1. Amplitude Modulation. Amplitude modulation in the form of ON-OFF keying of radio-telegraph transmitters is the oldest type of modulation. Today, amplitude modulation is widely used for those analog voice applications that require simple receivers (e.g., commercial broadcasting) and require narrow bandwidths.

In amplitude modulation the instantaneous amplitude of the carrier is varied in proportion to the modulating signal. The modulating signal may be a single frequency, or, more often, it may consist of many frequencies of various amplitudes and phases, e.g., the signals constituting speech. For a carrier modulated by a single-frequency sine wave of constant amplitude, the instantaneous signal $e(t)$ is given by

$$e(t) = E(1 + m \cos \omega_m t) \cos(\omega_c t + \phi) \quad (22)$$

where E is the peak amplitude of unmodulated carrier, m is the modulation factor as defined below, ω_m is the frequency of the modulating voltage (radians per second), ω_c

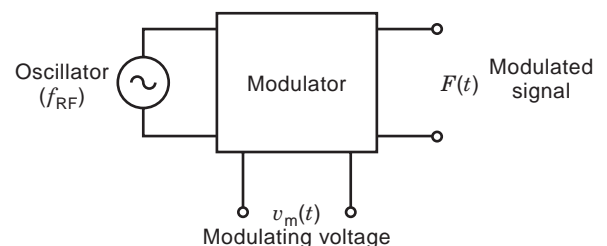


Figure 14. Blackbox view of a modulator.

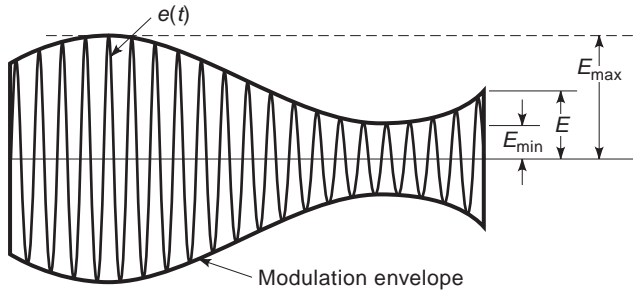


Figure 15. Amplitude-modulated carrier.

is the carrier frequency (radians per second), and ϕ is the phase angle of the carrier (radians).

The instantaneous carrier amplitude is plotted as a function of time in Fig. 15. The modulation factor m is defined for asymmetrical modulation in the following manner:

$$m = \frac{E_{\max} - E}{E} \quad (\text{upward or positive modulation}) \quad (23)$$

$$m = \frac{E - E_{\min}}{E} \quad (\text{downward or negative modulation}) \quad (24)$$

The maximum downward modulation factor, 1.0, is reached when the modulation peak reduces the instantaneous carrier envelope to zero. The upward modulation factor is unlimited.

The modulation carrier described by Eq. (22) can be rewritten as follows:

$$\begin{aligned} e(t) &= E(1 + m \cos \omega_m t) \cos(\omega_c t + \phi) \\ &= E \cos(\omega_c t + \phi) + \frac{mE}{2} \cos[(\omega_c + \omega_m)t + \phi] \\ &\quad + \frac{mE}{2} \cos[(\omega_c - \omega_m)t + \phi] \end{aligned} \quad (25)$$

Thus, the amplitude modulation of a carrier by a cosine wave has the effect of adding two new sinusoidal signals displaced in frequency from the carrier by the modulating frequency. The spectrum of the modulated carrier is shown in Fig. 16.

5.1.2. Angle Modulation. Information can be transmitted on a carrier by varying any of the parameters of the sinusoid in accordance with the modulating voltage. Thus, a carrier is described by

$$e(t) = E_c \cos \theta \quad (26)$$

where $\theta = \omega_c t + \phi$.

This carrier can be made to convey information by modulating the peak amplitude E_c or by varying the instantaneous phase angle θ of the carrier. This type of modulation is known as *angle modulation*. The two types of angle modulation that have practical application are phase modulation (PM) and frequency modulation (FM).

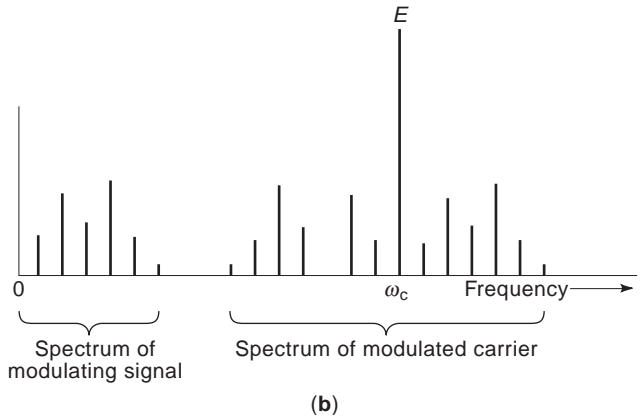
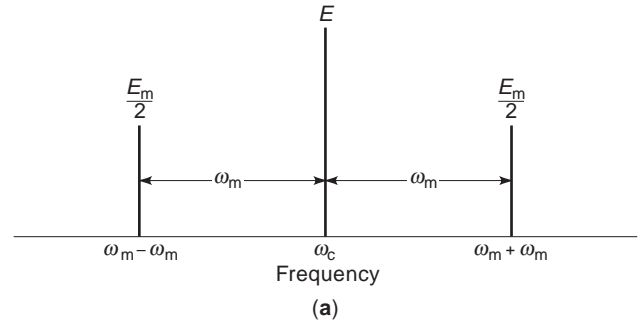


Figure 16. Frequency spectrum of an amplitude-modulated carrier: (a) carrier modulated by a sinusoid of frequency ω_m ; (b) carrier modulated by a complex signal composed of several sinusoids.

In phase modulation, the instantaneous phase angle θ of the carrier is varied by the amplitude of the modulating signal. The principal application of phase modulation is in the utilization of modified phase modulators in systems that transmit frequency modulation. The expression for a carrier phase-modulated by a single sinusoid is given by

$$e(t) = E_c \cos(\omega_c t + \phi + \Delta\phi \cos \omega_m t) \quad (27)$$

where $\Delta\phi$ is the peak value of phase variation introduced by modulation and is called the phase deviation, and ω_m is the modulation frequency (radians per second).

In frequency modulation, the instantaneous frequency of the carrier, that is, the time derivative of the phase angle θ , is made to vary in accordance with the amplitude of the modulating signal. Thus

$$f = \frac{1}{2\pi} \frac{d\theta}{dt} \quad (28)$$

When the carrier is frequency-modulated by a single sinusoid

$$f = f_{\text{RF}} + \Delta f \cos \omega_m t \quad (29)$$

where Δf is the peak frequency deviation introduced by modulation. The instantaneous total phase angle θ is

given by

$$\theta = 2\pi \int f dt + \theta_0 \tag{30}$$

$$\theta = 2\pi f_{RF}t + \frac{\Delta f}{f_m} \sin 2\pi f_m t + \theta_0 \tag{31}$$

The complete expression for a carrier that is frequency-modulated by a single sinusoid is

$$e(t) = E_c \cos \left(\omega_c t + \frac{\Delta f}{f_m} \sin 2\pi f_m t + \theta_0 \right) \tag{32}$$

The maximum frequency difference between the modulated carrier and the unmodulated carrier is the frequency deviation Δf . The ratio of Δf to the modulation frequency f_m is known as the modulation index or the deviation ratio. The degree of modulation in an FM system is usually defined as the ratio of Δf to the maximum frequency deviation of which the system is capable. Degree of modulation in an FM system is therefore not a property of the signal itself.

In digital wireless communication systems, Gaussian-filtered minimum-shift keying (GMSK) is the most popular, and four-level frequency-shift keying (4-FSK) and $\pi/4$ -shifted differential encoded quadriphase (or quadrature) phase-shift keying ($\pi/4$ -DQPSK) are also used. GMSK and 4-FSK are both frequency modulation, but $\pi/4$ -DQPSK is phase modulation.

5.1.3. Pulse Modulation. In pulse-modulated systems, one or more parameters of the pulse are varied in accordance with a modulating signal to transmit the desired information. The modulated pulse train may in turn be used to modulate a carrier in either angle or amplitude. Pulse modulation provides a method of time duplexing, since the entire modulation information of a signal channel can be contained in a single pulsetrain having a low duty cycle, i.e., ratio of pulse width to interpulse period, and therefore the time interval between successive pulses of a particular channel can be used to transmit pulse information from other channels.

Pulse modulation systems can be divided into two basic types: pulse modulation proper, where the pulse parameter which is varied in accordance with the modulating signal is a continuous function of the modulating signal; and quantized pulse modulation, where the continuous information to be transmitted is approximated by a finite number of discrete values, one of which is transmitted by each single pulse or group of pulses. The two methods are illustrated in Fig. 17. In quantized pulse modulation systems, the input function can be approximated with arbitrary accuracy by increase of the number of discrete values available to describe the input function. An example of a quantized pulse modulation system is shown in Fig. 18; the information is transmitted in pulse code groups, the sequence of pulses sent each period indicating a discrete value of the modulating signal at that instant. Typically, the pulse group might employ a binary number code, the presence of each pulse in the group

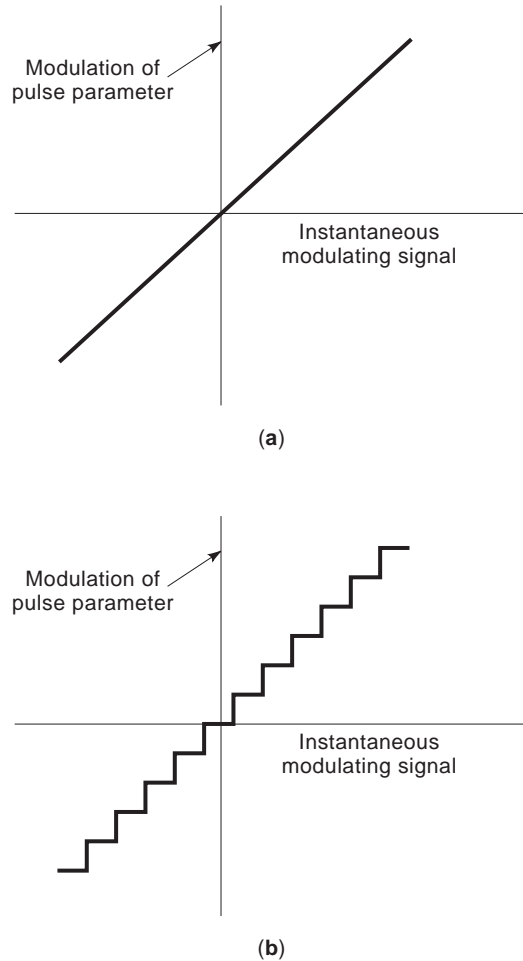


Figure 17. Input–output relationships of quantized and unquantized pulse modulation systems: (a) unquantized modulation system; (b) quantized modulation system.

indicating a 1 or 0 in the binary representation of the modulating signal.

The principal methods for transmitting information by means of unquantized pulse modulation are pulse-amplitude modulation (PAM; see Fig. 19), pulsewidth modulation (PWM), and pulse position modulation (PPM).

5.2. Frequency Translation

The most common form of radio receiver is the superheterodyne configuration shown in Fig. 20a. The signal input,

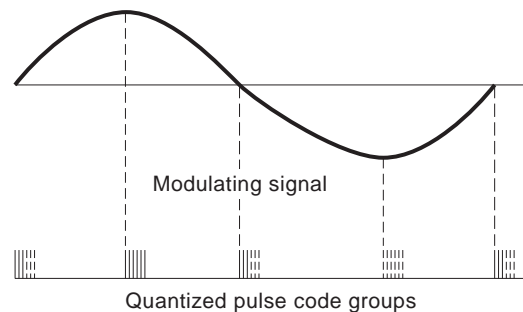


Figure 18. Example of a quantized pulse modulation system.

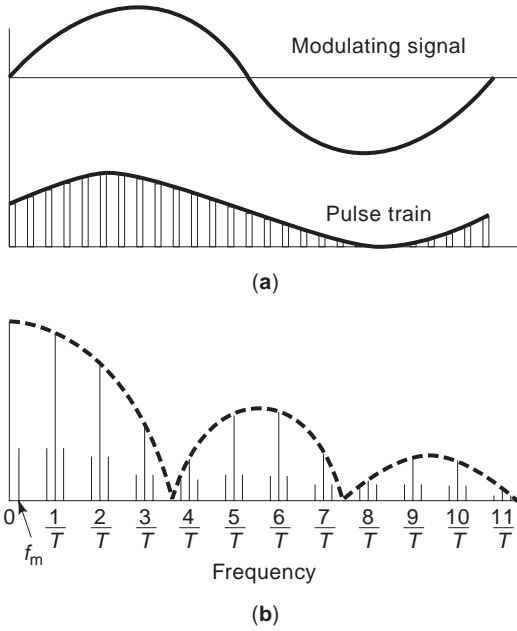


Figure 19. Pulse amplitude modulation: (a) amplitude-modulated pulsetrain; (b) frequency spectrum of the modulated pulse-train.

with a frequency ω_s , is usually first amplified in a tunable bandpass amplifier, called the *RF amplifier*, and is then fed into a circuit called the *mixer* along with an oscillator signal, which is local to the receiver, having a frequency ω_p . The LO is also tunable and is ganged with the input bandpass amplifier so that the difference between the input signal frequency and that of the LO is constant.

In operation, the mixer must achieve analog multiplication. With multiplication, sum and difference frequency components at $\omega_s \pm \omega_p$ are produced at the output of the mixer. Usually, the sum frequency is rejected by sharply tuned circuits and the difference frequency component is subsequently amplified in a fixed-tuned bandpass amplifier. The difference frequency is called the intermediate frequency (IF), and the fixed-tuned amplifier is called the *IF amplifier*. The advantage of this superheterodyne configuration is that most amplification and outband rejection occurs with fixed-tuned circuits, which can be optimized

for gain level and rejection. Another advantage is that the fixed-tuned amplifier can provide a voltage-controlled gain to achieve automatic gain control (AGC) with input signal level. In high-performance and/or small-size receivers, the filtering in the IF amplifier is obtained with electromechanical crystal filters.

To formalize the mixer operation, assume that both the input signal and the local oscillator output are unmodulated, single-tone sinusoids:

$$V_s = E_s \cos(\omega_s t) \tag{33}$$

$$V_p = E_p \cos(\omega_p t) \tag{34}$$

If the multiplier (mixer) has a gain constant K , the output is

$$V_0 = \frac{K}{2} E_s E_p [\cos(\omega_s - \omega_p)t + \cos(\omega_s + \omega_p)t] \tag{35}$$

The difference frequency, $\omega_s - \omega_p$, is denoted by ω_{if} .

If the input is a modulated signal, the modulation also is translated to a band about the new carrier frequency, ω_{if} . For example, if the input is amplitude-modulated,

$$\begin{aligned} V_s &= E_s(1 + m \cos \omega_m t) \cos \omega_s t \\ &= E_s \cos(\omega_s t) + \frac{m}{2} E_s \cos(\omega_s - \omega_m)t \\ &\quad + \frac{m}{2} E_p \cos(\omega_s + \omega_m)t \end{aligned} \tag{36}$$

The input can be represented as in Fig. 20b, with the carrier frequency term and an upper sideband and a lower sideband, each containing the modulation information.

For a linear multiplier, each of the input components is multiplied by the LO input, and the output of the multiplier contains six terms, as shown in Fig. 20c: the difference-frequency carrier with two sidebands and the sum-frequency carrier with two sidebands. The latter combination is usually rejected by the bandpass of the IF amplifier.

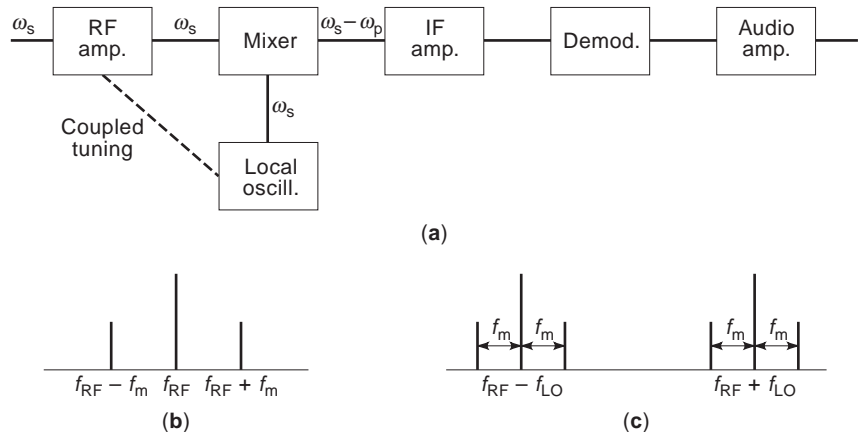


Figure 20. (a) The superheterodyne configuration; frequency spectra of (b) the input and (c) the multiplier output.

The series connection of the two cross-coupled, emitter-coupled pairs with a third emitter-coupled pair requires a high supply voltage, more than 2.0V. Therefore, many circuit design techniques for linearizing the low-voltage Gilbert cell have also been discussed.

6.1.2. Modified Gilbert Cell with a Linear Transconductance Amplifier. The modified Gilbert cell with a linear transconductance amplifier in Fig. 23 possesses a linear transconductance characteristic only with regard to the second input voltage V_y , because it utilizes a linear transconductance amplifier for the lower stage. Low-voltage operation is also achieved using the differential current source output system of two emitter-follower-augmented current mirrors. The general structure of the mixer is a Gilbert cell with a linear transconductance amplifier, since the cross-coupled emitter-coupled pairs that input the LO signal possess a limiting characteristic. To achieve the desired low distortion, the differential pair normally used as the lower stage of the cell is replaced with a superlinear transconductance amplifier. In practice, the linear input voltage range of the superlinear transconductance amplifier at a 1.9V supply voltage is 0.9V peak to peak for less than 1% total harmonic distortion (THD) or 0.8V for less than 0.1% THD.

The differential output current of the modified Gilbert cell with a linear transconductance amplifier is

$$\begin{aligned} \Delta I &= I^+ - I^- = (I_{C1} + I_{C3}) - (I_{C2} + I_{C4}) \\ &= 2G_y V_y \tanh\left(\frac{V_x}{2V_T}\right) \end{aligned} \tag{38}$$

where $G_y = 1/R_y$ and the DC common-base current gain factor α_F is taken as equal to one for simplification, since its value is 0.98 or 0.99 in current popular bipolar technology.

The product of the hyperbolic tangent function of the first input voltage and the second input voltage of the linear transconductance amplifier is obtained.

6.2. Quarter-Square Multipliers Consisting of Two Cross-Coupled Squaring Circuits

To realize a multiplier using squaring circuits the basic idea is based on the identity $(x + y)^2 - (x - y)^2 = 4xy$ or $(x + y)^2 - x^2 - y^2 = 2xy$. The former identity is usually expressed as

$$\frac{1}{4} [(x + y)^2 - (x - y)^2] = xy \tag{39}$$

The quarter-square technique based on the above identity has been well known for a long time.

The two input voltage ranges and the linearity of the transconductances of the quarter-square multiplier usually depend on the square-law characteristics of the squaring circuits and sometimes depend on the linearities of the adder and subtractor in the input stage. A quarter-square multiplier does not usually possess limiting characteristics with regard to both inputs.

6.3. Four-Quadrant Analog Multipliers with a Multiplier Core

The multiplier core can be considered as four properly combined square circuits. The multiplication is based on the identity

$$\begin{aligned} (ax + by)^2 + \left[(a - c)x + \left(b - \frac{1}{c} \right) y \right]^2 \\ - [(a - c)x + by]^2 - \left[ax + \left(b - \frac{1}{c} \right) y \right]^2 = 2xy \end{aligned} \tag{40}$$

where a , b , and c are constants.

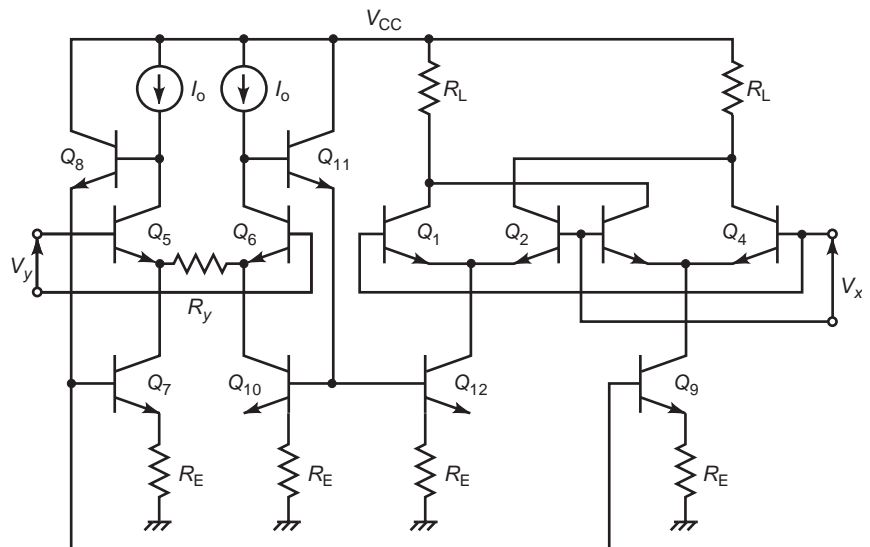


Figure 23. Modified Gilbert cell with a linear transconductance amplifier.

If each squaring circuit is a square-law element with another parameter z , the identity becomes

$$\begin{aligned} &(ax + by + z)^2 + \left[(a - c)x + \left(b - \frac{1}{c} \right) y + z \right]^2 \\ &- [(a - c)x + by + z]^2 \\ &- \left[ax + \left(b - \frac{1}{c} \right) y + z \right]^2 = 4xy \end{aligned} \tag{41}$$

In Eqs. (40) and (41), the parameters a , b , c , and z can be canceled out.

MOS transistors operating in the saturation region can be used as square-law elements. Four properly arranged MOS transistors with two properly combined inputs produce the product of the hyperbolic functions of the inputs. A cell consisting of four emitter- or source-common transistors biased by a single cell tail current can be used as a multiplier core.

6.3.1. Bipolar Multiplier Core. Figure 24a shows a bipolar multiplier core. The individual input voltages applied to the bases of the four transistors in the core can be expressed as $V_1 = aV_x + bV_y + V_R$, $V_2 = (a - 1)V_x + (b - 1)V_y + V_R$, $V_3 = (a - 1)V_x + bV_y + V_R$, $V_4 = aV_x +$

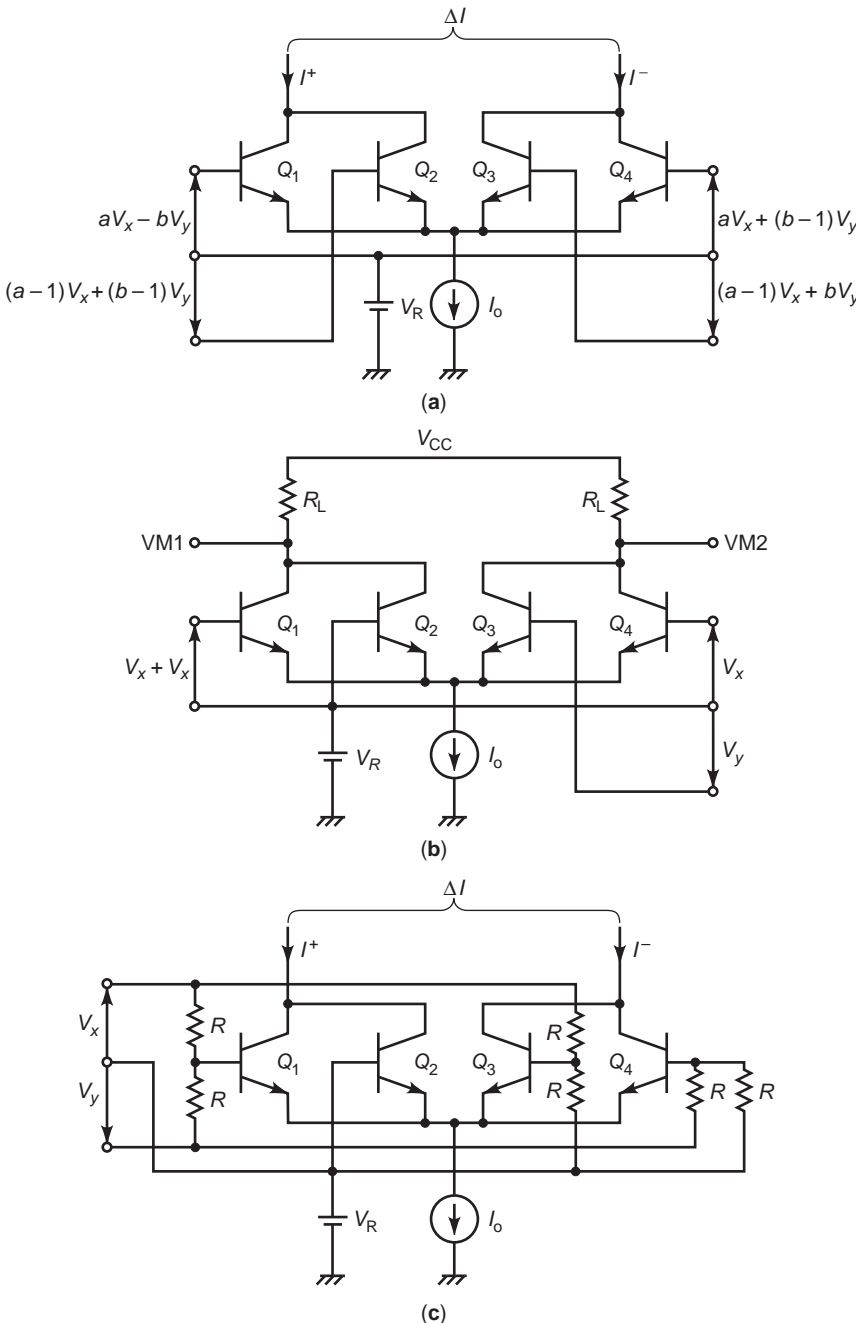


Figure 24. Bipolar multiplier: (a) general circuit diagram of core; (b) the core with the simplest combination of the two input voltages; (c) the bipolar multiplier consisting of a multiplier core and resistive dividers.

$(b-1)V_y + V_R$. The differential output current is expressed as

$$\begin{aligned} \Delta I &= I^+ - I^- = (I_{C1} + I_{C2}) - (I_{C3} + I_{C4}) \\ &= \alpha_F I_0 \tanh\left(\frac{V_x}{2V_T}\right) \tanh\left(\frac{V_y}{2V_T}\right) \end{aligned} \quad (42)$$

The parameters a and b are canceled out. The transfer function of the bipolar multiplier core is expressed as the product of the two transfer functions of the emitter-coupled pairs. The difference between Eqs. (42) and (38) is only in whether the tail current value is multiplied by the parameter α_F or by its square. Therefore, a bipolar multiplier core consisting of a quadritail cell is a low-voltage version of the Gilbert cell.

Simple combinations of two inputs are obtained when $a = b = \frac{1}{2}$, $a = \frac{1}{2}$, and $b = 1$, and $a = b = 1$ as shown in Fig. 24b. In particular, when $a = b = 1$, resistive voltage adders are applicable because no inversion of the signals V_x and v_y is needed (Fig. 24c).

6.3.2. MOS Multiplier Core. Figure 25a shows the MOS four-quadrant analog multiplier consisting of a multiplier core. Individual input voltages applied to the gates of the four MOS transistors in the core are expressed as $V_1 = aV_x + bV_y + V_R$, $V_2 = (a-c)V_x + (b-1/c)V_y + V_R$, $V_3 = (a-c)V_x + bV_y + V_R$, $V_4 = aV_x + (b-1/c)V_y + V_R$. The multiplication is based on the identity of Eq. (41).

Ignoring the body effect and channel-length modulation, the equations for drain current versus drain-to-source voltage can be expressed in terms of three regions of operation as

$$I_D = 0 \quad (43a)$$

for $V_{GS} \leq V_T$, the OFF region,

$$I_D = 2\beta \left(V_{GS} - V_T - \frac{V_{DS}}{2} \right) V_{DS} \quad (43b)$$

for $V_{DS} \leq V_{GS} - V_T$, the triode region, and

$$I_D = \beta (V_{GS} - V_T)^2 \quad (43c)$$

for $V_{GS} \geq V_T$ and $V_{DS} \geq V_{GS} - V_T$, the saturation region, where $\beta = \mu (C_o/2)(W/L)$ is the transconductance parameter, μ is the effective surface carrier mobility, C_o is the gate oxide capacitance per unit area, W and L are the channel width and length, and V_T is the threshold voltage.

The differential output current is expressed as

$$\begin{aligned} \Delta I &= I^+ - I^- = (I_{D1} + I_{D2}) - (I_{D3} + I_{D4}) \\ &= 2\beta V_x V_y (V_x^2 + V_y^2 + |V_x V_y| \leq I_0/2\beta) \end{aligned} \quad (44)$$

The parameters a , b , and c are canceled out. Four properly arranged MOS transistor with two properly combined inputs produce the product of two input voltages. Simple combinations of two inputs are obtained when $a = b = \frac{1}{2}$ and $c = 1$, $a = \frac{1}{2}$ and $b = c = 1$, and $(a = b = c = 1)$ as shown in Fig. 25b.

Figure 25c shows a CMOS four-quadrant analog multiplier consisting of only a multiplier core and an active voltage adder.

In addition, a multiplier consisting of the multiplier core in Fig. 25a and a voltage adder and subtractor has been implemented with a GaAs MESFET IC, and a useful frequency range from dc to UHF bands of 3 GHz was obtained for a frequency mixer operating on a supply voltage of 2 or 3 V.

7. RADIOFREQUENCY SIGNAL AND LOCAL OSCILLATOR

Figure 26 shows a block diagram of a communication system, showing modulation and demodulation. A wireless communication system will usually consists of an information source, which is modulated up to RF or microwave frequencies and then transmitted. A receiver will take the modulated signal from the antenna, demodulate it, and send it to an information “sink,” as illustrated in Fig. 26. The rate at which information can be sent over the channel is determined by the available bandwidth, the modulation scheme, and the integrity of the modulation-demodulation process.

Frequency synthesizers are ubiquitous building blocks in wireless communication systems, since they produce the precise reference frequencies for modulation and demodulation of baseband signals up to the transmit and/or receive frequencies.

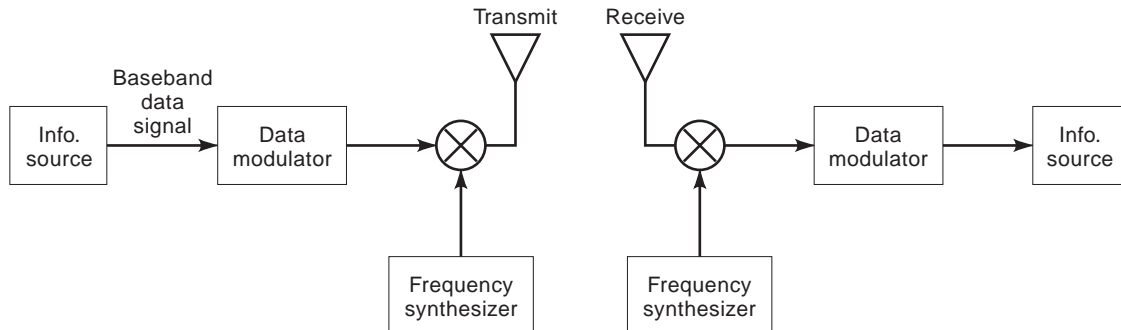


Figure 26. Block diagram of communications system, showing modulation and demodulation.

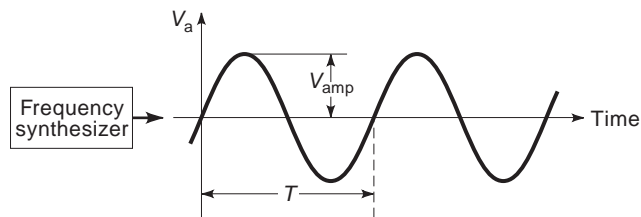


Figure 27. Block diagram of frequency synthesizer producing single-tone sinusoidal output.

A simple frequency synthesizer might consist of a transistor oscillator operating at a single frequency determined by a precise crystal circuit. Tunable transistor frequency sources rely on variations in the characteristics of a resonant circuit to set the frequency. These circuits can then be embedded in phase-locked loops (PLLs) to broaden their range of operation and further enhance their performance.

A representative view of a frequency synthesizer is given in Fig. 27 which shows a generic synthesizer producing a single tone of a given amplitude that has a delta-function-like characteristic in the frequency domain.

Indirect frequency synthesizers rely in feedback, usually in the form of the PLL, to synthesize the frequency. A block diagram of a representative PLL frequency synthesizer is shown in Fig. 28. Most PLLs contain three basic building blocks: a phase detector, an amplifier loop filter, and a voltage-controlled oscillator (VCO). During operation, the loop will acquire (or lock onto) an input signal, track it, and exhibit a fixed phase relationship with respect to the input. The output frequency of the loop can be varied by altering the division ratio (N) within the loop, or by tuning the input frequency with an input frequency divider (Q). Thus, the PLL can act as a broadband frequency synthesizer.

8. FREQUENCY SYNTHESIZER FIGURES OF MERIT

An ideal frequency synthesizer would produce a perfectly pure sinusoidal signal, which would be tunable over some specified bandwidth. The amplitude, phase, and frequency of the source would not change under varying loading, bias, or temperature conditions. Of course, such an ideal circuit is impossible to realize in practice, and a variety of performance measures have been defined over the years to characterize the deviation from the ideal.

8.1. Noise

The output power of the synthesizer is not concentrated exclusively at the carrier frequency. Instead, it is distrib-

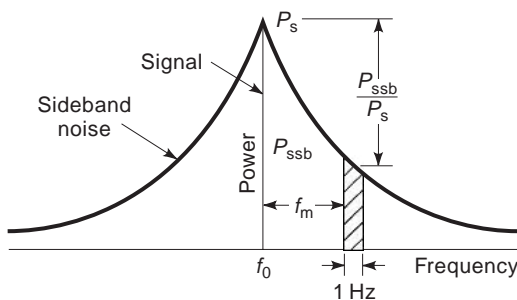


Figure 29. Phase noise specification of frequency source. The noise is contained in the sidebands around the signal frequency at f_0 .

uted around it, and the spectral distribution on either side of the carrier is known as the *spectral sideband*. This is illustrated schematically in Fig. 29. This noise can be represented as modulation of the carrier signal, and resolved into AM and FM components. The AM portion of the signal is typically smaller than the FM portion.

FM noise power is represented as a ratio of the power in some specified bandwidth (usually 1 Hz) in one sideband to the power in the carrier signal itself. These ratios are usually specified in “dBc/Hz” at some frequency offset from the carrier. The entire noise power can be integrated over a specified bandwidth to realize a total angular error in the output of the oscillator, and oscillators are often specified this way.

8.2. Tuning Range

The tuning range of an oscillator specifies the variation in output frequency with input voltage or current (usually voltage). The slope of this variation is usually expressed in megahertz per volt. In particular, the key requirements of oscillator or synthesizer tuning are that the slope of the frequency variation remain relatively consistent over the entire range of tuning and that the total frequency variation achieve some minimum specified value.

8.3. Frequency Stability

Frequency stability of an oscillator is typically specified in parts per million per degree centigrade (ppm/°C). This parameter is related to the Q of the resonator and the frequency variation of the resonator with temperature. In a free-running system this parameter is particularly important, whereas in a PLL it is less so, since an oscillator that drifts may be locked to a more stable oscillator source.

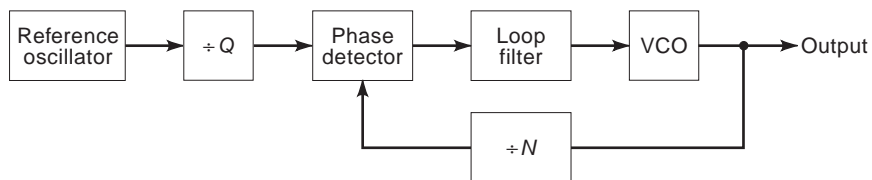


Figure 28. Indirect frequency synthesizer using a phase-locked loop.

8.4. Harmonics

Harmonics are output from the oscillator synthesizer that occur at integral multiples of the fundamental frequencies. They are typically caused by nonlinearities on the transistor or other active devices used to produce the signal. They can be minimized by proper biasing of the active device and design of the output matching network to filter out the harmonics. Harmonics are typically specified in “dBc” below the carrier.

8.5. Spurious Outputs

Spurious outputs are outputs of the oscillator synthesizer that are not necessarily harmonically related to the fundamental output signal. As with harmonics, they are typically specified in “dBc” below the carrier.

BIBLIOGRAPHY

1. A. A. Abidi, Low-power radio-frequency IC's for portable communications, *Proc. IEEE* **83**:544–569 (1995).
2. L. E. Larson, *RF and Microwave Circuit Design for Wireless Communications*, Artech House, Norwood, MA, 1996.
3. N. Camilleri et al., Silicon MOSFETs, the microwave device technology for the 90s, *1993 IEEE MTT-S Int. Microw. Symp. Digest*, June 1993, pp. 545–548.
4. C. Tsironis, R. Meierer, and R. Stahlman, Dual-gate MESFET mixers, *IEEE Trans. Microwave Theory Tech.* **MTT-32**: 248–255 (March 1984).
5. S. A. Maas, *Microwave Mixers*, 2nd ed., Artech House, Norwood, MA, 1993.
6. J. M. Golio, *Microwave MESFETs & HEMTs*, Artech House, Norwood, MA, 1991.
7. F. Ali and A. Gupta, eds., *HEMTs & HBTs: Devices, Fabrication, and Circuits*, Artech House, Norwood, MA, 1991.
8. D. Haigh and J. Everard, *GaAs Technology and Its Impact on Circuits and Systems*, Peter Peregrinus, London, 1989.
9. D. O. Pederson and K. Mayaram, *Analog Integrated Circuits for Communication—Principles, Simulation and Design*, Kluwer Academic, Norwell, MA, 1991.
10. W. Gosling, *R·A·D·I·O Receivers*, Peter Peregrinus, London, 1986.
11. K. Murota and K. Hirade, GMSK modulation for digital mobile telephony, *IEEE Trans. Commun.* **COM-29**:1044–1050 (1981).
12. Y. Akaiwa and Y. Nagata, Highly efficient digital mobile communications with a linear modulation method, *IEEE J. Select. Areas Commun.* **SAC-5**(5):890–895 (June 1987).
13. J. Eim binder, *Application Considerations for Linear Integrated Circuits*, Wiley, New York, 1970.
14. H. E. Jones, *Dual Output Synchronous Detector Utilizing Transistorized Differential Amplifiers*, U.S. Patent 3,241,078 (March 15, 1966).
15. B. Gilbert, A precise four-quadrant analog multiplier with subnanosecond response, *IEEE J. Solid-State Circ.* **SC-3**(4):365–373 (1968).
16. P. R. Gray and R. G. Meyer, *Analysis and Design of Analog Integrated Circuits*, Wiley, New York, 1977, pp. 667–681.
17. K. W. Kobayashi et al., InAlAs/InGaAs HBT X-band double-balanced upconverter, *IEEE J. Solid-State Circ.* **29**(10): 1238–1243 (1994).
18. F. Behbahani et al., A low distortion bipolar mixer for low voltage direct up-conversion and high IF frequency systems, *Proc. IEEE 1996 Bipolar Circuits Technology Meeting*, Sept. 1996, pp. 50–52.
19. H. Song and C. Kim, An MOS four-quadrant analog multiplier using simple two-input squaring circuits with source-followers, *IEEE J. Solid-State Circ.* **25**(3):841–848 (1990).
20. K. Kimura, A unified analysis of four-quadrant analog multipliers consisting of emitter and source-coupled transistors operable on low supply voltage, *IEICE Trans. Electron.* **E76-C**(5):714–737 (1993).
21. K. Bult and H. Wallinga, A CMOS four-quadrant analog multiplier, *IEEE J. Solid-State Circ.* **SC-21**(3):430–435 (1986).
22. K. Kimura, An MOS four-quadrant analog multiplier based on the multital technique using a quadritail cell as a multiplier core, *IEEE Trans. Circ. Syst. I Fund. Theory Appl.* **42**:448–454 (1995).
23. Z. Wang, A CMOS four-quadrant analog multiplier with single-ended voltage output and improved temperature performance, *IEEE J. Solid-State Circ.* **26**(9):1293–1301 (1991).
24. K. Kimura, A bipolar very low-voltage multiplier core using a quadritail cell, *IEICE Trans. Fund.* **E78-A**(5):560–565 (May 1995).
25. K. Kimura, Low voltage techniques for analog functional blocks using triple-tail cells, *IEEE Trans. Circ. Syst. I Fund. Theory Appl.* **42**:873–885 (1995).
26. R. Siferd, A GaAs four-quadrant analog multiplier circuit, *IEEE J. Solid-State Circ.* **28**(3):388–391 (1993).
27. B. Razavi, Challenges in the design of frequency synthesizers for wireless applications. *Proc. IEEE 1997 Custom Integrated Circuits Conf.*, May 1997, pp. 395–402.

MOBILE COMMUNICATION

TADEUSZ WYSOCKI

Curtin University of Technology

HANS-JÜRGEN ZEPERNICK

Cooperative Research Center for
Broadband

Telecommunications and
Networking

RALF WEBER

Ericsson Eurolab Deutschland
GmbH

The desire for mobility and for communication with others is deeply ingrained in human nature. The need to develop an efficient public mobile communication system has been driving a lot of researchers since the late nineteenth century. It is generally accepted that mobile communication (precisely speaking, mobile radiocommunication) was born in 1897, when Guglielmo Marconi gained a patent for his wireless telegraph. Since then, mobile communications have gone from the early stages at the beginning of the twentieth century, when mobile communication was widely used in navigation and in maintaining contacts with remotely traveling ships and airplanes, through

infancy of the 1950s and the 1960s, to maturity at the end of the twentieth century, when public mobile telephony, paging, and other mobile services are common place. There are several comprehensive readings available on each of those specific services [1–4], and this article does not pretend to cover all topics related to mobile communication. Rather, we concentrate on some specific issues that, in our opinion, allow the reader to understand major differences between mobile and stationary or fixed communications.

1. HISTORY

Mobile communication has always been used by people, particularly during military struggles, when commanders needed to pass their orders to remote troops in the middle of a battle. Several methods have been used, with horns and drums among the most popular. Different optical “mobile communication” systems based on so-called signal flags have also been used for maritime applications. All of those methods have been, however, of a limited range and small capacity. There were no major improvements in mobile communication until the birth of electromagnetic theory.

In the late nineteenth century, after the theoretical predictions made by Maxwell in his treatise on electricity and magnetism and Rudolf Hertz’s experimental work on the transmission and reception of electromagnetic waves, Guglielmo Marconi and some other researchers started to look into possible applications of electromagnetic radiation for communication purposes. Since then, radio communications have been used to save lives, win battles, generate new businesses, maximize opportunities, and so forth. From the introduction of public mobile cellular telephony in the 1980s, mobile communications have become elements of mass communication with the objective of providing a broad range of services similar to, and in some instances exceeding, those offered by the public switched telephone network (PSTN). The level of penetration for mobile phones varies among different countries, but in some countries it is already high.

Before the 1970s, numerous private mobile radio networks—citizen band (CB) radio, ham operator mobile radio, and portable home radio telephones—used different types of equipment utilizing diverse fragments of radio spectrum located in the frequency band from about 30 MHz to 3 GHz. Standardization started to take place in the 1970s with the development of the Nordic Mobile Telephone (NMT) system by Ericsson and the Advanced Mobile Phone Services (AMPS) by AT&T. Both systems have become *de facto* and *de jure* the technical standards for the analog mobile telephony as the so-called first-generation systems. Soon after the deployment of those first-generation systems, second generation, fully digital mobile cellular systems appeared on drawing boards throughout the world. The Groupe Spécial Mobile (GSM), pan-European, fully digital cellular telephony standard was developed in late 1980s. After its successful deployment, it began to be accepted as a standard for the second-generation mobile radio not only in Europe but

also in other parts of the world. The main competition for the GSM monopoly in digital mobile telephony has come from code-division multiple-access (CDMA) spread-spectrum technology, developed primarily for military applications. The CDMA-based IS-95 systems, and time-division multiple-access (TDMA)-based GSM systems have their powerful supporters and vigorous opponents, and it is not clear yet which approach is going to be adopted in the development of the third generation of mobile telephony or the future public land mobile telecommunication system (FPLMTS), which recently has been re-named International Mobile Telecommunications—2000 (IMT-2000).

2. OVERVIEW OF CONCEPTS

A typical mobile communication system consists of mobile terminals, base stations, mobile switching centers, and telecommunication channels. Those telecommunication channels are either of a fixed nature (cables or dedicated radiolinks), to provide connections between base stations and the mobile switching center, or mobile radio channels between mobile terminals and base stations servicing those terminals.

Unlike fixed telecommunication channels, the mobile radio channels are nonstationary and exhibit a high level of unpredictability with regard to channel characteristics. In addition, due to the nature of radiocommunication and low directivity of antennas used, there is always a possibility of strong interference from other users of the radio spectrum. All these factors need to be carefully taken into account while calculating a power budget for a mobile radio channel.

One of the specific features of mobile communication systems is the need to assign a free radio channel to the user requiring the connection. This is done during setup of the connection. This setup, combined with the limited frequency spectrum available for mobile services, means that the number of simultaneous calls within the coverage area of a single base station is highly limited. Therefore, before introduction of the cellular concept (which is explained later in the section on spectrum management), the number of simultaneous calls within a system covering sometimes a huge area was very low. For example, the single-base-station mobile system in New York City in the 1970s could only support a maximum of 12 simultaneous calls over one thousand square miles [5]. The concept of such a cellular system is illustrated in Fig. 1.

There are generally four different types of channels that are used for communication between the base station and mobiles: (1) forward voice channels (FVCs), used for voice transmission from the base station to mobiles; (2) reverse voice channels (RVCs), used for voice transmission from mobiles to the base station; (3) forward control channels (FCC), used for transmission of signaling data from the base station to mobiles; and (4) reverse control channels (RCC), used for transmission of signaling data from mobiles to the base station. The control channels transmit and receive data necessary to set up a call, moving it to an unused voice channel, and to manage the

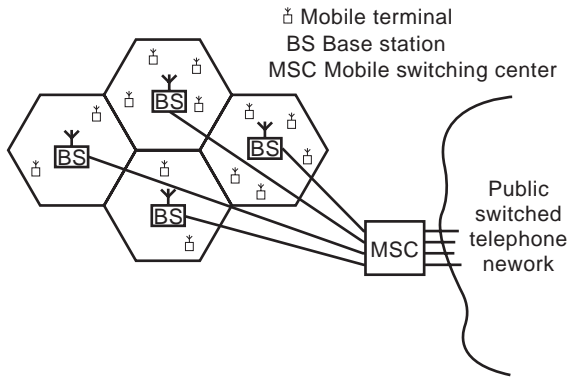


Figure 1. Configuration of a cellular system.

handovers between base stations. They are also used for constant monitoring of the system and for synchronization purposes.

The base station serves as a bridge between all mobile users in its coverage area and the mobile switching center (MSC). The MSC acts as a central switching point, closing the traffic among the connected base stations, and serves as a gateway to the PSTN. It also coordinates all activities of the base stations and accommodates all billing and maintenance functions. A typical MSC handles 100,000 cellular subscribers and 5000 simultaneous conversations [6].

3. CLASSIFICATION

Mobile communication systems are classified into generations in accordance with evolution of systems in time. Indicators for a generation are involved transmission techniques, supported services, and status of unification. First-generation systems were introduced in the early 1980s and used analog techniques basically for speech services. Second generation systems evolved in the late 1980s and are now in a mature form. They utilize digital techniques, and, apart from speech, they support some

low-rate data services. Second-generation systems may be further classified into cellular, cordless, and professional radio systems. Due to the wide range of second-generation systems and their immense complexity, we only summarize some air interface parameters of selected digital cellular systems in Table 1. Standards for third-generation systems are currently being developed to provide mobile multimedia telecommunications and universal coverage. In the following subsections, we will give a concise overview of mobile communication systems and refer to the literature for details.

3.1. First-Generation Systems

The first-generation cellular systems use analog frequency modulation (FM) for traffic channels, digital frequency shift keying (FSK) for signaling channels, and a frequency division duplex (FDD) method. In addition, frequency-division multiple access (FDMA) is employed to share the transmission medium. In the beginning, businesspeople were the main customers, but later acceptance in residential markets started to increase immensely. In 1981, the Scandinavian countries introduced the Nordic Mobile Telephone standard NMT-450 [7] and in 1986 the NMT-900 standard, where the numbers in the acronyms indicate the utilized frequency band in MHz. The AMPS system [8] was developed in the United States, and service opened in 1983. AMPS has been adapted by many countries, such as Canada and Australia. A variant of AMPS is the Total Access Communication system (TACS) deployed in 1985 in the United Kingdom, which basically uses a smaller channel spacing than AMPS. In 1986, the C-450 system [9] opened its service in Germany.

3.2. Second-Generation Systems

3.2.1. Cellular Systems

3.2.1.1. Global System for Mobile Communication.

Although mobile communication in most European countries was well covered by their individual analog cellular systems, incompatible standards made it impossible to

Table 1. Characteristics of Selected Second-Generation Systems

Mobile System	GSM	DCS-1800	DECT	IS-95
Frequency band				
MS → BS	890–915 MHz	1710–1785 MHz	1880–1990 MHz	824–849 MHz
BS → MS	935–960 MHz	1805–1880 MHz	1880–1900 MHz	869–894 MHz
Carrier spacing	200 kHz	200 kHz	1728 kHz	1250 kHz
Duplex spacing	45 MHz	95 MHz	0 Hz	45 MHz
No. of carriers	125	375	10	20
System bandwidth	2 × 25 MHz	2 × 75 MHz	20 MHz	2 × 25 MHz
Speech coder				
Full rate	13 kb/s RPE-LTP	13 kb/s RPE-LTP	32 kb/s ADPCM	8, 4, 2, 1 kb/s QCELP
Half rate	5.6 kb/s VSELP	4.5 kb/s VSELP		
Multiple access	TDMA	TDMA	TDMA	CDMA
Duplexing method	FDD	FDD	TDD	FDD
Modulation	GMSK ($BT^{\alpha} = 0.3$)	GMSK ($BT^{\alpha} = 0.3$)	GMSK ($BT^{\alpha} = 0.5$)	QPSK/BPSK
Frame bit rate	271 kbps	271 kbps	1.152 Mbps	1.288 Mbps
Frame length	4.615 ms	4.615 ms	10 ms	20 ms

^a BT^{α} : 3dB bandwidth and bit duration product of the Gaussian filter.

interwork among systems or share equipment. To overcome this deficiency, the Conférence Européenne des Postes et Télécommunications (CEPT) established in 1982 the Groupe Spécial Mobile to develop a pan-European standard. The outcome was the GSM system [10], which now stands for global system for mobile communication. The standard specifies a digital cellular system on the basis of a dedicated pan-European frequency band allocated at 900 MHz. GSM supports a variety of speech and low-rate data services. In 1991, the first GSM system opened and since then it has experienced tremendous popularity worldwide, as indicated by the more than 65 countries that have already adopted GSM. An extension of GSM is the Digital Cellular System—1800 (DCS-1800) standard allocated in the 1.8-GHz band. DCS-1800 has been designed to meet the requirements of personal communication networks (PCN).

3.2.1.2. Interim Standard 54 (IS-54). During the 1980s, increasing demand on cellular services was observed in the United States, approaching traffic capacity limits of analog AMPS. To satisfy the enormous capacity requirements, the Cellular Telecommunication Industry Association asked for a digital standard. As a result, IS-54 [11] has been developed and is also known as United States Digital Cellular (USDC). IS-54 is designed to coexist with analog AMPS in the same frequency band but to replace the analog system step by step. For that reason, IS-54 has to be upward compatible to AMPS and hence is sometimes referred to as digital AMPS (D-AMPS). With the used digital techniques and planned employment of a half-rate codec, IS-54 is expected to provide six times the traffic capacity than AMPS.

3.2.1.3. Interim Standard 95 (IS-95). Development of IS-95 was launched in 1991 after Qualcomm successfully demonstrated a CDMA digital cellular validation system. The IS-95 standard [12] specifies a direct-sequence CDMA digital cellular system. This wideband digital cellular standard employs a set of spreading sequences that are assigned to users. All users in the cellular system transmit in the same radio channel but using different sequences. Therefore, frequency planning is not required and can be thought of as replaced by planning how to allocate spreading sequences in different cells.

3.2.1.4. Personal Digital Cellular (PDC). The Japanese effort to increase capacity over analog systems is documented in a PDC air interface standard [13], which was issued in 1991. This digital cellular system has been allocated a different frequency band than the analog system. It supports speech, data, and short message services.

3.2.2. Cordless Systems

3.2.2.1. Cordless Telephony (CT2). The initial goal of cordless telephony was to provide wireless pay phone services with low-cost equipment but no support of incoming calls. These systems cover only a single cell with a radius of about 300 m outdoor and 50 m indoor. Most manufacturers in Europe agreed on a common air interface (CAI), which become the CT2/CAI standard [14]. It uses digital

techniques and replaces analog cordless telephony, which offered only a small number of channels. In Canada, CT2 + was developed to support incoming calls as well. By dedicating more carriers for signaling purposes, location management was practicable.

3.2.2.2. Digital European Cordless Telecommunications (DECT). The DECT standard [14] was developed by the European Telecommunications Standards Institute (ETSI) and has been allocated a guaranteed pan-European frequency. It is designed as a flexible interface based on open system interconnection (OSI) and was finalized in 1992. The system provides mobility in picocells with very high capacity. Speech and data services are supported where incoming and outgoing calls can be managed. Initially, DECT was intended for interworking with private automatic branch exchange (PABX) to provide mobility within the area of a PABX. Its application-independent interface allows also interworking with PSTN, integrated services digital network (ISDN), or even GSM. For operators of public networks, DECT can be employed to span the last mile to subscribers by radio local loop (RLL).

3.2.2.3. Personal Handy Phone Systems (PHS). In 1989, the Japanese Ministry of Posts and Telecommunications initiated the standardization process for another cordless system, which become the PHS standard [15]. Among other things, the standard defines the air interface, voice services, and data services. The system is designed for small cells, and it maintains incoming as well as outgoing calls. A special feature of PHS is that mobiles that are close enough may bypass the base station and communicate directly with each other.

3.2.3. Professional Mobile Radio. Besides cellular and cordless systems, a variety of professional mobile radio (PMR) systems have been designed for professional and private users. In 1988, the European Commission and ETSI initiated standardization of a PMR system known as trans-European trunked radio (TETRA). Applications include group calls within a fleet of users and fleet management as required by police, safety organizations, or taxi companies. Similarly, in the United States the so-called Associated Public Safety Communications Officers Project 25 (APCO 25) is specifically concerned with public safety radio services. There are a number of other PMR systems, such as European radio message (ERMES), digital short-range radio (DSSR), and terrestrial flight telephone system (TFTS), to mention only a few.

3.3. Third-Generation Systems

At present, mobile communications is realized by many kinds of competitive and incompatible standards, systems, and services. On the other hand, unification of cellular, paging, cordless, and professional mobile radio is desirable to manage limited physical resources, improve system quality, and keep up with the great demand for mobile services. Third-generation systems aim to provide unification and worldwide coverage.

3.3.1. Universal Mobile Telecommunication System. The European effort to support the same type of services anywhere and anytime is known as the Universal Mobile Telecommunication System (UMTS) and is described in Ref. 16. It is based on GSM, DCS-1800, and DECT. Standardization is concerned with air interface and protocol issues aiming for global coverage for speech, low-to-medium bit rate services, and multimedia capabilities. A major challenge is to achieve higher data rates, up to 2 mbps. In 1987, the European Union launched a program called Research and Development in Advanced Communications Technologies in Europe (RACE). RACE was supposed to investigate advanced options for mobile communications and in that way assist ETSI in standardization of UMTS. Several subprojects within RACE were concerned with advanced topics, as the following examples indicate. The advanced TDMA (ATDMA) project investigated antenna systems and equalization issues. An approach to increase data rate was undertaken in the Code Division Testbed (CODIT) project. Recently, an agreement was reached among European companies on the radio interface for UMTS based on wideband CDMA (W-CDMA) and time division CDMA (TD-CDMA) technologies [17]. Operation of UMTS is expected to commence in the beginning of the twenty-first century.

3.3.2. International Mobile Telecommunications—2000. In the mid-1980s, the International Telecommunications Union (ITU) began its studies of future public land mobile telecommunication systems, the goal of which is to support mobile communication anywhere, anytime. The goals are similar to those intended to be reached by UMTS, but under a worldwide perspective. The ITU approach is now called International Mobile Telecommunications—2000 (IMT-2000) [18], the former FPLMTS (the attached 2000 indicates the frequency band of operation in MHz as well as the year in which service is planned to open). At the World Administrative Radio Conference in 1992 (WARC-92), a bandwidth of 230 MHz in the 2 GHz frequency band was allocated worldwide to IMT-2000. A major objective of IMT-2000 is to offer users a small, inexpensive pocket communicator and provide for seamless roaming of a mobile terminal across various networks. Services range from voice to data and mobile multimedia applications or even Internet access. These services will be offered for a wide range of operating environments, such as indoor, outdoor, terrestrial, and satellite networks. ITM-2000 will utilize technologies like the asynchronous transfer mode (ATM) to provide broadband transport services.

3.3.3. Other Systems

3.3.3.1. Wireless Local Area Networks (WLANs). Mobile data of second-generation systems offers only low bit rate wireless data transmission but with wide-area mobility and roaming. UMTS and IMT-2000 are supposed to increase the bit rate to some 2 Mbps. On the other hand, for in-house and on-premises networking there is substantial demand for higher bit rates in the range of 20 Mbps, whereas mobility is required only in a restricted area. WLAN systems for such local networking are planned to complement third-generation systems and are considered a flexible and cost-

effective alternative to cable-based LANs. Since proprietary solutions are typically customized and rely on products of a particular equipment supplier, standardization of WLAN systems has been undertaken as follows. The high-performance radio local-area network (HIPERLAN) standard [19] was developed by ETSI. HIPERLAN achieves a bit rate of 20 Mbps and can be used to extend wired LANs such as Ethernet. Spectrum has been recommended in the 5- and 17-GHz bands. Access to the shared transmission channel is gained by a contention-based and collision avoidance strategy. All time-critical services are supported by best effort and, in principle, may achieve the same access priority. The Institute of Electrical and Electronics Engineers (IEEE) 802.11 standard [20] represents the first approach for WLAN products from an internationally recognized, independent organization. It defines the protocol for two types of networks—namely, adhoc and client/server networks. IEEE 802.11 operates in the industrial, scientific, and medical (ISM) band at 2.4 GHz using spread-spectrum modulation. The medium access control (MAC) uses a collision avoidance mechanism. The third major effort in the area of WLANs is known as wireless ATM (WATM) [21,22]. With ATM being a widely accepted standard for broadband networking, it is natural to extend this technology into the wireless domain. Accordingly, the ATM Forum is working toward a WATM standard. A WATM system will provide bandwidth on demand for low- and high-priority services, hence providing real support of time critical multimedia services. Furthermore, a WATM system will interwork seamlessly with wired ATM networks and can be expected to cooperate very well with IMT-2000.

3.3.3.2. Satellite Systems. Further improvement of coverage can be provided by satellite systems [23], which are a component of future-generation mobile systems. Low-Earth-orbit (LEO) satellite systems typically operate on orbits at an altitude of 700–1400 km, whereas medium-Earth-orbit (MEO) satellite systems have their orbits at about 10,000 km. Compared to geostationary satellite systems, LEO and MEO systems allow low-power handhelds and smaller antennas and offer a smaller round-trip delay between Earth and satellite. Both LEO and MEO systems employ a number of satellites that form a satellite network and offer worldwide coverage. Satellite systems can be used to cover remote areas that are out of range of a terrestrial cellular system or where a telephony system does not exist. The first generation of satellite personal communications networks (S-PCN) will basically support voice, data, facsimile, and paging. Promising candidates of LEO/MEO systems are Intermediate Circular Orbit (ICO) satellite cellular telephone systems, formerly known as Inmarsat-P, Odyssey, Globalstar, and Iridium. The second generation of S-PCN systems, such as the Teledesic approach, will evolve toward multimedia services and employ ATM technology as well.

4. MOBILE RADIO CHANNELS

Mobile radio channels considered to be a complex and severe transmission medium. Path loss often exceeds that of

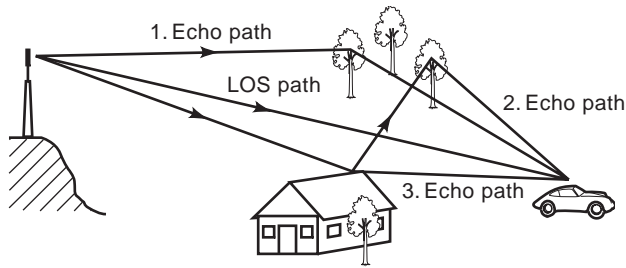


Figure 2. Illustration of multipath propagation typically experienced in a mobile radio environment. Signals between transmitter and receiver propagate along a line-of-sight (LOS) path and are scattered through several echo paths.

free space by several tens of decibels. Reflection, diffraction, scattering, and shadowing lead to fading and multipath reception (Fig. 2). Mobile radio channels are time variant, where signals fluctuate randomly as the receiver moves over irregular terrain and among buildings. Understanding channel behavior and development of channel models for a specific band is always vital for efficient system design.

4.1. Large-Scale Propagation Models

Propagation models that predict the average signal strength of a received signal at a given distance from the transmitter are called large-scale propagation models. These models are concerned with loss along the wave propagation path between the mobile and base stations. Extensive measurement campaigns have been undertaken to develop models for some typical environments. We distinguish roughly between rural, sub-urban, and urban environments.

4.1.1. Free-Space Model. The ideal large-scale model is free-space propagation, assuming that no objects or obstacles influence propagation. Free-space path loss is given by [24]

$$L_F = 10 \log G_t + 10 \log G_r - 20 \log f_c - 20 \log d - 32.44 \text{ dB} \quad (1)$$

where G_t and G_r are the transmitter and receiver antenna gain compared to an isotropic antenna, f_c is the carrier frequency in MHz, and d is the distance between the transmitter and receiver in km.

4.1.2. Okumura–Hata Model. Okumura [25] presented a graphical method to predict the median attenuation relative to free space for a quasismooth terrain. The model consists of a set of curves developed from measurements and is valid for a particular set of system parameters in terms of carrier frequency, antenna height, and so forth. After the free-space path loss has been computed, the median attenuation, as given by Okumura's curves, has to be added. Additional correction factors apply for different terrains. Later, Hata [26] transformed Okumura's graphical method into an analytical framework. The Hata model

for urban areas is given by the empirical formula

$$L_{50, \text{urban}} = 69.55 \text{ dB} + 26.16 \log f_c - 13.82 \log h_t - a(h_r) + (44.9 - 6.55 \log h_t) \log d \quad (2)$$

where $L_{50, \text{urban}}$ is the median path loss in dB. Equation (2) is valid for carrier frequencies f_c in the range from 150 to 1500 MHz, mobile antenna height h_r from 1 to 10 m, and base station antenna height ranging from 30 to 200 m. The distance d between mobile and base is supposed to be within 1–20 km. The correction factor $a(h_r)$ for mobile antenna height h_r for a small- or medium-sized city is given by

$$a(h_r) = (1.1 \log f_c - 0.7)h_r - (1.56 \log f_c) - 0.8 \text{ dB} \quad (3)$$

and for a large city it is given by

$$a(h_r) = \begin{cases} 8.29 [\log(1.54h_r)]^2 - 1.1 \text{ dB} & \text{for } f_c \leq 300 \text{ MHz} \\ 3.2 [\log(11.75h_r)]^2 - 4.97 \text{ dB} & \text{for } f_c \geq 300 \text{ MHz} \end{cases} \quad (4)$$

Equation (2) serves as the standard formula in urban areas and has to be modified for suburban areas:

$$L_{50, \text{suburban}} = L_{50, \text{urban}} - 2[\log(f_c/28)]^2 - 5.4 \text{ dB} \quad (5)$$

For rural areas, we have to use

$$L_{50, \text{rural}} = L_{50, \text{urban}} - 4.78(\log f_c)^2 - 18.33 \log f_c - 40.94 \text{ dB} \quad (6)$$

A uniform extension of these formulas for carrier the frequency range $1500 \text{ MHz} \leq f_c \leq 2000 \text{ MHz}$ and small cells, such as those of personal communications systems, is specified by the European Co-operative for Scientific and Technical research (COST-231) recommendation [27].

4.2. Wideband Characterization

To model the time and frequency dispersion of a mobile radio channel with respect to wideband transmission, a system theory approach can be utilized [28]. This approach is concerned with fading and multipath in the vicinity of a small area. A set of system functions provides a description in either the time or frequency domain. Due to the random nature of the radio channel, system functions describe stochastic processes.

4.2.1. Time-Variant Impulse Response and Autocorrelation Function. Bello [28] showed that a radio channel may be regarded as a linear time-variant systems. He introduced a set of continuous-time and continuous-frequency

system functions, each of which completely describes the channel and can be transformed into any of the remaining functions. For the sake of clarity, we assume hereinafter that signal spectra are narrow compared with carrier frequency and channel bandwidth. Thus, we can use a complex lowpass equivalent to represent a bandpass system [29]. In doing so, let us focus on the time domain and consider the input delay spread function $h(t, \tau)$, defined by

$$y(t) = \int_{-\infty}^{\infty} x(t - \tau)h(t, \tau) d\tau \quad (7)$$

where $x(t)$ and $y(t)$ denote the complex envelope of the transmitted and received signals, respectively. The input delay spread function $h(t, \tau)$ can be thought of as time-variant impulse response of the lowpass equivalent channel at time t due to unit input impulse applied in the past at time $t - \tau$.

Correlation functions provide significant insight into stochastic processes and are often used to avoid specification of multidimensional probability density functions. In this context, the autocorrelation function of the channel impulse response is given by [28]

$$R_h(t_1, t_2; \tau_1, \tau_2) = \overline{h(t_1, \tau_1)h^*(t_2, \tau_2)} \quad (8)$$

where $h(t, \tau)$ is assumed to be a random process without deterministic component, $\overline{h(\cdot)}$ denotes the ensemble average of $h(\cdot)$, and $*$ indicated a conjugate complex. Variables t_1 and t_2 denote time instants, whereas τ_1 and τ_2 denote delays. For many mobile radio channels Eq. (8) does not depend on absolute time but on time difference. In addition, scatterers may be regarded as uncorrelated. Such a channel is called a *wide-sense stationary uncorrelated scattering* (WSSUS) channel, and its autocorrelation function simplifies to [28]

$$R_h(t_1, t_2; \tau_1, \tau_2) = P_h(\Delta t; \tau_2)\delta(\tau_2 - \tau_1) \quad (9)$$

where $P_h(\Delta t; \tau_2)$ is a cross-power spectral density, $\Delta t = t_2 - t_1$ indicates time difference, and $\delta(\tau)$ denotes a unit impulse at time $\tau = \tau_2 - \tau_1$.

4.2.2. Time and Frequency Dispersion Parameters. In practice, a set of typical channel parameters is used to characterize the dispersive behavior of a mobile radio channel in the time and frequency domain. Similar to Bello's system approach of corresponding functions, time and frequency dispersion parameters possess dual representations in the frequency and time domain, respectively. These parameters can be obtained from measurements and employed for channel classification.

4.2.2.1. Delay Spread and Coherence Bandwidth. Because of multipath propagation, the impulse response of a mobile radio channel appears as a series of pulses rather than a single delayed pulse. A received signal suffers spreading in time compared to the transmitted signal. Delay spread can range from a few hundred nanoseconds inside buildings up to some microseconds in urban areas.

Delay-related parameters can be obtained from the power delay profile $P_h(\tau)$ [29], which is defined as the power spectral density for $\Delta t = 0$:

$$P_h(\tau) = P_h(\Delta t, \tau)|_{\Delta t=0} \quad (10)$$

Maximum excess delay is defined as the period between the time of the first arriving signal and the maximum time at which a multipath signal exceeds a given threshold. The first moment of a power delay profile is called mean excess delay m_τ and is defined by

$$m_\tau = \frac{\int_0^{\infty} \tau P_h(\tau) d\tau}{\int_0^{\infty} P_h(\tau) d\tau} \quad (11)$$

The square root of the second central moment of the power delay profile is referred to as root-mean-square (RMS) delay spread, σ_τ , and is defined by

$$\sigma_\tau = \sqrt{\frac{\int_0^{\infty} [\tau - m_\tau]^2 P_h(\tau) d\tau}{\int_0^{\infty} P_h(\tau) d\tau}} \quad (12)$$

The coherence bandwidth B_c translates time dispersion into the language of the frequency domain. It specifies the frequency range over which a channel affects the signal spectrum nearly in the same way, causing an approximately constant attenuation and linear change in phase. Coherence bandwidth is inversely proportional to rms delay spread:

$$B_c \propto \frac{1}{\sigma_\tau} \quad (13)$$

4.2.2.2. Doppler Spread and Coherence Time. Movement of a mobile station relative to a base station or movement of objects within the channel causes the received frequency at the mobile station to differ from the transmitted frequency due to Doppler shift. In a multipath environment, a mobile station receives signals from different paths. Its relative movement with respect to each path differs, which results in a range of Doppler shifts. The bandwidth over which dispersion of the transmitted frequency occurs is referred to as the Doppler spread, B_d . The time domain equivalent to Doppler spread B_d is called coherence time, T_c . It specifies a period over which the channel impulse response $h(t, \tau)$ is nearly time invariant. Coherence time is inversely proportional to Doppler spread:

$$T_c \propto \frac{1}{B_d} \quad (14)$$

4.2.3. Classification of Multipath Channels

4.2.3.1. Flat Fading. This type of fading is related to delay spread. It occurs when the signal symbol period is

much larger than rms delay spread. As a result, intersymbol interference (ISI) almost vanishes. In the dual domain, the signal bandwidth is narrow compared to the coherence bandwidth. The channel has a flat transfer function with almost linear phase, thus affecting all spectral components of the signal similarly.

4.2.3.2. Frequency Selective Fading. If the signal symbol period is much lower than rms delay spread, the receiver is able to resolve multipath components, and ISI impairs transmission. In that case, the bandwidth of the signal exceeds the coherence bandwidth, and various spectrum components may be affected differently. Frequency selective fading is also caused by delay spread.

4.2.3.3. Fast Fading. This type of fading is caused by motion in a mobile environment and hence relates to Doppler spread. Fast fading can be observed when significant changes in the channel impulse response occur within the signal symbol period. In other words, the bandwidth of the Doppler spectrum is wide compared with the signal bandwidth, which then causes significant signal distortion.

4.2.3.4. Slow Fading. In the case when the channel impulse response is almost time invariant for the duration of a signal symbol period, we observe a slow fading and only a minor signal distortion. The Doppler spread is then narrow compared to the signal bandwidth.

4.3. Narrowband Characteristics

We consider an unmodulated sinusoidal waveform being transmitted at carrier frequency f_c and described in complex notation by $x(t) = \exp(j2\pi f_c t)$, where $j = \sqrt{-1}$. The equivalent lowpass signal at the receiver can be written as [29]

$$\begin{aligned} y(t) &= y_I(t) + jy_Q(t) \\ &= \sum_{i=-\infty}^{\infty} a_i(t) \cdot \exp[j2\pi f_{d,i}t - j2\pi f_c \tau_i(t)] \end{aligned} \quad (15)$$

where $y_I(t)$ and $y_Q(t)$ denote, respectively, in-phase and quadrature components of the complex-valued signal $y(t)$, $a_i(t)$ is complex amplitude, $f_{d,i}$ is Doppler frequency, and $\tau_i(t)$ is delay of the i th multipath component.

4.3.1. Fading Distributions

4.3.1.1. Rayleigh Fading. Suppose there is no dominant path between transmitter and receiver, and all multipath components are multiply reflected to build a diffuse received signal. In that case, complex amplitude $a_i(t)$, Doppler frequency $f_{d,i}$, and delay $\tau_i(t)$ can be considered statistically independent of each other. The probability density function of the received signal envelope $r(t) = |y(t)| = \sqrt{y_I^2(t) + y_Q^2(t)}$ leads to a Rayleigh distribution

given by [24]

$$p_{\text{Rayleigh}}(r) = \frac{r}{\sigma_y^2} \exp\left(-\frac{r^2}{2\sigma_y^2}\right) \quad (16)$$

where $r \geq 0$ is the received signal envelope and $\sigma_y^2 = E\{y_I^2(t)\} = E\{y_Q^2(t)\}$ is the variance of the zero-mean and normally distributed processes, describing $y_I(t)$ and $y_Q(t)$. Mean m_r and variance σ_r of $r(t)$ are given by $m_r = E\{r(t)\} = \sqrt{\pi/2} \cdot \sigma_y$ and $\sigma_r^2 = (2 - \pi/2) \cdot \sigma_y^2$, respectively.

4.3.1.2. Rice Fading. Let the received signal contain a dominant component that might be caused by a line-of-sight (LOS) path or single reflected multipath components. In terms of an equivalent lowpass signal, we have to add a constant r_0 to the real part of $y(t)$ and thus $y(t) = [r_0 + y_I(t)] + jy_Q(t)$. The corresponding probability distribution function of the signal envelope $r(t) = \sqrt{[r_0 + y_I(t)]^2 + y_Q^2(t)}$ leads to a Rician distribution [24]

$$p_{\text{Rice}}(r) = \frac{r}{\sigma_y^2} \exp\left(-\frac{r^2 + r_0^2}{2\sigma_y^2}\right) I_0\left(\frac{r \cdot r_0}{\sigma_y^2}\right) \quad (17)$$

where $r_0 \geq 0$ is the peak amplitude of the dominant component and $I_0(\cdot)$ is the zero-order modified Bessel function of the first kind.

4.3.1.3. Lognormal Fading. When a mobile station moves within an area about the base station, the local-mean power P_r of the received signal varies about the area-mean power P_s due to shadowing effects. Measurements have shown that the logarithmic value $L_r = 10 \log(P_r)$ in dB of the local-mean power P_r is normal distributed about the logarithmic value $L_s = 10 \log(P_s)$ in dB of the area-mean power P_s . This gives rise to the call P_r being lognormal distributed, and the corresponding probability density function is given by [30]

$$\begin{aligned} p_{\text{lognormal}}(P_r) &= \frac{10 \log(e)}{P_r} \cdot \frac{1}{\sqrt{2\pi}\sigma_s} \\ &\times \exp\left\{-\frac{[10 \log(P_r) - L_s]^2}{2\sigma_s^2}\right\} \end{aligned} \quad (18)$$

where standard deviation σ_s in dB characterizes the shadowing effect.

5. SPECTRUM MANAGEMENT

The radiofrequency spectrum is a limited resource that has to be shared in some way among the communication community. With the increasing demand for mobile radio communication, regulations and methods for efficient spectrum usage are required. Frequency authorities such as the ITU and the Federal Communications Commission (FCC) play a vital part in allocating frequency bands to new systems and in worldwide coordination of the radio spectrum. Once a frequency band has been

licensed, the cellular concept enables spectrum efficiency by reusing frequency in spatial by distant areas. Bandwidth-efficient modulation schemes can be used to increase further the total number of available channels in a system.

5.1. Frequency Licensing

Spectrum planning is a hierarchical process that starts at the highest international level at the ITU and is covered by the WARC. This international framework is a base for national frequency planning and allocation. From the start of a licensing process to actual frequency allocation with specified services, often several years elapse. On the other hand, today's main requirements of licensing procedures are speed, transparency, fairness, efficiency, and conformity with government objectives. As a response, several national regulatory methods for licensing of frequency bands have been applied and are still used, depending on the local situation [31].

5.1.1. Over-the-Counter Allocation. This is the traditional method, which can be regarded as a first come, first served principle. Obviously, with this method there will be unsatisfied demand. In addition, there is no guarantee that those who apply first will be those who value the spectrum most highly or whose service is of greatest importance to the community. In cases where demand does not exceed supply (e.g., for many military applications), this approach is still favored.

5.1.2. Comparative Assessment. In this approach governments and regulators assess the relative merits of different applicants for a frequency band. The criteria are varied—for example, anticipated consumer benefits, the technology applied, or the perceived overall social worth of the service to be supplied. A regulator must be able to make judgments about the most valued use of a frequency band. Apparently, comparative assessment is neither transparent nor fast or even fair and should only be used when a decision can be easily reached (e.g., if there is no competition between providers due to a monopolistic market).

5.1.3. Lotteries. Lotteries involve a random distribution of licenses to different applicants of the same frequency band. Lotteries are quick and fair as long as all participants have the same weight and do not circumvent this by submitting multiple entries under different names. Even then lotteries might not be effective because the value of the service cannot be accounted for.

5.1.4. Tenders. Applicants provide sealed bid tenders for a desired frequency band. The advantages of this method are its fairness and transparency. The problem is that it is not effective in the sense that the most valued service will be gained by the company with the highest financial resources. This may lead to proprietary services if the final service in that band is not completely defined in advance. Otherwise, if the service is already defined, this approach is better than those previously mentioned. One

major disadvantage still remains: the high possibility of overvaluing the asset because the bids of others are not known.

5.1.5. Auctions. Auctioning of frequency bands combines the advantages of the tender approach with information about the bids of the applicants. In addition, government interests concerning enhanced competition can be taken into account by restricting the occupied amount of frequency bands for an applicant to a certain percentage. Sometimes the fairness of this approach is criticized because similar lots could be sold for very different prices. Furthermore, collisions may happen at auctions. To offer multiple frequency bands at the same time, the simultaneous multiple-round auction was developed. It seems that the latter method is one of the best for efficient and fair spectrum management. It fulfills most of the requirements mentioned previously and returns the pressure from the regulators back to the applicants. Thus, it is going to be applied in future licensing procedures in which an excess of demand over supply can be forecast (e.g., for third-generation mobile systems).

5.2. Frequency Reuse

The concept of frequency reuse is a core element of all cellular mobile radio systems [1,6]. It significantly increases system capacity, which may be indicated by the total number of available duplex channels. The frequency band allocated to a cellular system is organized into a finite number of frequency channels, each of which can be simultaneously reused in different geographic locations (so-called cells). In that way, a cellular system can serve more customers compared with the case when the whole system area is covered by just a single base station. On the other hand, reuse of frequency channels causes interference between those cells that use the same channel (this is called *cochannel interference*). It is a major task of cellular system design to maximize capacity and to minimize interference. Since capacity can be increased by using smaller cells and interference decreases with larger cells, a compromise is required.

In cellular system design, some idealized assumptions are made that ease the complex task of capacity and interference analysis. First, a hexagonal cell shape is normally proposed as a model to approximate the actual footprint of a base station. Thus, the whole coverage area of a cellular system can be represented by a homogeneous grid of hexagons. Because of this geometry, the number of cells in a cluster or cluster size can only take certain values and is given by

$$N = I^2 + IJ + J^2 \quad (19)$$

where the shift parameters I and J are nonnegative integers. Figure 3 shows the frequency reuse concept for a seven-cell cluster in which each letter denotes a set of frequencies. A certain cell is surrounded by adjacent channel neighbors. The nearest co-channel neighbor (say, to cell G) can be found by moving along a chain of $I = 2$ hexagons,

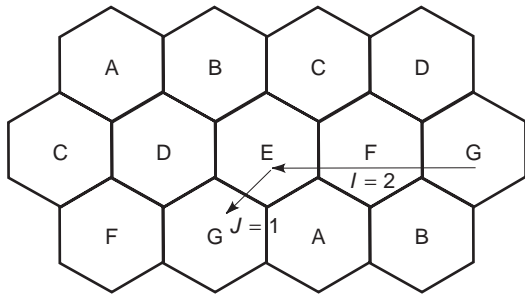


Figure 3. Illustration of the cellular concept by means of a seven-cell cluster. The seven frequencies reused in the system are labeled A through G. Shift parameters are $I = 2$ and $J = 1$.

turning 60° counter-clockwise, and finally moving in that new direction along $J = 1$ cells.

Here, we consider a homogeneous hexagonal cellular system in which cells are roughly of equal size. It turns out that cochannel interference does not depend on transmission power but on the ratio between distance D of a cell to the center of the nearest cochannel cell and radius R of a cell (Fig. 4). This parameter is called the *cochannel reuse ratio* and is given by

$$Q = D/R = \sqrt{3N} \tag{20}$$

A large cochannel reuse ratio means that transmission quality is high, since cochannel interference is kept low because of a reasonable spatial separation of cochannel neighbors. Large capacity can be obtained when the cluster size and correspondingly the cochannel reuse ratio is small.

Usually, cochannel interference can be quantified by computing the signal-to-interference ratio (SIR). For that purpose, let γ denote the path loss exponent and assume γ to be constant over the whole coverage area of the cellular system. In a mobile radio environment, γ typically ranges between two and four. In addition, assume that all base stations transmit the same power. Then the SIR at a mobile station can be estimated by

$$\frac{S}{I} = \frac{R^{-\gamma}}{\sum_{i=1}^{i_0} D_i^{-\gamma}} \tag{21}$$

where i_0 is the number of cochannel interfering cells. Let us now consider cochannel interfering cells from the first

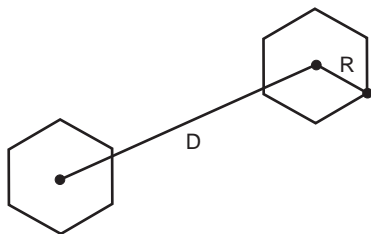


Figure 4. Interference geometry between two co-channel cells used to compute the signal-to-interference ratio assuming an idealized hexagonal cell shape. Cells are of radius R and have distance D from each other.

Table 2. Signal-to-Interference Ratio for Various Cluster Sizes

I	J	N	Q	S/I in dB	
				Eq. (22)	Eq. (23)
1	1	3	3.00	11.30	8.03
2	1	7	4.58	18.65	17.26
3	0	9	5.19	20.84	19.74
2	2	12	6.00	23.34	22.57

tier only and assume that all those base stations are at a distance D from the desired base station. Then the SIR can be approximated as

$$\frac{S}{I} = \frac{Q^\gamma}{i_0} = \frac{(D/R)^\gamma}{i_0} = \frac{(\sqrt{3N})^\gamma}{i_0} \tag{22}$$

Finally, in the worst-case scenario, in which the mobile station is located at the cell boundaries, the SIR can be approximated as

$$\frac{S}{I} = \frac{1}{2(Q-1)^{-\gamma} + 2Q^{-\gamma} + 2(Q+1)^{-\gamma}} \tag{23}$$

Table 2 shows SIR values for some typical cluster sizes. The pass loss exponent is taken as $\gamma = 4$, and the number i_0 of cochannel interfering cells in a fully developed system is about six. Subjective tests undertaken for voice services have shown that an $S/I = 18$ dB gives satisfactory quality. In a homogeneous hexagonal system, this requires a cluster size of at least seven.

Apart from frequency reuse, there are some other techniques to improve the capacity of a cellular system. Improved capacity is often required to adapt the initial system to an increasing demand on services or to better cover congested areas. Sectoring is such a technique and replaces omnidirectional antennas at a base station by several sector antennas. Most common is an arrangement of three or six sectors whereby a 120° or 60° directional antenna radiates within a certain sector. Due to less cochannel interferers in the first tier of a sectorized system, this approach decreases the signal-to-interference ratio and thus allows for a smaller cluster size (i.e., higher capacity). A second technique is called cell splitting, which basically reduces the cell sizes. In that way, more cells fit within an area, resulting in more available channels per area.

5.3. Digital Modulation Techniques for Mobile Communication

A modulation scheme for a mobile communication system should utilize the allocated frequency band and power as efficiently as possible. With regard to second-generation systems and the intended application of data services in future wireless systems, digital modulation techniques are a natural choice. Selection of an appropriate digital modulation scheme can be made on the basis of the following characteristics. The power density spectrum is defined as the relative power in a modulated signal versus

Table 3. Spectral Efficiency of Second-Generation Systems

System	Modulation Technique	Data Rate (kbps/s)	Channel Spacing (kHz)	Efficiency (bps/Hz)
GSM	GMSK ($BT^a = 0.3$)	270.8	200	1.35
IS-54	$\pi/4$ -DQPSK	48.6	30	1.62
IS-95	QPSK/BPSK	1288	1250	1.03
PDC	$\pi/4$ -DQPSK	42	25	1.68
CT-2	GMSK ($BT^a = 0.5$)	72	100	0.72
DECT	GMSK ($BT^a = 0.5$)	1152	1728	0.67
PHPS	$\pi/4$ -DQPSK	384	300	1.28
TETRA	$\pi/4$ -DQPSK	36	25	1.44

^a $BT = 3$ dB-bandwidth and bit duration product of the Gaussian filter.

frequency. It consists of a main lobe and several sidelobes, which indicate interference into adjacent channels. A modulation scheme can be further assessed by its robustness against interference and channel impairments, which is indicated by a low bit error rate. Bandwidth efficiency measures the bit rate that can be transmitted per unit of frequency bandwidth and is expressed as the number of bits per second per hertz (bps/Hz). Apart from that, implementation complexity and costs have to be considered as well. A desirable modulation scheme should achieve high bandwidth efficiency at a given bit error rate and simultaneously offer a narrow power density spectrum. Digital modulation schemes currently being used in second generation systems can be classified into phase shift keying (PSK) and continuous phase modulation (CPM).

The family of PSK schemes belongs to the class of linear modulation techniques [29]; that is, a modulating digital signal is used to vary linearly the amplitude of a transmitted signal. The most popular schemes within this family include quaternary phase shift keying (QPSK), offset QPSK (OQPSK), $\pi/4$ phase shift QPSK ($\pi/4$ -QPSK), and differentially encoded $\pi/4$ -QPSK, called $\pi/4$ -DQPSK. QPSK splits the baseband data signal into two pulsestreams (namely, in-phase and quadrature components), which reduces the data rate to half that of the baseband signal. The phase of the carrier takes one of four values (say, 0° , 90° , 180° , or 270° or an equally spaced but rotated constellation of these). Side lobes in the power density spectrum of a QPSK-modulated signal are usually suppressed by passing the signal through a front-end filter, but then the signal envelope will no longer have a constant envelope. When the filtered signal experiences a 180° shift in carrier phase, the envelope fluctuates significantly and even goes through zero. Such an envelope fluctuation will cause reappearance of sidelobes every time the filtered QPSK modulated signal passes a nonlinearity (e.g., a nonlinear amplifier). An improvement over QPSK offers the OQPSK modulation scheme, in which a shift of one bit delay is introduced to the quadrature component. As a result, in-phase and quadrature components have signal transitions at separate time instants, and thus shifts in carrier phase are limited to a maximum of $\pm 90^\circ$. Because 180° phase shifts have been removed, the envelope cannot go through zero any longer. Envelope fluctuations are less severe, and nonlinear amplification can be applied. Finally, $\pi/4$ -QPSK can be regarded as a compromise between

QPSK and OQPSK, which limits the maximum phase shift to $\pm 135^\circ$. $\pi/4$ -QPSK can be differentially encoded and is then called $\pi/4$ -DQPSK. The $\pi/4$ -DQPSK technique uses the phase shifts in the carrier instead of the phase to transmit information. It can be noncoherently detected, which is one of the reasons that $\pi/4$ -DQPSK has been employed in many digital mobile communication systems, such as IS-54, PDC, and PHS.

Improvement of OQPSK in terms of out-of-band radiation can be obtained from the CPM technique [32], which continuously varies the carrier phase and thus completely avoids discontinuous phase transitions. Further, all CPM schemes have constant carrier envelopes and hence allow for nonlinear amplification. Among the most popular CPM schemes are minimum shift keying (MSK) and Gaussian minimum shift keying (GMSK). MSK can be regarded as a special case of OQPSK in which the baseband signal uses half-sinusoidal pulses instead of a rectangular pulse shape (this produces the desired smooth phase transitions). Unfortunately, MSK does not have a power density spectrum as compact as desirable for mobile radio. A tighter spectrum can be achieved by passing the modulating signal through a premodulating pulse shaping filter. Following this concept, GMSK uses a filter with a Gaussian or bell-shaped transfer function. The compact power density spectrum of GMSK is gained at the expense of an increased irreducible bit error rate due to intersymbol interference. GMSK has been adopted for GSM, DECT, and CT-2.

Table 3 summarizes modulation techniques used in second-generation systems along with the achieved bandwidth efficiency. The most popular schemes are $\pi/4$ -DQPSK and GMSK. Note that the employed GMSK schemes differ in the 3 dB bandwidth and bit duration product BT of the Gaussian filter.

6. CONCLUSION

Mobile communication has already become an integral part of modern life and is one of the driving forces of telecommunications. Wireless access to global telecommunication can be expected to change the face of telecommunication even further. Apart from traditional voice services and low-rate data, future mobile communication will provide for multimedia services that are a mixture of voice, data, text, graphic, and video. Land mobile,

maritime, aeronautic, and satellite systems will not just coexist but will establish a global mobile system allowing users to communicate at any time and from anywhere in the world. Before this vision of a global mobile system can become reality, several technical challenges have to be resolved. Such resolution will require support from all areas of communication engineering, such as source and channel coding, bandwidth-efficient modulation, multiple access control, and protocol and security issues.

BIBLIOGRAPHY

1. W. C. Y. Lee, *Mobile Cellular Telecommunications*, McGraw-Hill, New York, 1995.
2. J. Tisal, *GSM Cellular Radio Telephony*, Wiley, New York, 1997.
3. A. D. Hadden, *Personal Communications Networks: Practical Implementation*, Artech House, Boston, 1995.
4. G. Calhoun, *Wireless Access and the Local Telephone Network*, Artech House, Boston, 1992.
5. G. Calhoun, *Digital Cellular Radio*, Artech House, Boston, 1988.
6. T. S. Rappaport, *Wireless Communications—Principles and Practice*, IEEE Press, Piscataway, NJ, 1996.
7. Nordic Mobile Telephone Group, *Nordic Mobile Telephone, System Description*, NMT Doc. 1. 1997, February 1978.
8. W. R. Young, Advanced mobile phone services: Introduction, background, and objectives, *Bell Syst. Tech. J.* **58**:1–14 (1979).
9. FTZ der Deutschen Bundespost, *Funkfernsprechdienst Netz C*, Technische Vorschriften, FTZ 171R60, Darmstadt, 1982.
10. European Telecommunications Standards Institute, *GSM Recommendations Series 01-12*, ETSI Secretariat, Sophia Antipolis Cedex, France, 1990.
11. Electronic Industries Association/Telecommunications Industrie Association, *Cellular System, Dual-Mode Mobile Station-Base Station Compatibility Standard*, EIA/TIA Interim Standard 54, 1991.
12. Electronic Industries Association/Telecommunications Industrie Association, *Mobile Station—Base Station Compatibility Standard for Dual-Mode Wideband Spread Spectrum Cellular System*, EIA/TIA Interim Standard 95, 1993.
13. Research and Development Center for Radio Systems, *Personal Digital Cellular System Common Air Interface*, RCR-STD 27B, Tokyo, Japan, 1991.
14. W. H. W. Tuttlebee, ed., *Cordless Telecommunications in Europe*, Springer-Verlag, Berlin, 1990.
15. Research and Development Center for Radio Systems, *Personal Handy Phone System: Second Generation Cordless Telephone System Standard*, RCR-STD 28, Tokyo, Japan, 1993.
16. S. Chia, The universal mobile telecommunication system, *IEEE Commun. Mag.* **30**(2):54–62 (1992).
17. European Telecommunications Standards Institute, *Agreement Reached on Radio Interface for Third Generation Mobile System*, UMTS (Universal Mobile Telecommunications System), press release, Tdoc 40/98, ETSI Secretariat, Sophia Antipolis Cedex, France, Jan. 29, 1998.
18. M. Callendar and T. F. La Porta eds., IMT-2000: Standards efforts of the ITU, *IEEE Personal Commun.* (special issue), **4**(4) (1997).
19. European Telecommunications Standards Institute, *Radio Equipment and Systems (RES)—High Performance Radio Local Area Network (HIPERLAN)*, technical report, DTR/RES-1003, ETSI Secretariat, Sophia Antipolis Cedex, France, 1993.
20. The Institute of Electrical and Electronics Engineers, *Wireless LAN Medium Access Control (MAC) and Physical Layer (PHY) Specification*, IEEE Draft Standard P802.11/D2.1-95/12, IEEE Press, Piscataway, NJ, 1995.
21. M. Naghshinen, ed., Wireless ATM, *IEEE Personal Commun.* (special issue) **3**(4) (1996).
22. T. R. Hsing et al. (eds.), Wireless ATM, *IEEE J. Select. Areas Commun.* (special issue) **15**(1) (1997).
23. E. Del Re et al. (eds.), Mobile satellite communications for seamless PCS, *IEEE J. Select. Areas Commun.* (special issue) **13**(2) (1995).
24. J. D. Parsons, *The Mobile Radio Propagation Channel*, Pentech Press, London, 1992.
25. T. Okumura, E. Ohmori, and K. Fukuda, Field strength and its variability in VHF and UHF land mobile services, *Rev. Electron. Commun. Lab.* **16**(9–10):825–873 (1968).
26. M. Hata, Empirical formula for propagation loss in land mobile radio services, *IEEE Trans, Vehic. Technol.*, **VT-29**:317–325 (1980).
27. European Cooperation in the Field of Scientific and Technical Research EURO-COST 231, *Urban Transmission Loss Models for Mobile Radio in the 900 and 1800 MHz Bands*, Revision 2, The Hague, Sept. 1991.
28. P. A. Bello, Characterization of randomly time-variant linear channels, *IEEE Trans. Commun.* **COM-11**:360–393 (1963).
29. J. G. Proakis, *Digital Communications*, McGraw-Hill, New York, 1994.
30. R. W. Lorenz, Field strength prediction method for a mobile telephone system using a topographical data bank, *IEE Conf. Proc.* **188**:6–11 (1980).
31. A. J. Shaw, Spectrum auctions: Are they the best approach? *Proc. 3rd Asia-Pacific Conf. Commun.*, Sydney, Australia, pp. 551–557.
32. J. B. Anderson, T. Aulin, and C.-E. Sundberg, *Digital Phase Modulation*, Plenum Press, New York, 1986.

MOBILE RADIO CHANNELS

RODNEY G. VAUGHAN
Simon Fraser University
Burnaby, British Columbia
Canada

1. INTRODUCTION

The term *mobile channel* refers to the transfer function of a radio link when one or both of the terminals are moving. The moving terminal is typically in a vehicle such as a car, or a personal communications terminal such as a cell-phone. Normally one end of the radio link is fixed, and this is referred to as the *base station*. In the link, there is usually multipath radiowave propagation, which is changing with time, or as a function of position of the moving terminal. The effects of this multipath propagation dominate the behavior and characterization of the mobile channel.

The radiofrequency of the link ranges from hundreds of kilohertz, as in broadcast AM radio, to microwave frequencies, as in cellphone communications. Indeed, even optical frequencies are used, as in an infrared link used for indoor computer communications. The kind of channel most often referred to as “mobile,” however, is that using microwave frequencies, and this article concentrates on the characteristics of a mobile microwave radio link. Much of the dynamic channel behavior can be scaled by the carrier frequency and by the speed of the mobile terminal.

Current spectral usage is a result of many different historical developments, so the bands used by mobile radio channels have evolved to be at many frequencies. For example, current vehicular and personal communications terminals mostly use frequencies around 900 MHz and 1.8 GHz. In the future, higher frequencies will be used. The frequency has a definitive bearing on the rate at which the channel changes.

Some examples of mobile channels include domestic cordless telephones; cellular telephones and radiotelephones; pagers; satellite communication terminals, including navigational services such as Global Positioning System (GPS) reception; and radio networks for local data communications. Finally, the reception by portable receivers of broadcast radio, at frequencies of a few hundred kilohertz (AM radio), are common forms of the mobile radio channel.

The use of mobile channels has grown very quickly since the early 1990s. This growth will continue. It is driven by a combination of consumer demand for mobile voice and data services and advances in electronic technology. A limiting factor to the growth is that many users

must share the radio spectrum, which is a finite resource. The spectral sharing is not only local; it is also international, and so spectral regulatory issues have also become formidable. The increasing pressure to use the spectrum more efficiently is also a driving force in regulatory and technical developments.

To a user, a mobile or personal communications system is simple: it is a terminal, such as a telephone, that uses a radio link instead of a wire link. The conspicuous result is that the terminal is compact for portability, and it has an antenna, although for personal communications the antenna is often no longer visible. To the communication engineer, however, the mobile terminal can be viewed as a component in an electrical circuit. The mobile channel is one link in the circuit, but this link is the most complex, owing to its use of radiowaves in complicated propagation environments and of radio signal-processing technology needed to facilitate wireless transmission among multiple users.

In mobile channels, efficient spectral utilization is a function of the basic limitations on controlling radiowave behavior in complicated physical environments, including the launching and gathering of the waves. Thus antennas and propagation are key topics, and their roles characterize the channel behavior.

2. THE MOBILE CHANNEL

The mobile channel covers many different transfer functions that have different properties. Figure 1 illustrates individual channels [1]. The figure shows half of a link,

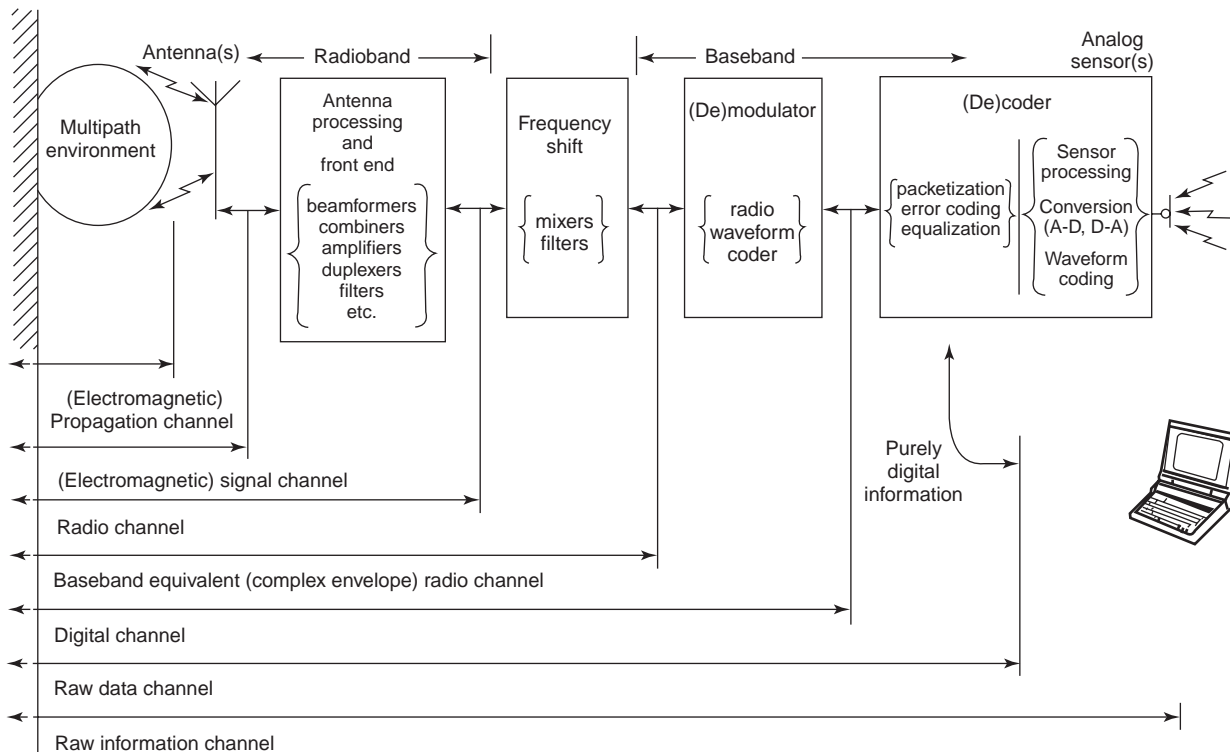


Figure 1. Various channels in a mobile communications link. The term “mobile channel” refers to the analog aspects of the channel, excluding modulation and coding.

with the other half essentially an inverse process. The multipath propagation environment represents the physical environment of the radio waves in the mobile channel. The flow of information is described here for transmission, but the description adapts readily to reception. A *raw information channel* refers to the transfer function that separates the transmitted and received raw information. For speech, for example, degradations of the immediate acoustical environment from reverberation and acoustic noise form part of the channel “seen” by the user at the receiving end. The quality of the information channel may be subjective, although standard metrics of distortion and signal-to-noise ratio can be applied for characterization. The electrical signal is often digitized for efficient transmission, and the *digital channel* is nonlinear, but its channel quality can be measured directly as a *bit error ratio* (BER). This digital form is sometimes rearranged by encoding techniques for more robust transmission of the information. The digital information is coded into analog waveforms and then mixed, or *heterodyned*, to the radio carrier frequency and transmitted via the antenna.

The distinguishing feature of the mobile channel is the changing multipath propagation between transmitter and receiver. The receiving antenna gathers the many incident electromagnetic waves from the multipath environment. These multipath contributions mutually interfere in a random, time-varying manner, and so statistical techniques are needed to characterize the channel. In the physical transmission media, the waves that bear the information are the signals of the *electromagnetic propagation channel*. The antenna reduces the signals from a vector form of orthogonal polarizations to a scalar voltage. The signal at the open-circuited receiving antenna terminal is the output of the *electromagnetic signal channel*. The antenna needs to be terminated in order to maximize the power received by the front end. The signal-to-noise ratio (SNR) is established at this point in the link, and the resulting signal is the output of the *radio channel*. The antenna is a critical part of the mobile channel, and it can control much of the channel behavior. The baseband equivalent form of the radio channel, which is the radio channel shifted in frequency to a lowpass spectral position, is the signal that engineers use for mathematical characterization and most electronic (including digital) signal processing. The analog form of the radio channel is what will be referred to from here on as the mobile channel.

2.1. Multiple Access for Mobile Channels

Most mobile communications systems are for multiple users, and a *multiple access* technique is required to allow the spectrum to be shared. In cellular systems, for example, the frequencies are reused at geographically spaced locations. For indoor systems, the frequency reuse spacing may be between floors. In a system design, the multiple access technique interacts with the choice of channel modulation and signal coding. The three basic techniques are frequency-division multiple access (FDMA), which has channels occupying different narrow bandwidths simultaneously; code-division multiple access (CDMA), in which

multiple users share wider band-widths simultaneously by using differently coded waveforms; and time-division multiple access (TDMA), in which users share a bandwidth by occupying it at multiplexed times. Some systems employ a combination of these techniques.

Multiple access is not a part of the mobile channel as such. However, the reader should remain aware that multiple access is part of the communications system and the choice of technique has an influence on the mobile channel bandwidth, its usage, and the type of signaling employed. Multiple access also brings in co- and adjacent-channel interference, in which the unwanted signals at a receiver may not be noiselike, but in fact be signals with very similar characteristics to the wanted signal. In systems with densely packed users, the system capacity is interference-limited.

3. MULTIPATH PROPAGATION EFFECTS

Multipath radiowave propagation is the dominant feature of the mobile channel. More often than not, the transmitted signal has no line-of-sight path to the receiver, so that only indirect radiowave paths reach the receiving antenna. For micro-wave frequencies, the propagation mechanisms are a mixture of specular (i.e., mirrorlike) reflection from electrically smooth surfaces such as the ground, walls of buildings, and sides of vehicles; diffraction from edges of buildings, hills, and other structures or formations; scattering from posts, cables, furniture, and other components; and diffuse scattering from electrically rough surfaces such as some walls, trees, and grounds.

Some multipath propagation occurs in nearly all communications links. The basic phenomenon is that several replicas of the signal are received, instead of one clean version. The result can be seen as television ghosts, for example. On transmission lines, reflections from mismatches on the line give the same effect, for example, echoes on telephone lines. On a long distance point-to-point radio link, a direct line-of-sight wave, a single ground bounce, and atmospherically refracted waves can all contribute to the received signal. When signal replicas are too close together to be discriminated and processed as discrete contributions, the received signal becomes distorted. This distortion limits the capacity of the channel. The phenomena is akin to the severe acoustic distortion known as the *railway station effect*, where increasing power output (volume) does not increase the intelligibility of the message. In digital communications, the distortion caused by multipath propagation creates an analogous effect; an increase in transmitted power does not decrease the BER as a simplistic implication of Shannon’s theorem might suggest. The amount and nature of the multipath propagation sets the level of power at which the BER becomes essentially independent of the SNR. The effect has often been referred to as the “irreducible BER,” but the use of signal processing, in particular equalization, can in fact reduce the BER further. Experimental examples of the irreducible BER in the digital channel are given below, but this article otherwise concerns the analog mechanisms and the statistical nature of the mobile channel.

3.1. Fading in the Mobile Channel

3.1.1. Fast Fading. The interference, or phase mixing, of the multipath contributions causes time- and frequency-dependent fading in the gain of the channel. The time dependence is normally from the changing position of the mobile terminal, and so is also referred to as *space dependence*. At a given frequency, the power of the received signal, and thus the gain of the mobile channel, changes with time. This changing SNR is called *signal fading* and is often experienced as audible “swooshing” or “picket fencing” when an FM station (with a radio frequency of about 100 MHz) is received by the antenna on a moving car. If the mobile terminal is stationary, the signal may continue to experience some fading, and this is caused by changes in the multipath environment, which may include moving vehicles and other objects.

In nearly all situations the changing mobile position dominates the time variation of the mobile channel. Usually, the multipath environment is taken, or at least modeled, as unchanging. This is called the *static multipath* assumption. In this case, a static mobile experiences an unchanging channel. If now the radiofrequency is swept, then the gain of the transfer function experiences fading similar to that due to changes in position, because the electrical path distances of the multipath components are frequency-dependent. For a continuous-wave (CW) signal, the time- and frequency-dependent fades can be some 40 dB below the mean power level, and up to 10 dB above the mean. This indicates the large dynamic range required of the receiver just to handle the multipath interference. This fading is variously called the *fast fading*, *short-term fading*, or *Rayleigh fading* after the Rayleigh distribution of the signal magnitude. The maximum density of fading is a fade about every half-wavelength on average, and this occurs typically in urban outdoor and indoor environments. The fast fading dominates the mobile channel characteristics and usage. For example, traditional amplitude modulation at microwave frequencies is not feasible, because for a fast-moving mobile terminal the fading interferes directly with the modulation.

3.1.2. Slow Fading. The dynamic range of the received signal is also affected by *slow fading*, also called *long-term fading* or *shadow fading*. This is superimposed on the fast fading. It is caused by shadowing of the radio signal to the scatterers as the mobile terminal moves behind large obstacles such as hills and buildings. The rate of the slow fading therefore depends on the large-scale nature of the physical environment. The basic short-term multipath mechanism remains unchanged. The dynamic range of the slow fading is typically less than that of the fast fading, being confined to about ± 10 dB for most of the time in urban and suburban environments. The total dynamic range for the fading therefore becomes about 70 dB. The distance-based path loss, as a mobile terminal roams near to and far from a base station, adds to this range.

3.2. Narrowband and Wideband

In a typical mobile microwave signal link, the *relative bandwidth* is small. This means that the spectral extent of

the signal is less than a few percent of the nominal carrier frequency. The fading within the frequency response of the transfer function is referred to as *frequency-selective fading*. If the bandwidth is sufficiently small so that all the frequency components fade together, then this is called a *flat fading* channel.

In the mobile channel context, a *narrowband* channel has flat fading and a *wideband* channel has frequency-selective fading. The use of a single frequency, or CW, for channel characterization is the limiting case of the narrowband channel. Historically, fading has been the principal observed characteristic of the mobile channel. Fast fading is merely one manifestation of the reception of several replica signals.

3.3. The Effect of Fading on the Digital Channel: Irreducible Bit Error Ratio

3.3.1. Timing Errors from Random Frequency Modulation. The digital channel in Fig. 1 is in principle the simplest channel to characterize experimentally, since it concerns a BER measure. The fading in the mobile channel has a particular effect on the BER curves, namely, the “irreducible BER” mentioned above. The example in Fig. 2 [2] shows curves of BER against carrier-to-noise ratio (CNR) from simulations of the narrowband mobile channel with carrier frequency 920 MHz. The static (no fading)

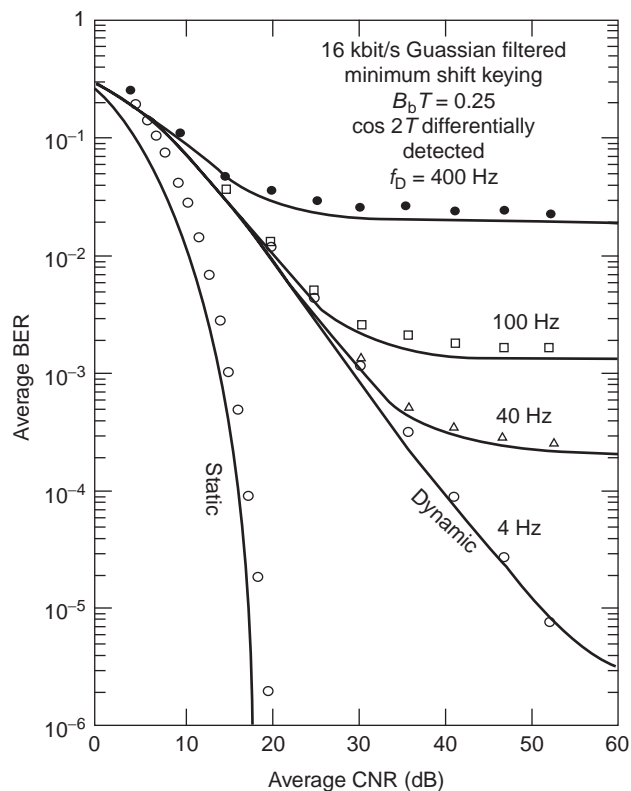


Figure 2. The irreducible BER for a digital mobile channel is attained when an increase of SNR does not improve the BER. The static (no fading) channel shows the classical waterfall shape of the Gaussian noise-limited channel, but as the fading rate increases, the form of the curve alters drastically. (From Ref. 2.)

curve shows the classical waterfall shape of the Gaussian channel. But the fading channel curves, shown with fading rate f_D , feature irreducible BERs, which occur at lower CNRs with increasing fading rate. The fading rate of 40 Hz corresponds to a mobile speed of about 40 km/h and a carrier frequency of 900 MHz. This corresponds approximately with using a cellphone from a moving car. The curves hold their basic form independently of the type of angle modulation used. The mechanism for the bit errors is timing error caused by the random FM, discussed below, imposed on the signal by the fading channel. The random FM causes jitter on the symbols after they have passed through the mobile channel.

3.3.2. Intersymbol Interference from Multiple Time Delays. As the signaling rate increases, an analogous irreducible BER effect occurs as a result of the several signal replicas arriving at different times. This spread of delays causes intersymbol interference when one dispersed symbol overlaps with other, similarly dispersed symbols. In analog parlance, this is called *dispersive distortion*. In the mobile channel the situation is complicated by the dispersion changing with time. The effect is depicted in the experimental example of Fig. 3 [3], where for a fixed fading rate of $f_D = 40$ Hz the increasing digital transmission rate experiences an increasing irreducible BER. As in Fig. 2, the effect is that the capacity of a given link cannot be increased by simply increasing the CNR, for example, by increasing the transmitted power. Signal processing is required.

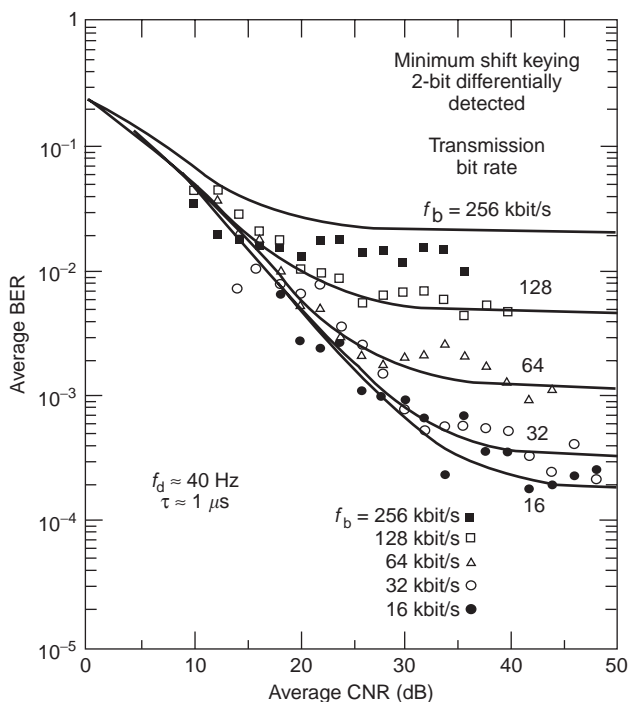


Figure 3. The irreducible BER caused by intersymbol interference. As the signaling rate increases relative to the spread of multipath propagation delay times, the irreducible BER increases. (From Ref. 3.)

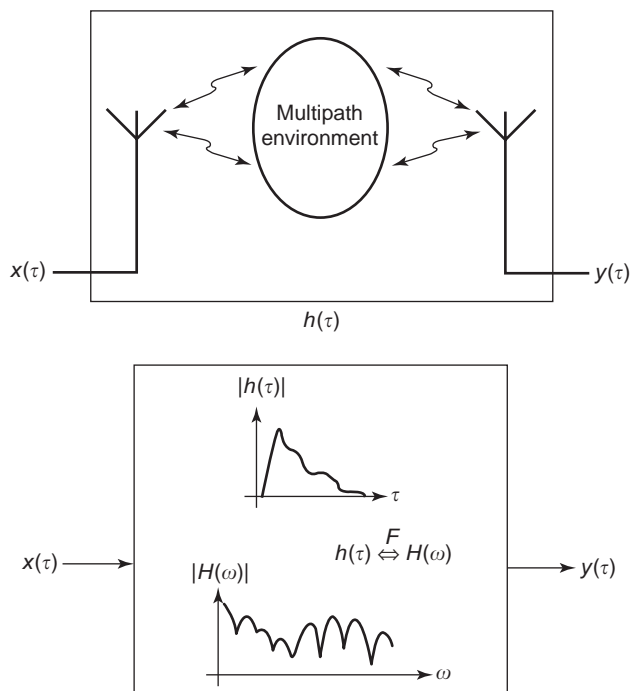


Figure 4. The static mobile channel transfer function. $x(\tau)$ and $y(\tau)$ are electronic signals before the transmitting antenna and after the receiving antenna, respectively. The impulse response can be found by Fourier transformation of a swept frequency measurement, for example.

3.4. Signal Processing for Mitigation of the Multipath Effect

Several signal-processing techniques can be applied to the mobile channel to reduce distortion and recover the capacity relative to the static channel. *Equalization* and *rake* systems basically attempt to gather the delayed signal replicas and recombine them into a single signal, which, ideally, is no longer distorted or faded. *Antenna diversity* uses multiple antenna elements to receive the same signal but with different multipath degradations, and combines the signals so that the resultant channel has better capacity than any of the channels from the individual antenna elements. A combination of the equalization, or rake, and antenna diversity methods is called *space-time processing*. All these techniques can be effective in improving the mobile channel. In fact, the use of antenna diversity offers very large potential capacities by effectively reusing the frequency at different positions in space.

3.5. The Mobile Channel as a Transfer Function

Figure 4 depicts a static mobile channel, which is taken as the baseband equivalent radio channel of Fig. 1. Recall that the effect of the antennas is included in the transfer function. The impulse response $h(\tau)$ and the transfer function $H(\omega)$ are related by Fourier transformation in the usual way, denoted $h(\tau) \leftrightarrow H(\omega)$. Here τ is the delay time and ω is the angular baseband equivalent frequency. The impulse response indicates the dispersive nature of the

channel, which causes distortion of the signals which are transmitted through it. This impulse response is modeled as a series of discrete delta functions below.

The example of Fig. 4 is for an instant in time t . As the mobile terminal moves, the delays and phases of the individual multipath contributions become functions of time. The impulse response and transfer function therefore become expressed mathematically as functions of time, that is, $h(\tau, t)$ and $H(\omega, t)$. If the scatterers in the multipath environment can be considered to be essentially stationary, then the time t and position z are related by the velocity V of the mobile: $z = Vt$. From now on the spatial variable z will be mostly used.

The following sections will develop, through the use of several assumptions about the channel, a double Fourier transform relation between the impulse response as a function of delay time and time (i.e., position) and the transfer function as a function of baseband angular frequency and Doppler frequency. Because of the variation of the transfer functions, the statistical parameters of the channel are relevant, and these also can be couched in terms of Fourier relations.

3.6. The Receiving Antenna in Multipath Transmission

The moving antenna combines the radiowave contributions, which have continuously changing delays, amplitudes, and polarizations. Deterministic analysis is not feasible except in simplistic situations, and to be able to interpret the statistical description requires an appreciation of multipath phenomena.

A base station transmitter is taken to emit power in a fixed radiation pattern. After multiple scattering, for example from many reflections, the polarization is changed in a random way and the electric (and magnetic) field has all three Cartesian components, independent of the transmitted polarization. These components can be independent functions of frequency and position. So the total incident electric field, at a point in space, can be written in baseband equivalent form [i.e., with a complex envelope, in which a factor of $\exp(j\omega_C t)$ is suppressed, where ω_C is the carrier frequency] as the complex vector

$$\begin{aligned} \mathbf{E}_1(\omega; x, y, z) = & E_x(\omega; x, y, z)\hat{x} + E_y(\omega; x, z)\hat{y} \\ & + E_z(\omega; x, y, z)\hat{z} \end{aligned} \quad (1)$$

in which the components, such as E_x , are complex scalars.

The introduction of an antenna promotes a change to spherical coordinates referred to the antenna orientation and position. The position is denoted with the single spatial variable z . The incident fields are now written as

$$\mathbf{E}_1(\omega, z; \theta, \phi) = E_\theta(\omega, z; \theta, \phi)\hat{\theta} + E_\phi(\omega, z; \theta, \phi)\hat{\phi} \quad (2)$$

The open circuit voltage of an antenna depends on both the incident field and the receiving pattern, $\mathbf{h}_a(\omega; \theta, \phi) = h_\theta(\omega; \theta, \phi)\hat{\theta} + h_\phi(\omega; \theta, \phi)\hat{\phi}$. This notation for the receiving pattern should not be confused with the symbol for the impulse response, $h(\tau, z)$. The open circuit

voltage is defined by

$$V_O(\omega, z) = \int_0^{2\pi} \int_0^\pi \mathbf{E}_1(\omega, z; \theta, \phi) \cdot \mathbf{h}_a(\omega; \theta, \phi) \sin \theta \, d\theta \, d\phi \quad (3)$$

and represents the transfer function of the electromagnetic signal channel.

By expanding the dot product, this transfer function is written in terms of the incident field components, which are now collectively detected as *standing waves*, and the receiving pattern components, as

$$\begin{aligned} H(\omega, z) = & \int_0^{2\pi} \int_0^\pi [E_\theta(\omega, z; \theta, \phi)h_\theta(\omega; \theta, \phi) \\ & + E_\phi(\omega, z; \theta, \phi)h_\phi(\omega; \theta, \phi)] \sin \theta \, d\theta \, d\phi \end{aligned} \quad (4)$$

This formula shows the inseparability of the antenna pattern and the incident fields in the definition of the mobile channel.

The antenna pattern is recognized as a filter in the spatial (including polarization) domain. The frequency dependence of the antenna pattern also represents a filter in the more familiar frequency domain. The space–frequency filter of the antenna is the difference between the vector electromagnetic propagation channel and the scalar electromagnetic signal channel of Fig. 1. If terminating (i.e., matching) the antenna has a negligible effect over the band of interest, then Eq. (4) represents the mobile channel.

4. CHANNEL MODEL USING DISCRETE EFFECTIVE SCATTERERS

Modeling the incident waves as emanating from discrete directions allows the convenience of using effective point sources. These are referred to as *effective scatterers*, because their scalar contribution is the physical incident wave weighted by the receiving pattern. The transfer function is written as the sum of effective scatterers, which have an amplitude a , a phase ψ , and a delay time τ for the information carried:

$$H(\omega, z) = \sum_i a_i \exp(j\psi_i) \exp(-j\omega_R \tau_i) \quad (5)$$

Here the radiofrequency is the sum of the carrier frequency (the center frequency of the radio band) and baseband equivalent frequency:

$$\omega_R = \omega_C + \omega \quad (6)$$

In the static situation, the terms in the transfer function containing the delays are constant and can be incorporated into the phases of the effective scatterers.

The effect of the moving terminal on the transfer function can be seen by considering an effective scatterer at a relatively large distance r_0 from it. The geometry is shown in Fig. 5. The mobile terminal moves a distance z along the spatial axis in the positive direction. The electrical

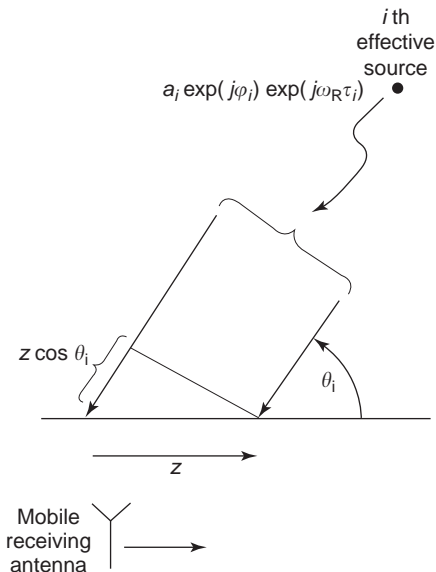


Figure 5. Point source with moving receiver. In a model of the channel, Eq. (5), the point source is not necessarily a physical scatterer, but can rather be considered as a point representation (an “effective scatterer”) that produces the waves received from a given angular direction.

distance to the i th effective scatterer changes from $k_R r_{0i}$, where k_R is the radiofrequency wavenumber, to

$$\begin{aligned} k_R r_i &\approx k_R r_{0i} - k_R z \cos \theta_i \\ &= \omega_R \tau_i - \frac{\omega_R}{c} \cos \theta_i z \\ &= \omega_R \tau_i - u_i z \end{aligned} \tag{7}$$

where

$$u_i = k_R \cos \theta_i \tag{8}$$

is the *spatial Doppler frequency* in radians per meter. The Doppler frequency in radians per second is

$$\omega_{Di} = u_i V = k_R V \cos \theta_i \tag{9}$$

Here u_i is a scaled directional cosine to the i th effective scatterer, and a receiver movement z produces a phase shift $u_i z$ in the signal from the scatterer.

The changing phase term of an effective scatterer at position z in Eq. (5) is

$$\omega_R \tau_i = \omega_C \tau_i + \omega \tau_i - \frac{\omega_C}{c} \cos \theta_i z - \frac{\omega}{c} \cos \theta_i z \tag{10}$$

The first term is independent of the position and baseband frequency, and can be incorporated in the phase of the scatterer. The last term is negligible, because in microwave communications we normally have a small relative bandwidth (i.e., $\omega/\omega_C \ll 1$). So within the approximations

above, the transfer function is

$$H(\omega, z) = \sum_i a_i \exp(j\psi_i) \exp[j(-\omega\tau_i + zu_i)] \tag{11}$$

Fourier transformation with respect to the baseband frequency ω gives the position-dependent impulse response as a function of the delay time and position,

$$h(\tau, z) = \sum_i a_i \exp(j\psi_i) \delta(\tau - \tau_i) \exp(ju_i z) \tag{12}$$

A further Fourier transformation, this time with respect to the position z , gives a function of delay time and spatial Doppler frequency, denoted

$$a(\tau, u) = \sum_i a_i \exp(j\psi_i) \delta(\tau - \tau_i) 2\pi \delta(u - u_i) \tag{13}$$

4.1. Fourier Transform Relations with Continuous Transfer Functions

The Fourier pair $a(\tau, u) \Leftrightarrow H(\omega, z)$ have the continuous form

$$H(\omega, z) = \frac{1}{2\pi} \int_0^\infty \int_{-k_C}^{k_C} a(\tau, u) \exp[j(-\omega\tau + zu)] du d\tau \tag{14}$$

$$a(\tau, u) = \frac{1}{2\pi} \int_{-\infty}^\infty \int_{-\infty}^\infty H(\omega, z) \exp[j(\omega\tau - zu)] d\omega dz \tag{15}$$

Note the mixed signs of the exponents. Moving in the negative z direction instead of the positive z direction, for example, changes the sign of the exponent zu in Eqs. (14) and (15).

From the double Fourier transform relation, there can be four complex functions that carry the same information for characterization of the mobile channel. These are denoted:

- $a(\tau, u)$, the scattering function in the time delay–spatial Doppler domain (referred to as the effective scattering distribution)
- $h(\tau, z)$, the impulse response in the delay–space domain (spatial spectrum)
- $A(\omega, u)$, the transfer function in the baseband frequency–spatial Doppler domain (frequency spectrum)
- $H(\omega, z)$, the transfer function in the baseband frequency–space domain (space–frequency spectrum)

The functions are related by the following single-dimensional Fourier transforms of the mobile channel:

$$\begin{aligned} a(\tau, u) &= \frac{1}{2\pi} \int A(\omega, u) e^{j\omega\tau} d\omega \\ A(\omega, u) &= \int a(\tau, u) e^{-j\omega\tau} d\tau \end{aligned} \tag{16}$$

$$h(\tau, z) = \frac{1}{2\pi} \int H(\omega, z) e^{j\omega\tau} d\omega \quad (17)$$

$$H(\omega, z) = \int h(\tau, z) e^{-j\omega\tau} d\tau$$

$$a(\tau, u) = \int h(\tau, z) e^{-jzu} dz \quad (18)$$

$$h(\tau, z) = \frac{1}{2\pi} \int a(\tau, u) e^{jzu} du$$

$$A(\omega, u) = \int H(\omega, z) e^{-jzu} dz \quad (19)$$

$$H(\omega, z) = \frac{1}{2\pi} \int A(\omega, u) e^{jzu} du$$

The amplitudes, phases, delays, and directions of the effective sources are randomly distributed, and the transfer function consequently behaves randomly, so a statistical approach is called for their characterization.

4.2. Averaging across a Transfer Function for Channel Gain

In terms of an individual channel transfer function, the total power, or *channel gain*, is given by

$$P^{(i)} = \frac{1}{L\omega_B} \int_L \int_{\omega_B} |H(\omega, z)|^2 d\omega dz \quad (20)$$

where L is an averaging distance or locus covering the positional averaging, and ω_B is an averaging bandwidth. Any of the abovementioned channel functions can be used to get the power in this way (Parseval's theorem). Integrating single variables gives the frequency-dependent power transfer function averaged over position

$$|H(\omega)|^2 = \frac{1}{L} \int_L |H(\omega, z)|^2 dz \quad (21)$$

and the position-dependent- (time-dependent) power transfer function averaged over the frequency band:

$$|H(z)|^2 = \frac{1}{\omega_B} \int_{\omega_B} |H(\omega, z)|^2 d\omega \quad (22)$$

This quantity is approximated in a receiver by the position-varying (or time-varying) received-signal strength indicator (RSSI) signal. However, in practice, the RSSI voltage is normally proportional to the logarithm of the channel power.

On averaging the power across a wideband channel, the total received power fades less than a narrowband component. This is the advantage of wideband modulation systems. Analogously, antenna diversity is used to reduce the fading by averaging the channel over samples of the spatial variable.

5. STATISTICAL BASIS OF A MOBILE CHANNEL

5.1. Power Spectra and Channel Correlation Functions

Assuming ergodicity so that the statistics remain second order, the *autocorrelation function*, denoted by R , of the effective scatterer distribution with respect to the delay times is written

$$R_a(\tau_1, \tau_2; u) = \langle a(\tau_1, u) a^*(\tau_2, u) \rangle \quad (23)$$

where the angular brackets denote averaging over all relevant realizations of the effective scattering distribution. This contrasts with the averaging over frequency or space for a single channel realization as in the previous section. The average power in the effective scattering distribution is

$$P(\tau, u) = R_a(\tau, \tau; u) = \langle |a(\tau, u)|^2 \rangle \quad (24)$$

Note that the averaging is of the powers, not of the complex values, of the $a(\tau, u)$.

This averaged power distribution can be expressed in several different statistical forms as seen below. Substituting Eq. (16) into Eq. (23) gives the Fourier transform

$$\begin{aligned} R_a(\tau_1, \tau_2; u) &= \frac{1}{4\pi^2} \int_{-\infty}^{\infty} \int_{-\infty}^{\infty} R_A(\omega_1, \omega_2; u) \exp[j(\omega_1\tau_1 - \omega_2\tau_2)] d\omega_1 d\omega_2 \end{aligned} \quad (25)$$

The inverse relation is

$$\begin{aligned} R_A(\omega_1, \omega_2; u) &= \int_0^{\infty} \int_0^{\infty} R_a(\tau_1, \tau_2; u) \exp[-j(\omega_1\tau_1 - \omega_2\tau_2)] d\tau_1 d\tau_2 \end{aligned} \quad (26)$$

Major simplifications are possible under certain assumptions, as follows.

5.1.1. Wide-Sense Stationarity in Frequency. The channel is now assumed to be *wide sense stationary in the frequency domain*. This means that the mean and correlation of $A(\omega, u)$ do not depend on the choice of frequency, ω , but on only the frequency difference, $\Delta\omega = \omega_2 - \omega_1$. This is a reasonable assumption for the frequencies within the small relative bandwidths of most mobile communications systems. Denote the autocorrelation of a wide-sense stationary (WSS) process using S , for example, by

$$\begin{aligned} R_A(\omega_1, \omega_2; u) &= R_A(\omega, \omega + \Delta\omega; u) \\ &= S_A(\Delta\omega; u) \quad (\text{WSS in } \omega) \end{aligned} \quad (27)$$

that is, the autocorrelation of the transfer function in the frequency-spatial Doppler domain is a power spectrum whose argument is the frequency difference. The symbols S and R are used to represent the correspondence of the power spectra S and the autocorrelation R of a process

that is WSS. As a result of the wide sense stationarity in ω , we can write Eq. (25) as

$$\begin{aligned} R_a(\tau_1, \tau_2; u) &= \frac{1}{4\pi^2} \int \int S_A(\Delta\omega; u) \exp(-j\Delta\omega\tau_2) \\ &\quad \times \exp[-j\omega_1(\tau_2 - \tau_1)] d\omega_1 d\Delta\omega \\ &= P(\tau_2, u) \delta(\tau_2 - \tau_1) \end{aligned} \quad (28)$$

where

$$P(\tau, u) = \frac{1}{2\pi} \int_{-\infty}^{\infty} S_A(\Delta\omega, u) \exp(j\Delta\omega\tau) d\Delta\omega \quad (29)$$

is the averaged power delay–Doppler frequency distribution of Eq. (24). The delta function in the autocorrelation of Eq. (28) is referred to as the *uncorrelated scattering* (US), and here means that a fading signal received at a given delay time is uncorrelated (when averaged over the relevant realizations) with a fading signal received at any other delay time. The wide-sense stationarity (via the $\Delta\omega$ factor) in the baseband frequency domain and the uncorrelated scattering in the delay time domain [the $\delta(\Delta\tau)$ factor] are equivalent characteristics.

5.1.2. Wide-Sense Stationarity in Space. Similarly, *wide-sense stationarity in the spatial domain* corresponds to uncorrelated scattering in the Doppler domain. This means that the fading signal at one spatial Doppler frequency u [or angle $\theta = \cos^{-1}(u/k_C)$] is uncorrelated with a fading signal received from any other spatial Doppler frequency. Denoting the spatial difference $\Delta z = z_2 - z_1$, we have

$$\begin{aligned} R_a(\tau; u_1, u_2) &= \iint S_h(\tau; \Delta z) \exp[j(z_2 u_2 - z_1 u_1)] dz_1 dz_2 \\ &= P(\tau, u_2) 2\pi \delta(u_2 - u_1) \end{aligned} \quad (30)$$

where the averaged power of the effective scattering distribution is expressed as

$$P(\tau, u) = \int S_h(\tau, \Delta z) \exp(-j\Delta z u) d\Delta z \quad (31)$$

5.1.3. Wide-Sense Stationary Uncorrelated Scattering Channel. Combining the space and frequency wide-sense stationary conditions, we have

$$\begin{aligned} R_a(\tau_1, \tau_2; u_1, u_2) &= \frac{1}{2\pi} \iint S_H(\Delta\omega, \Delta z) \exp[j(-\Delta\omega\tau_2 + \Delta z u_2)] \\ &\quad d\Delta\omega d\Delta z \delta(\tau_2 - \tau_1) 2\pi \delta(u_2 - u_1) \\ &= P(\tau_2, u_2) \delta(\tau_2 - \tau_1) 2\pi \delta(u_2 - u_1) \end{aligned} \quad (32)$$

where now

$$P(\tau, u) = \frac{1}{2\pi} \iint S_H(\Delta\omega, \Delta z) \exp[-j(\Delta\omega\tau - \Delta z u)] d\Delta\omega d\Delta z \quad (33)$$

The inverse Fourier transform is

$$S_H(\Delta\omega, \Delta z) = \frac{1}{2\pi} \iint P(\tau, u) \exp[j(\Delta\omega\tau - \Delta z u)] d\tau du \quad (34)$$

Thus the wide-sense stationarity conditions presented above result in the frequency–space correlation function being the double Fourier transform of the average power density of the effective scatterer distribution.

The term WSSUS was used by Bello [4] to describe tropospheric multipath channels containing scintillating scatterers being illuminated by static antennas. In the context of the mobile channel, the WSS refers to wide-sense stationarity in position, which implies uncorrelated scattering in the spatial Doppler frequency. The US refers to the delta function in delay time (effective sources at different delays are mutually uncorrelated), which implies WSS in the frequency domain.

The assumption of the WSSUS conditions in the channel allows the convenience of the double Fourier transform relations. However, in applying the Fourier relations for a given situation, the validity of the WSSUS model should always be questioned. The channel can often be arranged to be “sufficiently valid” for gaining useful insight and inferring channel behavior, by appropriately arranging the averaging. This averaging, denoted with the angular brackets, is often taken as several sampled records over short distances (tens of carrier wavelengths or several tens of fades) in order to stay within a given physical environment, followed by the power distribution averaging. Statistically, ensemble averaging implies many “realizations.” We can interpret this as several sampled records that should have uncorrelated data (e.g., well-separated spatial paths) within the same physical environment, or else as several records in different (i.e., independent) physical environments. The two cases are different. One case averages within a single environment; the other case averages over many different environments. Strictly speaking, the presence of multiple uncorrelated records in the same immediate environment does not truly satisfy the hypothesis of statistically independent records, because the scattering distribution is the same, that is, the signal sources constituting the physical scatterers are common to all the data records.

5.2. Key Relations for a Mobile Channel

Equations (14), (15) and, (33), (34) are key results for the mobile channel. They relate, respectively, by double Fourier transformation, a baseband channel transfer function $H(\omega, z)$ to an effective source distribution $a(\tau, u)$ that provides the incident multipath signals, and the average power spectral density of the channel $S_H(\Delta\omega, \Delta z)$ to the average power distribution of the effective scatterers,

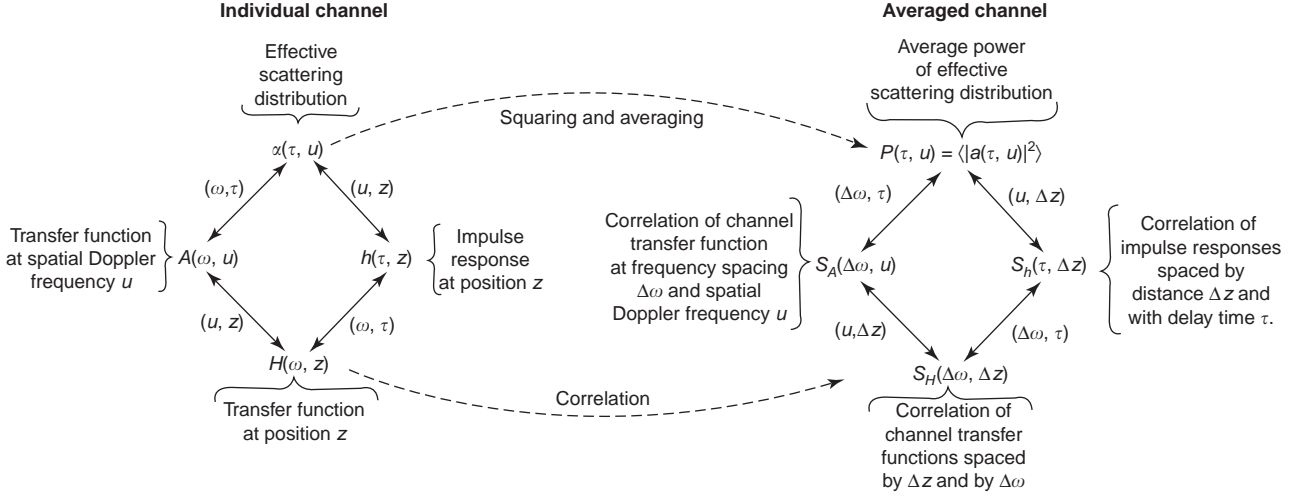


Figure 6. Fourier transform relations for the mobile channel functions and for their statistical representations under wide sense stationarity in frequency and position, $u = k_C \cos \theta$ is the spatial Doppler frequency, with θ the zenith angle with respect to the direction of motion z , and k_C the wavenumber of the radio carrier frequency. (From Ref. 1.)

$P(\tau, u)$. Figure 6 [1] depicts the relations between the functions.

5.3. Averaged Power Profiles

The more familiar single transformations also are of interest. Mathematically, we can put $\Delta z = 0$ in the frequency correlation

$$S_H(\Delta\omega) = S_H(\Delta\omega, \Delta z = 0) = \langle H(\omega, z_0) H^*(\omega + \Delta\omega, z_0) \rangle \quad (35)$$

from which Eq. (34) reduces to

$$S_H(\Delta\omega) = \int P(\tau) \exp(-j\Delta\omega\tau) d\tau \quad (36)$$

where the average power delay profile

$$P(\tau) = \int P(\tau, u) du \quad (37)$$

is the average power at delay τ , found by integrating over all spatial Doppler frequencies ($u = k_C$ to $u = -k_C$), that is, in all directions over the averaged power of the effective scattering distribution. In practice, the antenna performs this integration [recall that the effective scattering distribution $P(\tau, u)$ already includes the effect of the antenna]; for example, an omnidirectional antenna will gather the waves from all the directions. However, a single measurement from an antenna only accounts for a single realization of the effective scattering distribution—that is, for one point in the space of one environment. To estimate $P(\tau)$ from measurements, the averaging of the profile needs to be done over several different positions [i.e., several z_0 values in Eq. (35)], either in the same physical environment or in many different physical environments, as discussed above.

The frequency correlation function $S_H(\Delta\omega)$ is the Fourier transform of the average power delay profile $P(\tau)$

for the WSS channel with uncorrelated scattering. The inverse relation is

$$P(\tau) = \frac{1}{2\pi} \int S_H(\Delta\omega) \exp(j\Delta\omega\tau) d\Delta\omega \quad (38)$$

The Fourier relation in Eqs. (36) and (38) is identical to the relation between the transfer function and its impulse response, as in Fig. 4.

Similarly to the average delay profile, *the average spatial Doppler profile* is averaged over all delays:

$$P(u) = \int P(\tau, u) d\tau \quad (39)$$

$P(\tau)$ and $P(u)$ are sometimes called the *delay spectrum* and *Doppler spectrum*, respectively. Finally, the total power of the effective scatterers is given by

$$P = \iint P(\tau, u) d\tau du \quad (40)$$

Many details, extending to situations outside the mobile channel, may be found in Ref. 3.

5.3.1. Spreads. The *spread*, or second centralized moment, of a distribution is a standard characterizing parameter. For an instantaneous (i.e., snapshot, or unaveraged) channel distribution function, the instantaneous spread is the standard deviation of that function. For example, for a channel with a snapshot transfer function $h(\tau)$, the definition of the *instantaneous delay spread* is

$$\sigma_\tau^{(i)} = \sqrt{\frac{\int \tau^2 |h(\tau)|^2 d\tau}{\int |h(\tau)|^2 d\tau} - \left(\frac{\int \tau |h(\tau)|^2 d\tau}{\int |h(\tau)|^2 d\tau} \right)^2} \quad (41)$$

The (average) *delay spread*, denoted σ_τ , follows the same definition but uses the averaged distribution $P(\tau) = \langle |h(\tau)|^2 \rangle$ instead of $|h(\tau)|^2$. The analogous definition for the *Doppler spread* is

$$\sigma_u = \sqrt{\frac{\int u^2 P(u) du}{\int P(u) du} - \left(\frac{\int u P(u) du}{\int P(u) du}\right)^2} \quad (42)$$

It is important to note that it is the individual power distributions that are averaged to produce the power profiles, which are then used to produce the spreads. Statistically, it is wrong to calculate the spreads of individual channels, average these, and call the result the average spread.

5.3.2. Power Profile Examples. Two power profiles that are commonly used for modeling because of their simplicity, are the one-sided exponential

$$P(\tau) = \frac{1}{\sigma_\tau} \exp\left(-\frac{\tau}{\sigma_\tau}\right) \Leftrightarrow S_H(\Delta\omega) = \frac{1}{1 + j2\pi \Delta\omega \sigma_\tau} \quad (\tau \geq 0) \quad (43)$$

and the two-path

$$P(\tau) = \delta(\tau) + |a_2 \exp(j\alpha_2)|^2 \delta(\tau - \tau_2) \Leftrightarrow S_H(\Delta\omega) = 1 + |a_2 \exp(j\alpha_2)|^2 \exp(j\Delta\omega\tau_2) \quad (44)$$

which are shown in Fig. 7. The exponential is the most commonly used model.

The two-path model offers much insight into the mechanisms of the channel and is used in the following sections to develop the basic characteristics and parameters of

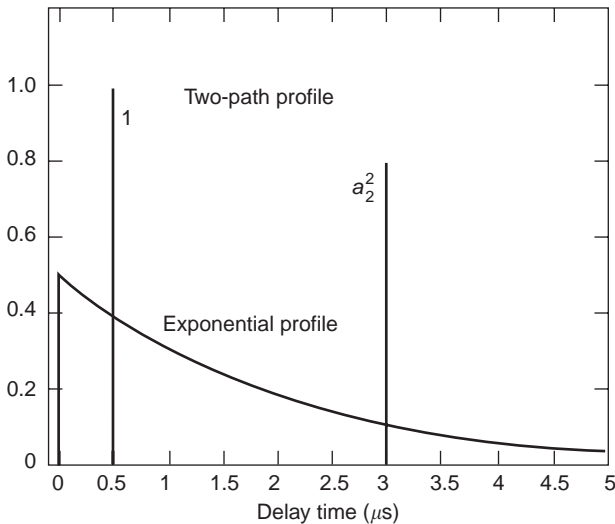


Figure 7. Examples of the exponential and the two-path models for the power delay profile. The two-path model comprises idealized discrete multipath contributions, whereas the exponential profile has a continuum of multipath contributions.

interest of the mobile channel’s behavior. It is later extended to the many-path situation. Liberties are taken with the mathematical use of the delta functions to allow convenient modeling.

6. THE TWO-PATH MODEL

The two-path model and its “statistics” (the model is treated statistically despite the situation being deterministic) produce and explain nearly all of the behavior that can be found in real-world mobile channels. Such a model is also used in point-to-point communications where there can be a direct wave with a single ground bounce. The term “two-path” refers to two effective sources. However, the introduction of the directions of the effective sources is delayed until later, since the directions have no bearing on the received signal while the receiver is static. The moving receiver introduces a changing frequency dependence, and the rate of change is determined by the directions. Understanding the behavior of the static model allows a smooth transition to understanding the many-path channel behavior.

6.1. Static Model for Frequency-Selective Fading

The two-path scenario is shown with its variation with frequency in Fig. 8. The impulse response, on setting $\tau_1 = 0$ and $\alpha_1 = 0$ for the first path, is

$$h^{(2)}(\tau) = \delta(\tau) + a_2 \exp(j\alpha_2) \delta(\tau - \tau_2) \quad (45)$$

and so represents a signal arriving with zero delay with normalized magnitude and zero phase, and a signal arriving at a delay of τ_2 with magnitude a_2 and phase α_2 . The transfer function is minimum phase when $a_2 \leq 1$, and is maximum phase (or in the general case, non-minimum phase) when $a_2 > 1$.

This model, which is static in the sense that the two effective scatterers are constant in amplitude and phase, needs no averaging to obtain the power profile. So $P(\tau) = \langle |h(\tau)|^2 \rangle = |h(\tau)|^2$ for the static case. The delay spread is thus the same as the instantaneous delay spread, and from Eqs. (44) and (41), is $\sigma_\tau^{(2)} = a_2 \tau_2 / (1 + a_2^2)$. The delay spread is not affected by time reversal or magnitude scaling of the power profile. In the two-path case, this means that a_2 can be replaced by $1/a_2$ (i.e., a

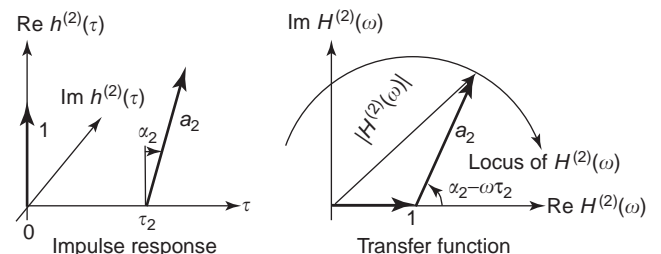


Figure 8. The impulse response of the static two-path model amplitudes 1 and a_2 , and a complex plane representation of the transfer function for the case $a_2 > 1$.

change from a minimum- to a maximum-phase channel) and the delay spread stays the same.

6.1.1. Transfer Function. The transfer function is obtained by Fourier transformation of Eq. (45), and is (the factor $1/2\pi$ is omitted for brevity)

$$H^{(2)}(\omega) = 1 + a_2 \exp[j(\alpha_2 - \omega\tau_2)] \quad (46)$$

where the delay difference is $\Delta\tau = \tau_2 - \tau_1 = \tau_2$. The in-phase component is the real part of the transfer function, $I(\omega) = 1 + a_2 \cos(\omega\tau_2 - \alpha_2)$, and similarly the quadrature part is $Q(\omega) = a_2 \sin(\omega\tau_2 - \alpha_2)$. Apart from the DC term, these are simply quadrature sinusoids. The phase of the second effective scatterer, α_2 , is now set to zero for brevity. The power transfer function is $|H(\omega)|^2 = 1 + a_2^2 + 2a_2 \cos(\omega\tau_2)$, and so the frequency fading behavior is periodic with period $1/\tau_2$ (Hz). The phase of the transfer function is

$$\phi^{(2)}(\omega) = \tan^{-1} \left(\frac{-a_2 \sin \omega\tau_2}{1 + a_2 \cos \omega\tau_2} \right) \quad (47)$$

which has a maximum rate of change when the power is a minimum. For the case $a_2 \leq 1$, the maximum and minimum values of the phase are $\pm \sin^{-1} a_2$. When $a_2 = 1$ and $\omega\tau_2 = n\pi$ (n is an integer), the phase changes by π over an infinitesimally small change in ω .

6.1.2. Group Delay. The group delay of a transfer function is the negative derivative of the phase with respect to frequency, $\tau_g(\omega) = -\partial\phi(\omega)/\partial\omega$. It approximates the time delay of the envelope of a narrowband signal after it has passed through a transfer function with phase $\phi(\omega)$ [5]. Changes in the group delay mean changes in the expected arrival times of information, such as symbols, at the receiver.

For a channel that contains many delay values, the received signal becomes distorted owing to the dispersion. For the two-path model, the group delay is found by differentiating Eq. (47) to be

$$\tau_g^{(2)}(\omega) = \frac{a_2\tau_2(a_2 + \cos \omega\tau_2)}{1 + a_2^2 + 2a_2 \cos \omega\tau_2} \quad (48)$$

For the minimum-phase case, this varies between $a_2\tau_2/(a_2 - 1)$ and $a_2\tau_2/(a_2 + 1)$. If different frequencies were sent through the channel, then these values are the extrema of the group delays that would be experienced. Figure 9 shows the in-phase and quadrature signals, the envelope and phase, and the group delay for the transfer function of a static two-path model.

6.1.3. Features of the Static Two-Path Model. The features from this deterministic model are frequency dependence with

- Smoothly varying in-phase and quadrature components
- Fading envelope

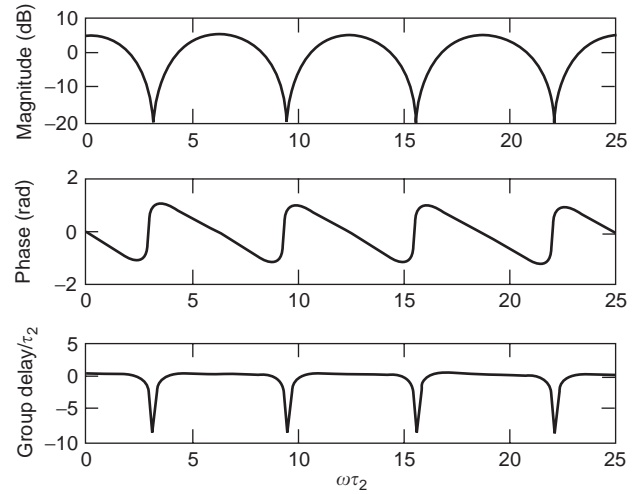


Figure 9. The periodic frequency selective channel behavior for the static two-path model. The receiver is at a fixed position. The magnitude shows fading, the phase is changing quickly at the fade frequencies, and the group delay is correspondingly large (and negative for $a_2 \leq 1$) at the fade frequencies.

- Sharp transitions of the phase of the transfer function, occurring when the envelope is at a minimum
- Possibility of both minimum-phase fades ($a_2 \leq 1$) and non-minimum-phase fades ($a_2 > 1$)
- Dispersive channel with sharp spikes in the group delay at the envelope minima

These transfer function variations are all periodic in the two-path model, but as seen below, the same effects occur also in the real-world channel, but with a random frequency and space dependence.

The reason for the phase behavior coinciding with the envelope is best seen from the locus of the signal in Fig. 8, where the envelope minima occur as the locus is passing closest to the origin, which is also when the phase is changing the quickest. For deep fades, the phase change is always nearly $\pm\pi$ (the sign depends on whether a_2 is less than or greater than one), and such phase jumps are also a characteristic of the many-path channel.

6.2. Moving Receiver

In a moving receiver, we can fix the frequency to a CW for simplicity and get behavior as in the static channel of Fig. 8, but with spatial (i.e., time, for a given mobile speed), instead of frequency, dependence. For a CW channel, the transfer function is

$$H^{(2)}(z) = 1 + a_2 \exp[j(\alpha_2 + \Delta u z)] \quad (49)$$

where $\Delta u = k_C(\cos\theta_2 - \cos\theta_1)$ is the spatial Doppler frequency difference between the two effective sources. The transfer function now has spatial periodicity with a period (in meters) of $2\pi/\Delta u$. For example, with sources exactly in front of ($\theta_1 = 0$) and behind ($\theta_2 = \pi$) the moving receiver, the periodicity is given by a spacing of exactly $z = \lambda_C/2$, that is, half the carrier wavelength.

6.3. Random Frequency Modulation

The spatial analogy to the group delay is the random FM, given in radians per meter by the derivative of the phase with respect to position as $\omega_R(z) = 2\pi\partial\phi(z)/\partial z$. The random FM is an angle modulation in the channel and will be applied to a signal borne by the channel. It means that angle modulation systems are affected as the receiver moves. In practice, the random FM is often too small to be noticed in a working system, but as carrier frequencies increase, the fading rate and the spectrum of random FM increasingly invades the signal band. In summary, the CW spatial mobile channel follows the same behavior as that in the frequency-dependent static channel, the transfer function signals shown in Fig. 9 apply with the abscissa $\omega\tau_2$ replaced with $z\Delta u$, and the group delay becomes the random FM (with the opposite polarity).

6.3.1. Two-Dimensional Transfer Function. The frequency and spatial dependences can be combined to give the two-dimensional transfer function, again with $\alpha_2 = 0$

$$H^{(2)}(\omega, z) = 1 + a_2 \exp[j(\Delta u z - \omega\tau_2)] \quad (50)$$

which explicitly indicates the two-dimensional nature of the fading. The range of angles Δu determines the spatial fading rate, and the range of delay times, $\Delta\tau = \tau_2$, determines the rate of fading in the frequency domain. The statistical equivalents of these quantities, the Doppler spread and the delay spread, are used for describing the average fading rates found in the real world many-path situation.

7. STATISTICAL APPROACH USING TWO-PATH MODEL

The statistical approach is required when there are too many paths to determine the channel, which is normally the case in mobile communications. The statistical approach to the two-path model also offers insight into the statistical behavior of the many-path case. In the static case, the transfer function of the two-path model assumes all its possible values as the relative amplitude a_2 and phase α_2 are varied. In practice, averaging is over the phase-mixing process, so here we fix the amplitude and average over the changing phase only. In the static case, the phase of the frequency-dependent transfer function can be changed by changing the frequency. In a mobile channel, the fixed-frequency transfer function is averaged over the varying phase by averaging over many positions.

Since the two-path transfer function has a symmetric, periodic envelope with half period π/τ_2 (rad), equally likely frequencies are expressed by a uniform probability density function (pdf) over one of the periods:

$$p_\omega(\omega) = \frac{\tau_2}{\pi}, n \frac{\pi}{\tau_2} \leq \omega \leq (2n + 1) \frac{\pi}{\tau_2} \quad (n \text{ any integer}) \quad (51)$$

The analogous expression for the moving receiver holds for equally likely positions (viz., $p_z(z) = \Delta u/\pi$). These pdfs allow the pdfs of the channel function to be calculated below.

7.1. Probability Density Function of Channel Power

For $a_2 < 1$ and equally likely frequencies, the pdf for the power $\gamma(\omega) = |H(\omega)|^2$ is, from function transformation of p_ω

$$Pr^2(\gamma) = p_\omega(\omega) \left| \frac{\partial\omega}{\partial\gamma(\omega)} \right| = \frac{1}{\pi\sqrt{(2a_2)^2 - [\gamma - (1 + a_2^2)]^2}} \quad (52)$$

where $1 + a_2^2$ and $(2a_2)^2$ are the mean and variance, respectively, of the power in the two-path channel.

7.2. Cumulative Density Function of Channel Power

The cumulative density function (cdf) is the integral of the pdf over its range values $(1 - a_2)^2$ to $(1 + a_2)^2$, and is written

$$\text{Prob}(\gamma^{(2)}(\omega) \leq \gamma_0) = 1 - \frac{1}{\pi} \cos^{-1} \left(\frac{\gamma_0 - (1 + a_2^2)}{2a_2} \right) \quad (53)$$

This probability approach is an alternative to the deterministic form $H^{(2)}(\omega)$ for characterizing the two-path channel. The approach is needed when a deterministic form is not available. The cdfs for the n -path model with all the $a_n = 1$ are given in Fig. 10 for $n = 2, 3, 8$. The eight-path case is very close, except at the tails of the distribution, to the Rayleigh distribution, which corresponds to the limiting case $n \rightarrow \infty$, discussed further below.

The pdf for the two-path case is centered at its mean, $1 + a_2^2$, and is confined to its limits, that is, between $(1 - a_2)^2$ and $(1 + a_2)^2$. At these limits, the pdf $p_\gamma^{(2)}$ goes to infinity. The many-path pdfs can behave the same way. This does not cause interpretation problems, however, since the probability of the power being at these limits is infinitesimal and the integral of the function of course maintains its unity value. For example, for $a_2 = 1$, the

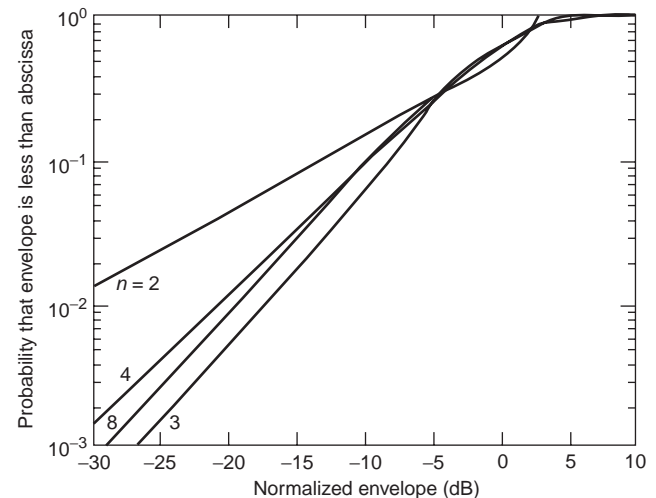


Figure 10. The cdf for the power of the $n = 2, 3, 4, 8$ channels, where all the multipath amplitudes are the same. The $n = 8$ model is essentially the same, for the cdf range displayed, as Rayleigh ($n \rightarrow \infty$) distribution, given in Fig. 14.

fades go exactly to zero in the transfer function. In the cdf of Fig. 10, the interpretation is that there is an infinitesimally small probability of the power being zero:

$$\text{Prob}(\gamma(\omega) \leq \gamma_0) \rightarrow 0 \text{ as } \gamma_0 \rightarrow 0, a_2 = 1 \quad (54)$$

A similar situation holds for the power approaching its maximum value $(1 + a_2)^2$:

$$\text{Prob}(\gamma(\omega) \leq \gamma_0) \rightarrow 1 \text{ as } \gamma_0 \rightarrow (1 + a_2)^2 \quad (55)$$

In the $a_2=1$ two-path example, the cdf diagram shows that for 10% of the frequencies the power transfer function is more than 13 dB below its mean value. The cdf curves are arranged so that the mean power always corresponds to 0 dB. A flat channel ($a_2 = 0$) would be represented by a line at $\gamma_0 = 0$ dB.

In summary, it is the phase difference between the source contributions that is the generic random variable for the statistical approach to the short-term variation of the power or envelope. In the static scenario, the averaging over the phase difference is implemented by varying the frequency. For the moving-receiver case, the CW transfer function is averaged over space. In the general case, the transfer function is a two-dimensional distribution with phase mixing causing fading in both frequency and position.

7.3. Coherence Bandwidth

An important parameter in a frequency-selective fading channel is the frequency separation for which the fading becomes effectively independent in the statistical sense. This frequency separation is determined by the auto-correlation of the channel transfer function. It is presented here as independent of frequency, that is, the channel is assumed to be WSS. The frequency correlation coefficient function, sometimes referred to as the *coherence function*, is

$$C(\Delta\omega) = \frac{S_H(\Delta\omega) - \langle H(\omega) \rangle \langle H^*(\omega) \rangle}{S_H(0) - \langle H(\omega) \rangle \langle H^*(\omega) \rangle} \quad (56)$$

and for the static two-path model with $a_2 = 1$, the magnitude of this is

$$|C^{(2)}(\Delta\omega)| = \left| \cos \frac{\Delta\omega\tau_2}{2} \right|, \quad a_2 = 1 \quad (57)$$

The coherence bandwidth Ω_C (rad/s) is defined as the frequency span from the maximum (unity) of the frequency correlation coefficient function to where the magnitude of the function first drops to a value C_C

$$|C(\Delta\omega = \Omega_C)| = C_C \quad (58)$$

as illustrated in Fig. 11.

C_C is taken by various authors from $1/e = 0.37$ to 0.9 [6–8]. A change of C_C scales the coherence bandwidth nonlinearly, so any results derived from some value of C_C

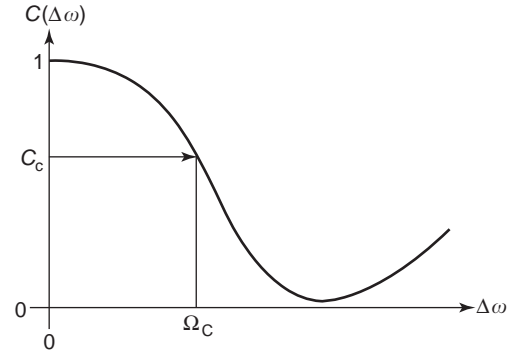


Figure 11. The definition of a coherence bandwidth Ω_C in terms of the frequency correlation coefficient function, or coherence function, and a correlation value of C_C . Narrowband channels, separated by a minimum frequency Ω_C , will display mutually uncorrelated fading in the sense that the correlation coefficient is $C_C < \sim 0.75$.

are also scaled in some way. The coherence function is periodic in $\Delta\omega$ for the two-path channel, since $H^{(2)}(\omega)$ is periodic. $\Omega_C^{(2)}$ is minimum for $a_2 = 1$, and for this case, the coherence bandwidth in hertz, $\Omega_C^{(2)}/2\pi$, can be written directly from Eqs. (57) and (58) as

$$B_{C,\text{Hz}}^{(2)} = \frac{1}{\pi\tau_2} \cos^{-1} C_C, \quad a_2 = 1 \quad (59)$$

The coherence bandwidth decreases with increasing delay difference between the two-path contributions, τ_2 . Also, the coherence bandwidth decreases with increasing relative amplitude a_2 . When a_2 is small, the coherence bandwidth becomes undefined, as the coherence function does not drop down to C_C .

7.4. Product of Coherence Bandwidth and Delay Spread

While the delay spread is a measure of the channel time dispersion, the coherence bandwidth is a measure of the fading rate with changing frequency. The ideal communications channel has a zero delay spread and infinite coherence bandwidth. For the two-path model, the delay spread increases while the coherence bandwidth decreases for increasing relative delay τ_2 and increasing relative amplitude a_2 . The coherence bandwidth and the delay spread are thus inversely related, but the exact relationship is not simple in the many-path case.

The product of these two parameters was taken for experimental channels using $C_C = 0.75$ [7], and an empirical law was found that $B\sigma_\tau$ was constant and approximately equal to $\frac{1}{8}$ (Gans' law). The constancy of the product can also be viewed as an uncertainty principle [5,9]. It gives a lower bound for the many-path channel as

$$B_{C,\text{Hz}}(C_C) \cdot \sigma_\tau \geq \frac{1}{2\pi} \cos^{-1} C_C \quad (60)$$

The equality holds for the two-path case with equal powers, as in Eq. (59), which corresponds to maximum delay spread.

For the two-path channel, the product $B_C^{(2)} \sigma_\tau^{(2)}$ does not exist for small a_2 , since $B_C^{(2)}$ does not exist. The dependence of this product on a_2 , is weaker than its dependence on the choice of C_C . The product $B_C^{(2)} \sigma_\tau^{(2)}$ is a minimum when a_2 is 1, that is, when the frequency fades are the deepest. In this case and for the value $C_C = 0.75$, the two-path product is in close agreement with Gans's law, $B_{C,Hz}^{(2)} \sigma_\tau^{(2)} = (1/2\pi) \cos^{-1} 0.75 \approx \frac{1}{8}$.

In the two-path model, then, the virtually constant value of the product allows the delay spread to be calculated from a measured correlation bandwidth, or vice versa. However, in a general many-path case, the expression for the coherence-bandwidth–delay-spread product must be heeded as a lower limit. It should always be borne in mind that the choice of C_C for the coherence bandwidth affects the value of the product. Because the delay spread is mathematically unbounded in the model (no limit is placed on τ_2), there is no theoretical upper limit for $B\sigma_\tau$ in the many-path case, even though the coherence bandwidth can simultaneously remain essentially constant. In practice, physical and practical considerations such as the space loss described below are imposed on the model and the delay spread and the product become bounded through these.

7.5. Correlation Distance

The correlation distance is the spatial counterpart of the coherence bandwidth. It is traditionally defined as the spatial displacement $d_d = \Delta z$ corresponding to when the spatial correlation coefficient, defined at a given frequency, decreases to some value. Instead of using the complex transfer function $H(z)$, analogously to using $H(\omega)$ for the coherence function, the envelope correlation coefficient function

$$\rho_r(\Delta z) = \frac{R_r(\Delta z) - \langle r \rangle^2}{R_r(0) - \langle r \rangle^2} \quad (61)$$

has been used traditionally, and the coefficient value is taken as $\rho_r(d_d) = 0.7$. The correlation distance is a measure of the spatial fading rate and therefore depends inversely on the spatial Doppler spread σ_u . The product of these, $d_d \sigma_u$, is lower bounded, but not with the same relationships as $B\sigma_\tau$.

8. MANY-PATH MODEL

The preceding discussion has touched several times on the many-path model. Many channel parameters for the three-path model can be derived deterministically. The three-path model has been of interest in point-to-point links because it matches the physical situation of a direct, a ground bounce, and a single atmospherically diffracted ray. It has been also used to help “randomize,” relative to the two-path model, a transfer function for a more realistic-looking (over two or three fades), but tractable, model. However, it otherwise offers little more insight into the channel behavior than does the two-path model. The statistics for the few-path (less than about 10) model are

rather complicated. When there are more than about 10 components of similar amplitude, however, the statistics follow, to a good approximation, the limiting case of a very large number of paths. The phase-mixing process of adding many random phasors gives, from the central limit theorem, the classical Rayleigh channel. The distribution functions are given below.

8.1. Phase Mixing with Many Random Contributions

Equations (11) and (12) describe the model. For a narrow band channel, the in-phase and quadrature components are Gaussian-distributed from the central limit theorem. It follows that: the distribution of the power is chi-square with 2 degrees of freedom (i.e., exponential), the envelope is Rayleigh-distributed, and the phase is uniformly distributed. The transfer function signals, as a function of position, are depicted in Fig. 12. The incident power is from all directions for this example. The figure can be compared with the signals from the two-path model, shown as a function of frequency in Fig. 9. The features of the channel are essentially the same as those in the two-path model, although the process is random. There are both minimum-phase and maximum-phase deep fades. Similarly, the random FM spikes have an associated polarity that is random.

8.1.1. Rayleigh Envelope and Uniform Phase. The signal representing the channel transfer function is represented as a complex Gaussian process. The in-phase component and quadrature components are denoted x and y , the envelope r , and the phase θ , and these are related as

$$x + jy = r e^{j\theta} \quad (62)$$

Here x and y are independent, zero mean Gaussians, so the pdf for each is (here for x)

$$p_x(x) = \frac{1}{\sqrt{2\pi}\sigma} \exp\left(-\frac{x^2}{2\sigma^2}\right) \quad (63)$$

where σ is the standard deviation of each component. The envelope and phase pdfs are established as independent with Rayleigh and uniform distributions respectively, through the steps

$$\begin{aligned} p_{r,\theta}(r, \theta) &= p_{x,y}(x, y) \left| \frac{\partial(x, y)}{\partial(r, \theta)} \right| \\ &= \frac{r}{\sigma^2} \exp\left(-\frac{r^2}{2\sigma^2}\right) \cdot \frac{1}{2\pi} \quad (r \geq 0) \\ &= p_r(r) \cdot p_\theta(\theta) \end{aligned} \quad (64)$$

The pdf of the phase is $1/(2\pi)$, so the mean phase is π and the standard deviation is $\pi/\sqrt{3}$. The averaged power is

$$\langle r^2 \rangle = \langle x^2 \rangle + \langle y^2 \rangle = 2\sigma^2 \quad (65)$$

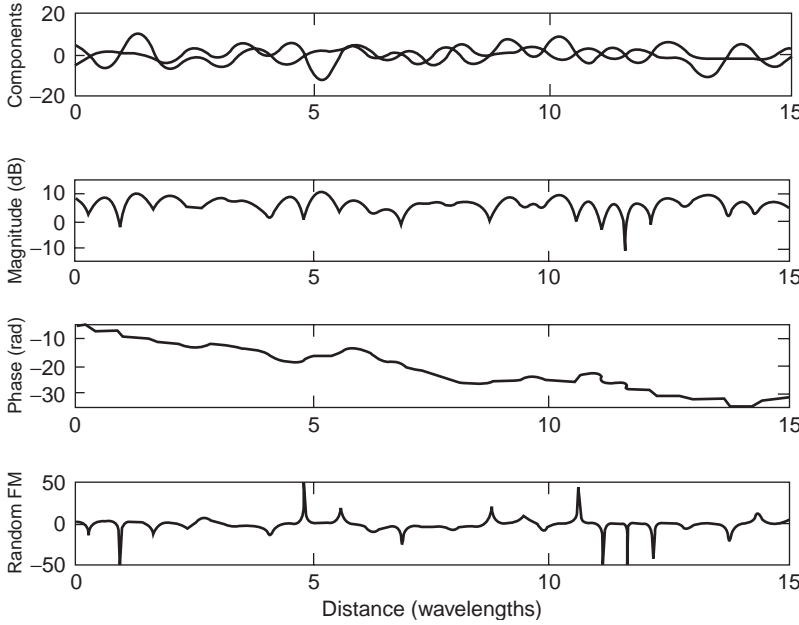


Figure 12. The signals of a many-path, narrow-band channel as a function of position. As the mobile receiver moves, the narrowband signal quantities vary in a way similar to the behavior of the plots. The in-phase and quadrature components comprise complex Gaussians, the magnitude or envelope is Rayleigh-distributed, the phase is uniformly distributed, and the random FM is Student- t -distributed.

and r^2 is recognized as having a chi-square distribution with 2 degrees of freedom,

$$p_{r^2}(r^2) = \frac{1}{2\sigma^2} \exp\left(-\frac{r^2}{2\sigma^2}\right) \quad (66)$$

The Rayleigh statistics are included in the more general Rice statistics, below.

8.1.2. Rice Envelope and Phase. Sometimes there is a single dominant effective source. This usually corresponds to a line-of-sight situation, which gives a single dominant effective scatterer. Multipath transmission still occurs, and the Rice distribution describes the statistics of the narrowband envelope. The Rice distribution results from one or both of the Gaussian processes having nonzero mean. These phase processes become

$$x_{\text{Ri}} = x + x_s, \quad y_{\text{Ri}} = y + y_s \quad (67)$$

where the x and y are zero-mean Gaussian and x_s and y_s are the respective means representing the dominant component (sometimes called the *specular*, or *coherent*, component, with x and y representing the *diffuse*, or *incoherent* component) of the signal. The phasor combination is shown in Fig. 13 in which $\phi = \tan^{-1}(y_{\text{Ri}}/x_{\text{Ri}})$ is the absolute phase of the Rice envelope r_{Ri} , and θ is the phase difference between r_{Ri} (Rayleigh component plus dominant component) and the dominant component r_s . The mean of the absolute phase of the process is $E(\theta + \phi)$. A coordinate rotation allows the phase to be defined as just θ .

From

$$(x_{\text{Ri}} - x_s)^2 + (y_{\text{Ri}} - y_s)^2 = r^2 = r_{\text{Ri}}^2 + r_s^2 - 2r_{\text{Ri}}r_s \cos \theta \quad (68)$$

the Rice pdf is

$$p_{r_{\text{Ri}},\theta}(r_{\text{Ri}}, \theta) = \frac{r_{\text{Ri}}}{2\pi\sigma^2} \exp\left(-\frac{r_{\text{Ri}}^2 + r_s^2 - 2r_{\text{Ri}}r_s \cos \theta}{2\sigma^2}\right) \quad (69)$$

The envelope and phase are thus statistically dependent, unlike the Rayleigh case. The $+\pi$ and $-\pi$ transitions that occur in the phase of the Rayleigh signal as the locus passes near the origin are now reduced to smaller values, which depend on the length of the envelope phasor component r_{Ri} . The Rice channel can be purely minimum phase when the dominant component is large enough.

The Rice k factor is the ratio of powers of the dominant component and the Rayleigh component:

$$k_{\text{Ri}} = \frac{r_s^2}{2\sigma^2} \quad (70)$$

When the dominant component r_s approaches zero, k_{Ri} approaches 0, and the distribution reduces to Rayleigh.

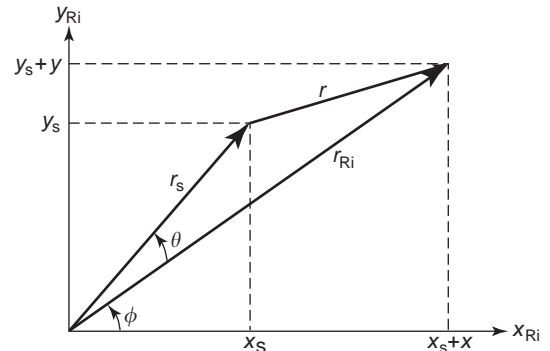


Figure 13. The Rice process has envelope r_{Ri} comprising the additive constant r_s and the Rayleigh envelope r . The phase of the Rice signal is θ .

Similarly, when the dominant component becomes very large, the Rice distribution for the envelope approaches Gaussian with mean r_s .

8.1.3. Rice Envelope. For convenience, the envelope is normalized by the Gaussian standard deviation:

$$r_{\text{Ri}}^{(n)} = \frac{r_{\text{Ri}}}{\sigma} \tag{71}$$

The envelope pdf is

$$\begin{aligned} p_{r_{\text{Ri}}}(r_{\text{Ri}}) &= \frac{r_{\text{Ri}}}{2\pi\sigma^2} \exp\left(-\frac{r_{\text{Ri}}^2 + r_s^2}{2\sigma^2}\right) \int_0^{2\pi} \exp\left(\frac{r_{\text{Ri}}r_s \cos \theta}{\sigma^2}\right) d\theta \\ &= \frac{r_{\text{Ri}}}{\sigma^2} \exp\left(-\frac{r_{\text{Ri}}^2 + r_s^2}{2\sigma^2}\right) I_0\left(\frac{r_{\text{Ri}}r_s}{\sigma^2}\right), r_{\text{Ri}} \geq 0 \end{aligned} \tag{72}$$

or in terms of $r_{\text{Ri}}^{(n)}$ and k_{Ri} ,

$$\begin{aligned} p_{r_{\text{Ri}}^{(n)}}(r_{\text{Ri}}^{(n)}) &= \frac{1}{\sigma} r_{\text{Ri}}^{(n)} \exp\left\{-\left[\frac{1}{2}\left(r_{\text{Ri}}^{(n)}\right)^2 + k_{\text{Ri}}\right]\right\} I_0\left(r_{\text{Ri}}^{(n)} \sqrt{2k_{\text{Ri}}}\right), r_{\text{Ri}}^{(n)} \geq 0 \end{aligned} \tag{73}$$

As k_{Ri} approaches infinity, the Rice pdf becomes a deltalike function, being a Gaussian with a variance approaching zero.

The Rice distribution is sometimes called Nakagami-Rice, in recognition of its independent development by Rice [10] and by Nakagami [11], who reported it in English at a later time. Because of its physical justification for many situations, the Rice distribution is the preferred one for short-term fading. Review material covering aspects of Rice’s work is presented in Refs. 12 and 13. The distribution for the random FM and group delay for the Rice channel is given by the Student t distribution [1,14].

The Rice envelope cumulative density function (cdf) is expressed as

$$\text{Prob}(r_{\text{Ri}} \leq r_0) = 1 - Q_1\left(\frac{r_s}{\sigma}, \frac{r_0}{\sigma}\right) \tag{74}$$

where Q is the Marcum Q function [15]. Further worthwhile discussion on the Q function is given in Refs. 1, 16, and 17. The Rice envelope cdf is sketched in Fig. 14 for values of the Rice k factor, including the Rayleigh case.

8.2. Lognormal Shadow Fading

Shadow fading has been found experimentally to be well described by the lognormal distribution. Whereas the Gaussian distribution results from the addition of many random variables, the lognormal distribution results from the product of many positive random variables. It follows that when Gaussian variables are expressed in logarithmic units, they then follow a lognormal distribution. The transformation of variables between the distributions is $z = e^x$, or $\ln z = x$. (z here is a variable, not distance.) If x is

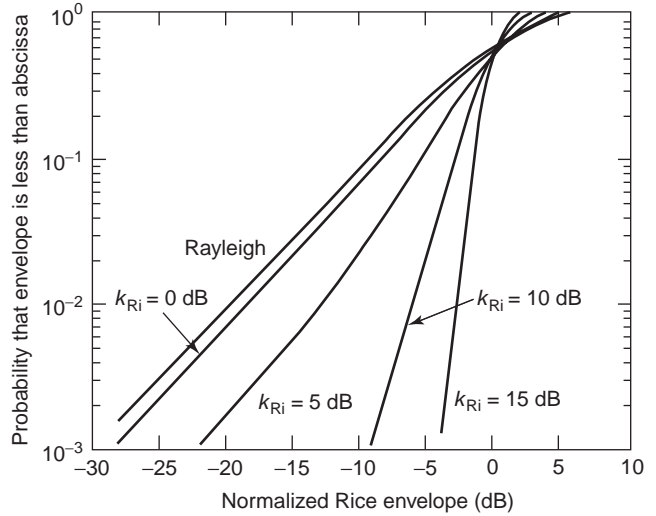


Figure 14. The Rice envelope cdf. For zero specular component, the distribution is Rayleigh, and approaches Gaussian (vertical line at 0 dB) for an asymptotically large specular component.

Gaussian, then z is lognormal. Alternatively stated, if z is lognormal, then $\ln z$ is Gaussian. The pdf of the lognormal distribution is found from the Gaussian pdf

$$p_1(z) = p_x(x) \left| \frac{\partial x}{\partial z} \right| = \frac{1}{\sqrt{2\pi}\sigma_{\ln z}} \exp\left(-\frac{(\ln z - m_{\ln z})^2}{2\sigma_{\ln z}^2}\right) \tag{75}$$

where $m_{\ln z}$ and $\sigma_{\ln z}^2$ are the mean and variance respectively of $\ln z$. The lognormal signal representing the local mean of the envelope looks like one of the phase components of Fig. 14, except that the scale would be in decibels rather than linear. Typically $\sigma_{\ln z}$ is 3–8 dB in urban environments.

8.3. Suzuki: Lognormal and Rayleigh

Combining the short-term Rayleigh and long-term lognormal distributions provides a model for the stochastic component of the path loss of a narrowband signal in mobile communications.

The lognormal distribution is over the mean of the envelope. This can be interpreted as Gaussian for the envelope mean in decibels. The Rayleigh envelope mean is linearly related to the Gaussian standard deviation, viz., $\langle r \rangle = \sqrt{\pi/2}\sigma$, so the lognormal distribution can be applied to the σ [18]. The distribution can be written

$$\begin{aligned} p_{\text{Su}}(r) &= \int_0^\infty \frac{r}{\sigma^2} \exp\left(-\frac{r^2}{2\sigma^2}\right) \cdot \frac{1}{\sqrt{2\pi}\sigma_l} \exp\left(-\frac{(\ln \sigma - m_l)^2}{2\sigma_l^2}\right) d\sigma \end{aligned} \tag{76}$$

No closed form has been found for the integral, which is a practical inconvenience when applying the Suzuki distribution. However, the distribution has the advantage of being based on a physical model for the envelope, and thus

offers good agreement with experimental results on large-scale records of envelopes of narrowband signals.

Many other distributions have been used to fit mobile channel fading [19]. Some have various advantages for mathematical manipulations or for the fitting of experimental data. Two are noteworthy because of their versatility. The Nakagami m [11] distribution has a single parameter that allows the shape of the distribution to be altered, in particular for small values of r . The generalized gamma distribution [20] has effectively two parameters that can independently adjust the shape of the small and large values of r .

9. PATH LOSS AND THE MOBILE CHANNEL

Much of the preceding discussion has been a statistical description of the behavior of the mobile channel. The interest in the envelope or power of the mobile transfer function is because this dominates the SNR of the received signal. The power is also referred to as the *channel gain*. How this ties in with the path loss is addressed in this section. In so doing, the discussion returns to the electromagnetic propagation and antenna issues of the opening sections.

Path loss is a well-defined concept originating from point-to-point radio links. It comes from the Friis transmission equation, which relates the transmitted and received powers (P_T, P_R respectively), the antenna gains (G_T, G_R respectively), and the path loss L :

$$\frac{P_R}{P_T} = G_T G_R \frac{1}{L} \quad (77)$$

Path loss is seen from this equation to be the reciprocal of the path gain. For frequency-independent antenna gains, the free space path loss for a separation distance d and wavelength $\lambda = c/f$ is

$$L_F = \left(\frac{4\pi d}{\lambda}\right)^2 = \left(\frac{4\pi f d}{c}\right)^2 \quad (78)$$

so that it varies as the frequency squared and the distance squared. The incident field strength is not dependent on frequency. In Eq. (77), the antennas are considered impedance- and polarization-matched.

9.1. Mean Path Loss and Mean Antenna Gain

In a mobile channel, the classical point-to-point situation does not apply. The received power and the receiving antenna gain become statistical quantities. The antenna's *mean gain* can be defined by the average gain into a well-defined distributed direction. The mean received power can be defined from a time average. The path loss is the time-varying quantity (because of the spatially dependent phase mixture of multipath propagation signals), and so the mean received power with Eq. (77) defines a *mean path loss*. Sometimes the term *mean effective gain* is used when comparing antennas by measuring their time-averaged received powers in the same environment. In this

context, it must be assumed that the transmitting power and the mean path loss are both common to each measurement record used for the averaging. The mean effective gains are then proportional to the mean received powers and include polarization mismatches. What is being measured is how well, on average, the vector antenna pattern is directed toward the vector distribution of incoming power from the measurement environments.

9.2. Scenario Models

Model distributions are used to approximate the average incident power incident power directions for various applications. For a mobile vehicle, for example, the Clarke scenario [21,22], given by

$$S^{(C)}(\theta, \phi) = S^{(C)}(\theta) = \delta(\theta - \pi/2) \quad (79)$$

is often used. This corresponds to a uniform source distribution at the horizon, surrounding the antenna. Transforming to the spatial Doppler variable results in the pdf

$$p_u^{(C)}(u) = \frac{1}{\pi \sqrt{k_C^2 - u^2}} \quad (80)$$

and this spatial Doppler spectrum is for the incident fields or the electromagnetic propagation channel (for one polarization), and also for the mobile channel if an omnidirectional (in the $\theta = \pi/2$ plane) antenna is used. The spatial Doppler spread is $\sigma_u^{(C)} = k_C/\sqrt{2}$ (rad/m). The spatial correlation coefficient for the envelope is $\rho_r^{(C)}(\Delta z) \approx J_0^2(k_C \Delta z)$, giving a 0.7 correlation distance of about 0.13 wavelengths and an average distance between fades of about 0.5 wavelength.

For a directional antenna, the spatial Doppler distribution corresponding to the pattern must be multiplied with Eq. (80) to get the spatial Doppler spectrum of the mobile channel. This is how the antenna pattern can control the mobile channel behavior. A single-lobed, directional pattern acts as a spatial Doppler bandpass filter and results in a decreased (relative to an omnidirectional pattern) Doppler spread, and therefore a decreased spatial fading rate. This effect can be seen with laser speckle, where the dark areas are the deep fades of energy, and the interspeckle distance, even though the frequency is optical, is sufficiently large to be visible to the eye because the spatial Doppler spread of the illuminating beam is so small.

BIBLIOGRAPHY

1. R. G. Vaughan and J. Bach Andersen, *Channels, Propagation and Antennas for Mobile Communications*, London: Peregrinus, 2003.
2. T. Miki and M. Hata, Performance of 16 kbits/s GMSK transmission with postdetection selection diversity in land mobile radio, *IEEE Trans. Veh. Technol.* **VT-33**(3):128–133 (1984).
3. K. Sakoh et al., Advanced radio paging service supported by ISDN, *Proc. Nordic Seminar on Digital Land Mobile Radio-communication*, Espoo, Finland, Feb. 1985, pp. 239–248.

4. P. A. Bello, Characterization of randomly time-variant linear channels, *IEEE Trans. Circuits Syst.* **CS-11**:360–393, (Dec. 1963).
 5. A. Papoulis, *Signal Analysis*, McGraw-Hill, New York, 1977.
 6. P. A. Bello and B. D. Nelin, The effect of frequency selective fading on the binary error probabilities of incoherent and differentially coherent matched filter receivers, *IEEE Trans. Circuits Syst.*, **CS-21**:170–186 (June 1963).
 7. M. J. Gans, A power spectral theory of propagation in the mobile-radio environment, *IEEE Trans. Veh. Technol.* **VT-21**(1):27–38 (Feb. 1972).
 8. D. C. Cox and R. P. Leck, Correlation bandwidth and delay spread multipath propagation statistics for 910 MHz urban mobile radio channels, *IEEE Trans. Commun.*, **Com-23**(11):1271–1280 (1975).
 9. B. H. Fleury, An uncertainty relation for WSS processes and its application to WSSUS systems, *IEEE Trans. Commun.* **Com-44**(12):1632–1635 (Dec. 1996).
 10. S. O. Rice, Mathematical analysis of random noise, *Bell Syst. Tech. J* (3) (1944); (1) (1945).
 11. M. Nakagami, The m -distribution—a general formula of intensity distribution of rapid fading, in W. C. Hoffman, ed., *Statistical Methods in Radio Wave Propagation*, Pergamon Press, Oxford, 1960.
 12. W. B. Davenport and W. L. Root, *An Introduction to the Theory of Random Signals and Noise*, McGraw-Hill, New York, 1958; reprinted, IEEE Press, Piscataway, NJ, 1987.
 13. D. Middleton, *An Introduction to Statistical Communications Theory*, McGraw-Hill, New York, 1960; reprinted, IEEE Press, Piscataway, NJ, 1997.
 14. J. Bach Andersen, S. L. Lauritzen, and C. Thomsen, Distributions of phase derivatives in mobile communications, *IEE Proc.* **137**(4):197–201 (1990).
 15. J. I. Marcum, A statistical theory of target detection by pulsed radar, *IRE Trans.* **IT-6**:59–267 (April 1960).
 16. S. Stein, M. Schwartz, W. R. Bennett, and S. Stein, *Communications Systems and Techniques*, McGraw-Hill, New York, 1966, Part III; reprinted, IEEE Press, Piscataway, NJ, 1996.
 17. J. G. Proakis, *Digital Communications*, McGraw-Hill, New York, 1983.
 18. H. Suzuki, A statistical model for urban radio propagation, *IEEE Trans. Commun.* **Com-25**(7):673–680 (July 1977).
 19. J. Griffiths and J. McGeehan, Interrelationship between some statistical distributions used in radio-wave propagation, *IEE Proc.* **129**(Part F)(6):411–417 (Dec. 1982).
 20. E. W. Stacy, A generalization of the gamma function, *Ann. Math. Stat.* **33**:1187–1192 (1962).
 21. R. H. Clarke, A Statistical theory of mobile radio reception, *Bell Syst. Tech. J.* **47**:957–1000 (1968).
 22. W. C. Jakes (ed.), *Mobile Microwave Communications*, New York: AT&T, 1974; reprinted, Piscataway, NJ: IEEE Press, 1989.
- W. C. Y. Lee, *Mobile Communications Engineering*, McGraw-Hill, New York, 1982.
- R. C. V. Macario, *Personal and Mobile Radio Systems*, IEE Telecommunications Series, 25, Peter Peregrinus, London: 1991.
- J. D. Parsons, *The Mobile Radio Propagation Channel*, Pentech Press, London, 1992.
- T. S. Rappaport, *Wireless Communications, Principles and Practice*, IEEE Press, New York, 1996.
- S. O. Rice, Statistical properties of sine wave plus random noise, *Bell Syst. Tech. J.* **27**:109–157 (1948).
- R. Steele, *Mobile Radio Communications*, Pentech Press, London, 1992.
- G. Stüber, *Principles of Mobile Communications*, Kluwer, Boston, 1996.
- R. G. Vaughan and J. Bach Andersen, *Channels, Propagation and Antennas for Mobile Communications*, Peter Peregrinus, London, 2003.

MOBILE SATELLITE COMMUNICATIONS

JOHN LODGE
 Communications Research
 Centre
 Ottawa, Ontario, Canada

Mobile satellite (MSAT) systems provide communications services to mobile and portable terminals using a radio-transmission path between the terminal and the satellite. An example of such a system, illustrating its typical components, is shown in Fig. 1. The mobile terminal may be installed in any one of a number of platforms including cars, trucks, railcars, aircraft, and ships. Alternatively, it could be a portable terminal with a size ranging from that of a handheld unit up to that of a briefcase, depending on the system and the service provided. Yet a third class could be small but fixed remote terminals serving functions such as seismic data collection and pipeline monitoring and control. A mobile satellite system requires one or more satellites with connectivity to the terrestrial infrastructure (e.g., to the public switched telephone network and to the various digital networks) supplied by one or more Earth stations. Typically, most of the communications traffic is between the mobile terminal and another terminal or application outside the mobile satellite system. However, most mobile satellite systems allow for mobile-to-mobile communications within the system. The Earth stations are coordinated by a control center in a way that shares the satellite transmission resources efficiently. Also, the control center may issue commands to the satellites via the Earth stations.

A number of radiolinks are required for such a system. Communication from the Earth station to the mobile terminal is said to be in the forward direction, whereas communication from the mobile terminal to the Earth station is said to be in the return direction. In both the forward and return directions, an uplink to the satellite and a downlink from the satellite are required, for a total of four radiolinks. The links between the Earth station and the satellite are sometimes referred to as *feeder links*, whereas

FURTHER READING

- H. L. Bertoni, *Radio Propagation for Modern Wireless System*, Prentice-Hall, Englewood Cliffs, NJ, 2000.
- J. K. Cavers, *Mobile Channel Characteristics*, Shady Island Press, Richmond, BC, 2003.
- W. C. Jakes, ed., *Mobile Microwave Communications*, AT&T, New York: 1974; reprinted, IEEE Press, Piscataway, NJ, 1989.

4. P. A. Bello, Characterization of randomly time-variant linear channels, *IEEE Trans. Circuits Syst.* **CS-11**:360–393, (Dec. 1963).
 5. A. Papoulis, *Signal Analysis*, McGraw-Hill, New York, 1977.
 6. P. A. Bello and B. D. Nelin, The effect of frequency selective fading on the binary error probabilities of incoherent and differentially coherent matched filter receivers, *IEEE Trans. Circuits Syst.*, **CS-21**:170–186 (June 1963).
 7. M. J. Gans, A power spectral theory of propagation in the mobile-radio environment, *IEEE Trans. Veh. Technol.* **VT-21**(1):27–38 (Feb. 1972).
 8. D. C. Cox and R. P. Leck, Correlation bandwidth and delay spread multipath propagation statistics for 910 MHz urban mobile radio channels, *IEEE Trans. Commun.*, **Com-23**(11):1271–1280 (1975).
 9. B. H. Fleury, An uncertainty relation for WSS processes and its application to WSSUS systems, *IEEE Trans. Commun.* **Com-44**(12):1632–1635 (Dec. 1996).
 10. S. O. Rice, Mathematical analysis of random noise, *Bell Syst. Tech. J* (3) (1944); (1) (1945).
 11. M. Nakagami, The m -distribution—a general formula of intensity distribution of rapid fading, in W. C. Hoffman, ed., *Statistical Methods in Radio Wave Propagation*, Pergamon Press, Oxford, 1960.
 12. W. B. Davenport and W. L. Root, *An Introduction to the Theory of Random Signals and Noise*, McGraw-Hill, New York, 1958; reprinted, IEEE Press, Piscataway, NJ, 1987.
 13. D. Middleton, *An Introduction to Statistical Communications Theory*, McGraw-Hill, New York, 1960; reprinted, IEEE Press, Piscataway, NJ, 1997.
 14. J. Bach Andersen, S. L. Lauritzen, and C. Thomsen, Distributions of phase derivatives in mobile communications, *IEE Proc.* **137**(4):197–201 (1990).
 15. J. I. Marcum, A statistical theory of target detection by pulsed radar, *IRE Trans.* **IT-6**:59–267 (April 1960).
 16. S. Stein, M. Schwartz, W. R. Bennett, and S. Stein, *Communications Systems and Techniques*, McGraw-Hill, New York, 1966, Part III; reprinted, IEEE Press, Piscataway, NJ, 1996.
 17. J. G. Proakis, *Digital Communications*, McGraw-Hill, New York, 1983.
 18. H. Suzuki, A statistical model for urban radio propagation, *IEEE Trans. Commun.* **Com-25**(7):673–680 (July 1977).
 19. J. Griffiths and J. McGeehan, Interrelationship between some statistical distributions used in radio-wave propagation, *IEE Proc.* **129**(Part F)(6):411–417 (Dec. 1982).
 20. E. W. Stacy, A generalization of the gamma function, *Ann. Math. Stat.* **33**:1187–1192 (1962).
 21. R. H. Clarke, A Statistical theory of mobile radio reception, *Bell Syst. Tech. J.* **47**:957–1000 (1968).
 22. W. C. Jakes (ed.), *Mobile Microwave Communications*, New York: AT&T, 1974; reprinted, Piscataway, NJ: IEEE Press, 1989.
- W. C. Y. Lee, *Mobile Communications Engineering*, McGraw-Hill, New York, 1982.
- R. C. V. Macario, *Personal and Mobile Radio Systems*, IEE Telecommunications Series, 25, Peter Peregrinus, London: 1991.
- J. D. Parsons, *The Mobile Radio Propagation Channel*, Pentech Press, London, 1992.
- T. S. Rappaport, *Wireless Communications, Principles and Practice*, IEEE Press, New York, 1996.
- S. O. Rice, Statistical properties of sine wave plus random noise, *Bell Syst. Tech. J.* **27**:109–157 (1948).
- R. Steele, *Mobile Radio Communications*, Pentech Press, London, 1992.
- G. Stüber, *Principles of Mobile Communications*, Kluwer, Boston, 1996.
- R. G. Vaughan and J. Bach Andersen, *Channels, Propagation and Antennas for Mobile Communications*, Peter Peregrinus, London, 2003.

MOBILE SATELLITE COMMUNICATIONS

JOHN LODGE
 Communications Research
 Centre
 Ottawa, Ontario, Canada

Mobile satellite (MSAT) systems provide communications services to mobile and portable terminals using a radio-transmission path between the terminal and the satellite. An example of such a system, illustrating its typical components, is shown in Fig. 1. The mobile terminal may be installed in any one of a number of platforms including cars, trucks, railcars, aircraft, and ships. Alternatively, it could be a portable terminal with a size ranging from that of a handheld unit up to that of a briefcase, depending on the system and the service provided. Yet a third class could be small but fixed remote terminals serving functions such as seismic data collection and pipeline monitoring and control. A mobile satellite system requires one or more satellites with connectivity to the terrestrial infrastructure (e.g., to the public switched telephone network and to the various digital networks) supplied by one or more Earth stations. Typically, most of the communications traffic is between the mobile terminal and another terminal or application outside the mobile satellite system. However, most mobile satellite systems allow for mobile-to-mobile communications within the system. The Earth stations are coordinated by a control center in a way that shares the satellite transmission resources efficiently. Also, the control center may issue commands to the satellites via the Earth stations.

A number of radiolinks are required for such a system. Communication from the Earth station to the mobile terminal is said to be in the forward direction, whereas communication from the mobile terminal to the Earth station is said to be in the return direction. In both the forward and return directions, an uplink to the satellite and a downlink from the satellite are required, for a total of four radiolinks. The links between the Earth station and the satellite are sometimes referred to as *feeder links*, whereas

FURTHER READING

- H. L. Bertoni, *Radio Propagation for Modern Wireless System*, Prentice-Hall, Englewood Cliffs, NJ, 2000.
- J. K. Cavers, *Mobile Channel Characteristics*, Shady Island Press, Richmond, BC, 2003.
- W. C. Jakes, ed., *Mobile Microwave Communications*, AT&T, New York: 1974; reprinted, IEEE Press, Piscataway, NJ, 1989.

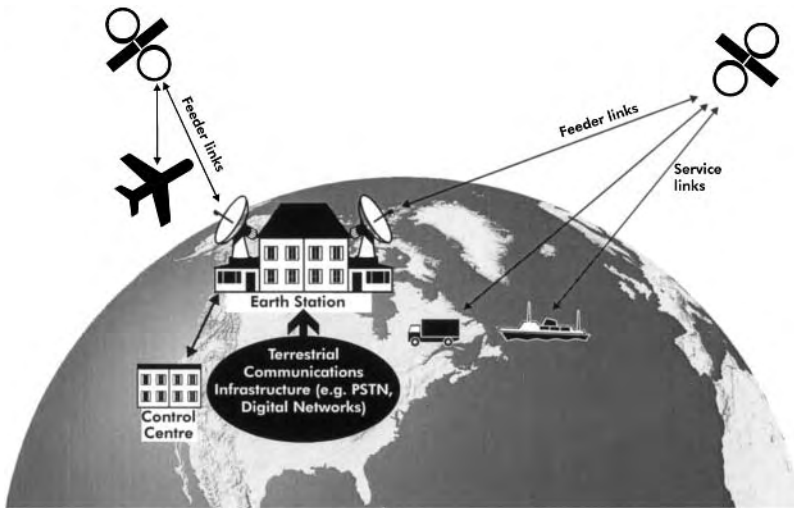


Figure 1. The major components of a mobile satellite system. Lines terminated with arrowheads indicate communication links.

the links between the mobile terminal and the satellite are typically referred to as *service links* or *mobile links*. In some of the more advanced satellite systems with multiple satellites, there are radiolinks between adjacent satellites called *intersatellite links*.

A wide variety of services and applications are supported by mobile satellite systems, with many more proposed. First- and second-generation systems are limited to data rates ranging from a few hundred bits per second (bps) to several tens of kilobits per second (kbps) and have concentrated their efforts on providing services that fall within categories such as telephone-quality speech, packet data communications, facsimile, generic asynchronous stream data, and paging. Third-generation systems are expected to be capable of transmission at rates up to several hundred kilobits per second and will be capable of delivering moderate-quality video and high-quality audio services. Increasingly, the services delivered by these systems will appear to be an extension of those available to users over the converging terrestrial systems.

Many satellites isolate selected frequency bands from the composite uplink signal using filtering, translate these selected bands to their downlink frequency band, amplify them, and then transmit them toward the Earth in the appropriate antenna beam. The term *transparent* satellite is used in this case. As an extension of this concept, some of the newer satellites use digital processing to select the uplink signal in a given frequency band, timeslot, and antenna beam, and then “switch” it to the desired downlink frequency band, timeslot, and antenna beam. The most sophisticated satellites demodulate the uplink transmissions and then process the resulting data signals in the same manner as a digital switch prior to modulation for downlink transmission. This type of satellite is sometimes referred to as a *regenerative satellite*.

A wide variety of mobile satellite terminals is commercially available. Here, we give only a few examples. Figure 2 shows a receive-only unit, manufactured by Skywave Mobile Communications Inc., that can be used to receive alphanumeric messages sent to a personal computer-based terminal, over the Inmarsat-D system. This system

is a high-penetration system and can receive messages even when moderate blockage of the satellite signal is occurring. The receiver is the small black rectangular object beside the laptop computer. The white disk-shaped object is the antenna, which has a magnetic base allowing it to be temporarily mounted on the roof of a vehicle. At other times, any flat surface will suffice.

A Mitsubishi MSAT telephone transceiver, mounted on the front wall of the trunk of a car, is shown in Fig. 3. The corresponding antenna subsystem, mounted on the car’s roof, is shown in Fig. 4. A third subsystem, which is not shown, is the user’s interface unit in the passenger compartment, including the telephone handset.

The major subsystems of the CAL Corporation’s satellite telephone terminal, for telephone communications to aircraft via MSAT, are shown in Fig. 5. Most of the terminal’s electronics are contained in the blackbox on the right-hand side. This box would normally be mounted



Figure 2. A receiver and antenna for the Inmarsat-D high-penetration messaging system. The receiver is shown connected to a laptop computer. (Reprinted with permission from Skywave Mobile Communications, Inc.)



Figure 3. A Mitsubishi MSAT telephone transceiver mounted on the front wall of the trunk of a car.

inside the pressurized cabin of the aircraft. The antenna subsystem is shown on the left-hand side, with its radome placed behind it. For this particular antenna, two short helices are used as the transducing elements in order to achieve the required amount of antenna gain while keeping the profile of the antenna low. The antenna is often mounted on the top of the fuselage, as is shown in Fig. 6. However, on some aircraft the top of the tail fin is a preferred location for antenna mounting.

1. MOBILE SATELLITE LINKS

We will start by considering the path of the radio signal as it travels from the satellite to the mobile terminal, that is, the downlink in the forward direction. A detailed discussion of this link will introduce the concepts necessary to understand more concise discussions pertaining to the



Figure 4. The antenna for a Mitsubishi MSAT telephone terminal, mounted on the roof of a car.

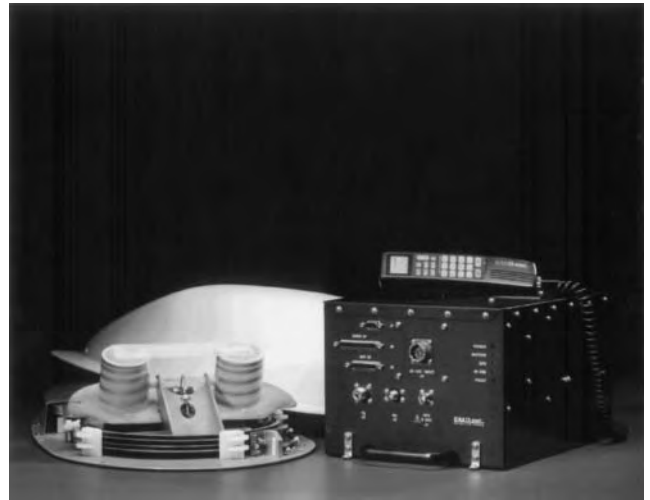


Figure 5. The major subsystems of the satellite telephone terminal, intended for use by aircraft with the MSAT system. (Reprinted with permission from CAL Corporation.)

other links of interest in a mobile satellite system. Radio-frequency bandwidth and electrical power are two scarce resources that tend to constrain the design of mobile satellite systems. In this section, the focus is primarily on power; efficient bandwidth utilization is partially addressed in subsequent sections. Clearly, downlink power will be limited because most satellites use solar power as their primary source of electrical power. Also, uplink power from the mobile terminal tends to be limited because such a terminal receives electrical power from either its own battery or that of the vehicle.

1.1. Line-of-Sight Transmission

At the satellite, the signal is amplified so that its average signal power is P_t dBW, at the input to the transmitting



Figure 6. A Cessna Citation jet aircraft, operated by the Ontario Air Ambulance Service, equipped with a mobile satellite communications terminal. The antenna subsystem can be seen mounted on top of the fuselage.

antenna. It is the transmitting antenna's function to spread that signal power as uniformly as possible over the desired coverage area on Earth's surface, while wasting as little power as possible outside this coverage area. This is directly analogous to the ability of the reflecting surface of a flashlight to focus the light from the bulb into a beam of light. A measure of the ability of the antenna to focus the radiation is its gain, which is the ratio of the flux density at the center of the coverage area to that value that would occur if the power had been radiated equally in all directions (i.e., isotropic radiation). This gain is a function of the size of the antenna, and for a circular parabolic antenna it is given by

$$G = 10 \log_{10} \frac{\Omega \pi^2 D^2}{\lambda^2} \text{dBi} \quad (1)$$

where Ω is the efficiency of the antenna (typically between 50% and 70%), D is the diameter in meters, and λ is the wavelength of the radiofrequency signal in meters. Other types of antennas will have differing gains, but Eq. (1) provides an order-of-magnitude estimate of the required antenna size to achieve a prescribed gain. This discussion assumes that a single beam is used to cover the desired area. For reasons that will be discussed later, it may be advantageous to cover the desired area with multiple overlapping beams, but using the same antenna superstructure. An example of one way to achieve this is to use a single large reflector with multiple feeds (i.e., source transducers) in different locations near the focal point of the reflector. Of course, increasing the number of beams increases the complexity of the satellite. The size and weight of the satellite's antennas are constrained by the need to maintain reasonable costs for the satellite and its launch. Nevertheless, advanced technology allows for surprisingly large antennas to be deployed in space. For example, the North American MSAT satellites have two elliptical antennas, measuring 6×5 m, and provide five beams covering all continental North America, the Caribbean Sea, and Hawaii. Some later systems have significantly larger antennas and can support more than 100 beams.

As the signal travels from the satellite to Earth, its flux density decreases as the square of the distance traveled. This power loss is referred to as the *free-space path loss* and is given by

$$L_p = 10 \log_{10} \frac{(4\pi d)^2}{\lambda^2} \text{dB} \quad (2)$$

where d is the distance traveled between the satellite and the mobile terminal. A geostationary orbit is a circular orbit for which the orbital radius, position, and velocity are such that the satellite remains in approximately the same location above the equator as Earth rotates. For a geostationary orbit, like that of MSAT, the radius is about 42,163 km, resulting in a typical propagation delay of greater than an eighth of a second to traverse from the satellite to the surface of Earth. At MSAT frequencies, the corresponding path loss is about 188 dB! The great

altitude of a geostationary satellite allows it to view about a third of the surface of the planet. Consequently, global coverage (with the exception of the polar regions) is possible with only three satellites. A larger number of satellites, in circular orbits at lower altitudes, can be used to provide global service with the advantages of lower path loss, shorter propagation delay, and lower launch costs on a per satellite basis. For reasons of satellite longevity, altitudes that avoid the Van Allen radiation belts are usually selected. The low-Earth orbits (LEOs) are located beneath the primary belt and have altitudes between 500 and 2000 km. Similarly, the medium-Earth orbits (MEOs) are located between the primary and secondary belts and have altitudes between 9000 and 14,000 km. The medium-Earth orbits are sometimes referred to as *intermediate circular orbits* (ICOs). Unlike systems that use geostationary orbits, these other systems typically use several distinct orbital planes, each of which is inclined with respect to the equator. A number of proposed systems have planned to use highly elliptical orbits (HEOs) instead of circular ones. The potential advantage of a HEO-based system is that it can provide high angle-of-elevation coverage to selected areas in the temperate zones (i.e., those parts of the world for which the demand for communications services is the greatest) with a moderate number of satellites. Despite this advantage, it does not appear that HEO systems will play a significant role in mobile satellite communications.

On reaching the terminal, the signal energy is collected by the receiving antenna and is converted by a transducer to an electrical signal. A typical example of a mobile satellite antenna designed for the MSAT system is shown in Fig. 7. Here, the transducing element is a short helical structure, similar to the element used for the land mobile satellite terminal and to each of the two elements for the aircraft mobile satellite terminal shown previously in this article. The white dome is a radome that is placed over the antenna to protect it. This antenna must be steered in azimuth but has a wide enough beam that steering in elevation is not necessary. Many mobile terminals use closed-loop antenna steering mechanisms, based on the received signal strength. The graybox shown in Fig. 7 contains a self-calibrating electronic compass that can be used to improve the antenna steering achievable using signal strength alone. Because of the fact that the physical rules describing the propagation of transmitting and receiving display a reciprocal relationship, an appropriate measure of the antenna's ability to collect the energy is the antenna gain, as described in the text near Eq. (1). Therefore, the average power of the received signal from the line-of-sight propagation path at the output of the receiving antenna is given by

$$P_r = 10 \log_{10} C = P_t + G_t - L_p + G_r \text{dBW} \quad (3)$$

where G_t is the gain of the transmitting antenna and G_r is the gain of the receiving antenna.

The signal's radiofrequency plays a major role in Eq. (3), with G_t , L_p , and G_r increasing with the square of the frequency. The net result is that the received power

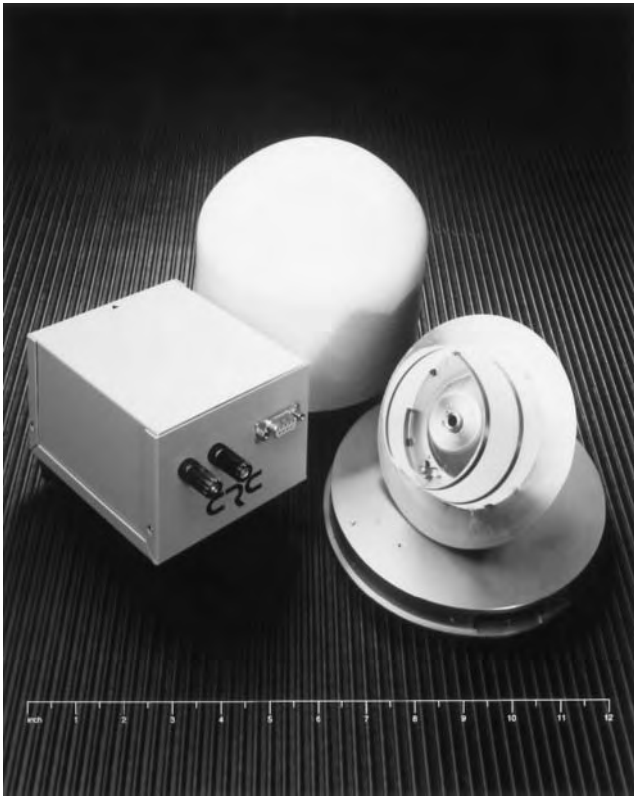


Figure 7. A prototype antenna system designed for the North American MSAT system. On the right-hand side of the foreground is the short helical antenna element. It can be steered in azimuth but is fixed in elevation. The box on the left-hand side is the antenna steering unit, and the radome is shown in the background.

also increases with the square of the frequency. Alternatively, if the received power is treated as the fixed parameter, smaller antennas could be used at higher frequencies. Some of this benefit for higher frequencies is offset by other propagation effects. For example, the lower frequencies (i.e., longer wavelengths) are more robust in the presence of blockage by collections of small obstacles such as foliage and rain. A second factor that is very important is the availability of an otherwise unused radio spectrum. At the international level, spectrum usage is determined by the International Telecommunications Union (ITU) at an ongoing series of World Administrative Radio Conferences (WARC). Then national bodies, such as the Federal Communications Commission (FCC) in the United States, license-specific service providers to offer the corresponding services within each country. A wide variety of frequency bands have been allocated for mobile satellite systems, typically with the larger allocations being at the higher carrier frequencies as a result of availability. Consequently, the systems that offer low-data-rate services are generally allocated lower frequency bands than do those offering high data rate services. For example, a number of systems offering low-rate store-and-forward messaging services communicate between the satellite and the mobile terminal in frequency bands between 100 and 400 MHz, although most of the systems offering medium-rate mobile satellite telephone services

use bands between 1.5 and 2.5 GHz, and many of the proposed systems for providing high-rate multimedia services plan to operate in bands between 20 and 30 GHz.

Because of the large path loss that is typical of satellite transmissions, the received power is very low. In fact, it is so low that the thermal noise in the receiving antenna and front end of the receiver must be accounted for. The resulting carrier-to-noise-spectral-density ratio is given by

$$10 \log_{10} \frac{C}{N_0} = P_r - T_r - k \text{dB} \cdot \text{Hz} \quad (4)$$

where T_r is the composite noise temperature of the receiver expressed (dBK) and k is Boltzmann's constant ($-228.6 \text{ dBW/K} \cdot \text{Hz}$). If the transmission is digital with a rate of R bps, the energy-per-bit-to-noise-spectral-density ratio is given by

$$\frac{E_b}{N_0} = \frac{C}{N_0 \cdot R} \quad (5)$$

Of course, thermal noise is not the only impairment that needs to be considered. Some of the other common impairments that are encountered by mobile satellite transmissions will be addressed in the following sections.

1.2. Multipath Propagation and Shadowing

In addition to the line-of-sight path, the signal can reach the receiving antenna by reflected paths from objects that are usually located nearby. Often, several distinct reflecting objects are in the field of view of the receiving antenna. If the differences in the propagation times for the various propagation paths (reflected and line of sight) are much less than the reciprocal of the bandwidth of the transmitted signal, the effect of the multipath propagation can be viewed as non-time-dispersive. This type of multipath propagation will affect the power and carrier phase of the received signal according to the nature of the superposition of the paths, but it will not distort its frequency content or introduce intersymbol interference in the case of a digital transmission. For land mobile satellite applications, measurements [1] taken in a frequency band near 1.8 GHz indicate that the difference in propagation times rarely exceeds 600 ns. Consequently, for signal bandwidths up to several hundred kilohertz, the multipath propagation can be considered non-time-dispersive. The following discussion is based on this assumption being valid. If the geometry of the paths change with time as a result of terminal motion, satellite motion, or motion of the reflecting objects, the power and carrier phase of the received signal will vary with time. This time-varying phenomenon is referred to as *fading*, or more specifically as *flat fading* for the non-time-dispersive case.

For the purpose of evaluating the performance of candidate transmission techniques, it is frequently desirable to model the propagation environment in a way that is suitable for numerical analysis and simulation. An approximation that is often made is to assume that the reflecting objects are adequately numerous and independent in

nature for the central-limit theorem to apply. Consequently the fading can be represented by a Gaussian process that is completely statistically characterized by its power spectral density. The power spectral density will be nonzero only over a bandwidth equal to the difference in frequency between the path with the greatest Doppler frequency shift and that with the least [2]. This type of fading model is referred to as *Rayleigh fading*. The combination of the line-of-sight path with the Rayleigh fading reflected path is referred to as *Rician fading*, which has the additional parameter called the carrier-to-multipath ratio (C/M), defined to be the ratio of the average signal power received over the line-of-sight path to that received over the reflected paths.

Another effect that can greatly affect the availability and performance of a mobile communication link is shadowing, the term given to blockage of the line-of-sight path. Such blockage occurs naturally in terrestrial mobile satellite environments as the moving vehicle passes by obstacles such as buildings, trees, and bridges. Many obstacles result in such severe attenuation of the line-of-sight signal that it is weaker than the reflected paths and can be ignored. A useful but simple model for shadowing is to switch between a good state (unshadowed) and a bad state (shadowed) with the typical time period for enduring each state being determined by the parameters of a two-state Markov model [3,4]. A transmission model corresponding to this discussion is shown in Fig. 8. A simple shadowing model is to apply a fixed attenuation selected on a shadowing event by shadowing event basis, using a lognormal distribution. If the shadowing is caused predominantly by foliage, the line-of-sight path may also be included with being subjected to attenuation according to another lognormal distribution [5]. Of course the values selected for the model's parameters depend on many issues, including angle of elevation to the satellite, type of terminal (e.g., land mobile, aircraft, marine, handheld), antenna gain pattern, vehicular velocity, satellite velocity, environment (e.g. urban, suburban, highway), and terrain.

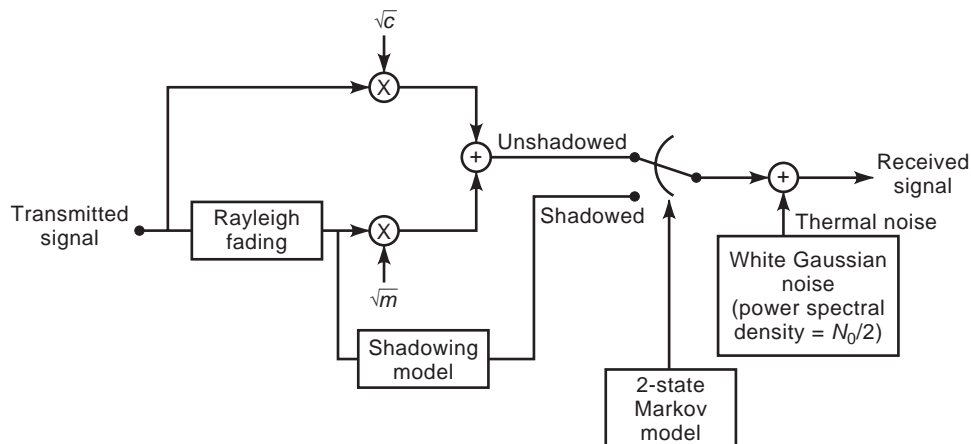


Figure 8. A useful model of fading and shadowing for the evaluation of mobile satellite transmission schemes. Here, c is the average power for the line-of-sight path and m is the average power for the reflected paths.

1.3. Other Sources of Degradation

Degradation to the received signal caused by thermal noise, multipath propagation, and shadowing have already been discussed. In many systems, these are the dominant sources of degradation, but there are a number of other ones that should be appreciated. Perhaps the next most important source of degradation is interference to the desired signal from other signals within the same system. If the interference is caused by another signal that is located in the same frequency channel as the desired signal, the interference is referred to as *cochannel interference*. For narrowband signals, cochannel interference is generally caused by interferers in other antenna beams for which the out-of-beam attenuation provided by the satellite antenna is not sufficiently great to render the interfering signal negligible. For spread spectrum signals, some of the cochannel interference may be due to other signals within the same beam. Interference to the desired signal can occur from signals in the adjacent frequency channels as a result of the fact that some of their transmitted energy falls outside of their allotted frequency channel. This type of interference is known as *adjacent-channel interference*.

For some mobile satellite systems, the ratio of the carrier frequency to the bit rate is many orders of magnitude. When this is the case, a nonnegligible amount of degradation can occur because the phase of the radiofrequency carrier differs significantly from its ideal value in a time-varying nature, which is the result of the electronic components in the system. This phenomenon is called *phase noise*. Common sources of phase noise include imperfect oscillators and frequency synthesizers, vibration of the mobile terminal's electronic circuitry (known as microphonics), and electronic steering of the mobile terminal's phased-array antenna.

Nonlinear power amplification, at several locations in a mobile satellite system, can cause degradation. In the case of the transmitting power amplifier in the mobile terminal, typically only a single carrier (signal) is present, and

the distortion of that signal by the amplifier's nonlinear behavior has two effects: (1) there will be a small reduction in the power efficiency of the desired transmission—for example, if the signal is digital, a little more transmit power will be necessary to achieve the required bit-error rate; and (2) the distortion will often broaden the power spectrum of the transmitted signal, resulting in increased interference in the adjacent channels.

Nonlinear distortion will also occur in the transmit power amplifiers of Earth stations and the satellites. Usually, many carriers will be amplified simultaneously. In this case, the result is a broadband noiselike signal caused by the intermodulation of the many carriers present in the amplifier.

Depending on the frequency band used by the given mobile satellite system, it may be necessary to account for effects such as ionospheric scintillation, tropospheric scintillation, gaseous absorption, and rain attenuation. In general, these effects become more severe for lower angles of elevation.

2. THE SIGNAL-PROCESSING PATH

In this section we discuss some of the signal-processing techniques that can be used to increase the efficiency with which the scarce resources of the radiofrequency spectrum and electrical power are used. Figure 9 shows a high-level block diagram of the processing stages for the transmitting side of the communication chain. The inverse operations are performed on the receiving side to recover the transmitted information. Here, we will discuss the blocks in this processing chain only to the level necessary for understanding their role in a mobile satellite context. More detailed treatment of many of these processing stages can be found elsewhere in this encyclopedia.

The first block in the chain is the information source. Examples include telephone-quality speech, data representing text, and multimedia signals representing a composite of audio, video, and data components. Regardless of the type of information that is to be transmitted, it is important to minimize the number of bits required to represent the information subject to constraints such as delay, processing complexity, and quality of the representation. This is the objective of the second block in the chain, entitled "source coding." Using telephone-quality speech as an example, the analog waveform can be accurately represented using a 64-kbps stream of data, by sampling the waveform at 8 kps (8000 samples per second) and giving each sample 8 bits of precision. However, using more recently developed speech-coding standardized techniques, the bit rate can be reduced a full order of

magnitude to 6.4 kbps without a significant reduction in speech quality [6]. Very efficient standardized low-rate videocoding techniques also exist [7]. Of course, the same techniques as are used for computer storage can be used to reduce the size of data and text files for mobile satellite transmission.

2.1. Error Control Coding

Error control coding introduces redundancy into the bitstream by increasing the total number of bits in such a way that each original bit influences several bits in the error-control-coded bitstream. This redundancy can then be used to correct (forward error correction coding) or detect (error detection coding) transmission errors at the receiver. We will consider forward error correction first. Even though the additional bits do result in an increase in the required number of bits to be transmitted, appropriate coding and decoding schemes will generally result in a net reduction in the transmitted power required to meet a given bit error rate. For first-generation mobile satellite systems, rate- $\frac{1}{2}$ constraint length 7 convolutional coding has been a fairly standard choice. Note that the rate is the ratio of the number of bits into the coder to those out of the coder. In some cases, punctured versions of this code have been used to achieve a higher coding rate, thereby improving bandwidth efficiency at the expense of power efficiency. A predominant reason for the popularity of this code is that it was one of the first fairly powerful error correction codes for which decoder integrated circuits, capable of processing soft decisions, were commercially available. For decoding in fast fading and shadowing conditions, the soft decision should incorporate channel state information so that the decoder assigns relatively less importance to bits that were received when the signal was faded or blocked.

The achievable coding gain is a strong function of the block length over which coding is performed, with larger blocks allowing for greater gains. For applications for which the packet or frame length is quite short (e.g., most packet data and low-rate speech applications) convolutional coding is still a good choice, although constraint lengths greater than 7 can be implemented now. Tail biting (i.e., encoding the input data in a circular buffer) can be performed to eliminate the overhead of transmitting extra bits to terminate the code's decoding trellis [8].

For applications for which the frame length is longer than a couple of hundred bits, turbo coding will be a strong candidate for future systems [9]. The performance of turbo coding improves as the block length increases; however, the end-to-end delay of the transmission system

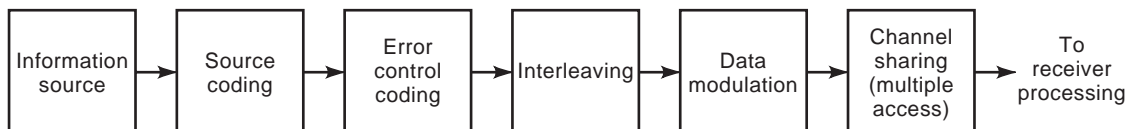


Figure 9. A high-level block diagram of the processing stages for the transmitting side of the communication chain.

increases with increasing block lengths. Consequently, only services that are tolerant of fairly large delays can benefit from the most power efficient error control coding. For rate- $\frac{1}{2}$ coding, Fig. 10 shows the performance for constraint length 9 convolutional coding (80-bit block) and turbo coding (512-bit block and 10,000-bit block). This turbo code uses 16-state recursive systematic convolutional codes as its component codes. These performance results assume antipodal signaling (e.g., ideal coherent binary phase shift keying); the only channel impairment is Gaussian noise.

In general, the benefit that can be achieved by error correction coding increases with increasing decoding complexity and block (i.e., codeword) size, and with decreasing code rate. One way to achieve a higher code rate, for a fixed decoding complexity, is to use puncturing [10]. Puncturing increases the code rate by selectively deleting some of the coded bits prior to transmission. In order to increase the code rate beyond 1 bit per symbol, it is necessary for the coder to map the input sequence of bits into a sequence of symbols for which the size of the symbol alphabet is greater than 2. A well-known technique for doing this is trellis-coded modulation [11,12]. Some forms of trellis-coded modulations are designed in such a way that standard convolutional decoder integrated circuits can be used to perform the decoding. These forms are referred to as *pragmatic trellis-coded modulations* [13]. An example of the tradeoff between power and bandwidth efficiency can be seen in Fig. 11. Here, all three codes are based upon the same convolutional code, where the rate- $\frac{1}{2}$ code is a constraint length 9 code, the rate- $\frac{3}{4}$ code is a punctured version of the rate- $\frac{1}{2}$ code, and the rate-1 code is a pragmatic trellis-coded modulation with the rate- $\frac{1}{2}$ code mapped into a four-level constellation.

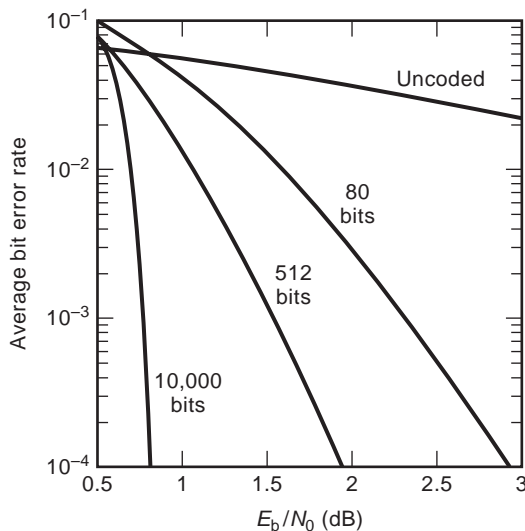


Figure 10. The performance of various rate- $\frac{1}{2}$ codes in an additive white Gaussian noise environment. Shown are simulation results for a constraint length 9 convolutional code with tail biting and a block size of 80 bits, and turbo coding with block sizes of 512 bits and 10,000 bits.

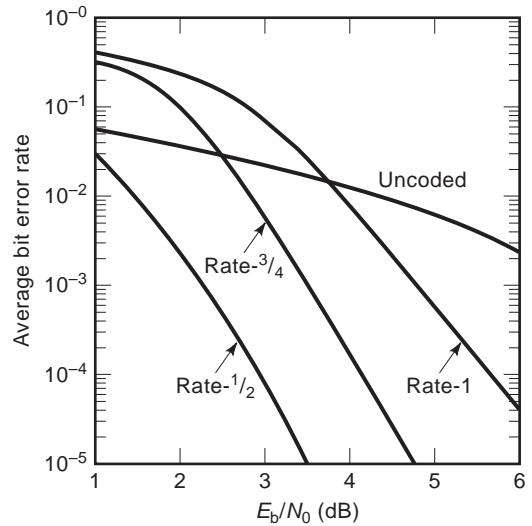


Figure 11. The performance of codes of differing rates in an additive white Gaussian noise environment. Shown are simulation results for the constraint length 9 rate- $\frac{1}{2}$ code; the rate- $\frac{3}{4}$ code, which is a punctured version of the rate- $\frac{1}{2}$ code; and the rate-1 code, which is a pragmatic trellis-coded modulation with the rate- $\frac{1}{2}$ code mapped into a four-level constellation.

Error detection coding is useful for services that are message- or frame-based, and it is important to know whether a given message or frame has been received correctly. In these cases a small field of parity bits (e.g., 16 parity bits) is appended to the message, with the parity bits generated using a cyclic redundancy code. At the receiver, if the parity bits computed from the received data bits do not agree with the received parity bits, the message is known to be in error. In some systems, a request will then be sent to the transmitter to retransmit the message.

Returning to error correction coding, many forward error correction codes are much better suited to correcting randomly distributed single errors than long bursts of errors, assuming that the average bit error rate is fixed. However, some impairments such as multipath fading cause error patterns that are bursty in nature. To the extent allowed by constraints such as message length and delay restrictions for the service, interleaving can be used between the coder and the modulator in an attempt to eliminate error bursts prior to decoding. Interleaving permutes the order of the coded symbols according to a rule that is known at both the transmitter and the receiver. After demodulation at the receiver, the deinterleaver performs the inverse permutation prior to passing the soft decisions to the decoder. By so doing, sequences of soft decisions corresponding to poor bursts of signal are broken up and mixed with soft decisions that were received under more favorable conditions.

2.2. Modulation

After interleaving, the sequence of coded symbols is modulated. Here, we restrict our consideration to linear modulation schemes. For a linear modulation scheme, the

transmitted signal is given by

$$\begin{aligned}
 s(t) &= \operatorname{Re} \left\{ \left[\sum_{i=0}^{N-1} a_i g(t - iT) \right] e^{j\omega_0 t} \right\} \\
 &= \left[\sum_{i=0}^{N-1} g(t - iT) \operatorname{Re}(a_i) \right] \cos(\omega_0 t) \\
 &\quad - \left[\sum_{i=0}^{N-1} g(t - iT) \operatorname{Im}(a_i) \right] \sin(\omega_0 t)
 \end{aligned} \quad (6)$$

where a_i ; $i=0, \dots, N-1$ is the sequence of complex modulation symbols, T is the symbol period, $g(t)$ is the unit pulse response of the pulse shaping filter and is assumed to be real, and ω_0 is the radian carrier frequency. In the second line of Eq. (6), the term inside the square brackets prior to “cos” is referred to as the in-phase component of the signal and the term inside the square brackets prior to “sin” is referred to as the quadrature component of the signal. For M -ary signaling, each a_i is selected from an alphabet of M complex numbers, with the modulus of each complex number representing the amplitude of the given symbol and the phase of each complex number representing the phase of the given symbol. The majority of mobile satellite communication systems use one or more forms of phase modulation. In the case of phase modulation, each a_i is selected from a symbol alphabet for which all elements have a modulus of 1. Therefore, only the phase of the symbol varies. Binary phase shift keying (BPSK) is popular for low-rate systems because of its robustness. For BPSK, each a_i is selected from the alphabet $\{1, -1\}$ which is purely real, and consequently a BPSK waveform has no quadrature component. A variation of BPSK, that is used in aeronautical satellite communications, is $\pi/2$ -BPSK for which subsequent symbols experience a relative phase shift of $\pi/2$ radians. For example, each a_i is selected from the alphabet $\{1, -1\}$ when i is even and from $\{j, -j\}$ when i is odd. When used with an appropriate choice of pulse shaping filter, such as a 40% square-root raised-cosine filter, the result is a waveform that suffers less spectral spreading when passed through a nonlinear amplifier, but enjoys all the robustness of standard BPSK. For systems requiring some additional spectral efficiency, some form of quadrature phase shift keying (QPSK) is usually selected. Standard QPSK can be thought of as two BPSK signals transmitted in parallel: one as the in-phase component and the other as the quadrature component. A variation of QPSK that is of some interest is $\pi/4$ -QPSK, for which subsequent symbols experience a relative phase shift of $\pi/4$ radians. The advantages of selecting $\pi/4$ -QPSK are similar to those described previously for $\pi/2$ -BPSK. Another variation of QPSK that is even more robust to nonlinear amplification is offset QPSK for which the symbol timing for the in-phase component is offset by half a symbol period relative to that of the quadrature component.

2.3. Multiple Access

Next we consider how the satellite resources of bandwidth and power can be efficiently shared between many users.

The sharing of the transmission medium between several users is referred to as multiple access (see MULTIPLE ACCESS MOBILE COMMUNICATIONS). We start from a highly idealized point of view, considering the case where there is only a single beam, perfect synchronization in both time and frequency have been achieved, and no interference is permitted between users.

First, let power be the only constraint. Each user can have as much bandwidth as desired but cannot exceed some fixed maximum value of transmit power. Under this constraint, each user attempts to maximize throughput (i.e., bit rate) subject to the requirement that the average bit error rate is better than some specified value. In general, lowering the coding rate allows for greater power efficiency and consequently a higher throughput for a given amount of power. The achievable region is illustrated by the area under the curve labeled “Power constraint” in Fig. 12. Note that the coding rate is expressed in bits per dimension, which takes into account the modulation and error control coding. This is the ratio of the number of bits into the error correction coder to the number of dimensions out of the modulator, over a fixed period of time. In Eq. (6), $\operatorname{Re}\{a_i\}$ and $\operatorname{Im}\{a_i\}$ can be considered as examples of dimensions in the signal space. It is well known that for a bandwidth of B and a time duration of T_s the number of available dimensions is $2BT_s$ [14].

Now let bandwidth be the only constraint considered. Clearly, the composite bit rate will increase linearly as the users increase their coding rate. The achievable region is illustrated by the area under the curve labeled “Bandwidth constraint” in Fig. 12. If both the power and bandwidth constraints are taken into account, there is an optimal code rate (assuming block size and decoding complexity are fixed) R_{opt} that maximizes the throughput of the system. If the system is operating at a lower rate, it is said to be bandwidth-limited, and if it is operating at a higher rate, it is said to be power-limited. With most of the early mobile satellite systems, the satellites were comparably weak, the demand for spectrum was low, and few devices were available to support coding rates below rate $\frac{1}{2}$. Consequently, most early systems were operating in the power-limited region. With newer systems, much more

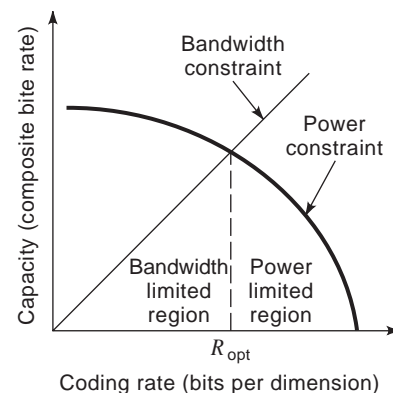


Figure 12. The tradeoff between capacity and coding rate subject to a power constraint and bandwidth constraint. R_{opt} is the coding rate that maximizes the capacity.

emphasis is now placed on achieving nearly optimum capacity in the system design.

One example of a set of dimensions (i.e., a basis) for the signal space is the time sample representation of the composite signal, with sampling being performed at the Nyquist rate. If sequential groups of these time samples are apportioned between the users, the sharing arrangement is called *time-division multiple access* (TDMA). Here, the mobile terminals must be fairly accurately synchronized in time so that bursts arriving at the satellite from different terminals can be tightly packed without interfering with each other. Typically, the required timing accuracy is achieved when the terminal requests to initiate communication by sending a short burst on a random access channel, for which accurate timing is not necessary. Then along with an assignment of a set of timeslots, the system sends the terminal an accurate clock correction that was calculated by the Earth station based on the measured time-of-arrival of the burst. Of course many other potentially useful bases exist. If nonoverlapping portions of the total bandwidth are apportioned between the users the arrangement is called *frequency-division multiple access* (FDMA). In this case, timing accuracy is no longer important, but narrower-band filtering is necessary and the lower data rates present on each carrier tend to make the system more susceptible to phase noise. If orthogonal codes are used to form the basis of the signal space, the sharing is called *code-division multiple access* (CDMA). In a synchronous CDMA system, the carriers must be synchronized in time to within a small fraction of a chip period so that orthogonality is maintained. In the forward direction, this is fairly straightforward to achieve if all the signals are originating from a single Earth station. In an asynchronous CDMA system, time synchronization is not required with the result that the signals are no longer truly orthogonal, resulting in some interference. In the return direction, achieving sufficiently accurate time synchronization among all the mobile terminals is quite challenging so asynchronous CDMA could be preferred over synchronous CDMA. Of course, combinations of these approaches are possible. Most of the mobile satellite systems to date have used FDMA. However, systems based on narrowband TDMA, which is a combination of FDMA and TDMA, are beginning to appear, even though CDMA is a strong candidate for systems with many beams or where there are severe power spectral density limitations.

More efficient use of both bandwidth and power can be achieved if the satellite's antenna system covers the desired area of Earth's surface with several smaller beams instead of one large one. The power efficiency of the link is improved as a result of the higher antenna gain associated with the smaller beams. With respect to frequency, the total allocated system bandwidth is divided into a number of distinct subbands, which need not be of equal bandwidth. As illustrated in Fig. 13, each beam is assigned a subband in such a manner that some desired minimum distance between beams with the same subband is maintained. The frequency reuse factor is the ratio of the number of beams to the number of distinct frequency subbands.

For most of the preceding discussion, it was assumed that no interference between users is permitted. In reality,

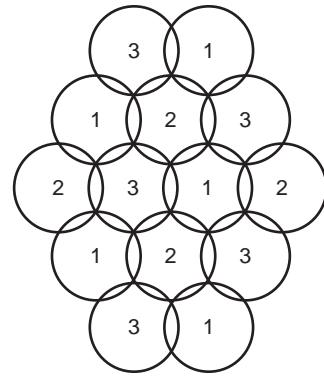


Figure 13. Total coverage area, consisting of multiple beams. In this case, there are 14 beams and the total frequency band is subdivided into three subbands. Two of the subbands are used in five beams, whereas the remaining subband is used in four. The resulting frequency reuse factor is 4.667.

some interference is unavoidable and may even be desirable to decrease system complexity and possibly to improve system capacity. For example, some CDMA systems allow each transmission to be completely asynchronous in chip timing and carrier phase relative to that of other users occupying the same frequency band and period in time. In this case, each transmission appears to be low-level broadband noise to the other users. Unlike the FDMA and TDMA systems for which the interference tends to be dominated by a small number of dominant interferers, the interference experienced by a user is the result of a very large number of other users resulting in a level of interference that is much less variable. Full statistical advantage can be taken of voice activation without the need for sophisticated dynamic channel assignment strategies. Powerful error correction coding allows for high levels of both intra- and interbeam interference. This results in the ability to reuse the same frequency bands in every beam and a corresponding high level of capacity in a multibeam satellite system [15].

Because interference is unavoidable, interference mitigation techniques are of interest. One example of such a technique is power control, for which the power of each user terminal is dynamically adjusted with the goal of providing it with just enough power to meet the required grade of service. Allowing terminals additional power would only serve to exacerbate the interference levels experienced in the system. A second example is the use of multiuser detection schemes (16).

3. PRESENT AND PLANNED SYSTEMS

Here the intent is to provide some examples of systems that are presently offering mobile satellite communications services and of those that are planned for the future. The systems discussed represent only a sampling and not an exhaustive summary.

Global mobile satellite communications got its start in 1976 when 3 Marisat satellites were launched and positioned at approximately equal intervals in geostationary orbits. In 1979, Inmarsat was formed to offer global

maritime satellite communications services. Inmarsat is a multinational organization that was created by the United Nations affiliated International Maritime Organization. Even though its original charter restricted its operation to maritime services, its charter was later extended to include aeronautical as well as land mobile and portable services. The nature of the Inmarsat organization continued to evolve with the goal of allowing it to offer an increasing array of mobile satellite services in a commercially competitive environment.

Inmarsat-A was the first system to offer commercial service on a global basis. Its terminals are relatively large and expensive; the typical antenna is a 1-m-diameter parabolic dish, and a terminal weight of around 35 kg is representative. Consequently, the majority of customers are large commercial users with most of the marine terminals installed on ocean-going ships and most of the portable terminals belonging to governments or news gathering organizations. Voice transmission was accomplished using analog frequency modulation, which is neither bandwidth nor power efficient by today's standards. Inmarsat has introduced several new voice and data systems that are based on more recent digital technologies. All Inmarsat's systems operate over geostationary satellites. The first of these new systems is the Inmarsat aeronautical system, which is based on the work of the International Civil Aviation Organization and the Airlines Electronic Engineering Committee.

The purpose of the aeronautical system is to provide comprehensive aeronautical communications services, including basic air traffic services, aeronautical operational control, and cabin telephone. Inmarsat began by providing the cabin telephone service, with other services to be phased in later. This system is unique in that it is the only mobile satellite system that has been designed in a manner consistent with Open System Interconnect (OSI) principles.

The Inmarsat-M and -B systems were developed in parallel and share a common protocol. The M system offers lower-cost and reduced weight (typically about 10 kg) terminals, which provide communications-quality voice (4.2 kbps voice coding rate with the addition of error control coding bringing the rate up to 6.4 kbps), low-speed data (2.4 kbps), and facsimile services. In addition to marine and land mobile terminals, portable terminals the size of a small briefcase (including the antenna) are available. Telephone booths based on Inmarsat-M technology, which are powered using solar panels, are used in underdeveloped parts of the world.

Inmarsat-B is the designated successor to Inmarsat-A for providing high-quality professional communications services. For operation within the global beam of a satellite, the mobile antenna requirements for the A and B systems are identical, with a typical gain of 20 dBi. Inmarsat-M terminals have smaller antennas, with gains of 14 and 12 dBi for marine and land mobile terminals, respectively. Also available are still smaller "mini-M" terminals that operate only in the higher gain beams provided by the Inmarsat-3 series of satellites, launched in 1996 and 1997.

Inmarsat-C was introduced in 1990 to support store-and-forward packet data services such as telex, electronic

mail, messaging, and position reporting. Even though only low-bit rates (600 bps) are supported, the terminals are small and inexpensive relative to those for the other Inmarsat systems. An antenna with a gain as low as 1 dBi will suffice.

A number of regional systems offer terminals and services similar to those of the mini-M system. One example is the North American MSAT system, for which Canada and the United States each launched a geostationary satellite. A number of future regional systems are planned for Asia and the Middle East, using extremely large geostationary satellites, which should be capable of delivering these services to handheld terminals, or higher data rate services to larger terminals.

These systems are alike in that they all use geostationary satellites, and the mobile terminals receive their signals in a band around 1550 MHz and transmit their signals in a band around 1650 MHz. Systems exist that use completely different frequency bands and in some cases orbits. We will begin with brief discussions of two systems that offer two-way messaging and position determination. These systems have targeted truck fleet management and cargo position reporting as primary application areas.

In 1990, the OmniTRACS system began full operation, providing two-way communications and position reporting services. It was licensed to operate on a secondary basis, which implies that it must not interfere with primary users, in the 12/14 GHz bands using existing geostationary satellites. The early start of service has allowed the OmniTRACS system to build up a large customer base. A number of novel spread-spectrum techniques are employed to safeguard against interfering with other systems.

The Orbcomm system plans to operate with a full constellation of 36 LEO satellites. The mobile terminals will receive their signals at about 138 MHz and transmit their signals at about 150 MHz. The system operators hope to achieve a competitive cost advantage by having small inexpensive satellites, low launch costs (as a result of the small satellites and low orbits), and lower terminal costs caused by the lower-frequency electronics.

A number of planned systems expect to offer handheld telephone services on a global basis. Three systems that deserve particularly close attention are Globalstar, Iridium, and ICO. Globalstar and Iridium are LEO systems with 48 and 66 active satellites in a full constellation, respectively. The ICO system will use 10 active MEO satellites. The multiple-access technique selected for ICO and Iridium is narrowband TDMA, whereas Globalstar will use CDMA. Iridium and Globalstar should be offering global services before the turn of the century, whereas ICO is expected to be a couple of years later.

Early in the next century, a number of satellite systems are planned to offer a broad range of services, including higher rate services that should effectively extend the digital network capabilities that will be available terrestrially. The highest profile of these is the Teledesic system. Originally, this system planned to use 840 LEO satellites! This has now been scaled back to a planned initial constellation of 288 LEO satellites.

For a number of reasons, position determination can be very important for a mobile satellite communication user. In fact, position determination is an integral part of many of the services such as vehicle fleet management and cargo tracking. Some terminals may use position information for antenna steering and to aid in the satellite and antenna beam handoff algorithms. Also, accurate position information is required for obtaining a license to offer service in some countries because the national authority insists on knowing if a call is being made within its territory. Some mobile satellite communications systems are capable of providing fairly coarse position estimation using the signals and satellites within the systems itself. However, accurate position determination is usually done by taking advantage of the Navstar global positioning system (GPS) (17).

The GPS system employs 24 satellites distributed in 6 orbital planes, each inclined by 55° with respect to the equator. These satellites are in 12h medium earth orbits. Even though the system is financed by the US Department of Defense, it is used globally for both civilian and military applications. In addition to the signals generated aboard the Navstar satellites, the Inmarsat-3 satellites have transponders that can relay ground-generated GPS-type signals. These additional signals can be used to improve the accuracy and reliability of the position estimates. A GPS receiver estimates the range to several satellites and then uses these estimates to determine its position by triangulation. Range estimates to Earth's three satellites are sufficient to provide two-dimensional position (i.e., on the Earth's surface or if the altitude is known) plus accurate time, whereas four satellites are required to provide three-dimensional position plus accurate time. Each Navstar satellite transmits in two frequency bands; the L_1 carrier is centered at 1575.42 MHz, and the L_2 carrier is centered at 1227.60 MHz. Frequency-dependent range estimates can be used to compensate for the effect of the ionosphere. The L_1 carrier is modulated with a short coarse/acquisition code (C/A code) at a chip rate of about 1 MHz and a longer precision code (P code) at a chip rate of about 10 MHz. The L_2 carrier is modulated with the P code only. The P code is dithered in a pseudorandom fashion so that precision is limited for users other than those in the U.S. military. In addition to the previously mentioned ranging codes, the carriers are modulated by a low-rate datastream carrying a navigation message that includes satellite position and satellite clock correction information. Typical civilian GPS receiver sets achieve a position accuracy of about 100 m and a time accuracy of about 10 ns. It is expected that the dithering of the P code will be eliminated within several years, allowing the accuracy for civilian sets to improve to better than 30 m.

4. TRENDS IN MOBILE SATELLITE SYSTEMS

Increasingly a broader range of services is being offered, with many of the new services requiring data rates that are higher than those currently available. Ultimately the services offered to mobile satellite users will be an extension of those that are available from terrestrial systems,

with the result that mobile satellite service offerings will be pulled along by the expansion and convergence that is occurring terrestrially. The upward trend in the data rates will necessitate increased use of the higher-frequency bands by mobile satellite systems.

In order to achieve the large numbers of users predicted by market studies, the trend toward smaller and less expensive terminals will need to continue. Small and simple antennas for the mobile terminals will be essential to achieve this goal. New systems must find ways to provide the extra power needed to offer the combination of higher data rates to smaller terminals. For systems based on geostationary satellites, this will require very powerful satellites with extremely large antennas. Because of reduced path loss, for systems using satellites in lower orbits, the size and power of the satellite can be traded off with the altitude of the orbit. Of course, as the altitude of the orbit decreases, the number of satellites needed to provide global coverage increases.

A large number of systems are in the planning stage, and one can expect fierce competition based on cost to the user, range of services, quality of services, and availability. Because it is usually not feasible to overcome blockage, satellite diversity to offer improved availability may become an important issue. Systems based on geostationary satellites will have an advantage for services requiring broad area coverage, such as point-to-multipoint communications, broadcasting, and wide-area paging. On the other hand, systems based on lower-Earth orbits will have an advantage for global point-to-point communications services, particularly if large transmission delays are undesirable. An example of such a service is global handheld telephony.

From the wide range of technologies and service offerings that characterize planned systems, it is clear that the field of mobile satellite communications is far from being mature.

BIBLIOGRAPHY

1. A. Jahn et al., Narrow- and wide-band channel characterization for land mobile satellite systems: Experimental results at L-band, *Proc. 4th Int. Mobile Satellite Conf.*, 1995, pp. 115–121.
2. W. Jakes, Multipath interference, in W. Jakes, ed., *Microwave Mobile Communications*, Wiley, New York, 1974.
3. E. Lutz et al., The land mobile satellite channel—recording, statistics, and channel model, *IEEE Trans. Veh. Technol.* **40**:375–386 (1991).
4. R. Barts and W. Stutzman, Modeling and simulation of mobile satellite propagation, *IEEE Trans. Anten. Propag.* **40**:375–381 (1992).
5. C. Loo, A statistical model for a land mobile satellite link, *IEEE Trans. Veh. Technol.* **VT-34**:122–127 (1985).
6. R. Cox and P. Kroon, Low bit-rate speech coders for multimedia communication, *IEEE Commun. Mag.* **34**(12):34–41 (1996).
7. K. Rijkse, H.263: Video coding for low-bit-rate communication, *IEEE Commun. Mag.* **34**(12):42–45 (1996).
8. H. Ma and J. Wolf, On tail biting convolutional codes, *IEEE Trans. Commun.* **COM-34**:104–111 (1986).

9. C. Berrou and A. Glavieux, Near optimum error correcting coding and decoding: Turbo-codes, *IEEE Trans. Commun.* **44**:1261–1271 (1996).
10. Y. Yasuda, K. Kashiki, and Y. Hirata, High rate punctured convolutional codes for soft Viterbi decoding, *IEEE Trans. Commun.* **COM-32**:315–319 (1984).
11. G. Ungerboeck, Trellis-coded modulation with redundant signal sets: Part I. Introduction, *IEEE Commun. Mag.* **25**(2):5–11 (1987).
12. G. Ungerboeck, Trellis-coded modulation with redundant signal sets: Part II. State of the art, *IEEE Commun. Mag.* **25**(2):12–21 (1987).
13. A. Viterbi et al., A pragmatic approach to trellis-coded modulation, *IEEE Commun. Mag.* **27**(7):11–19 (1988).
14. C. Shannon, Communications in the presence of noise, *Proc. IRE*, **37**:10–21 (1949).
15. K. S. Gilhousen et al., Increased capacity using CDMA for mobile satellite communications, *IEEE J. Select. Areas Commun.* **8**:503–514 (1990).
16. A. Duel-Hallen, J. Holtzman, and Z. Zvonar, Multiuser detection for CDMA systems, *IEEE Pers. Commun.* **2**(2):46–58 (1995).
17. M. Kayton, ed., *Navigation: Land, Sea, Air and Space*, IEEE Press, New York, 1990.

FURTHER READING

- J. Lodge and M. Moher, Mobile satellite systems, in J. D. Gibson, ed., *The Communication Handbook*, CRC Press, Boca Raton, FL, 1997, pp. 1015–1031.
- T. Logsdon, *Mobile Communications Satellites*, McGraw-Hill, New York, 1996.
- S. Kato, Personal communication systems and low earth orbit satellites, *Proc. Space Radio Sci. Symp.* U.R.S.I., Brussels, Belgium, 1995, pp. 30–42.
- W. Wu et al., Mobile satellite communications, *Proc. IEEE*, **82**(9):1431–1448 (1994).
- J. Lodge, Mobile satellite communications systems: Toward global personal communications, *IEEE Commun. Mag.* **29**(11):24–30 (1991).

MODE-MATCHING METHODS

F. ARNDT
University of Bremen
Bremen, Germany

1. INTRODUCTION

Due to its high efficiency, the mode-matching (MM) method has been applied for the calculation of waveguide structures already for a very long time. It is one of the oldest electromagnetics (EM)-based methods for the rigorous solution of waveguide discontinuity problems. In their historical papers 1944, Whinnery, Jamieson [1,2] and Robbins [2] calculated parallel-plate and coaxial transmission-line discontinuities, such as step junctions and diaphragms, already utilizing the typical character-

istic features of the method, which later was called the “mode-matching method”: expansion of the tangential electromagnetic field at the plane of discontinuity in terms of the corresponding waveguide modes, application of the (mode) matching conditions for tangential fields at the discontinuity, and utilization of the orthogonal properties of the waveguide modes for determination of the corresponding expansion coefficients.

Like nearly all important developments concerning the solution of electromagnetic problems, the work in Refs. 1 and 2 was—besides the original contributions of the authors—however, also a result of already available broad knowledge on the solution of waveguide problems contributed by many researchers. These included (to name only a few of them) Hahn’s analysis of cavity resonators [3] using a modal expansion method, Courant and Hilbert’s eigenfunction expansion and eigenfunction orthogonality theorem [4] (the general case of the well-known Fourier series expansion method), Stratton’s general waveguide modes solution approach constructed from superposition of elementary wavefunctions [5], the network formulation of microwave field theory and scattering matrix description of waveguide discontinuities during the 1940s at MIT, summarized by Marcuvitz et al. in [6,7], and the comprehensive contributions on integral equation formulations of the field problem of discontinuities and obstacles and its solutions by Schwinger at MIT, put together in Ref. 10. A compendious historical review of these early microwave field theory developments is given by Oliner [45].

The MM technique has been applied by Clarricoats and Slinn [13] and Wexler [14] to waveguide discontinuities using matrix notations and including the consideration of higher-order mode effects between discontinuities. Wexler called the method *modal analysis*, a notation that is also used in literature when referring to the MM technique. A MM technique utilizing an intermediate section for offset discontinuities has been introduced by Piefke [15] and Knetsch [17,18]. Convergence investigations have been carried out by Mastermann and Clarricoats [20], Lee et al. [22], Mittra et al. [23], and Chu et al. [58]. Lee et al. [22] used the term *mode-matching*, a term that is now widely adopted in the literature for this method, and is also used in the present article.

In 1960, Collin [11] applied the eigenfunctions expansion principle for the solution of the transverse cross section eigenvalue problem of inhomogeneous waveguides. Such applications are later referred to as “field matching” [91,92]. Field matching has found considerable applications during the 1980s for solving in particular microstrip and finline cross section eigenvalue problems, e.g., Kowalski, Pregla [21], Bornemann, Arndt [59,96]. For field matching, also special techniques have been applied, such as the transverse resonance method, Sorrentino [91], Sorrentino, Itoh [48], Bornemann, Arndt [96]. Hybrid combinations of the field-matching and MM methods have been applied for solving discontinuities at inhomogeneous waveguide structures by Arndt et al., Omar et al. [29,52,70,107]. The field-matching method, however, leads to numerically often inefficient indirect eigenvalue problems (e.g., to the necessity of search algorithms for the zeros of a determinant). For waveguide discontinuities

involving nonanalytical eigenvalue problems, therefore, other hybrid combinations, such as the MM/finite-element (MM/FE) method, Beyer, Arndt [123,129], Montejo-Garai, Zarpata [132], are preferred, where the FE cross section solution leads to a numerically more convenient standard explicit eigenvalue problem.

Arndt, Bornemann, Vahldiek applied 1981 [31] the MM method has been applied [131] for the rigorous analysis and optimization of E-plane metal-insert filters. A detailed description of the MM technique in terms of full-wave scattering matrix parameters for cascaded waveguide structures applied for optimized filters and transformers has been presented by Patzelt and Arndt [34]. The direct application of the full-wave scattering matrix (generalized scattering matrix, GSM) formalism [31,34] for cascaded waveguide discontinuities including evanescent modes leads to a numerically stable description of composed waveguide components and circuits also applicable to all higher-order modes.

Besides the GSM combination of discontinuities, the generalized admittance, e.g., [79] and generalized impedance matrices e.g., [121,146] (GAM, GIM) have been applied. Although there were initially some discussions regarding advantages and disadvantages with preference for GSM, GAM, or GIM combinations, all three formulations lead to nearly the same order of efficiency [142]. It is also worth mentioning that many new terms and formulations, introduced in many publications basically for the MM method, mostly describe the same (MM) approach with—at best—some only marginal modifications. This phenomenon obviously also results from the fact that the MM method can be interpreted [102] as a special case of Harrington's method of moments, [16] when using orthogonal eigenfunctions as basis functions.

Waveguide discontinuity problems for different port planes, with applications such as T-, X-, and six-port junctions, and magic tees, — have been solved by the MM method mostly either utilizing Kühn's resonator method [26] [e.g., 35,42,49,64,78,103,110,115] or Sharp's Green function technique [12] [e.g., 104,105]. A three-plane [7] MM method has been applied [101,140] by Zaki et al.

For scattering problems at the waveguide discontinuity to open space, the MM method has been used in conjunction with the method of moments [32,39,68,82,87] by Kühn, Hombach, James, and Arndt et al. The plane-wave spectrum in half-space combination is applied in [65] by Encinar, Rebolgar.

Although analytic solutions of the waveguide cross section eigenvalue problem for the application of the MM method, in addition to rectangular, circular, coaxial waveguides, have also been presented for elliptic waveguide discontinuities by Matras, Bungler, Arndt, Mongiardo, et al. [135,141,149], the applicability of the efficient MM method is greatly extended by using the MM/FE technique mentioned above [123,129,132]. In this way, for instance, the inclusion of waffle-iron, dual-mode, ridged waveguide, and combine filters is possible [142,143,148,154,160].

To extend the flexibility of the MM technique for applications to arbitrarily shaped planar waveguide structures, Reiter and Arndt introduced 1992 the boundary contour MM (BCMM) method [108,130]. A wideband modeling of planar waveguide structures is also possible

by the efficient boundary integral resonant-mode expansion (BIRME) method [138,139,153] (Conciauro et al., 1996). Arbitrarily shaped 3D waveguide structures can be included by a hybrid MM/method-of-moment (MM/MoM) technique, which was been introduced by Bungler, Arndt, 2000 [150].

Oliner stated in his overview [43] that the “network formulation of microwave field theory has been fundamental to the rapid progress made by the microwave community.” In view of the extremely high efficiency of the MM technique combined with the elegant completeness of the rigorous full-wave generalized scattering matrix formulations of waveguide circuits, I would like to append: MM techniques and their hybrid combinations are about to realize a microwave engineers' dream of achieving CAD tools for rigorous, optimized waveguide component designs within extremely short response times on a PC.

In this article, we will describe some basic relations of the MM method, and discuss some advanced aspects. Representative application examples will demonstrate the versatility and computational speed of the MM method.

2. THEORY

2.1. Mode Matching at a Step Discontinuity

Step discontinuities between two homogeneous waveguides (Fig. 1) are basic key building blocks, by which many other elements and components can be composed, including irises, transitions, bifurcations, iris filters, diplexers, and transformers. Moreover, the basic principles of the MM technique can be well elucidated at a step discontinuity.

At the plane of discontinuity $z=0$, the tangential electromagnetic field components E_{ti} , H_{ti} at the plane of discontinuity $z=0$ can either be described using Maxwell's equations directly (e.g., see Refs. 91 and 119 where explicit mode-matching formulations for some simple step discontinuities are given), or one can apply the more elegant description via vector potentials or Hertzian potentials (e.g. [11]). Matching of the tangential field components ultimately leads to a relation of forward (a_i)- and backward (b_i)-traveling or evanescent modes (also designated as incident or scattered modes) described by their amplitude coefficients a_i , b_i , respectively, which are advantageously normalized to the complex apparent power transmitted through the common aperture A of the discontinuity

$$a^2, b^2 = \iint_A \underline{\underline{E}}_{tp,r} \times \underline{\underline{H}}_{tp,r} dA \quad (1)$$

such that a mode amplitude of $a_i = 1\sqrt{W}$, $b_i = 1\sqrt{W}$, at $z=0$ transports an apparent power of amount 1 W through the cross-section A of the waveguide in forward (p) or backward (r) direction, respectively.

In this way, a more general description when matching the tangential field components along the transverse surface of the general step discontinuity from region I to II (Fig. 1) is possible, yielding directly the relation between

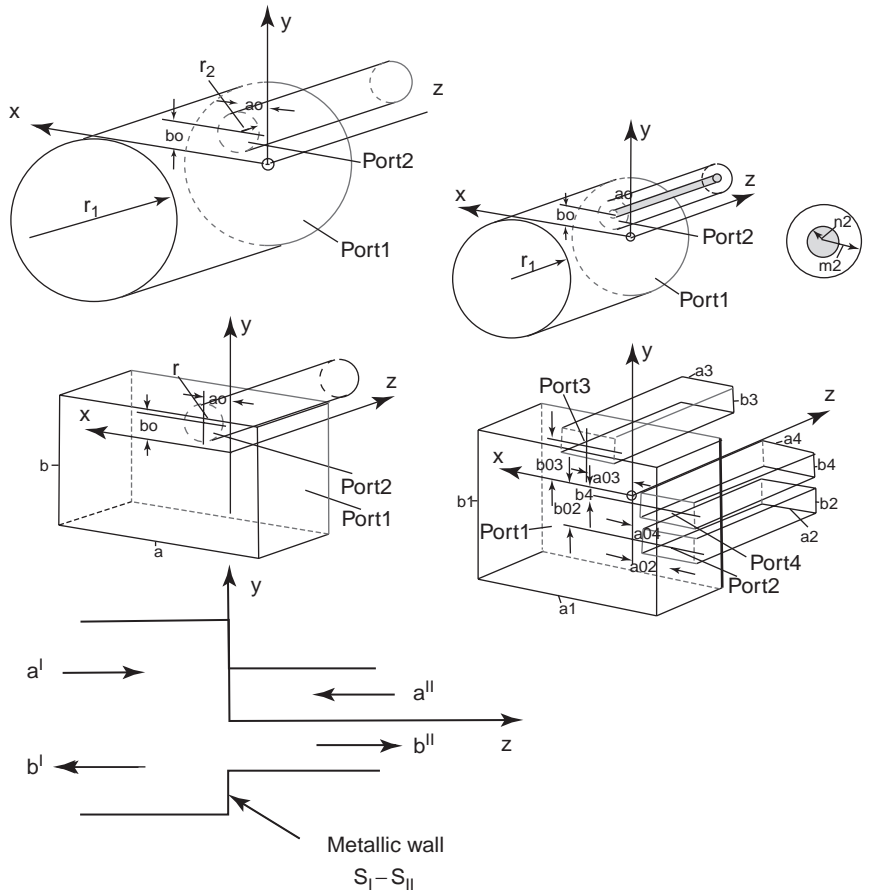


Figure 1. Some step discontinuity key building blocks between two homogeneous waveguides.

incident and scattered mode amplitude coefficients **a** and **b**, e.g. [34,142]

$$\sqrt{Z_i^I}(a_i^I + b_i^I) = \sum_{j=1}^{\infty} C_{ij} \sqrt{Z_j^{II}}(a_j^{II} + b_j^{II}) \quad i=1 \dots \infty \quad (2)$$

$$\sum_{i=1}^{\infty} C_{ij} \sqrt{Y_i^I}(a_i^I - b_i^I) = \sqrt{Y_j^{II}}(a_j^{II} - b_j^{II}) \quad j=1 \dots \infty,$$

where $Z = 1/Y$ are the modal wave impedances

$$Z_i = \frac{1}{Y_i} = \begin{cases} \frac{\omega\mu}{\beta_i} & \text{TE modes} \\ \frac{\beta_i}{\omega\epsilon} & \text{TM modes} \\ \sqrt{\frac{\mu}{\epsilon}} & \text{TEM modes} \end{cases} \quad (3)$$

with $j\beta = \gamma$, the propagation factor determined by the separation equation (7). The mode amplitude coefficients in (2) are related to the normalized voltages U and currents I introduced by Marcuvitz [7] by

$$\frac{U_i}{\sqrt{Z_i}} = u_i = a_i + b_i \quad (4)$$

$$I_i \sqrt{Z_i} = i_i = a_i - b_i$$

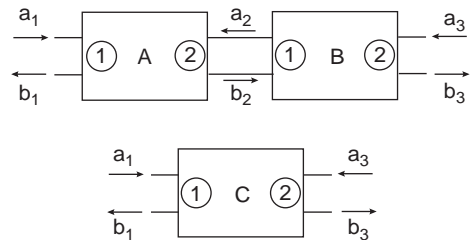


Figure 2. Scattering matrix combination of two cascaded structures.

C_{ij} in (2) are the elements of the frequency independent¹ coupling matrix

$$C_{ij} = \int_{S_{II}} \int \mathbf{e}_i^T \mathbf{e}_j^{II} dS = \int_{S_{II}} \int \mathbf{h}_i^{I*} \mathbf{h}_j^{II} dS \quad (5)$$

where \mathbf{e} and \mathbf{h} are the transversal eigenvectors

$$\mathbf{e} = \begin{cases} \mathbf{u}_z \times \nabla_t \Psi & \text{TE modes} \\ -\nabla_t \Psi & \text{TM and TEM modes} \end{cases} \quad (6)$$

$$\mathbf{h} = \mathbf{u}_z \times \mathbf{e}$$

¹Note that this holds only for this kind of structures like step discontinuities in z direction. For cavities, for instance, Fig. 3, C_{ij} relating to different planes are frequency dependent.

with \mathbf{u}_z is the unit vector in the z direction, and \mathbf{T} denotes the transposed. The potentials Ψ are for TE- and/or TM-mode solutions of the 2D Helmholtz equation

$$\nabla_t^2 \Psi + k_c^2 = 0 \quad (7)$$

with the separation condition

$$k_c^2 + \beta^2 = k^2 \quad (8)$$

where k is the free-space wavenumber, and $\nabla_t^2 = \nabla^2 - (\partial^2/\partial z^2)$ denotes the transversal Laplace operator. For TEM modes, Ψ are solutions of the Laplacian equation

$$\nabla_t^2 \Psi = 0 \quad (9)$$

The potentials Ψ are suitably normalized:

$$\iint_{S_j} \nabla_t^T \Psi_i \nabla_t \Psi_i dS = 1 \quad (10)$$

The Dirichlet and Neumann boundary conditions are

$$\begin{aligned} \Psi^{TM} = 0 \quad \Gamma_E & \quad \frac{\partial \Psi^{TM}}{\partial n} = 0 \quad \Gamma_M \quad (\text{TM modes}) \\ \frac{\partial \Psi^{TE}}{\partial n} = 0 \quad \Gamma_E & \quad \Psi^{TE} = 0 \quad \Gamma_M \quad (\text{TE modes}) \\ \Psi_i^{\text{TEM}} = \begin{cases} \text{const} \neq 0 & \Gamma_{Ei} \\ 0 \text{ else} & \Gamma_E \end{cases} & \quad \frac{\partial \Psi_i^{\text{TEM}}}{\partial n} = 0 \quad \Gamma_M \quad (i\text{th TEM mode}) \end{aligned} \quad (11)$$

where Γ denotes an electric (E) or magnetic (M) wall.

2.2. Generalized Scattering Matrix

Equation (2) can be represented in the form of a matrix equation by using either the incident and scattered mode amplitude coefficients \mathbf{a} and \mathbf{b}

$$\begin{aligned} \mathbf{a}^I + \mathbf{b}^I &= \mathbf{V}(\mathbf{a}^{II} + \mathbf{b}^{II}) \\ \mathbf{V}^T(\mathbf{a}^I - \mathbf{b}^I) &= \mathbf{a}^{II} - \mathbf{b}^{II} \end{aligned} \quad (12)$$

or by using the normalized voltages \mathbf{u} and currents \mathbf{i} (4)

$$\begin{aligned} \mathbf{u}^I &= \mathbf{V}\mathbf{u}^{II} \\ \mathbf{V}^T\mathbf{i}^I &= \mathbf{i}^{II} \end{aligned} \quad (13)$$

with

$$\begin{aligned} \mathbf{V} &= [\sqrt{\mathbf{Y}^I}] [\mathbf{C}] [\sqrt{\mathbf{Z}^I}] \\ \sqrt{\mathbf{Y}^I} &= \text{diag}(\sqrt{Y^I}) \\ \sqrt{\mathbf{Z}^I} &= \text{diag}(\sqrt{Z^I}) \end{aligned} \quad (14)$$

The formulation in terms of \mathbf{a} and \mathbf{b} (12) leads after rearranging the relations in terms of scattered and incident mode amplitude coefficients directly to the modal generalized scattering matrix (GSM)

$$\mathbf{b} = \mathbf{S}\mathbf{a} = \begin{bmatrix} \mathbf{S}_{11} & \mathbf{S}_{12} \\ \mathbf{S}_{21} & \mathbf{S}_{22} \end{bmatrix} \mathbf{a} \quad (15)$$

with the submatrices and $\mathbf{1}$ the unit matrix

$$\begin{aligned} \mathbf{S}_{11} &= -\mathbf{1} + \mathbf{V}\mathbf{S}_{21} \\ \mathbf{S}_{12} &= \mathbf{V}[\mathbf{1} + \mathbf{S}_{22}] \\ \mathbf{S}_{21} &= 2\mathbf{T}^{-1}\mathbf{V}^T \\ \mathbf{S}_{22} &= \mathbf{T}^{-1}[\mathbf{1} - \mathbf{V}^T\mathbf{V}] \\ \mathbf{T} &= \mathbf{1} + \mathbf{V}^T\mathbf{V} \end{aligned} \quad (16)$$

Note that only the inversion of submatrix \mathbf{T} is required.

From (12)–(16) it can be shown that the GSM \mathbf{S} has the interesting properties being symmetric and self-inverting:

$$\mathbf{S} = \mathbf{S}^T = \mathbf{S}^{-1}. \quad (17)$$

The generalized \mathbf{S} -matrix \mathbf{S} , which includes evanescent modes does not show the familiar unitarity relation for passive circuits. The unitarity holds only if relating to purely propagating waves. It can be shown, however, that the coupling matrix (5) is unitary also for the general case.

$$\mathbf{C}^T\mathbf{C} = \mathbf{1} \quad (17a)$$

Some of these rather well-known relations [18] are put together in Ref. 127, where it is also shown that other matching criteria, such as the conservation of the complex power used e.g., in Ref. 36, lead to identical mode-matching expressions similar to those of (12) and (13), see also Ref. 56. This follows finally from the general orthogonal properties relations for different E , H modes already given in Ref. 11.

In case of rectangular, circular, circular coaxial, and elliptical waveguide discontinuities, the cross section eigenvectors required for the MM technique are given analytically [7,9,11,13–122,141]. For more general cross sections, the corresponding eigenvalue problem can be solved numerically, where formulations by a 2D finite-element (FE) method [123,129,132] are preferred, leading to a fast convergent direct solution without requiring search algorithms that are usually necessary for cross section field matching, e.g., [29,96], or boundary integral approaches [137]. The powerful MM/FE method significantly extends the applicability of the MM method to a wide class of waveguide discontinuities and components, including waveguide structures with ridged, waffle-iron, arbitrarily shaped iris, combine cross-sections [142,143, 148,154,160].

For fastest convergence, it is shown [20,22,23,58] that for a step discontinuity, the ratio of the number of expansion modes used on both sides should be chosen according to the size of the different waveguide cross section areas. This ‘fastest convergence ratio’ [58] is conveniently given automatically when selecting a fixed cutoff frequency up to which all higher-order modes are included on both sides [142]. For usual step discontinuities, a cutoff frequency of about 10–40 times the highest analysis frequency has given excellent convergence and agreement with measurements [142].

For industrial microwave component design optimizations using rigorous EM methods, losses are commonly neglected, since an optimum solution for the lossless case leads also to the optimum solution for the lossy case. Moreover, finite measured insertion losses are due mainly to parameters that are often of a rather more statistical nature, such as ohmic contacts between halves of fabricated waveguide housings or surface roughness influences, than of a finite metal conductivity nature. Nevertheless, the MM method offers the possibility to include losses due to finite metallic conductivity, if required, by appropriate MM in a rather straightforward manner [145].

The complete required information for a multiport discontinuity (e.g., step-to-multiaperture waveguide; see Fig. 1) is inherently involved in the corresponding single discontinuity [83,85]. Hence, multiport discontinuities such as *n* furcations can be formulated by merely using corresponding matrix schemes utilizing the *S* matrix of a single step as submatrix [77,83,85].

2.3. Line Integral Formulation of Coupling Integrals

The frequency-independent coupling area integrals (5) can be formulated in terms of numerically somewhat more convenient line integrals by using the common definitions of the transversal eigenvectors (6) [142,156]:

$$\begin{aligned}
 & \frac{k^2 c_{II}}{k_{cII}^2 - k_{cI}^2} \oint_{\Gamma_{II}} \Psi^{II} \frac{\partial \Psi^I}{\partial n} dc && \text{TE-TE} \\
 & 0 && \text{TE-TE and TEM-TE} \\
 & - \oint_{\Gamma_{II}} \Psi^{II} \frac{\partial \Psi^I}{\partial \tau} dc && \text{TE-TE and TEM-TE} \\
 & \frac{k_{cI}^2}{k_{cI}^2 - k_{cII}^2} \oint_{\Gamma_{II}} \Psi^I \frac{\partial \Psi^{II}}{\partial n} dc && \text{TM-TM} \\
 & \oint_{\Gamma_{II}} \Psi^I \frac{\partial \Psi^{II}}{\partial n} dc && \text{TE-TE and TEM-TE} \\
 & 0 && \text{TEM-TM}
 \end{aligned} \tag{18}$$

In case of degenerate modes ($k_{cI} = k_{cII}$), an adequate expression for the limiting case $k_{cI} \rightarrow k_{cII}$ has to be taken into account [157].

2.4. Orthogonality of Eigenmodes

An important property of the transversal eigenvectors \mathbf{e} and \mathbf{h} (6) is their orthogonality [11]. In case of degenerate eigenmodes, that is, modes as a solution of (9) of same

cutoff frequency, namely, same eigenvalue ($k_{ci} = k_{cj}$), the orthogonality has to be enforced.

The scalar product of two eigenvectors be defined as follows:

$$\begin{aligned}
 \langle \mathbf{e}_i, \mathbf{e}_j \rangle &= \int_{\Omega} \int \mathbf{e}_i^T \mathbf{e}_j d\Omega = \int_{\Omega} \int \mathbf{h}_i^T \mathbf{h}_j d\Omega \\
 &= \int_{\Omega} \int \mathbf{u}_z^T (\mathbf{e}_i^T \times \mathbf{h}_j) d\Omega
 \end{aligned} \tag{19}$$

For orthogonal eigenvectors their scalar product is zero [11]. With (6), (7), and (11), we obtain after partial integration

$$\langle \mathbf{e}_i, \mathbf{e}_j \rangle = \begin{cases} \int_{\Gamma} \psi_i \frac{\partial \psi_j}{\partial n} d\Gamma + k_{cj}^2 \int_{\Omega} \psi_i \psi_j d\Omega \\ = \int_{\Gamma} \psi_j \frac{\partial \psi_i}{\partial n} d\Gamma + k_{ci}^2 \int_{\Omega} \psi_i \psi_j d\Omega \\ i, j \text{ of same mode type} \\ - \int_{\Gamma} \psi_i \frac{\partial \psi_j}{\partial t} d\Gamma = 0, \quad i \text{ TE}, j \text{ TM or TEM} \\ \int_{\Gamma} \psi_i \frac{\partial \psi_j}{\partial n} d\Gamma = 0, \quad i \text{ TM}, j \text{ TEM} \end{cases} \tag{20}$$

where “*t*” designates the tangential direction.

For the first case, the contour integrals are zero if *i* and *j* are of type TE or TM:

$$\langle \mathbf{e}_i, \mathbf{e}_j \rangle = 0, \quad k_{ci}^2 \neq k_{cj}^2 \quad \text{and} \quad i, j \text{ same mode type} \tag{21}$$

That is: Two eigenvectors are orthogonal if they are of different mode types or if they are of same mode type and have different cutoff frequencies. These features are summarized in Ref. 11.

For degenerate eigenmodes, two or more eigenvectors of the same type have the same eigenvalue (same cutoff frequency) and hence the same propagation factor (8). Therefore, any linear combination of degenerate eigenmodes is also a degenerate eigenmode [11]. As there are only a finite number of degenerate eigenmodes \tilde{e}_i , their orthogonality can be enforced by using the Gram–Schmidt orthogonalization [165], where e_i is the recursively determined new orthogonal eigenvector:

$$\begin{aligned}
 e_1 &= \tilde{e}_1 \\
 e_i &= \tilde{e}_i - \sum_j^{i-1} \langle \tilde{e}_i, e_j \rangle e_j
 \end{aligned} \tag{22}$$

$$\langle e_i, e_i \rangle = 1$$

2.5. Cascaded Elements

The generalized scattering matrix (GSM) of a cascaded microwave circuit *C* (Fig. 2) consisting of two partial components *A* and *B* is given by a straight-forward

numerically stable matrix combination, where $[1]$ is the unit matrix:

$$\begin{aligned} [S_{11}^C] &= [S_{11}^A] + [S_{12}^A][S_{11}^B][Q][S_{21}^A] \\ [S_{12}^C] &= [S_{12}^A]([1] + [S_{11}^B][Q][S_{22}^A])[S_{12}^B] \\ [S_{21}^C] &= [S_{21}^B][Q][S_{21}^A] \\ [S_{22}^C] &= [S_{22}^B] + [S_{21}^B][Q][S_{22}^A][S_{12}^B] \\ [Q] &= ([1] - [S_{22}^A][S_{11}^B])^{-1}. \end{aligned} \quad (23)$$

The GSM \mathbf{S}_e of a structure described by a GSM \mathbf{S} containing at all ports i homogeneous waveguide sections of lengths l_i is

$$\begin{aligned} [S_e] &= [D][S][D] \\ [D] &= [\text{diag}(\exp(-j\beta l_i))] \end{aligned} \quad (24)$$

In this way, based on the single-step discontinuity, a complete class of waveguide structures can conveniently be described, including transformers, irises, filters, diplexers, and polarizers. Typical examples can be found in the literature [31,33–35,37,38,42,46,47,49–51,53–55,60,63,64,66,67,74,78–106,109–126] an overview is also given in Refs. 119,142 and 153.

For modes below their cutoff frequencies, the propagation factor $\gamma = j\beta$ is real. It is therefore obvious that the numerical effort can be significantly reduced by considering only modes in the cascading process for which the amount of $\exp(-\gamma l)$ is higher than a defined limiting value. These modes, which contribute significantly, are called *accessible modes* [27]. The set of modes of higher number applied at the immediate discontinuity is called *localized modes*.

2.6. Generalized Admittance, Impedance Matrices

Besides the generalized scattering matrix GSM \mathbf{S} (15), the generalized admittance matrix (GAM) \mathbf{Y} , the generalized impedance matrix (GIM) \mathbf{Z} and the transmission matrix \mathbf{W} have been applied in the literature [57,79,104,105,121,122]. The GAM and GIM descriptions of a step discontinuity require additional waveguide sections of finite length at the ports. Based on normalized voltages and currents (4) and the relations (12), the corresponding expressions can be derived [57,79,104,105,121,122]. The relationships between \mathbf{S} , \mathbf{Y} , and \mathbf{Z} are given by

$$\begin{aligned} [Y] &= ([1] - [S])([1] + [S])^{-1} \\ [S] &= ([1] - [Y])([1] - [Y])^{-1} \\ [S] &= ([Z] - [1])([Z] - [1])^{-1} \end{aligned} \quad (25)$$

The transmission matrix \mathbf{W} is only applicable for same number of modes of the ports. Moreover, \mathbf{W} is numerically instable as the implied $\exp(-\gamma l)$ and $\exp(+\gamma l)$ expressions can exceed the available numerical range of the corre-

sponding computer for large γl . The \mathbf{S} , \mathbf{Y} , \mathbf{Z} formulations have their advantages and disadvantages. By selecting appropriate reference planes and applying adequate segmentation techniques [166,167], \mathbf{Y} , \mathbf{Z} can be set up for boundary enlargement and boundary reduction structures, respectively, without requiring the solution of an equation system [79,104,105,121,122,153]. On the other hand, for cascaded structures when taking the reduction according to accessible modes into account, \mathbf{Y} , \mathbf{Z} representations require the solution of an entire equation system of the form

$$(i_a) = ((y_{aa}) - (y_{al})(y_{ll}) - (\mathbf{1}))^{-1}(y_{la})(u_a) \quad (26)$$

where the subscripts “ a ” and “ l ” denote the corresponding accessible and localized terms, respectively. For the reduced \mathbf{Z} matrix, we obtain an identical expression. This is in contrast to the \mathbf{S} -matrix description, where we need only deleting the corresponding submatrix elements in (23).

The combination of \mathbf{Y} , \mathbf{Z} with an empty waveguide requires higher computational effort than the multiplication with diagonal matrices (24) for \mathbf{S} . Hence, a simple variation of the intermediate lengths, such as during optimization, is more time-consuming. Moreover, if a section length falls in the vicinity of half a wavelength of a propagating mode, there is the possibility of numerical instability in the expressions for \mathbf{Y} , \mathbf{Z} . Finally, as the generalized S matrix for describing the behavior of a microwave structure is usually desired, \mathbf{Y} - and \mathbf{Z} -matrix formulations have to be converted to the S matrix according to (25), which requires an additional matrix inversion. To sum up, it is meanwhile commonly adopted that the criterion of the computational effort, as seen on a global average, does not justify the exclusive preference for a specific matrix representation.

2.7. T-, X-, and Six-Port Junctions

Many waveguide components include structures with apertures in different planes (Fig. 3), such as corners and T and X junctions. Kühn’s resonator method [26] applied for the calculation of the S parameters of a waveguide corner leads, for instance, via superposition

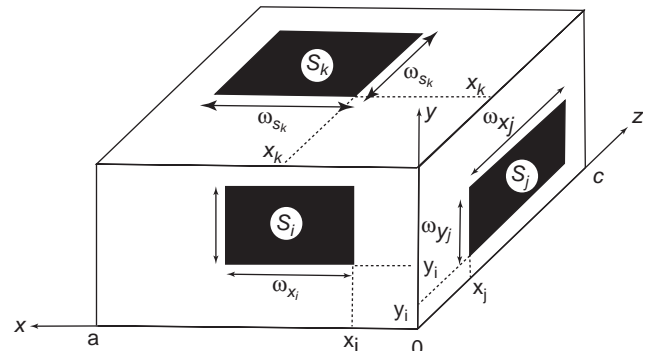


Figure 3. Rectangular cavity with port apertures in different planes.

of the two standing-wave solutions of short-circuited 90° degree waveguides of the two ports I and II in a common “resonator” region, to an equation system of the form [83,103]

$$\begin{pmatrix} \mathbf{a}^I - \mathbf{b}^I \\ \mathbf{a}^{II} - \mathbf{b}^{II} \end{pmatrix} = \begin{bmatrix} [D^I][Q] \\ [Q^T][D^{II}] \end{bmatrix} \begin{pmatrix} \mathbf{a}^I + \mathbf{b}^I \\ \mathbf{a}^{II} + \mathbf{b}^{II} \end{pmatrix} \quad (27)$$

where $[D]$ are diagonal matrices and $[Q]$ is a frequency-dependent matrix, which describes the coupling between the ports. Analog expressions can be derived for T-, X-, and six-port junctions [78,83,85,99,103,110,115].

Sharp’s [12] cavity method leads directly to generalized admittance expressions of the form

$$Y_{mn}^{eh(i,j)} = j\omega \iint_{S_j/S_i} \mathbf{n} \times \mathbf{e}_n^{h(j)}(\mathbf{r}) \underline{G}(\mathbf{r}, \mathbf{r}') \mathbf{h}_m^{h(i)}(\mathbf{r}') dr' \quad (28)$$

with the aperture eigenvectors (6), and the Green function G of the cavity. The corresponding descriptions for T-, X-, and six-port structures can be found in the literature [12,79,88,100,104,153].

Both formulations are nearly equivalent in terms of efficiency with the condition that for Sharp’s method both eigenfunctions of the apertures and the cavity Green function are given analytically.

2.8. Arbitrarily Shaped Planar Structures

Many waveguide components include arbitrarily shaped planar waveguide structures (Fig. 4), such as mitred bends, cylindrical posts, Y-junctions, steps or irises with finite radii, and shaped cavities. For such structures, the boundary contour MM method (BCMM) is applied [108,130]. The basic idea is to describe the arbitrarily shaped contour between the k -port apertures by a complete set of cylindrical mode functions, which leads to a set of linear equations

$$\mathbf{T}\boldsymbol{\alpha} = \mathbf{E}(\mathbf{a} + \mathbf{b}) \quad (29)$$

where the elements of the matrix \mathbf{T} are the coupling integrals of the field vectors of the cavity region. Because of the nonorthogonality of these field vectors at the

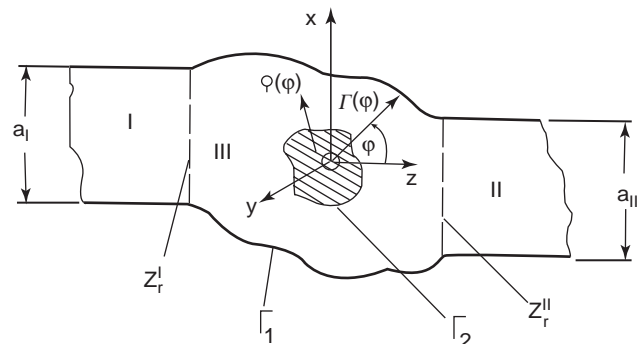


Figure 4. Arbitrarily shaped planar waveguide structure.

boundary, the matrix is not diagonal. The matrix \mathbf{E} describes the expansion of the electric field in the waveguide ports by cylindrical wavefunctions in the cavity region.

The excitation coefficients $\boldsymbol{\alpha}$ can be eliminated, which yields the generalized S -matrix at the k -port junction in the form

$$\mathbf{S} = (\mathbf{I} - \mathbf{C})^{-1}(\mathbf{I} + \mathbf{C}) \quad (30)$$

with

$$\mathbf{C} = \frac{1}{j\eta} \mathbf{E}^T \mathbf{T}^{-1} \mathbf{E} \quad (31)$$

η is the free space characteristic impedance. A second method for such structures is the hybrid MM/transfinite-element method [157], which has the advantage over the BCMM of higher flexibility, for example, as it is not restricted by possibly shaded regions in the description of the boundary region. In this way, septated T junctions, for instance, can also be efficiently calculated.

The boundary integral resonant-mode expansion (BIRME) method [138,139,153] is a third method, which applies a wideband pole expansion representation of the admittance matrix expressions. This method has been described [138,139,153] mainly for H -plane- or E -plane-type of modes, so far.

2.9. Arbitrarily Shaped Cross Sections

For arbitrarily shaped cross sections, such as for cross irises and ridged waveguide structures, the hybrid MM/finite-element (MM/FE) method is advantageously applied. This hybrid combination extends the applicability of the MM method to the inclusion of a comprehensive class of components [142], such as waffle-iron filters, dual-mode filters with coupling screws, and cross-irises.

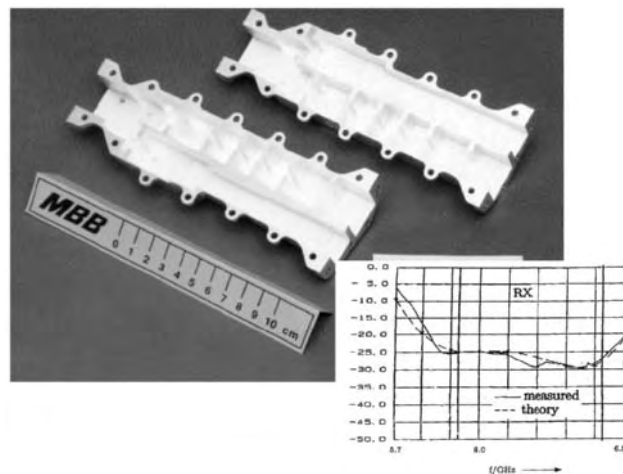


Figure 5. Optimized C-band satellite diplexer. Photograph and measured results by courtesy of MBB (now EADS), Prof. Fasold, Germany. (This figure is available in full color at <http://www.mrw.interscience.wiley.com/erfme>.)

2.10. Radiating Apertures and Arbitrarily Shaped 3D-Structures

Radiating apertures can be included in the MM method by applying a hybrid MM/method-of-moments (MoM) technique. The same is true for arbitrarily shaped 3D waveguide structures, such as partial-height posts within a partially open circular cavity (e.g., suitable for combline filter elements) [142,150,157,164].

3. SOME TYPICAL APPLICATION EXAMPLES

A classical satellite industry component example [90], illustrating the current state of the art design of advanced

microwave components by fast MM techniques and direct full-wave optimization, is the C-band diplexer shown in Fig. 5. The compact component (silver-plated aluminum housing) without tuning screws has been fabricated by a computer-controlled milling technique. For the optimization of such components, the evolution strategy [64] is advantageously applied. Typical MM method CPU speeds on standard PCs for such components showing excellent accuracy with measurements are in the order of merely fractions of a second per frequency point. This may illustrate the high computational power of the MM technique for the CAD and optimization of advanced waveguide components.

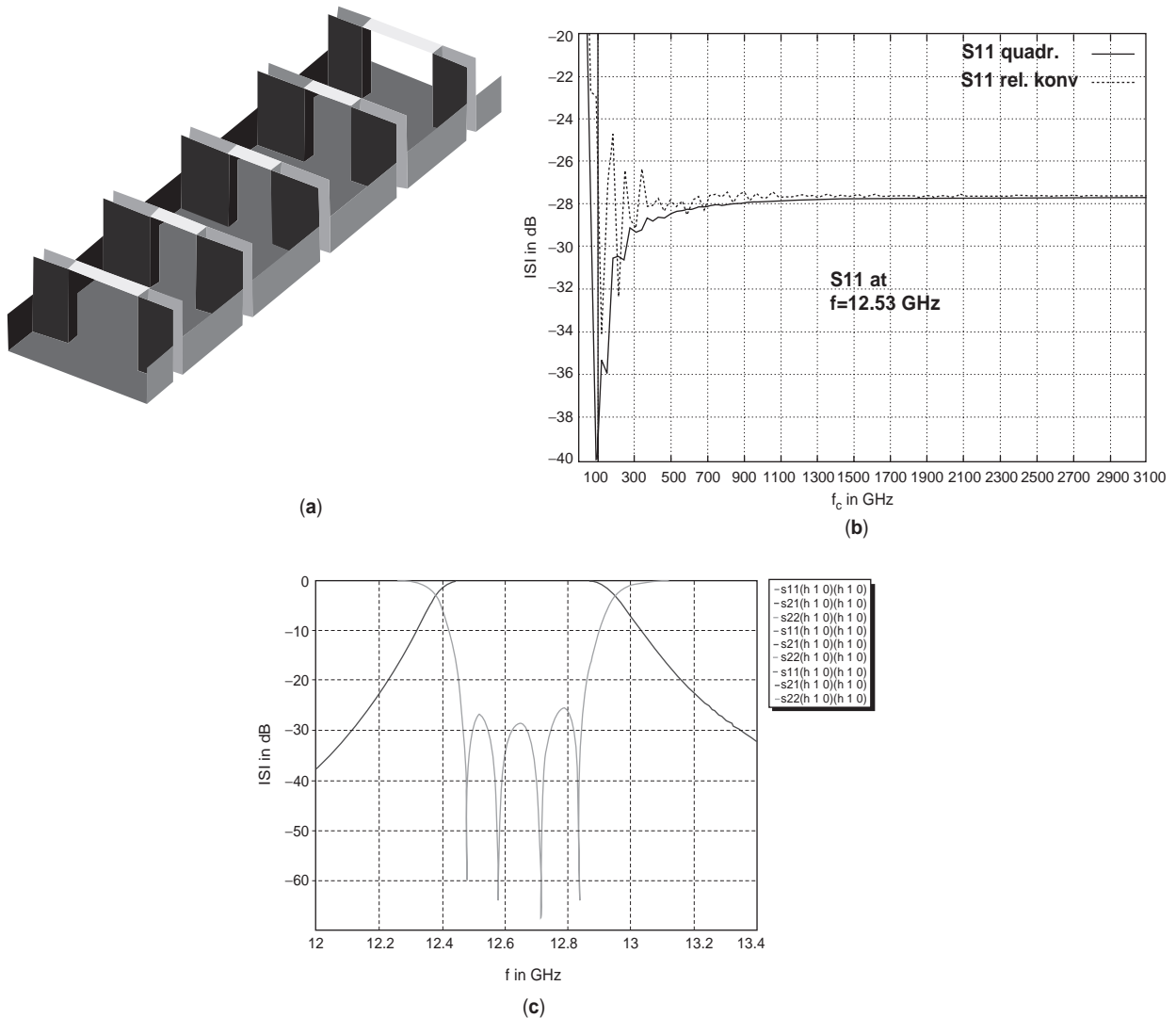


Figure 6. WR-75 H-plane iris filter example. Dimensions (mm): $a = 19.05$, $b = 9.525$, iris widths $a_1 = 9.600$, $a_2 = 6.385$, $a_3 = 5.860$, iris thickness $z_1 = 2$, resonator lengths $l_1 = 12.030$, $l_2 = 13.600$: (a) structure; (b) convergence behavior. Solid line—fastest convergence, localized modes at step discontinuity sides chosen according to given cutoff frequency f_c ; dashed line—number of localized modes identical on both sides. (c) S parameters: (1) for $f_c = 1100$ GHz, two accessible modes in resonator; (2) for $f_c = 3100$ GHz, two accessible modes in resonator; (3) for $f_c = 3100$ GHz, all localized modes in resonator (the results are identical within drawing accuracy). MM CPU speed for case 1:5 s, 500 frequency points (i.e., 10 ms/frequency point). PC: 3 GHz P4. (This figure is available in full color at <http://www.mrw.interscience.wiley.com/erfme>.)

The next example is a simple *H*-plane iris-coupled WR-75 waveguide filter (Fig. 6a), illustrating some basic features of the MM technique outlined in the previous section. Figure 6b shows the convergence behavior S_{11} as a function of cutoff frequency up to which all higher-order modes are taken into account. The fastest convergence (solid line) is achieved for choosing the number of modes at the discontinuity side according to given cutoff frequency f_c . In Fig. 6c, complete identity for the *S* parameters within drawing accuracy is demonstrated for the cases (1) $f_c = 1100$ GHz (70 localized modes, 2 accessible modes),

(2) $f_c = 3100$ (197 localized modes, 2 accessible modes), (3) $f_c = 3100$ (197 localized modes, 197 accessible modes). The MM CPU speed for this example (case 1) is ~ 10 ms per frequency point (3 GHz P4 PC) for the *S*-matrix formulation. The *Y*-matrix formulation leads to nearly identical speed (factor 1.2 slower), while for this example the *Z*-matrix formulation is about factor 4.2 slower.

On the basis of the MM techniques described above, many examples have been published in the literature showing the broad application potential of this efficient CAD technique. Typical waveguide components, which

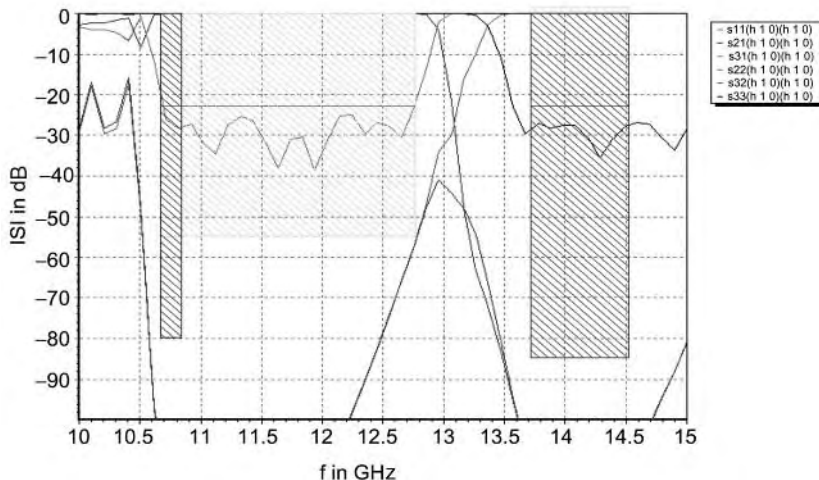
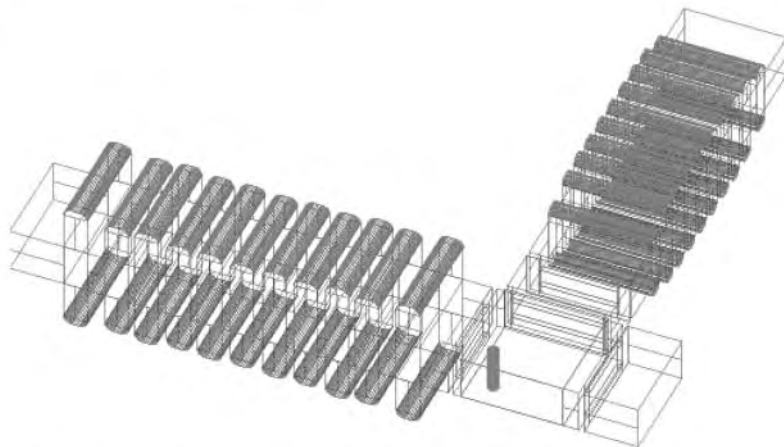
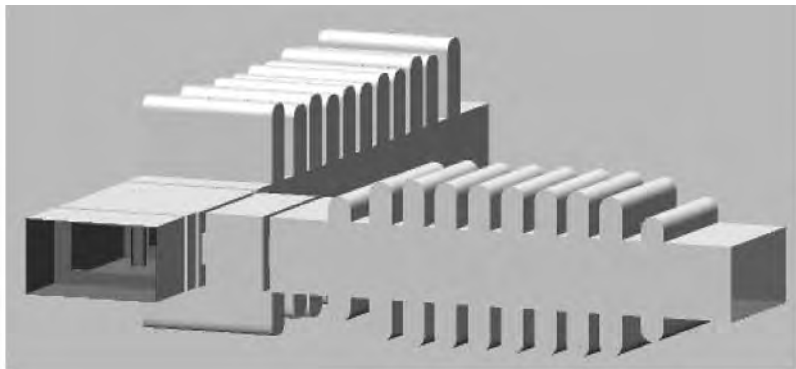


Figure 7. WR-75 diplexer with stub-loaded waveguide sections and post compensated T junction. Result of direct full-wave optimization by applying the MM technique. CPU speed: 0.5 s/frequency point, 3 GHz P4 PC, 19 modes. (This figure is available in full color at <http://www.mrw.interscience.wiley.com/erfme>.)

have been successfully designed by direct MM full-wave optimization, include many kinds of waveguide filters [31, 33, 34, 37, 38, 41, 46, 50, 61–63, 66, 67, 75, 76, 84, 89, 93, 96, 98, 99, 106, 109, 113, 117, 119, 123, 129, 132, 138, 139, 142, 143, 148, 153–155, 158, 160], mode sensors/converters [42, 55, 87, 113], transformers [47, 74, 95], couplers [35, 49, 64, 79, 88, 94, 97, 100, 104, 111, 119, 162, 163], polarizers [44, 53, 60], phase shifters [43, 51, 73, 80, 97, 105, 119, 145], diplexers [54, 83, 90, 119], multiplexers [81, 85, 124, 134, 143, 161] power dividers [77, 78, 142], and orthomode transducers [114, 119].

A typical WR-75 diplexer example, which includes some advanced MM elements, such as postcompensated T-junction and stub-loaded waveguides with rounded corners for convenient milling fabrication, is shown in Fig. 7. Because of the high CPU speed also for more complicated structures when applying the MM method (in this example ~ 0.5 s per frequency point; 3 GHz P4 PC), the direct full-wave optimization toward the given specifications is a straightforward task. The stubs are (instead of steps) modeled by X junctions; hence a rather low number of modes (19 higher-order modes in this example) has proved to be sufficient for convergence and excellent agreement with measurements.

The applicability of the MM method for waveguide components with arbitrarily shaped cross sections, for radiating structures, and for arbitrarily shaped 3D waveguide structures, is extended by hybrid techniques.

Because of the importance of these more recent extensions of the MM method [155, 157], CAD techniques based on hybrid methods are described in a separate article in this encyclopedia.

4. CONCLUSION

The mode-matching (MM) method is one of the oldest electromagnetics (EM)-based methods for the rigorous solution of waveguide discontinuity problems. The technical importance of the MM technique is its extremely high computational efficiency together with high accuracy and dynamic range. MM techniques and their hybrid combinations achieve CAD tools for rigorous, optimized waveguide component designs within extremely short response times on a PC. The article has presented an overview of the state of the art of MM techniques and described some more recent advances. The versatility and high calculation speed of the MM techniques is well documented in the literature in many examples, which have found widespread application in the microwave industry.

BIBLIOGRAPHY

- J. R. Whinnery and H. W. Jamieson, Equivalent circuits for discontinuities in transmission lines, *Proc. IRE* **32**:98–116 (Feb. 1944).
- J. R. Whinnery, H. W. Jamieson, and T. E. Robbins, Coaxial-line discontinuities, *Proc. IRE* **32**:695–709 (Nov. 1944).
- W. C. Hahn, A new method for the calculation of cavity resonators, *J. Appl. Phys.* **12**:62–68 (Jan. 1941).
- R. Courant and D. Hilbert, *Boundary problems of microwave physics (in German)*, Springer, Berlin, 1931.
- J. A. Stratton, *Electromagnetic Theory*, McGraw-Hill, New York, 1941.
- C. G. Montgomery, R. H. Dicke, and E. M. Purcell, *Principles of Microwave Circuits*, McGraw-Hill, New York, 1948.
- N. Marcuvitz, *Waveguide Handbook*, McGraw-Hill, New York, 1951.
- K. Kurokawa, The expansion of electromagnetic fields in cavities, *IRE Trans. Microwave Theory Tech.* **MTT-6**: 178–187 (April 1958).
- S. Ramo and J. R. Whinnery, *Fields and Waves in Modern Radio*, Wiley, New York, 1960.
- J. Schwinger and D. S. Saxon, *Discontinuities in Waveguides*, Gordon & Breach, New York, 1968.
- R. E. Collin, *Field Theory of Guided Waves*, McGraw-Hill, New York, 1960.
- E. D. Sharp, An exact calculation for a T-junction of rectangular waveguides having arbitrary cross-sections, *IEEE Trans. Microwave Theory Tech.* **MTT-15**:109–116 (Feb. 1967).
- P. J. B. Clarricoats and K. R. Slinn, Numerical solutions of waveguide-discontinuity problems, *Proc. IEE* **114**:878–886 (July 1967).
- A. Wexler, Solution of waveguide discontinuities by modal analysis, *IEEE Trans. Microwave Theory Tech.* **MTT-15**:508–517 (Sept. 1967).
- G. Piefke, The application of eigenfunction expansion to scattering problems in finite domains (in German), *Arch. El. Übertragungstechnik (AEÜ)* **22**:275–281 (May 1968).
- R. F. Harrington, *Field Computation by Moment Methods*, Macmillan, New York, 1968.
- H. D. Knetsch, Offset axes in circular waveguides with arbitrary radii (in German), *Arch. El. Übertragungstechnik (AEÜ)* **23**:23–32 (Jan. 1969).
- H. D. Knetsch, Contribution to the theory of stepped cross-section discontinuities of waveguides (in German), *Arch. El. Übertragungstechnik (AEÜ)* **22**:591–600 (Dec. 1968).
- K. Kurokawa, *An Introduction to the Theory of Microwave Circuits*, Academic Press, New York, 1969.
- P. H. Masterman and P. J. B. Clarricoats, Computer field-matching solution of waveguide transverse discontinuities, *Proc. IEE* **118**:51–63 (Jan. 1971).
- G. Kowalski and R. Pregla, Dispersion characteristics of shielded microstrips with finite thickness, *Arch. El. Übertragungstechnik (AEÜ)* **25**:193–196 (April 1971).
- S. W. Lee, W. J. Jones, and J. J. Campbell, Convergence of numerical solutions of iris-type discontinuity problems, *IEEE Trans. Microwave Theory Tech.* **MTT-19**:528–536 (June 1971).
- R. Mittra, T. Itoh, and T. S. Li, Analytical and numerical studies of the relative convergence phenomenon arising in the solution of an integral equation by the moment method, *IEEE Trans. Microwave Theory Tech.* **MTT-20**:96–104 (Feb. 1972).
- I. Wolff, G. Kompa, and R. Mehran, Calculation method for microstrip discontinuities and T-junctions, *Electron. Lett.* **8**:177–179 (April 1972).
- L. B. Felsen and N. Marcuvitz, *Radiation and Scattering of Waves*, Prentice-Hall, Englewood Cliffs, NJ, 1972.

26. E. Kühn, A mode-matching method for solving field problems in waveguide and resonator circuits, *Arch. El. Übertragungstechnik (AEÜ)* **27**:510–518 (April 1973).
27. T. Rozzi and W. F. G. Mecklenbräuker, Wide-band network modelling of interacting inductive irises and steps, *IEEE Trans. Microwave Theory Tech.* **MTT-23**:235–245 (Feb. 1976).
28. L. Lewin, The E-plane taper junction in rectangular waveguide, *IEEE Trans. Microwave Theory Tech.* **MTT-27**:560–563 (June 1979).
29. F. Arndt and G. U. Paul, The reflection definition of the characteristic impedance of microstrips, *IEEE Trans. Microwave Theory Tech.* **MTT-27**:724–731 (Aug. 1979).
30. F. Arndt, The orthogonal expansion method for solving electromagnetic scattering problems in finite millimeter-wave structures, *Proc. Colloque sur le Traitement du Signal et ses Applications*, Nice, 1981, pp. 593–598.
31. F. Arndt, J. Bornemann, D. Grauerholz, and R. Vahldieck, Low-insertion loss fin-line filters for millimeter applications, *EuMC Int. Microwave Symp. Digest*, Amsterdam, The Netherlands, Sept. 1981, pp. 309–314.
32. G. L. James, Analysis and design of TE₁₁-to-HE₁₁ corrugated cylindrical waveguide mode converters, *IEEE Trans. Microwave Theory Tech.* **MTT-29**:1059–1066 (Oct. 1981).
33. F. Arndt, J. Bornemann, D. Grauerholz, and R. Vahldieck, Theory and design of low-insertion loss fin-line filters, *IEEE Trans. Microwave Theory Tech.* **MTT-30**:155–163 (Feb. 1982).
34. H. Patzelt and F. Arndt, Double-plane steps in rectangular waveguide and their application for transformers, irises and filters, *IEEE Trans. Microwave Theory Tech.* **MTT-30**:771–777 (May 1982).
35. F. Arndt, D. Ellermann, H. W. Haeusler, and J. Strube, Field theory analysis and numerical synthesis of symmetrical multiple-branch waveguide couplers, *Frequenz* **36**:262–266 (Oct. 1982).
36. R. Safavi-Naini and R. H. McPhie, Scattering at rectangular-to-rectangular waveguide junctions, *IEEE Trans. Microwave Theory Tech.* **MTT-30**:2060–2063 (Nov. 1982).
37. J. Bornemann, R. Vahldieck, F. Arndt, and D. Grauerholz, Optimized low-insertion-loss millimetre-wave fin-line and metal insert filters, *Radio Electron. Eng. (Inst. IRE)* **52**:513–521 (Nov./Dec. 1982).
38. R. Vahldieck, J. Bornemann, F. Arndt, and D. Grauerholz, Optimized waveguide E-plane metal insert filters for millimeter-wave applications, *IEEE Trans. Microwave Theory Tech.* **MTT-31**:65–69 (Jan. 1983).
39. E. Kühn and V. Hombach, Computer-aided analysis of corrugated horns with axial ring or ring-loaded radial slots, *Proc. ICAP 83 Part I*, UK, March 1983, pp. 293–296.
40. J. Strube and F. Arndt, Three-dimensional higher-order mode analysis of transition from waveguide to shielded dielectric image guide, *Electron. Lett.* **19**:306–307 (April 1983).
41. J. Bornemann, F. Arndt, R. Vahldieck, and D. Grauerholz, Double planar integrated millimeter-wave filter, *Proc. 13th European Microwave Conf.*, Nürnberg, 1983, pp. 168–173.
42. H. Schmiedel and F. Arndt, Numerical synthesis of simple waveguide mode sensors, *Proc. 13th European Microwave Conf.*, Nürnberg, 1983, pp. 733–738.
43. F. Arndt, J. Bornemann, and R. Vahldieck, Design of multi-section impedance-matched dielectric-slab filled waveguide phase shifters, *IEEE Trans. Microwave Theory Tech.* **MTT-32**:34–39 (Jan. 1984).
44. F. Arndt, U. Tucholke, and T. Wriedt, Broadband dual-depth E-plane corrugated square waveguide polariser, *Electron. Lett.* **29**(11):458–459 (May 24, 1984).
45. A. A. Oliner, Historical perspectives on microwave field theory, *IEEE Trans. Microwave Theory Tech.* **MTT-32**:1022–1045 (Sept. 1984).
46. F. Arndt, J. Bornemann, R. Vahldieck, and D. Grauerholz, E-plane integrated circuit filters with improved stopband attenuation, *IEEE Trans. Microwave Theory Tech.* **MTT-32**:1391–1394 (Oct. 1984).
47. F. Arndt, U. Tucholke, and T. Wriedt, Computer-optimized multisection transformers between rectangular waveguides of adjacent frequency bands, *IEEE Trans. Microwave Theory Tech.* **MTT-32**:1479–1484 (Nov. 1984).
48. R. Sorrentino and T. Itoh, Transverse resonance analysis of finline discontinuities, *IEEE Trans. Microwave Theory Tech.* **MTT-32**:1633–1638 (Dec. 1984).
49. F. Arndt, B. Koch, H.-J. Orlok, and N. Schroeder, Field theory design of rectangular waveguide broad-wall metal-insert slot couplers for millimeter-wave applications, *IEEE Trans. Microwave Theory Tech.* **MTT-33**:95–104 (Feb. 1985).
50. F. Arndt, J. Bornemann, C. Piontek, and H. Schueler, Shunt-inductance-coupled waveguide filters with expanded second stopband, *Electron. Lett.* **21**(6):238–239 (March 1985).
51. F. Arndt, A. Frye, M. Wellnitz, and R. Wirsing, Double dielectric-slab-filled waveguide phase shifter, *IEEE Trans. Microwave Theory Tech.* **MTT-33**:373–381 (May 1985).
52. J. Strube and F. Arndt, Rigorous hybrid-mode analysis of the transition from rectangular waveguide to shielded dielectric image guide, *IEEE Trans. Microwave Theory Tech.* **MTT-33**:391–401 (May 1985).
53. F. Arndt, W. Tucholke, and T. Wriedt, Design of a wide-band compact square waveguide polariser, *Electron. Lett.* **21**(12):517–518 (June 1985).
54. F. Arndt, J. Bornemann, D. Grauerholz, D. Fasold, and N. Schroeder, Waveguide E-plane integrated-circuit diplexer, *Proc. Electron. Lett.* **21**:615–617 (July 1985).
55. H. Schmiedel and F. Arndt, Mode transducer utilizing asymmetric waveguide narrow-wall coupling, *Proc. 15th European Microwave Conf.*, Paris, Sept. 1985, pp. 737–742.
56. R. R. Mansour and R. H. McPhie, Scattering at an N-furcated parallel plate waveguide junction, *IEEE Trans. Microwave Theory Tech.* **MTT-33**:1052–1059 (Sept. 1985).
57. A. S. Omar and K. Schünemann, Transmission matrix representation of finline discontinuities, *IEEE Trans. Microwave Theory Tech.* **MTT-33**:765–770 (Sept. 1985).
58. T. S. Chu, T. Itoh, and Y.-C. Shih, Comparative study of mode-matching formulations for microstrip discontinuity problems, *IEEE Trans. Microwave Theory Tech.* **MTT-33**:1018–1023 (Oct. 1985).
59. J. Bornemann and F. Arndt, Calculating the characteristic impedance of finlines by transverse resonance method, *IEEE Trans. Microwave Theory Tech.* **MTT-34**:85–92 (Jan. 1986).
60. U. Tucholke, F. Arndt, and T. Wriedt, Field theory design of square waveguide iris polarizers, *IEEE Trans. Microwave Theory Tech.* **MTT-34**:156–160 (Jan. 1986).
61. J. Bornemann and F. Arndt, Metal-insert filters with improved characteristics, *IEE Proc.* **133**(Part H)(2):103–107 (April 1986).
62. J. Bornemann and F. Arndt, Metallic E-plane filter with cavities of different cutoff frequency, *Electron. Lett.* **22**:524–525 (May 1986).

63. F. Arndt, D. Heckmann, H. Semmerow, J. Bornemann, and R. Vahldieck, Stopband optimized E-plane filters with multiple metal inserts of variable number per coupling element, *IEE Proc.* **133**(Part H):169–174 (June 1986).
64. H. Schmiedel and F. Arndt, Field theory design of rectangular waveguide multiple-slot narrow wall couplers, *IEEE Trans. Microwave Theory Tech.* **MTT-34**:791–798 (July 1986).
65. J. A. Encinar and J. M. Rebollar, Convergence of numerical solutions of open-ended waveguide by modal analysis and hybrid modal-spectral techniques, *IEEE Trans. Microwave Theory Tech.* **MTT-34**:809–814 (July 1986).
66. R. Vahldieck, J. Bornemann, F. Arndt, and W. J. R. Hoefler, TE₁₀-mode filters formed by multilayered-dielectric slabs in waveguides below cut-off, *Proc. 16th European Microwave Conf.*, Dublin, Sept. 1986, pp. 275–280.
67. F. Arndt, J. Bornemann, D. Heckmann, C. Piontek, H. Semmerow, and H. Schueler, Modal-S-matrix method for the optimum design of inductively direct-coupled cavity filters, *IEE Proc.* **133**(Part H):341–350 (Oct. 1986).
68. F. Arndt, L. Bruenjes, R. Heyen, F. Siefken-Herrlich, and K. H. Wolff, Finite two dimensional array of rectangular waveguides including reactive elements, *Proc. JINA Conf.*, Nice, France, Nov. 1986, pp. 301–305.
69. R. R. Mansour and R. H. McPhie, An improved transmission matrix formulation of cascaded discontinuities and its application to E-plane circuits, *IEEE Trans. Microwave Theory Tech.* **MTT-34**:1490–1498 (April 1995).
70. A. S. Omar and K. Schünemann, The effect of complex modes at finline discontinuities, *IEEE Trans. Microwave Theory Tech.* **MTT-34**:1508–1514 (Dec. 1986).
71. K. Wolff, T. Wriedt, F. Arndt, and U. Tucholke, Hybrid field design of square potter horns, *Proc. 5th Int. Conf. Antennas and Propagation*, ICAP 87, March 1987, pp. 210–213.
72. A. S. Omar and K. F. Schünemann, Complex and backward-wave modes in inhomogeneously and anisotropically filled waveguides, *IEEE Trans. Microwave Theory Tech.* **MTT-35**:268–275 (March 1987).
73. J. Uher, F. Arndt, and J. Bornemann, Field theory design of ferrite-loaded waveguide nonreciprocal phaseshifters with multisection ferrite or dielectric slab impedance transformers, *IEEE Trans. Microwave Theory Tech.* **MTT-35**:552–560 (June 1987).
74. J. Bornemann and F. Arndt, Modal-S-matrix design of optimum stepped ridged and finned waveguide transformers, *IEEE Trans. Microwave Theory Tech.* **MTT-35**:561–567 (June 1987).
75. J. Uher, J. Bornemann, and F. Arndt, Ferrite tunable metal insert filter, *Electron. Lett.* **23**:804–806 (1986).
76. F. Arndt and R. Kasper, Field theory design of waveguide E-plane iris coupled low-pass filters, *SBMO Int. Microwave Symp. Digest*, Rio de Janeiro, July 1987, pp. 321–326.
77. J. Dittloff, J. Bornemann, and F. Arndt, Computer aided design of optimum E- or H-plane N-furcated waveguide power dividers, *Proc. 17th European Microwave Conf.*, Rome, Sept. 1987, pp. 181–186.
78. F. Arndt, I. Ahrens, U. Papziner, U. Wiechmann, and R. Wilkeit, Optimized E-plane T-junction series power dividers, *IEEE Trans. Microwave Theory Tech.* **MTT-35**:1052–1059 (Nov. 1987).
79. F. Alessandri, G. Bartolucci, and R. Sorrentino, Admittance matrix formulation of waveguide discontinuity problems: Computer-aided design of branch-guide directional couplers, *IEEE Trans. Microwave Theory Tech.* **MTT-36**:394–403 (Feb. 1988).
80. J. Dittloff, F. Arndt, and D. Grauerholz, Optimum design of waveguide E-plane stub-loaded phase shifters, *IEEE Trans. Microwave Theory Tech.* **MTT-36**:583–587 (March 1988).
81. J. Dittloff and F. Arndt, Rigorous design of septate E-plane multiplexers with printed circuit elements, *1988 IEEE MTT-S Int. Microwave Symp. Digest*, New York, May 1988, pp. 431–434.
82. F. Arndt, J. Tebbe, and H. Paradies, Reactively loaded rectangular waveguide arrays with unequal apertures, *Proc. JINA Conf.*, Nice, France, Nov. 1988, pp. 353–357.
83. J. Dittloff and F. Arndt, Computer-aided design of slit-coupled H-plane T-junction diplexers with E-plane metal-insert filters, *IEEE Trans. Microwave Theory Tech.* **MTT-36**:1833–1840 (Dec. 1988).
84. J. Uher, F. Arndt, and J. Bornemann, Computer-aided design and improved performance of tunable ferrite-loaded E-plane integrated circuit filters for millimeter wave applications, *IEEE Trans. Microwave Theory Tech.* **MTT-36**:1841–1849 (Dec. 1988).
85. J. Dittloff and F. Arndt, Rigorous field theory design of millimeter-wave E-plane integrated circuit multiplexers, *IEEE Trans. Microwave Theory Tech.* **MTT-37**:340–350 (Feb. 1989) (special issue on quasiplanar millimeter wave components and subsystems).
86. F. Arndt, K.-H. Wolff, J. Bruenjes, R. Heyen, F. Siefken-Herrlich, W. Bothmer, and E. Forger, Generalized moment method analysis of planar reactively loaded rectangular waveguide arrays, *IEEE Trans. Anten. Propag.* **AP-37**:329–338 (March 1989).
87. T. Wriedt, K.-H. Wolff, F. Arndt, and U. Tucholke, Rigorous hybrid field theoretic design of stepped rectangular waveguide mode converters including the horn transitions into halfspace, *IEEE Trans. Anten. Propag.* **AP-37**:780–790 (June 1989).
88. P. L. Carle, Multiport branch waveguide couplers with arbitrary power splitting, *1989 MTT-S Int. Microwave-Symp. Digest*, Long Beach, CA, Sept. 1989, pp. 317–320.
89. J. Bornemann and F. Arndt, Rigorous design of evanescent-mode E-plane finned waveguide bandpass filters, *1989 MTT-S Int. Microwave-Symp. Digest*, Long Beach, CA, June 1989, pp. 603–606.
90. F. Arndt, J. Dittloff, U. Papziner, D. Fasold, N. Nathrath, and H. Wolf, Rigorous field theory design of compact and light-weight broadband diplexers for satellite communication systems, *Proc. 19th European Microwave Conf.*, London, Sept. 1989, pp. 1214–1219.
91. T. Itoh, ed., *Numerical Techniques for Microwave and Millimeter-Wave Passive Structures*, Wiley, New York, 1989.
92. R. Sorrentino, ed., *Numerical Methods for Passive Microwave and Millimeter Wave Structures*, IEEE Press, New York, 1989.
93. F. Arndt, T. Duschak, U. Papziner, and P. Rolappe, Asymmetric iris coupled cavity filters with stopband poles, *1990 MTT-S Int. Microwave-Symp. Digest*, Dallas, May 1990, pp. 215–218.
94. F. Arndt, T. Sieverding, and P. Anders, Rigorous modal-S-matrix design of a new class of broadband 180-degree branch guide couplers, *1990 MTT-S Int. Microwave-Symp. Digest*, Dallas, May 1990, pp. 577–580.
95. J. Bornemann and F. Arndt, Optimum field theory design of stepped E-plane finned waveguide transformers of different

- inner cross-sections, *1990 MTT-S Int. Microwave-Symp. Digest*, Dallas, May 1990, pp. 1071–1074.
96. J. Bornemann and F. Arndt, Transverse resonance, standing wave, and resonator formulations of the ridge waveguide eigenvalue problem and its application to the design of E-plane finned waveguide filters, *IEEE Trans. Microwave Theory Tech.* **MTT-38**:1104–1113 (Aug. 1990).
 97. F. Arndt, T. Sieverding, and P. Anders, Optimum field theory design of broad-band E-plane branch guide phase shifters and 180-degree couplers, *IEEE Trans. Microwave Theory Tech.* **MTT-38**:1854–1861 (Dec. 1990).
 98. F. Arndt and U. Papziner, Modal-S-matrix design of microwave filters composed of rectangular and circular waveguide elements, *1991 MTT-S Int. Microwave Symp. Digest*, Boston, June 1991, pp. 535–538.
 99. F. Arndt and T. Sieverding, The rigorous CAD of aperture-coupled T-junction bandstop-filters, E-plane circuit elliptic-function filters and diplexers, *MTT-S Int. Microwave Symp. Digest*, Boston, June 1991, pp. 1103–1106.
 100. F. Alessandri, M. Mongiardo, and R. Sorrentino, Transverse segmentation: A novel technique for the efficient CAD of 2N-port branch-guide couplers, *IEEE Microwave Guided Wave Lett.* **1**:204–207 (Aug. 1991).
 101. X. P. Liang, A. Zaki, and A. E. Atia, A rigorous three-plane mode-matching technique for characterizing waveguide T-junctions, and its application to multiplexer design, *IEEE Trans. Microwave Theory Tech.* **MTT-39**:2138–2147 (Dec. 1991).
 102. J. J. H. Wang, *Generalized Moment Methods in Electromagnetics*, Wiley, New York, 1991.
 103. T. Sieverding and F. Arndt, Field theoretic CAD of open or aperture matched T-junction coupled rectangular waveguide structures, *IEEE Trans. Microwave Theory Tech.* **MTT-40**:353–362 (Feb. 1992).
 104. F. Alessandri, G. Bartolucci, and R. Sorrentino, Computer-aided design of beam forming networks for modern satellite antennas, *IEEE Trans. Microwave Theory Tech.* **MTT-40**:1117–1127 (June 1992).
 105. F. Alessandri, M. Mongiardo, and R. Sorrentino, A technique for the fullwave automatic synthesis of waveguide components: Application to fixed phase shifters, *IEEE Trans. Microwave Theory Tech.* **MTT-40**:1484–1495 (July 1992).
 106. J. Bornemann and F. Arndt, Modal-S-matrix design of metal finned waveguide components and its application to transformers and filters, *IEEE Trans. Microwave Theory Tech.* **MTT-40**:1528–1537 (July 1992).
 107. R. Ihmels and F. Arndt, Rigorous modal S-matrix analysis of the cross-iris in rectangular waveguides, *IEEE Microwave Guided Wave Lett.* **2**:400–402 (Oct. 1992).
 108. J. M. Reiter and F. Arndt, A boundary contour mode-matching method for the rigorous analysis of cascaded arbitrary shaped H-plane discontinuities in rectangular waveguides, *IEEE Microwave Guided Wave Lett.* **2**:403–405 (Oct. 1992).
 109. U. Papziner and F. Arndt, Field theoretical computer-aided design of rectangular and circular iris coupled rectangular or circular waveguide cavity filters, *IEEE Trans. Microwave Theory Tech.* **MTT-41**:462–471 (March 1993).
 110. T. Sieverding and F. Arndt, Modal analysis of the magic tee, *IEEE Microwave Guided Wave Lett.* **3**:150–152 (May 1993).
 111. T. Sieverding, J. Bornemann, and F. Arndt, Rigorous design of sidewall aperture couplers, *MTT-S Int. Microwave Symp. Digest*, Atlanta, June 1993, pp. 761–764.
 112. R. Keller and F. Arndt, Rigorous modal analysis of the asymmetric rectangular iris in circular waveguide, *IEEE Microwave Guided Wave Lett.* **3**:185–187 (June 1993).
 113. R. Ihmels and F. Arndt, Field theory CAD of L-shaped iris coupled mode launchers and dual-mode filters, *MTT-S Int. Microwave Symp. Digest*, Atlanta, June 1993, pp. 765–768.
 114. R. Ihmels, U. Papziner, and F. Arndt, Field theory design of a corrugated septum OMT, *MTT-S Int. Microwave Symp. Digest*, Atlanta, June 1993, pp. 909–912.
 115. T. Sieverding and F. Arndt, Rigorous analysis of the rectangular waveguide six-port cross junction, *IEEE Microwave Guided Wave Lett.* **3**:185–187 (June 1993).
 116. F. Arndt, U. Papziner, and R. Bohl, Field theory CAD of profiled corrugated rectangular or circular horns by an efficient full-wave modal-S-matrix method, *AP-S Int. Antennas and Propagation Symp. Digest*, Ann Arbor, MI, June 1993, pp. 1026–1029.
 117. W. Hauth, R. Keller, U. Papziner, R. Ihmels, T. Sieverding, and F. Arndt, Rigorous CAD of multiport coupled rectangular waveguide components, *EuMC Int. Microwave Symp. Digest*, Madrid, Sept. 1993, pp. 611–614.
 118. P. Guillot, P. Couffignal, and H. Baudrand, Improvement in calculation of some surface integrals: Application to junction characterization in cavity filter design, *IEEE Trans. Microwave Theory Tech.* **MTT-41**:2156–2160 (Dec. 1993).
 119. J. Uher, J. Bornemann, and U. Rosenberg, *Waveguide Components for Antenna Feed Systems: Theory and CAD*, Artech House, Boston, 1993.
 120. J. M. Rebollar, J. Esteban, and J. E. Page, Full-wave analysis of three and four-port rectangular waveguide junctions, *IEEE Trans. Microwave Theory Tech.* **MTT-42**:256–263 (Feb. 1994).
 121. M. Guglielmi, G. Gheri, M. Calamia, and G. Pelosi, Rigorous multimode network representation of inductive steps, *IEEE Trans. Microwave Theory Tech.* **MTT-42**:317–326 (Feb. 1994).
 122. M. Guglielmi and G. Gheri, Rigorous multimode network representation of capacitive steps, *IEEE Trans. Microwave Theory Tech.* **MTT-42**:622–628 (April 1994).
 123. R. Beyer and F. Arndt, Field-theory design of circular waveguide dual-mode filters by a combined mode matching finite element method, *EuMC Int. Microwave Symp. Digest*, Cannes, France, Sept. 1994, pp. 294–299.
 124. T. Sieverding and F. Arndt, Combined circuit-/field-theory CAD procedure for manifold multiplexers with circular cavities, *EuMC Int. Microwave Symp. Digest*, Cannes, France, Sept. 1994, pp. 437–442.
 125. R. Keller and F. Arndt, Rigorous CAD of rectangular aperture coupled circular waveguide multi-mode filters, *EuMC Int. Microwave Symp. Digest*, Cannes, France, Sept. 1994, pp. 1337–1342.
 126. A. A. Melcon and M. Guglielmi, Multimode network representation of two dimensional steps in rectangular waveguides, *EuMC Int. Microwave Symp. Digest*, Cannes, France, Sept. 1994, pp. 1943–1948.
 127. G. V. Eleftheriades, A. S. Omar, L. P. B. Katehi, and G. M. Rebeiz, Some important properties of waveguide junction generalized scattering matrices in the context of the mode matching technique, *IEEE Trans. Microwave Theory Tech.* **MTT-42**:1896–1903 (Oct. 1994).
 128. F. Alessandri, M. Mongiardo, and R. Sorrentino, Rigorous mode matching analysis of mitered E-plane bends in

- rectangular waveguide, *IEEE Microwave Guided Wave Lett.* **4**: 408–410 (Dec. 1994).
129. R. Beyer and F. Arndt, Efficient modal analysis of waveguide filters including the orthogonal mode coupling elements by an MM/FE method, *IEEE Microwave Guided Wave Lett.* **5**:9–11 (Jan. 1995).
 130. J. M. Reiter and F. Arndt, Rigorous analysis of arbitrarily shaped H- and E-plane discontinuities in rectangular waveguides by a full-wave boundary contour mode-matching method, *IEEE Trans. Microwave Theory Tech.* **MTT-43**:796–801 (April 1995).
 131. R. Beyer and F. Arndt, The generalized scattering matrix separation technique combined with the MM/FE Method for the efficient modal analysis of a comprehensive class of 3D passive waveguide circuits, *MTT-S Int. Microwave Symp. Digest*, Orlando, May 1995, pp. 277–280.
 132. J. R. Montejo-Garai and J. Zapata, Full-wave design and realization of multicoupled dual-mode circular waveguide filters, *IEEE Trans. Microwave Theory Tech.* **MTT-43**: 1290–1297 (June 1995).
 133. H.-W. Yao, K. A. Zaki, A. E. Atia, and R. Hershtig, Full wave modelling of conducting posts in rectangular waveguides and its applications to slot coupled combline filters, *IEEE Trans. Microwave Theory Tech.* **MTT-43**:2824–2380 (Dec. 1995).
 134. W. Hauth, R. Keller, T. Sieverding, U. Papziner, and F. Arndt, *Design of Compact Satellite-Channel Filters and Multiplexers*, HF Report, Feb. 1996, pp. 44–48 (in German).
 135. P. Matras, R. Bunger, and F. Arndt, Mode-matching analysis of the step discontinuity in elliptical waveguides, *IEEE Microwave Guided Wave Lett.* **6**:143–145 (March 1996).
 136. A. A. Melcon, G. Connor, and M. Guglielmi, New simple procedure for the computation of the multimode admittance or impedance matrix of planar waveguide junctions, *IEEE Trans. Microwave Theory Tech.* **MTT-44**:413–418 (March 1996).
 137. W. Schroeder and M. Guglielmi, Boundary integral equation approach to multi-mode Y-matrix characterization of multi-ridged sections in circular waveguide, *IEEE MTT-S Int. Microwave Symp. Digest*, San Francisco, CA, June 1996, pp. 1849–1852.
 138. G. Conciauro, P. Arconi, M. Bressan, and L. Peregrini, Wideband modelling of arbitrary shaped H-plane components by the “boundary integral-resonant mode expansion method,” *IEEE Trans. Microwave Theory Tech.* **MTT-44**:1057–1065 (July 1996).
 139. P. Arconi, M. Bressan, G. Conciauro, and L. Peregrini, Wideband modelling of arbitrary shaped E-plane components by the “boundary integral-resonant mode expansion method,” *IEEE Trans. Microwave Theory Tech.* **MTT-44**:2083–2092 (Nov. 1996).
 140. C. Wang and K. A. Zaki, Full-wave modeling of generalized double-ridged waveguide T-junctions, *IEEE Trans. Microwave Theory Tech.* **MTT-44**:2536–2542 (Dec. 1996).
 141. P. Matras, R. Bunger, and F. Arndt, Modal scattering matrix of the general step discontinuity in elliptical waveguides, *IEEE Trans. Microwave Theory Tech.* **MTT-45**:453–458 (March 1997).
 142. F. Arndt et al., Automated design of waveguide components using hybrid mode-matching/numerical EM building-blocks in optimization oriented CAD frameworks—state of the art and recent advances (invited paper), *IEEE Trans. Microwave Theory Tech.* **MTT-45**:747–760 (May 1997).
 143. R. Beyer, F. Arndt, and W. Hauth, Modal-block-LU-decomposition technique for the efficient CAD of ridged waveguide filters, *MTT-S Int. Microwave Symp. Digest*, Denver, June 1997, Vol. 3, pp. 1235–1238.
 144. R. Beyer and F. Arndt, Efficient hybrid mode-matching/finite-element (MM/FE) method for the design of waveguide components and slot radiators, *MTT-S Int. Microwave Symp. Digest*, Baltimore, June 1998, pp. 1275–1278.
 145. R. Keller, W. Hauth, F.-J. Goertz, F. Arndt, T. Sieverding, and U. Papziner, Fast and rigorous CAD of phase delay equalizers by mode matching techniques including losses, *MTT-S Int. Microwave Symp. Digest*, Baltimore, June 1998, Vol. 2, pp. 921–924.
 146. G. Gerini and M. Guglielmi, Efficient integral equation formulations for admittance or impedance representation of planar waveguide junctions, *MTT-S Int. Microwave Symp. Digest*, Baltimore, June 1998, Vol. 3, pp. 1747–1750.
 147. W. Wessel and F. Arndt, Mode-matching analysis of general waveguide multiport junctions, in *MTT-S Int. Microwave Symp. Digest*, Anaheim, CA, June 1999, pp. 1273–1276.
 148. F. Arndt, R. Beyer, W. Hauth, D. Schmitt, and H. Zeh, Cascaded wide stop band waffle-iron filter designed with a MM/FE CAD method, *EuMC Int. Microwave Symp. Digest*, Munich, Oct. 1999, pp. 186–189.
 149. M. Mongiardo, P. Russer, C. Tomassoni, and L. Felsen, Analysis of N-furcation in elliptical waveguides via the generalized network formulation, *IEEE Trans. Microwave Theory Tech.* **MTT-47**:2473–2478 (Dec. 1999).
 150. R. Bunger and F. Arndt, Moment-method analysis of arbitrary 3D metallic N-port waveguide structures, *IEEE Trans. Microwave Theory Tech.* **MTT-48**:531–537 (April 2000).
 151. A. P. Orfanidis, G. A. Kyriacou, and J. N. Sahalos, A mode-matching technique for the study of circular and coaxial waveguide discontinuities based on closed-form coupling integrals, *IEEE Trans. Microwave Theory Tech.* **MTT-48**:880–883 (May 2000).
 152. M. Mattes, A. A. Melcon, M. Guglielmi, and J. M. Mosig, Impedance representation of waveguide junctions based on the integral equation approach, *EuMC Int. Microwave Symp. Digest*, Oct. 2000, pp. 394–403.
 153. G. Conciauro, M. Guglielmi, and R. Sorrentino, *Advanced Modal Analysis. CAD Techniques for Waveguide Components and Filters*, Wiley, Chichester, UK, 2000.
 154. F. Arndt and J. Brandt, Fast hybrid MM/FE CAD tool for the design and optimization of advanced evanescent mode filters, *MIOP Int. Microwaves and Optronics Symp. Digest*, Stuttgart, May 2001, pp. 369–372.
 155. F. Arndt, J. Brandt, and J. Ritter, MM/FE/FD CAD method for the optimization of waveguide filters including structures of arbitrary shape and coax feeds, *EuMC Int. Microwave Symp. Digest*, London, Sept. 2001, pp. 319–322.
 156. G. Figlia and G. G. Gentili, On the line-integral formulation of mode-matching technique, *IEEE Trans. Microwave Theory Tech.* **MTT-50**:578–580 (Feb. 2002).
 157. F. Arndt, J. Brandt, V. Catina, A. Enneking, and J. Ritter, Fast hybrid MM/FE/transFE/MoM/FD CAD of waveguide components and aperture antennas (invited paper), *Proc. 18th Annual Review of Progress in Applied Computational Electromagnetics (ACES)*, Monterey, CA, March 2002, pp. 1-15–1-23.
 158. J. Kocbach and K. Folgero, Design procedure for waveguide filters with cross-couplings, *2002 Int. Microwave Symp. Digest*, June 2002, Vol. 3, pp. 1449–1452.

159. V. Crino, C. Tomassoni, and M. Mongiardo, Line-integral formulation of the hybrid MM/FEM technique, *IEEE MTT-S Int. Microwave Symp. Digest*, Seattle, WA, June 2002, pp. 2033–2036.
160. F. Arndt and J. Brandt, Direct EM based optimization of advanced waffle-iron and rectangular combline filters, *MTT-S Int. Microwave Symp. Digest*, Seattle, June 2002, pp. 2053–2056.
161. L. Accatino and M. Mongiardo, Hybrid circuit-full-wave computer-aided design of a manifold multiplexers without tuning elements, *IEEE Trans. Microwave Theory Tech.* **MTT-50**:2044–2047 (Sept. 2002).
162. F. Alessandri, M. Giordano, M. Guglielmi, G. Martirano, and F. Vitulli, A new multiple-tuned six-port Riblet-type directional coupler in rectangular waveguide, *IEEE Trans. Microwave Theory Tech.* **MTT-51**:1441–1448 (May 2003).
163. F. Arndt and J. Brandt, Multiport MM/FE technique for the efficient CAD of folded and cross-coupled rectangular combline filters, in *MTT-S Int. Microwave Symp. Digest*, Philadelphia, June 2003, pp. 287–290.
164. F. Arndt, V. Catina, and J. Brandt, Flexible hybrid MM/MoM technique for the CAD and optimization of arbitrarily shaped 3D waveguide components, *EuMC Int. Microwave Symp. Digest*, Munich, Oct. 2003, pp. 343–346.
165. W. H. Press, B. P. Flannery, S. A. Teukolsky, and W. T. Vetterling, *Numerical Recipes in Fortran*, Cambridge Univ. Press, Cambridge, UK, 1986.
166. T. Okoshi, Y. Uehara, and T. Takeushi, The segmentation method—an approach to the analysis of microwave planar circuits, *IEEE Trans. Microwave Theory Tech.* **MTT-24**: 662–668 (Oct. 1976).
167. R. Chadha and K. C. Gupta, Segmentations method using impedance matrices for analysis of planar microwave circuits, *IEEE Trans. Microwave Theory Tech.* **MTT-29**:71–74 (Jan. 1981).

MODULATION-DOPED FETs

LIANGHONG LIU
 HADIS MORKOÇ
 Virginia Commonwealth
 University
 Richmond, Virginia

1. INTRODUCTION

To some extent, the MODFET is the compound semiconductor analog of the ubiquitous MOSFET (metal oxide semiconductor field-effect transistor), which utilizes a pseudo-two-dimensional carrier gas, the concentration of which is modulated by a gate potential. In a MODFET, a higher-bandgap material with a high doping concentration (assumed to be n-type in this discussion) is grown on a lower-bandgap intrinsic material [1]. In practice, growth of a thin intrinsic layer of the high-bandgap material, known as the *intrinsic layer*, *setback layer*, or *spacer*, precedes growth of the rest of the high-bandgap material. Electrons diffuse from the doped higher-bandgap material to the lower-bandgap material where they are confined and form a conducting sheet, a two-dimensional electron

gas (2DEG). When the gate voltage is adequately high so that the source–drain channel is no longer depleted, the 2DEG is free to conduct in the intrinsic material. Because the undoped low-bandgap material has no donor atoms cluttered about, impurity scattering no longer inhibits the carrier mobility and saturation velocity. The spacer mentioned above serves to increase the channel mobility further by shielding the 2DEG from ionized impurities, although at the cost of decreased sheet carrier density.

Major refinements of the MODFET following its introduction have concentrated on improving the sheet carrier concentration through increased band discontinuity ΔE_c by adding and/or increasing the InAs mole fraction in the channel. The conventional MODFET uses AlGaAs and GaAs for the high-bandgap and low-bandgap materials, respectively, denoted as AlGaAs/GaAs, on a GaAs buffer. Carrier density and its confinement in the GaAs improve with increasing ΔE_c , induced by a larger Al mole fraction in $\text{Al}_x\text{Ga}_{1-x}\text{As}$. A technical problem, encountered in MODFETs, is the presence of DX centers whose concentration can be of the same order of magnitude with that of donors in the AlGaAs donor layer. Unfortunately, increased AlAs compositions exacerbate the DX center problem. Typically, DX center traps are mitigated by choosing an Al mole fraction less than 22% at the expense of reducing the conduction band discontinuity and thus the sheet electron concentration [2].

The PMODFET, or pseudomorphic MODFET, alleviates the DX center problem as well as providing a channel in InGaN with superior transport properties over GaAs. The structure is achieved by inserting a thin InGaAs layer between the GaAs buffer and the AlGaAs setback layer in otherwise conventional MODFET. The higher the In mole fraction in $\text{In}_x\text{Ga}_{1-x}\text{As}$, the higher the electron mobility within the 2DEG. Additionally, greater carrier confinement can be achieved with pseudomorphic systems because large conduction band discontinuities can be obtained between InGaAs and low-AlAs-mole-fraction AlGaAs. However, the thickness of the lattice mismatched InGaAs must be below the critical thickness beyond which misfit dislocations occur. The lattice constant, lattice mismatch, and the critical thickness are functions of the In mole fraction of the strained InGaAs layer; this limits the In mole fraction content to about 30% on GaAs. There are also the lattice-matched and pseudomorphic MODFETs based on InP substrates, which take advantage of the superior mobility and confinement properties of the AlInAs/InGaAs. Devices based on InP have exhibited the lowest noise figures yet achieved.

2. SYNOPSIS OF ANALYTICAL DESCRIPTION OF MODFETs

In MODFETs the carriers that form the channel in the lower-bandgap material are donated by the larger higher-bandgap material and/or provided by metal contacts. Since the mobile carriers and their parent donors are spatially separated, ionized impurity scattering is nearly eliminated, which leads to mobilities that are characteristic of nearly pure semiconductor. A Schottky barrier is then used to modulate the mobile charge that in turn

causes a change in the drain current. By virtue of the heterolayer construction, the gate can be placed very close to the conducting channel, which results in large transconductances [1]. A simplified analytical description of MOD-FET operation that shows quantitatively the effect of charge stored at the heterointerface on mobility and carrier velocity follows here. For its simplicity, while making the important points, the model of Drummond et al. [3] will be utilized. Simultaneous solutions of Poisson's and Schrödinger's expressions in the presence of bias must be numerically solved for a more accurate description.

The treatment will begin by stipulating that the amount of charge depleted from the barrier donor layer is equal to the charge accumulated at the interface while the Fermi level is kept constant across the heterointerface. For a visual description, refer to Fig. 1. The electron charge (or hole charge in the case of p-channel MODFET) depleted from the barrier layer is given by

$$n_s = \sqrt{\frac{2eN_d}{q}(\Delta E_c - E_{F2} - E_{F1}) + N_d^2 d_1^2} - N_d d_1 \quad (1)$$

where E_{F2} is the separation between the conduction band in the barrier layer and the Fermi level, N_d is the donor concentration in the barrier layer, ε is the dielectric permittivity of the barrier layer, ΔE_c is the conduction band discontinuity, E_{F1} is the Fermi level with respect to the conduction band edge in the channel layer, and d_1 is the thickness of the undoped layer in the barrier layer at the heterointerface. The electron charge stored at the heterointerface is given by

$$n_s = \frac{\rho kT}{q} \ln \left[(1 + e^{q/kT(E_{F1} - E_0)})(1 + e^{q/kT(E_{F1} - E_1)}) \right] \quad (2)$$

where $E_0 = \gamma_0 n_s^{2/3}$ and $E_1 = \gamma_1 n_s^{2/3}$ are the positions of the first and the second quantum states at the interface, a triangular well formed by the interfacial stored charge. The energy reference is the bottom of the conduction band edge in the smaller bandgap material.

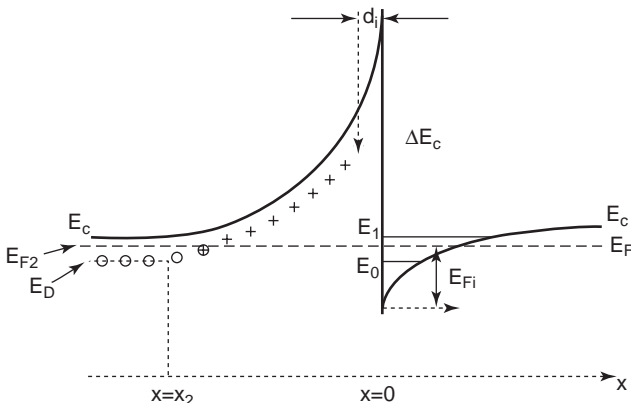


Figure 1. Equilibrium band diagram of a modulation-doped structure with Fermi level, quantum states, and the band discontinuity indicated.

We are assuming here that these lowest energy states are the only ones that are either filled or partially filled. The constants γ_0 and γ_1 , which are dependent on the effective mass of the channel material used, and ρ (density of states = $qm^*/\pi\hbar^2$) are derived in the triangular well. Depending on the value of the voltage applied, the gate on the surface of the barrier layer depletes some or all the stored charge at the interface. Simultaneously solving Eqs. (1) and (2) results in the determination of the Fermi level in case the interface sheet charge concentration is known, or the determination of the sheet charge concentration when the Fermi level is known. With a gate present, Eq. (1), which depicts the equilibrium situation, must be replaced with

$$n_s = \frac{\varepsilon}{qd} [V_g - (q\phi_b - qV_{p2} + E_{F1} - \Delta E_c)] \quad (3)$$

where ϕ_b is the Schottky barrier height of the gate metal deposited on the barrier layer, V_g is the gate to channel voltage, and $V_{p2} = qN_d d_d^2 / 2\varepsilon$. Here d_d is the thickness of the doped barrier layer, and $d = d_d + d_1$. Simultaneous solutions of Eqs. (2) and (3) give the interface charge concentration in the presence of a gate bias. Equation (3) can be conveniently reduced and expressed as

$$n_s = \frac{\varepsilon}{q(d + \Delta d)} (V_g - V_{\text{off}}) \quad (4)$$

with $V_{\text{off}} = \phi_b - \Delta E_c - V_{p2} + \Delta E_{F0}$ and $\Delta d = (\varepsilon a / q)$ ($= 80 \text{ \AA}$ for GaAs). Here the terms ΔE_{F0} and a are determined from the extrapolations. For example, ΔE_{F0} , which is a temperature-dependent quantity, is the residual value of the Fermi level and can be obtained from the extrapolation of the calculated Fermi level values versus the interface sheet charge to the zero sheet charge. The term a is slope of the curve, which is reasonably linear for a wide range of sheet charge except near the vanishing values, relating the Fermi level to the sheet charge, $E_{F1} = \Delta E_{F0}(T) + an_s$. For example, for the GaAs/AlGaAs case, $a \approx 0.125 \times 10^{-16} \text{ V/m}^2$, and $\Delta E_{F0} \approx 0$ at 300 K and 0.025 meV at $T \leq 77 \text{ K}$.

In a field-effect transistor, the drain bias produces a lateral field. In long-channel devices and/or for very small drain biases one normally makes the assumption that the channel voltage, which varies along the channel between the source and the drain and finally reaches a value equal to the drain voltage, is added to the gate potential. Doing so reduces Eq. (4) to

$$n_s = \frac{\varepsilon}{q(d + \Delta d)} (V_g - V_{\text{off}} - V(x)) \quad (5)$$

where $V(x)$ is the channel potential. For small values of $V(x)$, or of the electric field in the channel, we can assume that the constant mobility regime is in effect and that

$$I_d = qn_s \mu Z \frac{dV(x)}{dx} = \mu Z \frac{\varepsilon}{(d + \Delta d)} (V_g - V_{\text{off}} - V(x)) \frac{dV(x)}{dx} \quad (6)$$

where μ is the charge mobility and z is the width of the gate. By integrating Eq. (6) from the source to drain while keeping in mind that the drain current remains constant throughout the channel, one obtains

$$I_d = \beta \left(V_g' V_{ds} - \frac{1}{2} V_{ds}^2 \right) \quad (7)$$

where $V_g' = (V_g - V_{\text{off}})$ and $\beta = \mu Z \{ \varepsilon / [(d + \Delta d)L] \}$ and where L is the intrinsic channel length or more popularly, the gate length. The current reaches saturation when the drain voltage is increased so that the field in the channel exceeds its critical value, thereby causing the velocity to saturate. In that case the drain current is expressed as

$$I_{ds} = Z \frac{\varepsilon}{(d + \Delta d)} (V_g' - V_{ds}) v_s \quad (8)$$

where V_{ds} is the saturation drain voltage, I_{ds} is the saturation current, and v_s is the saturation velocity.

The treatment above is called the *two-piece model*, meaning an abrupt transition from the constant-mobility regime to the constant velocity regime. A more accurate picture is one where this transition is smoother. In that case a phenomenological velocity field relationship can be used to more accurately describe the MODFET operation. The simplest of all these expressions is one that neglects the peak in the velocity field curve and assumes a Si-like velocity field characteristic (see Fig. 7). One such expression is

$$v = \frac{\mu F(x)}{1 + \mu F(x)/v_s} \quad (9)$$

where $F(x)$ represents the electric field in the channel that is equal to $dV(x)/dx$. We must also point out that the field is not constant throughout the channel. To calculate the drain current, one must write the drain current as

$$\begin{aligned} I_d &= v Z \frac{\varepsilon}{(d + \Delta d)} [V_g - V_{\text{off}} - V(x)] \\ &= \frac{\mu dV(x)/dx}{1 + \frac{\mu dV(x)/dx}{v_s}} \frac{\varepsilon Z}{(d + \Delta d)} [V_g - V_{\text{off}} - V(x)] \end{aligned} \quad (10)$$

where $v_s = \mu F_{cr}$, where F_{cr} is the field where the velocity assumes its saturation value. By integrating Eq. (10) from the source end of the channel to the drain end, while keeping in mind that the drain current must be constant throughout, one can obtain an expression for the drain current following the mathematical steps of Ref. 4.

Integrating Eq. (10) from the source end of the gate to the drain end of the gate while keeping in mind that the current must remain constant throughout the channel, one obtains

$$I_d = \frac{\varepsilon Z}{(d + \Delta d)} \left(V_g V_d - \frac{1}{2} V_d^2 \right) \quad (11)$$

Note that if v_s , the saturation velocity, approaches ∞ , Eq. (11) reduces to Eq. (7), which is applicable for the constant mobility case, or the long-channel case. Following the procedure of Lehocvec and Zuleeg [4], the drain saturation current I_{ds} can be found by the mutual use of Eqs. (10) and (11) and assuming velocity saturation, as

$$I_{ds} = 2(V_g - V_{\text{off}})^2 \frac{\varepsilon Z}{L(d + \Delta d)} \frac{1}{\left\{ 1 + \left[\frac{2\mu(V_g - V_{\text{off}})}{v_s L} \right]^{1/2} \right\}^2} \quad (12)$$

The transconductance is an important parameter in FETs and is defined as

$$g_m = \left. \frac{\delta I_d}{\delta V_g} \right|_{V_d = \text{constant}}$$

In the saturation regime, the transconductance is expressed as

$$\begin{aligned} g_m^{\text{sat}} &= \left. \frac{\delta I_{ds}}{\delta V_g} \right|_{V_d = \text{constant}} \\ &= \mu Z \frac{\varepsilon}{(d + \Delta d)L} (V_g - V_{\text{off}}) \left[1 + \left(\frac{V_g - V_{\text{off}}}{v_s} \right)^2 \right]^{-1/2} \end{aligned} \quad (13)$$

The maximum transconductance is obtained when the sheet charge density is fully undepleted under the gate that leads to

$$g_m^{\text{max}} = \frac{q\mu Z n_s}{L} \left[1 + \left(\frac{q\mu n_s (d + \Delta d)}{\varepsilon v_s L} \right)^2 \right]^{-1/2} \quad (14)$$

For very short gate lengths, which represent all modern MODFETs fabricated presently, Eq. (14) reduces to

$$g_m^{\text{max}} = \frac{\varepsilon v_s Z}{d + \Delta d} \quad (15)$$

The measured transconductance is actually smaller than that given in Eq. (15) in that the source resistance, which will be defined shortly, acts as a negative feedback. Through circuit considerations, the measured, extrinsic transconductance is given by

$$g_m^{\text{max}}|_{\text{ext}} = \frac{g_m^{\text{max}}}{1 + R_s g_m^{\text{max}}} \quad (16)$$

High-speed devices are commonly analyzed by two-port scattering measurements performed generally in the range of 2–26 GHz by an on-wafer microwave probe station, although 60 GHz is possible, and this figure is constantly moving upward. From the scattering measurements one can obtain an equivalent circuit for diagnosis and circuit design. From the s parameters one deduces the

y parameters from which an equivalent circuit can be generated.

The transit time under the gate of a submicrometer MODFET is on the order of a few picoseconds. If this is the case, the charging time of the input and the feedback capacitance through the input resistance R_i in the equivalent circuit is substantial. Generally two parameters, the current gain cutoff frequency and maximum oscillation frequency, are figures of merit to gauge the expected high-frequency performance of an FET.

The current gain cutoff frequency, defined as the frequency at which the current gain goes to unity, is given by (since the feedback capacitance is negligible compared to the input capacitance)

$$f_T = \frac{g_m}{2\pi C_{gs}} = \frac{v_s}{2\pi L} \quad (17)$$

As can be seen and as mentioned above, the higher the saturation velocity and the smaller the gate length, the higher the f_T .

The maximum oscillation frequency, defined as the frequency at which the power gain goes to unity, is given by [5]

$$f_{max} = \frac{f_T}{2\sqrt{r_1 + f_T \tau_3}} \quad (18)$$

where $r_1 = (R_g + R_i + R_s)G_d$ and the feedback time constant $\tau_3 = 2\pi R_g C_{dg}$.

Having derived the simple analytical expressions, it is clear that with strained layers, one can increase the band discontinuities and thus the interface sheet carrier densities [Eq. (1)]. This, in turn, leads to larger current levels [Eq. (6)], as compared to the lattice-matched cases. Coupled with large sheet carrier concentrations, higher mobilities offered by the InGaAs alloy are exploited by the strained layer concept. A larger mobility through reduced source resistance leads to a larger transconductance [Eq. (15)], which in turn leads to larger current gains [Eq. (17)] at high frequencies and larger power gains [Eq. (18)]. Better carrier confinement at the heterointerface also aids in confining the carriers and has been shown experimentally to reduce the output conductance G_d . Therefore, the r_1 term discussed above can be reduced, leading to larger f_{max} values.

To analyze the carrier confinement effect, albeit under equilibrium conditions only, Ballingall et al. [6] solved the Schrödinger's and Poisson's equations simultaneously for GaAs/AlGaAs, $\text{In}_x\text{Ga}_{1-x}\text{As}/\text{AlGaAs}$ pseudomorphic, and lattice $\text{In}_{0.53}\text{Ga}_{0.47}\text{As}/\text{In}_{0.52}\text{Al}_{0.48}\text{As}$ MODFETs. As expected, the results clearly show that the larger is the conduction band discontinuity on the donor barrier side as well as on the buffer side, the tighter is the electron distribution. On GaAs substrates, the strained channel MODFET fares better. The confinement gets even better in the structure on InP substrates. If the InGaAs channel on InP contained more InAs than the lattice-matched composition, the confinement as well as the sheet carrier concentration would have been better.

Power gain is also aided by the reduction of parasitic resistances and the time constant τ_3 , which to a large extent depends on the geometry of the device. We will begin our discussion of experimental results by discussing the p-channel MODFETs first, followed by n-channel MODFETs.

3. POWER MODELING

An accurate modeling of device power performance in emerging semiconductor technologies is very useful in understanding how they stack up against more established semiconductor technologies and in determining in which applications they will have the greatest impact. In high-power semiconductor devices, it is imperative that the effect of temperature on device performance be accounted for accurately because power devices typically operate at elevated temperatures.

As in small-signal modeling, the first step in power modeling is to establish the basic device geometric factors that are needed to calculate the current voltage characteristics. Once these are known, the output characteristics superimposed with the load line can be used to get an estimate of the power level that can be obtained from the device provided that it is not limited by the input drive as shown in Fig. 2. In class A operation, the maximum power that can be expected from the drain circuit of a device is given by

$$P_{max} = \frac{I_{d,son}(V_b - V_{knee})}{8} \quad (19)$$

where $I_{d,son}$ is the maximum drain current, V_b is the drain breakdown voltage, and V_{knee} is the knee voltage as shown in Fig. 2. $I_{d,son}$ is the drain current with a small positive voltage on the gate electrode. The allowable positive gate voltage (≈ 1 V) will depend on the channel doping and the workfunction of the gate metal. The positive gate voltage is limited by the onset of forward Schottky diode current. Although Eq. (19) applies specifically to pentodelike devices such as FETs, the same approach would apply

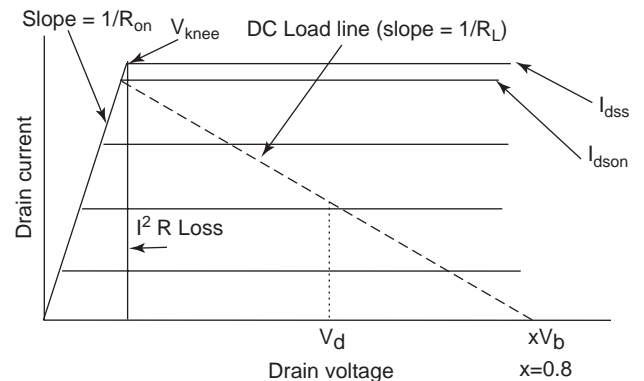


Figure 2. Output characteristics superimposed with the load line that can be used to get an estimate of the power level that can be obtained from the device provided that it is not limited by the input drive.

equally well to electronic devices with triodelike devices such static induction transistors (SITs) operated in the SIT mode, the pentodelike FET mode, or mixed mode. The DC load line shown in Fig. 2 would be used in a class A RF amplifier with the drain voltage $V_d = (V_b + V_{knee})/2$. The slope of the load line is $1/R_L$, where R_L is the value of the load resistance at the output of the FET.

To be of some value, the effect of junction temperature on the output characteristics must be taken into consideration. Temperature-dependent materials parameters, if known, can be used to calculate the output characteristics with respect to temperature. However, a more pragmatic approach, particularly when the aforementioned parameters and/or models required are not available, can be taken in which one measures the output characteristics of the device under consideration as a function of temperature. The junction temperature is critically dependent on the substrate thermal conductivity that is available for various substrates, including GaN [7]. The functional dependence of thermal conductivity on temperature is

$$\chi(T) = \chi(T_0) \left(\frac{T}{T_0} \right)^{-r} \quad (20)$$

where the coefficient r is 0.559, 0.443, 0.524, and 0.544 for Si, GaAs, SiC, and sapphire, respectively [8]. In Fig. 3, $\chi(T_0)$ has also been appropriately reduced to account for the doping of the substrate material.

4. PROCESSING

In an increasing manner, processing has become a central issue in device design and development. MODFETs represent a case of a buried-channel device and require special attention. The short gate lengths that generally accompany MODFETs necessitate unique approaches for the gate metal in an effort to keep the gate resistance from getting too large.

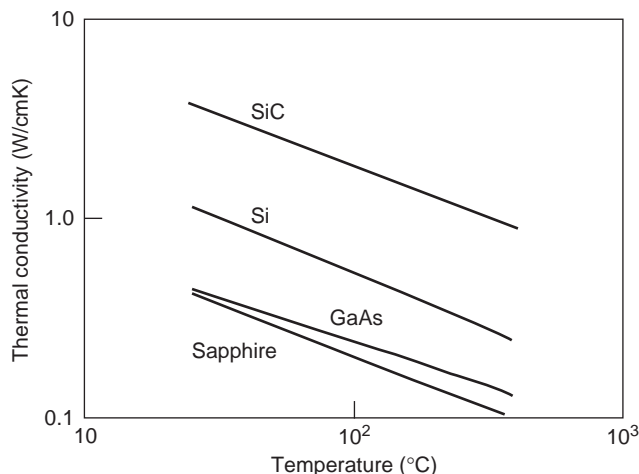


Figure 3. The thermal conductivity versus temperature of sapphire used for GaN devices, SiC used for some GaN devices, GaAs is used for GaAs based MODFETs, and Si for comparison.

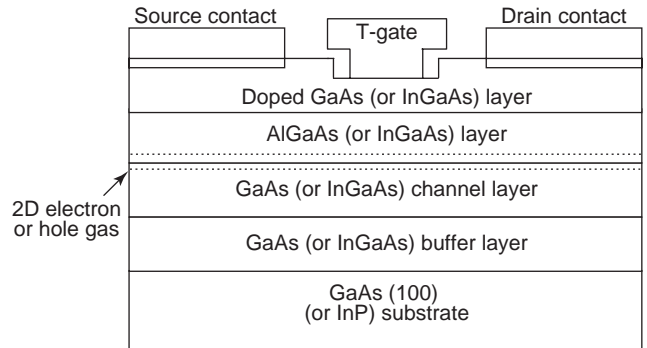


Figure 4. A cross-sectional representation of MODFET structures with the prominent “T” gate. Those within parenthesis indicate the materials used when the MODFET structure is on InP substrate. Other materials depict the case for GaAs substrates.

4.1. Gate Profile

High-performance devices require short gate lengths while keeping the gate resistance to a minimum. As shown in Fig. 4 in conjunction with a cross-sectional diagram of a MODFET structure, the T-shaped gate has proved highly beneficial because it combines low gate resistance with low gate capacitance. The upper, wide part of the T serves to reduce the gate resistance by virtue of its wide area, and the lower, narrow part of the T correspondingly reduces the gate capacitance through its narrow profile. Electron-beam (e-beam) lithography has been the favored method of fabrication, capable of submicron T-gate lengths [9]. Deep-UV lithography of submicrometer T-shaped gates has also been developed, overcoming the primary e-beam disadvantages of insufficient throughput and high cost [10]. The resist combines polymethylmethacrylate and polymethylisopropenylketone in a trilayer resist structure of PMMA/PMIPK/PMMA. Reliability studies with high-temperature accelerated failure tests have shown that the recess depth of the T-shaped gate plays a decisive role in device failure [11]. An unnecessarily deep gate recess will in time contribute to a sharp rise in the gate forward resistance due to the excess distance between the wide part of the T and its base. In order to avoid the consequent degradation of the gain and minimum noise figure, a gate recess depth less than 125 nm is sufficient. A single-etch gate recess method utilizes e-beam lithography followed by reactive-ion etching or electron cyclotron resonance plasma etching of the GaAs cap [12]. This represents an advance in simplicity over the more traditional double-gate recess process [13].

The Schottky barrier-related processes for GaN-based devices are nascent, but rapid progress is being made. Until recently it has been difficult to fabricate good quality single-crystal films on which a Schottky metal could be deposited, and properties of Schottky barrier could be studied. However, considerable progress has been made with Pt-GaN Schottky barriers [14,15] that have been successfully implemented in GaN-based MODFETs [16–21].

More recent success in growing good-quality single-crystal III–V GaN layers prompted the fundamental

electrical property studies of metal–semiconductor barriers on GaN. The formation of metal–semiconductor barriers is an essential element of a variety of semiconductor devices, particularly MODFETs. To obtain a large Schottky barrier height, metals with large work functions have been explored for rectifying metal contacts on GaN, including Au [22] and Pt [14]. Hacke et al. [22] obtained Au Schottky barriers on unintentionally doped n-GaN grown by hydride vapor phase epitaxy. The forward current ideality factor was $n_{\text{id1}} \sim 1.03$, and the reverse bias leakage current was $< 10^{-10}$ A at a reverse bias of -10 V. While the current–voltage measurement indicated the barrier height to be 0.844 eV, the capacitance measurements led to a value of 0.94 eV. However, the reported barrier height for Au/n-GaN ranges from 0.80 to 1.1 eV in various works. One possible cause is different surface treatment. Maffeis et al. [23] investigated the influence of premetallization surface preparation on the structural, chemical, and electrical of Au/n-GaN (i.e., Au/n-doped GaN) interfaces. The Schottky barrier with very low ideality factor (1.10) and high barriers (1.25 eV) was fabricated with ultra-high-vacuum (UHV) annealing at 600°C for 10 min [23].

Suzue et al. [14] have studied the Pt Schottky barriers on unintentionally doped N-GaN. Dependence of both current–voltage and capacitance–voltage characteristics on temperature was studied in the range from -195 to 42°C in an effort to gain insight about the current conduction mechanism. The excess current observed for small gate biases pointed to parasitic processes besides the thermionic emission over the Schottky barrier. This excess current is traditionally attributed to defects (generation recombination centers) and surface leakage current. The ensuing current is called the *Shockley–Read–Hall* (SRH) recombination current resulting from the midgap states. Preliminary investigations indicate that this excess current can be modeled very well with SRH current. Further experiments must be conducted to unravel the exact nature of the underlying processes involved. If one neglects this excess current, a barrier height of about 0.8 eV is deduced as opposed to about 1 eV deduced from the C/V (capacitance–voltage) measurements. Because of the excess current affecting the slope of the I/V (current–voltage) curve, the C/V measurement in this particular case is a closer representation of the metal barrier height. An examination of the C/V plots, however, indicated that under reverse bias condition, the capacitance depended insignificantly on the density of traps. The curves corresponding to all temperatures were largely linear, which yielded barrier heights ranging between 0.95 and 1.05 eV. Reduced capacitance with decreasing temperature is consistent with relatively deep donors. Binari et al. [24] studied titanium Schottky barriers on unintentionally doped n-GaN. The Schottky barrier heights estimated from the current–voltage and capacitance measurements were 0.58 and 0.59 eV, respectively. The ideality factor n_{id1} was about 1.28, and the diode series resistance $R_s = 100 \Omega$.

The ternary $\text{Al}_x\text{Ga}_{1-x}\text{N}$ is an essential component of nitride-based $\text{Al}_x\text{Ga}_{1-x}\text{N}/\text{GaN}$ heterostructure MODFET devices. In fact, the Schottky barriers are deposited on $\text{Al}_x\text{Ga}_{1-x}\text{N}$, which makes it imperative to investigate

metal $\text{Al}_x\text{Ga}_{1-x}\text{N}$, which so far have been lagging behind those on GaN in part because of the lack of good-quality layers. Khan et al. [25] reported the fabrication of Cr/Au Schottky barrier on N-doped AlGaIn. Moreover, Khan et al. [26] studied the Schottky barrier characteristics of the $\text{AuAl}_x\text{Ga}_{1-x}\text{N}$ system. A typical current–voltage characteristics of $\text{Al}_{0.14}\text{Ga}_{0.86}\text{N}$ Schottky diode had an ideality factor of 1.56 under reverse bias, and a threshold voltage of about 0.9 V at 0.1 A. The reverse bias leakage current was recorded to be marginally low (10^{-10} A) for a reverse bias of -10 V. Employing the current–voltage method, the barrier height and the electron affinity were determined to be 0.94 and 4.16 eV, respectively. From the C^{-2}/V plot the same barrier height and the electron affinity were deduced to be 1.3 ± 0.05 and 3.8 eV, respectively.

The measurement of barrier height to p-GaN is very difficult because of the lack of high-quality p-type epilayer and low resistance ohmic contact. The high I/V ideality factor prevents obtaining reliable barrier height from the I/V curves. In addition, these barriers obtained from I/V measurements are usually inconsistent with the ones from C/V measurements. Hartlieb et al. [27] fabricated a Pd/P-doped GaN Schottky barrier on chemical vapor cleaned p-type GaN surface. The final barrier height was 1.3 ± 0.1 eV. The difference between the predicted value (0.9 eV) and observed one arises from the interface dipole term, which is a result of the complicated interaction between extrinsic and intrinsic surface states as well as the contribution from metal-induced gap states. The work of Cao et al. [28] revealed that the removal of interfacial oxides causes the reductions in barrier height. It may partly explain considerable amount of scatter for contact properties reported in the literature.

In short, current conduction mechanism in metal–semiconductor structures is strongly affected by surface and bulk states. Deviations from an ideal ideality factor, such as the case here, are indicative of such states. The situation gets more complicated with AlGaIn and worsens as the AlN mole fraction is increased. Likewise, capacitance–voltage measurements also are affected by states that are charged, whether interface state or bulk state charge. As is the case in many facets of research and development, insights into the metal–nitride contacts will be gain in an evolutionary manner hinging on the developments in nitride layers.

4.2. Ohmic Contacts

Ohmic contact formation to the source and drain of a MODFET is complex because of the need for the ohmic contact to somehow penetrate the high-bandgap barrier layer. In case the contact metal does not penetrate through the barrier, ohmic conduction is realized by tunneling of electrons through the remaining AlGaAs barrier, models for which have been developed [29]. On the other hand, a contact with too large a lateral penetration causes short-circuiting to the gate. Several requirements should be fulfilled by a “good” ohmic contact. These requirements should include not only the short ohmic contact length mentioned above but also robust thermal stability and, of course, low contact resistance. A clear understanding and

control of the alloying reactions that occur at the metal–semiconductor interface and the effect of the wide-bandgap semiconductor on contact penetration are essential elements for optimizing the device and the ohmic contact process. Achieving all of these properties is not trivial. Also, different MODFET structures (e.g., AlGaAs/GaAs, AlGaAs/InGaAs, AlInAs/InGaAs) may interact distinctly with the metallization. Consequently, investigators have been forced to adjust their metallurgical mixes for ohmic contacts.

Alloyed ohmic contacts are the traditional ohmic contacts used for a MODFET's source and drain, and certainly are the MODFET ohmic contacts with the longest history of research behind them. Although AuGe/Ni/Au metallization has enjoyed favor as the typical ohmic contact on GaAs-type MODFETs, other similar metallizations under investigation, which address problems evident with AuGe/Ni/Au, may supplant it.

Nonalloyed ohmic contacts to the source and drain of the MODFET promise to become the ohmic contacts of choice for high-density integration. A short ohmic length with low parasitic source series resistance is a great advantage of nonalloyed ohmic contacts in high-density VLSI. Further, nonalloyed ohmic contacts suffer marginally from the orientation dependence of the specific contact resistance. The difference between the (011) and (00 $\bar{1}$) directions is very small, with insignificant variation. In contrast, alloyed ohmic contacts demonstrate a rather large difference in the specific contact resistance between the (011) and (00 $\bar{1}$) directions, as evidenced by electron microscope observations of the formation of the alloying region and the alloyed grain fluctuations in size [30,31]. The nonalloyed ohmic contact has been proscribed from actual use in a MODFET structure because of the necessarily high doping concentrations. Electron concentrations in the range of 10^{19} cm^{-3} are needed to enable electron tunneling (or, sufficient lowering of the Schottky barrier at the metal–semiconductor interface) with the result that the resistance offered by the heterojunction appears larger. The addition of a capping contact layer, typically a thin, heavily doped n-type InAs or InGaAs layer, is a common solution to enable nonalloyed ohmic contacts. This cap layer approach does have the drawback of requiring its removal for the subsequent gate metallization. A heavily Sn-doped GaAs contact layer has also been used, obviating the need for additional growth [32].

4.2.1. Contacts to III–V Nitrides Notably GaN. Ohmic contacts constitute a major obstacle in large bandgap semiconductors and thus to successful realization of GaN MODFETs. Early results for GaN indicate that ohmic contacts can be formed to both n- and p-type material. The contact resistances to n-type GaN using Al and Au metallizations [33] were in the range of 10^{-4} and $10^{-3}\ \Omega\cdot\text{cm}^2$. The current–voltage measurement revealed that while the as-deposited Al contacts were ohmic, the as-deposited Au contacts were rectifying, which became ohmic after annealing at 575°C. Using Ti/Au [34] and TiAl [35], specific contact resistivities of 7.8×10^{-5} and $8\times 10^{-6}\ \Omega\cdot\text{cm}^2$ were obtained, respectively. Nakamura et al. [36,37] used Au (and later Au/Ni) and Ti/Al as p- and

n-type contacts, respectively, in their LED (light-emitting diode) structures. Although no contact resistances were reported, an operating voltage of 4 V at 20 mA forward bias in a p-n junction device clearly demonstrates that reasonable contact resistances were obtained. Carrying the TiAl contact work one step further, Wu et al. [38] confirmed that, except at very high annealing temperatures, the ohmic contact suggested by Lin et al. [35] functions very effectively. At very high temperatures, Al of the metal contact melts and tends to ball up, resulting in rough surfaces and increased ohmic contact resistances as pointed out already by Lin et al. [35]. In an attempt to circumvent this difficulty, Wu et al. [38] designed a separate layer metallization method where a realignment and deposition of a second thin Ti layer, and a 2000-Å Au overlayer was carried out. Specific contact resistivities were in the range of $3.0\text{--}5.5\times 10^{-6}\ \Omega\cdot\text{cm}^2$ depending on the doping concentration in the semiconductor.

In an attempt to obtain an improved ohmic contact, Fan et al. [39] have designed a multilayer ohmic contact method. Utilizing a composite metal layer of Ti/Al/Ni/Au (150 Å/2200 Å/400 Å/500 Å), very low contact resistivities were obtained. Specifically, for n-GaN with doping levels between 2 and $4\times 10^{17}\text{ cm}^{-3}$, specific contact resistivities in the range of $\rho_s=1.19\times 10^{-7}\ \Omega\cdot\text{cm}^2$ and $8.9\times 10^{-8}\ \Omega\cdot\text{cm}^2$, respectively, were obtained. Calculation of the contact resistivity was based on the assumption that the semiconductor sheet resistance underneath the contacts remains unchanged, which is not true for nonalloyed contacts. As for the current conduction mechanism in these ohmic contacts, the large metal–semiconductor barriers diminish the possibility of thermionic emission-governed ohmic contacts to GaN. The alternative mechanism is naturally some form of tunneling that may take place if GaN is so heavily doped to cause a very thin depletion region. Tunneling is possible if, as a result of annealing, for example, at 900°C for 30 s, Al and Ti along with Ni undergo substantial interaction with each other and GaN. A cursory look would imply that Ti receives N from GaN, forming a metallic layer, while the lack of N on GaN provides the desired benefit of increased electron concentration through N vacancy formation. Al acts to passivate the surface and also possibly react with Ti forming TiAl. For details, the reader is referred to Ref. 7.

In contrast to n-GaN, stable ohmic contacts with low resistivity to p-GaN are much more difficult to achieve because of large workfunction of p-GaN, residual hydrogen passivation effect, and relatively low hole concentration. Ni-, Au-, Pd-, and Pt-based metal schemes with high workfunctions ($>5.0\text{ eV}$) have been widely investigated and currently relatively low resistivity in the order of 10^{-4} to $10^{-6}\ \Omega\cdot\text{cm}^2$ can be realized. Improved Ni/Au ohmic contacts to moderately doped p-GaN ($N_A=10^{17\sim 18}\text{ cm}^{-3}$) have been demonstrated by annealing in O_2/N_2 and resistivity as low as $4.0\times 10^{-6}\ \Omega\cdot\text{cm}^2$ was achieved [40–42].

5. CHANNEL DESIGN

Low-field mobilities in heterostructures rise and parasitic resistances decrease with decreasing temperature.

However, the conventional AlGaAs/GaAs MODFET exhibits the well-known collapse of the I/V characteristics and a strong threshold voltage shift [43]. The low-temperature behavior of the device is affected also by the altered behavior of the n-AlGaAs layer. As long as the Al mole fraction and the doping level are low, the activation energy of the donors is shallow. However, as the Al content exceeds 25% and the doping level exceeds $5 \times 10^{17} \text{ cm}^{-3}$, both of which are necessary for obtaining higher 2DEG and a better electron confinement in the channel, a large number of donors become deep, resulting in a freezeout of carriers, I/V collapse, and persistent photoconductivity at low temperatures. Replacing the doped n-AlGaAs layer with an n-GaAs/AlAs superlattice reduces these low-temperature effects [44]. Another novel improvement of the MODFET involves striping of the active channel. A striped-channel MODFET (SC-MODFET) is essentially the same as the conventional MODFET except that the source-to-drain region is divided into a number of narrow conducting channels referred to as wires. Thus an active AlGaAs/InGaAs layer grown on a GaAs substrate exhibits well-defined square well properties, providing good confinement of the 2DEG even at low sheet carrier density. In SC-MODFETs the 2DEG can be controlled in both vertical and lateral directions by the Schottky gate and the enhancement in transconductance is consistent with gate capacitance [45].

6. MODFET PERFORMANCE

To reiterate MODFET's performance is due to the conduction channel, which eliminates impurity scattering and unique capacitance voltage relationship. The PMODFET alleviates the DX center problem while using an InGaAs channel with superior transport properties over GaAs [46]. There is also the lattice-matched and pseudomorphic MODFETs based on InP substrates utilizing higher-mole-fraction InGaAs.

In the conventional III-V semiconductors, three types of MODFETs have been explored: those with GaAs channels on GaAs substrates, $\text{In}_x\text{Ga}_{1-x}\text{As}$ channels on GaAs substrates, and the high-InAs-mole-fraction InGaAs channels on InP substrates. The exploration has allowed the goals set for, for example, the W band (about 5 dB for gain and 4 dB for noise figures) to be well exceeded. With 0.15- μm gate devices [47], a 12.6-dB gain and minimum noise figure of 1.4 dB have been obtained at around 95 GHz. The associated gain at the bias point producing this extremely low noise figure is 6.6 dB. This value is remarkable and indicates the suitability of the InGaAs/InAlAs MODFET structure for operation near 100 GHz and beyond. Peng et al. [48] showed that the increase in the InAs mole fraction leads to an improvement in high-frequency performance. The results indicate that, as the InAs mole fraction is increased, for example, from zero to 65%, the current gain cutoff frequency increases by a factor of >2 , from about 110 to 260 GHz [49–58]. The current gain cutoff frequency corresponding to unity current gain, is an important parameter in logic gates. The maximum oscillation frequency (f_{max}), for which the maximum available gain of the

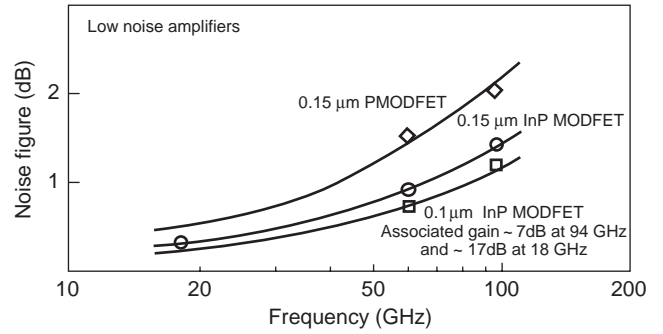


Figure 5. Minimum noise figure of pseudomorphic AlGaAs/InGaAs and InAlAs/InGaAs MODFETs with 0.15 μm for GaAs-based and 0.15, 0.1 μm for InP-based, gate lengths. (Courtesy of P. M. Smith, Lockheed Martin).

device goes to unity, is also an important factor for determining the electrical and microwave performance. This figure also shows that an increase in the InAs mole fraction leads f_{max} values, for example, for GaAs channel device to increase by about 30%, to about 350 GHz. With 53% mole fraction and a 0.15- μm gate length, it increases to a remarkable 405 GHz. The minimum noise levels from MODFETs based on GaAs and InP obtained at Lockheed Martin are shown in Fig. 5 through the courtesy of Dr. P. M. Smith.

Devices based on InP hold the highest f_t and f_{max} [59]. The promise held by PMODFETs was demonstrated with the development of 0.25- μm gate length [60]. The results obtained since show that f_t increases by a factor of >2 , from about 110 to 260 GHz, as the InAs mole fraction is increased from zero to 65% [61–64]. With the pseudomorphic approach, the f_{max} for a GaAs channel device is increased by $\sim 30\%$ to ~ 350 GHz [65]. With 53% mole fraction a remarkable 405 GHz was obtained with 0.15- μm gate devices [66]. Performance above 100 GHz has been measured by Tan et al. [67]. Using a 0.1- μm gate-length pseudomorphic $\text{In}_{0.52}\text{Al}_{0.48}\text{As}/\text{In}_{0.6}\text{Ga}_{0.4}\text{As}/\text{InP}$ structure, a noise figure of 1.3 dB and an associated gain of 8.2 dB at 95 GHz have been obtained. At 141.5 GHz, a D-band frequency, the device exhibited a gain of 7.3 dB.

The current gain cutoff frequency along with the maximum oscillation frequency f_{max} , the maximum transconductance g_{max} , and the maximum channel current I_{max} for some representative MODFETs are listed in Table 1.

6.1. Low-Noise Amplifiers

Low-noise amplifiers (LNAs) are required in a number of millimeter-wave and microwave applications, including radar, satellite communications, seekers, and minitions. LNAs are key components in the receiving portion of these systems. Recent advances in low-noise MODFET technology have significantly improved their performance, particularly for those at W-band frequency. Coplanar waveguides (CPWs) and conductor-backed coplanar waveguides (CBCPWs) are important alternatives to microstrip transmission lines for MMICs. These millimeter-wave monolithic CPW and CBCPW LNAs have been developed in a variety of forms, including a two-stage single-ended Q-band LNA, a 5–100-GHz distributed amplifier, a

Table 1. Full-Channel Current I_{\max} , Cutoff Frequency f_t , Maximum Oscillation Frequency f_{\max} , and Maximum Transconductance g_{\max} for Various MODFETs^a

MODFET Type	I_{\max} (mA/mm)	f_t (GHz)	f_{\max} (GHz)	g_{\max} (mS/mm)	Comments	Ref.
<i>GaAs-Based MODFETs</i>						
AlGaAs/GaAs MODFET	100	9	15	40 115	p-channel, $L = 0.25 \mu\text{m}$	68
AlGaAs/InGaAs/GaAs PMODFET	250	5	4		Vertically integrated with GRINCHSQW, $A = 2 \mu\text{m} \times 500 \mu\text{m}$	69
Unstrained InGaAs/InAlAs MODFET	250	15	56	335	$V_{\text{br,dg}} = 23.5 \text{ V}$, $A = 1 \mu\text{m} \times 10 \mu\text{m}$	70
AlGaAs/GaAs MODFET	275	72	144	330	CBE, $A = 0.2 \mu\text{m} \times 150 \mu\text{m}$	71
AlGaAs/InGaAs MODFET	300	15	59	224	$V_{\text{br,dg}} = 10 \text{ V}$, $L = 1.8 \mu\text{m}$	72
AlGaAs/InGaAs PMODFET	400	100	200	530	$A = 0.12\text{--}0.17 \mu\text{m} \times 75 \mu\text{m}$	73
AlGaAs/InGaAs PMODFET	400	100	200	530	7-dB gain at 90 GHz, $L = 0.2 \mu\text{m}$	74
InAlAs/InGaAs	400	45	115	700	Metamorphic on GaAs, triangular gate, $A = 0.4 \mu\text{m} \times 150 \mu\text{m}$	75,76
GaAs/InGaAs PMODFET	500 (77 K), 690	—	—	175 (77 K), 245	δ -doped, graded-channel, $A = 2 \mu\text{m} \times 100 \mu\text{m}$	77
DR PMODFET	525	50	100	360	$V_{\text{ds}} = 5 \text{ V}$, $V_{\text{br,dg}} = 11 \text{ V}$, $L = 0.25 \mu\text{m}$	78
AlGaAs/InGaAs PMODFET	550	100	200	640	12-nm SQW, $A = 0.2 \mu\text{m} \times 50 \mu\text{m}$	79
DR PMODFET	580	39	170	545	$L = 0.2 \mu\text{m}$	80
$2 \times$ heterostructure MODFET	600	90	200	500	$V_{\text{br,gd}} > 10 \text{ V}$, $A = 0.15 \mu\text{m} \times 80 \mu\text{m}$	81
AlGaAs/InGaAs PMODFET	630	110	230	653	$A = 0.15 \mu\text{m} \times 50 \mu\text{m}$	82
AlGaAs/InGaAs PMODFET	—	66	75	600	Enhancement mode, $L = 0.3 \mu\text{m}$	83
	—	66	75	450	Depletion mode	—
GaInP/GaAs PMODFET	—	17.8	23.5	163 (77 K), 213	$A = 1 \mu\text{m} \times 200 \mu\text{m}$	84,85
n-InGaP/InGaAs/GaAs	—	76	191	420	$A = 0.15 \mu\text{m} \times 200 \mu\text{m}$	86
<i>InP-based MODFETs</i>						
AlInAs/GaInAs/InP MODFET	350	22	75	240	Junction-modulated device, $A = 1 \mu\text{m} \times 15 \mu\text{m}$	87
GaInAs/AlInAs/InP PMODFET	700	80	—	500	$V_g = 0.4 \text{ V}$, $A = 0.25 \mu\text{m} \times 50 \mu\text{m}$, power modulation, $V_{\text{br,gd}} = 6.8 \text{ V}$	88
InAlP/InGaAs/InP PMODFET	800	86	>20	380	$A = 0.25 \mu\text{m} \times 50 \mu\text{m}$, Al mole fraction in InAlP = 0.25, $V_{\text{br,gd}} = 12 \text{ V}$	89
InP/InGaAs/InP MODFET	—	27	89	565	In mole fraction in InGaAs = 0.74, quantitative MODFET, $V_g = 5 \text{ V}$, $A = 1 \mu\text{m} \times 50 \mu\text{m}$	90

^aIn this table A is the cross-sectional area of the channel, L is the channel length, V_g is the gate voltage, and $V_{\text{br,gd}}$ is the gate-drain breakdown voltage. PMODFET is an abbreviation of pseudomorphic MODFET; DR denotes *double recessed*; SQW is an acronym for *single quantum well*.

W-band cascade amplifier, and a W-band four-stage single-ended CBCPW amplifier. These LNAs are particularly attractive for MMIC design because their properties of minimizing active device source inductance, increasing line-to-line isolation, improving on-wafer probe testing,

and simplifying MMIC processes. One major advantage of CPW LNA structures is that they can be fabricated together with microstrip-line and slotline components.

Fabrication of LNAs is performed primarily by making use of conventional n-AlGaAs/GaAs MODFETs. LNAs

Table 2. Frequency, Noise Figure, and Gain of Various MODFETs

MODFET Type	Frequency (GHz)	Noise Figure (dB)	Gain (dB)	Comments	Ref.
<i>InP-Based MODFETs</i>					
AlInAs-GaInAs-InP	2.0	0.5	35.0	2-stage MMIC	101
AlInAs-GaInAs/InP	7–11	1.2	22.0	—	102
AlInAs-GaInAs-InP	12.0	0.8	12.0	—	103
AlInAs-GaInAs-InP	18.0	0.7	—	$L^a = 0.1 \mu\text{m}$, planar-doped	104
AlInAs-GaInAs-InP	36	1.6	17	—	105
AlInAs-GaInAs-InP	40–45	0.2	33.0	$L = 0.1 \mu\text{m}$	106
AlInAs-GaInAs-InP	56–64	3.0	24	$L = 0.1 \mu\text{m}$	107
AlInAs-GaInAs-InP	60	1.9	13.0	—	93
AlInAs-GaInAs-InP	60	0.8	8.9	$L = 0.1 \mu\text{m}$	108
AlInAs-GaInAs-InP	92	—	9.2	—	93
AlInAs-GaInAs-InP	94	1.2	7.2	—	95
AlInAs-GaInAs-InP	95	1.3	8.2	$L = 0.1 \mu\text{m}$	109
AlInAs-GaInAs-InP	141.5	—	7.3	$L = 0.1 \mu\text{m}$	109
<i>GaAs-Based MODFETs</i>					
AlGaAs-InGaAs-GaAs	41–45	3.0	22	$x = 0.25$, $L = 0.15 \mu\text{m}$	110
AlGaAs-InGaAs-GaAs	112–115	6.3	12	2-stage LNA, $L = 0.1 \mu\text{m}$ planar, T-gate	111
AlGaAs-InGaAs-GaAs	2–20	>3.0	13	$L = 0.25 \mu\text{m}$, mushroom profile	112
AlGaAs-InGaAs-GaAs	91	3.4	8.7	2-stage, $0.15 \times 60 \mu\text{m}^2$	113
AlGaAs-InGaAs-GaAs	10	0.6	13	T-gate, $L = 0.3 \mu\text{m}$	114
n-In _{0.25} Ga _{0.75} P-In _{0.48} Ga ₀ GaAs	12	0.41	13	$0.15 \times 200 \mu\text{m}^2$	115
AlGaAs-InGaAs-GaAs	93–95	4.5–5.5	17	$L = 0.1 \mu\text{m}$, single-sideband noise	116
AlGaAs-InGaAs-GaAs	113	3.4	15.6	$L = 0.1 \mu\text{m}$	117
AlGaAs-InGaAs-GaAs	41–45	3.0	22	$L = 0.15 \mu\text{m}$ T-gate	118

^a L = channel length.

with these MODFETs, however, suffer from performance degradation. The latter stems from degradation of the performance of the conventional MODFETs with uniformly doped n-AlGaAs layer and channel length lower than $0.25 \mu\text{m}$ due to short-channel effects. To circumvent the degradation resulting from short-channel effects, the aspect ratio L/t , where L is the gate length and t is the thickness of the electron supply layer, is usually increased. This is achieved by lowering t , because a thin electron supply layer confines the 2DEG very effectively at the interface. InGaP-based MODFETs are particularly useful in this respect. The Schottky barrier height for this system is low and the charged DX centers practically absent. All these allow the thickness of the n-InGaP layer to be substantially reduced. Good carrier confinement thus achieved in the pseudomorphic quantum-well channel contributes to reducing short-channel effects. Because of this, InGaP/InGaAs/GaAs MODFETs may be improved alternatives to conventional AlGaAs/GaAs MODFETs. InP-based InAlAs/InGaAs/InP MODFETs may satisfy the same purpose. Recently, these MODFETs have demonstrated the lowest noise figures among all three-terminal solid-state devices. The lowest noise figures F_{\min} from various GaAs- and InP-based MODFETs [91–100] are depicted in Table 2. From this figure it may be noted that InP-based T-gate technology with noise figures below 1.0 dB has been realized.

6.2. Power Amplifiers

Power applications present another useful area in which the benefits of MODFETs can be exploited. A tabulation of power performance of some representative MODFETs,

metal semiconductor field effect transistors (MESFETs), and HBTs (heterojunction bipolar transistors) are shown in Table 3. From this table it may be noted that MODFETs demonstrate power performance better than that of MESFETs or HBTs.

High-power amplifications are necessary for achieving maximum reliability, minimum size and weight, high volume, low cost, and high performance of phased array systems such as radar, satellite communications transmitters, electronic warfare, seekers, and smart munitions. An efficient MODFET power amplifier should be not only cost-effective, but also yield superior power-added efficiencies (PAEs) and gain for phased-array systems applications. Chen et al. [121] developed 4-chip PMODFET K-band power modules that deliver 3.2W with a power added efficiency (PAE) of 35% at 3 dB compression, 10 dB saturated gain at 20 GHz, a 1-dB bandwidth of 1.7 GHz, and power density of 500 mW/mm. Such high-power modules are specially suited for spacecraft onboard applications. A $0.15\text{-}\mu\text{m}$ double-heterostructure InGaAs/AlGaAs/GaAs PMODFET has displayed a maximum transconductance over 500 mS/mm, a maximum current density over 600 mA/mm, a cutoff frequency of 90 GHz, and a maximum

Table 3. Comparison of Power Performance of GaAs-based MODFETs, MESFETs, and HBTs

Device	Power (W)	Gain (dB)	PAE (%)	Frequency (GHz)	Ref.
HBT	0.5	11	60	10	119
MESFET	8.0	9	40	10	119
PMODFET	10	13.5	63	2.45	120

oscillation frequency of 200 GHz [122]. This particular MODFET has been utilized in a V-band monolithic power amplifier with an output power of 313 mW (0.39 W/mm) with 8.95 dB power gain and 19.9% PAE at 59.5 GHz [123].

There is no doubt that AlGaAs/InGaAs/GaAs PMODFETs have demonstrated great potential as the microwave and millimeter-wave device for high-gain low-noise applications. However, there is still room for improvement. To further optimize the transmitter modules, the output power should be increased, which necessitates improvement of the power performance of PMODFETs. To this end, both the current drivability and the breakdown voltage must be increased. The breakdown voltage can be increased without deteriorating high-speed performance if the double-recess approach is employed [124] or if high-bandgap AlGaAs layers with lower mobility are used; perhaps a combination of both approaches may be viable. Alternatively, a highly p-doped, very thin surface layer in combination with GaInP as the wide-bandgap material can be used. Such a modification of device structure can lead to a distinct advantage over more typical AlGaAs/InGaAs PMODFETs [125]. Remarkably, a device with 1.8 μm gate length designed in this experiment shows a breakdown voltage of 4 V or higher, with all other parameters almost unchanged.

The main weakness of the InGaAs-based MODFETs is the impact ionization in the channel by hot electrons injected from the gate and that the weak Schottky barrier height on InAlAs allows large reverse-bias gate leakage current to flow, reducing the gate–diode breakdown. This prevents the $\text{In}_{0.53}\text{Ga}_{0.47}\text{As}$ -channel MODFETs from demonstrating high power performance. In order to address this issue, various modifications to both the gate and channel regions have been investigated. These modifications include variations in the gate contact layers, variations in the channel material, and variations in the doping strategy of the 2DEG. Three different approaches are undertaken to improve the gate barrier and the gate–drain breakdown voltage: (1) incorporation of a junction to modulate the 2DEG, (2) incorporation of an AlInP Schottky barrier, and (3) increasing of barrier height by increasing the Al mole fraction in the AlInAs Schottky barrier layer. In order to realize the junction-modulated MODFETs, a heavily doped p-type AlInAs layer is incorporated on top of the conventional MODFET structures. This results in high turnon voltage, low leakage current, and high reverse breakdown voltage. The increase in the barrier height by increasing the Al mole fraction of the AlGaAs, for example, from 48 to 70%, and a proper tailoring of the dopant concentration lead also to an increase in the turnon voltage from 0.5 to about 1.0 V.

The concept of regrown contacts [126] to a 2DEG has been tested in an InAlAs–InGaAs–InP MODFET [127]. It was noted that the improvement in barrier height that results from incorporating a junction between a surface p⁺ layer and the 2DEG leads to increase in the two-terminal gate–drain and the three-terminal OFF-state breakdown voltages. Further, the formation of a stable nonalloyed contact to the 2DEG by using selection regrowth of the source and the drain regions causes a reduction in the drain fields. Interestingly, all these improvements are achieved without sacrificing the full-

channel current and transconductance. The replacement of the InGaAs channel by the InP channel also provides a significantly large microwave power of 30 GHz or so, and a three-terminal ON-state breakdown voltage of 10 V. However, the same replacement accompanies deterioration in carrier mobility in the channel [128]. The formation of a composite bilayer channel, for which both doped and undoped InP along with a thin GaInAs layer are utilized, brings about improved microwave power up to about 60 GHz. One notable advantage of a composite channel over a conventional channel is that it enjoys the effect of high electron mobility of InGaAs and of high breakdown field and velocity of InP [129]. The effect of In mole fraction alternation of the InGaAs channel material on the electrical performance of the MODFETs has been carefully explored. This investigation points to the expected reduction in the electron effective mass in the channel as the In mole fraction is increased to about 60% or more. Thus the gain at submillimeter frequencies is increased [130]. The power performance and related properties of some representative MODFETs are presented in Table 4.

The expected frequency band of operation of low-noise GaAs and InP-based MODFET technologies is approaching 100 GHz. The lower-frequency end, particularly that of wireless communication arena, is challenged by MOSFET and SiGe technologies. While the digital telephone operation band is currently slated to be near 2 GHz, with the almost certain video transmission over the wireless systems in the future, this frequency is expected to be pushed upward. Burgeoning personal communication system (PCS) technology provides excellent opportunities for the devices discussed here.

Expected frequency bands of operation of low-noise GaAs and InP-based MODFET technologies are shown in Fig. 6 for 0.25, 0.15, and 0.1 μm gate lengths. In a more applications-specific format, Fig. 7 shows the possible applications of MODFET along with competing technologies, MESFET and HBT. As Fig. 7 indicates, the bulk of the applications can be satisfied by the GaAs-based pseudomorphic MODFETs (PMODFETs), particularly so for power applications. For any device to be considered for any application at all, the longevity requirements must be met. Results of accelerated lifetime investigations are shown in Figs. 8 and 9 for low-noise and power amplifiers. Clearly, even the InP devices, while not as good as those on GaAs substrates in terms of longevity, exhibit reasonable operating lifetimes.

The lower-frequency end, particularly that of the wireless communication arena, is challenged by MOSFET and SiGe technologies. Recently burgeoning PCS technology has provided excellent opportunities for electronic devices and in particular for the devices discussed here. While the digital telephone operation band is currently slated to be near 2 GHz, with the almost certain video transmission over the wireless systems in the future, this frequency is certain to be pushed upward. At present, digital telephone components for which compound semiconductors are being considered are power amplifiers (PAs), drivers, low-noise amplifiers (LNAs), mixers, and switches as shown in Fig. 10, which shows the RF section of such a telephone. Conflicting pressures are in effect in that on one hand in-

Table 4. Power Performance and Related Properties of Various MODFETs^a

MODFET Type	Frequency (GHz)	Gain (dB)	Power (mW)	PAE (%)	Comments	Ref.
<i>GaAs</i> -based MODFETs						
0.32 × 48-μm 2 × pulse doped-AlGaAs/GaAs MODFET	0.5–50	6.5	16 at 40 GHz	—	6-stage distributed, $V_{ds} = 4$ V, $f_t = 45$ GHz, $f_{max} = 110$ GHz, NF = 4.8 dB at 0.5–26.5 GHz	131
0.2 × 50-μm recessed AlGaAs/GaAs MODFET	2–52	9	2.5, max 12.6	—	Matrix distributed, 2-stage 4-section $V_{ds} = 3$ V	132
	2.45	13.5	10 W	63	—	133
0.25-μm × 8-mm DR MODFET	4	15.4	4.3 W	66	$g_m^{max} = 430$ mS/mm, $I_{max} = 450$ mA/mm, $V_{ds} = 8$ V	134
0.25 × 400-μm DR PMODFET	4.5	17.2	330	63	$V_{ds} = 8$ V, $g_m^{max} = 510$ mS/mm, $I_{max} = 540$ mA/mm,	135
0.7-μm × 3-mm 2 × AlGaAs/GaAs IMODFET	5.5	8.3	1.3 W	55	$g_m = 180$ mS/mm	136
0.25-μm × 1.12-mm recessed PMODFET	9	9.25	850	50	$V_{ds} = 5$ V, $g_m = 428$ mS/mm, $f_t = 50$ GHz, $I_{max} = 545$ mA/mm	137
0.35-μm PMODFET DR 2 × pulse-doped	10	10.4	870	59	$V_{ds} = 7$ V	138
0.25-μm PMODFET DR	10	10	970	70	Dry first recess etching, $V_{ds} = 8$ V	139
0.25-μm × 1.6-mm 2 × HJ PMODFET	12	14	2.2 W	39	2-stage	140
0.25-μm × 8-mm DR PMODFET, QW planar- and pulse-doped	12	10.8	6 W	52	$V_{ds} = 9$ V, $g_m = 420$ mS/mm, $I_{max} = 430$ mA/mm	141
GaAs/InGaAs/GaAs PMODFET	14.25	5	4.7 W	25	$V_{br} = 20$ V, $g_m = 224$ mS/mm	142
10.5-mm-wide GaAs/InGaAs/GaAs MODFET	14.25	lin. 8	4.7 W	25	$V_{ds} = 10$ V, $V_{br} = 25.7$ V	143
PMODFET	15	12	575	50	—	144
0.25-μm PMODFET	18	6.3	776	53	$I_{max} = 550$ mA/mm, $V_{ds} = 7$ V, $g_m = 350$ mS/mm, 2 × pulse-doped	145
0.25 × 50-μm PMODFET	18	8	20	59	$g_m = 554$ mS/mm, monolithic integration w/MODFET LNA	146
0.33 × 120-μm PMODFET	25	12.9	680	45	n^+ GaAs supply layer $I_{max} = 530$ mA/mm, $V_{ds} = 5$ V	147
0.25-μm PMODFET	30	8.5	500	40	2-stage cascaded	148
	31	11	141	40.3	2-stage cascaded	—
0.2-μm DR PMODFET	32	6	500	35	—	149
	44	4.3	494	30	—	—
0.15-μm PMODFET	34–36	9	1 W	20	$V_{ds} = 5$ V	150
	34–36	17	3 W	15	2-stage	—
0.25 × 900-μm PMODFET	35	3.2	658	24	—	151
0.15 × 50-μm PMODFET	35	9.0	32	51	—	152,153
0.2 × 80-μm/150-μm PMODFET	40	19.1	41	—	3-stage	154
0.2 × 600-μm DR 2 × pulse-doped PMODFET	40–45	10–11	500–725	10–17	First-pass, 3-stage, $V_{ds} = 5$ V	155
0.25 × 240-μm PMODFET	55	4.9	105	22	$g_m = 500$ mS/mm, $I_{max} = 540$ mA/mm	156
0.2 × 50-μm PMODFET	55	3.3	42	22.1	$g_m = 760$ mS/mm, $I_{max} = 800$ mA/mm	157
0.3 × 800-μm PMODFET	55	4.1	219	18	$f_t = 50$ GHz, $f_{max} = 92$ GHz, $I_{max} = 420$ mA, $g_m = 360$ mS	158
PMODFET 2 × heterostructure	59.5	8.95	313	19.9	2-stage, $V_{DS} = 5$ V	159
0.15 × 320-μm DR PMODFET	59.5–63.5	7	370	11	$V = 5$ V, $I_{sat} = 500$ mA/mm, $f_t > 75$ GHz	160
0.15 × 50-μm PMODFET	60	6.0	32	41	NF = 1.8 dB, associated gain = 6.4 dB	152,153
0.15 × 320-μm PMODFET	60	5.1	191	28.7	$V_{ds} = 5$ V	161
0.15 × 100-μm PMODFET	77	21	12	—	3-stage, $V_D = 3.5$ V, $f_t = 110$ GHz, $f_{max} = 200$ GHz	162

continue

Table 4. Continued

MODFET Type	Frequency (GHz)	Gain (dB)	Power (mW)	PAE (%)	Comments	Ref.
0.1 × 160-μm PMODFET	93.5	5.9	100	6.6	2-stage, $V_{DS} = 3.5$ V	163
0.1 × 40-μm PMODFET	94	7.3	10.6	14.3	$f_{max} = 290$ GHz	164
0.25-μm InGaAs/InP PMODFET	4	15	560	63	Composite channel	165
AlInAs/GaInAs/InP PMODFET	12	11.1	110	50	Double-doped channel	166
	12	11.0	288	40	—	—
AlInAs/GaInAs/InP PMODFET	20	7.1	516	47	Double-doped channel	167
AlInAs/GaInAs/InP PMODFET	20	10.5	20.5	52	$In_{0.47}Ga_{0.53}As$ channel	168
0.30-μm PMODFET	30	5.2	120	23	InP channel	169
<i>InP-Based MODFETs</i>						
0.15-μm AlInAs/GaInAs/InP PMODFET	60	4.9	155	30	δ -doped channel	170
0.20-μm AlInAs/GaInAs/InP PMODFET	60	4.2	145	24	Double-doped channel	—
0.15-μm GaInAs/InP PMODFET	60	—	170	30	Composite channel	171
0.15-μm InAlAs/InGaAs/InP MODFET	60	7.2	18.5 W	41	$Ga_{0.31}In_{0.69}As$ channel	168
0.25 × 400-μm AlGaAs/InGaAs/GaAs MODFET	34–36	12	500	32	2 × sided δ -doped 2-stage	172

^aIn the table V_{ds} is the drain–source voltage, V_{br} is the breakdown voltage, and NF is the noise figure.

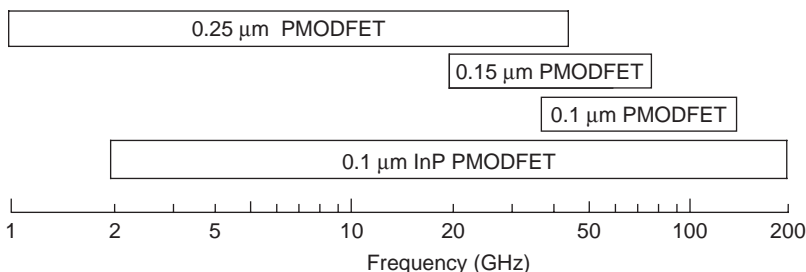


Figure 6. Frequency band of applications for MODFETs. (Courtesy of P. M. Smith of Lockheed Martin).

tegration is emphasized to simplify system assembly and reduce cost and on the other hand, more integration imposes application-specific designs and manufacture. Suppliers at the moments lean in the direction of less integration for wider range of applications for each part.

Cost considerations and manufacturing simplicity have favored the use of MESFETs especially for compound semiconductors for wireless operation. However with ever-increasing demands on performance and PAE to extend the battery operation coupled with advances in

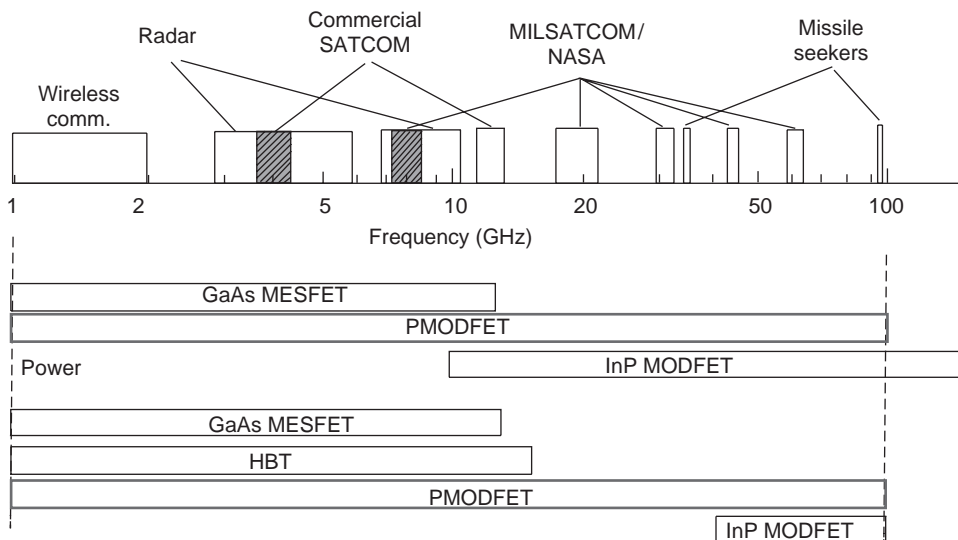


Figure 7. Possible applications of MESFET, MODFET and HBT technologies categorized by frequency of operation. (Courtesy of S. Komiak of Lockheed Martin.)

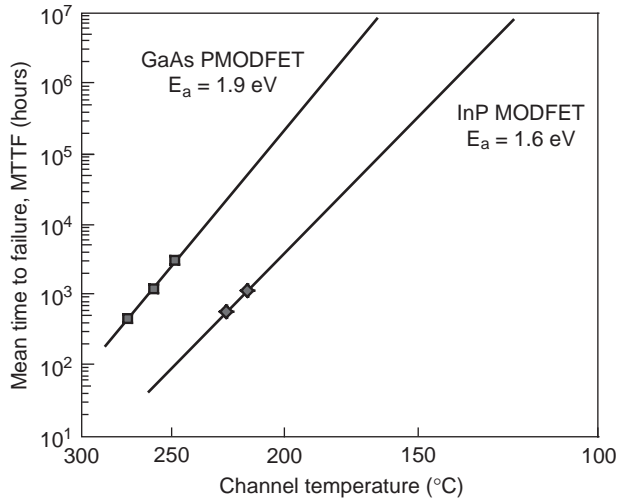


Figure 8. Accelerated lifetime tests for low-noise GaAs- and InP-based MODFETs. Activation energies of 1.9 and 1.6 eV are apparent for GaAs- and InP-based devices, respectively. (Courtesy of P. M. Smith of Lockheed Martin).

research, epitaxial technology with respect to production issues is paving the way for MODFETs. Companies such as Hewlett-Packard already produce large quantities of low-noise amplifiers and mixers on the same chip.

7. AlGaIn/GaN MODFETs

Semiconductor GaN-based field-effect transistors (FETs) are projected to be highly useful for amplification and switching in high-power and/or high-temperature environments. This optimism is justifiably fueled by the calculated large electron velocity and the robustness of the material. Other pertinent parameters include, but are not limited to, large thermal conductivity of GaN, type I

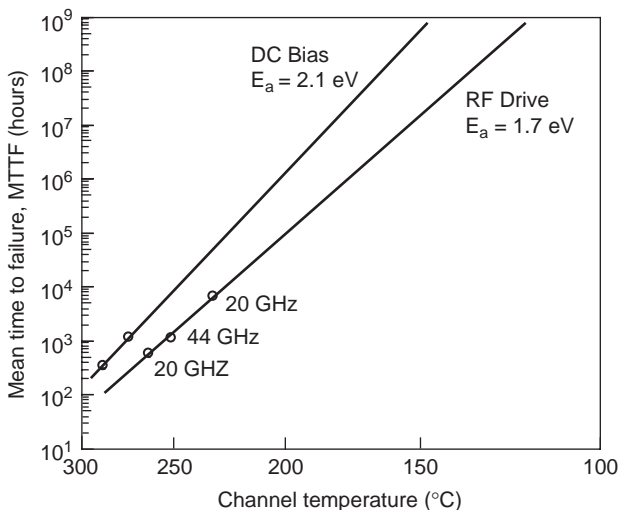


Figure 9. Accelerated lifetime tests for power GaAs-based PMODFETs. Activation energies of 2.1 and 1.7 eV are apparent for DC and RF biases, respectively. (Courtesy of P. M. Smith of Lockheed Martin).

heterojunctions, and large band discontinuities with resultant large interface carrier concentrations and large breakdown voltage, although this requires high-quality films [173,174]. Consequently, there has been a flurry of activity in GaN-based MODFETs [175–181]. The results are extraordinarily encouraging, and needless to say, research activity is on a rapid rise. These devices are receiving increased attention as the crystal growth techniques and processing methods advance to the point where the performance predicted by the material characteristics are beginning to be approached. The large conduction band offset between AlGaIn/GaN [182,183] possibly in conjunction with the strain-induced piezoelectric effect as alluded to in the literature [184–186] has enabled the realization of large measured carrier concentrations.

Electronic properties of modulation-doped structures based on the III-Nitride semiconductor system have been theoretically treated by Stengel et al. [187]. The structure considered for this particular study was a wurtzitic $\text{Al}_x\text{Ga}_{1-x}\text{N}/\text{GaN}$ -layered normal MODFET structure. For source and drain contacts, a scheme where the metal contact is deposited on $\text{Al}_x\text{Ga}_{1-x}\text{N}$ was considered with the well-justified assumption that contact metal penetrates down to the GaN layer, which hosts the two-dimensional electron gas. Because of conduction band discontinuity, the electrons diffusing from the larger-bandgap AlGaIn into the smaller-bandgap GaN form a triangular quantum well in the $\text{Al}_x\text{Ga}_{1-x}\text{N}/\text{GaN}$ interface.

7.1. Band Diagram for AlGaIn/GaN MODFETs

For illustrative purposes, the energy band diagram for a normally on (N-ON) MODFET, ignoring polarization effects as calculated by Stengel et al. [187] are shown in Fig. 11 for AlN mole fraction, $x = 0.25$, donor concentration in AlGaIn, $N_d = 10^{19} \text{ cm}^{-3}$, and the undoped layer thickness (spacer layer) in AlGaIn, $W_{sp} = 20 \text{ \AA}$. Also shown is the electron gas concentration at the heterointerface. For the calculations for N-ON MODFET, a gate bias of $V_g = 0.04 \text{ V}$, and doped AlGaIn layer thickness of $d = 200 \text{ \AA}$ were used. The two-dimensional electron gas (2DEG) does not extend to the AlGaIn region because of a high $\text{Al}_x\text{Ga}_{1-x}\text{N}/\text{GaN}$ conduction band discontinuity (more than 500 meV as compared to 142 meV for $\text{Al}_x\text{Ga}_{1-x}\text{As}/\text{GaAs}$ at $x = 0.3$). Because of this, and the fact that the amplitude of electron wavefunctions extending to the $\text{Al}_x\text{Ga}_{1-x}\text{N}$ is very low, a thinner spacer would be needed to achieve the optimal mobility in the 2DEG as a result of lower alloy scattering [188]. In spite of this, the effect of Coulombic scattering could presumably be opposite, especially because of the lower dielectric constant of GaN and AlGaIn, which leads to a higher scattering potential. Very precise calculations or experiments would be needed to resolve this matter. For the MODFET of Fig. 11, the quasi Fermi level in GaN is far above the lowest energy level, and the peak concentration of electron in the 2DEG is 10^{19} cm^{-3} . Also, some of the donor atoms (for z between -100 and -50 \AA) are now neutralized, and some electrons start to appear in the $\text{Al}_x\text{Ga}_{1-x}\text{N}$ region. For these reasons, a further rise in gate bias causes an increase not only in the donor neutralization but also in the electron concentration in

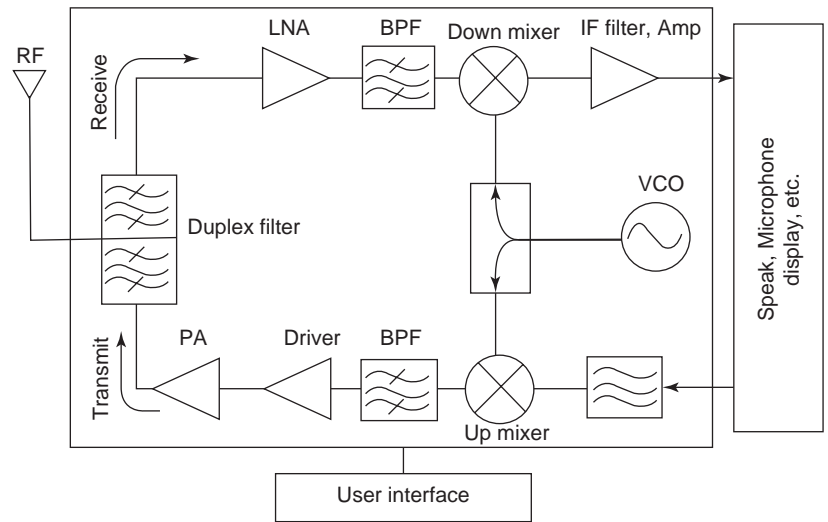


Figure 10. Mobile telephone cellphone RF section with areas of opportunity for compound semiconductor devices shown in bold lines. (After M. Golio of Motorola [234].)

$\text{Al}_x\text{Ga}_{1-x}\text{N}$. However, the 2DEG concentration remains unaltered.

Calculations employing typical parameters [7] for GaN and AlGaN indicate that the peak value of 2DEG concentration for $\text{Al}_x\text{Ga}_{1-x}\text{N}/\text{GaN}$ MODFETs is around $2\text{--}5 \times 10^{12} \text{ cm}^{-2}$. However, much larger values of n_{2D} have been measured, which is most likely due to ionization and redistribution of shallow charges caused by the piezoelectric effect. Figure 12 shows n_{2D}/V_g plots for various spacer thicknesses. As long as the unintentional doping level in the spacer layer is low, the effects of varying the AlN mole fraction x and W_{sp} on n_{2D} are essentially equivalent, because at the end of the spacer layer the value of $E_c - E_F$ is very close to $E_c(\text{interface}) - W_{sp}(dE_c/dz)(\text{interface})$. Experimental data describing the effect of the spacer-layer thickness on electron mobility in the 2DEG are needed in order to evaluate optimized values for this spacer layer.

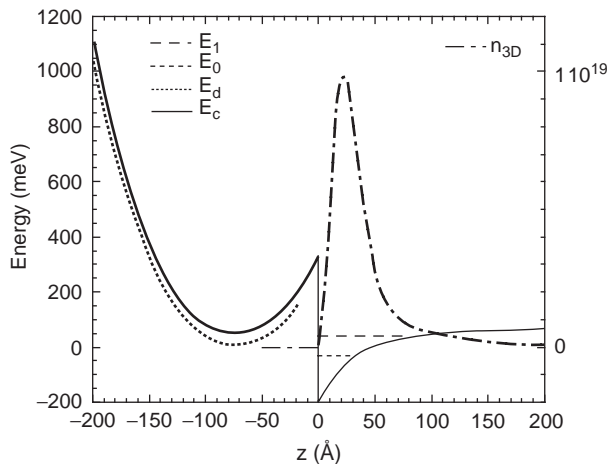


Figure 11. Band diagram for a normally-on MODFET. The origin of energy for these band diagrams is the Fermi level. The left side of $z = 0$ line corresponds to the AlGaN region and the right side, to the GaN. The donor level in AlGaN is represented by E_d ; the quantum energy levels in GaN are represented by E_0 and E_1 . The term E_c represents the conduction band edge in AlGaN and GaN layers.

One may, however, predict that these values for the $\text{Al}_x\text{Ga}_{1-x}\text{N}/\text{GaN}$ system would be smaller than those for the $\text{Al}_x\text{Ga}_{1-x}\text{As}/\text{GaAs}$ system, because the $\text{Al}_x\text{Ga}_{1-x}\text{N}/\text{GaN}$ system provides a deeper confinement, and the wavefunction of the 2DEG over a shorter range in $\text{Al}_x\text{Ga}_{1-x}\text{N}$ is nonzero.

Stengel et al. [187] calculated the variation of transconductance with gate bias for various channel lengths as shown in Fig. 13. When the channel length was decreased from 1 to $0.2 \mu\text{m}$, the peak transconductance increased from 420 to above 900 mS/mm. These very large values of transconductances are made possible when the values of both V_g and V_d were chosen to be small to avert the velocity saturation of the carriers. This was indeed very encouraging considering the fact that, for all practical purposes, MODFETs with reduced channel length are very desirable, and have lower leakage current at the operating point. Notably, the peak transconductance of these MODFETs is obtained for lower gate biases.

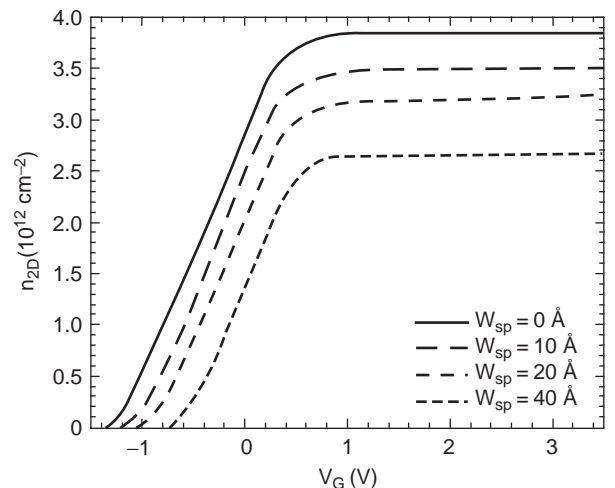


Figure 12. Plots of the 2DEG concentration as a function of the gate-source bias V_g for various values of the spacer layer thickness in $\text{Al}_x\text{Ga}_{1-x}\text{N}$.

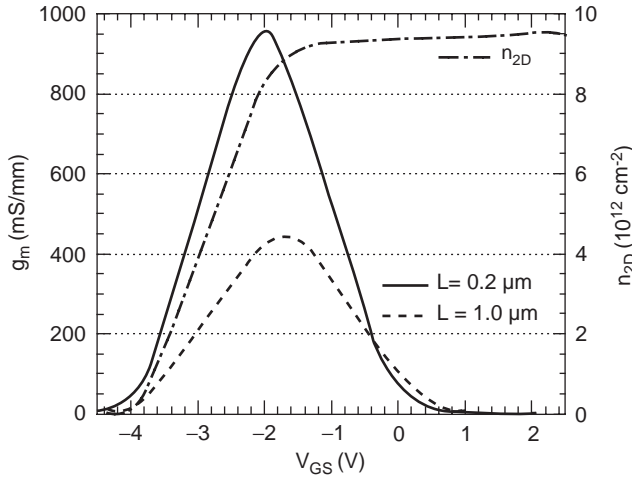


Figure 13. Variation of the transconductance g_m of MODFETs as a function of the gate-source bias V_g at the optimal value of the drain-source bias V_d (optimum value of V_d is defined to be the value at which transconductance peak reaches its maximum value) for each plot, for various values of the channel length L and values of 1 and $0.2\ \mu\text{m}$. The parameters used for the 2DEG are $d = 130\ \text{\AA}$, $N_d = 10^{19}\ \text{cm}^{-3}$, $W_{sp} = 20\ \text{\AA}$, $x = 0.25$, and $E_d = 45\ \text{meV}$.

The drain current can also be obtained from the model of Stengel et al. [187] as shown in Fig. 14. For a relatively relaxed geometry device, $L = 2\ \mu\text{m}$. The pinchoff depends on the relative values of the gate-source and the drain-source voltages. While the gate-source voltage tends to keep channel electrons stuck to the $\text{Al}_x\text{Ga}_{1-x}\text{N}/\text{GaN}$ surface, the drain-source voltage tends to drag them away to the drain. This competition between the gate-source and the drain-source voltages becomes increasingly imbalanced as the difference between them increases. Consequently, the length of the pinchoff region and hence the leakage become larger when the drain-source voltage becomes much larger than the gate-source voltage. This

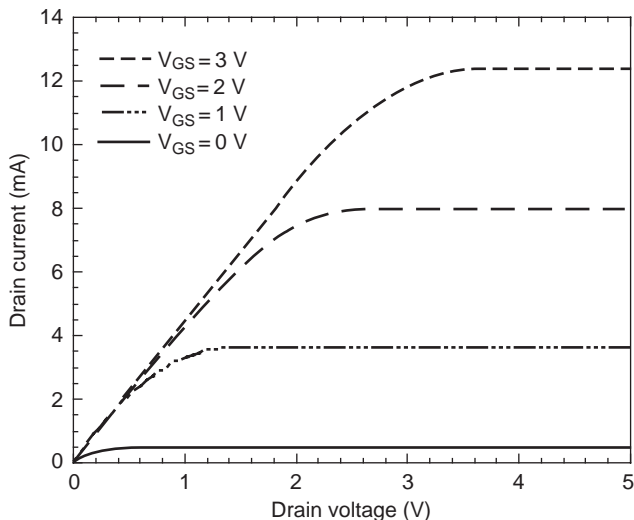


Figure 14. Calculated drain-source current I_d for AlGaIn/GaN MODFETs under various gate-source bias conditions (0, 1, 2, and 3 V).

causes a slight decrease in drain saturation current with increasing drain-source voltage V_d .

7.2. Performance of GaN MODFETs

As stated earlier, modulation-doped field-effect transistors utilize a two-dimensional carrier gas confined at an interface between two layers with an interfacial energy barrier such as $\text{AlGaAs}/\text{GaAs}$ and $\text{AlGaAs}/\text{InGaAs}$. A GaN MODFET taking advantage of the background donors in the AlGaN layer, which is not a controllable, to say the least, was reported. Congruent with the early stages of development and defect-laden nature of the early GaN and AlGaN layers, the MODFETs exhibited a low-resistance state and a high-resistance state both before and after application of a high drain voltage (20 V). As in the case of $\text{GaAs}/\text{AlGaAs}$ MODFETs, hot-electron trapping in the larger bandgap material at the drain side of the gate is primarily responsible for the current collapse. The negative electron charge accumulated as a result of this trapping causes a significant depletion of the channel layer, more probably a pinchoff, leading to a drastic reduction of channel conductance and decrease of the drain current. This continues to be effective until the drain-source bias is substantially increased, leading to a space charge injection and giving rise to an increased drain-source current.

7.2.1. Single Heterostructures. The DC drain characteristics of MODFETs with a gate length of $2\ \mu\text{m}$, gate width of $40\ \mu\text{m}$, and drain-source separation of $4\ \mu\text{m}$ are presented in Fig. 15. The maximum drain-source current I_{ds} corresponding to a drain-source voltage $V_{ds} = 3\ \text{V}$ and strong forward gate bias ($\sim 3\ \text{V}$) is about $500\ \text{mA}/\text{mm}$. The linear characteristics of the I/V curves demonstrate that the source and drain contacts of the MODFETs are highly ohmic. Good ohmic characteristics of the source and drain contacts probably led the present MODFETs to exhibit a substantially higher drain-source current. These MODFET with $2\text{-}\mu\text{m}$ gate lengths have room-temperature extrinsic transconductances of about $g_{em} = 185\ \text{mS}/\text{mm}$.

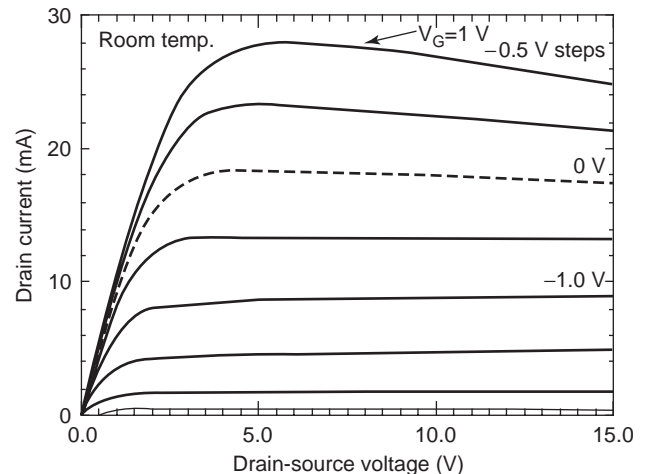


Figure 15. DC drain characteristics of a single-heterostructure MODFET with a gate length of $2\ \mu\text{m}$, gate width of $40\ \mu\text{m}$, and drain-source separation of $4\ \mu\text{m}$.

The peak value in the g_{em}/V_{gs} curve occurs at the gate-source voltage $V_{gs} = 1$ V and the drain-source voltage $V_{ds} = 4$ V. With increase in V_{gs} , there occurs higher accumulation of electrons in the active channel and a higher variation of I_{ds} with respect to V_{gs} at a certain value of V_{ds} . Consequently the transconductance increases with V_{gs} . However, when V_{gs} exceeds a certain limit, specifically, 4 V, the accumulation of electrons in the active channel no longer increases at the previous rate with increasing V_{gs} , and the voltage drop in the extrinsic circuit increases. As a result, the transconductance decreases with V_{gs} . The drain-source breakdown voltages are in the range of 100 V per 1- μ m spacing; the exact value depends on the layer design and quality of the layered structure.

7.2.2. Double Heterostructures. In order to increase the current capability of MODFETs, multi-2DEG structures are employed. In this case, the GaN layer is straddled by two doped AlGaIn that donate electrons to the channel, increasing the number of electrons available for current conduction. By Hall effect measurement, the mobility and sheet carrier densities in the two-dimensional electron gas (2DEG) were about 304 cm²/V-s and 3.7×10^{13} cm⁻², respectively, at room temperature. The sheet carrier concentration may have been affected by piezoelectric effect. A number of double heterochannel MODFETs (DHCMODFETs) with gate lengths of 1.5–1.75 μ m and gate width of 40 μ m have been reported.

The DC drain characteristics at room temperature of the DHCMODFET device with gate length of 1.5 μ m, gate width of 40 μ m, and drain-source separation of 3 μ m are presented here. The maximum drain-source current I_{ds} corresponding to a drain-source voltage $V_{ds} = 7$ V, $V_{gs} = 3.5$ V is about 1100 mA/mm, which is important as in high-power devices the input is momentarily forward-biased. The DHCMODFET has a room-temperature extrinsic transconductance $g_m = 270$ mS/mm. The value of the total resistance R_T extracted from the linear region of the I/V curves is 4 Ω mm. Near pinchoff, the drain breakdown voltage is about 80 V, indicating excellent power potential of the device. These measurements were made in a nitrogen-pressurized container to avoid possible oxidation of the contacts and probes. The maximum drain-source current and extrinsic transconductance of the DHCMODFET are 500 mA/mm and 120 mS/mm, respectively. These devices maintain reasonable output characteristics at temperatures as high as 500°C with maximum drain current and extrinsic transconductance values of 380 mA/mm and 70 mS/mm, respectively. Cool down back to room temperature restored the characteristics, which is indicative of the robustness of this material system and metallization employed.

7.3. Interface Roughness

The mobility in AlGaIn/GaN structures ranges from about 500 to over 2000 cm²/V-s, which is higher than that obtainable in bulk GaN, but may still be lower than that eventually expected. The charge state of defects in GaN and AlGaIn near the interface and geometric effects such as interface roughness may not be negligible. The AFM

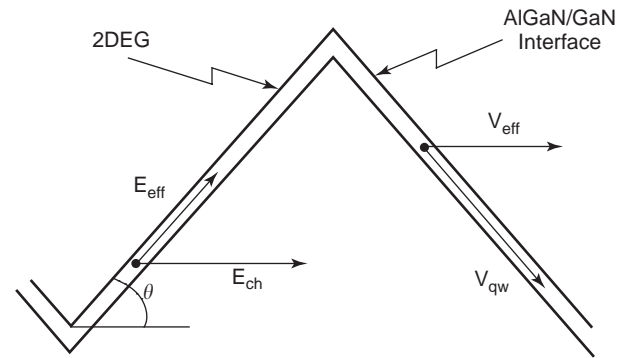


Figure 16. Schematic diagram showing three-dimensional surface and the reduction in electric field and velocity of the carriers in the channel.

(atomic force microscope) measurements indicate the presence of a 3D roughness on the surface of these samples. This roughness, combined with polarization effects, is likely to also have a strong effect on the mobility because it reduces the effective electric field on the electrons and the effective speed of electrons across the channel. As may be noted from Fig. 16, albeit somewhat exaggerated for the purpose of making the point, the effective field on the electrons in the channel is $E_{ch} \cos(\theta)$, and the effective velocity $V_{QW} \cos(\theta)$. The extent of the mobility reduction due to this effect may be calculated by taking an average over the surface, which would be difficult to perform analytically. However, for a qualitative understanding of this, we may consider the mean values of the measured roughness, which would yield $\theta = 60^\circ$ and the effective value of the mobility μ 0.25 times the original value, which may be considered to be a significant reduction in the mobility.

The value of the total resistance, $R_t = R_s + R_{ch} + R_d$, where R_s is the source area resistance, R_{ch} is the channel area resistance, and R_d is the drain area resistance, is extracted from the linear region of the I/V curves after accounting for the leakage from the gate. Using these values, we may calculate the intrinsic transconductance as a function of temperature. Assuming a long-channel operation, it would allow us to extract the μn_s product of the mobility μ and the sheet carrier concentration n_s from the intrinsic transconductance values. The same product μn_s may be extracted also from the values for R_T by assuming that the drain and source resistances are negligible. The analysis shows that the ohmic contacts do not really play a significant role in decreasing the transconductance at all temperatures. Therefore, the increase in these resistances should be due mostly to a decrease in the mobility-sheet carrier density product. Probably as a result of higher ionization of dopant atoms in n-AlGaIn, the 2DEG concentration increases slowly with increasing temperature. Thus, the observed decrease in transconductance and increase in the channel resistance is actually due to the decrease in the low field mobility and the saturation velocity. The mobility degradation caused by 3D surface roughness is not expected to have temperature dependence. Therefore, the decrease in transconductance by an increase in temperature may be an intrinsic

mechanism, most likely by polar optical phonon scattering, which is very effective at high temperatures.

7.4. RF Results

MODFETs have progressed to a point where microwave measurements have been performed on a variety of devices with gate length as wide as 2 μm and as narrow as about 0.2 μm. A typical MODFET structure with 2-μm gate lengths have been tested at small-signal *S*-parameter measurements were performed at bias conditions used for the power measurements, namely, 15 V, -2.5 V, and 20 mA for the drain voltage, gate voltage, and drain current, respectively. Short circuited current gain, maximum available power gain, and the unilateral gain calculated from the small-signal *S* parameters are shown in Fig. 17. Short-circuited current gain, maximum available gain, and unilateral gain as a function of frequency under bias conditions of $V_{ds} = 15$ V and $V_{gs} = -2.5$ V are presented. The I_{ds} at this bias was approximately 20 mA, which corresponds to 260 mA/mm. The unity current gain cutoff frequency (f_t) and maximum frequency of oscillation were 6 and 11 GHz, respectively, at both 15 and 30 V bias. Values in excess of 50 and 100 GHz have been reported for short-channel devices, respectively, at about 0.2 μm. The CW microwave power measurement results are presented in Fig. 18. The measurements were taken at 4 GHz with the input power swept from 5 to 18 dBm in 14 steps. The input and output matches, which were used during the power sweep, were determined by iterating between source and load pulls. The output match was selected to optimize the output power, and the input match was selected to maximize the delivered power. The devices were biased to $V_{ds} = 15$ V and $V_{gs} = -2.5$ V. The I_{ds} at this bias was approximately 20 mA, which corresponds to 260 mA/mm. From the figure, we see that the devices exhibited 6 dB gain for various input levels. The maximum output power was 20.6 dBm, and the peak PAE was 17.5%. This corresponds

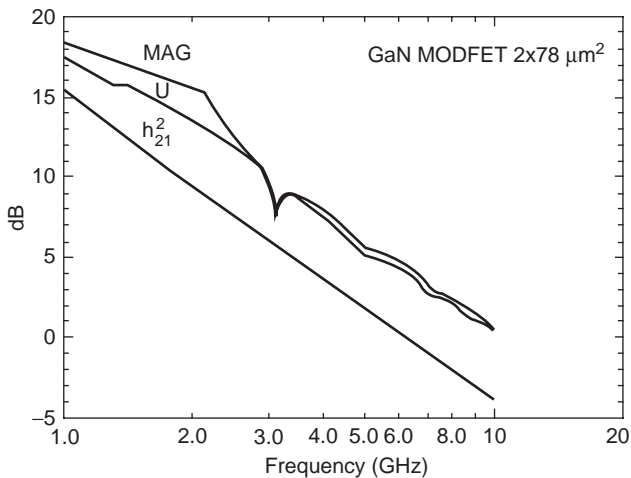


Figure 17. Short-circuited current gain, maximum available gain, and unilateral gain as a function of frequency under bias conditions of $V_{ds} = 15$ V and $V_{gs} = -2.5$ V. The I_{ds} at this bias was approximately 20 mA, which corresponds to 260 mA/mm.

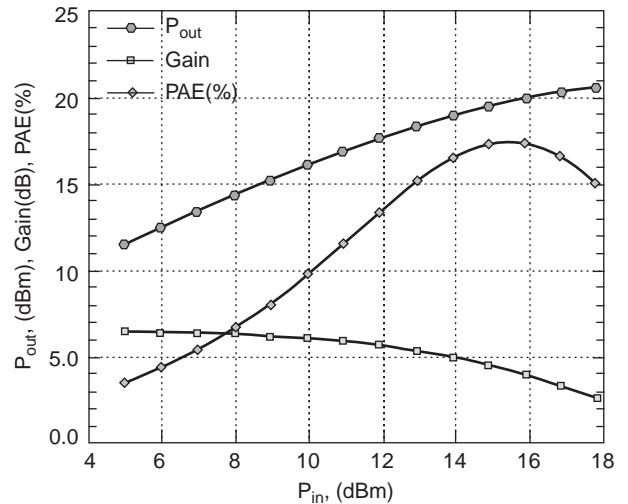


Figure 18. CW output power, power gain, and power-added efficiency versus input power level.

to a normalized output power density of 1.5 W/mm. Improved devices with shorter gate lengths have demonstrated normalized power levels of about 2.56 W/mm at X band, extrapolated from small-gate-width devices that sidesteps the thermal limitations imposed by sapphire substrates [179].

Inclusion of thermal limitations leads to the results shown in Fig. 19 for devices that compete in the high-power-device arena [8]. Since new device developments do in general compete with existing and alternative technologies, a brief account of competing technologies for the power arena will be given below. The Si MESFET analytical curve, modeled for its simplicity, is slightly above the SiC analytical curve and indicates a maximum power density of 0.35 W/mm at $V_{ds} = 7$ V, which is slightly lower than 0.39 W/mm. Since Si RF MESFETs are unavailable, commercial Si RF MOSFET results have been used for comparison instead. At low voltages the Si MOSFET data

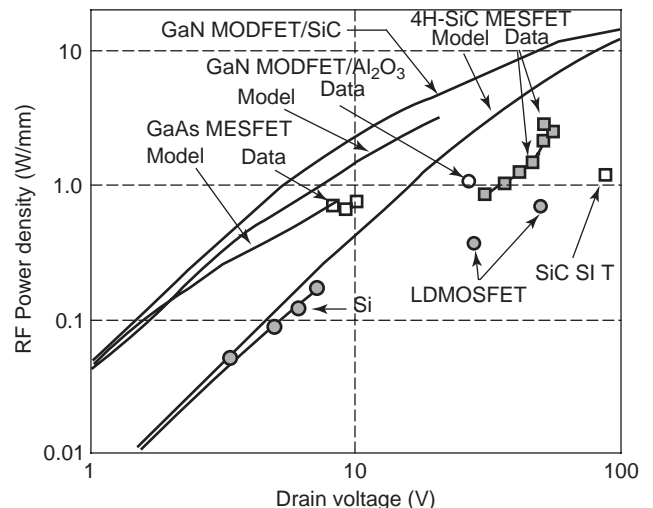


Figure 19. Simulated and experimental RF power density data for Si, GaAs, SiC, and GaN FET's. (After C. Weitzel et al. [8].)

parallel the analytical curve, suggesting the validity of the functional dependence of power density on drain voltage. Also shown are two higher power density data points at 0.4 W/mm, with $V_{ds} = 28$ V and 0.87 W/mm, with $V_{ds} = 48$ V. These higher power densities were obtained with specially designed RF power MOSFETs that incorporate lightly doped drains and field plates that significantly increase the breakdown voltage. The GaAs analytical curve shows the highest power density of all the devices at the lowest voltages primarily because of the higher electron mobility of GaAs. However, the low breakdown field limits the GaAs MESFETs drain voltage to about 8 V and power density to 0.63 W/mm, including thermal effects. Typical commercially available GaAs MESFET power densities are below 1 W/mm. However, high-performance GaAs FETs with more complex device cross sections have achieved power densities as high as 1.4 W/mm at 18 V. The SiC MESFET has a calculated maximum power density at 100 V both with and without factoring in thermal effects of 7.96 and 9.7 W/mm, respectively. The highest demonstrated continuous-wave power density 3.3 W/mm ($V_{ds} = 50$ V) for a SiC MESFET [189] is also shown for comparison. Additional SiC data again illustrate the functional dependence of power density on drain voltage. The GaN analytical results are highly dependent on the thermal conductivity of the substrate. With a sapphire substrate, the device is severely thermally limited to 2.24 W/mm at 30 V with a resulting channel temperature of $>400^\circ\text{C}$. The GaN results of analytical models are highly dependent on the thermal conductivity of the substrate. With a sapphire substrate, the device is severely thermally limited to 2.24 W/mm at 30 V with a resulting channel temperature of $>400^\circ\text{C}$. However, with a SiC substrate, the analysis predicts that a GaN MODFET could achieve 15.5 W/mm at 100 V while keeping the channel temperature at about 300°C [8].

GaN MODFET devices on conducting 6H-SiC substrates exhibited output characteristics that lacked the negative resistance (i.e., they exhibited good heatsinking). There have subsequently been a few reports of MODFET power devices on high-resistivity SiC [190–192] and p-type SiC [193] substrates with phenomenal improvement in power-handling capability notwithstanding the rapid progress on sapphire substrates. On sapphire, recent 0.7- μm -gate-length $\text{Al}_{0.5}\text{Ga}_{0.5}\text{N}/\text{GaN}$ MODFETs exhibited a current density of 1 A/mm, three-terminal breakdown voltages up to 200 V, and CW power densities of 2.84 and 2.57 W/mm at 8 and 10 GHz, respectively, representing a marked performance improvement for GaN-based FETs. Outstanding power levels are increasingly being achieved with near-0.5- μm or smaller gate lengths. To follow the evolution of the developments, a few examples are cited here. With 0.7- μm -gate-length devices on SiC substrates, where the gate–source spacing and gate–drain spacing were 0.5 and 0.8 μm , respectively, a total output power of 2.3 W in a device with a 1.28-mm gate periphery has been obtained [191]. The power gain at the 2.3-W output power point was 3.6 dB with a power-added efficiency (PAE) of 13.3% for a drain bias of 33 V. The current and power gain cutoff frequencies were 15 and 42 GHz, respectively. The contact resistance, although not the best, was between 2.6

and $3.5 \Omega \cdot \text{mm}$. The maximum normalized transconductance was 270 mS/mm, and the drain current was 293 mA/mm. Steady improvement in power performance has led to results at HRL laboratories with recordbreaking performance [194]. Typical DC characteristics include 600 mA/mm current performance and >60 V drain breakdown voltage. The current gain cutoff and maximum power gain cutoff frequencies measured were about 48 and 100 GHz, respectively, for -5.5 and 12.5 V gate and drain bias voltages, respectively. A minimum noise figure of 0.85 dB at 10 GHz with an associated gain of 11 dB is simply remarkable. Also, 6.3 W of CW output power was obtained at 10 GHz from a 1-mm-wide transistor device. More importantly, the power density remained nearly constant as the device size was scaled upward from a 0.1 mm width, where the device exhibits 6.5 W/mm, to 1.0 mm. These record-setting transistors were epitaxially grown AlGaIn/GaN heterostructures on seminsulating SiC (silicon carbide) substrates by MBE. HRL laboratories have expanded their work to amplifiers with several cells and showed very good power scalability up to 2 mm of total gate periphery [194]. Using 250-nm-gate devices, a CW output power of 22.9 W with an associated power-added efficiency of 37% was measured for an amplifier at 9 GHz with four 1-mm-gate periphery devices. Furthermore, the same authors [194] also showed a CW power density of 4 W/mm at 20 GHz, which is the state-of-the-art figure for any three-terminal solid state device at this frequency.

7.5. Anomalies in GaN/AlGaIn MODFETs

Field-effect transistors, in general, and modulation-doped field-effect transistors, in particular, exhibit anomalies in their output I/V characteristics. Among the causes of these anomalies are channel carriers being trapped in the wide-bandgap material and bulk, meaning the buffer layers. In addition surface states, if present and not passivated, could act to reduce the sheet conducting charge, particularly between the gate and the drain regions of the FETs [195]. Some AlGaAs/GaAs MODFETs, which are predecessors of the current AlGaIn/GaN MODFET, exhibit behavior similar to what was then termed “current collapse” [196]. This behavior was attributed to carrier injection from the channel to the AlGaAs at reasonably high fields where they are trapped at low temperatures. With below-the-gap light excitation, increasing temperature, and exchange of the source and drain terminals, the effect could be eliminated. The GaAs buffer layer for the AlGaAs/GaAs-based device is of high quality, so its trapping effect was not dominant. The surface states in the AlGaAs/GaAs device were not deemed to have a profound effect on the current voltage characteristics. However, it is always a prudent approach to passivate the surface states, as was done in the AlGaAs/GaAs device, as they greatly affect device operation with time. In the AlGaAs/GaAs variety, the trapping effect in the AlGaAs barrier was attributed to DX levels, which are caused by lattice-distorting defects, which causes massive change in the bandgap of the semiconductor at the local level, and their behavior could be described by a lattice coordination diagram. Since this effect reduced with lowering the AlAs mole fraction,

AlGaAs/InGaAs pseudomorphic modulation-doped FETs were developed [197], which are the dominant compound semiconductor FETs in industry at the moment, to mitigate the effect of DX centers.

In the AlGaN/GaN system, the surface states and/or defects play a much more important role due to polarization fields as the layers are on polar surfaces. Anomalous characteristics, such as the so-called current collapse, kinks in the I/V characteristics, and long-term instability, have haunted the device from the time of its early development. Preliminary investigations of these phenomena were undertaken some years earlier [198]. Now that these devices are strong contenders in the marketplace for systems applications, these phenomena are getting a good deal of attention. One of the anomalous behaviors is the drain current lag, which prevents attainment of RF power congruent with the DC output characteristics of the device. For a maximum drain voltage of 50 V (drain bias of 25 V) and maximum drain current of 1 A, one should normally get 6.25 and 12.5 W in class A and class B operations, respectively, assuming an ideal case with zero saturation voltage, and no thermal limitation. However, the observed values in the laboratory are, in general, substantially smaller. This is due to current lag which is basically a failure on the part of drain current to keep up with the gate bias voltage in response to a high-frequency large-signal gate modulation [199], attributed to surface states.

The drain current lag is schematically shown in Fig. 20, where the load line and quiescent operating conditions for class A operation are shown. Also shown are the extremes of DC current as governed by the load line. Current lag is meant to indicate that the RF current (shaded) fails to follow the gate bias and thus the drain current at high frequencies is lower than that measured under DC conditions. The RF current can be determined by the use of the so-called load-pull tuning. It can also be measured under active loading conditions with the use of a high-speed sampling scope for measuring the output RF voltage, in response to an RF input drive, wherein the voltage measured can be converted to current, knowing the load value.

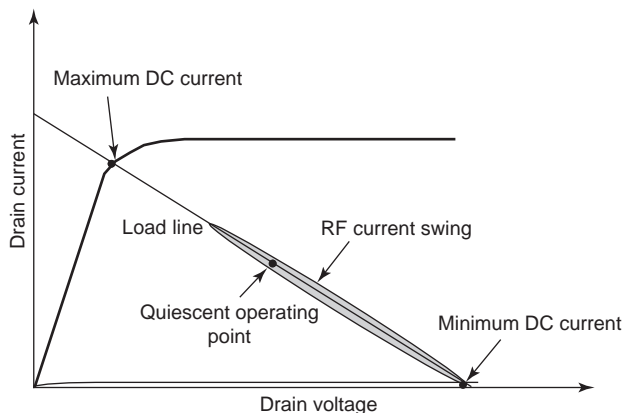


Figure 20. Schematic representation of RF current lag superimposed on top of DC drain I/V characteristics with a load line.

Traps are usually attributed to the current collapse. The loss of channel carriers as a result of being trapped at defects produces a large transverse electric field, which leads to the current collapse. The assumption is supported by the fact that light incident on the collapsed device photoionizes the trapped carriers and causes a restoration of the drain current [200,201]. The sudden removal of the current reduction at large V_{ds} (> 25 V) observed by Dietrich et al. [202] can also be explained by the field-enhanced carrier emission from traps.

The current lag can be measured as a function of frequency in the RF regime with an appropriate load line. Since the drain current does not follow the input stimulus due to surface traps, the term “lag” has been coined to describe the phenomenon. The surface must be appropriately passivated to avoid this degradation. The effective methods so far have been the use of low-temperature AlN [203] or Si_3N_4 [204] postgrowth and fabrication passivation layers. Better pinchoff characteristics, lower gate leakage current, reduction of current collapse, and increase of output power have been observed with surface passivation using Si_3N_4 [205–208]. However, whether surface state contributes significantly to current collapse remains unclear. If passivation alone is sufficient to eliminate the current lag, the issue of lattice distortion becomes an interesting one in that it raises the question as to whether the surface states are involved and if so, whether passivation layers also alter the strain picture.

7.6. Low- and High-Frequency Noise Performance

The low-frequency and high-frequency noise characteristics of GaN MODFETs are very important for the microwave applications of these devices. Investigation of the origin of noise is also important for understanding the physical processes taking place in the device. Although GaN MODFETs with excellent microwave performance have been fabricated for high-power and high-temperature applications, there is still little investigation on the noise properties.

7.6.1. Low-Frequency Noise. Low-frequency noise can be upconverted to high frequencies, limiting the performance of these transistors even in the microwave range. Low-noise electronics for communications necessitates some level of knowledge with respect to the origin of the processes responsible for low-frequency noise in GaN MODFETs. The low-frequency noise of GaN MODFETs usually exhibits flicker characteristics in the form of $1/f^\gamma$ dependence, where γ is close to 1. The dimensionless Hooge parameter α is commonly used, as shown as $\alpha = (S_I/I^2)f^\gamma N$, where f is frequency, N is the number of carriers, and S_I/I^2 is the relative spectral density of noise.

The first reported Hooge parameter (α) for the GaN MODFET has an approximate value of 10^{-2} [209]. Since then, transistors with low values of $\alpha \approx 10^{-4} \sim 10^{-5}$ have been reported [210–212], where the α parameter is comparable to that for commercial GaAs FET. It was observed that the noise level in GaN MODFETs is dependent on the structural perfection or the imperfection in the case may be. The noise level for MODFETs grown on sapphire sub-

Table 5. High-Frequency Noise Characterization of GaN MODFETs

Gate Length (μm)	Drain Bias (V)	Gate Bias (V)	f (GHz)	F_{\min} (dB)	Associated Gain (dB)	Ref.
0.15	6	≈ -3	10	0.60	13.5	218
0.25	10	-4	5/10	0.77/1.06	14/12	219
2	10	-1.5	2	0.58	14.13	220
0.12	10	-4.8	8	0.53	12.1	221

strates is one order of magnitude larger than those on SiC substrates [213,214]. In addition, Romyantsev et al. [214] observed that the noise spectrum for some samples on sapphire has a plateau at low frequencies, which is a characteristic feature of the generation–recombination (GR) noise. Only at very low noise levels (Hooge parameter on the order of 10^{-4}) does the contribution of generation–recombination noise become significant. It was found that GR noise for devices grown on sapphire has an activation energy $\Delta E \approx 0.42$ eV [214]. On the contrary, the temperature sensitivity for the noise level of devices grown on SiC is very weak, which is essential for high-temperature applications. Balandin et al. [215] reported $\Delta E \sim 0.85$ eV for transistors grown on sapphire and $\Delta E \sim 0.20$ – 0.36 eV for those grown on SiC. The trap densities for undoped and doped devices are $1.1 \times 10^{16} \text{ cm}^{-3}$ and $7.1 \times 10^{17} \text{ cm}^{-3}$, respectively [216]. Romyantsev et al. [217] reported a large activation energy $\Delta E \sim 0.8$ – 1.0 eV for GaN MODFET and MOS-MODFET (MODFET with SiO_2 whose role is prematurely likened to the gate dielectric in Si MOSFETs) grown on insulating 4H-SiC. The analysis indicates that the traps responsible for the observed GR noise could originate in the AlGaIn barrier layer, which has an estimated trap density of about $5 \times 10^{16} \text{ cm}^{-3}$.

7.6.2. High-Frequency Noise. Preliminary investigations of high-frequency noise performance have shown that GaN MODFETs have respectable microwave noise properties that are nearly comparable to those of AlGaAs/GaAs MODFETs. Table 5 displays studies of the microwave noise performance for GaN MODFETs. These encouraging results serve to motivate further investigation.

Lu et al. [222] also studied the effect of surface passivation on high-frequency GaN MODFET with $0.25 \mu\text{m}$ gate length. Although the gate leakage current was smaller after passivation, the noise measurements after passivation showed that the devices exhibited about 0.2–0.25 dB increase in F_{\min} . This was due mainly to the 1–1.5-dB decrease of associated power gain attributed to the increased C_{gs} and C_{gd} . It was concluded that the effect on microwave noise performance is a combination of effects of lower gate leakage current and higher surface dielectric constant.

7.7. Piezoelectric Effect

The III–V nitride semiconductors possess highly pronounced piezoelectric and spontaneous polarization properties. As such, any strain present in these crystals causes a distortion in atomic orbitals that leads to large polarization effects and must be taken into consideration, particularly in dealing with strained heterostructures. The

piezoelectric effect has become the focus of attention, with many claims including achievement of MODFET channels with no intentional doping anywhere in the entire heterostructure. It should be made clear that the resultant polarization field causes redistribution of the free and weakly bound charge, which could be mistakenly interpreted as bonus carriers [7]. The treatment must also include the charge redistribution in the presence of metal semiconductor contacts such as gate Schottky barriers and ohmic contacts. In positive strain (tensile strain), the direction of the polarization is from the anion, *B*-face, to the cation, *A*-face, sites. As can be easily imagined, if the growing nitride surface contains both polarities, the direction of the polarization vector would follow suit and would point either upward or downward depending on the spot. If the strain is tensile, then the polarization vector would be from the surface toward the substrate.

8. $\text{Si}_{1-x}\text{Ge}_x$ MODFET STRUCTURES

The advent of high-quality SiGe layers on Si substrates has paved the way for the exploration and exploitation of heterostructure devices in a Si environment. Tensile-strained Si films on strain-relieved SiGe buffer layers enable the formation of electron quantum wells, which exhibit enhanced electron mobilities. Compressively strained SiGe, or even pure Ge layers, can be used to create two-dimensional hole channels [223]. Silicon–germanium MODFETs have a significant high-frequency potential. Maximum oscillation frequencies of more than 100 GHz have been obtained. Capitalizing on the favorable band discontinuities outlined by Abstreiter et al. [224] Ismail et al. [225] reported encouraging values of electron mobility in a modulation-doped strained $\text{Si}_{0.7}\text{Ge}_{0.3}$ channel surrounded by $\text{Si}_{0.86}\text{Ge}_{0.14}$ donor layers. The cross-sectional view of this particular structure embedded into an FET structure is shown in Fig. 21. The electron mobilities measured were 1800, 9000, and 19,000 $\text{cm}^2/\text{V}\cdot\text{s}$ at room temperature, 77, and 1.4 K, respectively. The corresponding sheet electron densities are 1.2×10^{12} , 8.3×10^{11} , and $7.5 \times 10^{11} \text{ cm}^{-2}$, respectively. The layers were grown using UHV/CVD that offered a very low background impurity concentration in the intrinsic layers. As will be briefly mentioned below, the layered structures of this kind have been exploited for high transconductance modulation-doped FETs. Mii et al. [226] used a SiGe layer graded from 0% to 30% followed by a $\text{Si}_{0.7}\text{Ge}_{0.3}$ buffer layer, both of which were relaxed. A strained Si channel was grown on the $\text{Si}_{0.7}\text{Ge}_{0.3}$ buffer and capped with a doped $\text{Si}_{0.7}\text{Ge}_{0.3}$ layer. A maximum Hall mobility at 4 K of 125,000 $\text{cm}^2/\text{V}\cdot\text{s}$ has been obtained. The sheet electron

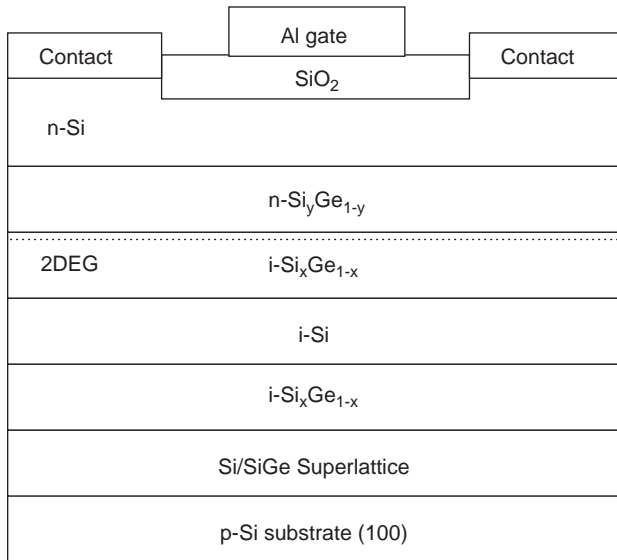


Figure 21. Schematic cross-sectional diagram of a strained layer SiGe/Si structure in conjunction with a MODFET device.

concentrations the heterostructure can sustain were 1.2×10^{12} at 300 K to 7.8×10^{11} at 77 K and below. Informal results indicate that mobilities close to $300,000 \text{ cm}^2/\text{V}\cdot\text{s}$ can be obtained, which compares with about $30,000 \text{ cm}^2/\text{V}\cdot\text{s}$ attainable in a Si/SiO₂ system. MODFETs with current gain cutoff and maximum oscillation frequency of about 32 and 40 GHz, respectively, have been reported in 0.5- μm -gate-length devices [227]. Aniel et al. [228] fabricated 100-nm T-gate strained Si/Si_{0.6}Ge_{0.4} n-MODFETs with new record performance, which has a cutoff frequency of 74 GHz at room temperature and maximum oscillation frequency of 107 GHz at room temperature. They also show a low noise figure NF_{min} of 0.4 dB and noise resistance of 52Ω at 2.5 GHz and room temperature. High quality Si/Si_{1-x}Ge_x/Si p-type modulation-doped double heterostructures with $x = 0.12$ and 0.15 have been grown using UHV/CVD by Wang et al. [229]. In this heterostructure, hole mobilities as high as $3700 \text{ cm}^2/\text{V}\cdot\text{s}$ at 14 K have been obtained with $x = 0.12$ and a Si spacer of 60 \AA for a sheet carrier concentration of $\sim 8 \times 10^{11} \text{ cm}^{-2}$. The values of hole mobility are roughly an order of magnitude higher than the highest values reported in p-type Si inversion layers and are most probably limited by remote ionized impurity scattering from the heavily doped Si layer, and/or the interfacial quality at the Si/SiGe heterointerface. Murakami et al. [230] utilized MBE grown a modulation-doped heterostructure where the strain at the heterointerface (p-Si_{0.5}Ge_{0.5}/Ge layers) is controlled by the Si composition ($1-x$) of the Si_{1-x}Ge_x buffer layer. When the Si composition is 25%, a hole mobility of $9000 \text{ cm}^2/\text{V}\cdot\text{s}$ at LN₂ temperature was achieved. Arafa et al. [231] have reported p-channel Si/SiGe MODFETs with extrinsic transconductances of 150 and 250 mS/mm for 1- and 0.25- μm -gate devices, respectively. As the gate length was reduced from 1 to 0.25 μm , the current gain cutoff frequency increased from 5 to 40 GHz. Preliminary devices with 0.1 μm gate lengths appear to show current gain cutoff frequencies of about 70 GHz. A cutoff frequency of 45 GHz, a maximum oscillation frequency of 81 GHz,

and an extrinsic transconductance of 142 mS/mm have been achieved on p-type SiGe MODFET with a 0.1 μm gate length. The minimum noise figure is 1.29 dB, while the associated power gain is 12.8 at 2 GHz [232]. The reader is referred to a review by König [233] for developments in both n-channel and p-channel SiGe-based FET technology. The more recent emphasis of SiGe technology is on bipolar and bipolarMOS (BiCMOS) technology, in which the Si bipolar devices and SiGe HBTs can be integrated for critical high-speed analog or digital functions.

9. CONCLUSIONS

In less than two decades (at the time of writing), the MODFET technology has evolved dramatically, from an interesting research innovation to an extremely formidable and yet practical device with numerous application areas, including wireless, low power communications, direct satellite broadcasting systems, millimeter-wave systems, and digital electronic systems. As is evident from the tables and figures presented in the body of the text, the MODFET has progressed to the point where the performance barriers thought to be insurmountable by three-terminal devices not long ago have been overcome with amazing dispatch. Although the GaAs channel MODFETs were formed the genesis of this unique device, the pseudomorphic MODFET with InGaAs channels has become the device of choice. Strained channel MODFETs with 80% InAs in their channel layers have shown current gain cutoff frequencies above 300 GHz. Again, strained channel MODFETs with 60% InAs in their channels exhibited measured power gain at 140 GHz. The data clearly indicate that the pseudomorphic MODFET has demonstrated increasingly enhanced electronic properties without compromising the breakdown voltage afforded by GaAs. Strained channel InGaAs MODFETs on GaAs substrates currently hold the power record. In concert with the gain and power performance, strained layer MODFETs on GaAs have shown a noise performance of 1.4 dB in the 90 GHz range. Despite the enhanced hole mobilities measured in compressively strained InGaAs, the p-channel MODFETs do not appear to have gained remarkably better performance. The bulklike properties away from the zone center and band mixing, which is very likely at high electric fields, are thought to be responsible for such a lack of enhanced performance.

Because of their large bandgaps, large high field electron velocity, large breakdown fields, large thermal conductivity, and robustness, wide-bandgap nitride semiconductors have gained considerable attention. The ensuing materials developments paved the way to AlGaIn/GaN MODFETs with superior power performance. CW power levels of about 6 W have been achieved at 10 GHz in devices with 1 mm gate periphery that are comparable to power densities extrapolated from smaller devices. When four of these devices were power combined in a single-stage amplifier, a CW output power of 22.9 W with a power-added efficiency of 37% was demonstrated at 9 GHz. On the noise figure front, a minimum noise figure of 0.85 dB with an associated gain of 11 dB at 10 GHz was obtained. A

discussion of the current collapse and the current lag occurring in GaN-based MODFETs has been presented. In closing, GaN-based MODFETs have made great strides and are continuing to do so despite the less than ideal materials properties. Anomalies in the current voltage characteristics at low and high frequencies observed in these devices are attributed to traps in the structure, surface states, and slow trapping processes associated with the field-induced lateral extension of the strain near the gate. It may be only a matter of time for inclusion of these devices in systems.

Relatively recent introduction of SiGe alloys propelled the Si technology into the realm of the heterojunction world. The new Si/SiGe system has provided a laboratory in which to study quantum phenomena and has led to an exploration into commercially important devices such as MODFETs. SiGe channel MODFETs with 0.2- μm gate lengths challenge the 100-GHz cutoff frequency benchmark. The f_{max} of n-type MODFETs peaked at 183 GHz in late 2001. Moreover, the MODFET phenomenon has expanded to include the emerging wide-bandgap GaN/AlGaIn semiconductor system, which already is beginning to demonstrate high-frequency (current and power gain cutoff frequencies of about 50 and 100 GHz, respectively) and high-power operation.

Acknowledgments

The research into MODFETs conducted by the author spanning nearly over two decades have been funded by the Air Force Office of Scientific Research (AFOSR) under the direction of Dr. G. L. Witt. The author's research in GaN MODFETs has been funded by AFOSR and the office of Naval Research (ONR) under the directions of Dr. G. L. Witt and Mr. M. Yoder, Dr. C. E. C. Wood, respectively. The author would like to thank his students and colleagues for collaboration, in particular Dr. T. J. Drummond. Finally, the grants from AFOSR (Dr. Todd Steiner), NSF (Drs. L. Hess and U. Varshni), and ONR (Dr. C. E. C. Wood, Mr. M. Yoder, and Dr. Y. S. Park), are acknowledged.

BIBLIOGRAPHY

1. H. Morkoç, H. Ünlü, and G. Ji, *Fundamentals and Technology of MODFETs*, Vols. I, II, Wiley, New York, 1991.
2. H. Morkoç, B. Sverdlov, and G. B. Gao, *Proc. IEEE*, **81**(4):492–556 (April 1993).
3. T. J. Drummond, H. Morkoç, K. Lee, and M. Shur, *IEEE Electron. Device Lett.* **EDL-3**:338–341 (1982).
4. K. Lehovec and R. Zuleeg, *Solid State Electron.* **13**:1415–1426 (1970).
5. C. A. Liechti, Microwave field effect transistors—1976, *IEEE Trans. Microwave Theory Tech.* **MTT-24**:279 (1976).
6. J. M. Ballingall, P. Ho, G. T. Tessmer, P. A. Martin, T. H. Yu, P. C. Chao, P. M. Smith, and K. H. G. Duh, Paper presented at the Fall Meeting of the Materials Research Society, Boston, *MRS Symp. Proc.* Vol. 160, 1990, pp. 759–770.
7. H. Morkoç, *Wide Bandgap Nitrides and Devices*, Springer, Heidelberg, 1999.
8. C. Weitzel, L. Pond, K. Moore, and M. Bhatnagar, *Proc. Silicon Carbide, III—Nitrides and Related Materials*, ICSI,

- Aug. 1997, Stockholm, Sweden, Trans Publications, Ltd; Materials Science Forum, Vols. 1998, pp. 264–268, 907–912.
9. K. Hosogi, N. Nakano, H. Minami, T. Katoh, K. Nishitani, and M. Otsubo, *Electron. Lett.* **27**:2011–2012 (1991).
10. E. Y. Chang, K. C. Lin, E. H. Liu, C. Y. Chang, T. H. Chen, and J. Chen, *IEEE Electron. Device Lett.* **15**:277–279 (1994).
11. T. Ishikawa, K. Hosogi, M. Katsumata, H. Minami, and Y. Mitsui, *IEICE Trans. Fund.* **E77-A**:158–165 (1994).
12. C. S. Wu, F. Ren, S. J. Pearton, M. Hu, C. K. Pao, and R. F. Wang, *Electron. Lett.* **30**:1803–1805 (1994).
13. C. K. Pao, G. L. Lan, C. S. Wu, A. Igawa, M. Hu, J. C. Chen, and Y. C. Shih, *IEEE Microwave Guided Wave Lett.* **2**:394–396 (1992).
14. K. Suzue, S. N. Mohamad, Z. F. Fan, W. Kim, Ö. Aktas, A. E. Botchkarev, and H. Morkoç, *J. Appl. Phys.* **80**(6):4467–4478 (Oct. 15, 1996).
15. S. N. Mohammad and H. Morkoç, Progress in quantum electronics, *Prog. Quant. Electron.* **20**(5/6):361–525 (1996) (a monograph).
16. H. Morkoç, Beyond SiC! III—V nitride based heterostructures and devices, in Y. S. Park, ed., *SiC Materials and Devices*, Willardson and Beer Series. (R. K. Willardson and E. R. Weber, eds.), Academic Press, 1998, Vol. 52, Chapter 8, pp. 307–394.
17. Ö. Aktas, W. Kim, Z. Fan, S. N. Mohammad, A. Botchkarev, A. Salvador, B. Sverdlov, and H. Morkoç, *Electron. Lett.* **31**(16):1389–1390 (1995).
18. Z. Fan, S. N. Mohammad, Ö. Aktas, A. Botchkarev, A. Salvador, and H. Morkoç, *Appl. Phys. Lett.* **69**(9):1229–1231 (Aug. 26, 1996).
19. S. N. Mohammad, Z. -F. Fan, A. Salvador, O. Aktas, A. E. Botchkarev, W. Kim, and Hadis Morkoç, *Appl. Phys. Lett.* **69**(10):1420–1422 (Sept. 2, 1996).
20. Z. Fan, C. Lu, A. Botchkarev, H. Tang, A. Salvador, Ö. Aktas, W. Kim, and H. Morkoç, *Electron. Lett.* **33**:814–815 (1997).
21. Ö. Aktas, Z. Fan, A. Botchkarev, M. Roth, T. Jenkins, L. T. Kehias, and H. Morkoç, *IEEE Elect. Device Lett.* **18**:293–295 (1997).
22. P. Hacke, T. Detchprohm, K. Hiramatsu, and N. Sawaki, *Appl. Phys. Lett.* **63**:2676–2678 (1993).
23. T. G. G. Maffei, M. C. Simmonds, S. A. Clark, F. Peiro, P. Haines, and P. J. Parbrook, *J. Appl. Phys.* **92**:3179 (2002).
24. S. C. Binari, H. B. Dietrich, G. Kelner, L. B. Roland, K. Doverspike, and D. K. Gaskill, *Electron. Lett.* **30**:909–910 (1994).
25. M. A. Khan, J. M. Van Hove, J. N. Kuznia, and D. T. Olson, *Appl. Phys. Lett.* **58**:2408–2410 (1991).
26. M. R. H. Khan, H. Nakayama, T. Detchprohm, K. Hiramatsu, and N. Sawaki, *Topical Workshop on III–V Nitrides Proc.* (Nagoya, Japan, 1995); *Solid State Electron.* **41**(2):259–266 (1997).
27. P. J. Hartlieb, A. Roskowski, R. F. Davis, W. Platow, and R. J. Nemanich, *J. Appl. Phys.* **91**:732 (2002).
28. X. A. Cao, S. J. Pearton, G. Dang, A. P. Zhang, F. Ren, and J. M. Van Hove, *Appl. Phys. Lett.* **75**:4130 (1999).
29. P. Roblin, J. Rice, S. Bibykurma, and H. Morkoç, *IEEE Trans. Electron. Devices* **ED-35**:1207–1213 (1988).
30. T. S. Kuan, P. E. Baston, T. N. Jackson, H. Rupprecht, and E. L. Wylie, *J. Appl. Phys.* **54**:6952 (1983).
31. A. A. Ketterson, F. Ponce, T. Henderson, J. Klem, and H. Morkoç, *J. Appl. Phys.* **57**:2305 (1985).

32. F. Ren, A. Y. Cho, D. L. Sivco, S. J. Pearton, C. R. Abernathy, *Electron. Lett.* **30**:912–914 (1994).
33. J. S. Foresi and T. D. Moustakas, *Appl. Phys. Lett.* **62**:2859–2861 (1993).
34. M. A. Khan, J. N. Kuznia, A. R. Bhattarai, and D. T. Olson, *Appl. Phys. Lett.* **62**:1786–1787 (1993).
35. M. E. Lin, Ma, F. Y. Huang, Z. Fan, L. Allen, and H. Morkoç, *Appl. Phys. Lett.* **64**:1003–1005 (1994).
36. S. Nakamura, T. Mukai, and M. Senoh, *Jpn. J. Appl. Phys.* **30**:L1998–L2000 (1991).
37. S. Nakamura, M. Senoh, and T. Mukai, *Appl. Phys. Lett.* **62**:2390–2392 (1993).
38. Y. Wu, W. Jiang, B. Keller, S. Keller, D. Kapolnek, S. Denbaars, and U. Mishra, *Topical Workshop on III–V Nitrides*, Sep. 21–23, Nagoya, Japan, 1995; *Proc. Solid State Electron.* **41**(2):75–78 (1997).
39. Z. Fan, S. Noor Mohammad, W. Kim, Ö. Aktas, A. E. Botchkarev, and H. Morkoç, *Appl. Phys. Lett.* **68**:1672–1674 (1996).
40. J. K. Ho, C. S. Jong, C. C. Chiu, C.-N. Huang, and K. K. Shih, *Appl. Phys. Lett.* **74**:1275 (1999).
41. J. K. Ho, C. S. Jong, C. C. Chiu, C.-N. Huang, K. K. Shih, L. C. Chen, F. R. Chen, and J. J. Kai, *J. Appl. Phys.* **86**:4491 (1999).
42. L. C. Chen, J. K. Ho, C. S. Jong, C. C. Chiu, K. K. Shih, F. R. Chen, J. J. Kai, and L. Chang, *Appl. Phys. Lett.* **76**:3703 (2000).
43. R. Fischer, T. J. Drummond, J. Klem, W. Kopp, T. Henderson, D. Perrachione, and H. Morkoç, *IEEE Trans. Electron. Devices* **ED-31**:1028–1032 (1984).
44. W. Brockerhoff, H. Meschede, W. Prost, K. Heime, G. Weimann, and W. Schlapp, *IEEE Trans. MTT* **37**(9):1380 (1989).
45. S. Bollaert, P. Legris, E. Delos, A. Cappy, P. Debray, and J. Blanchet, *IEEE Trans. Electron. Devices* **41**(10):1716–1724 (1994).
46. H. Morkoç, J. Klem, W. T. Masselink, T. Herderson, and A. Ketterson, *Semiconductor Device with Strained InGaAs Layer*, U.S. Patent 4,827,320; W. T. Masselink, A. Ketterson, J. Klem, W. Kopp, and H. Morkoç, *Electron. Lett.* **21**:937–939 (1985).
47. S. N. Mohammad and H. Morkoç, MODFETs: Operation, status and applications, in M. S. Shur, ed., *Compound Semiconductor Electronics: The Age of Maturity*, World Scientific, Singapore, 1996, pp. 25–84.
48. C. K. Peng, M. I. Aksun, A. A. Ketterson, H. Morkoç, and K. R. Gleason, *IEEE Electron. Device Lett.* **EDL-8**:24–26 (1987).
49. T. Henderson, M. I. Aksun, C. K. Peng, H. Morkoç, P. C. Chao, P. M. Smith, K. H. G. Duh, and L. F. Lester, *IEEE Electron. Device Lett.* **EDL-7**:649–651 (1986).
50. L. Lester, P. M. Smith, P. Ho, P. C. Chao, R. C. Tiberio, K. H. G. Duh, and E. D. Wolf, *IEEE IEDM Tech. Digest*, 1988, pp. 172–175.
51. N. Moll, A. Fischer-Colbrie, and M. Hueschen, *IEEE Trans. Electron Devices* **ED-34**:2357–2358 (1987).
52. A. N. Lepore, H. M. Levy, R. C. Tiberio, P. J. Taskar, H. Lee, E. D. Wolfe, L. F. Eastman, and E. Kohn, *Electron. Lett.* **24**:364–365 (1988).
53. P. C. Chao, P. M. Smith, K. H. G. Duh, J. M. Ballingall, L. F. Lester, B. R. Lee, A. A. Jabra, and R. C. Tiberio, *IEEE IEDM Tech. Digest*, 1987, pp. 410–413.
54. L. D. Nguyen, W. J. Schaff, P. J. Tasker, A. N. Lepore, L. F. Palmateer, M. C. Foisy, and L. F. Eastman, *IEEE Trans. Electron. Devices* **ED-35**:139 (1988).
55. K. Hikosaka, S. Sasa, N. Harada, and S. Kuroda, *IEEE Trans. Electron. Devices* **EDL-9**:241–243 (1988).
56. U. K. Mishra, A. S. Brown, S. E. Rosenbaum, C. E. Hooper, M. W. Pierce, M. J. Delaney, S. Vaughn, and K. White, *IEEE Electron. Device Lett.* **EDL-9**:647–649 (1988).
57. A. Fathimulla, J. Abrahams, T. Loughran, and H. Hier, *IEEE Electron. Device Lett.* **EDL-9**:328–330 (1988).
58. P. C. Chao, A. J. Tessmer, K. H. G. Duh, P. Ho, M. Y. Kao, P. M. Smith, J. M. Ballingall, S. M. Liu, and A. A. Tabra, *IEEE Elect. Device Lett.* **EDL-11**:59–62 (1990).
59. C. K. Peng, M. I. Aksun, A. A. Ketterson, H. Morkoç and K. R. Gleason, *IEEE Electron. Device Lett.* **EDL-8**:24–26 (1987).
60. T. Henderson, M. I. Aksun, C. K. Peng, H. Morkoç, P. C. Chao, P. M. Smith, K. H. G. Duh, and L. F. Lester, *IEEE Electron. Device Lett.* **EDL-7**:649–651 (1986).
61. L. D. Nguyen, W. J. Schaff, P. J. Tasker, A. N. Lepore, L. F. Palmateer, M. C. Foisy, and L. F. Eastman, *IEEE Trans. Electron. Device* **ED-35**:139 (1988).
62. P. C. Chao, A. J. Tessmer, K. H. G. Duh, P. Ho, M. Y. Kao, P. M. Smith, J. M. Ballingall, S. M. Liu, and A. A. Tabra, *IEEE Electron. Device Lett.* **EDL-11**:59–62 (1990).
63. A. Fathimulla, J. Abrahams, T. Loughran, and H. Hier, *IEEE Electron. Device Lett.* **EDL-9**:328–330 (1988).
64. P. C. Chao, A. J. Tessmer, K. H. G. Duh, P. Ho, M. Y. Kao, P. M. Smith, J. M. Ballingall, S. M. Liu, and A. A. Tabra, *IEEE Electron. Device Lett.* **EDL-11**:59–62 (1990).
65. L. Lester, P. M. Smith, P. Ho, P. C. Chao, R. C. Tiberio, K. H. G. Duh, and E. D. Wolf, *IEEE Int. Electron. Device Meeting Tech. Digest*, 1988, pp. 172–175.
66. P. C. Chao, A. J. Tessmer, K. H. G. Duh, P. Ho, M. Y. Kao, P. M. Smith, J. M. Ballingall, S. M. Liu, and A. A. Tabra, *IEEE Electron. Device Lett.* **EDL-11**:59–62 (1990).
67. K. L. Tan, D. C. Streit, P. D. Chow, R. M. Dia, A. C. Han, P. H. Liu, D. Garske, and R. Lai, *Int. Electron. Device Meeting Tech. Digest*, Washington, DC, Dec. 8–11, 1991, pp. 239–242.
68. H. Park, P. Mandeville, R. Saito, P. J. Tasker, W. J. Schaff, L. F. Eastman, *Proc. IEEE/Cornell Conf. Advanced Concepts in High Speed Semiconductor Devices and Circuits*, 1989, 101–110.
69. S. D. Offsey, P. J. Tasker, W. J. Schaff, L. Kapitan, J. R. Shealy, and L. F. Eastman, *Electron. Lett.* **26**:350–352 (1990).
70. N. C. Tien, J. Chen, J. M. Fernandez, and H. H. Wieder, *IEEE Electron. Device Lett.* **13**:621–623 (1992).
71. R. Kempter, H. Rothfritz, J. Plauth, R. Müller, G. Tränkle, and G. Weimann, *Electron. Lett.* **28**:1160–1161 (1992).
72. J. Dickmann, M. Berg, T. Hackbarth, R. Deufel, H. Daembkes, F. Scholz, and M. Moser, *Proc. IEEE/Cornell Conf. Advanced Concepts in High Speed Semiconductor Devices and Circuits*, 1989, pp. 529–538.
73. N. Camilleri, P. Chye, A. Lee, and P. Gregory, *Proc. IEEE Microwave and Millimeter-Wave Monolithic Circuits Symp.* 1990, pp. 27–30.
74. N. Camilleri, P. Chye, P. Gregory, and A. Lee, *IEEE MTT-S Tech. Digest* 1990, pp. 903–906.
75. P. Win, Y. Druelle, A. Cappy, Y. Cordier, D. Adam, J. Favre, *Proc. IEEE Cornell Conf. Advanced Concepts in High Speed Semiconductor Devices and Circuits*, 1993, pp. 511–519.

76. P. Win, Y. Druelle, P. Legry, S. Lepilliet, A. Cappy, Y. Cordier, and J. Favre, *Electron. Lett.* **29**:169–170 (1993).
77. H.-M. Shieh, W.-C. Hsu, R.-T. Hsu, C.-L. Wu, T.-S. Wu, *IEEE Electron. Device Lett.* **EDL-14**:581–583 (1993).
78. J. Perdomo, B. Hughes, H. Kondoh, L. Studebaker, G. Zhou, T. Taylor, C. Li, T. Ma, *Annual IEEE GaAs IC Symp. Digest*, 1992, pp. 203–206.
79. L. D. Nguyen, D. C. Radulescu, M. C. Foisy, P. J. Tasker, and L. F. Eastman, *IEEE Trans. Electron. Devices* **36**:833–838 (1989).
80. J. C. Huang, P. Saledas, J. Wendler, A. Platzker, W. Boulais, S. Shanfield, W. Hoke, P. Lyman, L. Aucoin, A. Miquelarena, C. Bedard, D. Atwood, *IEEE Electron. Device Lett.* **EDL-14**:456–458 (1993).
81. R. Lai, M. Wojtowicz, C. H. Chen, M. Biedenbender, H. C. Yen, D. C. Streit, K. L. Tan, and P. H. Liu, *IEEE Microwave Guided Wave Lett.* **3**:363–365 (1993).
82. L. D. Nguyen, P. J. Tasker, D. C. Radulescu, and L. F. Eastman, *IEDM Tech. Digest*, 1988, pp. 176–179.
83. M. Tong, K. Nummila, J. -W. Seo, A. Ketterson, I. Adesida, *Electron. Lett.* **28**:1633–1634 (1992).
84. Y. -J. Chan, and D. Pavlidis, *IEEE Trans. Electron. Devices* **ED-41**:637–642 (1994).
85. Y. -J. Chan, D. Pavlidis, M. Razeghi, and F. Omnes, *IEEE Trans. Electron. Devices* **ED-37**:2141–2147 (1990).
86. M. Takikawa and K. Joshin, *IEEE Electron Device Lett.* **EDL-14**:406–408 (1993).
87. J. B. Shealy, M. M. Hashemi, S. P. DenBaars, and U. K. Mishra, T. K. Liu, J. J. Brown, and M. Liu, *Proc. IEEE/Cornell Conference on Advanced Concepts in High Speed Semiconductor Devices and Circuits*, 1993, Aug. 2–4, pp. 548–556.
88. J. J. Brown, A. S. Brown, S. E. Rosenbaum, A. S. Schmitz, M. Matloubian, L. E. Larson, M. A. Melendes, and M. A. Thompson, *IEEE Trans. Electron Devices*, **ED-40**: 2111–2112, (1993).
89. J. J. Brown, M. Matloubian, T. K. Liu, L. M. Jelloian, A. E. Schmitz, R. G. Wilson, M. Liu, L. E. Larson, M. A. Melendes, and M. A. Thompson, *Proc. 6th Int. Conf. on InP and Related Materials*, 1994, March 27–31, pp. 419–422.
90. A. M. Kusters, A. Kohl, S. Brittner, V. Sommer, and K. Heime, *Proc. 6th Int. Conf. on InP and Related Materials*, 1994, March 27–31, pp. 323–326.
91. S. E. Rosenbaum, L. M. Jelloian, L. E. Larson, U. K. Mishra, D. A. Pierson, M. A. Thompson, T. K. Liu, and A. S. Brown, *IEEE Microwave Guided Wave Lett.* **3**(8) (1993).
92. S. E. Rosenbaum, C. S. Chow, C. M. Ngo, L. E. Rarson, and T. K. Liu, and M. A. Thompson, *IEEE Trans. MTT* 1103–1104 (1993).
93. P. C. Chao, M. S. Shur, R. C. Tiberio, K. H. G. Duh, P. M. Smith, J. M. Ballingall, P. Ho, and A. A. Jabra, *IEEE Trans. Electron. Devices* **ED-36**:461–473 (1989).
94. R. Lai, K. W. Chang, H. Wang, K. Tan, D. C. Lo, D. C. Streit, P. H. Liu, R. Dia, and J. Berenz, *Microwave Guided Wave Lett.* **3**(12) (1993).
95. K. H. Duh, P. C. Chao, S. M. J. Liu, P. Ho, M. Y. Kao, and J. M. Ballingall, *IEEE Microwave Guided Wave Lett.* **1**(5) (1991).
96. T. L. Tan, D. C. Streit, P. D. Chow, R. M. Dia, A. C. Han, P. H. Liu, D. Garske, and R. Lai, *IEEE IEDM Tech. Digest* 1991.
97. E. Y. Chang, K. C. Lin, E. H. Liu, C. Y. Chang, T. H. Chen, and J. Chen, *IEEE Electron. Devices Lett.* **EDL-15**:277–279 (1994).
98. M. Takikawa and K. Joshin, *IEEE Electron. Devices Lett.* **EDL-14**:409–411 (1983).
99. H. Wang, K. L. Tan, T. N. Ton, G. S. Dow, P. H. Liu, D. C. Streit, and J. Berenz, *IEEE MTT-S Tech. Digest*, 1993, pp. 783–785.
100. K. H. G. Duh, S. M. J. Liu, S. C. Wang, P. Ho, and P. C. Chao, *Proc. IEEE Microwave Millimeter Wave Monolithic Circuits Symp.* 1993, pp. 99–102.
101. S. E. Rosenbaum, L. M. Jelloian, L. E. Larson, U. K. Mishra, D. A. Pierson, M. A. Thompson, T. K. Liu, and A. S. Brown, *IEEE Microwave Guided Wave Lett.* **3**(8) (1993).
102. S. E. Rosenbaum, C. S. Chow, C. M. Ngo, L. E. Rarson, and T. K. Liu and M. A. Thompson, *IEEE Trans. MTT* 1103–1104 (1993).
103. S. E. Rosenbaum, L. M. Jelloian, L. E. Larson, and U. K. Mishra, *IEEE Microwave Guided Wave Lett.* **3**(8):265–267 (Aug. 1993).
104. P. C. Chao, M. S. Shur, R. C. Tiberio, K. H. G. Duh, P. M. Smith, J. M. Ballingall, P. Ho, and A. A. Jabra, *IEEE Trans. Electron. Devices* **ED-36**:461–473 (1989).
105. U. K. Mishra and J. B. Shealy, InP-based HEMTs: Status and potential, *Proc. 6th Int. Conf. InP and Related Materials*, March 27–31, 1994, pp. 14–17.
106. M. W. Pospieszalski, W. J. Lakatos, R. Lai, K. L. Tan, D. C. Streit, P. H. Liu, R. M. Dia, and J. Velebir, *IEEE MTT-S Tech. Digest*, 1993, pp. 515–518.
107. R. Lai, K. W. Chang, H. Wang, K. Tan, D. C. Lo, D. C. Streit, P. H. Liu, R. Dia, and J. Berenz, *Microwave Guided Wave Lett.* **3**(12) (1993).
108. K. H. Duh, P. C. Chao, S. M. J. Liu, P. Ho, M. Y. Kao, and J. M. Ballingall, *IEEE Microwave Guided Wave Lett.* **1**(5) (1991).
109. T. L. Tan, D. C. Streit, P. D. Chow, R. M. Dia, A. C. Han, P. H. Liu, D. Garske, and R. Lai, *IEEE IEDM Tech. Digest*, 1991.
110. K. H. G. Duh, S. M. J. Liu, S. C. Wang, P. Ho, and P. C. Chao, *IEEE Microwave and Millimeter-wave Monolithic Circuits Symp.*, 1993, pp. 99–102.
111. H. Wang, T. N. Ton, K. L. Tan, D. C. Garske, G. S. Dow, J. Berenz, M. W. Pospieszalski, and S. K. Pan, *IEEE J. Solid-State Circuits* **28**:988–993 (1993).
112. A. P. Long, S. J. Holmes, and R. H. Wallis, *Electron Lett.* **30**:422–423 (1993).
113. Y. Itoh, K. Nakahara, T. Sakura, N. Yoshida, T. Katoh, T. Takagi, and Yasuyuki. Ito, *IEEE Microwave Guided Wave Lett.* **5**:59–61 (1995).
114. E. Y. Chang, K. C. Lin, E. H. Liu, C. Y. Chang, T. H. Chen, and J. Chen, *IEEE Electron. Device Lett.* **EDL-15**:277–279 (1994).
115. M. Takikawa and K. Joshin, *IEEE Electron. Devices Lett.* **EDL-14**:409–411 (1983).
116. H. Wang, K. W. Chang, T. N. Ton, M. Biedenbender, S. T. Chen, J. Lee, G. S. Dow, K. L. Taang, and B. R. Allem, *IEEE Microwave Guided Wave Lett.* **3**:281–283 (1993).
117. H. Wang, K. L. Tan, T. N. Ton, G. S. Dow, P. H. Liu, D. C. Streit, and J. Berenz, *IEEE MTT-S Tech. Digest*, 1993, pp. 783–785.
118. K. H. G. Duh, S. M. J. Liu, S. C. Wang, P. Ho, and P. C. Chao, *Proc. IEEE Microwave Millimeter Wave Monolithic Circuits Symp.*, 1993, pp. 99–102.
119. F. A. Olson, *Microwave J.* 24 (Feb. 1995).
120. L. Aucoin, S. Bouthilette, A. Platzker, S. Shanfield, A. Bertrand, W. Hoke, P. Lyman, *15th Annual IEEE GaAs IC Symp. Digest*, 1993, pp. 351–353.

121. C. H. Chen, H. C. Yen, K. Tan, L. Callejo, G. Onak, D. C. Streit, P. H. Liu, and J. M. Schellenberg, *IEEE MTT-S Int. Microwave Symp. Digest*, 1993, pp. 1377–1380.
122. R. Lai, M. Wojtowicz, C. H. Chen, M. Biedenbender, H. C. Yen, D. C. Streit, K. L. Tan, and P. H. Liu, *IEEE Microwave Guided Wave Lett.* **3**:363–365 (1993).
123. R. E. Kasody, G. S. Dow, A. K. Sharma, M. V. Aust, D. Yamauchi, R. Lai, M. Biedenbender, K. L. Tan, and B. R. Allen, *IEEE Microwave Guided Wave Lett.* **4**:303–304 (1994).
124. M. Y. Kao et al., *IEDM Tech. Digest*, 1992, pp. 319–321; S. T. Fu et al., *IEEE MTT-S Tech. Digest*, 1993, pp. 1469–1472.
125. S. Kuroda, H. Suehiro, T. Miyata, S. Asai, I. Hanyu, M. Shima, N. Hara, and M. Takikawa, *IEEE IEDM Tech. Digest*, 1992, pp. 323–326.
126. A. Palevski, P. Solomon, T. F. Kuech, and M. A. Tischler, *Appl. Phys. Lett.* **56**:171–173 (1990).
127. J. B. Shealy, M. M. Hashemi, K. Kiziloglu, S. P. DenBaars, U. K. Mishra, T. K. Liu, J. J. Brown, and M. Liu, *IEEE Electron. Device Lett.* **EDL-14**:545–547 (1993).
128. M. Y. Kao, P. M. Smith, P. C. Chao, and P. Ho, *Proc. IEEE/Cornell Conf. Advanced Concepts in High-Speed Semiconductor Devices and Circuits*, 1991, pp. 469–477.
129. M. Matloubian, L. M. Jelloian, M. Lui, T. K. Liu, and M. Thompson, *IEEE IEDM Tech. Digest*, 1993, pp. 915–917.
130. O. Aina, M. Burgress, M. Mattingly, A. Meerschaert, J. M. O'Conner, M. Tong, A. Katterson, and I. Adishida, *IEEE Electron. Devices Lett.* **EDL-13** (May, 1992).
131. J. Perdomo, M. Mierzwinski, H. Kondoh, C. Li, and T. Taylor, *Proc. 11th Annual IEEE GaAs IC Symp.*, 1989, pp. 91–94.
132. R. Heilig, D. Hollman, and G. Baumann, *IEEE MTT-S Int. Micro-wave Symp. Digest*, Part 1, 1994, pp. 459–462.
133. L. Aucoin, S. Bouthilette, A. Platzker, S. Shanfield, A. Bertrand, W. Hoke, and P. Lyman, *15th Annual IEEE GaAs C Symp. Digest*, 1993, pp. 351–353.
134. S. T. Fu, W. F. Kopp, M. Y. Kao, K. H. G. Duh, P. M. Smith, P. C. Chao, and T. H. Yu, *IEEE MTT-S Int. Microwave Symp. Digest*, 1993, pp. 1469–1472.
135. M. -Y. Kao, S. -T. Fu, P. Ho, P. M. Smith, P. C. Chao, K. J. Nordheden, S. Wang, *IEEE IEDM Tech. Digest*, 1992, pp.319-321.
136. J. M. Van Hove, R. J. Schuelke, G. P. Thomas, J. D. Jörgenson, E. Y. Chang, R. M. Nagarajan, and K. P. Pande, *IEEE Electron. Device Lett.* **9**:530–532 (1988).
137. C. S. Wu, F. Ren, S. J. Pearton, M. Hu, C. K. Pao, and R. F. Wang, *Electron. Lett.* **30**:1803–1805 (Oct. 1994).
138. S. Shanfield, M. Schindler, L. Aucoin, A. Platzker, W. Hoke, P. Lyman, S. L. G. Chu, R. Binder, *14th Annual IEEE GaAs IC Symp.*, 1992, pp. 207–210.
139. S. Shanfield, A. Platzker, L. Aucoin, T. Kazior, B. I. Patel, A. Bertrand, W. Hoke, and P. Lyman, *IEEE MTT-S Int. Micro-wave Symp. Digest*, 1992, pp. 639–641.
140. D. Helms, J. J. Komiak, W. F. Kopp, P. Ho, P. M. Smith, R. P. Smith, and D. Hogue, *IEEE MTT-S Tech. Digest*, Part 2, 1991, pp. 819–821.
141. S. T. Fu, L. F. Lester, and T. Rogers, *IEEE MTT-S Int. Microwave Symp. Digest*, Part 2, 1994, pp. 793–796.
142. T. Fujii, S. Sakamoto, T. Sonoda, N. Kasai, S. Tsuji, M. Yamanouchi, S. Takamiya, and Y. Kashimoto, *13th Annual IEEE GaAs IC Symp. Tech. Digest*, 1991, pp. 109–112.
143. T. Sonoda, S. Sakamoto, N. Kasai, S. Tsuji, M. Yamanouchi, S. Takamiya, and Y. Kashimoto, *Electron. Lett.* **27**:1304–1305 (1991).
144. P. M. Smith, W. F. Kopp, P. Ho, P. C. Chao, R. P. Smith, K. Nordheden, and J. M. Ballingall, *Electron. Lett.* **27**:270–271 (1991).
145. D. Danzilio, L. K. Hanes, B. Lauterwasser, B. Ostrowski, and F. Rose, *14th Annual IEEE Gallium Aresnide IC Circuit Symp.*, 1992, pp. 255–257.
146. P. Saunier, H. Q. Tserng, H. D. Shih, and K. Bradshaw, *Electron. Lett.* **25**:583–584 (1989).
147. G. -G. Zhou, K. T. Chan, B. Hughes, M. Mierzwinski, and H. Kondoh, *IEEE IEDM Tech. Digest*, 1989, pp. 109–112.
148. H. Q. Tserng, P. Saunier, and Y. -C. Kao, *IEEE Microwave and Millimeter-Wave Monolithic Circuits Symp.*, 1992, pp. 51–54.
149. J. C. Huang, P. Saledas, J. Wendler, A. Platzker, W. Boulais, S. Shanfield, W. Hoke, P. Lyman, L. Aucoin, A. Miquelarena, C. Bedard, and D. Atwood, *IEEE Electron. Device Lett.* **EDL-14**:456–458 (1993).
150. M. V. Aust, B. Allen, G. S. Dow, R. Kasody, G. Luong, M. Biedenbender, and K. Tan, *IEEE Microwave and Millimeter-Wave Monolithic Circuits Symp.*, 1993, pp. 45–48.
151. P. M. Smith et. al., *Electron. Lett.* **25**:639–640 (1989).
152. P. M. Smith, M. Y. Kao, P. Ho, P. C. Chao, K. H. G. Duh, A. A. Jabra, R. P. Smith, and J. M. Ballingall, *IEEE MTT-S Digest*, 1989, pp. 983–986.
153. A. W. Swanson, P. M. Smith, P. C. Chao, K. H. Duh, and J. M. Ballingall, *Proc. IEEE MILCOM Symp.*, Part 3, 1989, pp. 744–748.
154. J. A. Lester, W. L. Jones, and P. D. Chow, *IEEE MTT-S Digest*, 1991, pp. 433–436.
155. W. Boulais, R. S. Donahue, A. Platzker, J. Huang, L. Aucoin, S. Shanfield, and M. Vafiades, *IEEE MTT-S Int. Microwave Symp. Digest*, Part 2, 1994, pp. 649–652.
156. K. L. Tan, D. C. Streit, R. M. Dia, S. K. Wang, A. C. Han, P.-M. D. Chow, T. Q. Trinh, P. H. Liu, J. R. Velebir, and H. C. Yen, *IEEE Electron. Device Lett.* **EDL-12**:213–214 (1991).
157. P. Saunier, R. J. Matyi, and K. Bradshaw, *IEEE Electron. Device Lett.* **EDL-9**:397–398 (1988).
158. S. Arai, H. Kojima, K. Otsuka, M. Kawano, H. Ishimura, and H. Tokuda, *13th Annual IEEE GaAs IC Symp. Tech. Digest*, 1991, pp. 105–108.
159. R. E. Kasody, G. S. Dow, A. K. Sharma, M. V. Aust, D. Yamauchi, R. Lai, M. Biedenbender, K. L. Tan, and B. R. Allen, *IEEE Microwave Guided Wave Lett.* **4**:303–304 (1994).
160. A. K. Sharma, G. Onak, R. Lai, and K. L. Tan, *Proc. IEEE Microwave and Millimeter-Wave Monolithic Circuits Symp.*, 1994, pp. 73–76.
161. R. Lai, M. Wojtowicz, C. H. Chen, M. Biedenbender, H. C. Yen, D. C. Streit, K. L. Tan, and P. H. Liu, *IEEE Microwave Guided Wave Lett.* **3**:363–365 (1993).
162. M. Schlechtweg, P. J. Tasker, W. Reinert, J. Braunstein, W. Haydl, A. Hülsmann, and K. Köhler, *Electron. Lett.* **29**:1119–1120 (1993).
163. T. H. Chen, K. L. Tan, G. S. Dow, H. Wang, K. W. Chang, T. N. Ton, B. Allen, J. Berenz, P. H. Liu, D. Streit, and G. Hayashibara, *Proc. 14th Annual IEEE GaAs IC Circuit Symp.*, 1992, pp. 71–74.
164. D. C. Streit, K. L. Tan, R. M. Dia, J. K. Liu, A. C. Han, J. R. Velebir, S. K. Wang, T. Q. Trinh, P.-M. D. Chow, P. H. Liu, and H. C. Yen, *IEEE Electron. Device Lett.* **EDL-12**:149–150 (1991).

165. T. Enoki, K. Arai, A. Kohzen, and Y. Ishii, InGaAs/InP double channel HEMT on InP, *Proc. Int. Conf. InP and Related Materials*, 1992.
166. M. Matloubian, L. D. Nguyen, A. S. Brown, L. E. Larson, M. E. Melendes, and M. Thompson, *IEEE MTT-S Tech. Digest*, 1991, pp. 721–724.
167. M. Matloubian, A. S. Brown, L. D. Nguyen, M. A. Melendes, L. E. Larson, M. J. Delaney, M. Thompson, R. A. Rhodes, and J. E. Pence, *Microwave Millimeter Wave Guided Wave Lett.* **3**(5):142–144 (1993).
168. M. Y. Kao, P. M. Smith, P. C. Chao, and P. Ho, *Proc. IEEE/Cornell Conf. Advanced Concepts in High-Speed Semiconductor Devices and Circuits*, 1991, pp. 469–477.
169. O. Aina, M. Burgess, M. Mattingly, A. Meerschaert, J. M. O'Conner, M. Tong, A. Ketterson, and I. Adishida, *IEEE Electron. Device Lett.* **EDL-13**(5):300–302 (1992).
170. M. Matloubian, A. S. Brown, L. D. Nguyen, L. E. Larson, M. J. Delaney, M. Thompson, R. A. Rhodes, and J. E. Pence, *IEEE MTT-S Tech. Digest*, Dec. 1993, pp. 535–538.
171. M. Matloubian, L. M. Jelloian, M. Lui, T. K. Liu, L. E. Larson, M. Le, D. Jang, and R. A. Rhodes, *Proc. Int. Conf. Millimeter and Sub-millimeter Waves and Applications*, 1993.
172. A. Kurdoghlian, C. S. Wu, W. Yau, J. Chen, M. Hu, C. Pao, and D. Bosch, *Proc. IEEE Microwave and Millimeter-Wave Monolithic Circuits Symp.*, 1993, pp. 97–98.
173. S. N. Mohammad, A. Salvador, and H. Morkoç, *Proc. IEEE*, **83**:1306–1355 (Oct. 1995).
174. H. Morkoç, S. Strite, G. B. Gao, M. E. Lin, B. Sverdlov, and M. Burns, *J. Appl. Phys. Rev.* **76**(3):1363–1398 (Aug. 1994).
175. Ö. Aktas, Z. F. Fan, S. N. Mohammad, A. E. Botchkarev, and H. Morkoç, *Appl. Phys. Letts.* **69**(25):3872–3874 (Dec. 16, 1996).
176. M. A. Khan, Q. Chen, M. S. Shur, B. T. Dermont, J. A. Higgins, J. Burm, W. Schaff, and L. F. Eastman, *Electron. Lett.* **32**:357–358 (Feb. 1996).
177. M. A. Khan, Q. Chen, J. W. Wang, M. S. Shur, B. T. Dermont, and J. A. Higgins, *IEEE Electron. Device Lett.* Vol. 17, No. 17, pp. 325–327, July 1996.
178. Y. F. Wu, B. P. Keller, S. Keller, D. Kapolnek, S. P. Denbaars and U. K. Mishra, *IEEE Electron. Device Lett.* Vol. 17, No. (9): pp. 455–457, (September 1996).
179. Y. -F. Wu, B. P. Keller, S. Keller, N. X. Nguyen, M. Le, C. Nguyen, T. J. Jenkins, L. T. Kehias, S. P. Denbaars, and U. K. Mishra, *55th Device Research Conf. Digest*, June 23–25, 1997, pp. 142–143.
180. S. J. Pearton, J. C. Zolper, R. J. Shul, and F. Ren, *J. Appl. Phys.* **86**:1–78 (1999).
181. Y.-F. Wu, B. P. Keller, P. Fini, S. Keller, T. J. Jenkins, L. T. Kehias, S. P. DenBaars, and U. K. Mishra, *IEEE Electron. Device Lett.* **19**(2):50–53 (1998).
182. G. A. Martin, S. T. Strite, A. Botchkarev, A. Agarwal, A. Rockett, W. R. L. Lambrecht, B. Segall, and H. Morkoç, *Appl. Phys. Lett.* **65**(5):610–612 (1994).
183. G. A. Martin, A. Botchkarev, A. Rockett, and H. Morkoç, *Appl. Phys. Lett.* **68**(10):2541–2543 (1996).
184. D. L. Smith, *Solid State Commun.* **57**:919 (1986).
185. A. Bykhovski, B. Gelmont, and M. Shur, *J. Appl. Phys.* **74**:6734 (1993).
186. G. A. Martin, Ph.D. thesis, Dept. Physics, Univ. Illinois, 1996.
187. F. Stengel, S. N. Mohammad, and H. Morkoç, *J. Appl. Phys.* **80**(5):3031–3042 (Sept. 1, 1996).
188. C. Weisbuch and B. Vinter, *Quantum Semiconductor Structures*, Academic Press, 1991.
189. K. E. Moore, C. E. Weitzel, K. J. Nordquist, L. L. Pond, III, J. W. Palmour, S. Allen, and C. H. Carter, Jr., *IEEE Electron. Device Lett.* **18**(2):69–70 (Feb. 1997).
190. S. T. Sheppard, K. Doverspike, W. L. Pribble, S. T. Allen, J. W. Palmour, L. T. Kehias and T. J. Jenkins, *IEEE Electron. Device Lett.* **20**(4):161 (1999).
191. G. J. Sullivan, M. Y. Chen, J. A. Higgins, J. W. Yang, Q. Chen, R. L. Pierson, and B. T. McDermott, *IEEE Electron. Device Lett.* **19**:198–199 (1998).
192. S. Binari, J. M. Redwing, G. Kelner, and W. Kruppa, *Electron. Lett.* **33**(3):242–243 (1997).
193. A. T. Ping, Q. Chen, J. W. Yang, M. A. Khan, and I. Adesida, *IEEE Electron. Device Lett.* **19**(2):54–56 (1998).
194. M. Micovic, A. Kurdoghlian, P. Janke, P. Hashimoto, D. W. S. Wong, J. S. Moon, L. McCray, and C. Nguyen, *IEEE Trans. Electron. Devices* **48**(3):591–592 (2001).
195. S. C. Binari, K. Ikossi-Anastasiou, J. A. Roussos, W. Kruppa, D. Park, H. B. Dietrich, D. D. Koleske, A. E. Wickenden, and R. L. Henry, Special Issue of *IEEE Electron. Devices* **48**:465–471 (2001).
196. R. Fischer, T. J. Drummond, J. Klem, W. Kopp, T. Henderson, D. Perrachione, and H. Morkoç, *IEEE Trans. Electron. Devices* **ED-31**:1028–1032 (1984).
197. W. T. Masselink, A. Ketterson, J. Klem, W. Kopp, and H. Morkoç, *Electron. Lett.* **21**:937–939 (1985).
198. W. Kruppa, S. C. Binari, and K. Doverspike, *Electron. Lett.* **31**:1951–1952 (1995).
199. C. Nguyen, N. X. Nguyen, and D. E. Grider, *Electron. Lett.* **35**:1380–1382 (1999).
200. P. B. Klein, J. A. Freitas, Jr., S. C. Binari, and A. E. Wickenden, *Appl. Phys. Lett.* **75**:4016 (1999).
201. P. B. Klein, S. C. Binari, J. A. Freitas, Jr., and A. E. Wickenden, *J. Appl. Phys.* **88**:2843 (2000).
202. R. Dietrich, A. Wieszt, A. Vescan, H. Leier, J. M. Redwing, K. S. Boutros, K. Kornitzer, R. Freitag, T. Ebner, and K. Thonke, *MRS Internet J. Nitride Semicond. Res.* **5**:2 (2000).
203. W. J. Schaff, J. Hwang, and B. Green, The effect of a MBE grown AlN surface layer on the DC and RF characteristics of GaN Heterojunction Field Effect Transistors, manuscript in preparation.
204. R. Vetury, N. Q. Zhang, S. Keller, and U. K. Mishra, Special Issue of *IEEE Electron. Devices* **48**:560–566 (2001).
205. X. Hu, A. Koudymov, G. Simin, J. Yang, M. Asif Khan, A. Tarakji, M. S. Shur, and R. Kaska, *Appl. Phys. Lett.* **79**:2832 (2001).
206. B. M. Green, K. K. Chu, E. M. Chumbes, J. A. Smart, J. R. Shealy, and L. F. Eastman, *IEEE Electron. Device Lett.* **21**:268 (2000).
207. A. V. Vertiatchikh, L. F. Eastman, W. J. Schaff, and T. Prunty, *Electron. Lett.* **38**:387 (2002).
208. W. Lu, V. Kumar, R. Schwindt, E. Piner, and I. Adesida, *Solid-State Electron.* **46**:1441 (2002).
209. M. E. Levinstein, F. Pascal, S. Contreras, W. Knap, S. L. Rumyantsev, R. Gaska, J. W. Wang, and M. S. Shur, *Appl. Phys. Lett.* **72**:3053 (1998).
210. J. A. Garrido, B. E. Foutz, J. A. Smart, J. R. Shealy, M. J. Murphy, W. J. Schaff, L. F. Eastman, and E. Muñoz, *Appl. Phys. Lett.* **76**:3442 (2000).

MONOLITHIC ANTENNAS

ANDERS RYDBERG
ERIK Öjefors
Uppsala University
Uppsala, Sweden

1. BACKGROUND AND APPLICATIONS

The use of high-microwave and millimeter-wave frequencies has to this date been restricted to professional applications, such as long-distance radiolinks and radar, due to the high cost of equipment and requirements for individual licenses for use of frequencies. The license-free 24-GHz, 60-GHz, and 77/79-GHz bands could, however, host mass-market consumer applications such as automobile anticollision radars, wireless LAN, and sensor devices, provided compact low-cost transceivers are made available. In conventional microwave technology for active antennas the RF frontend and the antenna are built on separate substrates, due to the size of the antenna structure. However, at millimeter-wave frequencies the small size of the antenna allows for monolithic integration between the antenna and the active chip. Such a close integration will eliminate the parasitics of interconnections in the package and promote the design of low cost wideband telecommunication and radar sensors.

It is not possible to obtain the high antenna gain required by long-range radars or radiolinks with an on-chip antenna of acceptable size. Thus, the on-chip antennas are suitable in short-range communication and sensor devices, where a low antenna gain is feasible due to the omnidirectional pattern usually required for such applications. By integrating the MMIC with the antenna in low-antenna-gain applications, advantages such as simplified packaging and considerable reduction of the space required by the radio frontend can also be achieved. One of the first trials in this respect was proposed in 1984 by Jain and R. Bansal in which a millimeter-wave (MMW) GaAs dipole antennas whose radiation characteristics could be controlled during fabrication and/or operation was to be integrated monolithically together with active devices [1]. In 1993 Robertson described a technique for employing radiating elements of a patch antenna on the backface of monolithic circuits [2], facilitating the integration between the active device and the antenna [3]. A small short-circuited H-shaped GaAs monolithic microwave integrated circuits (MMICs) patch antenna was presented by Singh et al. [4]. A new application of monolithic antennas was reported by the SiMICS Research Group, at the University of Florida, where a wireless interconnect system was proposed for clock distribution using on-chip antennas [5]. A V-band GaAs HEMT uniplanar monolithic integrated antenna and receiver frontend were presented by Chen et al. [6].

More recent advances in the realization of RF circuits using mature silicon technologies (RF CMOS and Si/SiGe HBT technologies) have led to a quantum leap in the complexity of monolithically integrated microwave circuits, even for frequencies of operation beyond 24 GHz.

211. M. E. Levinshtein, S. L. Rumyantsev, R. Gasja, J. W. Yang, and M. S. Shur, *Appl. Phys. Lett.* **73**:1089 (1998).
212. A. Balandin, S. Cai, R. Li, K. L. Wang, V. Ramgopal Rao, and C. R. Viswanathan, *IEEE Electron. Device Lett.* **19**:475 (1998).
213. S. Rumyantsev, M. E. Levinshtein, R. Gaska, M. S. Shur, A. Khan, J. W. Wang, G. Simin, A. Ping, and T. Adesida, *Phys. Stat. Sol. (A)* **176**:201 (1999).
214. S. Rumyantsev, M. E. Leevinshtein, R. Gaska, M. S. Shur, J. W. Yang, and M. A. Khan, *J. Appl. Phys.* **87**:1849 (2000).
215. A. Balandin, K. L. Wang, S. Cai, R. Li, C. R. Viswanathan, E. N. Wong, and M. Wojtowicz, *J. Electron. Mat.* **29**:297 (2000).
216. A. Balandin, Extraction of trap characteristics from excess noise in GaN devices, *Mat. Res. Soc. Symp. Proc.* **680**:E5.3.1 (2001).
217. S. L. Rumyanstev, N. Pala, M. S. Shur, E. Borovitskaya, A. P. Dmitriev, M. E. Levinshtein, R. Gaska, M. A. Khan, J. Yang, X. Hu, and G. Simin, *IEEE Trans. Electron. Devices* **48**:530 (2001).
218. N. X. Nguyen, M. Micovic, W.-S. Wong, P. Hashimoto, P. Janke, D. Harvey, and C. Nguyen, *Electron. Lett.* **36**:469 (2000).
219. A. T. Ping, E. Piner, J. Redwing, M. Asif Khan, and I. Adesida, *Electron. Lett.* **36**:175 (2000).
220. J. Deng, T. Werner, M. S. Shur, R. Gaska, A. Khan, G. Simin, and J. W. Wang, Int. Conf. Compound Semiconductor Manufacturing Technology, 2001.
221. W. Lu, J. Yang, M. Asif Khan, and I. Adesida, *IEEE Trans. Electron. Devices* **48**:581 (2001).
222. W. Lu, V. Kumar, R. Schwindt, E. Piner, and I. Adesida, *Solid State Electron.* **46**:1441 (2002).
223. G. L. Zhou and H. Morkoç, *Thin Solid Films*, **231**(1/2): 125–142 (Aug. 25, 1993); Special Issue: *Properties and Preparation of Emerging Device Heterostructures*, H. Morkoç, ed.
224. E. Abstreiter, H. Brugger, T. Wolf, H. Jorke and H. J. Herzog, *Phys. Rev. Lett.* **54**:2441–2444 (1985).
225. K. Ismail, B. S. Meyerson, and P. J. Wang, *Appl. Phys. Lett.* **58**(19):2117–2119 (1991).
226. Y. J. Mii, Y. H. Xie, E. A. Fitzgerald, D. Monroe, F. A. Thiel, B. E. Weir, and L. C. Feldman, *Appl. Phys. Lett.* **59**(13): 1611–1613 (1991).
227. K. Ismail, *IEEE IEDM Tech. Digest*, 1995, p. 509.
228. F. Aniel, M. Enciso-Aguilar, L. Giguere, P. Crozat, R. Adde, T. Mack, U. Seiler, Th. Hackbarth, H. J. Hertog, U. König, and B. Raynor, *Solid State Electron.* **47**:283 (2003).
229. P. J. Wang, B. S. Meyerson, F. F. Fang, J. Nocera, and B. Parker, *Appl. Phys. Lett.* **55**(22):2333–2335 (1989).
230. E. Murakami, K. Nakagawa, H. Etoh, A. Nishida and M. Miyao, *IEDM Tech. Digest*, 1990, pp. 375–378.
231. M. Arafa, K. Ismail, J. O. Chu, and I. Adesida, 54th Device Research Conference, Santa Barbara, CA, June 1996.
232. W. Lu, A. Kuliev, S. J. Koester, X. W. Wang, J. O. Chu, T. P. Ma, and I. Adesida, *IEEE Trans. Electron. Devices* **47**:1645 (2000).
233. U. König, N- and p-type Si-SiGe hetero FETs, *Proc. 8th IEEE Int. Symp. High Performance Electron Devices for Microwave and Optoelectronic Applications*, IEEE, Piscataway, NJ, 2000, pp. 1–7.
234. M. Golio, *Compound Semicond.* **1**(2):9–10 (1995).

211. M. E. Levinshtein, S. L. Rumyantsev, R. Gasja, J. W. Yang, and M. S. Shur, *Appl. Phys. Lett.* **73**:1089 (1998).
212. A. Balandin, S. Cai, R. Li, K. L. Wang, V. Ramgopal Rao, and C. R. Viswanathan, *IEEE Electron. Device Lett.* **19**:475 (1998).
213. S. Rumyantsev, M. E. Levinshtein, R. Gaska, M. S. Shur, A. Khan, J. W. Wang, G. Simin, A. Ping, and T. Adesida, *Phys. Stat. Sol. (A)* **176**:201 (1999).
214. S. Rumyantsev, M. E. Leevinshtein, R. Gaska, M. S. Shur, J. W. Yang, and M. A. Khan, *J. Appl. Phys.* **87**:1849 (2000).
215. A. Balandin, K. L. Wang, S. Cai, R. Li, C. R. Viswanathan, E. N. Wong, and M. Wojtowicz, *J. Electron. Mat.* **29**:297 (2000).
216. A. Balandin, Extraction of trap characteristics from excess noise in GaN devices, *Mat. Res. Soc. Symp. Proc.* **680**:E5.3.1 (2001).
217. S. L. Rumyanstev, N. Pala, M. S. Shur, E. Borovitskaya, A. P. Dmitriev, M. E. Levinshtein, R. Gaska, M. A. Khan, J. Yang, X. Hu, and G. Simin, *IEEE Trans. Electron. Devices* **48**:530 (2001).
218. N. X. Nguyen, M. Micovic, W.-S. Wong, P. Hashimoto, P. Janke, D. Harvey, and C. Nguyen, *Electron. Lett.* **36**:469 (2000).
219. A. T. Ping, E. Piner, J. Redwing, M. Asif Khan, and I. Adesida, *Electron. Lett.* **36**:175 (2000).
220. J. Deng, T. Werner, M. S. Shur, R. Gaska, A. Khan, G. Simin, and J. W. Wang, Int. Conf. Compound Semiconductor Manufacturing Technology, 2001.
221. W. Lu, J. Yang, M. Asif Khan, and I. Adesida, *IEEE Trans. Electron. Devices* **48**:581 (2001).
222. W. Lu, V. Kumar, R. Schwindt, E. Piner, and I. Adesida, *Solid State Electron.* **46**:1441 (2002).
223. G. L. Zhou and H. Morkoç, *Thin Solid Films*, **231**(1/2): 125–142 (Aug. 25, 1993); Special Issue: *Properties and Preparation of Emerging Device Heterostructures*, H. Morkoç, ed.
224. E. Abstreiter, H. Brugger, T. Wolf, H. Jorke and H. J. Herzog, *Phys. Rev. Lett.* **54**:2441–2444 (1985).
225. K. Ismail, B. S. Meyerson, and P. J. Wang, *Appl. Phys. Lett.* **58**(19):2117–2119 (1991).
226. Y. J. Mii, Y. H. Xie, E. A. Fitzgerald, D. Monroe, F. A. Thiel, B. E. Weir, and L. C. Feldman, *Appl. Phys. Lett.* **59**(13): 1611–1613 (1991).
227. K. Ismail, *IEEE IEDM Tech. Digest*, 1995, p. 509.
228. F. Aniel, M. Enciso-Aguilar, L. Giguere, P. Crozat, R. Adde, T. Mack, U. Seiler, Th. Hackbarth, H. J. Hertog, U. König, and B. Raynor, *Solid State Electron.* **47**:283 (2003).
229. P. J. Wang, B. S. Meyerson, F. F. Fang, J. Nocera, and B. Parker, *Appl. Phys. Lett.* **55**(22):2333–2335 (1989).
230. E. Murakami, K. Nakagawa, H. Etoh, A. Nishida and M. Miyao, *IEDM Tech. Digest*, 1990, pp. 375–378.
231. M. Arafa, K. Ismail, J. O. Chu, and I. Adesida, 54th Device Research Conference, Santa Barbara, CA, June 1996.
232. W. Lu, A. Kuliev, S. J. Koester, X. W. Wang, J. O. Chu, T. P. Ma, and I. Adesida, *IEEE Trans. Electron. Devices* **47**:1645 (2000).
233. U. König, N- and p-type Si-SiGe hetero FETs, *Proc. 8th IEEE Int. Symp. High Performance Electron Devices for Microwave and Optoelectronic Applications*, IEEE, Piscataway, NJ, 2000, pp. 1–7.
234. M. Golio, *Compound Semicond.* **1**(2):9–10 (1995).

MONOLITHIC ANTENNAS

ANDERS RYDBERG
ERIK Öjefors
Uppsala University
Uppsala, Sweden

1. BACKGROUND AND APPLICATIONS

The use of high-microwave and millimeter-wave frequencies has to this date been restricted to professional applications, such as long-distance radiolinks and radar, due to the high cost of equipment and requirements for individual licenses for use of frequencies. The license-free 24-GHz, 60-GHz, and 77/79-GHz bands could, however, host mass-market consumer applications such as automobile anticollision radars, wireless LAN, and sensor devices, provided compact low-cost transceivers are made available. In conventional microwave technology for active antennas the RF frontend and the antenna are built on separate substrates, due to the size of the antenna structure. However, at millimeter-wave frequencies the small size of the antenna allows for monolithic integration between the antenna and the active chip. Such a close integration will eliminate the parasitics of interconnections in the package and promote the design of low cost wideband telecommunication and radar sensors.

It is not possible to obtain the high antenna gain required by long-range radars or radiolinks with an on-chip antenna of acceptable size. Thus, the on-chip antennas are suitable in short-range communication and sensor devices, where a low antenna gain is feasible due to the omnidirectional pattern usually required for such applications. By integrating the MMIC with the antenna in low-antenna-gain applications, advantages such as simplified packaging and considerable reduction of the space required by the radio frontend can also be achieved. One of the first trials in this respect was proposed in 1984 by Jain and R. Bansal in which a millimeter-wave (MMW) GaAs dipole antennas whose radiation characteristics could be controlled during fabrication and/or operation was to be integrated monolithically together with active devices [1]. In 1993 Robertson described a technique for employing radiating elements of a patch antenna on the backface of monolithic circuits [2], facilitating the integration between the active device and the antenna [3]. A small short-circuited H-shaped GaAs monolithic microwave integrated circuits (MMICs) patch antenna was presented by Singh et al. [4]. A new application of monolithic antennas was reported by the SiMICS Research Group, at the University of Florida, where a wireless interconnect system was proposed for clock distribution using on-chip antennas [5]. A V-band GaAs HEMT uniplanar monolithic integrated antenna and receiver frontend were presented by Chen et al. [6].

More recent advances in the realization of RF circuits using mature silicon technologies (RF CMOS and Si/SiGe HBT technologies) have lead to a quantum leap in the complexity of monolithically integrated microwave circuits, even for frequencies of operation beyond 24 GHz.

The increase in complexity from a few to tens of active devices in typical III–V-based MMICs relatively recently to the hundreds of active devices possible in Si-based MMICs will enable the integration of advanced signal conditioning structures (phase and amplitude modulation) in a very compact fashion and close to the antenna. This also facilitates the interface with digital signal processing through on-chip interface circuitry. Si/SiGe BiCMOS technologies may enable the fully monolithic integration of digital signal processing and RF functions on a single chip. The discussion on monolithic antennas will thus be mostly devoted to silicon-based antennas, due to the strong progress in this area and the cost effective solutions compared to III–V technology.

2. PERFORMANCE ISSUES OF INTEGRATED ANTENNAS

One key requirement of the on-chip antennas is small size, due to the high cost of wafer space. For a typical square-shaped semiconductor die containing RF front-end circuitry, an area of $<10\text{ mm}^2$ ($3.3 \times 3.3\text{ mm}$) is usually desired. At 24 GHz, with a free-space wavelength of 12.5 mm, the die sidelength of such a chip would correspond to a quarter-wavelength.

The antenna gain for antennas is always lower than the directivity, due to conductor and substrate losses. The losses are characterized by the antenna efficiency and is defined as

$$\eta = \frac{P_{\text{rad}}}{P_{\text{in}}} \quad (1)$$

where P_{rad} is the radiated power P_{in} is the power at the antenna input terminals. Because of the fundamental limitations in antenna directivity mandated by the small size of integrated antennas, the efficiency is the most important figure of merit for such antennas. Thus, an important objective of the research on monolithic antennas is to maximize the radiation efficiency of small antennas by using micromachining methods compatible with the active circuits integrated on commercial, low-resistivity silicon substrates.

3. FABRICATION TECHNOLOGY

One objective in deriving the process technology for fabrication of monolithically integrated antennas is that the process should be compatible to a commercial foundry process. Although antennas have been integrated directly in MMIC processes, using the available metal layers, better performance and larger freedom in design of the antenna can be obtained by the use of micromachining postprocessing methods. The methods used to improve the efficiency are surface micromachining, application of the low-loss spinon polymer benzocyclobutene (BCB), and bulk micromachining. In the bulk micromachining BCB-coated silicon substrate is etched from the backside to release the BCB and form a membrane. This etching can be performed by either wet or dry etching methods.

3.1. Surface Micromachining

3.1.1. Processing of BCB Thick Dielectric. The substrate losses in low resistivity silicon wafers used for transmission lines and antennas can be reduced if a thick layer of a low-loss dielectric is deposited on the top of the wafer, before the transmission lines are metallized. A suitable dielectric is benzocyclobutane (BCB), which is a polymer with a dielectric constant $\epsilon_r = 2.65$ and low losses ($\tan \delta = 0.0005$) manufactured by Dow Chemicals. The BCB can be applied to the top of the wafer as a conventional photoresist, and thicknesses of 20–30 μm can be obtained if the polymer is applied in several subsequent spinon process steps. Photosensitive BCB is also available, allowing patterning of the polymer layer. The BCB is cured in a furnace at 250°C, and the top metallization is finally evaporated, electroplated, and patterned on top of the dielectric.

3.1.2. Silicon Bulk Micromachining. The term *bulk micromachining* refers to processes where parts of the bulk of the semiconductor substrate are selectively removed by etching processes. Two major techniques are used for bulk micromachining of silicon substrates: wet chemical etching [7] and dry etching [8].

In chemical wet etching the surface of the silicon wafer is masked by a durable mask, such as silicon nitride, with openings where a liquid is allowed to etch the substrate. Wet etching of silicon substrates can either be isotropic, where the etching progresses with the same rate in all directions, or anisotropic where the etch rate in certain directions is restricted by the (111) crystal planes in silicon. The anisotropic etch leaves slanted walls of etched cavities if a silicon wafer with the standard crystal orientation (100) is used. Anisotropic etching of silicon is a standard silicon micromachining process.

Dry etching is performed in an evacuated chamber where a plasma is generated and used to etch the silicon substrate. The wafer is masked by photoresist and patterned with photolithographic techniques to enable selective etching. In the commonly used deep-reactive-ion etching (DRIE) process by Bosch [8], the wafer is exposed to an alternating sequence of an etchant and a passivant. By the alternation between etching and passivation of the substrate the sidewalls of the etched holes are protected, thereby enabling high-aspect-ratio structures to be manufactured. Good control over the etching process and selectivity against the mask is also obtained.

3.2. Membrane Technology

Thin membranes of high-quality dielectric materials offer a way of integrating high-quality transmission-line structures and antennas [9] on silicon substrates. By suspending the conductors on membranes in air, an effective dielectric constant of close to one can be achieved. Low losses are also obtained since the silicon substrate is removed in the vicinity of the transmission lines or antenna conductors. A low-temperature membrane process, compatible with preprocessed semiconductor wafers, is obtained by combining the spinon BCB dielectric process with bulk micromachining. The BCB membrane is

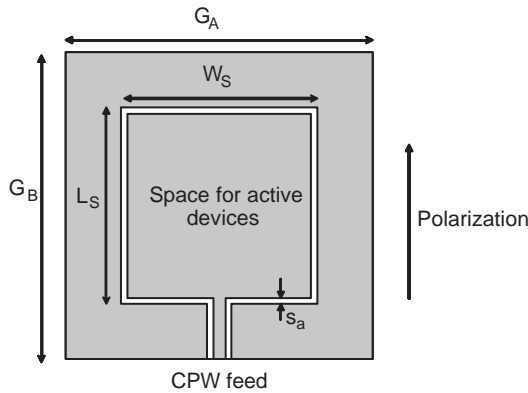


Figure 1. Integrated slot loop antenna.

released by backside etching of the wafer, using wet etching methods such as KOH or DRIE.

4. ANTENNAS

The antennas that will be described here are suitable for monolithic integration with active devices. Such antennas include the slot- and wire-loop antennas, the meandered dipole, and the patch antenna. The antennas discussed here have been implemented on surface and bulk micromachined low-resistivity silicon substrates.

4.1. Slot-Loop Antennas

The slot antenna consists of an aperture in a ground plane, where an electric field is excited across the slot. Using Booker's relation [10], the straight slot antenna can be considered to be the complementary antenna to the wire dipole and many of its properties, such as input impedance, can be directly calculated from the wire antenna equivalents.

By using micromachined membrane technology, high-performance slot antenna arrays have been built on silicon substrates [11]. The size needed for such antenna arrays, fully implemented on membranes, is, however, too large for monolithic integration on preprocessed SiGe wafers.

Because of their geometric properties, slot-loop antennas are particularly interesting for compact integration on chip (see Fig. 1) Slot-loop antennas integrated with active devices have been demonstrated in hybrid technology [12] and using high-resistivity silicon and bulk micromachining [13]. In order to minimize chip size, it is of interest to keep the antenna ground-plane dimensions as small as

possible without compromising the antenna performance. The influence of the dielectric substrate on the guided-slot wavelength is characterized using the effective dielectric constant ϵ_{eff} , as the relation between the free-space wavelength and the guided wavelength. The circumference of the slot-loop antenna is governed by the resonance condition of a total slot length of one guided wavelength [14] at the frequency of operation since the antenna is operated at the second resonance.

The slot-loop antenna is normally fed across one of the voltage maximums as illustrated with the CPW feed in Fig. 1. For a square slot loop on an infinite ground plane in free space, an input impedance of 250Ω can be calculated for an antenna in free space, using the Booker relation and published results for wire-loop antennas. Introduction of a dielectric substrate in the antenna will alter the input impedance at resonance as well as change the effective dielectric constant of the slotline and will include also conductive losses in the substrate.

4.1.1. Surface-Micromachined Slot-Loop Antenna. Using surface micromachining technology the characteristics of the slot-loop antennas can be improved. A surface-micromachined 24-GHz slot-loop antenna for integration with SiGe circuits on low-resistivity silicon wafer has been designed using a BCB process [14]. A square slot loop (see Fig. 1) was designed to maximize the area utilization given a specific loop length. A relatively narrow slot width $s_a = 20 \mu\text{m}$ was selected to maintain a slot mode despite the presence of a conductive silicon substrate. The antenna slot dimensions $L_s = W_s = 2000 \mu\text{m}$, equal to a total loop length of $1.14\lambda_g$, were chosen after HFSS (high-frequency structure simulator) simulation of the antenna, including the finite ground plane with the size $G_a = G_b = 3 \text{ mm}$. The antenna was realized on a $11\text{--}15\text{-}\Omega \cdot \text{cm}$ silicon wafer to simulate the substrate properties of preprocessed SiGe wafers. In the used surface micromachining method, a layer of BCB dielectric is spun on top of the silicon wafer, and shallow trenches are optionally formed in the silicon by frontside etching. The trenches are subsequently filled by the BCB dielectric layer, which extends the height over the silicon substrate by $10\text{--}20 \mu\text{m}$. The purpose of the spin-on BCB dielectric and the forming of the shallow trenches is to reduce the effective dielectric constant of the slotline and minimize substrate losses. A schematic sketch of the stacked layers together with an SEM view are shown in Fig. 2.

In Fig. 3 the return loss for antennas with identical metallizations with 10- and $20\text{-}\mu\text{m}$ -thick BCB layers are shown, as well as results for antennas with shallow trenches. The use of a thick BCB dielectric and the

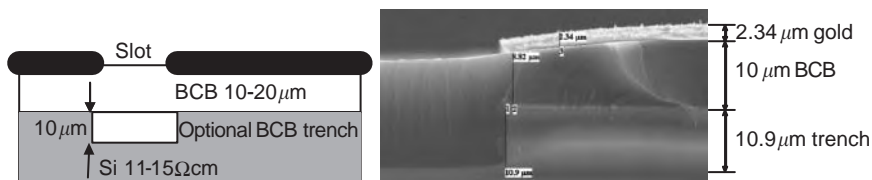


Figure 2. Surface micromachined slot-loop antenna on BCB layer and SEM view of the same.

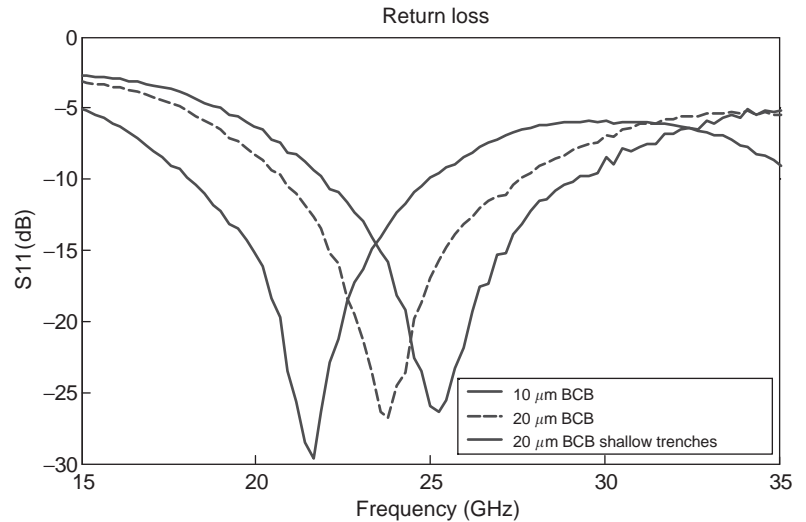


Figure 3. Return loss for surface-micromachined antennas with different BCB dielectric thickness and optional shallow trench. (This figure is available in full color at <http://www.mrw.interscience.wiley.com/erfme>.)

presence of micromachined shallow trenches reduces the effective dielectric constant and thus increases the frequency of resonance from 21 GHz for a thick 10- μm -thick BCB layer to 24 GHz for a 20- μm one.

The measured and simulated *E*- and *H*-plane radiation patterns for the slot-loop antenna are plotted in Fig. 4. Because of the low directivity of these small antennas, the coplanar wafer probe as well as the metallic wafer probe holder cause multiple reflections and shadowing problems that turn up as ripples in the measured patterns. The nulls in the radiation pattern are obtained in the plane of the antenna as predicted by theory.

4.2. Wire-Loop Antennas

The full-wavelength loop antenna can be considered as an alternative for an on-chip antenna (see Fig. 5). To enable compact integration of circuits on the same substrate as the antenna, the full membrane used in earlier approaches can be replaced by localized BCB membranes, here called “trenches”, under the wire loop as shown in Fig. 5. The loop dimensions are $W_L = L_L = 3000 \mu\text{m}$, with a loop wire width of $120 \mu\text{m}$ and a trench width of $W_{tr} = 360 \mu\text{m}$. The trenches are centred around the loop metallization. Two bridges of width $W_{br} = 200 \mu\text{m}$ are kept to maintain mechanical stability of the substrate. The bridges are placed at the current maxima of the loop to minimize capacitive coupling to the substrate in the vicinity of the voltage maxima. The radiation pattern is bidirectional as in the case of the slot-loop antenna, with a backlobe of a size comparable to that of the frontlobe. A property of the loop antenna is its inherently balanced feed, which makes the antenna suitable for integration with differential circuit topologies without the use of on-chip baluns. For integration on chip, the square loop antenna is of special interest since it can be placed around the edge of a chip with active components. The presence of active circuit ground planes in the center of the antenna will, however, reduce the radiation resistance and should therefore be considered in the antenna design. At the commonly used second resonance the input impedance of a thin-wire

square loop is $80 - j100$, thus requiring a total circumference of 1.15λ , for a resistive input impedance. The loop antenna can be modeled as a dual-resonance circuit where the series resonant circuit represents the useful second resonance. The measured input impedance of 70Ω is lower than the theoretical free-space value, indicated by the simulated values for the free-space case as shown in Fig. 6, due to the presence of the low-resistivity silicon substrate in the vicinity of the radiating loop. The wire-loop antenna has a radiation pattern similar to that of the half-wave dipole, but with a compressed *H*-plane pattern. The theoretical directivity [15] of the wire-loop antenna is 3.3 dBi. In an experimental setup a gain of 1.9 dBi has been obtained for the implemented antenna at 24 GHz. An annular loop antenna has been demonstrated on micromachined silicon substrate, using a BCB membrane to suspend the loop antenna in air [16].

4.3. Dipole Antennas

The dipole has been considered as a candidate for on-chip integration. On-chip dipole antennas for clock distribution have been demonstrated at 15 GHz on CMOS substrates [5] and on high-resistivity silicon substrates [17]. A 10-GHz dipole antenna has been integrated with a VCO (voltage-controlled oscillator) in a commercial BiCMOS process [18]. The balanced feed of the dipole is an advantage for integration with differential circuits. However, its length of a half-wavelength typically makes the dipole too large for integration on chip for applications in the 10–30 GHz frequency range. To reduce the size of a half-wave dipole antenna, the radiator can be meandered [19]. Meandering of an antenna with a certain wire length largely maintains its resonant frequency but reduces the radiation resistance. Since the loss resistance in the antenna remains relatively constant, the total efficiency of the antenna decreases. A meandered dipole, implemented on a BCB membrane to reduce substrate losses, is shown in Fig. 7. The length of the dipole L_{dip} is $3000 \mu\text{m}$ with a width W_{dip} of the meandered section of $500 \mu\text{m}$. The dipole was implemented on a BCB membrane with size $W_{tr} = 760 \mu\text{m}$,

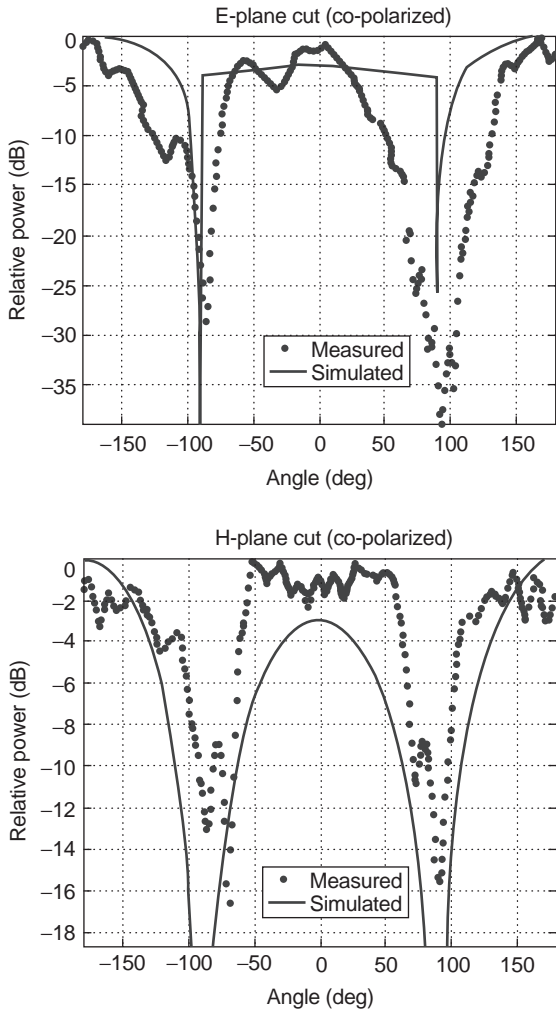


Figure 4. *E*- and *H*-plane measured and simulated radiation pattern, where -9° – 90° corresponds to topside of antenna. (This figure is available in full color at <http://www.mrw.interscience.wiley.com/erfme>.)

$L_{tr} = 3300 \mu\text{m}$. An additional antenna with a larger membrane, where the spacing between the silicon and the meandered line was increased from 125 to $425 \mu\text{m}$, was also designed. The theoretical directivity of a reduced-size

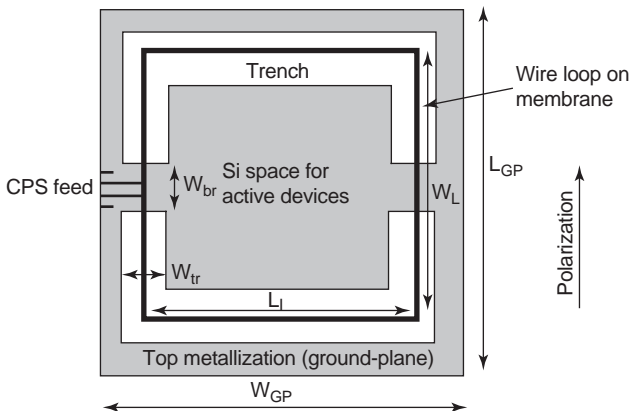


Figure 5. Wire-loop antenna with trenches etched in silicon wafer.

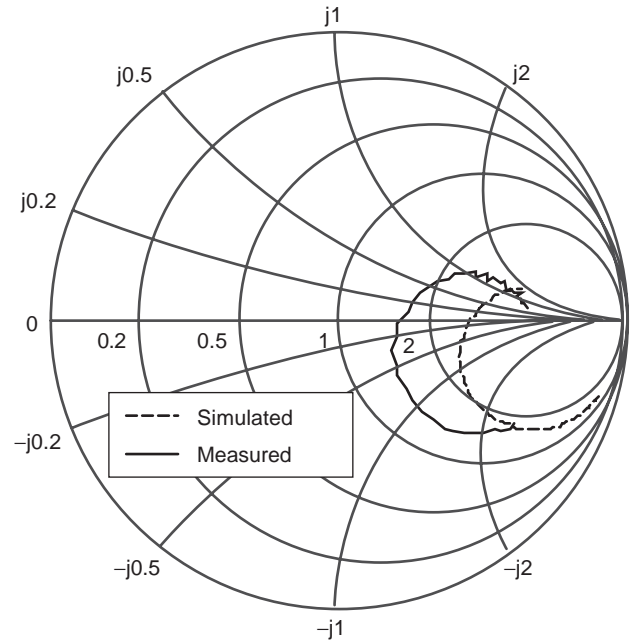


Figure 6. Wire-loop antenna with trenches, measured (solid line) and simulated (dashed line, silicon substrate effects not included); impedance 20–30 GHz. (This figure is available in full color at <http://www.mrw.interscience.wiley.com/erfme>.)

half-wave dipole in free space is bounded by the value 1.8 dBi for an infinitely short dipole and 2.1 dBi for a full-size half-wave dipole. The measured return loss is shown in Fig. 8, together with an IE3D [20] simulation considering the silicon substrate and a Momentum [21] simulation without the silicon substrate present. The measured impedance for the two different dipoles is plotted in Fig. 9 together with Momentum simulation results for an antenna without the silicon substrate present. The radiation resistance R_{rad} is reduced from the standard dipole value of 77Ω to 20Ω because of the meandering of the line. The meandered dipole can be accurately modeled for circuit codesign purposes by a standard series-resonant circuit with series resistances representing radiation and loss resistance. It should be noted that integrated antennas are not always required to have a 50Ω input impedance since the antenna and the active circuits can be codesigned. The radiation pattern for the *E* and *H* planes are shown in Fig. 10, where angles of 0 – 180° correspond to the topside of the wafer. The antenna beam pattern exhibits typical dipole characteristics with *E*-plane nulls at 0° and 180° and maxima in the broadside directions. The antenna gain was measured at

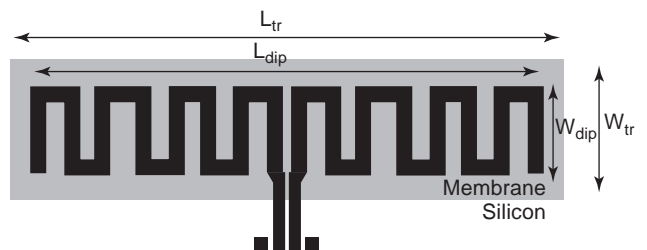


Figure 7. Meander dipole layout.

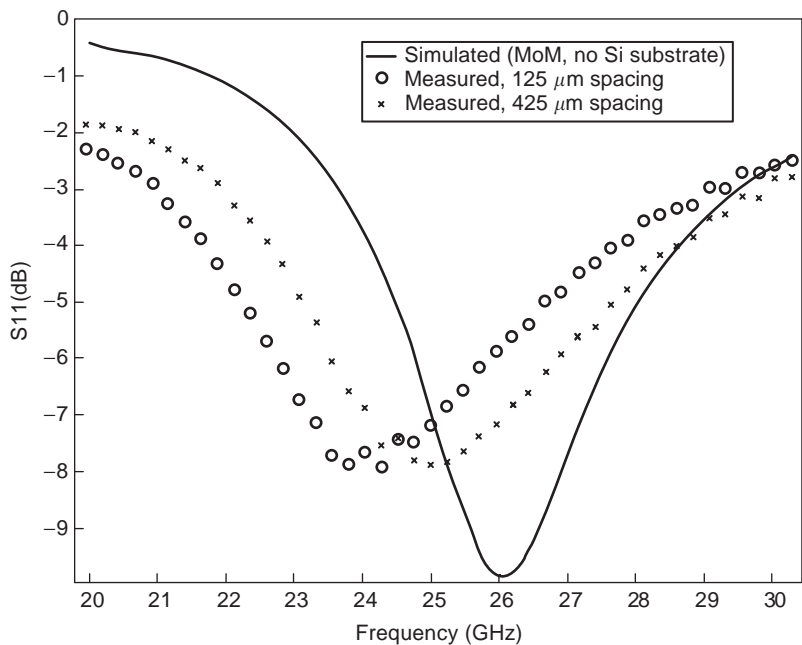


Figure 8. Measured and simulated (2D MoM; effects of silicon substrate not included) meander dipole antenna return loss.

24.14 GHz and found to be -1 dBi in a $50\text{-}\Omega$ system, which is in good agreement with the simulated gain of -0.2 dBi.

4.4. Patch Antennas

Patch antennas have been a common choice for integrated antennas in hybrid designs, due to their low profile and high gain. The normal patch antenna type consists of a wide metal patch on top of a grounded dielectric substrate.

By exciting a TM_{010} mode between the patch and the ground plane, radiating fringing fields will occur at two of the edges. A patch antenna manufactured on silicon will exhibit small bandwidth and poor performance due to the high dielectric constant of the substrate. Conductive losses in the silicon will lead to poor efficiency, thus requiring the use of high resistivity silicon, which is generally not compatible with standard SiGe bipolar and CMOS processes. A solution to these problems is offered by micromachining methods. The lossy silicon can be removed by backside etching of the substrate, thereby creating a cavity under the patch or by depositing a low-permittivity, low-loss dielectric such as BCB to the top of the wafer and realizing the patch on top of this layer.

Two micromachined patch antennas will be described, one 60-GHz aperture-fed patch antenna on a bulk micromachined high resistivity silicon substrate, suitable for a stacked wafer integration with an active transceiver module, and a differentially fed patch antenna developed on a thick BCB layer designed for wafer level integration with a 24-GHz differential SiGe oscillator [22,23].

4.4.1. Bulk Micromachined 60-GHz Patch Antenna. To increase the efficiency and bandwidth of such an antenna, part of the substrate beneath the patch could be removed using bulk micromachining techniques, thus reducing the effective dielectric constant of the substrate [22] (see Fig. 11). A well-known problem in the design of wideband patch antennas is that the requirements on the substrate are vastly different for the radiating patch element and the feedline (typically microstrip). By using aperture coupling between the patch and the feedline, a high-permittivity substrate could be chosen for the microstrip feed, while a substrate with a lower dielectric constant could be selected for the patch antenna element. Another advantage of aperture coupling over other feed types is that the feed network is shielded from the radiating side of the

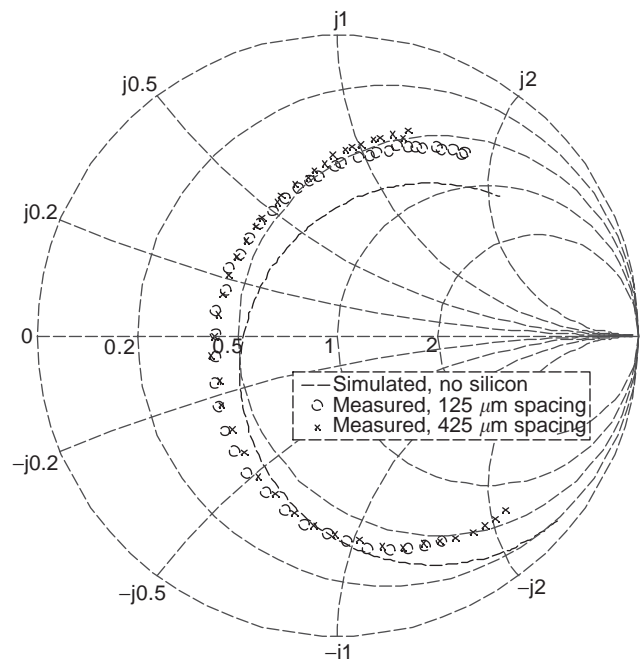


Figure 9. Measured and simulated (no silicon present) meander dipole antenna input impedance (20–30 GHz). (This figure is available in full color at <http://www.mrw.interscience.wiley.com/erfme>.)

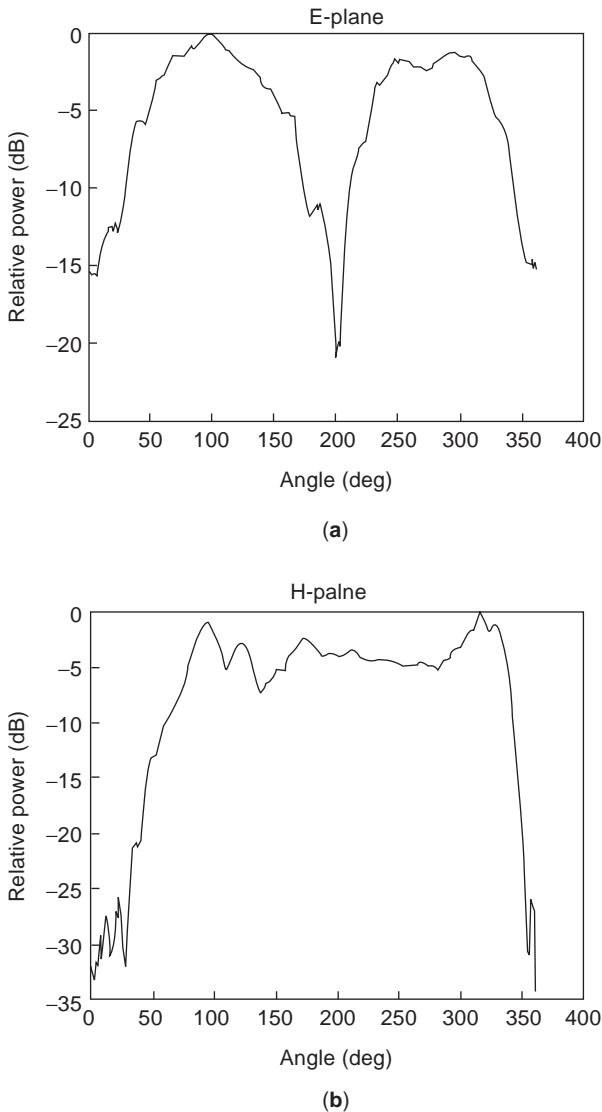


Figure 10. E-plane (a) and H-plane (b) radiation patterns.

elements by the ground plane. By combining silicon micromachining techniques and aperture feed, a highly efficient patch antenna can be made by stacking two silicon substrates on each other. A thick wafer is selected for the upper wafer to obtain good radiation characteristics where a cavity is opened underneath the patch. A thinner wafer is selected for the transmission lines, thus reducing the risk for substrate modes.

The effective dielectric constant of the mixed air–silicon patch substrate can be calculated using a quasistatic capacitor model presented by Papapolymerou et al. [24]. An

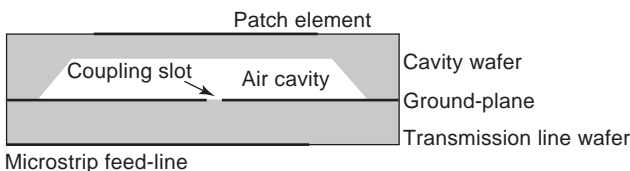


Figure 11. Micromachined silicon patch antenna.

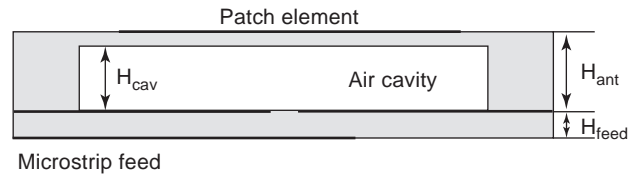


Figure 12. Side view of the micromachined patch antenna.

equivalent-circuit model of the rectangular aperture-coupled patch antenna based on transmission-line analysis has been presented by Himdi et al. [25]. By using an H slot instead of a rectangular one, the coupling can be improved, and the length of the slot can be well below the resonant region of the slot. An accurate transmission-line-based model for a H-slot feed-micromachined patch antennas was derived by Kurup et al. [26].

The antenna structure is shown in Figs. 12 and 13. A square patch was selected to allow for dual-polarization use (with a suitable feed network). A 50- μm -thick silicon membrane was selected as a compromise between surface-mode rejection and ease of manufacturing. The dielectric constant of 1.24 was calculated for a 254- μm -thick silicon substrate (H_{ant}) with a 200 μm deep cavity (H_{cav}). A patch antenna size of $W=L=1500 \mu\text{m}$ was determined for a 60 GHz resonance frequency. By selecting a $W_{\text{cav}}=L_{\text{cav}}=3 \text{ mm}$ large cavity underneath the patch element, most of the fringing fields were accommodated within the cavity, thus preventing excitation of surface waves. The microstrip line is aperture-coupled to the patch with an H-shaped slot with the dimensions $L_{\text{slot}}=1100 \mu\text{m}$, $L_{\text{H}}=600 \mu\text{m}$, and $W_{\text{slot}}=110 \mu\text{m}$. A $L_{\text{stub}}=0.45\text{-mm}$ -long quarter-wave stub is used to give the microstrip line a short-circuit termination after the slot. For measuring the antenna beam pattern a GaAs flip-chip diode was

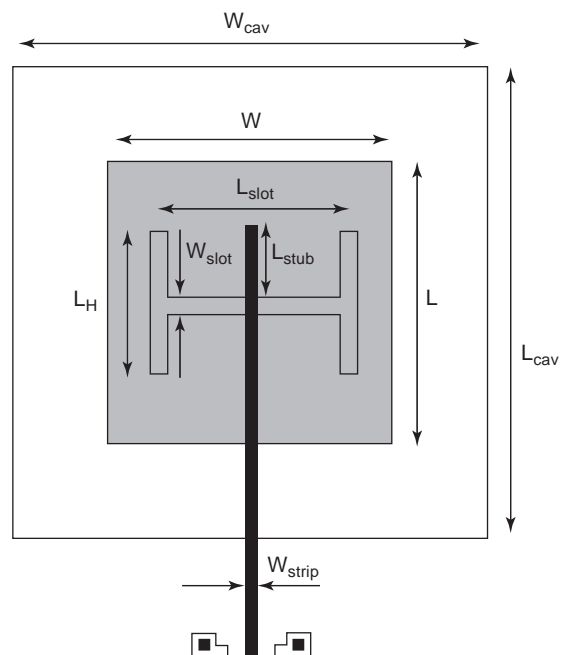


Figure 13. Top view of the micromachined patch antennas.

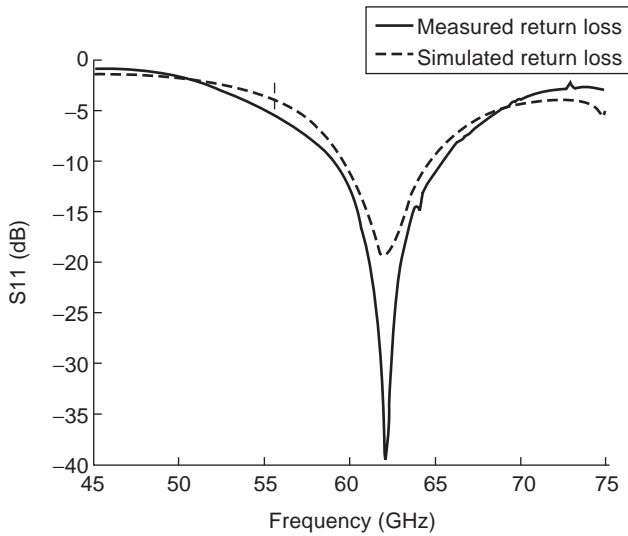


Figure 14. Antenna return loss.

connected to the end of the microstrip feedline in order to detect the received signal at the antenna terminals.

The patch antenna was manufactured on high-resistivity, double-polished, (100) silicon wafers. The wafer carrying the transmission lines and the slot was thinned from 254 to 100 μm (H_{feed}). The patch antenna elements were manufactured on a polished 254- μm -thick wafer.

The return-loss measured in this setup is shown in Fig. 14. From the measurements it can be seen that the antenna resonates at 62 GHz. The -10 dB bandwidth of the antenna is 6 GHz. No measurements of the radiation efficiency have been performed, but HFSS [21] simulations indicate 77% efficiency.

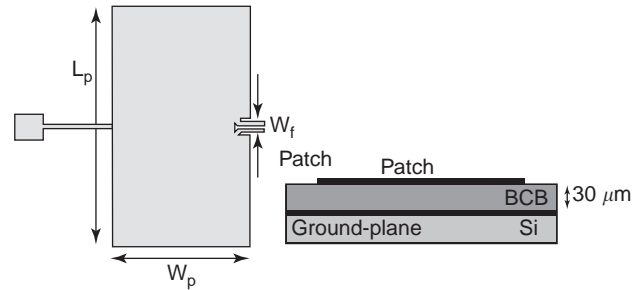


Figure 16. Differentially fed patch antenna on BCB layer.

The radiation pattern measurements for the vertical E plane and horizontal H plane are shown in Fig. 15 along with a HFSS simulation of the radiation pattern. A 50° half-power beamwidth obtained in the E plane. In the H plane the half-power beamwidth was measured to only 45° . A standing-wave minimum between the reference (measurement) antenna and the patch accounts for a drop in the received power at an 25° angle from the normal of the antenna pattern.

4.4.2. A Differentially Driven 24-GHz Patch Antenna. A differentially driven patch has been demonstrated [23] using a BCB thick layer dielectric on metallized silicon as the patch substrate (see Fig. 16). The antenna is 3848 μm (L_p) long and 1928 μm (W_p) wide, where the length determines the tuning frequency and the width, the impedance of the patch. Because of its size, this antenna is suited primarily for wafer-level integration with active devices at 24 GHz.

The antenna was manufactured by metallizing a ground plane on the silicon wafer and applying a 30- μm -thick BCB layer to act as a dielectric. Because of processing

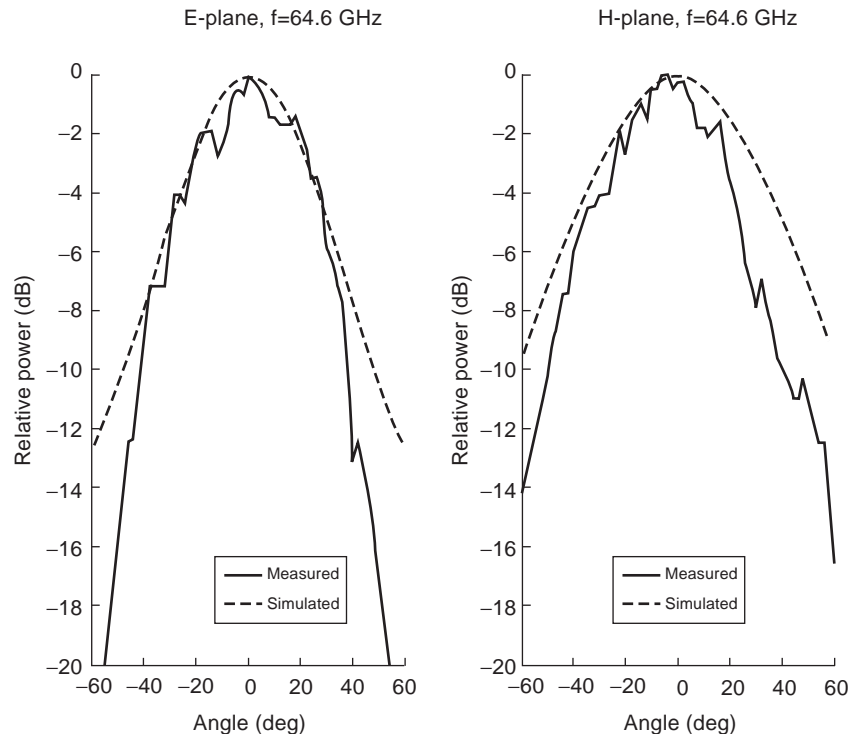


Figure 15. Antenna E - and H -plane radiation patterns.

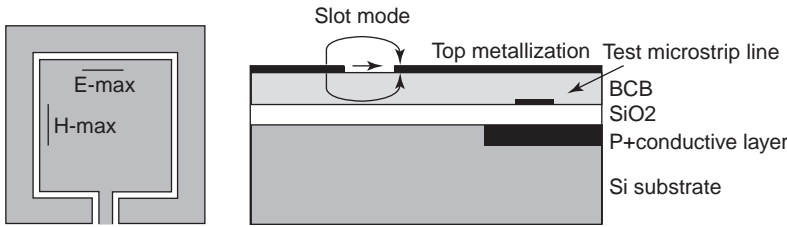


Figure 17. Crosstalk simulation setup.

constraints, it is difficult to obtain thicker layers of BCB, which imposes a limit on the obtainable bandwidth of the antenna. The patch metallization was added as the last step in the processing.

The patch antenna is differentially fed by a balanced transmission line positioned perpendicular to a normal microstrip feed. The short circuit of the balanced feedline presented by the patch induces currents parallel to the normal radiating mode of the antenna and thus couples to the patch mode. By adjusting the separation of the feed-point, the antenna impedance can be adjusted to a suitable value for the integrated active devices. The balanced feed offers compatibility with differential circuits and obviates the need for a connection from the active devices to the patch ground plane.

MoM simulations of the antenna yielded a directivity of 6.8 dBi and 0 dBi in gain when metallic and dielectric losses were included in the simulation, corresponding to an antenna efficiency of 20%. A 200 MHz bandwidth centered at 23.4 GHz was predicted by the simulations.

The measured antenna gain has not been reported, but an antenna integrated with a monolithic oscillator [23] yielded 5 dB less radiated power than the predicted value give the known oscillator output and antenna directivity, thus indicating reasonably good agreement with the simulated gain and efficiency. The main reason for the low efficiency of the antenna is the high Q value of the antenna caused by the limited obtainable thickness of the BCB dielectric used as the patch substrate.

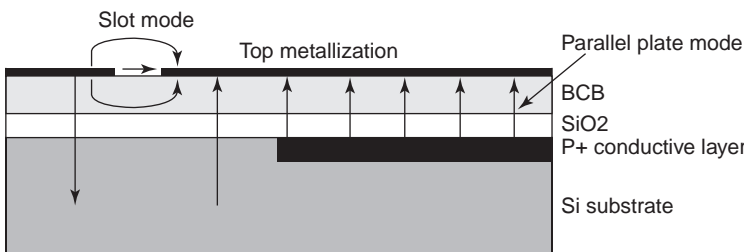


Figure 18. Parallel-plate-mode excitation.

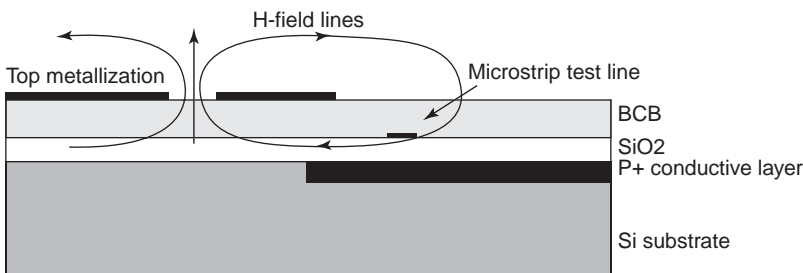


Figure 19. H -field configuration with finite antenna groundplane

5. CROSSTALK

If antennas are to be successfully integrated on the same chip as the active devices, the crosstalk between distributed and lumped elements in the active circuit and the on-chip antenna must be minimized. High levels of crosstalk can cause phase noise in on-chip oscillators and instabilities in receiver and transmitter chains as well as self mixing and DC offsets in zero-IF architectures.

Crosstalk between the circuits and the antenna in an integrated 24-GHz surface micromachined slot-loop antenna has been studied [27] for typical on-chip interconnects by electromagnetic simulations. Three cases were considered: no special crosstalk reduction scheme, truncation of antenna groundplanes, and short circuiting of the antenna ground plane to the circuit ground. The silicon substrates were assumed to have a low resistivity p^+ doping in the vicinity of the active devices, a feature common in commercial SiGe processes. A 200- μm -long microstrip testline, typical for an on-chip interconnect, was used as a testline and was placed parallel to the slots at different distances from the current and voltages maxima in the ring slot (see Fig. 17).

In the first case a parallel-plate mode was excited between the antenna ground planes and the conductive silicon substrate as shown in Fig. 18. This results in strong coupling; however, the coupling is relatively independent of the distance between the testline and the slotline that resulted.

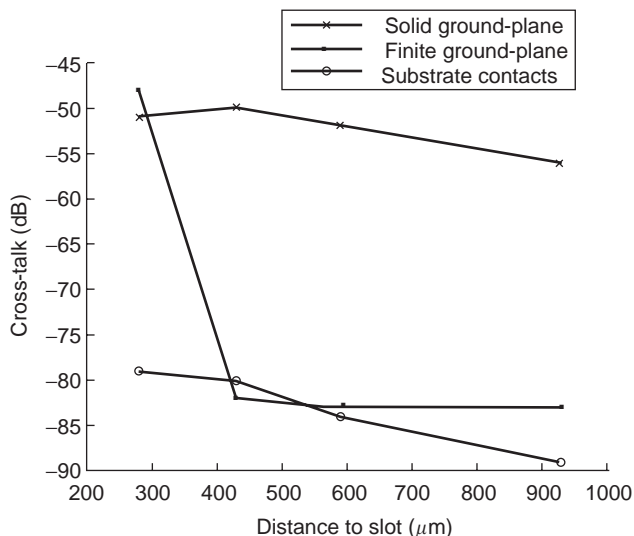


Figure 20. Simulated crosstalk at different distances from voltage maxima.

In the second case the antenna part of the antenna ground plane was removed over the area with the test interconnect line as shown in Fig. 19. By removing part of the ground plane, the performance of the slot antenna is compromised but the parallel-plate mode is prevented. However, as can be seen in Figs. 20 and 21, strong coupling is obtained when the test line is positioned close to the antenna slot, although the crosstalk decreases rapidly with increasing distance. The coupling was particularly strong close to the current maximums in the slot loop indicating primarily magnetic coupling as illustrated the H -field lines in Fig. 19.

The final case involved short-circuiting the parallel-plate mode by connecting the truncated ground plane with the conductive silicon substrate using via holes through the BCB dielectric. This grounding scheme eliminates the

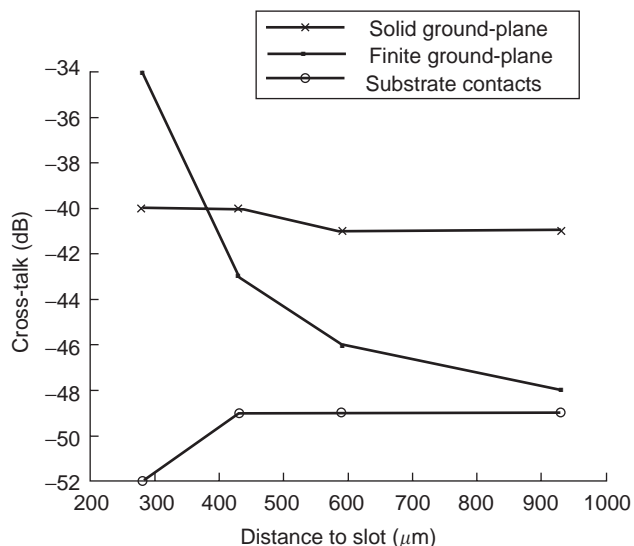


Figure 21. Simulated crosstalk at different distances from current maxima.

both parallel-plate modes and magnetic coupling, yielding low crosstalk, as can be seen in Figs. 20 and 21.

Acknowledgment

We would like to thank Dr. Katia Grenier, Mr. Fouad Bouchriha, and Prof. Robert Plana at CNRS/LAAS, Toulouse, France for the work on micromachined structures. We would also like to thank Dr. Jeurgem Berntgen and Dr. Winfried Rabe at Atmel Germany GmbH, Heilbronn, Germany for information on SiGe HBT processing. We would like to acknowledge Mr. Peter Lindberg at Uppsala University; Dr. Dhanesh Kurup, CPUM, Uppsala, Sweden; and the staff at EBS, University of Ulm, Ulm Germany, especially Mr. Peter Abele, Mr. Ertugrul Sönmez, and Prof. Hermann Schumacher for helpful discussions. This work was supported in part by the EU IST ARTEMIS project.

BIBLIOGRAPHY

1. F. C. Jain and R. Bansal, Monolithic antennas for millimeter wave GaAs integrated circuits, *Microwave Symp. Digest, MTT-S 84*(1):451–452 (1984).
2. I. D. Robertson, Millimetre-wave back-face patch antenna for multilayer MMICs, *Electron. Lett.* **29**(9):816–818 (1993).
3. I. D. Robertson, Millimetre-wave back-face patch antenna for multilayer MMICs, *Electron. Lett.* **29**(9):816–818 (1993).
4. D. Singh, C. Kalialakis, P. Gardner, and P. S. Hall, Small H-shaped antennas for MMIC applications, *IEEE Trans. Anten. Propag.* **48**(7):1134–1141 (2000).
5. B. A. Floyd, C.-M. Hung, and K. K. O, Intra-chip wireless interconnect for clock distribution implemented with integrated antennas, receivers, and transmitters, *IEEE J. Solid-State Circ.* **37**(5):543–552 (2002).
6. I.-J. Chen, H. Wang, and P. Hsu, A V-band GaAs HEMT uniplanar monolithic integrated antenna and receiver front end, *Microwave Symp. Digest, 2003 IEEE MTT-S Int. 2003*, Vol. 3, pp. 2023–2026.
7. K. E. Bean, Anisotropic etching of silicon, *IEEE Trans. Electron. Devices* **25**:1185–1193 (1978).
8. F. Lärmer and P. Schilp, *Method of Anisotropically Etching Silicon*, German Patent DE 4,241,045 (1994).
9. D. Neculoiu, A. Muller, P. Pons, L. Bary, M. Saadaoui, C. Buculescu, O. Andrei, R. Enachescu, D. Dubuc, K. Grenier, D. Vasilache, I. Petrini, and R. Plana, The design of membrane-supported millimeter-wave antennas, *Proc. Int. Semiconductor Conf. CAS, 2003*, Vol. 1, pp. 65–68.
10. H. G. Booker, Slot aeriels and their relation to complementary wire aeriels, *J. Inst. Electric. Eng.* 620–626 (1946).
11. P. Caudrillier, A. Takacs, O. Pascal, H. Aubert, P. Pons, and R. Plana, Compact circularly polarizing radiating element for Ka-band satellite communications, *Proc. IEEE Antennas and Propagation Society Int. Symp.*, 2002, Vol. 1, pp. 18–21.
12. K. Chang, *Microwave Ring Circuits and Antennas*, Wiley, New York, 1996.
13. Q. Chen, V. Fusco, M. Zheng, P. Hall, Silicon active slot loop antenna with micromachined trenches, *IEE Natl. Conf. Antennas and Propagation*, Conf. Publication 461, 1999, pp. 253–255.
14. E. Öjefors, F. Bouchriha, K. Grenier, and A. Rydberg, 24 GHz ISM-band antennas on surface micromachined substrates for

integration with a commercial SiGe process, *Proc. European Conf. Wireless Technology*, Munich, Germany, 2003.

15. C. A. Balanis, *Antenna Theory, Analysis and Design*, 2nd ed., Wiley, New York, 1997.
16. P. Abele, J. Konle, D. Behammer, E. Sonmez, K.-B. Schad, A. Trasser, and H. Schumacher, Wafer level integration of a 24 GHz and 34 GHz differential SiGe-MMIC oscillator with a loop antenna on a BCB membrane, *IEEE Microwave Symp. Digest*, 2003, Vol. 2, pp. 1033–1036.
17. A. B. M. H. Rashid, S. Watanabe, and T. Kikkawa, High transmission gain integrated antenna on extremely high resistivity Si for ULSI wireless interconnect, *IEEE Electron. Device Lett.* **23**:731–733 (Dec. 2002).
18. F. Touati and M. Pons, On-chip integration of dipole antenna and VCO using standard BiCMOS technology for 10 GHz applications, *Proc. Conf. European Solid-State Circuits, ESS-CIRC '03*, 2003, pp. 493–496.
19. H. Nakano, H. Tagami, A. Yoshizawa, and J. Yamauchi, Shortening ratios of modified dipole antennas, *IEEE Trans. Anten. Propag.* **32**:385–386 (April 1984).
20. *IE3D Release 10.1 User's Manual*, Zeland Software, Fremont, CA, 2004.
21. *Agilent High-Frequency Structure Simulator 5.6 User's Guide*, Agilent Technologies, Palo Alto, CA, 2000.
22. D. G. Kurup, A. Rydberg, and E. Öjefors, Design of millimeterwave micro-machined patch antennas for WLAN applications using a computationally efficient method, *Proc. European Microwave Conf. 2001*, London, Sept. 25–27, 2001, pp. 453–456.
23. P. Abele, E. Öjefors, K.-B. Schad, E. Sönmez, A. Trasser, J. Konle, and H. Schumacher, Wafer level integration of a 24 GHz differential SiGe-MMIC oscillator with a patch antenna using BCB as a dielectric layer, *Proc. European Microwave Conf. 2003*, pp. 293–296.
24. I. Papapolymerou, R. F. Drayton, and L. P. Katehi, Micromachined patch antennas, *IEEE Trans. Microwave Theory Tech.* **46**:295–306 (Feb. 1998).
25. M. Himdi, J. P. Daniel, and C. Terret, Transmission line analysis of aperture-coupled microstrip antenna, *Electron. Lett.* **25**:1229–1230 (1989).
26. D. G. Kurup, A. Rydberg, and M. Himdi, Transmission line model for field distribution in microstrip line fed H-slots, *Electron. Lett.* **37**:873–874 (2001).
27. E. Öjefors and A. Rydberg, Design and cross-talk simulations of on-chip antennas for integration in a SiGe process, *Proc. 4th Workshop on MEMS for Millimeterwave Communications (MEMSWAVE)*, Toulouse, France, July 2–4, 2003.

MONOLITHIC MICROWAVE INTEGRATED CIRCUITS (MMICs)

INDER J. BAHL
M/A-COM, Inc.
Roanoke, Virginia

Since the late 1980s, microwave technology has gone through a significant evolution to meet the necessary requirements for lower-cost solutions, circuit miniaturization, higher levels of integration, improved reliability, lower power consumption, low-voltage operation, and

high-volume applications. Component size and weight are prime factors in the design of electronic systems for satellite communications, phased-array radar (PAR), electronic warfare, and other airborne applications, whereas high volume and low cost drive the PAR and consumer electronics market. Monolithic microwave integrated circuits (MMICs) are the key to meeting these requirements. MMICs will play a significant role in consumer electronics dealing with information transfer, communications, automotive, and entertainment and successful deployment of the PAR systems for both commercial and military applications.

The first MMIC results for transmit/receive (T/R) modules using low-frequency silicon technology were reported in 1964. The results were not promising because the low resistivity of the silicon substrate produced insufficient isolation between the individual devices in the monolithic circuit. In 1976, the first monolithic X-band amplifier, based on the GaAs metal semiconductor field-effect transistor (MESFET), was developed. By 1980, many MMIC results using MESFETs for various circuits had been reported. Since that time, tremendous progress has been made in both MMIC developments and system applications. The outstanding progress in MMIC technology is attributed to the following:

1. Rapid development of GaAs material technology, including semiinsulating wafers, epitaxial growth, and ion implantation.
2. Advanced photo- or electron-beam (e-beam) lithography technology developed for Si ICs and directly applicable to GaAs ICs.
3. Excellent microwave properties of semiinsulating GaAs substrates, which permit easy isolation of devices for high-level integration [high dielectric constant ($\epsilon_r = 12.9$) and low loss ($\tan \delta = 0.0005$)].
4. The development of low-noise MESFETs and power MESFETs operating at up to 60 GHz have provided MMIC designers with versatile active circuit components.
5. Virtually any microwave solid-state circuit. They were realized using combinations of MESFETs, dual-gate MESFETs, Schottky barrier diodes, and switching MESFETs, each of which can be fabricated simultaneously using the same or similar process. HEMT MMICs provide enhanced performance in terms of noise figure, bandwidth, and frequency range. Using HEMT monolithic technology the frequency range was extended to 180 GHz.
6. High-electron-mobility transistors (HEMTs) and heterojunction bipolar transistors (HBTs), which are, in addition to MESFETs, the other most common active devices used in MMICs.
7. The development of good models for characterizing active devices and passive components.
8. The availability of commercial CAD tools for accurate simulation and optimization of microwave circuits.
9. The availability of on-wafer high-frequency test probes that permit both low-cost MMIC screening

and the collection of a large amount of statistically significant data without the cost and variability of packaging.

10. Government funding for technology development and maturation.
11. Expanding military and commercial applications.

The MESFET, commonly referred to simply as FET, is the most mature active device and is widely used in production applications. In addition to FETs, HEMT- and HBT-based MMICs are being produced in large volumes for military and commercial applications. With MMIC technology, a typical microwave subsystem can be produced on a single chip for less than \$100, while simpler single-function chips cost less than \$10. Some very simple MMIC chips are now produced in plastic packages for less than \$1.

Whereas most MMICs currently in production operate in the 0.5–30 GHz microwave range, applications covering the millimeter-wave (mmW) spectrum from 30 to 300 GHz are increasing. Monolithic technology is particularly suited for millimeter-wave applications through the elimination of the parasitic effects of bond wires that connect discrete components in conventional hybrid microwave integrated circuits (HMICs). In MMIC-based mmW subsystems, the cost can be lowered by a factor of 10 or more as compared to hybrid solutions.

Advantages of MMICs include low cost, small size, light weight, circuit design flexibility, broadband performance, elimination of circuit tweaking, high-volume manufacturing capability, package simplification, improved reproducibility, radiation hardness, improved reliability, and multifunction performance on a single chip. Indeed, the concept of implementing a subsystem on a chip became a reality through monolithic microwave technology.

IEEE Microwave and Millimeter-Wave Monolithic Circuits Symposium Digest, published from 1982 to 1996; *IEEE RFIC Symposium Digest*, published since 1997; and *IEEE GaAs IC Symposium Digest*, published since 1980 include comprehensive information on the design, fabrication, and performance of monolithic microwave and millimeter-wave integrated circuits as well as their applications. Several other books listed [1–19] deal with this subject either partially or exclusively.

1. MMIC FABRICATION

In fabricating MMICs, all active and passive circuit elements and interconnections are formed together on the surface of a semiinsulating substrate (usually gallium arsenide). Typically MMICs use microstrip and metal-insulator-metal (MIM) capacitors for the matching networks, whereas at low microwave frequencies, lumped inductors and MIM capacitors are commonly used. Via holes, metal-filled holes from the bottom of the substrate (ground plane) to the top surface of MMICs, provide low-loss and low-inductance ground connections. Figure 1 shows a three-dimensional view of an MMIC.

There are many ways to fabricate MMICs. MMICs using MESFET and HEMT are most commonly fabricated by

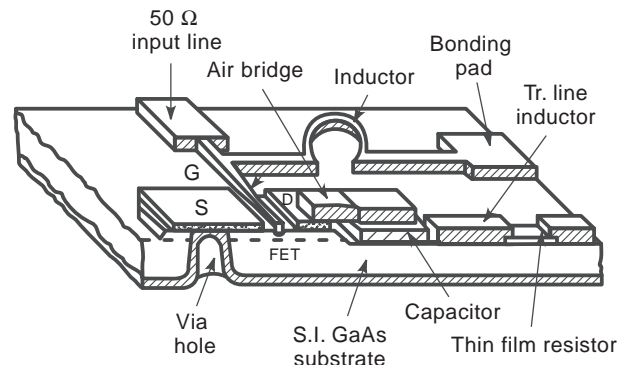


Figure 1. An MMIC three-dimensional view showing MESFET, inductor, capacitor, resistor, air bridge, via hole, and a microstrip section.

a recessed-gate process, but the self-aligned gate (SAG) process is gaining popularity because it permits the efficient fabrication of devices optimized for different functions (e.g., microwave small signal, microwave power, and digital) on the same wafer at the same time. The self-aligned gate process has demonstrated superior performance uniformity in a manufacturing environment. Figure 2 shows a SAG MESFET cross section along with salient features.

In order to give the reader an understanding of the relative complexity of GaAs MMIC manufacturing, a process flowchart for the SAG process is given in Fig. 3. The process for recessed-gate MMICs has many similarities. The process includes the fabrication of active devices, resistors, capacitors, inductors, distributed matching networks, airbridges, and via holes for ground connections through the substrate. Basic process steps are similar for any MMIC technology.

It should be noted that GaAs MMIC processing is less complex than silicon processing for devices operating at the low end of the microwave spectrum. Because silicon has inherently lower frequency capability and poorer isolation properties for integration purposes, more exotic processing is required to compete in the frequency region of overlap with GaAs applicability (1–2 GHz). For example, a silicon bipolar complementary metal oxide semiconductor (BiCMOS) process for such IC applications may require 2–3 times as many mask layers, adding significantly to the cost.

1.1. Active Layers

The MMIC process starts with the formation of an active layer on or into semiinsulating GaAs substrate. There are basically two methods of forming an n-type active layer: ion implantation and epitaxy. In the ion implantation technique, the dopant Si ions bombard the GaAs substrate in an area specified by a photolithographic photoresist pattern or mask. A suitable combination of energy and dose is used for the particular FET characteristics desired. During ion implantation, the crystal lattice of GaAs is damaged, and the implanted atoms come to rest at random locations with the material. A high-temperature

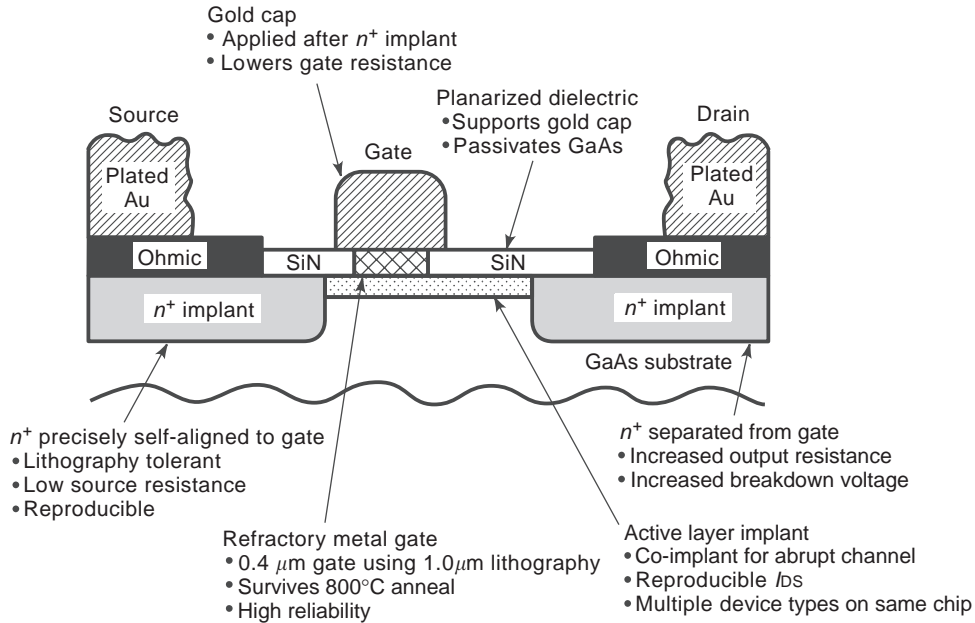


Figure 2. SAG FET cross section showing features to improve manufacturability.

($850\text{--}900^\circ\text{C}$) annealing step is performed to heal the lattice damage and allow the implanted atoms to move onto lattice sites. With this technique, different active-device types (with different active-layer properties) can be readily fabricated on the same wafer through respective selective implants defined by photoresist masks. This technique is well suited to high-volume production since the methods and equipment are nearly identical to those used in the silicon industry.

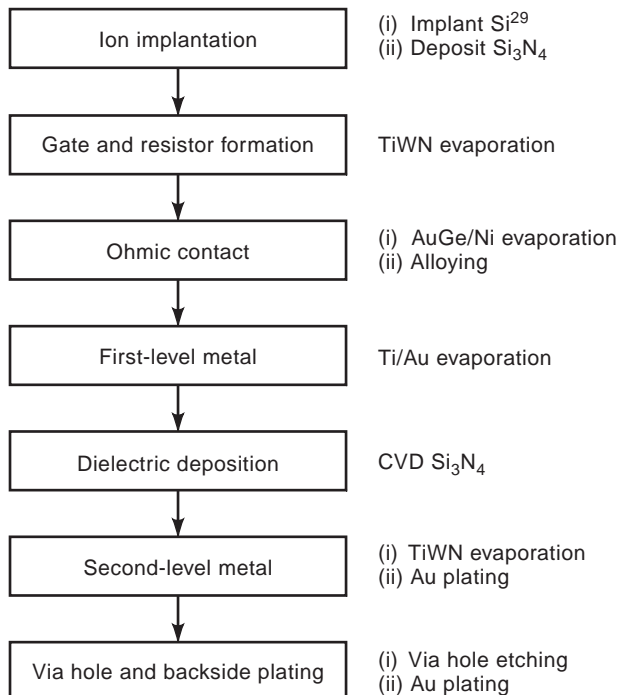


Figure 3. MMIC process flowchart for self-aligned gate process.

As discussed earlier, epitaxial devices are sometimes required for particular high-performance applications. In the epitaxial technique, additional GaAs (or other III-V compound) material layers are grown on the surface of the GaAs substrate in a manner that preserves the crystal structure. There are four basic types of epitaxy that have been used for GaAs: liquid-phase epitaxy (LPE), vapor-phase epitaxy (VPE), molecular-beam epitaxy (MBE), and metallorganic chemical vapor deposition (MOCVD). LPE is the oldest technique used to grow epitaxial layers on GaAs crystals, but it is not suitable for MMIC fabrication because of inherent surface roughness. VPE is typically used for GaAs power FETs. MBE is the most recent and powerful technique. Its advantage is that it can produce almost any epitaxial layer (III-V compound) composition, layer thickness, and doping with the highest possible accuracy and uniformity across a wafer. MOCVD has similar flexibility with the added advantage of being better suited to low-cost manufacturing; however, the material's electrical quality is not yet as good as that for MBE. The specified active areas are isolated either by mesa etching or by bombarding with ions, which increase resistivity by creating damage to the crystal lattice. A disadvantage of these techniques, relative to ion implantation, is that different device types generally require different epitaxial layers requiring not only multiple expensive growth runs but also relatively costly processing to isolate the different device types.

1.2. Schottky or Gate Formation

The quality and placement of the gate metal is critical to FET performance in both low-noise and power FETs. The choice of the gate metal is generally based on good adhesion to GaAs, electrical conductivity, and thermal stability. Recessed gate FETs utilize evaporated materials such as

TiPdAu or TiPtAu. SAG FETs [15] use a TiWN material, which forms a thermally stable, refractory Schottky gate in order to withstand the high-temperature annealing step, which is performed after the gate is in place. It is deposited by reactive sputtering.

Gate formation can be accomplished using optical lithography techniques for critical dimensions down to about 0.5 μm . Below 0.5 μm , the direct-write electron-beam lithography (EBL) method is often used. Although quite expensive because of the high cost of the equipment and relatively slow throughput, EBL provides a high degree of precision, making dimensions as small as 0.1 μm practical. The SAG technique uses lower-cost 1.0- μm optical lithography, along with a plasma underetch, to achieve 0.4 μm or smaller gate dimensions. Gate metalization is also used for thin-film resistors. Typical resistance values are about 10 Ω/square .

1.3. Ohmic Contact

Device ohmic contacts are made next. The purpose of an ohmic contact on a semiconductor material is to provide a good contact between the interconnect metal and the active channel at the semiconductor surface. The most common approach in industry to fabricate ohmic contacts on GaAs is by alloying gold and germanium (88% Au and 12% Ge by weight, with a melting point of 360°C). A thin layer of AuGe alloy, followed by a thin layer of Ni, is deposited by evaporation. The total layer thickness is about 2000 Å. The ohmic contact pads are defined by a photoresist mask and chemical liftoff of metal on the photoresist regions. The step is followed by alloying at 400°C in a hydrogen ambient.

1.4. First-Level Metal

Next a thick ($\sim 0.5\text{-}\mu\text{m}$) Ti/Au metal is overlaid on the gate by evaporation and liftoff. The metal reduces the gate resistance and also serves as a first-level metalization for MMIC fabrication (e.g., as a capacitor bottom plate or the interconnect metal under air bridges or crossovers).

1.5. Dielectric Deposition

Dielectric films are used in GaAs MMICs for passivation of active areas of FETs, diodes, and resistors; for MIM capacitors; and for crossover isolation. Silicon nitride (Si_3N_4) is commonly used as dielectric material, which is easily deposited either by plasma-assisted chemical vapor deposition or sputtering. The thickness of the dielectric film determines the capacitance per unit area of the MIM capacitor. The thickness is usually between 1000 and 3000 Å, and is optimized to have minimum pinholes, high breakdown voltage, and maximum possible capacitance. The capacitance value ranges from 240 to 1200 pF/ mm^2 with breakdown voltages from 16 V to greater than 60 V. Typical values for capacitance and breakdown voltage are 300 pF/ mm^2 and 60 V, respectively.

1.6. Second-Level Metal

Interconnection of components, airbridges, and the top plate of MIM capacitors is formed with the second-level

layer TiWN/Au metal system. In order to achieve low-resistance connections, gold plating (4.5 μm thick) is added to provide maximum current capability of about 10 mA/ μm of linewidth and a sheet resistance of less than 10 m Ω/square . Typical linewidths for microstrip line interconnects vary from 10 μm to 200 μm .

1.7. Backside Processing

Backside processing consisting of thinning by grinding or lapping, via-hole source ground contact finalization, and plating, is an important and cost-sensitive part of processing. In a production environment, a significant investment has been made in the wafer by the time the frontside processing is completed and the backside processing started. Also, several of the backside operations critically affect the circuit function and the yield as a whole. Typical functional yield for frontside processed MMICs is 90–95%, whereas for frontside- and backside-processed MMICs, yield numbers are 80–85%. After the frontside process, the wafer is thinned by a lapping technique from 600 μm to the required thickness, typically 100–125 μm for small-signal MMICs and 50–75 μm for power MMICs (to maximize heat dissipation). MMIC wafers may also be thinned down to 50–75 μm for frequencies greater than 50 GHz to minimize ground return parasitics. High-performance MMICs require low-inductance ground connections to the FET source and good thermal dissipation paths from the FET to its ground. In via-hole technology, holes are etched through GaAs substrate under each FET source connection as well as under other pads where ground connections are needed. Then the backside and the via-hole sidewalls are metallized. This provides a good connection from the frontside devices and components to the backside ground plane. This also eliminates the need for separate wire bonds to ground for each FET and other RF ground connections. The first check for a good circuit is automatic on-wafer testing with microwave probes. After identifying RF good ICs, the wafer is diced into chips.

2. MMIC SUBSTRATES

Any assessment of MMIC technology options available to the microwave designer will generally be in terms of chip size, weight, reliability, reproducibility, cost, maximum frequency of operation, and availability of a wide range of active devices for design flexibility. Various substrate materials used for MMICs are bulk silicon, silicon carbide, GaAs, InP, and GaN. Their electrical and physical properties are compared in Table 1. The semiinsulating property of the base material is crucial to providing higher device isolation and lower dielectric loss for MMICs. For example, even though bipolar silicon devices are capable of operating up to about 10 GHz, the relatively low resistivity of bulk silicon precludes monolithic integration for frequencies above the S band (2–4 GHz).

The GaAs FET as a single discrete transistor has been widely used in hybrid amplifiers (combining low noise, broadband, medium power, high power, high efficiency), mixers, multipliers, switching circuits, and gain control circuits. This wide use of GaAs FETs can be attributed to

Table 1. Comparison of Monolithic Integrated Circuit Substrates^a

Property	Silicon	SiC	GaAs	InP	GaN
Semiinsulating	No	Yes	Yes	Yes	Yes
Resistivity (Ωcm)	$10^3\text{--}10^5$	$>10^{10}$	$10^7\text{--}10^9$	$\sim 10^7$	$>10^{10}$
Dielectric constant	11.7	9.7	12.9	14	8.9
Electron mobility (cm^2/Vs)	1450	500	8500	4000	800
Saturation electrical velocity (cm/s)	9×10^6	2×10^7	1.3×10^7	1.9×10^7	2.3×10^7
Radiation hardness	Poor	Excellent	Very good	Good	Excellent
Density (g/cm^3)	2.3	3.1	5.3	4.8	—
Thermal conductivity ($\text{W/cm}^\circ\text{C}$)	1.45	4.3	0.46	0.68	1.3
Operating temperature ($^\circ\text{C}$)	250	>500	350	300	>500
Energy gap (eV)	1.12	2.86	1.42	1.34	3.39
Breakdown field (kV/cm)	≈ 300	≥ 2000	400	500	≥ 5000

^aPure materials at room temperature.

their high frequency of operation and versatility. All these benefits are automatically realized in MMICs as well. GaAs semiinsulating substrates provide isolation up to about 100 GHz. This, combined with much higher electron mobility (5–6 times that of silicon), enables GaAs MMICs to be produced for operation at up to 60 GHz. Additionally, MMICs at 94 GHz have been demonstrated using highly specialized HEMT devices epitaxially grown on semiinsulating GaAs. Hence, GaAs has been the technology of choice for most MMIC applications.

InP has been used for millimeter-wave monolithic integrated circuits using HEMTs, but very little work has been done on InP MMICs using MESFETs. The low Schottky barrier height of metals on n-type InP is a chronic impediment to the development of an InP MESFET technology of performance equivalent to that of GaAs. Pseudomorphic HEMTs fabricated on InP substrate exhibit much higher performance in terms of gain, noise figure, and power than does a GaAs-based HEMT of similar geometry. In this case, the InP substrate supports higher two-dimensional electron gas densities, resulting in high current and transconductance values. The high values of transconductance in InP HEMTs is responsible for ultralow noise figure, high gain, and high frequency of operation.

Except Si, all other substrate materials shown in Table 1 are called *compound semiconductors*. Silicon dominates the marketplace. GaAs is a distant second, with less mature technologies such as InP, SiC, and GaN only now emerging. For high-power and high-temperature applications, wide-bandgap materials with relatively high thermal conductivity, such as SiC and GaN, play a significant role. More recent advancements in the epitaxial techniques have made it possible to develop good active devices on these substrates, which is a prime requirement for any semiconductor material to be used as a substrate for MMICs.

3. TRANSMISSION LINES

The microstrip line and coplanar waveguide (CPW) are the two most commonly used transmission media in MMICs. The microstrip is more popular because of its quasi-TEM nature and excellent layout flexibility. Cross-

sectional views of these lines with physical parameters are shown in Fig. 4. Sections of microstrip lines and coplanar waveguides constitute the basic passive component building blocks of monolithic microwave integrated circuits. When the size of the microstrip section is reduced to dimensions much smaller than the wavelength, the section can be used as a lumped element. Examples of lumped microstrip elements are spiral inductors, thin-film resistors, and interdigital capacitors. Microstrip sections in lumped and distributed forms are commonly used in passive and active monolithic microwave integrated circuits.

Important parameters for designing these transmission lines are the characteristic impedance Z_0 , effective dielectric constant ϵ_{re} , attenuation constant α , discontinuity reactances, frequency dispersion, surface-wave excitation, and radiation. Several methods used to determine these parameters are summarized in Ref. 20. Basic properties such as Z_0 , ϵ_{re} , α , and maximum frequency of operation are briefly described here.

3.1. Microstrip

The microstrip propagation properties are controlled by conductor width W and substrate height h for a given dielectric constant value ($\epsilon_r = 12.9$ for GaAs). Figure 5 shows

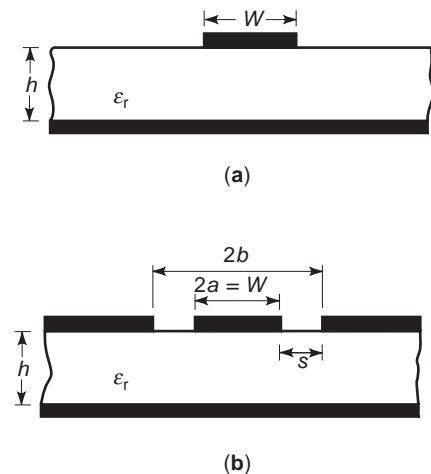


Figure 4. Transmission lines for MMICs: (a) microstrip; (b) coplanar waveguide.

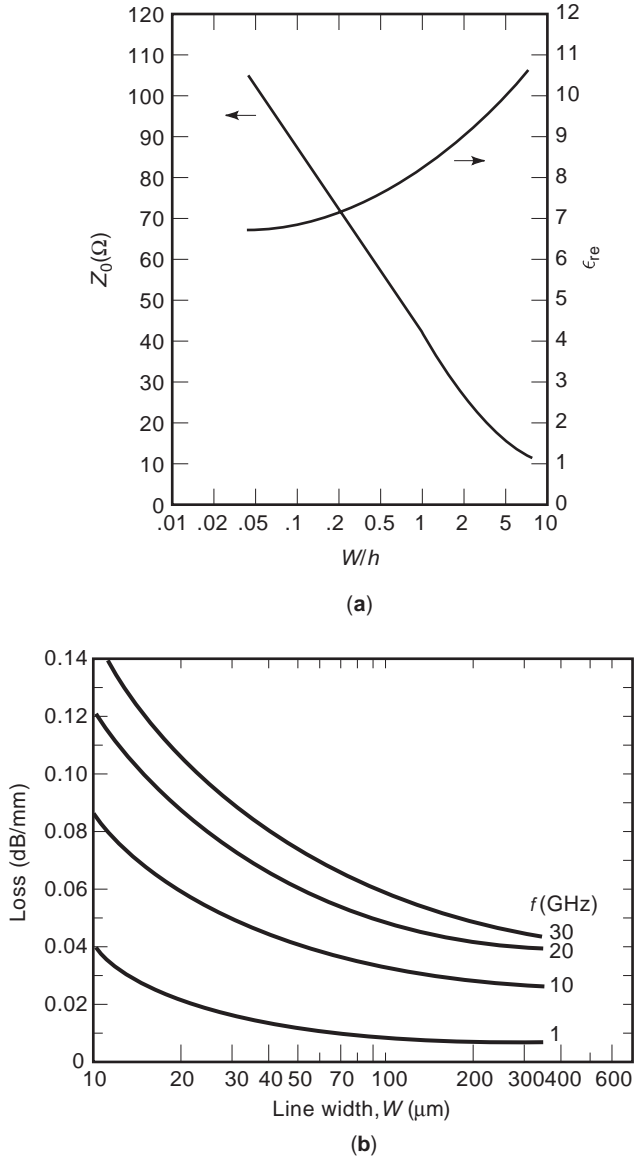


Figure 5. GaAs microstrip parameters: (a) characteristic impedance and effective dielectric constant; (b) attenuation constant measured as 1, 10, 20, and 30 GHz; substrate thickness of GaAs: 100 μm.

the variations of Z_0 , ϵ_{re} , and α . As an example, for a 50-Ω line on a GaAs substrate, the value of W/h is about 0.7.

The characteristic impedance value decreases when the strip width-to-height ratio W/h of the line increased. Wavelength in microstrip λ is related to ϵ_{re} by

$$\lambda = \frac{\lambda_0}{\sqrt{\epsilon_{re}}} \quad (1)$$

where λ_0 is the free-space wavelength.

The maximum frequency of operation of a microstrip transmission line is limited as a result of several factors including excitation of spurious modes, higher losses, pronounced discontinuity effects, low Q caused by radiation

from discontinuities, effect of dispersion on pulse distortion, tight fabrication tolerances, handling fragility, and, of course, technological processes. The frequency at which significant coupling occurs between the dominant quasi-TEM mode and the lowest-order surface-wave spurious mode is given by [20]

$$f_T = \frac{150}{\pi h} \sqrt{\frac{2}{\epsilon_r - 1}} \tan^{-1} \epsilon_r \quad (2)$$

where f_T is in gigahertz and h is in millimeters. Thus the maximum thickness of the GaAs substrate for microstrip circuits designed at 100 GHz is less than 0.3 mm.

The excitation of higher-order modes in a microstrip can be avoided by operating it below the cutoff frequency of the first higher-order mode, which is given approximately by [20]

$$f_c = \frac{300}{\sqrt{\epsilon_r}(2W + 0.8h)} \quad (3)$$

where f_c is in gigahertz and W and h are in millimeters. This limitation is applicable mostly for low-impedance lines that have wide microstrip conductors.

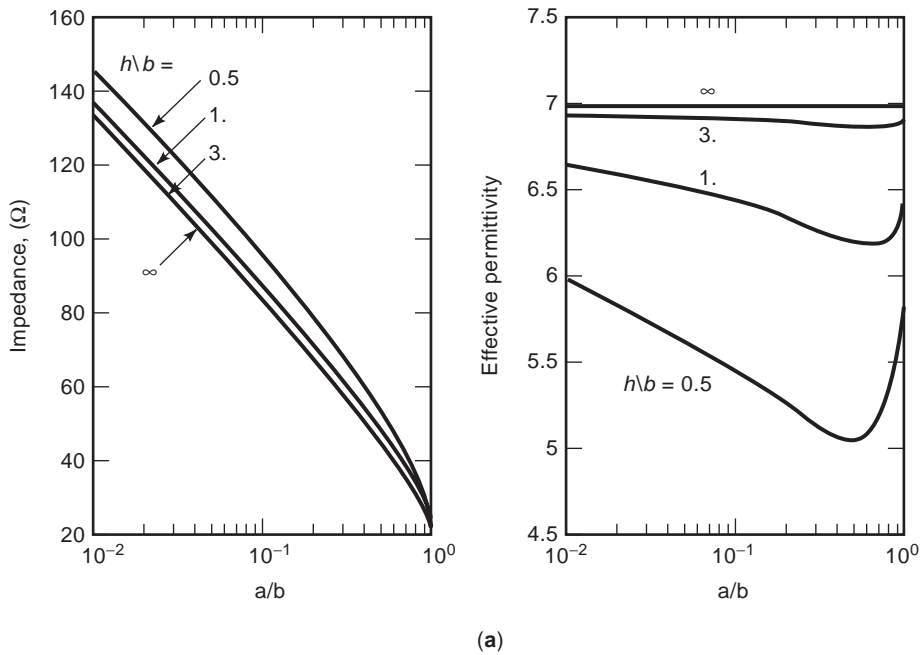
3.2. CPW

CPW properties are controlled by the center conductor width W and the spacing between the strip and the ground-plane conductor denoted by s in Fig. 4b. In a CPW, the substrate thickness generally used is large so that if the substrate has a conductor backing to improve the mechanical strength, it does not affect the electrical characteristics of the CPW. Figure 6 shows the variation of Z_0 , ϵ_{re} , and α as functions of the conductor width:gap separation ratio.

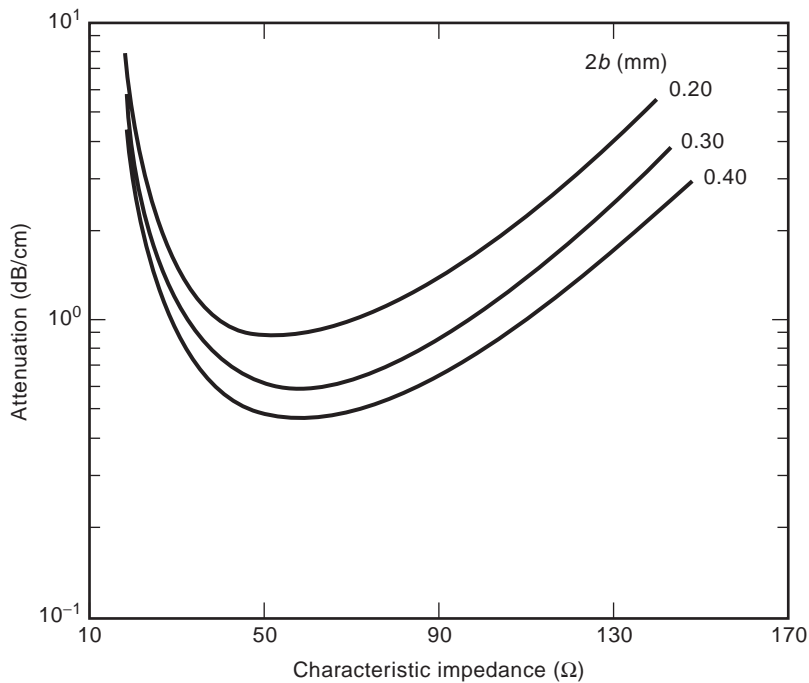
In addition to dielectric and ohmic losses, coupling of power to surface waves and radiation from unwanted (parasitic) modes contribute to the total loss of the coplanar lines. The parasitic mode in a coplanar waveguide is the odd mode with antiphase voltages in the two slots. This mode can be excited at discontinuities, and radiation may occur. Radiation from this mode can be minimized by maintaining symmetry of the circuits and thus avoiding its excitation or by using airbridges at regular intervals to short-circuit it out. In a conductor-backed coplanar waveguide, the parallel-plate waveguide modes are other parasitic modes. Surface waves or the substrate modes are the TM and TE modes supported by the substrate. Excitation of these modes can be avoided if a thin substrate is used such that the cutoff frequency of the surface modes is pushed above the operating frequency. This is achieved if the substrate thickness h is chosen such that

$$h \leq \frac{0.12\lambda_0}{\sqrt{\epsilon_r}} \quad (4)$$

where λ_0 and ϵ_r are respectively the free-space wavelength and dielectric constant of the substrate.



(a)



(b)

Figure 6. GaAs coplanar waveguide parameters: (a) characteristic impedance and effective dielectric constant; (b) attenuation constant.

CPW MMICs, compared with microstrip-based MMICs, can have lower loss at millimeter-wave frequencies by properly designing matching networks, require no via-hole technology for RF ground connections, and are more suitable for flip-chip mounting.

4. MMIC ACTIVE DEVICES

Since the first reported GaAs MMIC, the MESFET and the Schottky diode have been the workhorses for analog

integrated circuits (ICs). MESFET technology commonly uses $0.25\text{--}1.0\ \mu\text{m}$ gate lengths for microwave applications. MESFET low-noise and power MMICs demonstrate excellent performance at microwave frequencies. At the lower end of the microwave spectrum for new emerging wireless applications, GaAs FETs are more suitable, compared with bipolar transistors, because of their high-gain, low-noise figure and high power with good efficiency, excellent switching characteristics, and low-battery voltage (3–6 V) operation. However, increasing emphasis is being placed on new devices for better-performance and

higher-frequency operation. HEMT and HBT devices offer potential advantages in microwave and millimeter-wave IC applications, arising from the use of heterojunctions to improve charge transport properties (as in HEMTs) or p-n junction injection characteristics (as in HBTs). HEMTs appear to have a niche in ultra-low-noise and high-frequency (mmW) applications. The MMICs produced using novel structures such as pseudomorphic, lattice-matched HEMTs, also known as PHEMTs, have significantly improved the noise performance and high-frequency (up to 180 GHz) operation. PHEMTs that use multiple epitaxial III-V compound layers have shown excellent millimeter-

wave power performance from Ku through W bands. AlGaIn/GaN HEMT devices have demonstrated power densities greater than 5 times higher than that of conventional GaAs-based transistors [21,22]. HBTs are vertically oriented heterostructure devices and are gaining popularity as power devices. GaAs HBTs are extensively used as power devices for high-volume wireless applications because of their high gain, good efficiency, and single power supply low-voltage operation. They also offer better linearity and lower phase noise than do FETs and HEMTs. A cross-sectional view of the three basic device types (MESFET, HEMT, and HBT) is shown in Fig. 7. In a PHEMT

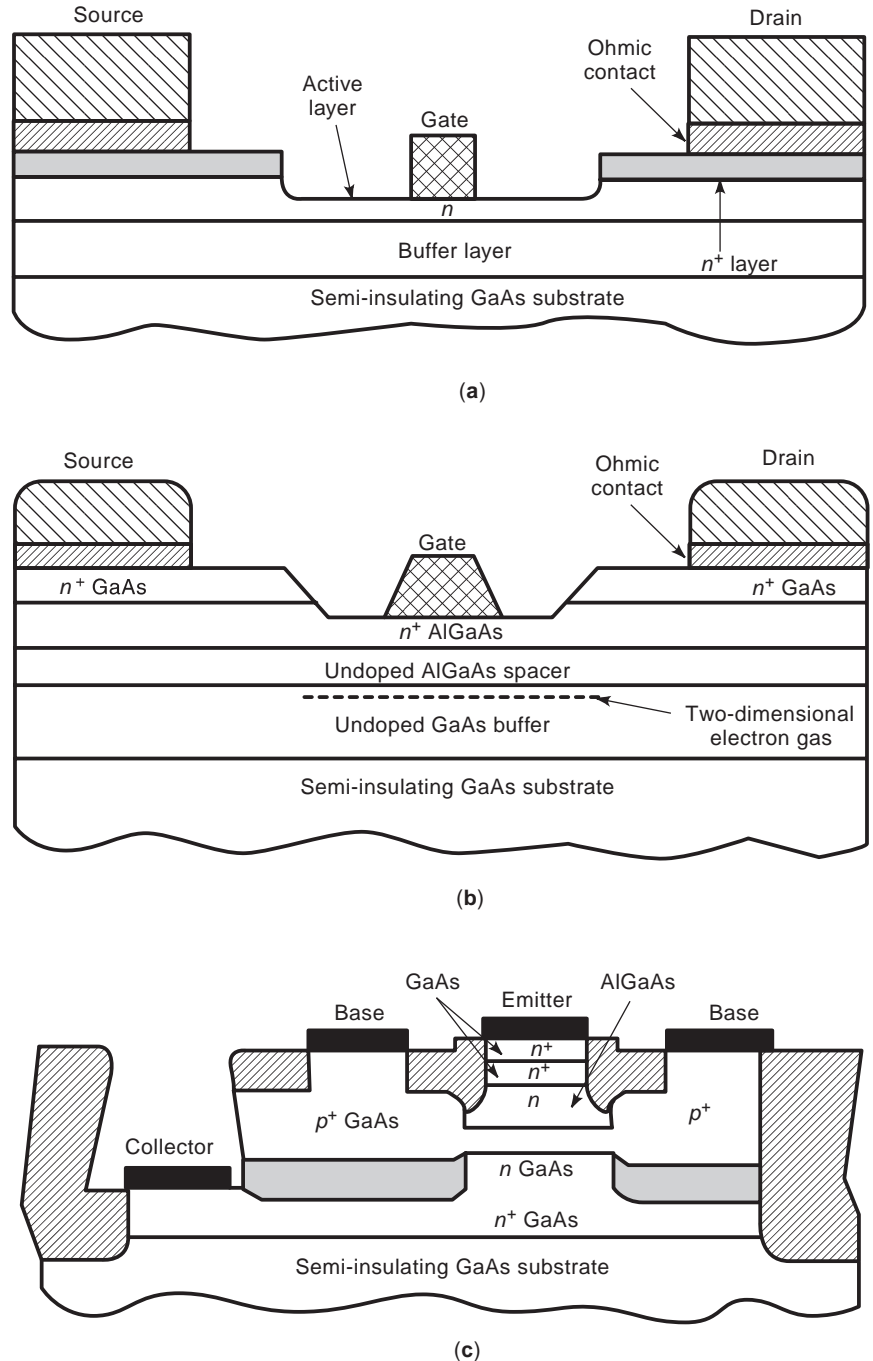


Figure 7. Schematic cross section of (a) MESFET, (b) HEMT, and (c) HBT.

structure there is another InGaAs active layer between the AlGaAs spacer and GaAs buffer that provides better carrier concentration in the channel than does a conventional HEMT structure.

MESFETs, HEMTs, and HBTs have been used to develop state-of-the-art circuit functions. GaAs-based MESFET, HEMT, and HBT devices are quite mature and versatile. These devices can be used for low-noise, switching, mixing, and power amplification depending on application requirements. For power circuits, where one needs much higher current, either a large number of cells are employed or larger gate periphery devices are used. Nearly all microwave circuit functions have now been realized as MMICs. Many of these functions have been demonstrated over the entire 1–100 GHz frequency range. Furthermore, many of these functions have been combined on a single chip to form portions of a microwave system. Examples of such single- and multifunction ICs are described in Section 9.

The upper frequency limit of MMICs is generally dictated by the active devices used. The performance of microwave transistors in MMIC technologies is improving every year. The performance of these devices (FETs, HEMTs, and HBTs) depends on the substrate material, process type, and channel physical dimensions. A commonly used figure of merit for devices is known as the *maximum frequency of oscillation* and denoted by f_{\max} . Generally, for amplifiers the maximum frequency of operation is about half of f_{\max} . For FETs on a GaAs substrate, a simplified expression for f_{\max} is given by [23]

$$f_{\max} = 38.05L^{-0.953} \quad (5)$$

where L is the gate length in micrometers. Thus, for FETs having gate length of 0.25 μm , the f_{\max} value is about 140 GHz. As reported in the literature, the f_{\max} values for a 0.1- μm -gate-length PHEMT on an InP substrate is about 600 GHz, and for a 1- μm emitter HBT it is about 170 GHz. A three-stage amplifier fabricated using a 0.1- μm PHEMT on an InP substrate has exhibited about 12 dB gain at 153–155 GHz [24].

5. COMPONENTS AND CIRCUITS

Monolithic microwave integrated circuits consist of passive components and active devices fabricated simultaneously on a semiinsulating substrate. Passive components can be divided into lumped and distributed categories, where “lumped” refers to components that are small with respect to the operating wavelength and “distributed” describes elements with sizes being comparable to the wavelength. Generally, monolithic design requires both lumped and distributed elements depending on its size, frequency of operation, types of circuit function, and cost. Examples of lumped elements [19,25], as shown in Fig. 8, are spiral inductors, thin-film resistors, interdigital capacitors, MIM capacitors, via holes, and airbridges. Distributed elements are commonly realized using sections of a microstrip transmission line or a coplanar waveguide. Lumped elements such as spiral inductors are usable in the microwave

frequency range where the size and bandwidth are critical parameters. Distributed elements are preferred in applications where lower loss and higher power-handling capability are important. However, thin-film resistors, capacitors, airbridges, and via holes are used in almost all microwave and millimeter-wave monolithic integrated circuits. The lumped elements have a lower Q than do the distributed elements, but they have the advantage of smaller size, ability of large impedance transformations, and wideband characteristics compared with distributed elements.

MMIC passive components include filters, impedance transformers, hybrids, couplers, power dividers/combiners, delay lines, and baluns. The design of such components has been thoroughly discussed in Refs. 8, 9, and 26–30. In order to predict the performance of microstrip passive components, the effect of junction and layout discontinuities and interaction effects between circuit elements caused by close proximity is usually included in the circuit analysis, with the help of electromagnetic (EM) field simulators. Figure 9 shows commonly used MMIC passive components.

In active MMIC components and subsystems, all interconnections are made along with active/passive devices on the semiinsulating semiconductor substrate, thereby eliminating discrete components and wire bond interconnects. MMIC active components use two types of devices: two-terminal devices referred to as *diodes*, such as Schottky and pin, and three-terminal devices, such as MESFET, HEMT, and HBT. Microwave circuits that use these devices include amplifiers, oscillators, multipliers, mixers, switches, phase shifters, attenuators, modulators, limiters, and many others used for receiver or transmitter applications covering microwave and millimeter-wave frequency bands. The theory and performance of most of these circuits have been well documented [1–18,31–34]. Figure 10 shows a physical layout of a broadband driver amplifier using FETs, microstrip lines, inductors, resistors, capacitors, via holes, and airbridges. Table 2 summarizes some of the key milestones in MMIC development [35]. This list is by no means exhaustive. Several examples of active circuits using various MMIC technologies are described in Section 9.

6. MMIC DESIGN

The design of MMICs requires state-of-the-art computer-aided design (CAD) tools. The need for increased design sophistication arises from the fact that the postfabrication tuning flexibility available in conventional hybrid microwave circuits is no longer present in the monolithically fabricated circuits. Consequently, a new design methodology is required. This includes development of accurately characterized standard library cells as well as subcircuits, accurate models for linear and nonlinear active devices, accurate passive component models, use of circuit topology and circuit elements that are more tolerant to process variations, tolerance centering of designs, proximity effect models, comprehensive simulation of complete circuits, and automatic RF testing of ICs on wafer. The latter is

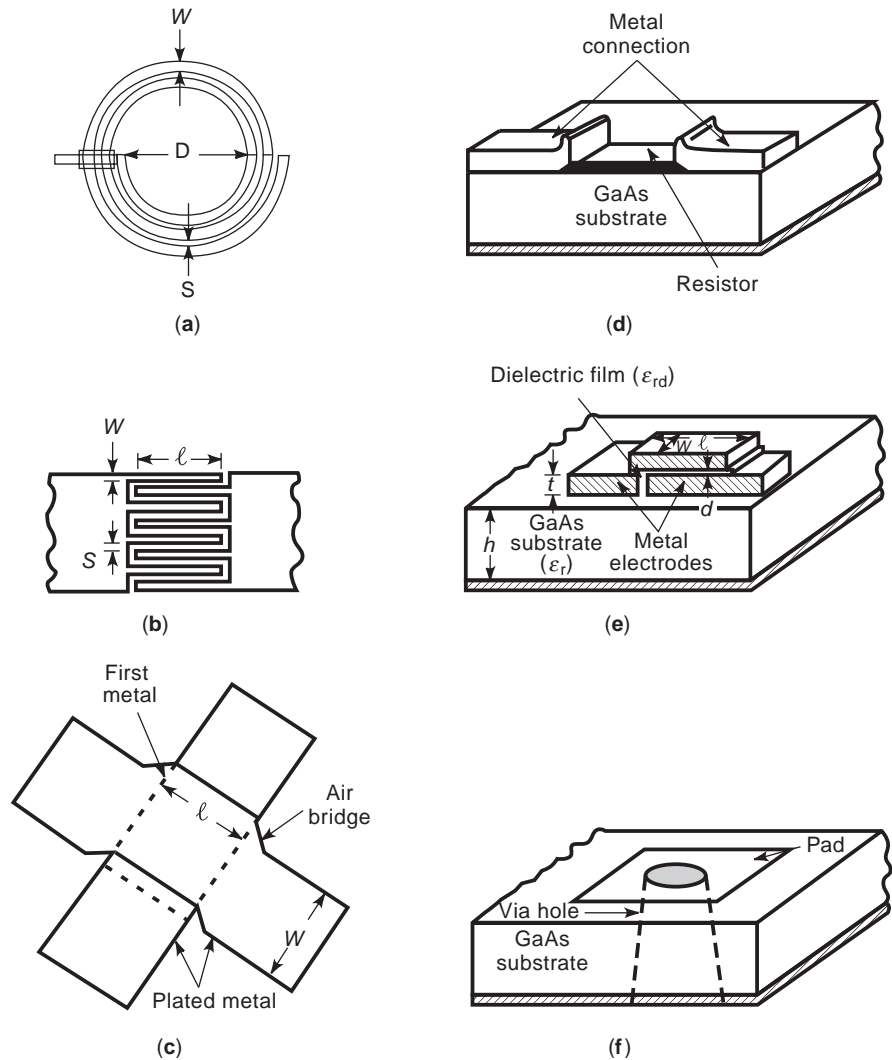


Figure 8. MMIC circuits use passive lumped elements: (a) spiral inductor; (b) interdigital capacitor; (c) airbridge crossover; (d) thin-film resistor; (e) MIM capacitor; (f) via hole.

needed in order to obtain sufficient statistical characterization data without having to do expensive mounting or packaging.

Figure 11 shows [36] a comprehensive CAD tool consisting of device, circuit, system simulators, and their accurate models (including physics-based and electromagnetic), and statistical design feature. Several microwave CAD tools are available to designers, including Agilent's ADS, Ansoft's Ansoft Designer, and Applied Wave Research's Microwave Office. A workstation-based MMIC CAD tool [37] is conceptually shown in Fig. 12. This interactive system will provide efficient coupling between the circuit simulation, the schematic captive/text editor, and the layout generator, greatly improving overall accuracy and reducing design cycle time. With such a system, first-pass design success for simple microwave functions should be achievable.

The evolution of a typical small-signal MMIC design generally follows the flow diagram depicted in Fig. 13. The design starts with the circuit specifications, which derive from the system requirements. System requirements also dictate the circuit topology along with the types of passive elements and active devices to be used (e.g., distributed or

lumped passive elements, single- or dual-gate FETs, and low-noise or power FETs). Comprehensive passive-element and active-device models developed by foundry or by users are used to simulate circuit functions. The final design is completed by taking into account layout discontinuities, interaction between the components, stability analysis in case of amplifiers, and circuit yield analysis by considering process variations. In the case of nonlinear circuit design, (e.g., power amplifier, oscillator, or mixer) an accurate nonlinear model for each device used is essential in order to design the circuit accurately.

7. EM SIMULATORS

The main contribution of electromagnetic (EM) simulators to MMIC CAD tools has been in the area of accurate modeling of passive circuit elements and components. These simulators are commonly used to model circuit elements such as microstrip and coplanar waveguide structures, discontinuities, and coupling between transmission-line sections and discontinuities, structures using multilayer dielectric and plating, inductors, capacitors, via holes, and

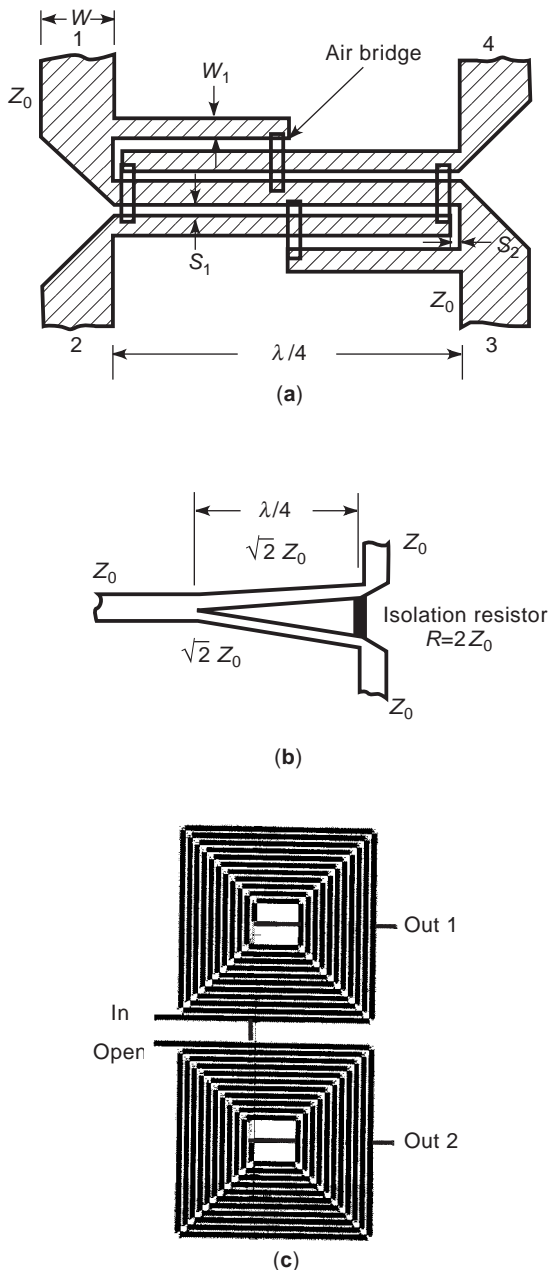


Figure 9. Typical MMIC passive components: (a) Lange coupler; (b) Wilkinson divider; (c) spiral Marchand balun.

crossovers. Passive components, such as filters, couplers, resonators, power dividers/combiners, baluns, matching impedance transformers, and several types of interconnects and packages, are accurately simulated using EM simulators. Accurate characterization of active-device parasitics also requires EM simulation. Another key and important role of EM simulators in successful MMIC design is the capability of incorporation of parasitic coupling effects among various parts of the circuit layout. Accurate evaluation of radiation and surface waves can be performed using simulators only. These effects become increasingly important as MMIC designs become more compact and are not easily incorporated using conventional

network-theory-based CAD tools. However, due to very large computation time, only a small portion of a circuit is analyzed using EM simulators, and the numerical results are combined with conventional CAD tools to obtain the response of the complete circuit. Most EM simulators work in the integrated simulation environment (i.e., they can be interfaced with microwave computer-aided design and engineering tools). Since the early 1990s, outstanding progress made on personal computers and workstations lead to commercial EM simulators.

7.1. Electromagnetic Simulation Methods

Several different field simulation methods have been used and described in the literature [38,39]. The most commonly used technique for planar structures is the method of moments (MoM), and for three-dimensional structures, the finite-element method (FEM) is usually used. Both these techniques perform EM analysis in the frequency domain. FEM, as compared to MoM, can analyze more complex structures but requires much more memory and longer computation time. There are several time-domain analysis techniques; among them, the transmission-line matrix (TLM) method and finite-difference time-domain (FDTD) method are commonly used. Fast Fourier transformation is used to convert time-domain data into frequency-domain results. An overview of commercially available EM simulators is given in Table 3. Here “planar” structure refers to 2D or 2.5D and “arbitrary” structure refers to full 3D configurations. More comprehensive information on these tools can be found in mid-late 1990s publications [40–42].

In EM simulators, Maxwell’s equations are solved in terms of electric and magnetic fields or current densities, which are in the form of integral-differential equations, by applying boundary conditions. When the structure is analyzed and laid out, the input ports are excited by known sources (fields or currents), and the EM simulator solves numerically the integral-differential equations to determine unknown fields or induced current densities. The numerical method involves discretizing (meshing) the space for evaluation of unknown fields or currents. Using FEMs, six field components (three electric and three magnetic) in an enclosed 3D space are determined, while MoMs results in current distribution on the surface of metallic structures.

7.2. Application to MMIC Design

All EM simulators are designed to solve arbitrarily shaped strip conductor structures and provide simulated data in single- or multiport S parameters, which can be read in a circuit simulator. To perform an EM simulation, the structure to be simulated is defined in terms of dielectric and metal layers, and their thicknesses and material properties. After creating the complete circuit/structure, the ports are defined, and the layout file is saved as an input file for EM simulations. Then an EM simulation engine is used to perform electromagnetic analysis. After the simulation is complete, the field or current information is converted into S parameters and saved for use with other CAD tools.

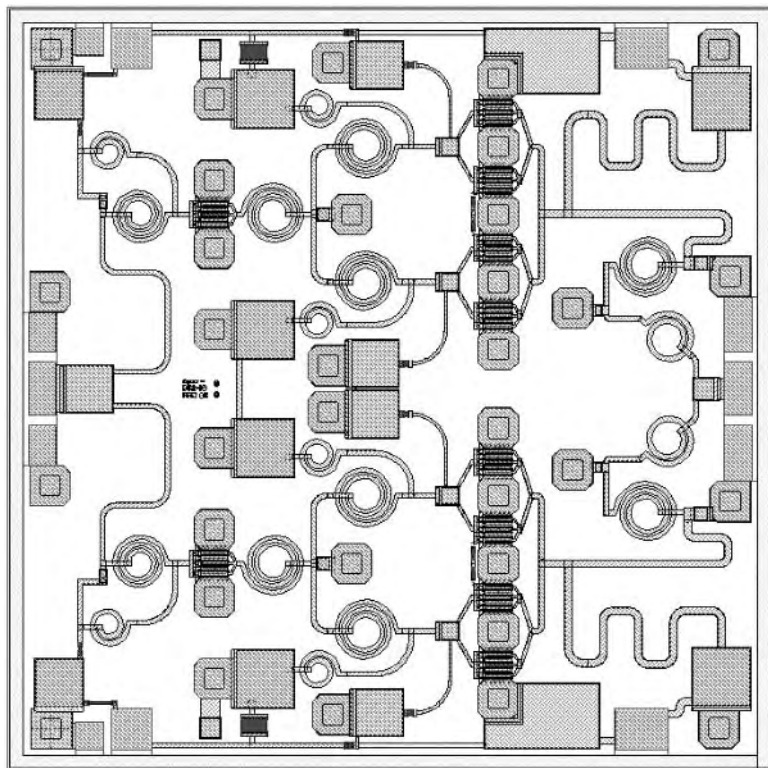


Figure 10. Physical layout of an MMIC amplifier using ten FETs, capacitors, resistors, inductors, microstrip as matching elements, and several vias.

EM simulators, although widely used, still cannot handle complex designs. There is considerable emphasis on achieving first-pass success of single- and multifunction MMICs in order to keep the MMIC development cycle time and cost low. Thus, microwave circuits should not only perform as individual components but also work as designed in the subsystem environment (e.g., T/R chip). This mandates comprehensive simulation of the complete chain including parasitic coupling effects between the closely spaced matching networks belonging to different microwave circuits. Although the advent of EM simulators has enhanced the accuracy of individual circuit functions, they are seldom used to perform comprehensive simulation of the complex MMIC chips such as T/R chips because of their large circuit size and very large CPU time. Thus, next-generation EM simulators are required to characterize compact and multilayer MMICs, highly integrated MMICs, multichip assemblies (MCAs), and for greater use of parallel computation and better integration with the circuit simulator so that they can become part of optimization. Advances in the numerical methods, computation speed, multiprocessor computations, and optimization techniques will set the course for EM simulators to become the microwave CAD tools of choice.

8. MODELING

The development of integrated CAD tools and accurate and comprehensive models for passive circuit elements and active devices was major activity during the 1980s and 1990s. Both play a key role in the successful development of MMICs. Passive circuit elements that have linear

models (independent of bias conditions and input power) include resistors, inductors, capacitors, via holes, airbridges/crossovers, transmission lines, discontinuities, and interaction effects. Active devices consist of diodes, and transistors (single- and dual-gate FETs and HEMTs, and HBTs). Transistors are of low noise, switching, and power types. Active devices use both linear and nonlinear (bias and input power-dependant) models. Figure 14 illustrates an attempt to summarize the current models for active devices and passive circuit elements. More comprehensive information on modeling can be found in several books [11,19,23,43] and other publications [44–47].

Basically there are three types of models:

1. Physics/EM-theory-based models
2. Analytical or hybrid models
3. Measurement-based models

These models are briefly described next.

8.1. Physics/Electromagnetic-Theory-Based Models

Development of accurate physics-based models for active devices that are derived in terms of doping profile and physical geometry are essential for establishing the link between the process and RF performance and for designing MMICs. These models consist of two parts: intrinsic and extrinsic. The intrinsic part deals with the active channel of the device, whereas the extrinsic part represents device pad/electrode parasitics, which are expressed in resistances, inductances, and capacitances. The intrinsic part of the model, the heart of the device, is obtained by

Table 2. Milestones in MMIC Development

Year	Function	Frequency Band	Substrate			Device Basis		
			Si	GaAs	InP	FET	HEMT	HBT
1965	PIN switch	X	●					
1968	Mixer/oscillator	V		●				
1974	Low-power amplifier	X		●		●		
1978	Power amplifier	X		●		●		
1979	Power combiner	X		●		●		
	Low-noise amplifier	K		●		●		
1980	Switches	X		●		●		
	Mixer/IF system	K _a		●		●		
1981	Direct-coupled amplifier	C		●		●		
	Traveling-wave amplifier	X		●		●		
	Signal generator	S		●		●		
	Oscillator	X		●		●		
	T/R module (multichip)	X		●		●		
1982	Phase shifter	X		●		●		
1984	T/R module (single-chip)	X		●		●		
	DBS receiver	X		●		●		
1985	Multioctave TWA	S-K _a		●		●		
	Receiver	C		●		●		
1986	Power amplifier	Q		●		●		
1987	Multioctave switch	DC-Q		●		●		
	Power amplifier	I-J		●		●		
1988	Low-noise amplifier	V					●	
1989	Power amplifier	X		●				●
	Power amplifiers	X, I-J		●			●	
1990	Multioctave TWA	5–100 GHz			●		●	
1991	Multioctave matrix amp.	S-K _a		●			●	
1992	LNA/power amplifier	W					●	
1994	Power amplifiers	I-J		●				●
2000	Low-noise receiver	183 GHz			●		●	
2002	24-W HPA ^a	16 GHz					●	
2003	10-W limiter/LNA	X		●		●		

^aSiC substrate.

solving device equations using appropriate boundary and bias conditions in the device channel (e.g., under the gate between the gate, source and drain electrodes). The semiconductor device equations are derived from the Boltzmann transport equation coupled to the solution of the Poisson equation. These equations, which are of partial-differential type and describe carrier transport properties

of the device, are solved numerically by using such techniques as finite differences or finite elements. The physical models also include device interface phenomena, quantum effects, effects of temperature and heterostructures, low-noise and high-field phenomena, electromagnetic interaction effects between electrodes, and many other effects. These models are of general nature but quite complex.

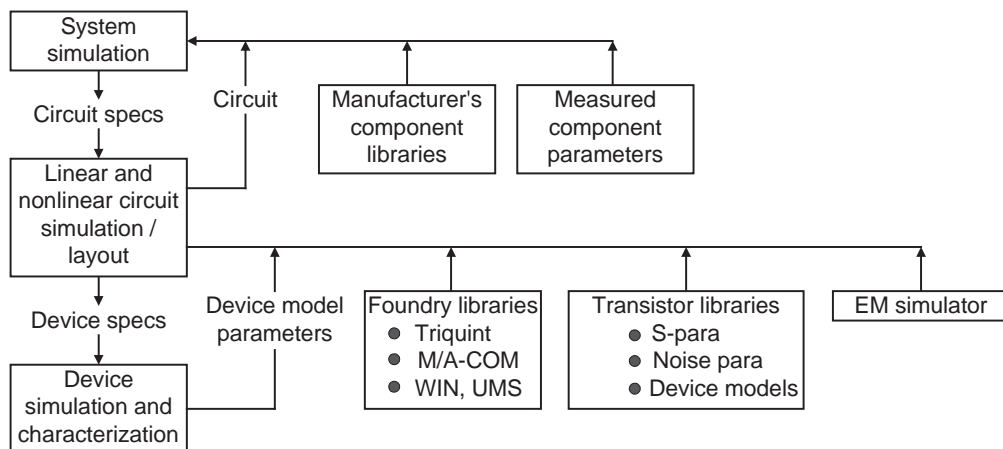


Figure 11. MMIC design system.

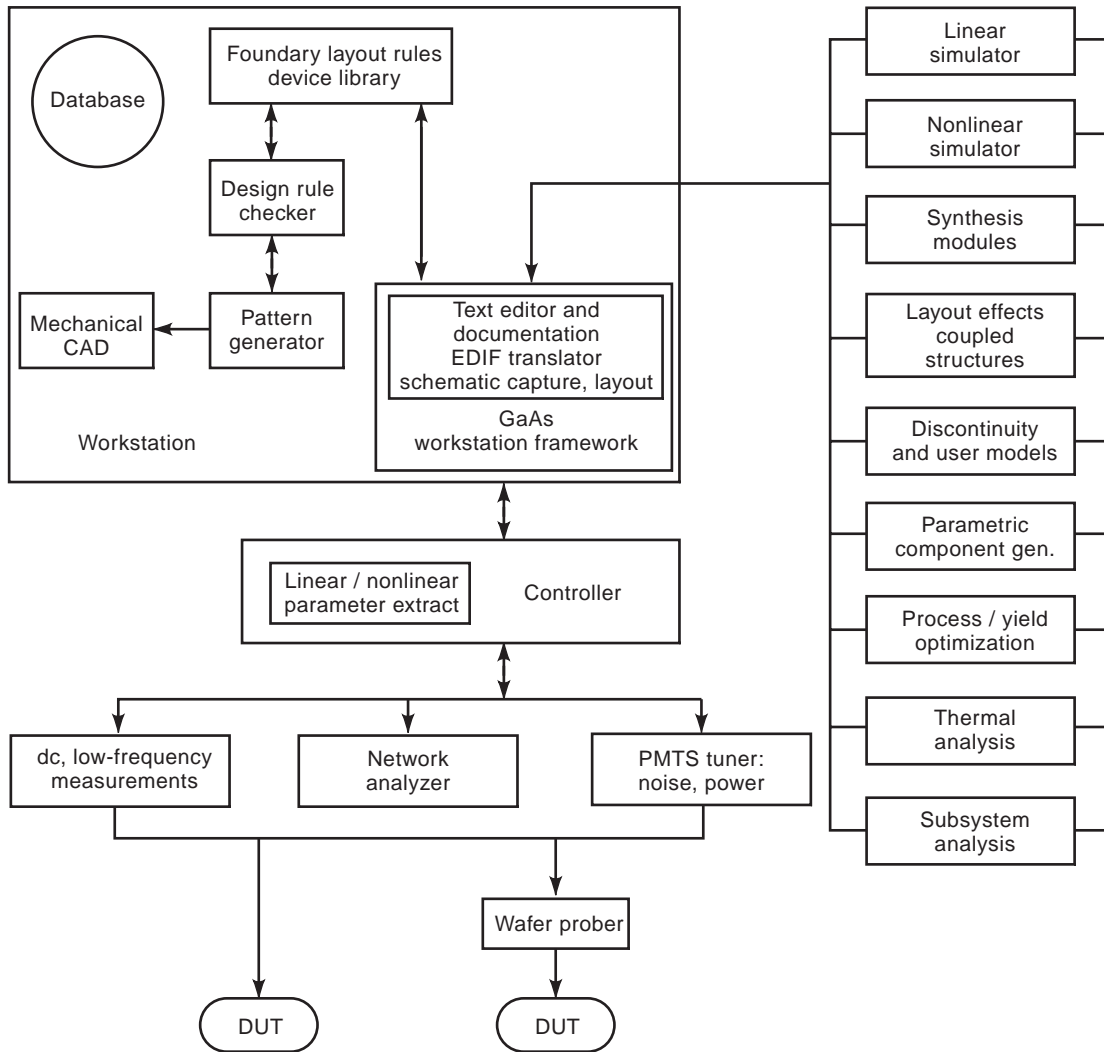


Figure 12. Next-generation MMIC workstation concept.

They include accurate parasitics and bias temperature and frequency dependence and can be used in time and frequency domains. The physical models are very useful for investigating the physical operation of active devices, predicting device performance as a function of process, material, and geometry. Thus, the device model helps in device studies, process control, and circuit yield and optimization. Any adjustment in the device can be achieved using the physics band model without costly fabrication experiments.

Because of lengthy execution times (physics-based analysis time increases rapidly with model complexity), the application of physical models is usually limited to device studies. Models are available for FETs, HEMTs and HBTs. Given sufficient computer resources, these models can become an integral part of microwave CAD tools.

8.2. Analytical or Hybrid Models

Analytical or hybrid models for passive-circuit elements and active devices are based on simple equivalent-circuit (EC) representation. Formulation of the model parameters

is based on simple equations whose values are obtained from the physics of the component, or DC or RF or both measurements. The analytical models fall between physics- and measurement-based techniques. Transmission lines and their discontinuities and nonlinear devices are generally represented by analytical models.

8.3. Measurement-Based Models

The most commonly used method of developing models for passive lumped elements and active devices is measurement of their DC characteristics and S parameters. This modeling approach gives quick and accurate results, although they are generally limited to just the devices measured. The component is represented by an equivalent-circuit model whose parameter values are extracted by computer correlation to the measured DC and S -parameter data.

The accuracy of the measurement-based models depends on the accuracy of the measurement systems, the calibration techniques, and the calibration standards. On-wafer measurements using high-frequency probes provide

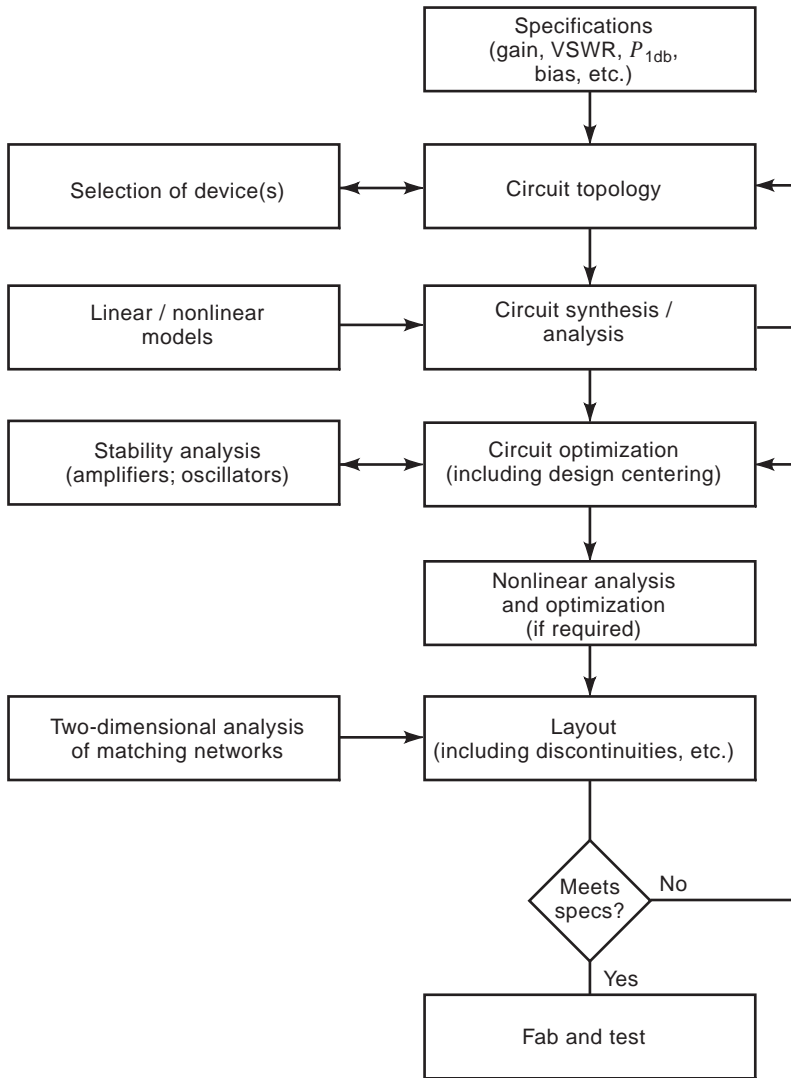


Figure 13. Typical flowchart for a MMIC design.

accurate, quick nondestructive, and repeatable results up to millimeter-wave frequencies. Various vector network analyzer calibration techniques are being used to determine a two-port error model that deembeds the device *S* parameters. The conventional short (circuit), open (circuit), load, and through (also termed *thru*) (SOLT)

calibration technique has proved unsatisfactory because the open and short reference planes cannot be precisely defined. The reference plane uncertainties for perfect short limit the accuracy of this technique. The line reflect match (LRM) calibration technique requires a perfect match on each port. The thru reflect line (TRL) calibration method is

Table 3. An Overview of Some Electromagnetic Simulators Used for MMICs

Company	Software Name	Type of Structure Three-Dimensional	Method of Analysis	Domain of Analysis
HP-EEsof	Momentum	Planar	FEM	Frequency
	HFSS	Arbitrary	FEM	Frequency
Sonnet Software	EM	Planar	MoM	Frequency
Jansen Microwave	Unisim	Planar	Spectral domain	Frequency
	SFMIC	Planar	MoM	Frequency
Ansoft Corporation	Maxwell 2D	Planar	MoM	Frequency
	Maxwell SI Eminence 3D	Arbitrary	FEM	Frequency
MacNeal-Schwendler Corp.	MSC/EMAS	Arbitrary	FEM	Frequency
Zeland Software	IE3D	Arbitrary	MoM	Frequency
Kimberly Communications Consultants	Micro-Stripes	Arbitrary	TLM	Time
Remco	XFDTD	Arbitrary	FDTD	Time

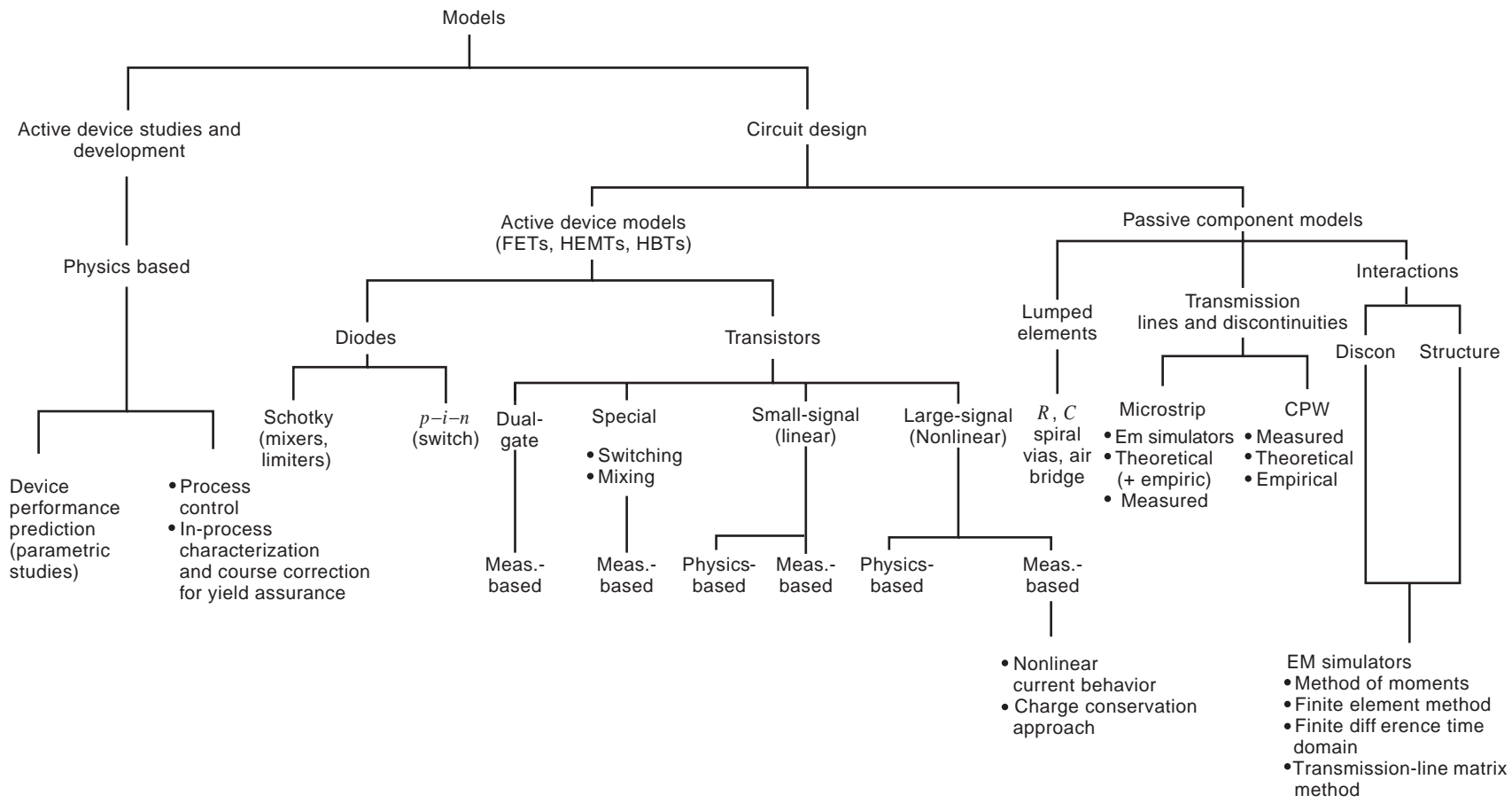


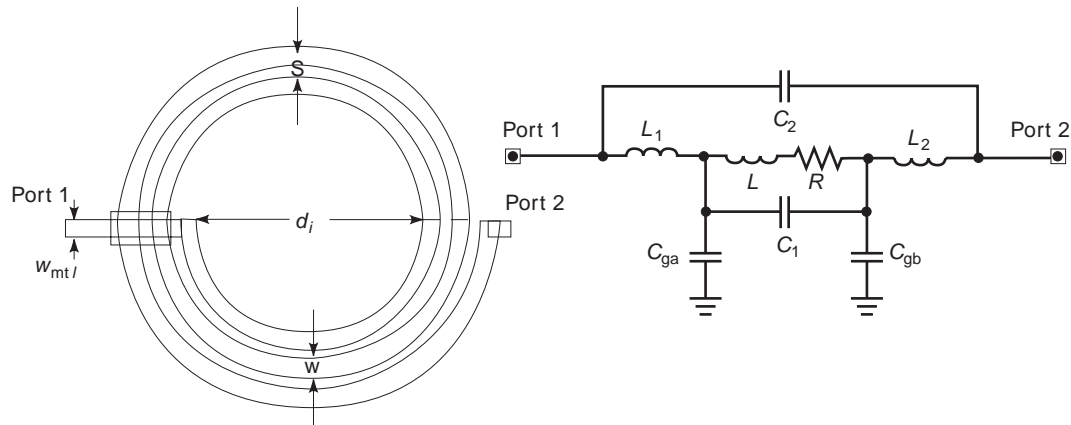
Figure 14. Spectrum of models and modeling techniques to support MMIC technologies.

based on the transmission-line calibration standards, which include non-zero-length thru and a reflect (open or short circuit) and delay-line standards (one or more dictated by the frequency range over which the calibration is performed). The advantage of TRL calibration lies in simple standards that can be placed on the same substrate as the components, ensuring a common transmission medium. This calibration technique accurately locates the reference planes and minimizes radiative crosstalk effects between the two probes because they are sufficiently far apart during the calibration procedure.

Measurement-based models fall into two groups: linear (passive-circuit elements and active devices for linear operation) and nonlinear (active devices for nonlinear operation such as mixing, power amplification, multiplication, and oscillation). In current measurement-based linear modeling, the components are electrically characterized

by measuring DC and RF parameters. A lumped-element equivalent-circuit model for each component that describes its frequency-dependent electrical characteristics is chosen. The lumped-element model parameter values are extracted by computer optimization to replicate the measured S parameters. Noise characterization of active devices is obtained by measuring on-wafer S parameters and noise parameters. The switching devices are modeled by two lumped-element equivalent-circuit models: one for when the device is in ON state (low-impedance state) and the second one for when the device is in OFF state (high-impedance state). The model parameter extraction is generally based on statistical data with average and standard deviation values that will help in centering designs for high yield.

As an example, an equivalent-circuit (EC) model for an inductor along with its physical layout is shown in Fig. 15.



Parameters	Units	1-511	2-511	3-511
Total inductance	nH	0.545	1.405	2.742
L	nH	0.249	0.985	2.138
L_1	nH	0.148	0.180	0.283
L_2	nH	0.148	0.240	0.321
C_1	pF	0.017	0.014	0.010
C_2	pF	0.008	0.009	0.0094
C_{ga}	pF	0.024	0.031	0.041
C_{gb}	pF	0.024	0.042	0.052
R_{dc}	Ω	0.370	0.600	1.100
Freq range	GHz	0–18	0–18	0–18

Dimensions	Units			
n_{turns} (number of turns)		1.5	2.5	3.5
d_i (inductor inside diameter)	μm	108	108	108
w (conductor width)	μm	20	16	12
s (conductor space)	μm	8	10	14
$w_{mt/1}$ (width of metal 1)	μm	18	18	18

Substrate thickness = 125 μm

$R = R_{dc} [1 + 0.125 \sqrt{f} (\text{GHz})] \Omega$
 Valid frequency range = 0–18 GHz
 Maximum current capacity = 35 mA

Figure 15. Physical layout and the equivalent-circuit model of spiral inductors (1.5, 2.5, and 3.5 turns).

This figure also includes model parameter values for three different inductors. An EC model for a MESFET is shown in Fig. 16a, and its parameter values are shown in Fig. 16b. This model describes basic linear operation of an FET, and the model reproduces the small-signal RF terminal characteristics of the device with good accuracy. The model is widely used to extrapolate *S* parameters to frequencies for which experimental data are not available and can be scaled to different sizes of the same device. The main disadvantages of the equivalent-circuit model are difficulty in scaling to different physical structures, limitation to single-bias condition, frequency independence of circuit elements, no time dependence feature, and the inherent limitation to linear circuits.

Many nonlinear equivalent-circuit models have been reported in the literature. All these models have the same basic configuration as shown in Fig. 16a and generate similar common-source DC or pulsed *I-V* curves that are in qualitative agreement with experimental data. Significant differences occur, however, in the quantitative behavior of the models, in comparison to both each other and experimental data. The differences in the various models are the expressions used to characterize the drain current generator and gate-source and the gate-drain

capacitances. Some of the most commonly mentioned models are Curtice, Curtice-Ettenberg, Stratz, Materka, and TOM [48-50].

The measurement-based models need to include terminal voltage-dependent equivalent-circuit elements such as I_{ds} (g_m, R_{ds}), C_{gs} , and C_{gd} as shown in Fig. 16 to accurately predict the nonlinear behavior of the active device.

Commonly used representation of the nonlinear MESFET model is given by

$$I_{ds} = (A_0 + A_1 V_1 + A_2 V_1^2 + A_3 V_1^3) \tanh(\alpha V_{ds}) \quad (6)$$

where

$$V_1 = V_{gs}[1 + \beta(V_{ds0} - V_{ds})] \quad (7a)$$

and

$$C_{gs} = C_{gs0} \cdot f(V_{gs}, V_{gd}) \quad (7b)$$

$$C_{gd} = C_{gd0} \cdot g(V_{gs}, V_{gd}) \quad (7c)$$

Here V_{gs} , V_{gd} , and V_{ds} are the terminal voltages between gate-source, gate-drain, and drain-source of the device,

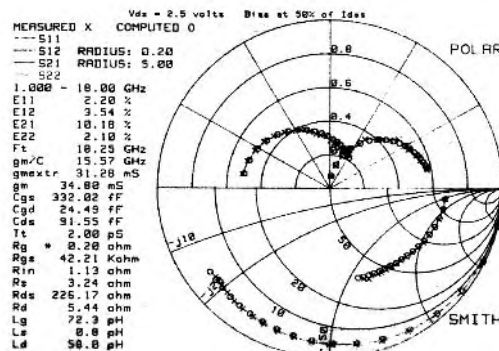
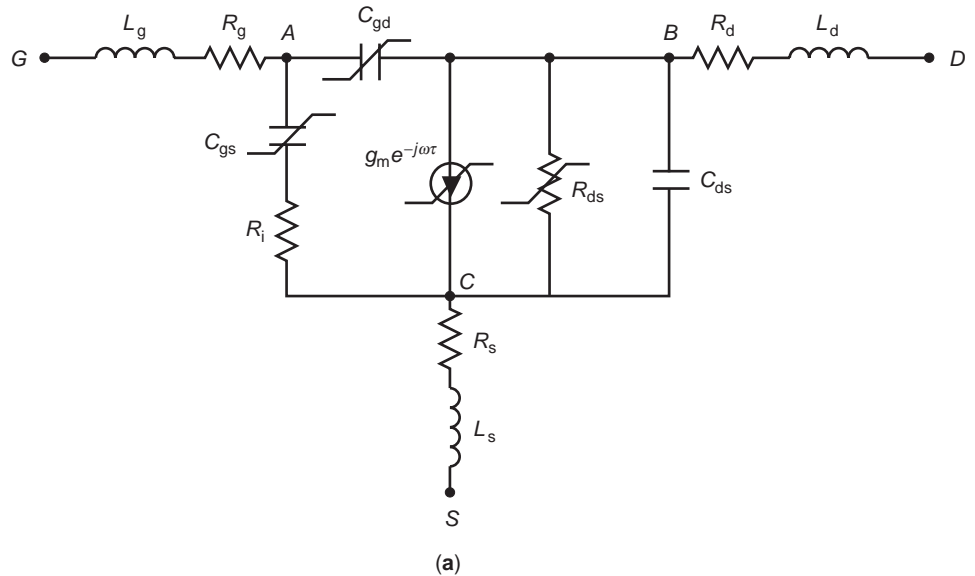


Figure 16. FET's small-signal equivalent-circuit model and typical model values for a 300- μm power FET biased at $V_{ds} = 2.5\text{ V}$, $I_{ds} = 50\% I_{ds0}$. Variable elements: C_{gs} , C_{gd} , g_m , and R_{ds} are strong functions of bias conditions.

(b)

respectively. The source of the FET is normally grounded. The A_i coefficients and constants α , β , and V_{ds0} are evaluated using measured DC or pulsed I - V data. The quantities C_{gs0} and C_{gd0} are extracted from the measured S parameter at the operating DC bias conditions, whereas f and g , which are functions of both V_{gs} and V_{gd} , are determined from measured S parameters over a large range of DC bias conditions to cover the full range of device operation.

Basically there are three steps in the development of nonlinear equivalent circuit models.

1. Extract coefficients for I_{ds} to match with measured I - V data. Important data are near the knee of the curves and break down near pinchoff.
2. Measure S parameters, extract small-signal model values, and derive coefficients for gate-source and gate-drain capacitances to describe its dependence on gate and drain voltages.
3. Validate model by comparing measured and simulated data with 50 input and output for P_{1dB} compression point and power levels for other harmonics. Simulations are generally carried out using harmonic balance analysis.

The main advantage of the equivalent-circuit models is the ease with which they can be integrated into radiofrequency (RF) circuit simulators. For linear operation (i.e., small-signal) the interface is direct because the entire device and circuit model are simulated in the frequency domain. For nonlinear applications, the device models are formulated in the time domain and are interfaced with the frequency-domain linear circuit simulators by means of the harmonic balance method (HBM). The RF performance obtained from these simulators can be satisfactory to good for a well-defined circuit, especially for mildly nonlinear applications such as a class A power amplifier not operating in hard saturation. The large-signal equivalent-circuit models generally do not scale well with varying operational conditions such as frequency or bias. As the circuit becomes increasingly nonlinear, simulator performance degrades.

The main disadvantage of the equivalent-circuit models is inherent inaccuracy resulting from simplifications in the model formulation, such as neglect of domain capacitance and the interdependencies of the nonlinear elements. In an actual device, all nonlinear elements are interdependent. For example, in a MESFET, it is not possible to change the device transconductance without also changing elements such as the gate-source capacitance. Perhaps the most significant limitation of the equivalent-circuit models, however, is the need to experimentally characterize the devices that are to be used. The devices must be designed, fabricated, and characterized before the CAD models can be defined. A change in any design parameter (such as gate width or channel impurity concentration) requires an almost complete recharacterization because scaling techniques are difficult to apply. This limits the designer's flexibility in obtaining optimum-performance integrated circuits where tailoring the device design for special applications would be desirable.

9. TYPICAL CIRCUITS AND PERFORMANCE

Since the early 1980s, tremendous progress has been made in amplifiers, including low noise, power, transimpedance, logarithmic, and limiting and variable gain. In addition to these amplifiers, control circuits, mixers, oscillators, and multifunction integrated circuits (MFICs) also have advanced the state of the art in microwave technology. Because this technology is growing rapidly, new examples of its application are constantly appearing. No attempt to include an exhaustive sampling is made; instead, a selection of circuits that have been developed for various applications will be described so that the diversity of the MMIC technology may be illustrated. Circuits chosen for exposition include low-noise amplifiers (LNAs), limiter/LNAs, power amplifiers, oscillators, mixers, phase shifters, and integrated multifunction circuits.

9.1. Low-Noise Amplifiers

A low-noise amplifier at a receiver front end sets the system noise figure. Narrowband and broadband LNAs are required depending on the system application. Table 4

Table 4. Best Reported InP HEMT MMIC LNA Results

Frequency (GHz)	Number of Stages	Minimum NF (dB)	Gain (dB)	NF over Band (dB)	Year Reported
2.3–2.5	3	0.4	35	0.5 maximum	1993
7–11	2	1.0	21	1.2 maximum	1993
19–22	3	1.1	38	1.2 maximum	1995
43–46	2	–	25	2.3 average	1993
43–46	3	1.9	22	2.0 average	1995
50	2	2.8	9	–	1994
63	2	3.0	18	–	1990
56–60	2	3.2	15	4.2 average	1992
56–64	3	2.7	25	3.0 average	1993
58–62	2	2.2	16	2.3 average	1995
75–110	3	3.3	11	5.0 maximum	1993
75–110	4	6.0	23	–	1993
92–96	3	3.3	20	4.4 maximum	1995
120–124	2	–	11	–	1994
142	2	–	9	–	1995

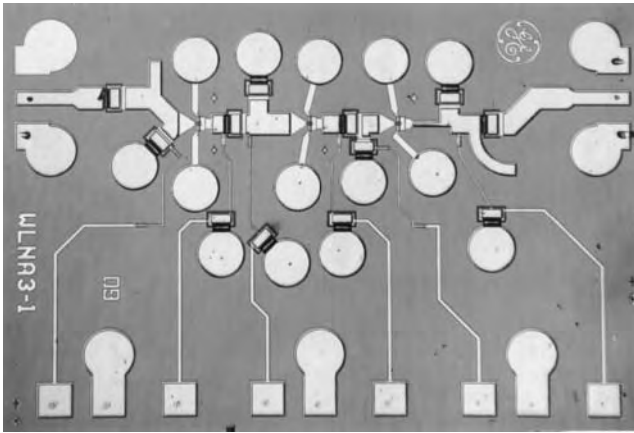


Figure 17. A three-stage 75–110-GHz PHEMT MMIC low-noise amplifier. Chip size is 5 mm^2 . (Reprinted with permission from P. M. Smith and IEEE © 1996.)

compares the state of the art in narrowband MMIC multistage LNAs developed using PHEMTs [51]. Noise figures of about 1 and 3.3 dB have been achieved at 10 and 94 GHz, respectively. A three-stage 75–110-GHz MMIC amplifier is shown in Fig. 17. For this chip, the best noise figure measured was 3.3 dB at the W band.

9.2. Limiter/LNA

Due to fine geometry used in MMIC transistors, these circuits are susceptible to damage from high-power spurious EM radiation. To protect the front-end receiver and maintain low noise figure, a high-power and low-loss limiter in front of an LNA is required. A novel high-power limiter/LNA that can handle greater than 10 W CW power at X band was developed [52] (see Fig. 18). The limiter/LNA design is a balanced configuration using Lange couplers with a Schottky diode limiter circuit followed by a two-stage LNA. High power termination resistor is also included on the chip. Typical measured performance shows gain greater than 14 dB, $\text{NF} < 2.7 \text{ dB}$, return loss better

than 20 dB, and output third-order intercept greater than 28 dBm over the 8.3–12 GHz frequency range.

9.3. Power Amplifiers

In comparison with power tubes, microwave power solid-state amplifiers are compact in size, lightweight, low-cost, more reproducible, and more efficient and reliable, and they operate at lower supply voltages. These amplifiers are used in transmitters and require much shorter warm-up time. Furthermore, no adjustment in the bias is required over long periods of operation. The performance of MESFET, PHEMT, and HBT amplifiers is constantly improving in terms of output power, power-added efficiency, linearity, and frequency. Microwave power amplifiers using monolithic technology look attractive for realizing tens of watts of power; these chips can be combined further using standard hybrid MIC techniques to obtain much higher power levels. High-efficiency operation of these circuits is becoming one of the most important factors for enhancing battery operating life in commercial communication applications and for reducing prime power and cooling requirements for advanced microwave and millimeter-wave systems. These characteristics are particularly useful for space and military applications where weight, size, and power-added efficiency requirements can impose severe limitations on the choice of components and systems. Figure 19 depicts [53] power performance for single-chip MMIC amplifiers at microwave and millimeter-wave frequencies, and a photograph of a 15 W amplifier chip using MESFET technology is shown in Fig. 20. This C-band amplifier achieved over 60% power-added efficiency [54].

9.4. Voltage-Controlled Oscillators and Mixers

Voltage-controlled oscillators (VCOs) and mixers are integral parts of receivers. Figure 21 shows a 28-GHz VCO developed using HBT technology [55]. Output power up to -5 dBm and tuning range up to 20% were achieved for this chip. Figure 22 shows a VCO mixer, which works as

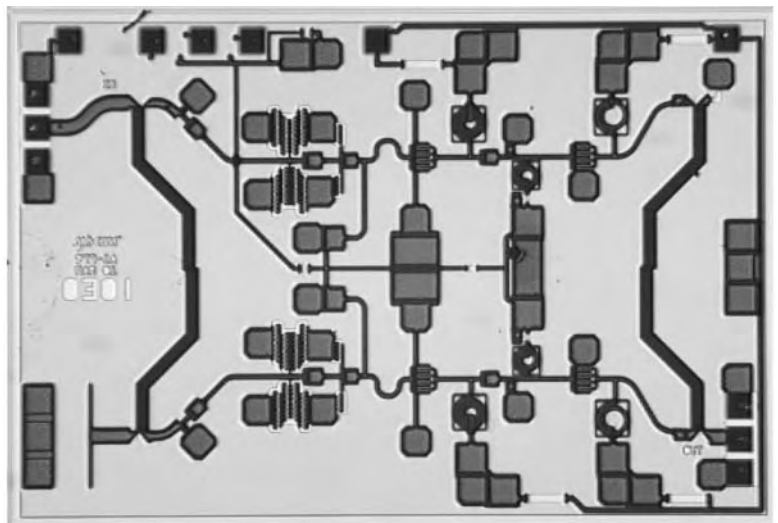


Figure 18. X-band 10-W limiter/LNA; chip size is 14 mm^2 . (Photograph courtesy of M/A-COM.)

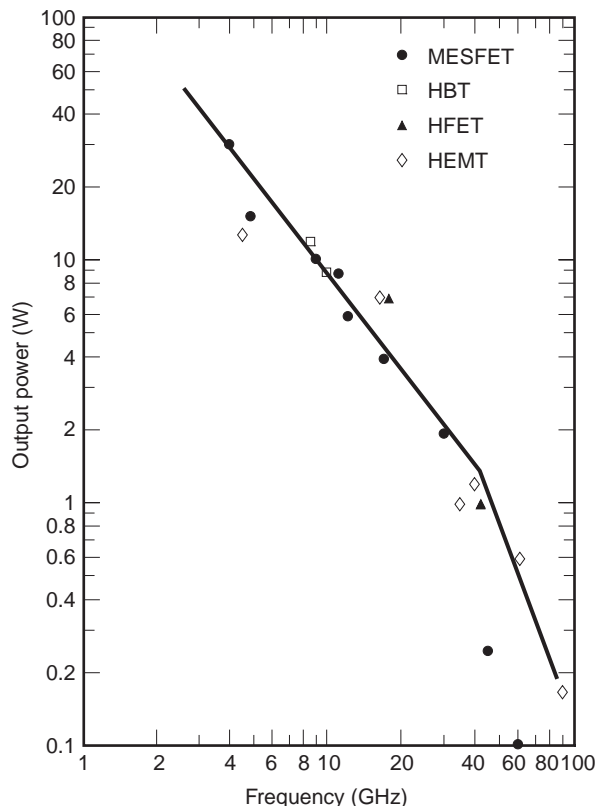


Figure 19. Performance status of single-chip power MMIC amplifiers using MESFET, HFET, HEMT, and HBT technologies. HFET: heterojunction FET.

an upconverter developed using GaAs HEMT-HBT IC technology [56]. The compact MMIC area is only 1 mm^2 . The VCO used HBT and provided 0 dBm output power over 28.5–29.3 GHz, whereas the active mixer used HEMT and achieved 6–9 dB conversion loss over a 31–39 GHz output frequency range.

9.5. Phase Shifter

One of the important elements in the TR module is the programmable multibit phase shifter. The scanning of the beam in phased-array radars is achieved by changing

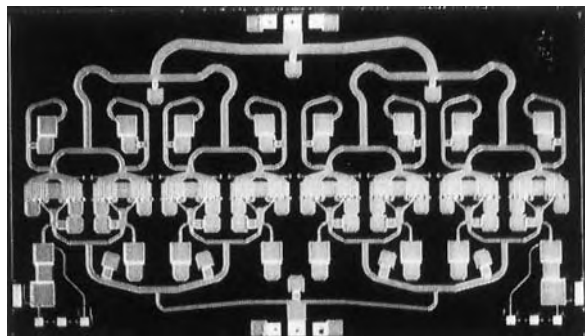


Figure 20. A C-band MESFET 15 W power MMIC amplifier. Chip size is 24 mm^2 . (Photograph courtesy of ITT Industries.)

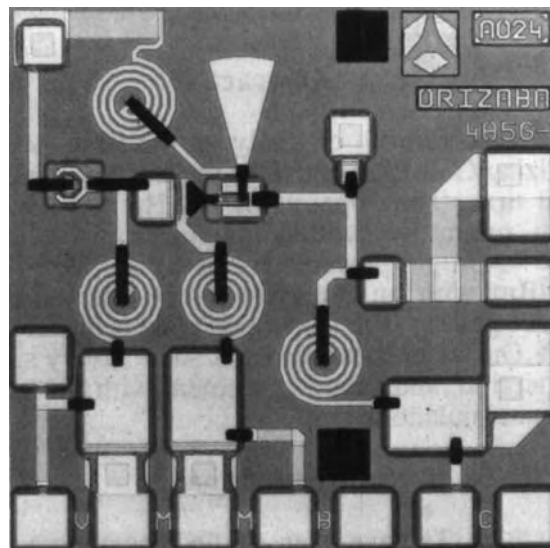


Figure 21. A 28-GHz HBT MMIC voltage-controlled oscillator. Chip size is 1 mm^2 . (Reprinted with permission from H. Blanck and IEEE © 1994.)

the phase of the RF signal fed to or received from each radiating element. For beamsteering, programmable bidirectional phase shifters are required to adaptively adjust transceiver phase in both the transmit and the receive modes. Figure 23 shows an X-band 6-bit digital phase shifter consisting of switching FETs and lowpass and highpass lumped-element networks. The phase shifter comprises 5.6° , 11.25° , 22.5° , 45° , 90° , and 180° bits cascaded in a linear arrangement. Typical measured insertion loss is 10 dB, VSWR is better than 2:1, RMS phase error is better than 6° , peak-to-peak gain variation is 3 dB, and input $P_{1\text{dB}}$ is 23 dBm, over the 8–12 GHz frequency range.

9.6. Multifunctional MMICs

Up until now, we have described single-function monolithic circuits. The next four examples represent highly integrated MMICs. A high level of integration at the MMIC chip level reduces the number of chips and results in low test and assembly costs, which in turn reduces the subsystem cost. The downside of high integration is higher nonrecurring engineering costs, and greater difficulty in optimizing each subcircuit's performance.

In active phased-array antennas, each antenna element consisting of a transmitter, a receiver, a radiator, and control circuitry is called a *transmit/receive module*. Thus, reducing the cost of GaAs IC-based transmit/receive modules is essential to the deployment of low-cost active phased-array radars. A complete C-band multifunction monolithic transceiver, containing 16 microwave circuits, has been developed [57] on a GaAs substrate measuring $10.8 \times 15.7 \text{ mm}^2$ (170 mm^2). The chip includes a class B 4-W power amplifier with 40% power-added efficiency, a high-power T/R switch, several SPDT switches, buffer amplifiers, a 6-bit programmable phase shifter, digital and analog attenuators, and an LNA with noise figure of

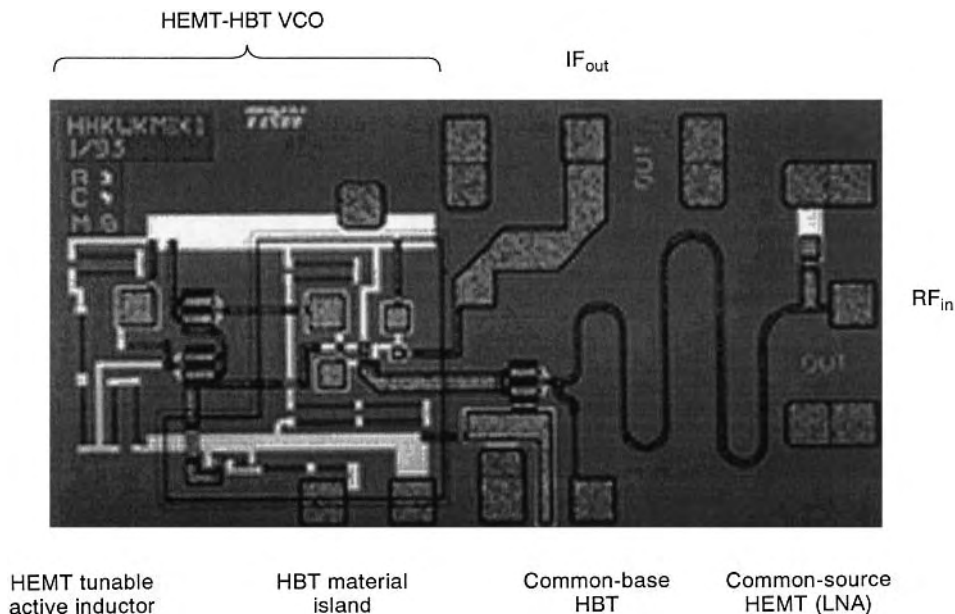


Figure 22. The HEMT-HBT VCO mixer. The compact MMIC is only 1.1 mm² in size. (Reprinted with permission from K. W. Kobayashi and IEEE © 1997.)

4.5 dB. Figure 24 is a photograph of the chip. The IC used 58 separate FETs, 87 via holes, 83 MIM capacitors, 153 resistors, 6 spiral inductors and 65 airbridges. A single 2–20-GHz T/R chip on GaAs has also been developed [58]. A photograph of the chip is shown in Fig. 25. The chip, which measures 17.6 mm², consists of T/R switches, driver amplifier, power amplifier, and LNA. A basic traveling-wave design approach was used for the amplifiers. The measured performance includes a maximum noise figure of 10 dB with associated gain of 18 dB and minimum power output of 200 mW with associated gain of 12 dB. This chip used 44 FETs, 60 via holes, 44 MIM capacitors, 69 resistors, and 60 spiral inductors. Typical yield for a circuit of this complexity exceeded 50%. A highly integrated

multifunction macro synthesizer chip has also been reported by Mondal et al. [59]. It has more than 30 RF building blocks, and some individual blocks operate through 40 GHz. This MMIC represents the highest level of integration on a single GaAs chip.

Microwave and millimeter-wave components, subsystems, and systems have been experiencing ever-increasing pressure to reduce costs to support the emergence of wireless and mobile communications applications and widespread use of phased-array radars. There is a need for new technologies to meet the challenge in size, performance, and cost requirements. GaAs monolithic 3D technology has made tremendous progress in achieving both performance and cost requirement goals. 3D technologies

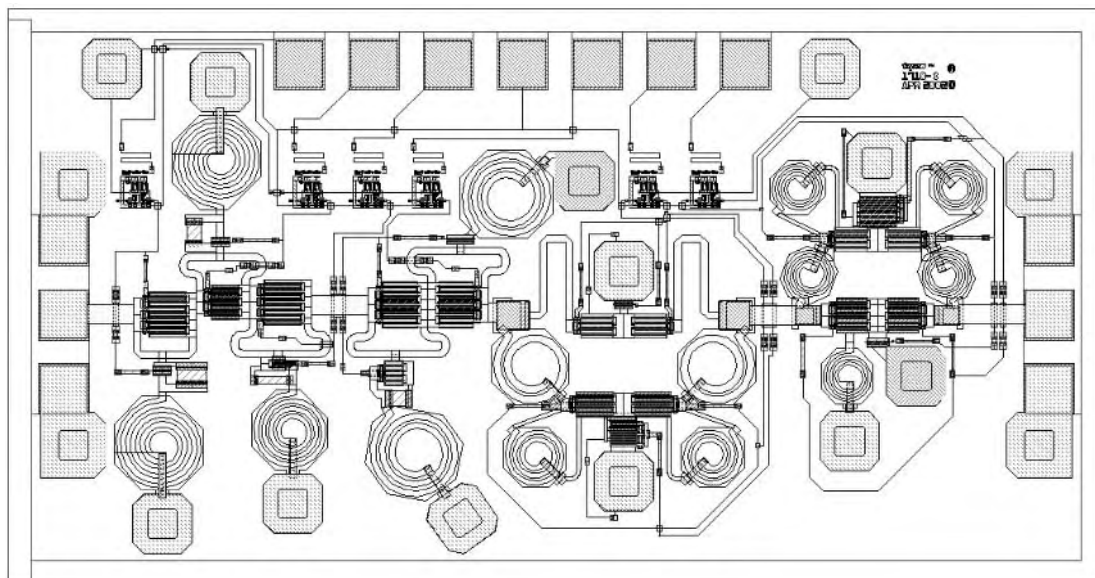


Figure 23. X-band 6-bit phase shifter; chip size is 4.5 mm².

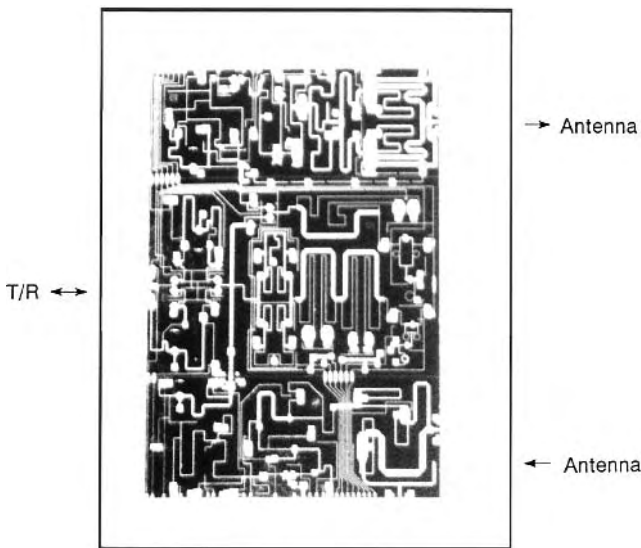


Figure 24. The 16-microwave function C-band TR chip. Chip size = 170 mm^2 . (Photograph courtesy of ITT Industries.)

provide another dimension in the integration and compaction of MMICs, where the matching networks, interconnects, and passive circuits are realized in a multilayer 3D volume. As an example, Fig. 26 shows a complete receiver [60], using low-noise amplifier, local oscillator amplifier, couplers, and voltage gain amplifier, and occupies only a 4 mm^2 chip area on GaAs when fabricated using 3D MMIC technology.

More recent advances in low-cost RF CMOS and SiGe HBT Si-based technologies offer great potential for very high-volume wireless applications. High RF performance of CMOS and HBT devices with large-scale integration capabilities make these technologies very attractive for low-cost solutions.

10. MMIC PACKAGING

Microwave packages and assembly techniques play a very important role in the performance, cost, and reliability of

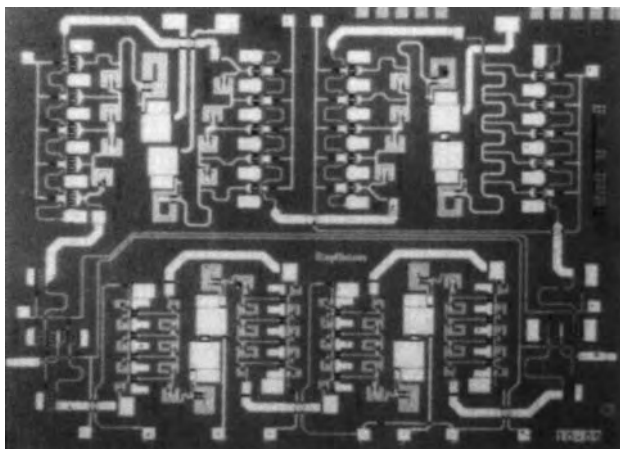


Figure 25. The broadband (2–20-GHz) TR chip (Reprinted with permission from M. J. Schindler and IEEE © 1990.)

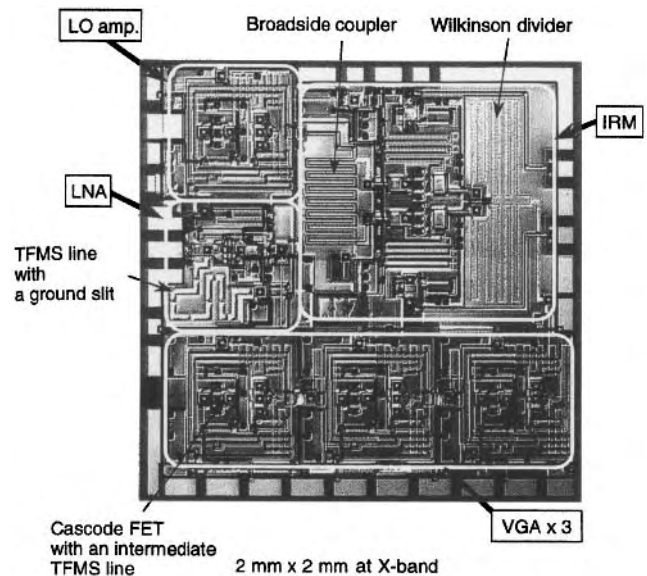


Figure 26. The 3D MMIC single-chip receiver. Chip size is 4 mm^2 (Reprinted with permission from I. Toyoda and IEEE © 1996.)

MMICs. Because MMICs represent state-of-the-art technology in terms of size, weight, performance, reliability, and cost, MMIC performance must not be compromised by packaging. The affordability requirement on packages mandates that their complexity be minimized. Minimizing both the number of dielectric layers and the overall size, dramatically improves electrical performance, production yields, and lower costs. However, a tradeoff exists between simplicity and the number of functional features in terms of costs. Some high-volume applications demand package costs as low as \$0.05 or \$0.10, whereas high-performance, low-volume applications can tolerate package costs (in the \$5 to \$25 range).

Many of the packaging considerations for MMICs are similar to those for hybrid MICs. Most ceramic/metal packages should meet the environmental requirements of MIL-S-19500 and test requirements of MIL-STD-750/883. The package must pass rigorous tests of hermetic properties, thermal and mechanical shock, moisture resistance, resistance to salt atmosphere, vibration and acceleration, and solderability. In order to minimize the effect of the package on MMIC performance, electrical, mechanical, and thermal modeling of packages must be performed.

The most important electrical characteristics of microwave packages are low insertion loss, high return loss and isolation, and no cavity or feedthrough resonance over the operating frequency range. When a chip or chip set is placed in the cavity of a microwave package, there should be minimum degradation in the chip's performance. Generally this cannot be accomplished without accurate electrical and electromagnetic modeling of the critical package elements. Microwave design must be applied to three parts of the package: RF feedthrough, cavity and DC bias lines. Of the three, the design of the RF feedthrough is the most critical in determining the performance of packaged MMIC chips.

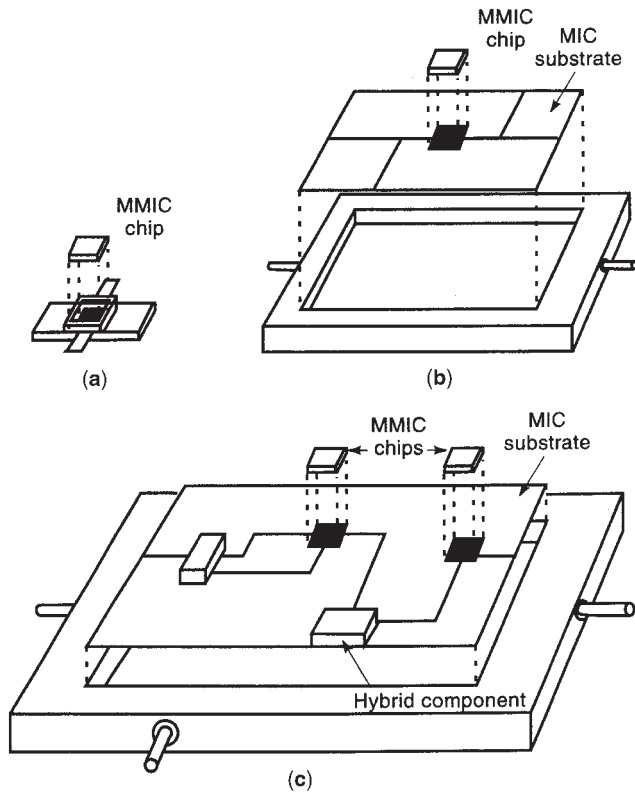


Figure 27. Three packaging-level details: (a) MMIC in package; (b) MMIC with support circuitry; (c) MMICs with hybrid and support circuitry.

MMIC packaging can be performed at three levels as shown [15] in Fig. 27. ICs can be mounted in individual packages; ICs can be packaged with support circuitry in a housing; or the ICs can be packaged at the subsystem level. The packaging requirements depend on the application at hand. For example, in wireless communications applications below 6 GHz, GaAs MMICs are being mounted into plastic packages in order to achieve low-cost goals. Because of relatively low power operation, thermally they are acceptable. For high-frequency, high-performance, and high-power applications, we require metal base ceramic packages, which have low thermal resistance, good hermetic properties, high power capability, and good reliability characteristics.

10.1. Ceramic Packages

The selection of the substrate material and thickness for ceramic packages depends on the electrical performance requirements, cost, and frequency range of interest. The substrate thickness is selected to match its height with MMIC thickness; otherwise, a pedestal for mounting MMIC chips is required because MMIC chips are about 4 mils thick. Microwave packages generally use 10–20-mil-thick alumina substrate, whereas millimeter-wave packages use 4–5-mil-thick quartz. A low-dielectric constant is generally preferred because it makes the package interconnects electrically insensitive and tolerant to microstrip dimensions and broadband frequency ranges and results

in a high yield. The microstrip width and thickness determine the characteristic impedance and the DC resistance, whereas the spacing between the two conductors on the same plane controls the crosstalk because of coupling. Generally, sufficient space between the MMIC, the package walls, and the lid is provided in order to prevent any interactions. The effect of the package lid on the MMIC characteristics is kept to a minimum by keeping the lid above the MMIC surface about 5 times the package substrate thickness. In very high-gain applications lids with absorbing materials are also used.

Several ceramic (alumina, Al_2O_3), beryllium oxide (BeO), and aluminum nitride (AlN) packages with metal base (Kovar, copper, copper-tungsten, or copper molybdenum) are now available. Their cost depends on package size, frequency of operation, and volume. Some of these packages can be used up to 40 GHz, and others can be obtained for less than \$3 in large volume. In small quantities, they cost between \$20 and \$50. Typically, the measured dissipative loss per RF feed is less than 0.5 dB at 20 GHz. These packages provide much higher frequency of operation, low leadframe inductance, very low ground connection inductance, and much lower thermal resistance than do the plastic packages. Ceramic-type packages are well suited for high-frequency small-signal, and high-power MMICs, whereas the plastic packages are commonly used for low-cost solutions at the lower end of the microwave frequency band.

10.2. Plastic Packages

Small-outline transistor (SOT) and small-outline integrated circuit (SOIC) plastic packages are commonly used. These packages are shown in Fig. 28. SOIC packages have 8–16 pins, and they work reasonably well up to 2 GHz. The measured dissipative loss in a SOIC 8-lead package is on the order of 0.2 dB at 2 GHz. In order to improve the RF performance and power dissipation for power ICs, customer-fused lead frames with low-signal lead parasitics, and reduced-ground bond inductance are being used in custom plastic packages. Plastic packages such as FQFP-16 can be used up to 18 GHz. Plastic-molded IC packages are described in two packaging handbooks [61,62]. The dielectric

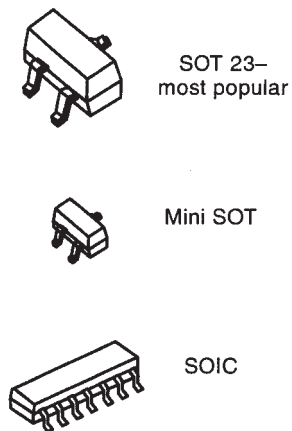


Figure 28. Plastic packages for RF and microwave applications.

constant and loss tangent values of the organic molding compound are about 3.7 and 0.01, respectively. The leadframe, which is the central support structure for ICs, is the backbone of a molded plastic package. Several different types of leadframe materials such as nickel-iron and copper-based alloys are being used. Their selection for a particular application depends on factors such as cost, performance, and ease of fabrication. The ICs are packaged using surface mounting techniques. SOIC packages are manufactured in quantities of over 10 billion per year, the material and packaging labor cost together are less than \$0.25 per package.

BIBLIOGRAPHY

- J. V. Dilozenzo and D. D. Khandelwal, eds., *GaAsFET Principles and Technology*, Artech House, Norwood, MA, 1982.
- R. S. Pengelly, *Microwave Field-Effect Transistors—Theory, Design and Applications*, Wiley, New York, 1982.
- R. Soares, J. Graffeuil, and J. Obregon, eds., *Applications of GaAs MESFETs*, Artech House, Norwood, MA, 1983.
- R. E. Williams, *Gallium Arsenide Processing Techniques*, Artech House, Norwood, MA, 1984.
- R. A. Pucel, ed., *Monolithic Microwave Integrated Circuits*, IEEE Press, Piscataway, NJ, 1985.
- D. K. Ferry, ed., *Gallium Arsenide Technology*, Howard Sams, Indianapolis, IN, 1985.
- N. G. Einspruch and W. R. Wisseman, *GaAs Microelectronics*, Academic Press, New York, 1985.
- I. J. Bahl and P. Bhartia, *Microwave Solid State Circuit Design*, 2nd ed., Wiley, Hoboken, NJ, 2003, Chap. 15.
- R. Soares, ed., *GaAs MESFET Circuit Design*, Artech House, Norwood, MA, 1989.
- J. Mun, ed., *GaAs Integrated Circuits: Design and Technology*, Macmillan, New York, 1988.
- P. H. Ladbrooke, *MMIC Design: GaAs FETs and HEMTs*, Artech House, Norwood, MA, 1989.
- R. Goyal, ed., *Monolithic Microwave Integrated Circuits: Technology and Design*, Artech House, Norwood, MA, 1989.
- F. Ali, I. Bahl, and A. Gupta, eds., *Microwave and Millimeter-Wave Heterostructure Transistors and Their Applications*, Artech House, Norwood, MA, 1989.
- F. Ali and A. Gupta, eds., *HEMTs and HBTs: Devices, Fabrication and Circuits*, Artech House, Norwood, MA, 1991.
- D. Fisher and I. Bahl, *Gallium Arsenide IC Applications Handbook*, Academic Press, San Diego, 1995.
- R. Goyal, ed., *High Frequency Analog Integrated Circuit Design*, Wiley, New York, 1995.
- M. Shur, ed., *Compound Semi-Conductor Electronics—The Age of Maturity*, World Scientific, Singapore, 1996.
- K. Chang, I. Bahl, and V. Nair, *RF and Microwave Circuit and Component Design for Wireless Systems*, Wiley, Hoboken, NJ, 2002.
- I. J. Bahl, *Lumped Elements for RF and Microwave Circuits*, Artech House, Norwood, MA, 2003.
- K. C. Gupta et al., *Microstrip Lines and Slotlines*, 2nd ed., Artech House, Norwood, MA, 1996.
- W. L. Pribble et al., Applications of SiC MESFETs and GaN HEMTs in power amplifier design, *IEEE MTT-S Int. Microwave Symp. Digest*, 2002, pp. 1819–1822.
- R. S. Pengelly, Improving the linearity and efficiency of RF power amplifiers, *High Freq. Electron.* 26–34 (Sept. 2002).
- J. M. Golio, *Microwave MESFETs and HEMTs*, Artech House, Norwood, MA, 1991.
- H. Wang et al., A 155-GHz monolithic InP-based HEMT amplifier, *IEEE Int. Microwave Symp. Digest*, 1997, pp. 1275–1278.
- V. K. Sathir, I. J. Bahl, and D. A. Willems, CAD compatible accurate models of microwave passive lumped elements for MMIC applications, *Int. J. Microwave Millim.-Wave Comput. Aided Eng.* 4:148–162 (1994).
- P. Bhartia and I. J. Bahl, *Millimeter Wave Engineering and Applications*, Wiley, New York, 1984.
- P. A. Rizzi, *Microwave Engineering Passive Circuits*, Prentice-Hall, Englewood Cliffs, NJ, 1988.
- K. Chang, ed., *Handbook of Microwave and Optical Components*, Wiley, New York, 1989, Vol. 1.
- D. M. Pozar, *Microwave Engineering*, 2nd ed., Wiley, Hoboken, NJ, 1998.
- R. Mongia, I. Bahl, and P. Bhartia, *RF and Microwave Coupled-Line Circuits*, Artech House, Norwood, MA, 1999.
- E. L. Kolberg, ed., *Microwave and Millimeter-Wave Mixers*, IEEE Press, New York, 1984.
- K. Chang, ed., *Handbook of Microwave and Optical Components*, Wiley, New York, 1990, Vol. 2.
- G. D. Vendelin et al., *Microwave Circuit Design Using Linear and Nonlinear Techniques*, Wiley, New York, 1990.
- K. Chang, *Microwave Solid-State Circuits and Applications*, Wiley, New York, 1994.
- E. C. Niehenke, R. A. Pucel, and I. J. Bahl, Microwave and millimeter-wave integrated circuits, *IEEE Trans. Microwave Theory Tech.* (50th anniversary issue) 50:846–857 (March 2002).
- M. B. Steer, J. W. Bandler, and C. M. Snowden, Computer-aided design of RF and microwave circuits and systems, *IEEE Trans. Microwave Theory Tech.* (50th anniversary issue) 50:996–1005 (March 2002).
- U. L. Rohde et al., MMIC workstations for the 1990s, *Microw. J.* (state-of-the-art reference) 32:51–77 (1989).
- T. Itoh, ed., *Numerical Techniques for Microwave and Millimeter-Wave Passive Structures*, Wiley, New York, 1989.
- R. Sorrentino, ed., *Numerical Methods for Passive Microwave and Millimeter-Wave Structures*, Wiley, New York, 1989.
- Special Issue on Engineering Applications of Electromagnetic Field Solvers, *Int. J. Microwave Millim.-Wave Comput. Aided Eng.* 5(1995).
- Special Issue on Automated Circuit Design Using Electromagnetic Simulators, *IEEE Trans. Microwave Theory Tech.* 45(11) (1997).
- A. Conrad and J. Browne, EM tools enhance simulation accuracy, *Microwaves RF* 36:133–136 (1997).
- R. Anholt, *Electrical and Thermal Characterization of MESFETs, HEMTs and HBTs*, Artech House, Norwood, MA, 1995.
- Special Issue on Process-Oriented Microwave CAD and Modeling, *IEEE Trans. Microwave Theory Tech.* 40 (1992).
- Special Issue on Computer-Aided Design of Nonlinear Microwave Circuits, *Int. J. Microwave Millim.-Wave Comput. Aided Eng.* 6 (1996).
- Special Issue on Optimization-Oriented Microwave Computer-Aided Design, *Int. J. Microwave Millim.-Wave Comput. Aided Eng.* 7 (1997).
- F. Bonani et al., Physics-based large-signal sensitivity analysis of microwave circuits using technological parametric

sensitivity from multidimensional semiconductor device model, *IEEE Trans. Microwave Theory Tech.* **45**:846–854 (1997).

48. D. Estreich, Nonlinear modeling for MMICs, *IEEE Microwave Millimeter-Wave Monolithic Circuits Symp. Digest*, 1987, pp. 93–96.
49. R. J. Trew, MESFET models for microwave CAD applications, *Int. J. Microwave Millim.-Wave Comput. Aided Eng.* **1**:143–158 (1991).
50. J. L. B. Walker, ed., *High-Power GaAs FET Amplifiers*, Artech House, Norwood, MA, 1993.
51. P. M. Smith, Status of InPHEMT technology for microwave receiver applications, *IEEE Trans. Microwave Theory Tech.* **44**:2328–2333 (1996).
52. I. J. Bahl, 10W CW broadband balanced limiter/LNA fabricated using MSAG MESFET process, *Int. J. RF Microwave Comput.-Aided Eng.* **13**:118–127 (2003).
53. I. J. Bahl, Solid state circuits, in R. C. Dorf, ed., *Electrical Engineering Handbook*, 2nd ed., CRC Press, Boca Raton, FL, 1997.
54. W. L. Pribble and E. L. Griffin, An ion-implanted 13 Watt C-band MMIC with 60% peak power added efficiency, *IEEE Microwave Millimeter-Wave Monolithic Circuits Symp. Digest*, 1996, pp. 25–28.
55. H. Blanck et al., Fully monolithic Ku and Ka-Band GaInP/GaAsHBT wideband VCOS, *IEEE Microwave Millimeter-Wave Monolithic Circuits Symp. Digest*, 1994, pp. 161–164.
56. K. W. Kobayashi et al., A novel monolithic HEMT-HBTKa-band VCO-mixer design, *IEEE RFIC Symp. Digest*, 1997, pp. 83–86.
57. C. Andricos et al., 4-Watt monolithic GaAsC-band transceiver chip, *GOMAC Digest*, 1991, pp. 195–198.
58. M. J. Schindler et al., A single chip 2–20 GHz T/R module, *IEEE Microwave Millimeter-Wave Monolithic Circuits Symp. Digest*, 1990, pp. 99–102.
59. J. Mondal et al., A highly multifunction macro synthesizer chip (MMSC) for applications in 2–18 GHz synthesized sources, *IEEE J. Solid State Circ.* **32**:1405–1409 (1997).
60. I. Toyoda, T. Tokumitsu, and M. Aikawa, Highly integrated three-dimensional MMIC single-chip receiver and transmitter, *IEEE Trans. Microwave Theory Tech.* **44**:2340–2346 (1996).
61. R. R. Tummala and E. J. Rayaszewski, eds., *Microelectronic Packaging Handbook*, Van Nostrand Reinhold, New York, 1989.
62. L. T. Manzione, *Plastic Packing of Microelectronic Devices*, Van Nostrand Reinhold, New York, 1990.

MONOPOLE ANTENNAS*

O. P. GANDHI
 G. LAZZI
 C. M. FURSE
 University of Utah
 Salt Lake City, Utah

This article describes the concepts underlying monopole antennas and their many applications, such as for broadcasting, car radios, and more recently for cellular

*See also section on Dipole Antennas

telephones. In its simplest form, the monopole antenna above an infinite ground plane shown in Fig. 1a can be considered as one-half of a corresponding double-length center-fed linear dipole shown for comparison in Fig. 1b. The current distribution for a vertical monopole antenna of height h is assumed to be a standing wave of the following form, in terms of the feedpoint current $I(0)$:

$$I(z') = \frac{I(0)}{\sin(kh)} \sin k(h - z') \tag{1}$$

for $0 \leq z' \leq h$. This occurs because the perfect ground plane creates an image of the monopole with a current distribution identical to that for the lower arm of the dipole. Together with this image, the monopole antenna appears to be a center-fed dipole for the upper half-space. There is negligible penetration of fields into a high conductivity ground for a monopole antenna, and all that

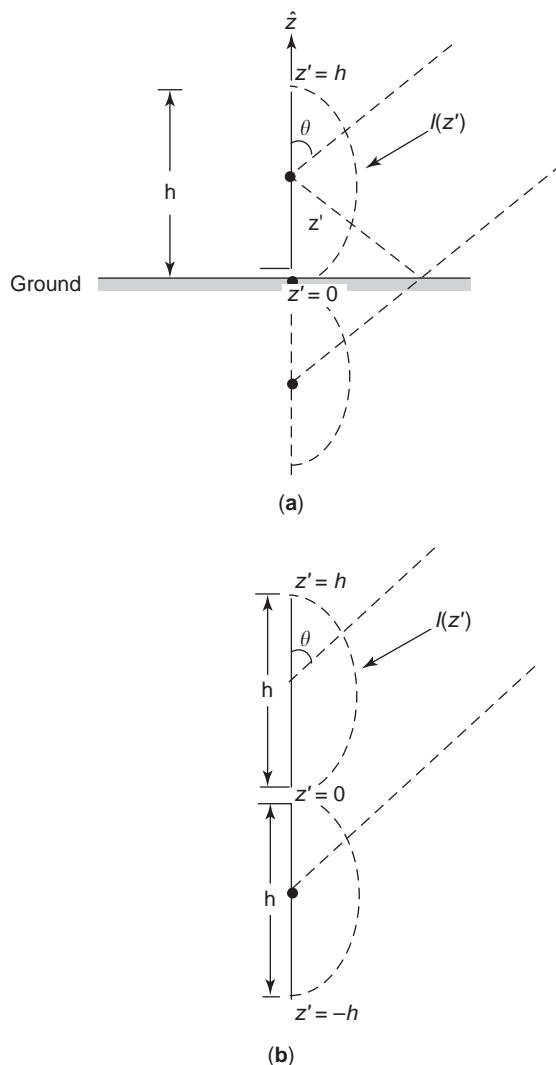


Figure 1. A vertical monopole antenna above ground (a) and the corresponding center-fed dipole (b). Shown also are the current variations $I(z')$ over the lengths of both the monopole and the corresponding dipole.

Table 1. Relationships between Monopole and Dipole Antennas

	Monopole Aboveground Length = h	Corresponding Dipole of Twice Length $L = 2h$
Radiation pattern	Same as that for the dipole but only for angle $0 \leq \theta \leq 90^\circ$	
Feedpoint reactance R_a	$R_a _{\text{monopole}} = \frac{1}{2}R_{a,d}(2h)$	$R_{a,d}$: function of length $L = 2h$ (see Fig. 2)
Feedpoint reactance X_a	$X_a _{\text{monopole}} = \frac{1}{2}X_{a,d}(2h)$	$X_{a,d}$: function of length $L = 2h$ (see Fig. 2)
Directivity D_a	$D_a _{\text{monopole}} = 2D_{a,d}(2h)$	$D_{a,d}$: function of length $L = 2h$

radiation is directed into the upper half-space, creating a power density for any angle θ (see Fig. 1) that is twice as high as that for a dipole radiating the same amount of power. This gives a directivity or gain of the monopole antenna that is twice that for the double-length dipole. Many of the other properties of a monopole antenna above ground are also related to those for the corresponding double-length dipole in a fairly simple manner.

In Table 1 we summarize the relationships between a monopole antenna of length h above ground and the corresponding dipole antenna of length $L = 2h$. A graph of the variation of the feedpoint resistance and reactance of the monopole antenna above ground is given in Fig. 2 as a function of length h/λ , where λ is the free-space wavelength at the radiation frequency [1]. Note that the reactance X_a depends on the conductor radius a , whereas the feedpoint resistance R_a is relatively independent of conductor radius a for thin antennas ($a/\lambda \ll 1$). The radiation patterns of a few typical monopole antennas are given in

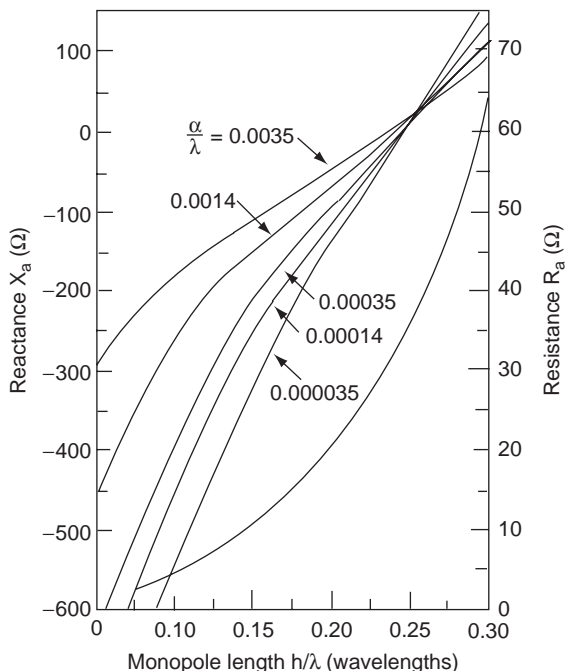


Figure 2. Variation of feedpoint R_a and reactance X_a for an end-fed monopole above ground as a function of height h/λ . (Source: E. C. Jordan and K. G. Balmain [1].)

Fig. 3. Because a monopole antenna is symmetric with respect to angle ϕ in the azimuthal plane (xy plane), these patterns are independent of angle ϕ and depend only on angle θ (see Fig. 1). The following relationship is given for

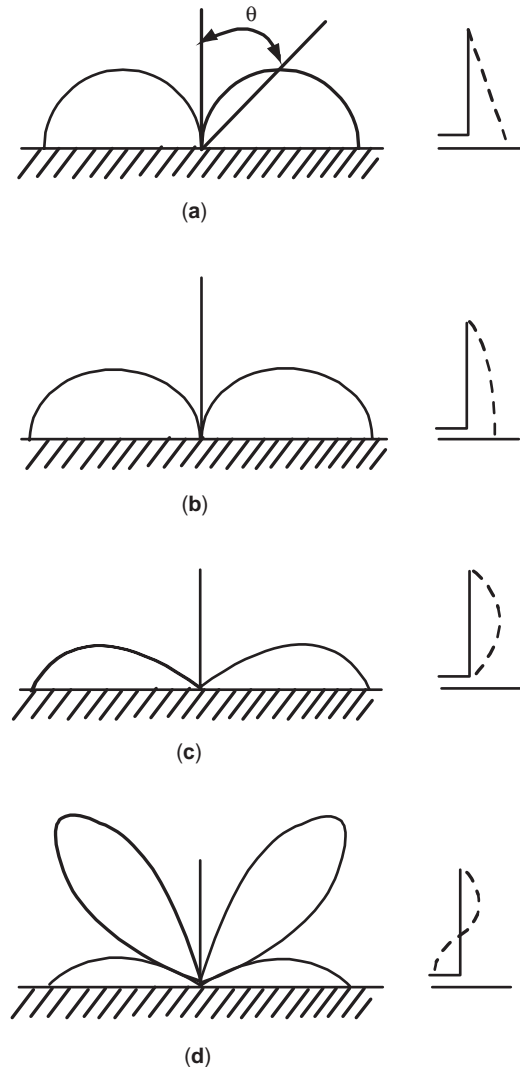


Figure 3. Radiation patterns for some typical end-fed vertical monopoles above infinite ground: (a) $h/\lambda = 0.05$ (short monopole); (b) $h/\lambda = 0.25$ (quarter-wave monopole); (c) $h/\lambda = 0.5$ (half-wave monopole); (d) $h/\lambda = 0.75$ ($3/4\lambda$ monopole). (Adapted from E. C. Jordan and K. G. Balmain [1].)

power density $S(\theta)$

$$S(\theta) = \frac{30 W}{\pi r^2 R_a} \frac{P^2(\theta)}{\sin^2(kh)} \quad (2)$$

where W is the radiated power, r is the distance to the field point, $k = 2\pi/\lambda$ is the propagation constant, and $P^2(\theta)$ is the pattern factor given by

$$P^2(\theta) = \left[\frac{\cos(kh \cos \theta) - \cos(kh)}{\sin \theta} \right]^2 \quad (3)$$

Because monopole antennas help reduce the length of the necessary dipole by a factor of 2 and result in directivities that are twice as large, vertical monopole antennas above ground are extensively used for amplitude-modulated (AM) broadcasting in the frequency range 535–1605 kHz. For this application, the wavelengths are long, on the order of 200–600 m, and the monopole antennas are immensely helpful in reducing the required height. It is necessary, of course, to create a good conductivity ground, which for dry or rocky soil conditions is often obtained by burying a conducting screen made of radially spread metal wires with angular separations of 2–3° that extend to a radius at least equal to the height of the antenna, but preferably 20–50% larger than this minimal requirement. This screen, called a *counterpoise*, is often buried a few inches below the surface of the natural ground but may also be left slightly above ground for rocky or otherwise difficult terrain.

1. EFFECT OF FINITE CONDUCTIVITY GROUND AND CURVATURE OF EARTH

Equation (2) gives the power density radiated from a monopole antenna for a ground of infinite conductivity and for flat earth. For finite conductivity ground, the power density at the earth surface diminishes more rapidly than the square of the distance r from the antenna given by Eq. 2. Furthermore, the rate at which the power density at the surface of the ground diminishes with distance is steeper at higher frequencies. The rate of reduction of the radiated power density as compared to Eq. (2) is also higher for lower-conductivity soil such as sandy or rocky lands and cities, rather than propagation over, for instance, seawater or marshy or pastoral lands. For distances in excess of about 1000 mi, there is a precipitous drop in the surface power density at all frequencies due to the increased effect of Earth's curvature [2].

Monopole antennas are also the antennas of choice for very low-frequency (VLF) (3–30 kHz) and low-frequency (LF) (30–300 kHz) communication systems. For these applications, the height h of the antenna is generally a small fraction of the wavelength. From Fig. 2, for small values of h/λ , the feedpoint resistance R_a is very small, on the order of a few ohms, and the ohmic losses resulting from the surface resistance of the antenna can be significant by comparison. This results in reduced antenna radiation

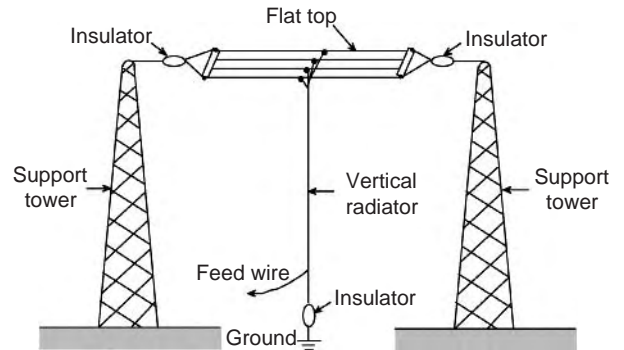


Figure 4. A top-loaded short-monopole antenna typical of VLF/LF communication systems.

efficiency η_a , given by the following equation:

$$\eta_a = \frac{R_a}{R_a + R_o} \quad (4)$$

where R_o is the effective ohmic resistance of the antenna.

Top loading of the monopole antenna illustrated in Fig. 4 is often used to improve the feedpoint or antenna-equivalent resistance R_a . Because the top set of wires acts as a capacitance to ground rather than the open end of the antenna, the current at the top of the antenna ($z' = h$) no longer needs to go to zero as it does for an open-ended monopole [from Eq. (1), $I = 0$ at $z' = h$]. The upper region of the antenna can, therefore, support a substantial radio frequency (RF) current, resulting in improved radiation efficiency. The antenna-equivalent resistance $R_a = 395 h^2/\lambda^2$ for open-ended short monopoles may be improved by a factor of 2–3 by use of top loading, resulting in higher radiation efficiency.

It should be mentioned that the various concepts discussed here are also usable at higher frequencies. Open-ended monopole antennas are, in fact, used up to ultra-high frequency (UHF) and microwave frequencies, where metallic conducting sheets, either solid or in the form of a screen, may be used in lieu of the ground to create the image antenna. A variety of top-loading “hats” illustrated in Fig. 5 may also be used at these higher frequencies.

Because a monopole antenna above ground or similar reflector acts as a dipole antenna, several of the concepts that are useful for dipole antennas are also used for the monopole antenna. Some of these concepts that are often used in practice are discussed next.

1.1. Folded Monopoles

A folded monopole antenna is illustrated in Fig. 6a, where the feedpoint is connected to arm 1, and arm 2 is grounded at the bottom end. For dipoles, this provides a method of increasing the feedpoint impedance given in the following relationship [3]

$$Z_i = (1 + c)^2 (R_a + jX_a) \quad (5)$$

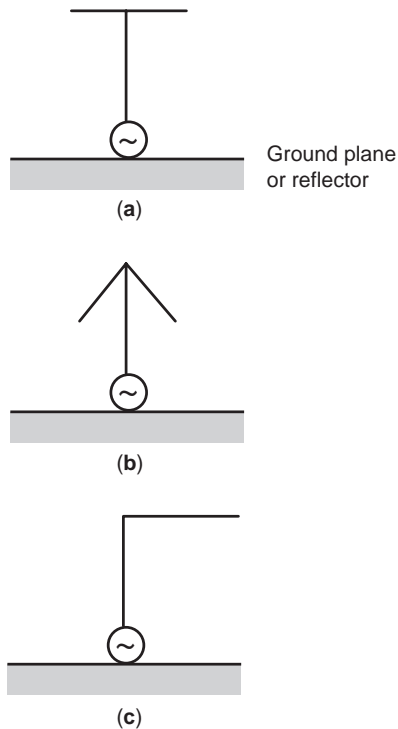


Figure 5. Some typical geometries used for top-loaded monopole antennas: (a) plate; (b) umbrella of wires; (c) inverted-L monopole.

where R_a and X_a plotted in Fig. 2 are the resistance and reactance of the single-arm (not-folded) monopole antenna, and the factor c is given approximately by

$$c \approx \frac{\ln(d/a_1)}{\ln(d/a_2)} \quad (6)$$

In Eq. (6), a_1 and a_2 are radii of wires or rods used for arms 1 and 2, respectively, and d is the center-to-center spacing between the two arms of the antenna, generally much smaller than the height of each of the arms. For a folded monopole antenna where equal radii arms are used, the feedpoint impedance is, therefore, 4 times higher than that for a monopole antenna that is not folded. This can be truly advantageous, because the feedpoint resistance may now be comparable to the characteristic impedance Z_0 of the transmission or feeder line, and the reactance of the antenna may easily be compensated by using a lumped element with a reactance that is negative of the reactance $(1+c)^2 X_a$ at the terminals of the folded monopole antenna.

1.2. Shunt-Fed Monopoles

A typical arrangement of a shunt-fed grounded monopole is shown in Fig. 6b. This corresponds to one-half of a delta match that is often used for dipoles. Because the base of the monopole is grounded for this arrangement, the antenna is fed typically 15–20% farther up on the antenna; the exact location is determined by matching the feeder line of characteristic impedance Z_0 , which is typically 200–600 Ω . Shunt-fed monopole antennas were often used in the early days of AM broadcasting when high-

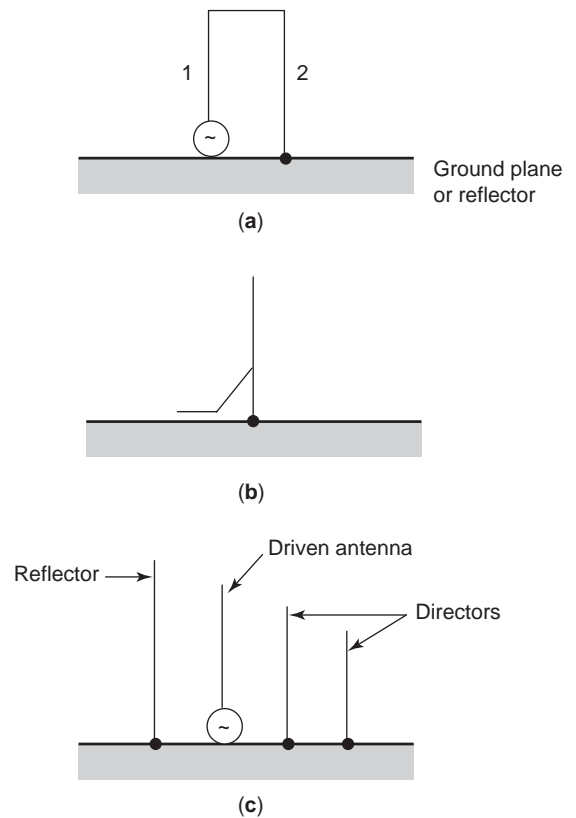


Figure 6. Some special adaptations of monopole antennas: (a) folded monopole antenna; (b) shunt-fed grounded monopole; (c) four-element Yagi–Uda array of monopoles.

quality insulators were not generally available and it was convenient to ground the tall steel/aluminum masts being used for monopole antennas. With the advent of high-compression-strength insulators, the masts are now more typically mounted on these insulators, and the monopole towers are fed at the base of these antennas.

1.3. Parasitic Monopoles

Much like the Yagi–Uda arrays of dipoles [3], parasitic monopoles of grounded elements are used to help direct the beams away from the reflector monopoles in the direction of director monopoles. An illustration of a four-element Yagi–Uda array of monopoles is shown as Fig. 6c. Forward gains on the order of 10–12 dB with front-to-back ratios of 5–8 dB may be obtained using such arrangements. One or more of the parasitic monopoles have also been occasionally used for beamshaping by AM broadcast stations. Two-element antenna arrays consisting of a parasitic reflector monopole and a driven monopole antenna have also been proposed for use in handheld wireless telephones (see, e.g., Ref. 4). If they are carefully designed, such antennas may allow electromagnetic fields to be partially directed away from the human head.

1.4. Arrays of Monopole Antennas

Like arrays of dipole elements, monopole arrays of equal or arbitrarily spaced and phased elements may be used for

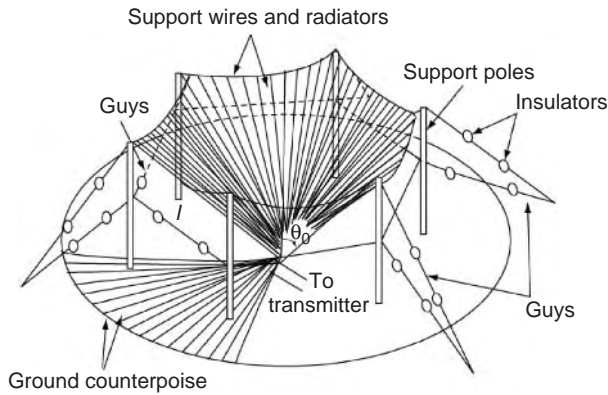


Figure 7. A conical monopole.

directing principal lobe(s) of radiation in desired directions. Arrays of monopole antennas are used for VLF/LF communications, for AM broadcasting, and, in general, for all frequencies up to microwave frequencies. AM broadcasters for non-clear-channel stations have, for example, used this technique to alter the diurnal and nocturnal radiation patterns by varying the phases and the magnitudes of excitations in the various elements.

1.5. Conical Monopole

A conical monopole, realized as a cone above a perfect ground plane, is commonly used because of its broadband properties. The cone may be either solid or built from a series of wires above a ground plane. Similar to conventional monopoles, the ground may also be built from a series of radial wires as shown in Fig. 7.

The analysis of this antenna may be done using either rigorous analytical solutions [5,6] or an approximate method [6]. The rigorous approach is based on a series expansion of transverse magnetic (TM) modes and is computationally complex. Numerical methods, based on the assumption that the antenna is built from a series of wires, have been commonly used for specific monopole arrangements.

An example of a conical monopole constructed of 60 evenly spaced wires above a ground plane is an antenna that has been in use by the U.S. Navy [7]. For use in the HF band 2–14 MHz, the dimensions of the monopole are $\ell = 30.6$ m, $a = 0.001$ m, and $\theta_0 = 45^\circ$ (see Fig. 7). The radius of the ground is approximately 37.5 m, constructed of 120 radial wires over average soil ($\epsilon_r = 15$ and $\sigma = 0.012$ S/m), and the radius of the screen wire is 0.002 m. This antenna performs over a 7:1 frequency band (2–14 MHz) with an input resistance varying from 44 to 64 Ω [6]. Because of the fairly narrow range of variation of input resistance, matching of this antenna to a 50- Ω line is possible over at least a 7–1 frequency range.

1.6. Monopole Antennas for Car Radio and Mobile Communications

Monopole antennas used for car radio and mobile communications commonly rely on the body of the vehicle to

provide the ground plane. Variations in the shape of the vehicle and placement of the antenna affect the radiation pattern and performance of these antennas [8]. For an antenna mounted on the automobile, it would no longer radiate isotropically in the horizontal plane but may radiate with a slightly higher gain in directions where the automobile body extends farther, thus simulating a wider ground plane in such directions.

For communication antennas in general, it is often desirable to have the shortest possible antenna. Although a quarter-wave monopole is easier to match, a shorter antenna has an associated capacitive reactance. This can, however, be canceled out by adding a loading coil (inductance) to the base of the antenna.

Another arrangement often used is to place an inductive coil at the center of the antenna [9]. Because of the altered current distribution along the length of the antenna (similar to a top-loaded monopole), this increases the feedpoint impedance of the end-fed antenna to roughly twice the value, making it easier to match to such an antenna. The value of the inductance needed at the center is approximately double that would be needed at the ends. This consequently increases the coil resistance.

In order to reduce the inductance of the loading coil required to match the antenna at either the center or top, a capacitive load (a small metal ball) may be added to the tip of the antenna.

In all this discussion of monopoles, we have assumed that the wave propagation from the antenna is over a perfectly conducting or infinite conductivity ground plane. This is hardly ever the case. For ground-wave propagation ($\theta = 90^\circ$) over a finite conductivity ground plane, the fields drop off more rapidly than $1/r^2$ given by Eq. (2). This effect is more pronounced for higher frequencies and is generally small only at very low frequencies less than a few tens of kilohertz. Also, as expected, the departure from the idealized Eq. (2) is more pronounced the lower the conductivity of the soil. Rocky and jagged hilly ground, for example, would result in a more rapid dropoff of the power density S along the ground plane than would propagation over seawater.

Yet another factor that has an impact on surface-wave propagation is the curvature of Earth. For distances larger than about 100 mi (62 km), the power density at the ground level diminishes very rapidly particularly for frequencies in excess of about 1 MHz.

2. EFFECT OF FINITE-SIZE GROUND PLANE ON IMPEDANCE AND RADIATION PATTERN

Whereas a ground plane of diameter 10 wavelengths or larger has a fairly small effect on the feedpoint impedance of a monopole antenna as compared to the values given in Fig. 2, a finite-size ground plane has a fairly significant effect on both the feedpoint impedance and radiation pattern [10].

An example of the effect on the radiation pattern is illustrated in Fig. 8a for the radiation pattern of a monopole antenna of a cellular telephone in free space. Since this monopole antenna is mounted on a plastic-covered

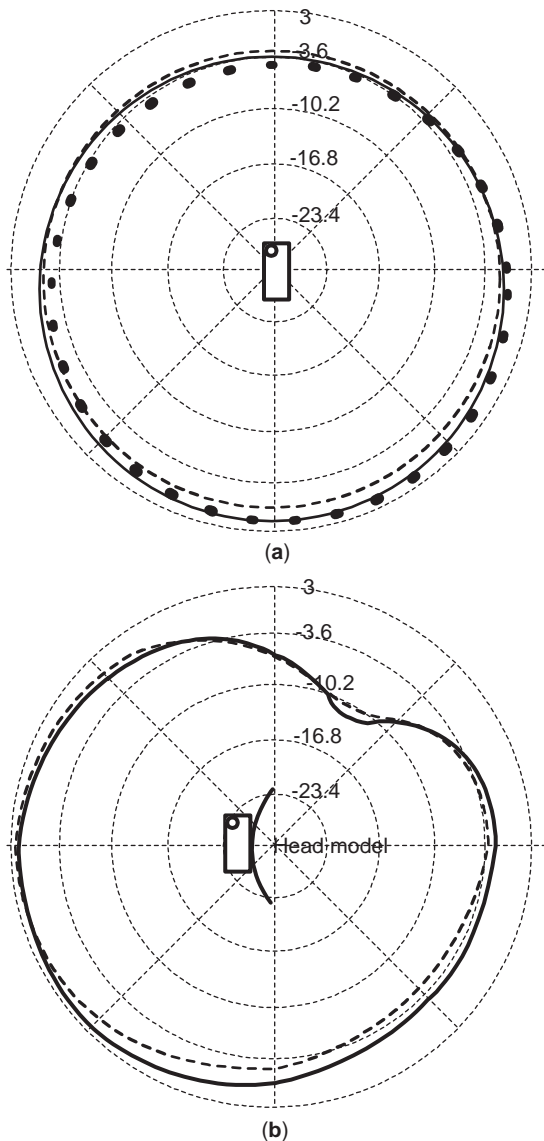


Figure 8. The computed and measured radiation patterns (in dBi) in the azimuthal plane for a commercial cellular telephone at 835 MHz (a) in free space and (b) held against the human head. (From Ref. 14.)

metal box of finite dimensions, only a finite-size ground plane of box shape is used for this radiator. One effect is to alter the radiation pattern (see Fig. 8a) from a perfect circle in the azimuthal plane to one that is crooked with a lower gain in the sector where the extent of the ground plane is minimal, specifically, on the side where the antenna shown by a circle in the inset of Fig. 8a is mounted. Also, the gain for this quarter-wave monopole antenna of about 1 dBi is considerably lower than 5.16 dBi (a factor of 3.28) for the same antenna mounted on a flat, infinite ground plane. The actual reason for this considerably reduced gain is that part of the energy is also radiated in the lower half-space for this vertical monopole antenna above the box while none would be radiated for this antenna mounted above an infinite ground plane.

3. MONOPOLE ANTENNAS FOR PERSONAL WIRELESS DEVICES

A monopole antenna with or without a helix has commonly been used for personal wireless devices, including cellular telephones [11]. Antennas of different lengths, typically from a quarter-wavelength to a half-wavelength at the irradiation frequency, have been used for handheld devices that operate at 800–900 MHz for cellular telephones and 1800–1900 MHz for PCS (personal communication system) devices. Often, these monopole antennas are in the form of a whip antenna that can be pulled out to its full length during a telephone conversation. At times, a short helical antenna is permanently mounted on the top of the handset through which the monopole antenna can be retracted and to which this monopole connects when it is completely pulled out, giving a monopole loaded with a helix at the bottom as the radiating antenna during telephone usage. Of necessity, these antennas use a finite-size reflecting plane, which is generally the metallic shielding box used either for the top RF section, or at times for the entire handset. Several authors have calculated and/or measured the radiation patterns of such monopole antennas mounted on a handset held in air or against the human head [12–14].

Figures 8a and 8b give the computed and measured radiation patterns in the azimuthal plane for a typical commercial telephone at the center-band frequency of 835 MHz in free space and in the presence of the human head, respectively [14]. This telephone uses a short helical antenna of diameter 4.2 mm, pitch 1.4 mm, and total length 16 mm. Dimensions of the handset are similar to those for many telephones and are approximately $2.4 \times 5.2 \times 14.7$ cm along the three axes, respectively. Fairly similar radiation patterns are also obtained for antennas using either monopoles or monopole–helix combinations. In the presence of the human head, gains on the order of 1.0–3.0 dBi are obtained away from the human head, with gains in directions through the head that are substantially lower due to absorption in the tissues of the head. Radiation efficiencies for monopole antennas used for personal wireless devices are typically on the order of 30–50%, with 30–50% of the power absorbed in the head and another 5–15% of the power absorbed in the hand [13,15].

4. MEDICAL APPLICATIONS

End-fed monopole antennas excited by a coaxial line have been used for a number of medical applications such as hyperthermia for cancer therapy [16] and cardiac ablation catheterization [17]. For these applications, both straight-wire and small-diameter helix monopoles have been used.

BIBLIOGRAPHY

1. E. C. Jordan and K. G. Balmain, *Electromagnetic Waves and Radiating Systems*, 2nd ed., Prentice-Hall, Englewood Cliffs, NJ, 1968, p. 543.
2. ITT Handbook, *Reference Data for Radio Engineers*, 5th ed., Howard Sams, Indianapolis, 1973, Chap. 26.

3. W. L. Stutzman and G. A. Thiele, *Antenna Theory and Design*, Wiley, New York, 1981.
4. O. P. Gandhi and J. Y. Chen, Electromagnetic absorption in human head from experimental 6-GHz hand-held transceivers, *IEEE Trans. Electromagn. Compat.* **37**:547–558 (1995).
5. C. T. Tai, On the theory of biconical antennas, *J. Appl. Phys.* **11**:55–1160 (1948).
6. R. W. P. King, *Theory of Linear Antennas*, Harvard Univ. Press, Cambridge, MA, 1956.
7. M. T. Ma and K. P. Spies, *A Simplified Formulation Computation for Conical Monopole Antennas*. U.S. Dept. Commerce Report OT 74-53, 1974.
8. D. E. Hicks, *CB Radio Antennas*, Howard Sams, Indianapolis, 1967.
9. *The A.R.R.L. Antenna Book*, The American Radio Relay League, West Hartford, CT, 1956.
10. R. C. Johnson and H. Jasik, *Antenna Engineering Handbook*, 2nd ed., McGraw-Hill, New York, 1984, Chap. 4.
11. R. Luebbers et al., FDTD calculation of radiation patterns, impedance and gain for a monopole antenna on a conducting box *IEEE Trans. Anten. Propag.* **40**:1577–1583 (1992).
12. M. A. Jensen and Y. Rahmat-Samii, EM interaction of handset antennas and a human in personal communications, *Proc. IEEE* **83**:7–17 (1995).
13. M. Okoniewski and M. A. Stuchly, A study of the handset Antenna and human body interaction, *IEEE Trans. Microwave Theory Tech.* **44**:1855–1864 (1996).
14. G. Lazzi et al., Comparison of FDTD-computed and radiation patterns of commercial mobile telephones in the human head. *IEEE Trans. Anten. Propag.* **46**:943–944 (1998).
15. O. P. Gandhi, G. Lazzi, and C. M. Furse, Electromagnetic absorption in the human head and neck for mobile telephones at 835 and 1900 MHz, *IEEE Trans. Microwave Theory Tech.* **44**:1884–1897 (1996).
16. J.-C. Camart et al., Coaxial antenna array for 915 MHz interstitial hyperthermia: Design and modelization–power deposition and heating pattern–phased array, *IEEE Trans. Microwave Theory Tech.* **40**:2243–2250 (1992).
17. S. Labonte et al., Monopole antennas for microwave catheter absorption, *IEEE Trans. Microwave Theory Tech.* **44**:1832–1840 (1996).

MONOPULSE TRACKING SYSTEMS

MANUEL SIERRA PEREZ
 JAVIER GISMERO MENOYO
 MANUEL SIERRA CASTAÑER
 ALBERTO ASENSIO LOPEZ
 Universidad Politecnica de
 Madrid
 Madrid, Spain

1. TRACKING SYSTEMS

The *tracking function* of a target in a radar system is found in two different types of systems:

1. Radar tracking while scanning
2. Tracking Radar

In type 1, surveillance radar equipped with a *data processor* having the necessary algorithms is used to forecast and filter the target positions encountered within its surveillance coverage. The system has an antenna with mechanical rotation that provides a directional radiation pattern that concentrates most of the radiated power into a narrow beam in azimuth (fan beam). The actual positions (range and azimuth) of targets obtained by the *detector* are the inputs to the radar data processor. The target data obtained during each antenna rotation period (scan) are first associated (if possible) with the active *tracks* in the processor (a *track* is a sequence of data belonging to the same target), through temporal and spatial correlation criteria. Once this association has been performed, the data are passed to the tracking filters [1,2] in order to perform the data filtering (accuracy improvement) and to forecast the future target position in the subsequent scan. The most common used tracking filters are the $\alpha\beta\gamma$ filter and the Kalman filter [1,2]. *Track-while-scanning* systems may use a double-radiation pattern so that the target azimuth is obtained through the output voltage of a monopulse processor that compares the pair of signals received through this pattern as described below.

The antenna subsystem in a tracking radar provides a directional radiation pattern that concentrates most of the radiated power into a narrow beam in both azimuth and elevation (pencil beam) to spatially isolate a single target and perform its tracking in range, azimuth, elevation, and/or Doppler parameters. The resolution cell size is inversely proportional to the transmitted bandwidth and the antenna physical dimension and is, in general, smaller than that in a surveillance radar. These systems normally have surveillance modes with sectorial and helicoidal scans used in the phase of target acquisition; however, usually there is another system that provides the coordinates of the target to track. Once the target has been acquired, the tracking radar provides the target coordinates at a much higher rate than does a surveillance radar. The system is equipped with range, elevation, and azimuth tracking loops for this purpose.

Range tracking is performed through the split-gate technique, which integrates the detected video signal in two contiguous windows (early–late). The signal needed by the loop filter is the difference between the outputs of the integrators. The system aims to keep the target between the two time windows, and hence if it works correctly, the target echo will be located in that position.

The angular tracking loops in both, elevation and azimuth can be used to obtain the antenna pointing error signal through three different techniques:

- Sequential lobing
- Conical scan
- Monopulse

The *sequential lobing* technique is based on switching the input to the receiver between the pair of signals obtained through a pair of pencil beams that, instead of pointing directly at the target, point slightly to one or the other side of the target in the desired angular coordinate. The

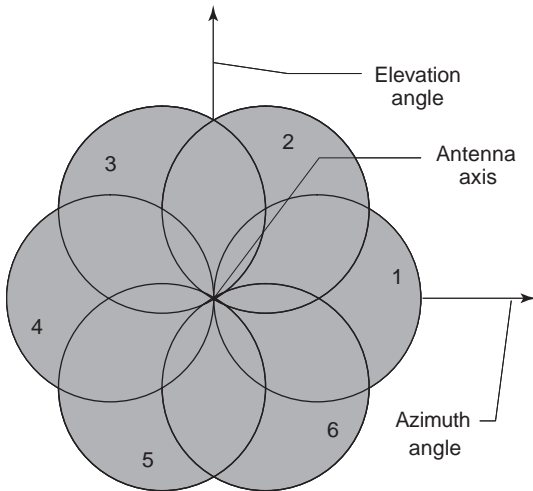


Figure 1. Conical scan in tracking antenna systems. (This figure is available in full color at <http://www.mrw.interscience.wiley.com/erfme>.)

difference in the amplitude of the received signals is proportional to the pointing error.

In a *conical scan* system, there is only a pencil beam rotating continuously in a circular path centered on the crossover axis at Ω rad/s. In this way the echoes produced by a target outside the pointing direction are amplitude-modulated by a sinusoid of angular frequency Ω rad/s as the amplitude of this modulation proportional to the error pointing of the system. Figure 1 shows the six beam prints in the angular coordinate plane around the boresight direction. All of these methods of measuring the target angle lose accuracy when some degree of pulse amplitude modulation exists, due to target or wave propagation pulse-to-pulse changes.

To avoid these and other problems, several simultaneous antenna patterns are used and two or more signal receivers are working at a time. This kind of system is called *simultaneous lobing* or the *monopulse system* [3,4].

2. MONOPULSE PRINCIPLE

The word *monopulse* was introduced to the radar terminology by H. T. Budenbom in 1946 to enhance the property of simultaneous lobe comparison to find the direction of a target with only one pulse, in contrast to other systems such as the switching lobe or the conical scan tracking systems, which require measurement of amplitude modulation through several pulses. Not only do radar systems use the monopulse principle to measure the direction of arrival (DoA) of a radio emission and not only can pulsed emissions be detected with this kind of receiver, but actually, most modern radar systems use this principle to accurately measure the target azimuth and elevation or to track its movement. One of the most important applications is the monopulse tracking radars, where the feedback of this information to the radar antenna servos allows one to follow the target position in both angular dimensions: elevation and azimuth.

In monopulse systems, the angle of arrival is measured by comparing the received signal through two antenna

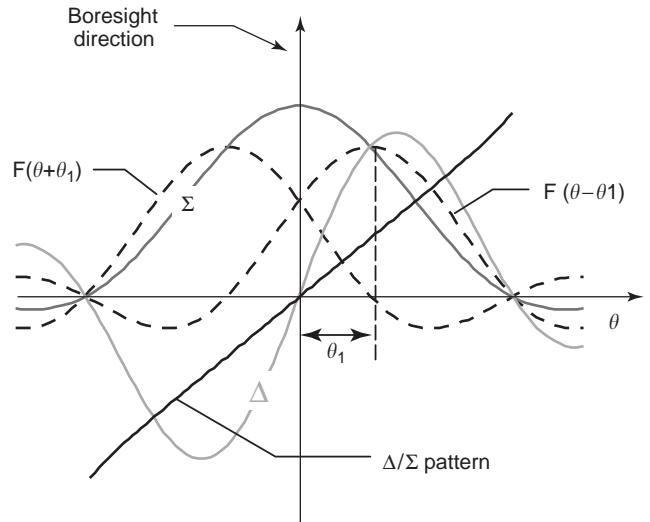


Figure 2. Sum and difference patterns with amplitude comparison. (This figure is available in full color at <http://www.mrw.interscience.wiley.com/erfme>.)

patterns: the so called “sum pattern or Σ pattern,” a directive pattern with a mainlobe pointing at the boresight direction, and the “difference or Δ pattern” a pattern with a deep null in the foresight direction and two mainbeams with phase opposition between them. These two beams, with radiation patterns $F(\theta - \theta_1)$ and $F(\theta + \theta_1)$, can be obtained by adding or subtracting two antenna patterns pointing in two directions at both sides of the main direction, as shown in Fig. 2. As the system uses relative amplitude and phase measurement, the value obtained is independent of the amplitude and phase of the incoming signal. On the other hand, if only one pulse is used to measure the arriving angle, errors due to rapid change of target position or pulse to pulse amplitude modulation are avoided in monopulse systems.

The method of measuring the angular distance to boresight is through the normalized difference function obtained as a ratio of the difference to the sum function (Δ/Σ). Figure 2 shows the normalized function in these patterns.

When two angular dimensions are controlled, the antenna must create a sum pattern and two difference patterns, one in each plane. To obtain these patterns, a four-lobe antenna pointing in four directions around the boresight can be used. Then the sum-and-difference patterns are obtained by combination of these mainlobes. Usually the combination of these lobes is obtained through RF circuits such as 180° hybrid circuits.

Another way to obtain a sum-and-difference pattern is combining the patterns of two equal antennas some distance apart to form an interferometer. Then, the phase difference between the two antenna received signals depends on the direction of arrival and hence, an OBA measurement system can be mounted. Usually sum and difference patterns can be obtained by adding or subtracting the two patterns, to obtain a sine or cosine array factor, as shown in Fig. 3.

To obtain a two-dimensional monopulse system, four antennas are combined. One sum pattern and two

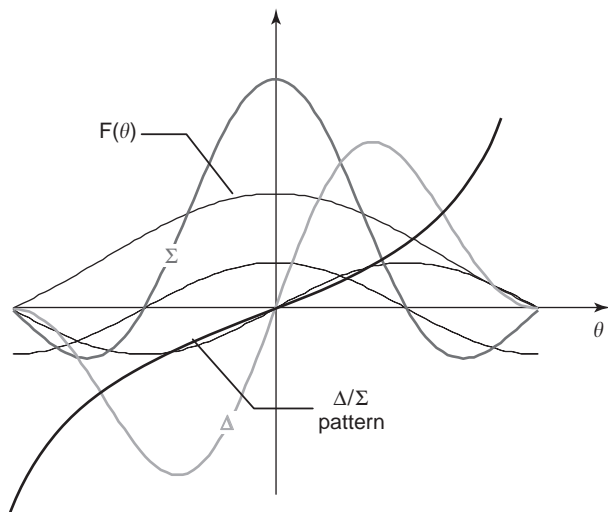


Figure 3. Sum and difference patterns obtained by phase comparison. (This figure is available in full color at <http://www.mrw.interscience.wiley.com/erfme>.)

difference patterns can be obtained as in the amplitude combination. Here the distance between antennas defines the angular beamwidth and the accuracy of the angle measurement. In general, as larger is the distance between antennas, the narrower is the beam and higher is the accuracy of the angle measurement.

In modern array antennas the sum and difference patterns can be designed specifically to obtain a highly linear normalized function combined with high directivity sum pattern, low lobe conditions, or a wide detection angle. All these characteristics can be controlled through the design of linear or plane arrays.

3. ANTENNAS IN MONOPULSE TRACKING SYSTEMS

Antenna design is a very important part in the design of successful monopulse tracking radar. The antenna must be capable of working in the specified bandwidth, with the desired polarization characteristics and generating the required radiation patterns. In fact, almost every kind of antenna (reflectors, arrays, horns, etc.) can be designed to

work for monopulse tracking systems. In this section, we will describe the main characteristics of antennas for monopulse systems. We will show some antenna designs and will finish with some general requirements for the antenna designer.

3.1. Antennas for Phase Comparison Monopulse Systems

One of the earliest and simplest monopulse systems was the phase comparison system. Transmitting and receiving antennas are usually different to avoid the use of duplexers. The transmitting antenna could be a parabolic reflector, while the receiving radiating system was typically composed of two parabolic reflectors for one angular direction monopulse performance. The monopulse system must have two antennas whose phase centers are displaced a required distance d . If the two antennas are equal, the amplitude patterns are identical, but the phase patterns differ by

$$\delta = \frac{2\pi}{\lambda} d \sin \theta \tag{1}$$

where d is the separation between both antennas, λ the wavelength, and θ the angle of arrival relative to broadside direction, as shown in Fig. 4.

If phases are considered with respect to the center of the antenna structure, the radiation patterns for both antennas can be expressed as the antenna pattern $P(\theta)$ multiplied by a phase factor as follows:

$$F_1(\theta) = P(\theta) \cdot \exp\left\{j\left[\frac{2\pi}{\lambda} \frac{d}{2} \sin \theta\right]\right\} \tag{2}$$

$$F_2(\theta) = P(\theta) \cdot \exp\left\{-j\left[\frac{2\pi}{\lambda} \frac{d}{2} \sin \theta\right]\right\}$$

Thus the angle of arrival is included in the difference in phase between both antenna patterns. Instead of processing the phase of both radiation patterns, it uses the more easily processed amplitude of the sum and difference

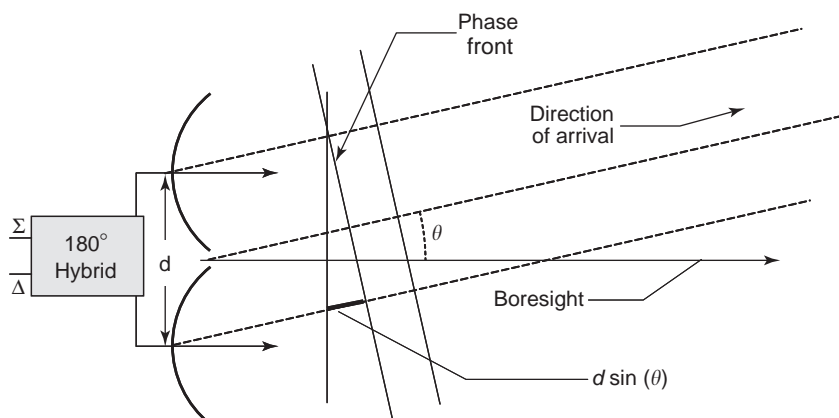


Figure 4. Interferometer array of two antennas. (This figure is available in full color at <http://www.mrw.interscience.wiley.com/erfme>.)

patterns:

$$\Sigma = 2P(\theta) \cos\left(\frac{2\pi d}{\lambda} \sin \theta\right)$$

$$\Delta = j2P(\theta) \sin\left(\frac{2\pi d}{\lambda} \sin \theta\right)$$
(3)

These sum and difference patterns can be obtained with a 180° or a 90° hybrid circuit as shown in the schematic in Fig. 4.

The usual antennas for this systems are parabolic reflectors because it is easy to obtain directive antenna patterns, low losses, and high bandwidths. If lower gains are required (<20 dBi), lens or horns can be used for phase comparison monopulse antennas.

Figure 5 shows a typical reflector antenna arrangement for a two-dimensional monopulse system. Here, the combination of the four antennas gives the main Σ pattern and differential combination of each two antennas allows formation of the two Δ patterns in both principal planes.

3.2. Antennas for Amplitude Comparison Monopulse Systems

The simplest monopulse system is amplitude comparison. Transmitting and receiving antennas can be one parabolic reflector: with one feed for transmitting channel and several for receiving channels, in order to avoid duplexing problems. The feeders can be horns, dipoles, or any other feeding antenna. The transmitting feed is in the focus, while the receiving antenna feeders have a lateral displacement from the reflector focus, so that both main-beams squint off in the broadside direction. The angle of arrival can be extracted from the relative amplitude from both feeders; for the broadside direction they are exactly

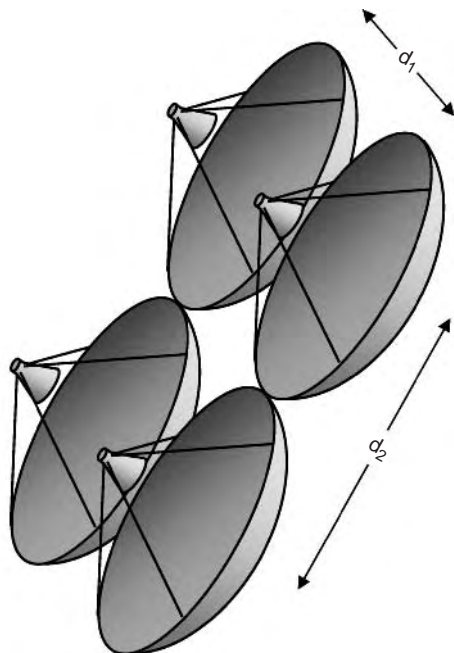


Figure 5. Four receiving parabolic reflectors for two-dimensional monopulse performance. (This figure is available in full color at <http://www.mrw.interscience.wiley.com/erfme>.)

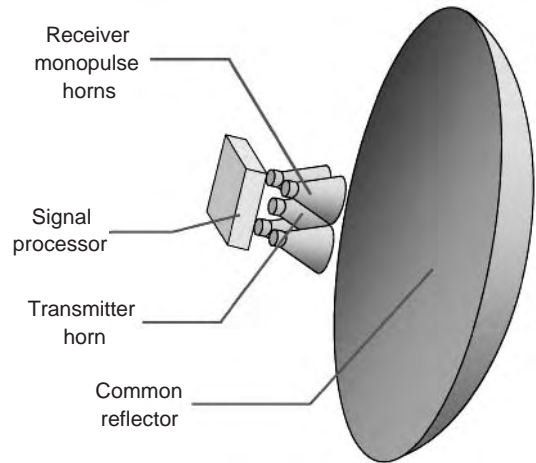


Figure 6. Reflector antenna with five horns used as transmitting and receiving terminals. (This figure is available in full color at <http://www.mrw.interscience.wiley.com/erfme>.)

the same, and the angle of arrival depends directly on the difference between both amplitude radiation patterns. The sum and difference patterns are obtained as follows:

$$\Sigma(\theta) = F(\theta - \theta_1) + F(\theta + \theta_1)$$

$$\Delta(\theta) = F(\theta - \theta_1) - F(\theta + \theta_1)$$
(4)

Physically the sum and difference patterns can be obtained through a 180° hybrid circuit such as the waveguide magic T or printed ring hybrid.

If monopulse performance in all directions is required, this can be obtained with five horns, with one transmitting feed placed in the focus of the reflector and four to form the reception systems with lateral displacements from the focus. Figure 6 is a drawing of this antenna system, while Fig. 7 represents the three-dimensional patterns of the four receivers.

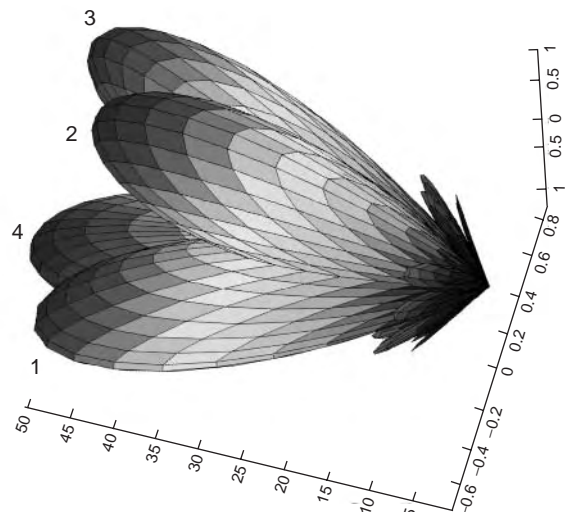


Figure 7. Schematic drawing of the four two-dimensional lobes around the antenna boresight. (This figure is available in full color at <http://www.mrw.interscience.wiley.com/erfme>.)

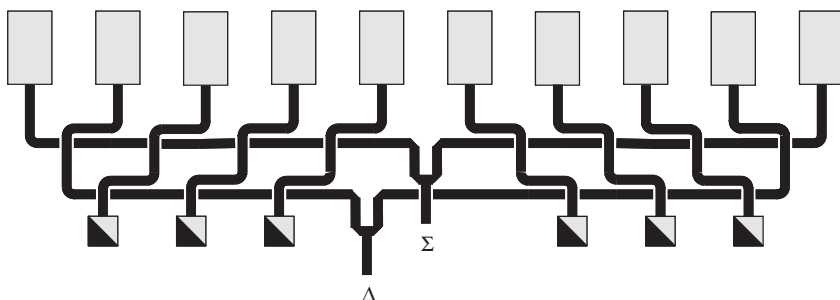


Figure 8. Feeding structure for monopulse array with independent Σ and Δ power distribution. (This figure is available in full color at <http://www.mrw.interscience.wiley.com/erfme>.)

feeders or a more complex cluster to improve some characteristics of the radiation pattern.

3.3. Array of Antennas as a Monopulse Antenna System

Arrays of antennas can be used exactly in the same way as reflector antennas if we consider that an array behaves as an aperture antenna to form a main pencil beam. In this sense a monopulse system can be arranged by a set of four panel arrays to form an interferometer monopulse antenna.

Because of the ability of array antennas to sweep the mainbeam in several directions of the space, a multibeam antenna array can also be built to perform similarly to the amplitude combination monopulse antenna.

Array antennas can obtain sum and difference radiation patterns directly, without processing the signals from two antenna panels or from two separated patterns pointing in two offset angles from boresight. In this antenna design, same radiating elements are used for sum and difference patterns, and two independent feeding structures are designed to obtain both patterns. The main advantage of this structure is the possibility of independent control of sum and difference patterns with the feeding networks.

In general, the array amplitude and phase distribution that produce high gain and low sidelobes for the sum pattern is different from the distribution needed for the difference pattern. Several designs have been studied to get a good monopulse function together with low sidelobes, such as those studied by Bayliss [5]. Once the designs of the sum and difference patterns are completed, the construction of feeding structures to obtain those array excitations

is another important problem. The solution of this problem depends greatly on the particular design, and one solution for linear arrays was reported by Kinsey [6], using a ladder structure of lines and hybrid couplers, like the scheme shown in Fig. 8 [7]. In this figure a printed patch antenna array is fed by two series feeding structure that use directional couplers to control the amplitude of each element. The phase is controlled by the length of the lines. The two lateral subarrays are fed by Wilkinson power dividers.

The elements of the array can be horns, dipoles, lens, slots, patch antenna, or any antenna that usually forms arrays. Of course, with a linear array only one plane monopulse performance is obtained. If both angular ranges are required, a planar one must be implemented.

Some kind of antennas and feeding structures behave as monopulse antennas with very simple physical arrangement. For instance, the antennas shown in Fig. 9 directly form sum and difference radiation patterns [8]. Figure 10 shows the measured radiation pattern in both amplitude and phase. This structure allows us to obtain both elevation and azimuth angles of arrival, with only two receiving signals. The antenna is based on a radial line with an array of slots placed on the radiating side. The antenna is 120mm in diameter and works in the 13.4–14 GHz band with left-hand circular polarization. The microstrip feeding structure on the backside is designed to excite the radial waveguide with two modes: one rotating mode to give the sum pattern and one coaxial mode to give the difference pattern, which behave as follows:

$$f_1(\theta, \phi) = \Sigma(\theta), \quad f_2(\theta, \phi) = \Delta(\theta)e^{j\phi} \tag{5}$$

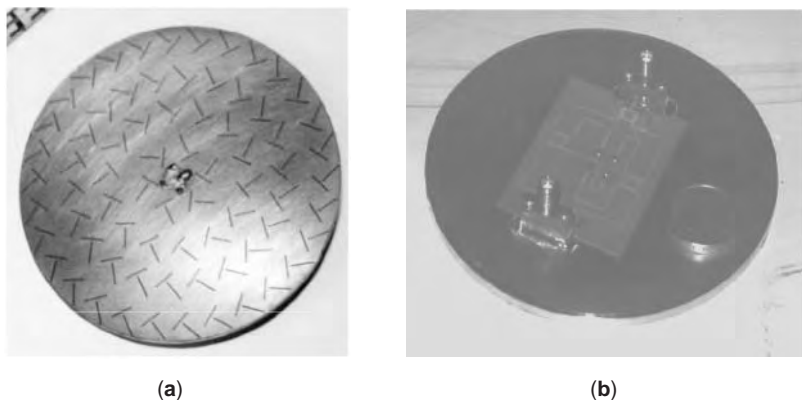


Figure 9. Radial slotline array as monopulse antenna: (a) radiating face; (b) feeding structure.

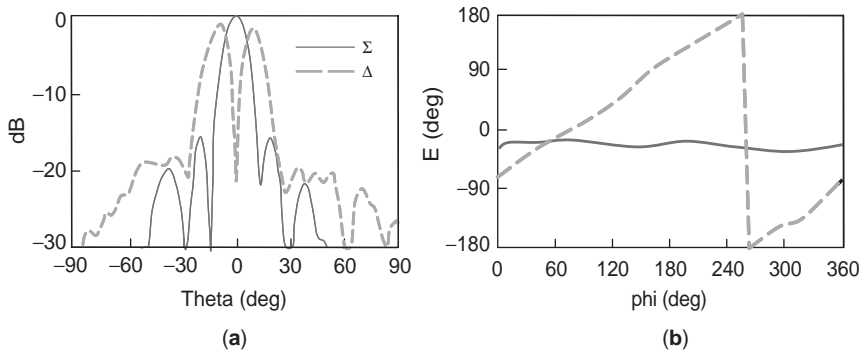


Figure 10. Sum Σ and difference Δ patterns: (a) amplitude for $\phi = 90^\circ$ at 13.7 GHz; (b) phase for $\theta = 9.4^\circ$ at 13.7 GHz. (This figure is available in full color at <http://www.mrw.interscience.wiley.com/erfme>.)

The elevation angle is obtained by comparing the amplitude of both radiation patterns and the azimuth angle, by comparing the phase for both radiation patterns, because the phase for the sum beam is uniform while the phase for the difference pattern is linear with azimuth angle of arrival.

3.4. Monopulse Antenna Parameters

To specify a monopulse antenna we have to determine two properties: the monopulse function, defined as the ratio between sum and difference patterns, and the conventional antenna parameters.

The first thing to take into account is the radiation pattern for both sum and difference patterns, defined as the spatial distribution of a quantity that characterizes the electromagnetic field generated or the signal received by an antenna. The most important parameters of the radiation pattern for monopulse performance are

- Angular range for monopulse performance, given by the angular distance between both maximum values of the monopulse function.
- Slope of the monopulse function. Usually the higher the slope, the lower the system error.
- Sidelobe levels outside the monopulse angular range. Outside the monopulse working range, it is important to have low sidelobe levels to avoid interference with or from other systems.
- Phase center. For amplitude monopulse systems, all the antennas must have the same phase center. For phase comparison monopulse systems, the angle of arrival is related to the position of the phase center of the antennas. In array systems, each element will have its own phase center.

Regarding other antenna parameters not specifically related to the monopulse application, we can mention the following:

- Frequency bandwidth. This is the frequency range within which the antenna has some specified behavior.
- Polarization. This is closely related to the radiation elements in array antennas and to feeders in reflector antennas. A cross-polar radiation pattern is the

spatial distribution of a quantity that characterizes the electromagnetic field generated by an antenna, in the polarization orthogonal to the desired one. This pattern can give a strong perturbation in the monopulse function and must be as low as possible.

- Gain. The gain was previously an important factor for the sum pattern. The gain is the difference (in dBi) between directivity (dBi) and antenna losses (dB). Directivity is closely related to the beamwidth of the radiation pattern; thus a compromise is required between monopulse angular range and sum pattern gain. The value of the gain for the difference pattern is much lower, and usually define the minimum signal we must receive for some specific error (sensitivity).
- Antenna matching to receiver. Antenna matching was previously measured in terms of reflection coefficient or standing-wave ratio. A good matching to receiver (typically 50 Ω) is required.

4. MONOPULSE PROCESSORS

The monopulse technique, also known as *simultaneous lobe comparison*, is used to measure the direction of arrival of active and passive electromagnetic radiation sources.

The monopulse processor is the subsystem that uses as input signals those received through the different antenna patterns and delivers an output signal containing information related to the target angular deviation with respect to the antenna axis [off-boresight angle (OBA)]. Although the processor could in principle deliver a signal error working directly with the antenna RF signals, the usual implementation starts with a special combination of these signals (through directional couplers, hybrids, and other specific radiofrequency elements) to form their linear combination, which we have called signals Σ and Δ (sum and difference signals). These new signals are applied to a pair of identical receivers and at the output of these receivers (at IF) is where the monopulse processor is usually found. The processor can share some hardware with the receiver, and part of the processing can be performed digitally together with other radar functions in the signal processing stages. Therefore it is correct to regard the monopulse processor more as a radar function than as an independent hardware unit. For the development of the

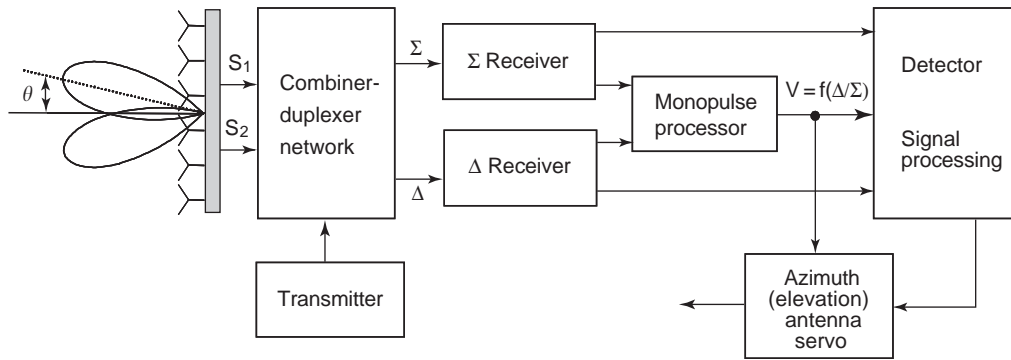


Figure 11. Monopulse location in a radar system.

monopulse function in one angular coordinate, two receivers are normally required as shown in Fig. 11.

In the design of a monopulse processor that functions with the Σ and Δ signals, it is not important whether they have been obtained by amplitude or phase comparison (except for the 90° phasing network that may be required) or the type of antenna used.

Often the Σ and Δ patterns are designed so that the Δ/Σ ratio will be an odd and nearly lineal function of the OBA in such a way that, for identical angular separations on both sides of the boresight, equal-magnitude outputs with opposite signs are produced. The linear property is specially sought for small OBAs since it simplifies the closed-loop functionality of the tracking system. Processor output must then depend on the complex ratio Δ/Σ (amplitude ratio, phase difference, or both) of the signals extracted from the antenna and not on their absolute amplitude or phase. This normalization will allow the output to depend only on the target OBA and not on the target range or radar cross section. However, this quotient represents a nonlinear operation, and the performance of any monopulse processor will depend on its correct implementation. In any case, in order to account for the nonideal behavior of the radiation patterns and the processor itself, its output signal (a voltage or digital word) must be calibrated for the specific radiation patterns of the antenna used. This calibration function or *monopulse function* $V_M = F(\Delta/\Sigma)$ allows the subsequent OBA estimation. In actual monopulse systems working with angular deviations of up to half the mainlobe width, a nonideal monopulse function is unavoidable.

4.1. Classification and Properties

Any subsystem able to deliver an output that depends on the ratio Δ/Σ can be considered as a monopulse processor. In tracking radars the outputs of the processor control the servos, allowing modification of both elevation and azimuth of the angular antenna position or pointing direction in order to situate the target in the axis of the system. In surveillance radars, the same output is used to complement the information relative to the axis of the antenna and improve the accuracy in angular estimation.

Although a large number of techniques are used to obtain a monopulse function as well as monopulse processor

implementations, all of which can be included in a first approach in one of two main classes:

1. Noncoherent processors, also known as *amplitude processors*. In these systems the amplitude of Δ and Σ signals is used to obtain the monopulse function.
2. Coherent processors, also known as *phase processors*. The information contained in the amplitude of Δ and Σ signals is transferred in some way to the phase of a new signal or signals on which it is easier to perform the processing.

In the following paragraphs some implementations of processors belonging to these categories are discussed. Obviously the number of possible variations is very large, but the ones described here are sufficiently representative to allow the reader to understand the underlying mechanisms used to obtain a valid monopulse function.

In order to compare the functionality and performances of the different processors, a pair of Δ and Σ signals is needed, as an ideal radiation pattern, applying them to the inputs of the processors. Here, Δ and Σ signals corresponding to the Jacovitti model [9] will be used, although other valid models could also be used [10]. In the Jacovitti model the amplitudes of Δ and Σ signals as a function of OBA are given by

$$G_\Sigma(\theta) = \frac{\sin\left(\frac{3\pi\theta}{2\theta_B}\right)}{\frac{3\pi\theta}{2\theta_B}} \left(1 - \left(\frac{3\theta}{2\theta_B}\right)^2\right)^{-1} \quad (6)$$

$$G_\Delta(\theta) = \frac{2\eta}{\pi} \sin\left(\frac{3\pi\theta}{2\theta_B}\right) \left(1 - \left(\frac{3\theta}{2\theta_B}\right)^2\right)^{-1} \quad (7)$$

where θ is the OBA, θ_B is the mainlobe width (defined at -3 dB below maximum), and η is the gain factor of the antenna.

Some properties of these functions are

1. Δ and Σ patterns intersect in angle $\theta = \theta_B/3\eta$.
2. The first null of the pattern is in $\theta = 1.5\theta_B$.
3. The Σ (sum) pattern is an even function of the OBA with respect to the origin and the Δ (difference)

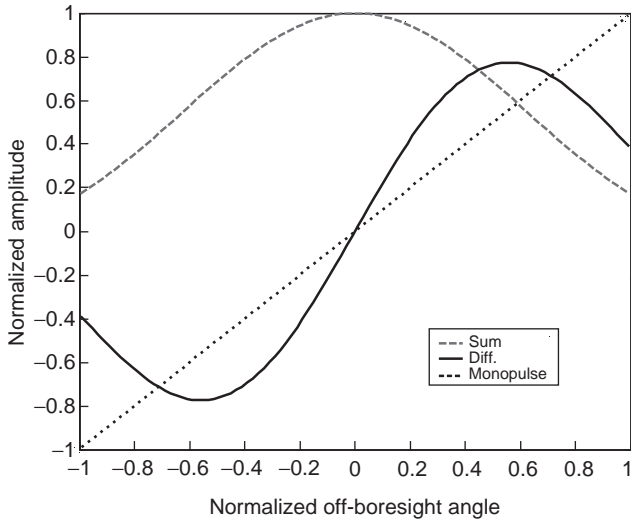


Figure 12. Sum, difference, and monopulse patterns for Jacovitti model. (This figure is available in full color at <http://www.mrw.interscience.wiley.com/erfme>.)

pattern is an odd function of the OBA. Therefore the sign of the Δ pattern gives the necessary information about the target position with respect to the boresight.

- The ratio of Δ and Σ patterns is a linear function of OBA:

$$\frac{G_{\Delta}(\theta)}{G_{\Sigma}(\theta)} = 3\eta \frac{\theta}{\theta_B} \quad (8)$$

Property 4 makes this a very convenient model for comparing processors since the monopulse function is the ideal one: a straight line. Figure 12 shows the sum and difference patterns (normalized with respect to the maximum amplitude of the Σ pattern) and its ratio or monopulse function (normalized with respect to 3η) as a function of a normalized OBA (θ/θ_B) for an antenna with $\theta_B = 2.4^\circ$ and $\eta = 0.74$.

4.2. Noncoherent Monopulse Processors

4.2.1. Noncoherent Processor Type 1. This processor is represented in Fig. 13.

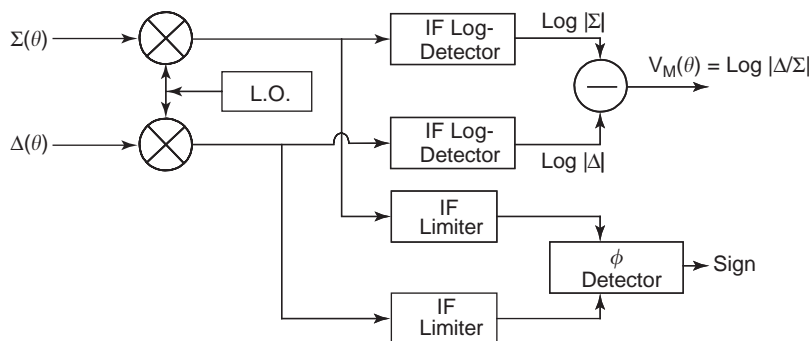


Figure 13. Noncoherent processor type 1.

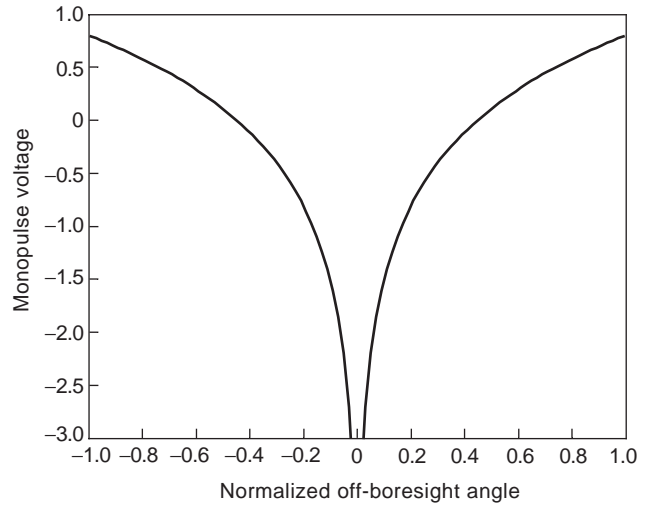


Figure 14. Monopulse function for noncoherent processor type 1.

The radiofrequency Σ and Δ signals are downconverted to IF and applied to a pair of logarithmic detectors. Their video outputs are subtracted to obtain the monopulse function $V_M(\theta) = \log(|\Delta|/|\Sigma|)$. This function, obviously, has no sign information since it is lost in the detectors, so an additional measurement is necessary from the phase difference of limited input signals in a conventional phase detector; if the phase detector output is positive, the target is at the right of boresight. Although the amplitude information of $|\Sigma|$ and $|\Delta|$ signals could be obtained through conventional video detectors (AM detectors), their limited dynamic range would be insufficient in most applications. Use of AGC (automatic gain control) circuits is not always possible as they are slow-acting and cause errors for off-axis targets whose echoes fluctuate in amplitude from pulse to pulse. In phase detection the limiters also allow the inputs to the phase detector to be of constant amplitude. Modern logarithmic detectors (some of them include the limiting function) have a dynamic margin in excess of 100 dB.

Figure 14 shows the monopulse function. The main disadvantage of this processor is a direct consequence of the null amplitude of the Δ signal in the boresight; the amplifier processing this signal tends to saturation. Furthermore the monopulse function is strongly nonlinear, so calibration will be a critical factor. On the other hand, this function is nonambiguous for any OBA.

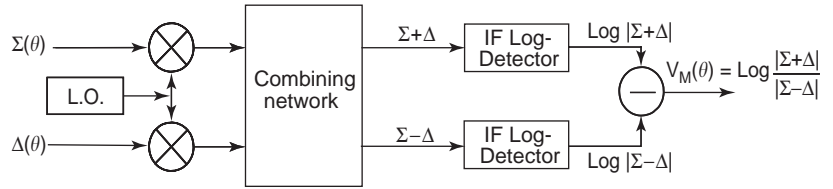


Figure 15. Noncoherent processor type 2.

4.2.2. Noncoherent Processor Type 2. In this processor Δ and Σ signals are combined before the logarithmic detection in order to obtain an odd function of OBA and to avoid the phase detection necessary otherwise. In a combining network the new signals $\Sigma + \Delta$ and $\Sigma - \Delta$ are formed and, as above, are applied to logarithmic detectors as shown in Fig. 15.

The resulting monopulse function $V_M(\theta) = \log(\text{abs}(\Sigma + \Delta)/\text{abs}(\Sigma - \Delta))$ is shown in Fig. 16, where this function's odd characteristic with respect to the OBA may be seen.

Figure 16 also shows the ideal monopulse function for comparison purposes. It must be mentioned that it is not important whether both functions are not equal, which simply implies a different (and more nonlinear) calibration function. The monopulse function obtained with this processor is nearly linear in the boresight vicinities, although is clearly nonlinear in the proximities of $\Sigma = \Delta$, showing, as before, saturation problems at this point. For $|\Sigma| < |\Delta|$ angles ($|\theta/\theta_B| > 0.42$ for the Jacovitti model used) the function is also ambiguous, so it is futile to calculate

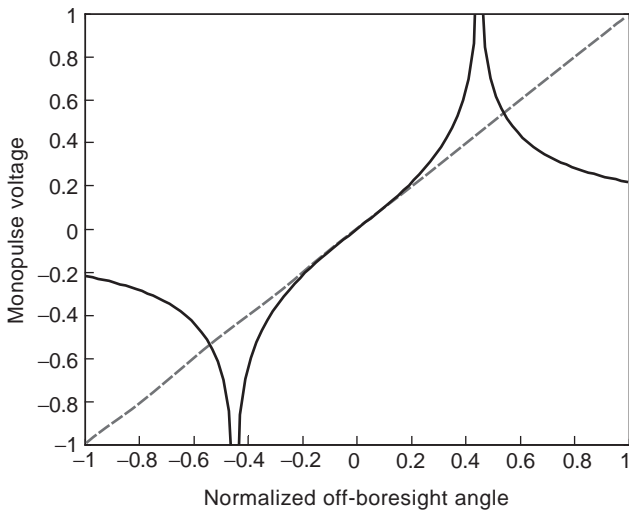


Figure 16. Monopulse function for noncoherent processor type 2. (This figure is available in full color at <http://www.mrw.interscience.wiley.com/erfme>.)

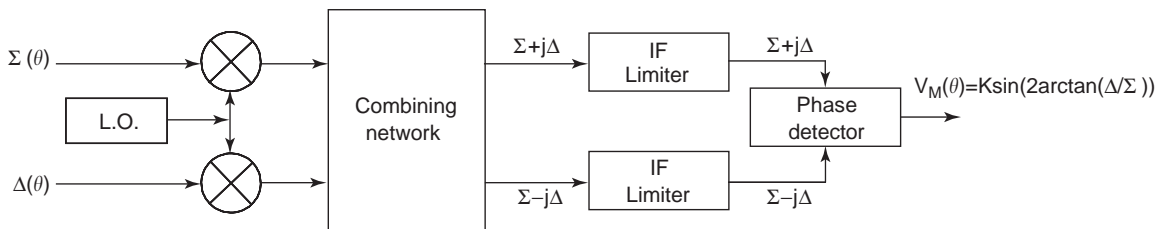


Figure 17. Coherent processor type 1.

the target OBA. From the tracking viewpoint, although ambiguous, the output polarity is the correct one, so the servos will guide the antenna in the right direction (in a nonlinear fashion).

4.3. Coherent Monopulse Processors

Coherent monopulse processors convert the amplitude information of Δ and Σ signals in phase information of a new set of signals for its subsequent easier processing.

4.3.1. Coherent Processor Type 1. Figure 17 shows a block diagram of this type of processor. A combining network forms the complex signals $\Sigma + j\Delta$ and $\Sigma - j\Delta$ that are applied to a pair of limiters prior to their phase detection to obtain the monopulse output voltage.

Effectively, as shown in the phasorial diagram in Fig. 18, the ratio between the amplitudes of Σ and Δ signals (the magnitude we are interested in measuring) is contained in the arctangent of the angle formed by the new signals. Supposing a sinusoidal characteristic for the phase detector, the output voltage (monopulse function) is given by

$$\begin{aligned}
 V_M(\theta) &= K \sin(\phi) = K \sin(\phi_1 + \phi_2) \\
 &= K \sin\left(\arctan\left(\frac{\Delta}{\Sigma}\right) + \arctan\left(\frac{\Delta}{\Sigma}\right)\right) \quad (9) \\
 &= K \sin\left(2 \arctan\left(\frac{\Delta}{\Sigma}\right)\right)
 \end{aligned}$$

Figure 19 shows the monopulse function obtained. In the vicinities of the boresight the function is linear and nonambiguous, but above angles for which $|\Sigma| < |\Delta|$, the ambiguity problem is also present, although the saturation problem is corrected.

4.3.2. Coherent Processor Type 2. In this processor the signals over which a phase detection is performed are Σ and $\Sigma + j\Delta$. A block diagram and monopulse function are shown in Figs. 20 and 21.

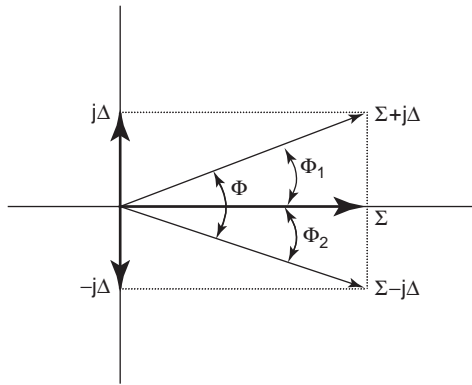


Figure 18. Relationship between angle and amplitude of signals.

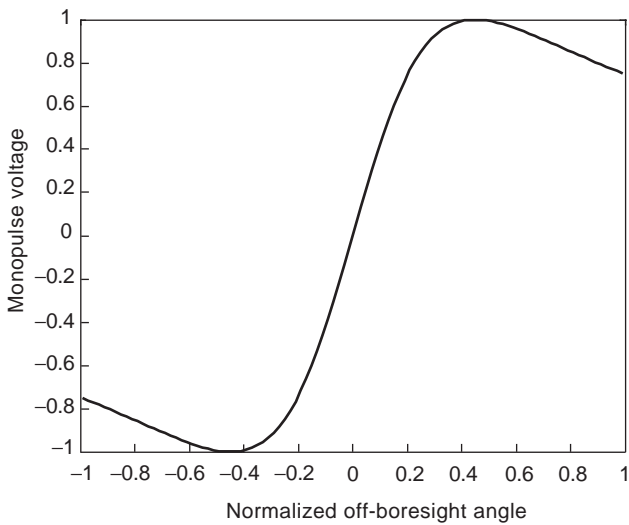


Figure 19. Monopulse function for coherent processor type 1.

This processor does not have the monopulse function ambiguity and/or saturation problems found in the other processor types. Furthermore, the linearity is maintained over a wider OBA range. These characteristics would seem to make it preferable to the others.

4.4. Nonideal Behavior

Any of the processors presented above could be used as a monopulse processor with a previous calibration of the output function. The monopulse functions shown have been obtained with supposed ideal components; however, in practice, there are a number of effects that should be analyzed since they are present to some extent in every real processor. Most representative of these effects are the thermal noise [characterized by the S/N ratio (SNR) of

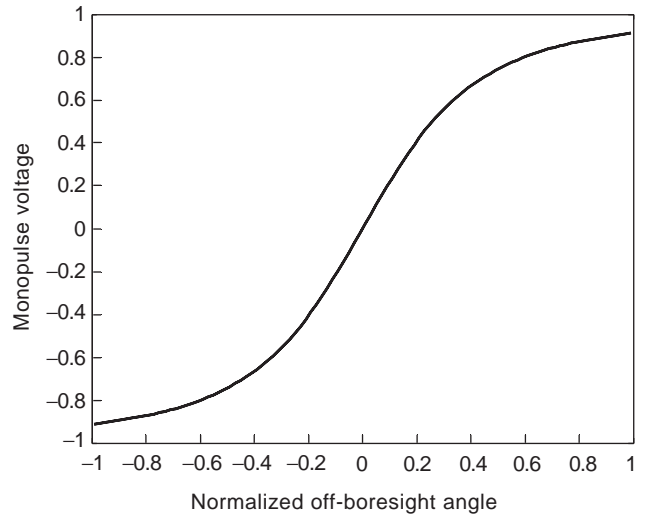


Figure 21. Monopulse function for coherent processor type 2.

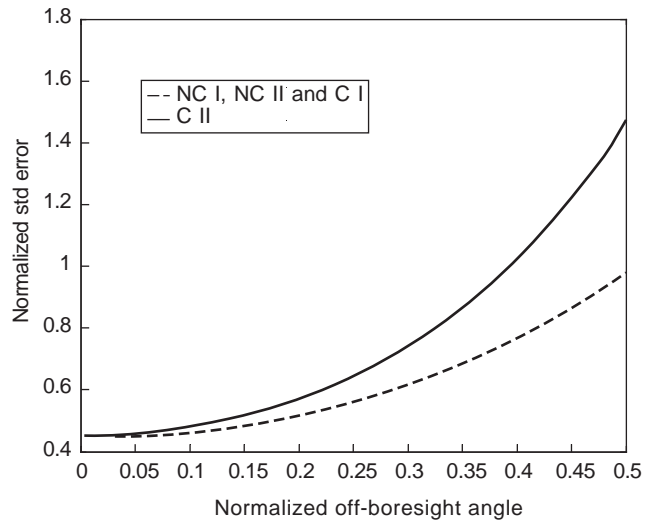


Figure 22. Error in angle estimation due to thermal noise.

processed signals] and amplitude imbalance and phase imbalance between Σ and Δ signals.

Deviations produced in the ideal monopulse function (that obtained supposing ideal components) due to these effects should be minimized. Processor choice is very important, as will be shown below.

4.4.1. Thermal Noise. If Σ and Δ are noisy signals (characterizing the noise as a Gaussian process with zero mean and standard deviation $\sigma_N = \sqrt{P_N}$, where P_N

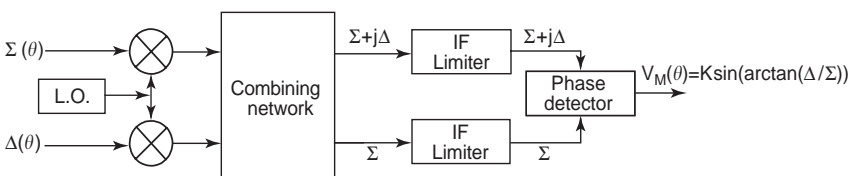


Figure 20. Coherent processor type 1.

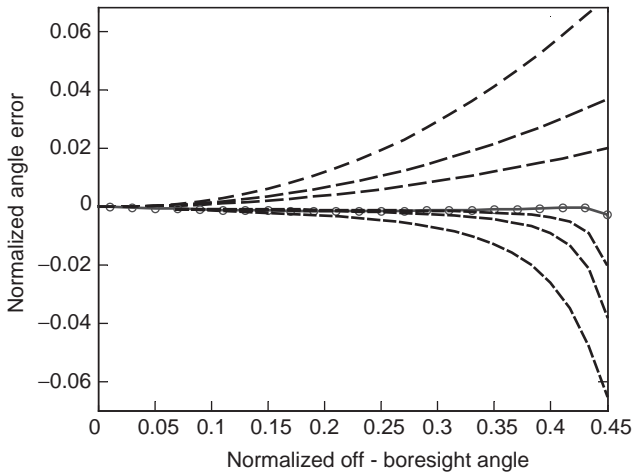


Figure 23. Normalized error versus OBA for noncoherent processor type 2 (dotted lines) and coherent processors types 1 and 2 (circles and dashed lines, respectively), for phases $\phi = 2.5^\circ, 4.5^\circ,$ and 8.5° . (This figure is available in full color at <http://www.mrw.interscience.wiley.com/erfme>.)

Table 1. Processor Performance Comparison

Processor Type:	Noncoherent		Coherent	
	1	2	1	2
Nonambiguous range	Total	$\Delta/\Sigma \leq 1$	$\Delta/\Sigma \leq 1$	Total
Linearity	1	3	2	4
Thermal noise	2	2	2	1
Phase imbalance	4	3	4	2

is the noise power), the angle estimation error is also a zero-mean Gaussian process with standard deviation given by (for the Jacovitti model)

$$\sigma_\varepsilon = \frac{\theta_B}{3\eta G_\Sigma(\theta/\theta_B)} (1 + 9\eta^2(\theta/\theta_B)^2)^{1/2} \left(\frac{1}{\sqrt{2\text{SNR}}} \right) \quad (10)$$

for noncoherent processors types 1 and 2 and coherent processor type 1. For coherent processor type 2, the standard error deviation is given by

$$\sigma_\varepsilon = \frac{\theta_B}{3\eta G_\Sigma(\theta/\theta_B)} (1 + 9\eta^2(\theta/\theta_B)^2) \left(\frac{1}{\sqrt{2\text{SNR}}} \right) \quad (11)$$

Figure 22 shows these errors normalized with respect to the noise power and θ_B ($\sigma_\varepsilon/(\theta_B\sigma_N) = \sigma_\varepsilon\sqrt{2\text{SNR}}/\theta_B$) as a function of normalized OBA (θ/θ_B).

For SNR = 20 dB and a radiation pattern with $\theta_B = 6^\circ$, the estimation error for an arrival angle of 2.4° (normalized OBA = 0.4) is about 0.4° for coherent processor type 2.

4.4.2. Precombinational Amplitude Imbalance. If the gains of Σ and Δ receivers are not identical prior to the combination of signals, an error will be induced in the angle estimation when denormalizing the monopulse function obtained since this function is processing an erroneous value for the Δ/Σ ratio.

Let us suppose that, in the diagram corresponding to noncoherent processor type 1, the Δ signal at the input is of the form $K\Delta$, where $K = 10^{(d/20)}$ is the amplitude imbalance between Σ and Δ receivers (d is the imbalance expressed in decibels). The output of the monopulse processor would be given by

$$V'_M = \log \left| \frac{K\Delta}{\Sigma} \right| \quad (12)$$

and, taking into account the relationship between Σ and Δ in the Jacovitti model

$$\frac{\Delta}{\Sigma} = 3\eta \frac{\theta}{\theta_B} \quad (13)$$

it is found that

$$V'_M = \log \left| \frac{K3\eta}{\theta_B} \theta \right| \quad (14)$$

This value includes the error due to the amplitude imbalance. The estimated angle through the calibrated monopulse function will be the θ' which delivers the same monopulse output through the ideal function

$$V'_M = \log \left| \frac{3\eta}{\theta_B} \theta' \right| \quad (15)$$

so the error in the angle estimation is $\varepsilon(\theta) = \theta' - \theta$. It is straightforward to represent this error in the form $\varepsilon(\theta) = (K - 1)\theta$. The same error is found in any of the processors presented, since, if ratio Δ/Σ is modified because of

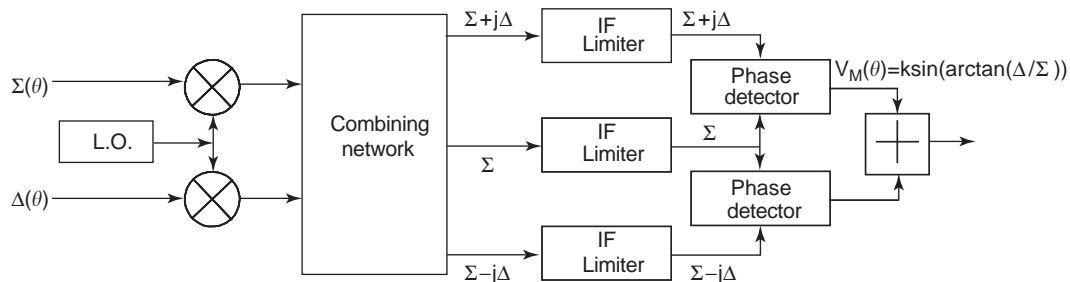


Figure 24. Coherent three-channel monopulse processor.

a gain imbalance, the underlying mechanism for measuring the angle is being modified. If there are no more error sources, any processor will give the same angle estimation (and thus the same error). For an imbalance of 1 dB and an OBA of 2.4° the error in the estimation is about 0.3° .

4.4.3. Precombinational Phase Unbalance. If the Δ signal suffers a phase deviation from the nominal, $\Delta' = \Delta e^{j\phi}$ (produced by different electrical lengths in Δ and Σ paths or different insertion phases of some component), the resultant monopulse function will be modified and, when denormalizing with respect the ideal one, an error in the angle estimation will be produced. In this case the error depends on the processor type. In noncoherent processor type 1 the resultant monopulse function is identical to the ideal since the amplitude of the phased signal is the same as that of the original one; thus the estimation error is null.

Figure 23 shows the normalized error ($\Delta\theta/\theta_B$) for the other three processors. Coherent processor type 1 is nearly immune to this source of error. Coherent type 2 suffers the maximum errors for angles near the boresight, although for all the processors the error is null in the boresight direction.

For the previous example (normalized OBA = 0.4, $\theta_B = 6$), Fig. 23 yields an error estimation of 0.17° for coherent processor type 2 if phase unbalance is only 4.5° .

Table 1 resumes different processors performances (where 1 denotes the worst and 4 denotes the best performance).

A coherent implementation known as a *coherent three-channel monopulse processor* combines the best properties of the processors listed in Table 1 at a cost of increased complexity, as may be seen in Fig. 24 [11].

The correct choice of processor for a given system will thus come from a tradeoff between performance and electronic complexity. Besides the traditional processors discussed here, there are a relatively large number of possible different structures. Among these, the I&Q processors (those based on in-phase–quadrature detection of sigma and delta signals) are probably the most attractive because of the versatility that they offer in subsequent digital processing, especially if pulse compression or spread-spectrum techniques are used [12].

BIBLIOGRAPHY

1. A. Farina and F. A. Studer, *Radar Data Processing*, Research Studies Press, Letchworth, Hertlezdshire, UK, 1986.
2. S. S. Blackman, *Multiple Target Tracking with Radar Applications*, Artech House, Norwood, MA, 1986.
3. D. R. Rhodes, *Introduction to Monopulse*, Artech House, Norwood, MA, 1982.
4. M. I. Skolnik, *Radar Handbook*, McGraw-Hill, New York, 1970.
5. E. T. Bayliss, Design of monopulse antenna difference patterns with low side lobes, *Bell Systems Tech. Journal* **47**:623–650 (May–June 1968).
6. R. R. Kinsey, Tandem Series-Feed System for Array Antennas, US Patent 8509577, April 1970.
7. R. C. Hansen, *Phased Array Antennas*, Wiley, New York, 1997.
8. M. Sierra-Castaner, M. Sierra-Perez, M. Vera-Isasa, and J. L. Fernandez-Jambrina, Low-cost monopulse radial line slot antenna, *IEEE Trans. Anten. Propag.* **51**(2):256–263 (Feb. 2003).
9. G. Jacovitti, Performance analysis of monopulse receivers for secondary surveillance radar, *IEEE Trans. Aerospace Electron. Syst.* **AES-19**(6):884–897 (Nov. 1983).
10. S. M. Sherman, *Monopulse Principles and Techniques*, Artech House, Norwood, MA, 1984.
11. D. Karp and M. L. Wood, *DABS Monopulse Summary*, FAA Report RD-76-219, Feb. 1977.
12. G. Ferreiro, M. Burgos, A. Asensio, J. Gismero, and J. L. Jimenez, Digital monopulse receivers for phase modulated signals, *Proc. 2003 Radar Conf.*, Adelaide, Australia.

MONTE CARLO ANALYSIS

PAOLO LUGLI
University of Rome

As the name suggests, the Monte Carlo (MC) method is based on the selection of random numbers [1–4]. In its present form, the method is attributed to Fermi, Von Neumann, and Ulam, who developed it for the solution of problems related to neutron transport. In principle, the MC method can be considered as a very general mathematical tool for the solution of a great variety of problems.

Among the various applications of the method, the following are probably the most important:

- Integrodifferential equations
- Matrix inversion
- Transport of nuclear particles
- Transport in semiconductors
- Modeling in semiconductor devices
- Process simulation

An important feature of the MC technique is that more precise results can be obtained by generating larger numbers of points. More generally, being based on random numbers, the results obtained with an MC procedure are never exact, but are rigorous in a statistical sense: The exact result lies in given intervals with given probabilities. The uncertainty of the results is strictly related to the variance of the possible outcomes, and it is smaller if the size of the sample (i.e., the amount of computations devoted to the solution of the problem) is larger. One basic element of the numerical procedure is the possibility to generate random numbers with given distributions starting from pseudorandom numbers uniformly distributed between 0 and 1. Modern computers provide sequences of numbers obtained with precise mathematical algorithms, starting from a given element (seed). For each seed, the sequence is perfectly predictable. However, it satisfies a large number of statistical test of randomness. Those pseudorandom numbers offer two great advantages: They

can be generated in a very fast way, and they are reproducible (which is essential, for example, in debugging a code).

The applications of MC methods can be divided into two major groups. One consists of the direct reproduction on a computer of the microscopic dynamics of the physical process in a system that is already statistical in nature. We use in this case the term "MC simulation." The second group consists of MC methods devised for the solution of well-defined mathematical equations or problems. In such cases, the methods provide a way of sampling a given statistical distribution. The majority of real cases are a mixture of the two extreme limits indicated above. The application to the study of semiconductor devices and processes is a good example. In fact, transport processes are statistical in nature, but are also accurately described by well-defined equations that may or may not correspond to the direct simulation of the physical system under examination. For instance, the MC solution of the Boltzmann transport equation (BTE) not only gives the distribution function that verifies the equation but also yields information that is lost in the BTE itself. On the other hand, the direct simulation is at times very inefficient, as, for example, in the analysis of situations that are rare in the actual physical system. In such cases it is necessary to distort the simulation by applying some more sophisticated MC techniques that reduce the variance of the quantity of interest, giving up partially the advantages offered by the direct simulation.

The applications of the MC methods that we will focus on are particularly important in light of the growth in the field of microelectronics achieved in recent years. Semiconductor devices are nowadays built with their active dimensions well below 1 μm . Metal oxide semiconductor field-effect transistor (MOSFET) technology has moved already into the 0.25 μm size, while high-electron-mobility transistors (HEMTs) are commercially available with 0.15 μm gate length. The reduction in size leads to a higher integration level as more devices can be put into a single chip. Such a push toward smaller and more powerful devices (which immediately translate into higher levels of integration and enhanced performance of the single devices as well as of the overall circuit) has been sustained by enormous advances in the area of fabrication and processing. A very precise control is nowadays possible on the device geometry and doping profile through techniques such as ion implantation, reactive-ion etching, and electron and X-ray lithography. Furthermore, new possibilities for novel devices are offered by the capability to grow nanometer layered structures with extremely high quality by molecular-beam epitaxy (MBE) and metal organic chemical vapor phase epitaxy (MOCVD). As we will see, MC approaches can be of great help in understanding and overcoming the limits of several technological or in attempting to improve the yield of integrated circuits. Moving into the submicron scale, many new physical phenomena become important that require a sophisticated theoretical treatment. There exists, therefore, a new challenge toward the understanding of the principles of operation of those novel devices. The MC method offers great advantages also in this direction.

Computer programs are extremely important for technology development. Computer-aided design (CAD) has become one of the keystones in microelectronics. The importance of such a field can be greatly appreciated focusing on the steps required for the fabrication of integrated circuits (ICs). The development of new technologies is traditionally driven by an experimental approach. A useful alternative is offered by software tools, which can lead to a speed up of the development cycle and a reduction of the development costs. In fact, those calculations can be considered as simulated experiments, which can be much faster and less expensive than real experiments. Furthermore, computer experiments allow a deep physical interpretation of the final results that leads to a better understanding of the problem at hand. This is particularly true for the MC simulations. The characteristic links between the different aspects of CAD can be summarized as follows [5]. The output of the process simulation is fed directly into a device simulation program, which determines the electrical characteristics and the performance of the device. At this stage, the interplay between process and device simulation can suggest improvements on the processing steps deduced from the simulated device performance. The output of the device simulator is then compacted in order to be inserted in a circuit simulation program, which determines the characteristics of the overall circuit. As this article will show, MC approaches are finding more widespread use as CAD tools, both at the level of device and at the level of process simulation.

Although it will not be possible to exhaust the complexity of the MC methods in such a short review, the present contribution is intended to give a critical overview of the MC algorithms used for device and process modeling and for circuit yield analysis. A more thorough investigation can be found in the references. For the MC simulation of semiconductor devices, a complete review can be found in Ref. 6.

1. MONTE CARLO DEVICE SIMULATION

The Monte Carlo technique is a fairly new tool in the area of device modeling, traditionally dominated by simulators based on drift-diffusion models or on balance-equation models (for an overview of the subject, see Refs. 7 and 8). The first MC application to the study of electronic transport in semiconductors is due to Kurosawa in 1966 [9]. Shortly afterward the Malvern group, in UK (Boardman, Fawcett, Hilsun, Swain, among others), provided the first wide application of the method to device simulation, focusing mainly on GaAs devices [10]. Applications to Si and Ge boomed in the 1970s, thanks to work performed at the University of Modena, Italy, and at IBM Yorktown, USA. The reviews in Refs. 4 and 11 provide a deeper historical and technical perspective. The great attention reserved in recent years to the MC analysis of devices is strictly connected to the availability of powerful and relatively inexpensive computers and workstations, which guarantee the necessary numerical resources for the computationally quite heavy simulations. Furthermore, with the recent advances in material growth, contact

deposition, and impurity control, devices have become more transparent from a physical point of view. Incidentally, this has provided physical systems of extreme interest. At the same time, MC algorithms have gained in sophistication and are now able to handle phenomena and systems of great complexity. These are two fundamental steps since the necessary input for an MC simulation of semiconductor materials and devices is an accurate microscopic description of the physical system under investigation. Many semiconductor devices can be nowadays simulated with the MC method, which is becoming more and more a very useful modeling tool.

The most common (and also the most interesting) simulation of a semiconductor device is performed for many particles in parallel [Ensemble Monte Carlo (EMC), procedure] and coupled to Poisson's equation in order to obtain the self-consistent potential related to the charge distribution given directly by the MC procedure. For systems of great complexity, a one-particle Monte Carlo (OPMC) simulation can be performed on a given fixed potential previously determined.

Since no a priori assumptions are needed on the form of the real- and k -space carrier distributions, an MC simulator is the only reliable tool for the investigation of those physical phenomena that critically depend on the shape of the distribution or on the details of its tail (such as electron injection over potential barriers). Furthermore, the MC technique allows us to focus on particular physical mechanisms that might be of importance with regard to the device performance (e.g., intercarrier scattering, impact ionization, generation-recombination, etc.). The price one has to pay are a very time-consuming algorithm and the requirement of a complete knowledge of the physical system under investigation. Often many assumptions have to be made in order to reduce the complexity of the model describing a given device.

1.1. The Monte Carlo Algorithm

In recent years, EMC simulations have been widely used to study the properties of semiconductor devices. Particular emphasis has been lately attributed to submicron structures, because of their performances in switching and high frequency operations [12]. Once the basic physics involved in the transport of such devices is known, EMC simulation provides a formidable tool to determine their limits and characteristics and can be very helpful in modeling. Together with the determination of the macroscopic properties of a device, EMC also gives a microscopic description of the local electric field, charge density, velocity distribution, and so on.

The basic steps of a standard EMC self-consistent device simulation are (see Fig. 1) as follows:

1. *Set up Geometry and Discretization Scheme.* Two parameters that play an important role in the choice of the time step and the grid size are the plasma frequency and the Debye length. For simple device geometry a one-dimensional description can be sufficient. Normally, MC simulations are performed using a two-dimensional grid (that is, assuming

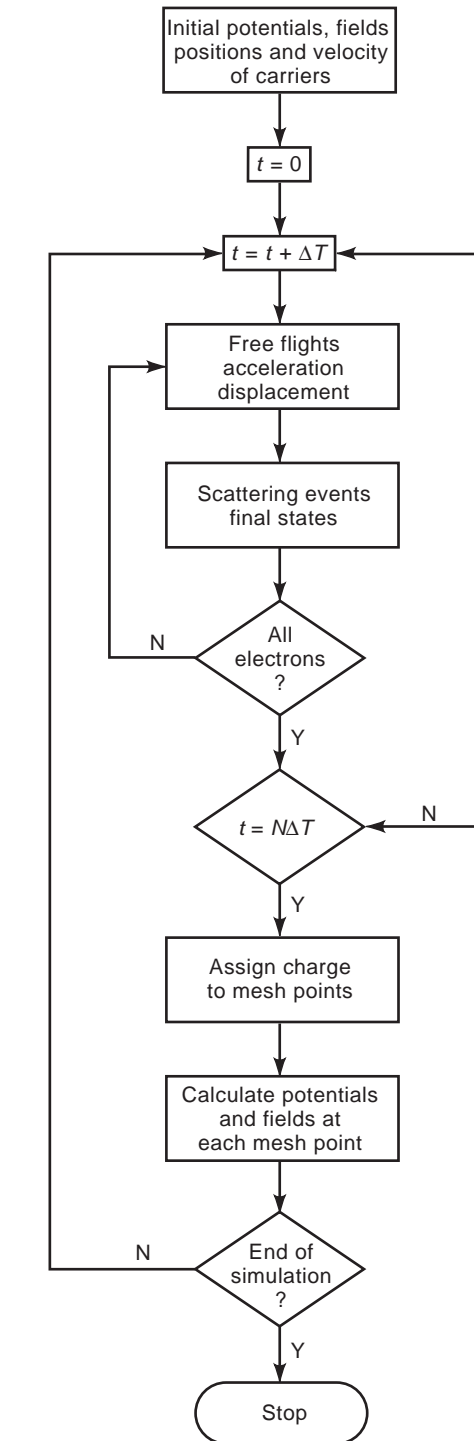


Figure 1. Flowchart of typical self-consistent MC device simulation.

homogeneity along the third direction). Since the simulation is inherently three-dimensional, there are no principal reasons that prevent a fully three-dimensional analysis.

2. *Charge Assignment.* The charge of each particle is assigned to a particular mesh point. Since it is not possible to simulate all the electrons present in a

real device, each simulated particle (also referred to as “superparticle”) represents a cloud of electrons for the purpose of estimating currents, charge, and field distributions. For all other purposes, each individual particle carries its elementary charge e . The doping charge is also added to the mesh according to its distribution. A sufficiently large number of simulated particles is needed to guarantee the statistical validity of the results and to reduce the level of numerical noise. Such a number depends on the dimensionality of the spatial grid, ranging typically from thousands of particles for one-dimensional descriptions, up to several tens of thousand particles for two- or three-dimensional systems.

3. *Potential Solution.* Poisson’s equation is solved to determine the electrostatic potential at the mesh points. In connection to EMC simulations, a finite-difference scheme is generally used, although some attempts to use a finite-element approach have been presented [13]. The solution can be obtained in several ways, among which we can list the Fourier analysis cyclic reduction, the conjugate gradient, the multigrid, and the direct matrix inversion methods. The first three methods provide effective algorithms that allow the inclusion of special boundaries. The latter requires a matrix inversion at the beginning of the simulation. The new potential is calculated with a simple matrix multiplication at fixed times during the simulation. The electrostatic field is then obtained from the potential with a finite-difference algorithm.
4. *Flights.* Each particle, now treated as an individual electron, undergoes the standard MC sequence of scattering and free flights, subject to the local field previously determined from the solution of the Poisson equation. The MC sequence is stopped at fixed times, at which the field is adjusted following the steps described above. The carrier dynamics is computed by solving Newton’s equations of motion in the crystal, described by its band structure. The length of a free flight is generated randomly according to the total scattering rate (i.e., the number of collisions per unit time). At the end of each flight, carriers scatter (with impurities, lattice vibrations, other carriers, etc.), with the probability of each event being weighted by its scattering rate (relative to the total one). Finally, a new state (i.e., the new energy, wavevector, occupied band) following the collision is determined according to the differential cross section of the process that has terminated the free flight. The scattering probability and the probability distribution of the final states are computed using quantum mechanics (starting from the so-called Fermi Golden Rule). A particular event (collision or no collision, which type of collision, which final state) is selected randomly, by comparing the probability of occurrence of that event to a random number.

The description of the problem is completed by setting initial and boundary conditions. The initial conditions are

not so important, since only the self-consistent steady-state result is usually retained. Boundary conditions are instead crucial, in particular in submicrometer devices, where contact properties drastically influence the behavior of the whole device.

The steady-state current is given directly by the net number of particles crossing one contact per unit time. More effectively, an extension of Ramo’s theorem to two-dimensional situations allows the calculation of the current in three terminal devices simply by summing the velocities of all particles found inside given portions of the device [14]. By performing several computer runs, it is possible to construct the I – V characteristics of the device. Important device parameters can also be extracted from the simulation. For example, the output resistance $R_{\text{out}} = \Delta V_{\text{ds}} / \Delta I_{\text{ds}}$ for constant gate bias V_{gs} and the transconductance $g_{\text{m}} = \Delta I_{\text{ds}} / \Delta V_{\text{gs}}$ for constant drain bias V_{ds} can be obtained from a series of runs, starting from normal operating conditions and varying the drain-to-source and gate-to-source biases, respectively. Parasitic elements can also be calculated, referring to an equivalent circuit description of the device. For example, the source-to-gate C_{sg} and source-to-drain C_{gd} capacitances are obtained by applying a step change respectively to the gate (ΔV_{gs}) and drain voltage (ΔV_{gd}) and $C_{\text{gs}} = \Delta Q_{\text{gs}} / \Delta V_{\text{gs}}$ and $C_{\text{gd}} = \Delta Q_{\text{gd}} / \Delta V_{\text{gd}}$, where ΔQ is the total equivalent charge flowing from the gate in response to the step potential. From the time dependence of the charge flow, it is also possible to estimate the parasitic source and drain resistance.

In an MC simulation, ohmic contacts are usually treated as ideal contacts, by maintaining a neutrality condition near the metal boundary. Due to such an assumption, the simulation results are those of an ideal intrinsic device. The comparison of the simulated characteristics with the one measured on real devices requires the consideration of a finite resistance for each ohmic contact. This can be done quite simply by scaling the simulated I – V characteristics using independently determined values of the contact resistances [15].

Traditionally, device simulators have been based on drift diffusion (DD) or hydrodynamical (HD) models. The basis of the two methods (as also the MC) is the Boltzmann transport equation. By taking the first three moments of BTE, three coupled equations are obtained which describe the spatial and temporal evolution of the average carrier concentration, velocity, and energy. Within the HD approach, the three equations are solved numerically, with some simplifying assumptions (such as the introduction of momentum and energy relaxation times for the equations of first and second moments). The DD approach assumes that carriers are always in equilibrium with the lattice temperature. Thus the energy equation drops out, and only the continuity equation is left, provided that the current density is expressed in a phenomenological way in terms of the carrier mobility and diffusivity. Clearly, the HD scheme is far superior to the DD one, since it can account (when all terms are considered) for carrier heating and nonhomogeneous distributions of the carrier temperature. The MC procedure stands on an even higher level, since it provides (also in nonhomogeneous, nonstationary

conditions) an exact solution of the Boltzmann equation. It correctly describes nonlocal effects (in space \mathbf{r} or time t) typical of situations where the field inside the device varies appreciably over lengths comparable with the electron mean free path, and the electrons at a given position carry information about the field value at another position. Unfortunately, the complexity and cost of each approach is inversely proportional to the refinement of the physical model it is based on. Therefore, the use of one approach or another depends on the specific device under investigation. The MC is the best technique to study situations where nonstationary effects are important (as, e.g., in submicrometer devices). It is safe to anticipate that as the tendency toward the miniaturization of devices will continue in the future, MC simulators will progressively extend their applicability. The success of MC in device modeling will ultimately depend on the compromise between two tendencies, one to use very sophisticated physical models (which lead to very costly but extremely accurate simulations), the other to rely on simplified models, sacrificing a bit of accuracy for a reduced complexity and cost of the algorithms. Along this line, it will be extremely useful to be able to combine different methods in order to fully exploit the potential of each approach. Examples of MC simulators present in the literature can be found in Refs. 16–42.

1.2. Special Features

In the following section, we focus on special aspects of the MC simulation that are not generally considered because of their difficulty, although they can be of great importance in the device performance.

1.2.1. Full Band Simulation. A physical description of the semiconductor band structure is needed as input to the MC simulation. Traditionally, bands have been described via nonparabolic dispersion relations, because this allows the analytical calculation of the differential and total scattering rates for a variety of scattering mechanisms. Furthermore, the calculation of the field-induced acceleration during a free flight is trivial. A typical example is the model used for GaAs [43], which includes a three-valley description of the conduction band (T, L, and X valley) and a description of the three valence bands (heavy, light, and split off holes). The nonparabolic dispersions are introduced with nonparabolicity factors treated as fitting parameters and adjusted as to reproduce a variety of experimental results, including those provided by time-resolved spectroscopy [6]. The carrier interaction with polar optical, acoustic, equivalent and nonequivalent intervalley, intraband and interband phonons, and ionized impurities can be easily considered. Unfortunately, nonparabolic dispersions provide an adequate band description only up to energies not too far from band edge (typically 1 eV or less). Thus, higher band states need to be described more accurately any time high-energy effects are important in a device (as, for instance, in the case of carrier injection above energy barriers, or when impact ionization occurs). The most popular approach is that based on a full band description, achieved via pseudopo-

tential methods [44]. The full $\varepsilon(\mathbf{k})$ dispersion is calculated numerically, either on the entire Brillouin zone or only on the irreducible wedge. The scattering rates are then calculated using directly the electronic states coming out of the numerical routine. The improvement in the band description level is paid in terms of computational time and memory required with respect to simpler band models.

1.2.2. Pauli Exclusion Principle. Electrons obey the Fermi–Dirac statistics and must satisfy the Pauli exclusion principle (PEP). This means that not all the states are available because only two electrons of opposite spin can reside in each state. This aspect is not very important in the nondegenerate case, and electrons are distributed in a large interval of states; in the degenerate case the problem becomes more conspicuous. For instance, GaAs electrons are degenerate at room temperature at densities around 10^{19} cm^{-3} . This is the case for many devices of interest. Degeneracy is equivalent to a many-body interaction which reduces the phase space available for the electron final state in an induced transition. If $p(\mathbf{k})$ and $p(\mathbf{k}')$ are the probabilities that the initial and final state are, respectively, occupied, the total rate of transition $P(\mathbf{k}, \mathbf{k}')$ between two different states is given by $P(\mathbf{k}, \mathbf{k}') = p(\mathbf{k})S(\mathbf{k}, \mathbf{k}')[1 - p(\mathbf{k}')]$. Normally a semiclassical MC procedure works with the approximation $p(\mathbf{k}') = 0$ because all the states are considered available as final states. The inclusion of the PEP is then essentially the inclusion of this term in the total scattering rate. In the EMC procedure, this is obtained very easily because the particle distribution is known step by step. The algorithm generating the distribution function is set up by multiplying the scattering probability by the correction factor $1 - p(\mathbf{k}')$; $p(\mathbf{k}')$ is determined self-consistently, and a rejection technique is used after selecting the final state without the correcting Pauli factor [45].

1.2.3. Contact Simulation. The simulation of contacts is one of the most serious problems in MC device simulations, due in part to the limited knowledge of the physics of contacts. On the other hand, contacts are of great importance in a number of semiconductor devices, whose applications range from high-speed logic to microwaves. As the dimensions of these devices reach the submicron limit, contacts become the limiting factor for the performance in the ballistic or quasiballistic mode of operation. In general, semiconductor devices do not operate under charge neutrality conditions. The net charge inside the device is directly related through Gauss' law to the flux of the electric field on the boundaries, and consequently to the potential inside the device. Therefore, charge neutrality (that is, conservation of the number of particles) cannot be enforced in the simulation. Rather, an appropriate handling of the boundaries is required to simulate a number of electrons that vary in time self-consistently with the potential distribution. Taking a field-effect transistor as an example, the most significant boundaries are at the source, drain, and gate electrodes. Source and drain contacts are usually treated as ideal ohmic contact by absorbing all the electrons that hit the electrodes and by injecting a number of electrons which maintain a neutral

region in the adjacency of the electrodes. The Schottky barrier at the gate is treated as a perfectly absorbing electrode with a potential equal to the applied potential minus the barrier height. Although commonly assumed, the above conditions have never really been tested. One attempt to deal with the problem of contacts in a simulation of a one-dimensional metal–n–n⁺ structure has been presented in Ref. 46.

1.2.4. Carrier–Carrier Scattering. Many devices are characterized by very high electron concentrations. In such a situation, one might have to worry about the possible influence of the interaction among the conducting electrons. A good example is provided by the heterojunction bipolar transistor (HBT), which will be examined later. In a standard device, such as a metal semiconductor field-effect transistor (MESFET) or HEMT, electrons are injected into the channel with a thermal energy distribution and a small initial velocity. In an HBT, electrons are injected from the emitter into the base, which they cross before being swept away from the high field at the base–collector junction. Due to the high doping (p-type) in the base region, electrons can be scattered by the collective excitations of the hole gas, as well as through normal binary collisions with the other electrons. Two main contributions to the carrier–carrier scattering can be identified:

- The individual carrier–carrier interaction via a screened Coulomb potential which accounts for two-body short-range interaction
- The electron–plasmon interaction, which accounts for the collective long-range behavior of the electron gas

In semiconductors, the plasmon energy at a reasonable electron density can be of the same order of magnitude as the characteristic phonon energies. In a device simulation, the scattering rates for electron–electron and electron–plasmon processes can be tabulated at the beginning of the simulation. Carrier–carrier scatterings are then treated as any other mechanisms in the MC algorithm, using appropriate rejection algorithms to account for the current carrier distribution function [47,48].

1.2.5. Optimization Procedures. An original, efficient algorithm has been implemented to calculate the appropriate duration of the free flights (depending on the actual carrier status). The method, which is based on a space-dependent definition of the scattering rate [49], leads to a drastic reduction in the number of self-scatterings, thus allowing a large savings in computation time (more than one order of magnitude compared with the conventional approaches). In areas where the electron population is very small, it is possible to extend a technique originally proposed by Phillips and Price [49], which allows one to obtain good statistics in rarely visited energy regions. Two situations are of particular interest. If a device presents regions with a high doping density N^+ connected to regions with low densities N^- , the carrier concentration will reflect (except at the interface between the different regions) the doping distribution. Therefore, most of the simulated carriers (roughly in the ratio N^+/N^-) will populate

the highly doped, low-field regions, requiring an extensive amount of computation for the simulation of a quasithermal distribution. This is the case, for example, of the MOSFET or a MESFET with ion implanted source and drain contacts. A similar case is found in k space, when we are interested in the population of high-energy states, which are rarely touched by the carriers but might cause very important physical phenomena (a typical example is the carrier injection into SiO₂ for the channel of a MOSFET). The latter situation is the one examined by Phillips and Price. The population of the high-energy states can be enhanced by generating a fixed number N of carrier histories every time one of the simulated particles enters the rarely populated region. Each one of the N generated particles will have the same initial condition (equal to the state of the “parent” particle at the moment of the multiplication) and a weight $1/N$ for the calculation of the average quantities. The multiplication algorithm can be repeated several times at higher energies, originating an “avalanche” of carriers that fill up the tail of the distribution function at higher and higher energies [35]. A similar multiplication technique has been also used in real space in Ref. 39. A peculiar situation is found when impact ionization phenomena are important. The knowledge of the high-energy tail of the carrier distribution function is then required. Furthermore, in the presence of carrier multiplication, the number of simulated particles would grow above the initially set value, diverging as breakdown is approached. A special multiplication technique for both energy and real space has been implemented [50], which is an extension of the approaches described above. Each particle is assigned a statistical weight that varies with its position in the device and its energy. With such approach, it is possible to account for regions with very different doping levels (as in bipolar transistors) and to obtain a reliable statistics of rare processes, keeping at the same time a constant number of particles.

1.3. Simulation Results

We show some results obtained by MC simulation of GaAs devices, leaving the interested reader to the variety of applications listed as references at the end of this article.

1.3.1. Heterojunction Bipolar Transistors. HBTs are receiving considerable attention because of their high-speed performance and high current-handling capability. The device shown in Fig. 2 has been simulated [43] and the results have been compared with measured data. By varying the base–collector voltage (in the common-base configuration), the electric field profile changes as depicted in Fig. 3. Very high values are reached in the collector region, with the maximum occurring at the base–collector interface. Electrons, injected from the emitter, cross the base where they strongly interact with the dense hole plasma. As they enter the collector, they are ballistically accelerated by the junction field, reaching velocities as high as 6×10^7 cm/s. The spatial extent of the velocity overshoot is limited to about 100 Å, as the electrons are rapidly scattered into the satellite valleys where they move at saturated velocity. Figure 4 indeed shows that

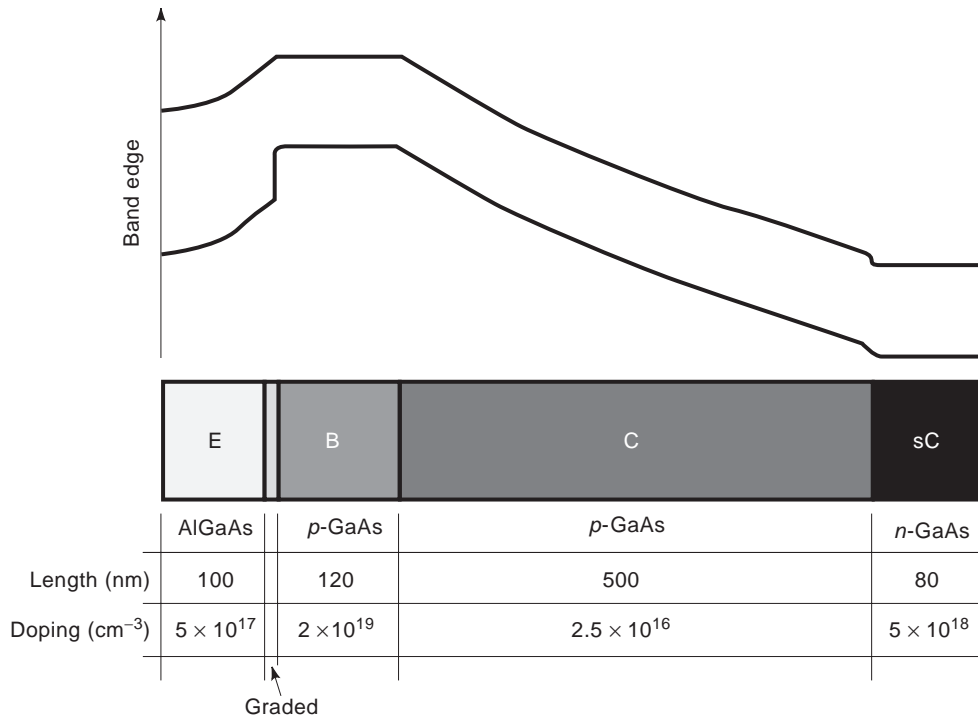


Figure 2. Energy band diagram and cross section of the simulated HBT.

for a collector voltage of 16 V, almost all electrons in the collector populate, in equal number, the L and X valleys. There, they are strongly heated by the collector field, obtaining the high values of average energy illustrated in Fig. 5. Correspondingly, the calculated $(M - 1)$ factor, which measures the relative increase of collector current due to multiplication phenomena, is around unity at this voltage, in excellent agreement with the measured value [43]. As V_{BC} is further increased, the holes created by primary ionization processes are in turn able to ionize, marking the onset of breakdown, which is predicted around 18 V.

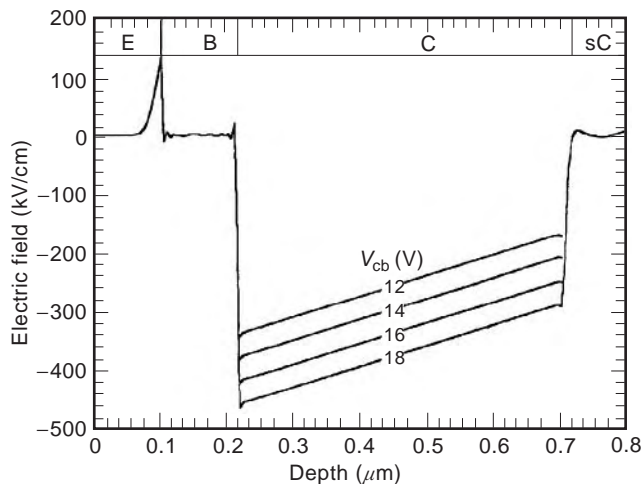


Figure 3. Electric field profile of the simulation HBT at various V_{BC} .

1.3.2. High Electron Mobility Transistors. HEMTs are extremely appealing for microwave low-noise applications. Their superior performance is due to the spatial separation of the electrons (confined in a small-gap channel layer, typically GaAs or InGaAs) from the donors (fixed in the large-gap region or regions surrounding the channel). In the simulated device [51] a special type of doping is considered, denoted δ -doping, where two dopant planes are located in the AlGaAs layers respectively above and below an InGaAs channel. The substrate material of the device is GaAs. Because of the different lattice constant of GaAs and InGaAs, strain is present in the channel region. This type of HEMT is referred to as “pseudomorphic HEMT.” Typical two-dimensional contour plots for a device with a gate length of 180 nm are shown in Figs. 6–9. The source-to-drain bias is 2 V. The potential distribution (Fig. 6) reveals that a high-field region exists in the channel between the end of the gate and the beginning of the cap layer (which is a doped GaAs region above the AlGaAs confining barrier, used in technology to reduce the capacitance and resistance at source–drain contact region). Entering this region, an electron becomes very hot, reaching average kinetic energies of few tenths of electronvolts, as indicated in the energy map of Fig. 7. Electron heating results in reduced confinement within the channel, since many of the electrons have sufficient energy to surmount the confining barrier. Furthermore, as a result of heating, the population of the upper L valley is very high in correspondence of the high-field region, as visible in Figs. 8 and 9 which show respectively the total and L valley electron concentrations. Because of the hot-electron-induced real-space transfer, the current flows through both the bottom AlGaAs layer (and partially

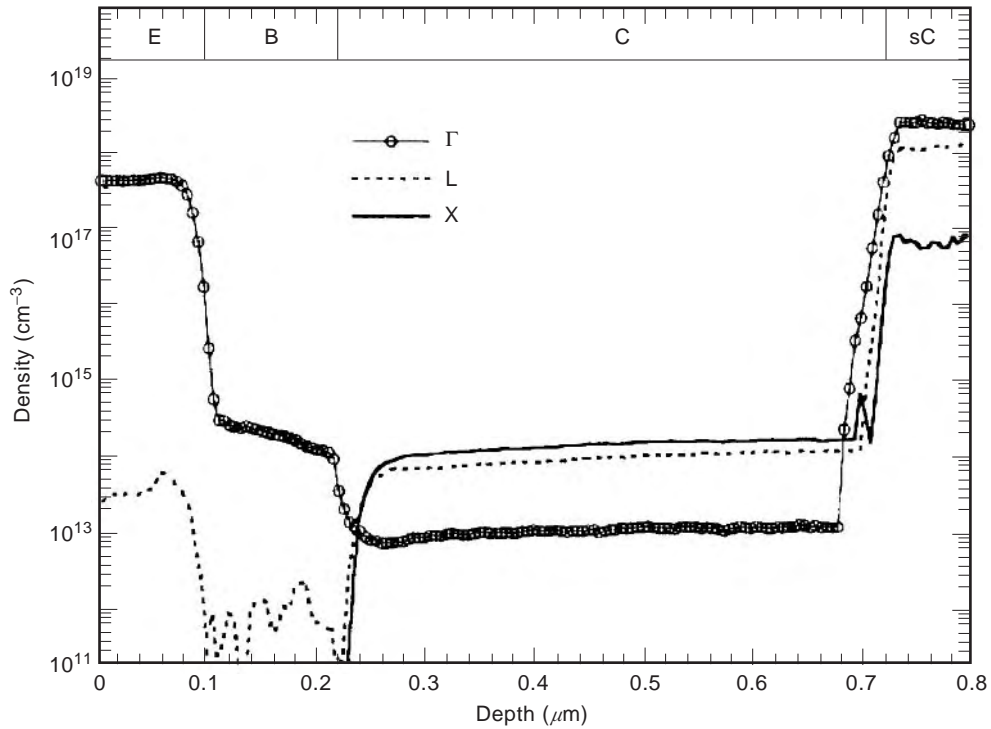


Figure 4. Electron concentration in the different valleys for $V_{BC} = 16$ V.

through the substrate) and the top AlGaAs barrier, which actually constitutes the access path to the drain cap region. The actual value of the electric field along the channel, along with the corresponding carrier drift velocity and average energy, is presented in Fig. 10. Due to the very

short gate length, the field reaches a peak value of 200 kV/cm, resulting in the strong electron heating discussed above and a remarkable velocity overshoot, which is in turn responsible for the excellent microwave performance of such devices.

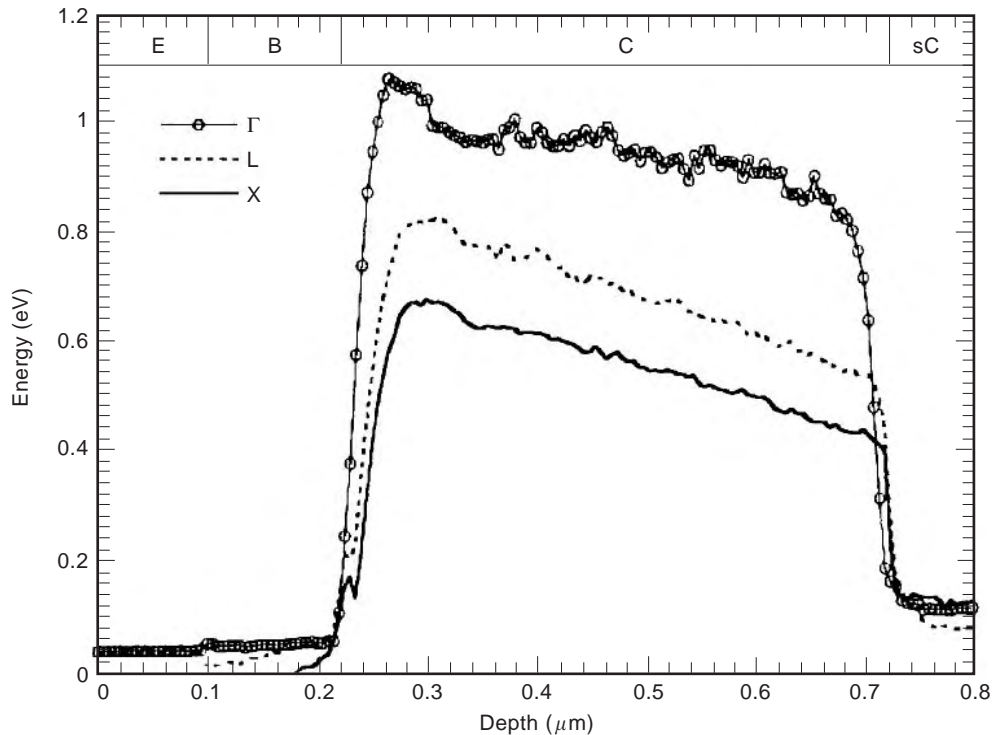


Figure 5. Electron average energy in the different valleys for $V_{BC} = 16$ V.

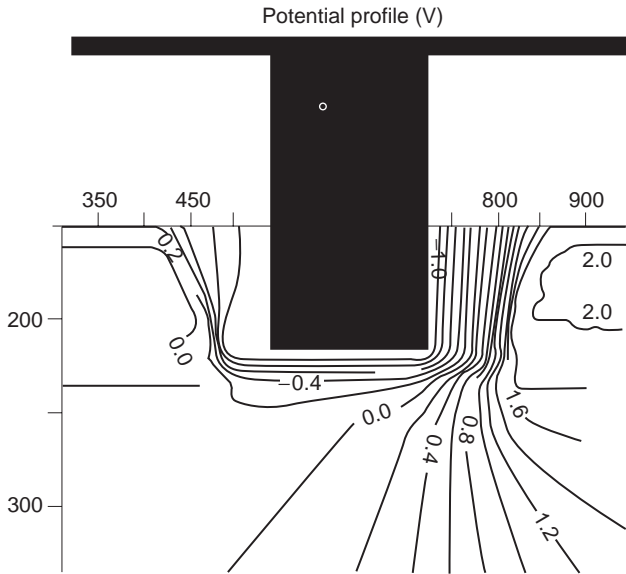


Figure 6. Two-dimensional plot of the equipotential lines for the simulated HEMT at a drain bias of 2 V.

2. MONTE CARLO PROCESS SIMULATION

We are going to discuss MC process simulation from the point of view of integrated circuit (IC) fabrication, since this is certainly the area where simulation plays the most important role. Many different interrelated steps contribute to the realization of the final product. The main processing steps can be classified into the following three categories:

1. Thermal processing and doping (ion implantation, predeposition, annealing, oxidation, epitaxial growth)
2. Pattern definition (reactive ion etching, deposition, evaporation, sputtering)
3. Pattern transfer (optical X-ray, electron-beam lithography)

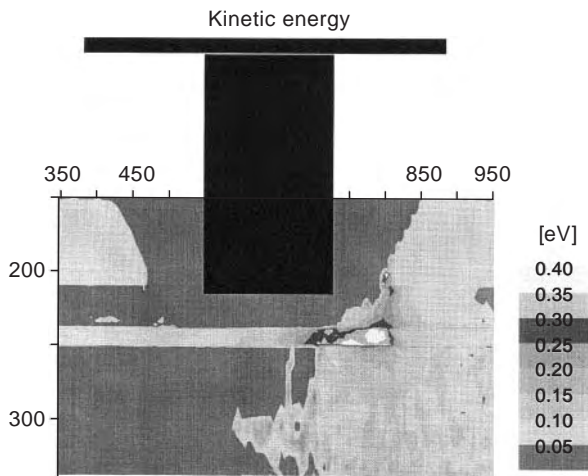


Figure 7. Two-dimensional representation of the electron average energy for the simulated HEMT at a drain bias of 2 V. The darkest region corresponds to an energy of 0.35 eV.

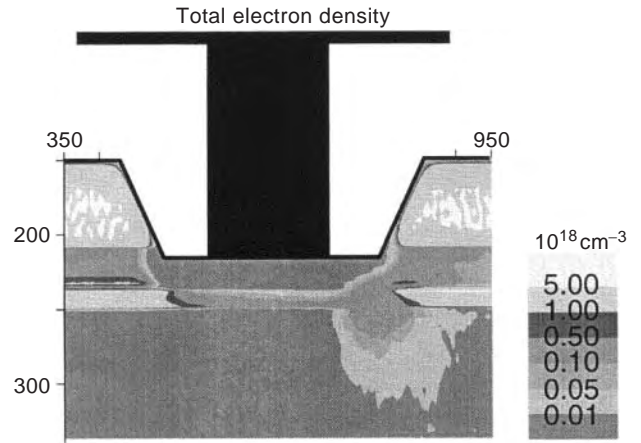


Figure 8. Two-dimensional representation of the total electron concentration for the simulated HEMT at a drain bias of 2 V. The darkest region corresponds to a density of $5 \times 10^{18} \text{ cm}^{-3}$.

Setting up mathematical models for each step requires the knowledge of very complex physical and chemical phenomena, such as, for instance, the redistribution of atoms or impurities into a given material, or the energy exchange between fast projectiles and the substrate they interact with. As we will see in the examples, some drastic approximations are made in order to define a tractable model.

As for the case MC device simulation, several analytical and numerical approaches exist in the literature that cover all the processing steps outlined above [5,52]. The MC technique has been very successful in some applications, especially those where the simulation can be reduced to a series of uncorrelated events describing the trajectories of projectiles against target atoms. This is the case of the examples we will discuss below—that is, ion implantation and electron beam lithography. Other

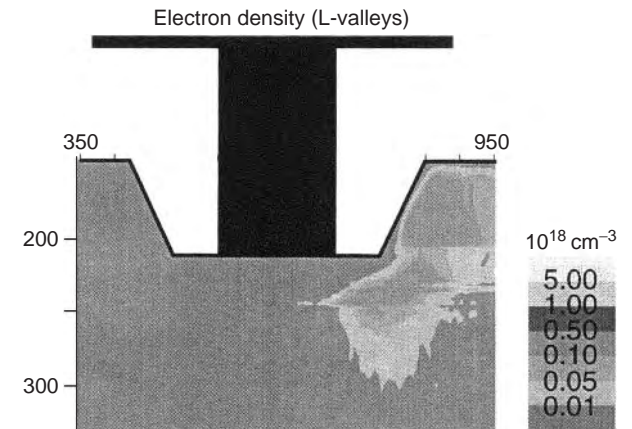


Figure 9. Two-dimensional representation of the L valley electron concentration for the simulated HEMT at a drain bias of 2 V. The darkest region corresponds to a density $5 \times 10^{18} \text{ cm}^{-3}$.

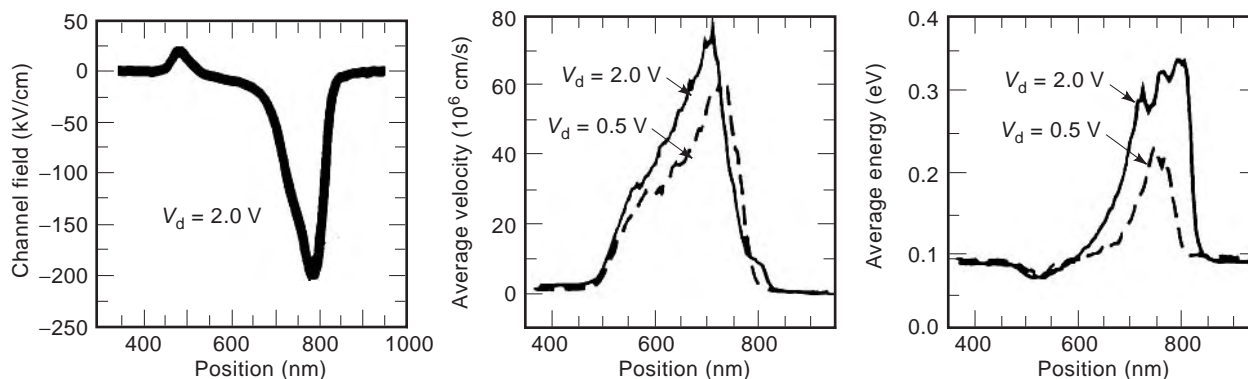


Figure 10. One-dimensional plot (along the channel direction) of the electric field (left), average velocity (center), and average energy (right) for two different drain voltages, respectively equal to 0.5 V (dashed lines) and 2 V (solid lines).

attempts have been made to use MC techniques to describe epitaxial growth [53,54].

As a general comment, we can say that once the mathematical model has been set up, the MC algorithm for process simulation presents fewer difficulties than the one for device simulation. This is because no self-consistency is required between internal potential and charge distribution and also because the transition probabilities are assumed to be constant between two successive stochastic events.

2.1. Ion Implantation

Ion implantation is one of the most important doping techniques for device fabrication, in particular for very-large-scale integration (VLSI) circuits. The successful application of this technique depends strongly on the ability to control the impurity profile for any implant condition. The three main processes involved in the penetration and slowing down of energetic ions into a material are

1. The energy loss via collisions with the target atoms. Thousands of atoms (called “recoils”) are displaced by each impinging ion. Local disorder and very high temperatures are reached in the region where the cascade occurs.
2. The thermalization of the excited zone, with possible diffusion of defects.
3. The long-range migration of defects.

Computer-aided design models for ion implantation fall into two broad categories: analytic distribution functions and MC methods. The former are computationally very inexpensive, but rely upon fits to experimental data to reproduce the observed profile of dopants ion and work well only for simple geometries in one dimension. In contrast, the MC approach attempts a first-principle calculation based on two-body scattering theory. Although computationally expensive, it can handle the most complicated structures.

An MC simulation offers the following advantages [55,56]:

- It accounts for implant profile discontinuities at the interface between different layers.
- It allows for a rigorous treatment of elastic scattering with the different types of atoms in a multiatomic target.
- It gives a full implant distribution rather than only a few of its moments.
- It can generate as-implanted profiles as a function of key parameters such as dose, energy, tilt, and rotation angles.
- It can include the recoil effect due to atoms that are knocked into deeper layers from an impinging ion.
- It allows the simulation of the defect generation due to ion implantation.

Furthermore, once a physically based model has been set up and verified, the MC method can be used to generate “experimental data” for semiempirical models that are highly computationally efficient and desirable in technology development and process optimization. Other important features of the MC simulation of ion implantation are its inherent three-dimensionality, the fact that ion backscattering is naturally accounted for, and the fact that both amorphous and crystalline targets can be considered. Those distinctive features make the MC simulation the most suitable approach to the study of ion implantation.

The MC simulation is performed by following a large number of individual ion histories; each of them is made up of collisions with target atoms, along with straight flights between them. The model relies on two main assumptions. The first is that the projectile interacts with one atom at a time, and thus multiple collisions can be neglected. Such a “binary collision” model breaks down at low energies, when deflections can occur even at greater distances from a target atom. The second approximation involves the mechanisms for energy and momentum losses. The contributions coming from electronic losses (where the incident ion is excited or ejects atomic electrons, with large energy and small momentum transfer) and from nuclear losses (originated from nearly elastic collisions with the target atoms, characterized by large exchange of momentum) are considered independent of each other. The

slowing down of the projectile results from the simple addition of the two effects. In the past, the basic theory to describe the penetration of charge particles into a solid was the one due to Lindhard, Scharff, and Schidøtt (LSS). The LSS theory has been successful in the prediction of primary ion range and damage distribution in amorphous semi-infinite substrates. Because of its assumption, it is not applicable to multilayers structures as often encountered in VLSI processing.

The simulation is made up of successive paths. After each of them, the energy of the ion is reduced by the amount of the electronic and nuclear losses, which are related to the momentum transfer to the target atom occurring during the collision. The history of each ion terminates either when its energy drops below a specified value or when the ion exits the target.

Different physical models can be used for the various phenomena involved in the energy loss process. An exhaustive review is found in [57]. A series of optimizations of MC procedures are discussed in Ref. 58. Such optimizations are crucial in order to overcome the major limitation of the MC approach—that is, the amount of computation needed to achieve an acceptable statistical accuracy.

A good example of a situation where the MC simulation works at its best is provided by channeling. If the target is crystalline in nature (and it is not damaged during the implantation process, as guaranteed by using low implant doses), then the stopping power of the medium is greatly reduced because of the large open spaces of the axial channels. The average ion penetration is then considerably increased with respect to amorphous targets. Although the number of ions that are well-channeled is considerably less than the number of the dechanneled ones, the well-channeled ions travel deep into the crystal and form a channeling tail in the resulting profile. It is the channeling tail that determines the junction depth. While the formulation of suitable transport equations for the channeling effect presents many problems, the direct MC simulation of the ion path through the target can be quite straightforward. The main obstacle is again the inadequacy of several available models for electronic stopping. Although still widely used, the LSS theory cannot properly describe channeling effects. Its shortcoming lies in the inability to account for the variation of electron densities between the atoms of the crystalline structure. In fact, an ion traveling along a crystal channel will experience less electronic stopping than another ion which more closely encounters the electron clouds of the target atoms. A proper model must therefore account for the electron distribution around each atom. For boron ions implanted in crystalline silicon, it has been shown that a combination of the two concepts of effective charge and proton stopping power lead to reasonable models. There, the solid-state Hartree–Fock theory with a muffin tin structure has been employed, with the assumption of a spherically symmetric electron distribution around the Si atoms. While such an assumption is fairly reasonable for boron, which has most of the bound electrons in *s* orbitals (i.e., with spherically symmetric distribution), it has been pointed out that a further improvement is needed for the implantation of

arsenic ions, where the electrons occupy *p* and *d* orbitals. One possibility is to calculate self-consistently the potential for the As projectile within the local density approximation, and then to determine the scattering phase shift and the scattering cross section needed in the simulation.

In the theoretical study of the implantation process, it is very important to be able to determine the cumulative damage imparted to the semiconductor crystal by the implanted ions. The MC simulation directly accounts for the effect of damage by explicitly simulating the formation of point defects, their recombination, and the effect that such defects have on each subsequently implanted ion [59,60]. The procedure is as follows. As the simulated ion travels through the crystal, target atoms that receive sufficient energy (15 eV for Si) leave their lattice site, forming a vacancy or an interstitial. The interstitials travel until they lose the energy gained from the incident ion. The location of interstitials and vacancies are recorded for each collision cascade. At the end of each of these cascades, the interstitials and vacancies within the cascade are annihilated if they are located within a specified capture radius of one another. Furthermore, the recombination with damage caused by previous cascades is taken into account via a statistical recombination algorithm. The defects that survive recombination are weighted to reflect the fraction of the overall dose that the simulated projectile represents, and then they are summed to obtain the simulated point defect distribution as a function of depth. This distribution is then used to modify the crystal structure that subsequent ions will cross by determining the rate of statistical creation of (1) interstitials at one of the eight interstitial sites in the diamond lattice unit cell and (2) vacancies on lattice sites. Such a model is inherently homogeneous, and it appropriately describes the damage caused by lighter ions, such as for instance boron, where the net formation of cumulative damage occurs by the overlap of the damage caused by individual cascades. Heavier ions, such as arsenic, can lead to local phase transitions from the crystalline to the amorphous phase. This can be simulated by considering the presence of highly localized disordered regions, which are formed whenever the relative number of displaced atoms during an ion cascade exceeds a specified value (for instance, 10% in the region under consideration).

The traditional MC approach described above is based on the calculation of a large number of independent ion trajectories, where each ion is followed from its entrance in the target material down to its stopping or exit point. Peripheral areas with low exposure (that is, with a dopant concentration that is order of magnitudes lower than the maximum values) cannot be adequately represented, because insufficient statistics is provided by the simulation. This is a typical situation where rare events can play an important role. An approach similar to the one already used in electronic transport simulation has been suggested [61]. The fundamental idea is to locally increase the number of calculated ion trajectories in areas with large statistical uncertainty. To this purpose, the simulated region is subdivided into layers, each characterized by a certain relative concentration level (with respect to the current maximum concentration achieved in the whole

region). For each simulated ions, a number of “check-points” is set up during the flight path. At a checkpoint, the local dopant concentration is calculated together with the global maximum concentration. The corresponding layer of fixed relative concentration is determined, and a “trajectory split point” is defined at the checkpoint if the ion has moved into a layer with lower relative concentration than the one touched at the previous checkpoint. The position, energy, and velocity of the ion are stored, and they are used to generate a series of virtual branches of the ion trajectory that start at this split point. In this way, a tree of virtual trajectories is formed for each regular ion, so that the peripheral areas of the dopant concentration are represented by a much higher number of ion trajectories and the statistical noise is reduced. To obtain the correct concentration, each branch is assigned a weight. The virtual trajectories are generated with the same model and parameters as the regular ones, with their initial condition (energy, velocity, and position) being determined by the regular ion characteristic at the checkpoint.

2.2. Electron-Beam Lithography

Electron-beam lithography (EBL) is the standard way of fabricating masks for optical and X-ray lithography. Furthermore, direct electron-beam writing on wafers is the only practical way to obtain ultrasmall linewidths. In EBL, finely focused beams are used to expose polymeric resist layers. The ultimate resolution obtainable is not limited by the characteristics of the incident beam but rather by the electronic scattering with the resist and the underlying substrate. Such scattering leads to the so-called proximity effect and can be subdivided into three distinct contributions, namely the forward scattering within the resist, the backscattering within the resist, and the backscattering from the substrate.

The actual process of electron scattering in solids is very complex, and simplifying models are needed to achieve quantitative results via numerical techniques. As for the case of ion implantation, the best approach is the MC simulation. In fact, the simulation is very similar to the one described before in this section. In the simplest model [62,63], electrons undergo a series of elastic scatterings with the target nuclei. They also suffer energy losses because of the inelastic scatterings with the target electrons. The elastic scattering is modeled using the screened Rutherford cross section, while in the inelastic contributions the energy is assumed to be lost continuously between two successive collisions according to Bethe’s formula. Between scattering events, the simulated electrons travel in a straight path, whose length is determined randomly according to the calculated cross sections. The sequence of free paths and scattering events is repeated until the electrons come to rest. Contrary to the ion implantation case, the quantity of interest here is the deposited energy rather than the position where the particle stops. It is, in fact, the energy passed by the incident electrons to the medium that creates the condition for the selective removal of the polymeric resist.

Several improvements have been suggested to the simple model described above. In particular, it was pointed

out [64] that the production of secondary electrons as a result of an ionization process caused by the incident beam has to be accounted for. Since the energy deposition is inversely proportional to the electron energy, the contribution of the secondary electrons (which are slower and move in a direction almost perpendicular to the incoming flux) can be significant. An hybrid model has been set up which includes a discrete energy loss mechanism corresponding to ionization, in addition to the continuous energy loss mechanism described above. A further refinement of the model has led to the use of Mott cross section for the treatment of elastic collisions [65]. Another improvement is needed in order to consider multilayered structures, as for instance those that serve as masks for X-ray lithography [66,67]. Such masks are obtained by direct writing via EBL on a thin resist, followed by pattern transfer in a thick resist multilevel structure. An example is shown in Fig. 11, where the radial profile of the energy deposited at the resist–substrate interface is plotted for three different values of the beam energy, namely, 20, 30, and 40 keV. The simulated multilayer is constituted by 10 nm of Al, 1000 nm of resist [polymethyl methacrylate (PMMA)], 20 nm of Au as base plating, 200 nm for Cr for adhesion purposes, and 2000 nm of Si substrate. The length of the free path has to be determined by taking into account the details of the electron dynamics— that is, the possibility for an electron to cross one or more layers during its path. Forward and backward contributions are shown separately in the figure, each characterized by its own range. The parameter η is the ratio between the energy deposited by backscattered versus forward scattered electrons. The MC results show that the ultimate resolution limit is set by forward scattering, which has a width of 90 nm at the interface. The backscattering contribution from the metal is important despite the reduced thickness of the layer, but can be eliminated by increasing the beam energy. The simulation results can be parameterized in order to predict the EBL resolution under various exposure conditions. This is done via the so-called proximity function, defined from a Gaussian fit to the MC data. By a numerical convolution of the proximity function with the

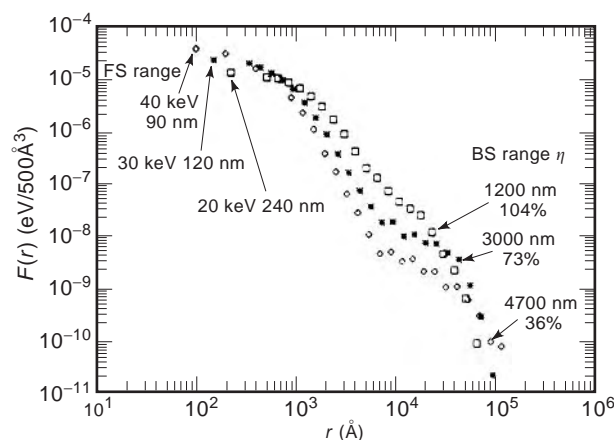


Figure 11. Radial distribution function of the total absorbed energy density for three different beam energies, with the relative contributions of forward scattering and backscattering.

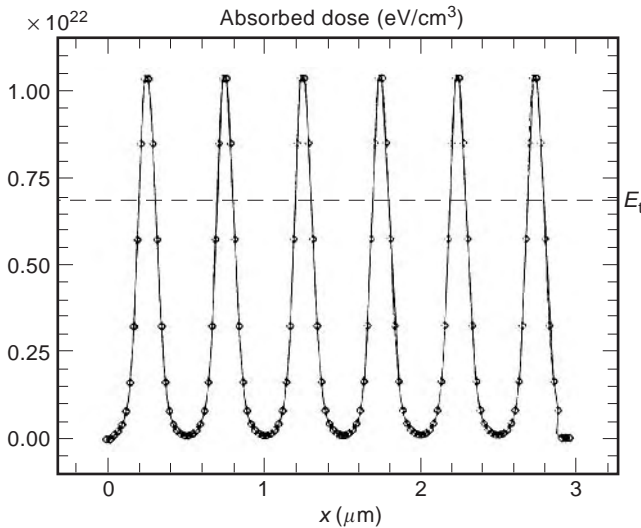


Figure 12. Profile of absorbed energy density for a nominal pattern of 5 lines/spaces of 0.1/0.4 μm .

experimental pattern, it is possible to calculate the absorbed energy densities correspondent to the experimental situations. Figure 12 shows the absorbed energy density profile for the structure considered before and after an electron energy of 40 keV. The nominal line/space dimension is 100/400 nm. By assuming (according to the “Threshold solubility model” [68]) that the solvent develops all the PMMA irradiated above the threshold energy E_t , the developed lines would be around 150 nm. This value reproduces very well the experimental findings.

3. MC ANALYSIS OF CIRCUIT YIELD

The number of transistors on a single chip is approximately doubling every 2 years, as predicted by Moore’s law. Such progress is sustained by the continuous drive toward smaller feature sizes, larger dies, and better packing efficiency. While technology allows a general reduction of the manufacturing costs per transistor, the level of investment to continuously upgrade such technology is becoming enormous. It is then vital for any manufacturer to improve the yield of the IC production. *Yield* can be defined as the ratio of the number of designs that pass the performance specifications to the total number of designs that are produced. Since the total number of designs produced might be large or unknown, yield is usually measured over a finite number of design samples or trails in the process known as yield estimation. As the number of trials become large, the yield estimate approaches the true design yield. Parameter values that have statistical variations are referred to as yield variables.

Statistical design techniques for ICs, including yield maximization and sensitivity minimization, are becoming increasingly important in IC technology development because cost effectiveness and competitiveness demand minimal experimental passes and short development times. A valuable statistical circuit simulation methodology must inherently predict device and circuit performance reliably

and efficiently, relate their performance to fabrication process parameters and account for the fluctuations of such parameters, and account for physical correlations among device model parameters. The use of numerical process and mixed-mode device/circuit simulators provides the needed capabilities for predicting the effects of technological variations on device/circuit performance. However, such an approach cannot be generally used for yield predictions or other statistical modeling due to the waste amount of computation time required. This is very efficiently done via MC techniques.

In general, there are two basic sources of yield loss in a fabrication process: local process faults and global process faults. The latter include, for instance, mask misalignment and linewidth variations. They can cause variations in speed and power consumption, thus affecting primarily parametric yield. The former include spot defects, such as oxide pinholes, extra metal, and extra or missing material defects. They affect functional yield, because they primarily affect circuit topology and can cause the chip to completely fail functionally. Local process faults are therefore called “catastrophic” faults. The most probable origin of such faults is the presence of dust particles, or in general some contaminant, on the mask or on the wafer surface. During the photolithographic processes, these particles lead to unexposed photoresist areas, or resist pinholes, thus causing unwanted material or unwanted etching of material on a layer. Although some crossover and coupling between the two types of faults occur, and manifest themselves at a circuit level, usually they are considered as uncorrelated and they are treated separately.

3.1. Catastrophic Yield

The effect of catastrophic faults on yield can be determined via a MC simulation made up of the following steps [69,70]: (1) generation of a chip sample, according to specified layout design rules, (2) generation and placement of defects on the layout, and (3) analysis of the modified layout for circuit faults. A filtering step prevents uninteresting faults to be considered. Many chip samples are generated in a simulation. The defect diameter, type, and spatial distribution on each sample are selected randomly according to the defect statistics observed in the fabrication line. Once the defects have been placed on the layout, a series of fault analysis procedures are performed by looking at the defect neighborhood in order to determine which type of circuit fault has occurred (if any): short, open, open device, shorted device, new via, new device due to extra metal, or new device due to extra active material. Out of the resulting faults, only those affecting functional yield are kept, the others being filtered out. Some faults can also be combined together into a composite fault. Both fault analysis and filtering operation are guided by defect models, which specify which circuit faults can be caused by each defect type, which layers interact with the defect, and how layers are electrically connected together. The resulting output is a chip sample containing a list of the circuit faults that have occurred on it during the simulated fabrication. The chip sample fault lists are summarized to record the frequency of each unique fault

combination and are then passed to an application post-processor when the simulation is completed. In a typical simulation, the random number generator can be called millions of times. It is therefore essential to use fast generation algorithms.

3.2. Parametric Yield

Parametric yield analysis is the process of varying a set of parameter values, using specified probability distributions, to determine how many possible combinations result in satisfying predetermined performance specifications. The design is simulated over a given number of trials in which the yield variables have values that vary randomly about their nominal values with specified probability distribution functions. The number of passing and failing trials are recorded, and these numbers are used to compute an estimate of the yield.

Statistical design is the process of (1) accounting for the statistical variation in the parameters of a design, (2) measuring the effects of these variations, and (3) modifying the design to minimize these effects. This can be achieved by resorting to a purely numerical process and device simulators [71], to macro- (response surface polynomials) models [72], or to a seminumerical mixed-mode device/circuit simulator coupled to a parameter evaluator [73]. In all three approaches, the first step is the specification of a set of measurable process parameters, which act as input variables for the simulation.

These variables have to be measurable, and they should be linked to more fundamental process parameters so that they can be used to control a fabrication process. For bipolar technology they can, for instance, be the base sheet resistivity, the epicollector doping density, and the effective surface recombination velocity at the emitter contact. The probability distribution for the input parameters has to be determined from measurements on different wafers and lots. In the second step, device model parameters are calculated, together with their variation following a given process fluctuation. In the example cited above for bipolar technology, model parameters can be the peak base doping density, the metallurgical base width, and the epicollector width. Seminumerical approaches resorting to analytical formulation of device operation can be used, or, as an alternative, extensive process simulations coupled to physical device simulations can be performed. Clearly, the first approach is fast and inexpensive, while the second can be computationally very demanding but is free from the deficiency intrinsic to compact and simplified process and device models. The third step consists of a mixed-level device/circuit simulation that predicts the performance of a given circuit and its variation with fluctuation of process parameters.

In the MC-based yield analysis a series of trials is run in which random values are assigned to the design's statistical variable of interest, a simulation is performed, and the yield specifications are checked against the simulated measurement values. The number of passing and failing simulations is accumulated over the set trials and used to compute the yield. The method is

widely used and well-accepted as a way to estimate yield. The strength of the method is twofold—the accuracy of the MC estimates is independent of the number of statistical variables, and no simplifying assumptions are needed on the probability distribution of either component parameters values or performance responses. The weakness of the method is that a full network simulation is required for each trial and that a large number of trials is required to obtain high confidence and an accurate yield estimate.

Multiple yield analysis can be performed in order to adjust the nominal value of the yield variables to maximize the yield estimate. This process is called yield optimization or design centering.

BIBLIOGRAPHY

1. J. M. Hammersley and D. C. Handscomb, *Monte Carlo Methods*, Methuen, London, 1964.
2. Yu. A. Shreider, ed., *The Monte Carlo Method*, Pergamon, Oxford, UK, 1966.
3. J. Spanier and E. M. Gelbard, *Monte Carlo Principles and Neutron Transport Problems*, Addison-Wesley, Reading, MA, 1969.
4. C. Jacoboni and L. Reggiani, *Rev. Mod. Phys.* **55**:645–705 (1983).
5. B. R. Penumalli, in W. L. Engl, ed., *Process and Device Modeling*, North-Holland, Amsterdam, 1986, p. 1.
6. C. Jacoboni and P. Lugli, *The Monte Carlo Method for Semiconductor Device Simulation*, Springer-Verlag, Vienna, 1989.
7. S. Selberherr, *Analysis and Simulation of Semiconductor Devices*, Springer-Verlag, Vienna, 1984.
8. G. Baccarani et al., in W. L. Engl, ed., *Process and Device Modeling*, North-Holland, Amsterdam, 1986, p. 107.
9. K. Kurosawa, *J. Phys. Soc. Jpn. (Suppl.)* **21**:424 (1966).
10. R. W. Hockney and J. W. Eastwood, *Computer Simulation Using Particles*, McGraw-Hill, New York, 1981.
11. P. J. Price, *Semiconduct. Semimetals*, **14**:249–308 (1979).
12. A. Yoshii and M. Tomizawa, in W. L. Engl, ed., *Process and Device Modeling*, North-Holland, Amsterdam, 1986, p. 195.
13. S. Babiker et al., *Solid-State Electron.* **39**:629–635 (1996).
14. V. Gruzinskis, S. Kersulis, and A. Reklaitis, *Semicond. Sci. Technol.* **6**:602 (1991).
15. S. Babiker et al., *IEEE Trans. Electron. Devices* **ED-43**, 2032–2034 (1996).
16. J. Zimmermann and E. Constant, *Solid-State Electron.* **23**:915 (1980).
17. A. Yoshii, M. Tomizawa, and K. Yokoyama, *IEEE Trans. Electron. Devices* **ED-30**:1376 (1983).
18. Y. Awano, K. Tomizawa, and N. Hashizume, *IEEE Trans. Electron. Devices* **ED-31**:448 (1984).
19. M. Tomizawa, A. Yoshii, and K. Yokoyama, *IEEE Electron. Devices Lett.* **EDL-6**:332 (1985).
20. P. Hesto, J. F. Pone, and R. Castagne, *Appl. Phys. Lett.* **40**:405 (1982).
21. Y. Park, T. Tang, and D. H. Navon, *IEEE Trans. Electron. Devices* **ED-30**:1110 (1983).

22. C. Moglestue, *IEEE Trans. Comput. Aided Design CAD-5*:326 (1986).
23. Y. Park, D. H. Navon, and T. Tang, *IEEE Trans. Electron. Devices ED-31*:1724 (1984).
24. M. A. Littlejohn et al., *J. Vacuum Sci. Technol. B* 1:449 (1983).
25. T. Wang, K. Hess, and G. J. Iafrate, *J. Appl. Phys.* 59:2125 (1986).
26. K. Brennan, *IEEE Trans. Electron. Devices ED-32*:2197 (1985).
27. S. E. Laux and M. V. Fischetti, *IEEE Electron. Devices Lett.* 9(9):467-469 (1988).
28. M. V. Fischetti and S. E. Laux, *Phys. Rev. B* 38:9721 (1988).
29. K. Yokoyama et al., *IEEE Trans. Electron. Devices ED-32*:2008 (1985).
30. T. Wang and K. Hess, *J. Appl. Phys.* 57:5336 (1985).
31. R. Fauquembergue et al., *Solid-State Electron.* 31:595 (1988).
32. M. Tomizawa, A. Yoshii, and K. Yokoyama, *IEEE Electron. Devices Lett.* EDL-5:362 (1984).
33. U. Ravaioli and D. K. Ferry, *IEEE Trans. Electron. Devices ED-33*:677 (1986).
34. K. Throngnumchai, K. Asada, and T. Sugano, *IEEE Trans. Electron. Devices ED-33*:1005 (1986).
35. E. Sangiorgi, B. Ricco, and F. Venturi, *IEEE Trans. Comput. Aided Design CAD-7*:259 (1988).
36. M. Tomizawa, K. Yokoyama, and A. Yoshii, *IEEE Trans. Comput. Aided Design CAD-7*:254 (1988).
37. S. Bandyopadhyay et al., *IEEE Trans. Electron. Devices ED-34*:392 (1987).
38. M. V. Fischetti and S. E. Laux, *IEEE Trans. Electron. Devices* 38:650 (1991).
39. I. Kizilyalli et al., *IEEE Trans. Electron. Devices ED-40*:234 (1993).
40. D. Park and K. Brennan, *IEEE Trans. Electron. Devices ED-37*:618 (1990).
41. J. G. Adams, T. Tang, and L. E. Kay, *IEEE Trans. Electron. Devices ED-41*:575 (1994).
42. P. Dollfus, *J. Appl. Phys.* 82:3911 (1997).
43. C. Canali et al., *IEEE Trans. Electron. Devices ED-43*:1769 (1996).
44. K. Hess, ed., *Monte Carlo Devices Simulation: Full Band and Beyond*, Kluwer, Boston, 1991.
45. P. Lugli and D. K. Ferry, *IEEE Trans. Electron. Devices ED-32*:2431 (1985).
46. U. Ravaioli et al., *IEEE Trans. Electron. Devices ED-32*:2097 (1985).
47. P. Lugli and D. K. Ferry, *Physica B* 129:532 (1985).
48. P. Lugli and D. K. Ferry, *IEEE Electron. Devices Lett.* EDL-6:25 (1985).
49. A. Phillips and P. J. Price, *Appl. Phys. Lett.* 30:528 (1977).
50. D. Liebig et al., *Microelectron. Eng.* 19:127 (1992).
51. P. Lugli et al., HEMT models and simulations, in R. Lee Ross, S. Swensson, and P. Lugli, eds., *Pseudomorphic HEMTs: Technology and Applications*, Kluwer, Dordrecht, 1996, pp. 141-163.
52. W. Fichtner et al., *Proc. IEEE* 72:96 (1984).
53. J. Singh, S. Dudley, and K. K. Bajaj, *J. Vacuum Sci. Technol. B* 4:878 (1986).
54. P. A. Maskym, *Semiconduct. Sci. Technol.* 3:594 (1988).
55. M. T. Robinson and D. G. Besco, *Phys. Rev. B* 9:5008 (1974).
56. A. M. Mazzone, *IEEE Trans. Comput. Aided Design CAD-4*:369 (1985).
57. H. Rysseel and J. P. Biersack, in W. L. Engl, ed., *Process and Device Modeling*, North-Holland, Amsterdam, 1986, p. 31.
58. G. Hobler, E. Langer, and S. Selberherr, *Solid-State Electron.* 30:445 (1987).
59. K. M. Klein, C. Park, and A. F. Tasch, *IEEE Trans. Electron. Devices ED-39*:1614 (1992).
60. S. Yang et al., *IEEE Trans. Semiconduct. Manuf.* 9:49 (1996).
61. W. Bohmayr et al., *IEEE Trans. Semiconduct. Manuf.* 8:402 (1995).
62. K. Murata, D. F. Keiser, and C. H. Ting, *J. Appl. Phys.* 52:4396 (1981).
63. D. C. Joy, *Microelectron. Eng.* 1:103 (1983).
64. S. Horiguchi et al., *J. Appl. Phys.* 39:512 (1981).
65. K. Murata et al., *J. Vacuum Sci. Technol. B* 5:124 (1987).
66. M. Gentili et al., *Microelectron. Eng.* 9:147 (1989).
67. P. Lugli, *IEEE Trans. Comput. Aided Design* 9:1164 (1990).
68. A. R. Neureuther, D. F. Keiser, and C. H. Ting, *IEEE Trans. Electron. Devices ED-26*:686 (1979).
69. H. Walker and S. W. Director, *IEEE Trans. Comput. Aided Design CAD-5*:541 (1986).
70. J. Khare and W. Maly, *IEEE Trans. Semiconduct. Manuf.* 9:518 (1996).
71. I. C. Kizilyalli et al., *IEEE Trans. Electron. Devices* 40:966 (1993).
72. M. O'Leary and C. Lyden, *IEEE J. Solid-State Circ.* 30:279 (1995).
73. H. Cho and J. Fossum, *Solid-State Electron.* 38:1065 (1995).

MONTE CARLO SIMULATION IN RELIABILITY

LAWRENCE M. LEEMIS
The College of William & Mary
Williamsburg, Virginia

Simulation is a generic term used loosely in engineering, with application areas ranging from flight simulators used in cockpit design to simulated annealing used in optimization. Simulation is presented here as a mathematical and computational technique used to analyze probabilistic models. Simulation can be divided into *Monte Carlo simulation*, where *static* models are analyzed; and *discrete-event simulation*, where *dynamic* models involving the passage of time are analyzed. Since simulation is presented here in the context of reliability modeling, Monte Carlo simulation models are emphasized.

Monte Carlo simulation methods are often used when analytic methods become intractable, and they typically give a modeler added insight into the structure of a problem. As reliability and lifetime models become less mathematically tractable, Monte Carlo methods will have increasing importance. Monte Carlo simulation techniques mirror the relative frequency approach for determining probabilities. The estimate for the probability of interest converges to the true value as the number of replications increases. This article considers methods for generating random lifetimes and random processes from probabilistic models. The basic methods are inversion [inverse cdf and inverse chf (see Section 1 for acronym definitions)], linear combination methods (composition and competing risks), majorizing methods (acceptance/rejection and thinning), and special properties.

The basic methods are followed by a discussion of order statistics. The generation of order statistics is useful for estimating measures of performance associated with series, parallel, and k -out-of- n systems. The accelerated life and proportional hazards lifetime models can account for the effects of covariates on a random lifetime. Variate generation for these models is a straightforward extension of the basic methods when the covariates do not depend on time. Variate generation algorithms for Monte Carlo simulation of nonhomogeneous Poisson processes are a simple extension of the inverse-chf technique. Methods for generating failure times for a repairable system modeled by a nonhomogeneous Poisson process are also reviewed.

1. PROBABILITY MODELS FOR LIFETIMES

In reliability modeling, a continuous positive random variable typically represents the lifetime of a component or system. The generic term “item” is used in this section to apply to either a component or a system. Several functions completely specify the distribution of a random variable. Five of these functions are useful in describing variate generation algorithms: cumulative distribution function (cdf), survivor function, probability density function (pdf), hazard function, and cumulative hazard function (chf). Other functions, not used here, include the characteristic function [1], density quantile function [2], mean residual life function [3], moment-generating function [4], and total time on test transform [5].

Although Monte Carlo simulation is applied here to problems in reliability, the techniques are applicable to any problem setting concerning random variables that can assume only positive values. Thus the setting here is actually “survival analysis” and includes fields as diverse as biostatistics, actuarial science, economics, and sociology.

This section considers techniques for generating random variates for Monte Carlo simulation analysis. Two textbooks [6,7] are devoted entirely to this topic. The purpose of this section is to review algorithms capable of transforming random numbers to *random variates* possessing known probabilistic properties for use in reliability studies. With the generation of random variates as a basis, several other topics, namely, generating order statistics, generating lifetimes from models with covariates, and generating point processes, are considered.

In the interest of brevity, we assume that a source of randomness is available (i.e., a stream of independent random numbers). These random numbers are uniformly distributed between 0 and 1, and most high-level programming languages now include a random-number generator. The random numbers are denoted by U , and the random variates (lifetimes) are denoted by T . Algorithms for generating the random numbers and desirable properties associated with random-number generators (such as insensitivity to parameter values, speed, memory requirements, relationship to variance reduction techniques) are reviewed by Schmeiser [8], as well as by many of the simulation textbooks that he references. Park and Miller [9] also overview Lehmer random-number generators, and L'Ecuyer, et al. [10] survey more recent work in random-number generation.

The discussion here is limited to generating *continuous*, as opposed to discrete or mixed, distributions. Generating variates from discrete distributions is useful for evaluation of certain types of reliability analysis tools such as fault trees. For simplicity, the examples are confined to the exponential and Weibull distributions, which have been chosen because of their tractability and widespread use. Any continuous lifetime distribution with a closed-form inverse cdf could have been used. Several reliability textbooks discuss Monte Carlo techniques [11–17].

The survivor function, also known as the *reliability function* and *complementary cdf*, is defined by

$$S(t) = P[T \geq t], \quad t \geq 0$$

which is a nonincreasing function of t satisfying $S(0) = 1$ and $\lim_{t \rightarrow \infty} S(t) = 0$. The survivor function is important in the study of *systems* of components since it is the appropriate argument in the structure function to determine system reliability [18]. $S(t)$ is the fraction of the population that survives to time t , as well as the probability that a single item survives to time t . For continuous random variables, $S(t) = 1 - F(t)$, where $F(t) = P[T \leq t]$ is the cdf.

When the survivor function is differentiable, the associated pdf is

$$f(t) = -S'(t), \quad t \geq 0$$

For any interval (a, b) , where $a < b$, we obtain

$$P[a \leq T \leq b] = \int_a^b f(t) dt$$

Finite mixture models for k populations of items may be modeled using the pdf

$$f(t) = \sum_{i=1}^k p_i f_i(t), \quad t \geq 0$$

where $f_i(t)$ is the pdf for population i and p_i is the probability of selecting an item from population i , $i = 1, 2, \dots, k$. Mixture models are used in composition, a density-based variate generation technique. Also, $H(t) = -\log S(t)$.

The hazard function, also known as the *rate function*, *failure rate*, and *force of mortality*, can be defined by

$$h(t) = \frac{f(t)}{S(t)}, \quad t \geq 0$$

The hazard function is popular in reliability work because it has the intuitive interpretation as the amount of *risk* associated with an item that has survived to time t . The hazard function is a special form of the complete intensity function at time t for a point process [19]. In other words, the hazard function is mathematically equivalent to the intensity function for a nonhomogeneous Poisson process, and the failure time corresponds to the first event time in the process. Competing risks models are easily formulated in terms of $h(t)$, as shown in the next section.

The cumulative hazard function can be defined by

$$H(t) = \int_0^t h(\tau)d\tau, \quad t \geq 0$$

If T is a random lifetime with cumulative hazard function H , then $H(T)$ is an exponential random variable with a mean of one. This result is the basis for the inverse-chf technique.

2. RANDOM LIFETIME GENERATION

Techniques for generating a single, continuous lifetime from a known parametric probabilistic model can be partitioned into density-based and hazard-based algorithms. Density-based algorithms may be applied to any random variable, whereas hazard-based algorithms can only be applied to nonnegative lifetimes. In this section, both types of algorithms are assumed to generate a nonnegative lifetime T .

The three classes of techniques for generating variates reviewed below are *inversion*, *linear combination methods*, and *majorizing methods*. For each class, there is a density-based method and a hazard-based method that are similar in nature. Examples of the use of all these techniques are given in Leemis and Schmeiser [20]. More recently, Devroye [21] reviewed variate generation techniques requiring just one line of code.

2.1. Inversion

The density-based inverse cumulative distribution function technique, or *inverse-cdf* technique, is based on the probability integral transformation which states that $F(T) \sim U(0, 1)$, where F is the cdf for the random lifetime T . Thus

$$T \leftarrow F^{-1}(U)$$

generates a lifetime T , where \leftarrow denotes assignment. If the cdf has a closed-form inverse, this method typically requires one line of computer code. If the inverse is not closed-form, numerical methods must be used to invert the cdf.

Example 1. Consider a Weibull distribution with scale parameter λ and shape parameter κ . The cdf is

$$F(t) = 1 - e^{-(\lambda t)^\kappa}, \quad t \geq 0$$

which has the closed-form inverse

$$F^{-1}(u) = \frac{1}{\lambda} [-\log(1 - u)]^{1/\kappa}, \quad 0 < u < 1$$

Thus, an algorithm for generating a Weibull random variate is

$$T \leftarrow \frac{1}{\lambda} [-\log(1 - U)]^{1/\kappa}$$

where $U \sim U(0,1)$. Most random-number generators currently in use do not return exactly 0 or exactly 1. If U is

generated so that 1 is excluded, $1 - U$ can be replaced with U for increased speed without concern over taking the logarithm of 0.

The inverse-chf technique is based on $H(T)$ being exponentially distributed with a mean of one. So

$$T \leftarrow H^{-1}(-\log(1 - U))$$

generates a single random lifetime T . This algorithm is easiest to implement if H can be inverted in closed form.

Example 2. Consider an arrangement of three identical components with independent and identically distributed Weibull lifetimes with parameters λ and κ as arranged in the block diagram in Fig. 1. Find the mean time to system failure.

It is possible to use both analytic and Monte Carlo techniques to solve this problem. Let T_1, T_2 , and T_3 be the lifetimes for the three statistically identical components; let T be the system lifetime; and let $S_i(t) = e^{-(\lambda t)^\kappa}$ be the survivor function for component i for $i = 1, 2, 3$ and $t \geq 0$. The system survivor function is

$$\begin{aligned} S(t) &= S_1(t)[1 - (1 - S_2(t))(1 - S_3(t))] \\ &= e^{-(\lambda t)^\kappa} [1 - (1 - e^{-(\lambda t)^\kappa})(1 - e^{-(\lambda t)^\kappa})] \\ &= 2e^{-2(\lambda t)^\kappa} - e^{-3(\lambda t)^\kappa}, \quad t \geq 0 \end{aligned}$$

Thus, the mean time to system failure is

$$E[T] = \int_0^\infty S(\tau)d\tau = \frac{\Gamma(1 + 1/\kappa)}{\lambda} (2^{1-1/\kappa} - 3^{-1/\kappa})$$

To solve the problem exactly as stated, this analytic solution is ideal. For many applications, however, a Monte Carlo solution can provide additional insight into a problem. Furthermore, a less restricted problem (e.g., with more complicated failure distribution or dependent component failure times) might not have a mathematically tractable analytic solution. A Monte Carlo estimate for the mean time to failure requires each component lifetime to be generated, and the inverse-chf technique is used here. The cumulative hazard function for the Weibull

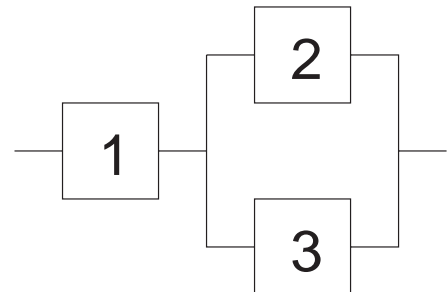


Figure 1. A block diagram for a three-component system.

distribution is

$$H(t) = (\lambda t)^\kappa, \quad t \geq 0$$

which has the closed-form inverse

$$H^{-1}(y) = \frac{1}{\lambda} y^{1/\kappa}, \quad y \geq 0$$

Thus an algorithm for generating a Weibull random variate is

$$T \leftarrow \frac{1}{\lambda} [-\log(1 - U)]^{1/\kappa}$$

which is identical to the inverse-cdf technique. In general, the inverse-cdf and inverse-chf techniques are interchangeable in this fashion. An algorithm to estimate the mean time to system failure using N system lifetimes is given below. Indentation is used to indicate nesting:

```

S ← 0
for i from 1 to N
    generate  $U_1, U_2, U_3 \sim U(0,1)$ 
     $T_1 \leftarrow \frac{1}{\lambda} [-\log(1 - U_1)]^{1/\kappa}$ 
     $T_2 \leftarrow \frac{1}{\lambda} [-\log(1 - U_2)]^{1/\kappa}$ 
     $T_3 \leftarrow \frac{1}{\lambda} [-\log(1 - U_3)]^{1/\kappa}$ 
     $T \leftarrow \min\{T_1, \max\{T_2, T_3\}\}$ 
     $S \leftarrow S + T$ 
A ← S/N
    
```

The variable S contains a cumulative sum of the system lifetimes, and A contains the average of the system lifetimes generated. The estimate for the average time to system failure A converges to the analytic result as the number of replications $N \rightarrow \infty$. This algorithm can be written more efficiently since the components have identical distributions. To save on the number of logarithms and exponentiations, properties such as $T_2 \geq T_3$ when $U_2 \geq U_3$ can be exploited so that only one Weibull variate needs to be generated for each system lifetime, based on the order of U_1, U_2, U_3 , as shown in the next example. The algorithm given above is inferior to the analytic method presented earlier in the example because it produces a *point estimator* A for the system reliability. It is appropriate to place a *confidence interval* around the point estimator in order to assess its accuracy [1].

A final example is given to illustrate an alternative way of generating the system lifetime of a coherent system [18] of components.

Example 3. Consider the same system as Example 2, which used three random numbers to generate a single system lifetime T . Thus the algorithm was not synchronized. A technique for achieving synchronization is illustrated in this example. The first step is to determine $\pi_i = P[T_i = T]$ for $i = 1, 2, 3$, which is the probability that component i is the component that “causes” system failure. Second, the conditional lifetime distribution of all components, given that they are the cause of failure, should be

determined, and a lifetime variate generated from the appropriate distribution. For the three-component example, we obtain

$$\pi_2 = P[T_3 < T_2 < T_1]$$

and, by symmetry

$$\pi_3 = P[T_2 < T_3 < T_1] = \pi_2$$

and

$$\pi_1 = 1 - \pi_2 - \pi_3$$

since $\pi_1 + \pi_2 + \pi_3 = 1$. The algorithm for generating a system lifetime from a single $U(0, 1)$ is given below. The U that is used in the last step of the algorithm has been rescaled so that it is conditionally $U(0, 1)$.

Setup

determine π_1, π_2, π_3
 find the conditional lifetime distributions for all components

Algorithm

```

generate  $U \sim U(0,1)$ 
if  $0 < U < \pi_1$ , then
     $J \leftarrow 1$  and  $U \leftarrow \frac{U}{\pi_1}$ 
if  $\pi_1 < U < \pi_1 + \pi_2$ , then
     $J \leftarrow 2$  and  $U \leftarrow \frac{U - \pi_1}{\pi_2}$ 
if  $\pi_1 + \pi_2 < U < 1$ , then
     $J \leftarrow 3$  and  $U \leftarrow \frac{U - \pi_1 - \pi_2}{\pi_3}$ 
generate  $T$  from conditional lifetime distribution  $J$  using  $U$ .
    
```

Inversion techniques exhibit some important properties:

- They are synchronized (i.e., one random number produces one lifetime).
- They are monotone (i.e., larger random numbers produce larger lifetimes).
- They accommodate truncated distributions.
- They can be modified to generate order statistics (useful for generating the lifetime of a k -out-of- n system, as shown in the next subsection).

2.2. Linear Combination Methods

Linear combination techniques are the density-based composition method and the hazard-based competing risks method. The composition method is viable when the pdf can be written as the convex combination of k density functions

$$f(t) = \sum_{j=1}^k p_j f_j(t), \quad t \geq 0,$$

where $\sum_{j=1}^k p_j = 1$. The algorithm is

```

choose pdf  $j$  with probability  $p_j, j = 1, 2, \dots, k$ 
generate  $T$  from pdf  $j$ 
    
```

The first step is typically executed using a discrete inversion algorithm.

The second linear combination technique is called *competing risks*, which can be applied when the hazard function can be written as the sum of hazard functions, each corresponding to a “cause” of failure

$$h(t) = \sum_{j=1}^k h_j(t), \quad t \geq 0$$

where $h_j(t)$ is the hazard function associated with cause j of failure acting in a population. The minimum of the lifetimes from each of these risks corresponds to the system lifetime. Competing risks is most commonly used to analyze series systems, but it can also be used in actuarial applications. The competing risks model is also used for modeling competing failure modes for components that have multiple failure modes. The algorithm is

```
generate  $T_j$  from  $h_j(t), j = 1, 2, \dots, k$ 
 $T \leftarrow \min\{T_1, T_2, \dots, T_k\}$ 
```

2.3. Majorizing Methods

The third class of techniques for generating random lifetimes is the majorizing techniques: the density-based acceptance/rejection and a modified version of thinning, which is hazard-based. In order to use acceptance/rejection, there must be a majorizing function $f^*(t)$ that satisfies $f^*(t) \geq f(t)$ for all $t \geq 0$. The pdf corresponding to $f^*(t)$ is

$$g(t) = f^*(t) / \int_0^\infty f^*(\tau) d\tau$$

The algorithm is

```
repeat
  generate  $T$  from  $g(t)$ 
  generate  $S \sim U(0, f^*(T))$ 
until  $S \leq f(T)$ 
```

Generating T may be done by inversion or any other method. The name *acceptance/rejection* comes from the loop condition; the random variate T is accepted for generation if $S \leq f(T)$ and rejected if $S > f(T)$.

Thinning was originally used by Lewis and Shedler [22] for generating the event times in a nonhomogeneous Poisson process. Thinning can be adapted to produce a single lifetime by ignoring all except the first event time generated. A majorizing hazard function $h^*(t)$ must be found that satisfies $h^*(t) \geq h(t)$ for all $t \geq 0$. The algorithm is

```
 $T \leftarrow 0$ 
repeat
  generate  $Y$  from  $h^*(t)$  given  $Y > T$ 
   $T \leftarrow T + Y$ 
  generate  $S \sim U(0, h^*(T))$ 
until  $S \leq h(T)$ 
```

Generating Y in the loop can be done by inversion or any other method. The term *thinning* comes from the fact that

T can make several steps, each of length Y , that are thinned out before the loop condition is satisfied.

2.4. Special Properties

The fourth class of techniques for generating random lifetimes is called *special properties*. It is neither density-nor hazard-based since it depends on relationships between random variables. Examples of special properties include generating an Erlang random variable as the sum of independent and identically distributed exponential random variables, and generating a binomial random variable as the sum of independent and identically distributed Bernoulli random variables. Examples of special properties associated with random variables are given in the encyclopedic work of Johnson et al. [23].

The four techniques described in this section are often combined in order to generate a variate from a particular distribution. Devroye [6] and Dagpunar [7] review variate generation techniques for some of the more intractable distributions (e.g., normal and gamma) that are not considered here. Most computer installations have access to subprograms capable of generating variates from a wide range of distributions.

The generation of independent univariate random variates provides the basis for Monte Carlo simulation analysis of reliability models. There are a number of directions that a section of this nature could take at this point. I have opted for surveying the following: generating order statistics, generating lifetimes for models with covariates, and generating nonhomogeneous Poisson processes. Other important topics include generating random vectors [17,24], civil engineering applications [13], mechanical engineering applications [17], fault-tree analysis [14], or discrete-event simulation [25].

3. ORDER STATISTIC GENERATION

In many reliability applications, the efficient generation of order statistics can be useful for generating a random system lifetime. Order statistics play a central role in the analysis of simple arrangements of systems consisting of n statistically identical components. Let T_1, T_2, \dots, T_n be the n independent failure times of components in a system, and let $T_{(1)}, T_{(2)}, \dots, T_{(n)}$ be the ordered failure times. If T denotes the system failure time, then $T = T_{(1)}$ for a series system, $T = T_{(n)}$ for a parallel system, and $T = T_{(n-k+1)}$ for a k -out-of- n system. The most straightforward approach to generating the system lifetime for these models is to generate the lifetimes of each component, sort the lifetimes, and then choose the appropriate order statistic. This approach is adequate when n is small and the lifetimes are simple to generate. When one or both of these conditions do not hold, the following results from the literature [26–29] can be used to generate order statistics more efficiently. The algorithms presented in this section are effective ways of decreasing the central processing unit (CPU) time to generate a system lifetime since only one inversion of F is necessary and no sorting is required.

The random variables $\min\{U_1, U_2, \dots, U_n\}$ and $1 - (1 - U)^{1/n}$ have the same distribution, where $U_i, i = 1,$

2, ..., n and U are independent random numbers. If the function $F^{-1}(u)$ can be evaluated in closed form or numerically, an algorithm to generate the system lifetime of a series system of identical components is

$$T \leftarrow F^{-1}(1 - (1 - U)^{1/n})$$

Since $\max\{U_1, U_2, \dots, U_n\}$ and $U^{1/n}$ have the same distribution, the system lifetime of a parallel system of statistically identical components can be generated by

$$T \leftarrow F^{-1}(U^{1/n})$$

Example 4. A system of n statistically identical components is arranged in parallel. If each component has an independent Weibull lifetime with scale parameter λ and shape parameter κ , devise a method to generate a system lifetime variate from a single random number U.

The inverse of the Weibull cdf is

$$F^{-1}(u) = \frac{1}{\lambda} [-\log(1 - u)]^{1/\kappa}, \quad 0 < u < 1.$$

A system lifetime T, which corresponds to the order statistic $T_{(n)}$, is generated by

$$T \leftarrow \frac{1}{\lambda} [-\log(1 - U^{1/n})]^{1/\kappa}$$

This is clearly faster than generating n Weibull variates and returning the largest generated.

The algorithm below generates order statistics efficiently for a k-out-of-n system when a beta variate generator is available.

generate $X \sim \text{beta}(n - k + 1, k)$
 $T \leftarrow F^{-1}(X)$

The variate generated corresponds to $T_{(n-k+1)}$. Efficient algorithms for generating beta variates are given by Law and Kelton [25].

4. ACCELERATED LIFE AND PROPORTIONAL HAZARDS MODELS

The effect of covariates (explanatory variables) on survival often complicates the analysis of a set of lifetime data. In a medical setting, these covariates are usually patient characteristics such as age, gender, or blood pressure. In reliability, covariates (such as the turning speed of a machine tool or the stress applied to a component) affect the lifetime of an item. Two common models to incorporate the effect of the covariates on lifetimes are the *accelerated life* and *Cox proportional hazards* models. This section describes algorithms for the generation of lifetimes that are described by one of these models.

The $q \times 1$ vector \mathbf{z} contains covariates associated with a particular item or individual. The covariates are linked to

the lifetime by the function $\psi(\mathbf{z})$, which satisfies $\psi(\mathbf{0}) = 1$ and $\psi(\mathbf{z}) \geq 0$ for all \mathbf{z} . A popular choice is $\psi(\mathbf{z}) = e^{\beta^T \mathbf{z}}$, where β is a $q \times 1$ vector of regression coefficients.

The cumulative hazard function for T in the *accelerated life* model is [19]

$$H(t) = H_0(t\psi(\mathbf{z}))$$

where H_0 is a baseline cumulative hazard function. When $\mathbf{z} = \mathbf{0}$, then $H_0 \equiv H$. In this model, the covariates accelerate [$\psi(\mathbf{z}) > 1$] or decelerate [$\psi(\mathbf{z}) < 1$] the rate at which the item moves through time. The cumulative hazard function for T in the *proportional hazards* model is

$$H(t) = \psi(\mathbf{z})H_0(t)$$

In this model, the covariates increase [$\psi(\mathbf{z}) > 1$] or decrease [$\psi(\mathbf{z}) < 1$] the failure rate of the item by the factor $\psi(\mathbf{z})$ for all values of t.

All the algorithms for variate generation for these models are based on the fact that $H(T)$ is exponentially distributed with a mean of one. Therefore, equating the cumulative hazard function to $-\log(1 - U)$ and solving for t yields the appropriate generation technique.

In the accelerated life model, since time is being expanded or contracted by a factor $\psi(\mathbf{z})$, variates are generated by

$$T \leftarrow \frac{H_0^{-1}(-\log(1 - U))}{\psi(\mathbf{z})}$$

In the proportional hazards model, equating $-\log(1 - U)$ to $H(t)$ yields the variate generation formula

$$T \leftarrow H_0^{-1}\left(\frac{-\log(1 - U)}{\psi(\mathbf{z})}\right)$$

In addition to generating individual lifetimes, these variate generation techniques can be applied to point processes. A renewal process, for example, with time between events having a cumulative hazard function $H(t)$ can be simulated by using the appropriate generation formula for the two cases shown above. These variate generation formulas must be modified, however, to generate variates from a nonhomogeneous Poisson process (NHPP).

In an NHPP, the hazard function $h(t)$ is analogous to the intensity function, which governs the rate at which events occur. To determine the appropriate method for generating variates from an NHPP, assume that the last event in a point process has occurred at time a. The cumulative hazard function for the time of the next event, conditioned on survival to time a, is

$$H_{T|T>a}(t) = H(t) - H(a), \quad t \geq a.$$

Table 1. Lifetime Generation in Regression Models

	Renewal	NHPP
Accelerated life	$T \leftarrow a + \frac{H_0^{-1}(-\log(U))}{\psi(\mathbf{z})}$	$T \leftarrow \frac{H_0^{-1}(H_0(a\psi(\mathbf{z})) - \log(U))}{\psi(\mathbf{z})}$
Proportional hazards	$T \leftarrow a + H_0^{-1}\left(\frac{-\log(U)}{\psi(\mathbf{z})}\right)$	$T \leftarrow H_0^{-1}\left(H_0(a) - \frac{\log(U)}{\psi(\mathbf{z})}\right)$

In the accelerated life model, where $H(t) = H_0(t\psi(\mathbf{z}))$, the time of the next event is generated by

$$T \leftarrow \frac{H_0^{-1}(H_0(a\psi(\mathbf{z})) - \log(1 - U))}{\psi(\mathbf{z})}$$

Equating the conditional cumulative hazard function to $-\log(1 - U)$, the time of the next event in the proportional hazards case is generated by

$$T \leftarrow H_0^{-1}\left(H_0(a) - \frac{\log(1 - U)}{\psi(\mathbf{z})}\right)$$

An example of the application of these algorithms to a particular parametric distribution is given by Leemis [30], who later extended the case where the covariates are time-dependent [31,32]. Table 1 summarizes the variate generation algorithms for the accelerated life and proportional hazards models (the last event occurred at time a). The $1 - U$ has been replaced with U in this table to save a subtraction, although the sense of the monotonicity is reversed.

The renewal and NHPP algorithms are equivalent when $a = 0$ (since a renewal process is equivalent to an NHPP restarted at zero after each event), the accelerated life and proportional hazards models are equivalent when $\psi(\mathbf{z}) = 1$, and all four cases are equivalent when $H_0(t) = \lambda t$ (the exponential case) because of its memoryless property.

5. GENERATING A NONHOMOGENEOUS POISSON PROCESS

This section describes two techniques for generating event times for NHPPs. Homogeneous Poisson processes and renewal processes are not considered since they are a straightforward generalization of the inversion algorithms. An NHPP is often suggested as an appropriate model for the failure times of repairable systems whose rate of occurrence of failures varies over time, as outlined elsewhere [4,33–35]. The repair time must be negligible in order to use an NHPP to approximate the probabilistic mechanism governing the sequence of failures. The two techniques considered here are *inversion*, which relies on a timescale transformation given by Cinlar [36], and *thinning*, developed by Lewis and Shedler [22].

An NHPP is a generalization of an ordinary homogeneous Poisson process with events occurring randomly over time at the rate of λ . Events occur over time at a rate defined by the *intensity function* $\lambda(t)$. The *cumulative*

intensity function is defined by

$$\Lambda(t) = \int_0^t \lambda(\tau) d\tau, \quad t > 0$$

and is interpreted as the mean number of events by time t .

5.1. Inversion

For cases where $\Lambda(t)$ can be inverted in closed form, or when it can be inverted numerically, Cinlar [36] showed that if E_1, E_2, \dots are the event times in a homogeneous Poisson process with rate 1 (often called a *unit* Poisson process), then $\Lambda^{-1}(E_1), \Lambda^{-1}(E_2), \dots$ are the event times for an NHPP with cumulative intensity function $\Lambda(t)$. This is a generalization of the result that formed the basis for the inverse-chf algorithm. An algorithm for generating the event times T_1, T_2, \dots , for an NHPP with cumulative intensity function $\Lambda(t)$ is

```

T0 ← 0
E0 ← 0
i ← 0
repeat
    i ← i + 1
    generate U ~ U(0,1)
    Ei ← Ei-1 - log(1 - U)
    Ti ← Λ-1(Ei)
until Ti ≥ S
    
```

The algorithm returns the event times T_1, T_2, \dots, T_{i-1} , where S is a prescribed termination time of the point process. The algorithm is valid because $-\log(1 - U)$ is the appropriate way (via inversion) of generating an exponential variate with a mean of one. As before, replacing $1 - U$ with U reduces the CPU time.

Example 5. The cumulative intensity function is given by

$$\Lambda(t) = (\lambda t)^\kappa, \quad t > 0$$

often known as the *power-law process* [34]. If $\kappa > 1$, the population of items is deteriorating; if $\kappa < 1$, the population of items is improving; and if $\kappa = 1$, the NHPP simplifies to a homogeneous Poisson process. Since the inverse cumulative intensity function is

$$\Lambda^{-1}(y) = \frac{1}{\lambda} y^{1/\kappa}, \quad y > 0$$

the last statement in the loop becomes $T_i \leftarrow (1/\lambda)E_i^{1/\kappa}$.

The techniques for estimating the cumulative intensity function for an NHPP from one or more realizations is too broad a topic to be reviewed here. Examples of parametric and nonparametric techniques for estimation and generating realizations for simulation models are given in the literature [37–39], and the paper by Leemis [39], is illustrated in the following example.

Example 6. This example considers nonparametric estimation of the cumulative intensity function of an NHPP from

one or more realizations and the associated algorithm for generating random variates. This method does not require the modeler to specify any parameters or weighting functions.

The cumulative intensity function is to be estimated from k realizations of the NHPP on $(0, S]$, where S is a known constant. Let n_i ($i = 1, 2, \dots, k$) be the number of observations in the i th realization, $n = \sum_{i=1}^k n_i$, and let $t_{(1)}, t_{(2)}, \dots, t_{(n)}$ be the order statistics of the superposition of the k realizations, $t_{(0)} = 0$ and $t_{(n+1)} = S$. Setting $\hat{\Lambda}(S) = (n/k)$ yields a process where the expected number of events by time S is the average number of events in k realizations, since $\Lambda(S)$ is the expected number of events by time S . The piecewise linear estimator of the cumulative intensity function between the time values in the superposition is

$$\hat{\Lambda}(t) = \frac{in}{(n+1)k} + \frac{n(t - t_{(i)})}{(n+1)k(t_{(i+1)} - t_{(i)})},$$

$$t_{(i)} < t \leq t_{(i+1)}; i = 0, 1, 2, \dots, n.$$

This estimator passes through the points

$$\left(t_{(i)}, \frac{in}{(n+1)k} \right),$$

for $i = 1, 2, \dots, n + 1$.

The rationale for using a linear function between the data values is that inversion can be used for generating realizations without having tied events. If the usual step function estimate of $\Lambda(t)$ is used, only the $t_{(i)}$ values could be generated.

Using inversion, the event times from a unit Poisson process, E_1, E_2, \dots , can be transformed to the event times of an NHPP via $T_i = \Lambda^{-1}(E_i)$. For the NHPP estimate considered here, the events at times T_1, T_2, \dots can be generated for Monte Carlo simulation by the algorithm below, given n, k, S and the superpositioned values:

```

i ← 1
generate  $U_i \sim U(0,1)$ 
 $E_i \leftarrow -\log(1-U_i)$ 
while  $E_i < \frac{n}{k}$  do
  begin
     $m \leftarrow \lfloor \frac{(n+1)kE_i}{n} \rfloor$ 
     $T_i \leftarrow t_{(m)} + [t_{(m+1)} - t_{(m)}] (\frac{(n+1)kE_i}{n} - m)$ 
     $i \leftarrow i + 1$ 
    generate  $U_i \sim U(0,1)$ 
     $E_i \leftarrow E_{i-1} - \log(1 - U_i)$ 
  end
end
    
```

Thus, it is a straightforward procedure to obtain a realization of $i - 1$ events on $(0, S]$ from the superpositioned process and $U(0,1)$ values U_1, U_2, \dots, U_i . Inversion has been used to generate this NHPP, so certain variance reduction techniques, such as antithetic variates or common random numbers, may be applied to the simulation output. Replacing $1 - U_i$ with U_i in generating the exponential variates will save CPU time, although the direction of the monotonicity is reversed. Tied values in the superposition do not pose any problem to this algorithm, although there may be tied values in the realization. As n increases, the amount of

memory required increases, but the amount of CPU time required to generate a realization depends only on the ratio n/k , the average number of events per realization.

If the inverse cumulative intensity function is not available, but a majorizing intensity function can be found, then thinning can be used to generate variates.

5.2. Thinning

In describing the basic techniques for variate generation, thinning was adapted to generate a single lifetime. Thinning was originally devised to generate the event times for an NHPP [22]. Assume that a majorizing intensity function $\lambda^*(t)$ exists such that $\lambda^*(t) \geq \lambda(t)$ for all $t \geq 0$. The algorithm is

```

 $T_0 \leftarrow 0$ 
 $i \leftarrow 0$ 
repeat
   $i \leftarrow i + 1$ 
   $Y \leftarrow T_{i-1}$ 
  repeat
    generate  $U_1, U_2 \sim U(0,1)$ 
     $Y \leftarrow Y - \log(1 - U_1)$ 
  until  $U_2 \leq \lambda(Y)/\lambda^*(Y)$ 
   $T_i = Y$ 
until  $T_i \geq S$ 
    
```

If the inside loop condition is not met, then this particular Y value is “thinned” out of the point process and not included as a failure time in the realization. Choosing a majorizing function that is close to the intensity function $\lambda^*(t)$ results in fewer passes through the inside loop, and hence reduces CPU time. Guo and Love [40] have adapted this algorithm for the generation of variates when covariates are included in the model.

The discussion in this article has focused primarily on variate generation for various Monte Carlo applications in reliability. The estimation of unknown parameters from data is an equally important topic that has not been considered here. Several authors [41–43] provide sections on a facet of discrete-event simulation known as ‘input modeling’, where the estimation of parameters is considered. Finally, Fishman [44] presents a comprehensive work on Monte Carlo simulation without taking the reliability modeling perspective that has been taken here.

SYMBOLS

T	a continuous nonnegative random variable
\sim	“is distributed as”
$f(t), F(t), S(t)$	the pdf, cdf, and survivor function of T
$h(t), H(t)$	the hazard function, cumulative hazard function of T
U	a random number [i.e., a $U(0,1)$ random variable]
λ	scale parameter for an exponential distribution
λ, κ	scale and shape parameters for a Weibull distribution

\log	natural logarithm
Γ	the gamma function
$T_{(i)}$	order statistic i
\mathbf{z}	a $q \times 1$ vector of covariates
β	a $q \times 1$ vector of regression coefficients
$\psi(\mathbf{z})$	link function
$\lambda(t)$	intensity function
$\Lambda(t)$	cumulative intensity function
E_1, E_2, \dots	homogeneous Poisson process event times
T_1, T_2, \dots	event times for an NHPP

BIBLIOGRAPHY

- R. Hogg and A. Craig, *Introduction to Mathematical Statistics*, 5th ed., Prentice-Hall, Englewood Cliffs, NJ, 1995.
- E. Parzen, Nonparametric statistical data modeling, *J. Am. Stat. Assoc.* **74**(365):105–131 (1979).
- G. B. Swartz, The mean residual life function, *IEEE Trans. Reliabil.* **R-22**:108–109 (1973).
- H. Ascher and H. Feingold, *Repairable Systems Reliability*, Marcel Dekker, New York, 1984.
- R. E. Barlow, Geometry of the total time on test transform, *Naval Res. Log. Quart.* **26**:393–402 (1979).
- L. Devroye, *Non-Uniform Random Variate Generation*, New York: Springer-Verlag, 1986.
- J. Dagpunar, *Principles of Random Variate Generation*, Oxford Science Publications, Oxford, 1988.
- B. Schmeiser, Simulation experiments, in D. P. Heyman and M. J. Sobel, eds., *Stochastic Models*, North-Holland, 1990.
- S. K. Park and K. W. Miller, Random number generators: Good ones are hard to find, *Commun. ACM* **31**(10):1192–1201 (1988).
- P. L'Ecuyer, R. Simard, E. J. Chen, and W. D. Kelton, An object oriented random-number package with many long streams and substreams, *Op. Res.* **50**(6):1073–1075 (2002).
- J. W. Foster, D. T. Phillips, and T. R. Rogers, *Reliability, Availability and Maintainability*, M/A Press, Beaverton, OR, 1981.
- H. Goldberg, *Extending the Limits of Reliability Theory*, Wiley, New York, 1981.
- M. E. Harr, *Reliability-Based Design in Civil Engineering*, McGraw-Hill, New York, 1987.
- E. J. Henley and H. Kumamoto, *Reliability Engineering and Risk Assessment*, Prentice-Hall, Englewood Cliffs, NJ, 1981.
- L. M. Leemis, *Reliability: Probabilistic Models and Statistical Methods*, Prentice-Hall, Englewood Cliffs, NJ, 1995.
- N. R. Mann, R. E. Schafer, and N. D. Singpurwalla, *Methods for Statistical Analysis of Reliability and Life Data*, Wiley, New York, 1974.
- S. S. Rao, *Reliability Based Design*, McGraw-Hill, New York, 1992.
- R. E. Barlow and F. Proschan, *Statistical Theory of Reliability and Life Testing*, To Begin With, Silver Springs, MD, 1981.
- D. R. Cox and D. Oakes, *Analysis of Survival Data*, Chapman & Hall, London, 1984.
- L. M. Leemis and B. W. Schmeiser, Random variate generation for Monte Carlo experiments, *IEEE Trans. Reliabil.* **R-34**:1, 81–85 (1985).
- L. Devroye, Random variate generation in one line of code, *Proc. 1996 Winter Simulation Conf.*, J. M. Charnes, D. J. Morrice, D. T. Brunner, and J. J. Swain, eds., Coronado, CA, 1996, pp. 265–272.
- P. A. W. Lewis and G. S. Shedler, Simulation of nonhomogeneous Poisson processes by thinning, *Naval Res. Log. Quart.* **26**(3):403–413 (1979).
- N. L. Johnson, S. Kotz, and N. Balakrishnan, *Continuous Univariate Distributions*, Vol. 1, Wiley, New York, 1994.
- R. A. Grimlund, Generating statistically dependent pairs of random variables: A marginal distribution approach, *Eur. J. Op. Res.* **57**(1):39–53 (1992).
- A. M. Law and W. D. Kelton, *Simulation Modeling and Analysis*, 3rd ed., McGraw-Hill, New York, 2000.
- W. R. Schucany, Order statistics in simulation, *J. Stat. Comput. Simul.* **1**:281–286 (1972).
- J. S. Ramberg and P. R. Tadikamalla, On the generation of subsets of order statistics, *J. Stat. Comput. Simul.* **6**:239–241 (1978).
- B. W. Schmeiser, Generation of the maximum (minimum) value in digital computer simulation, *J. Statist. Comput. Simul.* **8**:103–115 (1978).
- B. W. Schmeiser, The generation of order statistics in digital computer simulation: A survey, *Proc. 1978 Winter Simulation Conf.*, Miami, 1978, pp. 137–140.
- L. M. Leemis, Variate generation for the accelerated life and proportional hazards models, *Op. Res.* **35**(6):892–894 (1987).
- L. M. Leemis, L. H. Shih, and K. Reynertson, Variate generation for the accelerated life and proportional hazards models with time dependent covariates, *Stat. Probabil. Lett.* **10**(1):335–339 (1990).
- L. H. Shih and L. M. Leemis, Variate generation for a nonhomogeneous Poisson process with time dependent covariates, *J. Comput. Simul.* **44**:165–186 (1993).
- I. B. Gertsbakh, *Reliability Theory with Applications to Preventive Maintenance*, Springer-Verlag, New York, 2000.
- S. E. Rigdon and A. P. Basu, *Statistical Methods for the Reliability of Repairable Systems*, McGraw-Hill, New York, 2000.
- S. M. Ross, *Simulation*, 3rd ed., Academic Press, New York, 2002.
- E. Cinlar, *Introduction to Stochastic Processes*, Prentice-Hall, Englewood Cliffs, NJ, 1975.
- S. Lee, J. R. Wilson, and M. M. Crawford, Modeling and simulation of a nonhomogeneous Poisson process with cyclic features, *Commun. Stat.-Simul. Comput.* **20**(2/3):777–809 (1991).
- S. E. Rigdon and A. P. Basu, The power law process: A model for the reliability of repairable systems, *J. Qual. Technol.* **21**(4):251–260 (1989).
- L. M. Leemis, Nonparametric estimation of the intensity function for a nonhomogeneous Poisson process, *Manage. Sci.* **37**(7):886–900 (1991).
- R. Guo and C. E. Love, Simulating nonhomogeneous Poisson processes with proportional intensities, *Naval Res. Log.* **41**(4):507–522 (1994).
- J. Banks, J. S. Carson, B. L. Nelson, and D. M. Nicol, *Discrete-Event System Simulation*, 3rd ed., Prentice-Hall, Englewood Cliffs, NJ, 2001.
- P. Bratley, B. L. Fox, and L. E. Schrage, *A Guide to Simulation*, 2nd ed., Springer-Verlag, New York, 1987.
- A. F. Seila, V. C. Vlatko, and P. Tadikamalla, *Applied Simulation Modeling*, Thompson/Brooks/Cole, Belmont, CA, 2003.
- G. Fishman, *Monte Carlo Simulation: Concepts, Algorithms, and Applications*, Springer-Verlag, New York, 1996.

MOSFET MODELING

R. S. GUPTA
University of Delhi South
Campus
New Delhi, India
MRIDULA GUPTA
University of Delhi South
Campus
New Delhi, India
MANOJ SAXENA
University of Delhi
New Delhi, India

1. MOSFET AND ITS SMALL-SIGNAL ANALYSIS

1.1. Introduction

In 1925 and 1926 J. E. Lilienfeld filed Canadian and U.S. patent applications entitled *Method and Apparatus for Controlling Electric Current* [1] disclosing a semiconductor device using a gate electrode. Interest in the insulated gate field-effect transistor (IGFET) was revived by the successful experiments of Attalla *et al.* [2] in 1959, in passivating silicon surfaces through the use of grown SiO₂ layers. Kahng and Attalla [3] in 1960 proposed a Si-SiO₂ structure in which a metal gate was used to induce conduction between two normally reversed biased surface diodes. This is known as the *metal oxide semiconductor field-effect transistor* (MOSFET), as shown in Fig. 1.

In VLSI circuits, the MOSFET plays an important role because of its low fabrication cost, small size, and low power consumption. The important characteristics of a MOS transistor are bilateral symmetry, unipolarity, high input impedance, voltage controllability, and self-isolation. The property of bilateral symmetry render the source and the

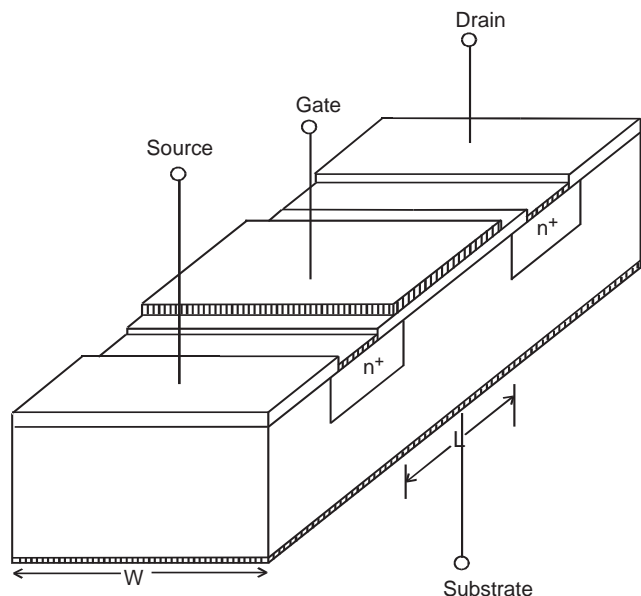


Figure 1. Three-dimensional view of MOSFET.

drain electrically interchangeable. Unipolarity allows conduction exclusively via one type of carriers. The input impedance is also high because of the gate oxide. There is no DC path between the gate and the other terminals. The input impedance is then extremely high and is primarily capacitive. Its DC resistance is greater than $10^{14} \Omega$, and it is a voltage-controlled device. At the beginning of the semiconductor era, manufacturers concentrated on the germanium devices, but the emphasis soon shifted to silicon, and it was on silicon substrates that the integrated circuit (IC) was developed. IC development has taken place in two main streams: bipolar and MOS technologies. At the outset, bipolar technology seemed to provide the most promising approach to fast logic arrays, but MOS technology holds the promise of higher levels of integration and the latest high-speed operation.

More recent developments in MOS technology include a large variety of new device architectures proposed to greatly improve MOS speed while retaining its high packing density. Thin-film fully depleted (FD) SOI (silicon on insulator) MOSFET is one promising option. The absence of latchup, the reduced parasitic source and drain capacitances, and the ease of forming shallow junctions are merely three obvious examples of the advantages presented by SOI technology over bulk. There are many other properties that allow SOI devices and circuits to exhibit performances superior to those of their bulk counterparts such as radiation hardness, high-temperature operation, improved transconductance, and subthreshold slope. The thin-film SOI can easily overcome many of the hurdles faced in implementation and isolation of the devices. As the scaling of the MOS transistor approaches the submicrometer regime, FD-SOI MOSFET, which shows no kink effect and has excellent short-channel effects (SCEs), seems to be a good alternative device structure [4].

According to the ITRS roadmap 2001, several new device features such as nonplanar or elevated S/D (source/drain) structures, strained heterostructures in the channel, vertical FETs, and other double-gate (DG) or a surrounding gate are viable alternatives to bulk CMOS for gate lengths down to 20 nm. However, due to complicated and innovative processing technology for DG-MOSFET, single-gate FD-SOI CMOS is a viable option.

Advances in process technology and device design has allowed Si-MOSFET to be applied successfully to RF circuits. To expedite VLSI circuit design and reduce manufacturing cost, it is important to model and predict circuit behavior in the early stages of technology development. For today's competitive analog designs, accurate DC and high-frequency (HF) AC models are needed. Modeling of parasitic elements and certain key issues such as low-frequency (LF) noise, generation-recombination (GR) noise, and noise at RF level is required to be incorporated in equivalent circuit. In this article small-signal analysis for Si-MOSFET with respect to the substrate effect is presented first. Modified expressions of power gain after incorporating the substrate effect are reported. In the next portion of the article, a drain current and capacitance model is developed after incorporating the fringing field effect. An equivalent circuit including the fringing field effect and gate inductance has a definite advantage of

physical significance to predict the admittance parameters. When the device length shortens, channel length modulation (CLM) takes place and increases the output conductance. Therefore, the CLM effect cannot be neglected. In the latter portion of the article, admittance and scattering parameters are derived after incorporating the CLM effect. Simple expressions of transconductance, scattering parameters, and power gain are presented incorporating the distributed gate inductance and the fringing field effects.

To achieve the VLSI goals of higher density and greater performance, MOSFET channel lengths continue to be reduced. However, hot-electron effects become more severe as channel length decrease. In order to reduce the hot-carrier effect, different drain engineered structures such as the lightly doped drain (LDD) and fully overlapped/lightly doped drain (FOLD) have been proposed. In FOLD structure, overlapping of the LDD region with the gate electrode is done to reduce the peak electric field; therefore this type of structure is not susceptible to spacer-enhanced degradation. The series parasitic resistance of FOLD structure is less than that of conventional LDD of equal reliability. Therefore, a two-dimensional analytical model to determine the intrinsic drain-source series resistance of FOLD MOSFET along with the I-V characteristics, drain conductance, transconductance, and cutoff frequency of the device has been discussed. In the concluding part of the article, a low-frequency (LF) noise model and generation-recombination (GR) model of FOLD MOSFET incorporating the voltage drop in the n^- region due to the parasitic resistance is studied.

1.2. RF MOSFET Modeling

The scaling of MOS devices has reduced channel length and/or width to submicrometer ranges. This reduction in device size has improved the circuit speed and increased circuit density. As these devices are scaled, various second-order effects such as fringing field effect, substrate effect, velocity saturation, and hot-carrier effect have come into existence. The enhanced performance of a device includes faster switching speed, lower power dissipation, and less circuit area. In developing a new device, modeling is very relevant when a totally new device concept is being developed or when an existing device is to be extended for a new task. The device model describes the terminal behavior of a device in terms of current-voltage, capacitance-voltage characteristics, and the carrier transport process, which takes place within the device. The models thus reflect device behavior in all regions of operations of the device [5]. Because of the 2D and 3D nature of the physical effects governing electrical behavior of a VLSI MOS transistor, it is very difficult to obtain closed-form analytical formulation, which is valid in all regions of operation. However, it is still possible to obtain closed-form analytical models, based on device physics, which are generally valid over a limited region of device operation.

Despite this limitation, such models are becoming increasingly important because of ease of computation. The models are categorized as (1) physical device models and (2) equivalent-circuit models. Physical device models can

be used to predict both terminal characteristics and transport phenomenon. The equivalent circuit models describe electrical properties of the device by connecting electrical circuit elements in such a way that the model simulates the electrical terminal behavior of the device [6]. The device model to be used in a circuit simulator should be accurate and simple so that it simulates actual transistor behavior over all regions of operation of interest.

1.3. Equivalent Circuit and Frequency Response

MOS transistors are by nature distributed elements. At present, most MOS circuits are designed as lumped-parameter systems, with the devices assumed to exhibit quasistatic behavior [7]. However, a careful look at the nonquasistatic behavior, RF operation of the MOS transistor is justifiable. The frequency response of a MOS device on the inversion region depends on the rate at which minority carriers can be supplied to, or removed from, the inversion region. In principle, at least, there appear to be a number of possible mechanisms [8–12] by which minority carriers can be supplied or removed when an AC source is applied, such as (1) generation-recombination (GR) centers within the depletion region, (2) changes in surface state occupancies, and (3) diffusion of minority carriers to and from the undepleted portions of the semiconductor. For n-type devices or p-type silicon devices in which care is taken to remove any oxide not covered by the metal gate for which the equivalent interface charge remains independent of bias, it appears that mechanism 1—generation-recombination within the depletion region—predominates. Measurements by Grove *et al.* [13] on both n- and p-type silicon devices have shown that the observed transition frequency to low-frequency type characteristics occurs at about 50 Hz for room-temperature conditions. Observations on the temperature dependence of the transition frequency indicate that the major source of generation-recombination corresponds to impurity centers having an activation energy equal to approximately half of the total bandgap. This is discussed by Sah *et al.* [14] as corresponding to the most effective energy level for GR within a space charge layer. Order-of-magnitude calculations [13–15] based on this mechanism yield a transition frequency very close to that observed. Hence it can be concluded that for this ideal form of MOS structure, mechanism 1 predominates.

For p-type silicon devices in which the oxide layer extends over an area greater than the metal gate area, the transition frequency between the two types of capacitance characteristics is often observed to be many orders greater than 100 Hz. The reason for this is that the positive oxide charge induces an inversion layer in all regions underlying the oxide, including those not covered by the metal.

The inversion layer can be considered as consisting of two parts: an intrinsic portion lying directly beneath the metal and an extrinsic portion consisting of those areas of the semiconductor covered by the oxide but not by the metal [10–12]. Usually, highly doped polysilicon is used as a material for making a gate in MOSFET, but insufficiently high doping in polysilicon gates becomes inevitable in modern CMOS process. But there is conflict in

requirements for low-energy ion implantation and various annealing conditions to achieve ultrashallow junctions. This results in a polydepletion width effect [16] in ultrathin oxide MOSFETs and as the polydepletion capacitance along with the oxide capacitance causes degradation of the inversion gate capacitance and transconductance. Further, metallic gates eliminate the polydepletion problem as well as boron penetration [17] through the gate oxide. Conventional alternative to amorphous silicon such as poly-SiGe or fine-grain columnar poly-Si seems to be a more promising option for 0.1–0.08 μm generation. Beyond these dimensions, metallic gates and high- K dielectrics seem to be mandatory as a result of gate leakage, boron penetration, polydepletion width effect, and oxide reliability [18].

1.3.1. Low-Frequency (LF) Characteristics. At low frequencies all circuit elements are lumped, since their physical dimensions are negligible compared with the wavelength of electromagnetic signals inside the components. In such a network, since Kirchhoff's voltage and current relationships are applicable, the current within any branch is the same at all points of the branch between its terminating nodes, and the voltage along any perfect conductor is constant and changes only at the components [19].

1.3.2. High-Frequency (HF) Characteristics. At higher frequencies, if the signal wavelength becomes comparable to the physical dimension of the components, then the spatial variations of voltages and currents along the wires and in the components must be considered. In such circuits, called *distributed networks*, Kirchhoff's laws are no longer valid and Maxwell's laws must be applied [20,21]. Another very important aspect of MOSFET is its RF and switching performance [22,23].

1.4. Small-Signal Analysis with Bulk Substrate Resistance Effect

Several methods of calculating the small-signal characteristics of JFET and MOSFET have been reported in the literature. These include the approximate power series [24,25] method and the exact [26–30] functional and computer method of solving the basic channel differential equations, and also the matrix method [31–35] of RC transmission-line analog solutions. Park *et al.* [36], Bagheri and Tsividis [37] and Das [38] did some work on modeling the distributed parameters along the channel length in which channel inductance was introduced. However, these models do not incorporate the distributed gate effect. In a model presented by Kim and Dutton [39] and Razavi *et al.* [40], the distributed nature of the gate region was modeled by treating the transistor as an array of smaller transistors connected together via a resistive gate.

Allam and Manku [41] presented a small-signal model for an integrated MOS transistor, which took into account the distributed nature of the gate structure. But they didn't consider the effect of gate inductance in their analysis from 0.1- to 1.0-GHz applications. The presence of a small bulk substrate resistance can cause an indirect excitation of the substrate, which can modify the overall

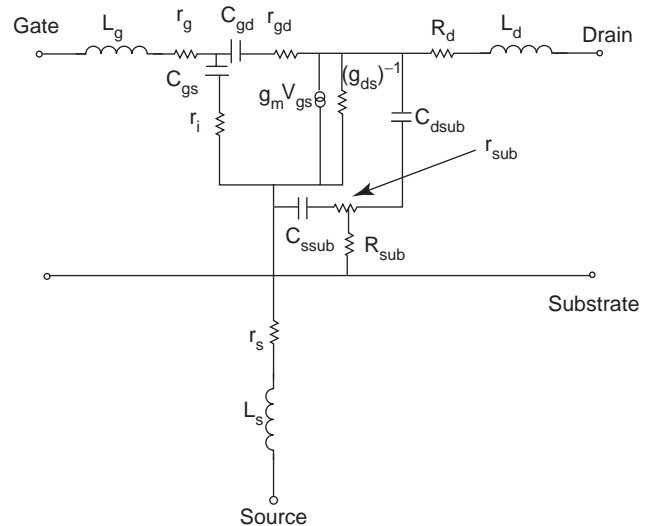


Figure 2. Equivalent circuit of MOSFET for small-signal analysis.

device characteristics. The equivalent circuit shown in Fig. 2 clearly indicates the influence of the substrate properties on frequency performance [42].

If an epitaxial active substrate layer is used on a very-low-resistivity bulk substrate material, the element R_{sub} can become negligible. Under these circumstances the contributions of the transfer admittance parameters Y_{13} and Y_{23} can be ignored when the source and substrate are short-circuited, but do not eliminate the physical substrate effects on admittance parameters Y_{21} and Y_{11} . The gate bulk capacitance, C_{gb} incorporated into C_{gs} for the same reason. Goswami *et al.* [42] developed a substrate-effect-dependent scattering parameter extraction of short-gate-length insulated gate field-effect transistor (IGFET) for microwave frequency applications in which the gate to drain capacitance has been considered only to evaluate admittance (Y) parameters. The expressions for Y parameters include the substrate effect on the device RF performance, and the new element added to this equivalent circuit is C_{sub} , which includes the effect of substrate.

The lossy element g_{bd} (substrate–drain conductance) has been neglected because of its reduced value in more recent technologies. The effect of channel charging resistance r_i and the gate–drain resistance r_{gd} are included in the analysis in addition to the well-known lumped elements. The drain–substrate capacitance (C_{dsub}) and source–substrate capacitance (C_{ssub}) will be in parallel when R_{sub} is taken to be negligible due to a very-low-resistivity bulk substrate material.

The variation of Y_{11} with frequency, including the substrate effect for devices with different dimensions ($L = 0.4 \mu\text{m}$ and $L = 1.6 \mu\text{m}$) is shown in Figs. 3a and 3b, respectively. For a given frequency, Y_{11} is greater when the substrate effect is taken into account. This is because with substrate effect the channel potential increases, leading to increase in the depletion layer width and thus reducing the capacitance. For a short-gate-length device, the substrate effect is more prominent because the capacitance is lower in comparison to large gate length. The value of Y_{11} is less for

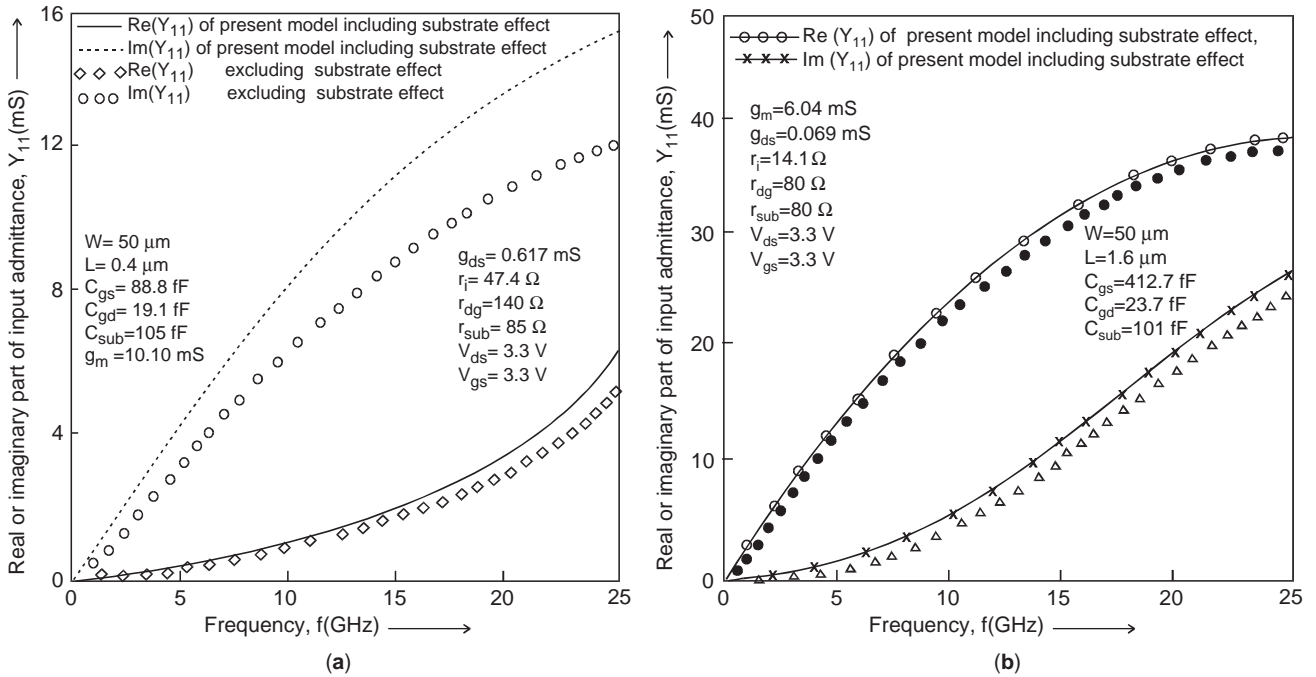


Figure 3. (a) Variation of input admittance parameter with frequency [$\diamond\diamond\diamond\diamond$ —Re (Y_{11}) of Ref. 43 excluding the substrate effect; $\circ\circ\circ\circ$ —Im (Y_{11}) of Ref. 43 excluding the substrate effect]; (b) variation of input admittance parameter with frequency [$\bullet\bullet\bullet\bullet$ —Re (Y_{11}) of Ref. 43 excluding the substrate effect; $\triangle\triangle\triangle\triangle$ —Im (Y_{11}) of Ref. 43 excluding the substrate effect].

short gate length because of decrease in capacitance. The reverse transfer admittance (Y_{12}) with and without the substrate effect shows a similar variation with frequency as without considering the substrate and can be seen in

Figs. 4a and 4b, respectively. Figure 5 shows variations of the forward transfer admittance parameter (Y_{21}), which is one of the important parameters used to calculate the gain of a device with frequency for the two different devices.

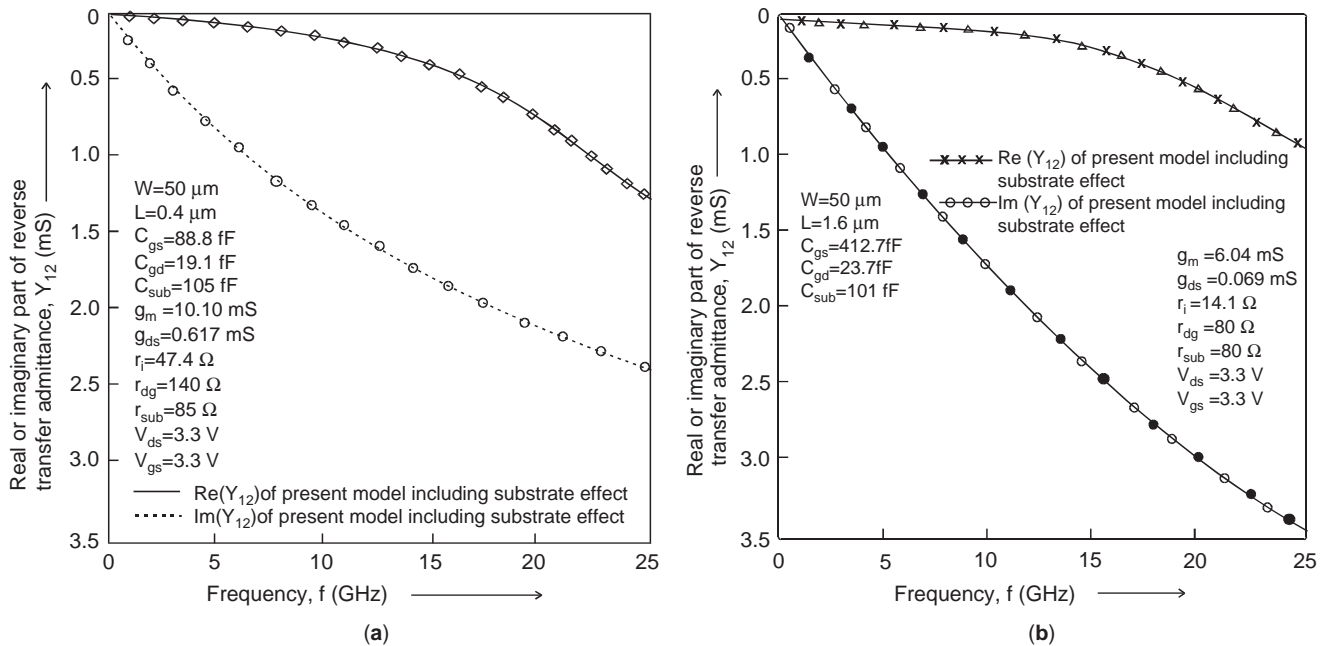


Figure 4. (a) Variation of reverse transfer admittance parameter with frequency [$\diamond\diamond\diamond\diamond$ —Re (Y_{12}) of Ref. 43 excluding the substrate effect; $\circ\circ\circ\circ$ —Im (Y_{12}) of Ref. 43 excluding the substrate effect]; (b) variation of reverse transfer admittance parameter with frequency [$\bullet\bullet\bullet\bullet$ —Re (Y_{12}) of Ref. 43 excluding the substrate effect; $\triangle\triangle\triangle\triangle$ —Im (Y_{12}) of Ref. 43 excluding the substrate effect].

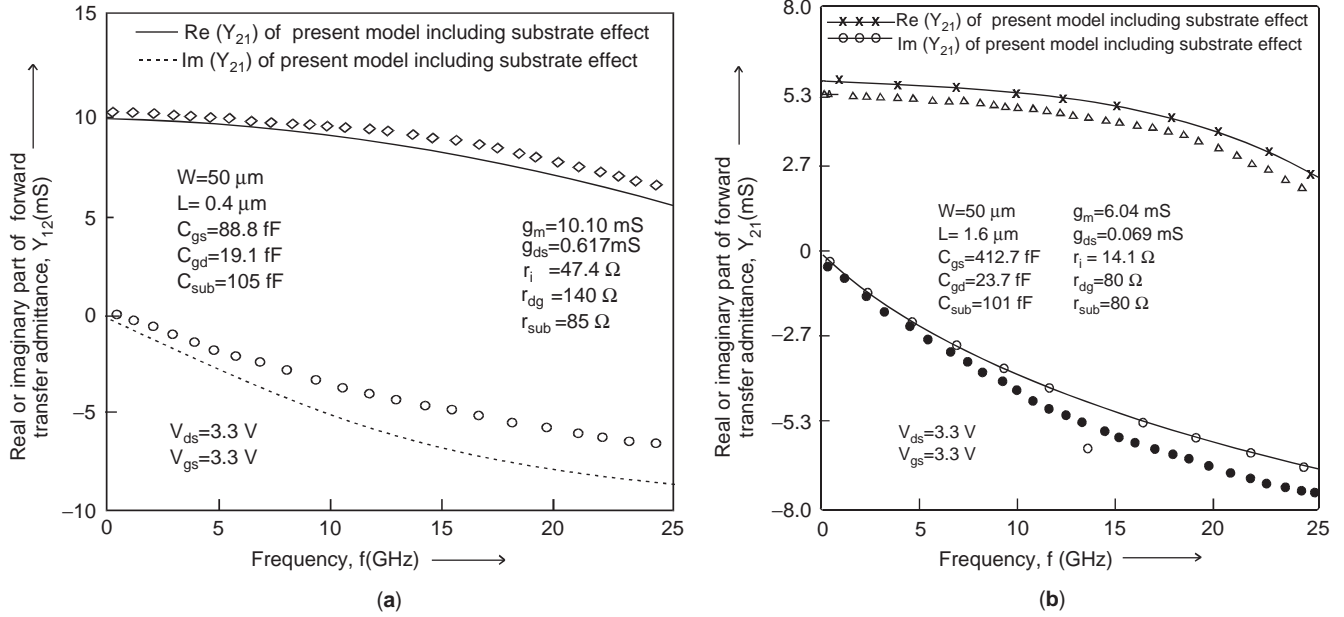


Figure 5. (a) Variation of forward transfer admittance parameter with frequency [$\diamond \diamond \diamond \diamond$ — $\text{Re}(Y_{21})$ of Ref. 43 excluding the substrate effect; $\circ \circ \circ \circ$ — $\text{Im}(Y_{21})$ of Ref. 43 excluding the substrate effect]; (b) shows variation of forward transfer admittance parameter with frequency [$\bullet \bullet \bullet \bullet$ — $\text{Im}(Y_{21})$ of Ref. 43 excluding the substrate effect; $\triangle \triangle \triangle \triangle$ — $\text{Re}(Y_{21})$ of Ref. 43 excluding the substrate effect].

Figure 5a shows that at a given frequency the value of the forward transfer admittance parameter (Y_{21}) incorporating the substrate effect is less, in comparison with excluding the substrate effect. This is because the substrate effect capacitance decreases, thereby increasing the channel charging resistance. At a given frequency it is observed that Y_{21} is less for short gate length because with decreasing gate length, gate–source capacitance decrease, thereby increasing the gate–source resistance, which in turn decreases Y_{21} . In case of Fig. 5b, the phenomenon is reverse for large gate length. At very high frequencies, Y_{21} decreases because of the decrease in time constant (resistance and capacitance).

The variations of output admittance Y_{22} with frequency is shown in Figs. 6a and 6b for different devices. It is observed that with the substrate effect one gets the lower value of Y_{22} at a given frequency because of decrease in depletion-layer capacitance as well as substrate capacitance.

1.5. Scattering Parameters

For a two-port network, the z, h parameters cannot be measured accurately at higher frequencies because the required short-and open-circuit tests are difficult to achieve over a broadband range of microwave frequencies. A set of parameters that is very useful in the microwave range is the scattering parameters (S parameters) [44,45]. The S parameter of short-gate-length IGFET for microwave frequency applications is required and as reported in Ref. 42, the equivalent-circuit model is scalable since all its elements have physical significance and new elements

added to this model are inclusive of the substrate effect, the overlap effect, the fringing field effect, and the effect of gate and drain contact pads. The final expressions of the various S parameters on the basis of Ref. 42 are discussed below. The S_{11} is given as

$$S_{11} \frac{b_1}{a_1} \Big|_{a_2=0} = \frac{\left\{ \frac{1 + s(C_{gd} + C_{gs})(r_i - 1) + sC_{gs}r_i(1 - sC_{gd})}{1 + s(C_{gd} + C_{gs})r_i + sC_{gs}r_i} \right\} A_2 + \frac{A}{B}}{\left\{ \frac{1 + s(C_{gd} + C_{gs})(r_i + 1) + sC_{gs}r_i(1 + sC_{gd})}{1 + s(C_{gd} + C_{gs})r_i + sC_{gs}r_i} \right\} A_2 - \frac{A}{B}} \quad (1a)$$

where

$$A = (1 + C_{gd}r_{gd})[-sC_{gd}g_m - s^2C_{gd}^2g_mr_{gd} + s^2C_{gd}^2 + s^3C_{gd}^2C_{gs}r_i] \quad (1b)$$

$$A_1 = \{1 - s^2C_{sub}^2r_{sub}(r_{sub} + r_0)\}(1 + sC_{gd}r_0) \quad (1c)$$

$$A_2 = \frac{F\{r_0 - (sC_{sub}r_{sub})^2r_0\} + A_1 + sC_{gd}r_0 - s^3C_{gd}^2C_{sub}^2r_{sub}^2r}{r_0F - s^2C_{sub}^2r_{sub}^2C_{gd}r_0 - s^3C_{sub}^2r_{sub}^2C_{gd}r_{dg}r_0} \quad (1d)$$

$$B = (1 + sC_{gd}r_{gd})^3(1 + sC_{gs}r_i) \quad (1e)$$

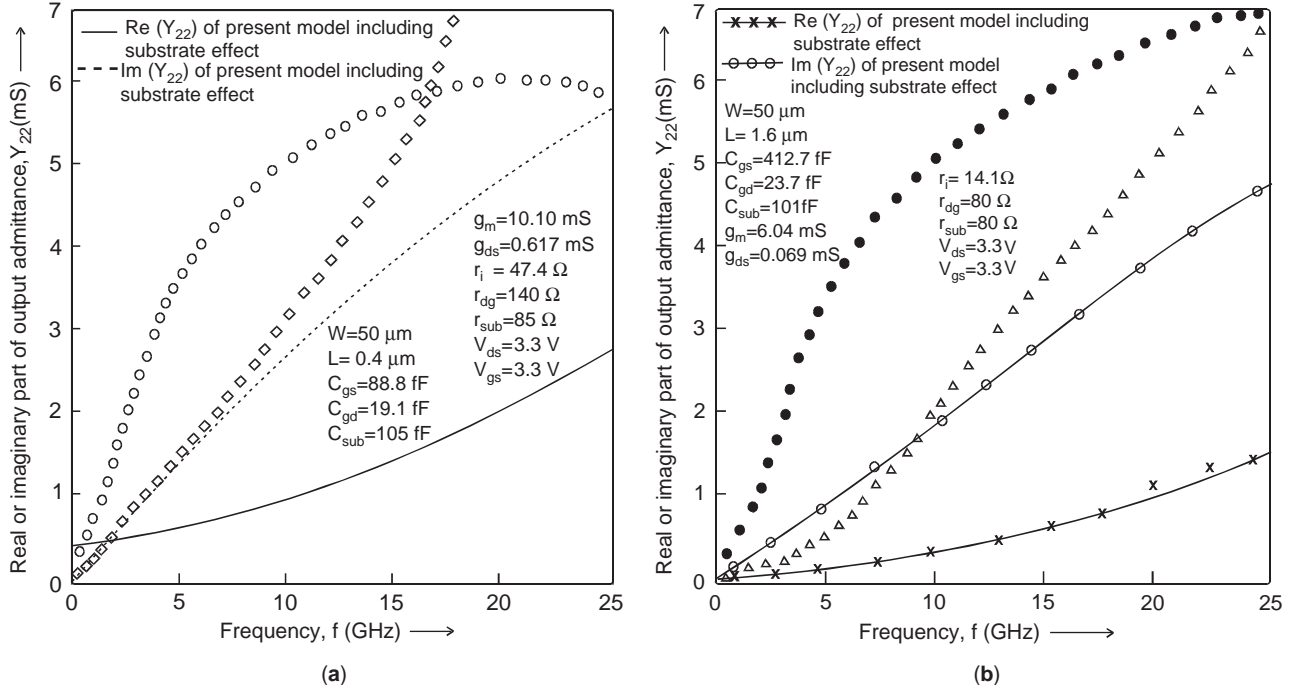


Figure 6. (a) Variation of output admittance parameter with frequency [$\diamond \diamond \diamond \diamond$ — $\text{Re}(Y_{22})$ of Ref. 43 excluding the substrate effect; $\circ \circ \circ \circ$ — $\text{Im}(Y_{22})$ of Ref. 43 excluding the substrate effect]; (b) variation of output transfer admittance parameter with frequency [$\bullet \bullet \bullet \bullet$ — $\text{Im}(Y_{22})$ of Ref. 43 excluding the substrate effect; $\triangle \triangle \triangle \triangle$ — $\text{Re}(Y_{22})$ of Ref. 43 excluding the substrate effect].

The reverse transmission scattering coefficient (S_{12}) is given as

$$S_{12} = \frac{b_1}{a_2} \Big|_{a_1=0} = \frac{\frac{2sC_{gd}}{1+sC_{gd}r_{gd}}}{\left\{ \frac{1+s(C_{gd}+C_{gs})(r_i+1)+sC_{gs}r_i(1+sC_{gd})}{1+s(C_{gd}+C_{gs})r_i+sC_{gs}r_i} \right\} (C/D) - C_1} \quad (2a)$$

$$C = (1 + C_{gd}r_{dg}) + \{1 - s^2C_{sub}^2r_{sub}(r_{sub} + r_0)\}(1 + sC_{gd}r_0) + sC_{gd}r_0 - s^3C_{gd}C_{sub}^2r_{sub}^2r \quad (2c)$$

$$D = (1 + sC_{gd}r_{dg}) - s^2C_{sub}^2r_{sub}^2C_{gd}r_0 - s^3C_{sub}^2r_{sub}^2C_{gd}r_{dg}r_0 \quad (2d)$$

The forward transmission scattering coefficient (S_{21}) is given as

$$S_{21} = \frac{b_2}{a_1} \Big|_{a_2=0} = \frac{2g_m F - sC_{gd}(1 + sC_{gs}r_0)}{\{(1 + sC_{gs})F\} \left\{ \frac{1 + s(C_{gd} + C_{gs})(r_i + 1) + sC_{gs}r_i(1 + sC_{gd})}{1 + s(C_{gd} + C_{gs})r_i + sC_{gs}r_i} \right\} E - E_1} \quad (3a)$$

where

where

$$E = \frac{(1 + sC_{gd}r_{dg}) + \{1 - s^2C_{sub}^2r_{sub}(r_{sub} + r_0)\}(1 + sC_{gd}r_0) + sC_{gd}r_0 - s^3C_{gd}C_{sub}^2r_{sub}^2r}{r_0(1 + sC_{gd}r_{dg}) - s^2C_{sub}^2r_{sub}^2C_{gd}r_0 - s^3C_{sub}^2r_{sub}^2C_{gd}r_{dg}r_0} \quad (3b)$$

$$C_1 = \frac{F \{ sC_{gd}g_m - s^2C_{gd}^2g_m r_{gd} + s^2C_{gd}^2 + s^3C_{gd}^2C_{gs}r_i \}}{F^3(1 + sC_{gs}r_i)} \quad (2b)$$

$$E_1 = \frac{FC}{F - s^2C_{sub}^2r_{sub}^2C_{gd}r_0 - s^3C_{sub}^2r_{sub}^2C_{gd}r_{dg}r_0} \quad (3c)$$

$$F = 1 + sC_{gd}r_{gd} \quad (3d)$$

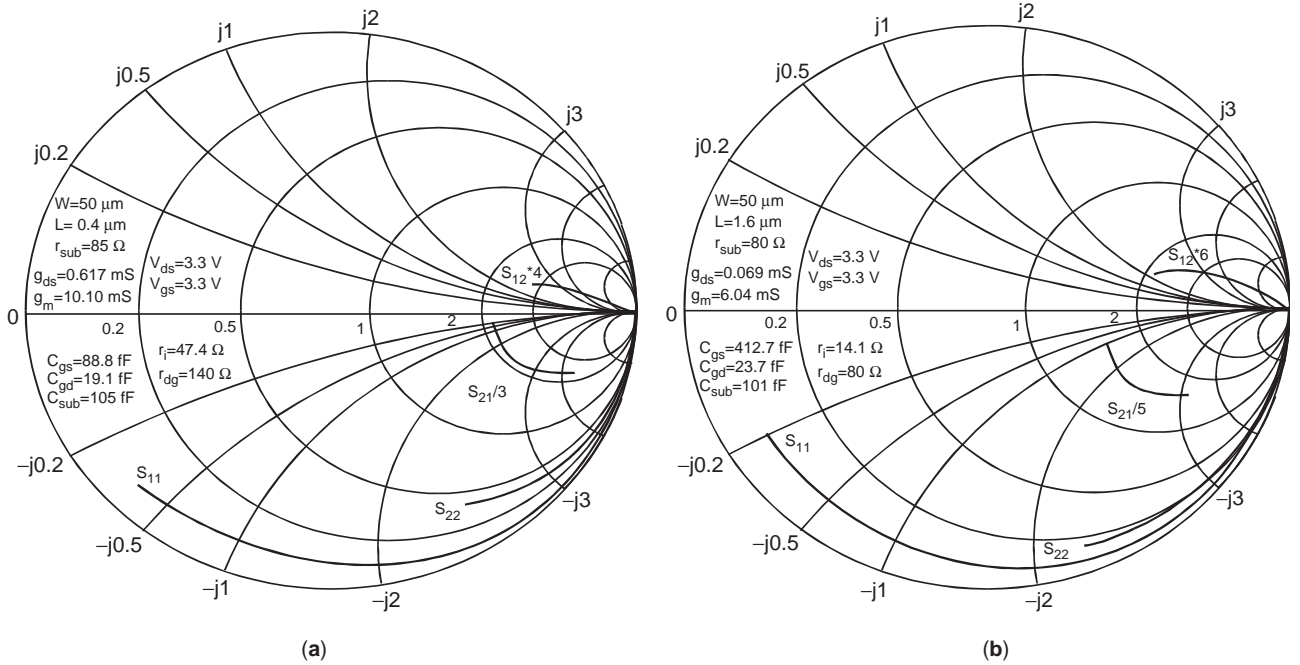


Figure 7. Variation of S parameter for (a) short-gate-length and (b) larger-gate length MOSFETs.

The output reflection scattering coefficient (S_{22}) is given as

$$S_{22} = \left. \frac{b_2}{a_2} \right|_{a_1=0}$$

$$= \frac{\left\{ \frac{1 + s(C_{gd} + C_{gs})(r_i + 1) + sC_{gs}r_i(1 + sC_{gd})}{1 + s(C_{gd} + C_{gs})r_i + sC_{gs}r_i} \right\} G_1 + A/B}{\left\{ \frac{1 + s(C_{gd} + C_{gs})(r_i - 1) + sC_{gs}r_i(1 - sC_{gd})}{1 + s(C_{gd} + C_{gs})r_i + sC_{gs}r_i} \right\} G_2 - \frac{A}{B}}$$

(4a)

where

$$G = s^2 C_{sub}^2 r_{sub}^2 C_{gd} r_0 + S^3 C_{sub}^2 r_{sub}^2 C_{gd} r_0 r_{gd} \tag{4b}$$

$$G_1 = \frac{r_0 F - G - FH + sC_{gd} \{r_0 - (sC_{sub} r_{sub})^2 r_0\}}{F \{r_0 - (sC_{sub} r_{sub})^2 r_0\}} \tag{4c}$$

$$G_2 = \frac{F \{r_0 - (sC_{sub} r_{sub})^2 r_0\} + A \times 1 + sC_{gd} r_0 - s^3 C_{gd} C_{sub}^2 r_{sub}^2 r}{r_0 F - s^2 C_{sub}^2 r_{sub}^2 C_{gd} r_0 - s^3 C_{sub}^2 r_{sub}^2 C_{gd} r_{dg} r_0} \tag{4d}$$

$$H = 1 - s^2 C_{sub}^2 r_{sub} (r_{sub} + r_0) + sC_{gd} r_0 \tag{4e}$$

For a given frequency, the imaginary part of Y_{22} for larger gate length ($L = 1.6 \mu\text{m}$) is greater than that for a shorter gate length ($L = 0.4 \mu\text{m}$) because C_{gd} and $r_0 [(g_{ds})^{-1}]$ for $L = 1.6 \mu\text{m}$ are more. But the real part of Y_{22} for $L = 0.4 \mu\text{m}$ is more than that of $L = 1.6 \mu\text{m}$ because r_{sub} is more for $L = 0.4 \mu\text{m}$. The scattering parameters are evaluated from admittance parameter, and their variations with frequency are shown in Figs. 7a and 7b for two different devices

with the substrate effect. The reflection scattering coefficient at port 1 (S_{11}) and the reflection scattering coefficient at port 2 (S_{22}) are less for short gate length ($L = 0.4 \mu\text{m}$) than for large gate length ($L = 1.6 \mu\text{m}$) because the input admittance (Y_{11}) and the reverse transfer admittance (Y_{12}) for short gate length are less than those for the large gate length.

Similarly, S_{21} and S_{12} for large gate length ($L = 1.6 \mu\text{m}$) are more than those for the short gate length ($L = 0.4 \mu\text{m}$). As the channel length decreases, the incident and reflected scattering parameters reduce but the variation in transmitted S parameters decreases.

1.6. Power Gain

Several definitions of power gain are important in the design of amplifiers. Consider the power flow from the generator to load as shown in Fig. 8, where M_1 and M_2 are lossless matching networks.

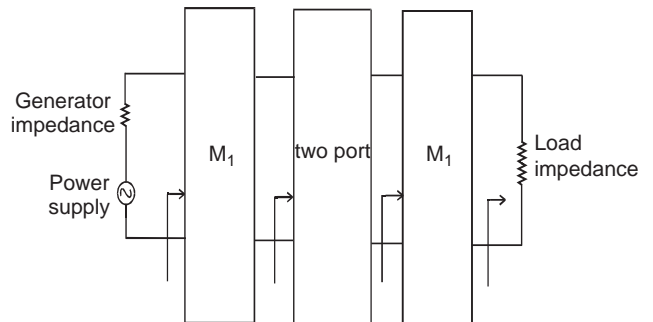


Figure 8. Available power and actual power for a two-port connected to a generator and a load.

The maximum stable power gain is given by

$$G_{ms} = \frac{|S_{21}|}{|S_{12}|} \quad (5)$$

This is the gain that can be achieved by resistively loading the two-port such that the stability factor (K) is unity and then simultaneously conjugately matching the input and output ports. For conditionally stable two-ports, the maximum stable gain is an upper limit in power gain that can be approached only as the input and output mismatch is reduced. If a simultaneous conjugate match is attempted, the two-port will oscillate if $K < 1$.

The unilateral power gain, which is the maximum available power gain when the two-ports are simultaneously conjugately matched and the two feedback parameters have been neutralized, has been developed. The conditions for unilateral gain are indicated in Fig. 9.

The unilateral power gain U_g , which is the maximum available power gain when the two ports are simultaneously conjugate-matched and the two feedback parameters have been neutralized, can be expressed in terms of S parameters [42] and is given as

$$U_g = \frac{\left[\frac{2g_m F - sC_{gd}(1 + sC_{gs}r_0)}{2sC_{gd}/(1 + sC_{gd})} - 1 \right]^2}{2K \left| \frac{2g_m F - sC_{gd}(1 + sC_{gs}r_0)}{2sC_{gd}/(1 + sC_{gd})} \right| - \operatorname{Re} \left(\frac{2g_m F - sC_{gd}(1 + sC_{gs}r_0)}{2sC_{gd}/(1 + sC_{gd})} \right)} \quad (6)$$

where K is the stability factor, given as

$$K = \frac{1 - |S_{11}|^2 - |S_{22}|^2 + |D|^2}{2|S_{12}| |S_{21}|} \quad \text{and } D = S_{11}S_{22} - S_{12}S_{21} \quad (7)$$

This gain is the highest possible gain that the active two-port could ever achieve. The frequency where the

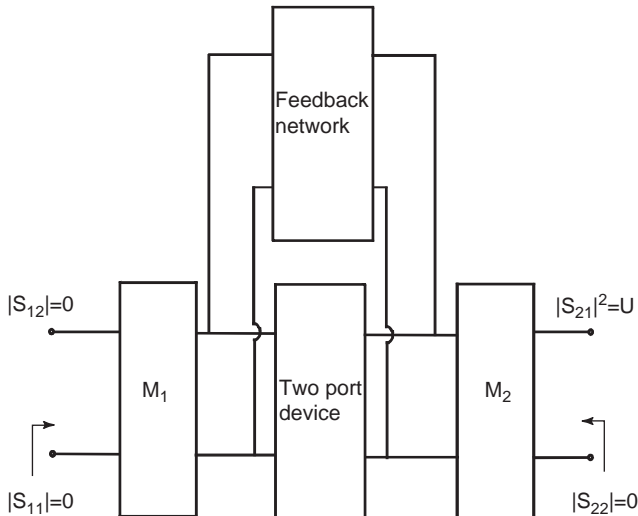


Figure 9. Condition for unilateral power gain.

unilateral gain becomes unity defines the boundary between an active and a passive network. This frequency is usually known as the *frequency of oscillation*. The maximum unilateral transducer power (G_{TUmax}), and unilateral figure of merit (U) are

$$G_{TU \max} = \frac{|S_{21}|^2}{(1 - |S_{11}|)^2(1 - |S_{22}|)^2} \quad (8a)$$

$$U = \frac{|S_{11}||S_{12}||S_{22}||S_{21}|}{(1 - |S_{11}|^2)(1 - |S_{22}|^2)} \quad (8b)$$

Figures 10a and 10b predict the variations of different gains and unilateral figure of merit with frequency. As the frequency increases, the power gain decreases for both devices. This is due to the decrease in admittance. For a given frequency the power gain for short gate length ($L = 0.4 \mu\text{m}$), as shown in Fig. 10a, is more than for large gate length ($L = 1.6 \mu\text{m}$), as shown in Fig. 10b, and is due to increase in transconductance. The power loss in the short-gate-length device is less than that in the large-gate-length device. The unilateral figure of merit is more for short-gate-length device, and the device becomes more unilateral when the gate length decreases.

Therefore, it can be concluded that as the gate length is reduced, the performance in the power gain increases. This shows that the circuits with small-gate-length devices are useful for microwave frequency applications.

2. SMALL-SIGNAL ANALYTICAL MOSFET MODEL WITH FRINGING FIELD EFFECT

2.1. Introduction

The design of analog and radiofrequency (RF) circuits in CMOS technology becomes increasingly difficult as device modeling faces new challenges in submicrometer processes and emerging circuit applications [46,47]. As the device geometry shrinks, various effects such as the reverse short-channel effect (RSCE), narrow-width effect, short-channel effect (SCE), and fringing field effect mix up with the circuit complexity and degrade the overall device performance [48,49]. The circuit designers need an accurate model in circuit simulation to describe the electrical characteristics of pocket implant process MOSFETs, incorporating RSCE, the hot-electron effect [50], the short-channel effect (SCE) [51], the narrow-width effect [52,53], and the fringing field effect [54,55]. Several methods of evaluating the small-signal characteristics have been reported [56–58]. The analytical results derived on the basis of a two-port model cannot be applied to many practical cases of high-frequency MOST structures. In MOS devices substrate doping is locally changed in the region between source and drain, and this is achieved by ion implantation. This results in variation of effective substrate doping concentration as one moves away from the channel/gate oxide interface toward bulk. Therefore, a complete drain current–voltage model [59] for small-geometry MOSFET with a nonuniformly doped (Gaussian) channel that covers the entire operating range and

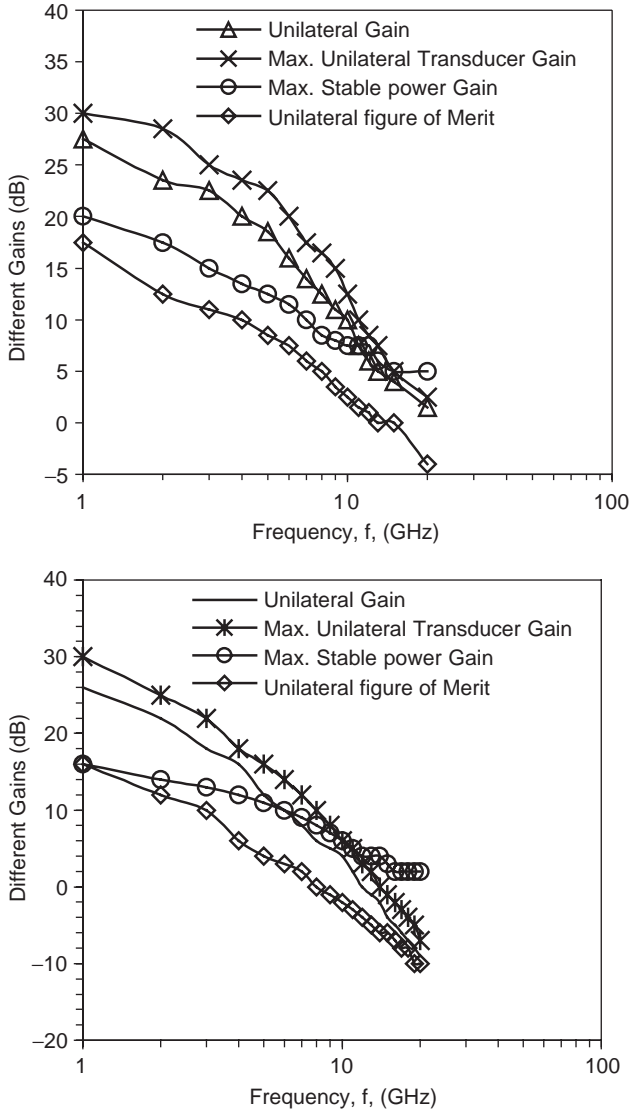


Figure 10. (a) Variation of different gains with frequency for short-gate-length MOSFET ($W = 50 \mu\text{m}$, $L = 0.4 \mu\text{m}$, $C_{gs} = 88.8 \text{ fF}$, $C_{gd} = 19.1 \text{ fF}$, $C_{sub} = 105 \text{ fF}$, $g_m = 10.10 \text{ mS}$, $g_{ds} = 0.617 \text{ mS}$, $r_i = 47.4 \Omega$, $r_{dg} = 140 \Omega$, $r_{sub} = 85 \Omega$, $V_{ds} = V_{gs} = 3.3 \text{ V}$); (b) variation of different gains with frequency for large-gate-length MOSFET ($W = 50 \mu\text{m}$, $L = 1.6 \mu\text{m}$, $C_{gs} = 412.7 \text{ fF}$, $C_{gd} = 23.7 \text{ fF}$, $C_{sub} = 101 \text{ fF}$, $g_m = 6.04 \text{ mS}$, $g_{ds} = 0.069 \text{ mS}$, $r_i = 14.1 \Omega$, $r_{dg} = 80 \Omega$, $r_{sub} = 85 \Omega$, $V_{ds} = V_{gs} = 3.3 \text{ V}$).

includes the fringing field effect is required for circuit simulation.

2.2. Drain Current Model

A MOSFET equivalent circuit used to evaluate various admittance parameters, including the fringing field effect for a RF amplifier, is shown in Fig. 11.

The drain current in MOSFET after incorporating fringing field effect [59] is

$$I_d = \frac{-\mu_{\text{eff}}W}{L} \int_{V_{ms}}^{V_{md}} Q_m dV \tag{9}$$

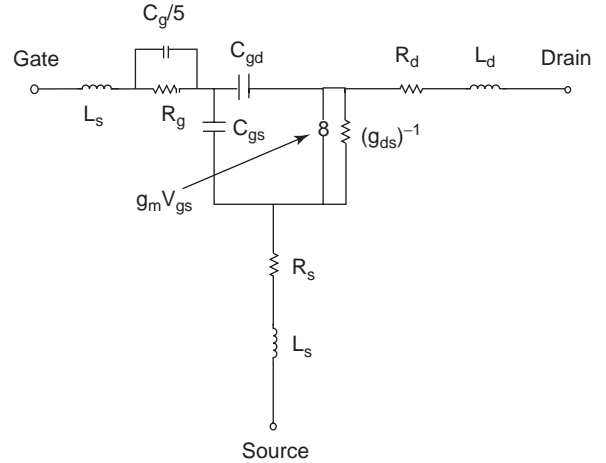


Figure 11. The equivalent circuit for evaluation of the admittance parameter.

where L and W are the channel length and width, respectively; μ_{eff} is the effective mobility [62]; and $V_{ms} = V_s + V_{bi}$ and $V_{md} = V_d + V_{bi}$ at the source and drain terminals, respectively. After incorporating all the charge density components, which are present in the short-geometry MOSFET, and the total charge density Q_m in the channel is now given by

$$Q_m = Q_i + Q_j + Q_s + \Delta Q_b \tag{10}$$

where Q_i is the inversion-layer charge [54], Q_j and Q_s are the p-n junction space charge density and the surface charge density, respectively, given as

$$Q_j = qNX_j = K_e \sqrt{V_m} \tag{11}$$

where the implanted layer is approximated by a rectangle of height N (doping per meter³) and width X_j (meter) further, $K_e = \sqrt{2eqN_e}$, $N_e = N_a N / (N_a + N)$, and $V_m = V + V_{bi}$. V takes the values V_s and V_d while V_m takes the values V_{ms} and V_{md} at the source and drain terminals, respectively. Then

$$\begin{aligned} Q_s &= -C_{ox}(V_{mg} - V_m) && V_{mg} > V_m && \text{(accumulation)} \\ &= qNX_s && V_T < V_{mg} < V_m && \text{(depletion)} \\ &= qNX_{sm} && V_{mg} < V_T && \text{(inversion)} \end{aligned} \tag{12}$$

where $V_{mg} = V_g - V_{fb} + V_{bi}$.

The surface space charge region thickness (X_s) is given by

$$X_s = \frac{K_n (\sqrt{V_m - V_{mg} + V_c} - \sqrt{V_c})}{qN} \tag{13}$$

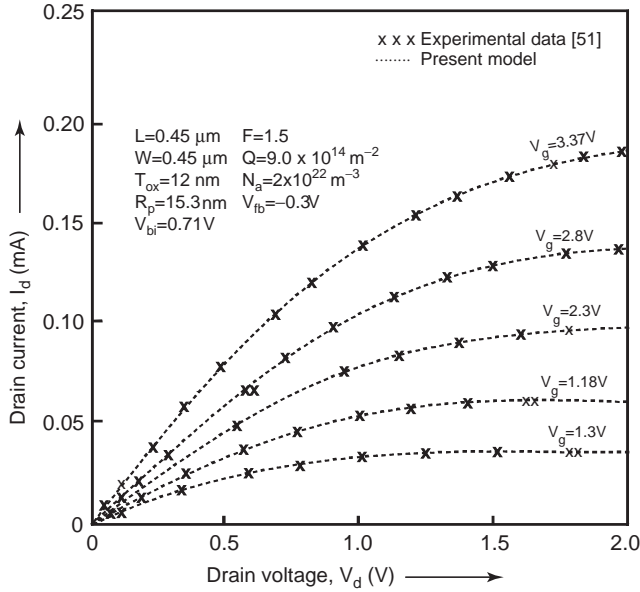


Figure 12. Drain current–drain voltage characteristics at different gate voltages.

where

$$V_c = \frac{qN\epsilon_{si}}{2C_{ox}^2} \quad \text{and} \quad K_n = \sqrt{2\epsilon_{si}qN} \quad (14)$$

When the inversion occurs at the surface, the space charge region X_s attains a maximum value X_{sm} given by $X_{sm} = (K_n\sqrt{V_m})/qN$. The term ΔQ_b is the increased charge density due to narrow gate width and shift of the threshold voltage and is given as [61]

$$\Delta Q_b = C_{ox} \left[\frac{0.17}{W} 10^{-6} V_{ms} + 1.5 \exp[-(10^6 \cdot W)] \sqrt{V_s + V_{bi}} \right] \quad (15)$$

Utilizing Eq. (10) in Eq. (9), the drain current is obtained after integrating the inversion-layer charge expression from source region to drain region [59]. The variation of drain current with drain to source voltage at different gate–source voltages is shown in Fig. 12.

It is seen that at a given V_g , I_d increases with V_d with increase in carrier mobility in the channel. Also at a given V_d , I_d is increasing with V_g because of the increase in inversion-layer charge. Fig. 13 shows the variation of drain current with gate voltage at different drain voltages. The theoretical result for $V_d = 0.05 \text{ V}$ is found to be in perfect agreement with experimental data [51]. The variation of drain current with gate width for different drain voltages is shown in Fig. 14. At a given V_d , the variation of I_d with W is linear and the slope of the line increases with V_d , which results in decrease in current at a faster rate at high value of V_d . Because of lateral diffusion of the depletion layer boundary toward the field oxide region, there will be an additional bulk side charge that results in a

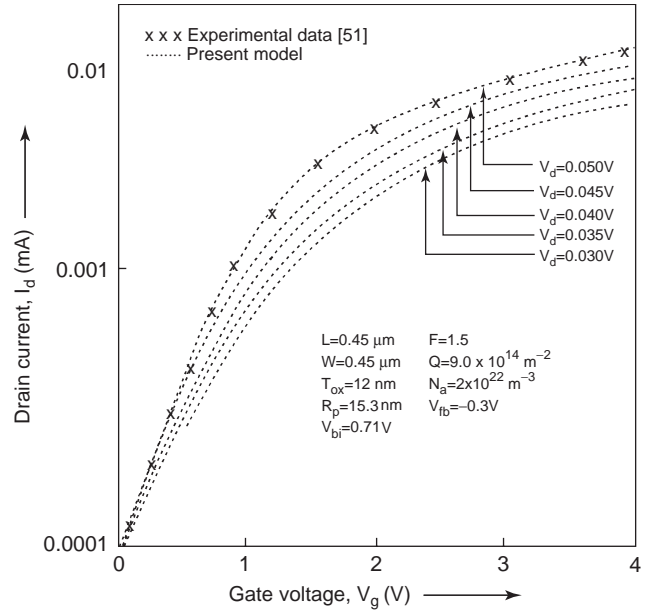


Figure 13. Drain current–gate voltage characteristics at different drain voltages.

decrease of channel current with the narrowing of gate width. With the increase in W , curves of a usual long-channel MOSFET are obtained. It is seen from Fig. 15, that as the channel length decreases I_d increases; this occurs because, with the shortening of channel length, the depletion region under the channel is widened. Therefore with the increase of potential at drain, the surface potential increases, which results in an increase of drain current.

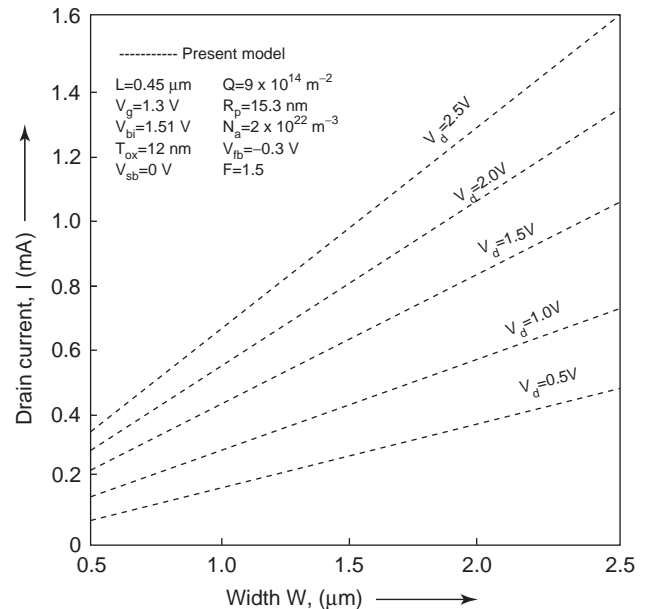


Figure 14. Variation of drain current with gate width at different drain biases.

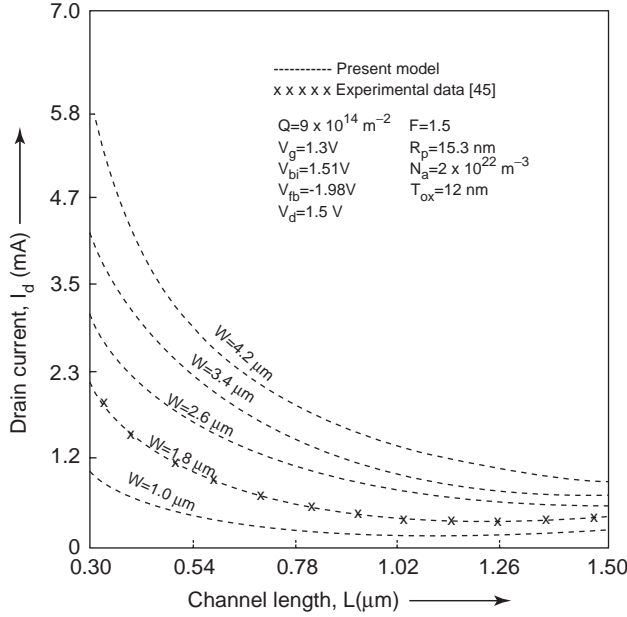


Figure 15. Variation of drain current with channel length at different gate widths.

2.3. Capacitance Model

The total charge in the gate side is obtained from the expression

$$Q_G = \frac{-\mu_{eff}W^2}{I_d} \int_{V_{md}}^{V_{ms}} Q_g Q_m dV_m \tag{16}$$

where Q_g is the gate accumulation charge density given as $Q_g = C_{ox}(V_{mg} - V_m)$. Substituting the values of Q_m from (10) and Q_g in expression (16), we get

$$Q_G = \frac{-\mu_{eff}W^2}{I_d} \left[C_{ox}Q_i \left\{ V_{mg}(V_{md} - V_{ms}) - \frac{(V_{md})^2 - (V_{ms})^2}{2} \right\} + K_e C_{ox} \left\{ \frac{2}{3} V_{mg} \left((V_{md})^{3/2} - (V_{ms})^{3/2} \right) - \frac{2}{5} V_{mg} \left((V_{md})^{5/2} - (V_{ms})^{5/2} \right) \right\} + (-C_{ox})^2 \left\{ (V_{mg})^2 (V_{md} - V_{ms}) + \frac{(V_{md})^3 - (V_{ms})^3}{3} - V_{mg}(V_{md})^2 - (V_{ms})^2 \right\} + Q_b C_{ox} \left\{ V_{mg}(V_{md} - V_{ms}) - \frac{(V_{md})^2 - (V_{ms})^2}{2} \right\} \right] \tag{17}$$

The gate-to-source capacitance (C_{gs}) and gate-to-drain capacitance (C_{gd}) are evaluated after incorporating the

fringing field effect are obtained as [59]

$$C_{gs} = \mu_{eff}W^2 \left(\left(-I_d \right)^{-2} \int_{V_{md}}^{V_{ms}} Q_g Q_m dV_m \right) \frac{dI_d}{dV_s} + \frac{1}{I_d} \frac{d}{dV_s} \left(\int_{V_{md}}^{V_{ms}} Q_g Q_m dV_m \right) \tag{18}$$

$$C_{gd} = \mu_{eff}W^2 \left(\left(-I_d \right)^{-2} \int_{V_{md}}^{V_{ms}} Q_g Q_m dV_m \right) \frac{dI_d}{dV_d} + \frac{1}{I_d} \frac{d}{dV_d} \left(\int_{V_{md}}^{V_{ms}} Q_g Q_m dV_m \right) - \frac{(-\theta\delta + \theta_c) \int_{V_{md}}^{V_{ms}} Q_g Q_m dV_m}{I_d [1 + \theta(V_g - V_t - \delta V_d) + \theta_b V_{sb} + \theta_c V_d]} \tag{19}$$

The variation of gate–source capacitance (C_{gs}) and gate–drain capacitance (C_{gd}) with drain current for a channel-length ($L = 0.8\text{-}\mu\text{m}$) and gate-width ($W = 60\text{-}\mu\text{m}$) device is shown in Fig. 16 as a function of saturation current.

It can be seen that C_{gd} is almost constant for higher-drain currents in saturation. It is obvious from the figure that C_{gd} , including the gate–drain capacitance and overlap capacitance, has a strong dependence on V_{gs} and consequently, from gate–drain bias conditions, C_{gd} is less dependent on V_{ds} , due to the reverse p-n junction depletion at the drain end. As in the case of C_{gs} , which is associated with gate oxide, capacitance in the depletion region near the source end is determined mainly by V_{gs} and is less V_{ds} dependent on and is almost constant in the saturation region. When drain current increases with increasing V_{gs} at saturation (at a fixed V_{ds}), the pinchoff point moves toward the drain end. Hence C_{gs} will increase

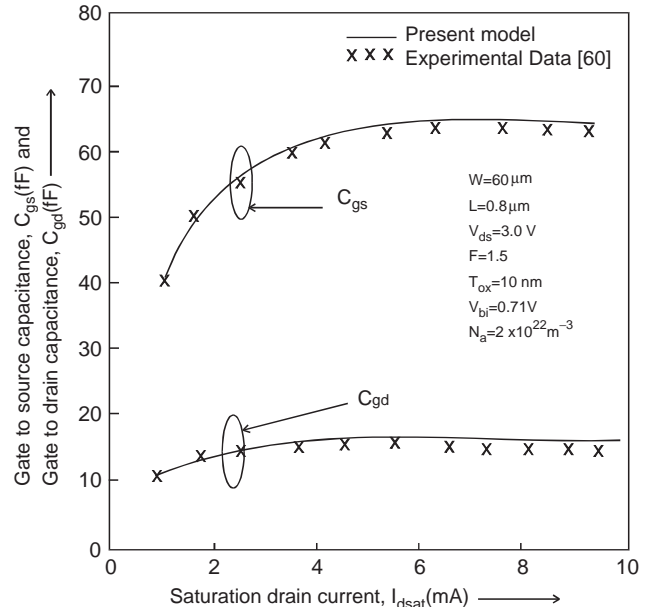


Figure 16. Variation of gate–source capacitance and gate–drain capacitance with saturation drain current (xxx—experimental data) [60].

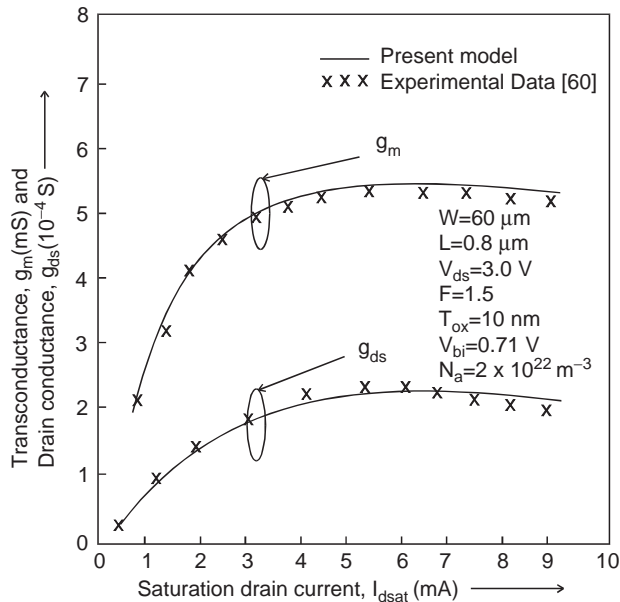


Figure 17. Variation of transconductance and drain conductance with saturation drain current (xxx—experimental data) [60].

with saturation drain current because of the increase in V_{gs} .

2.4. Transconductance and Cutoff Frequency Model

For optimization of FET in RF applications, the transconductance (g_m) plays a significant role, and is one of the most important indicators of device quality for microwave and millimeter-wave applications and in the linear region is given as [59].

$$g_m = \left. \frac{\partial I_d}{\partial V_g} \right|_{V_d = \text{constant}} \quad (20)$$

Figure 17 shows the variation of transconductance (g_m) and drain to source conductance (g_{ds}) with saturation drain current (I_{dsat}) of a device with $W/L = 60/0.8 \mu\text{m}$. The transconductance is evaluated from the first-order derivative of drain current versus gate–source bias characteristics in saturation at drain–source bias of 3 V. It can be seen that transconductance increases rapidly up to 3.0 mA and then increases slowly. The drain conductance increases gradually throughout the plot. The current gain cutoff frequency f_t is an important figure of merit for microwave semiconductor devices. It is the frequency at which the short-circuit current gain of the device falls to unity. It also indicates the ultimate speed of the device. Therefore, cutoff frequency (f_t), which is an indicator of device high-frequency performance, determines the utilizing switching speed of the device, given as [61].

$$f_t = \frac{g_m}{2\pi(C_{gs} + C_{gd})} \quad (21)$$

Although the cutoff frequency represents an important figure of merit of the device, it does not represent the lim-

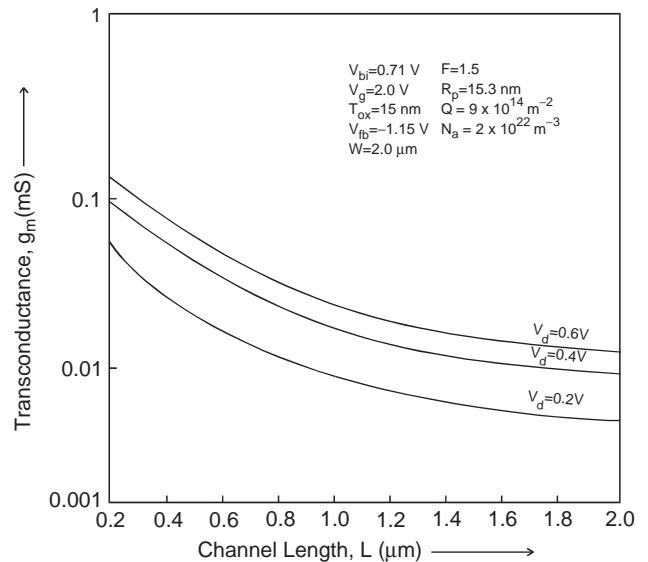


Figure 18. Variation of transconductance with channel length at different drain biases.

iting frequency of operation for microwave circuitry. However, for most microwave applications there is a figure of merit called *maximum frequency of oscillations* f_{max} that is than f_t more useful because microwave designers are typically concerned with power gain into conjugately matched conditions. Therefore, the maximum frequency of oscillation is defined as the frequency at which the unilateral power gain (U) of a device goes to unity.

The variation of I_d with gate width for a given channel length shows a variation similar to that seen in Fig. 14. Figure 18 shows a variation of transconductance with channel length at different drain voltages. For a given gate width and drain voltage, the transconductance increases with decrease in channel length, which is due to the increase in drain current as shown in Fig. 15. According to Fig. 19, as the width scales down, the transconductance decreases because of the decrease in drain current with channel width, as be seen from Fig. 14.

Figure 20 shows the variation of cutoff frequency (f_t) as a function of channel length. The operating frequency is found to be inversely proportional to the channel length. As the channel length reduces, the electron takes less time to cross the channel, which in turn increases frequency. According to Fig. 21, the cutoff frequency is directly proportional to the device width and can also be explained from Fig. 19.

2.5. Admittance (Y) Parameters

The kind of circuit shown in Fig. 11 has a definite advantage of physical significance in predicting the distributed gate resistance effect accurately. It is also convenient to represent its RF behavior as well as to simulate Y-parameter performance over a wide range of frequencies. The effective channel resistance is seen by the signal flowing via C_{gs} from gate to source. It is a representation of

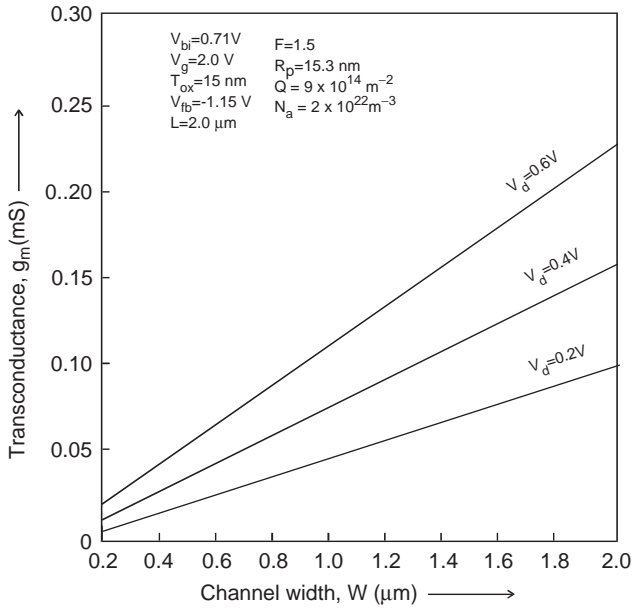


Figure 19. Variation of transconductance with channel width at different drain biases.

the distributed resistance of the channel and spreading bulk resistance, capacitively coupled to the channel, and is responsible for the real part of intrinsic Y_{11} . This element is important for matching in analog circuit designs.

The presence of distributed gate inductance (L_g) plays a vital role upto 1.0 GHz and cannot be ignored while using the device below 1.0 GHz. In an earlier model [41], the effect of gate inductance was neglected below 1.0 GHz. After incorporating the fringing field effect, gate resistance (R_g), and gate inductance, Goswami *et al.* [61] derived modified expressions for the input and output Y parameters, with

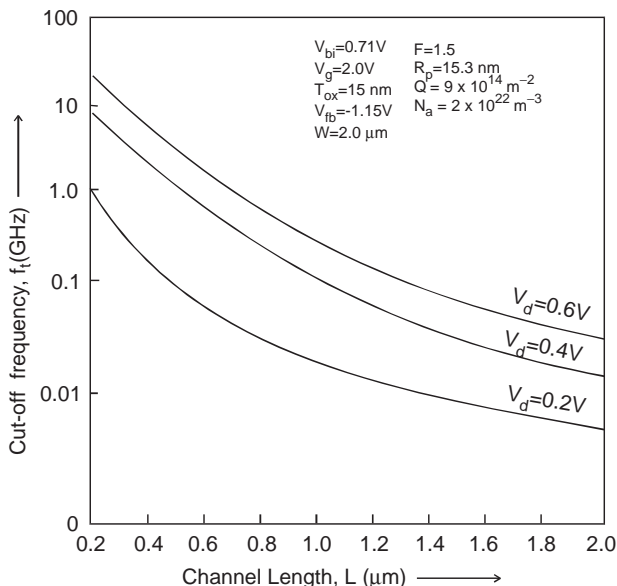


Figure 20. Variation of cutoff frequency with channel length at different drain biases.

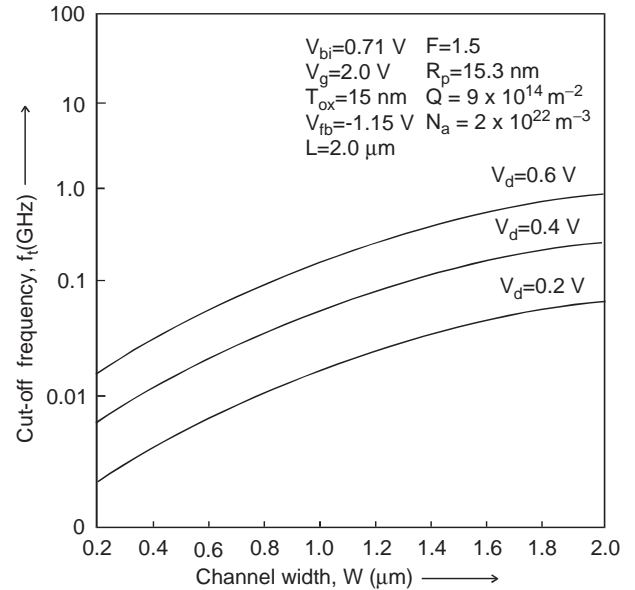


Figure 21. Variation of cutoff frequency with channel width at different drain biases.

and without incorporating the effect of gate inductance, which are applicable at low as well as at high frequencies for circuit applications. Table 1 shows Y parameters with and without incorporating the gate inductance. The total capacitance C_g is equal to the sum of C_{gs} and C_{gd} . Y_{ds} is admittance between source and drain; $s (=j\omega)$ is a complex number. γ is also a complex number and is given in Ref. 41.

As shows in Fig. 22, it is seen that in the frequency range $0.01 \text{ GHz} < f < 1.0 \text{ GHz}$, the real part of $\tanh[(sC_g(R_g + sL_g))/sC_g(R_g + sL_g)]$ is more, due to the effect of gate inductance (L_g), which is due to increase in the input impedance. In the frequency range greater than 1.0 GHz the effect of gate inductance is negligible and the gate becomes resistive.

Figure 23 shows variation of the input admittance Y_{11} with frequency. The real part of Y_{11} increases when distributed gate inductance is incorporated in the analysis, which results in increase in input impedance and thus in Y_{11} . A similar explanation can be given for decrease in the imaginary part of Y_{11} , which is shown in Fig. 24. Also, Y_{11} increases with the frequencies as it is directly related to frequency. The calculated value of Y_{11} without incorporating L_g matches the simulated data [41].

Figure 25 shows variation of the real part of reverse transfer admittance parameter (Y_{12}) with frequency. The real part of Y_{12} increases and the imaginary part of Y_{12} , shown in Fig. 26, decreases with the incorporation of distributed gate inductance. An explanation similar to that for Figs. 20 and 21 can be given for such type of variation of Y_{12} when the effect of L_g is considered. Y_{12} decreases with frequency, which is obvious from the expression of Y_{12} . This parameter is very small because the transistor is biased in the saturation region where C_{gd} is very small.

Variations of the real and imaginary parts of the forward transfer admittance parameter (Y_{21}) with frequency

Table 1. Y Parameter Relative to Inclusion or Exclusion of Gate Inductance in Analysis

Without Incorporating the Effect of Gate Inductance	Incorporating the Effect of Gate Inductance
$Y_{11} = s(C_{gd} + C_{gs}) \frac{\tanh(\gamma W)}{\gamma W}$	$Y_{11} = s(C_{gd} + C_{gs}) \frac{\tanh \sqrt{sC_g(R_g + sL_g)}}{\sqrt{sC_g(R_g + sL_g)}}$
$Y_{12} = -sC_{gd} \frac{\tanh(\gamma W)}{\gamma W}$	$Y_{12} = sC_{gd} \frac{\tanh \sqrt{sC_g(R_g + sL_g)}}{\sqrt{sC_g(R_g + sL_g)}}$
$Y_{21} = (g_m - sC_{gd}) \frac{\tanh(\gamma W)}{\gamma W}$	$Y_{21} = (g_m - sC_{gd}) \frac{\tanh \sqrt{sC_g(R_g + sL_g)}}{\sqrt{sC_g(R_g + sL_g)}}$
$Y_{22} = Y_{ds} + sC_{gd} + \frac{(g_m s C_{gd}) C_{gd}}{C_{gs} + C_{gd}} \left(1 - \frac{\tanh(\gamma W)}{\gamma W}\right)$	$Y_{22} = Y_{ds} + sC_{gd} + (g_m - sC_{gd}) C_{gd} \times \left[\left(\frac{\tanh \sqrt{sC_g(R_g + sL_g)}}{\sqrt{sC_g(R_g + sL_g)}} \right)^{-1} - 1 \right] \left(\frac{\tanh \sqrt{sC_g(R_g + sL_g)}}{\sqrt{sC_g(R_g + sL_g)}} \right)$

are shown in Figs. 27 and 28, respectively, and it can be seen that from 0.01 to 1.0 GHz the real part increases with decreasing frequency while the imaginary part decreases with decreasing frequency up to 0.1 GHz and then increases with decreasing frequency. The calculated results, without considering the effect of distributed gate inductance, are in close agreement with simulated data [41]. Figure 29 shows variation of the real part of the output admittance parameter with frequency. It is found that from frequency 0.01 to 1.0 GHz the real part of the output parameter (Y_{22}) incorporating the effect of gate inductance gives a larger value than without incorporating the gate inductance effect. Therefore the amplifier used up to 1.0 GHz should incorporate gate inductance to achieve better performance. Figure 30 shows variation of the

imaginary part of the output admittance parameter (Y_{22}) of the device with frequency.

2.6. Scattering Parameter

The downscaling of MOSFETs to deep-submicrometer dimensions and the resulting high unity-gain frequency make MOSFETs increasingly attractive for applications in IC used in RF analog electronics and wireless communications [63,64]. For efficient circuit design in the microwave and millimeter-wave bands the availability of an accurate and reliable device model is a key factor. The small-signal behavior of a MOSFET at higher frequencies around a bias point is usually determined by S parameters over its operational bandwidth. The S parameters are

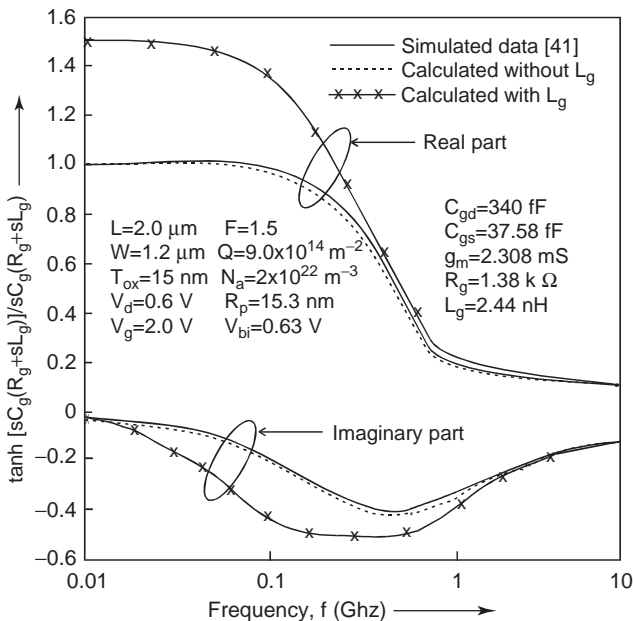


Figure 22. Variation of the $\tanh[(sC_g(R_g + sL_g))/sC_g(R_g + sL_g)]/sC_g(R_g + sL_g)$ with frequency.

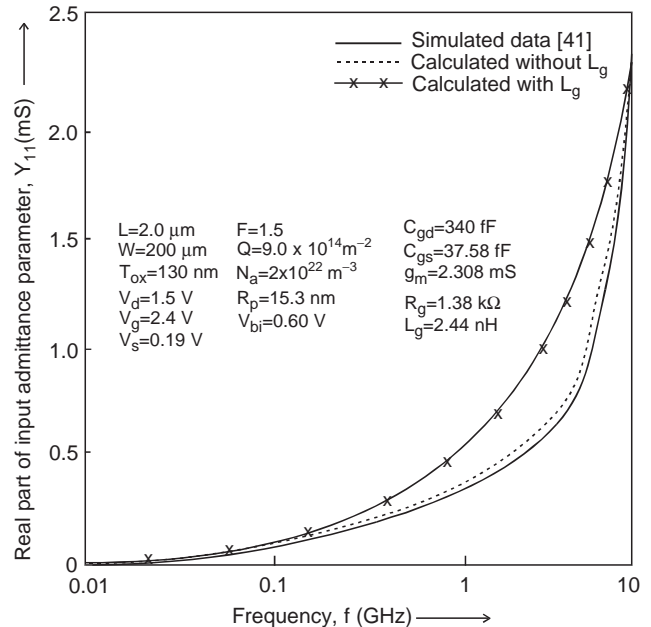


Figure 23. Variation of real part of input admittance parameter with frequency.

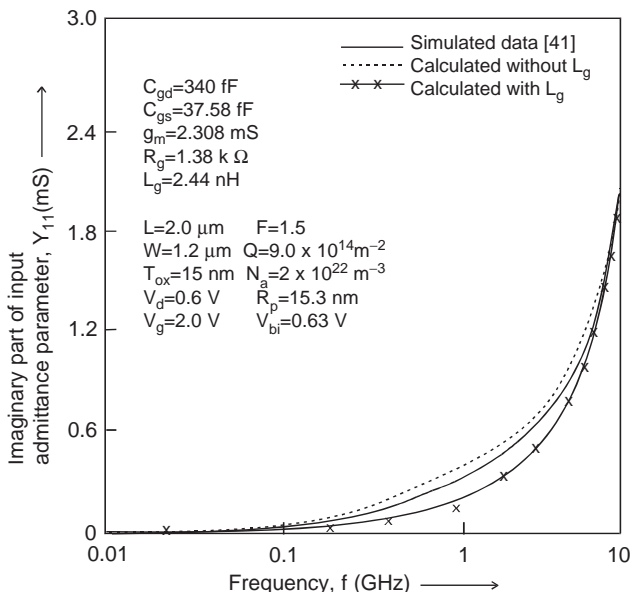


Figure 24. Variation of imaginary part of input admittance parameter with frequency.

used to represent the signal power gain and mismatch losses, as they are frequency-dependent, and therefore adequate representation of circuit elements over their entire operational ranges is essential for MMIC design [65,66]. Earlier models developed include the substrate effect and the gate-drain contact pad effect [59], for prediction of microwave characteristics of MOSFET. But in those models, *S*-parameter extraction incorporating the fringing field effect and the effect of distributed gate inductance was not done. When the device geometry is done in the submicrometer range, the fringing field effect comes into play. Therefore, simple expressions for *S* parameters

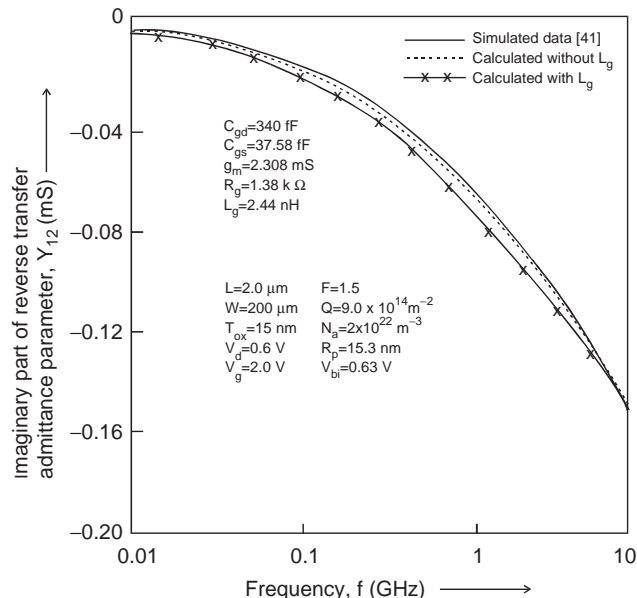


Figure 26. Variation of imaginary part of reverse transfer admittance parameter with frequency.

useful for circuit analysis and optimization are required that incorporate the distributed gate inductance and the fringing field effect. An equivalent circuit of short-channel MOSFETs with fringing field lines to evaluate the *S* parameters necessary in designing a RF amplifier was shown in Fig. 11. When the MOSFET geometry is small enough, the front-gate bias generates the fringing field, which results in an even stronger inversion along the sides of the wall of the edges than in the MOS interface. Therefore, as the device size shrinks and the contact pad is also scaled down, the fringing field effect and the effect of distributed gate inductance cannot be neglected. When

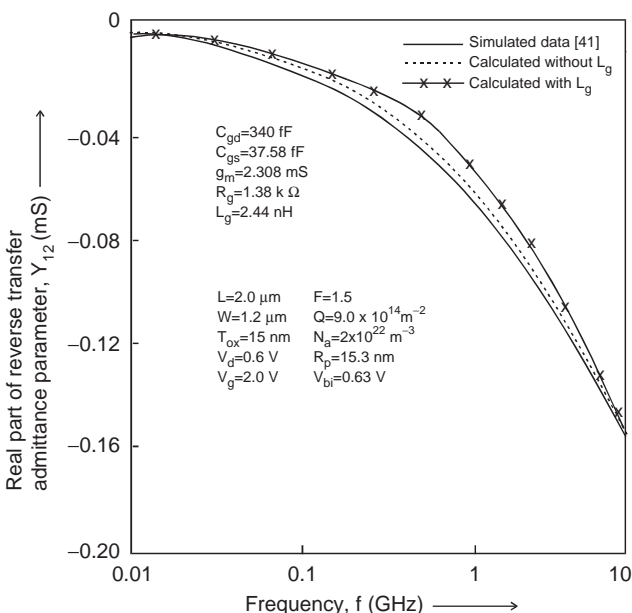


Figure 25. Variation of real part of reverse transfer admittance parameter with frequency.

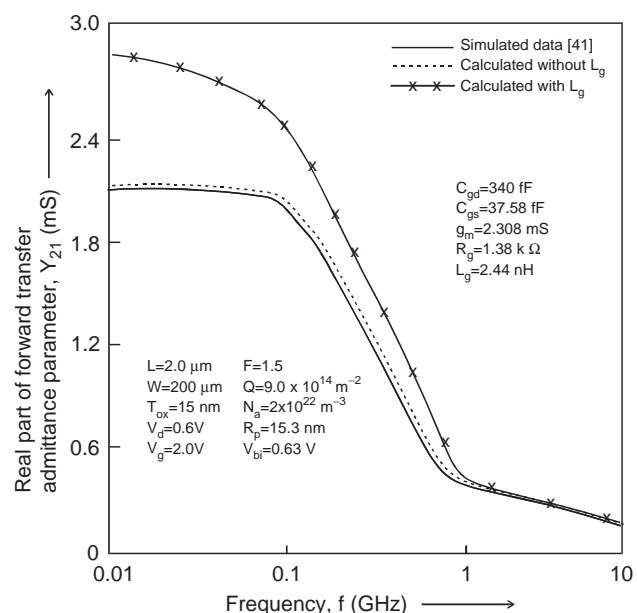


Figure 27. Variation of real part of forward transfer admittance parameter with frequency.

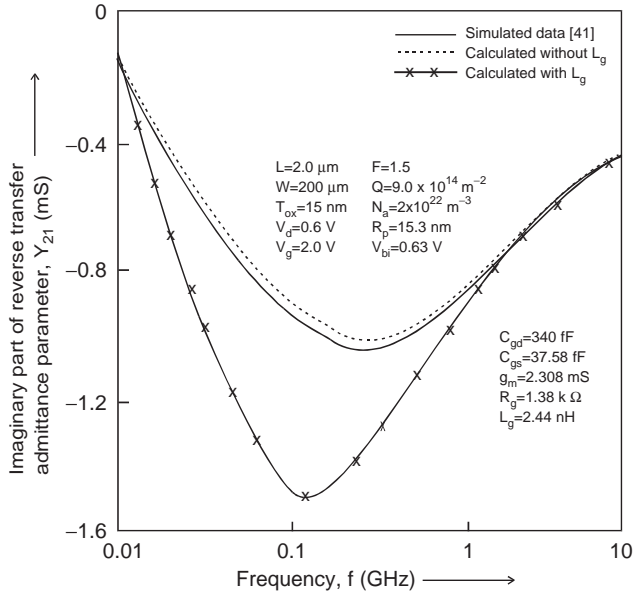


Figure 28. Variation of imaginary part of forward transfer admittance parameter with frequency.

the scattering concept is applied to lumped circuits, the S parameters [67] in terms of device parameters are given as

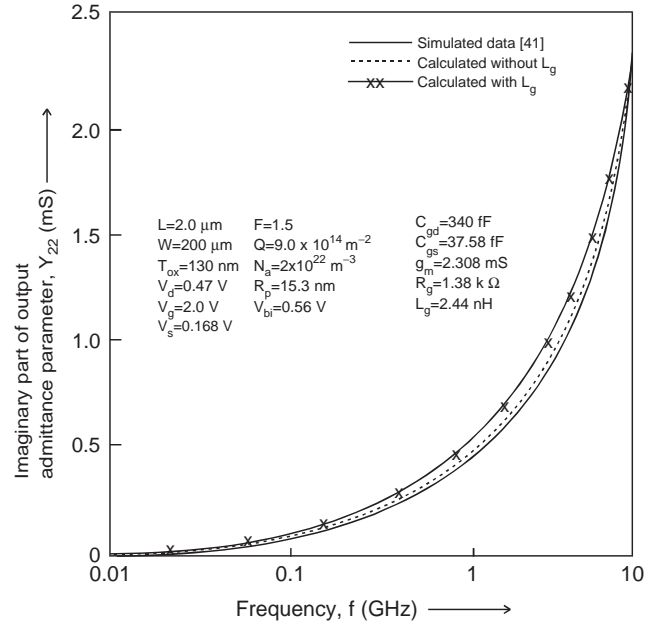


Figure 30. Variation of imaginary part of output admittance parameter with frequency.

where

$$S_{11} = \frac{\{\xi - s(C_{gs} + C_{gd}) \tanh \xi\} \{\xi(1 + g_{ds} + sC_{gd}) + (g_m - sC_{gd})C_{gd}(\xi - \tanh \xi)\} - sC_{gd}(g_m - sC_{gd}) \tanh^2 \xi}{(\xi + sC_g \tanh \xi)(\xi(1 + g_{ds} + sC_{gd}) + \beta) + s(C_{gs} + C_{gd})(R_g + sL_g) \tanh \xi} \quad (22)$$

$$\xi = \sqrt{sC_g(R_g + sL_g)} \quad (23)$$

$$\beta = (g_m - sC_{gd})C_{gd} \left[\left(\frac{\tanh \xi}{\xi} \right)^{-1} - 1 \right] \tanh \xi \quad (24)$$

Then S_{12} and S_{21} are given as

$$S_{12} = \frac{2sC_{gd}\xi \tanh \xi}{\{\xi + s(C_{gs} + C_{gd}) \tanh \xi\} \delta + sC_{gd}(g_m - sC_{gd}) \tanh^2 \xi} \quad (25)$$

where

$$\delta = \xi(1 + g_{ds} + sC_{gd}) + (g_m - sC_{gd})C_{gd}(\xi - \tanh \xi) \quad (26)$$

and

$$S_{21} = \frac{-2\xi(g_m - sC_{gd}) \tanh \xi}{\gamma + sC_{gd}(g_m - sC_{gd}) \tanh^2 \xi} \quad (27)$$

$$\gamma = \xi^2(1 + g_{ds} + sC_{gd}) + \xi sC_g \tanh \alpha + \xi(g_m - sC_{gd})C_{gd}(\xi - \tanh \xi) \quad (28)$$

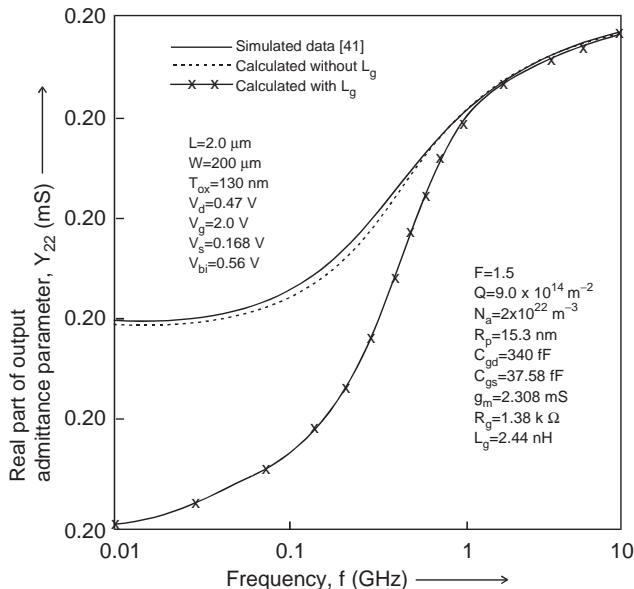


Figure 29. Variation of real part of output admittance parameter with frequency.

The reflection scattering coefficient at port 2 (S_{22}) is given as

$$S_{22} = \frac{\{\xi + s(C_{gs} + C_{gd}) \tanh \alpha\} \{(\xi(1 - g_{ds} - sC_{gd}) + \beta)\} - sC_{gd}(g_m - sC_{gd}) \tanh^2 \xi}{\gamma + sC_{gd}g_m \tanh^2 \xi - s^2C_{gd}^2 \tanh^2 \xi} \quad (29)$$

2.7. Power Gains

The unilateral power gain is given as

$$U_g = \frac{\left[\frac{2\xi(g_m - sC_{gd}) \tanh \xi}{2sC_{gd}\xi \tanh \xi} - 1 \right]^2}{2K \left| \frac{2\xi(g_m - sC_{gd}) \tanh \xi}{2sC_{gd}\xi \tanh \xi} \right| - \text{Re} \left(\frac{2\xi(g_m - sC_{gd}) \tanh \xi}{2sC_{gd}\xi \tanh \xi} \right)} \quad (30)$$

where K is the stability factor given in terms of scattering parameters as

$$K = \frac{1 - |S_{11}|^2 - |S_{22}|^2 + |D|^2}{2|S_{12}||S_{21}|} \quad (31)$$

$$D = S_{11}S_{22} - S_{12}S_{21} \quad (32)$$

The maximum unilateral transducer power G_{TUmax} , the unilateral figure of merit U , and the maximum stable power gain G_{ms} are given as

$$G_{TUmax} = \frac{|S_{21}|^2}{(1 - |S_{11}|^2)(1 - |S_{22}|^2)} \quad (33)$$

$$U = \frac{|S_{11}||S_{12}||S_{22}||S_{21}|}{(1 - |S_{11}|^2)(1 - |S_{22}|^2)} \quad (34)$$

$$G_{ms} = \frac{|S_{21}|}{|S_{12}|} \quad (35)$$

The variation of scattering parameters with frequency for the device with channel length $L = 0.8 \mu\text{m}$ incorporating the fringing field effect and distributed gate inductance is predicted in Fig. 31 for drain current of 6.0 mA with $L_g = 850 \text{ pH}$, $L_s = 0.1 \text{ pH}$ and $L_d = 240 \text{ pH}$. As a result of the wide channel width, the series inductance is caused mainly by the gate itself instead of interconnects. Therefore it is included in the analysis. Figure 32 predicts the variations of different gains and the unilateral figure of merit with frequency. As the frequency increases, the power gain decreases and is basically due to decrease in admittance.

It can be observed that at a given frequency, unilateral transducer power gain is the largest gain and is due to the positive stability factor of the device. The maximum stable power gain shows input/output mismatch, and it is found that as the frequency is increased, the input/output

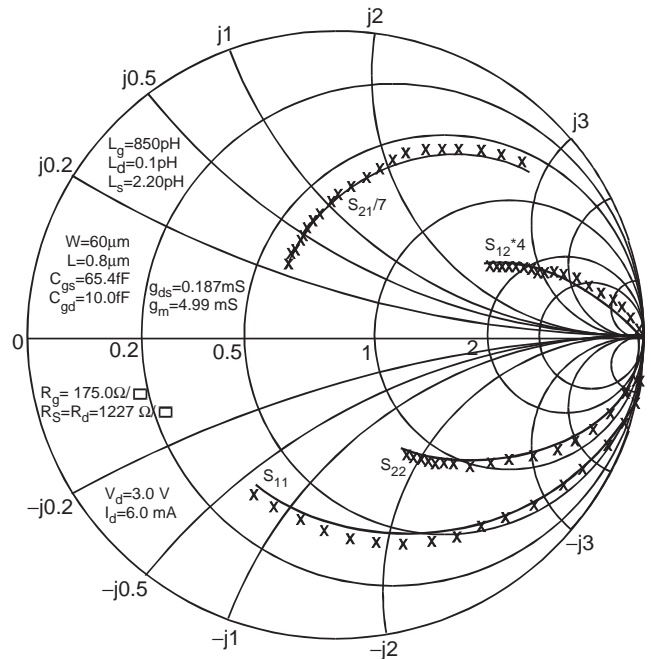


Figure 31. Variation of S parameter of MOSFET for a frequency range of 100 MHz–10 GHz (—present model; xxx—experimental data) [41].

mismatch decreases. Thus a simultaneous conjugate match has been obtained in the analysis. This shows that the circuit with a short-channel device is useful for microwave frequency applications. The unilateral figure of merit decreases with frequency but can be improved by reducing the gate length. Therefore high circuit performance can be obtained with small-gate-length devices.

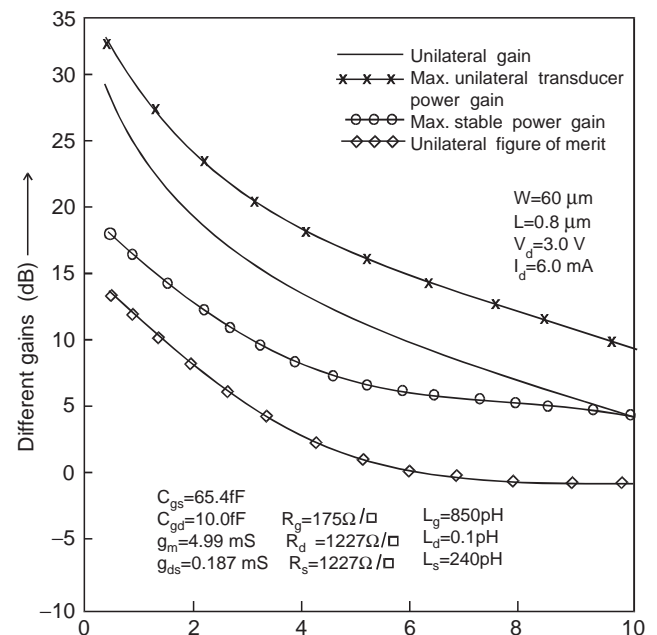


Figure 32. Variation of different gain with frequency.

3. SMALL-SIGNAL AC MOSFET MODEL FOR RF APPLICATIONS

3.1. Introduction

MOSFETs have been widely used in digital VLSI circuits as well as in analog circuits. But the MOSFET device models available in the circuit simulation programs are not adequate in some applications [68–71]. During RF operation, the transit time of carriers from source to drain in the MOSFET is comparable to the rise/fall time of the signals, and during RF switching, the charge in the MOSFET is in a transient condition and quasistatic assumptions of steady-state conditions are no longer valid.

A nonquasistatic (NQS) model predicts the source, drain, gate, and substrate currents, taking into account the inertia in the charge transport of carriers from source to drain and the charge distribution transient when fast turnon and turnoff voltages are applied to the device terminals [72]. One of the NQS models proposed by Oh et al. [73] is valid in all regions of operation (weak, moderate, and strong inversion). Unfortunately, this model requires the use of time-consuming boundary-value methods and therefore cannot be used in a circuit simulator. Turchetti and Masetti [74] developed a simplified CAD oriented model for MOSFETs that is essentially a strong inversion model, and except for the short-channel charge sharing effect, no other SCEs such as velocity saturation or mobility degradation are considered. Park et al. [36,69,75] developed a computationally efficient long-channel NQS model, but, this model does not factor in the 2D effects that determine the boundary conditions at the drain end of the channel or any other small-geometry effects. Quasistatic capacitance models [76] are traditionally used for transient circuit analysis by simulators such as SPICE. These models represent the MOSFET by voltage-dependent node capacitances, where the node capacitors are assumed to charge and discharge instantaneously with the applied bias. However, it is well known that node currents cannot change instantaneously with bias, therefore requiring NQS models to simulate this condition.

It is well known that, for frequencies higher than a given device-dependent limit, the current gain of a MOS transistor decreases quickly. This phenomenon is due to the fact that the modulation of the channel charge distribution to rapidly varying external potentials can no longer be considered instantaneous. Hence, neglecting these NQS effects can result in unpredictable behavior of RF circuits [77]. Earlier models developed include the substrate effect, fringing field effect, and gate–drain contact pad effect. However, when $V_d > V_{dsat}$, the channel pinchoff point, or the velocity pinchoff point starts to move toward the source. This movement is referred to as the *channel length modulation* (CLM) [62,78]. When the device length is large, this effect can be neglected. But as the device length shortens, the CLM takes place and provides an additional AC output current, which increases the output conductance. Therefore, a new model is required through which the relations between the AC small-signal Y parameter and the structure parameters of the MOSFET can be established by incorporating the CLM effect.

3.2. AC Characteristic Analysis

When a small AC voltage (v_g) is applied to the gate electrode, along with DC voltage (V_G), an electric field (AC and DC) is developed in the channel. The drift current in the channel consists of four components. The first is due to the DC sheet charge and DC potential gradient; the second component corresponds to the DC sheet charge and the AC potential gradient, while the third is related to the AC sheet charge and DC potential gradient. The latter two are the main components of AC currents in the MOSFET. The fourth one is a second-order term formed by the AC sheet charge and AC potential gradient. An AC current density per unit length is given by

$$j(x) = -\mu_{\text{eff}} Q_{\text{DC}} \frac{d\psi_{\text{AC}}}{dx} - \mu_{\text{eff}} q_{\text{AC}} \frac{d\psi_{\text{DC}}}{dx} + D_n \frac{dq_{\text{AC}}}{dx} \quad (36)$$

where ψ_{AC} is the AC potential and ψ_{DC} is the DC potential [12] and is given by

$$\psi_{\text{AC}} = \psi_0 e^{i\omega t} \quad (37)$$

$$\begin{aligned} \psi_{\text{DC}} = & \frac{\sin\left(\frac{\pi y}{2d}\right)}{\sinh\left(\frac{\pi L}{2d}\right)} \left(\frac{4V_1}{\pi} + \frac{16Kd^2}{\pi^3} \right) \sinh\left(\frac{\pi(L-x)}{2d}\right) \\ & + \left\{ \frac{4(V_1 + V_d)}{\pi} + \frac{16Kd^2}{\pi^3} \right\} \sinh\left(\frac{\pi x}{2d}\right) \\ & + \frac{1}{2} Ky^2 - Kdy + \psi_{s0} \end{aligned} \quad (38)$$

where $V_1 = V_{\text{bi}} - 2\phi_f$, $\psi_{s0} = 2\phi_f - V_d$, and $K = (qN_a/\epsilon_{\text{si}})$, where V_{bi} is the built-in potential of drain/source–body junction, $2\phi_f$ is the potential required to invert the surface, V_d is the DC drain voltage, d is the depletion-layer depth, L is channel length, and x y denote the position of charge carriers along channel length and depth, respectively. D_n is the diffusion coefficient for electrons, and μ_{eff} is the effective mobility given by

$$\mu_{\text{eff}} = \frac{\mu_0}{1 + \theta(V_g - V_{\text{th}}) + \theta_c V_d} \quad (39)$$

where θ is the mobility degradation coefficient, $\theta_c = (LE_c)^{-1}$, and E_c is the critical field. Q_{DC} is the DC sheet charge, q_{AC} is the AC sheet charge, and the total sheet charge is $Q = Q_{\text{DC}} + q_{\text{AC}}$.

The DC sheet charge is considered to be along x [79] and is given by

$$Q_{\text{DC}} = \left[V_d - V_g + V_{\text{th}} + V_w \left(\left(1 + \frac{V_d}{2\phi_f} \right)^{1/2} - 1 \right) \right] C_{\text{ox}} \quad (40)$$

where V_g is the DC gate voltage, N_a is the acceptor density, V_{th} is the threshold voltage, given [80] as

$$V_w = \frac{1}{C_{ox}} \sqrt{4\epsilon_{si}q\phi_f N_a} \quad (41)$$

$$V_{th} = V_{th0} + K_1(\sqrt{\phi_{s0}} - V_{bseff} - \sqrt{\phi_{s0}}) - K_2 V_{bseff} + K_1 \left(\sqrt{1 + \frac{N_{LX}}{L}} - 1 \right) \sqrt{\phi_{s0}} + (K_3 + K_{3b} V_{bseff}) \times \frac{T_{ox}}{W + W_0} \phi_{s0} \quad (42)$$

where V_{th0} is the threshold voltage for a long-channel device at zero backbias, T_{ox} is the thickness of gate oxide, ϕ_{s0} is termed as $2\phi_b$ and is given by $2V_t \ln(N_{ch}/n_i)$, N_{ch} is the doping concentration in the channel, n_i is the intrinsic carrier density, and K_3 , K_{3b} , W_0 , and N_{LX} are parameters as given in Ref. 80. In (42) the second and third terms describe the vertical nonuniform doping effect, and the fourth term includes the lateral nonuniform doping effect. Now the effective V_{bs} given by

$$V_{bseff} = V_{bc} + 5[V_{bs} - V_{bc} - \delta_1 + \sqrt{(V_{bs} - V_{bc} - \delta_1)^2 - 4\delta_1 V_{bc}}] \quad (43)$$

where $\delta_1 = 0.001$ and $V_{bc} = 0.9(\phi_{s0} - [(K_1)^2/4(K_2)^2])$:

$$K_1 = \gamma_2 - 2K_2 \sqrt{\phi_{s0} - V_{bm}},$$

$$K_2 = (\gamma_1 - \gamma_2) \frac{\sqrt{\phi_{s0} - V_{bx}} - \sqrt{\phi_{s0}}}{2\sqrt{\phi_{s0}}(\sqrt{\phi_{s0} - V_{bx}} - \sqrt{\phi_{s0}}) + V_{bm}}$$

with

$$\gamma_1 = \sqrt{\frac{2q\epsilon_{si}N_{ch}}{C_{ox}}} \quad \gamma_2 = \sqrt{\frac{2q\epsilon_{si}N_{sub}}{C_{ox}}}, \quad V_{bm} = -3.0 \text{ V},$$

$$V_{bx} = \phi_{s0} - \frac{qN_{ch}(X_t)^2}{2\epsilon_{si}}$$

where v_g is the AC voltage between gate and source and the AC sheet charge is given by

$$q_{AC} = (\psi(x) - v_g)C_{ox} \quad (44)$$

The current density equation given by (35) does not include the effect of generation of carriers in the depletion region on the AC current. Additionally, the variation of depletion region width with AC voltage is small when the surface is inverted. Therefore an AC current, which is generated in the depletion region, is of second order and is neglected.

The continuity equation is given by

$$\frac{\partial q_{AC}}{\partial t} = \frac{\partial j(x)}{\partial x} \quad (45)$$

Therefore, using (35), (44), and the assumption that DC potential varies with x and the channel is fully inverted, the right side of (45) becomes

$$\frac{\partial j(x)}{\partial x} = -\mu_{eff} Q_{DC} \frac{d^2 \psi_{AC}}{dx^2} - \mu_{eff} \left[q_{AC} \frac{d^2 \psi_{DC}}{dx^2} + \frac{d\psi_{DC}}{dx} \frac{dq_{AC}}{dx} \right] + D_n \frac{d^2 q_{AC}}{dx^2} \quad (46)$$

Using $\frac{\partial q_{AC}}{\partial t} = i\omega q_{AC}$ and $(d^2 q_{AC}/dx^2) = (d^2 \psi_{AC}/dx^2)C_{ox}$ in (32), we get

$$\frac{d^2 q_{AC}}{dx^2} - \frac{\mu_{eff}}{D_1} \left\{ -AB \frac{\sin(Ay)}{\sinh(AL)} + AB_1 \cosh(AL) \right\} \frac{dq_{AC}}{dx} - \frac{1}{D_1} \{ \mu_{eff} A^2 B_1 \sinh(AL) + i\omega \} q_{AC} = 0 \quad (47)$$

where $A = (\pi/2d)$, $B = (4V_1/\pi) + (16Kd^2/\pi^3)$, $B_1 = [4(V_1 + V_d)]/\pi + 16Kd^2/\pi^3$, and $D_1 = (\mu_{eff} Q_{DC}/C_{ox}) - D_n$.

Using (47) and $Q = Q_{DC} + q_{AC}$, D_1 comes out to be

$$D_1 = \mu_{eff}(V_d - V_g + V_{th} + V_w) \left(\left(1 + \frac{V_d}{2\phi_f} \right)^{1/2} - 1 - \frac{kT}{q} \right) \quad (48)$$

Using the boundary conditions

$$x = 0, \quad q_{AC} = -C_{ox}v_g \quad (49)$$

$$x = L, \quad q_a = (v_d - v_g)C_{ox} \quad (50)$$

$$q_{AC}(x) = \left\{ \frac{(v_d - v_g)C_{ox} + C_{ox}v_g e^{\delta L}}{e^{\delta L} - e^{\alpha L}} \right\} e^{\alpha x} + \left\{ \frac{(v_d - v_g)C_{ox} + C_{ox}v_g e^{\alpha L}}{e^{\delta L} - e^{\alpha L}} \right\} e^{\delta L} \quad (51)$$

where

$$\alpha = \frac{1}{2} \left[\left\{ \frac{\mu_{eff}}{D_1} \left\{ -AB \frac{\sin(Ay)}{\sinh(AL)} + AB_1 \cosh(AL) \right\} \right\} + \sqrt{\left\{ \frac{\mu_{eff}}{D_1} \left\{ -AB \frac{\sin(Ay)}{\sinh(AL)} + AB_1 \cosh(AL) \right\} \right\}^2 + \alpha_1} \right] \quad (52)$$

with

$$\alpha_1 = 4 \frac{1}{D_1} \{ \mu_{eff} A^2 B_1 \sinh(AL) + i\omega \} \quad (53)$$

$$\delta = \frac{1}{2} \left[\left\{ \frac{\mu_{\text{eff}}}{D_1} \left\{ -AB \frac{\sin(Ay)}{\sinh(AL)} + AB_1 \cosh(AL) \right\} \right\} - \sqrt{\left\{ \frac{\mu_{\text{eff}}}{D_1} \left\{ -AB \frac{\sin(Ay)}{\sinh(AL)} + AB_1 \cosh(AL) \right\} \right\}^2 + \alpha_1} \right] \quad (54)$$

The current density in the channel is obtained as

$$j(x) = \frac{D_n}{(e^{\delta L} - e^{\alpha L})} \left[\{(v_d - v_g) + v_g e^{\alpha L}\} C_{\text{ox}} \delta e^{\delta x} - \{(v_d - v_g) + v_g e^{\delta L}\} C_{\text{ox}} \alpha e^{\alpha x} \right] \quad (55)$$

Finally, the AC source current (i_s) is given by $i_s = i_d + i_g$. The AC source current (i_s) can be obtained using $i_s = Wj(x=0)$, and the AC drain current (i_d) is obtained as $i_d = Wj(x=L)$. Therefore the drain current and gate current, excluding the parasitic elements, can be obtained as

$$i_d = \frac{WD_n C_{\text{ox}}}{e^{\delta L} - e^{\alpha L}} \left[v_d (\delta e^{\delta L} - \alpha e^{\alpha L}) + v_g \times (\delta e^{(\alpha+\delta)L} - \delta e^{\delta L} + \alpha e^{\alpha L} - \alpha e^{(\delta+\alpha)L}) \right] \quad (56)$$

$$i_g = \frac{WD_n C_{\text{ox}}}{e^{\delta L} - e^{\alpha L}} \left[v_d (\delta - \alpha) + v_g (\delta e^{\alpha L} - \alpha e^{\delta L} - \delta + \alpha) \right] \quad (57)$$

3.3. Channel Length Modulation (CLM)

According to bulk charge theory [81], the DC drain current is given as

$$I_d = \frac{WC_{\text{ox}} \mu_{\text{eff}}}{L} \left[(V_g - V_{\text{th}}) V_d - \frac{V_d^2}{2} - \frac{4}{3} V_w \phi_f \right] \times \left[\left(1 + \frac{V_d}{2\phi_f} \right)^{3/2} - \left(1 + \frac{3V_d}{4\phi_f} \right) \right] \quad (58)$$

where L is a function of voltage (V_d) beyond the pinchoff point. Thus the variation of drain current (I_d) with V_d is given by

$$\frac{dI_d}{dV_d} = \frac{\partial I_d}{\partial L} \frac{\partial L}{\partial V_d} + \frac{\partial I_d}{\partial V_d} \quad (59)$$

This can be presented as an AC variation given by

$$i_{d0} = \left(\frac{\partial I_d}{\partial L} \frac{\partial L}{\partial V_d} + \frac{\partial I_d}{\partial V_d} \right) v_d \quad (60)$$

On differentiating (58) with respect to L , we get

$$\frac{\partial I_d}{\partial L} = -\frac{I_d}{L} \quad (61)$$

Also by differentiating (58) with respect to V_d , we get

$$\frac{\partial L}{\partial V_d} = -\frac{\xi}{2(2\phi_f + V_d - \gamma)} \quad (62)$$

where

$$\xi = \sqrt{\frac{2e_{\text{si}}(2\phi_f + V_d - \gamma)}{qN_a}} \quad (63)$$

$$\gamma = V_g - V_{\text{th}}$$

$$-V_w \left[\left\{ \left(\frac{V_g - V_{\text{th}}}{2\phi_f} \right) + \left(1 + \frac{V_w}{4\phi_f} \right)^2 \right\}^{1/2} - \left(1 + \frac{V_w}{4\phi_f} \right) \right] \quad (64)$$

Substituting $\partial I_d / \partial L$, $\partial L / \partial V_d$, and $\partial I_d / \partial V_d$ in (60) yields

$$i_{d0} = \frac{I_d \xi}{2L(2\phi_f + V_d - \gamma)} v_d = y_{22}^0 v_d \quad (65)$$

The drain current including the effect of channel length modulation is given as

$$i_d = \frac{WD_n C_{\text{ox}}}{e^{\delta L} - e^{\alpha L}} \left[v_d (\delta e^{\delta L} - \alpha e^{\alpha L}) + v_g (\delta e^{(\alpha+\delta)L} - \delta e^{\delta L} + \alpha e^{\alpha L} - \alpha e^{(\delta+\alpha)L}) \right] + y_{22}^0 v_d \quad (66)$$

3.4. Admittance Model

The equivalent-circuit model shown in Fig. 33 is scalable since all its elements have physical significance. The new elements added to this model are inclusive of the effect of CLM [83] and the overlap effect. The current-voltage

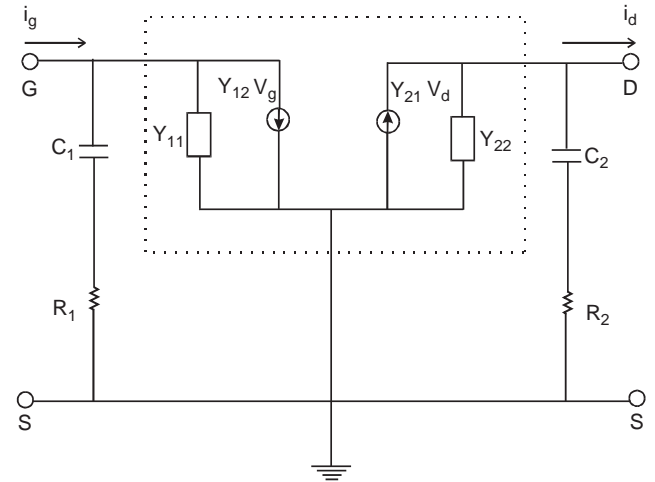


Figure 33. A small-signal equivalent-circuit model for Si-MOSFET.

equations that define the Y parameters are given as

$$i_g = Y_{11}v_g + Y_{12}v_d \quad (67)$$

$$i_d = Y_{21}v_g + Y_{22}v_d \quad (68)$$

The intrinsic Y parameters for the MOSFET are given as

$$Y_{11} = \frac{WD_n C_{ox}}{e^{\delta L} - e^{\alpha L}} [\delta e^{\alpha L} - \delta + \alpha - \alpha e^{\delta L}] \quad (69)$$

$$Y_{12} = \frac{WD_n C_{ox}}{e^{\delta L} - e^{\alpha L}} (\alpha - \delta) \quad (70)$$

$$Y_{21} = \frac{WD_n C_{ox}}{e^{\delta L} - e^{\alpha L}} [(\delta - \alpha)e^{(\alpha+\delta)L} - \delta e^{\delta L} + \alpha e^{\alpha L}] \quad (71)$$

$$Y_{22} = \frac{WD_n C_{ox}}{e^{\delta L} - e^{\alpha L}} [\delta e^{\delta L} - \alpha e^{\alpha L}] + Y_{22}^0 \quad (72)$$

Equations (69)–(72) describe the frequency dependence of the Y parameters for the MOSFET excluding parasitic parameters but including the CLM effect. The intrinsic Y parameters do not by themselves represent actual effects in a MOSFET. It is found that the input and output parasitic capacitances as well as resistances have to be incorporated to obtain total input and output admittances. Figure 33 shows the equivalent circuit used to evaluate the admittance parameters. A parasitic capacitance C_1 , which includes overlap capacitance between gate and source, is thus added along with resistance R_1 in series with C_1 . These elements are in parallel with the input circuit, and the total input admittance is given by

$$Y_{11} = \frac{WD_n C_{ox}}{e^{\delta L} - e^{\alpha L}} [\delta e^{\alpha L} - \delta + \alpha - \alpha e^{\delta L}] + R_1 C_1^2 \omega^2 + i\omega C_1 \quad (73)$$

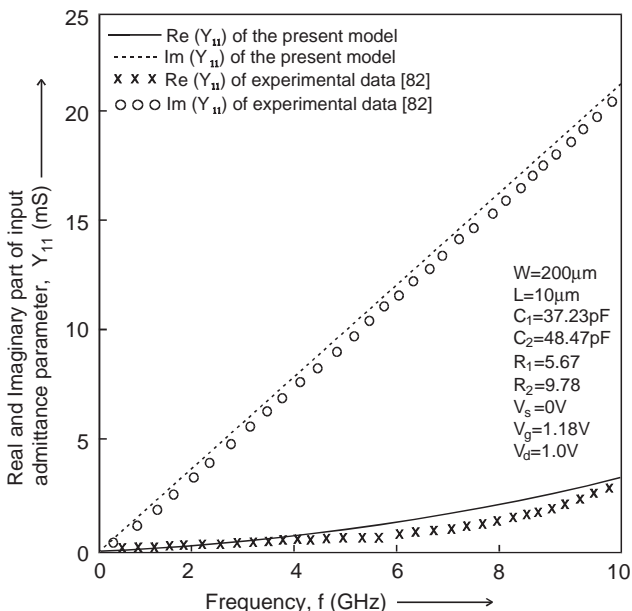


Figure 34. Variation of input admittance parameter with frequency.

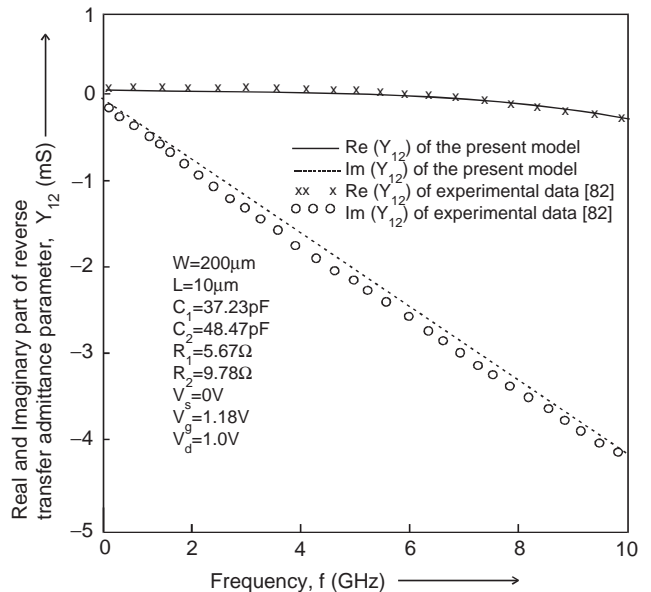


Figure 35. Variation of reverse transfer admittance parameter with frequency.

After incorporating the parasitic output capacitance C_2 , which includes the drain depletion region capacitance, along with a resistance R_2 in series with C_2 , we then consider the total output admittance, is given by

$$Y_{22} = y_{22}^0 + R_2 C_2^2 \omega^2 + i\omega C_2 + \frac{WD_n C_{ox}}{e^{\delta L} - e^{\alpha L}} [\delta e^{\delta L} - \alpha e^{\alpha L}] \quad (74)$$

Equations (73) and (74) show the frequency response of the MOSFET admittance parameters incorporating the CLM and parasitic elements [84].

Variation of the input admittance parameter (Y_{11}) with frequency up to 10 GHz for a device ($W = 200 \mu\text{m}$, $L = 10 \mu\text{m}$) is shown in Fig. 34. The real part of Y_{11} is proportional to

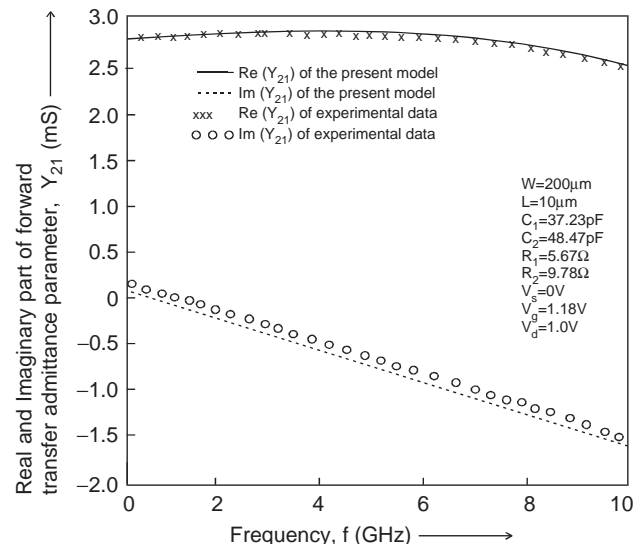


Figure 36. Variation of forward transfer admittance parameter with frequency.

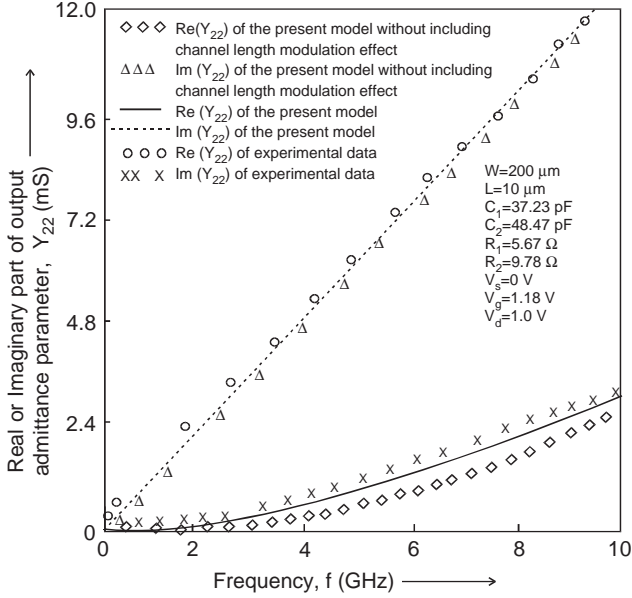


Figure 37. Variation of output admittance parameter with frequency.

the square of the frequency and the imaginary part of Y_{11} varies linearly. Figure 35 shows variation of the reverse transfer admittance parameter (Y_{12}) with frequency for $V_g = 1.18\text{ V}$ and $V_d = 1.0\text{ V}$. Excellent agreement with experimental data [82] is observed with minor deviation at high frequency due to CLM. As shown in Figure 36, at high frequencies, Y_{21} decreases with to the decrease in time constant. Figure 37 shows the variation of the output admittance (Y_{22}) with frequency for the same device. It can be seen clearly that the effect of CLM significantly contributes to the real part of Y_{22} at high frequencies.

3.5. Scattering Parameters

The input reflection scattering parameter coefficient (S_{11}) is given as [84,85]

$$S_{11} = \frac{\frac{1}{(e^{\delta L} - e^{\alpha L})^2} \{A_1 - (e^{\delta L} - e^{\alpha L})(R_1 C_1^2 \omega^2 + i\omega C_1)\} \{e^{\delta L} - e^{\alpha L}\} + WD_n C_{ox} (\delta e^{\delta L} - \alpha e^{\alpha L}) + A_2\} - A_4}{A_5 \{e^{\delta L} (1 + WD_n C_{ox} \delta) - e^{\alpha L} (1 + WD_n C_{ox} \alpha) + A_2\} + A_3 \{ \delta (e^{(\alpha + \delta)L} - e^{\delta L}) - \alpha (e^{(\alpha + \delta)L} - e^{\alpha L}) \}} \quad (75)$$

where

$$A_1 = (e^{\delta L} - e^{\alpha L}) - WD_n C_{ox} \{ \delta e^{\alpha L} - \alpha e^{\delta L} + \alpha - \delta \} \quad (76)$$

$$A_2 = (e^{\delta L} - e^{\alpha L}) (i\omega C_2 + R_2 C_2^2 \omega^2 + Y_{22}^0) \quad (77)$$

$$A_3 = \frac{W^2 D_n^2 C_{ox}^2 (\delta - \alpha)}{(e^{\delta L} - e^{\alpha L})^2} \quad (78)$$

$$A_4 = A_3 \{ (\delta - \alpha) e^{(\delta - \alpha)L} - (\delta e^{\delta L} - \alpha e^{\alpha L}) \} \quad (79)$$

$$A_5 = \frac{1}{(e^{\delta L} - e^{\alpha L})^2} \{ (e^{\delta L} - e^{\alpha L}) - WD_n C_{ox} \times \{ \delta e^{\alpha L} - \alpha e^{\delta L} + \alpha - \delta \} \} \quad (80)$$

The reverse scattering parameter (S_{12}) and the forward scattering parameter (S_{21}) are

$$S_{12} = \frac{2WD_n C_{ox} (\delta - \alpha) (e^{\delta L} - e^{\alpha L})}{\{A_1 - (e^{\delta L} - e^{\alpha L})(R_1^2 C_1^2 \omega^2 + i\omega C_1)\} B_1 - A_3 (e^{\delta L} - e^{\alpha L})^2 \{ (\delta - \alpha) e^{(\alpha + \delta)L} - (\delta e^{\delta L} - \alpha e^{\alpha L}) \}} \quad (81)$$

where

$$B_1 = A_2 + (e^{\delta L} - e^{\alpha L}) + WD_n C_{ox} (\delta e^{\delta L} - \alpha e^{\alpha L}) \quad (82)$$

and

$$S_{21} = \frac{2WD_n C_{ox} (e^{\delta L} - e^{\alpha L}) \{ (\alpha - \delta) e^{(\alpha + \delta)L} - \alpha e^{\alpha L} + \delta e^{\delta L} \}}{\{A_2 + (e^{\delta L} - e^{\alpha L}) + WD_n C_{ox} (\delta e^{\delta L} - \alpha e^{\alpha L})\} B_2 - A_3 (e^{\delta L} - e^{\alpha L})^2 \{ (\delta - \alpha) e^{(\alpha + \delta)L} - (\delta e^{\delta L} - \alpha e^{\alpha L}) \}} \quad (83)$$

where

$$B_2 = \{A_1 - (e^{\delta L} - e^{\alpha L})(R_1^2 C_1^2 \omega^2 + i\omega C_1)\} \quad (84)$$

The output scattering parameter (S_{22}) is given as

$$S_{22} = \frac{[\{ (e^{\delta L} - e^{\alpha L}) + WD_n C_{ox} (\delta e^{\delta L} - \delta + \alpha - \alpha e^{\alpha L}) + B_3 \} \{B_4 - (e^{\delta L} - e^{\alpha L})(i\omega C_2 + R_2 C_2^2 \omega^2 + Y_{22}^0)\} - B_5}{(A_1 + B_3) \{ (e^{\delta L} - e^{\alpha L}) + WD_n C_{ox} (\delta e^{\delta L} - \alpha e^{\alpha L}) \} A_2 + A_3 (e^{\delta L} - e^{\alpha L})^2 \{ (\delta - \alpha) e^{(\alpha + \delta)L} - (\delta e^{\delta L} - \alpha e^{\alpha L}) \}} \quad (85)$$

where

$$B_3 = (e^{\delta L} - e^{\alpha L}) (R_1 C_1^2 \omega^2 + iC_1 \omega) \quad (86)$$

$$B_4 = (e^{\delta L} - e^{\alpha L}) + WD_n C_{ox} (\delta e^{\delta L} - \alpha e^{\alpha L}) \quad (87)$$

$$B_5 = (e^{\delta L} - e^{\alpha L})^2 \{ (\delta - \alpha) e^{(\alpha + \delta)L} - (\delta e^{\delta L} - \alpha e^{\alpha L}) \} \quad (88)$$

Figure 38 shows the modeled S parameters of Si-MOSFET ($W = 200\ \mu\text{m}$, $L = 10\ \mu\text{m}$) at bias point of $V_g = 1.18\text{ V}$ and

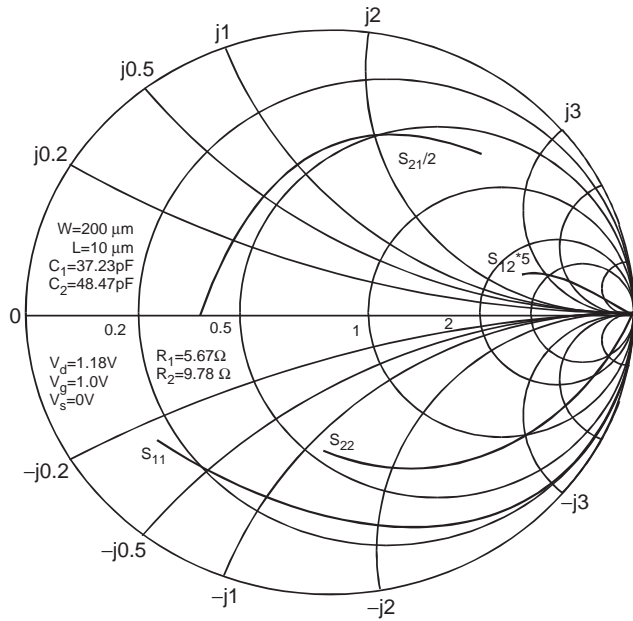


Figure 38. Variation of *S* parameter of MOSFET for a frequency range of 100 MHz–10 GHz.

$V_d=1.0V$ in the frequency range of 0.1–10.0 GHz. It is clear that the reflection scattering coefficient at gate (S_{11}) and the reflection coefficient at drain (S_{22}) are more than the transmitted *S* parameters. This occurs because as the channel length decreases, the input admittance and reverse transfer admittance also decrease. It can also be seen that the reverse scattering parameter has the higher magnitude than the forward scattering parameter.

Figure 39 predicts the variation of different gains and the unilateral figure of merit with frequency. It is observed

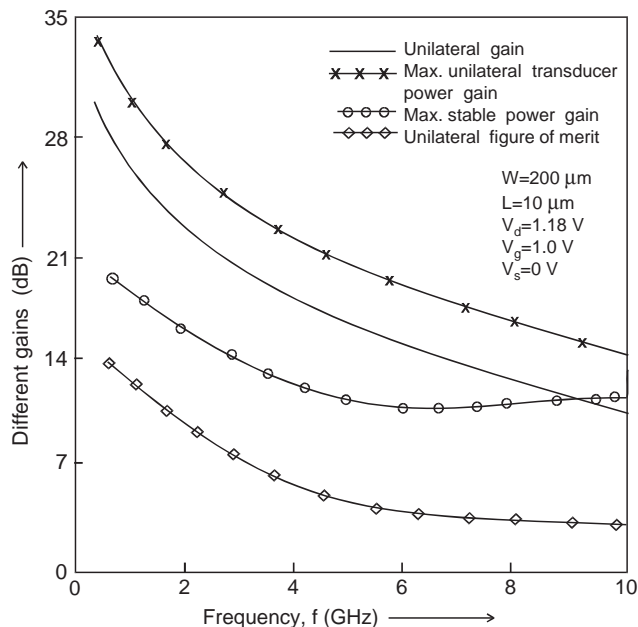


Figure 39. Variation of different gains with frequency.

that as the frequency increases, the power gain decreases and is basically due to decrease in admittance. For a given frequency, maximum unilateral transducer power gain is the largest gain and is due to the positive stability factor of the device. The maximum stable power gain shows the input/output mismatch, and it is found that as the frequency increases, the input and output mismatch decreases. Thus a simultaneous conjugate match has been obtained in the analysis. This shows that a circuit with a short-channel device is useful for RF application.

4. PARASITIC RESISTANCE AND ELECTRICAL CHARACTERISTIC OF FOLD MOSFET

4.1. Introduction

Various modifications to the transistor drain structure have been proposed to help counter this degradation using graded drain or lightly doped drain (LDD) devices [86–89]. The LDD structure can reduce the high-field effects in scaled-down devices by introducing n^- regions between the channel and n^+ source-drain. Since part of the high electric field can be absorbed into the n^- regions, this structure helps minimize the hot-carrier effect, for example. However, the n^- regions give large parasitic resistances that cause the reduction of device transconductance and the increase of saturation voltage [90]. One of the new approaches to drain engineering is the fully overlapped lightly doped drain (FOLD) structure. The angled ion implantation method has been applied to fabricate the n^- fully overlapped structure. From the reliability viewpoint, the greatest reduction in substrate current directly leads to the most reliable n^- design for the FOLD structure. The current path modulation phenomenon due to the trapped charge at the n^- extension region dominates the hot-carrier-induced characteristics change for the conventional LDD structure with the sidewall spacer. This phenomenon is minimized in the FOLD structure, due to its higher controllability of the gate electrode than the LDD structure at the n^- extension region.

4.2. The Series Resistance of the n^- Region

The schematic diagram with an equivalent circuit of a FOLD MOSFET structure, which is a combination of two buried-channel MOSFETS in series with an enhancement mode n -type MOSFET, is shown in Fig. 40, where R_s and R_d are the parasitic resistances of source and drain sides, respectively, including n^+ diffusion, contacts, and wiring series resistances. Taking the n^- region to be a buried-channel MOSFET, the drain current is expressed as [91]

$$I_{ds} = W(\mu_b Q_b + \mu_s Q_s) \frac{dV(y)}{dy} \tag{89}$$

where W is effective channel width, $\mu_b(\mu_s)$ is effective electron mobility of the conducting charge in the bulk (surface) of the n^- region, and Q_b and Q_s are the charge densities in the bulk and the surface, respectively.

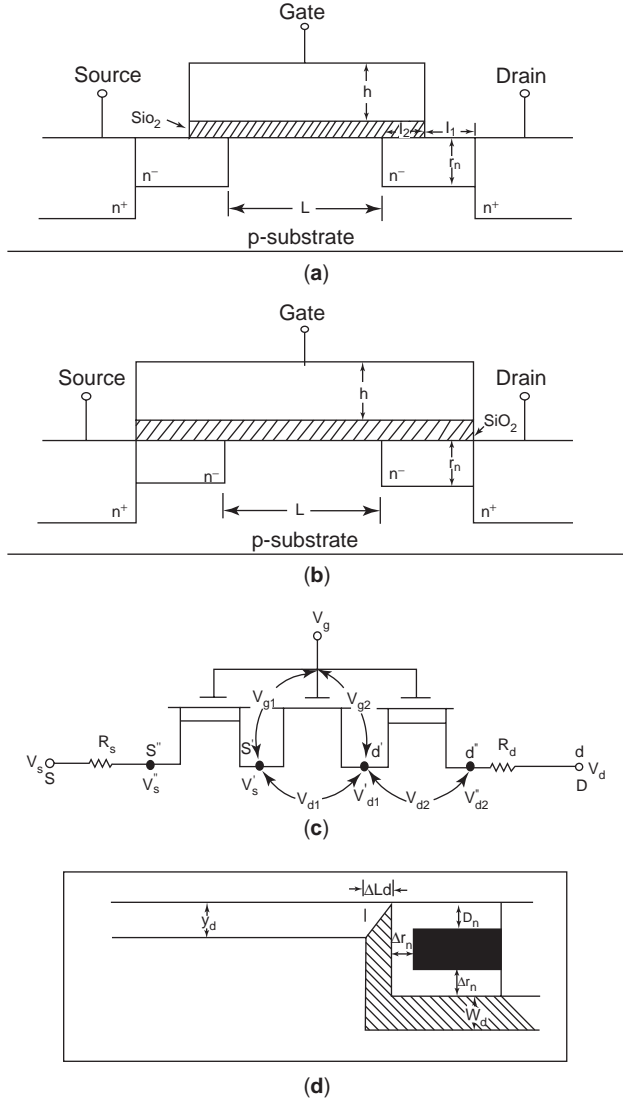


Figure 40. (a) Schematic diagram of the LDD structure; (b) schematic diagram of the FOLD structure; (c) equivalent circuit of the FOLD MOSFET; (d) schematic structure for calculating the geometrical factor and capacitance of the bulk in the n^- region.

In FOLD, it is assumed that the drain voltage is high and the depleted charges in the bulk of the n^- region are caused by the substrate and normal electric field from the gate. Therefore in the drain side, Q_b can be expressed as

$$Q_b(\text{FOLD}) = qN_d(r_n - \Delta r_n - D_n) \quad (90)$$

where r_n is the junction depth of the n^- region, Δr_n is the depletion depth of the bulk in the n^- region with respect to the substrate and is a function of potential [91], N_d is the average doping concentration in the n^- region, and D_n is the depletion depth of the n^- surface due to normal electric field. The surface charge Q_s is given as

$$Q_s = C(V_{g2} - V_{FBn} - V(y)) \quad (91)$$

$$V_{g2}(= V_g - V_d') \quad (92)$$

where V_{g2} is the voltage between gate and the intrinsic drain; V_{FBn} is flatband voltage of the n^- region, and C is the capacitance per unit area of the n^- region. Following Refs 92 and 93, the capacitance C for FOLD structure can be derived as

$$C(\text{FOLD}) = \frac{C_{of} + C_{ov} + C_{if}(\text{FOLD})}{r_n} \quad (93)$$

where

$$C_{ov} = \epsilon_{ox} \frac{(l_2 - \Delta r_n)}{\left(t_{ox} + \frac{\epsilon_{ox}}{\epsilon_{si}} D_n\right)} \quad (94)$$

$$C_{of} = \frac{2}{\pi} \epsilon_{ox} \ln \left(1 + \frac{h}{t_{ox}}\right) \quad (95)$$

$$C_{if}(\text{FOLD}) = \frac{2}{\pi} \epsilon_{ox} \ln \left(1 + \frac{(r_n - \Delta r_n - D_n)}{\left(t_{ox} + \frac{\epsilon_{ox}}{\epsilon_{si}} D_n\right)} \sin \left(\frac{2\epsilon_{ox}}{\pi\epsilon_{si}}\right)\right) \quad (96)$$

where l_2 and h denote overlap length and height of the gate electrode, respectively. For LDD with no overlap, C_{ov} is zero and $C_{if}(\text{FOLD})$ reduces to

$$C_{if}(\text{LDD}) = \frac{2}{\pi} \epsilon_{ox} \ln \left(1 + \frac{r_n}{t_{ox}} \sin \left(\frac{2\epsilon_{ox}}{\pi\epsilon_{si}}\right)\right) \quad (97)$$

Integrating Eq. (89) across the two ends of the n^- region near the drain, one gets

$$I_{ds}(l_1 + l_2) = W \left(\mu_b q N_d (r_n - \Delta r_n - D_n) V_{d2} + \mu_s C \right. \\ \left. \times \left(V_{g2} - V_{FBn} - \frac{V_{d2}}{2} \right) V_{d2} \right) \quad (98)$$

where $l_1(l_2)$ is without (with) overlapped length of the n^- region with respect to the gate

$$V_{d2}(= V_d'' - V_d') \quad (99)$$

V_{d2} is voltage drop in the n^- region near the drain side, V_d'' is n^- - n^+ junction voltage in the drain side. At large drain voltage, the depleted charges exist not only in the n^- /substrate junction but also in the n^- /channel junction. From charge-sharing scheme, the depleted charges in the bulk of the n^- region have the same amount of charge depleted in the substrate and channel regions (Fig. 40). The conducting charge density of the n^- region expressed in (90) is modified as

$$qN_d(r_n - \Delta r_n - D_n) = qN_d r_n f_b(\text{FOLD}) \quad (100)$$

where $f_b(\text{FOLD})$ is the geometric factor of the bulk in the n^- region and can be expressed as

$$f_b(\text{FOLD}) = 1 - \frac{N_a \left(W_d(l_1 + l_2) + \frac{\Delta L_d}{2}(2(W_d + r_n) - Y_d) \right)}{N_d r_n (l_1 + l_2)} \quad (101)$$

$$\Delta L_d = r_n \left(\sqrt{1 + \frac{2W_d}{r_n}} - 1 \right) \quad (102)$$

where W_d is effective depletion depth of the substrate with respect to the n^- region and Y_d is the depletion width in the channel region. On substituting

$$V_{d2} = I_{ds} R_{nd} \quad (103)$$

$$V_{gs2} - V_{FBn} - \frac{V_{d2}}{2} = V_{gs} - V_{ds} - V_{FBn} + I_{ds} \left(R_d + \frac{R_{nd}}{2} \right) \quad (104)$$

In Eq. (98) a quadratic equation for the resistance of the n^- region near the drain side (R_{nd}) is obtained and on simplifying

$$R_{nd} = \frac{l_1 + l_2}{W(\mu_b q N_d r_n f_{b0} + \mu_s C(\text{FOLD})(V_{gs} - V_{ds} - V_{FBn} + R_d I_{ds}))} \quad (105)$$

The term $R_d I_{ds}$ cannot be neglected in the high-current condition and can be approximated as

$$R_d I_{ds} = \frac{\mu_n C_{ox} W}{L} (V_{gs} - V_{t0}) R_d V_{ds} \quad (106)$$

Linearizing the geometric factor at the zero drain bias as

$$f_b = f_{b0} - S V_{ds} \quad (107)$$

where f_{b0} is the geometric factor at zero drain bias and S is the slope of the geometric factor versus drain voltage curve at zero drain bias. Putting (106) and (107) into (105), R_{nd} can be expressed as

$$R_{nd} = \frac{l_1 + l_2}{W(\mu_b q N_d r_n f_{b0} + \mu_s C(\text{FOLD})(V_{gs} - V_{FBn}) - G V_{ds})} \quad (108)$$

where

$$G = \mu_b q N_d r_n S + \mu_s C(\text{FOLD}) \left(1 - R_d \frac{\mu_n C_{ox} W}{L} (V_{gs} - V_{t0}) \right) \quad (109)$$

The resistance of the n^- region near the source side can be derived by the same method. In the general case, $V_{gs} - V_{FBn}$ is much greater than $I_{ds} R_s$. Therefore, the $I_{ds} R_s$ term can be neglected and the resistance of the n^-

region near the source side can be obtained as

$$R_{ns} = \frac{l_1 + l_2}{W(\mu_b q N_d r_n f_{b0} + \mu_s C(\text{FOLD})(V_{gs} - V_{FBn}))} \quad (110)$$

Figure 41 shows the simulated results of in-depth profiles of channel current density and schematic channel current path diagram at the drain edge for the LDD and FOLD structures. Filled circles and dashed-line arrows indicate the channel current profiles and paths with trapped electron charge above the n^- region. Open circles and solid-line arrows indicate the channel current profiles and paths without trapped charge. In case of LDD structure (Fig. 41a), the amount of channel current density at the surface is drastically decreased because of trapped electron charge at the n^- extension region. The peak channel current density at the drain edge shifts to about 10 nm depth from the surface. This result indicates that the LDD structure suffers from a peculiar degradation mode, since a charge is trapped above the n^- region. The trapped electron charge pushes the channel current path down from the surface. Consequently, the parasitic resistance at this region is modulated. Drain current is also modulated because of this effect. In the FOLD structure, in-depth profile and path of channel current density at drain edge are little affected by a trapped charge above the n^- extension region and are shown in Fig. 41b.

The decreasing ratio of the surface channel current density in the FOLD structure is smaller than that in the LDD structure. It is noted that the difference behavior of channel current density and channel current path between the LDD and FOLD structure is related to gate electrode controllability at the n^- extension region. The n^- extension region of the FOLD structure is fully controlled by the gate electrode. This leads to less channel modulation effect, caused by trapped electron charge at n^- extension region, and is also shown in Fig. 41b. The variation of parasitic resistances (R_{sd}) of FOLD and LDD structures with gate voltage at different drain voltages is plotted in Fig. 42. The results are compared with experimental data and are in excellent agreement. Because of the electrode controllability and higher n^- dose in the FOLD structure, less current flow modulation takes place. Consequently the parasitic resistance for FOLD is smaller than that for the LDD. In the present model outer and inner fringing capacitances and the depletion of the n^- surface, caused by the normal electric field from the gate have been considered. FOLD structure can achieve higher derivability than the LDD due to less parasitic resistance.

4.3. The I_d - V_d Characteristics

The drain current in the linear region can be written as

$$I_{ds} = \mu_n W Q_n \left(-\frac{dV(y)}{dy} \right) \quad (111)$$

where W is the effective channel width, μ_n is the electron mobility in the surface inversion layer along the channel direction, Q_n is the electron density per unit area along the channel direction, $V(y)$ is the potential distribution

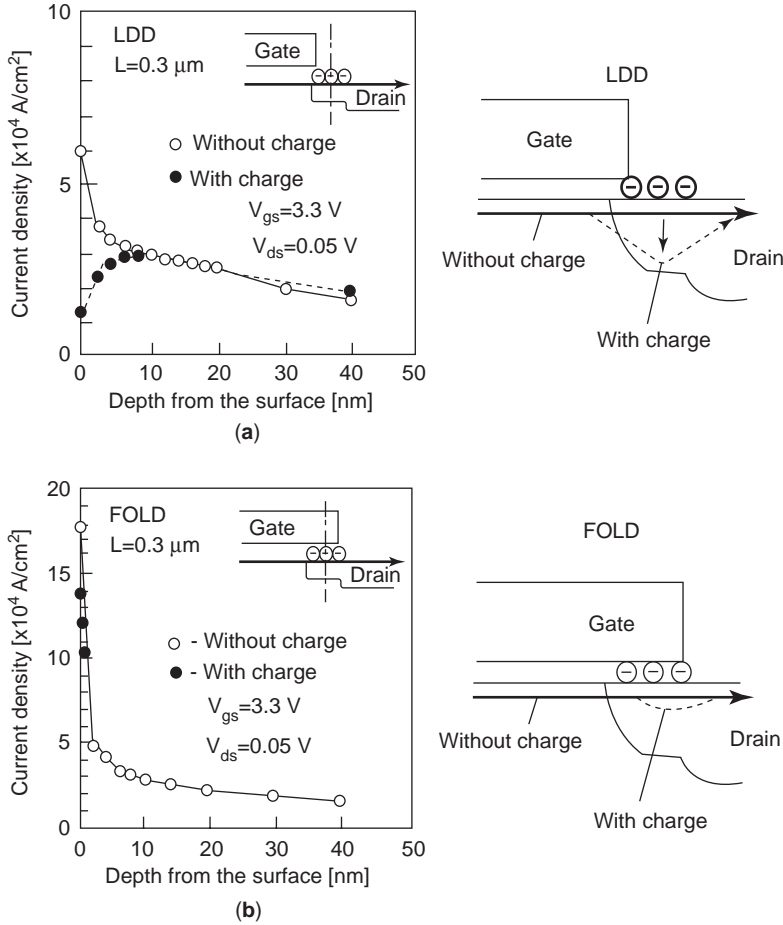


Figure 41. In-depth profiles for the channel current density at n^- region with or without fixed charge by two-dimensional device simulation: (a) LDD; (b) FOLD.

along the channel, and $E_1 = -dV(y)/dy$ is the electric field along the channel. The electron mobility μ_n in the surface inversion layer can be expressed as [94].

$$\mu_n = \frac{\mu_{n0}}{1 + \alpha|E_N| + \beta|E_L|} \quad (112)$$

where E_N is average transverse electric field across the channel, E_L is the longitudinal electric field along the inversion channel, μ_{n0} is the maximum electron mobility in the inversion layer, α is an empirical fitting parameter, $\beta = \mu_{n0}/v_{sl}$, where v_{sl} is the scattering-limited velocity. The average transverse electric field across the channel can be calculated by

$$E_N = \frac{E_1 + E_2}{2} \quad (113)$$

where E_1 is the transverse electric field at the SiO_2/Si interface and E_2 is the transverse electric field under the inversion layer. These two electric field components can be easily calculated using Gauss' law and are expressed as

$$E_1 = \frac{1}{\epsilon_{si}}(Q_B + Q_n) \quad (114)$$

$$E_2 = \frac{Q_B}{\epsilon_{si}} \quad (115)$$

where Q_B is the surface depletion charge density per unit area under the gate and ϵ_{si} is the dielectric permittivity of the bulk semiconductor. Therefore in a MOS structure

$$V_{gs} - V_{FB} - \phi_s = -\frac{Q_n + Q_B}{C_{ox}} \quad (116)$$

where V_{gs} the gate-source voltage, V_{FB} is the flatband voltage of the MOS capacitor without the surface implanted layer, ϕ_s is the surface potential along the channel with respect to the neutral substrate, and C_{ox} is the gate oxide capacitance per unit area. Substituting (113)–(116) into (112), one obtains

$$\mu_n = \frac{\mu_{n0}}{1 + \frac{\alpha C_{ox}}{2\epsilon_{si}} \left(V'_{gs} - V_{FB} - \phi_s + \frac{Q_B}{C_{ox}} \right) + \beta \left| \frac{dV(y)}{dy} \right|} \quad (117)$$

Substituting (117) into (111), and integrating along the channel, one gets

$$I_{ds} = \frac{\mu_n W C_{ox} \left(V'_{gs} - V_{th} - \frac{1}{2} V'_{ds} \right) V'_{ds}}{L \left(1 + \frac{\alpha C_{ox}}{2\epsilon_{si}} \left(V'_{gs} + V_{th} - 2(V_{FB} + 2\phi_F) - \frac{1}{2} V'_{ds} \right) + \left(\eta + \frac{\beta}{L} \right) V'_{ds} \right)} \quad (118)$$

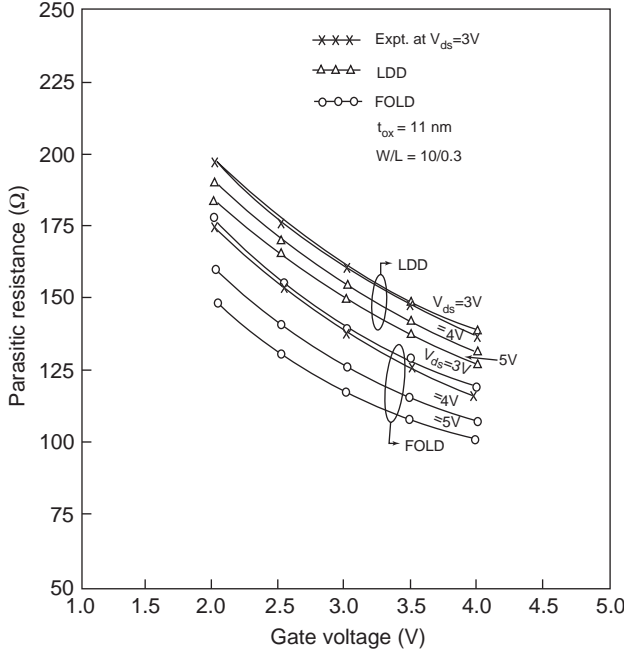


Figure 42. Parasitic resistance dependence on gate voltage for the optimized FOLD and the LDD structures [$N_a = 3.0 \times 10^{16} \text{ cm}^{-3}$, $N_d(\text{LDD}) = 1.8 \times 10^{17} \text{ cm}^{-3}$, $N_d(\text{FOLD}) = 1.3 \times 10^{17} \text{ cm}^{-3}$, $R_s = 13 \Omega$, $R_d = 13 \Omega$, $r_n = 0.15 \mu\text{m}$, $D_n = 0.05 \mu\text{m}$, $h = 0.16 \mu\text{m}$, $l_1(\text{FOLD}) = l_2(\text{LDD}) = 0$, $l_1(\text{LDD}) = l_2(\text{FOLD}) = 0.10 \mu\text{m}$, $V_{\text{BG}} = 1 \text{ V}$, $V_{\text{Fbn}} = -0.5 \text{ V}$, $t_{\text{ox}} = 11 \text{ nm}$, $\mu_n = 570 \text{ cm}^2/\text{V} \cdot \text{s}$, $\mu_b = 542.74 \text{ cm}^2/\text{V} \cdot \text{s}$, $\mu_s(\text{LDD}) = 542 \text{ cm}^2/\text{V} \cdot \text{s}$, $\mu_s(\text{FOLD}) = 562 \text{ cm}^2/\text{V} \cdot \text{s}$].

with

$$|Q_{\text{B,eff}}(V'_{\text{ds}})| = \frac{1}{L} \int_0^L |Q_{\text{B}}| dy = \frac{1}{V'_{\text{ds}}} \int_0^{V'_{\text{ds}}} |Q_{\text{B}}| dV(y) \quad (119a)$$

$$\frac{1}{2} V'_{\text{ds}} (1 - \gamma) = \frac{1}{L} \int_0^L V(y) dy \quad (119b)$$

$$V_{\text{th}} = V_{\text{FB}} + \phi_s + \frac{|Q_{\text{B}}|}{C_{\text{ox}}} \quad (119c)$$

$$\eta = \frac{\alpha C_{\text{ox}}}{4\epsilon_{\text{si}}} \gamma \quad (119d)$$

where γ is the correction factor, which is zero if the electric field along the inversion layer is constant. The threshold voltage no longer remains independent of drain bias and varies as

$$V_{\text{th}} = V_{t0} - k V_{\text{ds}} \quad (120)$$

where V_{t0} is the threshold voltage at zero drain bias and k is the slope of threshold voltage–vs drain voltage curve at zero drain bias [94]. Substituting (120) into (118), one

obtains

$$I_{\text{ds}} = \frac{\mu_n W C_{\text{ox}} (V'_{\text{gs}} - V_{t0} - \alpha V'_{\text{ds}}) V'_{\text{ds}}}{L \left(1 + \frac{\alpha C_{\text{ox}}}{2\epsilon_{\text{si}}} (V'_{\text{gs}} + V_{t0} - 2(V_{\text{FB}} + 2\phi_{\text{F}}) - b V'_{\text{ds}}) + \left(\eta + \frac{\beta}{L} \right) V'_{\text{ds}} \right)} \quad (121)$$

where $a = \frac{1}{2} - k$, $b = \frac{1}{2} + k$ and k is the slope of the threshold voltage versus V'_{ds} curve at zero drain bias. Using the following terminal relations, the drain–source current in the device can be obtained:

$$V'_{\text{gs}} = V_{\text{gs}} - I_{\text{ds}}(R_{\text{ns}} + R_{\text{s}}) = V_{\text{gs}} - I_{\text{ds}} R_{\text{st}} \quad (122)$$

$$V'_{\text{ds}} = V_{\text{ds}} - I_{\text{ds}}(R_{\text{ns}} + R_{\text{s}} + R_{\text{nd}} + R_{\text{d}}) = V_{\text{ds}} - I_{\text{ds}} R_{\text{t}} \quad (123)$$

According to Fig. 43, the FOLD structure shows drain current better than that of LDD structure. Figure 44 shows the behavior of drain current with channel length of both FOLD and LDD structure. It is demonstrated that the scaling down the device length increases the current driving capability and the FOLD promises better current driving capability.

According to the experimental data given in Ref. 89 a peak in the performance of FOLD MOSFET occurs at $L = 0.20 \mu\text{m}$. Below this length, performance suffers because of increase in the length of FOLD finger to maintain hot-electron reliability under the given conditions. Therefore $0.20 \mu\text{m}$ is the least technologically attainable length for the FOLD structure.

This peak in performance can be shifted to $L = 0.15 \mu\text{m}$ by introducing FOLD fingers only at the drain end to form

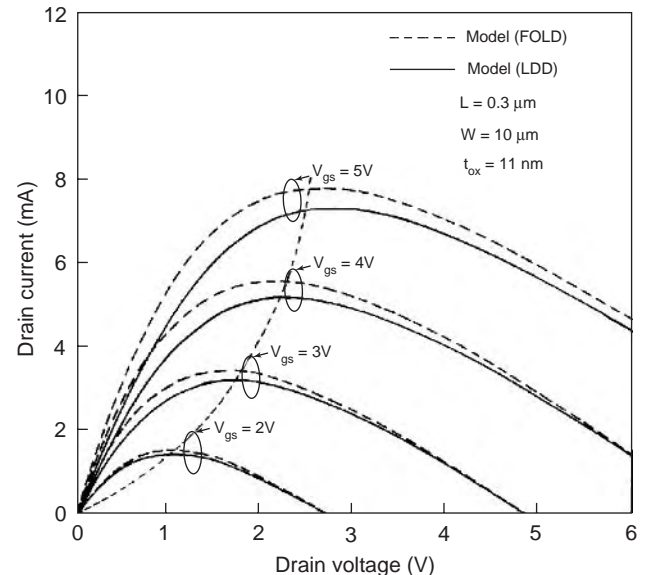


Figure 43. The $I_{\text{d}}-V_{\text{d}}$ characteristics of FOLD and LDD MOSFETs for different gate voltages ($\mu_n = 570 \text{ cm}^2/\text{V} \cdot \text{s}$, $\alpha = 8 \times 10^{-7} \text{ cm/V}$, $\beta = 4.90 \times 10^{-5} \text{ cm/V}$, $\eta = 2.05 \times 10^{-2} \text{ V}^{-1}$).

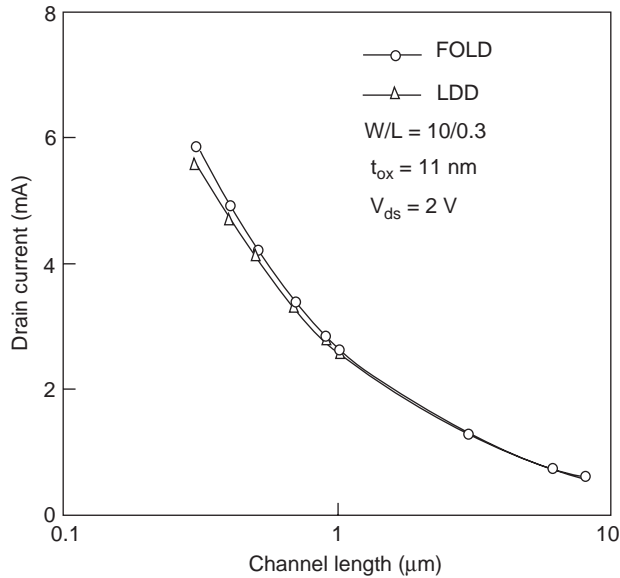


Figure 44. Variation of drain current with channel length ($\mu_n = 570 \text{ cm}^2/\text{V}\cdot\text{s}$, $\alpha = 8 \times 10^{-7} \text{ cm/V}$, $\beta = 4.90 \times 10^{-5} \text{ cm/V}$, $\eta = 2.05 \times 10^{-2} \text{ V}^{-1}$, $V_{ds} = 2 \text{ V}$, $V_{gs} = 2 \text{ V}$, $r_n = 0.15 \text{ }\mu\text{m}$).

asymmetric FOLD MOSFET. Drain voltage dependence of drain current at $V_{gs} = V_{ds}$ for the FOLD and the LDD structures is shown in Fig. 45. According to Fig. 46 shows that the drain current increases gradually as the gate voltage is increased above the threshold voltage. Figure 47 shows the variation of I_d - V_d characteristics of FOLD and LDD MOSFETs with different channel lengths. It is observed that the drain current increases with decrease in channel length. This clearly demonstrates the increased current driving capability of scaled-down devices. The figure also shows that the FOLD devices have a higher value of drain current compared with LDD MOSFETs.

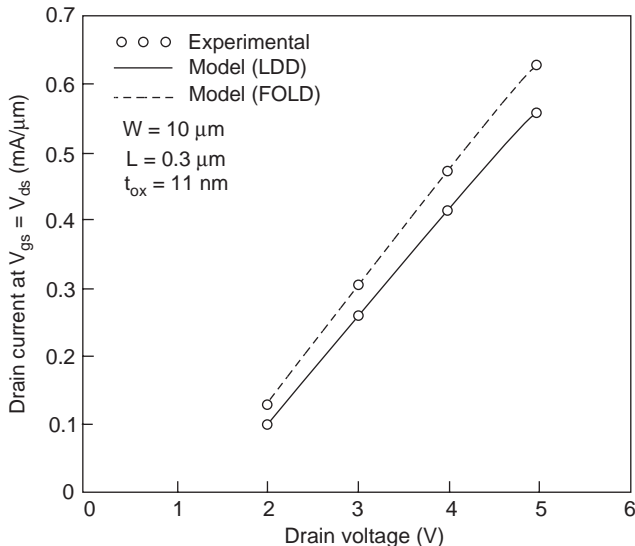


Figure 45. Drain voltage dependence of drain current $V_{gs} = V_{ds}$ for the FOLD and the LDD structures. (Experimental data from Ref. 95.)

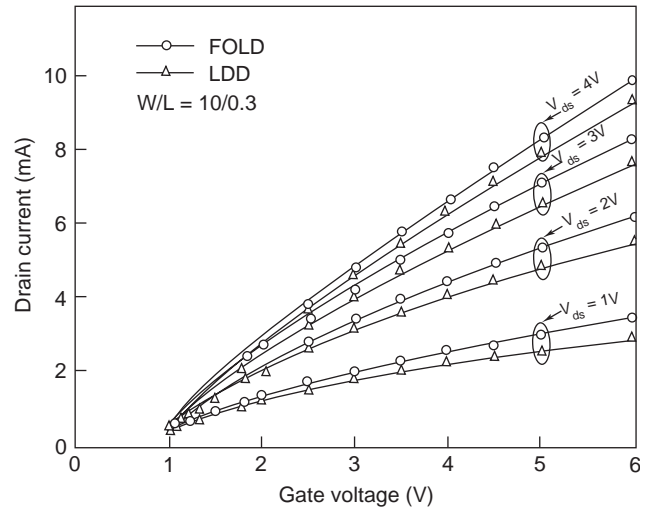


Figure 46. Gate voltage dependence of drain current at different drain voltages for FOLD and the LDD structures. ($\mu_n = 570 \text{ cm}^2/\text{V}\cdot\text{s}$, $\alpha = 8 \times 10^{-7} \text{ cm/V}$, $\beta = 4.90 \times 10^{-5} \text{ cm/V}$, $\eta = 2.05 \times 10^{-2} \text{ V}^{-1}$).

4.4. Transconductance

The transconductance (g_m) and drain conductance (g_d) of a FOLD MOSFET can be derived by from drain-source current [97]. The channel resistance is defined as

$$R_{ch} = \frac{1}{g_d} \quad (124)$$

4.5. Cutoff Frequency and Transit Time

The cutoff frequency is an important figure of merit of all microwave solid-state devices. It indicates the speed of

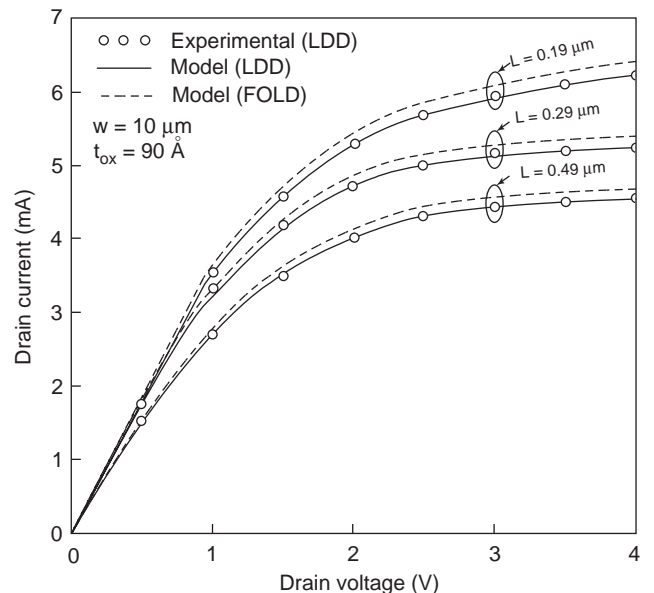


Figure 47. The I_d - V_d characteristics of FOLD and LDD MOSFETs for different channel lengths ($\mu_n = 570 \text{ cm}^2/\text{V}\cdot\text{s}$, $\alpha = 8 \times 10^{-7} \text{ cm/V}$, $\beta = 4.90 \times 10^{-5} \text{ cm/V}$, $\eta = 2.05 \times 10^{-2} \text{ V}^{-1}$) (Experimental data from Ref. 96.)

operation of a device. The cutoff frequency is estimated from the relation

$$f_c = \frac{g_m}{2\pi C_g} \tag{125}$$

where C_g is the gate capacitance and is expressed as

$$C_g(\text{FOLD}) = WL(C_{ox} + 2C_{if}(\text{FOLD}) + 2C_{of}) + 2W \frac{(l_2 - \Delta r_n)}{t_{ox} + \frac{\epsilon_{ox} D_n}{\epsilon_{si}}} \epsilon_{ox} \tag{126a}$$

In the no-overlap case C_g is given as

$$C_g(\text{LDD}) = WL(C_{ox} + 2C_{if}(\text{LDD}) + 2C_{of}) \tag{126b}$$

The transit time is defined as the finite time required for the carriers to travel from source to drain. Transit time represents the finite time taken by the carrier to travel from source to drain. It should represent the minimum delay for a given gate length since it assumes that electrons are traveling at their maximum velocity through the length of the channel. Here the transit time is directly evaluated from the cutoff frequency. The transit time for a FOLD MOSFET structure can be calculated from

$$\tau = \frac{1}{2\pi f_c} \tag{127}$$

where f_c is the cutoff frequency.

Figures 48–50 depict the transconductance and drain conductance variation of both FOLD and LDD devices with drain voltage. There is increase in transconductance due to the reduction in series resistance in FOLD. The drain conductance having a finite value at higher drain

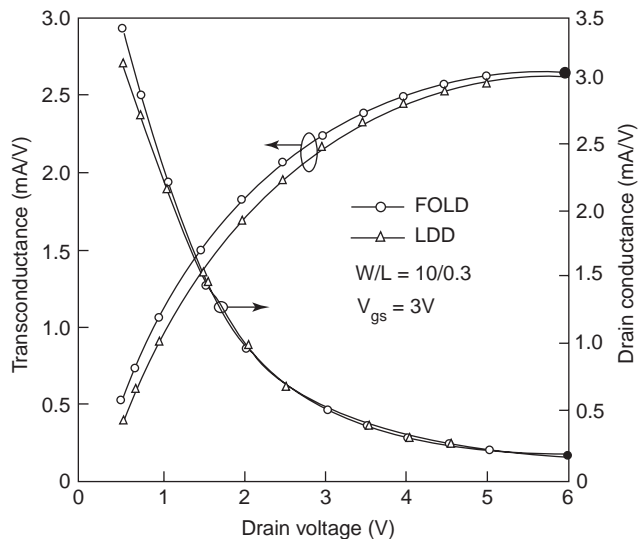


Figure 48. Variation of transconductance and drain conductance with drain voltage ($h = 0.16 \mu\text{m}$, $V_{gs} = 3\text{V}$, $\alpha = 8 \times 10^{-7} \text{cm/V}$, $\beta = 4.90 \times 10^{-5} \text{cm/V}$, $\eta = 2.05 \times 10^{-2} \text{V}^{-1}$, $\mu_n = 570 \text{cm}^2/\text{V}\cdot\text{s}$). (Experimental data from Ref. 96.)

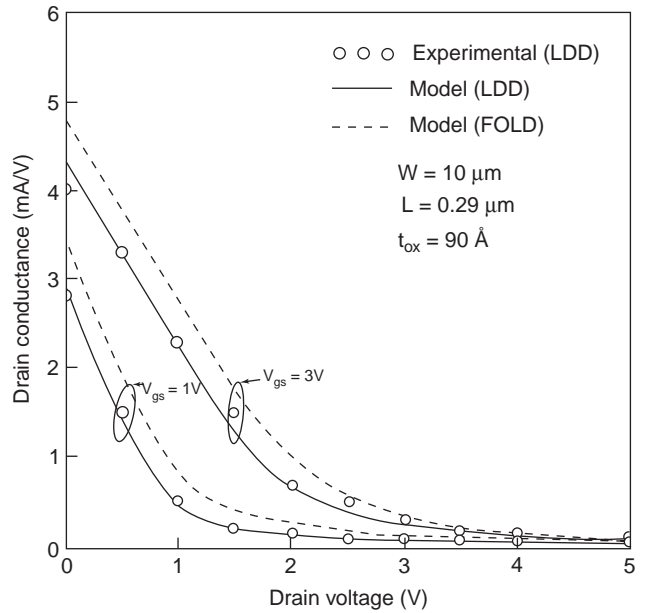


Figure 49. Variation of drain conductance with drain voltage ($h = 0.16 \mu\text{m}$, $\alpha = 8 \times 10^{-7} \text{cm/V}$, $\beta = 4.90 \times 10^{-5} \text{cm/V}$, $\eta = 2.05 \times 10^{-2} \text{V}^{-1}$, $\mu_n = 570 \text{cm}^2/\text{V}\cdot\text{s}$). (Experimental data from Ref. 96.)

voltages shows that the model is valid in the saturation regime of device operation. It is also demonstrated that the drain conductance is almost equal for FOLD and LDD MOSFETs at higher drain voltages.

This shows that the effect of series resistance is more prominent in the linear region of operation where the conductance degraded. Figure 51 depicts the transconductance variation of both FOLD and LDD devices with channel length. Transconductance increases as the channel length is reduced. FOLD structure has better transconductance.

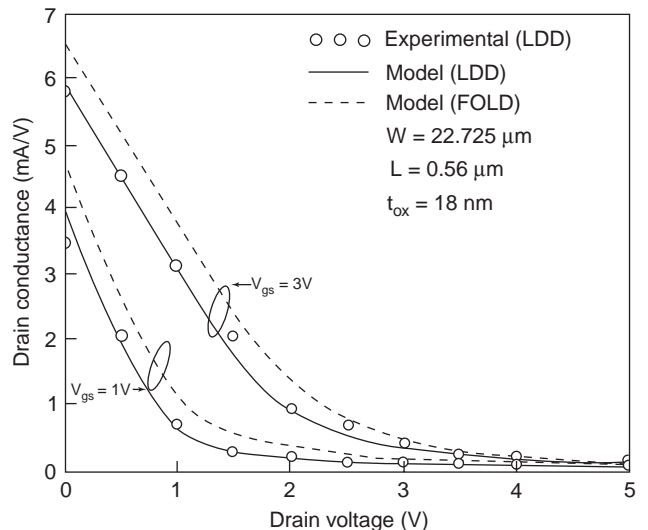


Figure 50. Variation of drain conductance with drain voltage ($h = 0.16 \mu\text{m}$, $\alpha = 8 \times 10^{-7} \text{cm/V}$, $\beta = 4.90 \times 10^{-5} \text{cm/V}$, $\eta = 2.05 \times 10^{-2} \text{V}^{-1}$, $\mu_n = 570 \text{cm}^2/\text{V}\cdot\text{s}$) (Experimental data from Ref. 96.)

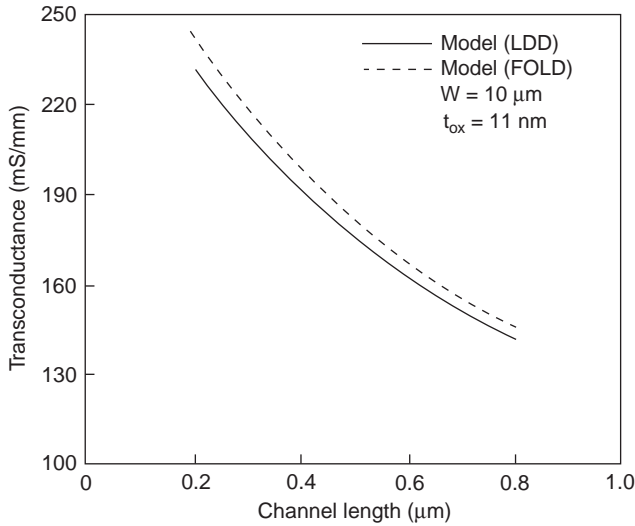


Figure 51. Variation of transconductance with channel length ($h = 0.16 \mu\text{m}$, $V_{ds} = 3 \text{V}$, $\alpha = 8 \times 10^{-7} \text{cm/V}$, $\beta = 4.90 \times 10^{-5} \text{cm/V}$, $\eta = 2.05 \times 10^{-2} \text{V}^{-1}$, $\mu_n = 570 \text{cm}^2/\text{V} \cdot \text{s}$).

It is evident from the Fig. 52 that the drain conductance increases and channel resistance decreases with gate voltage and the FOLD device shows higher drain conductance. The difference in conductance is less for lower gate biases. It is observed from Fig. 53 that the channel resistance increases with increase in drain voltage. Cutoff frequency also increases with drain voltage and becomes constant at higher drain voltage. It is also observed that the FOLD structure shows cutoff frequency lower than that of the LDD structure because of its larger fringing capacitance.

Fig. 54 shows the variation of cutoff frequency and transit time with channel length. It is evident from the

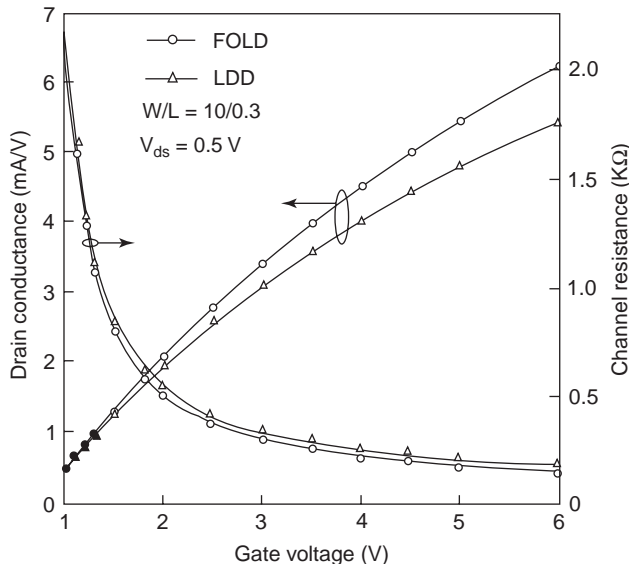


Figure 52. Variation of drain conductance channel resistance with gate voltage ($h = 0.16 \mu\text{m}$, $V_{ds} = 0.5 \text{V}$, $\alpha = 8 \times 10^{-7} \text{cm/V}$, $\beta = 4.90 \times 10^{-5} \text{cm/V}$, $\eta = 2.05 \times 10^{-2} \text{V}^{-1}$, $\mu_n = 570 \text{cm}^2/\text{V} \cdot \text{s}$).

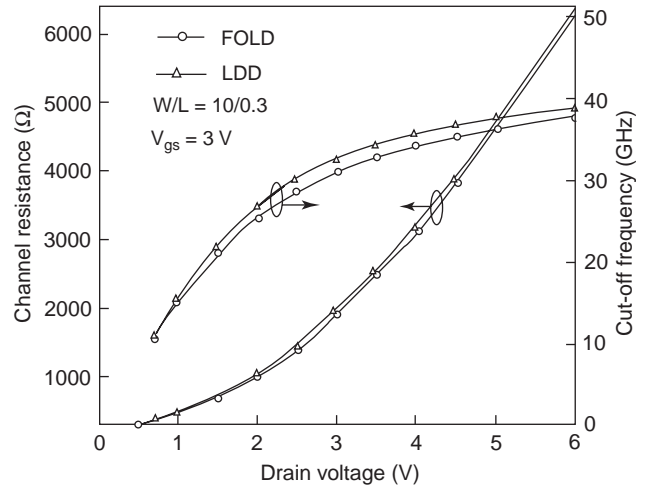


Figure 53. Variation of channel resistance and cutoff frequency with drain voltage ($h = 0.16 \mu\text{m}$, $V_{gs} = 3 \text{V}$, $\alpha = 8 \times 10^{-7} \text{cm/V}$, $\beta = 4.90 \times 10^{-5} \text{cm/V}$, $\eta = 2.05 \times 10^{-2} \text{V}^{-1}$, $\mu_n = 570 \text{cm}^2/\text{V} \cdot \text{s}$).

figure that the cutoff frequency shows a drastic increase with the channel length reduction when the channel length approaches the submicrometer region and the FOLD devices have a transit time larger than that of LDD device. Fig. 55 depicts the transit-time behavior with drain voltage. It is seen that the transit time decreases with increase in drain voltage and becomes constant at higher voltages.

Although FOLD structure has lower cutoff frequency and larger transit time, FOLD MOSFET is overall better than LDD MOSFET because

1. FOLD structure has lesser parasitic resistance than LDD.
2. This structure shows the better current driving capability due to the reduction in parasitic resistance.

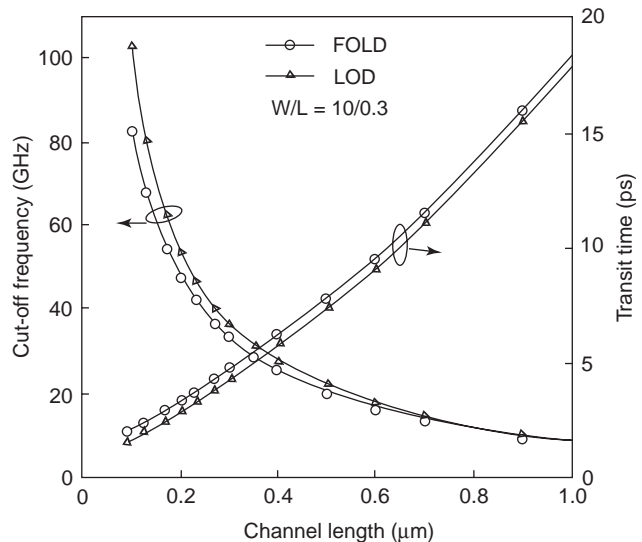


Figure 54. Variation of cutoff frequency and transit time with channel length ($h = 0.16 \mu\text{m}$, $V_{gs} = 3 \text{V}$, $\alpha = 8 \times 10^{-7} \text{cm/V}$, $\beta = 4.90 \times 10^{-5} \text{cm/V}$, $\eta = 2.05 \times 10^{-2} \text{V}^{-1}$, $\mu_n = 570 \text{cm}^2/\text{V} \cdot \text{s}$).

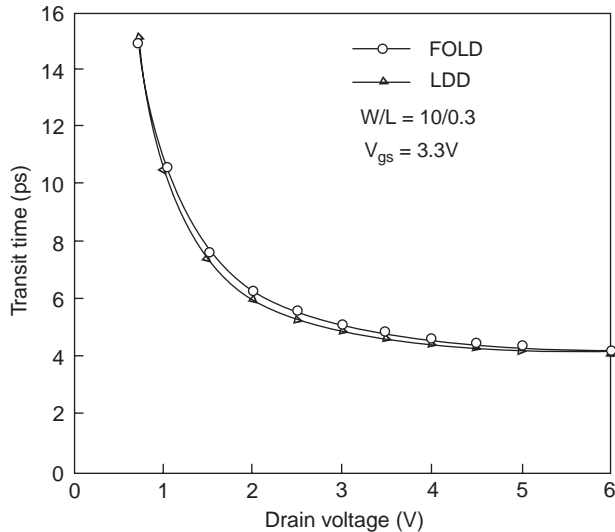


Figure 55. Variation of transit time with drain voltage ($h = 0.16 \mu\text{m}$, $V_{gs} = 3.3 \text{ V}$, $\alpha = 8 \times 10^{-7} \text{ cm/V}$, $\beta = 4.90 \times 10^{-5} \text{ cm/V}$, $\eta = 2.05 \times 10^{-2} \text{ V}^{-1}$, $\mu_n = 570 \text{ cm}^2/\text{V} \cdot \text{s}$).

The n^- extension region of the FOLD structure is fully controlled by the gate electrode. This leads to less channel modulation effect, caused by trapped electron charge at the n^- extension region. Therefore, the n^- extension design for reducing the substrate current is consistent with high reliability for FOLD structure in terms of reliability.

In the present analysis an analytical model for parasitic resistances (R_{sd}) has been developed for submicrometer FOLD MOSFET. The hot-carrier reliability for the optimized FOLD structure has been studied and compared with the optimized LDD structure. The parasitic resistance for FOLD structure is described considering the n^- region as a modified buried-channel MOSFET and the channel region as an intrinsic enhancement-mode n-type MOSFET. It is observed that the FOLD structure shows better results than that of the LDD structure because of reduction in series resistance.

5. LOW-FREQUENCY (LF) NOISE MODELS FOR FOLD MOSFET

5.1. Introduction

The response of a system to any force can be transient or steady-state in nature. In the absence of such a disturbance, the system exists in a state of equilibrium. However, even in this state parameters describing the system are actually fluctuating about their mean value. These fluctuations are popularly termed *noise*.

5.2. Different Types of Noise

5.2.1. Thermal Noise. This is due to the random motion of carriers in any conductor; as a consequence of this random motion, a fluctuating electromotive force (emf) $V(t)$ is developed across the terminals of the conductor. It is the dominant noise source in any device that is electrical in

nature and in thermal equilibrium with a temperature bath kept at a fixed temperature T .

5.2.2. Popcorn or “Burst” Noise. Popcorn noise, also called “burst” noise, was first discovered in semiconductor diodes and later reappeared in integrated circuits. If burst noise is amplified and fed into a loudspeaker, it sounds like corn popping, with thermal noise providing a background frying sound; thus the name “popcorn noise” [98]. The power density of popcorn noise has a $1/f^n$ characteristic, where n is typically 2.

5.2.3. Shot Noise. This noise occurs whenever a noise phenomenon can be considered as a series of independent events occurring at random. For example, in the case of emission of electrons by a thermionic cathode or by a photocathode, the emission of electrons consists of a series of independent random events; hence the emission currents show shot noise [99]. In p-n junctions and transistors the crossing of a junction by electrical carriers (electrons or holes) constitutes a series of independent random events; hence the currents in such devices show shot noise. This rule equally holds when transition occurs between two energy levels, such as in the generation and recombination of carriers in a semiconductor, or when photons are emitted by a laser. In each case one must ask what entities make up the series of independent random events that produce shot noise. The current carried by electrons emitted from a hot cathode in a vacuum diode, or by electrons that cross a potential barrier in a semiconductor are randomly generated. Random generation leads to fluctuations around the average current I :

$$S_I = 2qI \quad (128)$$

5.2.4. Generation–Recombination (GR) Noise. This noise occurs whenever free carriers are generated or recombine in a semiconductor material. The fluctuating rates of generation and recombination can be considered as a series of independent events occurring at random, and hence the process can be considered as a shot noise process [99]. As a consequence the number of carriers, and hence the resistance R , fluctuates. However, it is also useful to consider the fluctuation δn in the carrier density n as giving rise to a fluctuation δR in the resistance R of the device. This resistance fluctuation δR can be detected by passing a DC current I through the sample; the current I develops a fluctuating emf $V(t) = I\delta R(t)$ across its terminals, and this emf can be amplified and measured by standard techniques. The number of free electrons in the conduction band may fluctuate because of generation and recombination processes between the band and traps. The number fluctuations cause fluctuations in the conductance G , and, therefore, in the resistance R .

$$\frac{S_R}{R^2} = \frac{S_G}{G^2} = \frac{S_N}{N^2} = \frac{(\Delta N)^2}{N^2} \frac{4\tau}{1 + \omega^2\tau^2} \quad (129)$$

where τ is a relaxation time, characteristic of the trap, usually in the range from 10^{-6} to 10^{-3} s. If there is one

type of trap only, then the variance $(\Delta N)^2$ is given by

$$\frac{1}{(\Delta N)^2} = \frac{1}{N} + \frac{1}{X_n} + \frac{1}{X_p} \quad (130)$$

where X_n is the average number of occupied traps and X_p the average number of empty traps. The variance thus approximates the smallest of the quantities N, X_n, X_p . The complicated problem of a semiconductor with two kinds of traps, X and Y , has been solved [100–103].

5.2.5. 1/f Noise or Flicker Noise. Johnson discovered flicker noise in vacuum tubes in 1925, and this type of noise was interpreted by Schottky in 1926. Flicker noise [104] was found in a great variety of other components and devices. Because the spectrum varies as $1/f^\gamma$, with γ close to unity, one often uses the term *1/f noise* for “flicker noise”. This is a fluctuation in the conductance with a power spectral density proportional to $f^{-\gamma}$, where $\gamma = 1$ in a wide frequency range, usually measured from 1 Hz to 10 kHz. The spectral density cannot be exactly f^1 from $f = 0$ to $f = \infty$, since neither the integral of the power density nor the Fourier transform would be able to have finite values. Measurements down to 10^{-6} Hz showed that even there the spectrum still is f^1 [105].

5.3. Theory of Low-Frequency (LF) Noise

The study of LF noise in electronic devices in the past has received great attention, not only because noise limits circuit and devices performance. Two of the most frequently observed types of noise in semiconductors are (1) flicker and (2) generation–recombination (GR) noises. GR noise is due to random emission of electrons and holes from defect centers in the depletion region of the semiconductor.

For devices with high surface noise and low concentration of the Shockley–Read–Hall (SRH) centers, GR noise is usually overshadowed by the higher interfacial $1/f$ noise component. For Si MOSFETs there are three models explaining the observed $1/f$ noise: (1) fluctuation model [106,107], (2) mobility fluctuation model [108,109], and (3) combination of the number fluctuations and mobility fluctuations in an uncorrected or corrected manner [110–112]. Hung et al. [111] presented a unified flicker noise theory, which incorporates both the number fluctuation and the correlated surface mobility fluctuation mechanisms. The latter is attributed to the scattering effect of the fluctuating oxide charge. In addition, the $1/f^k$ spectrum where $0.7 < k < 1.2$ has also been found [113], and a modified McWhorter model has been presented to explain its frequency dependence.

5.4. Formulation of the Flicker Noise Model

Consider a section of the transistor channel with width W and length Δx . The coordinate system in use is defined in Fig. 56. Fluctuations in the amount of trapped oxide charge will introduce correlated fluctuations in the channel carrier number and mobility. The resulting fractional

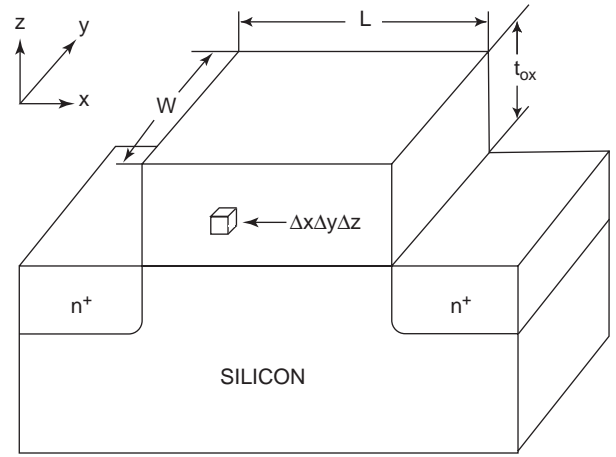


Figure 56. 1.55 MOSFET structure and coordinate system.

change in the local drain current can be expressed as

$$\frac{\delta I_{ds}}{I_{ds}} = - \left(\frac{\delta \Delta N}{\Delta N \delta \Delta N_t} + \frac{\delta \mu}{\mu \delta \Delta N_t} \right) \delta \Delta N_t \quad (131)$$

where $\Delta N = NW \Delta x$ and $\Delta N_t = N_t W \Delta x$, where N_t is the number of occupied traps per unit area. The ratio $\delta \Delta N / \delta \Delta N_t$ is the coupling coefficient of the fluctuation in channel carriers to fluctuation in occupied traps. At moderate to strong inversion, the coupling coefficient is virtually equal to unity [114]. To evaluate $\delta \mu / \delta \Delta N_t$, the relationship between the carrier mobility and the oxide charge density is needed.

A widely accepted model is the one based on the Matthiessen’s rule

$$\frac{1}{\mu} = \frac{1}{\mu_n} + \frac{1}{\mu_{ox}} = \frac{1}{\mu_n} + \alpha_1 N_t \quad (132)$$

where μ_{ox} is the mobility limited by oxide charge scattering and μ_n is the mobility limited by other scattering mechanisms [115,116]. It is expected that the scattering coefficient α_1 is a function of the local carrier density due to the screening effect as well as the distance of the trap from the interface [117]. Based on (132), it can be readily shown that

$$\frac{\delta \mu}{\delta \Delta N_t} = - \frac{\alpha_1 \mu^2}{W \Delta x} \quad (133)$$

and (131) becomes

$$\frac{\delta I_{ds}}{I_{ds}} = - \left(\frac{1}{N} + \alpha_1 \mu \right) \frac{\delta \Delta N_t}{W \Delta x} \quad (134)$$

It follows that the power spectral density of the local current fluctuations is

$$S_{M_d}(x, f) = \left(\frac{I_{ds}}{\Delta N} (1 + \alpha_1 \mu N) \right) S_{\Delta N_t}(x, f) \quad (135)$$

where $S_{\Delta N_t}(x, f)$ is the power spectral density of the mean-square fluctuation in the number of occupied traps over the area $W \Delta x$. According to the conventional number fluctuation theory [118], $S_{\Delta N_t}$ is given by

$$S_{\Delta N_t}(x, f) = \int_{E_v}^{E_c} \int_0^W \int_0^{t_{ox}} 4N_t(E, x, y, z) \Delta x f_t(1 - f_t) \times \frac{\tau(E, x, y, z)}{1 + \omega^2 \tau(E, x, y, z)^2} dx dy dz \quad (136)$$

where $N_t(E, x, y, z)$ is the distribution of the traps over the space and energy, $\tau(E, x, y, z)$ is the trapping time constant, $f_t = (1 + \exp(E - E_{fn})/kT)^{-1}$ is the trap occupancy function, E_{fn} is the quasi-Fermi level, $\omega = 2\pi f$ is the angular frequency, t_{ox} is the oxide thickness, and $(E_c - E_v)$ is the silicon energy bandgap.

To evaluate the integral in (136), two assumptions are made: (1) the oxide traps have a uniform spatial distribution near the interface, [i.e., $N_t(E, x, y, z) = N_t(E)$] and (2) the probability of an electron penetrating into the oxide decreases exponentially with the distance from the interface. As a result of the second assumption, the trapping time constant is given by

$$\tau = \tau_0(E) \exp(\gamma z) \quad (137)$$

where $\tau_0(E)$ is the time constant at the interface and γ is the attenuation coefficient of the electron wavefunction in the oxide [118]. WKB (Wentzel Kramer Brillouin) theory for carrier tunneling predicts that

$$\gamma = \frac{4\pi}{h} (2m^* \phi_B)^{1/2} \quad (138)$$

where m^* is the effective mass of the carrier in the oxide, h is Planck's constant, and ϕ_B is the tunneling barrier height faced by the carriers at the interface [118]. For the Si-SiO₂ system the value of γ is typically taken to be 10^8 cm^{-1} . Since $f_t(1 - f_t)$ in (136) behaves like a delta function around the quasi-Fermi level, the major contribution to the integral will be from those trap levels around E_{fn} . Thus $N_t(E)$ can be approximated by $N_t(E_{fn})$ and taken out from the integral. Replacing $f_t(1 - f_t)$ by $-kT df_t/dE$ and carrying out the integration yields

$$S_{\Delta N_t}(x, f) = N_t(E_{fn}) \frac{kTW\Delta x}{\gamma f} \quad (139)$$

The total drain current noise power turns out to be

$$S_{Id} = \frac{1}{L^2} \int_0^L S_{Id}(y, f) \Delta y dy \quad (140)$$

$$= \frac{kTI_{ds}^2}{W\gamma f L^2} \int_0^L N_t(E_{fn}) \left(\frac{1}{N} + \alpha_1 \mu_{n0} \right)^2 dy$$

where k is the Boltzmann constant, T is the absolute temperature, γ is the attenuation coefficient of the electron

wavefunction in the oxide, f is the frequency of the noise spectrum, α_1 is the scattering coefficient associated with the trapped charge, N_t is the trap density per unit energy, and E_{fn} is the quasi Fermi level. Using (111) and (117), Eq. (140) is modified for FOLD structure taking the series resistance into account to obtain

$$S_{Id} = \frac{kTI_{ds}}{W\gamma f L^2} \int_0^{V'_{ds}} \frac{(-\mu_{n0} W Q_n - \beta I_{ds})}{1 + \frac{\alpha C_{ox}}{2\epsilon_{si}} \left(V'_{gs} - V_{FB} - \phi_s + \frac{|Q_B|}{C_{ox}} \right)} \times N_t(E_{fn}) \frac{1}{N^2} (1 + \alpha_1 \mu_{n0} N)^2 dV(y) \quad (141)$$

where Q_n is the electron density per unit area along the channel direction given by

$$Q_n = qN = -C_{ox}(V'_{gs} - V_{th} - V(y)) \quad (142)$$

where q is the electron charge and N is the number of channel carriers per unit area. Threshold voltage no longer remains independent of drain bias and varies as

$$V_{th} = V_{t0} - KV(y) \quad (143)$$

where V_{t0} is the threshold voltage at zero drain bias, and K is the slope of threshold voltage-vs drain voltage curve at zero drain bias. Substitution of (143) in (142) gives

$$Q_n = -C_{ox}(V'_{gs} - V_{t0} - \lambda V(y)) \quad (144)$$

where $\lambda = 1 - K$ and α_1 and μ_{n0} are functions of the local carrier density, which by itself is a function of the local quasi-Fermi level. Using (142), (141) can be written as

$$S_{Id} = \frac{q^2 kTI_{ds}}{W\gamma f L^2} \int_0^{V'_{ds}} \frac{(-\mu_{n0} W Q_n - \beta I_{ds})}{1 + \frac{\alpha C_{ox}}{2\epsilon_{si}} \left(2(V'_{gs} - V_{FB} - \phi_s) + \frac{Q_n}{C_{ox}} \right)} \times \frac{N_t^*(E_{fn})}{Q_n^2} dV(y) \quad (145)$$

where

$$N_t^*(E_{fn}) = N_t(E_{fn})(1 + \alpha_1 \mu_n N)^2 \quad (146)$$

Using (144), one obtains

$$N_t^*(E_{fn}) = N_t(E_{fn}) \left(1 + \alpha_1 \mu_{n0} \frac{Q_n}{q} \right)^2 \quad (147)$$

$$\approx A_2 + B_2 Q_n + C_2 Q_n^2$$

where

$$A_2 = N_t, \quad B_2 = \frac{2\alpha_1 \mu_n N_t}{q}, \quad \text{and } C_2 \text{ is a fitting constant}$$

Also from (144) we obtain

$$dQ_n = C_{ox} \lambda dV \quad (148)$$

Therefore in the strong inversion regime, (145) can be written as

$$S_{Id} = \frac{q^2 k T I_{ds}}{W \gamma L^2} \int_{Q_{ns}}^{Q_{nd}} \frac{(-\mu_{n0} W Q_n - \beta I_{ds})}{1 + \frac{\alpha C_{ox}}{2 \epsilon_{si}} \left(2(V'_{gs} - V_{FB} - \phi_s) + \frac{Q_n}{C_{ox}} \right)} \left(\frac{1}{\lambda C_{ox}} \right) \times \left(\frac{A_2}{Q_n^2} + \frac{B_2}{Q_n} + C_2 \right) dQ_n \quad (149)$$

Therefore, S_{Id} and the drain voltage spectral density $S_{vd} = S_{Id}/g_d^2$ can be obtained from Equ. (149) and the derivation is given in Refs. 119 and 120.

The variations of S_{vd} and S_{Id} with drain voltage V_{ds} are shown in Figs. 57 and 58, respectively, with the gate voltage V_{gs} as a parameter. The oxide interface traps interact with the channel through carrier capture and generation, which causes a change in scattering rate when the trap becomes occupied. Therefore with the increase in drain voltage, the scattering phenomenon in the channel increases, thus increasing the noise.

In Fig. 59 S_{Id} increases with the gate voltage and saturates at higher gate and drain voltages. Figure 60 shows the variation of S_{vd} with gate voltage V_{gs} for LDD and FOLD devices with V_{ds} as a parameter. Since the trap concentration increases exponentially from midgap to band edges, a bias across the oxide will cause the tunneling of carriers to encounter more traps deeper into the oxide, which in turn will make the lower frequency region of the power spectrum more pronounced.

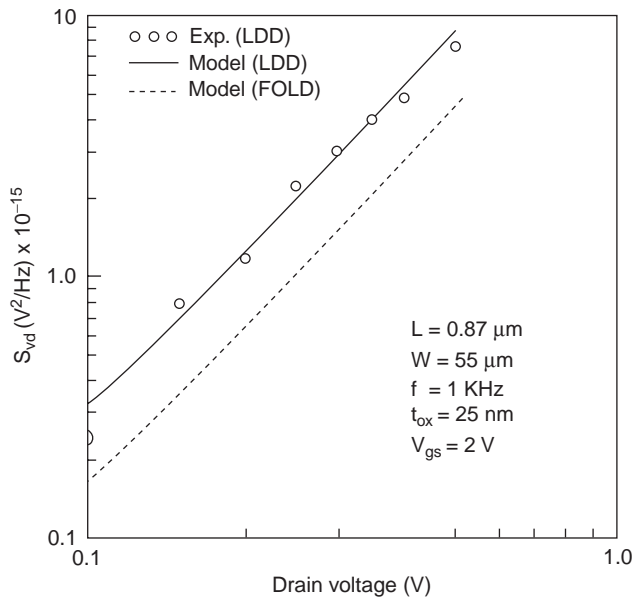


Figure 57. Variation of S_{vd} with V_{ds} ($\mu_{n0} = 604 \text{ cm}^2/\text{V} \cdot \text{s}$, $\gamma = 10^8 \text{ cm}^{-1}$, $\alpha_1 = 10^{-16} \text{ V} \cdot \text{s}$, $\eta = 5.05 \times 10^{-2} \text{ V}^{-1}$, $\alpha = 1.6 \times 10^{-7} \text{ cm V}^{-1}$, $\beta = 0.15 \times 10^{-6} \text{ cm/V}$).

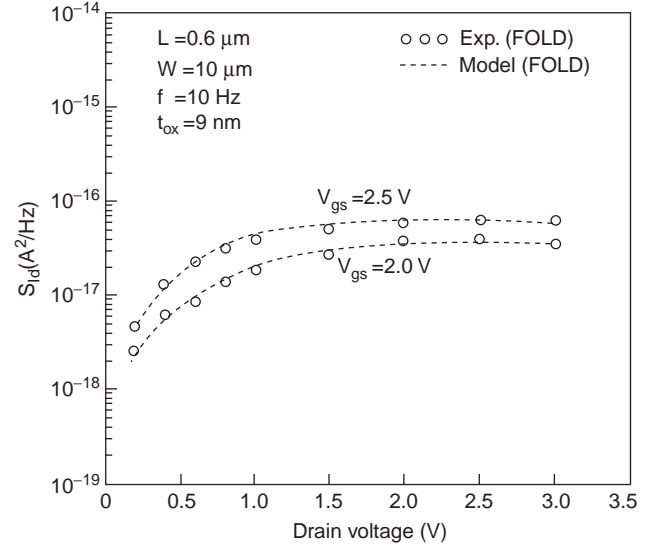


Figure 58. Variation of S_{Id} with V_{ds} ($\mu_{n0} = 600 \text{ cm}^2/\text{V} \cdot \text{s}$, $\gamma = 10^8 \text{ cm}^{-1}$, $\alpha_1 = 4 \times 10^{-15} \text{ V} \cdot \text{s}$, $\eta = 4 \times 10^{-2} \text{ V}^{-1}$, $\alpha = 8 \times 10^{-7} \text{ cm/V}$, $\beta = 3 \times 10^{-6} \text{ cm/V}$).

Therefore, as the gate bias increases, the slope of the power spectral density should increase. The comparison of the $1/f$ noise of the LDD and FOLD MOSFET is also shown in the figure. It is observed that the noise is less in FOLD MOSFET.

5.5. Formulation of the G-R noise model

It is assumed that the drain current spectral density contributed by the n^- regions is negligible compared with that produced in the intrinsic channel. Accounting for the

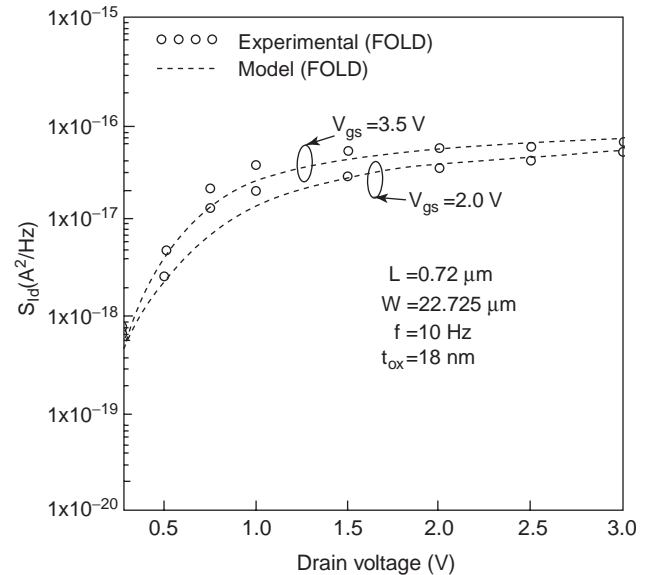


Figure 59. Variation of S_{Id} with V_{ds} at different V_{gs} ($\mu_{n0} = 600 \text{ cm}^2/\text{V} \cdot \text{s}$, $\gamma = 10^8 \text{ cm}^{-1}$, $\alpha_1 = 4 \times 10^{-15} \text{ V} \cdot \text{s}$, $\eta = 4 \times 10^{-2} \text{ V}^{-1}$, $\alpha = 8 \times 10^{-7} \text{ cm/V}$, $\beta = 3 \times 10^{-6} \text{ cm/V}$). (Experimental data from Ref. 122.)

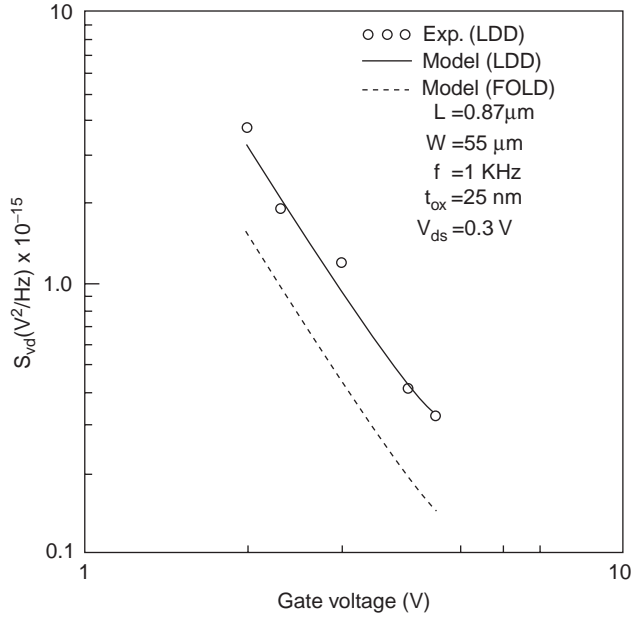


Figure 60. Variation of S_{vd} with V_{gs} ($\mu_{n0}=604 \text{ cm}^2/\text{V}\cdot\text{s}$, $\gamma=10^8 \text{ cm}^{-1}$, $\alpha_1=10^{-16} \text{ V}\cdot\text{s}$, $\eta=5.05 \times 10^{-2} \text{ V}^{-1}$, $\alpha=1.6 \times 10^{-7} \text{ cm/V}$, $\beta=0.15 \times 10^{-6} \text{ cm/V}$). (Experimental data from Ref. 121.)

field-dependent mobility and bias-dependent series resistance, the theory of low-frequency GR noise derived by Yau and Sah [123] can be modified. The drain current spectral density due to the GR process in the depletion region of a FOLD MOSFET can be written as

$$S_{I_{GR}} = \frac{4q^2 I_{ds} N_t}{C_{ox}^2 L} \int_0^{V'_{ds}} \frac{\mu_n}{V''_{gs} - V(y)} dV(y) \cdot \int_0^{W_d} f_t \frac{(1-f_t)t_{GR}}{1+\omega^2 t_{GR}^2} \left(1 - \frac{x}{W_d}\right) dx \quad (150)$$

where N_t is the trap density, f_t is the fraction of occupied defect centers, and t_{GR} is the fluctuation constant given in Ref. 124. If the depletion approximation is assumed, then f_t and t_{GR} can be approximately taken as constant, and one gets

$$S_{I_{GR}} = \frac{4q^2 I_{ds} N_t f_t (1-f_t) t_{GR}}{3C_{ox}^2 L (1+\omega^2 t_{GR}^2)} \int_0^{V'_{ds}} \frac{\mu_n}{V''_{gs} - V(y)} W_d dV(y)$$

$$W_d = \sqrt{\frac{2\epsilon_{si}}{qN_a} (2\phi_F + V(y))} \quad (151)$$

Using (111), (116), and (117), one gets

$$\frac{dV(y)}{dy} = \frac{I_{ds} + \frac{\alpha C_{ox} I_{ds}}{2\epsilon_{si}} \left(V'_{gs} - V_{FB} - \phi_{ss} + \frac{|Q_B|}{C_{ox}} \right)}{\left(\mu_{n0} W C_{ox} \left(V'_{gs} - V_{FB} - \phi_{ss} - \frac{|Q_B|}{C_{ox}} \right) - \beta I_{ds} \right)} \quad (152)$$

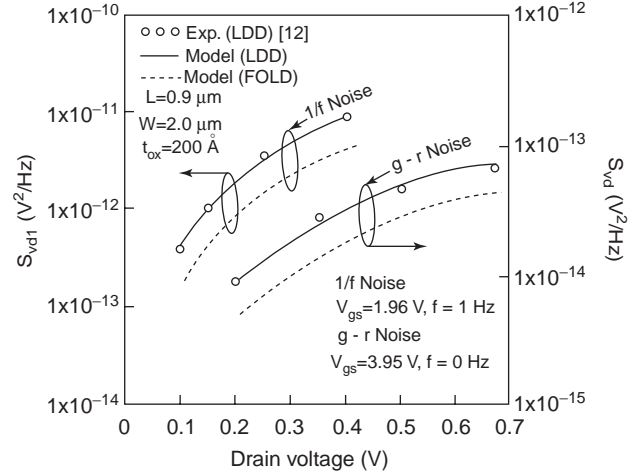


Figure 61. Variation of (S_{vd}) due to GR noise and (S_{vd1}) due to $1/f$ noise with V_{ds} ($\mu_{n0}=597.3 \text{ cm}^2/\text{V}\cdot\text{s}$, $N_t=7.99 \times 10^{11} \text{ cm}^{-3}$, $\eta=4.459 \times 10^{-2} \text{ V}^{-1}$, $\alpha=0.72 \times 10^{-6} \text{ cm/V}$, $\beta=4.9 \times 10^{-6} \text{ cm/V}$). (Experimental data from Ref. 125.)

After some mathematical manipulation of (117), μ_n can be rewritten as

$$\mu_n = \frac{\mu_{n0} \left(V''_{gs} - V(y) - \frac{\beta I_{ds}}{\mu_{n0} W C_{ox}} \right)}{(V''_{gs} - V(y)) \left(1 + \frac{\alpha |Q_B|}{\epsilon_{si}} + \frac{\alpha C_{ox}}{2\epsilon_{si}} (V''_{gs} - V(y)) \right)} \quad (153)$$

where

$$V_{t0} = V_{FB} + 2\phi_F + \frac{|Q_B|}{C_{ox}} \quad (154a)$$

$$V''_{gs} = V_{gs} - V_{t0} - I_{ds}(R_{ns} + R_s) = V'_{gs} - V_{t0} \quad (154b)$$

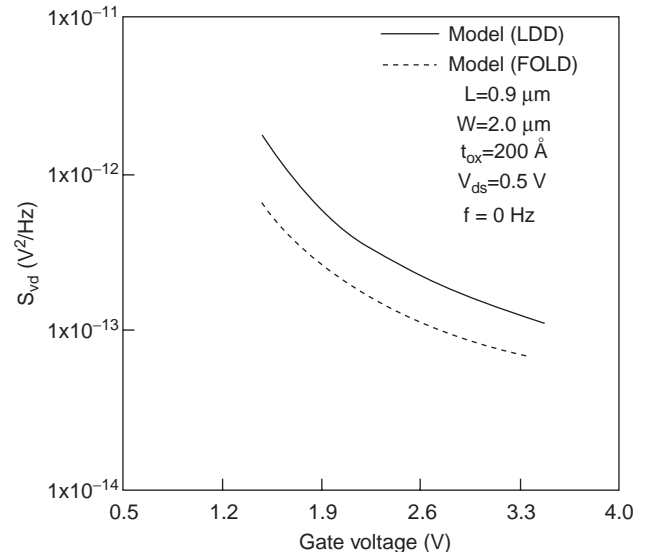


Figure 62. Variation of S_{vd} due to GR noise with V_{gs} ($\mu_{n0}=597.3 \text{ cm}^2/\text{V}\cdot\text{s}$, $N_t=7.99 \times 10^{11} \text{ cm}^{-3}$, $\eta=4.459 \times 10^{-2} \text{ V}^{-1}$, $\alpha=0.72 \times 10^{-6} \text{ cm/V}$, $\beta=4.9 \times 10^{-6} \text{ cm/V}$, $V_{ds}=0.5 \text{ V}$).

Substituting (154) into (152) and integrating, one gets the GR noise as a function of device terminal voltage [120]. The drain voltage spectral density due to the $1/f$ and GR noises in the intrinsic channel can be written as

$$S_{Vd} = \frac{(S_{1/f} + S_{IGR})}{g_d^2} \quad (155)$$

where g_d is the drain conductance and $S_{1/f}$ is the $1/f$ current noise. In Fig. 61 the variation of GR noise and $1/f$ noise with drain voltage is shown. It is found that the noises increase in direct proportion to drain voltage. The variation of GR noise with gate voltage is shown in Fig. 62. It is clear from the figure that GR noise decreases with increase in gate voltage. It is also observed that noise in a FOLD structure is less than that in a LDD MOSFET.

6. SUMMARY

The MOSFET plays an important role in the design of analog circuits. In designing a RF amplifier, it is necessary to explore the circuit parameters such as admittance parameters and scattering parameters. The small-signal behavior of a device at higher frequencies around a bias point is usually determined by scattering parameters over its operational bandwidth. The scattering parameters are used to represent the signal power gain and mismatch losses, as they are frequency-dependent, and an adequate representation of circuit elements over their whole operational ranges is essential for MMIC design. Therefore, there is a need for an optimized model that can account for these process parameter variations (such as basic physical effects of geometry) in addition to SCEs encountered in submicrometer Si MOSFET. There is also a need to develop an AC model to explore RF circuit performance of a MOSFET.

In the article, a comparative study has been made to explore the circuit parameters, and the results have been verified through the characterization. As device dimensions are scaled down, the long channel device characteristics are no longer retained. In order to retain the long-channel characteristics of submicrometer devices, it is proposed to incorporate the various SCEs such as narrow channel effect, mobility degradation effect, subthreshold degradation, substrate effect, and fringing field effect.

The microwave characteristics of short-gate-length MOSFET in terms of S parameters have been reported incorporating various effects such as substrate effect, fringing field effect and the effect of gate and drain contact pads. The results so obtained show that the circuits with shorter-gate-length devices are useful in RF circuit models. Since the analysis relates the intrinsic network parameters to the basic device physical parameters, it should be possible to exploit them not only for calculation of RF circuit performance of various types of MOS transistors but also to improve the device performance through proper design and optimization of the structure itself. Later, an analytical model of MOSFET for the drain characteristics is presented to show its variation with gate-source voltage. Besides this, a small-signal analysis

is carried out incorporating the SCEs and the effect of gate distributed inductance.

A detailed study of AC analysis of MOSFET from its current equations, obtained from analyzing the current continuity equation, is presented next. The design of RF CMOS ICs requires MOS transistor models that are accurate up to and beyond the gigahertz range. Simple expressions for Y parameters and S parameters are derived from the physics of the device incorporating the CLM effect, which is generated from decreasing the channel length and provides an additional AC output current. Therefore this effect enhances the output conductance. The model gives a better insight into the device frequency behavior at HF and for a direct extraction of RF model parameters. Modified expression of scattering parameters is also presented, including the fringing field effect and the effect of distributed gate inductance. The results so obtained show that the circuits for a short-channel-length device are useful in microwave frequency applications.

In Section 5, the parasitic resistance for a FOLD structure is considered as a combination of two buried-channel MOSFETs in series with an enhancement-mode MOSFET. Further, an analytic I_d-V_d model is also developed and the impact of series resistance on drain current is studied. It is found that the FOLD MOSFET has better current drivability than does the LDD MOSFET. Transconductance, drain conductance, channel resistance, cutoff frequency, and transit time are also studied. It is observed that the FOLD structure shows results better than those for the LDD structure because of reduced series resistance. An analytical model has been presented to characterize the $1/f$ and GR noise in the FOLD MOSFETs operating in the linear region. The $1/f$ noise model is developed on the basis of oxide-trap-induced carrier number and surface mobility fluctuations. The model takes into account the longitudinal and transverse field-dependent mobility and the series resistance of the n^- region. It is observed that the noise is less in FOLD MOSFET because of the lesser voltage drop in the n^- region.

BIBLIOGRAPHY

1. J. E. Lilienfeld, *Method and Apparatus for Controlling Electric Current*, U.S. Patent 1,745,175 (Jan. 28, 1930); Canadian application filed Oct. 1925; U.S. application filed Oct. 1926.
2. M. M. Attalla, E. Tannebaum, and E.J. Scheibner, Stabilization of silicon surfaces by thermally grown oxides, *Bell Syst. Tech. J.*, **39**:749–783 (May 1959).
3. D. Kahng and M. M. Attalla, Silicon-silicon dioxide field induced devices, Solid State Device Research Conf. Pittsburgh, PA, June 1960; see also references such as D. Kahng, A historical perspective on the development of MOS transistor and related devices, *IEEE Trans. Electron. Devices* **ED-23**:655–660 (1976); J. D. Meindl, Ultralarge scale integration, *ibid.*, **ED-31**:1555–1561 (1984).
4. J. P. Colinge, *Silicon-on-Insulator Technology: Materials to VLSI*, 2nd ed. Kluwer Academic, 1997.
5. K.W. Chai and J. J. Paulos, Unified non-quasi-static modeling of the long-channel four-terminal MOSFET for

- large- and small-signal analyses in all operating regimes, *IEEE Trans. Electron. Devices* **36**:2513–2520 (1989).
6. A. Goswami, A. Agrawal, M. Gupta, and R. S. Gupta, Admittance parameter extraction of short gate length MOS-FET including substrate effect for microwave frequency applications, *Proc. Progress in Electromagnetic Research Symp.*, Massachusetts (USA), 2000, pp. 1060.
 7. J. J. Paulos and D. A. Antoniadis, Limitations of quasi-static capacitance models for the MOS transistors, *IEEE Electron. Device Lett* **4**:221–224 (1983).
 8. K. Lehovec and A. Slobodsky, Impedance of semiconductor-Insulator-metal capacitors, *Solid-State Electron.* **7**:59–79 (1964).
 9. S. R. Hofstein, K. H. Zaininger, and G. Warfield, Frequency response of the surface inversion layer in silicon, *Proc. IEEE* **52**:971–972 (1964).
 10. H. Preier, Different mechanisms affecting the inversion layer transient response, *IEEE Trans. Electron. Devices.* **15**:990–997 (1968).
 11. D. R. Frankle, Some effects of material parameters on the design of space charge varactors, *Solid-State Electron.* **7**:59–79 (1964).
 12. K. N. Ratnakumar and J. D. Meindl, Short-channel MOST threshold voltage model, *IEEE J. Solid-State Circ.* **17**(5):937–948 (1982).
 13. A. S. Grove, E. H. Snow, B. E. Deal, and C. T. Sah, Simple physical model for the space-charge capacitance of metal oxide semiconductor structures, *J. Appl. phys.* **35**:2458–2460 (1964).
 14. C. T. Sah, R. N. Noyce, and W. Shockley, Carrier generation and recombination in p-n junction characteristics, *Proc. IRE.* **45**:1228–1243 (1957).
 15. A. S. Grove, B. E. Deal, E. H. Snow and C. T. Sah, Investigation of thermally oxidized silicon surfaces using metal-oxide-semiconductor structures, *Solid-State Electron.* **8**:145–163 (1965).
 16. C. H. Choi, P. R. Chidambaram, R. Kamankar, C. F. Machala, Z. Yu, and R. Dutton, Dopant profile and gate geometric effects on polysilicon gate depletion in Scaled MOS, *IEEE Trans. Electron. Devices* **49**(7):1227–1231 (July 2002).
 17. S. Horiuchi and J. Yamaguchi, Diffusion of boron in silicon through oxide layer, *Jpn. J. Appl. Phys.*, **1**:314–323 (1962).
 18. E. Josse and T. Skotnicki, Polysilicon gate with depletion-or-metallic gate with buried channel: what evil worse? *IEDM Techn. Digest*, 1999.
 19. H. G. Ansell, Networks of transmission lines and lumped reactances, *IEEE Trans. Circ. Theory.* **11**:214–223 (1964).
 20. A. Van der Ziel and J. W. Ero, Small-signal high frequency theory of field-effect transistors, *IEEE Trans. Electron. Devices.* **11**:128–135 (April 1964).
 21. R. S. Cobbold, *Theory and Application of Field Effects Transistors*, Wiley-Interscience, New York, 1970, pp. 336–339.
 22. P. J. V. Vandelloo and W. M. C. Sansen, Modeling of the MOS transistor for high frequency analog design, *IEEE Trans. Comput. Aided Design*, **8**(7):713–723 (1989).
 23. R. Pehlke, M. Schroter, A. Burstein, M. Matloubian, and M. F. Chang, High-frequency application of MOS compact models and their development for scalable RF model libraries, *Proc. IEEE Custom Integrated Circuits Conf.* 1998, pp 10.6.1–10.6.4.
 24. J. R. Hauser, Small-signal properties of field-effect devices, *IEEE Trans. Electron. Devices.* **12**:605–618 (Dec. 1965).
 25. B. Reddy and F. N. Trofimenkoff, FET high frequency analysis, *Proc. IEE (Lond.)*, **113**:1755–1762 (Nov. 1966).
 26. J. A. Geurst, Calculation of high-frequency characteristics of thin film transistors, *Solid State Electron.* **8**:88–90 (1965).
 27. W. Fischer, Equivalent circuit and gain of MOS field effect transistors, *Solid State Electron.* **9**:71–81 (1965).
 28. D. B. Candler and A. G. Jordan, A small signal analysis of insulated gate field effect transistor, *Int. J. Electron.* **19**:181–196 (1965).
 29. D. H. Treleven and F. N. Trofimenkoff, MOSFET equivalent circuit at pinch-off, *Proc. IEEE.* **54**:1223–1224 (1966).
 30. J. R. Burns, High-frequency characteristics of the insulated gate field effect transistor, *RCA Rev.* **28**:385–418 (1967).
 31. M. B. Das, Generalised high frequency network theory of field effect transistors, *Proc. IEE.* (Lond.) **114**:50–59 (1964).
 32. H. F. Jhantola and J. L. Moll, Design theory of a surface field effect transistor, *Solid-State Electron.* **7**:423–430 (1964).
 33. V. P. Popov and T. A. Bickart, RC transmission line with nonlinear controlled parameters-small-signal characteristics, *IEEE Trans. Circ. Syst.* **21**(2):268–270 (1974).
 34. T. Kacprazak, The method for determination small-signal admittance matrix of the RC transmission line with voltage-controlled parameters, *IEEE Trans. Circ. Syst.* **27**(4):318–320 (1980).
 35. Y. P. Tividis, MOSFET modeling for analog circuit CAD: problems and prospects, *IEEE J. Solid State Circ.* **29**:210–216 (1994).
 36. H. J. Park, P. K. Ko, and C. Hu, A nonquasi-static MOSFET model for SPICE-AC analysis, *IEEE Trans. Comput. Aided Design*, **11**(10):1247–1257 (1992).
 37. M. Bagheri and Y. P. Tividis, A small-signal dc-to high frequency nonquasistatic model for four-terminal MOSFET valid in all regions of operation, *IEEE Trans. Electron. Devices.* **32**(11):2383–2391 (1985).
 38. M. B. Das, High-frequency network properties of MOS transistors including the substrate resistivity effects, *IEEE Trans. Electron. Devices.* **16**(12):1049–1069 (1969).
 39. L. S. Kim and R. W. Dutton, Modeling of the distributed gate RC effect in MOSFET's, *IEEE Trans. Comput.-Aided Design.* **8**:1365–1367 (1989).
 40. B. Razavi, R. H. Yan, and K. F. Lee, Impact of distributed gate resistance on the performance of MOS devices, *IEEE Trans. Circ. Syst. I, Fund. Theory Appl.* **41**(11):750–754 (1994).
 41. E. A. Allam and T. Manku, A small-signal MOSFET model for radio frequency IC applications, *IEEE Trans. Comput.-Aided Design.* **16**(5):437–447 (1997).
 42. A. Goswami, A. Agrawal, S. Bose, S. Halder, M. Gupta, and R. S. Gupta, Substrate effect dependent Scattering parameter extraction of short gate length IGFET for microwave frequency applications, *Microwave Opt. Tech. Lett.* **24**(5):341–348 (2000).
 43. R. Sung, P. Bendix, and M. B. Das, Extraction of high-frequency equivalent circuit parameters of submicron gate-length MOSFET's, *IEEE Trans. Electron. Devices.* **45**(8):1769–1775 (1998).
 44. B. M. Guy, Z. Ouarch, M. Prigent, R. Quere, and J. Obregon, Direct extraction of a distributed nonlinear FET model from pulsed I-V/pulsed S-parameter measurements, *IEEE Microwave Guided Wave Lett.* **8**(2):102–104 (1998).
 45. S. Lee and H. K. Yu, A semi analytical parameter extraction of a SPICE BSIM3v3 for RF MOSFET's using S-parameters, *IEEE Trans. Microwave Theory Tech.* **48**(3):412–416 (2000).

46. N. Camilleri, J. Costa, D. Lovelace, and D. Ngo, Silicon MOSFET, the microwave device technology for the 90s, *IEEE MTT-S Digest*, 1993, pp. 545–548.
47. I. Yoshoda and M. Katsueda, Highly efficient 1.5 GHz band Si power MOS amplifier module, *IEICE Trans. Electron.* **E78-C**:979 (1995).
48. P. Yang and P. K. Chatterjee, SPICE modeling for small geometry MOSFET circuits, *IEEE Trans. Comput.-Aided Design*, **1**:169–182 (1982).
49. P. Yang, B. D. Epler, and P. K. Chatterjee, An investigation of the charge conservation problem for MOSFET circuit simulation, *IEEE J. Solid-State Circ.* **18**:128–138 (1983).
50. G. Baccarani, M. R. Wordeman, and R. H. Dennard, Generalised scaling theory and its application to 1/4 micrometer MOSFET design, *IEEE Trans. Electron. Devices*, **31**:452 (1984).
51. Y. Cheng, T. Sugif, K. Chen, and C. Hu, Modeling of small size MOSFETs with reverse short channel and narrow width effects for circuit simulation, *Solid-State Electron.* **41**(9):1227–1231 (1997).
52. R. S. Gupta and M. Bhatia, Inverse Narrow width effect and small geometry MOSFET threshold voltage model, *IEEE Trans. Electron. Device*, **ED-40**(3):681 (1993).
53. K. Ohe, S. Odanaka, K. Moriyama, T. Hori, and G. Fuse, Narrow-width effects of shallow trench-isolated CMOS with n^+ -polysilicon gate, *IEEE Trans. Electron. Devices*. **ED-36**(6):1110–1116 (June 1989).
54. R. Saleem, C. Thomas, S. Haldar, and R. S. Gupta, A fringing field dependent 2-D model for non uniformly doped short channel MOSFETs, *Int. J. Electron.* **86**(4):381–390 (1999).
55. R.S. Gupta, Maneesha, M. K. Khanna, and S. Haldar, An empirical, fringing capacitance threshold voltage model for short channel MOSFETs, *Solid-State Electron.* **39**:1687–1691 (1996).
56. D. Lovelace, J. Costa, and N. Camilleri, Extracting small signal model parameters of silicon MOSFET transistors, *IEEE MTT-S Tech. Digest*, 1994, pp. 864–868.
57. A. A. Abidi, Low-power radio frequency IC's for portable communications, *Proc. IEEE*. **83**(4):544–569 (1995).p
58. G. D. Dambrine, A. Cappy, F. Helidore, and E. Playez, A new method for determining the FET small-signal equivalent circuit, *IEEE Trans. Microwave Theory Tech.*, **36**:1151–1156 (1998).
59. A. Goswami, A. Agrawal, S. Haldar, M. Gupta, and R. S. Gupta, Fringing field dependent small geometry MOSFET model for radio frequency application, *Proc. Int. Workshop on Physics of Semiconductor Devices*, New Delhi, India, 1999, Vol. II, pp. 568–571.
60. C. H. Chen, M. J. Deen, Z. X. Yan, M. Schroter, and C. Enz, High frequency noise of MOSFETs II experiments, *Solid-State Electron.* **42**(11):2083–2092 (1998).
61. A. Goswami, A. Agrawal, C. T. Thuruthiyil, M. Gupta, and R. S. Gupta, Small-signal analytical MOSFET model for microwave frequency applications, *Microwave Opt. Tech. Lett.* **25**(5):346–352 (2000).
62. N. D. Arora, *MOSFET Models for VLSI Circuit Simulation*, Springer-Verlog, Vienna/New York, 1993.
63. G. Sodhini, P. K. Ko, and J. L. Moll, The effect of high fields on MOS device and circuit performance, *IEEE Trans. Electron. Devices*. **31**(10):1386–1393 (1984).
64. C. E. Biber, M. L. Schmartz, and T. Morf, Improvements on a MOSFET model for nonlinear RF simulation, *IEEE MTT-S Digest*, Denver, CO, 1997, pp. 865–868.
65. G. A. Hoile and H. C. Reader, Nonlinear MOSFET model for the design of RF power amplifier, *Proc. IEE*. **139**(5):574–580 (1992).
66. S. Lee and H. K. Yu, Accurate high-frequency equivalent circuit model of silicon MOSFET, *Electron. Lett.* **35**(17):1406–1407 (1999).
67. A. Goswami, M. Gupta, and R. S. Gupta, Analysis of scattering parameters and thermal noise of a MOSFET for its microwave frequency applications, *Microwave Opt. Technol. Lett.* **31**(2):97–105 (Oct. 20, 2001).
68. Y. Tsvividis and G. Masetti, Problems in the precision modeling of the MOS transistor for analog application, *IEEE Trans. Comput. Aided Design*. **3**:72–79 (1984).
69. H. J. Park, P. K. Ko, and C. Hu, A charge-conserving non-quasistatic MOSFET model for SPICE transient analysis, *IEEE IEDM Tech. Digest*, 1988, pp. 110–113.
70. E. Ward and R. W. Dutton, A charge-oriented model for MOS transistor capacitances, *IEEE J. Solid-State Circ.* **13**:703–707 (1978).
71. W. Budde and W. H. Lamfried, A charge sheet capacitance model based on drain current modeling, *IEEE Trans. Electron. Devices*. **37**:1678–1687 (1990).
72. M. F. Barciela, P. J. Tasker, Y. C. Roca, M. Demmler, H. Massler, E. Sanchez, C. C. Francos, and M. Schlechtweg, A simplified broad-band large-signal nonquasistatic table-based FET model, *IEEE Trans. Microwave Theory Tech.* **48**(3):395–405 (2000).
73. S. Y. Oh, D. E. Ward, and R. W. Dutton, Transient analysis of MOS transistors, *IEEE J. Solid-State Circ.* **15**(4):636–643 (1980).
74. C. Turchetti and G. Masetti, A CAD-oriented analytical MOSFET model high accuracy application, *IEEE Trans. Comput.-Aided Design*. **3**(2):117–122 (1984).
75. H. J. Park, P. K. Ko, and C. Hu, A non -quasistatic MOSFET model for SPICE, *IEEE IEDM Tech. Digest*, 1987, pp. 652–655.
76. R. Gharabagi and M. L. Nokali, Quasi-static model for the capacitances in short-channel MOSFETs, *Int. J. Electron.* **68**(2):181–193 (1990).
77. A. Goswami, A. Agrawal, M. Gupta, and R. S. Gupta, High frequency Y-parameters analysis of small geometry MOSFET for microwave frequency applications, *Proc. Int. Symp. Recent Advances in Microwave Technology*, Malaga, Spain, 1999, pp. 125–129.
78. M. Nokali and H. Miranda, A simple model for an MOS transistor in saturation, *Solid-State Electron.* **29**:591 (1986).
79. S. M. Sze, *Physics of Semiconductor Devices*, 2nd ed., Wiley, New York, 1981, pp. 480–482.
80. Y. Cheng et al., *BSIM3 Version 3 User's Manual*, Univ. California, Berkeley, Memo UCB/ERL M97/2, 1997.
81. Robert F. Pierret, Modular series on solid state devices, in *Field Effect Transistors*, Academic Press, Vol. IV, 1983.
82. S. H. M. Jen, C. C. Enz, D. R. Pehle, M. Schroter, and B. J. Sheu, Accurate modeling and parameter extraction for MOS Transistor valid up to 10GHz, *IEEE Trans. Electron. Devices*. **46**(11):2217–2227 (1999).
83. G. Sodhini, P. K. Ko, and J. L. Moll, The effect of high fields on MOS device and circuit performance, *IEEE Trans. Electron. Devices*. **31**(10):1386–1393 (1984).
84. A. Goswami, A. Agrawal, M. Gupta, and R. S. Gupta, Extraction of small-signal model parameters of silicon MOSFET for RF applications, *Microwave and Opt. Tech. Lett.* **27**(5):352–358 (Dec. 2000).

85. A. Goswami, *Substrate Effect Dependent Scattering Parameters Extraction and Small-Signal MOSFET Circuit Analysis for Microwave Frequency Applications*, Ph.D. dissertation, Univ. Delhi, New Delhi, India, 2000.
86. S. Ogura, P. Tsang, W. Walker, D. Critchlow, and J. F. Shepard, Design and characteristics of the LDD insulated gate field-effect transistor, *IEEE Trans. Electron. Devices*. **ED-27**:1359 (1980).
87. P. J. Tsang, S. Ogura, W. W. Walker, J. F. Shepard, and D. Critchlow, Fabrication of high performance LDD MOSFETs with oxide-sidewall spacer technology, *IEEE Trans. Electron. Devices*. **ED-29**: pp. 590 (1982).
88. E. Takeda, H. Kume, Y. Nakagome, T. Makino, A. Shimizu, and S. Asai, An As-P ($n^- - n^+$) double diffused drain MOSFET for VLSI, *IEEE Trans. Electron. Devices*. **ED-30**:652 (1983).
89. C. Duvvury, D. A. Baglee, M. C. Smayling, and M. P. Duane, Series resistance modeling for optimum design of LDD transistors, *IEDM Tech. Digest*, 1983.
90. D. A. Baglee, C. Duvvury, M. C. Smayling, and M. P. Duane, Lightly doped drain transistors for advanced VLSI circuit, *IEEE Trans. Electron. Devices*, **ED-32**(5):896 (1985).
91. G. S. Huang, and C. Y. Wu, An analytic I-V model for lightly doped drain (LDD) MOSFET devices, *IEEE Trans. Electron. Devices*. **ED-34**:1311–1322 (June 1987).
92. M. Inuishi, K. Mitsui, S. Kusunoki, H. Oda, K. Tsukamoto, and Y. Akasaka, Gate capacitance characteristics of gate/ n^- overlap LDD transistor with high performance and high reliability, *IEEE IEDM Tech. Digest*, 1991, pp. 371–374.
93. R. Shrivastava and K. Fitzpatrick, Simple model for the overlap capacitance of a VLSI MOS device, *IEEE Trans. Electron. Devices*. **ED-29**:1870–1875 (1982).
94. C. Y. Wu and Y. W. Dai, An accurate mobility model for the I-V characteristics of n-channel enhancement-mode MOSFETs with single-channel boron implantation, *Solid-State Electron*. **28**(12):1271 (1985).
95. F. Matsuoka, K. Kasai, H. Oyamatsu, M. Kinugawa, and K. Maeguchi, Drain structure optimization for highly reliable deep submicrometer n-channel MOSFET, *IEEE Trans. Electron. Devices*. **ED-4**:420–425 (1994).
96. S. L. Jang, S. S. Liu, and C. J. Sheu, A compact LDD MOSFET I-V model based on nonpinned surface potential, *IEEE Trans. Electron. Devices*. **ED-45**(12):2489–2498 (1998).
97. A. Kumar, E. Kalra, S. Haldar, and R. S. Gupta, A new analytical model to determine the drain-source series resistance of FOLD MOSFET, *Semicond. Sci. Technol.* **14**:489–495 (1999).
98. H. W. Ott, *Noise Reduction Techniques in Electronic Systems*, Wiley-Interscience, New York, 1976.
99. A. Van der Ziel, *Noise in Solid State Devices and Circuits*, Wiley-Interscience, New York, 1986.
100. K. M. van Vliet and J. R. Fasset, Fluctuations due to electronic transitions and transport in solids, in R. E. Burgess, ed., *Fluctuation Phenomena in Solids*, Academic, Press, New York, 1965, p. 267.
101. A. D. van Rhee, G. Bosman, and C. M. van Vliet, Decomposition of generation recombination noise spectra in separate Lorentzians, *Solid-State Electron*. **28**:457 (1985).
102. F. N. Hooge and L. Ren, On the generation–recombination noise, *Physica*. **B191**:220 (1993).
103. F. N. Hooge and L. Ren, On the variances of generation–recombination noise in a three-level system, *Physica B*, **B193**:31 (1994).
104. K. Amberiadis and A. van der Ziel, $1/f$ noise in diffused and ion implanted MOS capacitors, *Solid State Electron*. **26**:1009–1071 (1983).
105. T. G. M. Kleinpenning and A. H. de Kuyper, Relation between variance and sample duration of $1/f$ noise signals, *J. Appl. Phys.* **63**:43 (1988).
106. A. L. McWhorter, $1/f$ noise and germanium surface properties, in *Semiconductor Surface Physics*, Univ. Pennsylvania Press, Philadelphia, 1957, p. 207.
107. Z. H. Fang, S. Christoloveanu, and A. Chovet, Analysis of hot carrier induced aging from $1/f$ noise in short channel MOSFETs, *IEEE Electron. Device Lett.* **EDL-7**:371–373 (1986).
108. K. S. Rails et al., Discrete resistance switching in submicrometer silicon inversion layers: Individual interface traps and low frequency ($1/f$) noise, *Phys. Rev. Lett.* **52**(3):228 (1984).
109. C. Surya and T. Y. Hsiang, Surface mobility fluctuations in metal-oxide semiconductor field-effect transistors, *Phys. Rev.* **35**(12):6343 (1987).
110. R. Jayaraman and C. G. Sodini, A $1/f$ noise technique to extract the oxide trap density near the conduction band edge of silicon, *IEEE Trans. Electron. Devices*, **ED-36**:1773 (1989).
111. K. K. Hung, P. K. Ko, C. Hu, and Y. C. Cheng, A unified model for the flicker noise in metal-oxide-semiconductor field-effect transistors, *IEEE Trans. Electron. Devices*. **ED-37**(3):654–665 (March 1990).
112. A. D'Amico and P. Mazzetti, eds., *Proc. 8th Int. Conf. Noise in Physical Systems*, and the *4th Int. Conf. on $1/f$ Noise*, Rome, Sept. 1985; North-Holland, Amsterdam, 1986.
113. Z. Celik-Butler and T. Y. Hsiang, Spectral dependence of $1/f$ noise on gate bias in N-MOSFETS, *Solid-State Electron*. **30**:419–423 (1987).
114. G. Reimbold, Modified $1/f$ trapping noise theory and experiments in MOS transistors biased from weak to strong inversion-Influence of interface states, *IEEE Trans. Electron. Devices*. **ED-31**:1190 (1984).
115. A. Hartstein, A. B. Fowler, and M. Albert, Temperature dependence of scattering in the inversion layer, *Surf. Sci.* **98**:181 (1980).
116. S. C. Sun and J. D. Plummer, Electron mobility in inversion and accumulation layers on thermally oxidized silicon surfaces, *IEEE Trans. Electron. Devices*. **ED-27**:1497 (1980).
117. T. H. Ning and C. T. Sah, Theory of scattering of electrons in a nondegenerate semiconductor-surface inversion layer by surface-oxide charges, *Phys. Rev. B* **6**:4605 (1972).
118. S. Christensson, I. Lundstrom, and C. Svensson, Low frequency noise in MOS Solid transistors-I theory, *Solid-State Electron*. **11**:797 (1968).
119. A. Kumar, E. Kalra, S. Haldar, and R. S. Gupta, $1/f$ noise of fully overlapped lightly doped drain MOSFET, *IEEE Trans. Electron. Devices*. **47**(7):1426–1429 (July 2000).
120. A. Kumar, *An Analytical Model of Hot Carrier Immunized submicron Fully Overlapped Lightly Doped Drain MOSFET for VLSI/ULSI Applications*, Ph.D dissertation, Univ. Delhi, New Delhi, India.
121. S. L. Jang, Analytical low-frequency $1/f$ noise model for lightly doped drain MOSFETs operating in the linear region, *Solid-State Electron*. **36**(6):899–903 (1993).
122. S. L. Jang, H. K. Chen, and M. C. Hu, Low-frequency $1/f$ noise model for short channel LDD MOSFETs, *Solid-State Electron*. **42**(6):891–899 (1998).

123. L. D. Yau and C. T. Sah, Theory and experiments of low frequency generation-recombination noise in MOS transistors, *IEEE Trans. Electron. Devices*, **ED-16**:170–177 (1969).
124. C. T. Sah, The equivalent circuit model in solid state electronics, Parts I and II, *Proc. IEEE*, **55**:654–684 (May 1967).
125. S. L. Jang and P. C. Chang, Low-frequency noise characteristics of lightly doped drain MOSFETs, *Solid-State Electron.* **36**(7):1007–1010 (1993).

MULTIBEAM ANTENNAS

PETER BALLING
 ASC, Antenna Systems
 Consultant, ApS
 Taastrup, Denmark

A *multibeam antenna* (MBA) may be defined as an antenna with the ability to generate multiple independent beams simultaneously from a single aperture. MBAs play an increasingly important role. They add more functions to the systems that they are a part of, increase the capacity of communications systems, preserve the available frequency spectrum and other limited assets, and reduce interference.

This article is divided into three parts:

1. An introductory part (Sections 1–3) that briefly reviews MBAs for radar, satellite, and mobile base station applications and presents simple guidelines for the preliminary antenna sizing. We discuss the implementation of MBAs focusing on the beamforming techniques, giving a number of examples mainly from the satellite antenna field.
2. The central part (Section 4), which reviews the problem of forming simultaneous multiple beams from a common antenna aperture. Much of the early work considered arrays and investigated the limitations and implementation of passive MBA networks. Separate sections discuss the Stein limit of the maximum efficiency possible of an MBA and means to finding passive networks that will realize the Stein limit. The results are extended to array-fed reflector antennas considering also quasiorthogonal beams and dual- and multimode antenna systems.
3. The final part (Section 5), which considers array-fed offset reflector antenna systems, presenting simple design formulas and discussing performance limitations due to scan aberrations and polarization effects caused by the reflector offset. This part ends with a review of compensated dual-offset reflector antenna systems.

1. MULTIBEAM ANTENNA (MBA) APPLICATIONS

MBAs find use, for example, in radar and communication systems, with some typical beamshapes outlined in Fig. 1. A radar may need to illuminate a large sector in elevation with several beams of different widths, see the 1D eleva-

tion pattern cut in inset of Fig. 1a. A narrow high-gain beam is used near the horizon toward distant targets, with increasingly wider beams at higher elevation angles toward closer targets. This provides total coverage in elevation with a single antenna with a small number of beams.

Communication and broadcast satellites have beams tailored to the areas they serve on Earth. The service area is often served by several smaller beams to increase the antenna gain to meet the link budget and/or to increase the communications capacity of the satellite. Beams that are isolated spatially or by polarization can reuse the same frequency band, multiplying the communications capacity by the number of beams using the same band. Modern communication satellites in the geostationary orbit implement this *frequency reuse* by beams in two orthogonal polarizations, namely, either left-hand and right-hand circular polarization or two perpendicular linear polarizations. This technique requires a low level of cross-polarization in the service area and is termed *frequency reuse by polarization isolation*. Satellites with a large coverage reuse the frequency band by spatially separated copolarized beams. Then, the sidelobes falling in the frequency reuse areas must be low, and we talk about *frequency reuse by sidelobe isolation*. The 2D pattern contours in the inset of Fig. 1b indicate a global telecommunication coverage with two large “hemi” beams indicated by the solid line in one hand of polarization and two smaller “spot” beams indicated by the dotted line in the orthogonal hand of polarization.

Mobile communication satellites and satellites in lower Earth orbits designed to work with simpler terminal antennas on the ground use only a single polarization. These satellites often provide a large number of contiguous spot beams of simple shapes, and current mobile satellites may implement a large number of frequency reuses. The inset of Fig. 1c shows about 70 circular footprints and the total frequency bandwidth divided into seven subbands or colors indicated by numbers 1–7. Each subband may then be reused about 10 times.

Cellular mobile or wireless systems with omnidirectional antennas mimic this pattern of multiple spot beams with a base station serving each cell. Cells placed sufficiently far apart can reuse the frequency band. By shrinking the cells and deploying more base stations, the total communication capacity can in principle be increased almost indefinitely. However, this has been found to be a costly and difficult approach except in special dense areas. Therefore, advanced mobile base stations implement multiple beams either by switching between multiple fixed beams in azimuthal sectors or by using smart or adaptive antenna technology, ultimately allowing a single mobile user to be tracked by the base station. Mobile communications are complicated by the fact that the signal, particularly in urban areas, may propagate not only along the line of sight but also along multiple paths providing strong fading and other degradations, or there may be no direct signal. Multibeam base station antennas reduce multipath effects compared to omnidirectional antennas. Alternatively, smart antennas such as MIMO (multiple-input/multiple-output) systems may use the multipath interference to establish multiple independent paths between the

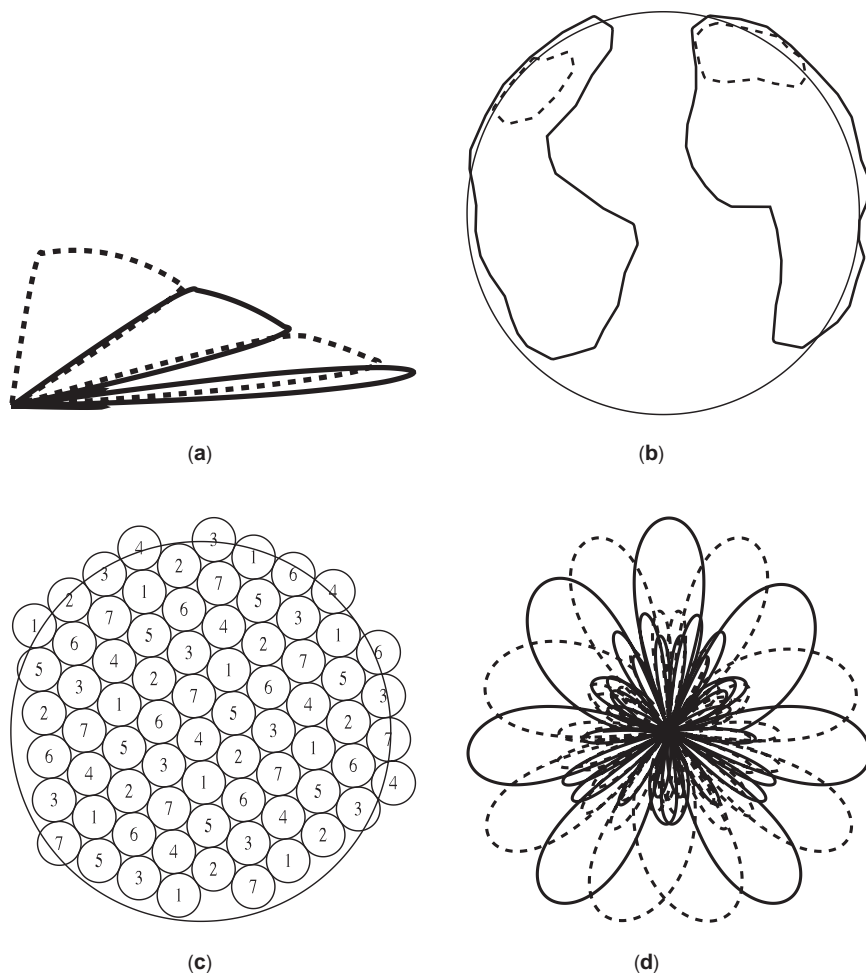


Figure 1. Examples of multibeam antenna applications and patterns: (a) 1D elevation pattern traces of search radar antenna; (b) 2D contours of satellite multiple contoured beam antenna; (c) 2D footprints of satellite multiple spot beam antenna; (d) 1D azimuth pattern traces of mobile base station antenna system.

base station and the mobile station. This requires more complex antenna systems also on the mobile terminal and signal processing [1,2]. MIMO systems are currently subject to intense research as a means to increase the communications capacity, but will not be dealt with in this article.

The inset of Fig. 1d illustrates the 1D pattern cuts of a base station antenna system consisting of three $\pm 60^\circ$ sector antennas with five beams each. Dotted and full lines are used as in inset (a) to distinguish adjacent beams. Some imperfections are evident:

1. The beams are not confined to the desired coverages, but extend into adjacent coverage areas via the finite-gain rolloff and sidelobes. This represents a power loss and an interference if beams reuse the same frequency band.
2. The beamshapes are not constant within their coverages, but intersect at a lower level, the *crossover level*, which often is at least 3 dB below the peak level. Thus, the quality of service will depend on the location in the coverage area even disregarding scattering and shadowing objects between the base station and the mobile terminal.

Similar imperfections due to gain rolloff, sidelobes, and other factors exist for the radar and satellite scenarios. Increasing antenna size and complexity can reduce the imperfections, but may result in unacceptable high costs and difficulties in accommodating the antenna system on the platform.

2. ANTENNA SIZING

The minimum gain that an MBA achieves over its service area depends on many factors such as the extent of the area and antenna size and complexity. Often a preliminary design must be carried out to assess the achievable performance. Some crude estimates may be obtained from tables for linear and circular aperture distributions presented in most antenna textbooks. See Milligan's book [3] for a large collection. These tables apply to antenna apertures that are large compared to the wavelength as the obliquity or Huygens' factor is neglected. Table 1 summarizes for a circular aperture of diameter D normalized with the wavelength λ the amplitude taper, the amplitude taper loss L_{ap} , the half-power beamwidth $\Delta\theta_3$, and the location θ_0 of the first null versus the level of the first sidelobe below peak level. The first line of the table applies to a

Table 1. Properties of Circular Aperture Distributions versus Sidelobe Level^a

Sidelobe (dB)	Taper (dB)	L_{ap} (dB)	$\Delta\theta_3/(\lambda/D)^\circ$	$\theta_0/(\lambda/D)^\circ$
17.6	0	0	59.0	69.9
20	4.3–4.5	0.09	61.7–61.8	75.1–86.5
25	10.7–12.4	0.50–0.60	66.3–67.3	85.2–86.5
30	14.9–19.3	0.92–1.19	69.8–72.2	94.2–97.9
35	17.8–25.8	1.23–1.75	72.3–76.8	101.9–109.5
40	24.4–32.0	2.00–3.08	78.4–81.0	– 121.1

^aLower limit is truncated Gaussian and upper limit, Hansen one-parameter distribution.

uniformly illuminated aperture, where the on-axis directivity is

$$D_0 = \left(\frac{\pi D}{\lambda}\right)^2$$

Ranges are given for the tapered illuminations. The lower limit corresponds to truncated Gaussian distributions and the upper limit, to the Hansen single-parameter distribution. These distributions are not optimum. (No null location is indicated for the Gaussian distribution with 40 dB sidelobe level where the inner sidelobes merge; the Gaussian distribution is not suitable for low sidelobe levels.) The table shows how lower sidelobes require a stronger aperture taper and result in a directivity loss and a wider beam. If the directivity and the beamwidth are to be maintained, a larger antenna is required. The difference $\theta_0 - \Delta\theta_3/2$ indicates the minimum separation between beams reusing the same frequency band. Hansen [4] and Duan and Rahmat-Samii [5] discuss more distributions also applicable to elliptical apertures. Table 2 summarizes properties of the Taylor circular n -bar distribution, which offers narrower beam and lower taper loss for the same peak sidelobe level than those presented in Table 1. It is derived from the uniform distribution by adjusting the first zeros near the main beam to provide n -bar roughly equal sidelobes at the specified level near the main beam. Farther out sidelobes decay as those of the uniform pattern. The values of n -bar in Table 2 have been chosen so that no peak occurs at the edge of the aperture. Antenna tolerance effects due to the array excitation errors, reflector surface errors, and other anomalies degrade in particular sidelobe levels. To implement a peak sidelobe level of 35 dB, it may be necessary to design for 40 dB or even lower sidelobes.

For a circular spot-beam coverage as in Fig. 1c, losses due to amplitude taper and beam crossover must be subtracted. Depending on the technology other losses due to

Table 2. Properties of Taylor Circular n -Bar Aperture Distribution versus Sidelobe Level

Sidelobe (dB)	n -Bar	Taper (dB)	L_{ap} (dB)	$\Delta\theta_3/(\lambda/D)^\circ$	$\theta_0/(\lambda/D)^\circ$
25	3	8.1	0.36	66.1	83.9
30	4	10.7	0.72	68.7	91.7
35	5	13.0	1.09	71.6	100.3
40	6		1.48	74.6	109.4

scan, spillover, tolerances, non-orthogonality of beams, mismatch, and other factors must be subtracted. Finally, Ohmic losses must be subtracted to obtain the antenna gain. For shaped-beam and contoured-beam coverages as in Figs. 1a and 1b, the relation between minimum gain and antenna size is more complex, but some simple expressions have been given by Badessi [6] and Balling [7] for contoured-beam antennas. Badessi derived an expression for the *minimum coverage area directivity*

$$\text{MCAD} = \frac{41253}{A + 67.5C/(D/\lambda)}$$

where A is the area in square degrees and C the contour length in degrees of a contoured beam. This expression neglects the effect of sidelobe isolation. DiFonzo [8] derived an expression for the reflector diameter required to achieve a sidelobe isolation of 27–30 dB between two frequency reuse areas

$$D = \frac{100\lambda}{\sigma}$$

where σ is the spacing between the two areas in degrees.

3. MBA IMPLEMENTATION

Array antennas and phased-array antennas are useful when the multiple beams cover a large angular field of view as in the case of radars, mobile base stations, and satellites in low and medium Earth orbits. Chapters in books by Mailloux [9] and Hansen [4] and Section 4 of this article treat multibeam array antennas, including the crucial problem of how to feed the array by a suitable *beamforming network* (BFN). For applications with a limited field of view as in the case of geostationary satellites, arrays are used as feeds in lens and in particular in offset-fed reflector antenna systems as discussed in book chapters by Ricardi [10] and Rusch et al. [11] and in Section 5 of this article. Satellite applications pose special problems due to the extreme environment during launch and in space and the long lifetimes and high reliability required—see the book by Kitsuregawa [12] and the book chapter by Han and Hwang [13]. Array-fed quasioptical systems provide the ultimately simple MBA when a single feed generates a beam so that no BFNs are required. In general, the feed array of a quasioptical system is smaller and has a smaller BFN than the corresponding direct radiating array.

A fundamental distinction exists between *passive antennas* with the RF amplification (transmitter or receiver) prior to the input of the BFN and *active antennas* with amplifiers at the radiating elements or distributed at various levels in the BFN. Active antennas allow higher losses and more flexibility in the beamforming and are required when the beamforming occurs at an intermediate frequency or by one of the more recently developed techniques such as optical and digital beamforming. Radar array antennas often use *transmit/receive modules* with power amplifier for transmit, low-noise amplifier (LNA) for receive, transmit/receive switch, variable attenuation,

and phase shift integrated with the radiating elements. Switching between receiving and transmit functions to use the same beamforming components for transmit and receive cannot be used in communication systems that receive and transmit continuously. Books by Kumar [14] and by Litva and Lo [15] discuss optical beamforming (OBF) and digital beamforming (DBF).

In OBF the RF signals are converted to optical signals by modulators or by direct modulation of laser diodes. The beamforming is carried out by an optical processor or a fiberoptic network that can provide the time delays required for wideband phased-array antennas. Photodetectors recover the RF signals after the beamforming. Alternatively, a coherent optical network may be used. Advantages includes small size and mass, wide bandwidth, flexible arrangement of the fibers, and low electromagnetic interference. Disadvantages are the power consumption and the significant conversion losses from RF to optical and back. OBF is expected to find use in advanced wireless communications and in radars.

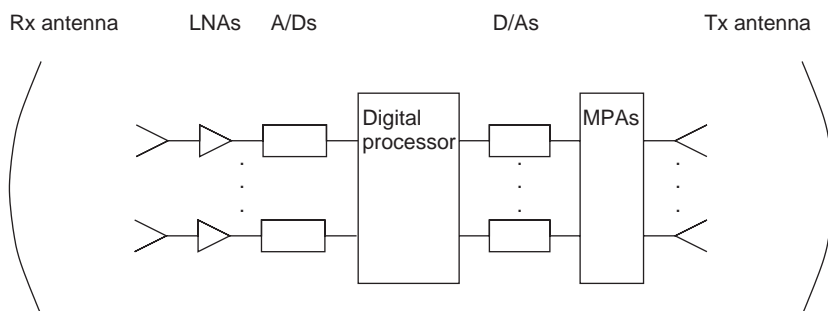
DBF is conceptually very simple and at the same time the ultimately capable approach. On receive, the RF signal is low-noise-amplified at each radiating element and converted to a digital stream by analog-to-digital (A/D) converters preserving the phase information. A digital processor applies the array antenna weights on the digital streams using either precalculated weights stored in the processor or, in smart systems, weights calculated by an adaptive algorithm to optimize some performance criterion or to track each single mobile terminal. Advantages include the very high flexibility at the level of the channels in a communication system and the ability to reset excitations to compensate, for example, for amplifier failures and component variations over temperature and age. The antenna may be upgraded by uploading new software and reconfigured by uploading new weights. Disadvantages include the high power consumption and the huge requirements to the high-speed digital processor for wideband signals. DBF's find use on board mobile commu-

nications satellites as discussed by Brain [16] and in radar antennas, and is a key technology for advanced mobile communications systems with and without MIMO [17]. Current DBF systems operate mainly at lower bands (L and S bands and below) and require lots of coaxial cable for interconnections. Some use of optical fiber links could be useful. Figure 2 illustrates the principal components of an active satellite receive/transmit DBF antenna system. The active transmit antenna part is discussed in more detail below.

Special problems relating to active antennas are to

- Achieve the required dynamic range
- Have amplifiers in adjacent paths track each other in amplitude and phase
- For active transmit antennas, limit the generation of intermodulation products while retaining an acceptable efficiency.

All carriers may be present in each power amplifier, which typically is a solid-state power amplifier (SSPA), and strict requirements to the linearity apply. This limits the amplifier efficiency achievable even though advanced linearization techniques are used. In contrast, passive antennas are often used in systems where the total frequency bandwidth is divided into channels, and the power amplification takes place channel by channel with at most very few carriers present in a channel. Then, the linearity requirements are less and the power amplification can be carried out at a much higher efficiency. In satellite communications, highly efficient traveling-wave tube amplifiers (TWTAs) are still being used, in particular with geostationary satellites at C and Ku band and above. One drawback of the channelized system is that output multiplexers (OMUXs) are required to combine the channels before the antenna beam ports. The insertion loss of the OMUX and the transmission lines required must be included when active and passive antenna



where a 4-by-4 MPA:

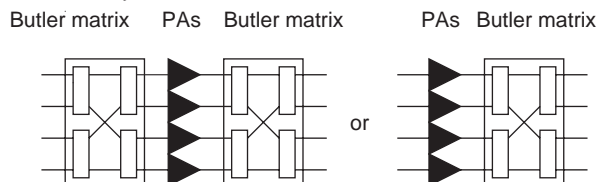


Figure 2. Simplified layout of active DBF receive/transmit reflector antenna system with multiport amplifiers on transmit. The diagram indicates LNAs, analog-to-digital converters (A/Ds), digital processor, digital-to-analog converters (D/As), power amplifiers (PAs), and ONETs.

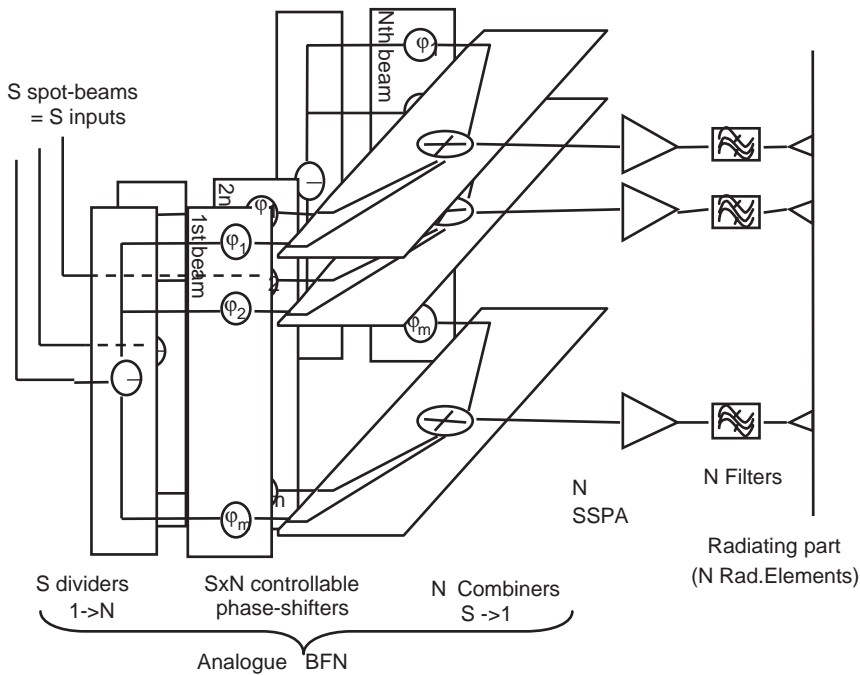


Figure 3. Diagram showing principle of Stentor Ku-band active Tx array BFN. (Courtesy of Alcatel Space.)

systems are compared. Nevertheless, channelized systems with passive antennas remain—since their introduction with Intelsat IV in 1971—popular with satellite operators as a satellite channel or transponder is a convenient unit to lease to service providers short of leasing the full satellite.

Satellites in low Earth orbits like Globalstar and Iridium at L and S bands often use active direct radiating arrays [18,19]. The mechanically steerable electronically zooming Ku-band antennas foreseen for Skybridge would keep the cell lattice fixed on Earth during the pass of the satellite [20]. The Globalstar and Iridium cell lattices move with the satellite requiring more handovers between beams. Lier and Jacomb-Hood [21] advocated active phased arrays for geostationary C- and Ku-band satellites. The active array allows more a compact low-power BFN technology with variable MMIC (microwave monolithic integrated circuit) and MEMS (microelectromechanical system) components. Figure 3 and 4 show a diagram and a photo of the Ku-band active Tx array BFN for the French Stentor technology satellite program. The photo shows the three beam ports, some MMICs, and some of the 48 output ports.

The SSPAs are located on the lower face of the radiating panel close to the radiating elements. In an active multibeam transmit antenna it is desirable to operate all power amplifiers at nominal power under all beam loading conditions to achieve optimum efficiency and minimize insertion phase variations. For multibeam transmit reflector antennas, this has led to the development of the *semiaactive antenna systems* or multiport antenna systems described by Roederer [22]. The feed array elements are not directly connected to power amplifiers, but separated from them by Butler matrix-type networks as indicated in Fig. 2. Typically 4×4 or 8×8 Butler matrices are used. The output (Butler) networks (ONETs) are always

required and must have low loss. The input (Butler) networks (INETs) are optional. By controlling the phases of the low-level equal-amplitude signals at the power amplifier inputs, the output power can be directed to the selected feeds to generate multiple pencil or contoured beams. DBF makes these beams reconfigurable.

Passive antenna technology is still very useful, in particular for geostationary satellite systems at C and Ku band and above, where wide frequency bands are used. An ultimate simple multibeam reflector antenna concept requiring no BFNs has become popular for Ka-band applications with each beam in a lattice as shown in Fig. 1c generated by a single feed; the feeds are distributed

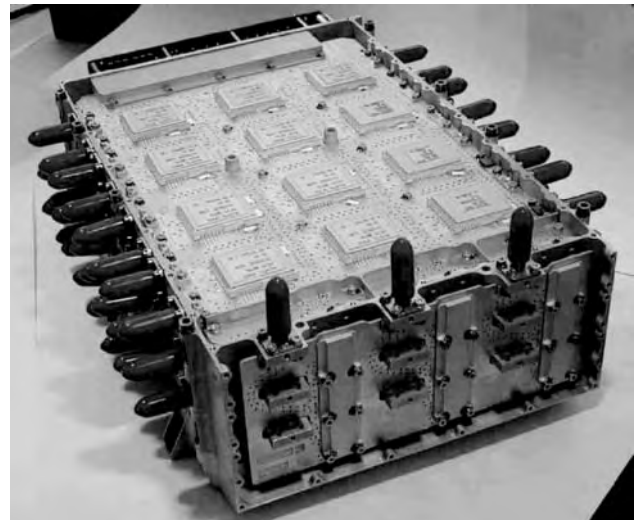


Figure 4. Stentor Ku-band active Tx array BFN with three fully reconfigurable beams over 48 output ports. (Courtesy of Alcatel Space.)

among three to four offset reflectors increasing the feed diameter by a factor of $\sqrt{3} - \sqrt{4}$, compared to the single-reflector case. The larger feed provides acceptable values of beam crossover losses and spillover losses [23].

In the general case each beam requires a BFN to excite a cluster of feeds. Many different BFN technologies are available such as rectangular waveguide, rectangular coaxial line, stripline, and microstrip. The main requirements are that it should be possible to make couplers and other components, the losses should be low for a passive antenna, the BFN must be able to handle the power required, the BFN must be stable with temperature, and the mass and volume must be acceptable. Waveguide is generally used at Ku band and above, and TEM line at C band and below. The literature on components in these technologies is very extensive, and excellent CAD software is available. Uher et al. [24] have published a book dedicated to waveguide BFN components. *Multipaction* and *passive intermodulation* (PIM) must be addressed in any high-power feed system—passive or active. *Electrostatic discharge* (ESD) may be a problem on a more general level. Consult Kitsuregawa's book [12] and other sources available. Otherwise, no fundamental problem should exist for fixed passive BFNs where array elements are used by only a single beam. The case where many array elements are used by more than one beam in the same polarization is the subject of the next section.

Antennas with *reconfigurable beams* where the BFN includes variable components have attracted much attention. This is an area where active antenna systems have considerable advantages over passive antenna systems. The active antenna performs the beamforming at low power levels, and compact MMIC or MEMS components or DBF technology can be used. A reconfigurable passive antenna must incorporate variable BFN components in the BFN at high power level on transmit and low loss on both transmit and receive. For passive antenna like the DSCS III lens antennas, Ricardi [9] discusses BFNs with ferrite circulator switches and variable ferrite phase shifters and power dividers. Attempts to transform the ferrite

technology to civilian applications have not been satisfactory. The ACTS 30- and 20-GHz Cassegrain reflector antenna systems use BFNs with latching ferrite waveguide switches to implement hopping spot beams [25]. The ACTS antenna subsystem is also unique by the high reflector surface accuracy (0.075 mm RMS for the 20-GHz 3.3-m main reflector) to implement frequency reuse by sidelobe isolation in the Ka band and the polarization sensitive subreflector systems to implement frequency reuse by polarization isolation. International satellites since Intelsat V have implemented reconfigurability by electromechanical coaxial or waveguide switches in the BFN. Kobayashi et al. [26] further developed the switched reconfigurability concept by combining small fixed sub-BFNs by switch couplers on the beam port side. The concept requires a minimum of variable BFN components and has been used on more recent satellites; see Bornemann et al. [27] and Paus et al. [28] for examples. Figure 5 illustrates an international communication satellite with reconfigurable coverages where the two hemi beams in the one hand of polarization are fixed, but the zone beams in the other hand of polarization may be changed by switches. This allows a satellite to be reconfigured for operation in different ocean regions. The BFNs are arranged in different layers of TEM line networks behind the feed array as indicated on the right side of the figure. Figure 6 shows one of the network layers and Fig. 7, a complete antenna system including BFNs, feed array, and reflector tested in a large compact range.

With satellite lifetimes of 13 years and more, reliability and availability are key issues. Variable BFN components and in particular active components are of concern. It is common practice to require redundancy for active components such as LNAs, SSPAs, and TWTAs. Similar concerns apply to mobile base station antenna systems as their complexity increases. During winter in cold climates, access may be difficult for long periods or even relatively short outages may be unacceptable. There is a large cost incentive in reducing the amount of maintenance required for a large number of widely dispersed base stations.

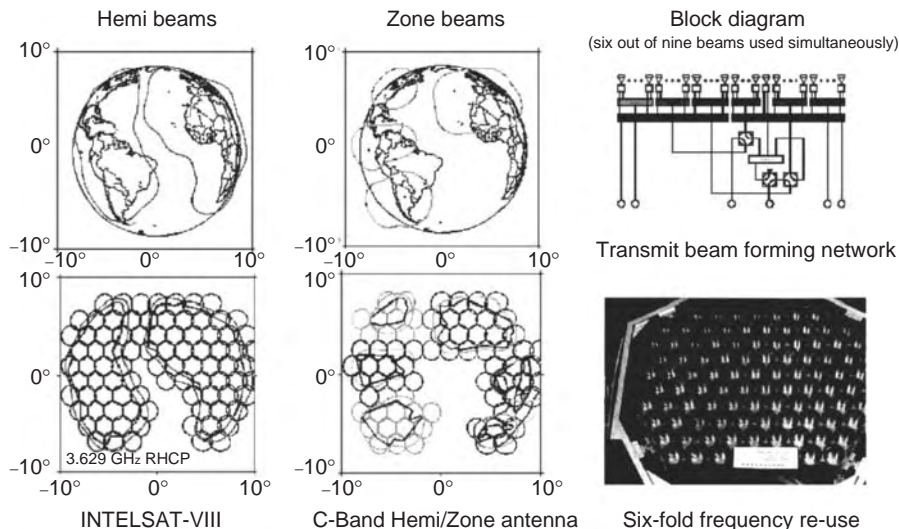


Figure 5. International C-band hemi/zone beam coverages on the left-hand side and a diagram of the reconfigurable BFNs and the feed array on the right-hand side. (Courtesy of EADS Astrium.)

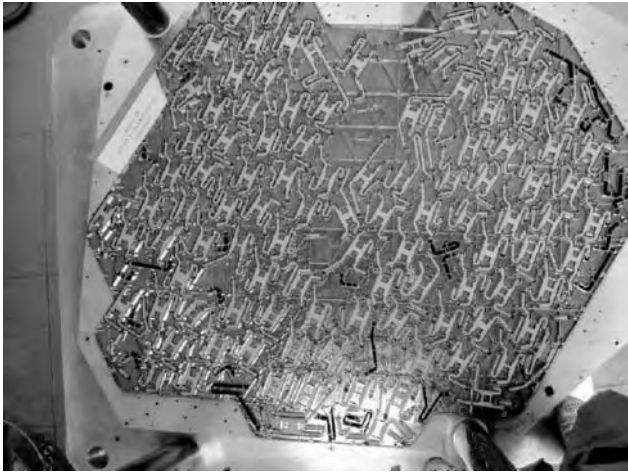


Figure 6. International C-band Tx TEM-line network layer with branchguide couplers. The scale is indicated by the human foot in the lower left corner. (Courtesy of EADS Astrium.)

4. ORTHOGONAL BEAMS

The problem of forming simultaneous multiple beams from a common aperture has received considerable interest. Much of the work considered arrays and in particular linear arrays and aimed at determining properties and limitations of the multibeam antenna networks assumed to be passive and their impact on the antenna performance. Many of the findings also apply to reflector antennas where the space feed mechanism may be viewed as a generalized network. One important antenna inefficiency to be added for reflectors is the feed array spillover loss. As already discussed, active antennas can overcome some of the inefficiencies of passive antennas, but at some cost.

Much of the work was carried out very early and is published in papers from 1961 and 1962. Shelton and Kelleher [29] found that the best multibeam pattern



Figure 7. International C-band Tx hemizone antenna system mounted on a satellite mockup during compact range tests. (Courtesy of EADS Astrium.)

configuration for a linear array of N elements occurs when the beams are equally spaced and the number of beams is equal to the number of elements. A scattering matrix analysis showed that the antenna network is lossless for only uniform illumination. Allen [30] extended the analysis and showed that unless one is willing to accept losses in addition to the normal Ohmic losses, the *complex array factor* of the beams must be mutually orthogonal over a period of the array factor. Kahn and Kurss [31] further extended the work demonstrating that the lossless network of the linear multibeam array results in some unique features; if the N beams shall be similar, the angular spacing between the beams is fixed. If the beams are not required to be similar, aperture illuminations will still have uniform phase progressions, but sinusoidal and cosinusoidal amplitude tapers generated by superposition of uniform distributions are possible.

White [32] showed that in a lossless passive antenna radiating multiple beams from a common aperture, the beams must be orthogonal in space so that the radiation pattern and the crossover levels cannot be specified independently. This result applies both to array antennas and to reflector antennas. White presented as examples 1D patterns from uniform, cosine, and cosine-squared distributions of width D . The beams for uniform distribution and sidelobe level 13.2 dB must be spaced λ/D in $u = \sin \theta$ space to be orthogonal with a crossover level of 3.9 dB. With cosine illumination, the beams with sidelobe level 23.0 dB must be spaced $2\lambda/D$, and the crossover level must be 9.5 dB. With cosine-squared distribution and 31.5 dB peak sidelobe level, the beam spacing must be $3\lambda/D$ and the crossover level must be only 15.4 dB. If one is forced to reduce the spacing to obtain satisfactory crossovers, the beams couple and the network will be lossy. White proposed three methods for solving this problem:

1. Split aperture decoupling
2. Resistive circuit decoupling
3. Active circuit decoupling

These solutions remain valid. Dividing the beams between several apertures is the solution being adapted in Ka-band satellite multibeam antenna systems with beams generated by single feeds distributed between three to four reflectors as described by Rao [23]. White proposed a decoupling networks with 3-dB hybrids and matched loads. For a 2D lattice of beams with cosine illumination and λ/D spacing with 2.1 dB crossover in the principal planes and 4.2 dB crossover in the diagonal plane, one-fourth of the power is radiated and three-fourths dissipated. For the cosine-squared illumination in both planes, only $\frac{9}{64}$ th of the power is radiated for the λ/D spacing. An active antenna with the amplification taking place at the array element before the resistive network overcomes these losses. On transmit, they occur at low level, and on receive, they do not affect the sensitivity.

4.1. The Stein Limit

Stein [33] quantified the effect of nonorthogonal beams and determined a fundamental limitation—the *Stein*

limit—of the maximum efficiency possible of an MBA. Stein considered a linear passive MBA network with M ports generating M beams. If the k th beam port is excited with a signal of unity power and all other beam ports terminated by matched loads, the complex vector far field is given by

$$\mathbf{E}_k(\theta, \phi) = q_k \mathbf{R}_k(\theta, \phi) \frac{e^{-jkr}}{r}$$

Here $\mathbf{R}_k(\theta, \phi)$ is termed the k th beam pattern and normalized such that

$$\int_{\Omega} \mathbf{R}_k^*(\theta, \phi) \cdot \mathbf{R}_k(\theta, \phi) d\Omega = 1$$

Then the total radiated power of the k th beam is

$$P_k = \int_{\Omega} r^2 \mathbf{E}_k^*(\theta, \phi) \cdot \mathbf{E}_k(\theta, \phi) d\Omega = |q_k|^2$$

With unit power incident, $|q_k|^2$ represents the radiation efficiency of the k th beam, and $1 - |q_k|^2$ network losses and power reflected back at all the beam ports. Given the M beam patterns, Stein defined as a measure of the beam overlaps the set of beam coupling factors

$$\beta_{kj} = \int_{\Omega} \mathbf{R}_k^*(\theta, \phi) \cdot \mathbf{R}_j(\theta, \phi) d\Omega$$

Here $\beta_{kk} = 1$ from the normalization, and also $\beta_{kj} = \beta_{jk}^*$ and $|\beta_{jk}| \leq 1$. Stein pointed out that the beam coupling factors do not define beam coupling simply in terms of overlap of the amplitude patterns. The fact that the beam patterns are complex-valued can be extremely important since variations in phase in the product being integrated can cause the integral to vanish even though the amplitude patterns may be identical. One such instance can occur when the locations on the radiating structure of the major currents exciting two beams are sufficiently disjoint. If a set of currents gives rise to a beam $\mathbf{R}_k(\theta, \phi)$ and this set of currents is translated the distance d , the new beam will have the form $\mathbf{R}_k(\theta, \phi) \exp(jkd \sin \psi)$, where ψ is the angle between the observation direction and the direction of translation. Another example is that of a “dual-mode antenna” where the phase patterns of two beams with overlapping amplitude patterns vary differently to make the integral vanish.

When all beam ports are excited with input signals x_k , the total radiated power is

$$P_{\text{rad}} = \sum_{k=1}^M \sum_{j=1}^M x_k^* q_k^* \beta_{kj} q_j x_j$$

Stein’s limit, based on the Hermitian and positive semi-definite properties of the matrix with elements $\Gamma_{kj} = q_k^* \beta_{kj} q_j$, states that the largest eigenvalue of this matrix cannot exceed unity: $\max \gamma_k \leq 1$.

Stein provided several examples. A simple and important result is obtained for the case when all beams have

equal radiation efficiencies, $q_k = q$ for all k . Then the eigenvalues of the matrix with elements Γ_{kj} are linearly related to the eigenvalues of the beam coupling matrix with elements β_{kj} by $\gamma_k = |q|^2 \beta_k$, and the Stein limit becomes $|q|^2 \leq 1/\max \beta_k$. Thus, the limitation on the radiation efficiency is determined directly from the beam overlap via the beam coupling matrix, independent of the MBA network. Since for all diagonal elements $\beta_{kk} = 1$, the sum of the diagonal elements (the trace of the matrix) is M . For any Hermitian matrix the sum of the eigenvalues equals the trace of the matrix. Thus, the largest eigenvalue must be equal to or exceed unity and $|q|^2 \leq 1$ with $|q|^2 = 1$ possible only if all eigenvalues are equal. This requires that all off-diagonal elements β_{kj} vanish, or that all beams be mutually orthogonal as previously pointed out by Allen and White. With two beams with equal radiation efficiencies, the eigenvalues are $\beta_{1,2} = 1 \pm \beta_{12}$ and the upper bound of the radiation efficiencies is for $\text{Re}(\beta_{12}) > 0$

$$|q|^2 \leq \frac{1}{1 + \beta_{12}}$$

The beam coupling factor for a uniformly illuminated line source of width D is

$$\beta_{12} = \text{sinc} \frac{\pi D(u_1 - u_2)}{\lambda}$$

Both Mailloux [9] and Hansen [4] provide more examples of beam coupling factors and further discussion. The beam coupling factor integral over the far field can be replaced by a summation of array excitation for omnidirectional array elements. Quite different beam overlap factors can be obtained for beams that differ only in their sidelobe structure, but have almost identical mainlobes. The same apply to the phase patterns that are seldom specified in a design. Most of the information on beam coupling factors applies to cases with a constant pattern phase.

4.2. MBA Network Realization

More recently DuFort [34,35] addressed the problem of finding a passive BFN that will realize the Stein limit. The first paper investigated the formation from a large linear array of a large number of identical low sidelobe beams in the Butler matrix directions with λ/D spacing, but with tapered distribution as considered previously by White. DuFort derived a simplified version of Stein’s limit for this case: “The maximum efficiency possible is the ratio of the average to the peak value of the aperture power distribution.” The network synthesis is based on Butler matrix networks with weights (attenuators and phase shifters) placed between the outputs of the Butler matrix and the array elements. The basic Butler matrix consists of 3-dB hybrid couplers and phase shifts and produces orthogonal beams with uniform excitations spaced $U = \lambda/D$ apart. Such beams and networks were considered by others [29,30,32] as discussed above. Figure 8 outlines an 8×8 Butler matrix network. The literature on Butler matrices

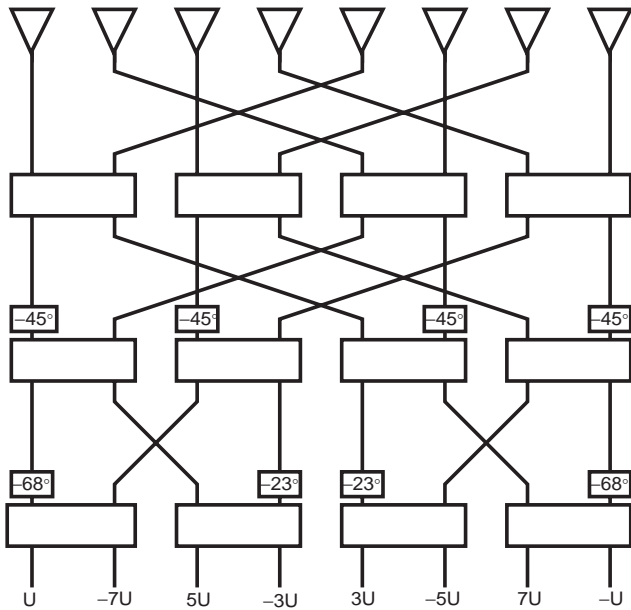


Figure 8. An 8×8 Butler matrix network with 3-dB hybrid couplers and phase shifts in degrees.

is very extensive [4,9,36]. DuFort showed that the optimum Stein limit efficiency can be achieved by placing attenuators in the array aperture. The network implements the optimum efficiency of $\frac{1}{2}$ for the cosine distribution in the 1D array as does White's network with hybrids and matched loads on the input of the orthogonal matrix network. In an alternative synthesis, DuFort placed the control elements on the input of the Butler matrix. This is advantageous when the number of beams is less than the number of array elements as in a limited scan case—in particular when an active antenna is used to compensate the beam coupling losses. A design with two types of 1–3 power dividers so that each beam uses three adjacent Butler matrix beams realizes a cosine squared on a pedestal with the optimum efficiency $|q|^2 = ((2+a)^2 + 2)/(4+a)^2$, where a is the pedestal height. For the case of no pedestal, DuFort's network achieves the optimum efficiency of $\frac{3}{8}$ for the linear array, as does White's two-stage network. The extension to Taylor n -bar distributions is more difficult and does not yield optimum results.

The second paper by DuFort [35] generalized the synthesis procedure. The desired complex radiation patterns or aperture distributions shall be specified, but can be arbitrary. The analysis leading to Klein's limit is extended into a synthesis procedure for the case of the general linear array. The analysis uses a weighted correlation matrix derived from the excitations specified over N array elements for M beams and specified weights for the efficiencies. The beam with the best efficiency is numbered one, and the others are allowed relative degraded efficiencies. Thus, DuFort's correlation matrix is a hybrid between Stein's beam coupling matrix with elements β_{kj} and the matrix with elements $\Gamma_{kj} = q_k^* \beta_{kj} q_j$ modified by the complex beam efficiency factors q_k . The synthesis is formulated in terms of the M eigenvalues λ_m and eigenvectors Ψ_m of the correlation matrix. The syn-

thesis procedure is expressed as a product of three matrices \mathcal{E} , \mathcal{T} and \mathcal{U}^\dagger , where the superscript \dagger denotes a conjugate transpose matrix. The \mathcal{E} matrix is an $M \times N$ matrix derived from the specified excitations, the efficiency weights, and the correlation matrix eigenvectors and eigenvalues. The \mathcal{T} matrix is an $M \times M$ diagonal matrix with elements $\sqrt{\lambda_m/\lambda_1}$. The \mathcal{U} matrix is an $M \times M$ diagonal matrix whose columns are the eigenvectors Ψ_m . The overall network is composed of three subnetworks—one subnetwork for each of the three matrices. The operation of the \mathcal{T} network may be performed by attenuators $\sqrt{\lambda_m/\lambda_1}$ between the input ports of the \mathcal{E} network closest to the array elements and the output ports of the \mathcal{U}^\dagger network. DuFort proposed to synthesize the \mathcal{E} and the \mathcal{U}^\dagger networks as Blass matrix networks and provided a synthesis procedure.

Figure 9 illustrates a *Blass matrix network* with eight feed ports and three beam ports. The network consists of directional couplers and phase shifters. Each beam is formed by a series-fed network. If the couplers have good isolation, the network for the beam closest to the array elements can be designed independent of the other beams. Other beams have spurious excitations due to the networks in front of them. For small coupling values, the magnitude of the spurious beams is reduced. The network suffers from losses in the loads terminating each line depending on how large coupling values are allowed at the end of the lines. The network can incorporate true time delays so that the beams will not squint with frequency as opposed to Butler matrix networks. See Butler [36], Hansen [4], and Mailloux [9] for further information on the network.

While DuFort had mainly radar applications as in Fig. 1a in mind, Wood [37] considered a satellite mobile application with beams in a hexagonal lattice as in Fig. 1c. Wood provided a simple formula to estimate the MBA orthogonality loss. A direct radiating array with N array elements provides M beams with array excitations c_j^i for

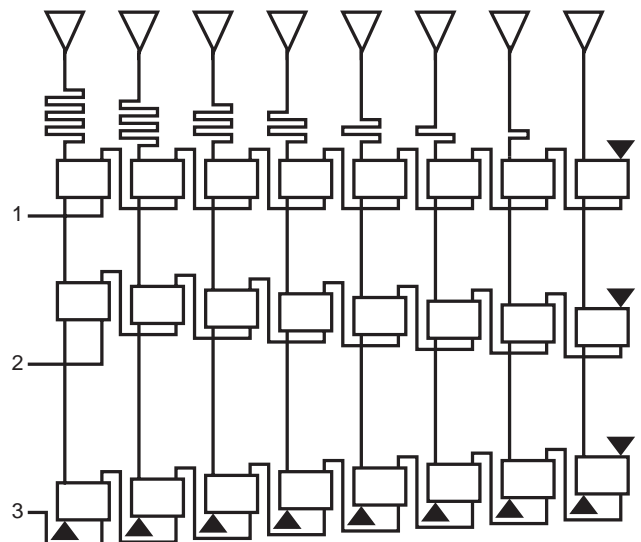


Figure 9. Blass matrix network with eight feed ports and three beam ports.

Table 3. Average Efficiency η_{MBA} and Network Efficiency η_{BFN} versus Aperture Dimension D and Crossover Level for Blass Matrix Network

D (λ)	Crossover Level (dB)	η_{MBA} (dB)	η_{BFN} (dB)	Largest Coupling (dB)
7.7	2.9	-4.1	-4.4	2.8
9.0	4.0	-3.3	-3.5	0.8
10.3	5.4	-2.5	-2.8	1.3
12.9	8.9	-1.4	-1.6	2.3

the j th element and the i th beam. By comparing the total array input power for the case where a beam is radiated at the time to the case where all beams are radiated simultaneously, Wood proposed the *MBA average efficiency*

$$\eta_{\text{MBA}} = \frac{\sum_{i=1}^M \sum_{j=1}^N c_j^i c_j^{i*}}{\max \sum_{i=1}^M \sum_{k=1}^M \sum_{j=1}^N c_j^i c_j^{k*}}$$

with a ‘‘cophasal beam’’ condition to maximize the denominator. A direct radiating array with 19 rectangular radiating elements in a hexagonal lattice with a Blass matrix network as in Fig. 9 is required to generate seven beams in a hexagonal lattice. Networks were designed for a 6.8 dB amplitude taper and a range of array aperture sizes. Table 3 summarizes the results comparing versus maximum aperture dimension D and crossover level the orthogonality loss predicted by the average efficiency η_{MBA} with the network efficiency η_{BFN} derived from the power dumped in the line terminations. The table also lists the largest coupling value in the networks and indicates that the networks are 0.2–0.3 dB less efficient than predicted by η_{MBA} . Wood attributed this difference to be representative of networks that avoid the 0 dB coupling limit and require the same total load power for each beam. Because of asymmetries in the beam overlap and in the network itself, it may be necessary to have a different total load power for each beam if the average efficiency η_{MBA} is to be achieved. Varying the aperture taper from 0 to -9.5 dB for the 10.3λ aperture increases the crossover level from 6.2 to 4.9 dB and improves the first sidelobe from 14.8 to 23.9 dB below peak, but also degrades η_{MBA} from -0.1 to -3.4 dB. The change in edge taper and sidelobe level degrades the networks efficiency by 3.3 dB even though the crossover level is improved only by 1.3 dB. In addition, the aperture efficiency is reduced by 0.5 dB.

Wood compared the array antenna with a 10.3λ -diameter offset reflector with seven feeds to generate the seven beams using one feed per beam. For the reflector antenna, the orthogonality loss mechanism is the spillover that occurs when part of the feed radiation is not intercepted by the reflector. The reflector antenna provided a crossover level of 6.4 dB and a spillover loss of 2.2 dB. This may be compared by the orthogonality loss of 2.0 dB derived from η_{MBA} for the 19-element array with the same edge taper.

4.3. Quasiorthogonal Beams

We assume an array-fed reflector antenna system with a network generating excitations sets for M beams over

N feeds. The excitation sets are given by vectors $\mathbf{c}^i = (c_1^i, \dots, c_N^i)$ for $i = 1, \dots, M$, where the excitations are normalized to unity power (i.e., $\sum_{j=1}^N c_j^i c_j^{i*} = 1$). If the network exists and is reciprocal and all ports are matched and isolated on both the feed and beam port side, the scattering matrix would take the form

$$\begin{pmatrix} b_1 \\ \vdots \\ b_N \\ b_{N+1} \\ \vdots \\ b_{N+M} \end{pmatrix} = \begin{pmatrix} 0 & \cdots & 0 & c_1^1 & \cdots & c_N^1 \\ \vdots & & \vdots & \vdots & & \vdots \\ 0 & \cdots & 0 & c_1^N & \cdots & c_N^N \\ c_1^1 & \cdots & c_N^1 & 0 & \cdots & 0 \\ \vdots & & \vdots & \vdots & & \vdots \\ c_1^M & \cdots & c_N^M & 0 & \cdots & 0 \end{pmatrix} \begin{pmatrix} a_1 \\ \vdots \\ a_N \\ a_{N+1} \\ \vdots \\ a_{N+M} \end{pmatrix}$$

where the port numbering begins on the feed port side. The specified excitation sets may have been determined by excitation optimizations separate for each beam and will then act as a reference solution for the multibeam antenna system. Depending on the specified excitation sets, the scattering matrix may not be realizable. If so, this will be corrected in an iterative procedure that changes the excitation sets as discussed below. For now we assume that received signals specified by the vector $(c_1^{i*}, \dots, c_N^{i*})$ equal to the complex conjugated i th excitation set are input on the feed ports. Then, the signal output on the k th beam port is

$$b_{N+k}^i = \sum_{j=1}^N c_j^k c_j^{i*}$$

For a lossless orthogonal network $b_{N+i}^i = 1$ and $b_{N+k}^i = 0$ for $k \neq i$. For a nonorthogonal network, the power $|b_{N+i}^i|^2$ represents the desired signal while the other power terms $|b_{N+k}^i|^2$ represent beam coupling losses due to the nonorthogonality of the network. This beam coupling loss (BCL) may be expressed by a set of beam port efficiencies. For the i th beam port we obtain the efficiency

$$\eta_{\text{BCL}}^i = \frac{|b_{N+i}^i|^2}{\sum_{k=1}^M |b_{N+k}^i|^2}$$

The procedure is repeated for all beam ports applying each time the appropriate complex-conjugated excitation set. For two identical excitation sets, $b_{N+1}^1 = b_{N+2}^1 = b_{N+1}^2 = b_{N+2}^2$, and the beam coupling loss is 3 dB. The expression for η_{BCL}^i is an alternative to Wood’s *MBA average efficiency*, but it provides an efficiency for each beam port rather than the average efficiency.

If the beam port efficiencies η_{BCL}^i are applied to the appropriate excitation sets in an iterative multibeam excitation optimization, the beam coupling loss will be traded off in the pattern optimization to achieve the best overall performance. A good starting point is the excitations derived for the case where the beams are provided by dedicated antennas. The *quasiorthogonal excitations* may be most useful when only a few feeds are shared between the beams and some losses can be tolerated. Unfortunately

there is no direct way of synthesizing the corresponding quasiorthogonal network apart from following the procedures outlined by DuFort and Wood. The network synthesis problem is addressed again at the end of the next section.

4.4. Dual- and Multimode Antennas

Previously, communications satellite contoured-beam reflector antenna systems were often so-called *dual-mode antennas* providing two identical beams in the same polarization—one beam used by the even numbered channels and the other by the odd numbered channels to relax the output multiplexer requirements. The Arabsat C-band transmit antenna described by Han and Hwang [13] is an example of a dual-mode antenna. Figure 10 outlines the principles of the antenna BFN with a 2–4 dual-mode converter with the even- and the odd-mode input ports and four sub-BFNs to connect to 13 circular waveguide feeds. The dual-mode converter consists of four quadrature hybrids and linelengths to provide the even- and the odd-mode excitation sets. The Arabsat BFN was implemented in barline technology (air stripline with solid conductor) and used “ratrace” couplers and not branchline couplers as indicated in the figure. The Arabsat BFN was divided into four network layers with the two layers closest to the feeds containing the four sub-BFNs for each of the two hands of circular polarization. The two last layers contain the dual-mode converters—one layer for each polarization. The connections between the layers eliminate the crossing lines in Fig. 10.

The sub-BFNs reduce the complexity of the dual-mode converter. The design of a general 2–13 converter is difficult, and the network will large requiring 23 hybrid

couplers with many paths through the network between the input and the output ports. The pathlengths must be approximately equal if the network is to operate over any significant bandwidth. A dual- or multimode converter synthesis procedure exists, but it provides a single-frequency design with no control of the coupling factors and the linelengths. The 2–4 converter with four hybrids is popular as it often provides a good tradeoff between performance and complexity. A more general converter is obtained by replacing the crossing lines between the four hybrids by a fifth hybrid—in particular if the coupling factors and linelengths are optimized as part of the excitation optimization. Then, the dual-mode converter usually has almost no impact on antenna performance. Sometimes 2–3 converters with only three hybrids are used providing sub-BFN excitations with phase offsets similar to $(\pm 0^\circ, \pm 60^\circ, \pm 120^\circ)$ often resulting in noticeable pattern degradations. A single hybrid is the ultimate simple dual-mode converter, but with phase offsets similar to $(\pm 0^\circ, \pm 90^\circ)$ at the two output ports and often unacceptable pattern degradations.

For linearly polarized antennas, the circular waveguide feeds are often replaced by larger rectangular waveguide feeds. This may replace a sub-BFN and several small feed with a single large feed, or at least significantly reduce the number of feeds per sub-BFN.

Another application of dual- or multimode antenna systems is to provide overlapping regional beams as in the case of the MSAT mobile communication satellite, which has six beams over North America and Hawaii. Four of the beams overlap and use three 2–3 mode converters to share feeds between adjacent beams [38]. A more complex scenario with four overlapping “linguistic” beams tailored to language zones in central parts of Europe was considered

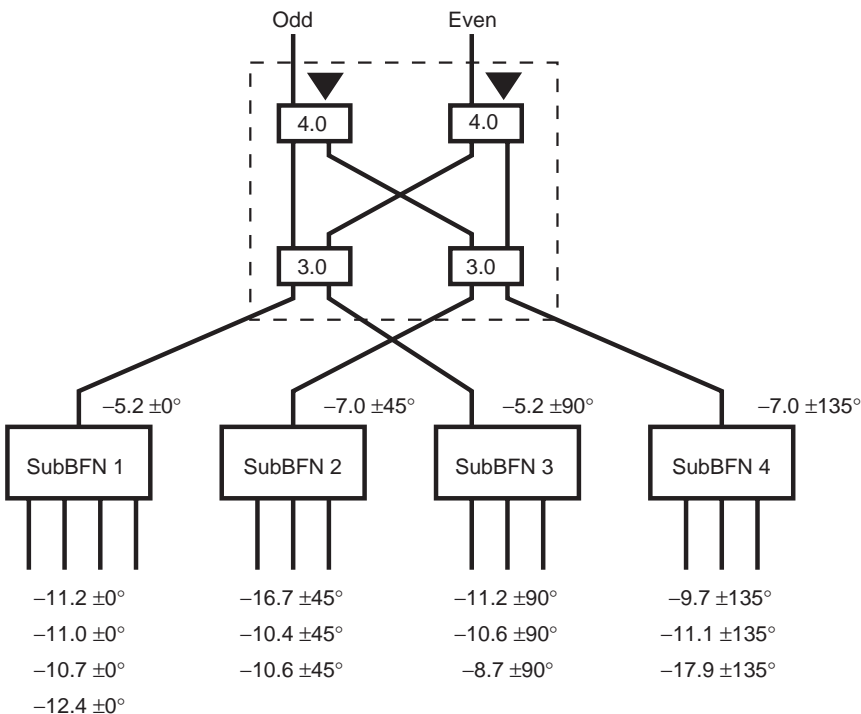


Figure 10. Dual-mode BFN with 2–4 dual-mode converter and 4 sub-BFNs connected to 13 feeds. The figure shows the coupling factors of the dual-mode converter hybrid couplers in decibels and the excitations of the two modes in decibels and degrees at the outputs of the dual-mode converter and of the sub-BFNs.

by LaFlame et al. [39]. This system required one 4–4, one 3–4, and one 2–3 mode converter. The 4–4 and 3–4 mode converters are complex and cause significant pattern degradations compared to the case with dedicated antennas for each beam.

Several approaches are available for synthesizing a dual- or multimode antenna. In one approach, the excitations for the overlapping beams are optimized applying orthogonality constraints, similar to $\sum_{j=1}^N c_j^k c_j^{i*} = 0$ for $k \neq i$ in the previous section between the excitations of the i th and the k th beams. Applying an orthogonality constraint directly to determine an excitation may not be the best approach. LaFlame et al. [39] use the orthogonality constraint indirectly by at each step in the iterative excitation optimization to improve only the beam with the worst performance and modify the other beams so that they remain orthogonal. Alternatively, the orthogonality condition may be applied “softly” via the *quasiorthogonal excitations* and *beam port efficiencies* η_{BCL}^i defined in the previous section. In any case, the excitation optimization should include sub-BFN arrangements adopted to simplify the network. Finally, a BFN must be found to realize the optimized excitation sets. There is no unique solution to this problem and typically the synthesis is carried out at a single frequency. Available synthesis methods progress as the Blass matrix network and Ruggerini’s *diagonalization BFN* [40] along similar lines. First a network of hybrid couplers and phase shifts is set up for the first beam. Then a network is set up for the next beam behind the first network. The second network attaches to the unused hybrid coupler ports of the first network and is determined such that it realizes the desired excitations at the feed ports in the presence of the network in front. The procedure is repeated for any remaining beam.

The synthesized network may be overly sensitive to component tolerances and bandwidth effects. A second synthesis approach is to derive as simply as possible approximate excitation sets, such as by a *quasiorthogonal excitation* optimization preferably identifying the most promising sub-BFN arrangement. Then, a template network is set up for the dual- or multimode part of the network and the component values are optimized using suitable models for the to fit the sub-BFN excitations found in the previous step. For a complex scenario like the MSAT scenario, several mode converting networks or matrices may have to be defined. When suitable mode converting networks with sufficient bandwidth have been identified, their network models are input and optimized in an overall excitations operating on the network component variables and any other excitations to determine the overall best antenna performance in terms of minimum coverage area directivity, sidelobe isolation, and other parameters versus antenna size and complexity.

5. OFFSET REFLECTORS

The offset paraboloidal reflector has emerged as the most popular quasioptic system used in multibeam antennas to reduce the size and the complexity of the array and the BFN for applications with a limited field of view as in the

case of geostationary satellites. The offset reflector is preferred to the center-fed reflector as the blockage by the feed array and its support is eliminated, and the interaction between the reflector and the feeds is reduced. The price paid is a more complex structure, where the reflector asymmetry generates a cross-polarization component for linearly polarized feeds or a small beam squint away from the offset plane for circularly polarized feeds—to the left for right-hand circular polarization and to the right for left-hand circular polarization when looking down the range.

As the array antenna far field is the Fourier transform of the array aperture field, the reflector far field is essentially the double Fourier transform or a replica of the feed array aperture field apart from near-field effects, scan degradations and a filtering of the feed array angular spectrum by the reflector aperture. While the beamsteering in the array is carried out by phase control, the beamsteering in the reflector is done by amplitude control and only the feeds in the vicinity of the image in the focal plane of a beam contribute to the beam. Thus, beams that do not overlap will tend to use feeds in spatially separated regions of the reflector focal plane. Beams away from the boresight suffer from scan degradations, which ultimately limit the angular region over which a reflector can be used. Increasing the focal length to aperture diameter (f/D) ratio reduces the scan degradations.

5.1. Multibeam Reflector Antenna Design

Book chapters by Rusch et al. [11] and Rahmat-Samii [41] provide information on the design and analysis of reflector antenna systems. The TICRA GRASP8/GRASP8W software [42] has become the industry standard for reflector antenna analysis. A number of simple beam models and design rules are available for the initial multibeam reflector antenna tradeoff and layout [6,7,23,43,44]. A brief summary is presented below.

We consider the offset paraboloidal reflector in Fig. 11 with aperture diameter D and focal length f . A number of

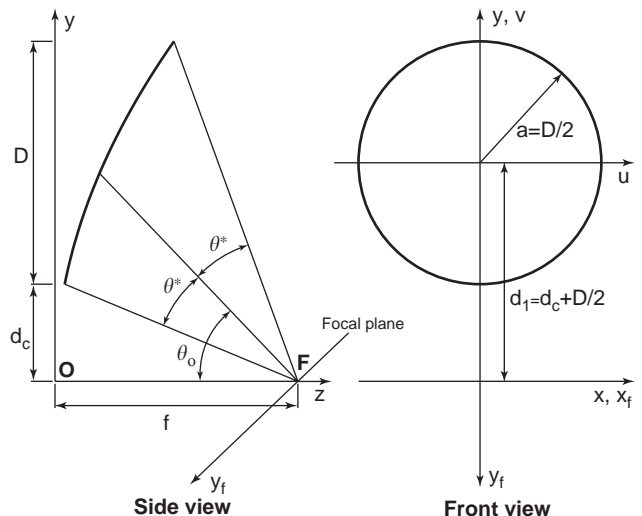


Figure 11. Side and front views of offset reflector with focus at F , apex at O , and $x_f y_f$ focal plane.

feeds placed in the tilted focal plane $x_f y_f$ each generates a pencil beam. If the maximum scan in the direction of the feed array is θ_{scan} and the ray from the lower edge of the reflector must clear the feed array by the angle θ_{clear} , the *reflector clearance* or offset must be

$$d_c = 2f \tan \frac{\theta_{\text{scan}} + \theta_{\text{clear}}}{2}$$

Different choices exist for the orientation of the feed array in the offset reflector. Mittra et al. [45] showed that the phase distortions of scanned feeds are minimized if the feed array points toward the reflector surface point whose projection into a plane perpendicular to the paraboloid axis is the center of the projected aperture. This provides the feed tilt angle

$$\delta = \arctan \left(\frac{d_1}{f - d_1^2/(4f)} \right)$$

Here we assume that the feed tilt angle is equal to the offset angle θ_o bisecting the angle subtended by the upper and lower reflector edges seen from the focus. This minimizes the spillover loss for the on-axis beam and slightly reduces cross-polarization effects. The offset angle and the subtended semiangle θ^* are determined from the offset height and aperture diameter (or vice versa) by

$$d_c = 2f \tan \frac{\theta_o - \theta^*}{2}$$

$$D + d_c = 2f \tan \frac{\theta_o + \theta^*}{2}$$

For an f/D ratio of 1 and an offset as large as $d_c/D = 0.5$, the angle δ is equal to 53.1° while θ_o and θ^* are 50.9° and 22.8° , respectively.

A feed element located at (x_j, y_j) in the focal plane gives rise to a pencil beam at (u_j, v_j) in antenna uv coordinates where

$$u_j = -\frac{B_{\text{df}} x_j}{f + d_1^2/4f} \pm \frac{\lambda \sin(\theta_o)}{4\pi f}$$

$$v_j = \frac{B_{\text{df}} y_j}{f + d_1^2/4f}$$

Here B_{df} is the *beam deviation factor* and d_1 the offset of the reflector center from the paraboloid axis. The denominator $f + d_1^2/(4f)$ is the distance from the focal point to the reflector center and acts as the “effective” focal length of the offset reflector. The second term on the right-hand side of the equation for u_j is the circular polarization beam squint. The upper sign applies for right-hand circular polarization and the lower sign, for left-hand circular polarization. No beam squint occurs for linear polarization where the term is omitted.

The beam deviation factor B_{df} depends on the aperture illumination $f(\rho)$. It may be derived from the expression

$$B_{\text{df}} = \frac{\int_0^a f(\rho)/(1 + (\rho/2f)^2)\rho^3 d\rho}{\int_0^a f(\rho)\rho^3 d\rho}$$

Table 4. Beam Deviation Factor B_{df} versus f/D Ratio for Uniform Illumination

f/D	0.7	1.0	1.3	1.6
B_{df}	0.922	0.960	0.976	0.984

derived by Ruze [46] under the condition of small feed displacements. The beam deviation factors derived for a center-fed reflector may be applied for an offset reflector if a larger “effective” focal length is used for the offset reflector as in the expressions above relating the feed location (x_j, y_j) and the beam location (u_j, v_j) . Rusch et al. [11] propose a slightly different “effective” focal length. For uniform illumination, the closed-form expression

$$B_{\text{df}} = 32 \left(\frac{f}{D} \right)^4 \left[\left(\frac{D}{f} \right)^2 - 16 \ln \left(1 + \frac{(D/f)^2}{16} \right) \right]$$

or ... $\frac{1}{16} \left(\frac{D}{f} \right)^2 \dots$

is obtained. Table 4 lists a few values of B_{df} versus f/D .

The *feed spillover* is important for multibeam reflector antennas as it must be traded off with the crossover loss between adjacent beams. For a Gaussian feed pattern with a half 10-dB feed pattern beamwidth θ_{10} , the *spillover loss* in dB is

$$L_{\text{spillover}} = 10 \log(1 - 10^{-(\theta^*/\theta_{10})^2})$$

As a beam is scanned away from the antenna boresight, a gain loss and a beam widening occur due to phase errors over the reflector aperture. The scan degradations depend for a given scan angle θ_{scan} on the D/λ ratio, the f/D ratio, the offset angle θ_o , and the aperture illumination. Following Dragone [47] and expanding the aperture phase errors in a power series and neglecting terms of order higher than 3, one obtains for the first-order *scan loss* in decibels due to *coma*, *astigmatism*, and an aberration with three periods in ϕ

$$L_{\text{scan loss}} \approx L_{\text{coma}} + L_{\text{astigmatism}} + L_3$$

where

$$L_{\text{coma}} = A(\alpha) \left[\frac{D}{\lambda} \left(\frac{D}{f} \right)^2 \sin \theta_{\text{scan}} \right]^2$$

$$L_{\text{astigmatism}} = B(\alpha) \left[\frac{DD}{\lambda f} \tan \frac{\theta_o}{2} \sin \theta_{\text{scan}} \right]^2$$

$$L_3 = C(\alpha) \left[\frac{D}{\lambda} \left(\frac{D}{f} \tan \frac{\theta_o}{2} \right)^2 \sin \theta_{\text{scan}} \right]^2$$

Table 5 provides expressions for $A(\alpha)$, $B(\alpha)$, and $C(\alpha)$ and numerical values versus edge taper for the aperture distribution $\alpha + (1 - \alpha)(1 - (\rho/a)^2)$. The expressions are approximate and neglect the dependence of the scan loss on the scan direction. A beam scanned away from the feed array suffers a higher scan loss than does a beam scanned

Table 5. Expressions and Numerical Values of Scan Loss Factors versus Aperture Taper for $\alpha + (1 - \alpha)(1 - (\rho/a)^2)$ Distribution

Factor	Expression	13 dB	10 dB	0 dB
$A(\alpha)$	$\frac{\pi^2}{2^{10}3 \ln 10} \frac{1 + 6\alpha + 3\alpha^2}{(1 + \alpha)(1 + 2\alpha)}$	0.001963	0.002076	0.002325
$B(\alpha)$	$\frac{5\pi^2}{2^5 3 \ln 10} \frac{1 + 3\alpha}{1 + \alpha}$	0.3048	0.3305	0.4464
$C(\alpha)$	$\frac{\pi^2}{2^9 \ln 10} \frac{1 + 4\alpha}{1 + \alpha}$	0.01296	0.01441	0.02093

toward the feed array. Nevertheless, the expressions indicate the impact of the antenna parameters on the scan loss and show that the astigmatism is most important for practical antenna geometries. A physical optics reflector antenna analysis program should be used to establish the actual antenna performance, and the expressions should be used only for qualitative comparisons. The scan loss is not a loss in radiated power as the BFN loss and the spill-over loss. It represents a loss in the resolution of the reflector due to the widening of the beams with increasing scan angle. The scan loss of the center-fed reflector is for the same aperture diameter, f/D ratio, and aperture illumination order of magnitude less than that of the offset reflector. The dominant scan aberration of the center-fed reflector is coma, which has a minor impact on the scan loss and mainly degrades the sidelobe performance. As the total scan loss is determined by a combination of coma, higher-order astigmatism, and spherical aberration, no simple expression exists for the scan loss of the center-fed reflector. Coma and astigmatism have ray optical interpretations; coma is related to the region on the far-field sphere with one or more rays from the feed reflected in the reflector surface. Similarly, astigmatism is related to the region with caustic effects where four edge-diffracted rays occur [48]. This observation provides an alternative explanation of why astigmatism for an off-axis feed is stronger in the offset reflector with its elliptical rim than in the center-fed reflector, where caustic phenomena occupy much smaller regions of the far-field sphere. It also indicates that surface shaping is not likely to reduce the astigmatism for the offset reflector. A dual-offset reflector with conic or shaped surfaces is required to improve the scan performance. Dual-offset reflectors with conic surfaces are discussed in Section 5.3 of this article. Albertsen et al. [49] compare different surface shaping techniques of dual-offset reflector antennas for improving the scan performance.

A beam generated by a single large feed in an offset reflector will suffer from significant degradations if scanned a sufficiently large number of beamwidths. Lam et al. [50] show that by replacing the single large feed by a cluster of smaller feeds with optimized excitations, the scan degradations may be reduced considerably. For an offset 108λ reflector scanned 10 beamwidth, the optimum directivity by a 7-element cluster and a 19-element cluster is respectively 8 and 12 dB higher than that of a single feed. When the feed cluster spacing is larger than 1λ , the

directivity found by conjugate field matching is similar to that found by optimization. For contoured beams generated by feed clusters, the excitation optimization may also partially compensate the scan aberrations.

5.2. Cross-Polarization Effects

We have already encountered Adatia and Rudge's [51] approximate formula for the circular polarization beam squint in the offset reflector

$$\psi_s = \pm \arcsin\left(\frac{\lambda \sin(\theta_o)}{4\pi f}\right)$$

stated to be accurate within 1.0% of the half-power beamwidth. The beam squint is to the left for right-hand circular polarization and to the right for left-hand circular polarization.

For linear polarization, each feed generates two cross-polar lobes, one on either side of the copolar beam center in directions perpendicular to the offset plane. Jacobsen's "reflector transformation" [52] gives for the ratio of the peak cross-polarization level (Cross-pol_{\max}) to peak copolarization level (Copol_{\max}) for a uniformly illuminated aperture

$$\frac{\text{Cross-pol}_{\max}}{\text{Copol}_{\max}} \approx 0.36\theta^* \tan\left(\frac{\theta_o}{2}\right)$$

The values $\theta_o = 35.23^\circ$ for the offset angle and $\theta^* = 23.23^\circ$ for the semiangle subtended by the reflector rim give a ratio of -27.2 dB. A similar expression, but with 0.36 replaced by 0.4 and θ^* by half the 10 dB feed beamwidth, was derived by Gans and Semplak [53] for reflector aperture fields (and far fields for the feed beamwidth small compared to θ^*). The cross-polar maxima occur about $0.73 \lambda/D$ radians from the copolar beam center and have opposite phases in phase quadrature with the copolar pattern. Several methods exist for reducing this cross-polarization, including

- Long f/D ratio and small offset angle,
- Dual-gridded reflector with polarization sensitive grid on the front shell and separate feed arrays for the two orthogonal linear polarizations (e.g., see Raab [54])
- Trimode feed horn including TM_{11} and TE_{21} mode as proposed by Rudge and Adatia [55]
- Feed array aligned with the paraboloid axis and the array factor squinted toward the offset reflector as proposed by Jacobsen [52]
- Planar polarization screen between the feed arrays and the reflector with either a parallel wire grid forming the angle $\theta_o/2$ with the xy plane as proposed by Chu [56] or a curved wire grid with more degrees of freedom for the screen tilt angle as proposed by Dragone [57]
- Cross-polarization cancellation between adjacent array feed elements with similar excitations as discussed by Balling et al. [58]

- Compensated dual-offset reflector with conic surfaces as discussed in the next section
- Dual-offset reflector with shaped surfaces to achieve a circular or elliptical beam with low cross-polarization as described by several authors [59–62]
- Dual-gridded subreflector with a polarization-sensitive grid on the front shell and a solid main reflector, and separate feed arrays for the two orthogonal linear polarizations as in the case of the ACTS 30 and 20 GHz Cassegrain reflector antenna systems [25]

5.3. Compensated Dual-Offset Reflectors

The scan degradations and the high cross-polarization levels for linear polarization of the offset reflector are reduced by a compensated dual-offset reflector antenna system. Tanaka and Mizusawa [63] established a condition that eliminates the linear polarization cross-polarization due to the reflector offset by adjusting the angles γ between the subreflector and the main reflector axis and ψ between the feed and the subreflector indicated for the offset Cassegrain and Gregorian systems in Fig. 12. A dual-offset reflector may with some limitations be represented by its *equivalent paraboloid*. The offset angle of the equivalent paraboloidal reflector is

$$\tan \frac{\theta_{o,eq}}{2} = \frac{e \sin((\psi - \gamma)/2) + \sin((\psi + \gamma)/2)}{e \cos((\psi - \gamma)/2) + \cos((\psi + \gamma)/2)}$$

where e is the eccentricity of the subreflector hyperboloid or ellipsoid. The equivalent offset angle $\theta_{o,eq}$ can take on any value, including zero. The condition $\theta_{o,eq} = 0$, which eliminates the cross-polarization and as shown by Dragone [47] most first-order scan aberrations including astigmatism, corresponds to a rotationally symmetric

equivalent paraboloid. The condition may be expressed as

$$\tan \psi = \frac{(1 - e^2) \sin \gamma}{(1 + e^2) \cos \gamma - 2e}$$

or in Adatia's [51] simplified form

$$\tan \frac{\psi}{2} = M \tan \frac{\gamma}{2}$$

where $M = (e + 1)/(e - 1)$ is the subreflector magnification. This condition is sometimes referred to as the *Mizugutch condition* as the paper by Tanaka and Mizusawa was not initially noticed outside Japan. Mizugutch et al. [59] spread the result and also present compact dual-offset reflector antenna systems with shaped surfaces for low cross-polarization, but allowing the feed axis to be kept parallel to the main reflector axis. Kitsuregawa and Mizugutch use notations that differ from Adatia's notation adopted in this article. Kitsuregawa uses angles $\alpha = \gamma$ and $\beta = \psi + \gamma$ with an eccentricity that changes sign for hyperboloidal and ellipsoidal and for concave and convex subreflectors. Mizugutch uses angles $\alpha = \psi$ and $\beta = \gamma$. In this article, the eccentricity is always positive, but the angles and the subreflector magnification may be negative. (An exception occurs for Cassegrain systems that use the concave branch of the hyperboloid. They are discussed below and require that the sign of the eccentricity in the formulas above be changed.) The Gregorian antenna in Fig. 12 has γ positive and ψ negative, whereas both angles are positive for the Cassegrain antenna. The Gregorian subreflector and main reflector are offset in opposite directions, making the Gregorian antenna more compact than the Cassegrain antenna. A main drawback of the Gregorian geometry is the scattering and spillover from the upper subreflector edge affecting the antenna far field close to the antenna boresight.

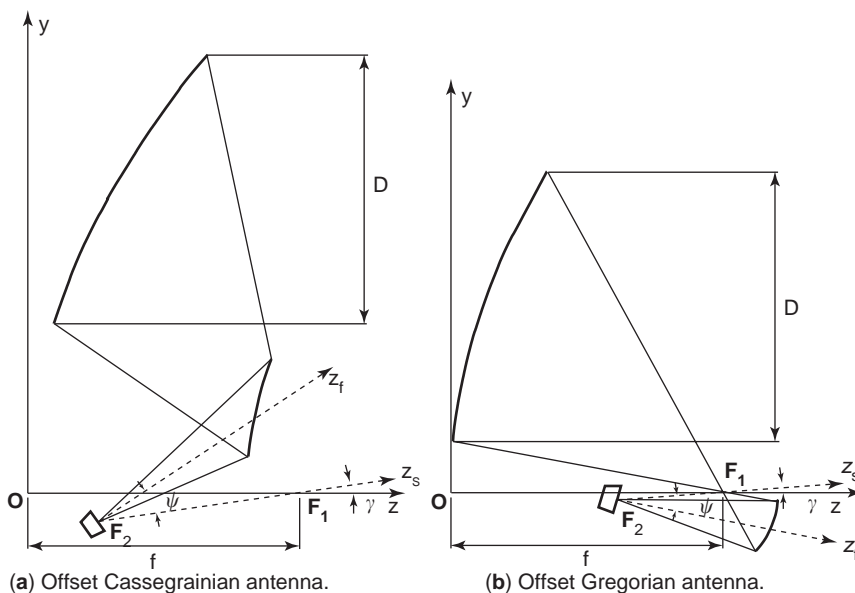


Figure 12. Compensated offset Cassegrain and Gregorian reflector antenna systems with $f/D = 1$ for main reflector: (a) Cassegrain system with $M = 3$, $\gamma = 8.45^\circ$, and $\psi = 25.00^\circ$; (b) Gregorian system with $M = -3$, $\gamma = 6.04^\circ$, and $\psi = -18.00^\circ$.

Alternatively, the subreflector magnification may be defined as the ratio of the equivalent paraboloid focal length to the main reflector focal length

$$M_{\text{eq}} = \frac{f_{\text{eq}}}{f} = \frac{e^2 - 1}{e^2 - 2e \cos \gamma + 1}$$

which differs from M for $\gamma \neq 0$.

The equivalent paraboloid is useful mainly for evaluating the case where the feed is placed at the focus and for determining in a first approximation the relation between feed positions in the focal plane and beam directions. The equivalent paraboloid should not be used to determine the scan degradations. For the offset Cassegrain and Gregorian systems in Fig. 12, rays for scanned beams will miss the small sub-reflectors. It is necessary to increase the subreflector size and the reflector offsets to prevent blockage and spillover. As described by Kitsuregawa [12], the subreflector and the feed array for scan angles as large as $\pm 10^\circ$ will be several times larger than the main reflector for a Cassegrain system. A Gregorian system can be more compact, but the subreflector will still be large. For both offset Cassegrain and Gregorian systems, the feed arrays cannot be planar for large scan angles. Rusch et al. [64] have evaluated the accuracy of the equivalent paraboloid for predicting the performance of offset Cassegrain and Gregorian antennas with a main reflector diameter of 100λ , subreflector diameter of about 20λ , main reflector f/D ratio of 0.625, subreflector magnifications of about 3 and -3 , and a feed taper of -10 dB toward the subreflector rim. For this case with no subreflector oversizing and the feed placed at the hyperboloid/ellipsoid focus, the subreflector diffraction causes a copolar loss of about 0.5 dB. The copolar sidelobes agree fairly well down to 30 dB below peak. Whereas the equivalent paraboloid predicts zero cross-polarization, the dual-reflector analyses predicts peak levels of about 32 and 38 dB below copolar peak for the Casse-

grain and the Gregorian antenna, respectively. Under scanned conditions, the agreement between the equivalent paraboloid and the dual-reflector analyses deteriorates rapidly. There are significant copolar differences for one beamwidth of scan, and gross differences at two and four beamwidths of scan. Thus, extreme care must be taken when applying the equivalent paraboloid under scanned conditions as would be required for multibeam antennas.

While classical offset Cassegrain and Gregorian systems can provide adequate performance for at least 10–12 beamwidths of scan within a $\pm 4^\circ$ field of view, the *front-fed offset Cassegrain* (FFOC) and *side-fed offset Cassegrain* (SFOC) in Fig. 13 are good candidates for applications with scan angles as large as $\pm 10^\circ$. For these systems, the subreflector is the concave branch of the hyperboloid with the magnification $M = (e - 1)/(e + 1)$ less than one. The feed arrays can be planar and will be smaller than for the classical offset Cassegrain and Gregorian systems. The subreflector size is comparable to that of the main reflector, but in particular the front-fed configuration allows a compact arrangement. Both the FFOC and the SFOC have unique scan properties due to the large focal length of the main reflector. The configurations seem to have been identified first by Tanaka and Mizusawa [63] and considered later by Dragone [65,66]. Makino et al. [67] and Jørgensen et al. [68] provided the extension to $\pm 10^\circ$ scan angles for the FFOC and the SFOC, respectively. The performance of the FFOC was experimentally validated and compared with that of an classical offset Gregorian with a large oversized subreflector.

For a 120λ main reflector aperture and 10° (17 beamwidths) scan, the SFOC scan loss is 2.1 dB in the worst direction, which is better than that of the offset Gregorian by 3 dB. The maximum linear polarization crosspolarization level of the SFOC is -38.0 dB calculated and -34.0 dB measured compared to -23 dB for the offset Gregorian. The feed horn provides a reflector edge level for the center beam of -15 dB and the feed used in the

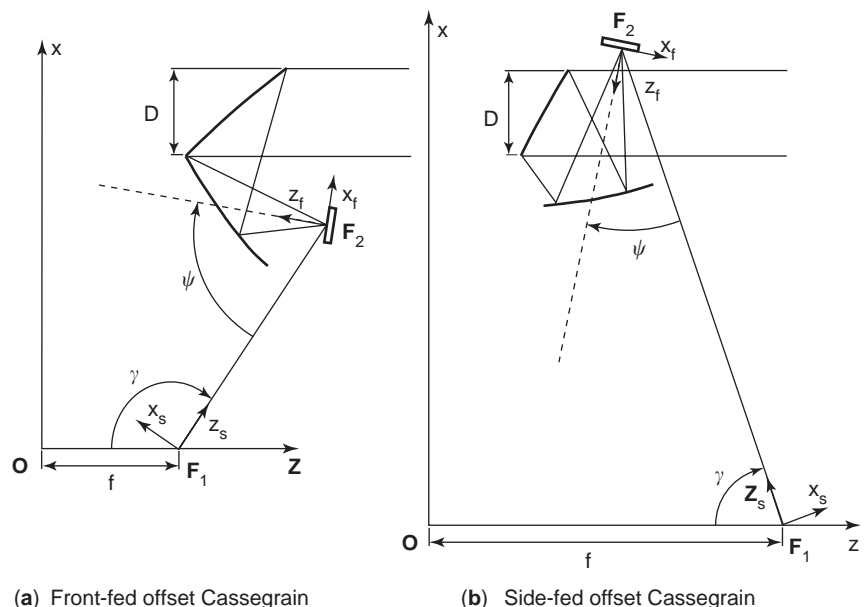


Figure 13. Offset Cassegrain antenna systems: (a) front-fed offset Cassegrain with $M = 0.344$, $\gamma = -123.61^\circ$, and $\psi = -65.37^\circ$; (b) side-fed offset Cassegrain with $M = 0.383$, $\gamma = -70.00^\circ$, and $\psi = -30.00^\circ$.

Table 6. Predicted Performance of the FFOC and SFOC Antenna Systems with 120λ Main Reflector Aperture

Scan Direction	Directivity (dBi)	Change (dB)	Sidelobe (dB)	Cross-polarization (dB)
<i>Side-Fed Offset Cassegrain</i>				
On axis	46.88	—	−18.50	−48.68
10° downward	46.52	0.36	−6.89	−38.06
10° upward	43.04	3.84	−14.80	−35.52
10° sideward	46.05	0.83	−12.42	−37.40
<i>Front-Fed Offset Cassegrain</i>				
On axis	46.42	—	−18.41	−54.78
10° downward	46.83	−0.41	−13.55	−40.20
10° upward	45.05	1.37	−15.67	−37.49
10° sideward	46.20	0.22	−15.95	−41.56

experiment had a cross-polarization level of about −40 dB. The FFOC performs even better with its larger main reflector f/D ratio. Table 6 compares the calculated FFOC and SFOC performance for the on-axis beam and the 10° beams scanned upward, sideward, and downward for 1.8λ feeds in the FFOC and 2.1λ feeds in the SFOC. For each case, Table 6 lists the peak directivity, the change in peak directivity from the on-axis beam, the peak sidelobe level, and the peak cross-polarization level.

The small feeds provide crossover levels close to 3 dB and would be used in a feed array where feeds are combined with BFNs to provide multiple contoured beams. Then, the high spillover losses of 4–5 dB on the feed element level would be reduced. The SFOC and FFOC provide a very high performance comparable to the copolar performance of single-offset reflectors with f/D ratios of about 2.6 and 5.6, respectively. Increasing the reflector diameter to 240λ and 480λ will increase the scan losses, which then may be reduced by optimizing the reflector surface shapes.

Only a limited number of FFOC and SFOC applications have been reported. The capability has so far exceeded the demand. Chandler et al. [69] proposed using four FFOCs in the Ka band to provide global multibeam coverage from a geostationary satellite using one feed per beam. While the SFOC may be applied in the same role [70], its main use has been for high-performance compact antenna test ranges as described by Dudok [71]. The excellent scan performance, low cross-polarization, and low diffraction in the large subreflector make the FFOC an excellent choice for this application, where it allows a large quiet zone to be implemented.

Acknowledgement

The author is grateful to Alcatel Space and Gérald Caille in supplying Figs. 3 and 4 with the Stentor Ku-band active Tx array and to EADS Astrium GmbH and Helmut Wolf in supplying Figs. 5–7 with international C-band hemi/zone reflector antenna systems.

BIBLIOGRAPHY

1. A. Lozano, F. R. Farrokhi, and R. A. Valenzuela, Lifting the limits on high-speed wireless data access using antenna arrays, *IEEE Commun. Mag.* **39**:156–162 (Sept. 2001).
2. R. D. Murch and K. B. Letaief, Antenna systems for broadband wireless access, *IEEE Commun. Mag.* **40**:76–83 (April 2002).
3. T. A. Milligan, *Modern Antenna Design*, McGraw-Hill, New York, 1985, Chap. 6.
4. R. C. Hansen, *Phased Array Antennas*, Wiley, New York, 1998, Chap. 8.
5. D.-W. Duan and Y. Rahmat-Samii, A generalized three parameter (3-P) aperture distribution for antenna applications, *IEEE Trans. Anten. Propag.* **AP-40**:697–713 (April 1992).
6. S. Badessi, Private communication, 1986.
7. P. Balling, Simple prediction of contoured beam antenna directivity, *CD-ROM Millennium Conf. Antennas and Propagation AP 2000*, (Davos, Switzerland), April 2000, paper 1563.
8. D. F. DiFonzo, Evolution of satellite antennas, *Proc. IEEE Int. Symp. Antennas and Propagation*, Albuquerque, NM 1982, pp. 358–361.
9. R. J. Mailloux, *Phased Array Antenna Handbook*, Artech House, Norwood, MA, 1994, Chap. 8.
10. L. J. Ricardi, Multiple beam antennas, in A. W. Rudge, K. Milne, A. D. Olver, and P. Knight, eds., *The Handbook of Antenna Design*, Peter Peregrinus, London, 1982, Vol. 1, Chap. 6.
11. W. V. T. Rusch, T. S. Chu, A. R. Dion, P. A. Jensen, A. W. Rudge, and W. C. Wong, Quasi-optical antenna design and application, in A. W. Rudge, K. Milne, A. D. Olver, and P. Knight, eds., *The Handbook of Antenna Design*, Peter Peregrinus, London, 1982, Vol. 1, Chap. 3.
12. Y. Kitsuregawa, *Advanced Technology in Satellite Communication Antennas: Electrical and Mechanical Design*, Artech House, Norwood, MA, 1990.
13. C. C. Han and Y. Hwang, Satellite antennas, in Y. T. Lo and S. W. Lee, eds., *Antenna Handbook*, Van Nostrand Reinhold, New York, 1993, Vol. 3, Chap. 21.
14. A. Kumar, *Antenna Design with Fiber Optics*, Artech House, Norwood, MA, 1996.
15. J. Litva and K.-Y. Lo, *Digital Beamforming in Wireless Communications*, Artech House, Norwood, MA, 1996.
16. J. R. Brain, The Inmarsat 4 mobile antenna system, *Proc. JINA 2002*, Nice, France, Nov. 2002, Vol. 2, pp. 333–336.
17. R. Arnott, S. Ponnekanti, C. Taylor, and H. Chaloupka, Advanced base station technology, *IEEE Commun. Mag.* **36**:96–102 (Feb. 1998).
18. F. J. Dietrich, P. Metzen, and P. Monte, The Globalstar cellular satellite system, *IEEE Trans. Anten. Propag.* **AP-46**:935–942 (1998).
19. J. J. Schuss, J. Upton, B. Myers, T. Sikina, A. Rohwer, P. Makriakias, R. Francois, L. Wardle, and R. Smith, The IRIDIUM

- main mission antenna concept, *IEEE Trans. Anten. Propag.* **AP-47**:416–424 (1999).
20. C. Mangenot, P. Lepeltier, F. Croq, and J. Maurel, Recent antenna developments at Alcatel Space Industries, in *CD-ROM ISAP 2000*, Fukuoka, Japan, Aug. 2000, paper 1A2-1; see also paper 1409 on CD-ROM AP2000, Davos, Switzerland, April 2000.
 21. E. Lier and A. Jacomb-Hood, Deployed and modular active phased array satellite antenna, *Proc. 18th AIAA Conf.*, Oakland, CA, April 2000, pp. 33–37; see also *IEEE Commun. Mag.* 40–47 (Dec. 2000).
 22. A. G. Roederer, Semi-active multimatrix reflector antennas, *Electromagnetics* **15**:123–132 (Jan. 1995).
 23. S. K. Rao, Design and analysis of multiple-beam reflector antennas, *IEEE Anten. Propag. Mag.* **41**:53–59 (Aug. 1999); see also *ibid.* **45**:26–34 (Aug. 2003).
 24. J. Uher, J. Bornemann, and U. Rosenberg, *Waveguide Components for Antenna Feed Systems: Theory and CAD*, Artech House, Norwood, MA, 1993.
 25. F. A. Regier, The ACTS multibeam antenna, *IEEE Trans. Microwave Theory Tech.* **MTT-40**:1159–1164 (1992).
 26. Y. Kobayashi, S. Makino, T. Noguchi, P. Balling, W. Bornemann, W. J. English, P. Neyret, and H.-H. Viskum, Flexible/reconfigurable 6 and 4 GHz antenna beam technology development, *Proc. JINA 1990*, Nice, France, Nov. 1990, pp. 399–402.
 27. W. Bornemann, M. Tromper, and L. L. Jensen, INTELSAT VIII antennas, *Proc. JINA 1994*, Nice, France, Nov. 1994, pp. 167–173.
 28. S. Paus, L. L. Jensen, N. Ratkorn, and H. Wolf, The INTEL-SAT-IX C-band hemi/zone antennas, in *CD-ROM AP2000*, Davos, Switzerland, April 2000, paper 0061.
 29. J. P. Shelton and K. S. Kelleher, Multiple beams from linear arrays, *IEEE Trans. Anten. Propag.* **AP-9**:154–161 (March 1961).
 30. J. L. Allen, A theoretical limitation on the formation of lossless multiple beams in linear arrays, *IEEE Trans. Anten. Propag.* **AP-9**:350–352 (July 1961).
 31. W. K. Kahn and H. Kurss, The uniqueness of the lossless feed network of a multibeam array, *IEEE Trans. Anten. Propag.* **AP-10**:100–101 (Jan. 1962).
 32. W. D. White, Pattern limitations in multiple-beam antennas, *IEEE Trans. Anten. Propag.* **AP-10**:430–436 (July 1962).
 33. S. Stein, On cross coupling in multiple-beam antennas, *IEEE Trans. Anten. Propag.* **AP-10**:548–557 (Sept. 1962).
 34. E. C. DuFort, Optimum low sidelobe high crossover multiple beam antennas, *IEEE Trans. Anten. Propag.* **AP-33**:946–954 (Sept. 1985).
 35. E. C. DuFort, Optimum networks for simultaneous multiple beam antennas, *IEEE Trans. Anten. Propag.* **AP-40**:1–7 (Jan. 1992).
 36. J. L. Butler, Digital, matrix, and intermediate-frequency scanning, in R. C. Hansen, ed., *Microwave Scanning Antennas*, Academic Press, 1966, Vol. 3, Chap. 3; now published by Peninsula Publishing, Los Altos, CA, 1985.
 37. P. J. Wood, Some extensions of the beam orthogonality concept for multi-beam antennas, *Proc. Conf. Antennas Communication*, Montreal, 1986, pp. 310–313.
 38. S. Gupta, Y. Patenaude, and C. Mok, MSAT L-band antenna subsystems, *Proc. JINA 1994*, Nice, France, 1994, pp. 196–201; see also *Proc. 15th AIAA Conf.*, San Diego, CA, 1994, pp. 559–567.
 39. D. LaFlame, P. Balling, J. Wu, N. Schröder, and H. Wolf, Multi-mode antenna optimization, *Proc. ESA Workshop on Advanced Beamforming Networks for Space Applications*, ESTEC, Noordwijk, The Netherlands, 1991, pp. 2.8.1–2.8.6; abbreviated version in *Proc. IEEE Int. Symp. Antennas and Propagation*, Chicago, 1992, pp. 1344–1347.
 40. G. Ruggerini, The diagonalisation BFN for satellite reflector antennas with simultaneous overlapped multiple coverages, *Proc. 8th Int. Conf. Antennas and Propagation*, Edinburgh, 1993, pp. 570–573.
 41. Y. Rahmat-Samii, Reflector antennas, in Y. T. Lo and S. W. Lee, eds., *Antenna Handbook*, Van Nostrand Reinhold, New York, 1993, Vol. 2, Chap. 15.
 42. K. Pontoppidan, ed., *Technical Description of GRASP8, TICRA*, Copenhagen, 2002 (the book and a student's version of GRASP8W is freely available from the TICRA Website www.ticra.com).
 43. Y. Rahmat-Samii and S. W. Lee, Directivity of planar array feeds for satellite reflector applications, *IEEE Trans. Anten. Propag.* **AP-31**:463–470 (May 1983); see also correction in **AP-32**:762 (1984).
 44. P. Balling, Spacecraft multi-beam and contoured-beam antennas, in R. J. Mailloux, ed., *Microwave Antennas for Avionics*, AGARD Lecture Series 151, 1987, pp. 4.1–4.23.
 45. R. Mittra, Y. Rahmat-Samii, V. Galindo-Israel, and R. Norman, An efficient technique for the computation of vector secondary patterns of offset paraboloid reflectors, *IEEE Trans. Anten. Propag.* **AP-27**:294–304 (May 1979).
 46. J. Ruze, Lateral-feed displacement in a paraboloid, *IEEE Trans. Anten. Propag.* **AP-13**:660–665 (Sept. 1965).
 47. C. Dragone, A first-order treatment of aberrations in Cassegrainian and Gregorian antennas, *IEEE Trans. Anten. Propag.* **AP-30**:331–339 (May 1982).
 48. P. Balling and W. Trachtman, Ray optical determination of scan properties of reflector antenna systems, *Proc. 3rd Int. Conf. Antennas and Propagation*, Norwich, 1983, pp. 322–325.
 49. N. C. Albertsen, K. Pontoppidan, and S. B. Sørensen, Shaping of dual reflector antennas for improvement of scan performance, *Proc. IEEE Int. Symp. Antennas and Propagation*, Vancouver, 1985, pp. 357–360.
 50. P. T. Lam, S. W. Lee, D. C. D. Chang, and K. C. Lang, Directivity optimization of a reflector antenna with cluster feeds: A closed-form solution, *IEEE Trans. Anten. Propag.* **AP-33**:1163–1174 (Nov. 1985); see also correction in **AP-33**:1473 (1986).
 51. N. A. Adatia and A. W. Rudge, Beam squint in circularly polarised offset reflector antennas, *Electron. Lett.* **11**:513–515 (Oct. 1975).
 52. J. Jacobsen, On the cross polarization of asymmetric reflector antennas for satellite applications, *IEEE Trans. Anten. Propag.* **AP-26**:276–283 (March 1977).
 53. M. J. Gans and R. A. Semplak, Some far-field studies of an offset launcher, *Bell Syst. Tech. J.* **54**:1319–1340 (Sept. 1975).
 54. A. R. Raab, Cross-polarisation performance of the RCA Satcom frequency re-use antenna, *Proc. IEEE Int. Symp. Antennas and Propagation*, Amherst, Oct. 1976, pp. 100–104.
 55. A. W. Rudge and N. A. Adatia, New class of primary-feed antennas for use with offset parabolic-reflector antennas, *Electron. Lett.* **11**:597–599 (Oct. 1975).
 56. T. Chu, Cancellation of polarization rotation in an offset paraboloid by a polarization grid, *Bell Syst. Tech. J.* **56**:977–986 (1977).
 57. C. Dragone, New grids for improved polarization diplexing of microwaves in reflector antennas, *IEEE Trans. Anten. Propag.* **AP-26**:459–463 (1978).
 58. P. Balling, H. Wolf, and M. van der Vorst, Crosspolarization suppression in large linearly polarized array-fed offset reflector antenna systems, *Proc. Int. ITG Conf. Antennas and COST 284 Workshop*, Berlin, Sept. 2003.

59. Y. Mizugutch, M. Akagawa, and H. Yokoi, Offset dual reflector antenna, *Proc. IEEE Int. Symp. Antennas and Propagation*, Amherst, 1976, pp. 2–5.
60. N. C. Albertsen, Off-set Cassegrain antenna optimized for frequency re-use, *Proc. IEEE Int. Symp. Antennas and Propagation*, Stanford, 1977, pp. 448–451.
61. B. S. Westcott, ed., *Shaped Reflector Antenna Design*, Research Studies Press, Letchworth, Hertfordshire, UK, 1983; see also B. S. Westcott and F. Brickell, Dual offset reflectors shaped for zero cross-polarisation and prescribed illumination, *J. Appl. Phys.* **12**:169–186 (1979).
62. G. Bjøntegaard and T. Petterson, An offset dual-reflector antenna shaped from near-field measurements of the feed horn: Theoretical calculations and measurements, *IEEE Trans. Anten. Propag.* **AP-31**:973–977 (1983).
63. H. Tanaka and M. Mizusawa, Elimination of cross-polarization in offset dual-reflector antennas, *Electron. Commun. Jpn.* **58B**(12):71–78 (1975).
64. W. V. T. Rusch, Y. R.-S. A. Prata, Jr., and R. A. Shore, Derivation and application of the equivalent paraboloid for classical offset Cassegrain and Gregorian antennas, *IEEE Trans. Anten. Propag.* **AP-38**:1141–1149 (1990).
65. C. Dragone, Offset multireflector antennas with perfect pattern symmetry and polarization discrimination, *Bell Syst. Tech. J.* **57**:2663–2685 (1978).
66. C. Dragone, Unique reflector arrangement with very wide field of view for multibeam antennas, *Electron. Lett.* **19**:1061–1062 (1983).
67. S. Makino, Y. Kobayashi, and T. Katagi, Front fed offset Cassegrain type multibeam antenna, *Proc. IEEE Int. Symp. Antennas and Propagation*, Vancouver, 1985, pp. 341–344.
68. R. Jørgensen, P. Balling, and W. J. English, Dual offset reflector multi-beam antenna for international communications satellite, *IEEE Trans. Anten. Propag.* **AP-33**:1304–1312 (1985).
69. C. Chandler, L. Hoey, D. Hixon, T. Smigla, A. Peebles, and M. Em, Ka-band communications satellite antenna technology, *Proc. 20th AIAA Conf.*, Montreal, Quebec, Canada, 2002, paper AIAA 2002–1988.
70. J.-M. Lopez, Brief overview of Ka-band satellite multibeam antenna work in France, *Int. ITG Conf. Anten.*, Berlin, Germany, Sept. 2003.
71. E. Dudok, New concepts and results in advanced antenna testing up to mm-waves: The compact antenna test range, *Proc. JINA 1990*, Nice, France, Nov. 1990, pp. 533–540.

MULTICONDUCTOR TRANSMISSION LINES

J. A. BRANDÃO FARIA
 Instituto Superior Técnico
 Lisbon, Portugal

1. INTRODUCTION

An important electrical engineering theme, the topic of wave propagation phenomena in multiconductor transmission lines (MTL) has been receiving attention since 1930 [1,2]. Interest in such a topic pervades many different areas where high-frequency regimes come into play, namely, powerline transients and powerline communications,

crosstalk and electromagnetic compatibility problems, electronic and microelectronic design, and packaging, as well as, naturally, in RF and microwave engineering.

In recent times the subject of multiconductor transmission lines has been growing in importance, particular attention being paid to the computation of the propagation characteristics of printed-circuit boards, high-speed interconnects, microstrip lines, and other components, with numerous applications in VLSI, MMICs, impedance-matching networks, pulseshaping devices, filters, and other microwave structures.

For an exact evaluation of transmission-line traveling-wave solutions, hybrid-mode full-wave analysis is often required. Nevertheless, quasistatic approaches based on transverse electromagnetic (TEM) parameters are ordinarily used. The latter yield very good results provided that two basic assumptions are fulfilled; the system's transverse dimensions are small compared to the operating wavelengths (higher-order modes excluded), and the longitudinal electromagnetic field components (due to system losses and dielectric inhomogeneity) are very small compared to the transverse ones. These assumptions are employed throughout this article, enabling the consistent use of such concepts as voltages and currents.

2. VOLTAGES AND CURRENTS IN MTLs

A multiconductor transmission line is defined by a set of $n + 1$ conductors running parallel to a longitudinal axis (z axis). Among the system conductors one of them is ordinarily chosen for reference (ground conductor, conductor 0).

Conductor voltages and conductor currents are defined at transverse planes (z constant). A function of t and z , conductor k voltage is defined as the line integral of the electric field vector \mathbf{E} from conductor k to conductor 0, the integration path \mathbf{s} lying on the z plane

$$v_k(z, t) = \int_{k0} \mathbf{E}(x, y, z, t) \cdot d\mathbf{s}, \quad \text{for } k = 1, 2, \dots, n \quad (1)$$

A function of t and z , conductor- k current is defined as the surface integral of the current density \mathbf{J}_k flowing in the conductor through its own cross section S_k , or, which is equivalent, the line integral of the magnetic field vector \mathbf{H} along an arbitrary closed path \mathbf{s}_k encircling the conductor, but, again, lying on the transverse plane

$$\begin{aligned} i_k(z, t) &= \int_{S_k} \mathbf{J}_k \cdot \mathbf{u}_z dS \\ &= \oint_{\mathbf{s}_k} \mathbf{H}(x, y, z, t) \cdot d\mathbf{s}, \quad \text{for } k = 1, 2, \dots, n \end{aligned} \quad (2)$$

where \mathbf{u}_z denotes the unit vector in the direction of the positive z axis (reference direction for positive currents).

The current intensity i_0 flowing in the reference conductor is not an independent variable, for it is related to

59. Y. Mizugutch, M. Akagawa, and H. Yokoi, Offset dual reflector antenna, *Proc. IEEE Int. Symp. Antennas and Propagation*, Amherst, 1976, pp. 2–5.
60. N. C. Albertsen, Off-set Cassegrain antenna optimized for frequency re-use, *Proc. IEEE Int. Symp. Antennas and Propagation*, Stanford, 1977, pp. 448–451.
61. B. S. Westcott, ed., *Shaped Reflector Antenna Design*, Research Studies Press, Letchworth, Hertfordshire, UK, 1983; see also B. S. Westcott and F. Brickell, Dual offset reflectors shaped for zero cross-polarisation and prescribed illumination, *J. Appl. Phys.* **12**:169–186 (1979).
62. G. Bjøntegaard and T. Petterson, An offset dual-reflector antenna shaped from near-field measurements of the feed horn: Theoretical calculations and measurements, *IEEE Trans. Anten. Propag.* **AP-31**:973–977 (1983).
63. H. Tanaka and M. Mizusawa, Elimination of cross-polarization in offset dual-reflector antennas, *Electron. Commun. Jpn.* **58B**(12):71–78 (1975).
64. W. V. T. Rusch, Y. R.-S. A. Prata, Jr., and R. A. Shore, Derivation and application of the equivalent paraboloid for classical offset Cassegrain and Gregorian antennas, *IEEE Trans. Anten. Propag.* **AP-38**:1141–1149 (1990).
65. C. Dragone, Offset multireflector antennas with perfect pattern symmetry and polarization discrimination, *Bell Syst. Tech. J.* **57**:2663–2685 (1978).
66. C. Dragone, Unique reflector arrangement with very wide field of view for multibeam antennas, *Electron. Lett.* **19**:1061–1062 (1983).
67. S. Makino, Y. Kobayashi, and T. Katagi, Front fed offset Cassegrain type multibeam antenna, *Proc. IEEE Int. Symp. Antennas and Propagation*, Vancouver, 1985, pp. 341–344.
68. R. Jørgensen, P. Balling, and W. J. English, Dual offset reflector multi-beam antenna for international communications satellite, *IEEE Trans. Anten. Propag.* **AP-33**:1304–1312 (1985).
69. C. Chandler, L. Hoey, D. Hixon, T. Smigla, A. Peebles, and M. Em, Ka-band communications satellite antenna technology, *Proc. 20th AIAA Conf.*, Montreal, Quebec, Canada, 2002, paper AIAA 2002–1988.
70. J.-M. Lopez, Brief overview of Ka-band satellite multibeam antenna work in France, *Int. ITG Conf. Anten.*, Berlin, Germany, Sept. 2003.
71. E. Dudok, New concepts and results in advanced antenna testing up to mm-waves: The compact antenna test range, *Proc. JINA 1990*, Nice, France, Nov. 1990, pp. 533–540.

MULTICONDUCTOR TRANSMISSION LINES

J. A. BRANDÃO FARIA
Instituto Superior Técnico
Lisbon, Portugal

1. INTRODUCTION

An important electrical engineering theme, the topic of wave propagation phenomena in multiconductor transmission lines (MTL) has been receiving attention since 1930 [1,2]. Interest in such a topic pervades many different areas where high-frequency regimes come into play, namely, powerline transients and powerline communications,

crosstalk and electromagnetic compatibility problems, electronic and microelectronic design, and packaging, as well as, naturally, in RF and microwave engineering.

In recent times the subject of multiconductor transmission lines has been growing in importance, particular attention being paid to the computation of the propagation characteristics of printed-circuit boards, high-speed interconnects, microstrip lines, and other components, with numerous applications in VLSI, MMICs, impedance-matching networks, pulseshaping devices, filters, and other microwave structures.

For an exact evaluation of transmission-line traveling-wave solutions, hybrid-mode full-wave analysis is often required. Nevertheless, quasistatic approaches based on transverse electromagnetic (TEM) parameters are ordinarily used. The latter yield very good results provided that two basic assumptions are fulfilled; the system's transverse dimensions are small compared to the operating wavelengths (higher-order modes excluded), and the longitudinal electromagnetic field components (due to system losses and dielectric inhomogeneity) are very small compared to the transverse ones. These assumptions are employed throughout this article, enabling the consistent use of such concepts as voltages and currents.

2. VOLTAGES AND CURRENTS IN MTLs

A multiconductor transmission line is defined by a set of $n + 1$ conductors running parallel to a longitudinal axis (z axis). Among the system conductors one of them is ordinarily chosen for reference (ground conductor, conductor 0).

Conductor voltages and conductor currents are defined at transverse planes (z constant). A function of t and z , conductor k voltage is defined as the line integral of the electric field vector \mathbf{E} from conductor k to conductor 0, the integration path \mathbf{s} lying on the z plane

$$v_k(z, t) = \int_{k0} \mathbf{E}(x, y, z, t) \cdot d\mathbf{s}, \quad \text{for } k = 1, 2, \dots, n \quad (1)$$

A function of t and z , conductor- k current is defined as the surface integral of the current density \mathbf{J}_k flowing in the conductor through its own cross section S_k , or, which is equivalent, the line integral of the magnetic field vector \mathbf{H} along an arbitrary closed path \mathbf{s}_k encircling the conductor, but, again, lying on the transverse plane

$$\begin{aligned} i_k(z, t) &= \int_{S_k} \mathbf{J}_k \cdot \mathbf{u}_z dS \\ &= \oint_{\mathbf{s}_k} \mathbf{H}(x, y, z, t) \cdot d\mathbf{s}, \quad \text{for } k = 1, 2, \dots, n \end{aligned} \quad (2)$$

where \mathbf{u}_z denotes the unit vector in the direction of the positive z axis (reference direction for positive currents).

The current intensity i_0 flowing in the reference conductor is not an independent variable, for it is related to

the remaining conductor currents through

$$i_0(z, t) = \int_{S_0} \mathbf{J}_0 \cdot \mathbf{u}_z dS = - \sum_{k=1}^n i_k(z, t) \quad (3)$$

3. TIME-DOMAIN EQUATIONS FOR LOSSLESS LINES

The application of Maxwell’s equations in integral form to the conductors of a loss-free multiconductor transmission-line structure of arbitrary small length yields [3,4]

$$\oint_{s_k} \mathbf{E} \cdot d\mathbf{s} = - \frac{\partial}{\partial t} \psi_k \rightarrow \frac{\partial}{\partial z} v_k(z, t) = - \sum_{j=1}^n L_{kj} \frac{\partial}{\partial t} i_j(z, t) \quad (4)$$

$$\int_{Sv_k} \mathbf{J} \cdot \mathbf{n}_e dS = - \frac{\partial}{\partial t} q_k \rightarrow \frac{\partial}{\partial z} i_k(z, t) = - \sum_{j=1}^n C_{kj} \frac{\partial}{\partial t} v_j(z, t) \quad (5)$$

where the per unit length external inductances L_{kj} (H/m) and the per unit length capacitances C_{kj} (F/m) take into account the distributed effects of magnetic and electric coupling among system conductors, respectively. These key parameters, which depend on the properties (permittivity ϵ and permeability μ) of the dielectric media that surrounds the conductors, are intrinsic to the geometry of the line configuration. Except for very simple cases, as, for example, MTLs comprising thin circular conductors, the evaluation of L_{kj} and C_{kj} generally requires the utilization of rather elaborated semianalytical or numerical techniques, [4].

By introducing two column vectors $\mathbf{v}(z, t)$ and $\mathbf{i}(z, t)$, that respectively gather all the conductor voltages and all the conductor currents,

$$\mathbf{v}(z, t) = \begin{bmatrix} v_1(z, t) \\ \vdots \\ v_k(z, t) \\ \vdots \\ v_n(z, t) \end{bmatrix}; \quad \mathbf{i}(z, t) = \begin{bmatrix} i_1(z, t) \\ \vdots \\ i_k(z, t) \\ \vdots \\ i_n(z, t) \end{bmatrix}$$

equations (4) and (5) can be written compactly in a convenient matrix form as

$$\frac{\partial \mathbf{v}}{\partial z} = - \mathbf{L}_e \frac{\partial \mathbf{i}}{\partial t}; \quad \frac{\partial \mathbf{i}}{\partial z} = - \mathbf{C} \frac{\partial \mathbf{v}}{\partial t} \quad (6)$$

where \mathbf{L}_e and \mathbf{C} are $n \times n$ matrices whose entries are the parameters L_{kj} and C_{kj} referred to above.

The per unit length external inductance and capacitance matrices in (6) are, both them, real symmetric positive-definite matrices [3,4].

In the particular case of MTLs with conductors surrounded by a homogeneous dielectric medium the matrix

pair \mathbf{L}_e and \mathbf{C} is related through

$$\mathbf{L}_e \mathbf{C} = \mathbf{C} \mathbf{L}_e = \mu \epsilon \mathbf{1} \quad (7)$$

where $\mathbf{1}$ is the $n \times n$ identity matrix (ones along the main diagonal).

If the cross section of the transmission line varies along the longitudinal coordinate z , or if μ or ϵ are functions of z , then the MTL will be classified as a nonuniform line. In such cases the inductance and capacitance matrices appearing in (6) and (7) become functions of z , $\mathbf{L}_e = \mathbf{L}_e(z)$ and $\mathbf{C} = \mathbf{C}(z)$.

The coupled pair of fundamental equations in (6) can be transformed in two other equations, one for \mathbf{v} and another for \mathbf{i} . By differentiating both sides of the two equations in (6) in order to z , one will get

$$\frac{\partial^2 \mathbf{v}}{\partial z^2} - \frac{d\mathbf{L}_e}{dz} \mathbf{L}_e^{-1} \frac{\partial \mathbf{v}}{\partial z} = \mathbf{L}_e \mathbf{C} \frac{\partial^2 \mathbf{v}}{\partial t^2} \quad (8)$$

$$\frac{\partial^2 \mathbf{i}}{\partial z^2} - \frac{d\mathbf{C}}{dz} \mathbf{C}^{-1} \frac{\partial \mathbf{i}}{\partial z} = \mathbf{C} \mathbf{L}_e \frac{\partial^2 \mathbf{i}}{\partial t^2} \quad (9)$$

The preceding results greatly simplify when uniform lines are considered since the terms involving $d\mathbf{L}_e/dz$ and $d\mathbf{C}/dz$ vanish. Further simplification arises in the case of MTLs with a homogeneous dielectric medium:

$$\frac{\partial^2 \mathbf{v}}{\partial z^2} = \mu \epsilon \frac{\partial^2 \mathbf{v}}{\partial t^2} \quad (10)$$

$$\frac{\partial^2 \mathbf{i}}{\partial z^2} = \mu \epsilon \frac{\partial^2 \mathbf{i}}{\partial t^2} \quad (11)$$

From (10) and (11) one immediately sees that line voltages and line currents obey the standard wave equation; the wave propagation velocity, common to all voltages and currents, given by $(\mu \epsilon)^{-1/2}$.

4. FREQUENCY-DOMAIN EQUATIONS FOR MTLs

The transmission-line equations presented in the preceding section are particularized now for the situation of time-harmonic fields, where all voltages and currents are assumed to vary sinusoidally in time with a given angular frequency ω . In order to exemplify the notation we write conductor k ’s voltage as

$$v_k(z, t) = V_k(z) \cos(\omega t + \phi_k(z)) = \text{Re}\{\bar{V}_k(z) e^{+j\omega t}\}$$

$$\bar{V}_k(z) = V_k(z) e^{j\phi_k(z)}$$

where \bar{V}_k is the complex amplitude associated with voltage v_k . This complex time-invariant quantity contains information about the magnitude V_k and phase angle ϕ_k of voltage v_k , both of which may vary along the line longitudinal coordinate z .

The consideration of time-harmonic regimes has two main advantages. On one hand, a great deal of simplification arises in the writing and solving of the transmission-line equations, since the time variable t disappears.

On the other hand, it easily allows for the incorporation of line losses (an important issue that cannot be dealt with in the framework of a pure time-domain formalism [5]).

The pair of equations in (6) for lossless MTLs translates to the frequency domain as

$$\frac{d}{dz}\bar{\mathbf{V}} = -j\omega\mathbf{L}_e\bar{\mathbf{I}} \quad (12)$$

$$\frac{d}{dz}\bar{\mathbf{I}} = -j\omega\mathbf{C}\bar{\mathbf{V}} \quad (13)$$

Generalization of these results to include conductor losses and dielectric losses is now possible by adding to the right-hand side of both equations new corrective terms as follows

$$\frac{d}{dz}\bar{\mathbf{V}} = -(\bar{\mathbf{Z}}_s + j\omega\mathbf{L}_e)\bar{\mathbf{I}} \quad (14)$$

$$\frac{d}{dz}\bar{\mathbf{I}} = -(\mathbf{G} + j\omega\mathbf{C})\bar{\mathbf{V}} \quad (15)$$

where $\bar{\mathbf{Z}}_s$ is the surface impedance matrix per unit length. The entries of this complex symmetric square matrix of order n are evaluated with the help of skin effect theory. By breaking down $\bar{\mathbf{Z}}_s$ into its real and imaginary parts, one finds

$$\bar{\mathbf{Z}}_s = \mathbf{R} + j\omega\mathbf{L}_i \quad (16)$$

where \mathbf{R} is the per unit length resistance matrix associated with line conductors finite conductivity, and \mathbf{L}_i is the per unit length internal inductance matrix associated with magnetic energy storage inside line conductors. For millimeter-wave and microwave applications, where the conductor skin effect penetration depth is of the order of micrometers, the frequency dependence of \mathbf{R} and \mathbf{L}_i is approximately of the type

$$\mathbf{R}(\omega) \propto \omega^{1/2}, \quad \mathbf{L}_i(\omega) \propto \omega^{-1/2}$$

In (15), \mathbf{G} denotes the per unit length conductance matrix, which is associated with dielectric media imperfections (conduction and polarization losses).

If we now define the longitudinal impedance matrix $\bar{\mathbf{Z}}$ (Ω/m) and the transverse admittance matrix $\bar{\mathbf{Y}}$ (S/m) such that

$$\bar{\mathbf{Z}} = \bar{\mathbf{Z}}_s + j\omega\mathbf{L}_e = \mathbf{R} + j\omega(\underbrace{\mathbf{L}_e + \mathbf{L}_i}_{\mathbf{L}}) \quad (17)$$

$$\bar{\mathbf{Y}} = \mathbf{G} + j\omega\mathbf{C} \quad (18)$$

we may rewrite (14) and (15) in the form

$$\frac{d}{dz}\bar{\mathbf{V}}(z) = -\bar{\mathbf{Z}}(\omega)\bar{\mathbf{I}}(z) \quad (19)$$

$$\frac{d}{dz}\bar{\mathbf{I}}(z) = -\bar{\mathbf{Y}}(\omega)\bar{\mathbf{V}}(z) \quad (20)$$

For the general case of nonuniform MTLs where $\bar{\mathbf{Z}}$ and $\bar{\mathbf{Y}}$ are functions of z , we obtain, in correspondence with (8) and (9)

$$\frac{d^2\bar{\mathbf{V}}}{dz^2} - \frac{d\bar{\mathbf{Z}}}{dz}\bar{\mathbf{Z}}^{-1}\frac{d\bar{\mathbf{V}}}{dz} = \bar{\mathbf{Z}}\bar{\mathbf{Y}}\bar{\mathbf{V}} \quad (21)$$

$$\frac{d^2\bar{\mathbf{I}}}{dz^2} - \frac{d\bar{\mathbf{Y}}}{dz}\bar{\mathbf{Y}}^{-1}\frac{d\bar{\mathbf{I}}}{dz} = \bar{\mathbf{Y}}\bar{\mathbf{Z}}\bar{\mathbf{I}} \quad (22)$$

From now on, throughout the remaining of this article, in order to alleviate the notation, we will drop the overbars indicating complex quantities.

5. SOLUTION OF TRANSMISSION-LINE EQUATIONS: MODAL DECOUPLING

Finding a solution to the frequency-domain transmission-line (TL) equations in (21) and (22) is a task that generally will require numerical integration techniques. However, a common procedure that is often used to analyze nonuniform MTLs consists in segmenting the global structure into a number of small longitudinal sections, each of which is a uniform MTL where \mathbf{Z} and \mathbf{Y} are assigned constant values, [3,4,6].

For the case of uniform line sections the set of equations in (21) and (22) reduces to a set of linear differential equations with constant coefficients

$$\frac{d^2\mathbf{V}}{dz^2} = \mathbf{Z}\mathbf{Y}\mathbf{V} \quad (23)$$

$$\frac{d^2\mathbf{I}}{dz^2} = \mathbf{Y}\mathbf{Z}\mathbf{I} \quad (24)$$

The much simpler equations in (23) and (24) have analytical solutions that ordinarily take the form of a superposition of natural modes of propagation involving exponential functions on z , [3,4,7–10], that is

$$\mathbf{V}(z) = \begin{bmatrix} V_1(z) \\ \vdots \\ V_k(z) \\ \vdots \\ V_n(z) \end{bmatrix} = \mathbf{T}\hat{\mathbf{V}}(z) \quad (25)$$

$$= \sum_{j=1}^n \mathbf{t}_j(\hat{\mathbf{V}}_j^{(f)} e^{-\gamma_j z} + \hat{\mathbf{V}}_j^{(b)} e^{+\gamma_j z})$$

$$\mathbf{I}(z) = \begin{bmatrix} I_1(z) \\ \vdots \\ I_k(z) \\ \vdots \\ I_n(z) \end{bmatrix} = \mathbf{W}\hat{\mathbf{I}}(z) \tag{26}$$

$$= \sum_{j=1}^n \mathbf{w}_j \hat{Y} w_j (\hat{\mathbf{V}}_j^{(f)} e^{-\gamma_j z} - \hat{\mathbf{V}}_j^{(b)} e^{+\gamma_j z})$$

where the complex amplitudes of the modal voltages $\hat{\mathbf{V}}_j^{(f)}$ and $\hat{\mathbf{V}}_j^{(b)}$ concerning the forward- and backward-propagating waves are determined upon consideration of boundary conditions. In (25), vector \mathbf{t}_j denotes the j th column of matrix \mathbf{T} ; likewise, in (26), vector \mathbf{w}_j denotes the j th column of matrix \mathbf{W} .

Voltages in the natural domain \mathbf{V} and voltages in the modal domain $\hat{\mathbf{V}}$, in (25), are related among them through a suitably chosen transformation matrix \mathbf{T} , which has the property of assuring the decoupling of the equation set defined in (23). Similarly, currents in the natural domain \mathbf{I} and currents in the modal domain $\hat{\mathbf{I}}$, in (26), are related among them through a suitably chosen transformation matrix \mathbf{W} , which has the property of assuring the decoupling of the equation set defined in (24):

$$\frac{d^2 \hat{\mathbf{V}}}{dz^2} = (\mathbf{T}^{-1} \mathbf{Z} \mathbf{Y} \mathbf{T}) \hat{\mathbf{V}} \tag{27}$$

$$\frac{d^2 \hat{\mathbf{I}}}{dz^2} = (\mathbf{W}^{-1} \mathbf{Y} \mathbf{Z} \mathbf{W}) \hat{\mathbf{I}} \tag{28}$$

For effective decoupling of equations to take place, the matrix products in parentheses must yield diagonal matrices. Since \mathbf{Z} and \mathbf{Y} are both symmetric matrices, we must find

$$\mathbf{T}^{-1} \mathbf{Z} \mathbf{Y} \mathbf{T} = \underbrace{\mathbf{T}^t}_{\mathbf{W}^{-1}} (\mathbf{Y} \mathbf{Z}) \underbrace{\mathbf{T}^{-1t}}_{\mathbf{W}} = \gamma^2$$

$$= \begin{bmatrix} \gamma_1^2 & & & & \\ & \ddots & & & \\ & & \gamma_j^2 & & \\ & & & \ddots & \\ & & & & \gamma_n^2 \end{bmatrix} \tag{29}$$

where superscript t denotes transposition.

From (29) we see that the transformation matrix for voltages and the transformation matrix for currents are not independent. Apart from an arbitrary normalizing matrix, these transformations are related to each other through

$$\mathbf{T}^t = \mathbf{W}^{-1} \tag{30}$$

Substituting (29) into (27) and (28) we find, for $j = 1, \dots, n$

$$\frac{d^2}{dz^2} \begin{Bmatrix} \hat{\mathbf{V}}_j \\ \hat{\mathbf{I}}_j \end{Bmatrix} = \gamma_j^2 \begin{Bmatrix} \hat{\mathbf{V}}_j \\ \hat{\mathbf{I}}_j \end{Bmatrix} \tag{31}$$

The solution of (31), concerning the modal voltage $\hat{\mathbf{V}}_j(z)$ and modal current $\hat{\mathbf{I}}_j(z)$ pertaining to mode j , can be put in the standard form of a sum of forward (f) and backward (b) propagating waves

$$\hat{\mathbf{V}}_j(z) = \hat{\mathbf{V}}_j^{(f)} e^{-\gamma_j z} + \hat{\mathbf{V}}_j^{(b)} e^{+\gamma_j z} \tag{32}$$

$$\hat{\mathbf{I}}_j(z) = \hat{Y} w_j (\hat{\mathbf{V}}_j^{(f)} e^{-\gamma_j z} - \hat{\mathbf{V}}_j^{(b)} e^{+\gamma_j z}) \tag{33}$$

where $\gamma_j = \alpha_j + j\beta_j$ stands for the propagation constant of mode j (α_j is the attenuation constant and β_j is the phase constant), and $\hat{Y} w_j$ stands for the characteristic wave admittance of mode j .

It should be stressed that, as a result of the frequency dependence of \mathbf{Z} and \mathbf{Y} , the transformation matrices \mathbf{T} and \mathbf{W} , as well as the diagonal matrices containing the propagation constants and characteristic wave admittances, all are, in general, frequency-dependent matrices. For the case of uniform MTLs such a dependence on the frequency is a smooth one.

The transformation matrix \mathbf{T} required to convert voltages from the natural domain to the modal domain is composed of n linearly independent column vectors (the eigenvectors of $\mathbf{Z} \mathbf{Y}$):

$$(\mathbf{Z} \mathbf{Y}) \mathbf{t}_j = (\gamma_j^2) \mathbf{t}_j \tag{34}$$

From a physical point of view, the entries of vector \mathbf{t}_j provide information about the voltages distribution among the conductors of the MTL when only mode j is present; likewise, the entries of vector \mathbf{w}_j provide information about the currents distribution among the conductors of the MTL when only mode j is present.

The diagonal matrix of characteristic wave admittances that we have referred to before

$$\hat{\mathbf{Y}}_W = \begin{bmatrix} \hat{Y} w_1 & & & & \\ & \ddots & & & \\ & & \hat{Y} w_j & & \\ & & & \ddots & \\ & & & & \hat{Y} w_n \end{bmatrix}$$

relates modal voltages to modal currents through

$$\hat{\mathbf{I}}^{(f)} = +\hat{Y}_W \hat{\mathbf{V}}^{(f)}, \quad \hat{\mathbf{I}}^{(b)} = -\hat{Y}_W \hat{\mathbf{V}}^{(b)} \quad (35)$$

The diagonal matrix \hat{Y}_W is determined from (19), or from (20), by imposing $\mathbf{V} = \mathbf{T}\hat{\mathbf{V}}$ and $\mathbf{I} = \mathbf{W}\hat{\mathbf{I}}$:

$$\frac{d\hat{\mathbf{V}}}{dz} = -\mathbf{T}^{-1}\mathbf{Z}\mathbf{W}\hat{\mathbf{I}}, \quad \frac{d\hat{\mathbf{I}}}{dz} = -\mathbf{W}^{-1}\mathbf{Y}\mathbf{T}\hat{\mathbf{V}}$$

Using (30), and taking into account the exponential dependence on $\pm\gamma z$ exhibited by the modal waves in $\hat{\mathbf{V}}(z)$ and $\hat{\mathbf{I}}(z)$ we find

$$\hat{Y}_W = \mathbf{T}'\mathbf{Z}^{-1}\mathbf{T}\gamma = \mathbf{T}'\mathbf{Y}\mathbf{T}\gamma^{-1} \quad (36)$$

Before we continue discussing the solution of the TL equations, an important subtle point must be addressed concerning the diagonalization of the \mathbf{ZY} matrix product, a key step that lies at the heart of the modal decoupling procedure—see (29) and (34).

We want to emphasize that despite the peculiar physical properties of \mathbf{Z} and \mathbf{Y} , no absolute aprioristic guarantees can be given of the success of the diagonalization operation in (29). Abnormal situations exist [3,11], which lead to singular transformation matrices \mathbf{T} , revealing a failure in the process of finding a complete set of n linearly independent eigenvectors \mathbf{t}_j . Such a failure is not of numerical or computational nature but is intrinsic to the constitution of the \mathbf{ZY} matrix itself.

Those abnormal cases—which fortunately are very rare—occur whenever \mathbf{ZY} is an irregular degenerate matrix [3] (a necessary, but not sufficient, condition for this to happen is that multiple eigenvalues γ are present). In such circumstances the solution to the problem involves the consideration of Jordan normal forms and modal groups [3,12]. The type of solution for line voltages and line currents can then include contributions of the type

$$(a_0 + a_1\gamma z + a_2(\gamma z)^2 + \cdots + a_{m-1}(\gamma z)^{m-1})e^{\pm\gamma z}$$

where γ is an irregular eigenvalue of order m , with $m \leq n$.

6. TRANSMISSION MATRIX OF UNIFORM MTLs

The results given in (25) and (26) allow the evaluation of MTL voltages and currents at any specific cross section z , thus enabling voltage and current variations to be followed along the entire length of the line section. In many applications this detailed knowledge is not necessary, as one may be concerned with voltages and currents only at the input and output terminals of the line. In this case the MTL structure is viewed as a blackbox, a $2n$ -port network whose internal constitution is not of concern.

In this section we obtain the transmission matrix (ABCD matrix) that characterizes a uniform MTL of

length ℓ :

$$\begin{bmatrix} \mathbf{V}_{\text{in}} \\ \mathbf{I}_{\text{in}} \end{bmatrix} = \underbrace{\begin{bmatrix} \mathbf{A} & \mathbf{B} \\ \mathbf{C} & \mathbf{D} \end{bmatrix}}_{\Phi} \begin{bmatrix} \mathbf{V}_{\text{out}} \\ \mathbf{I}_{\text{out}} \end{bmatrix} \quad (37)$$

The results in (25) and (26) can be rewritten in the form

$$\mathbf{V}(z) = \mathbf{T}e^{-\gamma z}\mathbf{T}^{-1}\mathbf{T}\hat{\mathbf{V}}^{(f)} + \mathbf{T}e^{+\gamma z}\mathbf{T}^{-1}\mathbf{T}\hat{\mathbf{V}}^{(b)} \quad (38)$$

$$\mathbf{I}(z) = (\mathbf{W}\hat{Y}_W\mathbf{T}^{-1})(\mathbf{T}e^{-\gamma z}\mathbf{T}^{-1}\mathbf{T}\hat{\mathbf{V}}^{(f)} - \mathbf{T}e^{+\gamma z}\mathbf{T}^{-1}\mathbf{T}\hat{\mathbf{V}}^{(b)}) \quad (39)$$

where the leading factor in the right hand side of (39)—a symmetric matrix—is the characteristic wave admittance matrix in natural coordinates

$$\mathbf{Y}_W = \mathbf{W}\hat{Y}_W\mathbf{T}^{-1} = \mathbf{Z}^{-1}\mathbf{T}\mathbf{Y}\mathbf{T}^{-1} = \mathbf{Y}\mathbf{T}\mathbf{T}^{-1} \quad (40)$$

where

$$\mathbf{T} = \mathbf{T}\gamma\mathbf{T}^{-1} = \text{SQRT}(\mathbf{ZY}) \quad (41)$$

It is also convenient to define the characteristic wave impedance matrix in natural coordinates, the inverse of \mathbf{Y}_W ,

$$\mathbf{Z}_W = \mathbf{Y}_W^{-1}$$

Imposition of the boundary conditions at $z=0$, $\mathbf{V}(0) = \mathbf{V}_{\text{in}}$ and $\mathbf{I}(0) = \mathbf{I}_{\text{in}}$, in (38) and (39), allow the determination of $\hat{\mathbf{V}}^{(f)}$ and $\hat{\mathbf{V}}^{(b)}$:

$$\hat{\mathbf{V}}^{(f)} = \frac{1}{2}(\mathbf{V}_{\text{in}} + \mathbf{Z}_W\mathbf{I}_{\text{in}}), \quad \hat{\mathbf{V}}^{(b)} = \frac{1}{2}(\mathbf{V}_{\text{in}} - \mathbf{Z}_W\mathbf{I}_{\text{in}})$$

Retrosubstitution of $\hat{\mathbf{V}}^{(f)}$ and $\hat{\mathbf{V}}^{(b)}$ into (38) and (39), followed by particularization for $z = \ell$, finally yields

$$\mathbf{V}_{\text{in}} = \text{COSH}(\Gamma\ell)\mathbf{V}_{\text{out}} + \text{SINH}(\Gamma\ell)\mathbf{Z}_W\mathbf{I}_{\text{out}} \quad (42)$$

$$\mathbf{I}_{\text{in}} = \mathbf{Y}_W \text{SINH}(\Gamma\ell)\mathbf{V}_{\text{out}} + \mathbf{Y}_W \text{COSH}(\Gamma\ell)\mathbf{Z}_W\mathbf{I}_{\text{out}} \quad (43)$$

where

$$\text{COSH}(\Gamma\ell) = \mathbf{T}(\cosh \gamma\ell)\mathbf{T}^{-1} \quad (44)$$

$$\text{SINH}(\Gamma\ell) = \mathbf{T}(\sinh \gamma\ell)\mathbf{T}^{-1}$$

Comparison established between (37) and (42), (43) permits identification of the submatrices \mathbf{A} , \mathbf{B} , \mathbf{C} , and \mathbf{D} that define the constitution of the transmission matrix Φ :

$$\mathbf{A} = \text{COSH}(\Gamma\ell) \quad (45)$$

$$\mathbf{B} = \mathbf{B}^\ell = \text{SINH}(\Gamma\ell)\mathbf{Z}_W \quad (46)$$

$$\mathbf{C} = \mathbf{C}^\ell = \mathbf{Y}_W \text{SINH}(\Gamma\ell) \quad (47)$$

$$\mathbf{D} = \mathbf{A}^\ell = \mathbf{Y}_W \text{COSH}(\Gamma\ell)\mathbf{Z}_W \quad (48)$$

We have shown above how the transmission matrix Φ can be obtained using previous knowledge of the transformation matrices and modal propagation parameters. The inverse problem poses no special difficulties, [3]; transformation matrices and modal propagation parameters are obtained straightforwardly from Φ with the help of (45)–(48).

7. TRANSMISSION MATRIX OF NONUNIFORM MTLs

The transmission matrix of a nonuniform MTL structure, characterized by per unit length longitudinal impedance and transverse admittance matrices $Z(z)$ and $Y(z)$ that vary along the line, can be analytically determined using various approaches.

It can be obtained by modeling the global structure as a cascade of many small uniform sections, after which the global Φ matrix is determined by multiplying the transmission matrices of the individual sections [3,4]

$$\Phi = \Phi_1 \Phi_2 \dots \Phi_k \dots \Phi_N \tag{49}$$

where N is the number of uniform sections into which the structure has been broken.

Alternatively, the A , B , C , and D submatrices can be evaluated by iterative numerical integration of transmission-line equations provided that both $Z(z)$ and $Y(z)$ are prespecified known functions of z , [13]. In fact, from (19) and (20)

$$\frac{d}{dz} \begin{bmatrix} \mathbf{V}(z) \\ \mathbf{I}(z) \end{bmatrix} = - \begin{bmatrix} \mathbf{Z}(z) & 0 \\ 0 & \mathbf{Y}(z) \end{bmatrix} \begin{bmatrix} \mathbf{I}(z) \\ \mathbf{V}(z) \end{bmatrix}$$

together with

$$\begin{bmatrix} \mathbf{V}_{in} \\ \mathbf{I}_{in} \end{bmatrix} = \begin{bmatrix} \mathbf{A}(z) & \mathbf{B}(z) \\ \mathbf{C}(z) & \mathbf{D}(z) \end{bmatrix} \begin{bmatrix} \mathbf{V}(z) \\ \mathbf{I}(z) \end{bmatrix}$$

leads to the problem of iteratively solving

$$\frac{d}{dz} \begin{bmatrix} \mathbf{A}(z) & \mathbf{B}(z) \\ \mathbf{C}(z) & \mathbf{D}(z) \end{bmatrix} = \begin{bmatrix} \mathbf{B}(z)\mathbf{Y}(z) & \mathbf{A}(z)\mathbf{Z}(z) \\ \mathbf{D}(z)\mathbf{Y}(z) & \mathbf{C}(z)\mathbf{Z}(z) \end{bmatrix}$$

Starting with the initial values $\mathbf{A}(0) = \mathbf{D}(0) = \mathbf{1}$, and $\mathbf{B}(0) = \mathbf{C}(0) = \mathbf{0}$, the process ends at $z = \ell$, yielding

$$\mathbf{A} = \mathbf{A}(\ell), \quad \mathbf{B} = \mathbf{B}(\ell), \quad \mathbf{C} = \mathbf{C}(\ell), \quad \mathbf{D} = \mathbf{D}(\ell)$$

Regardless of which technique is used, one will end up with a formulation as in (37):

$$\begin{bmatrix} \mathbf{V}_{in} \\ \mathbf{I}_{in} \end{bmatrix} = \begin{bmatrix} \mathbf{A} & \mathbf{B} \\ \mathbf{C} & \mathbf{D} \end{bmatrix} \begin{bmatrix} \mathbf{V}_{out} \\ \mathbf{I}_{out} \end{bmatrix} \tag{50}$$

However, for the general case of nonuniform MTLs, the submatrices A , B , C , and D no longer satisfy the very peculiar properties in (45)–(48), as now, in general, $\mathbf{A} \neq \mathbf{D}^t$, $\mathbf{B} \neq \mathbf{B}^t$, and $\mathbf{C} \neq \mathbf{C}^t$.

As shown elsewhere [14,15], the transmission matrix properties for nonuniform MTLs are

$$\mathbf{A}\mathbf{B}^t - \mathbf{B}\mathbf{A}^t = \mathbf{B}^t\mathbf{D} - \mathbf{D}^t\mathbf{B} = \mathbf{D}\mathbf{C}^t - \mathbf{C}\mathbf{D}^t = \mathbf{C}^t\mathbf{A} - \mathbf{A}^t\mathbf{C} = \mathbf{0} \tag{51}$$

$$\mathbf{A}\mathbf{D}^t - \mathbf{B}\mathbf{C}^t = \mathbf{D}^t\mathbf{A} - \mathbf{B}^t\mathbf{C} = \mathbf{1} \tag{52}$$

$$\det \begin{bmatrix} \mathbf{A} & \mathbf{B} \\ \mathbf{C} & \mathbf{D} \end{bmatrix} = \mathbf{1} \tag{53}$$

$$\begin{bmatrix} \mathbf{A} & \mathbf{B} \\ \mathbf{C} & \mathbf{D} \end{bmatrix}^{-1} = \begin{bmatrix} \mathbf{D} & -\mathbf{C} \\ -\mathbf{B} & \mathbf{A} \end{bmatrix}^t \tag{54}$$

As we will see next, by using suitable modal transformations defined at both the input and output terminals of the MTL structure, all submatrices A , B , C , and D can be brought into diagonal form. This allows the n -coupled MTL system to be broken down into a set of n uncoupled nonuniform single lines, whose modal parameters—propagation constants, characteristic forward-wave admittances, and characteristic backward-wave admittances—are easily determined.

The natural domain matrix equation in (50) is transformed into the modal domain as

$$\begin{bmatrix} \hat{\mathbf{V}}_{in} \\ \hat{\mathbf{I}}_{in} \end{bmatrix} = \begin{bmatrix} \hat{\mathbf{A}} & \hat{\mathbf{B}} \\ \hat{\mathbf{C}} & \hat{\mathbf{D}} \end{bmatrix} \begin{bmatrix} \hat{\mathbf{V}}_{out} \\ \hat{\mathbf{I}}_{out} \end{bmatrix} \tag{55}$$

where, according to our notation, quantities with a “hat” sign denote modal quantities.

The relationship between modal and natural domain quantities (voltages and currents) is defined through

$$\begin{aligned} \mathbf{V}_{in} &= \mathbf{T}_{in} \hat{\mathbf{V}}_{in}, \quad \hat{\mathbf{I}}_{in} = \mathbf{T}_{in}^t \mathbf{I}_{in} \\ \mathbf{V}_{out} &= \mathbf{T}_{out} \hat{\mathbf{V}}_{out}, \quad \hat{\mathbf{I}}_{out} = \mathbf{T}_{out}^t \mathbf{I}_{out} \end{aligned} \tag{56}$$

The diagonal modal matrices $\hat{\mathbf{A}}$, $\hat{\mathbf{B}}$, $\hat{\mathbf{C}}$ and $\hat{\mathbf{D}}$ in (55) are obtained from the corresponding ones in (50) through

$$\hat{\mathbf{A}} = \mathbf{T}_{in}^{-1} \mathbf{A} \mathbf{T}_{out} = \begin{bmatrix} \hat{a}_1 & & & & \\ & \ddots & & & \\ & & \hat{a}_j & & \\ & & & \ddots & \\ & & & & \hat{a}_n \end{bmatrix} \tag{57}$$

$$\hat{\mathbf{B}} = \mathbf{T}_{in}^{-1} \mathbf{B} \mathbf{T}_{out}^{-1t} = \begin{bmatrix} \hat{b}_1 & & & & \\ & \ddots & & & \\ & & \hat{b}_j & & \\ & & & \ddots & \\ & & & & \hat{b}_n \end{bmatrix} \tag{58}$$

$$\hat{\mathbf{C}} = \mathbf{T}_{\text{in}}^t \mathbf{C} \mathbf{T}_{\text{out}} = \begin{bmatrix} \hat{c}_1 & & & & \\ & \ddots & & & \\ & & \hat{c}_j & & \\ & & & \ddots & \\ & & & & \hat{c}_n \end{bmatrix} \quad (59)$$

$$\hat{\mathbf{D}} = \mathbf{T}_{\text{in}}^t \mathbf{D} \mathbf{T}_{\text{out}}^{-1t} = \begin{bmatrix} \hat{d}_1 & & & & \\ & \ddots & & & \\ & & \hat{d}_j & & \\ & & & \ddots & \\ & & & & \hat{d}_n \end{bmatrix} \quad (60)$$

where $\hat{a}_j \hat{d}_j - \hat{b}_j \hat{c}_j = 1$, for $j = 1 \dots n$.

The transformation matrices \mathbf{T}_{in} and \mathbf{T}_{out} , which apply respectively to the input and output terminals of the non-uniform MTL, are in general different from each other. They may happen to coincide only in very special cases, when certain symmetries exist (as always occurs with uniform lines).

Matrix \mathbf{T}_{in} is a similarity transformation that simultaneously brings $\mathbf{B}\mathbf{C}^t$ and $\mathbf{A}\mathbf{D}^t$ into diagonal form. Likewise, matrix \mathbf{T}_{out} is a similarity transformation that simultaneously brings $\mathbf{B}^t\mathbf{C}$ and $\mathbf{D}^t\mathbf{A}$ into diagonal form [16]:

$$\mathbf{T}_{\text{in}}^{-1}(\mathbf{B}\mathbf{C}^t)\mathbf{T}_{\text{in}} = \mathbf{T}_{\text{out}}^{-1}(\mathbf{B}^t\mathbf{C})\mathbf{T}_{\text{out}} = \hat{\mathbf{B}}\hat{\mathbf{C}} \quad (61)$$

$$\mathbf{T}_{\text{in}}^{-1}(\mathbf{A}\mathbf{D}^t)\mathbf{T}_{\text{in}} = \mathbf{T}_{\text{out}}^{-1}(\mathbf{D}^t\mathbf{A})\mathbf{T}_{\text{out}} = \hat{\mathbf{A}}\hat{\mathbf{D}} \quad (62)$$

The propagation parameters for mode j are determined using the information in (57)–(60) concerning the matrix entries \hat{a}_j , \hat{b}_j , \hat{c}_j , and \hat{d}_j , [16]:

Propagation constant $\gamma_j = \alpha_j + j\beta_j$:

$$\cosh(\gamma_j \ell) = \frac{\hat{a}_j + \hat{d}_j}{2} \quad (63)$$

Characteristic forward-wave modal admittance:

$$\hat{Y}w_j^{(f)} = \frac{e^{+\gamma_j \ell} - \hat{a}_j}{\hat{b}_j} = \frac{\hat{c}_j}{e^{+\gamma_j \ell} - \hat{d}_j} \quad (64)$$

Characteristic backward-wave modal admittance:

$$\hat{Y}w_j^{(b)} = \frac{\hat{a}_j - e^{-\gamma_j \ell}}{\hat{b}_j} = \frac{\hat{c}_j}{\hat{d}_j - e^{-\gamma_j \ell}} \quad (65)$$

It should be noted that, contrary to what happens with uniform MTLs, the characteristic forward- and backward-

wave modal admittances do not ordinarily coincide with each other when nonuniform structures are considered. Also, the propagation parameters, and transformation matrices characterizing nonuniform MTLs do not exhibit a smooth dependence on the frequency, as sharp variations are observed at the vicinity of certain critical frequencies, depending on the length of the TL structure [17].

BIBLIOGRAPHY

1. L. A. Pipes, Matrix theory of multiconductor transmission lines, *Phil. Mag. Soc.* **24**:97–113 (1937).
2. S. O. Rice, Steady state solutions of transmission line equations, *Bell Syst. Tech. J.* **20**:131–178 (1941).
3. J. B. Faria, *Multiconductor Transmission-Line Structures*, Wiley, New York, 1993.
4. C. R. Paul, *Analysis of Multiconductor Transmission Lines*, Wiley, New York, 1994.
5. J. B. Faria, On the time-domain transmission-line equations, *Microwave Opt. Technol. Lett.* **22**:194–197 (1999).
6. J. B. Faria, On the segmentation method used for analyzing nonuniform transmission lines: Application to the exponential line, *Eur. Trans. Electric. Power* **12**:361–368 (2002).
7. L. M. Wedepohl, Application of matrix methods to the solution of traveling-wave phenomena in polyphase systems, *Proc. Inst. Electric. Eng.* **110**:2200–2212 (1963).
8. C. Gary, Approche complete de la propagation multifilaire en haute frequence par utilisation des matrices complexes, *EDF Bulletin de la Direction des Etudes et Recherches* **3**/4:5–20 (1976).
9. G. T. Lei, G. W. Pan, and B. K. Gilbert, Examination, clarification and simplification of modal decoupling method for multiconductor transmission lines, *IEEE Trans. Microwave Theory Tech.* **43**:2090–2100 (1995).
10. C. R. Paul, Decoupling the multiconductor transmission line equations, *IEEE Trans. Microwave Theory Tech.* **44**:1429–1440 (1996).
11. J. B. Faria, Wave propagation in weakly coupled microstrip lines: An anomalous degenerate quasi-TEM solution, *Microwave Opt. Technol. Lett.* **2**:149–152 (1989).
12. J. B. Faria and J. B. Silva, Wave propagation in polyphase transmission lines: A general solution to include cases where ordinary modal theory fails, *IEEE Trans. Power Delivery* **1**:182–189 (1986).
13. A. Semlyen, Some frequency domain aspects of wave propagation on nonuniform lines, *IEEE Trans. Power Delivery* **18**:315–322 (2003).
14. L. M. Wedepohl and C. S. Indulkar, Wave propagation in non-homogeneous systems: Properties of the chain matrix, *Proc. Inst. Electric. Eng.* **121**:997–1000 (1974).
15. J. B. Faria, On the transmission matrix of 2n-port reciprocal networks, *Microwave Opt. Technol. Lett.* **33**:151–154 (2002).
16. J. B. Faria, A new generalized modal analysis theory for non-uniform multiconductor transmission lines, *IEEE Trans. Power Syst.* **19**:926–933 (2004).
17. J. B. Faria, Frequency-domain modal analysis of nonuniformly coupled transmission-line structures, *Microwave Opt. Technol. Lett.* **43**:186–189 (2004).

MULTIMODE EQUIVALENT NETWORK REPRESENTATIONS

MARCO GUGLIELMI
European Space Research and
Technology Centre
Noordwijk, The Netherlands

1. INTRODUCTION

The research carried out at the Radiation Laboratory of the Massachusetts Institute of Technology during World War II had a profound effect on the state of the art in the electromagnetic analysis of waveguide junctions and discontinuities [1,2].

One of the reasons for this significant effect was the use of *transmission-line formalism* to represent waveguide modes, and *single-mode equivalent circuits* to describe waveguide discontinuities (and junctions) as simple lumped circuit elements [3–5]. Following this approach, electromagnetic field problems could be solved by engineers with simple calculations based on network theory, while the development of the equivalent circuits themselves was carried out by researchers in the field. Engineers could then rapidly and effectively concentrate on the development of microwave equipment. As a result of this pioneering work, a number of equivalent network representations for a variety of waveguide discontinuities and junctions were then collected in the *Waveguide Handbook* [6].

Although single-mode equivalent networks are still extremely valuable tools, they do suffer from limitations that restrict their applicability. One of the most basic restrictions comes from the fact that they represent *distributed* discontinuities in terms of lumped elements as seen from the fundamental mode of the waveguide and therefore cannot account for *higher-order mode* interactions. If the *distance* between discontinuities is not sufficiently large, the higher-order mode interactions cannot be neglected and single-mode equivalent network representations are no longer valid.

Modern microwave and millimeter-wave equipment require extreme miniaturization of all components. Single-mode equivalent circuits must, therefore, be replaced by more advanced *multimode* representations that can correctly account for all higher-order mode interactions.

The objective of this article is to describe the basic theoretical steps leading to the formulation of multimode equivalent network representation of waveguide junctions. Both planar and arbitrary junctions are treated, progressing from the basic formulation to the formal solution of the relevant integral equations.

This article is intended as a guide to the development of practical solutions and can be of interest to both researchers and engineers in the microwave and millimeter-wave areas.

2. PLANAR JUNCTIONS

The problem under investigation is the planar junction between two arbitrary waveguides, as shown in Fig. 1. To

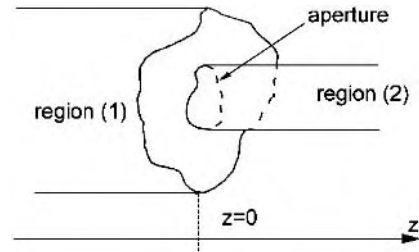


Figure 1. Planar junction between two arbitrary waveguides.

analyze this discontinuity, two formulations are possible, one leading to a multimode impedance and the other leading to a multimode admittance representation [7]. In this article, however, we will describe only the impedance formulation because of its superior computational performance [7].

The starting point is the imposition of the boundary conditions at the junction ($z = 0$ in Fig. 1), namely

$$\sum_{n=1}^{\infty} I_n^{(1)} \mathbf{h}_n^{(1)} = \sum_{n=1}^{\infty} I_n^{(2)} \mathbf{h}_n^{(2)} \quad (1)$$

where the index n covers both $TE_{m,n}$ and $TM_{m,n}$ modes, and where the superscripts (1) and (2) refer to regions (1) and (2) in Fig. 1. To proceed, we then separate the *accessible* from the *localized* modes by writing

$$\begin{aligned} \sum_{n=1}^{N^{(1)}} I_n^{(1)} \mathbf{h}_n^{(1)} - \sum_{n=N^{(1)}+1}^{\infty} V_n^{(1)} Y_n^{(1)} \mathbf{h}_n^{(1)} &= \sum_{n=1}^{N^{(2)}} I_n^{(2)} \mathbf{h}_n^{(2)} \\ &+ \sum_{n=N^{(2)}+1}^{\infty} V_n^{(2)} Y_n^{(2)} \mathbf{h}_n^{(2)} \end{aligned} \quad (2)$$

where $Y_n^{(\delta)}$ is the modal admittance. The next step is to add and subtract to (2)

$$\sum_{n=1}^{N^{(1)}} V_n^{(1)} \hat{Y}_n^{(1)} \mathbf{h}_n^{(1)} + \sum_{n=1}^{N^{(2)}} V_n^{(2)} \hat{Y}_n^{(2)} \mathbf{h}_n^{(2)} \quad (3)$$

where $\hat{Y}_n^{(\delta)}$ is defined as

$$\hat{Y}_n^{(\delta)} = (\hat{Z}_n^{(\delta)})^{-1} = \lim_{n \rightarrow \infty} Y_n^{(\delta)} = \begin{cases} \frac{-j|k_{t,n}^{(\delta)}|}{\omega\mu} & \text{for TE} \\ \frac{\omega\epsilon}{-j|k_{t,n}^{(\delta)}|} & \text{for TM} \end{cases} \quad (4)$$

The next step is to redefine the modal currents according to

$$\tilde{I}_n^{(1)} = I_n^{(1)} + V_n^{(1)} \hat{Y}_n^{(1)} \quad (5)$$

$$\tilde{I}_n^{(2)} = I_n^{(2)} - V_n^{(2)} \hat{Y}_n^{(2)} \quad (6)$$

so that (2) becomes

$$\begin{aligned} \sum_{n=1}^{N^{(1)}} \bar{\mathbf{I}}_n^{(1)} \mathbf{h}_n^{(1)} - \sum_{n=1}^{N^{(2)}} \bar{\mathbf{I}}_n^{(2)} \mathbf{h}_n^{(2)} &= \sum_{n=1}^{N^{(1)}} V_n^{(1)} \hat{\mathbf{Y}}_n^{(1)} \mathbf{h}_n^{(1)} \\ &+ \sum_{n=N^{(1)}+1}^{\infty} V_n^{(1)} Y_n^{(1)} \mathbf{h}_n^{(1)} + \sum_{n=1}^{N^{(2)}} V_n^{(2)} \hat{\mathbf{Y}}_n^{(2)} \mathbf{h}_n^{(2)} \\ &+ \sum_{n=N^{(2)}+1}^{\infty} V_n^{(2)} Y_n^{(2)} \mathbf{h}_n^{(2)} \end{aligned} \quad (7)$$

We now use the definition of modal voltage and write

$$V_n^{(\delta)} = \int_{cs} (\mathbf{u}_z \times \mathbf{E}) \cdot \mathbf{h}_n^{(\delta)*} ds' \quad (8)$$

where the electric field in the aperture ($\mathbf{u}_z \times \mathbf{E}$) can now be written as a linear combination of the *incident* accessible modes only (the modes that carry energy from one discontinuity to another)

$$(\mathbf{z}_0 \times \mathbf{E}) = \sum_{n=1}^{N^{(1)}} \bar{\mathbf{I}}_n^{(1)} \mathbf{M}_n^{(1)} - \sum_{n=1}^{N^{(2)}} \bar{\mathbf{I}}_n^{(2)} \mathbf{M}_n^{(2)} \quad (9)$$

This expression can now be substituted into (8) and (7), finally obtaining the integral equation

$$\begin{aligned} \mathbf{h}_n^{(\delta)} &= \int_{cs} \mathbf{M}_n^{(\delta)} \cdot \left[\sum_{m=1}^{N^{(1)}} \hat{\mathbf{Y}}_m^{(1)} \mathbf{h}_m^{(1)} \mathbf{h}_m^{(1)*} \right. \\ &+ \sum_{m=N^{(1)}+1}^{\infty} Y_m^{(1)} \mathbf{h}_m^{(1)} \mathbf{h}_m^{(1)*} \\ &+ \sum_{m=1}^{N^{(2)}} \hat{\mathbf{Y}}_m^{(2)} \mathbf{h}_m^{(2)} \mathbf{h}_m^{(2)*} \\ &\left. + \sum_{m=N^{(2)}+1}^{\infty} Y_m^{(2)} \mathbf{h}_m^{(2)} \mathbf{h}_m^{(2)*} \right] ds' \end{aligned} \quad (10)$$

The formulation is now concluded by recalling (8) and (9), to write

$$V_m^{(\gamma)} = \sum_{n=1}^{N^{(1)}} \bar{\mathbf{I}}_n^{(1)} \mathbf{z}_{m,n}^{(\gamma,1)} - \sum_{n=1}^{N^{(2)}} \bar{\mathbf{I}}_n^{(2)} \mathbf{z}_{m,n}^{(\gamma,2)} \quad (11)$$

where

$$\mathbf{z}_{m,n}^{(\gamma,\delta)} = \int_{cs} \mathbf{M}_n^{(\delta)} \cdot \mathbf{h}_m^{(\gamma)*} ds' \quad (12)$$

Equations (10) and (12) complete the formal solution of the problem in Fig. 1 in terms of the *finite* impedance multimode equivalent network shown in Fig. 2.

It is important to note that although the network representation derived involves only a limited number of accessible modes, the formulation described is rigorous in

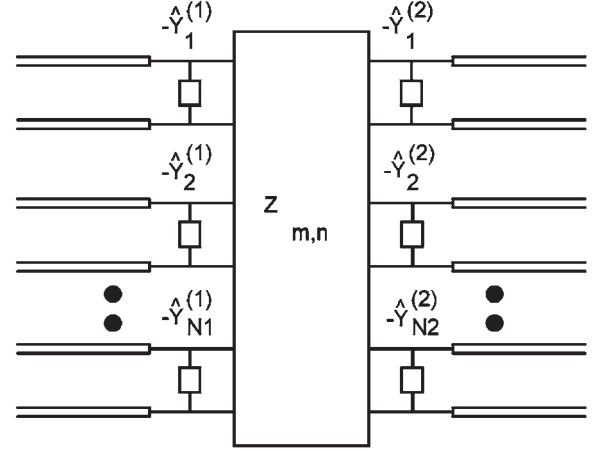


Figure 2. Multimode equivalent network representation of the waveguide step in Fig. 1.

principle since no approximations have been introduced. What needs to be done in practice in order to ensure accurate results is to explicitly include enough higher-order modes to correctly model the higher-order mode interactions between cascaded junctions.

Particularly simple equivalent network representations can be obtained for rectangular waveguide devices involving only inductive or capacitive discontinuities [8,9].

2.1. Offset and Multiple Discontinuities

The formulation described in the previous section is valid if the waveguide in region (2) is completely contained in the cross section of waveguide (1). The case shown in Fig. 3, however, can also be treated by using as basis functions for the method of moments (MoM) solution of (10) the mode functions of a waveguide with cross section equal to the common aperture. Furthermore, the same formulation can also be used if more than two waveguides are connected to each other, as in the case shown in Fig. 4 [10]. The only modification that is required is to define the unknown function $\mathbf{M}_n^{(\delta)}(s')$, and all the integrations, over the union of all of the common apertures AP :

$$AP = \bigcup_{q=2}^{NWG} ap^{(q)} \quad (13)$$

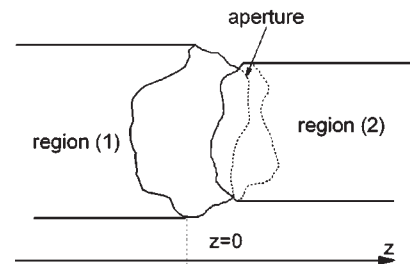


Figure 3. Offset waveguide step.

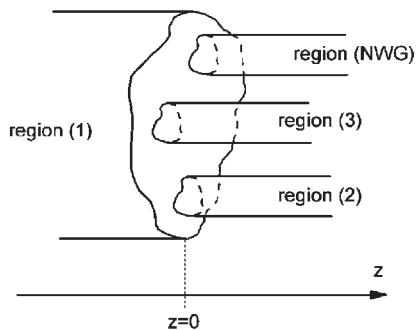


Figure 4. Multiple-aperture planar waveguide junction.

Taking this into account, we can write directly

$$\mathbf{h}_n^{(\delta)} u^{(\delta)} = \int_{AP} \mathbf{M}_n^{(\delta)} \cdot \sum_{q=1}^{NWG} \left[\sum_{m=1}^{N^{(q)}} \hat{Y}_m^{(q)} \mathbf{h}_m^{(q)} u^{(q)} \mathbf{h}_m^{(q)*} u^{(q)} + \sum_{m=N^{(q)}+1}^{\infty} Y_m^{(q)} \mathbf{h}_m^{(q)} u^{(q)} \mathbf{h}_m^{(q)*} u^{(q)} \right] ds' \quad (14)$$

$$\mathbf{z}_{m,n}^{(\gamma,\delta)} = \int_{AP} \mathbf{M}_n^{(\delta)} \cdot \mathbf{h}_m^{(\gamma)*} u^{(\gamma)} ds' \quad (15)$$

where NWG indicates the number of waveguides involved in the step, and the function $u^{(\delta)}(s)$ is denned as

$$u^{(\delta)} = \begin{cases} 1 & \text{for } s \in ap^{(\delta)} \\ 0 & \text{for } s \ni ap^{(\delta)} \end{cases} \quad (16)$$

The equivalent network obtained in this case is shown in Fig. 5. Once again, particularly simple representations can be obtained for inductive or capacitive multiple apertures in rectangular waveguide [10]

3. ARBITRARY WAVEGUIDE JUNCTIONS

The theory presented up to now is applicable to planar junctions where two or more waveguides are connected together at a planar interface that is orthogonal to the

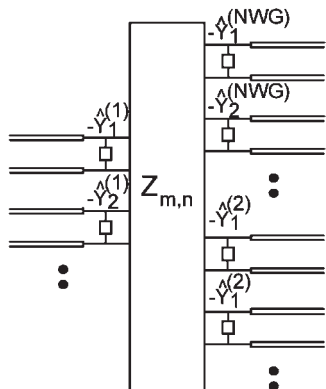


Figure 5. Multimode equivalent network for a multiple-aperture planar waveguide junction.

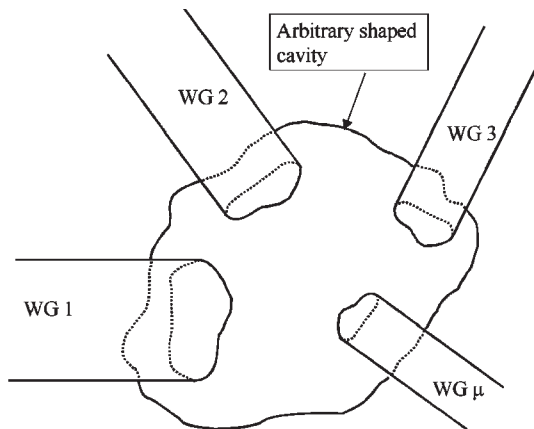


Figure 6. Waveguides joined by an arbitrarily shaped cavity.

propagation direction of the waveguides. Planar junctions of this type indeed cover the majority of engineering applications. However, an additional, more general type of junction is needed in order to cover *all* possible applications, namely, a junction where the connection between the waveguides is achieved with the help of a cavity, as shown in Fig. 6 [11]. The multimode equivalent network representation of this type of junction can be obtained with a simple modification of the formulation presented for the planar case. To start, we write the general expression of the magnetic field in the cavity based on Huygens' principle [12–14]

$$\mathbf{H}^{(c)}(\mathbf{r}) = \int_{(S)} \mathbf{G}^{(c)}(\mathbf{r}|\mathbf{r}') \mathbf{M}(\mathbf{r}') dS' \quad (17)$$

where

$$\mathbf{M}(\mathbf{r}) = \mathbf{n}(\mathbf{r}) \times \mathbf{E}^{(c)}(\mathbf{r}) \quad (18)$$

represents the magnetic currents in the apertures, the vector \mathbf{n} is directed outward from the cavity, and

$$\mathbf{G}^{(c)}(\mathbf{r}|\mathbf{r}') = j\omega\epsilon_0 \sum_{n=1}^{+\infty} \frac{\mathbf{h}_n^{(c)}(\mathbf{r}) \mathbf{h}_n^{(c)}(\mathbf{r}')}{k_0^2 - k_n^2} + \frac{j}{\omega\mu_0} \sum_{n=1}^{+\infty} \mathbf{g}_n^{(c)}(\mathbf{r}) \mathbf{g}_n^{(c)}(\mathbf{r}') \quad (19)$$

is the cavity's Green function described by solenoidal $\mathbf{h}_n^{(c)}$ and irrotational $\mathbf{g}_n^{(c)}$ modes [15].

Similar to what we did for the planar case, we now separate the modal expansion of the magnetic field in the ports in accessible ($I_k^{(\mu)}$) and localized ($Y_k^{(\mu)} V_k^{(\mu)}$) modes

$$\mathbf{H}^{(WG)}(\mathbf{r}) = \sum_{\mu=1}^N \sum_{k=1}^{N^{(\mu)}} I_k^{(\mu)} \mathbf{h}_k^{(\mu)}(\mathbf{r}) \delta_k^{(\mu)}(\mathbf{r}) + \sum_{\mu=1}^N \sum_{k=N^{(\mu)}+1}^{+\infty} Y_k^{(\mu)} V_k^{(\mu)} \mathbf{h}_k^{(\mu)}(\mathbf{r}) \delta_k^{(\mu)}(\mathbf{r}) \quad (20)$$

with

$$V_k^{(\mu)} = \int_{(S_{(\mu)})} \mathbf{h}_k^{(\mu)*}(\mathbf{r}) \mathbf{M}(\mathbf{r}) dS \quad (21)$$

and

$$\delta_k^{(\mu)}(\mathbf{r}) = \begin{cases} 1 & \text{if } \mathbf{r} \in S_{(\mu)} \\ 0 & \text{elsewhere} \end{cases} \quad (22)$$

where $Y_k^{(\mu)}$ denotes the characteristic admittance of mode k in port μ .

Applying the boundary condition of the magnetic field in the apertures, we find

$$\begin{aligned} & \sum_{\mu=1}^N \sum_{k=1}^{N^{(\mu)}} I_k^{(\mu)} \mathbf{h}_k^{(\mu)}(\mathbf{r}) \delta_k^{(\mu)}(\mathbf{r}) \\ &= \int_{(S)} [\mathbf{G}^{(\text{WG})}(\mathbf{r}|\mathbf{r}') + \mathbf{G}^{(c)}(\mathbf{r}|\mathbf{r}')] \mathbf{M}(\mathbf{r}') dS' \end{aligned} \quad (23)$$

with

$$\begin{aligned} & \mathbf{G}^{(\text{WG})}(\mathbf{r}|\mathbf{r}') \\ &= \sum_{\mu=1}^N \sum_{k=N^{(\mu)}+1}^{+\infty} Y_k^{(\mu)} \delta_k^{(\mu)}(\mathbf{r}) \mathbf{h}_k^{(\mu)}(\mathbf{r}) \mathbf{h}_k^{(\mu)*}(\mathbf{r}') \delta_k^{(\mu)}(\mathbf{r}') \end{aligned} \quad (24)$$

To continue, it is now again possible to model the magnetic current in the apertures as linear combination of the *incident* modes

$$\mathbf{M}(\mathbf{r}) = \sum_{v=1}^N \sum_{k=1}^{N^{(v)}} I_k^{(v)} \mathcal{M}_k^{(v)}(\mathbf{r}) \delta_k^{(v)}(\mathbf{r}) \quad (25)$$

leading to an integral equation for the new unknowns $\mathcal{M}_k^{(v)}$

$$\begin{aligned} \mathbf{h}_k^{(v)}(\mathbf{r}) &= \int_{(S)} [\mathbf{G}^{(\text{WG})}(\mathbf{r}|\mathbf{r}') \\ &+ \mathbf{G}^{(c)}(\mathbf{r}|\mathbf{r}')] \mathcal{M}_k^{(v)}(\mathbf{r}') dS' \end{aligned} \quad (26)$$

We complete the formulation by combining (21) and (25), and writing

$$V_k^{(\mu)} = \sum_{v=1}^N \sum_{l=1}^{N^{(v)}} \mathbf{Z}_{k,l}^{(\mu,v)} I_l^{(v)} \quad (27)$$

where

$$\mathbf{Z}_{k,l}^{(\mu,v)} = \int_{(S_{(\mu)})} \mathbf{h}_k^{(\mu)}(\mathbf{r}') M_l^{(v)}(\mathbf{r}') dS \quad (28)$$

is the generic expression for the elements of the multi-mode impedance representation of the cavity in terms of *accessible* modes only. The network representation shown

in Fig. 5 for the multiaperture case is directly applicable to this case as well.

It is important to note also in this case that the formulation is rigorous since no approximations have been introduced. The network representation will provide accurate results as long as enough higher-order modes are included to account for interactions between adjacent junctions in the waveguide arms.

4. FREQUENCY DEPENDENCE TREATMENT

To use the equivalent network representations derived, we must first solve the relevant fundamental integral equations. To this end, a convenient procedure, based on the method of moments, will be shown in a later section. One aspect, however, that deserves further attention is the frequency dependence of the kernel of the integral equations. The more complex the frequency dependence is, the longer will be the computing time required since the solution must be obtained for each point in frequency. In this section we describe a procedure that can be effectively used to greatly simplify the frequency dependence, thus reducing very substantially the computational effort required.

4.1. Planar Junction

For the case of the planar junction, we write

$$\begin{aligned} \mathbf{K}(s, s') &= \\ & \left[\sum_{m=1}^{N^{(1)}} \hat{Y}_m^{(1)} \mathbf{h}_m^{(1)} \mathbf{h}_m^{(1)*} + \sum_{m=N^{(1)}+1}^{\infty} Y_m^{(1)} \mathbf{h}_m^{(1)} \mathbf{h}_m^{(1)*} \right. \\ & \left. + \sum_{m=1}^{N^{(2)}} \hat{Y}_m^{(2)} \mathbf{h}_m^{(2)} \mathbf{h}_m^{(2)*} + \sum_{m=N^{(2)}+1}^{\infty} Y_m^{(2)} \mathbf{h}_m^{(2)} \mathbf{h}_m^{(2)*} \right] \end{aligned} \quad (29)$$

We then add and subtract the complement to infinity of the terms in (3), obtaining

$$\begin{aligned} \mathbf{K}(s, s') &= \left[\sum_{m=1}^{\infty} \hat{Y}_m^{(1)} \mathbf{h}_m^{(1)} \mathbf{h}_m^{(1)*} + \sum_{m=1}^{\infty} \hat{Y}_m^{(2)} \mathbf{h}_m^{(2)} \mathbf{h}_m^{(2)*} \right. \\ & - \sum_{m=N^{(1)}+1}^{\infty} \hat{Y}_m^{(1)} \left(1 - \frac{Y_m^{(1)}}{\hat{Y}_m^{(1)}} \right) \mathbf{h}_m^{(1)} \mathbf{h}_m^{(1)*} \\ & \left. - \sum_{m=N^{(2)}+1}^{\infty} \hat{Y}_m^{(2)} \left(1 - \frac{Y_m^{(2)}}{\hat{Y}_m^{(2)}} \right) \mathbf{h}_m^{(2)} \mathbf{h}_m^{(2)*} \right] \end{aligned} \quad (30)$$

With this procedure, the first two terms of (30) become static, while for the other two we can write

$$\lim_{m \rightarrow \infty} \left(1 - \frac{Y_m^{(\delta)}}{\hat{Y}_m^{(\delta)}} \right) = 0 \quad (31)$$

obtaining

$$\left(1 - \frac{\mathbf{Y}_m^{(\delta)}}{\hat{\mathbf{Y}}_m^{(\delta)}}\right) \simeq \sum_{p=1}^P B_{(2p)} \left(\frac{k_0}{k_{t,m}^{(\delta)}}\right)^{(2p)} \quad (32)$$

The expressions for the coefficient B_p can be found in Table 1.

Collecting all together, we have

$$\begin{aligned} \mathbf{K}(s, s') &= \hat{\mathbf{K}}(s, s') \\ &- \sum_{p=1}^P (k_0)^{2p} \hat{\mathbf{K}}_{2p}(s, s') \end{aligned} \quad (33)$$

where

$$\hat{\mathbf{K}}(s, s') = \sum_{m=1}^{\infty} \hat{\mathbf{Y}}_m^{(1)} \mathbf{h}_m^{(1)} \mathbf{h}_m^{(1)*} + \sum_{m=1}^{\infty} \hat{\mathbf{Y}}_m^{(2)} \mathbf{h}_m^{(2)} \mathbf{h}_m^{(2)*} \quad (34)$$

$$\begin{aligned} \hat{\mathbf{K}}_p(s, s') &= \sum_{m=N^{(1)}+1}^{\infty} \frac{B_{2p}}{(k_{t,m}^{(1)})^p} \hat{\mathbf{Y}}_m^{(1)} \mathbf{h}_m^{(1)} \mathbf{h}_m^{(1)*} \\ &+ \sum_{m=N^{(2)}+1}^{\infty} \frac{B_{2p}}{(k_{t,m}^{(2)})^p} \hat{\mathbf{Y}}_m^{(2)} \mathbf{h}_m^{(2)} \mathbf{h}_m^{(2)*} \end{aligned} \quad (35)$$

The result of this manipulation is that all the summations involved in the computation of the kernel are now frequency-independent, and need be computed only once outside the frequency loop.

4.2. Arbitrary Junction

Similar to what we have done for the planar discontinuity case, we will now simplify the frequency dependence of the integral equation in (26). To do so, we first divide the first part of (19) into two series, obtaining

$$\begin{aligned} &\sum_{n=1}^{+\infty} \frac{\mathbf{h}_n^{(c)}(\mathbf{r}) \mathbf{h}_n^{(c)}(\mathbf{r}')}{k_0^2 - k_n^2} \\ &= \sum_{n=1}^{N_0} \frac{\mathbf{h}_n^{(c)}(\mathbf{r}) \mathbf{h}_n^{(c)}(\mathbf{r}')}{k_0^2 - k_n^2} + \sum_{l=0}^{L_0} (k_0)^{2l} \\ &\times \sum_{n=N_0+1}^{+\infty} \frac{a_{l,n}}{(k_n^{(2l+1)})^2} \mathbf{h}_n^{(c)}(\mathbf{r}) \mathbf{h}_n^{(c)}(\mathbf{r}') \end{aligned} \quad (36)$$

where the second part includes the Taylor expansion of

$$\frac{1}{k_0^2 - k_n^2} = \sum_{l=0}^{L_0} a_{2l,n} (k_0)^{2l} \quad (37)$$

where $a_{2l,n} = -1$ for all l .

The upper summation limit N_0 has to be chosen such that $k_{N_0} > k_{\max}$ with $k_{\max} = 2\pi f_{\max}/c_0$ when f_{\max} denotes the maximum frequency that is used in the simulation. For all $k_n > k_{N_0+1}$, the term $1/(k_0^2 - k_n^2)$ is a well-behaved function that has no poles and can therefore be expanded

Table 1. TE and TM Expansion Coefficients B_p

P	TE	TM
2	$\frac{1}{2}$	$\frac{1}{2}$
4	$\frac{1}{8}$	$\frac{3}{8}$
6	$\frac{1}{16}$	$\frac{5}{16}$
8	$\frac{5}{128}$	$\frac{35}{128}$
10	$\frac{7}{256}$	$\frac{63}{256}$

into a rapidly converging Taylor series. The second series in the Taylor expansion term of (36), namely

$$\sum_{n=N_0+1}^{+\infty} a_{l,n} \mathbf{h}_n^{(c)}(\mathbf{r}) \mathbf{h}_n^{(c)*}(\mathbf{r}') \quad (38)$$

can be summed up after applying a method of moments on (26) to solve for the unknowns $\mathcal{M}_k^{(v)}$, so that for the frequency-dependent evaluation we only need to compute the outer series over l in (36).

The remaining portion of the kernel of (26), namely $\mathbf{G}^{(\text{WG})}$, can be treated as already shown for the planar junction case.

5. METHOD OF MOMENTS SOLUTION OF THE INTEGRAL EQUATION

The integral equations in (10), (14), and (26), must be solved before the equivalent network representations can be used. This can be easily done by using the method of moments (MoM), thereby effectively reducing the solution of a field problem to the solution of a linear system [16].

Since the application of the method of moments is essentially identical in all cases, we will outline here only the case of the planar junction. The procedure begins by rewriting the kernel (10) in the form

$$\begin{aligned} &\mathbf{h}_n^{(\delta)} \\ &= \int_{\text{cs}} M_n^{(\delta)} \cdot \left[\sum_{\gamma=1}^2 \sum_{m=1}^{\text{NKER}} \hat{\mathbf{Y}}_m^{(\gamma)} \mathbf{h}_m^{(\gamma)} \mathbf{h}_m^{(\gamma)*} \right. \\ &\quad \left. - \sum_{p=1}^P (k_0)^{2p} \left(\sum_{\gamma=1}^2 \sum_{m=N^{(\gamma)}+1}^{\text{NKER}} \frac{B_{2p}}{(k_{t,m}^{(\gamma)})^{2p}} \hat{\mathbf{Y}}_m^{(\gamma)} \mathbf{h}_m^{(\gamma)} \mathbf{h}_m^{(\gamma)*} \right) \right] ds' \end{aligned} \quad (39)$$

To implement the MoM solution of the integral equation, we first expand the unknown function using as the basis function the modes of the smallest waveguide

$$\mathbf{M}_n^{(\delta)} = \sum_{i=1}^{\text{NFUN}} \alpha_{i,n}^{(\delta)} \cdot \mathbf{h}_i^{(2)} \quad (40)$$

The integral equation is then reduced to a linear system by using Galerkin's procedure, thus obtaining

$$\sigma_{n,p}^{(\delta)} = \sum_{i=1}^{\text{NFUN}} \eta_{p,i} \alpha_{i,n}^{(\delta)} \quad (41)$$

where

$$\sigma_{n,p}^{(\delta)} = \int_{\text{cs}} \mathbf{h}_n^{(\delta)} \cdot \mathbf{h}_p^{(2)*} ds \quad (42)$$

and

$$\begin{aligned} & \eta_{p,i} \\ &= \sum_{\gamma=1}^2 \sum_{m=1}^{\text{NKER}} \hat{\mathbf{Y}}_m^{(\gamma)} \sigma_{m,p}^{(\gamma)} \sigma_{m,i}^{(\gamma)} \\ & - \sum_{p=1}^P (k_0)^{2p} \left(\sum_{\gamma=1}^2 \sum_{m=N^{(\gamma)}+1}^{\text{NKER}} \frac{B_{2p}}{(k_{t,m}^{(\gamma)})^{2p}} \right) \\ & \times \hat{\mathbf{Y}}_m^{(\gamma)} \sigma_{m,p}^{(\delta)} \sigma_{i,m}^{(\delta)} \end{aligned} \quad (43)$$

The formulation described is completely general and can therefore be used for any two-dimensional waveguide step for which we can compute the coupling integrals in (42). Once the solution of the system (41) is obtained, we can easily compute the impedance matrix, obtaining

$$\mathbf{Z}_{m,n}^{(\gamma,\delta)} = \sum_{i=1}^{\text{NFUN}} \alpha_{i,n}^{(\delta)} \sigma_{m,i}^{(\gamma)} \quad (44)$$

In the solution procedure outlined, all infinite sums are truncated to a finite number of terms. The relevant parameters are NFUN and NKER. Their values affect the accuracy of the solution. For most engineering applications, sufficient accuracy is obtained with NKER=400 and NFUN = $2N^{(\delta)}$. The number of modes $N^{(\delta)}$, on the other hand, depends on how close to each other the discontinuities are located in the actual waveguide device. An important feature of this approach is that the relative number of modes (modal ratios) chosen on each side of a step in the final network representation does not affect the final result. In fact, by increasing the total number of modes, the solution converges to the same result independently from the modal ratios.

The implementation of the solution procedure just described requires the computation of the coupling integrals in (42). This calculation can be carried out very efficiently for junctions involving canonical waveguide shapes (e.g., rectangular, circular, elliptical, coaxial) for which the modes are known in analytical form. The same consideration applies to arbitrary junctions involving resonators for which modes are known in analytical form (cubic, cylindrical, etc.). The procedure outlined, however, can also be used for junctions involving arbitrarily shaped waveguides or resonators for which we can compute the required coupling integrals [17].

6. APPLICATIONS

Following our theory, the first step in the analysis of any passive waveguide component is the decomposition of the component itself into a number of "uniform waveguide sections." The junctions between all the uniform waveguide sections—namely, the discontinuities—are then analyzed and characterized in terms of the multimode impedance matrix in Fig. 2, where the elements of $\mathbf{Z}_{m,n}$ are given by the theory discussed in this article. The next step is then to represent also the sections of uniform waveguide in terms of a multimode impedance matrix whose elements are given by simple network calculations (see, e.g., Ref. 6 or 17). The global equivalent network of the passive component can then be easily assembled by interconnecting the individual multimode impedance networks. In mathematical terms, what we obtain at the end of this process is a linear system with a sparse, block coefficient matrix containing all the separate multimode impedance matrices needed to represent the device under analysis [17]. The system thus obtained can then be easily inverted and the global electrical performance computed.

It is important to note that the process just described is inherently modular and is therefore very suitable for the development of advanced full-wave electromagnetic simulation programs. In the following sections we describe a few specific applications to show the very high level of accuracy that can indeed be achieved.

6.1. Inductive Filter

Microwave filters are among the most commonly used passive microwave components for both ground and space applications. One of the simplest and most commonly used microwave filter structures is the classic inductive filter in rectangular waveguides. In this class of filters, lengths of uniform rectangular waveguides are separated by thick inductive irises. The lengths of the waveguide act as resonators, and the inductive irises couple the energy from one resonator to the other. This type of structure is ideally suited for the application of the theory described in this article [8]. Figure 7 describes the structure of a five-pole filter that has been designed using software based on the

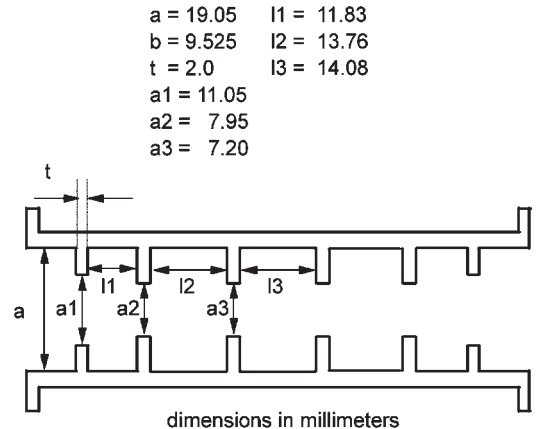


Figure 7. Classic inductive filter in rectangular waveguide.

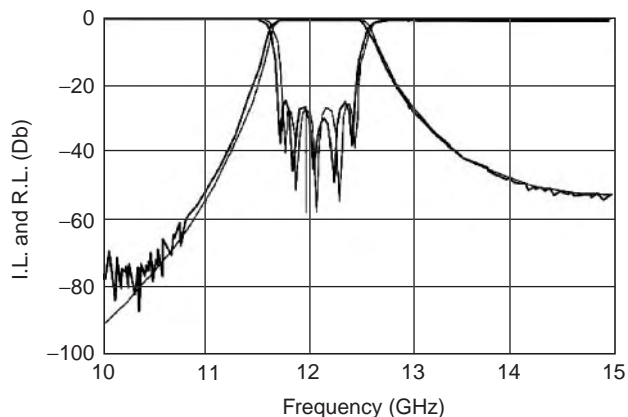


Figure 8. Measured and simulated performances of the inductive filter in rectangular waveguide.

theory described. Figure 8 shows a comparison between measured and simulated performances. As we can see, the agreement is indeed very good.

One important feature of this class of filters is that, using modern, high-accuracy manufacturing techniques, they can be realized without the need for any postmanufacture adjustment, or tuning, thereby greatly reducing the global cost of the filter.

6.2. Dual-Mode Inductive Filter

The next application we discuss is an inductive dual-mode filter. The difference between this structure and the previous one is that each physical cavity (a length of uniform waveguide) is used electrically 2 times. This particular feature allows for the implementation of advanced filter transfer functions that cannot be realized with the classic configuration [18]. Figure 9 shows the structure of an inductive dual-mode filter, while Fig. 10 shows the comparison between simulation and measurement.

6.3. Triple-Mode Filter

A further advancement with respect to the dual-mode filter described in the previous section is the triple-mode

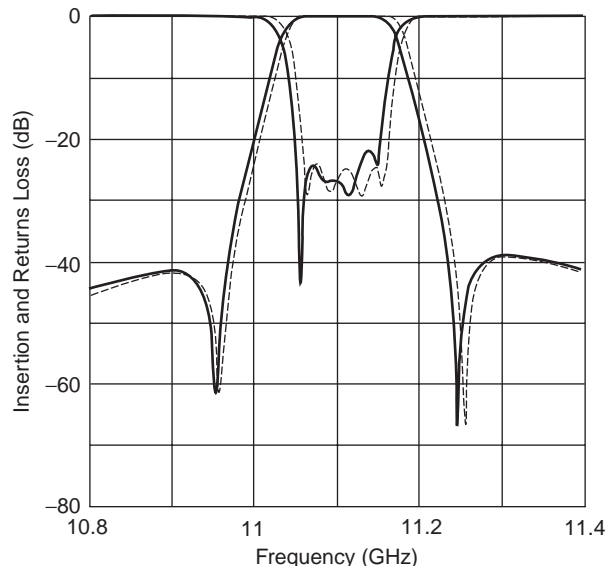


Figure 10. Measured (thick) and simulated performances of the dual-mode inductive filter in rectangular waveguide.

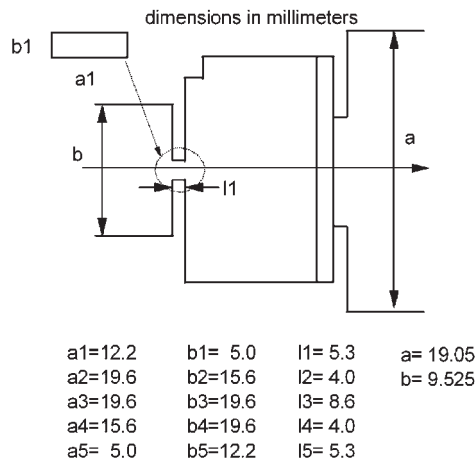


Figure 11. Longitudinal section of triple-mode filter in rectangular waveguide.

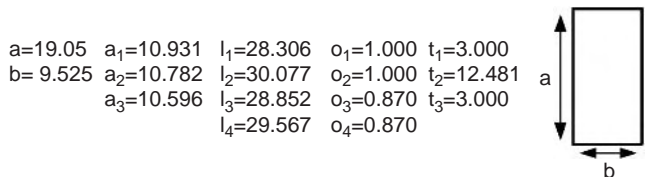
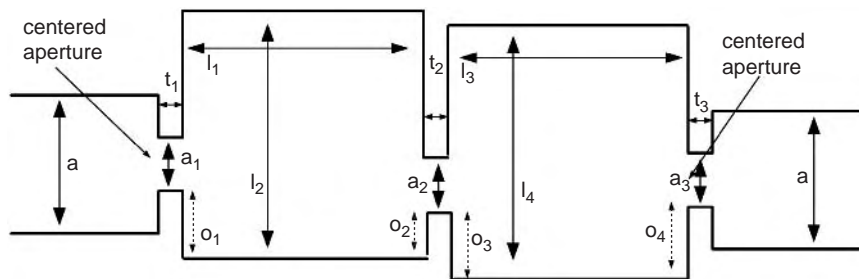


Figure 9. Dual-mode inductive filter in rectangular waveguide.



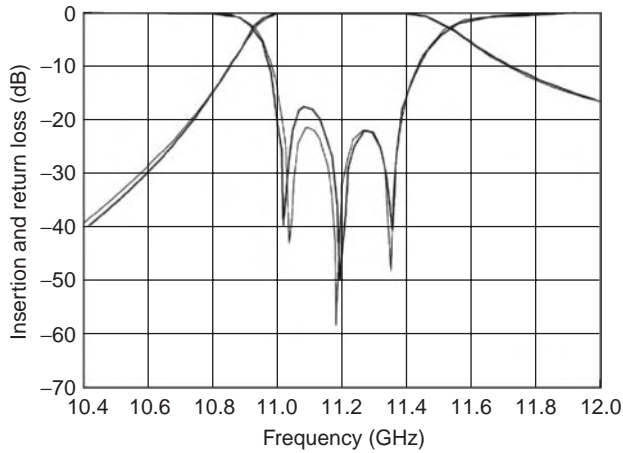
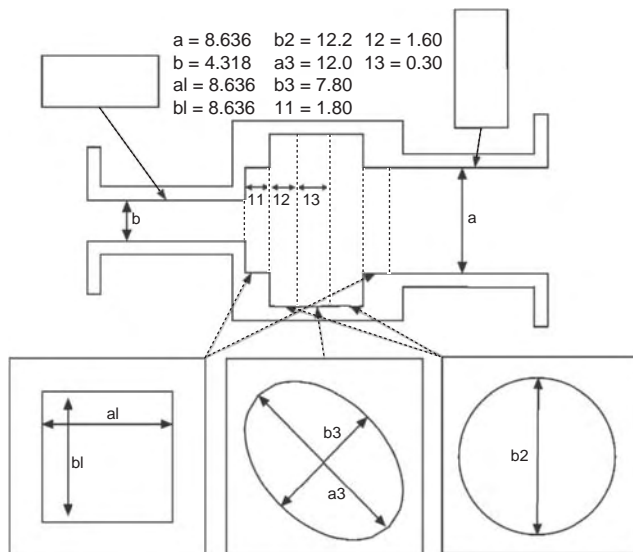


Figure 12. Simulated performance for triple-mode filter in rectangular waveguide compared with simulation from commercial finite-element software (thick).

filter. In this case, as the term *triple* indicates, the same physical cavity is used 3 times electrically. The result is an extremely compact filter that can be used to implement very selective filter transfer functions [19]. Figure 11 shows the structure of the filter, while Fig. 12 shows the comparison between the simulation based on the theory described in this article and the simulated response obtained using commercial finite-element software.

6.4. Waveguide Twist

Another type of passive microwave device that is sometimes required is the waveguide twist. A waveguide twist is needed whenever the polarization direction of a rectangular waveguide needs to be rotated. The structure shown in Fig. 13 can be effectively used to introduce a 90° rotation. Figure 14 shows a comparison between measured and simulated performances [20].



Drawing not to scale, dimensions in millimeters

Figure 13. Rectangular waveguide twist.

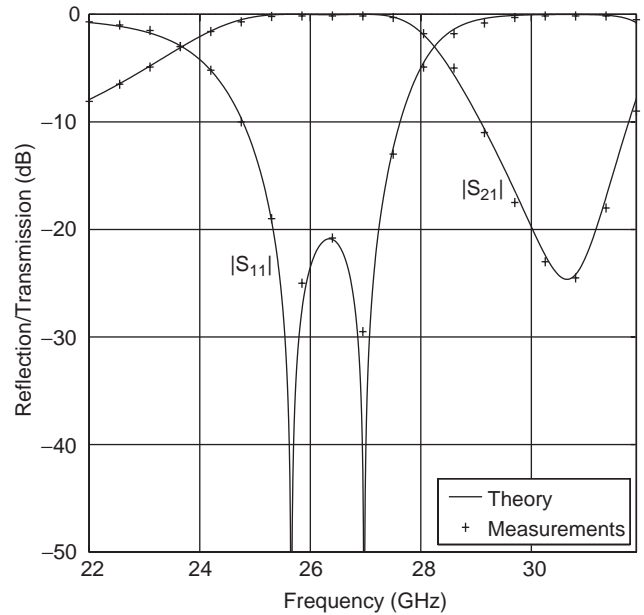


Figure 14. Measured versus simulated performances for the rectangular waveguide twist.

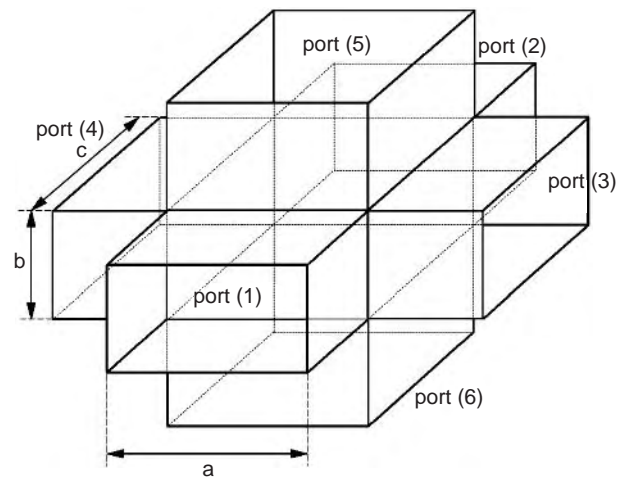


Figure 15. Cubic junction in rectangular waveguide.

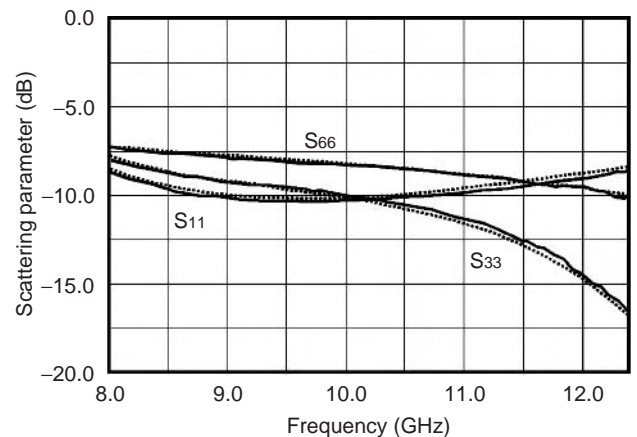


Figure 16. Measured versus simulated (dotted line) performances of a cubic junction in rectangular waveguide.

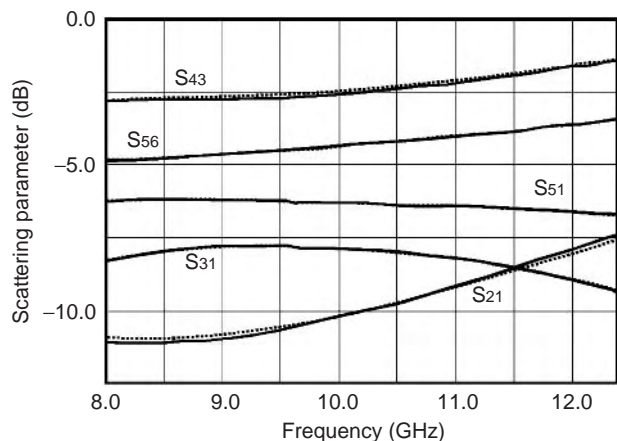


Figure 17. Measured versus simulated (dotted line) performances of a cubic junction in rectangular waveguide.

6.5. Cubic Junction

All the application examples reported so far have dealt with devices composed of cascaded uniform waveguide sections requiring the analysis of planar waveguide junctions. In the article, however, we have also discussed the theory of arbitrary waveguide junctions. As a last example, therefore, we now describe the analysis of the cubic junction shown in Fig. 15. This junction is particularly useful because it can be used to build very complex devices such as diplexers and output multiplexers where two or more microwave filters are combined in a single waveguide output. The comparison between measurements and simulation for this device is shown in Figs. 16 and 17 [11]. As we can see, very good agreement between simulation and measurements has indeed been achieved.

7. CONCLUSION

The multimode equivalent network representations described in this article can be used to analyze *all* waveguide junction problems of practical interest for microwave and millimeter-wave engineering applications. The formulations presented effectively reduce complex field problems to the computation of coupling integrals between the modes of the waveguides involved in the junctions, and to the solution of simple linear systems.

The theory presented in this article has a wide application scope, is rigorous, and leads to highly efficient numerical implementations. It constitutes, therefore, a very solid theoretical foundation for the development of advanced electromagnetic simulation programs needed for the analysis and design of modern complex waveguide devices and subsystems.

Acknowledgment

The author would like to acknowledge the contributions of the many graduate and postdoctoral students who contributed to the development and validation of the formulations described in this article. In particular, the author

would like to acknowledge the efforts and dedication of Alejandro Alvarez, Vicente Boria, Giampiero Gerini, Giorgio Gheri, Benito Gimeno, Gianluca Lastoria, Michael Mattes, and Antonio Panariello.

BIBLIOGRAPHY

1. Five years at the radiation laboratory, paper originally presented to the Members of the Radiation Laboratory by the Massachusetts Institute of Technology, Cambridge, 1946; reprinted for the 1991 IEEE MTT-S Int. Microwave Symp., Boston, June 10–14, 1991.
2. Special Centennial Issue, Historical Perspective of Microwave Technology, *IEEE Trans. Microwave Theory Tech.* **MTT-32**(9): (Sept. 1984).
3. J. Schwinger and D. S. Saxon, *Discontinuities in Waveguides*, notes on lectures by Julian Schwinger, Gordon & Breach Science, New York, 1968.
4. H. A. Bethe, Theory of diffraction by small holes, *Phys. Rev.* **66**(7/8):163–182 (1944).
5. L. Lewin, *Advanced Theory of Waveguides*, for *Wireless Engineer* by Iliffe & Sons, London, 1951.
6. N. Marcuvitz, *Waveguide Handbook*, MIT Radiation Laboratory Series, vol. 10, McGraw-Hill, New York, 1951.
7. G. Gerini, M. Guglielmi, and G. Lastoria, Efficient integral equation formulation for admittance or impedance representation of planar waveguide junctions, *IEEE 1998 MTT-S Digest*, 1998.
8. M. Guglielmi, G. Gheri, M. Calamia, and G. Pelosi, Rigorous multimode network numerical representation of inductive step, *IEEE Trans. Microwave Theory Tech.* **42**(2):317–326 (Feb. 1994).
9. M. Guglielmi and G. Gheri, Rigorous multimode network representation of capacitive steps, *IEEE Trans. Microwave Theory Tech.* **MTT-42**(4):622–628 (April 1994).
10. M. Guglielmi and G. Gheri, Multimode equivalent network representation of capacitive and inductive multiple posts, *IEE Proc. Microwave Antenn. Propag.* **142**(1):41–46 (Feb. 1995).
11. M. Mattes, A. Alvarez, M. Guglielmi, and J. R. Mosig, Impedance representation of waveguide junctions based on the integral equation approach, *Proc. 30th European Microwave Conf.* Paris, 2000.
12. R. E. Collin, *Field Theory of Guided Waves*, 2nd ed., IEEE Press, Piscataway, NJ, 1991.
13. K. Kurokawa, *An Introduction to the Theory of Microwave Circuits*, Academic Press, New York and London, 1969.
14. K. Kurokawa, The expansion of electromagnetic fields in cavities, *IRE Trans. Microwave Theory Tech.* **6**:178–187 (1958).
15. Y. Rahmat-Samii, On the question of computation of the dyadic Green's function at the source region in waveguides and cavities, *IEEE Trans. Microwave Theory Tech.* **23**:762–765 (Sept. 1975).
16. R. F. Harrington, Matrix methods for field problems, *IEEE Proc.* **55**(2):136–149 (Feb. 1967).
17. G. Conciauro, M. Guglielmi, and R. Sorrentino, *Advanced Modal Analysis, CAD Techniques for Waveguide Components and Filters*, Wiley, Chichester, UK, 2000.
18. M. Guglielmi, P. Jarry, E. Kerherve, O. Roquebrun, and D. Schmitt, A new family of all inductive dual mode filters, *Trans. Microwave Theory Tech.* **49**(10):1764–1769. (Oct. 2001).

19. G. Lastoria, G. Gerini, M. Guglielmi, and F. Emma, CAD of triple-mode cavities in rectangular waveguide, *IEEE Microwave Guided Wave Lett.* **8**(10):339–341 (Oct. 1998).
20. S. Cogollos, S. Marini, V. E. Boria, P. Soto, A. Vidal, H. Esteban, J. V. Morro, and B. Gimeno, Efficient modal analysis of arbitrarily shaped waveguides composed of linear, circular and elliptical arcs using the BI-RME method, *Trans. Microwave Theory Tech.* **51**(12):2378–2390 (Dec. 2003).

MULTIPLE ACCESS SCHEMES

MOSHE SIDI
Technion—Israel Institute of
Technology

Communication channels are major components of computer communication networks. They provide the physical mediums over which signals representing data are transmitted from one node of the network to another node. Communication channels can be classified into two main categories: point-to-point channels and shared channels. Typically, the backbone of wide-area networks (WAN) consists of point-to-point channels, whereas local-area networks (LAN) use shared channels.

Point-to-point channels are dedicated to connecting a pair of nodes of the network. They are usually used in fixed topology networks, and their cost depends on many parameters such as distance and bandwidth. An important characteristic of these channels is that nodes do not interfere with each other; in other words, transmissions between a pair of nodes has no effect on the transmissions between another pair of nodes, even if a node is common to the two pairs.

Shared channels are used when point-to point channels are not economical or not available or when dynamic topologies are preferable. In a shared channel, called also a broadcast channel, several nodes can potentially transmit and/or receive messages at the same time. Shared channels appear naturally in radio networks, satellite networks, and some local area networks (e.g., Ethernet). Their deployment is usually easier than point-to-point channels. An important characteristic of shared channels is that transmissions of different nodes interfere with each other; specifically, one transmission coinciding in time with another may cause none of them to be received. This means that the success of transmission between a pair of nodes is no longer independent of other transmissions.

To have successful transmissions in shared channels, interference must be avoided or at least controlled. The channel allocation among the competing nodes is critical for proper operation of the network. This article focuses on access schemes to such channels known as multiple access schemes. These schemes are nothing more than channel allocation rules that determine who goes next on the channel, aiming at some desirable network performance characteristics. Multiple-access schemes belong to a sublayer of the data link layer called the medium access control layer (MAC), which is especially important in LANs.

Multiple access schemes are natural not only in communication systems but also in many other systems such as computer systems, storage facilities, or servers of any kind, where resources are shared by a number of nodes. In this article we address mainly shared communication channels.

One way to classify multiple access schemes is according to the level of contention that is allowed among the nodes of the network. On the one hand, there are the conflict-free schemes that ensures that each transmission is successful, namely, it will not be interfered with by any other transmission. On the other hand, there are the contention-based schemes that do not guarantee that a transmission will be successful, namely, it might be interfered with by another transmission.

Conflict-free transmissions can be achieved by allocating the shared channel in an adaptive or nonadaptive (static) manner. Two common static allocations are the time-division multiple access (TDMA), where the entire available bandwidth is allocated to a single node for a fraction of the time, and the frequency-division multiple access (FDMA), where a fraction of the available bandwidth is allocated to a single node for all the time. Adaptive allocations are usually based on demands so that nodes that are idle use only little of the shared channel, leaving the majority of their share to other more active nodes. Adaptive allocations can be done by various reservation schemes using either central or distributed network control. Polling algorithms illustrate central control, whereas ring networks generally use distributed control based on token-passing mechanisms. It is important to note that idle nodes consume their portion of the shared channel when conflict-free schemes are used. The aggregate channel portion of idle nodes becomes significant when the number of potential nodes in the system is very large to the extent that conflict-free schemes might become impractical.

When contention-based schemes are used, it is essential to devise algorithms that resolve conflicts when they occur, so that messages are eventually transmitted successfully. Conflict resolution algorithms can be either adaptive or nonadaptive (static). Static resolution can be deterministic using some fixed priority that is assigned to the nodes, or it can be probabilistic when the transmission schedule for interfered nodes is chosen from a fixed distribution as is done in Aloha-type schemes and the various versions of carrier-sensing multiple-access (CSMA) schemes. Adaptive resolution attempt to track the system evolution and exploit the available information. For example, resolution can be based on time of arrival, giving highest (or lowest) priority to the oldest message in the system as is done in some tree-based algorithms. Alternatively, resolution can be probabilistic but such that the statistics change dynamically according to the extent of the interference. This category includes estimating the multiplicity of the interfering nodes and the exponential backoff scheme of the Ethernet standard. Note that when the population of potential nodes in the system increases beyond a certain amount and conflict-free schemes are useless, contention-based protocols are the only possible solution.

The goal of this article is to survey typical examples of multiple access schemes. These examples include TDMA, FDMA, Aloha, polling, and tree-based schemes. The allocated space for the topic of multiple access schemes in the encyclopedia (which is yet another shared resource) is just too tiny to include all the ingenious multiple access schemes that have been designed by researchers over the years. Interested readers should refer to books on the subject (e.g., Rom and Sidi [23], Hammond and O'Reilly [22], and to the international journals that have published papers on the subject).

1. BASIC MODEL

When multiple-access schemes are devised, a collection of nodes that communicate with each other or with a central node via a single shared channel is considered. In general, the ability of a node to hear the transmission of another node depends on the transmission power used, on the distance between the two nodes, and on the sensitivity of the receiver at the receiving node. We assume single-hop topologies in which all nodes hear one another, and whenever messages are transmitted successfully they arrive at their destinations.

The shared channel is the medium through which data are transferred from their sources to their destinations. The total transmission rate possible in the channel is C bits/s. We consider an errorless collision channel. Collision is a situation in which, at the receiver, two or more transmissions overlap in time wholly or partially. A collision channel is one in which all the colliding transmissions are not received correctly and must be retransmitted until they are received correctly. We assume that nodes can detect collisions. The channel is errorless in the sense that a single transmission heard at a node always received correctly. Other possible channels include the noisy channel in which errors may occur even if only a single transmission is heard at a node; furthermore, the channel may be such that errors between successive transmissions are not independent. Another channel type is the capture channel in which one or more of the colliding transmissions captures the receiver and can be received correctly. Yet another case is a channel in which coding is used so that even if transmissions collide the receiver can still decode some or all of the transmitted information.

The basic unit of data generated by a node is a message. It is possible, though, that because of its length, a message cannot be transmitted in a single transmission and must therefore be broken into smaller units called packets, each of which can be transmitted in a single channel access. A message consists of an integral number of packets, although the number of packets in a message can vary randomly. Packet size is measured by the time required to transmit the packet after access to the channel has been granted. Typically, all packets are of equal size, say, L bits.

The number of nodes that share the channel is denoted by M . When M becomes very large, the population of nodes is referred to as infinite population. Only contention-based schemes can cope with an infinite node population. The aggregate arrival process of new packets is assumed to be

Poisson with rate Λ packets/s. When the population is finite, the arrival rate to each node is $\lambda = \Lambda/M$ packets/s.

Nodes are generally not assumed to be synchronized and are capable of accessing and transmitting their messages on the shared channel at any time. Another important class of systems is that of slotted systems in which there is a global clock that marks discrete intervals of time called slots whose length is usually the time required to transmit a packet (i.e., $T=L/C$ s). In these systems, transmissions of packets start only at slot starts. The slot length is therefore $T=L/C$ s. Other operations, such as determining activities on the channel, can be done at any time.

In some models, nodes can tell if the shared channel is in use before trying to use it. If the channel is sensed as busy, no node will attempt to use it until it goes idle in order to reduce interference. Naturally, additional hardware is required at each node to implement the sensing ability. In other models, nodes cannot sense the channel before trying to use it. They just go ahead and transmit according to their access scheme. Only later can they determine whether the transmission was successful via the feedback mechanism. Feedback in general is the information available to the nodes regarding activities on the shared channel at prior times. This information can be obtained by listening to the channel, or by explicit acknowledgment messages sent by the receiving node. For every scheme, there exist some instants of time (typically slot boundaries or end of transmissions) in which feedback information is available. Common feedback information indicates whether a message was successfully transmitted or a collision took place or the channel was idle. Feedback mechanisms do not consume the shared channel sources because they usually use a different channel or are able to determine the feedback locally. Other feedback variations include indication of the exact or the estimated number of colliding transmission, or providing uncertain feedback (e.g., in the case of a noisy channel).

The important performance measures of multiple-access schemes are their throughput and delay. The throughput of the channel is the aggregate average amount of data that is transported successfully through the channel in a unit of time. The throughput equals the fraction of time in which the channel is engaged in the successful transmission of node data and will be denoted by S , and it is obvious that $S \leq 1$. In conflict-free access schemes, the throughput is also the total or offered load on the shared channel. However, in contention-based access schemes, the offered load on the shared channel includes transmissions of new packets as well as retransmissions of packets that collide with each other. The offered load is denoted by g (measured in packets per second) and, obviously, $g \geq \Lambda$. The normalized offered load [i.e., the rate (per packet transmission time) packets are transmitted on the channel] is denoted by $G = g \cdot T$ and, obviously, $G \geq S$.

Delay is the time from the moment a message is generated until it arrives successfully across the shared channel. Here one must distinguish between the node and the system measures because it is possible that the average delay measured for the entire system does not necessarily reflect the average delay experienced by any of the nodes.

In “fair” or homogeneous systems, we expect these to be almost identical. The average delay is denoted by D seconds, and its normalized version, grouped into units of packet transmission times, is denoted by \mathcal{D} (i.e., $\mathcal{D} = D/T = D \cdot C/L$).

Another important performance criterion is system stability. Unfortunately, some schemes’ characteristics may be such that some message generation rates, even smaller than the maximal transmission rate in the channel, cannot be sustained by the system for a long time. Evaluation of those input rates for which the system remains stable is therefore essential.

1.1. Ideal Access Scheme

Before introducing the various multiple-access schemes, let us consider an ideal scheme to use the shared channel. Ideally, transfer of the channel from one node to another can be accomplished instantaneously, without cost. Furthermore, whenever a node has data to transmit, some ingenious central controller knows this instantaneously and assigns the channel to that node in case the channel is idle. If the channel is busy, packets that arrive at the nodes are queued. For our purposes, the order in which packets of different nodes are served is not important. The performance of the ideal scheme serves as a bound to what can be expected from any practical access scheme.

The way the ideal scheme operates is identical to the operation of a single queue that is served by a single server, because packets do not interfere and because no time is wasted in transferring the channel use from one node to another. Because arrivals of new packets are according to a Poisson process and time is slotted, the performance of the ideal scheme is that of an $M/D/1$ queue. The throughput of an $M/D/1$ queue is just the utilization factor of the server as long as $S < 1$ (the stability condition), and it equals the offered load, in other words

$$S = G = \lambda T = \frac{\lambda \cdot M \cdot L}{C} \tag{1}$$

The normalized average delay of an $M/D/1$ queue is given by (as long as $S < 1$)

$$\mathcal{D} = 1 + \frac{S}{2(1 - S)} = \frac{2 - S}{2(1 - S)} \tag{2}$$

The Unit in the expression \mathcal{D} is the normalized transmission time of a packet, whereas $S/[2(1 - S)]$ is the normalized waiting time of a packet until being transmitted.

No access scheme can achieve throughput higher than S given in Eq. (1), and no access scheme can provide normalized average delays lower than \mathcal{D} given in Eq. (2). These quantities will serve as yardsticks in the sequel.

2. CONFLICT-FREE SCHEMES

Conflict-free schemes are designed to ensure that a transmission, whenever made, is not interfered with by any other transmission and is therefore successful. This is achieved by allocating the channel to the nodes without

any overlap between the portions of the channel allocated to different nodes. An important advantage of conflict-free access protocols in the ability to ensure fairness among nodes and the ability to control the packet delay—a feature that may be essential in real-time applications.

We consider both fixed-assignment schemes and dynamic schemes that guarantee no conflicts. In fixed-assignment schemes the channel allocation is predetermined (typically at network design time) and is independent of the demands of the nodes in the network. The most well-known fixed-assignment schemes are the frequency-division multiple access and the time-division multiple access. For both FDMA and TDMA, no overhead, in the form of control messages, is incurred. However, because of the static and fixed assignment, parts of the channel might be idle even though some nodes have data to transmit. Dynamic channel allocation schemes attempt to overcome this drawback by changing the channel allocation based on the current demands of the nodes. These schemes use some kind of reservation strategies based on either centralized or distributed polling.

2.1. Fixed Assignment

Both FDMA and TDMA are the oldest and most understood access schemes, widely used in practice. They are the most common implementation of fixed-assignment schemes.

With FDMA the entire available frequency band is divided into bands, each of which is used by a single node. Every node is therefore equipped with a transmitter for a given, predetermined frequency band and a receiver for each band (which can be implemented as a single receiver for the entire range with a bank of bandpass filters for the individual bands). With TDMA the time axis is divided into timeslots, preassigned to the different nodes. Every node is allowed to transmit freely during the slot assigned to it; that is, during the assigned slot the entire shared channel is devoted to that node. The slot assignments follow a predetermined pattern that repeats itself periodically; each such period is called a frame. In most TDMA implementations, every node has exactly one slot in every frame.

The main advantage of both FDMA and TDMA is that each transmission is guaranteed to be successful and no control messages are required. An additional advantage of FDMA is its simplicity—it does not require any coordination or synchronization among the nodes because each can use its own frequency band without interference. However, both FDMA and TDMA are wasteful, especially when the load is momentarily uneven, because when one node is idle, its share of the channel cannot be used by other nodes. Another drawback of FDMA and TDMA is that they are not flexible; adding a new node to the network requires equipment or software modification in every other node. In addition, both waste some portion of the channel to ensure no overlap (either in time or in bandwidth) in the transmissions of different nodes. FDMA uses guardbands between the subchannels, and TDMA uses guard times to separate the nodes.

Neglecting the channel waste resulting from guardbands or times, the throughput of FDMA and TDMA is

identical to that of the idealized schemes, because packets are never transmitted more than once. Therefore, we have for both

$$S = G = \Lambda T = \frac{\lambda \cdot M \cdot L}{C}$$

The delay characteristics of FDMA and TDMA are different. With FDMA the transmission rate of each node is C/M bps; therefore, the time to transmit a packet is $M \cdot L/C$ seconds. Each node can be modeled as an $M/D/1$ queue with arrival rate $\lambda = \Lambda/M$ and service time $M \cdot L/C$. The normalized average delay is therefore

$$\mathcal{D} = M \left[1 + \frac{S}{2(1-S)} \right] = M \frac{2-S}{2(1-S)}$$

which is M times larger than the normalized average delay of the ideal scheme.

With TDMA the transmission rate of each node is C bps, and the time to transmit a packet is L/C seconds. Each node can be modeled as an $M/D/1$ queue with arrival rate $\lambda = \Lambda/M$, but service is granted to the node only once a frame, namely every $M \cdot L/C$ seconds. The normalized average delay is therefore

$$\mathcal{D} = 1 + \frac{M}{2(1-S)}$$

Comparing the throughput delay characteristics of FDMA and TDMA, we note that

$$\mathcal{D}_{\text{FDMA}} = \mathcal{D}_{\text{TDMA}} + \frac{M}{2} - 1$$

We thus conclude that for any reasonable parameters, the TDMA-normalized average delay is always less than that of FDMA and the difference grows linearly with the number of nodes and is independent of the load. The difference stems from the fact that the actual transmission of a packet in TDMA takes only a single slot, whereas in FDMA it lasts the equivalent of an entire frame. This difference is somewhat offset by the fact that a packet arriving at an empty node may need to wait until the proper slot when a TDMA scheme is employed, whereas in FDMA transmission starts right away. It must be remembered, though, that at high throughput the dominant factor in the normalized average delay is inversely proportional to $(1-S)$ in both TDMA and FDMA; therefore, the ratio of the normalized average delays between the two schemes approaches unity when the load increases. Figure 1 depicts the delay throughput characteristics for TDMA and FDMA and the ideal access scheme for 50 users.

2.1.1. Further Reading. Many texts treating FDMA and TDMA are available [e.g.1,2] A good analysis of TDMA and FDMA can be found in Ref. 3. A sample path comparison between FDMA and TDMA schemes is carried out in Ref. 4 where it is shown that TDMA is better than FDMA not just on the average. A TDMA scheme in which the packets of each node are serviced according to a priority

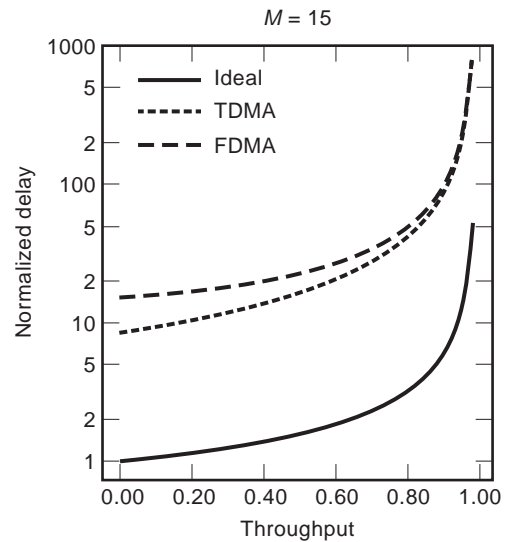


Figure 1. TDMA and FDMA performance.

rule is analyzed by De Moraes and Rubin [5]. The question of optimal allocation of slots to the nodes in generalized TDMA (in which a node can have more than one slot in a frame) is addressed in Itai and Rosberg [6], where the throughput of the network is maximized (assuming single buffers for each node), Hofri and Rosberg [7] where the expected packet delay in the network is minimized. Message delay (as opposed to packet delay) for generalized TDMA is analyzed by Rom and Sidi [8].

2.2. Dynamic Assignment

Static conflict-free protocols such as FDMA and TDMA schemes do not use the shared channel very efficiently, especially when the network is lightly loaded or when the loads of different nodes are asymmetric. The static and fixed assignment in these schemes cause portions of the channel to remain idle even though some nodes have data to transmit. Dynamic channel allocation schemes are designed to overcome this drawback. With dynamic allocation strategies, the channel allocation changes with time and is based on current (and possibly changing) demands of the various nodes. The better and more responsive use of the shared channel achieved with dynamic schemes does not come for free; it requires control overhead that is unnecessary with fixed-assignment schemes and consumes a portion of the channel.

To ensure conflict-free operation, it is necessary to reach an agreement among the nodes on who transmits in a given slot. This agreement entails collecting information as to which nodes have packets to transmit and an arbitration scheme that selects one of these nodes to transmit in the slot. Both the information collection and the arbitration can be achieved using centralized control or distributed control.

A representation example of schemes that use centralized control are polling schemes. The basic feature of polling schemes is the operation of a central controller that polls the nodes of the network in some predetermined

order (the most common is round-robin) to provide access to the shared channel. When a node is polled and has packets to transmit, it uses the whole shared channel to transmit its backlogged packets. With an exhaustive policy, the node empties its backlog completely, whereas with a gated policy it transmits only those packets that reside in its queue on the polling instant. The last transmitted packet contains an indication that the central controller can poll the next node. If a polled node does not have packets to transmit, the next node is polled. In between polls, nodes accumulate the arriving packets in their queues and do not transmit until polled.

The control overhead of polling schemes is a result of the time required to switch from one node to the next. The switching time, denoted by w , includes all the time necessary to transfer the poll (channel propagation delay, transmission time of polling and response packets, etc.). We let $\hat{w} = w/T$ denote the normalized switching time.

The throughput of a polling scheme is identical to that of an ideal scheme and is given by Eq. (1). The normalized average delay is given by

$$\mathcal{D} = 1 + \frac{S}{2(1-S)} + \frac{M\hat{w}(1-S/M)}{2(1-S)}$$

We note that the first two terms are just the normalized average delay of the ideal scheme and the third term reflects the overhead resulting from the switching times from one node to the next.

As an example of a distributed dynamic conflict-free scheme, we use the minislotted alternating priority (MSAP) scheme [9]. The MSAP scheme allows the nodes to determine in a distributed manner the order in which they'll use the shared channel, assuming the nodes are ordered according to some priority rule. Either the priority rule can be static or it can change in a round-robin manner in each slot.

MSAP is based on distributed reservations. To describe its operation, we need to define the slot structure. Let τ (seconds) denote the maximum system propagation delay, that is, the longest time it takes for a signal emitted at one end of the network to reach the other end. The quantity τ plays a crucial role in multiple-access schemes. Its normalized version is denoted by $a = \tau/T$. Let every slot consist of initial $M - 1$ reservation minislots, each of duration T , followed by another minislot. Only those nodes wishing to transmit in a slot take any action: a node that does not wish to transmit in a given slot remains quiet for the entire slot duration. Given that every node wishing to transmit knows its own priority, they behave as follows. If the node of the highest priority wishes to transmit in this slot, then it starts immediately. Its transmission consists of an unmodulated carrier for a duration of $M - 1$ minislots followed by a packet of duration T . A node of the i th priority ($2 \leq i \leq M$) wishing to transmit in this slot will do so only if the first $i - 1$ minislots are idle. In this case, it will transmit $M - i$ minislots of unmodulated carrier followed by a packet of duration T . The specific choice of the minislot duration ensures that when a given node transmits in a minislot all other nodes know it by the end of that minislot

allowing them to react appropriately. The additional minislot at the end allows the data signals to reach every node of the network. This is needed to ensure that all start synchronized in the next slot, as required by the reservation scheme.

The fraction of slots in which transmissions take place is ΛT . Because a fraction of $M\tau/(T + M\tau)$ of every slot is overhead, we conclude that the throughput of this scheme is

$$S = \Lambda T \frac{T}{T + M\tau} = \Lambda T \frac{1}{1 + Ma}$$

The normalized average delay is obtained by using standard analysis of priority queues, and it is given by

$$\mathcal{D} = (1 + Ma) \left\{ 1 + \frac{1}{2[1 - (1 + Ma)S]} \right\}$$

Figure 2 depicts the delay-throughput characteristics for the dynamic access schemes for 50 users.

2.2.1. Further Reading. The variants of polling schemes are numerous. Reference 10 contains the analysis of most of the basic schemes with a long list of reference that is complemented in Ref. 11. In Ref. 12 more advanced schemes are described along with some optimization considerations in the operations of polling schemes, such as the determination of the poll order of the nodes.

The MSAP scheme described previously represents an entire family of schemes that guarantees conflict-free transmissions using distributed reservation. All these schemes have a sequence of preceding bits serving to reserve or announce upcoming transmissions (this is known as the reservation preamble). In MSAP there are $M - 1$ such bits for every transmitted packet. An improvement to the MSAP scheme is the bit-map protocol described by Tanenbaum [13]. The idea is to use a single reservation preamble to schedule more than a single transmission;

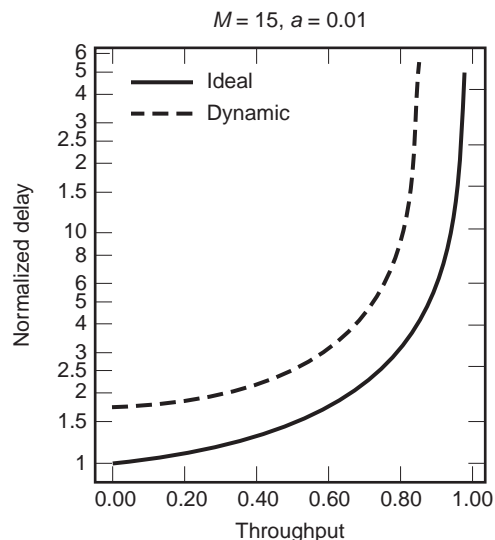


Figure 2. Dynamic access.

using the fact that all participating nodes are aware of the reservations made in the preamble. The bit-map scheme requires synchronization among the nodes that is somewhat more sophisticated than the MSAP scheme, but the overhead paid per transmitted packet is less than the overhead for MSAP. Another variation of a reservation scheme has been described by Roberts [14]. There, every node can make a reservation in every minislot of the reservation preamble, and if the reservation remains uncontested, that reserving node will transmit. If there is a collision in the reservation minislot, all nodes but the "owner" of that minislot will abstain from transmission. Altogether, this is a standard TDMA with idle slots made available to be grabbed by others. Several additional reservation and TDMA schemes are also analyzed by Rubin [4]. One of the most efficient reservation schemes is the broadcast recognition access method (BRAM) [15]. This is essentially a combination between the bit-map and the MSAP schemes. As with MSAP, a reservation preamble serves to reserve the channel for a single node, but unlike the MSAP, the reservation preamble does not necessarily contain all $M-1$ minislots. The idea is that nodes start their transmission with a staggered delay not before they ensure that another transmission is not ongoing (Kleinrock and Scholl [9] also refer to a similar scheme). Under heavy load BRAM reduced to regular TDMA.

3. CONTENTION-BASED SCHEMES

With the conflict-free schemes discussed earlier, every scheduled transmission is guaranteed to succeed. With contention-based schemes success of a transmission is not guaranteed in advance because whenever two or more nodes are transmitting on the shared channel simultaneously, a collision occurs and the data cannot be received correctly. This being the case, packets may have to be transmitted and retransmitted until eventually they are correctly received. Transmission scheduling is therefore the focal concern of contention-based schemes.

3.1. Pure and Slotted Aloha

The Aloha family of schemes is probably the richest family of multiple-access protocols. First of all, its popularity is the result of seniority because it was the first contention-based scheme introduced [16]. Second, many of these schemes are so simple that their implementation is straightforward. Many local-area networks of today implement some sophisticated variants of this family of schemes.

The pure Aloha scheme is the basic scheme in the family and it is very simple [16]. It states that a newly generated packet is transmitted immediately on generation, hoping for no interference by others. If two or more nodes transmit so that their packets overlap (even partially) in time, interference results, and the transmissions are unsuccessful. In this case every colliding node, independently of the others, schedules its retransmission to a random time in the future. This randomness is required to ensure that the same set of packets does not continue to collide indefinitely.

The Aloha scheme is very well suited to bursty traffic because a node does not hold the shared channel when it has no packets to transmit. The drawback of this scheme is that network performance deteriorates significantly as a result of excessive collisions at medium and high traffic intensities. The Aloha scheme is a completely distributed scheme that allows every node to operate independently of the others.

The exact characterization of the offered load to the channel for the pure Aloha scheme is extremely complicated. To overcome this complexity, it is standard to assume that the offered load forms a Poisson process (with rate g , of course). This flawed assumption is an approximation (as has been shown by simulation) that simplifies the analysis of Aloha-type schemes considerably and provides some initial intuitive understanding of the ALOHA scheme. Consider a packet (new or retransmitted) whose transmission starts at time t . This packet will be successful if no other packet is transmitted in the interval $(t - T, t + T)$ (this period of duration $2T$ is called the vulnerable period). The probability of this happening, that is, the probability of success P_s is the probability that no packet is transmitted in an interval of length $2T$. Because the transmission points correspond to a Poisson process, we have

$$P_s = e^{-2gT}$$

Now, packets are scheduled at a rate of g per second, of which only a fraction P_s are successful. Thus, the rate of successfully transmitted packets is gP_s . When a packet is successful, the channel carries useful information for a period of T seconds; in any other case, it carries no useful information at all. Because the throughput is the fraction of time that useful information is carried on the shared channel, we have

$$S = gTe^{-2gT} = Ge^{-2G}$$

This relation between S and G is typical to many Aloha-type schemes. For small values of G (light load), the throughput is approximately the offered load. For large values of G (heavy load), the throughput decreases rapidly because of excessive amount of collisions. For pure Aloha we note that for $G = \frac{1}{2}$, S takes on its maximal value of $1/2e \approx 0.18$. This value is referred to as the capacity of the pure Aloha channel. Figure 3 depicts the load throughput characteristics for the Aloha-type schemes.

We recall that for a system to be stable the long-term rate of input must equal the long-term rate of output meaning that stability requires $S = \Lambda T$. Larger values of Λ clearly cannot result in stable operation. Note, however, that even for smaller values of Λ there are two values of G to which it corresponds—one larger and one smaller than $\frac{1}{2}$. The smaller one is (conditionally) stable, whereas the other one is conditionally unstable, meaning that if the offered load increases beyond that point the system will continue to drift to higher load and lower throughput. Thus, without additional measures of control, the stable throughput of pure Aloha is 0 [17]. It is appropriate to note

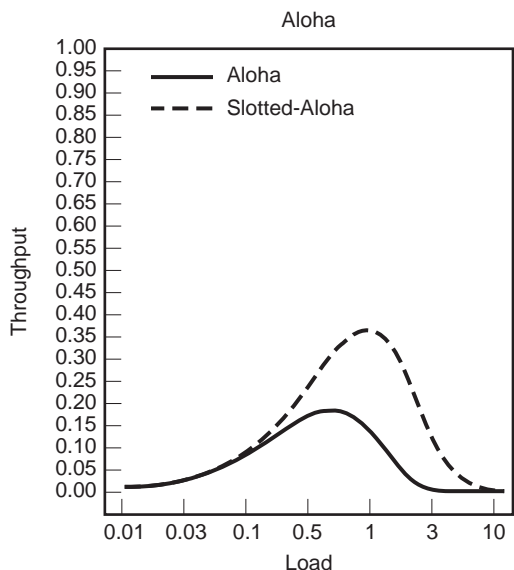


Figure 3. Throughput of Aloha and slotted Aloha.

that this theoretical instability is rarely a severe problem in real systems, where the long-term load, including, of course, the “off-hours” load, is fairly small, although temporary problems may occur.

The delay characteristic of the Aloha scheme can be approximated as follows. For each packet, the average number of transmission attempts until the packet is transmitted successfully is $G/S = e^{2G}$. Thus, the average number of unsuccessful transmission attempts is $G/S - 1 = e^{2G} - 1$. If a collision occurs, the node reschedules the colliding packet for some random time in the future. Let the average rescheduling time be B (seconds). Each successful transmission attempt requires T seconds and each unsuccessful transmission attempt requires $T + B$ seconds on the average. Therefore, the average delay is given by

$$\begin{aligned}
 D &= T + (G/S - 1)(T + B) \\
 &= T + (e^{2G} - 1)(T + B)
 \end{aligned}
 \tag{3}$$

and in a normalized form

$$\mathcal{D} = 1 + (e^{2G} - 1)(1 + B/T)$$

With pure Aloha, even if the overlap in time between two transmitted packets is very tiny, both packets are destroyed. The slotted Aloha variation overcomes this drawback, and it is simply pure Aloha with a slotted channel. Thus, two (or more) packets can either overlap completely or do not overlap at all, and the vulnerable period is reduced to a single slot. In other words, a slot will be successful if and only if exactly one packet is transmitted in that slot. Therefore

$$S = gTe^{-gT} = Ge^{-G}$$

This relation is very similar to that of pure Aloha, except of increased throughput. Channel capacity is $1/e \approx 0.36$

and is achieved at $G = 1$. These results were first derived by Roberts [14]. Similar to the pure Aloha scheme, the normalized average delay for the slotted Aloha scheme is

$$\mathcal{D} = 1 + (e^G - 1)(1 + B/T)$$

3.2. Carrier-Sensing Protocols

The Aloha schemes exhibit fairly poor performance, which can be attributed to the “impolite” behavior of the nodes, namely, whenever one has a packet to transmit it does so without consideration of others. It is clear that in a shared environment even little consideration can benefit all. Consider a listen-be-fore-talk behavior wherein every node, before attempting any transmission, listens whether somebody else is already using the channel. If this is the case, the node will refrain from transmission to the benefit of all; its packet will clearly not be successful if transmitted; furthermore, disturbing another node will cause the currently transmitted packet to be retransmitted, possibly disturbing yet another packet.

The process of listening to the shared channel is not that demanding. Every node is equipped with a receiver anyway, and every node can monitor the channel because it is shared. Moreover, to detect another node’s transmission does not require receiving the information; it suffices to sense the carrier that is present when signals are transmitted. The carrier-sensing family of schemes is characterized by sensing the carrier and deciding according to it whether another transmission is ongoing.

Carrier sensing does not yield conflict-free operation. Suppose that the channel has been idle for a while and that two nodes concurrently generate a packet. Each will sense the channel, discover that it is idle, and transmit the packet to result in a collision. “Concurrently” here does not really mean at the very same time; if one node starts transmitting it takes some time for the signal to propagate and arrive at the other node. Hence concurrently actually means within a time window of duration equal to signal propagation time. The maximum propagation time in the network is τ , and its normalized version is a , an important parameter that affects the performance of carrier sensing schemes. The larger this quantity is, collisions are more likely and the performance becomes worse.

All the carrier sensing multiple access schemes share the same philosophy: when a node generates a new packet, the channel is sensed, and if found idle the packet is transmitted without further ado. When a collision takes place, every transmitting node reschedules a retransmission of the collided packet to some other time in the future (chosen with some randomization to avoid repeated collisions) at which time the same operation is repeated. The variations on the CSMA scheme are caused by the behavior of nodes that wish to transmit and find (by sensing) the channel busy. Most of the basic variations were introduced and analyzed by Kleinrock and Tobagi [18–20].

In the nonpersistent versions of CSMA (NP-CSMA) a node that generated a packet and found the channel busy refrains from transmitting the packet and behaves exactly as if its packet collided [i.e., it schedules (randomly) the

retransmission of the packet to some time in the future]. With NP-CSMA, there are situations in which the channel is idle although one or more nodes have packets to transmit. The 1-persistent CSMA (1P-CSMA) is an alternative to NP-CSMA because it avoids such situations by being a bit more greedy. This is achieved by applying the following rule. A node that senses the channel and finds it busy persists to wait and transmits as soon as the channel becomes idle. Consequently, the channel is always used if there is a node with a packet. With the 1-persistent scheme, a collision may occur not only because of nonzero propagation delays but also when two nodes become ready to transmit in the middle of another node's transmission. In this case, both nodes will wait until that transmission ends and will begin transmission simultaneously, resulting in a collision.

For slotted operation, CSMA schemes use time slot of duration τ seconds, which is usually much smaller than the slot size of duration T seconds, used with slotted Aloha. However, like slotted Aloha, all nodes using slotted CSMA schemes are forced to start transmission at the beginning of a slot.

Beside the ability to sense the carrier, some local-area networks (such as Ethernet) have an additional feature, namely, that nodes can detect interference among several transmissions (including their own) while transmission is in progress and abort transmission of their collided packets. If this can be done sufficiently fast, then the duration of an unsuccessful transmission would be shorter than that of a successful one, thus improving the performance of the scheme. Together with carrier sensing, this produces a variation of CSMA that is known as CSMA/CD (carrier sensing multiple access with collision detection). The operation of all CSMA/CD schemes is identical to the operation of the corresponding CSMA schemes, except that if a collision is detected during transmission, the transmission is aborted and the packet is scheduled for transmission at some later time. For Ethernet networks this random delay is doubled (at most 16 times) each time the packet collides—a scheme known as binary exponential backoff. To ensure that all network nodes indeed detect a collision when it occurs, a consensus reinforcement procedure is used. This procedure is manifested by jamming the channel with a collision signal for a duration of τ_{cr} seconds, which is usually much larger than the time necessary to detect a collision. We let $\gamma = \tau_{cr}/\tau$.

The analysis of the throughput of CSMA schemes is rather complicated. It is based on computations of average lengths of idle and transmission periods. For NP-CSMA, we have

$$S = \frac{gTe^{-g\tau}}{g(T + 2\pi) + e^{-g\tau}} = \frac{Ge^{-aG}}{G(1 + 2a) + e^{-aG}}$$

For slotted NP-CSMA, we have

$$S = \frac{aGe^{-aG}}{1 - e^{-aG} + a}$$

For 1P-CSMA, we have

$$S = \frac{gTe^{-g(T+2\tau)}[1 + gT + g\tau(1 + gT + g\tau/2)]}{g(T + 2\tau) - (1 - e^{-g\tau}) + 1 + g\tau e^{-gT + \tau}}$$

$$= \frac{Ge^{-G(1+2a)}[1 + G + aG(1 + G + aG/2)]}{G(1 + 2a) - (1 - e^{-aG}) + (1 + aG)e^{-G(1+a)}}$$

For slotted 1P-CSMA, we have

$$S = \frac{Ge^{-G(1+2a)(1+a-e^{-aG})}}{(1+a)(1 - e^{-aG}) + ae^{-G(1+a)}}$$

For nonpersistent CSMA/CD, we have

$$S = \frac{Ge^{-aG}}{Ge^{-aG} + \gamma aG(1 - e^{-aG}) + 2aG(1 - e^{-aG}) + 2 - e^{-aG}}$$

For slotted nonpersistent CSMA/CD, we have

$$S = \frac{Ge^{-aG}}{Ge^{-aG} + \gamma aG(1 - e^{-aG} - aGe^{-aG}) + (2 - e^{-aG} - aGe^{-aG})}$$

Figure 4 depicts the load throughput characteristics for the CSMA-type schemes.

3.2.1. Further Reading. Numerous variations on the environment under which the Aloha and CSMA schemes operate have been addressed in the literature (see, e.g., Refs. 3, 13, and 21–23). For instance, various packet length distributions were considered by Abramson [24] and Ferguson [25] for Aloha and by Tobagi and Hunt [26] and for CSMA.

The assumption that, whenever two or more packets overlap at the receiver, all packets are lost is overly pessimistic. In radio networks the receiver might correctly receive a packet despite the fact that it is time overlapping

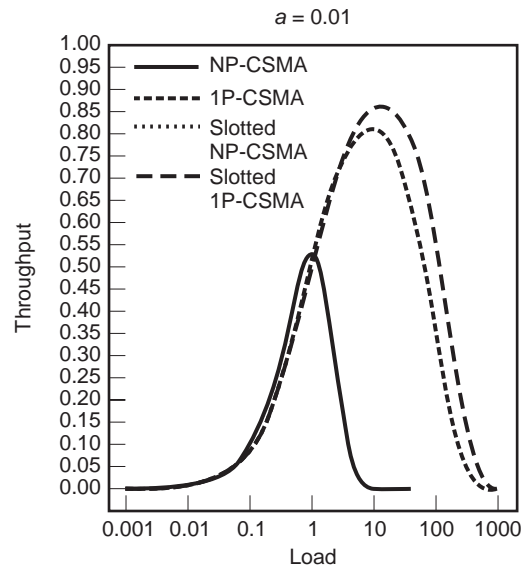


Figure 4. Throughput of CSMA versions.

with other transmitted packets. This phenomenon is known as capture and it can happen as a result of various characteristics of radio systems. Most studies [27,28] considered power capture (the phenomenon whereby the strongest of several transmitted signals is correctly received at the receiver). Thus, if a single high-powered packet is transmitted, then it is correctly received regardless of other transmissions. Hence, channel use increases.

Reservation schemes that allow contentions are designed to have the advantages of both the Aloha and the TDMA approaches. Examples of reservation schemes appear in Ref. 29, where the knowledge of the number of users is needed, or in Refs. 14 and 30, where they do not require this knowledge. Approximate analysis of a reservation Aloha protocol can be found in Lam [31].

Approximate analysis of the delay was presented by Ferguson [32] for Aloha and by Beurman and Coyle [33] for CSMA schemes. Instability issues of the Aloha protocol were first identified by Carleial and Hellman [34] and Lam and Kleinrock [35]. Later, similar issues were identified for the CSMA family of protocols by Tobagi and Kleinrock [20].

4. COLLISION RESOLUTION SCHEMES

The original Aloha scheme and its CSMA derivatives are inherently unstable in the absence of some external control. Looking into the philosophy behind the schemes, it is obvious that there is no sincere attempts to resolve collisions among packets as soon as they occur. Instead, the attempts to resolve collisions are always deferred to the future, with the hope that things will then work out, somehow, but they never do.

Another type of contention-based schemes with a different philosophy are collision resolution schemes (CRSs). In these schemes the efforts are concentrated on resolving collisions as soon as they occur. Moreover, in most versions of these schemes, new packets that arrive to the network are inhibited from being transmitted while the resolutions of collisions is in progress. This ensures that if the rate of arrival of new packets to the system is smaller than the rate at which collisions can be resolved (the maximal rate of departing packets—throughput), then the system is stable. The basic idea behind these schemes is to exploit in a more sophisticated manner the feedback information that is available to the nodes in order to control the retransmission process so that collisions are resolved more efficiently.

The most basic collision resolution scheme is called the binary-tree CRS (or binary-tree scheme) and was proposed by Capetanakis [36], Hayes [37], and Tsybakov and Mikhailov [38]. According to this schemes, when a collision occurs, in slot k , say, all nodes that are not involved in the collision wait until the collision is resolved. The nodes involved in the collision split randomly into two subsets, by (for instance) each flipping a coin. The nodes in the first subset, those that flopped 0, retransmit in slot $k+1$, whereas those that flipped 1 wait until all those that flipped 0 transmit their packets successfully. If slot $k+1$ is either idle or contains a successful transmission, the

nodes of the second subset (those that flipped 1) retransmit in slot $k+2$. If slot $k+1$ contains another collision, then the procedure is repeated (i.e., the nodes whose packets collided in slot $k+1$ flip a coin again and operate according to the outcome of the coin flipping, and so on). A node having a packet that collided (at least once) is backlogged.

The operation of the scheme can also be described by a binary tree in which every vertex corresponds to a time-slot. The root of the tree corresponds to the slot of the original collision. Each vertex of the tree also designates a subset (perhaps empty) of backlogged nodes. Vertices whose subsets contain at least two nodes indicate collisions and have two outgoing branches, corresponding to the splitting of the subset into two new subsets. Vertices corresponding to empty subsets or subsets containing one node are leaves of the tree and indicate an idle slot and a successful slot, respectively. For instance, consider a collision that occurs in slot 1. At this point it is neither known how many nodes nor who are the nodes that collided in this slot. Each of the colliding nodes flip a coin, and those that flipped 0 transmit in slot 2. By the rules of the scheme, no newly arrived packet is transmitted while the resolution of a collision is in progress, so that only nodes that collided in slot 1 and flipped 0 transmit in slot 2. Another collision occurs in slot 2, and the nodes involved in that collision flip a coin again. In this example, all the colliding nodes of slot 2 flipped 1 and therefore slot 3 is idle. The nodes that flipped 1 in slot 2 transmit again in slot 4, resulting in another collision and forcing the nodes involved in it to flip a coin once more. One node flips 0 and transmits (successfully) in slot 5, causing all nodes that flipped 1 in slot 4 to transmit in slot 6. In this example, there is one such node, and therefore slot 6 is a successful one. Now that the collision among all nodes that flipped 0 in slot 1 has been resolved, the nodes that flipped 1 in that slot transmit (in slot 7). Another collision occurs, and the nodes involved in it flip a coin. Another collision is observed in slot 8, meaning that at least two nodes flipped 0 in slot 7. The nodes that collided in slot 8 flip a coin and, as it happens, there is a single node that flipped 0, and it transmits (successfully) in slot 9. Then, in slot 10, transmit the nodes that flipped 1 in slot 8. There is only one such node, and its transmission is, of course, successful. Finally, the nodes that flipped 1 in slot 7 must transmit in slot 11. In this example, there is no such node; hence slot 11 is idle, completing the resolution of the collision that occurred in slot 7 and, at the same time, the one in the first slot.

It is clear from this example that each node, including those that are not involved in the collision, can construct the binary tree by following the feedback signals corresponding to each slot, thus knowing exactly when the collision is resolved. A collision is resolved when the nodes of the network know that all packets involved in the collision have been transmitted successfully. The time interval starting with the original collision (if any) and ending when this collision is resolved is called collision resolution interval (CRI). In the preceding example the length of the CRI is 11 slots.

The binary-tree protocol dictates how to resolve collisions after they occur. To complete the description of the

protocol, one must specify when newly generated packets are transmitted for the first time. One alternative, which is assumed all along (known as the obvious-access scheme), is that new packets are inhibited from being transmitted while a resolution of a collision is in progress. That is, packets that arrive to the system while a resolution of a collision is in progress, wait until the collision is resolved, at which time they are transmitted. In the example above all new packets arriving to the system during slots 1 through 11 are transmitted for the first time in slot 12.

Let L_n be the expected length of a CRI that starts with the transmission of n packets. From the operation of the scheme, it is clear that as long as the arrival rate of new packets into the system is smaller than the ratio n/L_n (for large n), the system is stable. When fair coins are used for splitting the users upon collisions, one can show that for every n

$$L_n \leq 2.886n + 1$$

yielding stable system for arrival rates that are smaller than 0.346.

The performance of the binary-tree protocol can be improved in two ways. The first is to speed up the collision resolution process by avoiding certain, avoidable, collisions. The second is based on the observation that collisions among a small number of packets are resolved more efficiently than collisions among a large number of packets. Therefore, if most CRIs start with a small number of packets, the performance of the protocol is expected to improve.

Consider again the example above. In slots 2 and 3 a collision is followed by an idle slot. This implies that in slot 2 all users (and there were at least two of them) flipped 1. The binary-tree protocol dictates that these users must transmit in slot 4, although it is obvious that this will generate a collision than can be avoided. The modified binary-tree protocol was suggested by Massey [39], and it eliminates such avoidable collisions by letting the users that flipped 1 in slot 2 in the preceding example, flip coins before transmitting in slot 4. Consequently, the slot in which an avoidable collision would occur is saved. In this case, fair coins yield a stable system for arrival rates smaller than 0.375, and biased coins increase this number up to 0.381.

When the obvious access is employed, it is very likely that a CRI will start with a collision among a large number of packets when the previous CRI was long. When the system operates near its maximal throughput, most CRIs are long; hence collisions among a large number of packets must be resolved frequently, yielding nonefficient operation. Ideally, if it were possible to start each CRI with the transmission of exactly one packet, the throughput of the system would have been 1. Because this is not possible, one should try to design the system so that in most cases a CRI starts with the transmission of about one packet. There are several ways to achieve this goal by determining a first-time transmission rule (i.e., when packets are transmitted for the first time). One way, suggested by Capetanakis [36], is to have an estimate on the number of

packets that arrived in the previous CRI and divide them into smaller groups, each having an expected number of packets on the order of one and handling each group separately. Another way, known as the epoch mechanism has been suggested by Gallager [40] and Tsybakov and Mikhailov [41]. According to this mechanism, time is divided into consecutive epochs each of length Δ slots. The i th arrival epoch is the time interval $[i\Delta, (i+1)\Delta]$. Packets that arrive during the i th arrival epoch are transmitted for the first time in the first slot after the collision among packets that arrived during the $(i-1)$ st arrival epoch is resolved. The parameter Δ is chosen to optimize the performance of the system. When $\Delta = 2.68$, the system is stable for arrival rates up to 0.429 if slots of sure collisions are not saved, and up to 0.462 if they are. A final enhancement of the epoch mechanism is to start a new epoch each time a collision is followed by two successful transmissions. This guarantees that each CRI will start with an optimal number of packets, and it yields the highest stable throughput known for multiple access systems—0.487.

4.1. Further Reading

Numerous variations of the environment under which collision resolution protocols operate have been addressed in the literature and excellent surveys on the subject appear in Refs. 42 and 43. Books by Bertsekas and Gallager [21] and Rom and Sidi [23] are also excellent sources on collision resolution protocols. Considerable effort has been spent on finding upper bounds to the maximum throughput that can be achieved in an infinite population model with Poisson arrivals and ternary feedback. The best upper bound known to date is 0.568 and is the work of Tsybakov and Likhanov [44]. Practical multiple access communication systems are prone to various types of errors. Collision resolution protocols that operate in the presence of noise errors, erasures, and captures have been studied in Refs. 45–49. Collision resolution protocols yielding high throughputs for general arrival processes (even if their statistics are unknown) were developed by Cidon and Sidi [50] and Greenberg et al. [51]. The expected packet delay of the binary-tree protocol has been derived by Fayolle et al. [52] and Tsybakov and Mikhailov [38]. Bounds on the expected packet delay of the algorithm with the epoch mechanism have been obtained in Refs. 41 and 53, and bounds on the packet delay distribution have been obtained in Refs. 54 and 55.

BIBLIOGRAPHY

1. J. Martin, *Communication Satellite Systems*, Prentice-Hall, Englewood Cliffs, NJ, 1978.
2. W. Stallings, *Data and Computer Communications*, Macmillan, New York, 1985.
3. J. F. Hayes, *Modeling and Analysis of Computer Communications Networks*, Plenum Press, New York, 1984.
4. I. Rubin, Access control discipline for multi-access communications channels: Reservation and TDMA schemes, *IEEE Trans. Inform. Theory* **IT-25**:516–536 (1979).

5. L. F. M. De Moraes and I. Rubin, Message delay for a TDMA scheme under a nonpreemptive priority discipline, *IEEE Trans. Commun.* **COM-32**:583–588 (1984).
6. A. Itai and Z. Rosberg, A golden ratio control policy for a multiple-access channel, *IEEE Trans. Autom. Control* **AC-29**:712–718 (1984).
7. M. Hofri and Z. Rosberg, Packet delay under the golden ratio weighted TDM policy in a multiple access channel, *IEEE Trans. Inform. Theory* **IT-33**:341–349 (1987).
8. R. Rom and M. Sidi, Message delay distribution in generalized time division multiple access (TDMA), *Probability Eng. Inform. Sci.* **4**:187–202 (1990).
9. L. Kleinrock and M. Scholl, Packet switching in radio channels: New conflict-free multiple access schemes, *IEEE Trans. Commun.* **COM-28**:1015–1029 (1980).
10. H. Takagi, *Analysis of Polling Systems*, MIT Press, Cambridge, MA, 1986.
11. H. Takagi, Queueing analysis of polling models, *ACM Comput. Surv.* **20**(1):5–28 (1988).
12. H. Levy and M. Sidi, Polling systems: Applications, modeling and optimization, *IEEE Trans. Commun.* **38**:1750–1760 (1990).
13. A. S. Tanenbaum, *Computer Networks*, 3rd ed., Prentice-Hall International Editions, Englewood Cliffs, NJ, 1996.
14. L. G. Roberts, ALOHA packet system with and without slots and capture, *Comput. Commun. Rev.* **5**(2):28–42 (1975).
15. I. Chlamtac, W. R. Franta, and K. D. Levin, BRAM: The Broadcast Recognizing Access Mode, *IEEE Trans. Commun.* **COM-27**:1183–1189 (1979).
16. N. Abramson, The ALOHA System—Another Alternative for Computer Communications, *Proc. Fall Joint Comput. Conf.* (1970), pp. 281–285.
17. G. Fayolle et al., The stability problem of broadcast packet switching computer networks, *Acta Informatica* **4**(1):49–53 (1974).
18. L. Kleinrock and F. A. Tobagi, Packet switching in radio channels: Part I—Carrier sense multiple-access modes and their throughput delay characteristics, *IEEE Trans. Commun.* **23**:1400–1416 (1975).
19. F. A. Tobagi and L. Kleinrock, Packet switching in radio channels: Part II—The hidden terminal problem in carrier sense multiple-access and the busy tone solution, *IEEE Trans. Commun.* **23**:1417–1433 (1975).
20. F. A. Tobagi and L. Kleinrock, Packet switching in radio channels: Part IV—Stability considerations and dynamic control in carrier sense multiple-access, *IEEE Trans. Commun.* **25**:1103–1119 (1977).
21. D. Bertsekas and R. Gallager, *Data Networks*, 2nd ed., Prentice-Hall International Editions, Englewood Cliffs, NJ, 1992.
22. J. L. Hammond and P. J. P. O'Reilly, *Performance Analysis of Local Computer Networks*, Addison-Wesley, Reading, MA, 1986.
23. R. Rom and M. Sidi, *Multiple Access Protocols; Performance and Analysis*, Springer-Verlag, New York, 1990.
24. N. Abramson, The throughput of packet broadcasting channels, *IEEE Trans. Commun.* **25**:117–128 (1977).
25. M. J. Ferguson, An approximate analysis of delay for fixed and variable length packets in an unslotted Aloha channel, *IEEE Trans. Commun.* **25**:644–654 (1977).
26. F. A. Tobagi and V. B. Hunt, Performance analysis of carrier sense multiple access with collision detection, *Comput. Networks* **4**(5):245–259 (1980).
27. J. J. Metzner, On improving utilization in Aloha networks, *IEEE Trans. Commun.* **24**:447–448 (1976).
28. N. Shacham, Throughput-delay performance of packet-switching multiple-access channel with power capture, *Perform. Eval.* **4**(3):153–170 (1984).
29. R. Binder, A dynamic packet switching system for satellite broadcast channels, *Proc. ICC'75*, (1975); pp. 41.1–41.5.
30. W. Crowther et al., A system for broadcast communication: Reservation-Aloha, *Proc. Int. Conf. Syst. Sci.*, (1973); pp. 371–374.
31. S. S. Lam, Packet broadcast networks—a performance analysis of the R-ALOHA protocol, *IEEE Trans. Comput.* **29**:596–603 (1980).
32. M. J. Ferguson, On the control, stability, and waiting time in a slotted Aloha, *IEEE Trans. Commun.* **23**:1306–1311 (1975).
33. S. L. Beuerman and E. J. Coyle, The delay characteristics of CSMA/CD networks, *IEEE Trans. Commun.* **36**:553–563 (1988).
34. A. B. Carleial and M. E. Hellman, Bistable behavior of ALOHA-type systems, *IEEE Trans. Commun.* **23**:401–410 (1975).
35. S. S. Lam and L. Kleinrock, Packet switching in a multicast broadcast channel: Dynamic control procedures, *IEEE Trans. Commun.* **23**:891–904 (1975).
36. J. I. Capetanakis, Tree Algorithm for Packet Broadcast Channels, *IEEE Trans. Inform. Theory* **25**:505–515 (1979).
37. J. F. Hayes, An adaptive technique for local distribution, *IEEE Trans. Commun.* **26**:1178–1186, (1978).
38. B. S. Tsybakov and V. A. Mikhailov, Free synchronous packet access in a broadcast channel with feedback, *Prob. Inform. Trans.* **14**(4):259–280 (1978).
39. J. L. Massey, *Collision Resolution Algorithms and Random-Access Communications Multi-User Communications Systems*, CISM Courses and Lectures Series (G. Longo, ed.), Springer-Verlag, New York, pp. 73–137, 1981 (also in UCLA Technical Report UCLA-ENG-8016, April 1980).
40. R. G. Gallager, Conflict resolution in random access broadcast networks, *Proc. AFOSR Workshop Commun. Theory Appl.*, Provincetown, Sept. 1978, pp. 74–76.
41. B. S. Tsybakov and V. A. Mikhailov, Random multiple packet access: Part-and-try algorithm, *Prob. Inform. Trans.* **16**:305–317 (1980).
42. R. G. Gallager, A perspective on multiaccess channels, *IEEE Trans. Inform. Theory* **31**:124–142 (1985).
43. B. S. Tsybakov, Survey of USSR contributions to multiple-access communications, *IEEE Trans. Inform. Theory* **31**:143–165 (1985).
44. B. S. Tsybakov and N. B. Likhonov, upper bound on the capacity of a random multiple access system, *Prob. Inform. Trans.* **23**(3):224–236 (1988).
45. I. Cidon and M. Sidi, The effect of capture on collision-resolution algorithms, *IEEE Trans. Commun.* **33**:317–324 (1985).
46. I. Cidon and M. Sidi, Erasures and noise in multiple access algorithms, *IEEE Trans. Inform. Theory* **33**:132–143 (1987).
47. I. Cidon, H. Kodesh, and M. Sidi, Erasure, capture and random power level selection in multiple-access systems, *IEEE Trans. Commun.* **36**:263–271 (1988).
48. M. Sidi and I. Cidon, Splitting protocols in presence of capture, *IEEE Trans. Inform. Theory* **31**:295–301 (1985).
49. N. D. Vvedenskaya and B. S. Tsybakov, Random multiple access of packets to a channel with errors, *Prob. Inform. Trans.* **19**(2):131–147 (1983).

50. I. Cidon and M. Sidi, Conflict multiplicity estimation and batch resolution algorithms, *IEEE Trans. Inform. Theory* **34**:101–110 (1988).
51. A. G. Greenberg, P. Flajolet, and R. E. Ladner, Estimating the multiplicities of conflicts to speed their resolution in multiple access channels, *J. ACM* **34**(2):289–325 (1987).
52. G. Fayolle et al., Analysis of a stack algorithm for random multiple-access communication, *IEEE Trans. Inform. Theory* **31**:244–254 (1985).
53. L. Georgiadis, L. F. Merakos, and P. Papantoni-Kazakos, A method for the delay analysis of random multiple-access algorithms whose delay process is regenerative, *IEEE J. Select Areas Commun.* **5**(6):1051–1062 (1987).
54. L. Georgiadis and M. Paterakis, Bounds on the delay distribution of window random-access algorithms, *IEEE Trans. Commun.* **COM-41**:683–693 (1993).
55. G. Polyzos and M. Molle, A queuing theoretic approach to the delay analysis for the FCFS 0.487 conflict resolution algorithm, *IEEE Trans. Inform. Theory* **IT-39**:1887–1906 (1993).

MULTIPLEXERS

RAAFAT R. MANSOUR
 University of Waterloo
 Waterloo, Ontario, Canada

1. INTRODUCTION

Multiplexers are used in communication system applications where there is a need to divide a wideband signal into a number of narrowband signals (channels). They are also employed to provide the opposite function, by combining several narrowband channels into a single wideband channel. Multiplexers are therefore known as *channelizers* or *combiners*. They find widespread use in many applications such as satellite payloads, wireless systems, and electronic warfare (EW) systems.

A two-channel version of the multiplexer is usually referred to as a *diplexer*, which is a component used in almost every communication wireless system. Figure 1 illustrates a simplified block diagram of the front end of a cellular base station. The purpose of the receive filter is to reject the out-of-band interference prior to low-noise

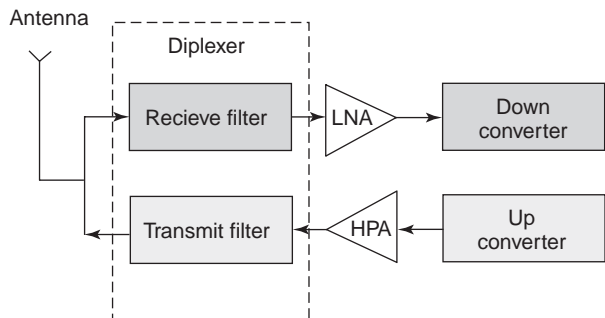


Figure 1. A simplified block diagram of the front end in base stations.

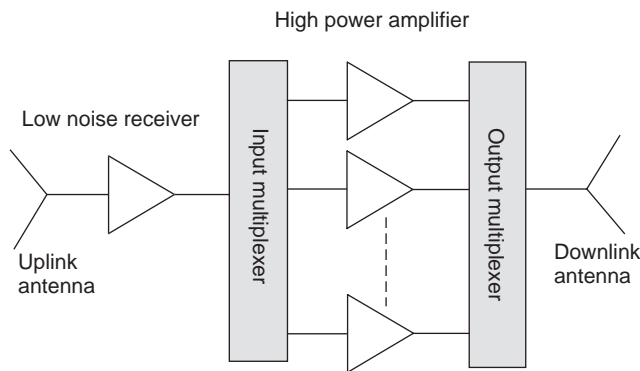


Figure 2. A simplified block diagram of a satellite payload.

amplification and downconversion. The transmit filter is used primarily to limit the out-of-band signals generated by the transmit portion of the base station. The transmit filter must have a very high level of rejection in the receive band in order to eliminate the possibility of intermodulation products being fed into the receiver through the common antenna. The receive and transmit filters are combined in the form of a diplexer to allow the receive and transmit functions to be used through a common antenna.

In satellite payloads, the input/output multiplexers are considered key components that determine the performance of the overall payload. Figure 2 illustrates a simplified block diagram of a conventional satellite payload system. It consists of receive/transmit antenna, low-noise receiver, input and output multiplexers and high-power amplifiers (HPAs). The payload acts basically as an orbiting repeater that receives, amplifies, and transmits. The practical constraints on high-power amplifiers require channelization of the received signal into a number of RF channels through the use of input multiplexers. The relatively narrowband channels are then amplified separately using high-power amplifiers and then recombined through the use of an output multiplexer for transmission back to ground. The typical number of filters for input multiplexers ranges from 36–60 filters, while the number of RF filters in output multiplexers typically ranges from 6 to 24 channels.

Multiplexers may also be used in wireless applications where the base station may need to transmit various frequency channels in different directions by using directive antennas. In this case, a multiplexer would be needed to separate the overall band transmitted into channels radiated in various directions. Another possible application of multiplexers in wireless base stations is in cases where the base station provides service to a number of independent operators who are licensed to operate only in specific channels within the band covered by the base station.

In EW systems, multiplexers may be used to construct switched filterbanks, which are essential building blocks in wideband receivers that operate in a hostile dense signal environment. In this case, switches are integrated with a multiplexer to allow the selection of a particular channel, allowing effectively the realization of a tunable filter with a variable bandwidth and a variable center frequency.

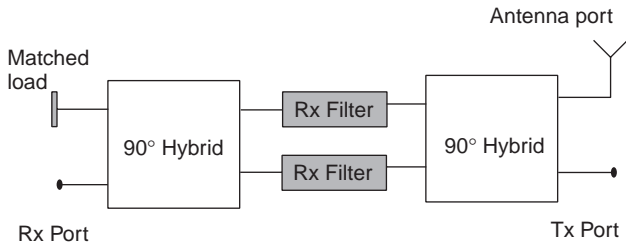


Figure 3. A diplexer implemented using the 90° hybrid approach.

2. DIPLEXER/DUPLEXER CONFIGURATIONS

The terms *diplexer* and *duplexer* have been used interchangeably by RF engineers for many years. The prefix “Di” is defined as twice or double, while the prefix “Du” is defined as two or dual. The term “Plex” is generated from the Latin word *plexus*, which means an interwoven combination of parts or elements. Thus, there is no basic difference in the meaning of the two terms. Traditionally, the term *duplexer* is used where the transmit and receive functions are combined in a single unit. A duplexer may be configured by coupling separate transmit and receive filters via a circulator or a switch or as an integrated unit with one common transmit/receive port as shown in Fig. 1. On the other hand, a diplexer is referred to as a unit that separates a composite signal into two separate channels. However, in view of IEEE publications on the subject since the early 1980s, one can clearly see that the two terms are often used interchangeably to describe the general case where the receive signal is isolated from transmit signal. In this article, we will use the term diplexer.

A simple form of a diplexer is shown in Fig. 3. It consists of two 90° hybrids and two identical filters. The filters are designed to operate within the receive band with enough isolation to reject the transmit band. The diplexer allows the use of one antenna for the receive (Rx) and transmit (Tx) signals. In view of the scattering matrix of the 90° hybrid [1], one can readily show that the signal received from the antenna port will be sent to the receive port while the signal from the transmit port will be reflected from the filters and will be directed to the antenna port. This diplexer configuration is bulky, requiring the use of two hybrids. However, it offers design simplicity and higher power handling capability.

Another approach to realize the diplexer is to use one filter for the receive channel and another one for the transmit channel. The two filters are then combined using a T junction. Figure 4a illustrates two coaxial filters combined together by a wire T junction, while Fig. 4b shows two iris waveguide bandpass filters combined together by a waveguide T junction. The interaction between the two filters in this case is very strong, requiring that the phase at the junction arms to be adjusted to make sure that the receive and transmit signals are integrated properly. In some applications such as radar systems, the receive and transmit signals do not exist simultaneously. In this case, a fast switch is used to replace the T junction, allowing the antenna to be connected to either the receive or the transmit circuits.

In diplexer applications, the insertion loss of the receive filter is an important factor since it contributes directly to the overall noise figure of the receiver that follows the diplexer. The insertion loss of the transmit filter is equally important since it impacts the power transmitted and the efficiency of the transmit system. A tradeoff exists among the loss, rejection and size of the filter. A high rejection, with a little effect on insertion loss and size, can be achieved by allocating several attenuation poles (rejection) in the appropriate band to increase the filter rejection. Typically, the insertion loss of the 90° hybrid approach is slightly higher than that of the T-junction combining approach. However, the 90° hybrid approach offers a higher power-handling capability. The reason is that the power-handling capability of the T-junction approach is determined by the power-handling capability of the transmit filter, while that of the hybrid approach is determined by the power handling capability of the 90° hybrid. Because of the buildup of energy inside the resonators, filters typically have less power-handling capability in comparison with 90° hybrids.

3. MULTIPLEXER CONFIGURATIONS

Since the early 1970s, several multiplexer configurations have been reported in the literature [2–17]. The most commonly used configurations are, hybrid-coupled multiplexers, directional filter multiplexers, circulator-coupled multiplexers, and manifold-coupled multiplexers. A summary of the advantages and disadvantages of these multiplexer configurations is given in Table 1 [9].

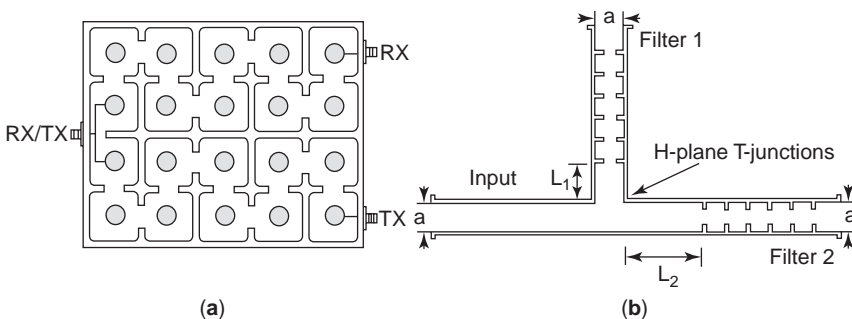


Figure 4. (a) A diplexer implemented using two coaxial filters and a wire T junction; (b) a diplexer implemented using two waveguide iris filters and T waveguide junction.

Table 1. A comparison between various multiplexer configurations

Manifold Multiplexer	Circulator Coupled MUX	Directional Filter MUX	Hybrid Coupled MUX
<i>Advantages</i>			
Requires one filter per channel	Requires one filter per channel	Requires one filter per channel	Amenable to modular concept
Most compact design	Simple to tune—no interaction between channel filters	Simple to tune—no interaction between channel filters	Simple to tune—no interaction between channel filters
Optimum if all present and future channels are assigned and installed at same time	Amenable to a modular concept	Amenable to modular concept	Total power in transmission modes as well as reflection mode is divided by the hybrid so that only 50% of the power is incident on each filter; power handling is thus increased and susceptibility to voltage breakdown is reduced
<i>Disadvantages</i>			
Tuning of the multiplexer can be time-consuming and expensive	Signals must pass in succession through circulators, incurring a loss per trip	Restricted to realize all-pole functions such as Butterworth and Chebyshev	Two identical filters and two hybrids are required for each channel
Not amenable to a flexible frequency plan; i.e., change of a channel frequency will require a new multiplexer design	Low-loss, high-power ferrite circulators are expensive	Difficult to realize bandwidths greater than 1%	Linewidths between hybrids and filters require precise balancing to preserve circuit directivity
	Higher level of passive intermodulation products than other configurations		The physical size and weight of the multiplexer is greater than other approaches

3.1. Hybrid-Coupled Approach

Figure 5 shows a layout of a hybrid-coupled multiplexer. Each channel consists of two identical filters and two identical 90° hybrids. The main advantage of the hybrid-coupled approach is that it is amenable to a modular concept minimizing the interaction between the channel filters. It also allows the integration of additional channels at a later date without disrupting the existing multiplexer design, which is a requirement in some systems. Another key advantage of this approach is that only half of the input power goes through each filter. Thus the filter design can be relaxed when using this type of multiplexer in high-power applications. Multiplexers employing this approach, however, have a relatively larger size since they require the use of two filters and two hybrids per channel. Another design consideration of such multiplexers is the phase deviation between the two filter paths that the two signals undergo before they add constructively at the

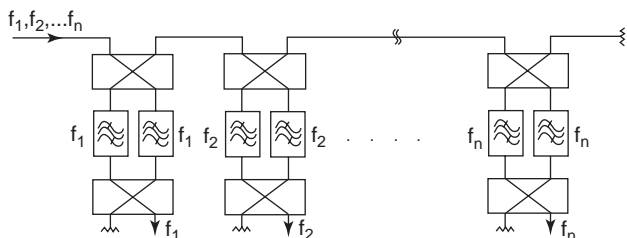


Figure 5. Layout of a hybrid-coupled multiplexer.

channel output. The structure therefore must be fabricated with tight tolerances to minimize the phase deviation, particularly in planar circuit applications where it is difficult to use tuning elements to balance the two paths.

3.2. Circulator-Coupled Approach

Each channel in this case consists of a channel-dropping circulator and one filter as shown in Fig. 6. This circulator-coupled approach has the same advantages as the hybrid-coupled approach in terms of amenability to modular integration and ease of design and assembly. The insertion loss of the first channel is the sum of the insertion loss of the channel filter as well as the insertion loss of the circulator. The subsequent channels exhibit a relatively higher loss due to the insertion loss incurred during each trip through the channel dropping circulators. Figure 7 shows a photo of a four-channel multiplexer employing four channel filters [14]. It consists of a stack of four circulators connected to stack of four filters by cables.

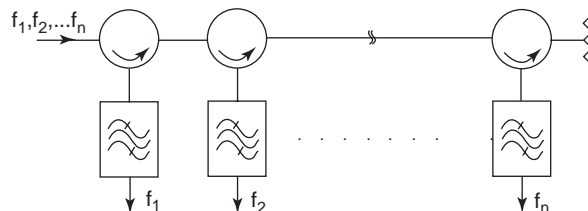


Figure 6. A circulator-coupled multiplexer.

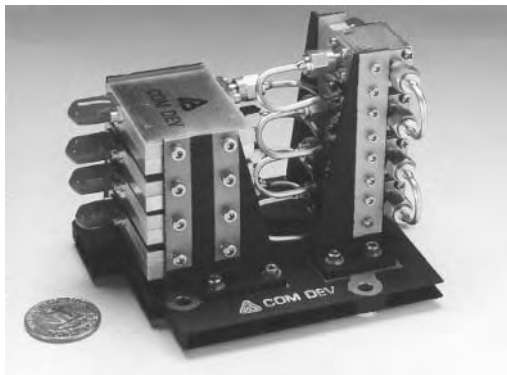


Figure 7. A four-channel circulator-coupled multiplexer [14].

3.3. Directional Filter Approach

Figure 8 illustrates a layout of a multiplexer realized by connecting directional filters in series. A directional filter is a four-port device where one port is terminated in a load. The other three ports of the directional filter essentially act as a circulator connected to a bandpass filter. Power incident at one port emerges at the second port with a bandpass frequency response, while the reflected power from the filter emerges at the third port. Directional filters, however, do not require the use of ferrite circulators. Figures 9a and 9b illustrate two possible approaches for realizing directional filters in waveguide and microstrip respectively [2]. The waveguide directional filter is realized by coupling rectangular waveguides operating in TE₁₀ modes to a circular waveguide filter operating in TE₁₁ modes. The microstrip version consists of one wavelength ring resonators coupled to one another and to two transmission lines. This multiplexing approach has the same advantages as the hybrid-coupled and circulator-coupled approaches. It is however limited to narrowband applications.

3.4. Manifold-Coupled Approach

The manifold-coupled approach shown in Fig. 10 is viewed as the optimum choice as far as miniaturization and absolute insertion loss are concerned. However, since interaction between filters on the manifold must be taken into account, manifold-coupled multiplexers are not amenable to a flexible frequency plan. Any changes in one of the channels will require a new multiplexer design. Moreover, as the number of channels increases, this approach becomes more difficult to implement. The manifold coupled multiplexer shown in Fig. 10 acts as a channelizer. It should be mentioned that the same configuration can be used as a combiner. Figure 11 is a photo of a four-channel multiplexer employing a waveguide manifold and four

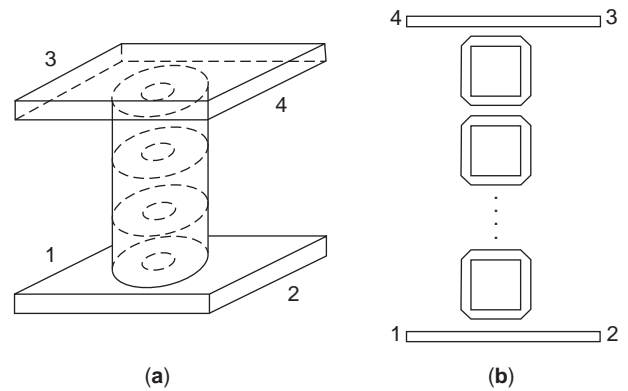


Figure 9. (a) A waveguide directional filter; (b) a microstrip directional filter.

dual-mode circular waveguide filters. The same figure also shows a miniature multiplexer employing a coaxial manifold and superconductive filters [17]. The manifold-coupled concept can be implemented as well in planar circuits as shown in Fig. 12, where three microstrip filters are integrated with a microstrip manifold [14]. In this particular case, one of the channels is connected directly to the manifold.

4. MULTIPLEXER DESIGN

The design of circulator-coupled multiplexers and hybrid-coupled multiplexers basically reduces down to the design of the individual channel filters. The same can be also stated for directional filter multiplexers. However, for the manifold-coupled multiplexer the interaction between the channel filters has to be taken into consideration over the whole band of operation. Manifold-coupled multiplexers can be built with non-contiguous channels where there is a frequency guardband between the channels. For such multiplexers, channel interaction is less and, as a consequence, their design and implementation is easier. However, in order to fully utilize the frequency spectrum, multiplexers are usually built with contiguous channels where there is a crossover between the adjacent channels at the 3-dB levels. The interaction between the channels for the contiguous case is obviously much stronger than the noncontiguous case, and the design of the channel filters must include the loading effects from adjacent channels as well as the loading effects of the manifold itself.

In designing manifold-coupled multiplexers, one can start with doubly terminated filters or singly terminated

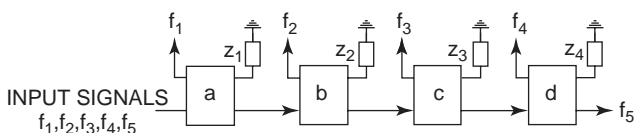


Figure 8. A directional filter multiplexer.

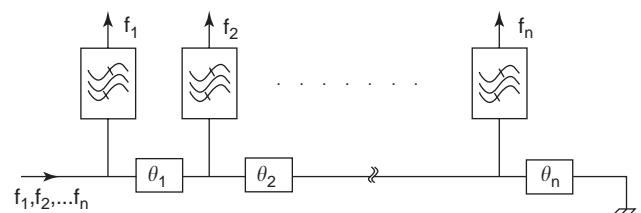


Figure 10. A manifold-coupled multiplexer.

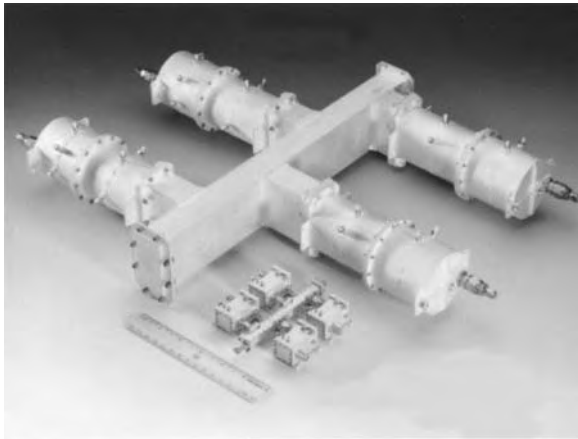


Figure 11. A C-band four-channel waveguide multiplexer in comparison with a four-channel multiplexer implemented using superconductor technology [17].

filters. Doubly terminated filters are generally used when designing noncontiguous multiplexers, whereas singly terminated filters are used for contiguous multiplexers. The doubly terminated filters are standalone filters, which are designed to terminate in loads at both ends. The singly terminated filters are synthesized to have a load only at one end and will only function as a filter if placed on the manifold. While several synthesis techniques have been published on the design manifold-coupled multiplexers [2–6], the focus since the early 1990s has been on the use of computer optimization.

To illustrate the design concept of manifold-coupled multiplexers, we consider the generalized filter network shown in Fig. 13, which is represented by a coupling matrix in the form

$$M = \begin{bmatrix} M_{11} & M_{12} & \dots & M_{1n} \\ M_{21} & M_{22} & \dots & M_{2n} \\ \vdots & & & \vdots \\ M_{n1} & M_{n2} & \dots & M_{nn} \end{bmatrix} \quad (1)$$

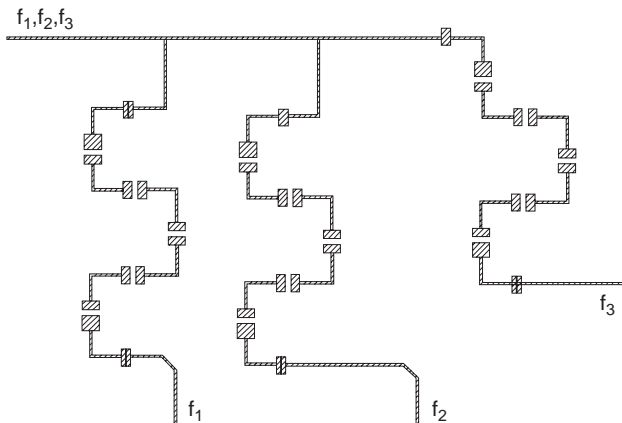


Figure 12. A three-channel multiplexer [14].

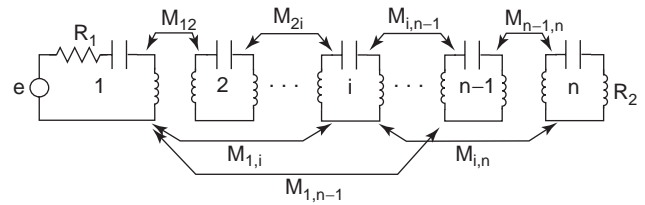


Figure 13. Coupling matrix representation of microwave filters.

where M_{ij} represents the coupling between resonators i and j . The diagonal elements relate to the resonance frequencies of the individual resonators and are zeros in the case of synchronously tuned filters. Following the analysis described in Ref. 18, one can obtain the scattering parameters of the filter in terms of coupling elements:

$$S_{21} = -2j\sqrt{R_1 R_2} [A^{-1}]_{n1} \quad (2)$$

$$S_{11} = 1 + 2jR_1 [A^{-1}]_{11} \quad (3)$$

where

$$A = \lambda I - jR + M \quad (4)$$

$$\lambda = \frac{f_0}{BW} \left(\frac{f}{f_0} - \frac{f_0}{f} \right) \quad (5)$$

where I is the identity matrix and R is a matrix with all elements zero, except $R_{11} = R_1$ and $R_{nn} = R_2$.

Consider the N -channel multiplexer shown in Fig. 14. The manifold consists of N T junctions connected in cascade and is terminated by a short circuit. The filters are spaced on the manifold and by $L(1), L(2), L(3) \dots L(N)$ and are placed away from the T junction by $W(1), W(2), W(3) \dots W(N)$ as shown in Fig. 14. With the knowledge of the scattering matrix of the T junction and the scattering matrices of the individual filters, one can use the generalized multiport technique given in Ref. 19, to calculate the overall scattering matrix of the multiplexer. Alternatively, the Y -parameter analysis given in Ref. 7 can be used to calculate the overall scattering matrix of the

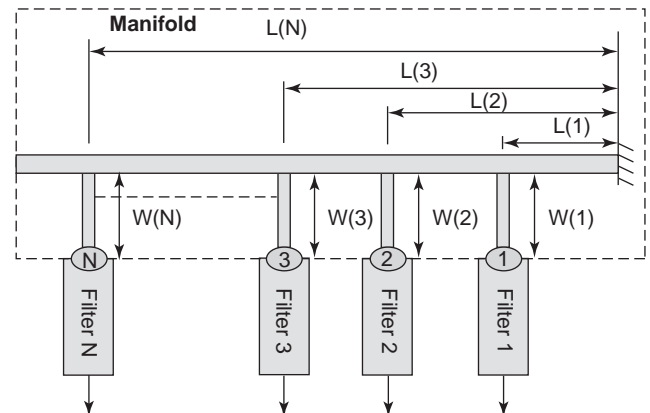


Figure 14. A layout of manifold-coupled multiplexer having N channels.

multiplexer. Our design objective is to find the manifold physical dimensions $L(1), L(2), L(3) \cdots L(N)$ and $W(1), W(2), W(3) \cdots W(N)$, as well as the coupling matrix of each of the N filters.

4.1. Noncontiguous Band Multiplexer

The design steps for the noncontiguous multiplexer given in this article are similar to those reported in Ref. 7, they can be summarized as follows:

Step 1 (Initial Dimensions). A good starting point for the noncontiguous manifold coupled multiplexer is to use doubly terminated filters; that is, the individual filters are designed as “standalone” filters to meet the bandwidth and return loss requirements. The coupling matrices for these filters can then be synthesized using Ref. 18. Equations (2)–(5) can then be used to calculate the scattering matrices of the filters.

Let $W(1) = W(2) = W(3) \cdots W(N) = W_0$ where W_0 is the minimum spacing that would allow the physical implementation of the channel filters on the manifold. Set $W_0 = 0$, if the channel filters can be attached directly to the manifold. Place the filters on the manifold such that the lowest frequency filter is closer to the short-circuited end of the manifold. Set the initial spacings L values according to:

$$L(0) = 0, L(k) - L(k - 1) = \lambda_{gk} / 2 \quad (6)$$

for $k = 1, 2, \dots, N$

where λ_{gk} is the guide wavelength at the center frequency f_{0k} of filter k .

Step 2 (Multiplexer Response). Using the given filter spacings L and the scattering matrices of the standalone filters, compute the frequency response of the multiplexer

by applying the generalized multiport analysis given in Ref. 19. If the multiplexer response meets the requirement, the design is complete and obviously nothing else needs to be done. Otherwise, find the filter j that satisfies the following:

$$|\rho(f_{0j})| = \max |\rho(f_{0k})| \text{ for } k = 1, 2, \dots, N \quad (7)$$

The filter j is basically the filter that has the worst return loss at the center frequency.

Step 3 (Filter Allocation). Change the spacing $L(j)$ of the filter according to the following rule. The filter is moved closer to the short circuit if a better return loss occurs at a frequency lower than midband frequency, and vice versa. The rule can be written as

$$\text{If } |\rho(f_{0j} - \Delta)| < |\rho(f_{0j})|, \text{ then} \quad (8)$$

$$L(j) = L(j) + \lambda_{gj} [1 - \lambda_1 / \lambda_{gj}]$$

$$\text{If } |\rho(f_{0j} + \Delta)| < |\rho(f_{0j})|, \text{ then} \quad (9)$$

$$L(j) = L(j) + \lambda_{gj} [1 - \lambda_2 / \lambda_{gj}]$$

where λ_1 and λ_2 are the guide wavelengths calculated at $(f_{0j} - \Delta)$ and $(f_{0j} + \Delta)$, respectively, and Δ is the filter bandwidth [7].

Step 4 (Iterations). Repeat steps 2 and 3 for a number of iterations. Typically this process converges, quickly leading to a multiplexer response with well-defined channels but with an input/output return loss that is the range of 8–12 dB (Fig. 15).

Step 5 (Multiplexer Optimization). The multiplexer performance can be improved by applying computer optimization. The optimization variables in this case would be

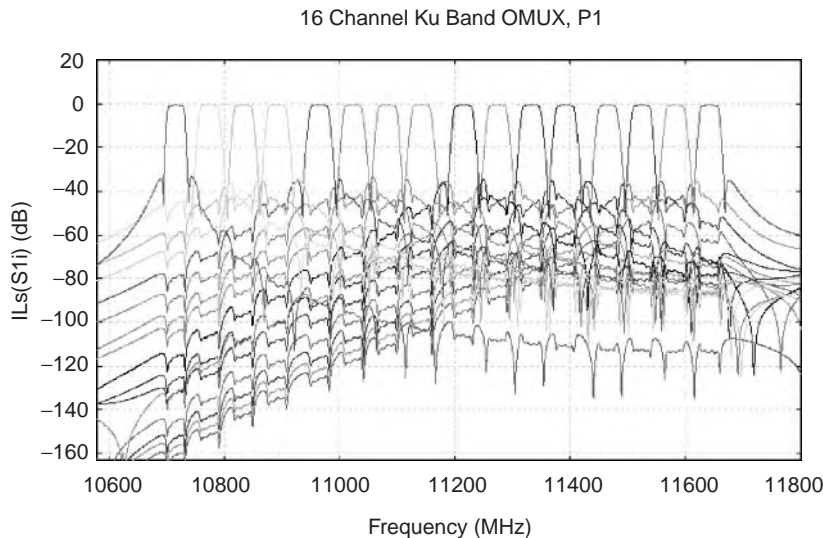


Figure 15. The performance of a 16-channel noncontiguous multiplexer designed using doubly terminated filters. (This figure is available in full color at <http://www.mrw.interscience.wiley.com/erfme>.)

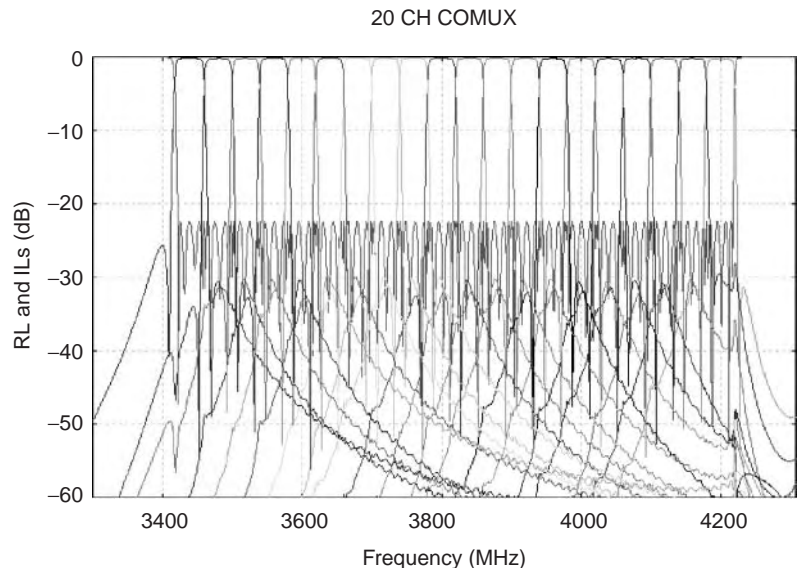


Figure 16. The optimized performance of a 20-channel contiguous multiplexer. (This figure is available in full color at <http://www.mrw.interscience.wiley.com/erfme>.)

$L(1), L(2), \dots, L(N)$ as well as $W(1)W(2), \dots, W(N)$. Typically, such a process leads to a multiplexer response that is very close to the optimum solution. Figure 16 shows a typical response of a noncontiguous three-channel multiplexer designed by using doubly terminated filters.

Step 6 (Multiplexer Fine Tuning). Fine tuning of the multiplexer requires optimization of all manifold physical dimensions L s and G s as well as the first few coupling elements of the filters (R_1, M_{12}). The initial values for the optimization variables could be the L and W values obtained from step 5 and the coupling matrices of the doubly terminated filters.

Step 7 (Overall Multiplexer Physical Dimensions). Once the optimized filter coupling elements are determined, the filter physical dimensions can be readily obtained. The problem reduces basically to the physical realization of filters for a given coupling matrix. An example for such realization is given in Refs. 21–23 for dielectric resonator filters.

The multiplexer design can certainly be achieved by skipping steps 2–4 and only applying steps 1, 5, 6, and 7, that is, to rely completely on computer optimization to achieve the goal. We have included steps 2–4 to illustrate that a reasonable performance in the case of noncontiguous multiplexers can be obtained by simply using manual tuning (on the computer) of the manifold spacings.

4.2. Design of Contiguous Band Multiplexers

The use of doubly terminated filters for the contiguous band multiplexer with an initial spacing of $\lambda/2$ does not usually lead to an acceptable response that can be reasonably tuned manually as the case of noncontiguous multiplexers. Two options can be followed in this case:

Option 1. Use doubly terminated filters and rely on computer optimization for both rough tuning and fine tuning. In some cases, it may be difficult to optimize the multiplexer since the starting point is usually far away from the final solution. In addition, it may lead to an inferior design in terms of group delay and loss variations. This design approach however may converge to the optimum solution by intelligently selecting the parameters to be optimized.

Option 2. Use singly terminated filter designs based on the synthesis procedure given in Ref. 20 or Refs. 2–6. Then use computer optimization to fine-tune the filter coupling elements as well as manifold physical dimensions. Figure 16 shows the performance of a 20-channel contiguous multiplexer [24] designed using option 2.

A detailed description of a design procedure for contiguous-band multiplexers is given in Ref. 25.

BIBLIOGRAPHY

1. D. Pozar, *Microwave Engineering*, Wiley, New York, 1998.
2. G. Matthaei, L. Young, and M. T. Jones, *Microwave Filters, Impedance Matching Networks and Coupling Structures*, Artech House, Norwood, MA, 1985.
3. J. D. Rhodes and R. Levy, A generalized multiplexer theory, *IEEE Trans. Microwave Theory Tech.* **MTT-27**:99–110 (1979).
4. J. D. Rhodes and R. Levy, Design of general manifold multiplexers, *IEEE Trans. Microwave Theory Tech.* **MTT-27**:111–123 (1979).
5. E. G. Cristal and G. L. Matthaei, A technique for the design of multiplexers having contiguous channels, *IEEE Trans. Microwave Theory Tech.* **MTT-12**:88–93 (Jan. 1964).
6. G. L. Matthaei and E. G. Cristal, Multiplexer channel separating units using interdigital and parallel coupled filters, *IEEE Trans. Microwave Theory Tech.* **MTT-13**:328–334 (March 1965).

MULTIRESOLUTION TECHNIQUE

7. A. E. Atia, Computer aided design of waveguide multiplexers, *IEEE Trans. Microwave Theory Tech.* **MTT-22**:322–336 (March 1974).
8. C. M. Kudsia, K. R. Ainsworth, and M. V. O'Donovan, Microwave filters and multiplexing networks for communication satellites in 1980s, AIAA, April 1980.
9. C. M. Kudsia et al., A new type of low loss 14 GHz high power combining network, *Proc. 9th European Microwave Conf.*, UK, Sept. 1979.
10. D. Doust et al., Satellite multiplexing using dielectric resonator filters, *Microwave J.* **32**(12):93–166 (Dec. 1989).
11. C. Kudsia, R. Cameron, and W. C. Tang, Innovation in microwave filters and multiplexing networks for communication satellite systems, *IEEE Trans. Microwave Theory Tech.* **MTT-40**:1133–1149 (June 1992).
12. S. Ye and R. R. Mansour, Design of manifold-coupled multiplexers using superconductive lumped element filters, *IEEE, MTT IMS*, 1994, pp. 191–194.
13. M. Guglielmi, Simple CAD procedures for microwave filters and multiplexers, *IEEE Trans. Microwave Theory Tech.* **MTT-42**:1347–1352 (July 1994).
14. R. R. Mansour et al., Design considerations of superconductive input multiplexers for satellite applications, *IEEE Trans. Microwave Theory Tech.* **MTT-44**:1213–1228 (July 1996).
15. G. Matthaei, S. Rohlfing, and R. Forse, Design of HTS lumped element manifold-type microwave multiplexers, *IEEE Trans. Microwave Theory Tech.* **MTT-44**:1313–1320 (July 1996).
16. R. R. Mansour et al., A 60 channel superconductive input multiplexer integrated with pulse-tube cryocoolers, *IEEE Trans. Microwave Theory Tech.* **MTT-48**(7):1171–1180 (July 2000).
17. R. R. Mansour, S. Ye, V. Dokas, B. Jolley, W. C. Tang, and C. Kudsia, System integration issues of high power HTS output multiplexers, *IEEE Trans. Microwave Theory Tech.* **MTT-48**:1199–1208 (July 2000).
18. A. E. Atia and A. E. Williams, Narrow band waveguide filters, *IEEE Trans. Microwave Theory Tech.* **MTT-20**:258–265 (April 1972).
19. K. C. Gupta, *Computer-Aided Design of Microwave Circuits*, Artech House, Dedham, MA, 1981.
20. R. J. Cameron, General coupling matrix synthesis methods for Chebyshev filtering functions, *IEEE Trans. Microwave Theory Tech.* **47**(4) (April 1999).
21. R. R. Mansour et al., Quasi dual mode resonators, *IEEE Trans. Microwave Theory Tech.* **MTT-48**:2476–2482 (Dec. 2000).
22. S. W. Chen and K. A. Zaki, A novel coupled method for dual-mode dielectric resonators and waveguide filters, *IEEE Trans. Microwave Theory Tech.* **38**(12):1885–1893 (Dec. 1990).
23. Y. Hui-Wen, K. A. Zaki, A. E. Atia, and R. Hershig, Full wave modeling of conducting posts in rectangular waveguides and its applications to slot coupled combline, *IEEE Trans. Microwave Theory Tech.* **43**(12):2824–2830 (Dec. 1995).
24. M. Yu, EM based smart design techniques for filters and multiplexers, paper presented at IEEE-IMS workshop on comparison of modern filter design techniques, Fort Worth, TX, June 2004.
25. R. G. Egri, A. E. Williams, and A. E. Atia, A contiguous-band multiplexer design, *IEEE MTT-S Int. Microwave Symp., Digest*, May 1983, pp. 86–88.

YINCHAO CHEN
 University of South Carolina
 Columbia, South Carolina
 QUNSHENG CAO
 University of Minnesota
 Minneapolis, Minnesota
 RAJ MITTRA
 Pennsylvania State University
 University Park, Pennsylvania

1. INTRODUCTION

The multiresolution time-domain (MRTD) scheme is a time-domain Maxwell solver based on electromagnetic field expansions in terms of scaling and wavelet functions [1,2], and has been extensively applied to various electromagnetic engineering applications [1–13]. The technique promises to significantly reduce the requirements on computational space and CPU time while at the same time it presents a unified field expansion structure that includes the finite-difference time-domain (FDTD) method and its higher-order versions. The MRTD scheme has been successfully applied to the analysis of fundamental guided-wave structures, microwave devices, scattering targets, and antenna applications. However, there are challenging issues that often hinder the implementation of the MRTD scheme for practical applications. For example, we cannot truncate a perfectly electric conducting (PEC) boundary by specifying a tangential electric field to zero for shielded structures, due to the coupling between cells resulting from high-order expansions of fields; another difficulty is that the orthogonal relations among scaling and wavelet basis functions are corrupted in an inhomogeneous region. This leads to great complexities when deriving field update equations for a structure with different materials that must be systematically solved in order to develop a generalized Maxwell MRTD solver.

In this article we begin by reviewing the foundation of the MRTD scheme—the multiresolution analysis (MRA), and then exploring the properties of the scaling functions and wavelets [14–28]. Also, we demonstrate the applications of the MRTD technique by analyzing a transverse electromagnetic (TEM) wave propagation in a dielectric layered stratified space and an integrated microwave circuit, which can be extended to solve electromagnetic engineering problems of general nature.

2. MULTIRESOLUTION ANALYSIS

This section will briefly present the fundamental concepts of the MRA, which serves as the conceptual foundation for the MRTD. To better understand the basic concept behind the definition of the MRA, we start by analyzing the structure of an electromagnetic field signal. In general, such a signal can be viewed as a composition of a smooth background embellished by fluctuation noises or details. The distinction between the smooth part and the details is

determined by the level of resolution. Therefore, at a given resolution level, a signal can be approximated by ignoring all the effects of fluctuations above that level. To better approximate the signal, we can progressively increase resolution levels and thus successively add finer detail to a coarse description of the signal. Eventually, when the resolution goes to infinity, we represent the original signal without any approximation error.

We can formulate the intuitive description above more precisely as follows. The resolution level, labeled by an integer s , has a corresponding scale set to 2^{-s} . The approximation of a signal $f(t)$ at level s is denoted by $f_s(t)$. When we increase the level to $s + 1$, we need to add the details, denoted by $d_s(t)$, to the signal at this new level in order to obtain the modified approximation, that is, $f_{s+1}(t) = f_s(t) + d_s(t)$. By repeating this procedure, we can recover the original signal $f(t)$ at infinity:

$$f(t) = f_s(t) + \sum_{k=s}^{\infty} d_k(t) \tag{1}$$

From a global perspective of the signal space, (1) indicates that we need to consider two sequences of subspaces $\{W_s\}$ and $\{V_s\}$, such that every $f(t)$ can be approximated at the resolution level $s + 1$ with $f_s(t)$ in the scale space V_s and $d_s(t)$ in the detail space W_s . Those subspaces will be the basic objects in our definition.

Our signal space is now considered as the space of square-integrable functions. Here we define a sequence of the resolution levels labeled by integers such that all details of signals on scales smaller than 2^{-s} will be ignored at the level s . Also, we define V_s as the subspace of the functions that contain the signal information down to the scale 2^{-s} . Formally, an MRA is just a sequence of V_s , which satisfies certain mathematical conditions.

Instead of beginning with a formal definition of MRA, we will first explain the meanings behind those fundamental conditions. We will clarify five fundamental properties that an MRA should possess.

2.1. Subspace Structure

The subspaces V_s should be constructed in a nested structure; information at the resolution level s is necessarily included in information at a higher resolution level; therefore, $V_s \subset V_{s+1}$ for all s . The difference between $f_{s+1}(t)$ and $f_s(t)$, denoted by $d_s(t) = f_{s+1}(t) - f_s(t)$, is the additional information on scales between 2^{-s} and $2^{-(s+1)}$. Since the best approximation in terms of V_s is given by the projection of the function onto V_s , we may expect that $d_s(t) \perp f_s(t)$. Accordingly, we can decompose the subspace V_{s+1} as $V_{s+1} = V_s \oplus W_s$, where W_s is the detail space at the resolution level s and is orthogonal to V_s , specifically, $W_s \perp V_s$. Repeating the decomposition, we obtain

$$V_{s+1} = W_s \oplus V_s = W_s \oplus W_{s-1} \oplus V_{s-1} = \dots = W_s \oplus W_{s-1} \oplus W_{s-2} \oplus \dots \oplus W_{s-s'} \oplus V_{s-s'} \tag{2}$$

These subspaces are mutually orthogonal. In fact, since $W_s \perp V_s$, we see that W_s is orthogonal to any subspace of V_s .

Since for $s' < s$, both $V_{s'}$ and $W_{s'}$ are contained in V_s and we thus have $W_s \perp V_{s'}$, and $W_s \perp W_{s'}$ when $s \neq s'$. In other words, any two detail spaces at different resolutions are orthogonal, and the detail space W_s is orthogonal to an approximation space $V_{s'}$ only when the detail space is at a higher resolution level.

2.2. Resolution of Functions

In the MRA, we describe all square-integrable functions at the finest resolution and only the zero function at the coarsest level. More precisely, as the resolution increases, we include an increasing number of details. As the resolution goes to infinity, the approximation can approach any original signal in the entire initial space $L^2(R)$. In other words, $\lim_{s \rightarrow \infty} V_s = \cup_s V_s$ should be dense in $L^2(R)$. On the other hand, as the resolution gets coarser, we remove more and more details of the signal. When $s \rightarrow -\infty$, only constant functions survive. Since functions have to be square-integrable, the zero function will be the only one left, that is, $\lim_{s \rightarrow -\infty} V_s = \cap_s V_s = \{0\}$.

2.3. Dilation of Function

This scale or dilation invariance of the space V_s is an important feature of the MRA. More explicitly, all V_s should be scaled versions of the central space V_0 . In fact, if a function $f(t)$ is in the space V_s , then $f(t)$ contains no details or fluctuations of scales smaller than 2^{-s} . Since $f(2t)$ is a function obtained from $f(t)$ with a squeezing factor of 2, it contains no details at scales smaller than $2^{-(s+1)}$. Therefore, $f(2t)$ is in V_{s+1} . Conversely, if $f(2t)$ is in V_{s+1} , then, by similar reasoning, $f(t)$ is in the space V_s . Therefore, $f(t) \in V_s \Leftrightarrow f(2t) \in V_{s+1}$.

2.4. Translation of Function

The translation or shift invariance of the space V_s is another important feature of the MRA. If we have a function $f(t) \in V_0$ and define $T_k f(t) = f(t - k)$, where $k \in Z$, then it is clear that the resolution level of $T_k f(t)$ should not change at all. Therefore, we require that V_0 be integral translation-invariant, that is, $T_k(V_0) \subset V_0$ for every integer k . Note that these properties yield the following result—if $f(t) \in V_0$, then $f(2^j t - k) \in V_j$ for all $k \in Z$.

2.5. Scaling Basis Functions

The final and the most important property we describe is the existence of a function ϕ whose set of integral translations forms a Riesz basis of the space V_0 [27]. The scale invariance condition then implies that $\{\phi(2t - k)\}_{k \in Z}$ forms a Riesz basis of V_1 . More generally, if we define $\phi_{s,k}(t) = 2^{s/2} \phi(2^s t - k)$, then $\{\phi_{s,k}(t)\}_{k \in Z}$ forms a Riesz basis of V_s . The function ϕ , which generates basis functions for all V_s , is called a *scaling function* of the MRA. This key feature is similar to the function $e^{j\omega t}$ that we use in Fourier analysis, where $e^{j\omega t}$ is the only function needed to generate an orthonormal basis.

On the basis of the preceding discussion, we now give the formal definition as follows. An MRA in $L^2(R)$ is

defined as a set of closed subspace V_s with $s \in \mathbb{Z}$ such that

1. $\dots \subset V_{-1} \subset V_0 \subset V_1 \subset \dots \subset L^2(\mathbb{R})$, that is, $V_s \subset V_{s+1}$ for all $s \in \mathbb{Z}$.
2. $\bigcap_{s=-\infty}^{+\infty} V_s = \{0\}$ and $\bigcup_{s=-\infty}^{+\infty} V_s$ is dense in $L^2(\mathbb{R})$.
3. $f(t) \in V_s$ if and only if $f(2t) \in V_{s+1}$.
4. If $f(t) \in V_0$, then $f(t-k) \in V_0$.
5. There exists a function $\phi(t) \in V_0$, called a *scaling function*, such that the set $\{\phi(t-k) | k \in \mathbb{Z}\}$ is a Riesz basis of V_0 .

If a scaling function actually generates an orthonormal basis, then we refer it to as an *orthonormal* scaling function. While the orthonormal bases are desirable, the orthogonality will strictly limit the possible scaling functions that we can use in practice. Therefore, a generalized orthonormal basis in the definition offers us greater flexibility. On the other hand, we can almost always use an orthogonalization procedure to produce an orthonormal scaling function from a Riesz scaling function, such that they generate the same V_s .

3. SCALING FUNCTIONS AND WAVELETS

The function $\phi(t)$ in the MRA definition is also called a father scaling function, as it generates bases for all V_s . In fact, based on the properties of the MRA, the sequence $\{\phi_{s,l}(t) = 2^{s/2} \phi(2^s t - l) | l \in \mathbb{Z}\}$ forms a Riesz basis of V_s for all s . It is clear from the definition that the scaling function plays a key role in MRA applications.

Since V_0 is contained in V_1 , we can represent $\phi(t)$ as a linear combination of the Riesz basis of V_1 :

$$\phi(t) = \sqrt{2} \sum_l h_l \phi(2t - l) \tag{3}$$

This is often called the “refinement” equation or the “dilation” equation. It plays a very important role in both the MRA theory and its applications. For example, it provides a way to construct fast algorithms to evaluate a scaling function at dyadic points [28]. This is often enough in many applications and is particularly useful when we do not know the scaling function itself explicitly.

On the other hand, when an orthonormal scaling function $\phi(t)$ is given, then the values of h_l can be easily found as follows:

$$\begin{aligned} & \sqrt{2} \int_{-\infty}^{+\infty} \phi(t) \phi^*(2t - n) dt \\ &= 2 \sum_l \int_{-\infty}^{+\infty} h_l \phi(2t - l) \phi^*(2t - n) dt \\ &= 2 \int_{-\infty}^{+\infty} h_n \phi(2t - n) \phi^*(2t - n) dt \\ &= \int_{-\infty}^{+\infty} h_n \phi(x) \phi^*(x) dx \\ &= h_n \end{aligned} \tag{4}$$

Since $V_s \subset V_{s+1}$, we may decompose V_{s+1} by $V_{s+1} = V_s \oplus W_s$. Recursive applications of this relation lead to

$$V_0 \oplus \sum_{s=0}^n W_s = \bigoplus_{s=-\infty}^n W_s = V_{n+1}, \text{ and } \bigoplus_{s=-\infty}^{+\infty} W_s = L^2 \tag{5}$$

Note that such W_s is not unique unless we require W_s to be the orthogonal complement space of V_s in V_{s+1} . We will assume that this is the case; that is, $W_s \perp V_s$, unless stated otherwise. This relation is referred to as an *orthogonal MRA* in some references where a general W_s is desired, although the terminology may be misleading as it does not require the scaling function of $W_s \perp V_s$ to generate orthogonal bases. However, it does imply that all W_s 's are mutually orthogonal as discussed before.

A function $\psi(t) \in W_0$ is called a *wavelet* (or *semiorthogonal wavelet*) of the MRA if the sequence $\{\psi_l(t) = \psi(t-l) | l \in \mathbb{Z}\}$ forms a Riesz basis of W_0 . It is called an *orthonormal wavelet* if the wavelet actually generates an orthonormal basis. Similar to $\phi(t)$, the function $\psi(t)$ is also called a “mother wavelet,” as $\psi(t)$ generates $\{\psi_{s,l} | l \in \mathbb{Z}\}$ to form Riesz bases for all W_s , where $\psi_{s,l}(t) = 2^{s/2} \psi(2^s t - l)$. Furthermore, since all W_s values are mutually orthogonal, the union of their Riesz bases, namely, $\{\psi_{s,l} | s, l \in \mathbb{Z}\}$, forms a Riesz basis of the whole space L^2 . In fact, it is often called a *semi-orthogonal basis* since $\psi_{s,l}(t) \perp \psi_{r,k}(t)$ for $s \neq r$. Once again, note that in general it is not necessary that the associated scaling function and wavelet be orthonormal, only $W_s \perp V_s$ and all W_s values are mutually orthogonal.

Since W_0 is contained in V_1 , the mother wavelet $\psi(t)$ can also be represented as a linear combination of the Riesz basis of V_1 :

$$\psi(t) = \sqrt{2} \sum_l g_l \phi(2t - l) \in V_1 \tag{6}$$

We call this the *wavelet equation*. Again, this equation plays a key role in wavelet construction, especially when it is used together with the refinement equation (3). Together (3) and (6) are often called *two-scale relations*.

We now turn to the question of how to generate a mother wavelet mathematically for a given MRA. Notice that existence of $\psi(t)$ is neither required nor guaranteed by the definition of the MRA; however, there is a procedure for producing an associated wavelet for a given $\phi(t)$. For example, if $\phi(t)$ is orthonormal, then $\psi(t)$ can be constructed using (6), as we can take $g_l = (-1)^l h_{1-l}^*$ in this case, where the values of h_k are the coefficients in the refinement equation (3). Note that $\psi(t)$ may not be uniquely generated in this manner.

4. TEM WAVE PROPAGATION

4.1. MRTD Modeling of TEM Wave Propagation

Based on the concepts of the MRA developed above, this section will demonstrate the principal procedure of the MRTD by analyzing a TEM wave propagation in a dielectric-layered space along the x (horizontal) axis. We consider an electromagnetic plane wave propagating

along the x direction and use a set of generalized formulations that include both the MRTD region and the anisotropic perfectly matched layers (APML) absorbing region [29–33]. We can then simplify the Maxwell equations as

$$\frac{\partial H_z}{\partial x} = -j\omega s_x D_y \tag{7}$$

$$D_y = \epsilon E_y \tag{8}$$

$$\frac{\partial E_y}{\partial x} = -j\omega\mu_0 s_x H_z \tag{9}$$

with

$$s_x = \begin{cases} 1 + \frac{\sigma_x}{j\omega\epsilon_0} & \text{in APML regions} \\ 1 & \text{in a non-APML region } (\sigma_x = 0) \end{cases} \tag{10}$$

where σ_x is the APML electric conductivity, and the permittivity ϵ is given as

$$\epsilon = \epsilon_0 \epsilon_y(x) = \begin{cases} \epsilon_0 \epsilon_y & \text{in the dielectric regions} \\ \epsilon_0 & \text{elsewhere} \end{cases} \tag{11}$$

Next, we expand the electromagnetic fields as follows:

$$\begin{aligned} E_y(x, t) = & \sum_{i,n=-\infty}^{+\infty} \left[\phi_y E_i^n \phi_i(x) \right. \\ & + \sum_{s=0}^{s_{\max}} \sum_{l=0}^{2^s-1} \psi_{yl}^s E_{i+2^{-s}(l+1/2)}^n \\ & \left. \times \psi_{s,i+2^{-s}(l+1/2)}(x) \right] h^n(t) \end{aligned} \tag{12}$$

$$\begin{aligned} D_y(x, t) = & \sum_{i,n=-\infty}^{+\infty} \left[\phi_y D_i^n \phi_i(x) \right. \\ & + \sum_{s=0}^{s_{\max}} \sum_{l=0}^{2^s-1} \psi_{yl}^s D_{i+2^{-s}(l+1/2)}^n \\ & \left. \times \psi_{s,i+2^{-s}(l+1/2)}(x) \right] h^n(t) \end{aligned} \tag{13}$$

$$\begin{aligned} H_z(x, t) = & \sum_{i,n=-\infty}^{+\infty} \left[\phi_z H_{i+1/2}^{n+1/2} \phi_i(x) \right. \\ & + \sum_{s=0}^{s_{\max}} \sum_{l=0}^{2^s-1} \psi_{zl}^s H_{i-1/2+2^{-s}(l+1/2)}^{n+1/2} \\ & \left. \times \psi_{s,i-1/2+2^{-s}(l+1/2)}(x) \right] h^{n+1/2}(t) \end{aligned} \tag{14}$$

where $\phi_y E_i^n$, $\psi_{yl}^s E_{i+2^{-s}(l+1/2)}^n$, $\phi_z H_{i+1/2}^{n+1/2}$, and $\psi_{zl}^s H_{i-1/2+2^{-s}(l+1/2)}^{n+1/2}$, are the field expansion coefficients in terms of scaling and wavelet functions. The basis functions $\phi(x)$, $\psi(x)$, $\psi_s(x)$, and $h(t)$ are, respectively, the Battle-Lemarie scaling, mother wavelet, s th-level wavelet,

and time rectangle pulse functions. The Fourier-transformed versions of the basis functions can be expressed as

$$\tilde{\phi}(\omega) = \left(\frac{\sin \frac{\omega}{2}}{\frac{\omega}{2}} \right)^4 \tag{15a}$$

$$\times \frac{1}{\sqrt{\left(1 - \frac{4}{3} \sin^2 \frac{\omega}{2} + \frac{2}{5} \sin^4 \frac{\omega}{2} - \frac{4}{315} \sin^6 \frac{\omega}{2} \right)}}$$

$$\tilde{\psi}(\omega) = e^{j(\omega/2)} \frac{\tilde{\phi}(\omega + 2\pi)}{\tilde{\phi}\left(\frac{\omega}{2} + \pi\right)} \tilde{\phi}\frac{\omega}{2} \tag{15b}$$

$$\tilde{\psi}_s(\omega) = e^{j(\omega/2)} \frac{\tilde{\phi}_s(\omega + 2\pi)}{\tilde{\phi}_s\left(\frac{\omega}{2} + \pi\right)} \tilde{\phi}_s\left(\frac{\omega}{2}\right) \tag{15c}$$

$$\tilde{\psi}_{s,i}(\omega) = 2^{(s/2)} \cdot e^{-j\omega 2^{-s}i} \cdot \tilde{\psi}(2^{-s}\omega) \tag{15d}$$

In order to illustrate their localized supports in both the space and frequency domains, the scaling functions $\phi(x)$ and $\tilde{\phi}(\omega)$, and the wavelet functions $\psi(x)$, $\psi_1(x)$, $\tilde{\psi}(\omega)$, and $\tilde{\psi}_1(\omega)$, have been, respectively, plotted in Figs. 1 and 2.

The orthogonal relations for the rectangular time pulse, scaling, and wavelet functions can be expressed as follows

$$\int_{-\infty}^{\infty} h^n(t) h^{n'}(t) dt = \delta_{n,n'} \Delta t \tag{16}$$

$$\int_{-\infty}^{\infty} \phi_i(x) \phi_{i'}(x) dx = \delta_{i,i'} \Delta x \tag{17}$$

$$\int_{-\infty}^{\infty} \psi_i^{s,l}(x) \psi_{i'}^{s',l'}(x) dx = \delta_{s,s'} \delta_{l,l'} \delta_{i,i'} \Delta x \tag{18}$$

where $\delta_{i,i'}$ is the Krönecker symbol representing unity when $i=i'$ and zero otherwise. To derive the MRTD update equations, we have to apply some intricate integral relations, which are summarized in the following:

$$\int_{-\infty}^{+\infty} \phi_i(x) \frac{\partial}{\partial x} \phi_{i'+(1/2)}(x) dx = \sum_{v=-\infty}^{+\infty} a(v) \delta_{i',i+v} \tag{19a}$$

$$a(v) = \frac{1}{\pi} \int_0^{+\infty} \left| \hat{\phi}(\omega) \right|^2 \omega \sin \left[\left(v + \frac{1}{2} \right) \omega \right] d\omega \tag{19b}$$

$$\int_{-\infty}^{+\infty} \phi_{j+(1/2)}(y) \frac{\partial \psi_{s,j'+2^{-s}(l+1/2)}(y)}{\partial y} dy \tag{20a}$$

$$= \sum_{v=-\infty}^{+\infty} d_{s,l}(v) \delta_{j',j+v}$$

$$\begin{aligned} d_{s,l}(v) = & \frac{1}{\pi} \int_0^{+\infty} \hat{\phi}(\omega) |\hat{\psi}_s(\omega)| \omega \\ & \times \sin \left[\omega \left(v - \frac{1}{2} + \frac{l}{2^s} + \frac{1}{2^{s+1}} \right) \right] d\omega \end{aligned} \tag{20b}$$

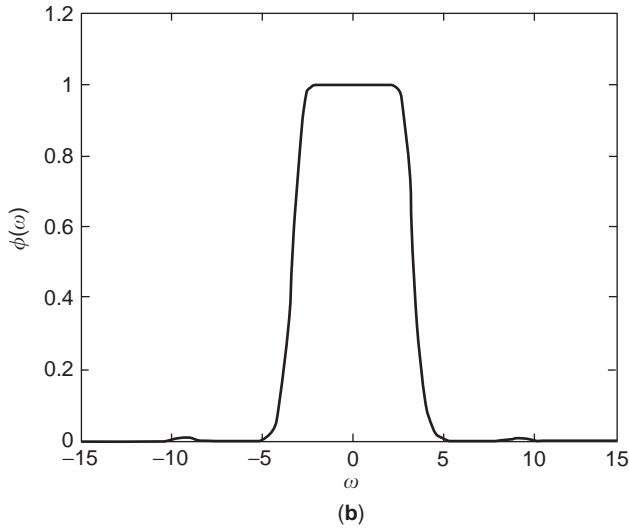
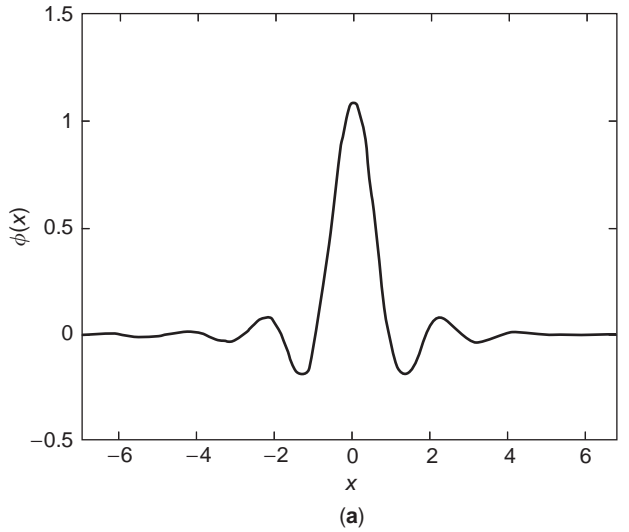


Figure 1. The cubic spline Battle-Lemarie scaling function in the (a) space domain and (b) spectral domain.

$$\int_{-\infty}^{+\infty} \psi_{s,j-(1/2)+2^{-s}[l+(1/2)]}(y) \frac{\partial \phi_{j'}(y)}{\partial y} dy = \sum_{v=-\infty}^{v=+\infty} c_{s,l}(v) \delta_{j',j+v} \quad (21a)$$

$$c_{s,l}(v) = \frac{1}{\pi} \int_0^{\infty} \hat{\phi}(\omega) |\hat{\psi}_s(\omega)| \omega \times \sin \left[\omega \left(v + \frac{1}{2} - \frac{l}{2^s} - \frac{1}{2^{s+1}} \right) \right] d\omega \quad (21b)$$

$$\int_{+\infty}^{+\infty} \psi_{s,i-(1/2)+2^{-s}[l+(1/2)]}(x) \times \frac{\partial \psi_{s,i'+2^{-s}'[l'+(1/2)]}(x)}{\partial x} dx = \sum_{v=-\infty}^{+\infty} b_{l',l}^{s,s'}(v) \delta_{i',i+v} \quad (22a)$$

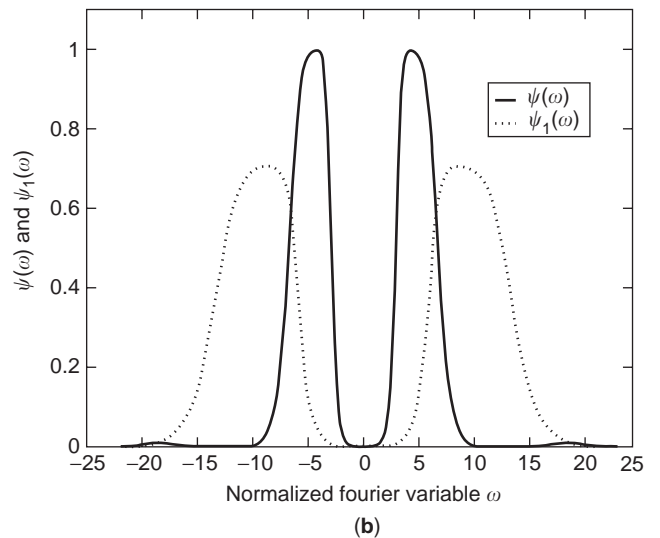
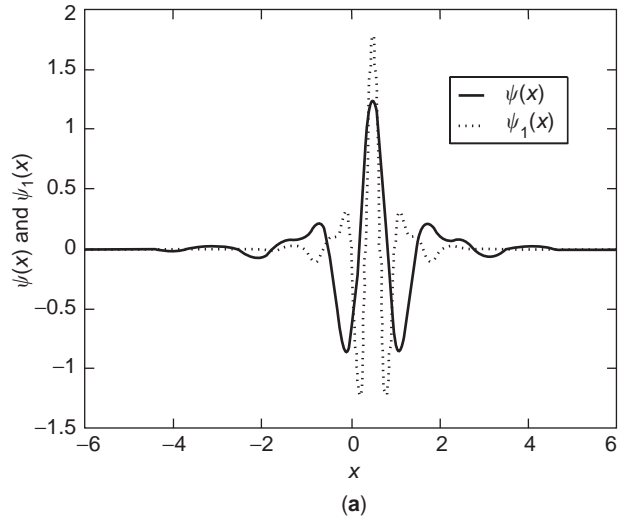


Figure 2. The cubic spline Battle-Lemarie wavelet functions with $s=0$ and $s=1$ in the (a) space domain and (b) spectral domain.

$$b_{l',l}^{s,s'}(v) = \frac{1}{\pi} \int_0^{\infty} |\tilde{\psi}_s(\omega)| |\tilde{\psi}_{s'}(\omega)| \omega \times \sin \left[\omega \left(v + \frac{1}{2} + \frac{l'}{2^{s'}} - \frac{l}{2^s} + \frac{1}{2^{s'+1}} - \frac{1}{2^{s+1}} \right) \right] d\omega \quad (22b)$$

Because of the localized nature of the Battle-Lemarie scaling and wavelet functions, the values of $a(v)$, $b_{l',l}^{s,s'}(v)$, $c_{s,l}(v)$, and $d_{s,l}(v)$ appearing in the equations above decrease exponentially with an increase in the absolute value of v . Although the summation index v in, (19a), (20a), and (21a) spans from positive to negative infinity, it is usually sufficient to truncate it at v_{\max} ($|v| \leq v_{\max}$; $v_{\max} = 9$), due to the fast convergent property of the scaling and wavelet functions. In addition, the symmetry of the coefficients, namely, $a(-1-v) = -a(v)$, $b_{l',l}^{s,s'}(-1-v) = -b_{l',l}^{s,s'}(v)$, $c_{s,l}(v) = c_{s,l}(v)$, and $d_{s,l}(v) = -d_{s,l}(v)$, can reduce the computational workload even more significantly in field update

Table 1. The Integral Coefficients $d_{s,l}(v)$ and $c_{s,l}(v)$ ($s = 1$)

v	$c_{1,0}(v)$	$c_{1,1}(v)$	$d_{1,0}(v)$	$d_{1,1}(v)$
-8	0.000077791	-0.000107917	-0.000107917	0.000077791
-7	-0.000154260	0.000216187	0.000216187	-0.000154260
-6	0.000313336	-0.000440914	-0.000440914	0.000313336
-5	-0.000625694	0.000906723	0.000906723	-0.000625694
-4	0.001348953	-0.001959836	-0.001959836	0.001348953
-3	-0.002586165	0.004273722	0.004273722	-0.002586165
-2	0.007532622	-0.011329640	-0.011329640	0.007532622
-1	-0.020265614	0.024321565	0.024321565	-0.020265614
0	0.030300911	-0.030300911	-0.030300911	0.030300911
1	-0.024321565	0.020265614	0.020265614	-0.024321565
2	0.011329640	-0.007532622	-0.007532622	0.011329640
3	-0.004273722	0.002586165	0.002586165	-0.004273722
4	0.001959836	-0.001348953	-0.001348953	0.001959836
5	-0.000906723	0.00088486	0.00088486	-0.000906723
6	0.000440914	-0.000313336	-0.000313336	0.000440914
7	-0.000216187	0.000154260	0.000154260	-0.000216187
8	0.000107917	-0.000077791	-0.000077791	0.000107917

equations. The values of $\alpha(v)$, $c_{0,0}(v)$, and $b_{0,0}^{0,0}(v)$ are listed in Ref. 2. The values of $d_{s,l}(v)$, $c_{s,l}(v)$, and $b_{l,l}^{s,s}(v)$ ($s = 1$) are summarized in Tables 1 and 2.

In these tables, we note that $b_{0,0}^{1,1}(v) = -b_{0,0}^{1,1}(v-1)$, if $v < 0$; $b_{0,1}^{1,1}(v) = -b_{0,1}^{1,1}(v-2)$, if $v < -1$; $b_{1,0}^{1,0}(v) = b_{0,0}^{0,1}(v)$; $b_{1,0}^{1,1}(v) = b_{0,1}^{1,1}(v)$, and $b_{1,1}^{1,1}(v) = b_{0,0}^{1,1}(v)$ for all values of v .

Substituting the field expansion in (12) through (14) into the governing equations (7) and (9), and applying Galerkin's method by using a scaling or wavelet function as a test function, we can derive time-domain update equations as follows:

$$\begin{aligned} \phi_y D_i^{n+1} &= \left(\frac{1 - \frac{\sigma_x \Delta t}{2\epsilon_0}}{1 + \frac{\sigma_x \Delta t}{2\epsilon_0}} \right) \\ &\times \phi_y D_i^n - \frac{1}{\left(1 + \frac{\sigma_x \Delta t}{2\epsilon_0}\right)} \left(\sum_{v=-9}^{+8} \alpha(v) \phi_z H_{i+v+(1/2)}^{n+(1/2)} \right) \end{aligned} \quad (23)$$

$$\begin{aligned} &+ \left. \sum_{s=0}^{s_{\max}} \sum_{l=0}^{2^s-1} \sum_{v=-9}^{+9} d_{s,l}(v) \psi_z^s H_{[i-(1/2)+v]+2^{-s}[l+(1/2)]}^{n+(1/2)} \right) \frac{\Delta t}{\Delta x} \\ \psi_y^s D_{i+2^{-s}[l+(1/2)]}^{n+1} &= \left(\frac{1 - \frac{\sigma_x \Delta t}{2\epsilon_0}}{1 + \frac{\sigma_x \Delta t}{2\epsilon_0}} \right) \\ &\times \psi_y^s D_{i+2^{-s}[l+(1/2)]}^n - \frac{1}{\left(1 + \frac{\sigma_x \Delta t}{2\epsilon_0}\right)} \end{aligned} \quad (24)$$

$$\begin{aligned} &\times \left(\sum_{v=-9}^{+9} c_{s,l}(v) \phi_z H_{i+v+(1/2)}^{n+(1/2)} \right) \\ &+ \sum_{s'=0}^{s_{\max}} \sum_{l'=0}^{2^{s'}-1} \sum_{v=-9}^{+9} b_{l',l'}^{s,s'}(v) \\ &\times \psi_z^s H_{[i+(1/2)+v]+2^{-s'}[l'+(1/2)]}^{n+(1/2)} \right) \frac{\Delta t}{\Delta x} \end{aligned}$$

$$\begin{aligned} \phi_z H_{i+(1/2)}^{n+(1/2)} &= \left(\frac{1 - \frac{\sigma_x \Delta t}{2\epsilon_0}}{1 + \frac{\sigma_x \Delta t}{2\epsilon_0}} \right) \phi_z H_{i+(1/2)}^{n-(1/2)} \\ &- \frac{1}{\mu_0 \left(1 + \frac{\sigma_x \Delta t}{2\epsilon_0}\right)} \left(\sum_{v=-9}^{+8} \alpha(v) \phi_y E_{i+v+1}^n \right) \\ &+ \sum_{s=0}^{s_{\max}} \sum_{l=0}^{2^s-1} \sum_{v=-\infty}^{+\infty} d_{s,l}(v) \\ &\times \psi_y^s E_{i+v+2^{-s}[l+(1/2)]}^n \left) \frac{\Delta t}{\Delta x} \end{aligned} \quad (25)$$

$$\begin{aligned} \psi_z^s H_{i-(1/2)+2^{-s}[l+(1/2)]}^{n+(1/2)} &= \left(\frac{1 - \frac{\sigma_x \Delta t}{2\epsilon_0}}{1 + \frac{\sigma_x \Delta t}{2\epsilon_0}} \right) \psi_z^s H_{i+(1/2)+2^{-s}[l+(1/2)]}^{n-(1/2)} \\ &- \frac{1}{\mu_0 \left(1 + \frac{\sigma_x \Delta t}{2\epsilon_0}\right)} \left(\sum_{v=-\infty}^{v=+\infty} c_{s,l}(v) \phi_y E_{i+v}^n \right) \\ &+ \sum_{s'=0}^{s_{\max}} \sum_{l'=0}^{2^{s'}-1} \sum_{v=-\infty}^{v=+\infty} b_{l',l'}^{s,s'} \psi_z^{s'} E_{i+v+2^{-s'}[l'+(1/2)]}^n \left) \frac{\Delta t}{\Delta x} \end{aligned} \quad (26)$$

These update equations are valid in all regions including both the APML and normal MRTD regions. We can easily obtain the update equations in a non-APML region by simply setting $\sigma_x \equiv 0$, ($s_x(x) \equiv 1$) in (23)-(26).

To further solve for the update equations for E fields, we apply the same discretization procedure for (8) and obtain

$$\epsilon_0 \sum_{i'=-\infty}^{+\infty} \left[(\epsilon_y^{\phi,\phi})_{i',i} \phi_y E_{i'}^n \right. \quad (27)$$

$$\begin{aligned} &+ \left. \sum_{s=0}^{s_{\max}} \sum_{l=0}^{2^s-1} (\epsilon_y^{\psi,\psi})_{i',i} \psi_y^s E_{i'+2^{-s}[l+(1/2)]}^n \right] = \phi_y D_i^n \\ \epsilon_0 \sum_{i'=-\infty}^{+\infty} \left[(\epsilon_y^{\psi,\phi})_{i,i'} \phi_y E_{i'}^n \right. \\ &+ \left. \sum_{s'=0}^{s_{\max}} \sum_{l'=0}^{2^{s'}-1} (\epsilon_{l,l'}^{s,s'} \psi_y^s)_{i,i'} \psi_y^{s'} E_{i'+2^{-s'}[l'+(1/2)]}^n \right] \\ &= \psi_y^s D_{i+2^{-s}[l+(1/2)]}^n \end{aligned} \quad (28)$$

with the dielectric-related coefficients defined as

$$\begin{aligned} (\epsilon_y^{\phi,\phi})_{i',i} &= \frac{1}{\Delta x} \int_{-\infty}^{+\infty} \epsilon_y(x) \phi_{i'}(x) \phi_i(x) dx \\ &= \delta_{i,i'} + \sum_{\alpha=0}^{\alpha_0} (\epsilon_y^\alpha - 1) \frac{1}{\Delta x} \int_{x_1}^{x_2} \phi_{i'}(x) \phi_i(x) dx \end{aligned} \quad (29a)$$

Table 2. The Integral Coefficients $b_{l,l'}^{s,s'}(v)$ ($s = 1$)

v	$b_{0,0}^{0,1}(v)$	$b_{0,1}^{0,1}(v)$	$b_{0,0}^{1,0}(v)$	$b_{0,0}^{1,1}(v)$	$b_{0,1}^{1,1}(v)$
-9	0.000068126	-0.000157979	-0.000157979	0.000062393	-0.000116529
-8	0.000143468	-0.000352128	-0.000352128	0.000217810	-0.000406512
-7	0.001101551	-0.001591902	-0.001591902	0.000760823	-0.001416527
-6	0.002106587	-0.004918699	-0.004918699	0.002663166	-0.004916515
-5	0.010876491	-0.018197365	-0.018197365	0.009390025	-0.016826645
-4	0.030774267	-0.062187652	-0.062187652	0.033934368	-0.054686440
-3	0.121900158	-0.216773548	-0.216773548	0.132668009	-0.142270550
-2	0.394611424	-0.739278550	-0.739278550	0.641536536	0.056428700
-1	1.225829337	-1.609301081	-1.609301081	5.039549683	0.000000000
0	1.609301081	-1.225829337	-1.225829337	-5.039549683	-0.056428700
1	0.739278549	-0.394611424	-0.394611424	-0.641536536	0.142270550
2	0.216773549	-0.121900158	-0.121900158	-0.132668009	0.054686440
3	0.062187653	-0.030774267	-0.030774267	-0.033934368	0.016826645
4	0.018197366	-0.010876491	-0.010876491	-0.009390025	0.004916515
5	0.004918699	-0.002106587	-0.002106587	-0.002663166	0.001416527
6	0.001591902	-0.001101551	-0.001101551	-0.000760823	0.000406512
7	0.000352128	-0.000143468	-0.000143468	-0.000217810	0.000116529
8	0.000157979	-0.000068126	-0.000068126	-0.000062393	0.000003339

$$\begin{aligned}
 ({}^s \varepsilon_y^{\phi,\psi})_{i,i'} &= \frac{1}{\Delta x} \int_{-\infty}^{+\infty} \varepsilon_y(x) \phi_i(x) \psi_{s,i'+2^{-s}[l+(1/2)]}(x) dx \\
 &= \sum_{\alpha=0}^{\alpha_0} (\varepsilon_y^\alpha - 1) \frac{1}{\Delta x} \int_{x_1^\alpha}^{x_2^\alpha} \phi_i(x) \psi_{s,i'+2^{-s}[l+(1/2)]}(x) dx
 \end{aligned} \tag{29b}$$

$$\begin{aligned}
 ({}^i \varepsilon_y^{\psi,\phi})_{i,i'} &= \frac{1}{\Delta x} \int_{-\infty}^{+\infty} \varepsilon_y(x) \psi_{s,i+2^{-s}[l+(1/2)]}(x) \phi_{i'}(x) dx \\
 &= \sum_{\alpha=0}^{\alpha_0} (\varepsilon_y^\alpha - 1) \frac{1}{\Delta x} \\
 &\quad \times \int_{x_1^\alpha}^{x_2^\alpha} \psi_{s,i+2^{-s}[l+(1/2)]}(x) \phi_{i'}(x) dx
 \end{aligned} \tag{29c}$$

$$\begin{aligned}
 ({}^{s,s'} \varepsilon_y^{\psi,\psi})_{i',i} &= \frac{1}{\Delta x} \int_{-\infty}^{+\infty} \varepsilon_y(x) \psi_{s,i'+2^{-s}[l'+(1/2)]}(x) \\
 &\quad \times \psi_{s,i+2^{-s}[l+(1/2)]}(x) dx \\
 &= \delta_{i,i'} \delta_{s,s'} \delta_{l,l'} + \sum_{\alpha=0}^{\alpha_0} (\varepsilon_y^\alpha - 1) \frac{1}{\Delta x} \\
 &\quad \times \int_{x_1^\alpha}^{x_2^\alpha} \psi_{i'+2^{-s}[l'+(1/2)]}(x) \psi_{s,i+2^{-s}[l+(1/2)]}(x) dx
 \end{aligned} \tag{29d}$$

where α_0 is the total number of dielectric regions and x_1^α and x_2^α are the beginning and end positions of the α th dielectric region.

For the sake of computational efficiency and simplicity, we expand all field quantities in terms of scaling functions for an entire computational region; we also expand wavelets with levels 0 and 1 in an extended discontinuity subregion where discontinuities exist and fields change dramatically. For example, for the α th dielectric region $[x_1^\alpha, x_2^\alpha] = [i_1 \Delta x, i_2 \Delta x]$ in a multilayer dielectric system we can truncate the wavelet expansions in the extended discontinuity subregion, $[(i_1 - M) \Delta x, (i_2 + M) \Delta x]$, by taking into account the stencil effect of the scaling and wavelet functions, where M is an adjustable integer dependent on accuracy requirements. The simplest choice is $M = 0$ for the crudest approximation. It is seldom necessary to set $M > 9$ because of the local support of scaling and wavelet functions. The value of M is usually designated by a suitable value to ensure enough accuracy, and in this research we set $M = 9$. Thus, we can rewrite the update equations (27) and (28) in matrix form

$$\begin{bmatrix} [\phi_y \mathbf{E}_i^n] \\ [\psi_{y0} \mathbf{E}_{i+(1/2)}^n] \\ [\psi_{y1} \mathbf{E}_{i+(1/4)}^n] \\ [\psi_{y1} \mathbf{E}_{i+(3/4)}^n] \end{bmatrix} = \frac{1}{\varepsilon_0} \sum_{i'=i_1-M}^{i_2+M} \begin{bmatrix} [{}^0 \varepsilon_{i,i'}^{\phi,\phi}] & [{}^0 \varepsilon_{i,i'+(1/2)}^{\phi,\psi}] & [{}^0 \varepsilon_{i,i'+(1/4)}^{\phi,\psi}] & [{}^1 \varepsilon_{i,i'+(3/4)}^{\phi,\psi}] \\ [{}^0 \varepsilon_{i+(1/2),i'}^{\psi,\phi}] & [{}^0 \varepsilon_{i+(1/2),i'+(1/2)}^{\psi,\psi}] & [{}^0 \varepsilon_{i+(1/2),i'+(1/4)}^{\psi,\psi}] & [{}^0 \varepsilon_{i+(1/2),i'+(3/4)}^{\psi,\psi}] \\ [{}^1 \varepsilon_{i+(1/4),i'}^{\psi,\phi}] & [{}^1 \varepsilon_{i+(1/4),i'+(1/2)}^{\psi,\psi}] & [{}^1 \varepsilon_{i+(1/4),i'+(1/4)}^{\psi,\psi}] & [{}^1 \varepsilon_{i+(1/4),i'+(3/4)}^{\psi,\psi}] \\ [{}^1 \varepsilon_{i+(3/4),i'}^{\psi,\phi}] & [{}^1 \varepsilon_{i+(3/4),i'+(1/2)}^{\psi,\psi}] & [{}^1 \varepsilon_{i+(3/4),i'+(1/4)}^{\psi,\psi}] & [{}^1 \varepsilon_{i+(3/4),i'+(3/4)}^{\psi,\psi}] \end{bmatrix}^{-1} \begin{bmatrix} [\phi_y \mathbf{D}_{i'}^n] \\ [\psi_{y0} \mathbf{D}_{i'+(1/2)}^n] \\ [\psi_{y0} \mathbf{D}_{i'+(1/4)}^n] \\ [\psi_{y1} \mathbf{D}_{i'+(3/4)}^n] \end{bmatrix} \tag{30}$$

where the coefficient matrix $[\epsilon_{i,i'}^{\phi,\phi}]$, for example, is given as follows

$$[\epsilon_{i,i'}^{\phi,\phi}] = \begin{bmatrix} (\epsilon_y^{\phi,\phi})_{i_1-M,i_1-M} & (\epsilon_y^{\phi,\phi})_{i_1-M,i_1-M+1} & \cdots & (\epsilon_y^{\phi,\phi})_{i_1-M,i_2+M-1} & (\epsilon_y^{\phi,\phi})_{i_1-M,i_2+M} \\ (\epsilon_y^{\phi,\phi})_{i_1-M+1,i_1-M} & (\epsilon_y^{\phi,\phi})_{i_1-M+1,i_1-M+1} & \cdots & (\epsilon_y^{\phi,\phi})_{i_1-M+1,i_2+M-1} & (\epsilon_y^{\phi,\phi})_{i_1-M+1,i_2+M} \\ \cdots & \cdots & \cdots & \cdots & \cdots \\ (\epsilon_y^{\phi,\phi})_{i_2+M-1,i_1-M} & (\epsilon_y^{\phi,\phi})_{i_2+M-1,i_1-M+1} & \cdots & (\epsilon_y^{\phi,\phi})_{i_2+M-1,i_2+M-1} & (\epsilon_y^{\phi,\phi})_{i_2+M-1,i_2+M} \\ (\epsilon_y^{\phi,\phi})_{i_2+M,i_1-M} & (\epsilon_y^{\phi,\phi})_{i_2+M,i_1-M+1} & \cdots & (\epsilon_y^{\phi,\phi})_{i_2+M,i_2+M-1} & (\epsilon_y^{\phi,\phi})_{i_2+M,i_2+M} \end{bmatrix} \quad (31a)$$

and $[\phi_y E_{i'}^n]$ is expressed as

$$[\phi_y E_{i'}^n]^T = [\phi_y E_{i_1-M}^n \quad \phi_y E_{i_1-M+1}^n \quad \cdots \quad \phi_y E_{i_2+M-1}^n \quad \phi_y E_{i_2+M}^n]^T \quad (31b)$$

As seen from Eq. (30), the fields at discrete points are coupled, and we have to update them by solving a matrix equation with dimensions of $4(i_2 - i_1 + 2M) \times 4(i_2 - i_1 + 2M)$ at each timestep. Note that all elements in the coefficient matrix (30) are constants for a specified system and that its elements can be calculated and stored in a constant array. Thus, we can update the E fields in (30) by simply performing a matrix multiplication if the inverse matrix of the coefficient matrix in (30) is saved as a constant matrix. Also note that the crudest approximation is to make the diagonal approximation and then (30) using the leapfrog update equations similar to those in the FDTD algorithm.

As shown in Fig. 3, we employ an APML to truncate both the entire computational domain for scaling functions (APML_s) and the internal extended discontinuity subregions (APML_w). To ensure adequate wave absorption in the x direction, we usually

choose the behavior of the APML conductivity σ_x as

$$\sigma_x = \sigma_{\max} \left| \frac{x - x_0}{d} \right|^\alpha \quad (32)$$

where x_0 is a starting position of the APML region in the x direction, d is the thickness of the APML region, and α is the power of the polynomial with the value of 2. The constant σ_{\max} is determined by the designated reflection coefficient for a wave to be normally incident on the APML wall

$$\sigma_{\max} = -\frac{\epsilon_0 v (\alpha + 1)}{2d} \ln(R(0)) \quad (33)$$

where v is the speed of electromagnetic wave propagation and $R(0)$ is the designated coefficient with normal incidence, here assuming $R(0) = 1.0 \times 10^{-8}$.

4.2. Application Results

As shown in Fig. 3, a plane TEM transient pulse, generated by exciting the E_y field, is incident on a dielectric slab characterized with the relative permittivity $\epsilon_y = 4$ and width $d = 9$ cm. The entire computational domain contains 100 cells with a cell size of $\Delta x = 7.5$ mm. The fields expanded with the scaling functions in the entire computational region are terminated by an APML at the two

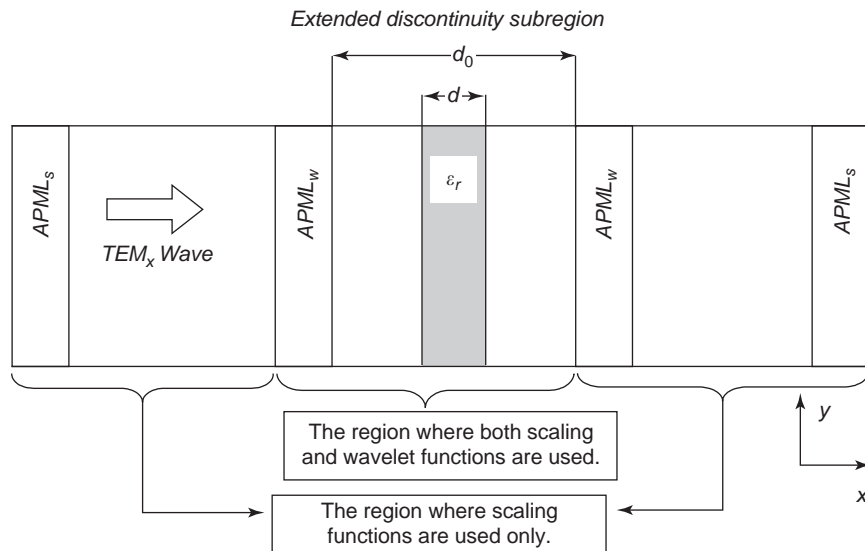


Figure 3. A TEM_x wave incident on a dielectric slab, where d is the width of the dielectric slab and d_0 is the extended dielectric region.

Table 3. Discretization in MRTD and FDTD Methods

	Δx (mm)	Δt (ps)	N_x (cell)	$N_{\text{PML},s}$ (cell)	$N_{\text{PML},w}$ (cells)
FDTD	1.5	2.5	512	N/A	N/A
S-MRTD	7.5	1.0	100	8	N/A
SW-MRTD ($s=0$)	7.5	1.0	100	8	5
SW-MRTD ($s=1$)	7.5	5.55	100	8	5

ends of the region, while those expanded with the wavelet expansion functions are defined only in the extended discontinuity subregion truncated with an APML_w . We observe excellent agreement among the results derived from the finite-difference time-domain (FDTD) method, the scaling function-based MRTD (S-MRTD), the scaling and wavelet function-based MRTD (SW-MRTD), and the analytic results. Table 3 lists the space and time discretization values of the system for the MRTD and FDTD computations.

It is found that the contribution to field magnitude from wavelets is much lower than that of scaling functions, and this is the reason why we only expand wavelets in an extended discontinuity region. In Figs. 4a and 4b, we present the reflection coefficients for a dielectric-layer system calculated by using the FDTD, S-MRTD, and SW-MRTD ($s=0,1$) methods. We observe excellent agreement between the results. We find that the SW-MRTD with $s=1$ shows the best accuracy with the relative error of 0.07% calculated at the peak as shown in Fig. 4b, and that the FDTD is the worst-case scenario with the relative error of 0.6% with respect to the analytic solution.

5. ANALYSIS OF MICROWAVE CIRCUITS

5.1. MRTD Modeling

In this section we study a generalized microwave circuit problem. For simplicity, we expand the electromagnetic fields only in terms of the Battle-Lemarie scaling function and ignore wavelet expansions. The governing equations thus include the pair of Maxwell two-curl equations

$$\nabla \times \vec{H} = \frac{\partial \vec{D}}{\partial t} \quad (34)$$

$$\nabla \times \vec{E} = -\mu_0 \frac{\partial \vec{H}}{\partial t} \quad (35)$$

and the defined constitutive relation relating the \vec{E} and \vec{D} fields:

$$\frac{\partial \vec{D}}{\partial t} = \bar{\sigma} \cdot \vec{E} + \epsilon_0 \bar{\epsilon}_r \cdot \frac{\partial \vec{E}}{\partial t} \quad (36)$$

For generality, we represent the relative permittivity and the conductivity as a diagonal tensor. Note that the printed planar microstrip circuits usually are inhomogeneous in the vertical direction (y axis) but homogenous in horizontal directions (x and z axes). Thus, the elements of the relative permittivity and conductivity can be ex-

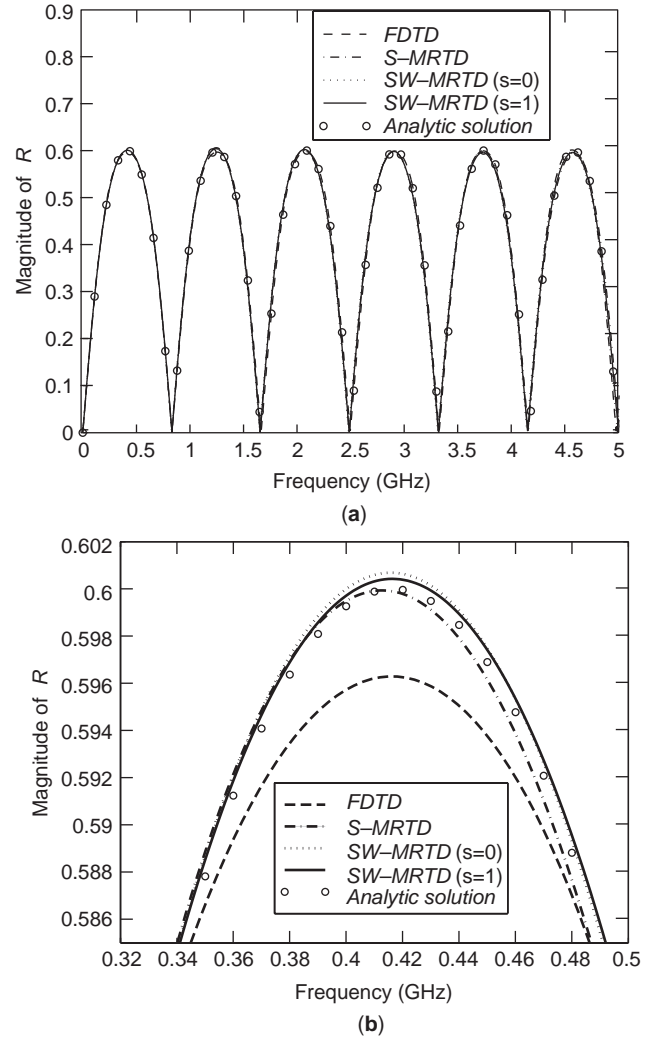


Figure 4. Magnitude of reflection coefficient R for a dielectric-layer slab system versus frequency ($d=9$ cm, $\epsilon_r=4.0$): (a) full frequency bandwidth of interest; (b) enlarged frequency response.

pressed as $\epsilon_i = \epsilon_i(y)$ ($i=x,y,z$) and $\sigma_i(x,y,z) = \sigma_\infty(x \in [x_1, x_2], y \in [y_1, y_2], z \in [z_1, z_2])$.

Next, we expand all the electric and magnetic field quantities in terms of the cubic spline Battle-Lemarie scaling function $\phi(x)$ in space and the rectangular pulse function $h(t)$ in time. For instance, all the x components of fields can be expressed as follows:

$$D_x(r, t) = \sum_{n,i,j,k=-\infty}^{+\infty} \phi_x D_{i+(1/2),j,k}^n \phi_{i+(1/2)}(x) \times \phi_j(y) \phi_k(z) h_n(t) \quad (37)$$

$$E_x(r, t) = \sum_{n,i,j,k=-\infty}^{+\infty} \phi_x E_{i+(1/2),j,k}^n \phi_{i+(1/2)}(x) \times \phi_j(y) \phi_k(z) h_n(t) \quad (38)$$

$$H_x(r, t) = \sum_{n,i,j,k=-\infty}^{+\infty} \phi_x H_{i,j+(1/2),k+(1/2)}^{n+(1/2)} \phi_i(x) \phi_{j+(1/2)}(y) \times \phi_{k+(1/2)}(z) h_{n+(1/2)}(t) \quad (39)$$

$$B_x(r, t) = \sum_{n,i,j,k=-\infty}^{+\infty} \phi_x B_{i,j+(1/2),k+(1/2)}^{n+(1/2)} \phi_i(x) \phi_{j+(1/2)}(y) \times \phi_{k+(1/2)}(z) h_{n+(1/2)}(t) \quad (40)$$

Note that both the electric fields E_x and D_x as well as the magnetic fields H_x and B_x are sampled at the same space points and time positions, respectively. Substituting the field expansions into Maxwell equations and applying the Galerkin's method, we obtain a set of field update equations. Typically, their x components read

$$\begin{aligned} \phi_x D_{i+(1/2),j,k}^{n+1} &= \phi_x D_{i+(1/2),j,k}^n \\ &+ \sum_m a(m) \left[\phi_z H_{i+(1/2),j+m+(1/2),k}^{n+(1/2)} \frac{\Delta t}{\Delta y} \right. \\ &\left. - \phi_y H_{i+(1/2),j,k+m+(1/2)}^{n+(1/2)} \frac{\Delta t}{\Delta z} \right] \end{aligned} \quad (41)$$

$$\begin{aligned} \phi_x H_{i,j+(1/2),k+(1/2)}^{n+(1/2)} &= \phi_x H_{i,j+(1/2),k+(1/2)}^{n-(1/2)} \\ &+ \frac{1}{\mu_0} \sum_m a(m) \left[\phi_y E_{i,j+(1/2),k+m+1}^{n+1} \frac{\Delta t}{\Delta z} \right. \\ &\left. - \phi_z E_{i,j+m+1,k+(1/2)}^{n+1} \frac{\Delta t}{\Delta y} \right] \end{aligned} \quad (42)$$

where the expansion coefficient $a(m)$ is as defined in (19). Note that the update equations so derived still retain the form of an explicit leapfrogging scheme similar to that of the FDTD, although they are more complex.

The microstrip line printed on a grounded dielectric substrate is a fundamental structure in planar printed millimeter-wave integrated circuits (MICs). We will derive the update equations for this type of MIC. For simplicity, both the printed microstrip-type circuits and the ground plane are assumed to be PECs, and infinitesimally thin as well.

In order to take into account of the coupling between cells in implementing the high-order expansions in the MRTD applications, we apply an image technique to truncate the PEC ground plane as shown in Fig. 5 [2,33]. Note that an imaginary image region must be constructed for PEC boundary truncation to account for the field contribution from the image structure although it would not require any additional computer resources.

Next, we consider a microstrip structure, in which a PEC strip and a dielectric substrate are defined inside the computational domain. We would like to point out that derived update equations such as (41) and (42) will not be sufficient to update fields in an inhomogeneous region, where the computational domain contains different materials, such as a PEC strip and a substrate. An additional update equation, including material parameters, must be derived from the constitutive relation. By expanding the

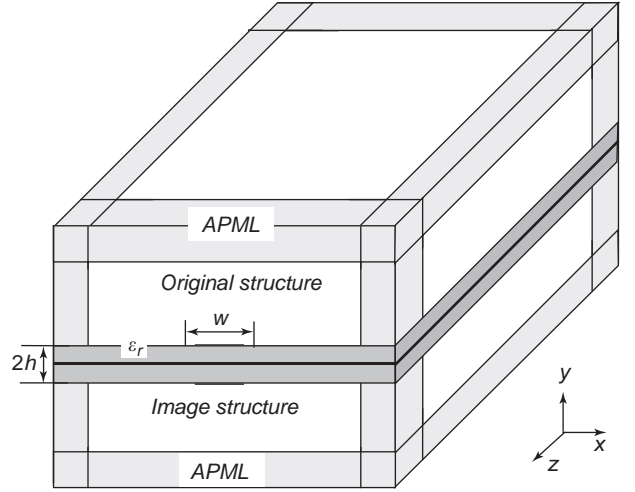


Figure 5. Computational domain for a grounded open microstrip-type structure using the MRTD scheme.

fields, substituting them into (36), and using Galerkin's method, we can obtain new update equations whose x -component relation reads

$$\begin{aligned} (\phi_x D_{i+(1/2),j,k}^{n+1} - \phi_x D_{i+(1/2),j,k}^n) &= \sum_{i',j',k'=-\infty}^{\infty} (\sigma_x)_{ii',jj',kk'} \frac{\Delta t}{2} (\phi_x E_{i'+(1/2),j',k'}^{n+1} + \phi_x E_{i'+(1/2),j',k'}^n) \\ &+ \epsilon_0 \sum_{j'=-\infty}^{\infty} (\epsilon_x)_{jj'} (\phi_x E_{i+(1/2),j',k}^{n+1} - \phi_x E_{i+(1/2),j',k}^n) \end{aligned} \quad (43)$$

where the coefficient $(\epsilon_x)_{jj'}$, defined as the element of the equivalent relative permittivity in the MRTD domain, is expressed as

$$\begin{aligned} (\epsilon_x)_{jj'} &= \frac{1}{\Delta y} \int_{-\infty}^{+\infty} \phi_j(y) \epsilon_x(y) \phi_{j'}(y) dy \\ &= \frac{1}{\Delta y} \int_{-\infty}^{+\infty} \phi \left(\frac{y}{\Delta y} - j \right) \epsilon_x(y) \phi \left(\frac{y}{\Delta y} - j' \right) dy \quad (44a) \\ &= \int_{-\infty}^{+\infty} \phi(y-j) \epsilon_x(y \Delta y) \phi(y-j') dy \end{aligned}$$

Similarly, the coefficient $(\sigma_x)_{ii',jj',kk'}$ is given as follows: is given as follows:

$$\begin{aligned} (\sigma_x)_{ii',jj',kk'} &= \frac{1}{\Delta x \Delta y \Delta z} \iiint_{\infty} \phi_{i+(1/2)}(x) \phi_{i'+(1/2)}(x) \phi_j(y) \\ &\times \phi_{j'}(y) \phi_k(z) \phi_{k'}(z) \sigma_x dx dy dz \\ &= \sigma_{\infty} \left(\int_{x_1}^{x_2} \phi_{i+(1/2)}(x) \phi_{i'+(1/2)}(x) \frac{dx}{\Delta x} \right) \\ &\times \left(\int_{y_1}^{y_2} \phi_j(y) \phi_{j'}(y) \frac{dy}{\Delta y} \right) \left(\int_{z_1}^{z_2} \phi_k(z) \phi_{k'}(z) \frac{dz}{\Delta z} \right) \\ &= \sigma_{\infty} \alpha_{i+(1/2),i'+(1/2)} \beta_{j,j'} \gamma_{k,k'} \end{aligned} \quad (44b)$$

In view of the localized feature of the basis functions, we have used a diagonal approximation in evaluating $a_{x,x'}$ ($\alpha = \alpha, \beta, \gamma; \chi = i + \frac{1}{2}j, k$); namely, we have replaced $\alpha_{i+(1/2),i' + (1/2)}\beta_{j,j'}\gamma_{k,k'}$ with $\alpha_{i+(1/2),i' + (1/2)}\beta_{j,j'}\gamma_{k,k'}\delta_{i,i'}\delta_{j,j'}\delta_{k,k'}$ in deriving update equations. Thus, (43) now becomes

$$\begin{aligned} & (\phi_x D_{i+(1/2),j,k}^{n+1} - \phi_x D_{i+(1/2),j,k}^n) \\ &= \left(\frac{\sigma_\infty \alpha_{i,i} \beta_{j,j} \gamma_{k,k} \Delta t}{2} \right) (\phi_x E_{i+(1/2),j,k}^{n+1} + \phi_x E_{i+(1/2),j,k}^n) \\ &+ \varepsilon_0 \sum_{j'=-\infty}^{\infty} (\varepsilon_x)_{j,j'} (\phi_x E_{i+(1/2),j',k}^{n+1} - \phi_x E_{i+(1/2),j',k}^n) \end{aligned} \quad (45)$$

where $\delta_{i,i'}$ is the Kronecker symbol representing unity when $i=i'$ otherwise zero. Furthermore, when the PEC strip is infinitesimally thin at the gridpoint j_0 , $\beta_{j,j}$ can be simply written as $\beta_{j,j}\delta_{j,j_0}$.

For an open grounded planar structure as shown in Fig. 5, all grids in the original region along the y direction are defined in the region $[0, N_y]$. Note that the summation index j' in (45) spans the original structure as well as all the image regions. However, all the image field quantities can be expressed in terms of fields in the original region bounded by $[0, N_y]$. According to the image principle [31], a tangential E field in the image region (parallel to the PEC ground plane) is oddly symmetric to its original field, while a tangential H field in the image region is evenly symmetric to its mirror field. Thus the summation (45) degenerates into a simpler form as

$$\begin{aligned} & (\phi_x D_{i+(1/2),j,k}^{n+1} - \phi_x D_{i+(1/2),j,k}^n) \\ &= \left(\frac{\sigma_\infty \alpha_{i,i} \beta_{j,j} \gamma_{k,k} \Delta t}{2} \right) \delta_{j,j_0} (\phi_x E_{i+(1/2),j,k}^{n+1} + \phi_x E_{i+(1/2),j,k}^n) \\ &+ \varepsilon_0 \sum_{j'=0}^{N_y} (\varepsilon_x^*)_{j,j'} (\phi_x E_{i+(1/2),j',k}^{n+1} - \phi_x E_{i+(1/2),j',k}^n) \end{aligned} \quad (46)$$

with

$$\sum_{j'=0}^{N_y} (\varepsilon_x^*)_{j,j'} = \sum_{j'=0}^{N_y} (\varepsilon_x)_{j,j'} - \sum_{j'=-N_y}^{-1} (\varepsilon_x)_{j,j'} \quad (47)$$

where the first term corresponds to the original circuits and the second one results from its image structure.

By taking the inverse operation of the equation in (46), we can obtain the update equation for the x -component of the E fields as follows:

$$\begin{aligned} \phi_x E_{i+(1/2),j,k}^{n+1} &= \sum_{j'=0}^{N_y} [A]_{j,j'} \phi_x E_{i+(1/2),j',k}^n \\ &+ \frac{1}{\varepsilon_0} \sum_{j'=0}^{N_y} [B]_{j,j'} (\phi_x D_{i+(1/2),j',k}^{n+1} \\ &- \phi_x D_{i+(1/2),j',k}^n) \end{aligned} \quad (48)$$

where the matrices $[A]$ and $[B]$ are given by

$$[A] = \left[[e_x^*]_{j,j'} + \frac{\sigma_\infty \alpha_{i,i} \beta_{j,j} \gamma_{k,k} \Delta t}{2\varepsilon_0} \delta_{j,j_0} \right]^{-1} \cdot \left[[e_x^*]_{j,j'} - \frac{\sigma_\infty \alpha_{i,i} \beta_{j,j} \gamma_{k,k} \Delta t}{2\varepsilon_0} \delta_{j,j_0} \right] \quad (49a)$$

$$[B] = \left[[e_x^*]_{j,j'} + \frac{\sigma_\infty \alpha_{i,i} \beta_{j,j} \gamma_{k,k} \Delta t}{2\varepsilon_0} \delta_{j,j_0} \right]^{-1} \quad (49b)$$

In common with the approach typically employed in the FDTD method, the MRTD algorithm can also accommodate different material parameters in the update equations for inhomogeneous computational regions, as is evident from the expressions given in (48) and (49).

5.2. APML Modeling

To truncate the computational domain, we apply an APML that incorporates the MRTD field expansions. For the sake of generality, we represent the relative permittivity and permeability as a diagonal tensor. Then, in a generalized APML medium, the Maxwell equations in the frequency domain become

$$\nabla \times \vec{H} = j\omega\varepsilon_0 \bar{\varepsilon} \cdot \vec{E} \quad (50)$$

$$\nabla \times \vec{E} = -j\omega\mu_0 \bar{\mu} \cdot \vec{H} \quad (51)$$

where the APML constitutive parameter matrix can be represented as

$$\bar{\varepsilon} = \begin{bmatrix} s_x^{-1} s_y s_z & 0 & 0 \\ 0 & s_x s_y^{-1} s_z & 0 \\ 0 & 0 & s_x s_y s_z^{-1} \end{bmatrix} \quad (52a)$$

with

$$s_\alpha = 1 + \frac{\sigma_\alpha}{j\omega\varepsilon_0} \quad (\alpha = x, y, z) \quad (52b)$$

By using the generalized differential matrix operators [34], the Maxwell equation can thus be written in matrix form for the APML region:

$$\begin{bmatrix} 0 & -\partial_z & \partial_y \\ \partial_z & 0 & -\partial_x \\ -\partial_y & \partial_x & 0 \end{bmatrix} \begin{bmatrix} H_x \\ H_y \\ H_z \end{bmatrix} = j\omega\varepsilon_0 \varepsilon_r \begin{bmatrix} s_y s_z s_x^{-1} & 0 & 0 \\ 0 & s_x s_z s_y^{-1} & 0 \\ 0 & 0 & s_x s_y s_z^{-1} \end{bmatrix} \begin{bmatrix} E_x \\ E_y \\ E_z \end{bmatrix} \quad (53)$$

$$\begin{bmatrix} 0 & -\partial_z & \partial_y \\ \partial_z & 0 & -\partial_x \\ -\partial_y & \partial_x & 0 \end{bmatrix} \begin{bmatrix} E_x \\ E_y \\ E_z \end{bmatrix} = -j\omega\mu_0 \begin{bmatrix} s_y s_z s_x^{-1} & 0 & 0 \\ 0 & s_x s_z s_y^{-1} & 0 \\ 0 & 0 & s_x s_y s_z^{-1} \end{bmatrix} \begin{bmatrix} H_x \\ H_y \\ H_z \end{bmatrix} \quad (54)$$

Note that s_x, s_y, s_z are parameters associated with wave attenuation in the x, y, z directions, respectively. Usually an APML region consists of a number of subregions, including APML faces, edges, and corners. As the most generalized case, we consider an APML corner where a wave is absorbed in all (x, y, z) directions. Since the three components of the E fields are similar, we need only to illustrate the x component.

Because of the reciprocal relation of $s_x(\alpha = x, y, z)$ appearing in Eqs. (53) and (54), we have to adopt a two-step approach by defining an electric flux density:

$$D_x = \left(\frac{1 + (\sigma_y/j\omega\epsilon_0)}{1 + (\sigma_x/j\omega\epsilon_0)} \right) \epsilon_0 \epsilon_r(y) E_x \quad (55)$$

With the frequency-time converter, $j\omega \Leftrightarrow (\partial/\partial t)$, we can convert (55) and the first equation of (53) into the time domain:

$$\frac{\partial D_x}{\partial t} + \frac{\sigma_z}{\epsilon_0} D_x = \frac{\partial H_z}{\partial y} - \frac{\partial H_y}{\partial z} \quad (56)$$

$$\epsilon_0 \epsilon_r \frac{\partial E_x}{\partial t} + \epsilon_0 \frac{\sigma_y}{\epsilon_0} E_x = \frac{\partial D_x}{\partial t} + \frac{\sigma_x}{\epsilon_0} D_x \quad (57)$$

By expanding all the fields in terms of the scaling functions in space and rectangular pulse function in time, substituting them into (56), (57), and then employing the Galerkin method, we can derive their corresponding update equations:

$$\begin{aligned} \phi_x D_{i+(1/2),j,k}^{n+1} &= \left(\frac{1 - (\sigma_z \Delta t / 2\epsilon_0)}{1 + (\sigma_z \Delta t / 2\epsilon_0)} \right) \phi_x D_{i+(1/2),j,k}^n \\ &+ \left(\frac{1}{1 + (\sigma_z \Delta t / 2\epsilon_0)} \right) \sum_m a(m) \\ &\times \left(\phi_z H_{i+(1/2),j+m+(1/2),k}^{n+(1/2)} \frac{\Delta t}{\Delta y} \right. \\ &\left. - \phi_y H_{i+(1/2),j,k+m+(1/2)}^{n+(1/2)} \frac{\Delta t}{\Delta z} \right) \end{aligned} \quad (58)$$

$$\begin{aligned} \phi_x E_{i+(1/2),j,k}^{n+1} &= \left(\frac{1 - (\sigma_y \Delta t / 2\epsilon_0)}{1 + (\sigma_y \Delta t / 2\epsilon_0)} \right) \phi_x E_{i+(1/2),j,k}^n \\ &+ \frac{1}{\epsilon_0} \left(\frac{1}{1 + (\sigma_y \Delta t / 2\epsilon_0)} \right) \sum_{j'=0}^{N_y} ([\epsilon_x^*]^{-1})_{j,j'} \\ &\times \left[\left(1 + \frac{\sigma_x \Delta t}{2\epsilon_0} \right) \phi_x D_{i+(1/2),j',k}^{n+1} \right. \\ &\left. - \left(1 - \frac{\sigma_x \Delta t}{2\epsilon_0} \right) \phi_x D_{i+(1/2),j',k}^n \right] \end{aligned} \quad (59)$$

Following the same procedure developed above, we can also obtain magnetic field equations in the frequency and time domains, whose x components read

$$B_x = \left(\frac{1 + (\sigma_y/j\omega\epsilon_0)}{1 + (\sigma_x/j\omega\epsilon_0)} \right) \mu_0 \mu_r H_x \quad (60)$$

$$-\frac{\partial B_x}{\partial t} - \frac{\sigma_z}{\epsilon_0} B_x = \frac{\partial E_z}{\partial y} - \frac{\partial E_y}{\partial z} \quad (61)$$

$$\mu_0 \mu_r \frac{\partial H_x}{\partial t} + \mu_0 \frac{\sigma_y}{\epsilon_0} H_x = \frac{\partial B_x}{\partial t} + \frac{\sigma_x}{\epsilon_0} B_x \quad (62)$$

Their associated/update equations now become

$$\begin{aligned} \phi_x B_{i,j+(1/2),k+(1/2)}^{n+(1/2)} &= \left(\frac{1 - (\sigma_z \Delta t / 2\epsilon_0)}{1 + (\sigma_z \Delta t / 2\epsilon_0)} \right) \phi_x B_{i,j+(1/2),k+(1/2)}^{n-(1/2)} \\ &+ \left(\frac{1}{1 + (\sigma_z \Delta t / 2\epsilon_0)} \right) \sum_m a(m) \\ &\times \left(\phi_y E_{i,j+(1/2),k+m+1}^n \frac{\Delta t}{\Delta z} \right. \\ &\left. - \phi_z H_{i,j+m+1,k+(1/2)}^n \frac{\Delta t}{\Delta y} \right) \end{aligned} \quad (63)$$

$$\begin{aligned} \phi_x H_{i,j+(1/2),k+(1/2)}^{n+(1/2)} &= \left(\frac{1 - (\sigma_y \Delta t / 2\epsilon_0)}{1 + (\sigma_y \Delta t / 2\epsilon_0)} \right) \phi_x H_{i,j+(1/2),k+(1/2)}^{n-(1/2)} \\ &+ \frac{1}{\mu_0 \mu_r} \left(\frac{1}{1 + (\sigma_y \Delta t / 2\epsilon_0)} \right) \\ &\times \left[\left(1 + \frac{\sigma_x \Delta t}{2\epsilon_0} \right) \phi_x B_{i,j+(1/2),k+(1/2)}^{n+(1/2)} \right. \\ &\left. - \left(1 - \frac{\sigma_x \Delta t}{2\epsilon_0} \right) \phi_x B_{i,j+(1/2),k+(1/2)}^{n-(1/2)} \right] \end{aligned} \quad (64)$$

We can derive the remaining MRTD update equations in the same manner for all the APML-face, edge, and corner regions.

5.3. Extraction of MIC characteristics

Most of the MIC characteristics can be extracted from the time or frequency domain voltages and currents. Since the time-domain-updated quantities in the MRTD do not

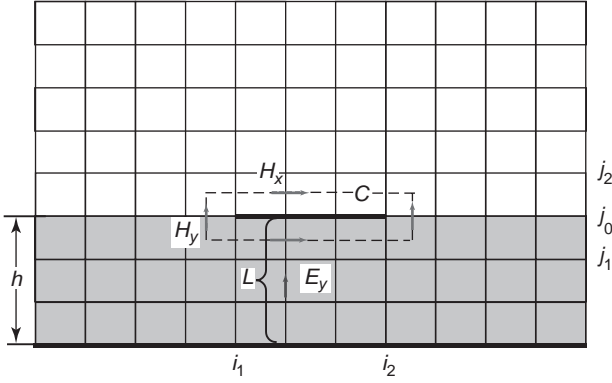


Figure 6. The integral paths C and L for the time-domain voltage and the current of a microstrip line.

represent fields but only the field expansion coefficients, we must first construct the total fields from these coefficients. For instance, the time-domain voltage for a microstrip line can be solved, as shown in Fig. 6, by taking an integration of E_y from the ground plane to the strip along an integral path L with the specified values of x_0 and z_0 . The time-domain voltage is then given as

$$\begin{aligned}
 V &= - \int_0^h E_y(x_0, y, z_0, t_0) dy \\
 &= - \sum_{l=0}^{N_s} \int_{l\Delta y}^{(l+1)\Delta y} \left[\iiint E_y(x, y, z, t) \delta(x - x_0) \right. \\
 &\quad \left. \times \delta(z - z_0) \delta(t - t_0) dx dz dt \right] dy \\
 &= - \sum_{l=0}^{N_s} \left[\int_{l\Delta y}^{(l+1)\Delta y} \sum_{i,j,k=-\infty}^{+\infty} \phi_y E_{i_0-i_j+(1/2),k_0-k}^n \phi(i) \phi(k) \right. \\
 &\quad \left. \times \phi_{j+(1/2)}(y) dy \right] \\
 &= - \sum_{l=0}^{N_s} \left[\sum_{i,j,k=-\infty}^{+\infty} \phi_y E_{i_0-i_j+l+(1/2),k}^n \phi(i) \phi(k) b(j) \Delta y \right]
 \end{aligned} \tag{65}$$

with

$$b(j) = \int_{-1/2}^{1/2} \phi(y-j) dy \tag{66}$$

where N_s is the number of cells counted from the ground plane to the PEC strip and $h = N_s \Delta y$. Note that the summation indices i, j, k must span all the real and image regions.

Similarly, we can solve the time-domain current by integrating the magnetic field intensity surrounding the strip along an enclosed contour C as shown in Fig. 6, and

described below

$$\begin{aligned}
 I &= \oint_C \vec{H} \cdot d\vec{l} \\
 &= \left[\int_{[i_1-(1/2)]\Delta x}^{[i_1+(1/2)]\Delta x} H_x(x, y_1, z_0, t_0) dx + \dots \right. \\
 &\quad \left. + \int_{[j_2-(1/2)]\Delta x}^{[j_2+(1/2)]\Delta x} H_x(x, y_1, z_0, t_0) dx \right] \\
 &\quad - \left[\int_{[i_1-(1/2)]\Delta x}^{[i_1+(1/2)]\Delta x} H_x(x, y_2, z_0, t_0) dx + \dots \right. \\
 &\quad \left. + \int_{[j_2-(1/2)]\Delta x}^{[j_2+(1/2)]\Delta x} H_x(x, y_2, z_0, t_0) dx \right] \\
 &\quad + \left[- \int_{[j_0-(1/2)]\Delta y}^{[j_0+(1/2)]\Delta y} H_y(x_1, y, z_0, t_0) dy \right. \\
 &\quad \left. + \int_{[j_0-(1/2)]\Delta y}^{[j_0+(1/2)]\Delta y} H_y(x_2, y, z_0, t_0) dy \right]
 \end{aligned} \tag{67}$$

where the first integration can be derived as

$$\begin{aligned}
 &\int_{[i_1-(1/2)]\Delta x}^{[i_1+(1/2)]\Delta x} H_x(x, y_1, z_0, t_0) dx \\
 &= \int_{[i_1-(1/2)]\Delta x}^{[i_1+(1/2)]\Delta x} \left[\iiint H_x(x, y, z, t) \delta(y - y_1) \right. \\
 &\quad \left. \times \delta(z - z_0) \delta(t - t_0) dy dz dt \right] dx \\
 &= \int_{[i_1-(1/2)]\Delta x}^{[i_1+(1/2)]\Delta x} \sum_{i,j,k=-\infty}^{+\infty} \phi_k H_{i_1-j,k_0-k}^{n+(1/2)} \phi(j) \phi(k) \phi_i(x) dx \\
 &= \sum_{i,j,k=-\infty}^{+\infty} \phi_k H_{i_1+i_{j_1-j},k_0-k}^{n+(1/2)} \phi(j) \phi(k) b(i)
 \end{aligned} \tag{68}$$

We finally have the time-domain current as follows:

$$\begin{aligned}
 I &= \sum_{l=i_1}^{i_2} \left[\sum_{i,j,k=-\infty}^{+\infty} (\phi_x H_{l+i_{j_1-j},k_0-k}^{n+(1/2)} \right. \\
 &\quad \left. - \phi_x H_{l+i_{j_2-j},k_0-k}^{n+(1/2)}) \phi(j) \phi(k) b(i) \right] \\
 &\quad + \sum_{i,j,k=-\infty}^{+\infty} [(\phi_y H_{i_2-i_{j_0+j},k_0-k}^{n+(1/2)} \\
 &\quad - \phi_y H_{i_1-i_{j_0+j},k_0-k}^{n+(1/2)}) \phi(i) \phi(k) b(j)]
 \end{aligned} \tag{69}$$

The two most important characteristics for a transmission line are the effective dielectric constant $\epsilon_{r,\text{eff}}$ and characteristic impedance Z_0 . The effective dielectric constant $\epsilon_{r,\text{eff}}$

defined as

$$\varepsilon_{r,\text{eff}}(\omega) = \frac{\beta^2(\omega)}{\omega^2 \varepsilon_0 \mu_0} \quad (70)$$

with

$$\beta(\omega) = \frac{1}{(z_j - z_i)} \text{angle} \left(\frac{\text{FFT}[V(z_i, t)]}{\text{FFT}[V(z_j, t)]} \right) \quad (71)$$

where z_i and z_j are two points along the transmission line separated by a distance $(z_j - z_i)$ and FFT denotes the fast Fourier transform to the time-domain voltage signals, $V(z_i, t)$ and $V(z_j, t)$. We find that it is not always necessary to extract the propagation characteristics using a post-processing algorithm [35] when the APMLs are used for mesh truncation.

Subsequently, the characteristic impedance Z_0 is calculated from

$$Z_0 = \frac{\text{FFT}\{V(z_i, t)\}}{\text{FFT}\{I(z_i, t)\}} \quad (72)$$

Apparently, both the time-domain voltages and currents can be solved at a specified position z_i , as mentioned previously.

On the basis of the defined voltage signals at each port, we can solve for the scattering parameters for a multiport

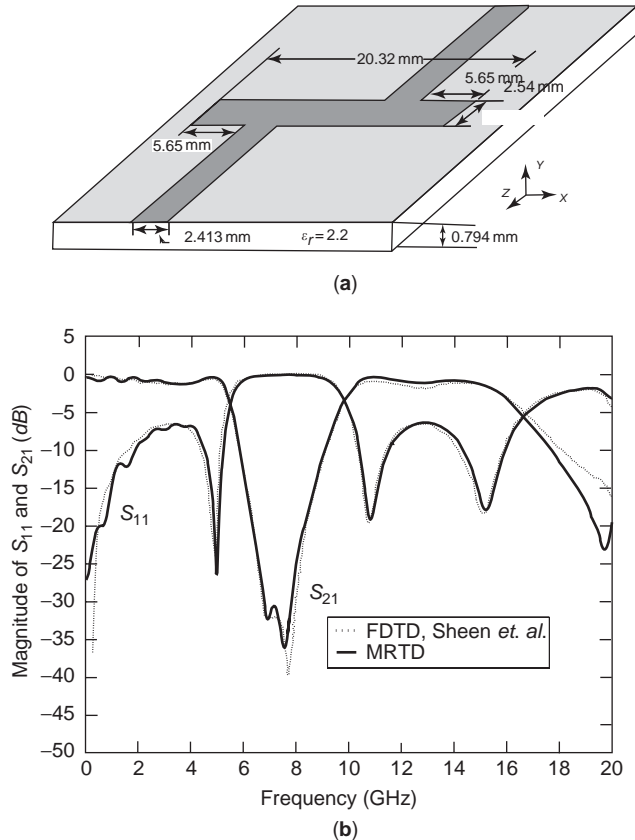


Figure 7. (a) Geometry and dimensions for a microstrip lowpass filter; (b) magnitudes of the S parameters S_{11} and S_{21} .

Table 4. Spatial and Time Discretization for a Microstrip Lowpass Filter

Discretization	MRTD	FDTD
Δx (mm)	0.8128	0.4064
Δy (mm)	0.3970	0.2650
Δz (mm)	0.8467	0.4233
Δt (ps)	0.3996	0.4410
$N_x \times N_y \times N_z$	$45 \times 10 \times 45$	$80 \times 16 \times 100$
VDR		15.82%
CPU time (s)	3553.77	19782.42c
TDR		17.96%

millimeter-wave integrated circuit. The scattering matrix coefficients in the frequency domain for a multiport system are defined as

$$[V]^- = [S][V]^+ \quad (73)$$

where $[V]^-$ and $[V]^+$ are the reflected and incident voltage vectors, respectively, and $[S]$ denotes the scattering matrix [36]. An arbitrary element on the scattering matrix S_{ij} can be derived from

$$S_{ij} = \frac{\text{FFT}\{V_i^-(t)\} \sqrt{Z_{0j}}}{\text{FFT}\{V_j^+(t)\} \sqrt{Z_{0i}}} \quad (74)$$

where $V_i^-(t)$ and $V_j^+(t)$ are the reflected and incident voltage signals defined at ports i and j , respectively and $\sqrt{Z_{0i}}$ and $\sqrt{Z_{0j}}$ are their corresponding characteristic impedance values at these two ports.

5.4. Application Results

Next we apply the developed MRTD technique to analyze a microstrip lowpass filter as shown in Fig. 7a. Six- and four-layer APMLs are used for termination of computational domain along the direction of wave propagation and other open walls; the image technique is employed for the ground plane termination.

The computational volume is discretized into $45 \times 10 \times 45$ cells as given in Table 4. The central strip segment is specified with the area of $25\Delta x \times 3\Delta z$, and the time update is terminated at $N_t = 4000$. We observe good agreement within a wide frequency range between the results of the scattering parameters derived from the MRTD and FDTD approaches [37], as seen in Fig. 7b. However, the MRTD approach requires much less computational CPU time (3,553.77 s) compared to that of the FDTD (19,782.42 s). A 333 MHz, a 128 M RAM Pentium II-MAX PC Compatible is used for all computations. The computational volume difference ratio (VDR) and CPU time difference ratio (TDR) between the MRTD scheme and the FDTD method are 15.82% and 17.96%, respectively.

6. CONCLUSIONS

In this article, we have introduced the fundamental concepts of MRA, scaling functions, and wavelets. On the basis of these concepts, we have developed a cubic spline

Battle–Lemarie scaling and wavelet function–based MRTD scheme, in conjunction with an APMML absorption boundary condition and an image technique, for generalized electromagnetic engineering applications. We have demonstrated the applications of the MRTD scheme by analyzing a TEM wave propagation in a dielectric-layered space and a microstrip lowpass filter. It is found that the developed MRTD scheme is highly efficient for all cases investigated and requires only a fraction of computational space and CPU time that are used in the FDTD techniques at the price of complexity in mathematical modeling. References 1–13 are on MRTD, Refs. 14–28 are on MRA, Refs. 29–33 are on APMML, and Refs. 34–37 are general.

Acknowledgment

The authors would like to thank Dr. Xian Wu for his comments and suggestions for the theory part of scaling functions and wavelets and Ms. Lori Donath for her great editing assistance.

BIBLIOGRAPHY

- M. Krumpolz and L. P. B. Katehi, New prospects for time domain analysis, *IEEE Microwave Guides Wave Lett.* **5**(11):382–384 (Nov. 1995).
- M. Krumpolz and L. P. B. Katehi, MRTD: New time domain schemes based on multiresolution analysis, *IEEE Trans. Microwave Theory Tech.* **44**(4):555–571 (April 1996).
- R. L. Roberson, E. M. Tentzeris, M. Krumpolz, and L. P. B. Katehi, Modeling of dielectric cavity structures using multiresolution time domain analysis, *Int. J. Numerical Modeling: Electron. Networks Devices Fields* **11**:55–68 (April 1998).
- R. L. Roberson, E. M. Tentzeris, M. Krumpolz, and L. P. B. Katehi, MRTD analysis of dielectric cavity structures, *Proc. IEEE MTT-S Digest*, 1996, pp. 1861–1864.
- C. D. Sarris, L. P. B. Katehi, and J. F. Harvey, Application of multiresolution analysis to the modelling of microwave and optical structures, *Opt. Quantum Electron.* **32**:657–679 (Aug. 2000).
- M. Fujii and W. J. R. Hoefer, A three-dimensional Haar-wavelet-based multiresolution analysis similar to the FDTD method-derivation and application, *IEEE Trans. Microwave Theory Tech.* **46**(12):2463–2475 (Dec. 1998).
- M. Fujii and W. J. R. Hoefer, Field-singularity correction in 2-D time-domain Haar-wavelet modelling of waveguide components, *IEEE Trans. Microwave Theory Tech.* **49**(4):685–691 (April 2001).
- Y. W. Cheong, Y. M. Lee, K. H. Ra, J. G. Kang, and C. C. Shin, Wavelet-Galerkin scheme of time-dependent inhomogeneous electromagnetic problem, *IEEE Microwave Guide Wave Lett.* **9**(8):297–299 (Aug. 1999).
- M. Fujii and W. J. R. Hoefer, Application of biorthogonal interpolating wavelet to the Galerkin scheme of time dependent Maxwell's equations, *IEEE Microwave Wireless Compon. Lett.* **11**(1) (Jan. 2001).
- T. Dogaru and L. Carin, Multiresolution time-domain using CDF biorthogonal wavelets, *IEEE Trans. Microwave Theory Tech.* **49**(5):902–912 (May 2001).
- Q. Cao and Y. Chen, Scaling-function based multiresolution time domain analysis for planar printed millimetre-wave integrated circuits, *IEE Proc. Microwaves Anten. Propag.* **148**(3):179–187 (June 2001).
- E. M. Tentzeris, A. Cangellaris, L. P. B. Katehi, and J. Harvey, Multiresolution time-domain (MRTD) adaptive schemes using arbitrary resolutions of wavelet, *IEEE Trans. Microwave Theory Tech.* **50**(2):501–516 (Feb. 2002).
- L. P. B. Katehi, J. F. Harvey, and E. Tentzeris, Time-domain analysis using multiresolution expansion, in A. Taflov, ed., *Advances in Computational Electrodynamics: The Finite-Difference Time-Domain Method*, Artech House, Boston, 1998, Chap. 3.
- G. Bachmam, L. Narici, and E. Beckenstein, *Fourier and Wavelet Analysis*, Springer, New York, 2000.
- A. Boggess and F. J. Narcowich, *A First Course in Wavelets with Fourier Analysis*, Prentice-Hall, Englewood Cliffs, NJ, 2001.
- R. N. Bracewell, *The Fourier Transform and Its Applications*, McGraw-Hill, New York, 1965.
- E. O. Brigham, *The Fast Fourier Transform and Its Applications*, Prentice-Hall, Englewood Cliffs, NJ, 1988.
- C. K. Chui, *An Introduction to Wavelets*, Academic Press, San Diego, CA, 1992.
- A. Cohen, Biorthogonal wavelets, in C. K. Chui, ed., *Wavelets: A Tutorial in Theory and Applications*, Academic Press, San Diego, 1992, pp. 123–152.
- I. Daubechies, *Ten Lectures on Wavelets*, SIAM, Philadelphia, PA, 1992.
- B. Jawerth and W. Sweldens, An overview of wavelet based multiresolution analysis, *SIAM Rev.* **36**(3):377–412 (1994).
- B. P. Lathi, *Linear Systems and Signals*, Berkeley-Cambridge Press, Carmichael, CA, 1992.
- S. G. Mallat, A theory for multiresolution signal decomposition: the wavelet representation, *IEEE Trans. Pattern Anal. Machine Intell.* **11**(7):674–693 (1989).
- S. G. Mallat, Multifrequency channel decompositions of images and wavelet model, *IEEE Trans. Acoust. Speech Signal Process.* **37**(12):2091–2110 (1989).
- Y. Meyer, *Ondelettes et Opérateurs*, I: *Ondelettes*, II: *Opérateurs de Calderón Zygmund*, III: (with R. Coifman), *Opérateurs Multilinéaires*, Hermann, Paris, 1990 (English translation of first volume, *Wavelets and Operators*, was published by Cambridge Univ. Press, 1993).
- Q. Cao and Y. Chen, Fundamental research on multiresolution time domain scheme and its application, *Electromagnetics.* **6**:485–496 (Aug.–Sept. 2001).
- A. Cohen, I. Daubechies, and J.-C. Feauveau, *Commun. Pure Appl. Math.* **45**:485 (1992).
- I. Daubechies, Orthogonal bases of compactly supported wavelets, *Commun. Pure Appl. Math.* **41**:909–996 (1988).
- J. P. Berenger, A perfectly matched layer for the absorption of electromagnetic waves, *J. Comput. Phys.* **114**:185–200 (Oct. 1994).
- Z. S. Sacks, D. M. Kingsland, R. Lee, and J. F. Lee, A perfectly matched layer anisotropic absorber for use as an absorbing boundary condition, *IEEE Trans. Anten. Propag.* **43**(12):1460–1463 (Dec. 1995).
- S. D. Gedney, An anisotropic perfectly matched layered-absorbing medium for the truncation of FDTD lattice, *IEEE Trans. Anten. Propag.* **44**(12):1630–1639 (Dec. 1996).
- E. M. Tentzeris, R. L. Robertson, M. Krumpolz, J. F. Harvey, and L. P. B. Katehi, PML absorbing boundary conditions for the characterization of open microwave circuit components

- using the multiresolution time-domain technique (MRTD), *IEEE Trans. Anten. Propag.* **47**(11):1709–1715 (Nov. 1999).
33. Q. Cao, Y. Chen, and R. Mittra, Multiple image technique (MIT) and anisotropic perfectly matched layer (APML) in implementation of MRTD scheme for boundary truncations of microwave structures, *IEEE Trans. Microwave Theory Tech.* **50**(6):1578–1589 (June 2002).
 34. Y. Chen, K. Sun, B. Beker, and R. Mittra, Unified matrix presentation of Maxwell's and wave equations using generalized differential matrix operators, *IEEE Trans. Educ.* **41**(1):61–69 (Feb. 1998).
 35. M. A. Schamberger, S. Kosanovich, and R. Mittra, Parameter extraction and correction for transmission lines and discontinuities using the finite-difference time-domain method, *IEEE Trans. Microwave Theory Tech.* **44**(6):919–925 (June 1996).
 36. D. M. Pozar, *Microwave Engineering*, Addison-Wesley, Reading, MA, 1993.
 37. D. M. Sheen, S. M. Ali, M. D. Abouzahra, and J. A. Kong, Application of the three-dimensional finite-difference time-domain method to the analysis of planar microwave circuits, *IEEE Trans. Microwave Theory Tech.* **38**(7):849–857 (July 1990).

NEGATIVE RESISTANCE

CLIFFORD A. KING
KWOK K. NG
Lucent Technologies

Resistance is the measure of allowed current passing through a component when a terminal voltage is applied. Ohm's law defines that the resistance is the ratio of the applied voltage to the resulting current:

$$R = \frac{V}{I} \quad (1)$$

This simple I - V relationship is shown in Fig. 1a. Sometimes a component deviates from having a linear relationship, resulting in a nonlinear curve. An example of a rectifier is shown in Fig. 1b. Such resistance is referred to as being nonlinear, as opposed to linear. It is also helpful to distinguish the static resistance (V/I) from the dynamic resistance or differential resistance (the slope of the I - V curve as dV/dI). So in a linear resistor, the static resistance is the same as the dynamic resistance ($V/I = dV/dI$), whereas in a nonlinear resistor, $V/I \neq dV/dI$.

It is understood that the term negative resistance refers to the dynamic characteristic, that is, the slope of the I - V curve (dV/dI) is negative. Notice that in the example of a common negative resistance (Fig. 1c), only dV/dI is negative, but the static resistance is always positive. That is why negative resistance and negative differential resistance are used interchangeably. Negative resistance can also be classified into two shapes: (1) N-shape negative resistance, as shown in Fig. 1c; and (2) S-shape negative resistance, as shown in Fig. 1d. The S-shape negative resistance is typical behavior of a switch.

Most of the devices exhibiting negative resistance have two terminals, but there are also devices with three or more terminals. An example is thyristor. The function of the extra terminal is to control the shape of the I - V characteristics between the two terminals that carry the majority of the current. Specifically, for the S-shape curve shown in Fig. 1d, the triggering (breakover) voltage or current before negative resistance sets in can be varied.

There is yet another group of devices where the negative resistance does not come from a negative slope in the I - V curve. In these devices, when an AC voltage is applied, the resulting AC current is not in phase with the applied voltage. The majority of this phase delay comes from the transit time of charge which is generated within the device and subsequently travels to the boundaries of the devices and to the terminals. For this reason, these devices are called transit-time devices. The phase relationship between the applied voltage and the resulting current is shown in Fig. 1e. The unique feature is that when the small-signal voltage is positive, the small-signal current is negative, giving rise to negative AC power

absorbed. So this type of negative resistance comes from \vec{V}/\vec{I} being negative, as opposed to dV/dI being negative. It is worthwhile to mention that both inductor and capacitor cause a phase shift between the AC voltage and current. The crucial requirement here is that in order to have net AC power gain, a phase shift or more than 90° is necessary, which is not achievable with either a capacitor or an inductor.

In the following sections, the negative resistance devices originating from dV/dI being negative are discussed, followed by their applications. Finally, similar discussions on the transit-time devices are presented.

1. TUNNEL DIODE

Tunneling is a quantum-mechanical process whereby electrons with insufficient energy to surmount a thin energy barrier tunnel directly through it. In a semiconductor p-n junction, significant tunneling occurs when both sides of the junction are heavily doped so that the depletion region (energy barrier) is thin. Also, since the tunneling process requires conservation of energy, the tunnel diode (Esaki diode) is fabricated such that both sides of the junction are degenerately doped so that states of equal energy exist on both sides of the junction (in the conduction and valence bands). Figure 2a illustrates the situation under low forward bias where the bottom of the conduction band on the n side and the top of the valence band on the p side overlap and significant tunneling occurs. At higher bias, the overlap becomes smaller and the tunneling current decreases, thereby producing the negative differential resistance (NDR) feature mentioned earlier. Eventually, at still higher forward voltages, when the overlap disappears as in Fig. 2b, the normal diffusion current becomes dominant and the current increases with bias once again. A useful figure of merit for NDR devices is the peak-to-valley ratio, which is a measure of the ratio of the peak current obtained just before the onset of NDR (point *B* in Fig. 1c) to the minimum current at the termination of the NDR region (point *C* in Fig. 1c). Peak-to-valley ratios of 3 to 20 are typical for semiconductor tunnel diodes.

2. RESONANT TUNNELING STRUCTURES

A semiconductor quantum well is a structure formed when materials with either a conduction or valence band discontinuity are joined such that the discontinuity creates a potential well. For example, a well formed in the conduction band is accomplished by sandwiching a layer of high-electron-affinity material in between layers of lower-electron-affinity material. The conduction band discontinuity serves as the barrier in the well. In the case of a resonant tunneling structure, the quantum well exists between two very thin, low electron affinity layers that have a large discontinuity and serve as the well barrier.

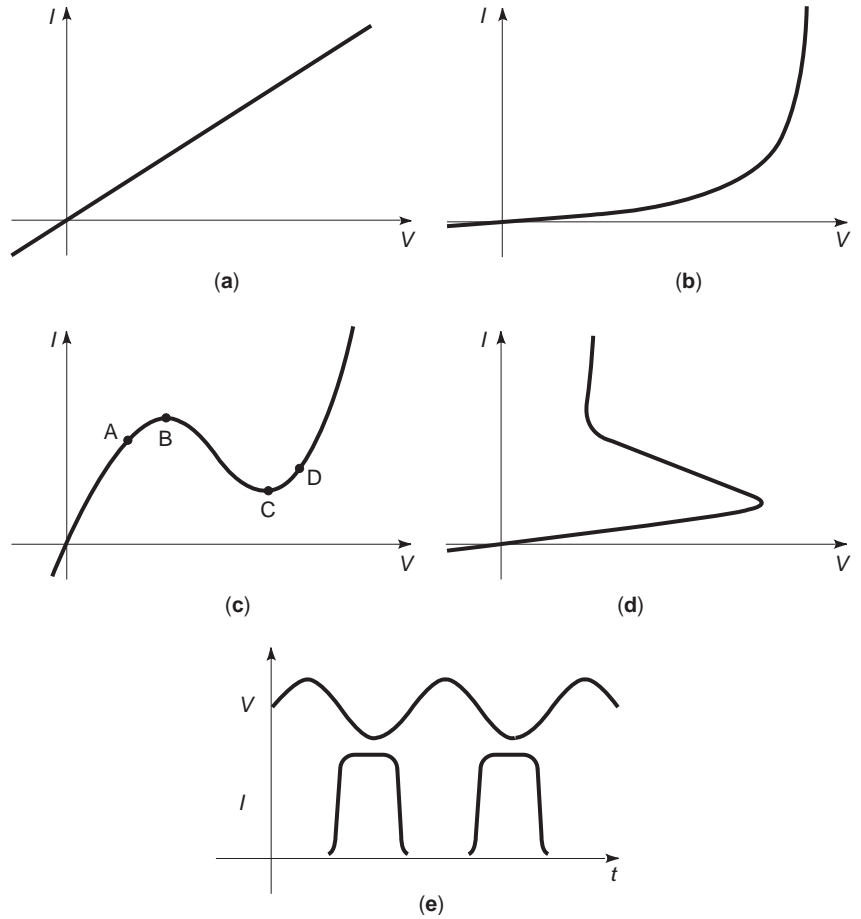


Figure 1. I - V relationship showing (a) linear resistance, (b) nonlinear resistance, (c) N-shape differential negative resistance, and (d) S-shape negative differential resistance; (e) in a transit-time device, negative resistance comes from the phase difference between terminal voltage and current.

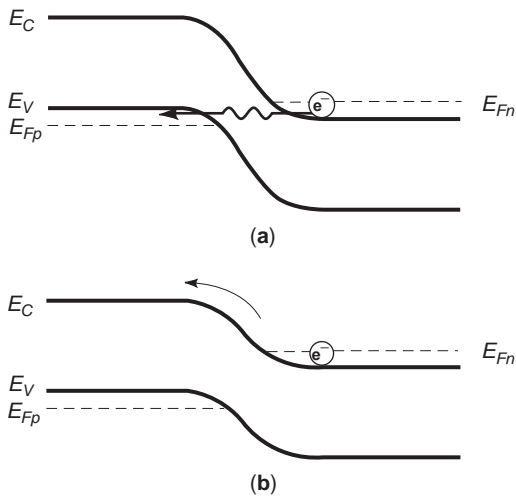


Figure 2. Band diagram showing how forward bias voltage affects the tunneling current in a tunnel diode. In (a), the junction is slightly forward biased so that there is still an overlap of states at the same energy in the conduction and valence bands. In (b), the forward bias is sufficient to remove the overlap and the current consists of carriers which surmount the barrier (diffusion current).

For example, in the GaAs/AlGaAs system, as shown in the inset of Fig. 3, the GaAs serves as the quantum well and the outside contact regions, while the barriers are made from AlGaAs. As the well is made thin, the continuum of states in the conduction band become discrete levels of subbands according to the following expression

$$E_n - E_C = \frac{h^2 n^2}{8m^* W^2}, \quad n = 1, 2, 3 \dots \quad (2)$$

where E_C is the conduction band edge, h is Planck's constant, m^* is the effective mass, and W is the thickness of the well. The band diagram of Fig. 3 shows how significant current flows only when E_C of the contact region aligns with the first subband energy. As the bias is further increased, the tunnel current diminishes, leading to a decrease in total current and thus an NDR region in the I - V characteristic. Depending on the depth of the well (height of the barriers), tunneling through higher subband energies can also occur, leading to additional NDR regions.

A resonant tunneling bipolar transistor (RTBT) results when the quantum well is placed within the emitter or base of a bipolar transistor. A resonant tunneling hot-electron transistor (RHET) has a similar structure without the emitter-base p-n junction. The advantages of such three-terminal structures are that the negative resistance

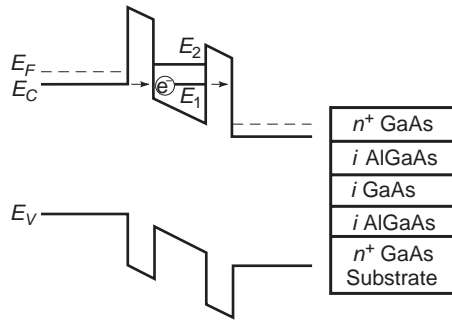


Figure 3. Band diagram of a resonant tunneling diode under bias conditions such that the conduction band edge aligns with the first subband level E_1 , causing a tunneling current to flow. The layer structure is shown in the inset.

is tunable by the base bias, and the output is isolated from the input.

3. SEMICONDUCTOR SWITCHES

A thyristor is a four-layer Si device consisting of an n-p-n-p structure. The structure is called a silicon controlled rectifier (SCR) when a gate contact is made to the middle p region, as shown in the inset of Fig. 4. As positive voltage is applied to the anode, a small reverse bias current flows until either the depletion regions of the central junctions join (a condition known as punchthrough), or avalanche multiplication occurs at the reverse biased junction. Beyond this “breakover voltage” (V_{BO}), a large current flows and the voltage across the device drops. An S-shape negative resistance region arises in this device as it switches from the high-impedance forward-blocking state to the low-impedance on state. With positive gate current, the breakover voltage is lowered, which is the mechanism used to trigger the device into the on state. Once the SCR

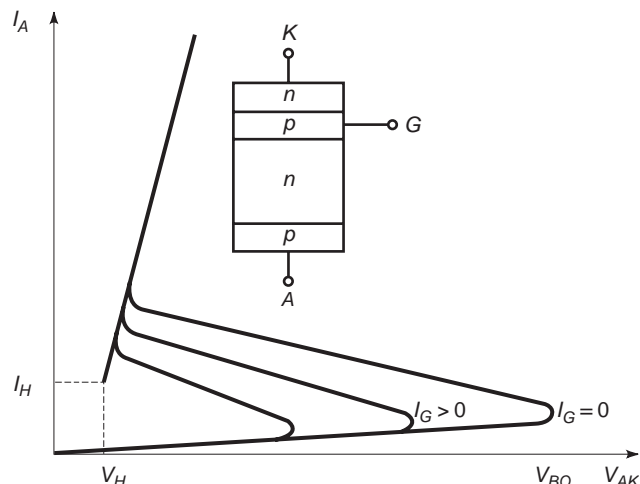


Figure 4. SCR current-voltage characteristics illustrating how positive gate current lowers the breakover voltage. The device structure is shown in the inset.

is switched on, an applied bias lower than the holding voltage (V_H) will turn the device off.

Other semiconductor switches which possess S-shape negative-resistance regions similar to the thyristor are the metal insulator semiconductor switch (MISS) and the planar doped barrier switch [1].

4. GUNN EFFECT AND THE TRANSFERRED ELECTRON DEVICE

The transferred electron device directly exploits a particular material property of semiconductors like GaAs and InP, which have lower mobility satellite valleys to which electrons transfer at high applied electric fields. A uniformly doped length of these materials display normal positive ohmic characteristics for low fields, but for applied voltages that cause the electric field to exceed some critical field a reduction in the current results, as more electrons are transferred to the low-mobility satellite valley. The critical electric field for GaAs is 3.2 kV/cm and 10.5 kV/cm for InP. This process of intervalley scattering can create instabilities within the semiconducting material with sufficient applied bias, which gives rise to microwave oscillations. The occurrence of these oscillations is known as the Gunn effect, named for its first observer.

The transferred-electron device (TED) or Gunn diode is simply composed of a length of material with two contacts on the ends. Planar structures grown on semiinsulating substrates are also possible. The essence of operation of the TED lies with the generation of a charge accumulation region within the device. Once an adequate bias is applied across the length of the device, an accumulation region will form in an area where there may be a crystal defect or a difference in doping—something that causes the electric field to be slightly larger than in the rest of the device. Once the fields in this region is sufficiently large to possess a negative differential mobility, a space charge instability will form and grow (either as a simple accumulation of electrons or a dipole consisting of electrons and ionized donors). Once the field in this unstable region rises above the point where it possesses a negative differential mobility, the dipole ceases to grow (matures) and continues to travel along the length of the device with the saturated drift velocity (v_{sat}). The result is charge pulses that arrive at the anode with a period of L/v_{sat} , where L is the length of the device. The transferred electron device is widely used as oscillator for 1–100-GHz applications.

5. REAL-SPACE TRANSFER DEVICES

Real-space transfer is similar to the Gunn effect described above, except that electrons are transferred to a lower-mobility material in real space at high fields rather than being transferred in momentum space. Unlike the Gunn effect, however, either electrons or holes can be transferred. In its most common implementation, a heterojunction barrier (e.g., AlGaAs/GaAs) and modulation doping form the basis of the structure. At low fields, carriers confined in the low-bandgap material flow from one contact to the other exhibiting normal ohmic behavior. At sufficiently

high bias, some carriers gain enough energy to surmount the barrier into the low-mobility, high-bandgap material. This transfer lowers the effective mobility and decreases the total current, which gives rise to an NDR region.

The charge injection transistor (CHINT) or negative-resistance field-effect transistor (NERFET) is a three-terminal device utilizing real-space transfer. The structure used in the Si/SiGe system is illustrated in Fig. 5. A lightly doped channel of low-bandgap material (SiGe) exists between source and drain. A barrier between the collector and the channel is formed by a layer of undoped Si, which has a larger bandgap than the SiGe. The inset of Fig. 5. illustrates the band structure of the CHINT device perpendicular to the channel. As voltage is applied between the source and drain, the carriers present in the channel produce a current flow just as in a normal FET. As the bias increases and the field across the channel increases, some carriers gain sufficient energy to surmount the barrier and are collected by the collector. This siphoning of carriers by the collector causes the total drain current to decrease with increasing drain voltage producing an NDR characteristic.

6. APPLICATIONS

The most common uses of negative resistance are for circuit applications in oscillators, amplifiers, memory, and active filters. An oscillator is made by combining a negative-resistance device together with a tuned *RLC* circuit so that the net resistance becomes zero. (The majority of *R* comes from parasitics.) The frequency of the oscillations is determined by the *LC* of the circuit. The series connection of a normal resistance and a negative resistance provides a simple example of a negative-resistance amplifier. By connecting a negative resistance (*-r*) in series with a normal resistor (*R*) as in Fig. 6a, and

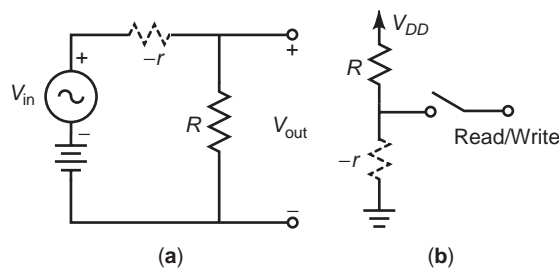


Figure 6. A simple negative-resistance amplifier is shown in (a), while (b) exhibits the use of a bistable negative-resistance device as a memory element.

taking the output across the normal resistor, the voltage ratio becomes

$$\frac{V_{out}}{V_{in}} = \frac{R}{R + (-r)} \tag{3}$$

which produces a voltage gain. Active filters for use on monolithic microwave integrated circuits (MMIC) are greatly improved with the use of a negative resistance to compensate for losses in inductors, transmission lines, and lossy dielectrics. In these filters, the negative resistance is combined with the *L* and *C* components to increase the overall quality factor (*Q*), which leads to a sharper cutoff at the frequency band edges. Memory circuits using negative resistance exploit the fact that these devices exhibit bistable behavior. Figure 6b shows an elemental memory circuit with a negative-resistance device loaded with a resistor *R* from a supply voltage *V_{DD}*. The *I-V* curve of Fig. 1c shows the two staple states, *A* and *D*, possible for a given load line. By forcing the voltage across the negative resistance device high or low, the circuit is forced to one or the other of the stable states.

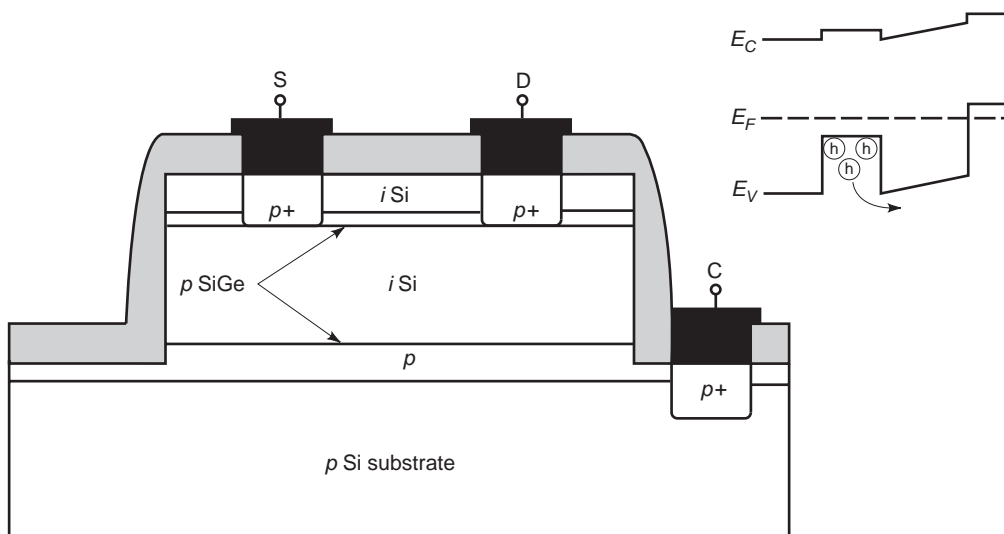


Figure 5. Charge injection transistor (CHINT) device structure for the Si/SiGe materials system. The top channel consists of small bandgap SiGe separated from the collector by an undoped Si barrier region. The inset schematically exhibits the device band diagram in the direction perpendicular to the channel.

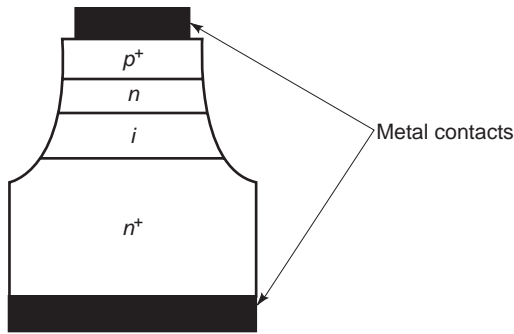


Figure 7. Structure of an IMPATT diode.

7. TRANSIT-TIME DEVICES

In a transit-time device, there are two important mechanisms. The first is the generation and buildup of charge within the device, followed by transit of these charges across the length of the device. Although the transit of charge is quite similar for different transit-time devices, the generation or injection of charge is quite different among them. These mechanisms include avalanche multiplication, thermionic emission, and tunneling. The most popular device among them is the IMPATT (impact ionization avalanche transit-time) diode. This discussion will be confined to the operation of the IMPATT diode. Other transit-time devices are BARITT (barrier injection transit-time) diode, TRAPATT (trapped-plasma avalanche-triggered transit) diode, DOVATT (double-velocity avalanche transit-time) diode, MITATT (mixed-tunnel-avalanche transit-time) diode, DOVETT (double-velocity transit-time) diode, TUNNETT (tunnel injection transit-time) diode, and QWITT (quantum-well injection transit-time) diode. Brief discussions on each of these can be found in Ref. 1.

An IMPATT diode can be realized by different physical structures. All of these are variations of a p-n junction. The most common is called the Read diode and is shown in Fig. 7. Common semiconductor materials are Si and GaAs. Here the p-n junction provides a high field for avalanche multiplication, and the large intrinsic layer is the region

where transit time is originated. The DC characteristics are shown in Fig. 8a. Notice that in the I - V curve, there is no region where the slope is negative. During operation, the diode is reverse biased with a DC value near the breakdown (V_{BD}), so that a small AC signal will drive it into avalanche multiplication. Referring again to Fig. 1e, the delay of current with respect to the voltage comes from two components. The first is the time it requires to build up the charge internally. The second is the transit time across this intrinsic region. This charge buildup time is a characteristic of avalanche multiplication, and it is absent in other injection mechanisms such as tunnelling and thermionic emission. That is why the IMPATT diode is more efficient in power generation compared with, for example, a BARITT diode. After the charge is generated, it traverses the intrinsic region with saturation velocity (v_{sat}). During the time of this transit, there is a continuous terminal current of magnitude

$$J = \frac{Q_A v_{sat}}{L} \quad (4)$$

where Q_A is the charge per area (cross-sectional) and L is the region of the intrinsic layer. The magnitude of Q_A is related to the magnitude and frequency of the AC signal and detailed derivation is beyond the scope of this article. Assuming that the transit time dominates the phase delay, the frequency of operation is given by

$$f = \frac{v_{sat}}{2L} \quad (5)$$

since the duration of the current pulse corresponds to the transit time of the charge packet, and this current pulse is roughly half of the cycle.

The main application of a transit-time diode is microwave generation in the 3–300 GHz range. The transit-time devices are the most efficient microwave oscillators in this frequency range. Usually a transit-time device is a discrete component and it is mounted in a resonator cavity. When a DC bias is applied to the device, an AC output is produced. Applications of these oscillators are in radar

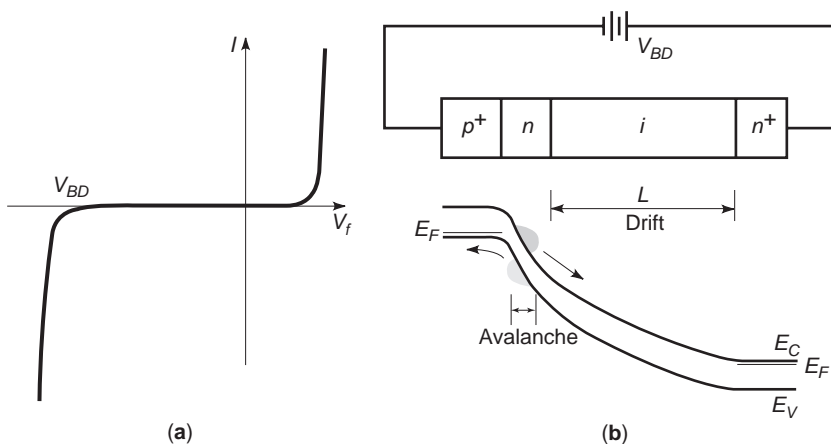


Figure 8. (a) The I - V curve of an IMPATT diode does not process a negative slope; (b) schematic diagram showing where the charge is generated (in this case by avalanche multiplication), and the region of charge transit.

systems and alarm systems. In high-power oscillators, a good heat sink is crucial.

BIBLIOGRAPHY

1. K. Ng, *Complete Guide to Semiconductor Devices*, McGraw-Hill, New York, 1995.

NEURAL NETWORKS FOR MICROWAVE CIRCUITS

QI-JUN ZHANG
MAKARAND DEO
JIANJUN XU
Carleton University
Ottawa, Canada

1. INTRODUCTION

Neural networks, also called *artificial neural networks* (ANNs), are information processing systems whose design was inspired by the studies of the ability of the human brain to learn from observations and to generalize by abstraction [1]. The fact that neural networks can be trained to learn arbitrary nonlinear input–output relationships from corresponding data has resulted in their use in a number of areas such as pattern recognition, speech processing, control, and biomedical engineering. In RF and microwave areas, ANN has been used to model passive and active devices to enhance circuit design. Neural networks can be trained using measured or simulated microwave device data, such as electromagnetic (EM) data for passive components and physics data for active devices. The trained neural networks become models of microwave devices and can be used in place of CPU-intensive EM/physics models to significantly speed up circuit design, while maintaining EM/physics-level accuracies. ANN-based modeling has been used to model a variety of passive and active components on both device and circuit levels [2]. ANN models can be realized in both frequency-domain and time-domain formats, compatible with the framework of existing CAD tools, including component’s geometric and physical parameters as optimization variables. ANN-based microwave models can be a pure neural network, or a knowledge-based neural network in which RF/microwave information is utilized together with neural networks.

The ANN modeling approach generally involves the following steps: (1) selecting appropriate ANN structure, (2) data generation and preprocessing, (3) ANN model training, (4) plugging the resultant neural model into a circuit simulator, and (5) simulation, optimization, and circuit design using ANN models. Each of these steps is elaborated in subsequent sections.

2. NEURAL NETWORK STRUCTURES

We describe neural network structural issues to better understand what neural networks are and why they have the ability to represent RF and microwave component behaviors. We study neural networks from the external input–output point of view, and also from the internal neuron information processing point of view. The most popularly used neural network structure, namely, the multilayer perceptron, is described in detail. The effects of structural issues on modeling accuracy are discussed.

2.1. Basic Components

A typical neural network structure has two types of basic components, namely, the processing elements and the interconnections between them [1]. The processing elements are called *neurons*, and the connections between the neurons are known as *links* or *synapses*. Every link has a corresponding weight parameter associated with it. Each neuron receives stimuli from other neurons connected to it, processes the information, and produces an output. Neurons that receive stimuli from outside the network are called *input neurons*; neurons whose outputs are externally used are called *output neurons*. Neurons that receive stimuli from other neurons and whose outputs are stimuli for other neurons in the network are known as *hidden neurons*. Different neural network structures can be constructed by using different types of neurons and by connecting them differently.

2.2. Neural Networks versus Conventional Modeling

The neural network approach can be compared with conventional approaches for a better understanding. The first approach is the detailed modeling approach (e.g., EM-based models for passive components and physics-based models for active devices), where the model is defined by a well-established theory. The detailed models are accurate but could be computationally expensive. The second approach is an approximate modeling approach, which uses either empirical or equivalent-circuit-based models for passive and active components. Evaluation of approximate models is much faster than that of the detailed models. However, the models are limited in terms of accuracy and input parameter range over which they can be accurate. Neural network approach is a new type of modeling approach where the model can be developed by learning from detailed (accurate) data of the RF/microwave component. After training, the neural network becomes a fast and accurate model representing the original component behaviors.

2.3. Multilayer Perceptrons Neural Network

2.3.1. Structure and Notation. Multilayer perceptrons (MLPs) is a popularly used neural network structure. In the MLP neural network, the neurons are grouped into layers. Let the total number of layers be L . The first layer is the input layer, the L th layer is the output layer, and layers 2 through $L - 1$ are hidden layers, as shown in Fig. 1.

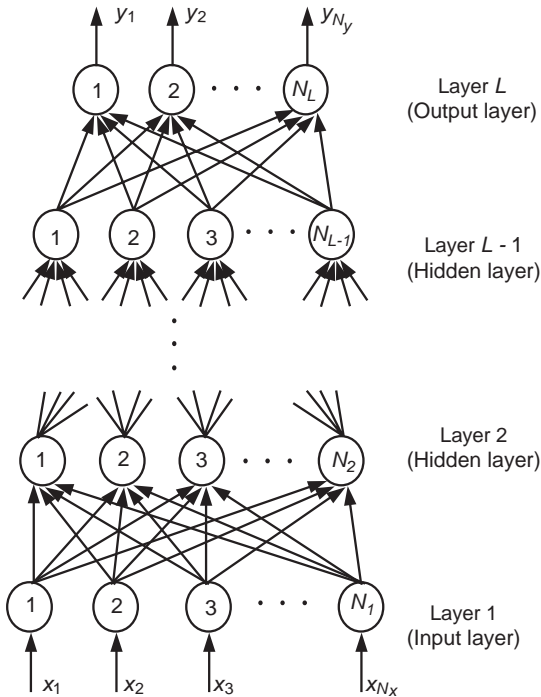


Figure 1. Multilayer perceptrons neural network structure. Typically, an MLP network consists of an input layer, one or more hidden layers, and an output layer. (Reprinted with permission from Ref. 1: Q. J. Zhang and K. C. Gupta, *Neural Networks for RF and Microwave Design*, Artech House Publishers, Norwood, MA, USA, 2000; www.artechhouse.com.)

2.3.2. Anatomy of Neurons. In the MLP network, each neuron processes the stimuli (inputs) received from other neurons. The process is done through a function called *activation function* in the neuron, and the processed information becomes the output of the neuron. Let z_i^l be the output of i th neuron of the l th layer, and let N_l be the number of neurons in the l th layer. Every neuron in the l th layer receives stimuli from the neurons of $l-1$ th layer: $z_1^{l-1}, z_2^{l-1}, \dots, z_{N_{l-1}}^{l-1}$. A typical i th neuron in the l th layer processes this information in two steps:

1. Each input is multiplied by the corresponding weight parameter, and the products are added to produce a weighted sum γ_i^l

$$\gamma_i^l = \sum_{j=0}^{N_{l-1}} w_{ij}^l z_j^{l-1} \quad (1)$$

where $w_{ij}^l, j > 0$, represent the weight of the link between j th neuron of the $(l-1)$ th layer and the i th neuron of the l th layer and w_{i0}^l represents the bias for the i th neuron of the l th layer.

2. The weighted sum in (1) is used to activate the neuron's activation function $\sigma(\cdot)$ to produce the final output of the neuron: $z_i^l = \sigma(\gamma_i^l)$. This output can, in turn, become the stimulus to neurons in the $(l+1)$ th

layer. The most commonly used hidden neuron activation function is the sigmoid function given by

$$\sigma(\gamma) = \frac{1}{1 + e^{-\gamma}} \quad (2)$$

Other functions that can also be used include the arc-tangent function and the hyperbolic tangent function. All these are smooth switch functions that are bounded, continuous, monotonic, and continuously differentiable. Input neurons use a relay activation function and simply relay the external stimuli to the hidden-layer neurons, $z_i^1 = x_i$, where x_i represents the i th external input to the MLP, $i = 1, 2, \dots, N_1$. In the case of neural networks for RF/microwave design, where the purpose is to model continuous electrical parameters instead of a binary relationship, a linear activation function can be used for output neurons. This makes it easier for the model to be trained since, according to the universal approximation theorem [3], a single layer of sigmoid functions in the hidden layer is sufficient to model the nonlinear input-output relationships. The linear activation function is defined as

$$\sigma(\gamma) = \gamma = \sum_{j=0}^{N_{l-1}} w_{ij}^l z_j^{l-1} \quad (3)$$

2.3.3. Feedforward Computation. Neural network feedforward computation is a process used to compute the output vector $\mathbf{y} = [y_1 \ y_2 \ \dots \ y_{N_y}]^T$ from the input vector $\mathbf{x} = [x_1 \ x_2 \ \dots \ x_{N_x}]^T$ and the weight vector \mathbf{w} , where N_x and N_y are numbers of external inputs and outputs of the MLP, respectively. Feedforward computation is useful not only during neural network training but also during the usage of the trained neural model. The external inputs are applied to the input neurons (i.e., the first layer) and the outputs from the input neurons are fed to the hidden neurons of the second layer. Continuing this way, the outputs of $(L-1)$ th-layer neurons are fed to the output-layer neurons (i.e., L th layer). During feedforward computation, neural network weights \mathbf{w} remain fixed. The computation is given by

$$z_i^1 = x_i, \quad i = 1, 2, \dots, N_1, \quad N_x = N_1 \quad (4)$$

$$z_i^l = \sigma \left(\sum_{j=0}^{N_{l-1}} w_{ij}^l z_j^{l-1} \right), \quad (5)$$

$$i = 1, 2, \dots, N_l, \quad l = 2, 3, \dots, L$$

$$y_i = z_i^L, \quad i = 1, 2, \dots, N_L, \quad N_y = N_L \quad (6)$$

Figure 2 shows physical representations of microstrip-line (passive) and FET (active) devices along with their corresponding neural models clearly showing choice of model inputs and outputs.

2.3.4. Speed and Accuracy of ANN Models. It may be noted that the simple formulas in (4)–(6) are now intended

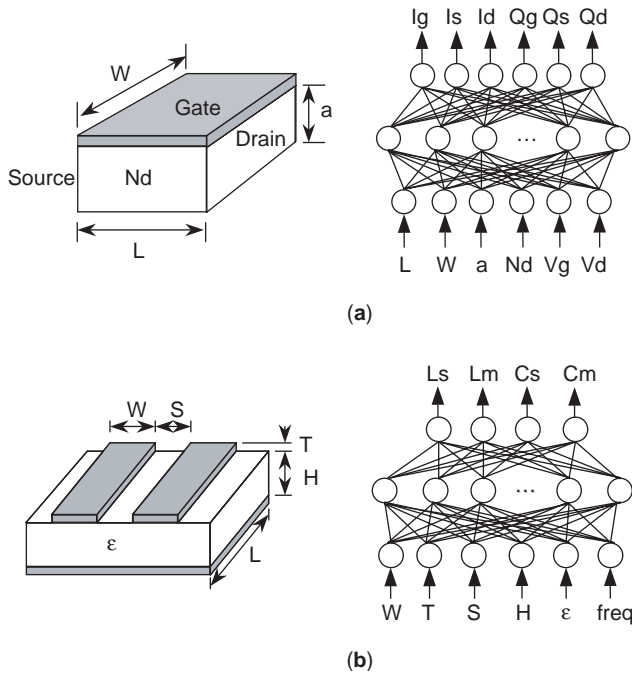


Figure 2. Physical models of (a) FET and (b) a microstrip line along with corresponding neural models.

for use as RF/microwave component models. It is evident that computation of these formulas is much easier than is numerical solution of theoretical EM or physics equations. This is why neural network models are much faster than detailed numerical models of RF/microwave components. The question of how such simple formulas for neural network can represent complicated behaviors can be answered by the universal approximation theorem.

The universal approximation theorem [3] states that there always exists a three-layer MLP neural network that can approximate any arbitrary, nonlinear, continuous, multidimensional function to any desired accuracy. This forms a theoretical basis for employing neural networks to approximate RF/microwave behaviors, which are functions of physical/geometric/bias parameters. MLP neural networks are distributed models; that is, no single neuron can produce the overall x - y relationship. For a given x , some neurons are switched to ON state, some are in OFF state, and others are in transition. This combination of neuron switching states enables the MLP to represent a given nonlinear input-output mapping. During the training process, the MLP weight parameters are adjusted, and at the end of training, they encode the component information from the corresponding x - y training data.

2.4. Other Neural Network Configurations

In addition to MLP, there are other ANN structures, such as radial basis function (RBF) networks, wavelet networks, and recurrent networks. In order to select a neural network structure for a given application, one starts by identifying the nature of the x - y relationship. Nondynamic modeling problems (or problems converted from dynamic to nondynamic using methods such as harmonic balance) can be solved using MLP, RBF, and wavelet

networks [1]. The most popular choice is the MLP. RBF and wavelet networks can be used when the problem exhibits highly nonlinear and localized phenomena (e.g., sharp variations). Time-domain dynamic behavior of nonlinear devices or circuits can be represented using recurrent neural networks (RNNs) [4] and dynamic neural networks (DNN) [5]. One of the most recent research directions in the area of microwave-oriented ANN structures is the knowledge-based network [6], which combines existing engineering knowledge (e.g., empirical equations and equivalent-circuit models) with neural networks.

3. ANN TRAINING

3.1. Defining ANN Inputs and Outputs

The first step toward developing a neural model is the identification of inputs (x) and outputs (y). Determination of the output parameters is based on the objectives of the neural network model. For example, real and imaginary parts of S parameters can be selected as outputs for passive component models, and currents and charges can be used for large-signal device models. Neural model input parameters are those device/circuit parameters (e.g., geometric, physical, bias, frequency) that affect the output parameter values.

3.2. Data Generation and Preprocessing

In this step, x - y sample pairs are generated using either simulation or measurement. The generated sample pairs could be divided into three sets, namely, training data, validation data, and test data. Training data is utilized to guide the training process, i.e., to update the neural network weight parameters during training. Validation data is used to monitor the quality of the neural network model during training and to determine stop criteria for the training process. Test data is used to independently examine the final quality of the trained neural model in terms of accuracy and generalization capability.

Scaling of data may also improve the training efficiency. Linear scaling of data can provide balance between different inputs (or outputs) whose values are different by orders of magnitude. Another scaling method is the logarithmic scaling, which can be applied to outputs with large variations in order to provide a balance between small and large values of the same output.

3.3. Formulation of Training Process

The most important step in neural model development is the neural network training. Let d_k be the k th sample of y in training data. We define neural network training error as

$$E_{T_r}(\mathbf{w}) = \frac{1}{2} \sum_{k \in T_r} \sum_{j=1}^{N_y} |y_j(\mathbf{x}_k, \mathbf{w}) - d_{jk}|^2 \tag{7}$$

where d_{jk} is the j th element of d_k , $y_j(\mathbf{x}_k, \mathbf{w})$ is the j th neural network output for input \mathbf{x}_k , T_r is the index set of all training data, and \mathbf{w} is the vector of neural network weight parameters.

The purpose of neural network training, in basic terms, is to adjust \mathbf{w} such that the error function $E_{T_r}(\mathbf{w})$ is minimized. Since $E_{T_r}(\mathbf{w})$ is a nonlinear function of the adjustable (i.e., trainable) weight parameters \mathbf{w} , iterative algorithms are often used to explore the \mathbf{w} space efficiently, beginning with an initialized value of \mathbf{w} and then iteratively updating it.

Neural network training algorithms commonly used in RF/microwave applications include gradient-based training techniques such as backpropagation, conjugate-gradient, and quasi-Newton methods. Global optimization methods such as simulated annealing and genetic algorithms can be used for increased quality of neural network training but at the cost of increased training time.

Neural network training process can be categorized into sample-by-sample training and batch-mode training. In sample-by-sample training also called *online training*, \mathbf{w} is updated each time a training sample is presented to the network. In batch-mode training, also known as *offline training*, \mathbf{w} is updated after each epoch, where an *epoch* is defined as a stage of training process that involves presentation of all the training data to the neural network once. The batch-mode training is more efficient because neural network weight update is done by considering errors in the entire training data. In the RF/microwave case, the data, which come from measurement or simulations, are typically offline so that batch data are available for training. Hence in RF/microwave modeling, batch-mode training is usually employed. A flowchart summarizing major steps in neural network training and testing is shown in Fig. 3 [7].

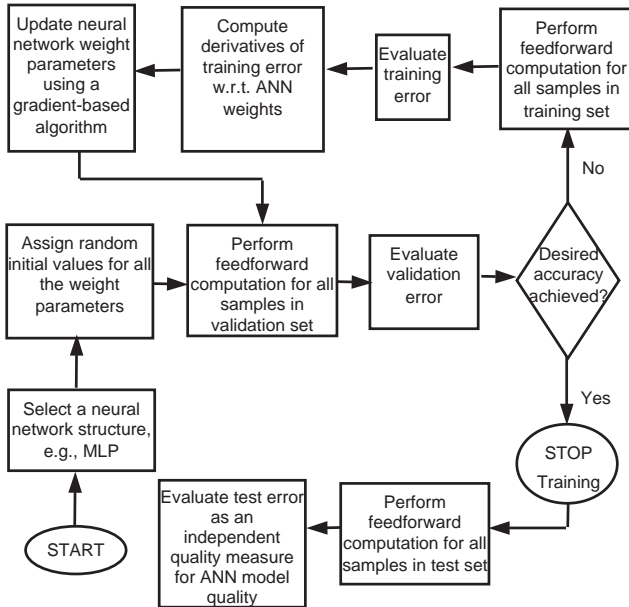


Figure 3. Flowchart demonstrating neural network training, neural model testing, and use of training, validation, and test datasets in ANN model development. (© 2003 IEEE, reprinted from Ref. 7 with permission from IEEE.)

3.4. Overlearning and Underlearning

The ability of a neural network to estimate output \mathbf{y}_k accurately when presented with input \mathbf{x}_k that is never seen during training (i.e., $k \notin T_r$) is called *generalization ability*. Let \hat{E}_V represent the validation error defined similarly to \hat{E}_{T_r} of (7) except that the dataset represents validation data instead of training data T_r . *Good learning* of a neural network is achieved when both training error (\hat{E}_{T_r}) and validation error (\hat{E}_V) have small values (e.g., 0.50%) and are close to each other. The ANN exhibits *overlearning* when it memorizes the training data but cannot generalize well (i.e., \hat{E}_{T_r} is small but $\hat{E}_V \gg \hat{E}_{T_r}$). Remedies for overlearning are, deleting a certain number of hidden neurons or adding more samples to the training data. The neural network exhibits *underlearning* when it has difficulties in learning the training data itself (i.e., $\hat{E}_{T_r} \gg 0$). Possible remedies are to add more hidden neurons or perturbing the current solution \mathbf{w} to escape from a local minimum of $E_{T_r}(\mathbf{w})$ and then continue training.

The automatic model generation (AMG) algorithm [8] automatically performs the model development process, including data generation with adaptive data sampling algorithm, training ANN, and determining the optimal number of hidden neurons by examining over- and underlearning. In this way, ANN models can be developed with minimum manual effort.

4. EM-ORIENTED NEURAL MODELING

4.1. Frequency-Domain Modeling

A frequency-domain neural model can represent Y or S parameters of a passive component with the speed of empirical models but with accuracy near detailed EM models [1]. Let \mathbf{x} represent an N_x vector containing the variables and \mathbf{y} represent an N_y vector containing the outputs (responses) of a passive component. For example, \mathbf{x} could contain geometric parameters such as length (L_R) and width (W_R) of an embedded resistor and signal frequency ω , and \mathbf{y} could contain corresponding Y or S parameters, as shown in Fig. 4.

Let \mathbf{f} represent a detailed EM relationship between \mathbf{x} and \mathbf{y}

$$\mathbf{y} = \mathbf{f}(\mathbf{x}) \quad (8)$$

to be modeled by a neural network. In general, \mathbf{f} can be accessible to microwave engineers in the form of a *data generator*:

$$\mathbf{d} = \mathbf{d}(\mathbf{x}) \quad (9)$$

For a given input \mathbf{x} , data generator $\mathbf{d}(\mathbf{x})$ can be used to compute and/or measure the outputs \mathbf{d} of the original problem. Data generation involves repetitive use of the data generator to obtain sample pairs $(\mathbf{x}_k, \mathbf{d}_k)$, where k is the sample index. These sample pairs are divided into training sets and test sets. The purpose of neural network

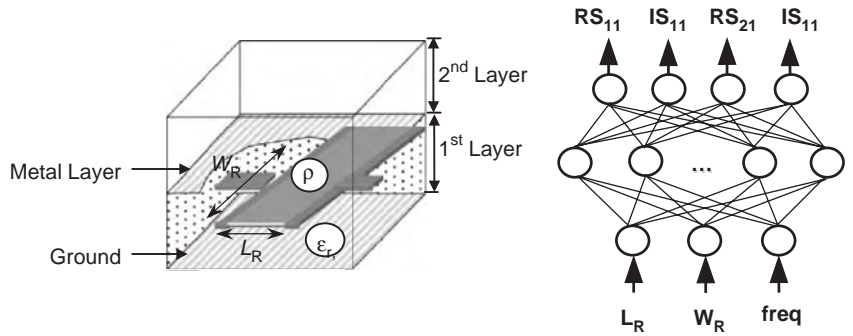


Figure 4. Geometric structure of embedded resistor and its neural model showing choice of inputs and outputs for the neural model.

modeling is to develop a fast neural model

$$y = f_{ANN}(x, w) \tag{10}$$

that accurately represents $f(x)$. Here, f_{ANN} is a neural network trained to learn samples of $f(x)$ from training data (x_k, d_k) , $k \in T_r$, and w is ANN weight vector. The trained fast neural model f_{ANN} can be used in place of CPU-intensive EM simulator during frequency-domain simulation and optimization.

4.2. Time-Domain Modeling

Time-domain models are important for CAD applications such as minimization of signal delay and crosstalk in high-speed VLSI interconnects. There is a need for time-domain models that include detailed EM effects. A time-domain neural model provides current/voltage relationships of a given passive component and their dependence on the component’s geometric parameters and time (t).

In a time-domain modeling approach, ANN can be used to provide coefficient values of the time-domain responses. Figure 5 explains the typical time-domain modeling approach.

For example, in the state space equation–neural network (SSE-NN) method [9], the frequency-domain and time-domain relations are given as follows:

$$H_{ij} = Y_{ij}(s) = \frac{b_0 + b_1s + \dots + b_{n-1}s^{n-1} + b_ns^n}{a_0 + a_1s + \dots + a_{n-1}s^{n-1} + s^n} \tag{11}$$

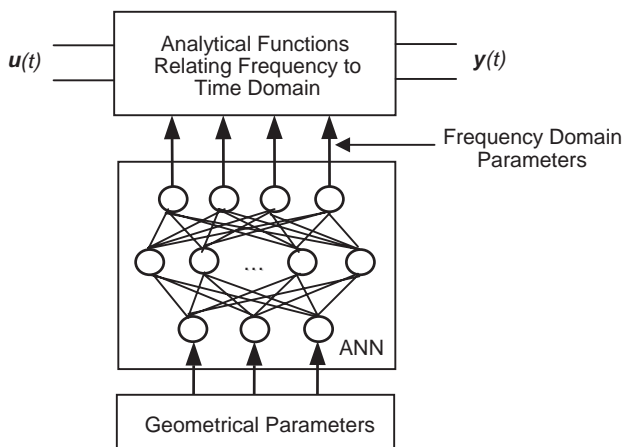


Figure 5. Time-domain EM-based ANN modeling approach.

This equation represents the Y-parameter transfer function between ports i and j of the EM structure. Here, s is the complex frequency and n represents the effective order of high-frequency behaviors of the passive component. The coefficients a_k , $k = 0, 1, \dots, n - 1$, and b_k , $k = 0, 1, \dots, n$ are related to physical/geometric parameters of the EM problem through an ANN. Following this, state space equations are used to express the time-domain responses as

$$\begin{cases} \dot{v}(t) = Av(t) + Bu(t) \\ i(t) = Cv(t) + Du(t) \end{cases} \tag{12}$$

where matrices A , B , C , and D are obtained by arranging the coefficients (i.e., the a and b values) estimated by ANN into a format specific to our choice of the transfer functions [9]; $v(t)$ represents state variables or voltages, and $u(t)$ and $i(t)$ are input voltage and output current waveforms, respectively. In summary, Eqs. (11) and (12) combined with a MLP form an EM based time-domain SSE-NN model of the passive component under consideration.

5. KNOWLEDGE-BASED NEURAL NETWORKS

The knowledge-based neural network (KBNN) approaches exploit the available microwave information in the form of empirical or equivalent-circuit models together with the neural models to develop fast and accurate hybrid EM-ANN models. The use of knowledge in neural networks helps reduce the amount of training data needed and enhance the extrapolation capability of the model. Here we summarize some of the major techniques developed to reduce the need for expensive data.

5.1. Difference Method (DM)

In this method, an ANN is trained to ascertain the difference between detailed EM data (obtained from simulator or measurements) and approximate model (equivalent-circuit and empirical relations) outputs [10]. The final model performs addition of equivalent-model output and the ANN output.

5.2. Knowledge-Based Neural Networks (KBNNs)

In this method, microwave knowledge in the form of empirical functions or analytical approximations is embedded into the neural network internal structure [6].

KBNN also accommodates multiple knowledge formulas in different regions of the parameter space using region definition neurons.

5.3. Prior Knowledge Input (PKI) Method

In this method, the empirical model outputs are used as inputs to the neural network model, in addition to the original problem inputs. In this case, the input–output mapping to be learnt by neural network is between the outputs of existing approximate model and the original problem [11].

5.4. Space-Mapped Neural Networks (SMNNs)

The SMNN concept divides the modeling problem into coarse-model part (empirical models) and fine-model part (EM or physics models). ANN is used to map the input parameters of the fine model into those of the coarse model. In this way, the coarse model aims to provide finer outputs by using suitably modified inputs with the help of mapping [12].

5.5. Equivalent Circuit–State Space Equation–Neural Networks (EC–SSE–NNs)

The difference between the equivalent-circuit model and actual EM data is represented by a state space model, and the state space model in turn is related to physical/geometric parameters by ANN. The final model output is the sum of approximated output of equivalent circuit and difference provided by the state space model. This technique is suitable for time-domain applications.

6. MODELING OF NONLINEAR RF/MICROWAVE DEVICES

For general nonlinear modeling problems, relationships between inputs and outputs of nonlinear circuits are not algebraic; they are related by differential equations. To model such relationships, two different categories of ANN-based approaches exist. The first category uses a combination of circuit and ANN models, where we rely on the circuit to define the dynamics and the ANN to define the nonlinearity. The second category uses dynamic or recurrent neural networks to directly represent the entire model, including both dynamic effect and nonlinearity. In the second category, we have a continuous time-domain formulation called *dynamic neural networks* (DNN) and a discrete time-domain formulation called recurrent neural networks (RNN).

6.1. Combined Circuit/ANN Approach for Nonlinear Device Modeling

In this approach, we use a known equivalent-circuit topology, but the nonlinear algebraic functions needed to describe the nonlinearities in the circuit branches are achieved by ANN. Figure 6 shows an FET model [13], where the function of the drain current with respect to gate and drain voltages is represented by an ANN. To train this model using DC and small-signal device data, an adjoint neural network [13] method can be used, which allows the ANN to learn the required derivative information between input and output neurons.

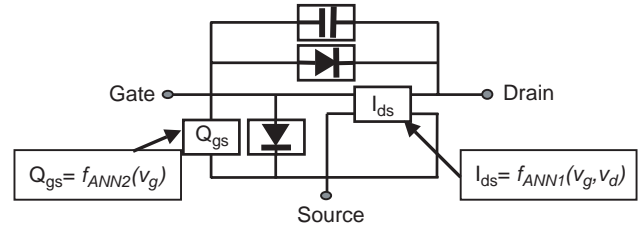


Figure 6. Neuron-based model of an FET where the nonlinear algebraic functions for current and charge are replaced by ANNs.

6.2. Continuous Time-Domain DNN Modeling

The DNN approach can be explained from the block schematic in Fig. 7. Let \mathbf{u} and \mathbf{y} be vectors of the input and the output signals of the nonlinear circuit, respectively. Let $\mathbf{y}^{(i)}(t) = d^i \mathbf{y}(t) / dt^i$ and $\mathbf{u}^{(j)}(t) = d^j \mathbf{u}(t) / dt^j$ represent the i th-order derivative of $\mathbf{y}(t)$ and the j th-order derivative of $\mathbf{u}(t)$ with respect to t , respectively. Let f_{ANN} represent a static multilayer perceptron (MLP) neural network. DNN is formulated as a reduced order representation of the original circuit [5]

$$\mathbf{y}^{(n)}(t) = f_{\text{ANN}}(\mathbf{y}(t), \mathbf{y}^{(1)}(t), \dots, \mathbf{y}^{(n-1)}(t), \mathbf{u}(t), \mathbf{u}^{(1)}(t), \dots, \mathbf{u}^{(n)}(t)) \quad (13)$$

where n is the effective order of the reduced model, $n < N_S$, and N_S is the order of the original nonlinear circuit. In this formulation, the signal flow from f_{ANN} input to output resembles differentiation; hence the model is referred to as a *differential dynamic neural network* (DDNN). In the integral DNN (IDNN) approach, the input–output relationship is reorganized as follows:

$$\mathbf{y}(t) = f_{\text{ANN}}(\mathbf{y}^{(1)}(t), \dots, \mathbf{y}^{(n)}(t), \mathbf{u}(t), \mathbf{u}^{(1)}(t), \dots, \mathbf{u}^{(n)}(t)) \quad (14)$$

Here the signal flow from f_{ANN} input to output resembles integration, as such the model is called *integral DNN* (IDNN).

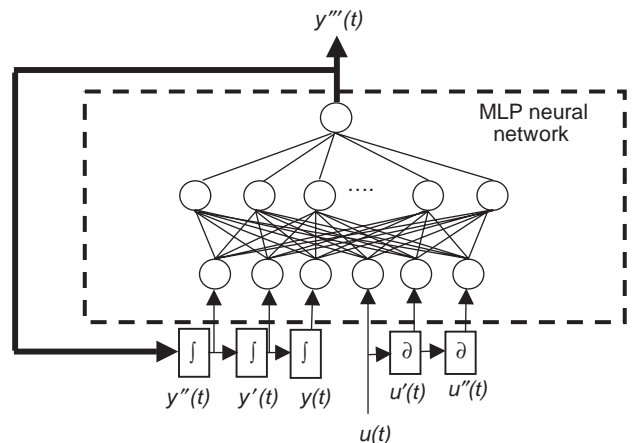


Figure 7. Dynamic neural network (DNN) for nonlinear circuit modeling in continuous time domain.

These two different formulations, DDNN and IDNN, are complementary formats of DNN and together form the DNN family. They can be used to represent the nonlinear microwave circuit behavior and can be used as models for high-level circuit and system design.

6.3. Discrete Time-Domain RNN Modeling

Recurrent neural networks (RNNs) are a special type of neural network with feedback from output to input and are capable of learning and then representing dynamic system behavior [4]. The nonlinear circuit modeling approach in discrete time domain using RNN is illustrated in Fig. 8. In order to derive a macromodel representing a nonlinear dynamic relationship, we first reformulate the original relationship in the discrete time domain with specific sampling rate into an input–output formulation as

$$\mathbf{y}(k) = \mathbf{g}(\mathbf{y}(k-1), \dots, \mathbf{y}(k-M_y), \mathbf{u}(k-1), \dots, \mathbf{u}(k-M_u), \mathbf{p}) \quad (15)$$

where k is the time index in the discrete time domain, $\mathbf{y}(k)$ is a simplified notation for $\mathbf{y}(k\tau)$, $\mathbf{u}(k)$ is a simplified notation for $\mathbf{u}(k\tau)$, τ is the time sampling interval, and \mathbf{g} is set of nonlinear functions. The terms \mathbf{y} , \mathbf{u} , and \mathbf{p} are vectors of output and input signals and circuit parameters, respectively. The number of delays M_y and M_u , of \mathbf{y} and \mathbf{u} , respectively, represent effective order of original nonlinear circuit as seen from input–output data. In the RNN approach, we use a neural network such as the MLP to represent the nonlinear function \mathbf{g} of (15). Furthermore, we use a reduced order representation such that M_y and M_u of (15) is replaced by n . In this way, the order of the RNN model is n , which can be much less than the order of the original circuit.

The input layer of the MLP contains buffered history of the circuit input and output signals, and the circuit parameter. Input and output waveforms of the original circuit are used as training data for RNN, which is trained by the backpropagation through time (BPTT) method.

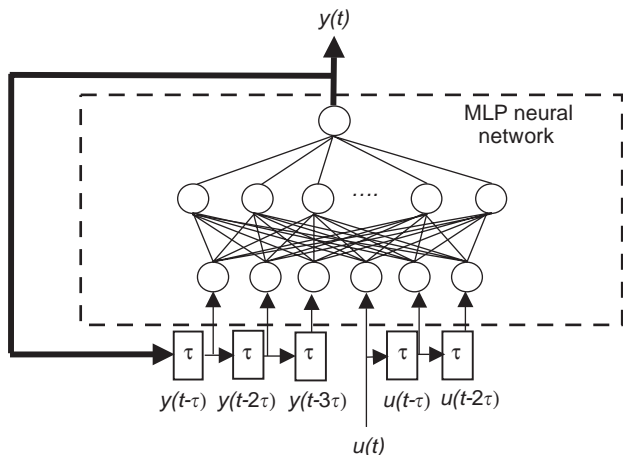


Figure 8. Recurrent neural network (RNN) for nonlinear circuit modeling in discrete time domain.

RNNs can be used to learn dynamics in both transient and steady-state stages [4].

7. USE OF ANN FOR CIRCUIT OPTIMIZATION

The trained ANN models for RF/microwave components can be used in circuit design and optimization [14]. If the ANN models have been trained from original EM/physics data, the use of such ANN models instead of original EM/physics models helps improve design speed while maintaining accuracy. To achieve this, the trained neural models are first incorporated into circuit simulators. An ANN model can be connected to other ANN models or any other models in the simulator to form a high-level circuit. During simulation, the circuit simulator passes input variables such as frequency and the physical parameters of a component to the ANN model, the ANN model then computes and returns the corresponding outputs of the neural network back to the simulator.

In case of knowledge-based ANN models, the knowledge part itself is usually already compatible with circuit simulator while the ANN part and its interaction with knowledge part can be incorporated into circuit simulator as functions of its weight parameters. While plugging DNN models, the dynamics can be represented by an equivalent circuit [5]. The combined circuit and ANN for such nonlinear models can then be implemented similarly to those of knowledge-based models.

Once the models are incorporated into the circuit environment, the device they represent can be optimized along with rest of the circuit with the model parameters as optimization variables. This approach allows the neural network inputs \mathbf{x} as optimization variables, for instance, physical/geometric parameters of the device or circuit. The performance optimization problem can be stated as minimization of errors between circuit responses and design specifications subject to electrical or physical/geometric constraints on the circuit elements.

Neural-network-based microwave optimization is especially significant for computationally expensive design tasks. It addresses the combined challenges due to (1) computational expenses of evaluating EM/physics effects in circuit components, (2) the size and complexities in today's RF/microwave circuits where the EM effects are present in many components at various levels of the design hierarchy, and (3) the need to repetitively vary physical/geometric parameters and re-evaluate EM/physics behaviors of all the components during design optimization. The use of neural network models helps to significantly accelerate EM/physics-based optimization.

BIBLIOGRAPHY

1. Q. J. Zhang and K. C. Gupta, *Neural Networks for RF and Microwave Design*, Artech House, Norwood, MA, 2000.
2. P. Burrascano, S. Fiori, and M. Mongiardo, A review of artificial neural networks applications in microwave computer-aided design, *Int. J. RF Microwave CAE* **9**:158–174 (1999).

3. K. Hornik, M. Stinchcombe, and H. White, Multilayer feedforward networks are universal approximators, *Neural Networks* **2**:359–366 (1989).
4. Y. Fang, M. Yagoub, F. Wang, and Q. J. Zhang, A new macromodeling approach for nonlinear microwave circuits based on recurrent neural networks, *IEEE Trans. Microwave Theory Tech.* **48**:2335–2344 (2000).
5. J. Xu, M. Yagoub, R. Ding, and Q. J. Zhang, Neural-based dynamic modeling of nonlinear microwave circuits, *IEEE Trans. Microwave Theory Tech.* **50**:2769–2780 (2002).
6. F. Wang and Q. J. Zhang, Knowledge-based neural models for microwave design, *IEEE Trans. Microwave Theory Tech.* **45**:2333–2343 (1997).
7. Q. J. Zhang, K. C. Gupta, and V. K. Devabhaktuni, Artificial neural networks for RF and microwave design- from theory to practice, *IEEE Trans. Microwave Theory Tech.* **51**:1339–1350 (2003).
8. V. K. Devabhaktuni, M. C. E. Yagoub, and Q. J. Zhang, A robust algorithm for automatic development of neural network models for microwave applications, *IEEE Trans. Microwave Theory Tech.* **49**:2282–2291 (2001).
9. X. Ding, V. K. Devabhaktuni, M. C. E. Yagoub, B. Chattaraj, M. Deo, J. Xu, and Q. J. Zhang, Neural network approaches to electromagnetic based modeling of passive components and their applications to high-frequency and high-speed nonlinear circuit optimization, *IEEE Trans. Microwave Theory Tech.* **52**:436–444 (2004).
10. P. M. Watson and K. C. Gupta, EM-ANN models for microstrip vias and interconnects in dataset circuits, *IEEE Trans. Microwave Theory Tech.* **44**:2495–2503 (1996).
11. P. M. Watson, K. C. Gupta, and R. L. Mahajan, Applications of knowledge-based artificial neural network modeling to microwave components, *Int. J. RF Microwave CAE* **9**:254–260 (1999).
12. J. W. Bandler, M. A. Ismail, J. E. Rayas-Sanchez, and Q. J. Zhang, Neuromodeling of microwave circuits exploiting space-mapping technology, *IEEE Trans. Microwave Theory Tech.* **47**:2417–2427 (1999).
13. J. J. Xu, M. C. E. Yagoub, R. Ding, and Q. J. Zhang, Exact adjoint sensitivity analysis for neural-based microwave modeling and design, *IEEE Trans. Microwave Theory Tech.* **51**:226–237 (2003).
14. A. H. Zaabab, Q. J. Zhang, and M. S. Nakhla, A neural network modeling approach to circuit optimization and statistical design, *IEEE Trans. Microwave Theory Tech.* **43**:1349–1358 (1995).

NOISE AND INTERFERENCE MODELING

GEOFFREY C. ORSAK
Southern Methodist University

Noise and interference are inevitable realities of collecting data or taking measurements in the real world. In some cases, the noise level may be so insignificant as to allow the engineer to ignore its effects. However, this situation generally occurs only in very controlled circumstances, such as those in the laboratory or when signal powers are exceptionally large relative to the noise.

Unfortunately, it is more generally the case that the noise and interference cannot be ignored. Rather, design and analysis must be done with careful attention to the corruptive effects of these disturbances. One way to ensure an effective final design is to have accurate models of the noise components of the signals of interest. Examples of the impact of high and low levels of noise on the observation of a sinusoid are shown in Fig. 1.

Modeling these effects can range from being relatively straightforward to being rather difficult if not impossible. To assist in this endeavor, it is the purpose of this article to describe various methods of characterizing noise and interference signals and to elaborate on some of the most popular models in practice today.

1. STATISTICAL DESCRIPTIONS OF NOISE

Because of its random nature, characterizing noise necessarily requires a variety of statistical methods. For applications involving the observation of continuous time or sampled signals, the most complete statistical description of the noise process is the so-called joint distribution of the process [1]. Throughout this article we will denote an arbitrary noise or interference signal by $x(t)$.

Definition 1. The n th-order joint distribution of $x(t)$, denoted $F_x(\mathbf{x}; \mathbf{t})$, is given by

$$F_x(\mathbf{x}; \mathbf{t}) = \Pr[x(t_1) \leq x_1, x(t_2) \leq x_2, \dots, x(t_n) \leq x_n] \quad (1)$$

where the length n vectors \mathbf{x} and \mathbf{t} represent the collections $\{x_1, x_2, \dots, x_n\}$ and $\{t_1, t_2, \dots, t_n\}$, respectively, and where, for example, $\Pr[x(t_1) \leq x_1]$ is the probability that the signal $x(t)$ at time t_1 is less than the constant x_1 . For $F_x(\mathbf{x}; \mathbf{t})$ to be completely defined, it must be computed for all collections of times t_1, t_2, \dots, t_n , vectors \mathbf{x} , and all integer values of n .

In modeling noise, one often wishes to know if the statistical characterization of the signal $x(t)$ changes with time. The most rigorous method for determining this important property is derived directly from the joint distribution.

If the joint distribution of the noise is shift-invariant, that is, if

$$\begin{aligned} \Pr[x(t_1) \leq x_1; x(t_2) \leq x_2, \dots, x(t_n) \leq x_n] \\ = \Pr[x(t_1 + \tau) \leq x_1; x(t_2 + \tau) \\ \leq x_2, \dots, x(t_n + \tau) \leq x_n] \end{aligned} \quad (2)$$

for all collections of times and vectors \mathbf{x} and for all choices of n , then $x(t)$ is said to be *strictly stationary*. In this case, the entire statistical description of the process is a function of only the relative locations of the samples with regard to one another rather than the absolute locations of the time samples.

Unfortunately, in general, determining $F_x(\mathbf{x}; \mathbf{t})$ for large values of n is almost always impractical. However it may often be the case that one has sufficient information so as

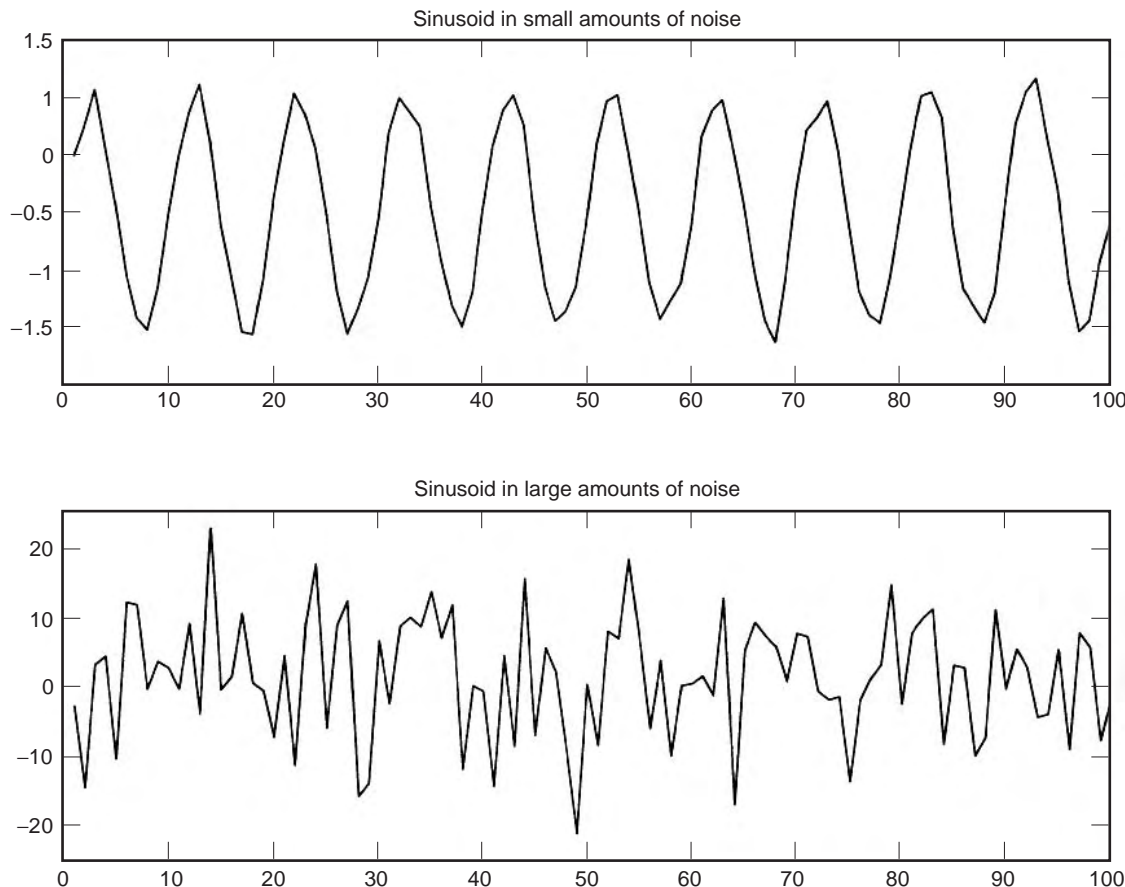


Figure 1. Plots of a common sinusoid embedded in low-level noise and high-level noise.

to be able to compute this important function for values of $n = 1$ or 2 . In this case we may introduce a weaker form of stationarity that has many important applications and uses in practice. This type of characterization is often referred to as the so-called *second-order* description of $x(t)$.

Under this characterization we seek to describe the mean and correlation of the noise signal rather than the instantaneous probabilities. Prior to presenting this definition, it is advantageous for us to supply the following definitions which will be used throughout the remainder of this article:

Definition 2. The amplitude probability density function of the signal $x(t)$ is given by

$$f_x(x; t) = \frac{\partial F_x(x; t)}{\partial x} \tag{3}$$

for all choices of x and
for all values of t

while the joint amplitude density function of $x(t)$ is given by

$$f_x(x_1, x_2; t_1, t_2) = \frac{\partial^2 F_x(x_1, x_2; t_1, t_2)}{\partial x_1 \partial x_2} \tag{4}$$

for all choices of x_1
and x_2 and for all t_1 and t_2

These two definitions completely characterize all the first- and second-order properties of $x(t)$ (e.g., mean values, signal energy and power, correlations and frequency content). In particular, the amplitude density function describes the statistical range of amplitude values of signal x at time t . Further, one should recall from basic probability theory [2] that the density functions $f_x(x; t)$ and $f_x(x_1, x_2; t_1, t_2)$ can be readily obtained from the n th joint distribution of the signal $x(t)$ given in Eq. (1) through simple limiting evaluations. Given these two density functions, we may define the second-order description of the noise or interference signal as follows:

Definition 3. The mean or average value of the noise as a function of time is defined as

$$\mu_x(t) = E[x(t)] \tag{5}$$

where the expectation is taken with respect to $f_x(x; t)$. The correlation function of the noise signal is defined as

$$R_x(t_1, t_2) = E[x(t_1)x^*(t_2)] \tag{6}$$

and where the expectation presented above is taken with respect to $f_x(x_1, x_2; t_1, t_2)$, and where x^* denotes the complex conjugate of $x(t)$.

If the mean function is a constant with respect to time (the average value of the noise does not change with time)

and the correlation function of the noise is a function of only the difference of times and not their absolute locations, that is, $R_x(t_1, t_2) = R_x(0, t_2 - t_1)$, then the noise is said to be *wide-sense stationary*. In this case we simplify the notation by letting the mean be μ and the correlation function be given by $R_x(\tau)$ where $\tau = t_2 - t_1$.

A signal $x(t)$ being wide-sense stationary implies that the average statistical properties as measured by the mean and the correlation function do not depend on when one observes the noise and interference. This is a very beneficial property since designers attempting to combat this noise are not required to include an absolute clock in their design, rather a fixed design will always be optimal.

As an important observation, one should note that if the noise happens to be strictly stationary, then the noise will also be wide-sense stationary. This is a direct consequence of the fact that the mean and correlation functions are expected values taken with respect to the first- and second-order joint density functions which, by supposition, are shift invariant. In general, the converse is not true. However, we will see later that among the most popular models for the noise, this will, in fact, be the case.

1.1. Power Spectral Density

Engineers are often more comfortable in describing or analyzing signals in the frequency domain as opposed to the statistical (or time) domain. This is equally true when dealing with random signals. However, random signals pose a few complications when one attempts to apply spectral techniques to them. This is a consequence of the fact that each time one makes an observation of this signal, the so-called noise *realization* (observation) is different and will therefore likely have a different spectrum. Moreover, many of these potential noise realizations might have infinite energy, and will therefore not have well-defined Fourier transforms.

Because of these complicating factors, we must consider the power spectrum (rather than the standard energy spectrum) averaged over all possible realizations to obtain a meaningful definition of the spectrum of a random signal. This approach leads to the well-known and often used *power spectral density* of the noise or interference as the basic frequency-domain description of $x(t)$.

To begin, assume that we only observe the noise signal $x(t)$ from $t = -T$ to $t = +T$ (we will later let T approach infinity to allow for the observation of the entire signal). The Fourier transform of this observed signal is

$$X_T(\omega) = \int_{-T}^T x(t)e^{-j\omega t} dt \quad (7)$$

We may then write the squared magnitude of $X_T(\omega)$ as follows:

$$|X_T(\omega)|^2 = \int_{-T}^T \int_{-T}^T x(t_1)x^*(t_2)e^{-j\omega(t_1-t_2)} dt_1 dt_2 \quad (8)$$

As described above, for the definition to have any utility, we need to compute the average magnitude squared power

spectrum, which requires that we must evaluate the expected value of $|X_T(\omega)|^2$ and then normalize this expectation by the length of the observation of $x(t)$ (this prevents the spectrum from blowing up with power signals). This leads to the following expression

$$\frac{1}{2T} E[|X_T(\omega)|^2] = \frac{1}{2T} \int_{-T}^T \int_{-T}^T R_x(t_1 - t_2) dt_1 dt_2 \quad (9)$$

$$= \int_{-T}^T \left[1 - \frac{|\tau|}{2T}\right] R_x(\tau) d\tau \quad (10)$$

where the second equation arises from a transformation of variables. The final step in the definition is to allow the observation window to grow to $(-\infty, +\infty)$, that is, to take the limit of Eq. (10) as T tends to infinity. From this we arrive at the following definition which holds for all wide sense stationary random signals.

Definition 4. The power spectral density of a wide sense stationary random signal $x(t)$ is given by

$$S_X(\omega) = \int_{-\infty}^{\infty} R_x(\tau)e^{-j\omega\tau} d\tau \quad (11)$$

Note that as a consequence of the preceding analysis, the power spectral density turns out to simply be the Fourier transform of the correlation function. Thus the correlation function of a random signal contains all the information necessary to compute the average spectrum of the signal and, furthermore, there is a one-to-one relationship between the average time dependency between samples (as measured by the correlation function) and the average frequency content in the signal.

The term “power spectral density” arises from the fact that $S_X(\omega)$ behaves like a probability density function. First, just like a standard density function, it is always nonnegative, and second, when integrated over a certain frequency range one obtains the average power of the signal over that frequency range. That is, computing the integral

$$\int_{-\omega_2}^{-\omega_1} S_X(\omega) d\omega + \int_{\omega_1}^{\omega_2} S_X(\omega) d\omega \quad (12)$$

results in the total power in the signal $x(t)$ between the frequencies ω_1 and ω_2 . (*Note:* We must consider both positive and negative frequencies.) This is just like the situation when one integrates a probability density function over a particular range to obtain the probability that the random variable will fall within that range.

Now given these few basic definitions, we may proceed to characterize various forms of noise or interference. From the statistical perspective, what differentiates various types of noise are, first and foremost, the specific joint distribution of the process. Since these joint density functions are exceedingly difficult to obtain, we are often relegated to comparing and classifying noise signals through $f_X(x; t)$ and $f_X(x_1, x_2; t_1, t_2)$, as well as the mean and correlation function or power spectral density.

2. NOISE MODELS

2.1. White Noise

White noise is a model used to describe any noise or interfering signal that has essentially equal power at all frequencies. More precisely, signals with a power spectral density given by

$$S_X(\omega) = \frac{N_0}{2} \text{ for all frequencies} \quad (13)$$

are said to be white because, similar to white light, these signals have equal power at all (visible) frequencies. Through simple integration it is easily shown that the amount of power contained in white noise over an angular frequency range of B radians per second is N_0B . (Note that the factor of 2 in the definition of the power spectral density accounts for the two-sided nature of the Fourier transform.)

It is important to note that this definition of white noise is not an explicit function of either the amplitude density function or the joint density function given in Eqs. (3) and (4), but rather a function of only the power spectral density of the signal. Thus, any noise source, irrespective of the specific forms of $f_X(x; t)$ and $f_X(x_1, x_2; t_1, t_2)$, can be white noise, so long as the power spectral density is a constant.

The corresponding correlation function of white noise is obtained through the inverse Fourier transform as

$$R_x(\tau) = \frac{N_0}{2} \delta(\tau) \quad (14)$$

where $\delta(\tau)$ is the familiar Dirac delta function [3]. Here one should observe from the above equation that white noise has zero correlation between all time samples of the signal, no matter how close the time samples are to one another. This does not imply that all samples of white noise are independent from one another, rather that they simply have zero correlation between them.

Unfortunately, by integrating the power spectral density over all frequencies we observe that the total power in white noise is infinite, which, of course, requires more energy than exists in the entire universe. Therefore, it is physically impossible for white noise to exist in nature. Yet, there are many noise processes which have essentially a constant power spectral density over a fixed and finite frequency range of interest, which suggests that white noise may be an appropriate and simplifying model. Yet, the real utility of the white noise model is in describing other “nonwhite” noise signals.

To demonstrate this, consider the output of a linear time-invariant system with frequency response $H(\omega)$ to a white-noise input. Under very general conditions, it can be shown [2] that this output, given by $y(t)$, is a noise signal with power spectral density given by

$$S_Y(\omega) = \frac{N_0}{2} |H(\omega)|^2 \quad (15)$$

Now, conversely, let us assume that we observe some nonwhite-noise signal with power spectral density $S_Y(\omega)$. If $\int \ln S_Y(\omega) / (1 + \omega^2) d\omega > -\infty$, then $y(t)$ can be modeled as the output of *some* linear time-invariant system with a white-noise input. That is, there will exist some well-defined system with frequency response given by $H(\omega)$ such that $N_0/2 |H(\omega)|^2 = S_Y(\omega)$. These processes are, in fact, physically realizable and constitute all random signals seen in practice. Thus, from a spectral perspective we may replace essentially all random signals seen in nature by a linear system driven by a white-noise signal.

2.2. Gaussian Noise

Gaussian noise is the most widely used model for noise or interference both in practice and in the scientific literature. There are two primary reasons for this: (1) many observations in nature follow the Gaussian law, and (2) the Gaussian density function is mathematically easy to analyze and manipulate.

The reason that so many natural observations are Gaussian arises from the so-called *central-limit theorem*. This theorem is stated as follows.

Theorem 1. Assume that Z_i are independent, and identically distributed random variables, each with mean μ_Z and finite variance σ_Z^2 . Then the so-called normalized sum given by

$$Y_n = \frac{1}{\sqrt{n}} \sum_{i=1}^{n-1} \frac{Z_i - \mu_Z}{\sigma_Z} \quad (16)$$

approaches a standard Gaussian random variable with mean equal to zero and unit variance, irrespective of the original distribution of the random variables Z_i .

What this very powerful theorem establishes is that if a particular observation of interest is a combination of infinitely many small and independent random components, then the combination, when properly normalized, is Gaussian Random variable with density function given by

$$f_x(x; t) = \frac{1}{\sqrt{2\pi}} e^{-x^2/2} \quad (17)$$

This might suggest that all natural observations are Gaussian since most physical phenomena are impacted by many random events; however, extensive experimental results establish otherwise [4]. Therefore, in addition to various forms of Gaussian noise, later in this article we will present a number of other “non-Gaussian” noise models.

Definition 5. A random noise signal is said to a Gaussian signal if all n th-order joint density functions are jointly Gaussian, that is, if all joint density functions are of the form

$$f_x(\mathbf{x}) = \frac{1}{(2\pi)^{n/2} \sqrt{\det(\mathbf{K})}} \times \exp \left[-\frac{1}{2} (\mathbf{x} - \boldsymbol{\mu})^T \mathbf{K}^{-1} (\mathbf{x} - \boldsymbol{\mu}) \right] \quad (18)$$

where the vector $\boldsymbol{\mu}$ and the matrix \mathbf{K} represent the mean vector and covariance matrix [2], respectively, of the vector $\mathbf{x}(t_1), \mathbf{x}(t_2), \dots, \mathbf{x}(t_n)$.

The important feature here is we see that for any value n , the joint statistics of a Gaussian signal are completely determined from the mean and correlation functions of $x(t)$. Furthermore, when the signal is in addition wide-sense stationary, then the joint statistics are shift invariant, and as such, the signal is also strictly stationary.

Gaussian noise is further differentiated by the nature of the mean functions and the correlation functions. When the correlation function is given by $R_X(\tau) = N_0/2\delta(\tau)$, then the signal is said to be *Gaussian White Noise*, which is the single most common model in noise analysis. In this case, each time sample will be independent from all others and have infinite variance. Other well-known Gaussian models that we describe below are Wiener noise, thermal noise, and shot noise.

2.3. Wiener Noise

The Wiener Process is the limiting case of a random-walk signal. A random walk is a popular abstraction for describing the distance an individual is from home when this individual randomly steps forward or backward according to some probability rule. The model is as follows. Every T seconds an individual will take a length s step forward with probability $\frac{1}{2}$ or a length s step backward with probability $\frac{1}{2}$. Therefore, at time nT , the position of the random walk will be $x(nT) = ks - (n-k)s$, where n is the total number of steps taken, and k is the number of forward steps taken. For large values of time, it can be shown using the DeMoivre–Laplace theorem [2] that

$$\Pr(x(nT) = ks - (n-k)s) \approx \frac{1}{\sqrt{n\pi/2}} e^{-(2k-n)^2/2n} \quad (19)$$

or that the location of the walker is governed approximately by a Gaussian law.

Now, let us extend this by considering the limiting case where the length of time between steps tends to zero ($T \rightarrow 0$). It is easy to show that $E[x^2(nT)] = ns^2 = ts^2/T$ for $t = nT$. To ensure that we do not have a variance going to zero (the walker stops) or blowing up (not physically realizable), let us also add the condition that the size of the steps be proportional to the square root of the time between steps, that is, $s^2 = \alpha T$. Then the well-known Wiener process is the signal $x(t)$, which is the limit of the random walk under these conditions. Examples of this are given in Fig. 2, where we have depicted realizations from three succeeding approximations to the Wiener process. In all figures, we have let the proportionality constant $\alpha = 1$. In Fig. 2a T and s equal 1, in Fig. 2b $T = 0.1$ and $s = \sqrt{0.1}$, and in Fig. 2c $T = 0.01$ and $s = 0.1$. One can see that as the approximation gets closer to the limiting value it becomes smoother (more continuous) and begins to exhibit long-term trends. This, of course, makes sense because the steps are getting much smaller and, as a consequence, it

takes longer periods of time of the walker (signal) to change positions (values).

It should be pointed out that as $T \rightarrow 0$, the position of the random walk at any point in time is the sum of infinitely many random steps, and therefore by the central-limit theorem, the location at any point in time is a Gaussian random variable with zero mean and variance given by αt .

To compute the correlation function of the Wiener process, we note that $x(t_2) - x(t_1)$ is independent of $x(t_1)$ because, by supposition, the random movements between times t_1 and t_2 are independent of the random movements up to time t_1 . From this it must be that

$$E[(x(t_2) - x(t_1))x(t_1)] = E[x(t_2) - x(t_1)]E[x(t_1)] = 0 \quad (20)$$

from which it is easy to show that $R_X(t_1, t_2) = \alpha t_1$ whenever $t_2 > t_1$. Determining the correlation of the case that $t_1 > t_2$ results in the final value for the correlation function of the Wiener process as

$$R_X(t_1, t_2) = \alpha \min(t_1, t_2) \quad (21)$$

One can readily see that the Wiener process is not wide-sense stationary and therefore does not have a computable power spectral density. Nevertheless, it is a highly useful, physically motivated model for Gaussian data with relatively smooth realizations and which exhibits long-term dependencies.

2.4. Thermal Noise

Thermal noise is one of the most important and ubiquitous sources of noise in electrical circuitry. It arises primarily from the random motion of electrons in a resistance and occurs in all electronic circuits not maintained at absolute zero degrees Kelvin. This resulting low-level noise is then scaled to significant levels by typical amplifiers used to amplify other low-level signals of interest.

To derive a model for thermal noise, let us assume that we have a conducting rod of length L and cross-sectional area A for which we expect to measure low-level random voltages. Let $V_{x,k}(t)$ denote the component of velocity in the x direction of the k th electron at time t . The total current denoted by $I(t)$ is the sum of all electron currents in the x direction

$$I(t) = \sum_{k=1}^{nAL} i_k(t) = \sum_{k=1}^{nAL} \frac{q}{L} V_{x,k}(t) \quad (22)$$

where n is the number of electrons per cubic centimeter and q is the charge of an electron. Let us assume that the average velocity of each electron is zero and that all electrons behave independently of one another and have an identical distribution. From this, it is easy to show that the correlation function of the current is given by

$$R_I(\tau) = \frac{nAq^2}{L} E[V_x(t)V_x(t+\tau)] \quad (23)$$

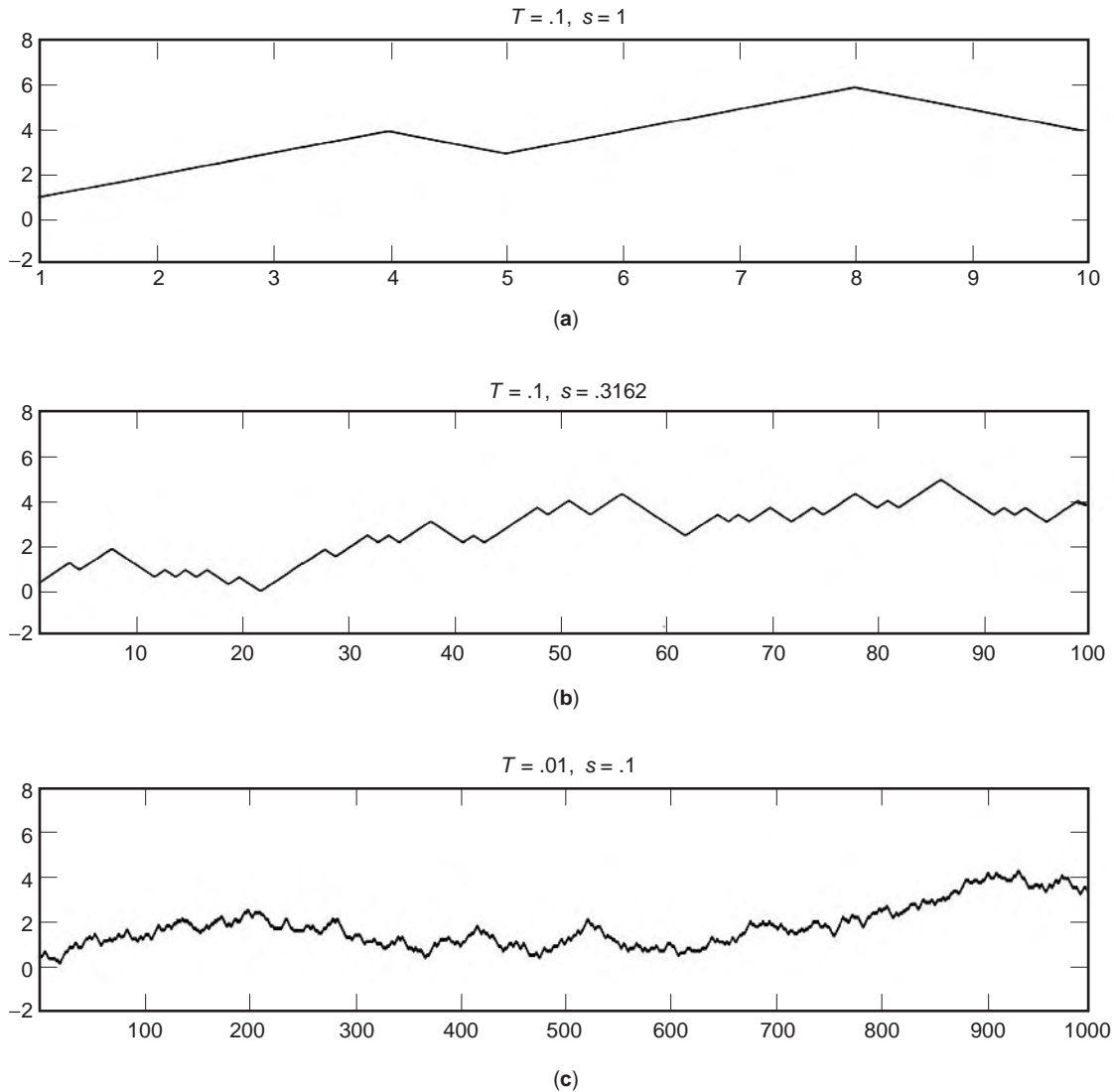


Figure 2. Plots of realizations from numerical approximations to the Wiener process for various values of s and T . In all cases, $\alpha = 1$. In (a), $T = 1$ and $s = 1$, in (b) $T = 0.1$ and $s = 0.3162$ and in (c) $T = 0.01$ and $s = 0.1$.

where we have dropped the subscript k for convenience. Assuming that electron collisions occur according to a Poisson law with intensity given by α [2] and that the average variance of the velocity of an electron is given by $k_B T/m$, where k_B is Boltzmann’s constant and m is the mass of an electron (from the equipartition theorem for electrons), it can be shown that

$$R_I(\tau) = \frac{kT}{R} \alpha e^{-\alpha|\tau|} \tag{24}$$

where R is the resistance of the rod. Recognizing that $E(t) = RI(t)$, we can easily obtain the correlation function of the voltage as

$$R_E(\tau) = kTR \alpha e^{-\alpha|\tau|} \tag{25}$$

Note that as the intensity of the electron collisions α increases, the correlation function begins to approach

a Dirac delta function, implying that the spectrum of thermal noise begins to better approximate white noise. Furthermore, we also observe that as we lower the temperature of the circuitry T , the power $R_E(0)$ in the thermal noise decreases proportionally. This, of course, suggests that if one wants to process very weak signals, for example, deep-space signals, then the circuitry must be cooled using some form of coolant. The central-limit theorem can be used to show that the voltage is very well approximated by a Gaussian process.

2.5. Shot Noise

Shot noise is used to model random and spontaneous emissions from dynamical systems. These spontaneous emissions are modeled as a collection of randomly located impulses (Dirac delta functions) given by $z(t) = \sum_i \delta(t - t_i)$, where the locations of the impulses in time

(t_i) are governed by a Poisson law with intensity λ which is then driven through some system.

The output of a system with impulse response $h(t)$ to the input $z(t)$ is said to be “shot noise.” From the convolution theorem, it is easily shown that this output is

$$x(t) = \sum_i h(t - t_i) \quad (26)$$

Using the properties of the Poisson law, it is easy to show that the mean value of shot noise is $\mu_x = \lambda H(0)$, where $H(\omega)$ is the frequency response (Fourier transform) of the system. The power spectral density function of $x(t)$ is given by

$$S_X(\omega) = \lambda^2 H^2(0) \delta(\omega) + \lambda |H(\omega)|^2 \quad (27)$$

Thus the frequency content of the shot noise is determined entirely by the system $h(t)$ and the intensity of the Poisson process, that is, average rate of emissions. As before, because $x(t)$ at large values of time is composed of the superposition of many random elements [see Eq. (26)] $x(t)$ is often modeled as a wide-sense stationary Gaussian random process with power spectral density given by Eq. (27).

3. NONGAUSSIAN MODELS

While the scope of the central-limit theorem might suggest otherwise, there are many datasets derived from the environment which do not conform well to the Gaussian model. Most of these data contain interfering signals emitted from a modest number of interferers or from interferers overlapping the signal of interest in the frequency domain in such a way that one could not easily remove these unwelcome elements by filtering.

Approaches to remedy this modeling problem fall into two categories: (1) generalize the Gaussian model to allow for statistical variation around the Gaussian process or (2) attempt to derive new statistical models directly from the physics of the problem. In both cases, most non-Gaussian specifications typically do not go beyond the amplitude probability density function given in Eq. (3) and power spectral density. This is due, in large part, to the severe complexity of merely specifying valid and useful joint probability functions with the desired amplitude density.

These non-Gaussian models for noise and interference generally differ statistically from Gaussian noise in the rate at which the so-called “tail” of the amplitude density tends to zero. More specifically, for Gaussian noise the amplitude probability density function is approximated by $e^{-x^2/2\sigma^2}$ for large values of $|x|$; that is, the tails (the probability density function from some large value to \pm infinity) of the amplitude density decay at an exponential rate with exponent equal to x^2 . From a physical point of view, this rate translates into the relative frequency of observing large amplitude values from the noise signal. That is, amplitude density functions with tails that decay to zero faster than the Gaussian tail give rise to datasets with fewer large values in the noise than one might see with Gaussian data. On the other hand, when the tail of the amplitude density decays slower than that of the Gaussian, one

is more likely to see large random values of the noise signal $x(t)$ than one would with Gaussian data. So, unlike differentiating noise models based on the spectrum of the noise, as seen in the preceding section, with non-Gaussian noise we typically differentiate various forms by the nature of the tail of the amplitude density function.

3.1. Generalized Gaussian Noise

The generalized Gaussian model is the most straightforward extension of the standard Gaussian model. In this case, the amplitude probability density function is given by

$$f_X(x; t) = a(p) \exp\left(-\left[\frac{|x|}{A(p)}\right]^p\right) \quad (28)$$

where the constant p parameterizes the density function and where $A(p) = \sqrt{[\Gamma(1/p)/\Gamma(3/p)]}$, $a(p) = p/[2 * \Gamma(1/p) * A(p)]$ and where $\Gamma(z)$ is the gamma function (generalized factorial). It should be noted that, irrespective of the value of p , the variance of the amplitude density function is held constant (in this case the variance is arbitrarily set to one). Plots of the amplitude density function for $p = 1, 2, 5, 50$ are depicted in Fig. 3. One can see that for small values of ($p < 2$), the tails of the density functions maintain relatively large values for large arguments. Conversely, for large values of ($p > 2$), the tails decay to zero quite rapidly.

From Eq. (28), it is easily recognized that for $p = 2$, the generalized Gaussian model results in a standard Gaussian model. Alternatively, when $p = 1$, we obtain the well-known *Laplacian* model for noise. In this case, the tail of the amplitude density function decays at a rate of $e^{-|x|}$, thus implying that one will likely observe many more large values of noise than one would see with Gaussian noise. In general, for $p < 2$ we obtain tails with more mass (more probability), resulting in “impulsive” data, while for $p > 2$ we obtain tails with less mass, resulting in datasets with very few outliers and more uniformly distributed over its range.

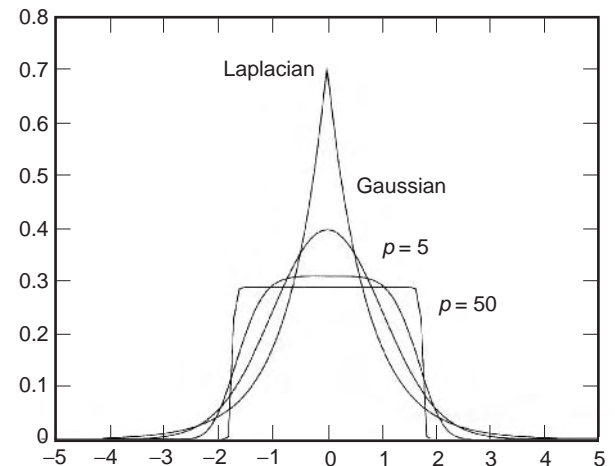


Figure 3. Plots of various specific amplitude density functions from the generalized Gaussian model.

To demonstrate the variation in the data under this model, Fig. 4 shows sample realizations from Laplacian noise ($p=1$), Gaussian noise ($p=2$), and generalized Gaussian noise ($p=50$). One can see that these datasets, all with a common variance (power), exhibit quite different behavior. The Laplacian noise better models interference which might contain spikes such as those produced by man-made devices, while $p=50$ might better model interference arising from signals with well-contained powers (Fig. 5).

3.2. Sub-Gaussian Noise

While in general one specifies a random signal through the joint distribution function, sub-Gaussian noise is specified through the joint characteristic function [2]. As a reminder, this function is simply the Fourier transformation of the joint density function and, as such, there exists a straightforward one-to-one relationship between characteristic functions and joint density functions. As opposed to the generalized Gaussian noise model, sub-Gaussian noise is parameterized in the exponent of the characteristic

function rather than the exponent of the amplitude density function [5].

Definition 6. A noise or interference signal is said to be an α -sub-Gaussian signal if for any positive integer n and time vector $\mathbf{t} = \{t_1, t_2, \dots, t_n\}$, the characteristic function of the joint density function of $[x(t_1), x(t_2), \dots, x(t_n)]$ is given by

$$\varphi(\mathbf{u}) = \exp\left(-\left[\frac{1}{2} \sum_{m,l=1}^n u_m u_l R(t_m, t_l)\right]^{\alpha/2}\right) \quad (29)$$

where $\alpha \in (1, 2]$ and where $R(t,s)$ is a positive definite function and where $\mathbf{u} = \{u_1, u_2, \dots, u_n\}$.

Importantly, if the parameter $\alpha = 2$ then the sub-Gaussian process is simply a Gaussian process. Otherwise, the noise signal corresponds to some signal which has been parameterized away from the Gaussian signal. In all cases other than $\alpha = 2$, the corresponding tail of the amplitude

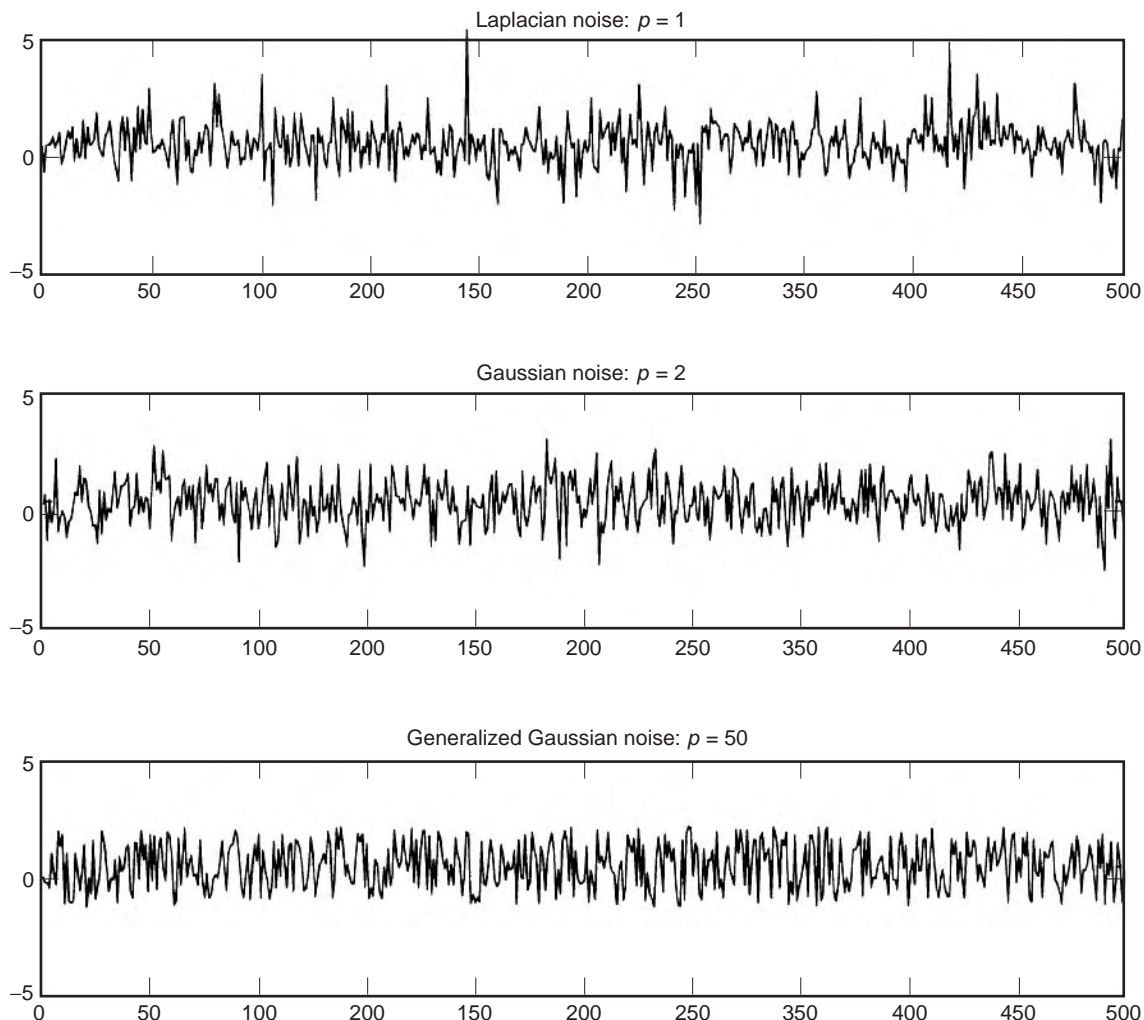


Figure 4. Plots of realizations from various density functions from the generalized Gaussian family of density functions.

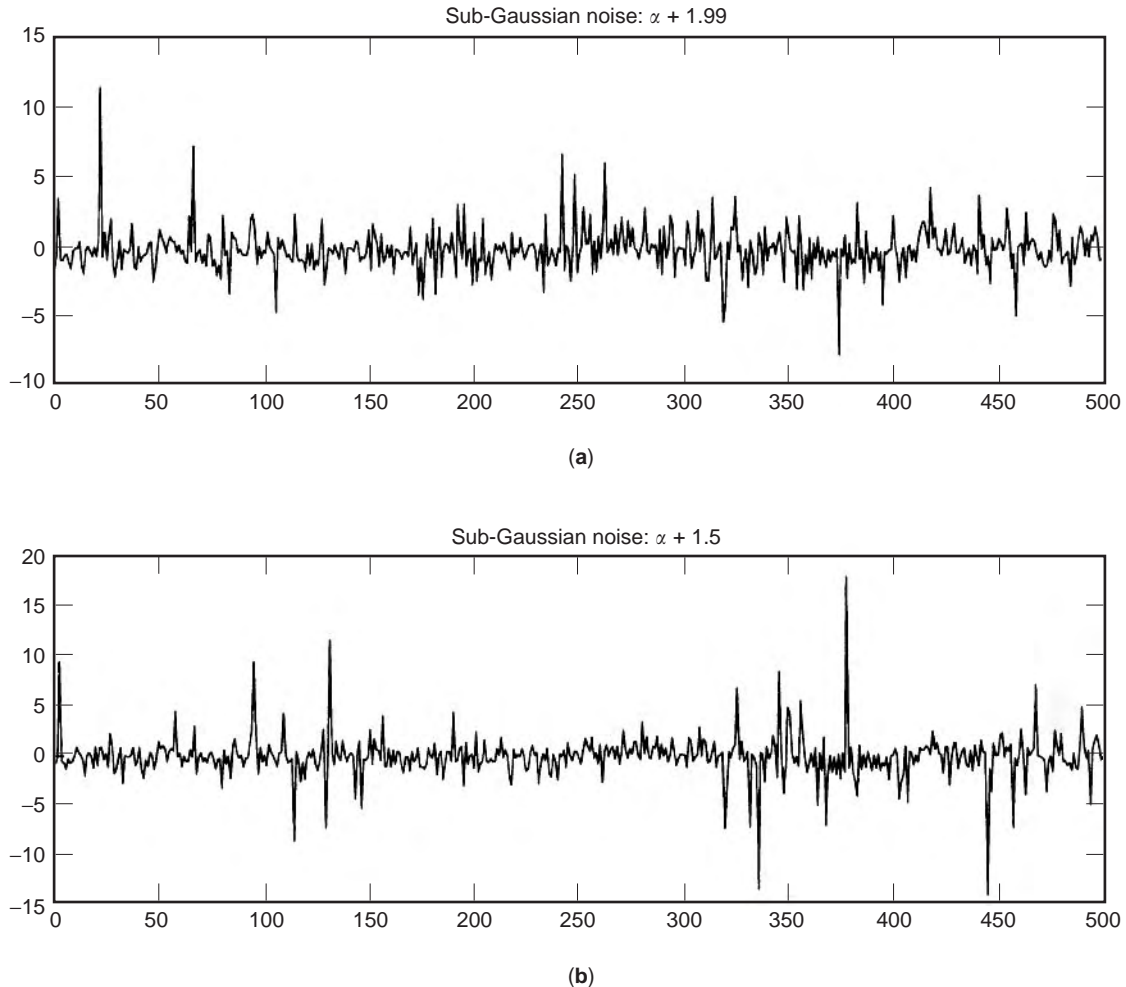


Figure 5. Plots of realizations from the sub-Gaussian noise family: (a) corresponds to $\alpha = 1.99$; (b) corresponds to $\alpha = 1.5$.

density function decays at a polynomial rate (rather than an exponential rate) which translates into many more very large amplitude values than one would typically see with pure Gaussian noise. Therefore this model might be appropriate for characterizing data that contain many impulses.

There are a number of important properties of sub-Gaussian process [6,7]. From a modeling point of view, the most significant is that any sub-Gaussian process can be expressed as the product of a Gaussian process scaled by a so-called $\alpha/2$ stable random variable. That is, if $x(t)$ is an α -sub-Gaussian signal, then

$$x(t) = S^{1/2}y(t) \quad (30)$$

where $y(t)$ is a Gaussian random process with zero mean and correlation function given by $R(t,s)$ and S is an independent, positive $\alpha/2$ -stable random variable. (A $\alpha/2$ -stable random variable is a random variable with characteristic function given by $\varphi(u) = \exp[-\gamma|u|^{\alpha/2}]$.) One interesting property of sub-Gaussian signals is that all samples from this signal are always dependent on one another. In addition, for $\alpha \neq 2$, it can be shown that samples from

$x(t)$ will have infinite variance, thus making this model somewhat problematic in terms of accurately representing the average power of an interference signal. Nevertheless, the sub-Gaussian noise model has been used extensively to model noise or interference with a significant number of outliers or impulses and, in some applications, it serves well as a replacement for shot noise as an efficient model.

3.3. Middleton Noise and Interference

Unlike either the generalized Gaussian model or the sub-Gaussian model, Middleton models have been derived directly from physical arguments. These models attempt statistically to characterize the amplitude density of the envelope [8] of a signal in the presence of various types of man-made interference after it has passed through the front end of the receiver. Importantly, these models are canonical, in the sense that they do not depend on the specific source of the interference—only the relative bandwidth of the interferers with respect to the receiver. Therefore, interferers such as powerlines, atmospheric noise, and various mechanical machines are all accommodated well by these very powerful models.

There are two basic forms of Middleton noise [9–11]. Class A noise represents the statistical interference when the bandwidth of the interfering signals are on the order of or smaller than the bandwidth of the front end of the receiver. In this case, transient effects from the receiver can be ignored.

Alternatively, class B noise considers the case where the receiver bandwidth is substantially smaller than the interference bandwidth and thus transient effects must be accounted for. In addition to class A and B noise, Middleton has introduced the notion of class C noise, which is simply a linear combination of both A and B noise [12].

3.3.1. Physical Model. For both class A and class B noise, it is assumed that there are an infinite number of potential sources of interference within reception distance of the receiver. The individual interfering signals are assumed to be of a common form, except for such parameters as scale, duration, and frequency, among others.

The locations and parameters of the interferers in the source field are assumed to be randomly distributed according to the Poisson law. The emission times for each source are also assumed to be random and Poisson distributed in time. Physically speaking, this implies that the sources are statistically independent both in location and emission time.

3.3.2. Class A Noise. As described above, the physical model for class A noise assumes that the bandwidth of the individual interfering signals is smaller than the bandwidth of the receiver (data collection system.) This allows for the simplification of ignoring all transient effects (ringing) in the output of the receiver front end.

Avoiding the tedious analysis and simply stating the result, the (approximate) amplitude probability density function under these assumptions was shown by Middleton [9] to be

$$f_x(x; t) = e^{-A} \sum_{m=0}^{\infty} \frac{A^m}{m!} \frac{1}{\sqrt{2\pi\sigma_m^2}} e^{-(x^2/2\sigma_m^2)} \quad (31)$$

where

$$\sigma_m^2 = \frac{m/A + \Gamma}{1 + \Gamma} \quad \text{and} \quad \Gamma = \sigma_G^2/\Omega \quad (32)$$

One can see from these equations that the class A model is parameterized in three parameters (A, Γ, Ω), each with physical significance. The parameter A is a measure of the impulsiveness of the interference and is given by the product of the average number of impulses emitted per unit time with the average duration of an impulse. Small values of A indicate a highly impulsive signal, since this would imply a small number of interferers each with very short pulses. For large values of A we have many interferers each with long duration and, thus, by the central-limit theorem, the interference is nearly a Gaussian process. The constant Γ quantifies the ratio of the intensity of the independent Gaussian component arising from

thermal or ambient noise (given by σ_G^2) to the mean intensity of the interference (given by Ω).

3.3.3. Class B Noise. Class B noise assumes that the bandwidth of the interfering signals is larger than the front-end bandwidth of the receiver. This assumption significantly complicates the analysis. In particular, one is required to use two separate models for small and large signal levels instead of a single model as in the class A model. Because of the level of detail required to describe this model, it is recommended that the interested reader seeking a precise definition be directed to the original work found in Ref. 9.

3.4. ε -Mixture Noise

One might observe from the preceding Middleton models that the amplitude density functions are infinite linear combinations of zero-mean Gaussian models. Interestingly, it has been well known in the statistics literature that appropriately scaled Gaussian density functions can be combined together to obtain nearly all valid amplitude density functions, so it is not surprising that this combination appears as a canonical representation of signal interference.

However, working with infinite sums of density functions requires much careful analysis. It is because of this that researchers have introduced a simplifying approximation to the Middleton class A Model, which is referred to as the ε -mixture model.

In this simplification, the amplitude probability density function of interference plus background or thermal noise is approximated by a combination of just two Gaussian density functions

$$f_x(x; t) = (1 - \varepsilon) \frac{1}{\sqrt{2\pi\sigma_\varepsilon^2}} e^{-(x^2/2\sigma_\varepsilon^2)} + \varepsilon \frac{1}{\sqrt{2\pi\gamma\sigma_\varepsilon^2}} e^{-(x^2/2\gamma\sigma_\varepsilon^2)} \quad (33)$$

where the constant ε determines the fraction of impulsivity found in the data and where γ represents the ratio of intensities of the impulsive component to nominal ambient noise. In order to maintain a fixed power level of σ^2 in the noise and interference model for all choices of ε and γ , the parameters must satisfy the following power constraint:

$$\sigma_\varepsilon^2 = \frac{\sigma^2}{1 - \varepsilon + \varepsilon\gamma} \quad (34)$$

Sample realizations from the ε -mixture model are depicted in Fig. 6. The top figure corresponds to purely Gaussian noise ($\varepsilon = 0$), while the middle and bottom figures correspond to $\varepsilon = 0.01$ and 0.1 , respectively. As one can see, as ε increases the average number of “impulses” (spikes in the data) increases, while the average power of background thermal noise decreases in accordance with Eq. (34). Therefore, this model offers some of the flexibility

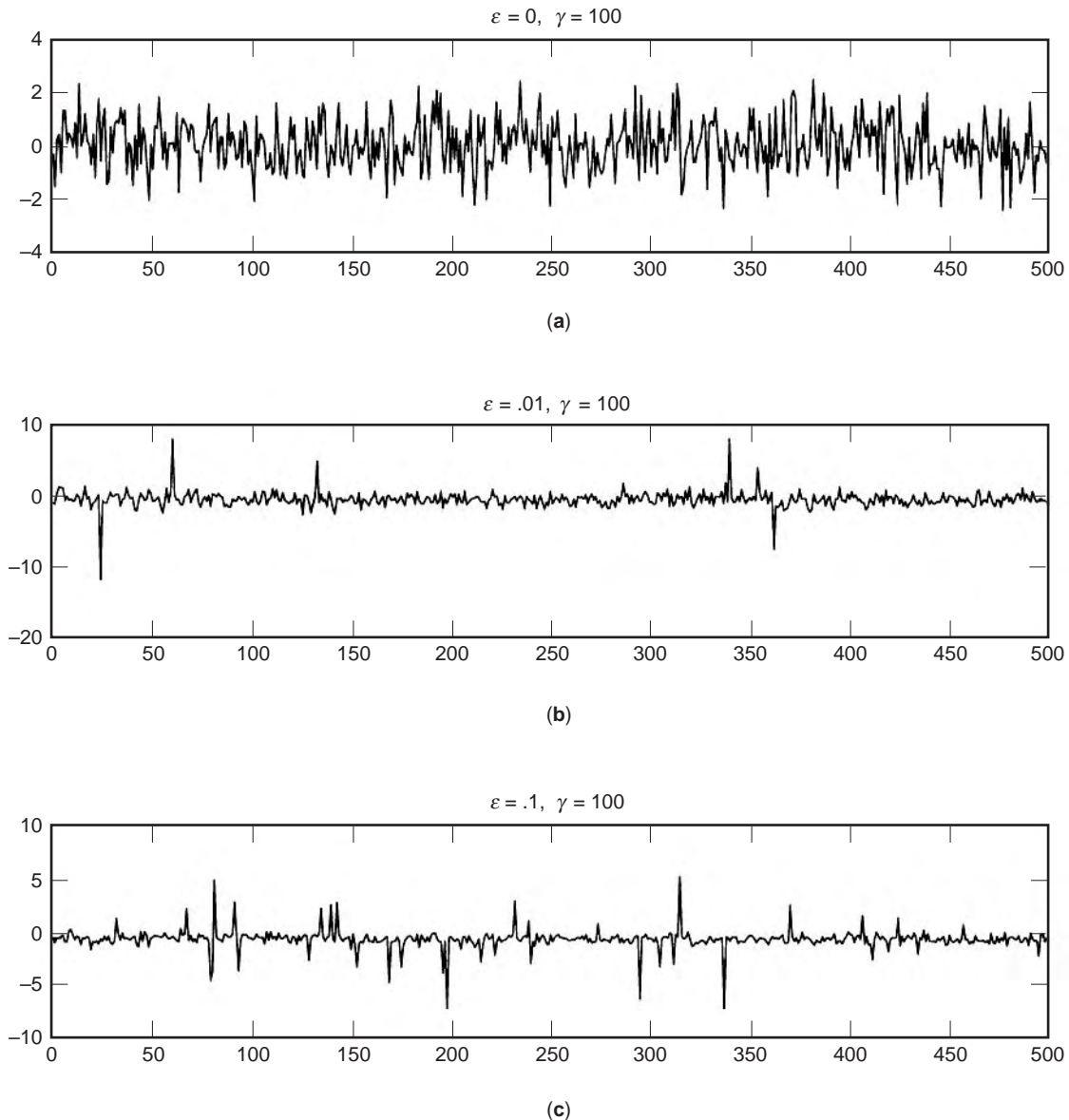


Figure 6. Plots of realizations from the ε -mixture noise family: (a) corresponds to $\varepsilon=0$ (pure Gaussian noise); (b) corresponds to $\varepsilon=0.01$ (a 1% chance of observing interference at any point in time); (c) corresponds to $\varepsilon=0.1$ (a 10% chance of observing interference at any point in time). One should observe that as ε increases, the empirical frequency of “impulses” arising from interference increases proportionally.

required by the Middleton models without the requisite computational complexity.

4. CONCLUSIONS

This article has described the basic techniques for characterizing noise and interference from both statistical and signal processing perspectives. These approaches have varied from the most analytic and fundamental (n th-order joint density or distribution functions) to more practical and data-oriented (means, correlation functions, and power spectral density).

The primary differentiation between various noise models has been based on the statistical characteristics of the signal. Of particular importance was the “Gaussianity” or non-Gaussianity of the signal. In many important applications, the central-limit theorem implies that the corruptive effects of noise will be well approximated by a Gaussian process. However, basic physical arguments, such as those found in Middleton’s work, also suggest that much of what we consider to be Gaussian noise is, in fact, substantially non-Gaussian. Moreover, it has been shown in much research that imposing the Gaussian model on data that are decidedly or marginally

non-Gaussian can have detrimental effects on the final designs. It is therefore critical that when one is dealing with data, particularly data arising from interfering sources, that the appropriate model be used and used accurately.

For readers interested in pursuing these topics further, one should begin with the important original work found in Ref. 13. Explicit models governing a wide variety of random phenomena can be found in Refs. 14–16. For an advanced treatment of random process in general, books by Doob [17] and Wong and Hajek [18] are excellent if not somewhat advanced treatments of the theory of random signals.

BIBLIOGRAPHY

1. R. M. Gray and L.D. Davisson, *Random Processes: A Mathematical Approach for Engineers*, Prentice-Hall, Englewood Cliffs, NJ, 1986.
2. A. Papoulis, *Probability, Random Variables, and Stochastic Processes*, McGraw-Hill, New York, 1984.
3. A. V. Oppenheim, A. S. Willsky, and I. T. Young, *Signals and Systems*, Prentice-Hall, Englewood Cliffs, NJ, 1983.
4. E. J. Wegman, S. C. Schwartz, and J. B. Thomas, eds., *Topics in Non-Gaussian Signal Processing*, Springer-Verlag, New York, 1989.
5. C. L. Nikias and M. Shao, *Signal Processing with Alpha-Stable Distributions and Applications*, Wiley, New York, 1995.
6. Y. Hosoya, Discrete-time stable processes and their certain properties, *Ann. Probab.* **6**(1):94–105 (1978).
7. G. Miller, Properties of certain symmetric stable distribution, *J. Multivariate Anal.* **8**:346–360 (1978).
8. J. G. Proakis, *Digital Communications*, 3rd ed., McGraw-Hill, New York, 1995.
9. D. Middleton, Canonical non-gaussian noise models: Their implication for measurement and for prediction of receiver performance, *IEEE Trans. Electromagn. Compat.* **EMC-21**: 209–220 (1979).
10. D. Middleton, Statistical-physical models of electromagnetic interference, *IEEE Trans. Electromagn. Compat.* **EMC-19**: 106–127 (1997).
11. D. Middleton, Procedures for determining the parameters of the first-order canonical models of class a and class b electromagnetic interference, *IEEE Trans. Electromagn. Compat.* **EMC-21**:190–208 (1979).
12. D. Middleton, *First-Order Non-Gaussian Class C Interference Models and Their Associated Threshold Detection Algorithms*, Tech. Report NTIA Contractor Rep. 87-39, Natl. Telecommunication Information Administration, 1987.
13. N. Wax, ed., *Noise and Stochastic Processes*, Dover, New York, 1954.
14. N. L. Johnson, S. Kotz, and A. W. Kemp, *Univariate Discrete Distributions*, 2nd ed., Wiley, New York, 1992.
15. N. L. Johnson and S. Kotz, *Continuous Univariate Distributions*, Vol. 1, Houghton-Mifflin, Boston, 1970.
16. N. L. Johnson and S. Kotz, *Continuous Univariate Distributions*, Vol. 2, Houghton-Mifflin, Boston, 1970.
17. J. L. Doob, *Stochastic Processes*, Wiley, New York, 1953.
18. E. Wong and B. Hajek, *Stochastic Processes in Engineering Systems*, Springer-Verlag, New York, 1985.

NOISE GENERATORS

SHAMBHU J. UPADHYAYA
State University of New York
at Buffalo

Noise is a broadbanded signal generated by environmental effects, such as lightning, or by man-made electrical devices. Two common categories of noise are thermal noise and shot noise. Looney [1] describes thermal noise as an electromotive force generated at the open terminals of a conductor due to the charges bound to thermally vibrating molecules. This type of noise is often referred to as Johnson noise in recognition of the first observations of the phenomenon [2]. On the other hand, shot noise is associated with the passage of current across a barrier. For instance, a circuit or an appliance that produces electric arcing produces noise. Shot noise was first described by Schottky using the analogy of a small shot patterning into a container [3]. Noise can be felt in audio systems as a crackle. Noise appears as white or black spots on a television screen.

Noise is generally characterized as a source of corruption of information and therefore is treated as an undesired signal. Noise contaminates informational signals to a certain extent by superimposing extraneous fluctuations that assume unpredictable values at each instant. Noise has been studied extensively in the literature because noise reduction is one of the major goals. A more compelling reason for the study of noise is its potential application in real life. These applications encompass biomedical engineering, electronic circuits, communication systems, cryptography, computers, electro-acoustics, geosciences, instrumentation, and reliability engineering. This article addresses the various noise generation techniques and implementing them in analog and digital circuit technology and concludes with a discussion of typical applications.

1. MODELING OF NOISE

A mathematical model of a phenomenon, such as noise, allows us to understand its generation, characteristics, and application well. We start with the observation that the structures of thermal and shot noise are similar, although their sources are different. Both types of noise can be represented as a random waveform consisting of a sequence of peaks randomly distributed in time. A noise signal can be modeled by a random process $X(t)$ with a probability distribution for the values of x it assumes. Any particular set of outcomes $\{(t, x_t)\}$ of the random variable X_t is called a realization of the noise process. An adequate characterization of such a random process can be often made with first- and second-order statistics. The first-order statistic of $X(t)$ is the expected value $E[X(t)]$ and the second-order statistic is the autocorrelation function $R_X(\tau) = E[X(t)X(t + \tau)]$, where E is the expectation operator. When the first- and second-order statistics do not change over time, the process is called wide-sense stationary [4].

Power spectral density, a standard measure used to describe a wide-sense stationary process, is defined as the Fourier transform of the autocorrelation function $R_X(\tau)$ [4]:

$$S_X(f) = \int_{-\infty}^{\infty} R_X(\tau) e^{-j2\pi f\tau} d\tau \quad (1)$$

With this modeling, we can analyze the spectra of noise. White noise is a wide-sense stationary process with zero mean. It has constant power spectral density over all frequencies. Stated another way, white noise is a process that is uncorrelated over time. The most mathematically tractable noise is the Gaussian wide-sense stationary process, where at each time t the probability distribution for the random variable $X_t = X(t)$ is Gaussian.

Colored noise is a variation of white noise that arises from the fact that actual circuits attenuate signals above certain frequencies. Therefore it makes sense to truncate the white noise spectral density at both extremes. Noise with this spectral characteristic is termed pink noise.

Apart from thermal noise and shot noise, a third category of noise observed in electronic systems is the $1/f$ noise. It is so called because the power spectral density of this noise varies with frequency as $|f|^{-\alpha}$, where α takes values between 0.8 and 1.2. This type of noise is exhibited by biological and musical systems in addition to electronics [3]. $1/f$ noise is variously called current noise, excess noise, flicker noise, semiconductor noise, and contact noise. It is applied in medical treatment and also in engineering, justifying the need for inclusion in our study.

2. NOISE GENERATION TECHNIQUES

Noise can be generated in many different ways. A diode tube operating at its saturation point produces broadband noise. A semiconductor diode is an inexpensive source of noise generation. When operated in the fully conducting region, the diode produces broadband noise. A current-carrying resistor produces thermal noise. It is necessary to condition noise signals by proper amplification, modulation, and filtering to suit one's application at a desired bandwidth. In our discussion of noise generation, we concentrate only on semiconductor techniques because approaches based on vacuum tubes are antiquated now.

The noise generation schemes range from simple mechanical techniques to electronic methods employing both analog and digital circuits. Inexpensive noise generators can be realized with discrete components and basic building blocks available in the IC market. We classify the noise generators into two categories, namely, analog and digital, based on their implementation.

2.1. Analog Techniques

Under this category, we discuss three different approaches: (1) a mechanical scheme, (2) amplifying inherent noise in op-amps, (3) oscillator method, and (4) using the chaotic behavior of deterministic systems.

2.1.1. Mechanical Approach. For audiofrequency noise, a very simple scheme can be devised at home or in the laboratory without any sophisticated circuits or components. Dunn [5] uses just a linen-covered phonograph and a foam-covered microphone. A piece of linen cloth is tied to the turntable and a foam-covered microphone is used to pick up the signal. As the turntable rotates, the microphone's foam cover rubs along the surface of the linen, producing sound with a nearly flat spectral density in the audiofrequency range of from 20 Hz to 20 kHz. Dunn shows that by using a good hi-fi microphone and a broadband amplifier, the output signal closely approximates white noise over the audiofrequency range. Other mechanical approaches include the use of gears and radioactive decay [6].

2.1.2. Amplification of Inherent Noise. The schematic of a relatively simple op-amp noise generator is shown in Fig. 1, which uses a single bipolar input amplifier and some discrete components. The principle used here to generate wideband noise is to amplify its own input noise in a decompensated op-amp [7]. Many op-amps have large $1/f$ input noise components. A bipolar input op-amp is chosen because bipolar devices exhibit much less $1/f$ noise than MOSFET devices.

In the figure, the op-amp is used as a fixed-gain stage amplifier with a closed-loop gain factor:

$$G = 1 + R_1/R_2 \quad (2)$$

If the input resistors R_2 and R_3 are chosen small, the thermal noise of the amplifier is forced to a small value. This choice of low values for the resistors also helps keep the amplifier's current noise component negligibly small when it is converted to voltage noise. Thus, the dominant noise of the circuit is the input voltage noise of the amplifier.

The choice of a single gain stage amplifier of the type shown in Fig. 1 results in a frequency-independent noise. This contrasts with multistage amplifiers, which may have peaks in the output noise response caused by frequency compensation effects. The values for resistors R_1 and R_2 can be designed by knowing the typical noise of the op-amp from datasheets and the required level of noise across the load R_L . The output is coupled through a blocking capacitor C_1 , which removes any amplified DC value at the output of the amplifier. However, the value of this

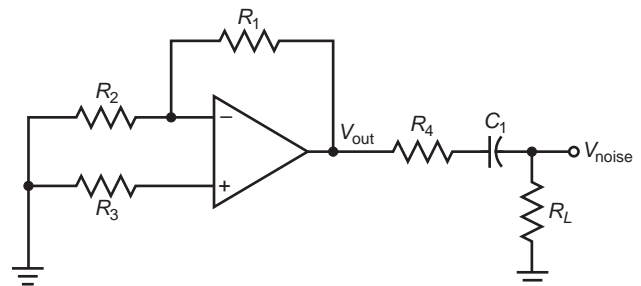


Figure 1. A simple analog noise generator based on amplification of op-amp input noise.

capacitor should be large enough to pass the lowest noise frequencies of interest. Interested readers may refer to Ref. 7 for a detailed circuit diagram and typical component values used to generate a noise of $50 \text{ nV}/\sqrt{\text{Hz}}$. Op-amp AD829 is used in the circuit that features flat voltage noise in the range from 100 Hz to 10 MHz.

2.1.3. Oscillator Method. A popular analog class of noise generators is the oscillator method [8], which samples the frequency noise or instability of free-running oscillators. In this scheme, the output of a fast oscillator is sampled on the rising edge of a slower clock using a D flip-flop. Oscillator jitter causes uncertainty in the exact sample values, ideally producing a random bit for each sample. For further details, readers may refer to Ref. 9.

2.1.4. Using Chaos in Deterministic Systems. Another elegant way of generating white noise is based on the observation that certain simple deterministic systems exhibit chaotic behavior [10]. The chaos or noise is generated by iterating a map either electronically or in a software program. A simple and most widely studied system for generating chaos is the logistic map [10] given by

$$x_{i+1} = 4\lambda x_i(1 - x_i), \quad i = 0, 1, 2, \dots, 0 \leq x_0 \leq 1 \quad (3)$$

The asymptotic behavior of the system described by the parabolic transfer function of Eq. (3) depends on the value of λ . McGonigal and Elmasry [11] show that values of λ between 0.89 and 1.0 result in oscillations without any detectable period. In fact, this is the region of chaotic behavior leading to power spectral density corresponding to white noise.

A noise generator can be implemented in hardware to test actual instruments or in software for simulation. McGonigal and Elmasry [11] use a multiplier and a difference amplifier to realize the term $x_i - x_i^2$ of the parabolic transfer function of Eq. (3). A variable-gain amplifier connected to the output of the differential amplifier, as shown

in Fig. 2, allows variation of λ . The iteration of the transfer function is realized by the feedback of the x_{i+1} signal as the next x_i input. The clock-driven multiplexer and the storage capacitors shown in the figure separate the impulses at the output of the circuit. During clock signal ck , the voltage on capacitor C_1 provides the input x_i whereas the resulting output x_{i+1} is stored on C_2 . During \bar{ck} , the roles of the capacitors are reversed leading to two iterations of the parabolic function in every clock cycle. The IC numbers and typical values of the discrete components are shown in the figure to generate a power spectrum from DC to 1 kHz. Experimental study in Ref. 11 confirms that the signal is uncorrelated in the chaotic region and that the power spectral density remains flat in this region. Interested readers may refer to Ref. 11 for further details of the circuit and a trace of the power spectrum.

The software implementation of the deterministic-chaotic, variably colored, noise generator is shown in Fig. 3. Colored noise is generated by organizing chaotic elements into a hierarchy and coupling them [12]. Each element of the hierarchy is modeled as a recursive loop whose output is a sequence of impulses. The unit delay element shown in the figure separates the instances of impulses of varying amplitude at the output. The gain unit and the nonlinear amplifier implement the map $x_{i+1} = g_{\lambda}f(x_i)$. The output at any instant becomes the input at the next instant. The initiator block is used only to set the amplitude of the first impulse and is then disconnected. This software setup yields sequences of impulses which are essentially aperiodic and hence noiselike from a practical point of view [12].

Researchers have used discrete, nonlinear, one-dimensional maps [13] that yield a transition between regions of chaotic motion to produce $1/f$ noise. The circuits used to implement such discrete maps are usually switched-capacitor type because discrete maps are described by nonlinear, finite-difference equations and they can be easily and accurately implemented by switched-capacitor circuits. Delgado-Restituto et al. [14] build a programmable

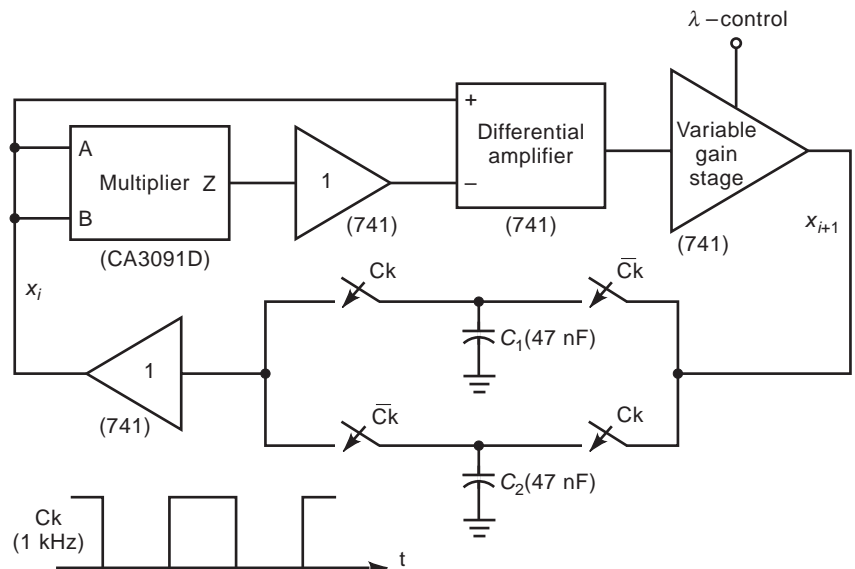


Figure 2. A low-frequency noise generator based on logistic map. (From Ref. 11, courtesy of IEEE, © 1987 IEEE.)

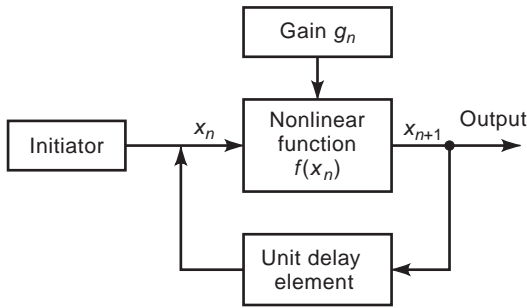


Figure 3. Block schematic of a software-based, deterministic-chaotic, variably colored noise generator.

prototype to generate colored noise to test systems with spectral density proportional to $1/f$. They use op-amps and switched capacitors to realize a chaotic, one-dimensional, piecewise-linear discrete map that yields a hopping transition between regions of chaotic motion. Murao et al. [15] propose a simple switched-capacitor circuit that realizes a one-dimensional, nonlinear, discrete map as opposed to a piecewise-linear approximation. With an IC and a couple of logarithmic and antilogarithmic amplifiers, they can synthesize a simple $1/f$ noise generator over a wide range of frequencies compared with the previous method of Delgado–Restituto et al. [14].

Of the four techniques of noise generation based on chaotic behavior of deterministic systems discussed here, the first is used for white-noise generation, whereas the next three implementations generate colored noise. Although colored noise is derived by properly filtering the output of white-noise sources [16], the direct methods described here are simpler and lend themselves to easy VLSI implementation. Some other simple IC-compatible chaos generators are found in Refs. 17 and 18.

2.1.5. Programmable Noise Generators. It is often desirable to have a programmable noise generator. The variability is achieved by multiplying the noise signal by a factor K and then passing the signal through a noise filter, as shown in Fig. 4. A linear phase filter passes frequencies between F_1 and F_2 , thus bandlimiting the filter output noise. In the simulated noise generator of Ref. 19, the output is sampled at a particular rate and stored in a data array. The statistics of the output data, such as mean, variance, min, and max are stored in another data array. This kind of programmable noise generator produces uniform Gaussian noise whose output noise power is set by adjusting the K factor shown in the figure.

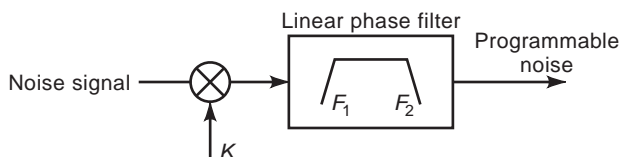


Figure 4. Structure of a programmable noise generator.

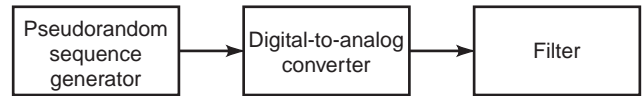


Figure 5. Block schematic of a basic digital noise generator.

2.2. Digital Techniques

The first-generation digital noise generators utilized random waveforms based on telegraph signals to obtain random noise [20]. For application in modern digital circuits, however, pseudo-random-number sequence generators provide a better basis. Pseudorandom numbers are generated with linear congruent algorithms [21]. If noise is needed in analog form, the numbers generated in binary form are converted to analog quantity. The analog output at the converter is essentially Gaussian white noise. This signal can be filtered appropriately to obtain colored noise. Figure 5 shows the block schematic of a digital noise generator.

2.2.1. Linear Feedback Shift Register as Random-Number Generator. The digital circuitry implementing the pseudo-random-number generator can be realized using a linear feedback shift register (LFSR). An LFSR consists of two basic digital building blocks, D-type flip-flops and exclusive-OR gates. The LFSR draws theory from cyclic error detecting codes [22] where all algebraic manipulations on polynomials are done in $GF(2)$, that is, Galois field-modulo-2 addition, subtraction, multiplication, and division of binary vectors. A k -stage LFSR generates at most $(2^k - 1)$ distinct binary patterns, which then repeat on themselves. In general, the length of the sequences generated depends on the size of the LFSR and the polynomial representing it. If the polynomial representing the LFSR is primitive [22], the LFSR generates a maximal length sequence $[(2^k - 1)$ vectors]. If the polynomial is irreducible but nonprimitive, then the length of the sequence is not maximal and depends on the initial contents of the LFSR, called the seed. The presence of internal memory in the LFSR makes the choice of the seed critical for nonprimitive case. In the primitive case, the seed does not affect the statistical properties of the output. However, if all of the flip-flops are set to zero, the LFSR remains dormant and is useless.

The upper block of Fig. 6 shows an LFSR implementation of a primitive polynomial of degree 6.

$$x^6 \oplus x \oplus 1 \quad (4)$$

where \oplus is the exclusive-OR operator. In this implementation of LFSRs, the output and selected internal stages of the LFSR corresponding to the nonzero terms of the polynomial are exclusive-ored and fed back to the input. The pseudorandom digital output sequence is plotted in Fig. 7. A clock frequency of 1 MHz is used to run the LFSR. Because a six-stage LFSR is used, the period of the pseudorandom output waveform is $63 \mu\text{s}$. For clarity the figure shows a couple of periods of the waveform.

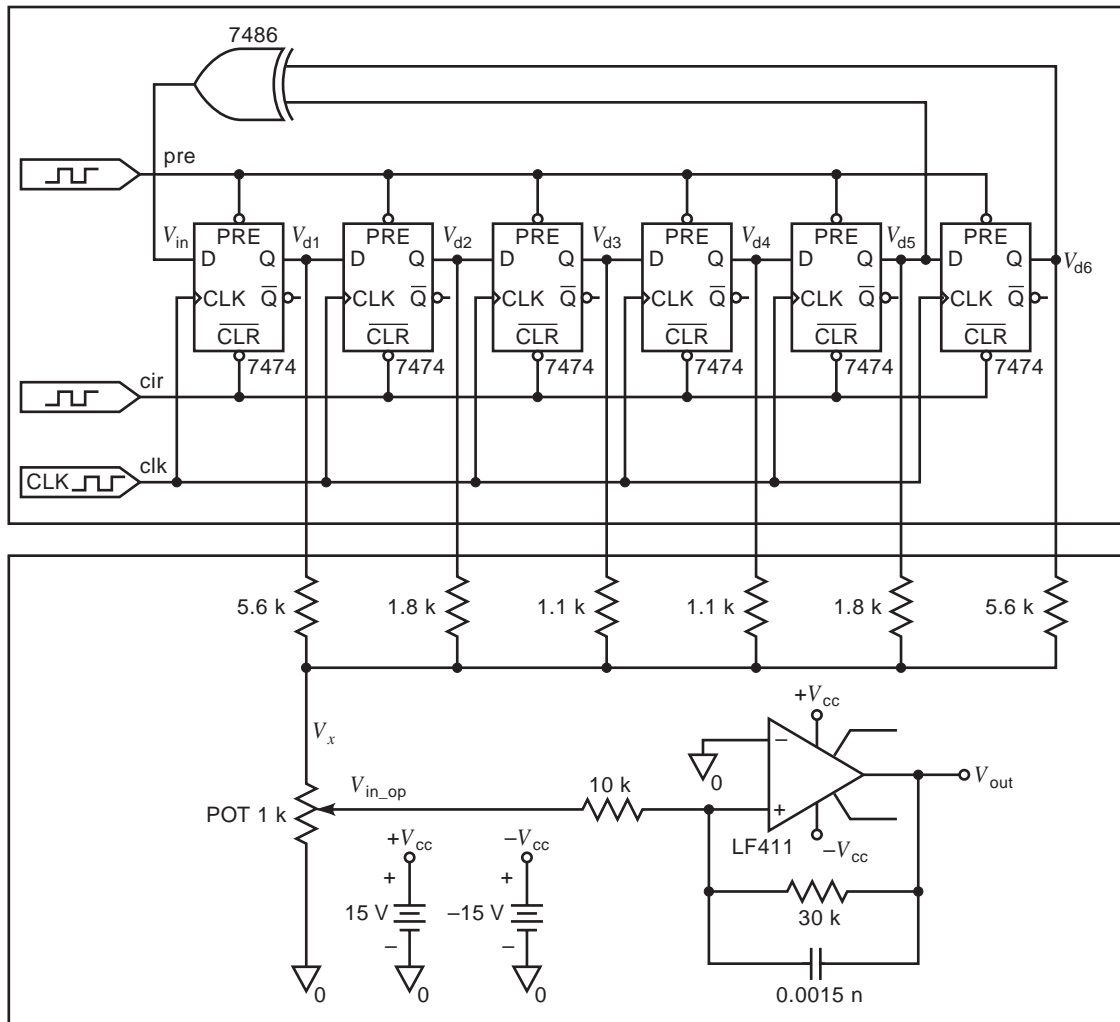


Figure 6. A six-stage linear feedback shift register with a resistive network for digital-to-analog conversion.

In the following, we describe several implementations of digital noise generators. They all have LFSRs as the basis for random number generation and use lowpass filtering to obtain the analog noise signal.

2.2.2. Analog Conversion by Time Integration. Alspector et al. [23] use a lowpass filter to convert the digital waveform at the outputs of the LFSR to a voltage signal. The cutoff frequency of the filter is kept at just a few percent of the clock frequency used to drive the LFSR. This arrangement has the effect of performing a time integration over many bits. If each bit is equally likely (i.e., a 0 or 1 with equal probability), as is the case in LFSRs, the value of this integration follows a binomial distribution that approaches Gaussian for a large number of bits. This creates a Gaussian pseudorandom noise source whose statistical properties are analogous to thermal or shot noise. A variable amplifier with gains low enough to avoid any coupling is used at the output.

2.2.3. Analog Conversion by a Resistive Network. D'Alvano and Badra [24] use a resistive network to convert the digital signal to an analog signal, as shown in the lower block of Fig. 6. The shift register outputs are linearly combined through the resistive network, which also plays the role of the coefficient set of a discrete-time FIR filter. These weights provide a lowpass transfer function with a raised-cosine impulse response. The output level at the filter is adjusted through a 1-k Ω trimmer.

The probability density function of the noise signal at the output can be predicted because of the random nature of the binary sequence generated at each of the shift register outputs. The random binary variables added to form the noise signal are statistically independent from one another. From the central-limit theorem [4], it follows that the probability density function of the signal at the output is asymptotically Gaussian.

To illustrate noise generation, we have performed a simulation using commercial software produced by MicroSim Corporation, USA. Figure 8 shows a trace of

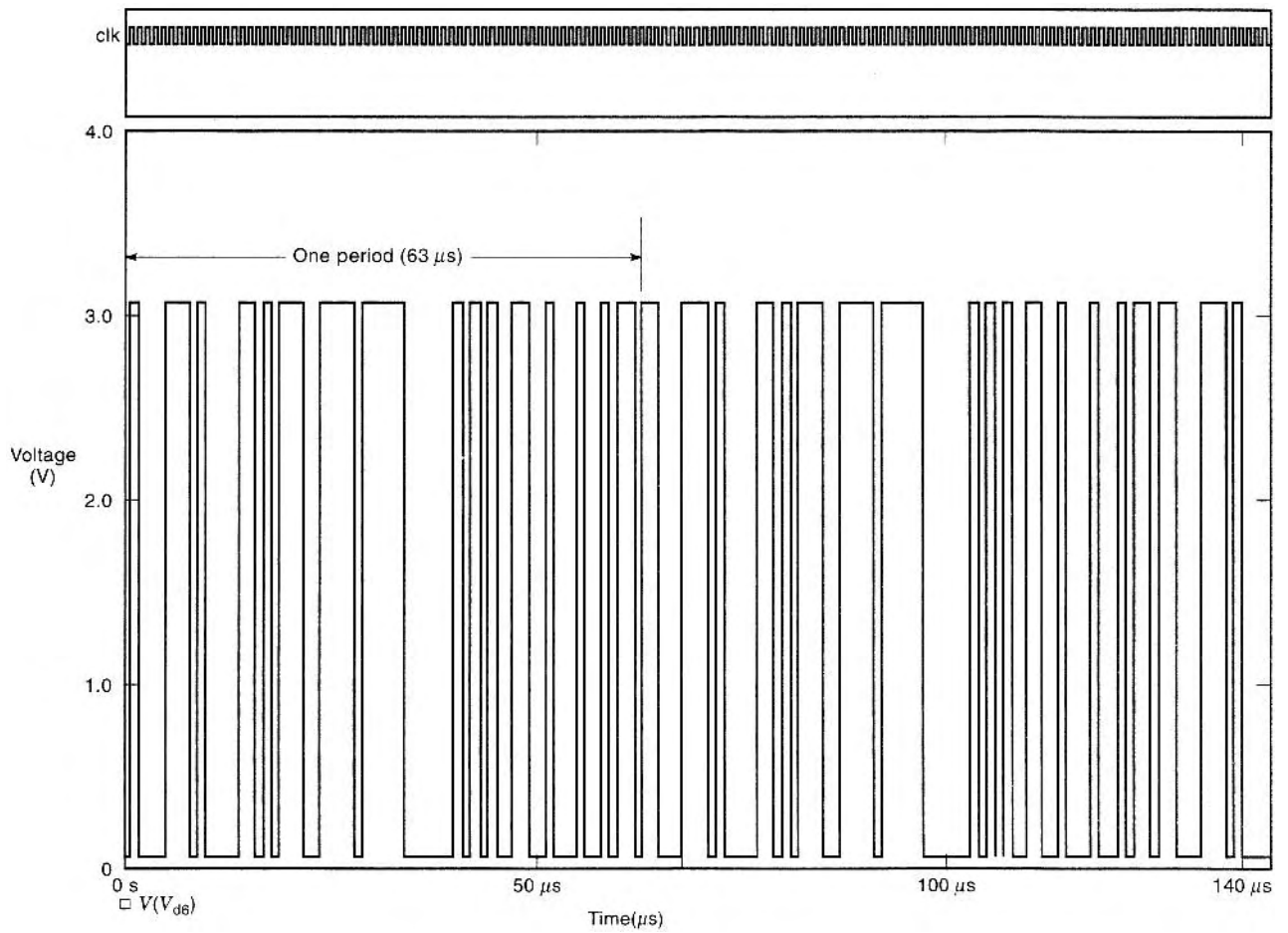


Figure 7. The waveform of the digital sequence at the output of LFSR.

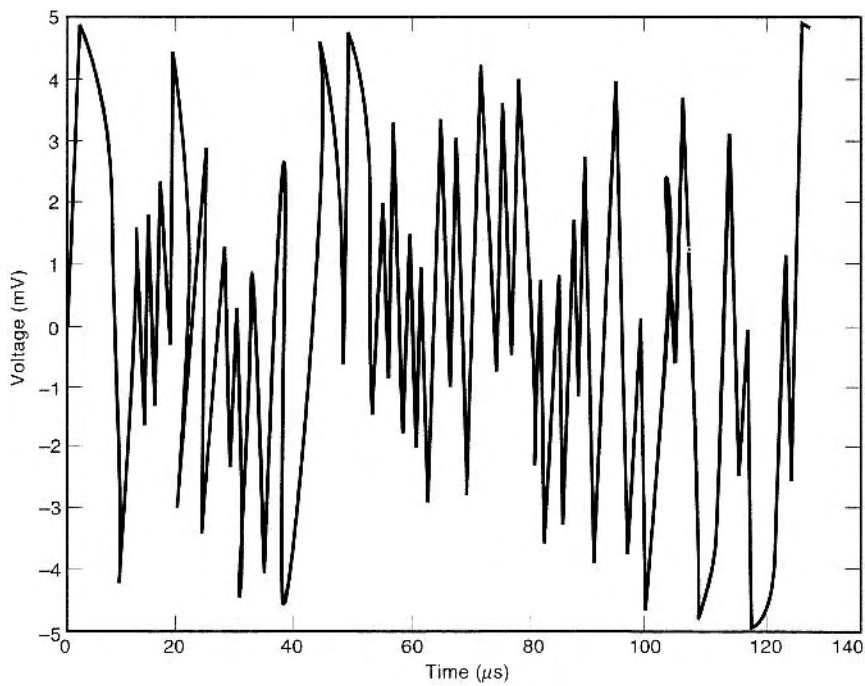


Figure 8. A simulation trace of an analog noise signal.

analog noise observed at the output of the op-amp (see Fig. 6). What is shown in Fig. 8 is repetitive noise. The periodicity in the noise is an undesirable feature, yet inevitable when small-size LFSRs are used for pseudo-random-number sequence generation. The periodicity can be broken by randomly changing the seed of the LFSR. The periodicity can also be improved by lengthening the shift register. Interested readers may refer to Ref. 24 for details of the circuit which produces truly random noise.

2.2.4. High-Frequency Noise Generation. A shift-register-based noise generator can be realized for RF noise power metrology [25]. Superconducting rapid, single-flux, quantum (RSFQ) logic [26] is used to meet the requirements of low noise and fast switching necessary to generate noise in the gigahertz range. In the RSFQ logic, the binary information is coded by flux quanta with the value $\phi_0 = h/2e$ in superconducting interferometers and is transmitted and processed as very short voltage pulses $V(t)$ of quantized area. The active circuit components are overdamped Josephson junctions (JJ), which need only dc bias currents set to values slightly below their critical currents. With these elements, SFQ pulses can be created, transmitted, reproduced, amplified, processed, and detected (25). The basic RSFQ logic elements for constructing complex digital circuits are available in current technology. Superconducting microstrip lines together with JJ technology allow transmitting picosecond waveforms with very low attenuation and dispersion. In a pseudorandom noise generator of this type, the logic enables the generation of pseudostatistical SFQ pulse sequences, operating as quasi-shot-noise sources.

2.2.5. Arrays of Noise Generators. It is often necessary to have an array of noise generators, especially in neural networks [25]. Although such noise generators can be designed with LFSRs, one should be careful to avoid any correlation among the outputs of these noise generators. Alspector et al. [23] accomplish this by tapping the outputs from various stages of the LFSR and processing them using exclusive-OR gates and lowpass filters. A cellular automata is used by Dupret et al. [27] to generate arrays of Gaussian white-noise sources. Cellular automata feature regular structure leading to compact VLSI layouts.

3. APPLICATION OF NOISE GENERATORS

Noise generators are used in a variety of testing, calibration, and alignment applications, especially with radio receivers. Some of the other applications are in digital communication, analog integrated circuit diagnosis, and learning processes of stochastic neural networks. In digital communication, noise is added as an “uncertainty” to a cryptographic exchange to confuse the information and to prevent unauthorized use or forgery. This is increasingly important in today’s electronic-commerce society. Random signals are also used for dithering in analog electronic circuits, forcing a signal to use the entire dynamic range of an analog system, one that reduces distortion. These

applications can be classified into four categories: noise used as a broadband random signal, measurements in which noise is used as a test signal, measurements in which noise is used as a probe into microscopic phenomena, and noise as a conceptual tool. This categorization of applications was first made by Gupta [28] and is used here. We include some examples and illustrations.

3.1. Noise as a Broadband Random Signal

This kind of signal is widely used in electronic countermeasures, microwave heating, simulation of random quantities, stochastic computing, and generation of random numbers. Noise generators are used to simulate random vibrations in mechanical systems. The combination of a random noise generator and a shake table is widely used to test the response of mechanical structures to random vibrations.

A well-known application of a high-power broadband noise generator is active jamming of radar and communication equipment. Radar jamming is called “active” if the jammer radiates a signal at the operating frequency of the radar system, as distinguished from “passive” jamming, which employs nonradiating devices like chaff. The broadband jamming signal can be generated either by a noise generator centered at the carrier frequency or by noise modulating a continuous-wave signal.

An interesting medical application is inducing sleep or anesthesia and suppressing dental pain in a technique called “audio-analgesia”. A dental patient listens to relaxing music via earphones, and switches to filtered random noise on feeling pain, increasing the intensity of noise as necessary to suppress pain. It is reported that audio-analgesia has about the same level of effectiveness as morphine [29].

In modern musical instruments, white-or color-noise generators are successfully used to generate the sound effect of desert wind, ocean surf, thunderstorm, lightning, and even the virtual cosmic background sound.

3.2. Noise as a Test Signal in Measurements

There are several cases of measurements where one needs a broadband signal with known properties like amplitude probability density and an autocorrelation function. Random noise is one such source and is ideal for measuring impulse response, insertion loss, linearity, and intermodulation of communication equipment, and in noise-modulated distance-measuring radar.

It is well known [4] that if a random signal $X(t)$ with auto-correlation function $R_X(\tau)$ is applied at the input of a linear system with an impulse response $H(t)$, the cross-correlation between the input and the resulting output $Y(t)$ is given by the convolution integral

$$R_{XY}(\tau) = \int_{-\infty}^{\infty} H(t)R_X(\tau - t) dt \quad (5)$$

This relationship can be used to calculate the impulse response $H(t)$ if R_X and R_{XY} are known. For causal, lumped, linear, time-invariant systems, this calculation

can be carried out algebraically. However, solving the integral equation for $H(t)$ is greatly simplified by using white noise as the input signal. If the bandwidth of the input signal is much larger than that of the system under test, $R_X(\tau)$ is effectively the impulse function $\delta(\tau)$, and the equation simplifies to

$$R_{XY}(\tau) = H(\tau) \quad (6)$$

Thus the impulse response is directly measured without involved calculation.

Spina and Upadhyaya [30] use the previous observation on impulse response measurement in testing and diagnosing analog VLSI. Here, a white-noise generator is used as input stimuli to the analog chip. At the output of the circuit under test, a pattern classifier which is usually an artificial neural network does the signature analysis and hence fault diagnosis. Alspector et al. [23] study application of noise as input to facilitate learning in parallel stochastic neural networks.

Noise is used in measuring linearity and intermodulation in a communication channel as follows. When a large number of telephone channels are to be carried by a coaxial cable or a broadband radiolink, any existing nonlinear distortions in the system introduce unwanted intermodulation products of the various components of the multiplexed signal. Calculation of the intermodulation noise so introduced is very difficult because of the large number of channels. Because statistical properties of white noise are similar to those of a complex multichannel signal with a large number of intermittently active channels, white noise is used to simulate such a signal. A bandlimited Gaussian white noise is introduced at the input into the system under test. The noise power in a test channel is measured first with all channels loaded with white noise and then with all but the test channel loaded with white noise. The ratio of the first to the second measurement is called the noise power ratio from which the channel noise due to intermodulation can be calculated. The spectral density of input noise can be shaped to match the signal under actual operating conditions.

The use of noise generators for checking system performance in manufacturing or in the laboratory is commonly known. The procedure can be extended to in-service monitoring of radar and communication equipment in the field because of the development of solid-state noise generators, which have smaller power consumption, weight, volume, radio frequency interference, turnon time, and turnoff time, but higher noise power output and reliability than gas discharge noise generators. As a result, the need for retuning or servicing the equipment is recognized before its performance becomes unacceptable. As the noise signal is very small and unrelated to all other signals, the monitoring can be carried out while the equipment is in operation, thus reducing the downtime due to checkups.

Noise is specifically used in the noise immunity test of several digital systems and TV pictures [31]. High-frequency noise generators are needed in RF noise power calibration.

The shift-register-based noise generator using RSFQ logic can function at frequencies up to 45 GHz (25) and can

be used for this purpose. Digital, pseudorandom numbers are also used to test a random collection of input possibilities with test circuits built on-chip.

3.3. Noise as a Probe into Microscopic Phenomena

Noise measurements can be used for estimating physical parameters related to microscopic phenomena, such as emission, recombination, or ionizing collision. Noise can also be used in testing semiconductors for uniformity and for estimating the reliability of semiconductor devices. Using noise in device reliability prediction has several advantages over conventional lifetime tests. Noise testing is nondestructive and does not take up a considerable fraction of the life of the device being tested. It also allows testing a specific individual device rather than measuring an average lifetime for a lot.

There are many ways in which measuring the noise in a device can be used to make reliability predictions. For instance, transistors with low $1/f$ noise exhibit longer lifespans, and reverse-biased p - n -junction diodes having a noise power spectral density with multiple peaks undergo rapid degradation. It has been found experimentally that the low-frequency $1/f$ noise output of a transistor increases by two or three orders of magnitude shortly before failure [28].

3.4. Noise as a Conceptual Tool

Noise is the motivating cause for developing new disciplines such as information theory, the statistical theory of communication, and circuit theory. It is also useful as a vehicle for theoretical investigations and for modeling other physical systems. For example, the concepts and principles developed with electrical noise have been used as guides in working with thermodynamics. Noise has been used as a tool for interpreting impedance in circuit theory. It has also led to the development of some analogies between quantum mechanics and the analyses of noisy circuits and systems and has helped simplify the concept of the quantum mechanical uncertainty principle. For further details, readers may refer to Ref. 28.

4. COMMERCIAL NOISE GENERATORS

A number of companies sell noise generators either as separate instruments or as part of an apparatus, such as a function generator. Table 1 lists the model numbers and the names of the manufacturers along with various features of the instruments, including noise range, the technique used in the design, and application areas where known. Some of the instruments are portable and battery-powered, whereas others are somewhat bulky. This list is not exhaustive and is provided only as a quick reference. The address of each company is provided in Table 2 as a ready reference. Although the internal circuitry of these noise generators is not available, the reader may refer to other guidebooks on electronics circuits, such as Ref. 32, which contains the circuit diagram of digital white-noise generators, thermal noise generators using incandescent lamp, and a simple diode noise generator.

Table 1. Commercial Noise Generators and Their Characteristics

Designation	Function	Name of Manufacturer	Noise Type and Range	Technique Used
AM700	Mixed signal audio measurement set	Tektronix	Shaped noise white and pink	Analog
3024	Very random noise generator	ACO Pacific, Inc.	White and pink (1.6 Hz–39 kHz)	Digital (pseudorandom)
SMT02	Signal generator	Rohde & Schwarz	500 kHz bandwidth	Not available
SMT03, 06				
IE-20B	Pink and white	Ivie Technologies, Inc.	Pink and white	Digital
PNG-2000	Portable noise generator	Research Electronics, Intl.	Audio frequency (300 Hz–3 kHz)	Not available
DS345	Waveform generator	Stanford Research Systems	White noise wideband (10 MHz)	Digital
DS360	Low-distortion function generator	Stanford Research Systems	White and pink	Digital
NG-1	Audible noise generator	Audio Technologies, Inc.	White and pink	Not available
PNG-7000	Precision noise generator	Noise/Com	Gaussian white noise	Not available
UFX7000	Broadband noise generator	Noise/Com	Broadband noise (10 Hz–40 GHz)	Not available

Table 2. Manufacturers of Noise Generators

Tektronix, Inc. 26600 SW Parkway P.O. Box 1000 Wilsonville, OR 97070 USA	Stanford Research Systems 1290-D Reamwood Avenue Sunnyvale, CA 94089 USA
ACO Pacific, Inc. 2604 Read Avenue Belmont, CA 94002 USA	ATI-Audio Technologies, Incorporated 328 W. Maple Avenue Horsham, PA 19044 USA
Rohde & Schwarz Muhldorfstrasse 15 81671 Munchen (Munich) Germany	Noise Com 64 E. Midland Avenue Paramus, NJ 07652 USA
Ivie Technologies, Inc. 1366 West Center Street Orem, UT 84057 USA	Tundra Semiconductor Corp. 603 March Road Kanata, Ontario K2K 2M5 Canada
Research Electronics International 15 South Old Kentucky Rd. Cookeville, TN 38501 USA	

Acknowledgments

The author acknowledges Yi-Hao Wang, Shu Xia, and Arshad Nissar for their help in the simulation effort.

BIBLIOGRAPHY

- C. Looney, Noise, in R. Dorf, ed., *The Electrical Engineering Handbook*, 2nd ed., CRC Press, Boca Raton, FL, 1997, pp. 1642–1653.
- J. Johnson, Thermal agitation of electricity in conductors, *Nature* **119**:50–51 (1927).
- M. Buckingham, *Noise in Electronic Devices and Systems*, Wiley, New York, 1983.
- A. Papoulis, *Probability, Random Variables, and Stochastic Processes*, 3rd ed., McGraw-Hill, New York, 1991.
- J. Dunn, White-noise generator, *Electron. Design* **44**:90 (1996).
- B. Schneier, *Applied Cryptography*, Wiley, New York, 1994.
- W. Jung, Simple wideband noise generator, *Electron. Design* **44**:102 (1996).
- L. Letham et al., A 128 K EPROM using encryption of pseudorandom numbers to enable read access, *IEEE J. Solid-State Circ.* **21**:881–889 (1986).
- C. S. Petrie and J. A. Connelly, A noise-based random bit generator IC for applications in cryptography, *Proc. Int. Symp. Circuits Systems*, June 1998, pp. 197–201.
- R. May, Simple mathematical models with very complicated dynamics, *Nature* **261**:459–467 (1976).
- G. McGonigal and M. Elmasry, Generation of noise by electronic iteration of the logistic map, *IEEE Trans. Circ. Syst. CAS-34*: 981–983 (1987).
- R. Bates and A. Murch, Deterministic-chaotic variably colored noise, *Electron. Lett.* **23**(19):995–996 (1987).
- R. Devaney, *An Introduction to Chaotic Dynamical Systems*, Benjamin/Cummings, Menlo Park, CA, 1986.
- M. Delgado-Restituto et al., A chaotic switched-capacitor circuit for $1/f$ noise generation, *IEEE Trans. Circ. Syst. I* **39**: 325–328 (1992).
- K. Murao et al., $1/f$ noise generator using logarithmic and antilogarithmic amplifiers, *IEEE Trans. Circ. Syst. I* **39**: 851–853 (1992).
- G. Corsini and R. Saletti, A $1/f^{\alpha}$ power spectrum noise sequence generator, *J. Solid State Circ.* **37**:615–619 (1988).
- M. Delgado-Restituto et al., Nonlinear switched-current CMOS IC for random signal generation, *Electron. Lett.* **29**:2190–2191 (1993).
- J. T. Bean and P. J. Langlois, A current-mode analog circuit for tent maps using piece-wise linear functions, *Proc. Int. Symp. Circuits Syst.*, 1994, pp. 125–128.
- F. Vitaljic, Programmable noise generator, *Electron. Design* **44**:122 (1996).
- H. Sutcliffe and K. Knott, Standard LF noise sources using digital techniques and their application to the measurement of noise spectra, *Radio Electron. Eng.* **40**:132–136 (1970).
- D. Knuth, *The Art of Computer Programming: Seminumerical Algorithms*, Addison-Wesley, Reading, MA, 1981, Vol. 2.
- W. Peterson and E. Weldon, *Error Correcting Codes*, 2nd ed., MIT Press, Cambridge, MA, 1972.
- J. Alspector et al., AVLSI efficient technique for generating multiple uncorrelated noise sources and its application to stochastic neural networks, *IEEE Trans. Circ. Syst.* **38**:109–123 (1991).
- F. D'alvano and R. Badra, A simple low-cost laboratory hardware for noise generation, *IEEE Trans. Educ.* **39**:280–281 (1996).
- W. Kessel, et al., Development of a rapid single-flux quantum shift register for applications in RF noise power metrology, *IEEE Trans. Instrum. Meas.* **46**:477–480 (1997).

26. K. Likharev and V. Semenov, RSFQ logic/memory family: A new Josephson-junction technology for sub-terahertz-clock-frequency digital systems, *IEEE Trans. Appl. Superconduct.* **1**:3–28 (1991).
27. A. Dupret, E. Belhaire, and P. Garda, Scalable array of Gaussian white noise sources for analogue VLSI implementation, *Electron. Lett.* **31**(N17):1457–1458 (1995).
28. M. Gupta, Applications of electrical noise, *Proc. IEEE* **63**: 996–1010 (1975).
29. K. Kryter, *The Effects of Noise on Man*, Academic Press, New York, 1970.
30. R. Spina and S. Upadhyaya, Linear circuit fault diagnosis using neuromorphic analyzers, *IEEE Trans. Circ. Syst. II, Analog Digit. Signal Process.* **44**:188–196 (1997).
31. T. Takagi, Composite noise generator as a noise simulator and its application to noise immunity test of digital systems and TV picture, *IEICE Trans. Commun.* **78B**(N2):127–133 (1995).
32. J. Markus, *Guidebook of Electronic Circuits*, McGraw-Hill, New York, 1974.

NOISE, HIGH-FREQUENCY

M. AGETHEN
 R. REUTER
 R. M. BERTENBURG
 W. BROCKERHOFF
 F. J. TEGUDE
 Innovative Processing AG
 (IPAG)
 Duisburg, Germany

1. INTRODUCTION

The high-frequency behavior of electronic devices is of major interest in the field of research and development. Beside the typical RF device parameters, such as the cutoff frequencies f_T and f_{max} , high-frequency noise behavior has to be considered for circuit design, especially if noise has a significant influence on the system performance, for instance, the sensitivity of receivers. By this means, there is a demand for simple but exact RF noise models that must consider the physically relevant noise phenomena with a significant contribution to the total noise behavior of the device.

After an introduction to various physical noise sources, a general description of noisy two-ports will be presented, followed by a brief presentation of a special measurement setup for RF noise in the range of 2–18 GHz with dependence on temperature (15–400 K). In Section 4 the RF noise phenomena in certain devices are examined and high-frequency noise models for heterostructure field-effect transistors (HFETs) and heterojunction bipolar transistors (HBTs) based on the material system InP are presented. For both devices the capabilities of the model presented will be proved by comparing measured and modeled RF noise parameters. In Section 5 modifications of the HFET noise model and applications of this RF noise model are presented.

2. NOISE THEORY

2.1. Physical Noise Sources

2.1.1. Thermal Noise. The most important and best-known noise mechanism is the thermal noise or *Johnson Noise* [1,2]. This process can be observed in all electrically conductive materials. Assuming a finite temperature $T(T > 0 \text{ K})$, the free electrons statistically move in these materials forced by their thermal energy. Because of scattering processes at lattice atoms, this movement leads to a statistical fluctuation of the voltage at the terminals of the conductor (e.g., a resistor R). The corresponding noise spectrum of the thermal noise is given as [1]

$$S_{th}(f) = 4kTR \quad (1)$$

where k is Boltzmann's constant ($k = 1.38 \times 10^{-23} \text{ W} \cdot \text{s/K}$). The measurable mean-square values of the thermal noise current $i_{th}^2(t)$ or the thermal noise voltage $v_{th}^2(t)$ per unit bandwidth Δf are given respectively as [3,4]

$$\overline{i_{th}^2(t)} = 4kT \frac{\Delta f}{R} \quad (2)$$

$$\overline{v_{th}^2(t)} = 4kTR \Delta f \quad (3)$$

2.1.2. Shot Noise. The phenomenon of statistical current fluctuations is called *shot noise*. Because of the quantization of electron charge e , the electron flow, which corresponds to the number of electrons per unit time, is not continuous. Using these assumptions it is possible to divide a current $i(t)$ into a DC component I_0 and an AC component $i_s(t)$. Assuming that Z as the average number of electrons per unit time, $i(t)$ can be written as

$$i(t) = I_0 + i_s(t) \quad (4)$$

where $I_0 = Ze$. The noise contribution caused by the AC current $i_s(t)$ is interpreted as an *ergodic* fluctuation phenomenon. A typical device dominated by shot noise is the vacuum diode with a pure metal cathode. However, the relations derived for this device can be applied to most semiconductor devices, as well. For those frequencies that are small compared to the reciprocal time period $1/\tau$ of the discrete current pulses, the single spectral contributions of each current pulse to the total noise spectrum are neglectable. In this case the *Schottky relation* is valid for the spectrum of shot noise:

$$S_S(f) = 2eI_0 \quad (5)$$

This spectrum is directly proportional to the mean DC current I_0 through the device. Generally, the *Schottky relation* is valid even for fast semiconductor devices and at very high frequencies. Equation (5) is also suitable to describe the related noise contribution due to gate leakage current I_{leak} in case of field-effect transistors, if I_0 is replaced by I_{leak} .

2.1.3. Avalanche Noise. Charge carrier multiplication in semiconductor devices can occur in regions of high

26. K. Likharev and V. Semenov, RSFQ logic/memory family: A new Josephson-junction technology for sub-terahertz-clock-frequency digital systems, *IEEE Trans. Appl. Superconduct.* **1**:3–28 (1991).
27. A. Dupret, E. Belhaire, and P. Garda, Scalable array of Gaussian white noise sources for analogue VLSI implementation, *Electron. Lett.* **31**(N17):1457–1458 (1995).
28. M. Gupta, Applications of electrical noise, *Proc. IEEE* **63**: 996–1010 (1975).
29. K. Kryter, *The Effects of Noise on Man*, Academic Press, New York, 1970.
30. R. Spina and S. Upadhyaya, Linear circuit fault diagnosis using neuromorphic analyzers, *IEEE Trans. Circ. Syst. II, Analog Digit. Signal Process.* **44**:188–196 (1997).
31. T. Takagi, Composite noise generator as a noise simulator and its application to noise immunity test of digital systems and TV picture, *IEICE Trans. Commun.* **78B**(N2):127–133 (1995).
32. J. Markus, *Guidebook of Electronic Circuits*, McGraw-Hill, New York, 1974.

NOISE, HIGH-FREQUENCY

M. AGETHEN
 R. REUTER
 R. M. BERTENBURG
 W. BROCKERHOFF
 F. J. TEGUDE
 Innovative Processing AG
 (IPAG)
 Duisburg, Germany

1. INTRODUCTION

The high-frequency behavior of electronic devices is of major interest in the field of research and development. Beside the typical RF device parameters, such as the cutoff frequencies f_T and f_{max} , high-frequency noise behavior has to be considered for circuit design, especially if noise has a significant influence on the system performance, for instance, the sensitivity of receivers. By this means, there is a demand for simple but exact RF noise models that must consider the physically relevant noise phenomena with a significant contribution to the total noise behavior of the device.

After an introduction to various physical noise sources, a general description of noisy two-ports will be presented, followed by a brief presentation of a special measurement setup for RF noise in the range of 2–18 GHz with dependence on temperature (15–400 K). In Section 4 the RF noise phenomena in certain devices are examined and high-frequency noise models for heterostructure field-effect transistors (HFETs) and heterojunction bipolar transistors (HBTs) based on the material system InP are presented. For both devices the capabilities of the model presented will be proved by comparing measured and modeled RF noise parameters. In Section 5 modifications of the HFET noise model and applications of this RF noise model are presented.

2. NOISE THEORY

2.1. Physical Noise Sources

2.1.1. Thermal Noise. The most important and best-known noise mechanism is the thermal noise or *Johnson Noise* [1,2]. This process can be observed in all electrically conductive materials. Assuming a finite temperature $T(T > 0 \text{ K})$, the free electrons statistically move in these materials forced by their thermal energy. Because of scattering processes at lattice atoms, this movement leads to a statistical fluctuation of the voltage at the terminals of the conductor (e.g., a resistor R). The corresponding noise spectrum of the thermal noise is given as [1]

$$S_{th}(f) = 4kTR \quad (1)$$

where k is Boltzmann's constant ($k = 1.38 \times 10^{-23} \text{ W} \cdot \text{s/K}$). The measurable mean-square values of the thermal noise current $i_{th}^2(t)$ or the thermal noise voltage $v_{th}^2(t)$ per unit bandwidth Δf are given respectively as [3,4]

$$\overline{i_{th}^2(t)} = 4kT \frac{\Delta f}{R} \quad (2)$$

$$\overline{v_{th}^2(t)} = 4kTR \Delta f \quad (3)$$

2.1.2. Shot Noise. The phenomenon of statistical current fluctuations is called *shot noise*. Because of the quantization of electron charge e , the electron flow, which corresponds to the number of electrons per unit time, is not continuous. Using these assumptions it is possible to divide a current $i(t)$ into a DC component I_0 and an AC component $i_s(t)$. Assuming that Z as the average number of electrons per unit time, $i(t)$ can be written as

$$i(t) = I_0 + i_s(t) \quad (4)$$

where $I_0 = Ze$. The noise contribution caused by the AC current $i_s(t)$ is interpreted as an *ergodic* fluctuation phenomenon. A typical device dominated by shot noise is the vacuum diode with a pure metal cathode. However, the relations derived for this device can be applied to most semiconductor devices, as well. For those frequencies that are small compared to the reciprocal time period $1/\tau$ of the discrete current pulses, the single spectral contributions of each current pulse to the total noise spectrum are neglectable. In this case the *Schottky relation* is valid for the spectrum of shot noise:

$$S_S(f) = 2eI_0 \quad (5)$$

This spectrum is directly proportional to the mean DC current I_0 through the device. Generally, the *Schottky relation* is valid even for fast semiconductor devices and at very high frequencies. Equation (5) is also suitable to describe the related noise contribution due to gate leakage current I_{leak} in case of field-effect transistors, if I_0 is replaced by I_{leak} .

2.1.3. Avalanche Noise. Charge carrier multiplication in semiconductor devices can occur in regions of high

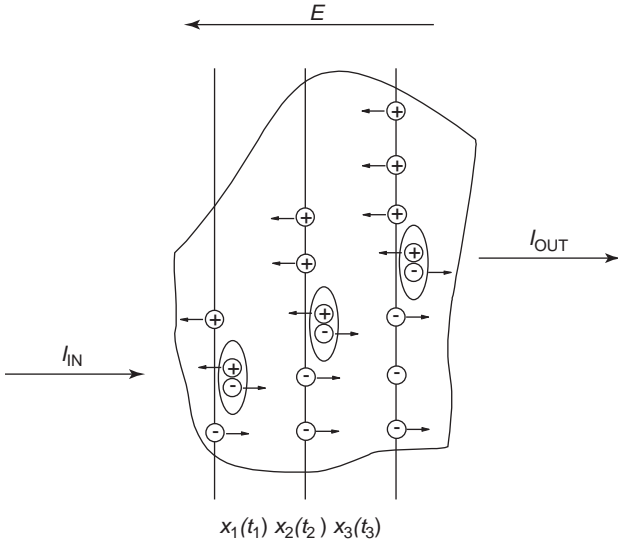


Figure 1. Model for the avalanche region at different locations and related timesteps $x_i(t_i)$ with input current I_{IN} and output current I_{OUT} .

electric field strengths. If the mean free path of carriers is long enough to achieve sufficient energy, additional electron–hole pairs are generated when colliding with lattice atoms (Fig. 1). This avalanchelike increase in the number of carriers often leads to a nonreversible degeneration of the device, known as *thermal breakdown*. If this process is limited, it becomes reversible and is often utilized to obtain special devices such as *avalanche photodiodes* (APD). In these devices the multiplication of optically generated electron–hole pairs enables a significant increase in the optical responsivity, hence receiver sensitivity. The corresponding noise contribution is called *avalanche noise*. The avalanche noise is characterized by two ionization factors, for electrons α and holes β , which describe the number of carriers generated per unit length. They are dependent on the location and electric field strength, respectively. Assuming that the input current I_{IN} shows shot noise and that the ionization coefficients for electrons and holes are equal, the following expression for the noise spectrum of the output current I_{OUT} can be derived [5]:

$$S_{I_{OUT}} = 2e I_{IN} M^3 \quad (6)$$

where M is the avalanche multiplication factor.

If the ionization coefficients are different but linearly dependent as in

$$\beta = c \cdot \alpha \quad (7)$$

where $c = \text{const}$ and the input current I_{IN} is caused by electrons only, the spectrum of the output current is derived by [6,7] as follows:

$$S_{I_{OUT}} = 2e I_{IN} M^3 \left[1 - (1 - c) \left(\frac{M - 1}{M} \right)^2 \right] \quad (8)$$

In the case of a pure hole current, c has to be replaced by $1/c$ in Eq. (8). As mentioned above, two restrictions have to be considered for the validity of both relations:

1. The spectrum of the injected current I_{IN} corresponds to that of shot noise only.
2. The length of the ionization region l_z is sufficient to achieve a high probability of collisions of the injected electrons with lattice atoms.

A modified relation is applicable to the phenomenon of impact ionization, which is of interest in conjunction with heterostructure FETs (see Section 4.1.3).

2.2. Noise in Linear Two-Ports

2.2.1. Equivalent Circuits for Noisy Impedances and Admittances. For physically related noise modeling of devices, a more generalized description of the single physical noise sources is necessary. The usual tool for noise calculations is the equivalent circuit, well known from RF modeling of devices. In the particular case of noise modeling all elements have to be treated as complex values.

The latter statement results in the fact that only devices assimilating real power are able to emit thermal noise power [8]. Replacing the real value R by the complex impedance $\mathbf{Z} = R + jX$ leads to the following equations for measurable frequency-dependent mean-square values of the thermal noise currents $i_{th}^2(t)$ and noise voltages $v_{th}^2(t)$ per unit bandwidth Δf .

$$\overline{i_{th}^2(t)} = 4kT \frac{\Delta f}{\Re\{\mathbf{Z}\}} \quad (9)$$

$$\overline{v_{th}^2(t)} = 4kT \Delta f \Re\{\mathbf{Z}\} \quad (10)$$

where the operator $\Re\{\}$ accesses the real part of the particular value.

In a similar way, more generalized relations for the thermal spectral noise densities can be derived using Eqs. (9) and (10) as follows:

$$S_{th,i} = \overline{i_{th}^2(t)} \frac{1}{\Delta f} = 4kT \frac{1}{\Re\{\mathbf{Z}\}} = 4kT \Re\{\mathbf{Y}\} \quad (11)$$

$$S_{th,v} = \overline{v_{th}^2(t)} \frac{1}{\Delta f} = 4kT \frac{1}{\Re\{\mathbf{Y}\}} = 4kT \Re\{\mathbf{Z}\} \quad \text{with} \quad (12)$$

$$\mathbf{Y} = \mathbf{Z}^{-1}$$

Finally, this leads to a description of physical noise processes based on a small-signal equivalent circuit. The individual noisy impedances or admittances can be described by either of two compatible equivalent circuits (Fig. 2):

1. A noise current source $i_{th}(f)$ and a noise-free ($T = 0$ K) admittance in parallel
2. A noise voltage source $v_{th}(f)$ and a noise-free ($T = 0$ K) impedance in series

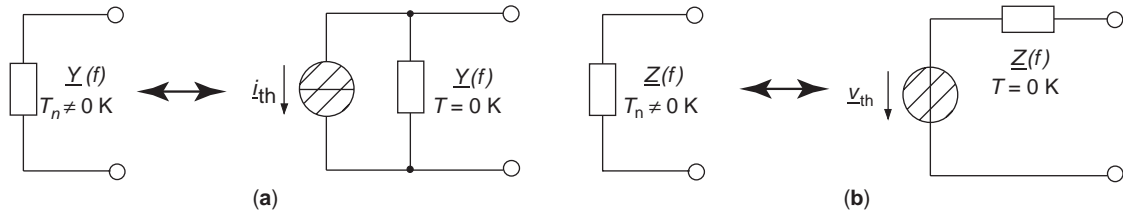


Figure 2. Equivalent circuits of noisy impedances or admittances: (a) noise current source; (b) noise voltage source.

If the derived temperature of the impedance or admittance is different from the ambient temperature of the device, it is called the *equivalent noise temperature* T_n .

Using this definition of the equivalent noise temperature, which in the first instance is valid for one-ports, together with the derived equivalent RF circuits, we can calculate the noise behavior of complex circuits and systems. Typically, however, possible correlations between the individual noise sources of the total system also have to be considered.

2.2.2. The Noise Figure. Unfortunately, the term *noise figure*, which was originally defined for the description of noisy networks [9] and is valid only under certain assumptions [10], sometimes leads to an overestimation of its real significance, especially in the case of discrete devices. Nevertheless, for systems the noise figure F is a more suitable parameter for noise characterization. The term *noise figure* suggests the formally defined *standard noise figure* F , which assumes an input noise signal that is not arbitrarily given, but related to the reference noise temperature of $T_0 = 290$ K, and hence an absolute value [11].

In this way, F is a value for two-port inherent noise and thus is independent of external conditions or terminations of the ports. A noise-free two-port is characterized by a noise figure of $F = 1$ or $F' = 0$ dB. Figure 3 shows the principal equivalent circuit for the definition of the (standard) noise figure. It consists of the noisy two-port connected to a load impedance Z_L , assumed to be noise-free ($T = 0$ K). The input is connected to a noisy source impedance Z_S ($T > 0$ K). Again, this impedance is represented by a voltage noise source and a noise-free impedance Z_S ($T = 0$ K).

With S_{n2v} as the noise spectrum at the output of the noisy two-port and S_{n20v} as the spectrum of the noise-free

two-port, F is defined by [8]

$$F = \frac{S_{n2v}}{S_{n20v}} \quad (13)$$

An equivalent equation can be derived using the noise current spectra instead.

2.2.3. Calculation of the Noise Figure F Using Noise Equivalent Circuits. The noise figure F of noisy linear two-ports can be calculated using equivalent circuits [12,13]. A very simple and appropriate description for a noisy two-port is the chain matrix or *ABCD* parameter description, respectively, with one current noise source and one voltage noise source at the input terminal (Fig. 4). In this way, the noise behavior of the total two-port can be modeled by only two noise sources that are chained to the input.

Using this equivalent circuit for the noisy two-port, the noise figure is given as:

$$F = 1 + \frac{S_{nv} + |Z_S|^2 S_{ni} + 2\Re\{Z_S S_{vi}\}}{4kT_0 R_S} \quad (14)$$

where

S_{nv} = voltage noise spectrum

S_{ni} = current noise spectrum

S_{vi} = cross-correlation spectrum between v_n and i_n .

The noise figure is independent of the input impedance of the two-port Z_{in} and the load impedance Z_L . However, the values of the spectra of the equivalent noise sources of the two-port as well as the cross-correlation spectrum, which describes the correlation between both noise sources, are required. Additionally, the noise figure depends on the

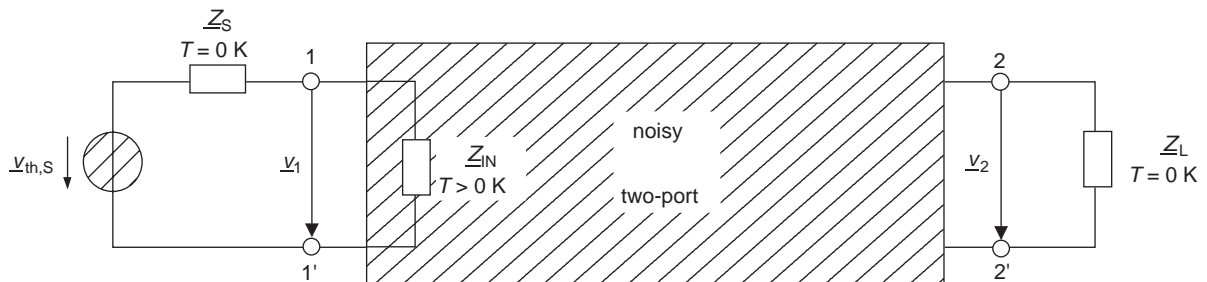


Figure 3. Equivalent circuit for definition of (standard) noise figure F .

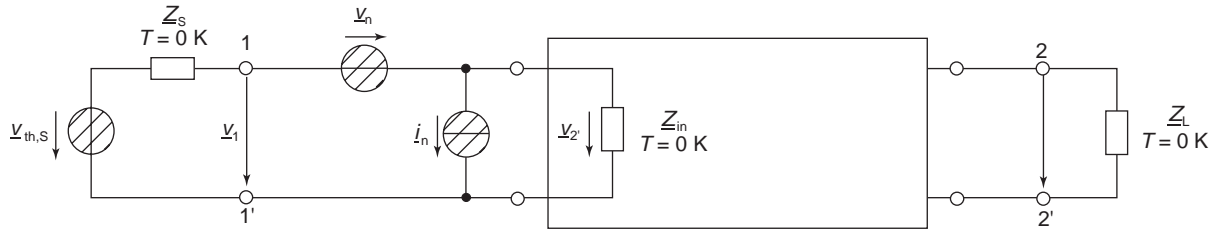


Figure 4. Noise equivalent circuit with noise current and noise voltage source “chained” at the input of the noise-free two-port.

source impedance Z_S . The value of the noise figure reaches a minimum at $F = F_{\min}$ for an optimal source impedance of $Z_S = Z_{S,\text{opt}}$. This is called *noise matching*. Unfortunately, the necessary impedances for noise matching differ from those for power matching. By this means, maximum available gain G_a of the two-port is actually not available, and a reduced power gain, the so-called *associated gain* G_{ass} , characterizes the two-port. Designing electronic circuits, which is always a compromise between *noise* and *power matching*, has to be realized.

2.2.4. Discussion of Noise Matching. As mentioned above, the noise figure is a function of the source impedance Z_S . Common measurement techniques for the determination of noise parameters are based on the relation given in Eq. (14). The dependence of F on deviations from the ideal matching condition can be described corresponding to [10] by

$$F = F_{\min} + \frac{R_n}{G_S} |Y_S - Y_{S,\text{opt}}|^2, \quad Y_S = G_S + jB_S \quad (15a)$$

or

$$F = F_{\min} + \frac{g_n}{R_S} |Z_S - Z_{S,\text{opt}}|^2, \quad Z_S = \frac{1}{Y_S} = R_S + jX_S \quad (15b)$$

using the equivalent noise conductance g_n with

$$g_n = R_n \cdot |Y_{S,\text{opt}}|^2 \quad (16)$$

Only four parameters—the minimum noise figure F_{\min} , the equivalent noise resistance R_n , and the real part $G_{S,\text{opt}}$ and the imaginary part $B_{S,\text{opt}}$ of the optimal generator (source) impedance—are necessary to completely describe the noise behavior of a linear two-port.

The term R_n is a measure for the sensitivity of the noise figure to deviations from the optimum source admittance $Y_{S,\text{opt}}$ or impedance $Z_{S,\text{opt}}$, respectively. By this means, R_n is a figure of merit regarding the noise behavior of the two-port. The equivalent noise resistance should be as small as possible to avoid a significant increase of noise if—depending on the actual application—the optimum noise matching ($Y_S = Y_{S,\text{opt}}$) has to be sacrificed for a potentially more important power matching at the input.

Usually, the admittance or impedance, respectively, are normalized and related to the characteristic impedance of the measurement setup Z_0 (typically $Z_0 = 50 \Omega$), which results in the following equation after transformation to the

Smith chart plane:

$$F = F_{\min} + 4r_n \frac{|\Gamma_S - \Gamma_{S,\text{opt}}|^2}{(1 - |\Gamma_S|^2)(1 + |\Gamma_{S,\text{opt}}|^2)} \quad (17)$$

where

- r_n = normalized equivalent noise resistance [$r_n = (R_n/Z_0)$]
- Γ_S = generator reflection coefficient
- $\Gamma_{S,\text{opt}}$ = optimum generator reflection coefficient for noise matching

Figure 5 shows a graphical interpretation of this equation, characterizing a paraboloidal surface, in the *Smith chart* plane. The minimum of the paraboloid represents the minimum noise figure F_{\min} at the optimum generator reflection coefficient $\Gamma_{S,\text{opt}}$. The latter can be derived by a perpendicular projection of the corresponding point onto the *Smith chart* plane. If Γ_S differs from $\Gamma_{S,\text{opt}}$, the noise figure F also rises. As discussed earlier, this increase is directly proportional to the value of the equivalent noise resistance R_n , which corresponds to the slope of the paraboloid at a specific point. In practice, this circumstance could imply an even higher priority to achieve a low R_n than an absolutely low F_{\min} , depending on several boundary conditions to be additionally considered.

3. RF NOISE MEASUREMENTS

Figure 6 shows a typical measurement setup that allows temperature-dependent noise figure measurements of two-ports in the temperature range of 15–400 K and frequency range of 2–18 GHz [14,15]. It comprises the *noise figure meter* (HP8970B) as the central unit and the calibrated *noise source* (HP346A) [16]. The *noise figure test set* (HP8971) and the *synthesizer* (HP8672A) are necessary to downconvert the measurement frequency to a frequency range of 10–1600 MHz, which the *noise figure meter* is able to directly process. To determine the four interesting noise parameters (F_{\min} , R_n , $G_{S,\text{opt}}$, and $B_{S,\text{opt}}$) of a linear two-port, the noise figures at various generator reflection coefficients Γ_S have to be measured [17,18].

These particular reflection coefficients can be achieved using a commercial *electronic tuner system* (see Fig. 6). The tuner subsystem consist of the *control unit* (NP5); the *mismatch noise source* (MNS), including the actual *tuner*; and the *remote receiver module* (RRM) with an integrated

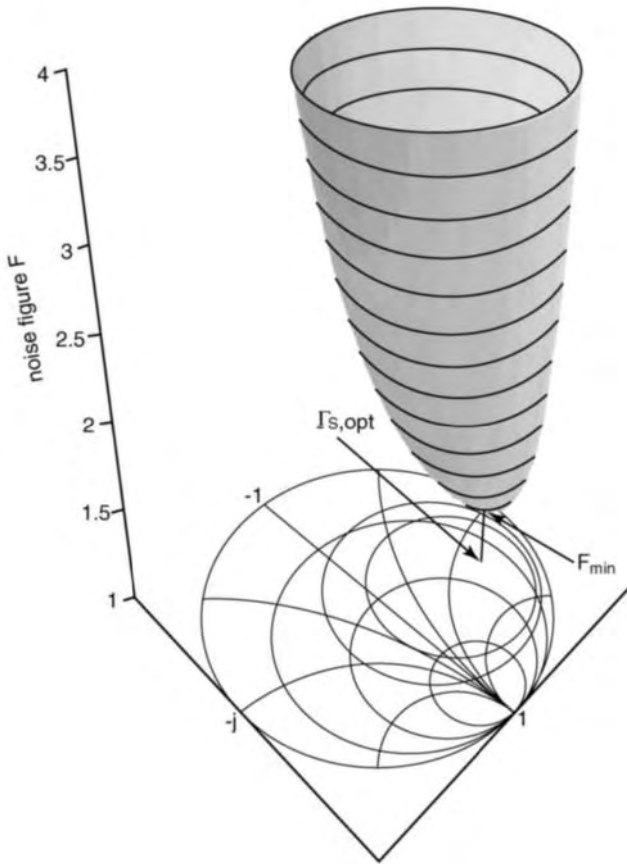


Figure 5. Noise figure F with dependence of generator reflection coefficient (here: $F_{\min} = 1.5$, $R_n = 50 \Omega$, $|\Gamma_{S,\text{opt}}| = 2/3$, $\text{Arg}\{\Gamma_{S,\text{opt}}\} = 60^\circ$).

low-noise preamplifier. Additionally, both elements (MNS and RRM) contain *RF switches* necessary for system calibration. These switches also enable the simultaneous measurement of the noise and the corresponding scattering parameters.

The complete system is controlled by a computer system that allows the evaluation of the data and the extraction of the specific noise parameters from the measured noise figures [16,19–22].

4. RF NOISE IN ELECTRONIC DEVICES

4.1. Noise in Heterostructure Field-Effect Transistors

4.1.1. Thermal Noise in HFET. The channel of a field-effect transistor (FET) can be interpreted as a controlled resistance. The thermal noise generated in this channel is the dominating noise contribution.

For an n-doped semiconductor, the well-known equation of the thermal noise current for a resistance R [cf. Eq. (2)] can be transformed to [23]

$$\overline{i_{\text{th}}^2(t)} = 4kT_{\text{eff}} \frac{1}{R_{\text{ch}}} \Delta f \quad (18)$$

where T_{eff} is the effective temperature in the semiconductor channel and R_{ch} is the resistance of the channel.

The geometric aspects of the channel resistance can be expressed as

$$R_{\text{ch}} = \frac{1}{\kappa} \frac{l}{A} \Rightarrow \frac{1}{R_{\text{ch}}} = \kappa \frac{A}{l} \quad (19)$$

where A is the cross-sectional area of the channel and l is the length of the current path through the semiconductor.

The conductivity κ can be calculated for purely n-type (p-type) conductivity as

$$\kappa = en_0\mu_0 \quad (20)$$

where n_0 is the electron (hole) concentration and μ_0 is the low-field mobility of electrons (holes).

In addition, the diffusion coefficient D_0 can be derived from *Einstein's relation* as

$$D_0 = \frac{kT\mu_0}{e} \quad (21)$$

Finally, this leads to a description of the thermal noise in the channel as

$$\overline{i_{\text{th}}^2(t)} = 4e^2 \frac{A}{l} n_0 D_0 \Delta f \quad (22)$$

In the case of high electric fields, as occur in the region between gate and drain, the conventional *Einstein's relation* [Eq. (22)] is no longer valid. The diffusion coefficient, the low-field mobility, as well as the effective noise temperature $T_{n,\text{eff}}$ of the channel become dependent on the electrical field strength E and the frequency f [24,25], leading to

$$\frac{kT_{n,\text{eff}}(E,f)}{e} = \frac{D_0(E,f)}{\Re\{\mu(E,f)\}} \quad (23)$$

As a result of the relation between the thermal noise attributed to a resistor and the equivalent description for a semiconductor channel, this is often called *diffusion noise*.

4.1.2. The Shot Noise in HFET. In principle, the shot noise of the drain current can be described using Eq. (5) (see Section 2.1.2) [26,27]. Especially in heterostructure field-effect transistors, the recombination of carriers underneath the space charge region leads to a significantly reduced shot noise [28,29].

Without further proof, it can be assumed that the channel shot noise contribution is negligible. Nevertheless, shot noise again becomes of major interest if the device suffers from gate leakage that generates an additional noise contribution to the channel noise (see Section 2.1.2).

4.1.3. Impact Ionization Noise in HFET. The assumptions for avalanche noise as presented in Section 2.1.3 are not valid in the case of HFET. Nevertheless, in the gate–drain region a kind of avalanche noise occurs caused by impact ionization processes due to the high electric field strengths. Especially in HFET based on layers

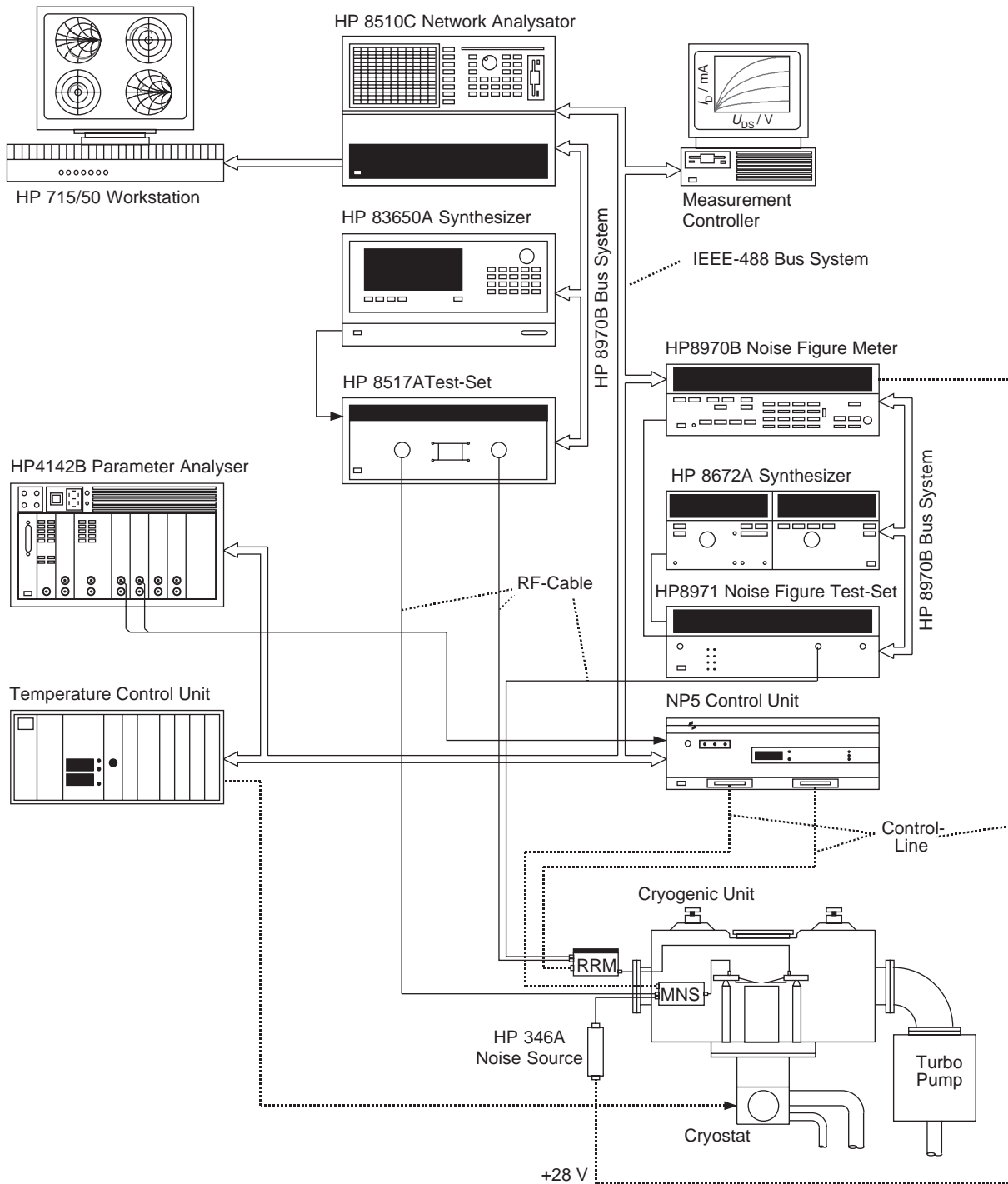


Figure 6. Measurement setup for RF noise parameters in the range 2–18 GHz with dependence of temperature (15–400 K).

with an advanced carrier mobility (e.g., InGaAs), this additional noise contribution can be observed as a result of the low bandgap of these channel materials. Typically, the area between gate and drain, where impact ionization can occur, is extremely small ($l \leq 100$ nm). Therefore, impact ionization leads to a moderate increase of the drain current I_D at high bias voltages

V_{DS} only. The corresponding noise, called *impact ionization noise*, differs from the basic avalanche noise because of the significantly smaller multiplication factor M [see Eq. (6)].

Using the same assumptions as in the case of avalanche noise, but regarding to the special geometric design of the HFET, the spectral density of the impact ionization

noise can be derived from [30,31]

$$S_{I_{OUT}} = M^2 S_{I_{IN}} + 2eI_{IN}\sigma^2 \quad (24)$$

where $S_{I_{IN}}$ is the density of the induced current I_{IN} and σ^2 the variance of the noise process.

4.2. RF Noise Model of InAlAs/InGaAs/InP HFET

Figure 7 shows a typical equivalent RF noise model for InAlAs/InGaAs/InP HFET [32]. It is based on an extended temperature noise model (TNM) [33], which takes into account the influence of gate leakage current on both, the RF and noise performance. Gate leakage is modeled by the additionally included resistances R_{pgd} and R_{pgs} . Moreover, this model considers the effects due to impact ionization [34,35]. This is enabled by an additional voltage-controlled current source $g_{m,im}$ and a RC combination in parallel to the output resistance. The current source is controlled by the voltage drop across the high-field region at the drain end of the gate, which is equal to the drain–gate voltage v_{dg} . The characteristic frequency dependence of the impact ionization effects on RF and noise behavior, respectively, are described by the combination of R_{im} and C_{im} . For noise modeling purposes an additional white-noise source i_{im} is included in parallel to the current source $g_{m,im}$. This arrangement of noise source and RC combination characterizes the frequency dependence of the externally available noise current $i_{im,ext}$. This impact ionization

source can be described by

$$\sqrt{i_{im,ext}^2} = \sqrt{i_{im}^2} \cdot \frac{1}{\sqrt{1 + \left(\frac{\omega}{\omega_0}\right)^2}}, \quad \omega_0 = \frac{1}{R_{im} \cdot C_{im}} \quad (25)$$

This formula describes the Lorentzian shape of the external noise current, which typically is attributed to carrier generation processes, thus substantiating the occurrence of impact ionization noted in Section 4.1.3.

4.3. Noise in Heterojunction Bipolar Transistors

For modeling of the high-frequency noise behavior of both *bipolar junction transistors* (BJTs) and *heterojunction bipolar transistors* (HBTs), the physical noise sources have to be defined in more detail. The most important noise phenomenon in all bipolar transistors is shot noise. In addition to this predominant effect, thermal noise due to parasitic resistances must also be considered.

Basically, a bipolar transistor consists of two combined p-n junctions. Figure 8 schematically represents the various current paths and components within a n-p-n bipolar transistor at active bias conditions. In this way, the base–emitter junction is forward-biased and the base–collector junction is reverse-biased. The electron current from the emitter towards the collector [line (a) in Fig. 8] is the dominating current component. Electrons induced by line (b). Holes are injected from the base into the emitter [line (c)]. Electrons are thermally generated in the base and holes within the emitter, respectively [lines (d), (e)].

In the case of the reverse-biased base–collector diode, the current components due to the thermal generation of electron–hole pairs have to be taken into account [Fig. 8 lines (f), (g)] only. All these current components can be combined, corresponding to Fig. 8, leading to four independent currents $I_1, I_2, I_3,$ and I_4 . The measurable currents at the

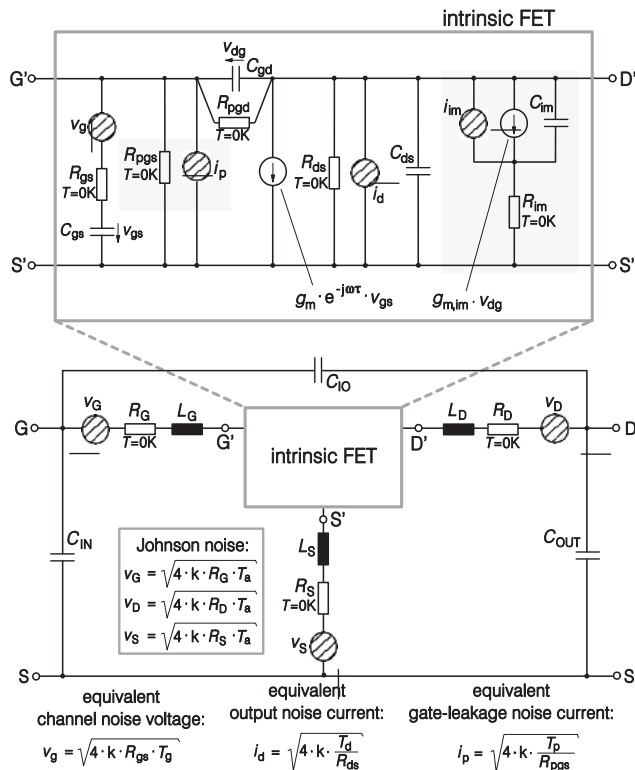


Figure 7. Intrinsic and extrinsic small-signal and noise equivalent circuit of HFET including modeling of gate leakage current and impact ionization on RF and noise behavior.

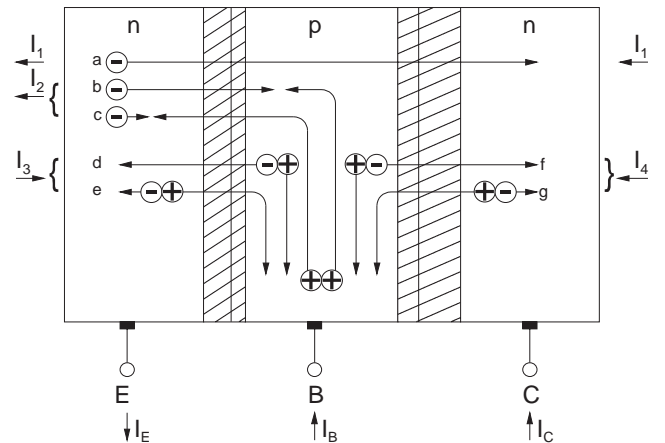


Figure 8. Current components and current flow in a n-p-n bipolar junction transistor.

terminals are then expressed as

$$I_E = I_1 + I_2 - I_3 \quad (26a)$$

$$I_C = I_1 + I_4 \quad (26b)$$

$$I_B = I_2 - I_3 - I_4 \quad (26c)$$

4.4. RF Noise Model of InGaAs/InP HBT

Figure 9 shows the typical three-mesa design of HBT based on III-V semiconductors [36]. The included T-like equivalent circuit can easily be found, associating all small-signal equivalent elements to a specific device region.

This extended small-signal equivalent circuit of HBT builds up the basis of the consistent small-signal and RF noise parameter model (Fig. 10). In the case of narrow-band noise, equivalent noise temperatures are associated with all resistances. In Fig. 10 all equivalent noise temperatures are included. As usual, the small-signal model is divided into two parts, an intrinsic one and an extrinsic one. The extrinsic resistances add only thermal noise; consequently their equivalent noise temperature is set to the ambient temperature T_A . The noise from the included RC combination R_{BP} and C_{BP} at the base contact (Fig. 10), taking into account a frequency dependence of the non-loyed ohmic base contact, is assumed to be thermal noise, too. As a consequence, only the four intrinsic equivalent noise temperatures have to be found for a complete RF noise parameter modeling of HBT. Additionally, with the help of these noise temperatures, a localization of various

noise sources and phenomena in specific HBT regions is possible.

4.5. Experimental Results and Verification of the Model for InAlAs/InGaAs/InP HFET

As an example of the applicability of the noise models discussed above, the RF noise behavior of a typical InAlAs/InGaAs/InP HFET with a gate length of $L_G = 0.7 \mu\text{m}$ and a gate width $W_G = 80 \mu\text{m}$ suitable for millimeter-wave and optoelectronic applications is presented. The material system has been selected to demonstrate the significance of both, the impact ionization in the InGaAs channel, and the gate leakage current. In contrast, typical GaAs-based HFET do not significantly suffer from those phenomena, mainly due to the larger bandgap of the corresponding materials [37,38].

All model parameters—the small-signal equivalent elements, equivalent noise temperatures (T_p, T_g, T_d), and equivalent impact ionization noise current (i_{im})—have been extracted using an optimization algorithm based on *simulated evolution* (evolution theory and genetic algorithms) [39–43]. These optimization strategies have to be applied because an analytical extraction of the model parameters from measured data (s parameters and noise parameters) is impossible because of the large number of model parameters and the complexity of the model.

4.5.1. RF-Performance. Figures 11 and 12 show both the measured and the modeled RF data in the frequency range from 45 MHz to 40 GHz, respectively. The good agreement demonstrate the applicability of the presented small-signal equivalent circuit including the significant effects of gate leakage and the impact ionization phenomena. The modeled parameters are calculated from the small-signal equivalent circuit, extracted from RF measurements using the *simulated evolution* described above. The corresponding bias conditions, geometry, performance data, and extracted small-signal equivalent elements are listed in Table 1.

Figure 13 shows the typical bias-dependent behavior of the extracted transconductance $g_{m,im}$ at room temperature ($T = 300 \text{ K}$). The low transconductance $g_{m,im}$ for small drain–source voltages V_{DS} demonstrates the negligible influence of impact ionization on RF performance at low V_{DS} corresponding to low fields in the HFET channel. With increasing V_{DS} , impact ionization and the inductive behavior of s_{22} occur, correlated with a drastically increased transconductance $g_{m,im}$.

4.5.2. Noise Behavior. The measured and modeled noise parameters ($F_{min}, R_n, g_n, G_{ass}, \Gamma_{opt}$) of the HFET are shown in Fig. 14. As a result of the Lorentzian shape of the external short-circuit noise current $i_{im,ext}$ [see Eq. (25)], corresponding to an upper frequency band limitation especially at low frequencies, a strong impact on the noise performance can be observed. The phenomenon of impact ionization now leads to an increase of the

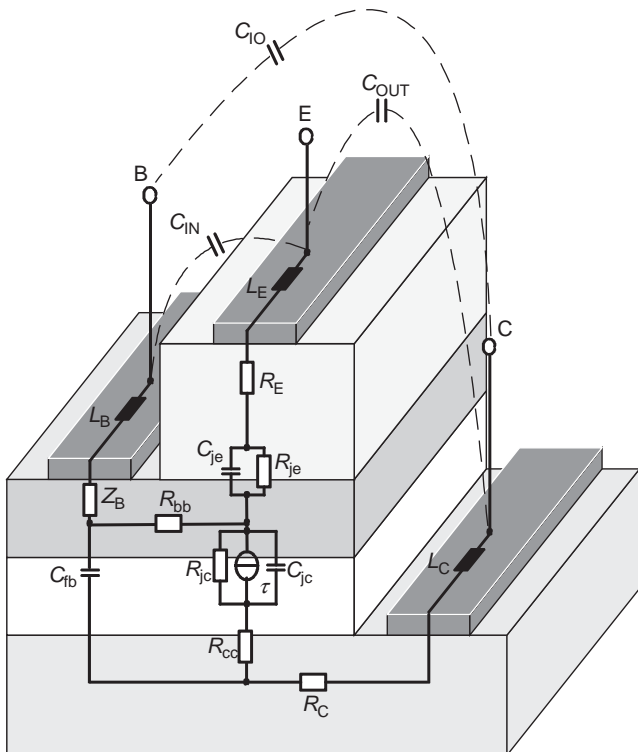


Figure 9. Typical three-mesa design of InP/InGaAs HBT.

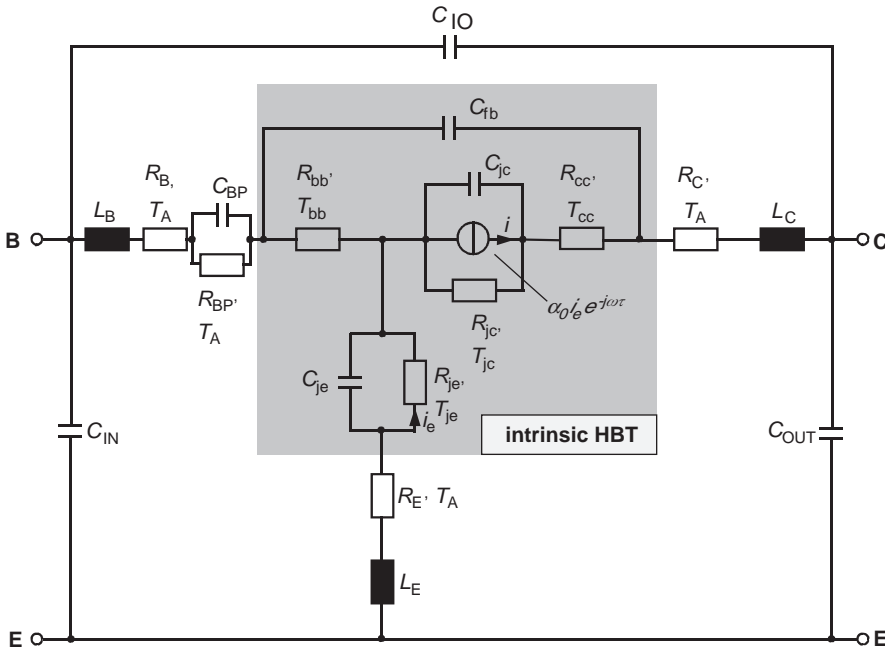


Figure 10. Consistent small-signal and RF noise parameter equivalent circuit of InP/InGaAs HBT.

minimum noise figure F_{min} . In particular, the increase of the minimum noise figure at low frequencies reflects the influence of the impact ionization process. In contrast to the influence of a gate leakage current [33], impact

ionization leads to higher optimum generator impedances and causes a sharp increase of the equivalent noise resistance R_n at low frequencies as well. The inductive behavior of the output path of the HFET also affects the associated gain G_{ass} and leads to a decrease at low frequencies. The three equivalent noise temperatures (T_g, T_p, T_d) and the equivalent impact ionization noise current i_{im} of the modeled extrinsic noise parameters are listed in Table 2.

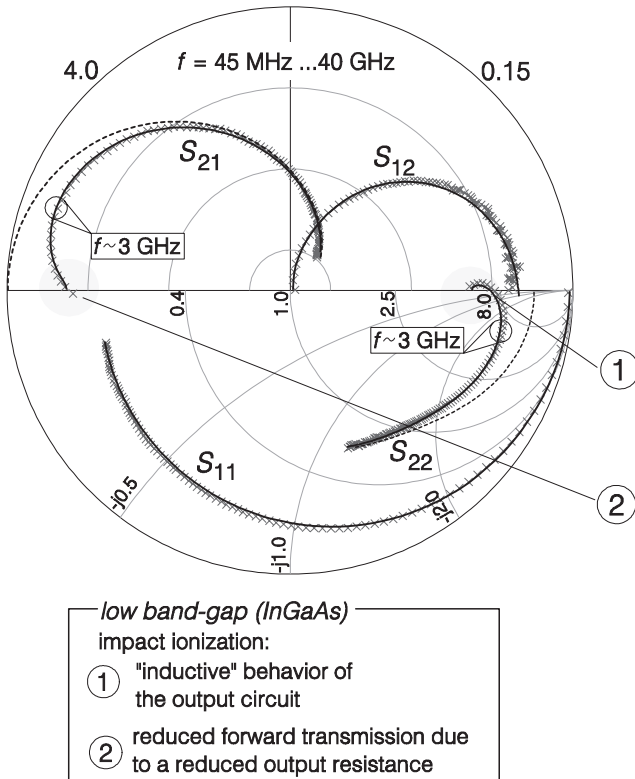


Figure 11. Measured (x) and modeled (■) scattering parameters versus frequency of an InAlAs/InGaAs/InP HFET at a bias condition where impact ionization occurs ($T = 300$ K, $V_{DS} = 1.5$ V, $V_{GS} = 0$ V, $L_g = 0.7$ μ m, $W_g = 80$ μ m). (This figure is available in full color at <http://www.mrw.interscience.wiley.com/erfme>.)

4.5.3. Intrinsic Equivalent Noise Sources. The intrinsic equivalent noise sources [44] of the HFET are strongly bias-dependent [32]. Figure 15 shows the drastic increase in the extracted impact ionization noise current i_{im} with higher drain-source voltages V_{DS} , while at low drain-source voltages ($V_{DS} < 0.7$ V) this component is negligible. In the latter case electron energies are smaller than those of the bandgap and are insufficient to generate electron-hole pairs. With increasing drain-source voltage ($> V_{DS} \approx 0.8$ V), impact ionization occurs and leads to additional noise currents that dominate the noise behavior of the transistor. This behavior reflects the strong correlation between impact ionization, bias condition, and generated total noise current. Because the level of the extracted impact ionization noise current i_{im} exceeds the equivalent shot noise drain current ($i_D = \sqrt{2eI_D}$) in a wide range of bias conditions, carrier multiplication [6,30,31] supposedly occurs in the high-field domain, leading to the following relation

$$i_{im} \propto f(M(E)) \cdot \sqrt{2eI_D} \quad (27)$$

where $f(M(E))$ reflects the dependence of the multiplication factor $M(E)$ on the electric field strength [30]. The relation between the multiplication factor $M(E)$ and the majority-carrier impact ionization rate per unit length

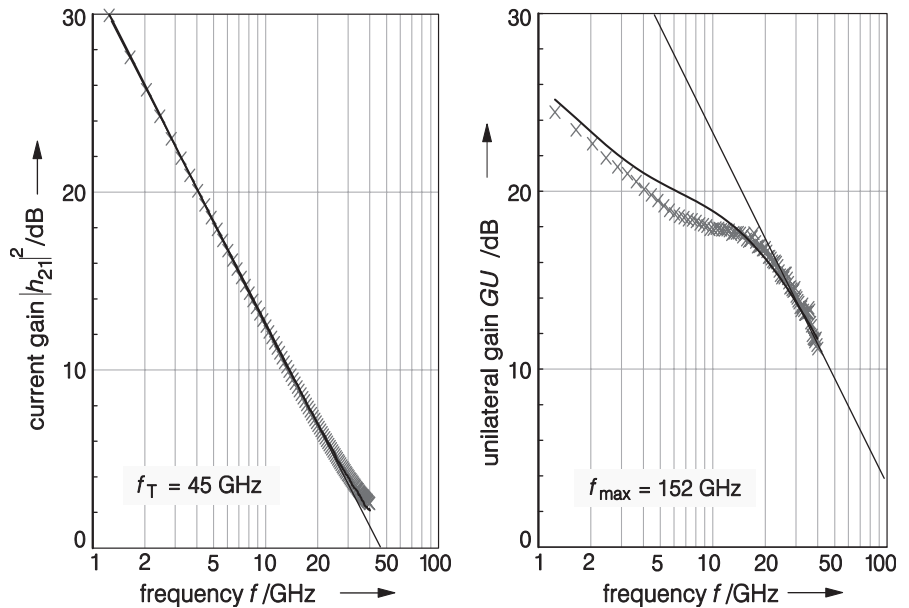


Figure 12. Measured (×) and modeled (■) current gain $|h_{21}|^2$ and unilateral gain GU versus frequency of an InAlAs/InGaAs/InP HFET at a bias condition where impact ionization occurs ($T=300$ K, $V_{DS}=1.5$ V, $V_{GS}=0$ V, $L_g=0.7$ μm , $W_g=80$ μm). (This figure is available in full color at <http://www.mrw.interscience.wiley.com/erfme>.)

$\alpha(x, E)$ can be described according to [30]

$$M(E) = \exp \left[\int_0^{L_{\text{eff}}} \alpha(\zeta, E) d\zeta \right] \quad (28)$$

where L_{eff} is the effective length of the impact ionization region.

Because of the position-dependent electric field strength and impact ionization rate, no simple analytical expression can be derived for the relation between bias conditions and the generated impact ionization noise current i_{im} .

The other equivalent intrinsic noise sources show the expected bias dependence [44] and reflect the strong correlation between equivalent intrinsic noise sources (i_d, i_p, v_g) and physical noise sources, such as shot noise drain current i_{sd} [see Eq. (29)] and shot noise gate current

i_{sg} [see Eq. (30)].

$$i_{\text{sd}} = \sqrt{2eI_D} \quad (29)$$

$$i_{\text{sg}} = \sqrt{2eI_G} \quad (30)$$

The equivalent output noise current i_d with dependence on the gate–source voltage V_{GS} versus the shot noise drain current is shown in Fig. 16. The equivalent noise current i_d is dominated by a reduced shot noise drain current [28]. The corresponding correlation is given by:

$$i_d = \sqrt{4k \frac{T_d}{R_{\text{ds}}}} \cong k_d \sqrt{2eI_D} + i_{d0} \quad (31)$$

with

$$k_d, i_{d0} = \text{const (value depending on the particular device)} \quad (32)$$

Table 1. Bias Conditions, Geometry, Performance Data, and Extracted Small-Signal Equivalent Elements of InAlAs/InGaAs/InP HFET

Bias conditions	
$V_{DS} = 1.5$ V, $V_{GS} = 0$ V,	
$I_D = 31.8$ mA, $I_G = -18$ μA	
Gate geometry	
$L_g = 0.7$ μm	
$W_g = 80$ μm	
Cutoff frequencies: $f_T = 45$ GHz, $f_{\text{max}} = 152$ GHz	
Small-signal equivalent elements	
$C_{\text{IN}} = 14.2$ fF, $C_{\text{IO}} = 4$ fF, $C_{\text{OUT}} = 28.2$ fF	
$R_G = 3$ Ω , $L_G = 63.1$ pH, $C_{\text{gs}} = 210.5$ fF	
$R_S = 8$ Ω , $L_S = 3.8$ pH, $L_D = 152$ pH	
$R_{\text{gs}} = 2.8$ Ω , $R_{\text{ds}} = 420$ Ω , $R_{\text{pgs}} = 12$ k Ω	
$R_D = 10$ Ω , $C_{\text{ds}} = 8.2$ fF, $R_{\text{pgd}} = 70.7$ k Ω	
$C_{\text{gd}} = 9.5$ fF, $g_m = 69$ mS, $\tau = 0.22$ ps	
$R_{\text{im}} = 38$ k Ω , $C_{\text{im}} = 1.42$ fF, $g_{m,\text{im}} = 4.26$ mS	

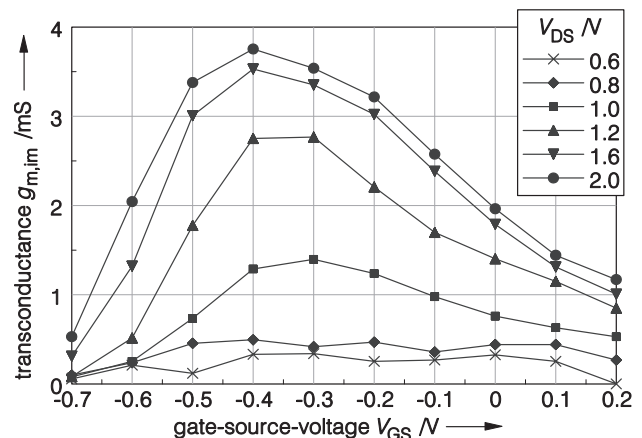


Figure 13. Impact ionization transconductance $g_{m,\text{im}}$ with dependence on the gate–source voltage V_{GS} , with the drain–source voltage V_{DS} as parameter; ($L_g=0.15$ μm , $W_g=100$ μm , $T=300$ K). (This figure is available in full color at <http://www.mrw.interscience.wiley.com/erfme>.)

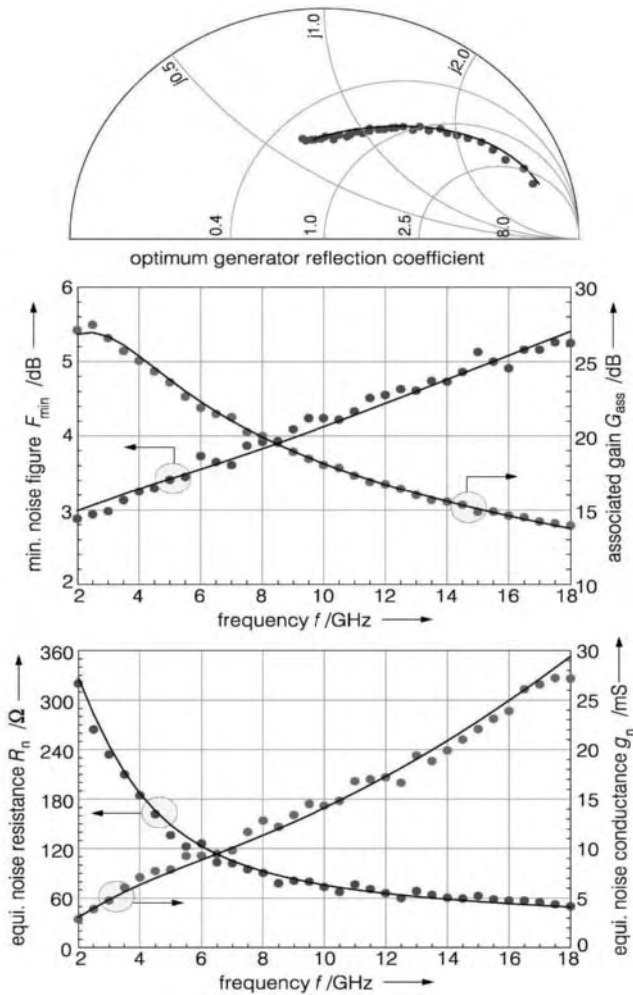


Figure 14. Measured (●) and modeled (■) noise parameters versus frequency of an InAlAs/InGaAs/InP HFET at a bias condition where impact ionization occurs ($V_{DS} = 1.5$ V, $V_{GS} = 0$ V, $I_D = 31.8$ mA, $L_g = 0.7$ μ m, $W_g = 80$ μ m, $T = T_a = 300$ K). (This figure is available in full color at <http://www.mrw.interscience.wiley.com/erfme>.)

The behavior of the equivalent channel noise voltage v_g (Fig. 17) with dependence on the gate–source voltage V_{GS} exhibits a behavior inversely proportional to that of the intrinsic current gain cutoff frequency f_T ($f_T = g_m / (2\pi(C_{gs} + C_{gd}))$). This is caused by a strong correlation of v_g with the intrinsic delay-time behavior of the HFET. A transformation of the equivalent channel noise voltage v_g , which is a characteristic value for the input circuit of the transistor, to a noise measure of the output circuit can be derived by multiplying v_g by the ratio of the square of the transcon-

Table 2. Extracted Equivalent Noise Temperatures and Noise Current of Modeled HFET^a

Equivalent-channel noise temperature: $T_g = 4014.9$ K
Equivalent output noise temperature: $T_d = 18007.84$ K
Equivalent gate leakage noise temperature: $T_p = 918.65$ K
Equivalent impact ionization noise current: $i_{im} = 146$ pA

^aParameters: $V_{DS} = 1.5$ V, $V_{GS} = 0$ V, $I_D = 31.8$ mA, $L_g = 0.7$ μ m, $W_g = 80$ μ m, $T = T_a = 300$ K.

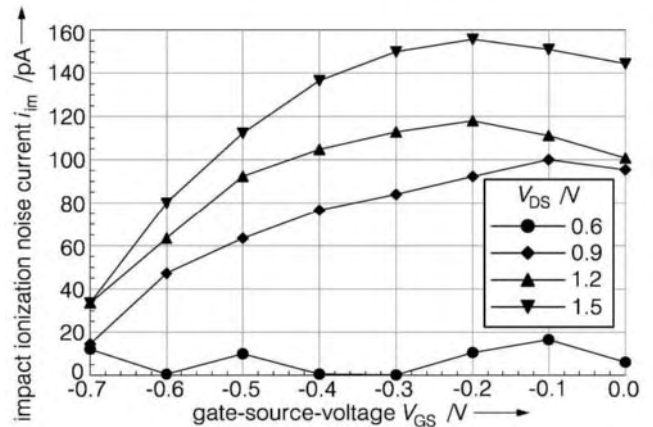


Figure 15. Extracted equivalent intrinsic impact ionization noise current i_{im} with dependence on gate–source voltage V_{GS} with drain–source voltage V_{DS} as parameter. (This figure is available in full color at <http://www.mrw.interscience.wiley.com/erfme>.)

ductance g_m to the intrinsic current gain cutoff frequency f_T . The transformed channel noise voltage demonstrates a behavior nearly proportional to that of the shot noise drain current (see Fig. 18). Using this transformation, the equivalent-channel noise voltage v_g can be expressed

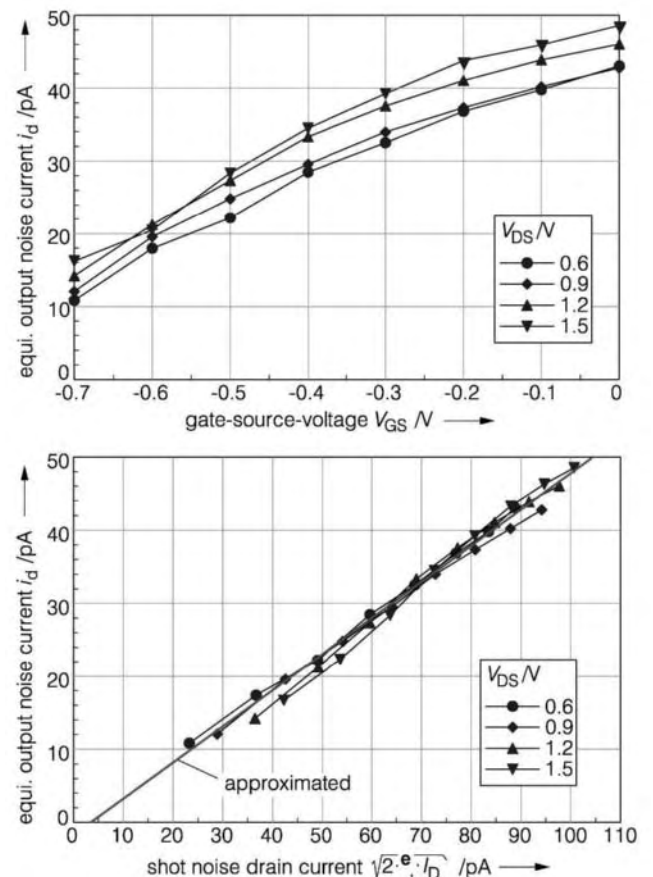


Figure 16. Extracted equivalent output noise current i_d with dependence on gate–source voltage V_{GS} (above) and on the shot noise drain current (below) with drain–source voltage V_{DS} as parameter. (This figure is available in full color at <http://www.mrw.interscience.wiley.com/erfme>.)

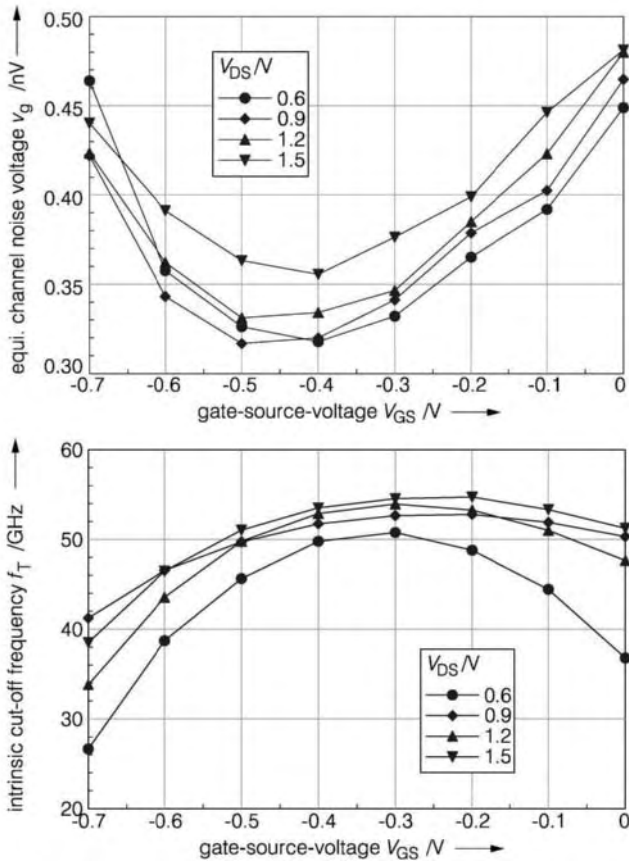


Figure 17. Equivalent channel noise voltage v_g (above) and intrinsic current gain cutoff frequency f_T (below) in dependence on gate–source voltage V_{GS} with drain–source voltage V_{DS} as parameter. (This figure is available in full color at <http://www.mrw.interscience.wiley.com/erfme>.)

by the following linear approximation

$$v_g \frac{g_m^2}{f_T} = \sqrt{4kT_g R_{gs}} \frac{g_m^2}{f_T} \cong k_g \sqrt{2eI_D} + i_{d1} \quad (33)$$

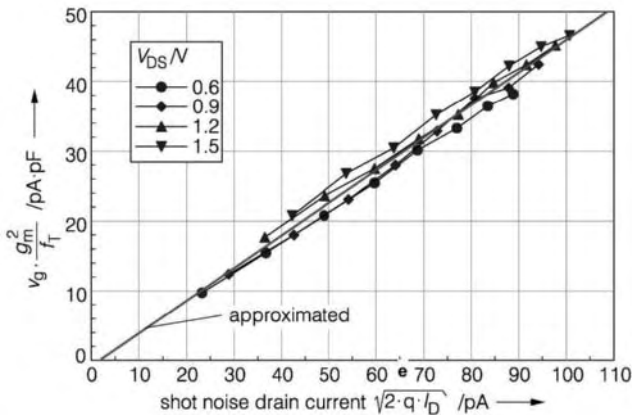


Figure 18. Extracted transformed equivalent channel noise voltage with dependence on the shot noise drain current with the drain–source voltage V_{DS} as parameter, respectively. (This figure is available in full color at <http://www.mrw.interscience.wiley.com/erfme>.)

with

$$k_g, i_{d1} = \text{const (value depends on the particular device)} \quad (34)$$

Figure 19 shows the equivalent gate leakage noise current i_p with dependence on the gate–source voltage V_{GS} versus the shot noise gate current. The equivalent gate leakage noise current i_p is nearly proportional to the shot noise gate current. This clearly demonstrates that a gate tunneling current causes pure shot noise [see Eq. (30)] [44]. The behavior described above leads to

$$i_p = \sqrt{4k \frac{T_p}{R_{pgs}}} \cong \sqrt{2eI_G} \quad (35)$$

These dependencies demonstrate the ability of the noise model presented above to separate the intrinsic noise sources, and the correlation to physical noise processes. Furthermore, only two independent noise parameter measurements are sufficient for extraction of the unknown parameters (k_g, k_d, i_{d0}, i_{d1}) in Eqs. (31)–(34).

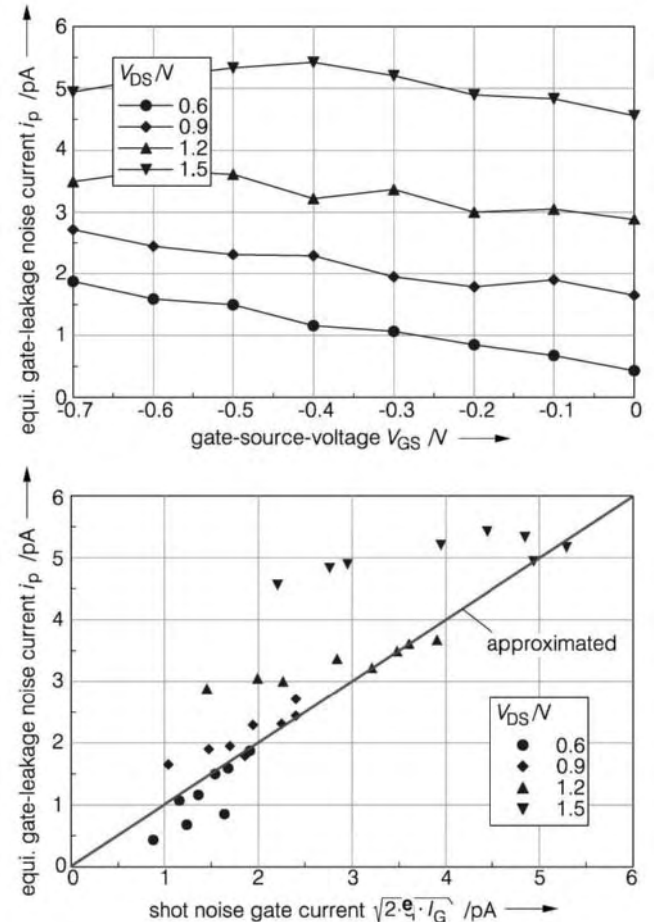


Figure 19. Extracted equivalent gate–leakage noise current i_p with dependence on gate–source voltage V_{GS} (above) and on shot noise gate current (below) with the drain–source voltage V_{DS} as parameter. (This figure is available in full color at <http://www.mrw.interscience.wiley.com/erfme>.)

With the extracted bias dependence of the small-signal equivalent elements and using Eqs. (31)–(35), the behavior of the channel noise voltage v_g , output noise current i_d as well as the equivalent gate leakage noise current i_p of the HFET can be derived for each bias condition at any frequency where $1/f$ noise is negligible.

4.5.4. Analytical and Scalable Noise Model for HFET.

When the influence of impact ionization and gate leakage current on the small-signal and noise performance can be neglected, the RF noise of HFET is dominated mainly by channel and output noise sources [see Eqs. (31) and (33)].

The parameters k_g and k_d are bias-independent but gate-geometry-dependent. To investigate the geometry dependence (gate length L_g and gate width W_g) of these parameters, the equivalent intrinsic noise sources of transistors with varying gate width and gate length have been extracted and analyzed in dependence on the shot noise drain current (Fig. 20). On the basis of these investigations, the following final analytical expressions can be derived for the intrinsic equivalent noise sources [45]:

$$\begin{aligned} i_{d,n} &= \sqrt{4k \frac{T_d}{R_{ds}}} \\ &\cong K_d \left(\sqrt{2e|I_D|} - \sqrt{2eI_{D,d}} \right) \end{aligned} \quad (36)$$

$$\begin{aligned} v_{g,n} &= \sqrt{4kT_g R_{gs}} \\ &\cong \frac{K_g W_g L_g f_T}{g_m^2} \left[\sqrt{2e|I_D|} - \sqrt{2eI_{D,g}} \right] \end{aligned} \quad (37)$$

In practice, the small influence of the parameters $I_{D,d}$ and $I_{D,g}$ can be neglected; thus, the following equations are sufficient for the prediction of the noise behavior:

$$i_{d,n} = \sqrt{4k \frac{T_d}{R_{ds}}} \cong K_d \cdot \sqrt{2e|I_D|} \quad (38)$$

$$\begin{aligned} v_{g,n} &= \sqrt{4kT_g R_{gs}} \\ &\cong K_g W_g L_g \sqrt{2e|I_D|} \frac{f_T}{g_m^2} \end{aligned} \quad (39)$$

A simplified intrinsic temperature noise model [46] is used to derive analytical expressions for all four noise

parameters:

$$F_{\min} = 1 + \frac{2}{T_0} \times \frac{f}{f_T} \sqrt{R_{gs} T_g \frac{T_d}{R_{ds}}} \quad (40)$$

$$R_{S,\text{opt}} = \frac{f_T}{f} \times \sqrt{R_{gs} T_g \frac{R_{ds}}{T_d}} \quad (41)$$

$$X_{S,\text{opt}} = \frac{1}{f} \frac{1}{2\pi C_{gs}} \quad (42)$$

$$R_n = \frac{1}{T_0} \left(R_{gs} T_g + \frac{T_d}{R_{ds}} \times \frac{1}{g_m^2} \right) \quad (43)$$

These estimations are sufficient for the geometry scaling of the intrinsic noise parameters of HFETs. Using these formulas and Eqs. (38) and (39), a correspondence between the intrinsic noise parameters and additional transistor parameters can be derived:

$$F_{\min} - 1 = \frac{f}{T_0} \times \frac{K_g K_d}{2k} W_g L_g \frac{2e|I_D|}{g_m^2} \quad (44)$$

$$R_{S,\text{opt}} = \frac{f_T}{f} \times \frac{K_g}{K_d} W_g L_g \frac{f_T}{g_m^2} \quad (45)$$

$$X_{S,\text{opt}} = \frac{1}{f} \times \frac{1}{2\pi C_{gs}} \quad (46)$$

$$R_n = \frac{1}{T_0} \times \frac{2e|I_D|}{4kg_m^2} \left[\left(K_g W_g L_g \frac{f_T}{g_m^2} \right)^2 + K_d^2 \right] \quad (47)$$

With these estimations for the gate length and gate width dependences, the behavior of the drain current I_D , the transconductance g_m , and the gate–source capacitance C_{gs} (Table 3), as well as the geometry dependence of the intrinsic noise parameters, can be obtained (Table 4).

4.6. Experimental Results and Verification of the Model for InP/InGaAs HBT

4.6.1. RF Performance of Devices Investigated. Devices under test are carbon doped InP/InGaAs self-aligned HBT with typical emitter areas $A_E = 20 \mu\text{m}^2$, $A_E = 40 \mu\text{m}^2$, and $A_E = 60 \mu\text{m}^2$ [47]. The carbon-doped p-(InGa)As:C base ($p > 10^{19} \text{cm}^{-3}$) is compositionally graded to increase current gain (Fig. 21) and transit frequency (Fig. 22), and a high-temperature in situ annealing sequence is carried out in TMAs/N₂ ambient at $T > 600^\circ\text{C}$ to activate the carbon doping in the base [48].

Figure 23 shows the capability of the model used to describe s parameters of the HBTs in the entire frequency range measured up to 40 GHz. To compare the three devices with respect to various emitter area A_E values, bias conditions are chosen in the active device region at constant collector-emitter voltage $V_{CE} = 1.2 \text{V}$ and constant current densities $S_E = I_C/A_E$. The range of current density increases from $S_E = 0.3 \times 10^4 \text{A/cm}^2$ up to $S_E = 6.7 \times 10^4 \text{A/cm}^2$. The results given in Fig. 23 show the measured and modeled s parameters for the three devices at high current

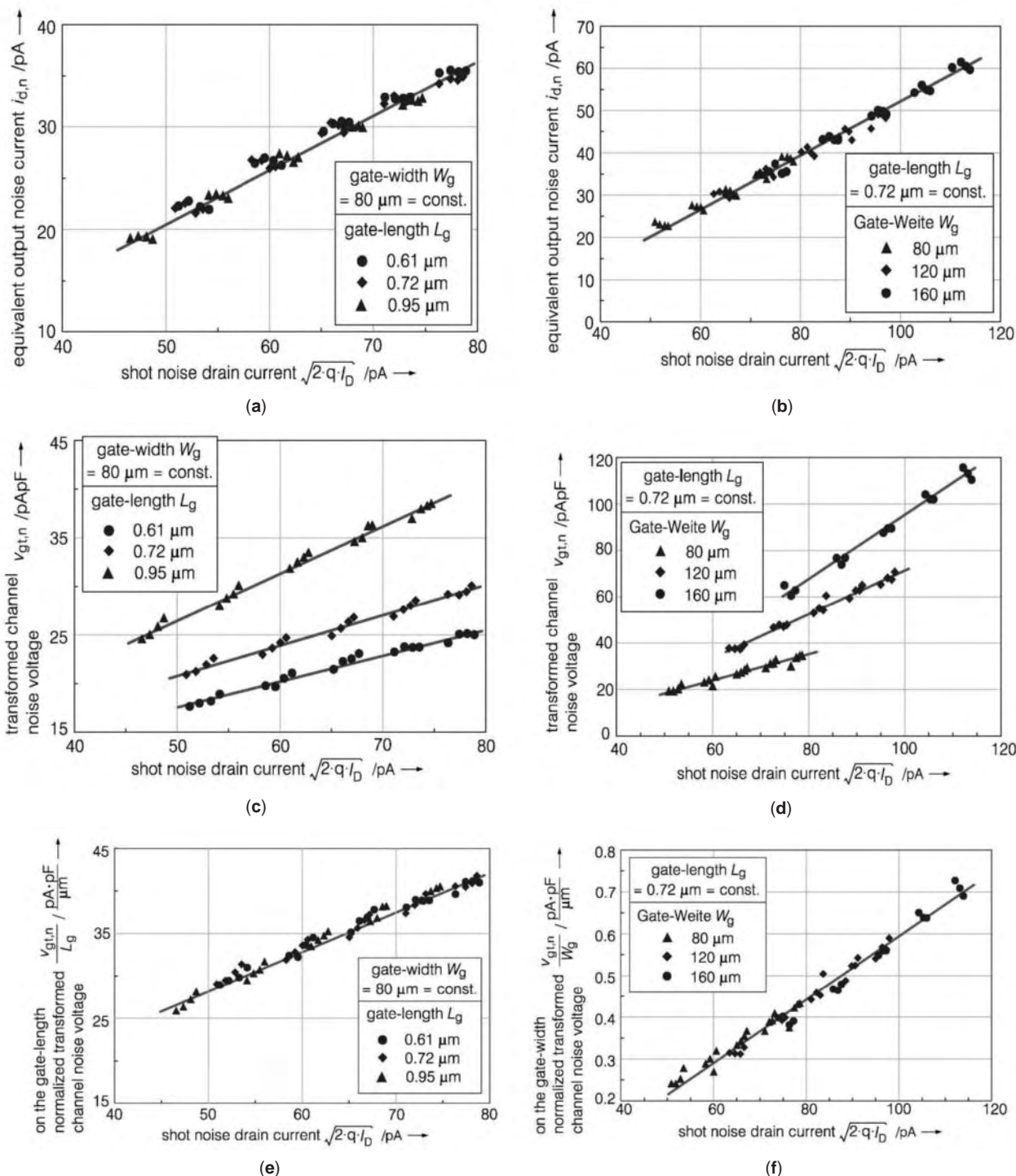


Figure 20. (a,b) Equivalent output noise current $i_{D,n}$ versus the shot noise drain current with (a) gate length L_G as a parameter and (b) gate width W_G as a parameter; (c,d) transformed equivalent channel noise voltage $v_{Gt,n}$ versus the shot noise drain current with (c) gate length L_G as a parameter and (d) gate width W_G as a parameter; (e,f) normalized transformed equivalent channel noise voltage $v_{Gt,n}$ versus the shot noise drain current (e) normalized on the gate length L_G and (f) normalized on the gate width W_G ($T = 300$ K, $V_{DS} = 0.9$ V up to 1.8 V, $V_{GS} = -0.3$ V up to 0.1 V). (This figure is available in full color at <http://www.mrw.interscience.wiley.com/erfme>.)

density $S_E = 5 \cdot 10^4$ A/cm². All small-signal equivalent elements are extracted by optimization strategies using multibias optimization [49]. These strategies take into account the bias independence of the extrinsic small-signal

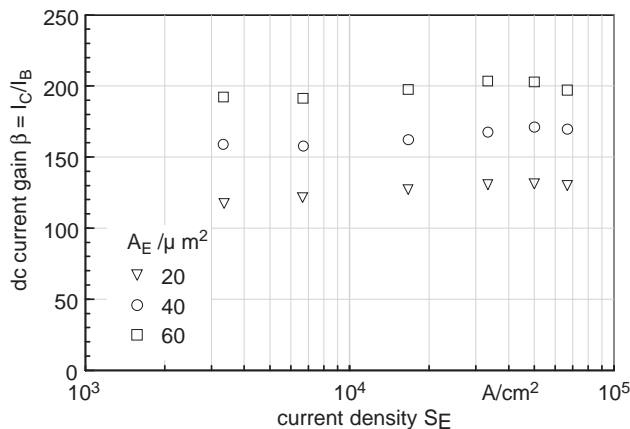
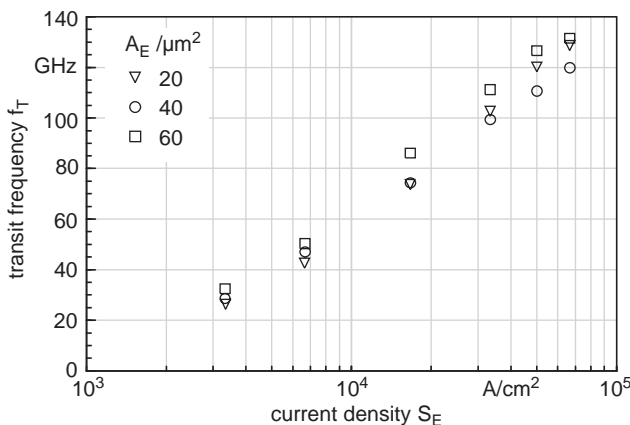
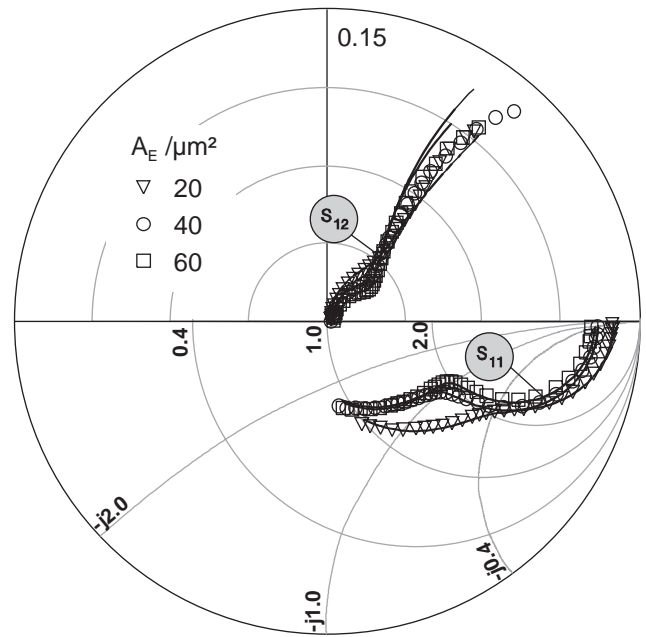
equivalent elements. All measured bias conditions are optimized simultaneously with the same extrinsic elements. The symbols in Fig. 23 represent the measured data; the solid lines, the modeled values.

Table 3. Scaling Properties of Some Small-Signal Equivalent Elements and Device Parameters

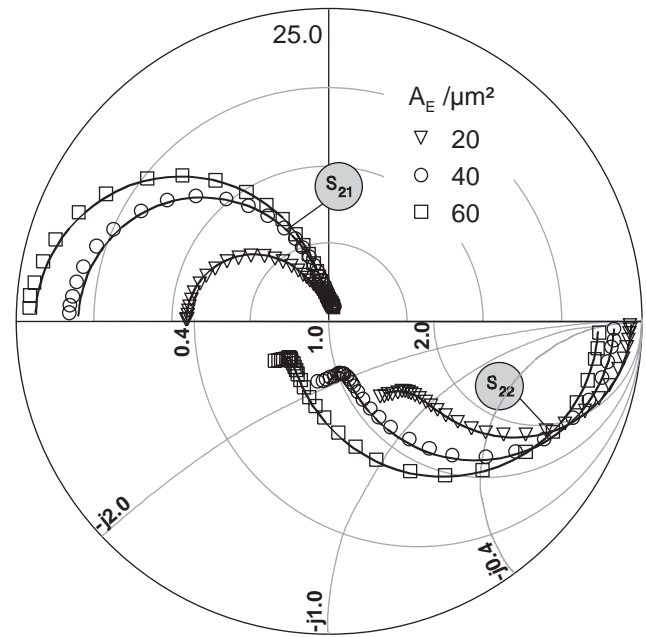
Gate Length Dependence	Gate Width Dependence
$g_m \neq f(L_g) = \text{const}$	$g_m \propto W_g$
$C_{gs} \propto L_g$	$C_{gs} \propto W_g$
$f_T \propto 1/L_g$	$f_T \neq f(W_g) = \text{const}$
$I_D \neq f(L_g) = \text{const}$	$I_D \propto W_g$

Table 4. Derived Scaling Behavior of the Intrinsic Noise Parameters

Gate Length Dependence	Gate Width Dependence
$F_{\min} - 1 \propto L_g$	$F_{\min} - 1 \neq f(W_g) = \text{const}$
$R_{Q,\text{opt}} \propto 1/L_g$	$R_{Q,\text{opt}} \propto 1/W_g$
$X_{Q,\text{opt}} \propto 1/L_g$	$X_{Q,\text{opt}} \propto 1/W_g$
$R_n \neq f(L_g) = \text{const}$	$R_n \propto 1/W_g$


Figure 21. DC current gain $\beta = I_C/I_B$ with dependence on current density S_E at $V_{CE} = 1.2$ V for the three different device geometries.

Figure 22. Extrinsic transit frequency f_T with dependence on current density S_E at $V_{CE} = 1.2$ V for the three different device geometries.


(a)



(b)

Figure 23. Measured (symbols) and modeled (lines) s parameters in frequency range from 45 MHz to 40 GHz at $V_{CE} = 1.2$ V and $S_E = 5 \times 10^4$ A/cm²: (a) s_{11} in Smith chart, s_{12} in polar diagram; (b) s_{22} in Smith chart, s_{21} in polar diagram.

4.6.2. Noise Behavior. To prove the consistency with RF noise parameter modeling, bias-dependent RF noise parameter measurements were performed for the same bias conditions.

First, the bias-dependent behavior of all noise parameters are given for the HBT with the smallest emitter area of $A_E = 20 \mu\text{m}^2$. Figures 24–26 show the measured and modeled RF noise parameters for three different current

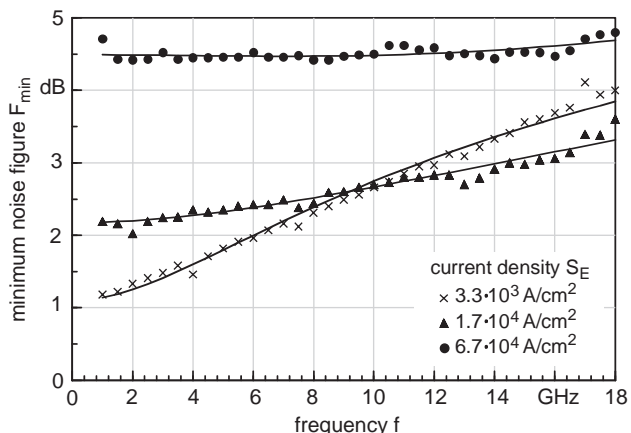


Figure 24. Measured (symbols) and modeled (lines) minimum noise figure F_{min} at constant $V_{CE} = 1.2$ V with dependence on current density S_E ($A_E = 20 \mu\text{m}^2$).

densities in the range from $S_E = 3.0 \cdot 10^3$ A/cm² up to $S_E = 6.7 \cdot 10^4$ A/cm² at constant collector-emitter voltage $V_{CE} = 1.2$ V in the active-device region. The model parameters factoring in RF noise behavior are optimized with the evolutionary algorithm as well. The small-signal equivalent elements, which were found during the abovementioned multibias optimization, were used and kept constant within the RF noise parameter optimization algorithm. As a consequence, only the four intrinsic equivalent noise temperatures of the intrinsic resistances have to be determined. The minimum noise figure F_{min} increases with rising collector current (Fig. 24). At low current density the value of the minimum noise figure is about $F_{min} = 1.3$ dB at $f = 2$ GHz for the devices investigated. The equivalent noise resistance is about $R_n = 175 \Omega$ at $f = 1$ GHz and decreases with higher frequencies. The noise resistance shows only minor dependence on collector current (Fig. 25). The last measured RF noise parameter is the optimum generator reflection coefficient Γ_{opt} . The magnitude of this reflection coefficient decreases with rising current density S_E (Fig. 26). This result shows the

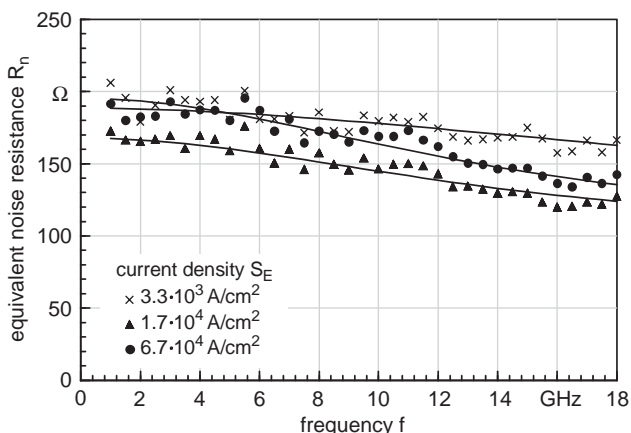


Figure 25. Measured (symbols) and modeled (lines) equivalent noise resistance R_n at constant $V_{CE} = 1.2$ V with dependence on current density S_E ($A_E = 20 \mu\text{m}^2$).

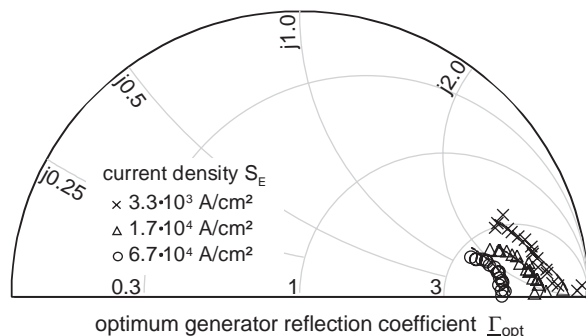


Figure 26. Measured (symbols) and modeled (lines) optimum generator reflection coefficient Γ_{opt} at constant $V_{CE} = 1.2$ V with dependence on current density S_E ($A_E = 20 \mu\text{m}^2$).

measurement difficulty in case of low currents because of the limited number of tuner states during noise parameter measurements, which show source reflection coefficients near the optimum generator reflection coefficient [18]. In addition to the three RF noise parameters given above, the associated gain g_{ass} is given with dependence on current density (Fig. 27). With rising current, RF gains of all the devices increase, which can be seen looking on the current density-dependent transit frequency (Fig. 22) and the associated gain.

Looking on the geometry dependence of HBT RF noise parameters, Figs. 28–30 show the measured and modeled RF noise parameters for the three devices with different emitter area A_E at the same bias condition in the active-device region with constant collector-emitter voltage $V_{CE} = 1.2$ V and constant high current density $S_E = 5 \cdot 10^4$ A/cm².

The HBTs show better RF noise performance for smaller emitter area. With increasing emitter area A_E , the minimum noise figure increases (Fig. 28), as does the equivalent noise resistance R_n (Fig. 29). Only the optimum generator reflection coefficient shows minimal influence on the emitter area of the device (Fig. 30). The devices with the smallest emitter area show the highest values of associated gain g_{ass} as well (Fig. 31).

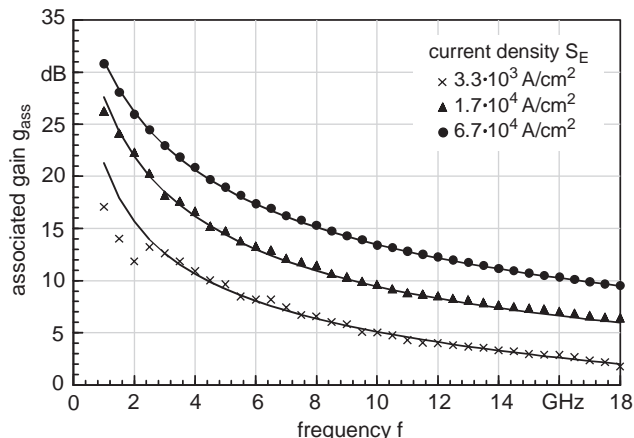


Figure 27. Measured (symbols) and modeled (lines) associated gain g_{ass} at constant $V_{CE} = 1.2$ V with dependence on current density S_E ($A_E = 20 \mu\text{m}^2$).

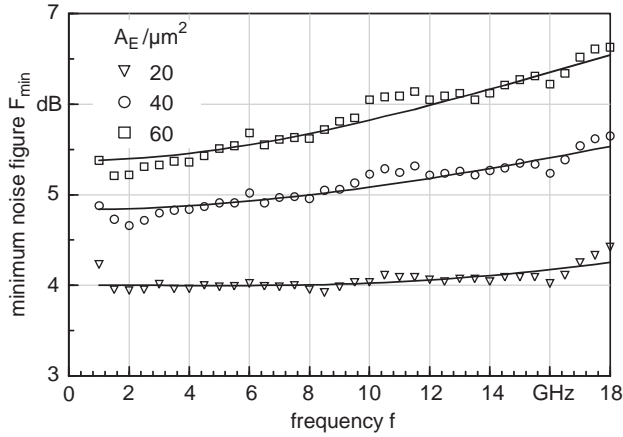


Figure 28. Measured (symbols) and modeled (lines) minimum noise figure F_{\min} with dependence on emitter area A_E at constant bias condition $V_{CE} = 1.2\text{ V}$ and $S_E = 5 \cdot 10^4\text{ A/cm}^2$.

4.6.3. Equivalent Intrinsic Noise Sources. With the extended bias and geometry-dependent modeling of RF parameters of HBT, the intrinsic noise sources of the model used can be investigated in detail. As a result of the small-signal and RF noise parameter model, a localization of various noise sources in the specific device regions is possible. With the optimization results of the bias and geometry-dependent modeling, the spectral densities of the four intrinsic noise current sources can be calculated (cf. Fig. 10). The intrinsic noise currents are calculated, knowing the values of the intrinsic resistances and the associated equivalent noise temperatures. Equations (48)–(51) are used for calculation of the following intrinsic noise currents: (1) the base noise current $i_{bb,n}$, based on the intrinsic base resistance R_{bb} in combination with T_{bb} ; (2) the base–emitter junction noise current $i_{je,n}$, using the values of the base–emitter junction resistance R_{je} and T_{je} ; (3) the base–collector junction noise current $i_{jc,n}$, which is calculated with base–collector junction resistance R_{jc} and T_{jc} ; and (4) the intrinsic collector noise current $i_{cc,n}$, known from combination of collector resistance R_{cc} and associated

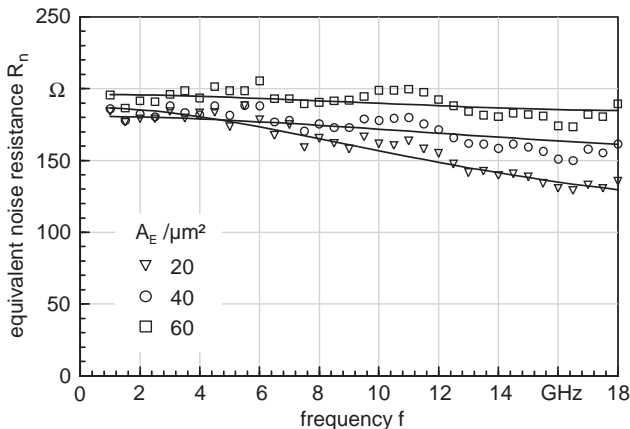


Figure 29. Measured (symbols) and modeled (lines) equivalent noise resistance R_n with dependence on emitter area A_E at constant bias condition $V_{CE} = 1.2\text{ V}$ and $S_E = 5 \cdot 10^4\text{ A/cm}^2$.

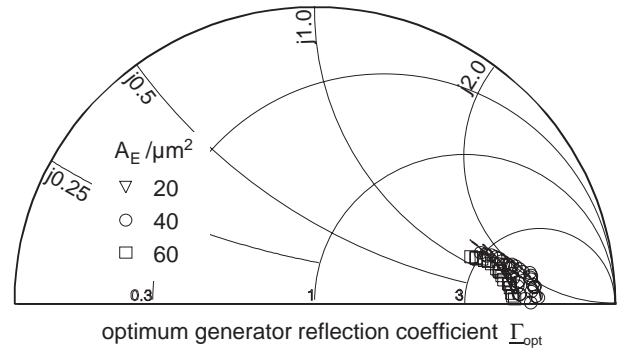


Figure 30. Measured (symbols) and modeled (lines) optimum generator reflection coefficient Γ_{opt} with dependence on emitter area A_E at constant bias condition $V_{CE} = 1.2\text{ V}$ and $S_E = 5 \cdot 10^4\text{ A/cm}^2$.

temperature T_{cc} :

$$i_{bb,n} = \sqrt{4k \frac{T_{bb}}{R_{bb}}} \quad (48)$$

$$i_{je,n} = \sqrt{4k \frac{T_{je}}{R_{je}}} \quad (49)$$

$$i_{jc,n} = \sqrt{4k \frac{T_{jc}}{R_{jc}}} \quad (50)$$

$$i_{cc,n} = \sqrt{4k \frac{T_{cc}}{R_{cc}}} \quad (51)$$

These calculated values are now plotted with dependence on bias condition; here we calculate the base $i_{B,S}$ and collector $i_{C,S}$ shot noise currents due to DC values with

$$i_{B,S} = \sqrt{2eI_B} \quad (52)$$

$$i_{C,S} = \sqrt{2eI_C} \quad (53)$$

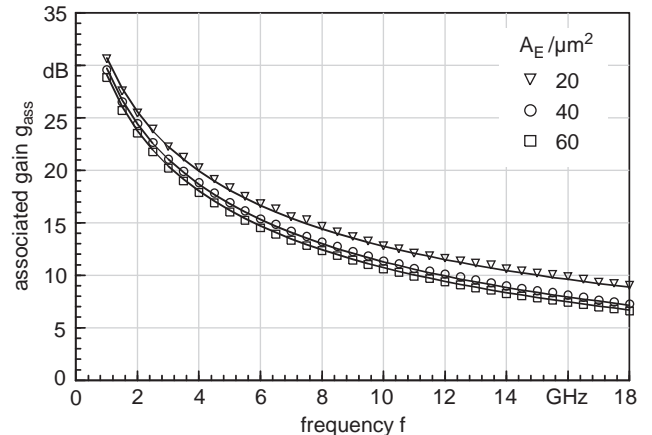


Figure 31. Measured (symbols) and modeled (lines) associated gain g_{ass} with dependence on emitter area A_E at constant bias condition $V_{CE} = 1.2\text{ V}$ and $S_E = 5 \cdot 10^4\text{ A/cm}^2$.

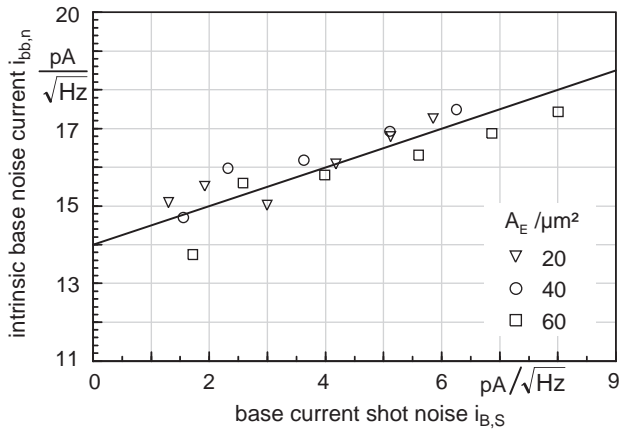


Figure 32. Extracted (symbols) intrinsic base noise currents with dependence on base current shot noise at constant $V_{CE} = 1.2$ V. Solid line represents linear fit.

Figure 32 shows the intrinsic base noise current $i_{bb,n}$ with dependence on base shot noise current $i_{B,S}$ of all HBT devices. The intrinsic base noise current shows a linear dependence on the shot noise due to extrinsic DC base current with a gradient of about 0.5. But a very high offset is obvious, which is correlated to the intrinsic noise source.

The other intrinsic noise currents show a strong influence on the shot noise of the DC currents. Figure 33 shows the intrinsic base–collector junction noise current $i_{jc,n}$, which is equal to the base current shot noise due to DC base current. The base–emitter junction noise $i_{je,n}$ (Fig. 34) and the intrinsic collector noise current $i_{cc,n}$ (Fig. 35) both are fully correlated to the DC collector current shot noise.

Interpreting the results achieved, all RF noise parameters of InP/InGaAs HBT can be modeled to fit only one equivalent noise temperature T_{bb} of the intrinsic base resistance R_{bb} . The other intrinsic equivalent noise temperatures can be calculated directly from the shot noise of the DC currents and the small-signal equivalent elements, which are known from s -parameter measurements. The number of unknown model parameters decreases. Addi-

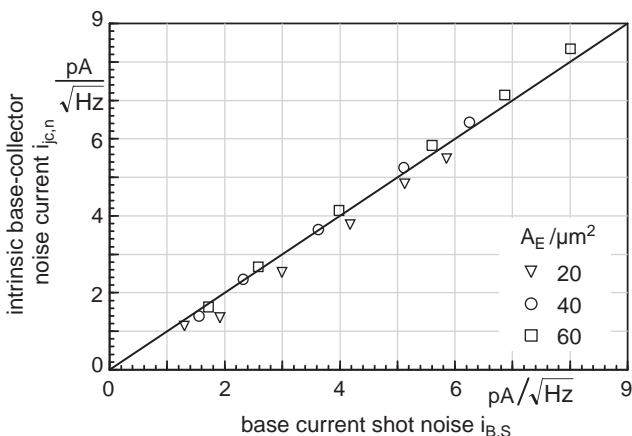


Figure 33. Extracted (symbols) intrinsic base–collector junction noise currents in dependence on base current shot noise at constant $V_{CE} = 1.2$ V. Solid line represents linear fit.

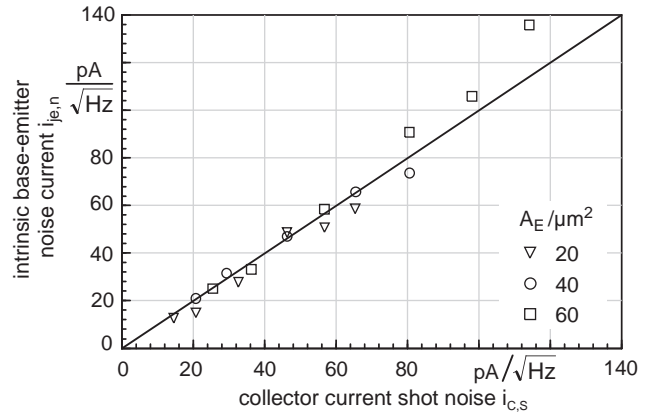


Figure 34. Extracted (symbols) intrinsic base–emitter junction noise currents with dependence on collector current shot noise at constant $V_{CE} = 1.2$ V. Solid line represents linear fit.

tionally, in case of noise modeling no emitter area scaling has to be taken into account. This scaling is included using the area-dependent small-signal equivalent elements only.

5. EXTENSION AND APPLICATION OF THE NOISE MODELS PRESENTED

5.1. Dual-Gate HFET in Cascode Configuration

Figure 36 shows a dual-gate HFET (DGHFET) and the corresponding equivalent circuit with the definition of extrinsic and intrinsic voltages and currents [50]. The DGHFET can be represented by two single-gate HFETs (SGHFETs), connected at the virtual node D_1 [51]. Consequently, the DGHFET can be separated into three parts (Fig. 37), all connected by a coupling network consisting of an additional resistance R_{coup} and a capacitance C_{coup} :

- The parasitic environment
- One single-gate HFET in common-source configuration
- One single-gate HFET in common-gate configuration

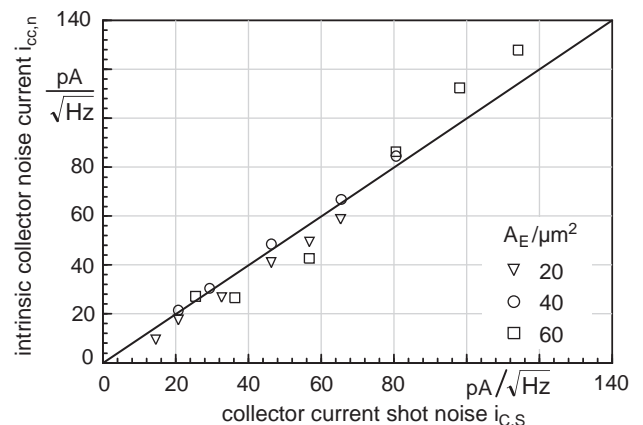


Figure 35. Extracted (symbols) intrinsic collector noise currents with dependence on collector current shot noise at constant $V_{CE} = 1.2$ V. Solid line represents linear fit.

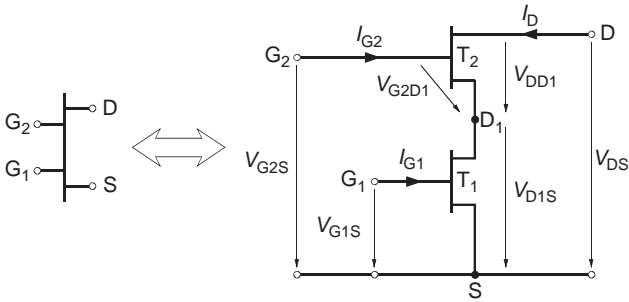


Figure 36. Dual-gate HFET and its equivalent circuit using two HFETs and defining extrinsic and intrinsic voltages and currents.

Correspondingly, the DGHFET can be modeled on the basis of the particular equivalent circuits of SGHFET described in Section 4.2. The small-signal equivalent elements as well as the noise temperatures and currents can also be extracted using the evolutionary algorithm [39].

Measured and modeled noise properties of a typical InP-based DGHFET are shown in Fig. 38 at two bias conditions, indicated in Table 5, with a comparable drain current. The modeled equivalent noise temperatures, the corresponding resistances and the extracted data of the noise sources (Table 5) demonstrate the influence of impact ionization with dependence on the bias condition.

Compared to single-gate HFET, the dual-gate HFET shows a reduced impact ionization noise component at comparable bias conditions [52]. Additionally, the RF performance of DGHFET corresponds to that of SGHFET. Moreover, even an increase of the unilateral gain and a reduced feedback can be obtained. Thus, dual-gate HFET are commonly used for mixers, oscillators, variable-gain amplifiers, and high-frequency applications such as OEICs or MMIC amplifiers [53].

5.2. Application of Noise Models for Circuit Design

The importance of reliable noise modeling of single devices is demonstrated below for an optoelectronic receiver circuit.

The necessary minimum optical input power $P_{opt,min}$ applied to an optoelectronic receiver in order to detect the original signal tolerating a certain error can be derived

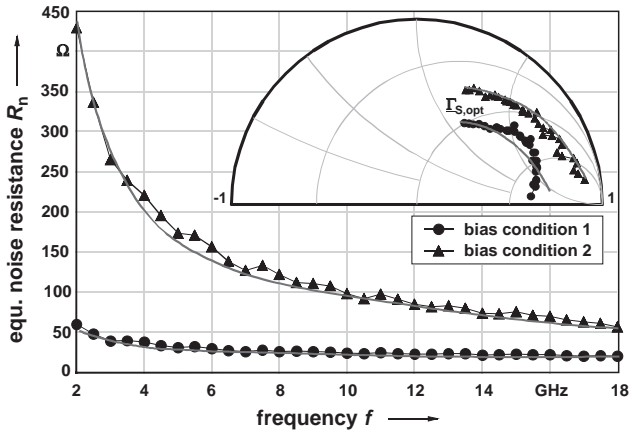
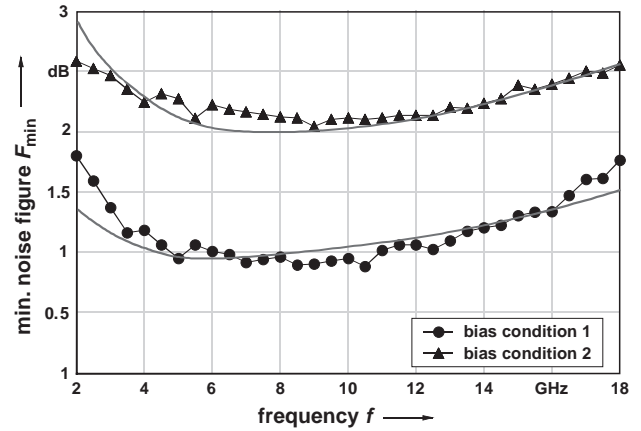


Figure 38. Measured and modeled noise parameter for bias conditions 1 ($V_{DS}=3\text{ V}$, $V_{G1S}=0.1\text{ V}$, $V_{G2S}=0.6\text{ V}$) (above) and bias conditions 2 ($V_{DS}=3\text{ V}$, $V_{G1S}=0\text{ V}$, $V_{G2S}=2.2\text{ V}$) (below). (This figure is available in full color at <http://www.mrw.interscience.wiley.com/erfme>.)

as [54]

$$P_{opt,min} = \frac{hc_0}{\eta e \lambda} Q \sqrt{i_{na}^2} \tag{54}$$

where

- h = Planck's constant
- c_0 = light velocity

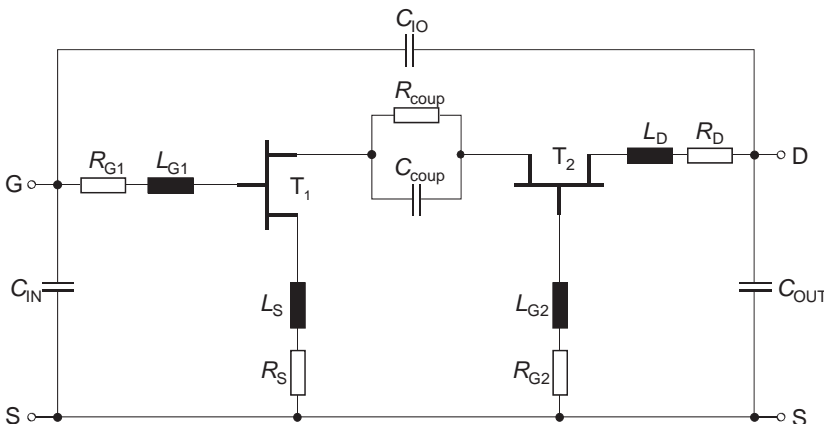


Figure 37. Small-signal equivalent circuit for a DGHFET in cascode configuration.

Table 5. Modeled Intrinsic Temperatures and Resistances Describing Noise Behavior of DGHFET

Bias Condition 1		Bias Condition 2	
$V_{DS} = 3 \text{ V}, V_{G1S} = 0.1 \text{ V},$		$V_{DS} = 3 \text{ V}, V_{G1S} = 0 \text{ V}, V_{G2S} = 2.2 \text{ V}$	
$V_{G2S} = 0.6 \text{ V}$			
$T_{g1} = 39215 \text{ K}, R_{gs1} = 2.9 \Omega$	$T_{g1} = 5323 \text{ K}, R_{gs1} = 0.98 \Omega$		
$T_{p1} = 587 \text{ K},$ $R_{pgs1} = 3.9 \times 10^5 \Omega$	$T_{p1} = 12337 \text{ K}, R_{pgs1} = 6.3 \times 10^5 \Omega$		
$T_{d1} = 6349 \text{ K}, R_{ds1} = 149.5 \Omega$	$T_{d1} = 38272 \text{ K}, R_{ds1} = 233.6 \Omega$		
$i_{im1} = 98 \text{ pA}$	$i_{im1} = 496 \text{ pA}$		
$T_{g2} = 5061 \text{ K}, R_{gs2} = 0.57 \Omega$	$T_{g2} = 4827 \text{ K}, R_{gs2} = 0.63 \Omega$		
$T_{d2} = 464 \text{ K}, R_{ds2} = 84.8 \Omega$	$T_{d2} = 300 \text{ K}, R_{ds2} = 277.8 \Omega$		
$i_{im2} = 9 \text{ pA}$	$i_{im2} = 0 \text{ pA}$		

η = quantum efficiency

λ = wavelength of the light

Q = the noise factor, which is $Q \approx 6$ for $\text{BER} = 10^{-9}$

$\sqrt{i_{na}^2}$ = the root mean square of the equivalent input noise current density

The noise factor Q is derived from probability calculations that consider the statistical nature of the noise signal as well as the pseudorandom characteristic of a real information signal. Q can be derived from the *Gaussian* probability integral where BER is the bit error rate of the detected digital signal behind the decision circuit:

$$\text{BER} = \frac{1}{2\pi} \int_Q^\infty e^{-x^2/2} dx \quad (55)$$

Typically, a bit error rate of $\text{BER} = 10^{-9}$ is assumed to be the maximum tolerable number of incorrectly detected bits per second. Hence, the corresponding noise factor equals

$$Q \approx 6|_{\text{BER} = 10^{-9}}.$$

The mean input noise current $\sqrt{i_{na}^2}$ is a function of numerous device- and circuit-related parameters. In particular, the noise sources of active devices—as discussed in earlier sections—have a dominant contribution at higher frequencies. The second important contribution comes from thermal noise currents generated in ohmic resistors that can be found at different locations of the receiver circuit itself. A closed formulation taking into account some of the small-signal related device parameters was derived

by [54] and can be written as

$$\overline{i_{na}^2} = \frac{4kT}{R_f} X_1 B + 2eI_L X_2 B + \frac{4kT\Gamma}{g_m} (2\pi C_T)^2 (f_c X_f B^2 + X_3 B^3) \quad (56)$$

where

X_1, X_2, X_3, X_f = special weight-functions (Personick integrals)

B = bit rate of the datastream

I_L = total leakage current (combination of dark current of photodetector (PD) and gate leakage current of input transistor)

g_m = transconductance of first transistor

C_T = total capacitance (usually $C_T = C_{gs} + C_{pd}$)

R_f = feedback resistance

f_c = corner frequency of $1/f$ noise contribution

Γ = channel noise factor (a function of transistor-related parameters)

In general, the primary aim of noise modeling in conjunction with circuit design and development is to enable a reliable estimation of the noise behavior of the total circuit.

As an example of the applicability of the abovementioned temperature noise model (TNM) for circuit noise simulation, the optoelectronic circuit shown in Fig. 39 is discussed. It consists of a four-stage traveling-wave amplifier (TWA) combined with a pin photodiode (PD) to form up a high-speed receiver module for transfer rates up to 35 Gbps (gigabits per second) [55,56]. The TWA comprises four HFET devices with varying gate widths, hence utilizing the scalability of the applied noise model. The single stages within the TWA are fed from an input transmission line that is connected to the PD (left side) and terminated by a resistor at the end (right side). The single line segments are built up as coplanar waveguides (CPWs) and are fed toward the transistor gate contact with airbridge interconnections treated as microstrip lines (MSLs) with $\epsilon_r = 1$. At the drain ends, again feeding MSL lines are connected to a CPW output transmission line, which is again terminated by a complex impedance (RC combination) at the opposite end of the RF output. Figure 40 shows a photograph of the realized receiver.

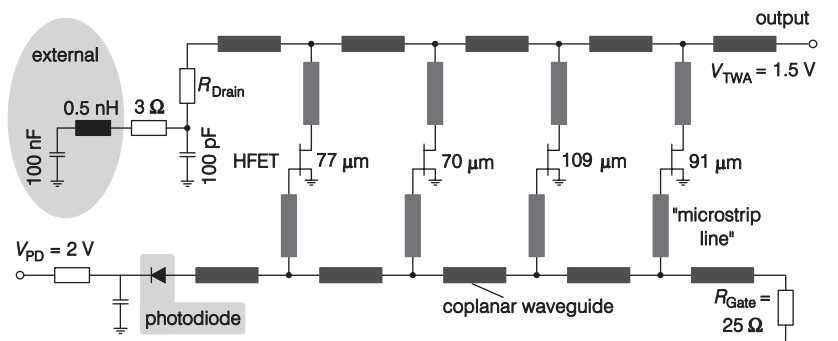


Figure 39. Circuit layout of a four-stage traveling-wave amplifier (TWA) combined with a pin photodiode (PD).

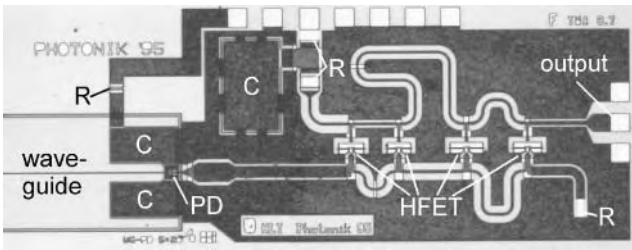


Figure 40. Photograph of realized optoelectronic receiver based on a TWA and waveguide fed pin photodetector (PD) in coplanar technique (C—RF-blocking capacitors, R—metal-film resistors).

The most interesting noise contributions are generated mainly by single HFET devices and the termination resistors. During circuit simulation that has been carried out using *microwave design systems* (Hewlett-Packard), noise behavior of the HFETs was considered using the TNM model. The inset in Fig. 41 depicts the transfer characteristic of the TWA derived from RF measurements up to 45GHz. In the particular case of optoelectronic receivers, the transimpedance is of major interest and is defined as follows with i_{ph} = photocurrent of detector generated by optical signal:

$$Z_T(f) = \frac{v_{out}}{i_{in}} = \frac{v_{out}}{i_{ph}} \quad (57)$$

The transfer characteristic is necessary for calculation of the equivalent input noise current $\sqrt{i_{na}^2} = \sqrt{\int i_{na}^2(f)df}$, which is not directly measurable. It has to be derived from measurements of the frequency-dependent noise factor F (or the absolute output noise power, respectively) by using the reverse transfer function $Z_T^{-1}(f)$ [57].

Both the validity and the reliability of the noise simulation are demonstrated in Fig. 41, where the simulated as well as the measured and recalculated frequency-dependent input noise current density $i_{na}(f)$ are depicted. The

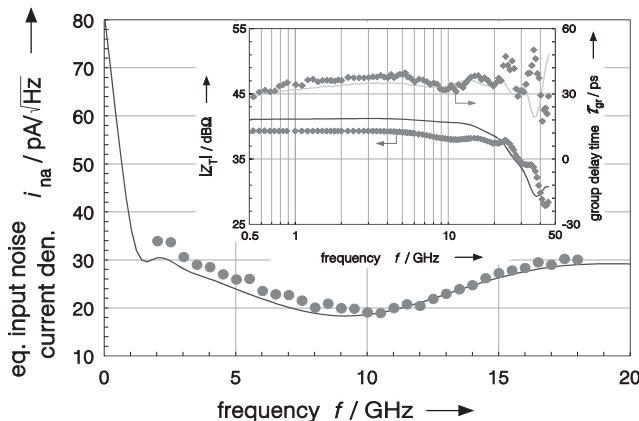


Figure 41. Measured (◆) and modeled (—) transfer characteristic of the TWA (transimpedance Z_T vs. frequency f). The inset shows the measured (●) and calculated (—) noise data (equivalent input noise current density i_{na} vs. frequency f). (This figure is available in full color at <http://www.mrw.interscience.wiley.com/erfme>.)

almost negligible differences between both curves clearly demonstrate the applicability and validity of the noise models employed, even for circuit noise simulations. Finally, these results enable the circuit designer to achieve reliable estimations of the total receiver sensitivity P_{min} using Eq. (54).

BIBLIOGRAPHY

1. H. Nyquist, Thermal agitation of electric charge in conductors, *Phys. Rev.* **32**:110–113 (July 1928).
2. J. B. Johnson, Thermal agitation of electricity in conductors, *Phys. Rev.* **32**:97–107 (July 1928).
3. H. Bittel and L. Storm, *Rauschen, Eine Einführung zum Verständnis elektrischer Schwankungserscheinungen*, Springer-Verlag, 1971.
4. R. Müller, *Rauschen, Halbleiter-Elektronik* **15** (1979).
5. A. S. Tager, Current fluctuations in a semiconductor (dielectric) under conditions of impact ionization and avalanche breakdown, *Sov. Phys. Solid State* **6**:1919–1925 (1965).
6. R. J. McIntyre, Multiplication noise in uniform avalanche devices, *IEEE Trans. Electron. Devices* **ED-13**(1):164–168 (1966).
7. R. J. McIntyre, The distribution of gains in uniformly multiplying avalanche diodes, *IEEE Trans. Electron. Devices* **ED-19**:703–713 (1972).
8. B. Schiek and H.-J. Siweris, *Rauschen in Hochfrequenzschaltungen*, Hüthig Buch Verlag, Heidelberg, 1990.
9. A. Neidenoff, *Lies, Damm Lies & The Noise Factor, Die falsche Auffassung von der Rauschzahl, Resümee einer Gegendarstellung zur heutigen Theorie und Praxis*, Hochschule für Technik und Wirtschaft des Saarlandes, 1994.
10. D. O. North, The absolute sensitivity of radio receivers, *RCA Rev.* **6**:332–343 (1942).
11. H. T. Friis, Discussion on “noise figures of radio receivers,” *Proc. IRE* **33**:125 (1945).
12. R. Q. Twiss, Nyquist’s and Thevenin’s theorems generalized for nonreciprocal linear networks, *J. Appl. Phys.* **26**(5): 599–602 (1955).
13. H. Hillbrand and P. H. Russer, An efficient method for computer aided noise analysis of linear amplifier networks, *IEEE Trans. Circuits Syst.* **CAS-23**:235–238 (1976).
14. H. Meschede, R. Reuter, J. Albers, J. Kraus, D. Peters, W. Brockerhoff, F. J. Tegude, M. Bode, J. Schubert, and W. Zander, On-wafer microwave measurement setup for investigations on HEMTs and high T_c superconductors at cryogenic temperatures down to 20 K, *IEEE Trans. Microwave Theory Tech.* **MTT-40**(12):2325–2331 (1992).
15. H. Meschede, J. Albers, R. Reuter, J. Kraus, D. Peters, W. Brockerhoff, F. J. Tegude, M. Bode, J. Schubert, and W. Zander, RF investigations on HEMTs at cryogenic temperatures down to 20 K using an on-wafer microwave measurement setup, *Proc., 22nd European Microwave Conf., EuMC-1992*, Vol. 1, Helsinki, Finland, Aug. 1992, pp. 151–156.
16. Hewlett-Packard, *Fundamentals of RF and Microwave Noise Figure Measurements*, Hewlett-Packard, Application Note 57-1.
17. H. Meschede, *Hochfrequenzcharakterisierung von Mikrowellentransistoren aus III-V-Halbleiternmaterial bei Temperaturen im Bereich von 20 K bis 300 K*, dissertation, Univ. Duisburg, VDI Verlag, Reihe 21, Elektrotechnik No. 144.
18. ATN Microwave Inc., *Operating Manual NP5B, 2–18 GHz Wafer Probe Test Set*, Oct. 1993.

19. A. Cappy, Noise modeling and measurement techniques, *IEEE Trans. Microwave Theory Tech.* **MTT-36**(1): 1–10 (1988).
20. E. F. Calandra, G. Martines, and M. Sannino, Characterization of GaAs-FETs in terms of noise, gain and scattering parameters through a noise parameter test set, *IEEE Trans. Microwave Theory Tech.* **MTT-32**(3):231–237 (1984).
21. A. C. Davidson, B. W. Leake, and E. Strid, Accuracy improvements in microwave noise parameter measurements, *IEEE Trans. Microwave Theory Tech.* **MTT-37**(12):1973–1978 (1989).
22. J. W. Archer and R. A. Batchelor, Fully automated on-wafer noise characterization of GaAs MESFETs and HEMTs, *IEEE Trans. Microwave Theory Tech.* **MTT-40**(2):209–216 (1992).
23. S. M. Sze, *Physics of Semiconductor Devices*, 2nd ed., Wiley, New York, 1981.
24. J.-P. Nougier, Fluctuations and noise of hot carriers in semiconductor materials and devices, *IEEE Trans. Electron. Devices* **ED-41**(11):2034–2049 (1994).
25. V. Bareikis, J. Liberis, I. Matulioniene, A. Matulionis, and P. Sakalas, Experiments on hot electron noise in semiconductor materials for high-speed devices, *IEEE Trans. Electron. Devices* **ED-41**(11):2050–2060 (1994).
26. A. van der Ziel, *Fluctuation Phenomena*, course, 1980.
27. A. van der Ziel, *Fluctuation Phenomena, Part II: Noise in Devices*, course, 1980.
28. J. R. Ragazzini, Noise and random processes, *Proc. IRE* **50**:1146–1151 (May 1962).
29. W. Kleen, Die untere Grenze des Verstärkerrauschens, Physikalische und technische Aspekte, *Physik in unserer Zeit*, **13**(1):14–21 (1982).
30. K. M. van Vliet and L. M. Rucker, Theory of carrier multiplication and noise in avalanche devices—Part I: One-carrier processes, *IEEE Trans. Electron. Devices* **ED-26**(5):746–751 (1979).
31. K. M. van Vliet, Theory of carrier multiplication and noise in avalanche devices—Part II: Two-carrier processes, *IEEE Trans. Electron. Devices* **ED-26**(5):752–764 (1979).
32. R. Reuter, M. Agethen, U. Auer, S. van Waasen, D. Peters, W. Brockerhoff, and F. J. Tegude, Investigation and modeling of impact ionization with regard to the RF- and noise behaviour of HFET, *IEEE Trans. Microwave Theory Tech.* **MTT-45**(6):977–983 (1997).
33. R. Reuter, S. van Waasen, and F. J. Tegude: A new noise model of HFET with special emphasis on gate-leakage, *IEEE Electron. Device Lett.* **EDL-16**(2):74–76 (1995).
34. R. Reuter, M. Agethen, U. Auer, S. van Waasen, T. Breder, W. Brockerhoff, and F. J. Tegude, A new RF- and noise model with special emphasis on impact ionization for HFET, *Proc. Microwave and Optronics, 9th Exhibition and Conf. High Frequency Engineering*, MIOP-1997, Sindelfingen, Germany, 1997, pp. 338–342.
35. R. Reuter, T. Breder, U. Auer, S. van Waasen, M. Agethen, and F. J. Tegude, On the temperature dependence of the impact ionization in HFET and the corresponding RF- and noise performance, *Proc. 8th Int. Conf. Indium Phosphide and Related Materials*, IPRM-1996, Schwäbisch-Gmünd, Germany, 1996, pp. 654–657.
36. D. Peters, W. Brockerhoff, R. Reuter, H. Meschede, A. Wiersch, B. Becker, W. Daumann, U. Seiler, E. Koenig, and F. J. Tegude, RF-characterization of AlGaAs/GaAs HBT down to 20 K, *Proc. 20th Int. Symp. GaAs and Related Compounds*, Freiburg, Germany, Aug. 1993, pp. 177–182.
37. U. Auer, R. Reuter, P. Ellrodt, W. Prost, and F. J. Tegude, Characterization and analysis of a new gate leakage mechanism at high drain bias in InAlAs/InGaAs heterostructure field-effect transistors, *Proc. Conf. Indium Phosphide and Related Materials*, IPRM-1996, Schwäbisch-Gmünd, Germany, 1996, pp. 650–653.
38. U. Auer, R. Reuter, P. Ellrodt, C. Heedt, W. Prost, and F. J. Tegude, The impact of pseudomorphic AlAs spacer layers on the gate leakage current of InAlAs/InGaAs heterostructure field-effect transistors, *IEEE Microwave Opt. Technol. Lett.* **11**(3):125–128 (Feb. 1996).
39. M. Agethen, R. Reuter, W. Brockerhoff, and F. J. Tegude, A new optimization strategy based on the theory of evolution for the RF-modeling of HFET, *Proc. Int. IEEE Workshop on Experimentally Based FET Device Modelling & Related Nonlinear Circuit Design*, Kassel, Germany, July 1997, pp. 4.1–4.5.
40. M. Agethen, R. Reuter, S. van Waasen, W. Brockerhoff, and F. J. Tegude, Theory of evolution: new optimization strategies for the modeling of HFET-RF-noise-parameters, *Proc. Microwave and Optronics, 9th Exhibition and Conf. High Frequency Engineering*, MIOP-1997, Sindelfingen, Germany, 1997, pp. 343–347.
41. J. Holland, *Adaption in Natural and Artificial Systems*, MIT Press, Cambridge, MA, 1992.
42. D. E. Goldberg, *Genetic Algorithms in Search, Optimization, and Machine Learning*, Addison-Wesley, Reading, MA, 1989.
43. Z. Michalewicz, *Genetic Algorithms + Data Structures = Evolution Programs*, Springer-Verlag, Berlin, 1992.
44. R. Reuter, S. van Waasen, D. Peters, U. Auer, W. Brockerhoff, and F. J. Tegude, A new temperature noise model of HFET with special emphasis on a gate-leakage current and investigation of the bias dependence of the equivalent noise sources, *Proc., 25th European Microwave Conf.*, EuMC-1995, Bologna, Italy, 1995, pp. 205–210.
45. R. Reuter and F. J. Tegude, A new analytical and scaleable noise model for HFET, paper presented at MTT-S-1998.
46. M. W. Pospieszalski, Modelling of noise parameters of MESFETs and MODFETs and their frequency and temperature dependence, *IEEE Trans. Microwave Theory Tech.* **MTT-37**(9):1340–1350 (1989).
47. U. Auer, S. O. Kim, M. Agethen, P. Velling, W. Prost, and F. J. Tegude, Fast fabrication of InP-based HBT using a novel coplanar design, *Electron. Lett.* **34**(19):1885–1886 (1998).
48. P. Velling, A comparative study of GaAs- and InP-based HBT growth by means of LP-MOVPE using conventional and non gaseous sources, *Progress Crystal Growth Charac. Mat.* (Dec. 2000).
49. M. Agethen, P. Velling, W. Brockerhoff, and F.-J. Tegude, Small-signal modelling of HBT using evolutionary multi-bias optimization algorithm, *Proc. 11th III-V Semiconductor Device Simulation Workshop*, IEMN, Villeneuve d'Ascq, France, May 1999.
50. F.-J. Tegude, W. Daumann, R. Reuter, and W. Brockerhoff, InAlAs/InGaAs/InP Dual-Gate-HFETs: New aspects and properties, *Proc. 9th Int. Conf. Indium Phosphide and Related Materials*, IPRM-1997, Cape Cod, MA, 1997, pp. 181–184.
51. L. Klapproth and G. Böck, Determination of the small-signal equivalent circuit elements from s-parameter measurements, *Proc. 8th Conf. and Exhibition on High Frequency Engineering, Microwave and Optronics*, May–June 1995, pp. 423–427.
52. W. Daumann, P. Ellrodt, W. Brockerhoff, R. M. Bertenburg, R. Reuter, U. Auer, W. Molls, and F. J. Tegude, InAlAs/InGaAs/InP HFET with suppressed impact ionization using

- dual-gate cascode-devices, *IEEE Electron. Device Lett. EDL-17*(10):488–490 (1996).
53. M. Schlechtweg, W. H. Haydl, A. Bangert, J. Braustein, P. J. Tasker, L. Verweyn, H. Massler, W. Bronner, A. Hülsmann, and K. Köhler, Coplanar millimeter-wave ICs for W-band applications using 0.15 μm pseudomorphic MODFETs, *IEEE J. Solid-State Circuits* **31**(10):1426–1434 (Oct. 1996).
 54. S. D. Personick, Receiver design for digital fiber optical communication systems, Parts 1 and 2, *Bell Syst. Technol. J.* **52**:843–886 (July–Aug. 1973).
 55. S. van Waasen, A. Umbach, U. Auer, H. -G. Bach, R. M. Bertenburg, G. Janssen, G. G. Mekonnen, W. Passenberg, R. Reuter, W. Schlaak, C. Schramm, G. Unterbösch, P. Wolfram, and F. J. Tegude, 27GHz bandwidth high-speed monolithic integrated optoelectronic photoreceiver consisting of a waveguide fed photo-diode and an InAlAs/ InGaAs-HFET-traveling wave amplifier, *IEEE J. Solid-State Circuits* **32**(9): 1394–1401 (1997).
 56. H.-G. Bach, A. Umbach, S. van Waasen, R. M. Bertenburg, and G. Unterbösch, Ultrafast monolithically integrated InP-based photoreceiver: OEIC-design, fabrication, and system application, *IEEE J. Select. Topics Quantum Electron.* **2**(2):418–423 (1996).
 57. R. M. Bertenburg, A. Clement, and F. J. Tegude, 40Gbit/s high sensitive optical receivers using photo detectors and TWAs: Design considerations and development, *Conf. Proc. Microwave and Optronics, 8th Exhibition and Conf. on High Frequency Engineering*, MIOP-1995, Sindelfingen, Germany, 1995, pp. 600–606.

NOISE, HOT CARRIER EFFECTS

ARVYDAS MATULIONIS
Semiconductor Physics Institute

Electric noise, or fluctuation in electric circuits, results from the discrete nature of charge carriers and their chaotic motion. Electric noise manifests itself as an acoustic noise in a telephone or a radio receiver, also as an irregular flickering on a television screen, known as a “snow-fall” flicker, and otherwise. In general, fluctuations are temporary deviations of variables (current, voltage, resistance, frequency, etc.) either from their long-term averages or from some regular time-dependent values of information-bearing signals. This article deals with electronic noise caused by electrons and holes in semiconductors. For simplicity, the term electrons will be used, unless mentioning holes is necessary for specific reasons.

Fluctuations are best understood for electron gas that is in thermodynamic equilibrium with lattice vibrations. The universal relations of Nyquist and Einstein, together with Ohm’s law, interrelate noise, current, and other electronic transport, including electron diffusion. These relations are sufficient to estimate the ultimate accuracy for electrical measurements and signal processing under near-equilibrium conditions. However, advances in instrumentation and communication technology increasingly depend on progress in microelectronics, where deviations

from equilibrium are essential, and the universal relations fail. High electric field enhances chaotic motion of electrons in devices and circuits. The customary name for this situation is *hot electrons*. Correspondingly, noise acquires features absent at equilibrium. Indeed, hot-electron noise differs from equilibrium, like a stormy sea differs from a mill pond. Measuring noise out of equilibrium provides new information about kinetic processes in electron gas—new as compared with that available from the average values of observables. As a result, investigation of hot electron noise proves to be a powerful tool for diagnosing nonequilibrium states in semiconductors subjected to high electric fields. Moreover, the knowledge obtained of the microscopic origin of hot-electron noise helps to control it and suggests how to eliminate some sources of excess noise through improvement of material technology and circuit design, thus contributing to development of highly sensitive low-noise devices.

1. HOT-ELECTRON VELOCITY FLUCTUATIONS

1.1. Electric Noise at Equilibrium and in Nonequilibrium State

1.1.1. Fluctuations at Equilibrium. Fluctuations have been under investigation since 1827, when R. Brown published the results of his observations on the endless irregular motion of microscopic particles suspended in a liquid. Numerous sophisticated investigations of this phenomenon, called Brownian motion, led to the conclusion that the mean kinetic energies of a Brownian particle and a molecule of the liquid were equal, provided enough care was taken not to disturb their thermal equilibrium. Moreover, fluctuations of position of a Brownian particle were found closely related to the viscosity of the surrounding liquid and the force of friction acting on the particle. Experiments on Brownian motion and its theory, developed by A. Einstein and M. Smoluchowski, were important arguments in favor of the molecular kinetic theory. The theory provided methodology to treat spreading of a cloud of particles (diffusion), friction, viscosity, and so on, in terms of velocity fluctuations. In particular, the Einstein relation associates the electron diffusion coefficient with electron mobility—the main electron transport parameter for a semiconductor in Ohm’s law for current flow. Nyquist [1], in 1928, related the spectral density of current fluctuations in a resistor to the dissipative part of its conductance, or resistance. The Nyquist theorem and Einstein’s relation together led to the fluctuation–diffusion relation, between electronic noise and electron diffusion.

In Nyquist’s derivation one can also trace ideas of Rayleigh (1900), who applied the equipartition theorem to the standing-wave modes of blackbody radiation. In some sense, the available noise power is a special low-frequency case of blackbody radiation. Under proper matching, a resistor emits noise power into the matched transmission line connected to a radiometer—a sensitive device to measure radiation power. At thermal equilibrium, noise is white over a wide range of frequencies, that is, the spectral density of noise power does not depend on frequency and is the universal function of the absolute temperature. Thus,

the noise radiometer serves as the absolute thermometer. (Visible and infrared radiation of a blackbody is used to measure the absolute temperature as well.) Provided noise power differs from thermal power, the equivalent noise temperature (or, simply, noise temperature) is introduced, in order to estimate the deviation from equilibrium. The logarithmic ratio, in decibels, of the noise temperature over the absolute temperature is widely used for the same purpose.

In 1951, Callen and Welton [2] completed the theory of fluctuations at equilibrium by formulating the general fluctuation-dissipation theorem, which expresses the spectral density of fluctuations in a physical system at a given frequency, in terms of the dissipative part of the response of the system to some external perturbation. Accordingly, calculation, or measurement, of the system of linear response at a given frequency provides data on the spectral density of fluctuations of the corresponding variable at the same frequency. Consequently, measurement of electric noise at equilibrium gives no complementary information, as compared with that available from impedance measurements. On the other hand, measuring electron mobility and electron density in a semiconductor is sufficient to determine its noise properties at equilibrium.

The thermodynamic arguments collapse for an open system, subjected to a continuous energy flow, when some energy is supplied from the external world and then dissipated back to the external world. No universal relation is valid between noise and impedance in this case. This statement has fundamental and practical consequences. First of all, investigation of fluctuations from the nonequilibrium state is a valuable tool for diagnosis of different mechanisms of dissipation: relaxation of momentum, energy, intervalley transfer, as well as free-carrier number relaxation, which are reflected in the noise spectrum pattern of a biased semiconductor. On the other hand, the failure of the fluctuation-dissipation theorem allows, to a certain extent, independent control of the response and the noise through variation of the applied field, frequency, semiconductor doping, ambient temperature, sample length, and so on. Such a study, aimed at finding the favorable conditions for coexistence of high drift velocity and low excess noise, is important for the development of high-speed, low-noise devices.

1.1.2. Excess Noise at Low Electric Fields. Hot-electron effects are negligible in low electric fields, where the electrons easily dissipate energy gained from the applied electric field, and the electron temperature remains approximately equal to that of the semiconductor lattice. Nevertheless, electric current disturbs equilibrium and changes fluctuation spectra. For example, fluctuations of resistance (already present at equilibrium) cause no noise at zero bias, but they modulate current and manifest themselves in a biased semiconductor.

Many sources of excess electric noise, such as flicker noise, generation-recombination noise, and shot noise need current to appear [3-5]. Flicker noise dominates at low frequencies, whereas generation-recombination noise is usually observed at intermediate frequencies. Shot noise is white over a wide range of frequencies. These

sources of excess noise are not observed in directions transverse to the current. On the contrary, the noise resulting from electron velocity fluctuations is observed in all directions. It exceeds the flicker and generation-recombination noise at high frequencies.

Shot noise is important when the current is controlled by a barrier: a p-n junction, a Schottky barrier, a heterojunction, a tunneling structure, nonuniformities of doping, nonohmic contacts, and so on. The universal Schottky formula [6] says that, for shot noise, the spectral density of current fluctuations is proportional to the current. Measurement of noise characteristics as a function of current. Measurement of noise characteristics as a function of current, frequency, and lattice temperature helps to distinguish different sources of excess noise, and suggests how to eliminate those of no interest. In particular, perfect ohmic contacts, uniform doping, and relatively high density of majority carriers, are prerequisites for avoiding interference of shot noise during experiments on hot-electron velocity fluctuations.

1.1.3. Electron Heating by Electric Field. A high electric field accelerates mobile electrons, and they accumulate excess energy. The steady state is reached when energy loss (usually at the lattice vibrations) compensates energy gain at a certain elevated mean energy of the electrons. The electron mean energy rising above its thermal equilibrium value—termed *hot electrons*—is specific to the electron behavior at high electric fields in semiconductors. The lattice temperature tends to increase as well, due to the Joule effect. However, the heat capacity of a semiconductor sample is much higher than that of the electron gas. Moreover, the lattice dissipates excess heat to the ambient, and the lattice temperature remains the same as (or only insignificantly higher than) the ambient temperature, provided a short voltage pulse is applied and the heat dissipation is efficient. The associated noise resulting from hot electrons is called hot-electron noise.

1.1.4. Hot-Electron Noise. Electronic processes inside the conduction band are fast, so the associated spectral features of excess noise appear at microwave frequencies. Therefore, it is quite natural that investigation of hot-electron noise at microwave and higher frequencies serves for diagnostics of fast and ultrafast processes in a semiconductor subjected to high electric fields. Microwave noise measurements usually deal with the noise power expressed in terms of the equivalent noise temperature. Another fluctuation characteristic is the spectral density of current fluctuations available from experimental data on noise temperature and small-signal microwave conductivity.

Experiments on hot-electron noise provide information on the anisotropy of kinetic energies in the longitudinal and transverse directions, the transverse and longitudinal diffusion coefficients of majority carriers, the energy relaxation time constant and its dependence on the applied electric field and lattice temperature, the intervalley transfer-time constants for equivalent and nonequivalent valleys, and other important kinetic parameters of electronic processes inside the conduction and valence bands.

1.2. Kinetic Theory of Fluctuations from Nonequilibrium State

1.2.1. Toward the Price Relation. Kinetic theory of hot-electron fluctuations in semiconductors is an important part of physical kinetics [7]. The crystal lattice presents an unperturbed thermal bath for the nonequilibrium electron gas in a semiconductor, allowing detailed treatment of hot-electron interaction with equilibrium phonons. This situation, and an understanding of the importance of fluctuations for the kinetic theory, immediately led to interesting results on hot electron fluctuations in semiconductors, reported by Lax [8], Price [9], Gurevich [10], Price [11], Gurevich and Katilius [12], and Kogan and Shul'man [13].

In particular, Price [11] extended to hot electrons the fluctuation–diffusion relation between the spectral density of current fluctuations caused by electron velocity fluctuations and the diffusion coefficient associated with fluctuations of position of the same electrons. The Price relation was proven to hold, despite the failure of the Einstein relation, Ohm's law, and the Nyquist theorem for hot electrons.

1.2.2. General Theory. Later results, obtained for the case of frequent electron–electron collisions, contradicted the earlier results, and Gantsevich et al. [14,15] and Kogan and Shulman [16] developed a self-consistent kinetic theory of fluctuations in a nonequilibrium case, based on the first principles of quantum mechanics and statistical physics. The theoretic apparatus of kinetic theory was generalized to obtain spectral properties of noise from statistical properties of collisions. The criteria of applicability of the theory were the same as for Boltzmann's equations used for response calculations. An important result obtained was [15] that the Price fluctuation–diffusion relation for hot electrons [11] had a narrower range of applicability than originally expected, with a high-density hot-electron gas being outside this range because of electron–electron collisions. The theory and its numerous applications to analytically tractable models are described in monographs [4,7] and review papers [17,18].

1.3. Hot-Electron Noise in Lightly Doped Semiconductors

1.3.1. Longitudinal and Transverse Noise. Developed theory and practical needs stimulated experimental investigation of hot-electron noise in semiconductors. Erlbach and Gunn [19] measured hot-electron noise temperature for n-type germanium in the transverse direction to the current. The resultant increase of the transverse noise temperature with the applied electric field indicated that the electrons were hot. Bryant reported on longitudinal noise temperature for n-type GaAs [20]. Avoiding possible contribution of generation–recombination noise, Bareikis et al. [21] measured the longitudinal noise temperature of hot carriers in n-type and p-type germanium [22] at microwave frequencies. Their study of longitudinal and transverse noise gave the first experimental evidence that noise temperature and spectral density of velocity fluctuations of hot carriers were anisotropic quantities. The experiment was performed on samples containing a

relatively low density of hot carriers, and the results were interpreted in terms of the Price fluctuation–diffusion relation with the correct conclusion [21] that the diffusion coefficient of hot carriers was anisotropic as well. (Some time later, Wagner, Davis, and Hurst observed the anisotropy of electron diffusion in ordinary gases at high electric fields [23].) So, microwave noise experiments demonstrated the possibility to obtain results on field-dependent longitudinal and transverse diffusion coefficients for majority carriers in uniform samples without introducing carrier density gradients, and this technique [21,22] was applied to investigate hot-electron diffusion in the principal semiconductors used in electronics [24,25]. The diffusion coefficient results obtained from microwave noise measurements were confirmed by experiments using other techniques [25].

1.3.2. Fluctuations in One-Valley Semiconductors. The physics of noise relates the observed fluctuations in macroscopic variables to the microscopic processes inside a semiconductor. For hot-electron scattering by acoustic phonons in a one-valley semiconductor, theory predicted a negative convective contribution to longitudinal current fluctuations resulting from energy fluctuations [11,12]. This phenomenon was experimentally confirmed in p-type germanium [22].

An essentially different contribution to longitudinal noise comes from inelastic scattering of hot electrons by optical phonons—the main energy loss mechanism at elevated electron energies. This scattering mechanism leads to resonant-type spectrum of velocity fluctuations in a narrow range of moderate electric fields at low lattice temperatures, as illustrated by experiments performed for p-type Ge and n-type InSb at 10 K lattice temperature [18,26]. Optical phonon scattering, dominating over a wide range of electric fields in n-type GaAs and InP, leads to a broad and relatively weak noise source resolved at liquid nitrogen and room temperatures [24].

1.3.3. Intervalley Fluctuations In Elementary Semiconductors. The conduction band of Ge and Si has several equivalent valleys, containing equal parts of the electron gas in equilibrium. An applied electric field introduces differences in the drift velocities and mean energies in the ellipsoidal valleys, oriented at different angles to the field, and the excess noise—hot-electron intervalley noise—appears [9]. It is anisotropic, with respect to the electric field direction and to the crystallographic orientation [27]. Intervalley noise and generation-recombination noise are examples of so-called partition noise [25].

1.3.4. Intervalley Fluctuations in Compound Semiconductors. The conduction band of direct-bandgap compound semiconductors differs essentially from that of silicon and germanium. Equilibrium electrons occupy the lowest single valley, where their mobility is high. The upper low-mobility valleys are usually empty at equilibrium (except for high lattice temperatures), and a high electric field is needed for their occupation. Intervalley transitions of hot electrons cause longitudinal fluctuations of drift velocity. Intervalley noise of this type dominates in GaAs [28] and

InP [29] at the subthreshold field for the Gunn effect. Sources of noise due to hot-electron transfer into satellite valleys located along the (111) and (100) directions (L and X valleys) were resolved in short submicrometer samples of n-type GaAs [30].

1.4. Monte Carlo Simulation of Fluctuations

Experimental studies demonstrate that hot-electron noise characteristics are sensitive to subtle details of the semiconductor band structure and scattering mechanisms. This stimulates the interpretation of experimental data, in terms of realistic semiconductor models. While analytical models perfectly illustrate the kinetic theory with deep insight into the physics of hot-electron noise, numerical techniques are useful in extracting quantitative information on the dominant kinetic processes inside the conduction band.

1.4.1. Simulation of Hot-Electron Fluctuations. The Monte Carlo method—a versatile numerical technique—introduces hot-electron velocity fluctuations into the simulation procedure in a natural way. The first calculation of hot-electron noise spectra by the Monte Carlo technique [31] was immediately followed by a paper [32] in which a better estimate of the scattering parameters of holes in the valence band of germanium was obtained by fitting the Monte Carlo simulation data to the experimental results. Simulation techniques and calculation of the spectral properties of hot-electron noise are described in a monograph [33] on Monte Carlo methods and their application to semiconductor devices. More recent developments and results with emphasis on hot-electron noise in semiconductor structures are discussed in review papers [34–36]. This Monte Carlo approach applies at low electron densities, and modified procedures are needed to treat fluctuations when electron–electron collisions are essential [37–39].

1.4.2. Simulation of Hot-Electron Diffusion. The Price fluctuation–diffusion relation, valid at low electron densities, provides another possibility to compare experimental data on hot-electron velocity fluctuations and numerical results for realistic models. Motion of individual electrons in real space, resulting in diffusive spreading of an electron cloud, was simulated by the Monte Carlo technique, and the diffusion coefficient available from this simulation was compared with data on spectral density of current fluctuations available from microwave noise measurements [24,25].

1.5. Effect of Electron–Electron Collisions

Electron–electron collisions are energy and momentum conserving; they have no direct effect on energy and drift velocity, but do influence these averages through other scattering mechanisms. For example, an electron–electron collision can assist emission of an optical phonon by one of the electrons supposing that each electron lacks energy for the emission before the collision. The associated loss of energy is essential. It causes a slow increase of hot-electron noise temperature at moderate electric fields and

cryogenic temperatures, as illustrated by comparing the results of Monte Carlo simulation with the experimental data for n-type GaAs [39]. Moreover, theory predicts that two-carrier collisions in hot-electron gas create additional correlation, and the additional term enters the fluctuation–diffusion relation [15,37].

1.6. Semiconductor Structures

1.6.1. Short Channel Effects. Modern microelectronics is shaped by small-size and low-dimension semiconductor structures. Investigation of hot-electron noise in such structures is important when one tries to minimize the associated excess noise at high speed of operation. Hot electrons fail to reach the steady state, corresponding to an infinitely long sample, provided the sample is short and the hot electrons leave the sample for the electrode early enough. As a result, a higher electric field is needed for the intervalley noise to appear in short samples [37]. In other words, at a fixed electric field, the intervalley noise is suppressed in short channels. The essential suppression of hot-electron noise in short channels has been demonstrated for lightly doped n-type GaAs [40] and InP [41], and for standard-doped n-type GaAs [42]. For a comparison with the results of Monte Carlo simulation, see Ref. 24.

1.6.2. Two-Dimensional Electron Gas Channels. In two-dimensional electron gas (2-DEG), the electrons are free to undergo planar motion, but their transverse freedom is limited by the heterojunction and electrostatic barriers. The degree of transverse freedom depends on the barrier height and the electron kinetic energy, the latter being easily controlled by the electric field applied in the plane of electron localization. This introduces sources of excess noise specific to low-dimensional channels [43,44]. Dependence of hot-electron noise on channel length is also important for low-noise operation of 2-DEG channels at microwave frequencies [44].

2. THEORETIC BACKGROUND

Hot-electron fluctuations depend on the details of kinetic processes taking place in a biased semiconductor. This requires consideration of the values in the nonequilibrium spectra that reflect these details. Definitions and relations appropriate for the nonequilibrium state and converging to the equilibrium states at zero bias are introduced in this section.

2.1. Correlation Function and Spectral Density of Fluctuations

Electric current in a semiconductor sample results from motion of the mobile electrons present in the sample. Random motion of individual electrons produces fluctuations of the current $\delta\mathbf{I}(t)$ around the time-independent mean value $\bar{\mathbf{I}}$. Let us consider N electrons in a uniform sample under steady-state, reached in a uniform static electric field \mathbf{E} . The time-dependent velocity of the all-electron mass center, averaged over the mobile electrons, or drift

velocity, is

$$\mathbf{v}_d(t) = \frac{1}{N} \sum_n^N \mathbf{v}_n(t) \quad (1)$$

where $\mathbf{v}_n(t)$ is the instantaneous velocity of the n th electron and t is time. Fluctuations of the drift velocity $\delta\mathbf{v}_d(t)$ around the time-independent mean value $\overline{\mathbf{v}_d(t)}$ are present in all directions:

$$\delta\mathbf{v}_d(t) = \mathbf{v}_d(t) - \overline{\mathbf{v}_d(t)} \quad (2)$$

The bar here and in the following designates the average over time. The fluctuating time-dependent drift velocity for a chosen model can be obtained from Monte Carlo simulation [33].

The quantity that yields important physical information on the size of the fluctuations and how they decay in time is the drift velocity autocorrelation function (see Ref. 4). In the direction of interest, the autocorrelation function is

$$\Phi(\tau) = \overline{\delta v_d(t) \delta v_d(t + \tau)} \quad (3)$$

where τ is the time difference between two observations and $v_d(t)$ is the drift velocity component in the chosen direction. The autocorrelation function value $\overline{\delta v_d^2(t)}$ at $\tau = 0$ is called variance. Correlation functions are available from the equations of fluctuation kinetics or from Monte Carlo simulation [17,18,33,34].

Fourier transformation of the drift velocity autocorrelation function [Eq. (3)] gives the spectral density of drift velocity fluctuations in the direction of interest (Wiener-Khinchine theorem) [3]:

$$S_v(\omega) = 4 \int_0^\infty \Phi(\tau) \cos(\omega\tau) d\tau \quad (4)$$

Electron velocity fluctuations induce voltage fluctuations on the sample terminals and current fluctuations in the circuit. It is a convention to deal with the open-circuit voltage fluctuations and the short-circuit current fluctuations unless otherwise mentioned. The current, which is usually measured outside the sample, can be related to the electron drift velocity inside the sample. In a similar way, the current fluctuations can be expressed in terms of the drift velocity and other fluctuations. In general, the relation is complicated, but it acquires a simple form in the case of a uniform electric field in a uniformly doped sample of constant cross section at high frequencies where electron number fluctuations can be ignored. Hence, the spectral density of current fluctuations S_I is proportional to that of drift velocity fluctuations

$$S_I(\omega) = e^2 n S_v(\omega) Q / L \quad (5)$$

where e is the elementary charge, n is the electron density, Q is the cross-sectional area, L is the sample length (interelectrode distance), ω is the circular frequency, and S_I

is determined in A^2s . Discussion of more complicated cases can be found elsewhere [34,36,45].

In general, the spectral density of current fluctuations is a tensor quantity, consisting of three diagonal and six off-diagonal components. A diagonal component results from the autocorrelation function of the time-dependent drift velocity component along the corresponding Cartesian axis [see Eq. (3)]. An off-diagonal component comes from the velocity covariation function [of a similar form as Eq. (3)], but containing the product of the time-dependent drift velocity components along two Cartesian axes. In an isotropic medium, for example, in an amorphous solid, the tensor of spectral density can be reduced to three diagonal nonzero components, the parallel to the applied electric field component and two transverse components; the latter two are equal to each other. In crystals, for example Si or Ge subjected to electric field, the off-diagonal components are also important.

2.2. Available Noise Power and Noise Temperature

Hot-electron velocity fluctuations and associated fluctuations of current dominate over other sources of fluctuations at microwave frequencies. The fluctuating, that is, time-dependent current, causes emission of electromagnetic waves into an open space or into the load (a coaxial cable, a waveguide, a coplanar line, etc.). Therefore, the semiconductor sample feeds the power into the load. The emitted noise power is of special importance in this frequency range, since the current fluctuation spectra (directly available from the velocity fluctuation spectra, in theory) are not measured at microwave frequencies directly. It is a convention to consider the emitted/absorbed noise power for matched impedances of the sample and the load, unless stated otherwise. Under this condition, the noise power is called the power available at the noise source or the available noise power.

The available noise power $P_n(f)$ emitted by a source of noise in a fixed frequency band Δf around a frequency $f = \omega/2\pi$ can be estimated by comparing it with the power radiated into the same frequency band by an absolutely blackbody kept at a known temperature. In case of equal powers at a given frequency, one can say that the equivalent noise temperature of the noise source at this frequency equals the absolute temperature of the reference blackbody. The equivalent noise temperature, or noise temperature, $T_n(f)$, multiplied by the Boltzmann constant k_B is, by definition, the power, per unit frequency band around the frequency f , dissipated by the sample into the matched load [4]:

$$T_n(f) = \frac{P_n(f)}{k_B \Delta f} \quad (6)$$

Hot-electron noise power depends on frequency, direction, electric field, and so on. This forces one to introduce frequency-, direction- and field-dependent equivalent noise temperature. In an isotropic medium, the nonequilibrium noise temperature differs in the directions parallel and transverse to the current. The hot-electron noise temperature $T_n(f)$ represents a property of an electron gas

differing from its energy temperature T_e , which is defined on the basis of the electron average energy, $T_e = (2/3)\langle \epsilon \rangle / k_B$.

In equilibrium, the noise temperature of the sample in question is independent of frequency over the wide range of frequencies, and equals the absolute temperature: $T_n = T_0$. The equilibrium noise spectrum is white (until $\omega \ll k_B T_0$; see Ref. 41), and the available noise power in this range of frequencies can serve for establishment of the absolute scale of temperature.

2.3. Spectral Density of Current Fluctuations and Noise Temperature

Noise power can be expressed in terms of spectral density of current fluctuations and impedances of the sample and the load. For the matched impedances one has

$$P_n(f) = \frac{1}{4} S_I(f) \operatorname{Re}\{Z(f)\} \Delta f \tag{7}$$

where S_I is the spectral density of current fluctuations determined under the short-circuit condition, and $Z(f)$ is the AC impedance of the sample around the DC bias point. (The matching of the sample and the load means that their impedances are equal.)

From Eqs. (6) and (7), the spectral density of short-circuit current fluctuations for hot electrons in a sample subjected to electric field E can be related to the noise temperature and the sample impedance

$$S_I(f, E) = \frac{4k_B T_n(f, E)}{\operatorname{Re}\{Z(f, E)\}} \tag{8}$$

where S_I , T_n , and Z are determined in a chosen direction (e.g., longitudinal or transverse to the electric field E for isotropic semiconductors). Thus, measurement of the impedance and the noise temperature are sufficient to obtain the experimental short-circuit value of current fluctuation spectral density for hot electrons. Since the same quantity is available from theory [see Eq. (5)], a comparison of the experimental data with the results of calculation is possible.

Voltage fluctuations are seldom considered at microwave frequencies. For completeness, note that the spectral density of voltage fluctuations on the sample terminals for the open circuit and the spectral density of current fluctuations under the short-circuit condition are inter-related, according to $S_V(f) = |Z(f)|^2 S_I(f)$.

2.4. Fluctuation–Dissipation Theorem and Its Extension

2.4.1. The Nyquist Theorem. As discussed above, the noise temperature at equilibrium equals the absolute temperature. Hence, for equilibrium it follows, from Eq. (8):

$$S_I(f) = 4k_B T_0 / \operatorname{Re}\{Z(f)\} \tag{9}$$

This relation is called the *Nyquist theorem* in the classical limit ($\hbar\omega \ll k_B T_0$). A sophisticated derivation of the Nyquist theorem can be found elsewhere [4].

2.4.2. The Einstein Relation. At equilibrium, the electron mobility and the diffusion coefficient are closely related according to the Einstein relation. For low-density nondegenerate electron gas, the relation is simplified to

$$D_0 = \mu_0 \frac{k_B T_0}{e} \tag{10}$$

where μ_0 is the low-field low-frequency electron mobility and D_0 is the zero-field diffusion coefficient in the expression for the diffusion current density, $j_d = -eD_0 \nabla n$, resulting from the electron density gradient ∇n .

2.4.3. Lorentz-Type Spectrum. The principle of energy equipartition means that the equilibrium mean energy contained in every degree of freedom equals $k_B T_0 / 2$. Applied to the mean energy of the all-electron mass center at equilibrium, the principle relates the drift velocity fluctuation variance in the direction of interest to the temperature

$$Nm \overline{v_d^2(t)} = k_B T_0 \tag{11}$$

where m is the electron effective mass.

For a rectangular sample, the variance of current at equilibrium can be presented as

$$\overline{I^2(t)} = e^2 N^2 \overline{v_d^2(t)} / L^2 = \frac{e^2 N}{m L^2} k_B T_0 \tag{12}$$

This equation relates equilibrium fluctuations of the current component in a given direction to the absolute temperature.

The electron momentum relaxation time τ_p in the simple expression for the low-field electron mobility,

$$\mu_0 = (e/m)\tau_p \tag{13}$$

determines the decay of corresponding fluctuations

$$\overline{\delta I(t) \delta I(t + \tau)} = \overline{\delta I^2} e^{-\tau/\tau_p} \tag{14}$$

Integration [see Eq. (4)] yields the frequency dependence of the spectral density of current fluctuations at equilibrium

$$S_I(\omega) = 4 \int_0^\infty \overline{\delta I^2} e^{-\tau/\tau_p} \cos(\omega\tau) d\tau = \overline{\delta I^2} \frac{4\tau_p}{1 + \omega^2\tau_p^2} \tag{15}$$

A spectral dependence like this is called a Lorentz spectrum.

Equations (12) and (15) lead to the Nyquist relation

$$S_I(\omega) = 4k_B T_0 e N \operatorname{Re}\{\mu(\omega)\} / L^2 \tag{16}$$

where the real part of AC mobility $\mu(\omega)$ is introduced:

$$\operatorname{Re}\{\mu(\omega)\} = \frac{(e/m)\tau_p}{1 + \omega^2\tau_p^2} \tag{17}$$

The electron mobility μ (determined by the momentum relaxation time constant τ_p) and the electron density n are the most important parameters of electron transport in semiconductors. According to the Nyquist relation, in the form of Eq. (16), the same parameters decide noise at equilibrium.

2.4.4. Fluctuation–Diffusion Relation. Velocity fluctuations of individual electrons cause fluctuations of their positions, resulting in diffusive spreading of a cloud of electrons, diffusion current, and other diffusion phenomena. As a result, an important relation exists between the diffusion coefficient and the spectrum of current fluctuations. Using the Einstein relation [Eq. (10)] and the Nyquist theorem [Eq. (16)] for $\omega\tau_p \ll 1$, one obtains [see Eq. (5)]:

$$S_v(0) = 4D_0 \quad (18)$$

So, the basic kinetic coefficients (mobility, diffusion coefficient) and spectral density of velocity fluctuations are interrelated through Nyquist [Eq. (16)], Einstein [Eq. (10)], and fluctuation–diffusion [Eq. (18)] relations at thermal equilibrium. Measurements or calculation of velocity fluctuation characteristics at equilibrium give no additional information not already available from the mobility.

2.5. Beyond the Fluctuation–Dissipation Theorem

Calculation of hot-electron noise is an independent problem of kinetic theory, which cannot be reduced to the calculation of the response of an electron system to external deterministic perturbation. So, in general, knowledge of the sample impedance is not sufficient for determination of excess noise. Nevertheless, under well-defined conditions, some useful relations can be applied to hot electrons in a biased semiconductor.

2.5.1. The Price Relation. Price [10] generalized the fluctuation–diffusion relation for a semiconductor subjected to a high electric field under the following conditions: (1) the system is electrically stable, that is, $\text{Re}\{\mu(E, f)\} > 0$; (2) two-carrier interaction is neglected; (3) the thermal bath is not perturbed; and (4) the electronic processes in the conduction band are essentially faster than those including energy levels in the gap (electron trapping) and the valence band (electron-hole recombination). It turns out that, as for the thermal equilibrium, the fluctuation–diffusion relations are valid for hot electrons

$$(S_v)_{xx} = 4D_{xx} \quad (19)$$

$$(S_v)_{xy} = 2(D_{xy} + D_{yx}) \quad (20)$$

where S_v stands for the tensor components of drift velocity fluctuation spectral density in the frequency range, where the maximum contribution comes from all intraband electronic processes.

Equations (19) and (8) lead to the equivalent form of the Price relation:

$$D_{xx}(E) = \frac{1}{e} k_B T_{nx}(E) \cdot \text{Re}\{\mu_{xx}(E)\} \quad (21)$$

where the hot-electron noise temperature T_{nx} is determined in the direction x , the electric field E being applied in any direction. The corresponding diagonal component of the real part AC mobility tensor, μ_{xx} , is determined at frequencies low, compared with the inverse time constants of the momentum relaxation and other relaxation processes inside the conduction band.

The Price relation is valid for hot electrons even when the Ohm, Einstein, and Nyquist relations do not hold. It is a useful relation for low-density, hot-electron gas, in contact with an unperturbed thermal bath of a semiconductor. The relation has suggested a convenient way to measure the components of the diffusion coefficient tensor for hot electrons, without introducing electron density gradient [21].

Further on, the diagonal components of the longitudinal and transverse directions to the applied electric field will be discussed (let the field be directed along the x axis): $(S_v)_{\parallel} = (S_v)_{xx}$ and $(S_v)_{\perp} = (S_v)_{yy}$.

2.5.2. Additional Correlation Due to Electron–Electron Collisions. The Price relation has been generalized [15] into

$$S_v = 4(D + \Delta) \quad (22)$$

where Δ is the tensor resulting from the additional correlation caused by the interelectron collisions [15,17,18,37]. The additional correlation arises only at nonequilibrium conditions, disappearing at equilibrium.

2.5.3. Excess Noise in Electron Temperature Approximation. Frequent electron–electron collisions establish hot-electron distributions governed by the electron temperature. In the electron temperature approximation for quasielastic scattering, the kinetic theory of fluctuations allows one to express the noise temperature in terms of conductivities, and lattice T_0 and electron T_e temperatures (13):

$$(T_n)_{\perp} = T_e \quad (23)$$

$$(T_n)_{\parallel} = T_e \left[1 + \frac{T_e}{4(T_e - T_0)} \left(\frac{\mu_{\parallel}}{\mu_{\perp}} + \frac{\mu_{\perp}}{\mu_{\parallel}} - 2 \right) \right] \quad (24)$$

where $(T_n)_{\parallel}$ and $(T_n)_{\perp}$ are the longitudinal and transverse noise temperatures, and μ_{\parallel} and μ_{\perp} are the longitudinal and transverse AC mobilities. Equations (23) and (24) hold at low microwave frequencies $\omega \ll \tau_e^{-1}$, provided the electron–electron collisions control the electron distribution in energy: $\tau_p \ll \tau_{ee} \ll \tau_e$ (here τ_{ee}^{-1} is the frequency of the interelectron collisions). It is noteworthy that the longitudinal excess noise depends on the small-signal mobilities in the longitudinal and transverse directions, this dependence disappearing in absence of hot-electron effects: when

either $T_e = T_0$ or Ohm's law holds and $\mu_{\perp} = \mu_{\parallel}$. One can notice a possible simplification at high electric fields, where $T_e \gg T_0$, the resultant expression demonstrating the same complex dependence on the deviations from Ohm's law.

2.6. Examples of Hot-Electron Fluctuation Spectra

In the previous section the main concepts, definitions, and important theoretic results on fluctuations near a non-equilibrium state were presented in the limit of low microwave frequencies. This section presents some examples of possible spectra of spatially homogeneous current fluctuations (for more details, see Ref. 18).

2.6.1. Convective Noise. Energy fluctuations contribute to fluctuations of current in the direction of a steady current. The contribution is easy to resolve in one-valley semiconductors in case of quasielastic scattering. Quasielastic scattering means that a collision changes the direction of the electron motion remarkably, with little effect on the absolute value of the electron velocity. The well-known example is electron scattering by acoustic phonons at not too low lattice temperatures; many collisions are needed for energy relaxation, so two time constants decide relaxation of fluctuations. They are the momentum relaxation time τ_p and the energy relaxation time τ_e ; the latter is larger than the first.

The spectral density of longitudinal current fluctuations in the presence of an external electric field contains the term due to energy fluctuation, resulting in the so-called convective contribution to noise [11,12]

$$S_I(\omega, E) = \frac{4\overline{\delta I^2}\tau_p}{1 + \omega^2\tau_p^2} + \frac{C}{1 + \omega^2\tau_e^2} \quad (25)$$

where C is the low-frequency ($\omega\tau_e \ll 1$) limit of the convective term. The latter is important, provided Ohm's law does not hold. The sign of deviation from Ohm's law decides the sign of C [12,16]: $C < 0$ in case of a sublinear current-voltage characteristic, and $C > 0$ for a superlinear one. The mobility decreases with increasing electron energy in lightly doped semiconductors. In this case, the convective contribution causes the partial suppression of current fluctuations in the longitudinal direction at frequencies $\omega\tau_e \sim 1$.

2.6.2. Intervalley and Real-Space Transfer Noise. In many-valley semiconductors the total number of electrons consists of the partial numbers corresponding to different valleys. Fluctuations of occupancies modulate the current and cause current fluctuations. Price [8] introduced the term *intervalley noise* to account for the extra contribution arising from the occupancy fluctuations.

Assuming that the intravalley processes are fast, as compared with the intervalley processes, the spectral density of velocity fluctuations in a chosen direction for a

simple two-valley model can be written as

$$S_v(\omega, E) = \frac{\bar{n}_1}{n} S_1 + \frac{\bar{n}_2}{n} S_2 + 4 \frac{\bar{n}_1\bar{n}_2}{n^2} \times (\bar{v}_1 - \bar{v}_2)^2 \frac{\tau_i}{1 + (\omega\tau_i)^2} \quad (26)$$

where τ_i is the intervalley relaxation time constant (inversely proportional to the squared intervalley coupling constant), n is the electron density, while $\bar{n}_1, \bar{v}_1, S_1$ and $\bar{n}_2, \bar{v}_2, S_2$ are the average electron densities, drift velocities, and spectral densities of velocity fluctuations in valleys of types 1 and 2, respectively. Consequently, hot-electron noise in a many-valley semiconductor is not equal to the sum of the corresponding intravalley contributions weighted by the partial numbers of electrons. The last term in Eq. (26) is always positive; it vanishes in two cases: for equivalent valleys, when $\bar{v}_1 = \bar{v}_2$, and at thermal equilibrium, when $\bar{v}_1 = 0$ and $\bar{v}_2 = 0$. Thus, current is necessary for the contribution from intervalley fluctuations, but electron heating is not necessary, in general. For example, at a relatively high lattice temperature, the transitions between nonequivalent valleys can lead to intervalley noise at low electric fields, without electron heating.

From Eqs. (19) and (26) one obtains a simplified expression for the intervalley diffusion

$$\Delta D = \frac{\bar{n}_1\bar{n}_2}{n^2} (\bar{v}_1 - \bar{v}_2)^2 \tau_i \quad (27)$$

Expressions given by Eqs. (26) and (27) are also suitable to describe excess noise and diffusion caused by transverse electron transitions from one layer to another in semiconductor structures containing layers with different electron mobilities. The related noise, appearing in the longitudinal direction, is called real-space-transfer noise.

3. EXPERIMENTAL TECHNIQUES

Noise spectroscopy, unlike the usual optical one, deals with relaxation, that is, aperiodic processes. Different electronic processes, characterized by relaxation times τ_m , cause steps at frequencies around $\omega\tau_m = 1$. Each step has a simple Lorentzian form, provided the decay of fluctuations is exponential. As mentioned, hot-electron noise results from the kinetic processes taking place inside the conduction band. Their relaxation times are in the picosecond and subpicosecond range. Therefore, microwave and higher frequencies serve best for experimental investigation of hot-electron fluctuation spectra. In this range of frequencies, other sources of noise, such as $1/f$ fluctuations, generation-recombination noise, and the like, do not mask hot-electron effects.

3.1. General Requirements

3.1.1. Samples. A semiconductor sample for hot-electron noise measurements at microwave frequencies is a nonlinear resistor. A typical shape is a rectangular

parallelepiped, with two Ohmic electrodes at its bases. For investigation of epitaxial conductive channels, coplanar ohmic electrodes are more convenient. The epitaxial sample is cut from a transmission-line-model structure. A standard coplanar configuration with different inter-electrode distances (often exploited to estimate contact resistance) is quite acceptable. Longitudinal and transverse noise temperatures can be measured by placing the sample oriented either normal or parallel to the wide walls of the waveguide. Fluctuations of current excite the H_{10} mode in the waveguide, and the AC electric field of the emitted noise, depending on the sample orientation, is either parallel or transverse to the bias field.

On-wafer microwave noise measurements can be performed using microprobes. Each microprobe consists of a central wire and two side wires attached for screening. Microprobes are connected to hard coaxial lines or waveguides, and are put in contact with the sample electrodes on the wafer.

3.1.2. Pulsed Measurements of Hot-Electron Noise. Spectral analyzers are now commercially available for a wide range of frequencies up to and including the V band of millimeter waves. They operate in a cw mode and support standard cw measurements of noise in semiconductor devices in many laboratories. However, investigation of hot-electron effects and other effects at high electric fields require pulsed rather than CW modes of operation. Pulsed measurements help to avoid thermal walkout, due to the Joule effect prevailing in a CW mode. The increase in the lattice temperature masks hot-electron effects. Unfortunately, spectral analyzers for pulsed measurements are not commercially available yet, and radiometric techniques operating at fixed frequencies are used to obtain the data specific to hot electrons. The noise power in the chosen frequency band Δf at frequency f is selected by a filter, then amplified and fed into a radiometer for noise power measurement.

3.1.3. Waveguide and Coaxial Techniques. Pulsed measurements of noise power impose several special requirements. The noise must be measured when the electric field is on, that is, when the radiometer is opened for a short time. One has to deal with a low and extremely short noise signal in the presence of high pulsed voltage, the latter penetrating into the noise-measuring circuit and disturbing the sensitive amplifier, unless the radiometric circuit is safely decoupled from the one which is used to heat the electrons. The decoupling is easily achieved at microwave frequencies. This frequency range is also useful for another reason—flicker and generation-recombination noise sources are cut off at microwaves and do not interfere with hot-electron noise measurements.

Measurement at high electric fields introduces a problem. The electric field changes the sample impedance and causes a mismatch of the sample to the load—the transmission line connecting the sample to the radiometer. The mismatch must be eliminated by changing the load impedance.

These problems have been solved by developing a waveguide-type short-time-domain gated modulation radiometer [47]. Low transmission losses in waveguides narrowband low-noise, high-gain parametric microwave amplifier available at microwave frequencies, efficient filtering out of parasitic signals, make a waveguide-type radiometer a valuable instrument for research of hot-electron fluctuations [18,24].

Coaxial techniques have also been widely used [19,20,27,29] (see also Ref. 24). The coaxial technique, using a wideband amplifier, appropriate filters, and pulsed bias, assures measurement of hot-electron noise over a wide range of frequencies, without changing the sample-holder hardware.

3.2. Waveguide-Type Short-Time-Domain Gated Radiometer

3.2.1. Radiometric Setup. Figure 1 presents a schematic view of the radiometric setup for hot-electron noise

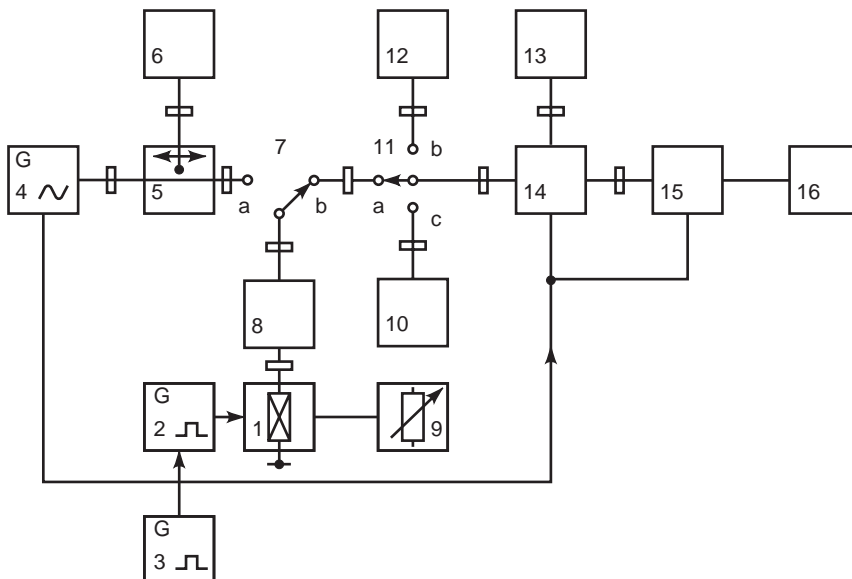


Figure 1. A schematic setup for hot-electron microwave noise power measurements: 1—the investigated sample in the waveguide; 2—the pulsed voltage generator; 3—the master generator; 4—the microwave generator; 5—the microwave line; 6—the SWR indicator; 7,11—the microwave switches; 8—the impedance transformer; 9—the resistance bridge; 10,13—the reference noise generators at $T_0 = 293$ K; 12—the reference noise generator at $T = (T_0 + 200)$ K; 14—the modulator; 15—the gated modulation radiometer; 16—the indicator.

measurements at microwave frequencies. The experimental procedure for determining the noise temperature T_n consists of two steps.

The first step is the measurement of the current–voltage characteristic and matching the waveguide impedance to that of the sample at each bias. The bias voltage pulses are typically from 1 to 5 μ s duration, fed at a 125 Hz repetition rate. The master generator 3 drives the pulse voltage generator 2 and the microwave generator 4. When microwave switch 7 (Fig. 3) is connected to port 7a, the microwave generator 4, the microwave line 5, and the transformer 8 are used to match the sample, that is, to reach the minimum standing microwave ratio. The resistance bridge 9 controls the sample resistance at each bias level.

The second step is the noise temperature measurement of the sample at a chosen bias. The switches 7 and 11 are connected to ports 7b and 11a, respectively. The noise signals from the sample 1 and the reference noise generator 13 are periodically fed into the input of the gated modulation radiometer, which is opened twice during the period of modulation: first, to connect the biased sample 1 to the radiometer, and for the second time to connect the reference noise generator 13. The difference between the signal levels is used to determine the noise temperature of hot electrons. The delay of the gating pulse ensures the noise power measurements before, during, and after the voltage pulse, if necessary. This is sufficient to control the channel overheat. The best matching data (transformer data) obtained for each bias are used. The standard noise reference sources 10 and 12 are connected to check the zero level (switch at port 11c) and the gain of the radiometer amplifiers (port 11b). The limit parameters of the X-band radiometer with 10^{-7} s gating time are as follows. The power sensitivity 10^{-15} W, the systematic error 0.25 dB, the noise temperature range up to $100 k_B T_0$.

3.2.2. Measured and Available Noise Power. The measured noise power data are sufficient to determine the available noise power, provided the sample is matched to the waveguide and the waveguide losses (and the associated waveguide related noise) are negligible. Since the sample impedance is field-dependent, the optimal conditions are not achieved over the wide range of electric field values. Losses and mismatch are corrected by additional microwave measurements.

3.2.3. Small-Signal Response and Current Fluctuations. The spectral density of current fluctuations $S_I(E)$ is determined from the data on noise temperature $T_n(E)$ and small-signal AC conductance $\text{Re}\{Y(E)\}$ of the sample, according to Eq. (8). Let us give a brief description of the technique to measure $\text{Re}\{Y(E)\}$, operating at the pulsed bias and using the same sample mounting, which is compatible with the gated radiometer. First, the standing-wave ratio $K(E, B=0)$ is measured at a strong electric field E at zero magnetic field at the ambient temperature. Then, the electric field is switched off, and the previous value of the standing-wave ratio is reached at zero electric field $K(E=0, B)=K(E, B=0)$, by changing the sample conductance with external magnetic field B or by changing

the lattice temperature. Now, the DC low-field conductance is measured in the standard way, at a very low DC electric field. Since a strong inequality holds at microwave frequencies, $(\omega\tau_p)^2 \ll 1$, one has $Y(\omega=0, E=0, B)=\text{Re}\{Y(\omega, E=0, B)\}$, where $Y(\omega, E=0, B)$ is the zero-field AC admittance at the microwave frequency in the magnetic field. The equality of the standing-wave ratios means that the small-signal microwave AC impedances are also equal, and $\text{Re}\{Y(\omega, E, B=0)\} = Y(\omega=0, E=0, B)$. Therefore, the required small-signal conductance at the microwave frequency under strong pulsed electric field E is available from the zero-field DC conductance, measured at a low electric field. This technique allows one to determine the small-signal conductance at the microwave frequency in the direction parallel and transverse to the bias field E .

3.2.4. Extremely High Electric Fields in Conductive Channels. Experimental study of hot-electron noise in conductive channels at extremely high electric fields is hindered by host crystal heating and thermal breakdown. A technique was developed to perform the measurements at fields up to the impact ionization threshold [30]. A nanosecond/microwave sample holder was designed to perform short-time-domain pulsed measurements of hot-electron noise power at microwave frequencies. The sample was placed into the coaxial part of the holder, enabling the application of 100 ns pulses of electric field along the channel. For coupling the investigated channel to the waveguide, a T-shaped antenna was used. Matching of the channel circuit to the waveguide was controlled by the standing-wave-ratio meter. The noise power emitted by the channel into the waveguide was compared with that of the “blackbody” radiation source kept at known temperature. This technique was applied to measure the equivalent noise temperature of hot electrons in the channel in the direction of the applied electric field. The average fields up to 300 kV/cm were reached in standard doped ungated GaAs channels for field-effect transistors.

4. EXPERIMENTAL RESULTS ON HOT-ELECTRON NOISE

Failure of the fluctuation–dissipation relation at nonequilibrium conditions means that spectra of noise are rich, containing many features, and knowledge of electron density and mobility is not sufficient to predict noise characteristics of a particular semiconductor subjected to a high electric field. Detailed information on excess noise is available, either from noise measurements or from realistic model calculations. This article contains the experimental results selected to illustrate the most specific effects of hot electrons on excess noise.

4.1. Anisotropy of Hot-Carrier Noise

4.1.1. Longitudinal and Transverse Noise Temperature. Hot-electron noise temperature T_n is an anisotropic quantity. The directions parallel and transverse to the steady current are not equivalent, even in the simplest case of a spherically symmetric band structure and isotropic scattering mechanisms. This is illustrated in Fig. 2, which presents the noise temperatures measured for p-type

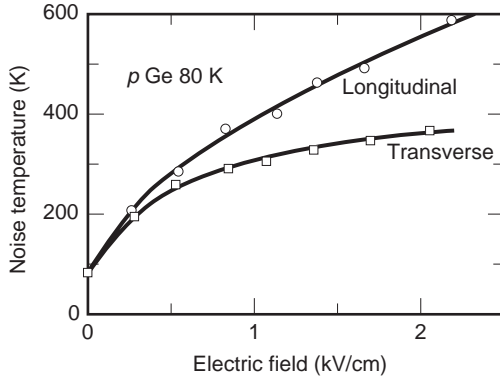


Figure 2. Equivalent noise temperature of hot holes increases with applied electric field in different ways when measured in the longitudinal and transverse directions to the steady current. Experimental data for p-type germanium [22] ($p = 1.5 \times 10^{14} \text{ cm}^{-3}$, $T_0 = 80 \text{ K}$). Solid curves are guides to the eye.

germanium at 9.6 GHz frequency and 80 K lattice temperature [21]. The origin of the transverse noise temperature is similar to that at equilibrium—it is closely related to the hole kinetic energy. Therefore, the measured transverse noise temperature gives experimental evidence that the holes become hot when subjected to a high electric field. This effect is not masked by contributions from the fluctuations that modulate the steady current flow and appear in the longitudinal direction.

4.1.2. Transverse Noise Temperature and Energy Relaxation. For a simple band structure in the carrier temperature approximation, the transverse noise temperature equals the carrier temperature; the latter is determined by the mean energy of carriers [see Eq. (23)]. Monte Carlo simulation shows this to be approximately true for holes in p-type germanium [31], where measurements of the transverse noise temperature can serve for estimation of the mean energy of hot holes, $\langle \varepsilon \rangle \approx (3/2)k_B(T_n)_\perp$, and of the energy relaxation time constant τ_e :

$$\tau_e = \frac{\langle \varepsilon \rangle - \langle \varepsilon_0 \rangle}{e(\bar{v}_d \mathbf{E})} \approx \frac{3}{2} \frac{k_B((T_n)_\perp - T_0)}{e(\bar{v}_d \mathbf{E})} \quad (28)$$

Figure 3 presents the dependence on the applied electric field of the energy relaxation time constant obtained for p-type Ge, according to Eq. (28) from the experimental data on the transverse noise temperature and the steady drift velocity \bar{v}_d [48]. Values exceeding 20 ps are obtained at low electric fields. As is often the case, the energy relaxation time constant decreases on carrier heating.

4.1.3. Tensor of Diffusion Coefficients. The first experimental results on diffusion coefficient tensor components for hot majority carriers were obtained using the noise technique [20]. The longitudinal and transverse hot-electron noise temperatures were measured at 9.6 GHz for n-type Ge, and the Price relation [Eq. (21)] was used to obtain the electric field dependence of the diffusion coefficient tensor components (see Fig. 4). The transverse

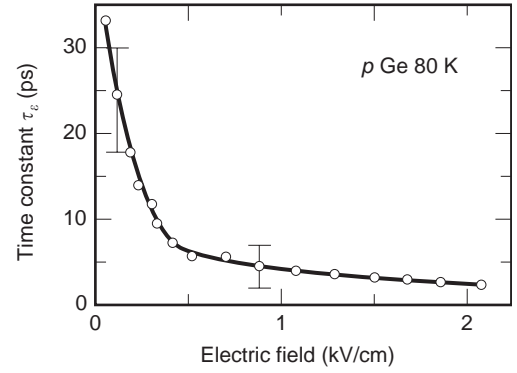


Figure 3. Hot-hole energy relaxation time constant τ_e in p-type germanium, deduced from the transverse noise temperature measured in the $\langle 110 \rangle$ direction for electric field applied in $\langle 1\bar{1}0 \rangle$ direction [48]. The time constant decreases as the electric field increases. Solid curve is a guide to the eye. $p = 1.5 \times 10^{14} \text{ cm}^{-3}$, $T_0 = 80 \text{ K}$.

component at nonequilibrium was found to exceed its value at equilibrium. The longitudinal component decreases as the electric field increases. As mentioned earlier (see Section 2.6.1), the energy fluctuations contribute to the longitudinal rather than the transverse fluctuations [see Eq. (25)]. Consequently, Fig. 4 gives experimental evidence of the negative contribution of the convective noise to the spectral density of longitudinal current fluctuations [11,12].

4.1.4. Comparison to Time-of-Flight Experiment. It would be interesting to compare the results on hot-carrier diffusion obtained by the noise technique with those available from other experiments. Time-of-flight technique (see Ref. 33) provides direct observation of longitudinal diffusion. In this technique, a sheet of electrons (or holes) drifts in an electric field in a semi-insulating plate placed into a charged condenser. The shape of the pulse of the condenser discharge current contains information on the average time of flight and its dispersion, where the latter

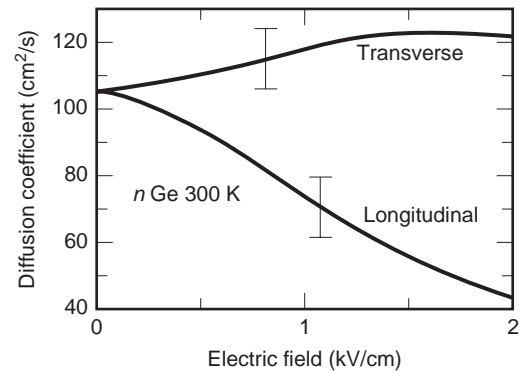


Figure 4. Hot-electron diffusion coefficients differ in the longitudinal and transverse directions to the steady current. Experimental data for n-type germanium [21] ($n = 2 \times 10^{14} \text{ cm}^{-3}$, $T_0 = 300 \text{ K}$).

is dependent on the sheet spreading, with hot-electron diffusion among other possible causes. Noise and time-of-flight experiments are difficult to perform on exactly the same material, because of almost incompatible requirements inherent in these techniques. Insulating or semi-insulating samples with rectifying contacts are preferable in the time-of-flight experiment, while the noise experiment must be performed on doped (better on lightly doped) samples with ohmic electrodes. As already mentioned, the latter requirements are important for matching the sample to the input circuit of the microwave radiometer, and in order to avoid contribution from shot noise. In spite of these difficulties, a few successful experiments have provided some valuable comparisons. Figure 5 compares the longitudinal tensor components of hot-hole diffusion coefficient available from noise (closed circles) and spreading (open circles) experiments, performed on silicon at 300 K [25]. The agreement is good throughout the range of electric fields, where the results are available from both experiments.

4.2. Excess Noise Spectra

As a rule, several kinetic processes contribute to longitudinal fluctuations. This leads to rich noise spectra, Lorentz-type contributions appearing as steps at $\omega \ll 1/\tau_m$. So, spectral investigation of excess noise in the current direction deserves more attention than that in the transverse direction. Herein-after the focus will be on the longitudinal fluctuations, longitudinal noise, and other longitudinal quantities. For simplicity, the subscript indicating the direction of measurements is omitted.

4.2.1. Generation-Recombination and Intervalley Noise in Silicon. Measurements of noise spectra at low frequencies necessitate application of long pulses of voltage, and the Joule effect limits the range of electric fields where hot-electron effects can be investigated experimentally. Figure 6 shows the spectral density of longitudinal current fluctuations measured in $\langle 100 \rangle$ direction for n-type silicon at 200 V/cm at 78 K temperature (Fig. 6, symbols, see Ref. 24). In addition to $1/f$ noise at low frequencies, two

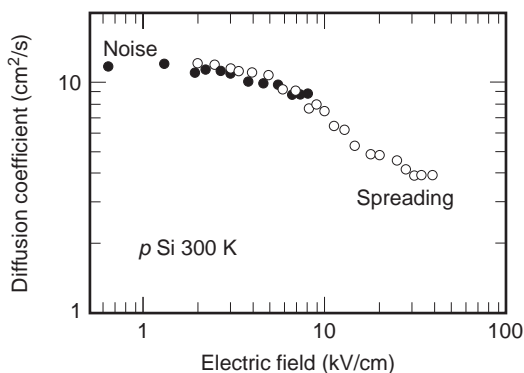


Figure 5. Longitudinal diffusion coefficient of hot holes in silicon at $T_0 = 300$ K: the results obtained from noise experiments (closed circles) match those available from spreading experiments (open circles) [25].

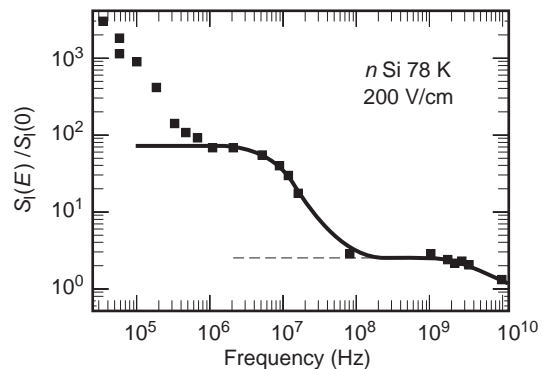


Figure 6. Experimental results on spectral density of longitudinal current fluctuations in n-type Si (squares [24]) in the frequency range from 1 MHz to 10 GHz can be described by two Lorentz-type contributions (curves) with the time constants $\tau_R = 20$ ns and $\tau_v = 50$ ps. $S_I \parallel \mathbf{E} \parallel \langle 100 \rangle$, $T_0 = 78$ K, $n = 3 \times 10^{13}$ cm $^{-3}$, $E = 200$ V/cm.

plateaus of the excess noise are resolved in the frequency range below 10 GHz. The fluctuations of electron number in the conduction band dominate at frequencies below 50 MHz, while the hot-electron fluctuations prevail at microwave frequencies. The solid curve is the fitted approximation, assuming 20 ns and 50 ps time constants for two Lorentz-type contributions [see Eq. (15)]. The hot-electron contribution (dashed curve) dominates in the frequency range $\omega\tau_R \gg 1$, where $\tau_R = 20$ ns is the time constant of the generation-recombination process.

4.2.2. Intervalley Noise, Comparison to Monte Carlo Data. Important information on the origin of hot-electron fluctuations in n-type Si at $\omega\tau_R \gg 1$ (Fig. 6) follows from comparison [44] of the longitudinal fluctuations measured in two directions of applied electric fields, $\mathbf{E} \parallel \langle 100 \rangle$ and $\mathbf{E} \parallel \langle 111 \rangle$ (see the open and closed circles in Fig. 7). Due to the conduction band structure of silicon, all valleys are oriented at the same angle to the electric field when the latter is applied along the $\langle 111 \rangle$ axis. Consequently, there is no intervalley noise in this configuration, but the intervalley noise is activated when the valleys are made nonequivalent, for example, for $\mathbf{E} \parallel \langle 100 \rangle$ [see Eq. (26)].

The results of Monte Carlo simulation of longitudinal velocity fluctuations [49] (Fig. 7, solid lines) give a satisfactory description of the experimental data (Fig. 7, symbols). In the configuration $\mathbf{E} \parallel \langle 111 \rangle$ (curve 3 of Fig. 7), corresponding to no intervalley noise, the convective noise leads to a negative contribution due to energy fluctuations at frequencies below $\omega \sim 1/\tau_e$ (11,12) [see Eq. (25)]. The results of Monte Carlo simulation allow one to estimate the energy relaxation time constant for this configuration: $\tau_e \approx 15$ ps at $E = 200$ V/cm, $T_0 = 78$ K (curve 3 in Fig. 7).

There is a competition of the convective and intervalley noise in the configuration $\mathbf{E} \parallel \langle 100 \rangle$. For the energy relaxation time constant in this configuration at $E = 200$ V/cm, $T_0 = 78$ K, one obtains $\tau_e \approx 5$ ps. The energy relaxation time constant appears to be shorter than the intervalley time constant $\tau_i \approx 50$ ps, and the local minimum is resolved at

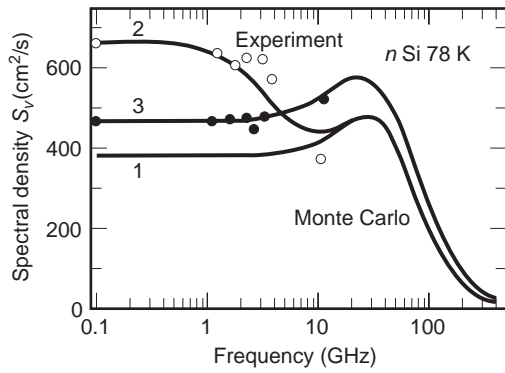


Figure 7. Experimental and simulated spectra of longitudinal velocity fluctuations of hot electrons in n-type Si at $T_0 = 78$ K, $E = 200$ V/cm [44] to illustrate the intervalley noise observed at frequencies below 10 GHz for the field \mathbf{E} applied along (100) axis, and the negative-convective-type contribution prevailing at frequencies below 20 GHz for $\mathbf{E} \parallel (111)$. Experimental results: $\mathbf{E} \parallel (100)$ (open circles), $\mathbf{E} \parallel (111)$ (closed circles). Results of Monte Carlo simulation 1— $\mathbf{E} \parallel (100)$, intervalley transitions neglected; 2— $\mathbf{E} \parallel (100)$, intervalley transitions included; 3— $\mathbf{E} \parallel (111)$ the intervalley transitions are included, but they do not contribute because $\bar{v}_1 = \bar{v}_2$; see Eq. (26).

frequencies $\tau_i^{-1} < \omega = 2\pi f < \tau_v^{-1}$, as evidenced by the Monte Carlo simulation data (curve 2 in Fig. 7).

As discussed in relation to Fig. 3, the energy relaxation time constant decreases as the electric field increases. The experimental data and the results of Monte Carlo simulation show [18] that the intervalley time constant τ_i in n-type Si becomes shorter at a higher electric field as well.

4.2.3. Hot-Carrier Effect on Generation-Recombination Noise. The Lorentz-type step at $\omega \sim \tau_R^{-1}$ due to generation–recombination fluctuations shifts toward higher frequencies at higher electric fields, as shown experimentally for p-type silicon at 77 K (see Ref. 25). This behavior is caused by the hot-hole effect on generation–recombination

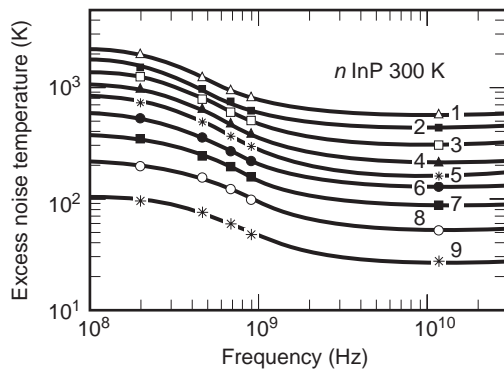


Figure 8. Lorentz-type contributions due to generation–recombination noise (curves) are important at $f < 1$ GHz and are not important at 10 GHz frequency, where the longitudinal excess noise temperature $(T_n)_{\parallel} - T_0$ results from hot electrons noise. Experimental data on lightly doped n-type InP ($n = 2.7 \times 10^{15} \text{ cm}^{-3}$) at $T_0 = 300$ K (29) (symbols): 1—10 kV/cm, 2—9 kV/cm, 3—8 kV/cm, 4—7 kV/cm, 5—6 kV/cm, 6—5 kV/cm, 7—4 kV/cm, 8—3 kV/cm, 9—2 kV/cm.

noise. Indeed, hole trapping and release probabilities (entering the time constant of the generation–recombination process) depend on the electric field and the hot-hole energy, in particular. For spectral analysis of the noise in p-type silicon, including hot-hole velocity fluctuations and the hot-hole effect on generation–recombination fluctuations, see review papers [25,34].

4.2.4. High Electric Fields. The hot-electron noise spectra at moderate fields in the frequency range down to 50 kHz (see Fig. 6) were obtained using long pulses of voltage. However, at high electric fields, the short-time-domain pulsed technique must be used in order to avoid lattice heating. This technique puts the limit on the frequency range $f \gg 1/\Delta t$, where Δt is the voltage pulse duration. As a result, the experimental noise spectra over the wide range of electric fields are available at high frequencies, usually exceeding 100 MHz [25,29,50].

The experimental results on frequency-dependent longitudinal noise temperature in n-type InP (29) (Fig. 8, symbols) can be interpreted in terms of sources of noise caused by generation–recombination and velocity fluctuations (Fig. 8, solid lines). At X-band microwave frequencies, where the contribution of generation–recombination noise is negligible, the kinetic processes inside the conduction band of InP contribute to the longitudinal noise. Again, 10 GHz frequency proves to be convenient to investigate details of hot-electron noise, its dependence on electric field, sample length, lattice temperature, and semiconductor parameters.

4.3. Intervalley Noise in n-Type GaAs and InP

4.3.1. Dependence on Intervalley Separation Energy. As is well known, the intervalley separation energy in InP is wider as compared with that of GaAs. Therefore, higher electric fields are required for hot-electron intervalley transfer, and the resultant noise to appear in InP [24,25]. The intervalley noise dominates at electric fields over 2 kV/cm in GaAs and over 6 kV/cm in InP (Fig. 9), which are below the threshold field for negative

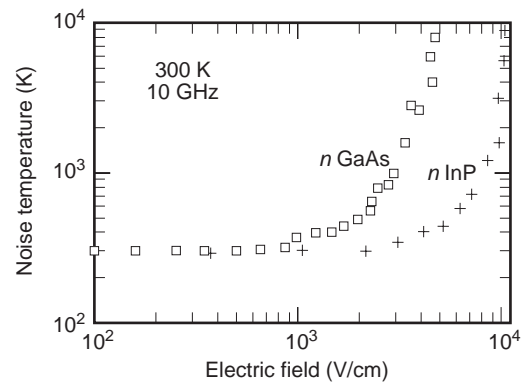


Figure 9. A higher intervalley separation energy causes the intervalley noise to appear at higher fields [24], as illustrated by experimental results on longitudinal noise temperature for n-type GaAs [squares, $\mu_0 = 7500 \text{ cm}^2/(\text{V} \cdot \text{s})$, $n = 0.9 \times 10^{15} \text{ cm}^{-3}$] and n-type InP [crosses, $\mu_0 = 4600 \text{ cm}^2/(\text{V} \cdot \text{s})$, $n = 3.2 \times 10^{15} \text{ cm}^{-3}$].

differential mobility due to the intervalley transfer, respectively, around 3.5 kV/cm and 12 kV/cm at 300 K. This is a good illustration that even a small number of high-energy electrons (available, e.g., at $E \sim 6$ kV/cm in InP) is essential for hot-electron noise.

4.3.2. Intervalley Coupling Constants. The intervalley contribution to the spectral density of velocity fluctuations is inversely proportional to the squared intervalley coupling constant [see Eq. (26) and the text following it]. This important parameter of hot-electron intervalley transfer can be estimated by comparing the experimental results with those obtained by model calculations. Monte Carlo simulation [31,51] predicted the intervalley-related maximum of the spectral density of longitudinal velocity fluctuations in n-type InP, to appear at around 8 kV/cm fields. Figure 10 compares the results of simulation with the experimental ones. The experimental results obtained on long samples (crosses 1 in Fig. 10; see Ref. 24) are in a reasonable agreement with those of simulation when the coupling constant 1.10^9 eV/cm is assumed (Fig. 10, solid line, [51]). A lower value of the coupling constant would be responsible for a longer intervalley time constant and the higher values of the intervalley contribution to $S_v(E)$ [see Eq. (26)], as illustrated by dashed curve 6 in Fig. 10.

The spectral density of intervalley fluctuations in lightly doped n-type GaAs [28] is essentially higher as compared with InP. This comparison suggests a low value of the intervalley coupling constant. The problem was considered in the framework of a three-valley (Γ -L-X) model, and a rather low Γ -L coupling constant, 1.8×10^8 eV/cm [52], was proposed. The model predicted a strong frequency dependence of S_v at around 10 GHz, which was not confirmed by the experimental data [50], and an intermediate value of

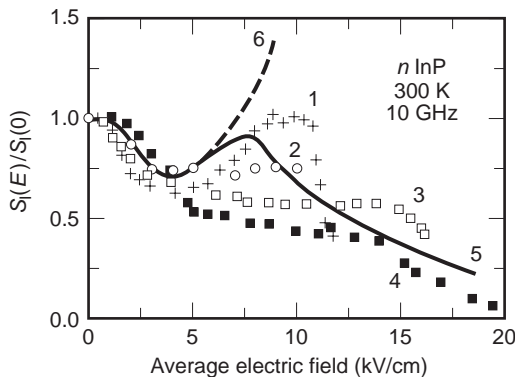


Figure 10. Normalized longitudinal spectral density of current fluctuations depends on sample length in the field range where the intervalley noise dominates in n-type InP. The experimental data on long samples (symbols 1) compared with the results of Monte Carlo simulation (curves 5 and 6) provide an estimate of the intervalley coupling constant. Experimental results for samples of different length L (symbols): 1— $L=10 \mu\text{m}$, $n=3.2 \times 10^{15} \text{ cm}^{-3}$, $\mu_0=4600 \text{ cm}^2/(\text{V}\cdot\text{s})$ [24], 2— $L=5 \mu\text{m}$, $n=2.7 \times 10^{15} \text{ cm}^{-3}$, $\mu_0=4500 \text{ cm}^2/(\text{V}\cdot\text{s})$ [28] 3— $L=5 \mu\text{m}$, $n=2.3 \times 10^{15} \text{ cm}^{-3}$, $\mu_0=4600 \text{ cm}^2/(\text{V}\cdot\text{s})$ [24], 4— $L=1.7 \mu\text{m}$, $n=5.4 \times 10^{15} \text{ cm}^{-3}$, $\mu_0=4500 \text{ cm}^2/(\text{V}\cdot\text{s})$ [23]. Results of Monte Carlo simulation for long samples [46] assuming different intervalley coupling constant (curves): 5— 1×10^9 eV/cm; 6— 3×10^8 eV/cm.

the Γ -L coupling constant, 3×10^8 eV/cm, was assumed to avoid contradictions of the three-valley model with the experimental data (see Ref. 24 and references cited therein).

4.3.3. Intervalley Noise Due to L and X Valleys in GaAs. Sources of hot-electron noise with threshold energies corresponding to the L and X valleys in n-type GaAs are resolved using nanosecond pulses of voltage applied to short channels. Figure 11 shows the excess noise temperature $\Delta T_n = T_n - T_0$, plotted as a function of voltage V at $T_0 = 293$ K ambient temperature [30]. As the channel length is $0.2 \mu\text{m}$, the average fields up to 300 kV/cm are reached in standard-doped GaAs channels ($3 \times 10^{17} \text{ cm}^{-3}$). The steep increase in current accompanies the increase in noise temperature at the highest fields—an experimental evidence for the impact ionization noise of hot electrons resolved in a conduction channel.

The $\Delta T_n(V)$ dependence can be decomposed into four sources of hot-electron noise; thin lines in Fig. 11 indicate possible contributions of each source. The lowest threshold appears at around 0.2 V; it results from the resonant scattering of hot electrons by the impurity levels located inside the conduction band [53] (see also Ref. 54). The thresholds at 0.3 and 0.5 V result from scattering of almost ballistically accelerated electrons into the L and X valleys of the conduction band (the L and X valley energies are close to 0.3 eV and 0.5 eV, respectively). The extrapolation of the experimental data on $\Delta T_n(V)$ obtained at the highest average fields yields the threshold energy for the impact ionization noise; the threshold energy, as expected, exceeds the forbidden gap.

The quasisaturation of hot-electron noise temperature takes place at the average electric fields, ranging from 50 to 200 kV/cm. This very specific noise behavior has been used to estimate the time constant for the Γ -X transfer experienced by the high-energy electrons present in the Γ valley at the energy $\varepsilon > \varepsilon_X \approx 0.5$ eV: $30 \text{ fs} < \tau_{\Gamma X} < 60 \text{ fs}$ [30]. This estimate, based on the hot-electron noise data, provides an independent confirmation of the results available from femto-second and cw luminescence data.

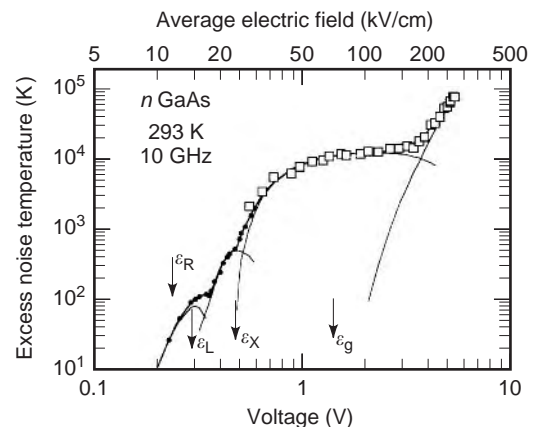


Figure 11. Four sources of hot-electron noise (activated at different threshold energies) are resolved in n-type GaAs channel of submicrometer length ($n=3 \times 10^{17} \text{ cm}^{-3}$, $L=0.2 \mu\text{m}$) at $T_0=293$ K [30]. Voltage pulse duration; $2 \mu\text{s}$ (dots), 100 ns (squares). Solid curve stands for the sum of the contributions given by the thin curves.

4.4. Suppression of Hot-Electron Noise In Short Samples

Time and space are needed for the complete development of fluctuations, and hot-electron noise depends on sample dimensions. Indeed, a hot electron spends limited time in a short sample and cannot acquire the energy accessible in a longer sample. Since the tail of the autocorrelation function [see Eq. (3)] is cut off, Eq. (4) leads to lower values of the spectral density. Hence, sources of noise caused by relatively slow kinetic processes and/or appearing at high threshold energies are suppressed in short samples. In other words, threshold-type sources of noise appear at higher electric fields in short samples.

4.4.1. Suppression of Intervalley Noise. Figure 12 illustrates the length-dependent behavior of hot-electron noise in lightly doped n-type GaAs [40]. There is no dependence of the noise temperature T_n on sample length L in long samples (symbols 1 and 2 of Fig. 12). However, the same noise temperature requires essentially higher electric fields in short samples (see symbols 2 and 3, 4 in Fig. 12). For a fixed average electric field, say, $V/L = 3$ kV/cm, the noise suppression exceeds 10 dB as the sample length L is reduced from 7.5 μm (symbols 2) to 1.5 μm (symbols 3).

A detailed interpretation of suppression is reached by comparing the experimental results with those obtained by Monte Carlo simulation. Figure 13 presents the spectral density of current fluctuations $S_I(E)$ normalized to its value at zero bias $S_I(0)$. The experimental data for n-type GaAs are presented by open symbols from 1 to 4. As noted earlier, the main source of current fluctuations in long samples at fields over 2 kV/cm results from hot-electron intervalley transfer. This source of fluctuations is heavily suppressed in a 1 μm sample (Fig. 13, points 4): the monotonously increasing dependence on electric field changes into a monotonously decreasing one, typical for one-valley semiconductors. Closed symbols in Fig. 13

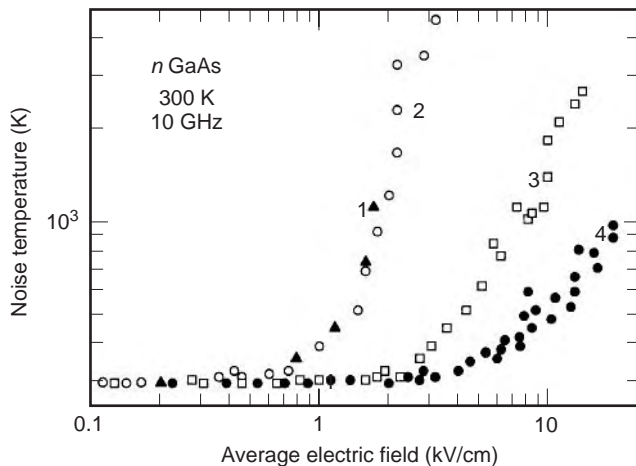


Figure 12. Suppression of the intervalley noise in short samples as illustrated by experimental results on longitudinal noise temperature of hot electrons in n-type GaAs at room temperature [28,40]. Samples length and other data: 1— $L = 1000 \mu\text{m}$, $\mu_0 = 6000 \text{ cm}^2/(\text{V}\cdot\text{s})$, 2— $L = 7.5 \mu\text{m}$, $n = 10^{15} \text{ cm}^{-3}$, $\mu_0 = 7500 \text{ cm}^2/(\text{V}\cdot\text{s})$, 3— $L = 1.5 \mu\text{m}$, $n = 10^{15} \text{ cm}^{-3}$, $\mu_0 = 7500 \text{ cm}^2/(\text{V}\cdot\text{s})$, 4— $L = 1 \mu\text{m}$, $n = 10^{15} \text{ cm}^{-3}$, $\mu_0 = 7500 \text{ cm}^2/(\text{V}\cdot\text{s})$.

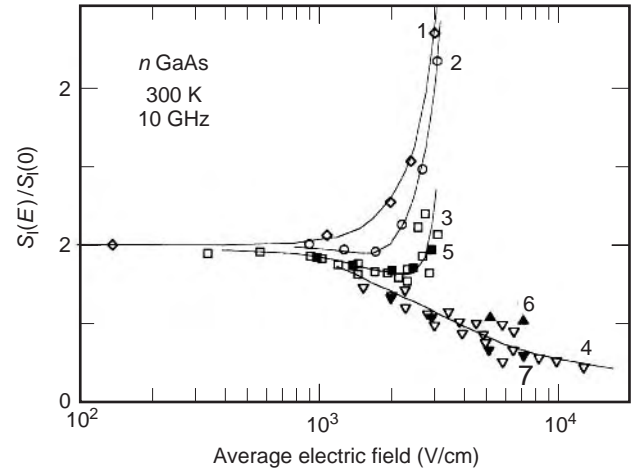


Figure 13. Transition from the monotonously increasing (diamonds 1) to the monotonously decreasing (open triangles 4) dependence on electric field of the normalized longitudinal spectral density of current fluctuations, illustrating suppression of the intervalley fluctuations in short (micrometer) samples. Experimental results correspond to lightly doped n-type GaAs (open symbols, curves are to guide the eye): 1— $L = 1000 \mu\text{m}$, $\mu_0 = 6000 \text{ cm}^2/(\text{V}\cdot\text{s})$, (28); 2— $L = 11 \mu\text{m}$, $\mu_0 = 5200 \text{ cm}^2/(\text{V}\cdot\text{s})$ [45]; 3— $L = 7.5 \mu\text{m}$, $\mu_0 = 7500 \text{ cm}^2/(\text{V}\cdot\text{s})$ [37], 4— $L = 1 \mu\text{m}$, $\mu_0 = 7500 \text{ cm}^2/(\text{V}\cdot\text{s})$ [37]. Monte Carlo simulation data (closed symbols) correspond to different values of sample length and Γ - L intervalley coupling constant [50]: 5— $L = 7.5 \mu\text{m}$, $1.8 \times 10^8 \text{ eV/cm}$, 6— $L = 1 \mu\text{m}$, $1.8 \times 10^8 \text{ eV/cm}$, 7— $L = 1 \mu\text{m}$, $1 \times 10^9 \text{ eV/cm}$.

correspond to Monte Carlo simulation of hot-electron fluctuations [55] (nonuniformity of the electric field and space charge fluctuations are taken into account). There is a reasonable agreement between the results of experiment and simulation.

In a similar way, the hot-electron intervalley fluctuations observed in long samples of n-type InP at fields over 6 kV/cm are suppressed in short samples (Fig. 10). Indeed, the maximum of spectral density in 10 μm samples (Fig. 10, crosses 1) diminishes and disappears as the sample length L is reduced down to 1.7 μm (symbols 4).

4.4.2. Critical Length for Noise Suppression. Under steady flow of current, hot electrons are constantly leaving the sample, and equilibrium electrons are entering at the cathode. This “exchange” opens an additional (external) energy loss mechanism by the hot electrons present in the sample. The external loss is negligible, as compared with the internal loss in long samples, but its relative weight increases when the sample length L is reduced. At a certain critical length the external loss assumes primary importance. It is evident that the critical length is shorter, provided the internal loss is greater.

Figure 14 compares the hot-electron noise temperature at a fixed average electric field, $V/L = 4$ kV/cm, for GaAs samples of different length and doping [53]. The results can be interpreted in terms of the critical lengths required for the electrons to gain the threshold energy of the dominant source of noise. The curves in Fig. 14 assume two critical lengths used as fitting parameters: L_1 stands for the lucky

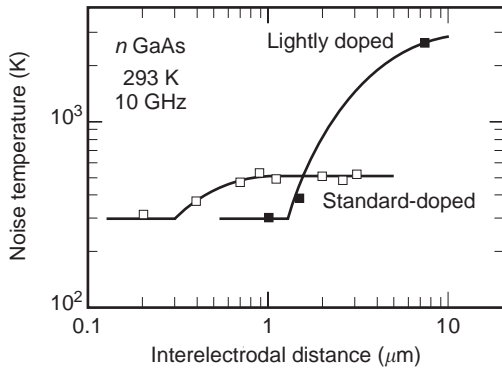


Figure 14. Suppression of hot-electron noise in short channels; essentially shorter lengths are needed for the suppression in the standard-doped n-type GaAs, as compared with the lightly doped samples, provided the same average electric field $V/L = 4 \text{ kV/cm}$ is applied [53]. Open squares— $n = 3 \times 10^{17} \text{ cm}^{-3}$, $\mu_0 = 4000 \text{ cm}^2/(\text{V} \cdot \text{s})$, closed squares— $n = 3 \times 10^{15} \text{ cm}^{-3}$, $\mu_0 = 7500 \text{ cm}^2/(\text{V} \cdot \text{s})$; solid curves are fitted approximations based on concepts of ballistic and dissipative critical lengths.

electrons, which do not undergo scattering events before they reach the threshold energy, and L_2 takes into account energy loss during electron acceleration to the same threshold energy. The curves correspond to $L_1 = 1.3 \mu\text{m}$, $L_2 = 3 \mu\text{m}$ for lightly doped (curve 1, Fig. 14) and to $L_1 = 0.3 \mu\text{m}$, $L_2 = 0.2 \mu\text{m}$ for standard-doped GaAs (curve 2). The critical lengths are shorter and the threshold energies are lower in the standard-doped GaAs channels.

4.5. Transition from Shot Noise to Hot-Electron Noise

So far uniformly doped samples with ohmic electrodes have been considered. These conditions favoring hot-electron noise rather than shot noise. However, most electronic devices contain barriers formed by nonuniform doping, surface charges, and heterojunctions. According to the Schottky formula [5] the spectral density of longitudinal current fluctuations due to shot noise increases proportionally to the constant current, while the corresponding dependence is steeper for hot electrons. In a diode, the shot noise prevails at low currents, but a transition to hot-electron noise can occur at high currents, unless the thermal breakdown takes place before the critical current is reached. The thermal breakdown has been avoided and the transition in question is observed in GaAs Schottky and planar-doped barrier diodes at high forward currents, by using short-time-domain radiometry of the noise power [56].

Figure 15 presents the spectral density of current fluctuations, S_I , measured [56] at 10 GHz frequency for the forward-biased GaAs Schottky diode and planar-doped barrier diode (PDBD). The measured spectral density is almost proportional to the current at very low current levels (Fig. 15), when the barrier controls the current and the shot noise dominates. The experimental points are close to the solid line (Fig. 15) standing for the Schottky formula $S_I = 2eI$. The sublinear dependence of $S_I(I)$ indicates onset of the screening effect of space charge of drift electrons. Eventually, at high currents, the sublinear

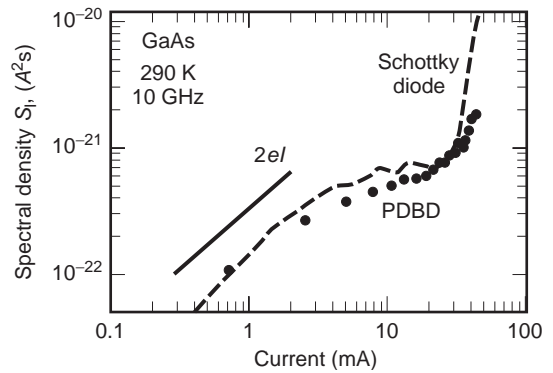


Figure 15. Spectral density of longitudinal current fluctuations of GaAs diodes demonstrates transition from shot noise to hot-electron noise at high forward currents [56]. Schottky diode (dashed line) and planar-doped barrier diode (PDBD, closed circles). Solid line is the Schottky formula for shot noise, $S_I = 2eI$.

dependence becomes superlinear. This change of the dominant source of fluctuations is accompanied by an onset of a different electron transport mechanism: the barrier diminishes and fails to control the current flow. These results give experimental evidence for transition to hot-electron-dominated noise in GaAs Schottky and planar-doped barrier diodes.

4.6. Noise in 2DEG Channels

Modern heterostructure growth technology provides a great variety of AlGaAs/GaAs, InAlAs/InGaAs, and InP/InGaAs channels for lattice-matched and pseudomorphic high-electron-mobility transistors (HEMT and PHEMT), containing two-dimensional electron gas (2DEG) confined in the quantum well (QW). High mobility of confined electrons is advantageous for fast operation of 2DEG channels. However, electron heating by an electric field applied along the channel is accompanied by enhanced chaotic motion of hot electrons in the plane of electron confinement, occupation of upper subbands, hot-electron deconfinement (real-space transfer) and other kinetic processes specific to a hot two-dimensional electron gas. The associated longitudinal fluctuations appear in QW channels [see Ref. 44]. Hot-electron velocity fluctuations due to real-space transfer have been resolved first in selectively doped AlGaAs/GaAs channels [40]. The experimental results are in reasonable agreement with the results of Monte Carlo simulation [57]. Moreover, the threshold field for this noise source increases as the heterobarrier height increases [58,59]. This supports the idea of transverse real-space transfer being responsible, among other factors, for the longitudinal fluctuations of current. A special case of real-space transfer is transverse tunneling of hot electrons across a thin barrier of AlAs, separating the 2DEG channel and the ionized donors in AlGaAs/GaAs/AlAs/GaAs structure. The associated longitudinal fluctuations are heavily suppressed in short channels [60]. The intersubband noise appears in δ -doped GaAs channels, where the upper subbands support higher electron mobilities as compared with more confined electronic states of the lower subbands. Dependence of hot-electron noise on the

quantum-well shape [61] is important in quasitriangular and quasirectangular quantum wells in InAlAs/InGaAs/InAlAs channels. These heterostructures can be heavily doped, in order to obtain high-density 2DEG useful for high-power applications. Heavy doping of the structures is accompanied by the excess fluctuations [62] absent in the low-density 2DEG.

4.6.1. Real-Space Transfer Noise. Figure 16 compares [59] the spectral density of longitudinal current fluctuations in GaAs samples and AlGaAs/GaAs single-heterojunction 2DEG channels. The local maximum of the spectral density appears (Fig. 16, squares and circles) at the intermediate fields $100 \text{ V/cm} < E < 2 \text{ kV/cm}$, which are low, as compared with the intervalley transfer field in GaAs. The height and position of the maximum depend on the Al mole ratio in the selectively doped AlGaAs layer: the source of fluctuations in question appears at a higher field (circles 2 in Fig. 16), when the hetero-barrier is higher. This is strong experimental evidence for hot-electron jumps from the QW into the AlGaAs layer and backward. The experimental data also show that this real-space transfer suppresses the intervalley fluctuations of hot electrons dominating in GaAs at fields over 2 kV/cm (see symbols and solid line in Fig. 16). The shape of the maximum is similar to that obtained by Monte Carlo simulation of the real-space transfer fluctuations [57], as illustrated by Fig. 17.

Interpret the maximum observed at 1 kV/cm field (Fig. 17, circles) in terms of Eq. (26). Since electron mobility is high in the quantum well channel and low in the adjacent doped layer of AlGaAs, the electron drift velocities \bar{v}_1 and \bar{v}_2 differ. The increase in electric field causes the monotonous decrease of electron density in the QW (the ratio \bar{n}_1/\bar{n}_2 decreases), and the maximum of spectral density forms at around $\bar{n}_1 \approx \bar{n}_2$ [see Eq. (26)]. Under assumption that $\bar{v}_1 - \bar{v}_2 \sim 10^7 \text{ cm/s}$ and $\bar{n}_1 \approx \bar{n}_2$, the real-space trans-

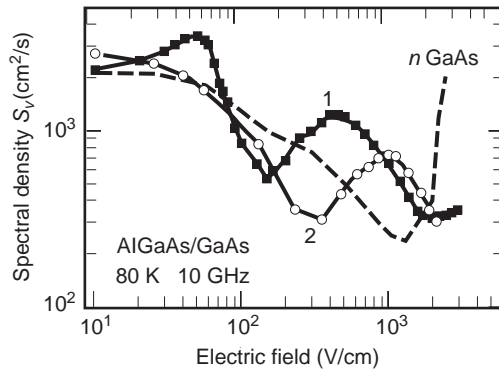


Figure 16. Spectral density of longitudinal velocity fluctuations in AlGaAs/GaAs quantum-well channels gives an experimental evidence for sources of fluctuations specific to two-dimensional electron gas (symbols) absent in GaAs samples (dashed curve) [58]. Al mole ratio in the spacer: 1–25% Al, $n = 6 \times 10^{11} \text{ cm}^{-2}$, $\mu_0 = 75,000 \text{ cm}^2/(\text{V}\cdot\text{s})$, 2–33% Al, $n = 2 \times 10^{11} \text{ cm}^{-2}$, $\mu_0 = 103,000 \text{ cm}^2/(\text{V}\cdot\text{s})$. Dashed line is for n-type GaAs [$n = 9 \times 10^{14} \text{ cm}^{-3}$, $\mu_0 = 77,000 \text{ cm}^2/(\text{V}\cdot\text{s})$]. Solid curves are guides to the eye.

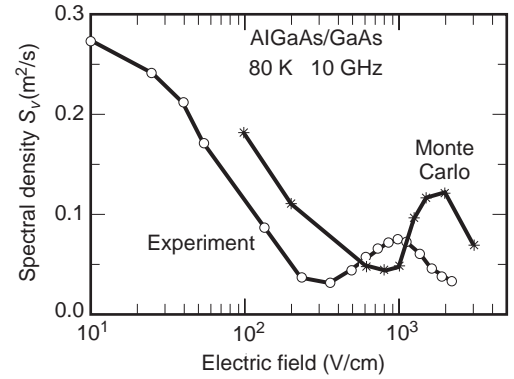


Figure 17. Real-space transfer in AlGaAs/GaAs channel causes the maximum of spectral density of longitudinal velocity fluctuations appearing at electric fields well below those for the intervalley transfer. Open circles stand for the experimental results [59]: AlGaAs/GaAs, 33% Al, $n = 2 \times 10^{11} \text{ cm}^{-2}$, $\mu_0 = 103,000 \text{ cm}^2/(\text{V}\cdot\text{s})$, $T_0 = 80 \text{ K}$. Stars stand for the results of Monte Carlo simulation for a simplified model of a quantum well channel [52]. Solid lines are guides to the eye.

fer time constant is estimated from the maximum value of the spectral density: $\tau \sim 5 \text{ ps}$ [59]. The time constant obtained is short; this enables observation of the real-space transfer at 10 GHz frequency and supports the idea of reversible real-space transfer.

4.6.2. Longitudinal Fluctuations Due to Transverse Tunneling. A triple-heterojunction AlGaAs/ δ -GaAs/AlAs/GaAs structure has been designed [60] to separate the 2DEG channel from the doped layer by the thin layer of AlAs. Strong excess noise appears [60] at electric fields well below those for the intervalley transfer (Fig. 18, symbols). The barrier of AlAs is high and thin; therefore, electron jumps over the barrier are excluded, but the high-energy electrons can penetrate it by tunneling. It has been concluded [60] that transverse tunneling is responsible for the steep increase in the longitudinal hot-electron noise

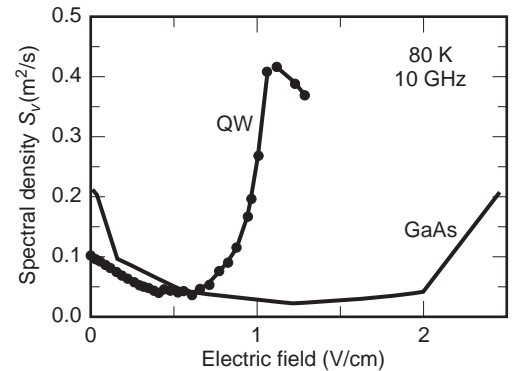


Figure 18. Contribution of transverse tunneling through a thin barrier of AlAs to the spectral density of hot-electron longitudinal velocity fluctuations, appearing in AlGaAs/ δ -GaAs/AlAs/GaAs quantum-well (QW) channel at electric fields well below those for the intervalley transfer [60]. Experimental data for the QW channel [closed circles, $n = 1.3 \times 10^{12} \text{ cm}^{-2}$, $\mu_0 = 35,000 \text{ cm}^2/(\text{V}\cdot\text{s})$, $T_0 = 80 \text{ K}$] are compared with those for bulk n-type GaAs (see Fig. 16).

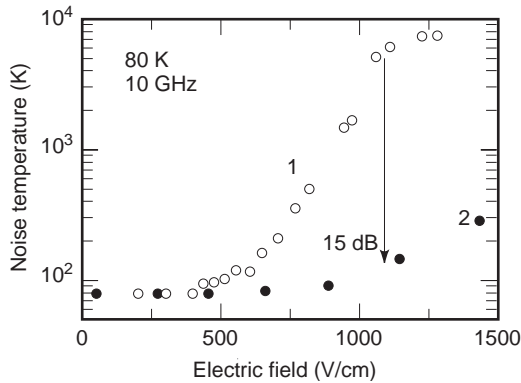


Figure 19. Experimental evidence for suppression (up to 15 dB at 1.1 kV/cm) of the longitudinal noise due to transverse tunneling of hot electrons in short AlGaAs/ δ -GaAs/AlAs/GaAs QW channels at 80 K [60]. Channel length: 1–18 μm , 2–3 μm . For the Hall effect data, see Fig. 18.

temperature (Fig. 19, open circles) and the maximum of spectral density of longitudinal velocity fluctuations (Fig. 18, closed circles) resolved at a field around 1 kV/cm at 80 K lattice temperature. In the framework of Eq. (26) under assumption $\bar{v}_1 - \bar{v}_2 \sim 2 \cdot 10^7$ cm/s, the time constant for the transverse tunneling is estimated to be $\tau \sim 10$ ps [60].

The transverse-tunneling-related noise source observed in a 18 μm channel at a 1 kV/cm field (open circles 1 in Fig. 19) is very weak in the 3- μm channel (closed circles 2). This strong dependence on channel length, being an illustration of suppression of hot-electron noise in short channels, suggests a way for an independent estimate of the transverse tunneling time constant using the electron transit time. The values for tunneling time constant estimated from these two independent experiments are in reasonably good agreement [60]. Similar results on the tunneling-time constant are available from luminescence data for resonant tunneling, while the nonresonant tunneling time constants are essentially longer.

5. SUMMARY

Hot-carrier noise in semiconductors, which is a special case of nonequilibrium noise, does not obey the fluctuation-dissipation theorem and other relations valid for electron gas at thermal equilibrium. Characteristics of hot-electron noise cannot be predicted from data on electron density and mobility measured at low electric fields; the noise spectra at high electric fields display features resulting from subtle details of semiconductor band structure and scattering mechanisms. Experimental investigation of these features at microwave frequencies, together with Monte Carlo simulation, provide the possibility to determine parameters (time constants, coupling constants, etc.) of fast kinetic processes in the conduction (or valence) band of a semiconductor subjected to a high electric field. Suppression of hot-electron noise, favoring low-noise operation of short channels at microwave frequencies, is shown experimentally and through Monte Carlo

simulation. A great variety of diverse sources of noise being resolved in low-dimensional channels demonstrates diagnostic possibilities of short-time-domain radiometry of hot-electron noise and high potentials of nanometric technology for development of high-speed, low-noise devices for electronics.

BIBLIOGRAPHY

1. H. Nyquist, Thermal agitation of electric charge in conductors, *Phys. Rev.* **32**(1):110–113 (1928).
2. H. B. Callen and T. A. Welton, Irreversibility and generalized noise, *Phys. Rev.* **83**(1):34–40 (1951).
3. A. van der Ziel, *Noise in Solid State Devices and Circuits*, Wiley, New York, 1986.
4. Sh. Kogan, *Electronic Noise and Fluctuations in Solids*, Cambridge Univ. Press, Cambridge, UK, 1996.
5. N. B. Lukyanchikova, *Noise Research in Semiconductor Physics*, in B. K. Jones, ed., Gordon & Breach Science Publishers, Amsterdam, 1997.
6. W. Schottky, Über spontane Stromschwankungen in verschiedenen Elektrizitätsleitern, *Ann. Phys.* **57**:541(1918).
7. E. M. Lifshitz and L. P. Pitaevski, *Physical Kinetics*, Pergamon, Oxford, UK, 1981.
8. M. Lax, Fluctuations from the nonequilibrium steady state *Rev. Mod. Phys.* **32**(1):25–64 (1960).
9. P. J. Price, Intervalley noise, *J. Appl. Phys.* **31**(6):949–953 (1960).
10. V. L. Gurevich, On current fluctuations in semiconductors near nonequilibrium steady state, *Zh. Eksp. Teor. Fiz.* **43**(5):1771–1781, 1962 [*Sov. Phys. – JETP* **16**(5):1252(1963)].
11. P. J. Price, Fluctuations of hot electrons, *Fluctuation Phenomena in Solids*, R. E. Burgess, ed., Academic Press, New York, 1965, pp. 355–379.
12. V. L. Gurevich and R. Katilius, Theory of hot electrons in an anisotropic semiconductor, *Zh. Eksp. Teor. Fiz.* **49**(4):1145–1156, 1965 [*Sov. Phys. – JETP* **22**(4):796 (1965)].
13. Sh. M. Kogan and A. Ya. Shul'man, Electric fluctuations in solid-state plasma at high electric fields, *Fiz. Tverd. Tela.* **9**(8):2259–2264 (1967) [*Sov. Phys. – Solid State* **9**:1771 (1968)].
14. S. V. Gantsevich, V. L. Gurevich, and R. Katilius, Current fluctuations in a semiconductor in high electric field, *Fiz. Tverd. Tela.* **11**(2):308–315 (1969) [*Sov. Phys. – Solid State* **11**(2):247, (1969)].
15. S. V. Gantsevich, V. L. Gurevich, and R. Katilius, Fluctuations in semiconductor in strong electric field and light scattering from hot electrons, *Zh. Eksp. Teor. Fiz.* **57**(2):503–519 (1969) [*Sov. Phys. – JETP* **30**(2):276 (1970)].
16. Sh. M. Kogan and A. Ya. Shul'man, Theory of fluctuations in nonequilibrium electron gas, *Zh. Eksp. Teor. Fiz.* **56**(3):862–876 (1969) [*Sov. Phys. – JETP* **29**(3):467 (1969)].
17. S. V. Gantsevich, V. L. Gurevich, and R. Katilius, Theory of fluctuations in nonequilibrium electron gas, *Rivista del Nuovo Cimento* **2**(5):1–87 (1979).
18. V. Bareikis et al., Fluctuation spectroscopy of hot electrons in semiconductors, in C. V. Shank and B. P. Zakharchenya, eds., *Spectroscopy of Nonequilibrium Electrons and Phonons*, Elsevier, Amsterdam, 1992, pp. 327–396.
19. E. Erlbach and J. B. Gunn, Noise temperature of hot electrons in germanium, *Phys. Rev. Lett.* **8**(7):280–282 (1962).

20. C. A. Bryant, Noise temperature of hot electrons in gallium-arsenide, *Bull. Am. Phys. Soc.* **9**(1):62 (1964).
21. V. Bareikis, I. Vaitkevičiūtė, and J. Požela, Fluctuations of hot current carriers in germanium, *Liet. Fiz. Rink.* **6**(3):437–440 (1966).
22. V. Bareikis, J. Pozhela, and I. Matulionienė, Noise and diffusion of hot carriers in p-Ge, *Proc. 9th Int. Conf. Physics Semiconductors* (S. M. Ryvkin, ed.), Nauka, Leningrad, 1968, pp. 760–765.
23. L. Huxley and R. Crompton, *The Diffusion and Drift of Electrons in Gases*, Wiley, New York, 1974.
24. V. Bareikis et al., Experiments on hot electron noise in semiconductor materials for high-speed devices, *IEEE Trans. Electron. Devices* **41**:2050–2060 (1994).
25. J. P. Nougier, Fluctuations and noise of hot carriers in semiconductor materials and devices, *IEEE Trans. Electron. Devices* **41**:2034–2049 (1994).
26. V. Bareikis et al., Noise and diffusivity of hot electrons in n-type InSb, *J. Physique* **4**(10)(Col. C7, Suppl.):215–220 (1981).
27. L. G. Hart, High field current fluctuations in n-type germanium, *Can. J. Phys.* **48**(5):531–542 (1970).
28. V. Bareikis et al., Microwave noise and the coupling constant for Γ and L valleys in the three-valley model of GaAs, *Fiz. Techn. Polupr.* **14**(7):1427–1429 (1980) [*Sov. Phys. Semiconduct.* **14**:847 (1980)].
29. D. Gasquet, M. Fadel, and J. P. Nougier, Noise of hot electrons in indium phosphide, *Proc. 7th Int. Conf. Noise Physical Systems and 1/f Fluctuations*, (M. Savelli, G. Lecoy, and J. P. Nougier, eds.), North Holland, Amsterdam, 1983, pp. 169–171.
30. V. Aninkevičius et al., Γ -X intervalley-scattering time constant for GaAs estimated from hot-electron noise spectroscopy data, *Phys. Rev. B* **53**(11):6893–6895 (1996).
31. G. Hill, P. N. Robson, and W. Fawcett, Diffusion and the power density fluctuations for electrons in InP by Monte-Carlo methods, *J. Appl. Phys.* **50**(1):356–360 (1979).
32. V. Bareikis et al., Calculation of noise in p-type Ge in a high electric field by the Monte-Carlo method, *Fiz. Techn. Polupr.* **13**(6):1123–1126 (1979) [*Sov. Phys.-Semiconduct.* **13**:658 (1979)].
33. C. Jacoboni and P. Lugli, *The Monte Carlo Method for Semiconductor Device Simulation*, Springer-Verlag, Vienna, 1989.
34. L. Varani and L. Reggiani, Microscopic theory of electronic noise in semiconductor unipolar structures, *Rivista del Nuovo Cimento*, **17**(Ser. 3)(7):1–110 (1994).
35. T. Kuhn et al., Monte Carlo method for the simulation of electronic noise in semiconductors, *Phys. Rev. B* **42**:5702–5713 (1990).
36. L. Reggiani et al., Modelling of small-signal response and electronic noise in semiconductor high-field transport, *Semiconduct. Sci. Technol.* **12**:141–156 (1997).
37. S. Dedulevich, Zh. Kancleris, and A. Matulis, Fluctuations and diffusion in a weakly heated electron gas, *Zh. Eksp. Teor. Fiz.* **95**(5):1701–1710 (1986) [*Sov. Phys.—JETP* **68**(5):982–987 (1989)].
38. L. Varani, Contribution of interparticles correlations to electronic noise in semiconductors, *Proc. 13th Int. Conf. Noise in Physical Systems and 1/f Fluctuations* (V. Bareikis and R. Katilius, eds.), World Scientific, Singapore, 1995, pp. 203–208.
39. A. Matulionis, R. Raguotis, and R. Katilius, Interparticle collisions and hot-electron velocity fluctuations in GaAs at 80 K, *Phys. Rev. B* **56**(4):2052–2057 (1997).
40. V. Bareikis et al., Velocity overshoot and suppression of diffusivity and microwave noise in short $n^+ - n - n^+$ structures of GaAs, in B. Källbäck and H. Beneking, eds., *High-Speed Electronics*, Springer, Berlin, 1986, pp. 28–31.
41. V. Bareikis et al., Long-range fluctuations of hot electrons in GaAs and InP at 80 K, *Proc. 10th Int. Conf. Noise Physical Systems and 1/f Fluctuations* (A. Ambrozy, ed.), Akademiai Kiado, Budapest, 1990, pp. 53–56.
42. V. Bareikis et al., Length dependent hot electron noise in doped GaAs, *Solid-State Electron.* **32**(12):1647–1650 (1989).
43. V. Aninkevičius et al., Real-space-transfer noise and diffusion in GaAs/AlGaAs heterostructure, *Proc. 11th Int. Conf. Noise Physical Systems and 1/f Fluctuations*, (T. Musha, S. Sato, and M. Yamamoto, eds.), Ohmsha, Tokyo, 1991, pp. 183–186.
44. V. Bareikis, R. Katilius, and A. Matulionis, High-frequency noise in heterostructures, *Proc. 13th Int. Conf. Noise Physical Systems and 1/f Fluctuations*, (V. Bareikis and R. Katilius, eds.), World Scientific, Singapore, 1995, pp. 14–21.
45. P. Shiktorov et al., Noise temperature of $n + nn +$ GaAs structures, *Phys. Rev. B* **54**:8821–8832 (1996).
46. C. W. Gardiner, *Quantum Noise*, Springer-Verlag, Berlin, 1991.
47. R. Šaltis, Gate Modulated Meter of Weak Pulse Signals with the Alternating Coefficient of Filing Sov. Patent 248063 (in Russian); *Bulletin Izobretenij*, **23** (1969).
48. V. A. Bareikis, A. P. Galdikas, and J. K. Požela, Noise, time of energy relaxation and diffusion of hot holes in p-germanium in the magnetic field, *Fiz. Techn. Polupr.* **11**(2):365–372 (1997) [*Sov. Phys.—Semiconduct.* **11**:210 (1977)].
49. V. Bareikis, V. Viktoravičius, and A. Galdikas, Noise dependence upon frequency in n-Si at high electric fields, *Fiz. Techn. Polupr* **16**(10):1868–1870 (1982) [*Sov. Phys.—Semiconduct.* **16**:1202 (1982)].
50. D. Gasquet et al., Diffusion noise of hot electrons in GaAs at 300 K, *Proc. Int. Conf. Noise Physical Systems and 1/f Noise* (A. d'Amico and P. Mazzetti, eds) Elsevier, Amsterdam, 1985, pp. 227–230.
51. C. Hammar and V. Vinter, Diffusion of hot electrons in indium phosphide, *Electron. Lett.* **9**(1):9–10 (1973).
52. V. Požela and A. Reklaitis, Diffusion coefficient of hot electrons in GaAs, *Solid State Commun.* **27**(11):1073–1077 (1978).
53. V. Bareikis et al., Impurity resonant scattering of hot electrons in GaAs, *Proc. 20th Int. Conf. Physics Semiconductors*, (E. M. Anastassakis and J. D. Joannopoulos, eds.), World Scientific, Singapore, 1990, pp. 2479–2482.
54. A. Matulionis et al., Microwave- and low-frequency fluctuations caused by DX-centres in GaAs and AlGaAs, *Proc. 14th Int. Conf. Noise Physical Systems and 1/f Fluctuations*, (C. Claeys and E. Simoen, eds.), World Scientific, Singapore, 1997, pp. 453–456.
55. D. Junevičius and A. Reklaitis, Monte Carlo particle investigations of noise in short $n^+ - n - n^+$ GaAs diodes, *Electron. Lett.* **24**(21):1307–1308 (1988).
56. J. Liberis et al., Microwave noise in unipolar diodes with nanometric barriers, *Proc. 14th Int. Conf. Noise Physical Systems and 1/f Fluctuations* (C. Claeys and E. Simoen, eds.), World Scientific, Singapore, 1997, pp. 67–70.
57. J. Zimmermann and Y. Wu, Diffusion coefficients of two-dimensional electron gas in heterojunctions, *Solid-State Electron.* **31**(3/4):367–370 (1988).
58. V. Aninkevičius et al., Comparative analysis of microwave noise in GaAs and AlGaAs/GaAs channels, *Solid-State Electron.* **36**(9):1339–1343 (1993).
59. V. Aninkevičius et al., Hot electron noise and diffusion in AlGaAs/GaAs, *Semiconduct. Sci. Technol.* **9**(5S):576–579 (1994).

60. V. Aninkevičius et al., Transverse tunnelling time constant estimated from hot-electron noise in GaAs-based heterostructure, *Solid State Commun.* **98**(11):991–995 (1996).
61. A. Matulionis et al., QW-shape-dependent hot-electron velocity fluctuations in InGaAs-based heterostructures, *Physica Status Solidi (b)* **204**(1):453–456 (1997).
62. V. Aninkevičius et al., Hot electron noise in InAlAs/InGaAs/InAlAs quantum wells, *Proc. 14th Int. Conf. Noise Physical Systems and 1/f Fluctuations* (C. Claeys and E. Simoen, eds.), World Scientific, Singapore, 1997, pp. 71–74.

NOISE, LOW-FREQUENCY

PETER H. HANDEL
University of Missouri St. Louis

Low-frequency noise, containing fluctuations of current or voltage with frequency components below 10 kHz, is mainly fundamental $1/f$ noise and sometimes nonfundamental $1/f$ noise. In addition, shot noise, generation–recombination (GR) noise, and thermal noise, which are important at higher frequencies, also extend to the low-frequency domain. All these forms of electronic noise, each defined below, are characterized by the mean squared current fluctuation $\langle(\delta I)^2\rangle$ [or $\langle(\delta V)^2\rangle \equiv \text{RMS } \delta V^2$ for voltage], measured in series with (or across) the device or sample under test, when a constant voltage (or current) is applied, except for thermal noise, which is present even in thermal equilibrium, with no bias applied. All the other forms of noise present in addition to thermal noise are also known as current noise and are absent in thermal equilibrium. Nevertheless, $1/f$ noise and GR noise also modulate the RMS level of the thermal noise currents (or voltages) in thermal equilibrium, while the available power remains constant at $k_B T$ per hertz, where $k_B = 1.38 \times 10^{-23}$ J/K is Boltzmann’s constant and T the absolute temperature. These two forms of current noise are also called modulation noise, because they modulate the resistance. If a bandpass filter is inserted between the measuring device (usually a quadratic meter) and the noise source, then the spectral density of the fluctuations, $\langle(\delta I)^2\rangle_f \equiv S_I(f)$ [or $S_V(f)$] is obtained by dividing the measured mean square by the bandwidth Δf of the filter.

1. SHOT NOISE

With the notable exception of $1/f$ noise, also known as excess noise, the various type of noise mentioned above were well known and understood in the third decade of the twentieth century through the works of J. B. Johnson, H. Nyquist, and W. Schottky. For instance, shot noise is caused, in vacuum tubes, electron beams, Schottky diodes, p-n junctions, and any other device carrying a current, by the discrete, atomistic nature of electricity. It is easily described as a Poisson process, and is given at low

frequencies by

$$S_I(f) = 2eI_0 \quad (1)$$

where e is the electric charge of the charge carriers and I_0 the average electrical current in the direction of their motion. For electrons both e and I_0 are negative. The mean squared current in a frequency interval Δf is thus $2eI_0 \Delta f$. The general formula is given by Carson’s theorem, which gives the spectral density of a random uncorrelated repetition of identical processes with spectrum $\phi(f)$ and repetition rate λ as

$$2\lambda|\phi(f)|^2 \quad (2)$$

The case with arbitrary correlations present between the moments t_0 of passage was treated by C. Heiden [1] and is usually not called shot noise. The elementary process in shot noise is the current $i(t - t_0)$ caused by the passage of a single carrier. Therefore

$$\phi(0) = \int_{-\infty}^{\infty} i(t - t_0) dt = e \quad (3)$$

is the total charge e transported by a single carrier. With $e\lambda = I_0$, Carson’s theorem then gives Eq. (1). The term “shot noise” recalls the noise caused by small shot (or raindrops) falling on a drum.

$1/f$ noise, however, remained shrouded in mystery, and fundamental $1/f$ noise was understood only after the advent of the quantum $1/f$ theory [2] in 1975. It turns out there is always fundamental $1/f$ noise [3,4] caused by the quantum $1/f$ effect (Q $1/f$ E), a new aspect of quantum mechanics as fundamental as space and time or existence itself. But there is also nonfundamental $1/f$ noise, characterized by accidental $1/f$ -like spectra arising from a fortuitous superposition of GR noise spectra. Both fundamental and nonfundamental $1/f$ noise types are important in practice, as we show below.

We briefly consider first GR and thermal noise here before tackling $1/f$ noise at an elementary level. Armed with an understanding of the basic low-frequency noise processes, we then proceed to practical device applications. Next, we delve into the quantum $1/f$ theory and finally consider briefly the epistemological and ontological origin of the $1/f$ spectra in general, trying to understand their much wider presence in nature, their ubiquitous character.

2. GENERATION–RECOMBINATION NOISE

GR noise is caused by the random generation and recombination or trapping and detrapping of current carriers in semi-conductors, being described by the (always one-sided) spectral density

$$S_I(f) = \frac{8\langle(\delta I)^2\rangle\pi\tau}{1 + \omega^2\tau^2} \quad (4)$$

60. V. Aninkevičius et al., Transverse tunnelling time constant estimated from hot-electron noise in GaAs-based heterostructure, *Solid State Commun.* **98**(11):991–995 (1996).
61. A. Matulionis et al., QW-shape-dependent hot-electron velocity fluctuations in InGaAs-based heterostructures, *Physica Status Solidi (b)* **204**(1):453–456 (1997).
62. V. Aninkevičius et al., Hot electron noise in InAlAs/InGaAs/InAlAs quantum wells, *Proc. 14th Int. Conf. Noise Physical Systems and 1/f Fluctuations* (C. Claeys and E. Simoen, eds.), World Scientific, Singapore, 1997, pp. 71–74.

NOISE, LOW-FREQUENCY

PETER H. HANDEL
University of Missouri St. Louis

Low-frequency noise, containing fluctuations of current or voltage with frequency components below 10 kHz, is mainly fundamental $1/f$ noise and sometimes nonfundamental $1/f$ noise. In addition, shot noise, generation–recombination (GR) noise, and thermal noise, which are important at higher frequencies, also extend to the low-frequency domain. All these forms of electronic noise, each defined below, are characterized by the mean squared current fluctuation $\langle(\delta I)^2\rangle$ [or $\langle(\delta V)^2\rangle \equiv \text{RMS } \delta V^2$ for voltage], measured in series with (or across) the device or sample under test, when a constant voltage (or current) is applied, except for thermal noise, which is present even in thermal equilibrium, with no bias applied. All the other forms of noise present in addition to thermal noise are also known as current noise and are absent in thermal equilibrium. Nevertheless, $1/f$ noise and GR noise also modulate the RMS level of the thermal noise currents (or voltages) in thermal equilibrium, while the available power remains constant at $k_B T$ per hertz, where $k_B = 1.38 \times 10^{-23}$ J/K is Boltzmann’s constant and T the absolute temperature. These two forms of current noise are also called modulation noise, because they modulate the resistance. If a bandpass filter is inserted between the measuring device (usually a quadratic meter) and the noise source, then the spectral density of the fluctuations, $\langle(\delta I)^2\rangle_f \equiv S_I(f)$ [or $S_V(f)$] is obtained by dividing the measured mean square by the bandwidth Δf of the filter.

1. SHOT NOISE

With the notable exception of $1/f$ noise, also known as excess noise, the various type of noise mentioned above were well known and understood in the third decade of the twentieth century through the works of J. B. Johnson, H. Nyquist, and W. Schottky. For instance, shot noise is caused, in vacuum tubes, electron beams, Schottky diodes, p-n junctions, and any other device carrying a current, by the discrete, atomistic nature of electricity. It is easily described as a Poisson process, and is given at low

frequencies by

$$S_I(f) = 2eI_0 \quad (1)$$

where e is the electric charge of the charge carriers and I_0 the average electrical current in the direction of their motion. For electrons both e and I_0 are negative. The mean squared current in a frequency interval Δf is thus $2eI_0 \Delta f$. The general formula is given by Carson’s theorem, which gives the spectral density of a random uncorrelated repetition of identical processes with spectrum $\phi(f)$ and repetition rate λ as

$$2\lambda|\phi(f)|^2 \quad (2)$$

The case with arbitrary correlations present between the moments t_0 of passage was treated by C. Heiden [1] and is usually not called shot noise. The elementary process in shot noise is the current $i(t - t_0)$ caused by the passage of a single carrier. Therefore

$$\phi(0) = \int_{-\infty}^{\infty} i(t - t_0) dt = e \quad (3)$$

is the total charge e transported by a single carrier. With $e\lambda = I_0$, Carson’s theorem then gives Eq. (1). The term “shot noise” recalls the noise caused by small shot (or raindrops) falling on a drum.

$1/f$ noise, however, remained shrouded in mystery, and fundamental $1/f$ noise was understood only after the advent of the quantum $1/f$ theory [2] in 1975. It turns out there is always fundamental $1/f$ noise [3,4] caused by the quantum $1/f$ effect (Q $1/f$ E), a new aspect of quantum mechanics as fundamental as space and time or existence itself. But there is also nonfundamental $1/f$ noise, characterized by accidental $1/f$ -like spectra arising from a fortuitous superposition of GR noise spectra. Both fundamental and nonfundamental $1/f$ noise types are important in practice, as we show below.

We briefly consider first GR and thermal noise here before tackling $1/f$ noise at an elementary level. Armed with an understanding of the basic low-frequency noise processes, we then proceed to practical device applications. Next, we delve into the quantum $1/f$ theory and finally consider briefly the epistemological and ontological origin of the $1/f$ spectra in general, trying to understand their much wider presence in nature, their ubiquitous character.

2. GENERATION–RECOMBINATION NOISE

GR noise is caused by the random generation and recombination or trapping and detrapping of current carriers in semi-conductors, being described by the (always one-sided) spectral density

$$S_I(f) = \frac{8\langle(\delta I)^2\rangle\pi\tau}{1 + \omega^2\tau^2} \quad (4)$$

Here τ is the lifetime of the carriers and $\omega = 2\pi f$. According to the Wiener–Kinchine theorem, the spectral density is the Fourier transform of the autocorrelation function

$$A(\tau) \equiv (I(t)I(t + \tau)) \quad (5)$$

and is given by

$$S(f) = 4 \int_0^\infty A(\tau) \cos(2\pi f \tau) d\tau \quad (6)$$

Equation (3) is obtained by Fourier transformation from the exponential autocorrelation function $A(\tau) = ((\delta I)^2) e^{-t/\tau}$, which describes, for instance, the exponential decay of the number of carriers that have not yet recombined at the time t . There is a term similar to Eq. (4) present in the spectral density of current noise in semiconductors, for each type of carrier.

Let N be the number of carriers of a certain type in a semiconductor sample in stationary conditions. In terms of the generation rate $g(N)$ and of the recombination rate $r(N)$, the general formulas for both the lifetime τ and the mean square entering in Eq. (4) are

$$\tau = \frac{1}{r'(N_0) - g'(N_0)}, \quad (7)$$

$$((\delta I)^2) \equiv \frac{I_0^2}{N_0^2} ((\delta N)^2) = \frac{I_0^2}{N_0^2} \tau g(N_0)$$

Here the prime denotes a derivative w.r.t. (with respect to) N . The derivatives are taken for $N = N_0 \equiv (N)$, and we have denoted (I) by I_0 . The following special cases are highlighted:

1. For a n-type semiconductor with N_d deep donors, the generation rate $g(N) = \gamma(N_d - N)$ is proportional to the number of neutral donors, $N_d - N$, while $r(N) = \rho N^2$, with constant γ and ρ , because there are N free electrons and N ionized donors. Therefore, one obtains

$$\tau = \frac{1}{\gamma + 2\rho N_0} = \frac{N_d - N_0}{\rho N_0(2N_d - N_0)} \quad (8)$$

$$((\delta N^2)) = \frac{N_0(N_d - N_0)}{2N_d - N_0}$$

2. For a near-intrinsic n-type semiconductor with N electrons, N_d donors (all ionized), and $P = N - N_d$ holes, we write $g = \text{const}$ because the fluctuations are due to the thermal generation of electron–hole pairs. In this case the recombination rate is $r = \rho NP = \rho N(N - N_d)$. Therefore

$$\tau = \frac{1}{\rho(N_0 + P_0)}, \quad ((\delta N)^2) = ((\delta P)^2) = \frac{N_0 P_0}{N_0 + P_0} \quad (9)$$

3. For a semiconductor with N_t traps and N trapped electrons, the trapping rate is proportional to the

number $N_t - N$ of empty traps, while the release rate is proportional to N . Therefore, $g(N) = a(N_t - N)$ and $r(N) = bN$. The constants a and b are determined by the equilibrium condition $a(N_t - N_0) = bN_0$, which yields $N_0 = [a/(a + b)]N_t$. Therefore

$$\tau = \frac{1}{a + b}, \quad ((\delta N)^2) = \frac{bN_0}{a + b} = \frac{abN_t}{(a + b)^2} \quad (10)$$

In this special case the rate g and r are not nonlinear functions of N and Eqs. (10) are therefore independent of N_0 . In this case, the fluctuation of N obeys the binomial distribution law.

3. THERMAL NOISE

Also known as Johnson (or Nyquist) noise, thermal equilibrium noise has a white (frequency-independent) spectrum at not too high frequencies. It is given in general, for a circuit component of impedance $Z = 1/Y$ of conductance $G = \text{Re } Y$ and resistance $R = \text{Re } Z$, by the Planck–Nyquist formula

$$S_I(f) = 4G \frac{hf}{e^{hf/kT} - 1} \approx 4kTG \quad (11)$$

$$S_V(f) = 4R \frac{hf}{e^{hf/kT} - 1} \approx 4kTR$$

Here $h = 6.62 \times 10^{-34} \text{ J} \cdot \text{s}$ is Planck's constant, and $k = 1.38 \times 10^{-23} \text{ J/K}$ is Boltzmann's constant. The thermal noise power available (for a matched load) is

$$S_a(f) = \frac{hf}{e^{hf/kT} - 1} \approx kT \quad (12)$$

With the exception of ultrahigh frequencies at very low temperatures, only the approximate forms are used in practice and are known as equivalent forms of the Nyquist formula. The amplitude distribution of thermal noise is Gaussian, with small deviations of fundamental origin caused by the $Q1/fE$ noise even in thermal equilibrium [4].

4. GENERAL INTRODUCTION TO $1/f$ NOISE

At low frequencies, the observed noise spectrum, in general, is roughly proportional to the reciprocal frequency, as Johnson first observed in 1925 in vacuum tubes. This $1/f$ noise accounts for most of the low-frequency noise. Low-frequency noise is therefore often considered synonymous with $1/f$ noise in practice. Schottky first called the $1/f$ noise “flicker noise” in 1926 and blamed it on a random flickering process on the surface of the cathode. In 1937 Schottky observed that flicker noise is suppressed by space charge in vacuum tubes to a larger extent than shot noise.

4.1. Nonfundamental $1/f$ Noise

A. L. McWhorter suggested in 1954 that $1/f$ noise in semiconductor samples and devices might arise from

transitions of electrons to and from traps in the oxide at the surface. The superposition of many Lorentzian spectra [Eq. (4)] resulting from traps with different exponential relaxation times τ in the interval $\tau_1 < \tau < \tau_2$ can yield a $1/f$ -like spectrum in a limited frequency domain if two conditions are satisfied, causing a nonfundamental, or accidental, $1/f$ noise, as mentioned above. The two conditions are (1) an electron is not allowed to interact with many traps at the same time and (2) the distribution of the characteristic times has a probability density c/τ . Indeed, one expects then an addition of power spectra

$$\begin{aligned} S_I(f) &= 8((\delta I)^2)\pi c \int_{\tau_1}^{\tau_2} \frac{\tau}{1 + \omega^2\tau^2} \frac{d\tau}{\tau} \\ &= 8((\delta I)^2) \frac{\pi c}{\omega} (\arctan \omega\tau_2 - \arctan \omega\tau_1) \quad (13) \\ &\approx 8((\delta I)^2) \frac{\pi^2 c}{\omega} \end{aligned}$$

The last approximation is valid only for $1/\tau_2 \ll \omega \ll 1/\tau_1$. There is strong evidence favoring a major contribution of this mechanism in MOSFETs from studies of the relaxation of slow surface states, particularly since the observed spectrum often differs slightly from $1/f$. The slow states are distributed uniformly in the oxide volume, which serves as gate insulation, at the surface of the semiconductor. This nonfundamental contribution is usually larger in MOSFETs than the fundamental $1/f$ noise. The constant c is proportional to the superficial density of slow surface states, which can in principle be determined from the slow relaxation of the surface charges, but is hard to determine in practice without measuring the $1/f$ noise. Therefore, Eq. (13) is difficult to apply in practice.

4.2. General Aspect of Fundamental $1/f$ Noise

In fact, $1/f$ noise was found in carbon resistors and microphones, in all semiconductors and semiconductor devices, in contacts (contact noise), in infrared detectors, in bolometers, in photodetectors, in piezoelectric transducers and sensors, in mixers, in thin metallic sheets, in Josephson junctions and SQUIDS, in electron beams in vacuum, in the rate of electron tunneling and cold emission, in the recombination and generation rates for current carriers in the bulk and on the surface of semiconductors, in the frequency fluctuations of quartz resonators and SAW devices and arrays, and so on. It is always observed when a bottleneck is present, causing an electrical current to be carried by only a few current carriers. This ubiquity of $1/f$ noise indicates that $1/f$ noise is “the way of life” for electric currents.

The ubiquitous character of $1/f$ noise inspired the development of a turbulence theory of it [5,6], which generalized Heisenberg’s hydrodynamic turbulence theory to the hydromagnetic plasma turbulence case. This theory yielded for the first time a universal $1/f$ spectrum from postulated instabilities of the laminar flow in the plasma of current carriers (electrons and holes in semi-

conductors). This physical theory was limited to homogeneous isotropic turbulence in an infinite, randomly stirred-up plasma of current carriers, and could therefore not be applied in practice. Nevertheless it demonstrated the fundamental nature of the $1/f$ spectrum caused by the universal feedback reaction of the electric current on itself via the electromagnetic field.

F. N. Hooge recognized that the turbulence theory [5,6] was the only physical theory of fundamental $1/f$ noise available at the time. This sparked experiments trying to verify $1/f$ -noise universality in the laboratory. In 1969 Hooge claimed, on the basis of his measurements, that the known inverse proportionality of $1/f$ noise with the volume of the sample under test becomes universal (i.e., with the same coefficient α_0 for any semiconductor, metal, or electrolyte) if the number of carriers N , rather than the volume of the sample (assumed to be homogeneous), is used in the denominator:

$$S_I(f) = \alpha_0^2 / Nf \quad (14)$$

This relation was known long before Hooge’s work, but the coefficient α_0 was considered dependent on the material, and the volume of the sample was used with preference in the denominator, instead of N . This was thought to be equivalent, because the volume is proportional to N . Early experiments seemed to support Hooge’s hypothesis, with a universal α_0 of 2–3 times 10^{-3} , but later experiments with smaller samples showed that Hooge was wrong, because any α_0 value from 10^3 down to 10^{-10} was shown to be possible. Although Hooge was proved wrong in his suggestion of a universal constant, his initial optimism helped accredit the notion of the fundamental nature of $1/f$ noise. The experimental “constant” α_0 was called the “Hooge parameter” [7] by A. van der Ziel, although it was in fact material-dependent, as had been assumed before Hooge. In 1974 the quantum $1/f$ theory derived Eq. (10) for the first time from first principles, allowing the exact calculation of α_0 , and explaining why small devices have α_0 values ranging from 10^{-5} to 10^{-10} . In 1982 it also explained why large devices have α_0 values close to 4×10^{-3} and why ferroelectric substances have α_0 values as large as 10^3 . This quantum-electrodynamics (QED) theory is presented here, first at an over simplified elementary level and with practical applications to devices, in order to clarify the physical basis and the new notions it introduces.

4.3. Elementary Introduction to Fundamental $1/f$ Noise

The main form of fundamental $1/f$ noise known at the present time is quantum $1/f$ noise, which is a manifestation of the coherent and conventional $Q1/fE$, representing a little-known new aspect of quantum mechanics. It can be obtained from a straightforward QED calculation of fundamental quantum fluctuations in cross sections, process rates, and electric currents, resulting from the author’s attempts to quantize the earlier turbulence theory. These attempts were necessitated by the absence of instabilities with zero threshold, which could otherwise trigger the

turbulence. They resulted in the discovery first of the conventional (1–4) and then of the coherent [3,8–10] quantum $1/f$ effect. The $Q1/fE$ was proven to be responsible for most of the $1/f$ noise observed in electronic devices, thereby allowing for a unified presentation of noise in electronic devices [7,11–22].

Other forms of fundamental $1/f$ noise are found in nature beyond the realm of electrophysics. Like the $Q1/fE$, these other forms of fundamental $1/f$ noise have been proved [23] to arise from a coincidence of nonlinearity and homogeneity in physical system. Just as in the case of the ontologically more fundamental $Q1/fE$, these other forms occur in systems that satisfy a universal sufficient criterion.

4.4. Simplified Derivation of the Conventional Quantum $1/f$ Effect

4.4.1. Definition. The $Q1/fE$ is a fundamental quantum fluctuation of all physical cross sections σ , process rates Γ , and currents j given by the universal formula $S(f) = 2\alpha A/fN$ (conventional quantum $1/f$ equation (16)) for small devices, and $S(f) = 2\alpha/\pi fN$ (coherent quantum $1/f$ equation [16,23,24]) for large devices. These two forms can be combined into a single large devices. These two forms can be combined into a single general formula, as we show below. Here $S(f)$ is the spectral density of fractional fluctuations in current, $\delta j/j$, in the scattering or recombination cross section $\delta\sigma/\sigma$, or in any other process rate $\delta\Gamma/\Gamma$. The number $\alpha \equiv e^2/\hbar c \approx \frac{1}{137}$ is Sommerfeld's fine structure constant, a basic number of our world depending only on Planck's constant \hbar , the charge of the electron, e , and the speed of light in vacuum c . The quantity $A \equiv 2(\Delta v/c)^2/3\pi$ is essentially the square of the vector velocity change Δv of the scattered particles in the scattering process whose fluctuations we are considering, in units of c . Finally, N is the number of particles used to define the notion of current j , of cross section σ or of process rate Γ .

4.4.2. Plan. We will present here first a back-of-the-envelope derivation of the conventional $Q1/fE$. After presenting some practical applications to devices, we present below first an elementary derivation and later a more rigorous derivation of both the conventional and coherent $Q1/fE$.

4.4.3. Origin. The physical origin of electrodynamic conventional quantum $1/f$ noise is easy to understand. Consider, for example, Coulomb scattering of current carriers (e.g., electrons) on a center of force, keeping in mind that electrons are described as probability amplitude waves ψ according to quantum mechanics. The scattered electrons reaching a detector at a given angle away from the direction of the incident beam are described by de Broglie waves ψ of a frequency corresponding to their energy. However, the electrons have energy loss amplitudes in the scattering process, due to the emission of bremsstrahlung into low-frequency photon modes. Therefore, part of the outgoing de Broglie waves are shifted to slightly lower frequencies. When we calculate the probability density $|\psi|^2$ in the scattered beam, we obtain also cross terms, linear in both the parts of ψ scattered with and without bremsstrahlung. These cross terms oscillate

with the same frequency as the frequency of the emitted bremsstrahlung photons. The emission of photons at all frequencies results therefore in probability density fluctuations at all frequencies. The corresponding quantum fluctuations of the current density $v|\psi|^2$ are obtained by multiplying the probability density fluctuations by the velocity v of the scattered current carriers. Finally, these current fluctuations, present in the scattered beam, will be noticed at the detector as low-frequency current fluctuations, and will be interpreted as fundamental fluctuations in the physical scattering cross section of the scatterer.

4.4.4. Derivation. For a simple semiclassical calculation of the conventional $Q1/fE$ along these lines, we start from the classical (Larmor) formula

$$P = 2q^2 a^2 / 3c^3 \quad (15)$$

for the power P radiated by a particle of charge q in the scattering process. The acceleration \mathbf{a} can be approximated by a delta function $\mathbf{a}(t) = \Delta v \delta(t)$ whose Fourier transform Δv is constant and is the change in the velocity vector of the particle during the almost instantaneous scattering process. The one-sided spectral density P_f of the emitted bremsstrahlung power

$$P_f = 4q^2 (\Delta v)^2 / 3c^3 \quad (16)$$

is therefore also constant, independent of frequency, but goes to zero for frequencies larger than the reciprocal duration of the scattering process. The number $4q^2 (\Delta v)^2 / 3\hbar f c^3$ of emitted photons per unit frequency interval is obtained by dividing by the energy $\hbar f$ one photon. The probability amplitude of photon emission

$$A_f = \left(\frac{4q^2 (\Delta v)^2}{3\hbar f c^3} \right)^{1/2} e^{i\gamma} \quad (17)$$

is given by the square root of this photon number spectrum, including also a phase factor $e^{i\gamma}$. The Schrödinger wavefunction Ψ of the scattered outgoing charged particles can be constructed from products of single-particle wavefunctions ψ . The beat term in the probability density $|\psi|^2$ is linear both in this bremsstrahlung amplitude A_f and in the nonbremsstrahlung amplitude, which does not depend on f . The spectral density of this beat term will therefore be given by the product of the squared probability amplitude $|A_f|^2 \ll 1$ of photon emission (proportional to $1/f$) with the squared nonbremsstrahlung amplitude $1 - |A_f|^2 \approx 1$, which is practically independent of f . The resulting spectral density of fractional probability density fluctuations is obtained by dividing $|\psi|^4$ and is therefore

$$\begin{aligned} |\psi|^{-4} S_{\delta|\psi|}^2(f) &= \frac{8q^2 (\Delta v)^2}{3\hbar f N c^3} \equiv \frac{2\alpha A}{fN} \\ &= j^{-2} S_j(f) = S_{\delta j/j}(f) = S_{\delta\sigma/\sigma}(f) \end{aligned} \quad (18)$$

where $\alpha = e^2/\hbar c$ is the fine-structure constant is $q = e$ is the elementary charge, $\hbar = h/2\pi$, and $\alpha A = 2e^2(\Delta v)^2/3\pi\hbar c^3$ is the bremsstrahlung coefficient, also known as the infrared exponent in quantum field theory. It is derived here as the quantum $1/f$ -noise coefficient in electrophysics.

The spectral density S_j of current density fluctuation $\delta j = v\delta|\psi|^2$ is obtained by multiplying the probability density fluctuation spectrum with the velocity $v = p/m$ of the outgoing particles. When we calculate the spectral density of fractional fluctuations in the scattered current j , the outgoing velocity simplifies or drops out, and therefore Eq. (18) also gives the spectrum of current fluctuation $S_j(f)$, as indicated above. Finally, the scattered particle current j per unit incoming flux is what we shall call the *physical scattering cross section* σ . This allows for the first equality in Eq. (18) after the identity sign.

The quantum $1/f$ noise contribution of each carrier is independent, and therefore the quantum $1/f$ noise from N carriers is N times larger; however, the current j will also be N times larger, and therefore in Eq. (1) a factor N was included in the denominator for the case in which the cross section fluctuation is observed on N carriers simultaneously. Finally, note that the simplified back-of-the-envelope derivation which led to Eq. (18) is similar to considering diffraction of a single photon in Young's diffraction experiment and then estimating the autocorrelation function and the spectral density in the probability fringes obtained on the screen, claiming it should apply to the diffraction pattern generated by a large number of photons. The correct way is based on the two-particle wavefunction, which is a product of two single-particle functions in the noninteracting case considered here. This yields the same result, replacing $|\psi|^4$ in the calculation with the physically reasonable squared absolute value of the two-particle wavefunction (see below).

4.4.5. Discussion. We have defined the physical cross section as the quantum-mechanical cross section plus the corresponding quantum fluctuations, which were eliminated in the calculation of the quantum-mechanical expectation value, which is usually defined as the cross section. Our new notion of *physical process rate* is defined in the same way. The physical quantities are the directly observed ones, because in the Q1/fE the quantum fluctuations become macroscopic—observable at low frequencies—due to the $1/f$ dependence.

Although the wavefunction φ of each carrier is split into a bremsstrahlung part and a nonbremsstrahlung part, no quantum $1/f$ noise can be observed from a single carrier. A single carrier will only provide a pulse in the detector. Many carriers are needed to produce the quantum $1/f$ noise effect, just as in the case of electron diffraction patterns, where each individual particle is diffracted, but unless we repeat the experiment many times, or use many particles, no diffraction pattern can be seen. A single particle only yields a point of impact on the photographic plate in diffraction, or a pulse in the detector in $1/f$ noise. While incoming carriers may have been Poisson distributed, the scattered beam will exhibit super-Poissonian statistics, or *bunching*, due to this new effect, the Q1/fE. The Q1/fE is thus a many-body or collective effect, at least a two-particle

effect, best described through the two-particle wavefunction and two-particle correlation function.

In conclusion, the conventional Q1/fE [1–4,6,8–15] is a fundamental fluctuation of physical cross sections and process rates, caused by the infrared-divergent coupling of current carriers to low-frequency photons (electrodynamic Q1/fE) and to other infraquanta, such as transverse phonons with piezoelectric coupling (lattice-dynamic Q1/fE), or electron–hole pairs on the Fermi surface of metals (electronic Q1/fE).

4.4.6. Application. The fundamental quantum $1/f$ fluctuations of physical cross section σ and process rates Γ are reflected in the collision frequency $\nu = 1/\tau$ and collision time τ of the carriers, and in various kinetic coefficients in condensed matter, such as the mobility μ and the diffusion constant D , the surface and bulk recombination speeds s , and recombination times τ_r , the rate of tunneling j_t , and the thermal diffusivity in semiconductors. Specifically, neglecting the energy distribution of the carriers or using appropriate averages, $\delta\sigma/\sigma = \delta\Gamma/\Gamma = \delta\nu/\nu = -\delta\tau/\tau = -\delta\mu/\mu = -\delta D/D$. Therefore, the spectral density of fractional fluctuations in all these coefficients is given also by Eq. (18) in a first approximation that neglects the statistical effects of the momentum distribution of the current carriers. This is true in spite of the fact that each carrier will undergo many consecutive scattering transitions in the diffusion process. The resulting quantum $1/f$ noise in the mobility and in the diffusion coefficient is most often practically the same as (and can never be smaller than) the quantum $1/f$ noise in a single representative scattering event that limits the mobility or the diffusion coefficient.

4.4.7. Coherent Effect. For large devices the concept of coherent-state Q1/fE was introduced by the author [23,24]. In this case the $1/f$ noise parameter α_0 as derived in the theory section below is given by

$$\alpha_0 = (\alpha_0)_{\text{coh}} = 2\alpha/\pi = 4.6 \times 10^{-3} \quad (19)$$

where $\alpha \approx \frac{1}{137}$ is the fine-structure constant as mentioned above. This is of the same order of magnitude as the empirical value $\alpha_0 = 2\text{--}3$ times 10^{-3} that Hooge and others found for large devices. It is obvious that Hooge's empirical value for α_0 is due to the coherent Q1/fE and has a fundamental origin.

4.4.8. Conventional Effect. For small samples or devices we consider conventional quantum $1/f$ noise [1–6,8–15], which is just the cross-section fluctuation introduced above in Eq. (18). In that case α_0 may be written

$$\alpha_0 = (\alpha_0)_{\text{conv}} = \frac{4\alpha(\Delta v)^2}{3\pi c^2} \quad (20)$$

This general principle is now illustrated on practical examples of materials and devices. The exact meaning of large and small is explained below and also in the theory section in terms of the parameters [24–26].

4.4.9. Simplified Application to Homogeneous Semiconductor Samples. In a homogeneous sample of length L , cross section A , volume $V=AL$, carrier mobility μ , carrier concentration n , and total number of carriers $N=nAL$, the conductance $C=n\mu eA/L$ and the resistance $R=1/C$ will exhibit quantum $1/f$ fluctuations with a spectral density $S_{\delta C/C}$ of fractional fluctuations $\delta C/C = -\delta R/R$ given by

$$S_{\delta C/C}(f) = S_{\delta R/R}(f) = S_{\delta\mu/\mu}(f) = \alpha_0/fN \quad (21)$$

4.4.9.1. Size Dependence. To calculate α_0 we first evaluate the parameter $s = nA \times 5.5 \times 10^{-13}$ cm introduced in the theory section below. If $s \geq 1$, coherent quantum $1/f$ noise is observed with $\alpha_0 = 2\alpha/\pi$.

If $s < 1$, Eq. (21) requires knowledge of $(\alpha_0)_{\text{conv}}$. The latter is calculated from Eq. (18) or (20) for each type of scattering that limits the mobility $\mu = e\tau/m^*$ of the carriers. Here τ is the mean collision time or scattering time of the carriers and m^* is their effective mass. In terms of the mean frequency of collisions $\nu = 1/\tau = \sigma\nu n_i$, one obtains $\mu = e/\nu m^* = e/\sigma\nu n_i m^*$. Here ν is the mean speed of the carriers between collisions, σ a scattering cross section, and n_i the concentration of scatterers.

4.4.9.2. Conventional Quantum $1/f$ Effect in the Mobility.

In general, Matthiessen's rule allows us to write, in terms of mobility,

$$\frac{1}{\mu} = \sum_j \frac{1}{\mu_j} \quad (22)$$

where μ_j is the mobility that would be obtained if only the j th scattering mechanism were present and limited the mobility. Applying a quantum $1/f$ fluctuation to Eq. (22), squaring, and averaging quantum-mechanically and statistically, we obtain as a reasonable first approximation

$$\frac{\delta\mu}{\mu^2} = \sum_j \frac{\delta\mu_j}{\mu_j^2}, \quad S_{\delta\mu/\mu}(f) = \sum_j \left(\frac{\mu}{\mu_j}\right)^2 S_{\delta\mu/\mu_j}(f) \quad (23)$$

Equation (20) yields the strongest conventional quantum $1/f$ noise for umklapp scattering, followed by the f and g forms of intervalley scattering or intervalley with umklapp scattering (in indirect bandgap semiconductors such as Si and Ge only), followed by normal phonon scattering, by neutral-impurity scattering, and by ionized impurity scattering. The corresponding terms in Eq. (23) reflect this hierarchy only partially, because of the factors $(\mu/\mu_j)^2$, which gauge the importance of each of the scattering processes in limiting the resultant mobility. To gain physical insight, the conventional Q $1/f$ E present in the various scattering processes is only estimated below and is actually calculated in the theory section in the second half of this article, taking into account the corrections introduced by the momentum distribution of the carriers and by the phonon distribution function at the temperature T .

4.4.9.3. Impurity Scattering. For instance, in the case of impurity scattering, n_i is. One obtains $S_{\delta\mu/\mu}(f) = S_{\delta\sigma/\sigma}(f)$. The physical scattering cross section σ , in turn, exhibits the Q $1/f$ E with the spectral density given by Eqs. (18) and (20):

$$S_{\delta\sigma/\sigma}(f)_i = \frac{4\alpha}{3\pi f N} \left\langle \left(\frac{\Delta v}{c}\right)^2 \right\rangle \approx \frac{3 \times 10^{-3}}{fN} \left(\frac{\hbar\Delta k}{m^*c}\right)^2 \quad (24)$$

The average quadratic velocity change of the electrons in a scattering process is smaller in impurity scattering than in lattice scattering, which includes normal phonon scattering, intervalley scattering in indirect-bandgap semiconductors with several valleys, and umklapp scattering, as well as optical phonon scattering. The Coulomb–Rutherford or Conwell–Weisskopf scattering cross section is proportional to $1/|\Delta k|^4$, which favors small-angle scattering. Nevertheless, there are a few larger-angle scattering events, which are most effective in limiting the mobility and which therefore are decisive in the exact evaluation of the Q $1/f$ E coefficient as a slow function of n_i , the concentration of impurities, given in the theory section below. This corresponds approximately to assuming randomizing collisions

$$\langle (\Delta v)^2 \rangle_i = 2(v^2) = 6k_B T/m^* \quad (25)$$

although impurity scattering is not randomizing. With m_0 representing the free-electron mass, we obtain this way

$$S_{\delta\mu/\mu}(f)_i = S_{\delta\sigma/\sigma}(f)_i = \frac{4\alpha}{3\pi f N} \left\langle \frac{6k_B T}{m^*c^2} \right\rangle \approx \frac{10^{-9}}{fN} \frac{Tm_0}{4m^*(100\text{ K})} \quad (26)$$

The quantum $1/f$ noise power present in impurity scattering is therefore proportional to T .

4.4.9.4. Normal Acoustic Phonon Scattering. For normal-phonon scattering, the product $\sigma\nu n_i$, has to be replaced by the lattice scattering rate Γ , given by an effective number of phonons times the squared phonon scattering matrix element, $|M|^2$. The latter exhibits quantum $1/f$ fluctuations, because the carriers emit bremsstrahlung photons in the scattering process. Therefore, if the mobility μ of electrons (of random velocity $v = \hbar k/m^*$) is limited by phonon scattering, we get

$$S_{\delta\mu/\mu}(f)_{\text{ap}} = S_{\delta\Gamma/\Gamma}(f)_{\text{ap}} = \frac{4\alpha}{3\pi f N} \left\langle \left(\frac{\hbar\Delta k}{m^*c}\right)^2 \right\rangle = \frac{3 \times 10^{-3}}{fN} \left\langle \left(\frac{\hbar\Delta q}{m^*c}\right)^2 \right\rangle \quad (27)$$

Here Δq is the acoustic-phonon momentum transfer in the scattering process, and the brackets indicate the average value. Using the linear approximation of the acoustic phonon dispersion relation $E_q = v_s q \hbar$, with v_s denoting the speed of sound, we obtain for a thermal phonon with

$$E_q = k_B T / 2$$

$$\langle (\hbar \Delta \mathbf{q} / m^* c)^2 \rangle = \left(\frac{k_B T}{2 v_s m^* c} \right)^2 = 1.25 \times 10^{-5} \left(\frac{m_0}{m^*} \right)^2 \quad (28)$$

we finally obtain

$$S_{\delta\mu/\mu}(f)_{\text{ap}} = \frac{3.75 \times 10^{-8}}{fN} \left(\frac{m_0}{m^*} \right)^2 \quad (29)$$

The mean squared momentum change and the $1/f$ noise are much larger (e.g., 50 times; see Fig. 1) for acoustic-phonon scattering, because impurity scattering is mainly small-angle scattering. A more rigorous treatment for the many types of scattering present in semiconductors, taking into account the corrections introduced by the momentum distribution of the carriers and the phonon distribution function at the temperature T , is given in the theory section in the second half of this article for the case of silicon.

4.4.9.5. Umklapp Scattering. In this case the momentum change is close to the smallest reciprocal lattice vector approximated by $\hbar G = 2\pi\hbar/a$, where a is the lattice constant. Therefore, Eq. (20) yields

$$(\alpha_{0u})_{\text{conv}} = \frac{4\alpha}{3\pi} \left(\frac{2\pi\hbar}{am^*c} \right)^2 = \frac{6 \times 10^{-8}}{fN} \left(\frac{m_0}{m^*} \right)^2 \quad (30)$$

for umklapp scattering.

4.4.9.6. Intervalley Scattering. In indirect-bandgap semiconductors the location of the energy minima of the conduction band in \mathbf{k} space is different from the location of the valence-band energy maxima. In thermal equilibrium electrons and holes are present close to the minima of the conduction and valence bands. Scattering processes

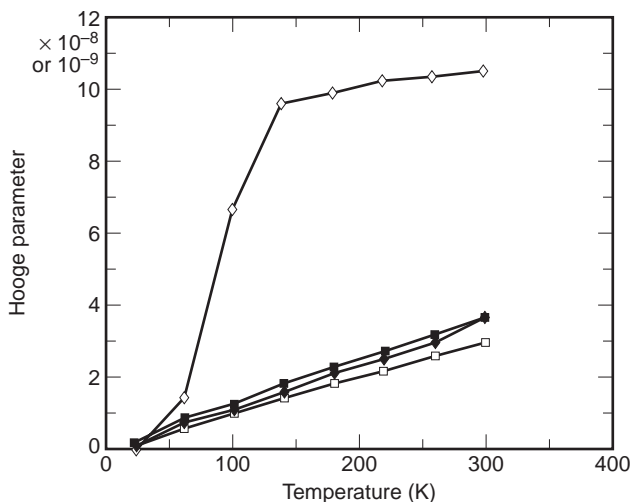


Figure 1. Acoustic Hooke parameter in units of 10^{-8} (open diamonds), and impurity Hooke parameter in units of 10^{-9} for three doping concentrations: 10^{21} (open squares), 10^{23} (solid diamonds), and 10^{24} (solid squares).

carrying electrons from one minimum (or valley) to the other are known as intervalley scattering. This is large-angle scattering, compared with normal (intervalley) scattering, and it is therefore affected by larger conventional quantum $1/f$ noise, almost as large as umklapp scattering. Indeed, for example, in Si the eight minima are located at $0.85G$ from the origin, where G is the smallest reciprocal lattice vector magnitude. For g processes, which scatter an electron to the valley symmetrically located on the other side of the origin, Eq. (30) remains valid with a correction factor of $(0.85)^2$. On the other hand, for f processes in Si, scattering electrons between neighboring valleys, the factor is 2 times smaller. There is also the possibility of intervalley scattering with umklapp, which requires a correction factor of $(1 - 0.85)^2$. Equation (20) thus yields for intervalley scattering with umklapp

$$(\alpha_{0iu})_{\text{conv}} = 0.0225 \frac{4\alpha}{3\pi} \left(\frac{2\pi\hbar}{am^*c} \right)^2 = \frac{1.35 \times 10^{-9}}{fN} \left(\frac{m_0}{m^*} \right)^2 \quad (31)$$

While this appears to indicate a lower contribution from these intervalley umklapp processes, the corresponding factor $(\mu/\mu_0)^2$ in Eq. (23) ensures a larger contribution to the resulting spectral density of quantum $1/f$ noise, $S_{\delta\mu/\mu}(f)$. Physically, this is caused by the scarcity of high-energy phonons able to bridge the momentum gap of $0.85G$.

5. CALCULATION OF THE CONVENTIONAL QUANTUM $1/f$ EFFECT IN HOMOGENEOUS SEMICONDUCTOR MATERIALS

A first-principles calculation of quantum $1/f$ cross-correlations, performed for the first time in 1987 by Handel [27], has yielded a slightly different result from earlier expectations. This same new form of the quantum $1/f$ cross-correlations was rederived with a different method by Van Vliet [15] in 1989. It differs from the old form used in the 1985 calculation of Kousik et al. [28] by a correction that is zero when the momentum changes of the two current carriers involved in the cross correlation are identical, but increases when the momentum differences caused by the scattering process are different. The correction is proportional to the squared difference of the two momentum changes. Handel and Chung [29] have repeated all calculations in the original paper by Kousik et al. [28], obtaining both for impurity scattering and for the various types of phonon scattering new analytical expressions that show a considerable increase of the final quantum $1/f$ noise. The results obtained are in general applicable both to direct- and to indirect-bandgap semiconductors.

5.1. Introduction

Handel and Chung [29] have performed an analytical calculation of mobility fluctuations in silicon and gallium arsenide, using the new quantum $1/f$ cross-correlations formula. This calculation is of major importance for the $1/f$ -noise-related optimization of the two types of materials, and of the many devices constructed with them for

military and civilian applications in the electronic and optoelectronic industries.

The new cross-correlation formula gives the cross-spectral density, which describes the way in which simultaneous quantum $1/f$ scattering rate fluctuation ΔW observed in the direction of the outgoing scattered wave vector \mathbf{K} are correlated with those in the \mathbf{K}' direction when the two corresponding incoming current carriers have the wavevectors \mathbf{K}_1 and \mathbf{K}_2 :

$$\begin{aligned} S_{\Delta W}(\mathbf{K}_1, \mathbf{K}'; \mathbf{K}_2, \mathbf{K}'; f) \\ = \frac{2\alpha}{3\pi f} \left(\frac{\hbar}{m^*c} \right)^2 W_{\mathbf{K}_1, \mathbf{K}'} W_{\mathbf{K}_2, \mathbf{K}'} \\ \times [(\mathbf{K}' - \mathbf{K}_1)^2 + (\mathbf{K}'' - \mathbf{K}_2)^2] \delta_{\mathbf{K}_1, \mathbf{K}_2} \end{aligned} \quad (32)$$

The form conjectured by us earlier had $2(\mathbf{K}' - \mathbf{K}_1)(\mathbf{K}'' - \mathbf{K}_2)$ in place of the rectangular bracket. The difference between the rectangular bracket and $2(\mathbf{K}' - \mathbf{K}_1)(\mathbf{K}'' - \mathbf{K}_2)$ is the perfect square $[(\mathbf{K}' - \mathbf{K}_1) - (\mathbf{K}'' - \mathbf{K}_2)]^2$. Therefore we expect the new results to be always larger than the results obtained on the basis of the previously conjectured form.

5.2. Impurity Scattering

For impurity scattering of electrons in solids, fluctuations $\Delta\tau$ of the collision times τ will cause mobility fluctuations

$$\Delta\mu_{\text{band}}(t) = \frac{e}{m^* \langle \langle v^2 \rangle \rangle} \sum_{\mathbf{K}} v_{\mathbf{K}}^2 \Delta\tau(t) n_{\mathbf{K}} \quad (33)$$

Where $\langle \langle v^2 \rangle \rangle$ is both average over all states of wave vectors \mathbf{K} , with occupation number $n_{\mathbf{K}}$, in the conduction band, and the thermal equilibrium average, of the squared carrier velocities. With the help of the relation

$$\frac{1}{\tau(\mathbf{K})} = \frac{V}{8\pi^3} \int \left(1 - \frac{\cos\theta'}{\cos\theta} \right) W_{\mathbf{K}, \mathbf{K}'} d^3K' \quad (34)$$

the mobility fluctuations are reduced to fluctuations of the elementary scattering rates $W_{\mathbf{K}, \mathbf{K}'}$, governed by Eq. (32). Here V is the volume of the normalization box, which disappears in the final result, and θ and θ' respectively the angles \mathbf{K} and \mathbf{K}' form with the direction of the applied field. One finally obtains, after tedious multiple integrations

$$\begin{aligned} \mu^{-2} S_{\Delta\mu}(f) &= \frac{256\pi\alpha\kappa^2\varepsilon^4\hbar^{12}}{3m^{*8}Z^4e^8N_i^2f} \\ &\times \sum_{\mathbf{K}} K^{10} \left(\ln(1+a^2) - \frac{a^2}{1+a^2} \right)^{-3} \\ &\left(\frac{2a^2+a^4}{1+a^2} - 2\ln(1+a^2) \right) F(E_{\mathbf{K}}) \\ &\times \left(\sum_{\mathbf{K}} v_{\mathbf{K}}^2 \tau(\mathbf{K}) F(E_{\mathbf{K}}) \right)^{-2} \end{aligned} \quad (35)$$

where $a = 2K/\kappa$, $\kappa^2 = e^2 n(T)/\varepsilon k_B T$, $n(T)$, is the electron concentration, $F(E_{\mathbf{K}}) = \exp(E_{\mathbf{F}} - E_{\mathbf{K}})$ for nondegenerate semiconductors, N_i is the concentration of impurities of charge Ze and ε is the dielectric constant. The corresponding partial Hooke parameter for impurity scattering is thus

$$\begin{aligned} \alpha_i &= \frac{4\sqrt{2\pi}\alpha\kappa\hbar^5 N_c}{3m^{*7/2}(k_B T)^{3/2}c^2} \\ &\int_0^\infty dx x^{11/2} e^{-x} \left(\ln(bx+1) - \frac{bx}{bx+1} \right)^{-3} \\ &\left(\frac{2bx+b^2x^2}{bx+1} - 2\ln(bx+1) \right) \\ &\times \left[\int_0^\infty dx x^3 e^{-x} \left(\ln(bx+1) - \frac{bx}{bx+1} \right)^{-1} \right]^{-2} \end{aligned} \quad (36)$$

This result is graphed in Fig. 1 for three different values of the donor concentration N_d and is compared with old results obtained by simply recalculating the old analytical expression [28]. As expected, the new cross-correlation formula leads to slightly higher α_i values than the previously conjectured expression. This was mentioned in connection with Eq. (32) above.

5.3. Electron Acoustic Phonon Scattering

In this case the calculation is similar, and leads to the result

$$\begin{aligned} \alpha_{ac} &= \frac{32\pi\alpha N_c m^* C_1^3 \hbar^3}{(3c^2 k_B T)^4} \left[\frac{1}{R^2} \int_1^\infty dx x^{-4} \right. \\ &\times \left(\frac{(x-1)^7}{7} + (R+1) \frac{(x-1)^6}{6} + R \frac{(x-1)^5}{5} \right) \\ &\times \left(\frac{(x-1)^5}{5} + (R+1) \frac{(x-1)^4}{4} + R \frac{(x-1)^3}{3} \right) \exp\left(-\frac{x^2}{4R}\right) \\ &+ \int_0^1 dx x^{-4} \left(\frac{(x+1)^5}{5} - \frac{(x+1)^6}{6} + \frac{(x-1)^5}{5} + \frac{(x-1)^6}{6} \right) \\ &\times \left(\frac{(x+1)^3}{3} + \frac{(x-1)^4}{4} + \frac{(x-1)^3}{3} - \frac{(x+1)^4}{4} \right) \\ &\exp\left(-\frac{x^2}{4R}\right) + \int_1^\infty dx x^{-4} \left(\frac{(x+1)^5}{5} - \frac{(x+1)^6}{6} \right) \\ &\left. \left(\frac{(x+1)^3}{3} - \frac{(x+1)^4}{4} \right) \exp\left(-\frac{x^2}{4R}\right) \right] \end{aligned} \quad (37)$$

where $R = k_B T/2m^* C_1^2$, C_1 is the deformation potential, and N_c is the effective density of states for the conduction band.

5.4. Nonpolar Optical Phonon Scattering

This time one obtains

$$\begin{aligned} \alpha_{\text{nonph}} = & \frac{8\pi\sqrt{2\hbar\omega_0}\alpha N_c\hbar^2}{3m^{*5/2}c^2\omega_0} \left[\int_0^\infty dx x^{5/2} \right. \\ & \times [(F+1)(x-1)^{1/2}\theta(x-1) + F(x+1)^{1/2}]^{-4} \\ & \times [(F+1)^2(x-1)(2x-1)\theta(x-1) \\ & \left. + F^2(x+1)(2x+1)\exp\left(-\frac{\hbar\omega_0x}{k_B T}\right)] \right] \\ & \times \left[\int_0^\infty dx x^{3/2} [(F+1)(x-1)^{1/2}\theta(x-1) \right. \\ & \left. + F(x+1)^{1/2}]^{-1} \exp\left(-\frac{\hbar\omega_0x}{k_B T}\right) \right]^{-2} \end{aligned} \quad (38)$$

where $F = [\exp(\hbar\omega_0/k_B T) - 1]^{-1}$, and ω_0 is the optical phonon frequency.

5.5. Polar Optical Phonon Scattering

Proceeding as in the cases of impurity and nonpolar optical-phonon scattering, we obtain

$$\begin{aligned} \alpha_{\text{poph}} = & \frac{8\pi\sqrt{2\hbar\omega_1}\alpha N_c\hbar^2}{3m^{*5/2}c^2\omega_1} \left(\int_0^\infty dx x^4 \right. \\ & \times \{F^2(x+1)^{1/2} \ln[2x^{1/2} + 2(x+1)^{1/2}] \\ & + (F+1)^2(x-1)^{1/2} \ln[2x^{1/2} \\ & \left. + (x-1)^{1/2}\theta(x-1)] \exp(-\hbar\omega_1x/k_B T) \right. \\ & \times \{(F+1)\text{arcsinh}[(x-1)^{1/2}\theta(x-1)] \\ & \left. + F \text{arcsinh}(x^{1/2})\}^{-4} \right) \end{aligned} \quad (39)$$

Here ω_1 is the longitudinal phonon frequency.

5.6. Intervalley Scattering

This type of scattering, present in indirect-bandgap semiconductors, transfers electrons from one of the six minima (or valleys) of the conduction band energy in \mathbf{k} space to one of the other five minima. Transitions between a valley and the nearest valley, which is along the same \mathbf{k} -space direction in the next copy of the first Brillouin zone in the periodic zone scheme, are of the umklapp type, and are called g processes. Transitions to the four valleys present in the same zone along the other two \mathbf{k} -space directions are called f processes. Repeating a previous calculation [31] on the basis of the new cross-correlation formula

Eq. (32), we obtain for g processes

$$\begin{aligned} \alpha_g = & \frac{8\pi\sqrt{2\hbar\omega_{ij}}\alpha N_c\hbar^2}{3m^{*5/2}c^2\omega_{ij}} \left[\int_0^\infty dx x^{5/2} \right. \\ & \times [(F+1)(x-1)^{1/2}\theta(x-1) + F(x+1)^{1/2}]^{-4} \\ & \times [(F+1)^2(x-1)(2x-1)\theta(x-1) \\ & \left. + F^2(x+1)(2x+1)\exp\left(-\frac{\hbar\omega_{ij}x}{k_B T}\right)] \right] \\ & \times \left[\int_0^\infty dx x^{3/2} [(F+1)(x-1)^{1/2}\theta(x-1) \right. \\ & \left. + F(x+1)^{1/2}]^{-1} \exp\left(-\frac{\hbar\omega_{ij}x}{k_B T}\right) \right]^{-2} \end{aligned} \quad (40)$$

where $\hbar\omega_{ij}$ is the phonon energy corresponding to the momentum difference required by the intervalley transition. For the corresponding f process we obtain (30)

$$\alpha_f = \left(\frac{k_0}{q_0}\right)^2 \alpha_g \frac{\hbar\omega_{ijf}}{k_B T} \quad (41)$$

where k_0/q_0 is the ratio between length of the position vector of a conduction band energy minimum in \mathbf{k} space, and twice the distance of the same minimum from the Brillouin zone boundary, 0.85/0.3 for silicon. $\alpha_g(\hbar\omega_{ijf}/k_B T)$ is calculated with the f momentum difference. There are three g -type alphas, α_{g1} , α_{g2} , and α_{g3} (from LA, TA, and LO phonons, respectively), and three f -type ones, α_{f1} (`<chemNamesilicon </chemName>`, α_{f2} , and α_{f3} (from TA, LA, and TO phonons). Their values are given in Fig. 2 and are a few times larger than the old values.

The various quantum $1/f$ contributions derived here can be approximately superposed to yield the resultant

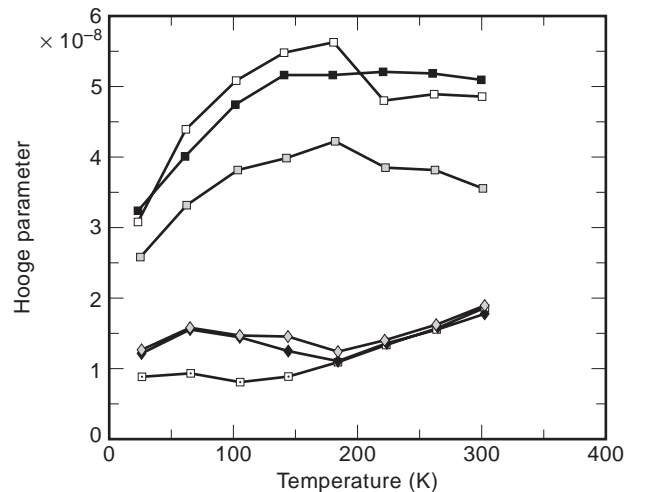


Figure 2. Hooke parameters for intervalley scattering in units of 10^{-8} for g processes (solid) and f processes (shaded).

quantum $1/f$ coefficient according to the rule

$$\alpha_H = \sum_j \left(\frac{\mu}{\mu_i} \right)^2 \alpha_i \quad (42)$$

In the next section we illustrate the application of these results to inhomogeneous semiconductor devices on the simplest case of p-n junctions. The case of transistors and other junction devices, as well as the cases of field-effect transistors, HEMTs, PBTs, and other devices, is presented in the literature (see, e.g., Ref. 16)

6. DERIVATION OF MOBILITY QUANTUM $1/f$ NOISE IN N^+P DIODES AND METAL-INSULATOR-SEMICONDUCTOR DEVICES

6.1. Mobility Quantum $1/f$ Noise in n^+p Diodes

For a diffusion limited n^+p junction the current is controlled by diffusion of electrons into the p region over a distance of the order of the diffusion length $L = (D_n \tau_n)^{1/2}$, which is shorter than the length w_p of the p region in the case of a long diode; τ_n is the lifetime of the electrons. Quantum $1/f$ fluctuations of the scattering rates, discussed in the previous section, will cause fluctuations in the local carrier mobility μ and diffusion constant $D = \mu kT/e$. If $N(x)$ is the number of electrons per unit length and D_n their diffusion constant, the electron current at x is

$$I_{nd} = -eD_n \frac{dN}{dx} \quad (43)$$

where we have assumed a planar junction and taken the origin $x=0$ in the junction plane. Diffusion constant fluctuations, given by kT/e times the mobility fluctuations, will lead to local current fluctuations in the interval Δx :

$$\delta \Delta I_{nd}(x, t) = I_{nd} \Delta x \frac{\delta D_n(x, t)}{D_n} \quad (44)$$

The normalized weight with which these local fluctuations representative of the interval Δx contribute to the total current I_d through the diode at $x=0$ is determined by the appropriate Green function and can be shown to be $(1/L) \exp(-x/L)$ for $w_p/L \gg 1$. Therefore the contribution of the section Δx is

$$\delta \Delta I_d(x, t) = \frac{\Delta x}{L} \exp\left(-\frac{x}{L}\right) I_{nd} \frac{\delta D_n(x, t)}{D_n} \quad (45)$$

with the spectral density

$$S_{\Delta I_d}(x, f) = \left(\frac{\Delta x}{L} \right)^2 \exp\left(-\frac{2x}{L}\right) \frac{I_{nd}^2 S_{D_n}(x, f)}{D_n^2} \quad (46)$$

For mobility and diffusion fluctuations the fractional spectral density is given by $\alpha_{Hnd}/(fN\Delta x)$, where the quantum $1/f$ coefficient α_{Hnd} for electronic diffusion or mobility is determined from quantum $1/f$ theory according to

Eq. (42). With Eq. (43) we then obtain

$$S_{\Delta I_d}(x, f) = \frac{\Delta x}{L^2} \exp\left(-\frac{2x}{L}\right) \left(eD_n \frac{dN}{dx} \right)^2 \frac{\alpha_{Hnd}}{fN} \quad (47)$$

The electrons are distributed according to the solution of the diffusion equation:

$$N(x) = [N(0) - N_p] \exp\left(-\frac{x}{L}\right) \quad (48)$$

$$\frac{dN}{dx} = -\frac{N(0) - N_p}{L} \exp\left(-\frac{x}{L}\right)$$

Substituting into Eq. (47) and simply summing over the uncorrelated contributions of all intervals Δx , we obtain

$$S_{I_d}(f) = \alpha_{Hnd} \left(\frac{eD_n}{L^2} \right)^2 \int_0^{w_p} \frac{[N(0) - N_p]^2 e^{-4x/L} dx}{[N(0) - N_p] e^{-x/L} + N_p} \quad (49)$$

We note that $eD_n/L^2 = e/\tau_n$. With the expression for the saturation current $I_0 = e(D_n/\tau_n)^{1/2} N_p$ and of the current $I = I_0 [\exp(eV/kT) - 1]$, we can carry out the integration

$$S_{I_d}(f) = \alpha_{Hnd} \frac{eI}{f\tau_n} \int_0^1 \frac{a^2 u^3 du}{au + 1} = \alpha_{Hnd} \frac{eI}{f\tau_n} F(a) \quad (50)$$

Here we have introduced the notation

$$u = \exp(-x/L), \quad a = \exp(eV/kT) - 1 \quad (51)$$

$$F(a) = \frac{1}{3} - \frac{1}{2a} + \frac{1}{a^2} - \frac{1}{a^3} \ln(1+a)$$

Equation (50) gives the diffusion noise as a function of the quantum $1/f$ noise parameter α_{Hnd} . A similar result can be derived for the quantum $1/f$ fluctuations of the recombination rate in the bulk of the p region. The result is the same, with α_{Hnd} replaced by α_{Hnr} .

6.2. Mobility Quantum $1/f$ Noise in Metal-Insulator-Semiconductor Devices

As an example of results on quantum $1/f$ noise in high-tech devices, we provide here without proof the results obtained by Handel for the $1/f$ -limited performance of metal-insulator-semiconductor (MIS) HgCdTe infrared detectors. The current density I in the detector contains a diffusion term I_d , a term I_r caused by recombination in the space charge region, a surface recombination term I_s , a tunneling term I_t , and a photovoltaic term caused by the creation of electron-hole pairs by photons:

$$I = I_d + I_r + I_s + I_t + q\eta\Phi$$

$$= qn_i \left[\frac{n_i}{n_0} \left(\frac{D_n}{\tau_n} \right)^{1/2} (e^{qV/kT} - 1) + \frac{W}{\tau} (e^{qV/2kT} - 1) + s \right] \quad (52)$$

$$+ I_t + q\eta\Phi$$

Here n_i is the intrinsic concentration, n_0 the concentration of acceptors on the p side, D_n and τ_n the diffusion constant and lifetime of minority carriers on the p side, W the width of the depletion region, $\tau = \tau_{p^0+n^0}$ the Shockley–Hall–Read lifetime, V the applied voltage, s the surface recombination speed, η the quantum efficiency, and Φ the incident flux of photons. With the exception of the last term, the terms in Eq. (52) are known as dark-current components.

We write the total dark-current fluctuation in the form

$$\delta I_d = \delta I_d + \delta I_r + \delta I_s + \delta I_{tb} + \delta I_{tc} + \delta I_{tsc} \quad (53)$$

and the spectral density of current fluctuations will be

$$S_{I_d} = S_{I_d} + S_{I_r} + S_{I_s} + S_{I_{tb}} + S_{I_{tc}} + S_{I_{tsc}} \quad (54)$$

Here we have lumped the recombination current on the back surface I_b together with the surface recombination (generation) current I_s . If we denote all the corresponding spectral densities of fractional fluctuations by a prime ($S'_{I_i} = S_{I_i}/I_i^2$), we obtain

$$\begin{aligned} S'_{I_d} = & (I_{dif}/I_d)^2 S'_{I_{dif}} + (I_{dep}/I_d)^2 S'_{I_{dep}} + (I_s/I_d)^2 S'_{I_s} \\ & + (I_{tb}/I_d)^2 S'_{I_{tb}} + (I_{tc}/I_d)^2 S'_{I_{tc}} + (I_{tsc}/I_d)^2 S'_{I_{tsc}} \end{aligned} \quad (55)$$

This equation was obtained by dividing the previous equation through I_d^2 , and shows that the biggest contribution will not necessarily come from the process with the highest fractional quantum $1/f$ noise, that is, with the highest $1/f$ noise coefficient. The weight of each type of noise is determined by the corresponding squared current ratio.

The detectivity of infrared detectors is limited in general by three types of noise: (1) current noise in the detector, (2) noise due to background photons (photon noise), (3) noise in the electronic system following the detector. We shall neglect here the background photon noise and the noise in the electronic system. The detectivity is defined as

$$D^*(\lambda, f) = \frac{(A\Delta f)^{1/2}}{\text{NEP}} \quad (\text{cm} \cdot \text{Hz}^{1/2}/\text{W}) \quad (56)$$

where A is the area of the detector; NEP is the noise equivalent power, defined as the RMS optical signal of wavelength λ required to produce an RMS noise voltage (current) equal to the RMS noise voltage (current) in a bandwidth Δf , and f is the frequency of modulation. The noise equivalent power is given by

$$\text{NEP} = \frac{h\nu}{\eta q} [S_{I_d}(f)\Delta f]^{1/2} \quad (57)$$

Therefore we obtain for the detectivity

$$D^*(\lambda, f) = \frac{q\eta\lambda}{hc} \left(\frac{A}{S_{I_d}(f)} \right)^{1/2} = \frac{q\lambda}{hc} [S_{I_d}(f)]^{-1/2} \quad (58)$$

We notice that $D^*(\lambda, f)$ is proportional to λ up to the peak wavelength λ_c . For $\lambda > \lambda_c$ we have $\eta = 0$ and thus $D^*(\lambda, f) = 0$. By substituting our result for S_{I_d} , we obtain the general expression for the detectivity as a function of various parameters of the MIS device.

Let us now evaluate the spectral density $S'(f)$ of fractional fluctuations in the various dark-current noise contributions per square centimeter of transversal detector (or gate) area, including also a numerical example for a MIS infrared detector. For a given detector, this needs to be divided by the area A of the detector to yield the corresponding fractional spectral densities: $S(f) = S'(f)/A$. Fractional fluctuations are dimensionless, so $S'(f)$ will have the dimension of a reciprocal frequency times a squared length unit, which simplifies when we divide by the area of the detector at hand. Let S'_{I_d} be the spectral density of fractional fluctuations in the noise caused by quantum $1/f$ fluctuations in diffusion, S'_{I_r} in bulk recombination, S'_{I_s} in surface recombination, and S'_{I_t} in tunneling. With $m_p^* = 0.55m_0$, $m_n^* = 0.02m_0$, $\tau_n = 10^{-6}$ s, $E_g = 0.1$ eV, $3kT/2 = 0.01$ eV, we obtain for a p-type MIS device with $w_p \gg L_d$

$$\begin{aligned} S'_{I_d} = & (\alpha_{Hnd} + \alpha_{Hnr}) \frac{e}{f\tau_n I_d} F(a) = \alpha_{\text{coh}} \frac{e^{1/2}}{f(kT\mu\tau_n)^{1/2} N_p} \frac{F(a)}{a} \\ = & \frac{4.6 \times 10^{-3}}{4fN_p} \frac{4 \times 10^{-10} C^{1/2}}{[(10^{-6} \text{ s})(1.5 \times 10^5 \text{ cm}^2/\text{V} \cdot \text{s})(4 \times 10^{-21} \text{ J})]^{1/2}} \\ = & \frac{1.8 \times 10^{-6} \text{ cm}^2}{f} \end{aligned} \quad (59)$$

$$\begin{aligned} S'_{I_r} = & \frac{\alpha_{\text{He}} e}{f(\tau_{n0} + \tau_{p0}) I_r} \tanh x = \frac{\alpha_{\text{He}} e}{feAwn_i \tanh x} \tanh x \\ = & \frac{\alpha_{\text{He}}}{feAwn_i} = \frac{4.6 \times 10^{-9} \text{ cm}^2}{f} \quad (x = eV/2kT) \end{aligned} \quad (60)$$

$$\begin{aligned} S'_{I_s} = & \frac{4\alpha}{3\pi m^* c^2} \left(\frac{3kT}{2} + \frac{eU}{2} + 0.1Ve \right) \frac{e \tanh x}{f(\tau_{n0} + \tau_{p0}) I_s} \\ = & \frac{4\alpha}{3\pi \times 0.02500,000} (0.025 + 0.5 + 0.5) \frac{e \tanh x}{feAwn_i (e^x - 1)} \\ = & \frac{7 \times 10^{-8} \text{ cm}^2}{f} \approx S_{I_b} \end{aligned} \quad (61)$$

$$\begin{aligned} S'_{I_{tb}} = & \frac{4\alpha E_g + 3kT/2}{3\pi m^* c^2} = \frac{4}{9.5 \times 137 \times 0.02500,000} \frac{0.11}{1} \\ = & \frac{3.310^{-8} \text{ cm}^2}{f} \end{aligned} \quad (62)$$

$$\begin{aligned} S'_{I_{tc}} = & \frac{4\alpha E_g + 3kT}{3\pi 2m^* c^2} = \frac{4}{9.5 \times 137 \times 0.02 \cdot 10^6} \frac{0.12}{1} \\ = & \frac{1.8 \times 10^{-8} \text{ cm}^2}{f} = S'_{I_{tsc}} \end{aligned} \quad (63)$$

S'_{I_d} was calculated in the small-bias limit for $w_p \gg L$, but $w_p = 0.25L$ gives the same result; the incoherent case with a lattice constant of 0.65 nm and $\Theta = 320$ K was also listed

above (because a 10- μm -thick device is very small, so it may be applicable), and would give $(1.8 \times 10^{-10} \text{ cm}^2)/f$ for a n-type device. Equations (60)–(63) would be reduced $m_p^*/m_n^* = 27.5$ times for n-type devices. We mention that S'_{I_s} has been calculated with the inclusion of a term of 10% of the applied gate voltage V in the kinetic energy of the carriers at the surface, and that for the back-surface recombination current this term has to be dropped in the similar expression for S'_{I_b} . However, we have neglected this here, because the surface recombination terms will not turn out to be important, as we will see below. The applied gate voltage was taken to be $V = 5 \text{ V}$. Calculating the fraction of each current, we obtain

$$\begin{aligned}
 (1 \text{ cm}^{-2})fS'_I(f) &= (20/132)^2 \times 1.8 \times 10^{-6} + (10/132)^2 \\
 &\quad \times 4.6 \times 10^{-9} + (3.6/132)^2 \times 7 \times 10^{-8} \\
 &\quad + (0.01/132)^2 \times 3.3 \times 10^{-8} + (80/132)^2 \\
 &\quad \times 1.8 \times 10^{-8} + (17.5/132)^2 \times 1.8 \times 10^{-8} \\
 &= 3.67 \times 10^{-8} + 2.6 \times 10^{-11} + 5.2 \times 10^{-11} \\
 &\quad + 1.9 \times 10^{-16} + 6.61 \times 10^{-9} + 3.17 \times 10^{-10} \\
 &= 4.37 \times 10^{-8} \tag{64}
 \end{aligned}$$

or for incoherent $1/f$ noise, 7.1×10^{-9} (p) and 3×10^{-10} (n). This value can be used in order to estimate the detectivity of the device in our example. Substituting into Eq. (57), we obtain with a quantum efficiency $\eta = 0.7$ and wavelength of $\lambda = 10 \mu\text{m}$

$$\begin{aligned}
 D^*(\lambda, f) &= \frac{\eta q \lambda}{hc} [S_{I_d}(f)]^{-1/2} \\
 &= \frac{(0.7 \times 1.6 \times 10^{-19} \text{ C})(10^{-5} \text{ m})}{(6.6 \times 10^{-34} \text{ J} \cdot \text{s})(3 \times 10^8 \text{ m/s})} \\
 &\quad \left(\frac{f}{(4.37 \times 10^{-8} \text{ cm}^2)(1.74 \times 10^{-6} \text{ A}^2/\text{cm}^4)} \right)^{1/2} \tag{65} \\
 &= (2 \times 10^7 \text{ cm} \cdot \text{Hz}^{1/2}/\text{W}) \times f^{1/2}
 \end{aligned}$$

or for incoherent $1/f$ noise, 5×10^7 (p) and 2.5×10^8 (n).

In conclusion we note that for the relatively large devices which we have considered, most of the quantum $1/f$ noise comes from fluctuations in diffusion and in the rate of tunneling via impurity centers in the bandgap. The effective mass of the carriers is present in the denominator of all quantum $1/f$ noise contributions except the coherent quantum $1/f$ fluctuation present in the diffusion current of large devices. In smaller devices the diffusion current will also be given by the conventional quantum $1/f$ formula, which contains the effective mass of the carriers in the denominator. For umklapp scattering the mass of the carriers in the denominator is squared. Consequently we

expect lower quantum $1/f$ noise from n-type devices, in which the minority carriers are holes, particularly if the devices are very small, say, below $10 \mu\text{m}$. We are now in a position to explain how “smart” ultralow-noise materials can be designed for specific classes of device applications (see Section 11).

7. DERIVATION OF THE CONVENTIONAL QUANTUM $1/f$ EFFECT

The simplified description of quantum $1/f$ noise was presented above in the elementary terms of Schrödinger’s statistical catalog model, without using second quantization. This approach is natural in view of the close connection between this new effect and diffraction, which is usually treated without second quantization, in the statistical catalog model based on the single-particle solution of the Schrödinger equation, normalized to the number of particles, N . Just as the superposition of elementary phase-shifted waves allows for the simplest and most intuitive description of diffraction through a slit, the description of quantum $1/f$ noise in terms of interference beats between slightly frequency-shifted scattered partial waves with bremsstrahlung energy losses will always provide the simplest and most elementary quantitative derivation of the $Q1/fE$, easily accessible even at the undergraduate level.

Below we now present the derivation of the $Q1/fE$ in a general form that determines the scattered current j from the observation of a sample of N outgoing particles. The minimal outgoing sample for defining particle–particle correlations in the scattered wave consists of two particles, and therefore the effect can be calculated for the case of two outgoing particles. Since the general derivation also yields a factor $1/N$ for bosons and a factor $1/(N-1)$ for fermions, and since the simplifying restriction to $N=2$ has given rise to some misinterpretations, a presentation of the general case of N bosons or N fermions will be of interest. We consider the case of bosons.

We start with the expression of the Heisenberg representation state $|S\rangle$ of N identical bosons of mass M emerging at an angle θ from some scattering process with various undetermined bremsstrahlung energy losses reflected in their one-particle waves $\varphi_i(\xi_i)$:

$$|S\rangle = (N!)^{-1/2} \prod_i d^3 \xi_i \varphi_i(\xi_i) \psi^\dagger(\xi_i) |0\rangle = \prod_i d^3 \xi_i \varphi_i(\xi_i) |S^0\rangle \tag{66}$$

where $\psi^\dagger(\xi_i)$ is the field operator creating a boson with position vector ξ_i , $\psi(\xi_i)$ is the field operator annihilating a particle, and $|0\rangle$ is the vacuum state, while $|S^0\rangle$ is the state with N bosons of position vectors ξ_i with $i = 1, \dots, N$. All products and sums in this section run from 1 to N , unless otherwise stated.

To calculate the particle density autocorrelation function in the outgoing scattered wave, we need the

expectation value of the operator

$$O(\mathbf{x}_1, \mathbf{x}_2) = \psi^\dagger(\mathbf{x}_1)\psi^\dagger(\mathbf{x}_2)\psi(\mathbf{x}_2)\psi(\mathbf{x}_1) \tag{67}$$

known as the operator of the pair correlation. This operator corresponds to a density autocorrelation function. The presence of two-particle coordinates in the operator O does not mean that we are considering two-particle interactions; it only means that the expectation value that we are calculating depends on the relative position of the particles. Using the well-known commutation relations for boson field operators,

$$\psi(\mathbf{x})\psi^\dagger(\mathbf{y}) - \psi^\dagger(\mathbf{y})\psi(\mathbf{x}) = \delta(\mathbf{x} - \mathbf{y}) \tag{68}$$

$$\psi(\mathbf{x})\psi(\mathbf{y}) - \psi(\mathbf{y})\psi(\mathbf{x}) = 0 \tag{69}$$

$$\psi^\dagger(\mathbf{x})\psi^\dagger(\mathbf{y}) - \psi^\dagger(\mathbf{y})\psi^\dagger(\mathbf{x}) = 0 \tag{70}$$

we first calculate the matrix element:

$$\begin{aligned} N| \langle S^o | O | S^o \rangle &= \sum'_{\mu\nu} \sum'_{mn} \delta(\eta_\nu - \mathbf{x}_1)\delta(\eta_\mu - \mathbf{x}_2)\delta(\xi_n - \mathbf{x}_1)\delta(\xi_m - \mathbf{x}_2) \sum_{(i,j)} \tag{71} \\ &\times \prod'_{ij} \delta(\eta_j - \xi_i) \end{aligned}$$

where $|S^o\rangle$ is the state with well-defined particle coordinates. Here the prime excludes $\mu = \nu$ and $m = n$ in the summations and excludes $i = m, i = n, j = \mu,$ and $j = \nu$ in the product. The summation $\sum_{(i,j)}$ runs over all permutations of the remaining $N - 2$ values of i and j . On the basis of this result we now calculate the complete matrix element

$$\begin{aligned} \langle S | O | S \rangle &= \frac{1}{N(N-1)} \sum'_{\mu\nu} \sum'_{mn} d^3\eta_\mu d^3\eta_\nu d^3\xi_m d^3\xi_n \\ &\times \varphi_\mu^*(\eta_\mu)\varphi_\nu^*(\eta_\nu)\varphi_m(\xi_m)\varphi_n(\xi_n)\delta(\eta_\nu - \mathbf{x}_1) \\ &\delta(\eta_\mu - \mathbf{x}_2)\delta(\xi_n - \mathbf{x}_1)\delta(\xi_m - \mathbf{x}_2) \\ &= \frac{1}{N(N-1)} \sum'_{\mu\nu} \sum'_{mn} \varphi_\mu^*(\mathbf{x}_2)\varphi_\nu^*(\mathbf{x}_1)\varphi_m(\mathbf{x}_1)\varphi_n(\mathbf{x}_2) \tag{72} \end{aligned}$$

The one-particle states are spherical waves emerging from the scattering center located at $x = 0$:

$$\varphi(\mathbf{x}) = \frac{C}{x} e^{iKx} \left(1 + \sum_{\mathbf{k},l} b(\mathbf{k},l) e^{-iqx} a_{\mathbf{k}l}^\dagger \right) \tag{73}$$

Here C is an amplitude factor, K the boson wave vector magnitude, and $b(\mathbf{k}, l)$ the bremsstrahlung amplitude for photons of wave vector \mathbf{k} and polarization l , while $a_{\mathbf{k}l}^\dagger$ is the corresponding photon creation operator, allowing the

emitted photon state to be created from the vacuum if Eq. (73) is inserted into Eq. (72). The momentum magnitude loss $\hbar q = Mck/K \equiv 2\pi Mf/K$ is necessary for energy conservation in the bremsstrahlung process. Substituting Eq. (73) into Eq. (72), we obtain

$$\begin{aligned} \langle S | O | S \rangle &= \left| \frac{C}{x} \right|^4 (N(N-1) \\ &+ 2(N-1) \sum_{\mathbf{k},l} |b(\mathbf{k},l)|^2 [1 + \cos q(x_1 - x_2)]) \tag{74} \end{aligned}$$

where we have neglected a small term of higher order in $b(\mathbf{k}, l)$. To perform the angular part of the summation in Eq. (74), we calculate the current expectation value of the state in Eq. (73) and compare it with the well-known cross sections without and with bremsstrahlung:

$$\mathbf{j} = \frac{\hbar \mathbf{K}}{Mx^2} \left[1 + \sum_{\mathbf{k},l} |b(\mathbf{k},l)|^2 \right] = \mathbf{j}_0 \left(1 + \alpha A \frac{df}{f} \right) \tag{75}$$

where the quantum fluctuations have disappeared; $\alpha A = (2\alpha/3\pi)(\Delta v/c)^2$ is the fractional bremsstrahlung rate coefficient, also known in QED as the infrared exponent; and the $1/f$ dependence of the bremsstrahlung part displays the well-known infrared catastrophe, that is, the emission of a logarithmically divergent number of photons in the low-frequency limit. Here Δv is the velocity change $\hbar(\mathbf{K} - \mathbf{K}_0)/M$ of the scattered boson, and $f = ck/2\pi$ the photon frequency. Equation (74) thus gives

$$\begin{aligned} \langle S | O | S \rangle &= \left| \frac{C}{x} \right|^4 (N(N-1) + 2(N-1)\alpha A \\ &\times [1 + \cos q(x_1 - x_2)] \frac{df}{f}) \tag{76} \end{aligned}$$

which is the pair correlation function, or density autocorrelation function, along the scattered beam with $df/f = dq/q$. The spatial distribution fluctuations along the scattered beam will also be observed as fluctuations in time at the detector, at any frequency f . According to the Wiener-Khinchine theorem, we obtain the spectral density of fractional scattered particle density ρ , (or current j , or cross section σ) fluctuations in frequency f or wave number q by dividing the coefficient of the cosine by the constant term $N(N - 1)$:

$$\rho^{-2} S_\rho(f) = j^{-2} S_j(f) = \sigma^{-2} S_\sigma(f) = \frac{2\alpha A}{fN} \tag{77}$$

where N is the number of particles or current carriers used to define the current j whose fluctuations we are studying. Quantum $1/f$ noise is thus a fundamental $1/N$ effect. The exact value of the exponent of f in Eq. (77) can be determined by including the contributions from all real and virtual multiphoton processes of any order (infrared radiative corrections), and turns out to be

$\alpha A - 1$ rather than -1 , which is important only philosophically, since $\alpha A \ll 1$. The spectral integral is thus convergent at $f=0$.

For fermions we repeat the calculation, replacing in the derivation of Eq. (10) the commutators of field operators by anticommutators, which finally yields in the same way

$$\rho^{-2}S_\rho(f) = j^{-2}S_j(f) = \sigma^{-2}S_\sigma(f) = \frac{2\alpha A}{f(N-1)} \quad (78)$$

which causes no difficulties, since $N \geq 2$ for particle correlations to be defined, and which is practically the same as Eq. (77), since usually $N \gg 1$. Equations (77) and (78) suggest a new notion of physical cross sections and process rates that contain $1/f$ noise and express a fundamental law of physics, important in most high-technology applications [16].

We conclude that the conventional quantum $1/f$ effect can be explained in terms of interference beats between the part of the outgoing de Broglie waves scattered without bremsstrahlung energy losses above the detection limit (given in turn by the reciprocal duration T of the $1/f$ noise measurement) on one hand, and the various parts scattered with bremsstrahlung energy losses; but there is more to it than that—exchange between identical particles is also important. This, of course, is just one way to describe the reaction of the emitted bremsstrahlung back on the scattered current. This reaction thus reveals itself as the cause of the quantum $1/f$ effect, and implies that the effect cannot be obtained with the independent boson model. The effect, just like the classical turbulence-generated $1/f$ noise, is a result of the scale-invariant nonlinearity of the equations of motion describing the coupled system of matter and field. Ultimately, therefore, this nonlinearity is the source of the $1/f$ spectrum in both the classical and the quantum form of the author's theory. We can say that the quantum $1/f$ effect is an infrared divergence phenomenon, this divergence being the result of the same nonlinearity. The new effect is, in fact, the first time-dependent infrared radiative correction. Finally, it is also deterministic in the sense of a well-determined wave function, once the initial phases γ of all field oscillators are given. In quantum-mechanical correspondence with its classical turbulence analog, the new effect is therefore a quantum manifestation of classical chaos, which we can take as the definition of a certain type of quantum chaos.

8. PHYSICAL DERIVATION OF THE COHERENT QUANTUM $1/f$ EFFECT

This effect arises in a beam of electrons (or other charged particles propagating freely in vacuum) from the definition of the physical electron as a bare particle plus a coherent state of the electromagnetic field. It is caused by the energy spread characterizing any coherent state of the electromagnetic field oscillators, an energy spread that spells nonstationarity, that is, fluctuations. To find the spectral density of these inescapable fluctuations, which are known to characterize any quantum

state that is not an energy eigenstate, we use an elementary physical derivation based on Schrödinger's definition of coherent states, followed by a rigorous derivation from a well-known quantum-electrodynamical propagator. The chaotic character of these fluctuations is discussed later.

The coherent quantum $1/f$ effect will be derived in three steps: First we consider a hypothetical world with just a single mode of the electromagnetic field coupled to a beam of charged particles; considering the mode to be in a coherent state, we calculate the autocorrelation function of the quantum fluctuations in the particle density (or concentration) that arise from the nonstationarity of the coherent state. Then we calculate the amplitude with which this one mode is represented in the field of an electron, according to electrodynamics. Finally, we take the product of the autocorrelation functions calculated for all modes with the amplitudes found in the previous step.

Let a mode of the electromagnetic field be characterized by the wave vector q , the angular frequency $\omega = cq$ and the polarization λ . Denoting the variables q and λ simply by q in the labels of the states, we write the coherent state [25,31,32] of amplitude $|z_q|$ and phase $\arg z_q$ in the form

$$\begin{aligned} |z_q\rangle &= \exp\left(-\frac{1}{2}|z_q|^2\right) \exp(z_q a_q^\dagger) |0\rangle \\ &= \exp\left(-\frac{1}{2}|z_q|^2\right) \sum_{n=0}^{\infty} \frac{z_q^n}{n!} |n\rangle \end{aligned} \quad (79)$$

Here a_q^\dagger is the creation operator that adds one energy quantum to the energy of the mode. Let us use a representation of the energy eigenstates in terms of Hermite polynomials $H_n(x)$:

$$|n\rangle = (2^n n! \sqrt{\pi})^{-1/2} \exp(-x^2/2) H_n(x) e^{i\omega t} \quad (80)$$

This yields for the coherent state $|z_q\rangle$ the representation

$$\begin{aligned} \psi_q(x) &= \exp\left(-\frac{1}{2}|z_q|^2\right) \exp\left(-\frac{x^2}{2}\right) \sum_{n=0}^{\infty} \frac{(z_q e^{i\omega t})^n}{[n!(2^n \sqrt{\omega})]^{1/2}} H_n(x) \\ &= \exp\left(-\frac{1}{2}|z_q|^2\right) \exp\left(-\frac{x^2}{2}\right) \exp(-z_q^2 e^{-2i\omega t} + 2xz_q e^{i\omega t}) \end{aligned} \quad (81)$$

In the last form the generating function of the Hermite polynomials was used. The corresponding autocorrelation function of the probability density function, obtained by averaging over the time t or the phase of z_q , is, for $|z_q| \ll 1$

$$\begin{aligned} P_q(\tau, x) &= \langle |\psi_q|_t^2 |\psi_q|_{t+\tau}^2 \rangle \\ &= [1 + 8x^2 |z_q|^2 (1 + \cos \omega\tau) - 2|z_q|^2] \exp(-x^2/2) \end{aligned} \quad (82)$$

Integrating over x from $-\infty$ to ∞ , we find the autocorrelation function

$$A^1(\tau) = 2^{-1/2}(1 + 2|z_q|^2 \cos \omega\tau) \tag{83}$$

This result shows that the probability distribution contains a constant background with small superposed oscillations of frequency ω . Physically, the small oscillations in the total probability describe self-organization, or bunching, of the particles in the beam. They are thus more likely to be found in a measurement at some times and places than at others along the beam. Note that for $z_q = 0$ the coherent state becomes the ground state of the oscillator, which is also an energy eigenstate, and therefore stationary and free of oscillations.

We now determine the amplitude z_q with which the field mode q is represented in the physical electron. One way to do this is to let a bare particle dress itself through its interaction with the electromagnetic field, by performing first-order perturbation theory with the interaction Hamiltonian

$$H' = A_\mu j^\mu = -\frac{e}{c} \mathbf{v} \cdot \mathbf{A} + e\phi \tag{84}$$

where \mathbf{A} is the vector potential and ϕ the scalar electric potential. Another way is to Fourier-expand the electric potential e/r of a charged particle in a box of volume V . In both ways we obtain

$$|z_q|^2 = \pi(e/q)^2(\hbar c q V)^{-1} \tag{85}$$

Considering now all modes of the electromagnetic field, we obtain from the single-mode result of Eq. (83)

$$\begin{aligned} A(\tau) &= C \prod_q (1 + 2|z_q|^2 \cos \omega_q \tau) = C \left(1 + \sum_q 2|z_q|^2 \cos \omega_q \tau \right) \\ &= C \left(1 + \frac{4V}{2^3 \pi^3} d^3 q |z_q|^2 \cos \omega_q \tau \right) \end{aligned} \tag{86}$$

Here we have again used the smallness of z_q , and we have introduced a constant C . Using Eq. (85) we obtain

$$\begin{aligned} A(\tau) &= C \left(1 + 4\pi \frac{V}{2^3 \pi^3} \frac{4\pi e^2}{V \hbar c} \frac{dq}{q} \cos \omega_q \tau \right) \\ &= C \left(1 + 2 \frac{\alpha}{\pi} \cos \omega\tau \frac{d\omega}{\omega} \right) \end{aligned} \tag{87}$$

Here $\alpha = e^2/\hbar c$ is the fine-structure constant $\approx \frac{1}{137}$. The first term in the large parentheses is unity and represents the constant background, or the dc part of the current carried by the beam of particles through vacuum. The autocorrelation function for the relative (fractional) density fluctuations, or for the current density fluctuations in the beam of charged particles, is obtained therefore by dividing the second term by the first term. The constant C drops out when the fractional fluctuations are considered.

According to the Wiener-Khinchine theorem, the coefficient of $\cos \omega\tau$ is the spectral density of the fluctuations, $S_{|\psi|}^2$ for the particle concentration, or S_j for the current density $j = e(k/m)|\psi|^2$:

$$S_{|\psi|}^2 \langle |\psi|^{-2} \rangle = S_j(j)^{-2} = 2 \frac{\alpha}{\pi f N} = 4.6 \times 10^{-3} f^{-1} N^{-1} \tag{88}$$

Here we have included in the denominator the total number N of charged particles that are observed simultaneously, because the noise contributions from each particle are independent. This result is related to the conventional $Q1/fE$ considered in the next section. A similar calculation yields the gravodynamical quantum $1/f$ effect (QGD $1/f$ effect) by substituting gravitons for the photons considered so far as infra-quanta.

9. RIGOROUS DERIVATION OF THE COHERENT QUANTUM $1/f$ EFFECT

The present derivation is based on the well-known new propagator $G_s(x' - x)$ derived relativistically [33,34] in 1975 in a new picture required by the infinite range of the Coulomb potential. The corresponding nonrelativistic form [35] was provided by Zhang and Handel (see Section 10.2.6):

$$\begin{aligned} &-i \langle \Phi_0 | T \psi_s(x') \psi_s^\dagger(x) | \Phi_0 \rangle \\ &\equiv \delta_{ss'} G_s(x' - x) \\ &= \frac{i}{V} \sum_{\mathbf{p}} \left(\exp i \frac{\mathbf{p} \cdot (\mathbf{r} - \mathbf{r}') - \mathbf{p}^2(t - t')/2m}{\hbar} \right) n_{\mathbf{p},s} \\ &\quad \times \left(-i \frac{\mathbf{p} \cdot (\mathbf{r} - \mathbf{r}')}{\hbar} + i(m^2 c^2 + \mathbf{p}^2)^{1/2} (t - t') \frac{c}{\hbar} \right)^{\alpha/\pi} \end{aligned} \tag{89}$$

Here $\alpha = e^2/\hbar c \approx 1/137$ is Sommerfeld's fine structure constant, $n_{\mathbf{p},s}$ the number of electrons in the state of momentum \mathbf{p} and spin s , m the rest mass of the fermions, $\delta_{ss'}$ the Kronecker symbol, c the speed of light, $x = (\mathbf{r}, t)$ any spacetime point, and V the volume of a normalization box. T is the time-ordering operator, which orders the operators in the order of decreasing times from left to right and multiplies the result by $(-1)^P$, where P is the parity of the permutation required to achieve this order. For equal times, T normal orders the operators, that is, for $t = t'$ the left-hand side of Eq. (89) is $i \langle \Phi_0 | \psi_s^\dagger(x) \psi_s(x') | \Phi_0 \rangle$. The state Φ_0 of the N electrons is described by a Slater determinant of single-particle orbitals.

The resulting spectral density coincides with the result $2\alpha/\pi f N$, derived directly in the section above from the coherent state of the electromagnetic field of a physical charged particle. The connection with the conventional quantum $1/f$ effect is discussed in the section.

To calculate the current autocorrelation function we need the density correlation function, which is also known

as the two-particle correlation function, and is defined by

$$\begin{aligned} & \langle \Phi_0 | T \psi_s^\dagger(x) \psi_s(x) \psi_s^\dagger(x') \Phi^{s'}(x') | \Phi_0 \rangle \\ &= \langle \Phi_0 | \psi_s^\dagger(x) \psi_s(x) | \Phi_0 \rangle \langle \Phi_0 | \psi_s^\dagger(x') \psi_s(x') | \Phi_0 \rangle \\ & \quad - \langle \Phi_0 | T \psi_s(x') \psi_s^\dagger(x) | \Phi_0 \rangle \langle \Phi_0 | T \psi_s(x) \psi_s^\dagger(x') | \Phi_0 \rangle \end{aligned} \quad (90)$$

The first term can be expressed in terms of the particle density of spin s , $n/2 = N/2V = \langle \Phi_0 | \psi_s^\dagger(x) \psi_s(x) | \Phi_0 \rangle$, while the second term can be expressed in terms of the Green function Eq. (89) in the form

$$\begin{aligned} A_{ss'}(x-x') &\equiv \langle \Phi_0 | \psi_s^\dagger(x) \psi_s^\dagger(x') \psi_s(x') \psi_s(x) | \Phi_0 \rangle \\ &= (n/2)^2 + \delta_{ss'} G_s(x'-x) G_s(x-x') \end{aligned} \quad (91)$$

The *relative* autocorrelation function $A(x-x')$ describing the normalized pair correlation independent of spin is obtained by dividing by n^2 and summing over s and s' :

$$\begin{aligned} A(x-x') &= 1 - \frac{1}{n^2} \sum_s G_s(x-x') G_s(x'-x) \\ &= 1 - \frac{1}{N^2} \sum_s \sum_{\mathbf{p}\mathbf{p}'} \\ & \quad \left(\exp i \frac{(\mathbf{p}-\mathbf{p}') \cdot (\mathbf{r}-\mathbf{r}') - (E_{\mathbf{p}} - E_{\mathbf{p}'})(t-t')}{\hbar} \right) n_{\mathbf{p},s} n_{\mathbf{p}',s} \\ & \quad \times \left(\frac{\mathbf{p} \cdot (\mathbf{r}-\mathbf{r}')}{\hbar} - (m^2 c^2 + \mathbf{p}^2)^{1/2} (t-t') \frac{c}{\hbar} \right)^{\alpha/\pi} \\ & \quad \times \left(\frac{\mathbf{p}' \cdot (\mathbf{r}'-\mathbf{r})}{\hbar} - (m^2 c^2 + \mathbf{p}'^2)^{1/2} (t'-t) \frac{c}{\hbar} \right)^{\alpha/\pi} \end{aligned} \quad (92)$$

Here we have used Eq. (89).

We now consider a beam of charged fermions (e.g., electrons), represented in momentum space by a sphere of radius p_F centered on the momentum \mathbf{p}_0 , which is the average momentum of the fermions. The energy and momentum differences between terms of different \mathbf{p} are large, leading to rapid oscillations in space and time, which contain only high-frequency quantum fluctuations. The low-frequency and low-wavenumber part A_1 of this relative density autocorrelation function is given by the

terms with $\mathbf{p} = \mathbf{p}'$:

$$A_l(x-x') = 1 - \frac{1}{N^2} \sum_s \sum_{\mathbf{p}} n_{\mathbf{p},s} \quad (93)$$

$$\begin{aligned} & \times \left| \frac{\mathbf{p} \cdot (\mathbf{r}-\mathbf{r}')}{\hbar} - (m^2 c^2 + \mathbf{p}^2)^{1/2} (t-t') \frac{c}{\hbar} \right|^{2\alpha/\pi} \\ & \approx 1 - \frac{1}{N} \left| \frac{\mathbf{p}_0 \cdot (\mathbf{r}-\mathbf{r}')}{\hbar} - \frac{m c^2 \tau}{\hbar} \right|^{2\alpha/\pi} \\ & \quad \text{for } p_F \ll \left| p_{03} - \frac{m c^2 \tau}{z} \right| \end{aligned} \quad (94)$$

Here we have used the mean value theorem, considering the $2\alpha/\pi$ power as a slowly varying function of \mathbf{p} and neglecting \mathbf{p}_0 in the coefficient of $\tau \equiv t-t'$, with $z \equiv |\mathbf{r}-\mathbf{r}'|$. The correlations propagate along the beam with a group velocity given by the average velocity \mathbf{p}_0/m of the particles in the beam, and with the phase velocity c^2/v . Using an identity in Ref. 36, we obtain from Eq. (94) with $\theta \equiv |\tau - \mathbf{p}_0 \cdot (\mathbf{r}-\mathbf{r}')/m c^2|$ the form

$$\begin{aligned} A_1(x-x') &= 1 - \frac{1}{N} \left| \frac{m c^2 \theta}{\hbar} \right|^{2\alpha/\pi} = 1 - \frac{1.25}{N} |\Theta|^{2\alpha/\pi} \\ &= 1 - \frac{1.25}{N} e^{(2\alpha/\pi) \ln \Theta} \\ &\approx 1 - \frac{1.25}{N} \left(1 + \frac{2\alpha}{\pi} \ln \Theta \right) \\ &= 1 - \frac{2.5}{N} + \frac{1.25}{N} \left(1 - \frac{2\alpha}{\pi} \ln \Theta \right) \\ &\approx \frac{N-2.5}{N} + \frac{1.25}{N} e^{-(2\alpha/\pi) \ln \Theta} \\ &= \frac{1}{N} \left(N - 2.5 + \frac{2.5\alpha}{\pi \cos \alpha} \int_0^{\cos \omega \Theta d\omega} \frac{\cos \omega \Theta d\omega}{\omega^{1-2\alpha/\pi}} \right) \end{aligned} \quad (95)$$

This indicates a $\omega^{-1+2\alpha/\pi}$ spectrum and a $1/(N-2.5)$ dependence of the spectrum of fractional fluctuations in density n and current j . The total error corresponding to the two linear approximations of exponentials in Eq. (95) is less than 1%, provided $|\ln \Theta| < 20$, or $(250,000)^{-1} \text{ h} < |\theta| < 250,000 \text{ h}$. Here $\Theta = \theta/(1 \text{ s})$, and ω is the circular Fourier frequency in radians per second. We have used $[(1 \text{ s}) m c^2 / \hbar]^{2\alpha/\pi} \approx 1.25$; this accounts also for the presence of the number 2.5 instead of the more usual number 2 in the final form. The form we have chosen here is more convenient for applications. The equivalent normal form would have been

$$\begin{aligned} A_1(x-x') & \approx \frac{1}{N} \left(N - 2 + \frac{2\alpha}{\pi \cos \alpha} \int_0^{\left(\frac{m c^2}{\hbar \omega} \right)^{2\alpha/\pi} \cos \omega \theta \frac{d\omega}{\omega}} \right) \end{aligned} \quad (96)$$

in which the error caused by the two linear approximations of exponentials would have been of the order of 20%, and in which the fractional power would also have been neglected

in the integrand for all purposes except for the theoretical question of the integrability of the $1/\omega$ spectrum.

The fractional autocorrelation of current fluctuations δj is obtained by multiplying Eq. (92) on both sides by $(ep_0/m)^2$ and dividing by $(enp_0/m)^2$, which is the square of the average current density j , instead of just dividing by n^2 . So it is the same as the fractional autocorrelation for quantum density fluctuations. The last form of Eq. (95) for the coherent quantum-electrodynamical chaos process in electric currents becomes

$$S_{\delta j/\delta j}(k) \approx \frac{2.5\alpha}{\pi\omega(N-2.5)}\omega^{2\alpha} \approx \frac{2.5\alpha}{\pi\omega N} = \frac{0.0058}{\omega N} \quad (97)$$

Being observed in the presence of a constant applied field, these fundamental quantum current fluctuations are usually interpreted as mobility fluctuations. Most of the conventional quantum $1/f$ fluctuations in physical cross sections and process rates are also mobility fluctuations, but some are also in the recombination speed or tunneling rate.

10. MORE RECENT RESULTS

Six developments are reported. They include (1) a first-principles proof of the absence of the $Q1/fE$ in the process of photogeneration of carriers in photodetectors, (2) the verification of the quantum $1/f$ noise theory in quartz resonators, (3) the application of quantum $1/f$ noise to explain the anisotropy observed for conventional quantum $1/f$ noise in mono-crystal silicon, (4) the derivation of the nonrelativistic propagator of QED, which predicts the presence of the coherent quantum $1/f$ effect, and (5) a clear formulation of the problem of transition between the coherent and conventional quantum $1/f$ effects. In addition we have improved our universal sufficient criterion for $1/f$ spectra in chaotic nonlinear systems, and (6) we have applied it to QED, obtaining the quantum $1/f$ effect as a consequence of the nonlinearity of the system formed by the charged particles together with the electromagnetic field.

10.1. Method Used

The derivation of the coherent nonrelativistic propagator of QED was performed in the picture introduced by Dollard in 1964, and uses the branchpoint propagator introduced later by Zwanziger and Kibble [33,34]. The derivation of the anisotropy of $1/f$ noise in monocrystalline silicon is based on the conventional quantum $1/f$ noise theory and the known structure of the conduction band of silicon in the Brillouin zone.

10.2. Results

Below we report the main results of the four [33,34] achievements mentioned above.

10.2.1. First-Principles Proof of the Absence of the Quantum $1/f$ Effect in the Photogeneration of Carriers in Photodetectors. Quantum $1/f$ noise is a fundamental aspect of quantum mechanics, representing universal fluctuations

of physical process rates R and cross sections σ given by the fractional (or relative) spectral density $S(f) = 2\alpha A/fN$. Therefore it is present in the process rates generating the dark current observed in junction photodetectors, such as *diffusion* (scattering cross sections fluctuate) in diffusion-limited junctions, and *recombination* in the recombination-limited regime. One is therefore tempted to expect similar fluctuations in the *photogeneration* of electron-hole pairs. However, as we show below, the corresponding quantum $1/f$ coefficient is zero, precluding the existence of quantum $1/f$ fluctuations in the photogeneration rate. Here N is the number of carriers used to define or measure the process rate or cross section considered.

For an arbitrary process involving a total of n incoming and outgoing charged particles, the nonrelativistic quantum $1/f$ coefficient is given [37] by

$$2\alpha A = \frac{4\alpha}{3\pi c^2} \sum_{i,j=1}^n \eta_i \eta_j q_i q_j (\mathbf{v}_i - \mathbf{v}_j)^2 \quad (98)$$

where the summation runs over the charges q_i and velocities \mathbf{v}_i of all incoming ($\eta_i = -1$) and outgoing ($\eta_i = 1$) particles (altogether n of them) in the process whose $Q1/fN$ we want to find, and α is Sommerfeld's fine structure constant, $e^2/\hbar c \approx \frac{1}{137}$. In a photogeneration process a photon ($q = 0$) is absorbed, and a pair of oppositely charged particles is generated ($\eta = 1$) with velocities \mathbf{v}_1 and \mathbf{v}_2 , which either are zero or quickly decay to zero in a time negligible with respect to the reciprocal frequency at which we calculate the quantum $1/f$ noise. Thus in our case there are no incoming charged particles, and $n = 0 + 2 = 2$. The coefficient αA of a photogeneration process is therefore zero:

$$\begin{aligned} \alpha A_{\text{ph}} &= (1, 1) + (2, 2) + (1, 2) + (2, 1) \\ &= 0 + 0 + \frac{4\alpha}{3\pi c^2} (\mathbf{v}_1 - \mathbf{v}_2)^2 \approx 0 \end{aligned} \quad (99)$$

All photogenerated carriers of the right sign are collected in the well of the charge-coupled device, although they may generate quantum $1/f$ voltage fluctuations on their way. Since usually only the number of carriers collected at readout matters, no quantum $1/f$ noise will be observed in a photoelectric CCD as long as the dark current is negligible with respect to the photocurrent. This is in agreement with the experiments performed by Mooney [38]. The same considerations apply to MIS photodetectors.

10.2.2. Verification of the Quantum $1/f$ Noise Theory in Quartz Resonators. According to the general quantum $1/f$ formula (2), $\Gamma^{-2} S_{\Gamma}(f) = 2\alpha A/f$, where $\alpha = e^2/\hbar c \approx 1/137$ and $A = 2(\Delta\mathbf{J}/ec)^2/3\pi$ is the quantum $1/f$ effect in any physical process rate Γ . Setting

$$\mathbf{J} = \frac{d\mathbf{P}}{dt} = \dot{\mathbf{P}} \quad (100)$$

where \mathbf{P} is the vector of the dipole moment of the quartz crystal, we obtain for the fluctuations in the rate Γ of phonon removal from the main resonator oscillation mode

of the crystal (by scattering on a phonon from any other mode of average frequency (ω) , or via a two-phonon process at a crystal defect or impurity, involving a phonon of average frequency (ω')) the spectral density

$$S_{\Gamma}(f) = \Gamma^2 4\alpha(\Delta\dot{\mathbf{P}})^2 / 3\pi e^2 c^2 \quad (101)$$

where $(\Delta\dot{\mathbf{P}})^2$ is the square of the dipole moment rate change associated with the process causing the removal of a phonon from the main oscillator mode. To calculate it, we write the energy W of the interacting resonator mode (ω) in the form

$$W = n\hbar(\omega) = 2 \frac{Nm}{2} \left(\frac{dx}{dt} \right)^2 = \frac{Nm}{e^2} \left(e \frac{dx}{dt} \right)^2 = \frac{m}{Ne^2} \varepsilon^2 \dot{\mathbf{P}}^2 \quad (102)$$

The factor 2 includes the potential energy contribution. Here m is the reduced mass of the elementary oscillating dipoles, e their charge, ε a polarization constant, and N their number in the quartz crystal. Applying a variation $\Delta n = 1$, we get

$$\frac{\Delta n}{n} = 2 \frac{|\Delta\dot{\mathbf{P}}|}{|\dot{\mathbf{P}}|}, \quad \text{or} \quad \Delta\dot{\mathbf{P}} = \frac{\dot{\mathbf{P}}}{2n}$$

Solving Eq. (102) for $\dot{\mathbf{P}}$ and substituting, we obtain

$$|\Delta\dot{\mathbf{P}}| = \left(\frac{N\hbar(\omega)}{n} \right)^{1/2} \frac{e}{2\varepsilon}$$

Substituting $\Delta\dot{\mathbf{P}}$ into Eq. (3), we get

$$\Gamma^{-2} S_{\Gamma}(f) = N\alpha\hbar(\omega) / 3n\pi mc^2 f \varepsilon^2 \equiv \Lambda / f \quad (103)$$

This result is applicable to the fluctuations in the loss rate Γ of the quartz.

The corresponding resonance frequency fluctuations of the quartz resonator are given by [39]

$$\omega^{-2} S_{\omega}(f) = \frac{1}{4Q^4} \frac{\Lambda}{f} = \frac{N\alpha\hbar(\omega)}{12n\pi mc^2 f \varepsilon^2 Q^4} \quad (104)$$

where Q is the quality factor of the single-mode quartz resonator considered, and (ω) is not the circular frequency of the main resonator mode, ω_0 , but rather the practically constant frequency of the average interacting phonon, considering both three-phonon and two-phonon processes. The corresponding $\Delta\dot{\mathbf{P}}$ in the main resonator mode has to be also included in principle, but is negligible because of the very large number of phonons present in the main resonator mode.

Equation (6) can be written in the form

$$S(f) = \beta V / f Q^4 \quad (105)$$

where, with a moderate value $(\omega) = 10^8 \text{ s}^{-1}$ and with $n = kT / \hbar(\omega)$, $T = 300 \text{ K}$, and $kT = 4 \times 10^{14}$

$$\beta = \frac{N}{V} \frac{\alpha\hbar(\omega)}{12n\pi\varepsilon^2 mc^2} = 10^{22} \frac{(1/137)(10^{-27} \times 10^8)^2}{12kT \times \pi \times 10^{-27} \times 9 \times 10^{20}} = 1$$

This is in very good agreement with experiment [40].

10.2.3. Application of Quantum 1/f Noise to Explain the Anisotropy of Conventional Quantum 1/f Noise in Monocrystalline silicon. The conduction band of silicon has six equivalent energy minima along the six $\langle 100 \rangle$ directions in the reciprocal lattice, which is bcc. These directions correspond to [111] in the direct lattice, which is fcc. If an electric field is applied along the [111] direct lattice axis, along which the energy minima are located, a lot of easy umklapp intervalley scattering processes (g processes) will take place along the direction opposing the applied field, because in the reciprocal lattice the minima are at $0.85K$ from the center of the first Brillouin zone, so there is only $0.3K$ to the next minimum in the neighboring zone. Here K is the distance between the center and the edge of the Brillouin zone. But umklapp processes are associated with the largest conventional $Q1/fE$, because in the expression $(4\alpha/3\pi)(\hbar\Delta k/mc)^2$ we have $\Delta k = G = 2\pi/a$ for umklapp, while normal scattering processes have smaller Δk . Therefore, the [111] direction will yield the highest quantum 1/f noise for identical currents applied in different directions in a Si mono-crystal. Experimentally it is well known that devices built on (100) silicon surfaces have lower 1/f noise than those built on (111) surfaces [41].

10.2.4. Derivation of the Nonrelativistic Propagator of Quantum Electrodynamics. The derivation of the coherent $Q1/fE$ by us [42] in second quantization was done on the basis of a new picture of QED introduced by Dollard, Zwanziger, and Kibble [29,31,33,34,43,44]. This new picture includes the long-range part of the Coulomb potential in the unperturbed Hamiltonian H_0 . The result is a more complicated free particle and a new propagator with a branch point instead of a pole. We used a nonrelativistic form of this new propagator and obtained the universal spectral density of fractional current fluctuations $S_{\delta j/j}(f) = 2\alpha/3\pi fN$, which we called the coherent $Q1/fE$. The purpose here is to derive this nonrelativistic propagator from the well-known relativistic propagator based on Dollard's picture.

Our derivation is similar to the derivation of the nonrelativistic equation from Dirac's theory of the electron. It is based on the distinction between the large and small components of the Dirac spinor.

The relativistic propagator $S(x' - x)$ in the equation

$$\theta(t' - t)\psi^\dagger(x') = i \int S(x' - x)\gamma_0\psi^\dagger(x)d^3x \quad (106)$$

is

$$S(x) = i(2\pi)^{-3} \int \frac{d^3\mathbf{p}}{2E} e^{ipx} (-ipx)^{\alpha/\pi} (i\gamma p - m) \quad (107)$$

and valid for very large time t' . In the nonrelativistic limit, the Dirac spinor can be written in the form

$$\psi^\dagger(x) = e^{-imc^2t'/h} \begin{bmatrix} \varphi(\mathbf{x}) \\ \chi(\mathbf{x}) \end{bmatrix} \tag{108}$$

So we get

$$\begin{aligned} & \vartheta(t' - t)\psi^\dagger(x') \\ &= i(-i) \iint \frac{d^3\mathbf{p}}{(2\pi)^3} \exp\left(i\frac{\mathbf{p}\cdot(\mathbf{x}' - \mathbf{x}) - E(t' - t) - mc^2t}{h}\right) \\ & \times (-ipx)^{\alpha/\pi} \frac{E\gamma_0 - ic\mathbf{p}\cdot\boldsymbol{\gamma} + mc^2}{2E} \beta \begin{bmatrix} \varphi(\mathbf{x}) \\ \chi(\mathbf{x}) \end{bmatrix} d^3\mathbf{x} \\ &= \iint \frac{d^3\mathbf{p}}{(2\pi)^3} \exp\left(i\frac{\mathbf{p}\cdot(\mathbf{x}' - \mathbf{x}) - E(t' - t) - mc^2t}{h}\right) \\ & \times (-ipx)^{\alpha/\pi} \frac{E + c\mathbf{p}\cdot\boldsymbol{\alpha} + \beta mc^2}{2E} \beta \begin{bmatrix} \varphi(\mathbf{x}) \\ \chi(\mathbf{x}) \end{bmatrix} d^3\mathbf{x} \end{aligned} \tag{109}$$

and then we have

$$\begin{aligned} & \vartheta(t' - t) \begin{bmatrix} \varphi(\mathbf{x}) \\ \chi(\mathbf{x}) \end{bmatrix} \\ &= \vartheta(t' - t)\psi^\dagger(x') e^{imc^2t'/h} \\ & \iint \frac{d^3\mathbf{p}}{(2\pi)^3} \exp\left(i\frac{\mathbf{p}\cdot(\mathbf{x}' - \mathbf{x}) - (E - mc^2)(t' - t)}{h}\right) \\ & \times (-ipx)^{\alpha/\pi} \frac{E + c\mathbf{p}\cdot\boldsymbol{\alpha} + \beta mc^2}{2E} \beta \begin{bmatrix} \varphi(\mathbf{x}) \\ \chi(\mathbf{x}) \end{bmatrix} d^3\mathbf{x} \\ &= \iint \frac{d^3\mathbf{p}}{(2\pi)^3} \exp\left(i\frac{\mathbf{p}\cdot(\mathbf{x}' - \mathbf{x}) - (E - mc^2)(t' - t)}{h}\right) \\ & \times (-ipx)^{\alpha/\pi} \left(\frac{1}{2} \begin{bmatrix} \varphi \\ \chi \end{bmatrix} + \frac{c\mathbf{p}}{2E} \cdot \begin{bmatrix} \sigma\chi \\ \sigma\varphi \end{bmatrix} + \frac{mc^2}{2E} \begin{bmatrix} \varphi \\ -\chi \end{bmatrix} \right) d^3\mathbf{x} \end{aligned} \tag{110}$$

Furthermore, after using the nonrelativistic limit spinor component relation

$$\chi \approx \frac{\boldsymbol{\sigma}\cdot\mathbf{p}}{2mc} \varphi \tag{111}$$

we get

$$\begin{aligned} & \vartheta(t' - t)\varphi^\dagger(x') \\ &= \int d^3\mathbf{x} \left[\int \frac{d^3\mathbf{p}}{(2\pi)^3} \exp\left(i\frac{\mathbf{p}\cdot(\mathbf{x}' - \mathbf{x}) - (\mathbf{p}^2/2m)(t' - t)}{h}\right) \right. \\ & \left. \times (-ipx)^{\alpha/\pi} \right] \varphi(\mathbf{x}) \end{aligned} \tag{112}$$

If we compare this with the equation

$$\vartheta(t' - t)\varphi(x') = i \int d^3\mathbf{x} G(x' - x)\varphi(x) \tag{113}$$

which defines the nonrelativistic propagator, we get for the latter

$$\begin{aligned} G(x' - x) &= -i \int \frac{d^3\mathbf{p}}{(2\pi)^3} \exp\left(i\frac{\mathbf{p}\cdot(\mathbf{x}' - \mathbf{x}) - (\mathbf{p}^2/2m)(t' - t)}{h}\right) \\ & \times (-ipx)^{\alpha/\pi} \end{aligned} \tag{114}$$

The propagator with a phase factor is

$$\begin{aligned} G(x' - x) &= -i \int \frac{d^3\mathbf{p}}{(2\pi)^3} \exp\left(i\frac{\mathbf{p}\cdot(\mathbf{x}' - \mathbf{x}) - (\mathbf{p}^2/2m)(t' - t)}{h}\right) \\ & \times (-i)^{\alpha/\pi + i\gamma} \left(-\frac{(m^2c^2 + \mathbf{p}^2)(t' - t)c}{h} + \frac{\mathbf{p}\cdot(\mathbf{x}' - \mathbf{x})}{h} \right)^{\alpha/\pi + i\gamma} \end{aligned} \tag{115}$$

This is just the nonrelativistic propagator used by us in the preceding section. It has a branchpoint instead of a pole. For $\mathbf{x} = \mathbf{x}'$

$$G = -i \left(i\frac{mc^2}{h}(t' - t) \right)^{\alpha/\pi + i\gamma} \left(\frac{m}{2\pi i(t' - t)} \right)^{3/2} \tag{116}$$

This propagator expresses the essence of our coherent Q1/f E.

10.2.5. Formulation of the Problem of Transition between the Coherent and Conventional Quantum 1/f Effects. From the beginning of the theory of fundamental 1/f noise in semiconductors and metals two situations were distinguished [45]. The first, applicable to small semiconductor samples and very small (mesoscopic) metallic samples, has most of the energy excess $Nmv_d^2/2$ present in the stationary state carrying a finite current through the sample (excess over the energy of the equilibrium state) contained in the sum of the individual kinetic energies of the N current carriers, $\sum_i mv_i^2/2$. Here the velocities v_i of the carriers of mass m contain a small drift term v_d . The second, applicable in larger semiconductor or metal samples, has most of that energy excess contained in the

collective magnetic energy of the current-carrying state, $(B^2 8\pi) d^3x = LI^2/2$. The ratio s of this magnetic energy to the kinetic energy excess is roughly equal [45,46] to the number of carriers N' per unit length of the sample, multiplied by the classical radius of the electron, $r_0 = e^2/mc^2$: $s = N'r_0$. This situation was considered already in our classical magnetic turbulence theory [45,47].

In the first situation conventional quantum $1/f$ noise is applicable for fluctuations in physical scattering cross sections σ , in physical process rates Γ , and in the mobility μ or diffusion coefficient D (the latter two only if exclusively limited by σ or Γ):

$$\sigma^{-2} S_\sigma(f) = \Gamma^{-2} S_\Gamma(f) = \mu^{-2} S_\mu(f) = 2\alpha A/fN \quad (s \ll 1) \quad (117)$$

because in this case the coherent, collective term in the Hamiltonian is negligible. In the second case, however, the coherent $Q1/fE$ [26] is dominant:

$$j^{-2} S_j(f) = \mu^{-2} S_\mu(f) = 2\alpha/\pi f N \quad (s > 1) \quad (118)$$

because the incoherent kinetic term can be neglected.

For the intermediate case, an interpolation formula was proposed [46]

$$j^{-2} S_j(f) = \mu^{-2} S_\mu(f) = \frac{2\alpha}{fN} \left(\frac{A}{s+1} + \frac{s}{\pi(s+1)} \right) \quad (119)$$

which is heuristic. The main purpose of Ref. 48 was to discuss various avenues to derive the correct form for the intermediary situation, and to consider initially the problem of coherent quantum $1/f$ noise in the $s \leq 1$ case.

For a finite sample or device Eq. (115) should be replaced by a propagator that approaches the classical free-particle propagator of the Schrödinger equation when the transverse sample size, or the number of particles per unit length of the sample, approaches zero. This would cause the coherent $Q1/fE$ to become very small compared with the conventional quantum $1/f$ noise present in the beam, due to the particular way in which the beam was generated. A formula like the interpolation in Eq. (119) would then express the fact that conventional quantum $1/f$ is always present, but is masked in larger samples by the coherent $Q1/fE$. However, a formula with a size-dependent infrared parameter intermediate between the coherent and conventional limits of α/π and αA , present in both the coefficient and the exponent, would express the same transition in a slightly different, physically more meaningful form:

$$j^{-2} S_j(f) = \mu^{-2} S_\mu(f) = \frac{2\beta}{f^{1-\beta} N} \quad \text{with } \beta = \frac{\alpha A}{s+1} + \frac{\alpha s}{\pi(s+1)} \quad (120)$$

So far we have not derived an expression equivalent to Eq. (120) in any way. However, the physical unity of coherent and conventional $Q1/fE$ s speaks in favor of a more sophisticated relation than Eq. (119). This same physical content can be expressed in a slightly different way by noting that Eq. (115) is equivalent to a energy-

momentum relation that is not sharp, allowing for quantum fluctuations of the rest mass of the charged particle, or of any other particle with infrared divergent coupling to a group of massless infraquanta. Describing these quantum fluctuations of the rest mass μ with the help of a distribution function $\rho(\mu)$ peaked at the measured rest mass m , we could attempt to write Eq. (115) in the form

$$\begin{aligned} & -i \langle \Phi_0 | T \psi_{s'}(x') \psi_s^\dagger(x) | \Phi_0 \rangle \\ & \equiv \delta_{ss'} G_s(x' - x) \\ & = \frac{i}{V} \sum_{\mathbf{p}} \left(\exp \frac{\mathbf{p} \cdot (\mathbf{r} - \mathbf{r}') - \mathbf{p}^2(t - t')/2m}{\hbar} \right) n_{\mathbf{p},s} \\ & \quad \times \left(-i \frac{\mathbf{p} \cdot (\mathbf{r} - \mathbf{r}')}{\hbar} + i(m^2 c^2 + \mathbf{p}^2)^{1/2} (t - t') \frac{c}{\hbar} \right)^{\alpha/\pi} \\ & = \frac{i}{V} \int d\mu \rho(\mu) \sum_{\mathbf{p}} \left(\exp i \frac{\mathbf{p}(\mathbf{r} - \mathbf{r}') - \mathbf{p}^2(t - t')/2m}{\hbar} \right) n_{\mathbf{p},s} \end{aligned} \quad (121)$$

The distribution function $\rho(\mu)$ can be used to transform various classical results calculated simply with the Schrödinger propagator into the corresponding quantum $1/f$ results.

To determine $\rho(\mu)$, we represent the nonrelativistic form [38] of the new QED propagator as a superposition of classical propagators, defined by an unknown mass distribution $\rho(\mu)$ that describes the fuzzy mass shell:

$$\begin{aligned} & \exp \left\{ \frac{im}{\hbar} \left[\mathbf{v} \cdot (\mathbf{r} - \mathbf{r}') - \left(c^2 + \frac{v^2}{2} \right) (t - t') \right] \right\} \\ & \cdot \left\{ \frac{im}{\hbar} \left[\mathbf{v} \cdot (\mathbf{r} - \mathbf{r}') - \left(c^2 + \frac{v^2}{2} \right) (t - t') \right] \right\}^{\alpha/\pi} \\ & = \int_0^\infty d\mu \rho(\mu) \exp \left\{ \frac{i\mu}{\hbar} \left[\mathbf{v} \cdot (\mathbf{r} - \mathbf{r}') - \left(c^2 + \frac{v^2}{2} \right) (t - t') \right] \right\} \end{aligned} \quad (122)$$

Let $u = (1/\hbar)[\mathbf{v} \cdot (\mathbf{r} - \mathbf{r}') - (c^2 + v^2/2)(t - t')]$. This allows us to simplify the equation presented above

$$\int_0^\infty d\mu \rho(\mu) e^{i\mu u} = e^{imu} (imu)^{\alpha/\pi} \quad (123)$$

When we used $\mu' = \mu - m$, the equation becomes

$$\int_{-m}^\infty d\mu' \rho'(\mu') e^{i\mu' u} = (imu)^{\alpha/\pi} \quad (124)$$

Because $\rho'(\mu')$ is different from zero only around $\mu' = 0$ or $\mu = m$, we can extend the domain of integration:

$$\int_{-\infty}^\infty d\mu' \rho'(\mu') e^{i\mu' u} = (imu)^{\alpha/\pi} \quad (125)$$

Let us take the derivative with respect to u . This yields

$$\int_{-\infty}^{\infty} d\mu' \rho'(\mu') e^{i\mu' u} \cdot i\mu' = \frac{(\alpha/\pi)(im)^{\alpha/\pi}}{u^{1-\alpha/\pi}} \quad (126)$$

We can further simplify this equation with the notation $\mu' \rho'(\mu') = X(\mu')$ and get

$$\int_{-\infty}^{\infty} d\mu' X(\mu') e^{i\mu' u} = \frac{(\alpha/\pi)m^{\alpha/\pi}}{(iu)^{1-\alpha/\pi}} \quad (127)$$

We can determine $X(\mu')$ by taking the Fourier transformation of the right-hand side:

$$\begin{aligned} X(\mu') &= \int_{-\infty}^{\infty} du \frac{(\alpha/2\pi^2)m^{\alpha/\pi}}{(iu)^{1-\alpha/\pi}} e^{-iu\mu'} = \frac{\alpha m^{\alpha/\pi}}{2\pi^2 i^{1-\alpha/\pi}} \int_{-\infty}^{\infty} du \frac{e^{-iu\mu'}}{u^{1-\alpha/\pi}} \\ &= \frac{\alpha m^{\alpha/\pi}}{2\pi^2 i^{1-\alpha/\pi}} \left(\int_{-\infty}^0 du \frac{\cos(\mu' u) + i \sin(\mu' u)}{u^{1-\alpha/\pi}} \right. \\ &\quad \left. + \int_0^{\infty} du \frac{\cos(\mu' u) + i \sin(\mu' u)}{u^{1-\alpha/\pi}} \right) \end{aligned} \quad (128)$$

$$\begin{aligned} &= \frac{\alpha m^{\alpha/\pi}}{2\pi^2 i^{1-\alpha/\pi}} \left(\int_0^{\infty} d(-u') \frac{\cos(-\mu' u') + i \sin(\mu' u')}{(-u')^{1-\alpha/\pi}} \right. \\ &\quad \left. (u' = -u) + \int_0^{\infty} du \frac{\cos(\mu' u) + i \sin(\mu' u)}{u^{1-\alpha/\pi}} \right) \\ &= \frac{\alpha m^{\alpha/\pi}}{2\pi^2 i^{1-\alpha/\pi}} \left(\int_0^{\infty} du' \frac{-\cos(-\mu' u') + i \sin(\mu' u')}{u'^{1-\alpha/\pi}} (-1)^{1-\alpha/\pi} \right. \\ &\quad \left. + \int_0^{\infty} du \frac{\cos(\mu' u) + i \sin(\mu' u)}{u^{1-\alpha/\pi}} \right) \\ &= \frac{\alpha m^{\alpha/\pi}}{2\pi^2 i^{1-\alpha/\pi}} \left([1 - (-1)^{1-\alpha/\pi}] \int_0^{\infty} du \frac{\cos(\mu' u)}{u^{1-\alpha/\pi}} \right. \\ &\quad \left. + i[1 + (-1)^{1-\alpha/\pi}] \int_0^{\infty} du \frac{\sin(\mu' u)}{u^{1-\alpha/\pi}} \right) \end{aligned} \quad (129)$$

$$\begin{aligned} &= \frac{\alpha m^{\alpha/\pi}}{2\pi^2 i^{1-\alpha/\pi}} \left([1 - (-1)^{1-\alpha/\pi}] \frac{\Gamma(\alpha/\pi)}{\mu'^{\alpha/\pi}} \cos \frac{\alpha}{2} \right. \\ &\quad \left. + i[1 + (-1)^{1-\alpha/\pi}] \frac{\Gamma(\alpha/\pi)}{\mu'^{\alpha/\pi}} \sin \frac{\alpha}{2} \right) \\ &\quad \text{(for } \mu' > 0) \\ &= \frac{\alpha m^{\alpha/\pi}}{2\pi^2 i^{1-\alpha/\pi}} \left([1 - (-1)^{1-\alpha/\pi}] \frac{\Gamma(\alpha/\pi)}{\mu'^{\alpha/\pi}} \cos \frac{\alpha}{2} \right. \\ &\quad \left. - i[1 + (-1)^{1-\alpha/\pi}] \frac{\Gamma(\alpha/\pi)}{\mu'^{\alpha/\pi}} \sin \frac{\alpha}{2} \right) \end{aligned} \quad (130)$$

(for $\mu' < 0$)

Because both $1 + (-1)^{1-\alpha/\pi}$ and $\sin(\alpha/2)$ are much smaller than $1 - (-1)^{1-\alpha/\pi}$ and $\cos(\alpha/2)$, we can just use

$$X(\mu') = [1 - (-1)^{1-\alpha/\pi}] \frac{\alpha \Gamma(\alpha/\pi) \cos(\alpha/2)}{2\pi^2 i^{1-\alpha/\pi}} \left(\frac{m}{\mu'} \right)^{\alpha/\pi} \quad (131)$$

for all practical purposes. We thus conclude that the mass distribution function has to be

$$\rho(\mu) = \frac{\alpha \Gamma(\alpha/\pi) \cos(\alpha/2)}{\pi^2 i^{1-\alpha/\pi}} \frac{m^{\alpha/\pi}}{(\mu - m)^{1+\alpha/\pi}} \quad (132)$$

This is a remarkable result. It allows us to approximate the effect of infrared radiative corrections on any electronic propagator by multiplying it by $\rho(\mu)$ and integrating over μ as was done with the free-particle propagator on the right-hand side of our first equation above. The result will represent an approximation of the physical electron's propagator corresponding to the problem at hand, that is, an approximation of the physical propagator including the infrared radiative corrections, which corresponds to the given potential in which the electron has to move, and which satisfies the given boundary conditions.

10.2.6. Application of the Universal Sufficient Criterion for $1/f$ Spectra in Chaotic Nonlinear Systems to Quantum Electrodynamics. The nonlinearity causing the $1/f$ spectrum of turbulence in both semiconductors and metals is caused by the reaction of the field generated by charged particles and their currents back on themselves. The same nonlinearity is present in QED, where it causes the infrared divergence, the infrared radiative corrections for cross sections and process rates, and the quantum $1/f$ effect. We shall prove this on the basis of our sufficient criterion for $1/f$ spectral density in chaotic systems.

Consider a beam of charged particles propagating in a well-defined direction, so that the Schrödinger equation describes the longitudinal fluctuations in the concentration of particles. Considering the nonrelativistic case, which is encountered in most quantum $1/f$ noise applications, we write in second quantization the equation of motion for the Heisenberg field operators ψ of the particles in the form

$$i\hbar \frac{\partial \psi}{\partial t} = \frac{1}{2m} \left(-i\hbar \nabla - \frac{e}{c} \mathbf{A} \right)^2 \psi \quad (133)$$

With the nonrelativistic form $\mathbf{J} = -i\hbar \psi^* \nabla \psi / m +$ (Hermitian conjugate), and with

$$\mathbf{A}(x, y, z, t) = \frac{\hbar}{2cmi} \cdot \frac{[\psi^* \nabla \psi - \psi \nabla \psi^*]}{|\mathbf{x} - \mathbf{x}'|} d^3 x' \quad (134)$$

where the small rectangular brackets are defined to include retardation, we obtain

$$i\hbar \frac{\partial \psi}{\partial t} = \frac{1}{2m} \left(-i\hbar \nabla - \frac{e\hbar}{2c^2 mi} \frac{[\psi^* \nabla \psi - \psi \nabla \psi^*]}{|\mathbf{x} - \mathbf{x}'|} d^3 x' \right)^2 \psi \quad (135)$$

At very low frequencies or wave numbers the second term in the large parentheses is dominant on the

right-hand side, being of order λ , while the first term is of order λ^{-1} when \mathbf{x} is replaced by $\lambda\mathbf{x}$, giving

$$i\hbar \frac{\partial\psi}{\partial t} = -\frac{1}{2m} \left(\frac{e\hbar}{2c^2m} \frac{[\psi^*\nabla\psi - \psi\nabla\psi^*]}{|\mathbf{x} - \mathbf{x}'|} d^3x' \right)^2 \psi \quad (136)$$

For \mathbf{x} replaced by $\lambda\mathbf{x}$, and \mathbf{x}' formally replaced by $\lambda\mathbf{x}'$, we obtain

$$\begin{aligned} i\hbar \frac{\partial\psi}{\partial t} &= -\frac{1}{2m} \left(\frac{e\hbar}{2c^2mi} \frac{[\psi^*(\nabla/\gamma)\psi - \psi(\nabla/\gamma)\psi^*]}{\lambda|\mathbf{x} - \mathbf{x}'|} \lambda^3 d^3x' \right)^2 \psi \\ &= \lambda^2 H\psi = \gamma^{-p} H\psi \end{aligned} \quad (137)$$

This satisfies our homogeneity criterion with $p = -2$, because if we also replace t with $\lambda^{-2}t$ on the left-hand side, λ drops out altogether, and the equation is invariant. Our sufficient criterion only requires homogeneity, with any value of the weight p , for the existence of a $1/f$ spectrum in chaos. Therefore, we expect partial self-ordering of the current carriers with long-range correlations leading to a universal $1/f$ spectrum of fundamental quantum current fluctuations (coherent quantum $1/f$ effect) and of fluctuations in physical cross sections and process rates, as derived in detail above. This is in agreement with the experimentally verified results of the quantum $1/f$ theory.

In conclusion, we realize that, both in classical and in quantum-mechanical nonlinear systems, the limiting behavior at low wave numbers is usually expressed by homogeneous functional dependences, leading to fundamental $1/f$ spectra on the basis of our criterion. This explains the ubiquity of the $1/f$ spectrum.

11. DEVELOPMENT OF SPECIAL MATERIALS FOR ULTRA-LOW-NOISE FET AND JUNCTION DEVICES

11.1. Fet Devices

Consider, for example, the class of devices that are homogeneous in the direction of the current flow, such as FETs, including JFETs, MODFETs, or HEMTs, and photoconductive detectors, as opposed to bipolar transistors, HJBTs, pn diodes, junction photodetectors, and other junction devices. The mobility quantum $1/f$ noise is determined in this class of devices by Eq. (57), with the various quantum $1/f$ coefficients α_i , given by the results presented earlier for impurity scattering, acoustic phonon scattering in indirect-bandgap semiconductors, various kinds of intervalley scattering with or without umklapp, and polar and nonpolar optical phonon scattering. Ionized impurity scattering consists of many small-angle scattering events, all with small velocity changes $\Delta\mathbf{v}$, and therefore also with a small value of the quantum $1/f$ coefficient α_i . On the other hand, intervalley scattering with or without umklapp causes large velocity changes, corresponding to wave vector changes of the order of the fundamental reciprocal lattice vector \mathbf{G} , and a large quantum $1/f$ coefficient of the order $(4\pi/3\pi)(\hbar G/mc)^2 = (4\pi/3\pi)(\hbar 2\pi/amc)^2$, where a is the lattice constant and m the effective mass of the

carriers. To reduce the $1/f$ noise of the resulting devices, one is interested in materials practically free of intervalley and umklapp scattering, even if this comes at the expense of a shorter lifetime of the carriers. One designs materials in which the mobility is limited mainly by ionized impurity scattering. If this is not practicable due to other constraints, one takes advantage of the inverse square dependence of the intervalley- and umklapp-scattering quantum $1/f$ coefficients and chooses the conduction type (n or p) and the host material in order to maximize m . Finally, the $1/N$ dependence also favors materials with a large concentration of ionized impurities.

11.2. Junction Devices

On the other hand, for materials designed for use in junction devices, the last form of Eq. (65) requires a large lifetime of the minority carriers in the low-doping part of the device. In this case, the material must have particularly low concentrations of recombination centers, of point defects, of dislocations, and of other lattice defects. For this class of devices the elimination of surface recombination currents through surface passivation is very important, because volume recombination is much less noisy according to our equations.

12. DEVICE OPTIMIZATION FOR ULTRALOW $1/f$ NOISE

After the design of optimal materials for each class of solids-state devices, the next objective is the use of these materials and of the quantum $1/f$ theory for practical device optimization. The following is the present list of our principles of optimal quantum $1/f$ noise design, which we currently use in creating new technological prototypes of devices:

1. Avoid coherent-state quantum $1/f$ noise by device size reduction below the coherent limit. This size limit is concentration-dependent, as seen from the expression for the coherence parameter $s = 2e^2 N' / mc^2 = 5 \times 10^{-13} \text{cm}^{-1} \times N'$ defined in Eq. (27). $N' = nA$ is the number of carriers per unit length of the device in the direction of current flow. A is the cross-sectional area of the current-carrying device, and n is the concentration of carriers. For $s \ll 1$ we expect conventional quantum $1/f$ noise, while for $s \gg 1$ the much larger coherent-state quantum $1/f$ noise is to be expected. In conclusion: think submicron, think transversely ultrasmall.
2. Avoid control of the device current or voltage by elementary cross sections or process rates tested by a small number of carriers only. Indeed, the number of carriers interrogating the cross section or process rate appears in the denominator of both the conventional and coherent quantum $1/f$ noise formulas. In particular, avoid current concentrations in bottle-necks, and current inhomogeneities. In junction devices higher lifetimes of the carriers lead to an increase in the number of carriers present in the sample that have tested the current-controlling

cross sections, and therefore lead to lower quantum $1/f$ noise.

3. Avoid control of a device exhibiting conventional quantum $1/f$ noise through elementary processes that involve large accelerations of the current carriers, or large velocity changes. The squared vector velocity change appears as a factor in the conventional quantum $1/f$ noise formula. For example, umklapp, intervalley, and lattice scattering are respectively worst, very bad, and bad, compared with ionized impurity scattering, in terms of the fractional mobility fluctuations they yield. For a given scattering mechanism, choosing current carriers with a large effective mass will in general reduce the conventional quantum $1/f$ noise, because for the same momentum transfers this results in smaller accelerations. Bulk recombination control of the current through a pn junction will lead to lower quantum $1/f$ noise than having the current controlled even in part by surface recombination, because the surface recombination centers are in a high-localized-field region at the interface between bulk and the passivation layer. Therefore, the best passivation is one that reduces the number and the cross section of the surface recombination centers, while also providing the smallest surface potential jump.

On this basis a detailed identification and analysis of the various noise sources can be performed. In a next step, a figure of merit can be defined on the basis of the mission specification for the devices in the focal plane array. Finally, material and design improvements are calculated and suggested, which optimize the figure of merit defined in the previous step. A similar sequence is applicable for quartz crystal resonators and SAW devices.

Use of these principles leads to lower $1/f$ device noise. The quantum $1/f$ theory can consequently be used for CAD optimization of $1/f$ device noise suppression.

13. DISCUSSION

We now have a clear understanding both of the general origin of fundamental $1/f$ spectra and of my practical engineering formulae $2\alpha A/fN$ and $2\alpha/\pi fN$ applicable to high-technology devices. No matter which device is concerned, if it is a high-technology device all trivial forms of instability and fluctuations have been eliminated, and the device will be limited in its performance by the fundamental quantum $1/f$ effect present in the elementary cross sections and process rates controlling the kinetics of the device. A Q1/E research institute is needed to translate these fundamental discoveries into valuable practical breakthroughs in modern high-technology applications.

Many contributions to this field are included in the Proceedings of the IV–VI International Symposia on Quantum $1/f$ Noise (1990, 1992, and 1994) and in the session on “ $1/f$ noise and quantum chaos” at the March 1992 meeting of the American Physical Society in Indianapolis. Continuing progress was reported in the

Proceedings of the International Conference on Noise in Physical Systems and $1/f$ Noise, which were published 1975–1996; see the reviews [26,49].

BIBLIOGRAPHY

1. P. H. Handel, $1/f$ Noise—an “infrared” phenomenon, *Phys. Rev. Lett.* **34**:1492–1494 (1975).
2. P. H. Handel, Quantum approach to $1/f$ noise, *Phys. Rev. A* **22**:745–757 (1980).
3. P. H. Handel, Low frequency fluctuations in electronic transport phenomena, in J. T. Devreese and V. van Doren, eds., *Proc. NATO Advanced Study Inst. Linear and Nonlinear Electronic Transport in Solids*, Plenum Press, New York, 1976, pp. 515–547.
4. P. H. Handel, *Arch. Elektron. Übertr.* **43**:261 (1989).
5. P. H. Handel, Quantum $1/f$ noise in the presence of a thermal radiation background, in C. M. Van Vliet and E. R. Chenette, eds., *Proc. II Int. Symp. 1/f Noise*, Gainesville Press, Univ. Florida, Orlando, 1980, pp. 96–110.
6. T. S. Sherif and P. H. Handel, Unified treatment of diffraction and $1/f$ noise, *Phys. Rev. A* **26**:596–602 (1982).
7. A. van der Ziel, The experimental verification of Handel’s expressions for the Hooge parameter, *Solid State Electron.* **31**:1205–1209 (1988).
8. P. H. Handel and D. Wolf, Characteristic functional of quantum $1/f$ noise, *Phys. Rev. A* **26**:3727–3730 (1982).
9. P. H. Handel and T. Sherif, Direct calculation of the Schrodinger field which generates quantum $1/f$ noise, in V. M. Savelli, G. Lecoy, and J. P. Nougier eds., *Proc. VII Int. Conf. Noise Physical Syst. III Int. Conf. 1/f Noise*, North-Holland, Montpellier May 17–20, 1983, pp. 109–112.
10. P. H. Handel, Effect of a finite mean free path on quantum $1/f$ noise, in C. M. Van Vliet ed., *Proc. IX Int. Conf. Noise Physical Syst.*, World Scientific, Teaneck, NJ, 1987, pp. 365–372, 419–422.
11. G. S. Kousik et al., Quantum $1/f$ noise associated with ionized impurity scattering and electron–phonon scattering in condensed matter, *Adv. Phys.* **34**:663–702 (1986); see also the continuation by G. S. Kousik et al., Quantum $1/f$ noise associated with inter-valley scattering in nondegenerate semiconductors, *Phys. Stat. Sol. (b)* **154**:713 (1989).
12. P. H. Handel and C. Eftimiu, Survival of the long time correlations in $1/f$ noise, *Proc. Symp. 1/f Fluctuations*, Tokyo Inst. Technol. Press, July 11–13, 1977, pp. 183–186.
13. P. H. Handel, Keldysh–Schwinger method calculation of $1/f$ low frequency current and cross section calculation, unpublished manuscript, 1979.
14. P. H. Handel, Quantum $1/f$ fluctuations of physical cross sections, *Phys. Rev.* (in press).
15. C. M. Van Vliet, Quantum electrodynamic theory of infrared effects in condensed matter. I, II, *Physica A* **165**:101–125, 126–155 (1990).
16. A. van der Ziel, Unified presentation of $1/f$ noise in electronic devices; fundamental $1/f$ noise sources, *Proc. IEEE* **76**:233–258 (1988) (review paper); *Noise in Solid State Devices and Circuits*, Wiley, New York, 1986, Chap. 11, pp. 254–277.
17. A. van der Ziel, Generalized semiclassical quantum $1/f$ noise theory. I: Acceleration $1/f$ noise in semiconductors, *J. Appl. Phys.* **64**:903–906 (1988).
18. A. van der Ziel, A. D. van Rheenen, and A. N. Birbas, Extensions of Handel’s $1/f$ noise equations and their

- semiclassical theory, *Phys. Rev. B* **40**:1806–1809 (1989); A. N. Birbas et al., Channel-length dependence of the $1/f$ noise in silicon metal–oxide–semiconductor field effect transistors, verification of the acceleration $1/f$ noise process, *J. Appl. Phys.* **64**:907–912 (1988).
19. A. H. Pawlikiewicz et al., Fundamental $1/f$ noise in silicon bipolar transistors, *Solid-State Electron.* **31**:831–834 (1988).
 20. A. van der Ziel and P. H. Handel, $1/f$ noise in n^+p diodes, *IEEE Trans. Electron. Devices* **ED-32**:1802–1805 (1985).
 21. A. van der Ziel et al., Review of the status of quantum $1/f$ noise in n^+p HgCdTe photodetectors and other devices, *J. Vacuum Sci. Technol. A. Vacuum Surf. Films* **A4**:2205 (1986).
 22. A. van der Ziel et al., $1/f$ noise characterization of n^+p and $n-i-p$ Hg_{1-x}Cd_x Te detectors, *J. Vacuum Sci. Technol. A. Vacuum Surf. Films* **A7**:550–554 (1989).
 23. P. H. Handel, Any particle represented by a coherent state exhibits $1/f$ noise, in M. Savelli, G. Lecoy, and J. P. Nougier eds., *Noise in Physical Systems and 1/f Noise*, North-Holland, Amsterdam, 1983, p. 97.
 24. P. H. Handel, Coherent states quantum $1/f$ noise and the quantum $1/f$ effect, *Noise in Physical Systems and 1/f Noise (Proc. VIIIth Int. Conf. Noise Physical Syst. and 1/f Noise)* New York: Elsevier, 1986, p. 469.
 25. P. H. Handel, Fundamental quantum $1/f$ noise in small semiconductor devices, *IEEE Trans. Electron. Devices* **41**:2023–2033 (1994).
 26. P. H. Handel, Coherent and conventional quantum $1/f$ effect, *Phys. Stat. Sol. (b)* **194**:393–409 (1996).
 27. P. H. Handel, Starting points of the quantum $1/f$ noise approach, *Phys. Rev B* (in press).
 28. G. S. Kousik et al., *Adv. Phys.* **34**:663–702 (1985).
 29. P. H. Handel and T. H. Chung, Graphical representation of quantum $1/f$ mobility fluctuation spectra in silicon, in P. H. Handel and A. L. Chung eds., *AIP Conf. Proc. 285*, AIP Press, 1992, pp. 176–179.
 30. G. S. Kousik et al., *Phys. Stat. Sol.* **154**:713–726 (1989).
 31. V. Chung, Infrared divergence in quantum electrodynamics, *Phys. Rev.* **140B**:1110–1122 (1965).
 32. J. M. Jauch and F. Rohrlich, *The Theory of Photons and Electrons*, Springer-Verlag, Heidelberg, 1976
 33. D. Zwanziger, *Phys. Rev. D* **7**:1082 (1973); *Phys. Rev. Lett.* **30**:934 (1973); *Phys. Rev. D*, **11**:3481, 3504 (1975).
 34. T. W. B. Kibble, *Phys. Rev.* **173**:1527 (1968); **174**:1882 (1968); **175**:1624 (1968); *J. Math. Phys.* **9**:315 (1968).
 35. Y. Zhang and P. H. Handel, in P. H. Handel and A. L. Chung eds., *Proc. 5th van der Ziel Conf. Quantum 1/f Noise and Other Low Frequency Fluctuations*, AIP Conf. Proc. 282, 1992, pp. 102–104.
 36. J. S. Gradshteyn and I. M. Ryzhik, *Table of Integrals, Series and Products*, Academic Press, New York, 1965, Sect. 3.761, Nos. 9, 7.
 37. P. H. Handel, Infrared divergences, radiative corrections, and bremsstrahlung in the presence of a thermal-equilibrium radiation background, *Phys. Rev.* **A38**:3082–3085 (1988), Eq. (7); see also, e.g., S. Weinberg, *Phys. Rev.* **140B**:516–524 (1965), Eqs. (2.26), (2.17) (Weinberg's notation for our quantum $1/f$ coefficient αA is just A , the infrared exponent).
 38. J. Mooney, Excess low-frequency noise in PtSi on p -type Si Schottky diodes, *IEEE Trans. Electron. Devices* **38**:160–166 (1991).
 39. P. H. Handel, Nature of $1/f$ frequency fluctuation in quartz crystal resonators, *Solid-State Electron.* **22**:875–876 (1979).
 40. F. L. Walls et al., A new model of $1/f$ noise in bulk acoustic wave quartz resonators, *Proc. 1992 IEEE Frequency Control Symp.*, 1992, pp. 327–333.
 41. A. van der Ziel, *Noise: Sources, Characterization, Measurement*, Prentice-Hall, Englewood Cliffs, NJ, 1970, p. 113.
 42. P. H. Handel, Coherent quantum $1/f$ effect in second quantization, *Quantum 1/f Noise & Other Low-Frequency Fluctuations in Electronic Devices*, AIP Publ. 282, 1993, pp. 29–31.
 43. J. D. Dollard, *J. Math. Phys.* **5**:729 (1965).
 44. P. P. Kluish and L. D. Faddeev, *Theor. Math. Phys. (USSR)* **4**:745 (1971).
 45. P. H. Handel, Instabilities, turbulence and flicker-noise in semiconductors, I, II, III, *Z. Naturforsch.* **21a**:561–593 (1966).
 46. P. H. Handel, Coherent states quantum $1/f$ noise and the quantum $1/f$ effect, in A. D'Amico and P. Mazzetti, eds., *Noise in Physical Systems 1/f Noise (Proc. VIIIth Int. Conf. Noise Physical Syst. 1/f Noise)*, Elsevier, New York 1986, p. 469.
 47. P. H. Handel, Turbulence theory for the current carriers in solids and a theory of $1/f$ noise, *Phys. Rev. A* **3**:2066 (1971).
 48. P. H. Handel, The nature of fundamental $1/f$ noise, in P. H. Handel and A. L. Chung, eds., *AIP Conf. Proc.* 285, AIP Press, 1992, pp. 162–171.
 49. P. H. Handel, $1/f$ noise universality in high-technology applications, in L. Maleki, eds., *Proc. 1994 IEEE Int. Frequency Control Symp.*, Boston, June 1–3, 1994, pp. 8–21.

FUTHER READING

- P. Fang et al., Noise and lifetime measurements in Si p^+ power diodes, *Solid-State Electron.* **32**:345–348 (1998) [obtains $\alpha_H = (4.0 \pm 0.8) \times 10^{-3}$ in, agreement with the coherent state quantum $1/f$ theory].
- P. H. Handel, Quantum $1/f$ noise in SQUIDS, in A. D'Amico and P. Mazetti, eds., *Proc. VIII Int. Conf. Noise Physical Syst. IV. Int. Conf. 1/f Noise*, Rome, 1985, pp. 489–490.
- P. H. Handel, *Quantum 1/f Noise in High Technology Applications Including Ultrasmall Structures and Devices*, AFOSR 1989–1993, Final Tech. Report 89–0416, May 14, 1994.
- P. H. Handel, The physical meaning of the quantum $1/f$ effect as a form of quantum chaos, in P. H. Handel and A. L. Chung, eds., *VI. van der Ziel Symp. on Quantum 1/f Noise and Other Low Frequency Fluctuations in Electronic devices*, Univ. Missouri, St. Louis, May 27–28, 1994, AIP Proc. 371, AIP Press, New York, 1996, pp. 44–47.
- Quantum $1/f$ effect in frequency standards, in P. H. Handel and A. L. Chung, eds., *VI. van der Ziel Symp. Quantum 1/f Noise and Other Low Frequency Fluctuations in Electronic Devices*, Univ. Missouri, St. Louis, May 27–28, 1994, AIP Proc. 371, AIP Press, New York, 1996, pp. 52–56.
- P. H. Handel and A. van der Ziel, Relativistic correction of the Hooge parameter for umklapp $1/f$ noise, *Physica B* **141**:145–147 (1986).
- P. H. Handel and F. L. Walls, Analysis of quantum $1/f$ effects in frequency standards, in L. Maleki ed., *Proc. 1994 IEEE Int. Frequency Control Symp.*, Boston, 1994, pp. 539–540.
- P. H. Handel and Y. Zhang, A bridge between coherent and conventional quantum $1/f$ noise, in P. H. Handel and A. L. Chung, eds., *VI. van der Ziel Symp. on Quantum 1/f Noise and Other Low Frequency Fluctuations in Electronic Devices* Univ.

Missouri, St. Louis, May 27–28, 1994, AIP Proc. 371, AIP Press, New York, 1996, pp. 48–51.

A. van der Ziel, Interpretation of Schwates's experimental data on secondary emission $1/f$ noise, *Physica B* **144**:195–205 (1986).

A. van der Ziel et al., Partition $1/f$ noise in pentodes and its quantum interpretation, *Physica B* **145**:195–204 (1987).

NONLINEAR CIRCUIT ANALYSIS

ALMUDENA SUÁREZ
University of Cantabria
Santander, Cantabria, Spain

1. INTRODUCTION

There is an increasing demand in modern communication systems for high-performance radiofrequency circuits. This fact, together with the common use of monolithic technologies, for which no modification is possible after manufacturing, requires the use of accurate and efficient simulation tools, in order to meet the circuit specifications. This simulation has added difficulties in the case of nonlinear circuits, such as those based on semiconductor devices, transistors, or diodes. The superposition principle does not hold in nonlinear circuits and so they exhibit characteristics, such as dependence on the input amplitude or the generation of harmonic frequencies, that are never observed in linear ones [1–3].

The self-sustained oscillation, exhibited by the oscillator circuits and also by unstable amplifiers, is possible only in nonlinear nonconservative systems. Other phenomena, exclusive to nonlinear systems, are the coexistence of solutions and the hysteresis, the oscillation synchronization with external sources, and the generation of subharmonic oscillations. Note that, although the special properties of the nonlinear circuits are sometimes undesired, they also make them the only choice for performing analog functions such as frequency mixing, frequency multiplication, oscillation, and frequency division.

In general, the nonlinear circuit will be described by a set of differential algebraic equations (DAEs) [4]. Two different kinds of circuits may be distinguished [1]: autonomous and nonautonomous. In an autonomous circuit, the DAEs do not explicitly depend on time, due to the absence of time-varying generators. This is the case of the free-running oscillators, which contain DC generators only. In a nonautonomous (forced) circuit, the DAEs explicitly depend on time, due to the existence of time-varying generators $g(t)$. Four main types of steady-state solutions are possible: the DC solution, the periodic solution, the quasiperiodic solution, and the chaotic solution. The periodic solution has one fundamental frequency only. The quasiperiodic solution has two or more incommensurable fundamentals, namely, two or more fundamental frequencies that cannot be rationally expressed in terms of a common period. It is the regime in which a frequency mixer

operates. Finally, the chaotic solution is neither periodic nor quasiperiodic, and, because of this nonperiodicity, it exhibits a continuous spectrum, at least for some frequency intervals [1].

Another essential characteristic of nonlinear circuits is the possible coexistence of two or more steady-state solutions for the same circuit values. Only the stable steady-state solutions are physically observed. A solution is stable when it is capable of recovering from small perturbations. For this reason, the stable solution is also called *robust* [1–3]. Since perturbations are always present in real life, nonrobust solutions cannot be obtained experimentally. As an example of coexistence of solutions with different stability properties, Fig. 1 shows the simulation of a free-running oscillator. As already mentioned, a free-running oscillator is an autonomous circuit and its equations can always be solved for a DC solution. In the case of Fig. 1, this DC solution is simply $v_{DC} = 0$, $i_{DC} = 0$, $\forall t$. If no initial value is provided to either of the two circuit nodes, the solution will remain at $v(t) = 0$, $i(t) = 0$ during the entire simulation interval. However, if the initial conditions differ from $v = 0$, $i = 0$, a transient will lead the circuit to the oscillating steady state. The DC solution is thus unstable. In contrast, the oscillating solution is stable. To show this, a perturbation is applied at $t = 5$ ns. This starts a transient that leads back to the oscillating solution.

Different methods exist for the simulation of nonlinear circuits. These methods can be classified into three main categories: time domain, frequency domain, and the more recent time–frequency methods. There are also analytical methods and numerical methods. The analytical methods, such as the describing function [2,5] or Volterra series [6,7], are very well suited for circuit design, since they give insight into the nonlinear behavior and enable an evaluation of its dependence on the circuit parameters. The describing function has been widely used for oscillator design, while the Volterra series is a good approach for identifying the linearity limiting factor of a given transistor technology. It is also very well suited for the analysis of

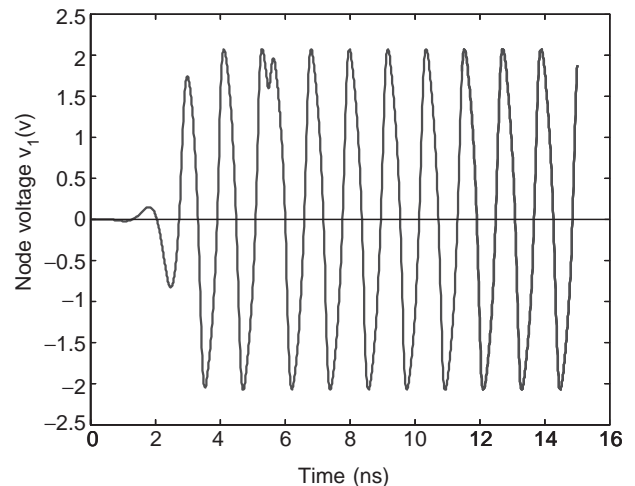


Figure 1. Coexistence of solutions in the cubic nonlinearity oscillator. The DC solution lies on the horizontal axis. Two perturbations are applied at $t = 0$ and $t = 5$ ns, respectively.

multitone signals and nonlinearities with memory. However, when the goal is to obtain an accurate solution, in terms of waveforms and spectral content, numerical iterative methods are generally preferred. These numerical simulation methods are the object of this contribution.

The nonlinear circuit can be simulated by applying integration algorithms to its corresponding DAE, from an initial condition [8–10]. This method, used in programs such as SPICE [10], provides the entire evolution of the circuit solution from the initial values to the steady state. Both the transient and steady state are simulated. However, the transient, which usually has little interest for the designer, may be too long in comparison with the solution period. To cope with this problem, the fast time-domain algorithms [11], such as the shooting [8,12,13] and finite-difference methods [11,13–15], perform the time-domain analysis of the steady state only, avoiding the transient. This is achieved using an additional constraint on the state of the solution. In the case of periodic regimes, the constraint imposes the equality of the circuit variables after one period. The fast time-domain methods are more difficult to apply to steady-state regimes of other kinds.

The distributed elements, with loss and frequency dispersion, are difficult to model and analyze in the time domain. The most general approaches use impulsive responses for the description of these elements, and the required convolution products may be long and inefficient, since the integration must be carried out from the initial time value. The linear elements are more easily described in the frequency domain, since it is generally simpler to obtain their response using phasor analysis. Taking this fact into account, the harmonic balance (HB) method [16–19] uses frequency-domain representations for the linear elements, lumped or distributed, maintaining the time-domain descriptions for the nonlinear devices. The circuit variables are represented by means of a Fourier series, with one or more fundamental frequency. Because of this representation, only the steady state is simulated. On the other hand, the use of a sinusoidal basis for the expression of the circuit signals restricts the applicability of the method to circuits with relatively mild nonlinearities. Regimes with fast time transitions are better analyzed in the time domain, with the shooting or finite-difference methods.

As already mentioned, only the stable steady-state solutions are physically observed. In the case of the time-domain integration, provided the integration step and the algorithm are properly selected, the steady-state solution obtained will be stable. This is due to the fact that the integration process follows the actual time evolution of the circuit solution (transient), up to the steady state (see Fig. 1). When using steady-state methods such as HB, the possible coexistence of steady-state solutions must be taken into account. It is possible to obtain a steady-state solution to which the circuit never evolves and, as a consequence, is never observed in practice. This situation is often faced in circuits such as power amplifiers. The designer simulates the desired periodic amplifier solution, which is actually unstable, and obtains a mixerlike spectrum in the measurement. This stable solution is due to the mixing of the signal delivered by the input generator with a self-oscillation. As can be gathered,

the verification of the solution stability will be essential for some analysis methods.

Because of the required Fourier series expression of the circuit variables, the HB technique cannot be applied to nonlinear circuits with modulated inputs. On the other hand, for a carrier frequency with a much higher value than the modulation bandwidth, the time-domain simulation may be inefficient or even impossible. However, in most of these circuits, two different timescales may be considered: one associated with the modulation signal (slower timescale) and the other associated with the high-frequency carrier (faster timescale). Because the circuit is periodic with respect to the time variable associated to the faster timescale, it will be possible to express the circuit variables in a harmonic series, with time-varying harmonic components, at the slower timescale. This is done in the envelope transient method [20,25]. The harmonic components become the unknowns of a system of differential algebraic equations. The advantage over the time-domain integration is its lower computational cost, since the equation system is integrated at the timestep of the slower timescale.

The objective of this contribution is to introduce and compare the different techniques for the numerical simulation of nonlinear circuits, showing the advantages and shortcomings of each of them, when applied to different kinds of circuits and regimes. In order to illustrate the different simulation techniques, a frequency divider will be used throughout this article. The frequency dividers are challenging circuits in terms of analysis, due to the variety of nonlinear operation modes [26] that they exhibit.

2. TIME-DOMAIN INTEGRATION

The most practical way to perform the time-domain analysis of a nonlinear circuit is to formulate the circuit as a system of differential algebraic equations (DAEs). But some facts must be taken into account. The distributed elements are originally described through partial differential equations, and are difficult to introduce in this formulation. To overcome this problem, the transmission lines may be segmented into lumped elements. Unfortunately, it has been shown that this segmentation often gives rise to numerical instabilities [27], that is, to artificial poles on the right-hand side of the complex plane. In addition, this technique cannot directly model the frequency-dependent parameters. A more general approach is the one based on the computation of the impulse responses of the linear elements from their frequency-domain descriptions [27,28]. Then, convolution products are calculated.

The transistors and diodes are usually described through lumped electrical models, containing linear and nonlinear elements. Examples of nonlinear elements are the voltage-controlled current $i(v)$ and junction capacitance $c_j(v)$ of a Schottky diode or the field-effect current $i_{ds}(v_{gs}, v_{ds})$ of a FET transistor, which is controlled by the gate-to-source voltage $v_{gs}(t)$, and the drain-to-source voltage $v_{ds}(t)$. The nonlinear elements are described through their instantaneous relationships with their control

variables, like the well-known diode–current model $i(t) = I_0(e^{\alpha v(t)} - 1)$, having I_0 and α as parameters. In the case of nonlinear capacitances, the model is written in terms of the associated nonlinear charge $q_j(v)$. In the case, for instance, of a junction capacitance, the nonlinear charge is given by $q_j(v) = -2C_{j0}\phi\sqrt{1 - v/\phi}$, with ϕ , the built-in potential and C_{j0} , the capacitance for $v = 0$. For the modeling of more complex nonlinearities, for example, some of those contained in FET or bipolar transistors, great research effort has been necessary. The most usual models can be found in Refs. 29 and 30. The nonlinear models must allow an efficient calculation of the circuit solution, with the existent simulation methods.

The modified nodal approach, obtained from the direct application to the circuit of Kirchhoff’s laws, allows a global formal expression of the DAE [8], which are written

$$\begin{aligned} \bar{i}(\bar{v}(t)) + \frac{d\bar{q}}{dt}(\bar{v}(t)) \\ + \int_{-\infty}^t \bar{h}(t - \tau)\bar{v}(\tau) d\tau + \bar{g}(t) = 0 \end{aligned} \tag{1}$$

where $\bar{v} \in R^P$ is the vector containing the node voltages and branch currents, $\bar{q} \in R^P$ is the vector of charges and fluxes, and $\bar{i} \in R^P$ is the vector of sums of currents (that enter each node) and branch voltages. The vector $\bar{h} \in R^P$ contains the impulsive responses, associated to the distributed elements, and $\bar{g}(t) \in R^P$ is the vector where the input generators are included. Whenever the relationship $\bar{q}(\bar{v})$ is invertible, it will be convenient to use \bar{q} as unknown, since this ensures the charge conservation [8].

As already mentioned, the impulsive responses in (1) are obtained from the inverse Laplace transforms of the distributed elements. In the general case of frequency-dependent distributed elements, the Laplace domain transfer functions are developed in Taylor series and approached using closed-loop Padé approximants [31,32]. The approximants can be expressed in partial fraction form. Then, the inverse Laplace transform provides a sum of exponentials in time domain that are used in the convolution calculation. To avoid the introduction of any artificial instability, all the poles of the computed approximation must have negative real parts [32].

For the practical solution of (1), the continuous-time variable t is discretized and replaced with the timepoints $[t_0, \dots, t_n, \dots, t_N]$. Then, the modified nodal equation is rewritten in terms of the discrete points t_n . At each point t_n , the convolution products are calculated through a discrete sum

$$\bar{i}(t_n) \cong \sum_{i=0}^{n-1} \bar{h}(t_n - t_i)\bar{v}(t_i)\Delta t_i \tag{2}$$

where $\Delta t_i = t_{i+1} - t_i$. For simplicity, a rectangular rule has been considered in (2), although other more efficient schemes of higher order are generally used in practice [33]. From (2), it is clear that the evaluation of the circuit response over the total simulation interval $[t_0, t_N]$ requires

$O(N^2)$ operations. Kapur et al. [33] proposed an algorithm to reduce the number of operations to $O(N \log(N))$.

Several algorithms exist for the numerical integration of (1). The difference between one and another is the way how the derivative $d\bar{q}/dt$ is approximated, in terms of the time samples t_n . A few of these algorithms will be shown here, for illustration. The forward and backward Euler approaches are, respectively, given by

$$\begin{aligned} \frac{d\bar{q}(\bar{v}(t_n))}{dt} &= \frac{\bar{q}(\bar{v}(t_{n+1})) - q(\bar{v}(t_n))}{h} \\ &\text{(forward Euler)} \\ \frac{d\bar{q}(\bar{v}(t_n))}{dt} &= \frac{\bar{q}(\bar{v}(t_n)) - q(\bar{v}(t_{n-1}))}{h} \\ &\text{(backward Euler)} \end{aligned} \tag{3}$$

where h is the timestep, initially assumed constant and such that $t_n = t_0 + nh$. In the forward Euler approach, the derivative at the time t_n involves the variable evaluated at the next timepoint t_{n+1} ; thus, the term “forward.” In the backward Euler approach, it involves the variable calculated at the previous timepoint t_{n-1} . The backward Euler algorithm is an implicit algorithm. An algorithm is called “implicit” when the point $\bar{q}(\bar{v}(n+1))$ is a function of itself:

$$\bar{q}(\bar{v}(t_{n+1})) = \bar{q}(\bar{v}(t_n)) + \frac{d\bar{q}(\bar{v}(t_{n+1}))}{dt} h \tag{4}$$

The implicit algorithms are generally more complicated in terms of computation. However, compared to the explicit algorithms, they offer better accuracy and improved stability properties [1]. This can be understood as the result of a feedback effect, due to the dependence of the point $\bar{q}(\bar{v}(t_{n+1}))$ on itself [see (4)].

The commonly used trapezoidal approximation estimates the derivative $d\bar{q}/dt$, using the average of its value at t_n and t_{n+1} . This provides the following relationship:

$$\begin{aligned} \frac{d\bar{q}(\bar{v}(t_{n+1}))}{dt} &= \frac{2}{h}(\bar{q}(\bar{v}(t_{n+1})) \\ &\quad - q(\bar{v}(t_n)) - \frac{d\bar{q}(\bar{v}(t_n))}{dt} \end{aligned} \tag{5}$$

The algorithms presented so far require one past point only, corresponding to the previous time t_n . There are also more complex multistep algorithms, which require two or more past points. A given algorithm has P order when the solution $\bar{q}(\bar{v}(t))$ and its P first time derivatives are continuous at the limits of the interval $[t_n, t_{n+1}]$. Thus, the integration is error-free for a system whose solution is a polynomial of the same order P or smaller order [1,34]. In particular, it is easily shown that the backward Euler algorithm has order 1, while the trapezoidal algorithm has order 2. The algorithms of higher order use more information about the system and are generally more exact. All the integration algorithms with similar formal structure are grouped in families, each member of a given family having

a different order P . A detailed classification of the different integration algorithms is given in Ref. 1.

The integration algorithm transforms the continuous-time system into a discrete-time system that is different for each particular algorithm. Particularizing the derivative in (1) to the trapezoidal approach (5), a discretized version of the modified nodal equation is obtained:

$$\begin{aligned} \bar{e}(t_{n+1}) \equiv & 2 \frac{(\bar{q}(\bar{v}(t_{n+1})) - \bar{q}(\bar{v}(t_n)))}{t_{n+1} - t_n} \\ & - \frac{d\bar{q}(\bar{v}(t_n))}{dt} + \bar{i}(\bar{v}(t_{n+1})) \\ & + \sum_{i=1}^n \bar{h}(t_{n+1} - t_i) \bar{v}(t_i) \Delta t_i + \bar{g}(t_{n+1}) = 0 \end{aligned} \quad (6)$$

This equation should provide the entire evolution of the circuit solution versus the time variable. The simulation starts with a DC analysis of the circuit, giving the initial value $\bar{v}(0)$. Then, the integration algorithm is applied from $t_0 = 0, \bar{v}(0)$, to obtain $\bar{v}(t_1)$ and recursively applied to obtain $t_{n+1}, \bar{v}(t_{n+1})$ from the knowledge of $t_n, \bar{v}(t_n)$ and all the past points, required for the calculation of the convolution products.

For the numerical determination of $\bar{v}(t_{n+1})$, an error function $\bar{e}(t_{n+1})$, equal to the term of the left-hand side, has been introduced in (6). Some tolerance limits in the circuit variables and a maximum error value, below which the solution $\bar{v}(t_{n+1})$ is considered to be a valid one, must be specified at the beginning of the process. This calculation can be carried out with the aid of the Newton–Raphson algorithm [1,8], which requires the computation of Jacobian matrix of the error function. Compared to other techniques, the advantage of the Newton–Raphson algorithm comes from the large value of the stepsize $\Delta t_{n+1} = t_{n+1} - t_n$ that it allows. As time evolves, the Newton–Raphson algorithm uses the result $\bar{v}(t_n)$ for the previous timepoint t_n as the initial guess for $\bar{v}(t_{n+1})$.

The truncation error of a given integration algorithm is due to the particular discretization method and can be defined as the error that would be present if the algorithm could be implemented with infinite precision [1]. For a multistep algorithm of order P , it can be expressed $\varepsilon_T = A_p h^{P+1}$ [1], where A_p is a real number that depends on the order P , the number of utilized past points, the particular time-domain equation, and the particular point $n + 1$ of the curve. In the trapezoidal rule ($P = 2$), the error is proportional to h^3 . In the backward Euler rule ($P = 1$), the error is proportional to h^2 . For sufficiently small h , the higher-order algorithms will be more accurate than the lower-order ones. The situation can, however, be reversed if the step h becomes too big. Provided the integration step is relatively small, it will be possible to use a larger stepsize with a higher-order algorithm.

For maximum efficiency of the algorithm, with the largest stepsize for a prefixed error tolerance, the stepsize must be adjusted during the integration process. The need for adjusting the stepsize comes from the fact that the truncation error ε_T changes at each timestep. Note, however, that, in multistep algorithms, the input past points

must be equally spaced in time. Thus, when the stepsize is changed, the evenly spaced points must be calculated, which will require additional computational effort.

These techniques have been applied to a frequency divider by 2, by harmonic injection. This circuit is basically an oscillator, whose second harmonic synchronizes with the input signal. Actually, the harmonic injection dividers exhibit a free-running oscillation, when no signal is delivered by the input generator. The divider that has been considered here, based on a MESFET transistor, is shown in Fig. 2. The generator frequency is about $f_{in} = 6$ GHz. The input network is a bandpass filter at this frequency. The output network is a bandpass filter about the divided frequency $f_{out} \cong 3$ GHz. The parallel LC network, at the source terminal, provides series feedback at the self-oscillation frequency. The drain-to-source LC branch attenuates the input frequency. The transistor is biased at $V_{GS} = -1.5$ V, $V_{DS} = 3$ V, near pinchoff, to take advantage of the quasiquadratic $i_{ds} \equiv i_{ds}(v_{gs})$ characteristic for an efficient mixing between the input frequency and the oscillation. This should provide the subharmonic frequency $\omega_{in}/2$. The nonlinear elements of the MESFET transistor, taken into account for the analysis, are the Schottky junction current $i_{gs} \equiv i_{gs}(v_{gs})$ and charge $q_{gs} \equiv q_{gs}(v_{gs})$; the drain-to-source current $i_{ds} \equiv i_{ds}(v_{gs}, v_{ds})$, which can be modeled through the Tajima equation [35]; and the drain-to-gate current $i_{dg} \equiv i_{dg}(v_{gs}, v_{ds})$, which can be modeled through a diodelike equation [29,30].

In the absence of external signal, a free-running oscillation takes place at $F_0 = 3$ GHz. Figure 3 shows the time-domain simulation of this oscillation, in terms of the voltage at the drain node. The oscillation startup required an initial condition to “escape” from the unstable DC solution. Note the long duration of the transient in comparison with the solution period (Fig. 3a). This duration is about 15 periods of the steady-state oscillation. The integration has been performed with the trapezoidal rule, with adjustable timestep. The minimum allowed timestep, along the integration interval, is $\Delta t = 1$ ps. Convergence fails when a larger value of this minimum step is chosen.

The criterion for the selection of the timestep is based on the number of iterations required to achieve convergence. If, for a time t_n , convergence is achieved with a smaller number of iterations than a certain prefixed value n_0 , the timestep for t_{n+1} is increased. The expanded view of Fig. 3b shows the steady-state waveform and the discrete timepoints. Figure 3c shows a comparison between the trapezoidal (solid line) and the backward Euler

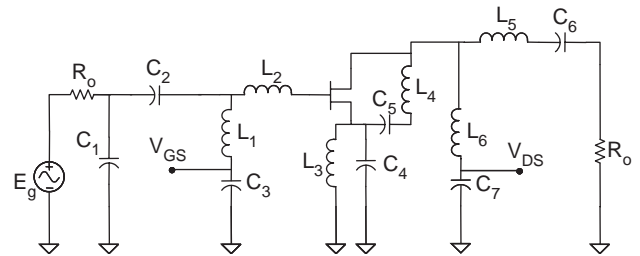


Figure 2. Schematic of a frequency divider by 2, with 6 GHz input frequency.

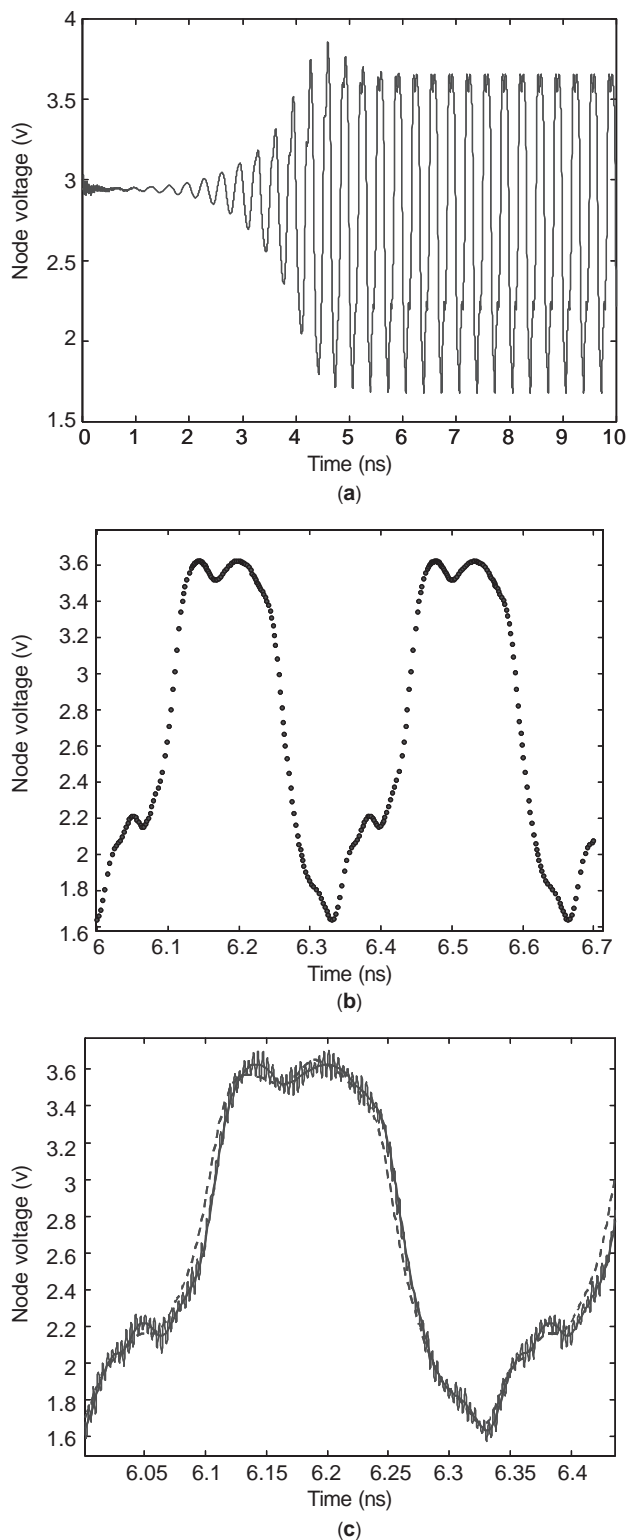


Figure 3. Time-domain integration of the circuit of Fig. 2, elements operating as a free-running oscillator: (a) transient and steady state; (b) expanded view of the steady-state waveform, showing the adjustment of the timestep; (c) comparison between the Euler integration rule (dashed line) and the trapezoidal rule (solid line) for fixed timestep $h = 1$ ps. For $h = 0.25$ ps, there is a numerical oscillation, in both cases. The one obtained for the trapezoidal rule has been superimposed.

(dashed line) integration rules, for fixed timestep $h = 1$ ps. To test the validity of this method, the integration step has been reduced to the unnecessarily small value $h = 0.25$ ps. For this small step, a numerical oscillation is obtained in both cases. The one resulting from the trapezoidal integration rule is shown in Fig. 3c.

The abovementioned numerical oscillation indicates the possible instability of the integration algorithms. As seen in the previous example, the unstable behavior is independent of the accuracy. It depends on the timestep and the particular algorithm. For a same continuous-time system, each algorithm gives rise to a different discrete-time equation. The stable solution of the continuous-time system may become an unstable solution of a particular discrete-time system. The stability properties of the different algorithms have been compared by applying them to a continuous first-order linear system [1], with a stable solution.

Generally speaking, the stable or unstable behavior of a given algorithm depends on the time constants of the original continuous-time system and the timestep h . With λ as the time constant of the original system, the different algorithms have different stability regions, in terms of λh [1]. These stability regions are usually larger for the implicit algorithms, due to the effect of feedback. Typically, the stability is not critical for the stepsizes that are commonly used by the designer. However, in some systems, called *stiff systems*, the step to satisfy the accuracy constraint lies within the instability region [1]. This is typical of systems with time constants of very different orders of magnitude.

3. FAST TIME-DOMAIN TECHNIQUES

As has been shown, the direct-integration methods provide the entire time evolution of the circuit solution, from the initial point t_0, \bar{v}_0 , including the transient and steady state. Generally, most of the simulation time is devoted to the transient. However, the circuit designers are usually interested in the steady-state solution only. Taking this into account, the fast time-domain methods directly address the steady-state regime. These methods use time-domain descriptions for both the linear and nonlinear elements. Therefore, if the circuit contains the distributed elements, the use of frequency-domain techniques is usually more convenient. But the fast time-domain analysis is possibly the best option for the simulation of strongly nonlinear periodic regimes in lumped-element circuits. Two different techniques will be briefly outlined here: the shooting methods and the finite differences in time domain.

3.1. Shooting Methods

The shooting methods [8,11–13] provide, through an optimization technique, a vector of initial conditions \bar{v}_0 , from which the circuit operates in the steady-state regime. Thus, no transient is obtained when integrating the nonlinear system (6) from \bar{v}_0 . The initial conditions are difficult to establish in the case of distributed elements, since these conditions must be specified throughout the entire

devices, which is done through the use of functions [13]. In case of periodic regimes, the solution at the end of the period must match this initial condition. Assuming initial time $t_0=0$, the two-point constraint $\bar{v}(0) - \bar{v}(T)=0$ is imposed, where T is the period of the solution. Of course, this boundary value constraint cannot be applied to quasiperiodic regimes. The so-called mixed frequency-time methods are a generalization of the shooting method, enabling the simulation of these quasiperiodic regimes [12].

A periodic steady state will be assumed here. Let the solution $\bar{v}(t)$ be expressed in terms of the initial value $\bar{v}(t_0)$ as $\bar{v}(t) = \bar{v}(t_0) + \bar{\phi}(\bar{v}(t_0), t_0, t)$, where $\bar{\phi}$ is the so-called state transition function [8,11]. Then, the shooting equation system is given by $\bar{\phi}(\bar{v}_0, 0, T) = 0$, which contains P equations in P unknowns. To obtain the transition matrix, it must be taken into account that $\bar{v}(t_{n+1})$ in (6) is an implicit function of $\bar{v}(t_n)$, assuming that no convolution terms are present. Thus, recursively integrating Eq. (6) from \bar{v}_0 , it will be possible to obtain numerically the function $\bar{\phi}(\bar{v}_0, 0, T)$. If the time interval $[0, T]$ is discretized in M values, such that $t_0=0$ and $t_{M-1}=T$, then Eq. (6) will be fulfilled at each of these values, even when the shooting equations are not satisfied.

A Newton-Raphson algorithm is used to solve the shooting equations $\bar{\phi}(\bar{v}_0, 0, T) = 0$ in terms of the initial conditions \bar{v}_0 . This requires calculation of the state-transition matrix over the shooting interval and determination of the Jacobian matrix $[J\phi] \equiv \partial\bar{\phi}(\bar{v}_0, 0, T)/\partial\bar{v}_0$, also called the *sensitivity matrix*. Thus, the circuit is solved through a two-level Newton-Raphson algorithm. The outer level corresponds to the shooting equations. The inner level is applied to the integration of the system (6), which is required for determination of the transition matrix. Note that the computational rapidly increases with the size of the circuit, so matrix-implicit iterative algorithms are usually applied.

3.2. Finite Differences in Time Domain

In the finite-difference time-domain (FDTD) method [11], the system (6) is combined with the periodicity condition $\bar{v}(t_0) - \bar{v}(t_{M-1}) = 0$, to obtain a global system, whose unknowns are the M time samples $v_p(t_n)$ ($n=0$ to $M-1$) of each P state variable. For a circuit containing lumped elements only and assuming a backward-Euler integration rule, the $P \times M$ equation system is written

$$\begin{aligned}
 & \frac{2}{h}(\bar{q}(\bar{v}(t_1)) - \bar{q}(\bar{v}(0)) + \bar{i}(\bar{v}(t_1)) + \bar{g}(t_1)) = 0 \\
 & \vdots \\
 & \frac{2}{h}(\bar{q}(\bar{v}(t_{n+1})) - \bar{q}(\bar{v}(t_n)) + \bar{i}(\bar{v}(t_{n+1})) + \bar{g}(t_{n+1})) = 0 \\
 & \vdots \\
 & \frac{2}{h}(\bar{q}(\bar{v}(T)) - \bar{q}(\bar{v}(t_{M-2})) + \bar{i}(\bar{v}(T)) + \bar{g}(T)) = 0 \\
 & \bar{v}(0) - \bar{v}(T) = 0
 \end{aligned} \tag{7}$$

where equal spacing h between the time samples has been considered. Compared with (6), in the subsystem composed by the $M-1$ first equations of (6), there are P additional unknowns, which correspond to the initial condition $\bar{v}(0)$. However, the periodicity condition $\bar{v}(0) - \bar{v}(t_{M-1}) = 0$ adds P more equations to the system. Thus, (7) is a well-balanced system of $P \times M$ equations in $P \times M$ unknowns, which is solved through the Newton-Raphson algorithm [11]. As in the case of the shooting methods, matrix-implicit iterative algorithms must be used for the analysis of large-size circuits.

The two cases of an autonomous or a nonautonomous circuit give rise to a difference in the solution of (7). In the case of a nonautonomous circuit, the time-varying input generator or generators $\bar{g}(t)$ set the conditions for the first point $t_0=0$, as these generators take the specific value $\bar{g}(0)$. In the case of an autonomous circuit (free-running oscillator), there are no time-varying input generators. Thus, there is no external reference, providing the initial value of the circuit variables at $t_0=0$. On the other hand, the solution period T is an unknown of the system, since the oscillation frequency is autonomously generated.

The autonomous circuit must be solved for T , in addition to $\bar{v}(0), \dots, \bar{v}(t_n), \dots, \bar{v}(T)$. However, because no external reference exists, one of the components of $\bar{v}(0)$ may take any value in the expected variation range, specifically, $v^1(0) = v_x$, which is arbitrarily assigned [14]. Thus, in the case of an autonomous circuit, there are $MP-1$ unknowns of the form $\bar{v}(t_n)$, with $n=0$ to $M-1$, plus the oscillation period T . So the system (7), in the case of an autonomous circuit, is also a well-balanced system.

Note that since the FDTD method directly provides the periodic steady state of the circuit, without passing through the transient, the solution obtained could be an unstable mathematical solution, to which the circuit never actually evolves. Taking this into account, the system (7) must be complemented with a stability analysis of the solution obtained. In the case of oscillator circuits, a DC solution coexists with the steady-state oscillation, as a mathematical solution. Thus, the initial values of the Newton-Raphson algorithm must be relatively close to the oscillating solution to avoid undesired convergence to the DC regime [14].

4. HARMONIC BALANCE

The HB technique [8,16-19], to be presented in this section, uses frequency-domain descriptions for the linear elements, while keeping the necessary time-domain description for the nonlinear elements. The use of a Fourier frequency basis for the representation of the circuit signals limits its application to relatively mild nonlinear regimes. This is due to the difficulties in the representation of fast time variations in a sinusoidal basis. Because of the use of Fourier series expansions for the circuit variables, HB analyzes only the steady-state solution. Convergence may be obtained to either stable or unstable solutions, so a complementary stability analysis will be necessary, as in the case of the FDTD analysis.

4.1. Formulation of the Harmonic Balance System

The HB method can be applied to periodic or quasiperiodic solutions only. It is assumed that the circuit variables can be expanded in a Fourier series, having a finite set of NF nonrationally related fundamentals $F_1 \dots F_{NF}$. In most practical circuits, the number of fundamentals is one or two. Examples of circuits with one fundamental frequency are the amplifiers and oscillators. A circuit with two fundamental frequencies is a frequency mixer.

Physical circuits have an intrinsic lowpass behavior, so it will be possible to truncate the Fourier series expansions of the circuit variables and keep only a certain number of harmonic terms. Let N be the total number of positive frequencies, resulting from the intermodulation products of the fundamental frequencies. The Fourier series expansions will have the general form

$$\bar{a}(t) = \sum_{k=-N}^N \bar{A}_k e^{j\omega_k t}; \quad \omega_k \equiv \bar{\lambda}_k^t \bar{\Omega}; \tag{8}$$

$$\bar{\Omega}^t = (2\pi F_1, 2\pi F_2, \dots, 2\pi F_{NF})$$

where $\bar{a}(t)$ stands for any of the circuit variables. The vector $\bar{\lambda}_k^t \in Z^{NF}$ contains the integer coefficients of the intermodulation product k . The subindex k ranges the resulting frequencies in increasing order $\omega_1 < \omega_2 < \dots < \omega_N$. Note that since we are dealing with real variables (in the time domain), the Fourier coefficients of (8) fulfill $A_k = A_{-k}^*$.

The Fourier series of a quasiperiodic signal may be truncated using different criteria. Two of the most common are the box truncation and the diamond truncation [7,36,37]. In the box truncation, positive integers nl_j are specified such that $|\lambda_j| \leq nl_j$ $1 \leq j \leq NF$. In the case of two fundamental frequencies, the representation of the selected pairs of coefficients λ_1, λ_2 (one vs. the other) provides a rectangle, which justifies the term used for this truncation criterion. In the diamond truncation, the criterion is $|\lambda_1| + |\lambda_2| + \dots + |\lambda_{NF}| \leq nl$, where nl is a previously imposed nonlinearity order. For two fundamental frequencies, the representation of the selected pairs of coefficients λ_1, λ_2 provides a diamond. It is easily shown that, in this case, the total number of positive frequencies is $N = nl(nl + 1)$.

The diamond truncation is generally more efficient than the box truncation, since for the same total number of frequency components it neglects components with higher order than any fundamental. Other truncation schemes can also be used. For instance, it is possible to assign a different order nl_j $1 \leq j \leq NF$ to each fundamental, while still imposing an overall truncation order $|\lambda_1| + |\lambda_2| + \dots + |\lambda_{NF}| \leq nl$. This technique is especially useful when there are significant differences in magnitude at the different fundamentals. Note that the a priori determination of the optimum truncation order is generally difficult. A saturation criterion can be applied, increasing nl or (nl_j) until no appreciable changes are obtained in the circuit solution. The error in the fulfillment of the Kirchhoff laws at the circuit nodes, in the time domain, can also be used to verify the validity of the series truncation.

Two different HB formulations are possible and will be introduced in the following text. The first formulation results from the direct introduction of the Fourier series expansions of the vector $\bar{v}(t), \bar{q}(t), \bar{i}(t),$ or $\bar{g}(t)$ into Eq. (1), taking into account the orthogonality of the Fourier basis. This formulation is known as *nodal harmonic balance* [8]. The size of the system is equal to the number of circuit nodes, multiplied by the number $(2N + 1)$ of spectral lines. Thus, a nonlinear system with a great number of unknowns may be obtained. The second formulation, known as *piecewise harmonic balance* [18], is based on a strict separation of the circuit elements into linear and nonlinear. This allows one to limit the set of unknowns to the control variables of the nonlinear elements only (instead of having to determine all the node voltages). The number of unknowns is reduced, at the expense of using linear impedances or admittances of higher order in ω .

4.1.1. Nodal Harmonic Balance. Let Fourier series expansions of the vectors $\bar{v}(t), \bar{q}(t), \bar{i}(t),$ and $\bar{g}(t)$, with the form (8), be considered. These expansions will be introduced into the modified nodal equation (2). Taking into account the orthogonality of the Fourier basis $e^{j\omega_k t}$, it will be possible to obtain a relationship between the harmonic components of $\bar{v}(t), \bar{q}(t), \bar{i}(t),$ or $\bar{g}(t)$. For a compact expression of this relationship, the set of Fourier coefficients will be written in the vector form

$$\bar{v}(t) \rightarrow \bar{V} = (\bar{V}_{-N}, \dots, \bar{V}_k, \dots, \bar{V}_N); \tag{9}$$

$$\bar{V}_k = (V_k^1, \dots, V_k^p, \dots, V_k^P)$$

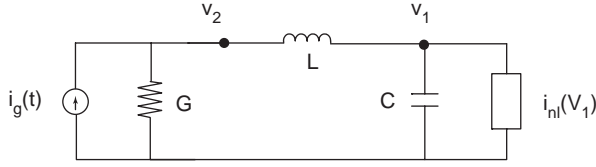
where k indicates the harmonic index and p , the index of the state variable. Similar expressions hold for $\bar{q}(t), \bar{i}(t),$ and $\bar{g}(t)$. Then, the relationship between the Fourier coefficients of the different sets of variables, constituting the HB equation, is

$$\bar{E}(\bar{V}) \equiv \bar{I}(\bar{V}) + [j\omega] \bar{Q}(\bar{V}) \tag{10}$$

$$+ [H(j\omega)] \bar{V} + \bar{G} = 0$$

where $[j\omega]$ is composed of diagonal matrixes of the form $j\omega_k [I_p]$, where $[I_p]$ is the identity matrix of P order. $\bar{E}(\bar{V})$ is an error function to be minimized in the solution process. Note that the convolution operation in (1) has become, in (10), a simple multiplication by the matrix $[H(j\omega)]$. This matrix contains the transfer functions of the different distributed elements. Provided the relationship $\bar{Q}(\bar{V})$ is globally invertible, it will be possible to express $\bar{I}(\bar{V}) \equiv \bar{I}(\bar{Q})$. Then the HB system can be reformulated using \bar{Q} as unknown. This technique ensures the charge conservation. Note that since the circuit variables are real, it is generally more convenient to limit the harmonic vectors $\bar{V}, \bar{I}, \bar{Q}, \bar{G}$ to the positive spectrum only. Then, real variables are used, instead of complex ones. The variables are given by the real and imaginary parts of each Fourier coefficient. The total number of unknowns (and equations) is $(2N + 1)P$.

As an example, Fig. 4 shows the nodal HB formulation of a simple nonlinear circuit. This circuit contains a



Nodal:
$$\begin{bmatrix} jC\omega_k & \frac{1}{R} \\ 1 & -1 - \frac{jL\omega_k}{R} \end{bmatrix} \begin{bmatrix} V_k^1 \\ V_k^2 \end{bmatrix} + \begin{bmatrix} I_{nk}(\bar{V}^1) \\ 0 \end{bmatrix} + \begin{bmatrix} -1 \\ jL\omega_k \end{bmatrix} I_{gk} = \bar{0}$$

Piecewise: $[1 - L\omega_k^2 + jRC\omega_k] V_k^1 + [R + jL\omega_k] I_{nk}(\bar{V}^1) - R I_{gk} = 0$

Figure 4. Comparison between the nodal and piecewise HB formulations of a simple nonlinear circuit.

one-port nonlinear element and an input generator. It has two nodes, so $P=2$. In turn, the subindex k goes from $-N$ to N , for N harmonic components. The number of HB unknowns is $2(2N+1)$. The same example will also be used later on to illustrate the piecewise HB formulation.

For a given value of the state variable vector \bar{V} , the corresponding $\bar{I}(\bar{V})$ and $\bar{Q}(\bar{V})$ are indirectly obtained through inverse (F^{-1}) and direct (F) Fourier transforms:

$$\begin{aligned} \bar{v} &= F^{-1}(\bar{V}) \rightarrow \bar{i} \equiv \bar{i}(\bar{v}), \bar{q} \equiv \bar{q}(\bar{v}) \\ &\rightarrow \bar{I} = F(\bar{i}), \bar{Q} = F(\bar{q}) \end{aligned} \quad (11)$$

For the practical calculation of the direct and inverse Fourier transforms, the time variable is discretized. Discrete Fourier transforms (DFTs) must be used. The algorithms for the calculation of these transforms, in the two cases of periodic and quasiperiodic signals, are the object of Section 4.2. The reader familiar with these algorithms can skip this section. The DFT algorithm requires a number M of discrete time samples in the vectors $\bar{v}(t)$, $\bar{q}(t)$, $\bar{i}(t)$, and $\bar{g}(t)$. The choice $M_{\min} = 2N + 1$, where N is the number of positive frequencies, gives rise to square transformation matrixes (see Section 4.2). However, oversampling is commonly used, to reduce aliasing. Then, the number of samples M is chosen between $2M_{\min}$ and $10M_{\min}$ [8]. The excess of time samples, with respect to the number $2N + 1$ of harmonic frequencies, gives rise to a rectangular Fourier transformation matrix, to which pseudoinversion techniques are applied.

The error function in (10) is usually minimized through the Newton–Raphson algorithm. Using this algorithm, the next-iteration vector \bar{V}^{j+1} is obtained from a linearization of the nonlinear system about the point \bar{V}^j , resulting from the iteration j . This is equated as

$$[JE]_j(\bar{V}^{j+1} - \bar{V}^j) = -\bar{E}^j(\bar{V}^j) \quad (12)$$

where $[JE]_j$ is the jacobian matrix of the error function in (10), evaluated at the previous iteration j . This Jacobian

matrix is given by

$$\begin{aligned} [JE] &\equiv \left[\frac{\partial \bar{E}}{\partial \bar{V}} \right] = \left[\frac{\partial \bar{I}(\bar{V})}{\partial \bar{V}} \right] \\ &+ [j\omega] \left[\frac{\partial \bar{Q}(\bar{V})}{\partial \bar{V}} \right] + [H(j\omega)] \end{aligned} \quad (13)$$

The algorithm requires an initial value \bar{V}^0 of the state variable vector. In a nonautonomous circuit, with low input generator amplitudes, \bar{V}^0 can be estimated by discarding the nonlinear effects in (10). This technique will not work properly in the case of input generators with high amplitude. A method to cope with this problem will be presented later.

To obtain the components of the matrixes $\partial I/\partial V$ and $\partial Q/\partial V$, the Fourier transformation matrix $[F]$ and the chain rule are used. As an example, let the element $i^r(\bar{v})$, $1 \leq r \leq P$, and the particular state variable v^p , $1 \leq p \leq P$, be considered. The box $\partial I^r/\partial V^p$, containing the derivatives of the harmonic components of i^r with respect to each harmonic component of v_p , is computed as follows

$$\frac{\partial \bar{I}^r}{\partial \bar{V}^p} = [F] \left[\frac{\partial i^r}{\partial v^p} \right] [F]^{-1} \quad (14)$$

Note that the calculation of $\partial I_N^r/\partial V_{-N}^p$ and $\partial I_{-N}^r/\partial V_N^p$ requires $4N + 1$ components in the Fourier series expansions of the derivatives. The box $\partial I^r/\partial V^p$ is full in the case of a nonlinear element $i^r(v^p)$. In the case of a linear element i^r , the box will be diagonal, since each harmonic component I_k^r depends only on the harmonic components of the same order k of the state vector \bar{v} . Since the vectors $\bar{i}(\bar{v})$ and $\bar{q}(\bar{v})$ include both linear and nonlinear elements, the calculations of the form (14) give rise to Jacobian matrix (13) with many zero terms. A matrix of this kind is called *sparse matrix* [38–40].

As already mentioned, the Newton–Raphson algorithm will have convergence problems in case of high input generator amplitude. A simple way to cope with this problem is to perform a general sweep in the amplitude of the RF generators, introducing a parameter η and expressing them as $\bar{G}_{RF}(\eta) = \eta \bar{G}_{RF}$. Then, the parameter η is varied between a very small value η_0 and 1, in discrete steps $\eta_n = \eta_0 + n\Delta\eta$ [3]. A complete HB resolution is carried out for each η_n , using the result of the previous analysis (for η_{n-1}) as the initial guess. Note that the circuit will operate in small signal for the initial parameter value η_0 . Thus, obtaining the HB solution for this initial value will be straightforward.

The Newton–Raphson algorithm (12) may be difficult to implement in the case of very large circuits, due to the large number of unknowns to be determined. This number of unknowns strongly increases in the case of quasiperiodic solutions. The matrix factorization required for the Jacobian inversion is very demanding in terms of computing time and memory storage. However, the natural sparsity of the system (14) enables the straightforward application of sparse matrix techniques for linear system

solution. This linear system is solved through preconditioned Krylov subspace methods [11,38]. If the GMRES [11] (generalized minimum residual) algorithm is applied, the Jacobian matrix $[JE]$ is not needed explicitly, since only matrix–vector products have to be computed.

4.1.2. Piecewise Harmonic Balance. In piecewise HB, the nonlinear elements of the circuit are initially identified [19]. These elements are considered as nonlinear controlled sources, and the set of all their control variables constitute the set of unknowns, to be determined in the solution process. As an example, in the circuit in Fig. 4, the only state variable is the voltage v_1 , controlling the nonlinear current i_{n1} . Compared to the nodal HB, the number of state variables has been reduced from two to one. Clearly, in piece-wise HB, the number of unknowns will be much lower than in the case of nodal HB. The Q different variables that control the nonlinear elements form the set of unknowns x_q , with $1 \leq q \leq Q$. The P nonlinear elements form a second set of variables y_p , with $1 \leq p \leq P$. Finally, the S independent generators of the circuit form a third set g_s , with $1 \leq s \leq S$.

Once the Fourier basis is established, three vectors \bar{X} , \bar{Y} , and \bar{G} , respectively containing the $2N + 1$ harmonic components of the different variables, x_q , y_p , and g_s , are defined. These vectors are organized in a manner similar to that for $\bar{v}(t)$ in (9). The HB system is easily obtained from the application to the circuit of the Kirchhoff laws, which provides a relationship between the three vectors $\bar{X}, \bar{Y}, \bar{G}$ [19]

$$\bar{H}(\bar{X}) = [A_x]\bar{X} + [A_y]\bar{Y}(\bar{X}) + [A_g]\bar{G} = 0 \tag{15}$$

where $[A_x]$, $[A_y]$, and $[A_g]$ are frequency-dependent linear matrixes, with respective orders $Q \times Q$, $Q \times P$, and $Q \times S$. These linear matrixes are block diagonal matrixes, at the different harmonic orders $-N \leq k \leq N$. The total number of equations is $(2N + 1)Q$, in $(2N + 1)Q$ unknowns. Using, again, the simple circuit of Fig. 4 as an example, it can be seen that the degree of the linear matrixes is 2 (in ω_k) in the piecewise formulation, while it was only 1 in the nodal formulation. In fact, the main advantage of the piecewise HB comes from the fact that the complexity of the linear network or the accuracy in the description of its elements may be arbitrarily increased, without increasing the number of unknowns of the nonlinear system.

Equation (15) is, in fact, a nonlinear equation, since the functions \bar{Y} and the state variables \bar{X} are nonlinearly related, through the (time-domain) transfer characteristics of the different nonlinear elements. The system (15) is numerically solved by minimizing the norm of the error function $\|\bar{H}\|$, through the Newton–Raphson algorithm. In contrast with the case of the nodal HB, the Jacobian matrix of the piecewise formulation is generally dense (not sparse). Artificial sparsity may be created by setting to zero selected elements of the matrix, according to a physical criterion [39]. However, a relatively high degree of sparsity is necessary for the sparse system solvers to operate efficiently. In a more recent work, an inexact Newton

approach enables the use of GMRES for the calculation of the inexact Newton update [40].

4.2. Algorithms for Calculation of the Discrete Fourier Transforms

From the point of view of the discrete Fourier transform (DFT) algorithms, two main types of signal may be distinguished: periodic and quasiperiodic. In the case of periodic signals, the techniques for the DFT are well known. In particular, the fast Fourier transform FFT reduces the number of operations involved in the transformation. These algorithms cannot be directly applied to quasiperiodic signals, and complementary approaches will be needed [36,41–45]. The main approaches are briefly summarized in the following paragraphs.

4.2.1. DFT of Periodic Signals. The case of a periodic signal $y(t)$, to be expressed in the form $y(t) = \sum_{k=-N}^N Y_k e^{jk2\pi f_0 t}$, will be considered initially. The $2N + 1$ coefficients Y_k may be calculated from the linear equation system that is obtained when considering $2N + 1$ timepoints t_n [41]. The resulting square system is as follows:

$$\begin{bmatrix} 1 & 1 & \dots & 1 & 1 & \dots & 1 \\ 1 & e^{j2\pi f_0 t_1} & \dots & e^{j2\pi N f_0 t_1} & e^{-j2\pi N f_0 t_1} & \dots & e^{-j2\pi f_0 t_1} \\ \vdots & \vdots & \dots & \vdots & \vdots & \vdots & \vdots \\ 1 & e^{j2\pi f_0 t_{2N}} & \dots & e^{j2\pi N f_0 t_{2N}} & e^{-j2\pi N f_0 t_{2N}} & \dots & e^{-j2\pi f_0 t_{2N}} \end{bmatrix} \times \begin{bmatrix} Y_0 \\ Y_1 \\ \vdots \\ Y_N \\ Y_{-N} \\ \vdots \\ Y_{-1} \end{bmatrix} = \begin{bmatrix} y(0) \\ y(t_1) \\ \vdots \\ y(t_{2N}) \end{bmatrix} \tag{16}$$

This system can be written in a more compact form: $[W]\bar{Y} = \bar{y}$. Provided the time instants t_n are calculated in such a way that $[W]$ is invertible, the Fourier transform of $y(t)$ will be given by $\bar{Y} = [W]^{-1}\bar{y}$. The timepoints t_n are

$$t_n = n \frac{1}{(2N + 1)f_0} \equiv nT_s \tag{17}$$

The frequency $f_s = (2N + 1)f_0$ is clearly the sampling frequency of the time-domain signal. With the point selection (17), the matrix $[W]$ is invertible and well conditioned. In order for a matrix to be well conditioned, its condition

number must be very close to unity. This number is calculated from the Euclidean norm of $[W]$ as $k_W = \frac{1}{\|W\|} \|W^{-1}\|$.

From the timepoint choice (17), and taking into account the harmonic relationship $f_k = kf_0$, the harmonic components of $y(t)$ can be written as

$$\begin{aligned} Y_k &= \frac{1}{2N+1} \sum_{n=0}^{2N} y(n) e^{\frac{-j2\pi}{2N+1} nk} \\ &= \frac{1}{M} \sum_{n=0}^{2N} y(n) (\Phi_M)^{nk} \end{aligned} \quad (18)$$

where $M=2N+1$ and $\Phi_M \equiv e^{-j2\pi/M}$. The fast Fourier transform (FFT) takes advantage of the periodicity of Φ_M , with respect to both n and k , to substantially reduce the number of operations involved in the calculation of the complete sequence Y_k .

4.2.2. DFT of Quasiperiodic Signals. In the case of periodic signals, the sample points are equally spaced within the signal period. Then the DFT has great accuracy since the rows of the transformation matrix $[W]$ are orthogonal and the matrix is well conditioned. In the case of quasiperiodic signals, the equally spaced timepoints give rise to the ill-conditioning of $[W]$. Thus, the DFT cannot be directly applied. Different methods for the calculation of the Fourier transform of quasiperiodic signals have been presented in the literature. The most efficient are summarized in the following paragraphs.

4.2.2.1. Almost-Periodic Fourier Transform. Kundert et al. [41], randomly obtain the timepoints t_n from a time interval equal to 3 times the period of the smallest nonzero frequency. Thus, a number M' of timepoints larger than M is generated. However, instead of oversampling, which would give rise to an increase in the computational cost, only M timepoints are selected from the original set of M' points. A variation of the Gram-Schmidt orthogonalization procedure is used for this selection. The selected M timepoints are those giving rise to the nearest-to-one condition number of the matrix $[W]$. However, the near orthogonality of $[W]$ can also be achieved using nonrandom selections of the sample points. Ngoya et al. [42] describe several strategies.

4.2.2.2. Frequency Remapping. The objective of the Fourier transform is determination of the frequency components of the nonlinear elements of the HB equations. Let the memoryless function $y \equiv y(\bar{x})$ be considered. It can be easily shown [43] that the Fourier coefficients of the nonlinear element Y_k , with $k = -N \dots N$, depend only on the Fourier coefficients of the state variables, grouped in the vector \bar{X} , and on the integer vector $\bar{\lambda}_k$ that generates the particular intermodulation product f_k , but do not depend on the frequency basis \bar{F} . They can actually be written $Y_k \equiv Y_k(\bar{X}, \bar{\lambda}_k)$. Thus, it will not be necessary to use the actual waveforms of the state variables $\bar{x}(t)$ to obtain the Fourier coefficients of $y(\bar{x})$. It will be possible to use simpler

artificial waveforms for the \bar{Y}_k calculation. A convenient choice for the frequency basis \bar{F}^{dl} would be one providing periodic artificial waveforms, to which the efficient FFT algorithm may be applicable. Thus, the actual fundamental frequencies $\bar{F}^t = (F_1 \dots F_{NF})$ are remapped to the artificial ones $(\bar{F}^{dl})^t = (F_1^{dl} \dots F_{NF}^{dl})$. Once the harmonic values \bar{Y}_k are determined, they will be assigned to the actual frequencies, given by $f_k = \bar{\lambda}_k^t \bar{F}$. For this calculation to be valid, the artificial basis \bar{F}^{dl} must generate $2N+1$ different frequencies $f_{kd} = \bar{\lambda}_k^t \bar{F}^{dl}$. These artificial frequencies are the *remapped frequencies*.

The value of the artificial fundamentals depends on the truncation criterion that is used for the Fourier series. For $NF=2$, the artificial fundamentals, in the two cases of box and diamond truncation, are respectively given by [36,37,43]

$$\left. \begin{aligned} F_1^{dl} &= \Delta f \\ F_2^{dl} &= (2nl+1)\Delta f \end{aligned} \right\} \text{box truncation}$$

$$\left. \begin{aligned} F_1^{dl} &= nl\Delta f \\ F_2^{dl} &= (nl+1)\Delta f \end{aligned} \right\} \text{diamond truncation} \quad (19)$$

where Δf is an arbitrary frequency, different from zero, and nl is the nonlinearity order.

4.2.2.3. Multidimensional Fourier Transform. Let a signal $x(t)$ and NF fundamental frequencies be considered. An artificial signal \tilde{x} can be defined, using a different time variable for each fundamental: $\tilde{x}(t_1, t_2, \dots, t_{NF})$. Then, the following equality is fulfilled: $x(t) = \tilde{x}(t, t, \dots, t)$. The artificial signal \tilde{x} is periodic in each time variable t_j . Considering a different truncation order nl_j , $1 \leq j \leq NF$ for each fundamental frequency, the NF -dimensional DFT is written [36,37,44]

$$\begin{aligned} X(\lambda_1, \lambda_2, \dots, \lambda_{NF}) &= \frac{1}{N_{\text{tot}}} \sum_{n_1=-nl_1}^{nl_1} \dots \sum_{n_{NF}=-nl_{NF}}^{nl_{NF}} x_{n_1} \dots x_{n_{NF}} \\ &\times \exp\left(-j2\pi \left(\frac{\lambda_1 n_1}{N_1} + \dots + \frac{\lambda_{NF} n_{NF}}{N_{NF}} \right)\right) \end{aligned} \quad (20)$$

where $N_j = 2nl_j + 1$, $1 \leq j \leq NF$, and $N_{\text{tot}} = \prod_{j=1}^{NF} N_j$.

Care must be taken in (20) to prevent aliasing when choosing the sampling orders. The multidimensional Fourier transform can be obtained through a sequential calculation of fast Fourier transforms, in the different time variables. However, the computational cost of these operations can be greatly reduced through the use of special algorithms [45]. For a nonlinear relationship $y = f(x)$, it is easily shown [36,37] that the samples of $y(t)$ can be obtained through $\hat{y}_{n_1, \dots, n_{NF}} = f(\tilde{x}_{n_1, \dots, n_{NF}})$, which is easily generalized to a nonlinear dependence on multiple state variables. Then, the Fourier coefficients of $y(t)$ can be determined through an expression formally identical to (20).

4.3. Analysis of Autonomous and Synchronized Circuits

As has been shown, the HB technique requires the provision by the designer of the set of fundamentals F_1, \dots, F_{NF} to be used in the Fourier series expansion of the circuit variables. In case of self-oscillations, the corresponding frequencies must be included in this basis. However, the existence or nonexistence of this oscillation and the value of the oscillation frequency depend on the circuit values, so the a priori determination of the frequency basis is not always an easy task. The designer might not even be aware of the existence of a self-oscillation in the circuit in question, as when simulating an unstable amplifier as if it operated in periodic regime.

But even when the entire frequency basis is correctly provided, there might still be problems for the simulation of autonomous or synchronized circuits. The reason is that, coexisting with the oscillating solution, there is always a mathematical solution, with no self-generated fundamentals. This mathematical solution is usually unstable and, thus, has no interest for the user. The most obvious example is the free-running oscillator, for which a DC solution always coexists with the oscillating one (see Fig. 1). In HB, the initial value \bar{X}^0 of the Newton–Raphson algorithm is essentially determined by the input generators. Therefore, the frequency terms involving self-generated fundamentals will have zero value in \bar{X}^0 and will remain so during the entire iterative procedure. Thus, the Newton–Raphson algorithm starting from \bar{X}^0 will converge to the nonoscillating solution, which is as mathematically correct as the other one.

The HB problems with autonomous and synchronized circuits can be circumvented through the use of complementary techniques, to avoid its undesired convergence to nonoscillating mathematical solutions. Then, HB becomes a very powerful method for the design of circuits such as oscillators and frequency dividers. To take full advantage of the technique, the designer must be aware of what he/she is actually facing. With this purpose, the dynamics of the forced oscillator is briefly outlined in Section 4.3.1, which will also allow a better understanding of the HB problems with the simulation of these circuits. The complementary analysis techniques will be presented in Section 4.3.2.

4.3.1. Dynamics of the Forced Oscillator. Let a free-running oscillator at the frequency F_0 be considered. The only fundamental F_0 of the circuit solution is an autonomous one. If an external periodic generator is connected to the circuit, different operation modes may be obtained, depending on the values of the frequency F_{in} and power P_{in} of the generator [3,46]. As an example, Fig. 5 shows the different operation regions of the forced oscillator of Fig. 4, in the plane defined by F_{in} and P_{in} . For small input power P_{in} , provided the input frequency F_{in} is not too close to F_0 , the two frequencies will coexist in the circuit, giving rise to a quasiperiodic regime at F_{in} , F_a . Note that the autonomous frequency F_a is slightly different from the free-running frequency F_0 , due to the influence of the input generator. The circuit operates like a self-oscillating mixer. If the input frequency F_{in} is relatively close to F_0 , then

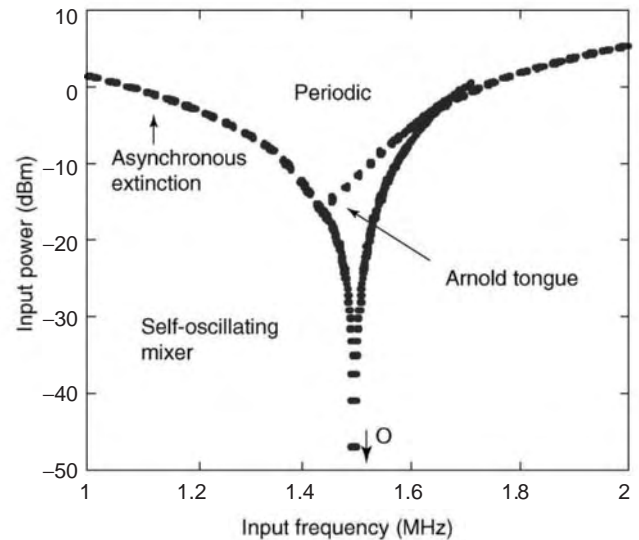


Figure 5. Global behavior of forced oscillators, in terms of the forcing generator frequency and power. Operation regions about F_0 of the oscillator in Fig. 4. (This figure is available in full color at <http://www.mrw.interscience.wiley.com/erfme>.)

the autonomous frequency F_a may be influenced by the input generator in such a way that both frequencies become the same and there is a constant phase relationship between the input signal and the self-oscillation. This phenomenon is called *synchronization*.

The synchronization band, in terms of the input frequency F_{in} , becomes wider as the power delivered by the input generator increases (see Fig. 5). The border of the synchronization region is a V-shaped curve in the plane defined by F_{in} and P_{in} , called the *Arnold tongue*. The lower vertex of the Arnold tongue is the free-running oscillation, occurring at the frequency F_0 , for zero input power P_{in} . The synchronized regime is a periodic regime with F_{in} as fundamental. Although the fundamental frequency is the same delivered by the input generator, the self-oscillation is still present in the circuit and, in general, gives rise to output power much higher than could be expected in a simple amplifier regime. Finally, note that for relatively high input power P_{in} at a frequency F_{in} not too close to F_a , the self-oscillation may be extinguished. This phenomenon, known as *asynchronous extinction*, gives rise to a simple forced regime.

The synchronization can also occur when the input frequency is close to any harmonic component, of k order, of the free-running frequency. Then $F_{in} = kF_a$, after synchronization. The harmonic synchronization principle is used for the design of analog frequency dividers. Thus, this kind of circuit operates in a synchronized regime in which the self-oscillation has become a subharmonic of the input signal. The synchronization is also possible when the input frequency is close to a subharmonic of the free-running oscillation frequency, that is, when $F_a = mF_{in}$. This is the principle of the subsynchronized oscillator, in which a stable subharmonic source is used to stabilize and reduce the phase noise of a noisier oscillator. The synchronization bands become narrower with the order k or m . Each

synchronization region in the plane F_{in}, P_{in} constitutes an Arnold tongue.

Figure 6a shows the periodic solution curves of the forced oscillator of Fig. 4, when represented in terms of the amplitude at the fundamental frequency. The point O indicates the free-running oscillation, obtained for zero input power. This solution coexists with a DC solution that, in the representation of the figure, would lie on the horizontal axis (abscissa). When the input generator power is injected, a synchronized solution curve is obtained around the free-running oscillation point. For small input power, this synchronization curve is closed. See, for instance, the curve obtained for $I_g = 7 \text{ mA}$, in the figure. This is in agreement with the fact that the synchronized solution has a limited bandwidth (see the Arnold tongue in Fig. 5).

The limits of the synchronization band are given by the infinite-slope points or turning points of this closed curve. Although the stability analysis is the object of the final

section (Section 6), it can be advanced that the turning points of a given solution curve always separate sections with different qualitative stability [3]. If the solution is originally stable, it becomes unstable after folding at a turning point. In Fig. 6a, only the upper section of the closed curve is stable. Note also that the closed curve coexists with a low-amplitude curve, obtained for the same input power and the same circuit values. It is an unstable solution, equivalent to the DC solution of the free-running oscillator. In this small amplitude solution, the circuit is not oscillating.

For higher input power, the closed synchronization curve widens, as gathered from the Arnold tongue of Fig. 5. For a certain input power, the upper curve and the lower curve merge. From that input power, only one curve is obtained. There is an intermediate range of input power for which the curve exhibits strong folding (see the curve for $I_g = 9 \text{ mA}$). For the lower input power values, the turning points will still be synchronization points. For higher input power, they will be simple jump points. At these points, the solution cannot continue evolving along the same section of the curve, due to its folding versus the parameter, and “jumps” to a different section. When the open periodic curves cross the locus, indicated with “asynchronous extinction” in Fig. 5, they become unstable. An autonomous frequency is generated and gives rise to a stable quasiperiodic regime. The autonomous frequency is, in fact, the self-oscillation frequency, reappearing in the circuit for input generator values of lesser influence.

In Fig. 6a, the circuit solution is quasiperiodic beyond the turning points (for the lower input power) and below the “asynchronous extinction locus” (for the higher input power). The quasiperiodic solution has two fundamental frequencies: the input frequency F_{in} and the oscillation frequency F_a . These quasiperiodic solutions have been represented in Fig. 6b, for the input current $I_g = 20 \text{ mA}$. Since there are two fundamentals, a path has been traced for each of them, showing the evolution of the corresponding harmonic amplitude. On the left-hand side, the synchronization is due to the asynchronous extinction of the autonomous fundamental, occurring at $F_{in} = 1.32 \text{ GHz}$. The solution is periodic in the input frequency interval 1.32–1.55 GHz. However, at $F_{in} = 1.55 \text{ GHz}$, it loses synchronization due to a turning point of the periodic curve (see Fig. 6a).

All the simulations in Fig. 6 have been carried through HB, using the techniques that will be presented in the following section. By default, the HB methods of Section 4.1 would miss many of the solutions represented in the figure. In the case of the free-running oscillator (zero input power), it would converge to the DC solution. When the input generator power is injected, two different cases must be distinguished. For low input power, it will converge to the low-amplitude curve, missing the actually synchronized solution. For higher input power, it will converge to the single periodic curve, but will not be able to circumvent the turning points for reasons that will be made clear later. The quasiperiodic solutions of Fig. 6b can never be obtained by default since convergence to the coexisting periodic solutions is much simpler, as these solutions are naturally forced by the input generators. In the case of low

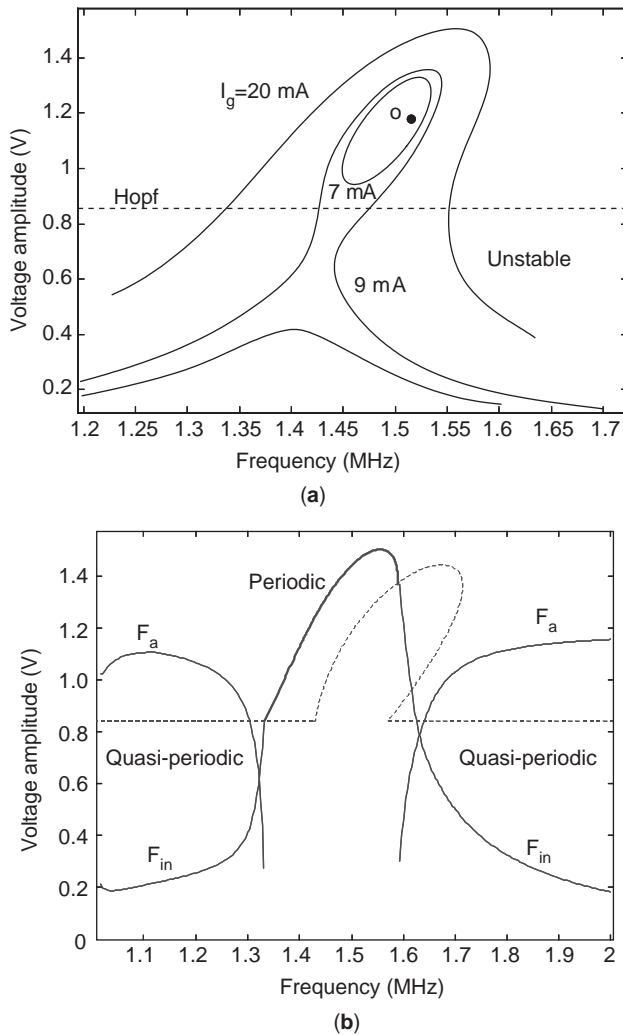


Figure 6. Solutions of the cubic nonlinearity oscillator: (a) for different values of the input generator current; (b) for the input current $I_g = 20 \text{ mA}$, including quasiperiodic simulations. (This figure is available in full color at <http://www.mrw.interscience.wiley.com/erfme>.)

input power, the periodic solution obtained will be the unstable low-amplitude curve. In the case of higher input power, the obtained periodic solution will be the unstable single curve.

4.3.2. Complementary Harmonic Balance Techniques. Different techniques have been proposed in the literature to cope with the HB difficulties when dealing with autonomous circuits [46–48]. In Ref. 46, taking into account the forced nature of ‘the HB method, an artificial generator is introduced at the self-generated fundamental. We shall refer to this artificial generator as the *auxiliary generator* [3,46]. Provided the auxiliary generator has a nonzero value, it will be able to initialize the harmonic components, involving the autonomous or synchronized fundamental. The solution obtained with the aid of this auxiliary generator must be the actual autonomous or synchronized solution, and must, of course, entirely agree with the one that would be obtained without the auxiliary generators.

Two different types of auxiliary generator are possible: voltage generators, connected in parallel at a circuit node, and current generators, connected in series at a circuit branch. The use of the voltage auxiliary generator is illustrated in Fig. 7, where it has been introduced in the frequency divider of Fig. 2. As formerly stated, the auxiliary generator operates at the autonomous or synchronized oscillation frequency. This will be written $F_{AG} = F_a$, where the subindex ‘a’ denotes, in general, ‘autonomous.’ We must also account for the fact that voltage generators and current generators are, respectively, short circuits and open circuits at frequencies different from those that they deliver. Thus, an ideal filter is necessary in each case, to avoid a major perturbation of the circuit, due to the short-circuiting/opening of the harmonic components. In the case of a voltage generator, the ideal filter is connected in series with this generator (see Fig. 7). The filter has a zero impedance value at the generator frequency $F_{AG} = F_a$ and infinite impedance at any other frequency (for which the generator will have no effect).

As already stated, to be of any use in determination of the circuit solution, the auxiliary generator must have no influence over this solution. To have zero influence, a voltage generator must exhibit a zero value of its current-to-voltage relationship at the delivered frequency. The non-perturbation condition will introduce additional constraints in the HB system. But there are also additional

variables. These variables depend on the type of regime, autonomous or synchronized, to be analyzed. Both cases are considered in the following text.

4.3.3. Autonomous Regime. In an autonomous regime, one of the fundamental frequencies is due to a self-oscillation of the circuit. As already indicated, for the analysis of this regime, an auxiliary generator is introduced at the frequency $F_{AG} = F_a$. Because the frequency F_a is autonomously generated by the circuit, its value will depend on the values of the circuit elements and the input generators, so it is not known a priori. It is, actually, one of the unknowns to be determined. The auxiliary generator will have an amplitude A_{AG} and a phase ϕ_{AG} . However, in an autonomous regime, the phase ϕ_{AG} can be anyone, in the sense that any phase value ϕ_{AG} gives rise, after the solution of the circuit, to the same waveforms of the circuit variables. For simplicity, the value $\phi_{AG} = 0$ will be considered.

As already mentioned, the auxiliary generator must not to perturb the steady state. The unknowns to be determined, in order to fulfill the nonperturbation condition, are the autonomous frequency, which is the same frequency delivered by the auxiliary generator, and the amplitude A_{AG} of this generator. In case of an auxiliary generator of voltage type, the nonperturbation conditions are the following:

$$\bar{Y}_{AG}(A_{AG}, F_{AG}) \equiv \begin{bmatrix} \text{Re} \left(\frac{I_{AG}}{A_{AG}} \right) \\ \text{Im} \left(\frac{I_{AG}}{A_{AG}} \right) \end{bmatrix} = \bar{0}, \tag{21}$$

$$V_{AG} \equiv A_{AG} e^{j0}$$

where I_{AG} is the current flowing through the auxiliary generator. The nonperturbation condition adds two more equations and two more unknowns to the HB system, which becomes

$$\bar{H}_B(\bar{X}, F_{AG}, A_{AG}) = \bar{0} \tag{22a}$$

$$\bar{Y}_{AG}(\bar{X}, F_{AG}, A_{AG}) = \bar{0} \tag{22b}$$

Note that a piecewise HB formulation has been considered, although the method can equally be applied when using a nodal formulation. The error function \bar{H}_B is the same function we have been dealing with in Section 5. Once the convergence is achieved, the voltage value at the auxiliary generator node (in case of a voltage generator) will be, at the oscillation frequency $V(F_A) = A_{AG} e^{j0}$. This value is independent of the presence or absence of the auxiliary generator, since, according to (22), this generator does not have any influence on the steady-state solution.

The auxiliary generator technique has been applied to the circuit of Fig. 2 in free-running oscillator regime. The fundamental frequency of the Fourier basis is $F_{AG} \equiv F_a$. The number of harmonic frequencies that has been taken into account is $N = 15$. Figure 8a shows the evolution of the real and imaginary parts of the admittance function Y_{AG} , versus the iteration number. Figure 8b shows the

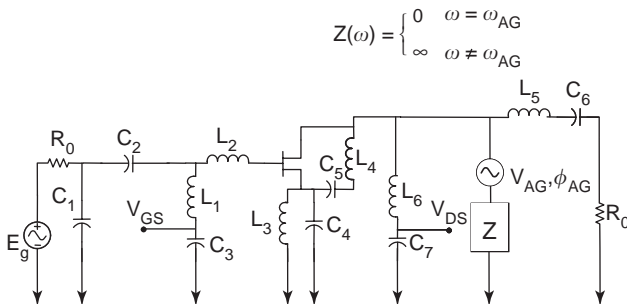


Figure 7. Auxiliary generators of voltage type, connected in parallel at a circuit node.

evolution of the frequency F_{AG} and the amplitude A_{AG} versus the iteration number. As can be appreciated, the initial values were relatively far from the actual solution. When the admittance function is equal to zero, F_{AG} agrees with the free-running oscillation frequency F_0 and A_{AG} with the node amplitude at the first-harmonic component. Figure 9 shows the resulting spectrum and waveform. As can be seen, the waveform (Fig. 9b) agrees with the one obtained through the time-domain analysis of Fig. 3.

4.3.4. Synchronized Regime. In the case of a synchronized regime, the self-oscillation frequency F_a is harmonically related to the input generator frequency F_{in} . There is also a constant-phase relationship between the two frequency components. For the analysis of this regime, an auxiliary generator will be introduced at the frequency at which the self-oscillation occurs. Since it is a synchronized regime, the frequency of the generator will be $F_{AG} \equiv F_a = F_{in}/k$. A similar relationship would hold in the case

$F_a = mF_{in}$. Since the frequency of the auxiliary generator is determined by F_{in} , it is no longer an unknown of the problem. In contrast, and as a result of the phase relationship between the oscillation and the input generator signal, the phase ϕ_{AG} of the auxiliary generator is no longer irrelevant and will be an unknown of the problem. The amplitude A_{AG} and phase ϕ_{AG} are unknowns to be determined through

$$\bar{H}_B(\bar{X}, \phi_{AG}, A_{AG}) = \bar{0} \tag{23a}$$

$$\bar{Y}_{AG}(\bar{X}, \phi_{AG}, A_{AG}) = \bar{0} \tag{23b}$$

with the auxiliary generator operating at the frequency $F_{AG} \equiv F_a = F_{in}/k$, in the case of a frequency divider or $F_{AG} \equiv F_a = mF_{in}$, in the case of a subsynchronized oscillator.

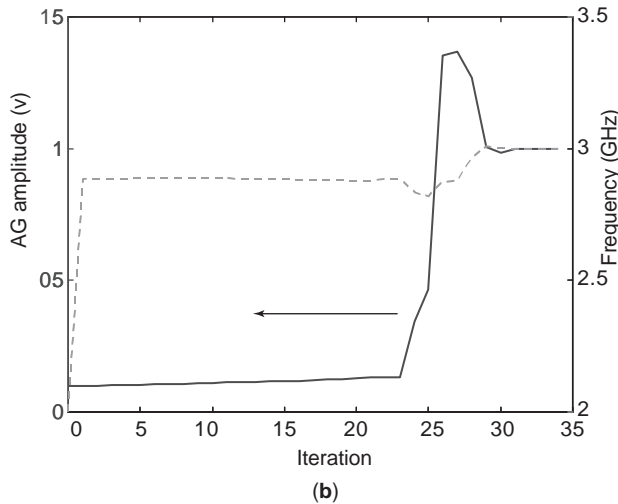
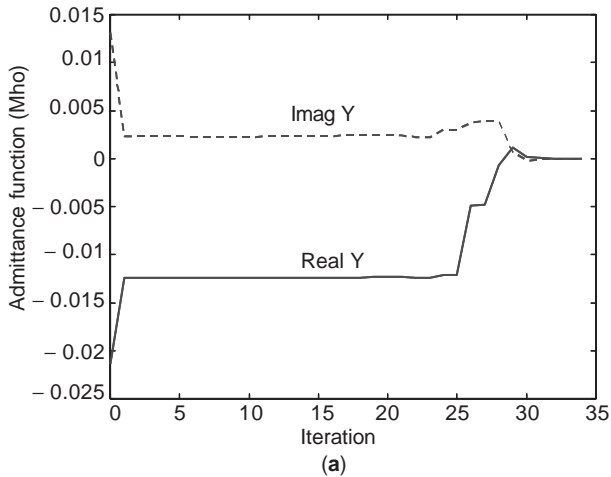


Figure 8. Application of the auxiliary generator technique to the circuit of Fig. 7, in free-running-oscillator regime, showing evolution of the (a) real and imaginary parts of the auxiliary generator admittance versus the iteration number and (b) auxiliary generator amplitude and frequency versus the iteration number.

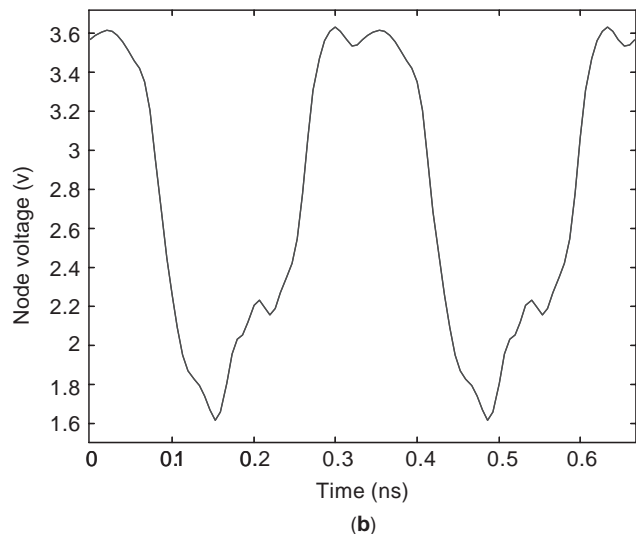
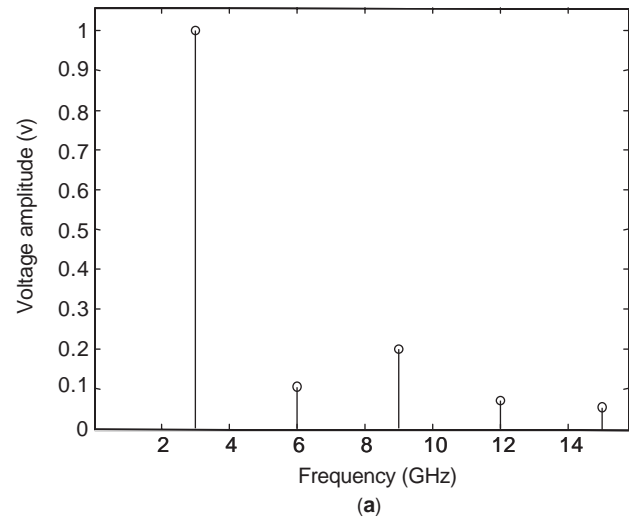


Figure 9. Results of application of the auxiliary generator technique to the circuit of Fig. 7, in free-running oscillator regime: (a) magnitude spectrum of the node voltage; (b) waveform.

The analysis technique has been applied to the divider circuit of Fig. 2. Now the input generator is connected, at a frequency F_{in} , about $2F_0$. The input amplitude is $V_{in} = 0.25$ V. The fundamental frequency of the Fourier series expansion is $F_{in}/2$. Again, the number of harmonic components is $N = 15$. The synchronized solution curve, in terms of the drain amplitude, versus the input frequency, has been traced in Fig. 10. For this relatively low input amplitude, a closed curve is obtained about the free-running oscillation. In agreement with the qualitative behavior of Fig. 6, there will also be a low-amplitude curve, with no frequency division (not represented). The upper section of the curve (between the two turning points) is stable, while the lower section is unstable.

In Fig. 11, the circuit has been analyzed for constant frequency $F_{in} = 6$ GHz and the same generator amplitude $V_{in} = 0.25$ V. The low-amplitude waveform of Fig. 11a at the nondivided frequency 6 GHz is the solution obtained through standard HB. The frequency-divided waveform is the solution obtained through the auxiliary generator technique. Figure 11b shows the time-domain analysis of the frequency-divided regime, with a long transient, in comparison with the solution period. Note the agreement of the resulting steady-state waveform with the divided solution of Fig. 11a.

For the input frequency $F_{in} = 5.6$ GHz, the solution lies on the left-hand side of the ellipsoidal curve of Fig. 10. The solution is not synchronized for these input conditions, and this is way it has not been represented. The input generator frequency F_{in} and the self-oscillation frequency F_a coexist and the circuit behaves as a self-oscillating mixer. Because of the existence of F_a as an independent fundamental, the circuit behaves in an autonomous regime that has been analyzed through (22). Note that a multitone analysis at the two fundamental frequencies F_{in} and F_{AG} is necessary. Here a diamond truncation of the spectrum has been used, with $nl = 7$. Figure 12a shows the

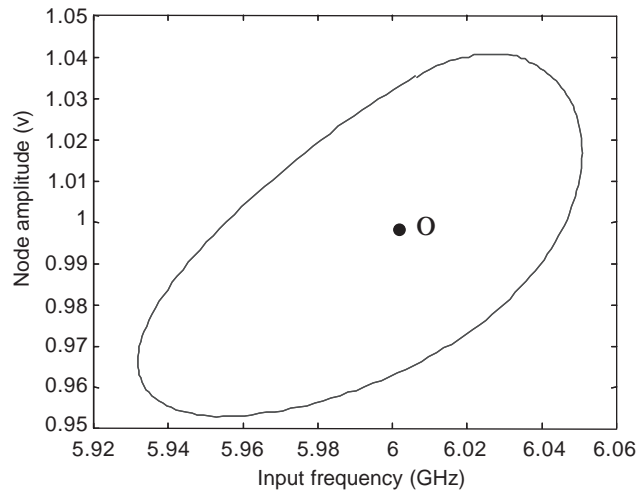


Figure 10. Synchronized solution versus the output frequency for $V_{in} = 0.25$ V. The upper portion of the closed curve is stable. The lower section of the solution curve is unstable. The point inside the curve corresponds to the free-running oscillation.

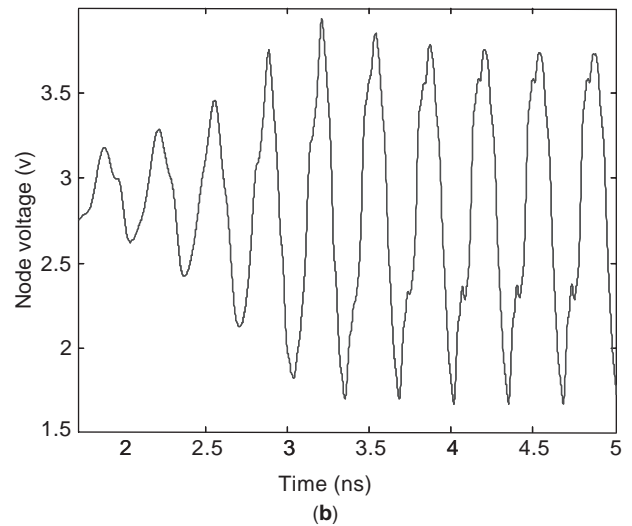
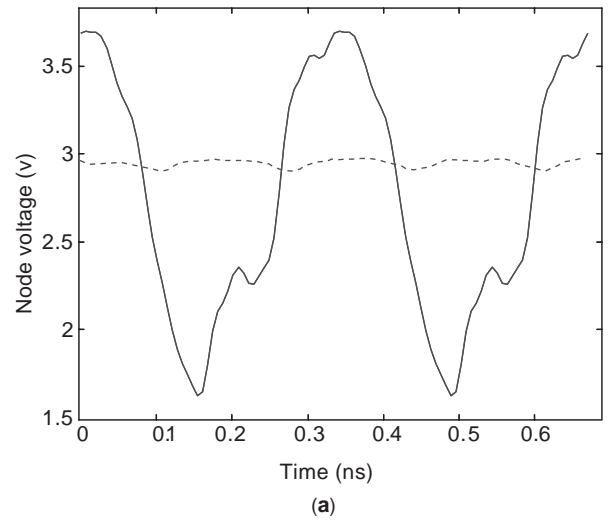


Figure 11. Simulation of the circuit of Fig. 2, operating as a frequency divider by 2: (a) the frequency-divided solution, obtained through the auxiliary generator technique, coexists with a non divided solution, obtained through standard HB simulation, with no auxiliary generator; (b) time-domain simulation of the frequency-divided regime.

evolution of the auxiliary generator frequency and amplitude versus the iteration number. Figure 12b shows the resulting quasiperiodic spectrum of the drain voltage.

For too close values of F_{in} and $2F_a$, differing, for instance, in just a few megahertz, the multitone HB will not be accurate, since this represents three orders of magnitude less than F_{in} and F_a . This kind of operation is obtained for input frequencies close to the border of the synchronization region. As will be shown, the envelope transient is very well suited for the simulation of this regime.

5. ENVELOPE TRANSIENT

Obviously, the HB method cannot be applied to the analysis of circuits with modulated input signals. This is due to the impossibility of representing the modulated variables

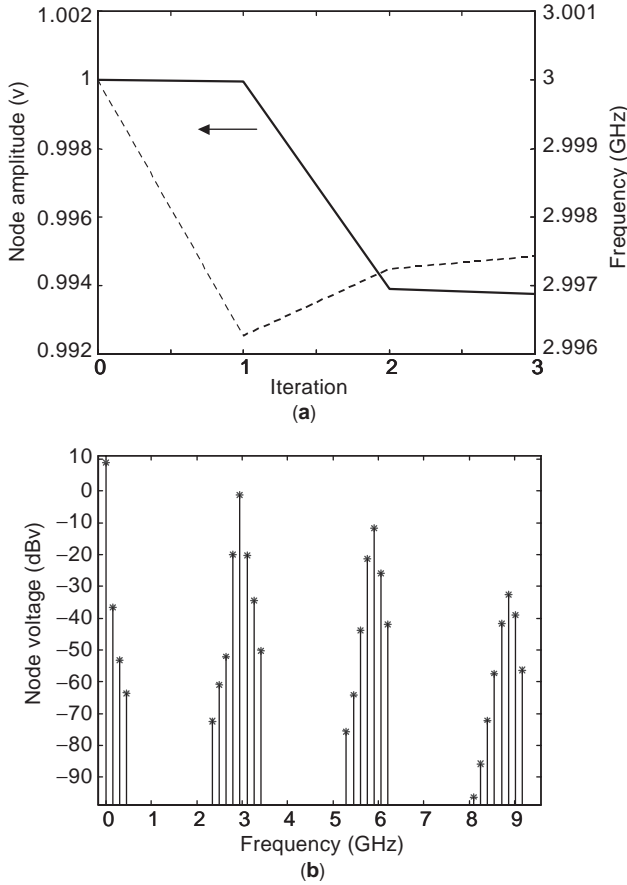


Figure 12. Auxiliary generator technique for analysis of the circuit in Fig. 2 in self-oscillating mixer regime: (a) evolution of the auxiliary generator amplitude and frequency versus the iteration number; (b) resulting quasiperiodic spectrum.

in a Fourier series. However, in most circuits with modulated inputs, it is possible to consider two different timescales. The faster timescale t_2 corresponds to the carrier, and the slower timescale t_1 corresponds to the modulation. The circuit is generally periodic in the “faster” time t_2 . Then, any state variable $a(t)$ can be expanded in a harmonic series of the form [20–25]

$$a(t_1, t_2) = \sum_{k=-N}^N A_k(t_1) e^{j\omega_k t_2} \quad (24)$$

where $A_k(t_1)$ are the slowly varying envelopes. In general, the frequencies ω_k will either be the harmonics of a single input frequency, in an amplifier, for instance, or the intermodulation products of an RF/IF input frequency and a local-oscillator frequency, in a frequency mixer.

According to (24), the circuit variables could be sampled using two different time rates t_1, t_2 . Of course, since the two timescales are fictitious, the variables $\bar{a}(t_1, t_2)$ will agree with $\bar{a}(t)$ only for $t_1 = t_2$. On the other hand, the envelopes must not overlap in order for the decomposition (24) to be unique in the basis $e^{j\omega_k t_2}$, $-N \leq k \leq N$.

When expressions of the form (24) are introduced in the HB system, the two time variables t_1, t_2 will require two

different derivative operators. However, as a result of the solution periodicity with respect to t_2 , for fixed t_1 , the derivative with respect to t_2 will simply be obtained through multiplication of the different harmonic terms by $j\omega_k$. This provides an algebraic system of differential equations in the harmonic terms $A_k(t_1)$, to be sampled (in the numerical integration) at a rate Δt_1 lower than that of the original system. This allows a significant reduction of the computational cost.

Two different cases may be considered, according to the type of HB formulation, nodal or piecewise, in which the expansions (24) are introduced. The two cases are analyzed in the following text.

5.1. Nodal Harmonic Balance

In the case of a nodal HB formulation [22,25], the envelope transient equation takes the form

$$\begin{aligned} \bar{I}(\bar{V}(t)) + [j\omega]\bar{Q}(\bar{V}(t)) + \frac{d}{dt}\bar{Q}(\bar{V}(t)) \\ + \int_{-\infty}^t \bar{H}(t-\tau)\bar{V}(\tau)d\tau + \bar{G}(t) = 0 \end{aligned} \quad (25)$$

where the subindex has been dropped from the time variable t_1 , for notation simplicity. For the numerical solution of (25), the time variable is discretized. Then the following system is obtained

$$\begin{aligned} \bar{I}(\bar{V}(t_{n+1})) + [j\omega]\bar{Q}(\bar{V}(t_{n+1})) \\ + \frac{\bar{Q}(\bar{V}(t_{n+1})) - \bar{Q}(\bar{V}(t_n))}{t_{n+1} - t_n} \\ + \sum_{i=0}^n \bar{H}(t_{n+1} - t_i)\bar{V}(t_i)\Delta t_i + \bar{G}(t_{n+1}) = 0 \end{aligned} \quad (26)$$

where a backward Euler integration rule has been considered. The system is integrated using the initial conditions $\bar{G}(t_0), \bar{V}(t_0)$. The initial condition may be obtained from a simple harmonic balance (with constant envelopes) at the initial time $t_0 = 0$. From this timepoint, the Newton-Raphson algorithm is applied to obtain the solution $\bar{V}(t)$ along the simulation interval $[0, T_s]$. Since Eq. (26) is a nonlinear harmonic relationship between $\bar{I}(t_{n+1}), \bar{Q}(t_{n+1}), \bar{V}(t_{n+1})$ and $\bar{G}(t_{n+1})$, the integration along $[0, T_s]$ involves a HB calculation for each timepoint t_{n+1} .

The major difficulty with the envelope transient, based on the nodal HB, comes from the need to compute the time-varying harmonic components of the impulsive responses $\bar{H}(t)$, which will necessitate, again, the use of Padé approximations, as in the case of the full time-domain analysis. However, the computation of the convolution products is much less demanding than in standard time-domain integration, since the models of the distributed elements can be narrowband about the harmonic frequencies ω_k .

5.2. Piecewise Harmonic Balance

When considering time-varying harmonic components in the piecewise HB equations, the following system is obtained [21,24]

$$\begin{aligned}
 & [A_x(jk\omega_0 + j\omega)]\bar{X}(t) + [A_y(jk\omega_0 + j\omega)]\bar{Y}(t) \\
 & + [A_g(jk\omega_0 + j\omega)]\bar{G}(t) = 0
 \end{aligned}
 \tag{27}$$

where ω is the frequency associated to the time variations in t_1 and, again, the subindex of this time variable has been dropped, $t_1 \equiv t$. Assuming slow variations of the harmonic components, the linear matrixes can be expanded in a Taylor series about $\omega = 0$. This Taylor expansion will necessarily limit the allowed envelope bandwidth. For $\omega \ll \omega_0$, a first-order Taylor expansion will be sufficient, providing the result

$$\begin{aligned}
 & [A_x(jk\omega_0)]\bar{X}(t) + \left[\frac{\partial A_x}{\partial jk\omega_0} \right] \frac{d\bar{X}(t)}{dt} \\
 & + [A_y(jk\omega_0)]\bar{Y}(t) + \left[\frac{\partial A_y}{\partial jk\omega_0} \right] \frac{d\bar{Y}(t)}{dt} \\
 & + [A_g(jk\omega_0)]\bar{G}(t) + \left[\frac{\partial A_g}{\partial jk\omega_0} \right] \frac{d\bar{G}(t)}{dt} = 0
 \end{aligned}
 \tag{28}$$

where the fact that the multiplication by $j\omega$ is equivalent to a time derivation in t_1 has been taken into account.

Because of the development of the linear matrixes in a first-order Taylor series, it will be valid only for slowly varying $\bar{X}(t), \bar{Y}(t), \bar{G}(t)$, that is, for narrowband harmonic components. This is a significant departure from the nodal formulation, which does not have this constraint. However, the formulation (28) requires neither the calculation of the distributed-element impulsive responses nor the computation of the convolution products. As a result, provided the envelopes are narrowband, which is usually the case, the piecewise formulation may be more efficient.

As an example, the envelope transient formulation has been applied to a transistor-based frequency mixer, with input frequency $F_{in} = 4$ GHz and local-oscillator frequency $F_0 = 3.5$ GHz. The input signal is CDMA-modulated, with 4 MHz bandwidth. Contrary to the previous examples, this circuit is forced. It is analyzed using a two-tone Fourier-series expansion, at F_{in} and F_0 , avoiding the harmonic relationship between the fundamentals. Diamond truncation is used, with $nl = 7$. The conditions for an accurate envelope transient simulation are fulfilled, since the envelope bandwidth, due to the CDMA modulation, is much narrower than the smallest frequency interval between the spectral lines $\Delta f/2 = (F_{in} - F_0) = 250$ MHz. Figure 13a shows the time-varying magnitude of the intermediate frequency component $F_{in} - F_0$, over the output 50 Ω load. Figure 13b shows the output power spectrum, in steady state. Note that this spectrum is centered about the frequency $f = 0$, since it has been calculated from the time varying envelope of the harmonic component $F_{in} - F_0$.

The envelope transient can be applied to the simulation of autonomous and synchronized regimes. However, as in

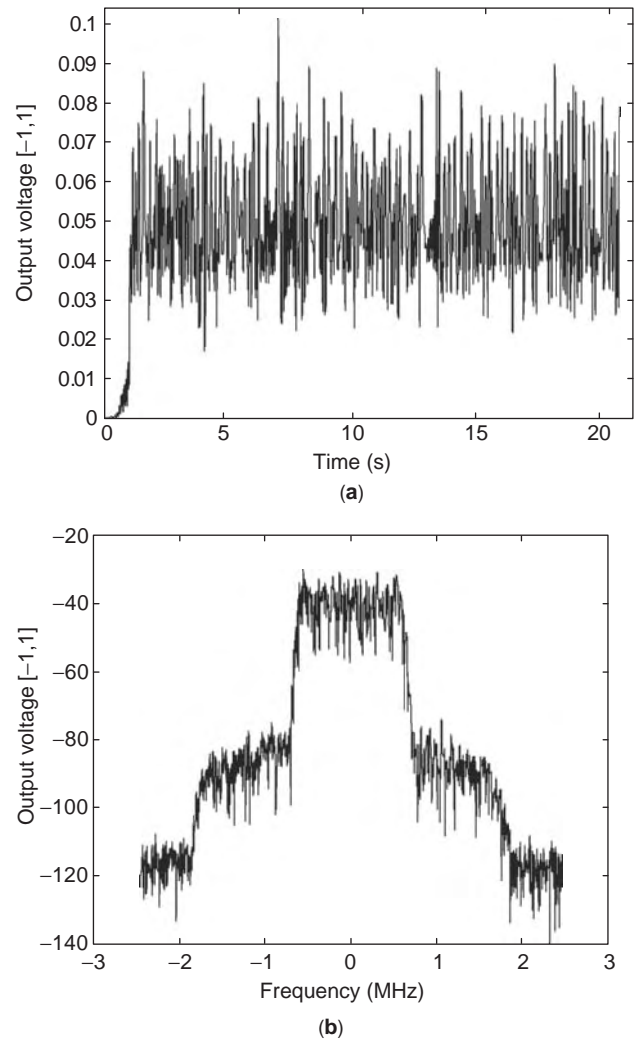


Figure 13. Frequency mixer with a CDMA input signal at $F_{in} = 4$ GHz. The frequency of the local oscillator is $F_0 = 3.5$ GHz: (a) magnitude of the time-varying envelope at the intermediate-frequency component $F_{in} - F_0$; (b) power spectrum about the frequency component $F_{in} - F_0$.

the case of standard HB, there may be simulation problems, due to the coexistence of the autonomous or synchronized solutions with a (generally unstable) mathematical solution, without self-oscillation. As in the case of the standard HB, the problem can be solved with the aid of auxiliary generators. This has been done in the bibliography in two different ways, indicated in the following text.

Assuming an auxiliary generator of voltage type, once the nonperturbation condition is fulfilled, the resulting generator voltage agrees with the node voltage. The same is true in terms of the branch current, in the case of a current generator. Thus, since we are dealing with the possibly modulated steady states, the value of the auxiliary generator should be time-varying. In the case of an autonomous regime, this generator would be represented by $A_{AG}(t), \omega_{AG}(t)$. In the case of a synchronized regime, it would be represented by $A_{AG}(t), \phi_{AG}(t)$. Taking this into account, Ngoya and coworkers imposed

the nonperturbation condition along the whole simulation interval $[0 - T_s]$ [21,24], as $\vec{H}_{AG}(A_{AG}(t), \zeta_{AG}(t)) = 0$, where $\zeta_{AG}(t)$ stands for either the auxiliary generator frequency or its phase, according to the type of regime. Thus, the auxiliary generator variables must be calculated at each timestep, along the simulation interval $[0 - T_s]$. This technique allows simulation of the oscillator transients [21,22].

A different technique has been developed [49] to avoid the computational complexity of the calculation of the time-varying values $A_{AG}(t), \zeta_{AG}(t)$, along $[0 - T_s]$. In this second technique, an auxiliary generator of constant value A_{AG_0}, ζ_{AG_0} is connected to the circuit at the initial point $t_0 = 0$ of the simulation interval only. The constant value A_{AG_0}, ζ_{AG_0} is determined from a HB analysis of the form (22) or (23), according to the type of regime. After $t_0 = 0$, the AG is disconnected from the circuit, letting it evolve according to its own dynamics, with no AG influence. In general terms, if the solution is stable, the circuit will evolve to it after removing the AG. In the case of an autonomous regime, the fundamental frequency of the frequency-series expansion (24) is kept constant to ω_{AG_0} , as this is the value resulting from the initial HB analysis, assuming constant harmonic terms A_k . When doing so, the frequency variation $\omega_a(t) - \omega_{AG}$ is naturally converted to phase variations of the harmonic terms $A_k(t)$ [3].

Two examples of application of the envelope transient to autonomous/synchronized circuits will be shown in the following paragraphs. The first example analyzes the effect of a modulated input phase at F_{in} , over the phase of the drain voltage, at the harmonic component $F_{in}/2$, in the frequency divider of Fig. 2. The input generator amplitude is $V_{in} = 0.25$ V, at the frequency $F_{in} = 6$ GHz. For these input generator conditions, the circuit operates in synchronized regime, as shown by the synchronization curve of Fig. 10. In the absence of any form of modulation, a constant value of the phase of the first-harmonic component $V[1]$ would be obtained. When the phase modulation is introduced, the phase of this harmonic responds to this modulation in the way shown in Fig. 14. The division by 2 of the phase increments should be noted. The same technique could be applied to more practical cases of modulated autonomous circuits.

The second example shows the application of the envelope transient technique to a near-synchronization regime, difficult to analyze through other techniques. According to Fig. 10, the circuit operates in this regime when the input frequency corresponds to values outside the ellipsoidal curve, but close to any of its two turning points. The input frequency and the oscillation frequency coexist in the circuit solution. Then, when using a frequency basis with ω_{in} as the only fundamental, the envelopes will oscillate at the difference frequency $|\omega_{in}/2 - \omega_a|$. Figure 15 shows the envelope transient simulation of the quasiperiodic solution for $F_{in} = 5.92$ GHz. The envelope oscillates at the difference frequency $F_a - F_{in}/2 = 8$ MHz (see Fig. 15a). The resulting dense spectrum about the first-harmonic component is shown in Fig. 15b. The demanding time-domain simulation of this regime is also shown in Fig. 15c, for comparison.

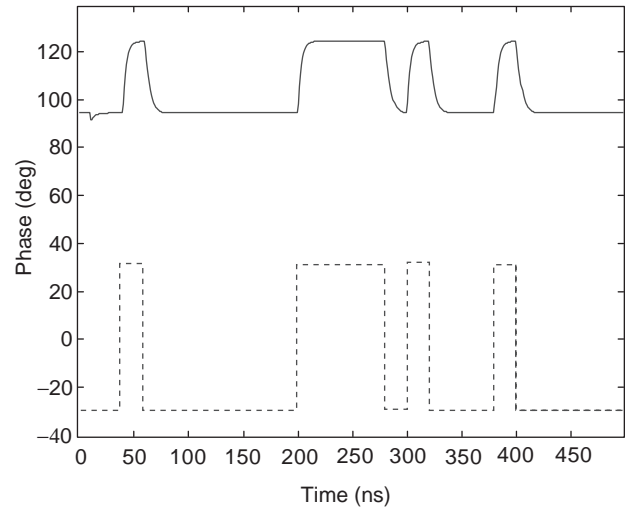


Figure 14. Effect of a modulated input phase on the solution of the circuit of Fig. 2, for $V_{in} = 0.25$ V, $F_{in} = 6$ GHz [dashed line—input modulation; solid line—phase of the harmonic component $V[1]$ of the drain voltage].

6. PARAMETRIC ANALYSIS AND STABILITY

Usually, the interest of the designer is not limited to obtaining the circuit solution for just a particular value of the input generator or generators, or the circuit elements. Instead, the designer generally wishes to know the circuit response versus a given parameter η , which may be the input generator power or frequency, or a bias voltage, for instance. In many cases, this parametric analysis is necessary in order to calculate the circuit operation ranges, in terms of frequency bandwidth, for instance, or to determine the possible coexistence of the desired regime with solutions of other type. As an example, the parametric analysis of the circuit of Fig. 2, versus the input frequency, allowed us to obtain its frequency-division band for $V_{in} = 0.25$ V (see Fig. 10).

The straightforward way to obtain the circuit response versus a parameter η is to carry out a sweep in this parameter. However, this direct sweep will generally lead to unsatisfactory results if the curve contains turning points. At the turning points (or infinite-slope points) the curve folds over itself, giving rise to a multivalued section, versus the parameter (see Fig. 6a). The turning points are intrinsic to the performance of frequency dividers and synchronized oscillators and are also commonly obtained in autonomous circuits of other nature, such as voltage-controlled oscillators.

The turning points of the solution curve can be circumvented using continuation methods. These methods assume that the solution is known for a particular value η_0 of the parameter. This initial point may have been obtained from a standard HB calculation or with the aid of auxiliary generators, in the case of an autonomous or synchronized regime. From this initial point, the solution variations versus η may be followed using different strategies. One of the most efficient techniques is the prediction–correction technique, with parameter switching [50].

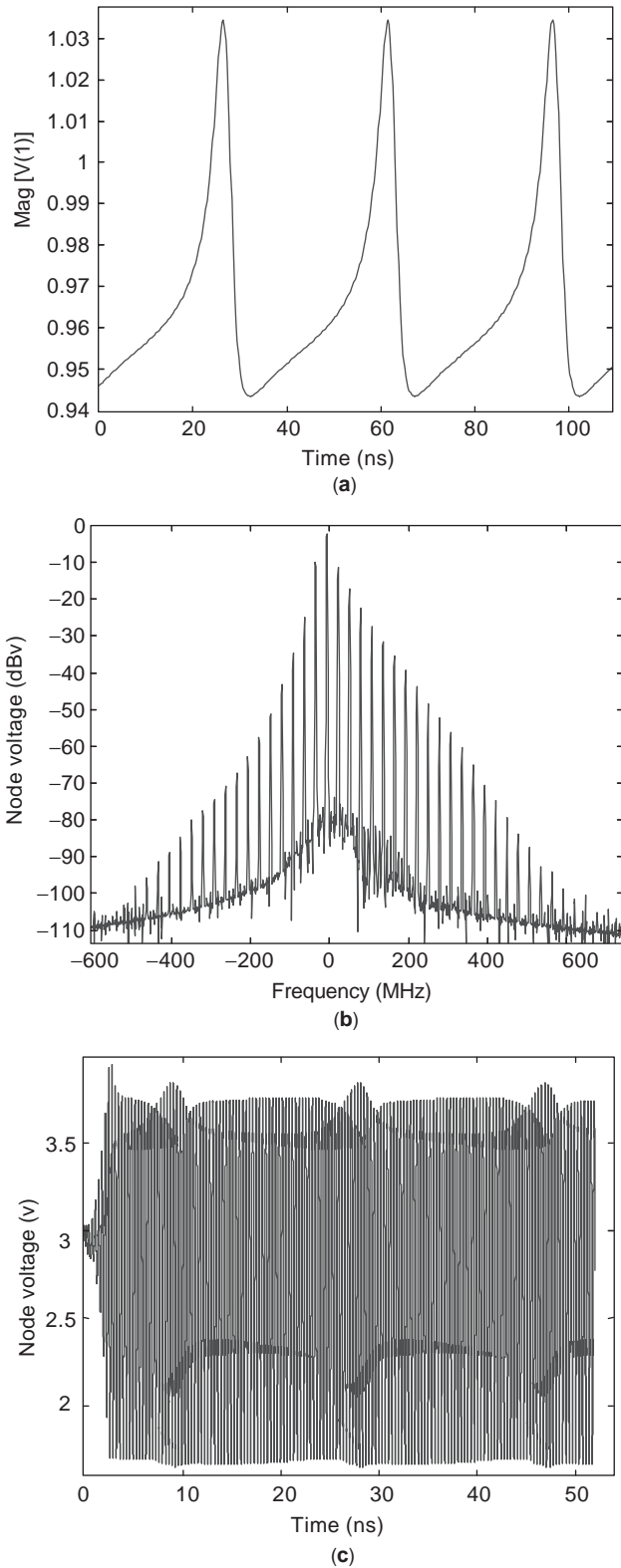


Figure 15. Envelope transient simulation of a near-synchronization solution; (a) slow oscillation of the magnitude of $V[1]$; (b) dense spectrum about the first-harmonic component; (c) time-domain simulation, for similar conditions.

The prediction–correction technique, with parameter switching, is applied from the initial solution point (η_0, \bar{X}_0) , considering a discrete step $\Delta\eta = h$. In this technique, once a solution point (η_n, \bar{X}_n) has been determined, the next one $(\eta_{n+1}, \bar{X}_{n+1})$ is estimated through the linearization of the HB system about the previous point (η_n, \bar{X}_n) . This constitutes the *prediction* stage of the technique. The estimated point will be called here $(\eta_{n+1,p}, \bar{X}_{n+1,p})$. It is calculated by differentiating the error function \bar{H} of the HB system

$$\begin{aligned} \Delta\bar{H} &= [JH]_n(\bar{X}_{n+1,p} - \bar{X}_n) + \frac{\partial\bar{H}}{\partial\eta}\bigg|_n(\eta_{n+1} - \eta_n) = 0 \\ \rightarrow \bar{X}_{n+1,p} &= \bar{X}_n - [JH]_n^{-1} \frac{\partial\bar{H}}{\partial\eta}\bigg|_n(\eta_{n+1} - \eta_n) \end{aligned} \quad (29)$$

where the Jacobian matrix $[JH]_n$ and the derivative of \bar{H} with respect to the parameter are evaluated at the preceding solution point n . The predicted point $(\eta_{n+1,p}, \bar{X}_{n+1,p})$ is not the actual solution point since the actual system $\bar{H}(\bar{X}, \eta) = 0$, unlike Eq. (29), is nonlinear. The point obtained through (29) is a linear estimation (prediction) of the solution for η_{n+1} .

At the *correction stage* of the continuation technique, the Newton–Raphson algorithm is applied for correction of the estimated point n , which is done for constant parameter value $\eta = \eta_{n+1,p}$. The input of this algorithm is the estimated solution $(\eta_{n+1,p}, \bar{X}_{n+1,p})$, which is used as the starting point: $\bar{X}_{n+1}^0 \equiv \bar{X}_{n+1,p}$. Unlike $\bar{X}_{n+1,p}$, the point resulting from the Newton–Raphson convergence $\bar{X}_{n+1} = \bar{X}_{n+1}^c$ is an actual solution point.

It is easily seen from (29) that the Jacobian matrix $[JH]$ becomes singular at any point of the curve with infinite slope of the solution curve or turning point. Because of this, the Newton–Raphson algorithm fails to converge in the neighborhood of the turning point. To cope with this problem, a parameter-switching algorithm [3,50] can be used. In this algorithm, the continuation parameter is, at sections of the curve, different from the actual circuit parameter η . In fact, at each prediction stage $(\eta_{n+1,p}, \bar{X}_{n+1,p})$, the predicted increments of the different variables (including the parameter η), $|\text{Re} \Delta X_{0n+1}^1|$, $|\text{Im} \Delta X_{0n+1}^1|, \dots, |\text{Re} \Delta X_{Nn+1}^Q|$, $|\text{Im} \Delta X_{Nn+1}^Q|, |\Delta\eta_{n+1}|$ are compared, taking the variable with the biggest increment as new analysis parameter.

If the new parameter is, for instance, $\text{Re} X_k^j$, the increment h is assigned to this variable. Therefore, this variable not considered as an unknown. Instead, the parameter increment $\Delta\eta_{n+1}$ is an unknown of the problem, to be determined in the resolution process. Note that taking the variable with the biggest increment as parameter prevents any unbounded growth of the circuit variables. Through this technique, points of infinite slope (turning points) become points of zero slope. The synchronization curves of Figs. 6 and 10 have been traced through the described prediction–correction technique, with parameter switching.

When dealing with HB simulations, the stability analysis of the obtained steady-state solutions is essential. This is even more so when two or more steady-state

solutions coexist for the same parameter values. To show the principles of the stability analysis through HB, a general steady-state solution \bar{X}_s will be considered. It may be a DC solution or a periodic or quasiperiodic solution, with frequency components ω_k , with $k = -N \dots N$. As already stated, a stable solution must be able to recover from small perturbations. To verify whether this is the case, a small perturbation of complex frequency $\sigma + j\omega$ has been considered [3,17,19]. The need for a complex frequency in the perturbation comes from the fact that the perturbed solution is no longer in steady state. Taking into account the smallness of the perturbation, the HB system can be linearized about \bar{X}_s , which provides the following characteristic equation:

$$\left\{ [A_x(k\omega_0 + \omega - j\sigma)] + [A_y(k\omega_0 + \omega - j\sigma)] \frac{\partial \bar{Y}}{\partial \bar{X}} \Big|_s \right\} \times \Delta \bar{X} = 0 \tag{30}$$

where $\partial \bar{Y} / \partial \bar{X} \Big|_s$ is the Jacobian of the nonlinear elements, with respect to the state variables, evaluated at the steady-state solution. In order for the variable increment $\Delta \bar{X}$ to be different from zero, the associated determinant must be singular:

$$\det[JH(\sigma + j\omega)] = 0 \tag{31}$$

For stability, all the determinant roots must be located on the left-hand side of the complex plane. This means that the perturbation will vanish exponentially in time (due to the negative sign of σ), in agreement with the definition of stability. Because of the (usually) very high order of the HB system, the direct calculation of these roots is a nearly impossible task. Instead, the Nyquist stability criterion is applied to (31). The Nyquist plot is obtained by performing a sweep in ω and tracing $\text{Im}[\det(j\omega)]$ versus $\text{Re}[\det(j\omega)]$. The number of unstable poles of the linearized system (30) agrees with the number of encirclements of the Nyquist plot about the origin of the complex plane. Examples of the application of this technique can be found elsewhere in the literature [3,17,19].

BIBLIOGRAPHY

1. T. S. Parker and L. O. Chua, *Practical Numerical Algorithms for Chaotic Systems*, Springer-Verlag, New York, 1989.
2. K. Ogata, *Modern Control Engineering*, Prentice-Hall, Englewood Cliffs, NJ, 1980.
3. A. Suárez and R. Quéré, *Stability Analysis of Nonlinear Microwave Circuits*, Artech House, Boston, 2003.
4. U. Ascher and L. Petzold, *Computer Methods for Ordinary Differential Equations and Differential-Algebraic Equations*, SIAM Press, Philadelphia, 1998.
5. L. Gustaffson, K. J. Lundstrom, and G. H. B. Hansson, On the use of the describing functions in the study of nonlinear active microwave circuits, *IEEE Trans. Microwave Theory Tech.* **20**(6):402–409 (June 1972).
6. S. Maas, *Nonlinear Microwave and RF Circuits*, Artech House, Boston, 2003.

7. J. C. Pedro and N. B. Carvalho, *Intermodulation Distortion in Nonlinear Microwave Circuits*, Artech House, Boston, 2003.
8. K. S. Kundert, Introduction to RF simulation and its application, *IEEE J. Solid State Circ.* **34**(9):1298–1319 (Sept. 1999).
9. M. I. Sohby and A. K. Jastrzebsky, Direct integration methods of nonlinear microwave circuits, *Proc. 15th European Microwave Conf.*, Paris, 1985, pp. 1110–1118.
10. L. W. Nagel, *SPICE 2: A Computer Program to Simulate Semiconductor Circuits*, Ph.D. Thesis ERL-M520, Univ. California, Berkeley, May 1975.
11. R. Telichevesky, K. Kundert, I. Elfadel, and J. White, Fast simulation of algorithms for RF circuits, *Proc. IEEE Custom Integrated Circuits Conf.*, 1996, pp. 437–444.
12. K. Kundert, Simulation methods for RF integrated circuits, *Proc. Int. Conf. Circuit Aided Design (ICCAD)*, 1997, pp. 752–765.
13. K. S. Kundert and A. Sangiovanni-Vicentelli, Finding the steady-state response of analogue and microwave circuits, *Proc. IEEE Custom Integrated Circuit Conf.*, 1998.
14. J. Bonet, P. Palá, and J. M. Miró, A discrete time approach to the steady-state analysis of distributed nonlinear autonomous circuits, *IEEE Trans. Circ. Syst.*, **47**(2):231–236 (Feb. 1998).
15. I. Maio and F. G. Canavero, Differential-difference equations for the transient simulation of lossy MTLs, *Proc. IEEE Int. Symp. Circuits and Systems (ISCAS)*, 1995, Vol. 2, pp. 1402–1415.
16. C. Camacho-Peñalosa, “Numerical steady-state analysis of nonlinear microwave circuits with periodic excitation, *IEEE Trans. Microwave Theory Tech.* **31**(9):724–730 (Sept. 1983).
17. V. Rizzoli and A. Neri, State of the art and present trends in nonlinear microwave CAD techniques, *IEEE Trans. Microwave Theory Tech.* **36**(2):343–356 (Feb. 1988).
18. V. Rizzoli, A. Lipparini, A. Constanzo, F. Mastroi, A. Neri, and S. Massoti, State of the art harmonic balance simulation of forced nonlinear microwave circuits by the piecewise technique, *IEEE Trans. Microwave Theory Tech.* **40**(1):12–28 (Jan. 1992).
19. R. Quéré, E. Ngoya, M. Camiade, A. Suárez, M. Hessane, and J. Obregon, Large signal design of broadband monolithic microwave frequency dividers and phase-locked oscillators, *IEEE Trans. Microwave Theory Tech.* **41**(11):1928–1938 (Nov. 1993).
20. J. Roychowdhury, Efficient methods for simulating highly nonlinear multi-rate circuits, paper presented at Design Automation Conf. Anaheim, CA, June 1997.
21. E. Ngoya and R. Larcheveque, Envelope transient analysis: A new method for the transient and steady state analysis of microwave communication circuits and systems, paper presented at IEEE Microwave Theory and Techniques Symp. (MTT-S), San Francisco, June 1996.
22. H. G. Brachtendorf, G. Welsch, and R. Laur, A novel time-frequency algorithm for the simulation of the steady state of circuits driven by multi-tone signals, *Proc. IEEE Int. Symp. Circuits and Systems*, Hong-Kong, June 1997, pp. 1508–1511.
23. H. G. Brachtendorf, G. Welsch, and R. Laur, A time-frequency algorithm for the simulation of the initial transient response of oscillators, *Proc. IEEE Int. Symp. Circuits and Systems (ISCAS)*, 1998, pp. 236–239.
24. E. Ngoya, J. Rousset, and D. Argollo, Rigorous RF and microwave oscillator phase noise calculation by the envelope transient technique, *Proc. IEEE Microwave Theory and Techniques Symp. (MTT-S)*, 2000, pp. 90–94.

25. J. C. Pedro and N. B. Carvalho, Simulation of RF circuits driven by modulated signals without bandwidth constraints, paper presented at IEEE Microwave Theory and Techniques Symp. (MTT-S), 2002.
26. J. Morales, A. Suárez, and R. Quéré, Accurate determination of frequency dividers operating bands, *IEEE Microwave Guided Wave Lett.* **6**(1):46–48 (Jan. 1996).
27. A. Dounavis, X. Li, M. Nakhla, and R. Achar, Passive closed-form transmission line model for general purpose circuit simulators, *IEEE Trans. Microwave Theory Tech.* **47**(12):2450–2459 (Dec. 1999).
28. J. Roychowdhury, A. R. Newton, and D. O. Peterson, Algorithms for the transient simulation of lossy interconnect, *IEEE Trans. Comput.-Aided Design Integrated Circ.* **13**(1):96–104 (Jan. 1994).
29. R. Anholt, *Electrical and Thermal Characterization of MESFETs, HEMTs and BTs*, Artech House, Norwood, MA, 1994.
30. J. M. Golio, *Microwave MESFETs and HEMTs*, Artech House, Norwood, MA, 1991.
31. L. T. Pillage and A. Rohrer, Asymptotic waveform evaluation for timing analysis, *IEEE Trans. Comput.-Aided Design Integrated Circ.* **9**:352–366 (April 1990).
32. P. Feldmann and R. W. Freund, Efficient linear circuit analysis by Padé approximation via the Lanczos process, *IEEE Trans. Comput.-Aided Design Integrated Circ.* **9**:352–366 (April 1990).
33. S. Kapur, D. E. Long, and J. Roychowdhury, Efficient time-domain simulation of frequency-dependent elements, *Proc. 1996 IEEE/ACM Int. Conf. Computer-Aided Design*, San Jose, CA, 1996, pp. 569–573.
34. K. S. Kundert and I. H. Clifford, Achieving accurate results with a circuit simulator, *Proc. IEE Colloq. "SPICE: Surviving Problems in Circuit Evaluation,"* June 1993, pp. 4/1–5. 155.
35. Y. Tajima, B. Wroma, and K. Mishima, GaAs FET large-signal model and its application to circuit design, *IEEE Electron. Devices* **28**(2) (Feb. 1981).
36. P. J. C. Rodrigues, *Computer Aided Analysis of Nonlinear Microwave Circuits*, Artech House, Norwood, MA, 1998.
37. B. Troyanovsky, *Frequency Domain Algorithms for Simulating Large Signal Distortion in Semiconductor Devices*, Ph.D. thesis, Stanford Univ., Nov. 1997.
38. R. W. Freund, Passive reduced-order modelling via Krylov-subspace methods, *Proc. 2000 IEEE Int. Symp. Computer-Aided Control System Design*, Anchorage, AK, Sept. 2000, pp. 261–266.
39. V. Rizzoli, F. Mastri, F. Sgallari, and V. Frontini, The exploitation of sparse-matrix techniques in conjunction with the piecewise harmonic balance method for nonlinear microwave circuit analysis, *Proc. IEEE Microwave Theory and Techniques Symp. (MTT-S)*, 1990, pp. 1295–1298.
40. V. Rizzoli, F. Mastri, C. Cecchetti, and F. Sgallari, Fast and robust inexact Newton approach to the harmonic-balance analysis of nonlinear microwave circuits, *IEEE Microwave Guided Wave Lett.* **7**(10):359–361 (Oct. 1997).
41. K. S. Kundert, G. B. Sorin, and A. Sangiovanni-Vicentelli, Applying harmonic-balance to almost periodic circuits, *IEEE Trans. Microwave Theory Tech.* **36**(2):366–378 (Sept. 1988).
42. E. Ngoya, J. Rousset, M. Gayral, R. Quere, and J. Obregon, Efficient algorithms for spectra calculations in nonlinear microwave circuit simulators, *IEEE Trans. Circ. Syst.* **37**(11):1339–1353 (Nov. 1990).
43. D. Hente and R. H. Jansen, Frequency-domain continuation method for the analysis and stability investigation of nonlinear microwave circuits, *IEE Proc.* **133**(Part H)(5):351–362 (Oct. 1986).
44. P. L. Heron and M. B. Steer, Jacobian calculation using the multidimensional fast Fourier transform in the harmonic balance analysis of microwave circuits, *IEEE Trans. Microwave Theory Tech.* **38**(4):429–431 (April 1990).
45. V. Rizzoli, C. Cecchetti, A. Lipparini, and F. Mastri, General-purpose harmonic balance analysis of nonlinear microwave circuits under multitone excitation, *IEEE Trans. Microwave Theory Tech.* **36**(12):1650–1659 (Dec. 1988).
46. A. Suárez, J. Morales, and R. Quéré, Synchronization analysis of autonomous microwave circuits using new global stability analysis tools, *IEEE Trans. Microwave Theory Tech.* **46**(5):494–504 (May 1998).
47. Y. Xuan and C. M. Snowden, A generalized approach to the design of microwave oscillators, *IEEE Trans. Microwave Theory Tech.* **35**(12):1340–1347 (Dec. 1987).
48. D. Elad, A. Majdar, and A. Bar-Lev, A new approach to the analysis and design of microwave feed-back oscillators, *Proc. European Microwave Conf.*, 1989, pp. 386–391.
49. E. de Cos, A. Suárez, and S. Sancho, Envelope transient analysis of self-oscillating mixers, *IEEE Trans. Microwave Theory Tech.* (in press).
50. L. O. Chua and A. Ushida, A switching parameters algorithm for finding multiple solutions of non-linear resistive circuits, *Int. J. Circ. Theory Appl.* **4**:215–239 (1976).

NONLINEAR CIRCUIT DESIGN

ALMUDENA SUÁREZ
University of Cantabria
Santander
Cantabria, Spain

1. INTRODUCTION

Circuits based on semiconductor devices are intrinsically nonlinear. The superposition principle does not hold, and the response depends on the values of the input signals. The linear assumption is valid for small excitation levels; however, as the input power increases, nonlinear effects, such as the gain saturation, or the generation of harmonic components, are observed [1–4]. These effects are undesired in circuits such as power amplifiers. However, essential functions in communication systems, such as frequency generation and frequency conversion, can be achieved only by means of circuits operating in nonlinear regime. Four examples of nonlinear circuits are frequency mixers [1–3,5], used for frequency conversion; oscillators [3,4,6]; frequency dividers [7,8]; and frequency multipliers [9,10]. Essential differences exist between their operation principles and characteristics, so specific design techniques should be used for each of them.

The design of circuits operating in the nonlinear regime is demanding. In case of forced circuits, the input generator level must be carefully chosen. Because of the

intrinsic generation of harmonic components, the harmonic loads will also have an influence on the circuit behavior. In case of autonomous circuits, the introduction of feedback networks is usually required and the stability considerations will be essential. In the past, analytical techniques such as describing function [3,11] or Volterra series [1,12] were used for an approximate analysis of the nonlinear circuits. Nowadays, iterative methods, such as harmonic balance [13,14] or envelope transient [15] (see also article titled NONLINEAR CIRCUIT ANALYSIS this encyclopedia), have taken the lead for accurate nonlinear analysis. However, they may be impractical and provide little intuition for circuit design, which should be complemented with systematic synthesis procedures. In contrast, analytical techniques enable a comprehensive design, with a clear identification of the most influential circuit elements and an approximate prediction of their effects on the circuit response. As an example, Volterra series [1,10] has allowed an analytical determination of the influence of the transistor nonlinearities on the intermodulation distortion. The method has been applied to the analysis of power amplifiers and, more recently, analysis of frequency mixers [1,5]. In turn, the describing function [3,11] can be used for an approximate oscillator design, at a specified oscillation frequency and output power, to be corrected at a later stage through harmonic balance simulations.

In this contribution, nonlinear synthesis techniques for frequency mixers, oscillators, frequency dividers, and frequency multipliers will be provided. The objective is not to present an exhaustive review of the possible circuit configurations; instead, the principles and implementation of modern design techniques will be emphasized. They will be illustrated by means of their application to simple, although practical, microwave circuits. Volterra series and describing function will be introduced, together with computer-aided tools, based on harmonic balance (HB). The use of auxiliary generators for oscillator optimization [16] or multiharmonic load pull [10,17,18] for oscillator and multiplier design will also be presented. Each section will start with some background about the particular nonlinear circuit. Then, the detailed design procedures will be presented.

2. FREQUENCY MIXERS

2.1. General Concepts about Frequency Mixers

An ideal frequency mixer is a signal multiplier. This instantaneous multiplication is used for the frequency downconversion or upconversion of a modulated signal. In the case of a frequency downconverter, the mixer will perform the frequency translation of a RF signal about the frequency ω_{RF} to a lower frequency, known as the *intermediate frequency* ω_{IF} . The RF signal is written, in terms of its lowpass equivalent $v_{\text{lp}}(t)$ [19] in the form $v_{\text{RF}}(t) = 2 \operatorname{Re}[v_{\text{lp}}(t)e^{j\omega_{\text{RF}}t}]$, where $v_{\text{lp}}(t)$ depends on the particular type of modulation. For downconversion to ω_{IF} , the RF signal must be multiplied by the one delivered by a local oscillator at the frequency ω_{LO} . For simplicity, only the case $\omega_{\text{RF}} > \omega_{\text{LO}}$ will be considered here, so $\omega_{\text{LO}} = \omega_{\text{RF}} - \omega_{\text{IF}}$. The local-oscillator signal constitutes the second input of the mixer circuit. Then, the ideal mixer

operation can be defined by the following expression:

$$\begin{aligned} v_{\text{IF}}(t) &= [2v_{\text{lp}}^{\text{r}}(t) \cos(\omega_{\text{RF}}t) \\ &\quad - 2v_{\text{lp}}^{\text{i}}(t) \sin(\omega_{\text{RF}}t)]V_{\text{LO}} \cos(\omega_{\text{LO}}t) \\ &= \operatorname{Re}[v_{\text{lp}}(t)V_{\text{LO}}e^{j(\omega_{\text{RF}}-\omega_{\text{LO}})t}] \\ &\quad + \operatorname{Re}[v_{\text{lp}}(t)V_{\text{LO}}e^{j(\omega_{\text{RF}}+\omega_{\text{LO}})t}] \end{aligned} \quad (1)$$

where the superscripts “r” and “i” respectively indicate the real and imaginary parts. Thus, the ideal mixer gives rise to two frequency terms at the difference and sum frequencies $\omega_{\text{IF}} = \omega_{\text{RF}} - \omega_{\text{LO}}$ and $\omega_{\text{RF}} + \omega_{\text{LO}}$. The sum frequency is generally far from the desired intermediate frequency ω_{IF} , so it is easily eliminated through filtering.

The ideal multiplier does not exist in practice, but it can be replaced with a properly selected nonlinear element, at a suitable operation point. Actually, using a Taylor series development about the operation point v_0 , a nonlinear voltage-controlled current characteristic $i(v)$ can be approximated by means of a power series $i(v) = i(v_0) + g_1v + g_2v^2 + \dots + g_Nv^N$. Introducing the signal $v(t) = V_{\text{RF}} \cos(\omega_{\text{RF}}t) + V_{\text{LO}} \cos(\omega_{\text{LO}}t)$ in this expansion, the terms $\omega_{\text{RF}} + \omega_{\text{LO}}$ and $\omega_{\text{RF}} - \omega_{\text{LO}}$ are obtained, together with undesired intermodulation products $m'\omega_{\text{LO}} + n\omega_{\text{RF}}$, with m' and n . The resulting frequency components form clusters about the different harmonic components ω_{LO} . It is generally more useful to express the intermodulation products in terms of ω_{LO} and ω_{IF} . When doing so, the indices have to be reorganized. Expressing $\omega_{\text{RF}} = \omega_{\text{LO}} + \omega_{\text{IF}}$, the new indexes will be $m\omega_{\text{LO}} + n\omega_{\text{IF}} = (m' + n)\omega_{\text{LO}} + n\omega_{\text{IF}}$.

It is easily shown that the use of $V_{\text{RF}} \ll V_{\text{LO}}$, where V_{RF} is the amplitude of the RF signal carrier, reduces the number of relevant intermodulation terms [1]. This is also the most usual case, since the RF input will generally correspond to a low-power received signal. The amplitude difference between the RF signal and the LO signal allows the use of the periodic oscillator solution (in the absence of RF input) as the quiescent point of the Taylor series expansion of the nonlinearity $i(v)$ [1,2]. Thus, the strongly nonlinear function is transformed into mildly nonlinear one, with periodic coefficients

$$\begin{aligned} i(v) &= i(v_{\text{LO}}(t)) + g_1(t)v_{\text{RF}}(t) \\ &\quad + g_2(t)v_{\text{RF}}(t)^2 + \dots + g_N(t)v_{\text{RF}}(t)^N \end{aligned} \quad (2)$$

with

$$g_k(t) = \frac{1}{k!} \frac{\partial^k i}{\partial v^k}(v_{\text{LO}}(t)), \quad k = 1, \dots, N$$

For moderate amplitude of the RF signal, the frequency conversion will be due to the linear term $g_1(t)v_{\text{RF}}(t)$, with $g_1(t)$ periodic at ω_{LO} , which gives rise to the two mixing terms $\omega_{\text{RF}} - \omega_{\text{LO}}$ and $\omega_{\text{RF}} + \omega_{\text{LO}}$.

2.2. Characteristics of Frequency Mixers

When carrying out a mixer design, the main characteristics to take into account will be the conversion loss or gain,

the spurious power level, the noise figure, and the intermodulation distortion. Each of these will be briefly introduced in the following paragraphs:

1. *Conversion Gain.* The mixer conversion gain is defined as the ratio $G_c = P_{IF}/P_{RF}$, where P_{IF} is the power delivered to the output load at the intermediate frequency and P_{RF} is the available RF power. This gain saturates from a certain RF power.

2. *Spurious Frequencies.* The spurious frequencies are the undesired intermodulation products of the form $m\omega_{LO} \pm n\omega_{IF}$, with $m \neq 0, n \neq 1$ [1]. One of spurious frequencies with highest amplitude is the *image frequency*. Assuming $\omega_{RF} > \omega_{LO}$, the image frequency will be $\omega_{IM} = \omega_{LO} - \omega_{IF}$. The term is derived from the fact that, in the spectrum, ω_{RF} and ω_{IM} are located on opposite sides of the local-oscillator signal, with equal frequency spacing ω_{IF} . The mixing of the image frequency with the local-oscillator frequency ω_{LO} gives rise to the same frequency ω_{IF} , which can have negative effects on the circuit behavior.

3. *Noise Figure.* The single-sideband noise figure of the frequency mixer [3,20,21] is the quotient of the input signal-to-noise ratio at the RF frequency, and the output signal-to-noise ratio at the IF frequency: $F_{mix} = (SNR)_{RF}/(SNR)_{IF}$. The input signal-to-noise ratio is calculated with the standard noise power kT_0B , where k is Boltzmann’s constant, T_0 the standard noise temperature, and B the noise bandwidth. The output noise at the IF will have contributions due to the conversion to this frequency of the input noise in all the harmonic terms $m\omega_{LO} + n\omega_{IF}$, especially at the image frequency ω_{IM} . It will also have contributions from the transistor noise sources and the circuit resistive elements [3]. The different contributions to the F_{mix} are easily distinguished in the following expression [20]:

$$F_{mix} = 10 \log \frac{E_n^2/R + KT_0(G_1 + G_2 + \dots + G_p)}{KT_0G_1} \quad (3)$$

where $G_1 \dots G_p$ indicate the conversion gain of the different intermodulation products, R is the output resistance, and

E_n^2 is the spectral density of the equivalent noise voltage at the output port, when no contributions from the input and output terminations are considered. For an accurate calculation of F_{mix} , the noise input due to the local oscillator should also be taken into account. Its effect on the IF noise power is included in the term $E_n^2(f)$.

4. *Intermodulation Distortion.* The intermodulation distortion is generally analyzed by considering two input RF carriers close in value ω_{RF1} and $\omega_{RF2} = \omega_{RF1} + \Delta\omega$ [1,2]. Then, assuming a signal of the form $v_{RF}(t) = V_{RF1} \cos(\omega_{RF1}t) + V_{RF2} \cos(\omega_{RF2}t)$, the higher-order terms $g_2(t)v_{RF}^2(t), g_3(t)v_{RF}^3(t), \dots$ in (2) will give rise to the intermodulation tones $m\omega_{LO} + p\omega_{IF1} + q\omega_{IF2}$. At the IF output, the frequencies will be $p\omega_{IF1} + q\omega_{IF2}$. The so-called intermodulation order IO is defined as the sum of the absolute values of the integer coefficients $IO = |p| + |q|$. Because of the proximity between the values of ω_{RF1} and ω_{RF2} , the frequencies ω_{IF1} and ω_{IF2} will also be close in value. Thus, the most dangerous intermodulation products will be third-order terms $2\omega_{IF1} - \omega_{IF2} = \omega_{IF1} - \Delta\omega$ and $2\omega_{IF2} - \omega_{IF1} = \omega_{IF2} + \Delta\omega$, since these will be the closest to the desired downconverted frequencies ω_{IF1} and ω_{IF2} .

For a better understanding of the intermodulation distortion, Fig. 1 shows a typical output power spectrum of a mixer circuit, in which two close input carriers, at the frequencies $f_{RF1} = 3.5 \text{ GHz} - 500 \text{ kHz}$ and $f_{RF2} = 3.5 \text{ GHz} + 500 \text{ kHz}$, have been introduced. The local oscillator frequency is $f_{LO} = 3 \text{ GHz}$, so the IF frequencies should be $f_{IF1} = 0.5 \text{ GHz} - 500 \text{ kHz}$ and $f_{IF2} = 0.5 \text{ GHz} + 500 \text{ kHz}$. As expected, the highest-amplitude tones are those corresponding to ω_{IF1} and ω_{IF2} . On each side of these tones, there are intermodulation terms of increasing odd order n , given by $\omega_{IF1} - k\Delta\omega$ and $\omega_{IF2} + k\Delta\omega$, with $k = (n - 1)/2$.

2.3. Realization of Frequency Mixers

Frequency mixers have traditionally been based on Schottky diodes [2,3]. Those devices do not have the charge accumulation limitations of bipolar devices, such as the PN diode, and the mixing function relies on the junction current $i(v) = I_s(e^{v/V} - 1)$. Then, the terms in (2)

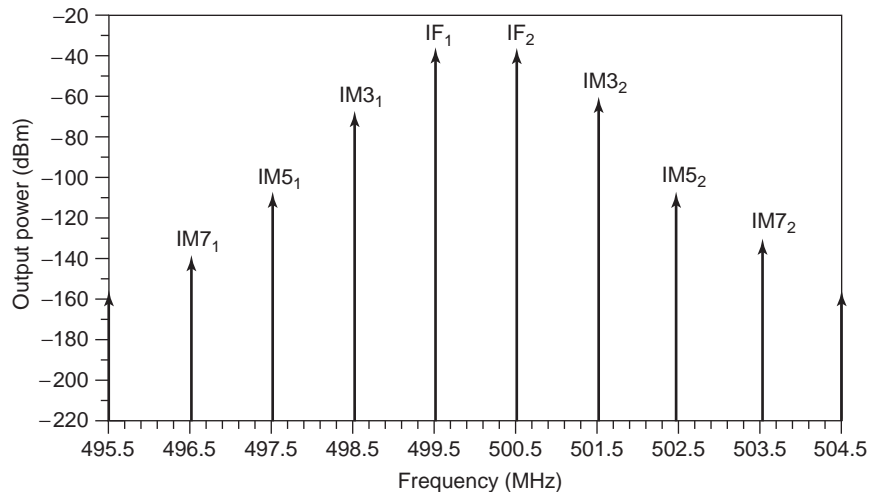


Figure 1. Typical mixer spectrum at the IF output.

are obtained by differentiating this function about the oscillator solution $V_{LO}(t)$. When using diodes as mixing elements, the amplitude of the downconverted signal is always smaller than that of the input RF signal, due to the diode passivity. The typical conversion loss is about 5 dB [3]. Balanced structures, based on hybrid couplers, are used for the isolation of the RF, LO, and IF signals. They also enable cancellation of the AM noise from the local oscillator and some undesired frequency terms, which are eliminated without filtering [3]. The singly balanced mixers are based on the use of two diodes connected to a 90° or 180° hybrid coupler. The doubly balanced mixers are based on the use of four diodes.

The transistors are active devices, so, under certain operation conditions, they can provide conversion gain. They also enable inherent input-output isolation. Both MESFET and bipolar transistors can be used for frequency mixing. The MESFET transistors are very common owing to the significant development of MMIC technology on GaAs substrate. Balanced structures, using two or four transistors, are also possible, to isolate the RF, LO, and IF signals and enable the cancellation of undesired frequency

terms. Different types of active FET mixer are possible [1,2], according to the port through which the LO and RF signals are injected.

In the *gate mixer*, the LO and RF signals are injected at the gate port. The IF signal is extracted through filtering from the drain port (see Fig. 2a). It is the most popular kind of FET mixer. Assuming that the amplitude of the RF input signal is small compared to the RF signal, the mixing will be mainly due to the product $g_m(v_{LO}(t))v_{RF}(t)$, where g_m is the transistor transconductance, evaluated with the local-oscillator signal as the only excitation. In turn, $v_{RF}(t)$ is the incremental voltage due to the input RF signal.

In the *resistive mixer*, the FET is biased in the triode region [2,5]. The mixing is due to the periodic variation of the channel conductance $g_{ds}(t)$ with the local-oscillator pumping (see Fig. 2b). Thus, the LO signal is introduced at the gate terminal, while the RF signal is introduced at the drain terminal. The mixing is due to the product $g_{ds}(t)v_D(t)$. The IF signal is extracted from the drain terminal. The main advantage of the resistive mixers is the low intermodulation level, due to the good linearity of the

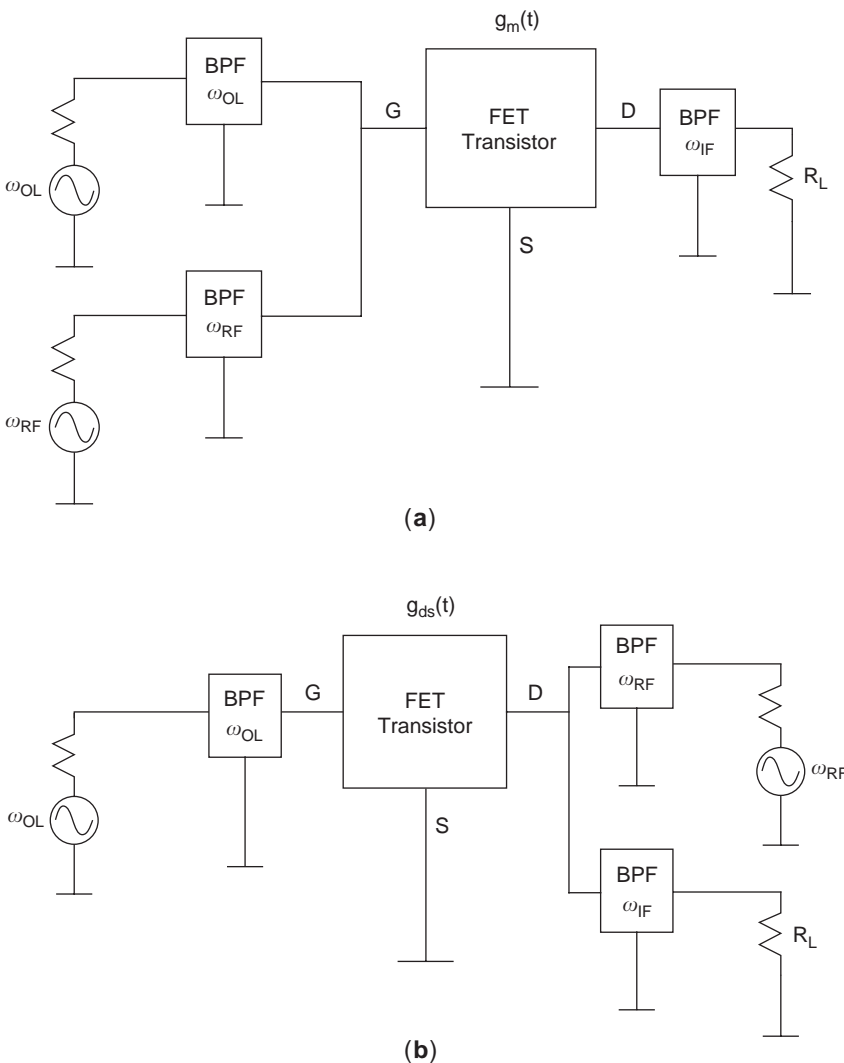


Figure 2. Two usual FET-based mixer configurations: (a) gate active mixer; (b) passive mixer.

channel resistance. The resistive mixers can also be realized in balanced topologies, with the same advantages as in the case of diodes.

2.4. Analysis of Frequency Mixers

Different techniques can be applied for the analysis and design of frequency mixers. The time-varying Volterra series, discussed in Section 2.5, enables an analytical evaluation of the influence of magnitudes such as the transistor bias voltages or the local-oscillator amplitude on the conversion gain and the intermodulation distortion. Thus, it is very helpful for an optimum selection of the operation conditions. However, its accuracy is limited to small amplitude of the input RF signal. For higher RF amplitude, iterative nonlinear analysis methods should be applied. Two-tone HB enables the accurate determination of the mixer conversion gain and spurious content [1] (see also NONLINEAR CIRCUIT ANALYSIS article). The envelope transient method enables an accurate analysis of the intermodulation distortion [1,22]. Next, the foundations of these two iterative methods are briefly summarized in order to provide an intuitive idea about their basic principles and to give the reader feeling for their circuit simulation capabilities.

2.4.1. Harmonic Balance. The HB method [15] uses frequency-domain representations for the linear elements and time-domain descriptions for the nonlinear devices. The circuit state variables are expressed in a Fourier series, with typically one or two fundamental frequencies. In the case of a frequency mixer, the two fundamentals will be ω_{LO} and ω_{IF} . The variables are written $v(t) = \sum_{m,n} V_{mn} e^{j(m\omega_{LO} + n\omega_{IF})t}$. Assuming a diamond truncation of this Fourier series [1] (again, see also NONLINEAR CIRCUIT ANALYSIS article), all the intermodulation products up to a certain nonlinearity order $nl = \max(|m| + |n|)$, by the user, will be considered. The direct and inverse Fourier transforms translate the circuit variables from one to another domain, which enables the frequency-domain expression of an error equation system $\bar{E}(\bar{V}) = 0$, where \bar{V} is the vector containing the harmonic components of the state variables. This technique enables an accurate prediction of the solution spectrum, with as many spurious terms as allowed by the nonlinearity order.

When the mixer circuit is analyzed through HB, the noise figure $F_{mix} = (SNR)_{RF} / (SNR)_{IF}$ can be determined using the conversion matrix approach [23]. Linear behavior with respect to the RF signal is assumed. When the noise perturbations are introduced, the HB equations are linearized about the nonlinear solution, at ω_{LO} , in the absence of RF input. The nonlinear current $\bar{I}(\bar{V})$ and charges $\bar{Q}(\bar{V})$ are replaced by their conversion matrixes, $[\partial \bar{I} / \partial \bar{V}]_0$, $[\partial \bar{Q} / \partial \bar{V}]_0$, evaluated at the solution at ω_{LO} [24]. These conversion matrixes are determined from the Fourier transforms of $g(t) = \partial i(t) / \partial v(t)$ and $c(t) = \partial q(t) / \partial v(t)$ [1]. The resulting perturbed system can be written

$$[Y(m\omega_{LO} + \omega_{IF})]_0 \Delta \bar{V}(m\omega_{LO} + \omega_{IF}) = \bar{I}_n(m\omega_{LO} + \omega_{IF}) \quad (4)$$

where the matrix $[Y]$ is easily calculated from the transistor conversion matrixes and the linear networks, evaluated at the sideband frequencies $m\omega_{LO} + \omega_{IF}$. The vector \bar{I}_n contains the equivalent noise current sources, obtained from their spectral power descriptions, in a normalized noise band of 1 Hz.

The perturbed state variables $\Delta \bar{V}$ are determined from the matrix inversion $[Y]_0^{-1}$. To obtain the power spectral density at the different harmonic terms, the noise correlation matrix $\bar{I}_n \bar{I}_n^*$, where the asterisk denotes *adjoint*, must be considered. The transistor intrinsic noise sources are correlated [21], which must be taken into account in the calculation of $\langle |\Delta V_{IF}|^2 \rangle$. The noise figure is determined from $F_{mix} = N_{IF} / (N_0 G_T)$, where N_{IF} is the noise output power. An example of application of this technique will be shown in Section 2.6.

2.4.2. Envelope Transient. The analysis of intermodulation distortion requires the consideration of two close input carriers ω_{RF1} and ω_{RF2} . The use of three-tone HB for this analysis is computationally expensive. The relatively recently introduced envelope transient method can be applied instead [15] (see also NONLINEAR CIRCUIT ANALYSIS article). This method relies on the use of two different time scales, one for the carrier frequencies and the other for the modulation signals. For the analysis of intermodulation distortion [22], the spacing between the two RF frequencies $\omega_m = \omega_{RF2} - \omega_{RF1}$ is taken as the modulation frequency of a unique carrier $\omega_{RF0} = (\omega_{RF1} + \omega_{RF2})/2$. The circuit variables are expressed in a Fourier series, with ω_{LO} and $\omega_{IF0} = \omega_{RF0} - \omega_{LO}$ as fundamentals, and slowly varying harmonic components, at the modulation rate, $v(t) = \sum_{m,n} V_{mn}(t) e^{j(m\omega_{LO} + n\omega_{IF0})t}$. When introducing this expression for the circuit variables in the HB equations, a differential equation system is obtained in the slowly varying components $\bar{V}(t)$. This system is efficiently integrated in much larger timestep than the one that would be required for a standard time-domain analysis.

As already stated, the dynamic Volterra series allows a comprehensive and optimized design and is less time-consuming than multitone HB and the envelope transient method. Because of its practical interest, the dynamic Volterra series will be presented in the next section. On the other hand, both harmonic balance and the envelope transient method are discussed in detail in the NONLINEAR CIRCUIT ANALYSIS article.

2.5. Volterra Series Analysis

The output of a linear, time-invariant system is related to its input through the impulse response $h(t)$, which characterizes the particular linear system [20]. For an input signal $i_g(t)$, the system output (circuit solution) is written $v_0(t) = \int_{-\infty}^{\infty} h(\tau) i_g(t - \tau) d\tau$. This kind of representation can be generalized to weakly nonlinear time-invariant systems. However, the superposition principle does not hold in nonlinear systems, and the overall effect of impulses applied at different time values must be taken into account [12]. The system output is expressed as

$v_0(t) = \sum_{n=1}^{\infty} v_{\text{on}}(t)$, where $v_{\text{on}}(t)$ is the n th-order solution:

$$v_{\text{on}}(t) = \int_{-\infty}^{\infty} \dots \int_{-\infty}^{\infty} h_n(\tau_1, \dots, \tau_n) i_g(t - \tau_1) \dots i_g(t - \tau_n) d\tau_1 \dots d\tau_n \quad (5)$$

The expression $v_0(t) = \sum_{n=1}^{\infty} v_{\text{on}}(t)$ constitutes the Volterra series representation of the solution, and the different functions $h_n(t_1, \dots, t_n)$ are the Volterra kernels [12]. The Volterra analysis is usually more convenient in terms of the transfer functions $H_n(\omega_1, \dots, \omega_n)$, associated with the different kernels $h_n(t_1, \dots, t_n)$. When these functions are used, the solution output, for an arbitrary input $i_g(t) = \sum_{p=-P}^P I_g^p e^{j\omega_p t}$, is given by

$$\begin{aligned} v_0(t) &= \sum_{n=1}^N v_{\text{on}}(t) \\ &= \sum_{n=1}^N \sum_{p_1=-P}^P \dots \sum_{p_n=-P}^P H_n(\omega_{p_1}, \dots, \omega_{p_n}) \\ &\quad I_g^{p_1} \dots I_g^{p_n} e^{j(\omega_{p_1} + \dots + \omega_{p_n})t} \end{aligned} \quad (6)$$

The Volterra series analysis can also be extended to time-varying weakly nonlinear systems. As evidenced by (2), this is the case of the mixer circuits, since their RF input signal usually has an amplitude much smaller than that of the local oscillator. The time-varying Volterra series is expressed as

$$\begin{aligned} v_{\text{on}}(t) &= \int_{-\infty}^{\infty} \dots \int_{-\infty}^{\infty} h_n(t, \tau_1, \dots, \tau_n) \\ &\quad \times i_g(t - \tau_1) \dots i_g(t - \tau_n) d\tau_1 \dots d\tau_n \end{aligned} \quad (7)$$

where the Volterra kernels have an extra time dependence on the variable t . The local oscillator solution is taken as the quiescent point and the kernels are periodic in t , with the same period as this local oscillator.

In the calculation of intermodulation distortion, two close RF signals, at ω_{RF1} and ω_{RF2} , are considered. As shown in (2), Taylor series developments, with the local-oscillator solution as the quiescent point, are used for the description of the nonlinear elements. The product of the nonlinearities by the RF inputs will generate current components at $m\omega_{\text{LO}} + p\omega_{\text{IF1}} + q\omega_{\text{IF2}}$, which are transformed to voltages at the circuit linear elements. Then, the independent voltages of the mixer solution can be expressed as [1]

$$\begin{aligned} v_0(t) &= \sum_{n=1}^N v_{\text{on}}(t) \\ &= \sum_{n=1}^N \sum_{p_1=-P}^P \dots \sum_{p_n=-P}^P H_n(t, \omega_{p_1}, \dots, \omega_{p_n}) \\ &\quad \times I_g^{p_1} \dots I_g^{p_n} e^{j(\omega_{p_1} + \dots + \omega_{p_n})t} \end{aligned} \quad (8)$$

where the transfer functions, associated with the different Volterra kernels, have been introduced. The input $i_g(t)$ represents an IF signal, with the general form $i_g(t) = \sum_{p=-P}^P I_g^p e^{j\omega_p t}$, where ω_p takes the values $-\omega_{\text{IF1}}$, $-\omega_{\text{IF2}}$, ω_{IF1} , ω_{IF2} . Because of their periodicity, it is possible to expand the transfer functions $H_n(t, \omega_{p_1}, \dots, \omega_{p_n})$ in a Fourier series at $m\omega_{\text{LO}}$ with m integer and varying between $-M$ and M . Then, the n th-order solution can be written [1] as follows:

$$\begin{aligned} v_{\text{on}}(t) &= \sum_{m=-M}^M \sum_{p_1=-P}^P \dots \sum_{p_n=-P}^P V_{mp_1 \dots p_n}^n \\ &\quad \times e^{j(m\omega_{\text{LO}} + \omega_{p_1} + \dots + \omega_{p_n})t} \end{aligned} \quad (9)$$

It should be noted that the frequencies ω_{p_1} to ω_{p_N} are not harmonically related to $m\omega_{\text{LO}}$. Each ω_{p_i} , with $i = 1 \dots N$, will take the values $-\omega_{\text{IF1}}$, $-\omega_{\text{IF2}}$, ω_{IF1} , ω_{IF2} .

In the harmonic input method, signals $I_g(t)$ of the form $e^{j\omega_{p_1} t}$, $e^{j\omega_{p_2} t}$, \dots , $e^{j\omega_{p_N} t} + \dots + e^{j\omega_{p_N} t}$ are introduced, in order to recursively determine the terms $V_{\text{on}}(t)$, from which the Volterra kernels are calculated. The calculation of $v_{01}(t)$ (sketched in Fig. 3a) requires the previous determination of the conversion matrixes of the different nonlinear elements. As is well known, this conversion matrix is obtained from the Fourier series expansion at $m\omega_{\text{LO}}$ of the derivatives $g(t) = \partial i / \partial v(v_{\text{LO}}(t))$ and $c(t) = \partial q / \partial v(v_{\text{LO}}(t))$, in case of capacitive nonlinearities. In Fig. 3a, a single nonlinear resistive-type element has been considered, with the first-order conversion matrix $[G_1]$. The direct application of Kirchhoff's laws provides a linear system in the frequency domain, from which the harmonic components of $v_{01}(t)$ are easily determined.

In order to determine the second term of the series $v_{02}(t)$, an input, of the form $e^{j\omega_{p_1} t} + e^{j\omega_{p_2} t}$, will be considered (see Fig. 3b). This calculation requires second-order derivatives of the nonlinear elements, of the form $g_2(t) = \partial^2 i / \partial v^2(v_{\text{LO}}(t))$. In time domain, this derivative should be multiplied by $v_{01}^2(t)$. This can easily be done, since the term $v_{01}(t)$ is already known from the preceding step. The resulting current $i_2(t) = g_2(t)v_{01}^2(t)$ will be considered as an external source (see Fig. 3b), and the second-order term $v_{02}(t)$ will be the new unknown. The system is linear in this term, which ensures a straightforward resolution.

The frequency-domain expression of $v_{02}(t)$ will contain the components $m\omega_{\text{LO}} + \omega_{p_1} + \omega_{p_2}$, with both ω_{p_1} and ω_{p_2} taking the values $-\omega_{\text{IF1}}$, $-\omega_{\text{IF2}}$, ω_{IF1} , ω_{IF2} . For the frequency-domain analysis of the circuit, a generalized conversion matrix of second order, obtained from the Fourier series expansion of $g_2(t) = \partial^2 i / \partial v^2(v_{\text{LO}}(t))$, must be used. Applying Kirchhoff's laws, a linear system is obtained in the harmonic components of $v_{02}(t)$.

The analysis above can be generalized up to the N^{th} order, with an input signal $e^{j\omega_{p_1} t} + e^{j\omega_{p_2} t} + \dots + e^{j\omega_{p_N} t}$ and requiring the Fourier series expansion of $g_N(t)$, to obtain the corresponding conversion matrix. As already stated, the most dangerous intermodulation terms are $2\omega_{\text{IF1}} - \omega_{\text{IF2}}$ and $2\omega_{\text{IF2}} - \omega_{\text{IF1}}$, so the Volterra series must be calculated up to a minimum order $N = 3$. The order should be higher for higher amplitude of the RF input signal.

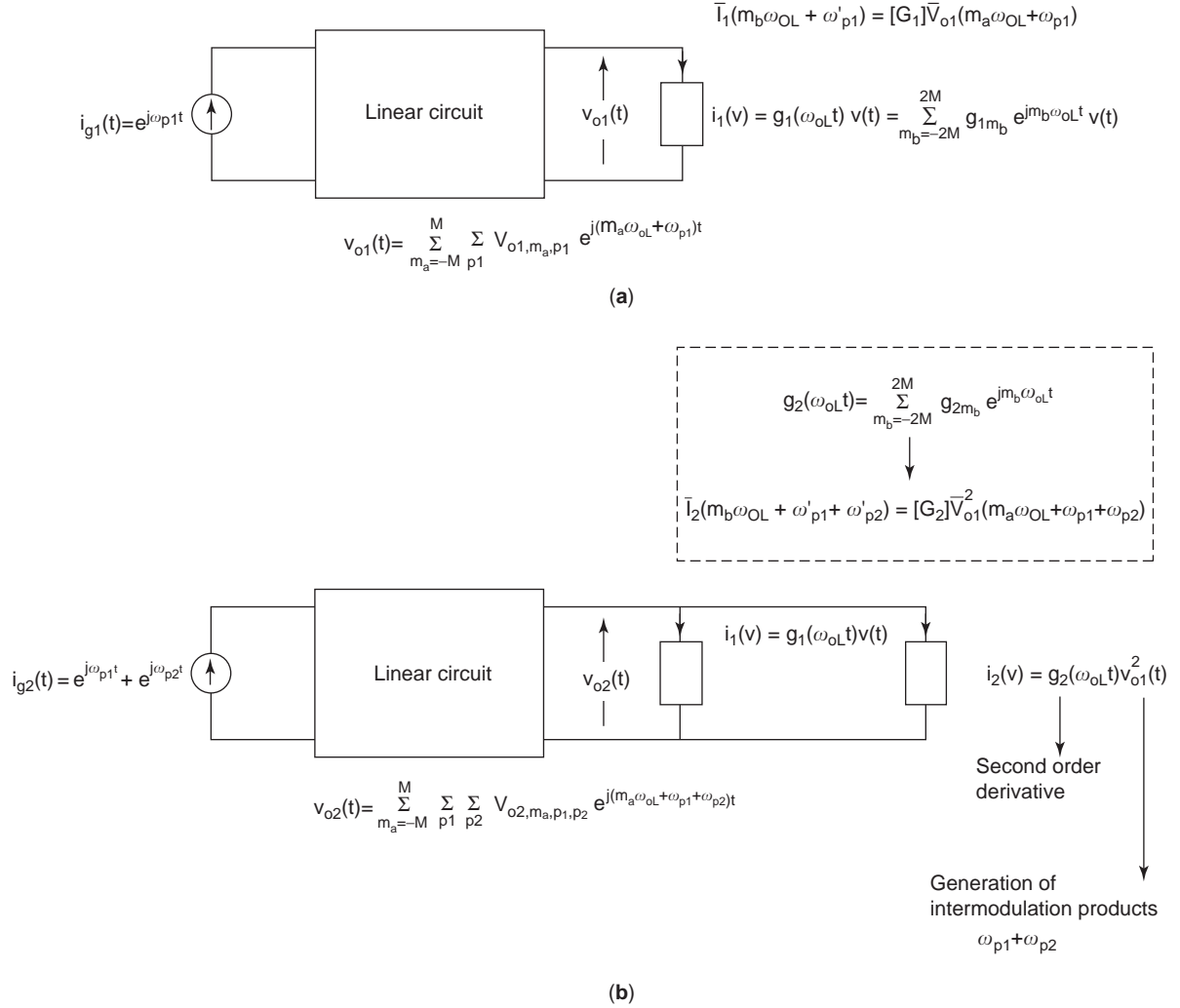


Figure 3. Calculation of the dynamic Volterra series up to second order.

The Volterra series enables the analytical evaluation of the influence of the bias point or the local-oscillator amplitude on the intermodulation distortion. Because of the complexity of this symbolic calculation, some circuit simplifications are necessary. For a given type of mixer, only the essential nonlinearities will be taken into account and most of the transistor parasitics will be ignored. The linear embedding of the mixer circuit is also simplified, assuming, for instance, that the input matching networks provide short circuits at all frequencies different from ω_{RF} and ω_{IM} , and that the output circuit provides short circuits at all frequencies different from ω_{IF} . This symbolic analysis has been carried out by other authors on both active and resistive mixers [1,5]. In the following example, the main results from this analysis are used for the design of a gate frequency mixer.

2.6. Gate Mixer Design

In the gate mixer, the LO and RF signals are injected at the gate port, while the IF signal is extracted through filtering from the drain port. The mixing will be due mainly to the periodic modulation of the transistor transconduc-

tance $g_m(t)$ by the LO signal. As already mentioned, a manageable analysis through time-varying Volterra series requires some circuit simplifications. Only the i_{DS} nonlinearity will be considered, assuming constant capacitances C_{gs} , C_{gd} , and C_{ds} . In the gate mixer, the transistor is usually biased in the saturation region, so, in most cases, the dependence of i_{DS} on the drain voltage may be ignored [1], which considerably reduces the complexity of the study. Regarding the linear embedding circuit, some additional assumptions are possible.

At the drain port, short circuits are imposed at both the RF and LO frequencies. At the gate port, a short circuit is considered at the IF frequency, which reduces the output noise. Under these assumptions, a simplified schematic is obtained in which the output power is directly proportional to the square of the I_{ds} current at the IF frequency. This can be determined from the first-order Volterra analysis [1]:

$$I_{ds}(\omega_{IF}) = G_{m1}V_{gs}(-\omega_{IM}) + G_{m,-1}V_{gs}(\omega_{RF}) + G_{dso}V_{ds}(\omega_{IF}) \quad (10)$$

The i_{DS} current has small dependence on the drain voltage, so the conversion gain will be optimized by maximizing of the harmonic term G_{m1} of the Fourier series expansion of $g_m(t) \equiv \partial i_{DS} / \partial v_{GS}(v_{LO}(t))$. The value of these terms will depend on the mixer bias point and the local-oscillator amplitude.

The second-order intermodulation terms $\omega_{IF2} - \omega_{IF1}$ and $\omega_{IF1} + \omega_{IF2}$, originating mainly from the second order derivative g_{m2} , will typically be far from the desired output frequencies ω_{IF1} , ω_{IF2} . In turn, the third-order intermodulation distortion, coming mainly from the third-order derivative g_{m3} , gives rise to the dangerous frequencies $2\omega_{IF1} - \omega_{IF2}$ and $2\omega_{IF2} - \omega_{IF1}$. The drain current at these intermodulation frequencies is obtained from a third-order Volterra series analysis of the circuit. It is approximately given by [1]:

$$I_{ds3}(2\omega_{IF1} - \omega_{IF2}) = G_{m3,-1} V_{gs1}^3 (2\omega_{RF1} - \omega_{RF2}) \quad (11)$$

Thus, in order to reduce the third-order intermodulation distortion, the first-harmonic component of the Fourier series expansion of $g_{m3}(t) \equiv \partial^3 i_{DS} / \partial v_{GS}^3(v_{LO}(t))$ must be minimized.

The results presented above have been applied to the design of a gate mixer, using the FET transistor CFY30. For the input network, a simple circuit topology has been chosen (see Fig. 4), with a power combiner, enabling the introduction of the RF and local-oscillator signals. The input frequencies considered here are $f_{RF} = 3.5$ GHz and $f_{OL} = 3$ GHz, with $f_{IF} = 0.5$ GHz. At the drain terminal, an open-circuited quarter-wave $\lambda/4$ line, at the local-oscillator frequency, is introduced, in order to suppress this frequency component from the mixer output. In addition, this $\lambda/4$ line reduces the variation of the drain-to-source voltage $v_{DS}(t)$ and thus ensures the mixer operation in the saturation region for all time values [1,3].

To take advantage of the analytical results (10) and (11), an accurate transistor model, enabling a reliable calculation of the nonlinear element derivatives up to third order, will be necessary. The Angelov model [24] has been used here, which is continuously differentiable. Using this model, the derivatives $g_1(t), g_2(t), g_3(t)$ are analytically calculated. The periodic quiescent point and its evolution versus each parameter of interest (e.g., V_{GS} or P_{LO}) are

initially determined through HB simulations. The waveforms $v_{gs}(t), v_{ds}(t)$, corresponding to each parameter value, are obtained through the inverse Fourier transform. This double set of waveforms (vs. the parameter) is introduced in the derivatives of the Angelov model. Different harmonic components of the Fourier transforms of these derivatives provide the factors in (10) and (11).

Initially, the influence of the gate bias voltage V_{GS} is considered, while setting the drain voltage to the constant value $V_{DS} = 2.5$ V and the local-oscillator power to the moderate value $P_{LO} = 0.8$ dBm. Figure 5 shows the variation of the amplitude of G_{m1} [first-harmonic component of $g_m(t)$] with this bias voltage. As can be seen, a maximum is obtained for $V_{GS} = -1$ V. Thus, maximum conversion gain should be expected for this gate bias. To verify this, a two-tone HB simulation has been carried out, obtaining the conversion gain from the direct calculation $G_c = P_{IF}/P_{RF}$. For this analysis, the RF power $P_{RF} = -18$ dBm has been considered, below the 1-dB gain compression, which occurs for $P_{RF} = 1.5$ dBm. The resulting G_c variation is also shown in Fig. 5, with good agreement with the Volterra series analysis, in terms of G_{m1} . After selection of the gate bias, input matching is carried out, by means of the transmission line and stub, represented in Fig. 4. This will increase the conversion gain.

In the case of FET devices, two different kinds of noise contributions can be considered: the intrinsic noise, modeled with two current sources i_g and i_d ; and the thermal noise, associated with parasitic resistive elements [21]. The i_g source is in parallel between the intrinsic gate and source terminals and has the mean-square value $\overline{i_g^2} = 4kTB\omega_{LO}^2 C_{gs}^2 S/g_m$. The i_d source is in parallel between the intrinsic drain and source terminals and has the mean-square value $\overline{i_d^2} = 4kTBg_m P$. The coefficients P and S depend on the drain current i_{ds} . Both g_m and C_{gs} are time-periodic at the local-oscillator period. For strong oscillator amplitude, P and S are also periodic. The two noise sources are thus cyclostationary. In the frequency domain, they give rise to harmonic terms $m\omega_{OL} + \omega_{IF}$. The two noise sources are frequency-correlated [22].

In Fig. 6, the conversion matrix approach has been applied for determination of the noise figure versus the LO power. As can be appreciated, it decreases with this power, because of the increase of conversion gain. In a detailed analysis, it was found that the largest noise contribution

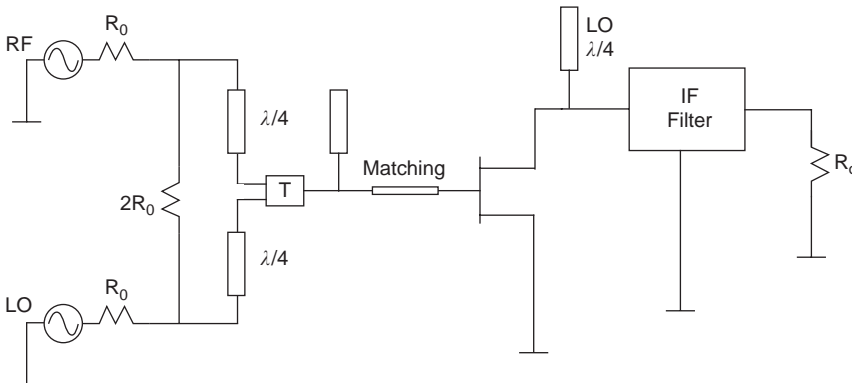


Figure 4. Classical topology of a gate mixer.

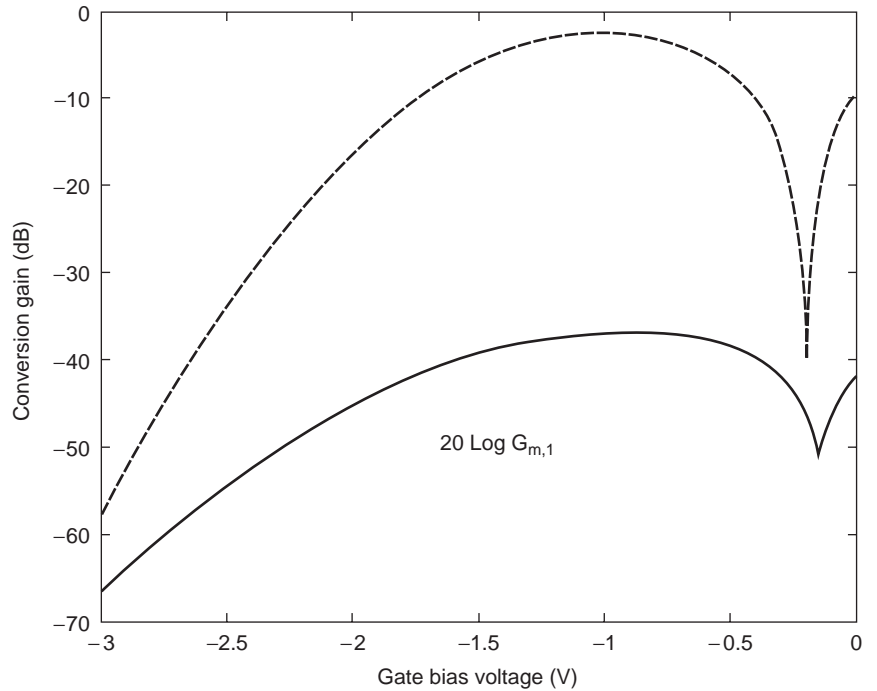


Figure 5. Variation of the mixer conversion gain with the gate bias voltage V_{GS} ; comparison with $G_{m,1}$ obtained through Volterra series analysis.

was due to the conversion to IF of the input noise, through the different gains in (3). The second largest contribution was the transistor source i_d . Next were the transistor resistive elements.

Figure 7 shows the mixer output power spectrum for $P_{RF} = -18$ dBm and $P_{LO} = 0.8$ dBm. It has been obtained through two-tone HB, using a diamond truncation of the Fourier series, with nonlinearity order $nl = 7$. The different spurious-frequency terms can be appreciated.

As already stated, the intermodulation distortion is analyzed by considering two closely spaced input carriers. For the gate mixer studied here, the two carriers are centered about $f_{RF} = 3.5$ GHz, with a frequency spacing of

$\Delta f = 100$ kHz. At the circuit output, two tones should be obtained about the intermediate frequency $f_{IF} = 0.5$ GHz, with the same frequency spacing $\Delta f = 100$ kHz. The frequency-translated carriers will be designed f_{IF1} and f_{IF2} , with $f_{IF1} < f_{IF2}$. As already seen in previous sections, the circuit nonlinearity gives rise to intermodulation tones of the form $pf_{IF1} + qf_{IF2}$, with p, q integers.

For the envelope transient analysis of Fig. 8, a two-tone HB formulation was used at the two fundamentals $f_{RF} = 3.5$ GHz and $f_{LO} = 3$ GHz. The frequency spacing between the tones $\Delta f = 100$ kHz was taken as the modulation frequency. The spectrum of Fig. 8 is centered about $f = 0$, because it is actually calculated from the Fourier transform of the harmonic component $V_{IF}(t)$. Thus, the line $f = 0$ represents the intermediate frequency f_{IF} , in similar manner to the low-pass equivalents of bandpass systems.

As already seen, the intermodulation distortion is highly dependent on the circuit operation point. The third-order intermodulation distortion, giving the two closest tones to the downconverted frequencies ω_{IF1} and ω_{IF2} , is determined mainly by $G_{m3,1}$, specifically, the first-harmonic component of the third-order derivative $g_{m3} = \partial^3 i_{ds} / \partial v_{gs}^3$ [see (11)]. The evolution of this harmonic component versus V_{GS} is shown in Fig. 9. As can be seen, a maximum of the $G_{m3,1}$ amplitude is obtained for $V_{GS} = -0.8$ V, while a substantial reduction is achieved for $V_{GS} = -0.4$ V. The results of this analysis have been verified through a sequential application of the envelope transient method. The third-order intermodulation tone $\omega_{IM3,1}$ has been followed along the entire V_{GS} interval, to obtain the curve superimposed in Fig. 9. As can be seen, there is very good agreement between the maximum and minimum of $G_{m3,1}$ and those corresponding to the tone $\omega_{IM3,1}$. The advantage

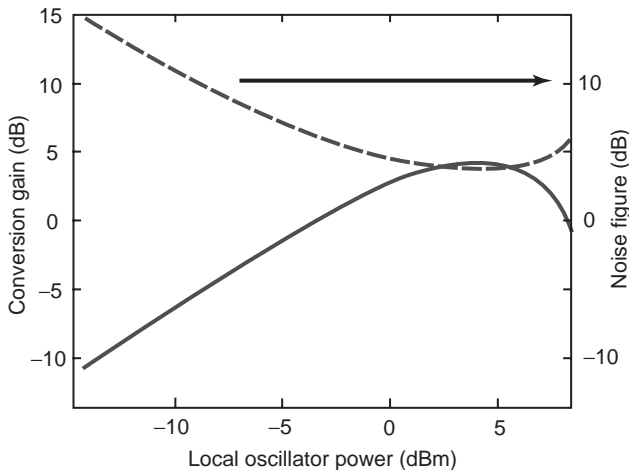


Figure 6. Variation of the conversion gain and noise figure versus the local-oscillator power, for $V_{GS} = -1$ V.

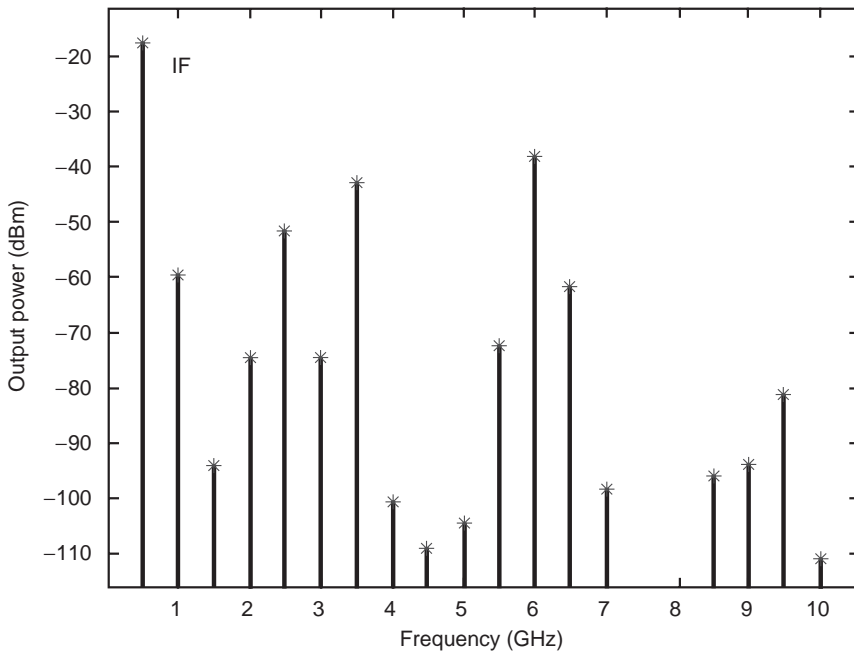


Figure 7. Output power spectrum of the frequency mixer.

of the Volterra series analysis is the short simulation time, compared to the envelope transient sweep, which is computationally very expensive.

3. OSCILLATOR SYNTHESIS

3.1. General Concepts about Oscillator Circuits

The oscillator circuit provides a time-varying, generally periodic solution, from DC sources only. In contrast to forced circuits, the fundamental frequency of the solution depends on the values of the circuit elements, bias sources, and other parameters, since it is not delivered to the circuit by any external source [4]. For this reason, the oscillation frequency will be an unknown of the circuit

equations. In the synthesis procedure, the values of the circuit elements will have to be determined in order to obtain the desired oscillation frequency and power.

The oscillator circuit is often modeled as the connection of a linear network and a nonlinear network [3,11]. The nonlinear network contains the active-device, feedback, and terminal elements, while the output resistive load is included in the linear network. With respect to this output load, the rest of the circuit must behave as an energy source at the desired oscillation frequency. Thus, the nonlinear network must exhibit negative resistance at the oscillation frequency, which is determined by the circuit resonance. To achieve this, a negative-resistance diode or a transistor is used in the oscillator design.

Since no RF generators are present in the oscillator circuit, its equations can always be solved for a DC solution. In a well-behaved oscillator, this solution will be unstable, that is, *nonrobust* versus perturbations [4]. Under any small perturbation, an oscillation of growing amplitude will begin as a result of the circuit resonance and the energy excess. The equilibrium state is enabled by the decrease of the negative resistance in all physical devices when the current amplitude increases beyond a certain level. Actually, it is the nonlinearity of the negative-resistance element that allows the establishment of the steady-state oscillation.

As already stated, even when the circuit oscillates, it can always be solved for a DC solution, besides the desired periodic solution [4]. The stability considerations for these two solutions are essential. From a mathematical point of view, the DC solution of this oscillator circuit must be unstable, having a pair of complex poles $\sigma \pm j\omega$, with $\sigma > 0$ and ω , in the order of the desired oscillation frequency ω_0 [4]. In turn, the steady-state oscillation must be stable, or robust versus perturbations, to be physically observed. No generators exist at the oscillation frequency ω_0 , so, in order for this frequency to be self-sustained, a pair of complex conjugate

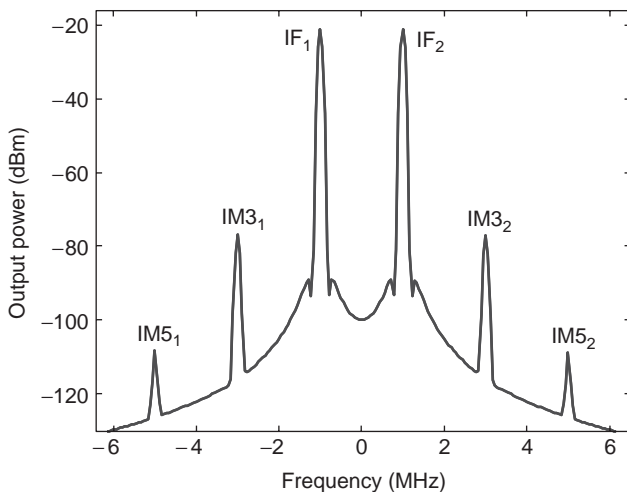


Figure 8. Intermodulation spectrum about the IF frequency $f_{IF} = 0.5$ GHz, obtained through the envelope transient method.

poles $\pm j\omega_0$ of the linearized system must be located on the imaginary axis. For stability, all the rest of the poles must be located on the left-hand side of the complex plane.

Another essential fact in oscillator circuits is that, since there is no external time reference for the self-oscillation (i.e., there exist no time varying generators in the circuit), the oscillating solution is invariant with respect to time translations. Any arbitrary timeshift to the oscillating solution obtained provides another solution of the oscillator equations [4]. There is a singularity in the system, corresponding to the existence of a pair of complex conjugate poles, located on the imaginary axis $\pm j\omega_0$. The invariance with respect to the time origin gives, in turn, an invariance of the phase reference. Thus, when a stable oscillator is perturbed, perturbations affecting the oscillator phase will remain in the steady-state solution [25].

The oscillator phase noise may be understood as the result of the phase shift accumulation, versus continuous perturbations, coming from the noise sources. The oscillator spectrum is not a delta at ω_0 [3], since the noise perturbations give rise to a power distribution about this frequency. When only phase noise is considered, the total power of the spectral distribution is the same as the one of the ideal line. The single-sideband phase noise spectral density at a certain frequency offset Ω is defined as the ratio between the sideband power at Ω , measured in 1 Hz bandwidth, and the carrier power.

3.2. Design Procedure

The oscillator circuits are most efficiently designed in the frequency domain, where impedance/admittance analysis can be easily applied for the evaluation of the oscillation startup and steady-state conditions. The distributed

elements of the linear networks are also more easily described in this domain. The oscillator design requires an initial choice of the active device. This device may be a negative-resistance diode or a transistor [3]. The three main types of negative-resistance diodes are tunnel, IMP-ATT (impact avalanche transit time), and Gunn diodes [26]. They allow higher oscillation frequencies than the transistor devices; however, at frequencies where the two types of devices are possible, the transistor-based oscillators are generally preferred. They usually enable lower phase noise values and have better stability properties. The diodes can also be difficult to match to the impedance values commonly used at microwave frequencies.

In the following, a systematic design procedure for oscillator circuits is presented. It will be illustrated by means of its application to the design of an oscillator, based on the MESFET CFY30, at the frequency $f_0 = 4.5$ GHz.

3.2.1. Oscillation Startup Conditions. The evaluation of the oscillation startup conditions is, in fact, an evaluation of the stability of its DC solution. As already stated, this solution has to be unstable, with two poles $\sigma \pm j\omega_0$ on the right-hand side of the complex plane. When using a transistor, it is convenient to start the oscillator design by calculating, for given bias conditions, the stability factor μ [27] about the desired oscillation frequency ω_0 . This factor depends on the transistor scattering parameters and, thus, on its bias point. When the transistor is unconditionally stable ($\mu > 1$) about the desired oscillation frequency, a different bias point can be attempted. However, to ensure sufficient negative resistance, it is convenient to use a feedback network. Reactive elements are generally chosen to avoid the introduction of unnecessary loss. Different feedback networks are possible. A simple topology is obtained through series feedback, with either a capacitance or an inductance, as shown in Fig. 10a.

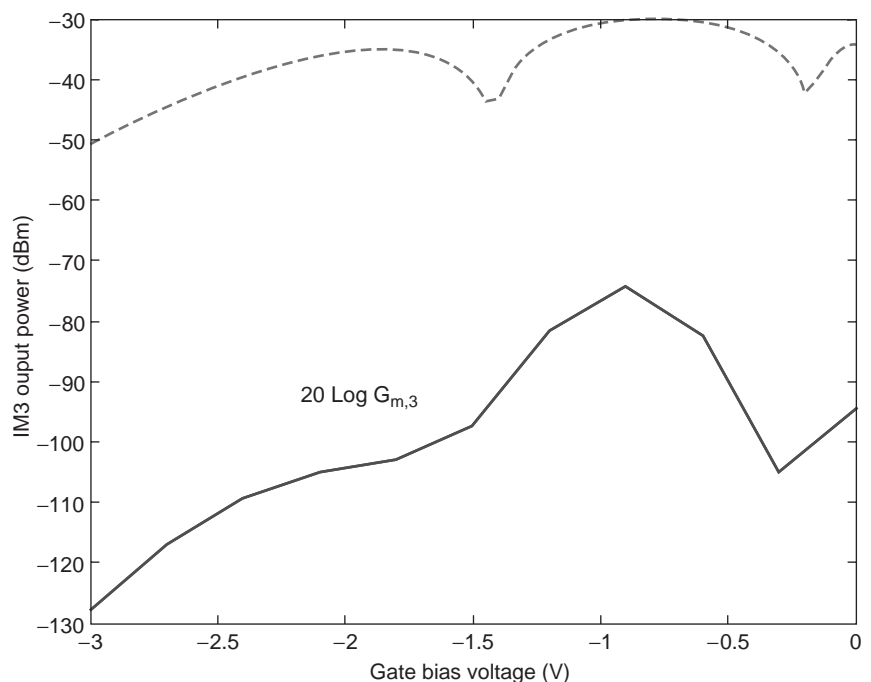


Figure 9. Variation of the third-order intermodulation distortion versus the gate voltage V_{GS} . Calculation from the envelope transient method, following the third-order intermodulation tone $\omega_{IM3,1}$. Comparison with the variation of $G_{m3,1}$.

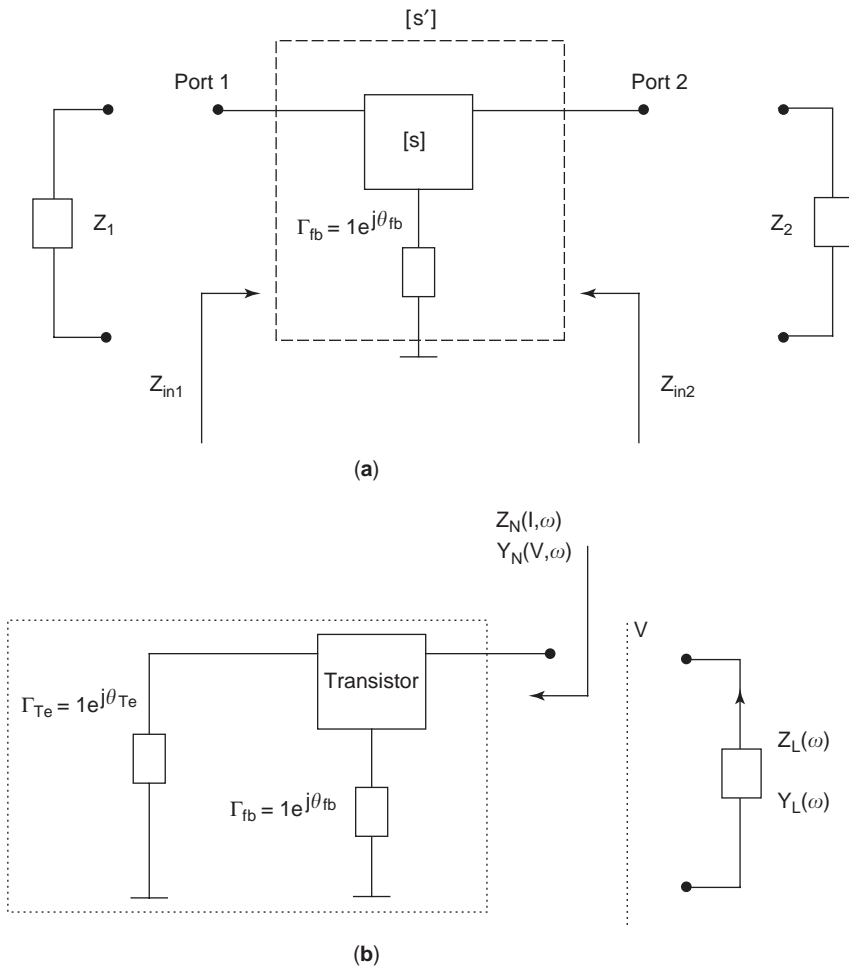


Figure 10. Transistor with series feedback to achieve negative resistance at the drain port: (a) two-port analysis; (b) one-port analysis, with a reactive terminal element at the gate port.

Topologies like the ones used in the Colpitts and Clapp–Gouriet oscillators [3,6] reduce the influence of the elements of the transistor model on the oscillation frequency.

A simple series feedback, at the transistor source, will be considered here (see Fig. 10a). A new two-port can be defined, including the transistor and the feedback elements. The two ports of the active network (including the feedback) will be denoted ports 1 and 2. The input impedance Z_{in1} at port 1 depends on the scattering parameters S , the feedback elements, and the circuit load at the other end Z_2 . In turn, the output impedance Z_{in2} at port 2 depends on S , the feedback elements, and Z_1 [3]. The oscillator synthesis can be carried out at either port 1 or port 2. The choice will depend on the particular oscillator configuration. Without loss of generality, port 2 will be selected here (see Fig. 10b).

The μ factor will now be analyzed, in the presence of series feedback, at the desired oscillation frequency ω_0 . To globally consider all the positive and negative reactive values, an ideal feedback element, defined by its reflection coefficient $\Gamma_{fb} = 1e^{j\theta_{fb}}$, will be used. For some values of θ_{fb} , a stability coefficient $\mu < 1$ will be obtained. Figure 11a shows the variation of μ versus θ_{fb} , for the transistor CFY30, when considering different values of gate bias. The drain voltage is in all cases $V_{DS} = 2.5$ V.

For $\mu < 1$, it will be possible to have source impedances such that $\text{Re}Z_{in2} < 0$. These are determined by tracing the

corresponding source stability circle on the Smith chart. This circle constitutes the border between the source impedances Z_1 for which $\text{Re}Z_{in2} < 0$ and those giving $\text{Re}Z_{in2} > 0$. For obvious reasons, provided the original scattering matrix of the transistor (referred to $50\ \Omega$) fulfills $|S_{22}| < 1$, the origin of the Smith chart will belong to the zone giving $\text{Re}Z_{in2} > 0$. The opposite is true for $|S_{22}| > 1$. Figure 11b shows the location of the stability circles, at the desired oscillation frequency $f_0 = 4.5$ GHz, for some θ_{fb} values, with $\mu < 1$.

In most cases, the impedance Z_1 is used to achieve the negative resistance only. It is often called *terminal impedance* Z_{Te} . For simplicity, and to avoid additional loss, a reactive value X_{Te} is usually chosen (Fig. 10b). However, in some cases, it will be necessary to consider a real part in Z_{Te} , especially when the objective is to synchronize the oscillator at a later stage, since the forcing generator, connected at port 1, will necessarily introduce a resistive value $\text{Re}Z_{Te} > 0$. If the oscillator is expected to operate in free-running regime, only Z_{Te} values on the border of the Smith chart will be selected. Although a single-terminal element (inductance or capacitance) will be considered here, it is also possible to use a resonator, with a high quality factor. As will be shown later, this reduces the phase noise spectral density.

As already mentioned, in order to fulfill the oscillation startup conditions, excess negative resistance and

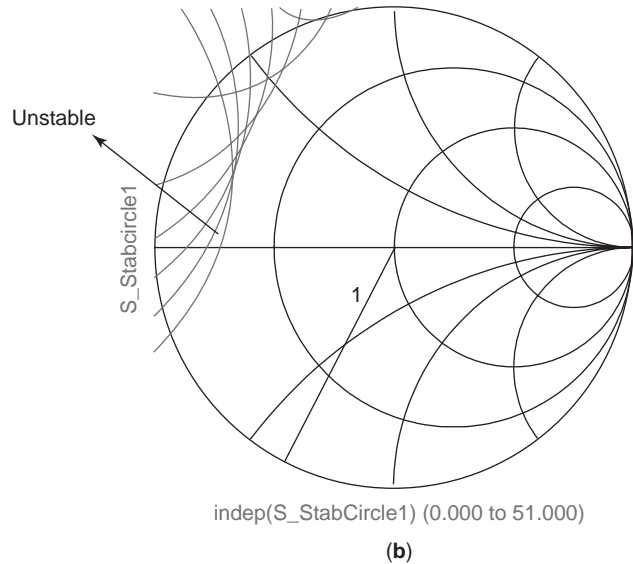
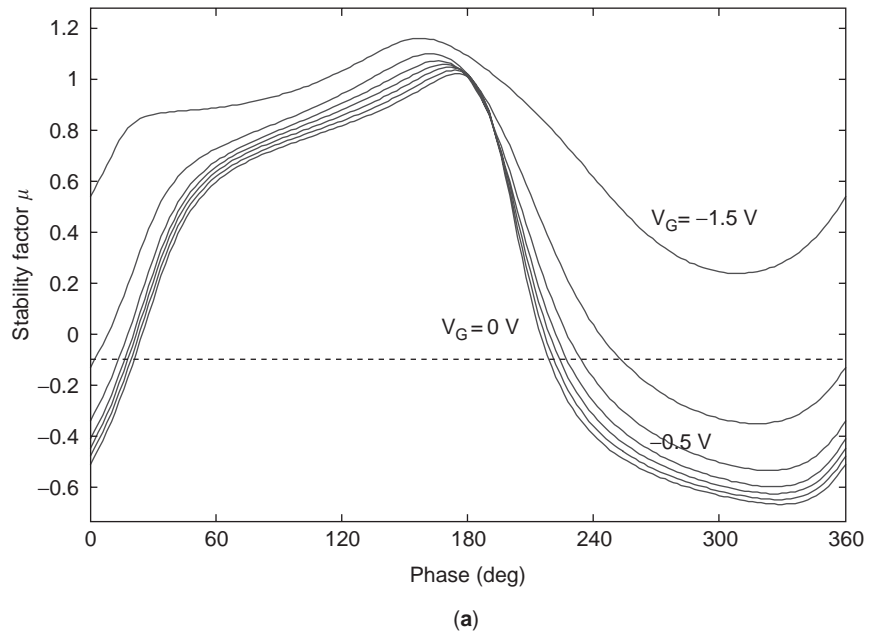


Figure 11. Analysis of potential instability of the series feedback topology in Figure 10: (a) variation of the stability factor μ versus the phase θ_{fb} for different values of the gate bias voltage; (b) regions in the Z_1 plane, providing negative resistance at the drain port, obtained for θ_{fb} values for which $\mu < 1$. (This figure is available in full color at <http://www.mrw.interscience.wiley.com/erfme>.)

resonance of the reactive elements must be achieved at port 2 in Fig. 10. This energy excess gives rise to the growth of the oscillation current. The oscillation startup conditions can also be evaluated in terms of the total impedance or the total admittance at port 2 (Fig. 10b). Actually, the connection of the linear and nonlinear networks of the oscillator circuit can be regarded as a series connection, which would require the sum $Z_{in2} + Z_2$, or as parallel connection, which would require the sum of the respective admittances $1/Z_{in2}$ and $1/Z_2$, specifically, $Y_T(V, \omega) = 1/Z_{in2} + 1/Z_2$, where V is the node voltage. Taking V as the independent variable, the negative-conductance excess, plus the resonance condition at ω_0 , will give rise to an oscillating transient of growing amplitude in this voltage variable. The choice of admittance functions is generally more convenient to make the design compatible with the later use of nonlinear simulation. Actually, the nonlinear circuit analysis is carried out using the node

voltages as the state variables. Thus, only admittance functions will be considered in the remainder of the text.

Analysis of Fig. 11b provides the values of the terminal impedance X_{Te} (on the border of the Smith chart) for which negative resistance (or conductance) is obtained at port 2 for different θ_{fb} values, with $\mu < 1$. However, it does not show the actual values of negative resistance/conductance. This requires an additional analysis that will allow the optimum selection of both the feedback and terminal element values. Again, to globally consider both inductive and capacitive values, this terminal impedance will be written $\Gamma_T = 1e^{j\theta_{Te}}$ (Fig. 10b). Renaming $Y_N \equiv 1/Z_{in2} = G_N + jB_N$, the variation of the function $G_N(\theta_{fb}, \theta_{Te})$, at the desired oscillation frequency ω_0 , will be analyzed by means of a double sweep in the two phases θ_{fb} and θ_{Te} .

Figure 12 shows the results of the application of the double-sweep technique to the MESFET oscillator, biased at $V_{GS} = -0.5$ V, $V_{DS} = 2.5$ V. The analysis frequency

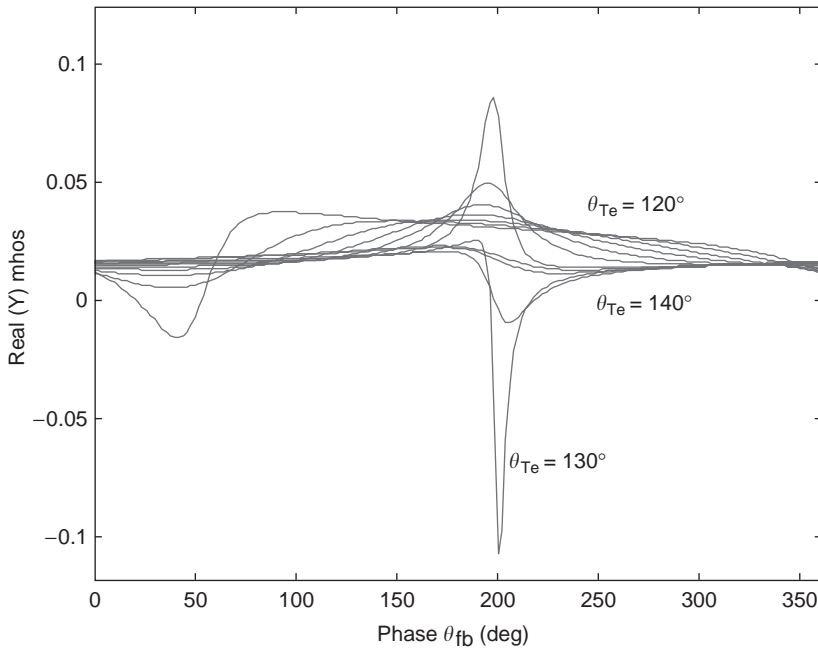


Figure 12. Conductance variation versus the phase of the reactive terminal and feedback elements, respectively, given by θ_T and θ_{fb} . (This figure is available in full color at <http://www.mrw.interscience.wiley.com/erfme>.)

agrees with the desired oscillation frequency $f_0 = 4.5$ GHz. Phase values between 0 and 180° will correspond to inductances, while phase values between 180° and 360° will correspond to capacitances. This distinction will be useful when a feedback or terminal element of a particular type is desired, as in the case of voltage-controlled oscillators (VCOs), for which a tuned capacitance is to be included as either terminal or feedback element. In the case of Fig. 12, the maximum conductance is obtained for the phase values $\theta_{fb} = 200^\circ$ and $\theta_{Te} = 130^\circ$. Thus, a capacitive feedback element $C = 4$ pF and an inductive terminal element $L = 0.82$ nH should be used.

After the choice of the optimum terminal and feedback elements, a load admittance $Y_L \equiv G_L + jB_L$ is connected to the nonlinear network

$$\begin{aligned} G_T(V \cong 0, \omega_0) &\equiv G_N(V \cong 0, \omega_0) + G_L(\omega_0) < 0 \\ B_T(V \cong 0, \omega_0) &\equiv B_N(V \cong 0, \omega_0) + B_L(\omega_0) = 0 \end{aligned} \quad (12)$$

where ω_0 is the desired oscillation frequency and $V \cong 0$ indicates small-signal voltage. These conditions establish the unbalance of the delivered and dissipated energy at the resonance frequency ω_0 . It is, in fact, an instability condition of the DC solution of the circuit at the selected bias point. In general, the circuit will evolve towards a stable oscillating solution for $(\partial B_T / \partial \omega)|_0 > 0$, as shown by Kurokawa [11]. In order to maximize the output power $P_o = \frac{1}{2} G_L V_o^2$, an empirical criterion is $G_L = -\frac{1}{3} G_N(V \cong 0, \omega_0)$.

In the case of the MESFET-based oscillator, $B_N(4.5 \text{ GHz}) = 0.069$ mhos. Thus, parallel inductance, of value $L = 0.511$ nH, should be introduced, to obtain $B_T = 0$. Figure 13 shows the fulfillment of the oscillation startup conditions at $f_0 = 4.5$ GHz. A design for specified output power P_o requires a nonlinear model of the active block $Y_N(V, \omega)$. The nonlinear oscillator design will be the object of the next section.

The sensitivity to perturbations of the oscillation frequency is smaller for higher slope of $B_T(\omega)$, at the resonance frequency ω_0 , as the oscillator quality factor Q is directly proportional to this derivative [28]. Thus, lower phase noise should be expected for larger $B_T(\omega)$. Dielectric resonators can be used to increase the Q factor [3,28]. They are made of ceramic material, being stable in temperature, with low loss and high dielectric constant. The resonator is placed in the neighborhood of a transmission line and is coupled to this line. Its equivalent circuit is a parallel resonant circuit, in series with the line, whose element values R , L , and C depend on the distance of the resonator from the transmission line and on the length of this transmission line that is actually coupled to the resonator [28].

As a final comment, it should be highlighted that in monolithic technologies, with high manufacturing reliability, the model parameters for different transistor devices will be very close in value. Thus, differential configurations can be used for oscillator design [29]. The negative resistance is provided by two transistors in cross-coupled configuration and biased by means of current source, at the emitter or source terminal. The resonance at the desired oscillation frequency may be achieved through an inductive divider and a capacitor, connected to the transistor collector or drain terminals. The technique presented here can also be used, with some modifications, for the types of steady-state design discussed in the following paragraphs.

3.2.2. Steady-State Design with One-Harmonic Accuracy. Assuming an ideal waveform $v(t) = V_o \cos(\omega_0 t)$, the steady-state oscillation condition, showing the balance between the delivered and dissipated energy, is given by

$$\begin{aligned} G_T(V_o, \omega'_0) &\equiv G_N(V_o, \omega'_0) + G_L(\omega'_0) = 0 \\ B_T(V_o, \omega'_0) &\equiv B_N(V_o, \omega'_0) + B_L(\omega'_0) = 0 \end{aligned} \quad (13)$$

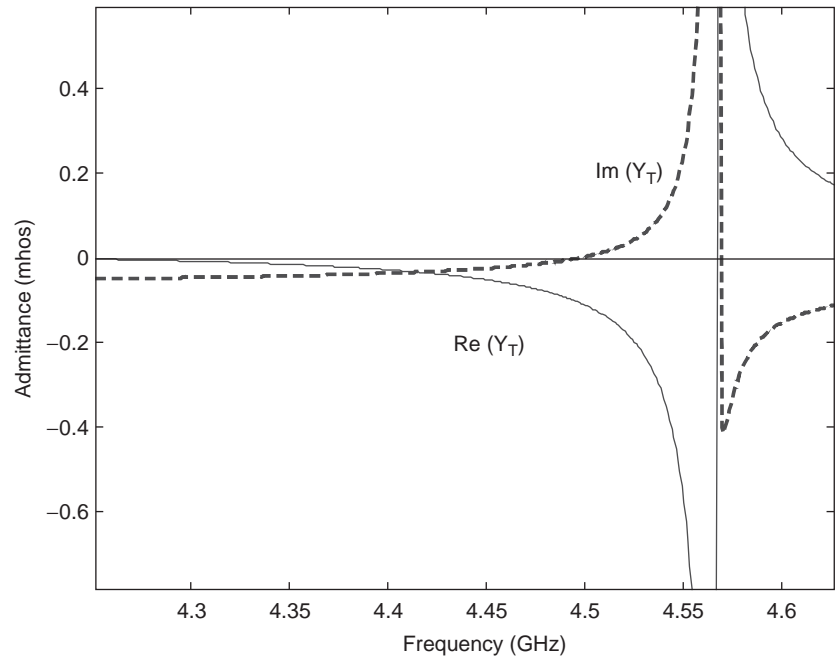


Figure 13. Fulfillment of the oscillation startup conditions for $f_0 = 4.5$ GHz. (This figure is available in full color at <http://www.mrw.interscience.wiley.com/erfme>.)

As shown in these equations, the steady-state oscillation frequency will generally be different from the desired value ω_0 , at which the startup condition (12) is evaluated. This is due to the nonlinear dependence of both G_N and B_N on the amplitude V . Unlike the startup condition (12), the steady-state equation (13) requires a nonlinear model $Y_N(V, \omega)$ for the admittance of the active device. This equation will enable the approximate calculation (with one-harmonic component) of the oscillation output power and frequency. After the initial design, based on (13), a rigorous nonlinear analysis should be carried out, taking into account a sufficient number of harmonic terms, which will have some influence on both the oscillation frequency and the power.

The nonlinear function $Y_N(V, \omega)$ can be determined either empirically or analytically. The empirical determination is carried out by measuring the scattering parameters with respect to the input amplitude V , in a frequency band about the expected oscillation frequency. The analytical determination relies on the *describing function* [3,11]. In order to mathematically define the describing function, the nonlinear element $i(v)$ will be considered, excited by a sinusoidal signal $v(t) = V \cos(\omega t)$. This will give rise to a current through the element $i(t)$, which, in general, will not be sinusoidal. The describing function $Y_N(V)$ is given by the ratio between the first harmonic of the current $i(t)$ and the amplitude V : $Y_N(V) = i(t)_{1st \text{ harm}}/V$.

The describing function enables an analytical design of the oscillator from the steady-state equation $Y_T = Y_N(V) + Y_L(\omega) = 0$. For relatively simple topologies, it will be possible to carry out an analytical calculation of the oscillator steady state V_0, ω_0 [4], as well as an evaluation of the oscillation startup and stability conditions (to be shown later). Conversely, it will be possible to impose the desired oscillation solution V_0, ω_0 and determine the values of two circuit elements η_1, η_2 , so as to satisfy $Y_T(\eta_1, \eta_2) = 0$. However, when multiple nonlinearities are present,

as is the case with the transistor devices, the overall calculation of Y_N is demanding. It requires an individual describing function for each nonlinear element. Thus, all the nonlinear elements should be replaced with their describing functions. The technique is described in detail in Ref. 3. Due to the complexity of the circuit equations, a numerical resolution of the steady state equation $Y_T(V, \omega) = 0$ or $Y_T(\eta_1, \eta_2) = 0$ will generally be necessary. An example is presented in the following paragraphs.

A simple sweep technique can be used for an oscillator design at ω_0 , with specified output power P_o . It is assumed that the values of terminal and feedback element, ensuring that $G_N(V \cong 0, \omega_0) < 0$ have already been determined using the technique described in Section 3.2.1. Then a sweep in V is carried out, tracing both the real and imaginary parts of Y_N versus this variable. In Fig. 14, the technique is applied to the MESFET oscillator. If the goal is to obtain an oscillation at V_0, ω_0 , a load admittance Y_L such that $G_L(\omega_0) = -G_N(V_0, \omega_0)$ and $B_L(\omega_0) = -B_N(V_0, \omega_0)$ should be chosen.

The design for specified output power P_o is carried out by adding the curve $-G_L = -(2P_o/V^2)$ to the representation of Fig. 14. Two different curves, $-G_{L1}(V)$ and $-G_{L2}(V)$, have actually been considered, respectively corresponding to the output power $P_o = 7$ dBm and $P_o = 9.16$ dBm. In the case of $-G_{L1}(V)$, two different intersection points are obtained with $-G_N(V_0, \omega_0)$. The first intersection point, with $V = 0.33$ V requires the load resistance $R_L = 1/G_L = 10.87 \Omega$. This low value is impractical for circuit implementation. The second intersection point, with $V = 0.78$ V, requires a load resistance $R_L = 62.5 \Omega$, which is much better suited for implementation. Thus, the second intersection point is kept for the design.

The nonlinear susceptance varies from $B_N = 0.11$ mho, in small signal, to $B_N = 0.073$ mho, at the desired oscillation point. Thus, the required susceptance value of the

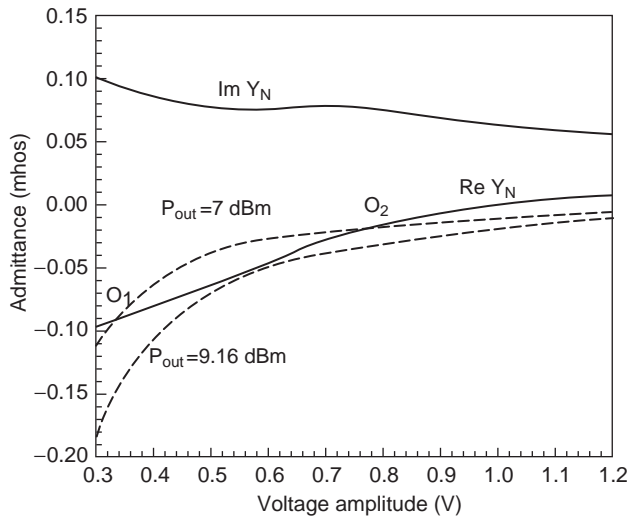


Figure 14. Approximate nonlinear design for specified output power, based on an amplitude sweep.

oscillator load will be $B_L = -0.073$ mho, which can be obtained with a parallel inductance, of value $L = 0.4845$ nH. Of course, for this design to be valid, the oscillation start-up conditions must still be fulfilled, with these load values, and the steady-state oscillation must be stable.

3.3. Steady-State Design Using CAD Tools

Provided HB software and a nonlinear model for the transistor device are available to the designer, an accurate oscillator synthesis can be carried out. The synthesis technique relies on the use of auxiliary generators, whose helpfulness for the analysis and design of oscillator circuits has been demonstrated in a number of works [4,8,16]. The auxiliary generator enables the evaluation of the impedance or admittance functions on which the oscillator synthesis is based.

The design using admittance equations requires an auxiliary generator of voltage type. This generator, of amplitude V_{AG} , is connected in parallel at the circuit node, at which the observation port is defined. In the case of the oscillator of Fig. 10, it would be connected between port 2 and ground, as shown in the sketch in Fig. 15. The auxiliary generator frequency will be ω_{AG} , while its phase, for the analysis of free-running oscillator circuits, may be ar-

bitrarily set to zero $\phi_{AG} = 0$. The voltage generator is connected in series to an ideal bandpass filter, exhibiting zero impedance at $\omega = \omega_{AG}$ and an infinite impedance at $\omega \neq \omega_{AG}$. The objective of this filter is to prevent the voltage generator from short-circuiting the frequency components different from $\omega = \omega_{AG}$.

Four different applications of the auxiliary generator technique to oscillator synthesis are presented next.

3.3.1. Approximate Nonlinear Design. The auxiliary generator enables a straightforward application of the approximate design technique described in Section 3.2.2 on HB software. Through simple Kirchhoff analysis, the ratio $Y_{AG} = I_{AG}/V_{AG}$, with I_{AG} entering the circuit, agrees with the sum $Y_N(V_{AG}, \omega_{AG}) + Y_L(\omega_{AG})$. As in the previous section, it is assumed that the values of terminal and feedback elements provide $G_N(V \cong 0, \omega_0) < 0$. For the approximate nonlinear design, the auxiliary generator frequency is $\omega_{AG} \equiv \omega_0$. Then, the transistor port 2 is loaded with a large resistor R , such that $Y_T(V, \omega) = Y_N + 1/R \cong Y_N(V, \omega)$ (see Fig. 15). A HB analysis is performed, sweeping the auxiliary generator amplitude from a small value to a few volts. The curves $\text{Re}(Y_{AG}(V, \omega_0))$ and $\text{Im}(Y_{AG}(V, \omega_0))$ are traced versus V . To obtain an oscillation at V_0, ω_0 , the load values $G_L = -\text{Re}(Y_{AG}(V_0, \omega_0))$ and $B_L(\omega_0) = -\text{Re}(Y_{AG}(V_0, \omega_0))$ should be selected. For specified output power, the curve $-G_L = -(2P_o/V^2)$, must be superimposed, which will enable an approximate design in the same manner as in Section 3.2.2.

3.3.2. Nonlinear Analysis. After implementation of the load circuit resulting from the approximate technique described in Section 3.3.1, the accuracy of the oscillator design is verified through a HB simulation. A sufficiently high number of harmonic components must be considered. Now, the auxiliary generator admittance function will be $Y_{AG} = Y_N + Y_L$, at $\omega = \omega_{AG}$, and $Y_{AG} = 0$ at $\omega \neq \omega_{AG}$, due to the ideal-filter action. If good accuracy has been obtained in the oscillator design, the ratio Y_{AG} , for $\omega_{AG} \equiv \omega_0$ and $V_{AG} \equiv V_0$, will be close to zero, $Y_{AG}(V_0, \omega_0) \cong 0$. Note that the harmonic termination mismatches will prevent the fulfilment of this oscillation condition.

The actual oscillator solution is obtained through the calculation/optimization of V_{AG}, ω_{AG} , in order to satisfy $Y_{AG} = 0$. This condition avoids the degenerate DC solution,

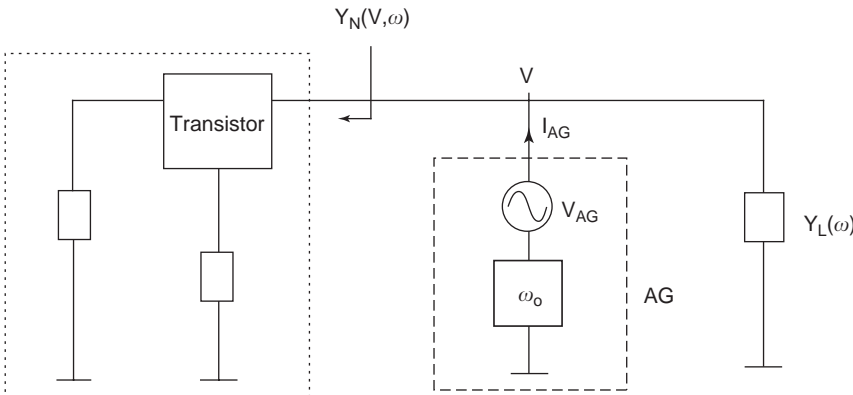


Figure 15. Auxiliary generator for oscillator analysis and design.

with $V_{AG} = 0$, that always coexists with the oscillating one. The condition $Y_{AG} = 0$ will be fulfilled for a first-harmonic amplitude V_0' and frequency ω_0' , where the prime signs point out the fact that the actual oscillation amplitude and frequency are different from those imposed at the design stage. Note that this approximate design was carried considering only one-harmonic component in the simulations. In the case of the MESFET oscillator, the oscillation frequency changes from $f_0 = 4.5$ GHz to $f_0' = 4.513$ GHz and the output power changes from $P_0 = 7$ dBm to $P_0' = 7.8$ dBm.

3.3.3. Nonlinear Optimization. The auxiliary generator can be used for a nonlinear optimization of the oscillator circuit, avoiding the shift from (V_0, ω_0) in the approximate design, to (V_0', ω_0') in the actual oscillator solution, when all the harmonic components are taken into account. For this purpose, the auxiliary generator amplitude and frequency are respectively set to $V_{AG} = V_0$ and $\omega_{AG} = \omega_0$. Then, two circuit elements η_1, η_2 , are optimized and/or calculated so as to satisfy $Y_{AG}(\eta_1, \eta_2) = 0$. This enables an accurate nonlinear design for prefixed oscillation power P_0 and frequency ω_0 .

The auxiliary generator technique is very useful for the sequential introduction of accurate models of the oscillator elements. It can be applied for the transmission-line implementation of lumped elements, avoiding any undesired shift of the oscillation frequency. This is done on an element-by-element basis. At each stage, the geometric dimensions of the new distributed element, length (l) and width (w), for instance, are optimized/calculated so as to fulfill $Y_{AG}(l, w) = 0$, with the auxiliary generator operating at the desired values $V_{AG} = V_0$ and $\omega_{AG} = \omega_0$. Accurate models for varactor diodes and packaged inductors or capacitors can also be progressively introduced, in a similar manner.

The technique described above has been used for the microstrip-line implementation of the terminal and load inductances of the MESFET oscillator (see Fig. 16a). In the MESFET oscillator, it has been used for the introduction of the DC block and feedback capacitor models, avoiding the shift of the oscillation frequency. The final oscillator solution, at exactly $f_0 = 4.5$ GHz, is shown in Fig. 16b, together with the experimental values.

3.3.4. Efficiency Maximization. The oscillator efficiency is defined as the ratio between the output power at ω_0 and the DC consumption: $E_{ff} = P_0/P_{DC}$. When high efficiency is required, a specific design technique is necessary to take this characteristic into account. The value of the oscillator load at different harmonic components has relevant influence on the efficiency, as shown by several authors [30,31]. Load pull can be used for the optimum selection of the harmonic impedances.

The load-pull system is implemented on HB software (see Fig. 17a). The load, at each harmonic component $n = 1 \dots N$, consists of an ideal bandpass filter, centered at $n\omega_0$ and terminated in a reflection coefficient $\Gamma_n = \rho_n e^{j\theta_n}$. The use of reflection coefficients is more convenient than the use of impedances or admittances, since all the possible passive terminations can be taken into account in the two

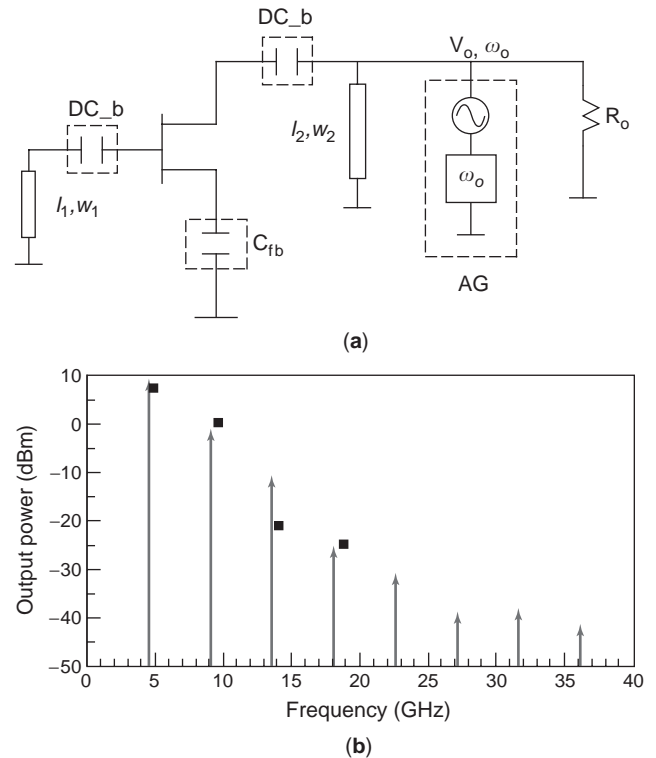


Figure 16. Oscillator circuit implemented on microstrip line using the auxiliary generator technique—accurate models have also been introduced for the packaged elements: (a) schematic; (b) output spectrum, with inclusion of experimental results.

bounded sweeps $\rho_n = 0 \dots 1$ and $\theta_n = 0 \dots 360^\circ$. The process starts with determination of the Γ_1 value, for maximum efficiency, when short-circuiting the higher harmonic terms, by making $\Gamma_n = 1 e^{j\pi}, n = 2 \dots N$. Note that, even when using these short-circuit terminations, the harmonic current still circulates inside the transistor device, as the i_{ds} current source is not short-circuited.

The optimum Γ_1 is determined through a double sweep in ρ_1, θ_1 . The auxiliary generator is maintained at the desired oscillation frequency ω_0 . The reactive feedback and terminal elements are calculated and/or optimized for each Γ_1 variation, in order to fulfill $Y_{AG} = 0$. Of course, because of the autonomous nature of the circuit, no solution will exist, for some Γ_1 values. Once the optimum Γ_1 has been determined, the influence of the higher-harmonic loads is analyzed, through consecutive sweeps, in the phases $\theta_2, \theta_3, \dots$. An example of application is shown in Fig. 17b, where the arrows indicate the order of the sweeps. The multiharmonic load will have to be implemented with a single passive network. An example of this implementation will be shown later, in Section 5.3. The fulfillment of the oscillation startup conditions must be verified for the final design.

3.4. Voltage-Controlled Oscillator

In a voltage-controlled oscillator (VCO), the oscillation frequency is tuned by modifying the bias voltage of a varactor diode. In reverse bias, the varactor diode is

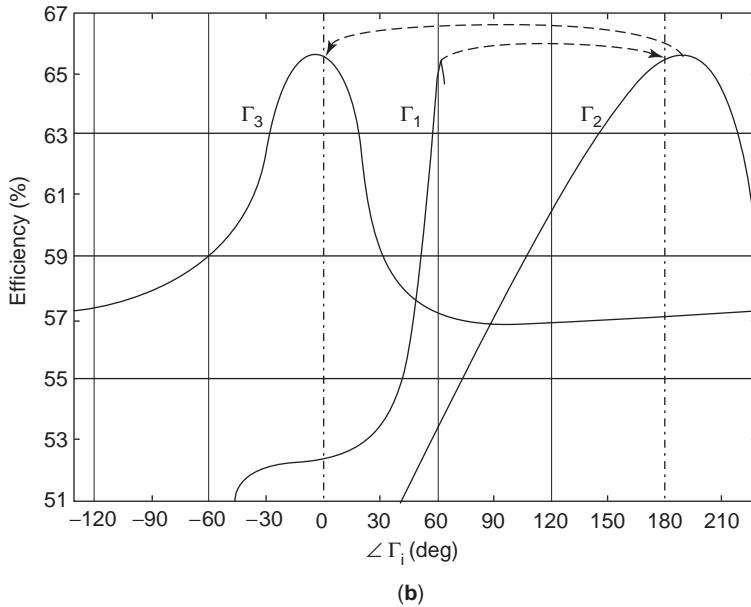
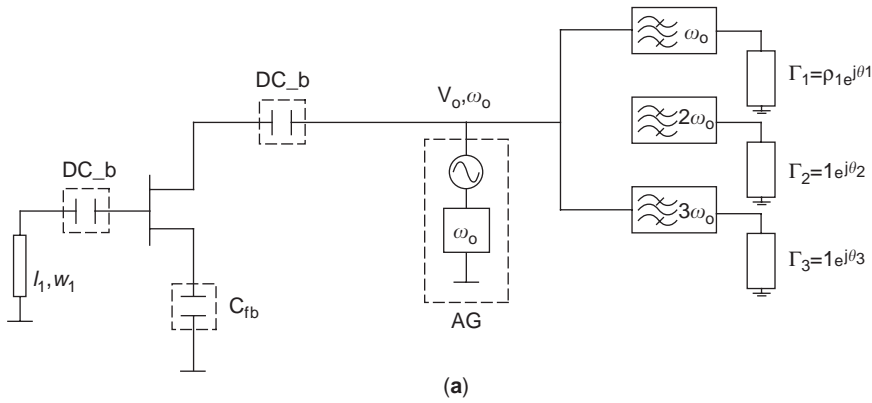


Figure 17. Load-pull system for maximization of the oscillator efficiency: (a) circuit schematic, with an ideal harmonic load; (b) maximization of the oscillator efficiency through the optimum selection of the harmonic loads.

essentially a voltage-dependent junction capacitance $C_j(v)$, in series with a loss resistance R_s . The junction capacitance varies according to $C_j(v) = C_{j0}/(1 - v/\phi_0)^{\gamma}$, where ϕ_0 is the built-in potential and C_{j0} is the capacitance value for zero bias voltage. The largest capacitance value is $C_{max} \cong C_{j0}$ and the region of maximum sensitivity corresponds to relatively small reverse-bias voltages.

The practical variation range is limited to $[C_{min} - C_{max}]$. With this given range, a simple technique can be applied to maximize the frequency-tuning interval [28]. The technique will be illustrated by means of its application to the FET oscillator circuit. The varactor diode is connected to a transistor terminal different from the one at which the series feedback is introduced. For source series feedback, it should be connected to the gate terminal, as the drain terminal provides the highest output power.

The transistor, together with the feedback and terminal elements, must exhibit negative conductance in a frequency interval containing the desired oscillation band (see Fig. 18a). For the approximate determination of this band, the small-signal susceptance $B(V \cong 0, \omega)$, seen from the varactor terminals, must be traced versus ω , together with the two straight lines $-C_{min}\omega$ and $-C_{max}\omega$. Then, the oscillation frequency interval is delimited by the two

intersection points of these two straight lines with the curve $B(\omega)$. This is shown in Fig. 18a, where the varactor diode has the capacitance variation range $C_{min} = 0.3 \text{ pF}$ to $C_{max} = 2 \text{ pF}$.

As shown in Ref. 28, the introduction of an inductor in parallel with $B(\omega)$ allows the flattening curve $B'(\omega) = B(\omega) - 1/(L\omega)$, which increases the frequency separation between the two intersection points. Provided the two points belong to the negative-resistance interval, a larger frequency-tuning range will be obtained. In Fig. 18a, the initial frequency bandwidth is $\Delta f = 734 \text{ MHz}$. After the introduction of the parallel inductance, the bandwidth increases to $\Delta f = 1.286 \text{ GHz}$. The nonlinear analysis of Fig. 18b, showing the variation of the oscillator frequency and power versus the varactor bias, confirms the validity of the technique. There is, however, a shift of the predicted band, due to nonlinear effects. The experimental values are in good agreement with the simulations.

3.5. Stability Analysis

As already mentioned, the startup condition (12), obtained from a small-signal impedance/admittance analysis, is, in

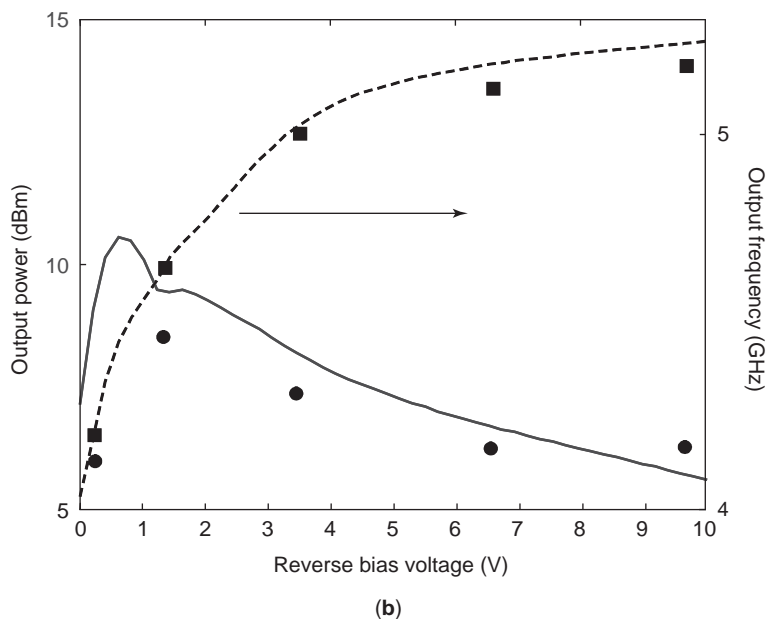
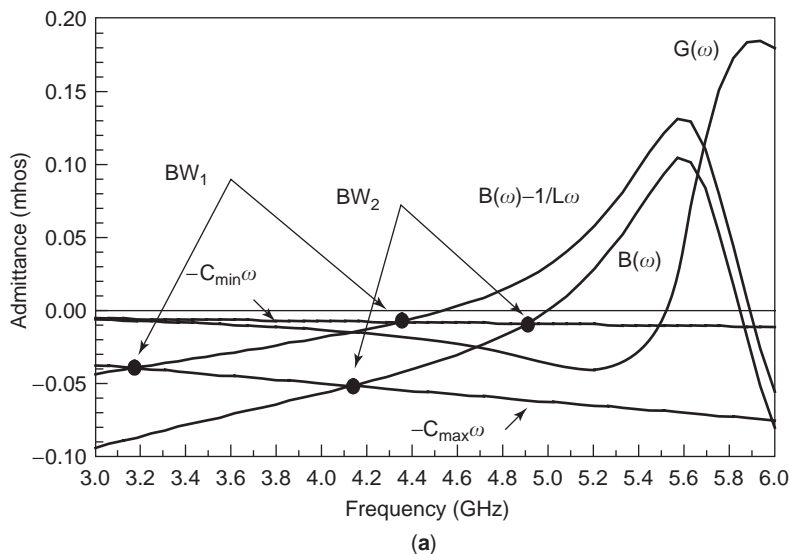


Figure 18. Design of a voltage-controlled oscillator: (a) method used to increase the frequency variation band, versus the varactor capacitance, through the introduction of an inductive element, in parallel; (b) frequency and output power variation versus the reverse bias voltage, obtained through a HB analysis. Experimental points are also included. (This figure is available in full color at <http://www.mrw.interscience.wiley.com/erfme>.)

fact, an instability condition of the DC solution. For a more rigorous analysis, a small-amplitude perturbation of complex frequency $\sigma + j\omega$ should be considered, in order to determine the value or number of unstable poles of the circuit linearization about the DC solution [4]. As already stated, for the oscillation startup, there must be a pair of unstable poles $\sigma \pm j\omega_0$, with $\sigma > 0$. Due to the complexity of the pole calculation, the Nyquist criterion is usually applied to the characteristic determinant associated with the linearized system.

The stability analysis of the steady-state oscillation is performed by considering a small-amplitude perturbation about this solution. The analysis is more difficult, due to the periodic nature of this steady-state regime. Two cases may be distinguished: a perturbation frequency satisfying $\omega = \omega_0 + \delta\omega$ and a perturbation frequency $\omega \neq \omega_0 + \delta\omega$. The first case enables the detection of instabilities giving rise to hysteresis phenomena. However, other instabilities,

such as the division by 2 of the fundamental frequency ω_0 or the onset of a second autonomous fundamental ω_a , nonharmonically related to the frequencies ω_0 , are also common.

The oscillator stability versus synchronous perturbations (fulfilling $\omega = \omega_0 + \delta\omega$) can be determined through the function proposed by Kurokawa [11]:

$$\xi = \frac{\partial G_T}{\partial V} \bigg|_0 \frac{\partial B_T}{\partial \omega} \bigg|_0 - \frac{\partial G_T}{\partial \omega} \bigg|_0 \frac{\partial B_T}{\partial V} \bigg|_0 \quad (14)$$

For $\xi > 0$, the solution will be stable against synchronous perturbations. For $\xi < 0$, it will be unstable. The stability function ξ can be easily evaluated with the aid of the same auxiliary generator that is used for the oscillator synthesis [32], the one satisfying $Y_{AG}(V_0, \omega_0) = 0$. The derivative calculation is carried out through increments in the two

variables V_{AG} and ω_{AG} , and the resulting values are introduced in (14). The stability condition can also be evaluated in a graphical manner. Defining the two vectors $\vec{Y}_v = [(\partial G_T/\partial V), (\partial B_T/\partial V)]_0$ and $\vec{Y}_\omega = [(\partial G_T/\partial \omega), (\partial B_T/\partial \omega)]_0$, the condition $\xi > 0$ is fulfilled for an angle $\vec{Y}_v \wedge \vec{Y}_\omega$ between 0 and 180°. In Fig. 19a, this condition is graphically verified for the MESFET oscillator circuit of Fig. 16a.

For the stability analysis when $\omega \neq \omega_0 + \delta\omega$, a small-amplitude perturbation of complex frequency $\sigma + j\omega$ should be considered, linearizing the HB equations about the steady-state periodic solution [4]. As already said, the free-running oscillator has a pair of complex conjugate poles, at the oscillation frequency $\pm\omega_0$. For stability, all the remaining

poles must have a negative real part. This may be verified by means of the Nyquist plot, tracing $\text{Im}[\det(\omega)]$ versus $\text{Re}[\det(\omega)]$, where $\det(\omega)$ is the determinant of the perturbed HB system. Since the oscillator system contains two poles at $\pm\omega_0$, the Nyquist plot of a stable oscillator solution must pass through the origin, without encircling it. This can be appreciated in the plot of Fig. 19b, showing the stability of the oscillator design of Fig. 16a.

The stability analysis of nonlinear regimes is seldom available in commercial HB. However, the user can perform this analysis externally, using auxiliary generators. For this purpose, a current generator of small amplitude I_p is introduced in parallel at a sensitive circuit node. The

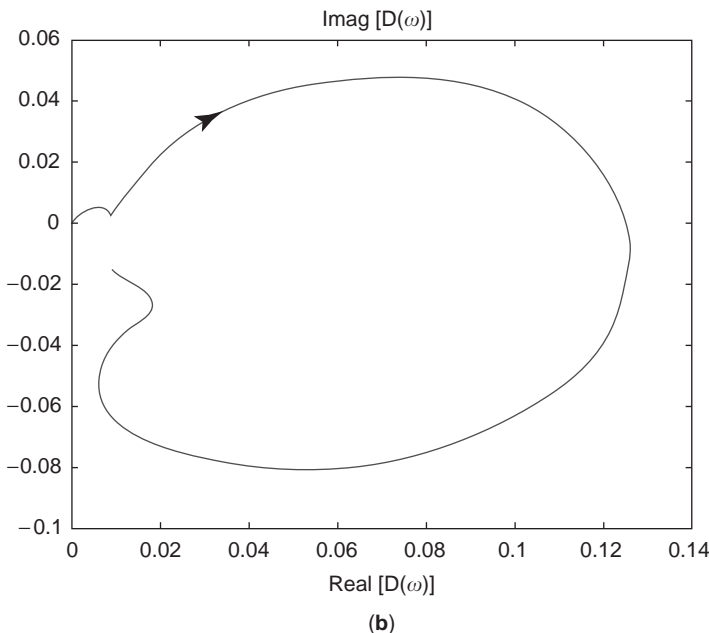
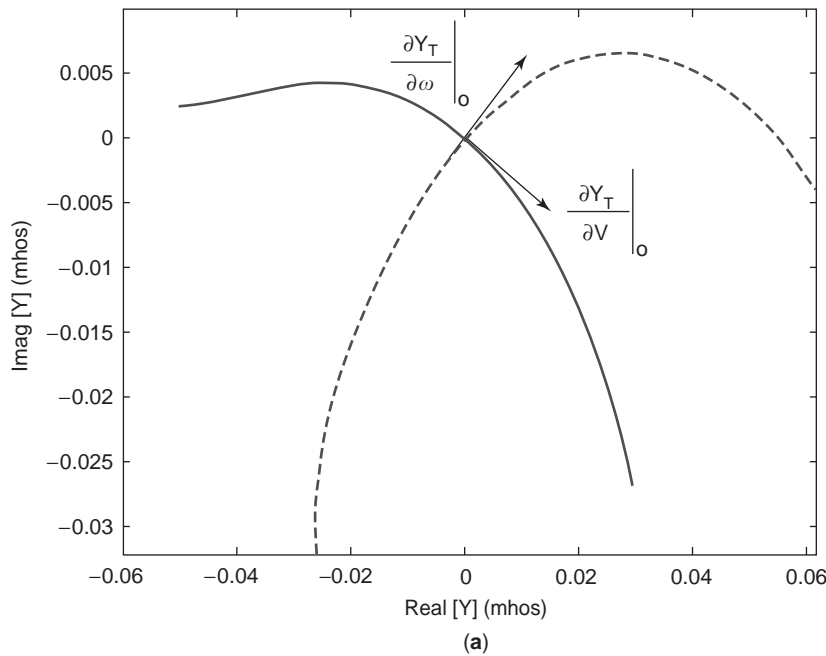


Figure 19. Stability analysis of steady-state oscillation: (a) verification of the fulfillment of stability condition versus synchronous perturbations; (b) full stability analysis per the Nyquist stability criterion.

nonperturbing AG, used for the determination of the steady-state solution, is also maintained in the circuit, at the steady-state oscillation values $V_{AG} \equiv V_0$ and $\omega_{AG} \equiv \omega_0$. The frequency of the additional current generator is ω_p , nonharmonically related to ω_0 . This generator plays the role of a small perturbation and will enable the linearization of the circuit about its nonlinear steady-state regime. A two-tone HB analysis is carried out, at the frequencies ω_0 and ω_p , although only first-order terms are kept in ω_p , due to the smallness of the perturbation [34].

By calculating the relationship between the current delivered by the generator (and entering the circuit) and V_p , through two-tone HB, the circuit total admittance at the frequency ω_p is determined, performing $Y(\omega_p) = I_p/V_p$ [34]. Through a sweep in the perturbation frequency ω_p , the possible fulfillment of the instability condition $Re Y(\omega_p) < 0, Im Y(\omega_p) = 0$ can be checked. The fulfillment of this condition for a given ω_p would give rise to the establishment of a steady-state regime at the two frequencies: ω_0 and $\omega_a \cong \omega_p$.

Note that the technique described above generalizes the impedance/admittance analysis, used in (12) for the evaluation of the oscillation startup conditions, from a DC solution, to the case of a circuit operating in a large-signal periodic regime. This analysis may fail in the case of a reduced sensitivity at the auxiliary generator location or pole-zero cancellations. For a more rigorous analysis, pole-zero identification techniques [34] should be applied to the closed-loop transfer function $Y(\omega_p) = I_p/V_p$.

3.6. Phase Noise

Noise perturbations, originating at the circuit resistive elements and semiconductor devices, give rise to amplitude and phase noise in the oscillator signal. Due to the autonomy of the solution, the latter will have the biggest influence on the oscillator spectrum. The oscillation frequency depends on the values of the circuit elements and is modulated by the noise sources, which gives rise to phase noise [11,23]. In addition, the oscillator nonlinearity is responsible for the conversion to the carrier frequency of the noise perturbations about DC and the different harmonic components.

The oscillator phase noise is thus the result of two different phenomena: carrier frequency modulation, which is the dominant effect for small frequency offset from the carrier; and frequency conversion, as in a mixer, which is the dominant effect for relatively high offset. Thermal noise sources, in the resistive elements, and shot and flicker noise, in the transistor devices, should be considered [3]. The spectral density of flicker noise varies as $1/\Omega$. Because of its high amplitude for small Ω , it will have great influence on the oscillator spectrum.

Using the describing function, an approximate expression of carrier modulation noise can be derived. As usual, the oscillator is represented by the parallel connection of a linear block and a nonlinear block, with the latter modeled by its describing function. For simplicity, only white-noise sources about the oscillation frequency ω_0 will be considered. The oscillator solution is assumed $v(t) = V_0 \cos(\omega_0 t)$, and the steady-state equation of the noise-free oscillator is

$Y_T(V, \omega) = G_T + jB_T = 0$. Now, a current white-noise noise source will be introduced in parallel with the linear and nonlinear blocks. Assuming small-frequency perturbations, the steady-state oscillator equation may be expanded in a Fourier series about the steady-state oscillation solution, which provides the system

$$\begin{aligned} \frac{\partial G_T}{\partial V} \Big|_0 \Delta V(t) + \frac{\partial G_T}{\partial \omega} \Big|_0 \Delta \omega(t) &= \frac{I_{nr}(t)}{V_0} \\ \frac{\partial B_T}{\partial V} \Big|_0 \Delta V(t) + \frac{\partial B_T}{\partial \omega} \Big|_0 \Delta \omega(t) &= \frac{I_{ni}(t)}{V_0} \end{aligned} \tag{15}$$

where $I_{nr}(t)$ and $I_{ni}(t)$ respectively represent the real and imaginary parts of the white-noise current, averaged over one period [11]. The time derivative of the amplitude increment is ignored in (15). As can be appreciated, the oscillator carrier becomes modulated by the noise sources.

To determine the oscillator phase noise, the previous linear system is solved for $\Delta \omega(t)$. Then the Fourier transform is calculated, also taking into account $\Delta \phi(\Omega) = \Delta \omega(\Omega)/(j\Omega)$. This provides the equation

$$\Delta \phi(\Omega) = \frac{G_v B_n(\Omega) - B_v G_n(\Omega)}{j\Omega(G_v B_\omega - G_\omega B_v)} \tag{16}$$

where $Y_v \equiv (\partial Y_T/\partial V)|_0$ and $Y_\omega \equiv (\partial Y_T/\partial \omega)|_0$, and G and B respectively stand for the real and imaginary parts of these quantities. Note that these derivatives are calculated at the steady-state unperturbed oscillation and agree with those already used in (14) to evaluate the oscillator stability. For calculation of the phase noise spectral density, multiplication of (16) by $\Delta \phi^*(\Omega)$ is necessary. The following expression is obtained:

$$|\Delta \phi(\Omega)|^2 = \frac{|I_n|^2(G_v^2 + B_v^2)}{\Omega^2 V_0^2 (G_v B_\omega - G_\omega B_v)^2} \tag{17}$$

where equal phase noise spectral density has been assumed at both sidebands. Note that the validity of (17) is restricted to small-frequency offset from the oscillator carrier. In agreement with the predictions by Leeson's model [3], white noise contributes as $1/\Omega^2$. On the other hand, an essential contribution to the denominator of (17) is the derivative B_ω . This derivative increases with the load quality factor Q , so, for larger Q , smaller phase noise should be obtained.

The reader can easily verify that the carrier modulation by the $1/\Omega$ noise is due essentially to the derivatives $\partial G_T/\partial V_{dc}$ and $\partial B_T/\partial V_{dc}$ and, contributes as $1/\Omega^3$. To obtain this result, the steady-state solution $v(t) = V_{DC} + V_0 \cos(\omega_0 t)$ must be assumed, formulating the steady-state equations at DC and the first harmonic component.

The HB analysis of the carrier modulation noise requires a mixed-mode formulation. In this formulation, the oscillation frequency ω_0 is added to the set of unknowns, which now becomes \vec{V} , ω_0 [23]. To balance the equations, and due to the oscillator autonomy, the real or imaginary part of one of the components of \vec{V} is arbitrarily set to zero.

In the presence of noise perturbations, the system becomes

$$\begin{bmatrix} \frac{\partial \bar{\mathbf{E}}}{\partial \bar{\mathbf{V}}} \end{bmatrix}_0 \Delta \bar{\mathbf{V}}(\Omega) + \begin{bmatrix} \frac{\partial \bar{\mathbf{E}}}{\partial \omega} \end{bmatrix}_0 \Delta \omega_0(\Omega) = \bar{\mathbf{I}}_n(\Omega) \quad (18)$$

where $\bar{\mathbf{E}}(\bar{\mathbf{V}}, \omega)$ is the vector of HB errors and $\bar{\mathbf{I}}_n(\Omega)$ is the vector containing the frequency descriptions of the noise currents. The calculation of the phase noise spectral density requires solving for $\Delta \omega_0(\Omega)$ and multiplying by the adjoint $\Delta \omega_0^*(\Omega)$, to be able to introduce the spectral densities and correlations of the noise sources $\bar{\mathbf{I}}_n(\Omega) \cdot \bar{\mathbf{I}}_n^*(\Omega)$. To obtain the phase noise, the relationship $\Delta \phi(\Omega) = \Delta \omega_0(\Omega) / (j\Omega)$ must also be taken into account. It must be emphasized that this phase noise calculation is valid only for small frequency offset Ω from the carrier. For larger frequency offset, the conversion matrix approach should be applied [24].

For the phase noise analysis of the VCO, a flicker noise source has been considered, in parallel with the gate terminal. In Fig. 20a, the function $B_T(\omega)$, at the same location, is represented for three different values of the varactor bias voltage: $V_b = 0, 4, 8$ V. In each case, the zero value of the frequency increment corresponds to the steady-state oscillation. The highest slope, indicating the largest quality factor, is obtained for $V_b = 4$ V, in the middle of the oscillation band. Figure 20b shows the phase noise spectral density, calculated through the carrier modulation approach. As can be seen, the lowest phase noise is obtained for $V_b = 4$ V. The experimental phase noise values were -86 dBc, at 100 kHz frequency offset, for $V_b = 4$ V and -79 dBc, at the same offset, for $V_b = 0$ V.

4. FREQUENCY DIVIDERS

4.1. General Concepts about Frequency Dividers

The output signal of a frequency divider [37] satisfies the relationship $\omega_{\text{out}} = \omega_{\text{in}}/N$, where ω_{in} is the input generator frequency. The frequency dividers are used mostly in the feedback loops of frequency synthesizers, to obtain a signal in the order of the reference frequency, whose phase will be comparable with that of the reference oscillator. A high-frequency signal can also be divided to be easily amplified and then multiplied again, to the original frequency range. Another possible application is the demodulation of FM signals with high modulation index and the demodulation of the PSK signals.

There are digital and analog dividers. The digital dividers, also called “static”, are based on logic circuits operating as cycle counters [37]. They perform the frequency-division cycle by cycle and enable broad division band. The basic divide-by-2 configuration uses a flip-flop, with feedback, to produce one output cycle for every two cycles of the input signal. The ripple counters, based on a chain connection of flip-flops, register the number of applied pulses in a binary form, which allows frequency division by the order $N = 2^n$, where n is the number of stages. The implementation of the logic gates requires a high number of transistors. Thus, the static dividers

typically contain many transistor devices. In contrast, the analog frequency dividers, also called “dynamic” [7], can be achieved with very small number of devices. They make use of phenomena inherent to the nonlinear dynamics of injected oscillators, nonlinear reactances or regenerative feedback configurations. The small number of devices enables lower phase noise than the static dividers. The disadvantage, compared to these dividers, is the narrow frequency bandwidth.

The three main types of analog dividers are parametric dividers, regenerative dividers and harmonic injection dividers. Their principles are briefly introduced in the following paragraphs.

4.1.1. Parametric Dividers. Parametric dividers make use of the capabilities of a nonlinear reactance to exhibit negative resistance under strong pumping from a periodic external source at a given frequency ω_{in} [38]. The negative resistance usually appears about $\omega_{\text{in}}/2$, which, together with a resonance at this frequency, gives rise to the establishment of a divide-by-2 solution. Actually, one of the main types of instability of a nonlinear periodic regime is the division by 2 of the fundamental frequency. A typical example of parametric division is the frequency division by 2 obtained through the pumping of a N varactor diode, with very nonlinear capacitance about $V = 0$ [38].

4.1.2. Regenerative Dividers. The operation of regenerative dividers can be represented with the feedback system of Fig. 21 [39], where a relatively high input generator amplitude E_{in} gives rise to a nonlinear steady-state regime at the delivered frequency ω_{in} . From certain input amplitude $E_{\text{in}0}$, the system instability at $\omega_0 \cong \omega_{\text{in}}/N$, plus the harmonic synchronization $N\omega_0 = \omega_{\text{in}}$, enable the frequency division by order N . This instability is favored by the feedback at $(N-1)\omega_0$ and the mixer action, which gives rise to a difference frequency term at ω_0 .

4.1.3. Harmonic Injection Dividers. The harmonic injection divider by N is basically an oscillator, whose N th-order harmonic $N\omega_0$ synchronizes with an external source [8]. In contrast with the parametric and regenerative dividers, harmonic injection dividers exhibit a self-oscillation in the absence of input signal. Since an oscillation signal with frequency in the order of the desired output frequency is already available, they enable frequency division from very low input power.

As can be gathered from the paragraphs above, the analog frequency dividers have an inherently autonomous nature, which makes them their synthesis difficult. Here nonlinear design techniques for analog dividers, based on the use of transistor devices, will be presented. Two main types of dividers will be studied: the regenerative divider and the harmonic injection divider.

4.2. Design of FET-Based Regenerative Frequency Dividers

Let the regenerative divider of Fig. 21 be considered. The instability conditions of the regime at ω_{in} , giving rise to the onset of $\omega_0 \cong \omega_{\text{in}}/N$, will be $|H(E_{\text{in}}, \omega_0)| > 1$ and $\angle H(E_{\text{in}}, \omega_0) = 2k\pi$, where H is the closed-loop transfer

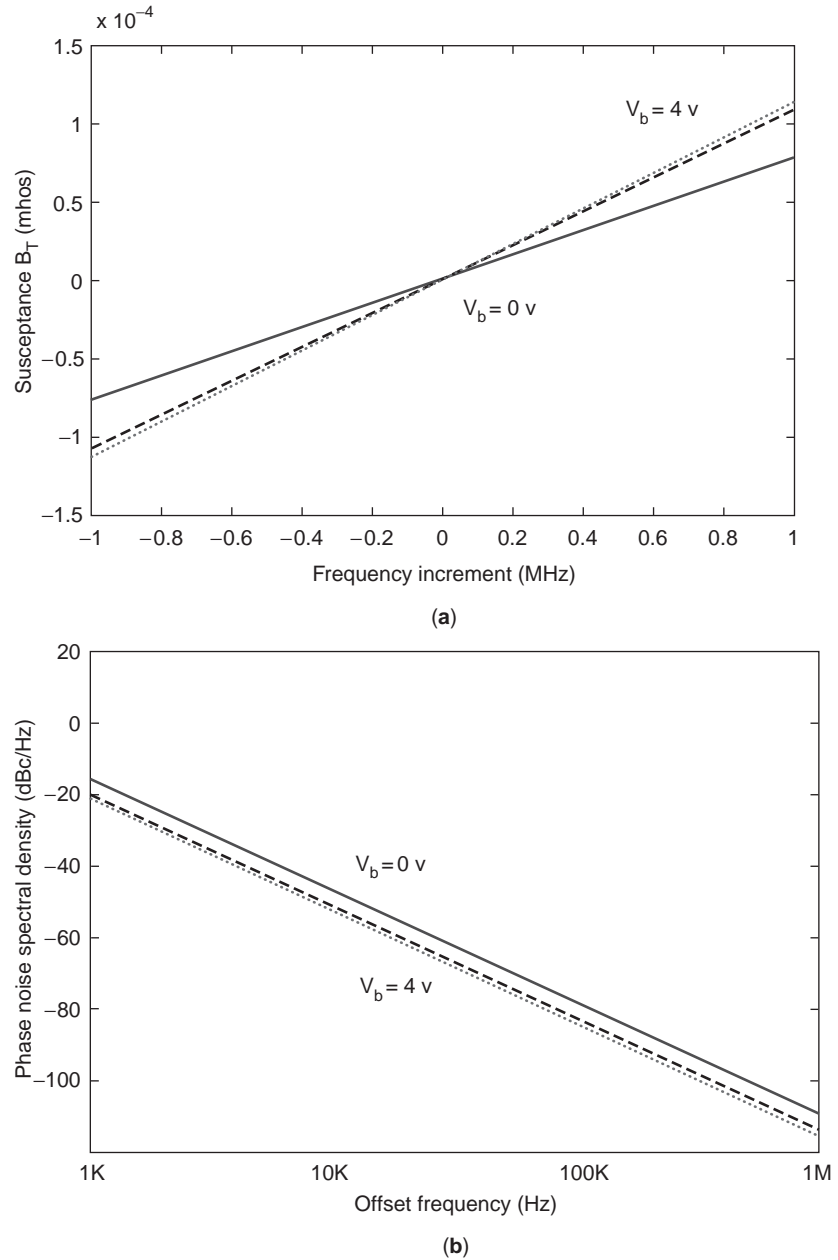


Figure 20. Phase noise analysis of the VCO: (a) variation of $B_T(\omega)$ about the oscillation frequency for three different values of the varactor bias, $V_b = 0$ V, 4 V, and 8 V; (b) analysis of phase noise spectral density with the carrier modulation approach.

function. These instability conditions will be fulfilled from a certain input amplitude E_{in0} . As appreciated in Fig. 21, the key elements for the onset of ω_0 are the feedback at

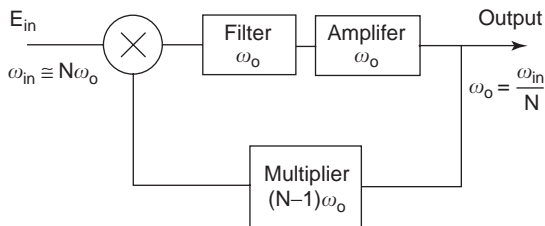


Figure 21. Operation principle of a regenerative frequency divider.

$(N - 1)\omega_0$ and the mixing of this frequency with the generator frequency at ω_{in} .

When using a FET transistor for the divider design, this device will perform both the mixing and amplification functions [7,40]. The transistor should be biased near pinchoff, where advantage can be taken of the quasiquadratic $I_{DS}(V_{GS})$ characteristic to efficiently perform the mixing function. As gathered from Fig. 21, the regenerative division by order 2 requires no frequency multiplier in the feedback loop and thus is easier to implement.

Figure 22 shows a general schematic of a FET-based frequency divider by 2, with series feedback. The input filter ensures the matching of the generator frequency ω_{in} . The transistor feedback $\omega_{in}/2$ enables the self-generation of this component. Finally, the output filter ensures the

matching to the load of this divided frequency. A divider configuration using parallel feedback is also possible [4]. Note that if a frequency divider by N is desired, the passive feedback network must be replaced by a multiplier by $N - 1$. As will be shown in Section 5, this multiplier can be implemented by means of a second transistor at a suitable bias point, together with a bandpass filter, for the selection of the harmonic component $(N - 1)\omega_{in}/2$.

Unlike the harmonic injection dividers, to be shown later, the regenerative divider does not oscillate in the absence of input generator signal. The quenching of the free-running oscillation may be achieved by reducing either the feedback amount or the transistor gain at $\omega_{in}/2$ [40]. It is generally more practical to limit the gain through a suitable selection of the transistor gate bias voltage. Let V_{GS0} be the threshold V_{GS} value, below which no oscillation is observed. The transistor must be biased with $V_{GS} < V_{GS0}$. Then, for relatively small input generator amplitude, the transistor gain is not sufficient to satisfy the instability conditions at $\omega_{in}/2$. As the input generator amplitude E_{in} increases, a larger fraction of the solution period satisfies $v_{GS}(t) > V_{GS0}$. Then, a threshold value E_{in0} may be reached, such that, for $E_{in} > E_{in0}$ the transistor gain at $\omega_{in}/2$ is large enough to fulfill the instability conditions $|H(E_{in}, \omega_{in}/N)| > 1$ and $\angle H(E_{in}, \omega_{in}/N) = 2k\pi$.

The instability condition for $E_{in} > E_{in0}$ may also be written in terms of the total admittance Y_T , at a sensitive circuit node (see Section 3). Note that it is the same function that had already been used for oscillator analysis and design. The regenerative divider will satisfy the following conditions:

$$\left. \begin{aligned} G_T(E_{in}, \frac{\omega_{in}}{2}) > 0 \\ B_T(E_{in}, \frac{\omega_{in}}{2}) = 0 \end{aligned} \right\} \text{for } E_{in} < E_{in0} \quad (19)$$

$$\left. \begin{aligned} G_T(E_{in}, \frac{\omega_{in}}{2}) < 0 \\ B_T(E_{in}, \frac{\omega_{in}}{2}) = 0 \end{aligned} \right\} \text{for } E_{in} > E_{in0}$$

Note that the resonance condition is easily satisfied, since the output filter and feedback networks are centered at this frequency.

The auxiliary generator technique, presented in Section 3, can be used for the evaluation of the conditions in (19). A voltage auxiliary generator, of small amplitude $V_{AG} = \varepsilon$ and frequency $\omega_{AG} = \omega_{in}/2$, is connected in parallel at a circuit node, while maintaining the input generator at the values E_{in}, ω_{in} . Then, the ratio between the current flowing through the AG (and entering the circuit) and the delivered voltage $Y_{AG} = I_{AG}/V_{AG}$ will agree with $Y_T = G_T + jB_T$. In contrast with the oscillator analysis, the AG phase ϕ_{AG} will now be a sensitive variable [4,41]. As shown in Ref. 42, the input amplitude threshold for the onset of the frequency division by 2 can be obtained through a double sweep in E_{in} and ϕ_{AG} , with the latter ranging between 0 and 180° .

Some efforts have been devoted to increasing the frequency bandwidth of the regenerative dividers. As an example, in Refs. 7 and 41, the input filter at ω_{in} is replaced by an amplifier at the same frequency, with broader bandwidth than the one expected for the frequency divider. The circuit elements are also tuned in a small-signal analysis, in order to decrease the frequency selectivity of the circuit, through a reduction of the positive slope $(\partial B_T/\partial \omega)|_{\omega_{in0}/2}$, where ω_{in0} is the central value of the input frequency band.

The HB simulation of frequency dividers is presented in detail in the NONLINEAR CIRCUIT ANALYSIS article, so only the essential aspects will be pointed out here. The major difficulty in this simulation comes from the coexistence of the frequency-divider solution at $\omega_{in}/2$, with a trivial solution, at the input generator frequency ω_{in} . The same auxiliary generator, used for the evaluation of (18), can be used to avoid undesired convergence to the solution at ω_{in} . The nonperturbation conditions will be as follows [4]:

$$\begin{aligned} Y_{AG}^r(V_{AG}, \phi_{AG}) &= 0 \\ Y_{AG}^i(V_{AG}, \phi_{AG}) &= 0 \end{aligned} \quad (20)$$

with $\omega_{AG} = \omega_{in}/2$. To obtain the frequency-division band versus the input generator frequency ω_{in} for given input power P_{in} , a sweep will be carried out in ω_{in} , calculating, at each sweep step, the auxiliary generator amplitude and phase V_{AG}, ϕ_{AG} .

As in the case of oscillator circuits, the AG technique can also be applied for the design of the frequency dividers. It will be possible to prefix the AG amplitude $V_{AG} \equiv V_{AG0}$ and input generator value E_{in}, ω_{in} and calculate and/or optimize two circuit parameters η_1, η_2 , together with ϕ_{AG} , in order to fulfill $Y_{AG} = 0$.

The auxiliary generator technique has been applied for a design of a frequency divider by 2, with 6 GHz input frequency. The MESFET transistor is biased with $V_{DS} = 3$ V and $V_{GS} = -1.5$ V, near pinchoff. In agreement with the block diagram in Fig. 22, the three main linear components of this divider circuit are an input filter at ω_{in} , an output filter at $\omega_{in}/2$, and a series feedback network at $\omega_{in}/2$. The simulation, for constant input power $P_{in} = 3.5$ dBm, is shown in Fig. 23a. The curve has been traced in terms of the average harmonic value. The undesired solution at ω_{in} can be observed. This solution is unstable between the two frequency values F_1 and F_2 and is stable outside this frequency interval. Figure 23b shows a comparison between simulated and experimental results, in terms of the output power.

4.3. Design of FET-Based Harmonic Injection Dividers

As already mentioned, the harmonic injection divider is basically an oscillator with one of its harmonic components synchronized with the input signal [4,8]. In contrast to the regenerative dividers, the circuit oscillates in the absence of input power. Using the block diagram of the regenerative divider (Fig. 21), a harmonic injection divider can also be obtained, if the system exhibits an oscillation at about ω_{in}/N , in the absence of input signal. In this case,

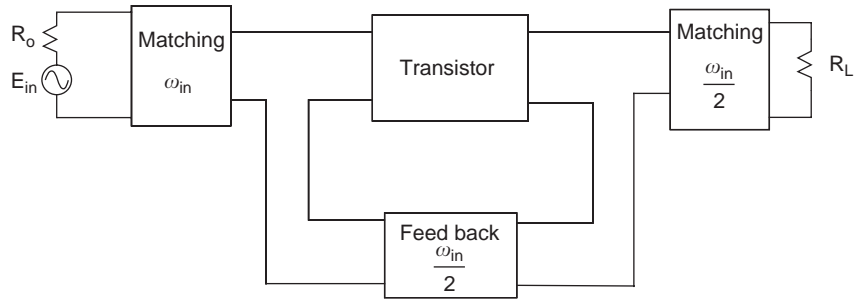
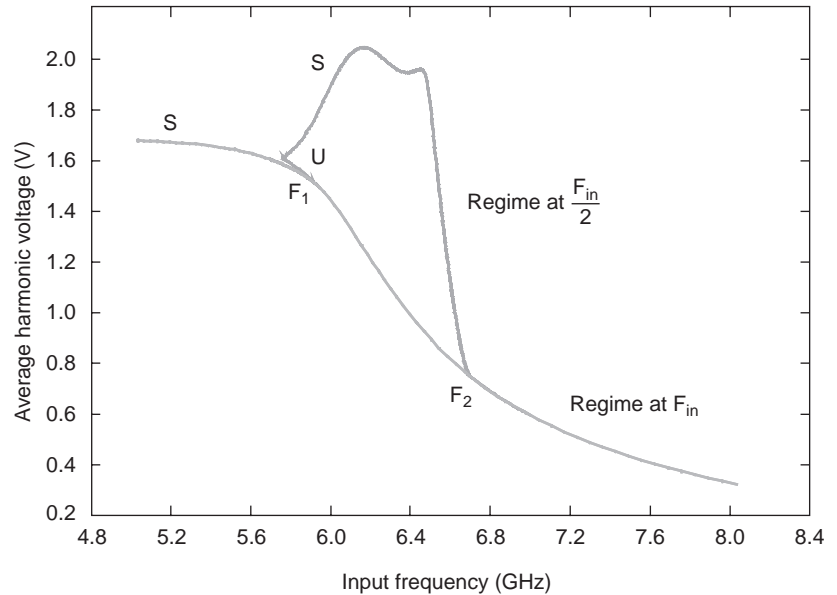


Figure 22. Block diagram of a FET-based analog frequency divider by 2.

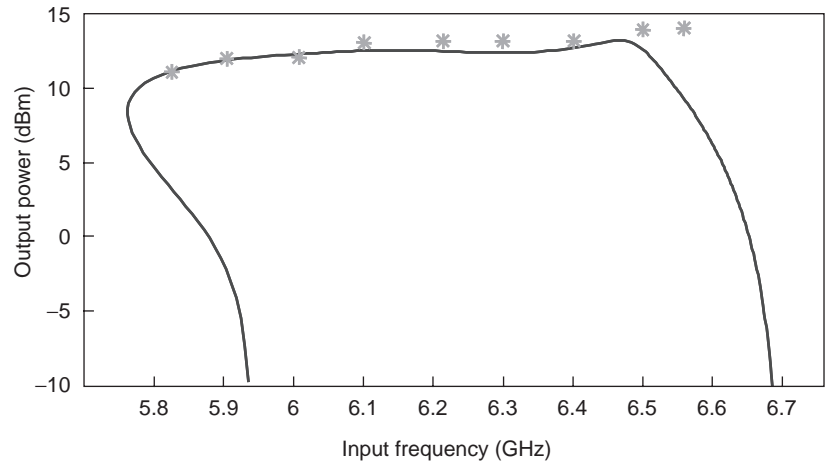
the division can be achieved from very low input power, through the synchronization of the N th-harmonic component of the self-oscillation with the input source. However, harmonic injection division can be obtained from much simpler topologies than the one in Fig. 21. Actually, any oscillator circuit can be used for this kind of division, since the harmonic synchronization is a natural nonlinear phenomenon occurring in all oscillatory systems excited by a

periodic external source. The problem is that, unless a careful design is carried out, the synchronization bandwidth may be extremely narrow. The bandwidth also decreases with the division order N .

The frequency-division band of a harmonic injection divider can be approximately predicted by means of the describing function. Prior to the connection of the input generator, at the harmonic frequency, the circuit



(a)



(b)

Figure 23. Analysis of a frequency divider by 2, with 6 GHz input frequency: (a) coexistence of divider solution with a nondivided solution at input generator frequency; (b) output power variation in frequency-division band, with measurements superimposed.

is assumed to behave as a free-running oscillator, fulfilling the steady-state oscillation condition, $Y_T = Y_N(V_0, \omega_0) + Y_L(\omega_0) = 0$, where Y_N is the describing function. Under the influence of the harmonic generator $i_g(t)$, the oscillation amplitude will become V_s and the oscillation frequency will be ω_s , satisfying the relationship $\omega_{in} = N\omega_s$, where ω_{in} is the input generator frequency. For the determination of the frequency-division band, the input current generator will be expressed as $i_g(t) = \text{Re}(I_g e^{j(\omega_{in} + \phi)t})$, where ϕ is the opposite of the phase shift between node voltage at ω_s and the input generator. The equation for the harmonic injection divider will be [8]:

$$Y_T(V_s, \omega_s, I_g e^{j\phi}) V_s e^{j0} = 0 \quad (21)$$

For small input amplitude I_g , a Taylor series expansion about the free-running oscillation point ($V_0, \omega_0, I_g = 0$) can be carried out

$$\begin{aligned} & \frac{\partial Y_T}{\partial V_0} \Delta V_s + \frac{\partial Y_T}{\partial \omega_0} \Delta \omega_s \\ & = - \left. \frac{\partial Y_T}{\partial I_g} \right|_0 I_g \cos \phi - \left. \frac{\partial Y_T}{\partial I_g} \right|_0 I_g \sin \phi \end{aligned} \quad (22)$$

with $\Delta \omega_s = \omega_s - \omega_0$ and $\Delta V_s = V_s - V_0$. The solution of (22) is an ellipse in the plane defined by ω_s and V_s , centered about the free-running oscillation point ω_0, V_0 . The infinite-slope points of the synchronization ellipse determine the frequency-division bandwidth [4,8]. This bandwidth is given by twice the maximum value of the increment $\Delta \omega_s$ versus the phase shift ϕ , in (22). Assuming a simplified dependence $Y_T = Y_r(V) + Y_i(\omega)$, the division bandwidth by order N can be approached: $\Delta \omega_N = I_g |\partial Y_i / \partial I_g|_0 \omega_0 / (Q G_L)$, where Q is the quality factor and G_L is the load resistance.

As in the case of regenerative dividers, the HB analysis of harmonic injection dividers by order N is carried out by means of an auxiliary generator at $\omega_{AG} \equiv \omega_{in}/N$, with phase ϕ_{AG} and amplitude V_{AG} [4,8]. If variation of a parameter is considered (e.g., the input frequency ω_{in}), the solution

curves are obtained by sweeping ϕ_{AG} , between 0 and $2\pi/N$, and calculating V_{AG} and the particular parameter at each sweep step, in order to fulfill $Y_{AG} = 0$.

Figure 24 shows the schematic of a harmonic injection divider by $N=4$, with 18 GHz input frequency. Source feedback (with the inclusion of a varactor diode) is used to achieve the free-running oscillation. A bias point V_{GS1}, V_{DS1} is initially selected, fitting the gate circuit so as to obtain negative resistance at the drain terminal about the required oscillation frequency $f_0 = 4.5$ GHz. To complete the oscillator design, a load circuit, enabling resonance at f_0 , is introduced at the drain port.

For the divider design, an auxiliary generator is introduced at the desired oscillation frequency and amplitude $\omega_{AG} \equiv \omega_0$ and $V_{AG} \equiv V_0$. Then, the load circuit is optimized so as to fulfill the nonperturbation condition $Y_{AG} = 0$. The bias point is also tuned, in order to increase the gate voltage magnitude at the harmonic component $(N-1)\omega_0$, which, for the divider by $N=4$, corresponds to $3\omega_0$. The closed synchronization curves obtained when the input-generator is connected are shown in Fig. 25a, where different values of input generator power have been considered. Experimental points are shown in Fig. 25b.

As already mentioned, harmonic injection dividers usually exhibit narrow synchronization bandwidth. In a 1999 study [43], injection-locking, phase-locking techniques [8] have been applied to increase the operation bandwidth of harmonic injection dividers. The techniques rely on the use of a low-frequency feedback loop, which is added to the already designed harmonic injection divider (Fig. 24). The loop allows the use of the low-frequency intermodulation term $|f_{in} - Nf_0|$, provided by the $I_{DS}(V_{GS})$ nonlinearity, to increase the sensitivity to the input generator and thus enlarge the synchronization bands.

The intermodulation term $|f_{in} - Nf_0|$ gives rise to a low-frequency error voltage $v_D(t)$ at the transistor drain terminal. This signal is extracted through a choke (see Fig. 24) and amplified in the feedback loop. The differential amplifier compares the low-frequency signal extracted from the drain terminal with a DC reference voltage. The amplifier output is connected to the varactor diode, and

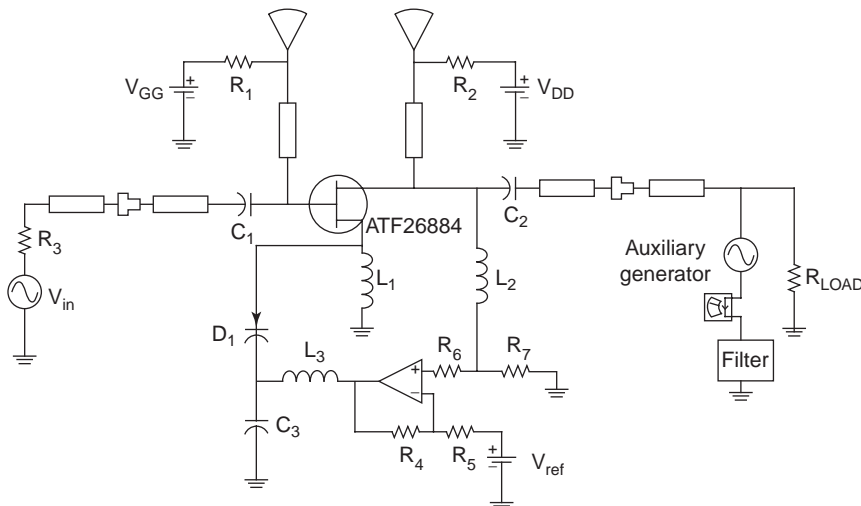


Figure 24. Harmonic injection divider by order $N=4$. The external low-frequency loop is introduced to increase the synchronization bandwidth through the combination of injection-locking and phase-locking effects [8,43].

this modifies the self-oscillation frequency so as to decrease the frequency error, as in a phase-locked oscillator. Thus, phase-locking techniques and harmonic injection are combined to increase the frequency-division bands. The enlargement of the synchronization bandwidth depends on the voltage gain G_a of the DC amplifier and the phase shift that this amplifier introduces in the low-frequency feedback signal [8,43].

In the case of the frequency divider studied here, the output of the feedback loop is connected to the cathode of the varactor diode. The application of the injection-locking, phase-locking technique enables, as shown in Fig. 25a, a substantial enlargement of the synchronization bandwidth. Measurements are shown in Fig. 25b.

5. FREQUENCY MULTIPLIERS

5.1. General Concepts about Frequency Multipliers

The signal generation is critical in communication systems, where high stability and low phase noise spectral density are required. At high frequencies, a common solution is the use of a low-noise source, at smaller frequency, and a frequency multiplier, to achieve the desired signal frequency ω_0 [10]. At the output, the phase noise spectral density roughly increases in $20 \log N$, where N is the multiplication factor, but, even so, the phase noise is generally lower than the one resulting from a direct oscillator design at ω_0 . More recent applications of multiplier circuits in communications systems include modulation

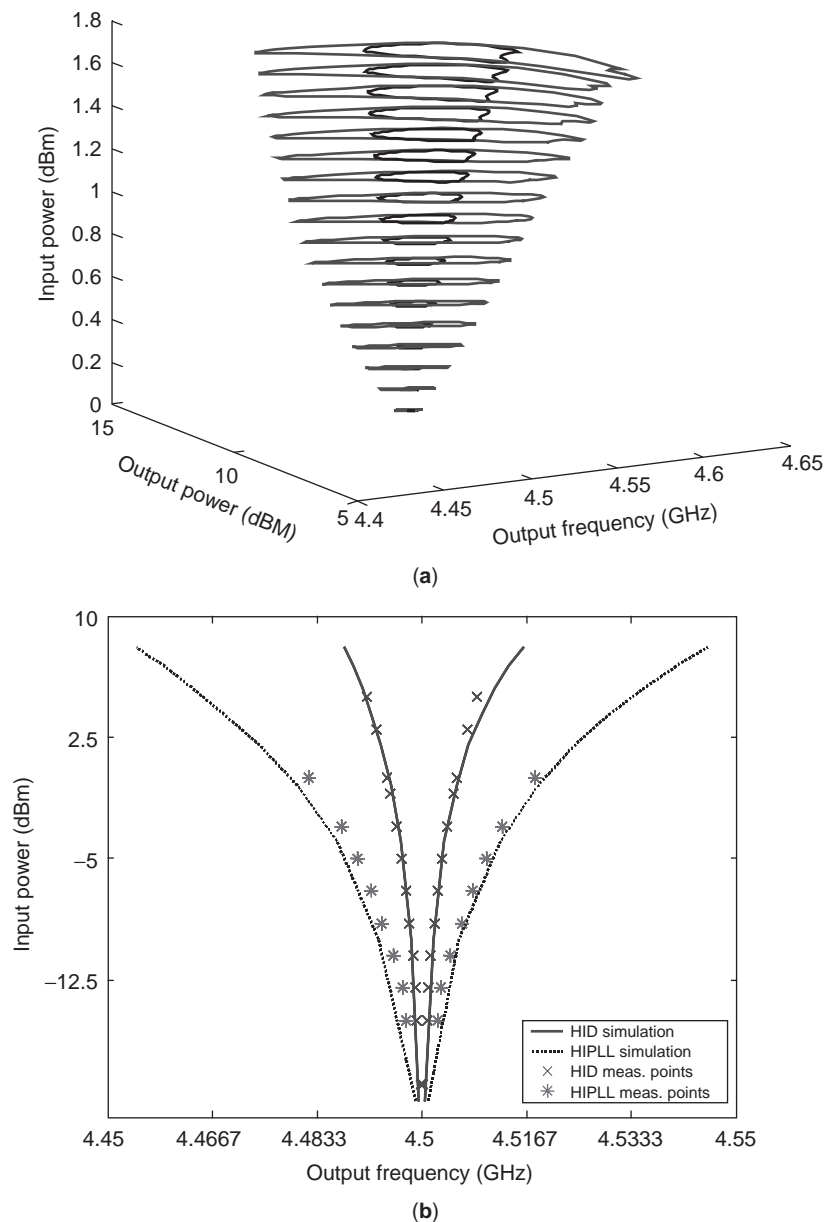


Figure 25. Response of the harmonic injection divider by $N=4$, with 18 GHz input frequency: (a) solution curves showing the frequency bandwidth for different values of the input generator power before and after the addition of the low-frequency feedback loop; (b) measurement of the synchronization bandwidth. (This figure is available in full color at <http://www.mrw.interscience.wiley.com/erfme>.)

and frequency translation. They can be used for direct modulation of FSK signals [44,45].

Frequency multipliers can be based on diodes or transistors. The diode multipliers enable a simple circuit design, with no need for biasing, and a broad operation band. Undesired harmonic components are suppressed through balanced configurations by phasing [9]. Unfortunately, conversion loss is high and thus frequency multipliers require high input power to achieve the necessary output power. The topologies employed may be difficult to integrate in the MMIC process. The transistor-based multipliers enable input-output isolation and are power-efficient. They are easily integrable in MMIC technology and can provide conversion gain [9,10]. By means of a single

FET, it is possible to obtain frequency multipliers up to order 5 or 6. Cascaded stages may be used for higher multiplication orders. In the following, a systematic design procedure for frequency multipliers is presented. The use of multiharmonic load pull for the optimization of the embedding linear networks is shown in Section 5.3.

5.2. FET-Based Multiplier Design

When using a FET transistor, the frequency multiplication by a factor N , is achieved by selecting a bias point, such that, under near-sinusoidal input voltage excitation at ω_0 , an output current is obtained, with high amplitude at the harmonic component $N\omega_0$. For optimal

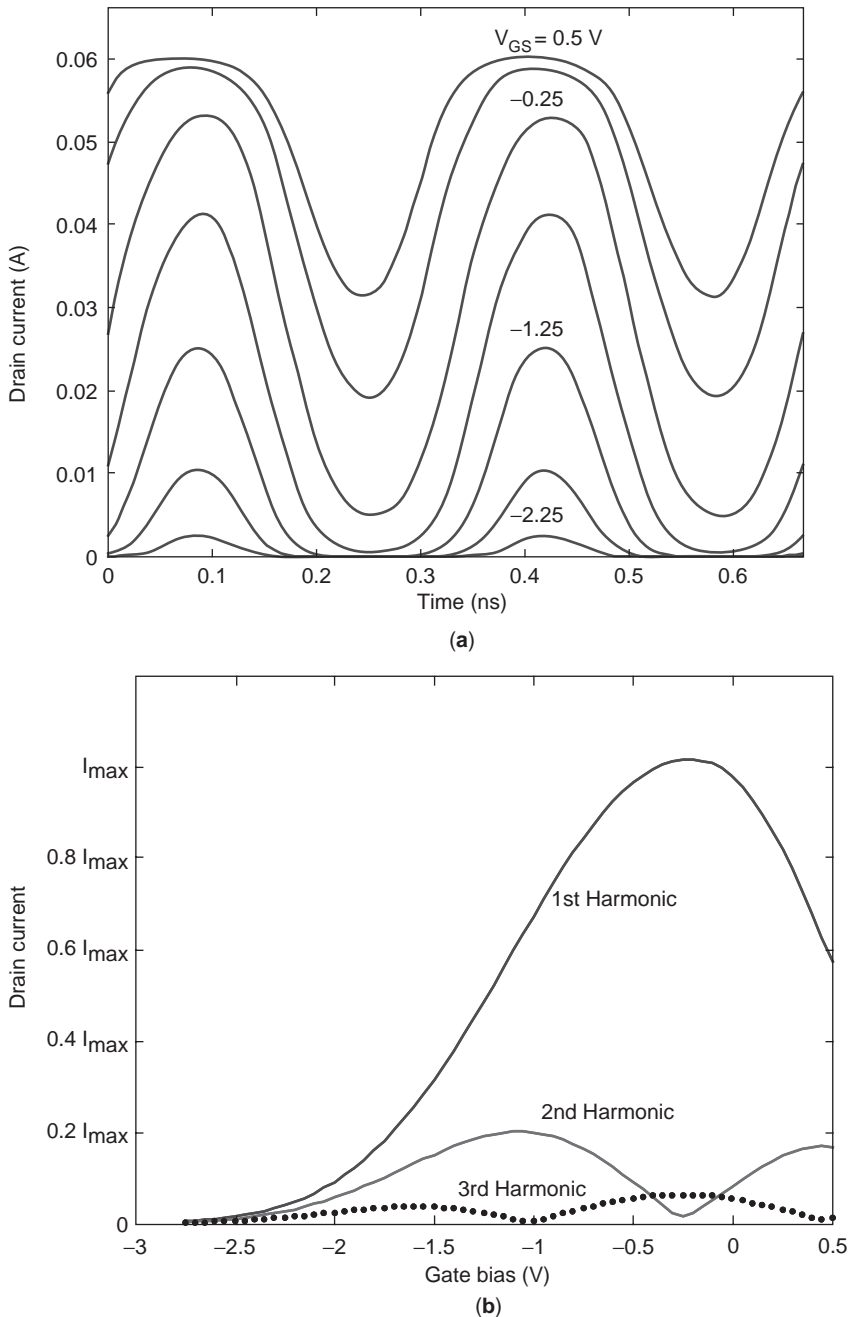


Figure 26. Selection of the gate bias voltage for the frequency multiplier: (a) drain current waveform for different gate bias values; (b) amplitude of the drain current harmonic components versus the gate bias voltage. (This figure is available in full color at <http://www.mrw.interscience.wiley.com/erfme>.)

performance, a transistor with a high maximum drain current value should be selected. The harmonic distortion is obtained by clipping the drain current waveform under relatively large input voltage excitation [9]. This can be done by biasing the transistor near forward conduction or by biasing the transistor near or below pinchoff. The latter choice is less hazardous for the transistor device. The transistor must be able to tolerate high reverse gate-to-drain voltage V_{GD} .

In Fig. 26a, a FET transistor, with $V_p = -1.5$ V, is considered. The figure shows the clipping of the $i_{ds}(t)$ waveform for different values of the gate bias and constant input power $P_{in} = 10$ dBm. For gate bias near forward conduction, the clipping takes place in the upper section of the $i_{ds}(t)$ waveform. Near or below pinchoff, the clipping takes place in the lower section. In the latter case, the conduction angle decreases for more negative gate bias and the peak value becomes smaller.

Let ω_0 be the multiplier input frequency. The conduction angle 2ϕ is defined as the fraction of 2π for which $\cos(\omega_0 t)$ is nonzero over one signal period $T = 2\pi/\omega_0$. In B class, $2\phi = \pi$; in C class, $2\phi < \pi$. However, very small conduction angles may be difficult to implement with FET devices. The amplitude of the different harmonic components of the drain current $I_{ds,n}$, where n is the harmonic order, depends on this conduction angle. For fixed drain bias voltage V_{DS} , this will depend on both the gate bias V_{GS} and the amplitude of the gate-to-source voltage waveform, which, in turn, depends on the input generator power and the input matching. Figure 26b shows the variation of the harmonic amplitude versus the gate bias. As an example, for the design of a frequency tripler $N=3$, the third-harmonic component must be maximized, which is done through the selection of the bias voltage $V_{GS} = -1.5$ V (see Fig. 26b).

Once the bias point and input amplitude are known, the input and output networks of the multiplier by N must be determined. In a simple design, the load impedance will consist of an output resistance, plus a parallel inductance L , calculated to resonate at $N\omega_0$ with the transistor output capacitance C_{ds} . The parallel resonant circuit $L-C_{ds}$ will act as a bandpass filter centred at $N\omega_0$. For a sufficiently

large quality factor, the harmonic components will be short-circuited [9]. The output resistance must provide sufficiently high output power at $N\omega_0$. On the other hand, the transistor input should also be matched to the input generator in order to maximize the conversion gain. However, an optimum design, exploiting all the capabilities of the transistor device, requires considering the influence of the device loads at the different harmonic frequencies. This can be done by means of the load-pull system, to be presented in the next section.

5.3. Harmonic Source/Load-Pull System

When using a HB simulator, a source/load-pull system may be implemented, in order to determine the optimum harmonic terminations. For the design of a multiplier by N , harmonic loads up to an order $n_{max} > N$ are considered at both the transistor input and output. Figure 27 shows the different harmonic blocks, each consisting of an ideal bandpass filter, centered at the particular harmonic component $n\omega_0$, plus a termination, given by a reflection coefficient of the form $\Gamma_n = \rho_n e^{j\theta_n}$, where $\rho_n \leq 1$, in order to ensure the load passivity. Initially, a perfect sinusoid at the input frequency ω_0 is imposed at the transistor gate, using short-circuit terminations in all the harmonic blocks, by making $\rho_n = 1, \theta_n = 180^\circ$, for $n > 1$. The first harmonic load is $Z_0 = 50 \Omega$, which is imposed, rendering $\Gamma_1 = 0$. In turn, a perfect sinusoid at the desired harmonic component $N\omega_0$ is imposed at the transistor output terminals, by making $\rho_n = 1, \theta_n = 180^\circ$, for $n \neq N$. Open-circuit terminations also reject undesired harmonic components, but they can give rise to high output voltages and thus to potential instability [6], so short circuits are preferred.

Using the harmonic terminations presented above, the harmonic load $\rho_{L,N}, \theta_{L,N}$ is optimized through a double sweep, keeping the values that maximize the output power at $N\omega_0$. This technique has been used here for the tripler design. The power variation is shown in Fig. 28a. The optimum values $\rho_{L,3}^o = 0.8, \theta_{L,3}^o = 120^\circ$ are kept for the following design stages. This reflection coefficient can be obtained through a resistance $R_3 = 111 \Omega$, in parallel with the inductance $L_3 = 1.608$ nH. The high resistance will

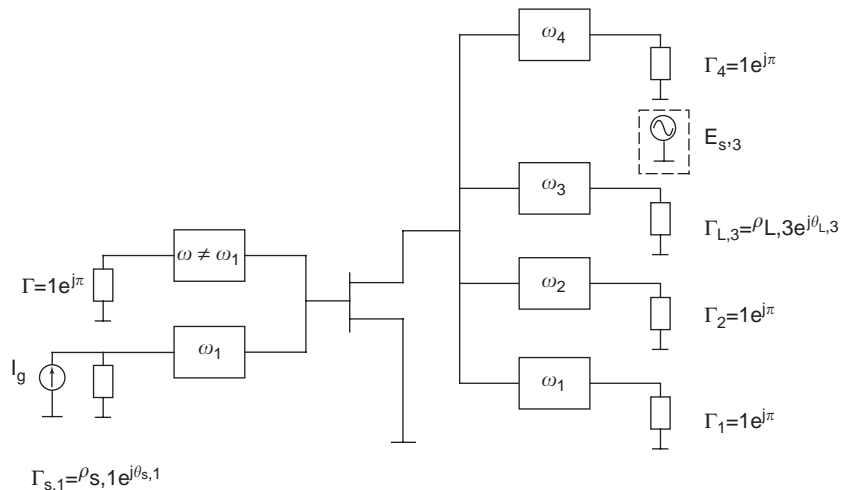


Figure 27. Harmonic load-pull system for the multiplier design. Instead of a reactive load Γ_3 , a substitution generator can also be used at this frequency component.

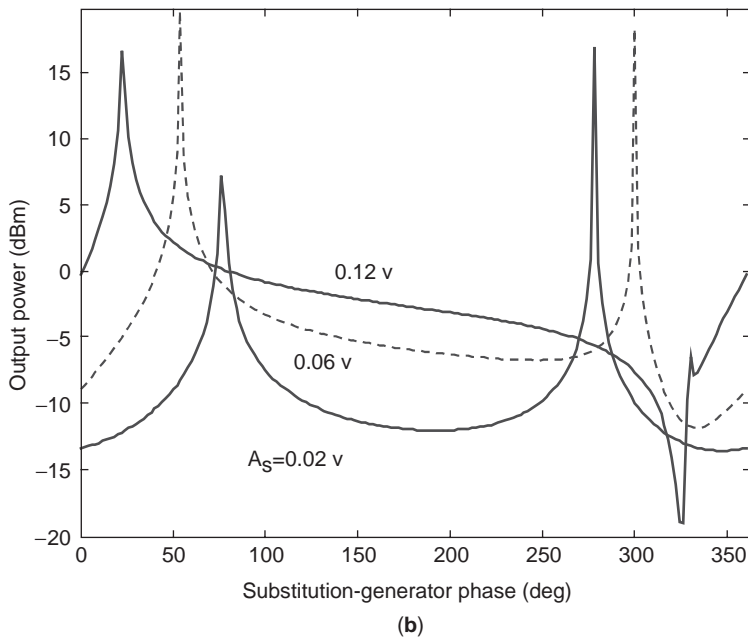
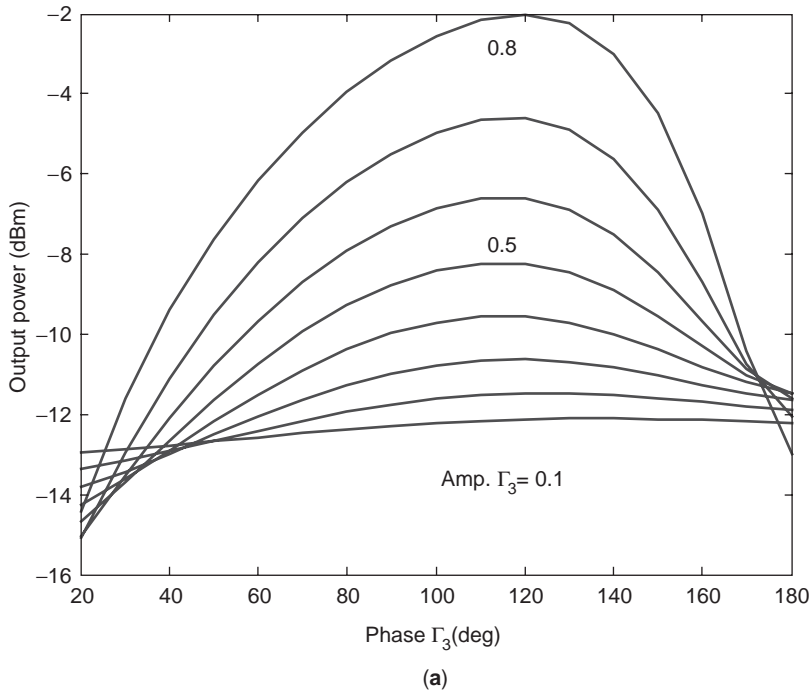


Figure 28. Selection of the optimum values of the third-harmonic load in terms of the amplitude and phase of the (a) reflection coefficient Γ_3 and (b) substitution generator. (This figure is available in full color at <http://www.mrw.interscience.wiley.com/erfme>.)

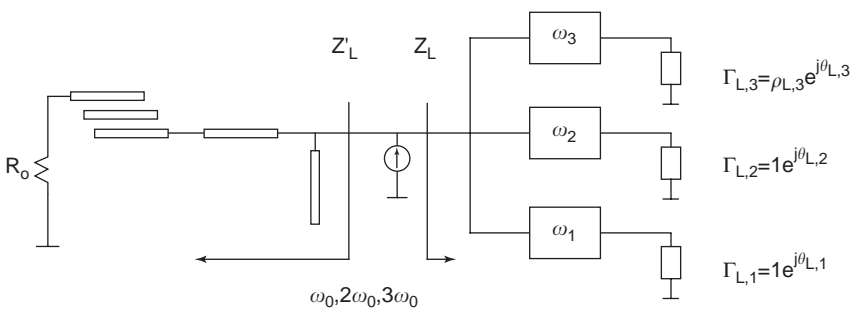


Figure 29. Arrangement for the distributed-line implementation of the multiharmonic load.

enable a large voltage swing at the third-harmonic component. The inductance enables the resonance with the transistor capacitive output, as already seen in Section 5.2.

A second option for determination of the optimum load value at the desired output frequency $N\omega_0$ is the use of a substitution generator [10] of voltage type, operating at $N\omega_0$ (see Fig. 27). This substitution generator is connected to the output of the bandpass filter at $N\omega_0$. Its amplitude and phase are $V_{s,N}, \phi_{s,N}$. To select the optimum generator values, a double sweep is performed in $V_{s,N}, \phi_{s,N}$, calculating, in each step, the output power by means of $P_N = [1/2\text{Re}(Z_{L,N})]V_{s,N}^2$, where $Z_{L,N} = V_{s,N}e^{j\theta_{s,N}}/I_N$ and I_N are the current entering the generator. To ensure that the load will be physically implementable at a later stage, the load must be passive; that is, the condition $\text{Re}(Z_{L,N}) > 0$ must be fulfilled.

Figure 28b shows the output power variations obtained through a double sweep in $V_{s,3}, \phi_{s,3}$. The peaks correspond to the sign changes in R_3 . Apparently, much higher values of the output power can be achieved through this technique. However, the output power increases fast as the resistance R_3 approaches the zero value and too low resistance values are not implementable. The practical values are, in fact, in the order of those obtained in the previous paragraph, through variation of $\rho_{L,3}, \theta_{L,3}$.

In a second design stage, the influence of the harmonic loading is analyzed. Note that when using short circuits $\rho_{L,n} = 1, \theta_{L,n} = 180^\circ$ at $n \neq N$, the harmonic currents still circulate inside the transistor device, reducing the efficiency and output power. The optimum operation would be obtained for short circuits at the internal drain source, instead of the transistor extrinsic drain terminal. In order to evaluate the influence of the first-harmonic load, this load is made equal to $\Gamma_{L,1} = 1e^{j\theta_{L,1}}$ and the phase $\theta_{L,1}$ is varied. The influence of other harmonic components may also be considered, although it generally will be small.

In a third design stage, the harmonic input network is synthesized in a single passive network. The first-

harmonic termination $\Gamma_1 = \rho_1 e^{j\phi_1}$ is calculated so as to match the RF generator to the transistor input. This will allow us to increase the conversion gain, which should be maximum for conjugate matching. The increase in conversion gain will enable a reduction of the input power, while maintaining the output power level. Note that the input is matched after the load circuit has been determined, since this load circuit affects the input impedance value. The influence of higher-harmonic components can also be analyzed, in similar manner. In the multiplier design carried out here, the matching of the input circuit has enabled a reduction of conversion loss from $L = 10$ dB to 4 dB, which is obtained for the impedance $Z_1 = 45 + j40 \Omega$.

In a final design stage, the multiharmonic networks should be implemented. In the case of the frequency tripler, the output load can be synthesized through the combination of a coupled-line bandpass filter at $3\omega_0$, a transmission line, and a stub [6]. The stub is an open-circuited quarter-wave line at $2\omega_0$, which ensures short-circuit terminations at all even harmonic terms. The coupled-line bandpass filter provides a 50Ω load at $3\omega_0$ and reactive impedances, with nearly 0 dB return loss, at the remaining harmonic components. The lengths of the transmission line and the stub should be determined so as to achieve the desired load impedance values at ω_0 and $3\omega_0$. This can be done as explained in the following paragraph.

The topology described for the passive network, containing the coupled-line bandpass filter, the transmission line, and the stub, is introduced in the circuit diagram of Fig. 29 [31]. The purpose is to obtain the values of the network elements through a simple optimization technique. A HB simulation, with the current generator delivering the three frequencies $\omega_0, 2\omega_0, 3\omega_0$, enables the simultaneous calculation of the impedance exhibited by the distributed network at these three frequency components. An error function is defined in terms of the difference between the ideal impedance values Z_L and those provided by the passive network Z_L' . The dimensions of the distributed passive network are optimized in order to minimize this error function. The final spectrum of the frequency tripler, after this implementation process, is shown in Fig. 30, where measurements are included.

BIBLIOGRAPHY

1. J. C. Pedro and N. B. Carvalho, *Intermodulation Distortion in Microwave and Wireless Circuits*, Artech House, Norwood, MA, 2003.
2. S. Maas, *Microwave Mixers*, Artech House, Norwood, MA, 1986.
3. G. D. Vendelin, A. M. Pavio, and U. L. Rohde, *Microwave Circuit Design*, J Wiley, New York, 1990.
4. A. Suárez and R. Quére, *Stability Analysis of Nonlinear Microwave Circuits*, Artech House, Norwood, MA, 2003.
5. J. A. Garcia, J. C. Pedro, M. L. de La Fuente, N. B. de Carvalho, A. Mediavilla, and A. Tazon, Resistive FET mixer conversion loss and IMD optimization by selective drain bias,

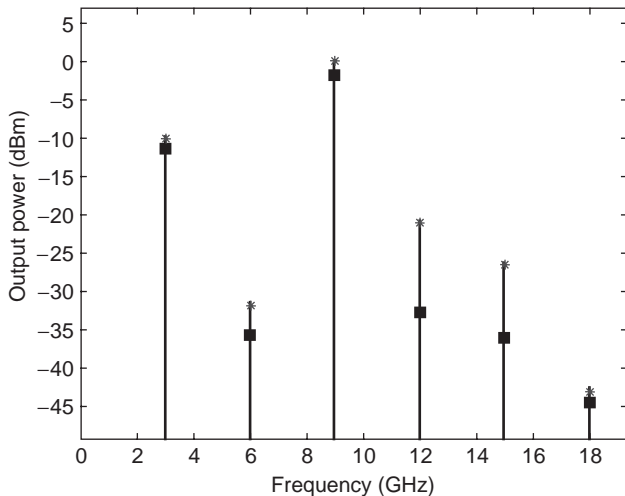


Figure 30. Output power spectrum of the frequency tripler, with measurements superimposed.

- IEEE Trans. Microwave Theory Tech.* **47**(12): 2382–2392 (Dec. 1999).
6. U. L. Rohde, Oscillator design for lowest phase noise, *Microwave Eng. Europe* 31–40 (May 1994).
 7. A. Suárez, E. Ngoya, P. Savary, M. Camiade, J. C. Sarkissian, and R. Quéré, Broadband design and simulation of frequency dividers in the millimetric band, *Proc. European Microwave Conf.*, Madrid, Sept. 1993, pp. 777–780.
 8. F. Ramírez, E. de Cos, and A. Suárez, Nonlinear analysis tools for the optimized design of harmonic-injection frequency dividers, *IEEE Trans. Microwave Theory Tech.* **51**(6): 1752–1762 (June 2003).
 9. D. M. Klymyshyn and Z. Ma, Active frequency-multiplier using CAD, *IEEE Trans. Microwave Theory Tech.* **51**(4): 1377–1385 (April 2003).
 10. B. Thibaud, D. Barataud, M. Campovecchio, J. M. Nebus, S. Tranchant, P. Quentin, and D. Floriot, CAD oriented design methods of frequency multipliers. Application to a millimeterwave MMIC PHEMT tripler and a microwave HBT doubler, *Proc. IEEE Int. Microwave Symp. MTT-S*, Anaheim, CA, June 1999, pp. 1747–1750.
 11. K. Kurokawa, Some basic characteristics of broadband negative resistance oscillator circuits, *Bell Syst. Tech. J.* 1937–1955 (July–Aug. 1969).
 12. W. J. Rugh, *Nonlinear System Theory, the Volterra/Wiener Approach*, Johns Hopkins Univ. Press, Baltimore, 1981.
 13. K. S. Kundert, Introduction to RF simulation and its application, *IEEE J. Solid-State Circ.* **34**(9):1298–1319 (Sept. 1999).
 14. V. Rizzoli, A. Lipparini, A. Constanzo, F. Mastri, A. Neri, and S. Massoti, State of the art harmonic balance simulation of forced nonlinear microwave circuits by the piecewise technique, *IEEE Trans. Microwave Theory Tech.* **40**(1):12–28 (Jan. 1992).
 15. E. Ngoya and R. Larcheveque, Envelope transient analysis: A new method for the transient and steady state analysis of microwave communication circuits and systems, *Proc. IEEE Int. Microwave Symposium MTT-S*, San Francisco, CA, June 1996, Vol. 3, pp. 1365–1368.
 16. S. Ver Hoeye, A. Suárez, and J. Portilla, Techniques for oscillator nonlinear optimization and phase-noise analysis using commercial harmonic balance software, *Proc. IEEE Int. Microwave Symp. MTT-S*, Boston, June 2000, Vol. 1, pp. 95–98.
 17. D. Barataud, M. Campovecchio, and J. M. Nebus, Optimum design of very high efficiency microwave power amplifiers based on time-domain harmonic load-pull measurements, *IEEE Trans. Microwave Theory Tech.* **49**(6):943–950 (June 2001).
 18. F. Blache, J. M. Nebus, P. Bouysse, and J. P. Villotte, A novel computerized multiharmonic active load-pull system for the optimization of high efficiency operating classes in power transistors, *Proc. IEEE Int. Microwave Symp. MTT-S*, 1995, Vol. 3, pp. 1037–1040.
 19. A. B. Carlson, *Communication Systems*, McGraw-Hill, New York, 1986.
 20. Kerr, Conversion loss and noise of microwave and millimetric wave mixers: Part 1—Theory, *IEEE Trans. Microwave Theory Tech.* **26**(2):49–55 (Feb. 1978).
 21. J. Dreifuss, A. Majdar, and A. Bar-Lev, Novel method for calculating the noise figure of microwave MESFET mixers, *IEE Proc. Microwaves Anten. Propag.* **136**(4):289–293 (Aug. 1989).
 22. E. de Cos, A. Suárez, and S. Sancho, Envelope transient analysis of self-oscillating mixers, *IEEE Trans. Microwave Theory Tech.* **52**(4):1090–1100 (April 2004).
 23. V. Rizzoli, F. Mastri, and D. Masotti, General noise analysis of nonlinear microwave circuits by the piecewise harmonic-balance technique, *IEEE Trans. Microwave Theory Tech.* **42**(5): 807–819 (May 1994).
 24. I. Angelov, H. Zirath, and N. Rorsman, Validation of a nonlinear transistor model by power spectrum characteristics of HEMTs and MESFETs, *IEEE Trans. Microwave Theory Tech.* **43**(5):1046–1052 (May 1995).
 25. A. Hajimiri and T. H. Lee, A general theory of phase noise in electrical oscillators, *IEEE J. Solid-State Circ.* **33**(2):179–194 (Feb. 1998).
 26. S. M. Sze, *Physics of Semiconductor Devices*, Wiley, New York, 1981.
 27. M. L. Edwards and J. H. Sinsky, A new criterion for linear 2-port stability using a single geometrically derived parameter, *IEEE Trans. Microwave Theory Tech.* **40**(12): 2303–2311 (Dec. 1992).
 28. R. Soares, J. Graffeulle, and J. Obregon, *Applications des Transistors a Effet de Champ en Arseniure de Gallium*, Eyrolles, Paris, 1984.
 29. Y. Sang-Woong et al., Cross-coupled differential oscillator MMICS with low phase-noise performance, *IEEE Microwave Wireless Compon. Lett.* **11**(12):495–497 (Dec. 2001).
 30. M. Lee, S. Yi, S. Nam, Y. Kwon, and K. Yeom, High efficiency harmonic loaded oscillator with low bias using a nonlinear design approach, *IEEE Trans. Microwave Theory Tech.* **47**(9): 1670–1679 (Sept. 1999).
 31. S. Ver Hoeye, F. Ramírez, and A. Suárez, Nonlinear optimization tools for the design of high-efficiency microwave oscillators, *IEEE Microwave Wireless Compon. Lett.* **14**(5):189–191 (May 2004).
 32. E. Palazuelos, A. Suárez, J. Portilla, and J. Barahona, Hysteresis prediction in autonomous microwave circuits using commercial software. Application to a Ku band MMIC VCO, *IEEE J. Solid-State Circ.* **33**(8):1239–1243 (Aug. 1998).
 33. A. Suárez, V. Iglesias, J. M. Collantes, J. Jugo, and J. L. García, Nonlinear stability analysis of microwave circuits using commercial software, *IEE Electron. Lett.* **34**(13):1333–1334 (June 1998).
 34. J. Jugo, J. Portilla, A. Anakabe, A. Suárez, and J. M. Collantes, Closed-loop stability analysis of microwave amplifiers, *IEE Electron. Lett.* **37**(4):226–228 (Feb. 15, 2001).
 35. A. Suárez, S. Sancho, S. Ver Hoeye, and J. Portilla, Analytical comparison between time and frequency domain techniques for phase-noise analysis, *IEEE Trans. Microwave Theory Tech.* **50**(10):2353–2361 (Oct. 2002).
 36. M. Bomford, Selection of frequency dividers for PLL applications, *Microwave J.* 159–167 (Nov. 1990).
 37. K. Ishii, H. Ichino, M. Togashi, Y. Kobayashi, and C. Yamaguchi, Very-high-speed Si bipolar static frequency dividers with new T-type flip-flops, *IEEE J. Solid-State Circ.* **30**(1): 19–24 (Jan. 1995).
 38. M. J. Hasler, Electrical circuits with chaotic behavior, *Proc. IEEE IEEE special issue on chaotic systems*, **75**:1009–1021 (Aug. 1997).
 39. C. Rauscher, Regenerative frequency division with a GaAs FET, *IEEE Trans. Microwave Theory Tech.* **32**(11):1461–1468 (Nov. 1984).
 40. R. Quéré, E. Ngoya, M. Camiade, A. Suárez, M. Hessane, and J. Obregón, Large signal design of broadband monolithic frequency dividers and phase-locked oscillators, *IEEE Trans. Microwave Theory Tech.* **41**(11):1928–1938 (Nov. 1993).

41. A. Suárez, J. Morales, and R. Quéré, Synchronization analysis of autonomous microwave circuits using new global stability analysis tools, *IEEE Trans. Microwave Theory Tech.* **46**(5):494–504 (May 1998).
42. J. M. Collantes and A. Suárez, Period doubling analysis and chaos detection using commercial harmonic balance simulators, *IEEE Trans. Microwave Theory Tech.* **48**(4):574–581 (April 2000).
43. H. C. Chang, A. P. Yeh, and R. A. York, Analysis of oscillators with external feedback loop for improved locking range and noise reduction, *IEEE Trans. Microwave Theory Tech.* **47**(8):1535–1543 (Aug. 1999).
44. D. M. Klymyshyn and S. Kumar, A simple GMSK modulator for microwave and millimeter-wave frequencies, *Microwave J.* **42**(2):88–104 (Feb. 1999).
45. M. Ugajin and T. Tsukahara, A 1-V 2.4-GHz FSK receiver with a complex BPF and a frequency doubler in CMOS/SOI, *Proc. IEEE Custom Integrated Circuits Conf.* 2003, pp. 151–154.

NOTCH ANTENNAS

RICHARD Q. LEE
 NASA Glenn Research Center
 Cleveland, Ohio

1. INTRODUCTION

A notch antenna, also known as a *tapered slot antenna* (TSA), is an endfire traveling-wave antenna. Like microstrip antennas, the TSA features low profile, light weight, easy fabrication by photoetching, conformal installation, and compatibility with microwave integrated circuits (MIC). Performance-wise, TSA has demonstrated multioctave bandwidth, moderate gain (7–10 dB), and symmetric *E*- and *H*-plane beam patterns. However, TSA lacks the versatility of microstrip antennas in terms of multifunction operations such as dual frequency and dual polarization and loses its planar architecture when used as circularly polarized antennas or in 2D arrays. The antenna was first proposed by Lewis et al. [1] in 1974. Since then, much technological advances have been made in both designs and applications. In designs, various numerical techniques have been developed and applied to aid the design of the TSA antennas [2–4]. Full-wave numerical techniques based on the method of moments are now commercially available, providing the ability to shorten the design cycle as have been demonstrated in a CAD benchmark demonstration [5]. In applications, TSAs have been used mainly for spatial power combining and as focal plane feed array for imaging reflector systems [6,7]. In more recent applications, TSA arrays capable of multifunction operations are emphasized. Examples of these include the dual-band dual-polarized TSA array of nested lattice architecture [8], and multifrequency full-duplex phased-array system with notch elements [9].

This article focuses on the most recent advances in TSA and their applications. In order to provide some basic

understanding of the design issues, the article begins with some discussions on the design of single tapered slot antennas. Then, TSA arrays and their applications will be highlighted.

2. BASIC GEOMETRIES

A typical TSA consists of a tapered slot section produced by the gradual widening of a slotline. The antenna, excited by a slotline feed, is fabricated on a metallization layer with or without a supporting dielectric substrate. The tapered slot section which constitutes the radiating region can take on any of three geometric profiles: (1) nonlinear taper (Vivaldi, tangential, or parabolic), (2) linear taper (LTSA), and (3) constant width (CWSA) [10]. The majority of previous studies have been focused on TSA with linear and exponential profiles. Prasad and Mahapatra [11] first introduced the linearly tapered slot antenna (LTSA) in 1979. Their antenna of about one free-space wavelength long was etched on a 25-mil alumina substrate. In the same year, Gibson [12] reported a TSA with exponentially tapered profile, also known as the “Vivaldi” antenna, which demonstrated a bandwidth of 8–40 GHz. The schematics of the LTSA and the Vivaldi antennas are shown in Fig. 1. In later years, most of the subsequent developments of TSA arrays are derived mainly from these two antenna types.

Figure 2 shows some typical radiation patterns of a relatively short TSA ($L \leq 2\lambda_0$). As shown, the *H*-plane pattern is significantly broader than the *E*- and the diagonal *D*-plane patterns. In general, the basic geometry of a TSA (length, taper profile, etc.) has strong effects on the radiation patterns. These effects will be discussed in a later section.

In order to facilitate integration of antenna and devices at sub-millimeter-wave frequencies, a new variant of the TSA, generally known as “V-antennas”, was introduced in 1979 for coupling radiation into diode mixers [13]. Years later, other applications of V-antennas were demonstrated at microwave frequencies [14,15]. These antennas with finite-width ground planes can enhance antenna performance by suppressing the surface waves. Another advantage of the V-antennas is its compatibility with uniplanar feed structures that allow one to excite the antenna

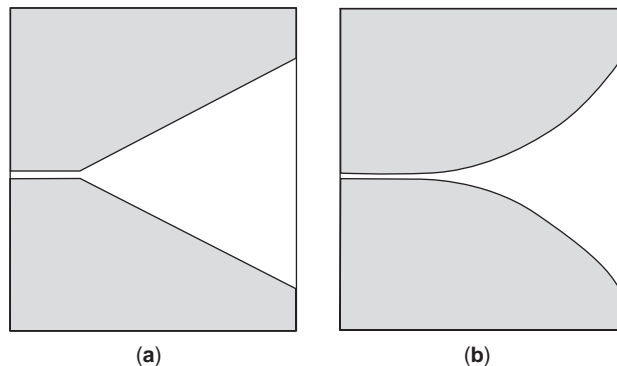


Figure 1. Schematics of (a) LTSA and (b) Vivaldi antennas.

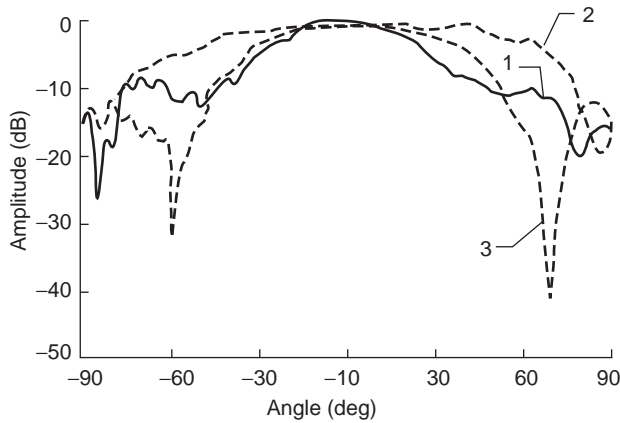


Figure 2. Typical radiation pattern for TSA of length $L = 0.93 \lambda_0$ and width $W = 0.68 \lambda_0$ tested at 11 GHz: 1— E plane; 2— H plane; 3— D plane.

with either a microstrip line or a waveguide [14]. The schematics of a V-LTSA and a V-Vivaldi excited by a coplanar stripline are shown in Fig. 3.

Another variant of the conventional TSA is the antipodal tapered slot antenna. In practice, the conventional planar TSA is fed by a balanced slotline. One serious drawback of the conventional TSA is in the fabrication and impedance matching of the slotline. Slotline fabricated on a low-dielectric-constant substrate has relatively high impedance, which makes matching to a microstrip feed very difficult. The antipodal TSA is designed to overcome this impedance-matching difficulty; however, it has exhibited very poor cross-polarization characteristics. The antenna is formed by gradually flaring the strip conductors of the balanced microstrip on opposite sides of the dielectric substrate with respect to the antenna axis, thus allowing the antenna to be directly fed by a microstrip feed [16]. To circumvent the high cross-polarization problem, a balanced antipodal Vivaldi consisting of three metallization layers was introduced. This new antenna, shown in Fig. 4, has demonstrated -15 dB lower cross-polarization across a 18–1 band as compared to the conventional Vivaldi antenna [17].

3. TSA DESIGN

For years, the design of TSA has been based primarily on empirical approach, which, as an initial step, could start with the following simple guidelines (where c is the veloc-

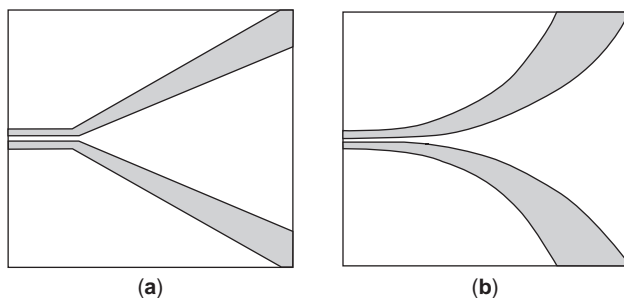


Figure 3. Schematics of (a) V-LTSA and (b) V-Vivaldi antennas.

ity of light, v is the velocity of field along the slot, and λ_0 is free-space wavelength):

Aperture width of the slot: $W \geq \lambda_0$

$1.05 \leq c/v \leq 1.2$

Effective thickness: $t_{\text{eff}} \leq 0.03 \leq \lambda_0$

Taper angle 2α typically $5\text{--}12^\circ$

Length of TSA L typically $2\text{--}12 \lambda_0$ wavelength.

With the availability of electromagnetic simulators, engineers can now check the accuracy of their designs before carrying out the actual fabrication and characterization. In general, design of the TSA involves two major tasks: (1) design of a broadband transition and feed structure with very wide frequency range and low return loss and (2) determining the dimensions and shape of the antenna in accordance with the required beamwidth, sidelobe, backlobe, and other parameters over the operating frequency range. The geometric parameters such as length, width, dielectric thickness, ground-plane size, and taper profile, which have direct impact on the impedance, directivity, bandwidth, and radiation pattern of the antenna will be discussed in the sections below.

3.1. Feeding Methods

Almost always planar tapered slot antennas such as LTSA and Vivaldi are excited by a slotline; thus, feeding a TSA requires building a transition between the slotline and other transmission media. In the case of microstrip or coaxial lines, the transition is a balun. In general, the transition should have small parasitic inductance and capacitance for wide bandwidth, and hence, electromagnetic coupling is preferred over wire bonding or solder connection. In the following, we will consider three basic feed structures: (1) coplanar waveguide (CPW), (2) microstrip line, and (3) coaxial lines.

3.1.1. Coplanar Waveguide-Feed. CPW possesses many useful design characteristics such as low radiation loss, less dispersion, and uniplanar configuration. In Ref. 10, we have presented several feeding techniques where the transmission media are CPW, which excite the TSA via electromagnetic coupling. Figure 5a shows a strip-to-slot coupled LTSA excited by a conductor-backed finite ground-plane CPW feed. In the figure, the distance L_s from the short termination of the slotline, as well as the distance L_w from the open termination of the extended center strip conductor to the CPW-to-slotline junction, is about a quarter-wavelength at the center frequency of 20 GHz; and Z_{os} and Z_{ow} are the characteristic impedances of the slotline and the CPW center strip conductor extension, respectively. The antenna has demonstrated a VSWR of 2–1 over nearly 3–1 bandwidth as indicated by the measured return loss shown in Fig. 5b.

The TSA can also be excited by direct slot-to-slot feeding where the CPW and the antenna are on the same side of the substrate. In order to excite the odd mode where the electric fields in both slots of the CPW have the same amplitude but opposite direction, a bondwire is usually placed across the slots to keep the two ground planes at equal potential. The CPW feed enables direct integration

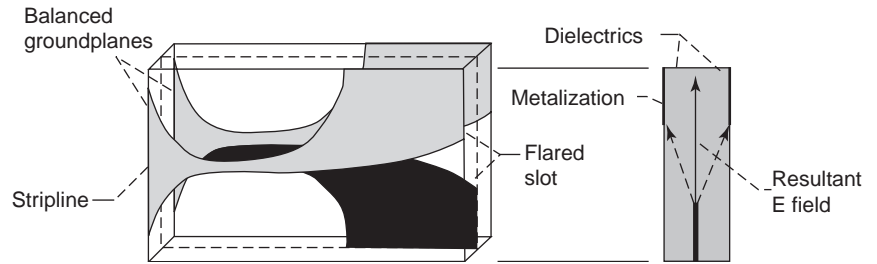


Figure 4. Balanced antipodal Vivaldi antenna. (From Ref. 17 with permission from IEE.)

of active solid-state devices with the antenna. Figure 6 shows the layout of a LTSA integrated with a FET amplifier that demonstrated a gain of more than 14 dB over a bandwidth of 1.75 GHz [18].

CPW can be designed as a tapered CPW with constant characteristic impedance, but with different ratio of slot to center strip widths [19]. This unique feature is useful for exciting twin tapered slot antennas of large separations.

Figure 7 shows the application of tapered CPW transitions to twin Vivaldi antennas to achieve pattern diversity for transponders and monopulse systems through even- and odd-mode excitations [20]. As shown, when the distance between the slotlines equal to $n\lambda_g$, where λ_g is the guide wavelength of the microstrip line, the even mode with in-phase electric fields is excited producing a maximum radiation in the broadside direction. Conversely, when the distance between the slotlines is $(2n + 1)\lambda_g/2$, the odd mode with opposite electric fields is excited, producing a minimum radiation in the boreside direction.

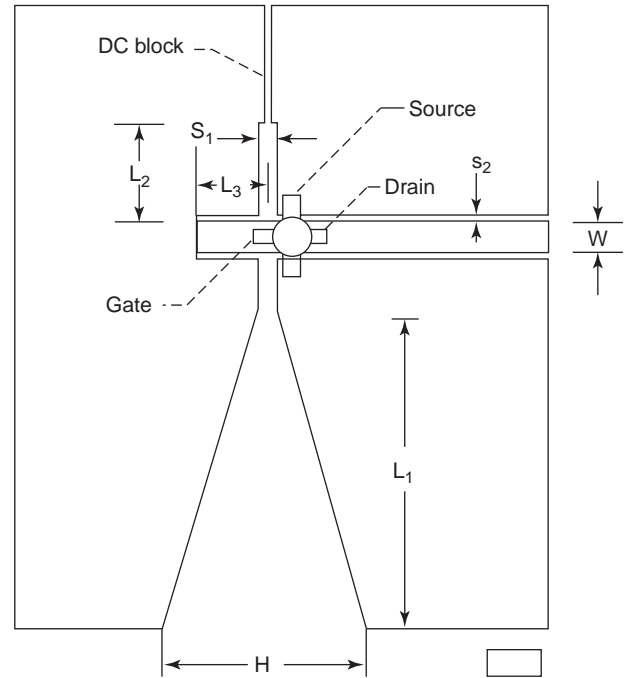


Figure 6. Circuit configuration of CPW cross-feed LTSA amplifier: $L_1 = 32$ mm, $L_2 = 8$ mm, $L_3 = 1.5$ mm, $S_1 = 0.5$ mm, $S_2 = 0.2$ mm, $H = 20.5$ mm, $W = 1.4$ mm. (From Ref. 18 with permission from IEE.)

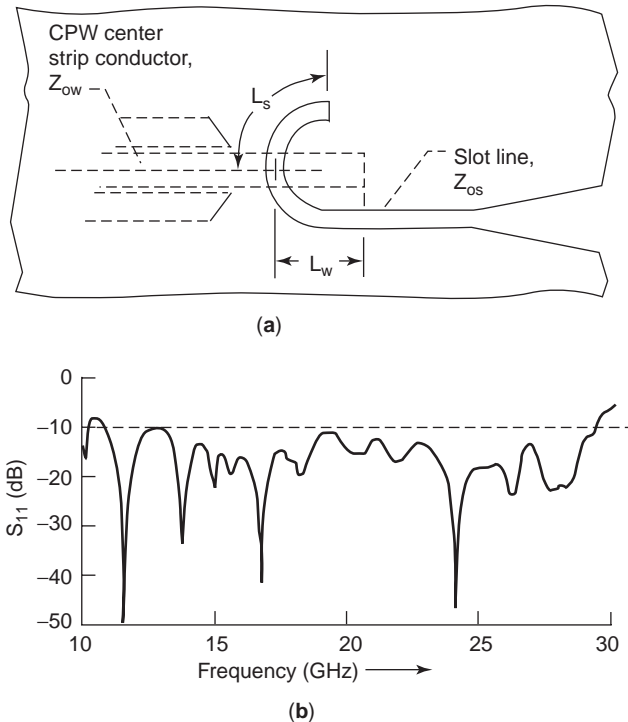


Figure 5. (a) CPW strip-to-slot transition; (b) measured return loss for the strip-to-slot coupled TSA.

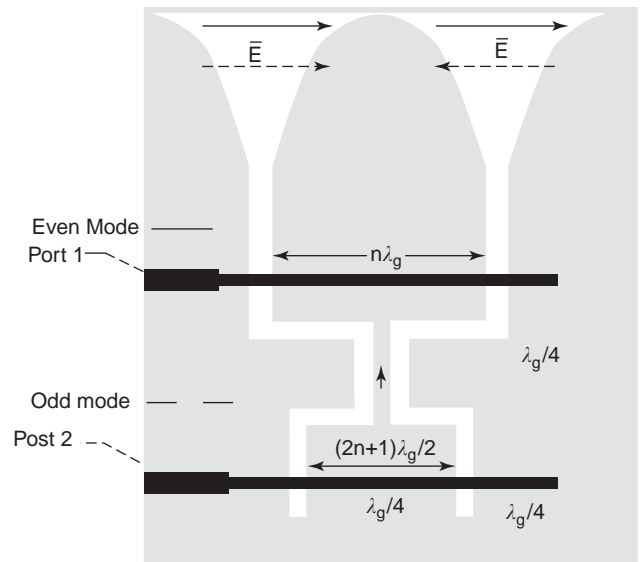


Figure 7. Twin LTSAs fed with tapered CPW transitions.

3.1.2. Microstrip Line Feed. Microstrip line is in widespread use in power combining circuit. Since microstrip line is an unbalanced line and slotline is a balanced line, feeding a TSA with a microstrip line requires a balanced-to-unbalanced transition (balun) to avoid compromising the broadband antenna performance. The most common microstrip/slot transition, the Marchand balun [21], has demonstrated a VSWR of 2–1 over an octave bandwidth with an integrated wideband V-Vivaldi antenna [22]. The transition and the corresponding transmission-line model are shown in Fig. 8. The balun consists of four quarter-wave sections with the end open-circuited section extended past the center of the slotline by about one-quarter of a guided wavelength. Further broadening of the bandwidth can be achieved when the microstrip is terminated by a radial stub and the slotline is terminated by an elliptical shaped cavity [10].

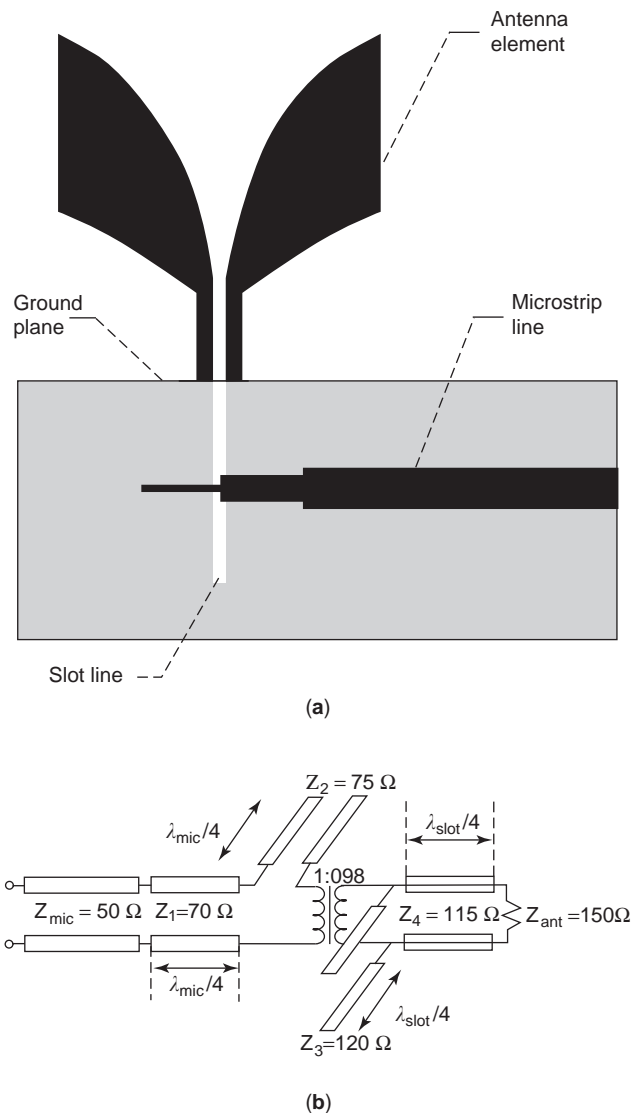


Figure 8. Schematic of (a) Marchand balun with interface to antenna element and (b) transmission-line model of the balun. (From Ref. 22 with permission from IEEE.)

The double-Y balun is another microstrip-to-slotline transition that has no inherent bandwidth limitation other than parasitic inductances and capacitances. As indicated in Fig. 9, the double-Y balun is based on the six-port double-Y junction that consists of three balanced and three unbalanced lines placed alternately around the center of the structure. For the balun to provide perfect transmission between an opposite balanced and unbalanced ports, opposite pairs of lines should have reflection coefficients with opposite phases, thus requiring one pair of lines to be short-circuited and the other, open-circuited. TSA with double-Y balun feed structure has achieved an impedance bandwidth of more than 2–1 [23].

The balun requirement often complicates the feed design and limits the antenna bandwidth if it is not designed properly. The V- and antipodal tapered slot antennas offer a way to circumvent this problem since they are not directly fed by a slotline. Figure 10 shows a V-LTSA with a uniplanar microstrip-to-coplanar stripline feed [24]. In the feed network, a microstrip line of characteristic impedance of 50Ω and width w_1 is coupled to two orthogonal microstrip lines of characteristic impedance of 70Ω and width w_2 through a quarter-wave impedance transformer of width w_1 . The mean pathlength of the folded loop “a through b” is equal to half a guide wavelength λ_g of the $70\text{-}\Omega$ microstrip line at the design frequency. However, for wideband operation, the mean pathlength needs to be increased to $0.638 \lambda_g$ to compensate for the right-angle bend parasitic elements. This design ensures that the signal phase from points a to b are 180° out of phase; thus the coupled microstrip lines are excited in the odd mode with the electric field predominantly across the gap S_2 . The dimension of S_2 is chosen such that the characteristic impedance of the coupled microstrip line is 50Ω . The measured return loss of the V-LTSA is better than 10 dB over the frequency range of 5–15 GHz.

Figure 11 shows an antipodal LTSA with a microstrip-to-balanced microstrip feed. The balanced microstrip is formed with the ground plane tapered to a width equal to the strip width w_l (0.71 mm), and the arc radius R_2 is

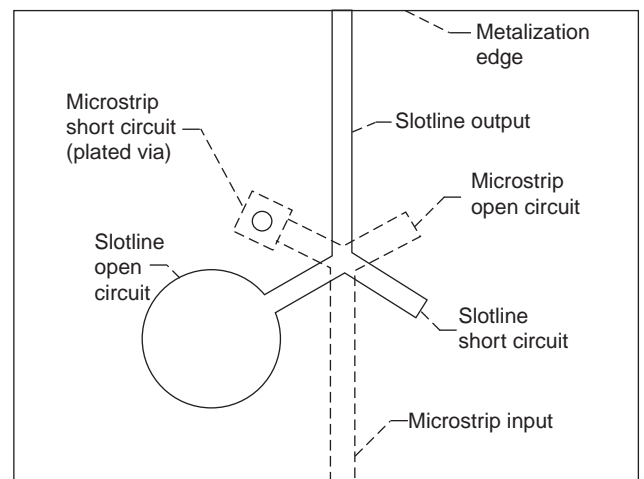


Figure 9. Double-Y microstrip-to-slotline transition.

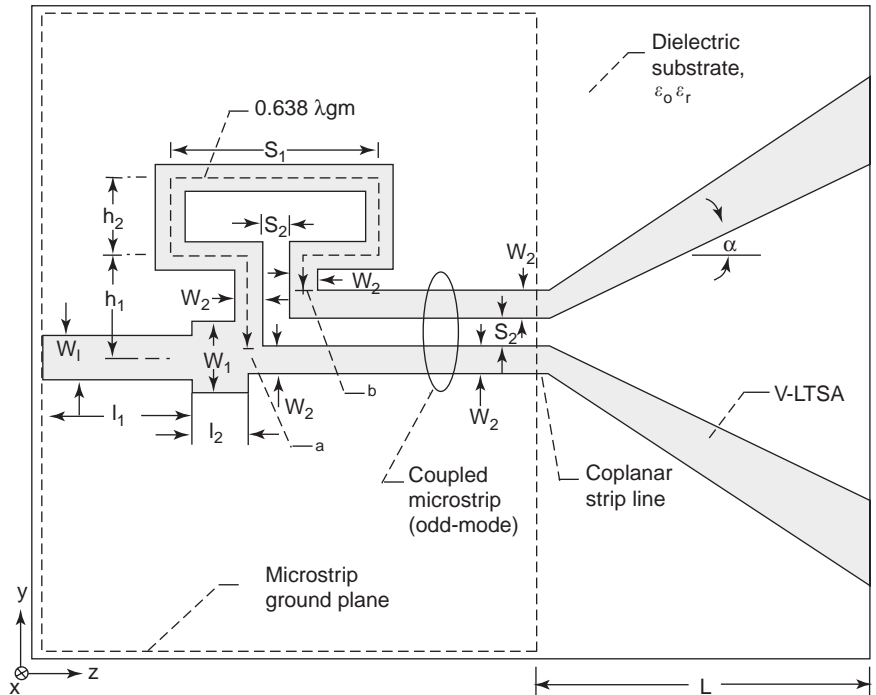


Figure 10. V-LTSA with a uniplanar microstrip line-to-coplanar stripline feed: $L = 50.8$ mm, $\alpha = 12.5^\circ$, $W_l = 0.229$ mm, $W_1 = 0.328$ mm, $W_2 = 0.102$ mm, $l_1 = 4.9$ mm, $l_2 = 2.771$ mm, $S_1 = 2.098$ mm, $S_2 = 0.102$ mm, $h_1 = 0.541$ mm, $h_2 = 1.339$ mm.

arbitrarily chosen to provide a smooth taper transition for matching the characteristic impedance of the conventional microstrip to the balanced microstrip.

The electric field lines at different cross sections along the feed and the antenna are illustrated in Fig. 12. The electric field lines, which are spread out in the conventional microstrip structure, concentrate between the metal strip of the balanced microstrip, and finally rotate while traveling along the LTSA. The field rotation inadvertently introduces higher cross-polarizations in these types of antennas. The antipodal LTSA has demonstrated over 4–1 (8–32 GHz) bandwidth for 2–1 VSWR at a design frequency of 18 GHz [25].

3.1.3. Coaxial Feed. Coaxial line is useful as a feed structure because of its compatibility with the slotline, coplanar microstrip, or balanced microstrip to form wide-band transitions; thus, it can be used to excite all three variants of TSA described above. The disadvantage is that it is not planar and has high losses at high frequencies. Further, coaxial line is an unbalanced feedline. All the currents flow inside the line, namely, the inner conductor and the inside of the shield. Feeding a balanced antenna with unbalanced coaxial feed may cause currents to flow on the outside the shield, which could result in significant power loss and serious distortion in radiation pattern. Since the magnitude of the current on the outside

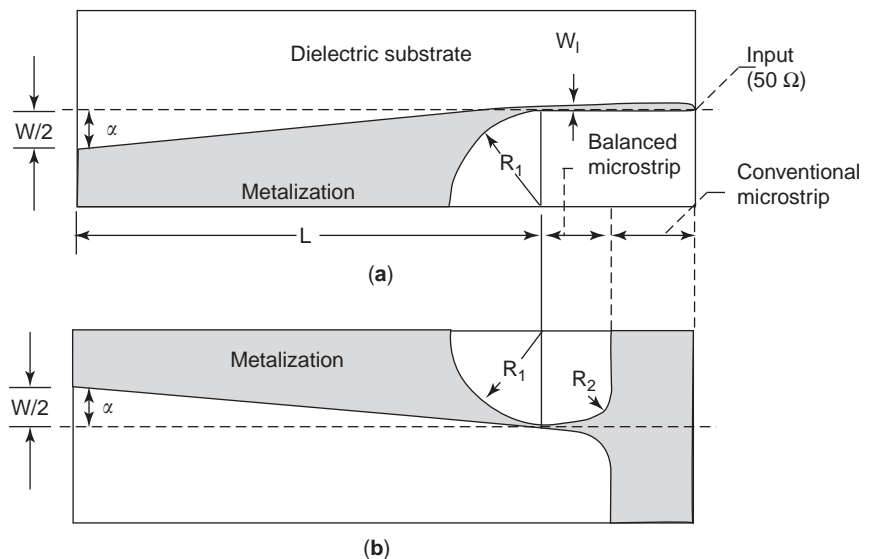


Figure 11. Antipodal LTSA and feed network: (a) top metallization; (b) bottom metallization.

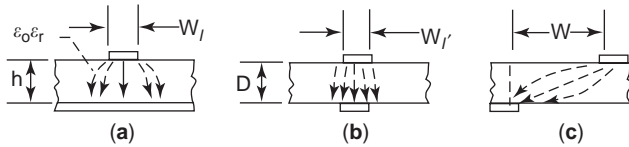


Figure 12. Electric field distribution at cross sections of (a) conventional microstrip, (b) balanced microstrip, and (c) antenna radiating edge.

shield is a function of the impedance to ground of the conductor, one common approach to cutoff the flow of current is with an open circuit that is created by placing a “skirt” a quarter-wavelength long around the outside shield and short-circuited to the shield at a quarter-wavelength away from the load.

The most direct way of exciting a TSA with a coaxial feed is to extend its center conductor over the slotline section of the TSA and anchor the coaxial feed with solder connection to the ground plane. An improved balun design that has direct application to V-antennas has been proposed [26]. The balun impedance is tapered by cutting open the outer wall of the coax so that the reflections at the input are minimized. The length of the balun is determined by the lowest operating frequency and the maximum reflection coefficient that occurs in the passband. Figure 13 shows the cross section of the tapered coaxial-line balun and its integration with a V-Vivaldi antenna.

4. RADIATION CHARACTERISTICS

A good understanding of the effects of the design parameters (length, width, dielectric thickness, ground-plane size, taper profile, etc.) on antenna characteristics would facilitate the task of antenna design. TSA is known to

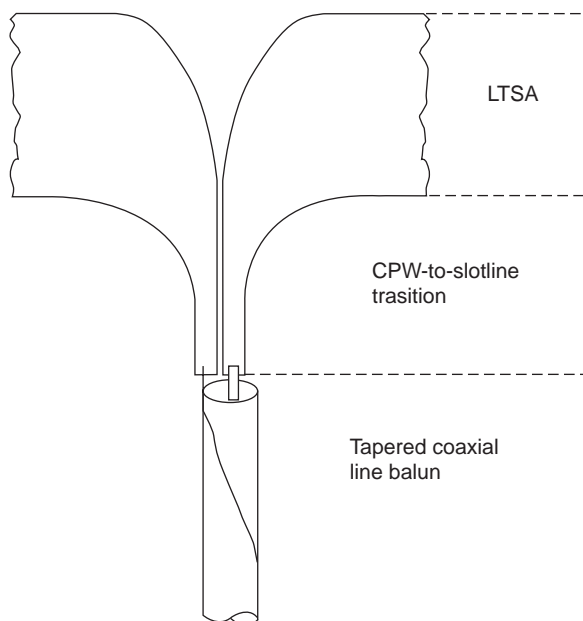


Figure 13. Coaxially-fed TSA with tapered coaxial line balun. (From Ref. 26 with permission from IEEE.)

have good performance over a wide bandwidth. In practice, the operating bandwidth is often limited by the slot-line-to-feedline transition and by the finite width of the antenna. To achieve wideband operation requires the TSA to operate in a traveling-wave mode with perfect impedance match at both the feed transition and the slot termination. In this section, some important characteristics of TSA, which are based on experimental data as well as from previous publications, will be presented.

4.1. Effect of Length, Width, and Taper Profiles

Tapered slot antennas radiate in the endfire direction with fairly symmetric radiation patterns, but have high cross-polarization levels in the diagonal plane. The lowest cross-polarization level in the diagonal plane is about 10–15 dB higher than that of the principal planes, which are typically better than -15 dB. In general, the cross-polarization characteristics of planar TSA are superior to those corresponding to their antipodal counterparts. Because this is a traveling-wave antenna, the phase velocity and guide wavelength λ_g varies with any change in the geometric and material parameters of the antenna, which in turn impacts the radiation characteristics of the antenna. The gain of a TSA increases with the length L of the antenna typically from a few decibels to over 10 dB as L increases from 2 to 5 λ_g [10]. Maximum measured gain of 16–17 dB with radiation efficiency of 80% has been reported for long TSA with L greater than $6\lambda_0$ [27]. Similarly, the beamwidths, which are inversely proportional to gain, decrease rapidly as the length is increased; however, the H -plane beamwidth varies more slowly in comparison to the E -plane beamwidth, particularly for L less than $5\lambda_g$.

The taper profile has been found to have strong effects on both the beamwidth and sidelobe level of the antenna. In general, the beamwidths are narrower for the CWSA, followed by the LTSA, and then Vivaldi for antennas with the same length, same aperture size, and on the same substrate. Similarly, the sidelobes are highest for the CWSA, followed by the LTSA, and the Vivaldi.

As a traveling-wave antenna, the H -plane beamwidth follows $1/\sqrt{L}$ dependence, while the E -plane beamwidth depends more on the aperture width or tapered angle [28]. Varying the tapered angle will change the phase velocity and hence λ_g , which will in turn change the E -plane beamwidth. Thus, constant beamwidth in both E and H planes can be achieved with proper choices of L and tapered angles. Gibson obtained approximately constant beamwidth in both E and H plane for a Vivaldi antenna fabricated on alumina substrate with tapered profile defined by [12]

$$y = \pm 0.125e^{0.052x}$$

where x and y are variables for the two principal axis of the rectangular coordinates. Approximately constant E - and H -plane beamwidths over a 6–8 GHz bandwidth have been demonstrated for a balanced antipodal antenna with elliptical radiating taper [17], and nearly identical E - and H -plane 3-dB beamwidth was observed for a LTSA with tapered angles in the range of 15–20° [29].

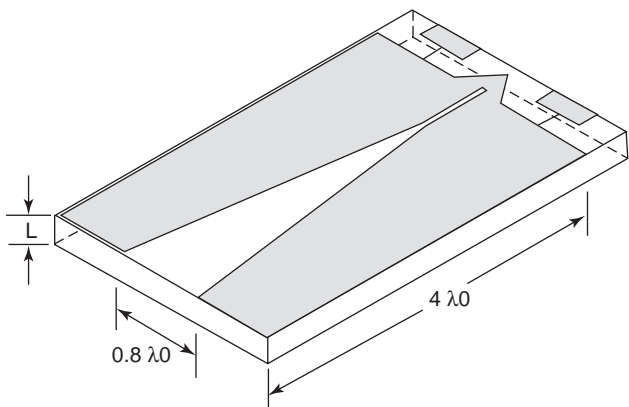


Figure 14. Micromachined tapered slot antenna. (From Ref. 32 with permission from IEEE.)

4.2. Effect of Dielectric

The performance of a TSA is sensitive to the thickness and dielectric constant of the dielectric substrate. The presence of a dielectric substrate has the primary effect of narrowing the mainbeam of the antenna. The effects of dielectric substrates on the *E*- and *H*-plane beamwidths of a Vivaldi antenna on polyethylene have been investigated at 18.5 GHz [30]. By varying substrate thickness from 10 to 15 and 27 mils, the *H*-plane beamwidths become narrower, while the *E*-plane beamwidths remain essentially constant, indicating that the dielectric has a strong effect on the *H* fields. Increasing the dielectric thickness generally results in increased gain, but with higher sidelobes. For good performance, a TSA should have an effective substrate thickness in the range of $0.0025\lambda_0 \leq t_{eff} \leq 0.028\lambda_0$ where $t_{eff} = t(\sqrt{\epsilon_r} - 1)$ is the effective thickness of the substrate. For substrate thickness above the upper bound of $0.028\lambda_0$, unwanted substrate modes develop that degrade the antenna performance, resulting in low efficiency and narrow bandwidth, particularly for dielectrics with high dielectric constants. Further, for millimeter-wave operations, the upper bound on the effective thickness constrains to using mechanically fragile substrates with thickness of only a few hundreds of micrometers. To overcome these problems, it has been proposed to fabricate notch antennas either on thick perforated substrates with an array of regularly and closely placed holes [31] or on photonic bandgap dielectrics

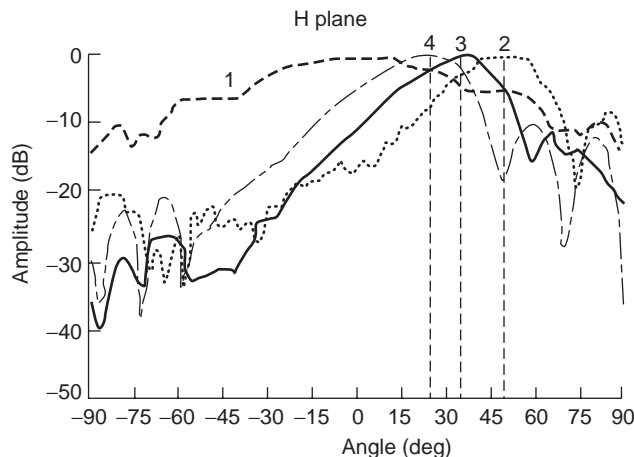


Figure 15. *H*-plane patterns at 11 GHz for a LTSA with a foam spacer: 1—with no ground plane; 2—with a ground plane and no spacer; 3—with a ground and a 0.3175-cm foam spacer; 4—with a ground plane and a 0.635-cm foam spacer.

as shown in Fig. 14 [32]. The former approach reduces the effective substrate thickness, while the latter approach suppresses the excitation of the surface modes.

4.3. Ground-Plane Effect

Placing a ground plane immediately below the TSA will cause the mainbeam to steer away from the endfire direction by about 50° in the *H* plane [10]. The amount of scan will be reduced as the distance between the ground plane and the antenna increases, and becomes negligible when the distance of separation is sufficiently large. For the *E*-plane patterns, no significant change was observed except that the TSA had to be tilted in the elevation to receive full power. Figure 15 shows measured *H*-plane patterns for a LTSA over a ground plane with a foam spacer in between.

5. IMPEDANCE CHARACTERISTICS

5.1. Input Impedance

The impedance characteristic of TSA is important for designing match transitions; yet very little information is

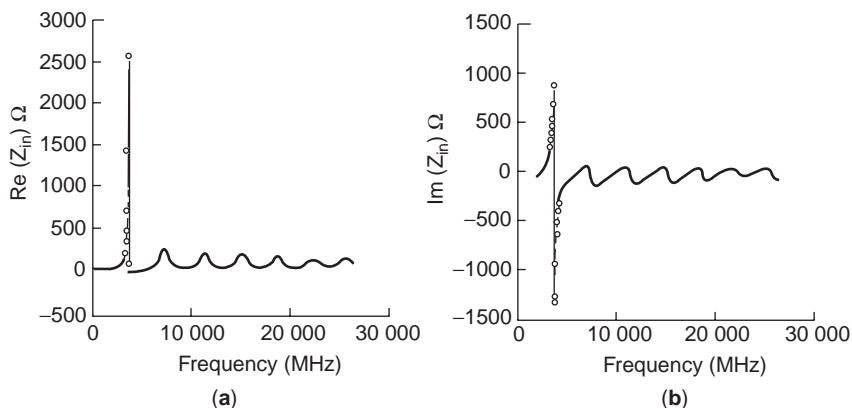


Figure 16. (a) Real and (b) imaginary parts of the input impedance ($\alpha = 5^\circ$ and $L = 2.54$ cm).

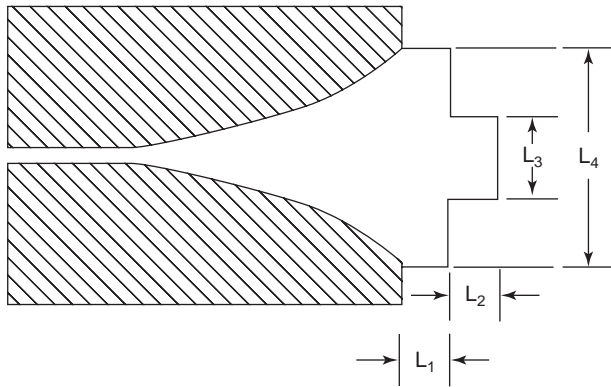


Figure 17. Vivaldi antenna with a dielectric impedance-matching transformer: $L_1 = 4$ mm, $L_2 = 4$ mm, $L_3 = 5$ mm, $L_4 = 10$ mm.

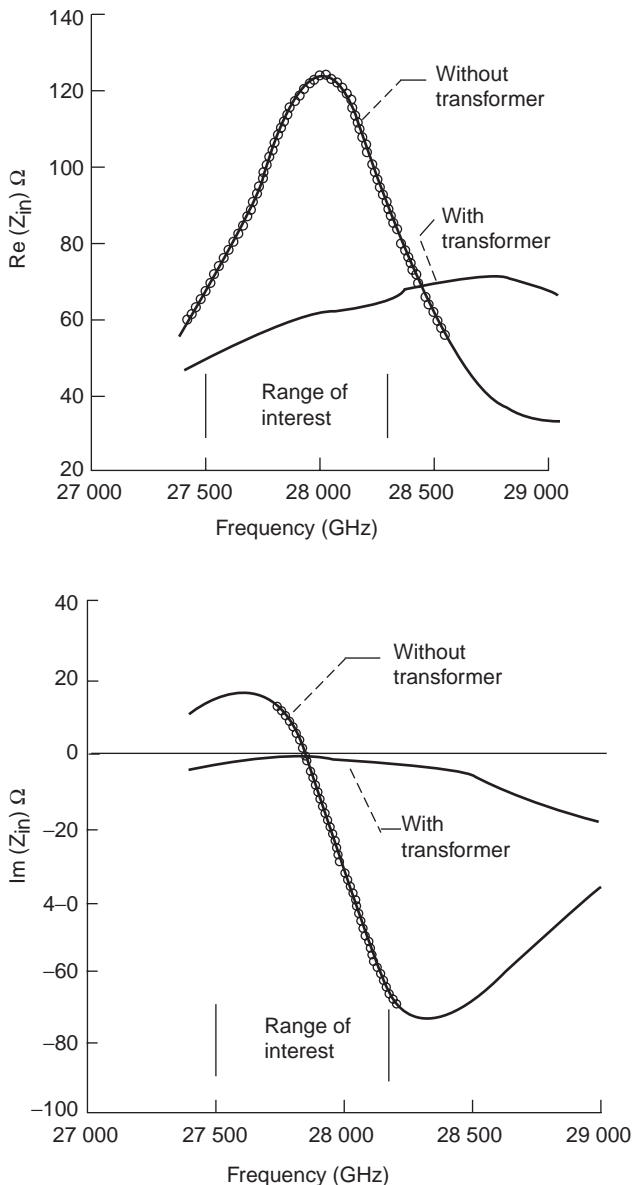


Figure 18. (a) Real and (b) imaginary parts of the input impedance.

available from previous publications. Based on conformal mapping method for a fin antenna without a dielectric, Yngvesson et al. reported that the impedance of a LTSA with thin dielectric is essentially constant at frequencies from 4 to 12.4 GHz and is close to 80 Ω [33]. In another study, the input impedance of LTSA was measured using a microwave wafer probe and a set of on wafer thru-reflect-line (TRL) slotline standards [34]. The LTSA was excited through a short length of a slotline by a ground-signal microwave probe (Picoprobe, Inc.). In the measurement, the reflection coefficient of the LTSA is deembedded from the measured reflection coefficient at the input terminal of the slotline using the NIST deembedded software [35]. Figure 16 shows the real and imaginary parts of the input impedance Z_{in} versus frequency for a LTSA with $\alpha = 5^\circ$ and $L = 2.54$ cm.

The impedance plot exhibits a series of resonance over the frequency band from 2 to 26.5 GHz. These resonances are caused by imperfect impedance match transitions at the feed end and the termination end of the LTSA. The first resonance mode at frequencies below 4 GHz has very large input impedance, typically over 1000 Ω , which could be caused by large electric fields associated with a very small W/λ_0 . For frequencies above 4 GHz, the impedances are bounded between 145 and 40 Ω with a mean value of about 92 Ω . Similar results were also obtained for LTSA of different lengths and tapered angles [10].

5.2. Impedance Matching

Impedance matching of TSA has commonly been performed at the feed end of the antenna. An approach illustrated in Fig. 17 for impedance matching at the termination end of the antenna has been proposed [36].

The new approach uses a two-step dielectric transformer to match the antenna to free space. The deembedded real

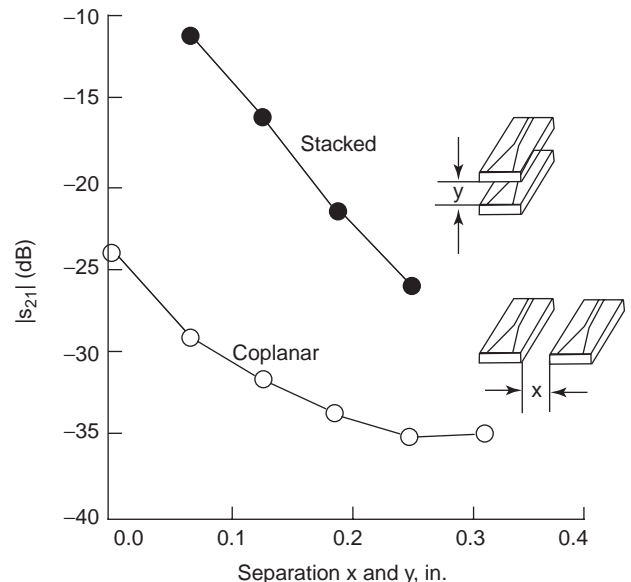


Figure 19. Measured mutual coupling between two LTSAs in coplanar and stacked arrangements as a function of separation.

and imaginary parts of the input impedance with and without the dielectric transformer are shown in Fig. 18.

5.3. Mutual Impedance

Mutual coupling can produce profound impacts on the performance of an antenna array, causing impedance mismatch and scanning blindness, particularly for antennas on thick dielectric substrates. In general, mutual coupling can occur between two TSAs arranged in either coplanar or stacked configurations. The mutual coupling between two LTSAs in close proximity and excited by two calibrated ground-signal microwave probes has been obtained from a *S*-parameter measurement of $|S_{21}|$ [37]. Figure 19 shows the measured mutual coupling between two LTSAs in coplanar and stacked arrangement as a function of separations. Results indicate that the mutual coupling decreases with the distance of separation.

The coupling coefficients as a function of frequencies were also measured first with the LTSAs fabricated on a continuous substrate and then repeated after a narrow slot was cut in the dielectric. In the latter case, coupling between antennas were confined to space waves only. Results indicate stronger mutual coupling for the TSAs on continuous substrate as a result of additional coupling through the supporting dielectric; however, both cases display decreasing $|S_{21}|$ with frequencies [10]. This is due to the fact that at higher frequencies the separation is electrically larger and separations between antennas are greater with respect to wavelengths.

6. TSA ARRAY AND APPLICATIONS

Over the years, many different applications of TSA arrays have been reported in the literature. TSA arrays have been successfully applied as focal-plane feed arrays for a multibeam imaging reflector system. For the same beamwidth, a TSA array occupies about 1/4 of the area of a feed array with waveguide elements; thus, an imaging system with TSA focal plane array can be designed to yield high angular resolution [27].

TSA arrays have also been advantageously used for spatial power combining to achieve power amplification and harmonic generation. In 1999 a 120-W, X-band spatially combined solid-state amplifier was demonstrated [6]. The spatial combiner consists of six identical “trays” with each containing four input/output broadband TSA integrated with four MMIC amplifiers via a slot-to-microstrip transition. Space power combining can be applied to large antenna aperture such as space-fed lens arrays. The concept of space power amplification has been demonstrated experimentally with a three-element LTSA array module. Figure 20 shows a photo of the array module and the measured *H*-plane pattern.

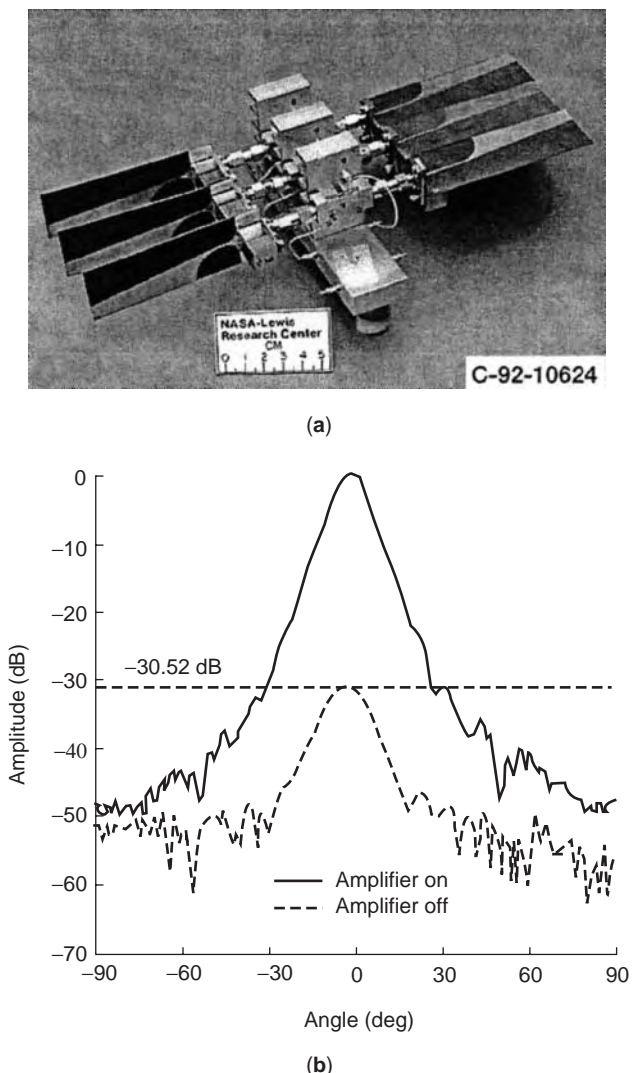


Figure 20. (a) Experimental three-element LTSA MMIC array module for space power amplification and (b) measured *H*-plane pattern.

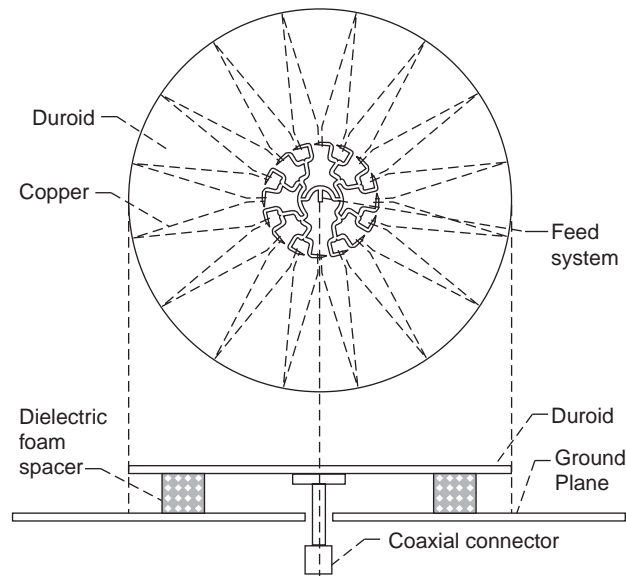


Figure 21. 16-element circular LTSA array.

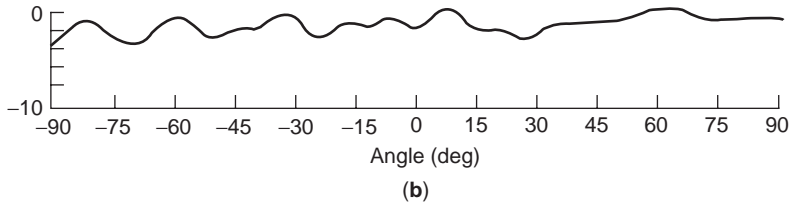
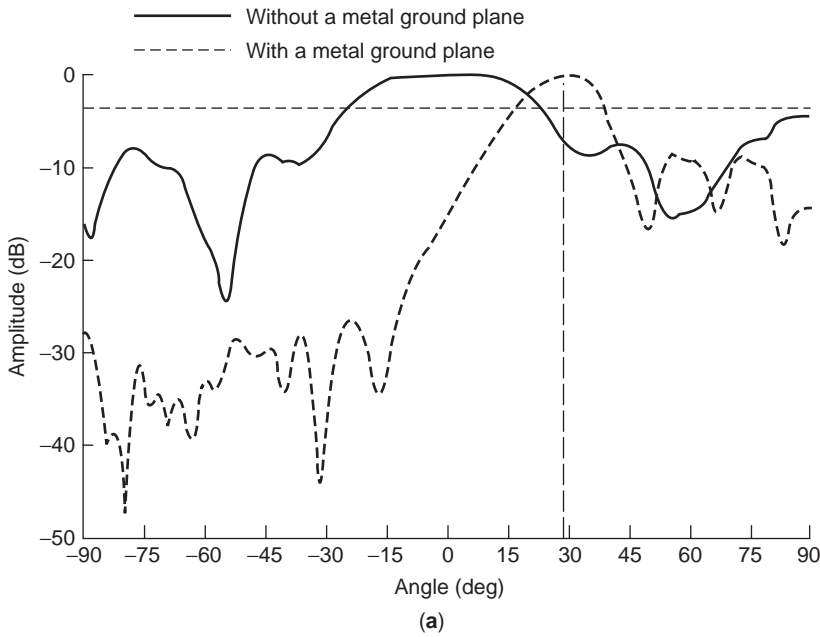


Figure 22. Measured patterns at 19 GHz: (a) *H*-plane; (b) *E*-plane.

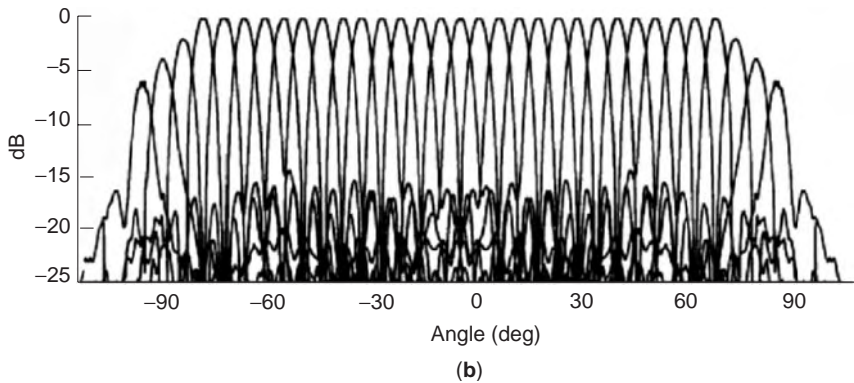
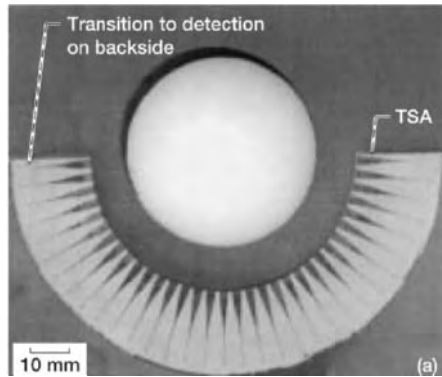


Figure 23. (a) 33-beam array with spherical Teflon lens; (b) measured *E*-plane pattern. (From Ref. 42 with permission from IEEE.)

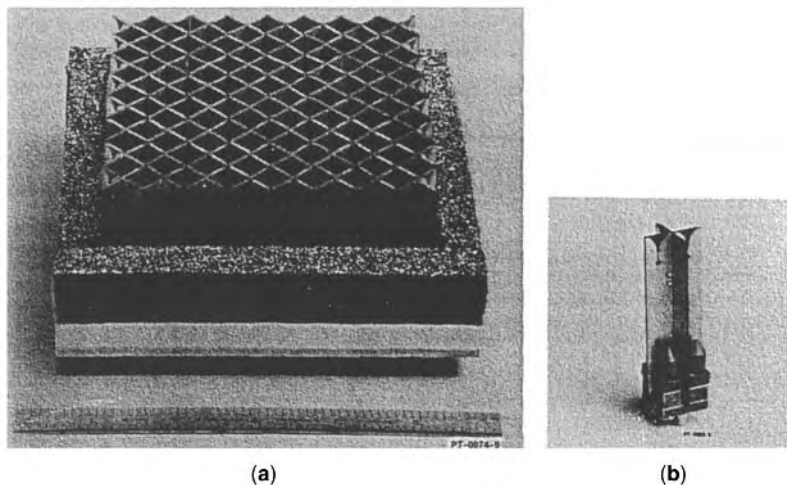


Figure 24. Photographs of dual-polarized TSA array: (a) 8×8 array; (b) orthogonal subarray element pair.

In this approach, an array of active antenna modules, constructed from nonplanar TSAs and monolithic microwave integrated circuit (MMIC) multistage GaAs power amplifiers, receives the signal at lower power and after amplification reradiates the signal into free space. Polarization diversity is employed to permit accurate measurement of the amplified signal radiated from the transmitting array. With the amplifiers turned on, the three-element active array module produced a gain of 30 dB at 20 GHz [38]. Replacing the MMIC multistage power amplifier with a broadband, GaAs MMIC distributed amplifier, frequency multiplication, and space power combining were demonstrated with the same active LTSA array module, which receives signals at 9.3 GHz, and after amplification, radiates the second harmonic signal into free space. Results indicated a fundamental-to-second-harmonic conversion efficiency of 8.1% [39]. For experimental details and measured results, the reader is referred to Ref. 10.

With the rapid development of the wireless industry, a K-band circular LTSA array, shown in Fig. 21, has been proposed for mobile communications [40]. The 16-element array is fed by a 1–16 microstrip line power splitter composed of T junctions and right-angle bends. The output ports of the splitter are electromagnetically coupled to the slotline of the LTSA through a microstrip-to-slotline transition with the slotline and microstrip line characteristic impedances chosen to be 120 and 100 Ω , respectively. The array was placed over a reflecting ground plane to displace the beam above the horizon, and foam spacers of different thickness are used to control the amount of scan. Figure 22 shows the measured *E*- and *H*-plane patterns for $0.286\lambda_0$ separation. As shown, the circular LTSA array produces an omnidirectional pattern in the azimuthal plane and a beam displacement of about 28° in the elevation plane.

Using a similar approach, an omnidirectional quasi-optical circular array of 12 Vivaldi-coupled oscillator elements has been designed for LMDS (local multipoint distribution services) applications [41]. The array, which

is powered from a single direct-current power supply, has demonstrated an 87% power combining efficiency, and 144 mW radiated power at 28 GHz.

TSA array has found applications in intelligent transportation systems. A wide-scan spherical lens antenna at millimeter-wave frequency (77 GHz) has been introduced for automobile radars [42]. The multibeam antenna system is composed of planar TSAs positioned around a homogeneous spherical Teflon lens. Beamscanning is achieved by switching between elements. Figure 23 shows a 33-beam spherical Teflon lens system that has demonstrated an angular resolution of 5.5° and -3.5 dB cross-over of adjacent beams.

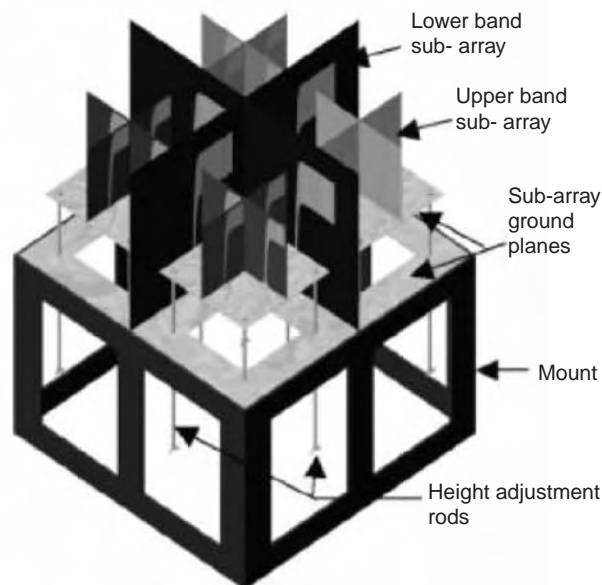


Figure 25. Sketch of a 20-element dual-band dual-polarized multilevel antipodal Vivaldi array. (From Ref. 8 with permission from IEEE.)

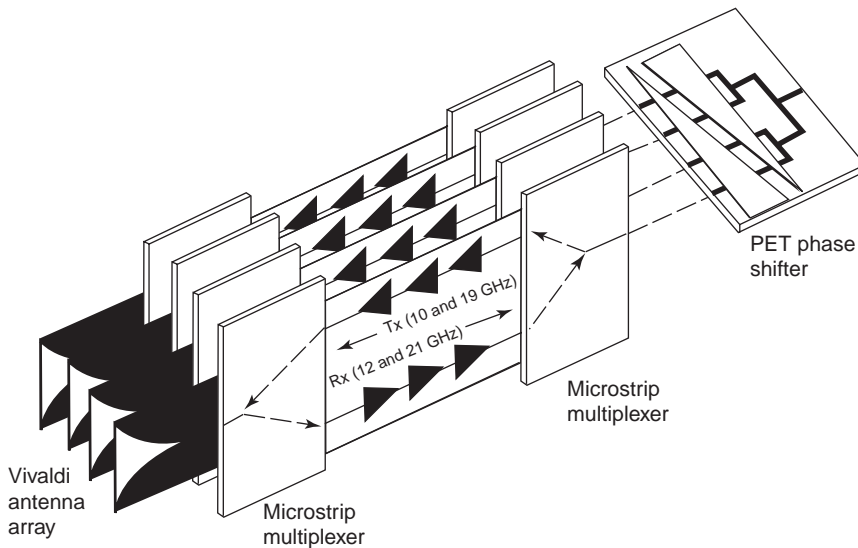


Figure 26. Multifrequency and full-duplex Vivaldi phased-array system with dual-PET phase controls. (From Ref. 9 with permission from IEEE.)

In shared aperture technology development where the functionality of several antennas are combined into one aperture using wideband multiple beam technology, dual-polarized tapered slot antennas with “double Y” microstrip-to-slotline transition have been used to achieve wideband operations [43]. To realize horizontal and vertical linear polarizations, two TSA elements of like polarization are first combined into a two-element subarray. Then, two such subarrays are joined at a 90° angle through a mechanical slot cut in the top of one subarray and the bottom of the other subarray to form a quad-element subarray module. Figure 24 shows an 8×8 array composed of quad-element subarray modules as building blocks. To obtain right- and left-hand circular polarization, the horizontal and vertical polarizations are combined with a 90° phase offset in a quadrature hybrid circuit.

Combining the functionality of several antennas into one shared aperture presents many technical challenges. In 2003 a dual-band dual-polarized nested antipodal Vivaldi array was developed for a new radiotelescope, the Square Kilometer Array (SKA) [8]. In order to meet the 5–1 bandwidth (0.8–4.0 GHz) requirement, the array consists of a lower-band and an upper-band subarray with each made up of different-size antipodal Vivaldi quad elements having overlapping bandwidths. The array of nested lattice architecture has multilevel ground planes that allow height adjustment to achieve optimization of the array performance. A sketch of a 20-element dual-band dual-polarized multilevel nested antipodal Vivaldi array is shown in Fig. 25.

In a more recent development of a low-cost, multifrequency and full-duplex phased-array transceiver that transmits at 10 or 19 GHz and receives at 12 or 21 GHz, Vivaldi antennas were used to achieve wideband performance. In addition, the system, as illustrated in Fig. 26, features a low-loss and low-cost multilayer phase shifter controlled by dual piezoelectric transducers (PETs) and four-channel microstrip multiplexers [9]. The array system has demonstrated scan angles of about 40° at 10–21 GHz using the PET phase controls. The use of PET

greatly simplifies the integration and high insertion loss problems generally associated with solid-state type phased shifters used in conventional phased arrays.

7. CONCLUSION

The objective of this article is to provide an overview of notch antennas including underlying principles and limitations, general design guidelines, performance characteristics, and new applications. Due to limited coverage, the article focuses mainly on LTSA and Vivaldi, while many other noteworthy works have not been able to include in the discussion. The general design guideline outlined here is intended as an initial step in the experimental or analytical processes leading to the final design. The discussions on feeding techniques and antenna characteristics are useful in understanding the design and the radiation process of notch antennas. Finally, the article ends with some more recent advances and innovative applications of TSA arrays based on shared aperture technology.

BIBLIOGRAPHY

1. L. R. Lewis, M. Fassett, and J. Hunt, A broadband stripline array element, *Proc. 1974 IEEE AP-S Int. Symp.*, Atlanta, GA, June 1974, pp. 335–337.
2. R. Janaswamy, An accurate moment method model for the tapered slot antenna, *IEEE Trans. Anten. Propag.* **37**(12):1523–1528 (Dec. 1989).
3. E. Thiele and A. Taflove, FD-TD analysis of Vivaldi flared horn antennas and arrays, *IEEE Trans. Anten. Propag.* **42**(5):633–641 (May 1994).
4. L. -C. Kuo, M. -C. Tsai, and H. -R. Chang, 3-D FDTD design simulation and experimental measurement of a Ka-band planar antipodal-linearly tapered slot antenna (ALTSA), *IEEE Microwave Wireless Compon. Lett.* **11**(9):382–384 (Sept. 2001).

5. CAD benchmark on a balanced antipodal Vivaldi antenna, *Microwave Engineering Europe* (<http://www.mwee.com/magazine/2000/CAD-nov.htm>), Oct. 2000.
6. N. -S. Cheng, P. Jia, D. B. Rench, and R. A. York, A 120-W X-band spatially combined solid-state amplifier, *IEEE Trans. Microwave Theory Tech.* **47**(12):2557–2559 (Dec. 1999).
7. T. L. Korzeniowski, D. M. Pozar, D. H. Schaubert, and K. S. Yngvesson, Imaging system at 94 GHz using tapered slot antenna elements, *Proc. 8th Int. Conf. Infrared and Millimeter Waves*, 1983, p. w6.3.
8. H. Loui, J. P. Weem, and Z. Popovic, A dual-band dual-polarized nested Vivaldi slot array with multilevel ground plane, *IEEE Trans. Anten. Propag.* **51**(9):2168–2175 (Sept. 2003).
9. T. -Y. Yun, C. Wang, P. Zepeda, C. T. Rodenbeck, M. R. Coutant, M. Li, and K. Chang, A 10–21 GHz, low-cost, multifrequency, and full-duplex phased-array antenna system, *IEEE Trans. AP-S* **50**(5):641–649 (May 2002).
10. K. F. Lee and W. Chen, *Advances in Microstrip and Printed Antennas*, Wiley-Interscience, New York, 1997, Chap. 9, p. 443.
11. S. N. Prasad and S. Mahapatra, A novel MIC slot line aerial, *Proc. 9th European Microwave Conf.*, Brighton, UK, 1979, pp. 120–124.
12. P. J. Gibson, The Vivaldi aerial, *Proc. 9th European Microwave Conf.*, Brighton, UK, 1979, pp. 101–105.
13. T. L. Hwang, D. B. Rutledge, and S. E. Schwarz, Planar sandwich antennas for submillimeter applications, *Appl. Phys. Lett.* **34**(1):9–11 (Jan. 1979).
14. R. N. Simons, N. I. Dib, R. Q. Lee, and L. P. B. Katehi, Integrated uniplanar transition for linearly tapered slot antenna, *IEEE Trans. Anten. Propag.* **43**(9):998–1002 (1995).
15. J. J. Lee and S. Livingston, Wide band bunny-ear radiating element, *1993 IEEE AP-S Int. Symp. Digest*, June 1993, pp. 1604–1607.
16. E. Gazit, Improved design of the Vivaldi antenna, *IEE Proc. Part H* **135**(2):89–92 (1988).
17. J. D. S. Langley, P. S. Hall, and P. Newham, Balanced antipodal Vivaldi antenna for wide bandwidth phased arrays, *IEE Proc. Anten. Propag.* **143**(2):97–102 (April 1996).
18. X. D. Wu and K. Chang, Compact wideband integrated active slot antenna amplifier, *Electron. Lett.* **29**(5):496–497 (March 1993).
19. G. Zheng, A. A. Kishk, A. W. Glisson, and A. B. Yakovlev, Slot antenna fed by a CPW line with tapered transition, *Microwave Opt. Technol. Lett.* **38**(6):465–467 (2003).
20. I. Linardou and C. Migliaccio, Twin Vivaldi antenna for transponders and monopulse systems, *Microwave Opt. Technol. Lett.* **27**(3):207–209 (Nov. 2000).
21. N. Marchand, Transmission line conversion, *Electronics* **17**:142–145 (1944).
22. A. B. Smolders and M. J. Arts, Wide-band antenna element with integrated balun, *1998 IEEE AP-S Int. Symp. Digest*, Atlanta, GA, June 1998.
23. V. Trifunovic and B. Jokanovic, Review of printed Marchand and double-Y baluns: Characteristics and application, *IEEE Trans. Microwave Theory Tech.* **42**(8):1454–1462 (Aug. 1994).
24. R. N. Simons, N. I. Dib, R. Q. Lee, and L. P. B. Katehi, Integrated uniplanar transition for linearly tapered slot antenna, *IEEE Trans. Anten. Propag.* **43**(9):998–1002 (1995).
25. R. N. Simons, R. Q. Lee, and T. D. Perl, Non-planar linearly tapered slot antenna with balanced microstrip feed, *1992 IEEE AP-S Int. Symp.* 1992, Vol. 4, pp. 2109–2112.
26. P. Knott and A. Bell, Coaxially-fed tapered slot antenna, *Electron. Lett.* **37**(18):1103–1104 (Aug. 2001).
27. K. Sigfrid Yngvesson, T. L. Korzeniowski, Y. -S. Kim, E. L. Kollberg, and J. F. Johansson, The tapered slot antenna—a new integrated element for millimeter-wave application, *IEEE Trans. Microwave Tech.* **37**(2):365–374 (Feb. 1989).
28. T. Thungren, E. L. Kollberg, and K. S. Yngvesson, Vivaldi antennas for single beam integrated receiver, *Proc. 12th European Microwave Conf.*, 1982, pp. 475–480.
29. P. S. Kooi, T. S. Yeo, and M. S. Leong, Parametric studies of the linearly tapered slot antenna (LTSA), *Microwave Opt. Technol. Lett.* **4**(5):200–206 (April 1991).
30. D. C. Hogg and W. E. Legg, A finline radiator, *Bell Syst. Tech. J.* **52**(7):1249–1253 (Sept. 1973).
31. J. S. Colbum and Y. Rahmat-Samii, Printed antenna pattern improvement through substrate perforation of high dielectric constant material: An FDTD evaluation, *Microwave Opt. Technol. Lett.* **18**(1):27–32 (May 1998).
32. T. J. Ellis and G. M. Rebeiz, MM-wave tapered slot antennas on micromachined photonic bandgap dielectrics, *1996 IEEE MTT-S Int. Symp. Digest*, 1996, pp. 1157–1160.
33. K. S. Yngvesson, D. H. Schaubert, T. L. Korzeniowski, E. L. Kolberg, T. Thungren, and J. F. Johnson, Endfire tapered slot antennas on dielectric substrate, *IEEE Trans. Anten. Propag.* **33**(12):1392–1400 (1985).
34. R. N. Simons and R. Q. Lee, Linearly tapered slot antenna impedance characteristics, *1995 IEEE AP-S Int. Symp. Digest*, 1995, Vol. 1, pp. 170–173.
35. NIST De-embedding software, *Program DEEMBED*, Rev. 4.04, 1994.
36. R. N. Simons and R. Q. Lee, Characterization of miniature millimeter-wave Vivaldi antenna for local multipoint distribution service, *49th ARFTG/MTT Conf. Digest*, 1997, pp. 95–99.
37. R. N. Simons and R. Q. Lee, On-wafer characterization of millimeter-wave antennas for wireless applications, *IEEE Trans. Microwave Theory Tech.* **47**(1):92–96 (Jan. 1999).
38. R. N. Simons and R. Q. Lee, Space power amplification with active linearly tapered slot antenna array, *Proc. 1993 IEEE MTT-S Int. Microwave Symp.* 1993, Vol. II, pp. 623–626.
39. R. N. Simons and R. Q. Lee, Spatial frequency multiplier with active linearly tapered slot antenna array, *Proc. 1994 IEEE MTT-S Int. Microwave Symp.* 1994, Vol. III, pp. 1557–1560.
40. R. N. Simons, E. Kelly, R. Q. Lee, and S. R. Taub, Radial microstrip slotline feed network for circular mobile communications array, *1994 IEEE AP-S Int. Symp. Digest*, 1994, Vol. 2, pp. 1024–1027.
41. M. J. Vaughan and R. C. Compton, 28 GHz omni-directional quasi-optical transmitter array, *IEEE Trans. Microwave Theory Tech.* **43**(10):2507–2509 (1995).
42. B. Schoenlinner, X. Wu, J. P. Ebling, G. V. Eleftheriades, and G. M. Rebeiz, Wide-scan spherical-lens antennas for automotive radars, *IEEE Trans. Microwave Theory Tech.* **50**(9):2166–2175 (Sept. 2002).
43. T. A. Axness, R. V. Coffman, B. A. Kopp, and K. W. O'Haver, Shared aperture technology development, *John Hopkins APL Tech. Digest* **17**(3):285–294 (1996).

ORTHOMODE TRANSDUCERS

G. G. GENTILI
 Milan Polytechnic
 Milan, Italy
 R. NESTI
 National Institute for
 Astrophysics
 Florence, Italy
 G. PELOSI
 S. SELLERI
 University of Florence
 Florence, Italy

1. INTRODUCTION

Orthomode transducers (OMTs) are microwave components commonly used in receivers and transmitters, especially in the microwave frequency range from about 1 GHz up to a few hundred gigahertz. Telecommunications and radio astronomy are typical operative environments using OMTs that thus serve both civilian and scientific applications.

This device works as a polarization diplexer; in transmitters, it combines two separate signals from separate input channels into two orthogonally polarized signals in a single output channel so that information is still separated, or, equivalently, the two signals are uncoupled. In receivers, it separates an incoming dual-polarized signal into two output channels, each carrying the information associated with one of the two polarization states of the input. The polarization state may be linear or circular; in this second case the OMT is more properly termed a *polarizer*.

An initial classification of OMT is given in the paper by Boifot et al. [1], while an excellent description of practical OMT and polarizer configurations is provided in the book by Uher et al. [2].

In the following we use the term *common port* to refer to the port where the two signals are mixed and *single-mode port*, to the other two ports.

The need for such a device originated primarily in (1) civilian applications, where resources in terms of frequency bands are very limited compared with the growing demands for new communication channels, thus generating interest in a device that doubles the number of channels in a given frequency band by using two separate polarizations and (2) modern scientific applications, such as astrophysics, to detect the polarization state of the signal coming from the sky, as this provide important information on fundamental cosmological parameters.

The aim of this article is to give fundamental information on OMT operative aspects, introducing few OMT models to help the reader understand the basic concepts of OMT architectures. Gaining this insight is very important because, unfortunately, analytical tools are not available to design OMTs in a direct and simple manner, so it is necessary to resort to computer software employing

numerical techniques to perform analysis and design. For this reason, numerical techniques are of primary importance, and an in-depth knowledge of these methods is fundamental for modern microwave engineers. Here there is space to give the reader only a brief insight into these techniques, but Itoh treats this argument in greater depth [3]. Finally, advanced OMT and polarizer design examples are presented to better illustrate the state of art of these devices.

2. ORTHOMODE TRANSDUCER FUNDAMENTALS

Because OMT operation is based on wave propagation in structures whose dimensions are of the order of the wavelength, OMT theory is based on the transmission-line approach, which is developed in the frequency-space domain. Also, even if—from a mechanical perspective—OMTs have three physical ports, the fact that the common port has two modes implies that, electrically speaking, the OMT schematic consists of a four-port device as shown in Fig. 1, with the two single-mode ports 3,4 and the two ports 1,2 at the common-port side.

OMTs are commonly characterized by means of the scattering coefficients [4] giving the ratio of the incident and reflected wave coefficients, which are complex quantities, at the various ports with a particular setting; where S_{ij} is the ratio between the amplitude of the field that comes out at port i and the amplitude of the incident field at port j , provided only port j is excited and any other port l , $l \neq j$, is connected to a matched load. A more meaningful parameter, from a physical perspective, is given by the square amplitude of the scattering coefficients: $|S_{ij}|^2$; this represents the fraction of the total power incident at port j which comes out from port i .

For an ideal OMT, referring to the sketch in Fig. 1, the scattering matrix is given by the following expression

$$S = \begin{bmatrix} 0 & 0 & e^{j\alpha} & 0 \\ 0 & 0 & 0 & e^{j\beta} \\ e^{j\alpha} & 0 & 0 & 0 \\ 0 & e^{j\beta} & 0 & 0 \end{bmatrix} \quad (1)$$

where α and β are, in general, real constants. We can see that it is matched at all the ports, with the diagonal

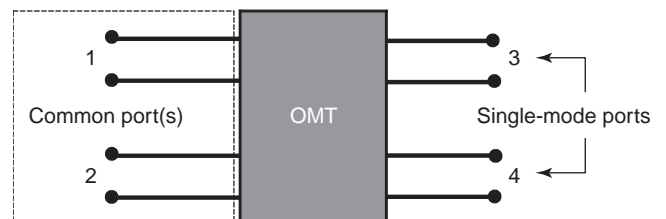


Figure 1. OMT schematic.

elements of S equal to zero. From the first row of S ($s_{13} = e^{j\alpha}$) we conclude that all the power incident at the single-mode port 3 comes out from port 1, which is associated with one of the two polarizations at the common port. Because of device reciprocity, the signal from port 1 must exit from port 3 ($s_{31} = s_{13} = e^{j\alpha}$). In a similar way ports 2 and 4 are coupled; thus $s_{24} = s_{42} = e^{j\beta}$. All the other entries of the S matrix are equal to zero in the ideal OMT. For practical OMTs, nonidealities are summarized in Table 1.

OMTs are formed by using essentially the following basic types of guiding structures: the rectangular, square, and circular waveguides; the microstrip line; and the coaxial cable. All these guiding structures support multi-mode field configuration, but, generally, in the operative OMT bandwidth, only the fundamental mode propagates. Each mode has its own electric and magnetic field distribution, knowledge of which, together with knowledge of the associated propagation constant, is fundamental in order to fully understand the behavior of OMTs and to obtain the required background for OMTs design. To satisfy this objective another aspect that must be developed with high accuracy is field polarization.

These arguments are discussed with sufficient accuracy here to enable the reader to understand the OMT aspects presented in this article, but we recommend a much more in-depth treatment for further details; for a very accurate description of field distribution and propagation in those kind of waveguides, we suggest Ref. 4, while for the full theory on field polarization, we recommend Ref. 5.

2.1. Coaxial Cable

Coaxial cable is used in OMTs as a single-mode port because its fundamental mode, as we shall see, has a single polarization configuration, avoiding the possibility of propagating two uncoupled signals. It is a structure allowing the propagation of electromagnetic (EM) energy in the whole frequency spectrum. The fundamental mode of propagation is transverse electromagnetic (TEM) with both the electric and magnetic field vectors on the plane orthogonal to the direction of propagation. As shown in Fig. 2, it is composed of two coaxial circular conductors of radii a and b , $b > a$, with, normally, a homogeneous dielectric material as interconductor medium to provide

Table 1. OMT Operative Parameters

Description	Scattering Coefficient
Reflection coefficient (return loss)	
Common port	$ S_{11} , S_{22} $ ($1/ S_{11} , 1/ S_{22} $)
Single-mode ports	$ S_{33} , S_{44} $ ($1/ S_{33} , 1/ S_{44} $)
Losses	
Channel 1	$1 - S_{31} ^2$
Channel 2	$1 - S_{42} ^2$
Isolation	
Channel crosstalk	$ S_{14} , S_{23} $
Common-port crosstalk	$ S_{12} $
Single-mode port crosstalk	$ S_{34} $

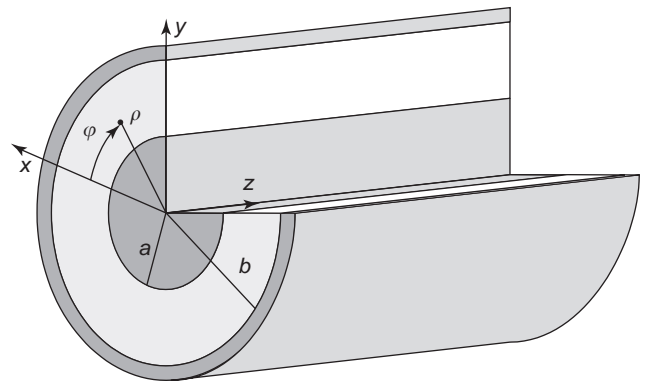


Figure 2. Coaxial cable: reference sketch.

mechanical stability. The structure is rotationally symmetric; a longitudinal slice is cut in the figure only to clarify the internal configuration. By applying a potential difference V_0 between the two conductors, a TEM field propagating in the medium can be expressed as follows:

$$\mathbf{E} = \frac{V_0}{\ln(b/a)} \frac{1}{\rho} \mathbf{u}_\rho e^{-j\beta z};$$

$$\mathbf{H} = Y_0 \mathbf{u}_z \times \mathbf{E};$$

$$a \leq \rho \leq b, \quad 0 \leq \varphi < 2\pi$$
(2)

The field, whose configuration is given in Fig. 3, is represented here in cylindrical coordinates ρ, φ, z , with unit vectors $\mathbf{u}_\rho, \mathbf{u}_\varphi, \mathbf{u}_z$, and the propagation is assumed e^{-jkz} type in only the z direction. The properties of the medium are expressed in the field impedance $Z_0 = Y_0^{-1} = (\mu/\epsilon)^{1/2}$, where ϵ and μ are, respectively, the dielectric permittivity and magnetic permeability of the dielectric material. The

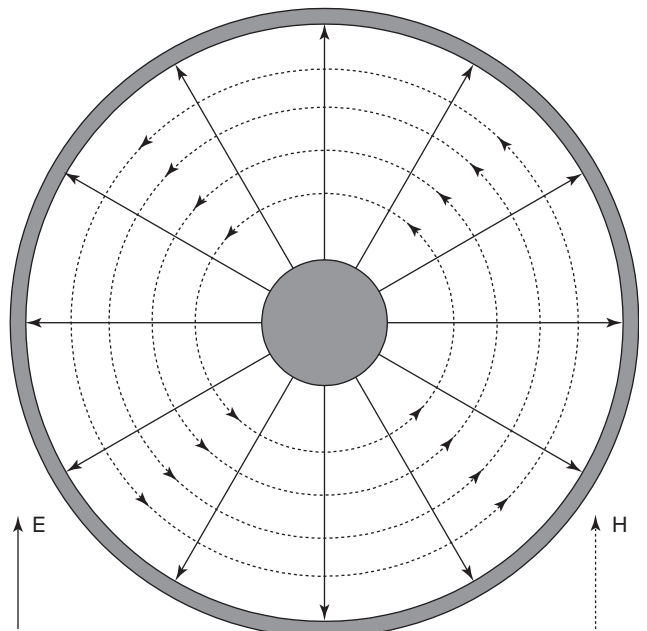


Figure 3. Coaxial cable: electromagnetic field distribution for the TEM fundamental mode.

electrical characteristics of the coaxial cable as a transmission line are expressed by the characteristic impedance $Z_c = Z_0 \ln(b/a)/(2\pi)$ and the propagation constant $\beta = k = \omega (\epsilon\mu)^{1/2}$ is equal to the medium wavenumber k and where $\omega = 2\pi f$ is the angular frequency (f is the frequency). The geometric parameters of the cable also determine the upper frequency limit; this is commonly associated with the cutoff frequency of the first higher-order mode (TE₁₁), which is given with very good accuracy by setting the cutoff wavelength equal to the circumference associated to the mean radius. Thus

$$\lambda_{11} = \pi(a + b); \Rightarrow f_{11} = \frac{c(\epsilon_r)^{-1/2}}{\lambda_{11}} = \frac{c(\epsilon_r)^{-1/2}}{\pi(a + b)} \quad (3)$$

where c is the light velocity in vacuum and ϵ_r the relative dielectric constant (i.e., the ratio between the permittivity of the dielectric material and the permittivity of vacuum). For a more in-depth treatment on coaxial cable higher-order modes, we suggest the book by Marcuvitz [6].

2.2. Microstrip Line

Like coaxial cables, the microstrip line (Fig. 4) is used essentially as a single-mode port as, in the same way, it supports a single fundamental mode, which propagates in the z direction from zero frequency upward. It is a structure belonging to the family of planar transmission lines that are used largely in modern microwave applications. As shown in Fig. 4, it is formed by a conducting strip of width w and thickness t placed on a dielectric substrate of relative dielectric constant ϵ_r and thickness h that is grounded on the other side by a conducting layer. The major advantages of the microstrip line are as follows:

- It can be fabricated using low-cost printed circuit board (PCB) technology with good mechanical tolerances in the microwave range.
- It allows very easy integration of elementary linear and nonlinear devices, making it possible to realize complex circuits directly on a single board; these circuits are commonly referred to as *integrated circuits*, while the single board is termed a “chip”.

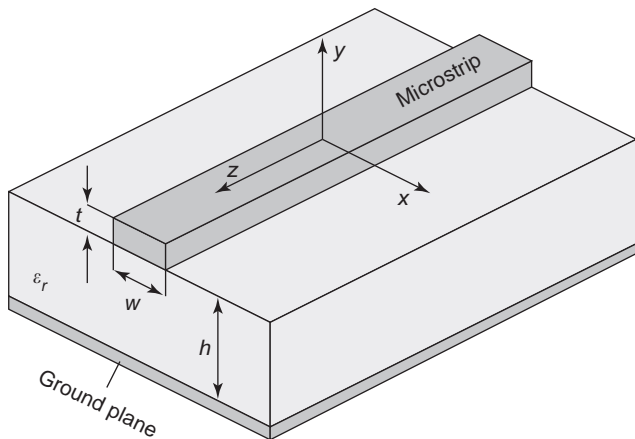


Figure 4. Microstrip line: geometry.

- It can be easily coupled with square or circular waveguides to form OMTs’.

The main drawbacks of the microstrip is that the medium in which the EM field propagates is nonhomogeneous. Differently from the coaxial cable, since the EM field propagates in both air and the dielectric material, the propagation constant does not depend linearly with the frequency, causing frequency distortion of wavepackets. The fundamental mode has the transverse field configuration shown in Fig. 5. Unfortunately there are no simple analytical solutions expressing the EM field distributions, but we would like to emphasize the close analogy with the coaxial cable, with the electric field lines directed mostly from one conductor to the other and the magnetic field lines as deformed circles around the smaller conductor. The strip guides the EM wave in the z direction whose energy is most concentrated in the dielectric medium, in the region between the strip itself and the ground plane, with such an effect emphasized by increasing ϵ_r . The fundamental mode is termed “quasi-TEM” because a longitudinal component of the associated EM field exists but is very small compared to the transverse ones. The characterization of the microstrip may be given, with very good approximation for our practical purposes, by using transmission-line concepts that are discussed later in this article; for a reader interested in more details, we suggest Refs. 4 and 7.

Although the transmission-line characterization is, in principle, quite simple, determined essentially by only two parameters, the characteristic impedance Z_c and the propagation constant of the fundamental mode β , closed formulas for these parameters are quite elaborate because of the complexity of the structure.

The propagation constant is usually expressed in terms of the *effective relative dielectric constant* ϵ_{e} , representing the dielectric constant of an equivalent homogeneous

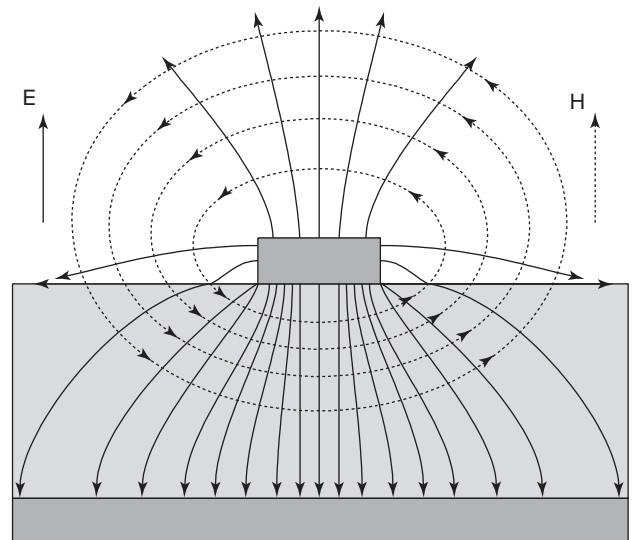


Figure 5. Microstrip line: field configuration of the quasi-TEM dominant mode.

TEM line, thus satisfying

$$\beta = \frac{\omega(\epsilon_e)^{-1/2}}{c} \tag{4}$$

The propagation factor is $e^{-j\beta z}(e^{+j\beta z})$ for waves traveling in the $+z$ ($-z$) direction.

The effective relative dielectric constant ϵ_e is a function of the geometry according to

$$\begin{cases} \epsilon_e = \frac{\epsilon_r + 1}{2} + \frac{\epsilon_r - 1}{2} \left[\left(1 + 12\frac{h}{w}\right)^{-1/2} + 0.04\left(1 - \frac{w}{h}\right)^2 \right] \frac{w}{h} \leq 1 \\ \epsilon_e = \frac{\epsilon_r + 1}{2} + \frac{\epsilon_r - 1}{2} \left(1 + 12\frac{h}{w}\right)^{-1/2} \frac{w}{h} \geq 1 \end{cases} \tag{5}$$

The characteristic impedance can also be expressed as a function of the effective relative dielectric constant ϵ_e , thus assuming different forms according to the ratio between the strip width w and the dielectric thickness h :

$$\begin{cases} Z_c = \frac{\mu c}{2\pi(\epsilon_e)^{1/2}} \ln\left(8\frac{h}{w} + 0.25\frac{w}{h}\right) \frac{w}{h} \leq 1 \\ Z_c = \frac{\mu c}{(\epsilon_e)^{1/2}} \left[\frac{w}{h} + 1.393 + 0.667 \ln\left(\frac{w}{h} + 1.444\right)\right]^{-1} \frac{w}{h} \geq 1 \end{cases} \tag{6}$$

These formulas give accuracy better than 1 percent for practical values of w , h , and ϵ_r [4].

To attain a better accuracy, the finite thickness t of the strip has to be considered. This can be done by replacing the actual strip width (w) and dielectric height (h) with the corresponding *effective* values w' and h' defined as

$$\begin{cases} w' = w + \frac{t}{\pi} \left[\ln\left(2\frac{h}{t}\right) + 1 \right] \\ h' = h - 2t \end{cases} \tag{7}$$

and by modifying the expression defining the effective dielectric constant ϵ_e as

$$\epsilon'_e = \epsilon_e - \frac{\epsilon_r - 1}{4.6} \frac{t/h}{(w/h)^{1/2}} \tag{8}$$

The upper frequency limit to prevent higher-order mode propagation is given by the following formula

$$f_c = \frac{150}{\pi h} \left(\frac{2}{\epsilon_r - 1}\right)^{1/2} \tan^{-1}(\epsilon_r) \tag{9}$$

where f_c is expressed in gigahertz and h in millimeters.

2.3. Rectangular Waveguide

The rectangular waveguide is the most versatile structure for OMT applications because it is used as both a single-mode port and a common port.

In contrast to the previous transmission lines, the rectangular waveguide does not support TEM (or quasi-TEM) propagation mode, and this fact has some important consequences:

- Rectangular waveguides cannot be characterized easily by resorting to circuit parameters such as like characteristic impedance and a propagation constant, but we have to use a full-field approach.
- The fundamental mode has a nonzero frequency cut-off below which no energy can be propagated.
- The propagation constant has a nonlinear variation with frequency causing signal dispersion; this effect is noticeable mainly in the lower side of the single-mode band.

Notwithstanding these drawbacks, the rectangular waveguide is widely used in the microwave range because

- Fields are known analytically, thus making available very simple, efficient, and accurate design tools.
- They exhibit very low losses and very high power-handling capabilities.
- They are inexpensive and easily machined structures.

Figure 6 shows the transverse section of a rectangular waveguide. The electromagnetic field excitation in a rectangular waveguide may be done in different ways. Microwave energy is able to propagate if the cutoff condition is satisfied. To determine this condition, we define the generic transverse eigenvalue:

$$\begin{aligned} k_{t,mn} &= [k_{xm}^2 + k_{ym}^2]^{1/2}, \\ k_{xm} &= \frac{m\pi}{a}; \\ k_{yn} &= \frac{n\pi}{b} \end{aligned} \tag{10}$$

which represents the wavenumber lower limit for both the TE_{mn} mode and the TM_{mn} mode under which the mode cannot propagate. Thus the cutoff condition for the two mn

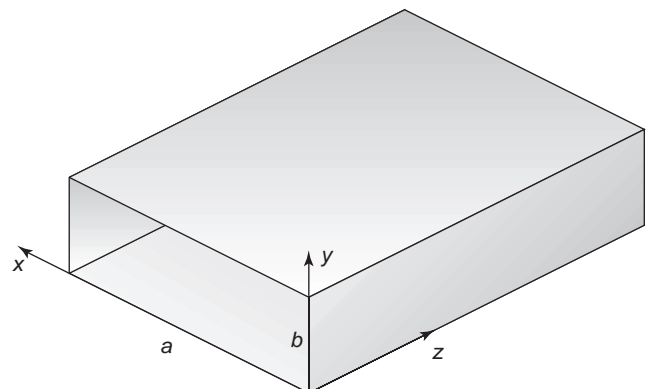


Figure 6. Rectangular waveguide: geometry.

modes is given by

$$k = \omega(\epsilon\mu)^{1/2} > k_{t,mn} \quad (11)$$

This relation gives directly the cutoff frequency f_c by

$$k = k_{t,mn} \Rightarrow f_c = \frac{ck_{t,mn}}{2\pi} \quad (12)$$

The propagation constant is given by

$$k_{mn} = -j(k_{t,mn}^2 - k^2)^{1/2} = \begin{cases} \beta > 0, & k > k_{t,mn} \\ -j\alpha, & \alpha > 0, k < k_{t,mn} \end{cases} \quad (13)$$

The propagation factor is $e^{-jk_{mn}z}(e^{+jk_{mn}z})$, for a wave traveling in the $+z$ ($-z$) direction. Each wave is associated with a complex wave intensity a_{mn} (b_{mn}), which is diff, in general, between TE_{mn} and TM_{mn} modes; finally, to obtain the total field, we have to consider another factor that accounts for the field dependence on the guide transverse section (xy):

For the TE_{mn} mode

$$\begin{cases} \mathbf{E}_{mn} = k_{yn} \cos(k_{xm}x) \sin(k_{yn}y)\mathbf{u}_x - k_{xm} \sin(k_{xm}x) \cos(k_{yn}y)\mathbf{u}_y \\ \mathbf{H}_{mn} = Y_{mn} \mathbf{u}_k \times \mathbf{E}_{mn} - \frac{k_{t,mn}^2}{j\omega\mu} \cos(k_{xm}x) \cos(k_{yn}y)\mathbf{u}_z \end{cases} \quad (14)$$

For the TM_{mn} mode.

$$\begin{cases} \mathbf{H}_{mn} = k_{yn} \sin(k_{xm}x) \cos(k_{yn}y)\mathbf{u}_x - k_{xm} \cos(k_{xm}x) \sin(k_{yn}y)\mathbf{u}_y \\ \mathbf{E}_{mn} = Z_{mn} \mathbf{H}_{mn} \times \mathbf{u}_k - \frac{k_{t,mn}^2}{j\omega\epsilon} \sin(k_{xm}x) \sin(k_{yn}y)\mathbf{u}_z \end{cases} \quad (15)$$

In these expressions $Y_{mn} = (k_{mn}/\omega\mu)$ is the TE field admittance, $Z_{mn} = (k_{mn}/\omega\epsilon)$ is the TM field impedance and \mathbf{u}_k is the unit vector associated to the direction of propagation ($\mathbf{u}_k = \pm \mathbf{u}_z$).

The fundamental mode in a rectangular waveguide is the TE_{10} mode, provided $a > b$. The field configuration of the TE_{10} mode is given in Fig. 7 showing no variation along the y coordinate and a sinusoidal taper with respect to the x coordinate.

The single-mode bandwidth for the rectangular waveguide depends on the value of b . If $a > 2b$, then the first higher-order mode is the TE_{20} and the relation between the cutoff frequencies of TE_{10} and TE_{20} is $f_{c20} = 2f_{c10}$; otherwise, in the case $b < a < 2b$ the first higher-order mode (TE_{01}) frequency is given by $f_{c01} = (a/b)f_{c10}$. In practice almost all the standard waveguides have $a = 2b$ giving the maximum bandwidth minimizing ohmic losses.

A particular configuration of the rectangular waveguide is used largely in OMT applications. In the case

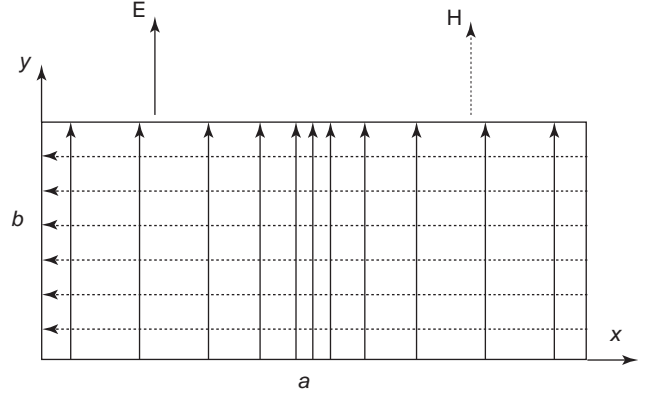


Figure 7. Rectangular waveguide: field configuration of the TE_{10} mode.

$a = b$, the square waveguide results with the properties that two uncoupled signals, having orthogonal field configurations, can propagate with the same propagation properties constituting a very attractive structure for OMT common ports. The two signals are associated with the TE_{10} and TE_{01} modes whose fields are represented in Fig. 8 showing a behavior the same as that of the standard waveguide fundamental mode. It is important to note that the single-mode bandwidth (or, in this case, more properly the double-mode bandwidth) of the square waveguide is less than half that of the standard waveguide, since the cutoff frequencies of both TE_{11} and TM_{11} are a $2^{1/2}$ factor greater than those of TE_{10} and TE_{01} . However, in structures with certain symmetries, these the first higher-order modes are not excited, so that the bandwidth can be increased in practice.

2.4. Circular Waveguide

The circular waveguide is another structure of interest because, like the square waveguide, it has very useful properties in use as a common port in OMTs.

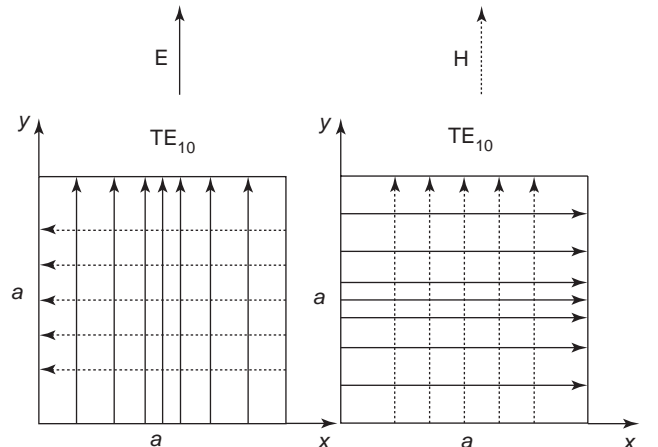


Figure 8. Square waveguide: field configuration of the TE_{10} and TE_{01} modes.

For the circular waveguide the same considerations given for the rectangular waveguide with respect to the non-TEM features of the fundamental mode are valid. While the square waveguide is better suited to feed pyramidal horns [8], the circular waveguide is better suited to feed circular horns [9] or corrugated circular horns [10]. The EM field propagation and configuration in a circular waveguide are often schematically represented as sketched in Fig. 9.

Similar to the rectangular waveguide, in a circular waveguide microwave energy is able to propagate if the cutoff condition is satisfied. In a circular waveguide the transverse eigenvalue generic expressions for the TE (h) case and the TM(e) case are different:

$$k_{t,mn}^h = \frac{p'_{mn}}{R}; \quad k_{t,mn}^e = \frac{p_{mn}}{R} \tag{16}$$

In these formulas p_{mn} and p'_{mn} are the n th zero of the m th-order Bessel function of first kind J and its derivative, respectively. New indices e and h are introduced here for the sake of brevity; the index indicates the longitudinal field component, which differs from zero, that is, $H_z \neq 0$ for TE modes (thus h) and $E_z \neq 0$ for TM modes (thus e). These zeros are obviously independent of frequency and geometry and are known and tabulated. The cutoff condition, the cutoff frequency, and the propagation constant for the e and h modes in a circular waveguide are again given by the same rectangular case formulas (11)–(13) with the position $k_{t,mn} = k_{t,mn}^h$ and $k_{t,mn} = k_{t,mn}^e$.

Also the propagation factor has the same expression $e^{\mp jk_{mn}^h z}$ ($e^{\mp jk_{mn}^e z}$), according to the direction of propagation $\pm z$ of the wave and the mode type, TE (TM). Each wave is associated with a complex coefficient, which varies, in general, between TE $_{mn}$ and TM $_{mn}$ modes; for instance, a TE $_{mn}$ wave propagating in the $+z$ direction is characterized by a factor $a_{mn}^h e^{-jk_{mn}^h z}$. Finally, to obtain the total field, we have to consider the transverse dependence whose analytical expression in circular waveguide is given as follows:

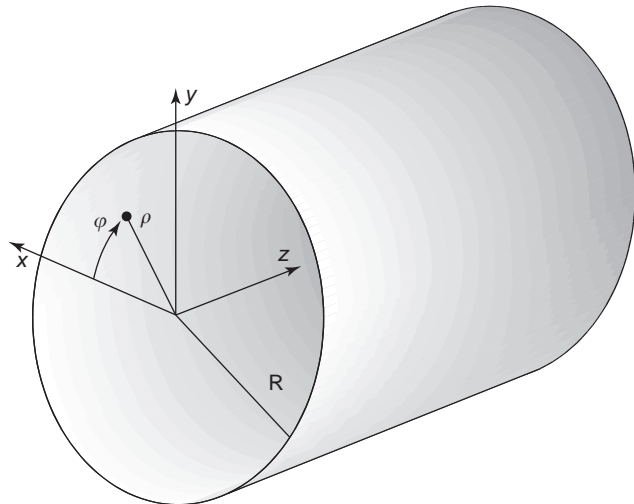


Figure 9. Circular waveguide: geometry.

For the TE $_{mn}$ mode

$$\begin{cases} \mathbf{E}_{mn} = \frac{m}{\rho} J_m(k_{t,mn}^h \rho) [V_{mn}^h \sin(m\phi) + H_{mn}^h \cos(m\phi)] \mathbf{u}_\rho \\ + \frac{\partial}{\partial \rho} J_m(k_{t,mn}^h \rho) [V_{mn}^h \cos(m\phi) - H_{mn}^h \sin(m\phi)] \mathbf{u}_\phi \\ \mathbf{H}_{mn} = Y_{mn}^h \mathbf{u}_k \times \mathbf{E}_{mn} - \frac{(k_{t,mn}^e)^2}{j\omega\mu} J_m(k_{t,mn}^h \rho) \\ \times [V_{mn}^h \cos(m\phi) - H_{mn}^h \sin(m\phi)] \mathbf{u}_z \end{cases} \tag{17}$$

and by

For the TM $_{mn}$ mode

$$\begin{cases} \mathbf{H}_{mn} = \frac{m}{\rho} J_m(k_{t,mn}^h \rho) [V_{mn}^e \cos(m\phi) - H_{mn}^e \sin(m\phi)] \mathbf{u}_\rho \\ - \frac{\partial}{\partial \rho} J_m(k_{t,mn}^e \rho) [V_{mn}^e \sin(m\phi) + H_{mn}^e \cos(m\phi)] \mathbf{u}_\phi \\ \mathbf{E}_{mn} = Z_{mn}^e \mathbf{H}_{mn} \times \mathbf{u}_k - \frac{(k_{t,mn}^e)^2}{j\omega\epsilon} J_m(k_{t,mn}^h \rho) \\ \times [V_{mn}^e \sin(m\phi) + H_{mn}^e \cos(m\phi)] \mathbf{u}_z \end{cases} \tag{18}$$

In these expressions $Y_{mn}^h = (k_{mn}^h / \omega\mu)$ is the TE field admittance, $Z_{mn}^e = (k_{mn}^e / \omega\epsilon)$ is the TM field impedance, and \mathbf{u}_k is the unit vector associated with the direction of propagation ($\mathbf{u}_k = \pm \mathbf{u}_z$). The V and H coefficients may be regarded to as normalization constants associated with one of the two independent polarization states in which each circular waveguide mode can exist, for $m > 0$; if $m = 0$, a unique polarization state does exist for each mode because the field is independent of the azimuth coordinate. In the case of the fundamental TE $_{11}$ mode, V and H may be interpreted as *vertical* and *horizontal*, associated with the direction of the electric field vector. The V and H field configurations are shown, respectively, in Figs. 10 and 11.

The fundamental TE $_{11}$ mode is associated with approximately $p'_{11} = 1.841$. The single-mode bandwidth for the rectangular waveguide does not depend on geometry, in contrast to the rectangular case, but it is fixed; the first higher-order mode is the TM $_{01}$ having approximately $p_{01} = 2.405$. The ratio between the cutoff frequencies of the TM $_{01}$ and the TE $_{11}$ modes equals the ratio of the associated zeros, so we have $f_{c01}^e = 1.3f_{c11}^h$, characterizing the bandwidth. Properties given by symmetric structures to produce, in practice, a larger bandwidth also exist in the circular waveguide, similarly to the square waveguide; in fact, we are interested mainly in circular waveguide structures having discontinuities only in the radial direction, implying that the first excited higher-order mode is the TM $_{11}$ mode having $p_{11} = 3.832$ and giving a fractional bandwidth of about $f_{c11}^e / f_{c11}^h = 2.08$.

For the same reasons regarding the TE $_{10}$ and TE $_{01}$ modes in a square waveguide, the properties of the V and H polarizations of the TE $_{11}$ mode (which we will refer to as TE $_{11v}$ and TE $_{11h}$) are very attractive for the common-port modes of OMTs.

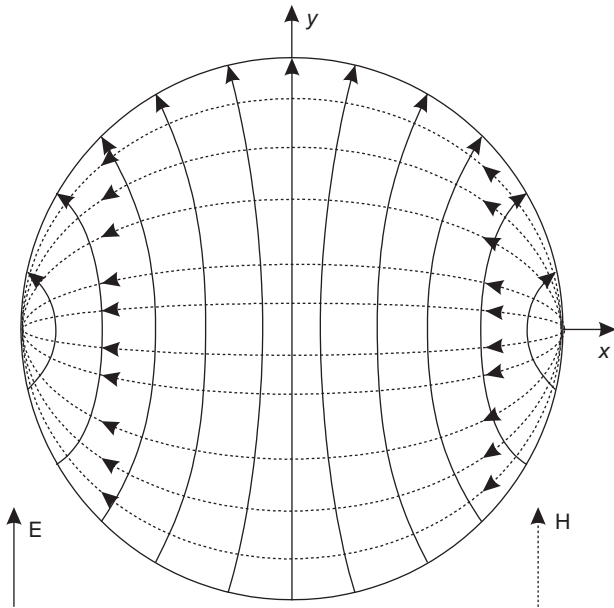


Figure 10. Circular waveguide: field configuration of the TE_{11v} mode.

3. PRACTICAL CONFIGURATIONS OF ORTHOMODE TRANSDUCERS

Different models of orthomode transducers have been developed, each matching a set of practical requirements, mainly electromagnetic requirements (return loss, ohmic losses, isolation, operative bandwidth) and mechanical/economical requirements (low cost, easy fabrication, easy

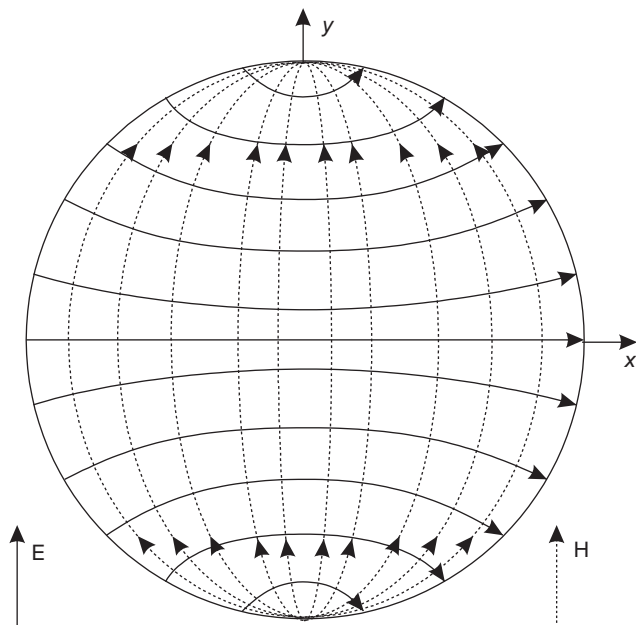


Figure 11. Circular waveguide: field configuration of the TE_{11h} mode.

interfacing with devices to which they are connected). Basic configurations will be shown in the subsequent sections.

We must note the importance of numerical methods in the computer-aided design of such devices. Many of these methods exhibit distinct features and have been developed through the increasing processing power of modern computers. Among these methods, in particular three are very useful in the design of the OMTs presented here—the finite-difference time-domain method (FDTD), the finite-element method (FEM), and the mode-matching (MM) method, each of which are only briefly introduced at this point. These three methods are particularly useful in solving electromagnetic boundary value problems in closed domains as in the case of OMTs.

The FDTD method is based on the finite-difference approximation applied directly to the differential form of Maxwell equations in the time domain and operating on a rectangular elementary cell-based mesh subdividing the entire domain of analysis. To give sufficient accuracy, these elementary cells should be small with respect to the minimum wavelength of the spectrum of the signal exciting the EM field. Also, the time elementary step, approximating the differential part of the derivative with respect to time in Maxwell equations, must satisfy certain constraints; specifically, it must be smaller than the ratio between the elementary cell dimension and the light velocity in the medium. Information regarding the boundary conditions, including the excitation signal, is the final requirement. FDTD leads directly to the solution with no matrix inversion; however, it is a bit time-consuming. Also, if the analysis is in the time domain, it is nevertheless possible to obtain frequency-related parameters, which in many cases are much more useful, using the fast Fourier transform algorithm.

FEM is actually a frequency-domain method also based on a discretization of the domain under analysis but giving more flexibility than FDTD in choosing the element cells, which may be of different shape and also within a single domain. This flexibility in the discretization is obtained at the expense of a more complex electromagnetic formulation. When boundary conditions are imposed, the EM problem becomes an algebraic linear system of equations that must be solved using conventional linear system methods. Since the system is sparse, very efficient solvers can be applied.

MM is a frequency-domain method based on the analytical field expansion into eigenfunctions in the region under analysis, leading, when boundary conditions are imposed, to an algebraic linear system, requiring in the solution the inversion of matrices that are quite full.

Nevertheless, when the geometry of the problem is simple, it is possible to describe it in terms of a cascade of waveguide sections (rectangular, circular, or coaxial), in which the solution of the Maxwell equations are known analytically, MM is perhaps the most suitable method, giving low calculation time and very high accuracy and requiring very low computation resources.

3.1. Coaxial-Cable-Coupled OMT

A very easy-to-fabricate and low-cost OMT is shown in Fig. 12. It is formed by the junction of two coaxial cables whose inner conductors intersect a circular waveguide section, where the axes of all three guiding structures are mutually orthogonal, with the coaxial external conductors electrically connected to the circular waveguide wall. On one side the waveguide is typically short-circuited by a metallic plane, while the common port is located on the other side and the two orthogonal modes TE_{11v} and TE_{11h} , associated with ports 1 and 2, respectively, can propagate. Inside the waveguide, the inner conductor of each coaxial cable is typically a quarter-wavelength long, and the distance of these cables from the waveguide short circuit is also about a quarter-wavelength. A square waveguide can replace the circular waveguide without changing the basic properties of this kind of OMT.

The ideal scattering behavior is given by the matrix (1), while the principle of operation is described in the following text. By the physical laws of the electromagnetic interaction between fields and their sources, in free space an electrical dipole radiates a field having an electric field that is oriented in the same general direction as the dipole with the property that in the far-field region the radial component tends to zero. In a bounded region, as in a waveguide, the situation is analogous; in the case of this OMT, if we consider the TE_{11v} mode (port 1) by the symmetry of its field configuration, we can note that it has a global resultant electric field that is directed vertically; thus it couples to the coaxial cable associated with port 3, with its inner conductor behaving as a vertical dipole; on the contrary, this field configuration ideally induces no currents on port 4, resulting in no field coupling between ports 1 and 4. By analogy, the TE_{11h} mode (port 2) couples to port 4 and does produce ideally no field excitation in the coaxial cable of port 3. If we assume

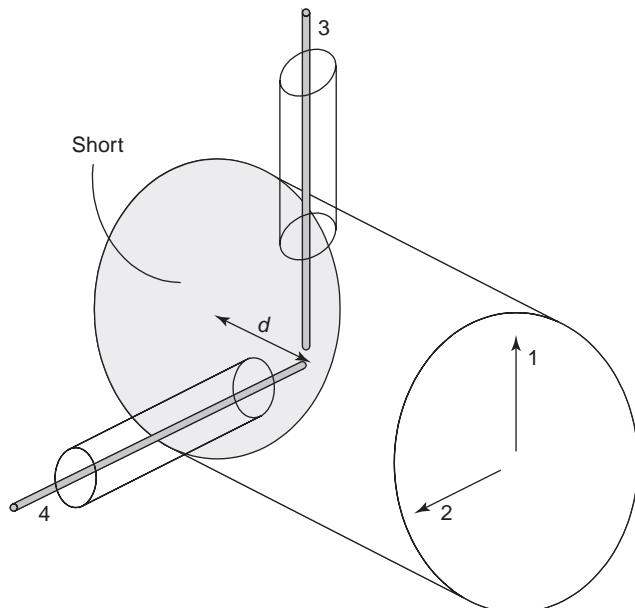


Figure 12. Coaxial-cable-coupled OMT: basic configuration.

perfect matching at the four ports and no coupling between ports 1 and 2 and between ports 3 and 4, we account for all the entries of the scattering matrix. This is, of course, ideal and untrue. It is very difficult to obtain perfect matching at all ports of this junction; a realistic value for measured junctions is $s_{ii} < (-15, -20)$ dB, and only if some matching elements, such as steps in a circular guide, are used, and this in a bandwidth no greater than 10–15%. Regarding the isolation between the uncoupled ports, we note that the azimuthal symmetry of the structure is of very high importance, avoiding the excitation of higher-order spurious modes, which results in a sensitive degradation of all the performance and a reduction in bandwidth. To be more precise, of prime importance is the symmetry with respect to the two polarization planes, which are the planes defined in the common-port waveguide by the field polarization of the two fundamental modes and the waveguide axis. In this case the structure configuration breaks the symmetries in the region of interaction with the coaxial cables, leading to severe performance degradation. On the other hand, one should observe that the presence of the short circuit does not violate any symmetry; it totally reflects only the incident mode without exciting any higher-order one.

3.2. Microstrip-Line-Coupled OMT

A more practical and widely used OMT device is shown in Fig. 13. It is formed by the junction of two microstrip lines on a common substrate, with the strips intersecting at 90° angles each other, as described in Section 3.1. Also, in this OMT the lines enter normal to the waveguide axis by the waveguide wall. The microstrip line is typically enclosed in a metallic box connected electrically to the waveguide wall; the lower side of this metallic box constitutes the microstrip ground plane, although in the region inside the waveguide the ground plane is usually removed to ensure conditions more favorable for optimum coupling. Also in

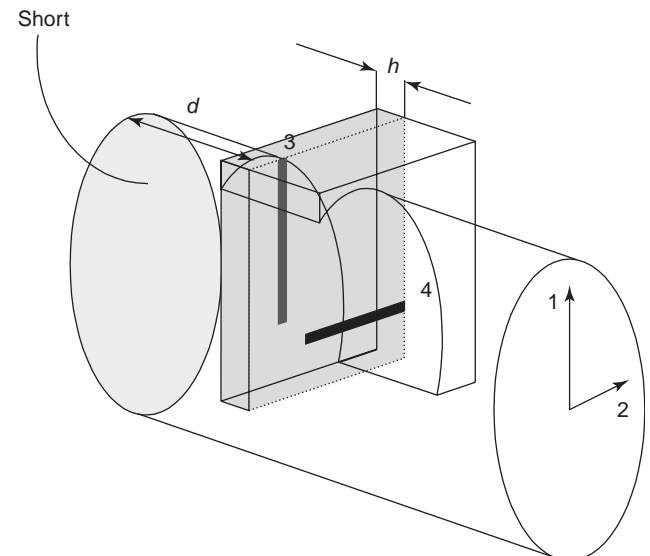


Figure 13. Microstrip-line-coupled OMT: basic configuration.

this configuration one side of the waveguide is typically short-circuited by a metallic plane while on the other side the two orthogonal modes TE_{11v} and TE_{11h} , associated with the ports 1 and 2, respectively, can propagate. The usual quarter-wavelength section is used in this case also, for both the length of the strips inside the waveguide and their distance from the short circuit ($d + h$ in Fig. 13), with care taken to consider the right wavelength. In the first case it is the wavelength in the microstrip; in the second case there is an appropriate combination, according to the lengths d and h of the respective regions, of the wavelengths in the waveguide both without and with the dielectric. A square waveguide can replace the circular waveguide without changing the basic properties of this type of OMT.

Regarding performance, we note that the optimization of the transition between a microstrip and a waveguide is currently a hotly debated point in scientific research. This is because this structure is used heavily in the front end of the receivers of the satellite TV broadcasting, directly connected to the horn feeding the 80-cm–1.2-m parabolic antenna on residential rooftops. In fact, satellite TV broadcasting uses, for each frequency band, two channels, V and H , differing only for the polarization, thus requiring an OMT to separate these two channels in the receiver.

Even if, in this case, the lack of symmetry with respect to the polarization planes does not provide high performance and broadband operation, this configuration nevertheless has two major advantages with respect to the coaxial cable configuration:

- It is very easy to fabricate matching networks with the present state-of-the-art microstrip technology using both lumped and distributed elements.
- It is very easy to accommodate on a microstrip the active circuitry to efficiently process the incoming radiofrequency signal, which requires low noise amplification as one of the first steps in preventing degradation of the signal-to-noise ratio. On a single microstrip card of a few centimeters, we can have the OMT part, matching networks, low-noise amplifiers, mixers, and other parts, with built-in hybrid microwave integrated circuit technology, so that the output signal from the microstrip is at such a low frequency that it can be transmitted through meters and meters of common TV coaxial cables for connection to the TV set without appreciably degrading the quality of the signal itself.

The principle of operation is basically the same as discussed in Section 3.1, with the coupling between TE_{11v} mode (port 1) and strip v (port 3) and between TE_{11h} mode (port 2) and strip h (port 4), thus providing the same ideal scattering matrix representation as shown in (1).

Regarding nonidealities, typical performance of this type of OMT in a 10–15% band exhibits a minimum of 15–20 dB return loss, a limit of 25–30 dB isolation between the various ports, and losses of a few tenths of a decibel.

3.3. Sidearm-Coupled OMT

A very widely used OMT is the one shown in Fig. 14, which we refer to as the *sidearm-coupled OMT*. It is developed entirely in the waveguide, a solution adopted when high performance (typically, return loss > 20 dB, isolation > 30 dB, losses < 0.2 dB) is desired. However, because of the asymmetry of the structure, the operative bandwidth is theoretically limited, in the square waveguide case, to the cutoff frequency f_{c11} of the TE_{11}/TM_{11} modes, giving a relative fractional bandwidth of about $(f_{c11} - f_{c10}) / (f_{c11} + f_{c10}) / 2 = 34\%$, where f_{c10} indicates the fundamental TE_{10} cutoff frequency. The version shown in Fig. 14 is based on the H -plane side coupling; an E -plane side coupling version also exists (see Fig. 15).

The H -plane side is associated with either of the two walls of the waveguide normal to the H plane, while the E -plane side is associated with each of the other two walls normal to the E -plane; for example, in the case of a TE_{10} single-mode standard waveguide with $a = 2b$, the H -plane sides are the walls associated with b while the E -plane sides are the ones associated with a . In both versions the common port and one of the rectangular single-mode ports are coaxial and the side port is orthogonal to them; this means that the structure exhibits geometric symmetries corresponding to very important electromagnetic properties that are of prime relevance in the proper operation of this type of OMT.

The H -plane sidearm-coupled OMT functions as follows. A vertically polarized TE_{10} wave (port 1) originating from the common port and crossing the side waveguide (port 4) excites, in this port, higher-order modes that, by symmetry, are $TE_{(m)(2n+1)} TM_{(m+1)(2n+1)}$, where m and n are integers. If this waveguide, in the operative band, is single-mode, the fundamental TE_{10} mode is not excited, thus resulting in the TE_{10} mode from the common port perceiving the side waveguide as a reactive load and no active power transfer between ports 1 and 4. On the other hand, traveling forward to port 3, this mode does excite a particular subset of modes, depending on the symmetries (E -plane, H -plane, or both), containing in any case the fundamental TE_{10} mode of port 3, which usually is a single-mode waveguide also in the operative band.

In the other case, the common-port horizontally polarized TE_{01} mode (port 2) does produce in port 4 a subset of

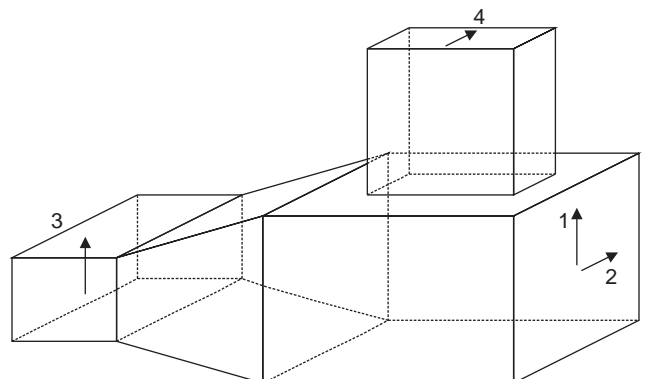


Figure 14. H -plane sidearm-coupled OMT: basic configuration.

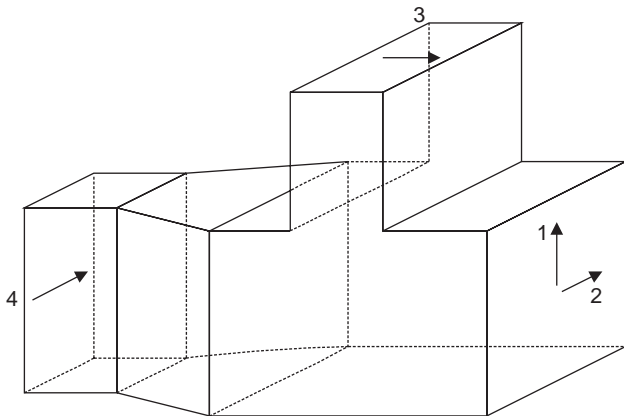


Figure 15. *E*-plane sidearm-coupled OMT: basic configuration.

modes $[TE_{(m)(2n)} TM_{(m+1)(2n+2)}]$ which, compatible with TE_{10} excitation, allows coupling between ports 2 and 4. On the other hand, port 3 behaves like a reactive load with respect to this common-port polarization, inducing a field expansion in modes $[TE_{(2m)(n)} TM_{(2m+2)(n+1)}]$.

The *E*-plane sidearm-coupled OMT obviously exhibits similar behavior but the electromagnetic coupling is of a different nature. If we again consider a vertically polarized TE_{10} wave (port 1) originating from the common port and crossing the side waveguide (now port 3), in this port it excites higher-order modes, which, when the a dimension of the side waveguide equals the side of the square of the common port section, are $TE_{1(n)}$ and $TM_{1(n+1)}$, where m and n are integers. If this waveguide, in the operating bandwidth, is single-mode, then only the fundamental TE_{10} mode can propagate. On the other hand, geometric symmetry implies that, if the a dimension of the through waveguide equals the side of the square common-port section, the modal expansion in port 4 is of the $TE_{0(2n+1)}$ type, not including this port fundamental TE_{10} mode. Thus the mode of port 1 perceives port 4 as a reactive load and active power transfer is allowed only between port 1 and port 3. The behavior of a horizontally polarized TE_{01} wave (port 2) in the *E*-plane sidearm-coupled OMT is essentially the same as that of the vertically polarized TE_{10} wave (port 1) in the *H*-plane sidearm-coupled OMT, also if the electromagnetic interactions between the ports are slightly different; that is, the side port is a reactive load and the active power from port 2 is coupled only to port 4.

Summarizing, because of the numbering unique to each port, these two kinds of OMT once again have the same ideal scattering matrix representation, as given in (1). In some applications this version of OMT is used with the common port in circular waveguide, basically exhibiting the same properties and performance, only giving a better mechanical interface when feeding, for example, a circular horn.

3.4. Finline-Based OMT

To enlarge the bandwidth (30–40%), an improved version of the OMT described in Section 3.3, with only a small performance degradation (typical values are 15 dB return loss, 30 dB isolation, and 0.5 dB loss), is obtained by

introducing a shaped metallic septum that constitutes in the common waveguide a tapered finline, coupled by a finline 90° *E*-plane band to the sidearm waveguide. This type of OMT [11], shown in Fig. 16, takes advantage of the finline waveguide properties. The single-mode bandwidth of a finline is a bit greater than that of the standard waveguide, depending essentially on the width between the ridges. Another feature of primary importance for the operation of the derived OMT is the fact that the electromagnetic field energy is concentrated increasingly in the region between the ridges, as this becomes smaller and smaller.

The principle of operation of the finline-based OMT is quite simple. A vertically polarized TE_{10} wave (port 1) coming from the common port is not perturbed by the presence of the metallic septum if its thickness is small with respect to the waveguide dimensions. The side waveguide can be seen as a reactive load because, by the *H*-plane symmetry of the problem, in this waveguide, which by assumption is single-mode in the OMT operative bandwidth, only the evanescent $TE_{(2m)(n)}$, $TM_{(2m+2)(n+1)}$ modes, with m and n integers, are excited. Thus the port coupling active power with port 1 is port 3.

In the other case, a horizontally polarized TE_{01} wave (port 2) originating from the common port is even more confined in the region closed to the gap between the finline center conductor as this gap becomes thinner. Approaching the sidearm junction, the curvature of the gap drives the electromagnetic energy to port 4, which propagates with a gradual transformation between a finline mode (in the region close to the junction) to a pure rectangular waveguide TE_{10} (in the region close to port 4). Regarding the coupling with the other port, the common-port TE_{01} mode, approaching the discontinuity, excites in port 3 a reactive field given (in this case we have *E*-plane symmetry) by the superposition of evanescent $TE_{(m)(2n+1)}$, $TM_{(m+1)(2n+1)}$ modes.

As a final consideration, we have an ideal scattering matrix for the finline-based OMT given by (1).

3.5. Dual-Junction-Based OMT

When higher performance levels are required in a broad band, an OMT with geometric symmetries on both *E* and

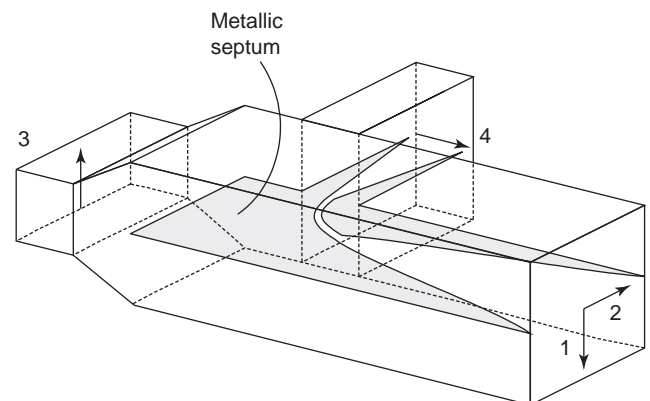


Figure 16. Finline-based OMT.

H planes is required. One of the most commonly used configurations of this type is the dual junction (Fig. 17), from which the dual-junction-based OMT is derived. The most important property responsible for its excellent electromagnetic behavior is that its dual-plane symmetry avoids excitation of the TE_{11} and TM_{11} modes, the first higher-order modes, and the most critical regarding performance degradation.

The dual-junction OMT consists of a common port, typically a square waveguide, coupling to two 90° lateral waveguides and two directly facing waveguides; the latter are obtained by simply splitting the common waveguide by means of a metallic septum.

To ensure high performance levels, the septum is shaped relative to the region of the side branches (Fig. 17) and to even further improve bandwidth and performance, two wire posts are placed in the center of the side waveguides parallel to the principal side.

The behavior of the dual-junction OMT is thus quite simple and partially analogous to that of, the E -plane sidearm-coupled OMT.

A vertically polarized TE_{10} wave (port 1) incident from the common port basically doesn't feel the presence of the metallic septum and is reactively loaded by port 4 (ports 4a and 4b), thus coupling with port 3 (ports 3a and 3b). This may be explained by noting that, because of the dual-plane symmetry, the modes excited in the discontinuity region of the waveguide intersection must have the same index parity of the excitation mode, namely, $TE_{(2m+1)(2n)}$, $TM_{(2m+1)(2n+2)}$, where m and n are integers. It is worth stressing, as mentioned above, that this modal subset does not contain TE_{11} and TM_{11} modes having, in the common-port square waveguide, cutoff frequencies a factor $2^{1/2}$ greater than in the fundamental mode. Furthermore, in the side waveguides this modal subset corresponds to a superposition of $TE_{(2m)(n)}$, $TM_{(2m+2)(n+1)}$ modes, not including the TE_{10} mode, and providing rationale for the reactive coupling given by the side waveguide to this polarization.

On the contrary, a horizontally polarized TE_{01} wave (port 2) incident from the common port basically perceives port 3 (3a and 3b) as a reactive load, exciting by symmetry $TE_{(2m)(n)}$, $TM_{(2m+2)(n+1)}$ modes. This polarization is driven by the particular shape of the upper part of the

metallic septum to port 4, in which the above mentioned modal expansion corresponds to an appropriate superposition of $TE_{(2m+1)(n)}$, $TM_{(2m+1)(n+1)}$ modes, including the TE_{10} mode and allowing ports 2–4 coupling.

To ensure a canonical OMT configuration, ports 3a and 3b, as well as ports 4a and 4b, must be combined to give a standard waveguide access to the OMT. If this appears quite simple for ports 3a and 3b by means of a stepped transformer, this is a bit more complex (and this is a consistently encountered drawback of this OMT) for ports 4a and 4b requiring E -plane or H -plane bends (or both) and a carefully designed combiner.

Typical performance levels for this OMT are >20 dB return loss and >35 dB isolation over a bandwidth approaching the $\sim 40\%$ standard waveguide bands.

4. EXAMPLE DESIGN OF A DUAL-JUNCTION-BASED OMT

To give the reader a clearer idea of practical applications, in this example we present a 20% band OMT operating at 30 GHz for a radio astronomy receiver, developed, built, and measured at the Institute of Radioastronomy of the Italian National Research Council.

The design is based on the dual junction with no posts and a triangle-shaped septum.

The prototype OMT, shown in Fig. 18, was fabricated by using aluminum material and then gold-plated with an approximate global dimension of 5 cm for the side cube. The sidearms are recombined through H -plane bends and a stepped combiner.

Figures 19 and 20 show the high performance levels of the overall OMT in comparison with the expected results for the standalone dual junction obtained by simulations with FEM-based commercial software.

In Fig. 19 the simulated reflection coefficient of the vertically polarized TE_{10} wave (port 1) of the dual-junction common port is shown together with the measured data of the corresponding measurement of the overall OMT and one of the coupled ports (V port = port 3).

Figure 20 shows analogous parameters of the horizontal polarization: the simulated reflection coefficient of the horizontally polarized TE_{01} wave (port 2) of the dual-junction common port, the measured data of the reflection coefficient of the same wave in the operative complete configuration and that in the coupled port (H port = port 4), which is the recombination of the side arms (4a and 4b).

It is worth noting the accuracy of the numerical method by comparing simulations with measured data; the dual-junction behavior is accurately predicted by the software, and the differences between the curves are due to the other components (bends, stepped transitions, combiner), which have been designed with much higher performance levels than in the dual junction itself. Thus the overall OMT has an oscillatory behavior of electromagnetic features across an approximately mean-value curve corresponding to dual-junction performance, according to in-phase or out-of-phase combinations of the scattered field, due to the different electrical lengths produced by changing the frequency.

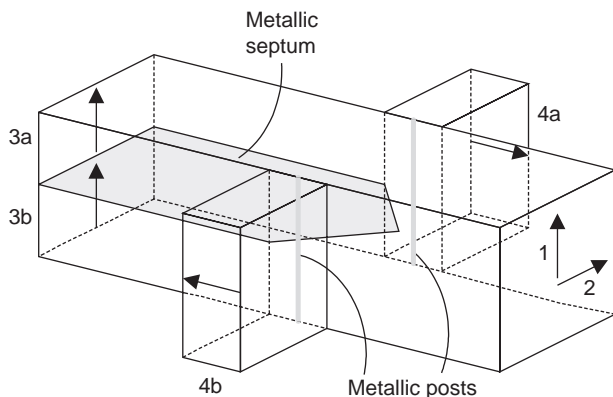
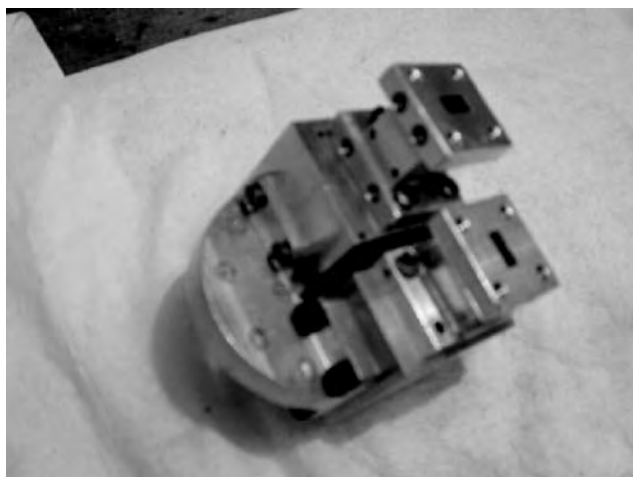
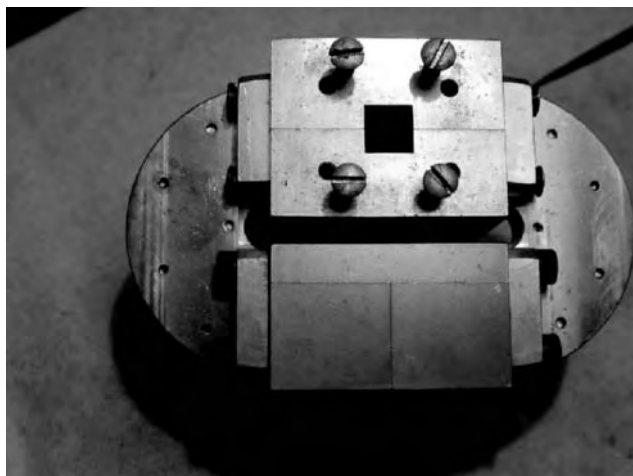


Figure 17. Dual-junction-based OMT.



(a)



(b)

Figure 18. Dual-junction-based 30 GHz OMT: side view (a); common-port view (b). (Courtesy of the Institute of Radioastronomy of the Italian National Research Council.)

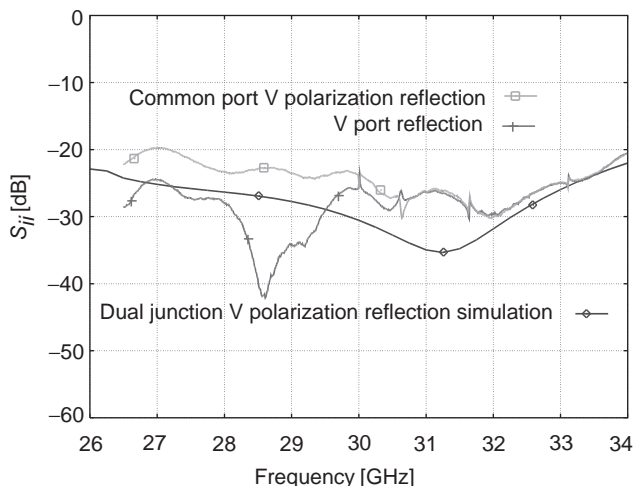


Figure 19. Dual-junction-based OMT: V-channel reflection coefficients.

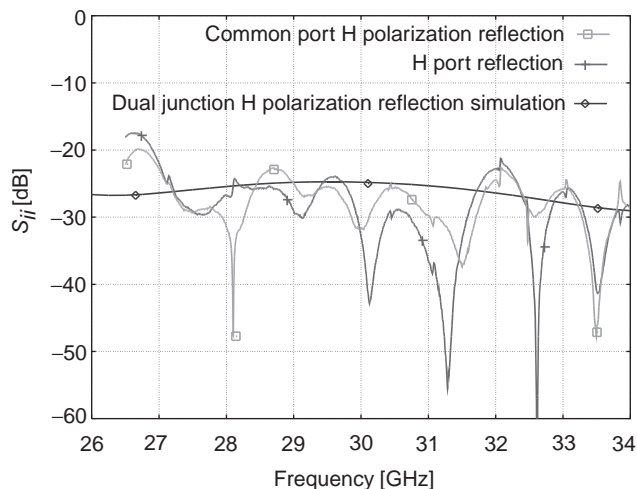


Figure 20. Dual-junction-based OMT: H-channel reflection coefficients.

These curves are, however, below -20 dB, with a mean value of approximately -25 dB, in a 20% band centered at 30 GHz. Losses were measured to be <0.4 dB for the vertical channel (ports 1–4) and <0.8 dB for the horizontal channel (ports 2–3).

5. POLARIZERS

Polarizers change the EM field polarization from linear to circular. They have, as do OMTs, three physical ports and may be represented with four electrical ports, as shown in Fig. 21, with two single-mode ports 3,4 and two ports 1,2 at the common physical port. In free space, a deterministic (nonrandom) monochromatic field has, in general, a transverse elliptical polarization. In frequency-domain phasor notation, in a generic point of the space, the elliptical polarization may be fully characterized by two complex orthogonal vectors with different amplitude and phase \mathbf{p} and \mathbf{q} , which are normal to the direction of propagation associated with a unit vector \mathbf{z} . The main physical meaning of this is that any elliptical polarization may be obtained as the superposition of two phase-shifted and orthogonal linearly polarized fields. In particular, when the phases of \mathbf{p} and \mathbf{q} are equal, we have a linearly polarized field in a particular direction depending on the amplitude relation between \mathbf{p} and \mathbf{q} . When \mathbf{p} and \mathbf{q} have the same amplitude and are 90° phase-shifted, we have a circularly polarized field, where the tip of the electric field describes a circumference as time varies.

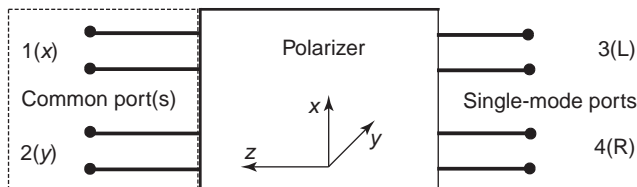


Figure 21. Polarizer schematic.

If the wave travels toward \mathbf{z} and

$$\frac{\mathbf{p} \times \mathbf{q}}{|\mathbf{p} \times \mathbf{q}|} = \mathbf{z} \quad (19)$$

then two independent circular polarization states are possible.

A right-hand circular polarization (RHCP) is obtained when the phase shift is as follows:

$$\arg(\mathbf{p}) - \arg(\mathbf{q}) = 90^\circ \quad (20)$$

We have a left-hand circular polarization (LHCP) if

$$\arg(\mathbf{p}) - \arg(\mathbf{q}) = -90^\circ \quad (21)$$

Once again suggesting Ref. 5 for a more in-depth treatment on field polarization, from a polarizer perspective, it is important to highlight the following properties of circular polarization:

1. Any deterministic and monochromatic field polarization may be obtained as the superposition of two independent circular polarizations: one LHCP and the other RHCP.
2. Waveguide circular polarizations (both LHCP and RHCP) are easily obtained in both circular and square waveguides by the superposition of the two fundamental modes, TE_{11v} and TE_{11h} in the circular waveguide, and TE_{10} and TE_{01} in the square waveguide, with the same amplitude and 90° phase-shifted.

Property 1 ensures that the polarizer can process any deterministic and monochromatic field configuration without any lack of representation, while property 2 basically allows us to adopt the same schematic notation used for OMTs, associating the ports of the common inputs 1 and 2 with the fundamental modes in the related waveguide: TE_{10} and TE_{01} in the square waveguide and TE_{11v} and TE_{11h} in the circular waveguide, respectively.

Thus, for an ideal polarizer, referring to the sketch in Fig. 21, the scattering matrix is given by the following expression:

$$S = 2^{-(1/2)} \begin{bmatrix} 0 & 0 & 1 & e^{j(\pi/2)} \\ 0 & 0 & e^{j(\pi/2)} & 1 \\ 1 & e^{j(\pi/2)} & 0 & 0 \\ e^{j(\pi/2)} & 1 & 0 & 0 \end{bmatrix} \quad (22)$$

We can see that it is matched at all the ports, with the diagonal elements of S equal to zero. From the third column of S we conclude that the power incident at the single-mode port 3 comes out 3 dB down from port 1 (x polarization) and port 2 (y polarization), with the x -polarization 90° retarded with respect to the y polarization, meaning that, as the outward travel of the wave is \mathbf{z} -directed, a pure LHCP is excited at the common port. From the fourth column we see analogously that, because this time the x polarization is retarded 90° in advance with

respect to the y polarization, at the common port a pure RHCP is excited.

Regarding the incident signals from the common port, it is more instructive to proceed in the following manner. If a pure LHCP polarization impinges on the common port, we can say that port 1 (x polarization) phasor is $2^{-(1/2)}$ while port 2 (y polarization) is 90° retarded with a phasor $2^{-(1/2)}e^{-j(\pi/2)}$. Thus, multiplying the scattering matrix by the incident vector associated with a common port incoming LHCP with unit power, we have

$$2^{-(1/2)} \begin{bmatrix} 0 & 0 & 1 & e^{j(\pi/2)} \\ 0 & 0 & e^{j(\pi/2)} & 1 \\ 1 & e^{j(\pi/2)} & 0 & 0 \\ e^{j(\pi/2)} & 1 & 0 & 0 \end{bmatrix} 2^{-\frac{1}{2}} \begin{bmatrix} 1 \\ e^{-j(\pi/2)} \\ 0 \\ 0 \end{bmatrix} \quad (23)$$

$$= \begin{bmatrix} 0 \\ 0 \\ 1 \\ 0 \end{bmatrix}$$

meaning that all the power comes from port 3, as expected by polarizer reciprocity. If the common-port incident wave is a unit power RHCP, we obtain analogously

$$2^{-(1/2)} \begin{bmatrix} 0 & 0 & 1 & e^{j(\pi/2)} \\ 0 & 0 & e^{j(\pi/2)} & 1 \\ 1 & e^{j(\pi/2)} & 0 & 0 \\ e^{j(\pi/2)} & 1 & 0 & 0 \end{bmatrix} 2^{-\frac{1}{2}} \begin{bmatrix} e^{-j\pi/2} \\ 1 \\ 0 \\ 0 \end{bmatrix} \quad (24)$$

$$= \begin{bmatrix} 0 \\ 0 \\ 0 \\ 1 \end{bmatrix}$$

confirming this time that RHCP is coupled to port 4.

Except for the channel crosstalk of the isolation OMT parameters of Table 1, all the other parameters are also meaningful for polarizers.

There is an additional parameter useful in describing polarizer nonidealities: the axial ratio (AR); that is the ratio, usually expressed in decibels, between the major and the minor axis of the polarization ellipse [thus $0 \leq \text{AR}(\text{dB}) < \infty$] of the elliptical polarization generated.

From an operative perspective, commonly used devices may be divided in two groups: double polarization conversion polarizers and septum polarizers.

5.1. Double-Polarization Conversion Polarizers

These devices are divided in two sections: a first section that converts two circularly polarized signals (LHCP, RHCP) in two linear and orthogonal polarizations (V, H) within a single common waveguide and an OMT (second section) of the already analyzed type, which splits the two linear polarizations into two separate waveguides.

Because we have already discussed OMTs, we will discuss only the first section, which is referred to as a *differential phase shifter* (DPS) because it introduces a 90° differential phase shift between the two fundamental modes.

A differential phase shift is given by the difference between two phase delays associated with each wave traveling from the input to the output of the device. As mentioned previously, 90° is the ideal differential phase shift of interest in the case of polarizers.

Operation of a DPS is shown in Fig. 22. If we assume that a structure exists having the property of introducing a 90° phase shift difference between an y -polarized signal and an x -polarized signal traveling from the input to the output port, it consequently transforms a LHCP signal incident at the input port in a linearly polarized, vertically directed ($V, \varphi = 45^\circ$) one, while converting a RHCP signal into a linearly polarized, horizontally directed ($H, \varphi = -45^\circ$) one, so that the two linear polarizations are orthogonal. These two linear polarizations V and H are associated, respectively, with the single-mode ports 3 and 4 of the OMT, so the scattering matrix of the resulting polarizer is the one given in (22).

If the ports are circular waveguides, there is no need to use any other device to complete the polarizer configuration using one of the OMT configurations shown earlier, but if the ports are square, a waveguide transition has to be used that rotates the square exactly 45° from input to output, by maintaining the same H or V direction of polarization. This transition from a square to a 45° -rotated square may be obtain by smooth tapering (Fig. 23) or by an

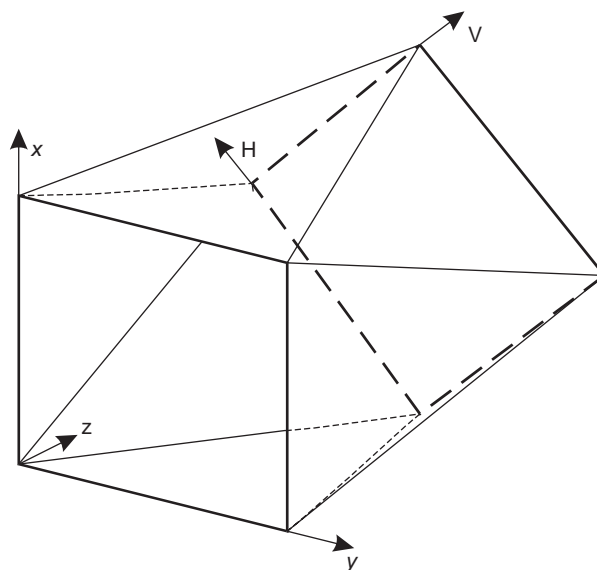


Figure 23. Square to 45° -rotated square transition.

abrupt junction, eventually with a circular section to improve performance.

Three of the most commonly used DPS configurations are shown in Fig. 24, in which the coordinate system is congruent with the one shown in Fig. 22. A simple rectangular waveguide (Fig. 24a) is an elementary DPS provided both the TE_{10} and the TE_{01} modes propagate. The polarization with the lower cutoff frequency has a greater propagation constant, so the phase shift between the two waves can be $\pm 90^\circ$ with an appropriate choice of the rectangular section length. An analogous circular waveguide port DPS can be obtained, as an optimum solution, with an elliptical waveguide section. This type of DPS is very simple, but in practice a differential phase shift close to 90° can be obtained only in a narrow band.

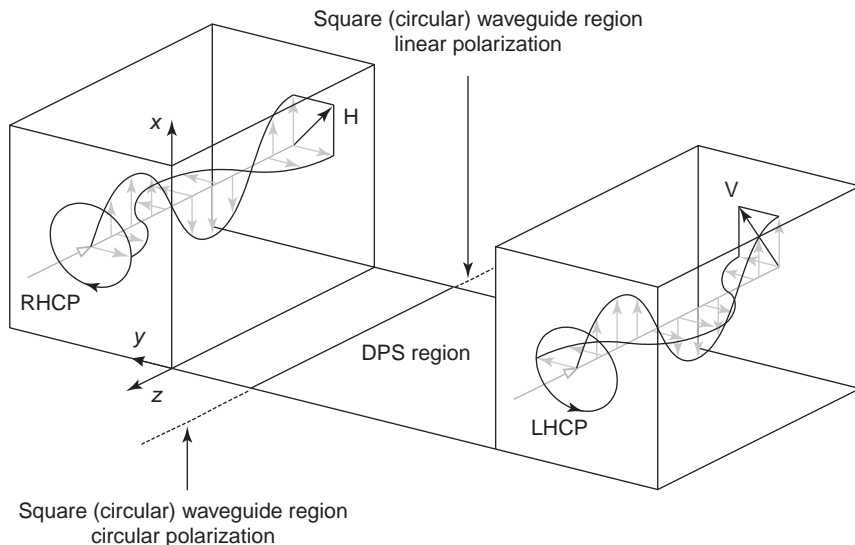


Figure 22. Differential phase shifter electromagnetic behavior.

An enlargement of the bandwidth may be obtained if we place an on-axis dielectric septum parallel to one of the two fundamental field polarizations (and orthogonal to the other) in a square (Fig. 24b) or circular waveguide. We obtain a DPS because the parallel component has a propagation constant greater than the one of the other polarization, obtaining again a $\pm 90^\circ$ differential phase shift by appropriate selection of the longitudinal length (z direction) of the septum.

However, the optimum solution for a DPS, with a broad band and without the problems encountered with dielectric materials (losses, mechanical interfacing, etc.), is the two-wall corrugated waveguide (Fig. 24c), which has an analogous configuration in circular waveguide using very thin elliptic section, more practically approximated by two transverse straight ridges, placed at 180° angles to each other, which partially fill the circular waveguide. The vertical x polarization, normal to the corrugations, has a propagation constant that is greater than the horizontal one, so in this case $\pm 90^\circ$ differential phase shift is also given by accurately designing the corrugation geometry. The dispersion characteristic (i.e., variation of the propagation constant with frequency) properties of the two polarizations give a very good flatness in the axial ratio curve with frequency, with two points at AR 0 dB very close in the frequency band, allowing the design of dual-band very-high-performance polarizers as well as broadband high-performance polarizers; in fact, the typical 40% standard waveguide band may be easily obtained by using these devices with an axial ratio below 1 dB.

5.2. Septum Polarizers

At the expense of a reduced operating bandwidth, a much more compact and simpler solution than any double-polarization conversion device is the septum polarizer, which is most commonly used in its square waveguide configuration (Fig. 25), but that exists also in circular, showing, in both cases, bandwidths of $\sim 12\text{--}15\%$.

This device can be called a “true” polarizing microwave junction, as the asymmetric triangular section performs the full double task, at least ideally, of differential phase-shifting the x and y polarizations of the common port and dividing, at the same time, the two recombined linear polarization signals into two separate waveguides.

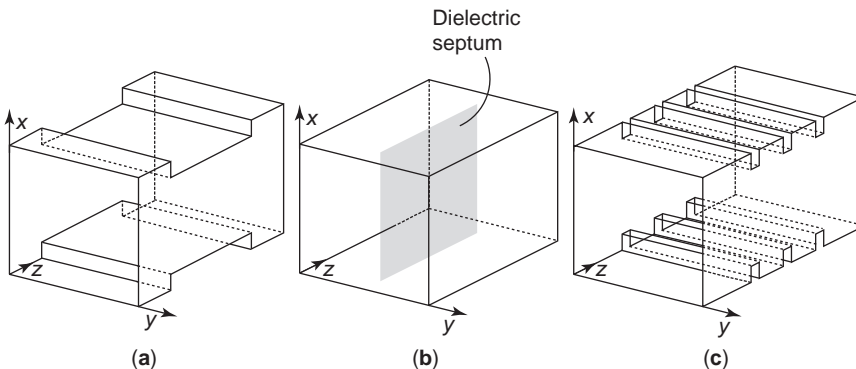


Figure 24. Differential phase shifter examples: rectangular waveguide (a), waveguide with a dielectric septum (b), two-wall corrugated waveguide (c).

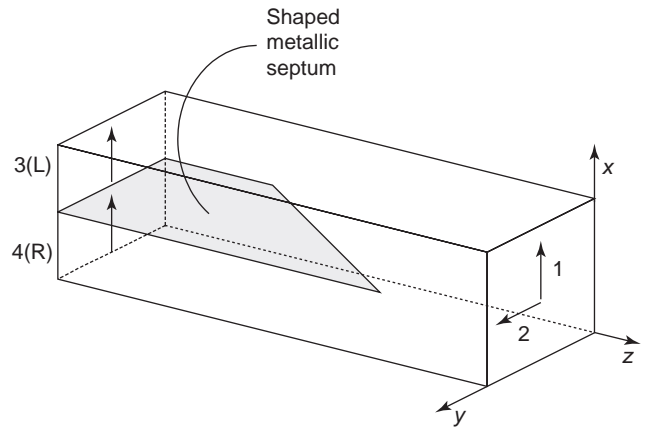


Figure 25. Septum polarizer.

Consider, for example, the RHCP signal in Fig. 26, whose principle of operation is as follows. The vertical ($-x$ in this case), polarization is not affected by the presence of the septum and travels almost unperturbed, dividing in the single-mode ports at 3 dB and in phase (with respect to the x direction); this is schematically shown in the right part of the RHCP sketch of Fig. 26. On the contrary, the shaped metallic septum significantly perturbs the propagation of the horizontal polarization ($-y$ in this case), causing electric field diffraction at the edge of the septum (left part of RHCP sketch in Fig. 26). Moreover, the field diffraction and the different propagation constant cause this $-y$ polarization to travel more slowly, thus retarding, ideally, at an angle of 90° with respect to the other $-x$ polarization. This behavior is schematically given by the successive dual chain of differently spaced field configurations and produces an in-phase combination at port 4(R) and an out-of-phase recombination at port 3(L) of the two polarizations if the incoming signal from the common port is RHCP, thus transferring its total power, ideally, to 4(R) and producing a null output signal from 3(L).

Explanation of the LHCP case is analogous to the difference that now the horizontal $-y$ polarization travels more slowly than the x polarization, thus retarding, ideally, at an angle of 90° with respect to the x polarization and producing a total power recombination at port 3(L) and a null signal at port 4(R). The scattering matrix representation of the septum polarizer, in the configuration shown in Fig. 25, is again given by (22).

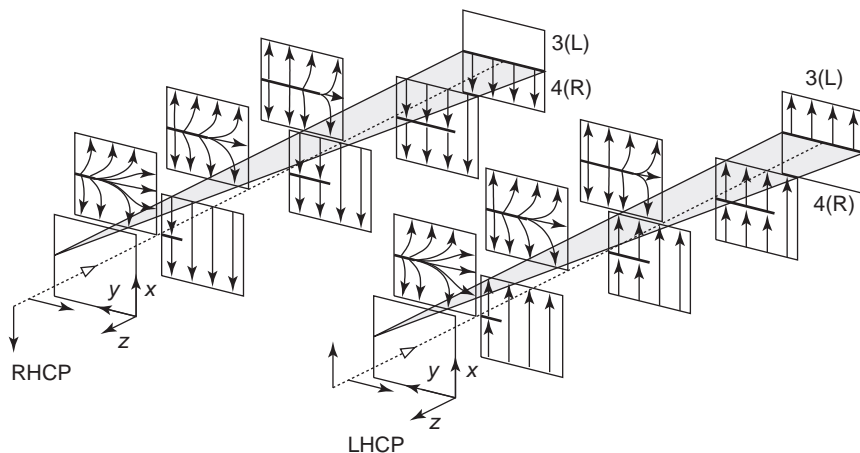


Figure 26. Septum polarizer electromagnetic behavior.

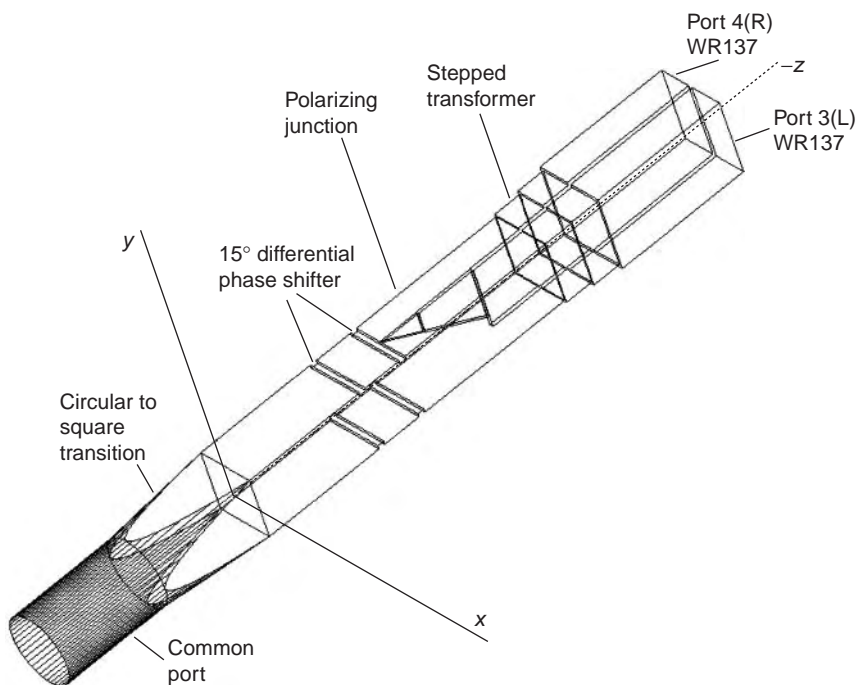


Figure 27. Septum polarizer design at 6.7 GHz.

6. EXAMPLE DESIGN OF A SEPTUM POLARIZER

As an example, the design of a septum polarizer, developed, built, and measured at the Institute of Radioastronomy of the Italian National Research Council, is given in this paragraph. The device, operating at 6.7 GHz in a room-temperature receiver for radio astronomy, has to be connected to a circular corrugated horn on one side and to a standard WR-137 waveguide-fed receiver on the other side. Thus it has a common port in circular waveguide and two single-mode ports in WR-137 rectangular waveguide as shown in Fig. 27. In this case, because the polarizing junction, formed by the metallic shaped septum region, is better designed in square waveguide, a circular to square-shaped transition has been designed. Moreover, as the polarizing junction provides only ~75° differential phase shifting, a two-wall corrugated waveguide providing 15° of further shifting, to obtain the

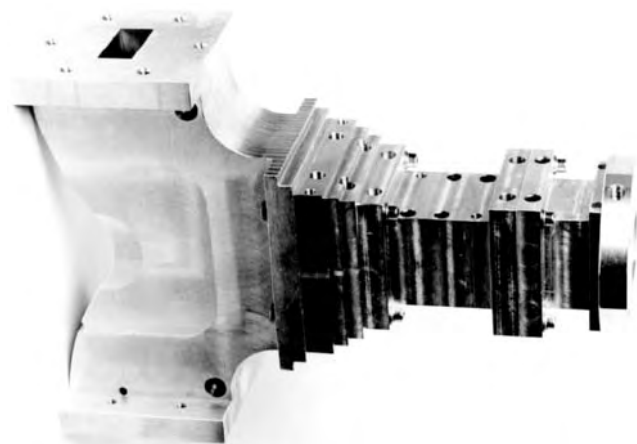


Figure 28. Septum polarizer at 6.7 GHz. (Courtesy of the Institute of Radioastronomy of the Italian National Research Council.)

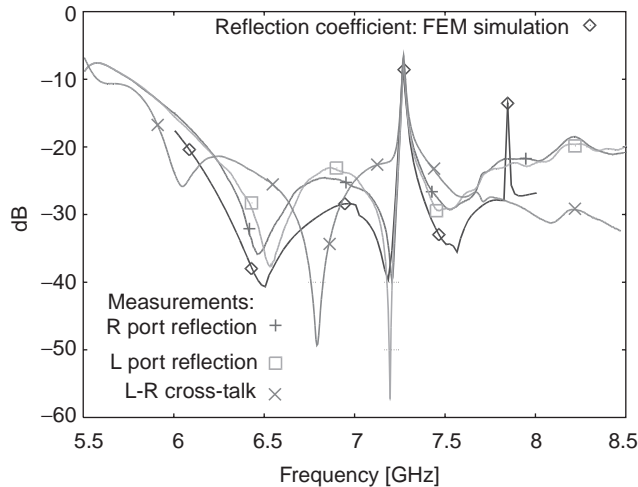


Figure 29. 6.7GHz septum polarizer electromagnetic performances.

desired 90° one, is introduced. The last complication in the design was the need to employ a stepped transition to connect the polarizing junction to the WR-137 standard waveguides.

The additional 15° could be achieved by carefully optimizing the septum profile. This can provide a more compact device, but having two separate components leads to greater design freedom and easier manufacturing.

An aluminum, direct-machined device has been fabricated on the basis of this design (Fig. 28) (the dimensions are about $50 \times 30 \times 15$ cm) and it was tested highlighting very good results in the 13% bandwidth centered at 6.7 GHz (Fig. 29), with an axial ratio below 0.8 dB and showing a very good agreement with expected results.

BIBLIOGRAPHY

1. A. M. Boifot, E. Lier, and T. Schaug-Pettersen, Simple and broadband orthomode transducer, *IEE Proc. H* **15**(6):396–400 (1990).
2. J. Uher, J. Bornemann, and U. Rosenberg, *Waveguide Components for Antenna Feed System: Theory and CAD*, Artech House, Norwood, MA, 1993.
3. T. Itoh, *Numerical Techniques for Microwave and Millimeter Wave Passive Structures*, Wiley, New York, 1989.
4. R. E. Collin, *Advanced Engineering Electromagnetics*, Wiley, New York, 1989.
5. J. D. Kraus, *Electromagnetics*, McGraw-Hill, Tokyo, 1984.
6. N. Marcuvitz, *Waveguide Handbook*, Dover, New York, 1965.
7. J. Bahl and P. Bhartia, *Microwave Solid State Circuit Design*, Wiley, New York, 1988.
8. C. A. Balanis, *Antenna Theory: Analysis and Design*, Wiley, New York, 1982.
9. W. L. Stutzman and G. A. Thiele, *Antenna Theory and Design*, Wiley, New York, 1982.
10. P. J. B. Clarricoats and A. D. Olver, *Corrugated Horns for Microwave Antennas*, Peter Peregrinus, London, 1984.
11. S. J. Skinner and G. L. James, Wide-band orthomode transducers, *IEEE Trans. Microwave Theory Tech.* **39**(2):294–300 (1991).

OSCILLATOR DESIGN

WOLFGANG MATHIS
PETER RUSSE
University of Hannover
Germany

1. INTRODUCTION

The development of electronic oscillators was closely related to the invention of the vacuum tube at the beginning of the twentieth century. First oscillator circuits were presented, for example, by Meissner, Hartley, Colpitts, and the basic ideas for a theory of such circuits were presented by Vallauri in 1917 [97]. In 1914 Zenneck considered an oscillatory arrangement with an arc as the active device and discussed nonlinear aspects of electronic oscillators by means of an energy balance equation. Unfortunately he did not derive the corresponding differential equations for the currents and voltages. A differential equation for a triode oscillator was presented for the first time by van der Pol in 1920. His studies became the starting point for a long series of research in mathematics, physics, as well as electrical engineering on oscillatory networks and systems. As a result a first monumental monograph about this subject was published by Andronov et al. [1] that included the essential aspects of the theory of oscillatory circuits and systems where these authors illustrated their theory by means of many examples. At the same time Krylov and Bogoliubov [55] published essential results on the analysis of oscillatory circuits. Both groups started from the work of van der Pol and used ideas and results from the work of the famous French mathematician and physicist Henry Poincaré. Short presentations of the history of these methods can be found in Sanders and Verhulst [86] and Mathis [66]. Although the results of these Russian authors were discussed several times in the literature, most of them were unknown to many researchers until the late 1960s. Maybe this is one of the reasons why, in contrast to the linear analysis of oscillatory circuits and systems, the details of the nonlinear theory due to the abovementioned Russian research groups were not included into a design theory of oscillators. We will show in this article that the design of oscillators can be clarified if their ideas are included.

2. FOUNDATIONS

2.1. Properties of Electrical Oscillators

In order to understand the difficulties related to electronic oscillators, it is useful to discuss the main properties of the behavior of such electronic circuits and consider some aspects of its modeling. It is well known that the basic behavior of an electronic oscillator should be characterized as follows: [79]:

- Some voltages and/or currents should behave in a periodic manner. The most essential shapes of the

output can be sinusoidal, sawtooth, and square waves.

- The oscillator frequency should be accurately determined.
- After a transient behavior the oscillator amplitude should be accurately determined and independent of the initial conditions.
- Perturbations of the oscillatory behavior in the steady state should have died out after some transient behavior.
- The oscillatory behavior should not be destroyed by parasitic circuit elements (structural stability).

From these qualitative properties the main features of electronic oscillators can be extracted and serve as main specifications:

- Oscillator frequency
- Oscillator amplitude
- Velocity of the startup and dying-out behavior

Obviously we have to add further properties if electronic oscillators will be designed. The signal-to-noise ratio and the stability of oscillator frequency and amplitude as well as the distortions with respect to a desired waveform are a few of these properties. Note that the basic behavior of electronic oscillators cannot be realized or modeled by using linear (time-invariant) circuits because these circuits have to be nondissipative (no Ohmic resistors are included) if periodic behavior is desired. Therefore the energy is conserved and their oscillatory amplitude depends on the initial conditions. Furthermore these linear (nondissipative) oscillator models are not structural stable (see characterization of oscillators) because the periodic behavior is destroyed by arbitrary small dissipative elements (e.g., Ohmic resistors). As a conclusion, mathematical models of electronic oscillators have to be nonlinear. In 1963 it was emphasized by Hale [40] that our knowledge of nonlinear systems is still far from being complete and only a few mathematical techniques are available to analyze such models. Although intensive research activities have been carried out in this area since the early 1970s, many problems still have to be solved to obtain a satisfying theory. Good illustrations of this statement can be found in Guckenheimer's discussion of the van der Pol equation [38].

2.2. Oscillator Models

Although linear LC circuits without dissipation are not suitable as a complete model for electronic oscillators, it is useful to start with such a circuit and to introduce the following changes:

- Compensation of the dissipation with negative resistors or positive feedback
- Comparison of the oscillator amplitude with a prescribed value in an implicit or explicit manner and control the negative resistor or the feedback

It should be emphasized that compensation is a linear technique whereas amplitude control by using parameter variation is an inherently nonlinear technique. These two steps can be described mathematically if we start from the differential equation for an LC circuit with a rather small resistor (dissipation)

$$\ddot{x} + \gamma\dot{x} + \omega_0^2 x = 0 \quad (1)$$

where γ is proportional to the (positive) resistance. Using a compensation technique the γ will be canceled. For example, this can be done by adding a negative resistor in series (or parallel) to the positive resistor with the same amount of resistance. If Eq. (1) is converted into the state space form $\dot{\mathbf{x}} = \mathbf{A}\mathbf{x}$ by the notations $x_1 := x$, $x_2 := \dot{x}$, it is easy to see that application of a compensation technique results in a pair of eigenvalues of \mathbf{A} on the imaginary axis. In more general cases the state space has a dimension $n > 2$ following more than two reactances. Usually the matrix \mathbf{A} has at least one pair of eigenvalues beside other eigenvalues with negative real parts. In Section 3.1 several approaches are discussed that can be used to find a set of parameters where a pair of eigenvalues with zero real part occur. Furthermore it should be emphasized that it is not necessary that we start with an LC circuit since it is possible, for example, to realize inductors in an active manner by means of resistors, capacitors, and (operational) amplifiers. In contrast to LC oscillators, these kinds of oscillators are called RC oscillators [e.g., 74]. The first RC oscillator was presented by Heegner [43] in 1927; see also Sidorowicz [91] further references.

If the resistor or, in other words, γ is controlled by the state variables (x, \dot{x}) , we get the following nonlinear differential equation:

$$\ddot{x} + \gamma(x, \dot{x})\dot{x} + \omega_0^2 x = 0 \quad (2)$$

Special choices of the function $\gamma = \gamma(x, \dot{x})$ lead to certain nonlinear oscillator models. In the next subsection this problem is discussed by means of the Poincaré–Andronov–Hopf theorem. As mentioned above, the van der Pol equation (vdP) was the first model of an oscillator circuit. The normalized version of this equation has the following form (with normalized $\omega_0^2 = 1$):

$$\ddot{x} + \varepsilon(x^2 - 1)\dot{x} + x = 0 \quad (3)$$

Note that this differential equation is of the abovementioned form. We mention that another differential equation of a similar type is the Rayleigh equation (R) (with normalized $\omega_0^2 = 1$):

$$\ddot{x} + \varepsilon(\dot{x}^2 - 1)\dot{x} + x = 0 \quad (4)$$

Unfortunately the equilibrium solution $\mathcal{O} := \{x(t) = 0 | t \in \mathbb{R}\}$ is the only solution that is known in exact terms. All other solutions and especially the periodic solution have to be calculated with perturbation methods. Therefore we consider a modified differential equation (with

normalized $\omega_0^2 = 1$)

$$\ddot{x} + \varepsilon(x^2 + \dot{x}^2 - 1)\dot{x} + x = 0 \quad (5)$$

with a periodic solution $x_p(t) := \{x(t) = \cos t | t \in \mathbb{R}\}$, which can be calculated in a simple manner. Obviously this solution is unique up to an additive phase φ and the periodic solution does not depend on the parameter ε . An advantage of this equation is that it can be interpreted very easily. For this reason $x_p(t)$ is represented in the state space ($x_1 := \dot{x}$, $x_2 := x$) as a circle. The state space representation of Eq. (5) is

$$\dot{x}_1 = -x_2 - \varepsilon(x_1^2 + x_2^2 - 1)x_1 \quad (6)$$

$$\dot{x}_2 = x_1 \quad (7)$$

Within this circle the (nonlinear) coefficient of the second term in Eq. (5) is negative and outside the circle the coefficient is positive. If this coefficient is constant both differential equations correspond to the descriptive equation of an *LC* circuit with linear damping that is an Ohmic resistor. If we assume the (nonlinear) coefficient in Eq. (5) to be constant for a moment, the first case corresponds to an *LC* circuit with a negative resistor and the second case, to a circuit with a positive resistor. From this heuristic point view it is easy to interpret the global behavior of Eq. (5). Although its solutions cannot be calculated analytically if the initial conditions are prescribed within or outside the circle x_p , the qualitative behavior of the differential equation follows from the analogy with an *LC* circuit with damping. We find that the amplitude of every solution that starts within the circle increases and approaches $x_p(t)$ as $t \rightarrow \infty$. On the other hand, the amplitude of every solution that starts outside the circle decreases and approaches to $x_p(t)$ as $t \rightarrow \infty$. From a physical point of view the two-dimensional state space of the differential equation (5) is decomposed by the circle x_p into two areas that have different meanings:

- The negative damping area (inner of the circle) where energy is supplied to the system
- The positive damping areas (outer of the circle) where energy is thrown away by the system

The periodic solution x_p can be interpreted as a dynamical equilibrium between the negative and the positive damping area. Stable periodic solutions of this kind are called *limit cycles* [e.g., 47]. In contrast to limit cycles, a stable equilibrium \mathcal{O} is embedded in a positive damping area. Both types of solutions are called *steady-state solutions*. In Fig. 1 the state space and the steady-state solutions of Eq. (5) are shown together with the damping area.

The physical situation of this rather special differential equation is the typical case in two-dimensional state space systems. In Fig. 2 we show the damping areas of the van der Pol equation and of the Rayleigh equation, which extend infinitely in the x_2 and x_1 directions, respectively. Obviously it is clear why sinusoidal solutions are impossible since the damping areas are not symmetric with respect to the unstable zero solution point.

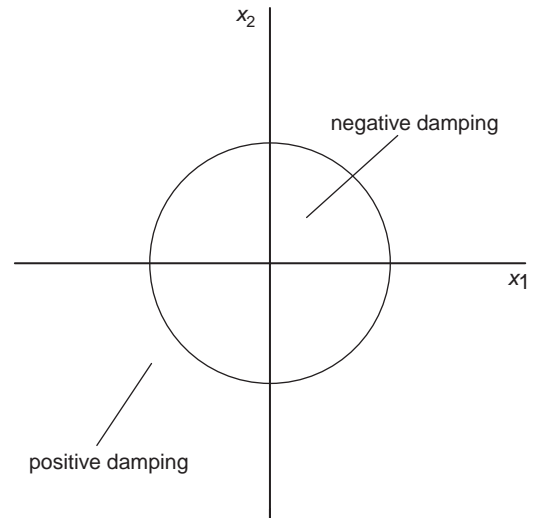


Figure 1. Negative damping area of the Rayleigh–van der Pol equation.

The parameter ε can be interpreted as a measure of deviation from the sinusoidal case. If $\varepsilon \ll 1$, we have a sinusoidal oscillator, which is discussed in the next sections. For large $\varepsilon \gg 1$, we obtain a relaxation oscillator that is considered in Section 3.4. The latter case is much more complicated from a mathematical point of view because circuits of this kind have to be described by differential-algebraic equations or analyzed by singular perturbation methods (see, e.g., Mathis [66]). However, the design of square-wave oscillators can be simplified if the transistors are modeled as switches. Such models are piecewise linear. In the case of sinusoidal oscillators an overall model is available.

2.3. The Mandelstam–Papalexi–Andronov Oscillator Model

Although the simple oscillator equations in the last section are very suitable for illustrating the physical

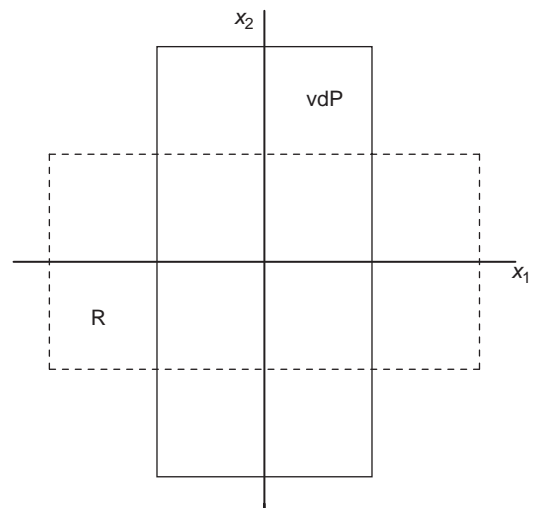


Figure 2. Damping areas: vdP—van der Pol Equation, R—Rayleigh equation.

rationale of periodic steady-state solutions, a more extensive model should be considered that includes additional parameters. From a systematic point of view a family of differential equations is considered that is parameterized by means of the mentioned parameter and the following questions are studied:

- Is there a subset of equations that permit a periodic steady-state solution?
- If yes, what is the critical value of the parameter where a qualitative change within the family arises?

These questions are crucial for the design of electronic oscillator circuits. Therefore these problems were studied around 1930 by Mandelstam et al. [63] and Andronov [64] using ideas from Poincaré’s theory of celestial mechanics. As a result, they proved a theorem including a criterion about the occurrence of a limit cycle in differential equations depending on a certain parameter. In the mathematical literature this theorem is known as the *Hopf bifurcation theorem* since Hopf reinvented this theorem in 1944 while studying problems in hydromechanics (see Arnold [11], p. 271 for further information about the reception of this theorem). The Mandelstam–Papalexi–Andronov oscillator model contains a parameter that is suitable for generating a limit cycle if a critical value is passed. In oscillator design this parameter corresponds to a circuit parameter (e.g., the load resistor). We will demonstrate the birth of a limit cycle before the Poincaré–Andronov–Hopf theorem is formulated. For this purpose a modification of Eq. (5) is used since it can be solved exactly. This equation is formulated in the state space representation [e.g., 77]:

$$\dot{x}_1 = -x_2 - (x_1^2 + x_2^2 - \mu)x_1 \tag{8}$$

$$\dot{x}_2 = x_1 - (x_1^2 + x_2^2 - \mu)x_2 \tag{9}$$

The parameter is included in another way. To solve this differential equation, we transform it into the magnitude and phase angle representation:

$$\dot{r} = \mu r - r^3 \tag{10}$$

$$\dot{\phi} = 1 \tag{11}$$

Obviously the system of two differential equations is decoupled, and in this case solutions of both equations are known. We have

$$r = r(t) = \sqrt{|\mu|} \frac{\exp \mu t}{\sqrt{1 + \exp 2\mu t}} \text{ and } \phi = \phi(t) = \phi_0 + t \tag{12}$$

In Fig. 3 the steady-state behavior of Eqs. (8) and (9) is illustrated for $\mu < 0$ and $\mu > 0$, and we find that in the latter case we have the desired limit cycle. The abovementioned critical parameter value is zero.

It can be shown that this case already describes a very general situation. If we consider n -dimensional systems of differential equations that describe more complicated electronic oscillators, the so-called center manifold

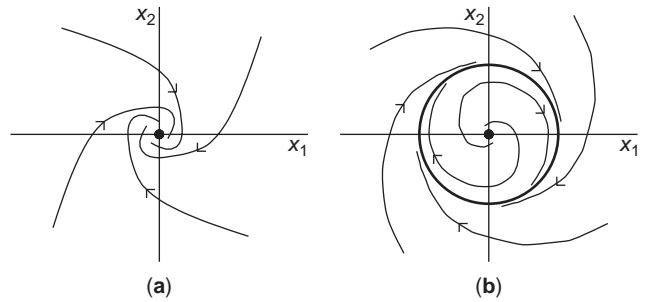


Figure 3. Bifurcation of a limit cycle: (a) $\mu < 0$; (b) $\mu > 0$.

theorem can be used to reduce the dimension of the system to 2. For details of this theorem, we refer to the monograph of Arrowsmith and Place [13]. Then the former case is obtained, but in this introductory article we cannot discuss further details and therefore the reader is referred to, for example, Hassard et al. [41]. In the following, the Poincaré–Andronov–Hopf theorem is formulated, which is very important for oscillatory circuits and systems.

Theorem 1 Poincaré–Andronov–Hopf. Let

$$\dot{x} = f(x, \mu) \tag{13}$$

a system of differential equations where $f(0, \mu) = 0$ for all μ in a neighborhood of 0. The Jacobian $D_x f(0, 0)$ of f in $(0, 0)$ has the eigenvalues $\lambda_{1,2} = \pm j\omega$ with $\omega \neq 0$ and other $n - 2$ eigenvalues λ_k with $\Re\{\lambda_k\} < 0$. Furthermore $(d/d\mu) \Re\{\lambda_1(\mu)\}|_{\mu=0} > 0$, and the equilibrium point 0 is a stable spiral in $\mu = 0$. Under these assumptions sufficiently small positive numbers μ_1 and μ_2 exist such that for all $\mu \in (-\mu_1, 0)$ the equilibrium point 0 is a stable spiral and for all $\mu \in (0, \mu_2)$ the equilibrium point 0 is an unstable spiral. In the last case the unstable spiral is surrounded by a stable limit cycle whose amplitude increases with μ .

If for some parameter value the assumption of this theorem are fulfilled, it is denoted as the Poincaré–Andronov–Hopf bifurcation point. Note that the necessary condition of imaginary eigenvalues of the Jacobian for the bifurcation point corresponds to the condition that the dynamical systems has to be nonhyperbolic in this point. We know from the Hartman–Grobman theorem (see, e.g., Arrowsmith and Place [13]) that only in this case can we expect a behavior of the system that is different from a linear system.

Instead of a proof (see, e.g., Hassard et al. [41] or Mathis [66]), this theorem is illustrated by the van der Pol equation.

Example 1. The van der Pol equation (3) can be formulated by a standard transformation $y = x$ into a system of differential equations of first order. Using the normalization $u := \sqrt{\epsilon}x$ and $v := \sqrt{\epsilon}y$, the following differential equations result:

$$\dot{u} = v \tag{14}$$

$$\dot{v} = -u - (u^2 - \epsilon)v \tag{15}$$

The eigenvalues of the Jacobian matrix are

$$\lambda_{1,2} = \frac{\varepsilon}{2} \pm \sqrt{\left(\frac{\varepsilon}{2}\right)^2 - 1} \tag{16}$$

and therefore $\lambda_{1,2} = \pm j$ (for $\varepsilon = 0$) and $(d/d\varepsilon)\Re\{\lambda_1(\varepsilon)\}|_{\varepsilon=0} = \frac{1}{2} > 0$. It can be shown that if $\varepsilon = 0$ the equilibrium point $(u, v) = (0, 0)$ is a stable spiral. It results from the Poincaré–Andronov–Hopf theorem that a stable limit cycle is generated for $\varepsilon > 0$ that encloses an unstable spiral. This oscillator model and the theorem was formulated for the first time by Andronov and his coworkers in 1934 while studying electronic oscillator circuits, but it was 1979 before Mees and Chua published theoretical considerations about oscillator design using this theorem [72]. On the other hand, a necessary condition of this theorem—Barkhausen’s oscillatory condition—was a known long time ago and became the basis of a linear design theory for oscillators.

3. DESIGN ASPECTS

3.1. The Linear Design Theory of Sinusoidal Oscillators

It is known from the Poincaré–Andronov–Hopf theorem that a pair of eigenvalues has to cross the imaginary axis whereas the other eigenvalues have to remain within the left half-plane of the complex plane. Obviously it is a necessary condition that oscillator circuits have a pair of eigenvalues on the imaginary axis for a certain value of some circuit parameter.

It was mentioned that all oscillatory criteria for sinusoidal oscillators known by electronic engineers are in essential criteria searching for nonhyperbolic cases, although this was never emphasized.

It is mentioned in Section 2.2 that this condition can be interpreted as the compensation step of oscillator design, which is possible in a linear manner using a linear negative resistor. This necessary assumption of the Poincaré–Andronov–Hopf theorem was already known since the first oscillator paper of Vallauri [97] in 1917 and during the following few years several variants of his results were published. One of the most popular criteria was the Barkhausen oscillatory condition (see, e.g., Millman and Grabel [74]). All these variants can be classified using the following topological structures of oscillator circuits:

- Negative impedance/admittance model
- Positive feedback model

and apply corresponding methods of network analysis. It has been known for a long time that these two models are equivalent from a network theoretical point of view. It is emphasized that many oscillator circuits contain tubes or transistors. In the case of tuned-circuit oscillators it is more efficient to describe the circuit as an active three-pole with a passive impedance embedding (see Fig. 4).

This was done for the first time in 1920 by Hazeltine [42]. He showed that the nature of the impedances $Z_1, Z_2,$

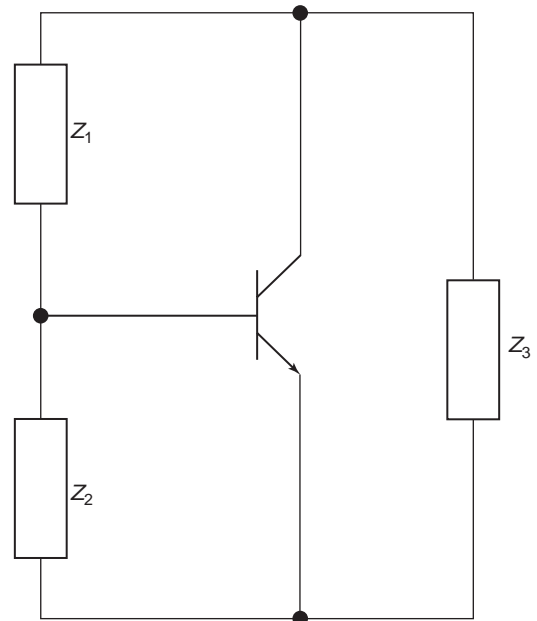


Figure 4. Active three-pole structure of transistor oscillators.

and Z_3 have to be capacitive and inductive, respectively. The reader will find systematic considerations about this subject in the books of Spence [93] and Cassagnol [19]. Since this rather restricted model for oscillator circuits can be reformulated in the form of a negative impedance/admittance model or the positive feedback model, we discuss the usage of the latter models in more detail. For this purpose we consider a rather simple oscillator circuit in order to avoid tedious calculations; further examples can be found in electronics textbooks [e.g., 74]. As the first step the network elements of a concrete oscillator circuit have to be associated with the defining blocks of the abovementioned models. In general this step includes some arbitrariness. The second step uses the conditions that a pair of eigenvalues with vanishing real parts have to occur where these conditions are formulated for the special topology of the models. As a result, we obtain (necessary) conditions for the occurrence of oscillations with respect to the oscillator frequency and the gain of the active elements parameterized by means of the network parameters of a concrete oscillator circuit. These conditions represent the linear part of the design of oscillator circuits.

Now we compile the corresponding conditions for the abovementioned oscillator models: [79, Chap. 1]:

- *Negative impedance model*—the real and imaginary parts R and X , respectively, of the model in Fig. 5 have to satisfy the conditions

$$R_g = -R_L, \quad X_g = -X_L \tag{17}$$

- *Negative admittance model*—the real and the imaginary parts G and B , respectively, of the model in

Fig. 5 have to satisfy the conditions

$$G_g = -G_L, \quad B_g = -B_L \quad (18)$$

- *Positive feedback model*—the open-loop gain consisting of the transfer functions $A(s)$ and $\beta(s)$, respectively, of the active block and the passive block (see Fig. 6) has to satisfy the condition

$$A \cdot \beta = 1 \Leftrightarrow \Re\{A \cdot \beta\} = 1, \quad \Im\{A \cdot \beta\} = 0 \quad (19)$$

- In the literature these conditions are called the *Barkhausen criterion* [74]. Instead of the decomposition of the complex equation into real and imaginary parts, a representation with magnitude and phase angle is preferred.

Of course, a network analysis in a straightforward manner leads to equivalent conditions for the occurrence of oscillations. For this purpose we consider the AC network model of an oscillator circuit that contains no independent sources and derive its network equations in the frequency domain. As a result we obtain a homogeneous system of linear equations

$$\mathbf{M}(j\omega)\mathbf{x} = \mathbf{0} \quad (20)$$

with the oscillation frequency $j\omega$ as the parameter. Note that an oscillator circuit contains only constant independent sources. Therefore these sources are omitted in the small-signal model. The matrix coefficients contain the network parameters. It is known from linear algebra that nontrivial solutions are obtained if the condition

$$\det(\mathbf{M}(j\omega)) = 0 \quad (21)$$

is satisfied. The equivalence of this expression with the other criteria can be shown. There is another method that is equivalent with a circuit analysis under certain conditions. In this case a transfer function is defined with

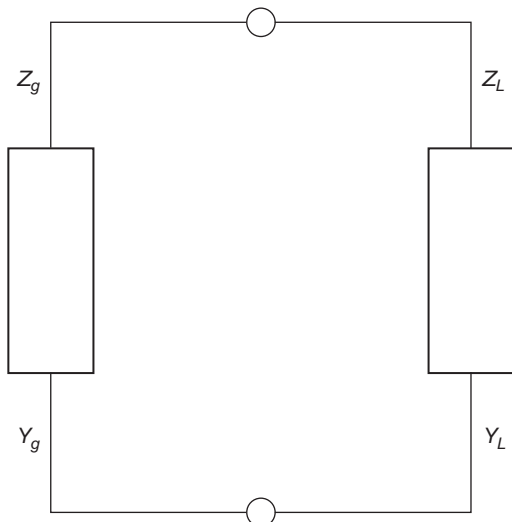


Figure 5. Negative impedance and admittance oscillator model.

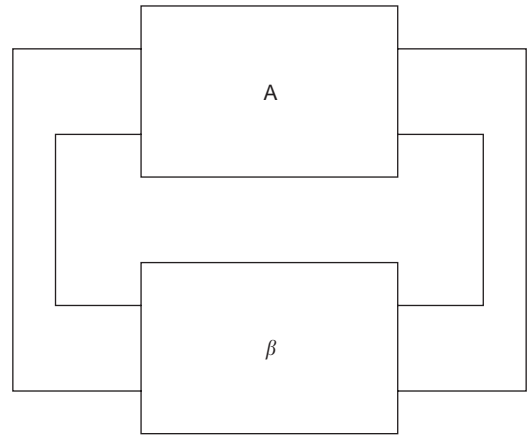


Figure 6. Feedback oscillator model.

respect to a (sinusoidal) input source and two terminal as the output port. This approach can be applied in a successful manner only if

- The input current or voltage source does not change the oscillator circuit substantially, that is, if we receive the initial circuit if the input source vanishes
- The circuit is controllable and observable with respect to the chosen input and output ports

The first condition is satisfied if we use a pliers entry and an independent voltage source or soldering-iron entry and an independent current source (see, e.g., Desoer and Kuh [26]). For the second condition a careful analysis of the circuit is needed before the two ports are chosen.

Example 2 Tunnel Diode Oscillator. [72]. The nonlinear network equations of the circuit in Fig. 7 can be formulated as (if $R \approx 0$)

$$\frac{d}{dt} \begin{pmatrix} i_L \\ \tilde{u}_C \end{pmatrix} = \begin{pmatrix} 0 & 1/L \\ -1/C & 0 \end{pmatrix} \begin{pmatrix} i_L \\ \tilde{u}_C \end{pmatrix} + \begin{pmatrix} 0 \\ (1/C)g(U_0 - \tilde{u}_C) \end{pmatrix} \quad (22)$$

where $\tilde{u}_C := U_0 - u_C$. Since the constant solution can be calculated in a simple manner as

$$i_L^0 = g(U_0), \quad \tilde{u}_C^0 = 0 (u_C = U_0) \quad (23)$$

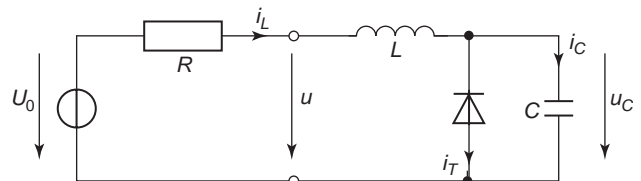


Figure 7. Tunnel diode oscillator model.

The AC network model (linearized network equations) can be derived where a distinction between large and small signal currents and voltages is omitted; g' is the derivative of g with respect to its argument. The transformation of this equation into the frequency domain leads to the following condition:

$$\det \begin{pmatrix} 0 & 1/L \\ -1/C & -(1/C)g'(U_0) \end{pmatrix} = \lambda^2 + \frac{1}{C}g'(U_0)\lambda + \frac{1}{LC} = 0 \quad (24)$$

The roots of this quadratic equation are

$$\lambda_{1,2} = -\frac{1}{2C}g'(U_0) \pm \sqrt{\left(\frac{1}{2C}g'(U_0)\right)^2 - \frac{1}{LC}} \quad (25)$$

and therefore a purely imaginary pair of eigenvalues is obtained if the condition

$$\frac{1}{C}g'(U_0) = 0 \quad (26)$$

is satisfied. In this case we have the oscillator frequency $\omega_0^2 = 1/(LC)$. We find from the tunnel diode characteristic that this is possible if the operating point of the diode is located in its maximum or minimum, where the derivative $g'(U_0)$ vanishes. If the AC network model of this tunnel diode circuit is interpreted as the negative conductance model, we find the oscillatory conditions

$$g'(U_0) = 0, \quad \omega_0 C - \frac{1}{\omega_0 L} = 0 \quad (27)$$

Obviously these conditions are equivalent to the former one. A negative-resistance model is not suitable in this example. If the negative-conductance model is assumed, a transfer function is determined if an extra (index E) independent sinusoidal voltage source U_E is located as an input quantity in series with the linearized tunnel diode resistor and the capacitor voltage U_C is used as output quantity; both U_E and U_C are represented in the frequency domain. The corresponding transfer function can be derived:

$$H(j\omega) = \frac{U_C}{U_E} = \frac{g'(U_0)j\omega L}{1 - \omega^2 LC + j\omega g'(U_0)L} \quad (28)$$

The zeros of the denominator are the eigenvalues of this circuit. Under the same condition ($g'(U_0) = 0$) on the voltage U_0 , we obtain a pair of imaginary eigenvalues and the oscillatory frequency $\omega^2 = 1/LC$. Finally we consider the approach where the positive feedback model is applied. For this purpose we reformulated the negative-conductance model such that the conductances $Y_g = g'(U_0)$ and $-Y_L(j\omega) = -1/Z_L(j\omega)$ become identical, that is, the sum of the admittances Y_g and Y_L has to be zero. By means of $Z_L(j\omega)$, an interpretation as a product is possible if the

sum is reformulated as

$$Y_g \cdot Z_L(j\omega) = g'(U_0) \cdot \frac{-1}{j\left(\omega_0 C - \frac{1}{\omega_0 L}\right)} = 1 \quad (29)$$

This is Barkhausen's condition if Y_g and $-Z_L(j\omega)$ are interpreted as transfer functions of a feedback model. Since this reformulation is derived by means of equivalent calculation steps, the same conditions for the occurrence of oscillations are obtained. Probably it is rather a problem of taste and/or experience which approach is used to derive the oscillatory conditions. For example, Parzen [79] discusses the design of tuned-circuit oscillators with transistors and therefore uses the abovementioned active three-pole representation with passive embedding. Based of this model, the author applies the negative-resistance/conductance model to calculate the oscillatory conditions. Mauro [71] prefers the positive feedback model and derives similar conditions for tuned-circuit oscillators as well as RC oscillators. In general both approaches can be used in a successful manner, and therefore the special choice makes no difference from a theoretical point of view.

3.2. The Nonlinear Design Aspects of Sinusoidal Oscillators

Although many aspects of the nonlinear theory of oscillator circuits are known, it is not trivial to make use of this knowledge to construct a systematic design concept for these circuits. At least theoretical results are suitable for a classification of oscillator circuits and for the construction of simulation tools. We will discuss these subjects in this and the following sections. Just as in other cases of circuit design, an oscillator circuit is determined if its network topology as well as its network parameters are known. A design process starts with some specifications of the desired oscillator circuit, and then we try to find an oscillator topology together with a certain set of network parameters in order to fit these specifications. For this purpose, the following approach can be used. Further details can be found in, for example, the monograph by Parzen [79].

1. *Basic specifications*, where the form of the oscillator behavior (sinusoidal, rectangle, triangle, etc.), frequency of the oscillator, the amplitude, and other parameters are considered
2. *Choice of the circuit devices*, where application of the oscillator circuit, the working temperature, and other factors are considered
3. *Choice of resonator type*, where the frequency stability, amplitude stability, variability of the frequency, and economic expense are accounted for
4. *Choice of the kind of limiting that maintains the oscillator amplitude*, where a self-limiter, an external limiting, or an automatic level control limiting can be chosen
5. *First draft of the oscillator circuit*, where the aspects listed above are considered

6. *Determination of circuit parameters*, where the actual circuit devices and its circuit parameters have to be chosen
7. *Optimization process*, where circuit simulations and/or an experimental realization are necessary— if the circuit does not meet the specifications, then some steps have to be repeated

This design outline shows that each design process of an oscillator circuit is a rather individual problem. However, we will add some remarks based on the theoretical considerations above. Although the frequency of an sinusoidal oscillator can be determined by a linear analysis (see the Barkhausen condition in Section 2.4), following the Poincaré–Andronov–Hopf theorem nonlinearities are essential for the functionality of oscillators (see Section 2.2). We already mentioned in Section 2.2 that a nonlinearity is necessary for limiting the amplitude, which can be done in one of three ways:

1. *Self-Limiting*. The inherent linearity of an active device (tube, transistor, operational amplifier, etc.) is used to build up a nonlinear differential equation with a stable limit cycle. In this case the amplitude is fixed implicitly by the type of nonlinear characteristic. The only thing that can be done is to calculate the amplitude with a suitable model of the nonlinear device.
2. *External Limiting*. This is a variant of the first case since the resonance circuit works in a linear mode and the limiting will be introduced by an additional device (Zener diode, symmetric clippers, thermistors, etc.).
3. *Automatic Level Control Limiting*. The rather natural approach to limiting is amplitude control, that is, measuring the amplitude, comparing it with a desired amplitude value, and controlling (if necessary) a circuit parameter that varies the damping of the circuit in the sense of a suitable control strategy. Even if the resonance circuit is approximately linear, the entire circuit, including the control part, is nonlinear because there is a coupling between at least one state variable and a circuit parameter. A suitable discussion for the construction of such control devices can be found in the monograph of Parzen [79] and the dissertation of Meyer-Ebrecht [73].

The first kind of limiting of the oscillator amplitude is a rather simple way to construct an oscillator circuit, but in this way the damping element is influenced by the large-signal gain factor. Unfortunately this gain factor varies with the instantaneous amplitude of the oscillator and results in spectral distortions. This is an essential disadvantage in the case of sinusoidal oscillators. If such an oscillator with low distortion is desired, the nonlinear damping should depend on an indefinite integral $\int x(t) dt$ of the amplitude $x(t)$ instead of the instantaneous amplitude. In mathematical terms, this statement can be formulated as follows if we restrict our discussion to an oscillator circuit of van der Pol type. Then the descriptive

equation is of the form

$$\ddot{x} + \gamma \left(\int x(t) dt \right) \dot{x} + \omega^2 x = 0 \quad (30)$$

instead of

$$\ddot{x} + \gamma(x)\dot{x} + \omega^2 x = 0 \quad (31)$$

Although the structure of an oscillator circuit and its amplitude stabilization are essential, analysis methods are necessary in order to calculate at least the amplitude and the frequency as a function of certain circuit parameters for a suitable design of sinusoidal oscillator. Since analytical solutions of the corresponding network equations of an oscillator are not available, perturbation methods have to be applied for this purpose. Several approaches are available:

- Perturbation methods
- Averaging methods or harmonic balance
- Describing function method
- Volterra series method

Most of the different variants of perturbation methods start with some Fourier polynomial and, based on this ansatz, a set of associated differential equations will be derived. Therefore these methods can be interpreted as time-domain methods, which are considered and illustrated in the monograph by Nayfeh [76]. Especially the first-order perturbation results are of some interest in practical oscillator design. Also the average or harmonic balance methods can be interpreted as time-domain methods. A very efficient variant of an average method that can be implemented in a computer algebra program uses Lie series [52]. It was applied for studying electronic oscillators by Keidies and Mathis [51]. Newer results for more complex oscillators (e.g., Clapp oscillator) were published by Prochaska and Mathis [80], where the average approach of Keidies and Mathis is combined with singularly perturbation method.

Another time-domain method can be interpreted as an extension of the convolution description of linear time-invariant input–output systems, which is called *Volterra series methods*. In this case a series of integrals is used as an ansatz and the coefficients are convolution kernels of higher order. Illustrations of this method are included in the paper by Chua and Tang [22].

An efficient iterative procedure for calculating the steady-state output waveform of almost sinusoidal nonlinear oscillators using the feedback formulation is presented by Buonomo and Di Bello [16]. In their paper this method is compared with the alternative methods of Mathis and Keidies as well as Chua and Tang. Just like the other methods, the interactive approach can be implemented by means of a computer algebra system, too.

Since frequency-domain methods are very successful in the case of linear time-invariant circuits and systems, many electrical engineers are very interested in

extensions of these approaches to nonlinear circuits and systems. The describing function method is very popular because it can be interpreted as an extension of the transfer function method that is a standard method in the analysis of linear time-invariant networks. We have to assume that only the first-harmonic part of the reaction of a nonlinear block to a sinusoidal input function is interesting because the other parts will be filtered out. If functionality of the sinusoidal oscillator is interpreted by the feedback structure in Fig. 6, this filter is realized within the feedback loop. Although the nonlinear block produces an entire spectrum of output frequencies as a reaction to a sinusoidal input function, only the first-harmonic part is essential for the functionality of a sinusoidal oscillator. Therefore the describing function method is illustrated by means of the feedback model of a sinusoidal oscillator, although extensions of the negative-impedance and admittance models, respectively, are possible [19]. We restrict our discussion to the case where only the A block in Fig. 6 contains nonlinear elements and the input signal is $x(t) = \hat{x} \cos \omega t$. Then a first-harmonic part can be extracted from the output signal

$$y(t) = y_1 \cos(\omega t + \varphi_1) + y_2 \cos(2\omega t + \varphi_2) + \dots \quad (32)$$

where we assume that no constant part is included in the output signal. Clearly the amplitudes y_1, y_2, \dots and the phases $\varphi_1, \varphi_2, \dots$ depend on \hat{x} and ω . The describing function is defined by

$$N(\hat{x}, \omega) = \frac{y_1(\hat{x}, \omega)}{\hat{x}} e^{j\varphi_1(\hat{x}, \omega)} \quad (33)$$

As a result, we obtain a generalization of the Barkhausen oscillatory condition

$$N(\hat{x}, \omega) \cdot \beta(\omega) = 1 \quad (34)$$

In many cases $N(\hat{x}, \omega)$ is independent of ω . Now $\beta(\omega)$ can be plotted as a single polar curve in the complex plane graduated in ω as well as the locus of $-1/N(\hat{x})$ graduated in \hat{x} . The intersection of these curves corresponds to a limit cycle whose stability properties can be studied. More details of this approach are included in the monograph by Mees [72], where the problems of this method are also discussed.

3.3. Theoretical Aspects of Noise in Oscillators

Obviously functionality of electronic oscillators and adaptation to specifications (frequency, amplitude, etc.) are a main subjects of oscillator design. Both subjects can be studied using concepts from the mathematical theory of dynamical systems. However, the amplitude of modern oscillator circuits is low and therefore the signal-to-noise ratio also can be low. Consequently, studying noise behavior of oscillator has become another main subject in oscillator design since the mid-1990s. In this section some theoretical aspects of noise in oscillators circuits will be discussed. In Section 5 advanced numerical

methods for noise analysis are described in further detail.

The first results in noise analysis of electrical oscillators were published as early as 1960 or so by Stewart, Edson, Mullen, Hafner, Lax, Leeson, and others; corresponding references can be found in the monograph by Hajimiri and Lee [39]. The popular Leeson model is discussed in the same book. However, more in-depth mathematical results about noise in oscillatory circuits were presented by the Russian researchers Kuznetsov, Stratonovich, and Tikhonov in the early 1950s; see a collection of papers by these authors [60].

More recently several papers have been published considering heuristic approaches on phase noise in electronic oscillators. Many material of that research is included in the books of Hajimiri and Lee [39] as well as Demir and Sangiovanni-Vincentelli [25]; the last book contains the framework of stochastic processes and stochastic differential equations. The main progress was done by Kärtner (a former Ph.D. student of the second author of this article) in his paper from 1990 [49], where he suggested a certain decomposition of limit cycle solutions. Many authors use Kärtner's device. A detailed description is contained in Section 5.

Another approach for analyzing noise in nonlinear systems uses the Stratonovich concept of nonlinear nonequilibrium thermodynamics. As a result, an exact noise theory for the probability density of a large class of nonlinear circuits was founded by Weiss and Mathis (overview and further references given in Ref. 69). Unfortunately it is restricted at first to reciprocal circuits such that a Langevin approach is discussed by these authors. On the basis of a Langevin description of oscillator circuits

$$dx = F(x)dt + \sigma(x)\xi \quad (35)$$

where ξ is a stochastic process with certain properties (e.g., stationary Gaussian process), Mathis and Prochaska [70] discuss a stochastic Andronov–Hopf bifurcation approach for nonlinear electronic oscillators using more recent mathematical results; see the monograph by Arnold [12] for an overview. The mathematical details of this approach are beyond the scope of this article, but there are in fact two types of bifurcation: (1) *P bifurcation*, where the quality of a probability density changed and (2) *D bifurcation*, where a so-called invariant measures that replace equilibrium solutions in deterministic cases changed. There are systems with *P* bifurcations but no *D* bifurcations and converse. Further interesting results can be expected using these mathematical concepts.

3.4. Design of Two-Port Oscillators

In the following we consider the two-port oscillator formed by a frequency-dependent linear feedback two-port and a nonlinear active two-port as depicted in Fig. 8. The output signal of the linear two-port is amplified in the non-linear active two-port and then feedback to the input of the linear two-port. A necessary condition for the occurrence

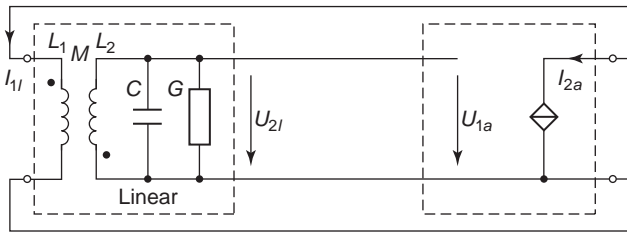


Figure 8. Two-port oscillator.

of a stationary harmonic oscillation is that the phase and the amplitude of the signal, after passing both two-ports, are unchanged. Due to the frequency-dependent linear feedback two-port, the phase condition is only fulfilled for one frequency. Because of the nonlinearity of the active two-port, the amplitude condition is fulfilled for only one value of the amplitude of the signal.

In our example we consider the simple model of an active two-port formed by a voltage-controlled current source. The voltage-current characteristic of the voltage-controlled current source is assumed to be nonlinear. If the active two-port contains additional linear elements, these elements may be moved to the linear two-port. In our example the linear frequency-dependent two-port consists of a transformer with the primary inductance L_1 , the secondary inductance L_2 , the mutual inductance M , a capacitor C , and a conductor G . The primary and secondary coils of the transformer are in antiphase and therefore $M < 0$. The secondary inductance L_2 and the capacitor C together form a parallel-resonant circuit. This inductor-coupled resonant circuit is the most compact model that we can establish for the linear feedback circuit. In more complex cases we can replace the reactive part of the feedback two-port by the canonical Foster representation [14]. In the neighborhood of the resonant frequency the essential part of the canonical Foster realization is given by a transformer-coupled resonant circuit as assumed in our model. In the case of small losses it is also possible to include the losses in this model [65]. The conductor G accounts for the losses in the passive and the active two-ports. At the resonant frequency of the parallel resonant circuit

$$\omega_0 = 1/\sqrt{L_2 C} \tag{36}$$

the phase change in the linear two-port is 180° . This compensates for the 180° phase change occurring in the active circuit and the phase condition for oscillation is fulfilled.

The nonlinear dependence of the output current $i_{2a}(t)$ of the linear two-port on its input voltage $u_{1a}(t)$ is given by

$$i_{2a}(t) = f(u_{1a}(t)) \tag{37}$$

The active two-port is considered to be frequency-independent. It is assumed that all reactive elements of the active element have been moved to the linear two-port. This can be done easily if the reactive elements are linear, and if it is possible to concentrate all reactive elements in

a π equivalent circuit. The relation between the spectra of the input current $I_{1l}(\omega)$ and the output voltage $U_{2l}(\omega)$ of the linear feedback network is given by

$$I_{1l}(\omega) = A_{21}(\omega)U_{2l}(\omega) \tag{38}$$

where A_{21} is the matrix element of the chain two-port representation. According to Fig. 8, we obtain $u_{1a} = u_{2l}$ and $i_{1l} = -i_{2a}$. Furthermore, we consider $i_{1l}(t) \circ \dots \bullet I_{1l}(\omega)$ and $u_{2l}(t) \circ \dots \bullet U_{2l}(\omega)$, where $(\cdot)(t) \circ \dots \bullet (\cdot)(\omega)$ denotes in a symbolic manner a pair of Fourier transformed functions in time and frequency domains.

We assume that in the oscillator circuit (Fig. 8) oscillations are excited by an initial perturbation. After some period of growth of amplitude due to the nonlinearity of the active element, the oscillator will saturate in a stationary state oscillating at a frequency ω_0 . In the case of a weak nonlinearity the oscillation exhibits only low harmonics. The linear feedback network acts as a bandpass filter and attenuates the harmonics. In the case of a sufficiently high Q factor of the resonant circuit and a weakly nonlinear active element, the transient of the oscillator from excitation to the stationary state exceeds the period of oscillation by orders of magnitude. We also can assume that the time constants governing the decay of the perturbation of the stationary state of the oscillator exceed the period of oscillation by orders of magnitude. Under these assumptions we can make for u_{2l} the ansatz

$$u_{2l}(t) = V(t) \cos(\omega_0 t + \varphi(t)) \tag{39}$$

where $V(t)$ and $\varphi(t)$ denote the amplitude and the phase of the oscillator signal. Due to the nonlinearity of the active two-port, the output amplitude I at the fundamental frequency ω_0 depends nonlinearly on the input amplitude V . With $\omega_0 t = \xi$, we obtain from (37) the fundamental frequency component of the output current:

$$I(V) = \frac{1}{\pi} \int_0^{2\pi} f(V \cos \xi) \cos \xi d\xi \tag{40}$$

This relation also holds for slowly time-varying amplitudes, and we obtain

$$i_{2a} = I(V(t)) \cos(\omega_0 t + \varphi(t)) \tag{41}$$

With $a_{21}(t) \circ \dots \bullet A_{21}(\omega)$ we obtain from (38) the relation between the input current in $i_{1l}(t)$ and the output voltage $u_{2l}(t)$ of the linear feedback circuit in the time domain:

$$i_{1l}(t) = \int_{-\infty}^{+\infty} a_{21}(t - t_1)u_{2l}(t_1) dt_1 \tag{42}$$

Representing (41) by

$$u_{2l}(t) = \Re\{V(t) \exp(j(\omega_0 t + \varphi(t)))\} \tag{43}$$

and expanding into a first-order power series yields

$$u_{2l}(t_1) = \Re\{[V(t) + (t_1 - t)(\dot{V}(t) + j\dot{\phi}(t)V(t))] \exp j \times (\omega_0 t_1 + \phi(t))\} \quad (44)$$

Inserting this expression into (42) gives

$$i_{1l}(t) = \Re\left\{V(t)e^{j\phi(t)} \int_{-\infty}^{+\infty} a_{21}(t - t_1)e^{j\omega_0 t_1} dt_1 - \right. \quad (45)$$

$$\left. (\dot{V}(t) + j\dot{\phi}V(t))e^{j\phi(t)} \int_{-\infty}^{+\infty} (t - t_1)a_{21}(t - t_1)e^{j\omega_0 t_1} dt_1\right\} \quad (46)$$

With the substitution $t - t_1 = t_2$ we obtain

$$i_{1l}(t) = \Re\left\{\left[V(t) \int_{-\infty}^{+\infty} a_{21}(t_2)e^{j\omega_0 t_2} dt_2 - \right. \quad (47)$$

$$\left. (\dot{V}(t) + j\dot{\phi}V(t)) \int_{-\infty}^{+\infty} t_2 a_{21}(t_2)e^{-j\omega_0 t_2} dt_2\right] e^{j(\phi(t) + \omega_0 t)}\} \quad (48)$$

Using $a_{21}(t) \circ \dots \bullet A_{21}(\omega)$ and $ta_{21}(t) \circ \dots \bullet jA'_{21}(\omega)$ with $A'_{21}(\omega) = dA_{21}(\omega)/d\omega$, we obtain

$$i_{1l}(t) = \Re\{[V(t)A_{21}(\omega_0) + (\dot{\phi}V(t) - j\dot{V}(t))A'_{21}(\omega_0)]e^{j(\omega_0 t + \phi(t))}\} \quad (49)$$

With (41) and $i_{1l} = -i_{2a}$, it follows

$$\Re\{[\Im(\mathfrak{B}(t)) + \mathfrak{B}(t)\Re(\omega) + (\phi\mathfrak{B}(t) - j\dot{V}(t))A'_{21}(\omega_0)]e^{j(\omega_0 t + \phi(t))}\} = 0 \quad (50)$$

Introducing the conductance G_0 and the susceptance B_0 by

$$G_0(\omega_0) = -\Re\{A_{21}(\omega_0)\}, \quad B_0(\omega_0) = -\Im\{A_{21}(\omega_0)\} \quad (51)$$

yields

$$I(V) - VG_0 - \dot{\phi}VG'_0 - \dot{V}B'_0 = 0 \quad (52)$$

$$VB_0 + \dot{\phi}VB'_0 - \dot{V}G'_0 = 0 \quad (53)$$

where the prime (\cdot)' denotes the derivative with respect to ω estimated for $\omega = \omega_0$. For the stationary state it follows that

$$I(V_0) - V_0G_0(\omega_0) = 0 \quad (54)$$

$$B_0(\omega_0) = 0 \quad (55)$$

We now investigate the influence of small perturbations V_1 of the stationary amplitude V_0 . With the ansatz

$$V = V_0 + V_1 \quad (56)$$

we linearize $I(V) - VG_0$ in a neighborhood of the stationary amplitude V_0 . With

$$I(V) - VG_0 \doteq I(V_0) + V_1I'(V_0) - V_0G_0 - V_1G_0 = V_1(I'(V_0) - G_0) \quad (57)$$

we obtain for small amplitude deviations V_1 from the stationary state the linear differential equation

$$\dot{V}_1 + \frac{B'_0(G_0 - I')}{B_0^2 + G_0^2} V_1 = 0 \quad (58)$$

The stationary state of oscillation is stable if any perturbation V_1 is decaying. This holds for

$$\frac{dB_0}{d\omega} \left(G_0 - \frac{dI}{dV}\right) > 0 \quad (59)$$

The relation between I and V may be expressed by a nonlinear transconductance S given by

$$S(V) = \frac{I}{V} \quad (60)$$

In this case the stability condition (59) can be written in the following form:

$$\frac{dB_0}{d\omega} \frac{dS}{dV} < 0 \quad (61)$$

For the Meissner oscillator with transformer feedback circuit according to Fig. 8, the parameters G_0 and B_0 are given by

$$G_0 = \frac{L_2}{|M|} G \quad (62)$$

$$B_0 = \frac{L_2}{|M|} \left(\omega C - \frac{1}{\omega L_2}\right) \quad (63)$$

The condition (55) yields the frequency of oscillation ω_0 in the stationary state according to (36). Due to (54), the stationary amplitude V_0 can be determined from

$$S(V_0) = \frac{L_2}{|M|} G \quad (64)$$

From

$$\left.\frac{dB_0(\omega)}{d\omega}\right|_{\omega=\omega_0} = 2 \frac{L_2 C}{|M|} \quad (65)$$

and (61) it follows that the stationary state of the two-port oscillator considered is stable for

$$\frac{dS}{dV} < 0 \quad (66)$$

that is, for a transconductance S that decreases with increasing amplitude V .

3.5. Design of Relaxation Oscillators

In Section 2.2 it was mentioned that the van der Pol equation is also suitable as a model for relaxation oscillators if $\epsilon \ll 1$ is considered. Unfortunately, analytical solutions are not available in this case, and for the derivation of approximative solutions advanced mathematical methods are necessary (see, e.g., Andronov et al. [1] or Mathis [66]). In Mishchenko and Rozov [83] the singular perturbation method is used to study relaxation oscillatory systems in a more sophisticated manner, but their approach is beyond the scope of this article. Therefore almost all design methods for relaxation oscillators are based on more simplified models for the active devices (e.g., transistors or operational amplifiers), and the transition part is not included in these considerations.

If the transistors are replaced by switches [e.g., 45], we obtain piecewise linear oscillator models; note that such models are nonlinear, as was always the case. Some disadvantages of this approach are known:

- The transient behavior to the steady state (or limit cycle) cannot be obtained in a simple manner.
- A limit cycle has to be assumed.
- The results are independent of certain parameters of the active devices.

However, under these assumptions simple design formulas can be derived since only linear (time-invariant) networks have to be analyzed. We illustrate this approach in the case of a symmetric multivibrator that is working in saturated mode. More complicated situations (e.g., if transistors are not working in saturated mode) will be found in the literature [e.g., 37].

Example 3 Symmetric Multivibrator. We consider the multivibrator shown in Fig. 9. Let us assume that at the initial instant $t = 0$, the left transistor T_1 conducts and the right transistor T_2 is cut off. If the voltage across the left capacitor is near zero while that across the right capacitor reaches the voltage U_0 , a switching event occurs. During

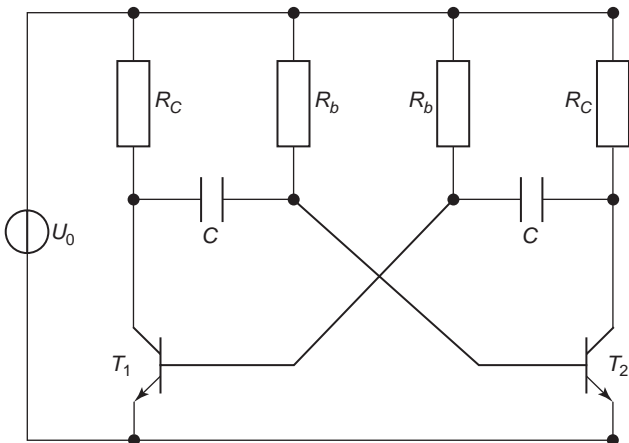


Figure 9. Symmetric multivibrator.

the commutation where T_1 switches to the cutoff state while T_2 changes to the conducting state, the left capacitor charges and the right capacitor discharges. The situation for $t > 0$ can be analyzed by means of a simple analysis of the network in Fig. 10. The following differential equation results

$$R_b C \frac{du_C}{dt} + u_C = U_0 \tag{67}$$

where $u_C(0) = U_0$. The solution is derived by well known calculations

$$u_C(t) = -U_0(1 - 2e^{-t/R_b C}) \tag{68}$$

A switching event takes place if $u_C(t)$ that corresponds to the base-emitter voltage of T_2 exceeds the cutoff voltage (which is simplified to zero in our case). From the solution above we have

$$t_{sw} : = R_b C \cdot \ln 2 \approx 0.69 \cdot R_b C \tag{69}$$

and therefore the period of the square wave is $T \approx 1.38 \cdot R_b C$. It is an easy matter to include cutoff and saturation quantities of the transistors [e.g., 19]. In the same way, results for other relaxation oscillators can be derived that include operational amplifiers or digital gates [see, e.g., Horenstein [45] or Kurz and Mathis [59]]. Furthermore, sawtooth wave oscillators can be analyzed if piecewise linear models of the active devices are used. The reader is referred to the literature for further details [e.g., 24].

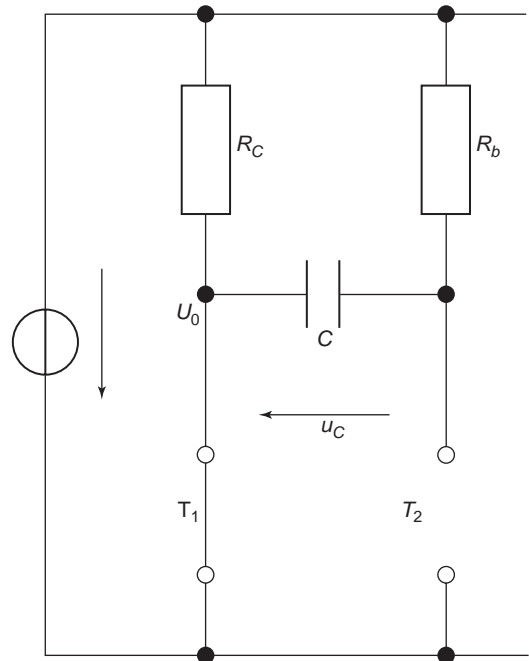


Figure 10. Dynamical operation.

4. ADVANCED MICROWAVE OSCILLATOR DESIGN TOOLS

4.1. Problems in Microwave Oscillator Design

Although this article is dedicated to design methods of all kinds of oscillators, the design of microwave oscillators has been studied intensively since 1989. Many results are published in the literature. Therefore an overview is presented in this section. But it should be mentioned that almost all methods can be used to design other kinds of oscillators. The design of monolithic integrated microwave and millimeterwave oscillators requires accurate and efficient tools for numerical modeling and optimization. Today the design of microwave oscillators in many cases is based on a linear analysis of the oscillation conditions. To predict and to optimize the oscillator output power or the oscillator spectral behavior, a nonlinear design approach is indispensable. The task of oscillator modeling can be separated into two parts:

- Nonlinear modeling of the unperturbed oscillator
- Modeling of the noise properties of the oscillator

The nonlinear modeling of the unperturbed oscillator may be done in the time domain by numerical integration [4,21,89], in the frequency domain using harmonic balance or Volterra series methods [20,46,61,81,82], or by using combined time-frequency domain methods [29,31,56,90]. Microwave oscillators may be subdivided into a linear embedding circuit and one or more nonlinear subcircuits. By this subdivision, the computational effort may be reduced considerably. The easiest approach is to subdivide the active element of the oscillator into a linear embedding network and one single nonlinear controlled source. In this way, the modeling may be improved compared with the linear approach, as shown, for example, in Refs. 27 and 36. This method is restricted to one single dominant nonlinearity in the oscillator circuit. A more accurate circuit modeling requires the inclusion of numerous nonlinear circuit elements in the simulation. Approximating the distributed elements within a broad but finite frequency interval by a lumped-element equivalent circuit facilitates the description of the unperturbed network by a set on nonlinear and autonomous first-order differential equations in the normal form

$$\frac{d\mathbf{x}}{dt} = \mathbf{f}(\mathbf{x}), \quad \mathbf{x} \in \mathbb{R}^N \quad (70)$$

The components of the vector \mathbf{x} are the state variables of the system. Time-domain integration of the network equations describing the equivalent lumped-element circuits usually yields an enormous computational effort, since the system of differential equations is usually high-dimensional and also exhibits high stiffness. One method for reducing of the computational effort is to combine time-domain and frequency-domain calculations [90]. The periodic steady-state solution can be found in the time domain by solving the periodic boundary value problem [4]. The solution obtained in the time domain is exact and

in this respect superior to harmonic balance. Using the multiple shooting algorithm of Bulirsch, the convergence of the time-domain boundary value problem may be improved [17,18]. Schwab has applied the time-domain boundary value method to the self-consistent determination of the steady-state solution of oscillators [89]. The time-domain method has the advantage that it is not necessarily restricted to a certain number of harmonics of the signals. The most common method for frequency-domain analysis of oscillators is the harmonic-balance method. Using the harmonic balance method a nonlinear system of equations

$$\mathbf{F}(\mathbf{X}, \omega_0) = \mathbf{0}, \quad \mathbf{X} \in \mathbb{C}^{n(2k+1)} \quad (71)$$

has to be solved. In this equation \mathbf{X} is the system state vector summarizing the signal amplitudes of n signals at the fundamental frequency ω_0 and at k harmonics [20,46,61,81,82]. The advantage of the harmonic-balance (HB) method is that distributed circuits can also be considered in the analysis. In the combined time/frequency-domain method, the oscillator circuit is subdivided into a linear circuit and a nonlinear circuit [56,90]. The linear part of the circuit is described in the frequency domain, whereas a state variable description in time domain is applied to the nonlinear part. This allows one to combine the advantage of frequency-domain and time-domain methods. In the linear part of the circuit, distributed circuit elements can also be considered.

4.2. Time-Domain Method

The computation of the steady-state solution of the oscillator by solving the initial value problem Eq. (87) for $t \rightarrow \infty$ has the disadvantage of high numerical effort. For most practical cases, interest is restricted to the periodic steady-state solution $\mathbf{x}(t) = \mathbf{x}(t + T^0)$ of the nonlinear oscillator waveform. The period of oscillation T^0 is not known. In order to determine the period of oscillation, we add T^0 as an additional variable to the state variables \mathbf{x} and introduce the normalized time variable $\tau = t/T^0$. We now have to solve the two-point boundary value problem for $\tau \in [0, 1]$:

$$\frac{d}{d\tau} \mathbf{x} = \mathbf{f}(\mathbf{x})T^0, \quad \frac{dT^0}{d\tau} = 0, \quad \tau = \frac{t}{T^0} \quad (72)$$

The $n + 1$ boundary conditions are

$$\mathbf{x}(0) = \mathbf{x}(1), \quad x_\kappa = a \quad (73)$$

where the latter condition fixes the phase of the limit cycle. Let us denote the solution of the initial value problem (72) at $\tau_{\mu+1}$ with the initial conditions \mathbf{s}_μ at τ_μ by $\mathbf{e}(\mathbf{s}_\mu, \tau_\mu, \tau_{\mu+1})$. The solution of the boundary value problem is equivalent to the determination of the zeros of the vector-valued function

$$\mathbf{G}(\mathbf{x}(0), T^0) = \begin{pmatrix} \mathbf{x}(\tau=0) - \mathbf{e}(\mathbf{x}(0), \tau_1=0, \tau_2=1) \\ x_k(0) - a \end{pmatrix} \quad (74)$$

This algorithm is called the “single-shooting method,” which generally has only a small domain of convergence. A better way to solve the boundary value problem is to use the multiple-shooting algorithm [17,18,90]. This algorithm is more stable and has a wider domain of convergence than does the single-shooting one. Using this method the region between the boundaries is divided into several subregions

$$0 = \tau_0 < \tau_1 < \dots < \tau_{\mu-1} < \tau_\mu = 1 \tag{75}$$

and for every subregion a starting point is chosen:

$$\begin{aligned} \mathbf{s}_0 &= \mathbf{x}(\tau = \tau_0) \\ \mathbf{s}_1 &= \mathbf{x}(\tau = \tau_1) \\ &\dots \end{aligned} \tag{76}$$

$$\mathbf{s}_{\mu-1} = \mathbf{x}(\tau = \tau_{\mu-1}) \tag{77}$$

These starting points are varied until a continuous solution fulfilling the boundary condition is found, which can easily be seen to be the zero of the vector-valued function

$$\mathbf{u}(\mathbf{s}_0, \mathbf{s}_1, \dots, \mathbf{s}_{\mu-1}) = \begin{pmatrix} \mathbf{e}(\mathbf{s}_0, \tau_0, \tau_1) - \mathbf{s}_1 \\ \mathbf{e}(\mathbf{s}_1, \tau_1, \tau_2) - \mathbf{s}_2 \\ \dots \\ \mathbf{e}(\mathbf{s}_{\mu-1}, \tau_{\mu-1}, \tau_\mu) - \mathbf{s}_0 \\ x_k(0) - a \end{pmatrix} \tag{78}$$

where the last two lines represent the boundary conditions and the others, the continuity conditions. Because of the special structure of Eq. (78), the zeros can be computed in a very efficient way [17]. To achieve starting values for T_0 and \mathbf{x} , the set of nonlinear differential equations (87) is linearized at the unstable stationary point \mathbf{x}_0 , with the Jacobian

$$\mathbf{J} = \left. \frac{\partial \mathbf{F}(\mathbf{x})}{\partial \mathbf{x}} \right|_{\mathbf{x}=\mathbf{x}_0} \tag{79}$$

with \mathbf{x}_0 given by $\mathbf{F}(\mathbf{x}_0) = 0$. Then T^0 and $\mathbf{x}(t)$ can be estimated by

$$\mathbf{x}(t) = a\mathbf{e}_v e^{j\lambda_v t}, \quad T^0 = \frac{2\pi}{\text{Im}\{\lambda_v\}} \tag{80}$$

where $\lambda_1, \dots, \lambda_n$ are the n eigenvalues and n_1, \dots, n_n the corresponding eigenvectors of the Jacobian $\mathbf{J} \cdot \lambda_v$ is the eigenvalue with $\text{Re}\{\lambda_v\} > 0$. The stiff-stable gear algorithm [21] has proved to be an effective method for numerical integration.

4.3. Frequency-Domain Method

Using the HB technique the steady state of the unperturbed oscillator may be computed in the frequency domain. The n state variables of the oscillator are

summarized in the state vector \mathbf{X} :

$$\mathbf{X} = (\mathbf{X}_1, \mathbf{X}_2, \dots, \mathbf{X}_n)^T \tag{81}$$

Since all state variables are periodic in the limit cycle, the time-domain state variables x_i can be expanded into Fourier series with the Fourier coefficients $X_{i,l}$. The frequency range considered is limited to k harmonics:

$$\begin{aligned} \mathbf{X}_i &= (X_{i,-k}, X_{i,-k+1}, \dots, X_{i,0}, \dots, X_{i,+k})^T \\ \text{with } \mathbf{X}_i &\in \mathbb{C}^{2k+1} \end{aligned} \tag{82}$$

The Fourier coefficients of the state variables \mathbf{X}^0 are determined by the solution of a nonlinear system of equations:

$$\mathbf{F}(\mathbf{X}^0, \omega_0) = \mathbf{0} \tag{83}$$

This nonlinear system of equations (83) with dimension $n(2k + 1)$ and $n(2k + 1)$ unknowns exhibits an infinite one-dimensional manifold of solutions since the phase of a free-running oscillator is arbitrary. The solution can be made unique by specifying the phase of one Fourier coefficient. The frequency of oscillation is an unknown variable and is also determined by solutions of the system equations.

4.4. Time/Frequency-Domain Method

Time-domain methods are efficient for the analysis of circuits exhibiting strong nonlinearities. However, it is not possible to include linear distributed circuits in the time-domain analysis. Especially in microwave oscillator design, the linear embedding circuits usually contain distributed circuits. The method described in the following is based on the subdivision of the oscillator network into the following two subsets:

- The linear embedding network
- The nonlinear subnetworks with neighboring low-pass structure

Therefore the network can be represented by a circuit model as shown in Fig. 11.

The linear embedding network may be described effectively in the frequency domain. The linear and nonlinear parts of the oscillator network are connected via a number of M ports. The port voltages and currents are described by the vector $\mathbf{U}(t) = [\mathbf{v}_T(t), \mathbf{i}_T(t)]^T$. Nonlinear resistors and nonlinear conductances are replaced by voltage and current sources and described in common with all other sources within the nonlinear subnetwork by the vector $\mathbf{U}(t) = [\mathbf{v}_0(t), \mathbf{i}_0(t)]^T$. In a subsequent step the linear and the nonlinear subnetworks are separated from each other, and the port voltages and currents represented by the vector $\mathbf{U}(t)$ are also replaced by voltage and current sources, as shown in Fig. 12.

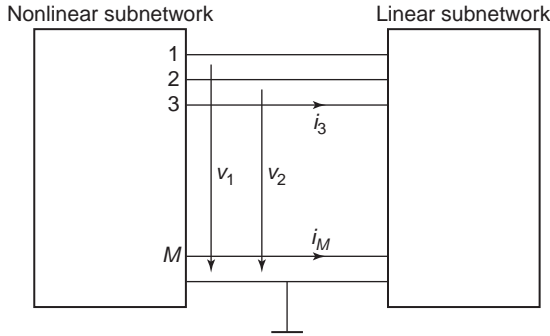


Figure 11. Linear and nonlinear parts of an oscillator network.

Based on the time-domain description [21], the nonlinear subnetwork is characterized by

$$\dot{\mathbf{x}} = \mathbf{A}\mathbf{x} + \mathbf{B}\mathbf{w} + \mathbf{C}\dot{\mathbf{w}} + \mathbf{D}\mathbf{l} \quad \mathbf{x} \in \mathbb{R}^N, \mathbf{l} \in \mathbb{R}^M \quad (84)$$

where \mathbf{x} are the independent state variables and \mathbf{w} is a function of the state variables and their time derivatives $\mathbf{w} = \mathbf{w}(\mathbf{w}, \dot{\mathbf{x}})$. The matrices \mathbf{A} , \mathbf{B} , \mathbf{C} , and \mathbf{D} , representing also nonlinear capacitors and inductors, depend on \mathbf{x} and $\dot{\mathbf{x}}$. Due to the dependence of the matrices $\mathbf{A}, \mathbf{B}, \mathbf{C}, \mathbf{D}$ and the vector \mathbf{w} on $\dot{\mathbf{x}}$, the system of differential equations (84) is implicit. This system of differential equations can be made explicit and put into the normal form by imposing the condition that the matrices $\mathbf{A}, \mathbf{B}, \mathbf{D}$ and vector \mathbf{w} depend only on \mathbf{x} and not on $\dot{\mathbf{x}}$. This condition is fulfilled if

- In the nonlinear subnetwork no current source is connected to a node that is connected only to current sources and to inductors.
- In the nonlinear subnetwork no voltage source is within a mesh containing only voltage sources and capacitors.

Under these conditions the matrix \mathbf{C} vanishes. If we also require that \mathbf{w} depends only on the system state variables \mathbf{x} and not on their time derivatives, we obtain from Eq. (84)

$$\dot{\mathbf{x}} = \mathbf{A}(\mathbf{x})\mathbf{x} + \mathbf{B}(\mathbf{x})\mathbf{w}(\mathbf{x}) + \mathbf{D}(\mathbf{x})\mathbf{l}(t) \quad (85)$$

The vector $\mathbf{c}^T(t) = [\mathbf{i}_r(t), \mathbf{u}_r(t)]$, dual to $\mathbf{l}(t)$ is given by

$$\mathbf{c}(t) = \mathbf{F}\mathbf{x} + \mathbf{G}\mathbf{w} + \mathbf{H}\mathbf{l} \quad (86)$$

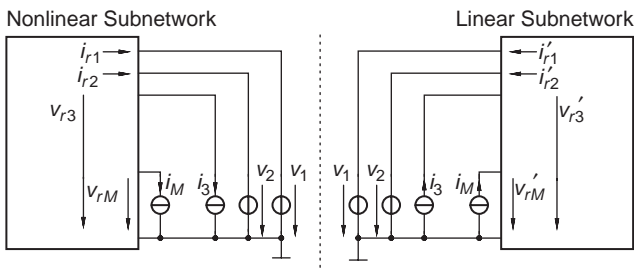


Figure 12. Separation of linear and nonlinear network parts.

By appropriate separation into a nonlinear and a linear subnetwork, large time constants originating, for example, from feedback loops or bias networks may be eliminated. As a result the differences between the time constants are smaller and the stiffness of the system is reduced considerably. If we treat the whole network totally in the time domain, the linear subnetwork does not exist and therefore the term $\mathbf{D}(\mathbf{x})\mathbf{l}(t)$ in Eq. (85) vanishes, and we obtain

$$\dot{\mathbf{x}} = \mathbf{A}(\mathbf{x})\mathbf{x} + \mathbf{B}(\mathbf{x})\mathbf{w}(\mathbf{x}) = \mathbf{F}(\mathbf{x}) \quad (87)$$

The nonlinear oscillator subnetwork is described by Eqs. (85) and (86). In addition to the periodic boundary condition $\mathbf{x}(t) = \mathbf{x}(t + T^0)$, the voltages and currents of $\mathbf{c}(t)$ and $\mathbf{c}'(t)$ must coincide. $\mathbf{c}'(t)$ may be expressed by

$$\mathbf{c}'(t) = \int_{-\infty}^{+\infty} \mathbf{V}(t)\mathbf{l}(t - t_1) dt_1 = \mathbf{V}(t) * \mathbf{l}(t) \quad (88)$$

where $\mathbf{V}(t)$ is the impulse response of the linear subnetwork. As in the previous section, we normalize the time variable with respect to T^0 and obtain

$$\frac{d\mathbf{x}}{d\tau} = (\mathbf{A}\mathbf{x} + \mathbf{B}\mathbf{w} + \mathbf{D}\mathbf{l})T^0, \quad \frac{dT^0}{d\tau} = 0, \quad \tau = tT^0 \quad (89)$$

Since the oscillator signals are assumed to be periodic, it is possible to represent the port variables $\mathbf{l}(t)$ by periodic Fourier series:

$$\mathbf{l}(t) = \sum_{v=-\infty}^{+\infty} (\mathbf{l}_{rv} + j\mathbf{l}_{iv})e^{j2\pi v\tau} \quad (90)$$

From Eq. (88) we obtain

$$\mathbf{c}'(t) = \sum_{v=-\infty}^{+\infty} \mathbf{V}_v(\mathbf{l}_{rv} + j\mathbf{l}_{iv})e^{j2\pi v\tau} \quad (91)$$

where \mathbf{V}_v is the hybrid matrix of the linear multiport, at the v th harmonic, which can be computed with standard linear network analysis methods. The Fourier series expansion representing the port variables is truncated after the k th element. In this case due to the sampling theorem it is necessary and sufficient that the condition $\mathbf{c}(t) = \mathbf{c}'(t)$ be fulfilled for $2K + 1$ discrete time values within the interval T^0 . We obtain

$$\mathbf{c}(\tau_v) = \mathbf{c}'(\tau_v), \quad \tau_v = \frac{v-1}{2K+2}, \quad v = 1, 2, \dots, 2K+1 \quad (92)$$

The solution of (92) and the periodic boundary condition may be expressed, similar to the solution in Section 4.2, as the solution of a boundary value problem. The state equations of the nonlinear subnetwork are therefore

expanded by $(2K + 1)M$ additional state equations:

$$\begin{aligned} \dot{\mathbf{x}} &= \mathbf{A}(\mathbf{x})\mathbf{x} + \mathbf{B}(\mathbf{x})\mathbf{w}(\mathbf{x}) + \mathbf{D}(\tau)\mathbf{l}(\tau)T^0 \\ \dot{T}_p &= 0 \\ \dot{L}_0 &= 0 \\ \dot{L}_1 &= 0 \\ &\dots \\ \dot{L}_k &= 0 \end{aligned} \tag{93}$$

The required $n + (2K + 1)m$ boundary conditions are

$$\begin{aligned} \mathbf{c}(\tau_v) - \mathbf{c}'(\tau_v) &= 0, \quad \tau_v = \frac{v-1}{2K+2}, \quad v = 1, 2, \dots, 2K+1 \\ \mathbf{x}(0) - \mathbf{x}(1) &= 0 \end{aligned}$$

Note that the boundary conditions are no longer given only at $\tau=0$ and $\tau=1$, but at $2K+2$ points at $\tau = [v - 1/(2K + 2)]$, $v = 1, \dots, 2K + 2$. Because of the special structure of the boundary value problem, the multiple-shooting algorithm can be adapted in a numerically efficient way [90].

5. NOISE IN OSCILLATORS

5.1. Problems in Microwave Oscillator Noise Analysis

Noise analysis of microwave oscillators is usually based on the assumption that the unperturbed state of the oscillator is almost sinusoidal. This allows the application of a describing function method for characterization of the nonlinear devices in the oscillator [35]. Based on this method, the noise behavior of microwave oscillators has been analyzed by several groups [28,57,58,92]. These methods were applied and extended to special cases [54,62,88]. They methods provided a good qualitative and to some extent also a quantitative description of the oscillator noise behavior. However, the applicability of these methods is restricted to simplified oscillator models, since the accuracy of the method depends on the validity of the approximation of the dynamic behavior of the nonlinear elements by a describing function [58]. Another severe limitation is that the upconversion of the low-frequency noise such as $1/f$ noise cannot be treated by these methods. Kärtner has developed a time domain method for noise analysis of oscillators, based on the solution of the Langevin equations [48,49]. Adding the noise terms to the normal form equations (70) yields

$$\frac{dx}{dt} = f(x, \zeta, y_1, \dots, y_M), \quad x \in \mathbb{R}^N, \zeta \in \mathbb{R}^k \tag{95}$$

The vector ζ describes white-noise sources, and y_1, \dots, y_M represent $f^{-\alpha}$ noise sources. Colored-noise sources may be derived from white-noise sources by inserting linear systems transforming the white-noise sources to colored noise. For considering $f^{-\alpha}$ noise sources infinite-dimen-

sional systems are required. However, as shown in Ref. 49, these infinite-dimensional systems may be treated with analytical formulas, so that $f^{-\alpha}$ noise sources may be treated by low computational effort. Using the perturbation method, the correlation spectra of the phase and amplitude noise due to white-noise sources as well as due to $f^{-\alpha}$ noise sources can be calculated. The method has been applied to bipolar transistor oscillators [48,49] to planar integrated microwave oscillators [34,78], and varactor tunable oscillators [33]. Frequency-domain noise analysis can be performed on the basis of the HB method [5–7]. Starting from the HB equations (71), we obtain a nonlinear system of equations:

$$F(X, \omega, N_T) = 0, \quad X_T \in \mathbb{C}^{n(2k+1)}, N_T \in \mathbb{C}^{r(2k+1)} \tag{96}$$

In this equation X_T is the system state vector summarizing the signal spectra of n signals at a frequency ω close to the fundamental frequency ω_0 and at k harmonics. The subscript “T” denotes that the signals are time-windowed [44,84]. The vector N_T summarized the r noise source spectra at a frequency ω and at k harmonics. The numerical solution of this equation is based on correlation matrix techniques. Combining of time- and frequency-domain techniques is also possible in noise analysis [9]. The phase noise is computed in the time domain. The linear subcircuits are described by noise multiports. This method again exhibits the advantages of the time/frequency-domain method. In Ref. 7 the results of measurements of designed and fabricated integrated oscillators are compared with the numerical simulations based on the methods discussed above. This paper [7] also considers a method to minimize oscillator phase noise by numerical optimization. Based on the computation of the oscillator steady state and spectral behavior in the time domain, single-sideband phase noise is minimized using a method of optimal control problems, a direct collocation algorithm [9,10].

Another essential aspect is the simulation of the startup behavior of oscillators. If the resonator is weakly damped, it is well known that many oscillations to the steady state occur. Although some analytical results are available (see, e.g., Ruzsnyak [85]) where a simplified model of a crystal oscillator is used, the corresponding simulation problem is very complicated [87]. Schmidt-Kreusel published an efficient solution for this problem that is based on the idea that the transient trajectory of a weakly damped oscillator consists of nearly closed trajectories in the state space. If only a few parts of this transient are approximated by periodic solutions, the envelope of the transient behavior can be calculated in a fast manner. This approach is described in detail by Mathis [67]. An alternative approach was published by Brachtendorf and Laur [15] that uses a certain kind of partial differential equations for calculating the envelope.

5.2. Description of Noisy Circuits

In linear noisy circuits we usually have to deal with stationary Gaussian noise signals. Such signals may be characterized completely by their correlation spectra [23].

For a signal $s(t)$ unlimited in time, the average power within the time interval of length $2T$ centered around t is given by

$$\frac{1}{2T} \int_{t-T}^{t+T} |s(t_1)|^2 dt_1 \tag{97}$$

If for large time intervals $2T$ the average power approaches a limit, which is independent from t , the signal $s(t)$ is called *stationary*. The average power $\langle P \rangle$ of a stationary signal can be exactly defined by

$$\langle P \rangle = \lim_{T \rightarrow \infty} \frac{1}{2T} \int_{-T}^{+T} |s(t)|^2 dt \tag{98}$$

We investigate the more general term

$$c_{ij}(\tau) = \lim_{T \rightarrow \infty} \frac{1}{2T} \int_{-T}^{+T} s_i(t) s_j^*(t - \tau) dt \tag{99}$$

The function $c_{ij}(\tau)$ is called a *correlation function*. For $i=j$, the function $c_{ii}(\tau)$ is the autocorrelation function of the signal $s_i(t)$ and for $i \neq j$ we have the cross-correlation function $c_{ij}(\tau)$ of the signals $s_i(t)$ and $s_j(t)$. With the time-windowed function $s_T(t)$ of the signal $s(t)$ defined by

$$s_T(t) = \begin{cases} s(t) & \text{for } |t| \leq T \\ 0 & \text{for } |t| > T \end{cases} \tag{100}$$

we can write Eq. (99) in the form

$$c_{ij}(\tau) = \lim_{T \rightarrow \infty} \frac{1}{2T} \int_{-\infty}^{+\infty} s_{iT}(t) s_{jT}^*(t - \tau) dt \tag{101}$$

The average power $\langle P \rangle$ of the signal $s_i(t)$ is given by

$$\langle P \rangle = c_{ii}(0) \tag{102}$$

We denote the Fourier transform of the time-windowed function $s_{iT}(t)$ with $S_{iT}(f)$:

$$s_{iT}(t) \circ \dots \bullet S_{iT}(f) \tag{103}$$

As mentioned before, the symbol $\circ \dots \bullet$ represents the correspondence between a pair of Fourier transforms. From Eq. (103), we obtain

$$s_{iT}(t) * s_{jT}^*(-t) \circ \dots \bullet S_{iT}(f) S_{jT}^*(f) \tag{104}$$

The symbol $*$ denotes the convolution operation

$$s_1(t) * s_2(t) = \int_{-\infty}^{+\infty} s_1(t_1) s_2(t - t_1) dt_1 \tag{105}$$

The correlation spectrum $C_{ij}(f)$, given by

$$C_{ij}(f) = \lim_{T \rightarrow \infty} \frac{1}{2T} S_{iT}(f) S_{jT}^*(f) \tag{106}$$

is the Fourier transform of the correlation function:

$$c_{ij}(\tau) \circ \dots \bullet C_{ij}(f) \tag{107}$$

$C_{ii}(f)$ with $i=j$ is the autocorrelation spectrum of the signal $s_i(t)$, and $C_{ij}(f)$ with $i \neq j$ is the cross-correlation spectrum of the signals $s_i(t)$ and $s_j(t)$. With the exception of a dimensional factor, $C_{ij}(f)$ is a spectral power density or a power spectrum. Since the autocorrelation function is a real and even function of τ , the autocorrelation spectrum is a real and even function of frequency. The cross-correlation function is complex. Changing the sign of the frequency or interchanging the indices i and j yields the complex conjugate of the correlation function:

$$2C_{ii}(f) \Delta f \tag{108}$$

The factor 2 results from considering both the positive and negative frequency parts. In general for random signals no amplitude spectra exist, whereas power spectra may be calculated also for random signals. For a stationary noise signal $s_{ni}(t)$ the Fourier integral does not exist. However, a correlation function

$$c_{ij}(\tau) = \lim_{T \rightarrow \infty} \frac{1}{2T} \int_{-\infty}^{+\infty} \langle s_{niT}(t) s_{njT}^*(t - \tau) \rangle dt \tag{109}$$

can be defined, in which the brackets indicate the statistical mean value over signals measured on an ensemble of identical circuits. If the signals $s_{ni}(t)$ and $s_{nj}(t)$ have zero mean value, in general, the mean value of the product $s_{ni}(t) s_{nj}^*(t - \tau)$ approaches 0 with arbitrary order for $\tau \rightarrow \infty$, so that the integral (109) and also its Fourier transform exist. Since the Fourier integral of a time-windowed function exists in general, the correlation spectrum may also be defined by

$$C_{ij}(f) = \lim_{T \rightarrow \infty} \frac{1}{2T} \langle S_{niT}(f) S_{njT}^*(f) \rangle \tag{110}$$

In this case, $T \rightarrow \infty$ has to be carried out after the ensemble averaging. The autocorrelation and cross correlation spectra $C_{ij}(f)$ of the noise sources of a linear network are given by

$$C_{ij}(f) = \lim_{T \rightarrow \infty} \frac{1}{2T} \langle S_{iT}(f) S_{jT}^*(f) \rangle \tag{111}$$

where $S_{iT}(f)$, $S_{jT}(f)$ are the spectra of the time-windowed signals of the noise sources. The correlation spectra $C_{ij}(f)$ can be combined in the correlation matrix

$$C(f) = \begin{bmatrix} C_{11}(f) & C_{12}(f) & \dots & C_{1n}(f) \\ C_{21}(f) & C_{22}(f) & \dots & C_{2n}(f) \\ \vdots & \vdots & & \\ C_{n1}(f) & C_{n2}(f) & \dots & C_{nn}(f) \end{bmatrix} \tag{112}$$

The correlation matrix $C(f)$ can be represented as the product of the column vector

$$\mathbf{S}_T(f) = \begin{bmatrix} S_{1T}(f) \\ \vdots \\ S_{nT}(f) \end{bmatrix} \quad (113)$$

and its Hermitian conjugate row vector

$$\mathbf{S}_T^\dagger(f) = [S_{1T}^*(f) \cdots S_{nT}^*(f)] \quad (114)$$

in matrix notation by

$$\mathbf{C}(f) = \lim_{T \rightarrow \infty} \frac{1}{2T} (\mathbf{S}_T(f) \mathbf{S}_T^\dagger(f)) \quad (115)$$

We now formally use the complex amplitudes $S_{iT}(f)$ in the same way as the amplitudes of deterministic signals. $S_{iT}(f)$ is the spectrum of a time-windowed noise signal. We can measure the noise signal within some finite interval of time, and we may calculate the spectrum of this sample. This specific sample of a noise signal has to be considered as a deterministic signal since we have exact knowledge of its time dependence. The transition from deterministic signals to random signals is done in our description by performing the ensemble average. After performing the ensemble average in the case of random signals, the decomposition of the correlation matrix into a product of a column vector and a row vector will be impossible. For example in the case of a signal vector describing independent random noise sources, the nondiagonal elements will be averaged out to zero and the correlation matrix will be diagonal. In general, the network equations have the following form in matrix notation:

$$\tilde{\mathbf{S}}_T(f) = \mathbf{M}(f) \mathbf{S}_T(f) \quad (116)$$

The coefficient matrix $\mathbf{M}(f)$ combines the complex amplitude vectors $\mathbf{S}_T(f)$ and $\tilde{\mathbf{S}}_T(f)$. Multiplying Eq. (116) from the right with its Hermitian conjugate, we obtain

$$\tilde{\mathbf{S}}_T(f) \tilde{\mathbf{S}}_T^\dagger(f) = \mathbf{M}(f) \mathbf{S}_T(f) \mathbf{S}_T^\dagger(f) \mathbf{M}^\dagger(f) \quad (117)$$

Performing the ensemble average on both sides and subsequently carrying out the transition $T \rightarrow \infty$, we obtain

$$\tilde{\mathbf{C}} = \mathbf{M}(f) \mathbf{C}(f) \mathbf{M}^\dagger(f) \quad (118)$$

This establishes a general rule for deriving equations for the correlation matrices from linear equations for the signal amplitudes. A linear noisy two-port may be characterized by two equivalent noise sources. These noise sources may be located at the input or at the output. If both equivalent noise sources are located at the same port, one noise source must be a voltage source in series with the port and the other source must be a current source in parallel with the port. If one equivalent noise source is assigned to every port, in general we may choose an equivalent current source or an equivalent voltage source at each port.

5.3. Noise in Two-port Oscillators

We analyze the noise behavior of the simple two-port oscillator shown in Fig. 13. The left two-port is the linear frequency-determining feedback two-port. In our example the feedback network of the Meissner oscillator was chosen. The right two-port is the nonlinear amplifying two-port. In our example, all internal noise sources of the linear two-port as well as the nonlinear two-port are summarized in the noise current source $I_{rT}(f)$. This equivalent noise source is obtained in the following way. In the first step, describe the noise properties of the linear feedback two-port by equivalent output noise located at its output and the noise properties of the active two-port by equivalent noise sources located at the input of the active two-port. To extract the noise parameters of the active two-port, we consider the active two-port to be linear. After connecting the output of the feedback two-port to the input of the active two-port, we can contract the four equivalent noise sources into one noise source $I_{rT}(f)$.

For the oscillator circuit depicted in Fig. 13, the following equations are valid:

$$I_{1T}(f) = A_{21}(f) V_{2T}(f) + A_{22}(f) I_{rT}(f) \quad (119)$$

$$I_{2aT}(f) = S(V) V_{1aT}(f) \quad (120)$$

$$V_{1aT}(f) = V_{2T}(f) \quad (121)$$

$$I_{1T}(f) = -I_{2aT}(f) \quad (122)$$

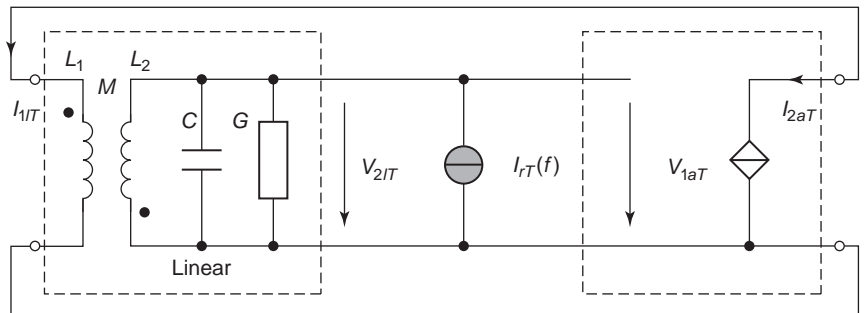


Figure 13. Noisy two-port oscillator.

The variables $I_{1T}(f)$, $V_{2T}(f)$, $V_{1aT}(f)$, and $I_{2aT}(f)$ are the noise current and voltage amplitudes at the ports of the two-ports. To investigate the oscillator noise behavior, we have to consider the nonlinear saturation properties of the active two-port. $A_{21}(f)$ and $A_{22}(f)$ are circuit parameters of the feedback two-port in chain representation. In our simple model we describe the active element by a nonlinear voltage-controlled current source. With the real amplitude V of the oscillator signal at the input of the nonlinear two-port, we describe the relation between input and output noise signals by the amplitude-dependent transconductance $S(V)$. From (119) to (122) we obtain

$$(A_{21}(f) + S(V))V_{2T}(f) + A_{22}(f)I_T^r(f) = 0 \quad (123)$$

The autocorrelation spectra $C^I(f)$ and $C^V(f)$ of the noise current source $I_T^r(f)$ and the voltage current source $V_T^r(f)$ are given by

$$C^I(f) = \lim_{T \rightarrow \infty} \frac{1}{2T} \langle I_T^r(f) I_T^{r*}(f) \rangle \quad (124)$$

$$C^V(f) = \lim_{T \rightarrow \infty} \frac{1}{2T} \langle V_{2T}(f) V_{2T}^*(f) \rangle \quad (125)$$

With (123) we obtain

$$C^V(f) = \frac{|A_{22}(f)|^2}{|A_{21}(f) + S(V)|^2} C^I(f) \quad (126)$$

For the Meissner oscillator the circuit parameters of the linear feedback two-port are given by

$$A_{21}(f) = -G_0 \left(1 + jQ \left(\frac{f}{f_0} - \frac{f_0}{f} \right) \right) \quad (127)$$

$$G_0 = \frac{L_2}{|M|} G \quad (128)$$

$$Q = \frac{2\pi f_0 C}{G} \quad (129)$$

$$A_{22}(f) = -\frac{L_2}{|M|} \quad (130)$$

where M is the mutual inductance of the transformer and L_2 is the inductance of the secondary coil. Substituting into (126), we obtain

$$C^V(f) = \left(\frac{L_2}{|M|} \right)^2 \frac{C^I(f)}{(G_0 - S)^2 + G_0^2 Q^2 \left(\frac{f}{f_0} - \frac{f_0}{f} \right)^2} \quad (131)$$

The power spectral density at the load conductance G is

$$W(f) = 2C^V(f)G \quad (132)$$

and the total power flowing into G is given by

$$\bar{P}_0 = \int_0^{+\infty} C^V(f) G df \quad (133)$$

With

$$\int_{-\infty}^{+\infty} \frac{dx}{a^2 + b^2 \left(x - \frac{1}{x} \right)^2} = \frac{\pi}{ab} \quad (134)$$

we obtain

$$\bar{P}_0 = \pi \frac{f_0 C^I}{Q(G_0 - S)} \quad (135)$$

The frequency deviation Δf from the carrier is given by $\Delta f = f - f_0$. For $\Delta f \ll f_0$ we can approximate

$$\frac{f}{f_0} - \frac{f_0}{f} \doteq 2 \frac{\Delta f}{f_0} \quad (136)$$

To characterize the oscillator noise, we introduce the *noise measure* M_r . The noise measure is the factor by which the power spectral density of a noise source exceeds the thermal noise. The autocorrelation spectrum of the equivalent noise source of a conductance G exhibiting thermal noise at a temperature T is given by $2kTG$. From this definition it follows that

$$M_r = \frac{C^I}{2kTG} \quad (137)$$

From (131), (132), (136), and (137) we obtain the power spectral density of the oscillator:

$$W(f) = \frac{4kTM_r G_0^2}{(G_0 - S)^2 + 4G_0^2 Q^2 \left(\frac{\Delta f}{f_0} \right)^2} \quad (138)$$

From (135) and (137) we obtain the average total power:

$$\bar{P}_0 = \frac{2\pi kTM_r G f_0}{Q(G_0 - S)} \quad (139)$$

We define the spectral width of the oscillator as the ratio of the average power \bar{P}_0 and the power spectral density $W(f_0)$ at the center frequency f_0

$$B = \frac{\bar{P}_0}{W(f_0)} \quad (140)$$

and obtain

$$B = \pi \frac{G_0 - S}{G_0} \frac{|M| f_0}{L_2 Q} \quad (141)$$

In the oscillator without noise, S equals G_0 , whereas in the noisy case $G_0 - S > 0$ is valid. The oscillator amplitude is determined by the nonlinear gain characteristics of the active element. It is only slightly influenced by the noise source. The ratio $G_0/(G_0 - S)$ is determined by the ratio of the saturation power \bar{P}_0 and the injected noise power. Using (139), we can express $G_0 - S$ by the ratio of the

power spectral density of the equivalent noise source and the saturation power of the oscillator and obtain

$$B = \frac{2\pi^2 f_0^2}{Q^2} \left(\frac{|M|}{L_2} \right)^2 \frac{kTM_r}{\bar{P}_0} \quad (142)$$

The spectral width of the oscillator is proportional to the noise measure M_r and proportional to the inverse of the saturation power and to the square of the quality factor Q of the resonant circuit. Low-noise design of oscillators requires a low-noise active element, a high quality factor of the active circuit, and a high saturation power of the oscillator. Since the amplitude of the oscillator is stabilized by the nonlinear saturation behavior of the oscillator, an oscillator exhibits primarily amplitude noise.

5.4. Noise Analysis in Frequency Domain

In the following a frequency-domain perturbation method for simulating the noise behavior of free-running microwave oscillators is presented [7]. The method is based on a piecewise harmonic-balance technique. The single-sideband phase noise of the oscillator is derived from the system equations. The method is limited to neither certain circuit topologies nor certain types of noise sources.

5.4.1. Fluctuations of the State Variables. In the frequency-domain method, noise sources may be considered by extending the nonlinear system of equations (83). Introducing the noise source vector $\mathbf{N}_T(\omega)$, which summarizes the time-windowed spectra of the noise sources the system equations now exhibit the following form:

$$\mathbf{F}(\mathbf{X}_T, \omega, \mathbf{N}_T) \equiv \mathbf{0} \quad (143)$$

The index “T” denotes the time-windowed signal spectra as defined in (103). The vector $\mathbf{N}_T \in \mathbb{C}^{r(2k+1)}$ summarizes the amplitudes at the fundamental frequency ω_0 and at the harmonics up to $k\omega_0$ of a number of r noise sources of arbitrary spectrum. In (143) all harmonics up to k th order, and their fluctuations are considered. This allows us to compute the complete correlation spectrum at the frequency deviation $\omega_m = \omega - \omega_0$. All noise processes, including the upconversion of low-frequency noise, are considered. Since the noise contribution is small compared with the deterministic part of the oscillator signal, the noise contribution may be considered as a first-order perturbation. From (143) we obtain

$$\mathbf{F}(\mathbf{X}_T, \omega, \mathbf{N}_T) + \mathbf{G}(\mathbf{X}_T^0, \omega)\mathbf{N}_T = \mathbf{0} \quad (144)$$

with $\mathbf{G}(\mathbf{X}_T^0, \omega) \in \mathbb{C}^{n(2k+1) \times r(2k+1)}$ and

$$\mathbf{G}(\mathbf{X}_T^0, \omega) \equiv \left. \frac{\partial \mathbf{F}(\mathbf{X}_T, \omega, \mathbf{N}_T)}{\partial \mathbf{N}_T} \right|_{\mathbf{X}_T = \mathbf{X}_T^0, \mathbf{N}_T = \mathbf{0}} \quad (145)$$

The matrix $\mathbf{G}(\mathbf{X}_T^0, \omega)$ describes the coupling of the noise sources \mathbf{N}_T with the system. It is assumed that noise sources effect only a small perturbation of the limit cycle

of the oscillator:

$$\begin{aligned} \mathbf{X}_T(\omega) &= \mathbf{X}_T^0(\omega) + \delta\mathbf{X}_T(\omega); \quad \omega = \omega_0 + \omega_m \\ \|\delta\mathbf{X}_T(\omega)\| &\ll \|\mathbf{X}_T^0(\omega)\|; \quad \omega_m \ll \omega_0 \end{aligned} \quad (146)$$

Therefore the system of nonlinear equations (144) may be linearized in the neighbourhood of the limit cycle, and we obtain

$$\mathbf{J}(\mathbf{X}_T^0, \omega)\delta\mathbf{X}_T + \mathbf{G}(\mathbf{X}_T^0, \omega)\mathbf{N}_T = \mathbf{0} \quad (147)$$

with the Jacobian matrix $\mathbf{J}(\mathbf{X}_T^0, \omega) \in \mathbb{C}^{n(2k+1) \times n(2k+1)}$ of the unperturbed system equations given by

$$\mathbf{J}(\mathbf{X}_T^0, \omega) \equiv \left. \frac{\partial \mathbf{F}(\mathbf{X}_T, \omega, \mathbf{0})}{\partial \mathbf{X}_T} \right|_{\mathbf{X}_T = \mathbf{X}_T^0} \quad (148)$$

This equation describes the perturbation of the oscillator by the noise sources. It includes the mixing of the injected noise signals \mathbf{N}_T with the unperturbed state variables \mathbf{X}_T^0 . From the solution of the linearized system of equations (147), the correlation spectra of the state variables may be computed. A problem arises from the fact that the Jacobian matrix $\mathbf{J}(\mathbf{X}_T^0, \omega_0)$ is singular for the limit cycle of the unperturbed system [4,102]. The linearized perturbed system equations cannot be solved by inversion or by LR decomposition. The lowest eigenvalue of the Jacobian is $\lambda_1 = 0$. A perturbation $\delta\mathbf{X}_T$ corresponding to the eigenvalue 0 of the Jacobian induces a perturbed solution $\mathbf{X}_T^0 + \delta\mathbf{X}_T$, which is again a solution of the system equations (143). The eigenvector corresponding to the eigenvalue $\lambda_1 = 0$ is tangent to the limit cycle. The fluctuations in direction of this eigenvector are the phase fluctuations. The subspace spanned by the other eigenvectors of the Jacobian is the space of the amplitude fluctuations. This subdivision of the eigenvector space of the Jacobian allows a clear and well-defined distinction between phase and amplitude fluctuations.

5.4.2. Solution of the System Equations Including Noise.

The Jacobian is singular at the steady state and for a small frequency deviation f_m of the carrier frequency the deviations of the matrix elements are small and the condition number of the Jacobian remains high [102]. The condition number *cond*, defined by

$$\text{cond}(\mathbf{J}) = \|\mathbf{J}\| \|\mathbf{J}^{-1}\| \quad (149)$$

provides a measure for the numerical error in the solution of a linear system of equations [18,32]. The expression $\|\mathbf{J}\|$ is the matrix norm of the Jacobian \mathbf{J} . The condition number of a matrix may be approximated by the ratio of the largest and the smallest eigenvalues of the matrix [32]. The largest eigenvalue is much larger than the frequency of oscillation f_0 because it is related to the fastest process of the system. The smallest eigenvalue is of the order of the frequency deviation f_m , as we will show later in (167). Therefore the condition number *cond* of the Jacobian is much larger than the ratio of the carrier

frequency to the frequency deviation of interest [50]

$$\text{cond}(\mathbf{J}(\mathbf{X}_T^0, 2\pi(f_0 + f_m))) \gg \frac{f_0}{f_m} \quad (150)$$

This means that the steady state of an oscillator has to be determined to a much higher precision than the inverse of the condition number to achieve a relative error smaller than 1 [18]. Considering a 10-GHz oscillator and a frequency deviation of $f_m = 10$ kHz, for instance, the condition number is much larger than 10^6 . To overcome the numerical problems, the Jacobian is linearized at the carrier frequency with respect to the frequency

$$\mathbf{J}(\mathbf{X}_T^0, \omega) = \mathbf{J}(\mathbf{X}_T^0, \omega_0) + \omega_m \mathbf{J}_\omega(\mathbf{X}_T^0, \omega_0) \quad (151)$$

with the abbreviation

$$\mathbf{J}_\omega(\mathbf{X}_T^0, \omega_0) \equiv \left. \frac{\partial \mathbf{J}(\mathbf{X}_T^0, \omega)}{\partial \omega} \right|_{\omega=\omega_0} \quad (152)$$

An eigenvalue decomposition [32] of the Jacobian with left- and right-sided eigenvectors is used. Thus the complete correlation spectra can be calculated in a numerically stable way. First we want to analyze the unperturbed Jacobian $\mathbf{J}_\omega(\mathbf{X}_T^0, \omega_0)$. The left- and right-sided eigenvectors of the Jacobian are denoted by \mathbf{V}_j^\dagger and \mathbf{W}_i and the eigenvalues with λ_j^V and λ_i^W , respectively.

$$\mathbf{V}_j^\dagger \mathbf{J}(\mathbf{X}_T^0, \omega_0) = \lambda_j^V \mathbf{V}_j^\dagger; \quad \mathbf{V}_j \in \mathbb{C}^{n(2k+1)} \quad (153)$$

$$\mathbf{J}(\mathbf{X}_T^0, \omega_0) \mathbf{W}_i = \lambda_i^W \mathbf{W}_i; \quad \mathbf{W}_i \in \mathbb{C}^{n(2k+1)} \quad (154)$$

The eigenvalues of the Jacobian are equal for a set of left- and right-sided eigenvectors:

$$\lambda_j^V = \lambda_i^W = \lambda_i \quad \text{for } i=j \quad (155)$$

The left- and right-sided eigenvectors satisfy the orthogonality relations [102]:

$$\mathbf{V}_j^\dagger \cdot \mathbf{W}_i = \delta_{ij} \quad \text{with} \quad \delta_{ij} = \begin{cases} 1 & i=j \\ 0 & i \neq j \end{cases} \quad (156)$$

According to these equations, the eigenvector \mathbf{V}_1 is orthogonal to all right-sided eigenvectors \mathbf{W}_i with the exception of \mathbf{W}_1 . The eigenvectors corresponding to the eigenvalue $\lambda_1 = 0$ are denoted with \mathbf{V}_1 and \mathbf{W}_1 . These eigenvectors will be investigated in the following in detail. The eigenvector \mathbf{W}_1 is determined by the steady-state solution [5,8]

$$\mathbf{W}_1 = j\omega_0 \mathbf{K} \mathbf{X}_T^0 \quad (157)$$

where $\mathbf{K} \in \mathbb{R}^{n(2k+1) \times n(2k+1)}$ is a matrix that has only nonvanishing diagonal elements consisting of the number

of the harmonics:

$$\mathbf{K} = \begin{bmatrix} -k & & & & & & \\ & -(k-1) & & & & & \\ & & \ddots & & & & \\ & & & +k & & & \\ & & & & -k & & \\ & \mathbf{0} & & & & \ddots & \\ & & & & & & k \end{bmatrix} \quad (158)$$

Figure 14 illustrates the meaning of the eigenvectors $\mathbf{v}_i(t)$ and $\mathbf{w}_i(t)$ in the time domain. The vector $\mathbf{v}_1(t) \circ \dots \bullet \mathbf{V}_1(f)$ is the tangent vector to the steady-state limit cycle $\mathbf{x}^0(t)$ and $\mathbf{w}_1(t) \circ \dots \bullet \mathbf{W}_1(f)$ is the normal vector defining a plane \mathcal{N} that is mapped onto itself by the unperturbed flux of the linearized set of differential equations (Poincaré map) [49].

The left-sided eigenvector \mathbf{V}_1 is determined via

$$\mathbf{J}^\dagger(\mathbf{X}_T^0, \omega_0) \mathbf{V}_1 = \mathbf{0} \quad (159)$$

which is a linear homogeneous system of equations and can be solved with a standard LU decomposition. The length of the vector \mathbf{V}_1 has to be normalized to satisfy (156):

$$\|\mathbf{V}_1\|_2 = \|\omega_0 \mathbf{K} \mathbf{X}_T^0\|_2^{-1} \quad (160)$$

The eigenvectors \mathbf{W}_i are a complete basis for the state space, and, due to (156), a multiplication of \mathbf{V}_1^\dagger with a vector within the state space is a projection onto the complementary space of the plane \mathcal{N} . This means that the projection operator $\mathbf{W}_1 \mathbf{V}_1^\dagger$ applied to any vector $\mathbf{z} = \sum_{i=1}^n a_i \mathbf{W}_i$ results in a vector with a tangential component a_1 with respect to the limit cycle. So if this projection operator $\mathbf{W}_1 \mathbf{V}_1^\dagger$ is applied to the noise sources in the state space $\mathbf{G}(\mathbf{X}_T^0, \omega) \mathbf{N}_T$, the contributions of the noise sources that cause a phase shift of the unperturbed

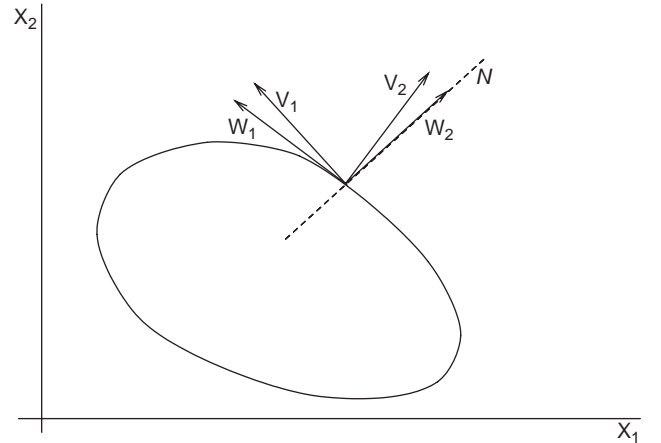


Figure 14. Limit cycle in a two-dimensional phase space.

steady state are separated. This will be shown in the following. For a small frequency deviation f_m the deviations of the elements of the Jacobian are small. Therefore the deviations of the eigenvalues and eigenvectors of the Jacobian are small, too [32]:

$$\lambda'_i = \lambda_i + \delta\lambda_i; \quad |\delta\lambda_i| \ll |\lambda_i| \quad (161)$$

$$\mathbf{V}'_j = \mathbf{V}_j + \delta\mathbf{V}_j; \quad \|\delta\mathbf{V}_j\|_2 \ll \|\mathbf{V}_j\|_2 \quad (162)$$

$$\mathbf{W}'_i = \mathbf{W}_i + \delta\mathbf{W}_i; \quad \|\delta\mathbf{W}_i\|_2 \ll \|\mathbf{W}_i\|_2 \quad (163)$$

The eigenvalues and eigenvectors of the perturbed Jacobian $\mathbf{J}'_\omega(\mathbf{X}_T^0, \omega_0)$ are denoted by a prime. It is sufficient to consider the deviations of the eigenvalues and eigenvectors up to the first order in ω_m :

$$\delta\lambda_i = \omega_m \mathbf{V}_i^\dagger \mathbf{J}'_\omega(\mathbf{X}_T^0, \omega_0) \mathbf{W}_i \quad (164)$$

$$\delta\mathbf{W}_i = \sum_{l=1, l \neq i}^{n(2k+1)} \frac{\omega_m}{\lambda_i - \lambda_l} (\mathbf{V}_l^\dagger \mathbf{J}'_\omega(\mathbf{X}_T^0, \omega_0) \mathbf{W}_i) \mathbf{W}_l \quad (165)$$

$$\delta\mathbf{V}_j = \sum_{l=1, l \neq j}^{n(2k+1)} \frac{\omega_m}{\lambda_j - \lambda_l} (\mathbf{V}_j^\dagger \mathbf{J}'_\omega(\mathbf{X}_T^0, \omega_0) \mathbf{W}_l) \mathbf{V}_l \quad (166)$$

The eigenvalue λ'_1 is of special interest since it is identical to the deviation $\delta\lambda_1$ from the lowest eigenvalue $\lambda_1 = 0$ of the unperturbed system. Using (157), we obtain

$$\lambda'_1 = \delta\lambda_1 = 2\pi f_m \mathbf{V}_1^\dagger \mathbf{J}'_\omega(\mathbf{X}_T^0, \omega_0) j2\pi f_0 \mathbf{K} \mathbf{X}_T^0 \quad (167)$$

The smallest eigenvalue of the perturbed Jacobian $\lambda'_1 = \delta\lambda_1$ is therefore of the same order of magnitude as the small frequency deviation ω_m . The inverse $\mathbf{J}'_\omega^{-1}(\mathbf{X}_T^0, \omega_0)$ of the Jacobian is represented by an eigenvalue decomposition with the eigenvalues and left- and right-sided eigenvectors of the Jacobian $\mathbf{J}'_\omega(\mathbf{X}_T^0, \omega_0)$:

$$\mathbf{J}'_\omega^{-1}(\mathbf{X}_T^0, \omega) = \sum_{i=1}^{n(2k+1)} \frac{1}{\lambda'_i} \mathbf{W}'_i \mathbf{V}'_i{}^\dagger \quad (168)$$

This inversion will not be calculated, because of the ill-conditioning of the Jacobian. We derive this equation to calculate the correlation spectrum of the state variable fluctuations. Later on we take into account the special eigenvalue λ'_1 , which causes the bad condition of the matrix and the problems associated with numerical inversion. The state variable fluctuations are given by

$$\delta\mathbf{X}_T = - \sum_{i=1}^{n(2k+1)} \frac{1}{\lambda'_i} \mathbf{W}'_i \mathbf{V}'_i{}^\dagger (\mathbf{G}(\mathbf{X}^0, \omega) \mathbf{N}_T) \quad (169)$$

5.4.3. Correlation Spectrum of the Oscillator Noise. The correlation spectra of the state variables $\mathbf{C}^{\delta X}(f)$ and the

noise sources $\mathbf{C}^N(f)$ are given by

$$\mathbf{C}^{\delta X}(f) = \lim_{T \rightarrow \infty} \frac{1}{2T} (\delta\mathbf{X}_T(f) \delta\mathbf{X}_T^\dagger(f)) \quad (170)$$

$$\mathbf{C}^N(f) = \lim_{T \rightarrow \infty} \frac{1}{2T} (\mathbf{N}_T(f) \mathbf{N}_T^\dagger(f)) \quad (171)$$

where the brackets denote the ensemble average. The correlation spectra of the state variables are derived using (170), (171), and the equation of the state variable fluctuations (169)

$$\begin{aligned} \mathbf{C}^{\delta X}(f) &= \sum_{i=1}^{n(2k+1)} \sum_{j=1}^{n(2k+1)} 1/(\lambda'_i \lambda'_j{}^*) \\ &\times (\mathbf{V}'_i{}^\dagger \mathbf{C}^{GN}(f) \mathbf{V}'_j) \mathbf{W}'_i \mathbf{W}'_j{}^\dagger \end{aligned} \quad (172)$$

with the abbreviation

$$\mathbf{C}^{GN}(f) = \mathbf{G}(\mathbf{X}_T^0, \omega) \mathbf{C}^N(f) \mathbf{G}^\dagger(\mathbf{X}_T^0, \omega) \quad (173)$$

The approximations of (164)–(166) for the eigenvalues and eigenvectors of the perturbed Jacobian are used to derive the correlation spectra of the state variable fluctuations. The term with the major contribution to the correlation spectrum is the term with $i=j=1$ due to the small eigenvalue $\lambda'_1 = \delta\lambda_1$ given in (167). This term denotes, as already described, the phase noise of oscillators. As the perturbation of the eigenvectors $\delta\mathbf{W}_1$ and $\delta\mathbf{V}_1$ are of the order of ω_m and therefore small compared with the unperturbed eigenvectors, they are negligible:

$$\mathbf{C}^{\delta X}(f) = \frac{(\mathbf{V}'_1{}^\dagger \mathbf{C}^{GN}(f) \mathbf{V}'_1) \mathbf{K} \mathbf{X}^0 \mathbf{X}^0{}^\dagger \mathbf{K}}{(2\pi f_m)^2 |\mathbf{V}'_1{}^\dagger \mathbf{J}'_\omega(\mathbf{X}^0, \omega_0) \mathbf{K} \mathbf{X}^0|^2} \quad (174)$$

Because of the special situation of the eigenvalue λ'_1 and the eigenvectors $\delta\mathbf{W}_1$ and $\delta\mathbf{V}_1$, the terms with $i=1$ and $j \neq 1$ or $i \neq 1$ and $j=1$ in (172) denote the amplitude phase correlation spectra. Finally the terms with $i \neq 1$ and $j \neq 1$ in (172) represent amplitude noise. These noise contributions are small compared with the phase noise, due to the larger eigenvalues, and are not taken into account in the following subsections.

5.4.4. Single-Sideband Phase Noise. The single-sideband phase noise $L(f_m)$ is the ratio between the noise power in a sideband of bandwidth 1 Hz at a frequency deviation $f_m = f - f_0$ from the carrier frequency and the total signal power P_s . The single-sideband phase noise $L(f_m)$ is equal for all state variables, and therefore we can choose any state variable x_i to calculate the single-sideband phase noise:

$$L(f_m) = P_{Ni}(f_m) / P_{Si} \quad (175)$$

In order to obtain the single-sideband phase noise at the fundamental frequency, the matrix element corresponding to the i th state variable is chosen that denotes the noise

power at the fundamental frequency. We have to select the element $|X_{i,1}^0|^2$ of the matrix $\mathbf{KX}^0\mathbf{X}^{0\dagger}\mathbf{X}$ and obtain for the noise power $P_{Ni}(f_m)$ in a 1 Hz bandwidth

$$\begin{aligned} P_{Ni}(f_m) &= 2\mathbf{C}^{\delta X}(f_0 + f_m)_{i,1}R_n \\ &= 2 \frac{|X_{i,1}^0|^2 R_n \mathbf{V}_1^\dagger \mathbf{C}^{GN}(f) \mathbf{V}_1}{(2\pi f_m)^2 |\mathbf{V}_1^\dagger \mathbf{J}_\omega(\mathbf{X}^0, \omega_0) \mathbf{KX}^0|^2} \end{aligned} \quad (176)$$

where R_n is a resistance of normalization. The signal power of the fundamental frequency is represented by

$$P_{Si} = 2|X_{i,1}^0|^2 \cdot R_n \quad (177)$$

With the definition of the single-sideband phase noise in (175), we derive an equation for $L(f_m)$ using the approximations of the noise power (176) and the signal power (177):

$$L(f_m) = \frac{1}{(2\pi f_m)^2} \cdot \frac{\mathbf{V}_1^\dagger \mathbf{C}^{GN}(f_0 + f_m) \mathbf{V}_1}{|\mathbf{V}_1^\dagger \mathbf{J}_\omega(\mathbf{X}^0, 2\pi f_0) \mathbf{KX}^0|^2} \quad (178)$$

where \mathbf{V}_1 is the solution of the homogeneous linear system of equations

$$\mathbf{J}^\dagger(\mathbf{U}_T^0, 2\pi f_0) \mathbf{V}_1 = \mathbf{0} \quad (179)$$

which can be obtained very easily with a standard LU decomposition of the Jacobian. The derivative of the Jacobian with respect to the frequency $\mathbf{J}_\omega^\dagger(\mathbf{U}^0, 2\pi f_0)$ can be calculated numerically, as we will show in our example. The denominator of the second term is constant for different frequency deviations and needs to be calculated only once. The numerator consists of the correlation spectrum of the noise sources multiplied by the vector \mathbf{V}_1^\dagger from the left side and by \mathbf{V}_1 from the right side. As we already described, this multiplication is a projection of all noise sources of the state space onto the tangent vector to the steady state. That means that the vector \mathbf{V}_1 selects the contributions of the noise sources that are tangential to the steady state and therefore induce phase noise. The noise sources, $1/f^\alpha$ -noise sources and white-noise sources, and their modulation are taken into account in the correlation matrix \mathbf{C}^{GN} . The correlation spectrum of a $1/f^\alpha$ -noise source decreases at 10α dB per decade, and therefore $L(f_m)$ decreases at $[20 + 10\alpha]$ dB/frequency decade. The single-sideband phase noise decreases at 20 dB per frequency decade due to white-noise sources because the correlation spectra of white-noise sources are constant with respect to the frequency. This method results in a numerically stable calculation of the phase noise of free-running oscillators, where all effects of the noise sources converted with harmonic signals are taken into account.

6. SYNCHRONIZATION OF OSCILLATORS

In the previous sections electronic oscillators without excitations were considered, but even in the early days

of oscillators undesired entrainment phenomena of forced oscillators were described by Möller [75] and others (see van der Pol [99]) around 1920. Although van der Pol mentioned forced oscillations in a 1920 paper, he considered circuits only with positive (differential) resistances. In 1922 Appleton [3] discussed “automatic synchronization” of forced triode oscillators (only another expression for entrainment), and in the following years this subject was studied in more detail (see van der Pol’s review paper [100]), but a sound mathematical basis of entrainment phenomena was not presented until the paper of Andronov and Vitt [2] in 1930, where again the mathematical ideas of Poincaré were used. A modern presentation can be found, for example, in the monograph by Jordan and Smith [47]. In 1945 Tucker [96] emphasized that

the synchronization (or entrainment) of oscillators was originally investigated because of difficulties experienced with early radio transmitters of “pull-in” to adjacent-station frequencies. Since then, however, the properties of oscillators under the influence of injected tones have been utilized in several ways.

He also mentioned ideas from his Ph.D. thesis about applications to carrier telephone systems and Kirschstein’s [53] miscellaneous applications in radio and other applications in communication engineering. Today many of these early applications of entrainment and synchronization of forced oscillators are discussed in the area of so-called phase-locked loops (see, e.g., Stensby [94] for further details and references). Although it seems that phase-locked-loop (PLL) circuits and forced electronic oscillators differ in their circuit structure a mathematical analysis shows similar phenomena in both circuits.

In this section some aspects of entrainment will be illustrated using the forced van der Pol equation (with normalized $\omega_0^2 = 1$)

$$\ddot{x} + \varepsilon(x^2 - 1)\dot{x} + x = \Gamma \cos \omega t \quad (180)$$

where $\varepsilon > 0$. Following Jordan and Smith [47], where van der Pol’s idea is used, we look for responses approximately of the form

$$x(t) = a(t) \cos \omega t + b(t) \sin \omega t \quad (181)$$

where a , b are slowly varying functions. Neglecting \dot{a} , \dot{b} , we obtain after some calculations a system of differential equations for the amplitude functions a and b

$$\begin{aligned} \left(2\omega - \frac{1}{2}\varepsilon ab\right)\dot{a} + \varepsilon\left(1 - \frac{1}{4}a^2 - \frac{3}{4}b^2\right)\dot{b} \\ = \varepsilon\omega a\left(1 - \frac{1}{4}r^2\right) - \Omega b \end{aligned} \quad (182)$$

$$\begin{aligned} -\varepsilon\left(1 - \frac{3}{4}a^2 - \frac{1}{4}b^2\right)\dot{a} + \left(2\omega + \frac{1}{2}\varepsilon ab\right)\dot{b} \\ = \Omega a + \varepsilon\omega b\left(1 - \frac{1}{4}r^2\right) + \Gamma \end{aligned} \quad (183)$$

where $\Gamma^2 = a^2 + b^2$ and $\Omega := \omega^2 - 1$. The periodic solutions with the frequency ω of the “input function” $\Gamma \cos \omega t$ (RHS of 180) correspond the equilibrium points ($\dot{a} = 0, \dot{b} = 0$) of these equations. Using the abbreviations $v = (\omega^2 - 1)/\varepsilon\omega$ (“detuning”) and $\gamma = \Gamma/\varepsilon\omega$, we obtain from the equilibrium equations the following condition for “response” solutions

$$r^2 \left\{ v^2 + \left(1 - \frac{1}{4}r^2 \right)^2 \right\} = \gamma^2 \tag{184}$$

Analysis of this polynomial equation shows that there are one or three real roots (since $r > 0$) depending on the parameter values v and γ . A graphical representation of r^2 in dependence of $|v|$ is called “response diagram,” which can be found, for example, in Jordan and Smith [47]. Based on these equilibrium points, a stability analysis has to be performed. As a conclusion it can be found that for certain values of the parameters v and γ around the frequency $\omega_0^2 = 1$ ($v = 0$) of the “free” oscillator (i.e., zero input function), there is a finite region (“lockin band”) of detunings v where a stable harmonic solution (with frequency ω) exists. This region of frequencies corresponds to the region of entrainment or synchronization. Outside this frequency region there are no stable harmonic solutions with the input frequency ω and in the $a - b$ -plane limit cycles appear. In Fig. 15 a variant of the response diagram is shown using the coordinates r and ω . A first curve subdivides the r, ω plane into the stable and unstable areas, whereas the semicircle above corresponds to the stable solutions of the polynomial equation (184). Moreover, the dashed lines confine the entrainment or synchronization region. These results were published by Andronov and Vitt [2] for the first time. Note that the forced van der Pol equation is nonlinear, and, in contrast to linear differential equations with constant coefficients where general solutions consist of a superposition of “free” and “forced” oscillations, this distinction makes no sense

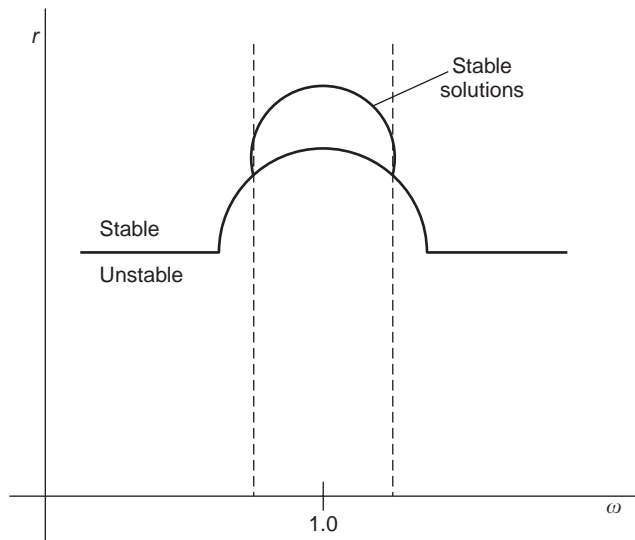


Figure 15. Response diagram of the van der Pol equation.

although it seems obvious if the frequencies ω_0 and ω are widely separated.

The abovementioned mathematical concept can be applied to discuss some basic aspects of entrainment/synchronization phenomena, but there are other effects (e.g., higher harmonics, subharmonics) where more involved techniques have to be applied. The reader is referred to the monograph of Jordan and Smith [47] for further details. For analysis of PLL circuits with its feedback structure, the monograph by Stensby [94] is very helpful.

Finally, we should mention that there is a close relationship between synchronization and chaotic behavior. This subject is contained in an interesting paper by Tsang et al. [95]. As a conclusion of their discussion, it can be emphasized that each circuit with synchronization properties is a potential candidate of a chaotic system.

7. MISCELLANEOUS PROBLEMS OF OSCILLATOR DESIGN

Besides the design problems discussed above, further problems are essential in the design of oscillators. Some of these problems are mentioned, but the reader is referred to the literature; for instance, the monographs by Parzen [79], Frerking [30], and Kurz and Mathis [59] contain many interesting design aspects. Several monographs are available that consider the design of microwave oscillators [e.g., 101]. We will discuss only some more general aspects of oscillator design. Spurious oscillations: Most spurious oscillations are caused by the parasitic inductances and capacitances in the active devices (e.g., transistors) or the physical layout for the components of the oscillator circuit. A main approach to avoid these oscillations is to introduce of additional damping (e.g., additional resistors). Parasitics that are related to the layout and a rather poor design can be reduced by an experienced designer since general rules to avoid it are not available. In crystal oscillators there is a tendency of spurious signals due to the crystal itself. For studying these effects a more complete model of the crystal with additional resonances (so-called modes) has to be considered [79].

Another effect is self-produced amplitude modulation of high-frequency oscillation; this effect is often denoted as “squegging.” The physical reason of squegging is related to an interaction between the time constant of the bias and coupling circuits and the time constants of the high-frequency tuned circuits of the oscillation part. Squegging occurs more frequently in self-limiting oscillators with low Q values than in crystal oscillators where a high Q is usual. Furthermore a suitable thermal design is necessary, especially if a crystal resonator is chosen. Some hints about this subject can be found in the literature [see, e.g., Kurz and Mathis [59]].

BIBLIOGRAPHY

1. A. A. Andronov, A. A. Vitt, and S. E. Khaikin, *Theory of Oscillators* (reprint of an extended edition of 1937), Dover, New York, 1966.

2. A. A. Andronov and A. A. Vitt, Theorie des Mitnehmens von van der Pol, *Archiv Elektrotechnik* **24**:99–110 (1930).
3. E. V. Appleton, The automatic synchronization of triode oscillators, *Proc. Cambridge Phil. Soc.* **21**:231 (1922).
4. T. J. Aprille and T. N. Trick, A computer algorithm to determine the steady state response of nonlinear oscillators, *IEEE Trans. Circ. Theory* **19**:131–139 (1972).
5. W. Anzill, F. X. Kärtner, and P. Russer, Simulation of the single sideband phase noise of oscillators, *Proc. 2nd Int. Workshop of the German IEEE MTT/AP Joint Chapter on Integrated Nonlinear Microwave and Millimeterwave Circuits*, Duisburg, Germany, Oct. 7–9, 1992, pp. 97–110.
6. W. Anzill and P. Russer, A general method based on harmonic balance techniques to simulate noise in free running oscillators, *IEEE MTT-S Int. Microwave Symp.*, Atlanta, GA, 1993, June 14–18, 1993, pp. 655–658.
7. W. Anzill and P. Russer, A general method to simulate noise in oscillators based on frequency domain techniques, *IEEE Trans. Microwave Theory Tech.* **41**(12):2256–2263 (Dec. 1993).
8. W. Anzill, F. X. Kärtner, and P. Russer, Simulation of the phase noise of oscillators in the frequency domain, *Arch. Elek. Übertragung. AE* **48**(1):45–50 (1994).
9. W. Anzill, *Berechnung und Optimierung des Phasenschwankens von Oszillatoren*, dissertation, Munich Technical Univ., 1995.
10. W. Anzill, O. v. Stryk, R. Bulirsch, and P. Russer, Phase noise minimization of microwave oscillators by optimal control, *IEEE MTT-S Int. Microwave Symp.*, Orlando, FL, May 16–May 20, 1995, pp. 1565–1568.
11. V. I. Arnold, *Geometrical Methods in the Theory of Ordinary Differential Equations*, Springer-Verlag, New York–Berlin–Heidelberg, 1983.
12. L. Arnold, *Random Dynamical Systems*, Springer-Verlag, Berlin–Heidelberg, 1998.
13. D. K. Arrowsmith and C. M. Place, *An Introduction to Dynamical Systems*, Cambridge Univ. Press, Cambridge, UK, 1990.
14. V. Belevitch, *Classical Network Theory*, Holden-Day, San Francisco, CA, 1968.
15. H. G. Brachtendorf and R. Laur, Multi-rate PDE methods for high Q oscillators, *Proc. 4th Circuits, Systems, Communications & Computers (CSCC) Conf.*, Athens, Greece, July 10–15, 2000.
16. A. Buonomo and C. Di Bello, Asymptotic formulas in nearly sinusoidal nonlinear oscillators, *IEEE Trans. Circ. Syst. I: Fund. Theory Appl.* **43**:953–963 (1996).
17. R. Bulirsch, *Die Mehrzielmethode zur numerischen Lösung von nichtlinearen Randwertproblemen und Aufgaben der optimalen Steuerung*, Carl-Cranz-Gesellschaft Heidelberg, Germany, 1971 (reprinted Technische Universität, Mathematisches Institut, Munich, Germany, 1985).
18. R. Bulirsch, and J. Stoer, *Introduction to Numerical Analysis*, Springer-Verlag, New York, 1980; *Differential Equations*, Prentice-Hall, Englewood Cliffs, NJ, 1971.
19. E. J. Cassagnol, *Semiconductors*, Vol. III, *Non-linear Electronics*, Philips Techn. Library, N. V. Gloeilampenfabrieken, Eindhoven, The Netherlands, 1968.
20. C.-R. Chang and M. B. Steer, Frequency-domain nonlinear microwave simulation using the arithmetic operator method, *IEEE Trans. Microwave Theory Tech.* **MTT-38**(8):1139–1143 (Aug. 1990).
21. L. O. Chua and P. Lin, *Computer-Aided Analysis of Electronic Circuits: Algorithms and Computational Techniques*, Prentice-Hall, Englewood Cliffs, NJ, 1975.
22. L. O. Chua and Y.-S. Tang, Nonlinear oscillation Volterra series, *IEEE Trans. Circ. Syst.* **CAS-29**:150–168 (1982).
23. W. B. Davenport and W. L. Root, *An Introduction to the Theory of Random Signals and Noise*, McGraw-Hill, New York, 1958.
24. J. Davidse, *Analog Circuit Design*, Prentice-Hall, New York, 1991.
25. A. Demir and A. Sangiovanni-Vincentelli, *Analysis and Simulation of Noise in Nonlinear Electronic Circuits and Systems*, Kluwer Academic, Boston–Dordrecht–London, 1998.
26. C. A. Desoer and E. S. Kuh, *Basic Circuit Theory*, McGraw-Hill, New York, 1969.
27. A. Dupuis, J. Hausner, and P. Russer, Hybrid integrated Ku-band VCO., *Proc. 19th European Microwave Conf.*, London, Sept. 4–7, 1989, pp. 1009–1014.
28. W. A. Edson, Noise in oscillators., *Proc. IRE* **48**:1454–1466 (1960).
29. M. Filleböck, M. Schwab, and P. Russer, Automatic generation of starting values for the simulation of microwave oscillators by frequency domain techniques, *IEEE Trans. Microwave Theory Tech.* **41**(5):809–813 (1993).
30. M. E. Frerking, *Crystal Oscillator Design and Temperature Compensation*, Van Nostrand Reinhold, New York, 1978.
31. T. Goeller, M. Schwab, and P. Russer, Efficient simulation of millimeter-wave IMPATT oscillators by FATE, a combined time- and frequency-domain method, *IEEE Microwave Guided Wave Lett.* **1**(11):343–345 (1991).
32. G. H. Golub and C. T. Loan, *Matrix Computations*, Johns Hopkins Univ. Press, Baltimore–London, 1989.
33. V. Güngerich, F. Zinkler, W. Anzill, and P. Russer, Reduced phase noise of a varactor tunable oscillator: Numerical calculations and experimental results, *Proc. IEEE MTT-S Int. Microwave Symp.*, Atlanta, GA, June 14–18, 1993, pp. 561–564.
34. V. Güngerich, J. Deuringer, W. Anzill, and P. Russer, Phase noise reduction of microwave oscillators by optimization of the dynamic behaviour, *Proc. MTT-S Int. Microwave Symp.*, San Diego, CA, May 23–27, 1994, pp. 953–956.
35. L. Gustafson, G. H. B. Hanson, and K. I. Lundstroem, On use of the describing functions in the study of nonlinear active microwave circuits, *IEEE Trans. Microwave Theory Tech.* **MTT-20**:402–409 (1972).
36. R. Gratzl, J. Hausner, and P. Russer, Nonlinear design approach of a broadband hybrid integrated Ku-band common source GaAs FET VCO, *Proc. Int. Microwave Symp.*, Dallas, TX, May 8–10, 1990, pp. 739–742.
37. P. R. Gray and R. G. Meyer, *Analysis and Design of Analog Integrated Circuits*, Wiley, New York, 1993.
38. J. Guckenheimer, Dynamics of the van der Pol equation, *IEEE Trans. Circ. Syst.* **CAS-27**:983–989 (1980).
39. A. Hajimiri and T. H. Lee, *Low Noise Oscillators*, Kluwer Academic, Boston–Dordrecht–London, 1999.
40. J. K. Hale, *Oscillations in Nonlinear Systems*, McGraw-Hill, New York, 1963.
41. B. D. Hassard, N. D. Kazarinoff, and Y.-H. Wan, *Theory and Applications of Hopf Bifurcation*, Cambridge Univ. Press, Cambridge, UK, 1981.
42. L. A. Hazeltine, Oscillating audio circuits, *Proc. Inst. Radio Eng.* **6**:63 (1918).
43. K. Heegner, Über Schwingungserzeugung mittels Elektronenröhren, welche Selbstinduktion nicht enthalten, *Jahrbuch drahtlosen Telegr. Teleph.* **29**:151 (1927).

44. H. Hillbrand and P. Russer, An efficient method for computer aided noise analysis of linear amplifier networks, *IEEE Trans. Circ. and Syst.* **CAS-23**:235–238 (1976).
45. M. N. Horenstein, *Microelectronic Circuits and Devices*, Prentice-Hall, Englewood Cliffs, NJ, 1996.
46. Y. Hu, J. J. Obregon, and J.-C. Mollier, Nonlinear oscillation via Volterra series, *IEEE Trans. Circ. Syst.* **CAS-29**(3): 150–168 (1982).
47. D. W. Jordan and P. Smith, *Nonlinear Ordinary Differential Equations*, 3rd ed., Oxford Univ. Press, Oxford, UK, 1999.
48. F. X. Kärtner, Determination of the correlation spectrum of oscillators with low noise, *IEEE Trans. Microwave Theory Tech.* **MTT-37**(1):90–101 (1989).
49. F. X. Kärtner, Analysis of white and $f^{-\alpha}$ noise in oscillators, *Int. J. Circ. Theory Appl.* **18**:485–519 (1990).
50. F. X. Kärtner, Noise in oscillating systems, *Proc. IEEE MTTAP Workshop Integrat. Nonlinear Microwave, Millimeter Wave Circuits (IN-MIC'92)*, Duisburg, 1992, pp. 61–75.
51. C. Keidies and W. Mathis, Application of symbolic methods to oscillator design, *Proc. 2nd SMACD'92, Conf.*, Florence, Italy, 1992, pp. 67–72.
52. U. Kirchgraber and E. Stiefel, *Methoden der analytischen Störungsrechnung und ihre Anwendung*, Teubner Verlag, Stuttgart, 1978.
53. F. Kirschstein, Die Mitnahme selbsterregter Schwingungen und ihre technische Verwertung, *Elektr. Nachrichtentech.* **20**:29–38 (1943).
54. R. Knöche, K. Schünemann, Noise in multiple-device oscillators, *Archiv Elektronik Übertragungstechnik* **36**(10):31–39 (1982).
55. N. M. Krylov and N. N. Bogoliubov, Einführung in die nichtlineare Mechanik, Verlag d. Akad. Wiss. Ukr. SSR, 1937.
56. S. K. Kundert and A. Sangiovanni-Vincentelli, *Steady State Methods for Simulating Analog and Microwave Circuits*, Kluwer Academic, Boston, 1990.
57. K. Kurokawa, Noise in synchronized oscillators, *IEEE Trans. Microwave Theory Tech.* **MTT-16**(4):234–240 (1968).
58. K. Kurokawa, Injection locking of microwave solid-state oscillators, *Proc. IEEE* **61**(10):1386–1408 (1973).
59. G. Kurz and W. Mathis, *Oszillatoren*, Hüthig Buch Verlag, Heidelberg, 1994.
60. P. I. Kuznetsov, R. L. Stratonovich, and V. I. Tikhonov, *Non-Linear Transformations of Stochastic Processes*, Pergamon Press, Oxford, 1965.
61. S. A. Maas, *Nonlinear Microwave Circuits*, Artech House, Norwood, MA, 1988.
62. K. März, Phasen- und Amplitudenschwankungen in Oszillatoren, *Archiv Elektronik und Übertragungstechnik* **24**(11):477–490 (1970).
63. L. Mandelstam and N. Papalexi, Über Resonanzerscheinungen bei Frequenzteilung, *Zeitschr. Physik* **72**:223–248 (1931).
64. L. Mandelstam, N. Papalexi, A. A. Andronov, S. Chaikin, and A. Witt, Exposé des recherches récentes, sur les oscillations non linéaires, *Zeitschr. Techn. Physik* **4**:81–134 (1935).
65. T. Mangold and P. Russer, Full-wave modeling and automatic equivalent-circuit generation of millimeter-wave planar and multilayer structures, *IEEE Trans. Microwave Theory Tech.* **MTT-47**(6):851–858 (June 1999).
66. W. Mathis, *Theorie Nichtlinearer Netzwerke*, Springer-Verlag, Berlin, 1987.
67. W. Mathis, An efficient method for the transient analysis of weakly damped crystal oscillators, *Proc. MTNS98*, Padova, Italy, July 6–10, 1998.
68. W. Mathis, Historical remarks to the history of electrical oscillators, *Proc. MTNS98*, Padova, Italy, July 6–10, 1998.
69. W. Mathis and L. Weiss, Noise analysis of nonlinear electrical circuits, in K. Antreich, R. Bulirsch, A. Gilg, and P. Rentrop, *Modeling, Simulation and Optimization of Integrated Circuits*, Birkhäuser Verlag, Basel, Switzerland, 2003, pp. 269–282.
70. W. Mathis and M. Prochaska, Deterministic and stochastic Andronov-Hopf bifurcation on nonlinear electronic oscillators, *Proc. NDES 2003*, Seoul, South Korea, May 18–21, 2003.
71. R. Mauro, *Engineering Electronics—a Practical Approach*, Prentice-Hall, Englewood Cliffs, NJ, 1989.
72. A. I. Mees, *Dynamics of Feedback Systems*, Wiley, Chichester, UK, 1981.
73. D. Meyer-Ebrecht, *Schnelle Amplitudenregelung harmonischer Oszillatoren*, dissertation TU Braunschweig, 1974.
74. J. Millman and A. Grabel, *Microelectronics*, McGraw-Hill, New York, 1987.
75. H. G. Möller, Über störungsfreien Gleichstromempfang mit dem Schwingaudion, *Jahrbuch Drahtl. Telegr.* **17**:256 (1921).
76. A. H. Nayfeh, *Introduction to Perturbation Techniques*, Wiley, New York, 1981.
77. G. Nicolis and I. Prigogine, *Self-Organization in Non-Equilibrium Systems*, Wiley, Chichester, UK, 1977.
78. G. R. Olbrich, T. Felgentreff, W. Anzill, G. Hersina, and P. Russer, Calculation of HEMT oscillator phase noise using large signal analysis in time domain, *IEEE-MTT Symp. Digest*, San Diego, CA, May 23–27, 1994, Vol. 2, pp. 965–968.
79. B. Parzen, *Design of Crystal and Other Harmonic Oscillators*, Wiley, New York–Chichester, 1983.
80. M. Prochaska and W. Mathis, On nearly sinusoidal solutions of singularly perturbed systems, *Proc. NDES 2004*, Evora, Portugal, May 9–13, 2004.
81. V. Rizzoli and A. Neri, State of the art and present trends in nonlinear microwave CAD techniques, *IEEE Trans. Microwave Theory Tech.* **MTT-36**(2):343–364 (Feb. 1988).
82. B. Roth, H. Sledzik, and A. Beyer, An improved method for the design and simulation of microwave oscillators, *Proc. West Germany IEEE MTT/AP Joint Chapter Workshop on Progress in Microwave CAD and in CAD Applications*, Ratingen, Oct. 26–27, 1989, pp. 208–224.
83. E. F. Mishchenko and N. K. Rozov, *Differential Equations with Small Parameters and Relaxation Oscillators*, Plenum Press, New York–London, 1980.
84. P. Russer and H. Hillbrand, Rauschanalyse von linearen Netzwerken, *Wissenschaftliche Berichte AEG-Telefunken* **49**:127–138 (1976).
85. A. Ruszynyak, Start-up time of CMOS oscillators, *IEEE Trans. Circ. Syst.* **CAS-34**:259–268 (1987).
86. J. A. Sanders and F. Verhulst, *Averaging Methods in Nonlinear Dynamical Systems*, Springer-Verlag, New York–Berlin–Heidelberg, 1985.
87. Ch. Schmidt-Kreusel, *Rechnergestützte Analyse von Quarzoszillatoren*, dissertation, Univ. Wuppertal, 1997.
88. K. F. Schünemann and K. Behm, Nonlinear noise theory for synchronized oscillators, *IEEE Trans. Microwave Theory Tech.* **MTT-27**(5):452–458 (1979).
89. M. Schwab, F. J. Zimmermann, P. Russer, F. X. Kärtner, and T. Göller, Steady state of a SAW stabilized bipolar oscillator obtained by solution of a boundary value problem, *Proc. 20th*

- European Microwave Conf.*, Budapest, Hungary, Sept. 10–13, 1990, pp. 1240–1245.
90. M. Schwab, Determination of the steady state of an oscillator by a combined time-frequency domain method, *IEEE Trans. Microwave Theory Tech.*, **MTT-39**(8):1391–1402 (Aug. 1991).
 91. R. S. Sidorowicz, An abundance of sinusoidal oscillators, *Proc. IEE* **119**:283–293 (1972),
 92. A. Spälti, Der Einfluss des thermischen Widerstandsrauschens und des Schroteffektes auf die Störmodulation von Oszillatoren, *Bull. Schweiz. Elektr. Vereins* **39**:419–427 (1948).
 93. R. Spence, *Linear Active Networks*, Wiley, London–New York, 1970.
 94. J. L. Stensby, *Phase-Locked Loops—Theory and Applications*, CRC Press, Boca Raton–New York, 1997.
 95. Y. S. Tsang, A. I. Mees, and L. O. Chua, Synchronization and chaos, *IEEE Trans. Circ. Syst.* **CAS-30**:620–626 (1983).
 96. D. G. Tucker, Forced oscillations in oscillator circuits, and the synchronization of oscillators, *J. IEE* **92**:226–234 (1945).
 97. G. Vallauri, Über die Wirkungsweise der in der drahtlosen Telegraphie benutzten Vakuumröhren mit drei Elektroden (Audion), *Jahrbuch Drahtlosen Telegraphie* **12**:349 (1917).
 98. B. L. van der Pol, A theory of the amplitude of free and forced triode vibrations, *Radio Rev.* **1**:701 (1920).
 99. B. L. van der Pol, Forced oscillations in a circuit with nonlinear resistance (reception with reactive triode), *Phil. Mag.* **3**:65–80 (1927); first published in the Dutch journal *Tijdschr. van het Nederlandsch Radiogenootschap* in 1924.
 100. B. L. van der Pol, The nonlinear theory of electrical oscillations, *Proc. Inst. Radio Eng. (IRE)* **22**:1051–1086 (1934).
 101. G. D. Vendelin, *Microwave Circuit Design Using Linear and Nonlinear Techniques*, Wiley, New York, 1990.
 102. J. H. Wilkinson, *The Algebraic Eigenvalue Problem*, Clarendon, Oxford, 1988.

PACKAGING RF DEVICES AND MODULES

Y. C. LEE
 WENGE ZHANG
 BINGZHI SU
 ZHIPING FENG
 K. C. GUPTA
 University of Colorado, Chong-
 IL Park, Kyocera America,
 Inc.

Initially implemented in military radar, microwaves have been used in communication, space, scientific, and commercial applications. The term *microwave* usually refers to the frequency spectrum ranging from 300 MHz to 300 GHz. Strictly speaking, the millimeter-wave (mm-wave) range begins at about 30 GHz; therefore, the term *radiofrequency* (RF) is used, instead of *microwave*, to represent both microwave (300 MHz–30 GHz) and mm-wave (30–300 GHz) frequency spectra.

Radiofrequency (RF) packaging is becoming more and more important because of the significant growth of military and commercial applications in wireless communication and sensing. Packaging strongly affects performance, cost, and reliability; it is a determining factor in application growth. Many RF packaging, issues are the same as those for microelectronic packaging, which are covered in other articles. However, RF packaging has three distinguishing features:

1. Table 1 lists application examples at frequencies ranging from 1 to 100 GHz [1]. There is another long list for frequencies less than 1 GHz. For such a wide spectrum of applications, it is not practical to develop a few “standard” packaging solutions to meet requirements that are usually frequency-dependent.
2. For frequencies higher than 1 GHz, the package strongly affects RF performance. It is a part of the circuit, not just a housing. The package parasitic becomes more critical as frequency increases [2,3].

Table 1. Examples of RF Applications at Frequencies from 1 to 100 GHz

Frequency(GHz)	Applications
1.9–2.1	Personal communication services (PCS)
4–8	Cooperative engagement military communication
5.1–5.3	Supernet band for PCS
12.4–12.7	Direct broadcast satellite (DBS)
20, 44	Military MILSTAR
27.5–30	Local multipoint distribution service (LMDS)
26–40	Military precision guided missiles
60	Wireless communication links
77	Vehicular collision avoidance radar
75–110	Concealed-weapon detection

3. The number of inputs/outputs (I/O) in RF packages is small, for instance, 6 I/Os or 12 I/Os; however, electromagnetic waves must be transmitted in and out with minimum losses.

RF packaging technologies have been driven by military applications; as a result, most packages are semicustom or custom designed for performance, reliability, and small volume manufacturing. With the growth of commercial applications, cost is becoming the predominant factor. As a result, plastic and low-cost ceramics are used for mass production of RF packages for PCS applications at frequencies around 2 GHz. They are being developed for higher frequencies around 5 GHz.

High-volume applications in mm-wave frequencies, for example, 23, 26, 30, 38, 60, and 77 GHz, are to be implemented in the near future. Packaging these RF devices and modules is critical to a successful implementation. Package complexity is increasing substantially in order to support these new commercial systems using microwave and millimeter-wave integrated circuits (MMICs), active antennas, antenna arrays, microelectromechanical systems (MEMSs), substrates with ferroelectric or superconductor or other novel components.

RF packaging technologies are advancing rapidly. This article provides basic knowledge to understand the technology advances. Most packaging issues common to those for microelectronics packaging will not be covered here, and they can be found in other articles. The following sections will focus on unique issues for RF packaging. Representative packages and assembly technologies will be reviewed. Critical consideration of RF performance and reliability will be introduced. The reliability section will cover both thermal management and mechanical integrity. A case study will be presented to illustrate a typical design procedure considering various factors. In addition, computer-aided-design (CAD) issues and advanced packaging concepts will be introduced, to understand future challenges.

1. RF PACKAGES

A typical microwave and mm-wave system is shown in Fig. 1. Signals are generated by an oscillator and transmitted from an antenna driven by an amplifier. The signals are received by another antenna and propagated to a receiver. There are many transmission-line components to interconnect these basic devices. In many cases, the transmission line is a part of the circuits. The trend is to integrate all the devices and components more and more using MMIC and advanced packaging technologies. High integration could eliminate layers of interconnects for cost reduction and performance enhancement.

Figure 2 shows an example of two levels of RF packaging. For a single-chip package, an RF device is connected to a package substrate through wire bonding or flip-chip soldering/bonding. Usually there are transmission lines

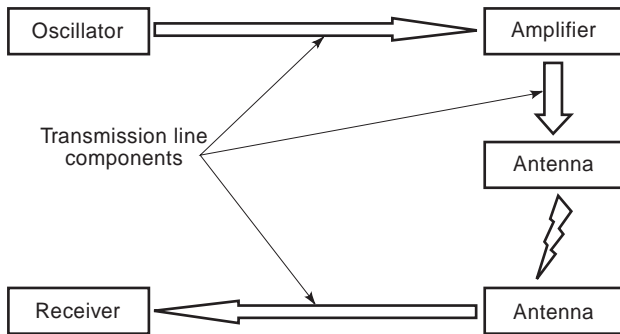


Figure 1. A typical microwave or millimeter-wave system consisting of major functional modules and circuits for signal transmitting and receiving. The integration of the oscillator, amplifier, and antenna is for signal transmitting. The integration of the antenna and receiver is for signal receiving. For high-frequency applications, the transmission-line components should be reduced as much as possible for high efficiency.

on the substrate; the lines are connected to the external ports through feedthroughs or vias. The external ports are connected to the next level board assembly. For a multichip RF module, bare-die devices and RF components are connected to a multilayer substrate with transmission lines as interconnects. These single-chip and multichip modules will be briefly reviewed in what follows (see Fig. 2).

1.1. Single-Chip Packages

Figure 3 shows a photo of a typical RF package with various components of a package shown in Fig. 4. The wall of housing is usually made of metal or ceramic. The feedthroughs are gold-coated leads passing through a metal or ceramic wall. With a metal wall, feedthroughs are isolated from the wall by glass. A gold plated Kovar (iron–nickel–cobalt alloy) or CuW (copper–tungsten) base is soldered to the bottom of the package, and a gold-plated Kovar lid is typically attached to the wall with AuSn (gold–tin) solder.

There are many different packaging approaches other than the example given above. Several factors should be addressed before an individual packaging method is chosen [4]:

- Low-loss electrical interconnect with impedance matching
- Dimensional stability and achievable tolerances
- Three-dimensional package characterization with antiresonance housing

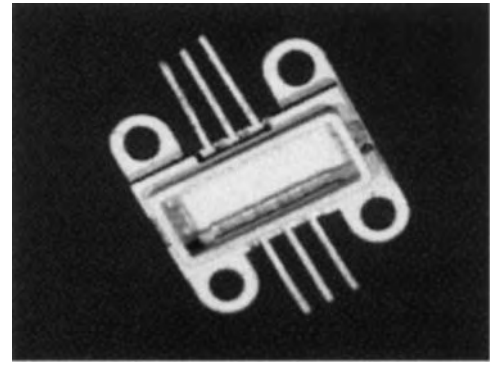
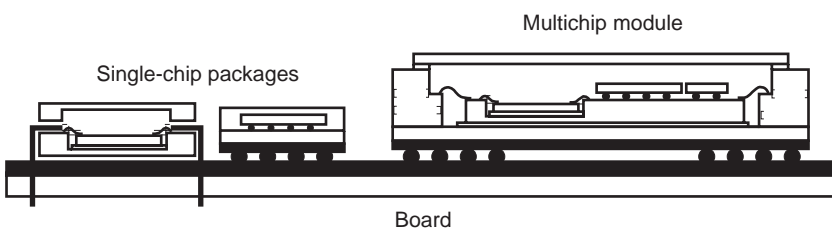


Figure 3. Photo of a typical single-chip RF package. Details of the package are described in Fig. 4.

- Electromagnetic shielding
- Efficient thermal management
- Matching of material properties for reliable connections
- System constraints such as size, weight, shape, hermeticity, or the special positioning of the package or modules in the array
- Test and validation
- Overall cost including assembly and rework as well as package manufacturability

With these considerations, a designer can choose a proper packaging solution. A summary of different packages are described below.

1.1.1. Package Materials. RF single-chip packages can be categorized by package material such as metal wall, ceramic wall, glass ceramic, and plastic packages. Their major characteristics are listed in Table 2 qualitatively, and a brief description is given in this section.

1.1.1.1. Metal Wall Package. The metal wall is usually Kovar coated with nickel and gold. Its feedthroughs for output leads are striplines isolated from the wall. Striplines are described later. A good package can be used up to 90 GHz with low insertion loss and excellent isolation. However, thermal performance is poor using Kovar and the cost can be high. Thermal performance can be enhanced substantially with a CuW base plate. To reduce cost, metal injection molding can be used for fabricating the metal housing [5].

Figure 2. Single-chip and multichip RF packages mounted on a board. The single-chip package can be through-hole or surface mount types. The multichip module can be assembled using wire bonding or flip-chip connections; the module can be mounted onto the board using through-hole or surface mount technologies. All the critical elements for the first- and the second-level packaging are shown in the figure.

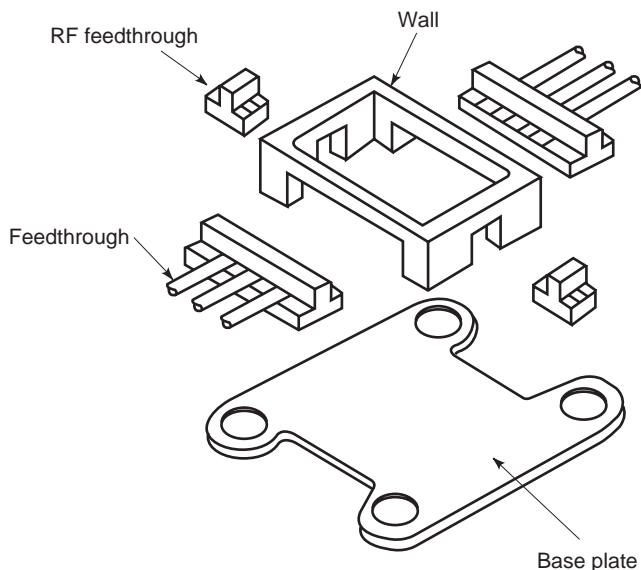


Figure 4. Structure of an RF package consisting of a wall, feedthroughs, and a baseplate. The baseplate carries the RF device that is connected to RF ports through wire bonding pads and feedthroughs. The metal wall is to provide electrical, thermal, and mechanical protection of the device.

1.1.1.2. Ceramic Wall Package. The ceramic wall is usually made by high-temperature cofired ceramic (HTCC) coated with nickel and gold. The process for HTCC is described in Ref. 6. The feedthrough conductor can be tungsten striplines without additional electrical isolation. A good package can be used up to 60 GHz with low insertion loss and good isolation. The package cost can be lower than that of the metal wall package's, but it may still be high.

1.1.1.3. Glass Ceramic Package. The package material is a compound mixing glass and alumina. It is also called low-temperature cofired ceramic (LTCC) with copper as the conductor. The substrate is ideal for surface mount package and multichip modules. A good package can be used up to 40 GHz with low insertion loss. Its cost is low because the use of copper as the conductor; however, without enhancement, its thermal performance can be poor.

Figure 5 shows a surface-mounted ceramic package with RF vias. The external ports can be designed for leadless chip carrier or ball-grid array (BGA) surface mount technologies. The insertion loss can be high, and the operation frequency is limited to a band between 18 and

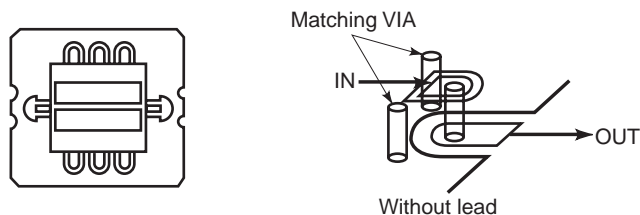


Figure 5. A surface mount package with RF vias. At the end of each port, the RF signal passes through the via to solder pad for surface mounting. No lead is needed for better RF performance because of short connections. Surface mount is important to automatic assembly of the package onto a board.

26 GHz. With higher frequencies, the typical $\lambda/4$ length scale is close to length scales of package discontinuities caused by bonding wires or joints, vias, walls, and other elements. To reduce the loss at a selected high-frequency band, the electromagnetic coupling at critical interfaces should be designed to smooth such discontinuities. Figure 6 is a package with coupling designed for 77 GHz.

1.1.1.4. Plastic Package. The plastic package is fabricated by injection molding of a device on a pedestal/lead-frame for die attachment and I/O leads. The package is excellent in manufacturability and ideal for surface-mount technology. However, it is usually used for frequencies less than 10 GHz due to high insertion loss. The manufacturing processes are the same as those for plastic packages used in microelectronics; however, the inductance of bonding wire and leadframe should be evaluated for high-frequency packages. A new premolded plastic package can enhance the performance, which is described later. The cost of a plastic package is low; however, it may not be lower than that of the glass ceramic package if both are designed for reach the same electrical performance.

1.1.1.5. Boards. The single-chip RF packages are generally mounted on a board. The board technologies are very similar to those for RF modules; these technologies are to be described in the next section.

1.2. Multichip Modules

Multichip module (MCM) technologies are being applied to design and manufacture RF modules. It is defined as a substrate of dielectric and conduction layers, on which integrated circuits (“chips”) and passive components (if any) are mounted directly on (or inside) the substrate, without

Table 2. Different Materials for Single-Chip RF Packages

	Metal Wall	Ceramic Wall	Glass Ceramic	Plastic
Features	Broadband	Broadband	Low loss	Low cost
	Low loss	Lower cost than metal wall	Suitable for single-chip and MCM	Suitable for high-volume applications
	Antiresonation	Low loss	Surface mount	Surface mount
Structure		Anticavity resonance	Suitable for high-volume applications	
	Excellent shielding	Good shielding		
	Excellent isolation	Good isolation	Excellent design flexibility	

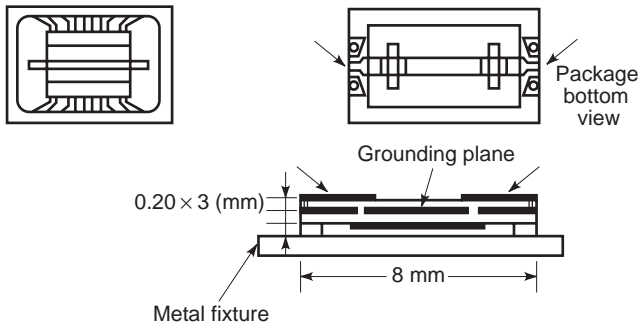


Figure 6. Structure of an electromagnetic coupling package. The top-layer microstrip line is coupled to the bottom one through the slot on the ground plane. The structure achieves the low insertion loss in a selected high frequency band. Such a specific RF design is important to reduce losses in millimeter-wave applications.

separate packaging for most of the active components. The entire MCM may be placed in a hermetic package much like a large single-chip carrier, or may be directly covered with a sealant material to protect the components from physical damage [7]. A good MCM example is shown in Fig. 7, which is a drawing of a photo taken from Ref. 8. The module consists of components on both sides. The front side has RF multicavities with all the MMICs and a large cavity with low-frequency components, for example, ASICs and discrete components for power supply and distribution. The backside is a nonhermetic area where all the surface mount components are assembled.

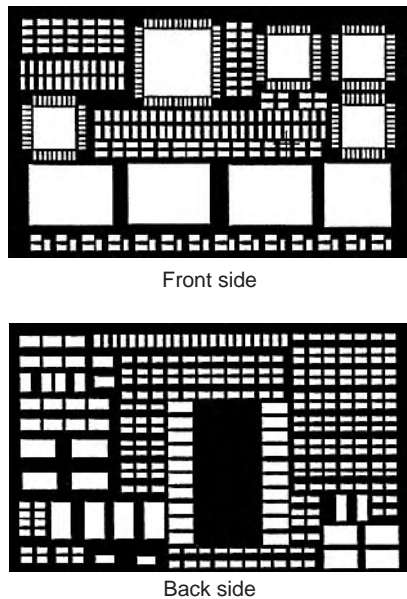


Figure 7. Substrate for a mixed multichip module. The frontside consists of low-frequency microelectronics and RF areas. Critical devices are sealed separately to avoid crosstalk. The backside is a nonhermetic area for all low-frequency surface mount components. A multichip module is much more complicated than single-chip packages; it is custom-designed and fabricated to interconnect many devices to reach specific targets on cost, performance, size, weight, or reliability.

Table 3. Advantages and Concerns for Single-Chip and Multichip Packaging

	Single Chip	MCM
Advantages	Each device testing Good yield as module Device to device isolation	Size reduction Lightweight Assembly cost reduction/cycle time reduction
	Hermeticity for individual device	Performance enhancement Reliability enhancement
Concerns	Volume manufactuability Electrical performance as module level	Power reduction Bare-die testing and yield Rework Use of via for RF line DC/RF shielding

The advantages and concerns of MCM and single-chip packaging are listed in Table 3. MCM technologies are emerging as a cost-effective technology for next-generation devices because of their advantages in small size, performance enhancement, better reliability, low power consumption, package cost reduction, and potential overall cost reduction for high-volume applications [9]. It is the predominant approach for mm-waves modules with frequencies higher than 30 GHz. However, its cost can be very high if manufacturing yield is low. With the establishment of MCM manufacturing infrastructure for microelectronics, the manufacturing barrier is being reduced substantially. In addition, sizes of single-chip packages are reduced significantly with chip-scale-package (CSP) technology. These packages for some RF and microelectronic devices can be integrated with other devices to form an MCM. It is anticipated that more MCM-based RF modules will be developed for size, weight, performance, power, or cost advantages in future.

MCMs can be fabricated using thin-film, thick-film, or thick/thin-film technologies. Typical substrate materials important to RF packaging are listed in Table 4 [10,11] for hard and Table 5 [12] for soft substrates.

1.2.1. Alumina/Glass Alumina. Alumina and glass alumina are popular substrates for MCMs. The fabrication of alumina substrate usually employs cofired technology, which includes low-temperature cofired ceramic (LTCC) and high-temperature cofired ceramics (HTCC). LTCC and HTCC are alumina/glass systems that differ in glass content (50% vs. 4%) and firing temperature (850°C vs. 1500°C). The LTCC firing temperature permits the use of silver, gold, and copper as conductors, while HTCC is limited to the use of a higher-melting-point refractory alloy, such as tungsten and molybdenum. LTCC substrates thus have lower sheet resistance but higher dielectric loss tangent. Their mechanical strengths and thermal conductivities are also lower than those of HTCC substrates. To achieve better cost/performance ratio, thin-film MCMs can use a harder alumina substrate, for example, A493, listed in Table 4, which has good RF, mechanical, and thermal

Table 4. Properties of Hard Substrate Materials

	CTE \times $10^{-6}/^{\circ}\text{C}$	Thermal Conductivity $\text{W/m} \cdot \text{K}$	Dielectric Constant ϵ_r (10 GHz)	Tan $\delta \times$ 10^{-4} (10 GHz)
Alumina (HTCC) ^a	6.9	20	9.1	12
Alumina thin film ^b	7.2	33	9.5	0.9
Glass ceramic ^c	5.9	2.5	5.7	12
ALN	4.7	150	8.6	53
BeO	9	260	6.7	40
Fused quartz	0.5	1.4	3.75	15
Sapphire	6	46.1	10.3	20
Si (high resistivity)	2.6	148	12	10–100
Gallium arsenide	5.7	58	12.9	16

^aAlumina A443 by Kyocera Corporation.

^bAlumina A493 by Kyocera Corporation.

^cGlass ceramic G-55 (GL550) by Kyocera Corporation.

Note: For properties of BeO the reader is referred to *Integrated Active Antennas and Spatial Power Combining* (J. A. Navarro, K. Chang, 1996). Properties of fused quartz, sapphire, and Si are covered in *Materials Handbook for Hybrid Microelectronics* (edited by Joseph Alison King, Artech House, 1988). Properties of gallium arsenide are listed in this table for reference.

properties. With thin-film technologies, low-temperature metals can be used for circuits. If planer passive components are needed, either HTCC or LTCC multilayer ceramic can be used as the substrate for thin film. Details on thin-film, thick-film, and thin/thick film-MCM technologies are given in other articles in this encyclopedia.

With single-layer or multilayer structures, different types of interconnect, for example, stripline, microstrip, and coplanar waveguide, can be used. Thermal conductivities of alumina and glass alumina substrate are usually poor. If needed, thermal performance can be enhanced by the use of metal plates, for example, CuW and Cu–Mo–Cu composites. Alternatively, AlN or BeO can be used.

1.2.2. BeO. Beryllium oxide or beryllia (BeO) is an alternative substrate material with an excellent thermal conductivity of 260 W/m · K. However, it is not widely used because of toxicity of outgasing during substrate fabrication. Also, its CTE is 9 ppm/°C, which is quite different from GaAs's CTE. In addition, BeO cannot be used to fabricate multilayer structures.

1.2.3. AlN. AlN, with a thermal conductivity of 150 W/m · K, is becoming an appealing alternative to alumina. Its coefficient of thermal expansion (CTE) of 4.7 ppm/°C, which is closer to silicon's and GaAs's CTE. It can be used for single-layer and multilayer thin-or thick-film technologies. AlN substrate also utilizes refractory metallizations, firing at 1800°C. AlN powders are currently more expensive than alumina and result in higher substrate cost. In addition, the electrical loss could be high and the thermal conductivity can be degraded substantially, with processing variations.

1.2.4. Polymers. Laminated substrates are being used widely for personal communication systems (PCS) appli-

Table 5. Properties of Soft Substrate Materials

	CTE \times $10^{-6}/^{\circ}\text{C}$	Thermal Conductivity $(\text{W/m} \cdot \text{K})$	Dielectric Constant ϵ_r (10 GHz)	Tan $\delta \times 10^{-4}$ (10 GHz)
PTFE ^a	17	0.257	2.33	13
Filled PTFE ^b	35	0.31	3.5	26
FR4 ^c	15.8	0.2	4.7	300
Polyimide ^d	16	0.043	4.2	150

^aDi clad 870 by Arlon Materials for electronics division.

^bAR 350 by Arlon Materials for electronics division.

^cFor properties of FR4 refer to *Microelectronics Packaging Handbook* [edited by R. R. Tummala and E. J. Rymaszewski, Van Nostrand-Reinhold, New York, 1989].

^d85N Arlon Materials for electronics division.

cations. Their well-established manufacturing infrastructure can be accessed by module designers. The typical substrates can be PTFE, FR4 and polyimide. Their properties are listed in Table 5. Their CTEs are very large and thermal conductivities are poor, so reliability issues should be considered during module design. For low-loss modules, PTFE with different fillers can be used.

In addition to the properties discussed above, another major concern regarding the materials is dimensional stability. RF performance is affected by the variations of dimensions such as the length and the width of a line, the shape of a line's cross section, the spacing among lines, the diameter of a via, surface roughness, and many other geometric parameters. In particular, performance in millimeter-wave modules is strongly dependent on dimensional stability. For these applications, HTCC, LTCC, and plastic packages might not be good choices; their structural shrinkage or expansion could cause performance degradation. Rigorous process control is needed to limit the dimensional change during manufacturing. Or, thin-film packages could be used. Even for the thin-film interconnects, tight process control or new processing techniques may be a needed. For example, reactive-ion etching (RIE) instead of a wet etching process may be used to fabricate a precise structure for superior performance [7].

1.3. Assembly Technologies

The first-level (device-to-package) assembly technologies are wire bonding, tape-automated bonding (TAB), and flip-chip soldering or bonding. The second-level (package-to-board) assembly technologies can be through-hole or surface mount. The surface-mounted packages can be leaded or leadless peripheral, ball-grid-array (BGA), chip-scale-package (CSP), or direct chip assembly (DCA). The major challenge to the assembly technology to control its effect on the package performance. Since the unique RF requirements of the second-level packaging are very similar to those of the first-level packaging, only the requirements for the wire bonding, TAB, and flip-chip assembly will be discussed.

1.3.1. Wire Bonding. Wire bonding technology is the earliest and by far the most prevalent technology (>90%) in use today. A typical microwave chip and wire intercon-

nect utilizes 18–25- μm diameter gold wire, which is ball or wedge bonded to gold-plated die and substrate bondpads. The very narrow wires are highly inductive at higher frequencies, and variations in wire length and loop shapes cause performance variations from module to module [13]. Length and impedance control are critical issues.

1.3.2. TAB. Tape-automatic bonding (TAB) technology is commonly utilized in commercial products requiring lightweight, thin packaging. TAB is typically a reel-to-reel process using solid copper tape or copper prepatterned on a polyimide film. The inner leads of the tape are bumped and bonded to the die pads. Finally, the bonded assembly is encapsulated and the outer leads are bonded to a printed wiring board [13]. The coplanar film carrier can be made for TAB RF packaging, which has an insertion loss of less than 0.2 dB/mm without resonance over the frequency range from DC to 30 GHz. The electrical performance of a GaAs MMIC module with coplanar film carrier is almost equal to that of an MMIC measured directly on wafer [14].

1.3.3. Flip-Chip Assemblies. Flip-chip technology provides a direct metallurgical interconnect between die bondpads and the substrate. Solder-bumped die are soldered or bonded directly to the substrate, providing an excellent electrical connection.

The thermal path is through the solder connection to the substrate. In the case of high-power GaAs MMICs, without the use of thermal bumps, this thermal path is usually inadequate for reliable operation [13]. However, flip-chip assembly is becoming more and more important with the following advantages [15–17]:

- Automated assembly
- Compact modules
- Minimum interconnect length
- Low inductance and discontinuity
- Compatibility with coplanar interconnects without the use of thin devices
- Efficient thermal management with the use of thermal bumps

RF packaging is very challenging because of the wide spectrum of operation frequencies and strong packaging effects on RF performance. For example, the number of I/Os is substantially less than those for microelectronics; however, it is still very difficult to switch from wire bonding to flip-chip assembly. Such a switch is a paradigm shift, demanding reconsideration of not only package but also device designs. The microstrip lines on an MMIC should be replaced by coplanar waveguides. More important, placement of high-power dissipation MESFETs or other devices should be close to the flip-chip joints. Trade-off considerations on RF performance and reliability must be taken into account before any package design. These two issues are to be discussed in the following sections.

2. PERFORMANCE OF RF PACKAGES

At microwave and higher frequencies, packaging can affect the RF performance of circuit significantly. RF parameters of the package are frequency-dependent. Insertion loss, return loss, package resonance frequency, and crosstalk caused by electromagnetic coupling are measures of RF performance. As frequency increases, packaging can become the limiting factor of electrical performance by degrading signal propagation, or by contributing to structural configuration that fosters cavity resonances or that propagates waveguide modes.

2.1. Single-Chip RF Package

Even though RF performance of multichip modules (discussed later) is superior [3] to that of single-chip package to some extent, the single-chip package is still useful due to several reasons [3]:

1. Electrical response of a packaged device is more reproducible and defined. Bondwire and mounting techniques affecting RF characteristics can be defined.
2. Die performance can be tested and validated.
3. Each package can be designed for machine handling.
4. Packages assembled are usually reworkable.

2.1.1. RF Structure of the Package. Figure 8 illustrates typical RF components for a single-chip package. An RF/MMIC chip (die) may be a single device or an integrated circuit consisting of several devices. The chip is bonded to pads on the substrate by using wire/ribbon bonding of flip-chip bonding technology. Transmission lines on the package substrate carry the signal in or out of the chip. Microstrip lines or coplanar waveguides (CPWs) can be used. Bias and control signal lines are also fabricated on

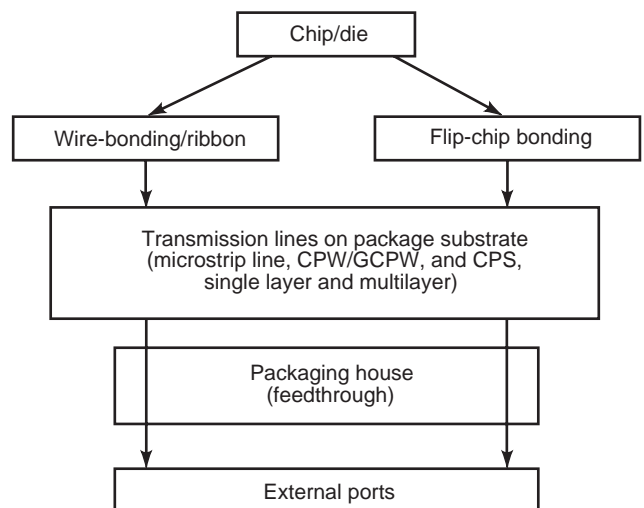


Figure 8. Block diagram of RF components for a general single-chip RF package. Each block represents a critical package element that affects the RF performance of a packaged RF device.

the package substrate. The package substrate can be either single-layer or multilayer. For a multilayer substrate, vertical vias are needed to carry the signal or DC power through different layers. The substrate is enclosed in the metal or ceramic housing with external ports. Feedthroughs are needed to carry the RF and other signals in and out through the package housing. A stripline structure is a common choice for these feedthroughs. External ports can be miniature coaxial connectors, through-hole leads, or solder joints for the next level packaging (see Fig. 2).

2.1.2. Bondwire and Flip-Chip Interconnect. Bondwires/ribbons and flip-chip interconnects provide electrical connections between a chip and a substrate. Figure 9 shows the comparison of effect of wire bond length and flip-chip interconnects on insertion and return losses. The insertion loss (S_{21}) in two-port RF circuits is found by driving port 1 with an incident wave of unit amplitude, and measuring the transmitted wave voltage amplitude, coming out of port 2, when port 2 is terminated in matched load to avoid reflection. The return loss (S_{11}) is, similar to the insertion loss, the ratio of the amplitude of the wave reflected from port 1 to the incident wave voltage amplitude to port 1 when port 2 is terminated in matched load. The return loss (S_{11}) and insertion loss (S_{21}) are widely used in RF engineering as measures of RF performance. As observed in Fig. 9, the flip-chip interconnect typically results in better performance, particularly for frequencies higher than 4 GHz [7]. Most of the discussions in the literature concentrate on S_{21} effects. However, to ensure a minimum amount of standing waves in the assembly and, hence, the most uniform behavior across a wide range of frequencies, S_{11} should be less than -20 dB across the entire passband of

interest. Here again, wire bonds of all lengths perform poorly in comparison with flip-chip interconnects for frequency above a few hundred megahertz.

2.1.2.1. Bondwire or Ribbons. Wire bonding is the most widely used method of connecting a chip to a package. A typical bondwire is around $300 \mu\text{m}$ long and $200 \mu\text{m}$ high. This length includes a margin of error due to (1) the height difference between the chip and the substrate, (2) chip contact pads' locations, and (3) an extra length needed to avoid a mechanical failure during thermal cycling. The inductance of the wire length may degrade the electrical performance of the RF chip. Wire bond inductance can be calculated using the following formula (18)

$$L_s = 5l \left[\ln \left(\frac{2l}{p} \right) - \frac{3}{4} \right]$$

where L_s is the self-inductance with the unit of nH, l is the length of the wire in inches, and p is the diameter of the wire in inches. Figure 10 shows calculated return loss and insertion loss of bondwire and bond ribbon interconnect versus normalized wire length L/λ_0 (19). An interconnect with a return loss better than -10 dB requires bondwires not longer than $0.033\lambda_0$, which is only $100 \mu\text{m}$ at 94 GHz. Bond ribbon has better performance; the limit on the length in this case is $0.063\lambda_0$ for -10 dB return loss (19).

2.1.2.2. Flip-Chip Interconnects. The use of CPW line on the chip and the substrate is the key step that allows applying flip-chip as an alternative interconnect technique for RF systems. In CPW, the ground conductors are on the same plane as the signal strip. Microstrip line is more

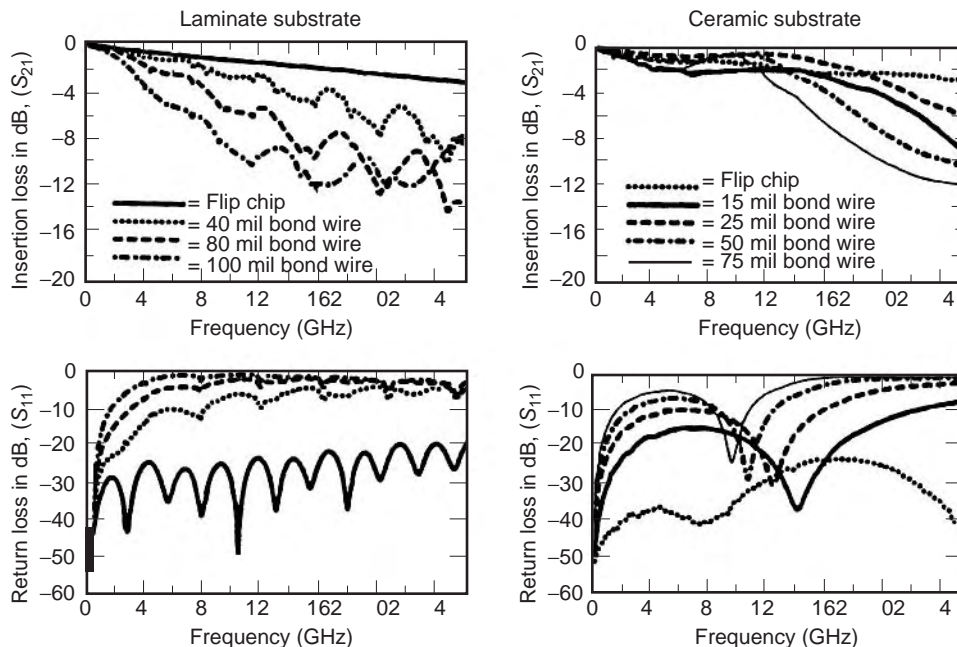


Figure 9. Insertion loss and return loss for flip-chip and bondwire interconnects with RF chips mounted on a laminate or a ceramic substrate. The losses are strongly dependent on the assembly technologies, substrate materials, and operating frequencies. This figure can be used to estimate losses in a typical RF package. (From Ref. 7, © IEEE 1997, reprinted with permission.)

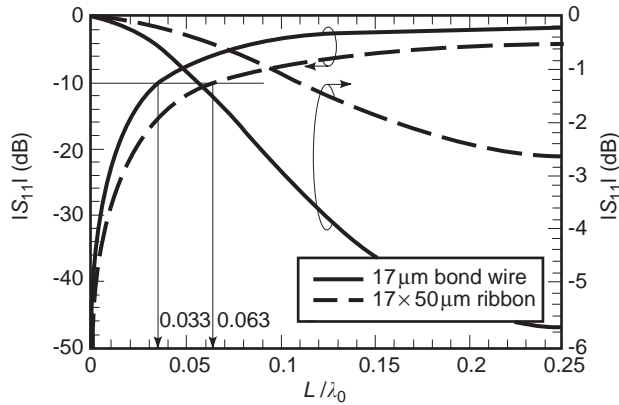


Figure 10. Calculated return and insertion losses of bondwire and bond ribbon interconnect versus normalized wire length L/λ_0 . This figure can be used to estimate the right wire length for desirable losses. (From Ref. 19, © IEEE 1996, reprinted with permission.)

commonly used in RF packages. Therefore, flip-chip interconnects are also used with microstrip. Because the ground conductor and signal strip line are not on the same plane in the microstrip line configuration, vias are needed to connect the ground planes on the chip and package substrate. Therefore, most of the comments in this section are limited to CPW flip-chips. Figure 11 shows the structure of flip-chip interconnect on CPW and microstrip lines. The bump height (50–75 μm) is small compared with the length of bondwire, and the bump diameter (40–150 μm) is larger than that of the bondwire. Therefore, a considerable improvement in the electrical interconnect properties is achieved. The return loss is less than -10 dB at 100 GHz for bump height 70 μm and bump diameter 40 μm [19]. However, chips are flipped so the substrate is very close to the chip. When the fields of the transmission lines on the chip interact with the mounting substrate, the RF performance of the chip can be affected for several reasons: (1) transmission lines on the chip, (2) the gap between the chip and the substrate, (3) the transition into the chip’s transmission lines, (4) chip thickness, (5) transmission lines or other structures on the substrate under chip, and (6) dielectric constants of the chip and the substrate. The change in line impedance for the flipped versus the unflipped cases is larger than 5% for microstrip line on GaAs with width 254 μm and airgap 100 μm [20]. When a CPW is used as the transmission line for MMICs, the fields in the CPW are well confined within the gaps on the CPW and narrower line widths and gaps are possible for a desired line impedance at the expense of higher transmission-line loss. The change in the impedance for CPW on GaAs is less than 0.53% up to 50 GHz with the width 14.2 μm, gap 15.42 μm, and airgap 100 μm [20]. As the airgap between the substrate and the chip is reduced, more field fringes into the substrate, which reduces the line impedance; the optimum airgap is about 100 μm for CPW with width 76.2 μm and gap 50.8 μm [20]. For protecting the chip from the environment and for increasing the connection reliability, an underfill epoxy can be used for flip-chip interconnects. The effect of underfill for RF

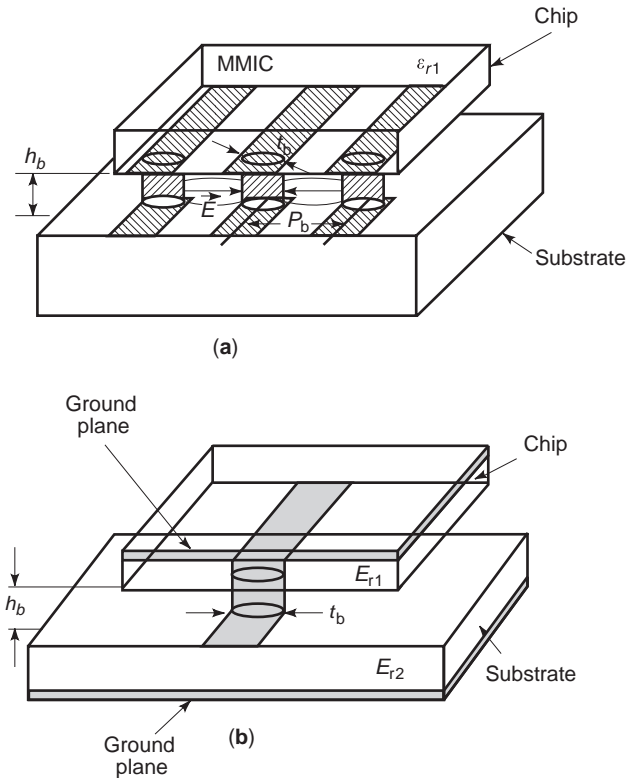


Figure 11. (a) Structure of flip-chip interconnect on a coplanar waveguide (CPW) with h_b as the bump height, P_b as the bump pitch, and t_b as the bump diameter. Three solder bumps are needed for one RF and two ground connections. (b) Structure of flip-chip interconnect on a microstrip line. A single solder bump is needed for the RF connection. (From Ref. 19, © IEEE 1996, reprinted with permission.)

performance of chips has been reported [16,17,21]. A lumped-element model of flip-chip joint is available [22].

2.1.3. Transmission Lines on Package Substrates. Microstrip line is widely used for MMICs and MCMs, but recently the CPW and coplanar strip (CPS) have been shown to be appealing alternatives. A brief discussion about microstrip line, CPW, and CPS is given below. Detail descriptions of these transmission lines are available in other articles in this encyclopedia.

2.1.3.1. Microstrip Line. The microstrip line is the most commonly used transmission line for MMICs; it is formed by a strip conductor of a width of W and thickness t , situated on the topside of a planar dielectric substrate and a ground conductor (see Fig. 12).

Given the dimensions of the microstrip line, the characteristic impedance can be calculated as [23].

$$Z_0 = \frac{60}{\sqrt{\epsilon_e}} \ln \left(\frac{8d}{W} + \frac{W}{4d} \right) \text{ for } 1 \geq W/d$$

$$= \frac{120\pi}{\sqrt{\epsilon_e} [W/d + 1.393 + 0.667 \ln(W/d + 1.444)]}$$

for $W/d \geq 1$

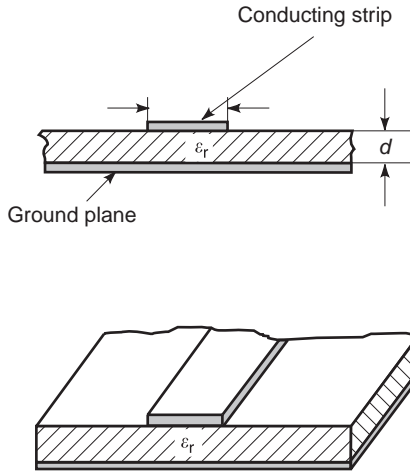


Figure 12. Geometry of a microstrip line with d as the substrate height, W as the width of the conducting strip, and ϵ_r as the relative dielectric constant of the substrate. The impedance of the line is determined by these three parameters.

where W is the width of the strip in microstrip line, d is the thickness of substrate, and ϵ_e is the effective dielectric constant of a microstrip line, which is given approximately by

$$\epsilon_e = \frac{\epsilon_r + 1}{2} + \frac{\epsilon_r - 1}{2} \frac{1}{\sqrt{1 + 12d/W}}$$

where ϵ_r is the dielectric constant of the substrate.

Given characteristic impedance Z_0 and dielectric constant ϵ_r , the W/d ratio can be found as

$$\begin{aligned} \frac{W}{d} &= \frac{8e^A}{e^{2A} - 2} \text{ for } W/d < 2 \\ &= \frac{2}{\pi} \left[B - 1 - \ln(2B - 1) + \frac{\epsilon_r - 1}{2\epsilon_r} \right. \\ &\quad \left. \times \left(\ln(B - 1) + 0.39 - \frac{0.61}{\epsilon_r} \right) \right] \\ &\text{for } W/d > 2 \end{aligned}$$

where

$$\begin{aligned} A &= \frac{Z_0}{60} \sqrt{\frac{\epsilon_r + 1}{2}} + \frac{\epsilon_r - 1}{\epsilon_r + 1} \left(0.23 + \frac{0.11}{\epsilon_r} \right) \\ \text{and } B &= \frac{377\pi}{2Z_0\sqrt{\epsilon_r}} \end{aligned}$$

Microstrip line is used for frequencies below 60 GHz with impedance ranging from 15 to 120 Ω [24]. Because the ground plane is usually fabricated on the backside of the chip or the component, it is necessary to fabricate via holes to connect ground bonding pads and the backside. Such via processing is expensive and susceptible to thermal mismatch-induced stresses.

2.1.3.2. CPW. The structure of a coplanar waveguide (CPW) is shown in Fig. 13. It consists of a signal conductor placed between two ground planes. All the three conductors are deposited on one side of a dielectric substrate. The dominant mode on a CPW is quasi-TEM at low frequencies [25]. For an ideal case, when the ground planes are very wide relative to the slot spacing S and the dielectric substrate is much thicker than S , the characteristics of the CPW can be determined by conformal mapping techniques [25]. The capacitance of the CPW is given by [25]

$$C = 4\epsilon_0 \frac{(\epsilon_r + 1)}{2} \frac{K(\kappa)}{K'(\kappa)}$$

where $K(\kappa)$ and $K'(\kappa) = K(\kappa')$ are the complete elliptical integrals of the first kind. The modulus $\kappa = S/(S + 2W)$ with gap S and width of signal conductor strip W . Consequently, the characteristic impedance is given by

$$Z_0 = \frac{120\pi K'(\kappa)}{\sqrt{\epsilon_e} K(\kappa)}$$

where ϵ_e is the effective dielectric constant for the CPW ($= (\epsilon_r + 1)/2$). Design equations for CPW with general dimensions are complex and available in Ref. 25, Section 2.1.4. Since the CPW is used in circuits with a higher integration density, attention has been paid to the effect of the distance between the top metal and CPW substrate and of the finite width of conductors on the line parameters [26].

The principal advantages of CPW are [27]: (1) easier construction using thicker substrates without via holes; (2) good grounding for integrated active devices; (3) compatibility with flip-chip assembly technology; (4) less radiation at discontinuities, low conductor loss in some cases, and less dispersion as compared with the microstrip line; and (5) reduced coupling between different lines in

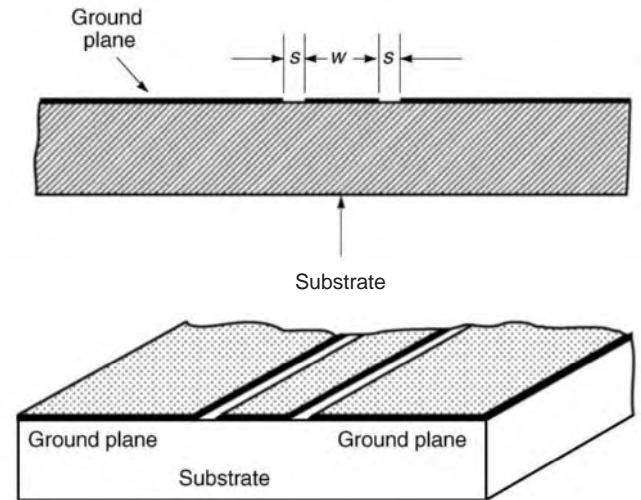


Figure 13. Structure of a CPW transmission line with W as the width of the center conducting strip and S as the spacing between the grounding plane and the center strip. The impedance of the line is determined by these two parameters and the effective dielectric constant of the substrate.

the same metallization layer [28]. One of major problems with CPW is that a balanced coupled-slotline mode can be excited at nonsymmetric discontinuities. This mode can be avoided by incorporating grounding straps between the ground planes, using either airbridges or underpasses [27]. Number and optimum placing of ground straps are issues of design.

2.1.3.3. Coplanar Strips. A coplanar strip (CPS) transmission line consists of a pair of strip conductors of width W and separated by a narrow slot of width S on a dielectric substrate, as shown in Fig. 14 [29]. As a balanced transmission line, it is ideally suited to balanced mixers and push-pull amplifiers. CPS has several advantages over conventional microstrip line and CPW [29]. It facilitates shunting as well as series mounting of active and passive devices and eliminates the need for wraparound/via holes, which introduce additional parasitic elements. In short, CPS has all the advantages of CPW. In addition, CPS makes efficient use of the wafer area, so the die size per circuit function is small. This results in lower cost and larger number of circuit functions for a given die size. Also, CPS propagation parameters are independent of the substrate thickness beyond a certain critical thickness that simplifies heatsinking and circuit packaging. CPS does not require grounding, which is an appealing feature for high-density interconnects. However, the lack of design information has severely restricted its use. More important, transitions from CPS to microstrip/CPW in real applications are very difficult because CPS is a balanced line without a ground plane.

2.1.3.4. Multilayer Substrate. A multilayer substrate consists of thin dielectric layers and metal conductors formed on a wafer surface. These metal transmission lines and ground planes are connected through vertical via holes. Using multiple dielectric and metal layers, it is possible to get an increased flexibility in circuit layouts, reduce the package size, get more flexible means of interconnect, and maintain low cost. Since the ground plane is used between the signal layers, the crosstalk among the signal lines is reduced. A typical multilayer substrate with microstrip lines and striplines (discussed later) is shown in Fig. 15 [30]. Analysis methods for mul-

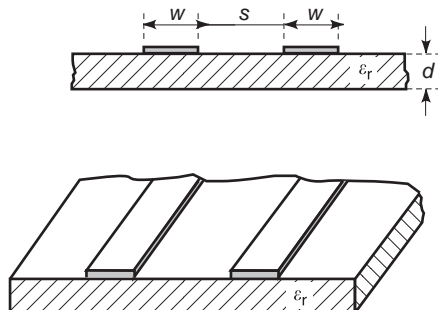


Figure 14. Structure of coplanar strip (CPS) transmission line with W as the width of each strip, S as the spacing between the strips, and d as the thickness of the dielectric substrate.

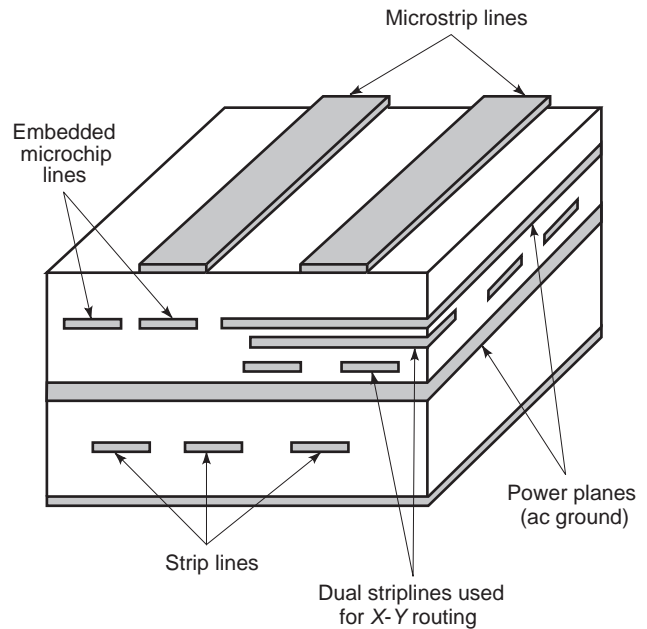


Figure 15. A typical multilayer substrate using microstrip lines and striplines as transmission lines. The substrate is used to interconnect RF packages or bare devices. (From Ref. 30, © ASME 1997, reprinted with permission.)

tilayer substrates can be found in Ref. 31. Additional discussions about the multilayer substrate will be presented later.

2.1.3.5. Crosstalk. When frequency increases, the signal energy is not confined to the transmission lines, but gets coupled from one line to others, including the DC powerlines. Coupling generally occurs in an unintended manner. The energy can be coupled to undesired propagating modes in the complicated waveguide structure formed by the package. This can result in spurious resonances in the package housing. A signal that is unintentionally coupled to the neighboring lines is called *crosstalk*, a term derived from telephone networks, where faint conversations might be heard from other lines.

Crosstalk actually arises from both the distributed capacitive and the inductive couplings of approximately equal magnitudes [32]. Although it may be easier to visualize the electric field of mutual capacitance between adjacent lines, it should be recognized that there is also a corresponding magnetic field coupling between the adjacent lines. When signal energy travels in one direction on the primary line, the portion of the signal coupled into the adjacent line travels in both directions. The magnetic coupling is important to understand the difference between the capacitive and inductive crosstalk at the two ends of a coupled line. The mutual capacitance coupling is in phase with the signal on the primary line at both ends. However, the inductively coupled lines are essentially the primary and secondary of a transformer due to mutual inductance coupling, although both sides of this transformer have only a single “turn”. Therefore, the two ends of the induc-

tively coupled secondary have opposite signal polarities [6]. Practical circuits often consist of numerous lines, which may be in proximity. Hence the space between lines should be considered for design of microstrip, CPW, or other interconnects in a package. A typical method for reducing spurious coupling is to restrict the routing of conductor lines on adjacent layers to orthogonal directions, so that signals cross only at 90° angles and the coupling is minimized. Also, in the multilayer structure the dielectric layers should be optimized in order to minimize coupling between the lines [33]. Grounded isolation lines, which convert the microstrip line into coplanar waveguide with finite size strips, can be used to reduced the coupling between lines in the same layer [26,34].

2.1.4. Housings for RF Packages. RF chips are generally enclosed in a package housing which is metallized on walls to shield the chips from outside EM fields. Because the package housing is almost completely metallized, it can be considered to be a rectangular metal waveguide cavity. Signal energy can be coupled to propagating modes in the complicated waveguide structure. Such a coupling may result in a resonance in the package with undesirable consequences such as power loss, poor isolation, and circuit instabilities. Therefore, package electrical performance is not only associated with the transmission-line design and functions of chips, but also affected by package housing geometry and intrinsic material properties [4].

The resonance frequencies of the TE_{mnl} or TM_{mnl} modes in a rectangular enclosure without a dielectric substrate is given by [23]

$$f_{mnl} = \frac{c}{2\pi} \sqrt{\left(\frac{m\pi}{a}\right)^2 + \left(\frac{n\pi}{b}\right)^2 + \left(\frac{l\pi}{d}\right)^2}$$

where *c* is the velocity of light and *a*, *b*, and *d* are the dimensions of the cavity in *x*, *y*, and *z* directions, respectively. If *b* < *a* < *d*, the TE₁₀₁ model will be the dominant resonant mode with the lowest resonance frequency *f*₁₀₁. In RF packages, to improve end-to-end isolation and raise cavity resonance frequencies, a large cavity is divided into some subcavities, with partition walls surface-mounted to the substrate and grounded with a row of vias [35]. For example, an empty package housing of 27.94 × 53.85 mm has a resonance frequency of about 6.0 GHz. But the resonance frequency of the 27.94 × 14.22 mm empty housing is approximately 11.8 GHz. When a dielectric substrate is inserted in the package cavity, the resonance frequency of the cavity is modified. If the substrate is placed in contact with the bottomwall of the package and has a thickness much smaller than the height of the package, the modified resonance frequency *f*_r is given by [36]

$$f_r = f_{101} \left[1 - \frac{d}{b} \left(\frac{\epsilon_r - 1}{\epsilon_r} \right) \right]^{1/2}$$

where *f*₁₀₁ is the resonance frequency for TE₁₀₁ mode, *d* is the thickness of the substrate, *b* is the cavity height, and *ε*_r is the dielectric constant of the substrate. In the formulas above, the effect of chips, imperfect cavity endwall (for

feedthroughs), and interconnections and passive circuits on the substrate on the resonance frequencies have not been considered. A full-wave simulation is needed to accurately predict the resonance frequencies of a package [35].

2.1.5. Feedthroughs/Ports in Housing. A design requirement of feedthroughs, which bring the signals through a package sidewall to external ports, is to provide controlled RF impedance and minimize the DC/RF losses. A stripline is used where a planar strip penetrates the dielectric-filled hole in the metal wall. Given the desired characteristic impedance of the stripline, spacing between the ground planes *b*, and dielectric constant *ε*_r, the ratio of the strip width *W* to the spacing *b* (see Fig. 16b) is given as [23]

$$\frac{W}{b} = \frac{30\pi}{\sqrt{\epsilon_r} Z_0} - 0.441 \text{ for } \sqrt{\epsilon_r} Z_0 < 120$$

$$\frac{W}{b} = 0.85 - \sqrt{1.041 - \frac{30\pi}{\sqrt{\epsilon_r} Z_0}} \text{ for } \sqrt{\epsilon_r} Z_0 > 120$$

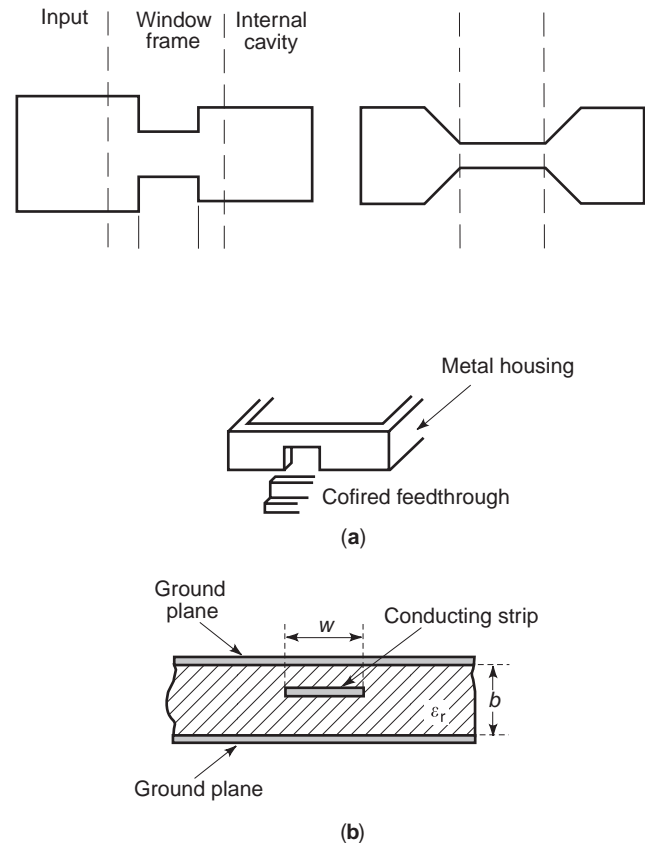


Figure 16. (a) Typical microstrip–stripline–microstrip feedthroughs. There are two different transitions to connect different linewidths. The tapered transition has lower losses than those with the sharp transition. A typical configuration for the transition consists of the metal housing and the cofired feedthrough. (b) Cross-section of a stripline commonly used for a feedthrough. (From Ref. 2, © Artech House 1989, reprinted with permission.)

Different microstrip–stripline–microstrip feedthroughs are shown in Fig. 16a. Loss properties of the ceramic substrate and physical dimensions of the feedthrough structure could attenuate the high-frequency signal as it travels along the feedthrough. Microstrip–stripline–microstrip feedthroughs behave like lowpass filters. The cut-off frequency is determined by the physical, geometric, and material properties of the structure [2,4]. Coaxial feedthroughs can also be used for RF packages [2].

2.2. RF Multichip Module (MCM) Packages

2.2.1. Types of MCMs for RF Circuits. Multichip modules are substrates of dielectric and conducting layers, on which integrated circuits (“chips”) and passive components (if any) are mounted directly on (or inside) the substrates, without separate packaging of each of the active components. That is, the chips are mounted “bare” onto the MCMs, which then provide the required power and ground, as well as all the signal interconnects and the electrical interface to the external environment. There are three kinds of MCMs:

1. Laminate MCMs (MCM-Ls) are manufactured through the lamination of sheet layers of organic dielectrics. These MCMs exhibit very low line losses up to relatively high frequencies because the lines are thick and wide; however, the vias are typical quite tall and also much wider than the lines, thus causing substantial impedance discontinuities and signal reflections for frequency components above 500 MHz.
2. Ceramic MCMs (MCM-Cs) are manufactured by stacking unfired layers of ceramic dielectric, onto which liquid metal lines are silk-screened using a metal ink process. The individual inked layers are then aligned, pressed together, and “cofired” at 800–900°C, or 1500°C to 1600°C into a solid planar structure. Vias in these MCMs are also tall and wide,

resulting in substantial impedance discontinuities and signal reflection for frequencies above 500 MHz.

3. Deposited MCMs (MCM-D) are manufactured through the deposition of organic or inorganic dielectrics onto a silicon or alumina support substrate. After each dielectric layer is deposited, one of several techniques is used to pattern metal lines as well as metal “vias,” which penetrate the dielectric layer to connect adjacent metal layers [7]. The chips are then mounted on the upper surface using wire bonding/TAB or flip-chip bonding technology. In MCM-D, line cross sections are smaller than those in MCM-C or MCM-L. The small cross section results in higher resistive line losses. However, the via heights are quite small, and the via cross sections are comparable to the linewidths, resulting in low levels of impedance discontinuity and signal reflections compared with the MCM-Ls and MCM-Cs.

2.2.2. Design Consideration

2.2.2.1. Multilayer Structure/Via for MCM. A multilayer structure is generally needed for an MCM. It is similar to the multilayer substrate for a single-chip package. Because there are more chips on a substrate, the multilayer substrate for an MCM is more complex than that for a single-chip package. Table 6 lists suggested number of layers for different design restrictions [7]. A large number of layers is not desirable because of manufacturing difficulty; four layers are typically used. Vias, interconnects between layers, are lossy (particularly at high frequency) and difficult to model accurately.

2.2.2.2. Power/Ground Noise. Power/ground noise becomes important when circuits are more complex and there are more circuit signal planes sharing one ground plane. A comprehensive understanding of this noise is being developed [37–39]. The noise is not a set of random fluctuations caused directly by the state switching of the

Table 6. Number of Layers versus Design Restrictions

Number of Metal Layers	Design Restrictions	Suggested Layer Assignments
1		
2	Digital systems up to 25–50 MHz; analog microwave designs using microstrip interconnects with no crossovers	1 routing/attach; 1 shared power/ground plane
3	Digital system up to 50 MHz with split-plane power delivery; analog microwave designs using microstrip interconnects	2 routing; 1 shared power/ground plane
4	Digital system up to 1 GHz; analog microwave system requiring microstrip and stripline interconnect.	2 routing; 1 shared power; 1 ground plane
5	Digital system up to 2.5 GHz; most analog microwave systems	2 routing; 1 shared power; 2 ground plane
6	Digital system up to 10–12 GHz; analog microwave systems up to 12–16 GHz	2 routing; 2 shared power; 2 ground plane
7	All digital and all analog or mixed signal designs are feasible	2 routing; 1 routing/attach; 1 power plane; 2 ground planes; 1 integrated small capacitor and/or embedded resistor layer
8	All digital and all analog or mixed signal designs are feasible	2 routing; 1 routing/attach; 2 power plane; 2 ground planes; 1 integrated small capacitor and/or embedded resistor layer

(From Ref. 7, © IEEE 1997, reprinted with permission.)

digital chips; but a complex resonance behavior of an essentially high Q circuit with a very large number of resonant modes, which are pumped by harmonic components in the state switching currents [37].

Many proposed next-generation analog or mixed-signal systems have been demonstrated to be exceptionally sensitive to noise in their power and ground planes [38]. These resonances must be characterized for a complete understanding of this phenomenon. Further, suppression of the resonant modes, at least within the signal passband of interest, is required [38,39].

2.3. EMC/EMI Considerations for RF Packages

Electromagnetic compatibility (EMC) and electromagnetic interference (EMI) issues have been studied for some time. However, only very simple models to characterize EMC/EMI have been proposed [40,41]. The conduction and radiation emission and susceptibility models are still at the component level, and need to be improved to reach the complexity level of real-world problems. The amount of EMI generated by a digital processor is directly related to the edge rates of the signals, the system clock rate, the total amount of switching current, and the size and shielding effectiveness of the device or system. Due to the complexity of an actual processor system, a combined deterministic and statistical approach is necessary to address these problems [7].

3. RELIABILITY

There are two issues related to RF package reliability. One is thermal management to control the temperatures of RF devices. The other is mechanical integrity to ensure reliable connections among different interfaces and low stresses in RF devices. Most thermal and mechanical considerations are the same as those for microelectronic packaging. However, there are unique requirements for RF packaging. These requirements are described in the following sections.

3.1. Thermal Management

Major thermal management challenges for RF packaging are associated with power MESFETs for transmitters. The unique requirements arise because of a very high heat flux.

- At high-frequency operations, power dissipation is high. A single GaAs FET (field-effect transistor) is capable of delivering a CW (continuous-wave) power output of 15 W at 10 GHz. When a few of these FETs are used along with other parts, this problem is compounded. For higher frequencies in the mm-wave spectrum, the combination of high-frequency and poor efficiency make thermal management a top packaging problem to solve. Heat flux higher than 300 W/cm^2 is not unusual [42], which is an order of magnitude higher than a high-power microprocessor's heat flux level.

- Thermal solutions have to meet constraints demanded by the selection of materials and structures for low-loss RF performance, reliable mechanical integrity, and cost. As shown in Tables 4 and 5, AlN has a high thermal conductivity but also high loss tangent and cost. In most cases, designers are not allowed to choose a high thermal conductivity material just for efficient heat removal.
- An RF device's electrical linearity and efficiency can strongly depend on its junction temperature. In some cases it is necessary to control the temperatures within a range rather than below an upper limit [43,44].
- GaAs, the major RF device material, is a poor thermal conductor. Its thermal conductivity of $50 \text{ W/m} \cdot \text{K}$ (at room temperature) is low and can be even lower at high temperatures. For example, at 150°C , GaAs's thermal conductivity can be as low as $31 \text{ W/m} \cdot \text{K}$ [43]. With low-conductivity GaAs, the power dissipated from the FET cannot be spread effectively. As a result, the heat flux to be removed is close to FET level rather than "chip" level, as usually assumed for silicon-based microelectronic chips with the thermal conductivity around $150 \text{ W/m} \cdot \text{K}$ at room temperature. In fact, wire bonded GaAs chips should be thinned, in order to use conductive material to spread the heat from FET directly to the package.

Heat conduction, convection, and radiation are three typical heat transfer mechanisms. For RF packages, heat conduction and convection are usually considered. To analyze the detail temperature distributions in a package, numerical computation is necessary. However, simple analytical solutions can provide a quick estimation to gain an insight into a thermal problem to be solved. A few useful formulas are to be described below.

For one-dimensional (1D) heat conduction through a component, for example, a plate, the thermal resistance is

$$R = \frac{L}{kA}$$

where L is the length of the component, A is the cross-sectional area of the component, and k is the heat conductivity of the component.

Similarly, for 1D analysis, the thermal resistance corresponding to heat convection can be expressed as

$$R = \frac{1}{hA}$$

where A is the surface area subject to heat convection, and h is convection heat transfer coefficient. Typically, h can be assumed to be around $5 \text{ W}/(\text{m}^2 \cdot \text{K})$ for natural air cooling and $20 \text{ W}/(\text{m}^2 \cdot \text{K})$ for forced air cooling in a desktop personal computer (PC) environment.

When different 1D components are thermally connected, a resistor network can be established to estimate their overall thermal performance. However, when two 1D components with different cross sections are connected, an additional thermal resistance, constriction resistance, needs to be considered. For instance, the additional ther-

mal resistance for a circular heat source in contact with a heat spreader is

$$R = \frac{1}{2\sqrt{\pi rk}}$$

where k is the thermal conductivity of the thermal spreader, and r is the radius of the circular heat source. Examples of how to use these formulas to estimate thermal performance will be presented in Section 4.

3.1.1. Plastic Packaging with Die Attachment. As stated by Pavio et al. [45], a plastic package enables source-to-ground assembly with semiconductor die. Thus, this arrangement supports the direct attachment of a transistor to the package heatsink (or actually a heat spreader). For the lower-power devices (1–2 W), the use of circuit board without additional heat spreading may be adequate. With increasing power levels, other options must be investigated. Figure 17 shows a die bonding to a conductive heat-sink, for example, a Cu slug [42]. Solder has to be used for thermally conductive die attachment, and the copper should be used for efficient heat spreading.

3.1.2. Ceramic Packaging with Die Attachment. Ceramics usually have a higher thermal conductivity compared with plastics and, in some conditions, can be directly used as heatsink. If the heat flux is very high, a more conductive heat spreader may be needed. For example, an AlN heat spreader can be inserted between a thinned GaAs chip and an alumina substrate, as shown in Fig. 18. More details on different materials for such heat spreading are to be discussed later on.

3.1.3. Flip-Chip Package. Flip-chip assembly is well known for its difficulty in removing heat from the chip. In fact, if the RF device is designed properly, the flip-chip assembly is thermally better than the wire bonded assembly. As shown by Gupta [42], the GaAs MESFET chips typically have a central active area of interdigitated source–gate–drain structures (Fig. 19), at which steady-state heat dissipation densities of up to 300 W/cm² are encountered. The prevalent interconnect/package scheme for these power amplifier chips involves die bonding to a

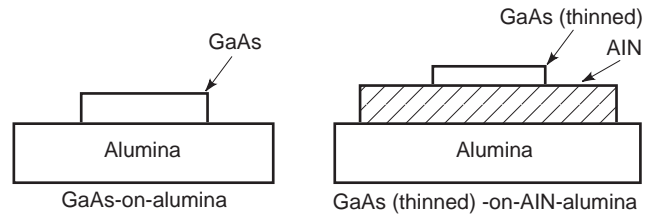


Figure 18. A high-conductivity AlN heat spreader used between thinned GaAs chip and alumina substrate to reduce thermal resistance. The AlN heat spreader has higher thermal conductivity and larger area than those of GaAs chip. Its insertion between the thinned GaAs and alumina reduces the thermal resistance between the heatsource and heatsink.

conductive heatsink, for example, a Cu slug (see Fig. 17). In order to remove intense heat through the die-bonded GaAs chip, additional care needs to be taken, due to the poor thermal conductivity of GaAs. In order to extract heat divergently through the back of the power amplifier chip to the Cu pedestal on which it is die-bonded, the die has to be thinned considerably (e.g., 50 μm) by back-grinding and chemical etching. Due to the brittleness of GaAs, this additional operation may involve yield loss after wafer fabrication.

Flip-chip interconnect is an alternative to the back-grinding of a GaAs chip. Because the active area of the GaAs chip is around the surface of the chip, flip-chip bumps can be used to directly remove the heat. In some conditions, where the power dissipated in the device is so high that the flip-chip bump may be not sufficient to remove the heat, a thermal bump has to be introduced to help remove the heat (Fig. 19). With a high-thermal-

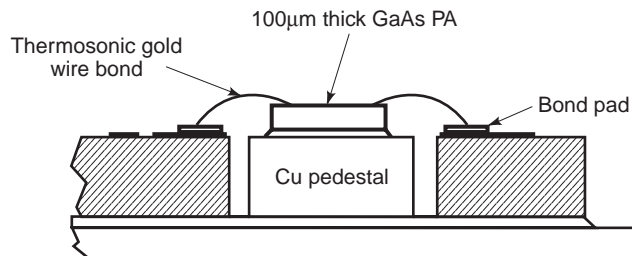


Figure 17. A typical packaging method for GaAs power amplifier chips using die bond to heatsink and gold–gold wire bond. The heat sink connected to the copper (Cu) pedestal is used to extract heat divergently through the back of the power amplifier. (From Ref. 42, © IEEE 1989, reprinted with permission.)

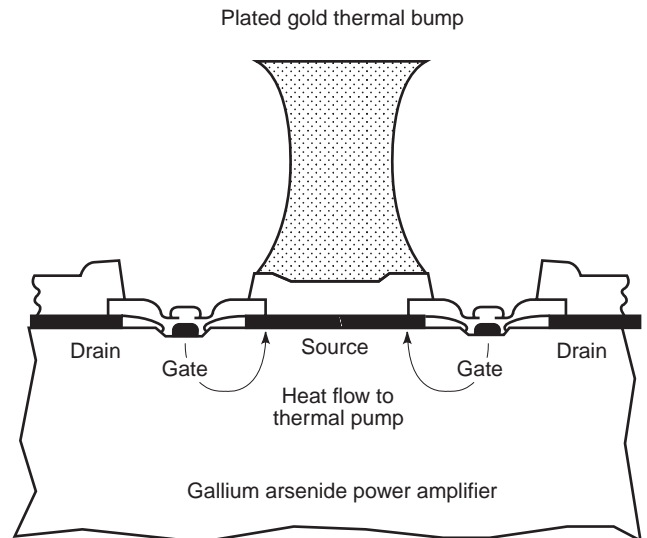


Figure 19. A gold-plated thermal bump on source fingers of a power amplifier. The thermal bump with high thermal conductivity is located close to the heatsource and is directly connected to a heatsink. This bump greatly reduces the thermal resistance between the heat source and heat sink. (From Ref. 42 © IEEE 1989, reprinted with permission.)

conductivity thermal bump (usually made by gold or silver), the thermal resistance from the GaAs chip to the heatsink substrate could be minimized.

3.2. Mechanical Integrity

Compared with microelectronic packaging, the mechanical integrity issues of RF packaging have the following unique features:

- The length scale of thermal mismatch is smaller. Typical sizes of RF chips and packages are smaller than those of microelectronic chips and packages. Therefore, thermal induced stresses/strains could be small.
- For efficient thermal management, mechanically poor materials have to be used for die attachment. For example, they may be highly conductive materials, such as solder, epoxy with added metal, or glass with added metal. In addition, any delamination could degrade heat conduction and increase temperature gradient across the die attachment. The increase could worsen the delamination and destroy the RF device.
- Mechanical solutions have to meet constraints demanded by the selection of materials and structures for low-loss RF performance, efficient thermal management, and cost. For example, underfill epoxy can enhance the fatigue life of flip-chip assembly using Duroid as the substrate [17]. However, the epoxy could degrade the RF performance with additional losses. If these losses are not acceptable, an alumina substrate needs to be used for reliable assembly without the underfill epoxy.
- GaAs is the main RF device with poor mechanical properties; it is brittle and susceptible to cracking. With its poor thermal conductivity, a large temperature gradient in the device can result from high power dissipation and damage the device.

RF packages have different mechanical characteristics, as mentioned above. However, the tradeoff design techniques are the same as those for microelectronic packaging. Delamination and fatigue are main concerns. These problems are well covered elsewhere, so only solder joint fatigue will be described briefly. Most discussions will focus on die cracking problem closely related to GaAs devices. The die cracking can occur at a die edge, at a via, and at a notch or a flaw due to stress concentration.

3.2.1. Solder Joint Fatigue. For a typical flip-chip assembly, the fatigue life of the solder joints is a major reliability concern. To estimate the solder fatigue life, numerical computation using finite-element methods (FEM) is necessary. However, some simple formulas can be used to illustrate the fatigue problem and to quickly estimate the fatigue life. The Coffin–Manson relationship is popularly used to estimate the fatigue life of a solder joint in a flip-chip assembly with different thermal expan-

sions of the chip and the substrate. It is expressed by

$$N_f = \frac{1}{2} \left(\frac{\Delta\gamma}{2\varepsilon_f} \right)^{-1/C}$$

where N_f is the fatigue life of the solder joint in terms of number of thermal cycles, $\Delta\gamma$ is total shear strain range, ε_f is fatigue ductility coefficient (which is the maximum strain resulting in a failure in one cycle; it is approximately 0.325 for Sn/Pb eutectic solder), and C is fatigue ductility exponent (which is 0.442 for the eutectic solder). The shear strain range caused by mismatch of thermal expansions of the chip and the substrate can be estimated by

$$\Delta\gamma = \frac{L(\alpha_1 - \alpha_2)\Delta T}{h_C}$$

where L is the distance between the solder joint and the neutral point of the assembly, α_1 is the CTE (coefficient of thermal expansion) of the substrate, α_2 is the CTE of the chip, and h_C is the height of the solder joint.

From these formulas, it is clear that solder fatigue problem is caused by the mismatch between chip's and substrate's thermal expansions during thermal cycling with temperature changes. To avoid the reliability problem, there are typically three design approaches: (1) to choose a substrate with CTE matched to that of the chip, (2) to control the distance from the solder joint to the neutral position, or (3) to increase solder joint height. More details of the solder fatigue will be illustrated in the section entitled Case Study.

3.2.2. Cracking at a Die Edge. Solder is commonly used in RF die attachment because of its high thermal conductivity. Since the CTEs of die, solder, and substrate/heat-sink are different, during thermal cycling, there is a large stress at the edge of the die. This stress, together with the imperfection of the die edge (caused by cutting), may result in a chip crack. Typically, there are vertical and horizontal cracks at the die edge. Vertical die cracks propagate under tensile stress and horizontal die cracks propagate under shear stresses at the edge. Horizontal edge cracks, developed from die-cutting damage, may propagate from the corner of the die to active chip elements and induce device failure. Or, it may propagate horizontally, causing the die to lift. Although die fracture is mainly governed by the size, shape, and defect locations in the die, voids in the attachment material or in the die-attach interface may also result in die fracture hyperverturing the thermal and stress transfer mechanisms [46]. Lee and Matija-sevic [47] developed a technique to produce void-free bonding between GaAs dice and alumina substrate using Au–Sn eutectic solder alloy, which reduced the possibility of chip crack greatly.

3.2.3. Cracking at a Via. For the die attachment using solder, the capillary action causes the vias to fill with molten solder during reflow. Due to the thermal expansion mismatch between the Si/GaAs chip and solder, the chip

may crack around vias during thermal cycling. The propagation of the crack could gradually damage the electrical performance of the device. Pavio [48] studied via cracking in a GaAs chip. The factors affecting the cracking are via size and shape. The problem can be eliminated by controlling the amount of solder which penetrates the via. A critical process window must be developed for each alloy to minimize the amount of solder filling the via, while maintaining sufficient coverage of solder die attachment for efficient thermal management. In addition, a small-size via can reduce the crack potential.

3.2.4. Cracking at a Notch or a Flaw on the Chip. Another cause for die cracking is the notches or the flaws on a chip. The fracture strength of brittle materials is dependent on several factors, the most important of which is the effect of stress concentration on notches and flaws. It is known from fracture mechanics that actual strengths for brittle materials will range $\frac{1}{10} - \frac{1}{1000}$ of that predicted theoretically, because flaws act as stress concentrators. Fractures occur because a crack (flaw) propagates due to the decrease in stored elastic energy associated with crack extension, exceeding the increase in surface energy associated with the formation of new surface. The flaws on the chip are caused by wafer slicing and thinning, which can reduce the mechanical strength of the Si/GaAs chip. Hawkins et al. [49] and Vidano et al. [50] studied the fracture strength of Si and GaAs chip, respectively. They showed that mechanical thinning followed by chemical thinning (etching) can improve chip strength, because the size and population of flaws were reduced by the chemical thinning.

Notches are different from flaws. Notches are features of the design. For example, a sharp angle exists between any two bonded plates with different sizes. The sharp angle would cause stress concentration that could result in crack initiation in a brittle plate.

3.2.5. Crack Prediction. Cracking is a major concern when it comes to ensuring a RF package's mechanical integrity. Unfortunately, there is lack of knowledge of how to control this problem using a quantitative analysis. To characterize cracks initiated from flaws, the stress-intensity approach can be used. For the flaw shown in Fig. 20 the stress intensity factor is $K_0 = \sigma\sqrt{\pi a}$ [51].

For a notch as a designed feature, however, there is no well-established approach. Dunn et al. developed a new approach to characterize stress intensities in a notch for microelectromechanical systems (MEMS) [52]. Such an approach may be useful to understand cracks induced by stress concentration around a notch. In their study, they combined modeling, analysis, and experimental results to establish the crack criteria for a notch. They used the stress intensity factor K to study crack initiation. Cracks initiate for a given notch configuration when the stress intensity factor reaches a critical level K_{cr} . They found K_{cr} to be similar for a given notch angle and material regardless of other geometric factors. Their method may be used to predict crack initiation at flaws or notches.

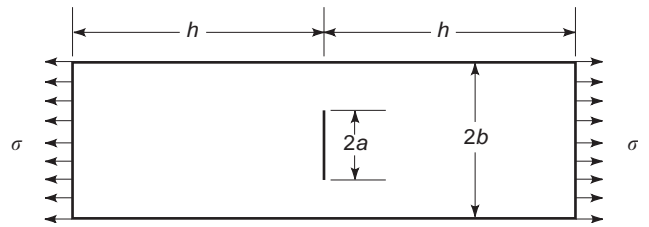


Figure 20. Plate of length $2h$, width $2b$, containing a central crack of length $2a$. Tensile stress σ acts in longitudinal direction and results in a stress intensity factor around the crack tip to be $K_0 = \sigma\sqrt{\pi a}$. When the stress intensity factor is higher than its critical value due to high stresses, the crack would propagate and break the plate.

4. CASE STUDY

This study illustrates a typical design procedure with a few key considerations for a RF package. The calculations are carried out using simple analytical solutions to get qualitative guidelines. Numerical computations may be needed for any quantitative designs.

4.1. Problem Definition

Figure 21 shows a flip-chip assembly with a GaAs chip soldered onto an alumina substrate. A metal wall encloses the assembly. CPW or microstrip lines can be used as the transmission lines on the substrate. Feedthrough is the transition from the substrate to the next level interconnects; it can be microstrip–stripline–microstrip or CPW–stripline–CPW. For CPW, there are three solder joints on each end of chip-to-substrate connection (see Fig. 11a). For a microstrip line, there would be a single solder joint at

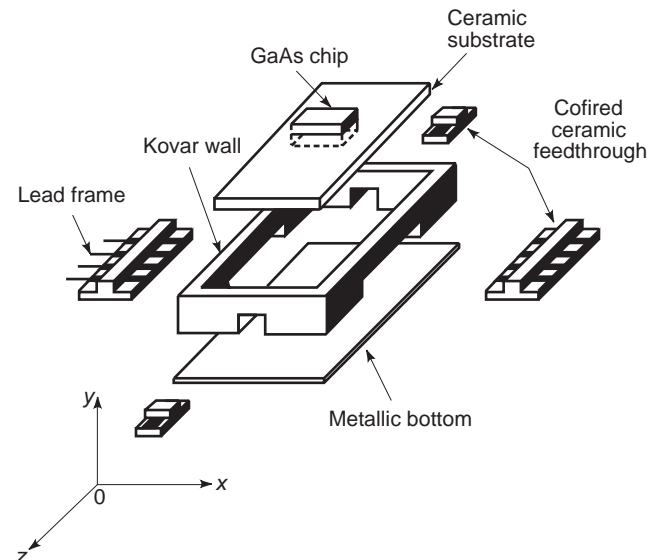


Figure 21. RF single chip package used in the case study. GaAs chip is flip-chip bonded on an alumina substrate with 6 solder joints for the case with a CPW and 2 solder joints for the case with a microstrip line. Feedthrough as shown is a microstrip–stripline–microstrip transition for RF signals. RF, thermal, and mechanical analyses are carried out in the case study to design the package.

each end (see Fig. 11b). All the critical dimensions and material properties taken from Table 3 are listed below.

- Cavity enclosing the flip-chip package—the size is $a \times b \times d = 14.4 \times 6 \times 24$ mm, where a , b , and d are housing dimensions in the x , y , and z directions, respectively.
- GaAs chip—thermal conductivity $k_{\text{chip}} = 48 \text{ W/m} \cdot ^\circ\text{C}$, CTE (coefficient of thermal mismatch) $\alpha_{\text{chip}} = 6.1 \times 10^{-6} \text{ mm/mm} \cdot ^\circ\text{C}$, and size $L_{\text{chip}} \times W_{\text{chip}} \times t_{\text{chip}} = 4.7 \times 1.13 \times 0.625$ mm.
- Ceramic substrate: $k_{\text{substrate}} = 20 \text{ W/m} \cdot ^\circ\text{C}$, $\alpha_{\text{substrate}} = 6.9 \text{ mm/mm} \cdot ^\circ\text{C}$, $L_{\text{substrate}} \times W_{\text{substrate}} \times t_{\text{substrate}} = 14.4 \times 24 \times 0.625$ mm, dielectric constant $\epsilon_r = 9.8$.
- Flip-chip solder joint: $k_{\text{joint}} = 53 \text{ W/m} \cdot ^\circ\text{C}$, height $H_{\text{joint}} = 75 \mu\text{m}$, diameter of the circular pad $d_{\text{pad}} = 150 \mu\text{m}$ (radius $r = d_{\text{pad}}/2 = 75 \mu\text{m}$), center-to-center distance of solder joints $p_x = 4$ mm and $p_z = 0.46$ mm.
- Air: $k_{\text{air}} = 0.03 \text{ W/m} \cdot ^\circ\text{C}$.

A complete analysis would be very complicated since many packaging effects are coupled. RF, thermal, and mechanical designs are to be studied only to address the following questions:

- What are the RF losses of the interconnects for operating frequencies below 10 GHz?
- What is the lowest resonance frequency of the housing?
- What is the feedthrough design for smooth transition?
- What would be the junction temperature for the GaAs chip dissipating 0.8 W with the substrate cooled by air with the convection heat transfer coefficient $h_{\text{conv}} = 20 \text{ W/m}^2 \cdot ^\circ\text{C}$ and $T_{\text{air}} = 25^\circ\text{C}$?
- What would be the fatigue life of the solder joints under thermal cycling from -25 to 125°C ?

4.2. RF Design

4.2.1. Losses in Interconnect. From Fig. 9, the losses can be estimated for a CPW and its associated flip-chip

solder joints. Using the same figure, the return loss is found to be less than 30 dB up to 8 GHz and the insertion loss could be found to be less than 1 dB. Such a loss is negligible if the GaAs chip has an amplifier with 10 dB gain.

4.2.2. Resonance Frequency of the Housing. The resonance frequency of the package housing can be calculated approximately by considering it as a rectangular waveguide cavity without a dielectric substrate. If dimensions shown in Fig. 22 are $b < a < d$, the dominant resonant mode (with lowest resonance frequency) is TE_{101} . Its corresponding resonance frequency can be calculated using the following formula taken from [23]. For the dimensions $a = 14.4$ mm, $b = 6.0$ mm, and $d = 24$ mm, the resonance frequency for the lowest TE_{101} mode is about 12.1 GHz, which is calculated as

$$f_{mnl} = \frac{c}{2\pi} \sqrt{\left(\frac{m\pi}{a}\right)^2 + \left(\frac{n\pi}{b}\right)^2 + \left(\frac{l\pi}{d}\right)^2}$$

$$f_{101} = \frac{3 \times 10^8}{2 \times 3.1416} \sqrt{\left(\frac{3.1416}{14.4 \times 10^{-3}}\right)^2 + \left(\frac{3.1416}{24.0 \times 10^{-3}}\right)^2}$$

$$= 12.1(\text{GHz})$$

where c is the speed of light and m, n, l are mode integers (1, 0, 1 for f_{101}).

However, with a dielectric substrate material located at the bottom of the housing, the resonance frequency should be modified. In this case, dielectric material is alumina with $\epsilon_r = 9.8$ and thickness $t_{\text{substrate}} = 0.625$ mm, the resonance frequency should be modified to be 11.5 GHz, which is calculated by using the following formula taken from [36]

$$f_r = f_c \left[1 - \frac{t_{\text{substrate}}}{b} \left(\frac{\epsilon_r - 1}{\epsilon_r} \right) \right]^{1/2}$$

$$= f_{101} \left[1 - \frac{0.625}{6} \left(\frac{9.8 - 1}{9.8} \right) \right]^{1/2} = 11.5(\text{GHz})$$

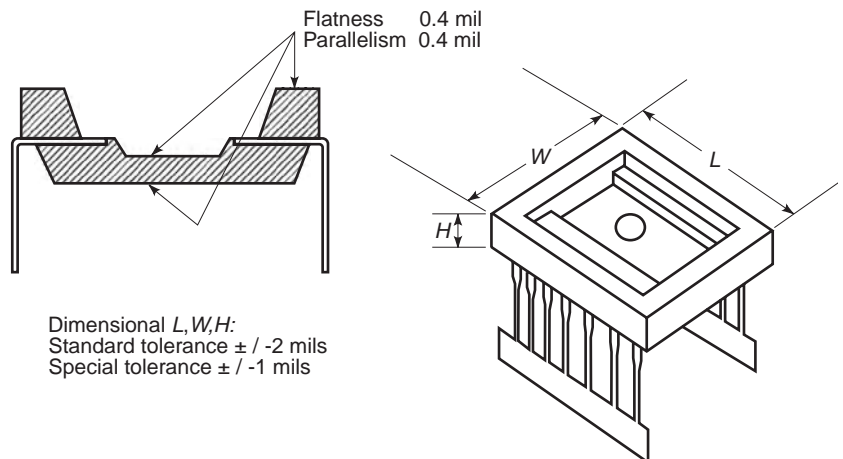


Figure 22. Premolded plastic package to increase applicable frequency. This package is different from typical injection-molded plastic packages with bondwires in air to control inductance variations. Bondwires are moved during the injection molding process; such movements are eliminated by the use of the premolded packages.

where f_{101} is the frequency without the dielectric effect; b is the height of the cavity in y direction (see Fig. 21).

The dielectric substrate reduces the resonance frequency from 12.1 to 11.5 GHz. In addition, the GaAs chip might cause another effect on the frequency. In this case, the chip is small compared with the housing, so the effect could be negligible. However, if the effect should be considered, for example, in the case of a multichip module, a full-wave simulation would have been conducted.

4.2.3. Feedthrough Design. A microstrip line is to be studied for this design consideration since it is the base transmission line for a feedthrough. For a CPW, it can be designed as a CPW–stripline–CPW transition [4] or CPW–shielded CPW–CPW transition [53]. A full-wave simulation is needed for CPW feedthrough structure design [53]. A common feedthrough for a microstrip line is for the transition from a 50- Ω microstrip line to a 50- Ω stripline as shown in Fig. 16. To design a 50- Ω microstrip line on the alumina substrate with thickness $t_{\text{substrate}} = 0.625$ mm and ϵ_r of 9.8, the width of the strip (W) can be calculated using a formula for $W/d < 2$ [23]

$$W = t_{\text{substrate}} \frac{8e^A}{e^{2A} - 2}$$

where

$$A = \frac{Z_0}{60} \sqrt{\frac{\epsilon_r + 1}{2}} + \frac{\epsilon_r - 1}{\epsilon_r + 1} \left(0.23 + \frac{0.11}{\epsilon_r} \right)$$

Hence, for this case

$$A = \frac{50}{60} \sqrt{\frac{9.8 + 1}{2}} + \frac{9.8 - 1}{9.8 + 1} \times \left(0.23 + \frac{0.11}{9.8} \right) = 2.13$$

$$W = 0.625 \times \frac{8 \times e^{2.13}}{e^{2 \times 2.13} - 2} = 0.61(\text{mm})$$

To design a 50- Ω stripline on the alumina substrate with the spacing between two ground planes $t_{\text{strip}} = 2t_{\text{substrate}} = 1.25$ mm and $\epsilon_r = 9.8$, the width of the strip (W) can be calculated as follows [23]:

For $\epsilon_r Z_0 > 120$

$$x = \frac{30\pi}{\sqrt{\epsilon_r} Z_0} - 0.441 = 0.16$$

$$W = t_{\text{strip}} \times (0.25 - \sqrt{0.6 - x}) = 0.23(\text{mm})$$

There is a clear mismatch between the width of the microstrip line (0.61 mm) and that of the stripline (0.23 mm). Typically, a taper section is used to connect these two transmission lines to decrease the return loss. The insertion loss of a typical feedthrough (a single microstrip–stripline–microstrip transition) can be less than 0.1 dB up to 20 GHz [4].

These three RF design considerations on interconnect losses, resonance frequency, and feedthrough are very critical to RF packaging. In addition, there are many other concerns that were discussed above. More general design methods are available in the literature [2,54–56].

4.3. Thermal Design

There are two approaches for thermal design. The simplest approach assumes no temperature gradients inside the GaAs chip. The substrate is cooled by air through convection heat transfer at the bottom surface; therefore, the main thermal path is from the chip to the bottom of the substrate through the solder joints. Its thermal resistance can be estimated using formulas described in the section on reliability/thermal management.

The thermal resistance of each solder joint is

$$R_{\text{joint}} = \frac{H_{\text{joint}}}{\pi r^2 k_{\text{joint}}}$$

For six joints, the thermal resistance is

$$\begin{aligned} R_{\text{joints}} &= \frac{1}{6} R_{\text{joint}} = \frac{H_{\text{joint}}}{6\pi r^2 k_{\text{joint}}} \\ &= \frac{75 \times 10^{-6}}{6\pi(75 \times 10^{-6})^2 \times 53} \\ &= 13(^{\circ}\text{C}/\text{W}) \end{aligned}$$

The thermal resistance of the air between the chip and the substrate is

$$\begin{aligned} R_{\text{air}} &= \frac{H_{\text{joint}}}{(L_{\text{chip}} W_{\text{chip}} - 6\pi r^2) k_{\text{air}}} \\ &= \frac{75 \times 10^{-6}}{(4.7 \times 10^{-3} \times 1.13 \times 10^{-3} - 6\pi(75 \times 10^{-6})^2) \times 0.03} \\ &= 480(^{\circ}\text{C}/\text{W}) \end{aligned}$$

The thermal resistance of the substrate (as a heat spreader) is

$$\begin{aligned} R_{\text{substrate}} &= R_{\text{constriction}} + R_{\text{conduction}} + R_{\text{convection}} \\ &= \frac{1}{6} \frac{1}{2\sqrt{\pi} k_{\text{substrate}}} + \frac{t_{\text{substrate}}}{L_{\text{substrate}} W_{\text{substrate}} k_{\text{substrate}}} \\ &\quad + \frac{1}{h_{\text{conv}} L_{\text{substrate}} W_{\text{substrate}}} \\ &= \frac{1}{12\sqrt{\pi} \times 75 \times 10^{-6} \times 20} \\ &\quad + \frac{0.625 \times 10^{-3}}{14.4 \times 10^{-3} \times 24 \times 10^{-3} \times 20} \\ &\quad + \frac{1}{20 \times 14.4 \times 10^{-3} \times 24 \times 10^{-3}} \\ &= 31 + 0.09 + 145 \\ &\approx 176(^{\circ}\text{C}/\text{W}) \end{aligned}$$

So the total thermal resistance is

$$\begin{aligned}
 R_{\text{total}} &= \frac{1}{\frac{1}{R_{\text{joints}}} + \frac{1}{R_{\text{air}}}} + R_{\text{substrate}} \\
 &= \frac{1}{\frac{1}{13} + \frac{1}{480}} + 176 \\
 &= 12.7 + 176 \\
 &\approx 189(^{\circ}\text{C/W})
 \end{aligned}$$

With GaAs chip power dissipation at $Q = 0.8\text{ W}$

$$\begin{aligned}
 T &= QR_{\text{total}} + T_{\text{air}} \\
 &= 0.8 \times 189 + 25 \\
 &= 176(^{\circ}\text{C})
 \end{aligned}$$

The chip temperature is estimated to be 176°C with the air temperature at 25°C . This temperature is too high to be acceptable. To reduce the temperature, it is important to understand the roles of major thermal elements. The thermal resistance across the airgap (480°C/W) is very large compared with the resistance through the solder joint (13°C/W). For a GaAs chip without temperature gradients, that is, with no heat conduction across the chip, the conduction through the airgap could be overlooked. On the other hand, the convection heat transfer results in a 145°C/W thermal resistance; it plays the dominant role for thermal design. The $20\text{ W}/(\text{m}^2 \cdot ^{\circ}\text{C})$ is a typical convection heat transfer coefficient for an air cooling system in a desktop personal computer (PC) environment. This value can be changed by using a heatsink, a different fan, or even different cooling medium such as liquid. If a small heatsink is added to double the surface area, it would reduce the chip temperature from 176°C to only 118°C , which may be acceptable for some applications. If this temperature is not acceptable or $T_{\text{air}} = 25^{\circ}\text{C}$ is not a good assumption because of higher inlet air temperature, additional thermal enhancement is needed. The enhancement can be accomplished by using a high-thermal-conductivity substrate to reduce the spreading resistance from 31°C/W to a lower value. Or, the convection can be further increased with more powerful air cooling or even liquid cooling.

The assumption of the chip without temperature gradients is reasonable for silicon chips; however, it may be unrealistic for a GaAs chip with a poor thermal conductivity. Let us calculate additional thermal resistance across the chip to understand this consideration. Assume the heatsource is a line source dissipating at the center of the chip; the additional thermal resistance from the chip center to the solder joints can be roughly calculated as

$$\begin{aligned}
 R_{\text{chip}} &= \frac{1}{4} \frac{p_x/2}{t_{\text{chip}}(W_{\text{chip}}/2)k_{\text{chip}}} \\
 &= \frac{4 \times 10^{-3}/2}{4 \times 0.625 \times 10^{-3} \times (1.13/2) \times 10^{-3} \times 48} \\
 &= 30(^{\circ}\text{C/W})
 \end{aligned}$$

where $P_x/2$ and $W_{\text{chip}}/2$ are for a quarter of the chip. The thickness t_{chip} of the GaAs is used to calculate the area for heat conduction. The $\frac{1}{4}$ is to convert the thermal resistance across a quarter of the chip into that across the entire chip. This additional thermal resistance is very large; it is the same as the spreading resistance in the substrate.

The corresponding total thermal resistance becomes

$$\begin{aligned}
 R_{\text{total}} &= 189 + 30 \\
 &= 219(^{\circ}\text{C/W})
 \end{aligned}$$

The highest temperature in the chip becomes

$$\begin{aligned}
 T &= QR_{\text{total}} + T_{\text{air}} \\
 &= 0.8 \times 219 + 25 \\
 &= 200(^{\circ}\text{C})
 \end{aligned}$$

The junction temperature increases 24°C if poor GaAs conduction is considered. Of course, the abovementioned different enhancement schemes have to be adopted to reduce the junction temperature.

This simple calculation illustrates a key challenge to thermal design in RF packaging. GaAs is a poor thermal conductor, and concentrated heatsources in GaAs could cause a major thermal problem if they are located far from solder joints.

The calculation also shows how difficult it is to estimate an accurate junction temperature using one-dimensional formulas for a three-dimensional configuration. Sometimes, contributions of important thermal elements might be neglected by wrong assumptions. Numerical simulation is always preferred if accuracy is crucial.

4.4. Reliability Design

The formulas

$$\Delta\gamma = \frac{L(\alpha_1 - \alpha_2)\Delta T}{h_C}$$

and

$$N_f = \frac{1}{2} \left(\frac{\Delta\gamma}{2\varepsilon_{f'}} \right)^{1/C}$$

are typically used to estimate the fatigue life of the flip-chip solder joints under thermal cycling. The life is strongly affected by the longest distance from the solder joints to the chip center (L), the mismatch between the chip's and the substrate's coefficients of thermal expansion ($\alpha_1 - \alpha_2$), and the temperature change (ΔT) during thermal cycling. With the dimensions and properties given and the temperature changing from -25°C to 125°C , the shear strain is

$$\begin{aligned}
 \Delta\gamma &= \frac{\sqrt{\left(\frac{P_x}{2}\right)^2 + \left(\frac{P_y}{2}\right)^2} (\alpha_{\text{substrate}} - \alpha_{\text{chip}})\Delta T}{H_{\text{joint}}} \\
 &= \frac{\sqrt{2^2 + 0.23^2} \times 10^{-3} \times (6.9 - 6.1) \times 10^{-6} \times [125 - (-25)]}{75 \times 10^{-6}} \\
 &= 0.0032
 \end{aligned}$$

The corresponding fatigue life the solder joint is

$$N_f = \frac{1}{2} \left(\frac{\Delta\gamma}{2\varepsilon_f} \right)^{1/C} = 0.5 \left(\frac{0.0032}{2 \times 0.325} \right)^{1/0.442} \\ = 8.3 \times 10^4 (\text{cycles})$$

The fatigue life, that is, number of thermal cycles, is very high because of the very small mismatch between the chip and the substrate. However, it should be noted that the formula used might not be valid for the case studied. The formula is derived for a flip-chip assembly dominated by a global mismatch caused by a large CTE difference between the chip and the substrate. With a very small global mismatch of $6.9 - 6.1 = 0.8 \times 10^{-6} \text{ mm/mm} \cdot ^\circ\text{C}$ in this assembly, the local mismatch between the solder and the GaAs chip may become the main failure cause. Unfortunately, there is no simple formula to estimate the fatigue life in a case strongly affected by a local mismatch. Numerical analysis is needed [57].

Although the 3.5×10^5 cycles predicted might not be accurate, the fatigue life is expected to be very high because of the very small global mismatch. If the substrate is changed to a polymer one, for example, Duroid (CTE = $14 \text{ mm/mm} \cdot ^\circ\text{C}$), the global mismatch is large and would reduce the fatigue life substantially. Under the same temperature range, the fatigue life with this large global mismatch can be estimated as follows. The shear strain is

$$\Delta\gamma = \frac{\sqrt{\left(\frac{P_x}{2}\right)^2 + \left(\frac{P_y}{2}\right)^2} (\alpha_{\text{substrate}} - \alpha_{\text{chip}}) \Delta T}{H_{\text{joint}}} \\ = \frac{\sqrt{2^2 + 0.23^2} \times 10^{-3} \times (14 - 6.1) \times 10^{-6} \times [125 - (-25)]}{75 \times 10^{-6}} \\ = 0.032$$

The corresponding fatigue life of the joint is

$$N_f = \frac{1}{2} \left(\frac{\Delta\gamma}{2\varepsilon_f} \right)^{1/C} = 0.5 \left(\frac{0.032}{2 \times 0.325} \right)^{1/0.442} \\ = 450 (\text{cycles})$$

The fatigue life is reduced substantially, and underfill epoxy might be used to enhance its reliability. However, underfill epoxy would affect RF performance, due to the change of the effective dielectric constants of the surrounding materials. A RF design is needed to identify potential problems for this use. A good tradeoff analysis can be found in Ref. 57.

The calculations were carried out using simple analytical solutions to review the basic design considerations. It is clear that qualitative guidelines could be obtained quickly. However, it is also clearly indicated that there are limitations of the formulas used. For a quantitative design, the designer must have a good background to select the right formulas for the estimation. Unfortunately, RF packaging involves many multidisciplinary consider-

ations; it is very unusual to train a designer with such a background. Advanced CAD tool integrating RF, thermal, mechanical, and other considerations is critical to the design of RF package.

5. CAD ISSUES FOR RF PACKAGING

Two outstanding CAD issues in RF package design need to be addressed fully and resolved in the near future. The first one is the integration of the design of RF circuits with the design of the package used for housing the circuit. Design tools for RF and microwave circuits have now reached a level of professional maturity. However, the CAD tools for millimeter-wave circuit design [58] have yet to arrive at a similar level of maturity. Even for RF and microwave frequencies, at the current state of the art, different approaches are used for simulation of circuits and for packages in which these circuits are housed. Network analysis-based software packages like Microwave Design System (MDS from HP) and Super Compact (from Compact Software Division of Ansoft Corp.) are used for circuit analysis. On the other hand, frequency-domain and time-domain electromagnetic simulation (EM) techniques (like HFSS and Momentum from HP, Em from Sonnet Software, Strata from Ansoft, and I3D from Zealand Software) are available for characterization of electronic packages at RF, microwave, and millimeter-wave frequencies. None of these approaches is, by itself, applicable for incorporating the effect of packages on performance of RF circuits, for designing of interconnects in the package assembly, or for design of passive embedded circuit functions in packages with multilayered dielectric substrates. Obviously, the network analysis approach, as such, cannot be applied to the RF package design; and three-dimensional field simulation approaches are not practical for analysis of complete RF circuit-package combinations because of impractical excessive computer memory and time requirements.

Two different approaches could possibly be used (and are being developed) for concurrent or integrated design of RF circuits and packages. The first one is based on network modeling of package effects [56,59–61]. In this approach, the significant effects of the package on circuit performance are modeled in terms of equivalent network representations. Rigorous electromagnetic analysis (or approximate field analysis based evaluations) is used for these equivalent network model derivations. These equivalent network models are then used in RF network simulators for design of RF circuits incorporating the effect of package on circuit performance. An alternative to the equivalent network model is the derivation of artificial neural network (ANN) models for packages, trained by EM simulation of the package, that could be coupled to RF circuit design software tools. Use of ANN modeling has been successfully carried out for incorporating difficult-to-model circuit components in microwave design [62,63], but so far it has not been implemented for incorporating the effect of packages in RF circuit design. It is expected that the network or ANN modeling of package effects will be

developed to a level appropriate for RF circuit designers to use it with commercially available RF circuit CAD tools.

The second approach for concurrent RF package and circuit design consists of using EM field simulators for package design and network simulators for circuit design (as is done separately now!) but linking the two simulators so that the design process can be carried out in an integrated manner. There have been some attempts [62–64] for interlinking diverse kinds of simulation tools. However, more of these have been directed toward analysis and design of integrated circuit–antenna modules. Design of integrated circuit–antenna modules is computationally similar to integrated package–circuit design. Just as package design needs to be based on EM field analysis (in contrast to the circuit design, which is based on network analysis), the design of antennas also needs EM field analysis. Thus the computational techniques developed for concurrent circuit–antenna design [65] are conceptually applicable to integrated circuit–package design also.

The second issue in the design of RF packages is the need for integration of thermal and mechanical design considerations with the electrical design of packages. Incorporation of thermal vias in RF circuit chips can affect the RF performance. Shape and dimensions of flip-chip bumps in RF circuit affect both the mechanical reliability and RF performance (because of the inductance introduced by flip-chip bumps). Use of underfill epoxy in flip-chip modules can change the characteristic impedances and insertion losses of transmission lines of RF chips. These are a few of the examples illustrating how mechanical, thermal, and electrical issues can be interrelated in the design of RF packages. Thus the CAD of RF packages calls for some sort of functional integration of electrical, thermal, and mechanical design tools.

CAD of RF packages is a developing area of research and commercial implementation. We can look forward to the arrival of these CAD tools in the near future.

6. ADVANCED PACKAGING CONCEPTS

Trends in packaging may be described in categories based on combinations of power and frequency. Table 7 describes eight such regions from low RF/low power (A1) to millimeter-wave/high power (D2). These regions of applications will be used to discuss different advanced packaging concepts. New materials include high thermal conductivity and low-loss materials. New packaging approaches include premolded plastic package, packages with passive components, and flip-chip assembly. In addition,

Table 7. Application Regions for RF Packaging

Frequency Range	Low RF 100– 800 MHz	High RF 800 MHz– 2 GHz	Microwave 2–30 GHz	Millimeter- Wave 30– 100 GHz
Power low (mW–10 W)	A1	B1	C1	D1
Power high (>10 W)	A2	B2	C2	D2

more challenging packaging technologies are being driven by new applications using active antennas, antenna arrays, RF photonics, RF microelectromechanical systems (MEMS), superconductors, and ferroelectric materials.

6.1. New Materials

6.1.1. High-Thermal-Conductivity Materials. There are instances where, although the total dissipation power requirement is low, devices have a heat concentrated area requiring local heat to be removed from a device surface. Thus aluminum nitride submounts with a surface mount configuration might be suitable in this area. An AlN grade with lower conductivity around 75 W/m · K can be used.

In the areas of high-power device packaging, thermal management is the predominant issue. The current heat-sinking materials have thermal conductivities between 150 W/m · K (for AlN, CuW, and CuMoCu) to 350 W/m · K (for Cu). Several studies are being pursued to investigate the development of diamondlike materials. Pure diamond has a thermal conductivity higher than 1000 W/m · K. An alternative is to develop cost-effective solutions using composite materials. Composites with thermal conductivities over 400 W/m · K are desirable.

6.1.2. Low-Loss Materials. Transmission loss α_{total} in high-frequency regions such as C1, D1, C2, and D2 is

$$\alpha_{\text{total}} = \alpha_r + \alpha_c + \alpha_d$$

where α_r is radiation loss dependent on package structure, α_c is conductor loss proportional to the length and inversely proportional to the square root of electrical conductivity, and α_d is dielectric loss proportional to loss tangent ($\tan \delta$). These loss components in packages become an issue in higher frequency regions such as C1 and D1 if the conducting path is long.

Materials development is required for ultra-low-loss tangent ceramics and plastics that are compatible with highly conductive line materials. Use of magnetic coupling to transfer electrical energy through dielectric materials without a conductive path can be used in the low-loss package solution in very-high-frequency regions such as C1, D1, C2, and D2.

6.2. New Packaging Approaches

6.2.1. Premolded Plastic Package. Currently, the plastic mold package is used in low-power regions at lower frequency (A1 and B1 regions). There are many attempts to increase the applicable frequency upward to the C1 region. Major issues in this area include wire bond inductance and control of the inductance. Thus the wire bonds must be in air, and this requires that a premold type of plastic should be used in this area, since it can create the necessary cavity structure in the package construction. An example of a premolded plastic package is shown in Fig. 22.

6.2.2. Flip-Chip Assembly. Various flip-chip applications are being developed, and flip-chip packaging is beginning to be utilized on the lower-power side. However,

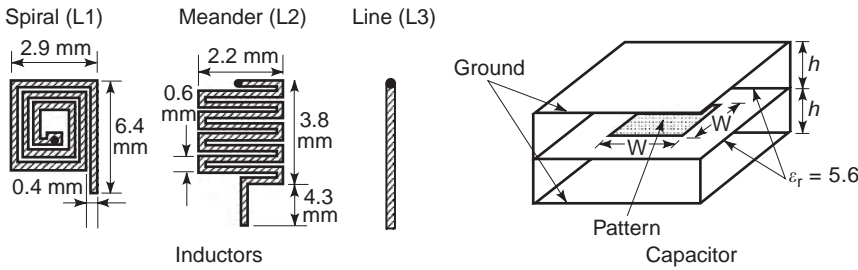


Figure 23. RF package with inductor and capacitor components integrated in a substrate. Such planar discrete components would reduce packaging costs. A large number of inductors and capacitors are commonly used as discrete components for RF modules. A high-density integration and batch processing of such planar components could result in a significant cost reduction.

high-power applications demand new solutions. The flip-chip configuration has the disadvantage of taking heat out of the back side since heat dissipation is very limited through the solder-ball-bonded face. Without a proper design, thermal resistance could be very high. In addition, devices have to be redesigned. See Section 3.1.3 or Ref. 66 for details.

6.2.3. Package with Passive Components. For some RF packaging, the future trend is in integration of passive devices into the package. In regions A1 and B1 there are many functional integration schemes being used, such as integration of impedance matching and use of L , R , and C filter functions within the package. The impedance-matching approach can reduce cost of the MMIC by fabricating matching circuits on the package instead of the MMIC. In some cases, the integration of passive components shown in Fig. 23 into the package could be easier and more cost-effective than integration into the active device.

6.3. New Applications

6.3.1. Active Antenna. As shown in Fig. 1, transmission lines interconnecting different RF devices are the limiting factors for RF performance. The trend for C1–D2 applications is to remove these lines by integrating RF devices and antennas into one active antenna. Figure 24 shows an

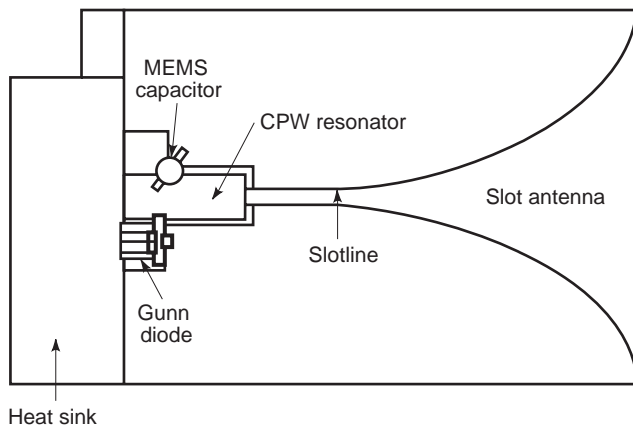


Figure 24. A tapered slot active antenna tuned by a variable capacitor. The device, transmission lines and antenna are integrated into a single module for high efficiency. The MEMS-based tunable capacitor could replace the varactor reported in Ref. 10 in order to enhance the quality factor (Q).

active slot antenna modified from a design taken from Ref. 10. The package itself is the active antenna, requiring integrated considerations of antenna, electrical, thermal, and mechanical designs.

6.3.2. Antenna Arrays. For applications in D1 and D2, device efficiency is very poor, so power combining using a resonant antenna array is necessary. Figure 25 shows a design similar to a quasioptical oscillator with frequency modulation obtained by a varactor array [67]. In addition to power combining, new functionality can be created by manipulating phases of waves [68]. Thousands of antenna elements are needed to achieve desirable functionality. The RF module is very complex and demands advanced MCM technologies.

6.3.3. RF Photonics. Another emerging area of integration is combination of optical and RF functions in devices and packages. RF characteristics of optoelectronic packages have already been identified as the major performance factors for gigahertz bandwidth. In addition, RF transceivers/optical transceivers can be integrated to form different module combinations for efficient transition between optical to wireless communication. Novel packaging concepts are being developed to accommodate this new challenging area.

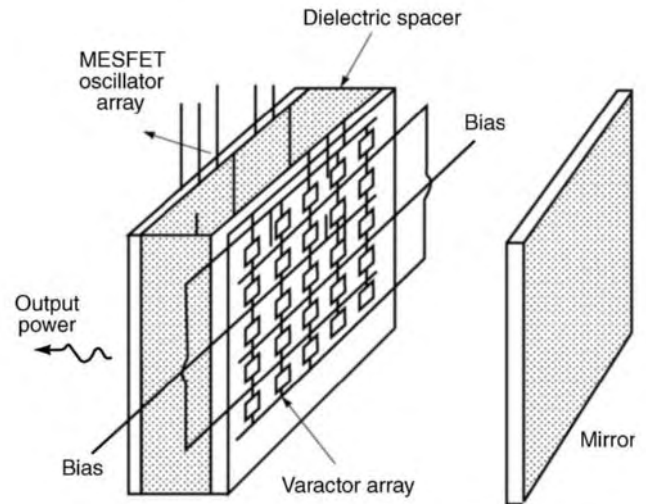


Figure 25. Quasioptical oscillator with frequency modulation. This is an example to use an antenna array to enhance power transmission efficiency. The power transmission through grid resonance is an effective approach for power combining.

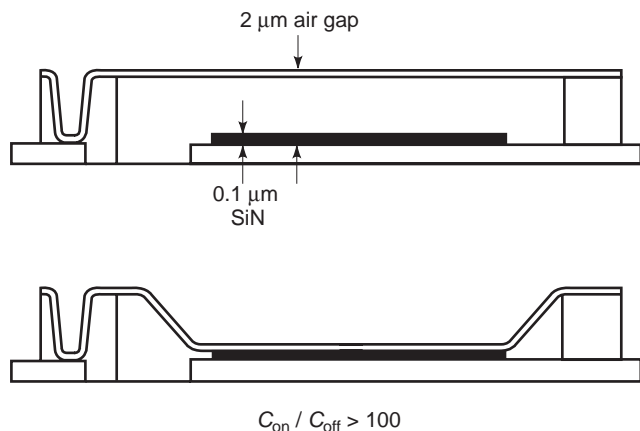


Figure 26. RF ON/OFF switches using MEMS. The capacitance ratio between the air dielectric layer and the silicon nitride layer could reach 100. The switching is controlled by electrostatic forces. In addition to ON/OFF switches, more complex MEMSs can be designed and fabricated for tunable capacitors, inductors, and multiway switches. MEMS technologies can also be used to fabricate precise RF circuits and packages.

6.3.4. RF Microelectromechanical Systems (MEMSs).

MEMSs can be used to fabricate low-loss switches, high- Q tunable capacitor, integrated high- Q inductors, and microscale vibrating mechanical resonators [69–71]. Through μm - or nm -level mechanical movements surrounded by air, the low-loss dielectric material, high- Q components could be designed and fabricated for applications in regions from C1–D2. Figure 26 shows RF switches using a thin diaphragm [1,69]. In the mm-wave region, RF performance is very sensitive to μm -level movements. Such sensitivity used to be a major manufacturing problem. Using an MEMS, however, the sensitivity could be tuned for frequency-agile electronics [70]. RF MEMSs are going to have an impact on low-cost, high- Q , frequency/phase-adaptable filters, circulators, conformal and phased-array antennas, oscillators, and phase shifters. For RF packaging involving MEMSs, new problems need to be overcome. For example, flip-chip assembly is the best approach to integrate MEMS with other RF devices and circuits; however, the silicon substrate used to fabricate MEMS has to be removed to achieve desirable RF performance [72].

Another interesting application of MEMS is the fabrication of RF circuits by silicon-based micromachining [73,74]. In this application, bulk silicon can be used to fabricate waveguide like circuit elements that simultaneously provide circuit function and package enclosures for MMIC and discrete components. Since silicon has good thermal conductivity, such structures are suitable for power devices. In addition, since air-filled cavities may be used to implement high- Q circuit elements, it is possible to fabricate many such circuits/packages out of an 8-inch (203 mm) wafer. This silicon-based micromachining technology is important to manufacture low-cost, precision circuits/packages for millimeter-wave applications.

6.3.5. Superconductor and Ferroelectric Materials. For very-high- Q modules, superconductor and ferroelectric new materials can be used. The high-temperature superconductor makes it possible to build low-loss structure and the ferroelectric gives a voltage variable dielectric [75]. The mixture of $\text{Ba}_{0.08}\text{Sr}_{0.92}\text{TiO}_3$ (BST) has shown to have both the desired large dielectric constant, for example, 17,000, and a large decrease in the dielectric constant, for example, 17,000 reduced to 6000, with an applied field of 25 kV/cm at 77 K. BST can be integrated with the superconductor $\text{YBa}_2\text{Cu}_3\text{O}_{7-x}$ (YBCO), because of the lattice match and chemical compatibility. The combinations have been used in a voltage-tunable oscillator, a phase shifter, and a voltage-tunable phase-array antenna system. In addition to typical issues for high- Q modules, the new materials and the new operation temperature at 77 K will demand very advanced RF packaging solutions.

7. SUMMARY

RF packaging is critical to the growth of applications of microwave and mm-wave modules and systems. The number of I/Os of RF packaging is not high; major packaging challenges result from two unique features:

1. Wide spectrum of operation frequencies ranging from kHz to hundreds of GHz
2. Packaging being a part of circuitry with strong effects on RF performance

This article reviews different RF single-chip and multichip packages, with an emphasis on their requirements that differed from those for microelectronics. It also discusses basic issues related to RF performance and package reliability in thermal management and mechanical integrity. To meet development needs, advanced packaging concepts are being created using new approaches and new materials. In addition, more challenging packaging technologies are being driven by new applications using active antenna, antenna arrays, RF photonics, RF microelectromechanical systems, superconductor, and ferroelectric materials.

BIBLIOGRAPHY

1. E. Brown, Microwave and millimeter-wave switches, 1997, DARPA Website (online).
2. B. Berson, F. Rosenbaum, and R. A. Sparks, MMIC packaging, in R. Goyal, ed., *Monolithic Microwave Integrated Circuits: Technology and Design*, Artech House, Norwood, MA, 1989, pp. 735–780.
3. D. Wein et al., Microwave and millimeter-wave packaging and interconnect methods for single and multiple chip modules, *IEEE GaAs IC Symp.*, 1993, pp. 333–336.
4. D. S. Wein, Advanced ceramic packaging for microwave and millimeter wave applications, *IEEE Trans. Anten. Propag.* **43**:940–948 (1995).

5. S. Chai et al., Low-cost package technology for advanced MMIC applications, *IEEE MTT-S Int. Microwave Symp.*, 1990, pp. 625–628.
6. S. Konsowski and A. Helland, *Electronic Packaging of High Speed Circuitry*, McGraw-Hill, New York, 1997, pp. 181–201.
7. B. K. Gilbert and G. W. Pan, MCM packaging for present and next generation high clock-rate digital and mixed-signal electronic system: Areas for development, *IEEE Trans. Microwave Theory Tech.* **45**:1819–1835 (1997).
8. C. Drevon, Mixed L.F./R.F. MCM, *IEEE Electron. Compon. Technol. Conf.*, San Jose, CA, 1997, pp. 497–501.
9. J. Hartung, Integrated passive components in MCM-Si technology and their applications in RF-systems, *Proc. Int. Conf. Multichip Modules High Density Packag.*, Denver, CO, 1998, pp. 256–261.
10. J. A. Navarro and K. Chang, *Integrated Active Antennas and Spatial Power Combining*, Wiley, New York, 1996, p. 15.
11. J. A. King, *Materials Handbook for Hybrid Microelectronics*, Artech House, Norwood, MA, 1988, pp. 106, 477, 516.
12. R. R. Yummala and E. J. Rymaszewski, *Microelectronics Packaging Handbook*, Van Nostrand Reinhold, New York, 1989, p. 36.
13. B. Dufour, M. McNulty, and S. Miller, Microwave multi-chip module utilizing aluminum silicon carbide with in situ cast components and high density interconnect technology, *Proc. Int. Conf. Multichip Modules*, Denver, CO, 1997, pp. 309–314.
14. H. Tomimuro et al., A new packaging technology for GaAs MMIC modules, *IEEE GaAs IC Symp.*, 1989, pp. 307–310.
15. P. Cameron et al., A flip chip high efficiency X-band HPA, *IEEE MTT-S Int. Microwave Symp. Digest*, 1997, pp. 889–892.
16. H. Kusamitsu et al., The flip-chip bump interconnect of millimeter-wave GaAs MMIC, *Proc. Int. Conf. Multichip Modules High Density Packaging*, Denver, CO, 1998, pp. 47–52.
17. W. Zhang et al., Study of RF flip chip assembly with underfill epoxy, *Proc. Int. Conf. Multichip Modules High Density Packaging*, Denver, CO, 1998, pp. 53–57.
18. A. J. Rainal, Computing inductive noise of chip packages, *AT&T Bell Lab. Tech. J.* **163**:177–195 (1984).
19. T. Kerms, Millimeter-wave performance of chip interconnects using wire bonding and flip chip, *IEEE MTT-S Int. Microwave Symp. Dig.*, 1996, pp. 247–250.
20. R. Sturdivant, Reducing the effects of the mounting substrate on the performance of GaAs MMIC flip chips, *IEEE Microwave Theory Tech. Symp. Digest*, 1995, pp. 1591–1594.
21. R. Sturdivant, C. Quan, and J. Wooldridge, Investigation of MMIC flip chips with sealants for improved reliability without hermeticity, *IEEE MTT-S Int. Microwave Symp. Digest*, 1996, pp. 239–242.
22. H. H. M. Ghouz and E.-B. El-Sharawy, An accurate equivalent circuit model of flip chip and via, *IEEE Trans. Microwave Theory Tech.* **44**:2543–2554 (1996).
23. D. M. Pozar, *Microwave Engineering*, Addison-Wesley, New York, 1990, Chap. 4.
24. I. Kneppo et al., *Microwave Integrated Circuits*, Chapman & Hall, London, 1994.
25. R. E. Collin, *Foundations for Microwave Engineering*, 2nd ed., McGraw-Hill, New York, 1992, pp. 175–176.
26. G. Ghione and C. U. Naldi, Coplanar waveguide for MMIC applications: Effect of upper shielding, conductor backing, finite-extent ground planes, and line to line coupling, *IEEE Trans. Microwave Theory Tech.* **35**:260–267 (1987).
27. I. D. Robertson, *MMIC Design*, IEE, London, 1995, p. 437.
28. C. Tzuang and T. Itoh, High speed pulse transmission along a slow wave CPW for monolithic microwave integrated circuits, *IEEE Trans. Microwave Theory Tech.* **35**:697–704 (1987).
29. R. N. Simons, N. I. Dib, and L. P. Katehi, Modeling of coplanar stripline discontinuities, *IEEE Trans. Microwave Theory Tech.* **44**:711–716 (1996).
30. V. K. Tripathi, Measurement based modeling of RF packages, *ASME Advances in Electr. Packag.*, Vol. 19-1, 1997, pp. 489–495.
31. C. Cho and K. C. Gupta, Design methodology for multilayer coupled line filters, *IEEE MTT-S Int. Microwave Symp. Digest*, 1997, pp. 785–788.
32. R. A. Matick, *Transmission Lines for Digital and Communication Networks*, McGraw-Hill, New York, 1969, Chap. 8.
33. J. Gilb and C. Balanis, Pulse distortion on multilayer coupled microstrip lines, *IEEE Trans. Microwave Theory Tech.* **37**:1620–1628 (1989).
34. L. Carin and K. Webb, Isolation effects in single and dual-plane VLSI interconnects, *IEEE Trans. Microwave Theory Tech.* **38**:396–404 (1990).
35. R. Clark, A. Agrawal, and S. Miiler, Simulation of multi-chip module package resonance using commercial finite electromagnetic software, *IEEE MTT-S Int. Microwave Symp. Digest*, 1995, pp. 1211–1214.
36. F. Ishitsuka and N. Sato, Low cost, high-performance package for a multi-chip MMIC module, *IEEE GaAs IC Symp.*, 1988, pp. 221–224.
37. G. Lei et al., Wave model solution to the ground/power plane noise problem, *IEEE Trans. Instrum. Meas.* **44**:300–303 (1995).
38. R. L. Thompson et al., An 8-bit 2.5 gigasample A/D converter multichip module for all-digital radar receiver for AN/APS 145 radar on Navy E2-C Airborne Early Warning Aircraft, *Proc. IEEE Multi-Chip Module Conf.*, Santa Cruz, CA, 1997, pp. 22–26.
39. G. Lei et al., Power distribution noise suppression using transmission line termination techniques, *Proc. 5th Top. Meet. Electric. Perform. Electron. Packag.*, Napa, CA, 1996, pp. 28–30.
40. R. Sorrentino and S. Pileri, Method of analysis of planar networks including radiation loss, *IEEE Trans. Microwave Theory Tech.* **MTT-29**:942–948 (1981).
41. R. B. Schulz, V. C. Plantz, and D. R. Brush, Shielding theory and practice, *IEEE Trans. Electromagn. Compat.* **30**:187–201 (1988).
42. D. D. Gupta, A novel active area bumped flip chip technology for convergent heat transfer from gallium arsenide power devices, *IEEE Trans. Compon. Packag. Manuf. Technol. A* **18**(1):82–86 (1995).
43. R. Sigliano and J. Danaher, Thermal performance heats up, *Adv. Packag.* 54–62 (May/June 1997).
44. T. Kole et al., Thermal modeling aids the design of packaged amplifiers, *Microwaves RF* 64–67 (Oct. 1997).
45. J. Pavio et al., Plastic packages hold power RF MOSFETs, *Microwaves RF* 209–214 (Dec. 1996).
46. P. Lall, M. G. Pecht, and E. B. Hakim, *Influence of Temperature on Microelectronics*, CRC Press, Boca Raton, FL, 1997, pp. 101–153.
47. C. C. Lee and G. S. Matijasevic, Highly reliable die attachment on polished GaAs surface using gold-tin eutectic alloy, *IEEE Trans. Compon. Hybrids Manuf. Technol.* **12**(3):406–409 (1989).

48. J. S. Pavio, Successful alloy attachment of GaAs MMIC's, *IEEE Trans. Electron. Devices* **34**:2616–2620 (1987).
49. G. Hawkins et al., Measurement of silicon strength as affected by wafer back processing, *25th Annu. Proc. Reliab. Phys.*, 1987, Cat. 87CH2388-7, pp. 216–223.
50. R. P. Vidano et al., Mechanical stress reliability factors for packaging GaAs MMIC and LSIC components, *IEEE Trans. Compon. Hybrids Manuf. Technol.* **12**:612–617 (1987).
51. C. R. Mischke and J. E. Shigley, *Mechanical Engineering Design*, 5th ed., McGraw-Hill, New York, 1989, Chap. 5.
52. M. L. Dunn, W. Suwito, and S. Cunningham, Fracture initiation at sharp notches: Correlation using critical stress intensities, *Int. J. Solids Struct.* **34**:3873–3883 (1997).
53. S. Yanaguchi et al., New module structure using flip-chip technology for high-speed optical communication ICs, *IEEE MTT-S Int. Microwave Symp. Digest*, 1996, pp. 243–246.
54. H. Wada and C. Makihara, High frequency package design technology using *S* parameter synthesise method, *IEEE Wireless Communication Conf.*, 1997, pp. 151–155.
55. M. Nachnani et al., A low-cost multichip (MCM-L) packaging solution, *IEEE / CHMT Int. Electron. Manufacturing Technol. Symp.*, 1993, pp. 464–470.
56. A. Stabban and K. C. Gupta, Effect of package on parasitic coupling among microstrip discontinuities in MMICs, *Int. J. Microwave Millimeter-Wave Comput. Aided Eng.* **1**:403–411 (1991).
57. Z. Feng et al., RF and mechanical characterization of flip-chip interconnects in CPW circuits with underfill, *IEEE MTT-S Int. Microwave Symp. Digest*, 1998, pp. 1823–1826.
58. K. C. Gupta, Emerging trends in millimeter-wave CAD, *IEEE Trans. Microwave Theory Tech.* **46**:747–755 (June 1998).
59. J. J. Burke and R. W. Jackson, A simple circuit model for resonant mode coupling in packaged MMICs, *IEEE MTT-S Int. Microwave Symp. Digest*, Boston, MA, June 1990.
60. K. C. Gupta, A network modeling approach for effects of metallic packages on microstrip circuit performances, *Proc. IEEE 3rd Topical Meeting on Electrical Performance of Electronic Packaging (EPEP)* 1994, pp. 159–162.
61. H. Cebi and K. C. Gupta, Effect of package shape on spurious coupling among microstrip discontinuities, *1996 IEEE MTT-S Int. Microwave Symp. Digest*, San Francisco, June, pp. 1823–1826.
62. V. A. Thomas et al., The use of SPICE lumped circuits as subgrid models for FDTD analysis, *IEEE Microwave Guided Wave Lett.* **4**(5):141–143 (1994).
63. K. Guillooard et al., A new global finite element analysis of microwave circuits including lumped elements, *IEEE Trans. Microwave Theory Tech.* **44**(12):2587–2594 (1996).
64. B. Bailargeat et al., Coupled localized and distributed elements analysis applying an EM software in the frequency domain, *1997 IEEE MTT-S Int. Microwave Symp. Digest*, Denver, CO, June 1997, pp. 1021–1024.
65. K. C. Gupta and P. S. Hall, *Integrated Circuit-Antenna Modules—Analysis and Design*, Wiley, New York, 1999.
66. P. Comeron et al., A flip chip high efficiency X-band HPA, *1997 IEEE MTT-S Int. Microwave Symp. Digest*, Denver CO, June 1997, pp. 889–892.
67. M. Kim et al., A 100-element HBT grid amplifier, *IEEE Trans. Microwave Theory Tech.* **41**:1762–1771 (1993).
68. W. A. Shiroma et al., A quasi-optical receiver with angle diversity, *IEEE MTT-S, Int. Microwave Symp. Digest* 1996, pp. 1131–1134.
69. C. Goldsmith et al., Micromechanical membrane switches for microwave applications, *IEEE MTT-S Int. Microwave Symp. Digest*, 1995, pp. 91–94.
70. H. D. Wu et al., MEMS designed for tunable capacitors, *IEEE MTT-S Int. Microwave Symp. Digest*, Baltimore, MD, 1998.
71. C. T. C. Nguyen, Microelectromechanical devices for wireless communication, *IEEE MEMS Workshop*, Germany, 1998.
72. R. S. Irwin et al., Quick prototyping of flip chip assembly with MEMS, *Proc. 44th Int. Instrum. Symp.*, Reno, NV, 1998, pp. 256–261.
73. R. M. Henderson and L. P. B. Katehi, silicon-based micromachined packages for discrete components, *IEEE MTT-S Int. Microwave Symp.*, 1997, pp. 521–524.
74. S. V. Robertson et al., A Si micromachined conformal package for a K-band low noise HEMT amplifier, *IEEE MTT-S Int. Microwave Symp.*, 1997, pp. 517–520.
75. F. S. Barnes et al., Some microwave applications of BaSrTiO₃ and high temperature superconductors, *Integr. Ferroelectric.* **8**:171–184 (1995).

PARALLEL ALGORITHMS AND COMPUTING FOR LARGE-SCALE ELECTROMAGNETIC SIMULATION

KING WAI LAM
 KA FAI CHAN
 CHI HOU CHAN
 City University of Hong Kong
 Kowloon, Hong Kong SAR,
 China

1. PARALLEL COMPUTING

Parallel computing can be performed with either shared- or distributed-memory multiprocessors [1,2]. Figures 1a and 1b show the schematic diagrams for shared-memory multiprocessor (SMMP) and distributed-memory multiprocessor (DMMP) architectures, respectively. In shared-memory multiprocessors, the architecture consists of a number of identical processors sharing a global main memory. The parallel processes are thread-controllable. Each runs on a separate processor and shares memory with other threads in the framework. The OpenMP [3] is a more recent application program interface (API) for writing multithreaded applications in shared-memory multiprocessor architecture. In distributed-memory multiprocessors, the architecture consists of a number of processors with individual memory that are interconnected via a communication network. The parallel processes run on separate processors and use message passing to communicate with each other. The MPI (message-passing interface) [4,5] and PVM (parallel virtual machine) [6] are the most popular message-passing libraries for programmers to write message-passing programs. As parallel computing has become more popular, many useful parallel packages suitable for science and engineering applications can now be downloaded freely from the Internet. The Fast

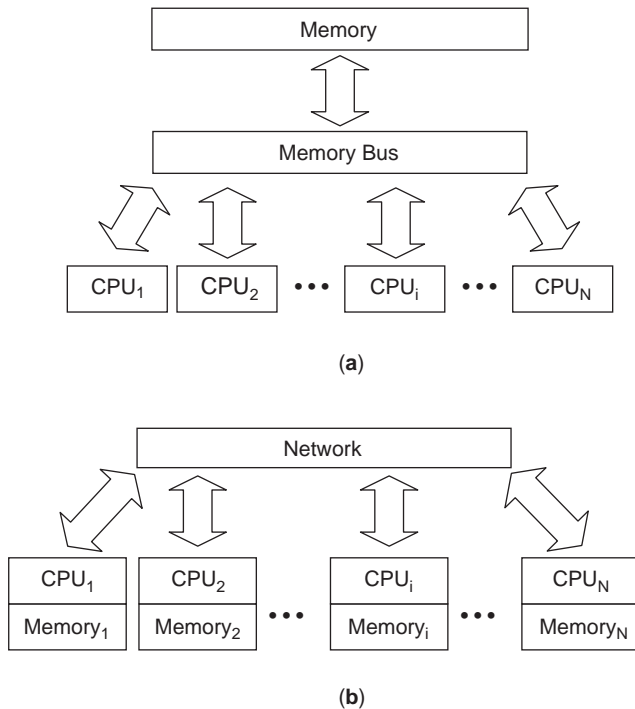


Figure 1. (a) Shared-memory multiprocessor architecture; (b) distributed-memory multiprocessor architecture.

Fourier Transform in the West (FFTW) [7] is one of these packages.

In this article, we will discuss some parallel algorithms and programming clues suitable for large-scale electromagnetic simulations in which the numbers of unknowns are too large for typical desktop computing. Readers are also referred to the work of Velamparambil et al. [8] for large-scale parallel computing. All the parallel computing techniques presented here are based on our experiences with self-built Beowulf clusters [9,10]. It is believed that these techniques are also applicable to other science and engineering applications. This article is outlined as follows. We will first describe the principle of parallel computing and the architecture of the Beowulf cluster in the City University of Hong Kong. Readers can then appreciate the cost-effectiveness of the Beowulf cluster, which is perhaps the easiest parallel computing platform that one can build by oneself. We will also discuss parallel implementation of commonly used computational techniques such as the finite-difference time-domain (FDTD) method [11] and the method of moments (MoM) [12]. Manipulations of full matrix as well as sparse matrix calculations will be described.

1.1. Principle of Parallel Computing

Regardless of the computing architecture, the principle of parallel computing is to decompose the large computational domain into smaller subdomains. Tasks in each subdomain are performed independently with minimum intercommunication among them. Each processing unit in the parallel computing platform will be tasked to

manipulate the computation for the corresponding identified domain. Results may need to be exchanged among processors via a message-passing library and API during the computation. There are two levels of parallelism: hardware-level parallelism and software-level parallelism.

1.1.1. Hardware-level Parallelism. Parallelism at this level is implemented by breaking down the load among multiple hardware components of the same category. Parallelism is attained by having the computational work done by these hardware components in parallel, and thus can achieve a higher computing performance. There are two types of hardware-level parallelism: fine-grained and coarse-grained parallelism. Fine-grained parallelism is achieved by performing the computing task with either one or multiple CPUs, while coarse-grained parallelism is achieved by a collection of systems. Hardware-level parallelism can further be classified by several sublevels, including the following:

- *CPU-Level Parallelism.* Multiple CPUs within the same machine to have computation work done in parallel.
- *Memory System Parallelism.* Instead of accessing the same memory pool through the same memory bus at the same time, memory access can be distributed by dividing the memory pool into independent memory blocks. The memory blocks and CPUs are connected through a crossbar memory access switch. Each memory access to different pieces of data can go through distinct access paths without interfering with memory access activities in the same system.
- *Input-Output Parallelism.* Usually input/output (I/O) channels and devices are bottlenecks in computational tasks, especially those with large data volume. Using multiple I/O channels and devices to serve the same I/O requests in parallel can increase throughput of data access.
- *System level parallelism.* This is a higher-level parallelism compared with the aforementioned parallelism categories. Computational tasks are decomposed into smaller, independent subtasks. Multiple nodes coordinate to work on independent subtasks in parallel. Linux clusters such as the Beowulf are included in this category.

1.1.2. Software-Level Parallelism. Software-level parallelization is one of the core parts of parallel computing. It features the ability to break up a problem into independent, self-contained parts that are solved by different hardware. Algorithms that can be parallelized can result in substantial speedup in execution. Problem domains of a serial nature (e.g., graphical user interface that waits for user input), or with more overhead than performance gain after parallelization, are unsuitable for parallelization. Whether a problem can be parallelized depends on whether we can take advantage of the following parallel application features:

- *Granularity.* —a measure of the size of problem fragments that can be accomplished independently without communicating with other fragments in the same problem domain
- *Data dependence.* —the data availability among problem fragments when some fragments have to wait for data available only from the remaining fragments
- *Control dependency.* —the data availability among problem fragments when some fragments have to wait for results of control conditions (e.g., execution of an expression that returns a true or false) available only from the remaining fragments

1.2. Schemes

There are various ways to construct a parallel computing platform; each has a different level of parallelism and thus limitation. However, there are two major streams in the development of parallel computing platform.

- *Shared-Memory Multiprocessor. (SMMP).* In this architecture, processors have equal access to the memory address space. There are multiple processors that access a shared-memory pool through a common memory access channel, usually via a bus or crossbar switch. Processors within the same machine communicate with each other through shared address space.
- *Distributed-Memory Multiprocessor. (DMMP).* In this architecture, each processor has its own memory module. Processors access their own memories and communicate with each other through message passing. Usually such a system is constructed from multiple systems, connected through high-speed network equipment. Processors access memory area in the corresponding machine and communicate with processors on other machines through high-speed networks.

In the SMMP model, various processors can reference the same variables and memory just as the single processor machine can. However, the system has to maintain the shared data integrity. In a DMMP model, the memory modules reside on separate machines, where they can be accessed. There is no data integrity issue among machines. The tasks of distributing data to various machines and reassembling the result collected from each machine are handled by software implementation. This requirement also adds communication complexity to the implementation, which does not exist in shared-memory multiprocessors [13]. On the other hand, well-designed distributed-memory multiprocessor software has better scalability for adding more machines [14]. Compared with the DMMP model, the SMMP model requires much more effort to scale up in both the hardware and software paradigms.

1.3. Beowulf Cluster

The Beowulf cluster is a distributed memory multiprocessor architecture. It usually consists of one server node and one or more client nodes connected together via Ethernet

or some other networks. Users access resources in the cluster by connecting to a single node while the rest of the cluster nodes are inaccessible from the outside world. Machines used in a cluster can be of identical models (a homogeneous cluster) or of different models (a heterogeneous cluster). It is commonly built by using commodity hardware components. Essential components include standard Ethernet adapters, Ethernet switches, and a personal computer (PC) that is capable of running a free operation system such as Linux. There is substantial benefit in price: performance ratio for Beowulf clusters compared to those traditional expensive supercomputers, at the expense of efforts in system management and software parallelization.

1.4. Cluster in CityU

In the Wireless Communications Research Center of CityU, parallel computing platforms are built by harnessing personal computers interconnected by a central network, forming a Beowulf cluster to solve large-scale electromagnetic problems. This kind of Beowulf architecture is well suited for scaling and is easy to implement with standardized programming models and without paying fees for an operating system.

1.4.1. Cluster Configuration. Figure 2 shows one of the Beowulf clusters in CityU. The schematic configuration is shown in Fig. 3. The cluster configuration consists of

- *1 Server Node.* —Intel Pentium IV 2.0GHz CPU, 1.5 GB (gigabyte) RAM, 36 GB Ultra 160 SCSI (small-computer system interface) hot-swap hard disk for RAID (redundant array of independent or inexpensive disks) 1 and 90 GB Ultra 160 SCSI hot-swap hard disk for RAID 5 storage disk, and sets of 3Com 3C905C 100 TX network interface cards
- *24 cluster nodes.* —dual Intel Pentium III 1GHz CPU, 2GB RAM, 18GB Ultra 160 SCSI hot-swap



Figure 2. Fourth generation of Beowulf Linux cluster in Wireless Communications Research Center, City University of Hong Kong.

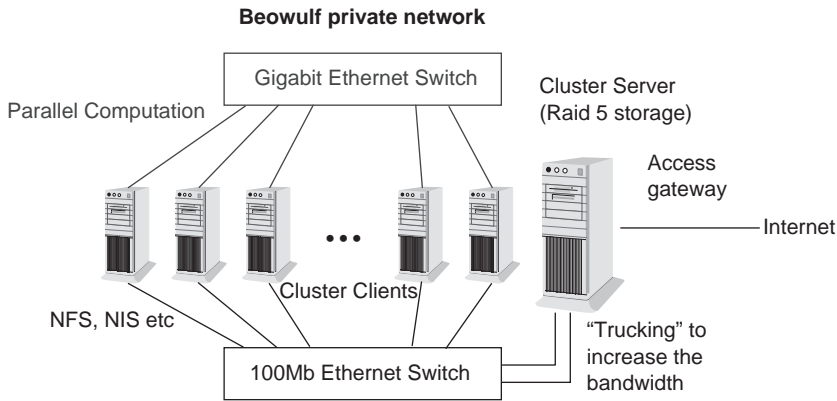


Figure 3. Schematic diagram illustrating configuration of a Beowulf Linux cluster.

hard disk, 1 set of 3Com 3C905C 100 TX network interface cards, and 1 set of 3Com 996B 1000TX Gigabit Fast Ethernet network interface cards

- *2 Ethernet switches.* —3Com Superstack 3 Switch 4924 24-port Gigabit Fast Ethernet network switch and 3Com Superstack 3 switch 4300 48-port Ethernet network switch
- *Cluster node operating system.* —RedHat Linux 8.0
- *Software packages*
 - Message-passing interface (MPI) [15]
 - Fast Fourier Transform West (FFTW) [7]
 - Basic linear algebra subprograms (BLASs) [16]
 - Linear algebra package* (LINPACK) [17]
 - Miscellaneous scientific and engineering software packages
 - Administrative and system monitoring software packages such as Cheops [18]

1.4.2. Design considerations. The server provides cluster-wide services, including Network File Services (NFS) for user home directories and common program depository, plus Network Information Services (NIS) for user information, and so on to all the client nodes. All the cluster nodes are connected through private gigabit and 100-Mb (megabit) Ethernet switches. Traffic among cluster nodes goes through the private network while the cluster is accessible through only one of the cluster nodes connected to Internet. The benefit of using private network is twofold:

- Network loading is incurred by interprocess communication and file access of the parallel applications running on the cluster. Performance of parallel applications running on other systems on the public network may be affected if such network loading is not isolated from the public network.
- Since only one cluster node is Internet-accessible, it is much easier to enforce the security of this single machine, rendering the cluster less vulnerable to network attacks. Furthermore, network protocols with low security level, such as NFS and NIS, are

protected against eavesdropping as they all go through the private network connection.

To further improve performance of inter-process communication and file access across the network, each cluster node possesses more than one network interface. The server node has three 100-Mb Ethernet network interfaces. One interface is used for Internet access to the cluster. The remaining two interfaces are used to access the private network through the 100-Mb Ethernet switch. They are bounded together to form a virtual network interface. This “trunking” method is adopted to double the communication bandwidth. Each client node has one Gigabit Ethernet card and one 100-Mb Ethernet card. All the client nodes are connected to the Gigabit Ethernet switch for interprocess communication of parallel computation applications. The 100-Mb Ethernet switch is used to connect the clients and server to provide NIS, NFS, and other services. In this way, two different network switches manage tasks related to parallel computation, I/O, and other file systems separately, and hence a more efficient and stable parallel computing platform can be achieved. To provide centralized storage for user data and application programs to be shared among all cluster nodes, a disk storage system is bundled with the server node. The storage system is configured as a “RAID 5” system, with which the storage system will continue to operate even after failure of any single hard disk. This configuration provides a secure and reliable way to protect the data and the system information, and avoids the storage system becoming a single point of failure for the entire cluster.

The cluster architecture deployment also provides (1) *high availability*—the cluster continues to operate regardless of single- or multiclient cluster node failure (hardware can be replaced without affecting the rest of the cluster) and (2) *upgradability*—new hardware and operating systems can be introduced into the cluster gradually by adding additional nodes, without making drastic changes to the entire cluster environment.

We now have some basic ideas about the parallel computing and components needed to build the parallel computing platform. In the following section, we will discuss some general parallel algorithms.

2. PARALLEL ALGORITHMS

In this section, we discuss several parallel algorithms and their implementations for the FDTD method and MoM on Beowulf PC clusters. Manipulations of full matrix as well as sparse matrix calculations are described.

2.1. Finite-Difference Time-Domain (FDTD) Method

The FDTD method was proposed by Kane Yee in 1966 [11]. It is one of the most popular simulation techniques in computational electromagnetics. It has broad applications, including electronic packaging, antennas and radiation, waveguiding structures, nonlinear problems in transmission lines with active devices, and other electromagnetic problems.

2.1.1. Theory of FDTD. Consider a free-space region that does not have either electric or magnetic current sources. The time-dependent Maxwell equation can be written as

$$\nabla \times \vec{E} = -\mu \frac{\partial \vec{H}}{\partial t} \quad (1)$$

$$\nabla \times \vec{H} = \sigma \vec{E} + \varepsilon \frac{\partial \vec{E}}{\partial t} \quad (2)$$

where \vec{E} and \vec{H} are the electric field and magnetic field, respectively. The magnetic permeability is denoted by μ , the electric permittivity by ε , and the electric conductivity by σ . In Cartesian coordinates, we can decompose the vector components of the curl operators in (1) and (2) as the following system of six coupled scalar equations:

$$\frac{\partial H_x}{\partial t} = \frac{1}{\mu} \left(\frac{\partial E_y}{\partial z} - \frac{\partial E_z}{\partial y} \right) \quad (3a)$$

$$\frac{\partial H_y}{\partial t} = \frac{1}{\mu} \left(\frac{\partial E_z}{\partial x} - \frac{\partial E_x}{\partial z} \right) \quad (3b)$$

$$\frac{\partial H_z}{\partial t} = \frac{1}{\mu} \left(\frac{\partial E_x}{\partial y} - \frac{\partial E_y}{\partial x} \right) \quad (3c)$$

$$\frac{\partial E_x}{\partial t} = \frac{1}{\varepsilon} \left(\frac{\partial H_z}{\partial y} - \frac{\partial H_y}{\partial z} - \sigma E_x \right) \quad (4a)$$

$$\frac{\partial E_y}{\partial t} = \frac{1}{\varepsilon} \left(\frac{\partial H_x}{\partial z} - \frac{\partial H_z}{\partial x} - \sigma E_y \right) \quad (4b)$$

$$\frac{\partial E_z}{\partial t} = \frac{1}{\varepsilon} \left(\frac{\partial H_y}{\partial x} - \frac{\partial H_x}{\partial y} - \sigma E_z \right) \quad (4c)$$

These six coupled partial-differential equations form the basis of the FDTD algorithm for general three-dimensional electromagnetic interactions. The Maxwell equations are discretized in a finite-difference timestepping manner by means of the Yee grid. The geometric position of the electric and magnetic field vector components in a unit Yee space lattice is shown in Fig. 4.

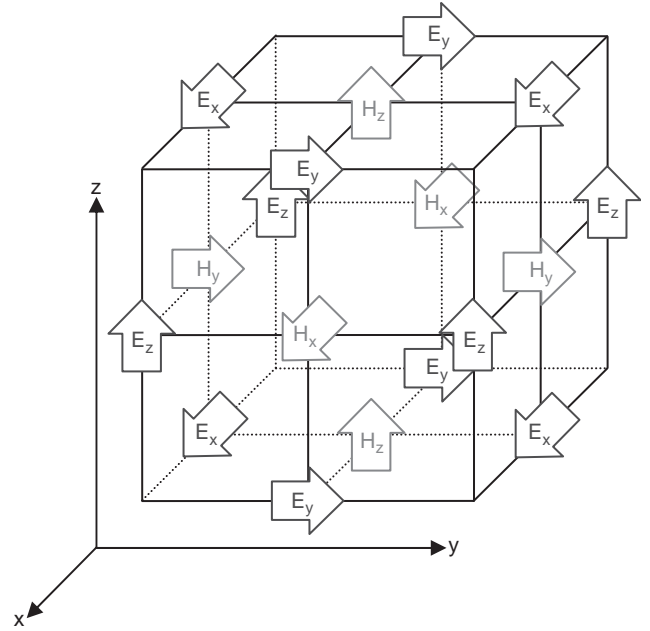


Figure 4. The Yee lattice.

If the space point in Yee's grid is uniform, we can define a gridpoint in the solution region as

$$(i, j, k) = (i \Delta x, j \Delta y, k \Delta z) \quad (5)$$

where Δx , Δy , and Δz are the spatial increments in x , y , and z directions, respectively. On the basis of this notation, any function F of space and time can be discretized as follows:

$$F^n(i, j, k) = F(i \Delta x, j \Delta y, k \Delta z, n \Delta t) \quad (6)$$

We adopt the central-difference approximation for both temporal and spatial derivatives with the second-order accuracy. Then the corresponding derivatives of function F can be expressed as follows:

$$\frac{\partial F^n(i, j, k)}{\partial x} = \frac{F^n(i + \frac{1}{2}, j, k) - F^n(i - \frac{1}{2}, j, k)}{\Delta x} + O((\Delta x)^2) \quad (7)$$

$$\frac{\partial F^n(i, j, k)}{\partial t} = \frac{F^{n+(1/2)}(i, j, k) - F^{n-(1/2)}(i, j, k)}{\Delta t} + O((\Delta t)^2) \quad (8)$$

With the notation in (7) and (8), we can express the components in (4a) as follows:

$$\frac{\partial E_x}{\partial t} \approx \frac{E_x^{n+1}(i, j, k) - E_x^n(i, j, k)}{\Delta t}, (n + \frac{1}{2}, i, j, k) \quad (9)$$

$$\frac{\partial H_z}{\partial y} \approx \frac{H_z^{n+(1/2)}(i, j + \frac{1}{2}, k) - H_z^{n+(1/2)}(i, j - \frac{1}{2}, k)}{\Delta y}, \quad (10)$$

$$(n + \frac{1}{2}, i, j, k)$$

$$\frac{\partial H_y}{\partial z} \approx \frac{H_y^{n+(1/2)}(i, j, k + \frac{1}{2}) - H_y^{n+(1/2)}(i, j, k - \frac{1}{2})}{\Delta z}, \quad (11)$$

$$(n + \frac{1}{2}, i, j, k)$$

$$\sigma E_x \approx \frac{E_x^{n+1}(i, j, k) + E_x^n(i, j, k)}{2}, \quad (12)$$

$$(n + \frac{1}{2}, i, j, k)$$

Thus

$$E_x^{n+1}\left(i + \frac{1}{2}, j, k\right) = \frac{\left(1 - \frac{\sigma \Delta t}{2\varepsilon}\right)}{\left(1 + \frac{\sigma \Delta t}{2\varepsilon}\right)} E_x^n\left(i + \frac{1}{2}, j, k\right) + \frac{\frac{\Delta t}{\varepsilon}}{\left(1 + \frac{\sigma \Delta t}{2\varepsilon}\right)} \times \left[\frac{H_z^{n+(1/2)}\left(i + \frac{1}{2}, j + \frac{1}{2}, k\right) - H_z^{n+(1/2)}\left(i + \frac{1}{2}, j - \frac{1}{2}, k\right)}{\Delta y} \right] - \frac{\frac{\Delta t}{\varepsilon}}{\left(1 + \frac{\sigma \Delta t}{2\varepsilon}\right)} \left[\frac{H_y^{n+(1/2)}\left(i + \frac{1}{2}, j, k + \frac{1}{2}\right) - H_y^{n+(1/2)}\left(i + \frac{1}{2}, j, k - \frac{1}{2}\right)}{\Delta z} \right] \quad (13a)$$

The y and z components of the electric field can be expressed as follows:

$$E_y^{n+1}\left(i, j + \frac{1}{2}, k\right) = \frac{\left(1 - \frac{\sigma \Delta t}{2\varepsilon}\right)}{\left(1 + \frac{\sigma \Delta t}{2\varepsilon}\right)} E_y^n\left(i, j + \frac{1}{2}, k\right) + \frac{\frac{\Delta t}{\varepsilon}}{\left(1 + \frac{\sigma \Delta t}{2\varepsilon}\right)} \times \left[\frac{H_x^{n+(1/2)}\left(i, j + \frac{1}{2}, k + \frac{1}{2}\right) - H_x^{n+(1/2)}\left(i, j + \frac{1}{2}, k - \frac{1}{2}\right)}{\Delta z} \right] - \frac{\frac{\Delta t}{\varepsilon}}{\left(1 + \frac{\sigma \Delta t}{2\varepsilon}\right)} \left[\frac{H_z^{n+(1/2)}\left(i + \frac{1}{2}, j + \frac{1}{2}, k\right) - H_z^{n+(1/2)}\left(i - \frac{1}{2}, j + \frac{1}{2}, k\right)}{\Delta x} \right] \quad (13b)$$

$$E_z^{n+1}\left(i, j, k + \frac{1}{2}\right) = \frac{\left(1 - \frac{\sigma \Delta t}{2\varepsilon}\right)}{\left(1 + \frac{\sigma \Delta t}{2\varepsilon}\right)} E_z^n\left(i, j, k + \frac{1}{2}\right) + \frac{\frac{\Delta t}{\varepsilon}}{\left(1 + \frac{\sigma \Delta t}{2\varepsilon}\right)} \times \left[\frac{H_y^{n+(1/2)}\left(i + \frac{1}{2}, j, k + \frac{1}{2}\right) - H_y^{n+(1/2)}\left(i - \frac{1}{2}, j, k + \frac{1}{2}\right)}{\Delta x} \right] - \frac{\frac{\Delta t}{\varepsilon}}{\left(1 + \frac{\sigma \Delta t}{2\varepsilon}\right)} \left[\frac{H_x^{n+(1/2)}\left(i, j + \frac{1}{2}, k + \frac{1}{2}\right) - H_x^{n+(1/2)}\left(i, j - \frac{1}{2}, k + \frac{1}{2}\right)}{\Delta y} \right] \quad (13c)$$

Similarly, the vector components of the magnetic field can be expressed as follows:

$$H_x^{n+(1/2)}\left(i, j + \frac{1}{2}, k + \frac{1}{2}\right) = H_x^{n+(1/2)}\left(i, j + \frac{1}{2}, k + \frac{1}{2}\right) + \frac{\Delta t}{\mu} \left[\frac{E_y^n\left(i, j + \frac{1}{2}, k + 1\right) - E_y^n\left(i, j + \frac{1}{2}, k\right)}{\Delta z} \right] - \frac{\Delta t}{\mu} \left[\frac{E_z^n\left(i, j + 1, k + \frac{1}{2}\right) - E_z^n\left(i, j, k + \frac{1}{2}\right)}{\Delta y} \right] \quad (14a)$$

$$H_y^{n+(1/2)}\left(i + \frac{1}{2}, j, k + \frac{1}{2}\right) = H_y^{n+(1/2)}\left(i + \frac{1}{2}, j, k + \frac{1}{2}\right) + \frac{\Delta t}{\mu} \left[\frac{E_z^n\left(i + 1, j, k + \frac{1}{2}\right) - E_z^n\left(i, j, k + \frac{1}{2}\right)}{\Delta x} \right] - \frac{\Delta t}{\mu} \left[\frac{E_x^n\left(i + \frac{1}{2}, j, k + 1\right) - E_x^n\left(i + \frac{1}{2}, j, k\right)}{\Delta z} \right] \quad (14b)$$

$$H_z^{n+(1/2)}\left(i + \frac{1}{2}, j + \frac{1}{2}, k\right) = H_z^{n+(1/2)}\left(i + \frac{1}{2}, j + \frac{1}{2}, k\right) + \frac{\Delta t}{\mu} \left[\frac{E_x^n\left(i + \frac{1}{2}, j + 1, k\right) - E_x^n\left(i + \frac{1}{2}, j, k\right)}{\Delta y} \right] - \frac{\Delta t}{\mu} \left[\frac{E_y^n\left(i + 1, j + \frac{1}{2}, k\right) - E_y^n\left(i, j + \frac{1}{2}, k\right)}{\Delta x} \right] \quad (14c)$$

It is noted from (13) and (14) that both electric field and magnetic field could be updated from the previous E and H fields. Following the timestepping expressions in (13) and (14), we can calculate the corresponding fields step by step. Many geometries of interest are defined in “open” regions where the spatial domain of the computed field is unbounded in one or more coordinate directions. Because of the finite size in computer memory, the finite-difference grid has to be truncated. Therefore, we need to define not only the field computation domain in a finite size that should be large enough to enclose the structure of interest but also a suitable boundary condition such that the simulation is capable of extending the outer perimeter to infinity and ensuring that the reflections of outgoing waves are minimized. Such artificial boundaries described by the mathematical expressions are known as the absorbing boundary conditions (ABCs). The most commonly used ABC includes Mur ABC [19] and perfectly matched layered ABC [20].

To ensure the stability and accuracy of FDTD computation, the size of Yee cell are typically $\frac{1}{10}$ th– $\frac{1}{20}$ th of the wavelength corresponding to the highest frequency of interest, and then the timestep must satisfy the following stability condition [21]

$$\Delta t \leq \frac{1}{c_{\max} \times \sqrt{\frac{1}{\Delta x^2} + \frac{1}{\Delta y^2} + \frac{1}{\Delta z^2}}} \quad (15)$$

where Δt is the timestep and c_{\max} is the maximum light velocity; Δx , Δy , and Δz are the size of the FDTD cube in x , y , and z directions, respectively.

The algorithm of FDTD calculation is shown in Fig. 5. The process of updating the magnetic and electric fields is the most time-consuming part of the calculation. This problem can be solved by means of parallel computing as discussed in the following subsection.

2.1.2. Parallel Implementation of FDTD. Although FDTD is a powerful tool for the analysis of time-domain problems and nonlinear problem with active devices, it requires a huge amount of computer memory and long computation time. This limits the use of FDTD in large-scale problems. In this subsection, we discuss how to implement the parallel computation of FDTD. The main idea is to decompose the single FDTD computation domain into several smaller domains. Each node in the Beowulf PC cluster will manipulate each of these domains and compute its corresponding electric and magnetic fields. The exchange of data occurs only at the interface of two different domains, and thus little communication time is required.

Figure 6 illustrates the concept of the FDTD domain decomposition and the mechanism of field exchange. Only three nodes in the parallel computing platform are used for illustrative purposes. As we can see in the figure, the FDTD computation domain is spatially decomposed into three regions of regular gridpoints along the z axis. Each node manipulates the computation for the corresponding region. On the basis of the FDTD algorithm, we need to update the E and H fields in each timestep. These E and H

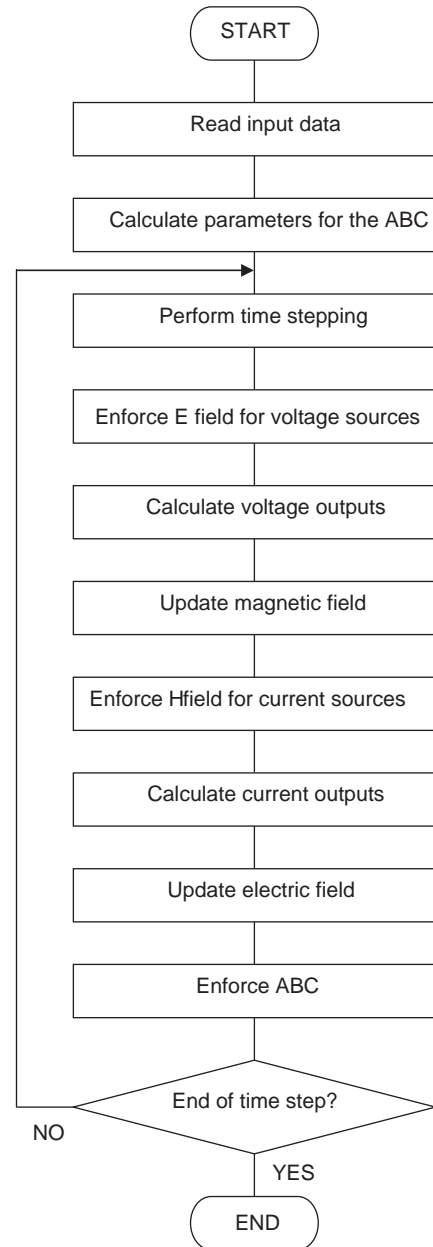


Figure 5. FDTD algorithm.

fields are computed with the corresponding adjacent neighboring E and H fields. Owing to the domain decomposition, some of the required E and H fields are not stored in the same computing node. They are calculated and stored in the adjacent node. When using the ABC, the first or last node needs to exchange E or H fields in either upper or lower slices of its domain only. The node in the center needs to exchange the calculated E and H fields in both upper and lower slices of its domain to its adjacent node for updating E and H fields in each timestep. Such field exchange process is handled by calling the message-passing interface (MPI) library. Referring to Fig. 6, we can see that the H_y field is used for updating the E_x field in each timestep. For the subdomain in node 1, the lower edge of the H_y field is missing. The upper slice of the H_y

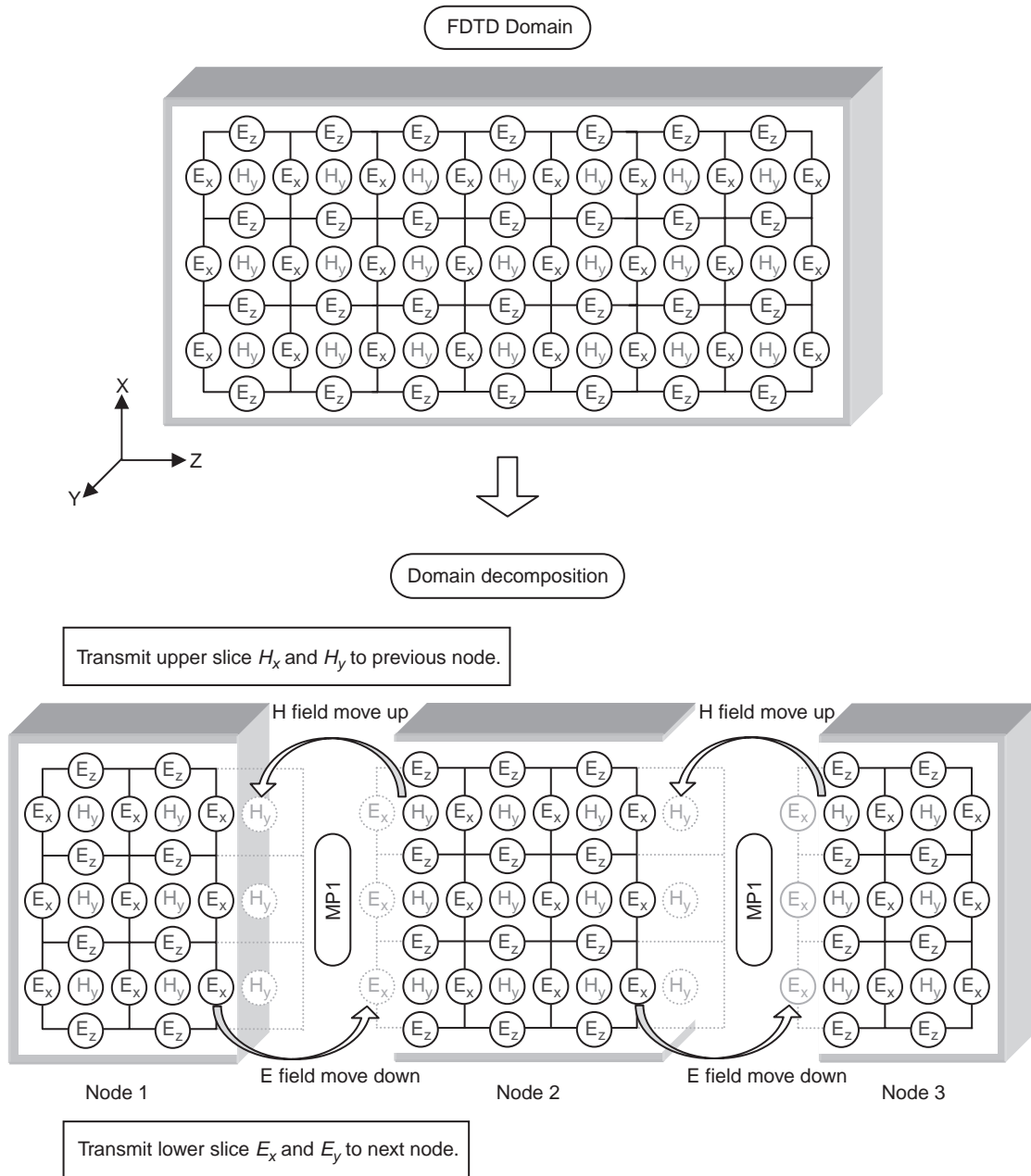


Figure 6. Domain decomposition by three computing nodes.

field in node 2's subdomain is needed to transfer the field information to node 1 for updating the E_x field. Similarly, the lower slice of the E_x field in node 1's subdomain will transfer the information to node 2 for updating the H_y field in each timestep.

To generalize the mechanism, Fig. 7 is a pictorial representation of the domain decomposition and field exchange mechanism. Assuming that M computing nodes are used, the FDTD computation domain is decomposed into M subdomains, equal or nearly equal in size, along the z -axis. The corresponding subdomain, which is rectangular in shape, and nonoverlapping, is computed completely independently of other nodes in the parallel computing platform. After the decomposition, only three

types of domain need to be handled separately: the first, center, and last regions, respectively, as shown in Fig. 7b. The field exchange mechanism for these three different regions are shown in Figs. 8, 9, and 10 respectively. In such an exchange mechanism, Eqs. (13) and (14) are used to update the E and H fields, respectively. The parallel-implemented FDTD codes for handling different regions are shown in Figs. 11 and 12. The data communication among all nodes is by means of using message-passing interface (MPI) library. To update the magnetic fields and electric fields in each timestep, MPI library calls such as `MPI_SEND` and `MPI_RECEIVE` are used. `MPI_SEND` and `MPI_RECEIVE` perform basic data communications (i.e., send and receive) among the nodes.

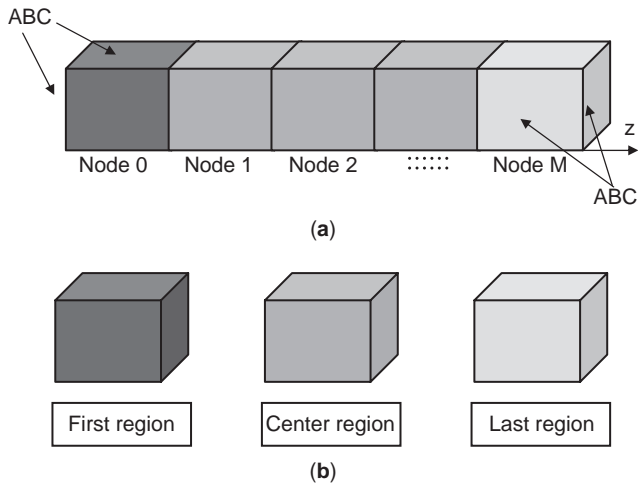


Figure 7. (a) Pictorial representation of domain decomposition into M nodes; (b) three types of region after domain decomposition. (This figure is available in full color at <http://www.mrw.interscience.wiley.com/erfme>.)

As an example, we will now analyze the active integrated antennas using parallel-implemented FDTD code.

2.1.3. Numerical Results (FDTD). Active integrated antennas have many military and commercial applications such as spatial or quasioptical power-combining arrays, phased arrays, and wireless communication systems. Since an active integrated antenna is a nonlinear antenna and operates with large-signal oscillations, it is difficult to predict the electromagnetic characteristics such as its stable oscillation modes and operating frequency. In this subsection, FDTD method is used to analyze the active integrated antenna problem [22–24]. The layout of an active integrated antenna array is shown in Fig. 13. The components of the active integrated antenna consist of Gunn diodes, radiating patches, two-stage $\lambda/4$ transformers, open tuning stubs, and adjacent coupling lines. Figure 14 shows the circuit model of the Gunn diode, and the equations of the Gunn diode operation [24,25] are also shown in Eqs. (16)–(20) and (22)

$$\frac{\epsilon}{\Delta t} E_z^{n+1}(i_s, j_s, k) = \frac{\epsilon}{\Delta t} E_z^n(i_s, j_s, k) + L[H_x, H_y] - \frac{I_d^{n+(1/2)}}{\Delta x \Delta y} \quad (16)$$

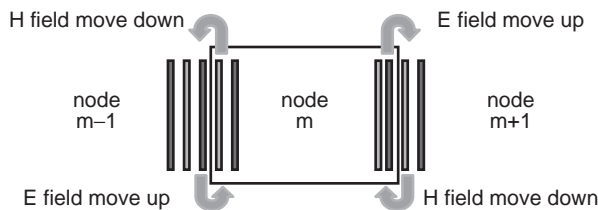


Figure 8. Pictorial representation for updating E field (red-colored bar) and H field (blue-colored bar) in the center region for each timestep in FDTD calculation. (This figure is available in full color at <http://www.mrw.interscience.wiley.com/erfme>.)

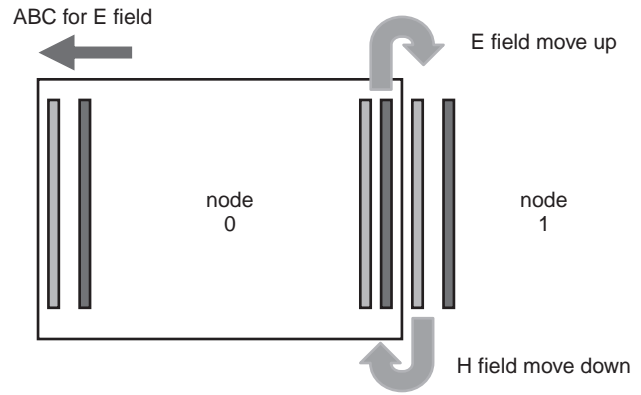


Figure 9. Pictorial representation for updating E field (red-colored bar) and H field (blue-colored bar) in the first region for each timestep in FDTD calculation. (This figure is available in full color at <http://www.mrw.interscience.wiley.com/erfme>.)

$$I_d^{n+(1/2)} = -I_d^{n-(1/2)} + \frac{2(V_s^n + V_z^n)}{R} \quad (17)$$

$$V_s^{n+1} = V_s^n - \frac{I_d^{n+(1/2)} + F(V_s^n)}{\frac{C}{\Delta t} + \frac{F'(V_s^n)}{2}} \quad (18)$$

$$V_z^n = \sum_{k=1}^3 E_z(i_s, j_s, k) \Delta z \quad (19)$$

$$F(V_s) = -G_1 V_s + G_3 V_s^3 \quad (20)$$

$$L[H_x, H_y] = \frac{H_x^{n+(1/2)}(i_s, j_s - 1, k) - H_x^{n+(1/2)}(i_s, j_s, k)}{\Delta y} + \frac{H_y^{n+(1/2)}(i_s, j_s, k) - H_y^{n+(1/2)}(i_s - 1, j_s, k)}{\Delta x} \quad (21)$$

where $G_1 = 0.0252 \Omega^{-1}$ and $G_3 = 0.0265 \Omega^{-1} V^{-2}$. The capacitance C is 0.2 pF, and the series resistance R is 1.0 Ω ; $F'(V_s)$ is a derivative of $F(V_s)$.

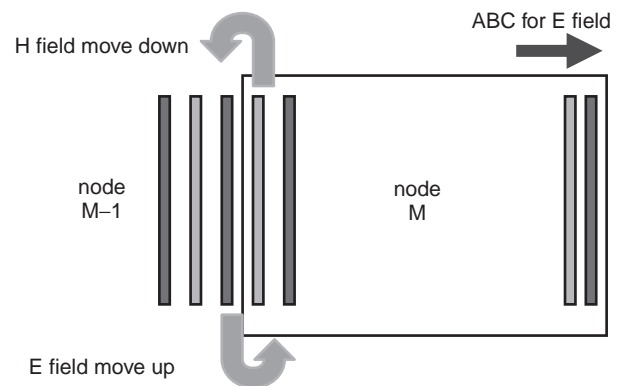


Figure 10. Pictorial representation for updating E field (red-colored bar) and H field (blue-colored bar) in the last region for each timestep in FDTD calculation, where M is the total number of processors used in the calculation. (This figure is available in full color at <http://www.mrw.interscience.wiley.com/erfme>.)

Updating Magnetic Field in the Center Regions

```

/**/ Update Hx, same calculation for Hy and Hz ***/
/**/ Hx : H-field in x ***/
/**/ Ez : E-field in z ; Ey : E-field in y ***/
/**/ Hmult1, Hmult2, Hmult3 : FDTD parameter ***/
FOR k=1 to Nz/N_nodes
  FOR j=1 to Ny
    FOR i=0 to Nx
      Hx(i,j,k)=Hmult1 x Hx(i,j,k)
        + Hmult2 x (Ez(i,j-1,k)-Ez(i,j,k))
        + Hmult3 x (Ey(i,j,k)-Ey(i,j,k-1))
    END FOR
  END FOR
END FOR
/**/ tUHx : store the upper slice of Hx ***/
k=the index of upper slice in z.
FOR j=1 to Ny
  FOR i=0 to Nx
    tUHx(i,j)=Hx(i,j,k)
  END FOR
END FOR

```

This upper slice will be send to the next region and will be used as a lower slice.

Send Upper Slice H Upward

```

/**/ nodeID (index of node) = 0,1,2...N ***/
/**/ N : number of node used ***/
IF (nodeID not equal to N-1) THEN
  Call MPI function MPI_SEND for sending upper slice of Hx (tUHx) to
    previous (nodeID-1) node
  Call MPI function MPI_SEND for sending upper slice of Hy (tUHy) to
    previous (nodeID-1) node
END IF
IF (nodeID not equal to 0) THEN
  Call MPI function MPI_RECV for receiving upper slice of Hx (tUHx) from
    next (nodeID+1) node
  Call MPI function MPI_RECV for receiving upper slice of Hy (tUHy) from
    next (nodeID+1) node
END IF

```

Receive Lower Slice H from Down Under

```

/**/ tLHx : store the lower slice of Hx ***/
k=the index of lower slice in z.
FOR j=1 to Ny
  FOR i=0 to Nx
    Hx(i,j,k) = tLHx(i,j)
  END FOR
END FOR
FOR j=0 to Ny
  FOR i=1 to Nx
    Hy(i,j,k) = tLHy(i,j)
  END FOR
END FOR

```

Figure 11. Parallel-implemented FDTD code to handle center region of the computation domain.

There is a narrow gap between two coupling lines. By short-circuiting the gap with a conductor and a resistor, respectively, the odd and even radiating mode can be obtained [26]. In order to reduce the CPU time, parallel-implemented FDTD code is used in the analysis. The simulation is performed on the Beowulf cluster depicted in Section 1.4. The active integrated antenna with four units operates at 12.4 GHz. The size of the computation domain $N_x \times N_y \times N_z$ is $235 \times 109 \times 16$ cells. The size of

each cell in the x , y , and z directions are 0.372, 0.392, and 0.392 mm, respectively. The narrow gap between coupling lines is connected with a 100- Ω resistor for providing an even radiating mode. The simulation is with Mur ABC. Figure 15 shows the voltage across the Gunn diodes. We can see that the voltages in the four units are in phase. The electric field component E_z at the dielectric-air interface at two different time instants are shown in Figs. 16 and 17, respectively. Figure 16 shows the in-phase

Similar Calculation for E Field

```

/**/ Update Ex, same calculation for Ey and Ez ***/
/**/ Ex : E-field in x ***/
/**/ Hz : H-field in z ; Hy : H-field in y ***/
/**/ Emult1, Emult2, Emult3 : FDTD parameter ***/
FOR k=1 to Nz/N_nodes
  FOR j=1 to Ny-1
    FOR i=1 to Nx
      Ex(i,j,k)=Emult1 x Ex(i,j,k)
      + Emult2 x (Hz(i,j+1,k)-Hz(i,j,k))
      + Emult2 x (Hy(i,j,k)-Hy(i,j,k-1))
    END FOR
  END FOR
END FOR

/**/ tLEx : store the lower slice of Ex ***/
k=the index of lower slice in z.
FOR j=1 to Ny-1
  FOR i=1 to Nx
    tLEx(i,j)=Ex(i,j,k)
  END FOR
END FOR

IF (nodeID not equal to 0) THEN
  Call MPI function MPI_SEND for sending upper slice of Ex (tLEx) for
  next (nodeID+1) node
  Call MPI function MPI_SEND for sending upper slice of Ey (tLEy) for
  next (nodeID+1) node
END IF
IF (nodeID not equal to N_nodes-1) THEN
  Call MPI function MPI_RECV for receiving upper slice of Ex (tLEx) for
  previous (nodeID+1)node
  Call MPI function MPI_RECV for receiving upper slice of Ey (tLEy) for
  previous (nodeID+1)node
END IF

/**/ tLEx : store the lower slice of Ex ***/
k=the index of upper slice in z.
FOR j=1 to Ny-1
  FOR i=1 to Nx
    Ex(i,j,k) = tLEx(i,j)
  END FOR
END FOR
FOR j=1 to Ny
  FOR i=1 to Nx-1
    Ey(i,j,k) = tLEy(i,j)
  END FOR
END FOR

```

Figure 11. (Continued).

behavior; Fig. 17 shows even radiating mode moment with different timestep.

We examine the parallel code with a different number of nodes in terms of speedup factor, efficiency, computation time, and time saving. Table 1 shows the overall performance of the parallel code with 30,000 timesteps. From the table, we can see that the computing time is reduced rapidly when the number of computing nodes is increased. The rate of change in CPU time with the number of computing nodes is shown in Fig. 18. Figure 19 shows the speedup factor of different number of nodes used. As we can see from the figure, the speedup factor is directly proportional to the number of computing nodes, as expected. For the ideal situation, it is expected that the speedup factor will be M , if M computing nodes are used.

However, that is not the case in practice. For example, as shown in the Figs. 18 and 19, the speedup factor is about 21 if 24 computing nodes are used. The discrepancy is due to the time spent for data communication among nodes for updating the E and H fields. The efficiency can reach almost 100% with the use of two or four computing nodes as indicated in Fig. 20. With a smaller number of nodes, the subdomain will be larger and the time for data communication among the nodes relatively shorter when compared to the remaining computation since most of the CPU time is spent computing the E and H fields. This is why the efficiency can be higher if a smaller number of nodes are used. However, when a smaller number of computing nodes are used, the speedup factor will be relatively low, as shown in Fig. 19. The saving in CPU

ABC on the Right and Left Faces

```

/**/ Ex : E-field in x      /**/
/**/ EzZ0n : ABC of Ex    /**/
/**/ smz1 : ABC parameter /**/
IF (nodelD equal to 0) THEN
  FOR i=1 to Nx
    FOR j=1 to Ny-1
      Ex(i,j,0)=ExZ0n(i,j,1)+ smz1*(Ex(i,j,1) - ExZ0n(i,j,0))
    END FOR
  END FOR
ENDIF
IF (nodelD equal to N_nodes-1) THEN
  k=Nz
  FOR i=1 to Nx
    FOR j=1 to Ny-1
      Ex(i,j,k)=ExZ0n(i,j,1) + smz1*(Ex(i,j,k-1) - ExZ0n(i,j,0))
    END FOR
  END FOR
ENDIF
ENDIF

```

Figure 12. Parallel-implemented FDTD code to handle first and last regions of the computation domain.

with a different number of computing nodes is shown in Fig. 21. It is obvious that the saving in CPU time is greater when the number of computing nodes increases.

2.1.4. FDTD Method with SPICE for Analyzing Electric Circuit. In the analysis of electric circuits, commercial software such as SPICE is commonly used. It is one of the most popular software packages for electric circuit analysis in both frequency and time domains. It provides a large number of models for complex electronic devices and libraries [27]. Many researchers have focused on combining the FDTD method with SPICE [28,29]. The FDTD method with SPICE (FDTD-SPICE) is one of the most powerful tools for analyzing integrated circuits, active antennas, and electromagnetic interference (EMI) problems. In this subsection, we will show the application of FDTD in circuit analysis by merging the FDTD method with SPICE. However, SPICE cannot directly merge FDTD domain because the input-output differences. In SPICE, the input and the output are voltage (V) and current (I), respectively. On the other hand, in FDTD, the input and the output are the electric field (E) and magnetic field (H), respectively. To solve this difficulty, we

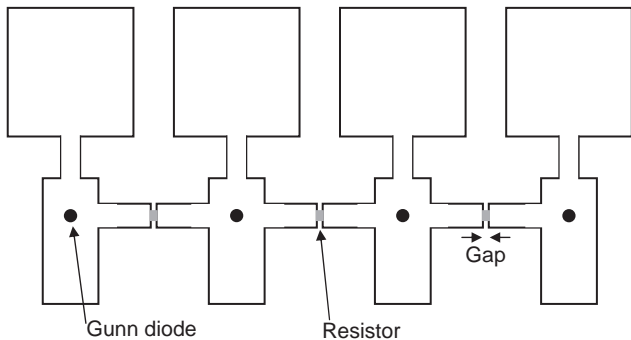


Figure 13. Layout of active integrated antenna.

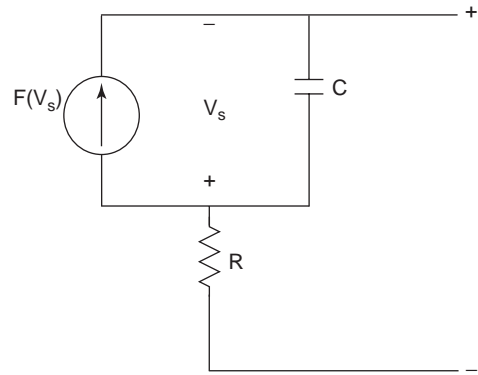


Figure 14. Circuit model of Gunn diode.

use the equivalent SPICE circuit as shown in Fig. 22. It is expressed by means of Ampere’s law, and the total current I is expressed in the following equation

$$C \frac{dV}{dt} + I(V) = I \tag{22}$$

where $I(V)$ is the current source, C is capacitance of an FDTD cell, and V is the voltage across the lumped element. At each timestep of updating the electric field in the FDTD computation, the information of $I(V)$ and C will be sent to SPICE for solving the lumped element, and then SPICE will send back the voltage of the lumped element to the FDTD module.

Figures 23 and 24 show the FDTD model and the layout of the simplified VHF amplifier circuit [30], respectively. The FDTD cell size is $d_x = d_y = d_z = 1$ mm and the relative dielectric constant is unity. The total number of timesteps in the calculation is 30,000. The impedances of the microstrip lines are 47.9Ω , and the two lines are separated by $2\frac{1}{2}$ times the width of the microstrip. The voltages at the input to the lumped transistor circuit and across the output resistor are shown in Fig. 25. The simulation results of FDTD-SPICE give good agreement with that of SPICE alone. The minimal difference between FDTD-SPICE and SPICE simulation is due to the separation between the microstrip line and parasitic coupling.

2.1.5. Matrix Manipulation of FDTD. If we cast the FDTD operation into matrix-vector manipulation, it is not difficult to see that each field-updating step requires matrix-vector multiplications and that the matrices are sparse ones as the field at an FDTD node is affected only by the nearby fields. This is one of the key characteristics of the partial-differential equation (PDE) approach. On the other hand, another popular tool in computational electromagnetics is the integral equation method in which the integral equation is cast into a matrix equation via the use of MoM. In contrast to the PDE approach, the resulting matrix is a full one. Parallel computing strategies are effective tactics in handling full-matrix solutions, particularly when the matrix size is large. Although the MoM matrix is denser than the FDTD matrix, it is often much smaller in size.

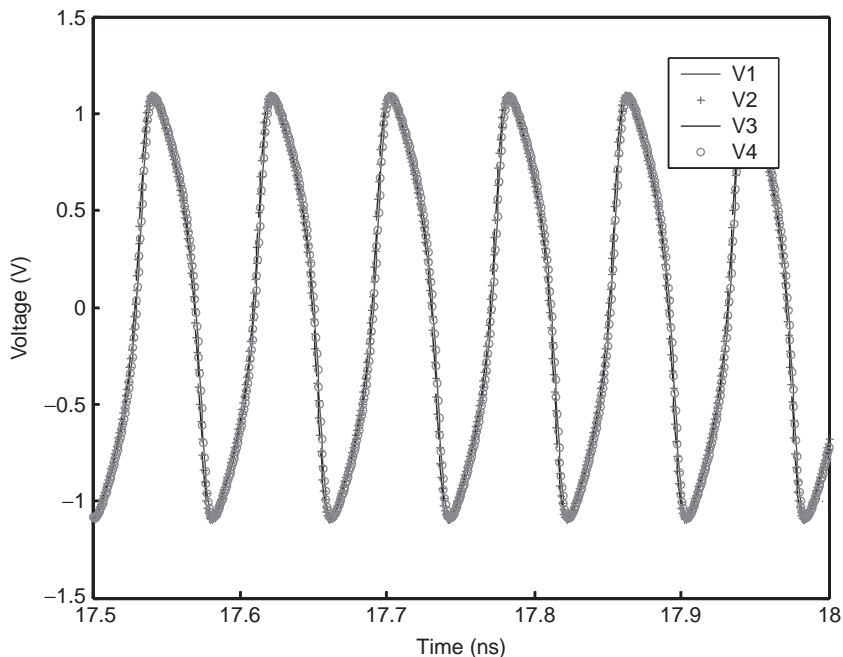


Figure 15. Stable voltage across Gunn diodes. (This figure is available in full color at <http://www.mrw.interscience.wiley.com/erfme>.)

In the following subsection, we will discuss two different scenarios when dealing with full-matrix solutions. In the first scenario a direct matrix inversion scheme is tractable. When the available computer memory resources are exhausted, we need to solve the full-matrix equation iteratively.

2.2. Method of Moments (MOM)

2.2.1. Introduction. The integral equation solver such as the method of moments (MoM) can be used to analyze many electromagnetic field problems, including those appearing in printed circuits and microstrip antennas.

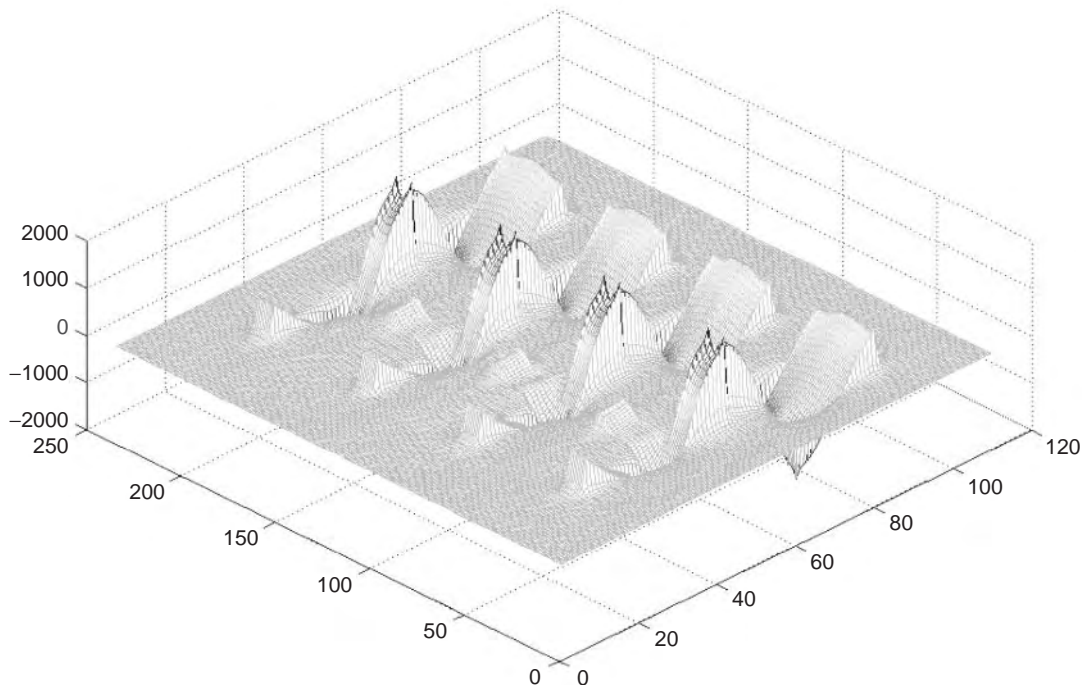


Figure 16. Electric field component E_z at dielectric-air interface. (This figure is available in full color at <http://www.mrw.interscience.wiley.com/erfme>.)

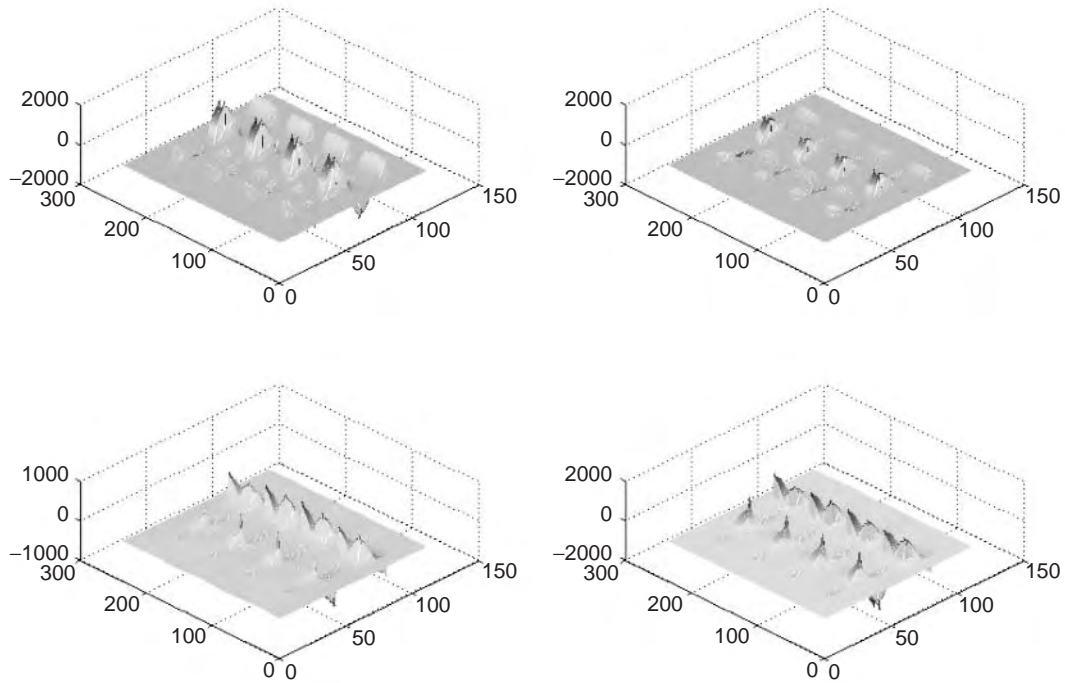


Figure 17. Electric field component E_z at dielectric–air interface at a different timestep. (This figure is available in full color at <http://www.mrw.interscience.wiley.com/erfme>.)

For these problems, the mixed potential integral equation (MPIE) formulation is often used. The MPIE is expressed as follows

$$\vec{E}^{\text{inc}} = j\omega\vec{A} + \nabla\phi \tag{23}$$

where \vec{E}^{inc} is the incident electric field and \vec{A} and ϕ are the vector and scalar potentials, respectively. The potentials can be expressed in terms of the unknown surface current density and the corresponding spatial domain Green

Table 1. Overall Performance of Parallel FDTD Code

Number of PCs	CPU Time (s)	CPU Time (min)	Speedup Factor	Efficiency (%)	Time Saving (%)
1	17382	289.7	1.0	100.0	0
2	8612	143.5	2.0	100.0	50.5
4	4323	72.1	4.0	100.0	75.1
8	2223	37.1	7.8	97.5	87.2
12	1525	25.4	11.4	95.0	91.2
16	1170	19.5	14.9	93.1	93.3
20	963	16.1	18.0	90.0	94.5
24	809	13.5	21.5	89.6	95.3

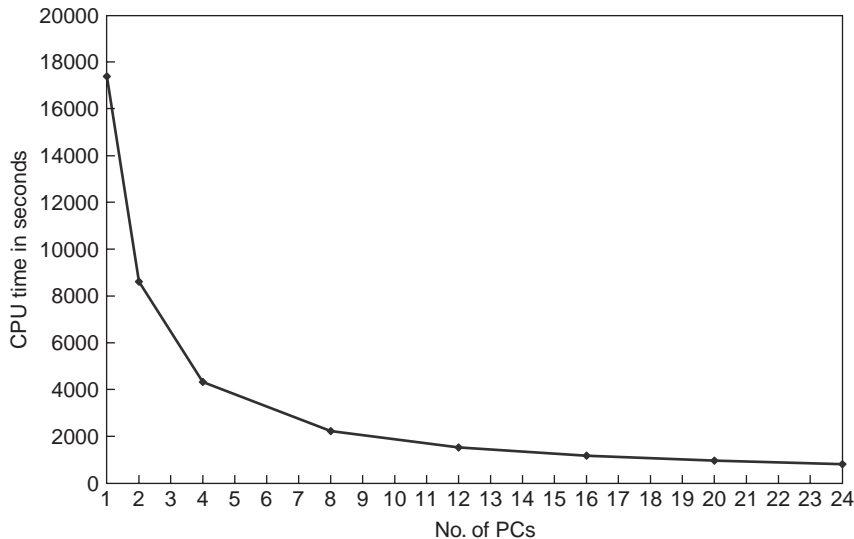


Figure 18. CPU time (s) with using different numbers of PCs.

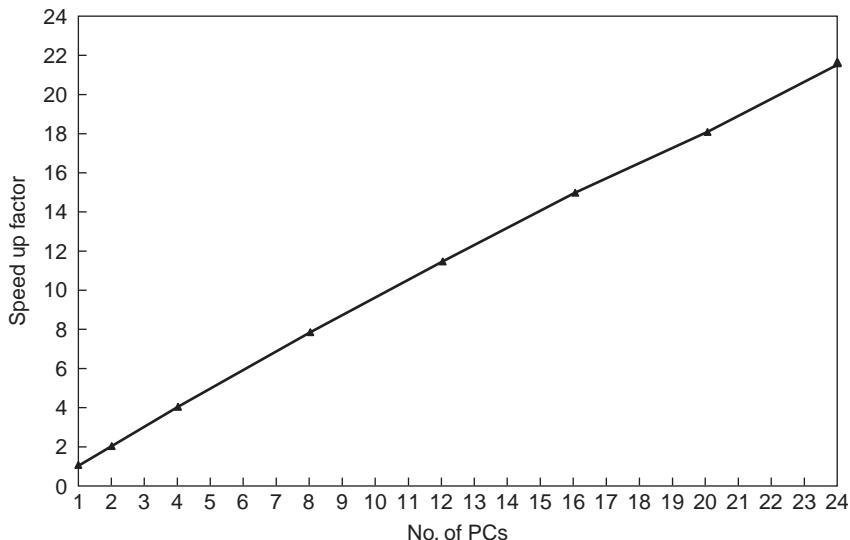


Figure 19. Speedup factor with different numbers of PCs.

functions as follows:

$$\vec{A}(\vec{r}) = \int_S dS' \vec{G}_a(\vec{r}, \vec{r}') \cdot \vec{J}(\vec{r}') \tag{24}$$

$$\phi(\vec{r}) = \int_S dS' \vec{G}_q(\vec{r}, \vec{r}') \nabla' \cdot \vec{J}(\vec{r}') \tag{25}$$

Applying different basis functions to the MPIE in conjunction with weighting functions, the matrix equation is obtained as

$$[Z]\{J\} = \{E^i\} \tag{26}$$

where $[Z]$ is the impedance matrix, $\{J\}$ is the unknown current vector, and $\{E^i\}$ is the known excitation vector. One of the commonly used basis functions is the Rao–Wilton–Glisson (RWG) basis function [31]. This matrix equation is a linear matrix equation, and direct matrix

inversion or an iterative method can be used to solve for the solution, depending on the available computer memory.

To demonstrate the effectiveness of parallel computing in solving large-scale electromagnetic problems, we consider the analysis of the microstrip reflectarray antenna and densely packed microstrip interconnects. The resulting matrix equation is extremely large in size, and it is difficult to solve by a direct matrix inversion method in a single computer due to the large computer memory requirement and extensive CPU time. To solve this problem, we implement parallel algorithms to solve the matrix equation on a parallel computing platform. The idea of the parallel algorithm is to divide the large matrix into several smaller portions. Each portion of the matrix is stored in its corresponding computing node, and therefore the memory burden can be alleviated. Each node computes only its portion of the matrix, and the overall CPU time is also reduced. The parallel algorithm is also im-

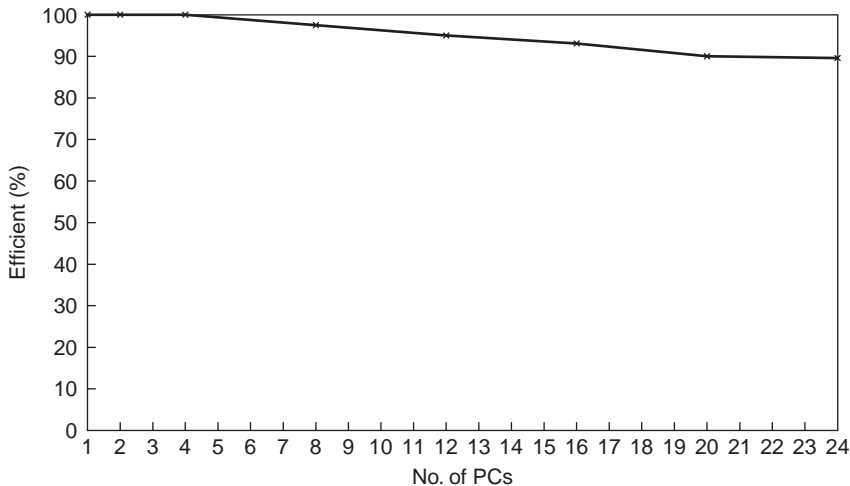


Figure 20. Efficiency with different numbers of PCs.

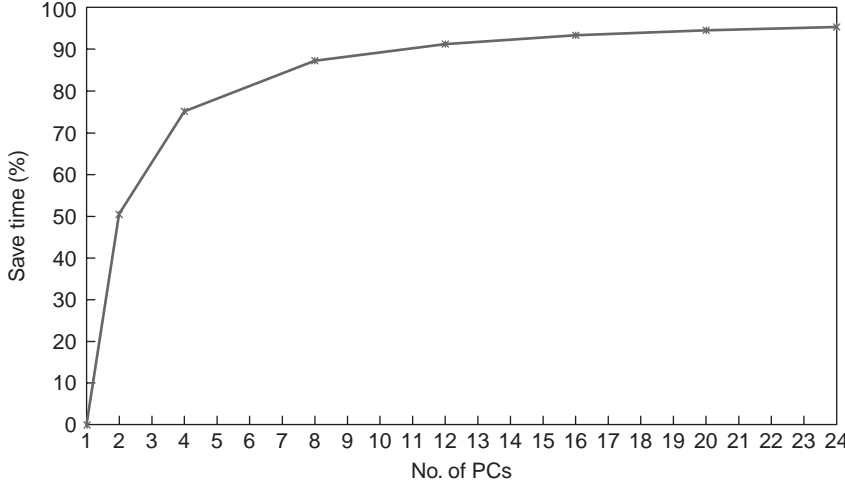


Figure 21. Time saving with different numbers of PCs.

plemented in matrix–vector multiplication form to speed up the computing time in the iterative solver. In the following subsection, we will discuss solving the matrix equation with both the Gaussian elimination method and *LU* decomposition. The parallel versions of the Gaussian elimination method and *LU* decomposition [32,33] are also considered. Then, we concentrate on discussing the parallel version matrix–vector multiplication [32,33] for iterative solutions. Finally, the sparse matrix canonical grid method [34], which is a fast solver, will be presented.

2.2.2. Methods for Solving a System of Linear Equations. The matrix equation representing the MPIE shown in (26) can be written as follows:

$$\begin{bmatrix} Z_{11} & Z_{12} & \cdots & Z_{1N} \\ Z_{21} & Z_{22} & \cdots & Z_{2N} \\ \vdots & \vdots & \ddots & \vdots \\ Z_{N1} & Z_{N2} & \cdots & Z_{NN} \end{bmatrix} \begin{bmatrix} J_1 \\ J_2 \\ \vdots \\ J_N \end{bmatrix} = \begin{bmatrix} E_1^i \\ E_2^i \\ \vdots \\ E_N^i \end{bmatrix} \quad (27)$$

In the following text, we will discuss full-matrix inversion methods for solving this linear matrix equation. Before we present their parallelized counterparts (Section 2.2.3), we will first concentrate on the conventional im-

plementation of the Gaussian elimination (Section 2.2.1) and *LU* decomposition (Section 2.2.2) methods.

2.2.2.1. Gaussian Elimination. There are two basic stages in the Gaussian elimination method. The first stage is to reduce the matrix into an upper triangular matrix. The form of the upper triangular matrix and its respective equations are shown as follows:

$$\begin{bmatrix} 1 & Z_{12}^{(1)} & \cdots & Z_{1N}^{(1)} \\ 0 & 1 & \cdots & Z_{2N}^{(2)} \\ \vdots & \vdots & \ddots & \vdots \\ 0 & 0 & \cdots & 1 \end{bmatrix} \begin{bmatrix} J_1 \\ J_2 \\ \vdots \\ J_N \end{bmatrix} = \begin{bmatrix} E_1^{i(1)} \\ E_2^{i(2)} \\ \vdots \\ E_N^{i(N)} \end{bmatrix} \quad (28)$$

$$Z_{kj}^{(k)} = \frac{Z_{kj}^{(k-1)}}{Z_{kk}^{(k-1)}} \quad (29)$$

$$Z_{ij}^{(k)} = Z_{ij}^{(k-1)} - Z_{ik}^{(k-1)} \times Z_{kj}^{(k)} \quad (30)$$

$$E_k^{i(k)} = \frac{E_k^{i(k-1)}}{Z_{kk}^{(k-1)}} \quad (31)$$

$$E_i^{i(k)} = E_i^{i(k-1)} - Z_{ik}^{(k-1)} \times E_k^{i(k)} \quad (32)$$

We rewrite (28) as

$$[U]\{J\} = \{\zeta^i\} \quad (33)$$

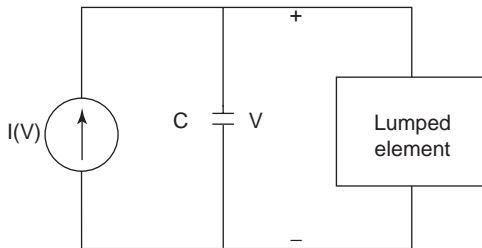


Figure 22. Equivalent SPICE circuit.

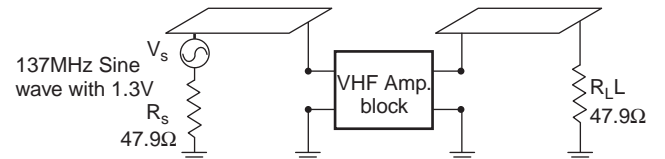


Figure 23. FDTD model.

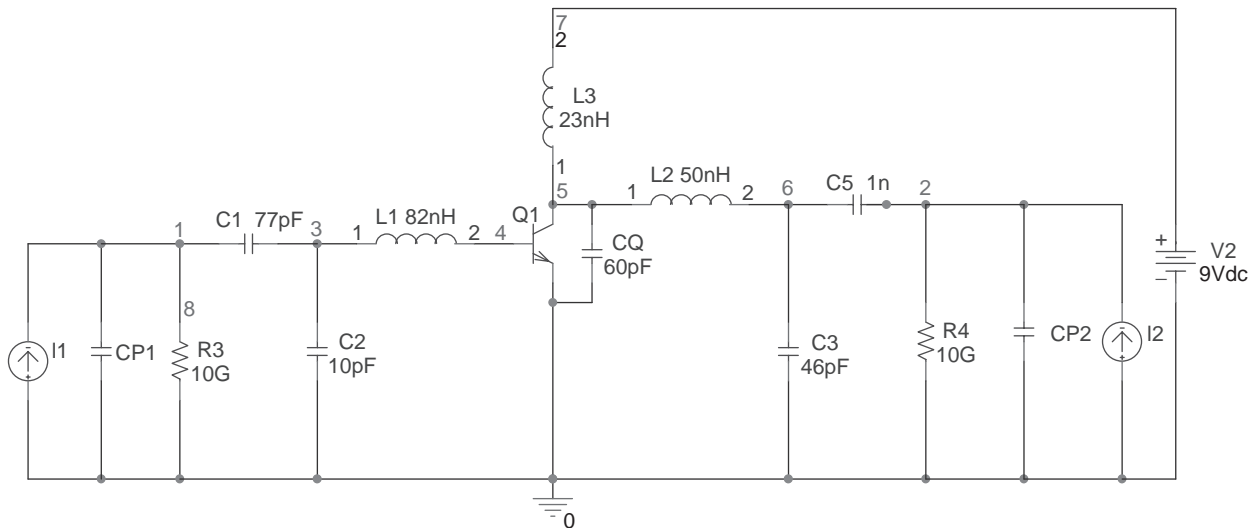


Figure 24. Layout of simplified VHF amplifier circuit.

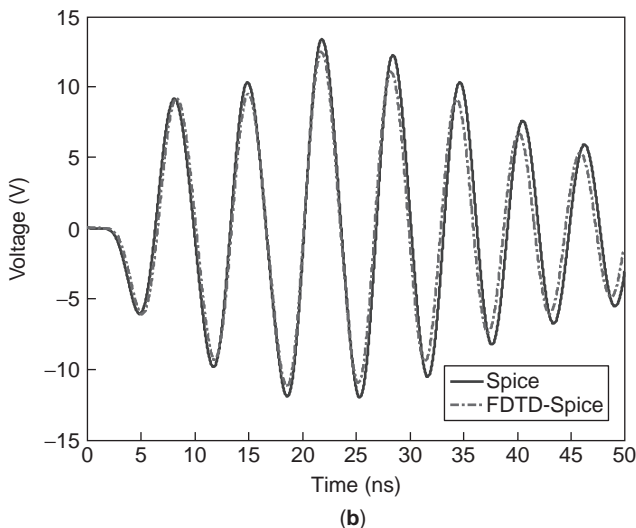
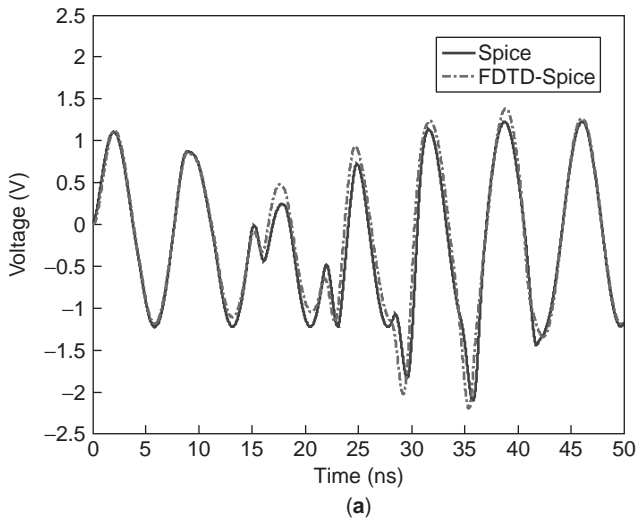


Figure 25. (a) Voltage at the input to the lumped transistor circuit; (b) voltage across the output resistor. (This figure is available in full color at <http://www.mrw.interscience.wiley.com/erfme>.)

where $[U]$ is the upper triangular matrix and k is the iteration step. In matrix $[U]$, the diagonal entries are equal to 1 and all the coefficients of the lower triangular matrix $[L]$ are set to 0. In the second stage, we apply the backsubstitution procedure to obtain the unknown currents $\{J\}$. The sequential Gaussian elimination algorithm is shown in Fig. 26. There are three nested loops. The outer loop is the iteration step and is controlled by the k variable. The remaining two loops are used to perform the Gaussian elimination calculation in each iteration step. After all the iteration steps, the backsubstitution extracts the solution $\{J\}$. The counter i of the loop is reversed and starts from N to 1. It is decreased by 1 in each looped step.

Figure 27 shows the sequential Gaussian elimination algorithm in detail. In the iteration $k = 1$, the first row of the matrix and E_1^i are divided by Z_{11} and the calculations

```

1:  /*** Gaussian elimination step ***/
2:  For k = 1 to N
3:    For j=k+1 to N
4:       $Z_{kj}=Z_{kj} / Z_{kk}$ 
5:    End For
6:     $E_k^i=E_k^i / Z_{kk}$ 
7:     $Z_{kk}=1$ 
8:
9:    For i=k+1 to N
10:     For j=k+1 to N
11:        $Z_{ij}=Z_{ij} - Z_{ik} \times Z_{kj}$ 
12:     End For
13:      $E_i^i=E_i^i - Z_{ik} \times E_k^i$ 
14:      $Z_{ik}=0$ 
15:   End For
16: End For
17: /*** Back-substitution step ***/
18: For i = N to 1 (decrease 1 in each step)
19:    $J_i = E_i^i$ 
20:   For j = i+1 to N
21:      $J_i = J_i - J_j Z_{ji}$ 
22:   End For
23: End For

```

Figure 26. Algorithm of sequential Gaussian elimination.

Initial state

$$\begin{bmatrix} Z_{11} & Z_{12} & Z_{13} & Z_{14} & E_1^i \\ Z_{21} & Z_{22} & Z_{23} & Z_{24} & E_2^i \\ Z_{31} & Z_{32} & Z_{33} & Z_{34} & E_3^i \\ Z_{41} & Z_{42} & Z_{43} & Z_{44} & E_4^i \end{bmatrix}$$

Iteration k = 1

$$\begin{aligned} Z_{1j}^{(1)} &= Z_{1j} / Z_{11} \leftarrow \begin{bmatrix} 1 & z_{12}^{(1)} & z_{13}^{(1)} & z_{14}^{(1)} & E_1^{i(1)} \\ 0 & z_{22}^{(1)} & z_{23}^{(1)} & z_{24}^{(1)} & E_2^{i(1)} \\ 0 & z_{32}^{(1)} & z_{33}^{(1)} & z_{34}^{(1)} & E_3^{i(1)} \\ 0 & z_{42}^{(1)} & z_{43}^{(1)} & z_{44}^{(1)} & E_4^{i(1)} \end{bmatrix} \rightarrow E_1^{i(1)} = E_1^i / Z_{11} \\ Z_{ij}^{(1)} &= Z_{ij} - Z_{1j}^{(1)} * Z_{i1} \leftarrow \begin{bmatrix} 1 & z_{12}^{(1)} & z_{13}^{(1)} & z_{14}^{(1)} & E_1^{i(1)} \\ 0 & z_{22}^{(1)} & z_{23}^{(1)} & z_{24}^{(1)} & E_2^{i(1)} \\ 0 & z_{32}^{(1)} & z_{33}^{(1)} & z_{34}^{(1)} & E_3^{i(1)} \\ 0 & z_{42}^{(1)} & z_{43}^{(1)} & z_{44}^{(1)} & E_4^{i(1)} \end{bmatrix} \rightarrow E_j^{i(1)} = E_j^i - Z_{i1}^{(1)} * E_1^{i(1)} \end{aligned}$$

Iteration k = 2

$$\begin{aligned} Z_{2j}^{(2)} &= Z_{2j}^{(1)} / Z_{22}^{(1)} \leftarrow \begin{bmatrix} 1 & z_{12}^{(1)} & z_{13}^{(1)} & z_{14}^{(1)} & E_1^{i(1)} \\ 0 & 1 & z_{23}^{(2)} & z_{24}^{(2)} & E_2^{i(2)} \\ 0 & 0 & z_{33}^{(2)} & z_{34}^{(2)} & E_3^{i(2)} \\ 0 & 0 & z_{43}^{(2)} & z_{44}^{(2)} & E_4^{i(2)} \end{bmatrix} \rightarrow E_2^{i(2)} = E_2^{i(1)} / Z_{22}^{(1)} \\ Z_{ij}^{(2)} &= Z_{ij}^{(1)} - Z_{2j}^{(2)} * Z_{i2}^{(1)} \leftarrow \begin{bmatrix} 1 & z_{12}^{(1)} & z_{13}^{(1)} & z_{14}^{(1)} & E_1^{i(1)} \\ 0 & 1 & z_{23}^{(2)} & z_{24}^{(2)} & E_2^{i(2)} \\ 0 & 0 & z_{33}^{(2)} & z_{34}^{(2)} & E_3^{i(2)} \\ 0 & 0 & z_{43}^{(2)} & z_{44}^{(2)} & E_4^{i(2)} \end{bmatrix} \rightarrow E_j^{i(2)} = E_j^{i(1)} - Z_{i2}^{(1)} * E_2^{i(2)} \end{aligned}$$

Iteration k = 3

$$\begin{aligned} Z_{3j}^{(3)} &= Z_{3j}^{(2)} / Z_{33}^{(2)} \leftarrow \begin{bmatrix} 1 & z_{12}^{(1)} & z_{13}^{(1)} & z_{14}^{(1)} & E_1^{i(1)} \\ 0 & 1 & z_{23}^{(2)} & z_{24}^{(2)} & E_2^{i(2)} \\ 0 & 0 & 1 & z_{34}^{(3)} & E_3^{i(3)} \\ 0 & 0 & 0 & z_{44}^{(3)} & E_4^{i(3)} \end{bmatrix} \rightarrow E_3^{i(3)} = E_3^{i(2)} / Z_{33}^{(2)} \\ Z_{ij}^{(3)} &= Z_{ij}^{(2)} - Z_{3j}^{(3)} * Z_{i3}^{(2)} \leftarrow \begin{bmatrix} 1 & z_{12}^{(1)} & z_{13}^{(1)} & z_{14}^{(1)} & E_1^{i(1)} \\ 0 & 1 & z_{23}^{(2)} & z_{24}^{(2)} & E_2^{i(2)} \\ 0 & 0 & 1 & z_{34}^{(3)} & E_3^{i(3)} \\ 0 & 0 & 0 & z_{44}^{(3)} & E_4^{i(3)} \end{bmatrix} \rightarrow E_j^{i(3)} = E_j^{i(2)} - Z_{i3}^{(2)} * E_3^{i(3)} \end{aligned}$$

Iteration k = 4

$$\begin{aligned} Z_{4j}^{(4)} &= Z_{4j}^{(3)} / Z_{44}^{(3)} \leftarrow \begin{bmatrix} 1 & z_{12}^{(1)} & z_{13}^{(1)} & z_{14}^{(1)} & E_1^{i(1)} \\ 0 & 1 & z_{23}^{(2)} & z_{24}^{(2)} & E_2^{i(2)} \\ 0 & 0 & 1 & z_{34}^{(3)} & E_3^{i(3)} \\ 0 & 0 & 0 & 1 & E_4^{i(4)} \end{bmatrix} \rightarrow E_4^{i(4)} = E_4^{i(3)} / Z_{44}^{(3)} \end{aligned}$$

Figure 27. Flow of Gaussian elimination computation.

in (29) and (31) are performed. The quantity Z_{11} is set to 1 after the end of the first-row computation, and other rows in the matrix are then computed by (30). All the remaining entries in the first column are set to 0. The right hand side of (33), $\{E^i\}$, except E_1^i , is computed according to (32). In the iteration $k = 2$, the computation is similar to the iteration $k = 1$, but the first row and column remain unchanged at this moment. According to (29) and (31), the second row of the matrix and E_2^i are divided by Z_{22} . The third row and below are computed by (30) and (32), and all the remaining entries in the second column are set to 0.

Similar procedures are performed in the next iteration step, following the same iteration algorithm.

2.2.2.2. LU Decomposition. The *LU* decomposition method is similar to the Gaussian elimination method. There are three steps for solving the matrix equation in *LU* decomposition method:

1. *LU* factorization: $[Z] = [L][U]$
2. Forward substitution: $[L]\{y\} = \{E^i\}$
3. Backward substitution: $[U]\{J\} = \{y\}$

The Gaussian elimination method combines steps 1 and 2. Therefore, we can delete lines 6, 7, 13, and 14 in Fig. 26, and thus variables i and j are interchanged. The algorithm for the *LU* decomposition method is subsequently obtained after these modifications. The corresponding computer algorithm is shown in Fig. 28. The required equations in *LU* decomposition method are

$$Z_{ik}^{(k)} = \frac{Z_{ik}^{(k-1)}}{Z_{kk}^{(k-1)}} \tag{34}$$

$$Z_{ij}^{(k)} = Z_{ij}^{(k-1)} - Z_{ik}^{(k)} * Z_{kj}^{(k-1)} \tag{35}$$

The LU decomposition implementation is shown in Fig. 29. In the iteration $k=1$, the first row remains unchanged. The first column is computed by (34). Other matrix coefficients are computed by (35). In the iteration $k=2$, the first row, second row, and first column are fixed. The second column is computed by (34), and the other matrix coefficients are computed by (35). In the next iteration, the computation repeats the procedure of iteration $k=2$. The total number of iteration is $N-1$. After all the iteration steps are computed, the new matrix appears as (36) when N is set to 4 to simplify our discussion:

$$\begin{bmatrix} Z_{11} & Z_{12} & Z_{13} & Z_{14} \\ Z_{21}^{(1)} & Z_{22}^{(1)} & Z_{23}^{(1)} & Z_{24}^{(1)} \\ Z_{31}^{(1)} & Z_{32}^{(2)} & Z_{33}^{(2)} & Z_{34}^{(2)} \\ Z_{41}^{(1)} & Z_{42}^{(2)} & Z_{43}^{(3)} & Z_{44}^{(3)} \end{bmatrix} \quad (36)$$

This matrix stores $[L]$ and $[U]$ matrices. The matrix can be separated into two matrices:

$$\begin{bmatrix} 1 & 0 & 0 & 0 \\ Z_{21}^{(1)} & 1 & 0 & 0 \\ Z_{31}^{(1)} & Z_{32}^{(2)} & 1 & 0 \\ Z_{41}^{(1)} & Z_{42}^{(2)} & Z_{43}^{(3)} & 1 \end{bmatrix}$$

Lower triangle matrix

$$\begin{bmatrix} Z_{11} & Z_{12} & Z_{13} & Z_{14} \\ 0 & Z_{22}^{(1)} & Z_{23}^{(1)} & Z_{24}^{(1)} \\ 0 & 0 & Z_{33}^{(2)} & Z_{34}^{(2)} \\ 0 & 0 & 0 & Z_{44}^{(3)} \end{bmatrix}$$

Upper triangle matrix

We apply the forward substitution with the lower triangular matrix to find $\{y\}$ and then the backward substitution for extracting the solution.

2.2.3. Parallel Gaussian Elimination Method. The Gaussian elimination method implemented with a parallel algorithm is discussed in this subsection. We assume that four computing nodes are used. The matrix is separated into several portions with several rows of the original matrix in each portion. Each node stores its portion of the matrix as shown in Fig. 30.

In the iteration $k=1$, node 1 computes the assigned row partitioned matrix. At that time, other nodes are idle and wait for the results in node 1. Data communication among all nodes is required after node 1 finishes its computation. Other nodes can now begin to compute the computation for the iteration $k=1$. In the iteration $k=2$, node 1 is idle and does not participate in any computation

```

1:  /** LU decomposition method **/
2:  For k = 1 to N-1
3:      For i=k+1 to N
4:          Zik=Zik / Zkk
5:      End For
6:
7:      For j=k+1 to N
8:          For i=k+1 to N
9:              Zij=Zij - Zik x Zkj
10:         EndFor
11:      End For
12: End For
13: /** Forward-substitution step **/
14: For i = 1 to N
15:     yi = 0
16:     For j = 1 to i-1
17:         yi = yi - yj Zij
18:     End For
19: End For
20: /** Back-substitution step **/
21: For i = N to 1 (decrease 1 in each step)
22:     Ji = 0
23:     For j = i+1 to N
24:         Ji = Ji - Jj Zij
25:     End For
26:     Ji = Ji / Ei
27: EndFor

```

Figure 28. Algorithm of LU decomposition.

and data communication. First, only node 2 computes the assigned row partitioned matrix. Other nodes are idle and wait for receiving results from node 2. Other nodes begin their computations after the data communication. In the iteration $k=3$ and $k=4$, the computation procedures are similar to the iteration $k=1$ and $k=2$ but the computation for iteration $k=4$ does not include any data communication. The parallel Gaussian elimination algorithm is slightly different from the sequential algorithm depicted in Fig. 26 and it is shown in Fig. 31.

2.2.4. Pipelined Parallel Gaussian Elimination. The parallel Gaussian elimination version mentioned above can reduce the memory requirement and computing time. However, the efficiency is not high because three nodes remain idle and continue to wait for one of the nodes to finish its computation during each iteration step. In order to enhance the computation efficiency, an asynchronous parallel version of the Gaussian elimination called *pipelined parallel Gaussian elimination* is used. The weakness of the synchronous parallel Gaussian elimination is that each node starts its computation after the previous node completes its computation. In contrast, each iteration k of the computation can be taken at the same time in the pipelined parallel Gaussian elimination and, thus, can further reduce the computing time. The procedure of the method is detailed in Fig. 32.

In Figs. 32b–32e, node 1 computes its partition. Other nodes are idle until node 1 finishes the first iteration. The row data will be sent to node 2 from node 1, but at that time other nodes are also idle. The received row data will be stored and passed to node 3. Similarly, other nodes store and pass the received data to the next node, namely, node 4. Node 2 starts its computation after passing the

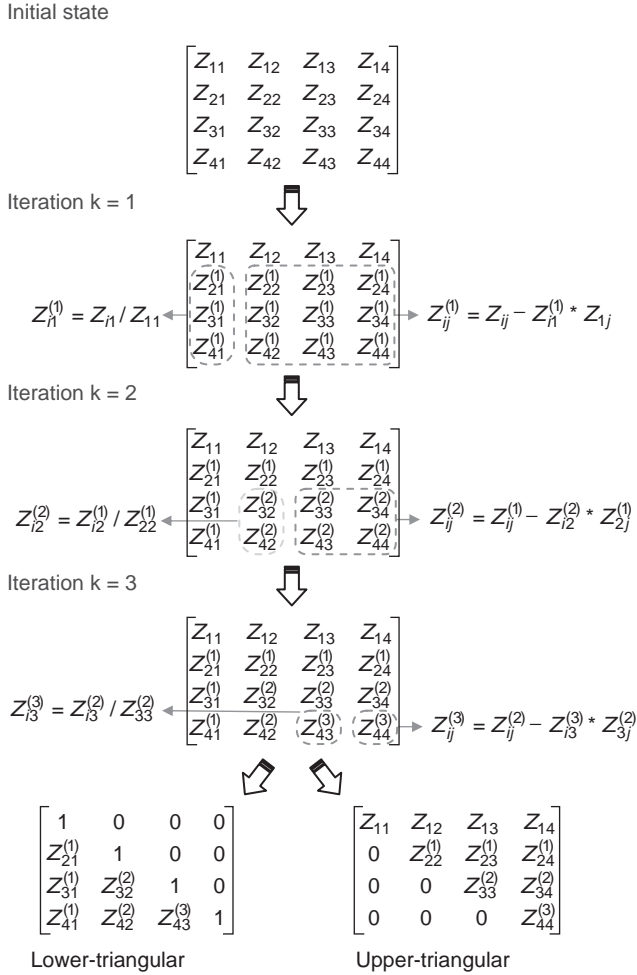


Figure 29. Flow of LU decomposition.

row data. Other nodes repeat similar procedure. In Fig. 32f, node 2 completes the computation of iteration $k=1$ and starts the computation of iteration $k=2$. At the same time, node 3 starts the computation of iteration $k=1$. Two iteration computations appear at the same time. In addition, node 4 passes the row data of iteration $k=1$. In Fig. 32g, data communication between nodes 2 and 3 appears after nodes 2 and 3 finish their respective iteration computation. Node 4 then starts the computation of iteration $k=1$. In Fig. 32h, node 4 completes the computation of the iteration and receives the row data of iteration $k=2$. Node 5 starts the computation of iteration $k=1$. In Fig. 32i, node 3 starts the computation of iteration $k=2$ and nodes 4 and 5 perform data communication. The iteration procedures continue until the upper triangular matrix is obtained by the pipelined parallel implementation as shown in Fig. 32q. The pipelined parallel algorithm is shown in Fig. 33.

The implementation of the parallel version of LU decomposition is slightly different from the parallel version of the Gaussian elimination. As we can see in Figs. 27 and 29, the computation of Gaussian elimination starts from the row of matrix $[Z]$. Both matrices $[Z]$

and $[E]$ are needed to involve in the calculation. On the other hand, the computation of LU decomposition starts from the column of matrix $[Z]$. Only matrix $[Z]$ is involved in the calculation. Therefore, a similar parallel LU decomposition algorithm as discussed above can be formulated using a modified-form parallel Gaussian elimination algorithm.

2.2.5. Numerical Results (Gaussian Elimination/ LU Decomposition). In this subsection, we will show the numerical results of implementing the Gaussian elimination and LU decomposition. Both results from sequential and parallel codes will be shown to illustrate the effectiveness of parallel computing. All the computations are performed on the parallel computing platform, which consists of 24 nodes of Pentium III 1-GHz processors. Figure 34 shows the CPU time for solving a full matrix with the Gaussian elimination. Results from the parallel Gaussian elimination and pipelined parallel Gaussian elimination methods as discussed in the previous subsection are also shown in the figure for comparison. As we can see from the figure, the CPU time for the sequential method radically increases when increasing the matrix size. On the other hand, both parallel methods can greatly reduce the CPU time. Figure 35 shows the speedup factors with both parallel methods versus the matrix size. We can see that the pipelined parallel Gaussian elimination method is higher in efficiency compared with the parallel Gaussian elimination method. The CPU times with the LU decomposition computation, including sequential, parallel, and pipelined parallel methods, are shown in Fig. 36. Similar to the results shown in Fig. 34, both parallel methods can essentially reduce the CPU time when dealing with a large matrix size. Again, the pipelined parallel LU decomposition method shows higher efficiency compared with the parallel LU decomposition method as shown in Fig. 37. We can see from Figs. 35 and 37 that the speedup factor is greater those that of the computing nodes used. This may be due to the loop overheads in sequential algorithms and insufficient cache size in the single computing node [35].

2.2.6. Matrix-Vector Multiplication. The parallel matrix-vector multiplication is introduced in this subsection. The sequential matrix-vector multiplication algorithm is to perform the calculation of $[Z]\{a\} = \{b\}$. Each of solution $\{b^i\}$ is equal to the dot product of row i of the matrix $[Z]$ with the column vector $\{J\}$. The sequential implementation is shown in Fig. 38. In the parallel matrix-vector multiplication algorithm, matrix $[Z]$ can be partitioned by either rows or by columns. The choice of partitioning by rows or columns mainly depends on the programming language used. For instance, since the arrays in C language are stored in row-major order, array elements in each row will store contiguously in memory. Thus, it is appropriate to choose partitioning by rows if C programming language is used. On the other hand, since the arrays in FORTRAN language are stored in column-major order, it is appropriate to choose partitioning by column if FORTRAN language is used. Both partitioning methods can distribute the required memory of storing the matrix

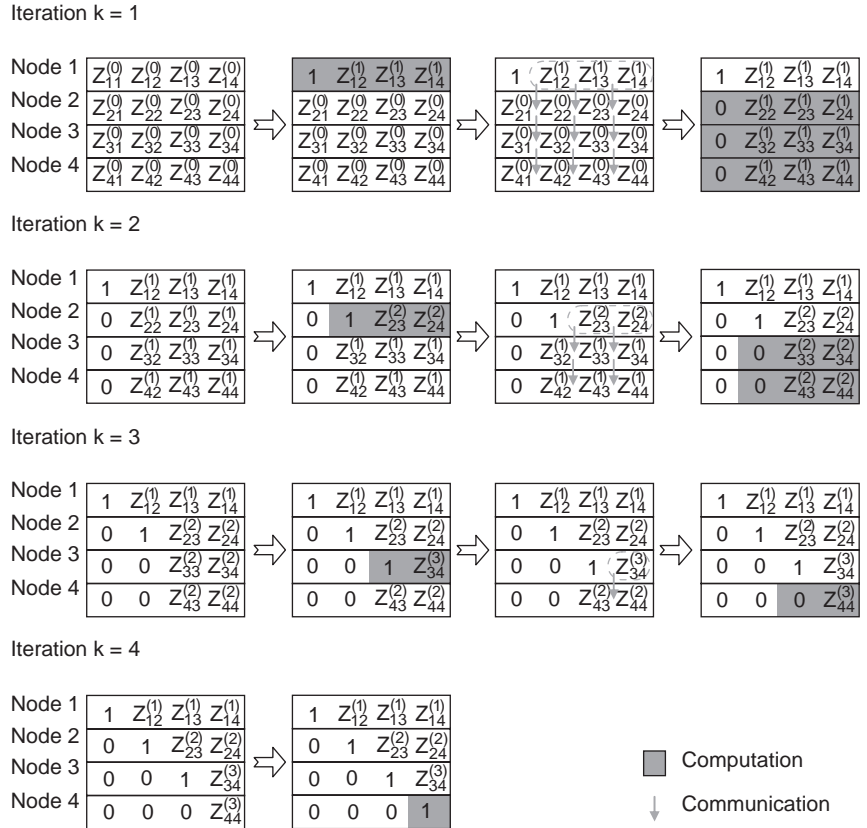


Figure 30. Workflow of parallel Gaussian elimination.

among the nodes. Therefore, the computation time can be shortened with the handling of a partitioned matrix in each node.

Suppose we adopt the row partitioning parallel algorithm to be implemented on an M -node parallel platform. Matrix $[Z]$ is partitioned into M portions of $[Z]$ by rows, and each portion is stored in its corresponding node. However, the whole vector $\{a\}$ is needed in each node as shown in Fig. 39. This should not be a problem as its size is only a small fraction of that of the partitioned portion of matrix $[Z]$. In the matrix-vector multiplication, each node computes only its portion of $[Z]$ and stores its results in $\{b^i\}$. For instance, node 1 computes only the result b_1^i and b_2^i . Similarly, entries in $\{b^i\}$ correspond to the row number of the partitioned matrix are computed in other nodes. However, as each node only computes a portion of $\{b^i\}$, the result is not complete. In order to compile the complete result of $\{b^i\}$ in each node, data communication among all nodes is required. We can use the callable MPI library MPI_ALLGATHER to collect the result $\{b^i\}$ from each node and broadcast the properly arranged $\{b^i\}$ to all nodes. The algorithm is shown in Fig. 40. If other nodes need the corresponding result of $\{b^i\}$ in each node, we can instead use the callable MPI library MPI_GATHER [5] in data communication. In that case, only node 0, the master node, gets the result of the entire $\{b^i\}$. The second partition method is the parallel column partition algorithm as shown in Fig. 41. Matrix $[Z]$ is partitioned by column, and the vector $\{a\}$ is partitioned by row. The result $\{b^i\}$ in

each node is obtained by matrix-vector multiplication. However, the result $\{b^i\}$ in each node is not complete as only some columns are involved in the matrix-vector multiplication. Therefore, we need to gather all $\{b^i\}$ in each node, sum them individually during the data communication, and broadcast the correct results $\{b^i\}$ to all nodes. In that case, we can use the callable MPI library MPI_ALLREDUCE. The algorithm is shown in Fig. 42. Similarly, the callable MPI library MPI_REDUCE can be applied instead in the data communication if the partial result of $\{b^i\}$ does not have to be distributed to all nodes.

2.2.6.1. Sparse Matrix Canonical Grid (SMCG) Method.

In the previous subsection, we discussed the parallel version of the matrix-vector multiplication. However, each node also requires a large memory to store its respective rows or columns of the matrix. In this subsection, we introduce another method, called the *sparse matrix canonical grid* (SMCG) method [36,37], to reduce the memory requirement and maintain speedy computation. The basic idea is the decomposition of the impedance matrix, which is divided into two parts: near interaction and far interaction. The near-interaction part corresponds to a sparse matrix, while that of the far interaction corresponds to a dense matrix. The sparse matrix-vector multiplication part is carried out in the conventional manner. In contrast, the dense matrix-vector multiplication part is computed efficiently using the fast Fourier transforms (FFTs).

```

1:  /** Parallel version Gaussian elimination step ***/
2:  n=N/number of nodes
3:  For k = 1 to N
4:      IF (iteration step k is for this node) THEN
5:          For j=k+1 to N
6:              Zkj=Zkj / Zkk
7:          End For
8:          Eik=Ek / Zkk
9:          Zkk=1
10:         Store the row k information
11:         For i=1 to n
12:             For j=k+1 to N
13:                 Zij=Zij - Zik x Zkj
14:             End For
15:             Eii=Ei - Zik x Eik
16:             Zik=0
17:         End For
18:         Send the stored row k information to all following node
19:     ELSE
20:         IF (iteration step k < the range of iteration step k in node) THEN
21:             Receive the row k information except node 1
22:             For i=1 to n
23:                 For j=k+1 to N
24:                     Zij=Zij - Zik x Zkj
25:                 End For
26:                 Eii=Ei - Zik x Eik
27:                 Zik=0
28:             End For
29:         End IF
30:     End IF
31: End
32: End
33: /** Back-substitution step ***/
34: Receive a part of output data from next except node N
35: For i = N to n*number of node+1 (decrease 1 in each step)
36:     Ji = Eii
37:     For j = i+1 to N
38:         Ji = Ji - Jj Zij
39:     End
40: End
41: Send a part of output data to pervious node except node 1
    
```

Figure 31. Algorithm for parallel Gaussian elimination method.

In the SMCG method [36,37], the impedance matrix can be represented as the sum of the strong neighborhood interactions sparse matrix $[Z^S]$ and the weak far-interaction dense matrix $[Z^W]$ as

$$[Z] = [Z^S] + [Z^W] \quad (37)$$

Figure 43 shows the relationship of the strong neighborhood interactions and weak far interactions.

Through Taylor expansion of the Green functions about uniformly spaced canonical gridpoints overlying the triangular discretization (see Fig. 44), we need to compute the Green function between the two centroids (x_i, y_i) and (x_j, y_j) of two interacting triangles. The Green function can be evaluated by either direct or indirect computation. The indirect Green function between the centroids of two interacting triangles includes three parts. The first part is from the point (x_j, y_j) to its nearest gridpoint (x_{j0}, y_{j0}) . The second and third parts are from gridpoint (x_{j0}, y_{j0}) to another gridpoint (x_{i0}, y_{i0}) and from (x_{i0}, y_{i0}) to (x_i, y_i) . This indirect computation corresponds to Taylor series expansion about the canonical gridpoints at (x_{j0}, y_{j0}) and (x_{i0}, y_{i0}) as shown in Fig. 44. The appropriate Green function can

be written as

$$\begin{aligned}
 G(\rho_{ij}) &= \sum_{m_1} \sum_{n_1} \sum_{m_2} \sum_{n_2} \frac{x_{d_i}^{m_1} y_{d_i}^{n_1} x_{d_j}^{m_2} y_{d_j}^{n_2}}{m_1! n_1! m_2! n_2!} \\
 &\times \frac{\partial^{m_1+m_2}}{\partial x_{i0}^{m_1+m_2}} \frac{\partial^{n_1+n_2}}{\partial y_{i0}^{n_1+n_2}} G(\sqrt{x_{d_{ij}}^2 + y_{d_{ij}}^2})
 \end{aligned} \quad (38)$$

where $x_{d_{ij}} = x_{i0} - x_{j0}$ and $y_{d_{ij}} = y_{i0} - y_{j0}$. It is not difficult to see that $G(\sqrt{x_{d_{ij}}^2 + y_{d_{ij}}^2})$ and its derivatives are translationally invariant. Consequently, (37) can be written as

$$\begin{aligned}
 \{[Z^S] + [Z^W]\}[I] &= \left\{ [Z^S] + \sum_{i=0}^k [Z^W_i] \right\} [I] \\
 &= [V]
 \end{aligned} \quad (39)$$

where k is the total number of terms in the expansion. We can solve Eq. (39) by an iteration method. The iterative solution is expedited by applying parallel computing

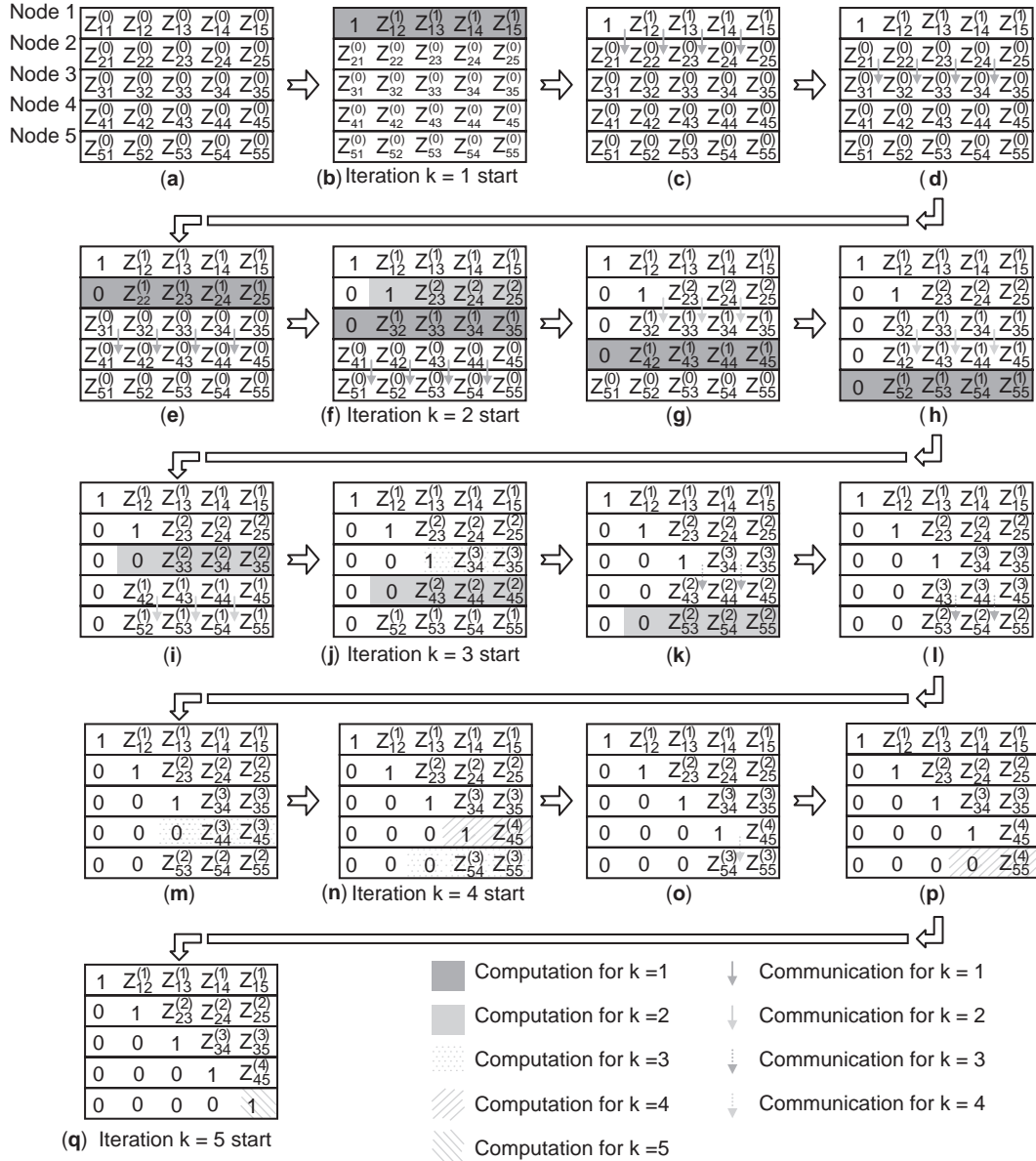


Figure 32. Workflow of pipelined parallel Gaussian elimination method.

techniques in the matrix–vector multiplication between $[Z]$ and the current vector in the n th iteration $[I_n]$. The first-order and higher-order solutions in the iterative procedure are defined as follows:

$$\{[Z^s] + [Z_0^w]\}I_1 = V \tag{40}$$

$$\{[Z^s] + [Z_0^w]\}I_{n+1} = V - \left\{ \sum_{i=1}^k [Z_i^w] \right\} I_n \tag{41}$$

From (41), more terms in the expansion series of $[Z^w]$ can be relocated to the left-hand side of the matrix equation to reduce the CPU time. Each order is solved by the biconjugate gradient (BCG) iterative solver [38].

The closed-form expressions of the spatial domain Green function [39] can be obtained by using the fast

Hankel transform (FHT) algorithm [40] and matrix pencil method [41]. Such closed-form expressions make the Taylor’s series expansion solvable analytically. Because of the translationally invariant kernels in the expanded Green functions, the weak matrix vector multiplication in the iterative procedure can be efficiently performed via the fast Fourier transforms. The matrix–vector multiplication corresponding to the far-interaction contributions can be written as

$$\begin{aligned} [Z^w][I_n] &= \left\{ \sum_{i=0}^K [Z_i^w] \right\} [I_n] \\ &= \left\{ \sum_{i=0}^K [T_i][G_i][T_{s_i}] \right\} [I_n] \end{aligned} \tag{42}$$

```

1:  /** Piplined parallel version Gaussian elimination step ***/
2:  n=N/number of nodes
3:  For k = 1 to N
4:    IF (iteration step k is for this node) THEN
5:      For j=k+1 to N
6:         $Z_{kj}=Z_{kj} / Z_{kk}$ 
7:      End For
8:       $E_k=E_k / Z_{kk}$ 
9:       $Z_{kk}=1$ 
10:     Store the row k information
11:     For i=1 to n
12:       For j=k+1 to N
13:          $Z_{ij}=Z_{ij} - Z_{ik} \times Z_{kj}$ 
14:       End For
15:        $E_i^i=E_i^i - Z_{ik} \times E_k^i$ 
16:        $Z_{ik}=0$ 
17:     End For
18:     Send the stored row k information to next node
19:   ELSE
20:     IF (iteration step k < the range of iteration step k in node) THEN
21:       Receive the row k information form previous node except node 1
22:       Send the stored row k information to next node except node N
23:       For i=1 to n
24:         For j=k+1 to N
25:            $Z_{ij}=Z_{ij} - Z_{ik} \times Z_{kj}$ 
26:         End For
27:          $E_i^i=E_i^i - Z_{ik} \times E_k^i$ 
28:          $Z_{ik}=0$ 
29:       End For
30:     End IF
31:   End IF
32: End
33: /** Back-substitution step ***/
34: Receive a part of output data from next except node N
35: For i = N to n*number of node+1 (decrease 1 in each step)
36:    $J_i = E_i^i$ 
37:   For j = i+1 to N
38:      $J_i = J_i - J_j Z_{ij}$ 
39:   End
40: End
41: Send a part of output data to pervious node except node 1

```

Figure 33. Algorithm for pipelined parallel Gaussian elimination method.

where the diagonal matrix $[T_s]$ corresponds to a premultiplication, while the other diagonal matrix $[T_t]$ corresponds to a postmultiplication. Note that the premultiplication corresponds to shifting the centroids of the basis triangles to their nearest gridpoints. The multiplication of the block-Toeplitz matrix corresponds to the inclusion of all

the interactions among the uniformly spaced canonical gridpoints. The final postmultiplication corresponds to translating the interactions at the gridpoints back to the centroids of the testing triangles. The multiplication with the block-Toeplitz matrix $[G_i]$ can then be performed via the FFT. It should be noted that some of the matrix-vector multiplications corresponding to the weak interactions are moved to the right-hand side of (39) to reduce the number of FFT operations in the iterative solution.

2.2.6.2. Parallel Version of the SMCG Method. The parallel code is implemented on the Beowulf parallel computer. The parallel code is written with the message-passing interface (MPI) [5] and the MPI version of the Fast Fourier Transform in West FFTW [7] is employed to perform the FFTs. The matrix is divided into subsections according to the number of computing nodes used. Figure 45 is a pictorial representation of the matrix decomposition. Note that N_{grid} represents the number of Cartesian canonical grid nodes used in the SMCG method and M the computing nodes used.

In regard to the sparse matrix-vector multiplication, the first advantage is that only a portion of the sparse

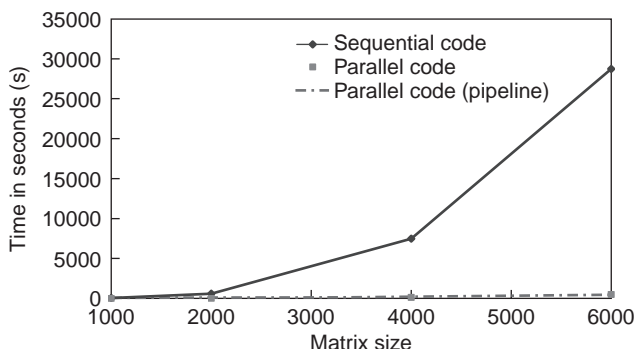


Figure 34. CPU times of Gaussian elimination methods. (This figure is available in full color at <http://www.mrw.interscience.wiley.com/erfme>.)

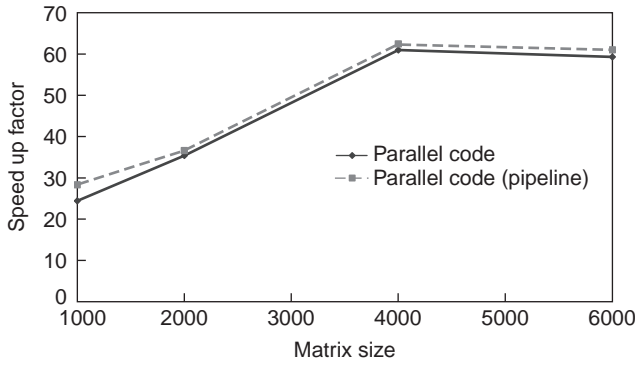


Figure 35. Speedup factor of parallel and pipelined parallel Gaussian elimination methods.

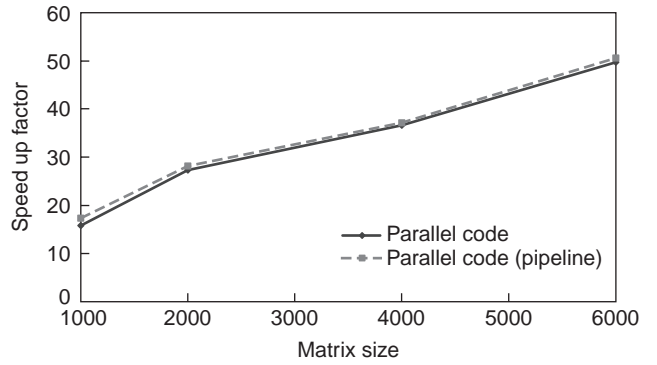


Figure 37. Speedup factor of parallel and pipelined parallel LU decomposition methods.

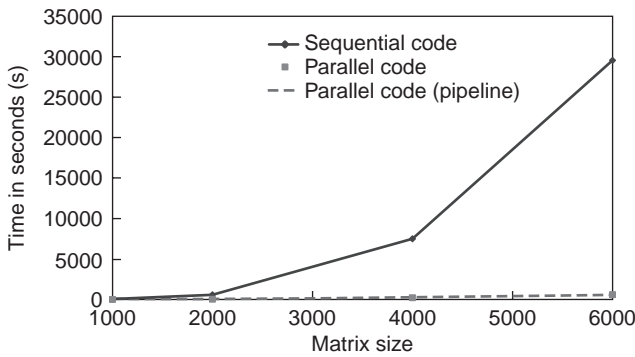


Figure 36. CPU times of LU decomposition methods.

```

1:   For i=1,N
2:     bii=0
3:     For j=1,N
4:       bij=bij+ Zij x ai
5:     End For
6:   End For
    
```

Figure 38. Algorithm of sequential matrix–vector multiplication.

matrix is stored in each computing node. Therefore, parallel computing can solve the problem with a huge number of unknowns. The other advantage is that each computing node computes only a portion of the sparse matrix and thus can reduce CPU time.

In computing the dense matrix–vector multiplication, we use FFTs to perform matrix–vector multiplication with block–Toeplitz matrix $[G_i]$ as in (42). The block Toeplitz matrix involves $2N_{\text{grid}} \times 2N_{\text{grid}}$ array elements, where N_{grid} is the number of gridpoints in x and y axes. We use

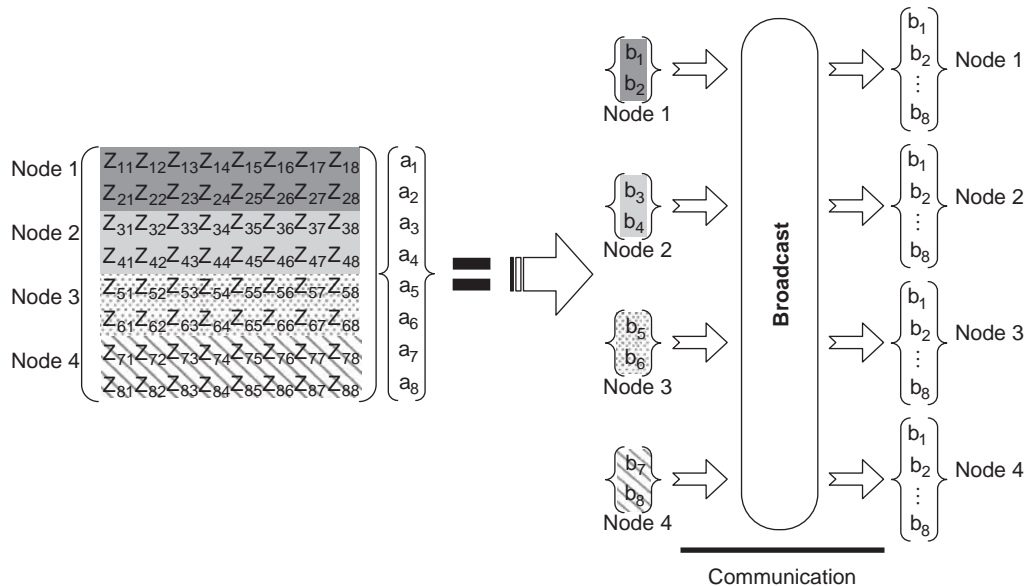


Figure 39. Implementation of parallel matrix–vector multiplication with row partitioning.

```

1: For i=1, N/number of nodes
2:   bi(1)=0
3:   For j=1,N
4:     bi(j)=bi(j)+ Zij x ai
5:   End For
6: End For
7: Call parallel library MPI_ALLGATHER
    
```

Figure 40. Algorithm for row-partitioned parallel matrix–vector multiplication.

FFT_w to compute the convolution between $[G_i]$ and the product of the diagonal matrix $[T_{s_i}]$ and $\{I_n\}$; therefore the matrix $[G_i]$ can be partitioned into M portions. Because of the distribution of $[G_i]$, each computing node handles only the corresponding elements of diagonal matrices $[T_s]$ and $[T_t]$ in the calculation of the matrix operation $[T_t][G_i][T_x]$. As a result, both CPU time and memory requirement can be reduced. However, if one of the nodes contains substantially larger amount of elements than other nodes, this node will reduce the overall speed of the computation.

2.2.6.3. Numerical results (MOM/SM/CG). In this subsection, we show two electromagnetic problems with implementation of the SMCG method. One is the densely packed interconnect problem, and the other one is the planar microstrip reflectarray. First, we discuss the densely packed interconnects using SMCG [37]. Figure 46 shows the top view of 12 densely curved microstrip lines. The microstrip structure contains a dielectric substrate backed by a ground plane. The thickness of the dielectric substrate is 1 mm, and the dielectric constant ϵ_r is 12.6. The length of each line is 6.2 mm, and the width is 0.3 mm. The canonical grid is set at $\Delta x = \Delta y = 0.1$ mm, which is about 30 points per linear dielectric wavelength. The first

```

1: For i=1, N/number of nodes
2:   bi(1)=0
3:   For j=1,n
4:     bi(j)=bi(j)+ Zij x ai
5:   End For
6: End For
7: Call parallel function MPI_ALLREDUCE
    
```

Figure 42. Algorithm for column-partitioned parallel matrix–vector multiplication.

and last lines are excited in our example. The amplitude of current density for each microstrip lines is shown in Fig. 47. From the figure, the mutual coupling effects and induced current on each line are observed. In this example

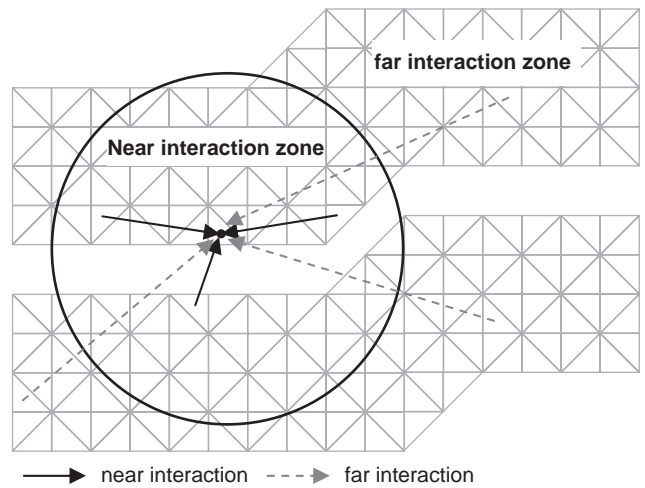


Figure 43. Near and far interactions.

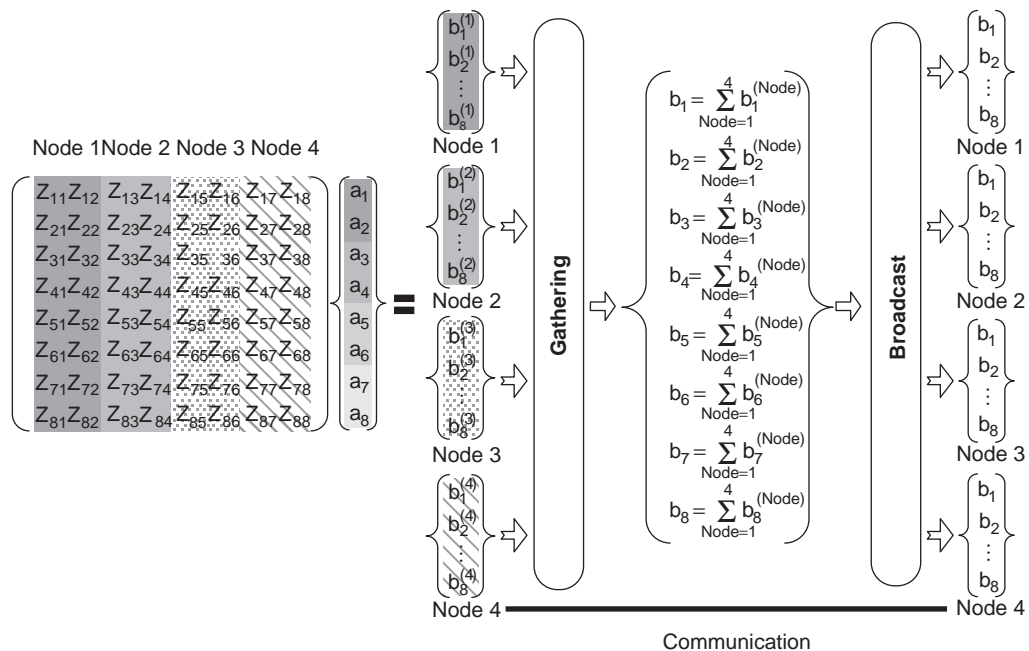


Figure 41. Implementation of parallel matrix–vector multiplication with column partitioning.

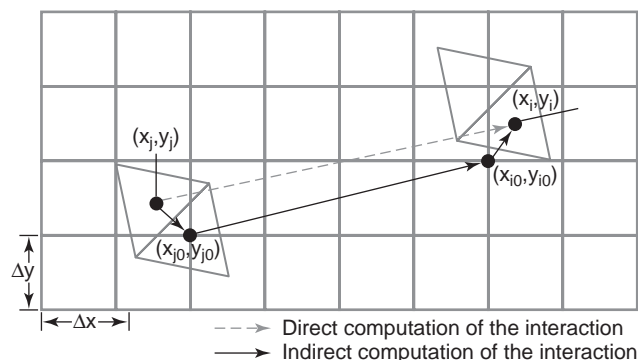


Figure 44. Canonical grid for Taylor series expansion.

with 8136 unknowns, 16 PCs each with a Pentium II 450-MHz processor and 256 MB of RAM are used. It takes about 5 min to complete the computation. The convergence of the biconjugate gradient method (BCGM) for each order is shown in Fig. 48. The convergence of percentage error is shown in Fig. 49.

Another microstrip problem with a large number of unknowns is also studied. The geometry and current distribution are shown in Fig. 50. There are 35,410 unknowns in this problem. The thickness and dielectric constant of the substrate are $h = 1$ mm and $\epsilon_r = 12.6$. The operation frequency is 30 GHz. The horizontal and vertical dimensions are 6.1 mm. Since the width of separation between adjacent small sections and the width of the hole are only 0.1 mm, the canonical grid is set at $\Delta x = \Delta y = 0.05$ mm. This structure is excited in the middle of the left-hand side. The parallel code is implemented in the parallel computer platform with eight Pentium II 600-MHz processors. The total CPU time for this problem is

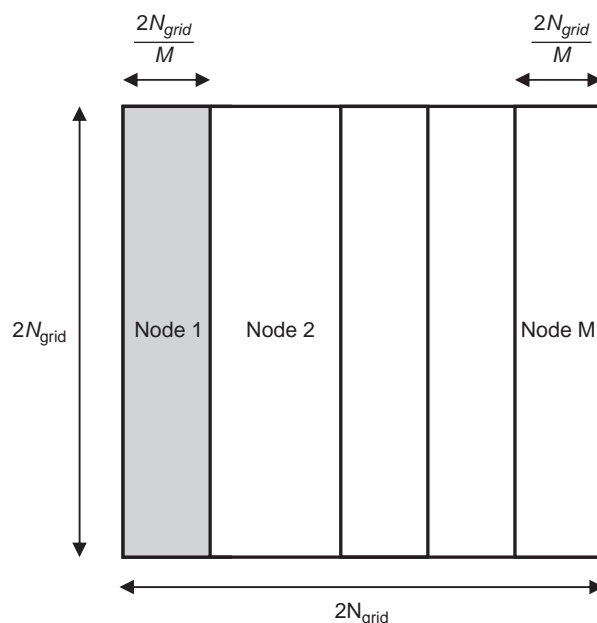


Figure 45. Pictorial representation of decomposition of block-Toeplitz matrix in SMCG method.

15.89 min. When the same code is run on the Beowulf with eight Pentium III 1-GHz processors, the total CPU time is reduced to 6.11 min. When 16 1-GHz processors are used, the total CPU time is 4.09 min.

Another example of using the SMCG method is the analysis of planar microstrip reflectarray. The reflectarray consists of 1117 dipoles printed on a Duroid 2.5 substrate, as described in Ref. 40. The design frequency is 24 GHz. The unit cell dimensions T_x and T_y are both equal to $0.4 \lambda_0$. It should be pointed out that the actual spacings of the

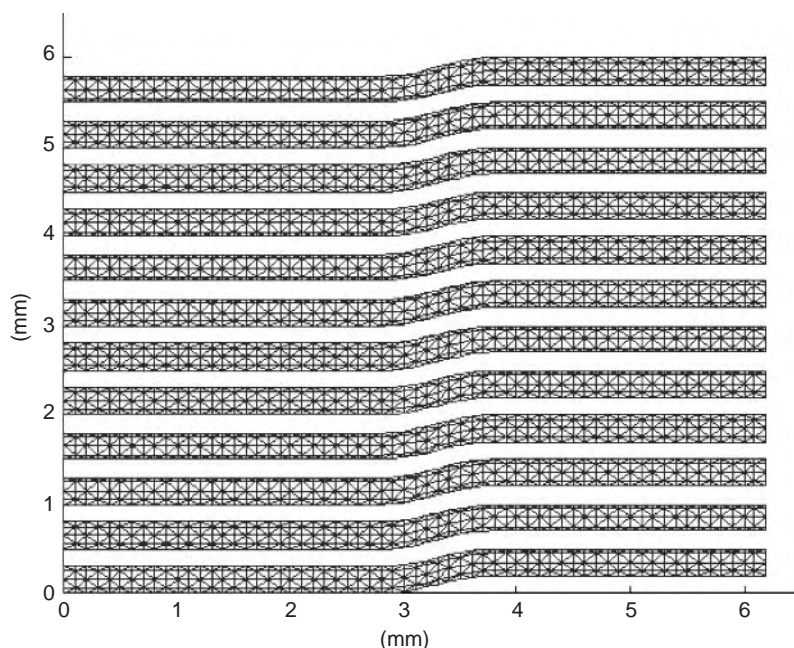


Figure 46. Geometry and discretization of microstrip lines. (This figure is available in full color at <http://www.mrw.interscience.wiley.com/erfme>.)

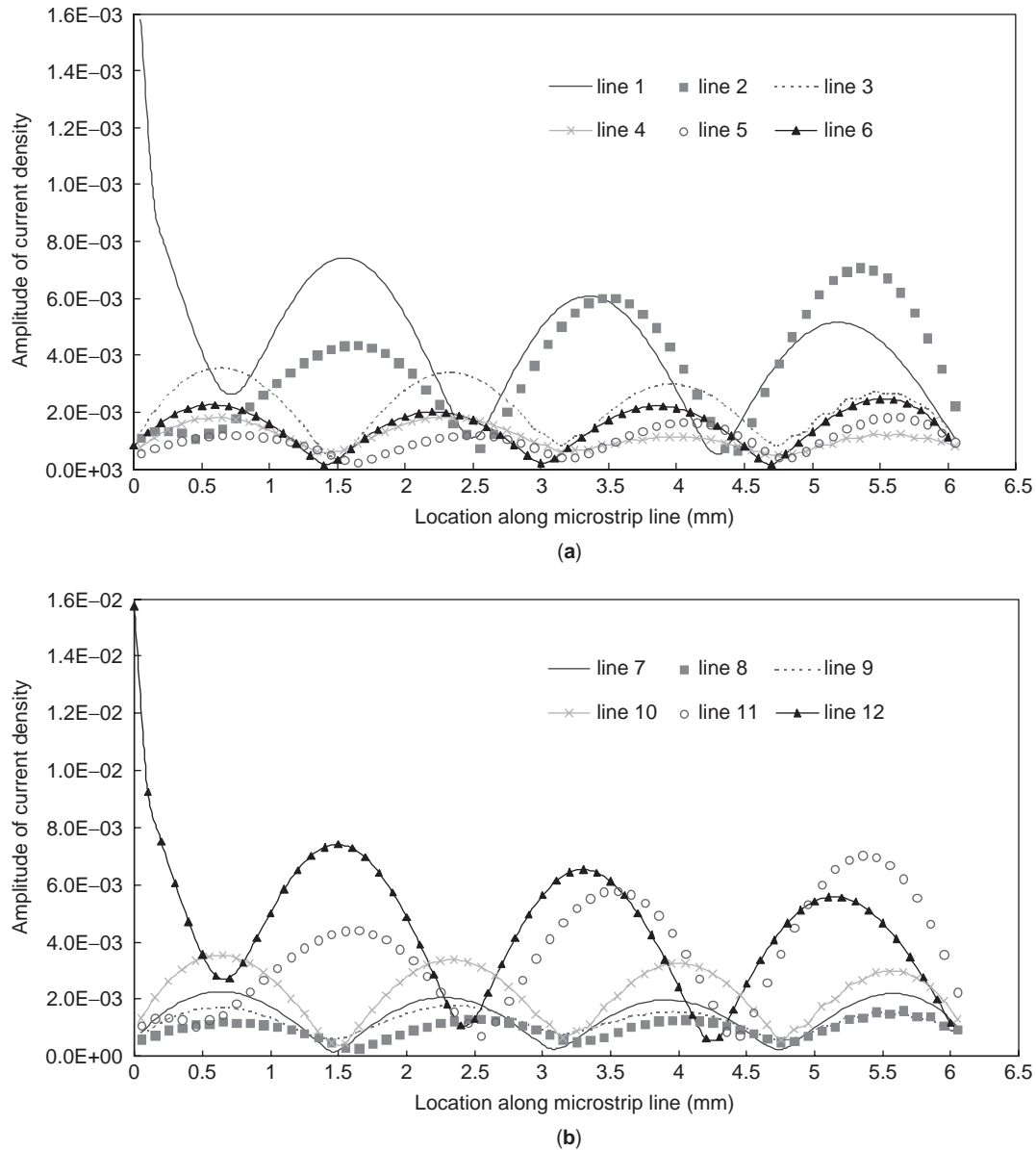


Figure 47. (a) Current distributions on microstrip lines 1–6; (b) current distributions on microstrip lines 7–12. (This figure is available in full color at <http://www.mrw.interscience.wiley.com/erfme>.)

canonical grid Δx and Δy are not necessarily equal. The dielectric constant and the thickness of the dielectric substrate are 2.5 and 0.76 mm, respectively. The layout of this dipole reflectarray is shown in Fig. 51. A rectangular horn with an aperture size of 10.7×4.3 mm is used to excite the reflectarray. The horn is located at $x_h = -216$ mm, $y_h = 0$ mm, $z_h = 160$ mm, as shown in Fig. 52. With eight nodes of dual Intel Pentium III 1-GHz processor and 23,676 unknowns, the computation time with the SMCG method for different number of discretization grids is shown in Table 2. The convergence of the BCGM for each order is shown in Table 3. As we can see from the tables, an increase in the number of canonical gridpoints also increases the computational time needed to perform the FFTs and hence leads to a longer total solution time.

The strong sparse matrix $[Z^s]$ in (37) is computed directly if the interactions are within the region $N_{near}\Delta x \times N_{near}\Delta y$. The convergence behaviors of each order of the SMCG method using 512×512 grids are shown in Fig. 53. The simulated radiation patterns in the $y-z$ plane are plotted in Fig. 54 with indistinguishable results using different canonical grid sizes. The experimental result, reported in Ref. 42, is also plotted in the same figure for comparison, and it is evident that the simulation and measured results compare well with each other.

Another reflectarray antenna consisting of 1117 square patches has been designed, fabricated, and measured. The design frequency was 28 GHz, and T_x and T_y were equal to $0.4 \lambda_0$. The dielectric constant and the thickness of the dielectric substrate were 2.94 and 0.76 mm, respectively. A

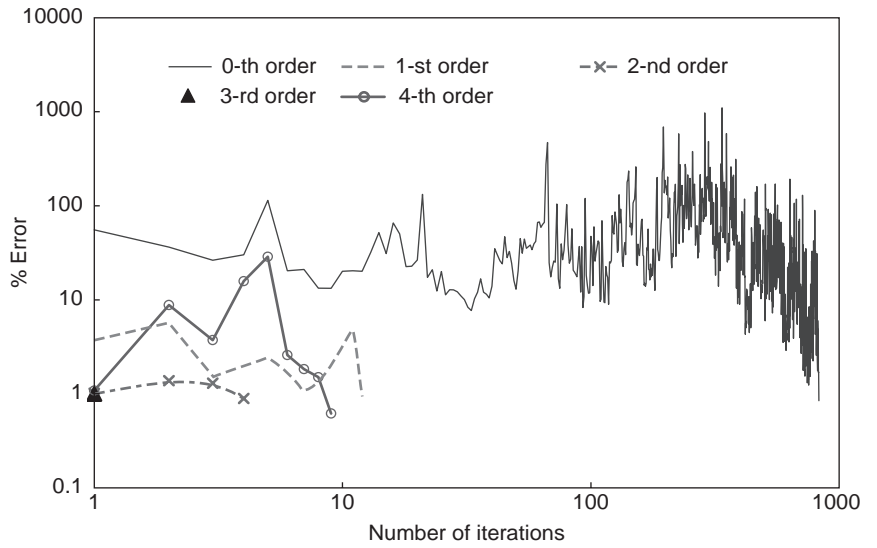


Figure 48. Convergence of BCGM for each order of SMCG method. (This figure is available in full color at <http://www.mrw.interscience.wiley.com/erfme>.)

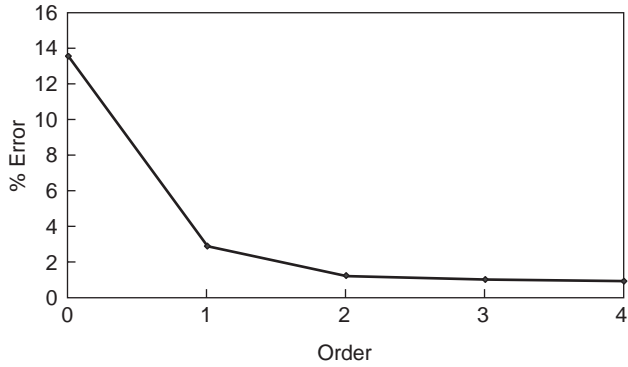


Figure 49. Convergence of SMCG method.

Table 2. SMCG Method for Different Numbers of Discretization Grids

Canonical Grid Size	Δx (mm)	Δy (mm)	N_{near}	CPU Time (min)
128×128	1.37796	1.53544	8	7.79
256×256	0.6863	0.7647	12	19.17
512×512	0.3425	0.3816	34	40.15
1024×1024	0.1711	0.1906	64	231.69

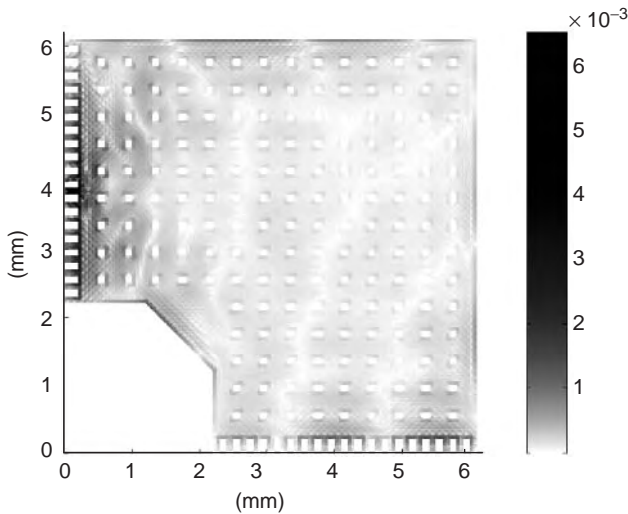


Figure 50. Top view of large-scale interconnect and current distribution.

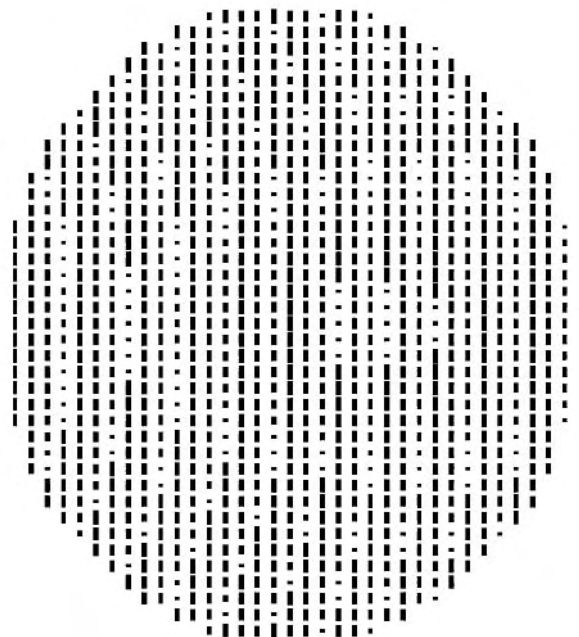


Figure 51. Layout of 1117-dipole-element reflectarray.

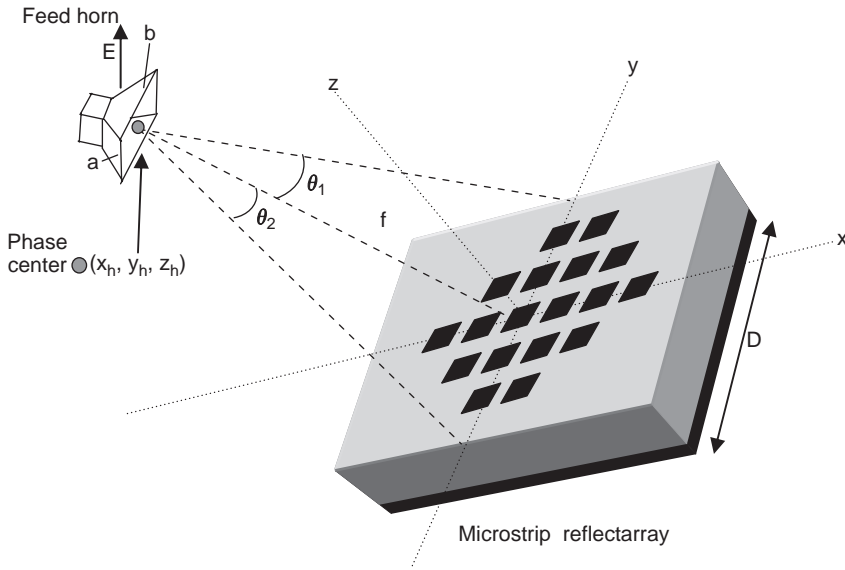


Figure 52. Reflectarray with offset feed horn.

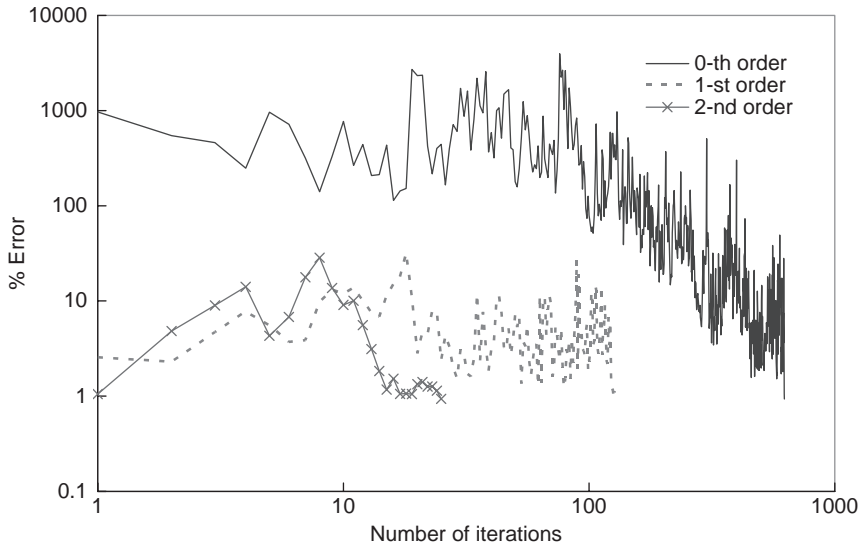


Figure 53. Convergence of SMCG method for 1117-dipole-patch-element reflectarray with 512×512 gridpoints. (This figure is available in full color at <http://www.mrw.interscience.wiley.com/erfme>.)

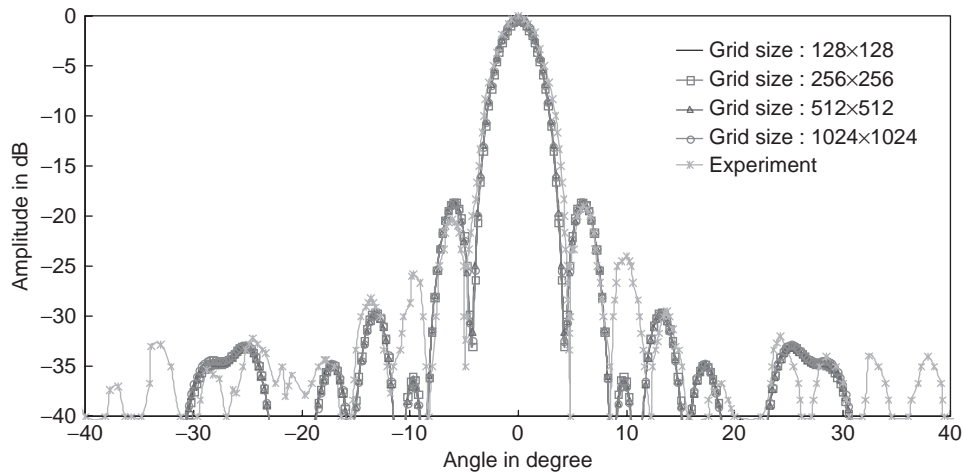


Figure 54. Comparison of SMCG simulation results of 1117 dipole-element reflectarray using different canonical grid sizes and experimental data. (This figure is available in full color at <http://www.mrw.interscience.wiley.com/erfme>.)

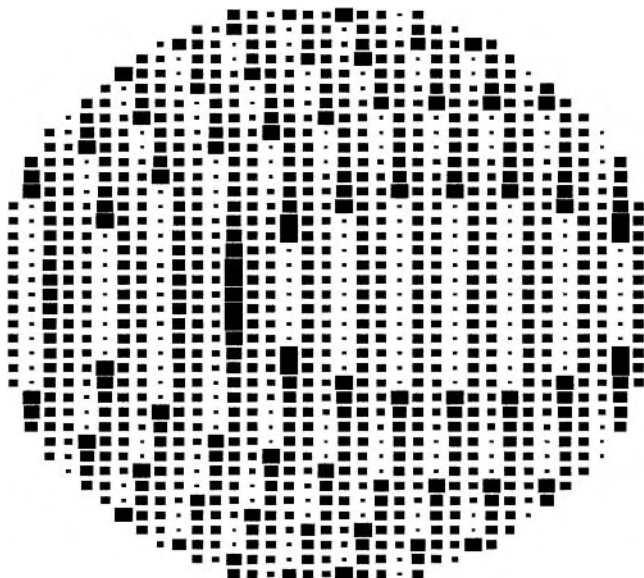


Figure 55. Layout of 1117-square-patch-element reflectarray.

rectangular feed horn with an aperture of 23.64×17.3 mm was offset-located to provide the necessary excitation. Although not shown here, the radiation pattern of the feed horn was measured to ensure that it radiates an adequate level of power when illuminating the reflect-

array. The mainbeam scan angle at -3 dB level is about $\pm 22^\circ$; hence the angles θ_1 and θ_2 in Fig. 52 should fall within the 22° limit. The location of the feed horn was chosen to be $x_h = -216$ mm, $y_h = 0$ mm, and $z_h = 160$ mm, so that the θ_1 and θ_2 angles were approximately 18° . The layout of a 1117-square-patch reflectarray is shown in Fig. 55. The measurement was performed with an NSI near-field measurement system.

With eight nodes of dual Intel Pentium III 1 GHz and 59,880 unknowns, the computational time with SMCG implemented on a 512×512 grid is approximately 121.7 min. The number of zeroth- and higher-order iterations needed are 1650, 308, and 99, respectively. The simulated and measured far-field patterns of a 1117-square-patch microstrip reflectarray in y - z plane are shown in Fig. 56. As we can see from the figure, there is a sharp mainbeam in the center, as desired. Although the first sidelobe of the pattern is not clearly observed in the measured result, the trend of the simulated peak location matches well with the measured result. The convergence behaviors of each order of the SMCG method using 512×512 grids are shown in Fig. 57.

As we can see from the examples above, the SMCG method implemented on parallel computers can efficiently handle and solve any large electromagnetic problem with a large number of unknowns.

Table 3. Convergence of the BCGM for Each Order

Canonical Grid Size	Number of Iterations							
	0th Order	1st Order	2nd Order	3rd Order	4th Order	5th Order	6th Order	7th Order
128×128	634	468	199	3	10	30	9	1
256×256	1090	433	67	1				
512×512	624	126	25					
1024×1024	1009	156						

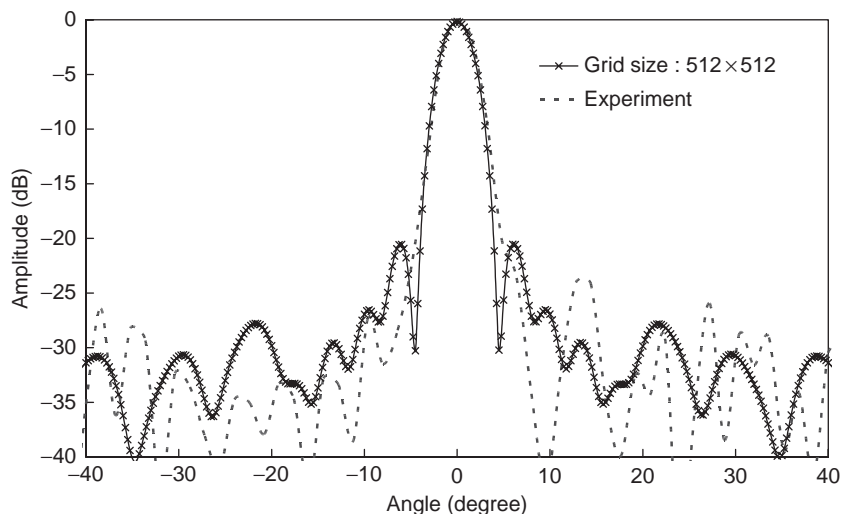


Figure 56. Radiation pattern of 1117-square-patch-element reflectarray. (This figure is available in full color at <http://www.mrw.interscience.wiley.com/erfme>.)

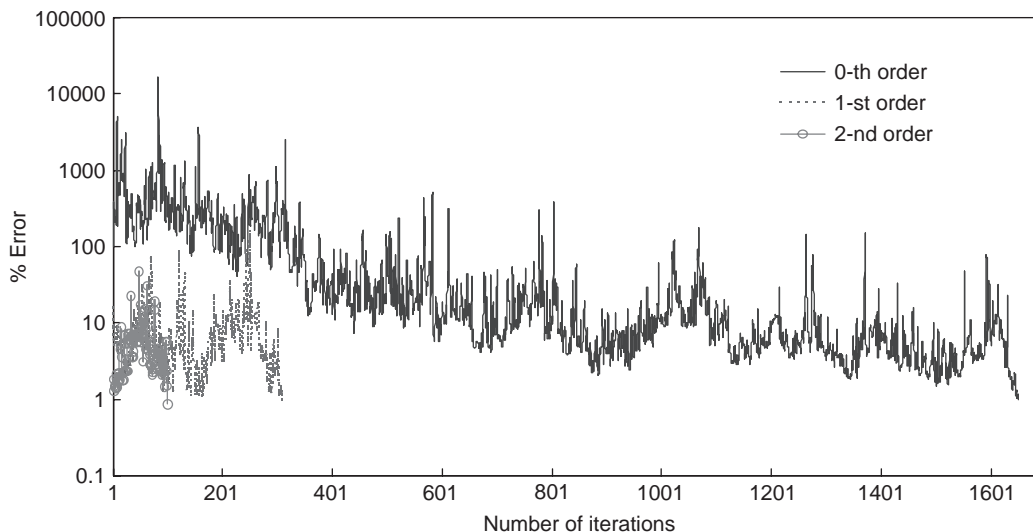


Figure 57. Convergence of SMCG method for 1117-square-patch-element reflectarray with 512×512 gridpoints. (This figure is available in full color at <http://www.mrw.interscience.wiley.com/erfme>.)

3. SUMMARY

In this article, we discuss some parallel algorithms and programming clues for solving large-scale electromagnetic problems on the Beowulf PC cluster. Parallel implementation of commonly used computational techniques such as FDTD and MoM methods are discussed in detail. Manipulation of FDTD calculation is one of the key characteristics of the PDE approach. In contrast to the PDE approach, the resulting matrix in MoM calculation is a full one. Several methods for solving a full-matrix solution are discussed. When the available computer memory resources are exhausted, we need to solve the full-matrix equation iteratively. We also discuss the SMCG method to reduce the memory requirement and maintain speedy computation of matrix-vector multiplication. Numerical examples presented are drawn from various applications of computational electromagnetics, and they are successfully solved by means of parallel computing, using various algorithms presented in this article.

ACKNOWLEDGMENT

The work presented in this article was supported in part by the Hong Kong Research Grant Council, Grant CityU 1031/97E.

BIBLIOGRAPHY

1. C. Leopold, *Parallel and Distributed Computing: A Survey of Models, Paradigms, and Approaches*, Wiley, 2001.
2. H. F. Jordan and G. Alaghband, *Fundamentals of Parallel Processing*, Prentice-Hall, 2003.
3. R. Chandra, L. Dagum, D. Kohr, D. Maydan, J. McDonald, and R. Menon, *Parallel Programming in OpenMP*, Morgan Kaufmann, 2000.
4. P. Pacheco, *Parallel Programming with MPI*, Morgan Kaufmann, 1996.
5. W. Gropp, E. Lusk, and A. Skjellum, *Using MPI: Portable Parallel Programming with the Message Passing Interface*, 2nd ed., MIT Press, 1999.
6. A. Geist, A. Beguelin, J. Dongarra, W. Jiang, R. Manchek, and V. S. Sunderam, *PVM: Parallel Virtual Machine: A Users' Guide and Tutorial for Network Parallel Computing*, MIT Press, 1994.
7. FFTW official homepage.
8. S. Velampambal, W. C. Chew, and J. M. Song, 10 million unknowns, is it that large, *IEEE Anten. Propag. Mag.* **45**(2):43–58 (April 2003).
9. The Beowulf Cluster Site, <http://www.beowulf.org>.
10. The Beowulf Underground, <http://www.beowulf-underground.org>.
11. K. S. Yee, Numerical solution of initial boundary value problems involving Maxwell's equations in isotropic media, *IEEE Trans. Anten. Propag.* **14**:302–307 (May 1966).
12. R. F. Harrington, *Field Computation by Moment Method*, IEEE Press, 1993.
13. Introduction to programming shared-memory and distributed-memory parallel computers, <http://www.acm.org/crossroads/xrds8-3/programming.html>.
14. D. HM Spector, *Building Linux Clusters*, O' Reilly, 2000.
15. MPICH—a portable MPI implementation of MPI, <http://www.unix.mcs.anl.gov/mpi/mpich/index.html>.
16. BLAS homepage, <http://www.netlib.org/blas/>.
17. LINPACK homepage, <http://www.netlib.org/linpack/>.
18. Cheops Network User Interface, <http://www.marko.net/cheops>.
19. G. Mur, Absorbing boundary conditions for the finite-difference approximation of the time-domain electromagnetic field equations, *IEEE Trans. Electromag. Compat.* **23**:377–382 (1981).
20. J. P. Berenger, A perfectly matched layer for the absorption of electromagnetic waves, *J. Comput. Phy.* **114**:185–200 (1983).
21. A. Taflov and M. E. Brodwin, Numerical solution of steady-state electromagnetic scattering problems using the time-

- dependent Maxwell's equations, *IEEE Microwave Theory Tech.* **MTT-23**(8):623–630 (Aug. 1975).
22. B. Toland, J. Lin, B. Houshmand, and T. Itoh, FDTD analysis of an active antenna, *IEEE Microwave Guided Wave Lett.* **3**(11):423–426 (1993).
 23. B. Toland, J. Lin, B. Houshmand, and T. Itoh, Electromagnetic simulation of mode control of a two-element active antenna, *IEEE MTT-S Int. Microwave Symp. Digest*, San Diego, CA, May 23–27, 1994, Vol. 2, pp. 883–886.
 24. Q. X. Chu, K. F. Chan, and C. H. Chan, Parallel FDTD analysis of active integrated antenna array, *Microwave Opt. Technol. Lett.* **34**(4):317–319 (Aug. 2002).
 25. Q. X. Chu, The FDTD analysis of MIC dielectric oscillator, *J. Electron.* **28**(4) (April 2000).
 26. J. Lin, T. Itoh, and S. Nogi, Mode switch in a two-element active array, *Antennas and Propagation Society International Symposium*, 1993. AP-S. Digest, **2**:664–667 (June 1993).
 27. K. John, *OrCAD Pspice and Circuit Analysis*, 4th ed., Prentice-Hall, Upper Saddle River, NJ, 2001.
 28. A. Witzig, C. Schuster, P. Regli, and W. Fichtner, Global modeling of microwave applications by combining the FDTD method and a general semiconductor device and circuit simulator, *IEEE Trans. Microwave Theory Tech.* **47**: 919–928 (June 1999).
 29. N. Matsui, N. Orhanovic, and H. Wabuka, FDTD_SPICE analysis of EMI and SSO of LSI ICs using a full chip macro model, *Proc. 2002 IEEE Int. Symp. Electromagnetic Compatibility*, Aug. 2002, Vol. 1, pp. 99–104.
 30. V. A. Thomas, M. E. Jones, M. Picket-May, A. Taflove, and E. Harrigan, The use of SPICE lumped circuits as sub-grid models for FDTD analysis, *IEEE Microwave Guided Wave Lett.* **4**(5) (May 1994).
 31. S. M. Rao, D. R. Wilton, and A. W. Glisson, Electromagnetic scattering by surfaces of arbitrary shape, *IEEE Trans. Anten. Propag.* **30**(3):401–418 (May 1982).
 32. M. J. Quinn, *Parallel Programming in C with MPI and OpenMP*, McGraw-Hill, 2004.
 33. V. Kumar, A. Grama, A. Gupta, and G. Karypis, *Introduction to Parallel Computing: Design and Analysis of Algorithms*, Benjamin/Cummings, 1994.
 34. L. Tsang, J. A. Kong, K. H. Ding, and C. O. Ao, *Scattering of Electromagnetic Waves: Numerical Simulations*, Wiley, 2001.
 35. M. D. Grammatikakis, D. F. Hsu, and M. Kraetzl, *Parallel System Interconnections and Communications*, CRC Press, 2001.
 36. C. H. Chan, C.-M. Lin, L. Tsang, and Y. F. Leung, A sparse matrix/canonical grid method for analyzing microstrip structures (invited paper), *IEICE Trans. Electron.* **E80-C**(11):1354–1359 (Nov. 1997).
 37. S.-Q. Li, Y.-X. Yu, C. H. Chan, K. F. Chan, and L. Tsang, A sparse-matrix/canonical grid method for analyzing densely packed interconnects, *IEEE Trans. Microwave Theory Tech.* **49**:1221–1228 (July 2001).
 38. F. Ling, C.-F. Wang, and J.-M. Jin, An efficient algorithm for analyzing large-scale microstrip structures using adaptive integral method combined with discrete complex-image method, *IEEE Trans. Microwave Theory Tech.* **48**(5):832–839 (May 2000).
 39. Y. L. Chow, J. J. Yang, D. G. Fang, and G. E. Howard, A closed-form spatial Green's function for the thick microstrip substrate, *IEEE Trans. Microwave Theory Tech.* **MTT-39**:588–593 (March 1991).
 40. N. B. Christensen, Optimized fast Hankel transform filter, *Geophys. Prospect.* **38**:545–568 (1990).
 41. T. K. Sarkar and O. Perira, Using the matrix pencil method to estimate the parameters of a sum of complex exponentials, *IEEE Anten. Propag. Mag.* **37**:48–55 (Feb. 1995).
 42. D. Pilz and W. Menzel, Full wave analysis of a planar reflector antenna, *Proc. 1997 Asia Pacific Microwave Conf.*, Dec. 1997, pp. 225–227.

PARAMETER ESTIMATION FROM ELECTROMAGNETIC SIMULATIONS USING SIGNAL MODELS

KRISHNA NAISHADHAM
Massachusetts Institute of
Technology
Lexington, Massachusetts

1. INTRODUCTION

Advances in digital and microwave electronics have resulted in increasing operating frequencies, reduction in circuit size, and the concomitant increase in circuit complexity. Design of microwave circuits and systems requires understanding the proximity interactions between components, effects of radiation, ohmic loss, and other properties, which are strongly dependent on the physical geometry, and cannot be predicted by circuit-theoretic approaches. Increasingly, full-wave electromagnetic (EM) simulation techniques, which calculate the EM field within and around the circuit, are being used in the analysis of high-speed digital circuits and microwave and millimeter-wave integrated circuits (MMICs). Commonly used simulation methods include the method of moments (MoM) [1], the finite-element method (FEM) [2], the finite-difference time-domain (FDTD) method [3], and the transmission-line matrix method [4]. Commercial software based on these methods is available to the microwave engineer. EM simulation, however, is typically computation-intensive and therefore finds use predominantly in microwave circuit analysis. It has attracted somewhat limited attention to the design and optimization of microwave circuits. Therefore, it is desirable to investigate means of improving the efficiency of full-wave methods so that they become more suitable to performing complex design-oriented tasks demanded by the increasing circuit complexity in the microwave industry.

It is instructive to conceptually understand how circuit parameters are calculated using full-wave methods in order to realize reasons for their limited use in design. In all these methods, the circuit parameters, such as admittance parameters of a matching transformer, are determined from the currents and voltages derived from the EM field within the circuit domain. In MoM, the surface of the circuit or scattering object (e.g., a microstrip antenna) is discretized into polygonal patch elements and the currents on these elements are determined by solving an

integrodifferential equation for the EM field on the surface. By using appropriate piecewise-approximate representation of the current within each patch, and forming moments involving pairwise current–field interactions between all the patches, a system of matrix equations is obtained that relates the patch currents to the impressed voltage or field. The matrix is dense (in fact *full*) because all the near-field and far-field interactions between the patch currents are accounted for. The currents are computed by solving such a linear system. Therefore, in design applications involving MoM simulations, one solves a large linear system of equations at *each design step* for the surface currents on the scattering object.

In FEM, a three-dimensional (3D) circuit region is divided into volume elements such as tetrahedra, and an energy functional, in the form of an integrodifferential operator equation, is formulated on the vector field components. Minimization of the functional determines the values of the field components within the region of interest. The unknown field is approximated by a polynomial function within each volumetric cell, and the Rayleigh–Ritz procedure is applied to minimize the functional, resulting in a system of linear equations. Although the procedure produces a sparse matrix because only the interactions between nearest neighbors need to be accounted for, FEM involves discretization of the volume around the circuit region all the way up to an artificial terminating boundary called the *absorbing boundary*. Thus, in design applications, FEM requires the solution of a large system of linear equations for the EM field in an entire 3D grid surrounding the object.

The FDTD method, first formulated by Yee [5], involves expressing Maxwell’s equations in finite difference form in an entire 3D spacetime lattice encompassing the scattering object, which is terminated in an absorbing boundary for open-region problems. The finite difference approximations are iteratively updated at each timestep for each spatial lattice point using an *explicit* method such as the marching-on-time or leapfrog algorithm. The spatial and temporal sampling increments are selected according to the Courant stability condition necessary (but not sufficient) for stability of the time-marching algorithm. Time-marching iterations are terminated when the desired steady-state response is observed. A major drawback of the FDTD method is that it is highly computer-intensive and suffers from lack of accuracy due to dispersion and other roundoff errors that accumulate in time and space. Therefore, unlike MoM and FEM, which have been coupled with optimization algorithms [6,7], the FDTD method has been used only in the analysis phase. Efforts to improve the accuracy and reduce the computational requirements have received significant attention more recently, and one such effort, related to extrapolation of time sequences, will be discussed in Section 2.

The TLM method exploits the relationship between EM field quantities in a computational volume and voltages and currents on equivalent transmission lines to solve boundary value problems applicable to microwave circuits. Equivalent transmission-line equations for the transverse electromagnetic (TEM) mode are derived from Maxwell’s equations and boundary conditions of the

problem. The TEM modal equations for voltage and current are expressed in finite difference form on a timespace lattice of transmission lines, terminated as necessary by an absorbing load, a short circuit, or an open circuit. Specific lattice points are excited by voltage or current pulses, and pulse propagation through the lattice is evaluated iteratively until a suitable convergence criterion is satisfied. The TLM method has a number of similarities with the FDTD method and thus suffers from the same drawbacks alluded to earlier.

From the summary above, it is evident that EM simulation methods are in general of limited value in microwave design unless their computational efficiencies can be improved. As a means to achieve this goal, it is desirable to investigate independent “signal” models, which accurately represent the circuit parameters of interest in the design space spanned by the full-wave simulation, and can be constructed from a limited number of EM simulations. Within this space, one can then utilize the model for computing the frequency response at each design iteration, thus minimizing the need for intensive computer simulations. This article focuses on the development and validation of such signal models.

We present techniques for modeling time-domain signatures in Section 2 and those applicable to frequency-domain data in Section 3. The emphasis is on practical implementation of the algorithms, rather than the underlying theory. The latter has been published in signal processing and control systems literature, and applicable references are cited throughout the article. Sufficient implementation details are included to enable the reader to generate computer programs for the algorithms with minimal effort. Microwave circuit and antenna examples are presented for both time- and frequency-domain models to illustrate the effectiveness of the proposed algorithms and to validate them. Important conclusions on the algorithms and their implementation are summarized in Section 4.

2. TIME-DOMAIN MODEL

The EM response of any scattering object can be conveniently represented as a sum of complex sinusoids whose amplitude and phase are closely related to parameters of interest (e.g., complex propagation constants on a transmission line and their modal response). This feature has been applied to signal modeling in EM with some success, particularly in time-domain methods such as the FDTD method. Signal processing techniques have been widely used to estimate microwave circuit parameters from time-domain EM simulations [8–13], and to characterize the system response from transient data extracted from simulations or measurements [14–17]. Important circuit parameters, such as quality factor of microstrip antennas [8], resonant frequencies of dielectric resonators [10], characteristic impedance and propagation constant of waveguides [12], and *S*-parameters of discontinuities [13], have been computed using these methods. In this section, we review how the complex exponential signal model can be constructed from a short time-varying data sequence computed by the FDTD method, and extrapolate

this model three- or fourfold to fill the remainder of the sequence [13]. Since the FDTD simulation is used for a relatively short time window compared to overall length of the final time signature, utilization of the signal model in the FDTD method improves its computational efficiency considerably. Although the signal model is demonstrated with the FDTD method because of its popularity in time-domain EM simulations, the model can be used to process the data generated by any time-domain simulation (see Ref. 18 for model-based extrapolation of time-domain MoM data), as well as measured data.

The FDTD technique is well-established as a versatile analytical tool for solving EM problems associated with characterizing scattering and radiation from microwave structures. However, it is also recognized that for accurate characterization of the underlying scattering modes of even relatively simple structures, very long time sequences (TSs) need to be computed. FDTD simulations are highly computation-intensive, and generation of these long TSs can be prohibitively expensive. The problem becomes particularly acute for high- Q structures with energy storage features such as cavities and cavity-backed apertures, which tend to manifest relatively long decay times requiring thousands of timesteps. The number of timesteps n_{\max} that are computed also increases with the maximum electrical size of the structure. Depending on the excitation and the structure being analyzed, in three dimensions, $n_{\max} \propto N^\beta$, where N is the number of volumetric grid cells used to model the structure and $\beta < 1$ [3]. As an example, for a box that measures $5\lambda \times 5\lambda \times 10\lambda$ at the highest operating frequency and divided into $50 \times 50 \times 100$ cubical cells (10 cells per wavelength), assuming that it takes the equivalent of five round-trip traverses across the maximum diagonal dimension of the box to achieve steady state, we estimate $n_{\max} = 2450$ and $\beta = 0.63$. A timestep $\Delta t = \Delta/2c$, where Δ is the space step and c is the speed of light, is used in the calculation above. Although n_{\max} appears to be relatively small, total simulation time can still be quite large, as the execution time for one temporal iteration over the whole object increases linearly with the number of spatial cells.

Several researchers have attempted to model time-domain EM data as the impulse response (IR) of an autoregressive moving-average (ARMA) transfer function [9–13]. The ARMA model involves both poles and zeros of the transfer function whereas the simpler AR model involves only poles [19–21]. In order to avoid long computation times and the associated cost, the ARMA or AR model of the TS is constructed from short “early” data records. The estimated (or trained) “model” is then used to predict the remainder of the TS by extrapolation.

Determination of ARMA parameters via IR fitting is a deterministic nonlinear optimization problem [21]. In EM literature, Prony’s method (PM) and its variations have played a dominant role in the “late time” extrapolation [8–12]. This is due primarily to the fact that PM approximates the true nonlinear modeling problem of minimizing the fitting error (FE), and converts it into a simpler linear estimation problem. In fact, it is shown in this section that PM actually optimizes an equation error (EE), which is a linearized approximation of the true nonlinear FE. As a

consequence, Prony’s approach suffers from certain drawbacks. Since it attempts to minimize an approximated error between the IR model and the simulated TD data, it tends to overmodel the system to achieve a close fit to the data. In fact, when there are deep nulls in the frequency domain magnitude spectra, significantly high model orders are needed to achieve a close fit. Furthermore, overmodeling may lead to instability, as demonstrated by simulated results in the sequel below.

The underlying assumption for system identification using PM (or linear predictor, stochastic AR/ARMA modeling, or similar approaches) is that the measured output TS can be characterized well as the response of a linear time invariant (LTI) system, represented by a ratio of polynomials. Figure 1 shows a typical input–output scenario of an unknown system to be modeled. System modeling using the output response of such a rational system can be categorized into two distinct classes, stochastic or deterministic, as summarized next:

- *Stochastic or Random Process.* In this case, usually only the output $y(n)$ is available for identification purposes. The input process $x(n)$ is either unavailable or cannot be measured, and is usually assumed to be “white noise” within the bandwidth of interest. Traditional stochastic modeling techniques assume that the process $y(n)$ is stationary and make use of its second-order statistics or autocovariance values to estimate the denominator and/or the numerator parameters of the unknown LTI system. A large class of “spectrum estimation” techniques belong to this category [19,20]. Interestingly, this inherent “random process” assumption has been made often, albeit implicitly, in extracting the poles of EM systems from transient response using Prony’s method [10,14,15], and the generalized pencil of functions (GPoF) method [16,17,22–24]. GPoF method utilizes certain properties of data and covariance matrices formed with the system response, whose generalized eigenvalues yield the poles.
- *Deterministic Process.* In this case, both the input excitation as well as the output sequence of the system are either known or can be measured [21]. The most common example is to estimate the system parameters from the output IR sequence [25–37]. The more general case, when both input and output sequences are directly used to estimate the unknown system parameters, is known as system identification, and has also received considerable attention [38–42]. Example applications of this deterministic approach to EM problems may be found in the literature [43–47].

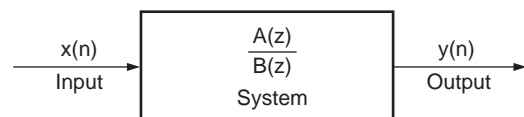


Figure 1. Rational transfer function system with input and output [13] (© IEEE 2001).

In modeling EM time-domain data, considerable research has focused on stochastic spectrum estimation based techniques [9,11,43–47]. As noted above, these methods implicitly assume the system input to be unknown white-noise sequence. However, limited attention has been given to deterministic IR modeling approaches. This is rather surprising, given that a known excitation sequence is used in EM analysis, which clearly implies that modeling the EM TS belongs more appropriately to the *deterministic* category. For example, in the FDTD analysis of EM scattering phenomena, a narrow Gaussian pulse is used as the input sequence. Since the pulse is sufficiently narrow in width, its bandwidth is much wider than the system bandwidth. Hence, the input can be essentially considered as an impulse, and the response can be categorized as a (deterministic) IR. Thus, the white noise input implicitly assumed in spectrum estimation-based techniques is neither necessary nor appropriate for FDTD signal modeling. We will show that a properly chosen deterministic model of the data represents time evolution of the FDTD signal more accurately, and leads to smaller model orders, than classical stochastic approaches.

There are other fundamental limitations in using stochastic spectrum estimation approaches for modeling EM signatures. It is well established that in spectrum estimation, AR parameter estimation is a linear problem (as in Prony-type algorithms) whereas estimating the MA part is a highly nonlinear optimization problem [19,20]. This perhaps explains why AR modeling has been the most common choice in EM literature. However, since AR models represent purely all-pole systems, they are known to be primarily effective for modeling “peaky” spectra, that is, systems with dominant poles. On the other hand, the response of microwave circuits such as filters and resonators often has deep nulls in the frequency domain. Clearly, the transfer functions of such structures must contain dominant zeros, which cannot be modeled well with poles *only*. In the absence of zeros in the assumed model, the pure AR approaches attempt to synthesize the nulls using significantly large numbers of poles away from the unit circle, leading to very high model orders [9,11,43–47]. Furthermore, the fundamental objective of modeling any unknown system is to seek the true underlying model fit with minimum possible number of parameters or model order (“principle of parsimony”). From that perspective, even if a large-order AR model can achieve a reasonably good fit, it does not necessarily produce the most efficient model characterization of an unknown system.

In general, in order to match a mixed spectrum containing both peaks and nulls, ARMA models are better suited than AR models [19–21]. We demonstrate in this article that if an appropriate *deterministic* ARMA model is assumed, and the model parameters are estimated by minimization of the true (nonlinear) IR model-fitting error (not the linearized “equation error” used in previous approaches), very close approximations to the measured TS can be achieved with significantly low model orders. It is interesting to note that unlike the stochastic spectrum estimation approaches, the numerator (MA) estimation problem in the deterministic case is *linear* whereas the

denominator (AR) estimation problem is *nonlinear* [21,36]. However, it has been shown [36] that the two problems can be decoupled without affecting the optimality properties of the true error criterion. The decoupling leads to two subproblems of reduced complexities. This approach, termed as the *decoupled optimal method* (OM), has been applied to model and extrapolate FDTD TSs [13], and will be described later.

In the representation of FDTD signals, we note that the TSs are highly oversampled because of the small sampling period necessitated by Courant’s stability condition. Hence, prior to modeling, the TSs need to be decimated by some decimation factor (DF). We have developed a frequency-domain approach for determining DFs that is based on acceptable level of aliasing caused by decimation [13]. The proposed approach is practically useful as it relies only on the “early” part of the FDTD TS to determine the DF. This approach will be illustrated with examples in Section 2.4.

This section on time-domain modeling is organized as follows. In Section 2.1, the EM time sequence model is defined and the modeling problem is stated. In Section 2.2, a few important “deterministic” model estimation approaches, applicable to FDTD sequences, are briefly reviewed. In Section 2.3, the decoupled optimal method for signal modeling is outlined, focusing on algorithm implementation rather than its theory. We also describe a practically useful data-driven criterion for model order selection. The effectiveness of the proposed approach is demonstrated in Section 2.4 with simulation results on high- Q structures such as a lowpass filter with sharp cut-off characteristics and a patch antenna.

2.1. Problem Statement

A general complex exponential model of the electromagnetic TD signal can be defined as the IR of an LTI system

$$h(n) = y(n) \triangleq \sum_{k=1}^p \alpha_k e^{(\sigma_k + j\omega_k)n\Delta t + j\phi_k}, \quad (1)$$

$$n = 0, 1, \dots, (N - 1)$$

where α_k , σ_k , ω_k , and ϕ_k denote the real amplitude, damping factor, frequency, and initial phase, respectively, of the k th exponential, and Δt is the sampling period. However, the time sequences generated by EM simulations are always real; that is, the exponentials occur in complex conjugate pairs. Consequently, these sequences can be represented as

$$h(n) \triangleq \sum_{k=1}^{p/2} \alpha_k e^{n\Delta t\sigma_k} \cos(\omega_k n\Delta t + \phi_k), \quad (2)$$

$$n = 0, 1, \dots, (N - 1)$$

Note that p has been assumed to be even without any loss of generality. If p is odd or if any frequency $\omega_k = 0$, there would be real components representing pure decay without any oscillation. Taking z transform on both sides of (1),

we obtain

$$H(z) = \sum_{k=1}^p \frac{A_k}{(1 - d_k z^{-1})} \quad (3)$$

where $A_k \triangleq \alpha_k e^{j\phi_k}$ denotes complex amplitudes and $d_k \triangleq \sigma_k + j\omega_k$. After summation of the p terms in the right-hand side, we obtain the transfer function (TF)

$$H(z) = \frac{a_0 + a_1 z^{-1} + \dots + a_{p-1} z^{-(p-1)}}{1 + b_1 z^{-1} + \dots + b_p z^{-p}} \triangleq \frac{N(z)}{D(z)} \quad (4)$$

where the coefficient of z^0 term in the denominator has been assumed to be unity. Note that the coefficients in this TF are real because all A_k and d_k occur in conjugate pairs. It is also noted that the TF in (4) represents a special case of a more general ARMA TF, given by

$$H(z) = \frac{a_0 + a_1 z^{-1} + \dots + a_{q-1} z^{-(q-1)} + a_q z^{-q}}{1 + b_1 z^{-1} + \dots + b_{p-1} z^{-(p-1)} + b_p z^{-p}} \quad (5)$$

where p and q denote the number of poles and zeros, respectively, and can have any arbitrary integer values, in general. When $p = q + 1$, the special ARMA TF in (4) is also known as “strictly proper” and classical Prony’s model belongs to this category. Another important special case is the purely autoregressive (AR) TF with $q = 0$. The transfer function $H(z)$ in (5) can be written equivalently in terms of its IR sequence as

$$H(z) = h(0) + h(1)z^{-1} + \dots + h(k)z^{-k} + \dots \quad (6)$$

which is aptly referred to as the *infinite impulse response* (IIR) TF. Stacking the first N significant samples of $H(z)$:

$$\mathbf{h} \triangleq [h(0) \quad h(1) \quad \dots \quad h(N-1)]^T \quad (7)$$

Next, let the vector containing the N samples of the simulated FDTD-TS (i.e., impulse response) be denoted as

$$\mathbf{h}_d \triangleq [h_d(0) \quad h_d(1) \quad \dots \quad h_d(N-1)]^T \quad (8)$$

According to Steiglitz [26], given a desired IR \mathbf{h}_d , “the ideal problem” of optimal estimation of the parameters a_i and b_i can be represented by the following model fitting error minimization

$$\begin{aligned} \min_{\mathbf{a}, \mathbf{b}} \|\mathbf{e}\|^2 &\triangleq \min_{\mathbf{a}, \mathbf{b}} \sum_{i=0}^{N-1} \left[h_d(i) - \left\{ \frac{N(z)}{D(z)} \right\} \delta(i) \right]^2 \\ &\triangleq \min_{\mathbf{a}, \mathbf{b}} \|\mathbf{h}_d - \mathbf{h}\|^2 \end{aligned} \quad (9)$$

where

$$\begin{aligned} \delta(i) &= \begin{cases} 1, & i = 0 \\ 0, & i \neq 0 \end{cases} \\ \mathbf{e} &\triangleq \mathbf{h}_d - \mathbf{h} \\ \mathbf{a} &\triangleq [a_0 \quad a_1 \quad \dots \quad a_q]^T \\ \mathbf{b} &\triangleq [1 \quad b_1 \quad \dots \quad b_p]^T \end{aligned} \quad (10)$$

The notation $\{N(z)/D(z)\}\delta(i)$, denotes the i th output when a “system” represented by $N(z)/D(z)$ is driven by the input $\delta(i)$. The estimation of the model parameters in (9) is known to be nonlinear in \mathbf{b} , and standard nonlinear optimization algorithms have been suggested [29–32]. Unlike these suboptimal methods, the decoupled OM presented in Ref. 13 does not modify the error criterion or the least-squares minimization of the nonlinear FE defined in (9). This optimal approach is general and has no restrictions on the numbers of poles and zeros, unlike other closely related methods [27,34,35], which are valid only for strictly proper TFs. In order to motivate the proposed approach, some of the important developments in deterministic system identification are briefly outlined next.

2.2. Overview of Deterministic System Identification

Over the last several decades, identification of unknown discrete-time linear systems received considerable attention [25–42]. Linear system modeling can be broadly categorized into two classes: nonparametric and parametric. Classical nonparametric models can be applied to IR sequence (e.g., the EM time sequence), frequency response, power spectral density (PSD) or periodogram, autocorrelation sequence, characteristic function, and other signals [19–21,48,49]. The major drawback of classical nonparametric models is that, more often than not, these representations are theoretically infinite in extent.

Parametric models such as rational transfer functions, exponential models and state space representations overcome the infinite-dimensionality problem of nonparametric models by parsimonious representation of systems in terms of a finite number of coefficients. The pole-zero or rational transfer function model is perhaps the most effective and practical representation of systems, and has been widely applied in the EM literature. Research on parameter estimation of rational transfer functions has evolved in four major directions. The first among the following four approaches listed below deals with modeling “random” processes, whereas the later three deal with “deterministic” scenarios:

1. In statistical and modern spectrum estimation literature, unknown systems, or rather their PSDs, are modeled using ARMA model identification methods [19,20]. The system parameters are estimated from the observed output data record only. Since the input to such systems cannot be observed, it is assumed as white noise for modeling convenience.

2. In control systems, the input and output signals of a plant are usually measurable. Hence, the system parameters are estimated from the known input/output record [38–42].
3. In digital filter design, the ideal filter specifications are given in the frequency domain in terms of the magnitude and phase responses in the passbands and stopbands, and classical methods are used for approximating IIR (or ARMA) filters, such as Butterworth, Chebyshev, and elliptic [21,48,49]. For arbitrary or nonclassical frequency-domain specifications, least-squares matching leads to general nonlinear optimization algorithms [29–31].
4. In data modeling, the least-squares fit between measured or simulated data and the desired IR is required. In this case, it becomes more appropriate to fit the data directly to the IR output of the rational transfer function model.

The FDTD modeling problem addressed in this work belongs to category 4 listed above. However, the time-domain algorithms for case 2 above may be appropriate if the Gaussian “input” pulse sequence is considered. Case 3 may also be applicable when frequency-domain simulated data characterize the unknown system (such as in FDFD and the finite-element methods). Hybrid algorithms combining any two or more of the three deterministic categories also appear feasible. Important theoretical developments leading to decoupled OM for rational model fitting are described next.

2.2.1. Kalman’s Method. In an early work on rational transfer function identification, Kalman suggested the solution of the following linear problem [40]:

$$\min_{\mathbf{a}, \mathbf{b}} \sum_{i=0}^{N-1} [\{D(z)\}h_d(i) - \{N(z)\}\delta(i)]^2 \quad (11)$$

The advantage of this modified error criterion is that it can be easily minimized in the least-squares sense with respect to the unknown coefficients in \mathbf{a} and \mathbf{b} , by solving a set of simultaneous linear equations. Apart from its simplicity, this approach is not known to possess any optimality property.

2.2.2. Prony-Based Methods. Prony’s work [50] was perhaps the first to recognize that the exponentials ($e^{j\omega k}$ terms) in (1) are the p roots of the polynomial $D(z)$ in (5). Making use of this fact, Prony converted the “nonlinear” problem of frequency (or “periodicity”) estimation into a “linear” problem of coefficient estimation. However, this was accomplished by bypassing the ideal model fitting error criterion in (9) and instead, an “equation error” is minimized. Using (4), we obtain

$$H(z)D(z) = N(z) \quad (12)$$

The LHS clearly represents a convolution operation. Hence, by equating the coefficients of same powers of z^{-1}

on both sides of (12), we obtain

$$\sum_{i=0}^p b_i h(k-i) = a_k \quad \text{for } k=0, 1, \dots, (p-1) \quad (13)$$

$$\sum_{i=0}^p b_i h(k-i) = 0 \quad \text{for } k=p, p+1, \dots \quad (14)$$

These equalities hold only if there is no error in modeling and the model parameters are exact. Otherwise, we get modeling or “equation errors” from (14):

$$e_{\text{eq}}(k) \triangleq \sum_{i=0}^p b_i h_d(k-i) \quad \text{for } k=p, p+1, \dots \quad (15)$$

In PM, the b_i coefficients are found by minimizing the squared sum of these equation errors:

$$\begin{aligned} \min_{\mathbf{b}} \sum_{k=p}^{N-1} e_{\text{eq}}^2(k) &\triangleq \min_{\mathbf{b}} \sum_{k=p}^{N-1} \sum_{i=0}^p b_i h_d(k-i) \\ &\equiv \min_{\mathbf{b}} \sum_{k=p}^{N-1} [\{D(z)\}h_d(k)]^2 \end{aligned} \quad (16)$$

Using matrix–vector representation, the equation error vector can be expressed as

$$\begin{aligned} \mathbf{e}_{\text{eq}} &\triangleq \begin{bmatrix} e_{\text{eq}}(p) \\ e_{\text{eq}}(p+1) \\ \vdots \\ e_{\text{eq}}(N-1) \end{bmatrix} \\ &\triangleq \begin{bmatrix} h_d(p) & h_d(p-1) & \cdots & \cdots & h_d(0) \\ \vdots & \ddots & \vdots & \ddots & \vdots \\ h_d(N-1) & h_d(N-2) & \cdots & \cdots & h_d(N-p-1) \end{bmatrix} \times \mathbf{b} \\ &\triangleq \mathbf{H}_2^p \mathbf{b} \end{aligned} \quad (17)$$

The minimization of the norm of this vector is also known as the “covariance method” of linear prediction [20,21]. The coefficients \mathbf{b} obtained by minimization of this criterion do not minimize the “ideal” FE criterion defined in (9), and hence these estimates are not optimum in that sense. There are two types of ARMA model identification techniques based on the denominator produced by PM, namely, Shank’s or Burrus–Parks methods.

2.2.2.1. Shanks’ Method. This is a two-step approach where the denominator coefficients are first estimated by

minimizing the equation error in (16) to form $\hat{D}(z)$ and then the numerator coefficients are found by minimizing the following modified fitting error norm [25]:

$$\min_{\mathbf{a}} \sum_{i=0}^{N-1} \left[h_d(i) - \left\{ \frac{N(z)}{\hat{D}(z)} \right\} \delta(i) \right]^2 \quad (18)$$

Note that the estimation of \mathbf{a} in (18) is a linear problem.

2.2.2.2. Burrus–Parks Method. This is also a two-step method closely related to Shank’s work [33]. The difference is only in the way the numerator coefficients are estimated. The denominator is found exactly in the same manner as Prony’s in (16). To obtain the numerator, the first q error samples are set to zeros, with the “best” available estimates used for the first q samples of $h_d(n)$. The elements of \mathbf{a} are then found from

$$a_k = \sum_{i=0}^k \hat{b}_i h_d(k-i) \quad (19)$$

It may be noted that the Matlab Signal Processing Toolbox uses this particular approach to estimate the numerator for its version of PM, and that subroutine function is called *prony*.

2.2.3. The Steiglitz–McBride Iterative Prefiltering Method. The “linear” methods described above completely modify the true criterion in (9) and minimize entirely different error criteria. In contrast, this approach attempts to remain within the framework of the original criterion in (9). In this method, an initial estimate $\hat{D}(z)$ of the denominator coefficients is first found by either Kalman’s method (11) or Shanks’ first step (16). Then the following modified fitting error criterion is optimized iteratively [41]:

$$\min_{\mathbf{a}, \mathbf{b}} \sum_{i=0}^{N-1} \left[\left\{ \frac{D(z)}{\hat{D}(z)} \right\} h_d(i) - \left\{ \frac{N(z)}{\hat{D}(z)} \right\} \delta(i) \right]^2 \quad (20)$$

The estimate $\hat{D}(z)$ obtained at the i th iteration step is used as prefilter for obtaining the estimates at the next iteration step. Note that (20) closely approximates (9) and both are exactly same if $D(z) = \hat{D}(z)$. But using (20), the unknown parameters in \mathbf{a} and \mathbf{b} can be estimated by solving a set of simultaneous linear equations. Further details on this method and its application in AR and ARMA model-based filter design may be found in Ref. 21.

2.3. Decoupled Optimal Method

The goal of this approach can be summarized as follows. Given a simulated (or measured) EM time sequence (8), estimate the coefficients of the numerator and denominator polynomials of the unknown rational transfer function (5) by minimizing the true IR model-fitting error [see Eq. (9)] in the least-squares sense. The approach presented below attempts to solve this multidimensional,

nonlinear optimization problem, as posed in (9), by optimizing with respect to the denominator and numerator coefficients.

As given by (9), the direct formulation reveals coupling between the numerator and denominator estimation problems. Shaw [36] showed that the joint FE optimization problem defined in (9) can be theoretically *decoupled* into two subproblems of *reduced* computational complexities. The approach, known as decoupled optimal method, is applicable to identification of rational models with *arbitrary* numbers of poles (p) and zeros (q). It has been shown that the nonlinear denominator subproblem possesses a weighted-quadratic structure that can be utilized to formulate an efficient *iterative* minimization algorithm. Unlike Steiglitz–McBride’s work, no iterations are needed to find the optimal numerator, which is estimated in a single step using a linear least-squares approach. The decoupled subcriteria of OM are known to possess *global optimality* properties [36]. A brief outline of OM follows, with details of implementation included in the Appendix at the end of this article.

It has been shown [36] that the nonlinear denominator criterion of OM has the following equivalent forms:

$$\begin{aligned} \min_{\mathbf{a}, \mathbf{b}} \|\mathbf{e}_{\text{OM}}(\mathbf{a}, \mathbf{b})\|^2 &\equiv \min_{\mathbf{b}} \|\mathbf{e}(\mathbf{b})\|^2 \\ &\triangleq \min_{\mathbf{b}} \|\mathbf{B}(\mathbf{B}^T \mathbf{B})^{-1} \mathbf{B}^T \mathbf{h}_d\|^2 \\ &= \min_{\mathbf{b}} \|\mathbf{h}_d^T \mathbf{B}(\mathbf{B}^T \mathbf{B})^{-1} \mathbf{B}^T \mathbf{h}_d\|^2 \\ &= \min_{\mathbf{b}} \mathbf{b}^T \mathbf{H}_2^T (\mathbf{B}^T \mathbf{B})^{-1} \mathbf{H}_2 \mathbf{b} \end{aligned} \quad (21)$$

where

$$\mathbf{B} \triangleq \begin{bmatrix} b_{q+1} & b_{q+2} & \cdots & b_p & \cdots & 0 \\ b_q & b_{q+1} & \cdots & b_{p-1} & \vdots & \cdots \\ \vdots & \vdots & \vdots & \vdots & \vdots & b_p \\ 1 & b_1 & \cdots & \cdots & \cdots & b_{p-1} \\ 0 & 1 & \cdots & \cdots & \cdots & \cdots \\ 0 & 0 & \cdots & b_1 & \cdots & \cdots \\ \cdots & \cdots & \cdots & 1 & \cdots & \cdots \\ 0 & 0 & \cdots & \cdots & \cdots & b_1 \\ 0 & 0 & \cdots & 0 & \cdots & 1 \end{bmatrix} \quad (22)$$

$\in \mathbf{R}^{N \times (N-q-1)}$

$$\mathbf{H}_2 \triangleq \begin{bmatrix} h_d(q+1) & h_d(q) & \cdots & h_d(0) & 0 & \cdots & 0 \\ h_d(q+2) & h_d(q+1) & \cdots & h_d(1) & h_d(0) & \cdots & 0 \\ \vdots & \vdots & \vdots & \vdots & \vdots & \vdots & \vdots \\ h_d(p) & h_d(p-1) & \cdots & \cdots & \cdots & \cdots & h_d(0) \\ \vdots & \vdots & \vdots & \vdots & \vdots & \vdots & \vdots \\ h_d(N-1) & h_d(N-2) & \cdots & \cdots & \cdots & \cdots & h_d(N-p-1) \end{bmatrix} \quad (23)$$

where $\mathbf{H}_2 \in \mathbf{R}^{(N-q-1) \times (p+1)}$. Note that, in deriving (21), no linearization approximation had been introduced at the outset. The criterion in (21) is nonlinear in \mathbf{b} but possesses a weighted-quadratic structure, where the weight matrix, $(\mathbf{B}^T \mathbf{B})^{-1}$ depends on the unknown parameters in \mathbf{b} . An iterative minimization scheme for this criterion has been developed [36], and the steps are summarized next.

2.3.1. Denominator Estimation. The nonlinear criterion for estimating the *denominator* in (21) is optimized in two steps.

Step 1: Initial Estimate of OM and Its Relation to Prony's. The initial estimate of \mathbf{b} is found by first setting $\mathbf{b} = [1 \ 0 \ 0 \ \cdots \ 0]^T$ to avoid the trivial solution. This is exactly equivalent to setting the “prefilter” matrix $(\mathbf{B}^T \mathbf{B})^{-1} = \mathbf{I}_{(N-q-1)}$ in (21). This modification or linearization leads to the following “equation error” (EE) criterion

$$\begin{aligned} \min_{\mathbf{b}} \|\mathbf{e}_{\text{eq}}(\mathbf{b})\|^2 &\triangleq \min_{\mathbf{b}} \|\mathbf{h}_d^T \mathbf{B} \mathbf{B}^T \mathbf{h}_d\|^2 \\ &= \min_{\mathbf{b}} \mathbf{b}^T \mathbf{H}_2^T \mathbf{H}_2 \mathbf{b} \end{aligned} \quad (24)$$

where the EE vector is defined as

$$\mathbf{e}_{\text{eq}}(\mathbf{b}) \triangleq \mathbf{B}^T \mathbf{h}_d = \mathbf{H}_2 \mathbf{b} \quad (25)$$

Interestingly, when $p = q + 1$, this equation error becomes

$$\begin{aligned} \mathbf{e}_{\text{eq}}^p(\mathbf{b}) &\triangleq \begin{bmatrix} h_d(p) & h_d(p-1) & \cdots & \cdots & h_d(0) \\ \vdots & \vdots & \vdots & \vdots & \vdots \\ h_d(N-1) & h_d(N-2) & \cdots & \cdots & h_d(N-p-1) \end{bmatrix} \\ &= \mathbf{H}_2^p \mathbf{b} \end{aligned} \quad (26)$$

Minimization of this error is exactly equivalent to the standard Prony method as well as the “covariance method” of AR modeling [19–21], both of which are commonly used in the EM literature. Note that \mathbf{H}_2^p in (26) is identical to the “data matrix” for Prony’s estimator in (17). Since the Prony’s estimator is a linearized special case of OM and, in fact, provides the initial estimate for OM iterations, it is fair to argue that OM would always outperform Prony-based methods. OM iteratively minimizes the modeling

error further to obtain a better fit. This will be demonstrated by the simulation examples later in this section.

Step 2: Phase 1 Iterations. Once the initial estimate of \mathbf{b} is available, the following criterion is iteratively optimized by utilizing the estimate obtained at the l th (previous) iteration to update the estimate at the $(l+1)$ th (present) iteration:

$$\min_{\mathbf{b}} \mathbf{b}^T \mathbf{H}_2^T (\mathbf{B}^{T(l)} \mathbf{B}^{(l)})^{-1} \mathbf{H}_2 \mathbf{b} \quad (27)$$

Details of this optimization are given in the Appendix.

2.3.2. Numerator Estimation. At convergence of the OM iterations, the optimum \mathbf{b}^o is used to find the minimized error as

$$\mathbf{e}_o \triangleq \mathbf{B}_o (\mathbf{B}_o^T \mathbf{B}_o)^{-1} \mathbf{B}_o^T \mathbf{h}_d \quad (28)$$

Using the optimal error, the “cleaned up” or optimum IR is found from

$$\mathbf{h}^o = \mathbf{h}_d - \mathbf{e}_o(\mathbf{b}) \quad (29)$$

The first q elements of this optimum IR are used for calculating the optimum \mathbf{a}^o as

$$a_k^o = \sum_{i=0}^k \hat{b}_i^* h^*(i-k), \quad k = 0, 1, \dots, q \quad (30)$$

Equations (27) and (30) are the two key formulas for estimating the coefficients of the denominator and numerator polynomials, respectively, of the unknown TF.

The decoupled estimation of \mathbf{a} and \mathbf{b} in OM belongs to a special class of nonlinear optimization problems that have been studied extensively by numerical analysts [51]. It has been shown [51] that in a non-linear error criterion, if some of the unknown variables are linearly related to the error and the other variables are nonlinearly related, and if these variables appear in a separable form, as in this case, then the two decoupled estimators in (27) and (30) are the *globally optimum estimators* for both sets of variables.

2.3.3. Computational Complexity. The major computational load of the algorithm is in performing the iterative refinement in (27), where, at each iteration step, one needs to invert an $(N-q-1) \times (N-q-1)$ matrix $(\mathbf{B}^T \mathbf{B})$. It may appear that this inversion should require $O[(N-q-1)^3]$ operations. However, $(\mathbf{B}^T \mathbf{B})$ is a symmetric banded Toeplitz matrix and many efficient algorithms are available for inverting such matrices [34,52,53]. Specifically, it has been shown that inversion of such banded Toeplitz matrices requires only operations of $O[N]$ [52]. Furthermore, numerical experimentation reveals that the iterations converge fairly quickly (5–10 iterations maximum).

2.3.4. Model-order Selection. As in any modeling problem, selection of the order of the underlying system is a critical issue. The difference between the desired and modeled signal, as defined in (9), is a combination of model mismatch error, measurement error and noise. If this error is Gaussian-distributed, then the minimization of the criterion in (9), as performed by OM, is the maximum-likelihood estimator (MLE) for this problem. In case of MLE, the Akaike information criterion (AIC) or minimum description-length (MDL) criterion are often used for order determination. However, it has been shown [54] that MDL is a consistent estimator of order, whereas AIC is inconsistent and that AIC often overestimates the model order. Hence, we propose to use MDL for order determination in combination with OM.

For the general ARMA (p, q) process, MDL is given by [54–56]

$$\begin{aligned} \text{MDL}(p, q) &= N \ln \sigma(p, q) + (p + q) \ln N; \quad p = 1, 2, 3, \dots, \\ q &= 0, 1, 2, \dots \end{aligned} \quad (31)$$

where N is the number of IR samples used and $\sigma(p, q)$ is the minimized error power as defined in (9) for a particular choice of p and q . According to [54–56], the optimal p and q correspond to the minimum value of $\text{MDL}(p, q)$. However, for Prony's case, $q = p - 1$ and the optimal p can be determined according to the minimum of

$$\text{MDL}(p) = N \ln \sigma(p) + (2p - 1) \ln N; \quad p = 1, 2, 3, \dots \quad (32)$$

These equations will be used in our simulations for comparing equivalent orders of OM and Prony's approaches. It may be noted that the first term in the MDL criterion is proportional to the error power that tends to diminish as p is increased, whereas the second term is a "penalty factor" that penalizes higher choice of p . As p is increased, $\text{MDL}(p)$ diminishes initially with the error. However, when p goes beyond the "true" model order, the second term dominates and pushes the value of $\text{MDL}(p)$ back up again. Hence, ideally, the plot of MDL is bowl-shaped and the optimum orders correspond to the bottom of the bowl.

2.4. Simulation Examples

In this section, we present results from Ref. 13 on modeling and extrapolation of FDTD simulated data for a microstrip lowpass filter and a microstrip patch antenna, comparing the performance of various algorithms, such as Prony's method, OM and AR modeling, in terms of model fidelity and accuracy. We also estimate the model order for each algorithm using the MDL criterion.

2.4.1. Lowpass Filter. In this section, the performance of OM is compared with that of a standard Prony-based algorithm provided with the Matlab signal processing toolbox. The FDTD-TS (time sequence) used for these simulations is shown in Fig. 2. This time-signature is sampled at the output port of a microstrip two-port lowpass filter

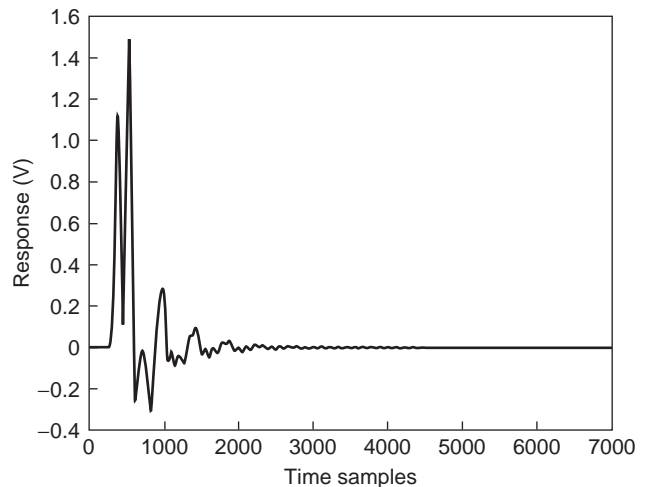


Figure 2. The raw FDTD time sequence of a microstrip lowpass filter [13] (© IEEE 2001).

(see Fig. 7 in Ref. 57 for the geometry). Both ports have a characteristic impedance of 50 Ω .

2.4.1.1. Determination of Decimation Factor (DF). The raw simulation is run with $\Delta t = 0.441$ ps, and hence, the total frequency range is $F = 1/\Delta t = 2267.6$ GHz. Clearly, the signal is oversampled and needs to be decimated because only 40 GHz (20 GHz on either side) is of interest for comparison with the measurements in Ref. 57. With appropriate decimation of the TS, the data processing required for modeling can be reduced considerably, and the effective model order will also be lower. However, the DF needs to be selected carefully so as not to cause any undesirable aliasing resulting from the decimation operation. The magnitude response of the filter shown in Fig. 3 indicates that in order to limit the aliasing below -50 dB, the one-sided bandwidth of the decimated signal cannot be less than 50 GHz. Hence, to limit aliasing effect to less than -50 dB, the filter TS can be safely decimated by a ratio of 22:1. Conservatively, we have chosen a DF of 10:1. The magnitude response in Fig. 3 validates that the DF choice of 10:1 is quite adequate for preserving the signal information, and will keep the alias level below -60 dB. In order to obtain the frequency domain plot in Fig. 3, only the *early-time* computed response (the first 2000 samples) were used, with sufficient zero padding as necessary for a smooth spectrum. This a priori selection of the DF before computing the entire TS presents a minor overhead to the FDTD simulation time, and is practically useful.

The FDTD simulation of the filter is terminated after 2000 timesteps (in contrast to 8000 in the original paper [57]). The first 1000 time samples, which correspond to transient data, are not considered in the signal processing; the samples between 1001 to 2000 are used for estimating the model. The selected 1000 samples are decimated by a factor of 10:1 to obtain the 100 modeling samples. Figure 4 shows the comparison of IR fit between an ARMA (6,5) model (sixth-order OM), and the standard Prony result (also sixth-order) for the decimated sequence. The corre-

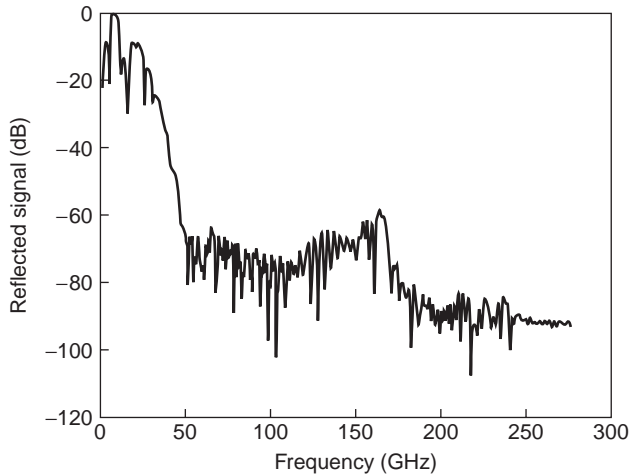


Figure 3. Frequency spectrum magnitude of the reflected signal for a lowpass filter [13] (© IEEE 2001).

sponding 1000-sample window of the raw FDTD-computed TS is also included in Fig. 4. While the ARMA model shows excellent agreement with the original raw data, Prony's model tracks the time signature rather poorly. The sixth-order model thus established has been used to extrapolate the TS from 2000 to 8000 (i.e., late-time data are extrapolated from an early-time model). Although not shown, excellent comparison between ARMA model and the reference solution in Ref. 57 has been observed for the entire TS of 8000 samples. The *entire* TS of 8000 samples is then Fourier-transformed to generate the frequency response. The prediction performance in the frequency-domain insertion loss S_{21} of the filter is shown in Fig. 5. The solid line corresponds to the measurements reported in Ref. 57, the dashed line to the sixth-order OM, and the dotted-dashed line to the sixth-order Prony. The measured data is in good agreement with the Fourier Spectrum of the original FDTD reference Signal of 8000 timesteps [57]. The results of direct FDTD analysis using

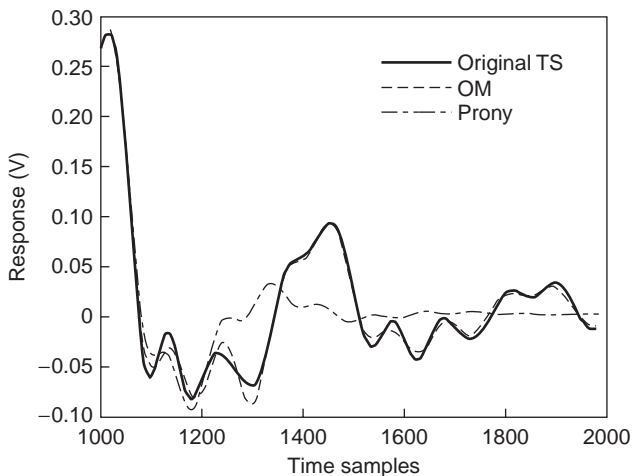


Figure 4. Comparison of the ARMA (6,5) model response for a lowpass filter using OM (dashed line), and Prony's method (dashed-dotted line), with the decimated FDTD reference solution (solid line) [13] (© IEEE 2001).

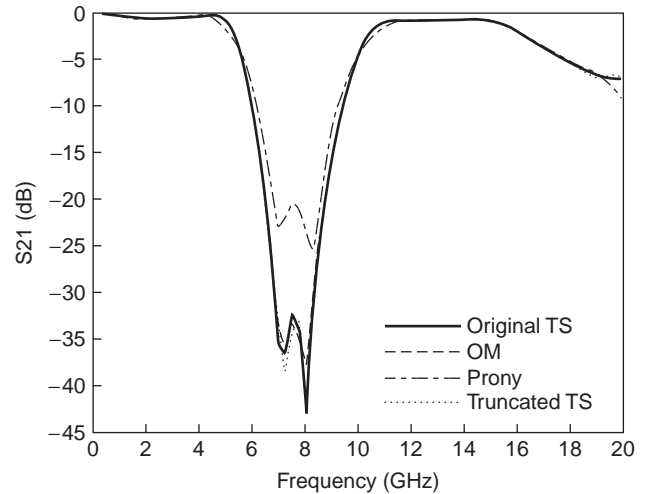


Figure 5. Comparison of frequency-domain insertion loss (S_{21}) for a lowpass filter, computed using extrapolated time sequences [13], with the measurements from Ref. 57 (© IEEE 2001).

only the initial 2000 timesteps are also included in Fig. 5 (dotted line) for comparison. Good corroboration between the spectrum of direct (truncated) FDTD sequence and the extrapolated model is not surprising given that the most significant spectral content is contained in the first 2000 temporal samples. Therefore, one could argue that good corroboration of FDTD-computed data with the measurements for the filter can be obtained by computing only 2000 samples and zero padding up to 8000. However, if we reduce the sample size to 1500, thereby discarding more of the significant spectral content, the discrepancy between spectra of truncated and extrapolated data increases, especially near the critical band in the vicinity of the notch [13].

The filter under consideration is a notch lowpass filter, designed with a notch frequency at 7.5 GHz and attenuation of -40 dB. The return loss S_{11} , also computed for both OM and Prony's models, is compared with the measurements from [57] in Fig. 6. It is observed that for the same

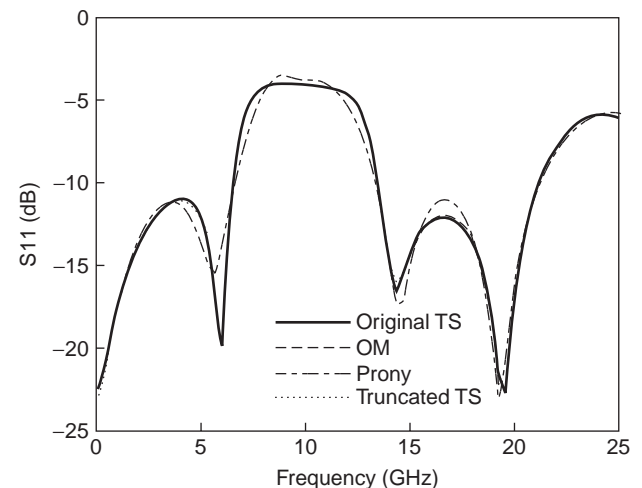


Figure 6. Comparison of frequency-domain return loss (S_{11}) for a lowpass filter, computed using extrapolated time sequences [13], with the measurements from Ref. 57 (© IEEE 2001).

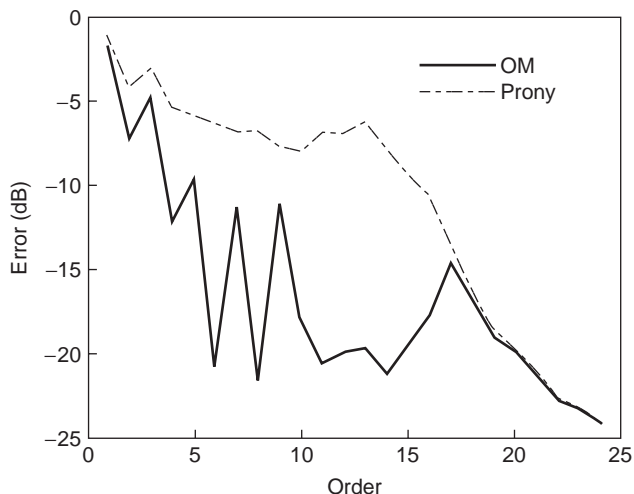


Figure 7. Comparison of a lowpass filter's model-fitting error for Prony's method with the error for OM [13] (© IEEE 2001).

low model order ($p=6$), OM outperforms the standard Prony model by a significant margin, and corroborates very well with the measurements. Again, it is observed that a truncated sequence of the initial 2000 samples predicts the return loss to the same accuracy as the extrapolated FDTD sequence, albeit with a 200 MHz shift in the resonant frequency at 15 GHz.

The IR fitting error defined in (9) was calculated for both methods with the model orders (p) ranging from 1 to 24, and the results are shown in Fig. 7. The figure shows that in order to obtain corroboration to the same degree of accuracy as achieved by OM with $p=6$ (-22 dB or better), the Prony's model order would have to be increased to $p=20$, as reported in Ref. 9. Figure 7 further suggests that the discrepancy between OM and Prony's model tends to diminish at higher model orders.

It may be noted that since PM does not minimize the true FE for the denominator, it needs extra poles to account for the notches in the frequency response. However, one needs to be careful about selecting too high an order because such "overmodeling" may lead to instability. This is depicted in Fig. 8, where the maximum pole radii in the case of PM are plotted for p ranging from 1 to 40. This figure clearly shows that at high orders, the largest pole radius pushes towards—and even exceeds—unity, which will render the estimated transfer function unstable. Standard stabilization approach by means of flipping the unstable poles inside the unit circle would not affect the magnitude response. However, such stabilization would alter the phase characteristics, the optimized impulse response, as well as the model fitting error, none of which may be desirable in practice.

That low values of p may be quite appropriate for this problem is further validated by the MDL criterion. Using the fitting errors shown in Fig. 7, the MDL(p) values were calculated for both OM and Prony's method at increasing orders, and the results are shown in Fig. 9. The figure indicates that in the case of OM, the values of MDL(6) and MDL(8) are about the same, and hence, the choice of $p=6$ for OM is justified.

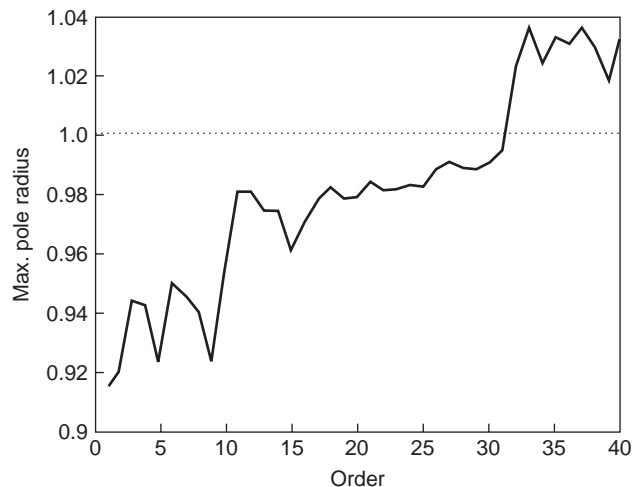


Figure 8. Maximum pole radius with increasing model order using Prony's method [13] (© IEEE 2001).

In summary, OM appears to be computationally more efficient, and gives better accuracy than Prony's method for FDTD data processing. For higher- Q and electrically large structures, the computational savings are expected to be much higher than for the filter studied.

2.4.1.2. Comparison with Pure AR Model. We note that the Matlab function *prony*, used for the comparisons given above actually produces ARMA models. This is because *prony* uses the Burrus–Parks version of Prony's method [33], where both the numerator and the denominator of the TF are estimated linearly. Hence, the Prony's results reported above are superior to what would otherwise be obtained if pure AR models had been used instead, as in Refs. 11 and 47, where no zeros at all are used to account for the notches. To illustrate this point, the fitting errors at different model orders are compared in Fig. 10 for pure AR models, ARMA and the Matlab function *prony*. Clearly, for

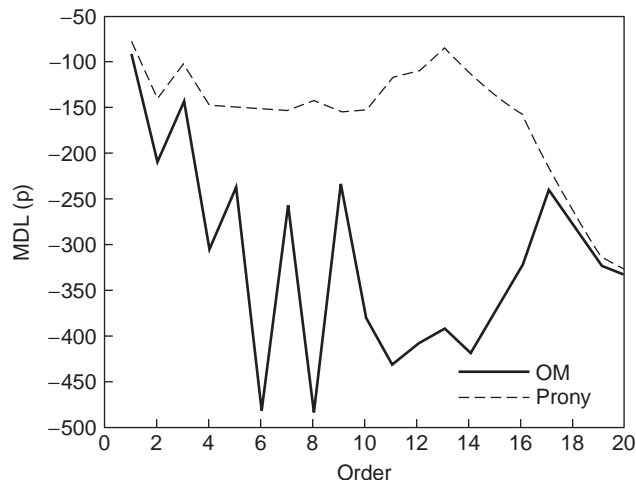


Figure 9. MDL criterion with increasing model order using OM and Prony's method on a lowpass filter [13] (© IEEE 2001).

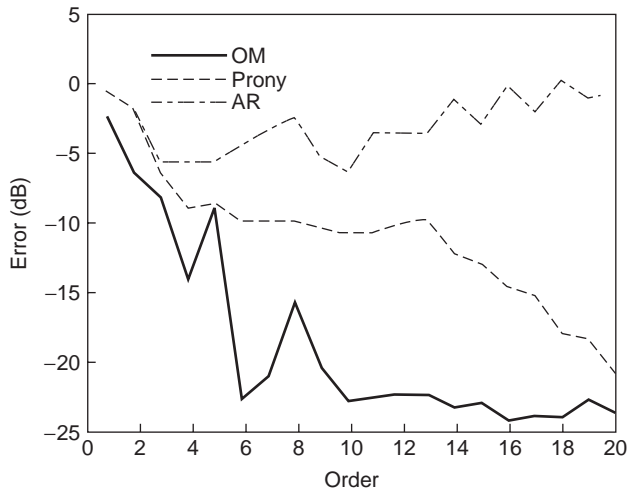


Figure 10. Comparison of model-fitting error for pure AR model with the error for Prony's method and that for OM [13] (© IEEE 2001).

the range of low orders depicted in Fig. 10, the performance of the AR models is poorer than either of the other two approaches. In fact, in order to obtain equivalent fit with the AR model for the same accuracy as the sixth-order OM, much longer training sequences and much higher filter orders need to be used [11,47].

2.4.2. Patch Antenna. Next, we consider modeling the field of a microstrip-line-fed patch antenna whose geometry is depicted in Fig. 3 of Ref. 57. The excitation is a Gaussian pulse of the same temporal parameters as indicated in Ref. 57. The raw simulation is run for 8000 timesteps ($\Delta t = 0.441$ ps) and produces the reference TS. The initial 1500 samples are discarded for transients and the samples between 1501 and 3000 are used for estimating the model. In this case also, the frequency range prior to decimation is $F = 1/\Delta t = 2267.6$ GHz. The magnitude spectrum of the reflected signal at the input port using the first 3000 samples is shown in Fig. 11. It indicates that in order

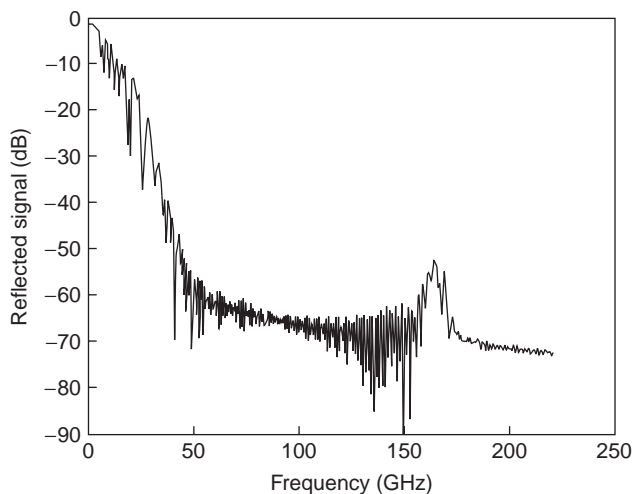


Figure 11. Frequency spectrum magnitude of the reflected signal for the patch antenna [13] (© IEEE 2001).

to limit aliasing to less than -50 dB, the one-sided bandwidth of the decimated signal in this case must be at least 45 GHz. Hence, this signal can be safely decimated by up to about 25:1 without any significant distortion due to aliasing. On the basis of this analysis, the signal was decimated with a ratio of 15:1. This structure has a narrower bandwidth and higher Q than does the filter example considered earlier.

Figure 12 compares the decimated reflected signal at the input port of the antenna with the ones produced by an ARMA (7,6) model (seventh-order OM) and the standard Prony method (also of seventh order). The models thus produced were then used to extrapolate the TS from 3000–8000 timesteps. The initial TS of transients between 1–1500 was added back. Because the antenna has a relatively high Q , it is reasonable to expect some compromise in accuracy between modeled and FDTD-computed TSs *with the low orders used*. However, even with $p = 7$, OM captures the details of the dominant early-time response very closely, and maintains a fairly good temporal corroboration overall. Prony's method, on the other hand, performs poorly for $p = 7$. The model fitting error is plotted as a function of the model order in Fig. 13. In order to obtain the same accuracy as the seventh-order OM, Prony's model would require an order of about 18. The MDL values for both methods are compared in Fig. 14, and once again, we clearly show that $p = 7$ is the optimal choice for OM in this case. Using the same late-time extrapolation approach as pursued for the filter, the frequency-domain return loss S_{11} of the patch antenna is computed for both OM and Prony's models, and compared in Fig. 15 with the measurements or equivalently, the spectrum of the original FDTD sequence of 8000 timesteps, reported in Ref. 57. It is observed that for the same order ($p = 7$), OM clearly outperforms Prony's in this case also, and corroborates quite well with measurements.

For comparison, we have also included in Fig. 15, the return loss computed from a truncated TS of the first 3000 timesteps. Although the discrepancy between the result in

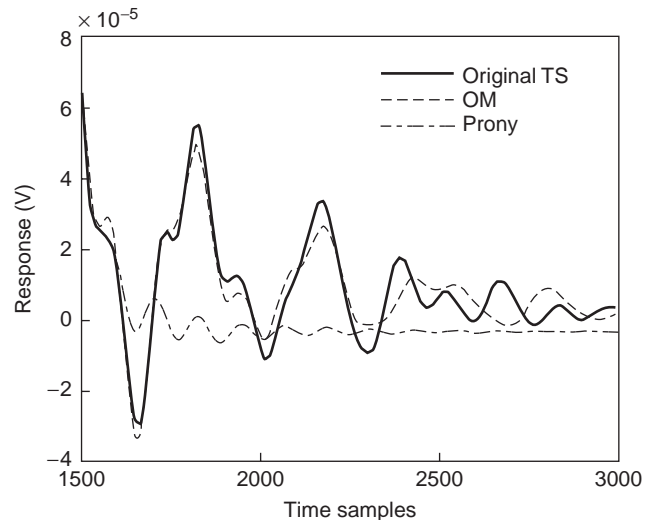


Figure 12. Comparison of the ARMA (7,6) model response for the patch antenna using OM (dashed line) and Prony's method (dashed-dotted line), with the decimated FDTD reference solution (solid line) [13] (© IEEE 2001).

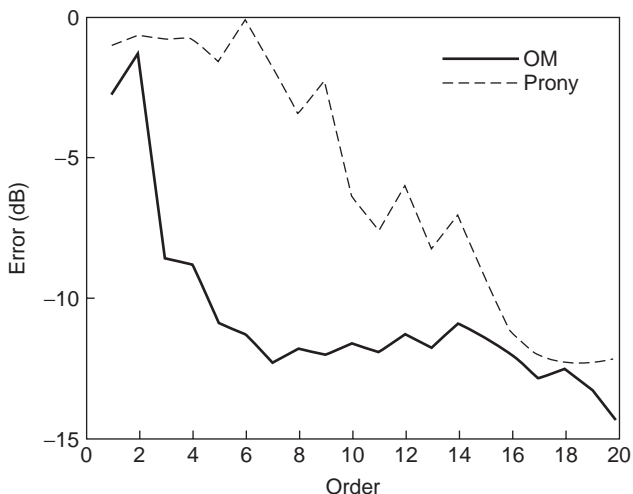


Figure 13. Comparison of the patch antenna's model-fitting error for Prony's method with the error for OM [13] (© IEEE 2001).

Ref. 57 (8000 steps) and the truncated TS appears to be negligible, it is emphasized that because of strong resonance, the tail for the patch antenna does not decay as rapidly as it does for the filter. Also, because of radiation, the pulse loses energy and experiences dispersion as it travels along the patch. These effects do not seem to influence the lower-frequency resonances as much as the high-frequency ones. To illustrate this, in Fig. 16 we have plotted return loss computed from both the truncated FDTD-TS (3000 timesteps) and the sequence used in Ref. 57 (8000 timesteps), over an extended frequency range. The discrepancy between the two results increases significantly above 41 GHz.

3. FREQUENCY-DOMAIN MODEL

In the previous section we described a robust technique for computing the poles and zeros of the ARMA transfer function in (5) by nonlinear optimization of the decoupled

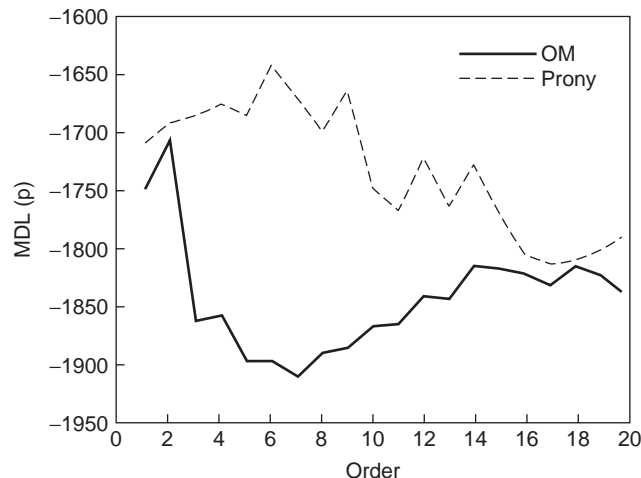


Figure 14. MDL criterion with increasing model order using OM and Prony's method on a patch antenna [13] (© IEEE 2001).

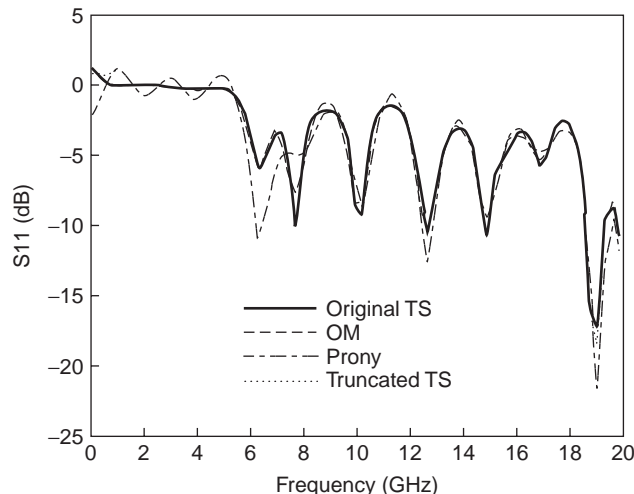


Figure 15. Comparison of frequency-domain return loss (S_{11}) for a patch antenna, computed using extrapolated time sequences [13], with measurements from Ref. 57 (© IEEE 2001).

denominator estimation problem followed by a least-squares solution of the numerator problem. Although nonlinear ARMA methods achieve a given model accuracy with lower model orders than do linear parameter estimation methods, their implementation is inherently complex, and the optimization can become impractical when many iterations are required for convergence. This becomes an issue, for example, in time-domain simulations when the transients established after the incoming wave first strikes the object decay slowly, and perhaps need to be partially included in the model. Another such example, where the transient tail decays very slowly, is the simulation of modes in a large, highly resonant cavity. Besides increasing the number of iterations needed for convergence of the nonlinear estimation methods, inclusion of transient data in the complex exponential model makes the amplitudes *time-de-*

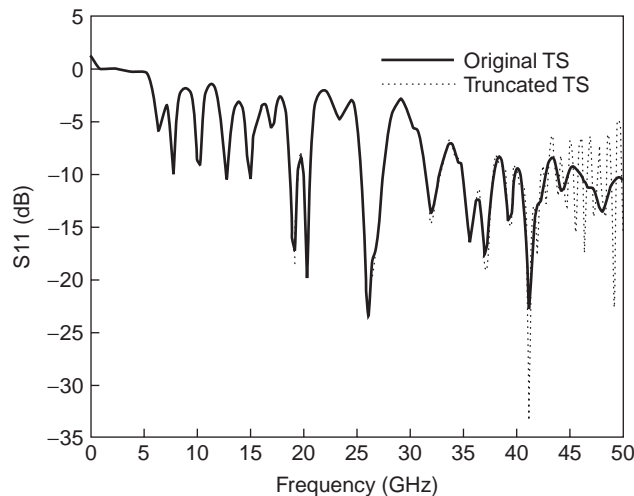


Figure 16. Comparison of frequency-domain return loss (S_{11}) for a patch antenna, computed using OM extrapolation on a truncated FDTD time sequence of 3000 timesteps [13], with the reference computation in Ref. 57 that employs 8000 timesteps (© IEEE 2001).

pendent. Well-established model-based parameter estimation techniques such as Prony's method, the generalized pencil-of-functions method, and OM do not allow for time- or frequency-dependent amplitudes. However, discarding transients in the simulation neglects important physics pertinent to the early-time response, namely, establishing the natural response of the object, which depends only on the object's geometric and physical features. As an example, consider the time-domain reflection from a dielectric slab. If the interaction with the back end of the slab is ignored for the moment (e.g., for a thick slab), the reflection coefficient is completely determined from the interaction between the incident pulse and the slab's front end. Ignoring the first few time samples in the reflected signal is tantamount to not capturing this interaction, and leads to a very erroneous estimate of the reflection coefficient. In this section, we present a robust state space method (SSM) to solve the underlying estimation problem of modeling frequency-domain (FD) signature from a circuit, antenna, or scatterer, in terms of complex exponentials. The amplitudes in the model have decay or growth constants that vary with frequency, and thus permit inclusion of the entire signal in model construction. The model parameters are estimated using concepts from linear system theory without any need for iterative solution. The signal model and its estimation using the SSM are shown to be stable and computationally efficient.

SSM has been introduced by Piou et al. for radar signal processing [58], and is based on linear estimation of all the model parameters. SSM signal processing is a subset of general techniques used to model the EM scattering of an object in the frequency domain in terms of scattering centers. These techniques, including multiple signal classification (MUSIC) [59] and estimation of signal parameters via rotational invariance techniques (ESPRIT) [60], have been used in radar signal processing for understanding scattering mechanisms, tracking, and target feature extraction. They are referred to as *superresolution* techniques because the resulting radar images potentially have better resolution than do conventional Fourier transform techniques. In contrast to MUSIC and ESPRIT, state space signal modeling provides an alternative representation of a rational transfer function that is popular in linear system and control theory. SSM seeks to achieve superresolution in the frequency domain by coherently processing wideband EM data, simulated or measured. The complex exponential terms in the model are interpreted in terms of *scattering centers*, whose amplitudes and time delay (or *range*) are made frequency-dependent to capture the dynamic wideband behavior of the scattering mechanism. The exponential model is cast in terms of a system of difference equations, and state space techniques are employed to solve for the model parameters (decay/growth constants and range) by determining the complex eigenvalues of the system's open-loop state matrix, constructed from the data samples. The modal amplitudes are subsequently obtained from a least-squares solution. Determination of the complex eigenvalues and their modal amplitudes allows one to compute the frequency response of isolated scattering centers on the object, such as the reflection from the frontface of the

dielectric slab alluded to earlier. Unlike previous signal modeling approaches, no part of the signal under consideration is discarded, and therefore the proposed SSM provides a robust state space model in lieu of full-wave simulation for microwave circuit synthesis.

The motivation of this study comes from the seminal work of Carl Baum who proposed the singularity expansion method (SEM) in 1976 [61]. SEM permits description of the distributed parameter problems of electromagnetics by the same pole-zero representations used in the analysis and synthesis of lumped circuits and linear control systems. SSM captures the essence of SEM by applying well-established control system theory to compute the poles and zeros of the rational transfer function that corresponds to the exponential signal model. As shown in Refs. 58 and 62, this algorithm performs robustly even in a low signal-to-noise-ratio (SNR) environment, and therefore, it can also be applied to extract physical parameters, such as dielectric constant, from *measured* data. The proposed approach is also expected to perform better than the existing time-domain extrapolation methods [e.g., 9,13] with respect to model order, stability, and fidelity. Unlike these methods, transients can be considered in the model, potentially capturing important physical phenomena neglected therein. For brevity, however, we restrict ourselves to frequency-domain modeling in this article, although the method is equally applicable for processing time-domain data.

This section on frequency-domain signal models is organized as follows. In Section 3.1, the state-space signal model is introduced. The next subsection presents solution of the difference equation that describes the model in terms of an ARMA transfer function. An alternative input-output description of the model in terms of state space representation is discussed in Section 3.3, and the system parameters are derived in Section 3.4. This method is applied to two practical problems in Section 3.5: (1) determination of dielectric constant of a lossy slab by isolating the leading-edge reflection and (2) isolation of creeping-wave modes by decomposition of the total EM-simulated field scattered by a dielectric-coated cylinder. The latter problem is relevant to calculation of mutual coupling in conformal antenna arrays.

3.1. Signal Model

In this subsection, we review the data sequence $y(k)$ that constitutes N uniformly spaced frequency samples, each represented as a sum of M complex sinusoids (or point scatterers) corrupted by white Gaussian noise $w(k)$. Over a given bandwidth, the signal measurements at these N frequencies can be modeled as

$$y(k) = \sum_{i=1}^M a_i p_i^k + w(k); \quad k = 1, \dots, N \quad (33)$$

where a_i refers to the amplitude of the i th scattering center and the complex pole p_i is given by

$$p_i = \exp \left[-\Delta f \left(\alpha_i + j \frac{4\pi}{c} R_i \right) \right] \quad (34)$$

where a_i , α_i , and R_i denote the amplitude, decay/growth parameter, and the range, respectively, associated with the i th scattering center. The parameter c refers to the speed of light, and Δf is the sampling interval. The range may alternatively be written in terms of the time delay τ_i to the i th scattering center as $\tau_i = (2R_i)/c$. In this article, the primary interest is in estimating the parameters embedded in the data sequence $y(k)$. The state space method presented in Refs. 58 and 62 provides an efficient computation of the decay/growth and range parameters from the eigenvalues of an open-loop matrix (see Section 3.3). Once these parameters are accurately estimated, the amplitudes a_i can readily be derived from the state space matrices using least-squares fit based on a modal decomposition method [58]. The state space formulation may be seen as an input–output relationship between the noise $w(k)$ and the data sequence $y(k)$. The best way to derive the state space matrices is to rewrite (33) as a difference equation and study its transfer function. The next subsection presents the difference equation that best describes the input–output relationship between $y(k)$ and $w(k)$, and the subsequent subsections summarize the derivation of the state-space matrices that allow for computation of the model parameters.

3.2. Transfer Function of the ARMA Model

The input–output relationship for the general ARMA transfer function describing the model in (33) is characterized by the difference equation

$$y(k) = \sum_{i=1}^m d_i y(k-i) + \sum_{j=1}^q b_j w(k-j) + b_0 w(k) \quad (35)$$

where $w(k)$ and $y(k)$ are the input and output, respectively. The transfer function $H(z)$ of the system described by (35) may be defined as

$$H(z) = \frac{Y(z)}{W(z)} = \frac{B_0(z)}{A_0(z)} \quad (36)$$

where

$$A_0(z) = 1 - \sum_{i=1}^m d_i z^{-i} \quad (37)$$

and

$$B_0(z) = b_0 + \sum_{j=1}^q b_j z^{-j} \quad (38)$$

The roots of the polynomial $A_0(z)$ are the poles of the system, whereas the roots of $B_0(z)$ determine the zeros. An interesting and popular special case of the ARMA model in (35) is the AR model, described by the input–output relationship

$$y(k) = \sum_{i=1}^m d_i y(k-i) + b_0 w(k) \quad (39)$$

The transfer function of the AR model is therefore given by

$$H(z) = \frac{b_0}{A_0(z)} \quad (40)$$

with $A_0(z)$ defined by (37). As the AR model is a special case of ARMA, the state space representation will be carried out on the ARMA model unless specified otherwise. In the next subsection, we present the state-space method for the ARMA model.

3.3. State Space Representation

The input–output description of the model in (33) is given alternatively by the difference equations

$$x(k+1) = Ax(k) + Bw(k) \quad (41)$$

$$y(k) = Cx(k) + w(k) \quad (42)$$

where $x(k) \in \mathcal{R}^{M \times 1}$ is the state, $A \in \mathcal{C}^{M \times M}$ is the system matrix, and $B \in \mathcal{C}^{M \times 1}$ and $C \in \mathcal{C}^{1 \times M}$ are constant matrices. The transfer function of the state space formulation is obtained by taking the z -transform of Eqs. (41) and (42), and evaluating the ratio $Y(z)$ to $W(z)$ as follows:

$$X(z) = (zI - A)^{-1}BW(z) \quad (43)$$

$$Y(z) = CX(z) + W(z) \quad (44)$$

where I is an identity matrix. Inserting (43) in (44), we obtain

$$Y(z) = C(zI - A)^{-1}BW(z) + W(z) \quad (45)$$

Thus

$$H(z) = C(zI - A)^{-1}B + 1 \quad (46)$$

Equation (46) shows that the ARMA model for a discrete-time process $y(k)$ in state space notation is related to the transfer function such that the poles of the model [i.e., the roots of the polynomial $A_0(z)$ in (37)] are the eigenvalues of the open-loop matrix A . Furthermore, the zeros [i.e., the roots of $B_0(z)$ in (38)] are the eigenvalues of the matrix $(A - BC)$. Next, we present a procedure to estimate the triplet (A, B, C) from a given data vector.

3.4. State Space Identification

Let the impulse response of the ARMA model be represented by (46). To identify the state space matrices (A, B, C) from the impulse response, we expand the matrix $(zI - A)^{-1}$ into an infinite series:

$$(zI - A)^{-1} = Iz^{-1} + Az^{-2} + A^2z^{-3} + \dots \quad (47)$$

Inserting (47) into (46) yields

$$Y(z) = 1 + CBz^{-1} + CABz^{-2} + CA^2Bz^{-3} + \dots \quad (48)$$

By invoking the definition of the z -transform, (48) may be written as

$$Y(z) = y(0) + y(1)z^{-1} + y(2)z^{-2} + y(3)z^{-3} \quad (49)$$

By comparing coefficients of the z^{-k} terms in Eqs. (48) and (49), we obtain the following sequence:

$$\begin{aligned} y(0) &= 1, \quad y(1) = CB, \\ y(2) &= CAB, \quad \dots \quad y(k) = CA^{k-1}B, \quad \dots \end{aligned} \quad (50)$$

Thus, the relationship between the impulse response of the model and the state space parameters for any positive k is defined by

$$y(k) = CA^{k-1}B \quad (51)$$

If we form a Hankel matrix H from the data samples, given by

$$H \triangleq \begin{bmatrix} y(1) & y(2) & y(3) & \dots \\ y(2) & y(3) & y(4) & \dots \\ y(3) & y(4) & y(5) & \dots \\ \vdots & \vdots & \vdots & \vdots \end{bmatrix} \quad (52)$$

then (51) indicates that H can be factored as

$$H = \begin{bmatrix} C \\ CA \\ CA^2 \\ \vdots \end{bmatrix} [B \quad AB \quad A^2B \quad \dots] \triangleq \Omega \Gamma \quad (53)$$

where, borrowing from linear system theory, Ω and Γ are known as *observability* and *controllability* matrices [63]. It is important to note that despite the infinite dimensions of H defined by (52), for a finite order filter of length M [see (33)], Ω and Γ can be truncated to M rows and M columns, respectively. Consequently H has finite rank $r \leq M$. For a given set of measurements the Hankel matrix H is, of course, always finite. In this case H may be considered to be an operator constructed from a set of measurements $y(k)$ that maps the past input vector w_- to the future output y_+ . In the remainder of this subsection, we present a method to compute the Hankel matrix and derive the state space matrices from a finite set of samples.

Let a set of measurements be defined by

$$y = [y(1) \quad y(2) \quad y(3) \quad \dots \quad y(N)] \quad (54)$$

and suppose that we want to derive the corresponding state space matrices. The first step in computing the triplet (A, B, C) is to form the matrix H from the available data

samples

$$H = \begin{bmatrix} y(1) & y(2) & \dots & y(L) \\ y(2) & y(3) & \dots & y(L+1) \\ \vdots & \vdots & \vdots & \vdots \\ y(N-L+1) & y(N-L+2) & \dots & y(N) \end{bmatrix} \quad (55)$$

where the parameter L denotes the correlation window, and it is heuristically chosen to be $L = \lfloor N/2 \rfloor$, with the brackets denoting the smallest integer less than or equal to the inserted quantity. The Hankel matrix given in (55) may be partitioned into signal and noise subspaces via a singular-value decomposition (SVD). Computing the SVD of H and rearranging its singular values σ_i in decreasing order yields

$$H = [U_{\text{sn}} \quad U_{\text{n}}] \begin{bmatrix} \Sigma_{\text{sn}} & 0 \\ 0 & \Sigma_{\text{n}} \end{bmatrix} \begin{bmatrix} V_{\text{sn}}^* \\ V_{\text{n}}^* \end{bmatrix} \quad (56)$$

In (56), the subscripts “sn” and “n” denote the signal and noise subspaces, respectively, and the superscript * refers to conjugate transpose. The matrices U_{sn} and U_{n} are the signal and noise components, respectively, of the left unitary matrix, V_{sn} and V_{n} are the signal and noise components, respectively, of the right unitary matrix, Σ_{sn} and Σ_{n} denote diagonal matrices, with the signal and noise singular values of H arranged in decreasing order along their main diagonals. For a given SNR, the appropriate threshold may be defined to discard the lowest-order singular values. To increase the accuracy of the state space matrices, the Hankel matrix H may be truncated by suppressing the noise singular values and their associated unitary matrix components. It is well known that an M -rank matrix that best approximates (56) in the spectral norm sense is obtained by retaining only the dominant components [58]:

$$\tilde{H} = U_{\text{sn}} \Sigma_{\text{sn}} V_{\text{sn}}^* \quad (57)$$

By using the balanced coordinate method proposed in Ref. 64, (57) may be further written as [also see (53)]

$$\tilde{H} = \tilde{\Omega} \tilde{\Gamma} \quad (58)$$

where the observability and controllability matrices are calculated as

$$\tilde{\Omega} = U_{\text{sn}} \Sigma_{\text{sn}}^{1/2} \quad \text{and} \quad \tilde{\Gamma} = \Sigma_{\text{sn}}^{1/2} V_{\text{sn}}^* \quad (59)$$

respectively. Then, the matrix $A \in \mathcal{C}^{M \times M}$ can be obtained either from $\tilde{\Omega}$ or $\tilde{\Gamma}$. If the derivation of A is based on the observability matrix, the following equation holds:

$$A = (\tilde{\Omega}_{-r1}^* \tilde{\Omega}_{-r1})^{-1} \tilde{\Omega}_{-r1}^* \tilde{\Omega}_{-r1} \quad (60)$$

The matrices $\tilde{\Omega}_{-r1}$ and $\tilde{\Omega}_{-r1}^*$ in (60) are obtained by deleting the first $\tilde{\Omega}$ and last rows ($r1$ and $r1$), respectively, of

$\tilde{\Omega}$. The state space matrix (or vector) C may next be computed from the observability matrix defined in (53):

$$C = \tilde{\Omega}(1, :) \quad (61)$$

In other words, vector C is given by the first row of $\tilde{\Omega}$. Likewise, the vector B may be computed as the first column of the controllability matrix defined in (53):

$$B = \tilde{\Gamma}(:, 1) \quad (62)$$

If the eigenvalues of A are assumed to be distinct, one has

$$\lambda\{A\} = \{\lambda_1, \lambda_2, \dots, \lambda_M\} \quad (63)$$

It is well known from spectral estimation theory [58] that the eigenvalues (λ_i) carry decay/growth and range information about the scattering object's features; magnitude and phase of the eigenvalues are related to α_i and R_i by

$$\alpha_i = -\frac{\log|\lambda_i|}{\Delta f} \quad \text{and} \quad R_i = -\frac{c\phi_i}{4\pi\Delta f} \quad (64)$$

respectively. In (64), Δf is the sampling frequency and ϕ_i refers to the phase of the eigenvalue λ_i . The amplitudes α_i ($i = 1, \dots, M$) are easily obtained from a least-squares fit to the data using the model in (33) with the parameters calculated in (64) [58].

3.5. Simulation Examples

3.5.1. Synthetic Noisy Data. We consider synthetic data involving four point scatterers, corrupted by complex white Gaussian noise $w(k)$ with variance σ_n defined by the peak signal-to-noise ratio

$$\text{SNR} = 20 \log \frac{\sigma_{\text{sn}}}{\sigma_n} \quad (65)$$

where σ_{sn} denotes the signal variance. The synthetic data are generated using Eq. (33) over the frequency range 3–10 GHz, with a sampling rate of 20.057 MHz. The SNR is 40 dB, and the signal parameters for the data are depicted in Table 1.

To test the effectiveness of the SSM algorithm in the presence of noise, we performed 200 independent trials using these signal parameters with SNR = 40 dB for each run. For each trial, the focus is on a segment of the data with 101 samples in the frequency range 5.5–7.5 GHz. To estimate the signal parameters, the Akaike information criterion (AIC) [65] is used to identify the number of scat-

tering centers (or model order). For each trial, the AIC detects the four signals embedded in the dataset that are estimated by the SSM. The average estimates of the signal parameters over the 200 trials is given in Table 2, showing good corroboration with the original data. The model thus constructed using the SSM with synthetic data over the 5.5–7.5 GHz frequency band is then extrapolated in both forward and backward directions to cover the entire frequency range 3–10 GHz. Excellent agreement is observed between both of the extrapolated models and the “truth” dataset for the complex amplitudes [known as I (in-phase) and Q (quadrature) channels in radar signal processing] over the extended frequency range. The pertinent plots, omitted here for brevity, may be found in Ref. 58.

Next, the same simulation was repeated, decreasing the SNR to 20 dB, and performing 200 trials as stated above. In each trial, AIC detects the four signals that are used to generate the dataset, and SSM estimates their complex amplitudes. The SSM algorithm filters a great deal of noise; therefore, we expect reasonably good corroboration between the estimates and the “truth” data even at this moderately low SNR. Indeed, Table 3 depicts such agreement for all the four scattering centers. The model thus constructed with synthetic data over the 5.5–7.5 GHz frequency band is then extrapolated in both forward and backward directions to cover the entire frequency range 3–10 GHz. Excellent agreement is observed between both of the extrapolated models and the “truth” dataset over the extended frequency range. Pertinent comparison plots may be found in Ref. 58.

3.5.2. Reflection from a Dielectric Slab. The reflection from a 15-mm-thick lossy slab with dielectric constant $\epsilon_r = (5, -0.01)$ is considered next, and it is shown that the response of the frontface of the slab can be isolated from the composite response using the SSM. The “truth” data consists of the Fresnel reflection coefficient for the slab, calculated at normal incidence over the 2–18 GHz frequency band. The dataset is Fourier transformed to obtain the composite response shown in Fig. 17. The transform employs distance to the scatterer (or range) instead of time, and this operation is also known as *pulse compression* or *range processing* [66]. Because the phase reference is at the front face, the pulse with peak at zero range is the first reflection off the slab front, the second pulse is the reflection off the backface, the third pulse is the rereflection off the front, and so on.

Next, a 20th-order state space AR model [see (33)] is computed from the simulated reflection data, and a single pole located at (1,0), with amplitude of 0.382 and phase π radians, is determined to have zero range. Thus, using only this pole in the AR transfer function, one can isolate the front face response of the slab. Figure 18 displays the frequency response of the isolated pulse along with that of the complete model, which is obtained by coherent addition of the response from all 20 poles. The interference between incident and reflected waves, causing the nulls at half-wavelength intervals, is evident. Although not shown, frequency response of the complete model coincides with the “truth” data. Because the leading reflection is isolated, the reflection coefficient of this pulse is the

Table 1. Signal Parameters for Synthetic Data

Scattering Center	Decay/Growth (α)	Time Delay (τ)	Amplitude ($ a $)
1	-0.9231×10^{-9}	2×10^{-9}	1
2	-0.2308×10^{-9}	6×10^{-9}	1
3	-0.3077×10^{-9}	1×10^{-8}	1
4	1×10^{-17}	14×10^{-9}	1

Table 2. Average Estimates of Signal Parameters over 200 Trials (SNR = 40 dB)

Scattering Center	Decay/Growth (α)		Time Delay (τ)		Amplitude ($ a $)	
	Estimates	% Error	Estimates	% Error	Estimates	% Error
1	-0.9118×10^{-9}	1.22	1.98×10^{-9}	1.0	0.997	0.3
2	-0.2084×10^{-9}	9.71	5.8×10^{-9}	3.33	1.03	3.0
3	-0.3318×10^{-9}	7.83	1.0×10^{-8}	0	0.995	0.5
4	0.51×10^{-16}	4.1	13.8×10^{-9}	1.43	1.0	0

same as that of the half-space problem. In other words, the ability to compute using the SSM the responses of different reflected pulses, isolated in range, provides a feature akin to time-domain gating in vector network analyzer measurements, *albeit* with simulated data. This feature has many applications, including determination of physical parameters from simulated (or measured) data. As an example, using the constant amplitude of S_{11} for the isolated pulse from Fig. 18 (with a phase of π), the slab's dielectric constant can be determined as

$$\epsilon_r = \left(\frac{1 - S_{11}}{1 + S_{11}} \right)^2 \quad (66)$$

This equation yields $\epsilon_r = 5 - j0.01$ *exactly*. Once the dielectric constant is known, using the distance d_{12} between the first two peaks in Fig. 17, the slab thickness can be determined as $d = d_{12} / \sqrt{\text{Re}(\epsilon_r)} = 34 / \sqrt{5} = 15.2$ mm, an error of 1.3%.

Next, the analysis shows how the proposed SSM algorithm works for moderately thin slabs when the resolution between the first two peaks in Fig. 17 becomes difficult. For example, when d is reduced to 5 mm, one obtains the range response in Fig. 19, which clearly shows impending merging of the two peaks. Because the first peak can still be isolated, this should result in an accurate dielectric constant. Indeed, the state-space AR model produces a pole with amplitude 0.384 and phase π at zero range, yielding the correct permittivity, thus illustrating qualitatively that the model is not sensitive to thickness variations within the extent of a range cell.

3.5.3. Coupling in a Conformal Array. Microstrip arrays conformal to cylindrically shaped substrates are important in radar and communication applications. Microstrip lines on such substrates serve to feed signal to the radiating elements, and are also used in baluns or couplers for matching the elements. Therefore, examining the modal

propagation on the surface of a cylindrical substrate can be useful. A primary source of coupling between the elements is azimuthal (or creeping) surface waves propagating along helical paths [67], which are not easily resolvable from the radiating space wave. Unlike the planar microstrip counterpart, the cylindrical surface waves do not exhibit pronounced resonance, and difficulty in their detection in the presence of noise is compounded by the fact that their amplitude is much smaller than that of the space wave. An example is the well-known Mie scattering from a sphere, in which the dominant creeping wave is 30 dB below the specularly reflected wave; subsequent creeping waves are considerably weaker. Therefore, isolation of creeping waves provides a challenging test for the SSM algorithm.

This article applies the superresolution SSM to resolve the creeping waves along the surface of a finite-length cylindrical microstrip substrate. Since the modal propagation characteristics are independent of the excitation, without loss of generality, we consider an incident plane wave, and compute the surface currents over a wide frequency band using the body-of-revolution method of moments (MoM) [68]. The radiated field is calculated from the currents as a function of incident angle and frequency. The data for specific angles, such as the specular aspect, contain, in addition to the space wave, the contribution from creeping waves launched at different locations on the substrate. Because the algorithm maps the origin of the creeping waves on the scatterer, one can ascertain in a practical situation not only the interelement coupling but also the source of such coupling. We believe that such an algorithm has significant potential for array optimization.

We consider a cylindrical substrate with a perfect electrically conducting (PEC) core of radius 10 mm, coated with a 4-mm-thick dielectric layer ($\epsilon_r = 3 - j0.6$). Figure 20 depicts the geometry along with schematic position of two conformal microstrip dipole elements, one active (A) and the other passive (P). The radiated field, observed broadside to the cylinder over the 2–12 GHz bandwidth, consists

Table 3. Average Estimates of Signal Parameters over 200 Trials (SNR = 20 dB)

Scattering Center	Decay/Growth (α)		Time Delay (τ)		Amplitude ($ a $)	
	Estimates	% Error	Estimates	% Error	Estimates	% Error
1	-0.9182×10^{-9}	0.53	1.92×10^{-9}	4.0	0.934	6.6
2	-0.2073×10^{-9}	10.18	5.73×10^{-9}	4.5	1.11	11.0
3	-0.343×10^{-9}	11.47	1.17×10^{-8}	17.0	0.987	1.3
4	0.87×10^{-16}	7.7	13.6×10^{-9}	2.86	1.04	4.0

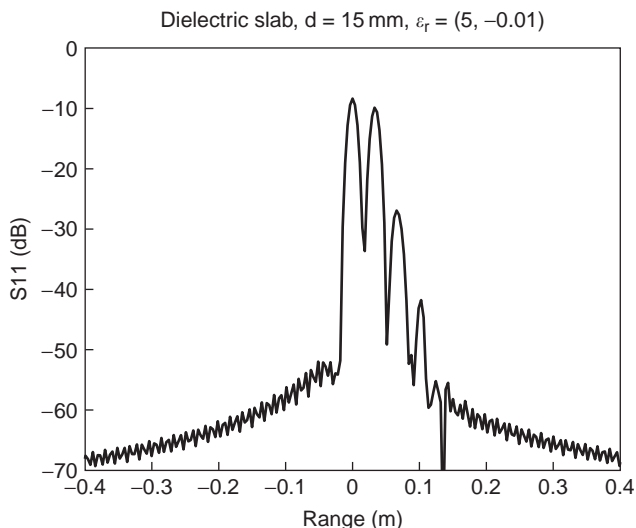


Figure 17. Range response of the reflection coefficient for a 15-mm-thick slab.

of two components: (1) the space wave directly reaching the field point from the active element and (2) the surface (creeping) wave that radiates as it traverses around the cylinder surface. The strength of the creeping wave is proportional to the coupling between the elements. The frequency-domain field data in the principal plane $\theta = 90^\circ$ are Fourier-transformed to obtain the composite response shown in Fig. 21. The first peak denotes the space wave, and the next one, about 35 dB lower, denotes the creeping wave. The range separation between the two peaks equals the arc length between the active and passive elements. The phase reference (zero range) is along the cylinder axis. Thus, the creeping wave originates from a fictitious line source on the opposite end of the cylinder at a range of 0.21 m (or one diameter), as one would expect from physical optics.

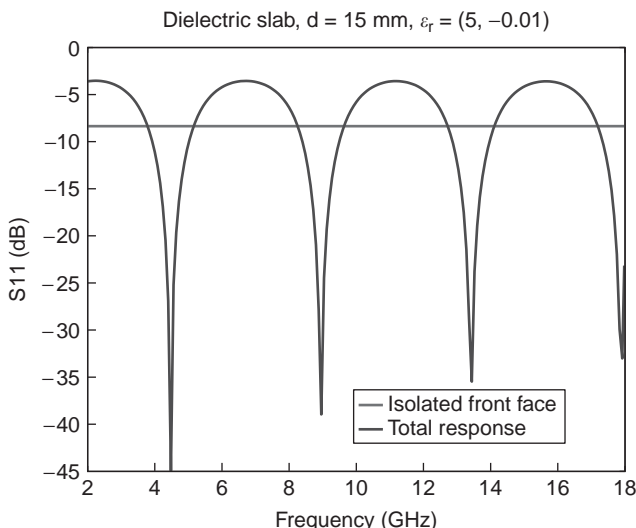


Figure 18. Frequency response of an isolated frontface reflection. (This figure is available in full color at <http://www.mrw.interscience.wiley.com/erfme>.)

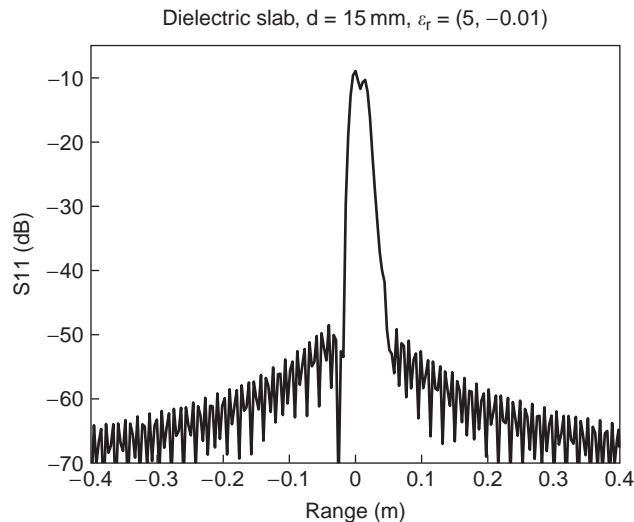


Figure 19. Range response of the reflection coefficient for a 5-mm-thick slab.

A 30th-order state space AR model [see (33)] is applied to the frequency-domain data, and the two wave spectra are extracted from the MoM data. The frequency response of the complete model is obtained by coherent addition of the response contributed by all the poles. Figure 22 depicts excellent corroboration between the model response and the original MoM data. The ripple up to 7.5 GHz is due to the interference between the space wave and the creeping wave in the direction of maximum radiation. As we shall show next, the latter cuts off around 7.5 GHz. An advantage of using range processing with SSM is the direct relation between range and pole locations. Thus, one may isolate a given mode (pulse) by simply adding contributions of only those poles that are associated with the range window of that pulse. By coherently summing the responses of only three poles whose range is centered on the creeping wave peak, we obtain the isolated response (model) shown in Fig. 23. For comparison, Fig. 23 also depicts an analytical solution derived in Ref. 67 by appealing to angularly propagating wave representation. Good agreement between the two at such low amplitude levels indicates the robustness, as well as the accuracy, of the SSM algorithm. In accord with Ref. 67, the creeping wave exhibits a high-frequency cutoff around 7 GHz, where it extinguishes and becomes trapped in the dielectric layer

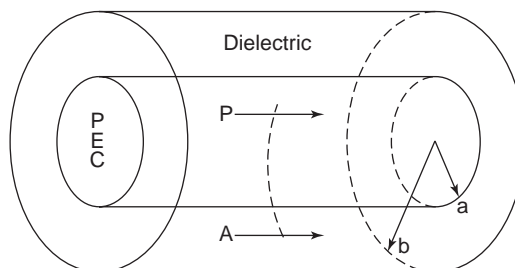


Figure 20. Radiating elements on a cylindrical substrate.

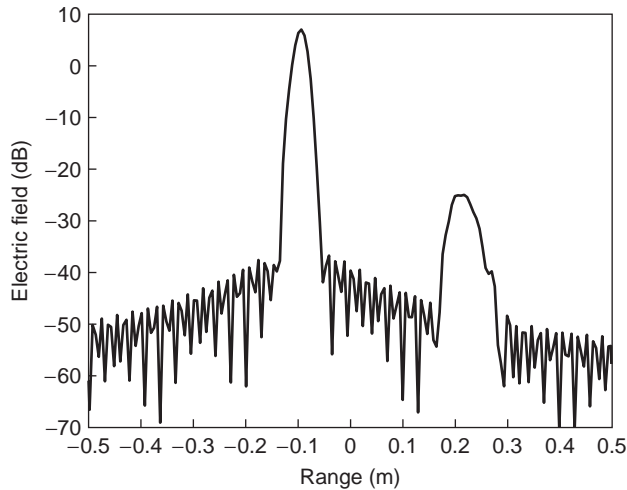


Figure 21. Range response for the radiated field.

(numerical cutoff is arbitrarily defined as the frequency at which the signal ≤ -30 dB). The trapped wave bounces back and forth internal to the layer, similar to a guided mode, and leaks outside tangentially on the surface as a result of curvature. Figure 23 indicates that the coupling between the elements can be neglected at the higher frequencies. The creeping-wave propagation constants and their modal amplitudes have also been calculated, giving considerable physical insight into the coupling. Calculation of these modal parameters will be discussed next.

3.5.3.1. Modal Propagation Constants. Because the exact path of the isolated creeping wave along the substrate surface can be determined from geometric considerations and the range plot, one can compute the attenuation and phase constants (or the complex propagation constant) of the mode using the SSM model. By computing the complex amplitude of the tangential field along the path using the SSM, the attenuation and phase constants have been ob-

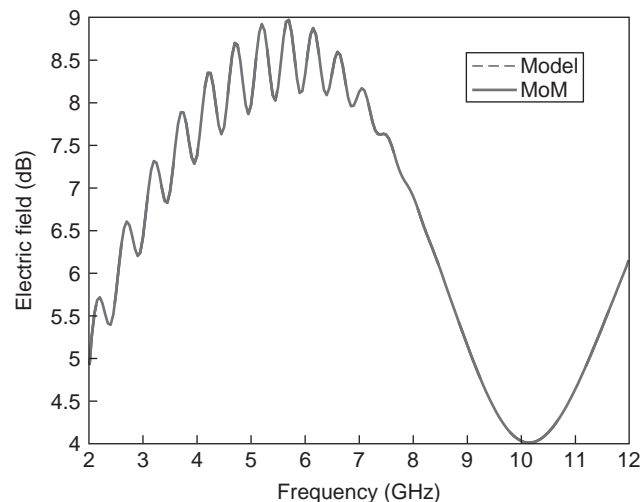


Figure 22. Frequency response comparison for the total field. (This figure is available in full color at <http://www.mrw.interscience.wiley.com/erfme>.)

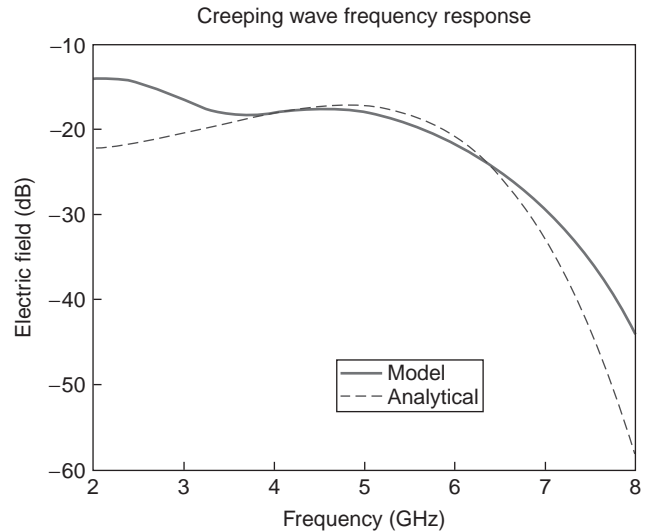


Figure 23. Comparison of the extracted creeping-wave response with the analytical solution in Ref. 67. (This figure is available in full color at <http://www.mrw.interscience.wiley.com/erfme>.)

tained as functions of frequency, and are plotted in Figs. 24 and 25 for the transverse electric (TE) and transverse magnetic (TM) modes, respectively. The TM modal field is extracted from the MoM simulation with horizontally polarized (or parallel to the cylinder axis) plane-wave incidence. The TE field corresponds to vertical polarization. It is noted that although the modes on a finite-length cylindrical microstrip substrate are hybrid in general, the TE-TM mode coupling can be neglected for broadside radiation, because the creeping-wave surface path has very small helicity.

As the creeping wave propagates, it attenuates by shedding energy tangentially because of curvature. The attenuation constant of the TE mode remains relatively constant until about 7.5 GHz and then increases rapidly with frequency, resulting in the trapped mode referred to earlier. Beyond the creeping-wave cutoff, there is very lit-

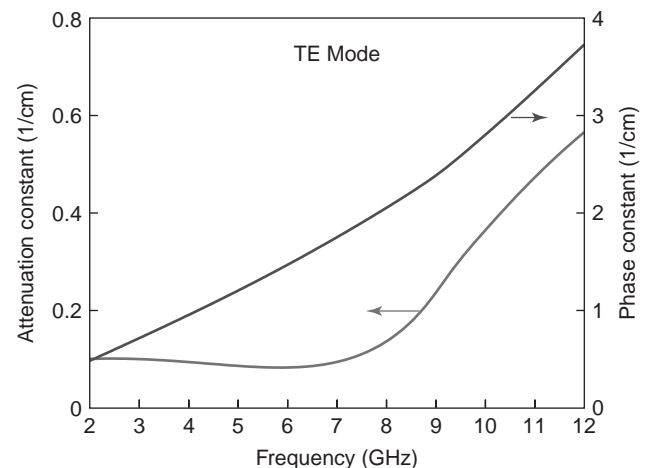


Figure 24. Creeping-wave attenuation and phase constants for the dominant TE mode. (This figure is available in full color at <http://www.mrw.interscience.wiley.com/erfme>.)

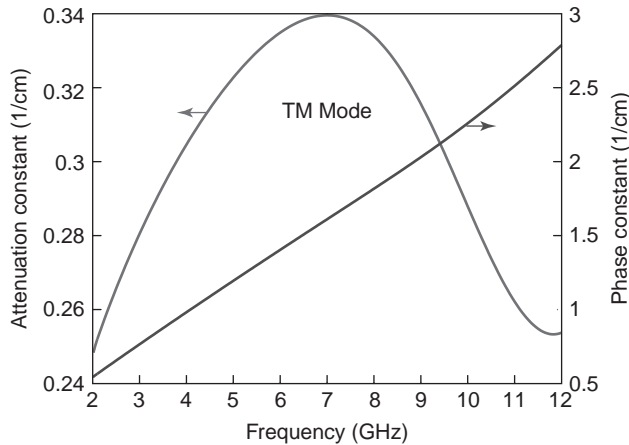


Figure 25. Creeping-wave attenuation and phase constants for the dominant TM mode. (This figure is available in full color at <http://www.mrw.interscience.wiley.com/erfme>.)

tle curvature-induced leakage, or in antenna terms, there is negligible interelement coupling due to the surface wave. From the phase constant plot, it is observed that dispersion exists at higher frequencies. The form of the attenuation curve, including the cutoff frequency, is in good agreement with the analytical results from Ref. 67. The relative variation of the amplitude over 10 GHz bandwidth is smaller for the TM mode than for the TE mode, and the TM mode does not exhibit high-frequency rolloff. Comparing the attenuation curves in Figs. 24 and 25, we conclude that the TE field is much stronger than the TM field. The TM field of the creeping wave is polarized tangentially to the cylinder surface, and becomes quite small for thin dielectric layers. In the limit of a PEC cylinder, this field should vanish.

4. CONCLUSIONS

We have presented signal models to represent EM signatures in both time and frequency domains. Time-domain data generated by FDTD simulations and frequency-domain data generated by the method of moments have been used to illustrate the effectiveness of the models. Various signal modeling approaches, including Prony's method, decoupled optimal method, and the state space spectral method, have been reviewed for their applicability to EM problems.

A classical ARMA identification technique has been described to model FDTD time sequences for resonant structures. The major focus of the discussion has been to demonstrate that, given a computed FDTD sequence, corresponding to an unknown transfer function with *arbitrary* number of poles and zeros, it is possible to obtain accurate match in time and frequency domains with relatively low model orders. It is shown that the multidimensional nonlinear optimization problem can be decoupled into two separate problems with reduced dimensionality, one of which is linear and the other, nonlinear. The inherent mathematical structure of the nonlinear denominator problem is utilized to design an efficient iterative compu-

tational algorithm for estimating the model from moderately early-time sequences. The simulation examples pertaining to a lowpass filter with sharp cutoff and a high-Q patch antenna demonstrate that low model orders are adequate to model the TSs of resonant structures.

A new method has been presented to model frequency-domain EM-simulated fields using a state space approach derived from control theory. The eigenvalues of the system matrix provide range and amplitude information of the field parameter, which allows for isolation of desired responses in the EM signature via pulse compression and spectral decomposition. This superresolution state space modeling approach has been applied to model and isolate modal EM responses from composite field data. Examples are presented to prove that the method can extract correct "design" parameters from the model, such as dielectric constant and mutual coupling. The proposed method is applicable to microwave circuit synthesis and optimization, where the state space model can potentially reduce the parameter domain and obviate the need for intensive EM simulations at each design iteration. The method has been applied to isolate the creeping-wave modes ensuing from wave propagation external to a cylindrical microstrip substrate. Amplitude variation along the creeping-wave ray path on the cylinder surface is used to calculate attenuation and phase constants of the dominant mode. The method has been validated by good corroboration between computed modal field and analytical data.

Acknowledgments

Research reported on the frequency-domain model was supported at MIT Lincoln Laboratory by the U.S. Army under Air Force Contract F19628-00-C-0002. Research reported on the time-domain model was performed while the author was on the Faculty at Wright State University, Dayton, and was partially supported by the U.S. Air Force Research Laboratory under Grant F33615-96-C-1810. Opinions, interpretations, conclusions, and recommendations expressed herein are those of the author, and are not necessarily endorsed by the United States government.

5. APPENDIX: COMPUTATIONAL ALGORITHM FOR OM

The criterion in (27) is nonlinear in \mathbf{b} and hence cannot be minimized directly. But instead of using standard nonlinear optimization techniques, the inherent mathematical structure of the criterion will be utilized to develop an iterative computational algorithm. The final form of the error vector in (27) is rewritten as

$$\begin{aligned}
 \mathbf{e}(\mathbf{b}) &= \mathbf{B}(\mathbf{B}^T \mathbf{B})^{-1} \mathbf{B}^T \mathbf{h}_d \\
 &\triangleq \mathbf{W} \mathbf{B}^T \mathbf{h}_d \\
 &= \mathbf{W} \mathbf{H}_2^p \mathbf{b} \\
 &= \mathbf{W}[\mathbf{g} : \mathbf{G}] \mathbf{b} \\
 &= \mathbf{W} \mathbf{g} + \mathbf{W} \mathbf{G} \hat{\mathbf{b}}
 \end{aligned} \tag{A.1}$$

where $\mathbf{W} \triangleq \mathbf{B}(\mathbf{B}^T \mathbf{B})^{-1}$, and \mathbf{H}_2^P is the Prony's data matrix defined in (17). If the matrix \mathbf{W} is treated as independent of $\hat{\mathbf{b}}$, one can minimize $\|\mathbf{e}(\mathbf{b})\|^2$ with respect to $\hat{\mathbf{b}}$ and obtain

$$\begin{aligned} \hat{\mathbf{b}} &= -(\mathbf{W}\mathbf{G})^\# \mathbf{W}\mathbf{g} \\ &= -(\mathbf{G}^T \mathbf{W}^T \mathbf{W}\mathbf{G})^{-1} \mathbf{G}^T \mathbf{W}^T \mathbf{W}\mathbf{g} \end{aligned} \quad (\text{A.2})$$

However, since \mathbf{W} does depend on the elements in $\hat{\mathbf{b}}$, it can be computed iteratively. At the $(i+1)$ th iteration, $\mathbf{W}^{(i)}$ is formed using the estimate of \mathbf{b} found in the i th iteration. This leads to the following iterative algorithm for computing \mathbf{b}^{i+1}

$$\mathbf{b}^{(i+1)} = \begin{bmatrix} 1 \\ \dots\dots\dots \\ -[\mathbf{X}^{(i)} \mathbf{G}]^{-1} [\mathbf{X}^{(i)}] \mathbf{g} \end{bmatrix} \quad (\text{A.3})$$

where

$$\begin{aligned} \mathbf{X}^{(i)} &\triangleq \mathbf{G}^T \mathbf{W}^{T(i)} \mathbf{W}^{(i)} \\ &= \mathbf{G}^T (\mathbf{B}^{T(i)} \mathbf{B}^{(i)})^{-1} \end{aligned} \quad (\text{A.4})$$

The iterations are continued until $\|\mathbf{b}_{i+1}^{i+1} - \mathbf{b}_i^i\|^2 < \delta$, where δ is an arbitrarily small number. It must be noted here that the iterations in (A.3) may not always converge to the absolute minimum of the error criterion in (9), and hence the estimated \mathbf{b} may not be the optimum one. This is because in (A.3) the variability of \mathbf{W} with respect to \mathbf{b} had been ignored while minimizing $\|\mathbf{e}(\mathbf{b})\|^2$. To achieve the optimum, the gradient of the complete expression of $\|\mathbf{e}(\mathbf{b})\|^2$ must be set to zero. If desired, this can be done in a second phase of the algorithm, which may be found in Ref. 36. However, the simulation examples in this article indicate that the first phase of iterations using (A.3) is adequate in bringing the estimate very close to the optimum. Once the estimates of \mathbf{b} converge, \mathbf{a} is computed by following the steps in (28)–(30).

BIBLIOGRAPHY

1. R. F. Harrington, *Field Computation by Moment Methods*, Macmillan, New York, 1968.
2. J. Jin, *The Finite Element Method in Electromagnetics*, John Wiley, New York, 1992.
3. A. Taflove, *Computational Electrodynamics: The Finite-Difference Time-Domain Method*, Artech House, Boston, 1995.
4. W. J. R. Hofer, The transmission-line matrix method—theory and applications, *IEEE Trans. Microwave Theory Tech.* **33**:882–893 (Oct. 1985).
5. K. S. Yee, Numerical solution of initial boundary value problems involving Maxwell's equations in isotropic media, *IEEE Trans. Anten. Propag.* **14**:302–307 (May 1966).
6. J. W. Bandler, R. M. Biernacki, Shao Hua Chen, P. A. Grobelny, and R. H. Hemmers, Space mapping technique for electromagnetic optimization, *IEEE Trans. Microwave Theory Tech.* **42**:2536–2544 (Dec. 1994).
7. High-Frequency Structure Simulator (HFSS), Version 9.2, Ansoft Technologies, Pittsburgh, PA, 2004.
8. J. L. Dubard, D. Pompei, J. Le Roux, and A. Papiernik, Characterization of microstrip antennas using the TLM simulation associated with a Prony-Pisarenko method, *Int. J. Num. Mod-el.* **3**(4):269–285 (Dec. 1990).
9. W. Ko and R. Mittra, A combination of FD-TD and Prony's methods for analyzing microwave integrated circuits, *IEEE Trans. Microwave Theory Tech.* **39**:2176–2181 (Dec. 1991).
10. J. A. Pereda, L. A. Vielva, A. Vegas, and A. Prieto, Computation of resonant frequencies and quality factors of open dielectric resonators by a combination of the FDTD and Prony's methods, *IEEE Microwave Guided Wave Lett.* **2**(11):431–433 (Nov. 1992).
11. J. Chen, C. Wu, T. K. Y. Lo, K. L. Wu, and J. Litva, Using linear and non-linear predictors to improve the computational efficiency of the FD-TD algorithm, *IEEE Trans. Microwave Theory Tech.* **42**:1992–1997 (Oct. 1994).
12. K. Naishadham and X. P. Lin, Application of spectral domain Prony's method to the FDTD analysis of planar microstrip circuits, *IEEE Trans. Microwave Theory Tech.* **MTT-42**:2391–2398 (Dec. 1994).
13. A. K. Shaw and K. Naishadham, ARMA-based time-signature estimator for analyzing resonant structures by the FDTD method, *IEEE Trans. Anten. Propag.* **49**:327–339 (March 2001).
14. M. L. VanBlaricum and R. Mittra, A technique for extracting the poles and residues of a system directly from its transient response, *IEEE Trans. Anten. Propag.* **AP-23**:777–781 (Nov. 1975).
15. M. L. VanBlaricum and R. Mittra, Problems and solutions associated with Prony's method for processing transient data, *IEEE Trans. Anten. Propag.* **AP-26**:174–182 (Jan. 1978).
16. A. J. Mackay and A. McCowen, An improved pencil-of-functions method and comparisons with traditional methods of pole extraction, *IEEE Trans. Anten. Propag.* **AP-35**:435–441 (April 1987).
17. Y. Hua and T. K. Sarkar, Generalized pencil-of-functions method for extracting poles of an EM system from its transient response, *IEEE Trans. Anten. Propag.* **AP-37**:229–234 (Feb. 1989).
18. S. M. Rao, *Time-Domain Electromagnetics*, Academic Press, San Diego, CA, 1999.
19. S. L. Marple, *Digital Spectral Analysis*, Prentice-Hall, Englewood Cliffs, NJ, 1987.
20. S. M. Kay, *Modern Spectral Estimation: Theory and Applications*, Prentice-Hall, Englewood Cliffs, NJ, 1988.
21. L. B. Jackson, *Digital Filters and Signal Processing*, MA: Kluwer Academic Publishers, Boston, 1986.
22. V. K. Jain, Filter analysis by pencil of functions, Parts I and II, *IEEE Trans. Circ. Syst.* **CAS-21**(5):574–583 (Sept. 1974).
23. V. K. Jain, T. K. Sarkar, and D. Weiner, Rational modeling by pencil-of-functions method, *IEEE Trans. Acoust. Speech Signal Process.* **ASSP-31**(3):564–573 (June 1983).
24. Y. Hua and T. K. Sarkar, Matrix pencil method for estimating parameters of exponentially damped/undamped sinusoids in noise, *IEEE Trans. Acoust. Speech Signal Process.* **ASSP-38**(5):814–824 (May 1990).
25. J. L. Shanks, Recursion filters for digital processing, *Geophysics* **32**:33–51 (1967).
26. K. Steiglitz, On the simultaneous estimation of poles and zeros in speech analysis, *IEEE Trans. Acoust. Speech Signal Process.* **ASSP-25**(3):229–234 (June 1977).

27. A. G. Evans and R. Fischl, Optimal least squares time-domain synthesis of recursive digital filters, *IEEE Trans. Audio Electroacoust.* **AU-21**:61–65 (1973).
28. E. R. Schulz, Estimation of pulse transfer function parameters by quasilinearization, *IEEE Trans. Autom. Control* **13**:424–426 (1968).
29. K. Steiglitz, Computer-aided design of recursive digital filters, *IEEE Trans. Audio Electroacoust.* **AU-18**(2):123–129 (June 1970).
30. F. Brophy and A. C. Salazar, Recursive filter synthesis in the time domain, *IEEE Trans. Acoust. Speech Signal Process.* **ASSP-22**(1):45–55 (Feb. 1974).
31. J. A. Cadzow, Recursive digital filter synthesis via gradient based algorithms, *IEEE Trans. Acoust. Speech Signal Process.* **ASSP-24**:349–355 (1976).
32. R. Fletcher and M. J. D. Powell, A rapidly convergent descent method for minimization, *Comput. J.* **6**:163–168 (1963).
33. C. S. Burrus and T. W. Parks, Time domain design of recursive digital filters, *IEEE Trans. Audio Electroacoust.* **AU-18**:137–141 (June 1970).
34. R. Kumaresan, L. L. Scharf, and A. K. Shaw, An algorithm for pole-zero modeling and spectral estimation, *IEEE Trans. Acoust. Speech Signal Process.* **ASSP-34**:637–640 (June 1986).
35. Y. Bressler and A. Macovski, Exact maximum likelihood parameter estimation of superimposed exponential signals in noise, *IEEE Trans. Acoust. Speech Signal Process.* **ASSP-34**(10):1081–1089 (Oct. 1986).
36. A. K. Shaw, Optimal identification of discrete-time systems from impulse response data, *IEEE Trans. Acoust. Speech Signal Process.* **42**(1):113–120 (Jan. 1994).
37. A. K. Shaw, Optimal estimation of the parameters of all-pole transfer-functions, *IEEE Trans. Circ. Syst. II:Analog Digital Signal Process.* **41**(2):140–150 (Feb. 1994).
38. L. Ljung, *System Identification: Theory for the Users*, Prentice-Hall, Englewood Cliffs, NJ, 1987.
39. T. Söderström and P. Stoica, *System Identification*, Prentice-Hall, Englewood Cliffs, NJ, 1987.
40. R. E. Kalman, Design of a self optimizing control system, *Trans. ASME* **80**:468–478 (1958).
41. K. Steiglitz and L. E. McBride, A technique for identification of linear systems, *IEEE Trans. Autom. Control* **AC-10**:461–464 (1965).
42. A. K. Shaw, A decoupled approach for optimal estimation of transfer function parameters from input-output data, *IEEE Trans. Signal Process.* **42**(5):1275–1278 (May 1994).
43. W. Kuempel and I. Wolff, Digital signal processing of time domain field simulation results using the system identification method, *IEEE MTT-S Digest*, Paper W-6, 1992, pp. 793–796.
44. Z. Bi, Y. Shen, K. Wu, and J. Litva, Fast FDTD analysis of resonators using digital filtering and spectrum estimation, *IEEE Trans. Microwave Theory Tech.* **MTT-40**(8):1611–1619 (Aug. 1992).
45. B. Houshmand, T. W. Huang, and T. Itoh, Microwave structure characterization by a combination of FDTD and system identification methods, *IEEE Microwave Guided Wave Lett.* **3**(8):262–264 (Aug. 1993).
46. T. W. Huang, B. Houshmand, and T. Itoh, Fast sequential FDTD diakoptics method using the system identification technique, *IEEE Microwave Guided Wave Lett.* **3**(10):378–380 (Oct. 1993).
47. J. Litva, C. Wu, K. L. Wu, and J. Chen, Some considerations for using the FDTD technique to analyze microwave integrated circuits, *IEEE Microwave Guided Wave Lett.* **3**(12):438–440 (Dec. 1993).
48. L. L. Scharf, *Statistical Signal Processing—Detection, Estimation and Time Series Analysis*, Addison-Wesley, Reading, MA, 1990.
49. A. V. Oppenheim and R. W. Schaffer, *Digital Signal Processing*, Prentice-Hall, Englewood Cliffs, NJ, 1975.
50. R. Prony, *Essai experimental et analytique etc.*, L'Polytechnique, Paris, 1 Cahier 2, 1795, pp. 24–76.
51. G. H. Golub and V. Pereyra, The differentiation of pseudoinverses and nonlinear problems whose variables separate, *SIAM J. Num. Anal.* **10**(2):413–432 (April 1973).
52. Y. B. Hua, The most efficient implementation of the IQML algorithm, *IEEE Trans. Signal Process.* **42**(8):2203–2204 (Aug. 1994).
53. M. P. Clark and L. L. Scharf, On the complexity of IQML algorithms, *IEEE Trans. Signal Process.* **40**(7):1811–1813 (July 1992).
54. M. Wax, *Detection and Estimation of Superimposed Signals*, Ph.D. dissertation, Stanford Univ., Stanford, CA, 1985.
55. J. Rissanen, Modeling by shortest data description, *Automatica*. **14**:465–471 (1978).
56. J. Rissanen, A universal prior for the integers and estimation by minimum description length, *Ann. Stat.* **11**:417–431 (1983).
57. D. M. Sheen, S. M. Ali, M. D. Abouzahra, and J. A. Kong, Application of the three-dimensional finite-difference time-domain method to the analysis of planar microstrip circuits, *IEEE Trans. Microwave Theory Tech.* **38**:849–857 (July 1990).
58. J. E. Piou, K. M. Cuomo, and J. T. Mayhan, *A state-space technique for ultrawide-bandwidth coherent processing*, MIT Lincoln Laboratory, Technical Report TR 1054, 1999.
59. J. W. Odendaal, E. Barnard, and C. W. I. Pistorius, Two-dimensional superresolution radar imaging using the MUSIC algorithm, *IEEE Trans. Anten. Propag.* **42**:1386–1391 (Oct. 1994).
60. M. L. Burrows, Two-dimensional ESPRIT with tracking for radar imaging and feature extraction, *IEEE Trans. Anten. Propag.* **52**:524–532 (Feb. 2004).
61. C. E. Baum, The singularity expansion method, in L. B. Felsen, ed., in *Transient Electromagnetic Fields*, Springer-Verlag, 1976.
62. J. E. Piou, K. M. Cuomo, and J. T. Mayhan, Ultra wide-band coherent processing, *IEEE Trans. Anten. Propag.* **47**:1094–1107 (June 1999).
63. K. Ogata, *Discrete-Time Control Systems*, Prentice-Hall, New York, 1987.
64. U. B. Desai and D. Pal, A realization approach to stochastic model reduction and balanced stochastic realizations, *Proc. 21st IEEE Conf. Decision and Control*, New York, 1992, pp. 1105–1112.
65. H. Akaike, A new look at stastical model identification, *IEEE Trans. Autom. Control* **19**(6):716–723 (1974).
66. D. L. Mensa, *High Resolution Radar Cross Section Imaging*, Artech House, Boston, 1991.
67. K. Naishadham and L. B. Felsen, Dispersion of waves guided along a cylindrically stratified medium, *IEEE Trans. Anten. Propag.* **41**:304–313 (March 1993).
68. J. R. Mautz and R. F. Harrington, H-field, E-field and combined-field solutions for conducting body of revolution, *Archiv fur Elektronik und Ubertragungstechnik (AEU)* **38**:157–164 (April 1978).

PASSIVATION

S. J. PEARTON
University of Florida
Gainesville, Florida

1. INTRODUCTION

Passivation layers are deposited over the entire top surface of Si or compound semiconductor wafers to form an insulating protective coating for the semiconductor. This procedure guards against environmental contamination that might lead to increased surface leakage currents, and also against mechanical damage during assembly and packaging. Some of the desirable properties of passivation-layer materials include good scratch protection of the underlying interconnect metallurgy, impermeability to moisture and alkali (Na^+ , K^+) ions, low stress ($<5 \times 10^8 \text{ dyn/cm}^2$, preferably compressive), conformal step coverage, and etchability with excellent uniformity and adhesion [1]. While thicker passivation layers would normally be desirable because of the improved mechanical protection they afford, there is generally an upper limit to the thickness in order to avoid cracking. The primary inorganic dielectric passivation films are SiO_2 and SiN_x , while polyimides and epoxy resins are used for low-cost polymer encapsulation. The thermal stability requirements are obviously lower for final passivation coatings than for interlevel dielectrics.

Patterns are formed in the passivation-layer material by either wet (for phosphosilicate glasses) or dry (for SiN_x or polymers) etching to enable electrical contact to the completed circuit. The area of these contact pads is sufficiently large ($100 \times 100 \mu\text{m}^2$) that wet etching is acceptable [2].

2. TYPES OF PASSIVATION LAYER

2.1. Phosphorous-Doped SiO_2 [Phosphosilicate Glass (PSG)]

The addition of P (2–6 at%) to SiO_2 reduces film stresses and improves the barrier properties for minimizing alkali and metallic ion contamination. If higher P contents are used, corrosion of the underlying metal may occur if moisture enters the circuit package; this results from reaction of moisture with PSG to form phosphoric acid (H_3PO_4). Electrochemical corrosion of Al interconnects will eventually lead to metallization failure.

These films are generally deposited by low-temperature chemical vapor deposition (CVD) (either at atmospheric pressure, at low pressure, or by plasma enhancement) with addition of phosphine (PH_3) to the gas flow to form P_2O_5 that is incorporated to form the PSG. The reactions are $\text{SiH}_4 + \text{O}_2 \rightarrow \text{SiO}_2 + 2\text{H}_2$; $4\text{PH}_3 + 5\text{O}_2 \rightarrow 2\text{P}_2\text{O}_5 + 6\text{H}_2$. Atmospheric-pressure CVD PSG has improved step coverage relative to undoped CVD SiO_2 [3]. The PSG may be flowed at temperatures $\geq 1000^\circ\text{C}$ to planarize the surface topography, although this is seldom done for passivation layers; only for interconnect isolation layers. The phosphorus content is controlled by the $\text{SiH}_4 : \text{PH}_3$ ratio in the gas flow. We emphasize that we

are dealing with films deposited from the gas phase, and not with the direct thermal oxidation of Si in either dry O_2 ($\text{Si} + \text{O}_2 \rightarrow \text{SiO}_2$) or steam ($\text{Si} + 2\text{H}_2\text{O} \rightarrow \text{SiO}_2 + 2\text{H}_2$), which is employed for the high-quality gate oxides in metal oxide semiconductor (MOS) devices. Oxides grown by thermal means range in thickness from 6 nm (tunneling oxides), 4–20 nm (gate oxide), 50–300 nm (capacitor dielectrics), 200–500 nm (mask oxide, surface passivation oxide), to 300–1000 nm (field oxide).

2.2. Silicon Nitride

Stoichiometric silicon nitride has the formula Si_3N_4 , but films deposited by plasma-enhanced CVD (PECVD) tend to contain large quantities of hydrogen (10–30 at%) and to be nonstoichiometric, and are thus collectively referred to as SiN_x . It is common as a passivation-layer material because of its scratch resistance and impermeability to moisture and alkali ions. In the case where it is deposited over Al metallization, the process temperature must be kept low, and PECVD is preferred [4]. These films generally have a relatively high compressive stress, which can lead to cracking or enhanced void formation in Al interconnects. There are three main applications for silicon nitride in VLSI technology: as a gate dielectric in metal nitride oxide semiconductor (MNOS) transistors, as a mask for selective oxidation of silicon, and as a final passivation layer for ICs. When used for the first two applications the silicon nitride is deposited by low-pressure CVD at 700–900°C through the reaction $3\text{SiCl}_2\text{H}_2 + 4\text{NH}_3 \rightarrow \text{Si}_3\text{N}_4 + 6\text{HCl} + 6\text{H}_2$. The dielectric strength of this material is generally $\sim 10^7 \text{ V/cm}$ with tensile stress $< 2 \times 10^{10} \text{ dyn/cm}^2$. The thermal stability is excellent, and usually only one IR band (at $\sim 870 \text{ cm}^{-1}$ due to Si = N bonds) is present. For passivation applications, the deposition is performed at 200–400°C through the reaction $\text{SiH}_4 + \text{NH}_3$ (or N_2) $\rightarrow \text{Si}_x\text{N}_y\text{H}_z + \text{H}_2$. The dielectric strength of this material is $\sim 6 \times 10^6 \text{ V/cm}$ with compressive stress $< 10^{10} \text{ dyn/cm}^2$. The thermal stability is variable, and two bands (due to Si = N at $\sim 870 \text{ cm}^{-1}$ and Si = Hat 2187 cm^{-1}) dominate the IR spectrum. The large hydrogen concentration may be detrimental, leading to threshold voltage shifts in devices and acceleration of hot-electron aging effects in MOS transistors. Lower hydrogen concentrations may be obtained when SiH_4/N_2 mixtures rather than SiH_4/NH_3 mixtures are employed in PECVD [5].

2.3. Silicon Oxynitrides

These are formed by reacting SiH_4 with N_2O and NH_3 mixtures, leading to $\text{SiO}_x\text{N}_y(\text{H}_z)$. These have alkali ion and moisture barrier properties similar to those of silicon nitride and are less permeable to these entities than are oxides. The stress of these films is intermediate between that of atmospheric-pressure CVD oxides (tensile) and plasma-deposited oxides and nitrides (compressive), and can be tailored by optimizing the deposition conditions. Typically PECVD oxynitride layers contain about half the hydrogen concentration found in PECVD nitrides.

Bilayers consisting of an initial PECVD oxide followed by PECVD nitride are becoming increasingly popular. The presence of the oxide reduces mechanical stress and

hydrogen content of the passivation layer, while the nitride overcoating provides a barrier for moisture and alkali ions. The dielectric films may then be coated with a polyimide for cushioning during loading of the individual die.

3. INTERLEVEL DIELECTRICS AND POLYIMIDES

Since individual transistors must be wired together with other circuit elements (resistors, inductors, capacitors) to complete the integrated circuit, connections between devices are critically important. Interconnections between devices are generally formed by covering the entire surface of the wafer, then masking the lines to be retained and etching away all the metal not being used. In connection of a die to external circuitry, the metallization on the Si surface terminates in a relatively large area referred to as a *bonding pad*, to which a wire can easily be attached. There are several requirements for an ideal metallization scheme, including low resistance, good adhesion, and ohmicity on Si. Aluminum is the most common metal employed, and gold is also used in some situations. Al and Cr adhere very well to SiO₂, especially if sintered at $\geq 300^\circ\text{C}$ to balance bonding [6].

The wiring delay may be the determining factor in the overall speed of a circuit, and therefore much attention is paid to the design of multiple wiring planes to minimize interconnect length. The multilayered metallization is isolated by interlevel dielectric layers, and a final passivation film is employed for environmental protection. In a metal oxide semiconductor transistor (MOSFET), for example, the total effective capacitance and resistance of the device at the gate and interconnect level produce an RC time constant τ_{RC} of [7]

$$\tau_{RC} = \frac{\rho}{t} = \frac{L^2 E_{ox}}{t_{ox}} \quad (1)$$

where ρ is the resistivity of the interconnect material, L its length, t its thickness, and E_{ox} and t_{ox} are the permittivity and thickness of the oxide that separates the interconnect from the semiconductor. Since the interconnect length increases with circuit complexity, multilevel designs must be employed to maintain circuit speed (schematic shown in Fig. 1).

On the basis of Eq. (1), we would ideally want a low dielectric constant insulation that was also as thick as possible. There are, however, many reasons why film thickness must be limited: (1) the metal levels are connected by holes etched into the intervening dielectric insulators, and to ensure metal continuity through these via holes, the overlying metal would also have to be made thicker (step coverage), and the intralevel capacitance would increase; and (2) it is difficult to etch high-aspect-ratio vias because of limitations in mask robustness and also in lithographic resolution in the type of thick resists needed to act as a mask for deep dielectric etching. This generally necessitates the use of bilevel or trilevel mask schemes, involving a thick imaging resist, a thin transfer layer, and a thick planarizing resist or polyimide. This adds considerably to process complexity, however.

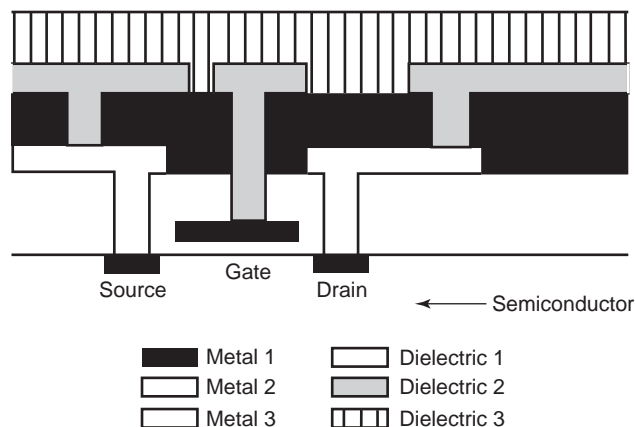


Figure 1. Simplified cross section of a three-level metal interconnect scheme on a metal oxide semiconductor transistor (after Ref. 7).

In addition to a low dielectric constant, it is desirable that the interlevel dielectrics have high breakdown strength ($\sim 10^7$ V/cm), high resistivity ($> 10^{12} \Omega \cdot \text{cm}$), low compressive stress, good adhesion, and impermeability to moisture and alkali ions.

3.1. Polyimides

These have reasonable thermal stability and lower dielectric constant (2.9–3.7) than do inorganic dielectrics such as SiO₂ (3.8–4.2) or Si₃N_{7,4}. They planarize underlying topography, but many polyimides absorb moisture on exposure to air, which in general increases the effective dielectric constant and semiconductor surface leakage. This is a major drawback, and it has been addressed by use of bilayer structures in which an inorganic dielectric is placed over the polyimide. However, this adds process complexity and may not gain much in terms of reducing the effective dielectric constant [8].

Polyimides generally have low stress and good step coverage, and deposition is by spin coating, which makes the process inexpensive, even though the polyimides themselves may be relatively expensive. As with photoresists, the prepolymer is applied to the wafer, and curing at elevated temperature is necessary to convert the precursor into the polyimide. Since the adhesion of polyimides to Al is poor, an adhesion promoter or thin layer of a material such as Cr is necessary to improve bonding to the metal. Moreover, moisture or outgassing from the polyimide may deform the metal overlayers.

Two further drawbacks are the lower thermal conductivity compared to inorganic dielectrics and the inferior resistivity and breakdown voltage of polyimides. Dry etching to form via holes is readily accomplished with O₂-based plasma chemistries.

3.2. Inorganic Insulators

Inorganic insulators in common use are based on undoped or B- or-P-doped SiO₂, or Si₃N₄ (or SiN_xH₄) or silicon oxynitrides, as discussed earlier. Spin-on glasses (SOGs) have good gap-filling/planarizing capabilities and are low-cost.

The most common form is siloxane SOG, a partially hydrolyzed mixture of tetrafunctional siloxane oligomer. While their gap-filling qualities are well established, alternative technologies such as low-pressure CVD with high-density plasmas or tetraethoxysilane (TEOS)/silane processes are attractive at small dimensions and high aspect ratios. Since many of the new materials being investigated are not strictly glasses, but dielectrics, they are referred to as *spin-on dielectrics* (SODs). Spin-on insulators are most commonly applied in processing of memory chips, which are more cost-sensitive and have a more suitable dense regular array geometry relative to logic chips [9].

The SOG films are typically sandwiched between two oxide layers which are usually $\sim 1000 \text{ \AA}$ thick; SOG is $\sim 3000 \text{ \AA}$ thick. If the top layer is subsequently chemically, mechanically (chemicomechanically) polished (CMP) for planarization, it is generally at least 1 \mu m thick, that is, as thick as the tallest underlying feature. This combination of gap filling with low dielectric constant spin-on glass, followed by CMP, is a promising technology for global planarization even at very small critical dimensions ($\leq 0.25 \text{ \mu m}$).

An area receiving a lot of attention is the issue of via poisoning, which occurs when the sidewall of an SOG feature is damaged during plasma ashing. When the SOG is damaged in this fashion, it can readily absorb moisture, which can outgas when the metal is in place and poison the via by leading to formation of metal oxides. These produce high via resistance. Excessive temperature ($> 500^\circ\text{C}$) as well as plasma exposure will cause a hydroscopic surface on an organic SOG, and the plasma ashing may lead to the presence of carbonaceous residues, which also create high via resistance.

Some newer organic, low-dielectric constant materials are formed to exhibit much improved moisture-generating characteristics, and a number of methods have been employed to eliminate via poisoning in conventional materials. These include Ar plasma exposure, ion-beam and electron-beam curing, and implantation of species such as As in order to produce a thin skin of silicatelike material on the sidewall that is impervious to moisture.

Low-dielectric-constant materials as replacements for polyimides or SiO_2 and Si_3N_4 are an avenue to improve chip speed and avoid crosstalk between adjacent metal lines [10]. The dielectric constant of PECVD SiO_2 (~ 4.2) can be reduced to around 3.5 by adding small amounts of fluorine. Poly arylene ethers have a dissociation constant of $K < 3$, while nanoporous silica (often classified as nanofoams and xerogels) have values under 2. A variety of low- K spin-on materials are under development. In addition, CVD low- K materials based on amorphous carbon, diamondlike carbon, or methyl silane/hydrogen peroxide, are under development. In most of these materials, direct contact with the metal is not desirable because of stress and hillock growth, and they are generally embedded in an oxide layer sandwich.

Currently the forecast for future trends in dielectric materials calls for K values of < 2.0 by 2004 [11]. These correspond to a capacitance in fF/um of 0.24 for feature sizes of 0.10 um and 6–8 metal layers. In the short term,

fluorinated silicon dioxide (F_xSiO_4) films are of great interest for intermetal dielectrics since they retain many of the properties of SiO_2 while achieving a modest reduction in dielectric constant. Since fluorine is the most electronegative and least polarizable element, incorporation of fluorine reduces the number of polarizable $\text{Si} = \text{OH}$ bonds and thus lowers the dielectric constant. Typical fluorine concentrations in these films range from 2 to 14 at%. The precursors for depositing F_xSiO_4 films are widely available and are inexpensive compared to alternatives such as fluorinated paralyenes. Moreover, the films are easily deposited in existing process tools, facilitating process integration.

A number of different inorganic precursors have been reported for depositing F_xSiO_4 films, including the following chemistries: $\text{Si}(\text{OC}_2\text{H}_5)_4$ with additional of NF_3 , CF_4 or C_2F_6 , SiF_4 with additions of SiH_4 , O_2 or N_2O , and $\text{FSi}(\text{OC}_2\text{H}_5)_3$ with additions of O_2 or H_2O . It is possible to produce stacked films using sequential deposition and a sequence of O_2 , C_2F_6 , and O_2 to form an oxide/fluorinated silicon dioxide/oxide structure. Deposition has been performed with predominantly plasma-enhanced CVD, but atmospheric pressure CVD has also proved effective. High-density plasma deposition appears very promising because simple precursor chemistries of SiH_4 , SiF_4 , and O_2 can be used that contain no carbon that might be incorporated. These films have low hydroxyl bond density and are generally reported to have dielectric constants lower than those of conventional PECVD films.

There is also an optimum fluorine concentration in F_xSiO_y films. While the dielectric constant decreases with increasing fluorine density, for values ≥ 15 at% the films are more susceptible to moisture absorption. This may result from an excessive number of dangling or weakly bound fluorine atoms. The stability of such films can be improved by either increasing the deposition temperature or applying an RF chuck bias to densify the film during deposition. The sandwich-type structures are obviously much more stable with respect to water absorption. The gap-filling ability and planarizability of F_xSiO_4 films appear to very good, with numerous reports of void-free gap filling for a 0.35-um space pattern with an aspect ratio of 3.8. Some authors have found that addition of C_2F_6 to PECVD TEOS films substantially improved the gap-filling characteristics. Other advantages of F_xSiO_4 films include reduced hillock formation in aluminum-alloy interconnections, longer lifetimes under bias stress, and lower Si/SiO_2 interface trap densities.

In summary, fluorinated SiO_2 has dielectric constants in the range 3.0–3.5 and is readily deposited using existing production equipment and relatively straightforward chemistries. The gap-filling properties for $< 0.5 \text{ um}$ feature sizes with aspect to ratio $> 2.3:1$ intermetal spacing is improved by fluorine addition to silicon dioxide.

4. TRENDS IN METALLIZATION

The semiconductor industry has relied on Al metallization from its inception in the early 1960s because it is a well-established, reproducible, low-cost technology. Early on it

was found that the electromigration resistance of Al could be improved by addition of small quantities of copper. However, improved metallization schemes are desirable. Table 1 shows some of the characteristics of the main contenders. Currently the most common scheme for interconnects is Al-based metallurgy embedded in an oxide/nitride dielectric, with refractory metal plugs for via connections. The Al alloys, CVD tungsten for plugs, with typical liners of Ti/W or Ti/TiN are well established and are basically industry standards.

There is extensive development on squeezing additional performance from the standard structures, including diffusion barriers for Al reflow, CVD tungsten for filling contacts or vias, use of CVD for the liner materials instead of physical vapor deposition (especially for $<0.30\text{-}\mu\text{m}$ vias, where coverage is a major challenge), improved Al deposition techniques and use of chemico-mechanical polishing (CMP) for global planarization. While CMP is well established for hard metals such as W and for dielectrics, there is still work to be done in perfecting its use for Al alloys and copper. The role of microstructures and voids in Al lines is critically important, as is the role of stresses on their reliability. New deposition techniques that might allow improved electromigration resistance, stress migration resistance, and improved yields, coupled with new developments in low-dielectric-constant materials, are the key focus.

4.1. Chemical Vapor Deposition of TiN

TiN is important as a liner material in via connections and serves as a nucleation layer to improve adhesion of W in these vias. It also prevents attack by WF_6 during W plug filling. Conformal deposition using the thinnest possible films is desirable in order to reduce interconnect stack thickness and via resistance, since TiN has a resistivity higher than that of any of the other components of the metallization (Ti, Al, and W). Moreover, the barrier properties must be thermally stable during the various thermal cycles encountered in a process sequence.

TiN films deposited by reactive sputtering (physical vapor deposition) generally have inadequate conformality

for $<0.5\text{-}\mu\text{m}$ applications with high aspect ratio. Collimated sputtering may not be able to produce sufficient sidewall coverage, and therefore there is a strong effort to develop CVD TiN [12].

The most common inorganic precursor is TiCl_4 , which is reduced by NH_3 to produce TiN deposition. Deposition temperatures below $\sim 550^\circ\text{C}$ lead to high concentrations of Cl incorporated in the films ($\sim 5\text{ at}\%$), and even at 700°C there may be $\sim 1\text{ at}\%$. The film resistivity increases with decreasing deposition temperature. Typical values of $85\ \mu\Omega\cdot\text{cm}$ are obtained at 700°C , similar to the values obtained by reactive sputtering. The incorporation of Cl is, of course, a potential corrosion issue with Al metallization. Electron Cyclotron Resonance (ECR) CVD can also be employed, but again temperatures above 400°C must be used to minimize Cl incorporation.

Use of metallorganic precursors enables lowering of the deposition temperature below 400°C so that not only the contact level, but also via, metal 2 and even higher layers can be metallized. The main precursor tried has been tetrakis(diethylamido)titanium, $\text{Ti}[\text{N}(\text{CH}_3)_2]_4$. A basic problem with all metalorganic precursors is incorporation of C, usually at the 2–3 at% level, and often poor step coverage. A new approach to overcome this is by thermal decomposition of $\text{Ti}[\text{N}(\text{CH}_3)_2]_4$ followed by an in situ N_2 plasma treatment. This produces excellent conformal coverage even at high aspect ratio with an absence of gas-phase reactions. Contacts consisting of W plugs with 200 Å CVD TiN as a glue layer performed very well using this TiN deposition process. The N_2 plasma treatment improves stability and reduces sensitivity to moisture uptake.

4.2. CVD of Tungsten

Conventional PVD techniques such as sputtering have problems with filling of high-aspect-ratio vias, and thus CVD is being pursued as a solution. The combination of blanket W CVD, followed by etchback is currently the best alternative to sputtered Al. The deposition occurs by the

Table 1. Properties of Potential Interlayer Metals (After ref. 7)

Property	Metal				
	Cu	Ag	Au	Al	W
Resistivity ($\mu\Omega\text{m}$)	1.67	1.59	2.35	2.66	5.65
Thermal conductivity (W cm^{-1})	3.98	4.25	3.15	2.38	1.74
Coefficient of thermal expansion $\times 10^6(^{\circ}\text{C})^{-1}$	17	19.1	14.2	23.5	4.5
Melting Point ($^{\circ}\text{C}$)	1085	962	1064	660	3387
Specific heat capacity ($\text{J Kg}^{-1}\text{K}^{-1}$)	386	234	132	917	138
Corrosion in air	Poor	Poor	Excellent	Good	Good
Adhesion to SiO_2	Poor	Poor	Poor	Good	Poor
Deposition					
Dry	X	X	X	Yes	Yes
Wet	Yes	Yes	Yes	Yes	Yes
Delay (ps/mm)	2.3	2.2	0.2	3.7	7.8
Self-diffusion					
Activation energy (eV)	2.19	1.97	1.81	1.48	5.47
Prefactor (D_0) (cm^2/s)	0.78	0.67	0.091	1.71	0.04

Source: After Ref. 7.

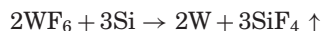
reduction of WF_6 :



This produces void-free filling of vias at typical pressures of 80 torr. Typical film resistivity is $\geq 10 \mu\Omega \cdot \text{cm}$, several times the bulk value ($5.65 \mu\Omega \cdot \text{cm}$ at 300 K), due to the columnar microstructure that traps fluorine. Reduction of the tungsten hexafluoride with B_2H_6 eliminates fluorine more efficiently than does H_2 alone [13].

CVD tungsten films have poor adhesion to SiO_2 , because of formation of tungsten oxide. This necessitates the use of TiN or TiW liners, which in addition prevent etching of the Si by WF_6 .

It is also possible to achieve selective tungsten CVD, which then eliminates the need for etchback, and for liner materials. The major issues with this technology are damage to the Si via cleaning prior to deposition and nonuniform via hole filling across large-area wafers. Silicon consumption through the reaction



occurs until a self-limiting growth of $\sim 200 \text{ \AA}$ of W is formed. Since WF_6 does not react with SiO_2 readily at low temperatures, it is straightforward to deposit W selectively on patterned wafers. To lower the deposition temperature, SiH_4 reduction is used in place of H_2 reduction.

An alternative to tungsten CVD is to employ Al sputtering and a reflow step. This can be achieved either by high-temperature Al sputtering, in which the vias fill because of the enhanced surface mobility, or by a cold sputter deposition and subsequent high-temperature sputtering. The reflow temperature is reduced from $\sim 480^\circ\text{C}$ for Al/0.5%Cu to as low as 300°C for Al/5%Ge/0.5%Cu, allowing efficient via and contact hole filling at relatively low temperatures using Al reflow sputtering. The filling characteristics of Al into vias is strongly dependent on the underlying film material. Al has poor wettability on SiO_2 , and poly Si, MoSi_2 , or Ti is generally used as a glue layer [14].

For process simplicity it would be desirable to have a single metallurgy for global interconnects, but no one material has the requisite sheet resistance, electromigration resistance, contact resistance to n^+ and p⁺ Si, adherence, step coverage, etchability, corrosion resistance, and availability of uniform, low-defect density deposition techniques. Al meets most of the requirements and hence is the most widely used. Layered metallizations are used, with the conductive layer as the middle layer [15]. The bottom layers are used for adhesion to the oxide and as barriers to Si. In the case of Al, layering with the refractories Ti, TiW, and TiN improved the reliability of the Al metallization, allowing its use to be extended to $0.18\text{-}\mu\text{m}$ critical-dimension devices.

4.3. Effect of Stress

Since Al films are typically deposited at $\sim 200^\circ\text{C}$, with Al plugs at 450°C , cooling to room temperature puts the

Al into tension because of its higher thermal expansion coefficient relative to the Si wafer. These stresses are generally high enough to cause plastic deformation, and stress relief may involve flow of material from the top surface to the bulk of the film. Spatially nonuniform flow may lead to voids that are failure sites during subsequent process steps.

After patterning of the Al, dielectric deposition typically around 400°C is performed, leading to compressive stresses in the Al lines that are larger in wider lines. These stresses may produce hillocks in the Al, which can be suppressed by addition of Cu to the Al alloy. Once the metal lines are encased in dielectric, they develop a uniform hydrostatic tensile stress that may be relieved by formation of voids. The addition of capping layers such as TiW or Ti can suppress these voids.

The basic causes of stress in interconnect structures are [16]

1. Thermal expansion coefficient differences with the Si
2. Deposition under nonequilibrium conditions
3. Changes in chemical composition (e.g., absorption of moisture in silica-based glasses or evolution of hydrogen from nitrides during heating)
4. Solid-state chemical reactions involving volume changes
5. Structural changes such as plastic flow, amorphous-to-crystalline transitions, or relaxation effects
6. Electromigration

The most obvious effects of mechanical stress are cracking of brittle materials, delamination of films, and formation of voids in metal lines.

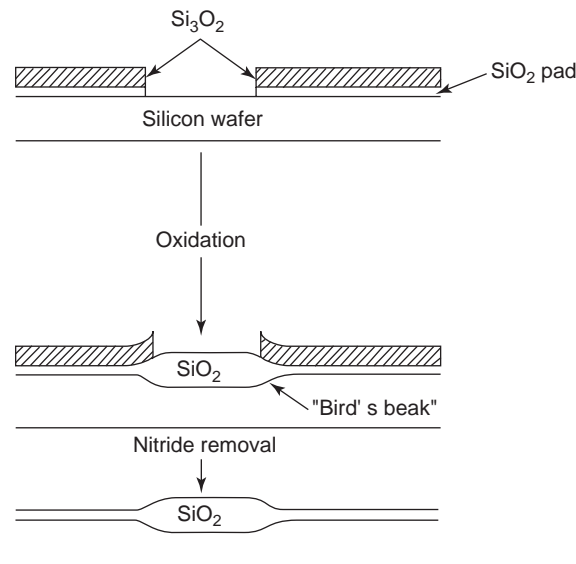


Figure 2. Simplified process sequence for localized oxidation of Si (after Ref. 1).

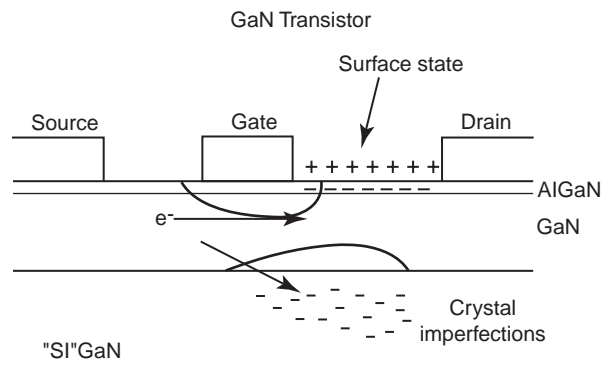


Figure 3. Schematic cross section of typical GaN-based high-electron-mobility transistor, showing degradation of current flow by depletion caused by surface traps.

5. ISOLATION TECHNOLOGIES

The two basic methods for device isolation and prevention of crosstalk are junction isolation, in which each active region of a transistor is surrounded by a reverse-biased pn junction, and oxide-based (insulator) technologies [1]. The former is employed for bipolar transistors and the latter for metal oxide semiconductor (MOS) circuits. The individual components of the circuit are interconnected by metal stripes that run across the oxide. Figure 2 shows a schematic of a simple local oxidation of silicon (LOCOS) process, in which a thin pad oxide is thermally grown (20–60 nm) to cushion the transition of stresses between the Si and the subsequently deposited nitride. The latter is generally put down by CVD to a thickness of 100–200 nm, and its purpose is to prevent oxidation, specifically, oxidation mask. The nitride/pad oxide is patterned by dry etching, and a channel-stop implant is performed in the field region. A field oxide is then grown by wet oxidation at $\sim 1000^\circ\text{C}$ for 2–4 h to create a thickness of oxidized Si of 300–1000 nm. There is some lateral oxidation under the edges of the nitride mask that tapers into the pad oxide (the “bird’s beak” encroachment). The nitride mask is then removed by wet etching. This simple process has a number of limitations for submicrometer technologies, including the lateral encroachment of the field oxide into the active device region, redistribution of the implanted

boron, poor surface topology, and width-dependent field oxide thickness. These have been addressed by a number of advanced LOCoS isolation processes and sidewall-masked isolation techniques.

6. PASSIVATION OF COMPOUND SEMICONDUCTORS

For microwave power amplification in satellite links and wireless communication applications, the AlGaIn/GaN high-electron-mobility transistor (HEMT) has emerged as the most promising device. A typical $\text{Al}_{0.3}\text{Ga}_{0.7}\text{N}/\text{GaN}$ HEMT shows a sheet carrier density up to $\sim 1.5 \times 10^{13} \text{ cm}^{-2}$ (roughly an order of magnitude higher than for GaAs HEMTs), a unity current gain frequency (f_T) of 65 GHz, and a maximum oscillation frequency (f_{max}) of 180 GHz. Output powers up to 9.8 W/mm at 8 GHz (power-added efficiency at 47%) have been reported for large periphery GaN HEMTs, while it has also been shown that these devices can achieve low microwave-added noise figures ($\text{NF} = 0.6 \text{ dB}$ at 10 GHz), while maintaining a large breakdown voltage ($> 60 \text{ V}$) and hence a large dynamic range.

One frequently reported problem in these devices is that the RF power obtained is still much lower than expected from the DC characteristics. This problem is manifested by a collapse in drain current or by frequency dispersions in the transconductance and output resistance, leading to severely reduced output power and power-added efficiency. Several mechanisms have been identified as the causes, including the presence of surface states between the gate and the drain that deplete the channel in this region over a time constant long enough to disrupt modulation of the channel charge during large signal operation or of trap states in the buffer layer (Fig. 3, top). Several studies have shown that the use of SiN_x passivation layers can be effective in reducing the effects of surface states. One drawback of typical plasma-enhanced chemical vapor deposited SiN_x is the high hydrogen content, which could migrate into the GaN or the gate metallization. Two alternative candidates for HEMT passivation are MgO and Sc_2O_3 , which are under development as gate dielectrics for GaN. A comparison of the properties of various dielectrics for compound semiconductors is shown in Table 2. In particular, the oxides have larger bandgaps (8 eV for MgO and 6.3 eV for Sc_2O_3) wider than the previously reported Gd_2O_3 (5.3 eV) and smaller

Table 2. Material Properties for GaN and Various Dielectrics

	GaN [1]	SiO_2 [2–4]	SiN_x [4]	AlN [5–7]	GGG [8]	Gd_2O_3 [8–10]	Sc_2O_3 [1–]	MgO [12,12]
Structure	W	A	A	W or A	A	B	B	N
Lattice constant	3.186	—	—	3.113	—	10.813	9.845	4.2112
Atomic spacing in the (111) plane	—	—	—	—	—	3.828	3.4807	2.978
Mismatch to GaN (%)	—	—	—	2.3	—	20.1	9.2	–6.5
T_{MP} (K)	2800	1900	2173	3500	2023	2668	2678	3073
Bandgap (eV)	3.4	9	5	6.2	4.7	5.3	6.3	8
Electron affinity (eV)	3.4	0.9	—	0–2.9	—	0.63	—	0.7
Workfunction (eV)	—	—	—	0.9–1.2	—	2.1–3.3	4	3.1–4.4
Dielectric constant	9.5	3.9	7.5	8.5	14.2	11.4	14	9.8

Key: W = wurtzite, A = amorphous, B = bixbyite, N = NaCl.

lattice mismatches to GaN (6.5% for MgO and 9.2% for Sc_2O_3 vs. 20% for Gd_2O_3). Layers of these materials deposited by molecular-beam epitaxy (MBE) on AlGaN/GaN HEMTs prevent much of the lag response found in unpassivated devices [17].

BIBLIOGRAPHY

1. S. Wolf and R. N. Tauber, *Silicon Processing for the VLSI Era*, Vol. 1, *Process Technology*, Lattice Press, Los Angeles, CA, 1986.
2. G. C. Schwartz, Interlevel dielectrics and passivating films, *Proc. Electronic Materials and Processing Seminar*, American Society for Metals, Metals Park, OH, 2001, pp. 49–66.
3. S. Mahajan, Defects in Si-processing, in L. Kimerling, ed., *Concise Encyclopedia of Semiconducting Materials and Related Technologies*, Peragamon Press, Oxford, 1992, pp. 78–84.
4. F. L. Riley, Silicon nitride: Bulk properties, in *Concise Encyclopedia of Semiconducting Materials and Related Technologies*, Peragamon Press, Oxford, 1992, pp. 458–461.
5. A. K. Sinha, Plasma deposited polycrystalline silicon nitride films, *Solid State Technol.* **23**:133 (1980).
6. *Process Technology for the 21st Century*, Semiconductor Consulting Services, Scottsdale, AZ, 1999.
7. S. P. Murarka and S. W. Hayes, *Crit. Rev. Solid State Mat. Sci.* **20**:87 (1995).
8. T. Nakano, Relationship between chemical composition and film properties of organic spin-on glass, *J. Electrochem. Soc.* **142**:918 (1995).
9. G. Samuelson, Polyimide for multilevel very large scale integration (VLSI), in E. D. Feit and C. W. Wilkins, eds., *Polymer Materials for Electronic Applications*, ACS Symp. Series, Vol. 184, American Chemical Society, Washington, DC, 1982, pp. 93–106.
10. R. K. Laxman, Low dielectrics: CVD fluorinated silicon dioxides, *Semicond. Int.* 71–74 (May 1995).
11. The National Technology Roadmap for Semiconductors 2002, Semiconductor Industry Association, San Jose, CA.
12. M. Eizenberg, CVD of TiN for sub-0.5 μm ULSI circuits, *MRS Bull.* **20**(11):38 (1995).
13. T. Ohba, CVD tungsten for vertical wiring, *MRS Bull.* **20**(11):46 (1995).
14. K. Kikuta and T. Kikkawa, *Extended Abstracts of the 53rd Autumn Meeting*, Vol. 2, The Japan Society of Applied Physics and Related Societies, 1993, pp. 720–721.
15. A. Sauter and W. O. Nix, in M. F. Doerner, W. C. Oliver, G. M. Pharr, and F. R. Brogen, eds., *Thin Films: Stresses and mechanical Properties II*, Materials Research Society, Pittsburgh, 1999, p. 15.
16. P. A. Finn, Mechanical stress in VLSI interconnections: Origins, effects, measurement and modelling, *MRS Bull.* **20**(11):70 (1995).
17. B. Luo et al., *Appl. Phys. Lett.* **80**:1661 (2001).
- G. W. Kaye and T. H. Laby, *Tables of Physical and Chemical Constants and Some Mathematical Functions*, 11th ed, Longmans, New York, 1956.
- C. T. Sah, *Fundamentals of Solid-State Electronics*, World Scientific, Singapore, 1991.
- S. M. Sze, *Physics of Semiconductor Devices*, 2nd edn., Wiley, New York, 1981.
- W. M. Yim, E. J. Stofko, P. J. Zanzucchi, J. I. Pankove, M. Ettenburg, and S. L. Gilbert, Epitaxially grown AlN and its optical band gap, *J. Appl. Phys.* **44**:292 (1973).
- W. L. Chin, T. L. Tansley, and T. Osotchan, Electron mobilities in gallium, indium, and aluminum nitrides, *J. Appl. Phys.* **75**:7365 (1994).
- M. S. Shur and M. A. Khan, GaN/AlGaN heterostructure devices: Photodetectors and field-effect transistors, *Mat. Res. Bull.* **22**(2):44 (1997).
- S. S. Derbeneva and S. S. Batsano, *Dokl. Chem.* **175**:710 (1967).
- S. S. Batsonov and E. V. Dulepov, *Sov. Phys. Solid State* **7**(4):995 (1965).
- K. A. Gschneider, *Rare Earth Alloys*, Izd. Mir, 1965.
- V. N. Abramov, A. N. Ermoshkin, and A. I. Kuznetsov, Optical properties and electron energy structure of Y_2O_3 and Sc_2O_3 , *Sov. Phys. Solid State*, **25**:981 (1983).
- N. Daude, C. Jouanin, and C. Gout, Electronic band structure of magnesium and calcium oxides, *Phys. Rev. B* **15**:2399 (1977).
- G. V. Samsonov, *The Oxide Handbook*, Plenum, New York, 1973, and references cited therein.

PERIODIC STRUCTURES

MAURIZIO BOZZI
University of Pavia
Pavia, Italy

1. INTRODUCTION

A structure is defined as being “periodic” when it can be obtained as the combination of infinite replicas of a “unit cell” appropriately shifted along translation vectors. According to the number of translation vectors, a periodic structure can be one-, two-, or three-dimensional. In particular, a one-dimensional periodic structure is simply a uniform linear array of identical elements; a two-dimensional periodic structure consists of a planar array of element arranged in a doubly periodic grid; in the case of three-dimensional periodic structure, the elements are arranged in a lattice.

In the real world any structure is limited in space and, therefore, rigorously periodic structures do not exist. Nevertheless, if an array is large enough, most of the inner elements practically “see” an infinite array environment, and for many applications their behavior can be well approximated by the uniform behavior of elements in an infinite periodic structure.

The reason for considering the infinite array model is that this permits a substantial reduction in the analysis computational complexity. In fact, the electromagnetic field inside a uniformly excited periodic structure is the same in any cell (apart from a phase shift), and therefore

FURTHER READING

- J. H. Edgar, ed., *Properties of Group III Nitrides*, Inspector, the Institution of Electrical Engineers, London, 1994.

the analysis of the whole structure can be reduced to an investigation of the unit cell. From the computational perspective, this often means a reduction in computing time and memory requirement roughly proportional to the square or cube of the number of array elements.

Periodic structures are widely used in the microwave and millimeter-wave ranges for a variety of applications in both circuits and antennas. They also find many applications in the infrared and optical regions. They are usually made of metal, dielectric, or a combination of both.

Periodic structures commonly used in the microwave range are described in Section 2, along with their operation principle, applications, and fabrication issues. The basic theory for the study of the propagation of electromagnetic waves in periodic structures is discussed in Section 3, where Floquet's theorem and Brillouin zones are discussed. Finally, Section 4 presents some numerical techniques, widely adopted for the analysis of periodic components operating in the microwave and millimeter-wave regions.

2. OPERATION PRINCIPLES OF PERIODIC STRUCTURES

This section presents some examples of periodic structures, widely used in the microwave and millimeter-wave

ranges. In particular, the geometry, operation principle, most commonly used fabrication techniques and most significant applications of these components are described and discussed at an introductory level.

Five classes of periodic structures are considered: periodically loaded transmission lines and polarizing grids (which are one-dimensional periodic structures), frequency-selective surfaces and quasioptical arrays (which are two-dimensional periodic structures), and metamaterials (which can be one-, two-, or three-dimensional periodic structures, depending on the applications).

2.1. Periodically Loaded Waveguides and Transmission Lines

Waveguides and transmission lines loaded at identical intervals with reactive elements are a simple example of one-dimensional periodic structures (see, e.g., Ref. 1, Chap. 8). The reactive elements adopted in these structures usually consist of metallic diaphragms that close a portion of the cross section of a waveguide or a coaxial line (Fig. 1).

Periodically loaded waveguides and transmission lines have two common properties:

1. They present a discrete set of passbands separated by stopbands, specifically, frequency bands where the elec-

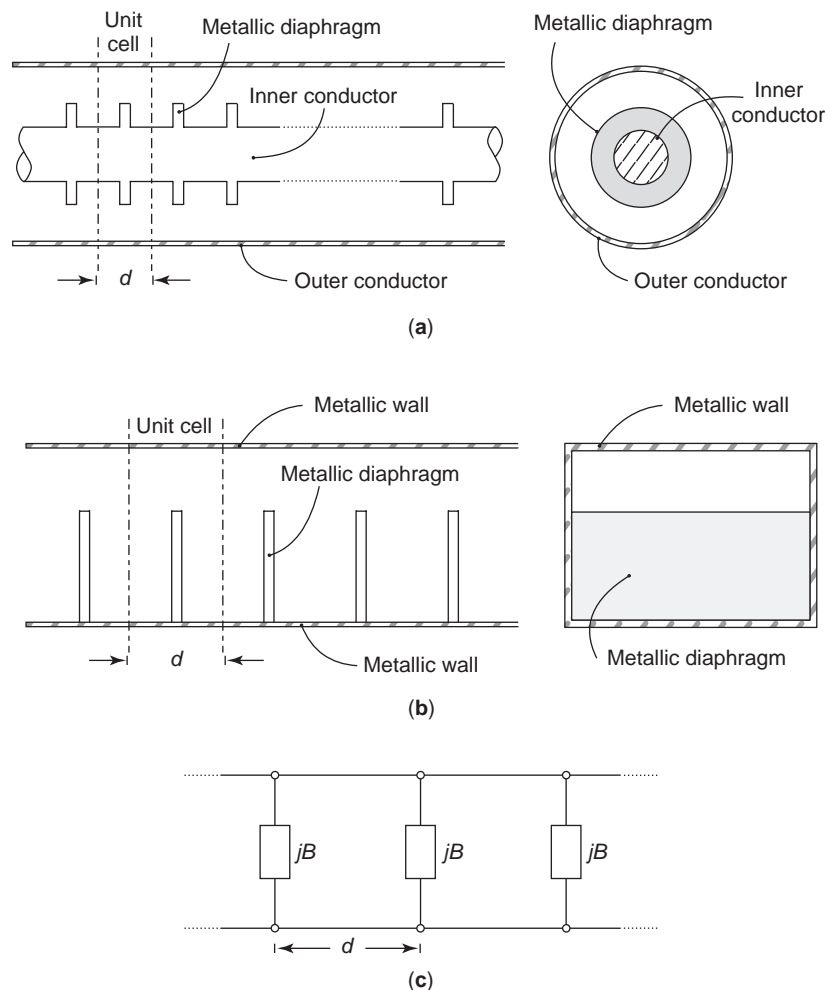


Figure 1. One-dimensional periodic structures: (a) side and front views of a coaxial line periodically loaded with circular diaphragms; (b) side and front views of a rectangular waveguide loaded with capacitive diaphragms; (c) lumped-element equivalent circuit, consisting of a transmission line loaded at intervals d by a lumped susceptance jB .

tromagnetic wave propagates in the structure without attenuation (except for metal losses), separated by frequency bands where the wave is highly attenuated and cannot propagate in the periodic structure. The physical explanation of this behavior can be easily understood by considering the equivalent circuit shown in Fig. 1c, where the periodic structure is modelled as the cascade of transmission-line sections with length d and lumped shunt susceptances jB . At those frequencies where the length d is a half-wavelength (or an integer number of half wavelengths), the transmission-line sections play no role and all susceptances are seen in parallel. Therefore, at these frequencies, the line is practically loaded with an infinite susceptance, and no power flows along the periodic structure. This property of periodically loaded transmission lines is particularly interesting for filtering purposes. To this aim, a tapered transition section is typically used for matching the periodic structure to the input/output transmission line [1]. The matching tapered section consists of a section of periodic structure, where the reactive loads gradually reduce to zero.

2. Periodically loaded transmission lines support the propagation of slow waves: waves with a phase velocity much smaller than the speed of light. This property can be easily understood by considering that the phase velocity of a smooth transmission line is given by

$$v_p = (LC)^{-1/2} \quad (1)$$

where C and L are the capacitance and the inductance per unit length, respectively. If the metallic diaphragm behaves as a lumped capacitance C_0 added at interval d (as shown in Fig. 1), the value of the capacitance per unit length is increased, whereas the inductance per unit length is unchanged. Therefore, the following phase velocity results:

$$v_p = \left[L \left(C + \frac{C_0}{d} \right) \right]^{-1/2} \quad (2)$$

The possibility of supporting slow waves is particularly important in traveling-wave-tube circuits and linear accelerators. In fact, in these applications, the electromagnetic field interacts with an electron beam, whose velocity is often 10–20% of the speed of light. Since an efficient interaction is obtained only when the two velocities are similar, a component able to support a slow wave is required [2].

2.2. Polarizing Grids

Polarizing grids are one-dimensional periodic structures, widely used in antennas and quasi-optical systems, and play an important role in polarization processing systems [3].

The simplest configuration of polarizing grids consists of an array of parallel conductors (round wires or flat strips), with dimension w and spacing g much smaller than the wavelength of the incident wave (Fig. 2a). When they are illuminated by an electromagnetic wave, these

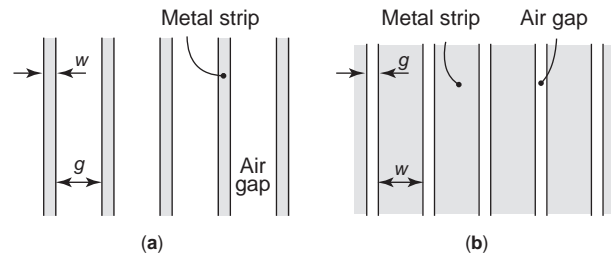


Figure 2. Polarizing grids: (a) inductive grid, consisting of narrow metal strips separated by wide gaps; (b) capacitive grid, consisting of wide metal strips separated by narrow gaps.

grids reflect completely the component of the incident field parallel to the wires, and are transparent for the component of the field perpendicular to the wires. Polarizing grids, operating in the millimeter- and sub-millimeter-wave regions, usually consist of slightly stretched metallic wires supported by a frame. In the microwave region, linear arrays of strips printed on a dielectric substrate are typically preferred.

If the condition that the wire spacing is much smaller than the wavelength is removed, polarizing grids exhibit a frequency-dependent behavior. In particular, at low frequency the component of the incident field parallel to the wires is completely reflected, whereas at high frequency the grid becomes practically transparent. When considering the field component parallel to the wires, the behavior of the grid can be modeled as a shunt inductance, which short-circuits the incident wave at low frequency, and plays no role at high frequency. Therefore, these components are named *inductive grids*.

The complementary structure, termed the *capacitive grid*, consists of a linear array of wide metal strips separated by narrow gaps (Fig. 2b). When considering the field component perpendicular to the gaps, this grid can be modeled as a shunt capacitance; the grid is practically transparent at low frequency, whereas it reflects most of the incident power at high frequency.

2.3. Frequency-Selective Surfaces (FSSs)

Frequency-selective surfaces are planar periodic structures, consisting of either an array of metallic patch elements patterned on a dielectric substrate (*capacitive FSS*; Fig. 3a), or a metallic screen perforated periodically with aperture elements (*inductive FSS*, Fig. 3b [4]). They are illuminated by an incident electromagnetic wave (which is considered planar and uniform in most cases), and their objective is to be transparent at some frequencies, and to reflect the incident wave in the specular direction at other frequencies.

When they are illuminated by a uniform plane wave, capacitive and inductive FSSs exhibit a nearly complementary behavior. At low frequency, the dimension of the array elements is much smaller than the wavelength; therefore, in the case of capacitive FSSs, the printed elements play no role and the periodic structure is practically transparent (apart from the reflection due to the dielectric substrate); conversely, in the case of inductive FSSs, the

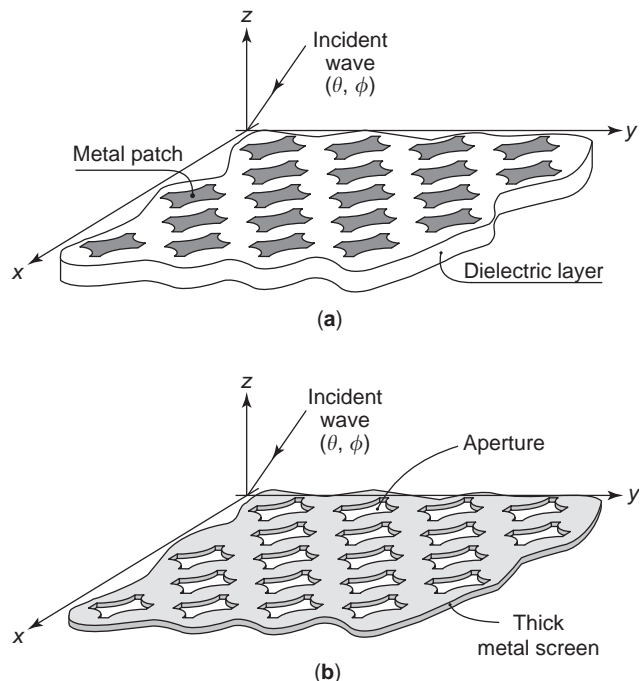


Figure 3. Frequency-selective surfaces with arbitrarily shaped elements: (a) capacitive FSS, consisting of a periodic array of metallic patches patterned on a dielectric substrate; (b) inductive FSS, consisting of a thick metallic screen perforated periodically with holes.

apertures are waveguides below cutoff and the structure practically behaves as a solid metallic mirror. When the frequency approaches the first element resonance, capacitive FSSs reflect completely the incident wave, whereas inductive FSSs are practically transparent. At frequencies higher than the first resonance, the reflected and transmitted fields are not a single uniform plane wave, due to the presence of grating lobes (or diffracted orders), which are additional plane waves propagating in different directions.

The frequency response of FSSs is determined mainly by the size and shape of the elements, their periodicity, the thickness and the dielectric permittivity of the substrate (for capacitive FSSs), the thickness of the metallic screen (for inductive FSSs), and the direction of incidence of the uniform plane wave. Different element shapes have been used in the design of FSSs (Fig. 4). In many cases, the elements have canonical shapes (rectangular or circular), due to their easier electromagnetic modeling. On the other hand, more complicated shapes can be adopted to obtain better performance, in terms of stability of the resonance frequency with the incidence angle, low cross-polarization level, large bandwidth, or small band separation. To this aim, the use of crosses, Jerusalem crosses, tripoles, rings and square loops have been proposed [5]. In the case of capacitive FSSs, the resonance frequency also depends on the dielectric permittivity and thickness of the substrate. In particular, for a given shape of the patch, the resonance frequency shifts down when increasing the dielectric permittivity of the substrate, since the dimension of the patch in terms of wavelengths increases.

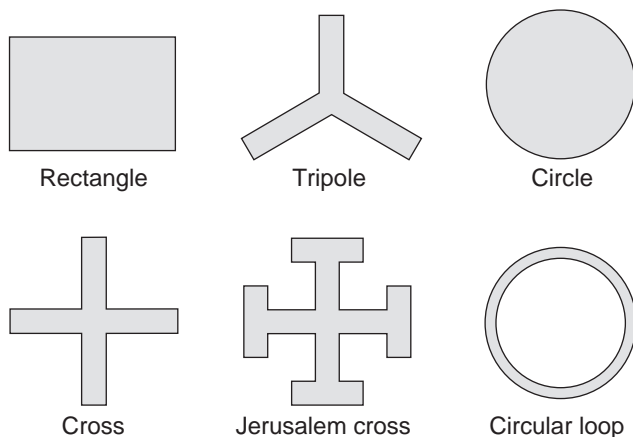


Figure 4. Different element shapes adopted in the design of frequency-selective surfaces.

Various manufacturing techniques can be chosen for the fabrication of FSSs. Capacitive FSSs can be obtained by photolithographic processing, with good accuracy and with no limitation in the element shape. Inductive FSSs operating in the microwave and millimeter-wave ranges are typically manufactured by the milling technique or by drilling, in the case of circular holes. Conversely, the fabrication of inductive FSSs intended for operation in the sub-millimeter-wave range is based mainly on galvanizing growth or laser cutting [6].

FSSs find a number of applications in the microwave and millimeter-wave regions for both scientific and commercial purposes. In the microwave region, FSSs are used as dichroic mirrors in large reflector antennas for radio-astronomy applications [7]. The feeding network of such antennas typically consists of beam-waveguide systems, and the FSS combines the beams generated by two feeds operating at different frequencies (Fig. 5). To this aim, the FSS is practically transparent at one frequency and behaves as a mirror at the other frequency. In this way, two feeds share the same reflector antenna, thus optimizing

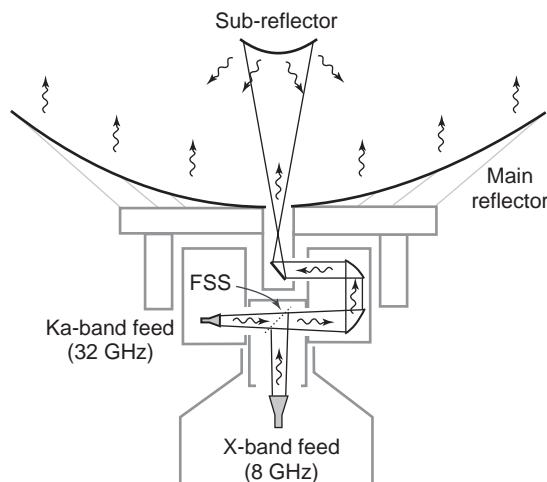


Figure 5. Reflector antenna using a frequency-selective surface for combining two feeds operating at different frequencies.

frequency reuse. For this kind of applications, the use of inductive FSSs is mostly preferred, due to lower losses and better power-handling capabilities. Another application of FSSs in the microwave region is the bandpass radome [8]; at the operating frequency the signal passes through the radome with minimum insertion loss, whereas at out-of-band frequencies the signal is reflected. Moreover, FSSs find wide commercial use in the screendoor of microwave ovens; the perforated metal screen reflects completely the microwave energy at 2.45 GHz, while allowing the light to pass through, thus permitting to see the food inside the oven. At higher frequency, FSSs are used as filters in quasi-optical systems, as diplexers, and as dichroic mirrors in laser cavities and in Fabry–Perot interferometers.

2.4. Metamaterials

Metamaterials are a new class of components, which have received a lot of attention since the 1990s for a variety of applications from the microwave to the optical regions [9]. They are based on artificially engineered periodic structures, and their objective is the modification of the electromagnetic properties of materials or the suppression of the electromagnetic wave propagation in certain frequency bands.

It is possible to identify three different classes of metamaterials: electromagnetic bandgap (EBG) structures, artificial magnetic conductors (AMCs), and double-negative (DNG) materials. However, because of the very recent origin of these components, no standard nomenclature is available yet.

EBG structures are periodic arrangements of dielectric and/or metallic elements, where the propagation of electromagnetic waves is inhibited in a certain frequency band. If the propagation is forbidden in all directions and for all polarizations, there is a full bandgap. The behavior of electromagnetic waves in EBG structures is analogous to the propagation of electrons in crystals; in the case of crystals, the periodic arrangement of atoms or molecules determines gaps in the energy band structure, so that electrons are forbidden to propagate with certain energies. Because of this analogy and since many applications were originally proposed in the field of optics, EBG structures are also indicated as photonic crystals (PCs) or photonic bandgap (PBG) structures. After some

discussions, the acronym EBG is becoming the standard term in the microwave community [10].

The idea of EBG structures was first proposed by Yablonoitch in 1987 [11], starting from studies in semiconductor theory. Moreover, Yablonoitch made the first prototype that exhibits a full electromagnetic bandgap in the microwave region [12]. It consists of a modified diamond structure, which is obtained by drilling a dielectric material along three appropriately chosen directions.

Different EBG configurations have been then proposed; they include metallodielectric structures, which are usually applied in the microwave and millimeter-wave ranges, and all-dielectric structures, which are preferred in the optical frequency range. Examples of metallodielectric EBG structures are two-dimensional arrays of metal patches patterned on a grounded dielectric slab. Conversely, an example of a one-dimensional dielectric EBG structure consists of a layered dielectric medium (Fig. 6a). Such structures have been used since long time as high-reflectivity mirrors in the infrared and optical regions: in fact, by choosing the correct thickness of the dielectric layers and their dielectric constants, it is possible to obtain very high reflection at a given frequency. This structure is known as a *Bragg stack*. More recently, two- and three-dimensional dielectric periodic structure have been proposed. In the 2D case, they are planar arrays of cylindrical rods in a square or hexagonal lattice (Fig. 6b), whereas in the 3D case they can be obtained by cross-stacking arrays of dielectric rods (Fig. 6c) and are known as “woodpile” structures [13].

Artificial magnetic conductors (AMCs) are planar periodic structures that reflect an incident plane wave without phase reversal, like a perfect magnetic conductor (i.e., the surface presents an infinite impedance). For this reason, AMCs are also termed *high-impedance surfaces*. AMCs are usually obtained by using metallodielectric planar periodic structures, which also exhibit EBG properties. Therefore, AMC and EBG structures will be discussed jointly here.

An interesting metallodielectric structure that presents EBG and AMC properties was proposed by Sievenpiper [14]. It consists of an array of hexagonal metal patches, patterned on a grounded dielectric substrate according to a triangular grid and connected to the ground plane by metallic vias (Fig. 7). Since the dimensions of the

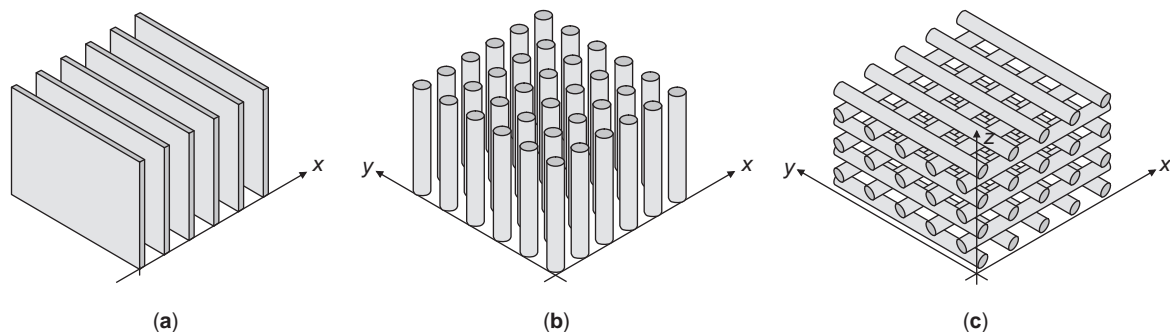


Figure 6. Examples of dielectric EBG structures: (a) stack of dielectric layers (1D structure); (b) planar array of dielectric rods (2D structure); (c) woodpile structure (3D structure).

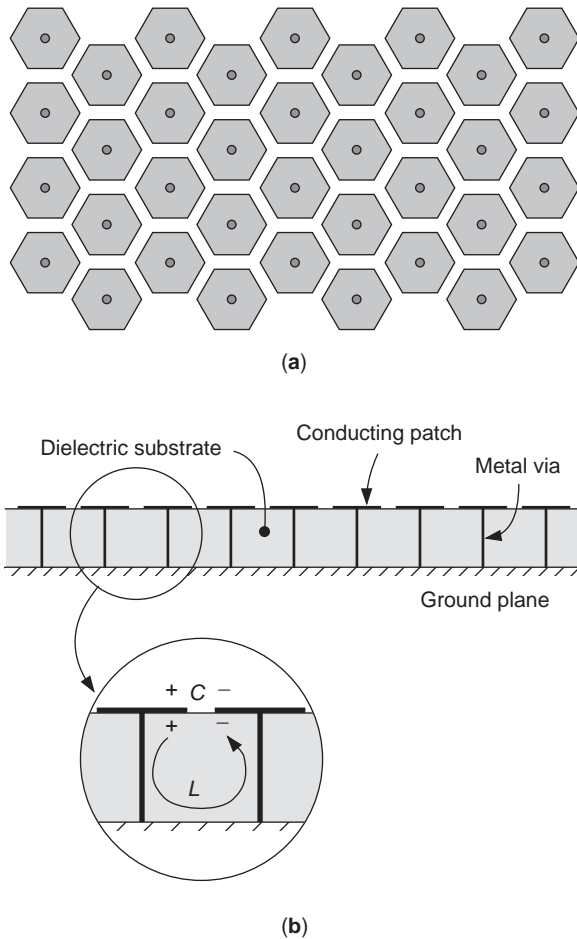


Figure 7. EBG structure consisting of an array of metallic mushrooms on a dielectric substrate: (a) top view; (b) side view.

unit cell are much smaller than the wavelength, many electromagnetic properties of this structure can be explained by using an equivalent-circuit model. The equivalent model is a parallel LC circuit, where the capacitance C is due to the gap between the metal patches and the inductance L depends on the loop through the metal vias and the ground plane (Fig. 7b). The impedance Z_p of the parallel LC circuits is given by

$$Z_p = \frac{j\omega L}{1 - \omega^2 LC} \quad (3)$$

where ω is the angular frequency. The value of the impedance is very large in a narrow band around the resonance frequency $\omega_0 = (LC)^{-1/2}$. At frequencies around ω_0 the currents on the surface radiate very efficiently, due to the resonance of the structure, and the structure suppresses the propagation of surface waves, thus exhibiting an EBG behavior. Moreover, at the same frequency, due to the large value of the impedance Z_p , the structure has high surface impedance, and therefore reflects the incident waves without the phase reversal that occurs in the case of conducting plates (AMC behavior).

Another significant metallodielectric EBG structure was proposed by Itoh and is the *uniplanar compact*

photonic bandgap (UCPBG) structure [15]. It is based on a two-dimensional periodic structure, patterned on a grounded dielectric substrate. The unit cell comprises a square patch connected to four thin metal strips with insets, located in the middle of each side of the square (Fig. 8). This structure can also be described as a complementary Jerusalem cross, since the top conducting plane is cut by an array of slots with a Jerusalem cross shape. In this case, the structure is planar, with no need of metal vias connecting the patches to the ground plane, thus resulting in a reduced fabrication complexity. The electromagnetic behavior of the UCPBG structure can be explained by its equivalent lumped-element circuit; also in this case, the equivalent model is a parallel LC circuit, where C represents the fringing capacitance of the gaps between the metal patches and the inductance L originates from the narrow metal strips connecting the patches.

One of the most important applications of EBG structures and AMCs in the microwave range is related to the design of printed antennas with high performance. In fact, standard patch antennas printed on dielectric substrates usually suffer from narrow bandwidth of operation, low gain, and limited radiation efficiency [16]. It is known that patch antennas exhibit good radiation efficiency when the thickness of the substrate is about a quarter-wavelength. With this particular substrate thickness, since the conducting ground plane reflects the incident wave with a phase reversal, the total phase shift of the round trip from the antenna to the ground plane and back to the antenna is equal to 360° (Fig. 9a). Therefore, the reflected wave is in phase with the direct wave, thus resulting in a constructive interference. Conversely, if the substrate thickness is smaller than a quarter-wavelength, the direct wave and the wave reflected by the ground plane

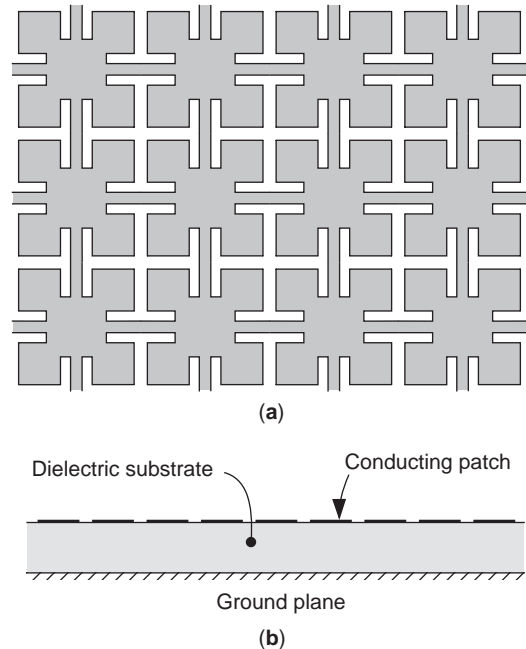


Figure 8. EBG structure consisting of an array of slots with a Jerusalem cross shape: (a) top view; (b) side view.

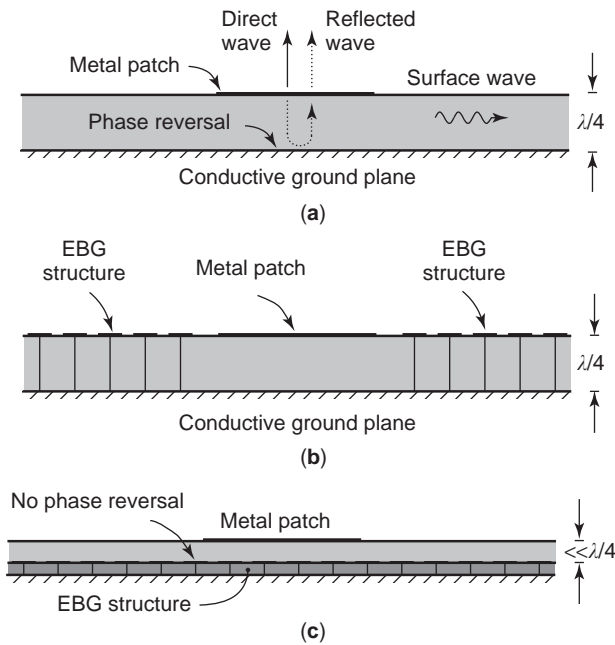


Figure 9. Patch antennas with EBG structures: (a) standard patch antenna on a thick dielectric substrate; (b) patch antenna surrounded by a periodic structure, which prevents the propagation of surface waves; (c) patch antenna located on a periodic structure, which creates a high-impedance surface (perfect magnetic conductor).

interfere in a destructive way, thus resulting in poor radiation efficiency. Also the antenna bandwidth depends on the substrate thickness, and can be improved by increasing the thickness. In both cases, when using thick substrates and high dielectric permittivity, the antenna couples power to surface waves, and its radiation efficiency deteriorates. Surface waves do not contribute to the primary radiation pattern, and therefore they reduce the radiated power. Moreover, surface waves are diffracted at the edges of the antenna substrate, thus deteriorating the radiation pattern of the antenna by increasing the sidelobes and the backward radiation. The performance of patch antennas can be improved by using an EBG structure, located around the antenna (Fig. 9b). The EBG structure is able to prevent the propagation of surface waves, thus permitting enhancement of the radiation efficiency and improvement of the radiation pattern [17]. Another solution is based on the use of an AMC below the antenna (Fig. 9c). In fact, the AMC is able to reflect the wave coming from the antenna with no phase reversal so that, if the antenna is located very close to the AMC, the direct and the reflected waves add constructively, and this leads to a good radiation efficiency [14]. This solution leads to the use of a substrate thickness much smaller than a quarter-wavelength, which permits substantially relaxation of the issue of the surface waves.

Besides these antenna applications, the use of EBG structures has been proposed for numerous significant applications in microwave circuits, in metallic waveguide, microstrip-line, and coplanar waveguide technologies. The

use of EBG structures has been proposed for implementing novel waveguides able to support a TEM mode [18]. In this waveguide, the top and bottom sides are standard metal layers, and represent an electric wall boundary condition, whereas the lateral sides consists of UCPBG structures, which behave as magnetic walls in a reasonably wide frequency band. The fundamental mode supported by this waveguide propagates with a phase velocity close to the speed of light, and presents TEM properties. The concept of the TEM waveguide was exploited in quasi-optical power amplifiers [19], since the TEM mode exhibits an almost uniform field distribution. In fact, illuminating the quasi-optical array with a uniform power density allows for increasing the overall saturation power of the amplifiers. EBG substrates have also allowed the design of stopband microstrip filters, with a sharp transition from the passband to the stopband [20]. A simple microstrip, located on a dielectric substrate with a periodically etched ground plane, presents a stopband at the frequencies where the periodic structure exhibits a high impedance. In fact, at those frequencies, the microstrip behaves as a narrow metal strip on a magnetic conductor, and this structure is not able to support the fundamental mode of a microstrip. The use of EBG was demonstrated to improve the performance of conductor-backed coplanar waveguides [15]. In fact, these structures suffer from leakage due to the propagation of the parallel-plate mode, which propagates between the ground plane and the upper conductor. By substituting the upper conductor with a UCPBG structure (Fig. 10), the propagation of the parallel-plate mode can be suppressed, thus reducing the losses of the coplanar waveguide mode. Another application of EBG structures is related to active circuits; they have been used to suppress the undesired harmonic frequencies in oscillators, mixers, and power amplifiers [21].

DNG materials are a very recent and promising class of the metamaterials. They include artificial materials that exhibit simultaneously negative real part of the effective electric permittivity and magnetic permeability in a given frequency band. Veselago considered these materials for the first time in the 1960s [22]; he theoretically showed from the Maxwell equations that such media exhibit a

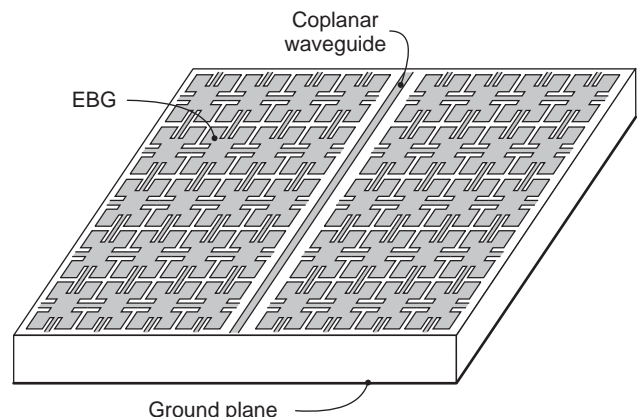


Figure 10. Conductor-backed coplanar waveguide integrated with EBG structure.

negative index of refraction. This means that the direction of the energy flow (Poynting vector) of a plane wave propagating inside the medium is antiparallel with the direction of the wave's phase velocity. In other words, the electric field, the magnetic field, and the propagation vector form a left-handed system, differently from ordinary materials, where they form a right-handed system. Because of these peculiarities, various names have been coined for this type of metamaterial, such as negative-index (of refraction) materials (NIMs), backward-wave (BW) media, and left-handed (LH) materials.

The first experimental verification of a DNG material operating in the microwave regime was reported in 2001 [23]. This artificial material uses an array of split-ring resonators (SRRs) to produce negative magnetic permeability and thin wire elements to produce negative electric permittivity in the same frequency band.

A potential application of DNG materials is the perfect lenses, proposed by Pendry [24]. It is a slab of negative-refractive-index material, which has the power to focus all Fourier components of a two-dimensional image, even those that do not propagate in a radiative manner. These perfect lenses could overcome the limitation of conventional lenses, whose resolution is limited by the wavelength. Another interesting application is based on the idea of subwavelength cavity resonators [25]. In fact, by combining a slab of DNG material and a layer of standard lossless dielectric medium, it is possible to obtain a one-dimensional cavity resonator whose dispersion relation do not depend on the sum of the thicknesses of the two slabs, but depends on the ratio of these thicknesses.

2.5. Quasioptical Arrays

Quasioptical components consist of planar arrays of patch or slot antennas patterned on a semiconductor substrate, monolithically integrated with active or nonlinear devices (Fig. 11). These components have received a lot of attention due to their great potential for applications in the

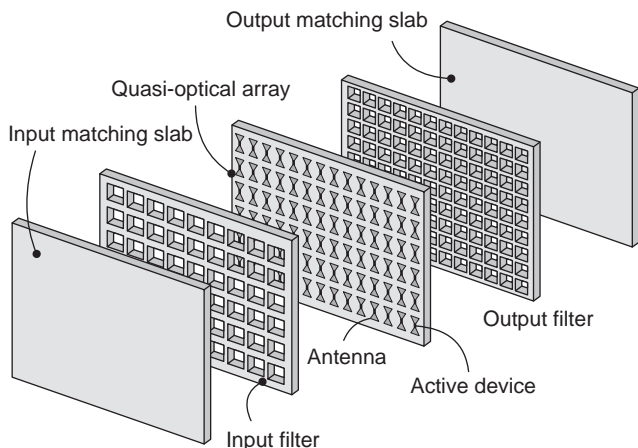


Figure 11. Quasioptical frequency multiplier, consisting of a planar array integrated with active and/or nonlinear devices; input and output filters (FSSs) are used for unidirectional operation, whereas dielectric slabs are used for input/output matching.

millimeter- and sub-millimeter-wave ranges [26]. At these frequencies, in fact, a technological gap still exists, between the mature technology of waveguide components in the microwave range and the optical technologies in the infrared and optical regions.

Quasioptical components performing a wide range of different operations have been proposed and experimentally verified. Among them, frequency multipliers [27], mixers [28], amplifiers [29], phase shifters [30], and oscillators [31] were proposed.

Quasioptical frequency multipliers (Fig. 11), for instance, are based on Schottky diodes or heterostructure barrier varactors, and use the nonlinear dependence of the junction capacitance versus the applied voltage. In such a way, they are able to convert a portion of the incident power from the fundamental frequency to the upper harmonic (typically second or third harmonic). The shape and size of the antennas where the nonlinear elements are located are designed in such a way, to couple all the incident power to the terminals of the devices and to guarantee their optimal conversion efficiency.

The use of quasioptical structures appears very promising for components and systems operating above 30 GHz. Quasioptics deals with the propagation in free space of electromagnetic beams, which are well collimated and have relatively small dimensions (when measured in wavelengths), transverse to the axis of propagation [3]. Quasioptical propagation is a very interesting method of propagation in the millimeter- and sub-millimeter-wave regions, which permits low power loss over very broad bandwidths. Conversely, traditional waveguide systems (e.g., metallic waveguides, coaxial cables, microstrip lines) present high losses when frequency increases, due to the finite conductivity of metallic conductors and the loss in dielectrics.

A key point of quasioptical components is the concept of power combining [32]. If a single device is limited in power for a specific application, the combination of a large number of identical devices (e.g., tens or hundreds) can easily overcome this limitation. In quasioptical systems, this combination can be easily performed, with no need of beamforming networks. Another significant advantage of these components over single-device structures is that, due to the large number of devices, their performance is subject to a graceful degradation in the case of failure of some devices. Moreover, quasioptical arrays are small and light, and therefore are particularly suitable to space applications. Monolithically integrated components are easier to fabricate than waveguide devices and less expensive in mass production. Finally, quasioptical systems performing complex functions can be realized by simply stacking arrays that perform elementary functions.

3. BASIC THEORY: FLOQUET'S THEOREM AND BRILLOUIN ZONE

This section presents two basic topics of the theory of periodic structures. The first topic is Floquet's theorem (or Bloch's theorem), which permits to determine the solution of the wave equation in a periodic structure. The deriva-

tion of the theorem is performed in the cases of one-dimensional and two-dimensional periodic structures. The second topic is the study of the Brillouin zones, which are very useful in the analysis of the propagation of electromagnetic waves in periodic structures. Some basic definitions are given, and the technique for drawing the Brillouin zones is described.

3.1. Floquet's Theorem

The basic theorem concerning the propagation of waves in a periodic medium was formulated by Gaston Floquet in 1883 [33]. Actually, Floquet's work deals with the solution of a differential equation with periodic coefficients, but perfectly applies to the analysis of 1D periodic structures. The generalization of this theorem for 2D and 3D cases is due to Felix Bloch in 1928 [34], who performed studies mainly in the field of quantum mechanics.

Let us first consider Floquet's theorem in one-dimensional periodic structures (see, e.g., Ref. 1, pp. 569–571). In a structure periodic along the z direction, it is possible to identify a unit cell, defined by two terminal parallel planes at a distance d (e.g., the planes $z=0$ and $z=d$; see Fig. 12). If we consider lossless structures, the fields at the terminal parallel planes have the same amplitude and differ for a phase shift, due to the propagation factor $e^{-\gamma d}$; the term γ is the propagation constant and can be written in the form $\gamma=j\beta$.

Since the choice of the terminal planes of the unit cell is arbitrary, the field in any point of the unit cell differs from the field in the corresponding point of another unit cell for a phase shift, due to the propagation factor $e^{-\gamma nd}$, where nd is the distance between the two cells (where n is an integer number). It results that

$$\begin{aligned}\mathbf{E}(x, y, z + nd) &= e^{-\gamma nd} \mathbf{E}(x, y, z) \\ \mathbf{H}(x, y, z + nd) &= e^{-\gamma nd} \mathbf{H}(x, y, z)\end{aligned}\quad (4)$$

Consequently, the electric and magnetic fields in a periodic structure are in the form

$$\begin{aligned}\mathbf{E}(x, y, z) &= e^{-j\beta z} \mathbf{E}_p(x, y, z) \\ \mathbf{H}(x, y, z) &= e^{-j\beta z} \mathbf{H}_p(x, y, z)\end{aligned}\quad (5)$$

where \mathbf{E}_p and \mathbf{H}_p are periodic functions of z with period d :

$$\begin{aligned}\mathbf{E}_p(x, y, z + nd) &= \mathbf{E}_p(x, y, z) \\ \mathbf{H}_p(x, y, z + nd) &= \mathbf{H}_p(x, y, z)\end{aligned}\quad (6)$$

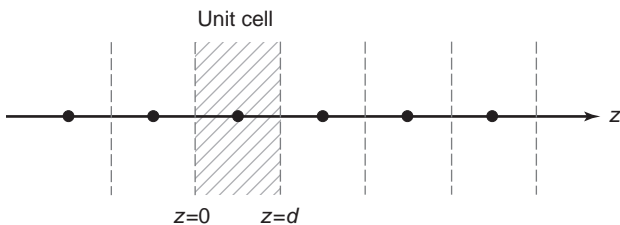


Figure 12. One-dimensional periodic structure.

Since \mathbf{E}_p is a periodic function, it can be expanded into a Fourier series

$$\mathbf{E}_p(x, y, z) = \sum_{n=-\infty}^{\infty} \mathbf{E}_{pn}(x, y) e^{-j2n\pi z/d} \quad (7)$$

where $\mathbf{E}_{pn}(x, y)$ are vector functions depending on x and y . By multiplying both sides of (7) by $e^{j2m\pi z/d}$, integrating over the unit cell (with z ranging from 0 to d), and exploiting the orthogonality of the exponential functions, we obtain

$$\mathbf{E}_{pn}(x, y) = \frac{1}{d} \int_0^d \mathbf{E}_p(x, y, z) e^{j2n\pi z/d} dz \quad (8)$$

By substituting (7) in (5), and using $\gamma=j\beta$, the electric field in a periodic structure can be expressed as

$$\mathbf{E}(x, y, z) = \sum_{n=-\infty}^{\infty} \mathbf{E}_{pn}(x, y) e^{-j\beta z - j2n\pi z/d} \quad (9)$$

$$= \sum_{n=-\infty}^{\infty} \mathbf{E}_{pn}(x, y) e^{-j\beta_n z} \quad (10)$$

where

$$\beta_n = \beta + \frac{2n\pi}{d} \quad (11)$$

It results that the electric field in a periodic structure can be written as a summation of terms, termed *spatial harmonics* or *Hartree harmonics*. For the n th harmonic, β_n represents the propagation phase constant, and the phase velocity v_{pn} is given by

$$v_{pn} = \frac{\omega}{\beta_n} = \frac{\omega}{\beta + 2n\pi/d} \quad (12)$$

where $\omega=2\pi f$ is the angular frequency. Moreover, the group velocity is given by

$$v_{gn} = \left(\frac{d\beta_n}{d\omega} \right)^{-1} = \left(\frac{d\beta}{d\omega} \right)^{-1} = v_g \quad (13)$$

and therefore does not depend on index n and is the same for all harmonics.

It is noted that both the propagation constant and the phase velocity can be positive or negative, according to the value of the integer number n . This means that in periodic structures some of the harmonics have phase velocity and group velocity opposite in sign [backward waves (BW_s)]. This property is exploited in BW traveling-wave-tube oscillators [2].

Let us now consider Floquet's theorem in two-dimensional periodic structures (see, e.g., Ref. 35, pp. 37–42). In a structure with double periodicity in the xy plane, the periodicity is described by a pair of translation vectors \mathbf{a} and \mathbf{b} . These translation vectors can either be orthogonal

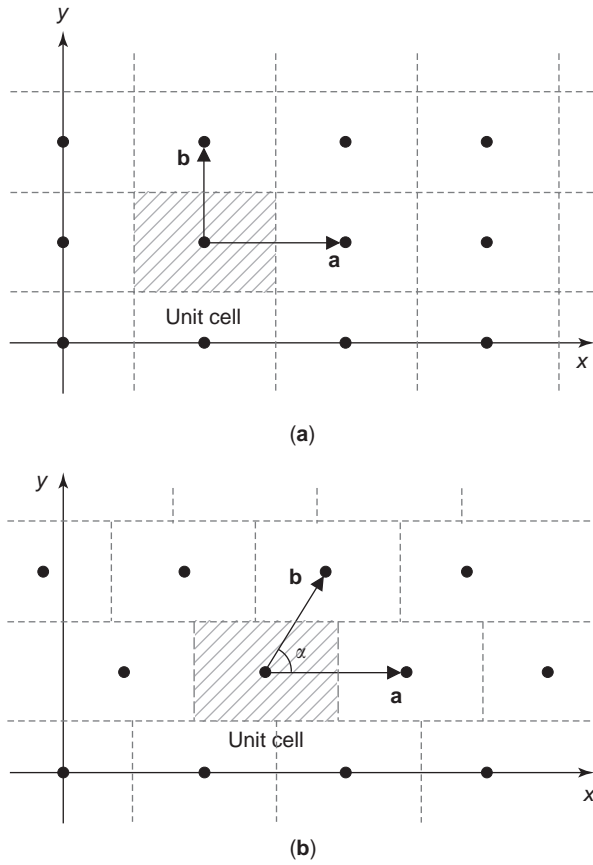


Figure 13. Two-dimensional periodic structure: (a) rectangular grid; (b) skewed grid.

(rectangular grid; Fig. 13a) or form an angle α (skewed grid; Fig. 13b).

The problem of the field representation is somehow similar to the study of metallic rectangular waveguides; in fact, it is convenient to formulate the problem in terms of scalar potentials, which are eigensolutions of the Helmholtz equation. The only difference is the boundary condition, which in this case is a periodicity condition instead of an electric wall condition.

We first consider the case of a rectangular grid (Fig. 13a). The scalar potential $\zeta(x, y, z)$ must satisfy the homogeneous scalar Helmholtz equation

$$\nabla^2 \zeta(x, y, z) + \kappa^2 \zeta(x, y, z) = 0 \tag{14}$$

and the periodicity condition

$$\zeta(x + a, y + b, z) = e^{-j(\psi_x + \psi_y)} \zeta(x, y, z) \tag{15}$$

where a and b represent the amplitude of the translation vectors \mathbf{a} and \mathbf{b} and ψ_x and ψ_y are the inter-element phase shift in the x and y directions, respectively. In the case of a two-dimensional array of elements illuminated by a uniform plane wave, the phase shift depends on the frequency

and the angle of incidence of the plane wave. In particular

$$\begin{aligned} \psi_x &= ka \sin \theta \cos \phi \\ \psi_y &= kb \sin \theta \sin \phi \end{aligned} \tag{16}$$

where (θ, ϕ) is the angle of incidence of the plane wave and k is the wavenumber at the operation frequency.

Similarly to standard waveguides, the behavior in the z direction is such that

$$\zeta(x, y, z) = e^{-\gamma z} \zeta(x, y) \tag{17}$$

where $\gamma = j\beta$ for propagating modes in the case of lossless structures. Therefore, by substituting (17) into (14), the Helmholtz equation is recast as follows

$$\nabla_T^2 \zeta(x, y) + (\kappa^2 - \beta^2) \zeta(x, y) = 0 \tag{18}$$

where ∇_T^2 is the transverse Laplace operator, and the boundary condition is derived directly from (15). By considering that

$$\beta^2 = \kappa^2 - \kappa_x^2 - \kappa_y^2 \tag{19}$$

and applying the technique of separation of variable

$$\zeta(x, y) = f(x)g(y) \tag{20}$$

the Helmholtz equation and its boundary condition can be split into x and y components:

$$\frac{\partial^2}{\partial x^2} f(x) + \kappa_x^2 f(x) = 0, \quad f(x + a) = f(x) e^{-j\psi_x} \tag{21}$$

$$\frac{\partial^2}{\partial y^2} g(y) + \kappa_y^2 g(y) = 0, \quad g(y + b) = g(y) e^{-j\psi_y} \tag{22}$$

Considering first function $f(x)$, a new function $f_p(x)$ is defined as

$$f_p(x) = f(x) e^{j(\psi_x/a)x} \tag{23}$$

It can be easily proved that $f_p(x)$ is a periodic function with period a . In fact

$$\begin{aligned} f_p(x + a) &= f(x + a) e^{j(\psi_x/a)(x+a)} e^{-j\psi_x} \\ &= f(x) e^{j(\psi_x/a)x} = f_p(x) \end{aligned} \tag{24}$$

Since $f_p(x)$ is periodic, it can be expanded into a Fourier series

$$f_p(x) = \sum_{m=-\infty}^{+\infty} f_{pm} e^{-j2m\pi x/a} \tag{25}$$

where f_{pm} are scalar coefficients. By substituting (25) in (23), the expression of function $f(x)$ can be obtained

$$f(x) = \sum_{m=-\infty}^{+\infty} f_{pm} e^{-jk_{xm}x} \quad (26)$$

where

$$\begin{aligned} \kappa_{xm} &= \frac{2m\pi + \psi_x}{a} \\ &= k \sin \theta \cos \phi + \frac{2m\pi}{a} \end{aligned} \quad (27)$$

The same derivation can be applied to function $g(y)$, where we obtain

$$g(y) = \sum_{n=-\infty}^{+\infty} g_{pn} e^{-jk_{yn}y} \quad (28)$$

where

$$\begin{aligned} \kappa_{yn} &= \frac{2n\pi + \psi_y}{b} \\ &= k \sin \theta \sin \phi + \frac{2n\pi}{b} \end{aligned} \quad (29)$$

Therefore, the eigenfunctions $\xi_{mn}(x, y)$ of the Helmholtz equation (18), with the proper normalization, are in the form

$$\xi_{mn}(x, y) = \frac{-j}{\sqrt{ab}} e^{-j(\kappa_{xm}x + \kappa_{yn}y)} \quad (30)$$

and the corresponding eigenvalues are

$$\kappa_{mn} = \sqrt{\kappa_{xm}^2 + \kappa_{yn}^2} \quad (31)$$

Once the eigensolutions of the Helmholtz equation have been determined, an orthonormal set of modal vectors, representing the proper modes of the waveguide with periodicity boundary conditions, can be determined. These modal vectors are termed *Floquet modes*. Similar to standard waveguide modes [36], TE and TM modes can be derived from scalar potentials. These modes propagate in the z direction with a propagation constant γ_{mn} given by

$$\gamma_{mn} = \begin{cases} \sqrt{\kappa_{mn}^2 - k^2} & \text{if } k < \kappa_{mn} \\ j\sqrt{k^2 - \kappa_{mn}^2} & \text{if } k > \kappa_{mn} \end{cases} \quad (32)$$

TM modes (denoted by the superscript prime) have the magnetic modal fields transverse to z ($H'_z = 0$), and their

electric and magnetic modal vectors are

$$\mathbf{E}'_{mn} = -\frac{\nabla_T \xi_{mn}}{\kappa_{mn}} \quad (33)$$

$$\mathbf{H}'_{mn} = -\mathbf{z} \times \frac{\nabla_T \xi_{mn}}{\kappa_{mn}} \quad (34)$$

and the corresponding modal admittance is

$$Y'_{mn} = \frac{jk}{\eta \gamma_{mn}} \quad (35)$$

TE modes (denoted by the superscript double prime) have the electric modal fields transverse to z ($E''_z = 0$), and their electric and magnetic modal vectors are

$$\mathbf{E}''_{mn} = -\frac{\nabla_T \xi_{mn}}{\kappa_{mn}} \times \mathbf{z} \quad (36)$$

$$\mathbf{H}''_{mn} = -\frac{\nabla_T \xi_{mn}}{\kappa_{mn}} \quad (37)$$

and the corresponding modal admittance is

$$Y''_{mn} = \frac{\gamma_{mn}}{j\eta k} \quad (38)$$

In case of $\psi_x = \psi_y = 0$ (e.g., in the case of a two-dimensional array illuminated by a plane wave with normal incidence, $\theta = 0$), the set of modes is not complete, and two additional TEM modes are needed [37]. The electric and magnetic modal vectors of the TEM modes can be derived from scalar potentials, which are the solutions of the Laplace equation with periodic boundary conditions. These modes, denoted by a superscript 0, have both electric and magnetic modal fields transverse to z ($E_z^0 = 0$ and $H_z^0 = 0$), and correspond to the fundamental modes of a rectangular waveguide with two electric walls and two magnetic walls. Their electric and magnetic modal vectors are

$$\mathbf{E}^0_{01} = \frac{\mathbf{x}}{\sqrt{ab}} \quad \mathbf{H}^0_{01} = \frac{\mathbf{y}}{\sqrt{ab}} \quad (39)$$

$$\mathbf{E}^0_{10} = \frac{\mathbf{y}}{\sqrt{ab}} \quad \mathbf{H}^0_{10} = \frac{-\mathbf{x}}{\sqrt{ab}} \quad (40)$$

and the corresponding modal admittance is

$$Y^0_{01} = Y^0_{10} = \frac{1}{\eta} \quad (41)$$

where η is the characteristic impedance of the medium ($\eta_0 = 377 \Omega$ in vacuum).

If translation vectors \mathbf{a} and \mathbf{b} are not orthogonal (i.e., they form an angle α ; Fig. 13b), the grid is not rectangular. In this case, the formulas derived in this section must be slightly modified. In particular, (29) is replaced by

$$\kappa_{yn} = k \sin \theta \sin \phi + \frac{2n\pi}{b \sin \alpha} - \frac{2m\pi}{a \tan \alpha} \quad (42)$$

and in (30), (39), and (40) the term

$$\frac{1}{\sqrt{ab}} \tag{43}$$

is replaced by

$$\frac{1}{\sqrt{ab \sin \alpha}}. \tag{44}$$

3.2. Brillouin Zone

Another important concept in the study of periodic structure is related to the definition of the direct lattice, the reciprocal lattice, and the Brillouin zone.

Let us first consider the study of the propagation characteristics of electromagnetic waves in one-dimensional periodic structures. As stated by the Floquet theorem, the solution of the propagation equation yields propagation constants $\beta_n = \beta + 2n\pi/d$ (with $n = \pm 1, \pm 2, \dots$) in addition to the fundamental mode. This is a direct consequence of the periodic characteristics of the structure. Because of these periodic characteristics, it is sufficient to study the propagation properties of the structure inside one period of the propagation phase constant β . The fundamental interval is usually defined by $-\pi < \beta d < \pi$. This fundamental interval contains all the information on the propagation characteristics of the electromagnetic waves in the periodic structure. All the replicas in other intervals contain redundant information.

The propagation characteristics of the wave in the fundamental interval, also termed the *first Brillouin zone*, are usually shown in the ω - β diagram (Fig. 14). This diagram permits us to identify the frequency bands where the structure exhibits passband behavior and those where it exhibits stopband behavior.

Let us now consider the case of two-dimensional periodic structures. This case is more significant than the one-dimensional case, has the same conceptual difficulties of the three-dimensional case, and is easier to discuss, anyway. Moreover, the two-dimensional case is by far the most

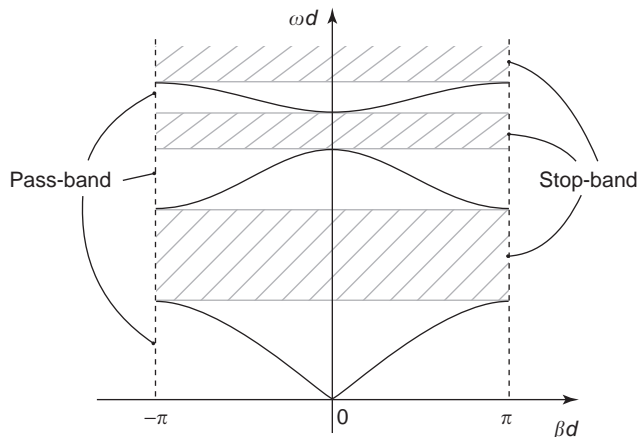


Figure 14. ω - β diagram of a one-dimensional periodic structure.

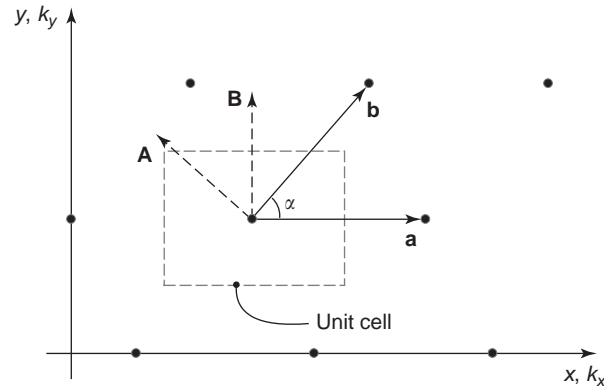


Figure 15. Direct and reciprocal lattice in a two-dimensional periodic structure.

important for microwave applications. A complete discussion of the three-dimensional case can be found in Ref. 38.

As already stated, a periodic structure can be described in terms of independent translation vectors, say, \mathbf{a} and \mathbf{b} , which form an angle α (Fig. 15). This means that each point of the structure is infinitely repeated at a particular distance, along the direction of the vectors \mathbf{a} and \mathbf{b} . More precisely, a lattice of points (named the Bravais lattice) can be defined

$$\mathbf{r} = l_1 \mathbf{a} + l_2 \mathbf{b} \tag{45}$$

where l_1 and l_2 are integer numbers. The translation vectors \mathbf{a} and \mathbf{b} permit us to define the unit cell of the periodic structure. It is evident that the choice of the vectors \mathbf{a} and \mathbf{b} is not unique. In fact, any linearly independent pair of vectors \mathbf{a}' and \mathbf{b}' , given by

$$\mathbf{a}' = m_1 \mathbf{a} + n_1 \mathbf{b} \tag{46}$$

$$\mathbf{b}' = m_2 \mathbf{a} + n_2 \mathbf{b} \tag{47}$$

where n_1, n_2, m_1 , and m_2 are integers, and $m_1/m_2 \neq n_1/n_2$, is still a satisfactory basis. The most common choice of primitive unit cell is the Wigner-Seitz unit cell, defined as the region of space closer to a particular point rather than to any other point of the Bravais lattice. The vectors \mathbf{a} and \mathbf{b} chosen in this way describe a lattice termed the *direct lattice*.

For each direct lattice it is possible to define a *reciprocal lattice* in the Fourier space. This is particularly important since the solution of many problems related to periodic structures is performed in the Fourier space. The reciprocal lattice is described by the vectors \mathbf{A} and \mathbf{B} , which must satisfy the following requirements:

$$\mathbf{a} \cdot \mathbf{B} = \mathbf{b} \cdot \mathbf{A} = 0 \tag{48}$$

$$\mathbf{a} \cdot \mathbf{A} = \mathbf{b} \cdot \mathbf{B} = 2\pi \tag{49}$$

Therefore, the vectors \mathbf{A} and \mathbf{B} are perpendicular to \mathbf{b} and \mathbf{a} , respectively, and their lengths are chosen in such a way

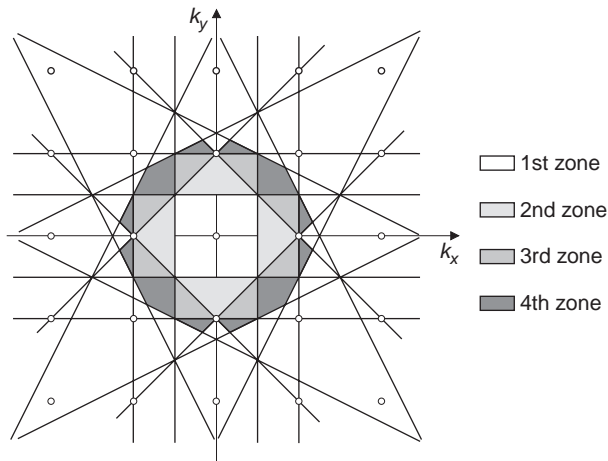


Figure 16. Graphical construction of Brillouin zones in the case of a square lattice.

that the product of corresponding vectors in the two spaces is 2π .

The Brillouin zones in the case of two-dimensional periodic structures can be obtained through a graphical method (Fig. 16); a point of the reciprocal lattice is chosen as the origin. Then, the construction is accomplished by drawing the perpendicular bisectors of reciprocal lattice vectors joining the origin to the nearest neighbors. The smallest closed polygon formed by these perpendicular bisectors represents the first Brillouin zone. In other words, the first Brillouin zone corresponds to the Wigner-Seitz cell of the reciprocal lattice.

Moving out from the origin, the upper Brillouin zones are sequentially encountered, which become increasingly fragmented. It can be easily seen by inspection that the fragments of the upper Brillouin zones can be mapped directly onto the first Brillouin zone by simple application of the translation vectors of the reciprocal lattice.

The redundancy can be further reduced by exploiting the symmetries. In a square lattice, for instance, the first Brillouin zone can be reduced to one-eighth (Fig. 17a). This smaller region, which contains no redundancy, is termed the *irreducible Brillouin zone*, and is identified by three special points: Γ (with coordinates $k_x = k_y = 0$), X (with coordinates $k_x = \pi/a$ and $k_y = 0$), and M (with coordinates $k_x = k_y = \pi/a$).

In the hexagonal lattice, the irreducible Brillouin zone is one-sixth of the first Brillouin zone (Fig. 17b). In this case, the three special points are Γ (with coordinates $k_x = k_y = 0$), M [with coordinates $k_x = 0$ and $k_y = 2\pi/(\sqrt{3}a)$], and K [with coordinates $k_x = 2\pi/(3a)$ and $k_y = 2\pi/(\sqrt{3}a)$].

Therefore, the analysis of the passband–stopband characteristics of a two-dimensional periodic structure can be performed by considering all the propagation constants in the irreducible Brillouin zone. In practice, since the band extremes of almost all the periodic structures occur at the boundary of the irreducible Brillouin zone, it is conventional to consider only the values of the propagation constant corresponding to the boundary of the irreducible Brillouin zone [39].

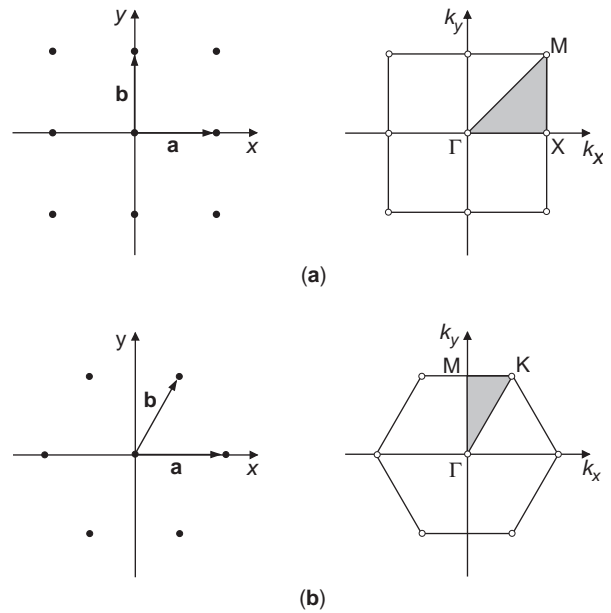


Figure 17. Direct and reciprocal lattice, with the irreducible Brillouin zone (gray region): (a) in the case of square lattice; (b) in the case of hexagonal lattice.

4. NUMERICAL TECHNIQUES FOR THE ANALYSIS OF PERIODIC STRUCTURES

The analysis of periodic structures applies to the solution of two basic modeling problems: (1) calculation of the reflected and transmitted fields, when the periodic structure is illuminated by a uniform plane wave with a given incidence angle; and (2) determination of the mode spectrum supported by the periodic structure, which is a discrete set of either propagating or leaky waves.

Analysis of these structures is usually performed under the periodicity approximation. By applying Floquet's theorem, the analysis of the complete structure reduces to investigation of the unit cell of the periodic structure, with the appropriate boundary conditions. Whichever numerical method is adopted for the analysis, this permits significant reduction of computing time.

Many numerical techniques have been developed for modeling of periodic structures. The equivalent-circuit model, discussed for certain cases in Section 2, is typically used only for a preliminary investigation, and is not accurate enough for a reliable modeling of the structure. Numerical techniques such as the integral equation method (IEM), the finite-element method (FEM), and the finite-difference time-domain (FDTD) method have been applied to the analysis of periodic structures, as well as a number of hybrid approaches, which are combinations of the aforementioned methods.

In this section, the most common numerical techniques adopted for the analysis of periodic transmission lines, frequency-selective surfaces, and electromagnetic band-gap structures are presented and briefly discussed.

4.1. Analysis of Periodic Transmission Lines

The study of the mode propagation is the basic problem in the analysis of one-dimensional periodic transmission lines. The aim of this study is the determination of the dispersion diagram, which represents the mode propagation constants versus frequency. In the case of a periodically loaded transmission line or waveguide (Fig. 1), the propagation characteristics of the modal fields can be obtained by using the \mathcal{ABCD} matrix [1].

Let us consider, as an example, a rectangular waveguide, periodically loaded with capacitive irises, whose unit cell is shown in Fig. 18a. The electric and magnetic fields on the ports of the unit cell, located at the terminal cross sections of the input and output waveguides, are expressed as a combination of N modes of the rectangular waveguide

$$\mathbf{E}_1 = \sum_{i=1}^N V_{1,i} \mathbf{e}_i \quad \mathbf{H}_1 = \sum_{i=1}^N I_{1,i} \mathbf{h}_i \quad (50)$$

$$\mathbf{E}_2 = \sum_{i=1}^N V_{2,i} \mathbf{e}_i \quad \mathbf{H}_2 = \sum_{i=1}^N I_{2,i} \mathbf{h}_i \quad (51)$$

where \mathbf{e}_i and \mathbf{h}_i are the electric and magnetic modal vectors of the rectangular waveguide, respectively, and $V_{p,i}$ and $I_{p,i}$ are the modal voltages and currents on the ports ($p = 1, 2$). The unit cell can be characterized through the \mathcal{ABCD} matrix, which relates the modal voltages and currents on the ports (Fig. 18b)

$$\begin{bmatrix} V_1 \\ I_1 \end{bmatrix} = \begin{bmatrix} \mathcal{A} & \mathcal{B} \\ \mathcal{C} & \mathcal{D} \end{bmatrix} \begin{bmatrix} V_2 \\ -I_2 \end{bmatrix} \quad (52)$$

where V_p and I_p are column vectors containing $V_{p,i}$ and $I_{p,i}$. The dispersion diagram is obtained, frequency by frequency, by imposing the periodicity of electric and magnetic fields at the ports of the unit cell. This leads to the following relation between modal voltages and currents at the ports

$$\begin{bmatrix} V_1 \\ I_1 \end{bmatrix} = e^{\gamma d} \begin{bmatrix} V_2 \\ -I_2 \end{bmatrix} \quad (53)$$

where d is the length of the unit cell (Fig. 18) and $\gamma = \alpha + j\beta$. Relation (53) is a phase shift condition when $\alpha = 0$ and an attenuation condition when $\beta = 0$. By combining (52) and (53), the following eigenvalue problem is obtained:

$$\begin{bmatrix} \mathcal{A} & \mathcal{B} \\ \mathcal{C} & \mathcal{D} \end{bmatrix} \begin{bmatrix} V_2 \\ -I_2 \end{bmatrix} = e^{\gamma d} \begin{bmatrix} V_2 \\ -I_2 \end{bmatrix} \quad (54)$$

For a given frequency, the eigenvalues of (54) give the propagation constant γ of the modes. The corresponding eigenvectors give the values of $V_{2,i}$ and $I_{2,i}$, representing the weight coefficients of the electric and magnetic fields at port 2 in terms of the modes of the rectangular waveguide.

Determination of the \mathcal{ABCD} matrix can be performed in different ways. Full-wave methods typically used for modeling waveguide components can be adopted for analysis of the unit cell. Approximated solution can also be found by using lumped-element modeling of the capacitive irises, as discussed by Collin [1].

4.2. Analysis of Frequency-Selective Surfaces

The aim of frequency-selective surface analysis is the determination of their scattering properties versus the frequency. In most cases, the analysis of FSSs is performed under the approximation of an infinite periodic array, illuminated by a uniform plane wave incident at a given angle. Under these hypotheses, the unit cell of the FSS is considered, and the analysis yields the reflection and transmission coefficients for the TE and TM fundamental Floquet modes.

A widely used approach for the analysis of FSSs is the integral equation method, which can be applied to both capacitive and inductive FSSs. Even if only capacitive FSSs are considered in this paragraph, the same approach can be applied to the analysis of inductive FSSs. The IEM is based on the formulation of an electric field integral equation, which is then solved by the method of moments (MoM) [4, Chap. 2]. Let us consider the unit cell of a capacitive FSS, consisting of a thin metallic patch printed on a dielectric substrate (Fig. 19). The transverse-to- z component of the scattered electric field is expressed in the

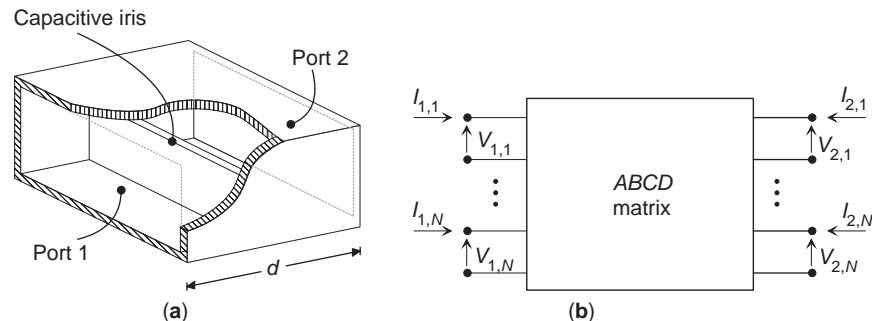


Figure 18. Unit cell of a waveguide periodically loaded with capacitive irises: (a) geometry of the unit cell considered in the analysis; (b) corresponding modeling through the \mathcal{ABCD} matrix.

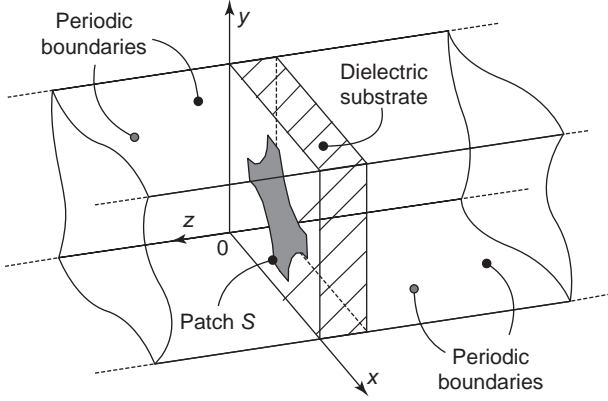


Figure 19. Unit cell of a capacitive frequency-selective surface.

form of a Green's integral

$$\begin{aligned} \mathbf{E}_{\text{scat}}^{\text{T}}(x, y, z) \\ = \int_S \underline{\mathbf{G}}(x, y, z, x', y', z') \cdot \mathbf{J}(x', y', z') dS' \end{aligned} \quad (55)$$

where \mathbf{J} is an unknown electric current density on the metallic patch, S is the surface of the patch, and $\underline{\mathbf{G}}$ is a dyadic Green function given by

$$\begin{aligned} \underline{\mathbf{G}}(x, y, z, x', y', z') \\ = \sum_{m,n} V_{mn}(z, z') \mathbf{E}_{mn}(x, y) \mathbf{E}_{mn}^*(x', y') \end{aligned} \quad (56)$$

where \mathbf{E}_{mn} denotes the transverse electric modal vector of the (m, n) th Floquet mode (TE, TM, or TEM), the asterisk denotes the complex conjugate, and function V_{mn} is determined by considering the equivalent modal transmission lines for the layered medium in the periodic cell. In the case of a metal patch located at the interface $z=0$, $V_{mn}(0, 0)$ represents the parallel of the impedance of the (m, n) th Floquet mode seen from $z=0$, looking toward the positive and to the negative directions of the z axis. By imposing the electric wall condition on the patch

$$\mathbf{E}_{\text{inc}}^{\text{T}}(x, y, 0) + \mathbf{E}_{\text{scat}}^{\text{T}}(x, y, 0) = 0 \text{ on } S \quad (57)$$

where $\mathbf{E}_{\text{inc}}^{\text{T}}$ is the transverse-to- z component of the electric field of the incident plane wave, and substituting (55) into (57), the following integral equation is obtained:

$$\begin{aligned} \mathbf{E}_{\text{inc}}^{\text{T}}(x, y, 0) \\ + \int_S \underline{\mathbf{G}}(x, y, 0, x', y', 0) \cdot \mathbf{J}(x', y', 0) dS' = 0 \text{ on } S \end{aligned} \quad (58)$$

The solution of (58) is obtained through MoM, which permits us to transform the integral equation into an algebraic matrix problem. By representing the unknown

current density \mathbf{J} as a combination of N vector basis functions \mathbf{f}_j

$$\mathbf{J}(x', y', 0) = \sum_{j=1}^N x_j \mathbf{f}_j(x', y') \quad (59)$$

and using the same set of functions as test functions, a matrix problem is obtained

$$[\mathbf{A}][\mathbf{X}] = [\mathbf{B}] \quad (60)$$

where matrices $[\mathbf{A}]$ and $[\mathbf{B}]$ have dimension $N \times N$ and $N \times 1$, respectively, and their entries are given by

$$A_{ij} = \sum_{m,n} V_{mn}(0, 0) \int_S \mathbf{f}_i(x, y) \cdot \mathbf{E}_{mn}(x, y) dS \quad (61)$$

$$\times \int_S \mathbf{f}_j(x', y') \cdot \mathbf{E}_{mn}^*(x', y') dS'$$

$$B_i = \int_S \mathbf{f}_i(x, y) \cdot \mathbf{E}_{\text{inc}}^{\text{T}}(x, y) dS \quad (62)$$

and $[\mathbf{X}]$ is the column vector of the unknown coefficients x_j . The solution of problem (60) is performed frequency by frequency and yields the unknown coefficients x_j , which are used in (59) to calculate the current density \mathbf{J} . Once \mathbf{J} is known, the transmission and reflection coefficients can be determined [4].

In the application of IEM, the choice of a suitable set of basis/test functions is a key point in the implementation of the algorithm, and has a significant impact on its performance. In fact, the dimension of matrix problem (60) is equal to the number N of basis functions used to represent \mathbf{J} , and the computing time for the solution of a matrix system increases with the square of the order of the matrix (N^2). Many authors have used subdomain basis functions (e.g., rooftops), which are piecewise linear functions defined on a small rectangular or triangular portion of S [4]. Rooftops have an analytical expression, are suited to analytically calculate the coupling integrals between basis functions and Floquet modal vectors appearing in (61), but usually a large number of rooftops are required to reach the convergence, and this leads to large matrix problems. Another possibility is the use of entire-domain basis functions, which are defined on the whole surface of patch S and satisfy the same boundary condition of \mathbf{J} on the boundary of S (i.e., they are tangential to the boundary). A set of "general-purpose" entire-domain basis functions comprises the electric modal vectors of a waveguide with a cross section S and with magnetic wall boundary condition. The use of these functions leads to more efficient algorithms, but these modal vectors are known analytically only for few canonical shapes of the cross section (e.g., rectangular and circular). Specialized entire-domain basis functions have been developed for a number of commonly used shapes (e.g., cross, tripole, and Jerusalem cross) [5],

but they are not flexible and need a customized implementation for each different patch shape. In the case of completely arbitrary shape of S , the entire-domain functions must be numerically calculated, and this requires the solution of the Helmholtz equation in S with Dirichlet or Neumann boundary conditions. Among the possible approaches, the use of the boundary integral–resonant mode expansion (BIRME) method [37,40] and FEM [41] have been recently proposed.

The efficiency of the IEM can be enhanced by improving the convergence of the series used to represent the Green function reported in (56). In fact, the basic formulation in terms of a series of Floquet modal vectors exhibits a rather slow convergence, and some hundreds of modes are typically needed. Even if the number of terms of the series is not related to the dimension of matrix $[A]$, the convergence rate of the Green function impacts the filling time of $[A]$, as evident from (61). Several methods have been proposed for accelerating the convergence of the series of the periodic Green function, based on the Ewald transformation [42], the Poisson summation formula [43], and the Shanks transformation [44].

In the case of FSSs with a complicate geometry (Fig. 20), the use of the IEM becomes unpractical, due to the problem of finding a proper expression of the Green function and a suitable set of basis functions. More flexible codes can be implemented by using the finite-element method [45,46] and the finite-difference time-domain method [47].

In FEM, the electromagnetic problem is formulated in terms of a functional, which must be minimized to find the electric and magnetic fields in the structure. The problem is solved by meshing the whole investigation volume with triangular prismatic elements, and expressing the electric field in terms of a set of edge-based expansion functions [46]. Since the scattering from FSSs is an open problem and the FEM problem must be solved in a limited domain,

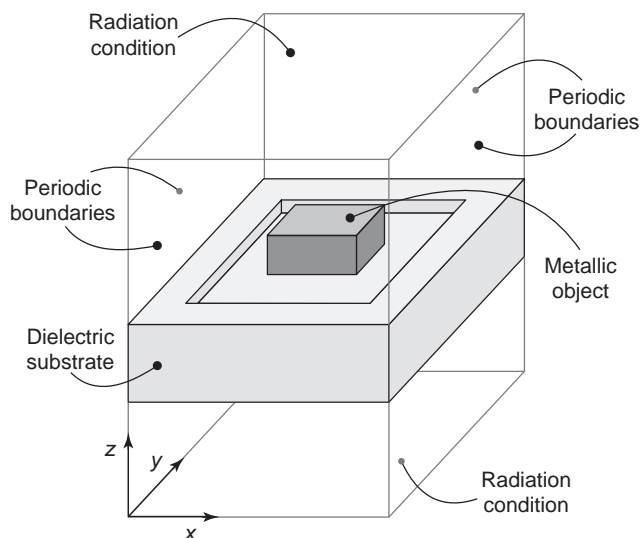


Figure 20. Unit cell of a frequency-selective surface with complicated geometry.

the investigation volume must be truncated by imposing a suitable set of boundary conditions (Fig. 20). In particular, the truncation in the x – y plane is performed by exploiting the periodicity of the structure, which turns into a phase shift relation between the fields on the opposite walls of the unit cell. On the top and bottom walls along the z direction, the domain must be truncated by imposing the radiation condition. To this aim, a possible approach is based on the perfectly matched layer (PML), a layer of artificial material that can be placed in close proximity to the FSS and can be used to absorb the scattered field [45]. Instead of using the PML, another approach consists in closing the top and bottom walls with an integral equation, resulting in a hybrid finite-element/boundary integral method [46]. The integral equation permits us to impose a rigorous boundary condition (instead of the approximate radiation condition obtained with the PML), but the resulting matrix is both partially sparse and partially dense, whereas the FEM/PML originates fully sparse matrices.

In the FDTD method [47], FSS analysis is performed by subsequent iterations in the time domain, until a steady-state is reached. The frequency response of the FSS is then obtained through a Fourier transform. Similar to the FEM, also in this case the fields must be evaluated in the whole volume of the domain, and therefore a truncation is required. The truncation in the x – y plane is performed by exploiting the periodicity of the FSS. Since the analysis is performed in the time domain, the phase shift condition turns into a time-delay condition. The truncation on the top and bottom walls along the z direction can be performed by using the absorbing boundary conditions (ABC), which simulates a radiation condition like the aforementioned PML.

With respect to the IEM, both FEM and FDTD method permit to analyze a much wider class of FSSs. Nevertheless, in the IEM the unknowns are defined only on the metallizations, whereas in both the FEM and the FDTD method volume meshing is required, resulting in a large number of unknowns. Consequently, FEM and FDTD method typically pay their flexibility with a significantly longer computing time and larger memory allocation requirements.

4.3. Analysis of Electromagnetic Bandgap Structures

The analysis of electromagnetic bandgap structures should provide two kinds of information. On the one hand, the mode spectrum of the electromagnetic waves which can propagate in the periodic structure must be determined; on the other hand, the phase of the reflection coefficient of the structure under plane-wave illumination needs to be calculated. The second problem is similar to the calculation of the frequency response of FSSs, and can be solved in the same way. Conversely, the techniques for determining the characteristics of the wave propagation are described in this section.

Most of the techniques used for the analysis of FSSs can be adapted to the calculation of the mode spectrum of EBG structures, but there is a substantial difference between the two analyses; whereas in the calculation of the

plane-wave response of FSSs the fields inside the structure are enforced by the incident plane wave, in the determination of the mode spectrum of EBG structures there are no incident fields, and therefore the analysis leads to an eigenvalue problem.

The IEM, already introduced for the calculation of the transmission and reflection properties of FSSs, can also be adopted for determining the bandgap characteristics of metallodielectric EBG structures (Figs. 7 and 8). In the case of FSSs, the boundary conditions are determined by the incident plane wave; for a given frequency and direction of incidence of the plane wave, the interelement phase shift can be calculated through (16). Conversely, in the case of EBG structures, the boundary conditions are enforced by the propagation constant of the mode propagating in the periodic structure. In practice, calculation of the dispersion diagram of EBG structures is performed by choosing a propagation constant (k_x, k_y) , which occurs at the boundary of the irreducible Brillouin zone (see Section 3), and searching the corresponding frequencies, which satisfy the fields equations and the boundary conditions in the unit cell [48]. For a given propagation constant (k_x, k_y) and frequency f , the IEM leads to the following matrix problem

$$[A][X] = [0] \quad (63)$$

where matrix $[A]$ is defined in (61), $[X]$ is the column vector of the unknown coefficients x_i used to represent the unknown current density \mathbf{J} , and $[0]$ is a column vector with the same dimension as $[X]$. Problem (63) has a non-trivial solution only if the determinant of matrix $[A]$ vanishes. In this case, the pair of the propagation constant (k_x, k_y) and the frequency f determine a point on the dispersion diagram. Since matrix $[A]$ depends on both the propagation constant and the frequency, and it is not possible to separate the two dependencies, an iteration is needed to find the dispersion diagram; for a given value of the propagation constant, the frequency is varied to search for the zeros of the determinant of $[A]$. This procedure is repeated for any value of the propagation constant that belongs to the boundary of the irreducible Brillouin zone.

When EBG structures with complicated geometry are considered (like a fully three-dimensional structure), the IEM method can still be applied. In this case, however, a volume integral equation is required, which can be solved by MoM [49]. This leads to large, fully dense matrix problems, which are typically computationally inefficient.

The FEM approach has been used for the modeling of EBG components [50,51]. Its formulation is similar to the one described in the case of FSSs. In order to truncate the analysis domain, both the PML and the integral equation have been adopted. Besides the advantages and disadvantages already discussed for the two truncation approaches, there is a further important difference in this case. In fact, the FEM/PML approach permits to determine the bandgap properties of the structure through the solution of a single-eigenvalue problem for each value of the propagation constant, with no need of a

frequency loop [51]. Conversely, when using the FEM in conjunction with the integral equation, the matrix equation must be repeatedly solved, in order to search for the desired frequency [50], similar to the case of the IEM.

Finite-difference methods have also been proposed in both the time and frequency domains (FDTD [52] and FDFD [53], respectively). Application of the FDTD method to the analysis of EBG structures [52] is similar to the approach described for modeling of FSSs, and the Fourier transform of the steady-state solution yields a peak at those frequencies that are close to the frequency of an eigenmode. The finite-difference methods provide high flexibility in the geometry of the components, but are usually very time-consuming.

Acknowledgment

The author wishes to thank Prof. Luca Perregrini from the University of Pavia (Pavia, Italy) for his useful suggestions and for the final revision of the manuscript.

BIBLIOGRAPHY

1. R. E. Collin, *Foundation for Microwave Engineering*, McGraw-Hill, New York, 1992.
2. P. M. Lapostolle and A. L. Septier, *Linear Accelerators*, North Holland, Amsterdam, 1970.
3. P. F. Goldsmith, *Quasioptical Systems: Gaussian Beam Quasioptical Propagation and Applications*, IEEE Press, New York, 1998.
4. T. K. Wu, *Frequency Selective Surface and Grid Array*, Wiley, New York, 1995.
5. R. Mittra, C. H. Chan, and T. Cwik, Techniques for analyzing frequency selective surfaces—a review, *Proc. IEEE* **76**(12):1593–1615 (Dec. 1988).
6. M. Bozzi, L. Perregrini, J. Weinzierl, and C. Winnewisser, Design, fabrication and measurement of frequency selective surfaces, *Opt. Eng.* **39**(8):2263–2269 (Aug. 2000).
7. P. Besso, M. Bozzi, L. Perregrini, L. Salghetti Drioli, and W. Nickerson, Deep space antenna for Rosetta mission: Design and testing of the S/X-band dichroic mirror, *IEEE Trans. Anten. Propag.* **AP-51**(3):388–394 (March 2003).
8. B. A. Munk, *Frequency Selective Surfaces: Theory and Design*, Wiley-Interscience, New York, 2000.
9. *IEEE Trans. Anten. Propag.* **AP-51**(10) (special issue on metamaterials) (Oct. 2003).
10. A. A. Oliner, Periodic structures and photonic-band-gap terminology: Historical perspectives, *Proc. 29th European Microwave Conf.*, Munich, Germany, 1999, Vol. 3, pp. 295–298.
11. E. Yablonovitch, Inhibited spontaneous emission in solid-state physics and electronics, *Phys. Rev. Lett.* **58**(20):2059–2062 (May 1987).
12. E. Yablonovitch, Photonic band-gap structures, *J. Opt. Soc. Am. B* **10**(2):283–295 (Feb. 1993).
13. H. S. Sozuer and J. P. Dowling, Photonic band calculations for woodpile structures, *J. Modern Opt.* **41**(2):231–239 (Feb. 1994).
14. D. Sievenpiper, L. Zhang, R. F. Jimenez Broas, N. G. Alexopolous, and E. Yablonovitch, High-impedance electromag-

- netic surfaces with a forbidden frequency band, *IEEE Trans. Microwave Theory Tech.* **MTT-47**(11):2059–2074 (Nov. 1999).
15. F.-R. Yang, K.-P. Ma, Y. Qian, and T. Itoh, A uniplanar compact photonic-bandgap (UC-PBG) structure and its applications for microwave circuits, *IEEE Trans. Microwave Theory Tech.* **MTT-47**(8):1509–1514 (Aug. 1999).
 16. D. M. Pozar, Considerations for millimeter wave printed antennas, *IEEE Trans. Anten. Propag.* **AP-33**(9):740–747 (Sept. 1983).
 17. R. Gonzalo, P. de Maagt, and M. Sorolla, Enhanced patch-antenna performance by suppressing surface waves using photonic-bandgap substrates, *IEEE Trans. Microwave Theory Tech.* **MTT-47**(11):2131–2138 (Nov. 1999).
 18. F.-R. Yang, K.-P. Ma, Y. Qian, and T. Itoh, A novel TEM waveguide using uniplanar compact photonic-bandgap (UC-PBG) structure, *IEEE Trans. Microwave Theory Tech.* **MTT-47**(11):2092–2098 (Nov. 1999).
 19. M. Belaid and K. Wu, Spatial power amplifier using a passive and active TEM waveguide concept, *IEEE Trans. Microwave Theory Tech.* **MTT-51**(3):684–689 (March 2003).
 20. T. Lopetegi, M. A. G. Laso, M. J. Erro, M. Sorolla, and M. Thumm, Analysis and design of periodic structures for microstrip lines by using the coupled mode theory, *IEEE Microwave Wireless Compon. Lett.* **12**(11):441–443 (Nov. 2002).
 21. V. Radisic, Y. Qian, Member, and T. Itoh, Broad-band power amplifier using dielectric photonic bandgap structure, *IEEE Microwave Guided Wave Lett.* **8**(1):13–14 (Jan. 1998).
 22. V. G. Veselago, The electrodynamic of substances with simultaneously negative values of ϵ and μ , *Sov. Phys. Uspekhi* **10**(4):509–514 (Jan.–Feb. 1968).
 23. R. A. Shelby, D. R. Smith, and S. Schultz, Experimental verification of a negative index of refraction, *Science* **292**:77–79 (April 2001).
 24. J. B. Pendry, Negative refraction makes a perfect lens, *Phys. Rev. Lett.* **85**(18):3966–3969 (Oct. 2000).
 25. N. Engheta, An idea for thin subwavelength cavity resonators using metamaterials with negative permittivity and permeability, *IEEE Anten. Wireless Propag. Lett.* **1**:10–13 (2002).
 26. R. A. York and Z. B. Popovic, *Active and Quasi-Optical Arrays*, Wiley, New York, 1997.
 27. A. Moussessian, M. C. Wanke, Yongjun Li, Jung-Chih Chiao, J. S. Allen, T. W. Crowe, and D. B. Rutledge, A terahertz grid frequency doubler, *IEEE Trans. Microwave Theory Tech.* **MTT-46**(11):1976–1981 (Nov. 1998).
 28. J. B. Hacker, R. M. Weikle II, M. Kim, M. P. De Lisis, and D. B. Rutledge, A 100-element planar Schottky diode grid mixer, *IEEE Trans. Microwave Theory Tech.* **MTT-40**(3):557–562 (March 1992).
 29. M. Kim, E. A. Sovero, J. B. Hacker, M. P. DeLisis, Jung-Chih Chiao, Shi-Jie Li, D. R. Gagnon, J. J. Rosenberg, and D. B. Rutledge, A 100-element HBT grid amplifier, *IEEE Trans. Microwave Theory Tech.* **MTT-41**(10):1762–1771 (Oct. 1993).
 30. W. W. Lam, H. Z. Chen, K. S. Stolt, C. F. Jou, N. C. Luhmann, Jr., and D. B. Rutledge, Millimeter-wave diode grid phase shifters, *IEEE Trans. Microwave Theory Tech.* **MTT-36**(5):902–907 (May 1988).
 31. B. Jongsuck, Y. Aburakawa, H. Kondo, T. Tanaka, and K. Mizuno, Millimeter and submillimeter wave quasi-optical oscillator with Gunn diodes, *IEEE Trans. Microwave Theory Tech.* **MTT-41**(10):1851–1855 (Oct. 1993).
 32. J. W. Mink, Quasi-optical power combining of solid-state millimeter-wave source, *IEEE Trans. Microwave Theory Tech.* **MTT-34**(2):273–279 (Feb. 1986).
 33. G. Floquet, Sur les équations différentielles linéaires à coefficients périodiques (Linear differential equations with periodic coefficients), *Ann. École Norm. Sup.* **12**:47–88 (1883).
 34. F. Bloch, Über die Quantenmechanik der Electronen in Kristallgittern (Quantum mechanics of electrons in crystal lattices), *Z. Physik* **52**:555–600 (1928).
 35. N. Amitai, V. Galindo, and C. P. Wu, *Theory and Analysis of Phased Array Antennas*, Wiley-Interscience, New York, 1972.
 36. L. B. Felsen and N. Marcuvitz, *Radiation and Scattering of Waves*, Prentice-Hall, Englewood Cliffs, NJ, 1973.
 37. M. Bozzi, L. Perregrini, J. Weinzierl, and C. Winnewisser, Efficient analysis of quasi-optical filters by a hybrid MoM/BI-RME method, *IEEE Trans. Anten. Propag.* **AP-49**(7):1054–1064 (July 2001).
 38. L. Brillouin, *Wave Propagation in Periodic Structures; Electric Filters and Crystal Lattices*, 2nd ed., Dover, New York, 1953.
 39. J. Joannopoulos, R. Meade, and J. Winn, *Photonic Crystals: Molding the Flow of Light*, Princeton Univ. Press, Princeton, NJ, 1995.
 40. M. Bozzi and L. Perregrini, Analysis of multilayered printed frequency selective surfaces by the MoM/BI-RME method, *IEEE Trans. Anten. Propag.* **AP-51**(10):2830–2836 (Oct. 2003).
 41. W. A. Imbriale, Analysis of a thick dichroic plate with arbitrarily shaped holes, *IPN Progress Report*, Jet Propulsion Lab, Pasadena, CA, Aug. 2001.
 42. K. E. Jordan, G. R. Richter, and P. Sheng, An efficient numerical evaluation of the Green's function for the Helmholtz operator on periodic structures, *J. Comput. Phys.* **63**:222–235 (1986).
 43. R. E. Jorgenson and R. Mittra, Efficient calculation of the free-space periodic Green's function, *IEEE Trans. Anten. Propag.* **AP-38**(5):633–642 (May 1990).
 44. S. Singh, W. F. Richards, J. R. Zinecker, and D. R. Wilton, Accelerating the convergence of series representing the free space periodic Green's function, *IEEE Trans. Anten. Propag.* **AP-38**(12):1958–1962 (Dec. 1990).
 45. I. Bardi, R. Remski, D. Perry, and Z. Cendes, Plane wave scattering from frequency-selective surfaces by the finite-element method, *IEEE Trans. Magn.* **MAG-38**(2):641–644 (March 2002).
 46. T. F. Eibert, J. L. Volakis, D. R. Wilton, and D. R. Jackson, Hybrid FE/BI modeling of 3-D doubly periodic structures utilizing triangular prismatic elements and an MPIE formulation accelerated by the Ewald transformation, *IEEE Trans. Anten. Propag.* **AP-47**(5):843–850 (May 1999).
 47. P. Harms, R. Mittra, and Ko Wai, Implementation of the periodic boundary condition in the finite-difference time-domain algorithm for FSS structures, *IEEE Trans. Anten. Propag.* **AP-42**(9):1317–1324 (Sept. 1994).
 48. H. D. Yang, R. Kim, and D. R. Jackson, Design consideration for modelless integrated circuit substrates using planar periodic patches, *IEEE Trans. Microwave Theory Tech.* **MTT-48**(12):2233–2239 (Dec. 2000).
 49. H. D. Yang, Characteristics of guided and leaky waves on multilayer thin-film structures with planar material gratings, *IEEE Trans. Microwave Theory Tech.* **MTT-45**(3):428–435 (March 1997).

50. L. Zhang and N. G. Alexopoulos, Finite-element based technique for the modeling of PBG materials, *Electromagnetics* **19**(3):225–239 (May–June 1999).
51. L. Zhang, *Numerical Characterization of Electromagnetic Band-Gap Materials and Applications in Printed Antennas and Arrays*, Ph.D. thesis, Univ. California, Los Angeles, 2000.
52. R. Coccioli, F.-R. Yang, K.-P. Ma, and T. Itoh, Aperture-coupled patch antenna on UC-PBG substrate, *IEEE Trans. Microwave Theory Tech.* **MTT-47**(11):2123–2130 (Nov. 1999).
53. H. D. Yang, Finite difference analysis of 2-D photonic crystals, *IEEE Trans. Microwave Theory Tech.* **MTT-44**(12):2688–2695 (Dec. 1996).

PERMITTIVITY AND MEASUREMENTS

V. KOMAROV
 S. WANG
 J. TANG
 Washington State University

1. INTRODUCTION

Propagation of electromagnetic (EM) waves in radio frequency (RF) and microwave systems is described mathematically by Maxwell's equations with corresponding boundary conditions. Dielectric properties of lossless and lossy materials influence EM field distribution. For a better understanding of the physical processes associated with various RF and microwave devices, it is necessary to know the dielectric properties of media that interact with EM waves. For telecommunication and radar devices, variations of complex dielectric permittivity (referring to the dielectric property) over a wide frequency range are important. For RF and microwave applicators intended for thermal treatments of different materials at ISM (industrial, scientific, medical) frequencies, one needs to study temperature and moisture content dependencies of the permittivity of the treated materials.

Many techniques have been developed for the measurement of material permittivity. Some general descriptions of those methods are provided in the literature [1–4]. The measurement results for diverse dielectric media are compiled in the literature [5–7].

The objective of this article is to provide a brief description of basic physical theory for the measurement of permittivity associated with three popular experimental methods and to review the permittivities for different materials. Most of these data are taken from the literature, but some of permittivity data were measured in Biological Systems Engineering Department of Washington State University. The measurements were conducted by means of open-ended coaxial probe method with commercial instrumentation.

2. THEORY OF PERMITTIVITY

Permittivity is a quantity used to describe dielectric properties that influence reflection of electromagnetic waves at interfaces and the attenuation of wave energy within materials. In frequency domain, the complex relative permittivity ϵ^* of a material to that of free space can be expressed in the following form:

$$\epsilon^* = \epsilon' - j\epsilon'' \quad (1)$$

The real part ϵ' is referred to as the *dielectric constant* and represents stored energy when the material is exposed to an electric field, while the dielectric loss factor ϵ'' , which is the imaginary part, influences energy absorption and attenuation, and $j = \sqrt{-1}$. One more important parameter used in EM theory is a tangent of loss angle: $\tan \delta_e = \epsilon''/\epsilon'$. Mechanisms that contribute to the dielectric loss in heterogeneous mixtures include polar, electronic, atomic, and Maxwell–Wagner responses [7]. At RF and microwave frequencies of practical importance and currently used for applications in material processing (RF 1–50 MHz and microwave frequencies of 915 and 2450 MHz), ionic conduction and dipole rotation are dominant loss mechanisms [8]:

$$\epsilon'' = \epsilon''_d + \epsilon''_\sigma = \epsilon''_d + \frac{\sigma}{\epsilon_0 \omega} \quad (2)$$

where subscripts “d” and “ σ ” stand for contributions due to dipole rotation and ionic conduction, respectively; σ is the ionic conductivity in S/m of a material, ω is the angular frequency in rad/s, and ϵ_0 is the permittivity of free space or vacuum (8.854×10^{-12} F/m). Dielectric lossy materials convert electric energy at RF and microwave frequencies into heat. The increase in temperature (ΔT) of a material can be calculated from [9]

$$\rho C_p \frac{\Delta T}{\Delta t} = 5.563 \times 10^{-11} f E^2 \epsilon'' \quad (3)$$

where C_p is the specific heat of the material in $\text{J kg}^{-1} \text{ }^\circ\text{C}^{-1}$, ρ is the density of the material in kg/m^3 , E is the electric field intensity in V/m, f is the frequency in Hz, Δt is the time duration in seconds, and ΔT is the temperature rise in the material in $^\circ\text{C}$. It is clear from Eq. (3) that the rise in temperature is proportional to the material's dielectric loss factor, in addition to electric field intensity squared, frequency, and treatment time.

In dielectric materials, the electric field strength decreases with distance z from the surface and is written as

$$E = E_0 e^{-\alpha z} \quad (4)$$

The attenuation factor α depends on the dielectric properties of the material [5] and is given by

$$\alpha = \frac{2\pi}{\lambda_0} \left[\frac{1}{2} \epsilon' \left(\sqrt{1 + \left(\frac{\epsilon''}{\epsilon'} \right)^2} - 1 \right) \right]^{1/2} \quad (5)$$

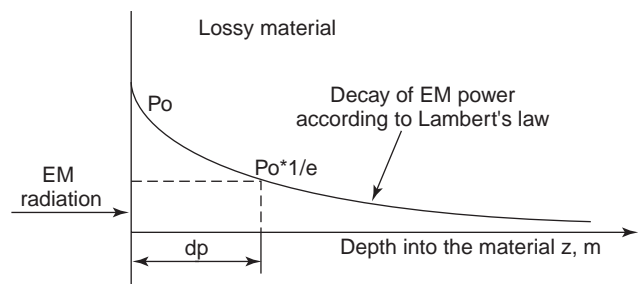


Figure 1. Typical penetration depth inside a large-sized material (larger than the wavelength).

where λ_0 is the free-space wavelength. Substituting Eq. (4) into power equation Eq. (3), one obtains

$$P = P_0 e^{-2\alpha z} \tag{6}$$

Penetration depth of microwave and RF power is defined as the depth where the power is reduced to $1/e$ ($e = 2.718$) of the power entering the surface (Fig. 1). The penetration depth d_p in meters of RF and microwave energy in a lossy material can be calculated by [5]

$$d_p = \frac{c}{2\pi f \sqrt{2\epsilon' \left[\sqrt{1 + \left(\frac{\epsilon''}{\epsilon'}\right)^2} - 1 \right]}} \tag{7}$$

where c is the speed of light in free space (3×10^8 m/s). After obtaining the dielectric properties, the penetration depths of electromagnetic energy into selected materials can be calculated at the required frequency. Given fixed dielectric properties, the penetration depth of a material is inversely proportional to frequency. It is, therefore, expected that in general deeper penetration corresponds to lower frequencies, and that higher frequencies result in greater surface heating. It should be noted that the

dielectric properties of lossy materials vary with frequency but penetration depth does not vary exactly as $1/f$. Nevertheless, EM waves with short wavelength do not penetrate deeply into most moist media [7], where the dielectric constants and loss factors are relatively high.

2.1. Frequency Effect

Dielectric properties of materials are affected by many factors, including frequency, temperature, and moisture content. Dielectric properties can vary significantly with frequency, which will be discussed in detail in this section. The frequency-dependent trend of dielectric properties can provide important information of the material characteristics. In theory, electric conduction and various polarization mechanisms (including dipole, electronic, ionic, and Maxwell–Wagner) contribute to the dielectric loss factor (Fig. 2). For moist dielectric materials ionic conductivity plays a major role at lower frequencies (e.g., < 200 MHz), whereas both ionic conductivity and dipole rotation of free water play a combined role at microwave frequencies. Maxwell–Wagner polarization arises from buildup of charges in the interface between components in heterogeneous systems. The Maxwell–Wagner polarization effect peaks at about 0.1 MHz [7], but in general, its contribution is small compared to that of ionic conductivity. For low-moisture media, bound water plays a major role in dielectric heating in the frequency range between 20 and 30 GHz [10,11] at room temperature (20°C) [12].

For a pure liquid, the Debye model [13] describes the frequency-dependent dielectric properties in the rectangular form

$$\epsilon^* = \epsilon_\infty + \frac{\epsilon_s - \epsilon_\infty}{1 + \omega^2 \tau^2} - j \frac{(\epsilon_s - \epsilon_\infty) \omega \tau}{1 + \omega^2 \tau^2} \tag{8}$$

where ϵ_∞ is the infinite or high frequency relative permittivity, ϵ_s is the static or zero-frequency relative permittivity, and τ is the relaxation time in seconds of the material. In general, the larger the molecules, the longer

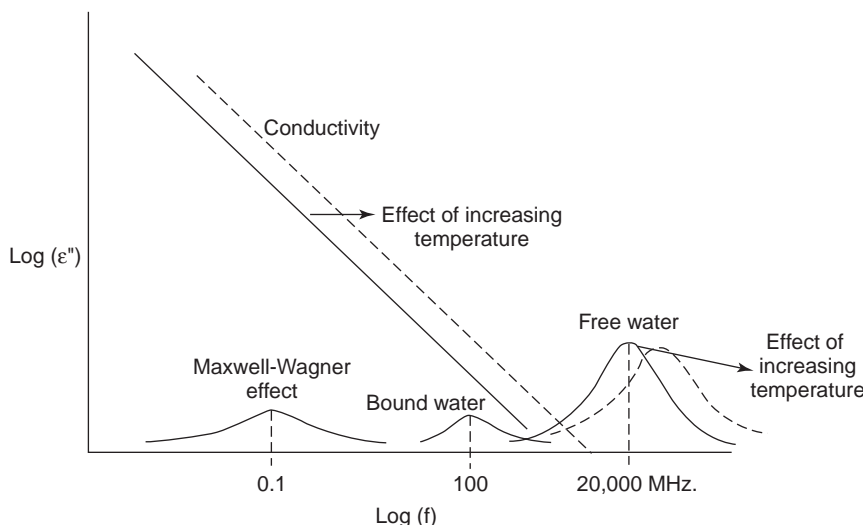


Figure 2. Contributions of various mechanisms of the loss factor (ϵ'') of moisture materials as a function of frequency (f) [12].

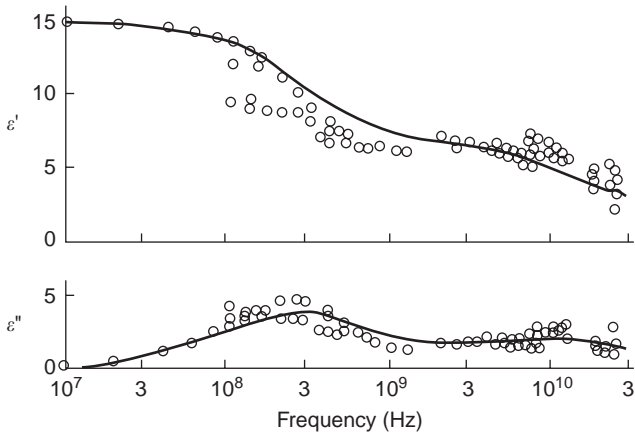


Figure 3. Dielectric constant (ϵ') and loss factor (ϵ'') as a function of frequency for packed lysozyme samples containing nearly two layers of bound water at 25°C [10].

the relaxation time. For a pure liquid, such as water, the dielectric loss factor reaches the maximum at a critical frequency related to the relaxation time ($f_c = 1/2\pi\tau$). Water molecules are polar, and the most important constituent that contributes to the dielectric properties of moist dielectrics. Water molecules bound to the surface of polar materials in monolayers or multilayers have much longer relaxation times than do free water molecules. For example, the relaxation time of bound water in different food materials at 20°C is determined to be between 0.98 and 2.00 ns, corresponding to a peak in ϵ'' at ~ 100 MHz, whereas the relaxation time τ of free water in those foods at 20°C is between 0.0071 and 0.00148 ns, corresponding to a peak in ϵ'' at around 16000 MHz [14]. Harvey and Hoekstra [10] found that ϵ'' of monolayer bound water in lysozyme at 25°C peaked at 300 MHz and ϵ'' for the second layer bound water peaked at about 10000 MHz. The two dispersions observed in Fig. 3 correspond to the first and second layers of bound water, respectively.

Figure 4 shows a good example of Debye dielectric relaxation for butyl alcohol at 20°C with single relaxation time measured with an open-ended coaxial probe connect-

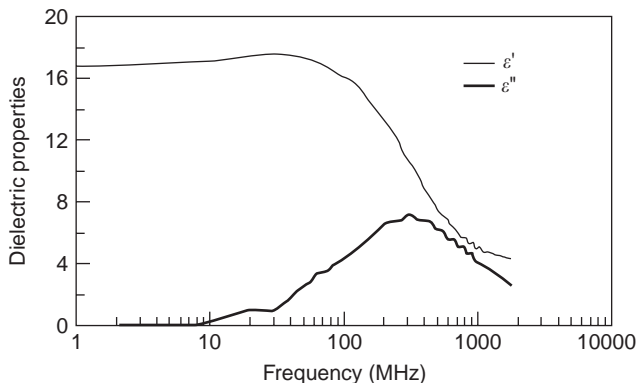


Figure 4. Dielectric constant (ϵ') and loss factor (ϵ'') of butyl alcohol at 20°C [19].

ed to an impedance analyzer [19]. At low frequencies, in a static region, where the dipoles have time to follow the variations of the applied field, the dielectric constant of butyl alcohol has a value of ~ 17 . The loss factor is small for both high and low frequencies and reaches a peak at the relaxation frequency of ~ 250 MHz.

Similar frequency-dependent permittivity can be found in water, methanol, and ethanol and can be expressed in the following relationships, respectively [15]:

$$\begin{aligned}\epsilon^* &= 5.62 + \frac{74.59}{1 + jf/17.0 \times 10^9} \text{ (water)} \\ \epsilon^* &= 5.76 + \frac{27.89}{1 + jf/2.709 \times 10^9} \text{ (methanol)} \\ \epsilon^* &= 4.44 + \frac{20.84}{1 + jf/0.826 \times 10^9} \text{ (ethanol)}\end{aligned}\quad (9)$$

Frequency-dependent characteristics of complex biological materials, including moist foods, cannot be described with simple mathematical expressions.

2.2. Temperature Effect

Temperature of a material has a significant effect on the dielectric properties. Generally, the loss factor increases with increasing temperature at low frequencies due to ionic conductance and decreases with increasing temperature at high frequencies due to free-water dispersion (Fig. 2). In multidispersion materials, for example, the transition is gradual because of the combined effects of relaxation and the ionic conduction and there is a U-shape frequency response in ϵ'' (Fig. 6). Debye related the relaxation time for the spherical molecule to viscosity and temperature as the result of randomizing agitation of the Brownian movement [5]

$$\tau = V \frac{3\nu}{kT} \quad (10)$$

where ν is the viscosity, T is the absolute temperature, V is the volume, and k is a constant. For nonspherical water molecules, we may have the following relation

$$\tau \propto \frac{\nu}{T} \quad (11)$$

while the viscosity of all fluid decreases with increasing temperature [16]

$$\nu = \nu_0 e^{E_a/R_g T} \quad (12)$$

where E_a is activation energy and R_g is the universal gas constant. Therefore, as temperature rises, relaxation time for water decreases. The shifting of the relaxation time toward a lower value (thus the frequency at the maximum ϵ'' shifts toward a higher value as temperature increases) reduces the value of ϵ'' for water at a fixed microwave frequency (Fig. 5). For example, as the relaxation time τ decreases with increasing temperature, the dispersion peak moves to higher frequencies and the loss factor of

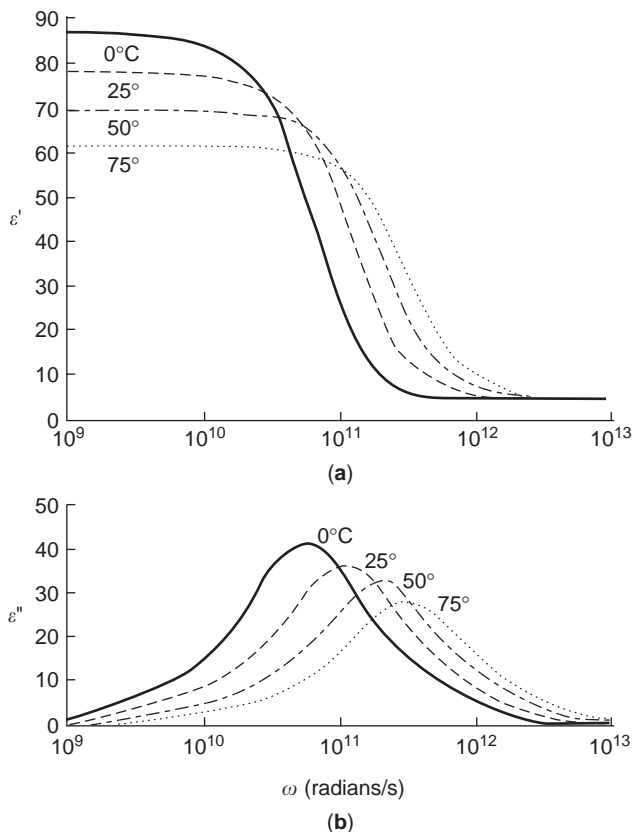


Figure 5. Effect of temperature on dielectric constant (ϵ') and loss factor (ϵ'') of free water ($\omega = 2\pi f$, where f is frequency in Hz) [22].

pure water at 2450 MHz decreases with increasing temperature. The dielectric constant ϵ' of free water also decreases with increasing temperature as the result of increased Brownian movement.

The dielectric loss factor ϵ''_{σ} due to conduction decreases with increasing frequency as shown in Eq. (2). The

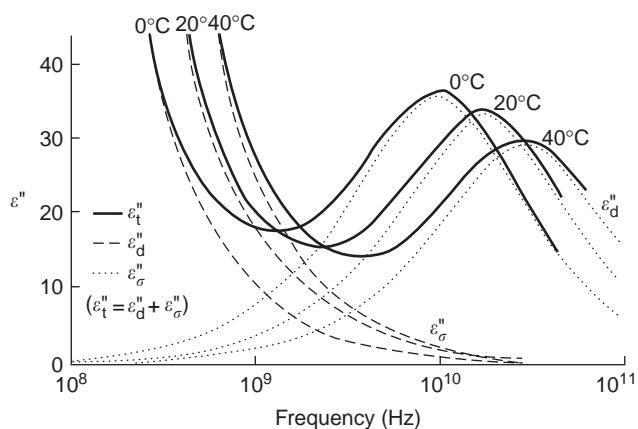


Figure 6. Effect of temperature on dielectric loss factor (ϵ'') of 0.5N aqueous sodium chloride at three temperatures [18].

contribution of ϵ''_{σ} to the overall loss factors is smaller at 2450 MHz than at 915 Hz (Fig. 6). The electric conductivity σ in ionic solutions increases with temperature due to decreased viscosity and hence increased ion mobility [17]. Therefore, based on Eq. (2), ϵ''_{σ} also increases with temperature (Fig. 6). At 915 MHz the dielectric constant of ionic solutions generally increases with temperature.

The dielectric properties of high-moisture-content substances change with temperature [19]. An example of the dielectric loss factor (ϵ'') of fifth-instar codling moths measured at five temperatures is shown in Fig. 7. The loss factor decreases with increasing frequency, reaching about 12 at 1800 MHz. The loss factor of codling moth larvae increases with temperature, especially at low frequencies. This is due mainly to the increase in ionic conduction at high temperatures [12]. Increasing dielectric loss factor with temperature often results in a well-known phenomenon, commonly referred to as “thermal runaway” [7], in which a preferentially heated subject in an EM field accelerates heating as its temperature rises.

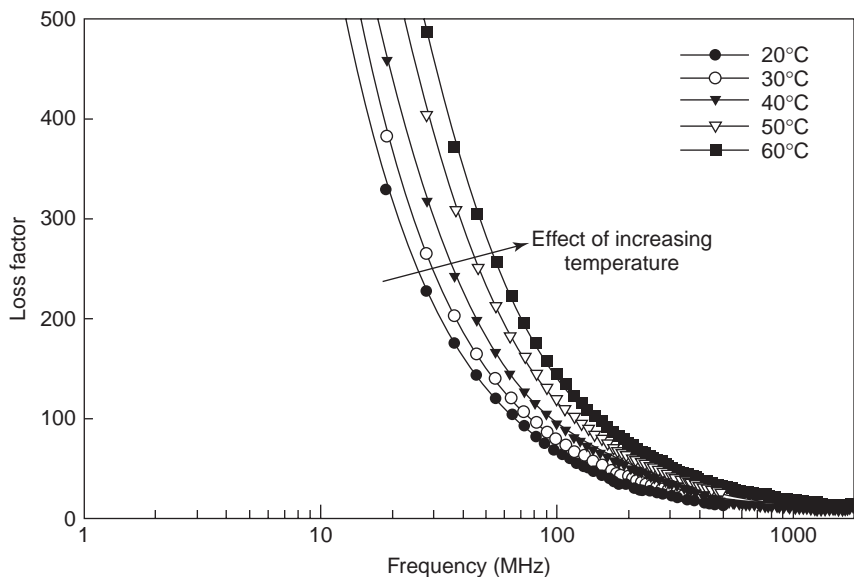


Figure 7. Dielectric loss factor of codling moth larvae (slurry) at five temperatures [19].

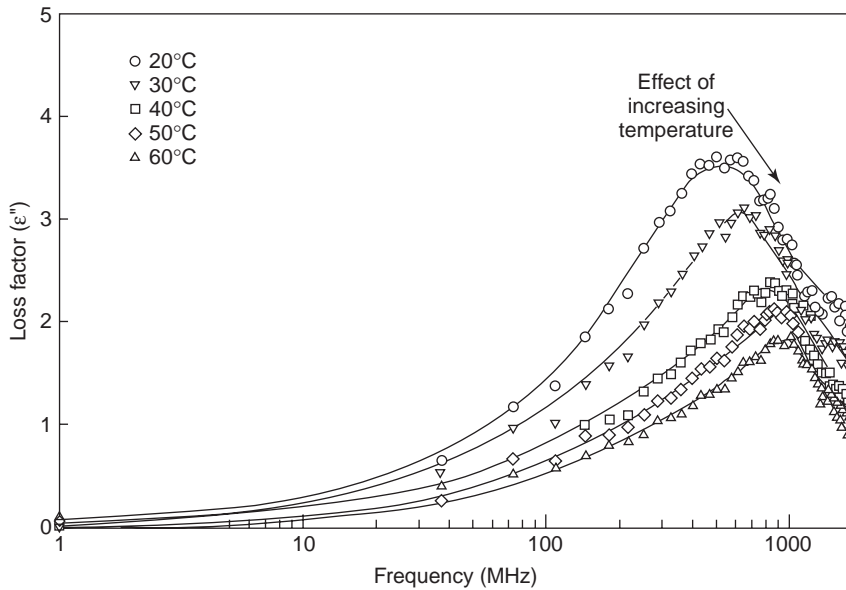


Figure 8. Dielectric loss factor of walnut kernels as a function of frequency at five temperatures [19].

Figure 8 shows the loss factor of a typical dry nut (walnut kernels) over the frequency range from 1 to 1800 MHz at five temperatures. The ϵ'' values are less than 1 at frequencies below 50 MHz. The ϵ'' values peak in the range between 500 and 1000 MHz. The peak value of ϵ'' for walnut kernels decreases with increasing temperature, while the frequency corresponding to the peak ϵ'' shifts to a higher value. This temperature-dependent trend is typical of polar molecules [20]. At any selected frequency in the tested range, the loss factor of the walnut kernel generally decreases with increasing temperature; that is, for a given EM field intensity, higher temperature walnuts will absorb less energy than cooler ones, resulting in improved heating uniformity.

Ice is almost transparent to microwaves (Table 1). When a lossy material is frozen, both dielectric constant and loss factor are significantly reduced; the degree of reduction depends, to a large extent, on the amount of water in the unfrozen state and the ionic conductivity of the free water.

2.3. Moisture Effect

Moisture content is one of the major components of most biological materials. In general, the higher the moisture content, the larger the dielectric constant and loss factor of the materials [20, 22, 23]. Water in moist dielectric materials can be divided, in descending mobility, into (1) water held in intercellular space or capillaries, (2) multilayer

water, and (3) monolayer water that is tightly bound to the polar sites. The free-water molecules have dielectric properties similar to those of liquid water, while the bound water exhibits icelike dielectric properties. Dielectric properties of biomaterials, in general, decrease rapidly with decreasing moisture content to a critical moisture level. Below this moisture level, the reduction in loss factor is less significant because of the bound water (Fig. 9). During microwave drying, the wetter parts of biomaterials

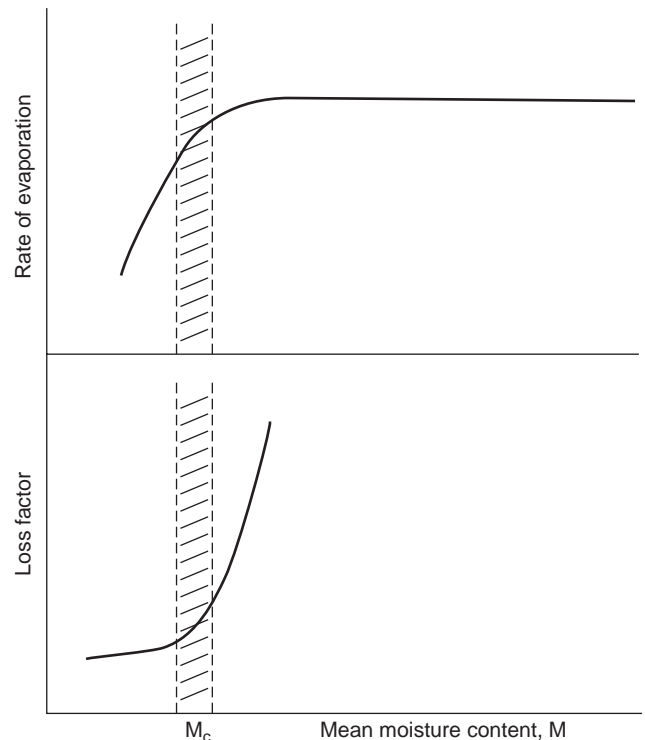


Figure 9. Rate of evaporation and dielectric loss factor as affected by food moisture content [7].

Table 1. Dielectric Properties of Water and Ice at 2450 MHz

State of Water	Relative Dielectric Constant (ϵ')	Loss Factor (ϵ'')	Loss Tangent ($\tan \delta$)
Water (25°C)	78	12.5	0.16
Ice	3.2	0.0029	0.0009

Source: Ref. 21.

absorb more microwave energy and tend to level off the uneven moisture distribution.

3. MEASUREMENT PRINCIPLES AND METHODS

3.1. Open-Ended Coaxial Probe Method

Open-ended coaxial probe (OCP) method is currently one of the most popular techniques for measuring of complex dielectric permittivity of many materials. Nondestructive, broadband (RF and microwave ranges), and high-temperature ($\leq 1200^\circ\text{C}$) measurements can be performed with this method using commercially available instrumentation. Its well-developed theory makes it possible to obtain sufficiently accurate results for both medium-loss and high-loss media [24–26].

Figure 10 illustrates an OCP system used at Washington State University. It consists of an automatic network analyzer (ANA) with a calibration kit, custom-built test cell, a programmable circulator, a coaxial cable, and a personal computer connected to the ANA through a special bus. The material under study is placed in a stainless steel pressureproof test cell. The probe is kept in close contact with the sample during the measurements via a stainless steel spring and piston. A thin rigid stainless steel thermocouple probe passes onto the center of the sample to measure sample temperature. The programmable circulator pumps a temperature-controlled liquid (90% ethylene glycol and 10% water by volume) through the water jacket of the test cell, allowing the sample inside to be heated and cooled.

The sensing element of an OCP system is an open-ended cylindrical coaxial line that is excited by transverse electromagnetic (TEM) wave. Parameters (amplitude and phase) of incident and reflected signals are detected by the ANA. The complex dielectric permittivity is determined according to the reflected coefficient ($\Gamma = \Gamma' - j\Gamma''$) as follows [27]

$$\begin{aligned}\varepsilon' &= (A_{ef})^{-1} \left\{ \frac{-2\Gamma''}{(1 + \Gamma')^2 + \Gamma''^2} \right\}; \\ \varepsilon'' &= (A_{ef})^{-1} \left\{ \frac{1 - \Gamma'^2 - \Gamma''^2}{(1 + \Gamma')^2 + \Gamma''^2} \right\}\end{aligned}\quad (13)$$

where A_e is the empirical coefficient dependent on characteristic impedance of the probe and sample size. In order to eliminate the influence of reflections caused by transmission-line discontinuities, a calibration procedure is utilized. The EM characteristics of the measurement system are analyzed using three standard terminations (open, short, and $50\ \Omega$). Then any material with well-known dielectric properties such as deionized water, for example, is tested. The actual reflection coefficient differs from reflection coefficient measured using ANA (Γ_m) [25]

$$\Gamma = \frac{\Gamma_m - a_{11}}{a_{22}(\Gamma_m - a_{11}) + a_{12}} \quad (14)$$

where a_{11} is the directivity error, a_{12} is the frequency response error, a_{22} is the source match error. Taking into account propagation constant (γ) and distance from the connector to the probe head (z) we can calculate a_{ij} in terms of S parameters of the connector:

$$a_{11} = S_{11}; a_{12} = S_{12}S_{21}e^{-2\gamma z}; a_{22} = S_{22}e^{-2\gamma z} \quad (15)$$

In the inverse coaxial probe model, it is assumed that a sample has a semiinfinite size. A few additional conditions must be satisfied to avoid measurement error in the OCP method:

- Minimize thermal expansion of both conductors of coaxial line at high temperatures.
- Intimate contact between the probe and the sample; liquid sample may flush the probe and the surface roughness of solid sample should be less than $0.5\ \mu\text{m}$ [28].
- Minimize disturbance caused by temperature, vibration, or any other external factors after calibration and during measurement.

The OCP method is very well suited for liquids or soft solid samples. It is accurate, fast, and broadband (from 0.2 to up to 20 GHz). The measurement requires little sample preparation. A major disadvantage of this method is that it is not suitable for measuring materials with low dielectric property (plastics, oils, etc.).

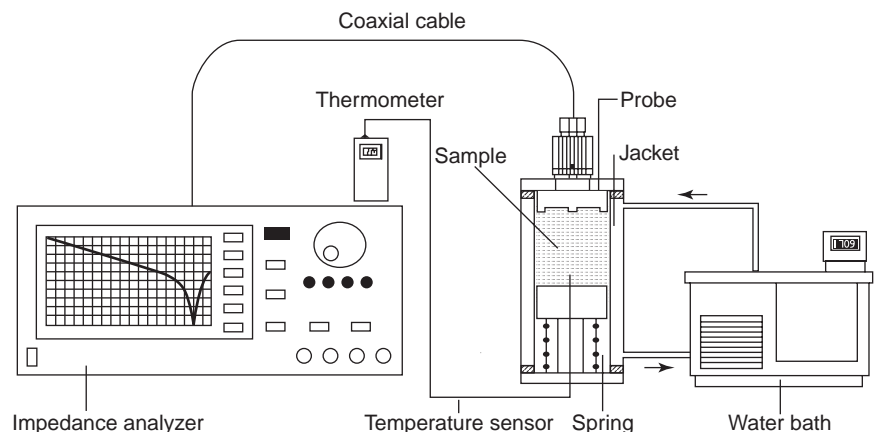


Figure 10. Schematic diagram of experimental setup realizing open-ended coaxial probe method [19].

3.2. Transmission-Line Method

The transmission-line method (TLM) belongs to a large group of nonresonant methods of measuring complex dielectric permittivity of different materials in a microwave range [7,51]. Several modifications to this method exist, including the free-space technique [29], the open-circuit network method (see previous section), and the short-circuited network method. Usually three main types of transmission lines are used as the measurement cell in TLM: rectangular waveguide, coaxial line, and microstrip line.

Consider the distribution of the TEM wave in a short-circuited coaxial line partially filled with a lossy material under study (Fig. 11). Analyzed sample is placed near the short-circuited end of the transmission line. The dielectric properties of the sample are determined using the following expressions

$$\begin{aligned} \epsilon' &= \left(\frac{\lambda}{2\pi d}\right)^2 (x^2 - y^2) + \left(\frac{\lambda}{\lambda_{qc}}\right)^2; \\ \epsilon'' &= \left(\frac{\lambda}{2\pi d}\right)^2 2xy \end{aligned} \tag{16}$$

where λ is the free-space wavelength, λ_{qc} is the quasicutoff wavelength, d is the sample thickness (Fig. 11), $x = \text{Re}(Z_{in})$ and $y = \text{Im}(Z_{in})$, and Z_{in} is the input impedance of the short-circuited line

$$Z_{in} = \frac{K_t^2 + tg^2(2\pi/\lambda_a l)}{K_t[1 + tg^2(2\pi/\lambda_a l) + j(1 - K_t^2)tg(2\pi/\lambda_a l)]} \tag{17}$$

where l is the distance between the dielectric surface and the first minimum of the standing wave, λ_a is the wavelength in unloaded part of transmission line, and K_t is the traveling-wave coefficient that is calculated when $K_t \geq 0.4$

as

$$K_t = \sqrt{\frac{E_{min}}{E_{max}}} \tag{18}$$

and when $K_t < 0.4$ as

$$K_t = \frac{\sin(2\pi\Delta x/\lambda_a)}{\sqrt{((E/E_{min}) - 1) \sin(2\pi\Delta x/\lambda_a)}} \tag{19}$$

where E_{min} and E_{max} are the minimum and maximum values of electric field amplitude (see Fig. 11) and $2\Delta x$ is the distance between two points along transmission line on both sides of minimum where measured data are equal and determined from $E = m^2 E_{min}$ ($2 < m < 10$ is the empirical coefficient found from the calibration procedure).

Dielectric permittivity of lossy media may be also successfully measured employing a two ports coaxial cell with a sample placed in the middle of transmission line, so that the TEM wave could propagate from the input port to the output port. Impedance changes and propagation characteristics (S parameters) of the TEM wave measured by means of ANA in empty and partially loaded transmission line lead to determination of the dielectric properties of lossy material. Basic principles of this technique are given in Ref. 30.

In general, a TLM measurement system is more expensive for the same range of frequency than the open-ended coaxial probe system, and the measurements are more difficult and time-consuming. The method described above gives a good accuracy for high-loss materials. But it has rigid requirements on sample shape and sizes. In particular, the sample shape needs to precisely fit the cross section of the transmission line. In some cases, in order to increase accuracy, it is necessary to measure several samples of various thicknesses. Despite these drawbacks, TLM is still widely used in microwave measuring engineering because of its simplicity. Using coaxial line as a

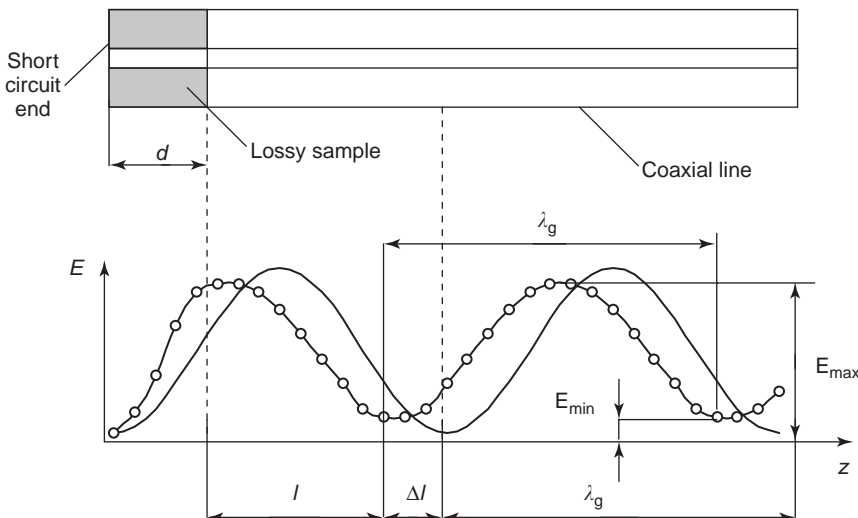


Figure 11. Electric field pattern of TEM wave in empty (solid lines) and partially loaded (lines with circles) short coaxial waveguide. Equations (16)–(19) explain all parameters used in this figure.

basic unit of measurement cell makes this method sufficiently broadband. The accuracy of this method is generally between that of the OCP method and that of the resonance cavity method.

3.3. Resonant Cavity Method

Resonant cavity methods are also widely utilized in measuring complex dielectric permittivity of lossy materials. The most popular resonant cavity method is the perturbation method (PM), which is based on a comparative analysis of certain EM characteristics between empty and a partially loaded rectangular or cylindrical resonance cavity [31]. A schematic diagram of an experimental setup of PM is shown in Fig. 12.

According to PM theory [32,33], dielectric permittivity and losses of a sample under study are determined as follows:

$$\epsilon' = 1 + A^{-1} \frac{V_c \Delta f}{V_s f_0}; \quad \epsilon'' = B^{-1} \frac{V_c}{V_s} \left(\frac{1}{Q_1} - \frac{1}{Q_0} \right) \quad (20)$$

where f_0 and Q_0 are the resonance frequency and Q factor of the empty cavity, f_1 and Q_1 are the resonance frequency and Q factor of the cavity with a sample, V_c is the cavity volume, V_s is the sample volume; and $\Delta f = f_0 - f_1$. A and B are the coefficients that depend on several parameters: shape, sizes, and location of the sample in the cavity, and configuration and excited operating mode of the cavity. In some cases, A and B may be found analytically for a lossy sheet material placed in a rectangular cavity with

operating mode TE_{103} [31], or they may be determined empirically with calibration of the experimental setup. Equation (20) is valid when three main assumptions are satisfied [32]: (1) the dielectric sample does not disturb the general distribution of the EM field in the cavity, (2) metallic wall losses do not influence the resulting losses in the cavity, and (3) Q_0 and Q_1 are measured at the same frequency. Appropriate location of the sample is also a very important factor that affects the accuracy of the measurement. Preliminary numerical modeling of the microwave setup with lossy dielectric material inside the cavity may be a useful approach for determining an optimum sample position in this case [31]. Sometimes, measurement errors are possible when there are airgaps between the specimen and the conducting parts of the metallic resonator.

There are also some restrictions in using conventional resonance PM for measuring the dielectric loss tangent of low-loss media. If conduction losses in cavity walls are higher than (or comparable to) the dielectric losses of the specimen, the resonator Q factor may change and one will not obtain the correct values of ϵ'' . In this case, application of hybrid high-order modes called whispering-gallery modes [34] or a special calibration procedure of Q factor characterization as a function of frequency [32] can help to eliminate the drawbacks of this method.

PM is more accurate than the waveguiding methods. It is particularly suited for medium-loss and low-loss materials and substances. Precisely shaped small-sized samples are usually used with this technique. But PM provides dielectric properties measurements only at a fixed

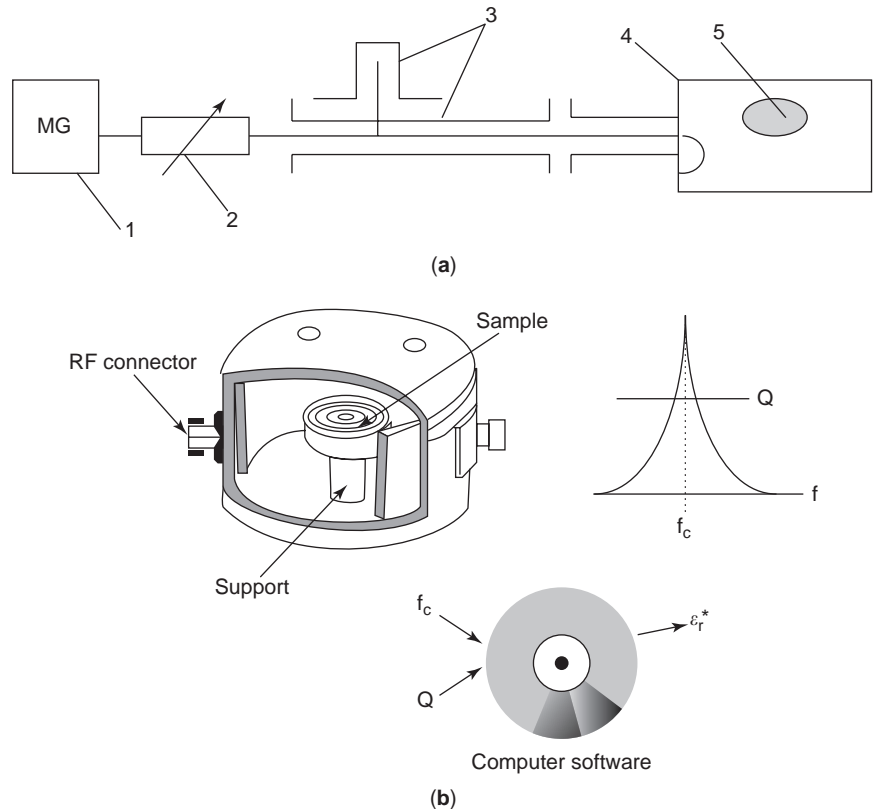


Figure 12. (a) Microwave system for measuring dielectric properties of lossy materials: microwave generator (1), attenuator (2), wavemeter (3), cavity resonator (4), and sample (5); (b) closeup view of a sample, cavity, and related principles for the measurement.

frequency. Commercial systems from Hewlett-Packard are more expensive than the open-end coaxial probe system.

4. PERMITTIVITY OF ORGANIC AND INORGANIC MATERIALS

4.1. Foodstuff and Agricultural Products

Numerous data are reported in the literature on the dielectric properties of biomaterials, especially food materials. This section only summarizes the dielectric properties for some typical materials commonly used in food processing. Table 2 lists electrical property data for different salt solutions, fruits, and codling moth larvae at 27 MHz RF and 915 MHz microwave. Air and deionized water do not absorb much electromagnetic energy at these two frequencies due to near-zero dielectric loss factors. Dielectric and conductivity properties increase with increasing salt content. However, dielectric constant decreases both with frequency and salt content at 915 MHz.

Dielectric properties of dry food solids, fats, and oils are very low and are relatively independent of frequency and temperature. The dielectric properties of selected oils and low-moisture-content food solids are listed in Table 3.

Figure 13 shows the effect of temperature on the dielectric loss factor of selected foods at 3000 MHz [37]. The high salt content in the ham makes the dielectric properties of this product quite different from those of the remaining materials in the graph. Due to ionic polarization,

the dielectric loss factors increase with temperature above the freezing point, which is contrary to the trend of dielectric properties of other foods in which loss mechanisms are determined mostly by the dipole polarization of free water. One advantage of the decreased loss factor with increasing temperature is the so-called temperature leveling effect. When a certain portion of a food is overheated, the loss factor of that part is reduced, which results in less conversion of microwave energy to heat at that part of the food and helps reduce nonuniform spatial temperature distribution.

When thawing frozen foods at relatively high microwave power levels, one often experiences the thermal runaway phenomenon, in which certain areas of the food are overheated while the other areas are still frozen. This is because faster thawing of a portion of food due to uneven heating dramatically increases the loss factor of that part of the food due to the high loss factor of free water (Fig. 13), which in turn increases microwave absorption, causing more uneven heating. In practice, a low microwave power level is often used in microwave thawing so that heat conduction can reduce nonuniform temperature distribution. In industrial tempering (a process that brings deep-frozen products from -30° or -10°C to a few degrees below freezing point for further processing) of large blocks of meat or fish, convective surface cooling at below freezing temperature is often used to reduce thermal runaway.

Figure 14 shows the dielectric properties of Red Delicious apples as a function of frequency at three selected

Table 2. Electrical Conductivity (σ) and Dielectric Properties at 27 and 915 MHz of Lossy Materials at Room-Temperature Conditions

Materials	$\sigma \times 100$ (S/m)	At 27 MHz RF		At 915 MHz	
		ϵ'	ϵ''	ϵ'	ϵ''
Air	~ 0	1.0	~ 0	1.0	~ 0
Water					
Distilled/deionised	$0.5\text{--}1.1 \times 10^{-2}$	80.1	0.03	78.4	3.6
Fresh (tapwater, Pullman, WA, USA)	3.25	79.6	18.9	78.8	4.5
+ 0.05% salt (common salt, Nail)	13.3	80.3	75.1	78.9	6.4
+ 0.10%	23.1	80.6	126.6	79.0	8.2
+ 0.15%	32.0	81.5	178.5	78.7	9.9
+ 0.20%	40.5	82.1	226.3	78.6	11.5
+ 0.25%	49.8	83.6	276.0	78.6	13.3
+ 0.50%	92.5	88.0	524.3	78.1	21.8
+ 1.0%	173	99.2	985.8	77.3	37.2
+ 2.0%	333	126.1	1866	75.7	67.1
Sea	400	—	—	—	—
Apples:					
McIntosh/Winesap	1.05–1.33	—	—	—	—
Fuji	0.86–1.3	—	—	—	—
Red Delicious (juice)	18.5	79.5	138.9	74.7	9.9
Apples (flesh)	—	64.3	80.8	56.9	8.9
Immature apple (juice)	43.0	87.5	248.9	77.2	13.5
Cherries:					
Bing, Rainier (flesh)	—	87.6	185.4	69.7	14.3
Sweetheart (juice)	42.0	—	—	—	—
Vegetables pieces	6–10	—	—	—	—
Fruit pieces	5–15	—	—	—	—
Insect: codling moth (5th instars)	31.0	125.2	458.3	59.9	22.4

Source: Ref. 35.

Table 3. Dielectric Constant (ϵ') and Loss Factor (ϵ'') of Oil and Selected Food Solids

Products	T (°C)	Frequency (Hz)				
		10 ⁶	10 ⁷	10 ⁸	10 ⁹	
Soybean salad oil	25	ϵ'		2.85	2.62	
		ϵ''		0.159	0.168	
	49	ϵ'		2.88	2.71	
		ϵ''		0.138	0.174	
	82	ϵ'		2.86	2.72	
		ϵ''		0.092	0.140	
Cotton oil	25	ϵ'		2.83	2.64	
		ϵ''		0.174	0.175	
	49	ϵ'		2.87	2.70	
		ϵ''		0.134	0.174	
	Flour (Mc = 3.2%)	0	ϵ'	2.8	2.8	
			ϵ''	0.184	0.184	
40		ϵ'	3.5	2.7		
		ϵ''	0.196	0.235		
70		ϵ'	4.0	3.2		
		ϵ''	0.160	0.275		
Skimmed milk powder	0	ϵ'	2.1	1.9		
		ϵ''	0.038	0.040		
	40	ϵ'	2.1	1.8		
		ϵ''	0.044	0.054		
	70	ϵ'	2.4	2.0		
		ϵ''	0.067	0.072		

Source: Ref. 36.

moisture contents and two measured temperatures. At a high moisture content (70% wet basis), ϵ' decreases with increasing frequency, while ϵ'' decreases to a minimum value and then increases with frequency (Figs. 14a and 14d). The gradual reduction in ϵ' of high-moisture-content samples with increasing frequency is likely caused by the dispersion of water molecules. In a single dispersion system (e.g., pure water), this transition takes place in a narrow frequency range and follows the Debye equation

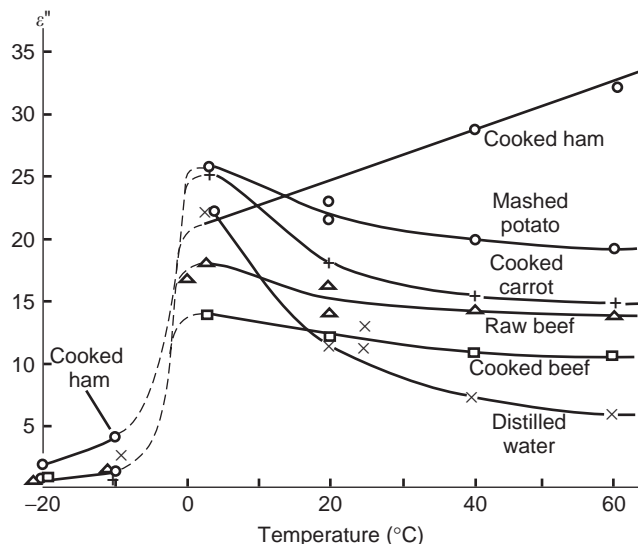


Figure 13. Dielectric loss factor (ϵ'') of selected foods at 3000 MHz as affected by temperature [37].

[Eq. (8)]. In multidispersion food systems, the transition is gradual because of the combined effects of relaxation and ionic conduction. A minimum ϵ'' is observed at 1000 MHz (Fig. 14a) at 22°C. The frequency corresponding to the minimum ϵ'' shifts to about 2000 MHz at 60°C (Fig. 14d). This shift can be related to the temperature response of both the free-water dispersion and the ionic conduction.

Figure 15 shows the dielectric constant ϵ' and loss factor ϵ'' of apples at 915 and 2450 MHz as a function of moisture content (MC). In general, ϵ' and ϵ'' decreases with decreasing moisture content. In a drying process, as the drying progresses, water dipole becomes less mobile, resulting in reduced loss factor. Reduced moisture content during drying also reduces ionic conductivity, as a small amount of free water is available as the solvent. In addition, air voids in apple samples as a result of dehydration contribute to the low values of both ϵ' and ϵ'' .

Salty products (e.g., macaroni and cheese) have, on the other hand, much larger loss factors than do fresh fruits (Table 4). In addition, the loss factor of fresh fruits and macaroni and cheese increases sharply with increasing temperature, especially at low frequency (e.g., 27 MHz).

There has been increasing interest in using RF and microwave energy as a new thermal treatment method for postharvest insect control in agricultural commodities [36–40]. Knowledge of dielectric properties of insects and commodities is necessary in guiding development, improvement, and scaleup of RF and microwave treatment protocols. Table 5 summarizes the mean values of the dielectric constant and the loss factor of apples, almond, cherry, grapefruit, orange, and walnut as a function of temperature at 27 and 915 MHz. The dielectric constant and the loss factor of fresh fruits at 27 MHz are significantly higher than those at 915 MHz. The loss factor of fresh fruits increases with increasing temperature at 27 MHz and remains nearly constant at 915 MHz, similar to the pattern shown in Fig. 7. However, the temperature effect on dielectric properties of almond and walnut is different from that on fresh fruits as shown in Fig. 8. The peak value of the loss factor decreases and corresponding frequency shifts to larger values with increasing temperature.

Mean values of the dielectric constant and the loss factor of selected insect larvae as a function of temperatures at 27, 40, 915, and 1800 MHz are listed in Table 6. Both the dielectric constant and the loss factor for insects increased with increasing temperature at 27 MHz, but remained almost constant at 915 MHz. This is due mainly to the increase in ionic conduction at high temperatures [12]. The loss factor of insects at 27 MHz decreased in order at all temperatures: Mexican fruitfly, navel orangeworm, codling moth, and Indian meal moth.

Compared to codling moth larvae, the loss factor values of walnuts are much smaller because of high oil content and less moisture in walnut kernels. It is clear from Figs. 7 and 8 that the difference in the value of the ϵ'' between codling moth larvae and walnut kernels is much larger at lower frequencies than at microwave frequencies, suggesting a better potential for preferential heating of insects

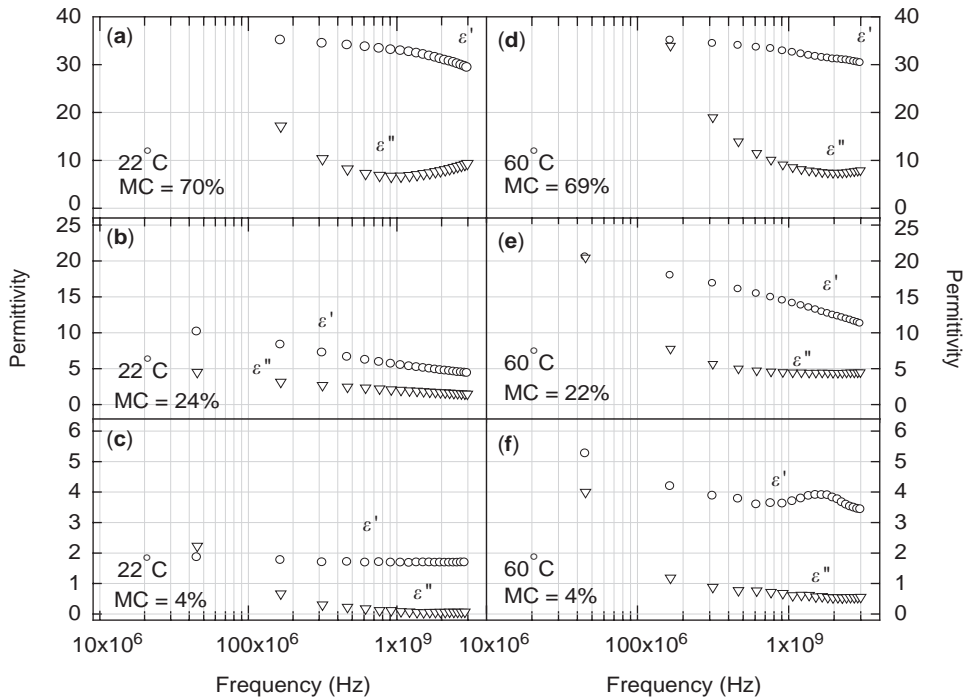


Figure 14. Dielectric properties of Red Delicious apples at three moisture contents and two temperatures [20].

in walnuts when using lower-frequency treatments. A theoretical model and experimental evidence have been provided [18] to support the hypothesis that insect larvae can be preferentially heated in dry nuts by 27 MHz RF

heating for pest control. This differential heating makes possible in the development of practical RF pest control treatments that the walnut industry can use to replace chemical fumigation.

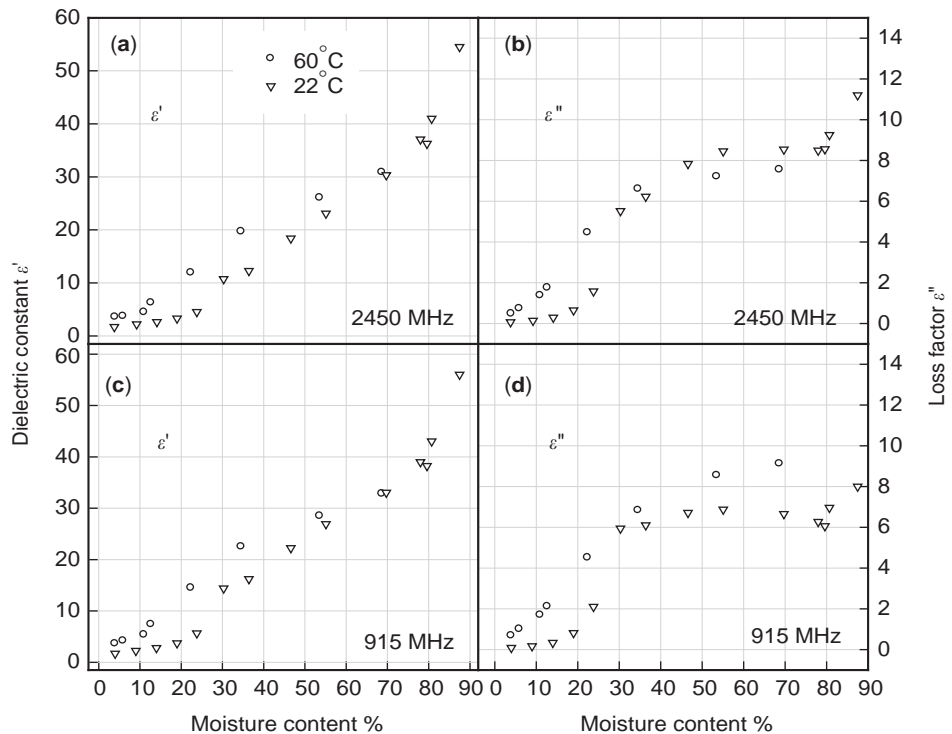


Figure 15. Dielectric properties of Red Delicious apples at 915 and 2450 MHz as influenced by moisture content on a wet basis [20].

Table 4. Dielectric Properties of Macaroni and Cheese

T (°C)		27 MHz	40 MHz	915 MHz	1800 MHz
20	ϵ'	70.90 ± 8.96	65.27 ± 8.29	40.23 ± 3.71	38.77 ± 5.41
	ϵ''	400.03 ± 55.18	273.47 ± 37.76	21.33 ± 3.81	17.40 ± 3.39
30	ϵ'	72.40 ± 9.09	66.53 ± 8.52	40.87 ± 3.18	39.07 ± 5.35
	ϵ''	486.57 ± 66.47	331.40 ± 45.06	23.47 ± 4.26	17.90 ± 3.46
40	ϵ'	72.87 ± 8.22	66.63 ± 7.65	40.90 ± 2.88	39.30 ± 5.10
	ϵ''	593.50 ± 63.65	403.13 ± 43.11	27.30 ± 5.51	19.03 ± 3.21
50	ϵ'	72.67 ± 8.87	66.27 ± 8.20	40.53 ± 3.07	38.90 ± 5.16
	ϵ''	688.70 ± 67.08	466.53 ± 45.38	29.77 ± 5.55	19.70 ± 3.03
60	ϵ'	73.07 ± 8.55	66.13 ± 7.91	40.03 ± 3.00	38.53 ± 5.08
	ϵ''	800.30 ± 57.46	541.43 ± 38.88	32.87 ± 5.21	20.93 ± 2.71
70	ϵ'	74.03 ± 8.03	66.67 ± 7.51	40.07 ± 2.70	38.17 ± 4.89
	ϵ''	921.37 ± 62.49	622.73 ± 42.61	36.23 ± 4.76	22.23 ± 2.49
80	ϵ'	73.83 ± 8.13	65.67 ± 7.43	39.53 ± 2.39	37.57 ± 4.92
	ϵ''	1060.27 ± 55.75	716.17 ± 37.55	39.70 ± 4.75	23.67 ± 2.44
90	ϵ'	76.67 ± 8.37	67.17 ± 7.34	40.67 ± 4.88	37.17 ± 4.60
	ϵ''	1208.60 ± 67.57	815.70 ± 45.29	43.23 ± 3.30	25.23 ± 1.40
100	ϵ'	80.93 ± 5.59	69.90 ± 4.75	40.67 ± 4.38	37.13 ± 4.52
	ϵ''	1382.23 ± 117.32	932.73 ± 78.84	48.17 ± 2.55	27.57 ± 0.84
110	ϵ'	83.23 ± 4.91	71.13 ± 3.60	40.37 ± 4.48	36.77 ± 4.67
	ϵ''	1536.13 ± 164.25	1035.87 ± 110.15	52.37 ± 3.04	29.57 ± 1.36
121.1	ϵ'	84.33 ± 5.26	71.07 ± 4.17	38.93 ± 4.82	35.57 ± 4.84
	ϵ''	1712.80 ± 172.76	1154.57 ± 115.96	57.40 ± 3.64	31.87 ± 1.75

Source: Ref. 11.

4.2. Biological Tissues

High-frequency EM energy is widely used in medical treatments, including physiotherapeutic, diagnostics, rapid rewarming of cryopreserved tissues, pharmacology, reflex therapeutic, blood sterilization, and hyperthermal treatment of cancer [42–45].

The main mechanism for the interaction between EM waves and biological tissues is the same as in foodstuffs: oscillation of polar water molecules (H_2O) and ions. Part of water in biological tissues is linked with albumen (0.3–0.4 g of water on 1 g of albumen), and at relaxation frequencies specific electrical conductivity (σ) of “linked” water sometimes is higher than σ of pure water.

Biological tissues (biotissues) are divided into two main groups: materials with high and low water contents; muscles (73–78%), liver (75–77%), kidneys (76–78%), brain (68–73%), skin (60–76%), lung (80–83%), eye ($\leq 89\%$) compile the first group. Fat (5–10%) and bone (8–16%) tissues may be included in the second group. Moisture content in blood is higher than in other tissues ($\leq 83\%$).

Complex dielectric permittivity of some biological materials at room temperature and 2450 MHz taken from Refs. 46 and 47 is represented in Table 7. Bloodflow seldom influences their dielectric properties, excluding tissues with high blood volume (kidneys) or low moisture content (fat). Experimental results [48] have shown that measured data of ϵ' and ϵ'' of biotissues in vivo (directly in organism) and in vitro (in the test tube) almost coincide at frequencies higher 100 MHz.

A new technology of microwave diagnostics based on measurement of $\epsilon' - j\epsilon''$ of normal and invalid tissues has been proposed [49]. Permittivity of infected gall ($\epsilon' = 63$ – 65 ; $\epsilon'' = 17$ – 19) is higher than that of normal gall ($\epsilon' = 60$; $\epsilon'' = 15$).

4.3. Wood and Fibrous Materials

Most fibrous materials are organic cellulose-based substances; such as wood, paper, cartoon, fabric, and fibers. Wood is highly hygroscopic and anisotropic. The dielectric properties of wood depend on type of wood, density, moisture content, and temperature [50,51]. Normal moisture content of wood is between 8 and 12%.

According to generalized electrophysical model of wood samples proposed [51], one can consider a second-order tensor for evaluation of its complex dielectric permittivity

$$\begin{aligned}
 & \|\epsilon' - j\epsilon''\| \\
 & = \begin{vmatrix} \epsilon'_{LL} - j\epsilon''_{LL} & \epsilon'_{LR} - j\epsilon''_{LR} & \epsilon'_{LU} - j\epsilon''_{LU} \\ \epsilon'_{RL} - j\epsilon''_{RL} & \epsilon'_{RR} - j\epsilon''_{RR} & \epsilon'_{RU} - j\epsilon''_{RU} \\ \epsilon'_{UL} - j\epsilon''_{UL} & \epsilon'_{UR} - j\epsilon''_{UR} & \epsilon'_{UU} - j\epsilon''_{UU} \end{vmatrix} \quad (21)
 \end{aligned}$$

where L , R , and U are the longitudinal, radial and tangential axes of anisotropy, respectively. Rotation of electric field vector (\vec{E}) on a 180° angle does not change the dielectric properties of wood materials; that is L , R , and U are the principal axes of anisotropy, and the tensor in Eq. (21) may be simplified as follows:

$$\|\epsilon' - j\epsilon''\| = \begin{vmatrix} \epsilon'_L - j\epsilon''_L & 0 & 0 \\ 0 & \epsilon'_R - j\epsilon''_R & 0 \\ 0 & 0 & \epsilon'_U - j\epsilon''_U \end{vmatrix} \quad (22)$$

When \vec{E} is arbitrarily oriented in space and forms an angle ϑ_1 with L , angle ϑ_2 with R and angle ϑ_3 with U closed-form

Table 5. Dielectric Properties (Mean±STD) of Fruits and Nuts at Five Temperatures and Four Frequencies

Material	Temperature (°C)	Dielectric Constant				Loss Factor			
		Frequency (MHz)				Frequency (MHz)			
		27	40	915	1800	27	40	915	1800
Apple (GD ^a)	20	72.5±0.6	72.6±0.7	74.3±0.8	67.4±0.9	120.4±2.1	80.5±1.5	8.5±0.8	9.9±0.1
	30	71.3±0.8	71.3±0.8	72.3±0.7	66.0±0.9	143.9±2.0	96.4±1.4	8.5±1.1	8.7±0.0
	40	69.7±0.8	69.6±0.8	70.0±0.8	64.1±0.9	171.8±2.6	115.3±1.7	8.2±0.9	7.6±0.0
	50	68.1±0.8	67.9±0.8	67.8±1.0	62.1±1.0	202.2±3.3	135.8±2.2	8.3±0.6	6.9±0.1
	60	66.5±0.8	66.4±0.9	65.6±1.0	60.1±1.0	234.1±4.3	157.4±2.7	8.7±0.3	6.7±0.1
Apple (RD ^a)	20	74.6±0.6	74.7±0.5	77.0±0.0	70.4±0.5	92.0±0.9	61.1±0.8	10.0±1.4	10.8±0.2
	30	72.7±0.8	72.8±0.7	74.5±0.2	68.3±0.4	109.1±0.6	72.8±0.6	9.4±1.8	9.4±0.7
	40	70.6±0.8	70.8±0.8	71.5±0.1	66.1±0.5	130.7±1.1	87.5±0.8	10.0±2.5	8.3±0.7
	50	68.7±0.9	68.7±0.8	68.9±0.2	64.0±0.5	153.8±1.6	103.1±1.3	9.8±2.8	7.4±0.8
	60	66.8±1.0	66.8±0.8	67.1±0.5	62.0±0.8	178.6±2.3	119.9±1.6	8.9±1.9	6.7±0.7
Almond	20	5.9±0.1	5.9±0.1	1.7±0.9	5.8±0.2	1.2±0.2	1.5±0.2	5.7±0.5	2.9±0.8
	30	5.7±1.7	5.9±1.8	3.2±2.3	3.4±2.3	0.6±0.2	1.1±0.6	6.4±1.8	3.4±0.9
	40	5.8±1.6	6.1±1.9	3.3±2.0	3.6±2.1	0.6±0.1	1.0±0.5	6.0±1.3	3.5±0.7
	50	5.8±1.6	6.2±1.8	3.4±0.5	4.2±1.6	0.6±0.3	1.1±0.6	5.7±0.1	3.4±0.2
	60	6.0±1.5	6.3±1.8	3.1±1.4	3.9±2.3	0.7±0.1	1.1±0.4	6.4±1.3	3.0±1.2
Cherry	20	91.2±0.1	85.0±0.4	73.7±0.1	70.9±0.1	293.0±4.3	198.5±2.9	16.4±0.0	16.0±0.2
	30	91.4±0.9	84.0±0.8	72.0±0.3	69.7±0.3	363.1±11.2	245.7±7.6	17.2±0.5	15.1±0.6
	40	91.0±2.0	82.4±1.6	69.6±0.7	67.8±0.6	44.01±26.6	297.5±18.0	18.3±1.0	14.6±0.9
	50	89.6±3.6	79.9±2.7	66.7±1.6	65.2±1.5	501.9±37.2	338.9±25.1	19.3±1.4	14.2±1.1
	60	89.8±5.5	78.5±3.8	64.1±1.8	62.8±1.6	565.4±54.0	381.8±36.6	20.4±1.9	14.1±1.4
Grape Fruit	20	89.0±5.1	82.7±1.8	72.7±2.5	72.1±1.2	202.4±9.3	137.8±7.0	12.1±0.0	12.6±0.1
	30	90.3±6.8	81.9±2.7	70.8±2.3	70.2±1.1	242.6±8.9	165.2±6.9	12.5±0.2	11.5±0.2
	40	91.9±9.2	81.4±4.0	68.5±2.1	68.2±1.1	291.4±9.0	198.4±7.3	13.3±0.4	10.9±0.2
	50	93.8±11.3	80.9±5.2	66.1±2.1	66.0±0.9	345.3±7.8	235.2±6.9	14.2±0.3	10.7±0.2
	60	96.5±14.0	80.8±6.6	63.7±2.0	63.7±0.8	401.1±5.8	273.3±5.8	15.5±0.3	10.7±0.2
Orange	20	84.0±0.1	81.0±0.1	72.9±1.9	72.5±0.1	223.3±0.6	151.6±0.3	16.5±2.8	14.8±0.5
	30	82.2±0.3	78.5±0.3	70.6±1.8	70.7±0.3	267.9±1.8	181.6±1.1	17.8±2.7	13.9±0.5
	40	80.2±0.7	75.7±0.6	68.0±2.1	68.6±0.4	318.0±5.3	215.3±3.4	18.7±3.0	13.1±0.5
	50	78.0±0.5	72.7±0.4	66.1±0.6	65.6±0.2	367.7±5.0	248.6±3.4	17.5±1.2	12.3±0.2
	60	75.8±0.9	69.9±0.6	63.2±0.7	62.7±0.3	418.4±6.5	282.8±4.3	18.4±1.2	12.2±0.2
Walnut	20	4.9±0.0	4.8±0.0	2.2±1.6	2.1±0.7	0.6±0.0	0.7±0.1	2.9±0.1	1.8±0.2
	30	5.0±0.1	4.9±0.1	2.1±0.3	2.7±0.2	0.5±0.1	0.6±0.1	2.6±0.1	1.6±0.2
	40	5.1±0.1	5.1±0.1	3.0±0.1	3.2±0.0	0.4±0.0	0.6±0.1	2.3±0.1	1.3±0.2
	50	5.2±0.1	5.1±0.0	3.4±0.0	3.5±0.0	0.3±0.1	0.5±0.1	2.0±0.0	1.1±0.1
	60	5.3±0.0	5.2±0.0	3.8±0.0	3.7±0.0	0.4±0.1	0.5±0.0	1.8±0.0	1.0±0.1

^aGD, Golden Delicious; RD, Red Delicious

Source: Ref. 41.

expressions for calculation of ϵ' and $\tan \delta_e$ are derived as follows [51]:

$$\epsilon' = \epsilon'_L \cos^2 \vartheta_1 + \epsilon'_R \cos^2 \vartheta_2 + \epsilon'_U \cos^2 \vartheta_3 \quad (23)$$

$$\tan \delta_e = tg \delta_{eL} \cos^2 \vartheta_1 + tg \delta_{eR} \cos^2 \vartheta_2 + tg \delta_{eU} \cos^2 \vartheta_3 \quad (24)$$

The measured dielectric constant of Douglas fir at 2450 MHz as a function of moisture content [MC (%)] and temperature (°C) is shown in Fig. 16 [50]. Here \vec{E} is oriented parallel to wood fibers. Dependencies ϵ' (MC) and ϵ'' (MC) at 9210 MHz for the same type of wood and softwood hembal when $T=23^\circ\text{C}$ and $0 \leq \text{MC}\% \leq 28$ are presented in Ref. 52.

Density of wood [ρ (g/cm³)] may also influence $\epsilon' - j\epsilon''$. Experimentally obtained functions ϵ' (ρ , MC, T) and ϵ'' (ρ , MC, T) for $0.3 \leq \rho \leq 0.8$, $0 \leq \text{MC} \leq 60$, $20 \leq T \leq 90$ for various

RF and microwave frequencies are given in Ref. 51. These functions are valid for the cases when \vec{E} is perpendicular to wood fibers.

4.4. Resins and Plastics

According to the classification proposed in Ref. 53, resins and plastics are divided into three main groups: (1) no polar high-frequency (HF) dielectrics, including polyethylene, polypropylene, and polyester (2) weak polar and polar HF and low-frequency (LF) dielectrics, including polyformaldehyd, rubbers, and polybutadiene; and (3) polar LF dielectrics such as polyamide, epoxide, and polyvinylchloride.

Rubber-based resins are multimolecular substances described by the formula $(\text{C}_5\text{H}_8)_m$, where m is the number of molecular chains. Vulcanization (heating of rubber after mixing with sulfur containing matters) of crude rubber allows improving its heatproof properties. The dielectric

Table 6. Dielectric Properties (Mean ± STD) of Four Insect Larvae at Five Temperatures and Four Frequencies

Material	Temperature (°C)	Dielectric Constant				Loss Factor			
		Frequency (MHz)				Frequency (MHz)			
		27	40	915	1800	27	40	915	1800
Codling moth	20	71.5 ± 0.9	64.9 ± 0.9	47.9 ± 0.2	44.5 ± 0.1	238.1 ± 0.1	163.3 ± 0.4	11.7 ± 0.1	12.0 ± 0.2
	30	71.5 ± 0.1	63.9 ± 0.2	45.9 ± 0.9	42.9 ± 0.9	277.8 ± 8.5	190.2 ± 5.4	12.5 ± 0.4	11.7 ± 0.3
	40	73.8 ± 0.1	64.5 ± 0.1	44.6 ± 0.6	41.6 ± 0.4	332.4 ± 16.3	227.5 ± 10.5	13.9 ± 0.5	11.9 ± 0.3
	50	79.3 ± 1.1	68.5 ± 1.6	45.6 ± 1.5	42.7 ± 1.5	422.5 ± 5.9	288.6 ± 4.4	16.5 ± 0.3	13.2 ± 0.3
	60	84.5 ± 2.5	71.5 ± 2.9	45.0 ± 2.4	41.9 ± 2.2	511.3 ± 26.6	349.1 ± 18.3	19.1 ± 1.0	14.2 ± 0.7
Indian-meal moth	20	81.3 ± 1.9	69.1 ± 0.9	39.9 ± 0.4	37.5 ± 0.5	210.9 ± 4.8	149.0 ± 3.7	13.4 ± 1.4	10.6 ± 0.6
	30	85.8 ± 2.7	72.0 ± 1.4	39.2 ± 0.0	36.9 ± 0.1	244.1 ± 3.7	172.4 ± 3.0	14.3 ± 1.4	10.6 ± 0.8
	40	94.4 ± 1.5	77.3 ± 0.9	37.6 ± 0.8	35.5 ± 0.9	268.7 ± 25.1	190.9 ± 16.9	15.2 ± 2.1	10.6 ± 1.2
	50	103.7 ± 0.8	83.7 ± 0.5	37.2 ± 1.3	35.3 ± 1.4	314.0 ± 42.8	223.1 ± 28.1	16.9 ± 2.4	11.4 ± 1.5
	60	113.0 ± 3.3	90.4 ± 2.2	37.8 ± 1.6	35.6 ± 1.7	397.4 ± 57.8	280.7 ± 37.9	19.9 ± 2.8	12.8 ± 1.7
Mexican fruitfly	20	90.3 ± 13.6	71.2 ± 0.3	48.5 ± 3.4	47.0 ± 0.7	343.9 ± 15.1	230.9 ± 5.9	17.5 ± 2.0	13.3 ± 1.7
	30	105.1 ± 21.5	87.2 ± 12.1	47.3 ± 3.5	45.5 ± 0.4	384.7 ± 15.2	272.2 ± 18.2	21.3 ± 3.9	13.9 ± 1.9
	40	117.4 ± 28.2	95.4 ± 16.6	46.4 ± 2.9	44.7 ± 0.8	446.1 ± 19.0	316.5 ± 22.4	24.2 ± 5.1	14.5 ± 2.2
	50	128.7 ± 33.6	102.9 ± 20.0	45.7 ± 2.3	44.1 ± 1.4	521.8 ± 32.1	370.7 ± 33.0	26.8 ± 5.7	15.4 ± 2.5
	60	141.2 ± 37.5	111.5 ± 22.8	44.5 ± 2.0	43.0 ± 1.6	582.2 ± 28.1	414.5 ± 31.7	29.4 ± 5.9	16.5 ± 2.7
Navel orange worm	20	80.2 ± 0.3	68.6 ± 0.4	44.5 ± 1.3	42.2 ± 1.4	307.8 ± 4.9	212.6 ± 3.1	16.1 ± 0.1	12.7 ± 0.0
	30	83.6 ± 1.5	70.4 ± 1.0	43.6 ± 0.4	41.5 ± 0.7	359.7 ± 10.5	248.0 ± 7.5	17.5 ± 0.6	12.9 ± 0.4
	40	87.7 ± 2.1	72.7 ± 1.6	42.8 ± 0.1	40.7 ± 0.1	419.4 ± 17.3	288.8 ± 12.0	19.2 ± 0.9	13.4 ± 0.6
	50	92.8 ± 1.6	75.9 ± 1.2	42.3 ± 0.4	40.2 ± 0.1	480.3 ± 24.5	330.8 ± 16.5	21.2 ± 1.0	14.1 ± 0.6
	60	99.4 ± 0.0	80.1 ± 0.0	42.2 ± 0.1	40.0 ± 0.0	562.7 ± 3.3	386.7 ± 2.2	24.0 ± 0.1	15.5 ± 0.0

Source: Ref. 41.

constant of rubbers in a microwave range has been studied in several works [5,53,54]. For example, temperature dependencies of $\epsilon'(T)$ and $\epsilon''(T)$ of stearine butadiene rubber (SBR) at 2800 MHz are represented in Ref. 7. These dependencies may be approximated with polynomial expressions:

$$\begin{aligned} \epsilon' &= 0.1172 \times 10^{-9}T^5 - 0.6167 \times 10^{-7}T^4 + 0.121 \times 10^{-4} \times T^3 \\ &\quad - 0.001088T^2 + 0.03727T + 8.821 \\ \epsilon'' &= -0.27561 \times 10^{-11}T^6 + 0.163672 \times 10^{-8}T^5 \\ &\quad - 0.38772 \times 10^{-6}T^4 + 0.46581 \times 10^{-4}T^3 - \\ &\quad - 0.0029782 \times T^2 + 0.096531 \times T - 0.971 \end{aligned} \quad (25)$$

Similar functions for cured and vulcanized nitrile butadiene rubber (NBR) at 2450 MHz have been measured [54] (see Fig. 17). Experimental data of the complex dielectric permittivity of some rubbers at various frequencies have also been given [5].

Resins such as polyamide and polyimide have wide practical applications in modern microelectronics electrical, and aerospace engineering. The dielectric properties of

some of these materials at microwave frequencies have been studied closely. In particular, $\epsilon'(T)$ and $\epsilon''(T)$ of Nylon-6 at 2450 MHz have been obtained [55]. These results are represented in Fig. 18.

Plastic dielectrics have weak interaction with EM fields because of their nonpolar molecular structure. Plastics are often used as package material for foods treated by microwaves. Most of plastics have a very weak linear dependence on temperature at RF and microwave frequencies. For example, the dielectric permittivity and loss factor of plastic materials have been analyzed in by Von Hippel [5] at 10,000 MHz: $2.5 \leq \epsilon' \leq 6$; $\tan \delta_e \leq 0.05$. Table 8 lists the dielectric permittivities of selected plastic materials at 2450 MHz.

4.5. Ceramics

Ceramics are widely applied in many areas of science and engineering because of their unique features such as high temperature stability of physical properties, low wearability, thermal conductivity, and weight. Dielectric properties of selected ceramics as a function of temperature and frequency have also been studied [5]. The dielectric constant of ceramic may be sufficiently low (Mullite, $\epsilon' < 10$), average

Table 7. Dielectric Permittivity (ϵ') and Loss Factor (ϵ'') of Biotissues at 2450 MHz and Room Temperature

Tissue	Eye	Brain	Fat	Muscle	Kidneys	Skin	Blood
$\epsilon' - j\epsilon''$	30 - j8	32 - j15.5	5 - j0.99	46 - j13.5	44.5 - j14.9	43 - j14	65 - j19.5

Sources: Refs. 46 and 47.

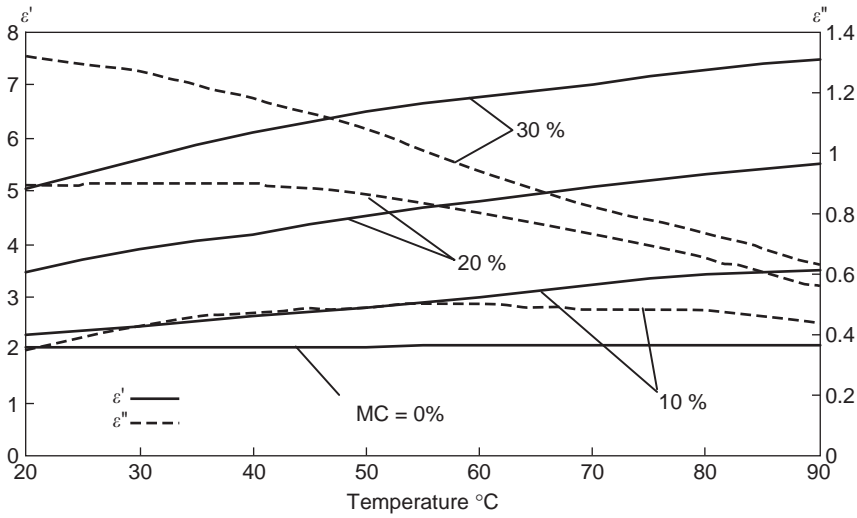


Figure 16. Dielectric permittivity (ϵ') and loss factor (ϵ'') of Douglas fir at different moisture content [50].

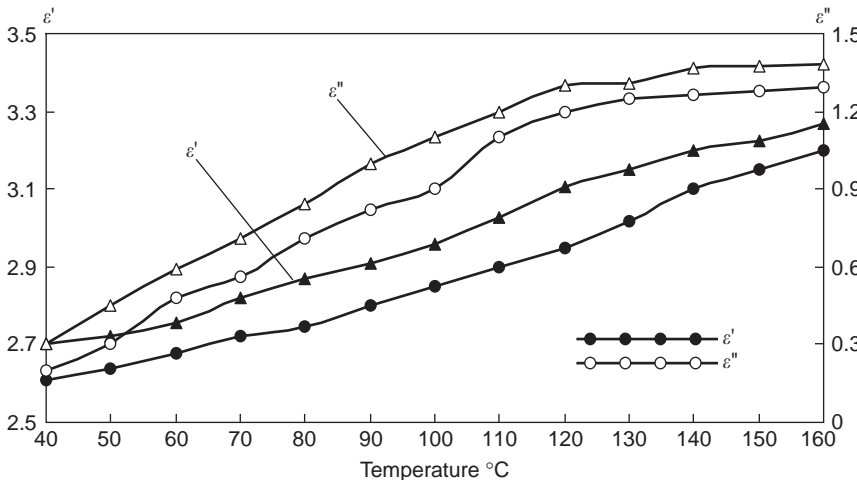


Figure 17. Dielectric permittivity (ϵ') and loss factor (ϵ'') of nitrile butadiene rubber: crude rubber (lines with triangles), vulcanized rubber (lines with circles) [54].

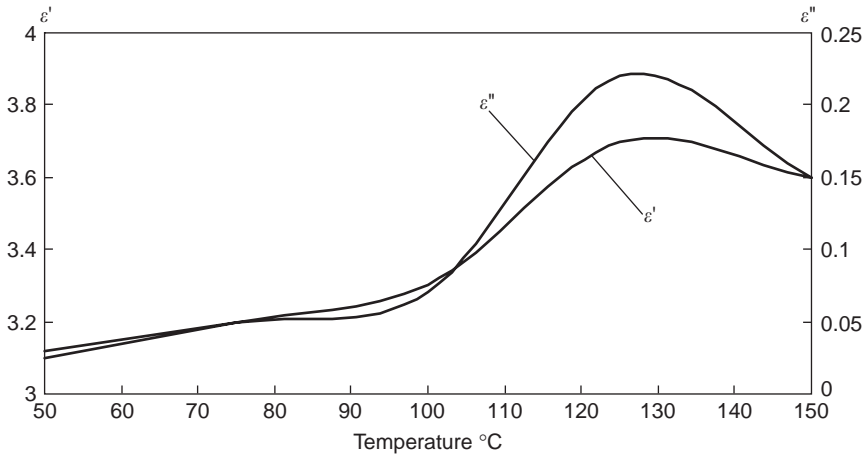


Figure 18. Dielectric permittivity (ϵ') and loss factor (ϵ'') of Nylon-6 [55].

Table 8. Dielectric Permittivity (ϵ') and Loss Factor (ϵ'') of Plastics [5,7] at 2450 MHz

Material	China	Ultem	Polyetilene	Polystirol	Teflon	Glass
$\epsilon' - j\epsilon''$	$5.7 - j0.05$	$3.5 - j0.0013$	$2.2 - j0.004$	$2.5 - j0.001$	$2.05 - j0.002$	$7.6 - 0.156$

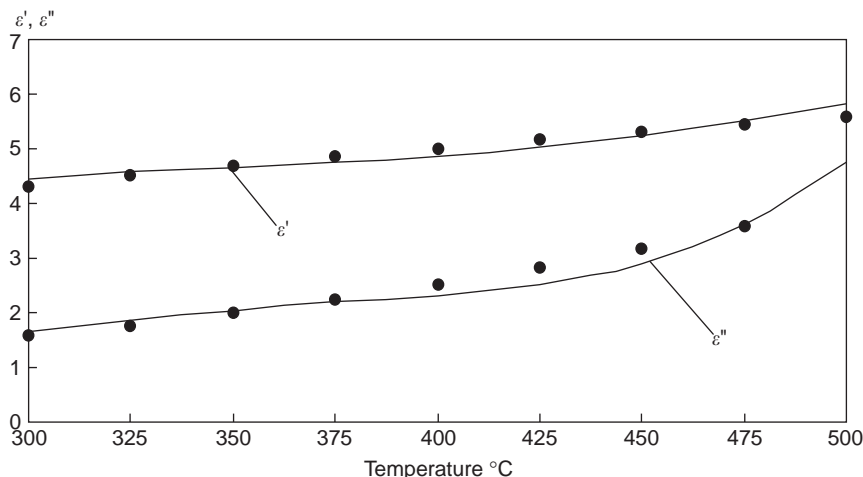


Figure 19. Dielectric permittivity (ϵ') and loss factor (ϵ'') of zeolite ceramics: experiment (solid lines) and approximation (black circles) [59].

Table 9. Dielectric Permittivity (ϵ') and Loss Factor (ϵ'') of Ceramic Materials

f (MHz)	$T = 500^\circ\text{C}$		$T = 1000^\circ\text{C}$		$T = 1200^\circ\text{C}$	
	ϵ'	ϵ''	ϵ'	ϵ''	ϵ'	ϵ''
915	9.13	0.022	10.47	0.66	13.32	3.83
2450	9.13	0.087	10.86	0.53	12.66	2.01

Source: Ref. 56.

Table 10. Dielectric Permittivity (ϵ') and Loss Factor (ϵ'') of Some Soils

Soil	MC = 4%		MC = 12%		MC = 20%	
	1 GHz	3 GHz	1 GHz	3 GHz	1 GHz	3 GHz
Sand ($\epsilon' - j\epsilon''$)	$3.33 - j0.13$	$3.05 - j0.26$	$11.6 - j0.78$	$10.8 - j1.04$	$20.3 - j1.17$	$19.4 - j1.96$
Clay ($\epsilon' - j\epsilon''$)	$3.05 - j0.78$	$2.88 - j0.73$	$12.5 - j4.30$	$11.4 - j2.35$	$22.2 - j8.87$	$19.2 - j4.43$

Source: Ref. 64.

Table 11. Dielectric Permittivity (ϵ') and Loss Factor (ϵ'') of Selected Minerals [66] at 2450 MHz

Mineral	$T = 25^\circ\text{C}$		$T = 100^\circ\text{C}$		$T = 200^\circ\text{C}$		$T = 300^\circ\text{C}$	
	ϵ'	ϵ''	ϵ'	ϵ''	ϵ'	ϵ''	ϵ'	ϵ''
Chalcoite	16.72	1.64	17.14	1.76	15.46	1.52	11.82	1.12
Chalcopyrite	11.01	8.02	11.41	10.20	11.20	12.5	9.01	1.41

(titanic ceramics N1400-110, N750T, $30 \leq \epsilon' \leq 150$) or high (TiO_2 , CaTiO_3 and LaAlO_3 , $\epsilon' > 200$).

The complex dielectric permittivity of ceramics Hilox-882, which consists of Al_2O_3 , SiO_2 , MgO , CrO_2 , and CaO at two microwave frequencies and three temperatures, is shown in Table 9 [56]. An analytical model that describes the behavior of ϵ' and ϵ'' of composite ceramics in temperature range $0 < T < 2500$ at 2450 MHz has been derived [57]

$$\epsilon = \epsilon_{in} + 10^{-4}(T - 25) - j \cdot 10^{-3}(T - 25) \quad (26)$$

Where $\epsilon_{in} = 3.9 - j0.46$ is the initial value at $T = 25^\circ\text{C}$.

Several types of ceramics—aluminosilicate and zirconia fibre board, alumina, Ni-Zn-ferrite, and PZT ceramics—

were analyzed at 2422 MHz by Hamlin et al. [58], who treated these materials by microwave in a cylindrical applicator with operating mode TM_{010} .

Measured values of $\epsilon'(T) - j\epsilon''(T)$ at 3000 MHz for soda lime glass (Corning 0080), borosilicate glass, Mullite MV20, cupric oxide, aluminum nitride, zeolite Fig. 19, alumina cement AC56, zirconia cement, and felt can be found in Ref. 59. Some of these dependencies (zeolite) may be approximated by expressions:

$$\begin{aligned} \epsilon' &= 0.250933T^{0.499713}, \\ \epsilon'' &= 0.383887e^{0.0047014 \cdot T} \quad R^2 = 0.962 \end{aligned} \quad (27)$$

Where R^2 is the coefficient of determination. Both equations are valid when $300 < ^\circ\text{C} < 500$. The dielectric constant of Mullite MV20 $\epsilon'(T) = 5.3 \sim 7.8$, $\epsilon''(T) = 0.05 \sim 1.3$, $400 \leq ^\circ\text{C} = 1300$ at 915 MHz has been investigated [60].

4.6. Soils and Minerals

Moisture dependent dielectric constants of many soils (sandy, high-clay, loami and etc.) over RF and microwave frequency ranges have been published by several authors [61–64]. Most of these studied have been carried out in the temperature range ($5 \leq ^\circ\text{C} \leq 25$) for fixed values of soils density. As an example in Table 10, complex dielectric permittivity of two types of soils is listed for different moisture content at two microwave frequencies [64].

At 2450 MHz all dry sandy soils may be classified on three groups according to the value of loss factor: sands with low losses ($\epsilon'' = 0.0075$), sands with average losses ($0.011 \leq \epsilon'' \leq 0.031$), and sands with high losses ($0.05 \leq \epsilon'' \leq 0.1$) [65]. Dry clay soils are characterized by $3.91 \leq \epsilon' \leq 4.21$ and $0.14 \leq \epsilon'' \leq 0.32$. Dielectric properties of loami soils with moisture content: $2 \leq \text{MC} \leq 50\%$ and $3.49 \leq \epsilon' \leq 32.53$ and $0.22 \leq \epsilon'' \leq 1.3$.

EM fields are used today in mining industry, geology, road building technologies, and so on. Determination of dielectric properties of minerals allows more accurate mathematical modeling of physical processes of EM waves interaction with lossy media. The open-end-coaxial line method has been utilized [63] for measuring $\epsilon'(f, T) - j\epsilon''(f, T)$ of over 60 minerals in the temperature range $25\text{--}325^\circ\text{C}$ and frequency range $300 \leq f, \text{MHz} \leq 3000$. Some of these experimental data at 2450 GHz are given in Table 11. Most minerals exhibit increasing values of ϵ' and ϵ'' versus temperature, except for minerals presented in Table 11 which have complicated dependencies $\epsilon'(T)$ and $\epsilon''(T)$ [66].

5. CONCLUSION

Wide applications of dielectric materials require the knowledge of their dielectric properties. We have represented data about dielectric permittivity for some of these materials in RF and microwave ranges. Many of the experimental results given in Section 4 have been implemented in mathematical models of RF and microwave technological applicators developed at Washington State University.

Three main factors—frequency, temperature and moisture content—which significantly influence the value of $\epsilon' - j\epsilon''$ are analyzed in details. In many cases, the non-linear characteristic of temperature dependences of dielectric permittivity dictates that the physical processes in RF and microwave systems are highly coupled EM and heat conduction problem. A major challenge in RF and microwave heating research and development is to design RF applicators and microwave cavities that provide uniform E -field patterns in treated materials. With precise measurements of dielectric and thermal

properties for different materials, great success of new designs in industrial implementations will be expected in the future.

BIBLIOGRAPHY

1. M. N. Afsar, J. R. Birch, and R. N. Clarke, The measurement of the properties of materials, *Proc. IEEE* **74**:183–199 (1986).
2. J. Krupka and R. G. Geyer, Loss-angle measurement, *Wiley Encyclopedia of Electrical and Electronics Engineering Online*, Wiley, New York, 1999.
3. S. Aditya and A. Arokiaswami, Microwave measurement instrumentation, *Wiley Encyclopedia of Electrical and Electronics Engineering Online*, Wiley, New York, 1999.
4. R. Bartnikas, Dielectric measurement, *Wiley Encyclopedia of Electrical and Electronics Engineering Online*, Wiley, New York, 1999.
5. A. Von Hippel, *Dielectrics and Waves*, Wiley, New York, 1954.
6. P. S. Neelakanta, *Handbook of Electromagnetic Materials: Monolithic and Composite Versions of Their Application*, CRC Press LLC, Boca Raton, FL, 1995.
7. A. C. Metaxas and R. J. Meredith, *Industrial Microwave Heating*, Peter Peregrinus, London, 1983.
8. S. Ryyänen, The electromagnetic properties of food materials: A review of the basic principles, *J. Food Eng.* **29**:409–429 (1995).
9. S. O. Nelson, Review and assessment of radio-frequency and microwave energy for stored-grain insect control, *Trans. ASAE* **39**:1475–1484 (1996).
10. S. C. Harvey and P. Hoekstra, Dielectric relaxation spectra of water adsorbed on lysozyme, *J. Phys. Chem.* **76**:2987–2994 (1972).
11. Y. Wang, T. Wig, J. Tang, and L. M. Hallberg, Dielectric properties of food relevant to RF and microwave pasteurization and sterilization, *J. Food Eng.* **57**:257–268 (2003).
12. J. Tang, H. Feng, and M. Lau, Microwave heating in food processing, in X. Young and J. Tang, eds., *Advances in Bioprocessing Engineering*, World Scientific, 2002.
13. P. Debye, *Polar Molecules*, The Chemical Catalog Co., New York, 1929.
14. S. Mashimo, S. Kuwabara, S. Yagihara, and K. Higasi, Dielectric relaxation time and structure of bound water in biological materials, *J. Phys. Chem.* **91**:6337–6338 (1987).
15. P. Gregory, R. N. Clarke, T. E. Hodgetts, and G. T. Symm, *RF and Microwave Dielectric Measurements upon Layered Materials Using Reflectometric Coaxial Sensor*, Natl. Phys. Lab. Report DES 125, 1993.
16. C. W. Macosko, *Rheology, Principles, Measurements, and Applications*, VCH Publishers, Cambridge, UK, 1994.
17. J. G. Trump, Dielectric materials and their applications, in A. R. von Hippel, ed., *Dielectric Properties and Waves*, Wiley, New York, 1954.
18. B. D. Roebuck and S. A. Goldblith, Dielectric properties of carbohydrate-water mixtures at microwave frequencies, *J. Food Sci.* **37**:199–204 (1972).
19. S. Wang, J. Tang, R. P. Cavalieri, and D. Davis, Differential heating of insects in dried nuts and fruits associated with radio frequency and microwave treatments, *Trans. ASAE* **46**:1175–1182 (2003).

20. H. Feng, J. Tang, and R. P. Cavalieri, Dielectric properties of dehydrated apples as affected by moisture and temperature, *Trans. ASAE* **45**:129–135, 2002.
21. R. F. Schiffmann, Food product development for microwave processing, *Food Technol.* **40**:94–98 (1986).
22. R. E. Mudgett, Dielectric properties of foods, in R. V. DeCarreau, ed., *Microwaves in the Food Processing Industry*, Academic Press, New York, 1985.
23. S. O. Nelson, J. Forbus, and K. Lawrence, Permittivity of fresh fruits and vegetables at 0.2 to 20 GHz, *J. Microwave Power Electromagn. Energy* **29**:81–93 (1994).
24. M. A. Stuchly and S. S. Stuchly, Coaxial line reflection methods for measuring dielectric properties of biological substances at radio and microwave frequencies—a review, *IEEE Trans. Instrum. Meas.* **29**:176–183 (1980).
25. D. V. Blackham and R. D. Pollard, An improved technique for permittivity measurement using a coaxial probe, *IEEE Trans. Instrum. Meas.* **46**:1093–1099 (1997).
26. G. P. Otto and W. C. Chew, Improved calibration of a large open-ended coaxial probe for dielectric measurements, *IEEE Trans. Instrum. Meas.* **40**:742–746 (1991).
27. J. de los Santos, D. Garsia, and J. A. Eiras, Dielectric characterization of materials at microwave frequency range, *Mater. Res.* **6**:97–101 (2003).
28. M. Arai, J. G. P. Binner, and T. E. Cross, Estimating errors due to sample surface roughness in microwave complex permittivity measurements obtained using a coaxial probe, *Electron. Lett.* **31**:115–117 (1995).
29. D. K. Ghodgaonkar, V. V. Varadan, and V. K. Varadan, A free space method for measurement of dielectric constants and loss tangents at microwave frequencies, *IEEE Trans. Instrum. Meas.* **37**:789–793 (1989).
30. C. C. Courtney, Time-domain measurement of the electromagnetic properties of materials, *IEEE Trans. Microwave Theory Tech.* **46**:517–522 (1998).
31. V. V. Komarov, and V. V. Yakovlev, Modeling control over determination of dielectric properties by perturbation technique, *Microwave Opt. Technol. Lett.* **39**(6):443–446 (2003).
32. L. Chen, C. K. Ong, and B. T. Tan, Amendment of cavity perturbation method for permittivity measurement of extremely low-loss dielectrics, *IEEE Trans. Instrum. Meas.* **48**:1031–1037 (1999).
33. A. W. Kraszewski and S. O. Nelson, Observation on resonant cavity perturbation by dielectric objects, *IEEE Trans. Microwave Theory Tech.* **40**:151–155 (1992).
34. J. Krupka, D. Cros, M. Auburg, and P. Guillon, Study of whispering gallery modes in anisotropic single-crystal dielectric resonators, *IEEE Trans. Microwave Theory Tech.* **42**:56–61 (1994).
35. J. N. Ikediala, J. Hansen, J. Tang, S. R. Drake, and S. Wang, Development of saline-water-immersion technique with RF energy as a postharvest treatment against codling moth in cherries, *Postharvest Bio. Technol.* **24**:25–37 (2002).
36. M. Kent, *Electrical and Dielectric Properties of Food Materials*, COST 90bis Production, Science and Technology Publishers, Hornchurch, Essex, UK, 1987.
37. N. E. Bengtsson and P. O. Risman, Dielectric properties of foods at 3 GHz as determined by a cavity perturbation technique, *J. Microwave Power EM Energy* **6**:107–123 (1971).
38. J. Tang, J. N. Ikediala, S. Wang, J. Hansen, and R. Cavalieri, High-temperature-short-time thermal quarantine methods, *Postharvest Bio. Technol.* **21**:129–145 (2000).
39. S. Wang, J. N. Ikediala, J. Tang, J. Hansen, E. Mitcham, R. Mao, and B. Swanson, Radio frequency treatments to control codling moth in in-shell walnuts, *Postharvest Bio. Technol.* **22**:29–38 (2001).
40. S. Wang, J. Tang, J. A. Johnson, E. Mitcham, J. D. Hansen, R. Cavalieri, J. Bower, and B. Biasi, Process protocols based on radio frequency energy to control field and storage pests in in-shell walnuts, *Postharvest Bio. Technol.* **26**:265–273 (2002).
41. S. Wang, J. Tang, J. A. Johnson, E. Mitcham, J. D. Hansen, G. Hallman, S. R. Drake, and Y. Wang, Dielectric properties of fruits and insect pests as related to radio frequency and microwave treatments, *Biosyst. Eng.* **85**:201–212 (2003).
42. C. C. Lu, H. Z. Li, and D. Gao, Combined electromagnetic and heat conduction analysis of rapid rewarming of cryopreserved tissues, *IEEE Trans. Microwave Theory Tech.* **MTT-48**:2185–2190 (2000).
43. F. A. Gibbs, Clinical evaluation of a microwave/radiofrequency system (BSD Corporation) for induction of local and regional hyperthermia, *Int. J. Microwave Power EM Energy* **16**:185–192, (1981).
44. J. C. Lin, S. Hirai, C. L. Chiang, W. L. Hsu, J. L. Su, and Y. J. Wang, Computer simulation and experimental studies of SAR distributions of interstitial arrays of sleeved-slot microwave antennas for hyperthermia treatment of brain tumors, *IEEE Trans. Microwave Theory Tech.* **MTT-48**:2191–2198 (2000).
45. M. F. Iskander and C. H. Durney, Microwave methods of measuring changes in lund water, *Int. J. Microwave Power EM Energy* **18**:265–275 (1983).
46. M. A. Stuchly and S. S. Stuchly, Dielectric properties of biological substances—tabulated international, *Int. J. Microwave Power EM Energy* **15**:19–26 (1980).
47. R. Pethig, Dielectric properties of biological materials: Biophysical and medical applications, *IEEE Trans. Electric. Insul.* **EI-19**:453–474 (1984).
48. A. Kraszewski, M. A. Stuchly, S. S. Stuchly, and A. M. Smith, In vivo and in vitro dielectric properties of animal tissues at radio frequencies, *Electromagnetics* **3**:421–432 (1982).
49. S. B. Kumar, K. T. Mathew, U. Raveendranath, and P. Augustine, Dielectric properties of certain biological materials at microwave frequencies, *Int. J. Microwave Power EM Energy* **36**:67–75 (2001).
50. W. Tinga, *Multiphase Dielectric Theory Applied to Cellulose Mixtures*, Ph.D. thesis, Univ. Alberta, Canada, 1969.
51. G. I. Torgovnikov, *Dielectric Properties of Wood and Wood Based Materials*, Springer-Verlag, Berlin, 1993.
52. W. A. Voss, Factors affecting the operation of high-power microwave heating systems for lumber processing, *IEEE Trans. Indust. Gener. Appl.* **GE-20**:234–243 (1966).
53. D. M. Kazarnovskiy and S. A. Yamanov, *Radio Engineering Materials*, Vishaya Shkola Issue, Moscow, 1972 (in Russian).
54. J. M. Catala-Civera, S. Giner-Maravilla, D. Sanchez-Hernandez, and E. de las Reyes, Pressure-aided microwave rubber vulcanization in a ridged three-zone cylindrical cavity, *Int. J. Microwave Power EM Energy* **35**:92–104 (2000).
55. F. Liu, I. Turner, E. Siores, and P. Groombridge, A numerical and experimental investigation of the microwave heating of polymer materials inside a ridge waveguide, *Int. J. Microwave Power EM Energy* **31**:71–82 (1996).
56. M. Arai et al., Elevated temperature dielectric property measurements: Results of a parallel measurement program,

- Proc. Symp. Microwave Theory Appl. Mater. Process. II* **36**:539–546, 1993.
57. J. Braunstein, K. Connor, S. Salon, and L. Libelo, Investigation of microwave heating with time varying material properties, *IEEE Trans. Magn.* **MAG-35**:1813–1816 (1999).
 58. M. G. Hamlin, A. L. Bowden, and N. G. Evans, Measurement and use of high temperature dielectric properties in ceramic processing, *Proc. Int. Conf. Microwave and High-Frequency Heating'95*, Cambridge, UK, 1995, pp. 11–14.
 59. W. Xi and W. Tinga, Error analysis and permittivity measurements with re-entrant high-temperature dielectrometer, *Int. J. Microwave Power EM Energy* **28**:104–112 (1993).
 60. W. Xi and W. Tinga, A high temperature microwave dielectrometer, *Proc. Symp. Microwave Theory Appl. Mater. Process.* **34**:215–224 (1991).
 61. P. Hoekstra and A. Delaney, Dielectric properties of soils at UHF and microwave frequencies, *J. Geophys. Res.* **79**:1699–1708 (1974).
 62. J. E. Hipp, Soil electromagnetic parameters as a function of frequency, soil density and soil moisture, *Proc. IEEE* **62**:98–103 (1974).
 63. J. R. Wang and T. J. Schmutge, An empirical model for the complex dielectric permittivity of soils as a function of water content, *IEEE Trans. Geosci. Remote Sens.* **GE-18**:288–295 (1980).
 64. A. M. Shutko, *Microwave Radio Sensing of Water Surfaces and Soils*, Nauka, Moscow, 1986 (in Russian).
 65. L. V. Gonchariva, V. I. Barinova, U. M. Egorov and V. M. Fedorov, Dielectric properties of disperse soils in microwave range, *Proc. Int. Conf. Application of Microwave Energy in Technology and Science*, Saratov, Russia, 1991, pp. 104–105 (in Russian).
 66. J. B. Salsman, Measurement of dielectric properties in the frequency range of 300 MHz to 3 GHz as a function of temperature and density, *Proc. Symp. Microwave Theory Appl. Mater. Process.* **34**:203–214 (1991).

PERSONAL AREA NETWORKING WITH BLUETOOTH

S. ZEADALLY
 A. KUMAR
 Wayne State University
 High Speed Networking
 Laboratory
 Detroit, Michigan

1. INTRODUCTION

Since the early 1990s, we have witnessed wide proliferations and acceptance of wireless communication technologies in society. Coupled with this major technological development, the rapid decrease in the prices of wireless technologies is paving the way for new networking paradigms such as wireless local-area networking and wireless personal-area networking. Wireless personal-area networking, the focus of this article, enables a user-centered network concept where an individual user, surrounded by a collection of devices (cellphone, laptops, palm pilot, etc),

communicates wirelessly with them and through them with external networks and devices. The wireless personal-area network (WPAN) communication infrastructure should enable a variety of personal communication-enabled devices to be connected to networks anytime, anywhere, and (through) any media [8]. The idea of networking within the personal space exists in different solutions, including body-area network (BAN) [2,3], Picoradio [4], IrDA [5], and HomeRF [6]. The central concepts that led to the convergence of these solutions are wireless connectivity, cable replacement, and embedded low-power and low-cost radio.

Many wireless systems and devices such as cellular phones, personal digital assistants, pagers, and other portable devices have proliferated in contemporary society. However, they are often used separately and their applications do not interact. One of the goals of PANs [7,8] is to enable such a diverse set of devices to exchange information in a seamless, friendly, and efficient way. One of the emerging short-range wireless networking technologies that shows promise as an enabling technology for realizing PANs is the more recent industry-standard Bluetooth [9]. Bluetooth evolved from the need to replace wires in short-range communications (e.g., serial cable between computers and peripherals) with short-range wireless links among small form factor mobile devices. Bluetooth has a transmission range of approximately 10 m in a free propagation environment and operates in the unlicensed 2.4-GHz ISM (industrial, scientific, medical) band. To increase robustness to interference, Bluetooth uses a frequency-hopping technique where the carrier frequency is changed for every packet transmission. To minimize complexity and reduce the cost of transceivers, the signals are modulated using Gaussian frequency shift keying (GFSK) and transmitted in one of 79 channels by a pseudorandom sequence hopped through the 79 channels at a rate of 1600 hops per second.

2. BLUETOOTH TECHNOLOGY AND WIRELESS PERSONAL-AREA NETWORKING STANDARDS

2.1. Bluetooth Technology

Bluetooth enables the creation of ad hoc networks based on the concept of master/slave devices and provides full-duplex transmissions using a slotted time-division duplex (TDD) scheme. Master-to-slave transmissions always start in an even-numbered slot, whereas slave-to-master transmission starts in an odd-numbered timeslot. The master controls data transmission of up to seven slaves using a polling mechanism. Slaves cannot communicate with each other in Bluetooth. Transmission is only between a slave and a master or vice versa. Slaves are allowed to transmit only after being polled. The device that initiates the connection is defined as the “master”. Three configurations are supported by Bluetooth: point-to-point connection, point-to-multipoint (known as a *piconet*), and multiple interconnected piconets with overlapping areas forming a *scatternet*. A Bluetooth unit can simultaneously be a slave of multiple piconets, but a master in only one, and can transmit and receive data in one piconet at a time,

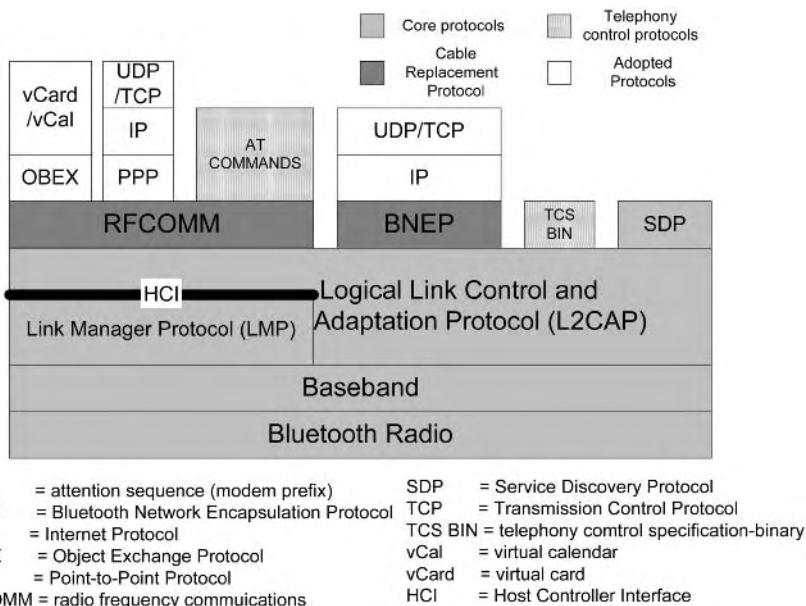


Figure 1. Bluetooth protocol stack.

which implies that time-division multiplexing is needed for participation in multiple piconets. All these characteristics make Bluetooth a strong candidate for establishing PANs. Figure 1 illustrates the Bluetooth protocol stack. Bluetooth is based on a high-performance, low-cost integrated radio transceiver.

Baseband is the physical layer that manages functions such as error correction, packet handling, paging and inquiry to access Bluetooth devices, and Bluetooth security. The baseband transceiver supports a TDD scheme. The Link Manager Protocol (LMP) performs link setup and configuration, authentication, encryption management, and other functions. The Logical Link and Control Adaptation (L2CAP) layer hides the functionalities of Bluetooth lower layers. L2CAP supports protocol multiplexing, provides connection-oriented and connectionless data services to upper layers, and performs segmentation and reassembly operations to and from smaller baseband packets. In addition, L2CAP also supports point-to-multipoint links. The Service Discovery Protocol (SDP) allows Bluetooth applications to discover services available in a Bluetooth environment. Higher-layer protocols such as RFCOMM, OBEX, and TCP/IP can also be used for

Bluetooth to support legacy applications. The Host Controller Interface (HCI) layer provides an interface to access the hardware capabilities of Bluetooth.

Bluetooth supports two types of links between the master and the slave(s): the synchronous connection-oriented (SCO) link and the asynchronous connectionless (ACL) link. The SCO link is a symmetric point-to-point link between a master and a single slave and is typically used for sensitive traffic such as voice. The SCO link (such as between a headset and a cellular handset) reserves two consecutive timeslots: one for transmission and one for reception at fixed intervals. A master can support up to three SCO links to one or different slaves outside its piconet. The slave can support three SCO links from the same master or two links from different masters in their respective piconets. SCO links are symmetric and yield a maximum of 64 kbps (kilobits per second) in both directions. L2CAP supports only ACL links and packet sizes up to 64 kB (kilobytes). The ACL link is point-to-multipoint between a master device and up to seven slaves. ACL links can support both symmetric and asymmetric connections, and ACL packets can be broadcast to all slaves in a piconet. ACL links offer speeds up to 723.2 kbps downlink and

Table 1. ACL Packet Types

Type	Payload Header (bytes)	User Payload (bytes)	FEC	CRC	Symmetric Maximum Rate (kbps)	Asymmetric Maximum Rate (kbps)	
						Forward	Reverse
DM1	1	0-17	2/3	Yes	108.8	108.8	108.8
DH1	1	0-27	No	Yes	172.8	172.8	172.8
DM3	2	0-121	2/3	Yes	258.1	387.2	54.4
DH3	2	0-183	No	Yes	390.4	585.6	86.4
DM5	2	0-224	2/3	Yes	286.7	477.8	36.3
DH5	2	0-339	No	Yes	433.9	723.2	57.6
AUX1	1	0-29	2/3	No	185.6	185.6	185.6

simultaneously 57.6 kbps uplinks for ACL. All ACL packets shown in Table 1 use CRCs (cyclic redundancy checks), and in the presence of errors they are retransmitted. The Bluetooth standard offers a range of data packet types: DH_x and DM_x . The H-type packets have higher payloads whereas the M-type packets support medium payloads but include forward error correction (FEC) for error recovery in noisy operating conditions. The baseband controller can be configured to select the packet type. Actually, the strategy is if a higher-layer (i.e., L2CAP layer and above) packet exceeds the size of the DH or DM packets, the next DH or DM packet of the minimum size is chosen. This method improves link utilization and also reduces overhead.

2.2. WPAN Standards

Future WPANs will require innovative system solutions and appropriate network design architectures to provide mobile users local and global access with high availability, low power, and minimal infrastructure requirement. To achieve these objectives, the IEEE has created the IEEE 802.15 [10] working group, which concentrates on developing consensus standards for WPANs or short-distance wireless networks. The activities within the IEEE 802.15 working group are divided into various task groups, each of which focuses on a different issue; task group 1 deals with Bluetooth, task group 2 deals with coexistence issues between WPANs (802.15) and wireless local-area networks (WLANs) (802.11), task group 3 deals with high-rate (≥ 20 -Mbps) WPANs, task group 3a is chartered to work on higher-speed (≥ 110 -Mbps) WPANs, and task group 4 is investigating a low-data-rate solution (< 0.25 Mbps) with multimonth to multiyear battery life, and very low complexity. We summarize the IEEE 802.15 standards in Table 2.

It is worthwhile pointing out also that IEEE has also approved four projects concerning IEEE 802.15 WPAN standards. These projects deal with a wireless mesh topology standard for WPAN devices and modifications to the high-rate WPAN standard so that it supports wireless multimedia applications more effectively. The task groups include IEEE 802.15.5, which will develop an architectural framework for interoperable, stable, and scalable wireless mesh topologies for WPAN devices. The mesh topologies are expected to extend network coverage without increasing transmission power or receiver sensitivity.

These topologies also aim to improve reliability through route redundancy, simpler network configuration, and longer battery life. The 802.15.3b group deals with modifications of IEEE 802.15.3 to improve ease of implementation and interoperability while maintaining backward compatibility. The 802.15.4a group is expected to design alternate WPAN physical-layer specifications to meet the evolving needs of ultra-low-complexity, ultra-low-cost, ultra-low-power WPAN communications. It will provide for precision to one meter or less, improved communications range, improve link robustness, and the ability to support mobility. The IEEE 802.15.4 standard will be revised by the 802.15.4-REVb group to remove ambiguities and will be extended to support shared time base distribution and new frequency allocations in Europe, China, and Japan.

3. SEAMLESS CONNECTIVITY OF BLUETOOTH TO IP-BASED NETWORKS

The proliferation of IP over all kinds of networks today makes it necessary to support Bluetooth applications over IP-based networks. However, an IP-over-Bluetooth profile was not specified in the Bluetooth specifications. There are currently two ways of running IP-based applications over Bluetooth; one approach is to use the LAN profile [11], and the other approach is to use the PAN profile [12].

3.1. LAN and PAN Profiles

The LAN profile defines how Bluetooth-enabled devices can access services of a LAN using the IETF Point-to-Point Protocol PPP [13] as shown in Fig. 2. A frequent topology used consists of a LAN access point (LAP), which is a Bluetooth device that provides the services of a PPP server, and a data terminal (DT), which is a Bluetooth device that acts as a PPP client. Using appropriate PPP mechanisms, a suitable IP address is negotiated between the LAN access point and the data terminal.

The PAN profile describes how two or more Bluetooth-enabled devices can form an ad hoc network and how the same mechanism can be used to access a remote network through a network access point [12]. It uses the Bluetooth Network Encapsulation Protocol (BNEP) [14] to provide networking capabilities for Bluetooth devices. BNEP encapsulates packets from various networking protocols,

Table 2. IEEE 802.15 Standards

IEEE Standard	Area Covered	Data Rate	Potential Applications
802.15.1	Bluetooth	1 Mbps	Speakers, microphones, headsets, printers, cellphones, PDAs, sensors, etc.
802.15.2	Coexistence between Bluetooth and 802.11	N/A	N/A
802.15.3	High-rate WPAN	> 20 Mbps	Low-power, low-cost solutions for portable consumer digital imaging and multimedia applications
802.15.3a	Higher-rate WPAN	> 110 Mbps	Streaming and other multimedia applications
802.15.4	Low-rate WPAN	2.4 GHz—250 kbps; 868/915 MHz—20/10 kbps	Sensors, smart badges, interactive toys, remote controls, home automation

Source: Ref. 1.

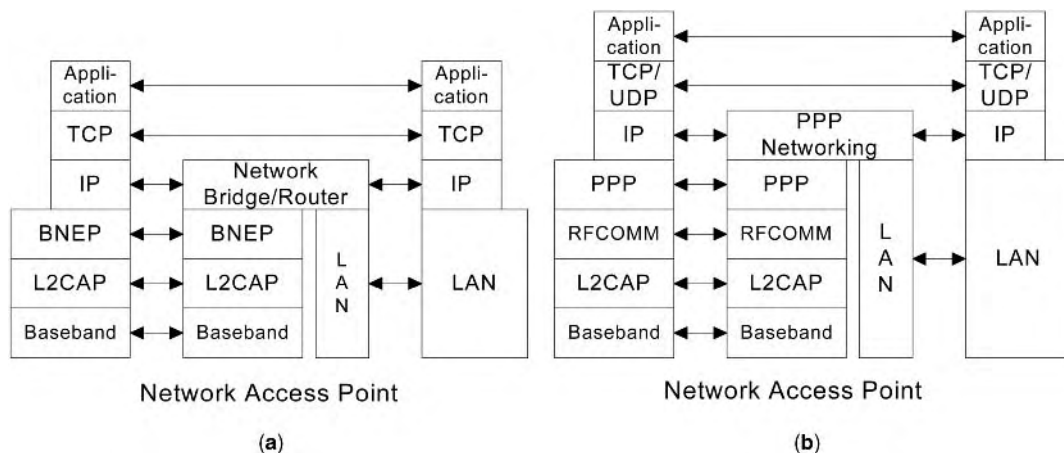


Figure 2. PAN profile using Bluetooth Network Encapsulation Protocol (BNEP) (a) versus LAN access profile (using PPP and RFCOMM) (b).

which are transported directly over L2CAP. BNEP includes support for common networking protocols such as IPv4, IPv6, IPX, and other existing or emerging networking protocols supported by IEEE 802.3/Ethernet encapsulation. BNEP removes and replaces the Ethernet header with the BNEP header, leaving the Ethernet payload unchanged. Both the BNEP header and the Ethernet payload are encapsulated by L2CAP.

3.2. IPv6-Enabled Bluetooth Devices

Depletion of IPv4 addresses is one of the reasons for the development of IPv6. IPv6 also defines *stateful* and *stateless* autoconfiguration [15]. Stateful autoconfiguration is the IPv6 equivalent of DHCP. DHCPv6 is used to pass out addressing and service information in the same way as DHCP is used in IPv4. The stateless configuration works as follows. Appending the interface’s identifier to the well-known link-local prefix forms a link-local address. The node then verifies that this tentative address is unique by sending neighbor solicitation messages. The next phase of autoconfiguration involves obtaining a router advertisement or determining that no routers are present. If routers are present, they will send router advertisements that specify what sort of autoconfiguration a host should do.

We need to exploit the IPv6 feature of autoconfiguration to enable Bluetooth devices to automatically connect to an IPv6-based Internet. This facility enables seamless connectivity as users of Bluetooth-enabled devices such as handheld PDAs and cellphones can roam around a variety of networks—ad hoc networks network hotspots and traditional fixed networks in the home and the office. Most users of these handheld devices will not have the expertise to reconfigure IP parameters. Another incentive for Bluetooth device manufacturers to support IPv6 is the upcoming support for Bluetooth in Windows XP, which will have native Bluetooth support. From a home networking point of view, the IPv6 autoconfiguration feature is also desired [16,17].

3.3. Effect of LAN and PAN Profiles with IPv4, and IPv6 Protocol Stacks on Latency

Our experimental testbed consists of an IPv6 network. The Bluetooth device that acts as a master consists of two interfaces—one is an Ethernet interface that connects it to an IPv6 local-area network and the other is a Bluetooth interface. The Bluetooth master is configured as a router. When a Bluetooth device (slave) establishes a connection to the Bluetooth master, an interface is created on the slave side. The Bluetooth slave is autoconfigured over this interface. The slave can access the IPv6 network without requiring any further configuration from the user. A single Bluetooth piconet consists of one master and up to seven slaves. If such a configuration is performed, all the slaves can access the IPv6 network and can communicate with each other.

We used various performance metrics to explore the impact of PAN and LAN profiles, IPv4, and IPv6 on data and voice transmissions to IP-enabled Bluetooth devices. It is useful for application designers and developers of IP-based Bluetooth applications to know whether the LAN or the PAN profile gives optimal Bluetooth performance. We used latency (measured using Netperf [18]) as the performance metric. Our testbed consisted of two identical laptops (each with an Intel Pentium III, 789-MHz processor, 512 MB of RAM) and one iPAQ pocket PC, all running BlueZ [19] protocol stack, with the laptops running Red Hat 9 Linux operating system, and the pocket PC running Familiar v0.7 Linux operating system. Both laptops and the pocket PC were equipped with BL-500 Bluetooth network adapters (from Brainboxes) and they all had support for both IPv4 and IPv6 protocol stacks as well as PAN and LAN profiles. For the latency tests, we used the two laptops and experimented with packet sizes in the range 64–1600 bytes. The reason for this choice for the packet size range stems from observations that most packet sizes on networks and the Internet are within this range [20].

Figure 3 shows one-way latency results (round-trip latency test measures how long it takes a packet to travel from one host to another and back to the originating host.

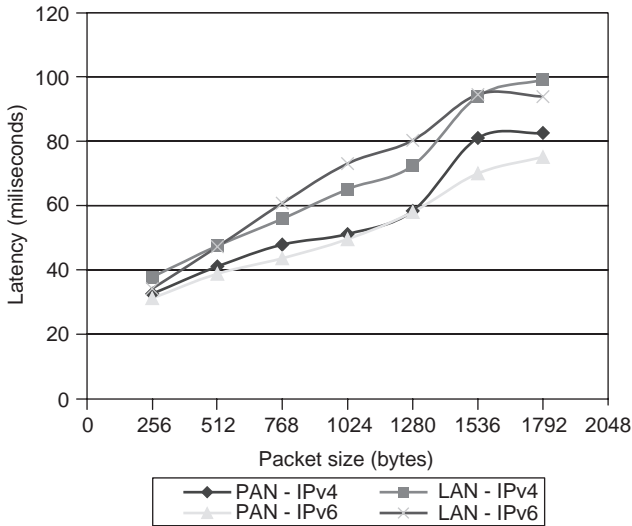


Figure 3. Latency using LAN and PAN profiles over IPv4 and IPv6 protocol stacks. (This figure is available in full color at <http://www.mrw.interscience.wiley.com/erfme>.)

One-way latency is half of the round-trip latency) obtained with raw data for LAN and PAN over IPv4 and IPv6. For both IPv4 and IPv6, we obtained better (i.e., lower) latencies with PAN compared to LAN. In fact, a close look at the results shown in Fig. 3 reveals that latency of PAN transmission ranges from 14% to 21% and 8% to 32% lower than LAN transmission in the case IPv4 and IPv6, respectively. The serial bit transmission characteristic associated with PPP probably accounts for the higher delays obtained with LAN packetized transmissions.

3.4. Voice Delivery to IPv4 and IPv6-Enabled Bluetooth PDAs

There has been a lot of interest recently (as of 2004) in delivering voice over IP-based networks. For Voice over IP (VoIP) to become reality and widely deployed, we need to support voice transmission and delivery on an *end-to-end* basis. It is no longer sufficient to support VoIP over wired networks only. In fact, the wide proliferation of wireless networks require VoIP support to extend to wireless net-

work segments frequently connected to wired LAN and the Internet. In addition, we should also be capable of delivering voice a range of popular devices such as PDAs and cellular phones. Only when these conditions are satisfied will a true end-to-end VoIP deployment be possible to mobile, handheld devices associated with mobile users. We investigate the deployment of a VoIP implementation that supports these goals—the wireless network under consideration being the Bluetooth network, and the iPAQ pocket PC running, the familiar v0.7 Linux operating system. In addition, we exploit IPv6 in our VoIP implementation to achieve seamless connectivity (i.e., with zero configuration) and delivery of voice to Bluetooth handheld devices connected to IP-based networks.

We experimented with various CODECS, namely G721 (yielding a bit rate of 32 kbps), G723 (yielding a bit rate of 24 kbps) and G723 (yielding a bit rate of 40 kbps). We experimented with two different voice packet sizes (40 and 20 ms) in our voice tests. The 20-ms voice packet size translates to 120, 160, and 200 bytes with G723 (yielding a bit rate of 24 kbps), G721 (yielding a bit rate of 32 kbps), and G723 (yielding a bit rate of 40 kbps), respectively. It is worthwhile explaining how the 20-ms voice packet size used translates to 120 bytes with a G723 CODEC. For a voice recording of 20 ms, a sampling rate of 8000 samples per second, stereo (two channels), a sample size of 16 bits (linear PCM) we get an uncompressed voice packet size of 640 ($20 \times 8000 \times 2 \times 16/8 \times 1000$) bytes. This yields an encoded (compressed) voice packet size output of 120 bytes with the G723 CODEC. In the case of the 40 ms voice packet size translates to 240 bytes, 320 bytes, and 400 bytes with G723, G721, and G723, respectively. To assess the voice quality delivered by the iPAQ running IP and connected to a Bluetooth network, we used end-to-end delay and jitter of the voice delivered.

3.4.1. End-to-End Voice Delay with IPv4 and IPv6. The results shown in Fig. 4 demonstrate that on average we obtained an end-to-end delay of about 60–70 ms in the voice delivery. This is well below the recommended end-to-end delay by ITU Recommendation G.114 [21], which recommends that the maximum one-way end-to-end delay acceptable by most users should be within 150 ms [22,23] to achieve the same speech quality as a normal telephone

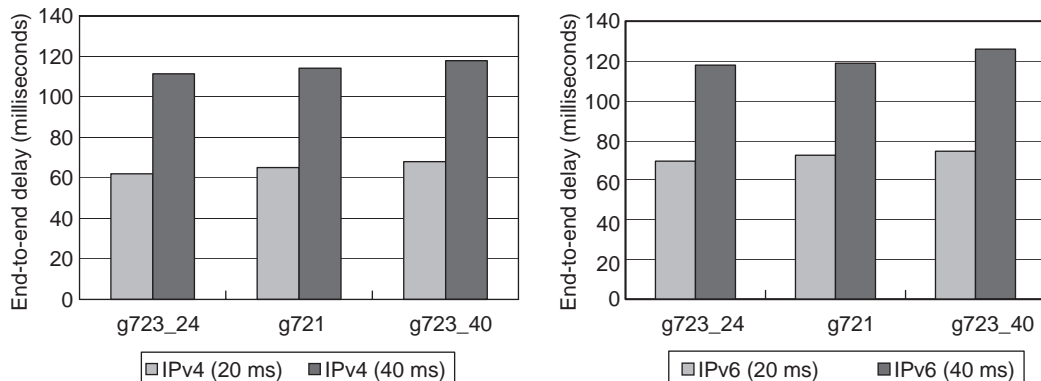


Figure 4. End-to-end delay of voice using different CODECs over IPv4, IPv6 stacks on iPAQ. (This figure is available in full color at <http://www.mrw.interscience.wiley.com/erfme>.)

conversation. Interestingly, the end-to-end delay results over IPv6 are also very similar to those obtained with IPv4 despite extra overheads (such as larger addresses) with IPv6. Furthermore, from these results, we also note that the execution of the IPv6 stack on the iPAQ does not really introduce any performance degradations in voice performance. These latency results demonstrate the feasibility of delivering high-quality voice over Bluetooth to IPv6-enabled handheld devices such as iPAQs. Another observation worth noting is that the smaller of the voice packet size (i.e., 20 ms) yields the lowest end-to-end delay. As far as the CODECs are concerned, we found that the G723 (yielding a bit rate of 24 kbps) yields the best (i.e., lowest) voice delay performance among the CODECs tested. In the case of jitter, we obtained on average 28–30 ms and 51–54 ms with voice packet sizes of 20 and 40 ms, respectively, with the three CODECs tested. The 20 ms voice packet size yields the lowest jitter, which is well below the recommended jitter for excellent voice quality. Karam and Tobagi [24] found that for best voice quality, the jitter experienced by voice should be at most 50 ms so that the playback at the receiver end remains smooth.

4. COEXISTENCE OF BLUETOOTH AND IEEE 802.11 WLANs

Various radiofrequency technologies such as Bluetooth and IEEE 802.11 WLANs are being adopted at a rapid pace in academic office spaces, buildings, and campuses. One of the major issues arising out of the coexistence of these radiofrequency (RF) systems is the possibility of interference on each other. Various performance studies [25–28] have been conducted by several research groups, including the IEEE 802.15 working group to investigate the impact of IEEE 802.11 on Bluetooth transmissions. Gollmie et al. [28] investigated the effect of several factors, such as transmitted power, offered load, packet size, hop rate, and error correction on performance. They found that power control may have limited benefits in an interference environment. Increasing the Bluetooth transmission power even 10 times is not sufficient to reduce Bluetooth packet loss. They also found that short packets lead to less packet loss for Bluetooth at the cost of causing more interference on wireless LANs. Sriskanthan et al. [29] propose an application of Bluetooth technology in home automation and networking environment. Initially, due to lack of Bluetooth products, most, if not all empirical analyses were based solely on *simulations* that do not really capture the problems often arising in typical *real, physical* networking environments. To address this issue and distinguish our efforts from those previously undertaken, we present *practical* performance results using real Bluetooth and 802.11 networks. We conducted several tests to explore the influence of IEEE 802.11 interference on Bluetooth communication performance using raw data transfers and audio/video streaming. We used performance metrics such as time taken to stream audio/video and throughput in the case of raw-data transfers. We measured the raw application-to-application TCP/IP throughput using Netperf. For the interference measurement

tests, we used TCP/IP data transmission as the interfering traffic and we ensured that the interfering traffic remained present until the end of the test under consideration. This ensures that we do measure the actual performance in the presence of interference.

The testbed we used in our experiments includes four identical laptops (each with an Intel Pentium III, 789-MHz processor, 512 MB of RAM), one 802.11 wireless Ethernet access point, and one AXIS 9010 Bluetooth access point. Two laptops were each equipped with a Xircom Credit Card Bluetooth adapter. The other two laptops were each equipped with a Dell TrueMobile 1150 Series wireless PCI adapter. Thus, on the Bluetooth network, we used two Bluetooth laptops connected to each other via the Bluetooth access point. We used the other two laptops on the 802.11 network connected via the 802.11 access point. It is worthwhile pointing out that in our tests we used a link rate of 1 Mbps for the 802.11 network. We could have used 11 Mbps link speed but we wanted to have comparable link speed with Bluetooth to avoid introducing further parameters that could affect our results and their interpretations. The Bluetooth specification specifies a maximum throughput of about 720 kbps [9].

4.1. Application Throughput without Interference

We first investigated the best performance achievable with Bluetooth and IEEE 802.11 technologies under conditions when each is operating on its own (i.e., without any interference from the other technology). We varied the distance between the two laptops and measured the effect of distance on the application throughput. The Bluetooth technology is expected to deliver uniform performance within 10 m range. Our experiment indeed reveals negligible changes in the throughput with increasing distance between the Bluetooth nodes (as shown in Fig. 5). We obtained similar results with increasing distance between the 802.11 wireless nodes. However, we obtained around 680 kbps (68% link utilization) with 802.11 transmissions compared to Bluetooth transmissions where we obtained around 200 kbps (only ~28% link utilization).

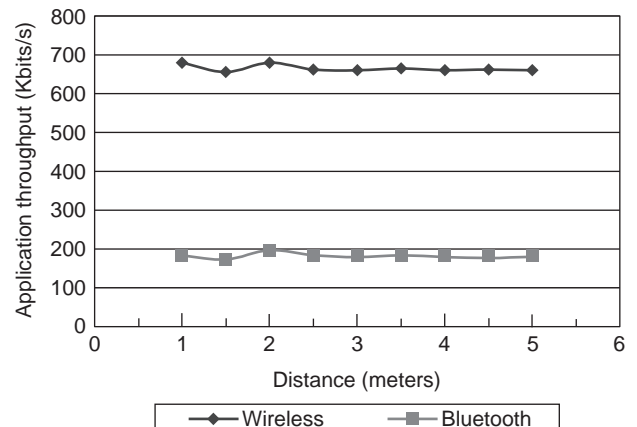


Figure 5. Variation of throughput of Bluetooth and 802.11 nodes with distance. The throughput of each was measured on its own (without interference).

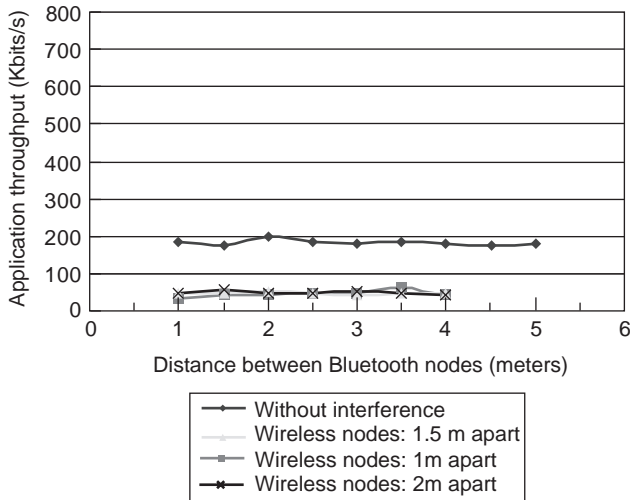


Figure 6. Throughput of Bluetooth in the presence of interference caused by 802.11 LAN transmissions. The 802.11 nodes are set at distances of 1, 1.5, and 2 m apart. (This figure is available in full color at <http://www.mrw.interscience.wiley.com/erfme>.)

4.2. Application Throughput with Interference

Figures 6 and 7 show variations in throughput using Bluetooth and 802.11 nodes. It is interesting to note from Fig. 7 that in the presence of interfering Bluetooth traffic, there is almost *no* impact on the 802.11 wireless transmission rate, which yields almost the same application throughput for different distances between the Bluetooth nodes. However, the converse is not true for the performance observed with Bluetooth in the presence of competing 802.11 LAN traffic. In this case, as Fig. 6 illustrates, we obtained much lower performance (~50 kbps) with Bluetooth compared to the case with no interference. This translates to almost a *fourfold* degradation in Bluetooth throughput in the presence of 802.11 LAN interference traffic.

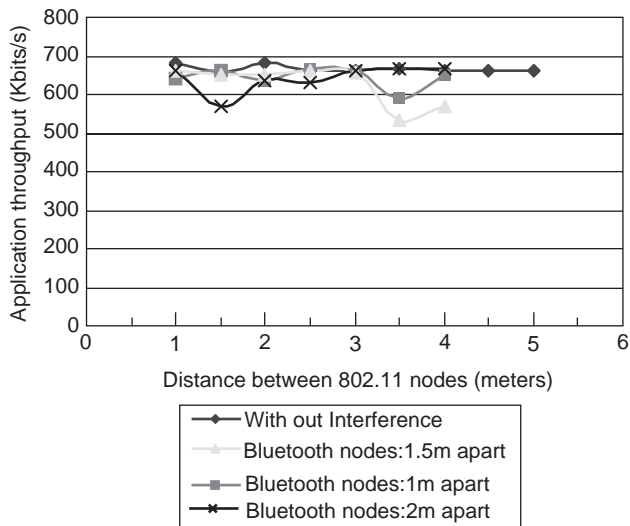


Figure 7. Throughput of 802.11 node in the presence of Bluetooth interference. The distances between the two Bluetooth nodes are set at 1, 1.5, and 2 m. (This figure is available in full color at <http://www.mrw.interscience.wiley.com/erfme>.)

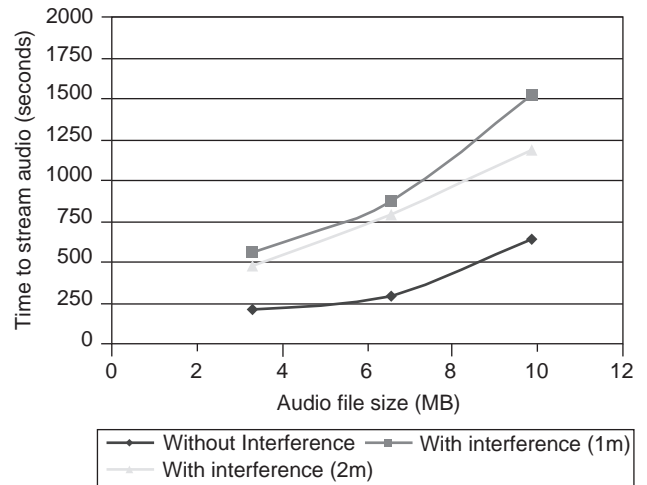


Figure 8. Time taken to stream different audio file sizes. (This figure is available in full color at <http://www.mrw.interscience.wiley.com/erfme>.)

4.3. Audio/Video Streaming

We investigated the impact of interference on Bluetooth devices performing audio/video streaming. The streaming test used different file sizes between two Bluetooth nodes. One node (at the client side) had Windows Media Player for audio/video streaming and playback. The other Bluetooth node (the server side) was configured as a Web server using Microsoft Information Services). Audio and video were streamed from one Bluetooth node to the other via the Bluetooth access point (connected to the local LAN).

Figures 8 and 9 show the audio/video streaming results. For both audio and video, we report the *time taken* to stream and play the audio (using Windows Media Audio format) or video (using Windows Media Video format).

Figures 8 and 9 show that the time taken to stream continuous media increases by almost 3 times for video and almost 2 times for audio in the presence of 802.11 traffic interference. The closer the 802.11 wireless nodes are to the Bluetooth devices, the higher the interference

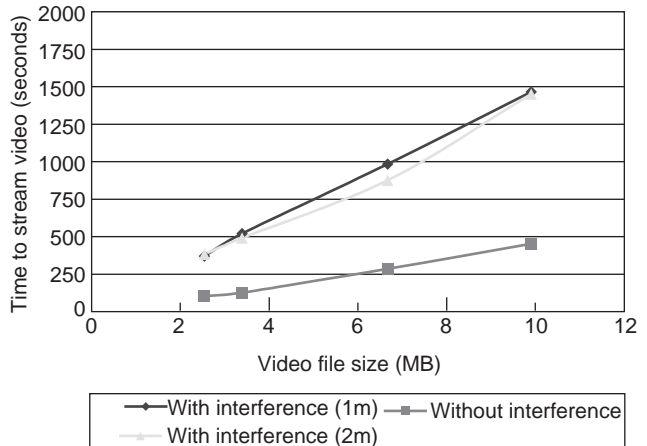


Figure 9. Time taken to stream different video file sizes. (This figure is available in full color at <http://www.mrw.interscience.wiley.com/erfme>.)

leading to slightly higher times for a distance of one meter compared to a distance of two meters.

It is clear from the experimental results that the interference caused by 802.11 traffic on Bluetooth transmissions is significant and seriously impedes performance of the latter. We speculate some possible explanations for the Bluetooth performance degradation. A Bluetooth channel is divided into timeslots, each 625 μs in length. Bluetooth packets may extend up to five timeslots depending on the packet type in use, and the frequency remains fixed for the duration of the packet. In the presence of 802.11 traffic, Bluetooth shares the same frequency band, and a static packet format may lead to low efficiency since multislot packets are more likely to face interference for longer durations, thereby decreasing Bluetooth throughput. This is a direct result of the fact that Bluetooth lacks the ability to automatically adapt to meet changing channel conditions. Another possible explanation could be due to increased retransmissions by the sender because of frequent timeouts for not receiving acknowledgments since these acknowledgments also compete with 802.11 traffic for channel access.

We explored the performance of individual DH_x and DM_x (where x can have values 1,3,5) packet types in the presence and absence of IEEE 802.11 interference. We used the results (shown in Fig. 10) obtained as the basis to change the packet type in the design of a novel dynamic implementation that will improve Bluetooth performance in the presence of 802.11 traffic. We observe from the results of Fig. 10, in the absence of IEEE 802.11 interference, DH₅ and DM₅ yield maximum throughput and in the presence of IEEE 802.11 interference, DM₅ gives a maximum throughput of 269 kbps (L2CAP MTU is 2016 bytes).

The L2CAP MTU field represents the largest L2CAP payload, in bytes, that the originator of a request can accept for that channel. The default MTU value is 672 bytes. This default MTU is selected based on the payload carried by two DH₅ packets (2 × 341 = 682 bytes), excluding the baseband ACL headers (2 × 2 = 4 bytes) and L2CAP header (6 bytes). Each Bluetooth profile specifies a particular L2CAP MTU. For example, the PAN profile requires a minimum L2CAP MTU of 1691 bytes [12]. We performed another preliminary experiment between two Bluetooth

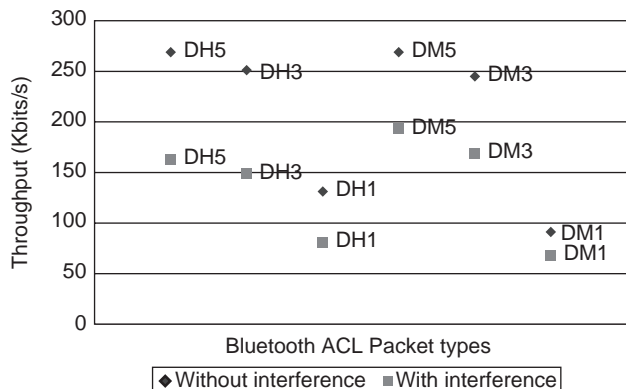


Figure 10. Performance of ACL packet type. (This figure is available in full color at <http://www.mrw.interscience.wiley.com/erfme>.)

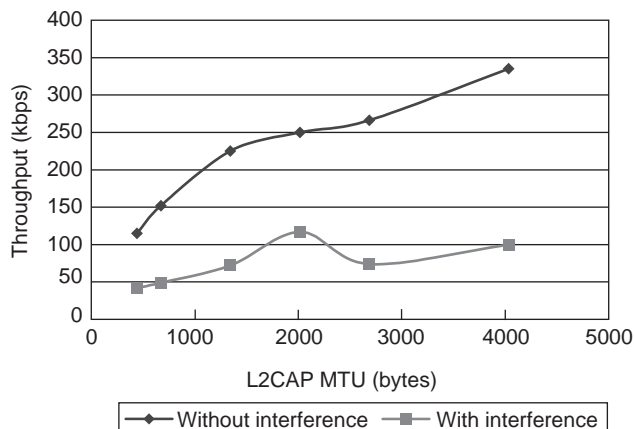


Figure 11. Variation of throughput with L2CAP MTU. (This figure is available in full color at <http://www.mrw.interscience.wiley.com/erfme>.)

devices to study the optimal L2CAP maximum transmission unit (MTU) value. The L2CAP MTU value was varied and we calculated the corresponding throughput by measuring using the time taken to transfer a fixed number of packets for an L2CAP client-server socket program. The results are shown in Fig. 11. In the absence of interference, the throughput increases with increase in MTU. In the presence of interference, an L2CAP MTU of 2016 bytes (3 times the default value of 672 bytes) yields the best throughput (120 kbps) and shows a 140% increase in throughput over the default L2CAP MTU value of 672 bytes (50 kbps).

4.4. Novel Dynamic Approach to Improve Bluetooth Performance in the Presence of Interfering 802.11 LAN Traffic

We designed and implemented a scheme that enables robust Bluetooth transmissions that is minimally affected by 802.11 interference traffic. Our proposed design works at the L2CAP layer of Bluetooth and dynamically adapts the ACL packet type to improve Bluetooth performance. It is worthwhile pointing out that we also investigated several other parameters such as the L2CAP flush timeout, ACL MTU, and transmission window size, but none of them really showed significant performance improvements that mitigate the interference effects of 802.11 traffic. Two parameters, namely, the L2CAP MTU and the ACL packet type, yield considerable improvement in the performance of Bluetooth even in the presence of interference. We therefore exploited these parameters in our implementation.

4.4.1. Implementation. To implement a design that dynamically adapts the Bluetooth transmission parameters according to dynamic conditions requires access to the Bluetooth stack or the underlying Bluetooth hardware. Since we are using commercially available Bluetooth hardware adapters, we do not have access to the link manager, baseband layer, or the radio layer. Other researchers and designers also face similar constraints. Consequently, if we were to modify Bluetooth, we could do so only at the application layer or at the kernel layer. We chose a kernel implementation (at the L2CAP layer) for

our proposed scheme since it allows us to modify the Bluetooth stack and secondly, the modified stack can be used by others without modifying their Bluetooth applications. Furthermore, the implementation could have also been implemented using higher-layer sockets such as RFCOMM, but such a layer would not be used by all the other Bluetooth profiles, and any improvements obtained would be limited to that profile only.

We used the BlueZ Bluetooth protocol stack running on Red Hat Linux version 9. The Host Controller Interface (HCI) provides a uniform command method for accessing the underlying Bluetooth hardware capabilities. HCI link commands provide the host with the ability to control link layer connections to other Bluetooth devices. These commands enable the link manager (LM) to exchange LMP commands with remote Bluetooth devices. The HCI firmware implements the HCI commands for the Bluetooth hardware by accessing the baseband/link manager commands, hardware status registers, control registers, and event registers. Several layers may exist between the HCI driver on host system and the HCI firmware on the Bluetooth hardware. These intermediate layers (such as the Host Controller Transport Layer) provide the ability to transfer data. Bluetooth ACL packet types and sizes are selected by the baseband layer which, as mentioned previously, is not accessible to the user or host device driver software. However, it is possible to force the baseband layer to use a particular packet type by using the link command `Change_Connection_Packet_Type`.

Our implementation relies on the dynamic adaptation of packet sizes during a Bluetooth transmission subjected to interference caused by IEEE 802.11 LAN traffic. We established a connection between a Bluetooth slave and a Bluetooth master on L2CAP connection-oriented sockets. Using the previous results illustrated in Figs. 10 and 11, our implementation of the proposed dynamic approach works as follows. In the initial phase, our implementation chooses the ACL packet size to avoid overheads due to padding. For instance, if the user payload is less than 10 bytes, our implementation chooses a DM_1 packet. If the user payload is greater than 177 bytes, our implementation chooses DM_5 rather than DM_3 since better performance is obtained with DM_5 in the presence of interference.

At various stages during transmission, our implementation periodically calculates the throughput delivered and simultaneously obtains the link quality (an indicator of how much interference is taking place). To obtain the link quality, we exploit the HCI command `Get_Link_Quality`, which returns a value for the current link quality (in the range 0–255) of the ACL link between the two Bluetooth devices. The higher the value returned, the better is the link quality. From the preliminary experiments, we found that the value of the link quality is above 230 in the absence of IEEE 802.11 interference traffic but below 215 in the presence of 802.11 traffic.

Our implementation periodically checks the link quality and the actual throughput value obtained for that signal quality. Depending on the value of the throughput obtained, the packet size chosen by the baseband layer is varied accordingly using the HCI command `Change_Connection_Packet_Type` (as explained earlier) to yield the

highest throughput. Basically, the dynamic implementation changes the ACL packet type to DM_5 if the user payload is greater than 120 bytes or if the user payload is between 20 and 120 bytes, DM_3 is chosen. If the user payload is less than 20 bytes, DH_1 is selected (rather than DM_1 since in the presence of interference DH_1 yields higher performance). One issue that we faced during the implementation is the rate at which we check the link quality and measure the actual throughput experienced. We have implemented a timer function to perform the periodic sampling at small enough intervals to ensure a smooth adaptation based on actual channel conditions.

4.4.2. Evaluation of Dynamic Approach. To evaluate our implementation, we conducted file transfer performance tests that measured the time taken to perform file transfers with and without interference, with and without using the dynamic implementation. For the interference measurement tests, we used TCP/IP data transmission as the interfering traffic. We ensured that the interfering traffic remained present for the duration of the test under consideration thereby making sure that we measure the actual performance in the presence of interference.

The testbed used in our experiments included four identical laptops (each with an Intel Pentium III, 789-MHz processor, with 512 MB of RAM) running Linux Red Hat 9 operating system, and one 802.11 wireless Ethernet access point. Two of the laptops were each equipped with a Brainboxes BL-500 Bluetooth adapter using the BlueZ (the official Bluetooth protocol stack for Linux). The other two laptops were each equipped with a Dell TrueMobile 1150 Series wireless PCI adapter. Thus, on the Bluetooth network, we used two Bluetooth laptops connected to each other via ACL link. The Bluetooth specification specifies a maximum throughput of ~ 720 kbps. We used the other two laptops on the 802.11 network connected via the 802.11 access point. We performed experiments with link speed of 1 Mbit/s for the 802.11 network to have comparable link speed to Bluetooth transmissions.

4.4.3. File Transfer Performance. We executed a file transfer application and measured the time taken to transfer different file sizes. The results we obtained are shown in Fig. 12. In the absence of interference, we found that the time taken when the dynamic implementation is used is close to the case when it is not used. This demonstrates that the dynamic implementation does not really introduce significant overheads to the overall performance delivered to users. When Bluetooth is subjected to 802.11 traffic interference, for the different file sizes tested, we obtained a performance improvement (in terms of time taken to transfer files) of 51–85% over the case when our dynamic implementation is not used.

As mentioned previously, the experimental tests were conducted by transferring a fixed number of packets. The time measured is the time taken to transfer all the packets. For the L2CAP program (without our dynamic packet size adaptation implementation), more time is taken in the presence of interference. However, our implementation improves the performance of Bluetooth in the presence of interference, and therefore the time taken to

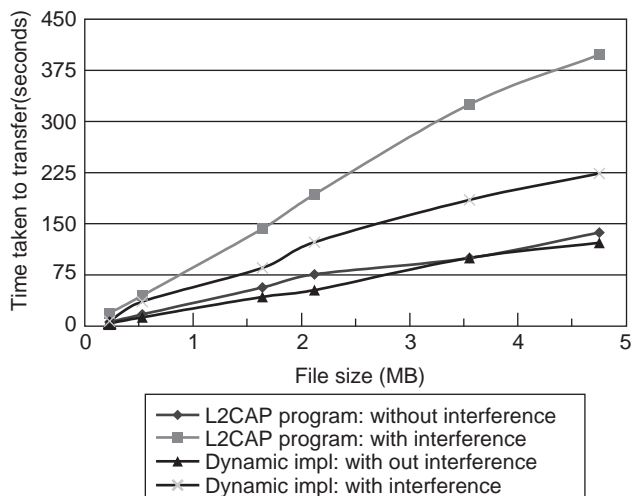


Figure 12. Time taken for file transfers using and without using the dynamic implementation in the presence and absence of 802.11 traffic interference. (This figure is available in full color at <http://www.mrw.interscience.wiley.com/erfme>.)

transfer the same number of packets is smaller. It is worthwhile noting that our proposed dynamic packet size adaptation needs to be implemented at the L2CAP layer. Our approach is designed using L2CAP sockets as we had no access to Baseband. However, Bluetooth ACL packets are defined at the Baseband layer. We dynamically configure the Baseband layer to use a particular packet type by using HCI Commands. Given direct access to the Baseband layer, the dynamic packet size adaptation can be implemented at the Baseband layer.

5. MULTIMEDIA SUPPORT OVER BLUETOOTH

Audio/video streaming applications have become increasingly popular. Advances in hardware and software technologies are making it possible to support these applications types on a wide range of devices. We expect future deployment of devices such as Bluetooth-enabled personal digital assistants (PDAs) and pocket PCs will support a wide variety of streaming applications involving audio and video [30].

5.1. Audio/Video Distribution Transport Protocol (AVDTP)

The Audio/Video (A/V) Distribution Protocol [31] defines the transport protocol and procedures that enable the distribution of advanced audio and video content of high quality on ACL channels. The basic audio functionality in Bluetooth only supports uncompressed voice connection with pulse-code modulation (PCM), and a bandwidth of 64 kbps is assigned to each voice connection. The term “advanced audio” should be distinguished from “Bluetooth audio,” which indicates distribution of narrowband voice on SCO channels as defined by the Bluetooth Baseband specification [9]. A typical usage case for AVDTP is the streaming of music content from a stereo music player to headphones or speakers. The audio data are compressed in an appropriate format for efficient use of the limited

bandwidth. The SCO link allocates a fixed bandwidth between the master and the slave. The master maintains the SCO link by using reserved slots at regular intervals. The basic unit of reservation is two consecutive slots (one in each transmission direction). The reservation of slots by SCO links leaves very limited piconet bandwidth for the other ACL links in the piconet. Furthermore, it is worthwhile noting that the transmission of audio/video over the Internet requires the support of an audio encoding/decoding scheme and a packet-switched network connection—which is not offered by the SCO connection. Therefore, in order to support the transfer of high-quality A/V data using limited bandwidth and a packet transfer mode, ACL channel is a better alternative.

The Audio Video Working group has defined a Bluetooth profile that allows streaming of high-quality mono or stereo audio directly over L2CAP from another device. This profile, the Advanced Audio Distribution Profile (A2DP) [32], is based on the Generic Audio/Video Profile Distribution Profile (GAVDP) [33], which in turn uses Audio/Video Distribution Transport Protocol (AVDTP). AVDTP specifies the transport protocol for audio and video distribution and streaming over the Bluetooth air interface using ACL links. AVDTP provides rules and procedures to provide high-quality isochronous communication (required for the transmission of clock-dependent processes) for the transfer of A/V data. Figure 13 shows the protocol stack model for AVDTP. The transport mechanism and message formats of the AVDTP are based on the Real-time Transport Protocol (RTP).

AVDTP defines the signaling mechanism between Bluetooth devices for stream setup and media streaming of audio or video using ACL links. A/V streaming and signaling setup messages are transported via L2CAP packets. A dedicated Protocol/Service Multiplexer (PSM) value (the PSM value for AVDTP is 25) is used to identify L2CAP packets that are intended for AVDTP. AVDTP applies point-to-point signaling over connection-oriented L2CAP channel set up in advance between two devices participating in A/V streaming.

Before A/V applications transport A/V streams over a Bluetooth link, AVDTP performs A/V parameter negotiation. Based on the result of this negotiation, applications transfer A/V content. Figure 14 shows the AVDTP architecture (as defined by the AVDTP specification). We summarize the major functions of the AVDTP components below:

- *Stream manager*—provides the following functions: streaming, media framing, timestamp management,

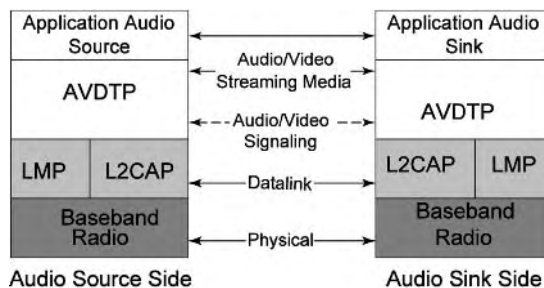


Figure 13. AVDTP protocol model and the Bluetooth protocol stack.

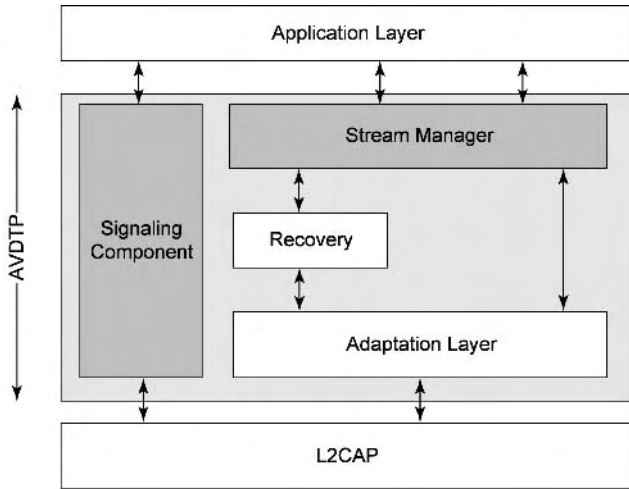


Figure 14. AVDTP architectural components in the Bluetooth protocol stack.

media packet sequence numbering, reporting of packet loss to higher layers, and calculation of jitter

- *Recovery component*—provides no FEC and equal FEC
- *Adaptation layer*—performs header compression and multiplexing to allow several transport sessions to be multiplexed onto one transport channel
- *Signaling*—provides the discovery of application and transport service capability, stream negotiation, stream connection establishment, stream connection teardown, stream suspension and resumption

AVDTP represents a scalable architecture with different support levels of services provided to the upper layer. The services provided to the application layer are defined as the *application service capabilities*. This comprises of negotiation and configuration of source CODECs, content protection systems, and support of media synchronization. The *transport service capabilities* correspond to more specifically transport related “services” inside the A/V transport layer. These comprise framing and segmentation, encapsulation, reporting of delivery performance, packet loss detection, packet recovery, robust header compression, and multiplexing transport sessions to transport

channels. Transport services are broadly classified into following services: basic, recovery, reporting, and adaptation (multiplexing and robust header compression).

We have designed and implemented the AVDTP protocol for multimedia support in Bluetooth. However, in this article, we focus on the delivery of audio only. Our design supports the specification of the AVDTP protocol as defined by Bluetooth SIG and implements the following:

- A means to discover the capabilities of the devices, as well as the means to negotiate for A/V stream setup as well as the establishment and tearing down of a stream
- Mechanisms that associate data with timing information required for playback of media streams at the receiver side
- Capability to report “quality of service” and status of transport of media packets to the application layer (i.e., reporting the status of transport of media packets to the application)
- Mechanisms to optimize the use of available bandwidth
- Mechanisms to minimize the transmission delay for real-time streams
- Independent functions for use on devices of limited complexity (although this feature is not yet fully supported; only MP3 CODEC is supported in our current implementation)

Our current AVDTP implementation does not yet provide recovery mechanisms and functions to reduce the overhead of the headers in the transport protocol.

5.2. Implementation of AVDTP for Bluetooth

We have implemented only the *signaling* and the *stream manager* (shown in Fig. 15) components, which together constitute the *basic service* transport functionality of AVDTP for Bluetooth devices. When AVDTP is configured for basic services, two main functions are performed: stream discovery and negotiation and media streaming using signaling and the stream manager. The signaling procedure requires ACL link between a pair of interconnected

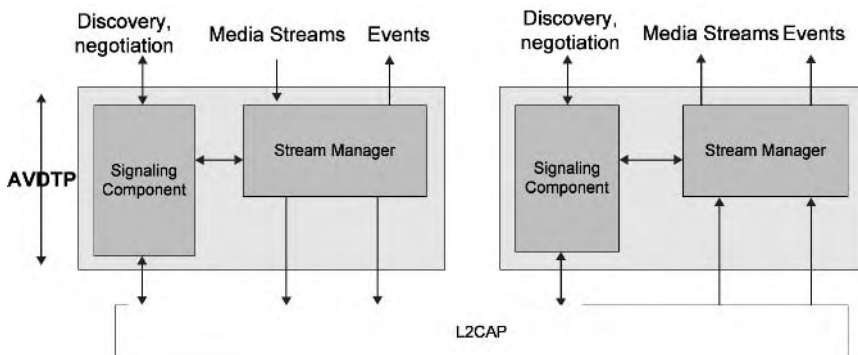


Figure 15. Implementation of the AVDTP basic service components.

devices. Transactions are performed on a connection-oriented channel established between communicating devices, and consist of bidirectional asynchronous message exchanges. To establish a stream, the upper layer requests the *signaling component* to discover, configure, and establish streams. After establishing the *stream* (a Bluetooth A/V stream represents the logical end-to-end connection of media data (audio or video) between two A/V devices), the upper layer can send or receive streaming media.

In our design, the *stream manager* is the core component of AVDTP, and it performs the following functionalities: setting up application service capability of the service endpoint based on the upper layer description of audio data, initiating the signal interface, setting up transport service parameters, framing of the audio data, media packet sequence numbering, buffering of the data at receiver end, reporting of packet loss to upper layer, jitter calculation, and timestamp management. In addition to the components we have implemented for the basic service, we have also included an L2CAP interface component, which can be used to set L2CAP and Host Controller Interface (HCI) layer parameters based on the transport service capability. The L2CAP interface component initiates the L2CAP layer commands to connect, listen, send, and receive audio data. Establishment of the connection-oriented L2CAP channels, used for media streaming, is initiated by the application layer. These channels are set up and released by AVDTP. Once the stream has been established, the application layer starts A/V streaming.

The application layer initiates the streaming procedure by registering itself with AVDTP as a stream endpoint (SEP). A SEP is a concept used to expose the available application capabilities. The application registers its SEP in AVDTP to allow other devices to discover and connect to it and is assigned a unique SEID (the SEID represents the cross device reference to a specific stream). This reference is used in the signaling transactions between peer AVDTP entities. The application also specifies the role of acceptor/initiator (ACP/INT) and the mode Source/Sink (SRC/SNK) of communication while registering with AVDTP. AVDTP returns a stream handle (represents a top-level reference to a stream), which is exposed to the application layer and represents the *stream context* associated with that stream. The application then provides the application service capability information to the A/V transport layer (AVDTP). This information typically comprises of the audio CODEC type supported by the application and its properties. The application on one Bluetooth device initiates streaming by setting up a connection-oriented link, established by a signaling procedure, to another Bluetooth device over the L2CAP layer. As illustrated in Fig. 16, the stream endpoint discovery command (optional) retrieves the type and the identifier (SEID) for one stream endpoint, or jointly multiple stream endpoints present in the particular Bluetooth device. Since SEID is needed as a reference in subsequent procedures, the stream endpoint discovery must be first invoked. However, the discovery procedure is not needed for repeated configuration attempts. The “stream get capabilities” (optional) procedure is also optional, as an initiator can guess the capabilities of the acceptor and directly invokes the *stream configuration* procedure. The

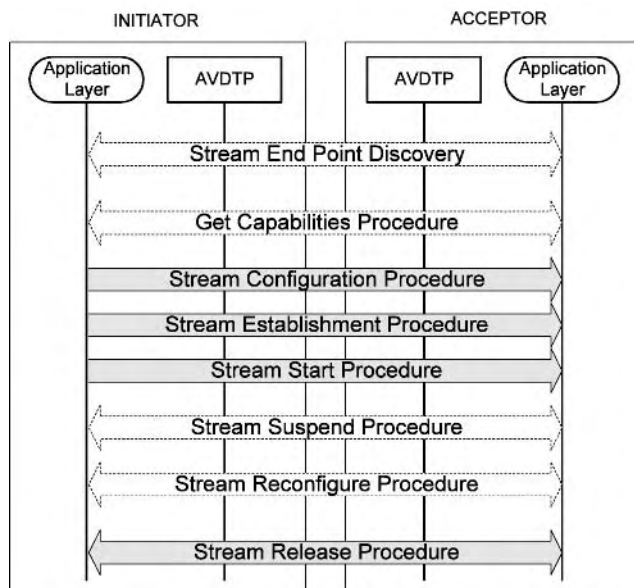
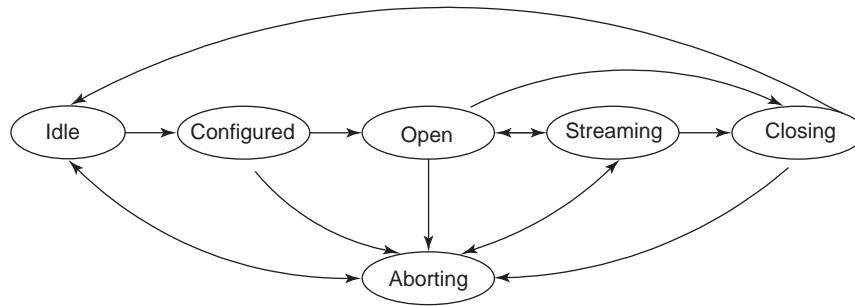


Figure 16. Signaling procedure implemented in our AVDTP design. Stream configuration, establishment, start, and release functions are mandatory, but the others optional.

“stream get capabilities” procedure can be triggered by any of the devices with no effect on the stream endpoint states. Either or both devices may initiate a stream by calling the *stream configuration procedure*, *stream establishment procedure*, and the *stream start procedure*. The *stream configuration* procedure constitutes a dedicated connection between peer stream endpoints in both devices. The stream configuration procedure also establishes the set of application and transport service parameters to be used during the transfer of audio/video content. These parameters include the audio CODEC capability—the media CODEC supported by source and sink. The most suitable audio CODEC parameter is selected and based on the audio CODEC capability; the media packet header requirements and the media payload format are defined by the AVDTP entity. Only the initiator of a stream configuration procedure may be the initiator of the *stream establishment* and *stream start* procedures and performs streaming over the configured SEP. After the start procedure has completed, both the devices may trigger any of the “stream suspend,” “stream reconfigure,” or “*stream release*” procedures. The use of “stream suspend” and “stream reconfigure” procedures depends on the application. The AVDTP state diagram is illustrated in Fig. 17.

Once the signaling procedure is executed, a streaming session will be established via AVDTP between the source and sink devices, ready to send and receive data respectively. The source device starts sending the audio data to the A/V transport layer where data are encapsulated in a frame with a media header (based on the RTP format), and sent to the L2CAP layer for the transmission over the air interface using an ACL link. The L2CAP layer adds an L2CAP header, one of the fields of which has a *PSM* to identify the connection at the receiving end. At the receiver side, the A/V transport layer retrieves media



Idle : AVDTP has been initialized

Configured : Initiator has successfully configured an Acceptor's Stream End Point

Open : INT and ACP have opened stream end-point Session on a stream end point.

Streaming : INT and ACP have established a Streaming

Closing : INT and ACP are closing stream end-point.

Aborting : INT and ACP have requested to abort the stream establishment.

Figure 17. The AVDTP state diagram.

packets from the L2CAP layer and checks the validity of the data received. If the packet received is a media packet, then the receiver-specific information (such as packet loss, jitter calculation, payload received, etc.) is updated. The media header part is stripped off and audio data are sent to the application layer for playback. After audio streaming is performed, a signaling command is sent from source to the sink to indicate the stream end and close the streaming connection.

6. BLUETOOTH SECURITY

The ad hoc nature and wireless characteristic of Bluetooth make authentication, authorization, and privacy important issues that need to be dealt when deployed in WPANs. Proper resource access and usage, reliable user identification, and accounting functionalities all need to be efficiently supported in WPANs.

Four different entities (shown in Table 3) are used to implement security at the link layer [34] in Bluetooth: a public address that is unique for each user, two secret keys, and a random number different for each new transaction are used. The secret keys are derived during initialization and are never disclosed. Normally, the

encryption key is derived from the authentication key during the authentication process. Each time encryption is activated, a new encryption key is generated.

However, the Bluetooth security architecture, although relatively simple, suffers from several weaknesses. Several authors [35–37] have identified and demonstrated several security flaws, including:

Spoofing through Keys. A simple attack, although not so simple to implement in practice, is a “man-in-the-middle attack” to steal identification and encryption keys before the start of a session [37]. The identification and keys can then be used to impersonate and/or eavesdrop on communications. This problem is, of course, not specific to Bluetooth as most key exchange systems are prone to this type of attack. One way to mitigate such an attack in all systems is to include support for a digital certificate-based authentication system. Another approach, applicable to Bluetooth, is to make it difficult for an attacker to lock onto the frequency used for communication. Making the frequency hopping intervals and patterns reasonably unpredictable can help to prevent an attacker from locking onto the device’s signal.

Spoofing through a Bluetooth Address. Each Bluetooth device has a unique address, allowing users to have some trust in the identity of the device at the other end of the transmission. Once a device identifier is associated with a user of the device, an intruding device can change its address to match the device address of the user. The intruder can then impersonate the user with the spoofed address.

PIN Length. Another vulnerability relates to the PIN (personal identification number) itself [37]. Most devices have extremely short (usually four decimal digits) PINs. This is itself is a security weakness,

Table 3. Entities Used in Authentication and Encryption Procedure in Bluetooth

Entity	Number of bits (bits)
Bluetooth address	48
Private user key, authentication	128
Private user key, encryption configurable length (byte-wise)	8–128
Random number for each transaction	128

although it is a property of the implementation and not the specification. Attackers can exhaustively search through the set of short PINs to determine a key.

Location Attacks. If a device is in discoverable mode, then it will respond to inquiries unless other baseband activity prohibits it. When responding to an inquiry, a slave transmits its identity on the baseband. Therefore, an attacker can determine the location and movements of victim devices by maintaining geographically distributed devices that continuously inquire all devices entering within their reach, and recording the identities given in the responses. Since devices use the same identities all the time, this allows the attacker to determine their movements [37].

Clearly, if Bluetooth technology is to be widely deployed as a strong enabler for WPANs, we need to improve the current security features to make it more robust to various kinds of intruder attacks.

7. CONCLUSIONS

The WPAN networking paradigm, coupled with IP as an integration mechanism, will play a fundamental role in supporting a user-centered network concept that provides seamless access to local and global networking capabilities. In this article, we focused on Bluetooth as an enabler for WPANs. We described and discussed mechanisms and novel approaches that enable Bluetooth to provide efficient WPAN support. Our focus areas dealt with crucial issues such as seamless IP connectivity to other IP-based networks, coexistence with IEEE 802.11b WLANs, and support for high-quality audio transmission over new protocols such as AVDTP. However, major drawbacks of the Bluetooth technology such as poor scalability, adaptability, and weak security, along with the dynamic nature of WPANs, present further research design challenges that need to be addressed before the WPAN networking paradigm can be fully integrated into widely deployed network solutions. Novel technical solutions are required for low-cost, low-power system architectures, physical-layer access techniques, middleware and adaptive protocols, and security, as well as human aspects (dealing with friendly communication with devices using face recognition or voice recognition technologies and health issues with the various wireless technologies) [8].

Acknowledgments

This work was supported by an equipment grant from Wayne State University, and grants from Microsoft Corporation (Seattle), Ixia Corporation, and OPNET. We would like to express our gratitude to Monica Brockmeyer and Farshad Fotouhi for making the wireless equipment available to us to conduct our tests. We thank Aruna Banda for her help, support, and contribution to the implementation of the dynamic approach for Bluetooth. We also thank the anonymous reviewers for their comments and suggestions. We are grateful to Kai Chang and Cassie

Craig for their kind help, support, patience, and understanding during the preparation of this manuscript.

BIBLIOGRAPHY

1. G. Roberts, *Overview of WPAN Working Group, Task Groups, and Study Groups*, IEEE 802.15, 03053r0, Jan. 2003.
2. L. Gavrilovska and R. Prasad, B-PAN—a new network paradigm, *Proc. WPMC'01*, Aalborg, Denmark, Sept. 2001, pp. 1135–1140.
3. V. Dam et al., From PAN to BAN: Why body area networks, *Proc. WWRP*, Helsinki, Finland, May 2001.
4. PicoRadio, <http://www.gigascale.org/picoradio>.
5. IrDA, <http://www.irda.org/>.
6. HomeRF Working Group, <http://homerf.org/>.
7. T. Zimmerman, *Personal Area Networks (PAN): Near-Field Intra-Body Communication*, M.S. thesis, MIT Media Lab, Cambridge, MA, 1995.
8. R. Prasad and L. Gavrilovska, Personal area networks (key-note speech), *Proc. EUROCON 2001*, Brastislava, July 2001, pp. 3–8.
9. Bluetooth SIG, *Specification of the Bluetooth System*, core version 1.1, Feb. 2001.
10. IEEE 802.15, <http://grouper.ieee.org/groups/802/15>.
11. Bluetooth SIG, *Bluetooth Local Area Networking Profiles, Specification of the Bluetooth System v1.0* (version 1.0), May 2001.
12. Bluetooth SIG, *Bluetooth Personal Area Networking Profiles, Specification of the Bluetooth System*, v1.0, May 2003.
13. W. Simpson, *The Point-to-Point Protocol (PPP)*, RFC 1661, July 1994.
14. Bluetooth SIG: *Bluetooth Network Encapsulation Protocol (BNEP) Specification, Specification of the Bluetooth System*, v1.0, May 2003.
15. S. Thomson and T. Narten, *IPv6 Stateless Address Auto-configuration*, IETF RFC 2462.
16. T. Kyntaja et al., Wireless residential network based on IPv6, *Proc. 5th Int. Symp. Wireless Personal Multimedia Communications*, Vol. 2, 2002, pp. 596–600.
17. Y. Tajika et al., Networked home appliance system using Bluetooth technology integrating appliance control/monitoring with Internet service, *Proc. IEEE Int. Conf. Consumer Electronics*, June 2003, pp. 142–145.
18. R. Jones, Netperf, www.netperf.org/netperf/NetperfPage.html.
19. BlueZ, Official Linux Bluetooth Protocol stack, <http://bluez.sourceforge.net>.
20. K. Thompson, G. Miller, and M. Wilder, Wide-area Internet traffic patterns and characteristics, *IEEE Network* 11(6) (Nov./Dec. 1997).
21. ITU-T Recommendation G.114: *One Way Transmission Time*, ITU, Feb. 1996.
22. W. Kampichler and K. Goeskha, Plain end-to-end measurement for local area network voice transmission feasibility, *Proc. IEEE Model. Anal. Simul. Comput. Telecommun. Syst.* 235–240 (2001).
23. A. Maropoulou, F. Tobagi, and M. Karam, Assessment of VoIP quality over Internet backbones, *Proc. IEEE INFOCOM'02*, June 2002.

24. M. Karam and F. Tobagi, Analysis of the delay and jitter of voice traffic over the Internet, *Proc. IEEE INFOCOM'01*, 2001, pp. 824–833.
25. N. Golmie, *IEEE P802.15 Working Group for Wireless Personal Area Networks*, Natl. Inst. Standards and Technology, MD, IEEE 802.15-01/00144r0.
26. N. Golmie, N. Chevrollier, and I. Elbakkouri, Interference aware Bluetooth packet scheduling, *Proc. GLOBECOM'01*, San Antonio, TX, Nov. 2001.
27. N. Golmie, R. VanDyck, and A. Soltanian, Interference of Bluetooth and IEEE 802.11: Simulation modeling and performance evaluation, *Proc. 4th Int. Workshop on Modeling, Analysis, and Simulation of Wireless and Mobile Systems, MSWIM'01*, Italy, July 2001.
28. N. Golmie et al., Interference evaluation of Bluetooth and IEEE 802.11b systems, *ACM Wireless Networks J.* (special issue) **9**(3): 201–211 (May 2003).
29. N. Sriskanthan, F. Tan, and A. Karande, Bluetooth based home automation system, School of Computer Engineering, Nanyang Technology Univ., <http://www.ee.ncue.edu.tw/note/data/o/7/91.pdf>.
30. C. Bisdikian, P. Bhagwat, and N. Golmie, eds., Wireless personal area networks, *IEEE Network* (special issue) **15**(5) (Sept./Oct. 2001).
31. Bluetooth SIG, *Audio/Video Distribution Transport Protocol Specification*, v1.00a draft, Bluetooth Audio Video Working Group, 2002.
32. Bluetooth SIG, *Advanced Audio Distribution Profile*, v1.00a draft, 2002.
33. Bluetooth SIG, *Generic Audio Video Distribution Profile (GAVDP)*, April 2002.
34. Bluetooth Special Interest Group, *The Bluetooth Specification*, v.1.1, Feb. 22, 2001, <http://www.bluetooth.com/developer/specification/specification.asp>.
35. C. Hager and S. Midkiff, An analysis of Bluetooth security vulnerabilities, *Proc. IEEE Wireless Communications and Networking Conf. (WCNC'03)*, New Orleans, LA, March 2003, Vol. 3, pp. 1825–1831.
36. C. Hager and S. Midkiff, Demonstrating vulnerabilities in Bluetooth security, *Proc. IEEE Global Telecommunications Conf. (GLOBECOM'03)*, San Francisco, CA, Dec. 2003, Vol. 3, pp. 1420–1424.
37. M. Jakobsson and S. Wetzel, Security weaknesses in Bluetooth, *Proc. Cryptographer's Track at RSA Conf. (CT-RSA 2001)*, Lecture Notes in Computer Science 2020, Berlin, Springer, Germany, 2001.

applied effectively to many cases. Electromagnetic problems expressed in integral form are particularly useful for obtaining approximate solution and developing general theory. Two techniques usually used for integral equations are (1) the variational method and (2) the perturbation method. The variational procedure gives an approximate value to the desired quantity rather than the changes in the quantity. The formula is relatively insensitive to the variations in an assumed field for which there is an exact or correct field.

2. PERTURBATION METHODS

The meaning of the term *perturbation* is the disturbance or a slight change. Perturbation methods are simple and accurate for calculating changes in some quantity due to small changes in the problem. Many of the electromagnetic field problems can be very effectively solved by this simple method. The method involves two situations, namely, the “unperturbed” and “perturbed” states. In the unperturbed problem the solution is known. The perturbed problem is slightly different from the unperturbed one. There are two cases of perturbation: perturbation of cavity walls and cavity material perturbation. Although many researchers [1–4] handled the perturbation problems in many different ways, it was R. F. Harrington [5] who made a systematic and almost exhaustive theoretical study on the perturbation problem.

2.1. Perturbation of Cavity Walls

A *cavity resonator* can be formed by a conductor carrying a surface S and enclosing a lossless region τ , as shown in Fig. 1a. A deformation of the original cavity changes the cavity surface to S' and volume to τ' (Fig. 1b) such that $\Delta S = S - S'$ and $\Delta\tau = \tau - \tau'$. The change in the resonant frequency due to the change in the cavity wall can be determined by analyzing Maxwell's integral equations [6]. Let E_0, H_0 , and ω_0 , represent the electric and magnetic fields and the resonant frequency of the original cavity, respectively, and E, H , and ω represent the corresponding quantities of the perturbed cavity. The *field equations* are satisfied in both cases:

$$-\nabla \times E_0 = j\omega_0\mu H_0 \quad -\nabla \times E = j\omega\mu H \quad (1)$$

$$\nabla \times H_0 = j\omega_0\varepsilon E_0 \quad \nabla \times H = j\omega\varepsilon E \quad (2)$$

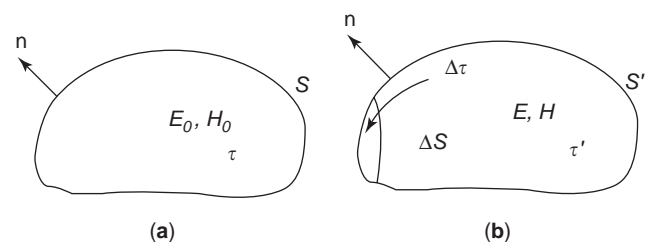


Figure 1. Perturbation of cavity walls in an original cavity (a) and a perturbed cavity (b).

PERTURBATION THEORY

K. T. MATHEW
 Cochin University of Science and
 Technology
 Cochin, India

1. INTRODUCTION

Electromagnetic field problems can be expressed and solved mathematically in differential or integral equation forms. The differential form leads to an exact solution of the mathematical problems. But this approach cannot be

The permittivity and permeability of the medium are assumed to be lossless.

Multiplying Eq. (2) scalarly by E_0^* and the conjugate of E_0 and the conjugate of Eq. (1) by H as

$$E_0^* \cdot \nabla \times H = j\omega \epsilon E_0^* \cdot E \tag{3}$$

$$-H \cdot \nabla \times E_0^* = -j\omega_0 \mu H_0^* \cdot H \tag{4}$$

applying the identity

$$\nabla \cdot (M \times N) = N \cdot \nabla \times M - M \cdot \nabla \times N$$

and adding Eqs. (3) and (4), we get

$$\nabla \cdot (H \times E_0^*) = j\omega \epsilon E \cdot E_0^* - j\omega_0 \mu H_0^* \cdot H \tag{5}$$

Similarly, we obtain

$$\nabla \cdot (H_0^* \times E) = j\omega \mu H \cdot H_0^* - j\omega_0 \epsilon E_0^* \cdot E \tag{6}$$

Adding Eqs. (5) and (6) and integrating the sum throughout the volume of the perturbed cavity, we obtain

$$\begin{aligned} & \iiint_{\tau} [\nabla \cdot (H \times E_0^*) + \nabla \cdot (H_0^* \times E)] d\tau \\ &= j(\omega - \omega_0) \iiint_{\tau} (\epsilon E \cdot E_0^* + \mu H \cdot H_0^*) d\tau \end{aligned} \tag{7}$$

Applying the divergence theorem on left-hand-side (LHS) terms, the resulting equation is

$$\begin{aligned} & \oiint_{S'} (H \times E_0^*) ds + \oiint_{S'} (H_0^* \times E) ds \\ &= j(\omega - \omega_0) \iiint_{\tau} (\epsilon E \cdot E_0^* + \mu H \cdot H_0^*) d\tau \end{aligned} \tag{8}$$

Since $n \times E = 0$ on S' , second term on the LHS is reduced to zero.

Therefore

$$\begin{aligned} & \oiint_{S'} (H \times E_0^*) ds \\ &= j(\omega - \omega_0) \iiint_{\tau} (\epsilon E \cdot E_0^* + \mu H \cdot H_0^*) d\tau \end{aligned} \tag{9}$$

Since $n \times E_0 = 0$ on S , we have

$$\oiint_S (H \times E_0^*) ds = 0$$

and hence the LHS of the equation can be written as

$$\begin{aligned} & \oiint_{S'} (H \times E_0^*) ds - \oiint_S (H \times E_0^*) ds \\ &= \oiint_{S' - S} H \times E_0^* \cdot ds = - \oiint_{\Delta S} H \times E_0^* \cdot ds \end{aligned} \tag{10}$$

Negative sign is taken to indicate that ds is extended outward. Thus the Eq. (9) can be rearranged as follows:

$$\begin{aligned} & - \oiint_{\Delta S} H \times E_0^* \cdot ds = j(\omega - \omega_0) \\ & \iiint_{\tau} (\epsilon E \cdot E_0^* + \mu H \cdot H_0^*) d\tau \\ \omega - \omega_0 &= \frac{j \oiint_{\Delta S} (H \times E_0^*) \cdot ds}{\iiint_{\tau} (\epsilon E \cdot E_0^* + \mu H \cdot H_0^*) d\tau} \end{aligned} \tag{11}$$

This expression gives the change in resonant frequency due to an inward perturbation of the cavity walls.

An approximation to the perturbation equation is to be made by replacing E and H by the unperturbed fields E_0 and H_0 . If the perturbation of the field due to the deformation of the cavity is shallow and smooth, the approximation is very reasonable and won't affect the accuracy of the result substantially. Thus

$$\oiint_{\Delta S} (H \times E_0^*) \cdot ds \approx \oiint_{\Delta S} (H_0 \times E_0^*) \cdot ds$$

Applying the Poynting theorem for the conservation of complex power, this expression leads to

$$\oiint_{\Delta S} (H_0 \times E_0^*) \cdot ds = j\omega_0 \iiint_{\Delta \tau} (\epsilon |E_0|^2 - \mu |H_0|^2) d\tau \tag{12}$$

Substituting E_0, H_0 for E, H in the denominator in Eq. (11), the perturbation equation becomes

$$\frac{\omega - \omega_0}{\omega_0} \approx \frac{\iiint_{\Delta \tau} (\mu |H_0|^2 - \epsilon |E_0|^2) d\tau}{\iiint_{\tau} (\mu |H_0|^2 + \epsilon |E_0|^2) d\tau} \tag{13}$$

The numerator represents the electric and magnetic energies removed by perturbation, while the denominator is proportional to the total energy stored in the cavity. In terms of energy, the perturbation equation is changed to

$$\frac{\omega - \omega_0}{\omega_0} \approx \frac{\Delta \bar{W}_m - \Delta \bar{W}_e}{W} \tag{14}$$

where $\Delta \bar{W}_m$ and $\Delta \bar{W}_e$ are time-average magnetic and electric energies originally contained in $\Delta \tau$ and W is the total energy stored in the original cavity. If $\Delta \tau$ is small, the $\Delta \bar{W}$ values can be approximated to $\Delta \tau$ times the energy densities. Similarly the W can be written as τ times the space average energy density \dot{w}

$$\frac{\omega - \omega_0}{\omega_0} = \frac{(\bar{w}_m - \bar{w}_e)\Delta \tau}{\dot{w}\tau} = C \frac{\Delta \tau}{\tau} \tag{15}$$

where C is a constant depending on the geometry of the cavity and the position of perturbation. Thus an inward

perturbation will increase the resonant frequency if it is made at a point of large H (high value of \bar{w}_m) and lower the resonant frequency if it is made at a point of large E (high \bar{w}_e). The opposite behavior will occur from an outward perturbation. The greatest resonant frequency will result when the perturbation is at a position of maximum E and zero H . Vice versa for minimum resonant frequency shift.

2.2. Cavity Material Perturbation

This case is more significant than the previous one as far as the practical applications are concerned. The resonant frequency of the cavity is changed due to the perturbation of the material within the cavity. Figures 2a and 2b represent the situation before and after the perturbation of the cavity. μ and ε respectively are the permeability and permittivity of the medium of the original cavity. In the perturbed cavity the parameters of the medium are changed to $\mu + \Delta\mu$ and $\varepsilon + \Delta\varepsilon$. The field equations in the two cases are

$$\begin{aligned} -\nabla \times \mathbf{E}_0 &= j\omega_0 \mu \mathbf{H}_0 & -\nabla \times \mathbf{E} &= j\omega(\mu + \Delta\mu) \mathbf{H} \\ \nabla \times \mathbf{H}_0 &= j\omega_0 \varepsilon \mathbf{E}_0 & \nabla \times \mathbf{H} &= j\omega(\varepsilon + \Delta\varepsilon) \mathbf{E} \end{aligned} \quad (16)$$

Take the conjugate of the first equation and multiply it scalarly by \mathbf{H} and the last equation scalarly by \mathbf{E}_0^* . Add these resulting equations to give rise to

$$\nabla \cdot (\mathbf{H} \times \mathbf{E}_0^*) = j\omega(\varepsilon + \Delta\varepsilon) \mathbf{E} \cdot \mathbf{E}_0^* - j\omega_0 \mu \mathbf{H}_0^* \cdot \mathbf{H}$$

Similarly we get

$$\nabla \cdot (\mathbf{H}_0^* \times \mathbf{E}) = j\omega(\mu + \Delta\mu) \mathbf{H} \cdot \mathbf{H}_0^* - j\omega_0 \varepsilon \mathbf{E}_0^* \cdot \mathbf{E}$$

Add the two equations above and integrate throughout the cavity to get

$$\begin{aligned} \iiint_{\tau} [\nabla \cdot (\mathbf{H} \times \mathbf{E}_0^*) + \nabla \cdot (\mathbf{H}_0^* \times \mathbf{E})] d\tau &= \\ \iiint_{\tau} j\{[\omega(\varepsilon + \Delta\varepsilon) - \omega_0 \varepsilon] \mathbf{E} \cdot \mathbf{E}_0^* &+ \\ + [\omega(\mu + \Delta\mu) - \omega_0 \mu] \mathbf{H} \cdot \mathbf{H}_0^*\} d\tau & \end{aligned} \quad (17)$$

with $n \times \mathbf{E}$ and $n \times \mathbf{E}_0$ on S , both equal to zero. Then apply the divergence theorem to the LHS, and it vanishes to zero

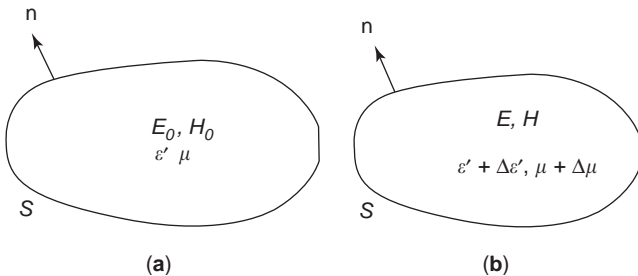


Figure 2. Perturbation of matter in an original cavity (a) and a perturbed cavity (b).

as

$$\begin{aligned} 0 &= \iiint_{\tau} \{[\omega(\varepsilon + \Delta\varepsilon) - \omega_0 \varepsilon] \mathbf{E} \cdot \mathbf{E}_0^* \\ &+ [\omega(\mu + \Delta\mu) - \omega_0 \mu] \mathbf{H} \cdot \mathbf{H}_0^*\} d\tau \\ 0 &= (\omega - \omega_0) \iiint_{\tau} [\varepsilon \mathbf{E} \cdot \mathbf{E}_0^* + \mu \mathbf{H} \cdot \mathbf{H}_0^*] d\tau \\ &+ \omega \iiint_{\tau} [\Delta\varepsilon \mathbf{E} \cdot \mathbf{E}_0^* + \Delta\mu \mathbf{H} \cdot \mathbf{H}_0^*] d\tau \\ \frac{\omega - \omega_0}{\omega} &= - \frac{\iiint_{\tau} (\Delta\varepsilon \mathbf{E} \cdot \mathbf{E}_0^* + \Delta\mu \mathbf{H} \cdot \mathbf{H}_0^*) d\tau}{\iiint_{\tau} (\varepsilon \mathbf{E} \cdot \mathbf{E}_0^* + \mu \mathbf{H} \cdot \mathbf{H}_0^*) d\tau} \end{aligned} \quad (18)$$

In the limit, as $\Delta\varepsilon \rightarrow 0$ and $\Delta\mu \rightarrow 0$, we can approximate \mathbf{E} , \mathbf{H} , ω by $\mathbf{E}_0, \mathbf{H}_0, \omega_0$ to obtain

$$\frac{\omega - \omega_0}{\omega_0} \approx - \frac{\iiint_{\tau} (\Delta\varepsilon |\mathbf{E}_0|^2 + \Delta\mu |\mathbf{H}_0|^2) d\tau}{\iiint_{\tau} (\varepsilon |\mathbf{E}_0|^2 + \mu |\mathbf{H}_0|^2) d\tau} \quad (19)$$

This equation states that a small increase in ε and/or μ decreases the resonant frequency. In terms of energy stored in the fields, the above perturbation equation becomes

$$\frac{\omega - \omega_0}{\omega_0} \approx - \frac{1}{W} \iiint_{\tau} \left(\frac{\Delta\varepsilon}{\varepsilon} \bar{w}_e + \frac{\Delta\mu}{\mu} \bar{w}_m \right) d\tau$$

where \bar{w} is the energy density and W is the total energy stored in the original cavity.

Let us take $\Delta\varepsilon = \varepsilon - \varepsilon_0$ and $\Delta\mu = \mu - \mu_0$:

$$\begin{aligned} \frac{\omega - \omega_0}{\omega} &= - \frac{\iiint_{\tau} [(\varepsilon - \varepsilon_0) \mathbf{E} \cdot \mathbf{E}_0^* + (\mu - \mu_0) \mathbf{H} \cdot \mathbf{H}_0^*] d\tau}{\iiint_{\tau} (\varepsilon_0 \mathbf{E} \cdot \mathbf{E}_0^* + \mu_0 \mathbf{H} \cdot \mathbf{H}_0^*) d\tau} \\ &= - \frac{\iiint_{\tau} [(\varepsilon - \varepsilon_0) \mathbf{E} \cdot \mathbf{E}_0^* + (\mu - \mu_0) \mathbf{H} \cdot \mathbf{H}_0^*] d\tau}{2 \iiint_{\tau} \varepsilon_0 \mathbf{E} \cdot \mathbf{E}_0^* d\tau} \end{aligned} \quad (20)$$

If the element is introduced into an of E -field region, then

$$\frac{\omega - \omega_0}{\omega} = - \frac{\iiint_{\tau} [(\varepsilon - \varepsilon_0) \mathbf{E} \cdot \mathbf{E}_0^*] d\tau}{2 \iiint_{\tau} \varepsilon_0 \mathbf{E} \cdot \mathbf{E}_0^* d\tau} \quad (21)$$

The approximation applied for the fields under original and perturbed conditions are that $\Delta\varepsilon$, $\Delta\mu$, and $\Delta\tau$ all be small. But the restrictions on $\Delta\varepsilon$ and $\Delta\mu$ can be removed by applying certain procedures at the expense of further complication. We have to apply constraint to the shape of the

sample and location. We assume that the internal field of $\Delta\tau$ is related to the field external to $\Delta\tau$ in the same manner as for static fields. This assumption is justifiable as the Helmholtz equation can be approximated by Laplace' equation in a small region compared to wavelength [7]. Four special cases of dielectric samples are considered for relating the internal and external fields. Thus E_{int} for a slab with E normal to it is given by

$$E_{\text{int}} = \frac{1}{\epsilon_r} E_{\text{ext}}$$

and for a long thin cylinder with E along the axis, the relation is $E_{\text{int}} = E_{\text{ext}}$; for E normal to the axis of the circular cylinder, we obtain

$$E_{\text{int}} = \frac{2}{1 + \epsilon_r} E_{\text{ext}}$$

Finally for E normal to a small sphere, we have

$$E_{\text{int}} = \frac{3}{2 + \epsilon_r} E_{\text{ext}}$$

where ϵ_r is the relative permittivity given by $\epsilon_r \epsilon_0 = \epsilon$.

The modified field in the quasistatic approximations can be substituted for E in the numerator of the general equation. The denominator remains unaltered as the contribution from $\Delta\tau$ is small compared to that from the rest of τ . For $\Delta\mu = 0$ (pure dielectric), the quasistatic correction to the perturbation formula is

$$\frac{\omega - \omega_0}{\omega_0} \approx - \frac{\iint \Delta\epsilon E_{\text{int}} \cdot E_0^* d\tau}{2 \iint \epsilon |E_0|^2 d\tau} \quad (22)$$

This equation is most valuable for solving problems for which the exact solution is not known. The validity of the above equation can be checked by applying to problem for which an exact solution is known. Perturbation method in conjunction with the quasistatic approach gives excellent accuracy to the solution of the problem. By simply measuring the shift in resonant frequency caused by the introduction of a dielectric sample in the cavity resonator, the constituent parameters of matter can be determined.

2.3. Waveguide Perturbations

Cavity perturbation equations are efficient tools to determine the dielectric and magnetic parameters of materials. The techniques developed for the evaluation of these parameters based on the perturbation theory are called *cavity perturbation techniques*. From the analysis of the perturbation equation it is clear that the knowledge about the frequency shift and resonant frequency as well as the information of the field are necessary for the determination of the parameters. This necessitates the use of standard resonant cavities such as waveguide (rectangular or circular cross section) or coaxial cables. Let us consider cylindrical waveguides first and then rectangular wave-

guide which are widely used as *cavity resonators*. The cross section along the Z axis is constant. At the cutoff frequency a waveguide is a two-dimensional resonator. We can apply perturbation formula to waveguides at cutoff. The waveguide cavity resonator is constructed with a section of a waveguide bounded by two $z = \text{const}$ (constant) planes with conducting sheets. Since the fields are independent of z axis, the surface integrals over these two cross sections cancel each other. For the integral equation $\iint (H \times E_0^* + H_0^* \times E) \cdot ds$, the surface integral only over the wall is needed. Hence the cutoff frequency ω_c and the change in cutoff frequency $\Delta\omega_c$ due to an inward perturbation of the waveguide cavity wall are related as

$$\frac{\Delta\omega_c}{\omega_c} \approx \frac{\iint_{\Delta S} (\mu |H_0|^2 - \epsilon |E_0|^2) ds}{\iint_S (\mu |H_0|^2 + \epsilon |E_0|^2) ds} \quad (23)$$

The approximation is due to the fact that the perturbed fields E and H are replaced by unperturbed fields E_0 and H_0 for small perturbations. An inward perturbation of the waveguide walls at a position of high E will lower the cutoff frequency, while that at a position of high H will raise the cutoff frequency. An example of waveguide cavity wall perturbation is the ridge waveguide [8], formed from the rectangular waveguide by adding ridges along the center of the top and bottom walls. Such ridges will lower the cutoff frequency of the dominant mode and will raise the cutoff frequency of the next-higher mode. The ridges also decrease the characteristic impedance of the guide, and hence they are used for impedance matching.

Likewise, the material perturbation in a waveguide cavity at cutoff can be treated in a similar way to develop the formula. We can obtain the exact formula for the change in cutoff frequency due to a change of parameters of matter enclosed by the waveguide cavity resonator. It is

$$\frac{\Delta\omega_c}{\omega_c} = - \frac{\iint (\Delta\epsilon E \cdot E_0^* + \Delta\mu H \cdot H_0^*) ds}{\iint (\epsilon E \cdot E_0^* + \mu H \cdot H_0^*) ds} \quad (24)$$

It is clear that an increase in ϵ or μ decreases the cutoff frequency of a waveguide. If $\Delta\epsilon$ and $\Delta\mu$ are small, we can replace the perturbed field by the original field:

$$\frac{\Delta\omega_c}{\omega_c} \approx - \frac{\iint (\Delta\epsilon |E_0|^2 + \Delta\mu |H_0|^2) ds}{\iint (\epsilon |E_0|^2 + \mu |H_0|^2) ds}$$

But for large values of $\Delta\epsilon$ and $\Delta\mu$ but of small spatial extent, the quasistatic approximation can be made. For a nonmagnetic case

$$\frac{\Delta\omega_c}{\omega_c} \approx - \frac{\iint \Delta\epsilon |E_0|^2 ds}{\iint (\epsilon |E_0|^2 + \mu |H_0|^2) ds}$$

So far the perturbed waveguide cavity is assumed to be homogeneous. When the cavity is filled with a nonhomogeneous medium, the perturbation formula for a wall perturbation and material perturbation is given by

$$\beta - \beta_0 = -j \frac{\oint_{\Delta c} (\hat{\mathbf{E}}_0^* \times \hat{\mathbf{H}}) \cdot \mathbf{n} \cdot d\mathbf{l}}{\iint_{S^1} (\hat{\mathbf{E}}_0^* \times \hat{\mathbf{H}} + \hat{\mathbf{E}} \times \hat{\mathbf{H}}_0^*) \cdot \mathbf{u}_Z ds} \quad (25a)$$

$$\beta - \beta_0 = \omega \frac{\iint_S (\Delta\epsilon \hat{\mathbf{E}} \cdot \hat{\mathbf{E}}_0^* + \Delta\mu \hat{\mathbf{H}} \cdot \hat{\mathbf{H}}_0^*) ds}{\iint_S (\hat{\mathbf{E}}_0^* \times \hat{\mathbf{H}} + \hat{\mathbf{E}} \times \hat{\mathbf{H}}_0^*) \cdot \mathbf{u}_Z ds} \quad (25b)$$

where β_0 and β are phase shift constants in the two cases. The field configuration within the waveguide depends on the cross section of the waveguide, which can easily be found from the dimension of the waveguide. The derivation for the material perturbation equation in a waveguide is given in the Appendix.

Many experimental techniques have been developed based on the theory of perturbation for the determination of the dielectric and magnetic properties of materials. Of the two types of cavity perturbation the latter has more practical applications. The work of R. A. Waldron [9] is worth mentioning in the development of perturbation theory in this direction. According to his concept, it is assumed that the fields in the perturbed case due to a sample is the sum of the unperturbed fields E_0, H_0 and additional fields E_1, H_1 with a frequency change $\delta\omega$. Starting from the fundamental equations of Maxwell and applying the vector identity, we have

$$\text{Curl } E_0 = - \frac{\delta B_0}{\delta t} = -j\omega B_0$$

$$\text{Curl } (E_0 + E_1) = -j(\omega + \delta\omega)(B_0 + B_1)$$

Subtracting, we obtain

$$\text{Curl } E_1 = -j[\omega B_1 + \delta\omega(B_0 + B_1)]$$

Similarly

$$\text{Curl } H_1 = j[\omega D_1 + \delta\omega(D_0 + D_1)]$$

Following the same procedure of Harrington, we get

$$\begin{aligned} (E_0 \cdot \nabla \times H) + (H_0 \cdot \nabla \times E) &= j\omega[E_0 \cdot D_1 - H_0 \cdot B_1] \\ &+ j\delta\omega[(E_0 \cdot D_0 - H_0 \cdot B_0) \\ &+ (E_0 \cdot D_1 - H_0 \cdot B_1)] \end{aligned} \quad (26)$$

For the sample outside

$$B_0 = \mu_0 H_0, \quad B_1 = \mu_0 H_1$$

$$D_0 = \epsilon_0 E_0, \quad D_1 = \epsilon_0 E_1$$

and for the sample inside

$$B_1 = \mu_0[\mu_r(H_0 + H_1) - H_0]$$

$$D_1 = \epsilon_0[\epsilon_r(E_0 + E_1) - E_0]$$

For gyromagnetic material, inside the sample B_1 becomes

$$B_1 = \mu_0\{[\mu_r](H_0 + H_1) - H_0\}$$

Use the vector identity

$$\begin{aligned} \nabla \cdot [(H_0 \times E_1) + (E_0 \times H_1)] \\ &= E_1 \cdot \nabla \times H_0 - H_0 \cdot \nabla \times E_1 \\ &+ H_1 \cdot \nabla \times E_0 - E_0 \cdot \nabla \times H_1 \end{aligned}$$

Substituting for curl E and curl H in this expression and rearranging, we get

$$\begin{aligned} H_0 \cdot \nabla \times E_1 + E_0 \cdot \nabla \times H_1 \\ &= j\omega(E_1 \cdot D_0 - H_1 \cdot B_0) \\ &- \nabla \cdot [(H_0 \times E_1) + (E_0 \times H_1)] \end{aligned} \quad (27)$$

Equating (27) to the LHS of Eq. (26), we obtain

$$\begin{aligned} j\omega(E_1 \cdot D_0 - H_1 \cdot B_0) - \nabla \cdot [(H_0 \times E_1) \\ &+ (E_0 \times H_1)] = j\omega(E_0 \cdot D_1 - H_0 \cdot B_1) \\ &+ j\delta\omega[(E_0 \cdot D_0 - H_0 \cdot B_0) \\ &+ (E_0 \cdot D_1 - H_0 \cdot B_1)] \end{aligned}$$

Let V_0 be the volume of cavity and V_1 the volume of the sample. Thus $(V_0 - V_1)$ is the part of the cavity not occupied by the sample. Integrate equation over the volume V_0

$$\begin{aligned} j\omega \iiint_{V_0} (E_1 \cdot D_0 - H_1 \cdot B_0) dV \\ &- \iiint_{V_0} \nabla \cdot [(H_0 \times E_1) + (E_0 \times H_1)] dV \\ &= j\omega \iiint_{V_0} (E_0 \cdot D_1 - H_0 \cdot B_1) dV \\ &+ j\delta\omega \iiint_{V_0} [(E_0 \cdot D_0 - H_0 \cdot B_0) \\ &+ (E_0 \cdot D_1 - H_0 \cdot B_1)] dV \end{aligned} \quad (28)$$

If the inner surface of the cavity is perfectly conducting, the divergence integral on the LHS is zero. The contribution from the region $(V_0 - V_1)$, the region of the cavity outside the sample, to the first term of LHS and the right-hand side (RHS) is the same.

Thus we only require the contribution to these integrals from the region V_1 . When $\delta\omega \ll \omega$, E_1 and H_1 are small compared with E_0 and D_0 and in the neighborhood of

the sample, the contribution to the integral will be small. So there is no harm to neglect the second integral of the RHS of the equation above. Thus Eq. (28) becomes

$$\frac{\delta\omega}{\omega} = \frac{\iiint_{V_1} [(E_1 \cdot D_0 - E_0 \cdot D_1) - (H_1 \cdot B_0 - H_0 \cdot B_1)] dV}{\iiint_{V_0} (E_0 \cdot D_0 - H_0 \cdot B_0) dV} \tag{29}$$

Knowing the field and measuring the frequency shift, dielectric parameters are determined assuming that the influence of the sample at the magnetic field is negligible. Thus the general expression for the frequency shift is given by

$$\frac{\delta\omega}{\omega} = \frac{\iiint_{V_1} (E_1 \cdot D_0 - E_0 \cdot D_1) dV}{2 \iiint_{V_0} E_0 \cdot D_0 dV} \tag{30}$$

The sample size should be uniform over a volume large compared to that of the sample.

Sample size will be selected to have small $\delta\omega/\omega$ value. This is particularly important for high-loss materials. In order to use the perturbation theory for the evaluation of dielectric and magnetic parameters, the concept of complex frequency shift was introduced. A waveguide cavity resonator is equivalent to a resonant circuit, and the complex resonant frequency shift $d\Omega$ and resonant frequency ω_0 are related to the quality factor Q of the resonator by the expression [10,11]

$$\frac{\delta\Omega}{\omega_0} = \frac{\delta\omega}{\omega_0} + \frac{j}{2} \left(\frac{1}{Q_1} - \frac{1}{Q_0} \right) \tag{31}$$

Q_0 and Q_1 are quality factors of empty cavity and cavity with perturbing sample. Thus in the perturbation theory $\delta\omega/\omega_0$ is replaced by $\delta\Omega/\omega_0$.

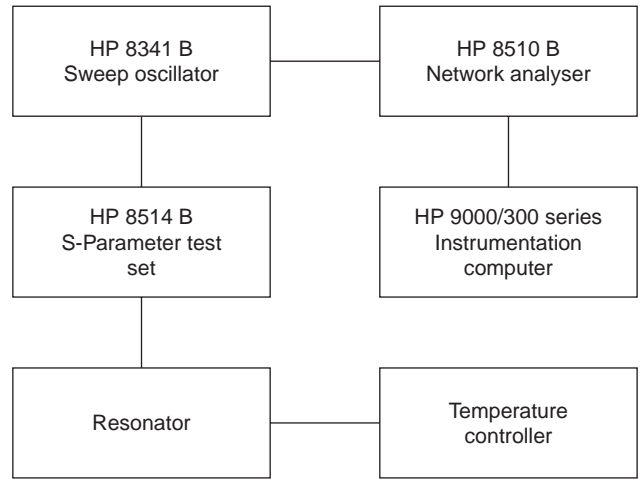


Figure 3. Block diagram of experimental setup.

3. MEASUREMENT TECHNIQUES

A block diagram of the experimental set up for the measurement of dielectric and magnetic parameters of materials is shown in Fig. 3. The experimental setup consists of a cavity resonator, HP8510C/8714ET network analyzer assembly and an interfacing computer.

3.1. Rectangular Waveguide Cavity Resonator

The closed section of a rectangular waveguide constitutes a cavity resonator. The cavity resonator can be of transmission or reflection type. A transmission-type cavity resonator [12] is shown in Fig. 4. Electromagnetic energy is coupled to the cavity through coupling irises at the ends of the cavity. A nonradiating slot is provided at the broadwall of the cavity for the introduction of the sample. On exciting the cavity resonator in the TE_{10p} mode, a typical resonant frequency spectrum is obtained. The cavity resonates at different frequencies depending on its dimensions. The basic principle involved in the technique is that the field within the cavity resonator is perturbed by in-

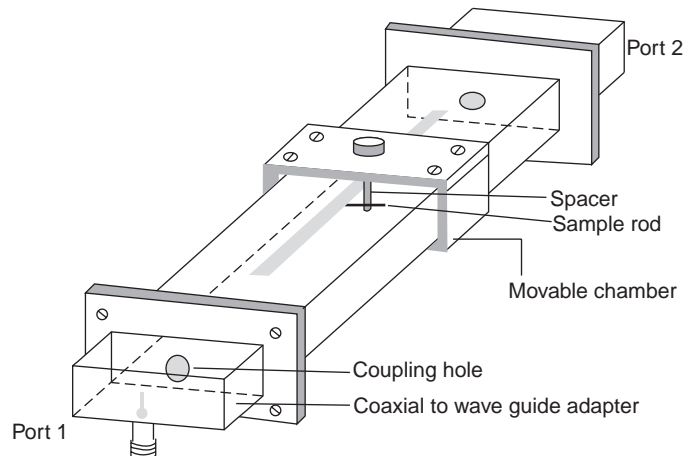


Figure 4. Schematic diagram of rectangular cavity resonator.

roduction of the dielectric sample through the nonradiating slot. The resonant frequency and the quality factor of the cavity get shifted because of perturbation. The determination of the complex permittivity and conductivity is based on the theory of perturbation. When the sample is introduced into the cavity, the relative complex frequency shift of the resonator is given as [5]

$$\frac{d\Omega}{\omega_0} \approx \frac{(\bar{\epsilon}_r - 1)\epsilon_0 \int_{V_s} E \cdot E_0^* dV + (\bar{\mu}_r - 1)\mu_0 \int_{V_s} H \cdot H_0^* dV}{\int_{V_c} (D_0 \cdot E_0^* + B_0 \cdot H_0^*) dV} \quad (32)$$

where E_0 is the electric field in the unperturbed cavity, E is the electric field in the perturbed cavity, D is the displacement current density, and H_0 , H , and B the respective magnetic quantities. $\bar{\epsilon}_r$ is the relative complex permittivity of the sample. But $\bar{\epsilon}_r = \bar{\epsilon}'_r - j\bar{\epsilon}''_r$ where $\bar{\epsilon}'_r$ the real is part of the complex permittivity and $\bar{\epsilon}''_r$ is the imaginary part of the complex permittivity. μ is the permeability. The numerator of Eq. (32) represents the total energy stored in the sample and the denominator represents the total energy stored in the cavity.

3.1.1. Dielectric Parameters. When a dielectric material is introduced in a cavity resonator at the position of maximum electric field, the contribution of magnetic field for the perturbation is minimum. The field perturbation due to the introduction of dielectric sample at the position of maximum electric field is related as

$$\frac{d\Omega}{\omega_0} \approx \frac{(\bar{\epsilon}_r - 1) \int_{V_s} E \cdot E_{0 \max}^* dV}{2 \int_{V_c} |E_0|^2 dV} \quad (33)$$

where $d\Omega$ is the complex frequency shift, V_s and V_c are the volumes of the sample and the cavity resonator, respectively. The complex frequency shift is related to the quality factor as

$$\frac{d\Omega}{\omega_0} = \frac{d\omega}{\omega_0} + \frac{j}{2} \left(\frac{1}{Q_s} - \frac{1}{Q_c} \right) \quad (34)$$

where Q_s and Q_c are the quality factors of cavity resonator with and without the sample.

Quality factor Q is given by $Q = f/\Delta f$, where f is the resonant frequency and Δf is the corresponding 3 dB bandwidth. For a small sample, we assume that $E = E_0$, which is one of the assumptions taken in the theory of perturbation. For dominant TE_{10p} mode in rectangular waveguide [6], we have

$$E_0 = E_{0 \max} \sin \frac{\pi x}{a} \sin \frac{p\pi z}{d}, \quad p = 1, 2, 3, \dots \quad (35)$$

$E_{0 \max}$, a , and d are the peak values of E_0 , the broader dimension and the length of the waveguide cavity resonator, respectively.

From Eqs. (33)–(35), we get

$$\epsilon'_r - 1 = \frac{f_c - f_s}{2f_s} \left(\frac{V_c}{V_s} \right) \quad (36)$$

$$\epsilon''_r = \frac{V_c}{4V_s} \left(\frac{Q_c - Q_s}{Q_c Q_s} \right) \quad (37)$$

The real part, ϵ'_r of the complex permittivity is usually known as the *dielectric constant*. The imaginary part, ϵ''_r of the complex permittivity is associated with dielectric loss of the material. The effective conductivity, σ_e is given as

$$\sigma_e = \omega \epsilon''_r = 2\pi f \epsilon_0 \epsilon''_r \quad (38)$$

The dielectric loss of a material will be usually expressed by a term loss tangent or $\tan \delta$ as

$$\tan \delta = \epsilon''_r / \epsilon'_r \quad (39)$$

3.1.2. Magnetic Parameters. When a magnetic material is introduced at the position of maximum magnetic field [12], the perturbation equation becomes

$$\frac{d\Omega}{\omega_0} = - \frac{\int_{V_s} \Delta\mu (H \cdot H_0^*) dv}{2\mu_0 \int_{V_c} |H_0|^2 dv} \quad (40)$$

where V_s and V_c are the volumes of the sample and cavity respectively, $\Delta\mu = \bar{\mu} - \mu_0$ and $\bar{\mu} = \bar{\mu}_r \mu_0$. But $\bar{\mu}_r = \mu'_r - j\mu''_r$. Thus Eq. (40) becomes

$$\frac{d\Omega}{\omega_0} = - \frac{\int_{V_s} (\bar{\mu}_r - 1) H \cdot H_0^* dv}{2 \int_{V_c} |H_0|^2 dv} \quad (41)$$

The components of the magnetic field for the TE_{10n} modes are

$$H_x = -C \frac{\beta a}{\pi} \sin \left(\frac{\pi x}{a} \right) \sin(\beta z)$$

$$H_z = C \cos \left(\frac{\pi x}{a} \right) \sin(\beta z)$$

The denominator of Eq. (41) becomes

$$\begin{aligned} \int_{V_c} |H_0|^2 dV &= \int_{V_c} H_x^2 dV + \int_{V_c} H_z^2 dV \\ &= \frac{C^2 V_0}{4} \frac{\lambda_g^2 + 4a^2}{\lambda_g^2} \end{aligned}$$

The numerator of Eq. (41) is reduced to

$$(\bar{\mu}_r - 1) \int_{V_s} \mathbf{H} \cdot \mathbf{H}_0^* dV = (\bar{\mu}_r - 1) \frac{4C^2 a^2 V_s}{\lambda_g^2}$$

Thus

$$\frac{d\Omega}{\omega_0} = -(\bar{\mu}_r - 1) \frac{8a^2}{(\lambda_g^2 + 4a^2)} \frac{V_s}{V_c} \quad (42)$$

Equating the real and the imaginary parts of (42), we obtain

$$(\mu'_r - 1) = \frac{(\lambda_g^2 + 4a^2) f_c - f_s V_0}{(8a^2) f_s V_s} \quad (43)$$

$$\mu''_r = \frac{(\lambda_g^2 + 4a^2) V_c}{16a^2} \left(\frac{1}{Q_s} - \frac{1}{Q_c} \right) \quad (44)$$

Q_s and Q_c are the quality factors of the cavity with and without the sample in the cavity, and f_s and f_c are the resonant frequencies of the cavity with and without the sample on the sample holder. λ_g is the guided wavelength. For the TE_{10n} mode, $\lambda_g = 2d/n$, where d is the length of the cavity and $n = 1, 2, 3, \dots$

3.2. Coaxial Transmission-Line Resonator

The experimental procedure is the same as that explained in Section 3.1. The coaxial transmission-line resonator consists of a circular waveguide that operates below cutoff for the TM_{01} mode. A typical coaxial transmission-line resonator is shown in Fig. 5. Along the waveguide axis there is a removable center conductor. Thus the TEM mode can propagate up to the end of the center conductor. The standing-wave field components of the resonant TEM mode are obtained by combining the forward and backward propagating waves (in cylindrical coordinate

system $\{\rho, \phi, z\}$)

$$E_{\rho s}^0 = \frac{Ae^{j\beta z}}{\rho} + \frac{Be^{-j\beta z}}{\rho} \quad (45)$$

$$H_{\phi s}^0 = -\frac{Ae^{j\beta z}}{\eta\rho} + \frac{Be^{-j\beta z}}{\eta\rho}$$

where η is the free-space impedance and A and B are constants. The boundary conditions require that $E_{\rho s}^0$ vanish at $z = 0$, which is the fixed end of the center conductor. At $z = L$ (where L is the length of the center conductor), the maximum field corresponding to resonance occurs. The first condition gives $A = -B$, while the second gives the resonance condition. Now the preceding equations become

$$E_{\rho s}^0 = 2j \frac{A}{\rho} \sin \beta z = jE_{av} \sin \beta z$$

$$H_{\phi s}^0 = -2 \frac{A}{\eta\rho} \cos \beta z = -\frac{E_{av}}{\eta} \cos \beta z \quad (46)$$

Since ρ varies from a to b (from the surface of the center conductor to the inner radius of the resonator), the average field acting on the sample may be considered. Thus E_{av} is the average electric field. The electrical energy stored in the cavity is

$$W_e = \frac{\epsilon_0}{2} \int_{V_c} E_{\rho s}^0{}^2 dV$$

On substituting the value of $E_{\rho s}^0$ from (46), we get

$$W_e = \frac{\epsilon_0}{2} \int_0^{2\pi} \int_a^b \int_0^L E_{av}^2 \sin^2 \beta z \rho d\rho d\phi dz \quad (47)$$

Here b is the inner radius of the outer conductor and a is the radius of the center conductor.

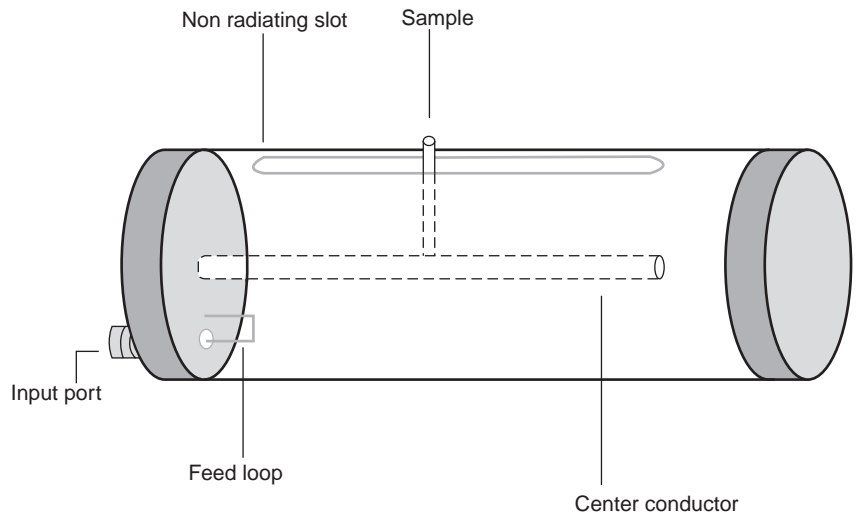


Figure 5. Schematic diagram of coaxial cavity resonator.

When the dielectric sample is introduced at the position of maximum electric field, the relative frequency shift is given by [13,14]

$$\frac{d\Omega}{\omega_0} \approx \frac{(\bar{\epsilon}_r - 1) \int_{V_s} \epsilon_0 E_{\rho s \max} \cdot E_{\rho s \max}^{0*} dV}{4W_e} \quad (48)$$

Substituting for W_e , we obtain

$$\begin{aligned} \frac{d\Omega}{\omega_0} &\approx \frac{(\bar{\epsilon}_r - 1) \int_{V_s} E_{\rho s \max} \cdot E_{\rho s \max}^{0*} dV}{2 \int_0^{2\pi} \int_a^b \int_0^L E_{av}^2 \sin^2 \beta z \rho d\rho d\phi dz} \quad (49) \\ &\approx \frac{(\bar{\epsilon}_r - 1) V_s}{\pi L (b^2 - a^2)} \end{aligned}$$

For a small volume of the sample, $E_{\rho s \max} = E_{\rho s \max}^0 = E_{av} \cdot V_s = \pi r r^2 (b - a)$, where r is the inner radius of the capillary tube. However, $\bar{\epsilon}_r = \epsilon'_r - j\epsilon''_r$:

$$\frac{d\Omega}{\omega_0} \approx -\frac{(\epsilon'_r - 1)r^2}{L(b+a)} + \frac{j\epsilon''_r r^2}{L(b+a)} \quad (50)$$

Equating the real and imaginary part of (50), we obtain

$$(\epsilon'_r - 1) = \frac{L(b+a)}{r^2} \frac{(f_c - f_s)}{f_s} \quad (51)$$

$$\epsilon''_r = \frac{L(b+a)}{2r^2} \left[\frac{1}{Q_s} - \frac{1}{Q_c} \right] \quad (52)$$

4. SOURCES OF ERROR AND ACCURACY CONSIDERATION

In general cavity resonator techniques based on perturbation theory offer an accurate method of measurement for the study of dielectric and magnetic properties of materials. The main sources of experimental error are high relative resonant frequency shift, decrease in Q factor of the cavity, and irregular shape of the materials. Study shows that the perturbation condition is satisfied mostly when the relative frequency shift is of the order of 1 in 1000 and, the decrease in the quality factor due to the introduction of the sample by a factor of 10–15%. This shows that the sample size will vary for different materials (low, medium, and high loss). The assumption that the fields in the cavity under perturbed and unperturbed conditions are the same [14–17] will be valid only when the sample size satisfies the conditions mentioned above. A comparative study of the dielectric parameters of water using perturbation technique and other rigorous technique is given in Table 1 [12].

Table 1. Comparison of Dielectric Parameters of Water Obtained with Cavity Perturbation Technique and the Rigorous Method

Frequency (GHz)	Rectangular Cavity Perturbation Technique		Rigorous Method (Wei and Sridhar) [21]	
	ϵ'_r	ϵ''_r	ϵ'_r	ϵ''_r
2.44	78.58	7.01	78.14	7.12
2.68	76.56	7.90	75.46	8.24
3.29	74.47	11.98	74.12	11.27
3.63	74.06	14.89	73.88	15.12
3.98	72.88	16.20	73.22	16.56
5.10	72.13	16.45	72.27	16.89
5.63	70.61	17.69	71.94	17.45
6.93	67.53	21.57	69.56	22.17
8.57	64.10	24.35	65.09	25.44
10.14	60.29	27.97	61.50	29.18
10.97	58.47	29.23	59.72	30.25

5. PRACTICAL APPLICATIONS OF PERTURBATION THEORY

Perturbation theory finds application in industrial, scientific, and medical (ISM) research. For the development of new materials for various applications, especially in microelectronics and MMICs, thorough knowledge about the dielectric and magnetic properties of the test materials is essential. Low- and medium-frequency measurements are rather simple and well established. Measurements in UHF and microwave frequency ranges need special attention. Cavity perturbation techniques are assumed to be most accurate. This technique is very important in the case of samples (solid, liquid, or gaseous), which are available in extremely small quantities. Biological samples such as bile and pancreatic juice are examples [18,19]. More recent study reveals that imaging of materials using perturbation technique [20] has been effectively applied in *medical imaging*.

6. APPENDIX: DERIVATION FOR MATERIAL PERTURBATION EQUATION IN A WAVEGUIDE

The unperturbed fields in a waveguide can be written as follows:

$$E_0 = E_{0 \max} e^{j\omega t - \gamma_0 z}$$

$$H_0 = H_{0 \max} e^{j\omega t - \gamma_0 z}$$

$$E = E_{\max} e^{j\omega t - \gamma z}$$

$$\nabla \times E_0 = -j\omega\mu_0 H_0$$

$$\nabla \times H_0 = j\omega\epsilon_0 E_0$$

$$\nabla \times E = -j\omega\mu_0 H \quad (\text{exterior to the sample})$$

$$= -j\omega\mu H \quad (\text{interior to the sample})$$

$$\nabla \times H = j\omega\epsilon_0 E \quad (\text{exterior to the sample})$$

$$= j\omega\epsilon E \quad (\text{interior to the sample})$$

The same procedure for derivation of the frequency shift in the preceding cases is employed here also. It can be easily shown that

$$\gamma_p - \gamma_u = \frac{\omega \int_{\Delta_s} [(\mu - \mu_0)H \cdot H_0^* + (\varepsilon - \varepsilon_0)E \cdot E_0^*] ds}{\int_S \mu_0 H \cdot H_0^* + \varepsilon_0 E \cdot E_0^* ds}$$

If the sample is a lossy medium

$$\gamma_p = \beta_p - j\alpha_p$$

$$\gamma_u = \beta_u \quad \text{for free space}$$

$$\gamma_p - \gamma_u = (\beta_p - \beta_u) - j\alpha_p$$

For a nonmagnetic material $\mu = \mu_0$ and

$$\varepsilon - \varepsilon_0 = \bar{\varepsilon}_r \varepsilon_0 - \varepsilon_0 = \varepsilon_0(\bar{\varepsilon}_r - 1), \quad \bar{\varepsilon}_r = \varepsilon'_r - j\varepsilon''_r$$

$$\beta_p - \beta_u = \frac{\omega \int_{\Delta_s} (\varepsilon'_r - 1)E \cdot E_0^* ds}{2 \int_S E \cdot E_0^* ds}$$

$$\alpha_p = \frac{\omega \varepsilon'' \int_{\Delta_s} E \cdot E_0^* ds}{2 \int_S E \cdot E_0^* ds}$$

Putting $E = E_0$, we obtain

$$\beta_p - \beta_u = \frac{\omega(\varepsilon'_r - 1) \int_{\Delta_s} |E_0|^2 ds}{2 \int_S |E_0|^2 ds}$$

$$\alpha_p = \frac{\omega \varepsilon'' \int_{\Delta_s} |E_0|^2 ds}{2 \int_S |E_0|^2 ds}$$

Thus the insertion of a nonmagnetic dielectric material in to a uniform waveguide will produce a phase shift and attenuation between the incoming and outgoing waves. This property is utilized in the design of phase shifters and strip attenuators.

Cavity perturbation theory can be modified to obtain an expression for the frequency shift for a ferrite material. It is assumed that a ferrite is sufficiently small to cause only a small perturbation in the resonant cavity. Thus the frequency shift

$$\frac{\delta\omega}{\omega} = \frac{\int_{\text{sample}} (E_1 \cdot D_0 - E_0 \cdot D_1 + H_0 \cdot B_1 - H_1 \cdot B_0) dv}{\int_{\text{cavity}} (E_0 \cdot D_0 - H_0 \cdot B_0) dv}$$

will be modified as

$$\frac{\delta\omega}{\omega} = \frac{\int_{\text{sample}} [(\chi^e \cdot H) \cdot H - \chi_e^e E \cdot E] dv}{\int_{\text{cavity}} (\varepsilon_0 E_0 \cdot E - \mu_0 H_0 \cdot H) dv}$$

where χ^e and χ_e^e are the external forms of the tensor susceptibility and dielectric susceptibility, respectively.

BIBLIOGRAPHY

1. H. A. Bethe and J. Schwinger, NDRC Report D1-117, Cornell Univ. March 1943.
2. E. G. Spencer, R. C. Lecrow, and L. E. Ault, Note on cavity perturbation Theory, *J. Appl. Phys.* **28**:130-132 (1957).
3. M. E. Brodwin and M. K. Parsons, New approach to the perturbation of cavity resonators by homogeneous, isotropic spheres, *J. Appl. Phys.* **36**:494, 504 (1964).
4. S. H. Chao, Measurement of microwave conductivity and dielectric constant by the cavity perturbation method and their errors, *IEEE Trans. Microwave Theory Tech.* **MTT-33**:519-526 (1985).
5. R. F. Harrington, *Time-Harmonic Electromagnetic Fields*, McGraw-Hill, New York, 1961.
6. E. Jordan and K. Balmain, *Electromagnetic Waves and Radiating Systems*, Prentice-Hall, New Delhi, India, 1990.
7. B. I. Bleaney and B. Bleaney, *Electricity and Magnetism*, Oxford Univ. Press, Oxford, UK, 1957.
8. S. B. Cohn, Properties of ridge waveguide, *Proc. IRE* **35**(8):783-788 (1947).
9. R. A. Waldron, Perturbation theory of resonant cavities, *Proc. Inst. Electric. Eng.* **107-C**: 272-274 (1960).
10. A. Parkash, J. K. Vaid, and A. Mansingh, Measurement of dielectric parameters at microwave frequencies by cavity perturbation technique, *IEEE Trans. Microwave Theory Tech.* **MTT-27**:791-795 (1979).
11. R. A. Waldron, *Theory of Guided Electromagnetic Waves*, Van Nostrand, London, 1970.
12. K. T. Mathew and U. Raveendranath, Cavity perturbation techniques for measuring dielectric parameters of water and other allied liquids, in H. Baltes, W. Gopel, and J. Hesse, eds., *Sensors Update*, Vol. 7, Wiley-VCH, Germany, 2000.
13. U. Raveendranath and K. T. Mathew, New cavity perturbation technique for measuring complex permeability of ferrite materials, *Microwave Opt. Technol. Lett.* **18**:241-243 (1998).
14. U. Raveendranath, S. Bijukumar, and K. T. Mathew, Broadband coaxial cavity resonator for complex permittivity measurements of liquids, *IEEE Trans. Instrum. Meas.* **IM-49**:1305-1312 (2000).
15. S. Li, C. Akyel, and R. G. Bosisio, Precise calculations and measurement on the complex dielectric constant of lossy materials using TM₀₁₀ cavity perturbation techniques, *IEEE Trans. Microwave Theory Tech.* **MTT-29**:1041-1047 (1981).
16. R. G. Carter, Accuracy of microwave cavity perturbation measurements, *IEEE Trans. Microwave Theory Tech.* **MTT-49**(5):918-923 (2001).
17. L. Chen, C. K. Ong, and B. T. G. Tan, A resonant cavity for high-accuracy measurement of microwave dielectric properties, *Meas. Sci. Technol.* **7**:1255-1259 (1996).
18. S. Bijukumar, K. T. Mathew, U. Raveendranath, and P. Augustin, Dielectric properties of certain biological materials

- at microwave frequency, *J. Microwave Power Electromagn. Energy* (USA) **36**:67–75 (2001).
19. D. A. Stone and M. P. Robinson, Total body water measurements using resonant cavity perturbation techniques, *Phys. Med. Biol.* **49**:1773–1788 (2004).
 20. J. F. Zurcher, Material imaging with the use of microwave cavity perturbation technique, *Microwave Opt. Technol. Lett.* **33**(2):106–112 (2002).
 21. Z. Wei and S. Sreedhar, *IEEE Tran. Microwave Theory Tech. MTT-39*:526–531 (1991).

PHASE LOCKED LOOPS

GÉZA KOLUMBÁN
 Budapest University of
 Technology and Economics
 Hungary

1. INTRODUCTION

Although the first description of the phase-locked loop (PLL) was published by Appleton [1] in 1923, the PLL did not attract widespread attention until much later. Today PLLs of various types are used extensively in electrical engineering, from telecommunication systems to measurement equipment.

Depending on the loop components, especially on the operation of the phase detector, analog, digital, and hybrid PLLs are distinguished. The behavior of these circuits is described by differential, difference, and mixed integro-difference equations.

Even though applications of PLLs require a variety of circuit configurations, and the mathematical models mentioned above require different kinds of mathematical treatment, their behavior can be approximated and studied by means of a simple feedback structure. Unfortunately, the behavior of this structure is complicated to analyze because it is nonlinear, may contain edge-triggered digital circuits, and is driven by random noise. In many cases, analytical results are not available in closed form; they are often buried in complicated mathematics that cannot be assimilated easily by the circuit designer. On the other hand, the design of PLLs for many applications can be performed successfully on the basis of a simple linearized model and by means of a few rules of thumb. In this article the essential elements and secondary effects of loop behavior are clearly differentiated, the key assumptions and approximations involved in the analysis are highlighted, and the conditions under which the approximations are valid are collected. The main goals are to provide a survey of PLL theory and applications and to summarize the most important design rules and equations.

If the PLL must operate in a noisy environment, then an analog multiplier has to be used as phase detector (PD) to get the best noise performance. The PLL built with an analog multiplier is called an *analog phase-locked loop* (APLL). The other phase detectors such as digital or

edge-triggered circuits have much worse performance in a noisy environment. This is why APLLs are used to build amplifiers, demodulators and carrier recovery circuits.

The other important PLL application is frequency synthesis, where the reference signal has very high spectral purity. In frequency synthesis the edge-triggered phase detectors such as sample-and-hold and phase-frequency detectors offer the best system parameters.

The article is organized according to these applications. Section 1 is devoted to APLL theory. First the baseband model is developed, then the linear theory of APLL (tracking, modulation, and noise) is discussed. Finally, the most important nonlinear effects (acquisition, cycle slips, hang-up) are surveyed. Section 2 discusses the most common PLL applications. Section 3 is devoted to frequency synthesis, where both the sampling (sample-and-hold-type PD) and charge-pump (phase-frequency detector with charge pump) PLLs are considered. These phase detectors are edge-triggered circuits; the discrete-time operation makes the analysis of these PLLs very complex. The problem of discrete-time operation arising from the application of edge-triggered circuits is discussed and design methods are given.

2. ANALOG PHASE-LOCKED LOOP

In an APLL, all loop components are analog circuits and the phase detector is an analog multiplier. The APLL operation is modeled by an ordinary differential equation.

The APLL was the first, and is the most widely studied, version of the PLLS. Many excellent books [2–11], two IEEE special issues [12,13], and a tutorial [14] have been devoted to the theory and applications of the APLL.

In many applications, the block diagram of an APLL has to be completed with extra loop components such as frequency divider and mixer. That is why the results developed for the APLL cannot be used directly in many cases. However

- APLL theory is very well developed and is relatively easy to understand.
- Equations describing the loop behavior in different applications can be developed in closed form.
- Having understood the operation of the APLL, it is easy to study more complex PLL configurations.
- If the closed-loop bandwidth [defined later by Eq. (37)] is at least 10 times less than the frequency of the input signal, then the theory of any kind of PLLs even including edge-triggered circuits may be approximated by the APLL theory.

This section presents a *concise* treatment of the APLL. First, the baseband model for the APLL is developed. Then the linear APLL theory is discussed. In the majority of applications, the APLL operates in its linear region. The linear theory can be applied only if the *phase-locked* condition has been achieved and is maintained. Under phase-locked condition the average input and voltage-

controlled oscillator (VCO) frequencies are exactly equal and the VCO phase tracks the input phase.

The phase-locked condition is achieved as a result of a highly nonlinear, acquisition process. In the last part of this section, the most important aspects of nonlinear APLL theory are surveyed.

2.1. Basic Loop Configuration

A PLL is a feedback system that continuously tries to track the phase of an input signal. It contains a *phase detector*, a time-invariant linear *loop filter*, and a *voltage-controlled oscillator* the oscillator to be synchronized. As shown in Fig. 1, the phase detector compares the phase of input signal against the phase of VCO output and produces an error signal. This error signal is then filtered, in order to remove noise and other unwanted components of the input spectrum, and the filter output controls the instantaneous VCO frequency.

A nonzero output voltage must be provided by the PD in order to change the VCO frequency if the input frequency differs from the VCO center frequency. Consequently, the PLL tracks the phase of input signal with some phase error. However, this phase error can be kept very small in a well-designed PLL.

Figure 1 shows a few important telecommunication applications of a phase-locked loop; it may be used to demodulate both phase- (PM) and frequency- (FM) modulated signal, to implement an FM modulator, or for recovery of carrier signal.

2.1.1. Acquisition and Tracking. In every application, the PLL tracks the phase of an input signal. However, before a PLL can track, it must first reach the phase-locked condition.

In general, the VCO center frequency ω_0 differs from the frequency ω_i of input signal. Therefore, first the VCO frequency has to be tuned to ω_i by the loop. This process is called *frequency pull-in*. Then the VCO phase has to be adjusted according to the input phase. This process is known as *phase lock-in*.

In connection with acquisition and tracking, three important loop characteristics are defined.

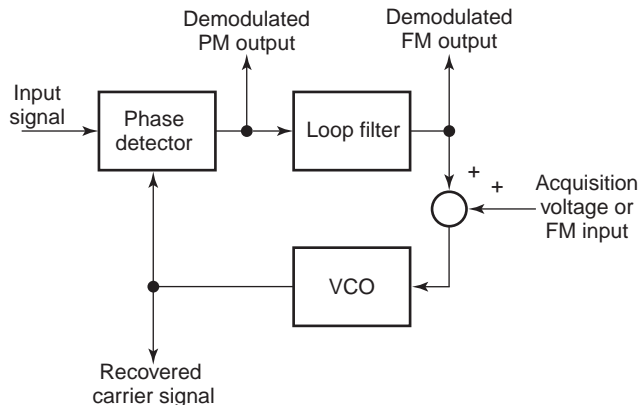


Figure 1. APLL block diagram showing inputs and outputs for various telecommunication applications.

2.1.1.1. Pull-in Range. $\Delta\omega_P = |\omega_i - \omega_0|$ is the maximum initial frequency difference between the input and VCO center frequencies in both positive and negative directions, for which the PLL eventually achieves the phase-locked condition. The pull-in range is related to the dynamics of the APLL.

2.1.1.2. Lockin Range. $\Delta\omega_L = |\omega_i - \omega_0|$ is the frequency range over which the PLL achieves the phase-locked condition without cycle slips. Cycle slips will be defined later.

2.1.1.3. Holdin Range. Suppose that the phase-locked condition has been achieved in the PLL. Now vary the input frequency ω_i slowly, and the VCO frequency will follow it. The holdin range $\Delta\omega_H = |\omega_i - \omega_0|$ is determined by the lower and upper values of ω_i for which the phase-locked condition is lost. The holdin range represents the maximum static tracking range and is determined by the saturation characteristics of the nonlinear loop elements in the PLL.

2.2. Loop Equation and Nonlinear Baseband Model

The block diagram of the APLL to be studied is shown in Fig. 2, where $F(p)$ denotes the transfer function of the loop filter. In the equations developed in this article, the time variable t is suppressed for conciseness where it does not cause misunderstanding. In order to write the differential equations in compact form, the differentiation d/dt in the time domain is denoted by the multiplication of *Heaviside operator* p . If the transfer function $F(s)$ of a linear network is given in the complex frequency domain s , then $F(p) = F(s)|_{s=p}$. For more details on the Heaviside operator, see p. 73 in Ref. 6.

It is assumed in the APLL analysis that the loop components are linear; the only source of nonlinearity is the phase detector. The instantaneous VCO frequency may be varied about its center value ω_0 by the VCO control voltage $v_c(t)$.

Almost all signals and random processes appearing in electrical engineering may be considered narrowband [15]. Let the input signal

$$s(t, \Phi) = \sqrt{2}A \sin \Phi \tag{1}$$

be a narrowband signal, where $A(t)$ describes the *amplitude modulation* produced at the transmitter on purpose

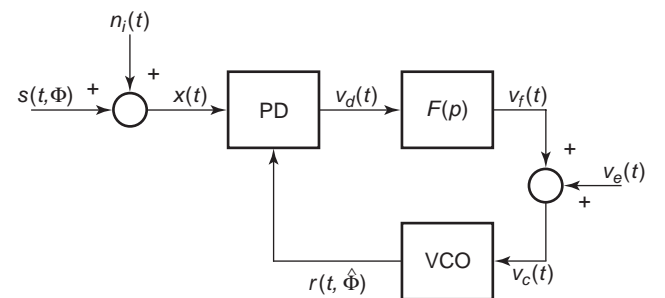


Figure 2. APLL block diagram indicating the additive input noise that corrupts the input signal.

and/or caused by the time-varying channel through which the signal is transmitted. Let the phase of the incoming signal be expressed with respect to the VCO center frequency as

$$\Phi = \omega_0 t + \theta_i \quad (2)$$

where $\theta_i(t)$ is the *input phase modulation* produced at the transmitter and/or caused by the channel. Note that $\theta_i(t)$ also incorporates the input frequency error $\Delta\omega_i = \omega_i - \omega_0$.

As shown in Fig. 2, the incoming signal $s(t, \Phi)$ is corrupted by additive input noise $n_i(t)$. In almost all applications, the additive input noise is a narrowband random process centered about ω_0 . By means of the analytic signal approach [15], narrowband random processes or signals can be expressed as a product of a slowly varying complex envelope and a sinusoidal carrier. For example, an arbitrary narrowband signal $w(t)$ centered about ω_0 can be expressed in terms of a complex envelope $\tilde{w}(t)$ as

$$w(t) = \text{Re}\{\tilde{w}(t) \exp(j\omega_0 t)\} \quad (3)$$

Since the carrier frequency component has been removed, the complex envelope is a slowly varying function

$$\tilde{w}(t) = w_I(t) + jw_Q(t) \quad (4)$$

where $w_I(t)$ and $w_Q(t)$ are the low-frequency *in-phase* and *quadrature components* of the narrowband signal $w(t)$.

Let $n_i(t)$ be modeled by a narrowband Gaussian random process of zero mean and symmetric power spectral density. Then the sample function of the narrowband noise can be expressed from Eqs. (3) and (4) in *canonical form* [6,15] as

$$n_i = \sqrt{2}[n_I \cos(\omega_0 t) - n_Q \sin(\omega_0 t)] \quad (5)$$

The in-phase and quadrature components are

$$n_I = \frac{1}{\sqrt{2}}[n_i \cos(\omega_0 t) + \hat{n}_i \sin(\omega_0 t)] \quad (6)$$

and

$$n_Q = \frac{1}{\sqrt{2}}[\hat{n}_i \cos(\omega_0 t) - n_i \sin(\omega_0 t)] \quad (7)$$

where $\hat{n}_i(t)$ is the Hilbert transform of $n_i(t)$ [15].

The VCO output is also a narrowband signal

$$r(t, \hat{\Phi}) = \sqrt{2}V_o \cos \hat{\Phi} \quad (8)$$

where $\hat{\Phi}(t)$ is the loop estimate of $\Phi(t)$ that can be expressed, with respect to the VCO center frequency, as

$$\hat{\Phi} = \omega_0 t + \theta_o \quad (9)$$

In Eqs. (8) and (9) V_o and $\theta_o(t)$ denote the RMS amplitude and phase of the VCO output, respectively.

The PD multiplies the input signal $x(t) = s(t, \Phi) + n_i(t)$ and VCO output $r(t, \hat{\Phi})$ and produces both difference- and sum-frequency terms. The PD always contains a lowpass filter that eliminates the sum-frequency component. By means of simple trigonometric identities the PD output is obtained

$$\begin{aligned} v_d &= AV_o \sin \theta_e + V_o(n_I \cos \theta_o + n_Q \sin \theta_o) \\ &= K_d[A \sin \theta_e + N(t, \theta_o)] \end{aligned} \quad (10)$$

where the *phase error* is defined by

$$\theta_e(t) = \Phi(t) - \hat{\Phi}(t) = \theta_i(t) - \theta_o(t) \quad (11)$$

and $K_d = V_o$, a dimensionless quantity, is the gain of PD. The *equivalent phase noise process* is defined by

$$N(t, \theta_o) = n_I \cos \theta_o + n_Q \sin \theta_o \quad (12)$$

For the statistical properties of $N(t, \theta_o)$, refer to the following subsection.

From Eqs. (10) and (12), two conclusions may be drawn:

- Even in the noise-free case, the PD output depends not only on the phase error $\theta_e(t)$ but also on the amplitude $A(t)$ of incoming signal.
- The equivalent noise process $N(t, \theta_o)$ is independent of $\theta_e(t)$; it appears as an additive term in the PD output.

The instantaneous VCO frequency $\dot{\theta}_o(t) = d\theta_o(t)/dt$ referenced to ω_0 is related to its input through

$$\dot{\theta}_o = K_v v_c + \dot{\Psi}_2 = K_v(v_f + v_e) + \dot{\Psi}_2 \quad (13)$$

where $v_c(t) = v_f(t) + v_e(t)$ denotes the VCO control voltage, $v_f(t) = F(p)v_d(t)$ is the output voltage of the loop filter, $v_e(t)$ denotes the external control voltage, K_v is the VCO gain in $\text{rad/V} \cdot \text{s}$, and $\Psi_2(t)$ denotes the VCO jitter, that is, the VCO phase noise.

Taking into account the transfer function of the loop filter, the output phase is obtained from Eqs. (10) and (13) as

$$\theta_o = \frac{KF(p)}{p}[A \sin \theta_e + N(t, \theta_o)] + \frac{K_v}{p}v_e + \Psi_2 \quad (14)$$

where $K = K_d K_v$ defines the *loop gain* in $\text{rad/V} \cdot \text{s}$. Substituting Eq. (14) into Eq. (11), the following nonlinear stochastic integro-differential equation is obtained

$$\dot{\theta}_e = \theta_i - \frac{KF(p)}{p}[A \sin \theta_e + N(t, \theta_o)] - \frac{K_v}{p}v_e - \dot{\Psi}_2 \quad (15)$$

which describes the operation of APLL. In general, the input phase modulation $\theta_i(t)$ consists of three terms

$$\theta_i = d + M + \Psi_1 \quad (16)$$

where $d(t)$ describes the Doppler effect appearing in the channel, $M(t)$ is the digital or analog phase/frequency modulation, and $\Psi_1(t)$ denotes the jitter, that is, phase noise of the transmitter oscillator.

The loop equation given by Eq. (15) has two important features. Due to the introduction of a phase error, the high-frequency terms have been dropped and all signals involved in the loop equations have become low-frequency signals, that is, slowly varying functions. This means that instead of angle-modulated signals, only their modulation has to be considered and in computer simulation the lowest sampling frequency may be used. A further advantage, the phase error approach simplifies the problem to be studied in many cases. For example, Eq. (15) becomes an autonomous differential equation during acquisition that is relatively easy to study.

Note that, in an implemented APLL, the phase error does not exist as an explicit variable; it has been introduced only to derive a simple mathematical model for the APLL. However, if $\theta_e(t)$ is known, then all signals appearing in a built APLL can be expressed easily by the equations developed above.

The baseband model of the APLL can be developed from Eq. (15) as shown in Fig. 3. The sinusoidal nonlinearity in Eq. (15) is due to the particular type of PD and the sinusoidal VCO and input waveforms. However, other kinds of PD and signals may be also applied. Fortunately, the unified baseband model shown in Fig. 3 remains valid for each loop configuration if the loop nonlinearity $g(\cdot)$ is selected according to the actual PD characteristics and $n_g(t)$ describes the equivalent noise process for the case to be studied. If an analog multiplier is used as the PD and the signals are sinusoidal, then $g(\cdot) = \sin(\cdot)$ and $n_g(t) = N(t, \theta_o)$. Lindsey and Chie have collected $g(\cdot)$ and $n_g(t)$ for many other loop configurations [11].

Note that the input and output of baseband model are not measurable signals but are the input and output phase modulations, respectively. If the real input and output signals have to be determined, then $s(t, \Phi)$ and $r(t, \hat{\Phi})$ are obtained from Eqs. (1) and (8).

2.3. Statistical Properties of Equivalent Noise

In order to use the baseband model in PLL analysis and design, the statistical properties of equivalent noise

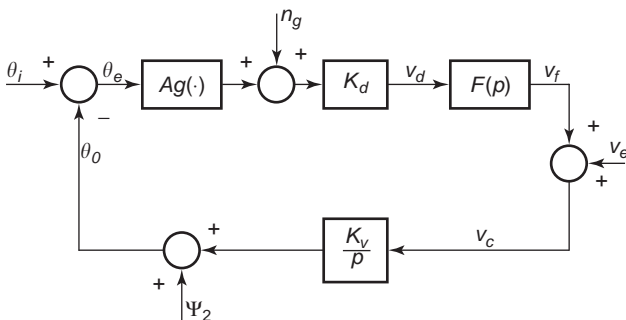


Figure 3. Unified baseband model of APLL.

process $N(t, \theta_o)$ must be known. This subsection summarizes the properties of the in-phase and quadrature components of $n_i(t)$ and gives the statistical properties of $N(t, \theta_o)$

The additive input noise is modeled by a narrow-band Gaussian random process with zero mean. It may be expressed either in canonical form or as a sinusoidal signal

$$n_i = \sqrt{2} [n_I \cos(\omega_0 t) - n_Q \sin(\omega_0 t)] = \sqrt{2} N_n(t) \cos(\omega_0 t + \theta_n) \tag{17}$$

where the envelope $N_n(t)$ and phase $\theta_n(t)$ processes are defined by

$$N_n(t) = \sqrt{n_I^2(t) + n_Q^2(t)} \text{ and} \tag{18}$$

$$\theta_n(t) = \tan^{-1} \left[\frac{n_Q(t)}{n_I(t)} \right]$$

Note that the envelope $N_n(t)$ differs from the complex envelope defined by Eq. (3). If the power spectral density of $n_i(t)$ is symmetric about ω_0 , then a very simple relationship exists between the autocorrelation functions of $n_i(t)$ and $N_n(t)$

$$R_n(\tau) = 2r(\tau) \cos(\omega_0 \tau) \tag{19}$$

where $R_n(\tau)$ and $r(\tau)$ denote the autocorrelation functions of $n_i(t)$ and $N_n(t)$, respectively.

If $n_i(t)$ has a symmetric power spectral density about ω_0 , then the most important properties of the in-phase $n_I(t)$ and quadrature $n_Q(t)$ components of $n_i(t)$ are as follows [10,15]:

1. If $n_i(t)$ is a Gaussian process, then both $n_I(t)$ and $n_Q(t)$ are also Gaussian.
2. If $n_i(t)$ has zero mean, then both $n_I(t)$ and $n_Q(t)$ have zero-mean values. Note that $n_i(t)$ is a bandpass signal, consequently, it always has zero mean.
3. The in-phase and quadrature components have the same variance as the narrowband noise $n_i(t)$.
4. The correlation functions of $n_I(t)$ and $n_Q(t)$ may be expressed [6] as

$$\overline{n_I(t)n_I(t+\tau)} = \overline{n_Q(t)n_Q(t+\tau)} = r(\tau) \tag{20}$$

$$\overline{n_I(t)n_Q(t+\tau)} = \overline{-n_Q(t)n_I(t+\tau)} = 0$$

5. where overbar symbolizes the time-averaging operation. The first equation shows that the autocorrelation functions of $N_n(t)$, $n_I(t)$, and $n_Q(t)$ are equal to each other, while the second one means that $n_I(t)$ and $n_Q(t)$ are independent.

6. Both the in-phase and quadrature noise components have the same power spectral density that is related to the power spectral density $S_N(f)$ of $n_i(t)$ as

$$S_I(f) = S_Q(f) = \begin{cases} \frac{1}{2}[S_N(f - f_0) + S_N(f + f_0)], & -B \leq f \leq B \\ 0, & \text{elsewhere} \end{cases} \quad (21)$$

where $S_N(f)$ occupies the frequency band $f_0 - B \leq |f| \leq f_0 + B$ and $f_0 > B$.

To complete the APLL baseband model, the statistical properties of $N(t, \theta_o)$ have to be determined. The problem is that the equivalent noise depends not only on $n_i(t)$ but also on $\theta_o(t)$. Due to the closed loop, the noise modulates the VCO and $\theta_o(t)$ also becomes a random process. Because the PD is nonlinear, the fluctuations in $\theta_o(t)$ intermodulate with the incoming signal and additive input noise $n_i(t)$.

The nonlinear operation of the PD makes exact analysis impossible, so some kind of approximation must be used. Viterbi [3] introduced two assumptions in order to get a simple but useful result:

1. The additive bandpass noise $n_i(t)$ has a symmetric power spectral density.
2. The bandwidth of $n_i(t)$ is much wider than that of $\theta_o(t)$.

The bandwidth of $\theta_o(t)$ is determined by the noise bandwidth of the loop, which will be defined later. Since the APLL noise bandwidth is always much less than the bandwidth of $n_i(t)$, the correlation time [6] of the additive input noise is much less than that of the output phase. Consequently, $\theta_o(t)$ can be thought of as a slowly varying function compared to $n_i(t)$ and the two processes are approximately independent [3].

Under these assumptions the equivalent noise process can be approximated by white noise. The process $N(t, \theta_o)$ shall be treated as though it were white so that $\theta_o(t)$ embedded in $N(t, \theta_o)$ does not enter into the APLL analysis, either linear or nonlinear. Thus, if the additive input noise $n_i(t)$ is white with spectral density $N_0/2$, then the power spectral density of the equivalent noise $n_g(t)$ indicated in Fig. 3 is uniform with value $N_0/2$.

Fortunately, the assumptions listed above are valid for almost all practical APLL applications and the design of different circuit configurations operating in either the linear or nonlinear region can be performed on the basis of a simple baseband model.

2.4. Linear Operation of the APLL

Linear APLL theory is used extensively in designing APLLs for different applications from telecommunication to measurement engineering. Many system parameters used in circuit development and characterization are introduced and defined in the linear theory.

The linear operation of APLL assumes that

- The phase-locked condition has been achieved and is maintained.
- The phase error remains in the neighborhood of its quiescent value, that is, one may write

$$g(\theta_e) \approx g(\theta_{ss}) + \left. \frac{dg(\theta_e)}{d(\theta_e)} \right|_{\theta_{ss}} \Delta\theta_e,$$

where θ_{ss} is the quiescent value of $\theta_e(t)$ and $\Delta\theta_e(t)$ denotes its perturbation.

In this section the linear baseband model for the APLL is developed and then the APLL transfer functions are defined. After evaluating the stability properties, the tracking (transient and modulation) behavior and noise performance of the APLL are studied using the linear baseband model.

2.4.1. Linear Baseband Model. As shown above, the behavior of the APLL is described by a nonlinear stochastic differential equation

$$\dot{\theta}_e = \theta_i - \frac{KF(p)}{p} [Ag(\theta_e) + n_g] - \frac{K_v}{p} v_e - \Psi_2 \quad (22)$$

where $g(\cdot)$ describes all nonlinearities of the loop and $n_g(t)$ denotes the equivalent noise process. Recall that the linear approximation may be used only if the APLL operates under phase-locked condition.

First the quiescent value of the phase error must be determined. Let $n_g(t) = \Psi_2(t) = 0$, and let the input phase modulation be

$$\theta_i = (\omega_i - \omega_0)t + \theta_{i0} = \Delta\omega_i t + \theta_{i0}$$

where $\Delta\omega_i$ is the initial frequency detuning and θ_{i0} denotes the phase of the incoming signal. Taking into account that under steady-state conditions all signals are constant and that the Heaviside operator p means d/dt in the time domain, the quiescent value θ_{ss} of $\theta_e(t)$ may be obtained from Eq. (22) as

$$\theta_{ss} = g^{-1} \left(\frac{\Delta\omega_i - K_v v_{e0}}{KF(0)A} \right) \quad (23)$$

where v_{e0} denotes the external DC VCO control voltage and $F(0)$ is the DC gain of the loop filter.

If the phase error remains in the neighborhood of θ_{ss} , then $g(\Delta\theta_e) \approx dg(\theta_e)/d\theta_e|_{\theta_{ss}} \Delta\theta_e$, where $\Delta\theta_e = \theta_e - \theta_{ss}$. Let $K_g = dg(\theta_e)/d\theta_e|_{\theta_{ss}}$ be lumped with K_d . To show explicitly the dependence of APLL transfer functions on the amplitude of input signal, A is not lumped with K_d .

From Eq. (22) the linear loop equation for phase error is obtained as

$$\dot{\theta}_e = \theta_i - \frac{KF(p)}{p} \left(A\theta_e + \frac{n_g}{K_g} \right) - \frac{K_v}{p} v_e - \Psi_2 \quad (24)$$

where, in order to have a compact notation, $\theta_e(t)$ is not distinguished from its perturbation $\Delta\theta_e(t)$, and the new

value of loop gain is $K=K_gK_dK_v$. Note that K_g is measured in rad^{-1} and the new value of loop gain K is given in $(V \cdot s)^{-1}$. The output phase is obtained as

$$\theta_0 = \frac{KF(p)}{p} \left(A\theta_e + \frac{n_g}{K_g} \right) - \frac{K_v}{p} v_e - \Psi_2 \tag{25}$$

The linear baseband model is constructed from Eqs. (24) and (25). Although every built APLL is nonlinear, the linear model shown in Fig. 4 is valid in many applications, where after acquisition the APLL must operate in the linear region in order to avoid distortion.

2.4.2. Transfer Functions. The transfer function concept gives a simple tool to express the output signal(s) of a linear system in the complex frequency domain. Let the Laplace transform variable be denoted by s and let the Laplace transform of a signal be denoted by a capital letter.

In order to describe the behavior of APLL by means of transfer functions, Eq. (24) has to be rearranged as

$$\Theta_e(s) = [1 - H(s)] \left[\Theta_i(s) - \frac{K_v}{s} V_e(s) - \Psi_2(s) \right] - H(s) \frac{N_g(s)}{AK_g} \tag{26}$$

and substituting Eq. (11) into Eq. (25) the output phase has to be expressed as

$$\Theta_o(s) = H(s) \left[\Theta_i(s) + \frac{N_g(s)}{AK_g} \right] - [1 - H(s)] \left[\frac{K_v}{sV_e(s)} - \Psi_2(s) \right] \tag{27}$$

where $\Psi_2(s)$ denotes the Laplace transform of $\Psi_2(t)$.

Note that only two transfer functions are required to characterize the APLL completely, namely, the *closed-loop transfer function*

$$H(s) = \frac{AKF(s)}{s + AKF(s)} \tag{28}$$

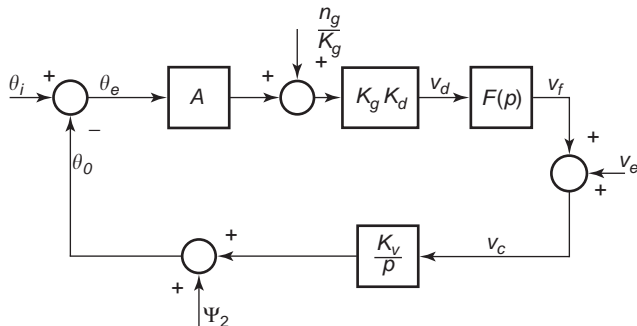


Figure 4. Linear baseband model of APLL.

and *error function*

$$1 - H(s) = \frac{s}{s + AKF(s)} \tag{29}$$

The closed-loop transfer and error functions have lowpass and highpass characteristics, respectively. The parameters of $H(s)$ and $[1 - H(s)]$ are determined by the loop filter $F(s)$, the loop gain K , and the RMS amplitude of the input signal. If $A(t)$ varies as a result of either amplitude modulation or a time-varying channel, then both $H(s)$ and $[1 - H(s)]$ also vary with time. In the majority of applications, this time dependence is not allowed; consequently, an AGC circuit preceding the APLL must be used in order to fix the amplitude of the input signal.

APLLs are classified according to the type and order of the loop. Let

$$G(s) = \frac{AKF(s)}{s} \tag{30}$$

denote the open-loop transfer function. The loop type is determined by the number of poles at the origin, that is, by the number of perfect integrators in $G(s)$, while the loop order is equal to the number of poles in $G(s)$.

The derivation of closed-loop APLL parameters is shown here to the two most important loop filter configurations. The closed-loop parameters for other loop filter configuration are given in Table 1.

First-Order, Type 1 Loop. In the simplest case $F(s) = 1$, that is, no loop filter is used. The first-order APLL is very rarely used in real applications but plays an important role in understanding the APLL operation. Substituting $F(s) = 1$ into Eqs. (28) and (29), the closed-loop transfer function

$$H(s) = \frac{1}{1 + \frac{s}{AK}} \tag{31}$$

and error function

$$1 - H(s) = \frac{\frac{s}{AK}}{1 + \frac{s}{AK}} \tag{32}$$

are obtained. The transfer function $H(s)$ has a lowpass characteristic with a well-defined 3 dB bandwidth, called the *closed-loop bandwidth*. Note that the closed-loop bandwidth $\omega_{3dB} = AK$ varies with the amplitude A of the input signal. The disadvantage of a first-order APLL is that only one free design parameter is available. The loop gain K determines all parameters of the APLL. For example, the quiescent phase error θ_{ss} given by Eq. (23) and the closed-loop bandwidth appearing in Eq. (31) may not be selected independently of each other; a small θ_{ss} results in a large closed-loop bandwidth. It is not possible to

Table 1. Parameters of Linearized APPLs (B_L Denotes APPL Noise Bandwidth)

Loop Order	Type	Loop Filter $F(s)$	Key Parameters	$H(s)$
First	1	1	$\omega_{3\text{ dB}} = AK$ $B_L = AK/4$	$\frac{4B_L}{s + 4B_L}$
Second	1	Passive lag filter $\frac{1}{1 + s\tau_1}$	$\omega_n^2 = AK/\tau_1$ $2\zeta\omega_n = 1/\tau_1$	$\frac{\omega_n^2}{s^2 + 2\zeta\omega_n s + \omega_n^2}$
		Passive lag-lead filter $\frac{1 + s\tau_2}{1 + s\tau_1}$	$B_L = AK/4$ $\omega_n^2 = AK/\tau_1$ $2\zeta\omega_n = \frac{1 + AK\tau_2}{\tau_1}$	$\frac{\left(2\frac{\zeta\omega_n - \omega_n^2}{AK}\right)s + \omega_n^2}{s^2 + 2\zeta\omega_n s + \omega_n^2}$
Third	2	Active filter $\frac{1 + s\tau_2}{s\tau_1}$	$\omega_n^2 = AK/\tau_1$ $2\zeta\omega_n = \frac{AK\tau_2}{\tau_1}$	$\frac{2\zeta\omega_n s + \omega_n^2}{s^2 + 2\zeta\omega_n s + \omega_n^2}$
			$B_L = \frac{\omega_n}{2} \left[\zeta \left(1 - \frac{\omega_n}{2AK\zeta} \right)^2 + \frac{1}{4\zeta} \right]$ $B_L = \frac{\omega_n}{2} \left(\zeta + \frac{1}{4\zeta} \right)$	$B_L = \frac{5}{6} B_0$

implement simultaneously a small tracking error and a small closed-loop bandwidth.

Second-Order, Type 2 Loop. The circuit diagram of the most frequently used active loop filter is shown in Fig. 5. Because of the finite DC gain, the transfer function of the loop filter

$$F(s) = \frac{1 + s\tau_2}{s\tau_1} \quad (33)$$

may not be implemented, but is approximated closely by an operational amplifier. The time constants in Eq. (33) are $\tau_1 = R_1 C$ and $\tau_2 = (R_1 + R_2)C$. A loop implemented with an active loop filter is often referred to as an *ideal second-order APPL*. After substituting Eq. (33) into Eqs. (28) and (29), the closed-loop trans-

fer function

$$H(s) = \frac{2\zeta\omega_n s + \omega_n^2}{s^2 + 2\zeta\omega_n s + \omega_n^2} \quad (34)$$

and the error function

$$1 - H(s) = \frac{s^2}{s^2 + 2\zeta\omega_n s + \omega_n^2} \quad (35)$$

are obtained, where the *natural frequency* ω_n and the *damping factor* ζ of loop are given by

$$\omega_n = \sqrt{\frac{AK}{\tau_1}} \quad \text{and} \quad \zeta = \frac{\tau_2\omega_n}{2} \quad (36)$$

The closed-loop bandwidth can be expressed as

$$\omega_{3\text{ dB}} = \omega_n \sqrt{2\zeta^2 + 1 + \sqrt{(2\zeta^2 + 1)^2 + 1}} \quad (37)$$

The magnitudes of the APPL frequency response and error response are plotted in Figs. 6 and 7, respectively, for several values of damping factor. Note that $H(s)$ and $[1 - H(s)]$ really have lowpass and highpass characteristics, respectively, as claimed.

The quiescent value of the phase error, the APPL transient behavior, and the closed-loop bandwidth are in the three basic APPL parameters that have to be selected in

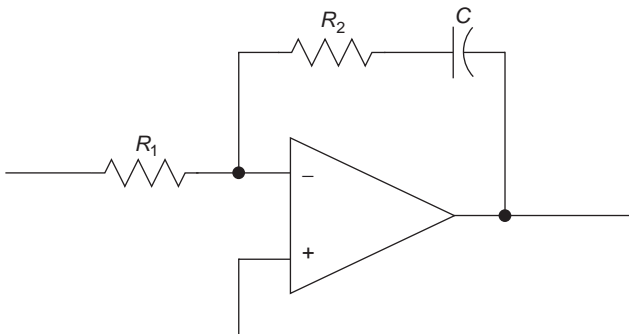


Figure 5. Circuit diagram of the most widely used active loop filter.

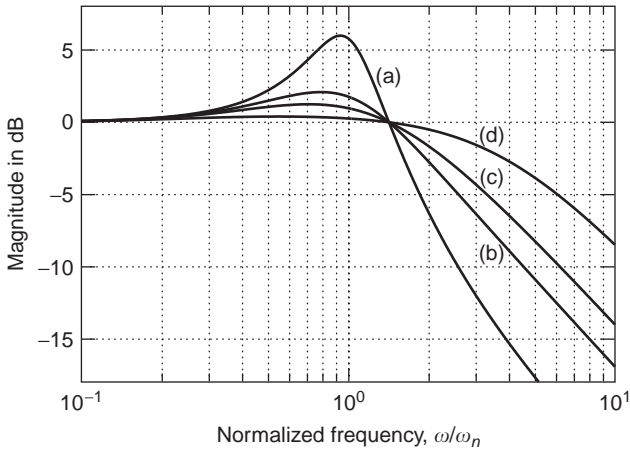


Figure 6. Frequency response of APLL implemented with an active loop filter for several values of damping factor: (a) $\zeta = 0.3$; (b) $\zeta = 0.707$; (c) $\zeta = 1$; (d) $\zeta = 2$.

design of every APLL. The main advantage of the ideal second-order APLL is that these parameters may be chosen independently of each other:

- The high DC gain of the operational amplifier ensures that $\theta_{ss} \approx 0$; furthermore, θ_{ss} does not depend on A .
- Equation (37) shows that ω_n may be calculated from the required closed-loop bandwidth and damping factor. Then AK/τ_1 is calculated from ω_n using Eq. (36).
- The transient behavior of the loop is controlled by the damping factor. From Eq. (36), τ_2 may be calculated.

A further advantage of second-order loop is that it is unconditionally stable for all values of loop gain. However, note that all closed-loop parameters depend on the RMS amplitude of the input signal.

Other loop filters are also used in built APLL circuits. A short summary of loop parameters and closed-loop trans-

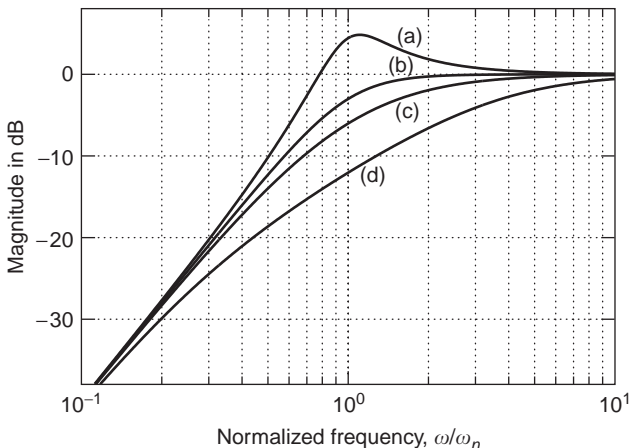


Figure 7. Error response of an ideal second-order APLL for various values of damping factor: (a) $\zeta = 0.3$; (b) $\zeta = 0.707$; (c) $\zeta = 1$; (d) $\zeta = 2$.

fer functions is given in Table 1 for different loop filter configurations.

2.4.3. Stability Considerations. So far, stability of the APLL has been assumed. A necessary and sufficient condition for stability is that all the poles of the closed-loop transfer function given by Eq. (28) lie in the left half-plane. As shown by Eq. (28), the positions of the poles vary as the loop gain is changed.

The poles of the first- and second-order APLLs always lie in the left half-plane; that is, these circuits are unconditionally stable. However, the third-order APLL may become unstable for low values of AK [10]. Because $A(t)$ is the RMS amplitude of the input signal, a third-order APLL may become unstable for weak signals, even if it is stable under normal operating conditions. The unconditional stability of the second-order APLL makes it popular in situations where the amplitude of the input signal is not constant.

A complete APLL analysis may be performed graphically by means of Bode plots [10]. Its features are as follows:

- All the important closed-loop parameters appear as distinctive points on the Bode plot.
- Loop stability and stability margin may be checked.
- Effect of variation in loop parameters such as loop gain, and pole and zero frequencies of loop filter on closed-loop APLL parameters may be tracked easily.

The Bode plot consists of a pair of graphs, where both the magnitude and phase of the open-loop transfer function are plotted. The frequency ω_B , where the open-loop gain becomes 0 dB, is a good approximation of the closed-loop bandwidth. The Bode criterion for stability is that the absolute value of the phase of $G(j\omega)$ at ω_B must be less than 180° , in case of the APLLs the typical phase shift is 135° that gives a phase margin of 45° .

The open-loop transfer function for the most commonly used second-order APLL implemented with the active loop filter is

$$G(s) = AK \frac{F(s)}{s} = AK \frac{1 + s\tau_2}{s^2\tau_1} \tag{38}$$

Figure 8 shows the Bode plot, where pole and zero frequencies and the most important closed-loop parameters are also indicated. Note that the absolute value of the phase shift never exceeds 180° ; that is, this loop is unconditionally stable. The Bode plot shows that the damping factor is controlled by the zero frequency of the loop filter. Placing the zero at the unity-gain point ω_B yields a damping factor $\zeta = 0.5$. The natural frequency ω_n is assigned by the frequency at which the extension of the -40 dB/decade line segment crosses the unity-gain ordinate.

Since

$$H(s) = \frac{G(s)}{1 + G(s)} \tag{39}$$

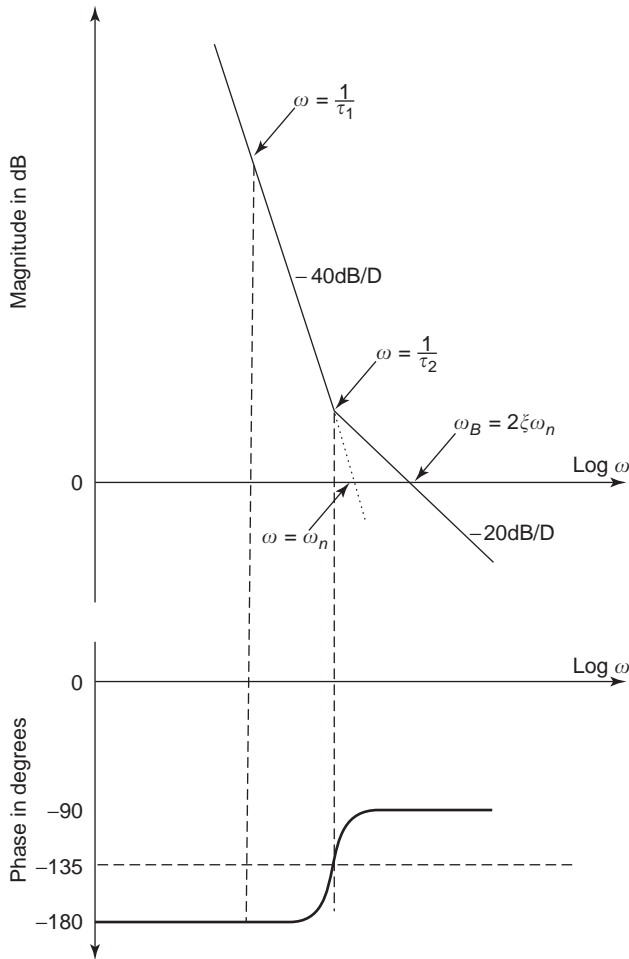


Figure 8. Bode plot of ideal second-order APLL.

the closed-loop transfer function may be also determined graphically from the Bode plot. For $\omega \ll \omega_n |G(s)| \gg 1$ and $H(s) = 1$, while for $\omega \gg \omega_n |G(s)| \ll 1$ and $H(s) = G(s)$.

The open-loop transfer function depends on the amplitude of incoming signal, as shown by Eq. (38). If A varies, then the Bode plot has to be shifted up or down along the vertical axis. In these cases both ω_n and ζ vary, but the second-order APLL remains stable for any amplitude of input signal.

2.4.4. Linear Tracking. The phase of input signal must be tracked with a small phase error. To evaluate the track-

ing properties of APLL, the phase error response to different input phases $\theta_i(t)$ has to be determined. Three cases are considered here:

1. Transient response to phase step, frequency step, and frequency ramp
2. Sinusoidal modulation
3. Modulation with an arbitrary stationary process

From Eq. (26) we obtain the phase error response to the input phase

$$\Theta_e(s) = [1 - H(s)]\Theta_i(s) = \frac{s}{s + AKF(s)}\Theta_i(s) \quad (40)$$

Recall that this linear approximation is valid for perturbations of variables about their quiescent values and requires $\theta_e(t)$ to remain small enough both during the transient and under steady-state conditions. For the sinusoidal PD and if $\theta_{ss} = 0$, the magnitude of phase error has to be less than 1 radian. Then the approximation $\sin \theta_e \approx \theta_e$ may be used.

The excitations described by *phase step*, *frequency step*, and *frequency ramp* are of the form

$$\theta_i(t) = \left(\Delta\theta_i + \Delta\omega_i t + \Delta\dot{\omega}_i \frac{t^2}{2} \right) u(t) \quad (41)$$

where $u(t)$ is the unit step function. The steady-state value of phase error may be expressed by means of the final value theorem of Laplace transform

$$\lim_{t \rightarrow \infty} \theta_e(t) = \lim_{s \rightarrow 0} s[1 - H(s)]\Theta_i(s) \quad (42)$$

The steady-state value of phase error for different loop filter configurations are summarized in Table 2. Note that the overall phase error is the sum of θ_{ss} and the phase error is given in Table 2.

A heuristic derivation of the steady-state phase response to a frequency step input helps to understand better the APLL operation. In steady-state, the input and VCO frequencies are equal. The control voltage needed to retune the VCO by $\Delta\omega_i$ is $\Delta\omega_i/K_v$. Since the DC gain of the loop filter is $F(0)$, the steady-state value of the PD output is $\Delta\omega_i/K_v F(0)$. The phase error required to produce this

Table 2. Steady-State Values of Phase Error Response to a Few Commonly Encountered Excitations

Loop			Steady-State Phase Error Response in radians to		
Order	Type	Loop Filter $F(s)$	Phase Step	Frequency Step	Frequency ramp
First	1	1	0	$\frac{\Delta\omega}{AK}$	∞
Second	1	$\frac{1+s\tau_2}{1+s\tau_1}$	0	$\frac{\Delta\omega}{AK}$	∞
		$\frac{1+s\tau_2}{s\tau_1}$	0	0	$\frac{\Delta\dot{\omega}}{\omega_n^2}$

output voltage is

$$\theta_e = \frac{\Delta\omega_i}{AK_d K_v F(0)} = \frac{\Delta\omega_i}{AKF(0)} \quad (43)$$

Table 2 shows the most important advantage of the ideal second-order APLL. In real applications, the frequency of the input signal always differs from the VCO center frequency. Even if an ideal integrator cannot be implemented, the high DC gain of the operational amplifier used in the active loop filter keeps the steady-state phase error extremely small, regardless of the magnitude of frequency error. Because of the *constant* and *almost zero* phase error,

- PD gain becomes constant and the closed-loop APLL parameters do not depend on the frequency error.
- $\sin \theta_e \approx \theta_e$, and the widest linear region of the analog multiplier can be exploited.

The error responses of APLL to different inputs may be calculated by taking the inverse Laplace transform of Eq. (40) or may be found in the literature. For a good survey, see Ref. 11, Table III, p. 19.

Next the error response to *angle-modulated inputs* is determined. For sinusoidal input phase modulation

$$\theta_i(t) = \Delta\theta \sin(\omega_m t) \quad (44)$$

where $\Delta\theta$ is the peak phase deviation and ω_m denotes the modulation frequency.

The steady-state phase error response may be calculated from Eq. (40) as

$$\theta_e(t) = |1 - H(\omega_m)| \Delta\theta \sin(\omega_m t + \Theta) \quad (45)$$

where the gain $|1 - H(\omega_m)|$ and phase shift Θ are given by

$$|1 - H(\omega_m)| e^{j\Theta} \equiv [1 - H(s)]_{s=j\omega_m} \quad (46)$$

For input frequency modulation

$$\theta_i(t) = \int_0^t \Delta\omega \sin(\omega_m \tau) d\tau = \frac{\Delta\omega}{\omega_m} \cos(\omega_m t) \quad (47)$$

where $\Delta\omega$ denotes the peak frequency deviation. The phase error is

$$\theta_e(t) = |1 - H(\omega_m)| \frac{\Delta\omega}{\omega_m} \cos(\omega_m t + \Theta) \quad (48)$$

where $|1 - H(\omega_m)|$ and Θ are given by Eq. (46).

The normalized error response to the input frequency modulation is shown in Fig. 9 for the first-order [where $F(s) = 1$] and ideal second-order loops. The high-frequency asymptote is the same for both loops, but the responses are completely different below ω_n , namely, the second-order APLL ensures a much smaller tracking error than the first-order loop. Recall that if the APLL is used to process

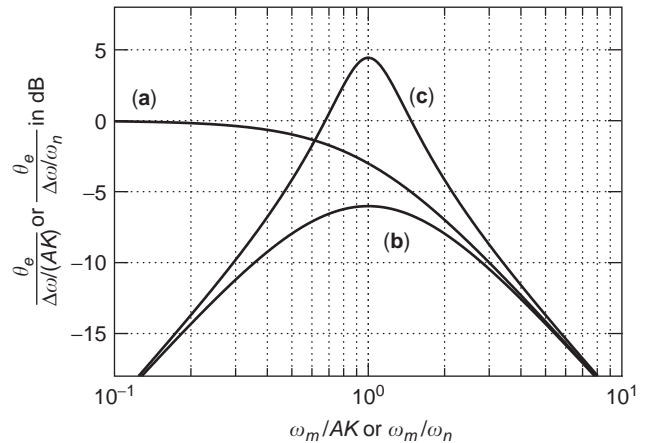


Figure 9. Phase error generated by sinusoidal FM in a (a) first-order and ideal second-order APLL for (b) $\zeta = 1$ and (c) $\zeta = 0.3$. The modulation frequency ω_m and the peak frequency deviation $\Delta\omega$ are normalized to AK in the first-order loop and to ω_n in the second-order loop. To make the figures comparable, $AK = \omega_n$.

angle-modulated signals, then a smaller phase error results in less distortion.

Inspection of Figs. 7 and 9 shows that the tracking error becomes very large at ω_n in the second-order loop for small damping factors. Recall that the linear approximation can be used only if the phase error remains small enough, even at ω_n .

It has been assumed above that the input angle modulation is produced by a single sinusoidal signal. In general, the modulating signal is a random process and all that may be known are its mean and covariance function. In this case the aim is to determine the power spectral density and variance of the phase error process caused by the input PM and FM.

Let the *input phase modulation process* $\theta_{i,PM}(t)$ be a wide-sense stationary process with zero mean and power spectral density $S_{i,PM}(\omega)$. As shown in Ref. 3, the power spectral density of the phase error process in steady-state may be expressed as

$$S_{e,PM}(\omega) = |1 - H(\omega)|^2 S_{i,PM}(\omega) \quad (49)$$

and its variance is

$$\sigma_{e,PM}^2 = \frac{1}{2\pi} \int_{-\infty}^{\infty} S_{e,PM}(\omega) d\omega \quad (50)$$

The variance of $\theta_e(t)$ represents the mean-square value of the phase error process, which must be kept small for almost all t in order to make the linear model valid. If the input of the phase modulator generating $\theta_i(t)$ is a stationary random process of zero mean and power spectrum $S_m(\omega)$, then

$$S_{i,PM}(\omega) = K_{PM}^2 S_m(\omega) \quad (51)$$

where K_{PM} is the modulator gain. Substituting Eq. (51) into Eq. (49), the parameters of the phase error process may be expressed.

In the case of FM, the input phase modulation is

$$\theta_i(t) = K_{\text{FM}} \int_0^t m(\tau) d\tau \quad (52)$$

where K_{FM} denotes the modulator gain. Even if the modulating process $m(t)$ is stationary, its integral will not necessarily be, so that the relationship between the power spectral densities of the input frequency modulation process and the phase error process may not be expressed. However, Viterbi [3] has shown that the power spectrum of the phase error process may be obtained as

$$S_{e,\text{FM}}(\omega) = K_{\text{FM}}^2 \frac{|1 - H(\omega)|^2}{\omega^2} S_m(\omega) \quad (53)$$

where $S_m(\omega)$ is the power spectrum of $m(t)$. The variance of the phase error process is

$$\sigma_{e,\text{FM}}^2 = \frac{1}{2\pi} \int_{-\infty}^{\infty} S_{e,\text{FM}}(\omega) d\omega \quad (54)$$

2.4.5. Noise Performance for High SNR. A narrowband additive input noise $n_i(t)$ can be modeled by an equivalent noise process $n_g(t)$ entering the baseband model after the PD nonlinearity $g(\cdot)$ as shown in Fig. 3. If an analog multiplier is used as the PD, then $n_g(t) = N(t, \theta_o)$. The statistical properties of $N(t, \theta_o)$ have been summarized earlier: if $n_i(t)$ has a symmetric power spectral density of $N_0/2$ and the bandwidth of $\theta_o(t)$ is much less than that of $n_i(t)$, then the equivalent noise $n_g(t)$ is a Gaussian process with uniform spectral density $N_0/2$. Furthermore, if the variance of phase error caused by noise and input angle modulation, if any, is sufficiently small, then the linear baseband model shown in Fig. 4 may be used to evaluate the noise performance of the APLL. Provided that the linear model is valid, the superposition theorem holds and the effect of noise and input angle modulation may be determined independently of each other.

The equivalent-noise process having a power spectral density $S_N(\omega) = N_0/2$ is stationary in the wide sense with zero mean. Let the point where $n_g(t)$ is applied to the loop be considered as input, and let $\theta_e(t)$ and $\theta_o(t)$ be considered as outputs. The magnitude of the two frequency responses is obtained as

$$\left| \frac{K_d K_v F(\omega)}{j\omega + AK_d K_v F(\omega)} \right| = \frac{|H(\omega)|}{A} \quad (55)$$

Consequently, the power spectral densities of the phase error $S_{e,N}(\omega)$ and the output phase $S_{o,N}(\omega)$ processes become

$$S_{e,N}(\omega) = S_{o,N}(\omega) = |H(\omega)|^2 \frac{N_0}{2A^2} \quad (56)$$

from which is obtained the variances of the phase error and the output phase

$$\sigma_{e,N}^2 = \sigma_{o,N}^2 = \frac{N_0}{2A^2} \frac{1}{2\pi} \int_{-\infty}^{\infty} |H(\omega)|^2 d\omega \quad (57)$$

Let the noise bandwidth B_L of the loop be defined as the bandwidth of an ideal lowpass filter, whose output variance is $\sigma_{e,N}^2$ when it is driven with Gaussian white noise of power spectral density $N_0/2A^2$:

$$B_L = \frac{1}{2\pi} \int_0^{\infty} |H(\omega)|^2 d\omega \quad (58)$$

Then Eq. (57) becomes

$$\sigma_{e,N}^2 = \sigma_{o,N}^2 = \frac{N_0 B_L}{A^2} \quad (59)$$

To suppress noise, B_L has to be chosen as small as possible. The noise bandwidths for the most important loop filter configurations are given in Table 1.

Noise bandwidth for the ideal second-order loop is plotted against damping in Ref. 9,10 (see Fig. 3.3 on p. 32). The minimum B_L is achieved for $\zeta = 0.5$, but the noise bandwidth does not exceed the minimum by more than 25% for any damping between 0.25 and 1.0.

Since the input additive noise and angle modulation are independent processes, the total variance of phase error is the sum of Eqs. (50) and (57) for PM and the sum of Eqs. (54) and (57) for FM. For PM

$$\sigma_e^2 = \sigma_{e,\text{PM}}^2 + \sigma_{e,N}^2 = \frac{1}{2\pi} \int_{-\infty}^{\infty} |1 - H(\omega)|^2 S_{i,\text{PM}}(\omega) d\omega + \frac{N_0 B_L}{A^2} \quad (60)$$

The linear approximation can be used only if the total variance of $\theta_e(t)$ is small enough. For the ideal second-order loop, σ_e^2 has to be less than 0.2 [10]. If, in addition to the input noise and angle-modulation, other random processes such as VCO noise or frequency modulation of the VCO output signal are present then the effects of these processes must also be accommodated in σ_e^2 by applying the technique described above.

Since there is no real signal in the baseband model of the APLL, an unambiguous definition of the signal-to-noise ratio (SNR) in the loop may not be given. The variance of the phase error is used by Viterbi [3] and Lindsey [6] to define the SNR in APLL:

$$\text{SNR}_L = \frac{A^2}{2B_L N_0} \quad (61)$$

2.5. Nonlinear Operation of the APLL

The linear theory of the APLL has been very well developed and is easy to use. In the majority of circuit design

and development, the linear APLL model is applied and the nonlinearity is considered only as an unwanted effect.

However, there are situations where the nonlinear APLL model has to be considered, for example, if the lock limits or acquisition properties have to be determined, if the APLL operates at low SNR, and so forth.

In contrast to the linear APLL theory, a unified theory describing the nonlinear operation of APLL in closed form does not exist. Many times heuristic arguments are used to solve a nonlinear problem. The details of nonlinear mathematical analysis are beyond the scope of this article. In this section only the most important aspects of nonlinear APLL theory will be discussed; the interested reader should refer to the literature for further details. The latest results on nonlinear analysis may be found in three IEEE publications [11–13], while the nonlinear APLL theory is given in many excellent books [3–10].

2.5.1. Nonlinear Tracking in the Absence of Noise. It is assumed in this subsection that the phase-locked condition has been achieved, but the frequency or phase of input signal is changed. First the hold-in range is determined; then the nonlinear transient response to a phase or/and frequency step is determined by means of the phase-plane portrait. Only the noise-free case is considered here.

The input frequency error was defined by Eq. (2) as $\Delta\omega_i = \omega_i - \omega_0$. The *hold-in range* is equal to the input frequency error, which can be tracked by the APLL, that is, for which the phase-locked condition is maintained. Mathematically the hold-in range is equal to the maximum frequency error for which Eq. (15) has a steady-state solution

$$\sin \theta_e = \frac{\Delta\omega_i - K_v v_{e0}}{AKF(0)} = \frac{\Lambda_0}{AKF(0)} \tag{62}$$

where v_{e0} is a DC voltage, $\Lambda_0 = \Delta\omega_i - K_v v_{e0}$ denotes the initial equivalent frequency detuning, and $F(0)$ is the DC gain of loop filter. Because the sine function cannot exceed unit magnitude, the hold-in range is

$$|\Delta\omega_H - K_v v_{e0}| = AKF(0) \tag{63}$$

The physical meaning of “hold-in range” is that the PD output voltage is bounded and so the maximum VCO frequency detuning is also bounded.

Equation (63) states that the holdin range can be made arbitrarily large by using very high loop gain K . Of course, this is not entirely correct because some other loop component will then saturate before the phase detector. In the ideal second-order loops, generally saturation of the loop amplifier limits the hold-in range. Note that the hold-in range is a *static parameter*; that is, its value does not depend on the order of APLL.

Consider next the nonlinear tracking properties, that is, the *dynamics* of a first-order APLL in the absence of noise. Substituting $F(p) = 1$, $N(t, \theta_o) = \Psi_2 = 0$ and $d\theta_i/dt = \Delta\omega_i$ into Eq. (15), a nonlinear differential equation is

obtained:

$$\frac{d\theta_e}{dt} = \Delta\omega_i - K_v v_{e0} - AK \sin \theta_e = \Lambda_0 - AK \sin \theta_e \tag{64}$$

Solution of this autonomous nonlinear differential equation gives the transient response of APLL.

Assume that the APLL is operating in steady-state when the input phase is suddenly changed. To get the nonlinear transient response to the input phase step $\theta_{i01}(t)$, Eq. (64) must be solved. The initial value θ_{e0} of phase error depends on the phase error measured under the previous steady-state conditions and θ_{i0} .

The APLL dynamics may be determined graphically in the phase plane shown in Fig. 10 for the first-order APLL, where the *frequency error* $\hat{\theta}_e = d\theta_e/dt$ is plotted as a function of θ_e . A plot of a single solution in the phase plane is called a *trajectory*. The trajectory starts from the initial value θ_{e0} of the phase error and goes to its steady-state value for which $d\theta_e/dt = 0$. An ensemble of trajectories emerging from different initial conditions is known as *phase-plane portrait* or *flow*. A trajectory shows the dynamics of a loop against time as it settles (or fails to settle) toward an equilibrium.

As shown in Fig. 10, all trajectories of a first-order APLL coincide with each other. Let the trajectory start from an initial phase error θ_{e0} . If $d\theta_e/dt$ is positive for that value of θ_{e0} , then the phase error increases as a function of time. In fact, the APLL follows the trajectory plotted in Fig. 10 and moves toward the right until it reaches the steady-state for which $d\theta_e/dt = 0$. Similarly, if $d\theta_e/dt$ is negative for θ_{e0} , then the phase error decreases until it reaches the steady-state conditions. A point belonging to steady-state is stable, if after a small perturbation of θ_e in either direction, the system tends to return to the steady-state. The stability of steady-state phase errors is also shown in Fig. 10.

Since almost all phase detectors have a periodic characteristic, they cannot distinguish a phase step of $\Delta\theta_i + 2\pi n$, $n = 1, 2, 3 \dots$ from one of $\Delta\theta_i$. Therefore, the APLL never loses lock when it is driven by a pure phase step, irrespective of the magnitude of the loop order.

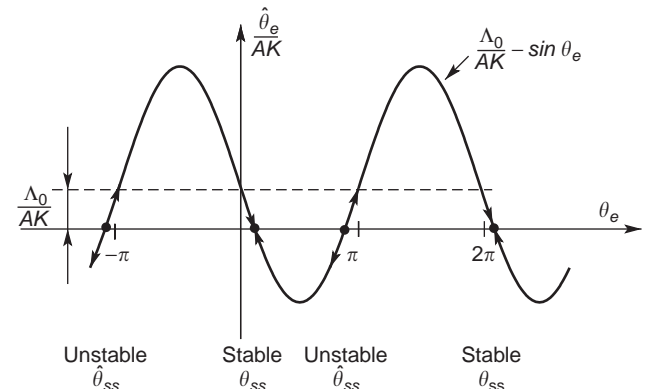


Figure 10. Phase-plane portrait for first order APLL, where the stability of steady-state phase errors θ_{ss} is also shown.

In the first-order APLL, a frequency step breaks the lock if, and only if, the frequency error exceeds the holdin limit. In this case, the phase-locked condition cannot be recovered and the APLL remains unlocked.

To obtain the phase-plane trajectories for the ideal second-order APLL, first the time variable has to be eliminated in Eq. (15). Substitution of $F(p) = (p\tau_2 + 1)/p\tau_1$ and

$$\theta_i(t) = \Delta\omega_i t + \theta_i$$

into Eq. (15) gives

$$\frac{d^2\theta_e}{dt^2} + \left(AK \frac{\tau_2}{\tau_1} \cos \theta_e \right) \frac{d\theta_e}{dt} + \frac{AK}{\tau_1} \sin \theta_e = 0 \quad (65)$$

Letting $t = \tau/[AK(\tau_2/\tau_1)]$ so that $(d\theta_e/dt) = AK(\tau_2/\tau_1)(d\theta_e/d\tau)$, and taking into account that $AK(\tau_2/\tau_1) \neq 0$, Eq. (65) may be rewritten as

$$\frac{d^2\theta_e}{d\tau^2} + \cos \theta_e \frac{d\theta_e}{d\tau} + \frac{\tau_1}{AK\tau_2^2} \sin \theta_e = 0 \quad (66)$$

Dividing Eq. (66) by $\dot{\theta}_e = d\theta_e/d\tau$ and recognizing that $(d^2\theta_e/d\tau^2) = (d^2\dot{\theta}_e/d\tau)$, the first term in Eq. (66) becomes $\dot{\theta}_e/d\theta_e = (d\dot{\theta}_e/d\tau)/(\dot{\theta}_e/d\tau) = d\dot{\theta}_e/d\theta_e$. Eliminating τ in Eq. (66), the phase error θ_e and the normalized frequency error $\dot{\theta}_e$ may be treated as independent variables:

$$\frac{d\dot{\theta}_e}{d\theta_e} = -\cos \theta_e - \frac{\tau_1}{AK\tau_2^2} \frac{\sin \theta_e}{\dot{\theta}_e} \quad (67)$$

To get the phase-plane portrait, the solution of Eq. (67) must be determined for different initial conditions. The phase-plane trajectories for an ideal second-order APLL are shown in Fig. 11.

The phase-plane portrait of an APLL with periodic phase detector characteristic is also periodic with the same period in variable θ_e , but is aperiodic in $\dot{\theta}_e$. Trajec-

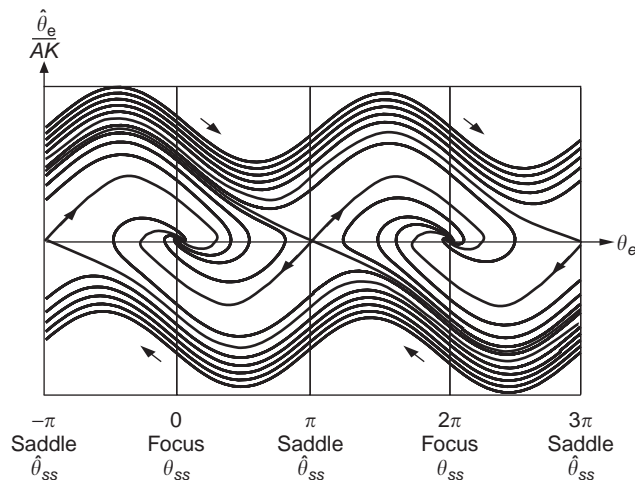


Figure 11. Phase-plane trajectories of the ideal second-order APLL for $\zeta = 0.707$.

tories proceed as a function of time clockwise only as marked by arrows in Fig. 11. Intersection of trajectories may occur only at *singular points*, which assign the possible steady-state solutions of loop equation. Both stable and unstable singular points appear; equilibrium occurs at stable singularities. In a second-order APLL, an equilibrium is called a *stable node* or *stable focus* if the loop is overdamped ($\zeta > 1$) or underdamped ($\zeta < 1$), respectively. The steady-state phase-locked conditions which are reached asymptotically are called *equilibria*.

The unstable singularity is called a *saddle point*. Even if the loop state gets just into a saddle point, where it is in equilibrium, it cannot remain there, because any disturbance, such as noise, will displace it slightly and then the saddle point repels the loop state.

A trajectory that terminates on a saddle point is called *separatrix*.

Consider a stable singular point and the two separatrices that terminate on the two adjacent saddle points. If the initial conditions lie between these separatrices and the initial phase error is in the 2π interval centered about the stable equilibria to be achieved, then the trajectories emerging from these initial conditions will terminate at that equilibrium point without cycle slip. If the initial conditions lie outside these separatrices, then the loop slips one or more complete cycles before achieving the phase-locked condition.

We are now ready to evaluate the nonlinear transient graphically for a second-order APLL. First, the initial conditions have to be determined from the input phase and frequency steps, and the previous steady-state conditions. Then the initial conditions have to be plotted on the phase-plane portrait, and the trajectory emerging from them gives the actual transient response of APLL.

The phase-plane portrait is a very useful tool for the determination of APLL dynamics. Phase-plane portraits for other loop configurations can be found in Refs. 3 and 6.

2.5.2. Acquisition Behavior in the Absence of Noise.

Before a PLL can track, it must first acquire the phase-locked condition. In general, the PLL quiescent frequency differs from the frequency of the incoming signal. Therefore, first the VCO frequency has to be tuned to the incoming frequency by the loop. This process is called *frequency pull-in*. Then the VCO phase has to be adjusted according to the input phase. This process is known as *phase lock-in*.

The two parts of acquisition process may be identified by checking the cycle slips between the input and VCO phases. During phase lock-in, cycle slips do not occur.

Acquisition is inherently a highly nonlinear phenomenon. It starts from given initial conditions (initial phase and frequency errors), and no external excitation is applied. This means that acquisition may be described by an autonomous nonlinear differential equation and it may be studied by the phase-plane portrait introduced in the previous subsection.

If the loop acquires lock by itself, the process is called *self-acquisition*. If it is assisted by extra circuits, it is called *aided acquisition*. Since self-acquisition is relatively

slow and unreliable, acquisition-aids are often used. For a good survey of different aided acquisition techniques, see Ref. 10.

The acquisition behavior of a first-order APLL is modeled by Eq. (64). Under steady-state conditions $d\theta_e/dt = 0$ and the phase error becomes

$$\theta_{ss} = \sin^{-1}\left(\frac{\Lambda_0}{AK}\right) \pm 2n\pi, \quad n = 0, 1, 2, \dots$$

$$\hat{\theta}_{ss} = -\sin^{-1}\left(\frac{\Lambda_0}{AK}\right) + (1 \pm 2n)\pi, \quad n = 0, 1, 2, \dots$$
(68)

provided $|\Lambda_0| \leq AK$. Figure 10 shows that the equilibrium points denoted by θ_{ss} and $\hat{\theta}_{ss}$ are stable and unstable, respectively. If the phase error is equal to $\hat{\theta}_{ss}$, then any perturbation in either direction, caused by noise, for example, will cause θ_e to move until it reaches the next stable equilibrium. If $|\Lambda_0| > AK$, no stable equilibrium exists and the loop never reaches the phase-locked condition, but $\theta_e(t)$ moves along a sinusoidal trajectory.

Figure 10 and Eq. (68) show that an infinitely large number of equilibrium points exist. Since every cycle of the trajectory has a stable equilibrium, $\theta_e(t)$ cannot change by more than one cycle before phase-locking. Thus the pull-in and lock-in ranges are equal; consequently, cycle slipping never occurs during acquisition in the first-order loop.

The phase transients of the first-order APLL during acquisition are shown in Fig. 12 for different values of the initial phase error θ_{i0} . Note that for small θ_{i0} , the loop operation remains near the equilibrium and the phase transient is almost exponential, as expected from the linear theory of the APLL. However, if $\theta_{i0} > 135^\circ$, the waveforms diverge considerably from exponential and the acquisition time becomes very long. The acquisition parameters of the first-order loop are given in Table 3.

The first-order loop always achieves the phase-locked condition without cycle slips. The same is not valid for the second- and higher-order loops; for these, the lock-in range is smaller than the pull-in range.

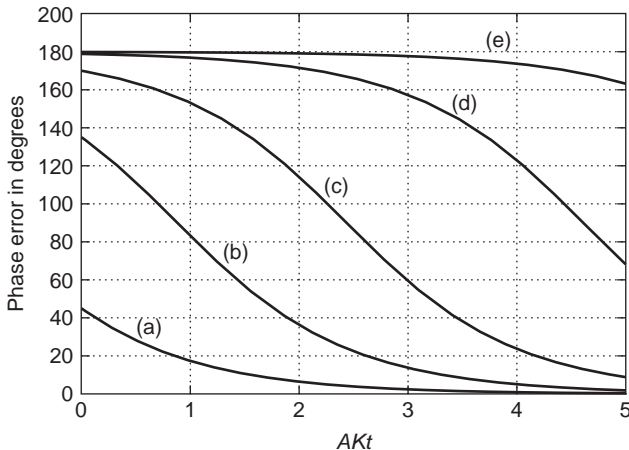


Figure 12. Acquisition behavior of first-order APLL. The frequency detuning $\Lambda_0 = 0$ and the initial values of phase error θ_{i0} are (a) 45° , (b) 135° , (c) 170° , (d) 178.86° , and (e) 179.886° .

Table 3. Acquisition parameters of First- and Second-Order APPLs

Loop Order	Loop Filter $F(s)$	Pull-in Range (rad/s)	Pull-in Time (s)
First	1	AK	$\frac{8}{AK}$
Second	$\frac{1+s\tau_2}{1+s\tau_1}$	$2\sqrt{AK\zeta\omega_n}$	$\frac{\Lambda_0^2}{2\zeta\omega_n^3}$
	$\frac{1+s\tau_2}{s\tau_1}$	∞	$\frac{\Lambda_0^2}{2\zeta\omega_n^3}$

The acquisition behavior of ideal second-order APLL is described by Eq. (67). The trajectories and steady-state phase error ($\theta_{ss} = \pm 2\pi n, n = 0, 1, 2, \dots$) may be determined from the phase-plane portrait shown in Fig. 11.

Gardner has proposed a simple method to estimate the lock-in range of higher order PLLs [10]. Let $F(\infty)$ denote the high-frequency asymptotic gain of loop filter, for a second-order loop $F(\infty) = \tau_2/\tau_1$. If the deviation of the input frequency from the VCO center frequency is greater than $1/\tau_2$, then the second-order loop behaves like a first-order one, with loop gain $K = K_d K_v F(\infty)$. As a useful engineering approximation, the lock-in range of higher-order loops is approximated by the lock-in range of the first-order one with equivalent gain $F(\infty)$. If $v_{e0} = 0$, then

$$\omega_L \approx \pm AKF(\infty)$$
(69)

The frequency pull-in, or simply pull-in, is much slower than the lock-in process. The acquisition problem cannot be solved in closed form; some approximation must be used. Richman has developed a model [16] for the analysis of the pull-in process.

Consider an ideal second-order APLL. The loop filter can be divided into two parallel paths

$$F(s) = \frac{1+s\tau_2}{s\tau_1} = \frac{1}{s\tau_1} + \frac{\tau_2}{\tau_1}$$
(70)

as shown in Fig. 13. Note that there is a high-frequency AC path from the PD output to the VCO input with flat gain of τ_2/τ_1 and a DC path that contains a perfect integrator.

The pull-in process may be understood easily by plotting the relevant spectra in the loop. Initially, the input

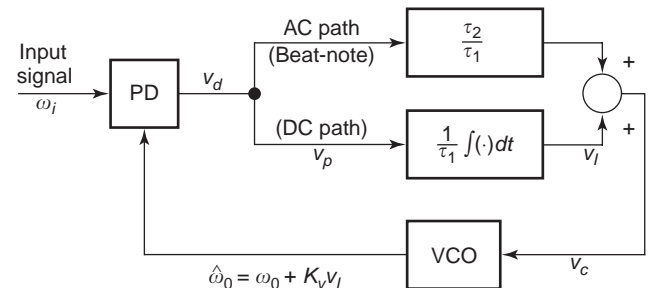


Figure 13. Pullin model for the ideal second-order APLL.

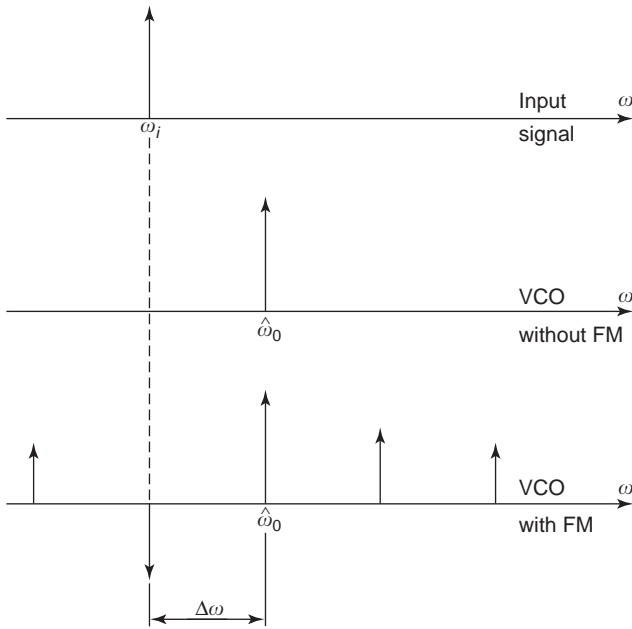


Figure 14. Pullin spectra. The instantaneous center VCO frequency is denoted by $\hat{\omega}_0$.

and VCO frequencies are ω_i and $\hat{\omega}_0$, respectively, as shown by the upper two traces of Fig. 14. Let $\hat{\omega}_0(t)$ denote the instantaneous VCO frequency, which is a slowly varying function, and which is determined by the integrator output v_1 . The frequency difference $\Delta\omega = \hat{\omega}_0 - \omega_i$ is called the *beatnote*.

The analog multiplier used as phase detector generates the beatnote, which gets through the AC path and modulates the VCO, generating FM sidebands as shown in the lower trace of Fig. 14. Observe that the FM sideband ($\hat{\omega}_0 - \Delta\omega$) coincides with ω_i and produces a negative DC voltage at the PD output denoted by v_p in Fig. 13. This DC voltage is integrated by the DC path and the slowly varying output $v_1(t)$ of integrator pushes $\hat{\omega}_0$ toward ω_i . The pull-in process is terminated when $\hat{\omega}_0 = \omega_i$.

Many approximate formulas for pull-in limits and pull-in time have been developed by different authors for various loop configuration. For a good survey, see Sect. 5.3 of Ref. 10. Formulas giving the acquisition parameters of first- and second-order loops are given in Table 3.

2.5.3. Hangup Phenomenon. APLLs occasionally have extremely long acquisition time that cannot be tolerated in many applications. In these cases, the loop seems to stick for a long time at a certain value of phase error before moving toward the phase-locked condition. This phenomena is known as the *hangup effect* [17].

Due to the periodicity of PD characteristic, the loop equation has two steady-state solutions in every period. The locations of steady-state solutions have been called the *normal equilibrium null* (stable steady-state) and *reverse null* (unstable steady-state) by Gardner [10].

Consider an APLL implemented with an analog multiplier and assume that $\Lambda_0 = 0$, that is, that the steady-state

phase error is zero. The phase trajectories originating near 180° remain in that vicinity for a long time before decaying toward equilibrium at 0° .

Figure 12 shows the hangup phenomenon for a first-order APLL. It must be emphasized that the hangup effect appears in every APLL, independently of the loop order.

It is obvious from Fig. 13 that the rate of VCO control voltage is proportional to the DC output v_p of the phase detector. The slowly varying v_p may be considered as a restoring force. If v_p is very small, as occurs near the reverse null, the restoring force is also small and the loop converges extremely slowly toward the phase-locked condition.

2.5.4. False Lock to Data Sidebands. The recovery of suppressed carriers is also performed by PLLs. The most commonly used circuit configurations will be discussed later. Since the carrier is completely suppressed in these systems, the carrier recovery circuit must regenerate a harmonic of the carrier (squaring loop) or, equivalently, must generate a phantom carrier (Costas loop). In both solutions, the loop operation may be modeled by a nonlinear operation followed by a CW tracking loop.

In addition to the regenerated signal, discrete frequency components spaced by integer multiples of half the symbol rate also appear about the desired frequency because of the nonlinear operation [18,19]. If the quiescent frequency of the VCO is close enough to one of these sidebands, then the loop will lock onto that spectral component instead of the desired frequency. This phenomenon is called *false lock to data sidebands*. The probability of false lock is especially high when the SNR_L is high.

2.5.5. APLL Behavior in the Presence of Noise. When a built APLL is tested in the presence of noise and the SNR_L is reduced below ~ 7 dB, the fluctuation in phase error, called “phase jitter”, becomes greater than predicted from Eq. (60). In this section, the behavior of the APLL for low SNR_L when the linear approximation is no longer applicable is briefly discussed and the most important conclusions for circuit designers are drawn¹.

We have seen that PLLs have an infinitely large number of stable equilibrium points. At low SNR_L , the phase error migrates among the different stable equilibrium points; that is, the *probability density function* (pdf) of θ_e appears as a multimodal function with each mode centered about a stable equilibrium point. Consequently, the phase error process is nonstationary and the pdf of phase error has an unbounded variance. Unfortunately, the phase error process cannot be treated mathematically.

The migration among different equilibrium points causes cycle slipping in the built APLL, which is not allowed in many applications such as coherent communication.

Tikhonov [20,21] and Viterbi [22] have shown that the phase error process reduced by modulo- 2π is stationary

¹The loop operation can be described in the presence of noise by a nonlinear stochastic differential equation [see Eq. (15)]. An exact nonlinear theory for APLL may be developed by means of Fokker-Planck theory [6]. The solution of the Fokker-Planck equation gives the pdf for the *reduced phase error process* in closed form.

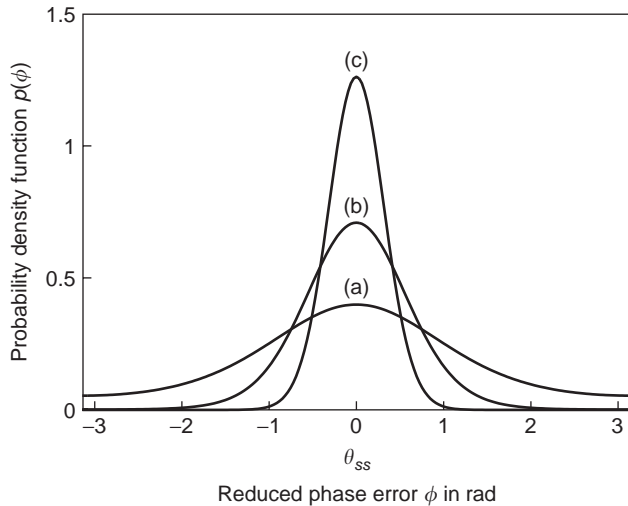


Figure 15. Probability density functions of reduced phase error for a first-order APLL with zero detuning. The curves are given for SNR_L values of (a) 0 dB, (b) 5 dB, and (c) 10 dB.

and possesses a bounded variance. The APLL behavior for low SNR_L may be analyzed by considering the cycle slipping as an independent problem and by calculating the pdf of reduced phase error process.

The reduced phase error process has a Tikhonov pdf as shown in Fig. 15 for the first-order APLL [3]. Lindsey has shown in [6] that pdf of reduced phase error process of higher-order loops may also be approximated by the Tikhonov distribution. For a comparison of measured and calculated distributions, refer to Ref. 7.

Cycle slips in the carrier recovery circuit are very important since they destroy the performance of digital telecommunication systems. Cycle slips may occur either in isolated form or in bursts [23].

Consider a first-order APLL with zero detuning. Using the Fokker–Plank technique, Lindsey [6] has shown that the mean time between cycle slips is

$$\tau = \frac{\pi^2 \alpha I_0(\alpha)}{2B_L} \quad (71)$$

where $\alpha = 4A/(N_0K)$ and $I_0(x)$ denotes the zeroth-order modified Bessel function. Observe that τ is inversely proportional to the noise bandwidth of the APLL; that is, for efficient carrier recovery a narrowband loop must be used.

Equation (71) can approximate the mean time between cycle slips in higher-order APLLs if the parameter α is modified appropriately [6]. A better theory, giving more accurate results, has been published in Ref. 24; for measured data, refer to Ref. 23.

3. PLL APPLICATIONS

The PLL is one of the most commonly used circuits in electrical engineering. This section discusses the most important PLL applications and gives guidelines for the de-

sign of these circuits. A detailed discussion of different applications is beyond the scope of this article; for a comprehensive survey, see Refs. 11 and 14.

The baseband model of the analog phase-locked loop and its linear theory were discussed in the previous sections. In all PLL applications, the phase-locked condition must be achieved and maintained. In order to avoid distortion, many applications require operation in the linear region; that is, the total variance of the phase error process resulting from noise and modulation must be kept small enough. If the PLL operates in the linear region then the linearized baseband model may be used in circuit design and development.

Recall that only the PD output, VCO control voltage, input phase $\theta_i(t)$, and output phase $\theta_o(t)$ appear in the PLL baseband model. All these signals are low-frequency signals. The RF input and output signals may be expressed from $\theta_i(t)$ [see Eqs. (1) and (2)] and $\theta_o(t)$ [see Eqs. (8) and (9)], respectively.

Amplitude-modulated (AM) signals may not be generated or processed by PLLs; even more, the PLL may be used to reject input AM.

In order to achieve the best circuit performance, different phase detectors are used in the different applications, and many of them are edge-triggered. A PLL may contain other edge-triggered circuits, such as a frequency divider, for example. The operation of PLLs including edge-triggered circuits may not be described exactly by the simple APLL model. However, Gardner has shown that the APLL theory may be used as a good approximation of the real operation if the closed-loop bandwidth is less than one-tenth of the input frequency [25].

Sampling involved in edge-triggered operation and non-linearity always increase the noise level. Consequently, if the input SNR is low, then an analog multiplier has to be used as PD to get the best noise performance.

In addition to the conventional applications, new applications for the various PLLs have been published. It has been shown that both the analog [26] and sampling [27] PLLs may exhibit chaotic behavior. Bernstein and Lieberman have proposed the application of an ideal sampling PLL for random number generation [28]. The quality of generated random numbers has been evaluated by the run test in Ref. 29.

3.1. Tracking Bandpass Filter for Angle-Modulated Signals

Because of their temperature dependence, narrowband bandpass filters cannot be implemented by conventional analog filters. In other applications, the carrier frequency of angle-modulated signals to be selected varies. These problems may be overcome if a PLL tracking the carrier is used as a bandpass filter. The PLL separates the spectrum of the angle-modulated signal from other interfering signals, or limits the transmitted spectrum to within specified bounds. The relationship between the input and output phase modulation is determined by the closed-loop transfer function

$$\Theta_o(s) = H(s)\Theta_i(s) \quad (72)$$

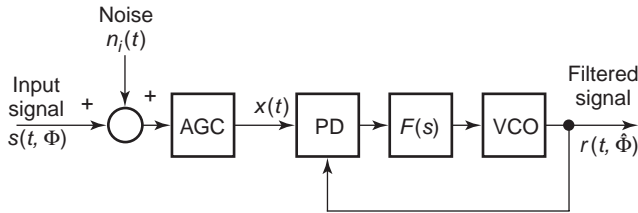


Figure 16. PLL configuration for bandpass tracking filter and CW carrier recovery. The AGC circuit is used to keep the input amplitude, that is, the loop parameters, constant.

The filter characteristic is determined by the closed-loop transfer function. A further advantage of the PLL bandpass tracking filter is that it rejects the amplitude modulation; that is, it may also be used as a limiter.

The block diagram of a bandpass tracking filter is shown in Fig. 16. If the loop parameters depend on the amplitude of the input signal, an AGC (automatic gain control) circuit must precede the PD in order to keep the filter parameters constant. Note that the problems of and the difficulties associated with the design and implementation of a high-frequency bandpass filter are reduced to the design and implementation of a baseband loop filter. The design of PLL bandpass filters is discussed in detail in Ref. 30.

3.2. CW Carrier Recovery

In every coherent receiver, the carrier has to be recovered from the noisy input signal [15]. Here, it is assumed that the carrier is present all the time in the received spectrum; the recovery of a suppressed carrier will be considered later. The aim of CW carrier recovery is to retrieve the carrier and to suppress as much noise, modulation, and interference as possible. The CW carrier recovery circuit is a narrowband bandpass tracking filter implemented by a PLL as shown in Fig. 16.

The noise-free recovery of a carrier in a noisy environment requires a very narrowband PLL [see Eq. (59)]. As shown in Table 3, the acquisition properties of narrowband PLLs are very poor. This problem may be eliminated by using two different loop bandwidths: a wide one during acquisition and a narrow one in steady-state, after the phase-locked condition has been achieved [10].

The Doppler effect must also be considered in many carrier recovery circuits. The ideal second-order PLL may track a frequency ramp, but the reduction of tracking error requires a wide loop bandwidth (see Table 2). Unfortunately, the noise-rejection performance of a PLL is inversely proportional to the loop bandwidth. For low SNR, this contradiction may be solved by using third- or higher-order loop configurations [31].

3.3. PLL Frequency Divider and Multiplier

The PLL may be used as a frequency divider if a frequency multiplier is placed into the feedback path as shown in Fig. 17, where M denotes the frequency multiplier ratio.

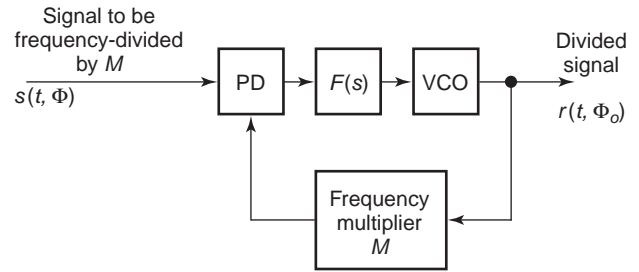


Figure 17. Block diagram of a PLL frequency divider.

Let ω_i denote the frequency of input signal $s(t, \Phi)$. Under phase-locked conditions the PLL divides the input frequency by M :

$$r(t, \Phi_o) = \sqrt{2} V_o \cos \Phi_o = \sqrt{2} V_o \cos\left(\frac{\omega_i}{M} t + \theta_o\right)$$

When the carrier frequency of an angle modulated signal is divided, its modulation frequency f_m does not change, but its phase/frequency deviation is divided by M :

$$\Theta_o(s) = \frac{1}{M} H(s) \Theta_i(s)$$

The closed-loop transfer function $H(s)$ is given by Eq. (28), but the frequency multiplier in the feedback path increases the loop gain:

$$K = MK_g K_d K_v$$

The PLL may be used as a frequency multiplier if, instead of the multiplier, a frequency divider with division ratio of N is placed into the feedback path in Fig. 17. Again, the modulation frequency of an angle modulated signal does not change, but the carrier frequency and the phase/frequency deviation is multiplied by N :

$$\Theta_o(s) = NH(s) \Theta_i(s)$$

where the loop gain is

$$K = \frac{K_g K_d K_v}{N}$$

3.4. PLL Amplifier for Angle-Modulated Signals

The high-gain amplifiers operating in the extremely high-frequency bands are very expensive. The PLL may be used for amplification of angle-modulated signals, the signal to be amplified is applied to the PLL input and the VCO output is the amplified signal. The gain is determined by the ratio of VCO output and PLL input powers. Note that the amplification is performed in the baseband. In addition to amplification, the PLL also operates as a limiter and filter for the incoming angle-modulated signals.

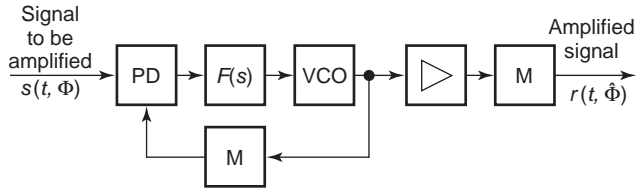


Figure 18. Amplification of angle-modulated high-frequency signals by PLL.

Sometimes it is cheaper to implement the VCO and power amplifier below the input frequency band, as shown in Fig. 18. Due to the frequency multiplier placed in the feedback path, the VCO output frequency is f_i/M , where f_i is the input frequency. The input phase/frequency deviation is also divided by M ; however, the modulating frequency remains unchanged. The frequency multiplier following the power amplifier restores the original carrier frequency and its phase/frequency deviation.

3.5. Frequency Synthesis and Angle Modulation by PLL

Signals with high-frequency stability and high spectral purity are often required in electrical engineering. In many applications, the frequency of generated signal must be varied by a digital code.

The PLL is widely used in frequency synthesis to generate spectrally pure signals and, if necessary, to operate as an analog or digital frequency or phase modulator. Frequency multiplication or division and frequency addition or subtraction may be performed using a PLL in conjunction with programmable frequency dividers and mixers as shown in Fig. 19. As a result, the output frequency f_o depends on the reference f_R and offset f_S frequencies, and moreover, on the division ratios of frequency dividers. In frequency synthesis, the PLL input is called *reference signal* and its frequency is denoted by f_R . To optimize the system performance, a multiloop circuit configuration [32] is frequently used.

In frequency synthesis, the dominant noise sources are the VCO, frequency dividers, mixers, and phase detectors. The main design goals are to minimize the output phase noise, to avoid the generation of spurious output signals, and to minimize the unwanted output FM caused by the periodic output of the phase detector. These requirements

can be satisfied with special PD configurations, such as a sample-and-hold phase detector or a phase-frequency detector with a charge-pump circuit. The operation of these edge-triggered PDs will be discussed later.

Many system-level aspects must be considered during the development of frequency synthesizers, a detailed discussion of these questions may be found in Refs. 32–35.

In addition to frequency synthesis, PLLs may be also used as an FM or PM modulator. The corresponding transfer functions for FM and PM are

$$s\Theta_o(s) = [1 - H(s)]K_v V_{FM}(s) \tag{73}$$

$$\Theta_o(s) = H(s) \frac{N}{AK} V_{PM}(s)$$

where K_v and $N/(AK)$ are the gains of the FM and PM modulators, respectively. The closed-loop error $[1 - H(s)]$ and transfer $H(s)$ functions are given by Eqs. (29) and (28), respectively. The only difference is that the frequency synthesizer has a frequency divider in the feedback path; consequently, the loop gain becomes

$$K = \frac{K_g K_d K_v}{N} \tag{74}$$

3.6. Coherent Demodulation by APLL

The noise performance of coherent demodulators is better than that of their noncoherent counterparts [15]. A circuit configuration that is suitable for coherent PM, FM, and AM demodulation is shown in Fig. 20.

3.6.1. PM Demodulator. Assume first that the input signal $s(t, \Phi)$ is phase-modulated and $a(t) = A = \text{constant}$. The demodulated PM signal appears at the output of the phase detector

$$V_d(s) = [1 - H(s)]AK_d \Theta_i(s) \tag{75}$$

where $\Theta_i(s)$ denotes the input PM and AK_d is the gain of the PM demodulator. The demodulated PM signal is multiplied by the closed-loop error function, which has a high-pass characteristic. Distortion is avoided if the closed-loop

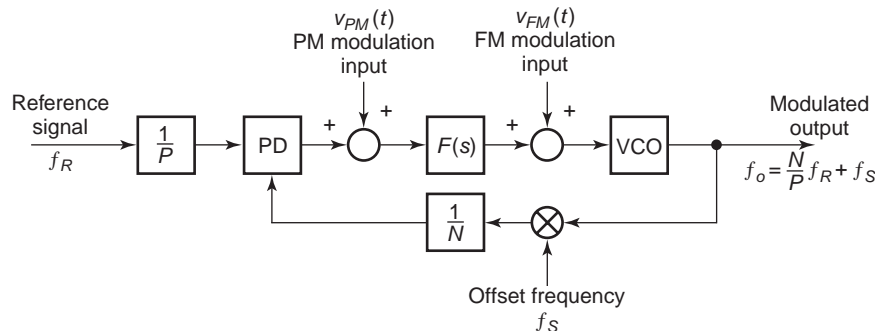


Figure 19. Frequency synthesis by phase lock.

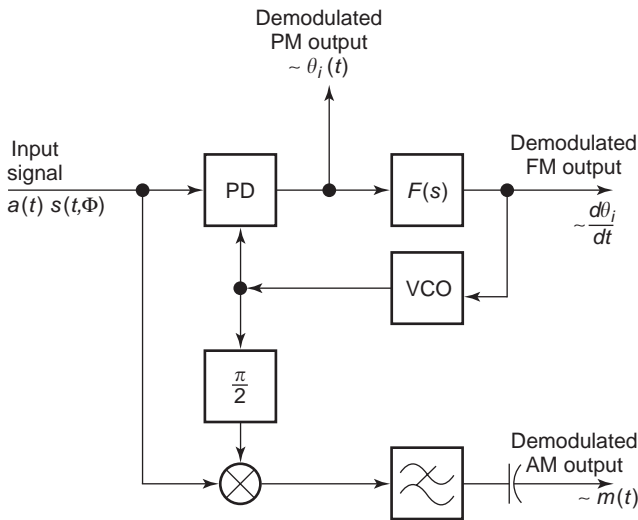


Figure 20. Coherent PM, FM, and AM demodulation by APLL.

bandwidth is less than the lowest modulation frequency. The other source of distortion is the PD nonlinearity. This type of distortion does not appear if the total variance of the phase error given by Eq. (60) remains small enough.

3.6.2. FM Demodulator. Assume that a frequency-modulated input signal is applied to the PLL input. Due to the phase-locked condition, the VCO frequency follows the incoming frequency. Since the instantaneous VCO frequency is proportional to the VCO control voltage, the FM modulation may be recovered from the VCO control voltage. By means of the transfer function concept, the demodulated signal is obtained

$$V_c(s) = H(s) \frac{1}{K_v} s \Theta_i(s) \quad (76)$$

where $1/K_v$ is the gain of the FM demodulator. This equation shows that the FM demodulator output, that is, the VCO control voltage, is proportional to the input FM if the closed-loop bandwidth exceeds the highest modulation frequency.

The distortion caused by the PD nonlinearity is reduced by feedback; consequently, the PD distortion is not critical. However, the VCO transfer function must be linear in order to get an FM demodulator with low distortion.

3.6.3. AM Demodulator. Let the input signal be amplitude-modulated

$$x(t) = [1 + m(t)] \sqrt{2} A \sin(\omega_c t + \theta_{i0}) \quad (77)$$

where $m(t)$ carries the information, and A , ω_c , and θ_{i0} are constants. The PLL demodulator contains a carrier recovery circuit (see the PLL in Fig. 20) and an AM demodulator (see the analog multiplier and lowpass filter in Fig. 20). Since the PLL needs an input signal to be tracked

continuously, the spectrum of the AM signal must contain a carrier component.

The carrier is recovered by the PLL, its VCO output is

$$r(t, \hat{\Phi}) = \sqrt{2} V_o \cos(\omega_c t + \theta_{i0}) \quad (78)$$

This signal is multiplied by the AM input signal. The lowpass filter selects the difference-frequency output of multiplier and the DC blocking capacitor removes its DC component. The demodulated signal is obtained as

$$AV_o m(t) \quad (79)$$

where AV_o is the gain of the AM demodulator.

3.7. Suppressed Carrier Recovery Circuits

In digital telecommunications, the optimum detection of transmitted data requires that both carrier and clock signals be available at the receiver [15]. The carrier and clock recovery circuits are used to retrieve these signals from the noisy digitally modulated received waveform.

In order to maximize the power efficiency, modern digital modulation techniques suppress the carrier completely; consequently, all transmitted energy resides in the data sidebands. Narrowband PLLs cannot be used for carrier recovery, because the carrier frequency is missing from the input spectrum.

The missing carrier can be regenerated by nonlinear circuits called *regenerators*. The regenerator may be placed before the narrowband PLL as an entirely separate circuit, or it may be included in the loop. Examples for the first and second solutions are the squaring and Costas loops, respectively.

Many factors have to be considered during the selection and development of a suppressed carrier recovery circuit [36]. Here, only the basic operating principles of these circuits are surveyed. Interested readers should refer to the literature [7,10,36–39].

For the sake of simplicity, only *binary phase shift keying* (BPSK) modulation is considered here. In BPSK, the binary information to be transmitted is mapped to the phase of a sinusoidal carrier. If the data bit is a “1,” the phase of the carrier is zero; while if the data bit is a “0,” the carrier phase becomes -180° . If the probabilities of “1”s and “0”s are equal, then the carrier is completely suppressed. In the noise-free case, the received signal may be expressed in the form

$$v_i(t) = m(t) \sin(\omega_c t + \theta_i) \quad (80)$$

where ω_c is the carrier frequency and the carrier phase θ_i is arbitrary but constant. The binary datastream is given by $m(t) = \pm 1$. Three basic types of carrier recovery circuits are discussed in the next subsection: the *squaring loop*, the *Costas loop* and the *inverse modulator*.

3.7.1. Squaring Loop. In this case, the nonlinear operation is performed by a square-law device, that is, a frequency doubler circuit. As shown in Fig. 21, the nonlinear operation precedes the narrowband APLL. From Eq. (80)

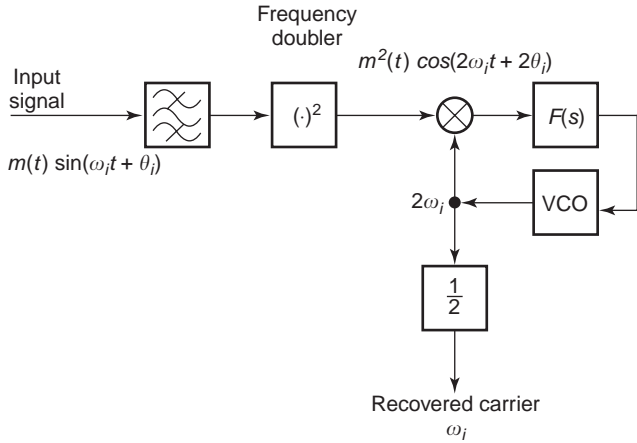


Figure 21. Suppressed carrier recovery by squaring loop.

the output of frequency doubler circuit is obtained:

$$v_x(t) = v_i^2(t) = \frac{1}{2} m^2(t) [1 - \cos(2\omega_i t + 2\theta_i)] \tag{81}$$

Since $m(t) = \pm 1$, then $m^2(t) = 1$ and

$$v_x(t) \sim \cos(2\omega_i t + 2\theta_i) \tag{82}$$

Equation (82) shows that, after the frequency doubler, a conventional narrowband PLL can be used to recover the second harmonic of the carrier. Finally, the double-frequency output of the PLL is frequency divided by 2, in order to recover the original carrier.

3.7.2. Costas Loop. In the squaring loop the nonlinear operation is performed in the RF band. The Costas loop offers an alternative solution, where the BPSK modulation is removed in the baseband.

The block diagram of Costas loop is shown in Fig. 22. The circuit contains *in-phase* (I-arm) and *quadrature* (Q-arm) channels and an analog multiplier, that is, a phase detector that precedes the loop filter. The I and Q arms consist of an analog multiplier and a lowpass filter.

To understand the operation of the Costas loop, assume that the phase-locked condition has been achieved and

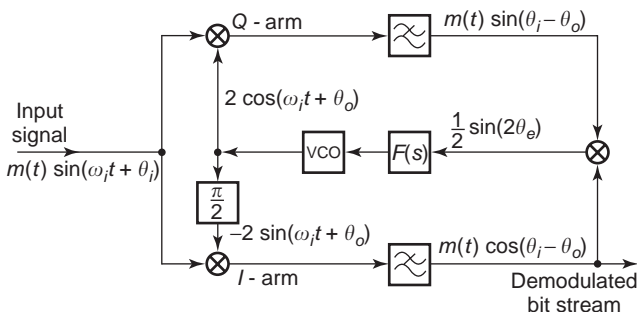


Figure 22. Demodulation of BPSK signal by a Costas loop.

that the VCO output is

$$2 \cos(\omega_i t + \theta_o) \tag{83}$$

The outputs of lowpass filters in the Q and I arms are $m(t) \sin(\theta_i - \theta_o)$ and $m(t) \cos(\theta_i - \theta_o)$, respectively. Taking into account that $m^2(t) = 1$, the output of the baseband multiplier is obtained as

$$\frac{1}{2} m^2(t) \sin[2(\theta_i - \theta_o)] = \frac{1}{2} \sin(2\theta_e) \tag{84}$$

By comparing Eqs. (10) and (84) we conclude that, except for a constant multiplier, the output of the baseband multiplier in a Costas loop is equal to the PD output of a conventional APLL in the noise-free case. Consequently, the Costas loop behaves like an APLL.

In addition to carrier recovery, the Costas loop demodulates the incoming BPSK signal. If the phase error is small, then the output of the lowpass filter in the I arm becomes

$$m(t) \cos(\theta_i - \theta_o) \approx m(t) \tag{85}$$

3.7.3. Inverse Modulator. Two slightly different versions of the inverse modulator or remodulator may be found in the literature [10]. The terms inverse modulator and remodulator are used interchangeably and indiscriminantly. As an example, the operation of an inverse modulator is discussed here.

The block diagram of an inverse modulator contains demodulator and modulator circuits, as shown in Fig. 23. Assume that the PLL involved has achieved the phase-locked condition and that the VCO output is

$$2 \cos(\omega_i t + \theta_o) \tag{86}$$

Then the output of the demodulator is obtained as

$$m(t - t_d) \cos(\theta_i - \theta_o) \tag{87}$$

where $(\theta_i - \theta_o)$ is the phase error of the PLL and t_d denotes the time delay of the lowpass filter involved in the demodulator. This demodulated signal modulates the recovered carrier in the modulator and produces an output

$$2m(t - t_d) \cos(\theta_i - \theta_o) \cos(\omega_i t + \theta_o) \tag{88}$$

which is multiplied in the phase detector by the delayed input signal $m(t - t_d) \sin(\omega_i t + \theta_i)$. The input signal has to be delayed in order to cancel the effect of delay in the demodulator.

Neglecting the sum frequency component, the PD output is obtained:

$$m^2(t - t_d) \cos(\theta_i - \theta_o) \sin(\theta_i - \theta_o) \approx \sin(2\theta_e) \tag{89}$$

As in Eq. (84), this signal can be considered as the PD output of an equivalent PLL. Observe that if the phase

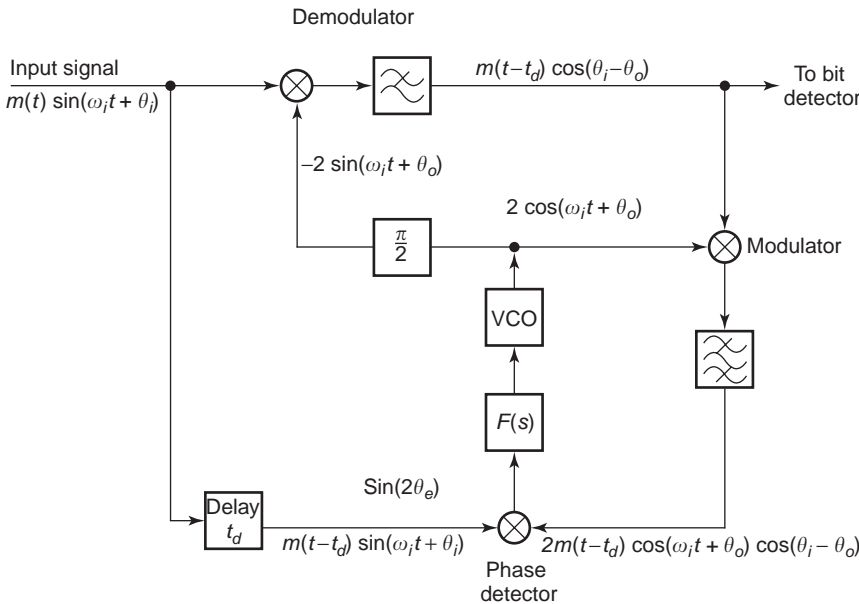


Figure 23. Block diagram of an inverse modulator.

error is small enough, then the demodulator output is equal to $m(t - t_d)$.

3.8. Clock Recovery Circuit

The timing information, that is, the clock signal, also has to be recovered in a digital telecommunication system [7,36]. There are two basic classes of clock recovery circuits, but a PLL can be recognized behind both solutions.

The clock frequency component is regenerated from the incoming signal via some nonlinear operation in the first class of clock recovery circuits. These approaches offer the simplest solution, but their performance is only suboptimal. These solutions are analogous to the squaring loop used in suppressed carrier recovery. Examples for these circuits are the cross-symbol synchronizer [40] and the squaring loop symbol synchronizer [41].

The other class of clock recovery circuits is based on *maximum a posteriori estimation* (MAP) techniques [7,42]. Many variants of this technique are currently

used; they differ mainly in the phase detector (also called *clock error detector*) characteristics. The operation of the early-late gate clock recovery circuit [43], as an example, is discussed here.

The block diagram of the early-late gate clock recovery circuit is shown in Fig. 24. The circuit contains a pair of gated integrators called *early* and *late* gates, each performing its integration over a time interval of $T/2$. The input bitstream is

$$\sum_n a_n p(t - nT) \tag{90}$$

where T is the symbol duration and $p(t)$ denotes a rectangular pulsewidth duration T . Integration by the early and late gates are performed during the $T/2$, just before and after, respectively, the estimated location of data transition. Gate intervals adjoin each other, but do not overlap.

Waveforms are shown in Fig. 25 to clarify the operation of the clock recovery circuit. If the timing error is zero,

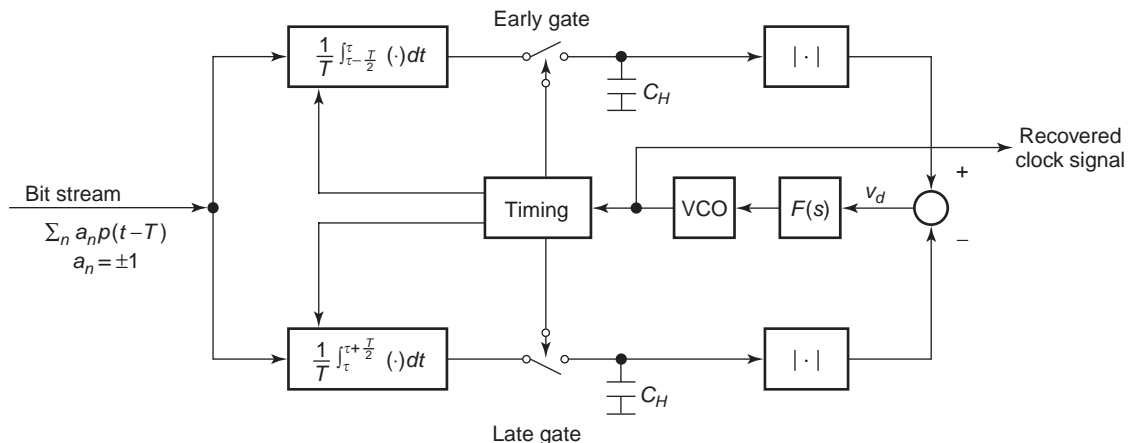


Figure 24. Block diagram of the early-late gate clock recovery circuit.

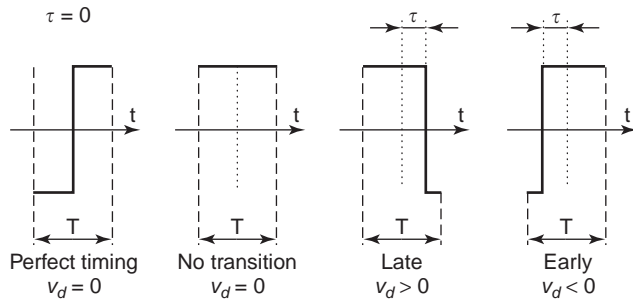


Figure 25. Typical waveforms in the early-late gate clock recovery circuit.

then the data transition falls just on the boundary between the operation of the early and late gates. In this case, the estimated and incoming data transitions coincide with each other, and the output of the two integrators, stored in the hold capacitors C_H , are equal. As a result, the error voltage $v_d(t)$ becomes zero.

Because the error voltage is produced from the absolute values of the integrator outputs, it is also zero if the data transition is missing.

If a transition of input data does not coincide with the estimated time instant of a transition, then a timing error denoted by τ in Fig. 25 appears. In this case, the data transition does not fall on the boundary of operation of the early and late gates, but occurs within the operation interval of one of gates as shown in Fig. 25. Since the input signal changes its polarity during the gate operation, the associated integration reaches a magnitude smaller than that for the other gate, where a transition does not occur. Comparing the magnitudes of the two integrators gives the error voltage $v_d(t)$, which is used after lowpass filtering to control the VCO frequency.

4. FREQUENCY SYNTHESIS BY PHASE LOCK

In addition to the desired DC voltage, a periodic signal appears at the output of phase detectors in steady-state. This periodic signal is attenuated, but cannot be completely suppressed by the lowpass filter included in the phase detector, and the loop filter. The periodic signal getting through the loop filter to the VCO input causes unwanted frequency modulation of the output signal; that is, sidebands appear around the generated signal.

A frequency synthesizer has to generate a signal with very high spectral purity; consequently, both phase noise and unwanted sidebands must be extremely low. The unwanted output FM, or sidebands, caused by the periodic PD output may not be reduced by the feedback since the digital frequency divider used in the feedback path eliminates this FM under steady-state conditions [35]. More exactly, due to the edge-triggered operation of frequency dividers, feedback does not exist for the output FM if the modulation frequency is equal to lf_R , where $l = 1, 2, 3, \dots$ and f_R denotes the reference frequency.

The sampling and charge-pump PLLs offer the best system performance in frequency synthesis. A sample-

and-hold-type phase detector is used in the sampling, as well as a phase-frequency detector with charge-pump circuit in the charge-pump PLLs. These are edge-triggered circuits, where the information is transmitted only at discrete-time instants.

Another source of discrete-time operation is the edge-triggered digital frequency dividers.

If a PLL contains edge-triggered circuit(s), then its mathematical model becomes an integrodifferential equation. These loops are called “hybrid PLLs” in the literature. Unfortunately, the integrodifferential equations may be solved only very rarely in closed form. This is why the analysis of these mixed-signal circuits is a very difficult problem.

In the development of sampling and charge-pump PLLs, intuitive extension of APLL theory, which may be used if the closed-loop bandwidth of PLL is less than one-tenth of reference frequency, and heuristic considerations are frequently used. However, these approximations obscure the special benefits and problems arising from the mixed-signal operation.

4.1. Sampling Phase-Locked Loop

The sampling phase-locked loop (SPLL) is used mainly in frequency synthesis [33–35]. The unique feature of the SPLL is that the sample-and-hold phase detector produces a pure DC output in steady-state [35]. The only source of a periodic signal at the PD output is the feedthrough of the digital signal, which controls the sampling switch. SPLL frequency synthesizer offers the following features:

- The loop filter may be omitted; consequently, a very short frequency switching time can be achieved.
- The unwanted output FM, that is, the sidebands, are extremely low.

4.1.1. Sample-and-Hold Phase Detector. The sample-and-hold PD shown in Fig. 26 is an edge-triggered circuit, that is, a sequential phase detector. Let f_R denote the frequency of the reference signal. The first stock generates block generates the sampled signal $v_R(t)$, which is synchronized with the reference signal. The sampled signal may have any shape; assume that it is a sawtooth waveform in our case. Since the PD is edge-triggered, this sawtooth waveform converts the time interval elapsed between the transitions of the reference and sampling signals into a voltage. The sampling switch is driven by the feedback signal, that is, by the divided VCO output. The switch is closed at the sampling time instants $t_k, k = 0, 1, 2, \dots$ and

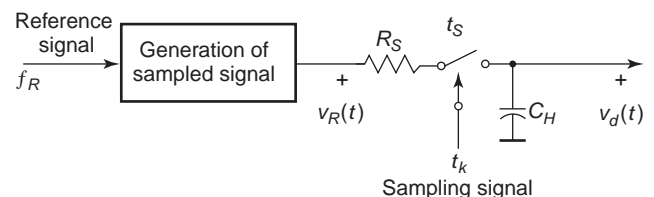


Figure 26. Simplified circuit diagram of sample-and-hold phase detector.

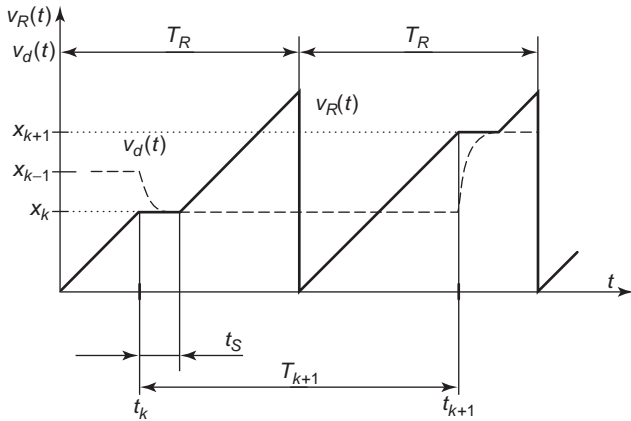


Figure 27. Waveforms in the sample-and-hold phase detector, $T_R = 1/f_R$.

the voltage of the hold capacitor C_H becomes equal to the instantaneous value of the sampled signal. Note that the voltage $v_d(t)$ of the hold capacitor, which is the PD output, is linearly proportional to the time elapsed between transitions of the reference and sampling signals, that is, to the phase error. The capacitor C_H holds this voltage until the next sampling time instant.

The sampling switch may be implemented by an integrated CMOS or discrete FET switch. In both cases, the switch has a series resistance modeled by R_S in Fig. 26. Due to R_S , a finite sampling time is required to charge up or discharge the hold capacitor. The sampling switch is closed at the sampling time instant t_k and remains closed during the sampling time t_S .

The sampled signal $v_R(t)$ and PD output $v_d(t)$ are plotted by solid and dashed lines, respectively, in Fig. 27. When the sampling switch is closed, the PD output voltage $v_d(t)$ varies exponentially from its previous value to the new one. The time constant $R_S C_H$ of the sampling switch has to be much less than the sampling time t_S . Note that the sampled signal is kept constant during the finite sampling time t_S . This must be done in order to avoid the appearance of a periodic signal at the PD output in steady-state.

Figure 28 shows the waveforms of sample-and-hold phase detector in steady-state. Since the sampled signal (solid line) is kept constant during the finite sampling time, the PD output (dashed line) becomes a pure DC voltage under phase-locked conditions.

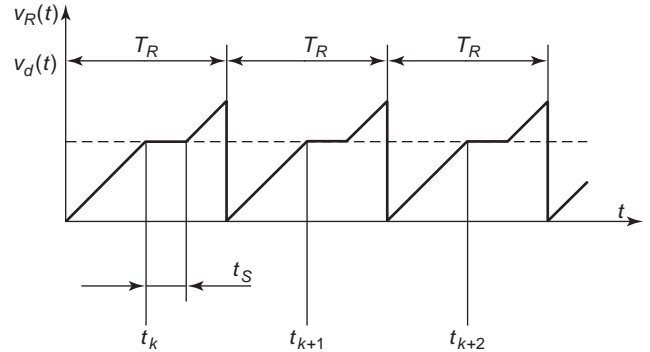


Figure 28. Steady-state waveforms in the sample-and-hold phase detector. [Note: If the sampled signal $v_R(t)$ (solid line) is kept constant during t_S , then the PD output $v_d(t)$ (dashed line) becomes a pure DC voltage.]

More details on the sample-and-hold phase detector and its design are given in Refs. 34 and 35.

4.1.2. SPLL Loop Equation. A block diagram of the SPLL is shown in Fig. 29. The sinusoidal reference signal $s(t)$ corrupted by noise $n_i(t)$ synchronizes a sawtooth waveform in the phase detector. The sampled signal $v_R(t)$ is kept constant during the finite sampling time t_S , as shown in Fig. 27. The PD output $v_d(t)$ is an *analog signal* that is processed by an analog loop filter $F(s)$. The instantaneous VCO frequency is controlled by $v_c(t)$ and is divided by a frequency divider; the division ratio is N . The sampling time instants t_k are determined by the frequency divider output.

The waveforms of sample-and-hold PD are shown in Fig. 27. Let x_k denote the value of the sampled signal at t_k and assume that $R_S C_H \ll t_S$. When the sampling switch is closed, the PD output voltage $v_d(t)$ changes from x_{k-1} to x_k . In the time interval $[t_k + t_S, t_{k+1})$ the sampling switch is open, that is, $v_d(t) = x_k$.

Due to sampling, subharmonic locking is also possible in the SPLL. In subharmonic locking, one sample is taken every M th reference period; that is, in steady-state the output frequency becomes

$$f_o = \frac{N}{M} f_R$$

To derive the governing equation, first the sampling time instants have to be expressed as a function of VCO

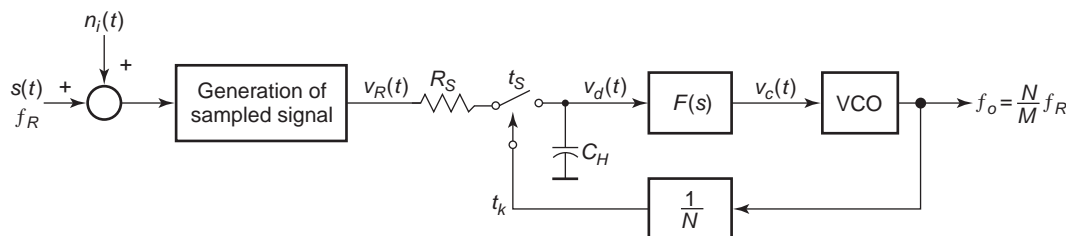


Figure 29. Block diagram of SPLL. A frequency divider with a division ratio of N is placed in the feedback path to control the output frequency.

output phase. Let $T_{k+1} = t_{k+1} - t_k$ denote the time elapsed between two adjacent sampling time instants. Due to the edge-triggered operation of frequency divider, the phase of VCO signal increases by $2\pi N$ radians between two adjacent sampling time instants. If $t_0 = 0$, then the time instant of the k th sampling may be expressed by means of the steady-state output frequency as

$$\frac{N}{M} \omega_R t_k + \theta_{ok} = 2\pi N k \tag{91}$$

where $\theta_{ok} = \theta_o(t)|_{t=t_k} = \theta_o(t_k)$ is the phase modulation of the VCO output at t_k . The sampling time instants are obtained from Eq. (91)

$$t_k = \left(k - \frac{\theta_{ok}}{2\pi N} \right) M T_R, \quad k = 1, 2, 3, \dots \tag{92}$$

Next the synchronization of the sampled signal with the reference signal has to be modeled. Let ω_R , φ_{R0} , and $\hat{\theta}_R(t)$ denote the frequency, phase, and phase modulation, respectively, of the reference signal:

$$s(t) = \sqrt{2} V_R \sin[\omega_R t + \varphi_{R0} + \hat{\theta}_R(t)] \tag{93}$$

The synchronization of the sampled signal is edge-triggered; that is, a new voltage ramp is started at each positive zero crossing of the noisy reference signal. Because the signal-to-noise ratio is extremely high at the PD input, false triggering does not occur and the synchronization process may be described by

$$s(t_n) + n_i(t_n) = 0 \quad \text{and} \quad \left. \frac{ds(t)}{dt} \right|_{t=t_n} > 0 \tag{94}$$

where $t_n, n = 0, 1, 2, \dots$ denotes the starting time instants of voltage ramps. To get t_n , Eq. (94) has to be solved. In the general case, this synchronization and the sampling at t_k are independent of each other. This means that the value of the sampled signal at t_k depends on two variables, n and k , where n describes the synchronization, while k appears as a result of sampling. A governing equation in closed form can be developed only if a relationship between k and n is found.

It has been shown [44] that if cycle slipping does not occur, then $n = Mk$, and the independent variable n may be eliminated from the equations. Henceforth, we assume that cycle slipping does not occur in the SPLL.

Knowing t_n , we may express the sampled signal as

$$v_R(t) = \sum_{n=0}^{\infty} \hat{g}(t - t_n) \tag{95}$$

where the nonlinear periodic function $\hat{g}(\cdot)$ describes the shape of the sampled signal.

The time instants t_n are influenced by both the additive noise $n_i(t)$ and the phase modulation $\hat{\theta}_R(t)$ of the reference signal. Both effects may be incorporated in the equivalent input phase modulation [44] if the signal-to-noise ratio is high at the PD input and if the phase deviation of $\hat{\theta}_R(t)$ is

small:

$$\begin{aligned} \theta_{Rk} &= \varphi_{R0} + \hat{\theta}_R \left(k M T_R - \frac{\varphi_{R0}}{\omega_R} \right) \\ &+ \frac{1}{\sqrt{2} V_R} n_i \left(k M T_R - \frac{\varphi_{R0}}{\omega_R} \right) \end{aligned} \tag{96}$$

Then, by linearizing Eq. (94), the starting time instants of the voltage ramps may be expressed as

$$t_n = M k T_R - \frac{\varphi_{Rk}}{\omega_R} \tag{97}$$

Let the phase error θ_{ek} be defined according to conventional PLL terminology

$$\theta_{ek} = \theta_{Rk} - \frac{M}{N} \theta_{ok} \tag{98}$$

By substituting Eqs. (92) and (97) into Eq. (95), the sampled signal is obtained at the k th sampling time instant:

$$x_k = v_R(t_k) = \hat{g}(t_k - t_n) = g(\theta_{ek}) \tag{99}$$

Finally, using Eqs. (91) and (98) and the definition of T_{k+1} , the phase error is obtained as

$$\theta_{ek} = \theta_{Rk} - \omega_R \frac{z^{-1}}{1 - z^{-1}} (M T_R - T_{k+1}) \tag{100}$$

Equation (100) is the governing equation of the SPLL. Its main advantage is that it contains only those variables that are well known from the PLL baseband models [14]. However, the baseband model can be determined only if T_{k+1} is found in closed form.

According to Fig. 27, the time interval T_{k+1} may be divided into two distinct periods; from t_k to $(t_k + t_S)$ the sampling switch is closed, while from $(t_k + t_S)$ to t_{k+1} the switch is open. This means that the topology of the SPLL is changed at t_k and at $(t_k + t_S)$; consequently, the SPLL is a time-varying circuit. A time-varying circuit may be analyzed by the event-driven approach, where the next sampling time instant t_{k+1} is predicted from the state of the SPLL measured at t_k .

Since the VCO output is a sinusoidal signal and the frequency divider is edge-triggered, the variation in the VCO phase is $2\pi N$ between t_k and t_{k+1} . Let ω_0 denote the VCO center frequency. The variation in the VCO phase between t_k and t_{k+1} is

$$\begin{aligned} \int_{t_k}^{t_{k+1}} [\omega_0 + K_v v_c(t)] dt &= \omega_0 T_{k+1} \\ &+ K_v \left[\int_{t_k}^{t_k + t_S} v_c(t) dt + \int_{t_k + t_S}^{t_{k+1}} v_c(t) dt \right] \equiv 2\pi N \end{aligned} \tag{101}$$

Calculation of the $(k + 1)$ th sampling time instant requires the solution of this integro-difference equation.

In general, Eq. (101) cannot be solved in closed form. The solution is available only if Eq. (101) is separated into

a pure difference and a pure differential equation. This separation may be done in the following cases [44]

- If the dominant time constant of the open-loop transfer function is much less than t_S .
- If the dominant time constant of the open-loop transfer function is much greater than T_k .
- If the SPLL remains in the neighborhood of its quiescent point during the operation.

Fortunately, at least one of these conditions is almost always valid in practical situations.

For the sake of simplicity, only the SPLL implemented without loop filter is considered in this article. For more complex SPLL configurations (passive lag-lead filter, double sampling SPLL), refer to Ref. 44.

When the loop filter is omitted, $F(s) = A_0$ and the dominant time constant is $R_S C_H$, which is much less than t_S . The time elapsed between two adjacent sampling time instants is obtained as follows:

$$T_{k+1} = \frac{2\pi N + A_0 K_v (x_k - x_{k-1}) R_S C_H}{\omega_0 + A_0 K_v x_k} \quad (102)$$

4.1.3. Nonlinear Baseband Model. The SPLL outputs are analog signals. Equations (100) and (99) give the signals at the sampling time instants only, the analog signals have to be expressed in terms of x_k . Inspection of Fig. 27 shows that the PD output voltage $v_d(t)$ may be generated from x_k by means of a zero-order hold circuit followed by an RC lowpass filter. Note that the sampling is not uniform in the SPLL; consequently, the hold time of zero-order hold circuit varies during the operation.

The discrete part of the nonlinear baseband model is constructed from Eqs. (100) and (99) as shown in Fig. 30.

To get the signals in the continuous-time domain, the discrete-time signal x_k has to be converted to an analog signal by a zero-order hold circuit. The time constant of sample-and-hold circuit is accounted by a lowpass filter (see R_S and C_H in Fig. 30) and the analog PD output $v_d(t)$ appears at the output of this lowpass filter. The time interval T_{k+1} may be calculated from Eq. (102) if the loop filter is omitted. Recall that expressions for T_{k+1} are given in Ref. 44 for other loop configurations.

Recall that θ_{Rk} is the equivalent input phase modulation in Fig. 30, which, according to Eq. (96), incorporates both the phase modulation $\hat{\theta}_R(t)$ of reference signal and additive input noise $n_i(t)$. The phase modulated reference signal was given by Eq. (93).

Because of the systematic application of conventional PLL terminology, the nonlinear baseband model of SPLL shown in Fig. 30 is very similar to the baseband models that have been developed for analog and digital PLLs in the literature. The most important properties of the SPLL baseband model are

- Due to the edge-triggered operation of sample-and-hold PD and frequency divider, the feedback operates in the discrete-time domain.
- The signals measured in a built SPLL are analog signals; consequently, each signal is expressed in the continuous-time domain.

4.1.4. Linear SPLL Theory. To get the linear SPLL baseband model, first the quiescent value of phase error has to be determined. In phase-locked condition $T_{k+1} = MT_R$, and the phase error is obtained from Eqs. (102) and (99) as

$$\theta_{ss} = g^{-1} \left[\frac{1}{A_0 K_v} \left(\frac{N}{M} \omega_R - \omega_0 \right) \right]$$

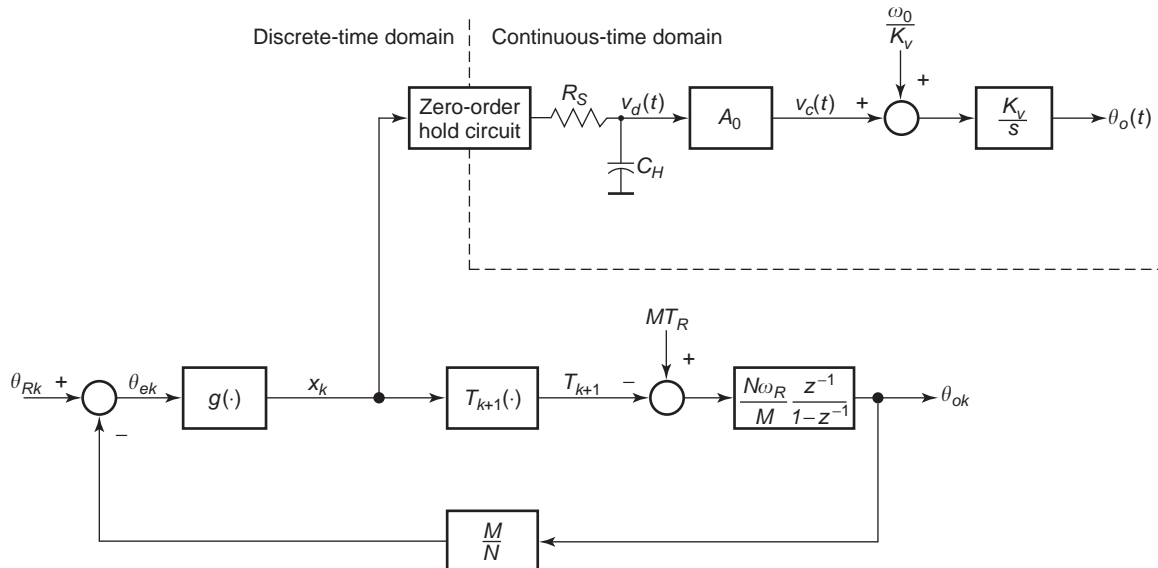


Figure 30. Nonlinear baseband model of SPLL for $F(s) = A_0$. The dashed line separates the discrete- and continuous-time domains.

One of the most important design parameters of an SPLLL is the loop gain that appears in many design equations. In the case of the SPLLL, it is defined by the following equation:

$$G_0 = \left. \frac{dg(\theta_e)}{d\theta_e} \right|_{\theta_e = \theta_{ss}} \frac{A_0 K_v}{N f_R} \tag{103}$$

The SPLLL implemented without a loop filter is stable [44] if

$$M^2 G_0 < \frac{2}{1 - 2B_1} \tag{104}$$

where

$$B_1 = \frac{R_S C_H}{M T_R}$$

If the phase error remains in the neighborhood of θ_{ss} , then the nonlinear baseband model may be linearized. For the sake of simplicity, assume that $\varphi_{R0} = 0$ in Eq. (96). Then

$$\begin{aligned} \theta_{Rk} &= \hat{\theta}_R(kMT_R) + \frac{1}{\sqrt{2}V_R} n_{ik}(kMT_R) \\ &= \hat{\theta}_{Rk} + \frac{1}{\sqrt{2}V_R} n_{ik} \end{aligned} \tag{105}$$

From Eq. (105) and Fig. 30, the linear SPLLL baseband model may be constructed as shown in Fig. 31. In the figure

$$G(z) = \frac{(1 - B_1)z + B_1}{z}$$

is the transfer function of sample-and-hold phase detector and

$$K_v M T_R \frac{z^{-1}}{1 - z^{-1}}$$

gives the VCO transfer function in the discrete-time domain. To have compact notations in Fig. 31 and in the linear SPLLL analysis, the variables are not distinguished from their perturbations. Note that besides the equivalent input phase modulation θ_{Rk} , both the phase modulation $\hat{\theta}_{Rk} = \hat{\theta}_R(kMT_R)$ of the reference signal and noise $n_{ik} = n_i(kMT_R)$ corrupting the reference signal are shown explicitly in the linear SPLLL baseband model.

The SPLLL transfer functions are derived from the linear baseband model. The equations shown here are valid for the SPLLL built without a loop filter; for more complex SPLLL configurations, refer to Ref. 44.

Similar to the APLL theory, the output phase modulation of SPLLL at the sampling time instants may be expressed as

$$\Theta_o(z) = H(z)\hat{\Theta}_R(z)$$

where $H(z)$ is the closed-loop transfer function, $\hat{\Theta}_R(z)$ and $\Theta_o(z)$ denote the z-transform of input $\hat{\theta}_{Rk}$ and output θ_{ok} , respectively, phase modulation. Since the SPLLL is a feedback system, its closed-loop transfer function is obtained by applying the rules of block diagram algebra to Fig. 31:

$$H(z) = \frac{N}{M} M^2 G_0 \frac{(1 - B_1)z + B_1}{z^2 - [1 - M^2 G_0(1 - B_1)]z + M^2 G_0 B_1} \tag{106}$$

In many applications, the output phase modulation must also be expressed in the continuous-time domain. Transforming x_k from the discrete- to the continuous-time

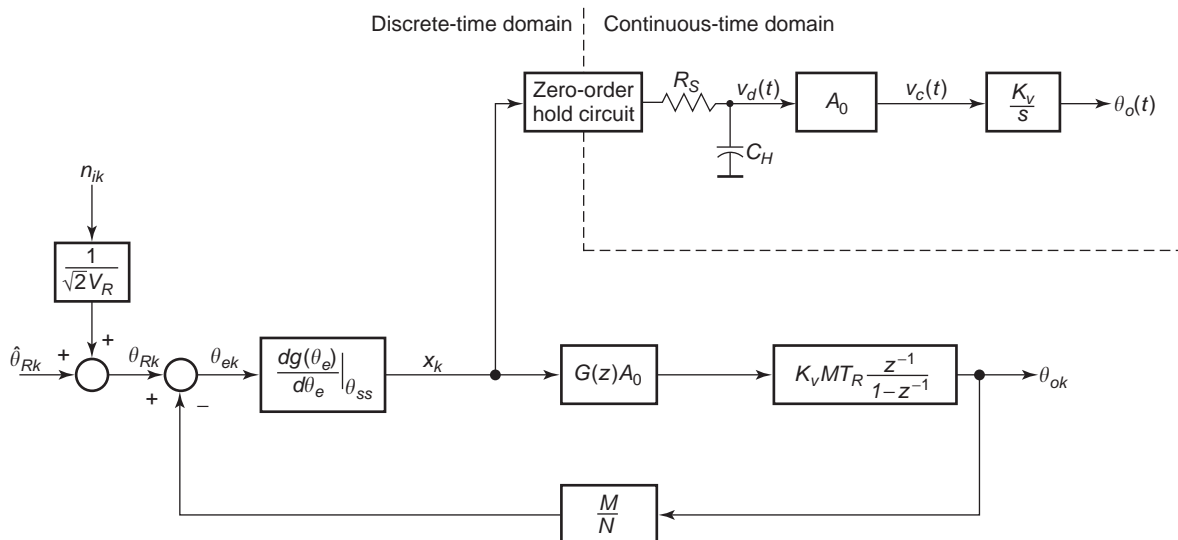


Figure 31. Linear baseband model of SPLLL for $F(s) = A_0$.

domain by a zero-order hold circuit as shown in Fig. 31, and taking into account the effect of the phase detector, loop-amplifier, and VCO, the Fourier transform of the output phase modulation is obtained [45] as

$$\Theta_o(\omega) = \left[1 - \frac{M}{N} H(z) \Big|_{z=e^{j\omega MT_R}} \right] A(\omega) \sum_{n=-\infty}^{\infty} \hat{\Theta}_R \left(\omega - n \frac{\omega_R}{M} \right) \quad (107)$$

where $A(\omega)$ gives the relationship between x_k and the Fourier transform of the output phase modulation

$$A(\omega) = \frac{N}{M} \frac{M^2 G_0}{j\omega MT_R} \frac{\sin\left(\frac{\omega MT_R}{2}\right)}{\frac{\omega MT_R}{2}} \frac{1}{1 + j\omega R_S C_H} e^{-j(\omega MT_R/2)} \quad (108)$$

Assume that the SPLL reference signal is an angle-modulated signal where the modulation frequency is low. Since in Eq. (107)

$$\lim_{\omega \rightarrow 0} \left[1 - \frac{M}{N} H(z) \Big|_{z=e^{j\omega MT_R}} \right] A(\omega) = \frac{N}{M} \quad (109)$$

the SPLL multiplies the input phase/frequency deviation by N/M , but leaves the modulation frequency ω unchanged. Recall that this effect was also observed in the APLL frequency multiplier.

A harmful consequence of edge-triggered PD operation is that the output phase noise is increased by overlapping. To examine this effect, assume that the noisy reference signal is bandlimited by an ideal lowpass filter with cutoff frequency of

$$\omega_L = \left(L + \frac{1}{2} \right) \frac{f_R}{M}$$

where L is an arbitrary integer. This filter passes the reference signal without any distortion but limits the bandwidth of additive Gaussian white noise $n_i(t)$ characterized by its power spectral density $N_0/2$. The power spectral density of output phase process is obtained from Eq. (107):

$$S_{\Theta_o, N}(\omega) = (2L + 1) \left| 1 - \frac{M}{N} H(z) \Big|_{z=e^{j\omega MT_R}} \right|^2 |A(\omega)|^2 \frac{N_0}{4V_R^2} \quad (110)$$

Inspecting Eqs. (110) and (109), two important conclusions are drawn that are valid to every frequency synthesizer using edge-triggered phase detector:

1. Sampling causes overlapping, and this effect multiplies the power spectral density of input noise by a factor of $(2L + 1)$. Consequently, a filter must be used

before each edge-triggered PD to limit the bandwidth of $n_i(t)$.

2. If a frequency divider is used in the feedback path, then it multiplies the power spectral density of input noise by a factor of N/M in the vicinity of output frequency.

To illustrate that the APLL theory may not be used for the design of an SPLL if the closed-loop bandwidth is not much less than f_R , the frequency response of a built SPLL to input phase modulation was predicted from Eq. (107) and measured. The parameters of SPLL under test were $R_S = 100 \Omega$, $C_H = 1 \text{ nF}$, $t_S = 1.4 \mu\text{s}$, $N = 3000$, and $f_R = 33.33 \text{ kHz}$.

Since the deviation of output phase modulation was kept low to make the linear approximation valid, the sideband-to-carrier ratio J_1/J_0 at the VCO output was calculated and measured. Recall that the levels of sidebands are given by the Bessel functions in PM and that for small values of phase deviation $\Delta\theta$

$$J_0(\Delta\theta) \approx 1, \quad J_1(\Delta\theta) \approx \frac{\Delta\theta}{2} \quad \text{and}$$

$$J_n(\Delta\theta) \approx 0 \quad \text{for } n \geq 2$$

The calculated (solid, dashed, and dotted lines) and measured (marked by crosses) frequency responses of the SPLL implemented without a loop filter to the phase modulation $\hat{\theta}_R(t)$ of the reference signal are shown in Fig. 32. The results are compared for three values of loop gain: $G_0 = 0.67$ (solid line), $G_0 = 1.0$ (dashed line), $G_0 = 1.5$ (dotted line). J_1/J_0 denotes the sideband-to-carrier ratio at the VCO output. The frequency axis $f_0 = f_o/f_R - N$ shows the frequency detuning from the carrier normalized to the reference frequency.

Figure 33 shows the calculated (solid line) and measured (marked by crosses) frequency response of an SPLL

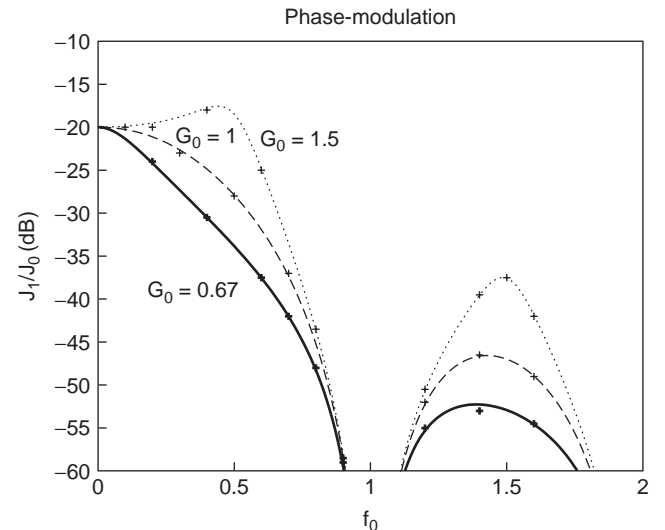


Figure 32. Frequency response of the SPLL implemented without loopfilter to the input phase modulation. The phase deviation of input PM was 6.67×10^{-5} rads.

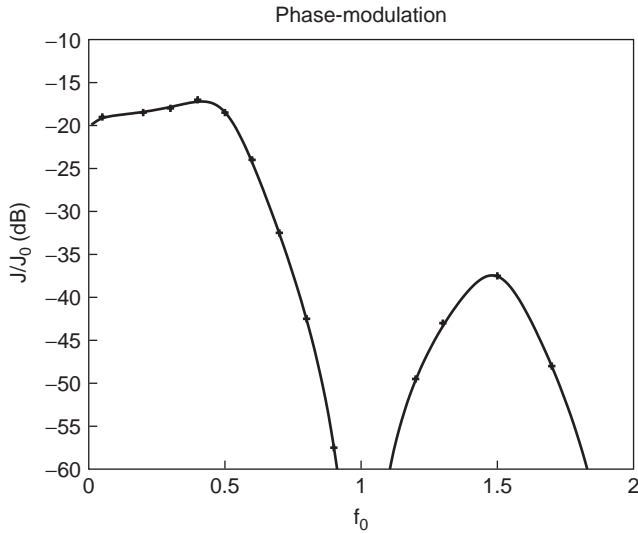


Figure 33. Frequency response of the SPLL implemented with a passive lead-lag filter to the input phase modulation. The phase deviation of input PM was 6.67×10^{-5} rads.

implemented with a passive lag-lead filter

$$F(s) = \frac{1 + sR_2C}{1 + s(R_1 + R_2)C}$$

to $\hat{\theta}_R(t)$. The parameters of the loop filter were $R_1 = 6.8 \text{ k}\Omega$, $R_2 = 680 \Omega$ and $C = 220 \text{ nF}$. The loop gain defined by Eq. (103) was $G_0 = 16.5$.

Figures 32 and 33 show clearly that a simple extension of APLL theory cannot be used for the design of a sampling phase-locked loop. For example, first- and second-order APLLs have a lowpass frequency response to the input phase modulation. If the APLL is implemented without a loop filter, then the loop gain G_0 controls the closed-loop bandwidth. These effects cannot be observed in Figs. 32 and 33. Even more, high-attenuation poles appearing in the SPLL frequency response at the entire multiples of the reference frequency (see Figs. 32 and 33), do not occur in analog PLLs. The real SPLL frequency responses are even qualitatively different from that one predicted from the APLL theory.

It was also shown that the stability properties of the SPLL may not be predicted from classical APLL theory [44]. For example, it is obvious from Eq. (104) that even an SPLL implemented without a loop filter may become unstable.

4.2. Charge-Pump Phase-Locked Loop

The PLL acquisition incorporates the frequency pullin and phase lockin processes. In higher-order PLLs, the pullin time may be extremely long; worse still, for many loop configurations there is no guarantee that the phase-locked condition will be ever reached. This problem may be overcome by means of a *phase-frequency detector* (PFD) [46] that operates as a phase detector under phase-locked condition, but provides a frequency-sensitive signal to aid frequency pullin when the loop is out of lock.

As shown in Table 2, a type 2 PLL is required to elicit a zero steady-state phase error response to a frequency step input. Unfortunately, an integrator cannot be implemented if the input of loop filter is a voltage.

In the charge-pump phase-locked loop (CP-PLL) [10,35,47], a charge-pump (CP) circuit converts the PFD output into current that charges up or discharges the loop filter capacitor. The current sources of charge pump and the capacitor of loop filter together constitute an integrator, the CP-PLL is the only phase-locked loop that implements a type 2 feedback loop.

The CP-PLL is the most frequently used PLL configuration in frequency synthesis because:

- The pull-in and hold-in ranges of CP-PLL are identical.
- Theoretically, the output of charge pump circuit is zero in steady-state (an explanation will be given in sec. 4.2.2), consequently, it does not generate unwanted output FM.
- The PFD characteristic has the widest linear region (4π rad) among the phase detectors.

4.2.1. Phase-Frequency Detector With Charge Pump

The simplified block diagram of a phase-frequency detector with charge pump is shown in Fig. 34. It contains an edge-triggered logic circuit (the phase-frequency detector) and a charge pump, which includes two controlled current sources I_U and I_D . The PFD and charge-pump circuit together constitute the PFD-CP phase detector. Note, that the output of PFD-CP phase detector is not a voltage but a current $i_d(t)$.

Assume that the state of the sequential-logic PFD circuit is controlled by the rising edges of reference $s(t)$ and frequency-divided VCO output $r(t)$ signals connected to the R and F inputs, respectively. The PFD has two outputs U and D; if one of them is high, then the other is low.

If the edge of the R input leads that of the F input, then the edge of R input sets the U output high unless the

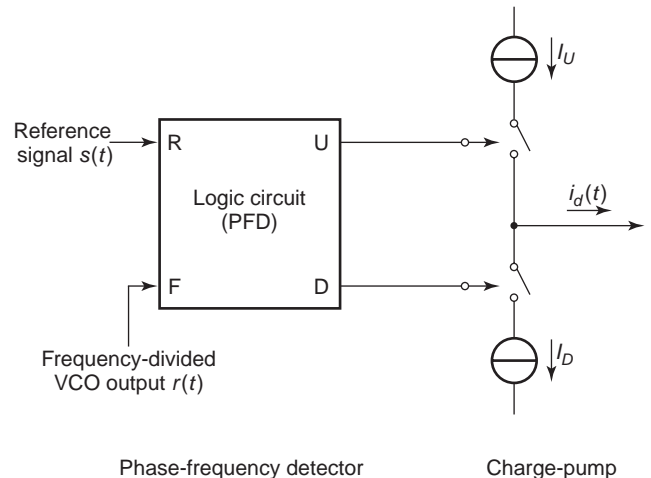


Figure 34. Simplified circuit diagram of the PFD-CP phase detector. Recall that the phase-frequency detector and charge-pump circuit together constitute the PFD-CP phase detector.

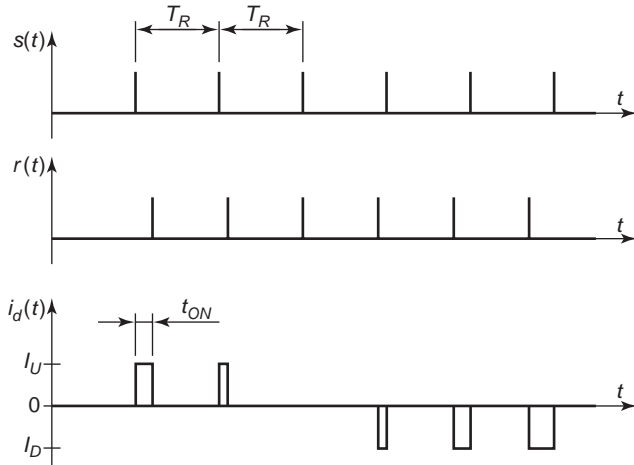


Figure 35. Input and output signals of the PFD-CP phase detector.

U-output is already high, in which case the R input has no effect. The next edge of the F input resets the U output low. As long as the R input leads the F input, the D output is low. If the F input leads the R input, then the edge of the F input sets the D output high and the next edge of the R input resets the D output low. As long as the F input leads the R input, the U output remains low.

The current sources I_U and I_D are controlled by the U and D outputs of PFD. Note that both current sources may never be switched on simultaneously. The input and output waveforms of the PFD-CP phase detector are shown in Fig. 35, where t_{ON} denotes the width of current pulses generated by the charge-pump circuit.

Based on Fig. 35, the operation of PFD with charge pump may be summarized as follows. This phase detector is an edge-driven circuit, and its output $i_d(t)$ is a series of current pulses. The sign of pulses is determined by the sign of frequency error, while their duration is proportional to the phase error. If the edges of R and F inputs coincide with each other, that is, if the phase error is zero, then the PFD-CP phase detector has no output $i_d(t)$.

4.2.2. CP-PLL Operation. The block diagram of CP-PLL is shown in Fig. 36. Note that an impedance $Z_F(s)$ is used as loop filter; this impedance converts the discrete-time current output $i_d(t)$ of PFD-CP phase detector into the analog VCO control voltage $v_c(t)$. The loop filter may be either passive or active; for the sake of simplicity, the CP-PLL configuration incorporating a PFD with charge-pump and a passive loop filter is considered here. For other loop configurations, refer to Ref. 25. To get a first-order loop filter and to have a zero² in the open-loop transfer function, the impedance $Z_F(s)$ is implemented by a series connection of a resistor R and a capacitor C .

Consider the noise-free case and assume that the reference signal $s(t)$ in Fig. 36 is an unmodulated signal. Consider the CP-PLL acquisition process and assume that the reference frequency f_R is greater than the frequency-

divided VCO frequency f_o/N initially. Figure 35 shows that the sign of output current pulses $i_d(t)$ of PDF-CP phase detector is determined by the sign of frequency error $f_R - f_o/N$. If $f_R > f_o/N$, then positive current pulses appear at the PDF-CP phase detector output that charge up the loop filter capacitor C , that is, increase the VCO frequency. In a locked CP-PLL under steady-state, the VCO output frequency f_o and VCO control voltage $v_c(t)$ are constant; consequently, $i_d(t) = 0$. It means that the steady-state phase error is zero as claimed in sec. 4.2.

The zero steady-state phase error is extremely important in the frequency synthesizer applications. If the phase error is zero, then $i_d(t) = 0$ and the VCO input is free from the periodic signal of period T_R that would produce an unwanted output FM, that is, sidebands in the output signal. Recall that the unwanted output FM caused by the periodic PD output may not be attenuated by the PLL feedback since the digital frequency divider eliminates this FM.

Unfortunately, in an implemented CP-PLL the phase error must exceed a certain limit to avoid crossover distortion [35]. The unwanted FM appearing due to the finite phase error may be attenuated but not fully eliminated by an additional capacitor connected in parallel with $Z_F(s)$ [25].

Similarly to the SP-PLL, the CP-PLL is a time-varying circuit. The PFD-CP phase detector is an edge-triggered circuit, its discrete-time output is converted into the continuous-time domain by the impedance $Z_F(s)$. An exact analysis and baseband model must take into account the variations in the loop topology.

Unfortunately, an exact CP-PLL baseband model has not yet been published. A time-averaged and linearized model has been developed by Gardner [25]; that baseband model, discussed in Section 4.2.3, is an intuitive extension of APLL theory that may be used successfully in circuit design if the closed-loop bandwidth calculated from the model is less than one-tenth of reference frequency f_R .

4.2.3. Time-Averaged Linear Baseband Model of the CP-PLL. To get an approximate but simple CP-PLL baseband model, Gardner linearized each nonlinear CP-PLL block independently from one another and removed the discrete-time operation by time averaging.

Assume that the CP-PLL is locked, and let

$$\Phi(t) = \omega_R t + \theta_R(t) \quad \text{and}$$

$$\hat{\Phi}(t) = \frac{\Phi_o(t)}{N} = \omega_R t + \frac{\theta_o(t)}{N}$$

denote the phases of reference $s(t)$ and frequency-divided VCO $r(t)$ respectively, signals. According to the PLL terminology, let

$$\theta_e = \theta_R - \frac{\theta_o}{N} \quad (111)$$

define the phase error. Recall that in the CP-PLL shown in Fig. 36, the quiescent value of phase error is zero.

²This zero is used to set the stability margin, that is, to control the loop dynamics.

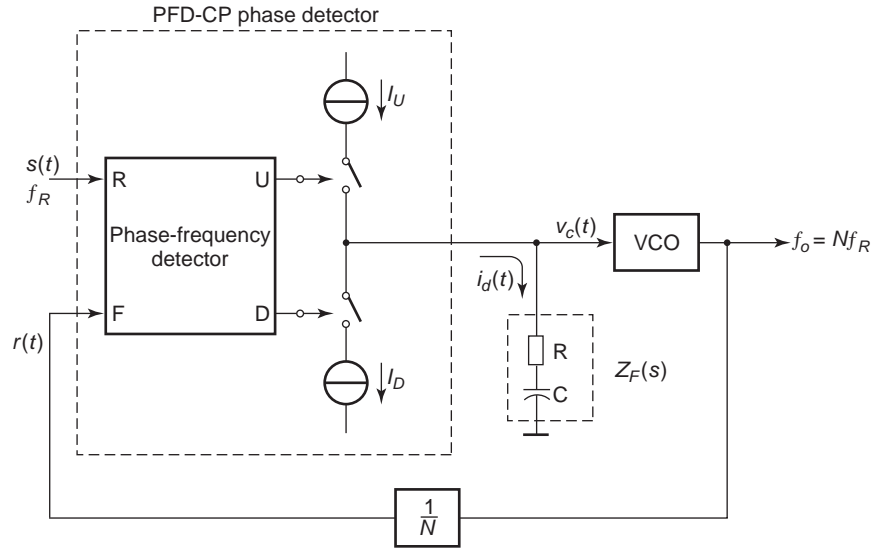


Figure 36. Block diagram of CP-PLL implemented with an impedance $Z_F(s)$. The steady-state output frequency f_o is controlled by the division ratio N of frequency divider.

The width of PD output current pulses may be approximated by

$$t_{ON} \approx \frac{\theta_e}{2\pi} T_R = \frac{1}{\omega_R} \left(\theta_R - \frac{\theta_o}{N} \right) \quad (112)$$

Note that the sign of t_{ON} depends on the sign of phase error; if the VCO signal leads the reference one, then $t_{ON} > 0$; if the edges of two signals coincide with one another, then $t_{ON} = 0$; otherwise $t_{ON} < 0$. Equation (112) is exact if the VCO signal leads the reference one, but otherwise it is an approximation. The approximation arises out of the fact that the phase of VCO signal varies during the time interval t_{ON} . The error caused by this approximation is negligible if the closed-loop bandwidth of CP-PLL calculated from the linear baseband model is much less than the reference frequency f_R .

In the majority of applications, narrowband CP-PLLs are used. If the closed-loop CP-PLL bandwidth is less than one-tenth of reference frequency f_R , then the state of the CP-PLL changes by only a very small amount on each reference cycle. If one is not interested in the CP-PLL behavior within a single reference cycle, then the time-averaging technique may be used. As a result, the effect of time-varying operation is removed and the CP-PLL loop equation becomes a pure differential equation.

Assume that the absolute values I_P of the currents provided by the two current sources of charge pump are identical and apply the time-averaging technique to the output current $i_d(t)$ of PFD-CP phase detector. The average error current over a reference cycle is

$$i_d^{AV}(t) = \frac{1}{T_R} \int_{T_R} i_d(t) dt = I_P \frac{t_{ON}}{T_R} \quad (113)$$

Substituting Eq. (112) into Eq. (113), the following relationship between average error current and phase error is

found:

$$i_d^{AV}(t) = \frac{I_P}{2\pi} \theta_e$$

Let $I_d^{AV}(s)$ denote the Laplace transform of $i_d^{AV}(t)$. Then, taking into account the transfer functions of loop filter and VCO, the output phase is obtained as

$$\Theta_o(s) = \frac{K_v}{s} V_c(s) = \frac{I_P}{2\pi} Z_F(s) \frac{K_v}{s} \Theta_e(s) \quad (114)$$

From Eqs. (111) and (114) the phase error

$$\Theta_e(s) = [1 - H(s)] \Theta_R(s) \quad (115)$$

and the output phase

$$\Theta_o(s) = NH(s) \Theta_R(s) \quad (116)$$

are obtained, where the closed-loop transfer function takes the form

$$H(s) = \frac{\frac{I_P K_v}{2\pi N} Z_F(s)}{s + \frac{I_P K_v}{2\pi N} Z_F(s)} \quad (117)$$

The time-averaged linear CP-PLL baseband model constructed from Eqs. (115) and (114) is depicted in Fig. 37.

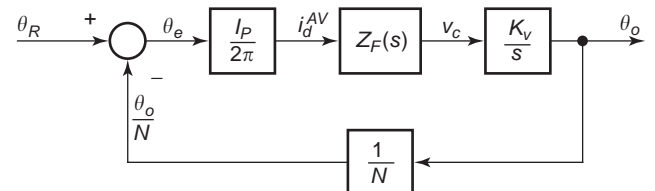


Figure 37. Time-averaged linear baseband model of CP-PLL.

A comparison of Eqs. (115), (116) and (117), respectively, to Eqs. (26), (27) and (28) shows that time-averaged linear baseband model of CP-PLL is an extension of linear APLL theory. This relationship may be also recognized by comparing Fig. 37 to Fig. 4.

A second-order type-two feedback loop is implemented with the most frequently used passive loop filter shown in Fig. 36. In this case the closed-loop transfer function becomes

$$H(s) = \frac{2\zeta\omega_n s + \omega_n^2}{s^2 + 2\zeta\omega_n s + \omega_n^2} \quad (118)$$

where the natural frequency ω_n and the damping factor ζ are given by

$$\omega_n = \sqrt{\frac{I_P K_v}{2\pi N C}} \quad \text{and} \quad \zeta = \frac{\tau\omega_n}{2}$$

and where $\tau = RC$.

The linear baseband model shown in Fig. 37 may be successfully used in the development of CP-PLL circuits until the closed-loop bandwidth calculated from Eq. (118) is less than one-tenth of f_R . However, never forget that the time-averaged model is based on an approximation that has the most serious consequence on the loop stability.

Equation (118) suggests that the CP-PLL shown in Fig. 36 is unconditionally stable. Unfortunately, this is not true. Gardner [25] showed that this CP-PLL would go unstable for large loop gain.

Let the loop gain be defined by

$$K = \frac{I_P K_v}{2\pi N} R$$

The exact characteristic equation, which includes the effect of edge-triggered operation, takes the form [25]

$$D(z) = (z-1)^2 + (z-1) \frac{2\pi K}{\omega_R} \left(1 + \frac{2\pi}{\omega_R \tau}\right) + \frac{4\pi^2 K}{\omega_R^2 \tau}$$

The CP-PLL implemented with a passive loop filter is stable if the roots of characteristic equation lie inside the unit circle in the z plane.

4.2.4. Crossover Distortion. Timing uncertainties in the edge-triggered PFD together with the finite risetimes and fall times cause an error in the amount of charge delivered by the charge pump to the loop filter capacitor. This error may be neglected for large phase error, but it changes severely the gain of PFD-CP phase detector about the zero-phase error. Egan observed more than ± 20 dB variations in the PD gain in this crucial small phase error region [48]. This variation in PD gain has a serious influence on closed-loop CP-PLL parameters and, even worse, may cause a stability problem. This effect is called *crossover distortion* [35]. To avoid crossover distortion, the phase error must exceed a minimum value in steady-state. The phase error region that may not be used is called the dead zone [47].

The phase error may be increased by connecting a resistor in parallel with $Z_F(s)$ in Fig. 36. But recall that,

because of the nonzero phase error, a periodic signal appears at the VCO input that causes an unwanted output FM, that is, sidebands at the CP-PLL output.

4.2.5. Exact Analysis of the CP-PLL. The time-averaging approach was used in the previous subsection to develop a baseband model and transfer functions for the CP-PLL. The transfer functions facilitate the design of a CP-PLL, but the time averaging neglects the discrete nature of the loop. Consequently, the validity of that model is limited, and application of the model may result in a disagreement between the predicted and measured CP-PLL behavior.

Event-driven models have been published for the CP-PLL more recently. These models are exact and take into account the discrete-time operation of CP-PLL. Their disadvantage is that a baseband model and transfer functions cannot be developed from these equations; consequently, these models may be used only in computer simulations. The detailed discussion of the event-driven models goes beyond the scope of this article, the interested readers should refer to the papers mentioned below.

Paemel published an event-driven model for the CP-PLL implemented with a first-order passive loop filter in 1994 [49]. Based on the order of edges of reference and frequency-divided VCO signal, Paemel distinguished four different situations. Two state variables and, according to the four possible orders of edges, four nonlinear difference equations were used to describe the behavior of CP-PLL. The equations developed are also valid for the transient analysis and, even more, if the loop is out of lock.

Another event-driven model was developed for the CP-PLL implemented with a first-order passive loop filter by Hedayat et al. in 1997 [50]. Later the validity of that model was extended to the second-order passive loop filter [51]. According to the three possible output of the PFD-CP phase detector (up, down, no output current), a set of three nonlinear difference equations was used to model the operation of CP-PLL. These equations may be used to write a computer program to simulate the behavior of CP-PLL under various conditions.

5. CLOSING REMARKS

The goal of this article was to survey the theory and the most important applications of phase-locked loops. The main emphasis was put on the APLL theory and frequency synthesis. The former is relatively easy to understand and is the basis of every other PLL analysis. The latter is crucial in RF engineering since frequency synthesizers are used everywhere from telecommunication systems to measurement equipment.

While the APLL theory has been very well established, the theory of the hybrid PLLs including both analog and edge-triggered circuits is subject to continuous development. For example, it has been shown [52] that false lock limits the pull-in range of SPLL implemented with a first-order loop filter. For the latest results in the field of PLLs, refer to Ref. 53.

The majority of PLLs developed recently (as of 2004) are used in integrated circuits. The discussion of special

requirements arising from the IC implementation goes beyond the scope of this article, for a good survey, refer to Ref. 54.

Acknowledgment

This work was supported by the National Scientific Research Foundation of Hungary (OTKA) under grant number T-038083.

BIBLIOGRAPHY

1. E. V. Appleton, Automatic synchronization of triode oscillators, *Proc. Cambridge Phil. Soc.*, **21**(Part III):231 (1922-1923).
2. A. V. Balakrishnan, *Advances in Communication Systems*, Academic Press, New York, 1965.
3. A. J. Viterbi, *Principles of Coherent Communication*, McGraw-Hill, New York, 1966.
4. J. J. Stiffler, *Theory of Synchronous Communication*, Prentice-Hall, Englewood Cliffs, NJ, 1971.
5. J. Klapper and J. T. Frankle, *Phase-Locked and Frequency-Feedback Systems*, Academic Press, New York, 1972.
6. W. C. Lindsey, *Synchronization Systems in Communications*, Prentice-Hall, Englewood Cliffs, NJ, 1972.
7. W. C. Lindsey and M. K. Simon, *Telecommunication Systems Engineering*, Prentice-Hall, Englewood Cliffs, NJ, 1973.
8. A. Blanchard, *Phase-Locked Loops*, Wiley, New York, 1976.
9. W. C. Lindsey and M. K. Simon, eds. *Phase-Locked Loops and Their Applications*, IEEE Press, New York, 1978.
10. F. M. Gardner, *Phase-Lock Techniques*, 2nd ed., Wiley, New York, 1979.
11. W. C. Lindsey and C. M. Chie, eds., *Phase-Locked Loops*, IEEE-Press, New York, 1986.
12. F. M. Gardner and W. C. Lindsey, *IEEE Trans. Commun.* (special issue on synchronization) **COM-28** (Part I) (Aug. 1980).
13. W. C. Lindsey and C. M. Chie, *IEEE Trans. Commun.* (special issue on synchronization) **COM-30** (Oct. 1982).
14. S. C. Gupta, Phase-locked loops, *Proc. IEEE* **63**:291-306 (Feb. 1975).
15. S. Haykin, *Communication Systems*, 3rd ed., Wiley, New York, 1994.
16. D. Richman, Color carrier reference phase synchronization accuracy in NTSC color television, *Proc. IRE* **42**:106-133 (Jan. 1954).
17. F. M. Gardner, Hangup in phase-locked loops, *IEEE Trans. Commun.* **COM-25**:1210-1214 (Oct. 1977).
18. G. Hedin, J. K. Holmes, W. C. Lindsey and K. T. Woo, Theory of false lock in Costas loops, *IEEE Trans. Commun.* **COM-26**:1-12 (Jan. 1978).
19. S. T. Kleinberg and H. Chang, Sideband false-lock performance of squaring, fourth-power, and quadriphase Costas loops for NRZ signals, *IEEE Trans. Commun.* **COM-28**:1335-1342 (Aug. 1980).
20. V. I. Tikhonov, The effect of noise on phase-locked oscillator operation, *Autom. Remote Control* **20**:1160-1168 (1959).
21. V. I. Tikhonov, Phase-lock automatic frequency control, *Autom. Remote Control* **21**:209-214 (1960).
22. A. J. Viterbi, Phase-locked loop dynamics in the presence of noise by Fokker-Planck techniques, *Proc. IEEE* **51**:1737-1753 (Dec. 1975).
23. G. Aschied and H. Meyr, Cycle slips in phase-locked loops: A tutorial survey, *IEEE Trans. Commun.* **COM-30**:2228-2241 (Oct. 1982).
24. D. Ryter and H. Meyr, Theory of phase tracking system of arbitrary order: Statistic of cycle slips and probability distribution of the state vector, *IEEE Trans. Inform. Theory* **IT-24**:1-7 (Jan. 1978).
25. F. M. Gardner, Charge-pump phase-lock loops, *IEEE Trans. Commun.* **COM-28**:1849-1858 (Nov. 1980).
26. G. Kolumbán and B. Vizvári, Nonlinear dynamics and chaotic behavior of the analog phase-locked loop, *Proc. NDES*, 1995, pp. 99-102.
27. G. Kolumbán and B. Vizvári, Nonlinear dynamics and chaotic behavior of the sampling phase-locked loop, *IEEE Trans. Circ. Syst.* **CAS-41**:333-337 (April 1994).
28. G. M. Bernstien and M. A. Lieberman, Secure random number generation using chaotic circuits, *IEEE Trans. Circ. Syst.* **CAS-37**:1157-1164 (Sept. 1990).
29. B. Vizvári and G. Kolumbán, Quality evaluation of random numbers generated by chaotic sampling phase-locked loops, *IEEE Trans. Circ. Syst.* **CAS-44** (1997).
30. H. J. Blinchook and G. R. Vaughan, All-pole phase-locked tracking filters, *IEEE Trans. Commun.* **COM-30**:2312-2318 (Oct. 1982).
31. P. H. Lewis and W. E. Weingarten, A comparison of second, third and fourth order phase-locked loops, *IEEE Trans. Aerospace Electron. Syst.* **AES-3**:720-727 (July 1967).
32. U. L. Rohde, *Digital PLL Frequency Synthesizers: Theory and Design*, Prentice-Hall, Englewood Cliffs, NJ, 1983.
33. V. F. Kroupa, *Frequency Synthesizers: Theory, Design and Applications*, Wiley, New York, 1973.
34. V. Manassewitsch, *Frequency Synthesizers: Theory and Design*, Wiley, New York, 1980.
35. W. F. Egan, *Frequency Synthesis by Phase Lock*, 2nd ed., Wiley, New York, 1999.
36. I. Frigyes, Z. Szabó, and P. Ványai, *Digital Microwave Transmission*, Elsevier Science Publishers, Amsterdam, 1989.
37. M. Moeneclaey, Linear phase-locked loop theory for cyclostationary input disturbances, *IEEE Trans. Commun.* **COM-30**:2253-2259 (Oct. 1982).
38. C. L. Weber and W. K. Alem, Demod-remod coherent tracking receiver for QPSK and SQPSK, *IEEE Trans. Commun.* **COM-28**:1945-1954 (Dec. 1980).
39. W. R. Braun and W. C. Lindsey, Carrier synchronization techniques for unbalanced QPSK signals, Parts I and II, *IEEE Trans. Commun.* **COM-26**:1325-1341 (Sept. 1978).
40. R. D. McCallister and M. K. Simon, Cross-spectrum symbol synchronization, *Proc. ICC'81*, 1981, pp. 34.3.1-34.3.6.
41. J. K. Holmes, Tracking performance of the filter and square bit synchronizer, *IEEE Trans. Commun.* **COM-28**:1154-1158 (Aug. 1980).
42. H. L. Van Trees, *Detection, Estimation and Modulation Theory*, Wiley, New York, 1968.
43. M. K. Simon, Nonlinear analysis of an absolute value type of early-late-gate bit synchronizer, *IEEE Trans. Commun.* **COM-18**:589-596 (Oct. 1970).
44. G. Kolumbán, *Design of Sampling Phase-Locked Loops: Model and Analysis*, C.Sc. thesis, Hungarian Academy of Sciences, Budapest, 1989.
45. G. Kolumbán, Frequency domain analysis of sampling phase-locked loops, *Proc. IEEE-ISCAS'88*, Helsinki-Espoo, June 1988, pp. 611-614.

46. J. I. Brown, A digital phase and frequency-sensitive detector, *Proc. IEEE* **59**:717 (April 1971).
47. B. Razavi, *RF Microelectronics*, Prentice-Hall, Upper Saddle River, NJ, 1998.
48. W. F. Egan, Test your charge-pump phase detectors, *Electron. Design* **12**:134–137 (June 7, 1978).
49. M. V. Paemel, Analysis of a charge-pump PLL: A new model, *IEEE Trans. Commun.* **COM-42**:2490–2498 (July 1994).
50. C. D. Hedayat, A. Hachem, Y. Leduc, and G. Benbassat, High-level modeling applied to the second-order charge-pump PLL circuit, *Texas Instrum. Tech. J.* **14**(2):99–107 (March–April 1997).
51. C. D. Hedayat, A. Hachem, Y. Leduc, and G. Benbassat, Modeling and characterization of the 3rd order charge-pump PLL: A fully event-driven approach, *Analog Integr. Circ. Signal Process.* **19**(1):25–45 (April 1999).
52. Z. Szabó and G. Kolumbán, How to avoid false lock in SPLL frequency synthesizers, *IEEE Trans. Instrum. Meas.* **52**(3):927–931 (June 2003).
53. B. Razavi, *Phase-Locking in High Performance Systems: From Devices to Architectures*, Wiley and IEEE Press, NJ, 2003.
54. B. Razavi, ed., *Monolithic Phase-Locked Loops and Clock Recovery Circuits*, Wiley and IEEE Press, NJ, 1996.

wireless communication systems such as cellphones, require these building blocks [1]. Based on a frequency standard, the synthesizer provides a stable reference frequency for the system.

Synthesizers are used to generate frequencies with arbitrary resolution covering the frequency range from audio to millimeter-wave. Today, simple frequency synthesizers consist of a variety of synthesizer chips, an external voltage-controlled oscillator (VCO), and a frequency standard. For high-volume applications, such as cellphones, cordless telephones, walkie-talkies, or systems where frequency synthesizers are required, a high integration is desired. The requirements for synthesizers in cordless telephones are not as stringent as in test equipment. Synthesizers in test equipment use customized building blocks and can be modulated to be part of arbitrary waveform generators [2].

The VCO typically consists of an oscillator with a tuning diode attached. The voltage applied to the tuning diode tunes the frequency of the oscillator. Such a simple system is a phase-locked loop (PLL). The stability of the VCO is the same as the reference. There are single-loop and multiloop PLL systems. Their selection depends on the characteristic requirements. Figure 1 shows the block diagram of a single-loop PLL [3].

The PLL consists of a VCO, a frequency divider, a phase detector, a frequency standard, and a loop filter [4–7].

There are limits to how high the frequency division ratio can be. Typically, the loop where the RF frequency is divided below 1 kHz, becomes unstable. This is because microphonic effects of the resonator will unlock the system at each occurrence of mechanical vibration. At 1 GHz, this would be a division ratio of one million. To avoid such high division ratios, either multiloop synthesizers are created or a new breed of PLL synthesizers called fractional- N division synthesizers will be considered. At the same time, direct digital synthesis is being improved. Using direct digital synthesis in loops can also overcome some of the difficulties associated with high division ratios. There are

PHASE LOCKED OSCILLATORS AND FREQUENCY SYNTHESIZERS

ULRICH L. ROHDE
Synergy Microwave Corporation
Paterson, New Jersey

1. INTRODUCTION

Frequency synthesizers are found in all modern communication equipment, and signal generators, particularly

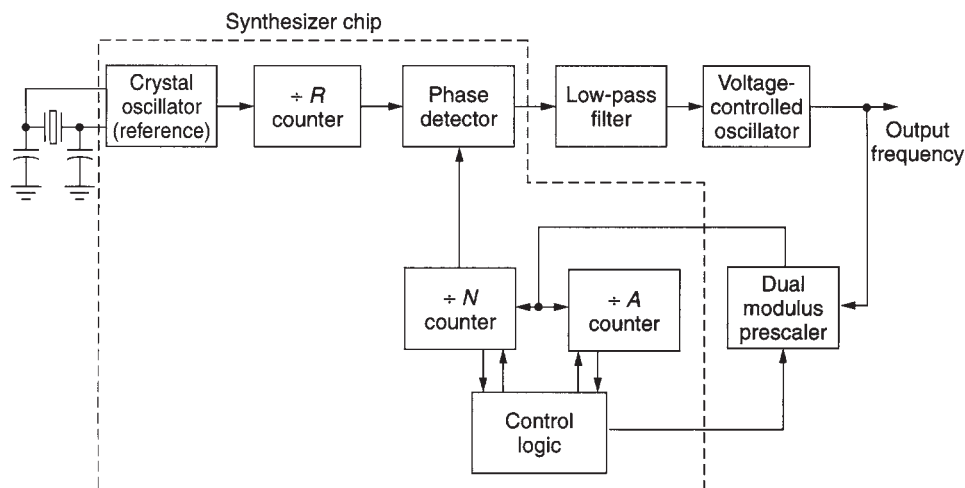


Figure 1. Block diagram of an integrated frequency synthesizer. In this case, the designer has control over the VCO and the loop filter; the reference oscillator is part of the chip. In most cases (up to 2.5 GHz), the dual-modulus prescaler is also inside the chip.

46. J. I. Brown, A digital phase and frequency-sensitive detector, *Proc. IEEE* **59**:717 (April 1971).
47. B. Razavi, *RF Microelectronics*, Prentice-Hall, Upper Saddle River, NJ, 1998.
48. W. F. Egan, Test your charge-pump phase detectors, *Electron. Design* **12**:134–137 (June 7, 1978).
49. M. V. Paemel, Analysis of a charge-pump PLL: A new model, *IEEE Trans. Commun.* **COM-42**:2490–2498 (July 1994).
50. C. D. Hedayat, A. Hachem, Y. Leduc, and G. Benbassat, High-level modeling applied to the second-order charge-pump PLL circuit, *Texas Instrum. Tech. J.* **14**(2):99–107 (March–April 1997).
51. C. D. Hedayat, A. Hachem, Y. Leduc, and G. Benbassat, Modeling and characterization of the 3rd order charge-pump PLL: A fully event-driven approach, *Analog Integr. Circ. Signal Process.* **19**(1):25–45 (April 1999).
52. Z. Szabó and G. Kolumbán, How to avoid false lock in SPLL frequency synthesizers, *IEEE Trans. Instrum. Meas.* **52**(3):927–931 (June 2003).
53. B. Razavi, *Phase-Locking in High Performance Systems: From Devices to Architectures*, Wiley and IEEE Press, NJ, 2003.
54. B. Razavi, ed., *Monolithic Phase-Locked Loops and Clock Recovery Circuits*, Wiley and IEEE Press, NJ, 1996.

wireless communication systems such as cellphones, require these building blocks [1]. Based on a frequency standard, the synthesizer provides a stable reference frequency for the system.

Synthesizers are used to generate frequencies with arbitrary resolution covering the frequency range from audio to millimeter-wave. Today, simple frequency synthesizers consist of a variety of synthesizer chips, an external voltage-controlled oscillator (VCO), and a frequency standard. For high-volume applications, such as cellphones, cordless telephones, walkie-talkies, or systems where frequency synthesizers are required, a high integration is desired. The requirements for synthesizers in cordless telephones are not as stringent as in test equipment. Synthesizers in test equipment use customized building blocks and can be modulated to be part of arbitrary waveform generators [2].

The VCO typically consists of an oscillator with a tuning diode attached. The voltage applied to the tuning diode tunes the frequency of the oscillator. Such a simple system is a phase-locked loop (PLL). The stability of the VCO is the same as the reference. There are single-loop and multiloop PLL systems. Their selection depends on the characteristic requirements. Figure 1 shows the block diagram of a single-loop PLL [3].

The PLL consists of a VCO, a frequency divider, a phase detector, a frequency standard, and a loop filter [4–7].

There are limits to how high the frequency division ratio can be. Typically, the loop where the RF frequency is divided below 1 kHz, becomes unstable. This is because microphonic effects of the resonator will unlock the system at each occurrence of mechanical vibration. At 1 GHz, this would be a division ratio of one million. To avoid such high division ratios, either multiloop synthesizers are created or a new breed of PLL synthesizers called fractional- N division synthesizers will be considered. At the same time, direct digital synthesis is being improved. Using direct digital synthesis in loops can also overcome some of the difficulties associated with high division ratios. There are

PHASE LOCKED OSCILLATORS AND FREQUENCY SYNTHESIZERS

ULRICH L. ROHDE
Synergy Microwave Corporation
Paterson, New Jersey

1. INTRODUCTION

Frequency synthesizers are found in all modern communication equipment, and signal generators, particularly

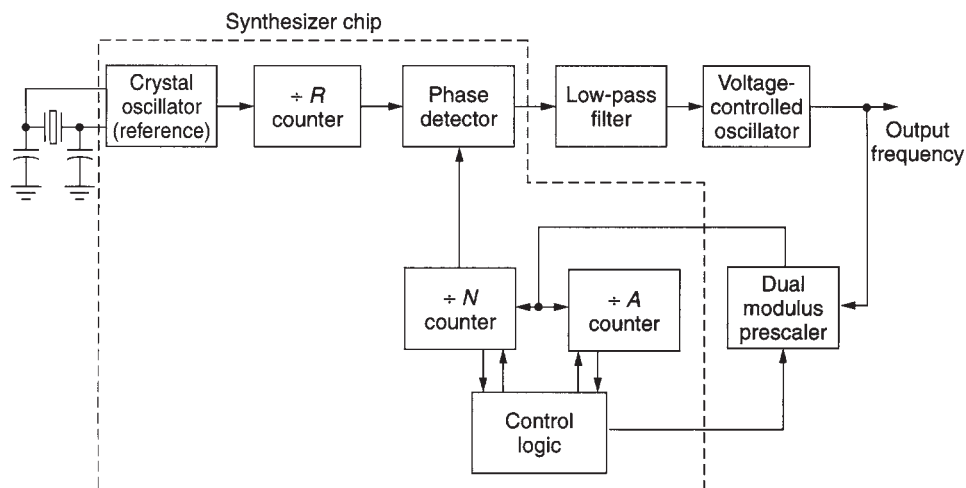


Figure 1. Block diagram of an integrated frequency synthesizer. In this case, the designer has control over the VCO and the loop filter; the reference oscillator is part of the chip. In most cases (up to 2.5 GHz), the dual-modulus prescaler is also inside the chip.

also combinations of techniques that I would like to refer to as “hybrid synthesizers.” They will be covered here.

The quality of the system, or signal generator, is determined by the properties of the synthesizer and, of course, its building blocks. There are a variety of parameters in characterizing the synthesizer. To name a few important ones, we need to worry about the frequency stability, spurious suppression, and phase noise characteristics. The frequency resolution of the synthesizer tends to be covered by the switching speed and its spurious response. A lot of research is put into developing the ideal synthesizer, whatever ideal means. For portable applications such as cellphones, size and power consumption are real issues, as well as the cost of the system. As mentioned, there are several competing approaches. In particular, there is a race between the fractional-*N* division synthesizer and the direct digital synthesis. The fractional synthesizer allows for generation of the output frequencies, which are not exact integers of the reference frequency. This results in an average frequency and problems with spurious sidebands. The direct digital synthesis uses a look-up table to construct a sine wave, and the size of the lookup table and the sample rate determine the quality of the signal and its output frequency.

2. FREQUENCY SYNTHESIZER FUNDAMENTALS

There are several approaches to “synthesize” a frequency, as we already mentioned. Probably the first and the oldest approach is the direct frequency synthesis, where a bank of crystals, as frequency standards, will be used to generate output frequencies. Such a system is called “frequency-incoherent.” There is no phase coherency among the various oscillators [8].

A simple example of direct synthesis is shown in Fig. 2. The new frequency $\frac{2}{3} f_0$ is realized from f_0 by using a divide-by-3 circuit, a mixer, and a bandpass filter. In this example, $\frac{2}{3} f_0$ has been synthesized by operating directly on f_0 .

Figure 3 illustrates the form of direct synthesis module most frequently used in commercial frequency synthesizers of the direct form. The method is referred to as the “double-mix-divide” approach.

An input frequency f_{in} is combined with a frequency f_1 , and the upper frequency $f_1 + f_{in}$ is selected by the bandpass filter. This frequency is then mixed with a switch-selectable frequency $f_2 + f^*$ (in the following, f^* refers to any one of 10 switch-selectable frequencies). The output of the second mixer consists of the two frequencies $f_{in} + f_1 + f_2 + f^*$ and $f_{in} + f_1 - f_2 - f^*$; only the higher frequency term appears at the output of the bandpass filter. If the

frequencies f_{in} , f_1 , and f_2 are selected so that

$$f_{in} + f_1 + f_2 = 10f_{in} \tag{1}$$

then the frequency at the output of the divide by 10 will be

$$f_{out} = f_{in} + \frac{f^*}{10} \tag{2}$$

The double-mix-divide module has increased the input frequency by the switch-selectable frequency increment $f^*/10$. These double-mix-divide modules can be cascaded to form a frequency synthesizer with any degree of resolution. The double-mix-divide modular approach has the additional advantage that the frequencies f_1 , f_2 , and f_{in} can be the same in each module, so that all modules can contain identical components.

A direct frequency synthesizer with three digits of resolution is shown in Fig. 4. Each decade switch selects one of 10 frequencies $f_2 + f^*$. In this example, the output of the third module is taken before the decade divider.

For example, it is possible to generate the frequencies between 10 and 19.99 MHz (in 10-kHz increments), using the three module synthesizer, by selecting

$$f_{in} = 1 \text{ MHz}$$

$$f_1 = 4 \text{ MHz}$$

$$f_2 = 5 \text{ MHz}$$

As

$$f_{in} + f_1 + f_2 = 10 f_{in} \tag{3}$$

the output frequency will be

$$f_0 = 10 f_{in} = f_3^* + \frac{f_2^*}{10} + \frac{f_1^*}{100} \tag{4}$$

As f^* occurs in 1-MHz increments, $f_1^*/100$ will provide the desired 10-kHz frequency increments.

Theoretically, either f_1 or f_2 could be eliminated provided that

$$f_{in} + f_1 \text{ (or } f_2) = 10f_{in} \tag{5}$$

but the additional frequency is used in practice to provide additional frequency separation at the mixer output. This frequency separation eases the bandpass filter requirements. For example, if f_2 is eliminated, $f_1 + f_{in}$ must equal $10f_{in}$ or 10 MHz. If an f_1^* of 1 MHz is selected, the output of the first mixer will consist of the two frequencies 9 and

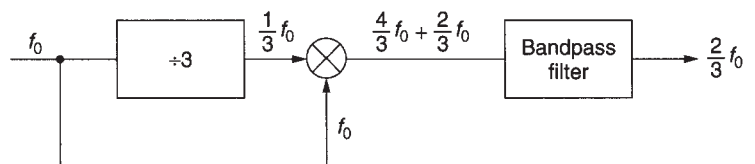


Figure 2. Direct frequency generation using the mix-and-divide principle. It requires excessive filtering.

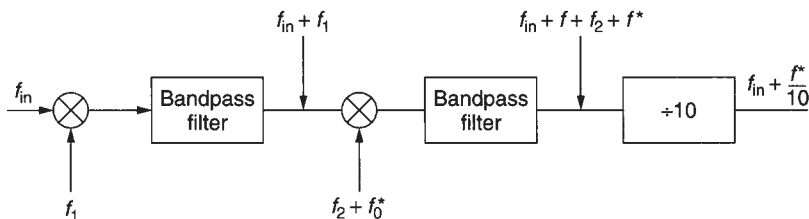


Figure 3. Direct frequency synthesizer using a mix-and-divide technique to obtain identical modules for high resolution.

11 MHz. The lower of these closely spaced frequencies must be removed by the filter. The filter required would be extremely complex. If, instead, a 5-MHz signal f_2 is also used so that $f_{in} + f_1 + f_2 = 10$ MHz, the two frequencies at the first mixer output will (for an f_1^* of 1 MHz) be 1 and 11 MHz. In this case, the two frequencies will be much easier to separate with a bandpass filter. The auxiliary frequencies f_1 and f_2 can be selected in each design only after considering all possible frequency products at the mixer output.

Direct synthesis can produce fast frequency switching, almost arbitrarily fine frequency resolution, low phase noise, and the highest-frequency operation of any of the methods. Direct frequency synthesis requires considerably more hardware (oscillators, mixers, and bandpass filters) than do the two other synthesis techniques to be described. The hardware requirements result in direct synthesizers being larger and more expensive. Another disadvantage of the direct synthesis technique is that unwanted (spurious) frequencies can appear at the output. The wider the frequency range, the more likely that the spurious components will appear in the output. These disadvantages are offset by the versatility, speed, and flexibility of direct synthesis.

2.1. PLL Synthesizer

The most popular synthesizer is based on PLL [9]. An example of such a PLL-based synthesizer is shown in Fig. 5. In preparing ourselves for hybrid synthesizers, it needs to be noted that the frequency standard can also be replaced

by a direct digital synthesizer (DDS). The number of references for synthesizers seems endless, but the most complete and relevant ones are given at the end. It's also very important to monitor the patents. If any incremental improvements are achieved there, the inventors immediately try to protect them with a patent. The following will give some insight into the major building blocks used for PLL and hybrid synthesizers. It should be noted that most designers use a combination of available integrated circuits, and most of the high-performance solutions are due to the careful design of the oscillator, the integrated/low-pass filter, and the systems architecture. All of these items will be addressed, particularly the fractional- N synthesizer, which requires a lot of handholding in the removal of spurious products. How does the PLL work? According to Fig. 5, we have a free-running oscillator, which can operate anywhere from audio to millimeter wave. The output is typically sinusoidal. The VCO also is occasionally called a VTO (voltage-tuned oscillator), which drives an output stage and a pulseshaping stage to prepare the signal to drive a frequency divider chain. The frequency divider chain consists of silicon germanium or GaAs dividers to reduce the signal below 1000 MHz. At these frequencies, either silicon-based dividers or CMOS dividers can take over. The frequency divider, typically part of an integrated circuit, is a synchronous divider, which is programmable over a large range. Division ratios as low as four and as high as one million are possible [10].

The output of the frequency divider is fed to a phase comparator, which in most cases is actually a phase-frequency detector. The phase-frequency detector compares

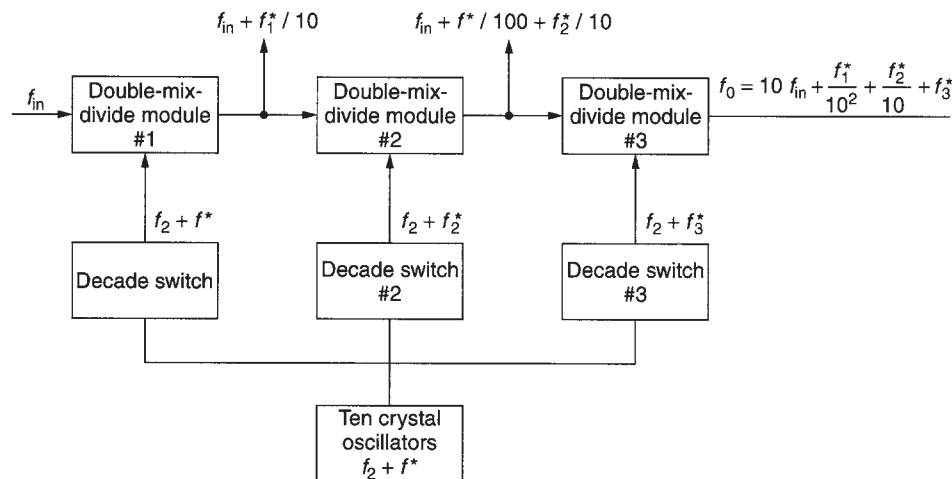


Figure 4. Phase-incoherent frequency synthesizer with three-digit resolution.

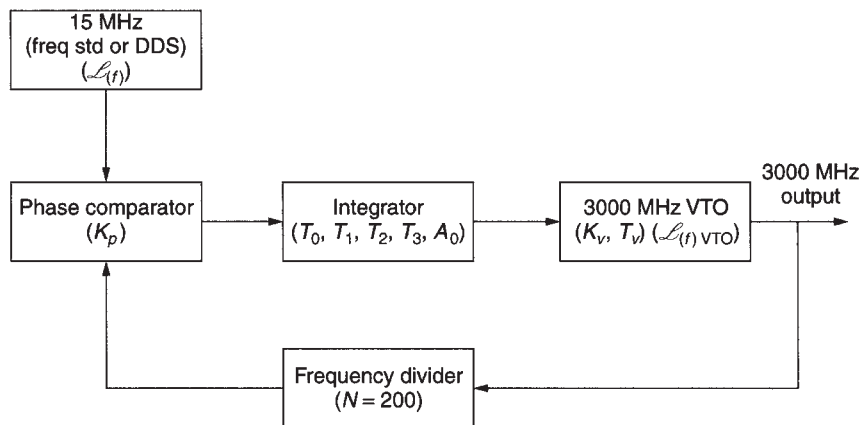


Figure 5. Block diagram of a PLL synthesizer driven by a frequency standard, DDS, or fractional-*N* synthesizer for high resolution at the output. The last two standards allow a relatively low division ratio and provide quasiarbitrary resolution.

the output of the frequency divider, which typically is the same magnitude as the reference frequency, with a reference frequency, which is derived from a frequency standard. Frequency standards come as precision standards such as atomic frequency standards, followed by oven-controlled crystal oscillators, to temperature-compensated crystal oscillators. Sometimes even simple crystal oscillators will do the trick. The output from the phase comparator is a dc voltage typically between 1 and 25 V, which is applied to the tuning diode of the VTO or VCO. This tuning voltage is modulated by the differences of the two prior to lock. The frequency detector portion of the phase-frequency comparator jams the voltage to one extreme, charging the capacitors and integrator and acquiring frequency lock. After frequency lock is obtained, the control voltage will change the frequency at the output to have a fixed phase relationship compared to the reference frequency. The advantage of having a frequency detector in parallel to a phase detector is that the system always requires frequency lock [11,12].

2.2. Fractional-*N* Phase-Locked Loops

The principle of the fractional-*N* PLL synthesizer has been around for a while. In the past, implementation of this has been done in an analog system [13,14]. It would be ideal to be able to build a single-loop synthesizer with a 1.25-MHz or 50-MHz reference and yet obtain the desired stepsize resolution, such as 25 kHz. This would lead to the much smaller division ratio and much better phase noise performance. Figure 6 shows the block of an analog fractional-*N* synthesizer.

An alternative would be for *N* to take on fractional values. The output frequency could then be changed in fractional increments of the reference frequency. Although a digital divider cannot provide a fractional division ratio, ways can be found to accomplish the same task effectively.

The most frequently used method is to divide the output frequency by *N* + 1 every *M* cycles and to divide by *N* the rest of the time. The effective division ratio is then

N + 1/*M*, and the average output frequency is given by

$$f_0 = \left(N + \frac{1}{M} \right) f_r \tag{6}$$

This expression shows that *f*₀ can be varied in fractional increments of the reference frequency by varying *M*. The technique is equivalent to constructing a fractional divider, but the fractional part of the division is actually implemented using a phase accumulator. The phase accumulator approach is illustrated in Section 6. This method can be expanded to frequencies much higher than 6 GHz using the appropriate synchronous dividers. For more details, see Section 6 [15–53].

2.3. Digital Direct Frequency Synthesizer

The digital direct frequency uses sampled data methods to produce waveforms [54–69].

The digital hardware block provides a datastream of *K* bits per clock cycle for DAC. Ideally, the DAC is a linear device with glitch-free performance. The practical limits of the DAC will be discussed later in this article. The DAC output is the desired signal plus replications of it around the clock frequency and all of the clock’s harmonics. Also

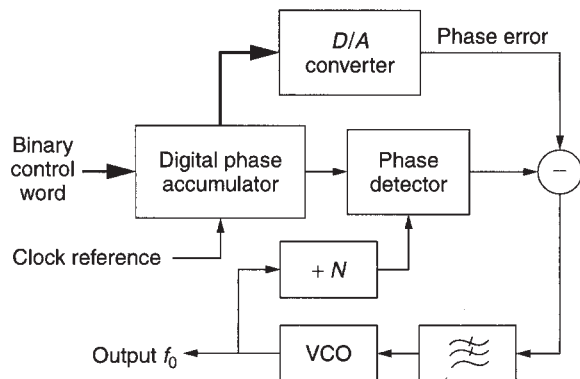


Figure 6. Simplified block diagram of an analog fractional-*N* synthesizer.

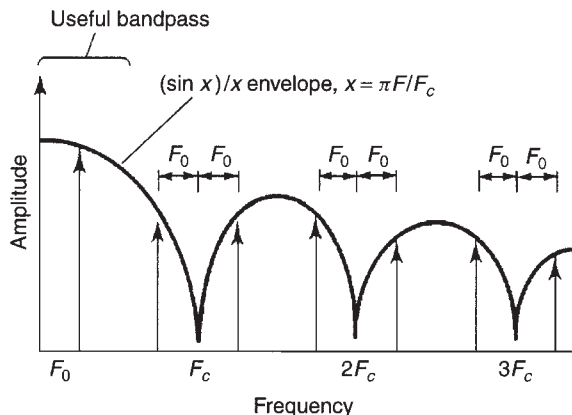


Figure 7. Ideal DAC output with F_0 , a sampled-and-held sine wave, at its output. Notice the $(\sin x)/x$ envelope rolloff. As F_0 moves up in frequency, an aliased component $F_c - F_0$ moves down into the passband.

present in the DAC output signal is a small amount of quantization noise from the effects of finite math in the hardware block. Figure 7 shows the frequency spectrum of an ideal DAC output with a digitally sampled sine-wave datastream at its input. Note that the desired signal, F_0 (a single line in the frequency domain), is replicated around all clock terms. Figure 8 shows the same signal in the time domain.

The DAC performs a sample-and-hold operation as well as converting digital values to analog voltages. The sample occurs on each rising edge of the clock; the hold occurs during the clock period. The transfer function of a sample-and-hold operator is a $(\sin x)/x$ envelope response with linear phase. In this case, $x = (\pi F/F_{\text{clock}})$.

It should be noted that the sinc function rolloff affects the passband flatness. A 2.4 dB should be expected at 40% of F_{clock} .

Referring to Fig. 9, the output of the DAC is passed through a lowpass filter (LPF). With proper attention to design, an LPF may be realized that has linear phase in a flat passband with width of $0.4F_{\text{clock}}$. With this design, the maximum available bandwidth is achieved. For example,

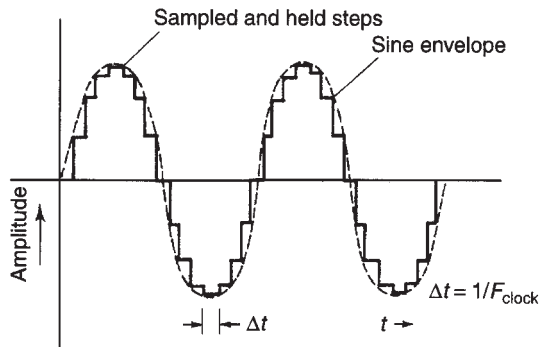


Figure 8. Samples/cycle sine wave. This is typical of a single-tone DAC output. $F_0 = F_{\text{clock}}/16$ after lowpass filtering; only the sine envelope is present. The LPF removes the sampling energy. Each amplitude step is held for a clock period.

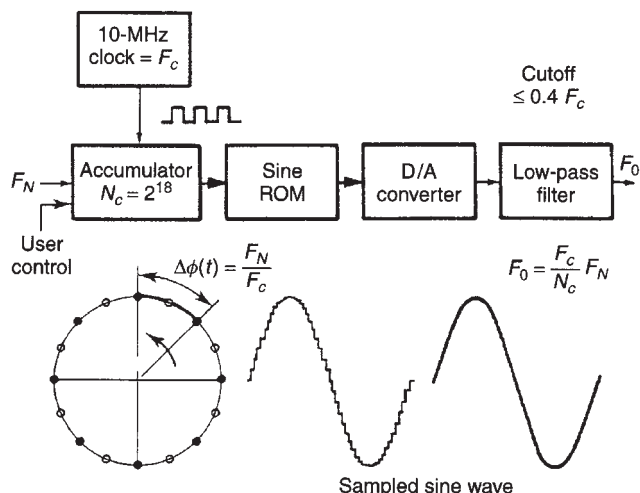


Figure 9. Direct digital frequency synthesizer.

with $F_{\text{clock}} = 125 \text{ MHz}$, the useful synthesized bandwidth of about 50 MHz is attained. The LPF output is the desired signal without any sampling artifacts. Viewing the LPF strictly as a device to remove sampling energy, it is obvious why the output contains only the desired signal. It is also instructive to view the LPF from the time domain. From this point, the LPF may be seen as the perfect interpolator. It fills the space between time samples with a smooth curve to reconstruct perfectly the desired signal.

In the design of a DDS, the following guidelines apply:

- The desired frequency resolution determines the lowest output frequency f_L .
- The number of D/A conversions used to generate f_L is $N = 4k = 4f_U/f_L$ provided that four conversions are used to generate f_U ($P = 4$).
- The maximum output frequency f_U is limited by the maximum sampling rate of the DDS, $f_U \leq \frac{1}{4}T$. Conversely, $T \leq \frac{1}{4}f_U$.

To generate nf_L , the integer n addresses the register, and each clock cycle kn is added to the content of the accumulator so that the content of the memory address register is increased by kn . Each kn th point of the memory is addressed, and the content of this memory location is transferred to the D/A converter to produce the output sampled waveform.

To complete the DDS, the memory size and length (number of bits) of the memory word must be determined. The wordlength is determined by system noise requirements. The amplitude of the D/A output is that of an exact sinusoid corrupted with the deterministic noise due to truncation caused by the finite length of the digital words (quantization noise). If an $(n + 1)$ -bit wordlength (including one sign bit) is used and the output of the A/D converter varies between ± 1 , the mean noise from the quantization will be

$$\rho^2 = \frac{1}{12} \left(\frac{1}{2}\right)^{2n} = \frac{1}{3} \left(\frac{1}{2}\right)^{2(n+1)} \tag{7}$$

The mean noise is averaged over all possible waveforms. For a worst-case waveform, the noise is a square wave with amplitude $\frac{1}{2}(\frac{1}{2})^n$ and $\rho^2 = \frac{1}{4}(\frac{1}{2})^{2n}$. For each bit added to the wordlength, the spectral purity improves by 6 dB.

The main drawback of a low-power DDS is that it is limited to relatively low frequencies. The upper frequency is directly related to the maximum usable clock frequency; today, the limit is about 1 GHz. DDS tends to be noisier than other methods, but adequate spectral purity can be obtained if sufficient lowpass filtering is used at the output. DDS systems are easily constructed using readily available microprocessors. The combination of DDS for fine frequency resolution plus other synthesis techniques to obtain higher-frequency output can provide high resolution with very rapid setting time after a frequency change. This is especially valuable for frequency-hopping spread-spectrum systems.

In analyzing both the resolution and signal-to-noise ratio (or rather signal-to-spurious performance) of the DDS, one has to know the resolution and input frequencies. As an example, if the input frequency is approximately 35 MHz and the implementation is for a 32-bit device, the frequency resolution compared to the input frequency is $35\text{E}6 \div 2^{32} = 35\text{E}6 \div 4.294967296\text{E}9$ or $0.00815\text{Hz} \approx 0.01\text{Hz}$. Given the fact that modern shortwave radios with a first IF of about 75 MHz will have an oscillator between 75 and 105 MHz, the resolution at the output range is more than adequate. In practice, one would use the microprocessor to round it to the next increment of 1 Hz relative to the output frequency.

As to the spurious response, the worst-case spurious response is approximately $20 \log 2^R$, where R is the resolution of the digital/analog converter. For an 8-bit A/D converter, this would mean approximately 48 dB down (worst case), as the output loop would have an analog filter to suppress close-in spurious noise. Modern devices

have a 14-bit resolution. Fourteen bits of resolution can translate into $20 \log 2^{14}$ or 80 dB, worse case, of suppression. The actual spurious response would be much better. The current production designs for communication applications, such as shortwave transceivers, despite the fact that they are resorting to a combination of PLLs and DDSs, still end up somewhat complicated. By using 10 MHz from the DDS and using a single-loop PLL system, one can easily extend the operation to above 1 GHz but with higher complexity and power consumption. This was shown in Fig. 5. Figure 10 shows a multiple loop synthesizer using a DDS for fine resolution.

3. IMPORTANT CHARACTERISTICS OF SYNTHESIZERS

The following sections list the parameters used to describe the performance of the synthesizer. These are referred to as *figures of merit*.

3.1. Frequency Range

The output frequency of a synthesizer can vary over a wide range. A synthesizer signal generator typically offers output frequencies from as low as 100 kHz to as high as several gigahertz. The frequency range is determined by the architecture of the signal generator as the system frequently uses complex schemes of combining frequencies in various loops. A standard loop-based synthesizer has a frequency range typically less than 1–2, as an example, 925–1650 MHz.

3.2. Phase Noise

Oscillators unfortunately are not clean, but the various noise sources in and outside of the transistor modulate the VCO, resulting in energy or spectral distribution on both

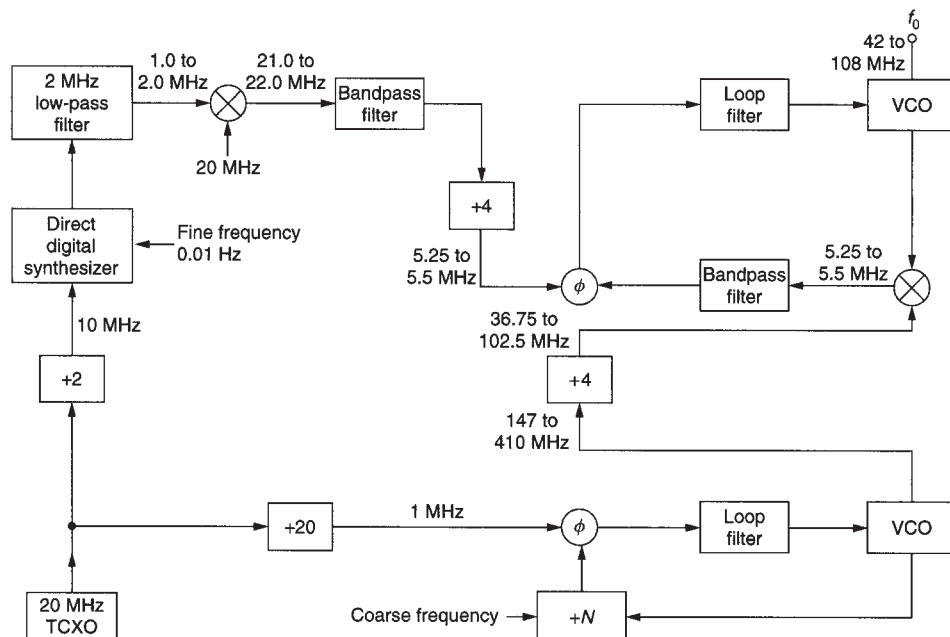


Figure 10. A multiple-loop synthesizer using a DDS for fine resolution.

sides of the carrier. This occurs via modulation and conversion. The noise, or better, FM noise is expressed as the ratio of output power divided by the noise power relative to 1 Hz bandwidth measured at an offset of the carrier. Figure 11 shows a typical phase noise plot of a synthesizer. Inside the loop bandwidth, the carrier signal is cleaned up, and outside the loop bandwidth, the measurement predicts the performance of the VCO itself.

3.3. Output Power

The output power is measured at the designated output port of the frequency synthesizer. Practical designs require an isolation stage. Typical designs require one or more isolation stages between the oscillator and the output. The output power needs to be flat. Although the synthesized generator typically is flat with only 0.1-dB \pm deviation, the VCO can vary as much as ± 2 dB over the frequency range.

3.4. Harmonic Suppression

The VCO inside a synthesizer has a typical harmonic suppression of better than 15 dB. For high-performance applications, a set of lowpass filters at the output will reduce the harmonic contents to a desired level. Figure 12 shows a typical output power plot of a VCO.

3.5. Output Power as a Function of Temperature

All active circuits vary in performance as a function of temperature. The output power of an oscillator over a temperature range should vary less than a specified value, such as 1 dB.

3.6. Spurious Response

Spurious outputs are signals found around the carrier of a synthesizer that are not harmonically related. Good, clean synthesizers need to have a spurious-free range of 90 dB, but these requirements make them expensive. Although

oscillators typically have no spurious frequencies besides possibly 60 and 120 Hz pickup, the digital electronics in a synthesizer generate a lot of signals, and when modulated on the VCO, are responsible for these unwanted output products. (See also Fig. 11).

3.7. Stepsize

The resolution, or stepsize, is determined by the architecture.

3.8. Frequency Pushing

Frequency pushing characterizes the degree to which an oscillator’s frequency is affected by its supply voltage. For example, a sudden current surge caused by activating a transceiver’s RF power amplifier may produce a spike on the VCO’s DC power supply and a consequent frequency jump. Frequency pushing is specified in frequency/voltage form and is tested by varying the VCO’s DC supply voltage (typically ± 1 V) with its tuning voltage held constant.

3.9. Sensitivity to Load Changes

To keep manufacturing costs down, many wireless applications use a VCO alone, without the buffering action of a high reverse-isolation amplifier stage. In such applications, frequency pulling, the change of frequency resulting from partially reactive loads, is an important oscillator characteristic. Pulling is commonly specified in terms of the frequency shift that occurs when the oscillator is connected to a load that exhibits a nonunity VSWR (such as 1.75, usually referenced to 50 Ω), compared to the frequency that results with unity-VSWR load (usually 50 Ω). Frequency pulling must be minimized, especially in cases where power stages are close to the VCO unit and short pulses may affect the output frequency. Such poor isolation can make phase locking impossible.

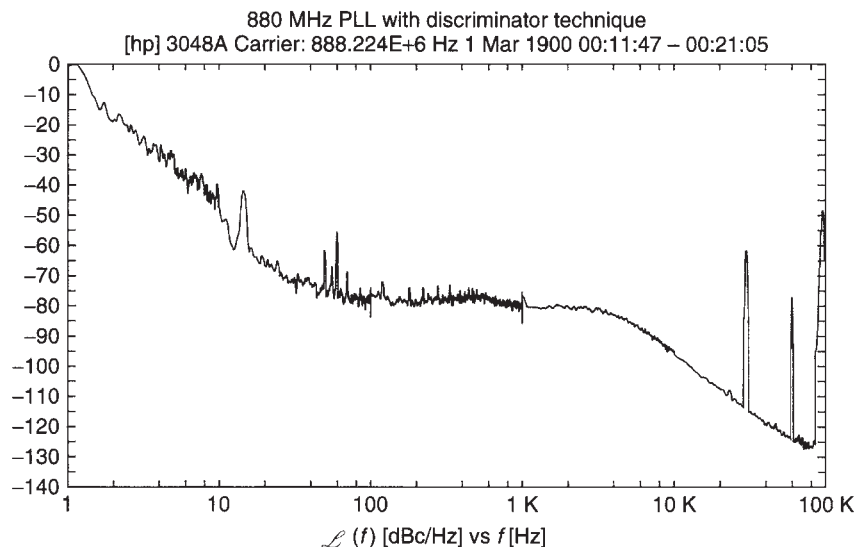


Figure 11. Measured phase noise of an 880-MHz synthesizer using a conventional synthesizer chip.

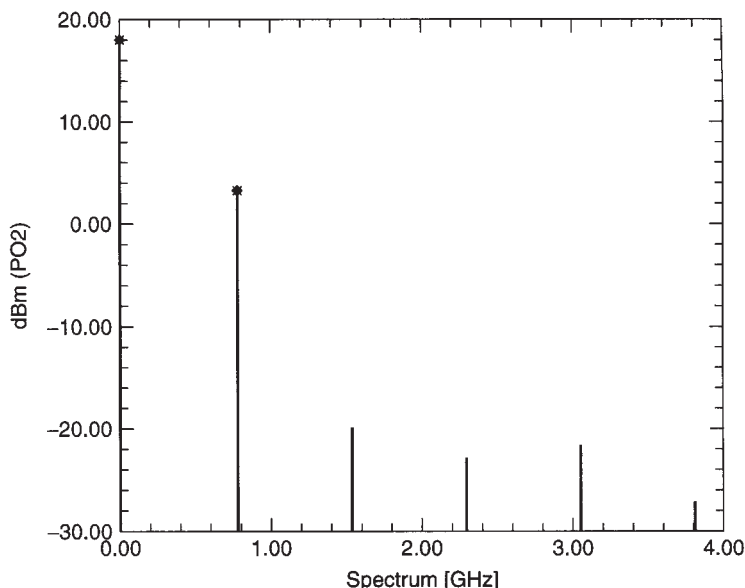


Figure 12. Predicted harmonics at the output of a VCO.

3.10. Tuning Sensitivity

This is a VCO parameter also expressed in frequency/volt- age and is not part of a synthesizer specification.

3.11. Posttuning Drift

After a voltage step is applied to the tuning diode input, the oscillator frequency may continue to change until it settles to a final value. Posttuning drift is one of the pa- rameters that limits the bandwidth of the VCO input.

3.12. Tuning Characteristic

This specification shows the relationship, depicted as a graph, between the VCO operating frequency and the tun- ing voltage applied. Ideally, the correspondence between operating frequency and tuning voltage is linear.

3.13. Tuning Linearity

For stable synthesizers, a constant deviation of frequency versus tuning voltage is desirable. It is also important to make sure that there are no breaks in tuning range, for example, that the oscillator does not stop operating with a tuning voltage of 0 V.

3.14. Tuning Sensitivity and Tuning Performance

These data, typically expressed in megahertz per volt (MHz/V), characterize how much the frequency of a VCO changes per unit of tuning voltage change.

3.15. Tuning Speed

This characteristic is defined as the time necessary for the VCO to reach 90% of its final frequency on the application of a tuning voltage step. Tuning speed depends on the in-

ternal components between the input pin and the tuning diode, including, among other things, the capacitance present at the input port. The input port’s parasitic ele- ments determine the VCO’s maximum possible modula- tion bandwidth.

3.16. Power Consumption

This characteristic conveys the DC power, usually speci- fied in milliwatts and sometimes qualified by operating voltage, required by the oscillator to function properly [70].

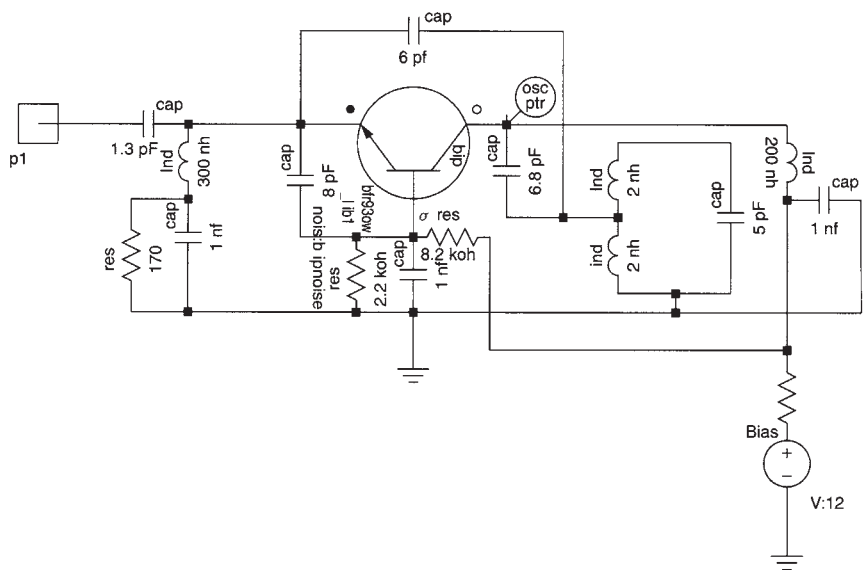
4. BUILDING BLOCKS OF SYNTHESIZERS

4.1. Oscillator

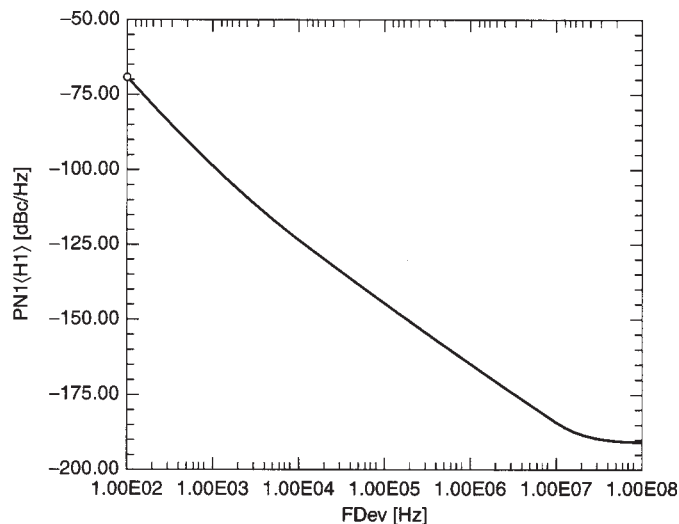
An oscillator is essentially an amplifier with sufficient feedback so that the amplifier becomes unstable and be- gins oscillation. The oscillator can be divided into an am- plifier, a resonator, and a feedback system [71]. One of the most simple equations describes this. It describes the in- put admittance of an amplifier with a tuned circuit at the output described by the term Y_L :

$$Y_{11}^* = Y_{11} - \frac{Y_{12} \times Y_{21}}{Y_{22} + Y_L} \tag{8}$$

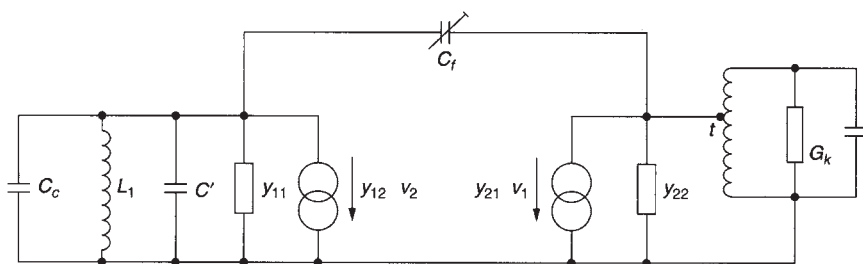
The feedback is determined by the term Y_{12} , or in practical terms, by the feedback capacitor. The transistor oscillator (Fig. 13a) contains a grounded base circuit. For this type of oscillator, using microwave transistors, the emitter and collector currents are in phase. That means that the input circuit of the transistor needs to adjust the phase of the oscillation. The transistor stage forms the amplifier, the tuned resonator at the output determines the frequency of oscillation, and the feedback capacitor provides enough energy back into the transistor so that oscillation can



(a)



(b)



(c)

Figure 13. (a) A grounded base VHF/UHF oscillator with a tuned resonator tapped in the middle to improve operational Q ; (b) the predicted phase noise of the oscillator in Fig. 13a; (c) the equivalent circuit of the oscillator configuration of Fig. 13a. For the grounded base configuration, emitter and collector currents have to be in phase. The phase shift introduced by C_f is compensated by the input tuned circuit.

occur. To start oscillation, the condition, relative to the output, can be derived in a similar fashion from the input:

$$Y_{22}^* = (Y_{22} + Y_L) - \frac{Y_{12} \times Y_{21}}{Y_{11} + Y_T} \quad (9)$$

If the second term of the equation on the right side is larger than the first term on the right of the = sign, then $\text{Re}(Y_{22}^*)$ is negative and oscillation at the resonant frequency occurs.

This oscillator circuit is good for low-frequency applications, but the Colpitts oscillator is preferred for

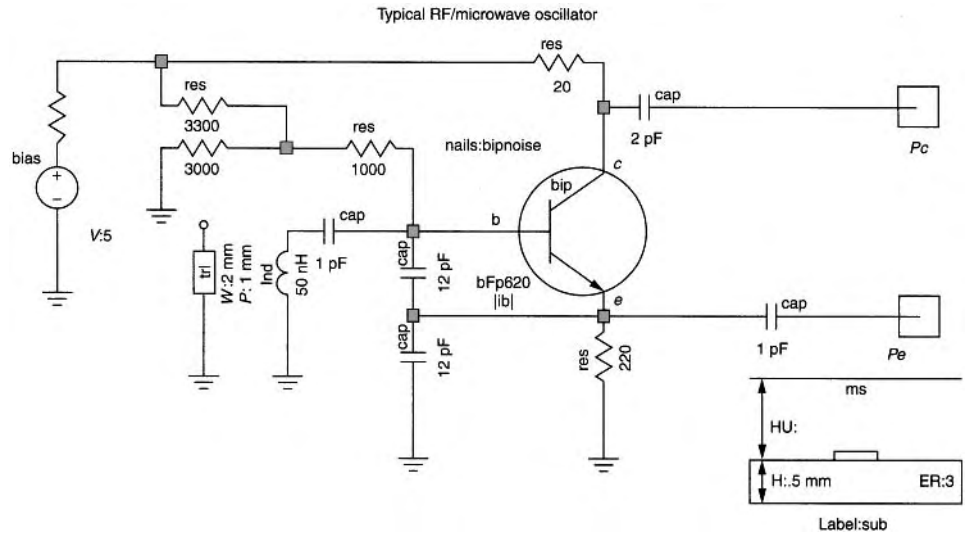


Figure 14. Colpitts oscillator using a coil inductor or a transmission line as a resonator. In this case, all the physical parameters of the transmission line have to be provided.

higher frequencies. The Colpitts oscillator works by rotating this circuit and grounds the collector instead of the base. The advantage of the Colpitts oscillator is the fact that it is an emitter follower amplifier with feedback and shows a more uniform gain of a wider frequency range (see Fig. 14). Oscillators with a grounded emitter or source have more stability difficulties over wider frequency ranges.

Depending on the frequency range, there are several resonators available. For low frequencies up to about 500 MHz, lumped elements such as inductors are useful. Above these frequencies, transmission-line-based resonators are microwave resonators, which are better. Very small oscillators use printed transmission lines. High-performance oscillators use ceramic resonators (CROs), dielectric resonators (DROs), and surface acoustical wave resonators (SAWs), to name only a few. The frequency standard, if not derived from an atomic frequency standard, is typically a crystal oscillator. Even the atomic frequency standards synchronize a crystal against an atomic resonance to compensate for the aging of the crystal. Figure 15a shows a circuit of a crystal oscillator with typical component values that are based on a 10-MHz third overtone AT cut crystal. Q is the ratio of stored energy divided by dissipated energy. The Q of the crystal can be as high as one million. The figure of merit Q is defined by $\omega L/R$. In our case, $\omega L/R$ is

$$\frac{2\pi \times 1Hy \times 10E6}{50} = 1.25 \text{ million}$$

Therefore, the resulting Q is 1.25 million. Typical resonator Q values for LC oscillators are 200; for structure-based resonators like ceramic resonators or dielectric resonators, Q values of 400 are not uncommon.

An oscillator operating at 700 MHz is shown in Fig. 15a, including its schematic. CAD simulation was used to determine the resonance frequency phase noise and the harmonic contents, shown in Fig. 15b. The output power

can be taken off either the emitter, the emitter that provides better harmonic filtering, or from the collector that provides smaller interaction between the oscillator frequency and the load. This effect is defined as frequency pulling. The tuned capacitor can now be replaced by a voltage-dependent capacitor. A tuning diode is a diode operated in reverse. Its PN-junction capacitance changes as a function of applied voltage.

A two-port oscillator analysis will now be presented. It is based on the fact that an ideal tuned circuit (infinite Q), once excited, will oscillate infinitely because there is no resistance element present to dissipate the energy. In the actual case where the inductor Q is finite, the oscillations die out because energy is dissipated in the resistance. It is the function of the amplifier to maintain oscillations by supplying an amount of energy equal to that dissipated. This source of energy can be interpreted as a negative resistor in series with the tuned circuit. If the total resistance is positive, the oscillations will die out, while the oscillation amplitude will increase if the total resistance is negative. To maintain oscillations, the two resistors must be of equal magnitude. To see how a negative resistance is realized, the input impedance of the circuit in Fig. 16 will be derived.

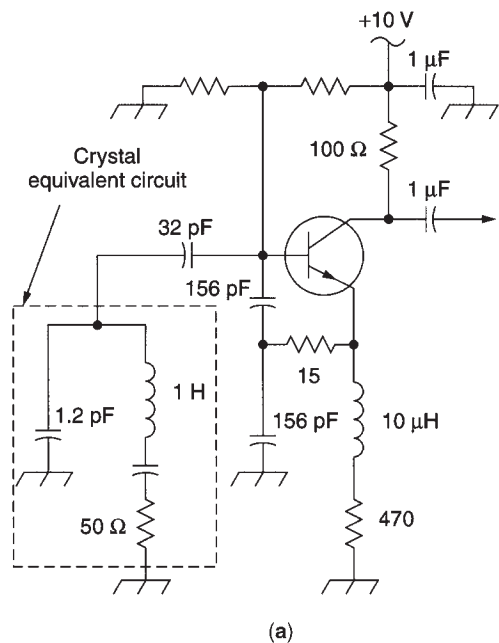
If Y_{22} is sufficiently small ($Y_{22} \ll 1/R_L$), the equivalent circuit is as shown in Fig. 16. The steady-state loop equations are

$$V_{in} = I_{in}(X_{C1} + X_{C2}) - I_b(X_{C1} - \beta X_{C2}) \tag{10}$$

$$0 = -I_{in}(X_{C1}) + I_b(X_{C1} + h_{ie}) \tag{11}$$

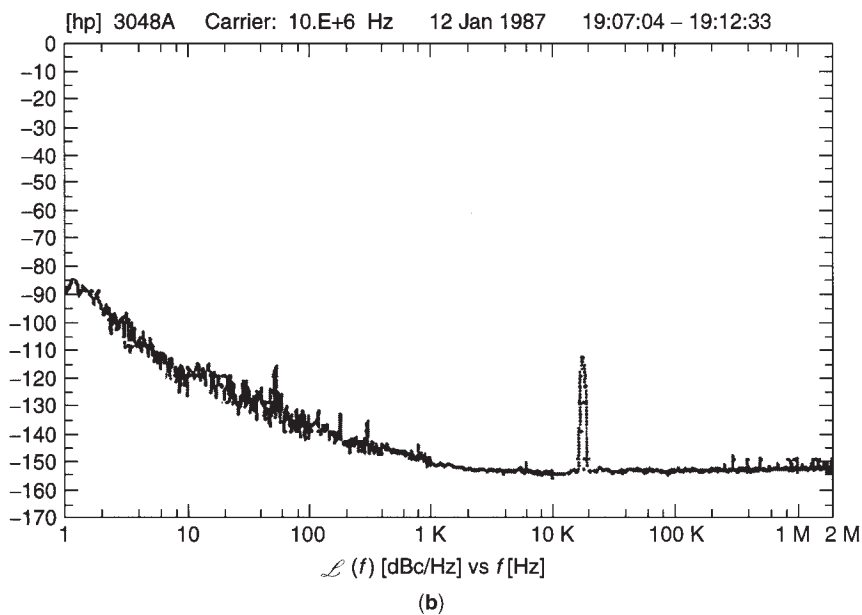
After I_b is eliminated from these two equations, Z_{in} is obtained as

$$Z_{in} = \frac{V_{in}}{I_{in}} = \frac{(1 + \beta)X_{C1}X_{C2} + h_{ie}(X_{C1} + X_{C2})}{X_{C1} + h_{ie}} \tag{12}$$



(a)

Typical-noise curve for R 10 MHz frequency standard



(b)

Figure 15. (a) Abbreviated circuit of a 10-MHz crystal oscillator; (b) measured phase noise for this frequency standard by HP of Fig. 15a.

If $X_{C_1} \ll h_{ie}$, the input impedance is approximately equal to

$$Z_{in} \approx \frac{1 + \beta}{h_{ie}} X_{C_1} X_{C_2} + (X_{C_1} + X_{C_2}) \quad (13)$$

$$Z_{in} \approx \frac{-g_m}{\omega^2 C_1 C_2} + \frac{1}{j\omega [C_1 C_2 / (C_1 + C_2)]} \quad (14)$$

That is, the input impedance of the circuit shown in Fig. 17 is a negative resistor,

$$R = \frac{-g_m}{\omega^2 C_1 C_2} \quad (15)$$

in series with a capacitor,

$$C_{in} = \frac{C_1 C_2}{C_1 + C_2} \quad (16)$$

which is the series combination of the two capacitors.

With an inductor L (with the series resistance R_S) connected across the input, it is clear that the condition for sustained oscillation is

$$R_S = \frac{g_m}{\omega^2 C_1 C_2} \quad (17)$$

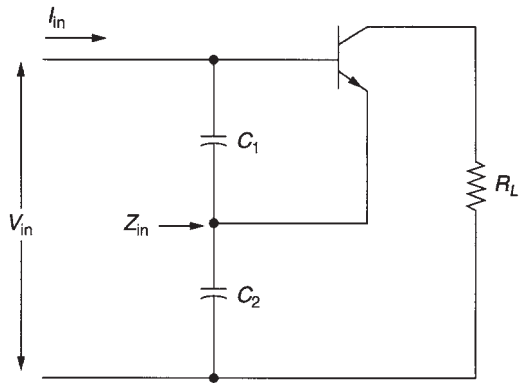


Figure 16. Calculation of input impedance of the negative-resistance oscillator.

and the frequency of oscillation is

$$f_o = \frac{1}{2\pi\sqrt{L[C_1C_2/(C_1 + C_2)]}} \tag{18}$$

This interpretation of the oscillator readily provides several guidelines that can be used in the design. First, C_1 should be as large as possible so that

$$X_{C_1} \ll h_{ie} \tag{19}$$

and C_2 is to be large so that

$$X_{C_2} \ll \frac{1}{Y_{22}} \tag{20}$$

When these two capacitors are large, the transistor base-to-emitter and collector-to-emitter capacitances will have a negligible effect on the circuit's performance. However, there is a maximum value of the capacitances because

$$r \leq \frac{g_m}{\omega^2 C_1 C_2} \leq \frac{G}{\omega^2 C_1 C_2} \tag{21}$$

where G is the maximum value of g_m . For a given product of C_1 and C_2 , the series capacitance is at maximum when

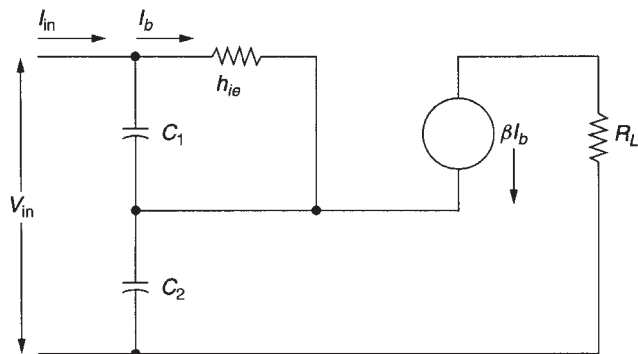


Figure 17. Equivalent small-signal circuit of Fig. 16.

$C_1 = C_2 = C_m$. Thus

$$\frac{1}{\omega C_m} > \sqrt{\frac{r}{G}} \tag{22}$$

Design rule:

$$C_2 = C_1 \times \left| \frac{Y_{21}}{Y_{11}} \right| \tag{23}$$

This equation is important in that it shows that for oscillations to be maintained, the minimum permissible reactance $1/\omega C_m$ is a function of the resistance of the inductor and the transistor's mutual conductance, g_m . Figure 18 shows the resonant and oscillation condition for optimum performance. The negative real value should occur at $X = 0$!

An oscillator circuit known as the *Clapp circuit* or *Clapp-Gouriet circuit* is shown in Fig. 19. This oscillator is equivalent to the one just discussed, but it has the practical advantage of being able to provide another degree of design freedom by making C_o much smaller than C_1 and C_2 .

It is possible to use C_1 and C_2 to satisfy the condition of Eq. (20) and then adjust C_o for the desired frequency of oscillation ω_o , which is determined from

$$\omega_o L - \frac{1}{\omega_o C_o} - \frac{1}{\omega_o C_1} - \frac{1}{\omega_o C_2} = 0 \tag{24}$$

Figure 20 shows the Clapp-Gouriet oscillator. Like the Colpitts, the Clapp-Gouriet obtains its feedback via a capacitive voltage divider; unlike the Colpitts, an additional capacitor series tunes the resonator. The Pierce oscillator, a configuration used only with crystals, is a rotation of the Clapp-Gouriet oscillator in which the emitter is at RF ground [72-75].

4.1.1. Phase Noise. An estimate of the noise performance of an oscillator is

$$\mathcal{L}(\omega_m) = \frac{1}{8} \frac{FkT}{P_{sav}} \frac{\omega_0^2}{\omega_m^2} \left(\frac{P_{in}}{\omega_0 W_e} + \frac{1}{Q_{unl}} + \frac{P_{sig}}{\omega_0 W_e} \right)^2 \left(1 + \frac{\omega_c}{\omega_m} \right)$$

Phase perturbation

Resonator Q

Flicker effect

Input power/reactive power ratio

Signal power/reactive power ratio

(25)

This equation is based on work done by Dieter Scherer of Hewlett-Packard about 1978. He was the first to introduce the flicker effect to the Leeson equation by adding the AM-to-PM conversion effect, which is caused by the nonlinear capacitance of the active devices [76]. Figure 21 shows details of the noise contribution. This equation must be

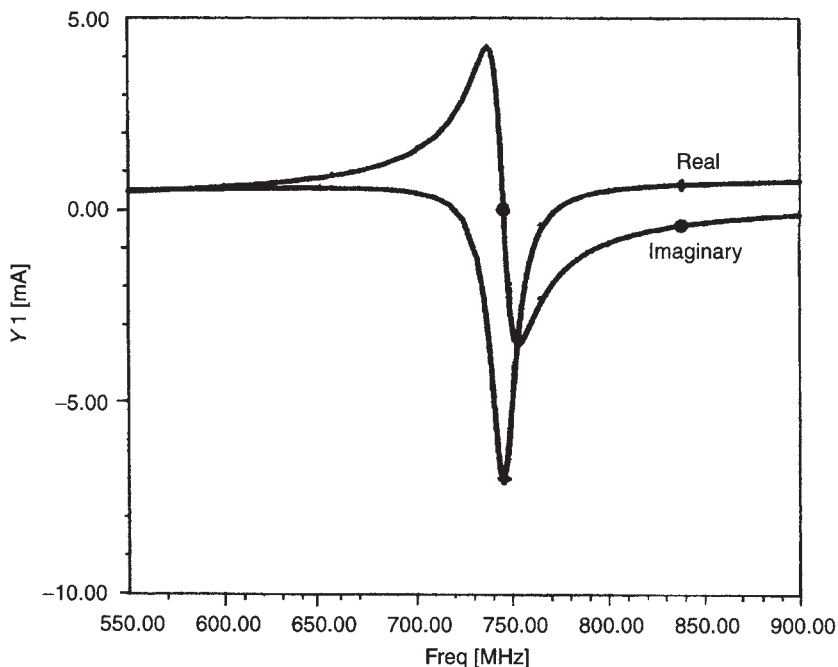


Figure 18. The CAD-based linearized currents. Conditions for oscillation are $X=0$ and $R<0$.

further expanded:

$$\mathcal{L}(f_m) = 10 \log$$

$$\times \left\{ \left[1 + \frac{f_0^2}{(2f_m Q_{load})^2} \right] \left(1 + \frac{f_c}{f_m} \right) \frac{FkT}{2P_{sav}} + \frac{2kTRK_0^2}{f_m^2} \right\} \quad (26)$$

where

$\mathcal{L}(f_m)$ = ratio of sideband power in 1 Hz bandwidth at f_m to total power in decibels

f_m = frequency offset

f_0 = center frequency

f_c = flicker frequency

Q_{load} = loaded Q of the tuned circuit

F = noise factor

kT = 4.1×10^{-21} at 300 K₀ (room temperature)

P_{sav} = average power at oscillator output

R = equivalent noise resistance of tuning diode (typically 200 Ω–10 kΩ)

K = oscillator voltage gain

Table 1 shows the flicker corner frequency f_c as a function of I_C for a typical small-signal microwave BJT. $I_{C(max)}$ of this transistor is about 10 mA.

Note that f_c , which is defined by AF and KF in the SPICE model, increases with I_C . This gives us a clue about how f_c changes when a transistor oscillates. As a result of the bias point shift that occurs during oscillation, an oscillating BJT's average I_C is higher than its small-signal I_C . KF is therefore higher for a given BJT operating as an oscillator than for the same transistor operating as a small-signal amplifier. This must be kept in mind when considering published f_c data, which are usually determined under small-signal conditions without being qualified as such. Determining a transistor's oscillating f_c is best done through measurement—operate the device as a high- Q UHF oscillator (we suggest using a ceramic-resonator-based tank in the vicinity of 1 GHz), and measure its close-in (10 Hz–10 kHz) phase noise versus offset from the carrier. f_c will correspond to a slight decrease in the slope of the phase noise versus offset curve. Generally, f_c varies with device type as follows: silicon JFETs, 50 Hz and higher;

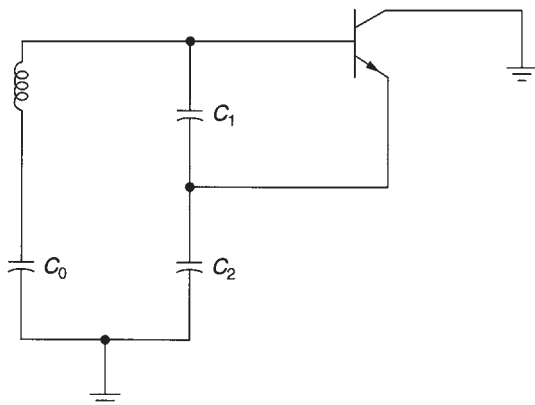


Figure 19. Circuit of a Clapp-Gouriet oscillator.

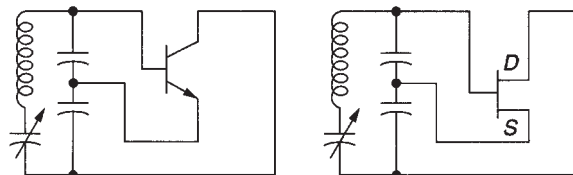


Figure 20. Clapp-Gouriet oscillator.

Table 1. Flicker Corner Frequency f_c as a Function of I_C

I_C (mA)	f_c (kHz)
0.25	1
0.5	2.74
1	4.3
2	6.27
5	9.3

Source: Motorola

microwave RF BJTs, 1–10 kHz (as above); MOSFETs, 10–100 kHz; GaAs FETs, 10–100 MHz. Figure 22 shows the phase noise of oscillators using different semiconductors and resonators.

The additional term introduces a distinction between a conventional oscillator and a VCO. Whether the voltage- or current-dependent capacitance is internal or external makes no difference; it simply affects the frequency.

For a more complete expression for a resonator oscillator’s phase noise spectrum, we can write

$$\begin{aligned}
 S_\phi(f_m) = & \frac{\alpha_R F_0^4 + \alpha_E \left(\frac{F_0}{2Q_L}\right)^2}{f_m^3} \\
 & + \frac{\left(\frac{2GFkT}{P_0}\right) \left(\frac{F_0}{2Q_L}\right)^2}{f_m^2} \\
 & + \frac{2\alpha_R Q_L F_0^3}{f_m^2} \\
 & + \frac{\alpha_E}{f_m} + \frac{2GFkT}{P_0}
 \end{aligned} \tag{27}$$

where

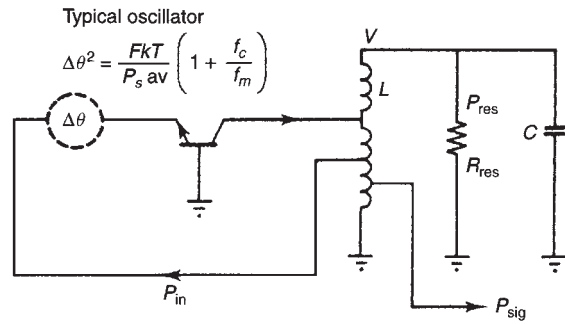
- G = compressed power gain of the loop amplifier
- F = noise factor of the loop amplifier
- k = Boltzmann’s constant
- T = temperature in Kelvin
- P_0 = carrier power level (in watts) at the output of the loop amplifier
- F_0 = carrier frequency in hertz
- f_m = carrier offset frequency in hertz

$Q_L (= \pi F_0 \tau_g)$ = loaded Q of the resonator in the feedback loop

α_R and α_E = flicker noise constants for the resonator and loop amplifier, respectively [77–86]

4.2. Frequency Divider

The output from the VCO has to be divided down to the reference frequency. The reference frequency can vary from a few kilohertz to more than 100 MHz [87–89]. A smaller division ratio provides better phase noise. Most of the frequency dividers are either off-the-shelf devices or custom devices. A typical frequency divider consists of a CMOS synchronous divider that can handle division ratios as low as 5 and as high as 1 million. The division ratio



For $f_m < \frac{f_o}{2Q_{load}}$

$$\mathcal{L}(f_m) = \frac{1}{2} \frac{1}{\omega_m^2} \left(\frac{\omega_o}{2Q_{load}} \right)^2 \frac{FkT}{P_{sav}} \left(1 + \frac{f_c}{f_m} \right)$$

$$\begin{aligned}
 Q_{load} &= \frac{\omega_o W_e}{P_{diss, total}} = \frac{\omega_o W_e}{P_{in} + P_{res} + P_{sig}} \\
 &= \frac{\text{Reactive power}}{\text{Total dissipated power}}
 \end{aligned}$$

Maximum energy in C or L: $W_e = \frac{1}{2} C V^2$

$$\mathcal{L}(\omega_m) = \frac{1}{8} \frac{FkT}{P_{sav}} \frac{\omega_o^2}{\omega_m^2} \left(\frac{P_{in}}{\omega_o W_e} + \frac{1}{Q_{uni}} + \frac{P_{sig}}{\omega_o W_e} \right) \left(1 + \frac{\omega_c}{\omega_m} \right)$$

Phase perturbation
Resonator Q
Flicker effect

Input power over reactive power
Signal power over reactive power

Figure 21. Diagram for a feedback oscillator showing the key components considered in the phase noise calculation and its contribution.

is determined by the number of dividers. Typical CMOS dividers end at 250 MHz. To extend the frequency range by using an asynchronous divider means to extend the frequency range up to several gigahertz, but then the frequency resolution is compromised. This prescaler has to be

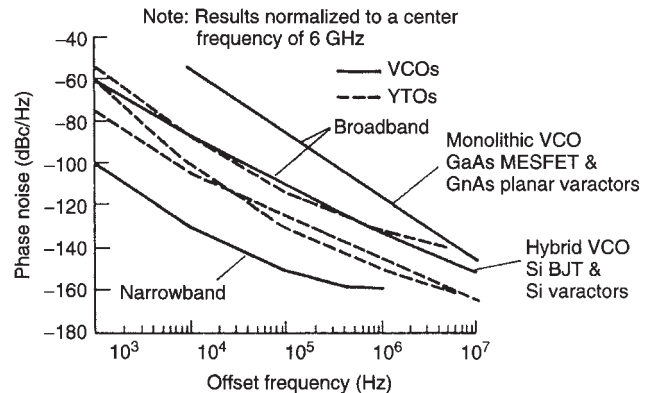


Figure 22. Phase noise of oscillators using different semiconductors and resonators.

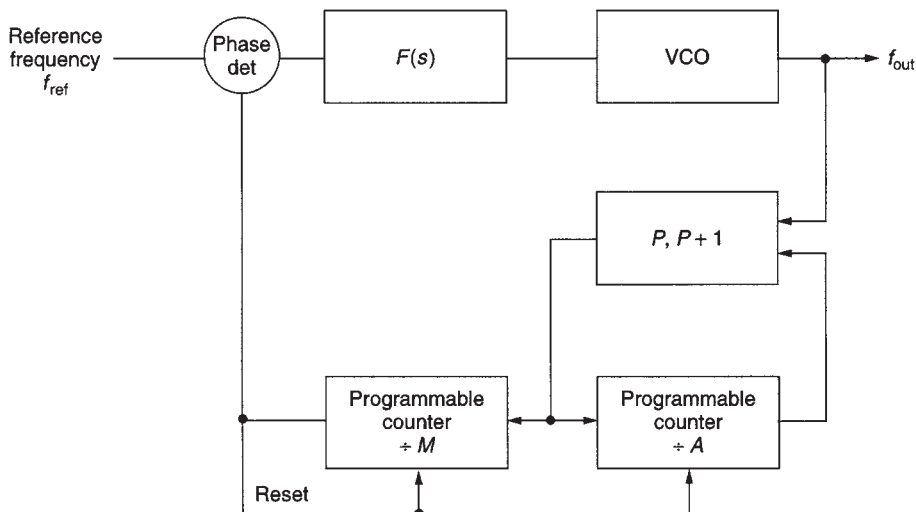


Figure 23. System using dual-modulus counter arrangement.

a synchronized counter that has to be clocked by the main divider, but because of propagation delays, this can become difficult to achieve and can introduce phase jitter. A way around this is to use a dual modulus prescaler that toggles between two stages, dividing by N and dividing by $N + 1$. Dual modulus counters are available in numbers like 5/6, 10/11, and 20/21.

Consider the system shown in Fig. 23. If the $P/(P + 1)$ is a 10/11 divider, the A counter counts the units and the M counter counts the tens. The mode of operation depends on the type of programmable counter used, but the system might operate as follows. If the number loaded into A is greater than zero, then the $P/(P + 1)$ divider is set to divide by $P + 1$ at the start of the cycle. The output from the $P/(P + 1)$ divider clocks both A and M . When A is full, it ceases count and sets the $P/(P + 1)$ divider into the P mode. Only M is then clocked, and when it is full, it resets both A and M , and the cycle repeats.

$$(M - A)P + A(P + 1) = MP + A \tag{28}$$

Therefore

$$f_{out} = (MP + A)f_{ref} \tag{29}$$

If A is incremented by one, the output frequency changes by f_{ref} . In other words, the channel spacing is equal to f_{ref} . This is the channel spacing that would be obtained with a fully programmable divider operating at the same frequency as the $P/(P + 1)$ divider.

For this system to work, the A counter must underflow before the M counter does; otherwise, $P/(P + 1)$ will remain permanently in the $P + 1$ mode. Thus, there is a minimum system division ratio, M_{min} , below which the $P/(P + 1)$ system will not function. To find that minimum ratio, consider the following.

The A counter must be capable of counting all numbers up to and including $P - 1$ if every division ratio is to be

possible, or

$$A_{max} = P - 1 \tag{30}$$

$$M_{min} = P \text{ because } M > A \tag{31}$$

The divider chain divides by $MP + A$; therefore, the minimum systems division ratio is

$$\begin{aligned} M_{min} &= M_{min}(P + A_{min}) \\ &= P(P + 0) = P^2 \end{aligned} \tag{32}$$

Using a 10/11 ratio, the minimum practical division ratio of the system is 100.

In the system shown in Fig. 23, the fully programmable counter, A , must be quite fast. With a 350-MHz clock to the 10/11 divider, only about 23 ns is available for counter A to control the 10/11 divider. For cost reasons, it would be desirable to use a TTL fully programmable counter, but when the delays through the ECL-to-TTL translators have been taken into account, very little time remains for the fully programmable counter. The 10/11 function can be extended easily, however, to give a $+N(N + 1)$ counter with a longer control time for a given input frequency, as shown in Figs. 24 and 25. Using the 20/21 system shown in Fig. 24, the time available to control 20/21 is typically 87 ns at 200 MHz and 44 ns at 350 MHz. The time available to control the 40/41 (Fig. 25) is approximately 180 ns at 200 MHz and 95 ns at 350 MHz.

Figure 26 shows the block diagram of an advanced digital synthesizer block, which is produced by analog devices. There are numerous manufacturers of such chips on the market. Figure 25 gives some insight into the frequency divider system. The top accepts input from a frequency standard, also referred to as a *reference signal*, which is reduced to a number between 5 kHz and 20 MHz. The use of a high-frequency reference requires a higher division ratio, but typically these reference frequencies are also used for some other mixing processes. The 24-bit input

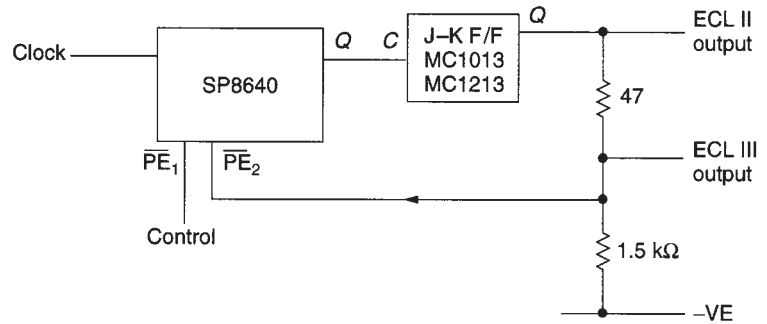


Figure 24. Level shifting information for connecting the various ECL₂ and ECL₃ stages.

register controls both the reference divider and the frequency divider. The frequency divider uses a prescaler like 5/6 or 10/11, and its output is applied to the phase frequency detector. The multiplex unit on the right is doing all the housekeeping and providing information like block, detect, and others. The divider typically has very little control over this portion of the synthesizer, and it's a constant battle to find better parts. Very few high-end synthesizers use custom IC's. To have those built is typically very costly and is cost-effective only if the frequency resolution required is not provided by any other chip on the market. Most of the high-end fractional-*N* synthesizer chips fall in this category.

4.3. Phase Detector

The phase detector at minimum consists of a phase sensitive circuit such as a double-balanced mixer [90–93]. Such a simple circuit has two disadvantages: (1) it's not sensitive to frequency changes and (2) the DC output level is only 0.7V per diode in the ring, and therefore, a poor signal-to-noise ratio can be expected. Today, modern circuits use a phase discriminator with a charge-pump output. The phase frequency is edge triggered and sensitive to both phase and frequency changes. Figure 27 shows a digital phase frequency discriminator with a programmable delay. Under locked condition, the charge pump does not supply current. Under unlocked condition, the current at the point CP charges or discharges a capacitor, which is

part of the integrated system and smoothes the output voltage to become ripple-free. The output from the reference divider is a pulsetrain with a small duty cycle, and the input from the frequency divider(/*N*) is a pulse train with a very small duty cycle. The duty cycle typically is as short as a division ratio is high. So, for a division ratio of 1000, the duty cycle is 0.1%, but the repetition frequency is equal to the output. The charge output, therefore, is also a very narrow train of pulses that are fed to the loop filter. The phase detector has to deal with complicated issues like zero crossings causing instability. The best phase frequency detectors are either TTL or CMOS because they have a larger voltage output swing. In some cases, the charge pump is built from discrete components if a very high performance is required.

4.4. Loop Filter

Loop filters range from a simple lowpass filter to a complex arrangement of active filters. Figure 28 shows the configuration and frequency response of passive and active loop filters. Figure 29 shows an arrangement of more complex filters, including their calculations. The charge pumps can frequently lift with a purely passive filter, as seen in Fig. 30; however, the DC gain of the active filters provides better close-in phase noise and tracking. There may be a penalty if the active circuit is noisy; however, the latest available operation amplifiers have sufficient performance [94].

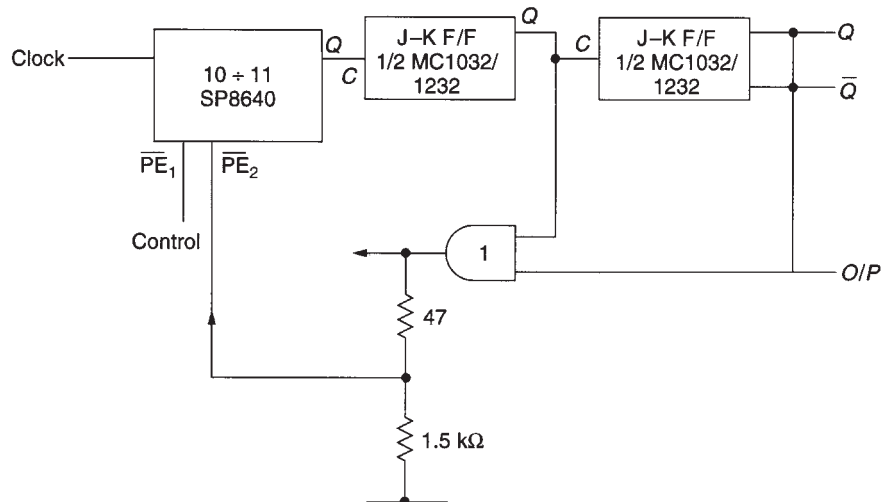


Figure 25. Level shifter diagram to drive from ECL₂ and ECL₃ levels.

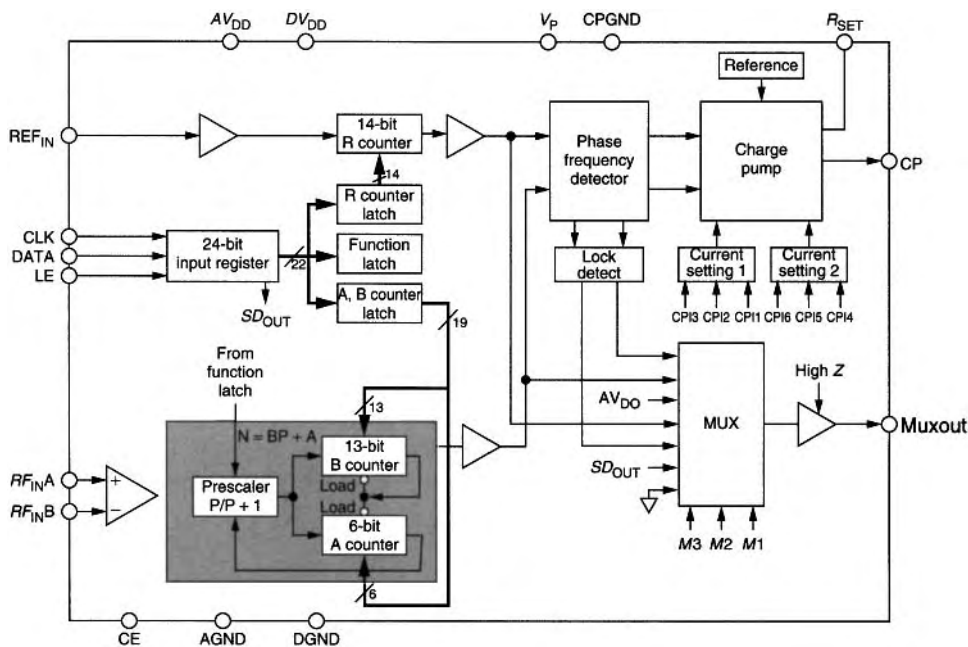


Figure 26. Shows the block diagram of an advanced digital fractional-*N* synthesizer.

5. PHASE LOCKED LOOP DESIGNS

5.1. The Type 2, Second-Order Loop

The following is a derivation of the properties of the type 2, second-order loop. This means that the loop has two integrators—the diode and the operational amplifier—and it

is built with the order of 2, as can be seen from Fig. 29. The basic principle to derive the performance for higher-order loops follows the same principle, although the derivation is more complicated. Following the math section, we will show some typical responses [95].

The type 2, the second-order loop uses a loop filter in the form

$$F(s) = \frac{1}{s} \frac{\tau_2 s + 1}{\tau_1} \tag{33}$$

The multiplier $1/s$ indicates a second integrator, which is generated by the active amplifier. In Table 1, this is the type 3 filter. The type 4 filter is mentioned there as a possible configuration but is not recommended because, as stated previously, the addition of the pole of the origin creates difficulties with loop stability and, in most cases, requires a change from the type 4 to the type 3 filter. One can consider the type 4 filter as a special case of the type 3 filter, and therefore, it does not have to be treated separately. Another possible transfer function is

$$F(s) = \frac{1}{R_1 C} \frac{1 + \tau_2 s}{s} \tag{34}$$

with

$$\tau_2 = R_2 C \tag{35}$$

Under these conditions, the magnitude of the transfer function is

$$|F(j\omega)| = \frac{1}{R_1 C \omega} \sqrt{1 + (\omega R_2 C)^2} \tag{36}$$

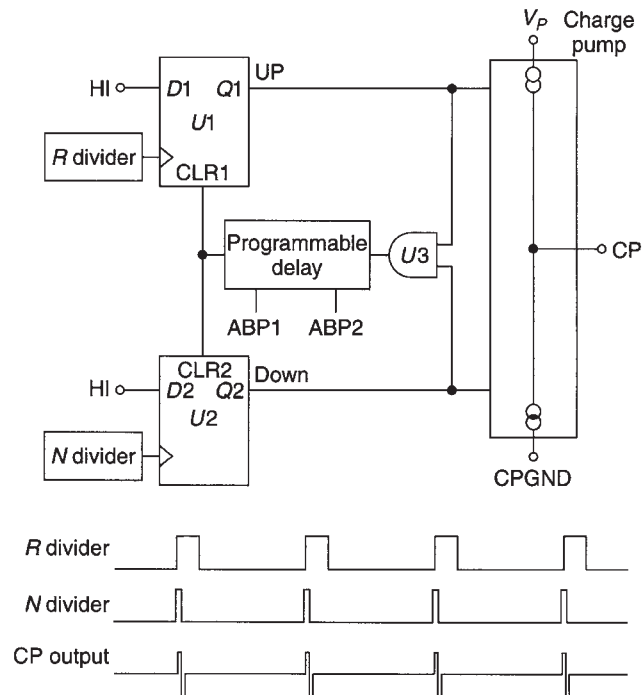


Figure 27. A digital phase frequency discriminator with a programmable delay.

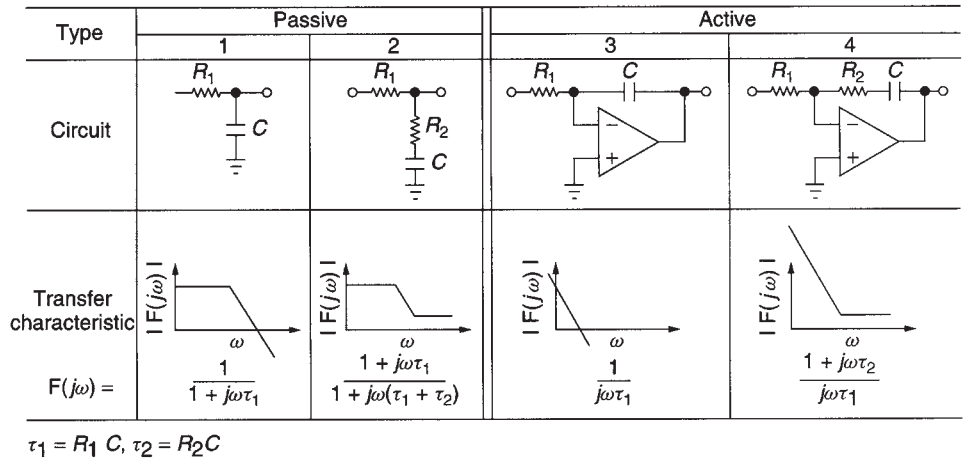


Figure 28. Circuit and transfer characteristics of several PLL filters.

and the phase is

$$\theta = \arctan(\omega\tau_2) - 90^\circ \tag{37}$$

and

$$R_2 = \frac{\tau_2}{C} \tag{41}$$

Again, as if for a practical case, we start off with the design values ω_n and ζ , and we have to determine τ_1 and τ_2 . Taking an approach similar to that for the type 1, second-order loop, the results are

$$\tau_1 = \frac{K}{\omega_n} \tag{38}$$

The closed-loop transfer function of a type 2, second-order PLL with a perfect integrator is

$$B(s) = \frac{K(R_2/R_1)[s + (1/\tau_2)]}{s^2 + K(R_2/R_1)s + (K/\tau_2)(R_2/R_1)} \tag{42}$$

By introducing the terms ζ and ω_n , the transfer function now becomes

$$\tau_2 = \frac{2\zeta}{\omega_n} \tag{39}$$

$$B(s) = \frac{2\zeta\omega_n s + \omega_n^2}{s^2 + 2\zeta\omega_n s + \omega_n^2} \tag{43}$$

and

with the abbreviations

$$R_1 = \frac{\tau_1}{C} \tag{40}$$

$$\omega_n = \left(\frac{K R_2}{\tau_2 R_1}\right)^{1/2} \text{ rad/s} \tag{44}$$

Passive lead-lag	Passive lead lag with pole	Active integrator	Active integrator with pole
$F(s) = \frac{s\tau_2 + 1}{[s(\tau_1 + \tau_2) + 1]}$ $\tau_1 = R_1 C_2; \tau_2 = R_2 C_2$	$F(s) = \frac{s\tau_2 + 1}{[s(\tau_1 + \tau_2) + 1](s\tau_3 + 1)}$ $\tau_1 = R_1 C_2; \tau_2 = R_2 C_2;$ $\tau_3 = (R_2 R_1) C_3$	$F(s) = \frac{s\tau_2 + 1}{s\tau_1}$ $\tau_1 = R_1 C_2; \tau_2 = R_2 C_2;$	$F(s) = \frac{s\tau_2 + 1}{s\tau_1(s\tau_3 + 1)}$ $\tau_1 = R_1(C_2 + C_3); \tau_2 = R_2 C_2;$ $\tau_3 = (R_2 R_1) C_3$
Type 1.5, 2 nd order (low gain)	Type 1.5, 3 rd order (low gain)	Type 2, 2 nd order (high gain)	Type 2, 3 rd order (high gain)

Figure 29. Implementation of different loop filters.

Integrator	Integrator with poles	Integrator with 2 poles
$F(s) = R_1 \frac{s\tau_1 + 1}{s\tau_1}$ $\tau_1 = R_1 C_1$	$F(s) = R_1 \frac{s\tau_1 + 1}{s\tau_1(s\tau_2 + 1)}$ $\tau_1 = R_1 C_1; \tau_2 = R_2 \left(\frac{C_1 C_2}{C_1 + C_2} \right)$	$F(s) = R_1 \frac{s\tau_1 + 1}{s\tau_1(s\tau_2 + 1)(s\tau_3 + 1)}$ $\tau_1 = R_1 C_1; \tau_2 = R_1 \frac{C_1 C_3}{C_1 + C_3};$ $\tau_3 = R_2 C_2$
Type 2, 2 nd order	Type 2, 3 rd order	Type 2, 4 th order

Figure 30. Recommended passive filters for charge pumps.

and

$$\zeta = \frac{1}{2} \left(K\tau_2 \frac{R_2}{R_1} \right)^{1/2} \quad (45)$$

and $K = K_0 K_o / N$.

The 3 dB bandwidth of the type 2, second-order loop is

$$B_{3dB} = \frac{\omega_n}{2\pi} \left[2\zeta^2 + 1 + \sqrt{(2\zeta^2 + 1)^2 + 1} \right]^{1/2} \text{ Hz} \quad (46)$$

and the noise bandwidth is

$$B_n = \frac{K(R_2/R_1) + 1/\tau_2}{4} \text{ Hz} \quad (47)$$

Again, we ask the question of the final error and use the previous error function,

$$E(s) = \frac{s\theta(s)}{s + K(R_2/R_1)\{[s + (1/\tau_2)]/s\}} \quad (48)$$

or

$$E(s) = \frac{s^2\theta(s)}{s^2 + K(R_2/R_1)s + (K/\tau_2)(R_2/R_1)} \quad (49)$$

As a result of the perfect integrator, the steady-state error resulting from a step change in input phase or change of magnitude of frequency is zero.

If the input frequency is swept with a constant range change of input frequency ($\Delta\omega/dt$), for $\theta(s) = (2\Delta\omega/dt)/s^3$, the steady-state phase error is

$$E(s) = \frac{R_1}{R_2} \frac{\tau_2(2\Delta\omega/dt)}{K} \text{ rad} \quad (50)$$

The maximum rate at which the VCO frequency can be swept for maintaining lock is

$$\frac{2\Delta\omega}{dt} = \frac{N}{2\tau_2} \left(4B_n - \frac{1}{\tau_2} \right) \text{ rad/s} \quad (51)$$

The introduction of N indicates that this is referred to the VCO rather than to the phase/frequency comparator. In the previous example of the type 1, first-order loop, we referred it only to the phase/frequency comparator rather than to the VCO.

Figure 31 shows the closed-loop response of a type 2, third-order loop having a phase margin of 10° and with the optimal 45° .

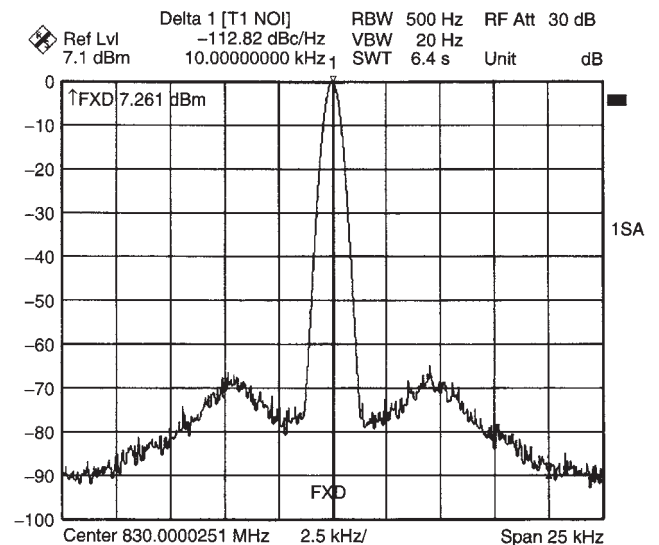


Figure 31. Measured spectrum of a synthesizer where the loop filter is underdamped, resulting in ≈ 10 dB increase of the phase noise at the loop filter bandwidth. In this case, we either do not meet the 45° phase margin criterion or the filter is too wide, so it shows the effect of the upconverted reference frequency.

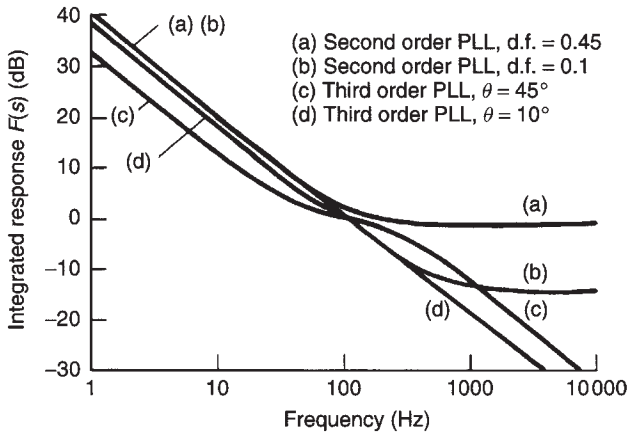


Figure 32. Integrated response for various loops as a function of the phase margin.

A phase margin of 10° results in overshoot, which in the frequency domain would be seen as peaks in the oscillator noise-sideband spectrum. Needless to say, this is a totally undesirable effect, and as the operational amplifiers and other active and passive elements add to this, the loop filter has to be adjusted after the design is finalized to accommodate the proper resulting phase margin ($35\text{--}45^\circ$). The open-loop gain for different loops can be seen in Figs. 32 and 33.

5.2. Transient Behavior of Digital Loops Using Tristate Phase Detectors

5.2.1. Pullin Characteristic. The type 2, second-order loop is used with either a sample/hold comparator or a tristate phase/frequency comparator.

We will now determine the transient behavior of this loop. Figure 34 shows the block diagram.

Very rarely in the literature is a clear distinction between pullin and lockin characteristics or frequency and phase acquisition made as a function of the digital phase/frequency detector. Somehow, all the approximations or linearizations refer to a sinusoidal phase/frequency comparator or its digital equivalent, the exclusive-OR gate.

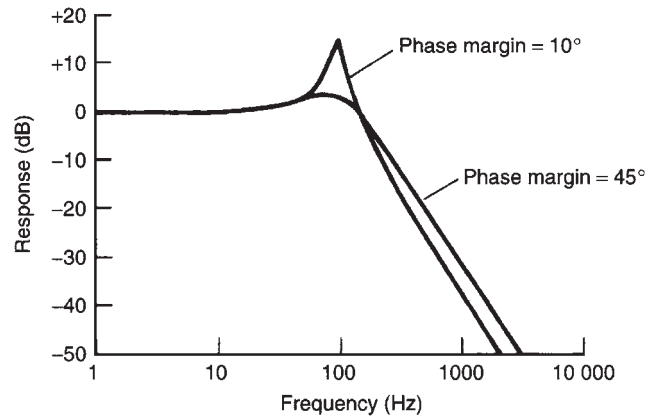


Figure 33. Closed-loop response of a type 2, third-order PLL having a phase margin of 10° .

The tristate phase/frequency comparator follows slightly different mathematical principles. The phase detector gain is

$$K'_d = \frac{V_d}{\omega_0} = \frac{\text{phase detector supply voltage}}{\text{loop idling frequency}}$$

and is valid only in the out-of-lock state and is a somewhat coarse approximation to the real gain, which, due to non-linear differential equations, is very difficult to calculate.

However, practical tests show that this approximation is still fairly accurate. Definitions are

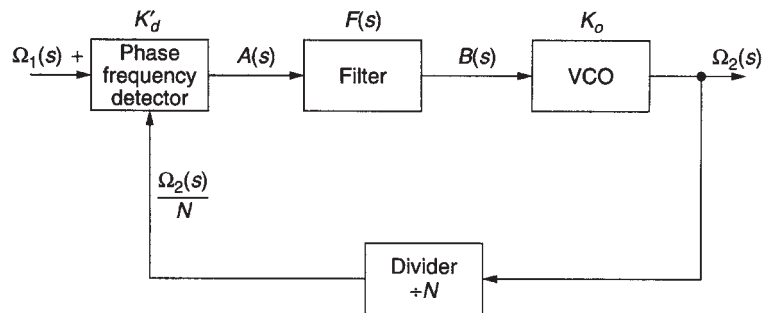
$$\Omega_1(s) = \mathcal{L}[\Delta\omega_1(t)] \text{ (reference input to } \delta/\omega \text{ detector)}$$

$$\Omega_2(s) = \mathcal{L}[\Delta\omega_2(t)] \text{ (signal VCO output frequency)}$$

$$\Omega_e(s) = \mathcal{L}[\omega_e(t)] \text{ (error frequency at } \delta/\omega \text{ detector)}$$

$$\Omega_e(s) = \Omega_1(s) - \frac{\Omega_2(s)}{N}$$

$$\Omega_2(s) = [\Omega_1(s) - \Omega_e(s)]N$$



Note: The frequency transfer const. of the VCO = K_o (not $\frac{K_o}{s}$, which is valid for phase transfer only.)

Figure 34. Block diagram of a digital PLL before lock is acquired.

From the circuit above, we obtain

$$\begin{aligned} A(s) &= \Omega_e(s)K'_d \\ B(s) &= A(s)F(s) \\ \Omega_2(s) &= B(s)K_o \end{aligned}$$

The error frequency at the detector is

$$\Omega_e(s) = \Omega_1(s)N \frac{1}{N + K_oK'_dF(s)} \quad (52)$$

The signal is stepped in frequency:

$$\Omega_1(s) = \frac{\Delta\omega_1}{s} \quad (\Delta\omega_1 = \text{magnitude of frequency step}) \quad (53)$$

Active Filter of First Order. If we use an active filter

$$F(s) = \frac{1 + s\tau_2}{s\tau_1} \quad (54)$$

and insert this in Equation (51), the error frequency is

$$\Omega_e(s) = \Delta\omega_1N \frac{1}{s \left(N + K_oK'_d \frac{\tau_2}{\tau_1} \right) + \frac{K_oK'_d}{\tau_1}} \quad (55)$$

Utilizing the Laplace transformation, we obtain

$$\omega_e(t) = \Delta\omega_1 \frac{1}{1 + K_oK'_d(\tau_2/\tau_1)(1/N)} \exp \left[-\frac{t}{(\tau_1N/K_oK'_d) + \tau_2} \right] \quad (56)$$

and

$$\lim_{t \rightarrow 0} \omega_e(t) = \frac{\Delta\omega_1N}{N + K_oK'_d(\tau_2/\tau_1)} \quad (57)$$

$$\lim_{t \rightarrow \infty} \omega_e(t) = 0 \quad (58)$$

Passive Filter of First Order. If we use a passive filter

$$\lim_{t \rightarrow \infty} \omega_e(t) = 0 \quad (59)$$

for the frequency step

$$\Omega_1(s) = \frac{\Delta\omega_1}{s} \quad (60)$$

the error frequency at the input becomes

$$\begin{aligned} \Omega_e(s) &= \Delta\omega_1N \left\{ \frac{1}{s [N(\tau_1 + \tau_2) + K_oK'_d\tau_2] + (N + K_oK'_d)} \right. \\ &\quad \left. + \frac{\tau_1 + \tau_2}{s [N(\tau_1 + \tau_2) + K_oK'_d\tau_2] + (N + K_oK'_d)} \right\} \quad (61) \end{aligned}$$

For the first term, we will use the abbreviation A , and for the second term, we will use the abbreviation B :

$$A = \frac{1/[N(\tau_1 + \tau_2) + K_oK'_d\tau_2]}{s \left[s + \frac{N + K_oK'_d}{N(\tau_1 + \tau_2) + K_oK'_d\tau_2} \right]} \quad (62)$$

$$B = \frac{\frac{(\tau_1 + \tau_2)}{N(\tau_1 + \tau_2) + K_oK'_d\tau_2}}{s + \frac{N + K_oK'_d}{N(\tau_1 + \tau_2) + K_oK'_d\tau_2}} \quad (63)$$

After the inverse Laplace transformation, our final result becomes

$$\mathcal{L}^{-1}(A) = \frac{1}{N + K_oK'_d} \left\{ 1 - \exp \left[-t \frac{N + K_oK'_d}{N(\tau_1 + \tau_2) + K_oK'_d\tau_2} \right] \right\} \quad (64)$$

$$\mathcal{L}^{-1}(B) = \frac{\tau_1 + \tau_2}{N(\tau_1 + \tau_2) + K_oK'_d\tau_2} \exp \left[-t \frac{N + K_oK'_d}{N(\tau_1 + \tau_2) + K_oK'_d\tau_2} \right] \quad (65)$$

and finally

$$\omega_e(t) = \Delta\omega_1N [\mathcal{L}^{-1}(A) + (\tau_1 + \tau_2)\mathcal{L}^{-1}(B)] \quad (66)$$

What does the equation mean? We really want to know how long it takes to pull the VCO frequency to the reference. Therefore, we want to know the value of t , the time it takes to be within 2π or less of lock-in range.

The PLL can, at the beginning, have a phase error from -2π to $+2\pi$, and the loop, by accomplishing lock, then takes care of this phase error.

We can make the reverse assumption for a moment and ask ourselves, as we have done earlier, how long the loop stays in phase lock. This is called the *pullout range*. Again, we apply signals to the input of the PLL as long as the loop can follow and the phase error does not become larger than 2π . Once the error is larger than 2π , the loop jumps out of lock.

When the loop is out of lock, a beat note occurs at the output of the loop filter following the phase/frequency detector.

The tristate phase/frequency comparator, however, works on a different principle, and the pulses generated and supplied to the charge pump do not allow the generation of an ac voltage. The output of such a phase/frequency detector is always unipolar, but relative to

the value of $V_{batt}/2$, the integrator voltage can be either positive or negative. If we assume for a moment that this voltage should be the final voltage under a locked condition, we will observe that the resulting DC voltage is either more negative or more positive relative to this value, and because of this, the VCO will be “pulled in” to this final frequency rather than swept in. The swept-in technique applies only in cases of phase/frequency comparators, where this beat note is being generated. A typical case would be the exclusive-OR gate or even a sample/hold comparator. This phenomenon is rarely covered in the literature and is probably discussed in detail for the first time in the book by Roland Best [9].

Let us assume now that the VCO has been pulled in to final frequency to be within 2π of the final frequency, and the time t is known. The next step is to determine the lockin characteristic.

5.2.2. Lockin Characteristic. We will now determine the lockin characteristic, and this requires the use of a different block diagram. Figure 5, of the section on frequency synthesizer fundamentals shows the familiar block diagram of the PLL, and we will use the following definitions:

$$\theta_1(s) = \mathcal{L}[\Delta\delta_1(t)] \text{ (reference input to } \delta/\omega \text{ detector)}$$

$$\theta_2(s) = \mathcal{L}[\Delta\delta_2(t)] \text{ (signal VCO output phase)}$$

$$\theta_e(s) = \mathcal{L}[\delta_e(t)] \text{ (phase error at } \delta/\omega \text{ detector)}$$

$$\theta(s) = \theta_1(s) - \frac{\theta_2(s)}{N}$$

From the block diagram, the following is apparent:

$$A(s) = \theta_e(s)K_d$$

$$B(s) = A(s)F(s)$$

$$\theta_2(s) = B(s) \frac{K_o}{s}$$

The phase error at the detector is

$$\theta_e(s) = \theta_1(s) \frac{sN}{K_oK_dF(s) + sN} \tag{67}$$

A step in phase at the input, where the worst-case error is 2π , results in

$$\theta_1(s) = 2\pi \frac{1}{s} \tag{68}$$

We will now treat the two cases using an active or passive filter:

Active Filter. The transfer characteristic of the active filter is

$$F(s) = \frac{1 + s\tau_2}{s\tau_1} \tag{69}$$

This results in the following formula for the phase error at the detector:

$$\theta_e(s) = 2\pi \frac{s}{s^2 + (sK_oK_d\tau_2/\tau_1)/N + (K_oK_d/\tau_1)/N} \tag{70}$$

The polynomial coefficients for the denominator are

$$a_2 = 1$$

$$a_1 = (K_oK_d\tau_2/\tau_1)/N$$

$$a_0 = (K_oK_d/\tau_1)/N$$

and we have to find the roots W_1 and W_2 . Expressed in the form of a polynomial coefficient, the phase error is

$$\theta_e(s) = 2\pi \frac{s}{(s + W_1)(s + W_2)} \tag{71}$$

After the inverse Laplace transformation has been performed, the result can be written in the form

$$\delta_e(t) = 2\pi \frac{W_1e^{-W_1t} - W_2e^{-W_2t}}{W_1 - W_2} \tag{72}$$

with

$$\lim_{t \rightarrow 0} \delta_e(t) = 2\pi$$

and

$$\lim_{t \rightarrow \infty} \delta_e(t) = 0$$

The same can be done using a passive filter.

Passive Filter. The transfer function of the passive filter is

$$F(s) = \frac{1 + s\tau_2}{1 + s(\tau_1 + \tau_2)} \tag{73}$$

If we apply the same phase step of 2π as before, the resulting phase error is

$$\theta_e(s) = 2\pi \frac{[1/(\tau_1 + \tau_2)] + s}{s^2 + s \frac{N + K_oK_d\tau_2}{N(\tau_1 + \tau_2)} + \frac{K_oK_d}{N(\tau_1 + \tau_2)}} \tag{74}$$

Again, we have to find the polynomial coefficients, which are

$$a_2 = 1$$

$$a_1 = \frac{N + K_oK_d\tau_2}{N(\tau_1 + \tau_2)}$$

$$a_0 = \frac{K_oK_d}{N(\tau_1 + \tau_2)}$$

and finally find the roots for W_1 and W_2 . This can be written in the form

$$\theta_e(s) = 2\pi \left[\frac{1}{\tau_1 + \tau_2} \frac{1}{(s + W_1)(s + W_2)} + \frac{s}{(s + W_1)(s + W_2)} \right] \tag{75}$$

Now we perform the inverse Laplace transformation and obtain our result

$$\delta_e(t) = 2\pi \left(\frac{1}{\tau_1 + \tau_2} \frac{e^{-W_1 t} - e^{-W_2 t}}{W_2 - W_1} + \frac{W_1 e^{-W_1 t} - W_2 e^{-W_2 t}}{W_1 - W_2} \right) \tag{76}$$

with

$$\lim_{t \rightarrow 0} \delta_e(t) = 2\pi$$

with

$$\lim_{t \rightarrow \infty} \delta_e(t) = 0$$

When analyzing the frequency response for the various types and orders of PLLs, the phase margin played an important role. For the transient time, the type 2, second-order loop can be represented with a damping factor or, for higher orders, with the phase margin. Figure 35 shows the normalized output response for a damping factor of 0.1 and 0.47. The ideal Butterworth response would be a damping factor of 0.7, which correlates with a phase margin of 45° .

5.3. Loop Gain/Transient Response Examples

Given the simple filter shown in Fig. 36 and the parameters as listed, the Bode plot is shown in Fig. 37. This approach can also be translated from a type 1 into a type 2

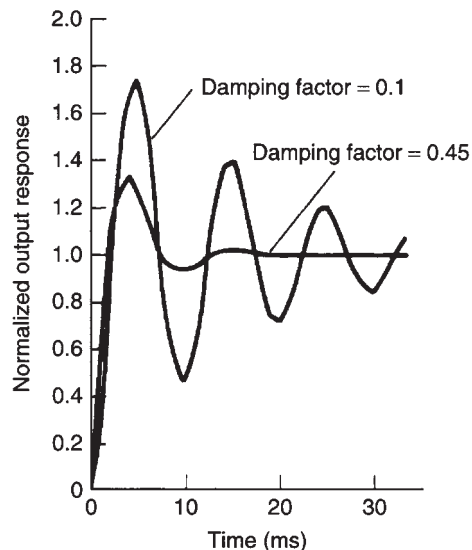


Figure 35. Normalized output response of a type 2, second-order loop with a damping factor of 0.1 and 0.05 for $\Omega_n = 0.631$.

filter as shown in Fig. 38 and its frequency response as shown in Fig. 39. The lockin function for this type 2, second-order loop with an ideal damping factor of 0.707 (Butterworth response) is shown in Fig. 40. Figure 41 shows an actual settling-time measurement. Any deviation from ideal damping, as we'll soon see, results in ringing (in an underdamped system), or, in an overdamped system, the voltage will crawl to its final value. This system can be increased in its order by selecting a type 2, third-order loop using the filter shown in Fig. 42. For an ideal synthesis of the values, the Bode diagram looks as shown in Fig. 43 and its resulting response is given in Fig. 44.

The order can be increased by adding an additional low-pass filter after the standard loop filter. The resulting system is a type 2, fifth-order loop. Figure 45 shows the Bode diagram or open-loop diagram, and Fig. 46 shows the locking function. By using a very wide loop bandwidth, this can be used to clean up microwave oscillators with

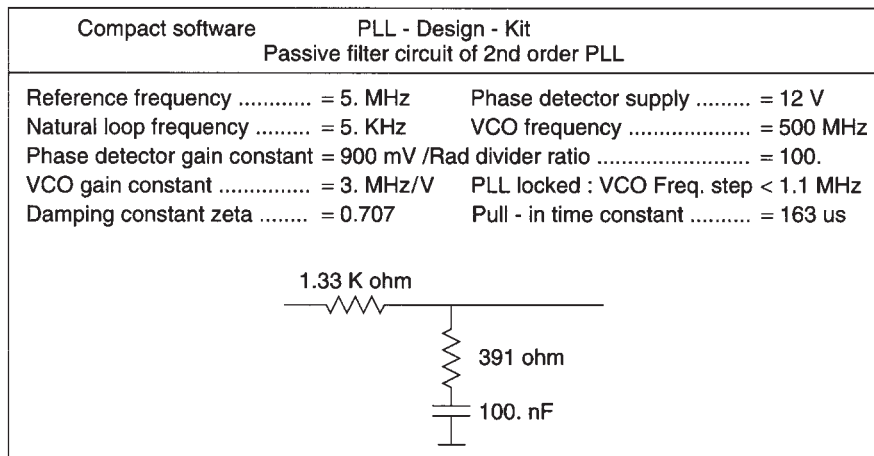


Figure 36. Loop filter for a type 1, second-order synthesizer.

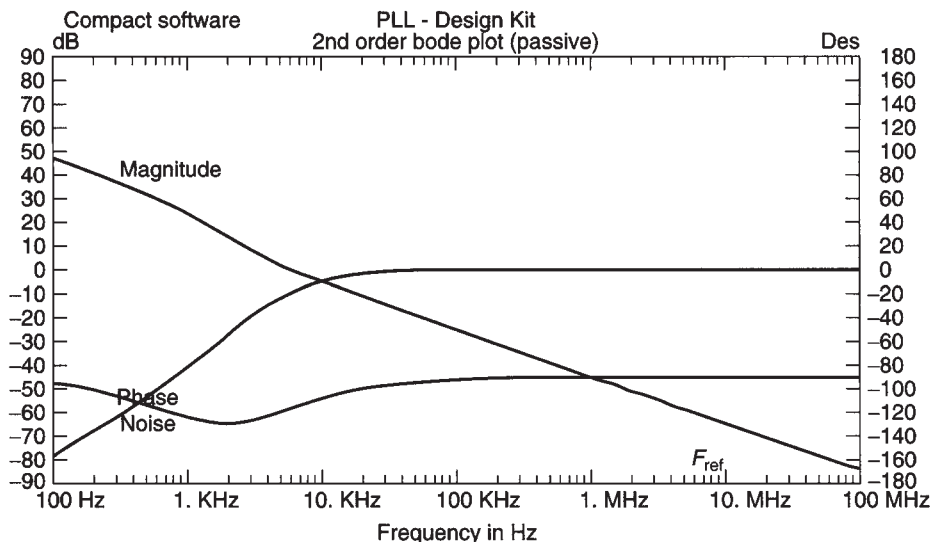


Figure 37. Type 1, second-order loop response.

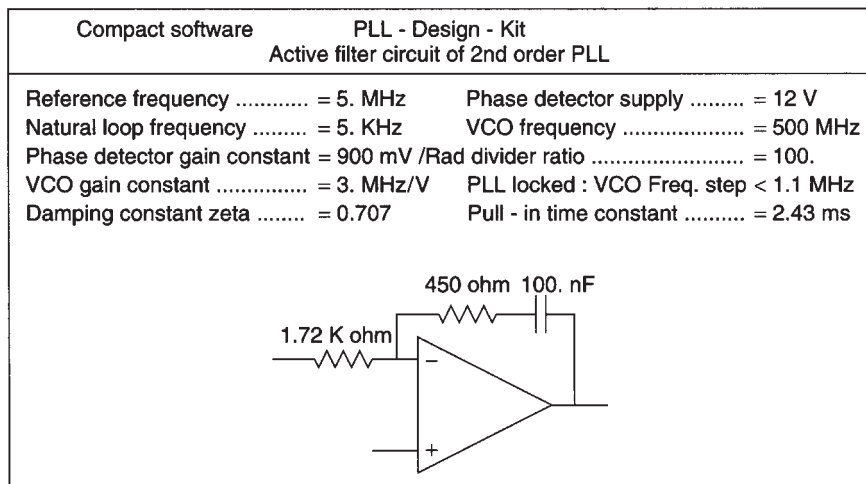


Figure 38. Loop filter for a type 2, second-order synthesizer.

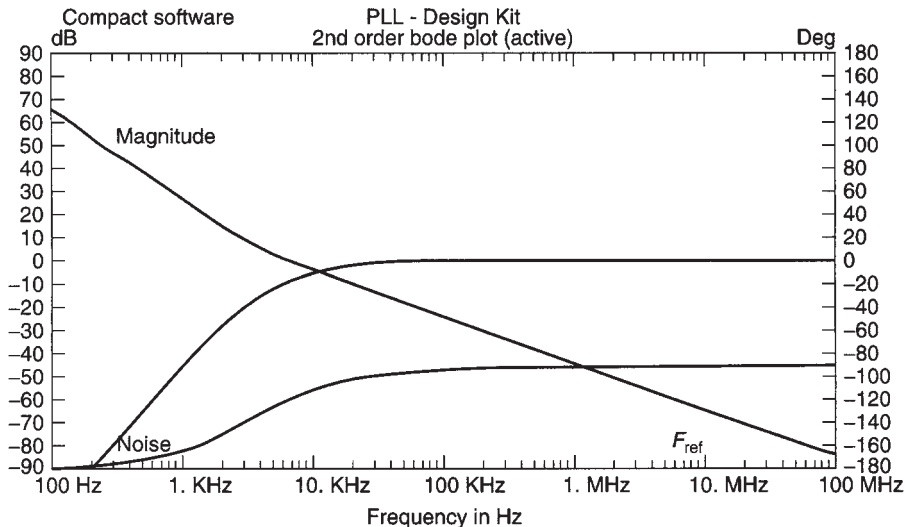


Figure 39. Response of the type 2, second-order loop.

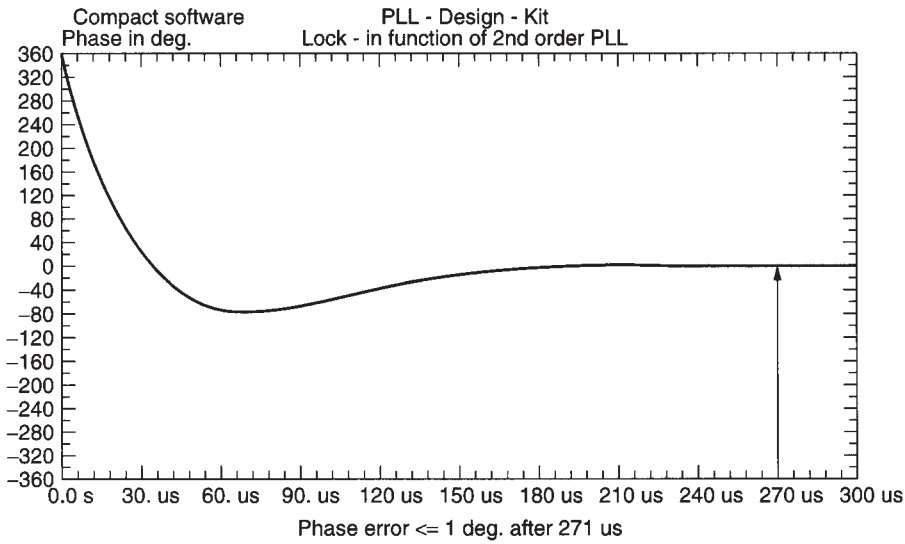


Figure 40. Lockin function of the type 2, second-order PLL. It indicates a lock time of 271 μ s and an ideal response.

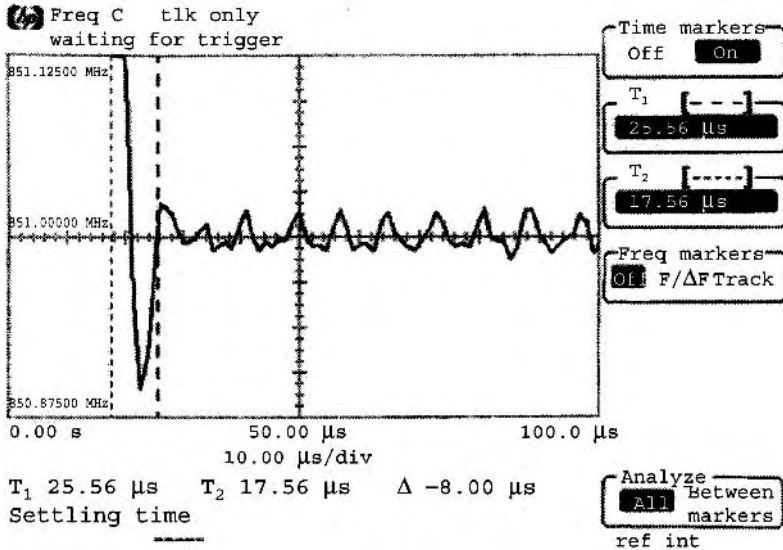


Figure 41. Example of settling-time measurement.

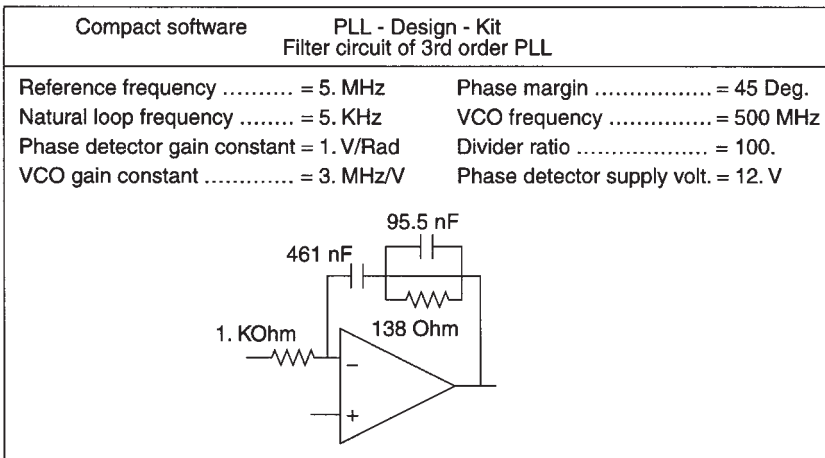


Figure 42. Loop filter for a type 2, third-order synthesizer.

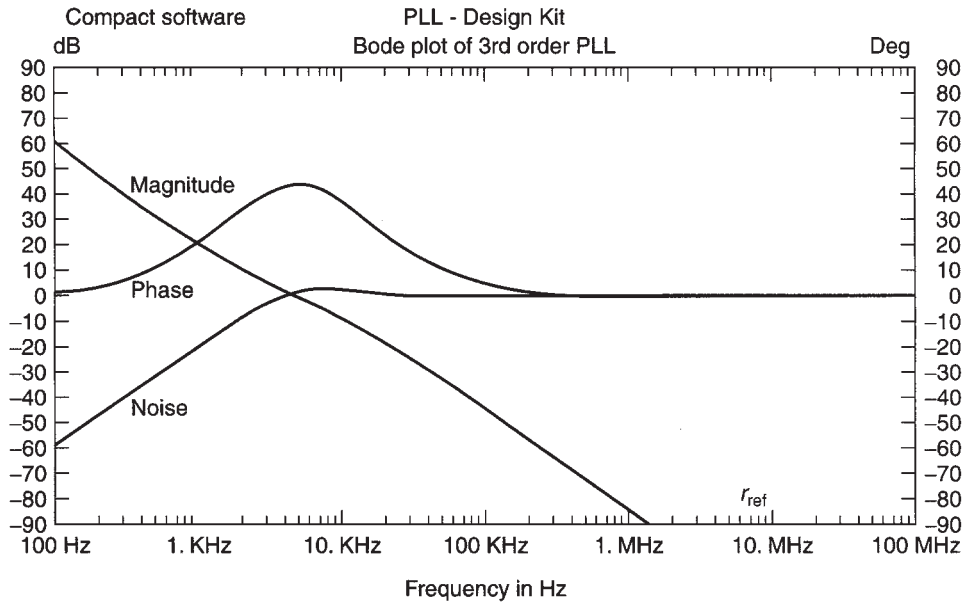


Figure 43. Open-loop Bode diagram for the type 2, third-order loop. It fulfills the requirement of 45° phase margin at the 0 dB crossover point, and it corrects the slope down to -10 dB gain.

inherent comparatively poor phase noise. This cleanup has a dramatic influence on the performance.

By deviating from the ideal 45° to a phase margin of 33°, one obtains the already-mentioned ringing, as is evident from Fig. 47. The time to settle has grown from 13.3 to 62 μs.

To more fully illustrate the effects of nonideal phase margin, Figs. 48–51 show the lock-in function of a different type 2, fifth-order loop configured for phase margins of 25°, 35°, 45°, and 55°, respectively.

I have already mentioned that the loop should avoid “ears” (Fig. 31) with poorly designed loop filters. Another interesting phenomenon is the tradeoff between loop bandwidth and phase noise. In Fig. 52, the loop band-

width has been made too wide, resulting in a degradation of the phase noise, but provides faster settling time. By reducing the loop bandwidth from about 1 kHz to 300 Hz, only a very slight overshoot remains, improving the phase noise significantly. This is shown in Fig. 53.

5.4. Practical Circuits

Figure 54 shows a passive filter that is used for a synthesizer chip with constant current output. This chip has a charge-pump output, which explains the need for the first capacitor.

Figure 55 shows an active integrator operating at a reference frequency of several megahertz. The notch filter

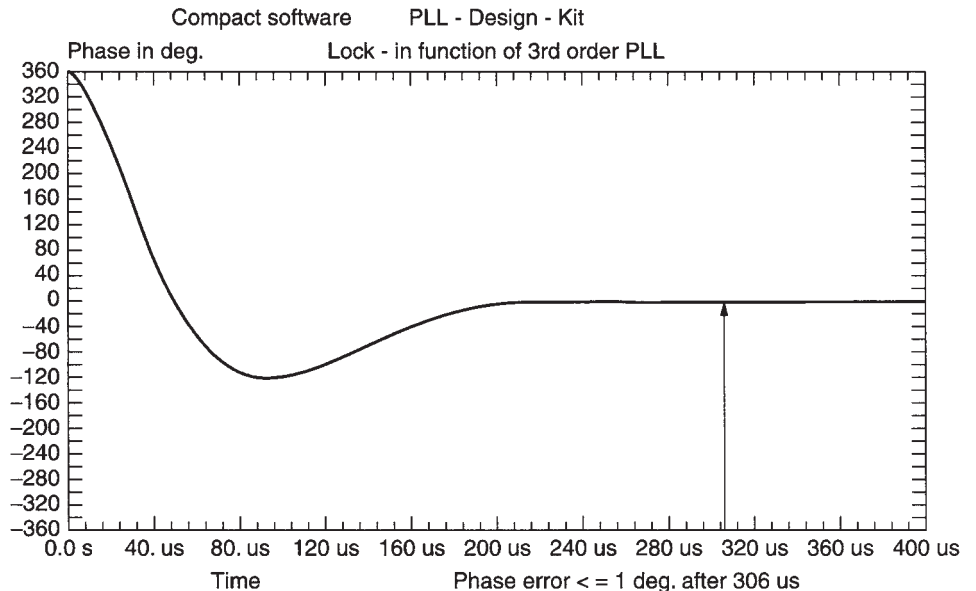


Figure 44. Lockin function of the type 2, third-order loop for an ideal 45° phase margin.

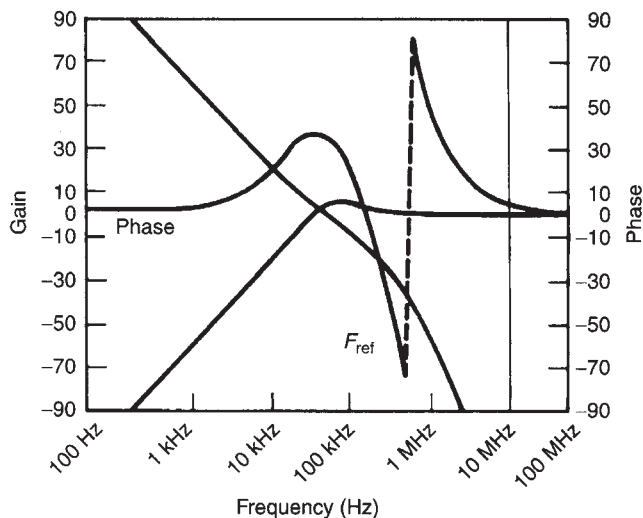


Figure 45. Bode plot of the fifth-order PLL system for a microwave synthesizer. The theoretical reference suppression is better than 90 dB.

at the output reduces the reference frequency considerably. The notch is about 4.5 MHz.

Figure 56 shows the combination of a phase/frequency discriminator and a higher order loop filter as used in more complicated systems, such as fractional division synthesizers.

Figure 57 shows a custom-built phase detector with a noise floor of better than -168 dBc/Hz.

6. THE FRACTIONAL-N PRINCIPLE

The principle of the fractional- N PLL synthesizer was touched previously in Section 2. The following is a numerical example for better understanding.

Example 1. Considering the problem of generating 899.8 MHz using a fractional- N loop with a 50-MHz

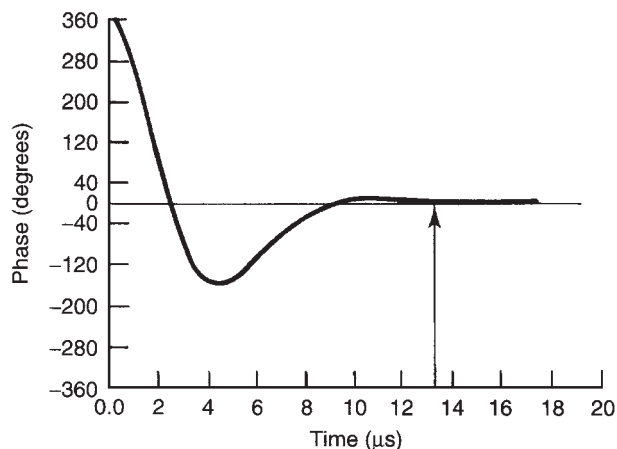


Figure 46. Lockin function of the fifth-order PLL. Note that the phase lock time is approximately $13.3 \mu\text{s}$.

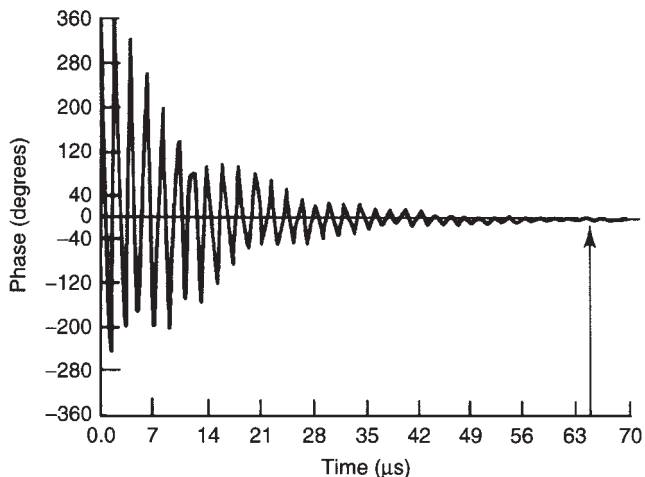


Figure 47. Lockin function of the fifth-order PLL. Note that the phase margin has been reduced from the ideal 45° . This results in a much longer settling time of $62 \mu\text{s}$.

reference frequency,

$$899.8 \text{ MHz} = 50 \text{ MHz} \left(N + \frac{K}{F} \right)$$

The integral part of the division N has to be set to 17, the fractional part K/F needs to be $\frac{996}{1000}$ (the fractional part K/F is not a integer), and the VCO output has to be divided by $996 \times$ every 1000 cycles. This can easily be implemented by adding the number 0.996 to the contents of an accumulator every cycle. Every time the accumulator overflows, the divider divides by 18 rather than by 17. Only the fractional value of the addition is retained in the phase accumulator. If we move to the lower band or try to generate 850.2 MHz, N remains 17 and K/F becomes $\frac{4}{1000}$. This method of using fractional division was first introduced by using analog implementation and noise cancellation, but today, it is implemented totally as a digital approach. The necessary resolution is obtained from the dual modulus prescaling, which allows for a well-established method for achieving a high-performance frequency synthesizer operating at UHF and higher frequencies. Dual-modulus prescaling avoids the loss of resolution in a system compared to a simple prescaler; it allows a VCO step equal to the value of the reference frequency to be obtained. This method needs an additional counter, and the dual-modulus prescaler then divides one or two values depending on the state of its control. The only drawback of prescalers is the minimum division ratio of the prescaler for approximately N^2 . The dual-modulus divider is the key to implementing the fractional- N synthesizer principle. Although the fractional- N technique appears to have a good potential of solving the resolution limitation, it is not free of having its own complications. Typically, an overflow from the phase accumulator, which is the adder with the output feedback to the input after being latched, is used to change the instantaneous division ratio. Each overflow produces a jitter at the output frequency, caused by the fractional

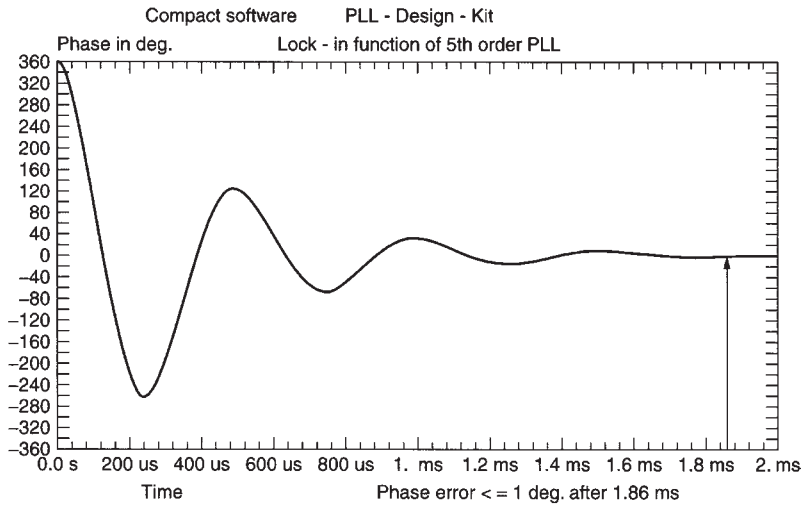


Figure 48. Lockin function of another type 2, fifth-order loop with a 25° phase margin. Noticeable ringing occurs, lengthening the lockin time to 1.86 ms.

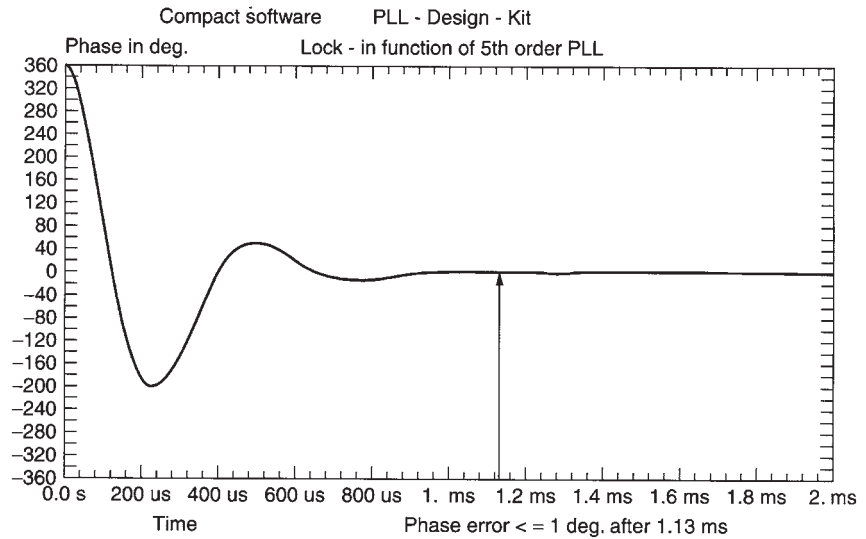


Figure 49. Lockin function of the type 2, fifth-order loop with a 35° phase margin. Ringing still occurs, but the lockin time has decreased to 1.13 ms.

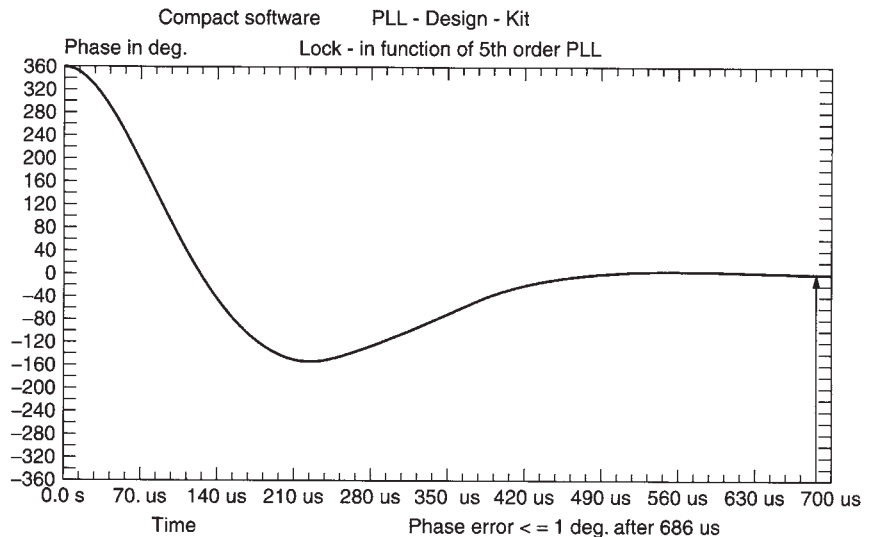


Figure 50. Lockin function of the type 2, third-order loop with an ideal 45° phase margin. The lockin time is 686 μs.

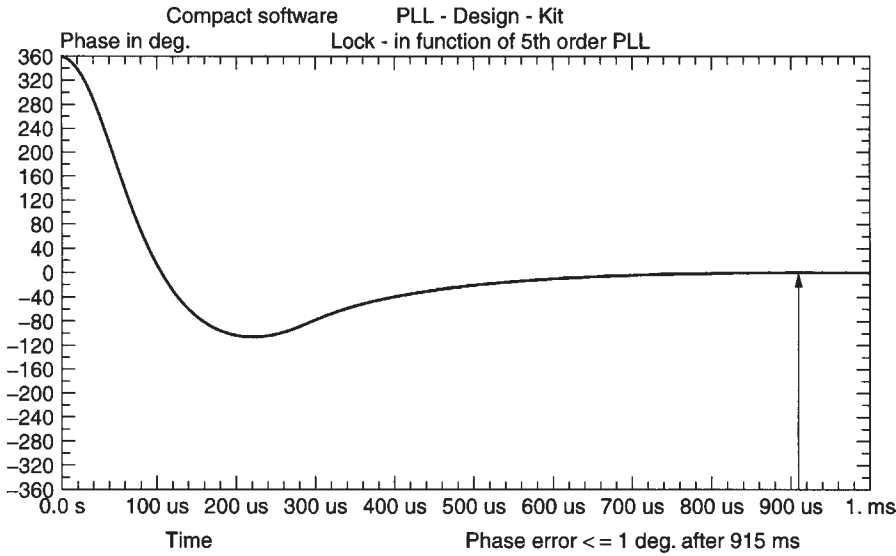


Figure 51. Lockin function of the type 2, fifth-order loop, for a 55° phase margin. The lock-in time has increased to 915 μs.

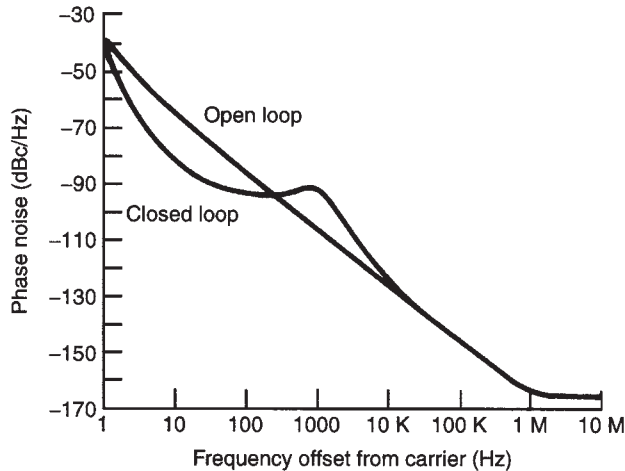


Figure 52. Comparison between open- and closed-loop noise prediction. Note the overshoot of around 1 kHz off the carrier.

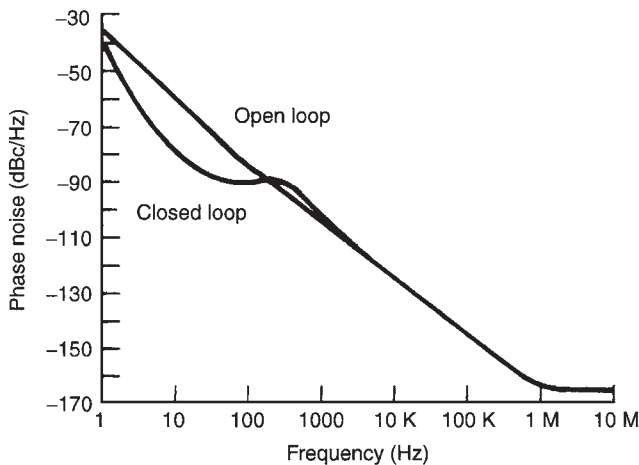


Figure 53. Comparison between open- and closed-loop noise prediction. Note the overshoot at around 300 Hz off the carrier.

division, and is limited to the fractional portion of the desired division ratio.

In our case, we had chosen a stepsize of 200 kHz, and yet the discrete sidebands vary from 200 kHz for $K/F = \frac{4}{1000}$ to 49.8 MHz for $K/F = \frac{996}{1000}$. It will become the task of the loop filter to remove those discrete spurious components. Although in the past the removal of the discrete spurs has been accomplished by using analog techniques, various digital methods are now available. The microprocessor has to solve the following equation:

$$N^* = \left(N + \frac{K}{F}\right) = [N(F - K) + (N + 1)K] \quad (77)$$

Example 2. For $F_0 = 850.2$ MHz, we obtain

$$N^* = \frac{850.2 \text{ MHz}}{50 \text{ MHz}} = 17.004$$

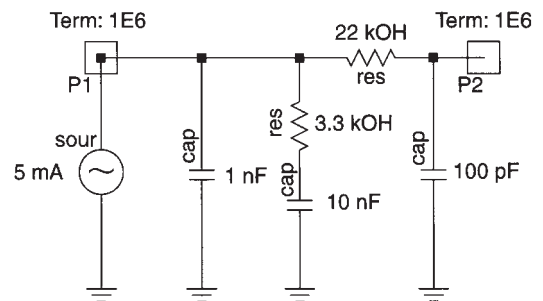


Figure 54. Type 1 high-order loop filter used for passive filter evaluation. The 1-nF capacitor is used for spike suppression as explained in the text. The filter consists of a lag portion and an additional lowpass section.

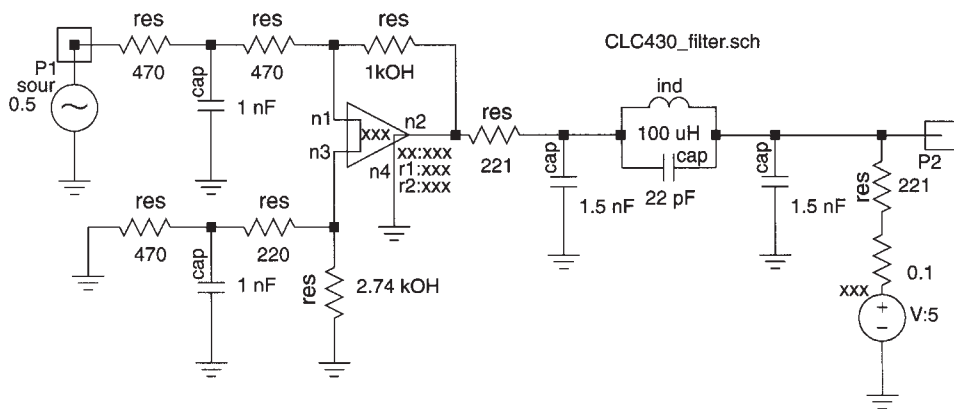


Figure 55. A type 2 high-order filter with a notch filter to suppress the discrete reference spurs.

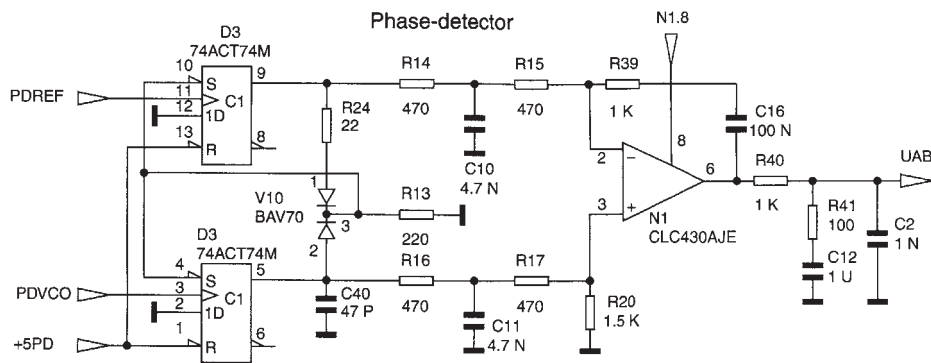


Figure 56. Phase/frequency discriminator including an active loop filter capable of operating up to 100 MHz.

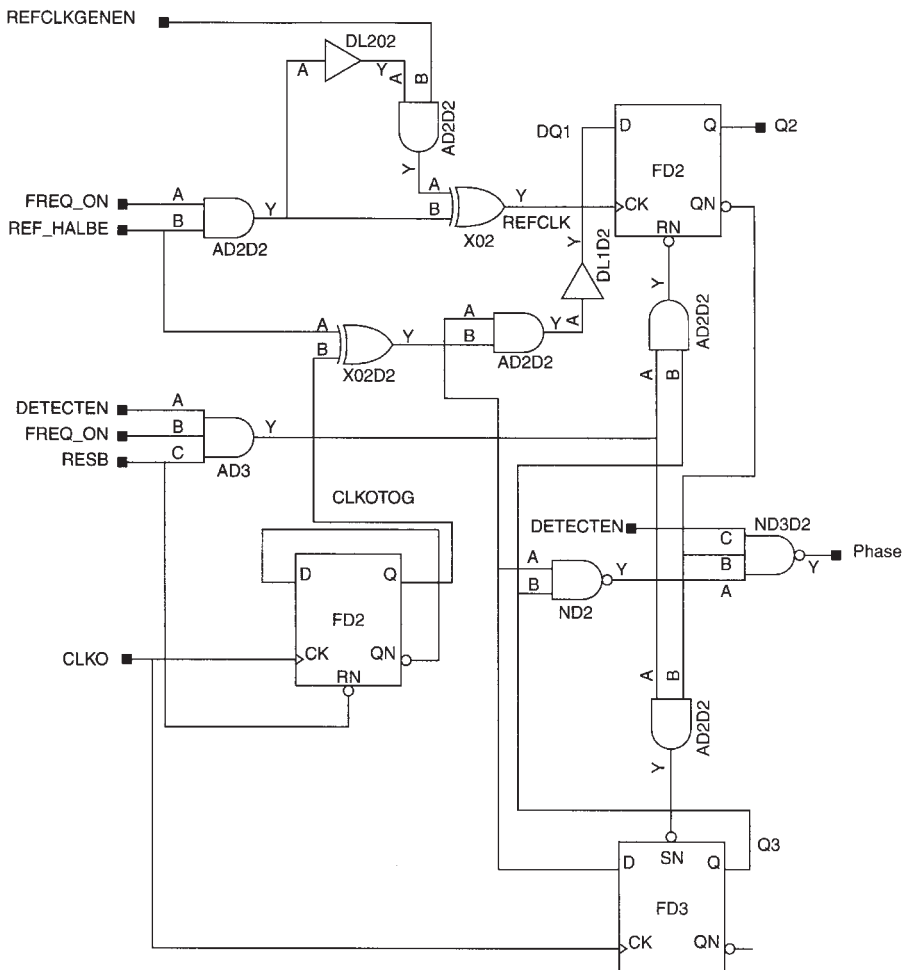


Figure 57. Custom-built phase detector with a noise floor of better than -168 dBc/Hz. This phase detector shows extremely low phase jitter.

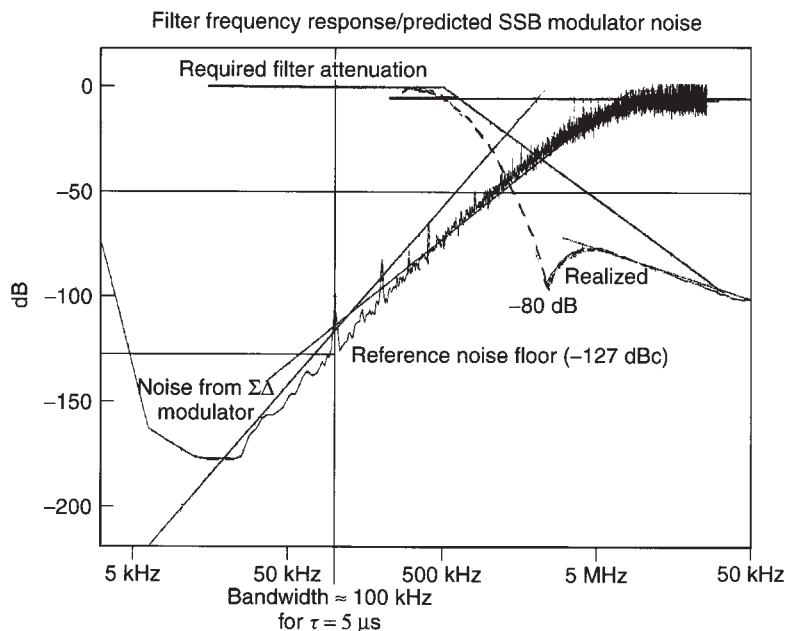


Figure 58. The filter frequency response/phase noise analysis graph shows the required attenuation for the reference frequency of 50 MHz and the noise generated by the sigma-delta converter (three steps) as a function of the offset frequency. It becomes apparent that the sigma-delta converter noise dominates above 80 kHz unless attenuated.

Following the formula above, we further obtain

$$N^* = \left(N + \frac{K}{F} \right) = \frac{[17(1000 - 4) + (17 + 1) \times 4]}{1000}$$

$$= \frac{[16932 + 72]}{1000} = 17.004$$

$$F_{out} = 50 \text{ MHz} \times \frac{[16932 + 72]}{1000}$$

$$= 846.6 \text{ MHz} + 3.6 \text{ MHz}$$

$$= 850.2 \text{ MHz}$$

Table 2. Modern Spur Suppression Methods

Technique	Feature	Problem
DAC phase estimation	Cancel spur by DAC	Analog mismatch
Pulse generation	Insert pulses	Interpolation jitter
Phase interpolation	Inherent fractional divider	Interpolation jitter
Random jittering	Randomize divider	Frequency jitter
Sigma-delta modulation	Modulate division ratio	Quantization noise

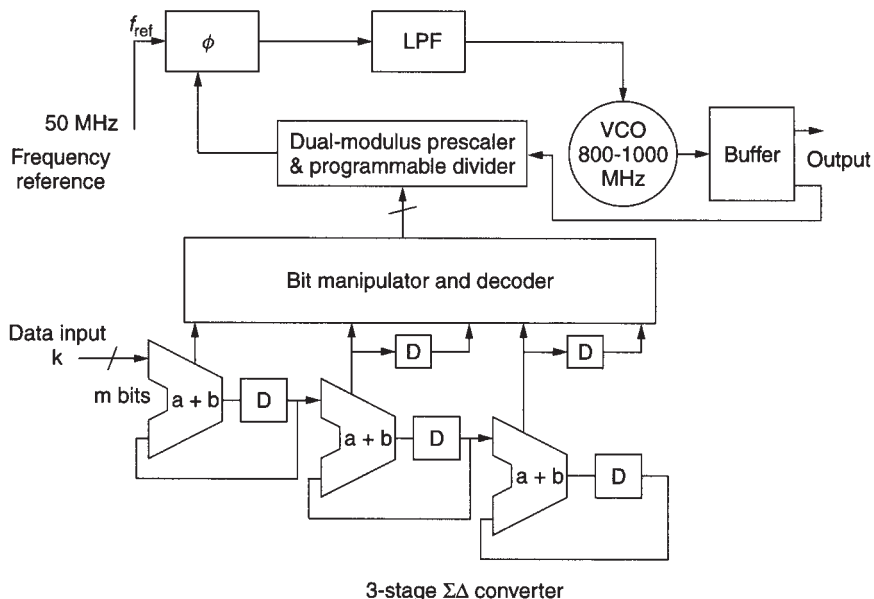


Figure 59. Block diagram of the fractional-*N* synthesizer built using a custom IC capable of operation at reference frequencies up to 150 MHz. The frequency is extensible up to 3 GHz using binary ($\div 2, \div 4, \div 8$, etc.) and fixed-division counters.

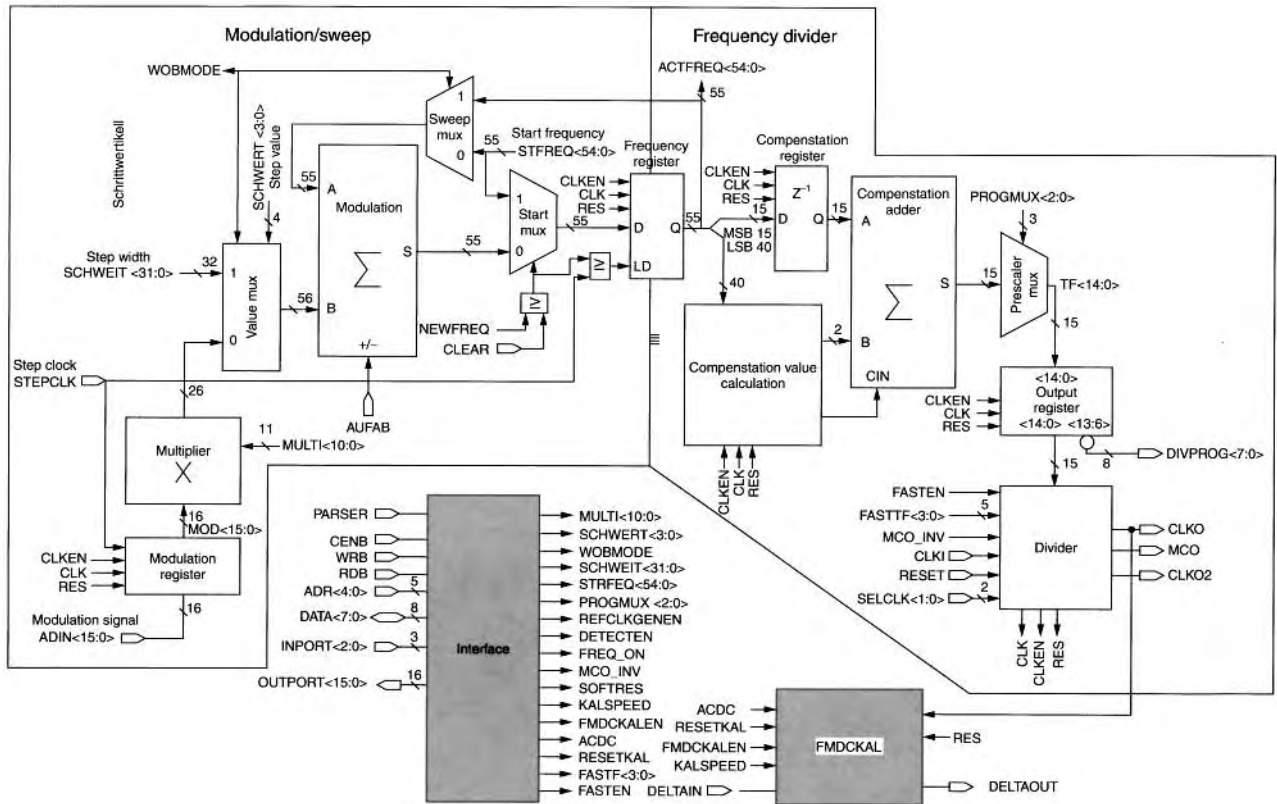


Figure 60. Detailed block diagram of the inner workings of the fractional-*N*-division synthesizer chip.

By increasing the number of accumulators, frequency resolution much below 1 Hz stepsize is possible with the same switching speed.

There is an interesting, generic problem associated with *all* fractional-*N* synthesizers. Assume for a moment that we use our 50-MHz reference and generate a 550-MHz output frequency. This means that our division factor is 11. Aside from reference-frequency sidebands (± 50 MHz) and harmonics, there will be no unwanted spurious frequencies. Of course, the reference sidebands will be suppressed by the loop filter by more than 90 dB. For reasons of phase noise and switching speed, a loop bandwidth of 100 kHz has been considered. Now, taking advantage of the fractional-*N* principle say that we want to operate at an offset of 30 kHz (550.03 MHz). With this new output frequency, the inherent spurious-signal reduction mechanism in the fractional-*N* chip limits the reduction to about 55 dB. Part of the reason why the spurious-signal suppression is less in this case is that the phase-frequency detector acts as a mixer, collecting both the 50-MHz reference (and its harmonics) and 550.03 MHz. Mixing the 11th reference harmonic (550 MHz) and the output frequency (550.03 MHz) results in output at 30 kHz; as the loop bandwidth is 100 kHz, it adds nothing to the suppression of this signal. To solve this, we could consider narrowing the loop bandwidth to 10% of the off-

set. A 30 kHz offset would equate to a loop bandwidth of 3 kHz, at which the loop speed might still be acceptable, but for a 1-Hz offset, the necessary loop bandwidth of 100 Hz would make the loop too slow. A better way is to use a different reference frequency—one that would place the resulting spurious product considerably outside the 100-kHz loop filter window. If, for instance, we used a 49-MHz reference, multiplication by 11 would result in 539 MHz. Mixing this with 550.03 MHz would result in spurious signals at ± 11.03 MHz, a frequency so far outside the loop bandwidth that it would essentially disappear. Starting with a VHF, low-phase-noise crystal oscillator, such as 130 MHz, one can implement an intelligent reference-frequency selection to avoid these discrete spurious signals. An additional method of reducing the spurious contents is maintaining a division ratio greater than 12 in all cases. Actual tests have shown that these reference-based spurious frequencies can be repeatedly suppressed by 80–90 dB.

6.1. Spur Suppression Techniques

Although several methods have been proposed in the literature, the method of reducing the noise by using a sigma-delta modulator has shown to be most promising. The concept is to get rid of the low-frequency phase error by rapidly switching the division ratio to eliminate the grad-

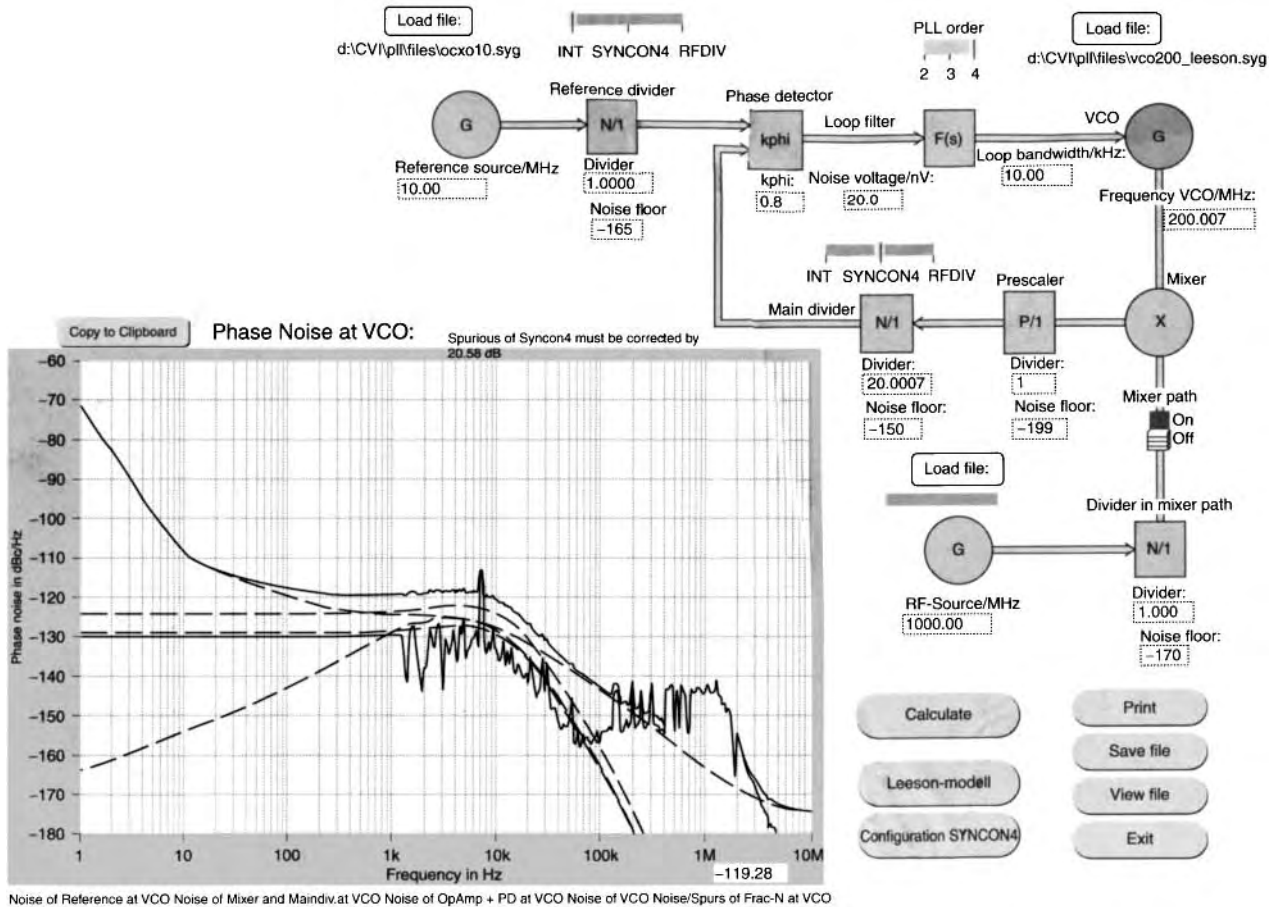


Figure 61. Composite phase noise of the fractional-*N* synthesizer system, including all noise and spurious signals generated within the system. The discrete spurious of 7 kHz is due to the non-linearity of the phase detector. Its value needs to be corrected by 20.58 dB to a lesser value because of the bandwidth of the FFT analyzer.

ual phase error at the discriminator input. By changing the division ratio rapidly between different values, the phase errors occur in both polarities, positive as well as negative, and at an accelerated rate that explains the phenomenon of high-frequency noise pushup. This noise, which is converted to a voltage by the phase/frequency discriminator and loop filter, is filtered out by the lowpass filter. The main problem associated with this noise shaping technique is that the noise power rises rapidly with frequency. Figure 58 shows noise contributions with such a sigma-delta modulator in place.

On the other hand, we can now, for the first time, build a single-loop synthesizer with switching times as fast as 6 μs and very little phase-noise deterioration inside the loop bandwidth, as seen in Fig. 58. As this system maintains the good phase noise of the ceramic-resonator-based oscillator, the resulting performance is significantly better than the phase noise expected from high-end signal generators. However, this method does not allow us to increase the loop bandwidth beyond the 100-kHz limit, where the noise contribution of the sigma-delta modulator takes over.

Table 2 shows some of the modern spur suppression methods. These three-stage sigma-delta methods with larger accumulators have the most potential.

The power spectral response of the phase noise for the three-stage sigma-delta modulator is calculated from

$$L(f) = \frac{(2\pi)^2}{12 \times f_{ref}} \times \left[2 \sin\left(\frac{\pi f}{f_{ref}}\right) \right]^{2(n-1)} \text{ rad}^2/\text{Hz} \quad (78)$$

where *n* is the number of the stage of the cascaded sigma-delta modulator. Equation (78) shows that the phase noise resulting from the fractional controller is attenuated to negligible levels close to the center frequency, and further from the center frequency, the phase noise is increased rapidly and must be filtered out prior to the tuning input of the VCO to prevent unacceptable degradation of spectral purity. A loop filter must be used to filter the noise in the PLL loop. Figure 58 showed the plot of the phase noise versus the offset frequency from the center frequency. A fractional-*N* synthesizer with a three-stage sigma-delta modulator as shown in Fig. 59 has been built. The

synthesizer consists of a phase/frequency detector, an active lowpass filter (LPF), a voltage-controlled oscillator (VCO), a dual-modulus prescaler, a three-stage sigma-delta modulator, and a buffer. Figure 60 shows the inner workings of the chip in greater detail.

After designing, building, and predicting the phase noise performance of this synthesizer, it becomes clear that measuring the phase noise of such a system becomes tricky. Standard measurement techniques that use a reference synthesizer will not provide enough resolution because there are no synthesized signal generators on the market sufficiently good enough to measure such low values of phase noise. Therefore, a comb generator is needed that would take the output of the oscillator and multiply this up 10–20 times.

Figure 61 shows a simulated phase noise and termination of spurious outputs for the fraction- N -division synthesizer with $\Sigma\Delta$ converter. At the moment, it is unclear if the PLL with DDS or the fractional- N -division synthesizer principle with $\Sigma\Delta$ converter is the winning approach. The DDS typically requires two or three loops and is much more expensive, while the fractional- N approach requires only one loop and is a very intelligent spurious removal circuit, and high-end solutions are typically custom built [96–111].

BIBLIOGRAPHY

- U. L. Rohde and J. Whitaker, *Communications Receivers*, 3rd ed., McGraw-Hill, New York, Dec. 2000.
- L. E. Larson, *RF and Microwave Circuit Design for Wireless Communications*, Artech House, Norwood, MA, 1996.
- U. L. Rohde, *Microwave and Wireless Synthesizers: Theory and Design*, Wiley, New York, Aug. 1997.
- W. F. Egan, *Frequency Synthesis by Phase Lock*, Wiley-Interscience, New York, 1981.
- F. Gardner, *Phaselock Techniques*, 2nd Edition, Wiley-Interscience, New York, 1979.
- J. Gorski-Popiel, *Frequency Synthesis: Techniques and Applications*, IEEE, New York, 1975.
- V. F. Kroupa, *Frequency Synthesis: Theory, Design, and Applications*, Wiley, New York, 1973.
- V. Manassewitsch, *Frequency Synthesizers: Theory and Design*, Wiley, New York, 1976.
- Roland E. Best, *Phase-Locked Loops: Theory, Design, and Applications*, McGraw-Hill, New York, 1989.
- P. Danzer, ed., AC/RF sources (oscillators and synthesizers), in *The ARRL Handbook for Radio Amateurs*, 75th ed., ARRL, Newington, 1997, Chap. 14.
- C. R. Chang and U. L. Rohde, The accurate simulation of oscillator and PLL phase noise in RF sources, *Proc. Wireless '94 Symposium*, Santa Clara, CA, Feb. 15–18, 1994.
- M. M. Driscoll, Low noise oscillator design using acoustic and other high Q resonators, *Proc. 44th Annual Sympo. Frequency Control*, Baltimore, MD, May 1990.
- U. L. Rohde, Low-noise frequency synthesizers fractional N phase-locked loops, *Proc. SOUTHCON/81*, Jan. 1981.
- W. C. Lindsey and C. M. Chie, eds., *Phase-Locked Loops*, IEEE Press, New York, 1986.
- A. Albarello, A. Rouillet, and A. Pimentel, *Fractional-Division Frequency Synthesizer for Digital Angel-Modulation*, Thomson-CSF, U.S. Patent 4,492,936 (Jan. 8, 1985).
- C. Attenborough, *Fractional- N Frequency Synthesizer with Modulation Compensation*, Plessey Overseas Ltd., Ilford, UK, U.S. Patent 4,686,488 (Aug. 11, 1987).
- R. J. Bosselaers, *PLL Including an Arithmetic Unit*, U.S. Patent 3,913,928 (Oct. 1975).
- R. G. Cox, *Frequency Synthesizer*, Hewlett-Packard Company, U.S. Patent 2,976,945.
- J. A. Crawford, *Enhanced Analog Phase Interpolation for Fractional- N Frequency Synthesis*, Hughes Aircraft Company, Los Angeles, CA, U.S. Patent 4,586,005 (April 29, 1986).
- A. T. Crowley, *PLL Frequency Synthesizer Including Fractional Digital Frequency Divider*, RCA Corporation, New York, U.S. Patent 4,468,632 (Aug. 28, 1984).
- A. P. Edwards, *Low Phase Noise RF Synthesizer*, Hewlett-Packard Company, Palo Alto, CA, U.S. Patent 4,763,083 (Aug. 9, 1988).
- B. G. Goldberg, *Digital Frequency Synthesizer*, Sciteq Electronics, Inc., San Diego, CA, U.S. Patent 4,752,902 (June 21, 1988).
- B. G. Goldberg, *Digital Frequency Synthesizer Having Multiple Processing Paths*, U.S. Patent 4,958,310 (Sept. 18, 1990).
- B. G. Goldberg, *Programmable Fractional- N Frequency Synthesizer*, Sciteq Electronics, Inc., San Diego, CA, U.S. Patent 5,224,132 (June 29, 1993).
- B. G. Goldberg, Analog and digital fractional- n PLL frequency synthesis: A survey and update, *Appl. Microwave Wireless* 32–42. (June 1999).
- W. G. Greken, *Digital Frequency Synthesizer*, General Dynamics, U.S. Patent 3,882,403.
- A. W. Hietala and D. C. Rabe, *Latched Accumulator Fractional N Synthesis with Residual Error Reduction* Motorola, Inc., Schaumburg, IL, U.S. Patent 5,093,632 (March 3, 1992).
- L. Jackson, *Digital Frequency Synthesizer*, U.S. Patent 3,734,269 (May 1973).
- T. Jackson, *Fractional- N Synthesizer*, Plessey Overseas Ltd., Ilford, UK, U.S. Patent 4,758,802 (July 19, 1988).
- T. Jackson, *Frequency Synthesizer of the Fractional Type*, Plessey Overseas Ltd., Ilford, UK, U.S. Patent 4,800,342 (Jan. 24, 1989).
- T. Jackson, *Improvement In or Relating to Synthesizers*, Plessey Overseas Ltd., Ilford Essex, UK, Eur. Patent 0214217B1 (June 6, 1996).
- T. Jackson, *Improvement In or Relating to Synthesizers*, Plessey Overseas Ltd., Ilford, Essex, UK, Eur. Patent WO86/05046 (Aug. 28, 1996).
- N. J. R. King, *Phase Locked Loop Variable Frequency Generator*, Racal Communications Equipment Ltd., UK, U.S. Patent 4,204,174 (May 20, 1980).
- N. G. Kingsbury, *Frequency Synthesizer with Fractional Division Ratio and Jitter Compensation*, Marconi Company Ltd., Chelmsford, UK, U.S. Patent 4,179,670 (Dec. 18, 1979).
- C. A. Kingsford-Smith, *Device for Synthesizing Frequencies Which Are Rational Multiples of a Fundamental Frequency*, Hewlett-Packard Company, Palo Alto, CA, U.S. Patent 3,928,813 (Dec. 23, 1975).
- F. L. Martin, *Frequency Synthesizer with Spur Compensation*, Motorola, Inc., Schaumburg, IL, U.S. Patent 4,918,403 (April 17, 1990).

37. F. L. Martin, *Frequency Synthesizer with Spur Compensation*, Motorola, U.S. Patent 4,816,774 (March 28, 1989).
38. K. D. McCann, *Frequency Synthesizer Having Jitter Compensation*, U.S. Philips Corp., New York, U.S. Patent 4,599,579 (July 8, 1986).
39. B. M. Miller, *Multiple-Modulator Fractional-N Divider*, Hewlett-Packard Company, U.S. Patent 5,038,117 (Aug. 6, 1991).
40. E. J. Nossen, *Digitized Frequency Synthesizer*, RCA Corp., New York, U.S. Patent 4,206,425 (June 3, 1980).
41. O. Peña, SPICE tools provide behavioral modeling of PLLs, *Microwaves RF* 71–80 (Nov. 1977).
42. V. S. Reinhardt and I. Shahriary, *Spurless Fractional Divider Direct Digital Frequency Synthesizer and Method*, Hughes Aircraft Company, Los Angeles, CA, U.S. Patent 4,815,018 (March 21, 1989).
43. J. Remy, *Frequency Synthesizer Including a Fractional Multiplier*, Adret Electronique, Paris, France, U.S. Patent 4,458,329 (July 3, 1984).
44. T. A. D. Riley, *Frequency Synthesizers Having Dividing Ratio Controlled Sigma-Delta Modulator*, Carleton Univ., Ottawa, Canada, U.S. Patent 4,965,531 (Oct. 23, 1990).
45. W. P. Shepherd, D. E. Davis, and W. F. Tay, *Fractional-N Synthesizer Having Modulation Spur Compensation*, Motorola, Inc., Schaumburg, IL, U.S. Patent 5,021,754 (June 4, 1991).
46. W. J. Tanis, *Frequency Synthesizer Having Fractional-N Frequency Divider in PLL*, Engelman Microwave, U.S. Patent 3,959,737 (May 25, 1976).
47. J. N. Wells, *Frequency Synthesizers*, Marconi Instruments, St. Albans, Hertfordshire, UK, Eur. Patent 0125790B2 (July 5, 1995).
48. J. N. Wells, *Frequency Synthesizers*, Marconi Instruments Ltd., St. Albans, UK, U.S. Patent 4,609,881 (Sept. 2, 1986).
49. C. E. Wheatley III, *Digital Frequency Synthesizer with Random Jittering for Reducing Discrete Spectral Spurs*, Rockwell International Corp., El Segundo, CA, U.S. Patent 4,410,954 (Oct. 18, 1983).
50. M. A. Wheatley, L. A. Lepper, and N. K. Webb, *Frequency Modulated Phase Locked Loop with Fractional Divider and Jitter Compensation*, Racal-Dana Instruments Ltd., Berkshire, UK, U.S. Patent 5,038,120 (Aug. 6, 1991).
51. R. O. Yaeger, *Fractional Frequency Divider*, RCA Corp., Princeton, NJ, U.S. Patent 4,573,176 (Feb. 25, 1986).
52. U. L. Rohde, A high performance synthesizer for base stations based on the fractional-N synthesis principle, *Microwaves RF Mag.* (April 1998).
53. U. L. Rohde and G. Klage, Analyze VCOs and fractional-N synthesizers, *Microwaves RF* (Aug. 2000).
54. R. Hassun and A. Kovalic, An arbitrary waveform synthesizer for DC to 50 MHz, *Hewlett-Packard J.* (Palo Alto, CA) (April 1988).
55. L. R. Rabiner and B. Gold, *Theory and Application of Digital Signal Processing*, Prentice-Hall, Englewood Cliffs, NJ, 1975, Chap. 2.
56. H. T. Nicholas and H. Samuelli, An analysis of the output spectrum of direct digital frequency synthesizers in the presence of phase-accumulator truncation, *Proc. 41st Annual Frequency Control Symp.*, IEEE Press, New York, 1987.
57. L. B. Jackson, Roundoff noise for fixed point digital filters realized in cascade or parallel form, *IEEE Trans. Audio Electroacoust.* **AU-18**:107–122 (June 1970).
58. Technical Staff of Bell Laboratories, *Transmission Systems for Communication*, Bell Labs, Inc., 1970, Chap. 25.
59. A. Kovalick, *Apparatus and Method of Phase to Amplitude Conversion in a SIN Function Generator*, U.S. Patent 4,482,974.
60. C. J. Paull and W. A. Evans, Waveform shaping techniques for the design of signal sources, *Radio Electron. Eng.* **44**(10) (Oct. 1974).
61. L. Barnes, Linear segment approximations to a sinewave, *Electron. Eng.* **40** (Sept. 1968).
62. R. Hassun and A. Kovalick, *Waveform Synthesis Using Multiplexed Parallel Synthesizers*, U.S. Patent 4,454,486.
63. D. K. Kikuchi, R. F. Miranda, and P. A. Thysel, A waveform generation language for arbitrary waveform synthesis, *Hewlett-Packard J.* (Palo Alto, CA) (April 1988).
64. H. M. Stark, *An Introduction to Number Theory*, MIT Press, Cambridge, MA, 1978, Chap. 7.
65. W. Sagun, Generate complex waveforms at very high frequencies, *Electron. Design* (Jan. 26, 1989).
66. G. Lowitz and R. Armitano, Predistortion improves digital synthesizer accuracy, *Electron. Design* (March 31, 1988).
67. A. Kovalic, Digital synthesizer aids in testing of complex waveforms, *EDN Mag.* (Sept. 1, 1988).
68. G. Lowitz and C. Pederson, RF testing with complex waveforms, *RF Design* (Nov. 1988).
69. C. M. Merigold, in K. Fehrer, ed., *Telecommunications Measurement Analysis and Instrumentation*, Prentice-Hall, Englewood Cliffs, NJ, 1987.
70. *Synergy Microwave Corporation Designer Handbook*, Specifications of Synthesizers, 2001.
71. G. Vendelin, A. M. Pavio, and U. L. Rohde, *Microwave Circuit Design Using Linear and Nonlinear Techniques*, Wiley, New York, Jan. 1990.
72. J. A. Crawford, *Frequency Synthesizer Design Handbook*, Artech House, Norwood, MA, 1994.
73. D. B. Leeson, Short-term stable microwave sources, *Microwave J.* 59–69 (June 1970).
74. J. Smith, *Modern Communication Circuits*, McGraw-Hill, New York, 1986, pp. 252–261.
75. J. S. Yuan, Modeling the bipolar oscillator phase noise, *Solid State Electron.* **37**(10):1765–1767 (Oct. 1994).
76. D. Scherer, Design principles and test methods for low phase noise RF and microwave sources. *RF Microwave Measurement Symposium and Exhibition*, Hewlett-Packard.
77. S. Alechno, Analysis method characterizes microwave oscillators, *Microwaves RF* 82–86 (Nov. 1997).
78. W. Anzill, F. X. Kärtner, and P. Russer, Simulation of the single-sideband phase noise of oscillators, *Proc. 2nd Int. Workshop of Integrated Nonlinear Microwave and Millimeterwave Circuits*, 1992.
79. N. Boutin, RF oscillator analysis and design by the loop gain method, *Appl. Microwave Wireless* 32–48 (Aug. 1999).
80. P. Braun, B. Roth, and A. Beyer, A measurement setup for the analysis of integrated microwave oscillators, *Proc. 2nd Int. Workshop of Integrated Nonlinear Microwave and Millimeterwave Circuits*, 1992.
81. C. R. Chang et al., Computer-aided analysis of free-running microwave oscillators, *IEEE Trans. Microwave Theory Tech.* **39**:1735–1745 (Oct. 1991).
82. P. Davis et al., Silicon-on-silicon integration of a GSM transceiver with VCO resonator, *1998 IEEE Int. Solid-State Circuits Conf. Digest Tech. Papers*, 1998, pp. 248–249.
83. P. J. Garner, M. H. Howes, and C. M. Snowden, *Ka-Band and MMIC pHEMT-based VCO's with low phase-noise proper-*

- ties, *IEEE Trans. Microwave Theory Tech.* **46**:1531–1536 (Oct. 1998).
84. A. V. Grebennikov and V. V. Nikiforov, An analytic method of microwave transistor oscillator design, *Int. J. Electron.* **83**:849–858 (Dec. 1997).
 85. A. Hajimiri and T. H. Lee, A general theory of phase noise in electrical oscillators, *IEEE J. Solid-State Circ.* **33**:179–194 (Feb. 1998).
 86. Q. Huang, On the exact design of RF oscillators, *Proc. IEEE 1998 Custom Integrated Circuits Conf.*, 1998, pp.41–44.
 87. Fairchild Data Sheet: *Phase/Frequency Detector, 11C44*, Fairchild Semiconductor, Mountain View, CA.
 88. Fairchild Preliminary Data Sheet: *SH8096 Programmable Divider-Fairchild Integrated Microsystems*, April 1970.
 89. U. L. Rohde, *Digital PLL Frequency Synthesizers—Theory and Design*, Prentice-Hall, Englewood Cliffs, NJ, Jan. 1983.
 90. W. Egan and E. Clark, Test your charge-pump phase detectors, *Electron. Design* **26**(12):134–137 (June 7, 1978).
 91. S. Krishnan, Diode phase detectors, *Electron. Radio Eng.* 45–50 (Feb. 1959).
 92. Motorola Data Sheet: *MC12012*, Motorola Semiconductor Products, Inc. Phoenix, AZ, 1973.
 93. Motorola Data Sheet: *Phase-Frequency Detector, MC4344, MC4044*.
 94. U. L. Rohde and D. P. Newkirk, *RF/Microwave Circuit Design for Wireless Applications*, Wiley, New York, April 2000.
 95. W. C. Lindsey and M. K. Simon, eds., *Phase-Locked Loops & Their Application*, IEEE Press, New York, 1978.
 96. W. Z. Chen and J. T. Wu, A 2 V 1.6 GHz BJT phase-locked loop, *Proc. IEEE 1998 Custom Integrated Circuits Conf.*, 1998, pp. 563–566.
 97. J. Craninckx and M. Steyaert, A fully integrated CMOS DCS-1800 frequency synthesizer, *1998 IEEE Int. Solid-State Circuits Conf. Digest Tech. Papers*, 1998, pp. 372–373.
 98. B. De Smedt and G. Gielen, Nonlinear behavioral modeling and phase noise evaluation in phase locked loops, *Proc. IEEE 1998 Custom Integrated Circuits Conf.*, 1998, pp. 53–56.
 99. N. M. Filiol et al., An agile ISM band frequency synthesizer with built-in GMSK data modulation, *IEEE J. Solid-State Circ.* **33**(7):998–1007 (July 1998).
 100. Fujitsu Microelectronics, Inc., *Super PLL Application Guide*, 1998.
 101. Hewlett-Packard Application Note 164-3, *New Technique for Analyzing Phase-Locked Loops*, June 1975.
 102. V. F. Kroupa, ed., *Direct Digital Frequency Synthesizers*, IEEE Press, New York, 1999.
 103. S. Lo, C. Olgaard, and D. Rose, A 1.8 V/3.5 mA 1.1 GHz/300 MHz CMOS dual PLL frequency synthesizer IC for RF communications, *Proc. IEEE 1998 Custom Integrated Circuits Conf.*, 1998, pp. 571–574.
 104. G. Palmisano et al., Noise in fully-integrated PLLs, *Proc. 6th AACD 97*, Como, Italy, 1997.
 105. B. H. Park and P. E. Allen, A 1GHz, low-phase-noise CMOS frequency synthesizer with integrated LC VCO for wireless communications, *Proc. IEEE 1998 Custom Integrated Circuits Conf.*, 1998, pp. 567–570.
 106. B. Sam, Hybrid frequency synthesizer combines octave tuning range and millihertz steps, *Appl. Microwave Wireless* 76–84 (May 1999).
 107. M. Smith, *Phase Noise Measurement Using the Phase Lock Technique*, Wireless Subscriber Systems Group (WSSG) AN1639, Motorola.
 108. V. von Kaenel et al., A 600 MHz CMOS PLL microprocessor clock generator with a 1.2 GHz VCO, *1998 IEEE Int. Solid-State Circuits Conf. Digest Tech. Papers*, 1998, pp. 396–397.
 109. Motorola MECL Data Book, 1993, Chapter 6, “Phase-Locked Loops.”
 110. U. L. Rohde, Low noise microwave synthesizers, WFFDS: Advances in microwave and millimeter-wave synthesizer technology, *Proc. IEEE-MIT-Symp.*, Orlando, FL, May 19, 1995.
 111. U. L. Rohde, Oscillator design for lowest phase noise, *Microwave Eng. Europe* 35–40 (May 1994).

PHASE NOISE AND MEASUREMENTS

HENG-CHIA CHANG
RF System, Blue 7
Communications, Inc.
Fremont, California

1. INTRODUCTION TO PHASE NOISE THEORY

In modern communications phase noise has challenged the wireless communication circuits and systems on the performance. Phase noise has been known to limit the operating range, precision, and sensitivity of various communication systems, such as the radars and satellite communications. Before characterizing the phase noise and its limit on the systems, one must know some mathematical expressions and terminology of phase noise. Here we are only interested in phase noise (or phase fluctuation) and neglect amplitude fluctuation. The signal of interest can be expressed as

$$\begin{aligned} v(t) &= A \cos(\theta(t)) = A \cos(\theta_0(t) + \delta\theta(t)) \\ &= A \cos(2\pi f_0 t + \delta\theta(t)) = A \cos(2\pi(f_0 + \delta f)t) \end{aligned} \quad (1)$$

where A is the amplitude of the voltage signal, θ_0 the signal phase, and f_0 the signal frequency, respectively. $\delta\theta(t)$ and $\delta f(t)$ are the phase and frequency fluctuation of the signal around the nominal phase $\theta_0(t) = 2\pi f_0 t$ and frequency f_0 , respectively. The averaged output power of the signal expressed in (1) is $P_0 = A^2 / (2R_L)$, where R_L is the output load resistance in the measurement system.

The phase noise of the signal can be characterized in either frequency or time domain. In the frequency domain, phase noise is related to the spectral density of the phase or frequency fluctuation in the signal [2–8]. In the time domain, the phase noise is characterized by using the jitter instead, as the zero crossing of the signal is easily

measured. In the following, we characterize the phase noise only in the frequency domain.

1.1. Phase Noise Expression

Phase or frequency fluctuations in the signals can be characterized in frequency domain by using Fourier transform. From (1), one has

$$\delta\theta(t) = 2\pi\delta f(t)t \tag{2}$$

Because such fluctuations are random or stochastic in nature, one needs to calculate the power spectral density of the phase fluctuation $\delta\theta(t)$ [or frequency fluctuation $\delta f(t)$]. From the Wiener–Khintchine theorem, the autocorrelation and power spectral density of $\delta\theta(t)$ are defined as

$$R_\theta(\tau) \equiv \langle \delta\theta^*(t)\delta\theta(t + \tau) \rangle$$

$$S_\theta(\omega_m = 2\pi f_m) \equiv \int_{-\infty}^{\infty} R_\theta(\tau)e^{-j\omega_m\tau} d\tau = F_\tau[R_\theta(\tau)] \tag{3}$$

respectively, where $\langle \rangle$ is the ensemble average, (*) is the complex conjugate, and τ is the time delay. The Fourier transform of (2) is defined as

$$F_t[\delta f(t)] = \tilde{\delta f}(f_m) = \int_{-\infty}^{\infty} \delta f(t)e^{-j2\pi f_m t} dt$$

$$= F_t \left[\frac{1}{2\pi} \frac{d(\delta\theta(t))}{dt} \right] = \frac{1}{2\pi} (j2\pi f_m) \tilde{\delta\theta}(f_m) \tag{4}$$

where F_t denotes the Fourier transform of t from the time domain to the frequency domain, (\sim) the spectral variable, f_m is the noise offset frequency relative to the carrier frequency f_0 , and the subscript “m” denotes the modulation caused by the noise source.

The phase fluctuation $\delta\theta(t)$ is assumed ergodic random process, where the time average is equal to its ensemble

average. Thus, one has

$$R_\theta(\tau) = \langle \delta\theta^*(t)\delta\theta(t + \tau) \rangle$$

$$= \int_{-\infty}^{\infty} \delta\theta^*(t)\delta\theta(t + \tau) dt$$

$$= \int_{-\infty}^{\infty} \left[\int_{-\infty}^{\infty} \tilde{\delta\theta}^*(\omega_m) e^{-j\omega_m t} d\omega_m \right]$$

$$\left[\int_{-\infty}^{\infty} \tilde{\delta\theta}(\omega'_m) e^{j\omega'_m(t + \tau)} d\omega'_m \right] dt$$

$$= \int_{-\infty}^{\infty} \int_{-\infty}^{\infty} \int_{-\infty}^{\infty} \tilde{\delta\theta}^*(\omega_m) \tilde{\delta\theta}(\omega'_m) e^{j(\omega'_m - \omega_m)t} e^{j\omega'_m\tau} dt d\omega_m d\omega'_m$$

$$= \int_{-\infty}^{\infty} \int_{-\infty}^{\infty} \tilde{\delta\theta}^*(\omega_m) \tilde{\delta\theta}(\omega'_m) \delta(\omega'_m - \omega_m) e^{j\omega'_m\tau} d\omega_m d\omega'_m$$

$$= \int_{-\infty}^{\infty} \tilde{\delta\theta}^*(\omega_m) \tilde{\delta\theta}(\omega_m) e^{j\omega_m\tau} d\omega_m$$

$$= \int_{-\infty}^{\infty} |\tilde{\delta\theta}(\omega_m)|^2 e^{j\omega_m\tau} d\omega_m$$

$$= F_{\omega_m}^{-1} [|\tilde{\delta\theta}(\omega_m)|^2] \tag{5}$$

where $\int_{-\infty}^{\infty} e^{j(\omega'_m - \omega_m)t} dt = \delta(\omega'_m - \omega_m)$ and $F_{\omega_m}^{-1}$ is the inverse Fourier transform of ω_m from the frequency domain to the time domain. Then the power spectral density of the phase fluctuation $\delta\theta(t)$ becomes

$$S_\theta(\omega_m = 2\pi f_m) = F_\tau[R_\theta(\tau)]$$

$$= F_\tau[F_{\omega_m}^{-1} [|\tilde{\delta\theta}(\omega_m)|^2]]$$

$$= \langle |\tilde{\delta\theta}(\omega_m)|^2 \rangle \tag{6}$$

In typical phase noise measurements, the power spectral density of the phase fluctuation (or phase noise) is measured relative to the averaged signal power P_0 at the carrier frequency $\omega_0 = 2\pi f_0$. One can obtain the spectral density of the phase fluctuations (i.e., the phase noise or

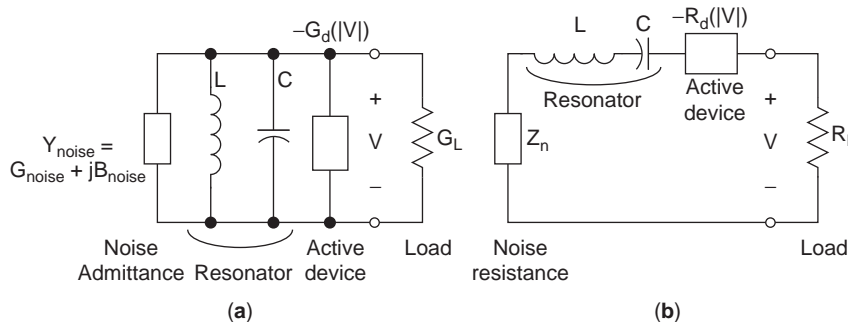


Figure 1. The oscillator phase noise model with noise admittance or resistance dependent on the oscillator equivalent circuits.

PM noise) and frequency fluctuations (i.e., FM noise)

$$S_{\theta}(f_m) \equiv \langle |\tilde{\delta}\theta(f_m)|^2 \rangle / P_0 \quad (7)$$

$$\begin{aligned} S_f(f_m) &\equiv \langle |\tilde{\delta}f(f_m)|^2 \rangle / P_0 = f_m^2 \langle |\tilde{\delta}\theta(f_m)|^2 \rangle / P_0 \\ &= f_m^2 S_{\theta}(f_m) \end{aligned} \quad (8)$$

respectively.

1.2. Free-Running Oscillator Result

The oscillator has been the driving force of modern communication systems, and it can be modeled by the equivalent circuits shown in Figs. 1a and 1b to obtain important phase noise features. The active device is modeled by a negative conductance or resistance embedded in parallel or series-resonant circuits, respectively. The negative conductance $-G_d(|V|)$ or resistance $-R_d(|V|)$ is assumed to be independent of frequency, but dependent on the oscillation signal amplitude nonlinearly. Here we only use the parallel-resonant circuit model to derive the noise as illustration. The noise source of the oscillator can be modeled by adding the noise conductance or resistance [7,8]. The same derivation can be applied to series-resonant oscillator model. The circuit equation of parallel-resonant oscillator model is

$$C \frac{dV}{dt} + \frac{1}{L} \int V dt + (G_L - G_d(|V|) + Y_n)V = 0 \quad (9)$$

The integral of this equation can be approximated by integration by parts [6] to give

$$\int V dt = -\frac{2jV}{\omega_0} + \frac{1}{\omega_0^2} \frac{dV}{dt} + \dots \quad (10)$$

By substituting (10) into (9), $\omega_0^2 = 1/(LC)$, and $Q = \omega_0 C/G_L$ (the Q factor of a parallel-resonant circuit), one can obtain

$$\frac{dV}{dt} = j\omega_0 V - \frac{\omega_0}{2Q} \left(1 - \frac{G_d(|V|)}{G_L}\right) V - \frac{\omega_0 Y_n}{2QG_L} V \quad (11)$$

where the Q factor of the oscillator is high enough so that the oscillation frequency is close to ω_0 . The output signal of the oscillator can be expressed as

$$V(t) = A(t)e^{j\theta(t)} \quad (12)$$

where $A(t)$ and $\theta(t)$ are the amplitude and phase, respectively. Then the imaginary and real parts of (11) with (12) become the phase and amplitude dynamics

$$\frac{d\theta}{dt} = \omega_0 - \frac{\omega_0}{2Q} B_n \quad (13)$$

$$\frac{dA}{dt} = -\frac{\omega_0}{2Q} \left(1 - \frac{G_d}{G_L}\right) A - \frac{\omega_0}{2Q} G_n A \quad (14)$$

respectively, where $G_n = G_{\text{noise}}/G_L$ and $B_n = B_{\text{noise}}/G_L$. The amplitude saturation constant α is modeled as

$$1 - \frac{G_d(|V|)}{G_L} \approx -\mu_p \left(1 - \frac{A^2}{\alpha^2}\right) \quad (15)$$

and the subscript ‘‘p’’ denotes the parallel-resonant oscillator model.

For noise analysis, the equations above are perturbed by substituting $A \rightarrow \hat{A} + \delta A$ and $\theta \rightarrow \hat{\theta} + \delta\theta$ into (13) and (14), where $(\hat{A}, \hat{\theta})$ are the steady-state solutions to (13) and (14) and $(\delta A, \delta\theta)$ are the amplitude and phase fluctuations, respectively. Assuming small fluctuations, the equations can be linearized around $(\hat{A}, \hat{\theta})$ to become

$$\frac{d\delta\theta(t)}{dt} = -\frac{\omega_0}{2Q} B_n(t) \quad (16)$$

$$\begin{aligned} \frac{d\delta A(t)}{dt} &= -\frac{\omega_0}{2Q} \mu_p \left(1 - \frac{3\hat{A}^2}{\alpha^2}\right) \delta A(t) \\ &\quad - \frac{\omega_0}{2Q} \hat{A} G_n(t) \end{aligned} \quad (17)$$

where $\omega_{3\text{dB}} = \omega_0/(2Q)$ is the half the full-width half-maximum frequency of the oscillator. By Fourier transforming these equations, one can obtain

$$\frac{J\omega_m}{\omega_{3\text{dB}}} \tilde{\delta}\theta = -\tilde{B}_n \quad (18)$$

$$\left[\frac{J\omega_m}{\omega_{3\text{dB}}} - \mu_p \left(1 - 3\frac{\hat{A}^2}{\alpha^2}\right) \right] \tilde{\delta A} = -\hat{A} \tilde{G}_n \quad (19)$$

Therefore, from the previous phase noise expressions one can obtain the PM noise of single free-running oscillator

$$\langle |\tilde{\delta}\theta|^2 \rangle_{\text{uncoupled}} = \frac{\langle |\tilde{B}_n|^2 \rangle}{(\omega_m/\omega_{3\text{dB}})^2} \quad (20)$$

and the AM noise

$$\langle |\tilde{\delta A}|^2 \rangle_{\text{uncoupled}} = \frac{\hat{A}^2 \langle |\tilde{G}_n|^2 \rangle}{(\omega_m/\omega_{3\text{dB}})^2 + \mu_p^2 \left(3\frac{\hat{A}^2}{\alpha^2} - 1\right)^2} \quad (21)$$

where α and \hat{A} are the free-running oscillator amplitude and the steady-state amplitude after coupling, respectively.

These results have the same form as those in Kurokawa’s and Schlosser’s papers [4,5]. Note that for most oscillators, noise close to the carrier ($\omega_m \ll \omega_{3\text{dB}}$) is dominated by phase noise. This somewhat justifies our neglect of amplitude noise and AM-to-PM conversion [8]. The result (20) features prominently in the following derivations.

1.3. Leeson's Model and Noise Admittance/Resistance

The noise admittance (or noise resistance) has been used to model the intrinsic oscillator noise sources, and the theory matches very well with the experimental results. However, Leeson's oscillator model, shown in Fig. 2, has often been used because it explains the power-law spectral density of the phase noise in real oscillators. Here we will compare our oscillator noise admittance (or resistance) model with Leeson's oscillator model and determine the equivalence between these two models.

The Leeson's model consists of an amplifier with a feedback loop. The amplifier has a noise figure F , and the feedback is a tank circuit with a transfer function

$$L(\omega_m) = \frac{1}{1 + j \left(\frac{\omega_m}{\omega_{3\text{dB}}} \right)} \quad (22)$$

where $\omega_{3\text{dB}} = \omega_0/2Q$ is the half the 3 dB bandwidth of the resonator tank circuit, and Q is the Q factor of the resonator, and ω_0 is the free-running oscillator frequency and the center resonance frequency of the resonator. The power spectral density of the ergodic internal oscillator phase uncertainty is

$$\overline{\tilde{V}_n^2}(\omega_m) = FkTB \quad (23)$$

and the phase fluctuation spectral density in Leeson's model is

$$\begin{aligned} \langle |\tilde{\delta}\theta_0(\omega_m)|^2 \rangle &= \frac{\overline{\tilde{V}_n^2}(\omega_m)}{|1 - L(\omega_m)|^2} \\ &= FkTB \left(1 + \left(\frac{\omega_{3\text{dB}}}{\omega_m} \right)^2 \right) \end{aligned} \quad (24)$$

where k is the Boltzmann constant, T is the absolute temperature of the oscillator, and $B = 1$ for a 1 Hz bandwidth. Under the standard room temperature, $kTB = -174$ dBm/Hz. In (23) $(-)$ denotes the time average of the signal. If the noise offset frequency $\omega_m < \omega_{3\text{dB}}$, the oscillator phase noise is $\overline{\tilde{V}_n^2}/(\omega_m/\omega_{3\text{dB}})^2$. If the noise offset frequency $\omega_m > \omega_{3\text{dB}}$, the oscillator phase noise becomes the thermal noise floor $\overline{\tilde{V}_n^2}$, and the feedback inside the oscillator has no effect.

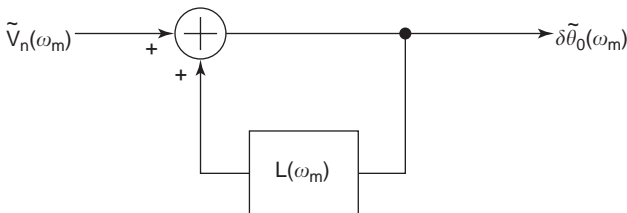


Figure 2. Leeson's model for oscillator phase noise.

The phase noise of the single free-running oscillator from the oscillator noise admittance/resistance model is

$$\begin{aligned} \langle |\tilde{\delta}\theta_0(\omega_m)|^2 \rangle &= \langle |\tilde{\delta}\theta_i(\omega_m)|^2 \rangle_{\text{uncoupled}} \\ &= \frac{\langle |\tilde{\mathbf{B}}_n(\omega_m)|^2 \rangle}{\left(\frac{\omega_m}{\omega_{3\text{dB}}} \right)^2} \end{aligned} \quad (25)$$

After comparing Leeson's model with our noise admittance model, we have

$$\langle |\tilde{\mathbf{B}}_n(\omega_m)|^2 \rangle = FkTB \quad (26)$$

In the oscillator admittance/resistance model, the thermal noise floor is not included in the derivation. One can include the thermal noise floor into the noise expression by multiplying the correction factor

$$\text{Correction factor} = \frac{1 + \left(\frac{\omega_{3\text{dB}}}{\omega_m} \right)^2}{\left(\frac{\omega_{3\text{dB}}}{\omega_m} \right)^2} \quad (27)$$

with our phase fluctuation spectral density $\langle |\tilde{\delta}\theta_0(\omega_m = 2\pi f_m)|^2 \rangle$, and then we have the same results as Leeson's model. If $1/f$ flicker noise contribution is considered, one can set

$$\langle |\tilde{\mathbf{B}}_n(\omega_m)|^2 \rangle = FkTB \left(1 + \frac{\omega_c}{\omega_m} \right) \quad (28)$$

where ω_c is the corner frequency for $1/f$ flicker noise.

In the typical phase noise measurements, the normalized [in 1 Hz bandwidth (BW)] single-sideband noise power, \mathfrak{L} in dBc/Hz, is often used, and it is defined as

$$\mathfrak{L}(f_m) = \frac{N(1 \text{ Hz BW})}{P_0} \quad (29)$$

where $N(1 \text{ Hz BW})$ is the noise power with corrections at f_m (where $f_m = \omega_m/(2\pi)$ is the noise offset frequency in Hz), and P_0 is the carrier power.

The relationship between $\mathfrak{L}(f_m)$ and $\langle |\tilde{\delta}\theta_0(\omega_m)|^2 \rangle$ can be written as

$$\mathfrak{L}(f_m) = \frac{\langle |\tilde{\delta}\theta_0(\omega_m = 2\pi f_m)|^2 \rangle}{2P_0} \quad (30)$$

where the factor of 2 is used, because $\mathfrak{L}(f_m)$ is the single-sideband noise power instead of double sideband, and P_0 is the averaged oscillator power at carrier frequency. Therefore, the spectral density of phase fluctuation is

defined as

$$S_{\theta}(f_m) = \frac{\langle |\tilde{\delta}\theta_0(\omega_m = 2\pi f_m)|^2 \rangle}{P_0} \tag{31}$$

$$= 2\mathfrak{L}(f_m)$$

where S_{θ} is in the unit of rad^2/Hz .

From the preceding definitions, if the $1/f$ flicker noise and thermal noise floor are included in our oscillator model, the measured oscillator phase noise becomes

$$\mathfrak{L}(f_m) = \frac{FkTB}{2P_0} \left(1 + \frac{f_c}{f_m} \right) \left(1 + \left(\frac{f_{3\text{dB}}}{f_m} \right)^2 \right)$$

$$= \underbrace{\frac{FkTB}{2P_0}}_{\text{thermal noise floor}} + \underbrace{\frac{FkTB}{2P_0} \left(\frac{f_c}{f_m} \right)}_{\text{flicker phase noise}} \tag{32}$$

$$+ \underbrace{\frac{FkTB}{2P_0} \left(\frac{f_{3\text{dB}}^2}{f_m^2} \right)}_{\text{thermal phase noise}} + \underbrace{\frac{FkTB}{2P_0} \left(\frac{f_c f_{3\text{dB}}^2}{f_m^3} \right)}_{\text{upconverted } 1/f \text{ noise}}$$

where f_m is the noise offset frequency in Hz. The first term in this equation is thermal noise floor, the second term is flicker phase noise, the third term is thermal phase noise (which is our main concern), and the fourth term is upconverted $1/f$ noise or flicker phase noise in the oscillator phase noise. The SSB phase noise with different noise source contributions versus the noise offset frequency is shown in Fig. 3. Here one can find that the noise admittance/resistance model is consistent with Leeson’s model.

2. MEASUREMENT TECHNIQUES

Phase noise measurement is very important for testing and verifying the design of circuits and systems. However, the phase noise measurement often takes much time and money for the related expensive equipments. Many sophisticated techniques are used to obtain the phase noise results. Here the author only explains several popular methods and the related basic ideas, including the

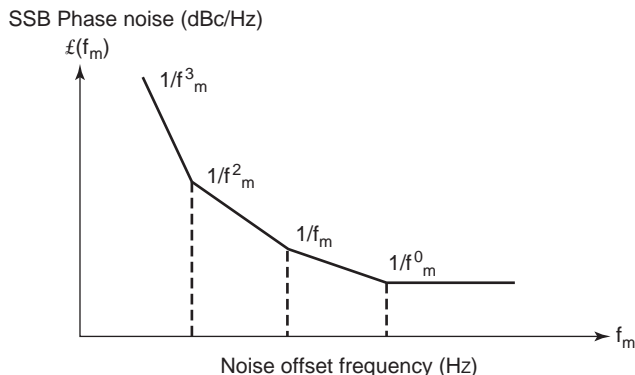


Figure 3. The SSB (single-sideband) oscillator phase noise spectrum versus the noise offset frequency.

spectrum analyzer, frequency discriminator, and double-balanced mixer methods.

2.1. Spectrum Analyzer

The spectrum analyzer is the most direct way to measure the phase noise of the device under test. The spectrum analyzer needs to have enough dynamic range for the input signal, and its internal local oscillator phase noise of the spectrum analyzer is less than the device under test [9–12]. The output frequency of the device under test is also required to be reasonably stable during the test. The measured phase noise by spectrum analyzer can be obtained from (29)

$$\mathfrak{L}(f_m) = 10 \log_{10}(P_{\text{SSB}}) - 10 \log_{10}(P_0) \tag{33}$$

where P_{SSB} is the single-sidedband noise spectral power reading and P_0 is the carrier spectral power reading from the spectrum analyzer.

The schematic diagram of the typical spectrum analyzer is shown in Fig. 4. Several factors affect the measurement sensitivity. There is an input attenuator in the spectrum analyzer, and it should be set to minimum (or zero) in order to increase the signal-to-noise ratio (SNR) for optimum measurement sensitivity. The resolution bandwidth (RBW) also affects the SNR, and it should be set to minimum for optimum SNR of the measurement system. The RBW is the bandwidth of the intermediate-frequency (IF) filter following the first gain stage (or the mixer) of the analyzer. After setting the input attenuation and RBW to minimum, one can set the video bandwidth (VBW) to minimum in order to view the signal close to the noise level, even though the video bandwidth does not affect the noise level. The video bandwidth is the bandwidth of the video filter used to reduce or smooth out the fluctuation of the input noisy signal displayed on the screen of the analyzer.

However, Eq. (33) is not complete because several correction factors are not included. The nonideal IF filter has a filter rolloff, which affects the IF bandwidth and then the resolution bandwidth. The correction factor due to the IF filter rolloff is expressed as $-10 \log_{10}(c_1 \cdot \text{RBW})$, where c_1 is the parameter dependent on the specific spectrum analyzer. The spectrum analyzer has logarithmic IF gain stage that amplifies the noise peaks less than the rest of the noise signal. The correction factor due to the logarithm IF gain stage is c_2 . Thus, the modified phase noise is

$$\mathfrak{L}(f_m) = 10 \log_{10}(P_{\text{SSB}}) - 10 \log_{10}(P_0)$$

$$- 10 \log_{10}(c_1 \cdot \text{RBW})$$

$$+ c_2 \tag{34}$$

The factors c_1 and c_2 depend on different spectrum analyzer designs and their specifications.

2.2. Frequency Discriminator

The frequency discriminator method is a sensitive technique used to measure $S_f(f_m)$. The measurement setup of

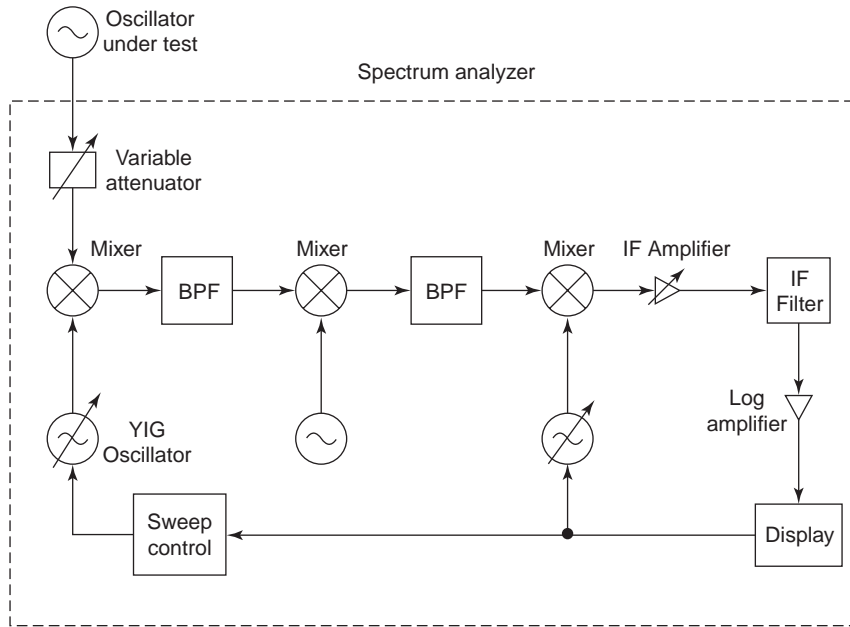


Figure 4. The spectrum analyzer method for phase noise measurement.

frequency discriminator method is shown in Fig. 5a and 5b. The signal of the oscillator under test is $V_1(t) = A_1 \cos(\omega_1 t + \delta\theta_1(t))$, and that of the reference oscillator is $V_2(t) = A_2 \cos(\omega_2 t + \delta\theta_2(t))$. These two signals are mixed and passed through the lowpass filter and the frequency discriminator. Several methods are used to implement the frequency discriminator. In Fig. 5(a) one

can use the op-amp to implement the frequency discriminator with transfer function $H(s) = -sRC$, and $s = j\omega$. The output signal of the discriminator is $V_{fd}(t) = K'(\omega_1 - \omega_2) + K'd(\delta\theta_1(t) - \delta\theta_2(t))/dt$. In Fig. 5(b) a delay-line cable, a phase shifter, a power divider, and a mixer are used as a frequency discriminator. The output signal of the discriminator is $V_{fd}(t) = K'(\omega_1 - \omega_2) + K'(\delta\theta_1(t) - \delta\theta_1(t - \tau) +$

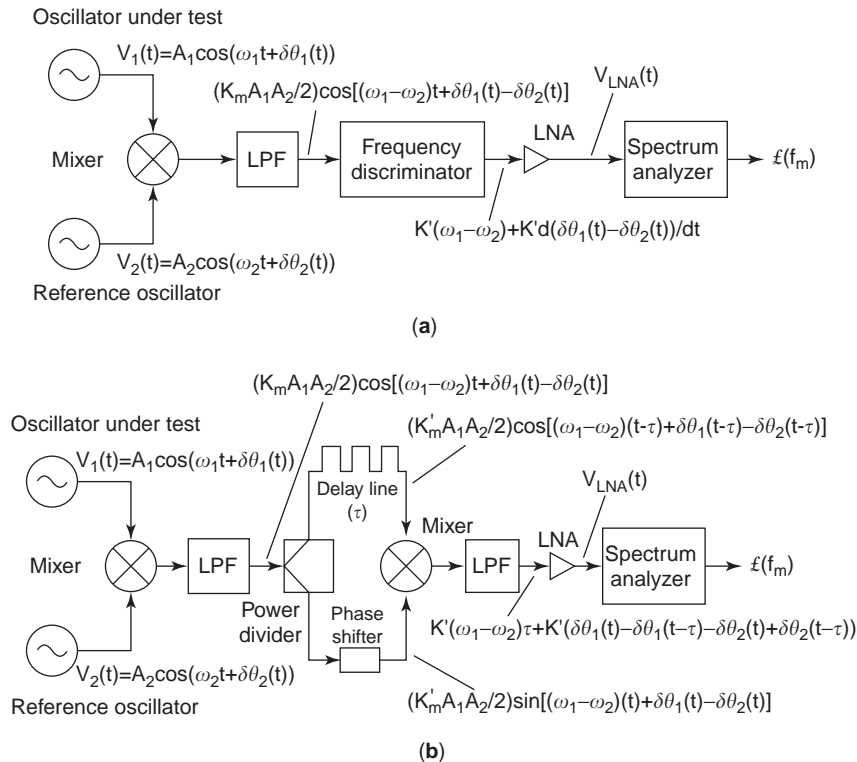


Figure 5. The frequency discriminator method for phase noise measurement.

$\delta\theta_2(t) - \delta\theta_2(t - \tau) \approx K'(\omega_1 - \omega_2) + K'\tau d(\delta\theta_1(t) - \delta\theta_2(t))/dt$, where the approximation $\delta\theta(t - \tau) \approx \delta\theta(t) - \tau d(\delta\theta(t))/dt$ is used. The delay τ of the delay-line cable can be measured by the time-domain reflectometer. The signal after the LNA can be expressed as $V_{LNA}(t) = K(\omega_1 - \omega_2) + Kd(\delta\theta_1(t) - \delta\theta_2(t))/dt$. The parameter K includes the signal amplitudes of the device under test and the reference oscillator signal, the mixer, the frequency discriminator conversion gain, and the LNA gain. The phase noise (or frequency noise) introduced by the LNA is assumed negligible as compared to the device under test or the reference oscillator signal. The signal $K(\omega_1 - \omega_2)$ can be treated as a DC offset and filtered out, as long as the output frequencies ω_1 and ω_2 are reasonably stable.

The output signal of the LNA, $Kd(\delta\theta_1(t) - \delta\theta_2(t))/dt = K(\delta f_1(t) - \delta f_2(t))$, is applied to a low-frequency spectrum analyzer. In the frequency domain, the desired signal becomes $K(\tilde{\delta f}_1(f_m) - \tilde{\delta f}_2(f_m))$, where (\sim) is a spectral variable and f_m is the noise offset frequency relative to the carrier frequency. Since the frequency fluctuations $\tilde{\delta f}_1(f_m)$ and $\tilde{\delta f}_2(f_m)$ are uncorrelated, the combined RMS (root-mean-squared) $\tilde{\delta f}_{RMS} = K\sqrt{|\tilde{\delta f}_1(f_m)|^2 + |\tilde{\delta f}_2(f_m)|^2}$. The spectrum analyzer normally displays the spectral power, and the display is $(\tilde{\delta f}_{RMS})^2 = (K)^2(|\tilde{\delta f}_1(f_m)|^2 + |\tilde{\delta f}_2(f_m)|^2)$. The phase (or frequency) fluctuation of the reference oscillator is much less than that of the device under test [i.e., $|\tilde{\delta f}_2(f_m)| \ll |\tilde{\delta f}_1(f_m)|$], and $(\tilde{\delta f}_{RMS})^2 \approx (K)^2|\tilde{\delta f}_1(f_m)|^2$. The low-frequency spectrum analyzer with more exquisite embedded functions can calculate the noise sideband power relative to the carrier power to obtain $\xi(f_m) = S_\theta(f_m)/2 = S_f(f_m)/(2f_m^2)$ from (8).

2.3. Double-Balanced Mixer

The double-balance mixer method shown in Fig. 6 is also a sensitive method used to measure the phase noise without frequency discriminator [1,9]. The frequency difference error is used to lock the reference oscillator to the device under test. The reference oscillator frequency can be tuned as close to the device frequency under test (i.e., $\omega_1 \cong \omega_2$) in order to maintain constant phase difference

between the input signal phase and the reference oscillator phase. The output signal of the lowpass filter becomes $V_{LPF}(t) = -(K_m A_1 A_2 / 2) \sin(\delta\theta_1(t) - \delta\theta_2(t)) \approx -(K_m A_1 A_2 / 2)(\delta\theta_1(t) - \delta\theta_2(t))$, where $(\delta\theta_1(t) - \delta\theta_2(t))$ is assumed very small, and K_m includes the mixer conversion gain and the filter gain. The spectrum analyzer normally displays the spectral power, and the display is $(\tilde{\delta f}_{RMS})^2 = (K_m A_1 A_2 / 2)^2 (|\tilde{\delta f}_1(f_m)|^2 + |\tilde{\delta f}_2(f_m)|^2)$. The phase (or frequency) fluctuation of the reference oscillator is much less than that of the device under test [i.e., $|\tilde{\delta f}_2(f_m)| \ll |\tilde{\delta f}_1(f_m)|$] and $(\tilde{\delta f}_{RMS})^2 \approx (K)^2|\tilde{\delta f}_1(f_m)|^2$. The reference oscillator noise can track that of the device noise under test inside the loop bandwidth. The noise of those two oscillators has no correlation outside the loop bandwidth. However, the Q factor of the stable reference oscillator is very high and its phase noise is very low from (20), so its tuning range is very small. The double-balanced mixer method is suitable for the device under test only with operating frequency as close as possible to that of the reference oscillator.

For the these measurement methods, one can find that the spectrum analyzer is the most direct method, but requires some correction factors on the test results. The frequency discriminator and double-balanced mixer methods also require good mixers, lowpass filter, bandpass filters, and LNAs (low-noise amplifiers). The double-balanced mixer method is more suitable for the input signal stable frequency as close as possible to the reference oscillator frequency. Figure 7 is the illustrated measured phase noise result of the X-band microwave oscillator fabricated in microstrip circuit, and the frequency discriminator method is used.

3. CONCLUSIONS

Phase noise has been a very important design consideration in modern communication systems. The phase noise in the oscillators has dominated the system performance and one must characterize the oscillator phase noise by theory and measurement. The brief phase noise theory

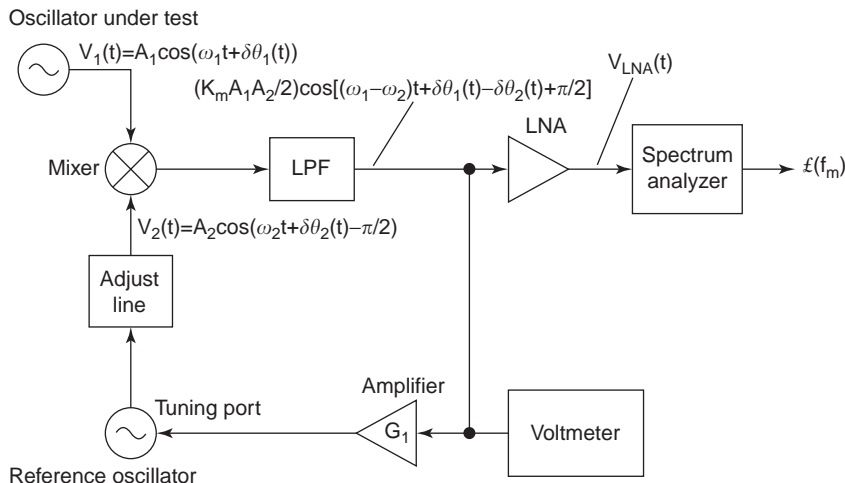


Figure 6. The double-balanced mixer method for phase noise measurement.

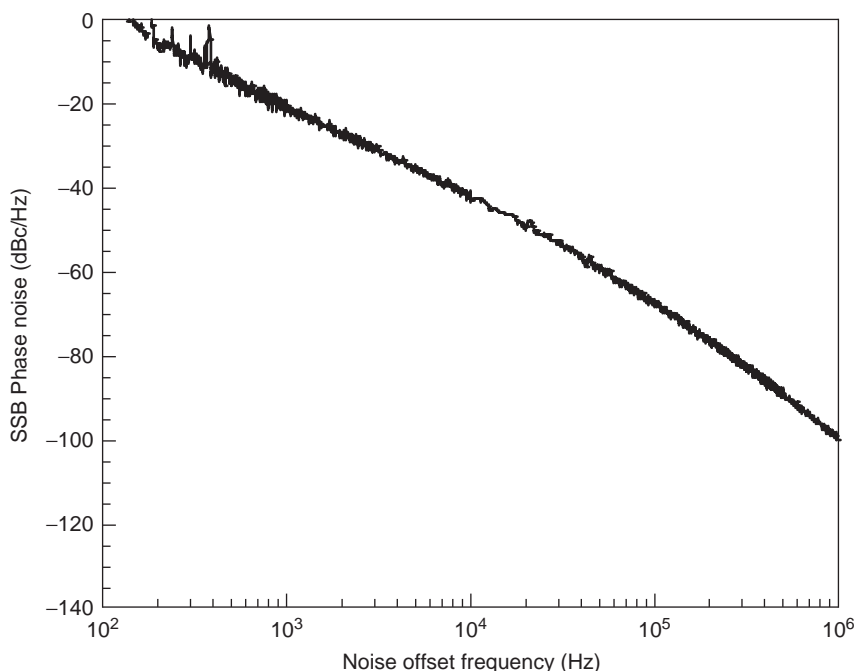


Figure 7. The measured phase noise result of the microwave oscillator fabricated in microstrip circuits operating at X band. The phase noise results is obtained from the frequency discriminator method.

and measurement techniques are presented in this article. The oscillator phase noise can be modeled by using either the noise conductance (or resistance) or Leeson's model [2–8], as the consistence between these two models is illustrated.

Several popular measurement methods are illustrated and explained, including the Spectrum analyzer, frequency discriminator, and double-balanced mixer method [9–13]. The advantages and disadvantages of these methods are explained. One can obtain accurate phase noise results by using one of the measurement methods described above carefully after considering the limits and requirements of each method. There are many phase noise model and theory in the literature, and the readers can find more details and references in the review and tutorial articles [1,14–18].

BIBLIOGRAPHY

1. NIST Technical Note 1337, *Characterization of Clocks and Oscillators*, D. B. Sullivan, D. W. Allan, D. A. Howe, and F. L. Walls, eds., 1990.
2. D. B. Leeson, A simple model of feedback oscillator phase noise spectrum, *Proc. IEEE*, **54**:329–330 (1966).
3. S. Hamilton, FM and AM noise in microwave oscillators, *Microwave J.* **21**:105–109 (June 1978).
4. K. Kurokawa, Noise in synchronized oscillators, *IEEE Trans. Microwave Theory Tech.* 234–240 (April 1968).
5. W. O. Schlosser, Noise in mutually synchronized oscillators, *IEEE Trans. Microwave Theory Tech.* **MTT-16**:732–737 (Sept. 1968).
6. A. E. Siegman, *Lasers*, University Science Books, California, 1986.
7. T. Makino, M. Nakajima, and J.-I. Ikenoue, Noise reduction mechanism of power combining oscillator system, *Electron. Commun. Jpn.* **62-B**(4):37–44 (1979).
8. H.-C. Chang, X. Cao, U. K. Mishra and R. A. York, Phase noise in coupled oscillators: Theory and experiment, *IEEE Trans. Microwave Theory Tech.* **45**(5):604–615 (May 1997).
9. G. D. Vendelin, A. M. Pavio, and U. L. Rohde, *Microwave Circuit Design using Linear and Nonlinear Techniques*, Wiley, 1990, Chap. 6.
10. M. Engleson, *Modern Spectrum Analyzer Theory and Applications*, Artech House, 1984.
11. Hewlett-Packard, *HP 3048A Option 301 Operation Manual*, Phase Noise Measurement System, 1995.
12. Agilent, *Spectrum Analyzer Measurements and Noise*, Application Note 1303.
13. Agilent, *Pulsed Carrier Phase Noise*, Application Note 1309.
14. A. Demir, A. Mehrota, and J. Roychowdhury, Phase noise in oscillators: a unifying theory and numerical methods for characterization, *IEEE Trans. Circ. Syst. II* **47**:655–674 (May 2000).
15. A. Hajimiri and T. Lee, A general theory of phase noise in electrical oscillators, *IEEE Trans. Solid-State Circ.* **33**(2): 179–194 (Feb. 1998); corrections to A general theory of phase noise in electrical oscillators, *IEEE Trans. Solid-State Circ.* **33**(6):928 (June 1998).
16. T. Lee and A. Hajimiri, Oscillator phase noise: A tutorial, *IEEE J. Solid-State Circ.* **35**(3): 326–336 (March 2000).
17. B.-G. Goldberg, *Digital Frequency Synthesis Demystified*, LLH Publishing, 1999.
18. C. W. Gardiner, *Handbook of Stochastic Methods*, Springer-Verlag, Berlin, 1983.

PHASE SHIFTERS

FRANCO DE FLAVIIS
University of California at
Los Angeles

A microwave phase shifter is a two-port device capable of producing a true delay of a microwave signal flowing through it. The produced time delay can be fixed or adjustable, and the phase shifter is accordingly called fixed phase shifter or tunable phase shifter. The geometry of the phase shifter is intimately related to the guiding structure that is used to design it and is also related to the operational frequency. Most phase shifters are realized in waveguides or in planar structures. Electrically, a phase shifter can be characterized by its scattering parameters matrix. The scattering matrix for an ideal phase shifter (see Fig. 1) takes the form

$$S = \begin{bmatrix} 0 & e^{-j\phi_1} \\ e^{-j\phi_2} & 0 \end{bmatrix} \quad (1)$$

The signal arriving at port 1 will appear at port 2 with a phase shift ϕ_1 without being reflected at port 1 and with no attenuation, while the signal arriving at port 2 will appear at port 1 with phase shift ϕ_2 and without reflection or attenuation.

In general, $\phi_1 \neq \phi_2$ and the phase shifter is called non-reciprocal, and if $\phi_1 = \phi_2$ the phase shifter is called reciprocal. In practice it is impossible to achieve perfect matching at the two ports (no reflection) and to avoid some attenuation while the signal flows through the phase shifter. For these reasons the scattering matrix of a real phase shifter can be written in general as

$$S = \begin{bmatrix} S_{11} & |S_{21}|e^{-j\phi_1} \\ |S_{12}|e^{-j\phi_2} & S_{22} \end{bmatrix} \quad (2)$$

The attenuation of the microwave signal due to the presence of the phase shifter can be calculated from its S parameters, and it is expressed in decibels as

$$(\text{Insertion loss})_1 = 20 \log |S_{21}| \quad (3)$$

$$(\text{Insertion loss})_2 = 20 \log |S_{12}| \quad (4)$$

The subscripts 1 and 2, respectively, refer to the phase shifter when the input signal is at port 1 or port 2. The mismatch is expressed as standing-wave ratio (VSWR) at

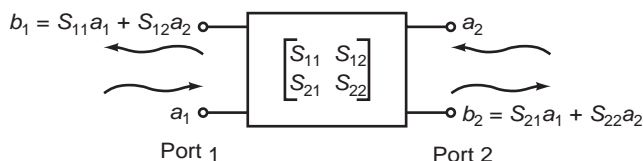


Figure 1. Phase shifter viewed as a two-port device.

each port and is given by

$$(\text{VSWR})_1 = \frac{1 + |S_{11}|}{1 - |S_{11}|} \quad (5)$$

$$(\text{VSWR})_2 = \frac{1 + |S_{22}|}{1 - |S_{22}|} \quad (6)$$

In order to evaluate the performance of a phase shifter, it is necessary to introduce a quality factor. For a phase shifter operating at a specific frequency we can define a *figure of merit* as the ratio between the maximum phase shift (in degrees) and the corresponding attenuation in dB at that frequency. This parameter can be expressed as

$$\text{figure of merit} = \frac{\Delta(\text{phase } S_{21})}{|S_{21}|} \quad (7)$$

The performance of a phase shifter can be measured using a standard S parameter setup, including a network analyzer and a test-set of calibration standards suitable for the specific guiding structure [1].

1. PHASE SHIFTER CLASSIFICATION

A first classification of a phase shifter can be based on its phase shifting capability, according to which it can be identified as fixed or adjustable. A fixed phase shifter will provide a constant phase change between the two ports, while an adjustable phase shifter will provide a phase change between the ports which can be controlled mechanically or electrically. Further classification for the adjustable type is based on electrical performance and operational principle. Within the adjustable phase shifters we can distinguish between those where the phase change is achieved through a mechanical tuning and those where the change is obtained with an electrical signal. Furthermore, for the electrically tunable type we can distinguish between those where the phase can be changed continuously (analog) and those where the phase can only be changed by discrete steps (digital). Figure 2 shows a graphical classification of different types of phase shifters.

2. PHASE SHIFTER PERFORMANCE

In the evaluation of a phase shifter performance, besides the quantities derived from its S parameters such as insertion loss, quality factor, and VSWR, other quantities are important for practical design. Below we discuss such parameters and their corresponding meaning.

- *Operational Bandwidth.* This is defined as the 3 dB bandwidth (2), which is expressed as the frequency range in which the insertion loss is contained within 3 dB change.
- *Power-Handling Capabilities.* This is expressed as the maximum power that can flow in the phase shifter without overheating its components or without introducing nonlinear phenomena due to the amplitude

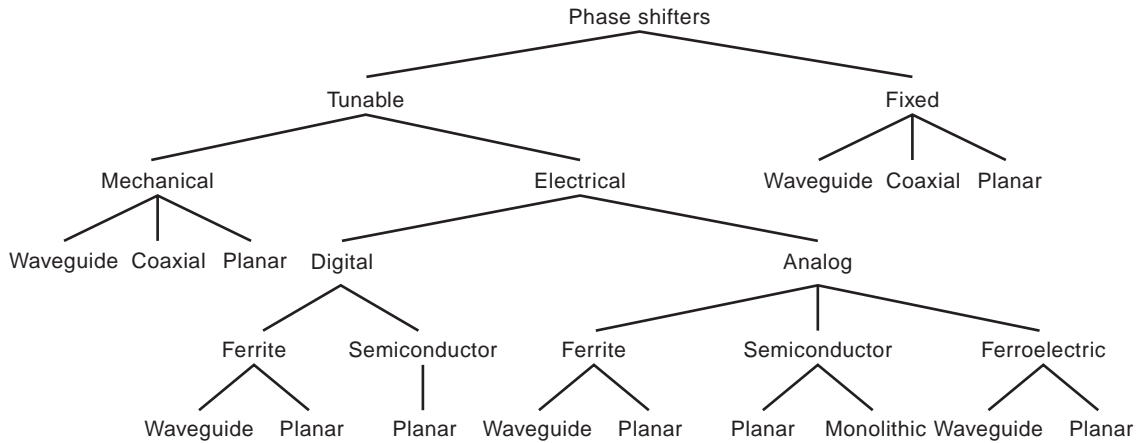


Figure 2. Phase shifter classification chart.

of the microwave field. This second limitation is particularly important for phase shifters which employ discrete devices such as field-effect transistors (FETs) or diodes.

- *Switching Speed.* This is the time needed by the phase shifter to switch between two different states, usually at the two ends of the achievable phase shift (larger allowable jump).
- *Temperature Sensitivity.* This expresses the sensitivity in terms of degree of phase shift degradation per °C change. This parameter should be small to avoid the necessity to adopt thermal compensation.
- *Physical Size.* This parameter can be very important, especially when the phase shifter is employed in a radar system where thousands of units are required. Physical dimensions and weight must be minimized even at the cost of other parameters. As an example, think of a radar system that needs to be mounted on the frontside of a jet fighter.

3. FIXED PHASE SHIFTERS

A fixed phase shifter must provide a constant phase change between its two ports. Theoretically any transmission line would be suitable for producing such a function as illustrated in Fig. 3. For instance, in the X band [1] a coaxial cable could be used as a fixed phase shifter, while in the Ku band a waveguide can be employed for the same purpose. In many applications, it is desirable to achieve a differential phase shift between two lines having the same

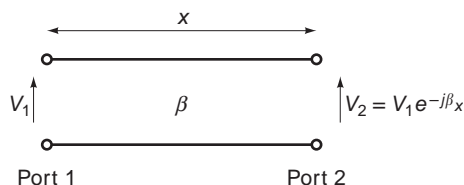


Figure 3. Transmission line acting as a phase shifter.

length. For this purpose, lines with different time delays must be used. A possible approach to this problem is to change the propagation constant of the line, loading it with lumped or distributed elements. So if β_1 is the propagation constant of the unloaded line and β_2 is the propagation constant of the loaded one, the achieved differential phase shift will be given by [3]

$$\Delta\phi = (\beta_1 - \beta_2)x \tag{8}$$

where x is the length of the line. So the basic idea in the realization of this type of phase shifter is to change the propagation constant of the transmission line by properly loading it. As an example, consider the realization of a fixed phase shifter in circular waveguide geometry. The waveguide is loaded with metal inserts as shown in Fig. 4. The equivalent circuits for the loaded and unloaded cases, assuming that the guide is operating with the fundamental mode TE_{11} [4], are reported in Fig. 5. Both lines have the same length, and the differential phase shift between the two TE_{11} modes is related to the normalized suscep-

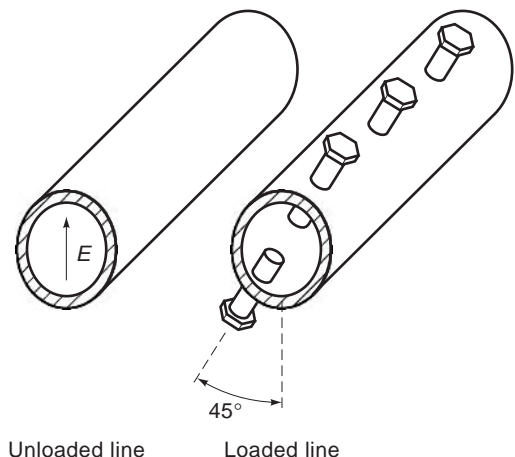


Figure 4. Loaded circular waveguide.

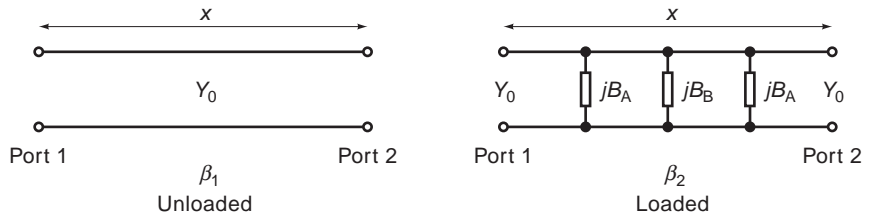


Figure 5. Equivalent circuits for loaded and unloaded circular waveguides operating with the fundamental mode.

tance of the loads [5] by the following equations:

$$\bar{B}_B = \frac{B_B}{Y_0} = \frac{\sin 2\beta x - \sin(2\beta x + \Delta\phi)}{\sin^2 \beta x} \quad (9)$$

$$\bar{B}_A = \frac{B_A}{Y_0} = \frac{\sin \Delta\phi \cos \beta x - (1 - \cos \Delta\phi) \sin \beta x}{\sin \beta x \sin(2\beta x + \Delta\phi)} \quad (10)$$

The use of Eqs. (9) and (10) allows one to design the loads necessary to achieve a desired phase shift. Using a similar concept, depending on the transmission line geometry, different type of loads can be devised as shown in Fig. 6. A quarter-wave transformer is used to avoid reflection at the load interface. Figures 6a and 6b show realization in circular waveguide geometry using dielectric or metallic loads, while Figs. 6c and 6d are rectangular waveguide geometry using dielectric loads.

4. MECHANICALLY TUNED PHASE SHIFTERS

Mechanically tunable phase shifters are capable of varying the signal delay in a transmission line using some

moving parts. The specific geometry depends on the operational frequency and on the guiding structure. As an example, three classical implementations—a coaxial cable, a waveguide, and a microstrip line, respectively—are outlined below.

4.1. Coaxial Cable Phase Shifter

In a coaxial cable the dominant mode is TEM (see ELECTROMAGNETIC FIELD MEASUREMENT) [6], so the phase of the signal propagating over a length between two cable endpoints is given by

$$\phi = \frac{\omega\sqrt{\epsilon_r}}{c} x \quad (11)$$

where x is the cable length, ω is the operating frequency, ϵ_r is the dielectric constant of the inner core of the cable, and c is the speed of light in free space. A Δx change in its length will produce a change in phase ($\Delta\phi$) between the two cable endpoints expressed by

$$\Delta\phi = \frac{\omega\sqrt{\epsilon_r}}{c} \Delta x \quad (12)$$

Figure 7 illustrates a section view of this type of phase shifter. To allow for the stretch, the coaxial cable has concentric airlines which can slide one into another, maintaining the characteristic impedance of the cable constant while changing length.

4.2. Waveguide Phase Shifter

In waveguide geometry, one way of obtaining a tunable phase shift without changing its length is to change the effective dielectric constant in some region of the guide, inserting a movable dielectric slab. Figure 8 illustrates one version of this mechanical tunable phase shifter. The insertion of the flap in the center of the waveguide, where the electric field is maximum assuming that the fundamental mode is propagating, will delay the signal, producing a phase shift. This type of device is only usable with some restrictions, since the thickness of the flap and its dielectric constant must be calculated to avoid the propagation of higher-order modes (i.e., TE_{30}). A simple equation for the design of this type of phase shifter, which avoids higher modes, was proposed by Gardiol [7] and leads to the following relation:

$$\sqrt{\epsilon_r} \tan[\pi(a - d)/\lambda_c] = \cot(\pi\sqrt{\epsilon_r}d/\lambda_c) \quad (13)$$

Based on the same concept, it is possible to have a movable dielectric inside a rectangular waveguide operating with

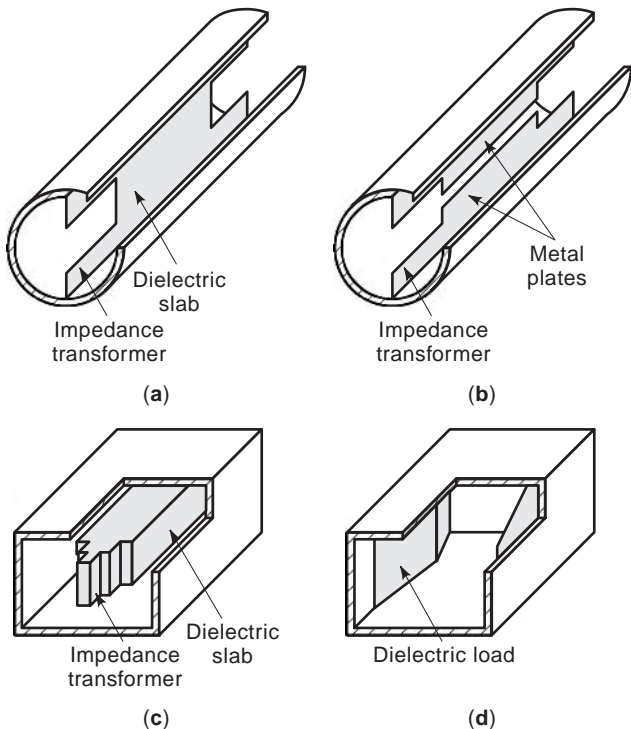


Figure 6. Different types of loaded transmission line.

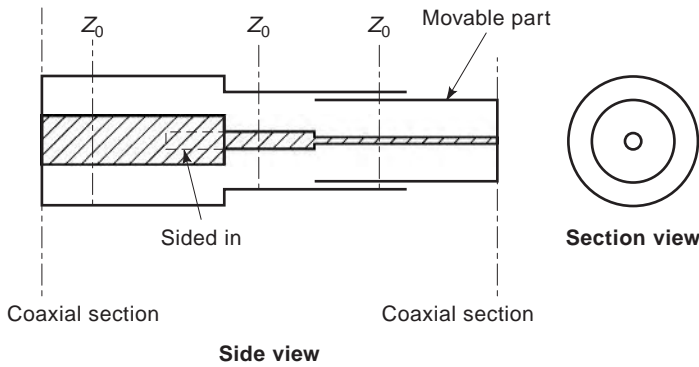


Figure 7. Mechanically tuned coaxial phase shifter.

the fundamental mode TE_{10} as shown in Fig. 9, where the interaction of the field with the dielectric will be maximum when the plate is in the center of the guide (maximum delay corresponding to maximum phase shift) and minimum when it is on the sidewalls. Proper design of the $\lambda/4$ transformer [8] is necessary to avoid reflections at the phase shifter interface.

4.3. Microstrip Phase Shifter

For the microstrip geometry a mechanically tuned phase shifter was proposed by Joines [9]. In this geometry it is possible to achieve a phase shift by changing the dielectric constant of the substrate above and below the strip as depicted in Fig. 10.

The change in the dielectric constant will induce a change in the propagation constant, and consequently different phase shifts will be achieved. This structure is attractive because it yields a continuous phase shift while maintaining the characteristic impedance constant. If we observe its section view depicted in Fig. 10, we notice that by a proper design of the thicknesses t_1 and t_2 , accordingly with the dielectric constant [9], it is possible to keep the characteristic impedance of the strip constant while changing its propagation constant.

These are just a few examples of mechanically tunable phase shifters; of course, many others are possible, but the basic concept on which they operate is the same and can be summarized as follows. In order to obtain a phase shift, it is necessary to delay the electric signal independently from the type of guiding structure used. This can be achieved in two ways; one way is to change the *physical length* of the transmission line Δx that produces a delay of

the signal at the output port, inducing a phase shift change given by $\Delta\phi = \beta\Delta x$. In the second case, a change of the *wave propagation velocity* obtained by changing the propagation constant of the line $\Delta\beta$ will produce a phase shift at the output port given by $\Delta\phi = \Delta\beta x$.

5. ELECTRICALLY TUNED PHASE SHIFTERS

In electrically tuned phase shifters the phase change is controlled by an electric signal (driving signal) such as a voltage or a current. Since no moving parts are involved in the phase control process, electrically controlled phase shifters can achieve faster phase shift compared to mechanical ones. They can be subdivided into two major categories—*digital* and *analog*—depending on the type of control on the phase shift they provide. One of the most important application of electrically tuned phase shifters is the so-called phased-array system. A phased-array system is an array of antennas of which by electronically controlling the phase of the electromagnetic signal at each antenna element one can change its pointing direction. As an example, let us consider a linear array of antenna as illustrated in Fig. 11. If all the elements are excited with the same phase signal, the radiated signal adds coherently and forms a wave front parallel to the array direction (line joining all the elements). The beam pointing direction is perpendicular to the wavefront, so the radiated beam will point in a broadside direction. In a phased array, this direction is adjustable by acting on the phase of the electromagnetic signal at the aperture of each radiating element. In a linear array with equispaced elements the beam can

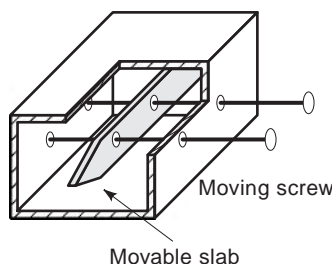


Figure 9. Dielectric loaded rectangular waveguide phase shifter.

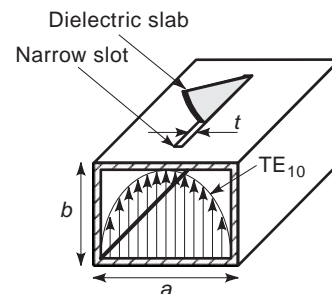


Figure 8. Mechanically tuned waveguide phase shifter.

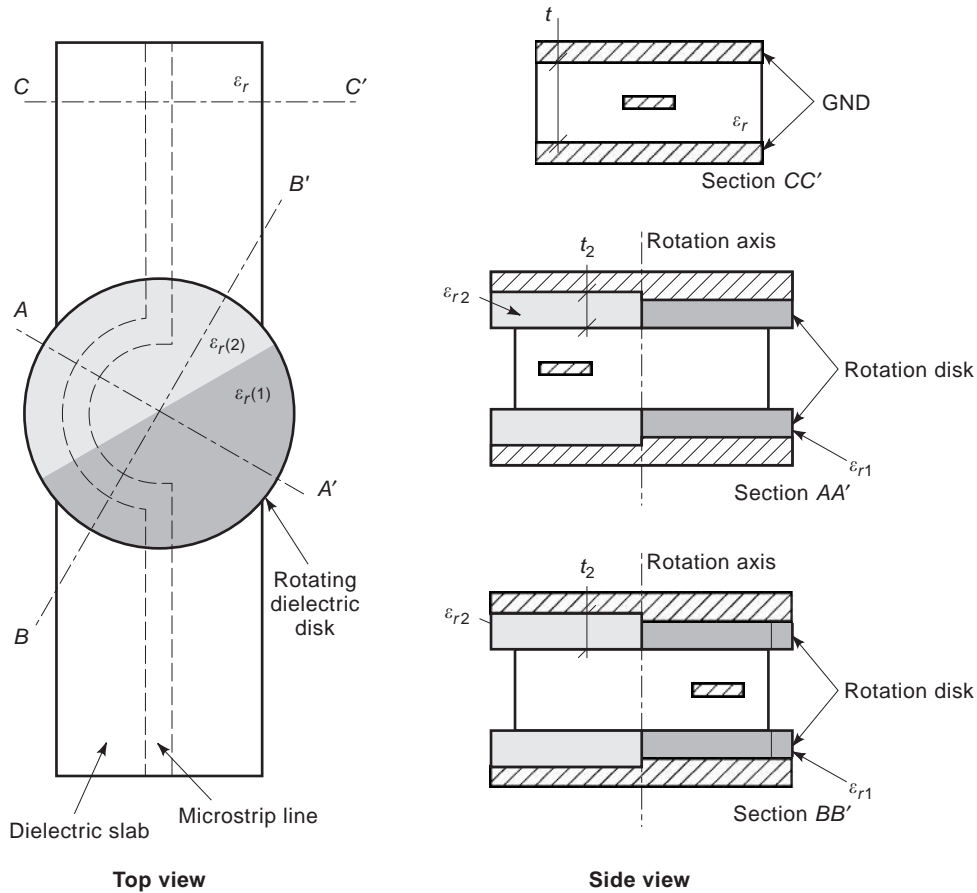


Figure 10. Microstrip mechanically tuned phase shifter.

be steered by introducing a progressive phase shift between successive elements. If θ_0 is the scan angle with respect to the broadside direction, then the phase delay to be introduced between adjacent antenna apertures can be calculated from

$$\Delta\phi = \frac{\omega}{c} d \sin \theta_0 \tag{14}$$

where d is the element spacing and c is the free space light speed. For scanning the beam continuously, $\Delta\phi$ is varied by analog phase shifters; and for switching the beam from one scan angle to another, $\Delta\phi$ is varied in discrete steps by digital phase shifters. The same principle applies to planar array for achieving three-dimensional scanning and switching.

5.1. Digital Phase Shifters

Digital phase shifters use electronic devices such as pin diodes or FETs as switching elements; this allows the digital phase shifter to direct the microwave signal through paths of different length, obtaining in this way the phase shift. The use of a pin diode as a switching circuit allows biasing of the diode forward (to obtain a trough) or reverse (to obtain an open circuit) by means of a dedicated bias circuitry. In a similar way, an FET channel can be switched

on or off by proper bias [10]. The use of FETs and diodes allows four basic designs. The simplest one is shown in Fig. 12, where the shift is obtained by switching the signal between two different length transmission lines; Fig. 12 also shows a microstrip implementation of this type. The phase shift is proportional to the difference between the length of the two lines and is given by $\Delta\phi = \Delta x\beta$. In a similar way, as shown in Fig. 13, the use of different loads on the transmission lines, which are switched on and off by the diodes, allows a phase change between the biased and unbiased condition ($\Delta\phi$) related to the impedance of the line (Z_0) and to the susceptance of the loads (B) according to the relation [5]

$$\Delta\phi = 2 \arctan \left(\frac{B_n}{1 - B_n^2/2} \right) \tag{15}$$

where $B_n = Z_0 B$. A microstrip implementation of this circuit is also shown in Fig. 13; the reactive and inductive loads are obtained using open stubs of different length, and their values can be calculated for a given susceptance using [11]

$$B = Z_s \cot \left(\frac{2\pi f \sqrt{\epsilon_r} l_s}{c} \right) \tag{16}$$

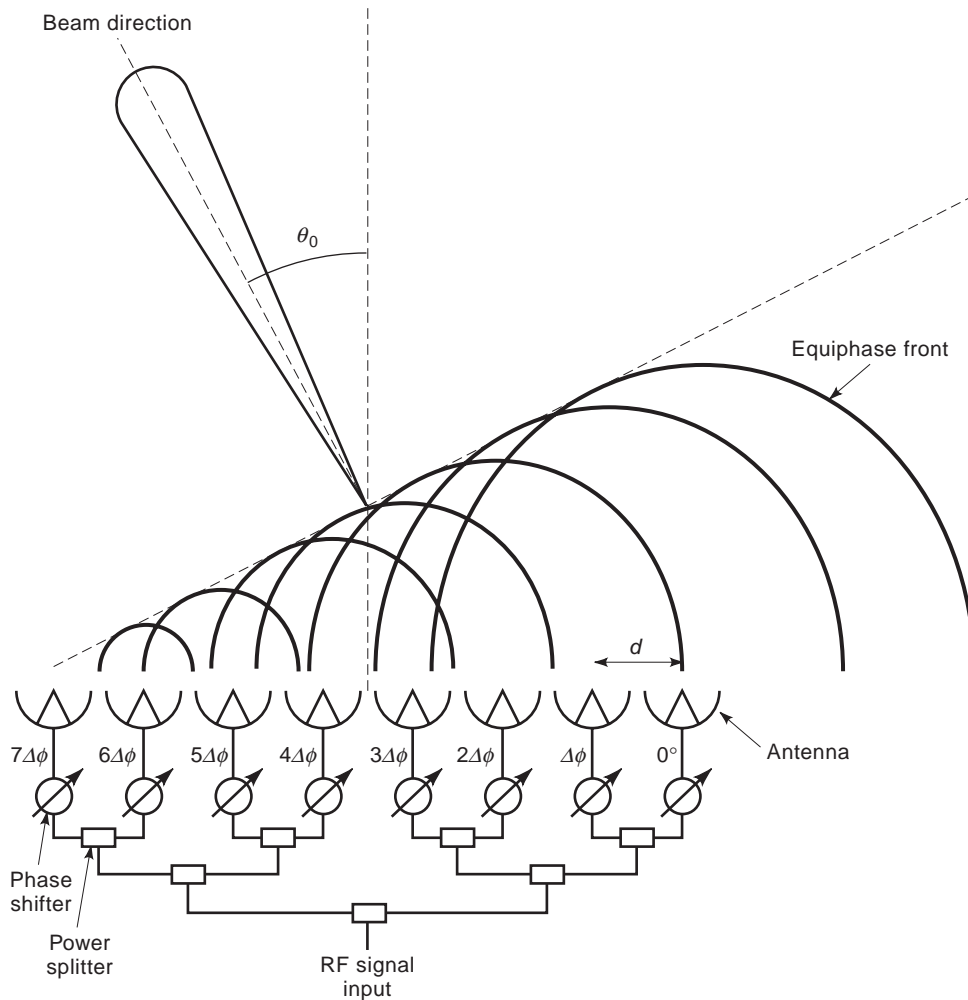


Figure 11. Beamsteering concept using a phase shifter at each radiating element.

where Z_s is the stub impedance, f is the operation frequency, ϵ_r is the relative dielectric constant, l_s is the stub length, and c is the speed of light in free space. Another design using a pin diode in combination with a 90° hybrid circuit is illustrated in Fig. 14. In this case the differential phase shift obtained between the biased and unbiased condition is given by

$$\Delta\phi = \beta \frac{x}{2} \tag{17}$$

The bias circuit must be designed carefully here, in order to avoid degradation of performance and direct-current (DC) leaks. The bias circuit must allow biasing of all the active devices independently, while insulating the DC biasing signal from the radiofrequency (RF) signal. A simple design for a microstrip topology is illustrated in Fig. 15. The two DC blocks are acting as series capacitors for the RF signal, allowing the RF to go through the diode while stopping the DC component from the rest of the circuit. The two $\lambda/2$ high-impedance microstrip lines are operating as an open stub [11]. At the microstrip junction they will result in an open circuit transparent to the microwave

signal while allowing the DC signal to provide the necessary bias for the diode. The high impedance of the open stub makes it look like an open circuit for a larger bandwidth [11].

The use of FETs as a switching element is similar to that of the pin diode: The source and drain are grounded (only for the DC signal). In the off state, the gate-source and the gate-drain capacitances are equal. Because of this, the drain is not isolated from the gate terminal. In real circuits, the bias network is configured so as to provide high impedance for the RF at the gate terminal. This is achieved by using a lowpass filter such that it presents an effective RF open at the gate. This arrangement is shown in Fig. 16.

Because digital phase shifters only allow discrete phase jumps, a cascade of them must be used when high resolution in the phase change is desired. Figure 17 shows a typical arrangement and the corresponding phase shift states for a 4-bit phase shifter, capable of giving phase jumps with an increment of 22.5° and a maximum phase shift of 360° . By increasing the number of phase shifters, higher resolution is achievable. The maximum achievable resolution will obviously depend on the number of phase

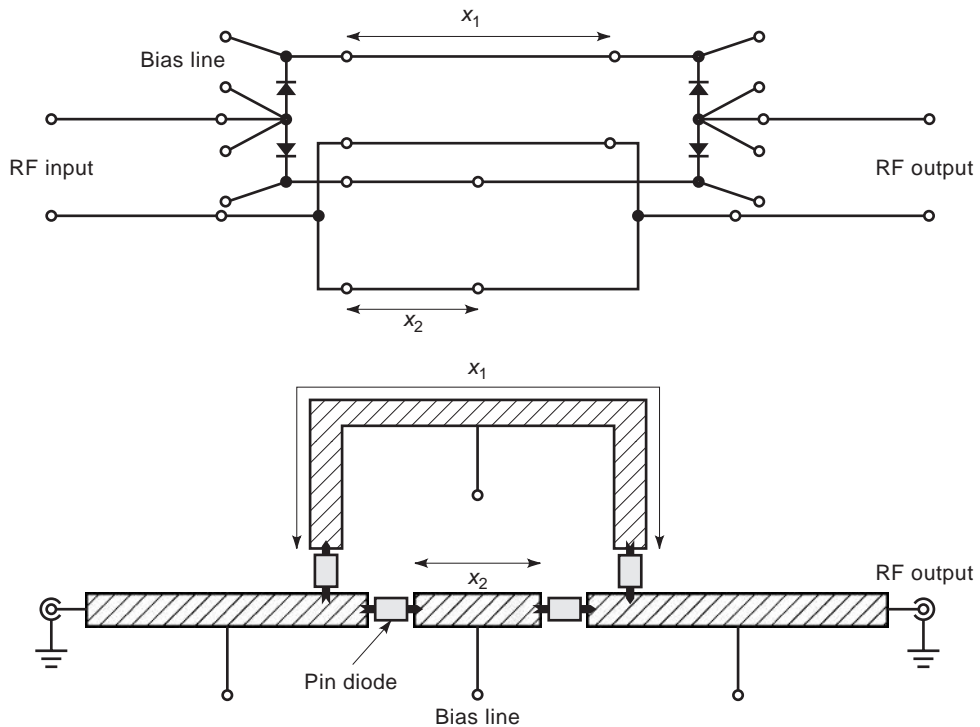


Figure 12. Pin diode type of electrically controlled digital phase shifter.

shifters and is expressed by the relation

$$\Delta\phi_{\min} = \frac{2\pi}{2^n} \quad (18)$$

where n is the number of discrete phase shifters.

5.2. Analog Phase Shifters

Analog phase shifters allow time-delay control of a microwave signal by using an electric driving signal. They differ from digital phase shifters due to their capability to pro-

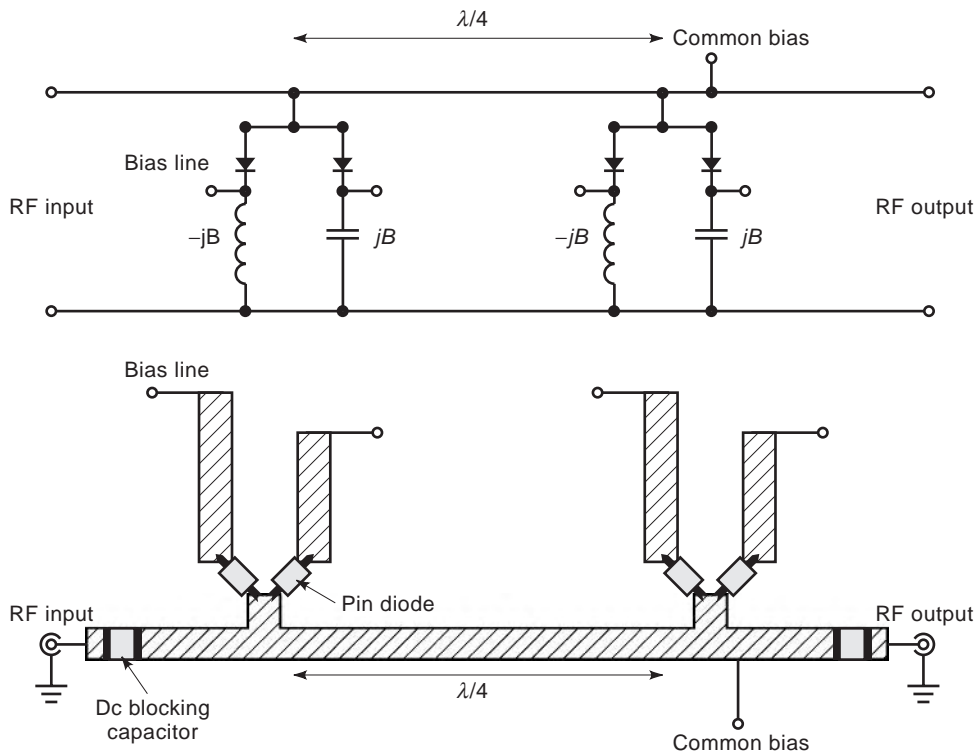


Figure 13. Loaded pin diode electrically tuned digital phase shifter.

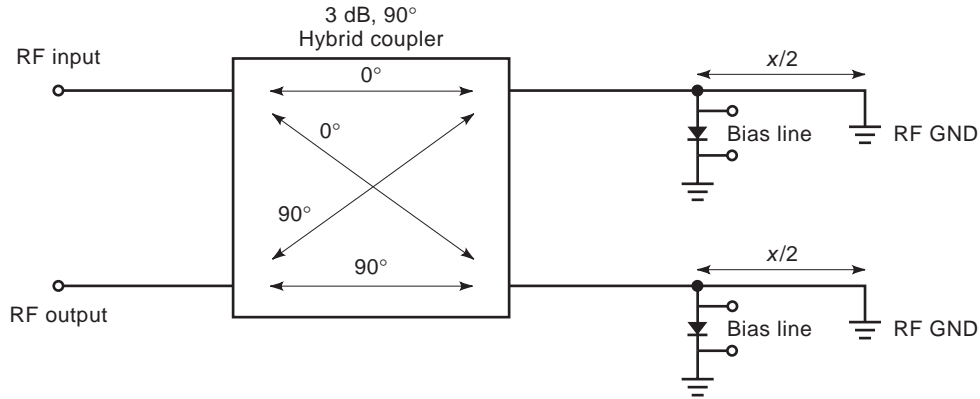


Figure 14. Pin diode and 90° hybrid circuit type of electrically controlled digital phase shifter.

vide continuous phase delay control. This characteristic is very attractive when a fixed phase resolution is impractical to use. Consider as an example the received signal coming from a broadcast TV, as illustrated in Fig. 18. Because a multiple reflection path exist, a double image is received. One possible solution to overcome the problem is to use two receiving antennas and by proper adjustment of the phase difference between them eliminate the reflected signal. Because of the random nature of the delay, only a continuous adjustable phase shifter can be employed.

Electrically analog tunable phase shifters can be subdivided in three major subcategories as illustrated in Fig. 2. A description of the operational principle for each of them is provided below.

5.3. Ferrite Phase Shifters

Ferrite phase shifters are employed in a waveguide or a planar structure. They operate using the ferrite property of nonlinear dependence between magnetization (B) and magnetic field (H). Ferrites are nonlinear and nonreciprocal magnetic materials composed of a mixture of divalent metal and iron oxide having the general chemical structure



where M is a divalent metal such as manganese, magnesium, nickel, or iron. They exhibit a hysteresis $B-H$ dependence as reported in Fig. 19. To explain how ferrites are used in phase shifters, it is not necessary to describe in detail the material properties, which are well documented in Refs. 12 and 13. The nonlinear $H-\mu$ dependence will be exhibited as shown in Fig. 19. The permeability at specific magnetization value (H^*) can therefore be calculated as

$$\mu = \mu_0 + \left. \frac{\partial B}{\partial H} \right|_{H=H^*} \tag{20}$$

In general the ferrite permeability takes the form of a tensor because of the nonreciprocal behavior. The elements of this tensor are a function of the applied magnetic field. When the magnitude or direction of the magnetic field is changed, the permeability of the ferrite changes, thereby changing the propagation constant of the electromagnetic wave. Phase shift is a consequence of the change in the propagation constant brought about by electronically controlling the applied magnetic field. For a more extensive and complete treatment of ferrite properties at microwave frequencies, see Refs. 14 and 15. As direct application of this concept, a waveguide ferrite loaded phase shifter is described. The geometry of the device is shown in Fig. 20, the magnetization of the ferrite is achieved using a

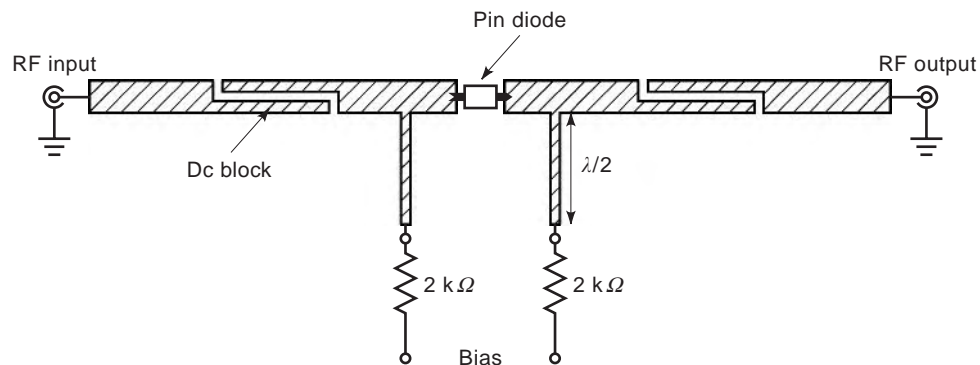


Figure 15. Bias circuit of pin-diode-type phase shifter.

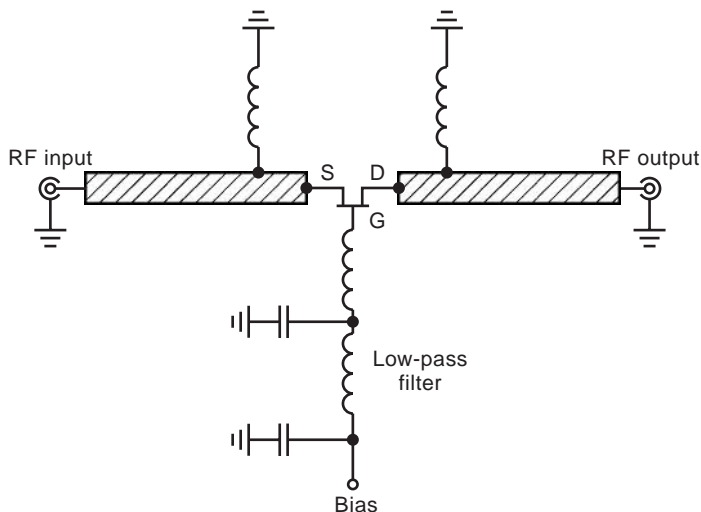
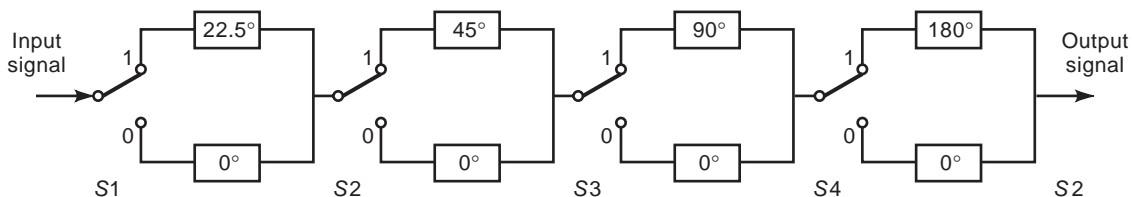


Figure 16. Bias circuit for an FET type of phase shifter.

current loop around the ferrite slab (with the aid of a biasing wire). The ferrite is placed in the waveguide in such a way to maximize the interaction with the existing magnetic field in the guide. For waveguide operating with the fundamental mode (TE_{10}), the magnetic field will be maximum at $\frac{1}{4}$ and $\frac{3}{4}$ of the longitudinal section of the guide [6] as illustrated in Fig. 20. Because the magnetic field has opposite direction at those sections, an asymmetric bias (see Fig. 20) will be necessary in order to obtain a phase shift. This is done using a current flowing in the two wires in opposite directions. Another concept is to use different geometries as illustrated in Fig. 21. The cross section depicted in Fig. 21a is an extension of the one shown in

Fig. 20; the difference is that the ferrite is placed where the maximum magnetic field exists at the bottom and top of the guide. This allows a reduction of the mismatch with the empty waveguide, making easier the design of the matching circuit. Also in this case as illustrated in the figure, a differential bias of the ferrite must be used. Figure 21b is also based on a similar concept; but the asymmetric bias is replaced by an asymmetric geometry, so the ferrite is only placed on one side of the guide. Further improvement toward the matching for this structure is obtained in the case of Fig. 21c. Several versions of a planar structure that employ ferrites as tunable elements have been proposed [16–18]. Even though in principle



Switch state S1 S2 S3 S4	Phase shift
0 0 0 0	0°
1 0 0 0	22.5°
0 1 0 0	45°
1 1 0 0	67.5°
0 0 1 0	90°
1 0 1 0	112.5°
0 1 1 0	135°
1 1 1 0	157.5°
0 0 0 1	180°
1 0 0 1	202.5°
0 1 0 1	225°
1 1 0 1	247.5°
0 0 1 1	270°
1 0 1 1	292.5°
0 1 1 1	315°
1 1 1 1	337.5°

Figure 17. Diagram of 4-bit phase shifter and corresponding switching scheme.

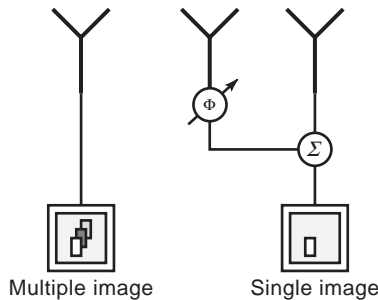
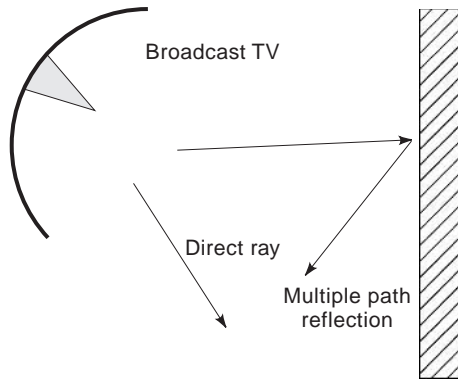


Figure 18. Phase shift recovering for a multiple-path reflected signal.

those structures work, most ferrite phase shifters currently constructed use waveguide geometry.

Another operational principle for the ferrite reciprocal phase shifters is to use Faraday rotation to produce time delay of microwave signal. This type of phase shifter was at first proposed by Reggia and Spencer [19] and is illustrated in Fig. 22. Several modifications of the original form were proposed later, but the basic operative principle remains the same. In this phase shifter a longitudinal ferrite toroid is placed in the longitudinal section of a rectangular waveguide (see Fig. 22). The magnetic biasing field is produced by an external magnetization circuit. It is well known that when a linearly polarized wave propagates in a ferromagnetic rod, the plane of polarization of the wave in the rod rotates. Now if the rod is placed inside a rectangular waveguide with one of its dimension at cutoff, then the rotational effect is suppressed (for small-size rod). Reggia and Spencer have demonstrated large changes in insertion phase with external magnetic field bias for the transmitted power. They also demonstrated that the phase variations are independent of the propagation

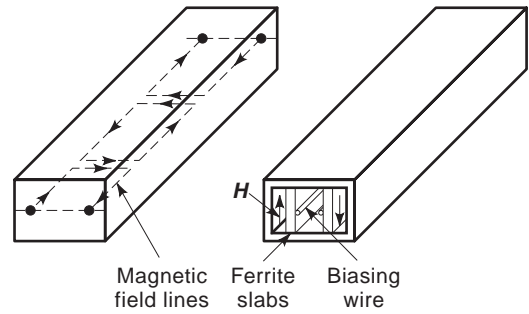


Figure 20. Nonreciprocal waveguide ferrite phase shifter.

direction. Many other authors investigated the theory beyond this effect [20,21]. Practical design of the Reggia-Spencer phase shifter is mostly based on approximate equations [22] that consider the phase shift as a consequence of a small perturbation in the effective permeability.

5.4. Ferroelectric Phase Shifters

In ferroelectric phase shifters the phase shift capability of ferroelectric materials results from the fact that if we are below their Curie temperature [23,24] (see FERROELECTRICS), the dielectric constant of such a material can be modulated under the effect of an electric bias field. Particularly, if the electric field is applied perpendicularly to the direction of propagation of the electromagnetic signal, the propagation constant ($\beta = 2\pi/\lambda$) of the signal will depend on the bias field since $\beta = 2\pi\sqrt{\epsilon_r}/\lambda_0$ and $\epsilon_r = \epsilon_r(V_{\text{bias}})$. The total wave delay will become a function of the bias field, and therefore this will produce a phase shift $\Delta\phi = \Delta\beta l$, where l is the length of the line. Two major implementations of a ferroelectric phase shifter have been used: waveguide geometry and planar structures. In waveguide geometry the ferroelectric material is placed inside a waveguide as illustrated in Fig. 23. A voltage is applied to the center conductor, creating a vertical electric field to the grounded flange. The matching layer must be placed on either side of the sample to couple the RF energy in and out of the material. These rectangular layers of dielectric are needed in the design of the phase shifter because of the impedance mismatch between air and the high permittivity ferroelectric. One problem in the use of this type of setup is the high bias required (typically 1–2kV) due to the thickness of the material. Ferroelectrics require a bias

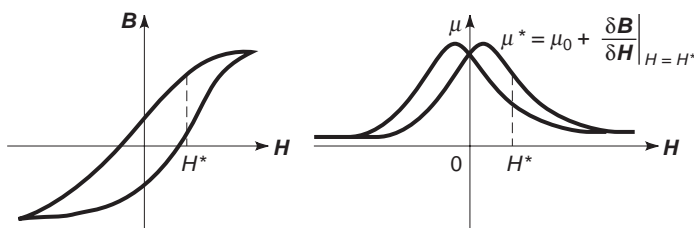


Figure 19. Nonlinear $B-H$ dependence and correspondent $\mu-H$ dependence.

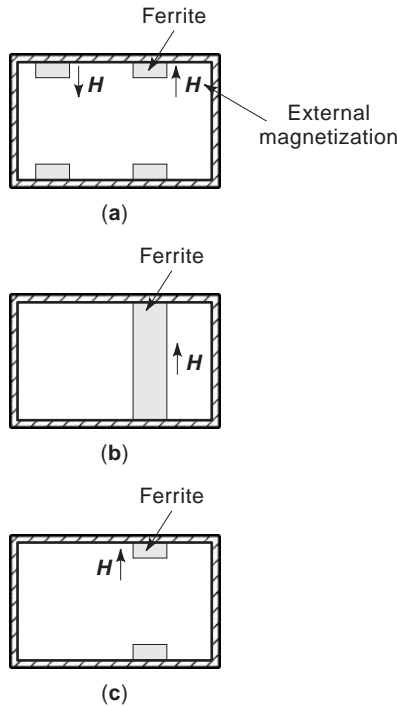


Figure 21. Different types of nonreciprocal waveguide ferrite phase shifter.

voltage of the order $2\text{--}4\text{V}/\mu\text{m}$ in order to significantly change their dielectric constant [25,26].

Use of the planar type of ferroelectric material in microstrip geometry avoids this problem as demonstrated in Ref. 27. The geometry is illustrated in Fig. 24. The active part of the device consists of a microstrip line printed on a ferroelectric substrate whose dielectric constant is changed by bias. The length of the strip determines the maximum phase shift achievable for a fixed change of the propagation constant ($\Delta\beta$), associated with the maximum bias voltage. The complete design of this type of phase shifter is reported in Ref. 28. To reduce the required bias, the ferroelectric material has a thickness of the order of $0.1\text{--}0.2\text{ mm}$, allowing bias voltage of a few hundred volts. As in the case of the pin-diode phase shifter, attention must be dedicated to the design of the biasing circuit, to avoid leakage of the DC voltage in the RF circuit.

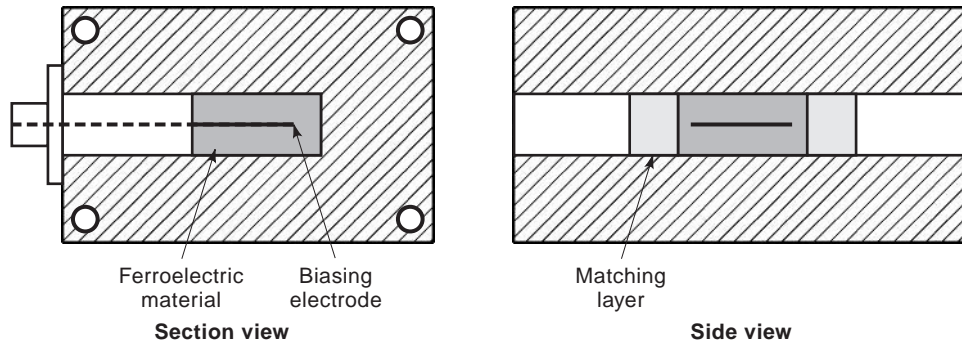


Figure 23. Waveguide ferroelectric type of analog phase shifter.

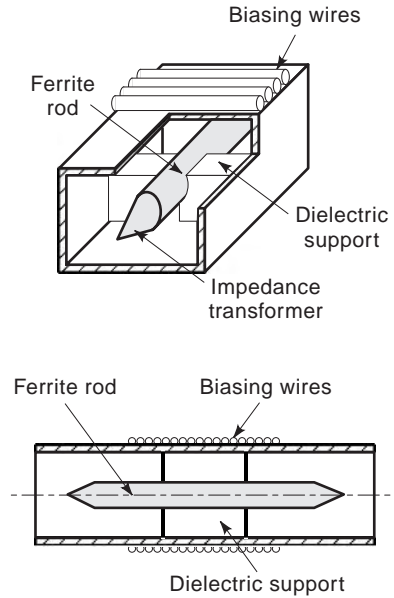


Figure 22. Reggia-Spencer reciprocal ferrite phase shifter.

5.5. Varactor Diode Phase Shifter

In varactor diode phase shifters a varactor diode is used as a variable-capacitance element. This variable capacitance is obtained through a voltage-tuned capacitance of the diode under a reverse-bias condition [24]. The varactor diode is used in combination with a hybrid coupled circuit as illustrated in Fig. 25a. The $3\text{ dB } 90^\circ$ hybrid circuit is symmetrically terminated with the diodes. If X is the reactance of the diode, the reflection coefficient can be calculated as [11]

$$\Gamma = \frac{jX/Z_0 - 1}{jX/Z_0 + 1} \tag{21}$$

and the corresponding phase of the reflection coefficient is given by

$$\phi = \pi - 2 \arctan(X/Z) \tag{22}$$

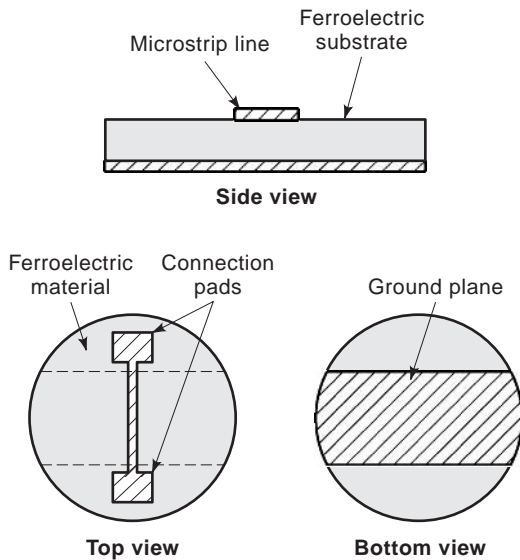


Figure 24. Microstrip ferroelectric type of analog phase shifter.

where Z_0 is the characteristic impedance of the transmission line ($50\ \Omega$ typically). We notice that in order to obtain a phase variation in the range going from 0 to 2π , the reactance of the diode must go from $-\infty$ to 0 to $+\infty$ and the maximum change of phase is obtained when $X=0$. Hence, in order to obtain a maximum phase shift, the diode must be connected in series with an inductive load to allow resonance ($X=0$); this can be achieved with a stub as illustrated in Fig. 25b for a microstrip realization. The

impedance of the reflecting termination (diode and stub) is given by

$$Z = R_d + j\left(Z_s \tan \beta l_s - \frac{1}{\omega C_d}\right) \quad (23)$$

where R_d and C_d are the equivalent parameters of the diode, and Z_s and l_s are the stub characteristic impedance and length, respectively. The associated reflection coefficient is calculated from

$$\Gamma = \frac{R_d - Z_0 + jX}{R_d + Z_0 + jX} \quad (24)$$

As the bias voltage changes from 0 to a negative value, C_d goes from $C_{d,max}$ to $C_{d,min}$, giving a change of X expressed by

$$\Delta X = \frac{1}{\omega C_{d,min}} - \frac{1}{\omega C_{d,max}} \quad (25)$$

For such change of X the correspondent phase change can be obtained as

$$|\Delta\phi| = 4 \arctan\left(\frac{\Delta X}{2Z_0}\right) \quad (26)$$

Also at $X=0$ (resonance condition) a maximum insertion loss due to R_d will occur. The corresponding attenuation in

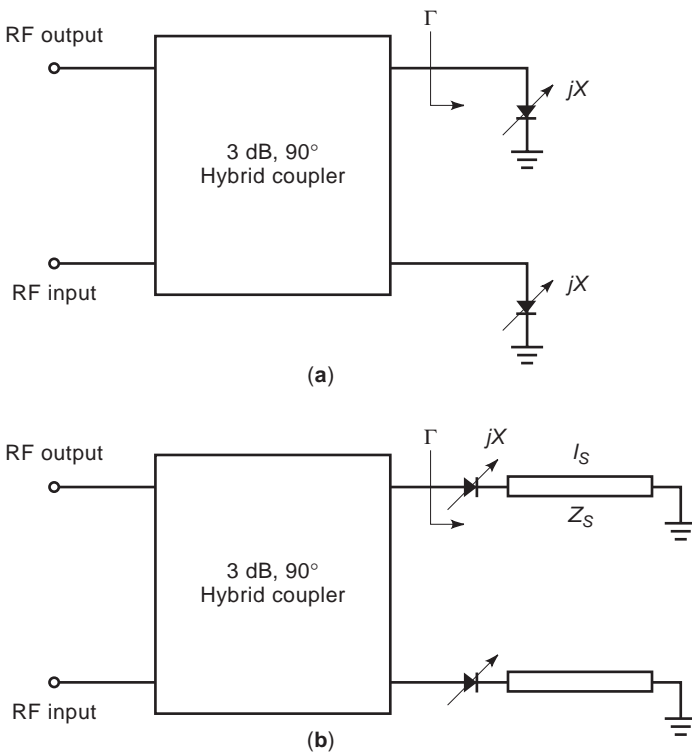


Figure 25. Varactor-based tunable phase shifter.

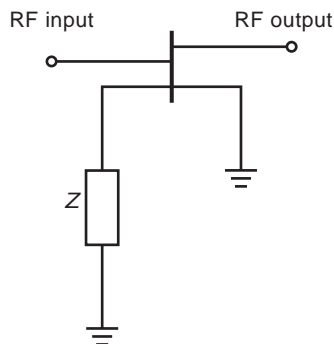


Figure 26. Active FET-type phase shifter.

this circumstance is

$$\alpha_{\text{dB}} = 20 \log_{10} \left(\frac{1 + R_d/Z_0}{1 - R_d/Z_0} \right) \quad (27)$$

The figure of merit (F) for the analyzed structure is calculated as

$$F = \frac{|\Delta\phi|_{\text{deg}}}{\alpha_{\text{dB}}} \quad (28)$$

A possible improvement of the presented structure can be obtained using two series varactor diodes as presented in Ref. 29. the operational principle remains the same, but a larger change in the capacitance is obtained.

5.6. Active Phase Shifter

Use of FET in an analog phase shifter [30] allows one to take advantage of the gain of the FET at microwave frequencies, while producing the time delay at the same time. Figure 26 shows the topology of this kind of phase shifter. The phase variation in the transmission coefficient (S_{21}) is achieved by controlling the bias voltage at the gate of the FET. The bias voltage is applied on the second gate of the FET, while a fixed inductive load is connected to it. The bias voltage will change the capacitance between the first gate (G_1) and the source, and this will change the amplitude and phase of the S_{21} . One limitation of this topology is the narrow bandwidth that is achieved. Use of more complicated topologies as reported in Ref. 31 will allow larger bandwidth and larger phase shifting capabilities.

Acknowledgements

The author wishes to thank Professor N. G. Alexopoulos of the Electrical and Computer Engineering Department at the University of California, Irvine, for useful suggestions.

BIBLIOGRAPHY

1. M. Sucher and J. Fox, *Handbook of Microwave Measurements*, Polytechnic, New York, 1963.
2. G. D. Vendelin, A. M. Pavio, and U. L. Rohde, *Microwave Circuit Design Using Linear and Nonlinear Techniques*, Wiley, New York, 1990.

3. R. E. Collin, *Foundations for Microwave Engineering*, McGraw-Hill, New York, 1966.
4. R. E. Collin, *Field Theory of Guided Waves*, 2nd ed., IEEE Press, New York, 1991.
5. R. Winnery and V. Durez, *Campi e Onde nell' Elettronica per le Comunicazioni*, Milan, 1984.
6. C. A. Balaniis, *Advanced Engineering Electromagnetics*, Wiley, New York, 1989.
7. F. E. Gardiol, Higher order modes in dielectrically loaded rectangular waveguides, *IEEE Trans. Microwave Theory Tech.* **MTT-16**:919–924 (1969).
8. N. Marcuvitz, *Waveguide Handbook*, Peter Peregrinus, London, 1986.
9. W. T. Joines, A continuously variable dielectric phase shifter, *IEEE Trans. Microwave Theory Tech.* **MTT-19**:729–732 (1971).
10. P. R. Gray and R. G. Meyer, *Analysis and Design of Analog Integrated Circuits*, Wiley, New York, 1993.
11. G. Gonzalez, *Microwave Transistor Amplifiers*, Prentice-Hall, Englewood Cliffs, NJ, 1984.
12. G. P. Rodrigue, Magnetic materials for millimeter wave applications, *IEEE Trans. Microwave Theory Tech.* **MTT-11**:351–356 (1963).
13. J. Smith and H. P. J. Wijn, *Ferrites*, Phillips' Technical Library, New York, 1959.
14. G. L. Matthaei, L. Young, and E. M. T. Jones, *Microwave Filters, Impedance Matching Networks, and Coupling Structures*, Artech House, Dedham, MA, 1980.
15. J. J. Green and F. Sandy, Microwave characterization of partially magnetized ferrites, *IEEE Trans. Microwave Theory Tech.* **MTT-22**:641–645 (1974).
16. R. R. Jones, A slow-wave digital ferrite strip transmission line phase shifter, *IEEE Trans. Microwave Theory Tech.* **MTT-14**:684–687 (1966).
17. L. R. Whicker and R. R. Jones, A digital latching ferrite strip transmission line phase shifter, *IEEE Trans. Microwave Theory Tech.* **MTT-13**:781–784 (1965).
18. W. M. Libbey, Characteristic of a microstrip two meander ferrite phase shifter, *IEEE Trans. Microwave Theory Tech.* **MTT-21**:483–487 (1973).
19. F. Reggia and E. G. Spencer, A new technique in ferrite phase shifting for beam scanning of microwave antennas, *Proc. IRE* **45**:1510–1517 (1957).
20. P. A. Rizzi and B. Gatlin, Rectangular guide ferrite phase shifter employing longitudinal magnetic fields, *Proc. IRE* **47**:1130–1137 (1959).
21. W. E. Hord, F. J. Rosenbaum, and C. R. Boyd, Theory of the suppressed-rotation reciprocal ferrite phase shifter, *IEEE Trans. Microwave Theory Tech.* **MTT-16**:902–910 (1968).
22. K. J. Button and B. Lax, Perturbation theory of the reciprocal ferrite phase shifter, *Proc. IRE* **109B** (1962).
23. M. E. Lines and A. M. Glass, *Principles and Applications of Ferroelectrics and Related Materials*, Clarendon Press, Oxford, UK, 1977.
24. C. Kittel, *Introduction to Solid State Physics*, Wiley, New York, 1986.
25. T. Mitsui and S. Nomura, Landolt–Bornstein: Numerical data and functional relationship in science and technology, *Ferroelectr. Related Subst.* **16** (1981).
26. R. Pepinsky, *Physics of Electronic Ceramics*, Marcel Dekker, New York, 1972.

27. F. De Flaviis et al., Ferroelectric materials for microwave and millimeter wave applications, *Proc. SPIE Smart Struct. Mater.* **2448**:9–21 (1995).
28. F. De Flaviis, O. M. Stafsudd, and N. G. Alexopoulos, Planar microwave integrated phase shifter design with high purity ferroelectric materials, *IEEE Trans. Microwave Theory Tech.* **45**:963–969 (1997).
29. B. T. Henoeh and P. Tamm, A 360° reflection type diode phase modulator, *IEEE Trans. Microwave Theory Tech.* **MTT-29**:103–105 (1971).
30. C. Tsironis and P. Harrop, Dual gate GaAs MESFET phase shifter with gain at 12 GHz, *Electron. Lett.* **16**:553–554 (1980).
31. M. Kumar, R. J. Menna, and H. Huang, Broadband active phase shifter using dual-gate MESFET, *IEEE Trans. Microwave Theory Tech.* **MTT-29**:1098–1102 (1981).

PHOTONIC BAND GAP (PBG)

ALEJANDRO MARTÍNEZ
 AMADEU GRIOL
 PABLO SANCHIS
 JAVIER MARTÍ
 Universidad Politécnica de
 Valencia
 Valencia, Spain

1. INTRODUCTION

In 1987, E. Yablonovitch suggested that a dielectric medium with a periodic index of refraction in the three dimensions would make it feasible to inhibit the spontaneous emission from an excited atom, provided a sufficient refractive index contrast was achieved [1]. This phenomenon occurs because the periodicity of the medium gives rise to a frequency region where electromagnetic (EM) radiation is suppressed regardless of the wavevector (direction of incidence). This frequency region is usually called the *photonic bandgap* (PBG) as it is the classical wave equivalent to the electronic bandgap for electrons in semiconductors. Since this seminal work, the number of publications related to PBG materials and applications has doubled every year.

The first step after the publication of the Yablonovitch's work was intended to find a three-dimensional (3D) composite that could allow a complete 3D PBG. The microwave regime was chosen to fabricate the first 3D structures because they can be more easily manufactured and tested than their optical counterparts, taking into account that the fundamental length is on the order of millimeters instead of micrometers. The first choice was a face-centered cubic (fcc) lattice of air spheres in a high-index ($n = 3.5$) dielectric material as the rounded shape of the Brillouin zone of the fcc lattice contributes to the appearance of a full 3D PBG [2]. Following this approach, a number of structures with different filling factors and refractive indices were fabricated and tested owing to the lack of numerical tools that could ease the design. For one of these structures (86% filling factor), Yablonovitch was

able to identify experimentally a 1-GHz-width 3D PBG centered at 15 GHz between the first two bands [2], which validated his own theoretical predictions 2 years earlier. These experimental results were confirmed by two theoretical works in which the photonic band diagram of the structure measured in Ref. 2 was calculated by employing a plane-wave expansion (PWE) method with a scalar approximation of the EM fields [3,4]. However, after this apparent success several authors pointed out that if a full-vector approximation were used to obtain the photonic bands by means of the PWE approach, the PBG observed experimentally would be merely a pseudo-PBG [5,6], due to degeneracy of the first bands near the W and U symmetry points. These disappointing theoretical results gave rise to some controversy but, at the end of 1990, the first structure possessing a complete 3D PBG was discovered: the diamond lattice of dielectric spheres [7]. From this discovery until the present the investigation field related to PBG materials has experienced such a growing interest that many authors have pointed out that these materials could give rise to a technological revolution similar to that caused by semiconductors in the mid twentieth century [8].

2. FUNDAMENTALS OF PHOTONIC BANDGAP

PBG materials can be classified as one-dimensional (1D), two-dimensional (2D), or (3D) depending on the directions of periodicity of the index of refraction. A 3D PBG structure is necessary to achieve a complete PBG. However, 2D PBG structures such as planar photonic crystals that can have an in-plane PBG [9] have attained great success as they are easier to fabricate (use of conventional techniques employed in microelectronics) and to test than 3D ones such as inverted opals [10] or woodpile structures [11,12].

As mentioned above, PBG materials can be designed to work in any spectral regime, from microwaves to infrared frequencies, due to the scaling properties of the Maxwell equations [13]. The materials must have only an appropriate index of refraction and low absorption losses in the selected spectral regime. For example, materials such as silica, silicon, or III–V composites are commonly used to implement PBG circuits working at optical frequencies [9–12,14]. On the other hand, in the microwave regime the most extensive choice has been the use of alumina (Al_2O_3) because of its high refractive index and low absorption losses [15]. 2D and 3D lattices of alumina rods have been widely used to study PBG-based phenomena [16–20] that have been demonstrated experimentally first in the microwave domain and then in the optical domain, for the reasons explained previously. For example, the existence of localized modes and the guiding of light through linear defects were first demonstrated in the microwave regime using 2D lattices of alumina rods [12,21]. Some years later, these same phenomena were measured in the optical domain using more sophisticated procedures [22].

The two most important EM properties of PBG structure are (1) the existence of the PBG where no propagation states exist owing to the destructive interaction between multiple EM waves reflected and refracted in all interfaces

of the composite and (2) the existence of EM modes that can propagate without scattering through the periodic composite despite the high-index contrast at the materials interfaces. These modes propagate in the form of Bloch waves [23]: a plane wave modulated by a periodic function with a periodicity the same as that of the PBG structure. Because of the property of wavevector conservation, a Bloch wave can propagate losslessly through a perfectly periodic dielectric structure. The photonic bands of a PBG composite show all the Bloch modes that can propagate in the composite and thus fully characterize the EM behavior of the PBG structure. The photonic bands of a given PBG structure can be obtained from the so-called master equation [13]

$$\nabla \times \left(\frac{1}{\varepsilon(\mathbf{r})} \nabla \times \mathbf{H}(\mathbf{r}) \right) = \left(\frac{\omega}{c} \right)^2 \mathbf{H}(\mathbf{r}) \quad (1)$$

where $\varepsilon(\mathbf{r})$ is the permittivity in the region under consideration, $\mathbf{H}(\mathbf{r})$ is the magnetic field, ω the optical frequency, and c the light speed in vacuum. A detailed procedure on how to obtain Eq. (1) can be found in Ref. 13.

To better understand the EM properties of PBG composites, let us analyze a typical PBG structure: a 2D arrangement of high-index cylinders with radius r in air forming a hexagonal lattice with lattice constant a , such as that shown in Fig. 1a. The structure is formed by the periodic repetition of the unit cell (see Fig. 1b) in a plane. The high-symmetry directions are denoted as ΓM and ΓK . Figure 1c depicts the first Brillouin zone in the reciprocal space corresponding to the hexagonal lattice, including the high-symmetry points and the irreducible Brillouin zone (highlighted triangle). All these concepts are similar to those employed in solid-state physics to describe the electronic properties of crystals [24]. In a 2D PBG structure such as that depicted in Fig. 1a, EM modes can be classified into transverse electric (TE) and transverse magnetic (TM) polarizations as the system is invariant under reflections through the plane perpendicular to the cylinders' axes [13]. In general, it is assumed that the waves are confined in the plane of periodicity, so the wave vector in the normal direction is zero. For TM (TE) modes the electric (magnetic) field is parallel to the rods' axes and the magnetic (electric) field is in the periodicity plane. The behavior of TM and TE modes is quite different; a PBG may exist for TE modes and not for TM ones, or vice versa. Furthermore, a periodic structure of high-index cylinders in air (such as that shown in Fig. 1) benefits the appearance of PBGs for TM modes, whereas a 2D lattice of air-holes in a high-index material has PBGs mainly for TE modes [13]. Figure 2a shows the photonic bands of the structure described in Fig. 1 for TM modes. The bands have been obtained by employing the PWE method to solve Eq. (1) [7]. The parameters have been chosen as $r = 0.133a$ and $\varepsilon = 10.3$, as in the PBG circuits described below. On the horizontal axis (abscissa) the wavevector at the boundary of the irreducible Brillouin zone is represented; on the vertical axis (ordinate) the frequency of the modes is represented in normalized units of a/λ , where λ is the wavelength in vacuum. It is usual to represent the

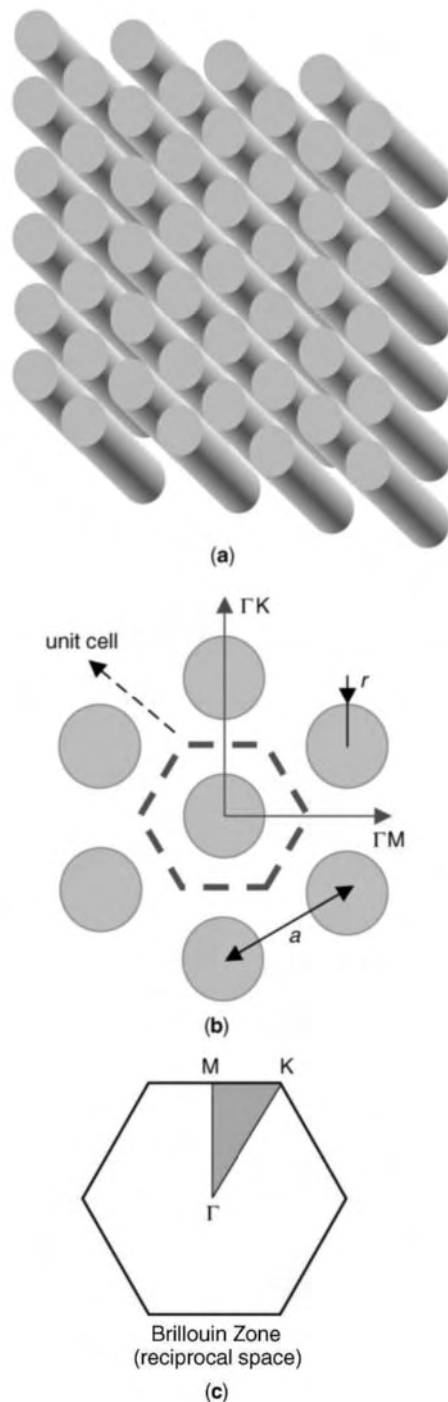


Figure 1. (a) Schematic of a 2D PBG structure consisting of high-index cylinders in air distributed in a hexagonal arrangement; (b) hexagonal lattice of the PBG structure, showing the unit cell, the lattice constant a , and the high-symmetry directions ΓM and ΓK ; (c) Brillouin zone of the hexagonal lattice in the reciprocal space, with the high-symmetry points (Γ , M , and K) and the irreducible Brillouin zone (highlighted triangle). (This figure is available in full color at <http://www.mrw.interscience.wiley.com/erfme>.)

photonic bands in terms of these normalized dimensionless units, as this representation is independent of the frequency regime where the PBG structure works. From the band diagram and properly selecting a , the PBG

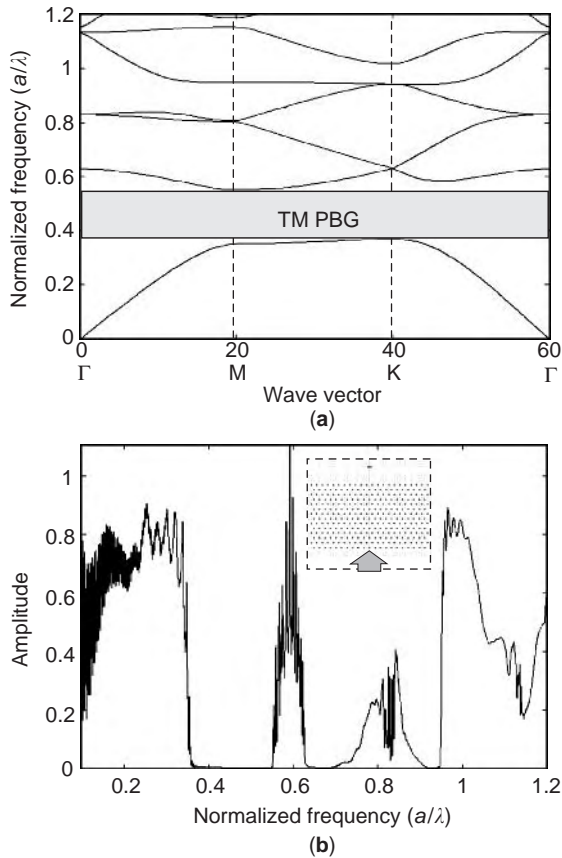


Figure 2. (a) Photonic bands of a 2D hexagonal PBG structure of cylinders ($\epsilon = 10.3$, $r = 0.133a$) in air (PWE method); (b) transmission response of the previous PBG structure along the ΓM direction (seven layers) obtained with an FDTD method. (This figure is available in full color at <http://www.mrw.interscience.wiley.com/erfme>.)

structure can be designed to have a PBG in a given frequency range (from microwaves to the infrared). Figure 2a shows a frequency range of $0.37\text{--}0.55 [a/\lambda]$ where no photonic bands exist regardless of the wavevector. Then, in this region there exists a PBG for TM-polarized waves. This can also be demonstrated by obtaining the transmission spectrum of the proposed PBG structure. To this end, the finite-difference time-domain (FDTD) method [25] can be employed. This method allows one to resolve numerically the Maxwell equations in the time domain in a finite spatial region. Figure 2b shows the transmission spectrum of a PBG structure such as that whose photonic bands are shown in Fig. 2a. The wave propagates along the ΓM direction and the crystal has a thickness of seven layers in this direction (see inset of Fig. 2b). It can be observed that there is a low-transmission region corresponding to the TM PBG shown in Fig. 2a. The ripple in the transmission region between 0.55 and $0.63 [a/\lambda]$ (where the second photonic band is excited) is due to the reflectivity at both facets of the PBG structure that behaves as a Fabry–Perot cavity. There are two other low-transmission regions ($0.63\text{--}0.76 [a/\lambda]$ and $0.86\text{--}0.95 [a/\lambda]$) corresponding to pseudo-PBGs in the ΓM direction, that is, PBGs that exist for wavevectors along ΓM but not along ΓK , which can also be identified in the photonic bands. The total transmission in a PBG or a pseudo-PBG is not actually zero because the PBG structure has a finite thickness and modes with frequencies inside the PBG are evanescent inside the crystal and their amplitudes decrease exponentially as they enter the crystal. This can be observed in more detail in Fig. 3, which shows the distribution of the electric field component parallel to the cylinder axis when a plane wave impinges on the PBG structure under study. Two different cases are taken into account; in Fig. 3a the frequency of the wave is $0.58 [a/\lambda]$, so there exists an allowed Bloch mode (see Fig. 2a) that is excited when the

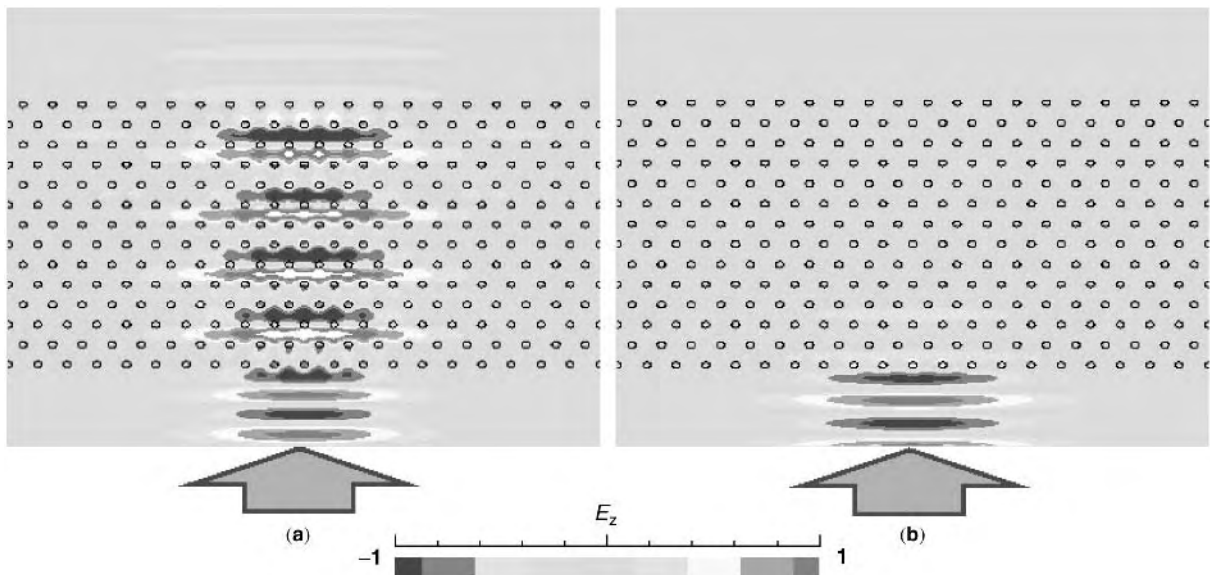


Figure 3. Distribution of the vertical component of the electric field (TM polarization) for a 2D hexagonal PBG structure of cylinders ($\epsilon = 10.3$, $r = 0.133a$) in air when a monochromatic wave impinges from above and is directed upward along the ΓM direction: (a) $0.58 [a/\lambda]$ (guided band); (b) $0.5 [a/\lambda]$ (inside the PBG). (This figure is available in full color at <http://www.mrw.interscience.wiley.com/erfme>.)

plane wave enters the crystal; in Fig. 3b the frequency is $0.5 [a/\lambda]$, inside the PBG, so the incident wave cannot enter the crystal as there is no mode that can be excited and the wave is mainly reflected backward whereas a exponentially attenuated signal penetrates inside the crystal in the form of an evanescent wave.

Most of the applications related to PBG composites are related to the insertion of defects inside the otherwise periodic structure, as occurs with the doping of impurities in semiconductors. For example, the insertion of a point defect in a 3D PBG composite breaks the 3D periodicity and can give rise to the presence of a localized EM mode with frequency inside the PBG. This phenomenon was first investigated by Yablonovitch et al., who developed a PBG structure known as a *Yablonovite*, which was the first structure to experimentally demonstrate a complete 3D PBG [21]. Yablonovitch et al. inserted impurities in this composite by adding (acceptor modes) and removing (donor modes) a given quantity of high-index material and noticed that a narrow peak appeared in the transmission spectrum due to the existence of a localized mode inside the defect [26]. Such defects can be used as optical microcavities (or photon boxes) and allow the confinement of light in volumes on the order of $(\lambda/2)^3$.

Linear defects can also be inserted giving rise to EM modes (which can also be classified as acceptors and donors) confined along a line. This fact can be used to implement optical waveguides with a field transverse width of about $\lambda/2$ [13]. In contrast to conventional optical integrated waveguides, in which light confinement is achieved by index guiding (a dielectric core is sandwiched between claddings with a refractive index lower than that of the core material), using PBG linear defects, it becomes feasible to guide light through air waveguides. This has several advantages over guiding light through dielectric materials: reduction of absorption losses, reduction of nonlinear effects, and higher power transmission. However, the most important characteristic of PBG waveguides is that they allow bending of light through sharp bends with negligible losses as the radiation outside the line defect is suppressed because of the existence of the PBG [17,27]. In this way, PBG structures are considered as the main candidates to miniaturize optical components to the order of several wavelengths, which could give rise to the development of nanophotonics technology, in the same way that semiconductors made feasible the widely known microelectronics technology.

3. PHOTONIC BANDGAP IN THE MICROWAVE REGIME: PROPERTIES AND APPLICATIONS

As stated previously, PBG composites can be designed to have a PBG in the microwave regime if the lattice constant ($a \sim \lambda/2$) and the dielectric material are properly chosen. A number of PBG structures, components, and functionalities have been analyzed in the microwave regime, due the relatively easy mode of fabrication (sizes of the order of centimeters) and test (mature measure instruments in the megahertz and gigahertz ranges). The first experiments were aimed at demonstrating the exis-

tence of a 2D PBG for in-plane wavevectors (as in Ref. 16) or a complete 3D PBG (as in Ref. 21). The following target was to demonstrate the existence of localized defect modes, as done in Ref. 26 for cavities and in Ref. 17 for linear waveguides. The demonstration of the feasibility of guiding EM waves through line defects was a key step as a great number of devices and components (in both microwave and optical regimes) are implemented making use of waveguides.

Among all the passive components and applications that have been proposed to implement functionalities of use in optical devices and networks, the Y junction, the directional coupler, and the Mach-Zehnder interferometer (MZI) can be considered as the key building blocks because they enable almost all the applications necessary in these networks (filters, routers, demultiplexers, power combiners/splitters) to be implemented. All these components can be created in a PBG lattice of alumina cylinders and tested using conventional microwave instruments, such as horn antennas and a network analyzer, in order to characterize their performance. In the following paragraphs, these components, as well as two kinds of conventional PBG waveguides that can be used to implement them, are separately described and analyzed.

3.1. PBG Waveguides

As mentioned above, a waveguide can be created in a PBG structure by inserting a line defect that alters the otherwise periodic structure. For example, a ΓK -oriented row of rods can be removed in a 2D hexagonal lattice of high-index cylinders in air, as shown schematically in Fig. 4a. This kind of waveguide is usually referred to as W1 waveguide. In this case, the line defect arises from the removal of high-index dielectric material, so it gives rise to a decreased-index waveguide. Insertion of the defect produces that a single donor mode appears inside the PBG [13]. On the other hand, if the defect is created by adding high-index material, then an increased-index waveguide is obtained, which is inherently multimode. Decreased-index waveguides are preferred as they are single-mode and allow a high efficiency in processes such as guiding through sharp bends or power splitting in Y junctions [27,28]. On the other hand, increased-index waveguides are inherently multimode, which gives rise to undesired phenomena when the translational symmetry of the waveguide is broken (bends, cavities, Y junctions) because higher-order

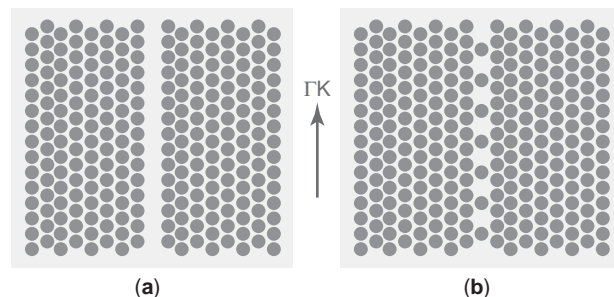


Figure 4. Schematics of (a) a W1 waveguide and (b) a CCW inserted along the ΓK direction in a hexagonal lattice of high-index cylinders in air. (This figure is available in full color at <http://www.mrw.interscience.wiley.com/erfme>.)

modes become excited, degrading the performance of the structure [29].

A waveguide can also be created by inserting a chain of evenly spaced strongly confined microcavities, a structure which is commonly referred to as *coupled-cavity waveguide* (CCW) [18,30,31]. A CCW can be created in a PBG lattice by removing one of each of two cylinders along a certain direction, as shown schematically in Fig. 4b. Light propagation in CCWs can be explained as photon hopping between nearby cavities, due to overlapping of the tightly confined modes. The separation d between cavities must be large enough to ensure that the modes are weakly coupled and the eigenmode of the field in the waveguide remains essentially the same as in an isolated cavity (in Fig. 4b, $d = 2a$). This picture is exactly the classical wave analogous of the tight-binding (TB) approach employed in solid-state physics to describe the electronic properties of solids. From the TB formalism and taking into account that interaction occurs only between consecutive defects along the waveguide, the dispersion relation of a CCW can be expressed as [30]

$$\omega(k) = \Omega[1 + \kappa \cos(kd)] \quad (2)$$

where ω is the angular frequency, k is the wavevector along the direction of the waveguide, Ω is the angular eigenfrequency of an isolated cavity, and κ is the hopping parameter. Owing to the periodicity of the structure along the waveguide direction, the wavevector k is folded into the region $[0, \pi/d]$, so the TB model of the CCW band [Eq. (2)] depends on only two parameters: Ω and κ . The width of the CCW band $\Delta\omega$ may be obtained as $\Delta\omega = 2|\kappa|\Omega$. The most promising features of CCWs are the feasibility of tuning the central frequency of the CCW guided band by modifying the cavities and the 100% transmission of light through sharp bends over their entire bandwidth if the cavity mode has a proper symmetry [30].

Figure 5 shows the measured TM-polarized transmission response (normalized with respect to free-space

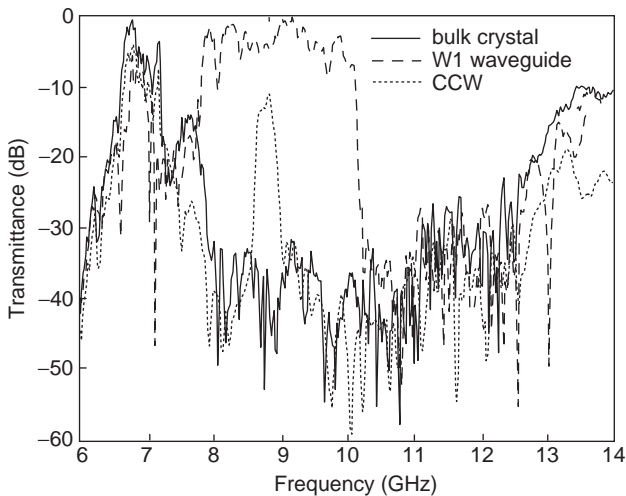


Figure 5. Experimental TM-polarized transmission response (normalized with respect to free-space transmission) of a bulk hexagonal crystal of alumina cylinders, a W1 waveguide, and a CCW (parameters: $\epsilon = 10.3$, $r = 0.133a$, $a = 1.5$ cm).

transmission) of a ΓK -oriented bulk structure composed of alumina rods (with the same parameters considered above: $\epsilon = 10.3$, $r = 0.133a$, and $a = 1.5$ cm), and both a W1 waveguide and a CCW inserted in such a structure as shown in Fig. 4. When no defects are inserted, a PBG appears between approximately 7.4 and 13 GHz for in-plane propagation and ΓK incidence. However, if the line defects are introduced, a passband appears inside the rejected band. It can be noticed that the passband is wider and has more amplitude in the case of the W1 waveguide. This is because the dispersion relation of a W1 waveguide is wider and has a higher slope (which means a higher group velocity), so the coupling efficiency from free space is higher and the insertion loss smaller. When bends are introduced, a CCW shows a better behavior than a W1 waveguide, due to the propagation mechanism. In any case, 120° sharp bends can be introduced with high efficiency of power transmission. A more detailed analysis of the performance of bending in these waveguides can be found in Refs. 27 and 29 for a W1 waveguide and in Ref. 31 for a CCW. Both kinds of waveguides are used to implement the structures described below.

3.2. Directional Coupler

A directional coupler (DC) can be created by setting closely two parallel 2D PBG waveguides [32,33]. The main advantage of this approach relies on achieving strong coupling due to the narrow separation between both waveguides. Figure 6 shows a scheme of a 1×2 DC implemented on a 2D hexagonal lattice of alumina rods, as that considered previously in the study of the PBG waveguides. Both waveguides are of the W1 kind. Because of the close proximity between waveguides, the guided mode of an isolated waveguide splits up into two guided modes with even and odd symmetries with respect to the plane equidistant from both waveguides [32]. These modes have different propagation constants β_{even} for the even mode and β_{odd} for the odd mode respectively, which gives rise to an EM power interchange between both waveguides as an EM wave travels along the structure. In order to quantify this effect, the coupling coefficient of the structure is defined as $\kappa = |\beta_{\text{even}} - \beta_{\text{odd}}|/2$. Thus, a higher mismatch of the propagation constants produces a higher κ , which means a stronger mode coupling. This also yields a shorter coupling length, which is defined as $L_c = 2\pi/|\beta_{\text{even}} - \beta_{\text{odd}}|$ and represents the length that light needs to jump from one

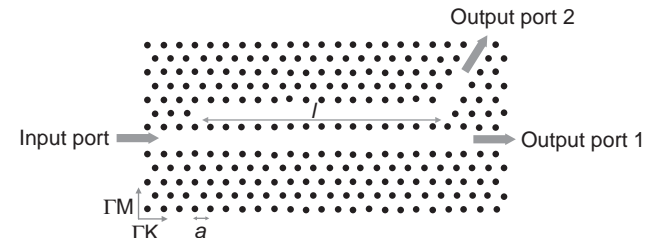


Figure 6. Schematic layout of the directional coupler. The waveguides are created along the ΓK direction of the hexagonal structure. The total coupling length is l , and the lattice constant is a .

waveguide to the other and return back to the first one. The transmission response of the coupler depends on the coupling coefficient and the overall length of the coupling region l (see Fig. 6). The normalized power related to the power injected into the input port at both output ports can be written as $P_{o1}/P_i = \cos^2(\kappa l)$ and $P_{o2}/P_i = \sin^2(\kappa l)$, respectively. Figure 7a shows both β_{even} and β_{odd} as a function of the frequency for the directional coupler shown in Fig. 6 and assuming the parameters previously considered. Both propagation constants were obtained by employing the PWE method. Figure 7b shows the calculated normalized coupling coefficient $\kappa \cdot a$ of the proposed coupler. From Fig. 7b it is observed that very high coupling coefficients are obtained mainly in the range between 8.2 and 8.6 GHz, so very short coupling lengths are achieved [34]. For example, at a frequency of 8.5 GHz ($\lambda = 3.53$ cm) the normalized coupling coefficient is $\kappa \cdot a = 0.38$, so the coupling length becomes as short as $3.5\lambda = 12$ cm. Since an overall length of $L_c/4$ is needed to distribute the signal equally between both waveguides, it becomes clear that 3-dB power splitters with a length in the order of the wavelength of the propagating signal can be achieved using PBG technology [34]. It should be emphasized that the same principles may be used to implement ultrashort couplers at

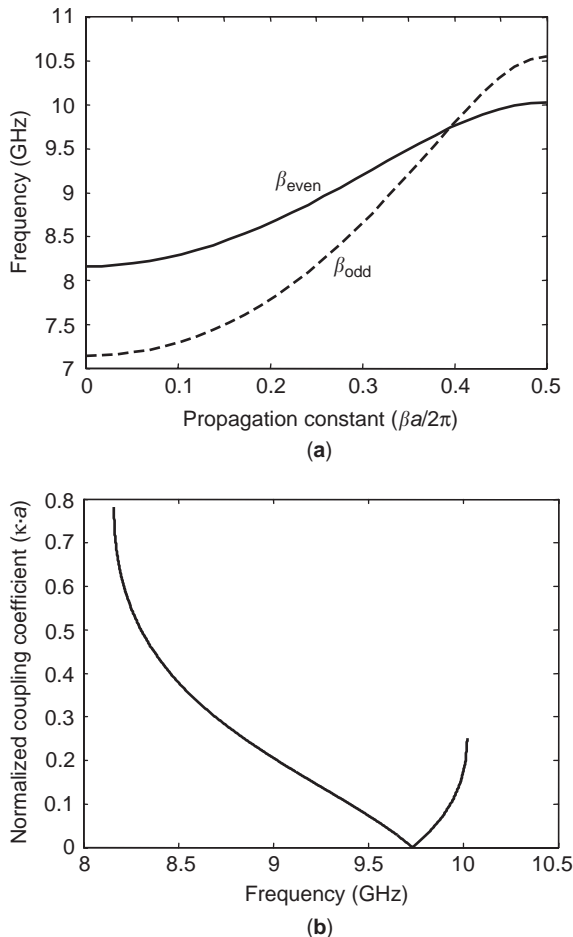


Figure 7. (a) Propagation constant of the even (solid line) and odd (dashed line) modes of the PBG coupler; (b) normalized coupling coefficient ($\kappa \cdot a$) as a function of frequency.

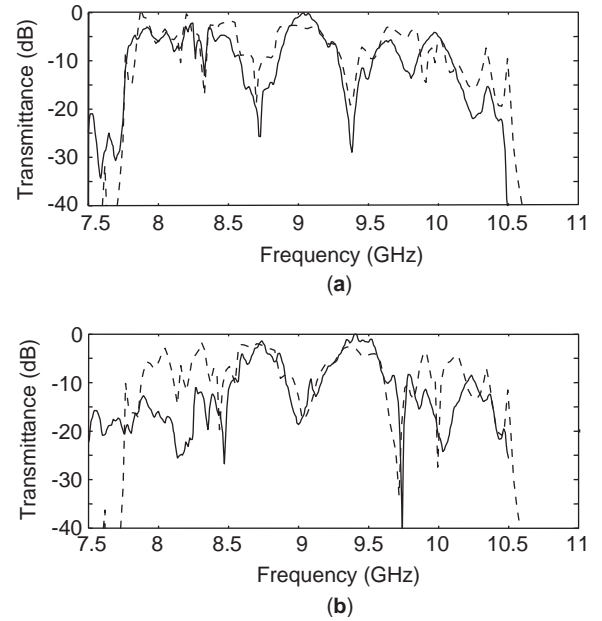


Figure 8. Simulated (dashed line) and measured (solid line) transmission frequency response at output port 1 (a) and output port 2 (b).

optical frequencies, so, in principle, it would be feasible to achieve 3-dB power splitters in the optical domain ($\lambda = 1550$ nm) with lengths around $2 \mu\text{m}$.

The coupler structure was measured and also simulated using the FDTD method. Figure 8a shows the simulated and measured transmission responses at output port 1 of the coupler. From Fig. 8a, it can be observed that the simulated transmission notches inside the guided transmission band appear at 8.7008 and 9.3717 GHz whereas the measured ones appear at 8.723 and 9.383 GHz, respectively. On the other hand, Fig. 8b shows the simulated and measured transmission responses at output port 2 of the coupler. In this case, and from Fig. 8b, the simulation notches appear at 8.44, 9.04, and 9.718 GHz whereas the measured notches appear at 8.475, 9.005, and 9.743 GHz, respectively. A very good agreement between simulation and experimental results is observed in both cases. In addition, it can be noticed that the maximum transmission points in one waveguide correspond to minimum ones in the other one, as expected from the coupler behavior. The small differences observed between simulated and measured results are due mainly to the limitations arising from the experimental setup (undesired reflections, small variations of the rod diameter) and the spectral resolution (4 MHz) of the employed network analyzer. These results confirm that PBG waveguide DCs in the optical domain could be used for wavelength-dependent applications such as demultiplexers or interleavers.

3.3. Y Junction

Power splitters are key building blocks in photonic multifunctional devices and systems. There are mainly two different approaches to equally split up the power of an incoming signal into two output ports: using either a DC

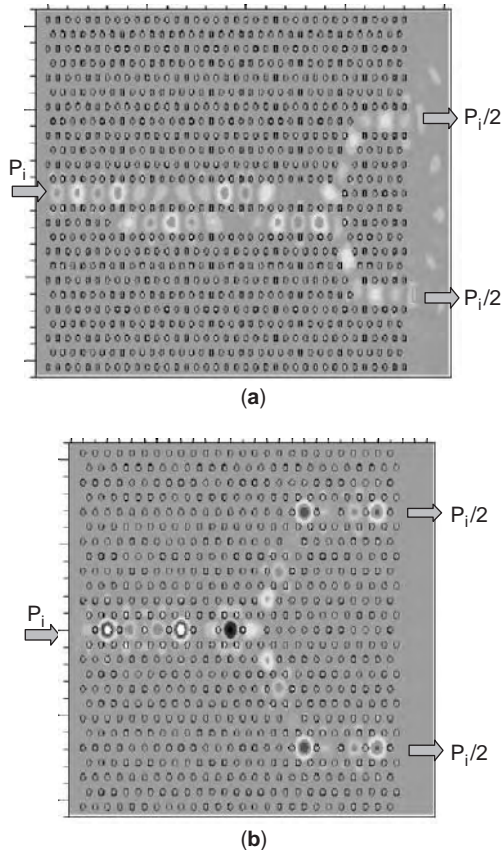


Figure 9. Distribution of the vertical component of the electric field (TM polarization) in two different PBG structures that allow 3 dB power splitting: (a) DC; (b) Y junction. The results are obtained by means of the FDTD method. (This figure is available in full color at <http://www.mrw.interscience.wiley.com/erfme>.)

or a Y-junction structure [35]. The performance of both structures is schematically shown in Fig. 9, which depicts the distribution of the vertical components of the electric field (TM polarization) in a 3-dB splitter based on (a) a DC and (b) a Y junction obtained by means of the FDTD method. It should be noted that in the first approach (Fig. 9a) the relative phase shift between output signals is 90° whereas in the latter (Fig. 9b) both output signals are in phase. The performance of a Y junction working as 3 dB power splitter implemented in a PBG structure (120° and 180° between output waveguides) has been demonstrated in the microwave regime using CCWs [18]. As the mode in the input waveguide has even symmetry (assuming that the fundamental mode of this waveguide is excited), the even supermode of the system formed by the two output waveguides is excited, so there is no phase shift between outputs. However, an alternative structure can be implemented that allows a 180° phase shift between output ports [34]. Figure 10 shows a schematic of this alternative power splitter implemented on a hexagonal lattice of alumina rods in air, as in the previous examples. The coupler section (dashed rectangle in Fig. 10) consists of two CCWs as those shown in Fig. 4b. Thereby, this section of the overall splitter structure can be seen as a CCW coupler. Each CCW forming the coupler consists of N cavities

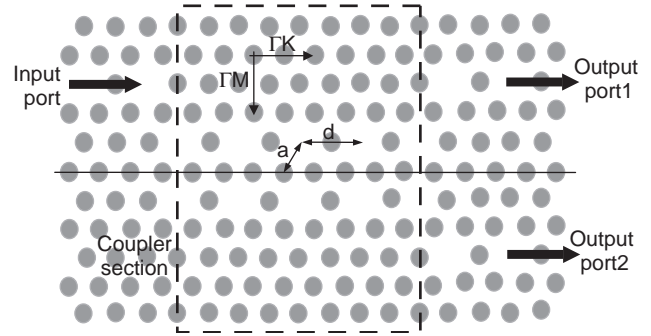


Figure 10. Schematic of the proposed 180° phase shift power splitting structure implemented on a hexagonal PBG lattice of high-index cylinders.

(in Fig. 10, $N = 5$ cavities) with a d spacing between adjacent ones. A single CCW is used to inject signal into one of the CCWs comprising the coupler, whereas two CCWs are used as output ports. The proximity between CCWs in the coupler section gives rise to the splitting of the guided mode of an isolated CCW into two modes with even and odd symmetries, as in the case of the DC previously analyzed. The band structures of an isolated CCW and the CCW coupler obtained by using the PWE method for TM modes are shown in Fig. 11. The parameters are the same as the previously considered. From Fig. 11 it can be seen that the splitting of the isolated mode when the coupler is created is very strong and the modes of the coupler are almost completely separated in two frequency ranges, which can be explained by considering that the coupling strength in the transverse direction of the waveguides (ΓM) is of similar order as the coupling strength in the longitudinal direction, (ΓK), due to the propagation caused by photon hopping between cavities. Periodic power transfer between waveguides in DCs can be achieved only for the frequency range where both coupler modes coexist and have different propagation constants, so in the

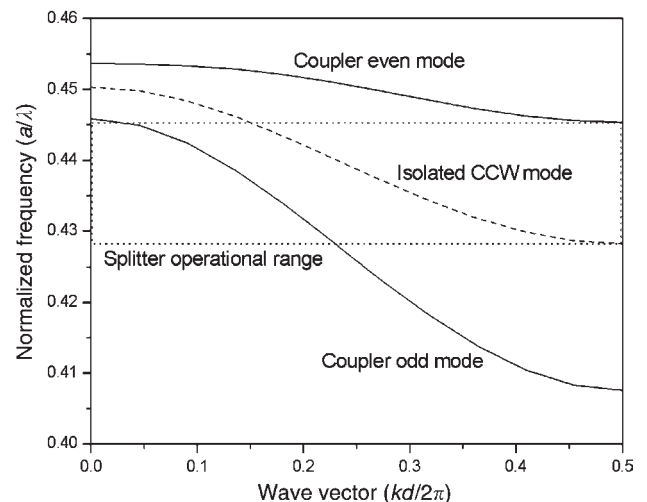


Figure 11. Band structure of the guided modes for an isolated CCW (dashed curve) and the CCW coupler (solid curves).

proposed CCW coupler power interchange is achieved only in a very narrow frequency range around $0.446 [a/\lambda]$, which drastically limits its operation as a conventional DC. However, the behavior of the CCW coupler may be exploited to implement a power splitter as that shown in Fig. 10. From Fig. 11 it may be observed that in the frequency range between 0.4076 and $0.4454 [a/\lambda]$ only the odd mode can propagate through the CCW coupler. If this mode is excited by means of an external CCW as shown in Fig. 10, the frequency working range of the splitter is restricted to the dotted rectangle depicted in Fig. 11. Signals propagating through the output CCWs have a relative phase shift of 180° because of the odd symmetry of the mode. As both signals travel through the same length, they are synchronized and there is no time delay between them, which results in a technique suitable for high-speed signals.

Figure 12 shows the distribution of the electric field component parallel to the rods of a monochromatic wave with frequency $0.44 [a/\lambda]$ in the proposed structure with $N = 6$ obtained by means of the FDTD method. In Fig. 12 it can be seen that there is a 180° phase shift between the field in each CCW coupler branch because maxima (white) in the upper cavities correspond to minima (black) in the lower cavities, and vice versa. CCWs provide the added advantage of implementing sharp bends with negligible losses, which allows spatial separation of the branches of the coupler. Simulated transmission spectra for different lengths demonstrated that the power splitting occurs regardless of the coupler length (even for $N = 1$), although, for example, for $N = 2$ the response was slightly impaired because of the strong interaction between input and output CCWs. Anyway, it can be stated that the overall splitter length can be very small (e.g., for $N = 4$ the total length of the coupling section is $\sim 4a < 2\lambda$), resulting in a very compact structure.

The splitting structure depicted in Fig. 10 was experimentally characterized in the microwave regime using the same procedure that in the DC case. Figure 13 shows the measured transmission (a) amplitude and (b) phase for a splitter with $N = 4$ cavities. Different spectral regions

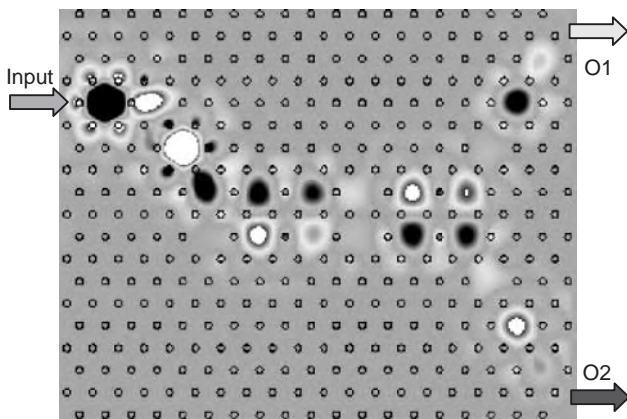


Figure 12. Distribution of the vertical component of the electric field of a monochromatic wave in the splitter ($N=6$) for a frequency $0.44 [a/\lambda]$ obtained with a 2D FDTD simulation.

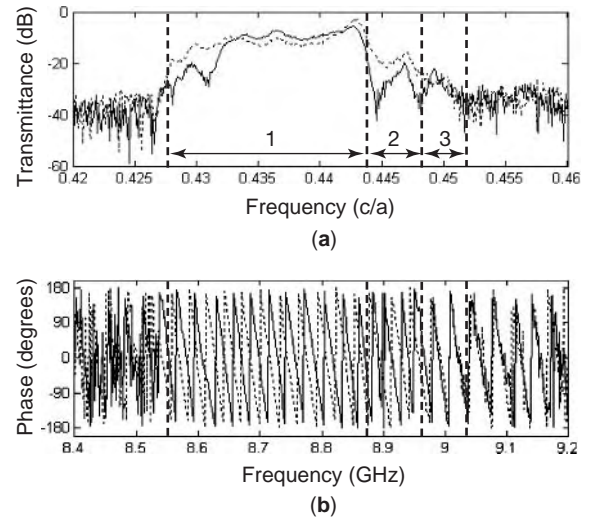


Figure 13. Experimental transmission of the 180° phase shift power splitting structure: (a) amplitude and (b) phase for both output ports 1 (solid curves) and 2 (dashed curves).

are separated by vertical dotted lines in Fig. 13. Region 1 highlights the 180° phase shift power splitting range, where only the odd mode exists and the input power is equally split up between the outputs, in good agreement with the theoretical results and confirming the feasibility of employing the proposed structure as a 3-dB power splitter. In region 2, the difference on transmitted power between the two output ports is attributed to the interaction between the odd and the even modes, so the structure does not work any longer as a splitter. Finally, in region 3 only the even mode is excited and both outputs are balanced again, so this structure can also work as a conventional Y-junction-based 3-dB power splitter. The different power transmission at the outputs observed in Fig. 13a is due mainly to external reflections, finiteness of the structure in the vertical direction, and inaccuracies in the implementation of the physical structure, as in the DC case. In Fig. 13b a phase difference near 180° between output ports is observed in region 1, confirming the theoretical and simulation results. The EM splitting covers a spectral range over 300 MHz, which means a relative splitter operational range of 3.45%. In region 3, around 9 GHz, only the even mode is excited so the outputs are in phase, as shown in Fig. 13b. The low transmittance in region 3 compared to region 1 can be explained by taking into account the flatness of the dispersion relation of the even mode. It should be highlighted that a 50% power splitting over the frequency range indicated in Fig. 11 is achieved, which contrasts clearly with splitters implemented using DCs in which perfect 50% splitting is possible in only a limited frequency range, due to the frequency-dependent behavior of the coupling coefficient (see Figs. 7 and 8).

3.4. Mach-Zehnder Interferometers

Mach-Zehnder interferometers (MZIs) have been widely used to implement a huge variety of optical devices such as filters, demultiplexers, switches, and intensity

modulators. A MZI makes use of two interfering paths of different lengths to resolve different wavelengths at the outputs. The reduction of the overall size of an interferometric structure can be achieved by using PBG waveguides and in particular, CCWs because the effective length of these waveguides can become very large for a reduced number of cavities because of their small group velocity [36].

Figure 14a shows a scheme of a 2×2 MZI consisting of two 3-dB DCs connected through two optical waveguides with different lengths, L and $L + \Delta L$. Assuming that optical power is injected only into input port 1, the transfer function of the MZI may be basically expressed as

$$\begin{pmatrix} T_{11}(f) \\ T_{21}(f) \end{pmatrix} = \begin{pmatrix} \sin^2 \frac{\beta \Delta L}{2} \\ \cos^2 \frac{\beta \Delta L}{2} \end{pmatrix} \quad (3)$$

where β is the propagation constant of the guided mode in the waveguides. As mentioned previously, guided modes in CCWs have very low group velocities, even one or two orders of magnitude lower than in conventional index-guiding waveguides, reaching their maximum at the band center and decaying to zero at both band edges [37]. This means that light propagates slowly through the CCW and the effective length of the guide becomes very large compared to its actual length, so very large phase shifts between both paths can be attained using very short CCWs. Furthermore, one can accurately control the transmission properties of these guides by using the TB approach expressed in Eq. (2), from which the propagation constant of the guided mode in a CCW may be written as

$$\beta(f) = \frac{1}{d} \arccos \left(\frac{f - f_0}{\kappa f_0} \right) \quad (4)$$

where f_0 is the eigenfrequency of an isolated cavity and f is the frequency.

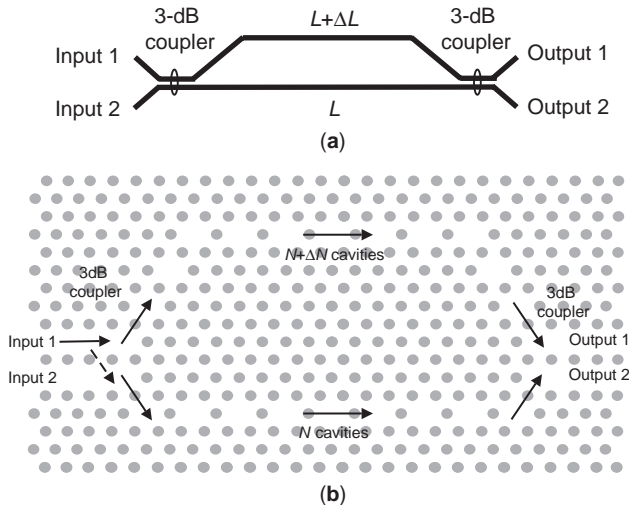


Figure 14. (a) Scheme of a 2×2 MZI; (b) scheme of a MZI employing DCs and CCWs in a 2D PBG structure of alumina cylinders.

Figure 14b depicts the scheme of a MZI implemented using CCWs. Input and output DCs are formed by two parallel PBG waveguides and should be properly designed to achieve 3 dB power splitting, using the procedure explained in Section 3.2. CCWs are implemented as two chains consisting of N and $N + \Delta N$ d -spaced coupled cavities, respectively. Then the path difference can be written as $\Delta L = \Delta N d$ and the MZI transfer function can be expressed as

$$\begin{pmatrix} T_{11}(f) \\ T_{21}(f) \end{pmatrix} = \begin{pmatrix} \sin^2 \left(\frac{\Delta N}{2} \arccos \left(\frac{f - f_0}{\kappa f_0} \right) \right) \\ \cos^2 \left(\frac{\Delta N}{2} \arccos \left(\frac{f - f_0}{\kappa f_0} \right) \right) \end{pmatrix} \quad (5)$$

The transfer function of the CCW-based MZI given by (5) depends on only three parameters: the eigenfrequency of an isolated cavity (f_0), the hopping parameter (κ), and the difference in the number of cavities (ΔN). Both f_0 and κ depend on the physical structure of the CCW and may be easily obtained from band structure calculations. Thereby, ΔN may be considered as a design parameter of the interferometric effect that may be chosen to achieve the requirements of a specific MZI-based functionality.

Figure 15 shows the amplitude responses of CCW-based MZIs with different ΔN values obtained from Eq. (5). To emphasize the interferometric effect, the intrinsic CCW transmission response is not considered in Fig. 15. It should be noticed that in the frequency region around f_0 , the $\arccos(\cdot)$ function has an almost linear response, which gives rise to evenly spaced channels at the MZI outputs. In this frequency range the spacing $\Delta \nu$ between demultiplexed channels may be obtained from (5) as $\Delta \nu = \pi \kappa f_0' \Delta N$, so as the parameters f_0 and κ depend on the CCW

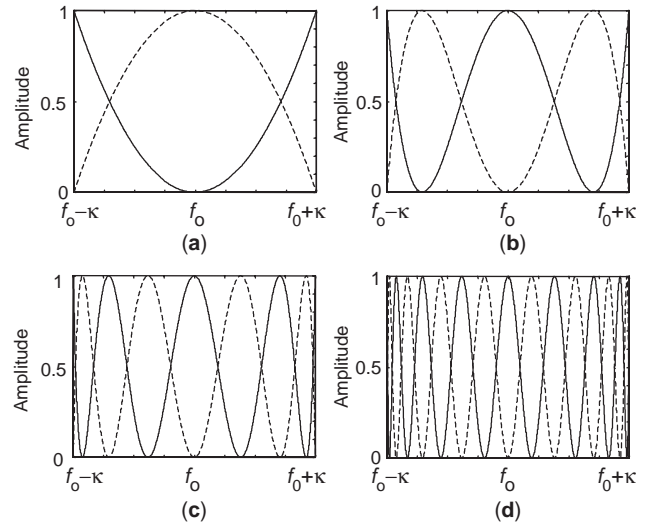


Figure 15. Theoretical CCW-based MZI transmission responses for (a) $\Delta N = 2$, (b) $\Delta N = 4$, (c) $\Delta N = 8$, and (d) $\Delta N = 16$ resulting from the theoretical model. Dotted and solid lines stand for output ports 1 and 2, respectively.

structure, the MZI response for demultiplexing applications may be designed by properly choosing ΔN .

A CCW-based MZI such as that shown in Fig. 14b was implemented on the 2D hexagonal lattice of alumina rods in air and tested, as in the case of the previously mentioned structures. Y junctions instead of 3-dB DCs were used to both divide and combine the input signal due to the difficulty in implementing DCs in the experimental structure. In this case, the transfer function of the 1×1 MZI can be expressed as $T_{11}(f) = \cos^2(\beta\Delta L/2)$. From this transfer function it can be noticed that $\Delta N/2$ transmission notches appear at the MZI output due to the interference between different paths. Figure 16 shows the experimental transmission responses for (a) $\Delta N=2$ and (b) $\Delta N=4$. The MZI response is depicted as solid line, whereas the transmission response of one of the CCWs forming the corresponding MZI is shown as dotted line. In addition, in Fig. 16 the frequencies of the transmission notches expected from theoretical calculations are set in dotted vertical lines. A very good agreement is observed between theoretical and experimental results. From Fig. 16, for $\Delta N=2$ the calculated value of the transmission notch is

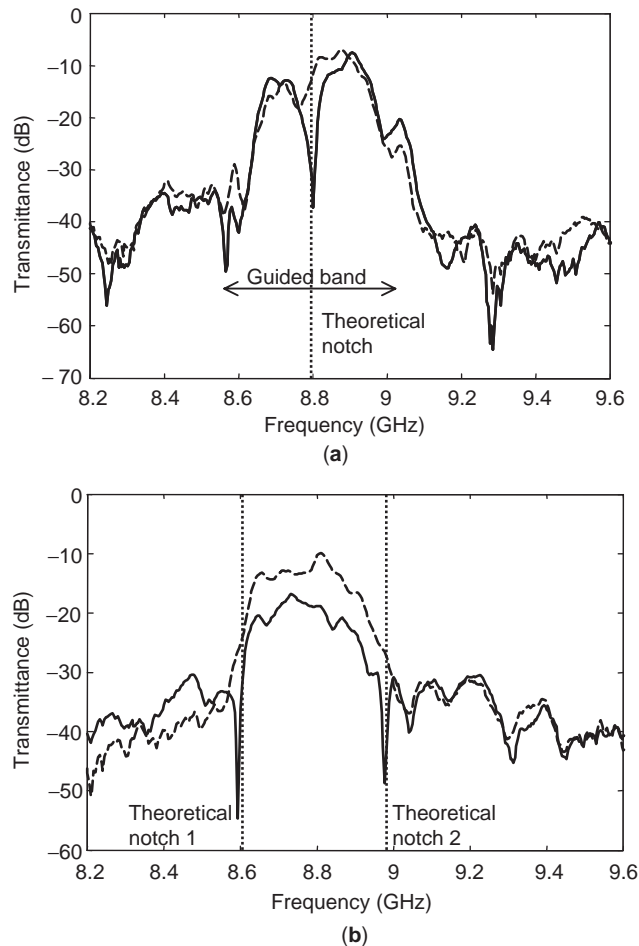


Figure 16. Experimental transmission response of the CCW-based MZI (solid line) and one of two CCWs constituting the MZI (dashed line) for (a) $\Delta N=2$ and (b) $\Delta N=4$. The theoretical frequencies of the transmission notches are shown as vertical dotted lines.

8.79 GHz and the measured frequency is 8.802 GHz, while for $\Delta N=4$ the theoretical notches are 8.6066 and 8.9734 GHz and the experimental notches appear at 8.594 and 8.978 GHz, respectively. The small differences observed are also due mainly to the limitations arising from the experimental setup and the spectral resolution of the network analyzer.

4. PHOTONIC BANDGAP IN MICROSTRIP LINES

4.1. Brief Introduction to PBG Structures Implemented in Microstrip Technology

PBG structures have also been demonstrated at microwave frequencies but employing microstrip or coplanar technologies instead of 2D and 3D lattices of high-index rods. The first approach to implement PBG structures in microstrip technology consisted of creating periodic structures by drilling a periodic pattern of rods through the substrate [38,39]. In 1998, Radisic et al. demonstrated a convenient way to implement PBG microstrip structures by etching a three-rod periodic pattern of circles in the ground plane of a microstrip line [40]. Later, it was demonstrated that only one-rod of etched circles could be employed to develop high quality PBG structures due to the high confinement of the electric field above the microstrip line [41]. This property allows one to design meander PBG microstrip structures with improved behavior and reduced size as demonstrated in Ref. 42.

A periodic PBG microstrip line can be considered and studied as a 1D grating. This correspondence allows us to employ Bragg condition and coupled-mode theory [43] to control the physical parameters of the designed PBG structure in order to obtain a bandgap with desired parameters in terms of central frequency and bandwidth. Further equivalencies between physical parameters of the PBG microstrip line and those of the grating were reported [44]. Furthermore, this equivalency led to novel PBG microstrip approaches, including apodized [44–46] and chirped [47] structures. On the other hand, circuital models based on the modification of the microstrip-line inductance introduced by the periodic patterns can also be employed to characterize and design periodic PBG structures in microstrip technology as reported in Ref. 48.

Other etched geometries besides circles have also been suggested to implement PBG microstrip structures with better performances and further applications [50–52]. Furthermore, continuous etched patterns in the ground plane of the microstrip lines were proposed to achieve PBG microstrip structures, avoiding the formation of spurious bandgaps that typically appears in PBG structures based on discrete patterns. In this way, Laso et al. [49] demonstrated that the combination of several raised sinus patterns etched in the ground plane of a microstrip line could be employed to obtain PBG microstrip structures with multiple-frequency-tuned bandgaps at desired frequencies.

Finally, PBG microstrip structures with an unperturbed ground plane have been also proposed. In this kind of structure the bandgap is achieved by varying the microstrip-line impedance, which is wide relative to the linewidth [47,53]. These concepts can be easily translated

to other planar technologies as reported in Ref. 54, where PBG structures are achieved using coplanar technology.

4.2. Nonperiodic Structures

All the patterns described in Section 4.1, which are employed for the implementation of PBG microstrip structures, are periodic. However, it is interesting to analyze the behavior and properties of nonperiodic patterns. So, in Ref. 55 nonperiodic patterns of etched circles in the ground plane of a 50-Ω microstrip line were proposed in order to obtain multiple tuned frequency bandgaps and new PBG microstrip circuit applications. These nonperiodic PBG topologies are based on breaking the etched circles periodicity (defects insertion) as shown in Fig. 17, which depicts the three nonperiodic structures that were studied in Ref. 55. When a single defect is inserted in the periodic pattern, a resonance appears inside the initial bandgap of the unperturbed PBG structure [56]. The frequency of this resonance depends on the defect size, referred to as *ad* in Fig. 17. As this basic structure (defect) is repeated along the microstrip ground plane, a splitting of the single defect resonance into *n* resonances takes place, where *n* is the number of introduced defects. This splitting effect may be explained by using the TB theory, as it can be considered that there is a CCW formed by *n* cavities along the microstrip line [19]. In addition, it may be demonstrated that this splitting effect depends mainly on the spacing between defects *d* in Fig. 17, obtaining a higher frequency splitting by increasing the coupling between defect modes when the defects are closely placed.

Figure 18 shows respectively the *S*₂₁ parameter obtained experimentally (thick line) and by FDTD simulation (thin line) for the three structures depicted in Fig. 17. As can be observed in Fig. 18, the maximum frequency splitting (Fig. 18c) corresponds to the closer defect inser-

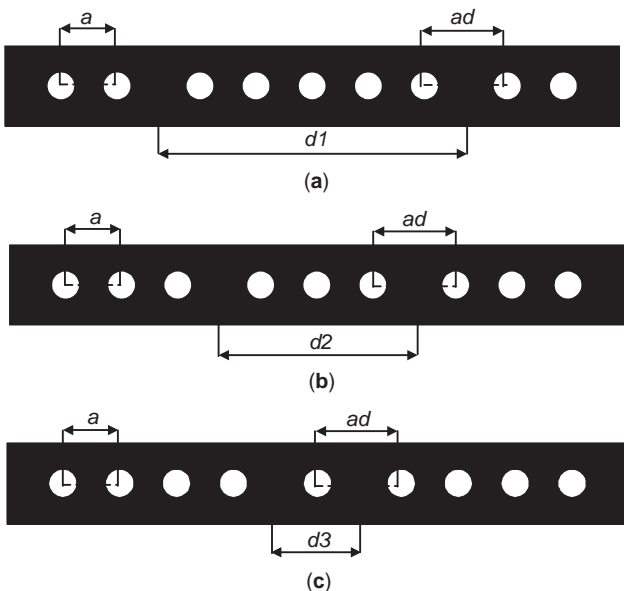


Figure 17. Microstrip PBG ground-plane topologies with two defects and (a) weak coupling, (b) medium coupling, and (c) high coupling between defect modes.

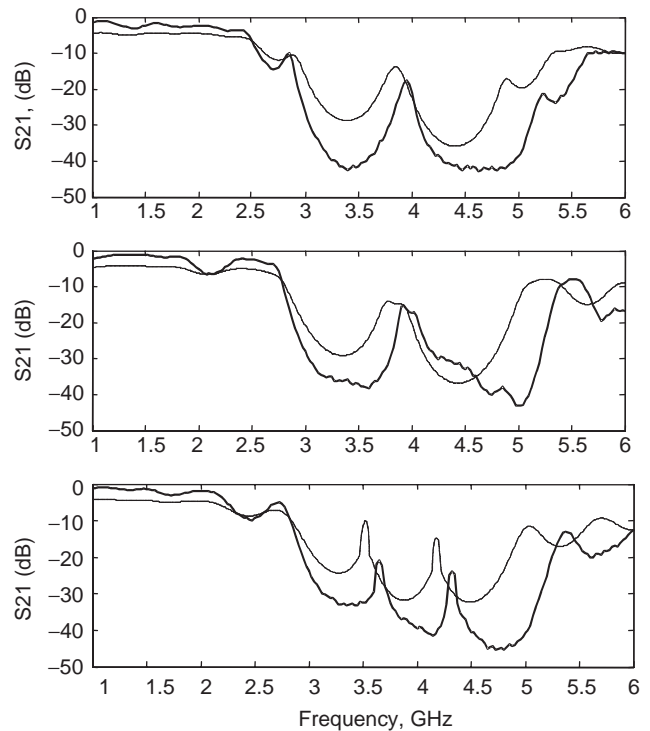


Figure 18. Simulated (thin line) and measured (thick line) *S*₂₁ parameter for topologies in Fig. 14.

tion as expected. The results shown in Fig. 18 report on a verification of the TB theory applied to PBG microstrip technology, and its application for multiple tuned bandgap structures has been demonstrated. Other applications of CCWs in microstrip lines are envisaged, such as bandpass filters, channelizers, or phase shifters.

4.3. PBG Microstrip Structures Applied to Harmonic Suppression in Bandpass Filters

PBG-microstrip structures have been employed for spurious suppression in bandpass filters based on coupled line sections [52,57–59]. Furthermore, a PBG-microstrip circuit based on etching a circle pattern in the circuit ground plane has been proposed to reject second-order harmonics in multistage coupled ring bandpass filters [60]. As shown in Fig. 19, two topologies were employed for harmonic suppression: PBG inside and out of microstrip-coupled rings. The topology depicted in Fig. 19a incorporates a PBG microstrip structure at the output feeding line. This PBG microstrip structure based on etching a periodic pattern of circles in the ground plane was designed to obtain a bandgap centered at the second harmonic of the coupled ring bandpass filter. Conversely, Fig. 19b depicts the filter topology when the PBG structure is etched in the ground plane of one of the two bandpass filter rings. In such a structure harmonic suppression is achieved by cascading two rings, one of which is an embedded PBG ring to obtain a lower frequency-shifted second-harmonic (slow-wave effect) in comparison to a simple ring as reported in Ref. 60. Both filters shown in Fig. 19 were physically implemented

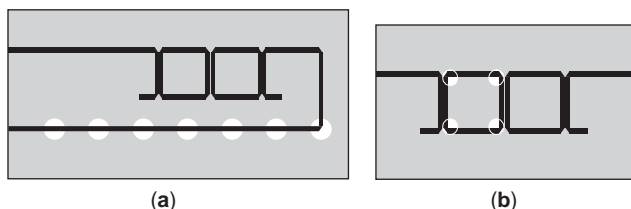


Figure 19. Microstrip ring filter layouts with electromagnetic bandgap (EBG) structures out of the rings (a) and inside a ring (b).

on a fiberglass substrate with a relative permittivity of 4.41 and a substrate dielectric height of 1.6 mm.

Figure 20a shows the S_{11} and S_{21} parameters of the filter topology depicted in Fig. 19a, obtained by FDTD simulation (dashed line) and experimental measurements (solid line). It can be observed that a second-harmonic suppression of nearly 30 dB is achieved. On the other hand, Fig. 20b depicts the scattering parameters of the filter topology shown in Fig. 19b, obtained by FDTD simulation (dashed line) and measurements (solid line). From Fig. 20b it can be observed that a second-harmonic suppression ratio higher than 20 dB is now achieved without any size penalty of the overall composed circuit. In addition, insertion losses lower than 3 dB (a lower figure may be obtained by using better dielectric substrates) and return losses of nearly 12 dB with a flat passband and a sharp rejection band are also obtained. Finally, it should be pointed out that other PBG microstrip structures have also been employed for harmonic suppression in microstrip multistage coupled ring bandpass filters [61].

5. PBG STRUCTURES IN THE OPTICAL REGIME

Although extensive work has been done most recently on PBG structures in the microwave regime, it is in the op-

tical regime (infrared, near infrared, visible) where these systems can find real applications that justify the interest that they have received. In this way PBG materials are expected to be the main candidates for the realization of high-density photonic integrated circuits. Microscale photonic integrated circuits are expected to become key components in all-optical networks in order to address the increasing data traffic, which is currently limited by components performed in the electronic domain. Most of the processing functionalities, such as routing and switching, are still performed in the electrical domain, limiting the maximum data transmission rate in this kind of network. Current photonic integrated circuits are limited to replacing microelectronics circuits because of their large size and relative simplicity. More recent results show that key components in photonic integrated circuits as directional couplers and Mach-Zehnder devices have still lengths in the order of millimeters [62–64]. However, a large variety of functionalities based on compact PBG structures have also been reported and experimentally demonstrated, thus proving its advantages with respect to conventional photonic devices.

Resonant cavities and waveguides have been the subject of a significant research effort as they are the basic components in photonic integrated circuits. On the basis of these components, different passive functionalities have been proposed and demonstrated, such as sharp bends [22,65], Y junctions [66–68], add drop filters [14,69], or demultiplexers and multiplexers [70,71], and also active ones, such as all-optical switches [72], ultra-low-threshold lasers [73,74], or high-efficiency light-emitting diodes (LEDs) [75,76]. Transmission through CCWs has also been demonstrated in the optical regime [77] in 2D planar PBG structures. Figure 21a–21c shows SEM micrographs of a sharp bend, a Y junction, and a CCW fabricated on an 8-in silicon-on-insulator (SOI) wafer (220 nm top silicon with 1 μm of silica) using 248-nm-

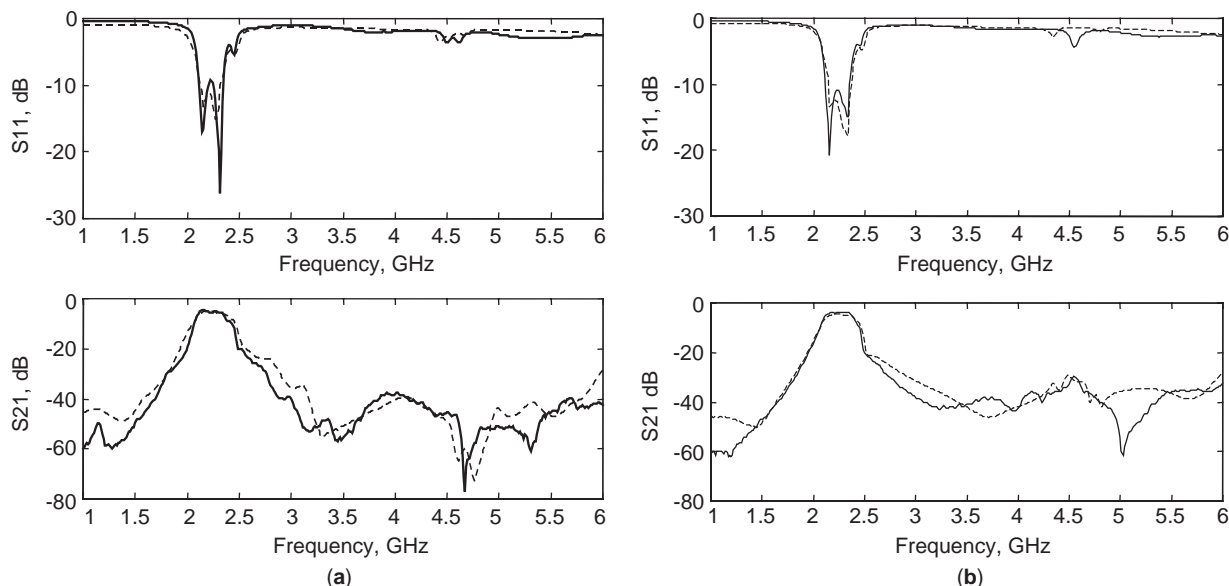


Figure 20. Simulated (dashed line) and measured (solid line) S -parameter results: (a) for the topology in Fig. 17a; (b) for topology in Fig. 17b.

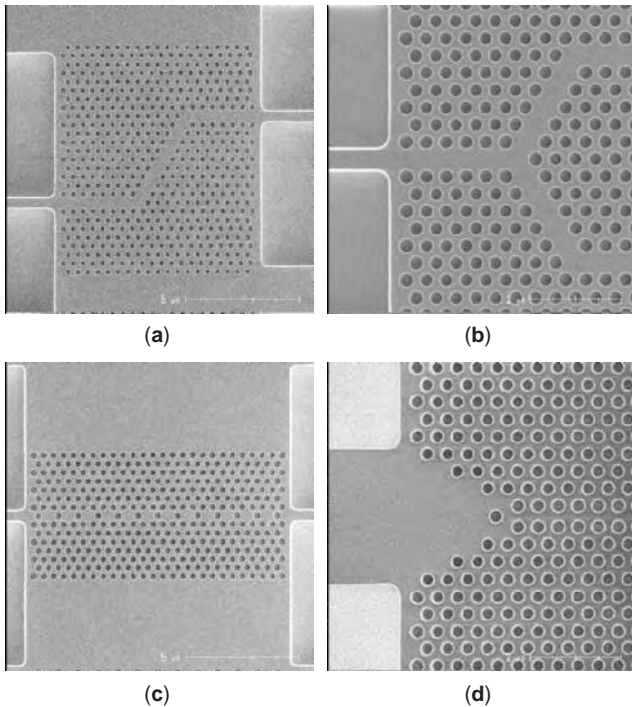


Figure 21. SEM micrographs of (a) sharp bend, (b) Y junction, (c) CCW, and (d) optimized PBG waveguide taper which were fabricated on a silicon-on-insulator (SOI) substrate.

deep UV lithography [78], as examples of PBG structures fabricated to work in the optical regime.

On the other hand, efficient coupling into and out of PBG circuits is a key step in the way to a definitive commercial deployment of this technology. Coupling losses are due to the mode mismatch between the PBG and external waveguides. In PBG waveguides, light propagation is determined by Bloch modes, whereas in conventional dielectric waveguides this method relies on index contrast guiding. A large variety of coupling techniques and structures have been proposed for efficient interfacing fiber and wide-dielectric waveguides to the narrower PBG waveguides [79–86]. It is important to highlight the PBG waveguide tapers, which are a promising approach because of their small coupling length and high coupling efficiencies achieved in a broad frequency range [87–91]. Figure 21d shows a SEM micrograph of an optimized PBG waveguide taper where a localized defect is inserted within the taper, significantly increasing the transmission efficiency [92,93]. It is also worth mentioning the importance of an efficient coupling between different blocks or functionalities inserted in a PBG optical circuit. Thereby, crosstalk reduction, particularly in waveguide intersections, are of interest to reduce the circuit size. Broadband bandwidth and low crosstalk intersections have been proposed as a means to effectively utilize the interesting properties derived from PBG structures [94,95]. In addition, efficiency coupling into and out of CCWs is also mandatory in order to eliminate the undesired resonances of the transmission spectrum, which generate ripples in the group velocity that may distort the transmission of ultrashort pulses [96–98].

Finally, it is important to mention the role of the third dimension in 1D and 2D PBG structures. In these structures, the confinement of light in the vertical direction is usually achieved by total internal reflection, as in conventional integrated waveguides. However, diffraction losses appear in practical PBG circuits because of the presence of roughness and other impairments [99,100]. Therefore, a thorough understanding of out-of-plane losses as well as techniques to eliminate them is important for enabling commercial device applications.

BIBLIOGRAPHY

1. E. Yablonovitch, Inhibited spontaneous emission in solid-state physics and electronics, *Phys. Rev. Lett.* **58**:2059–2062 (1987).
2. E. Yablonovitch and T. J. Gmitter, Photonic band structure: The face-centered-cubic case, *Phys. Rev. Lett.* **63**:1950–1953 (1989).
3. K. M. Leung and Y. F. Liu, Photonic band structures: The plane wave method, *Phys. Rev. B* **41**:10188–10190 (1990).
4. S. Satpathy, Z. Zhang, and M. R. Salehpour, Theory of photon bands in three-dimensional periodic dielectric structures, *Phys. Rev. Lett.* **64**:1239–1242 (1990).
5. K. M. Leung, and Y. F. Liu, Full vector wave calculation of photonic band structure in face-centered-cubic dielectric media, *Phys. Rev. Lett.* **65**:2646–2649 (1990).
6. Z. Zhang and S. Satpathy, Electromagnetic wave propagation in periodic structures: Bloch wave solution of Maxwell's equations, *Phys. Rev. Lett.* **65**:2650–2653 (1990).
7. K. M. Ho, C. T. Chan, and C. M. Soukoulis, Existence of photonic gaps in periodic dielectric structures, *Phys. Rev. Lett.* **65**:3152–3155 (1990).
8. J. D. Joannopoulos, P. R. Villeneuve, and S. Fan, Photonic crystals: Putting a new twist on light, *Nature (London)* **386**:143–149 (1997).
9. T. F. Krauss, R. M. de la Rue, and S. Brand, Two-dimensional photonic-bandgap structures operating at near-infrared wavelengths, *Nature (London)* **382**:699–702 (1996).
10. A. Blanco, E. Chomski, S. Grubtchak, M. Ibsate, S. John, S. W. Leonard, C. Lopez, F. Meseguer, H. Miguez, J. P. Mondia, G. A. Ozin, O. Toader, and H. M. van Driel, Large-scale synthesis of a silicon photonic crystal with a complete three-dimensional bandgap near 1.55 micrometres, *Nature (London)* **405**:437–440 (2000).
11. S. Noda, K. Tomoda, N. Yamamoto, and A. Chutinan, Full three-dimensional photonic bandgap crystals at near-infrared wavelengths, *Science* **289**:604–606 (2000).
12. S. Y. Lin, J. G. Fleming, D. L. Hetherington, B. K. Smith, R. Biswas, K. M. Ho, M. M. Sigalas, W. Zubrzycki, S. R. Kurtz, and J. Bur, A three-dimensional photonic crystal operating at infrared wavelengths, *Nature (London)* **394**:251–253 (1998).
13. J. D. Joannopoulos, R. D. Meade, and J. N. Winn, *Photonic Crystals: Molding the Flow of light*, Princeton Univ. Press, 1995.
14. S. Noda, A. Chutinan, and M. Imada, Trapping and emission of photons by a single defect in a photonic bandgap structure, *Nature (London)* **407**:608–610 (2000).
15. Y. Pastol, G. Arjavalingam, J. M. Halbout, and G. V. Kopcsay, Absorption and dispersion of low-loss dielectrics measured with microwave transient radiation, *Electron. Lett.* **25**:523–524 (1989).

16. S. L. McCall, P. M. Platzman, R. Dalichaouch, D. Smith, and S. Schultz, Microwave propagation in two-dimensional lattices, *Phys. Rev. Lett.* **67**:2017–2020 (1991).
17. S. Y. Lin, E. Chow, V. Hietala, P. R. Villeneuve, and J. D. Joannopoulos, Experimental demonstration of guiding and bending of electromagnetic waves in a photonic crystal, *Science* **282**:274–276 (1998).
18. M. Bayindir, B. Temelkuran, and E. Ozbay, Photonic-crystal-based beam splitters, *Appl. Phys. Lett.* **77**:3902–3904 (2000).
19. M. Bayindir, B. Temelkuran, and E. Ozbay, Tight-Binding description of the coupled defect modes in three-dimensional photonic crystals, *Phys. Rev. Lett.* **84**:2140–2143 (2000).
20. M. Bayindir, B. Temelkuran, and E. Ozbay, Propagation of photons by hopping: A waveguiding mechanism through localized coupled-cavities in three dimensional photonic crystals, *Phys. Rev. B* **61**:R11–R55 (2000).
21. E. Yablonovitch, T. J. Gmitter, and K. M. Leung, Photonic band structures: The face-centered cubic case employing non-spherical atoms, *Phys. Rev. Lett.* **67**:2295–2298 (1991).
22. T. Baba, N. Fukaya, and J. Yonekura, Observation of light propagation in photonic crystal optical waveguides with bends, *Electron. Lett.* **35**:654–655 (1999).
23. F. Bloch, Über die quantenmechanik der electronen in kristallgittern, *Z. Physik* **52**:555–600 (1928).
24. C. Kittel, *Introduction to Solid State Physics*, Wiley Text Books, 1995.
25. A. Taflove, *Computational Electrodynamics: The Finite-Difference Time-Domain Method*, Artech House, Norwood, MA, 1995.
26. E. Yablonovitch, T. J. Gmitter, R. D. Meade, A. M. Rappe, K. D. Brommer, and J. D. Joannopoulos, Donor and acceptor modes in photonic band structures, *Phys. Rev. Lett.* **67**:3380–3383 (1991).
27. A. Mekis, J. C. Chen, I. Kurland, P. R. Villeneuve, and J. D. Joannopoulos, High transmission through sharp bends in photonic crystal waveguides, *Phys. Rev. Lett.* **77**:3787–3790 (1996).
28. S. Fan, S. G. Johnson, J. D. Joannopoulos, C. Manolatu, and H. A. Haus, Waveguide branches in photonic crystals, *J. Opt. Soc. Am. B* **18**:162–165 (2001).
29. A. Chutinan and S. Noda, Waveguides and waveguide bends in two-dimensional photonic crystal slabs, *Phys. Rev. B* **62**:4488–4491 (2000).
30. A. Yariv, Y. Xu, R. K. Lee, and A. Scherer, Coupled-resonator optical waveguide: A proposal and analysis, *Opt. Lett.* **24**:711–713 (1999).
31. U. Peschel, A. L. Reynolds, B. Arredondo, F. Lederer, P. J. Roberts, T. F. Krauss, and P. J. I. de Maagt, Transmission and reflection analysis of functional coupled cavity components, *IEEE J. Quantum Electron.* **38**:830–836 (2002).
32. A. Martínez, F. Cuesta, and J. Martí, Ultrashort 2-D photonic crystal directional couplers, *IEEE Photon. Technol. Lett.* **15**:694–696 (2003).
33. M. Koshiba, Wavelength division multiplexing and demultiplexing with photonic crystal waveguide couplers, *IEEE/OSA J. Lightwave Technol.* **19**:1970–1975 (2001).
34. F. Cuesta, A. Griol, A. Martínez, and J. Martí, Experimental demonstration of photonic crystal directional coupler at microwave frequencies, *Electron. Lett.* **39**:455–456 (2003).
35. A. Martínez, F. Cuesta, A. Griol, D. Mira, J. García, P. Sanchis, R. Llorente, and J. Martí, Photonic-crystal 180° power splitter based on coupled-cavity waveguides, *Appl. Phys. Lett.* **83**(15):3033–3035 (2003).
36. A. Martínez, A. Griol, P. Sanchis, and J. Martí, Mach-Zehnder interferometer employing coupled-resonator optical waveguides, *Opt. Lett.* **28**:405–407 (2003).
37. A. Martínez, A. García, P. Sanchis, and J. Martí, Group velocity and dispersion model of coupled-cavity waveguides in photonic crystals, *J. Opt. Soc. Am. A* **20**:147–150 (2003).
38. I. Rumsey, M. Piket-May, and K. Kelly, Photonic bandgap structures used as filters in microstrip circuits, *IEEE Microwave and Guided Wave Lett.* **8**:336–338 (1998).
39. V. Radisic, Y. Quian, and T. Itoh, Broad-band power amplifier using dielectric photonic bandgap structure, *IEEE Microwave Guided Wave Lett.* **8**:13–14 (1998).
40. V. Radisic, Y. Qian, R. Coccioli, and T. Itoh, Novel 2D photonic bandgap structure for microstrip lines, *IEEE Microwave Guided Wave Lett.* **8**:69–71 (1998).
41. F. Falcone, T. Lopetegui, and M. Sorolla (1-D and 2-D photonic bandgap microstrip structures, *Microwave Opt. Technol. Lett.* **22**:411–412 (1999).
42. A. D’Orazio, M. de Sario, V. Gadaleta, V. Petruzzelli, and F. Prudenzeno, Meander microstrip photonic bandgap filter using a Kaiser tapering window, *Electron. Lett.* **37**:1165–1167 (2001).
43. T. Lopetegui, M. A. G. Laso, M. J. Erro, M. Sorolla, and M. Thumm, Analysis and design of periodic structures for microstrip lines by using the coupled mode theory, *IEEE Microwave Wireless Compon. Lett.* **12**:441–443 (2002).
44. M. J. Erro, M. A. G. Laso, T. Lopetegui, D. Benito, M. J. Garde, and M. Sorolla, Modelling and testing of uniform fiber Bragg grating using 1-D photonic bandgap structures in microstrip technology, *Fiber Integr. Opt.* **19**:311–325 (2000).
45. A. D’Orazio, M. de Sario, V. Petruzzelli, F. Prudenzeno, and F. Renna, Compact tapered photonic bandgap microstrip lowpass filters, *Electron. Lett.* **38**:1107–1109 (2002).
46. N. C. Karmakar, M. N. Mollah, and S. K. Padhi, Improved performance of a nonuniform ring patterned PBG-assisted microstrip line, *Proc. IEEE Antennas and Propagation Soc. Int. Symp.*, 2002, Vol. 2, pp. 848–851.
47. M. A. G. Laso, T. Lopetegui, M. J. Erro, D. Benito, M. J. Garde, M. A. Muriel, M. Sorolla, and M. Guglielmi, Chirped delay lines in microstrip technology, *IEEE Microwave Wireless Compon. Lett.* **11**:486–488 (2001).
48. J. P. Kim and W. S. Park, Microstrip lowpass filter with multislots on ground plane, *Electron. Lett.* **37**:1525–1526 (2001).
49. M. A. G. Laso, T. Lopetegui, M. J. Erro, D. Benito, M. J. Garde, and M. Sorolla, Multiple-frequency-tuned photonic bandgap microstrip structures, *IEEE Microwave Guided Wave Lett.* **10**:220–222 (2000).
50. F.-R. Yang, K.-P. Ma, Y. Quian, and T. Itoh, A novel low-loss slow-wave microstrip structure, *IEEE Microwave Guided Wave Lett.* **8**:372–374 (1998).
51. D. Ahn, J.-S. Park, C.-S. Kim, J. Kim, Y. Quian, and T. Itoh, A design of the lowpass filter using the novel microstrip defected ground structure, *IEEE Trans. Microwave Theory Tech.* **49**:86–93 (2001).
52. I. Chang and B. Lee, Design of defected ground structures for harmonic control of active microstrip antennas, *Proc. IEEE Antennas and Propagation Soc. Int. Symp.*, 2002, Vol. 2, pp. 852–855.
53. T. Lopetegui, M. A. G. Laso, J. Hernandez, M. Bacaicoa, D. Benito, M. J. Garde, M. Sorolla, and M. Guglielmi, New microstrip wiggly-line filters with spurious passband suppression, *IEEE Trans. Microwave Theory Tech.* **49**:1593–1598 (2001).

54. F. Martin, F. Falcone, J. Bonache, T. Lopetegui, M. A. G. Laso, and M. Sorolla, New periodic-loaded electromagnetic bandgap coplanar waveguide with complete spurious pass-band suppression, *IEEE Microwave Wireless Compon. Lett.* **12**:435–437 (2002).
55. A. Griol, D. Mira, A. Martínez, J. Martí, and J. L. Corral, Microstrip multistage coupled ring bandpass filters using photonic bandgap structures for harmonic suppression, *Electron. Lett.* **39**:68–70 (2003).
56. J. S. Foresi, P. R. Villeneuve, J. Ferrera, E. R. Thoen, G. Steinmeyer, S. Fan, J. D. Joannopoulos, L. C. Kimerling, H. I. Smith, and E. P. Ippen, Photonic-bandgap microcavities in optical waveguides, *Nature (London)* **390**:143–145 (1997).
57. F.-R. Yang, K.-P. Ma, Y. Quian, and T. Itoh, A uniplanar compact photonic-bandgap (UC-PBG) structure and its applications for microwave circuits, *IEEE Trans. Microwave Theory Tech.* **47**:1509–1514 (1999).
58. F.-R. Yang, Y. Quian, R. Coccioli, and T. Itoh, Analysis and application of coupled microstrips on periodically patterned ground plane, *Proc. IEEE MTT-S Digest*, 2000, Vol. 3, pp. 1529–1532.
59. J. S. Park, J. S. Yun, and D. Ahn, A design of the novel coupled-line bandpass filter using defected ground structure with stopband performance, *IEEE Trans. Microwave Theory Tech.* **50**:2037–2043 (2002).
60. A. Griol, D. Mira, A. Martínez, J. Martí, and J. L. Corral, Multiple frequency photonic bandgap microstrip structures based on defects insertion, *Microwave Opt. Technol. Lett.* **36**:479–481 (2003).
61. A. Griol, D. Mira, J. Martí, and J. L. Corral, Harmonic suppression in microstrip multistage coupled ring bandpass filters using defected ground structures, *Microwave Opt. Technol. Lett.* **39**:351–353 (2003).
62. C. Z. Zhao, E. K. Liu, G. Z. Li, Y. Gao, and C. S. Guo, Zero-gap directional coupler switch integrated into a silicon-on-insulator for 1.3-mm operation, *Opt. Lett.* **21**:1664–1666 (1996).
63. R. L. Espinola, M.-C. Tsai, J. T. Yardley, and R. M. Osgood, Fast and low-power thermo-optic switch on thin silicon-on-insulator, *IEEE Photo. Technol. Lett.* **15**:1366–1368 (2003).
64. A. Liu, R. Jones, L. Liao, D. Samara-Rubio, D. Rubin, O. Cohen, R. Nicolaescu, and M. Paniccia, A high-speed silicon optical modulator based on a metal-oxide-semiconductor capacitor, *Nature (London)* **427**:615–618 (2004).
65. M. Tokushima and H. Yamada, Light propagation in a photonic-crystal-slab line-defect waveguide, *IEEE J. Quantum Electron.* **38**:753–759 (2002).
66. S. Y. Lin, E. Chow, J. Bur, S. G. Johnson, and J. D. Joannopoulos, Low-loss, wide-angle Y splitter at similar to 1.6- μm wavelengths built with a two-dimensional photonic crystal, *Opt. Lett.* **27**:1400–1403 (2002).
67. S. Boscolo, M. Midrio, and T. F. Krauss, Y-junctions in photonic crystal channel waveguides: High transmission and impedance matching, *Opt. Lett.* **27**:1001–1003 (2002).
68. Y. Sugimoto, N. Ikeda, N. Carlsson, K. Asakawa, N. Kawai, and K. Inoue, Light-propagation characteristics of Y-branch defect waveguides in AlGaAs-based air-bridge-type two-dimensional photonic crystal slabs, *Opt. Lett.* **27**:388–390 (2002).
69. S. Fan, P. R. Villeneuve, J. D. Joannopoulos, and H. A. Haus, Channel drop tunnelling through resonant states, *Phys. Rev. Lett.* **80**:960–963 (1998).
70. M. Koshiba, Wavelength division multiplexing and demultiplexing with photonic crystal waveguide couplers, *IEEE J. Lightwave Technol.* **19**:1970–1975 (2001).
71. S. Boscolo, M. Midrio, and C. G. Someda, Coupling and decoupling of electromagnetic waves in parallel 2-D photonic crystal waveguides, *IEEE J. Lightwave Technol.* **38**:47–53 (2002).
72. S. Lan and H. Ishikawa, Coupling of defect pairs and generation of dynamical bandgaps in the impurity bands of nonlinear photonic crystals for all-optical switching, *J. Appl. Phys.* **91**:2573–2577 (2002).
73. O. Painter, R. K. Lee, A. Scherer, A. Yariv, J. D. O'Brien, P. D. Dapkus, and I. Kim, Two-dimensional photonic band-gap defect mode laser, *Science* **284**:1819–1821 (1999).
74. K. Sakoda, K. Ohtaka, and T. Ueta, Low-threshold laser oscillation due to group-velocity anomaly peculiar to two- and three-dimensional photonic crystals, *Opt. Express* **4**:U1–U9 (1999).
75. S. H. Fan, P. R. Villeneuve, J. D. Joannopoulos, and E. F. Schubert, High extraction efficiency of spontaneous emission from slabs of photonic crystals, *Phys. Rev. Lett.* **78**:3294–3297 (1997).
76. H. Y. Ryu, J. K. Hwang, Y. J. Lee, and Y. H. Lee, Enhancement of light extraction from two-dimensional photonic crystal slab structures, *IEEE J. Sel. Topics. Quantum. Electron.* **8**:231–237 (2002).
77. S. Olivier, C. Smith, M. Rattier, H. Benisty, C. Weisbuch, T. Krauss, R. Houdré, and U. Oesterlé, Miniband transmission in a photonic crystal coupled-resonator optical waveguide, *Opt. Lett.* **26**:1019–1021 (2001).
78. W. Bogaerts, V. Wiaux, D. Taillaert, S. Beckx, B. Luyssaert, P. Nienstman, and R. Baets, Fabrication of photonic crystals in silicon-on-insulator using 248-nm deep UV lithography, *IEEE J. Select Topics Quantum Electron.* **8**:928–934 (2002).
79. A. Mekis and J. D. Joannopoulos, Tapered couplers for efficient interfacing between dielectric and photonic crystal waveguides, *IEEE J. Lightwave Technol.* **19**:861–865 (2001).
80. W. Kuang, C. Kim, A. Stapleton, and J. D. O'Brien, Grating-assisted coupling of optical fibers and photonic crystal waveguides, *Opt. Lett.* **27**:1604–1606 (2002).
81. H. Kosaka, T. Kawashima, A. Tomita, T. Sato, and S. Kawakami, Photonic-crystal spot-size converter, *Appl. Phys. Lett.* **76**:268–270 (2000).
82. P. E. Barclay, K. Srinivasan, M. Borselli, and O. Painter, Experimental demonstration of evanescent coupling from optical fibre tapers to photonic crystal waveguides, *Electron. Lett.* **39**:842–844 (2003).
83. E. Miyai, M. Okano, M. Mochizuki, and S. Noda, Analysis of coupling between two-dimensional photonic crystal waveguide and external waveguide, *Appl. Phys. Lett.* **81**:3729–3731 (2002).
84. D. W. Prather, J. Murakowski, S. Shi, S. Venkataram, A. Sharkaw, C. Chen, and D. Pustai, High-efficiency coupling structure for a single-line-defect photonic-crystal waveguide, *Opt. Lett.* **27**:1601–1603 (2002).
85. D. Taillaert, W. Bogaerts, P. Bienstman, T. F. Krauss, P. Van Daele, I. Moerman, S. Versteuyft, K. De Mesel, and R. Baets, An out-of-pale grating coupler for efficient butt-coupling between compact planar waveguides and single-mode fibers, *IEEE J. Quantum Electron.* **38**:949–955 (2002).
86. Y. Xu, R. Lee, and A. Yariv, Adiabatic coupling between conventional dielectric waveguides and waveguides with discrete translational symmetry, *Opt. Lett.* **25**:755–757 (2000).
87. T. D. Happ, M. Kamp, and A. Forchel, Photonic crystal tapers for ultracompact mode conversion, *Opt. Lett.* **26**:1102–1104 (2001).

88. A. Talneau, M. Mulet, S. Anand, and Ph. Lalanne, Compound cavity measurements of transmission and reflection of a tapered single-line photonic crystal waveguide, *Appl. Phys. Lett.* **82**:2577–2579 (2003).
89. P. Pottier, I. Ntakis, and R. M. De La Rue, Photonic crystal continuous taper for low-loss direct coupling into 2D photonic crystal channel waveguides and further device functionality, *Opt. Commun.* **223**:339–347 (2003).
90. P. Bienstman, S. Assefa, S. G. Johnson, J. D. Joannopoulos, G. S. Petrich, and L. A. Kolodziejski, Taper structures for coupling into photonic crystal slab waveguides, *J. Opt. Soc. Am. B*, **20**:1817–1821 (2003).
91. M. Dinu, R. L. Willett, K. Baldwin, L. N. Pfeiffer, and K. W. West, Waveguide tapers and waveguide bends in AlGaAs-based two-dimensional photonic crystals, *Appl. Phys. Lett.* **83**:4471–4473 (2003).
92. P. Sanchis, J. Martí, A. García, A. Martínez, and J. Blasco, High efficiency coupling technique for planar photonic crystal waveguides, *Electron. Lett.* **38**:961–962 (2002).
93. P. Sanchis, J. Martí, J. Blasco, A. Martínez, and A. García, Mode matching technique for highly efficient coupling between dielectric waveguides and planar photonic crystal circuits, *Opt. Express* **10**:1391–1397 (2002).
94. S. G. Johnson, C. Manolatou, S. Fan, P. R. Villeneuve, J. D. Joannopoulos, and H. A. Haus, Elimination of cross talk in waveguide intersections, *Opt. Lett.* **23**:1855–1857 (1998).
95. S. Lan and H. Ishikawa, Broadband waveguide intersections with low cross talk in photonic crystal circuits, *Opt. Lett.* **27**:1567–1569 (1998).
96. S. Lan, S. Nishikawa, H. Ishikawa, and O. Wada, Design of impurity band-based photonic crystal waveguides and delay lines for ultrashort optical pulses, *J. Appl. Phys.* **90**:4321–4327 (2001).
97. P. Sanchis, J. García, A. Martínez, F. Cuesta, A. Griol, and J. Martí, Analysis of adiabatic coupling between photonic crystal single-line-defect and coupled-resonator optical waveguides, *Opt. Lett.* **28**:1903–1905 (2003).
98. T. Yang, Y. Sugimoto, S. Lan, N. Ikeda, Y. Tanaka, and K. Asakawa, Transmission properties of coupled-cavity waveguides based on two-dimensional photonic crystals with a triangular lattice of air holes, *J. Opt. Soc. Am. B* **20**:1922–1926 (2003).
99. W. Bogaerts, P. Bienstman, D. Taillaert, R. Baets, and D. De Zutter, Out-of-plane scattering in photonic crystal slabs, *IEEE Photon. Technol. Lett.* **13**:565–567 (2001).
100. H. Benisty, D. Labilloy, C. Weisbuch, C. Smith, T. F. Krauss, D. Cassagne, A. Beraud, and C. Jouanin, Radiation losses of waveguide-based two-dimensional photonic crystals: Positive role of the substrate, *Appl. Phys. Lett.* **76**:532–534 (2000).

PIEZOELECTRIC TRANSDUCER CONTROLLED CIRCUITS

TAE-YEOUL YUN
Hanyang University
Seoul, Korea

1. INTRODUCTION

Tunable microwave circuits can be realized in many techniques, but whatever the method of tuning may be, they

must conserve as much as possible their original S -parameter magnitudes or output characteristics over a tuning range [1]. Most tunable microwave circuits and antennas described in the literature fall into four basic types [2]: mechanically [3–5], magnetically [6–10], electrically [11–15], and optically [16,17] tunable circuits. In addition, the most recently reported are microelectromechanical systems (MEMS) [18,19], providing mechanical tuning with electrically controlled methods using electrostatic forces. The MEMS with movable metal overlays seems to have a low loss and wide tuning range for limited circuit applications such as phase shifters and switches. A new method introduced in this article is also a kind of electromechanical tuning method using a piezoelectric transducer (PET) or actuator [20–22]. The PET is a piezoelectric ceramic, deflected by an applied voltage [23]. A dielectric or metal perturber attached to the PET can introduce wide tunability, low loss, low cost, and easy fabrication for various microwave circuits. Advantages of the PET tuning method will be demonstrated for the largest tuning range to date in a bandpass filter, resonator, and dielectric resonator oscillator (DRO) based on a low-loss PET-controlled phase shifter concept.

A wideband, low-loss phase shifter is an important component in a phased array for beamsteering and beamforming, timing recovery circuits, phase equalizers for data channels, and other applications. Published results [10,14,16] were narrowband, lossy, or providing small phase shift. A new phase shifter has been presented using dielectric perturbation on the microstrip line, electrically controlled by the PET [20]. The PET-controlled dielectric layer perturbs the electromagnetic fields of the microstrip line. The dielectric perturber attached to the PET can be easily moved in the z -axis direction, as shown in Fig. 1a. In this article, an optimized PET phase shifter will be presented with the largest phase shift and the lowest loss to date. In addition, from the PET-controlled phase shifter idea, a new tunable bandpass filter and ring resonator are presented on the microstrip line with simulation and measurement data. The dielectric perturber produces shielding effect on the microstrip line for reducing the radiation loss [24].

One-dimensional (1D) photonic bandgap (PBG) resonators have been reported using varactors for electronic tuning [25]. This resonator is based on the Fabry–Perot resonator consisting of a center resonant line with two sides of PBG reflectors. Even though a flip-chip varactor having very small parasitic effects was used, the quality (Q) factor was still degraded. In this article a new electronically tunable 1D PBG resonator is proposed using the PET-controlled perturber over the resonant line. The dielectric or metal perturber attached under the PET can perturb the electromagnetic fields at the center of the resonant line. This changes the line capacitance, which produces exactly the same effect as with a varactor. Thus the distance of the airgap between the perturber and resonant line determines the operating frequency. This new method is successfully demonstrated with wideband tuning of the resonant frequency with little Q -factor degradation.

The dielectric resonator oscillator (DRO) is widely used for stable microwave sources because of its good temper-

88. A. Talneau, M. Mulet, S. Anand, and Ph. Lalanne, Compound cavity measurements of transmission and reflection of a tapered single-line photonic crystal waveguide, *Appl. Phys. Lett.* **82**:2577–2579 (2003).
89. P. Pottier, I. Ntakis, and R. M. De La Rue, Photonic crystal continuous taper for low-loss direct coupling into 2D photonic crystal channel waveguides and further device functionality, *Opt. Commun.* **223**:339–347 (2003).
90. P. Bienstman, S. Assefa, S. G. Johnson, J. D. Joannopoulos, G. S. Petrich, and L. A. Kolodziejski, Taper structures for coupling into photonic crystal slab waveguides, *J. Opt. Soc. Am. B*, **20**:1817–1821 (2003).
91. M. Dinu, R. L. Willett, K. Baldwin, L. N. Pfeiffer, and K. W. West, Waveguide tapers and waveguide bends in AlGaAs-based two-dimensional photonic crystals, *Appl. Phys. Lett.* **83**:4471–4473 (2003).
92. P. Sanchis, J. Martí, A. García, A. Martínez, and J. Blasco, High efficiency coupling technique for planar photonic crystal waveguides, *Electron. Lett.* **38**:961–962 (2002).
93. P. Sanchis, J. Martí, J. Blasco, A. Martínez, and A. García, Mode matching technique for highly efficient coupling between dielectric waveguides and planar photonic crystal circuits, *Opt. Express* **10**:1391–1397 (2002).
94. S. G. Johnson, C. Manolatos, S. Fan, P. R. Villeneuve, J. D. Joannopoulos, and H. A. Haus, Elimination of cross talk in waveguide intersections, *Opt. Lett.* **23**:1855–1857 (1998).
95. S. Lan and H. Ishikawa, Broadband waveguide intersections with low cross talk in photonic crystal circuits, *Opt. Lett.* **27**:1567–1569 (1998).
96. S. Lan, S. Nishikawa, H. Ishikawa, and O. Wada, Design of impurity band-based photonic crystal waveguides and delay lines for ultrashort optical pulses, *J. Appl. Phys.* **90**:4321–4327 (2001).
97. P. Sanchis, J. García, A. Martínez, F. Cuesta, A. Griol, and J. Martí, Analysis of adiabatic coupling between photonic crystal single-line-defect and coupled-resonator optical waveguides, *Opt. Lett.* **28**:1903–1905 (2003).
98. T. Yang, Y. Sugimoto, S. Lan, N. Ikeda, Y. Tanaka, and K. Asakawa, Transmission properties of coupled-cavity waveguides based on two-dimensional photonic crystals with a triangular lattice of air holes, *J. Opt. Soc. Am. B* **20**:1922–1926 (2003).
99. W. Bogaerts, P. Bienstman, D. Taillaert, R. Baets, and D. De Zutter, Out-of-plane scattering in photonic crystal slabs, *IEEE Photon. Technol. Lett.* **13**:565–567 (2001).
100. H. Benisty, D. Labilloy, C. Weisbuch, C. Smith, T. F. Krauss, D. Cassagne, A. Beraud, and C. Jouanin, Radiation losses of waveguide-based two-dimensional photonic crystals: Positive role of the substrate, *Appl. Phys. Lett.* **76**:532–534 (2000).

PIEZOELECTRIC TRANSDUCER CONTROLLED CIRCUITS

TAE-YEOUL YUN
Hanyang University
Seoul, Korea

1. INTRODUCTION

Tunable microwave circuits can be realized in many techniques, but whatever the method of tuning may be, they

must conserve as much as possible their original S -parameter magnitudes or output characteristics over a tuning range [1]. Most tunable microwave circuits and antennas described in the literature fall into four basic types [2]: mechanically [3–5], magnetically [6–10], electrically [11–15], and optically [16,17] tunable circuits. In addition, the most recently reported are microelectromechanical systems (MEMS) [18,19], providing mechanical tuning with electrically controlled methods using electrostatic forces. The MEMS with movable metal overlays seems to have a low loss and wide tuning range for limited circuit applications such as phase shifters and switches. A new method introduced in this article is also a kind of electromechanical tuning method using a piezoelectric transducer (PET) or actuator [20–22]. The PET is a piezoelectric ceramic, deflected by an applied voltage [23]. A dielectric or metal perturber attached to the PET can introduce wide tunability, low loss, low cost, and easy fabrication for various microwave circuits. Advantages of the PET tuning method will be demonstrated for the largest tuning range to date in a bandpass filter, resonator, and dielectric resonator oscillator (DRO) based on a low-loss PET-controlled phase shifter concept.

A wideband, low-loss phase shifter is an important component in a phased array for beamsteering and beamforming, timing recovery circuits, phase equalizers for data channels, and other applications. Published results [10,14,16] were narrowband, lossy, or providing small phase shift. A new phase shifter has been presented using dielectric perturbation on the microstrip line, electrically controlled by the PET [20]. The PET-controlled dielectric layer perturbs the electromagnetic fields of the microstrip line. The dielectric perturber attached to the PET can be easily moved in the z -axis direction, as shown in Fig. 1a. In this article, an optimized PET phase shifter will be presented with the largest phase shift and the lowest loss to date. In addition, from the PET-controlled phase shifter idea, a new tunable bandpass filter and ring resonator are presented on the microstrip line with simulation and measurement data. The dielectric perturber produces shielding effect on the microstrip line for reducing the radiation loss [24].

One-dimensional (1D) photonic bandgap (PBG) resonators have been reported using varactors for electronic tuning [25]. This resonator is based on the Fabry–Perot resonator consisting of a center resonant line with two sides of PBG reflectors. Even though a flip-chip varactor having very small parasitic effects was used, the quality (Q) factor was still degraded. In this article a new electronically tunable 1D PBG resonator is proposed using the PET-controlled perturber over the resonant line. The dielectric or metal perturber attached under the PET can perturb the electromagnetic fields at the center of the resonant line. This changes the line capacitance, which produces exactly the same effect as with a varactor. Thus the distance of the airgap between the perturber and resonant line determines the operating frequency. This new method is successfully demonstrated with wideband tuning of the resonant frequency with little Q -factor degradation.

The dielectric resonator oscillator (DRO) is widely used for stable microwave sources because of its good temper-

ature stability, small size, compactness, low price, and other advantages. In addition, the electronically tunable DRO or voltage-controlled DRO (VCDRO) has many applications in communication and radar systems, and frequency-hopping spread-spectrum circuits. Several methods have been used to tune the resonant frequency of DR [2] and DRO: mechanical [5], ferrite, varactor [12,13], PIN diode, and optical [17]. The mechanical method using a dielectric disk perturbation was able to maintain good performance over a wide tuning range [2]. The DRO oscillation frequency can be tuned by perturbing the DR's electromagnetic fields. This tuning can be achieved by varying the airgap between the DR and the dielectric (or metallic) disk above the DR, using the PET. The PET-controlled VCDRO is demonstrated to obtain the largest tuning range up to date.

2. DESIGN AND EXPERIMENTS

2.1. Tunable Phase Shifter

The new phase shifter of Fig. 1a consists of microstrip-line substrate (dielectric constant of ϵ_{r1}), airgap ($\epsilon_{r2} = 1$), and perturber (ϵ_{r3}). To calculate the capacitance of perturbed microstriplike transmission lines, the variational method was used [26]. The capacitance variations correspond to variations in effective dielectric constant, characteristic impedance (Z_c), and propagation constant. A dispersion formula is found from curve fitting [27,28], which is used for optimizing the PET-controlled phase shifter to reduce the control voltage with smaller size and larger phase shift. The substrate optimized for the microstrip line is RT/duroid 6010.8 with a dielectric constant of 10.8, thick-

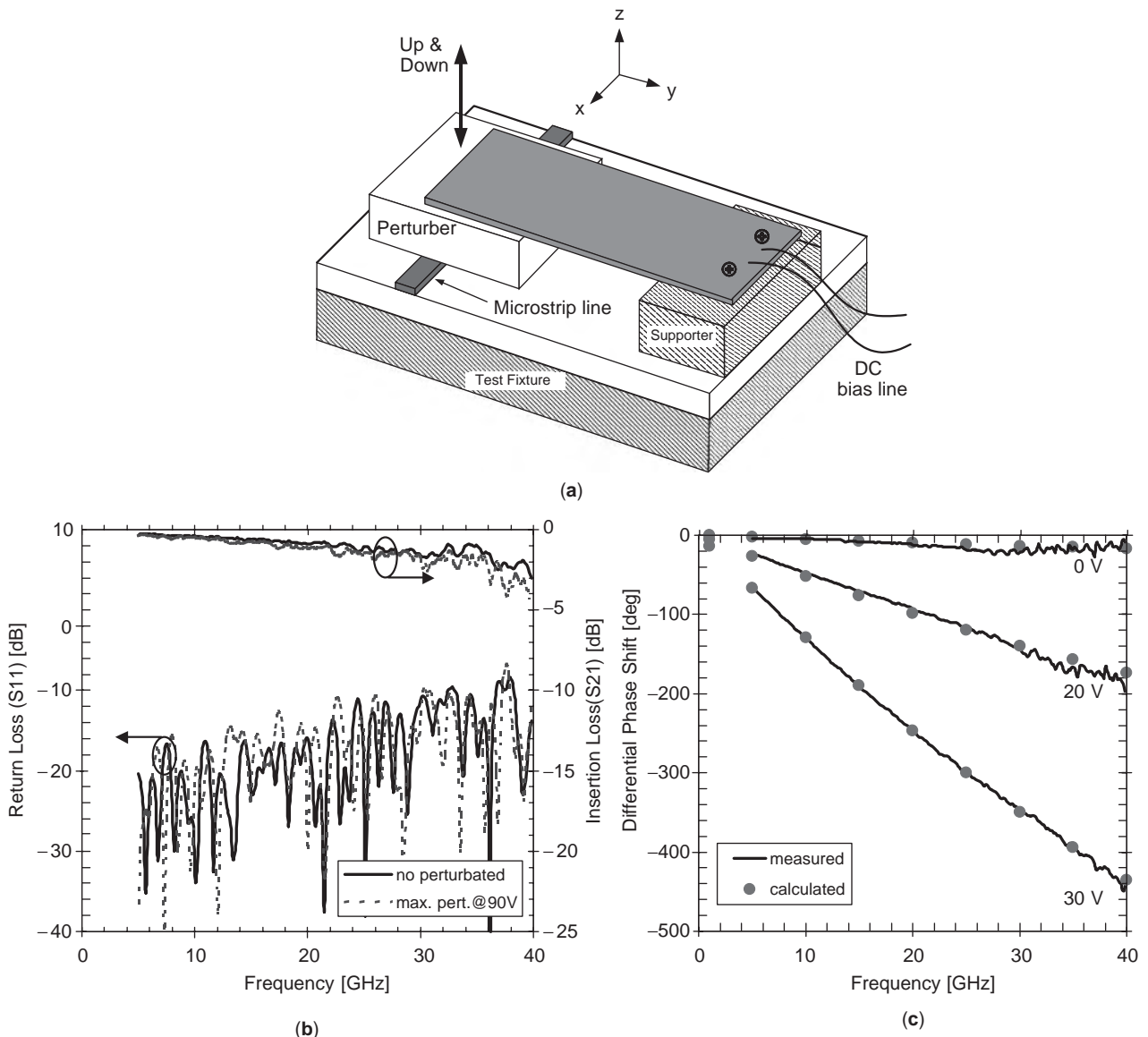


Figure 1. A PET-controlled phase shifter: (a) configuration; (b) S parameters; (c) phase shifts versus frequencies with different PET voltages, with a substrate of $\epsilon_r = 10.8$, thickness = 10 mil, microstrip width = 5 mil, and perturber of $\epsilon_r = 10.8$ and length = 1.2 in. (This figure is available in full color at <http://www.mrw.interscience.wiley.com/erfme>.)

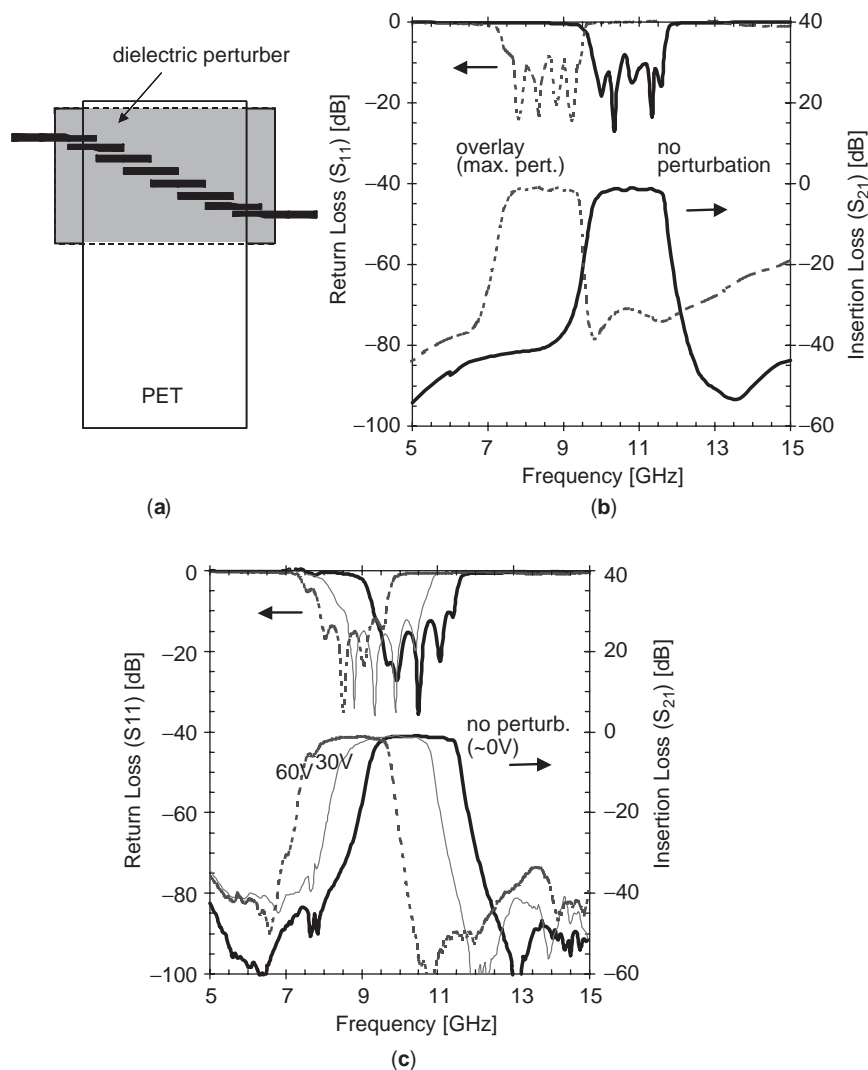


Figure 2. A tunable bandpass filter: (a) configuration—top view; (b) simulated S parameters; (c) measured S parameters with different PET voltages, with a substrate of $\epsilon_r = 10.8$, thickness = 25 mil, microstrip width = 22 mil, and perturber of $\epsilon_r = 10.8$. (This figure is available in full color at <http://www.mrw.interscience.wiley.com/erfme>.)

ness of 10 mil, and width of 5 mil. The dielectric perturber has a dielectric constant of 10.8, height of 50 mil, and length of 1.2 inch. The microstrip-line width of 5 mil is designed for a high Z_c of $64\ \Omega$ at 40 GHz to compensate for the decreased Z_c by dielectric perturbation. At maximum perturbation, when the dielectric perturber is placed on the microstrip line, Z_c is close to $50\ \Omega$. This will maintain good impedance matching without any external matching circuit. The PET measures 2.75 in (length) \times 1.25 in (width) \times 0.085 in (thickness including a supporter) with a composition of lead zirconate titanate. This size makes a large capacitance of 290 nF and a relatively slow response time of 5 ms. Smaller size can be used to make a compact unit and improve the tuning time.

“Thru reflect line” (TRL) calibration was used to remove the coaxial connector-to-microstrip-line transition effect for S -parameter measurement of HP8510. But an imperfect calibration and/or surface-wave generation caused a fluctuation in the insertion loss (S_{21}) near 37 GHz, as shown in Fig. 1b. Except for the fluctuation of S_{21} , the maximum perturbation-added loss is less than 2 dB, and

thus the total loss is less than 4 dB up to 40 GHz. The return loss (S_{11}) is less than -15 dB over all frequency range and about -10 dB near 40 GHz. S -Parameter magnitudes are not much affected by the dielectric perturbation.

Figure 1c shows measured differential phase shifts with varying frequencies and PET voltages and how S_{21} of the microstrip line with a PET-controlled perturber exhibits a phase shift from -450° to -20° at 40 GHz with respect to the unperturbed condition. The amount of phase shift depends on PET deflection, which is controlled by varying the applied voltage from 0 to 30 V. There is no deflection (or no perturbation) at 0 V and full downward deflection (or maximum perturbation) at 90 V. This is called a *top-down alignment*, the reverse of the *bottom-up alignment* used in Refs. 20–22. The calculated phase shift agrees very well with measured data at each PET-controlled voltage. Between 30 and 90 V of the control voltage, the additional phase shifts becomes small. The phase shift at 90 V is almost saturated and shows -480° . Thus the DC bias is required only up to 30 V. This DC voltage can be further decreased if the alignment is

improved or a narrower microstrip line and thinner substrate are used.

The optimized PET phase shifter has three advantages compared with the previously reported results [20,22]; the bias voltage range is reduced from 90 to 30 V, the size is reduced from 1.8 to 1.2 in, and the phase shift curves are more linear with respect to frequency, even though the S parameters and phase shifting performance are similar. In addition, a phase shift/insertion loss ratio of 229°/dB at 25 GHz and 287°/dB at 35 GHz are achieved. The results are better than those reported in Refs. 15 and 19.

2.2. Tunablebandpass Filter and Ring Resonator

A seven-section, parallel-coupled microstrip bandpass filter was designed, as shown in Fig. 2a. The dielectric perturber is large enough to cover the whole filter and is attached under the PET. Details of design parameters for

the filter are not described here but can be found in Ref. 29. The hand-calculated design is confirmed using IE3D, a moment method full-wave electromagnetic simulator produced by Zeland Software. In Fig. 2b, multilayer simulation results of S parameters are shown with and without perturbation, near the center frequency of 10 GHz. A wide tuning range of 2.315 GHz or 24% was achieved in the simulation without S -parameter degradation. The measured results are shown in Fig. 2c and agree very well with the simulation. The slight difference of filter responses between simulation and measurement may be caused by fabrication inaccuracy and long, bent 50 Ω input/output microstrip lines to balance two ports on a test fixture that were not considered in the simulation. A measured tuning range is 1.675 GHz or 17.5%, which is slightly smaller than the simulated result because of nonperfect overlay or perturbation. The tuning range should be increased if the filter substrate is designed using a lower dielectric con-

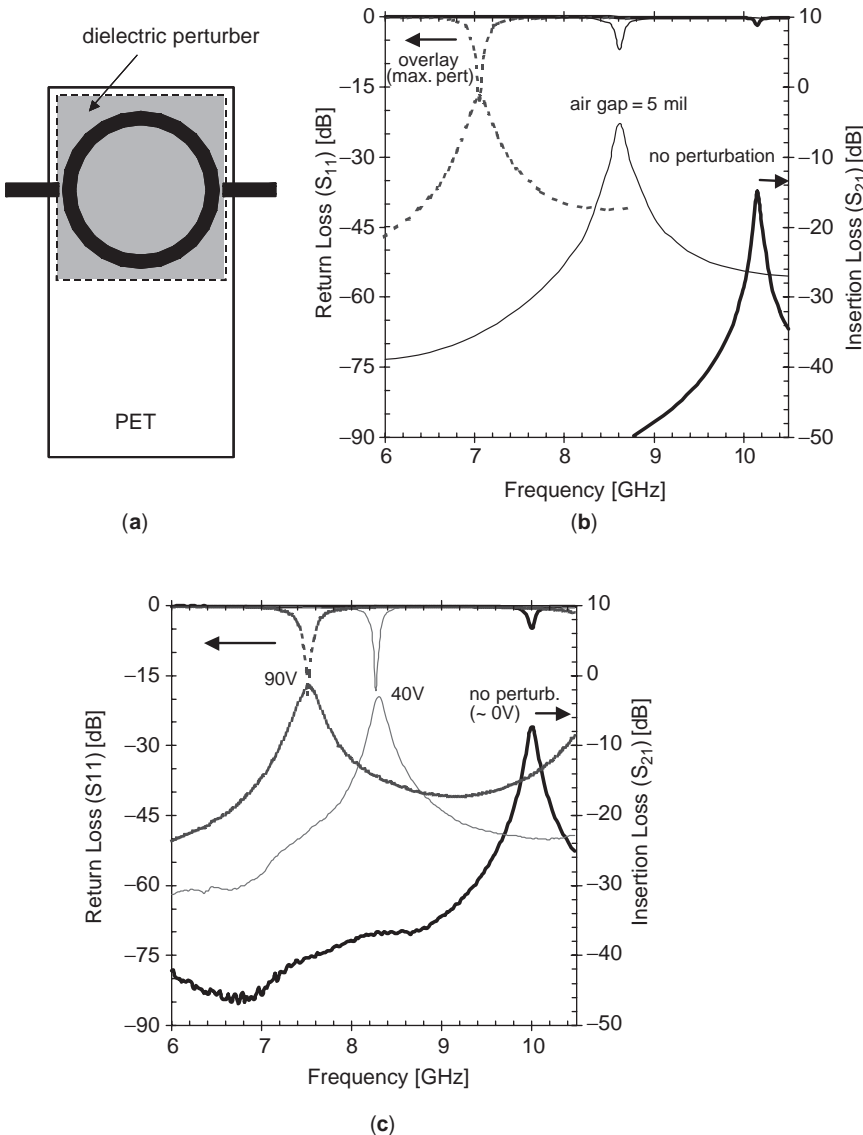


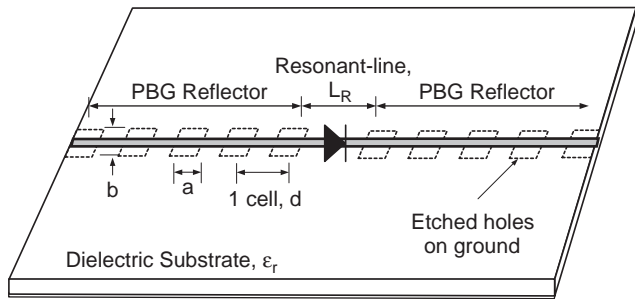
Figure 3. A tunable ring resonator: (a) configuration—top view; (b) simulated S parameters; (c) measured S parameters with different PET voltages, with a substrate of $\epsilon_r = 2.33$, thickness = 20 mil, microstrip width = 50 mil, ring coupling gap = 5 mil, and perturber of $\epsilon_r = 10.8$. (This figure is available in full color at <http://www.mrw.interscience.wiley.com/erfme>.)

stant material. This idea is demonstrated in the following PET-tuned ring resonator.

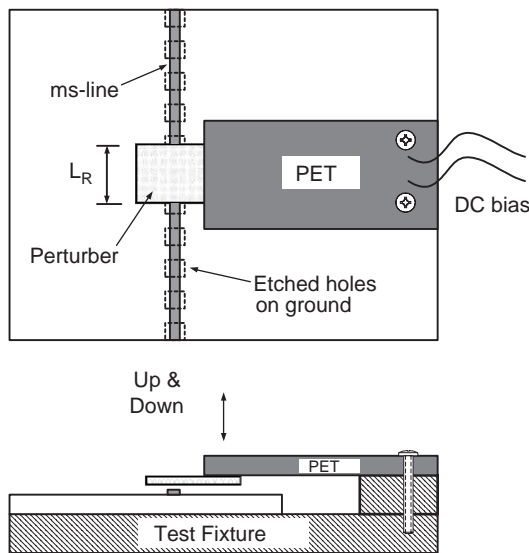
In Fig. 3, the PET tuning feasibility for the microstrip ring resonator is demonstrated with simulation and measurement. As mentioned above, a lower dielectric constant of $\epsilon_r = 2.33$ was used for the microstrip substrate to increase the tuning range. The second resonant frequency of the ring resonator was designed near 10 GHz and tuned over 3.1 GHz or 36% with maximum perturbation in the simulation, as shown in Fig. 3b. The measured results in Fig. 3c show a tuning range of 2.5 GHz or 28.5%; the range is greatly improved by using the lower-permittivity-material substrate. Although not shown, experiments indicated a tuning range of 1.35 GHz or 14.7% with a microstrip substrate of $\epsilon_r = 10.8$. Note that the radiation and mismatch losses are gradually reduced by overlaying of dielectric perturber, as shown in Figs. 3b and 3c and as suggested in Ref. 24.

2.3. Tunable One-Dimensional (1D) Photonic Bandgap (PBG) Resonator

The 1D PBG structure consists of a 50-Ω microstrip conductor line and etched square holes on the ground plane,



(a)



(b)

Figure 4. Tunable 1D PBG resonator configurations: (a) varactor-tuned; (b) PET-tuned.

as shown in Fig. 4a. This has results similar to those obtainable for an alternately high low characteristic impedance line or air holes drilled through the substrate along the microstrip line [25]. When a varactor is mounted in a resonant line, the variable capacitance is used to change the resonant frequency (f_0). The substrate used is a RT/duroid 6010.5 with dielectric constant 10.5, length 2 in., thickness 25 mil, and linewidth 22 mil. Slot size ($a = b$) 100 mil, spacing (d) 200 mil, and resonant-line length ($L_R = 1.5d$) of 300 mil are chosen. As a result of the varactor-tuned PBG resonator, a wideband tuning capability of ~20% near 10 GHz is measured with a maximum loaded $Q(Q_L)$ of only 77. The low intrinsic Q of the varactor near 10 GHz is the main reason for the low Q_L . With the same structure as that of the 1D PBG resonator, the PET is used instead of the varactor to change the resonant frequency by perturbation of the electromagnetic fields on the resonant line, as shown in Fig. 4b. The airgap distance between the perturber and the resonant line is controlled by varying the DC bias of the PET from 0 to 90 V.

Both metal and dielectric perturbations can be used to tune the 1D PBG resonator. To investigate effects of metal and dielectric perturbers on the resonant frequency, a variational analysis [26] was developed and compared with measured results as shown in Fig. 5. A micrometer head was used for measuring the accurate distance of the airgap. The resonant frequency depends on the effective length of resonant line, which can be easily calculated from the line capacitance and effective dielectric constant obtained from variational analysis. As can be seen from Fig. 5, metal perturbation increases the resonant frequency whereas dielectric perturbation decreases the resonant frequency. This is because metal perturbation decreases the effective dielectric constant and dielectric perturbation increases the effective dielectric constant of the perturbed resonant. The calculated and measured results of dielectric perturbation agree very well. But metal perturbation

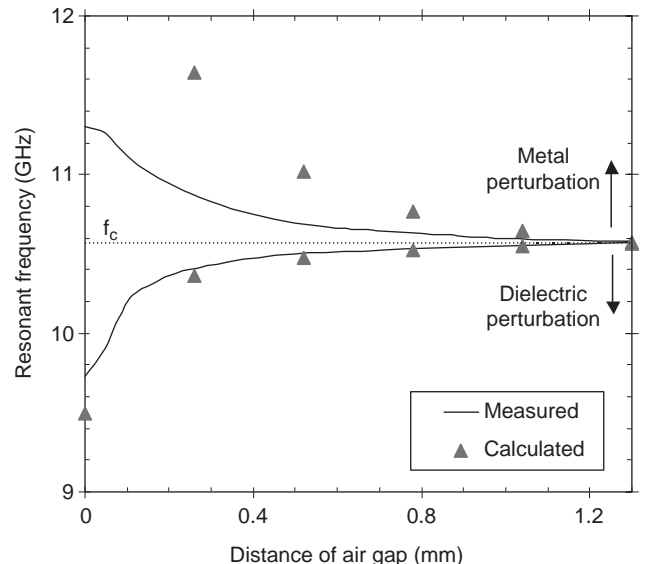


Figure 5. Micrometer-head-controlled perturbation on 1D PBG resonator, to compare measurement with calculation data.

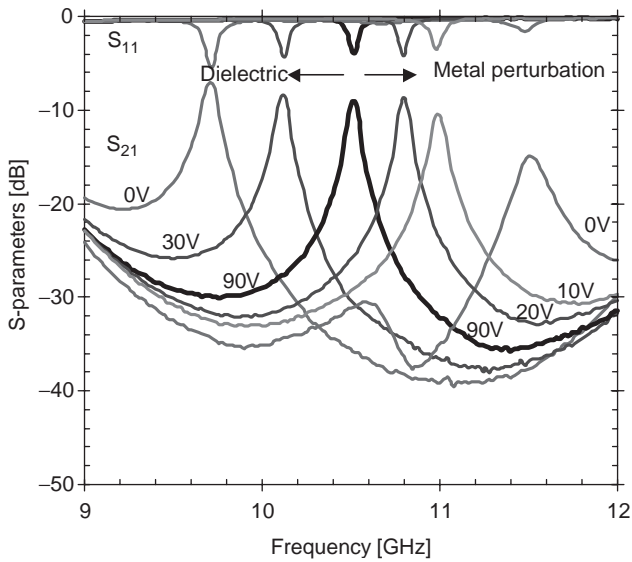


Figure 6. A PET-controlled tunable 1D PBG resonator, measured S parameters with different PET voltages, with a substrate of $\epsilon_r = 10.8$, thickness = 25 mil, microstrip width = 22 mil, perturber of $\epsilon_r = 10.8$, and thickness = 50 mil. (This figure is available in full color at <http://www.mrw.interscience.wiley.com/erfme>.)

results are somewhat different. This discrepancy can be attributed to the distortion that occurs in the quasi-TEM field of the microstrip line when the metal perturber is very close to the resonant line. The above variational analysis may not be accurately predicting this situation.

Insertion loss (S_{21}) and return loss (S_{11}) are measured for the PET-controlled metal and dielectric perturbation on the 1D PBG resonator, as shown in Fig. 6. In order to avoid short-circuiting the metal perturber and microstrip line at 0 V, an airgap of ~ 0.1 mm is added for the metal perturbation. Tuning capability is from -8.2% to $+9\%$ at 10.6 GHz. A maximum insertion loss increase is 1.6 dB and Q_L is larger than 100 for both perturbations. Measured Q_L is 148.5 at 10.6 GHz for the unperturbed condition under 90 V applied bias.

2.4. Tunable Dielectric Resonator Oscillator (DRO)

As shown in Fig. 7a, the DRO consists of a MESFET feedback-type oscillator with a DR. To perturb electromagnetic fields of the DR and thereby tune the oscillation frequency, a dielectric or metal perturber disk attached to the PET moves vertically above the DR puck as the DC bias voltages is varied from 0 to 90 V. A commercial DR (Trans-Tech) of $\epsilon_r = 30.09$ and a MESFET (Agilent, ATF-26836) are used. To obtain an optimum power level and a more

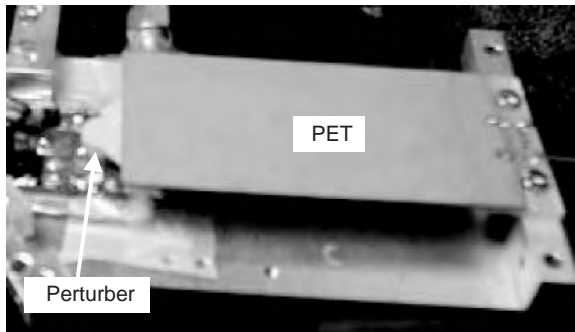
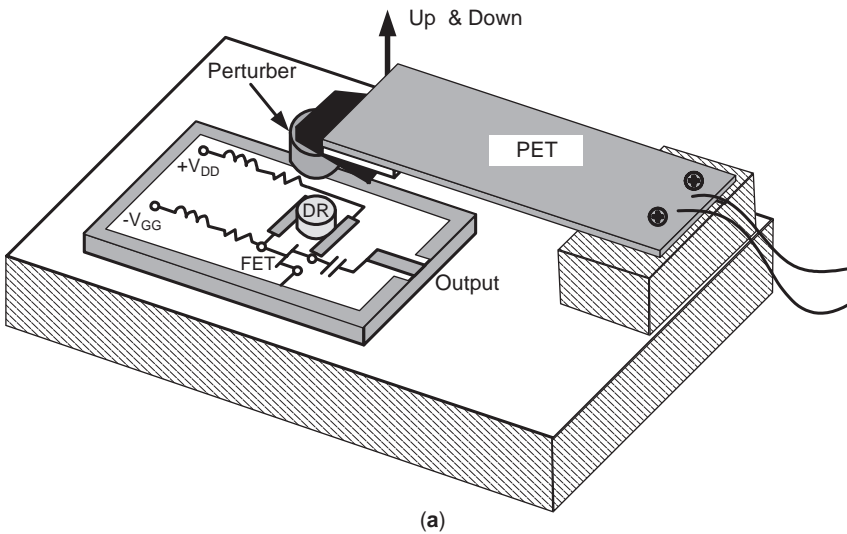


Figure 7. A PET-controlled VCDRO: (a) configuration; (b) photograph.

stable oscillation, the DR locations between two microstrip lines and bias conditions are adjusted. DC biases of $V_{GG} = -0.8\text{ V}$, $V_{DD} = 12\text{ V}$, and $I_{DS} = 30\text{ mA}$ are applied. A drain resistor of $100\ \Omega$ is used. The dielectric perturber has a dielectric constant of 10.8, diameter of 0.3 in, and thickness of 0.1 in. The perturber's size affects the tuning bandwidth. So as not to change the normal circuit operation, the perturber diameter is chosen very similarly with the DR puck diameter. Figure 7b shows a photograph of the PET-controlled VCDRO.

Measured results are shown in Fig. 8. A bottom-up alignment method was used, which means a minimum perturbation and deflection at 0 V and a maximum perturbation and deflection at 90 V. The use of dielectric and metal perturbation results in the tuning of the oscillation frequency from 11.54 to 11.97 GHz or -2.0 to $+1.7\%$ about the center frequency of 11.78 GHz. There is a gap

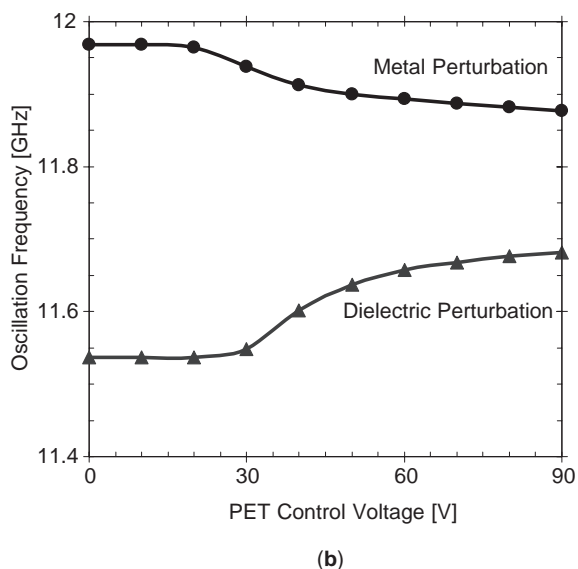
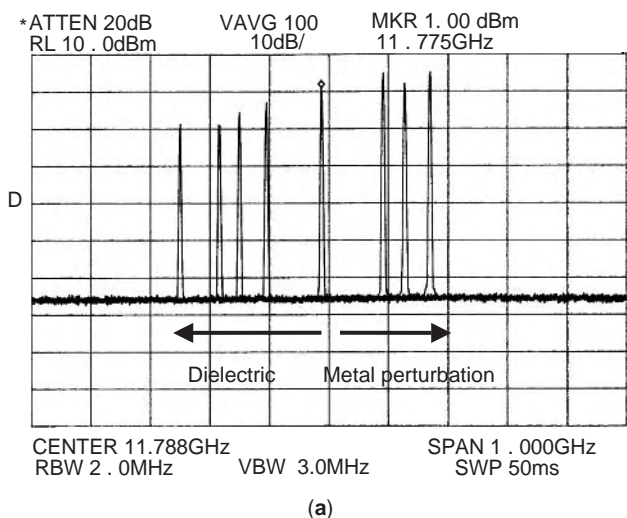


Figure 8. PET-controlled VCDRO results with the dielectric and metal perturbation: (a) spectrum analyzer display of tuning the oscillation frequency; (b) oscillation frequencies versus PET-controlled voltages.

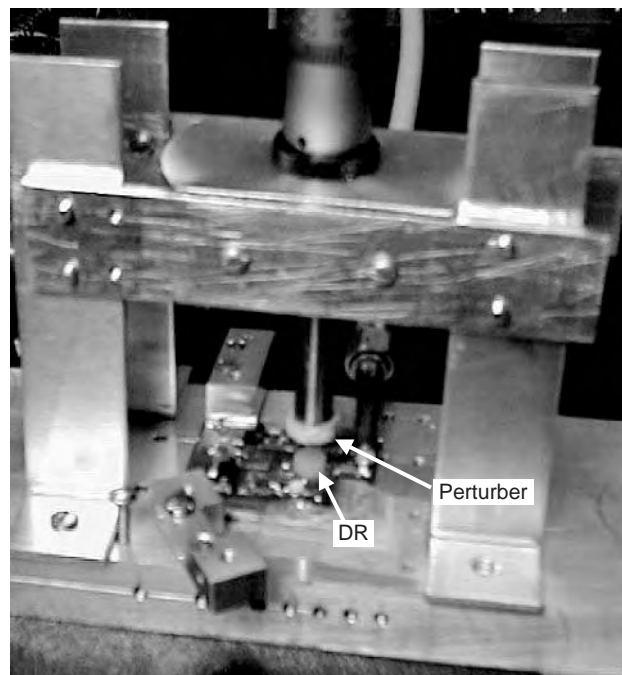


Figure 9. A photograph of mechanical tuning using a micrometer-head-controlled DRO.

without tuning from 11.7 to 11.87 GHz as shown in Fig. 8b because the DRO was not designed for PET tuning and it was difficult to align the PET exactly on the DR. The metal perturbation may increase the stored magnetic energy in the DRO with respect to the electrical energy, which results in increased oscillation frequency. Increase in resonant frequency can be also explained by a metal cavity wall movement inward. The dielectric perturbation effect can, in contrast, also be explained [2]. Material with a dielectric constant of >10.8 for the perturber may produce a wider tuning range [5]. Ideally the VCO output power level remains constant, but all practical purposes the PET and metal or dielectric perturber cause the output power level to fluctuate from -5 to $+2.9\text{ dBm}$. The output power level without perturbation is $+1.45\text{ dBm}$.

For comparison, a mechanical tuning using a micrometer head was set up as shown in Fig. 9, and the results are given in Fig. 10. The micrometer-head-controlled DRO produces more ideal perturbation results due to better alignment and the smaller effect on the circuit by the micrometer head movement. A tuning bandwidth ranging from -3.1 to $+1.6\%$ with a power level variation of 4.5 dB has been achieved. The results are slightly better than with the electronic tuning.

3. DISCUSSION

Although PET-controlled microwave circuits are a new technology with much promise, for use in any commercial systems, certain practical considerations need to be investigated such as uniformity, reproducibility, survivability,

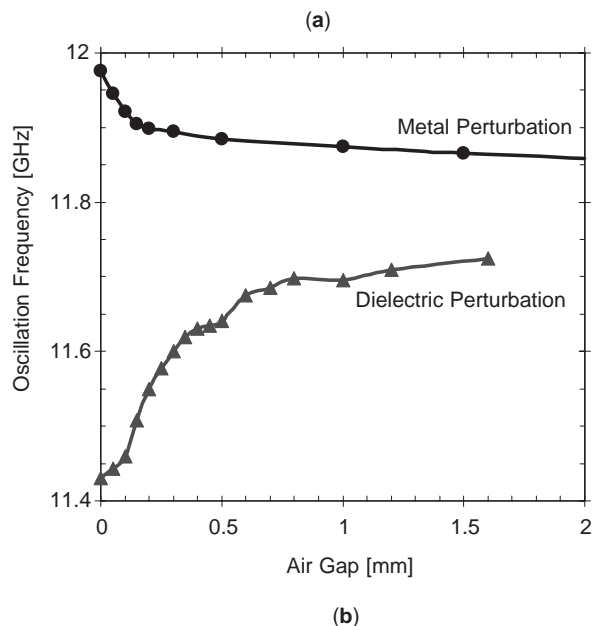
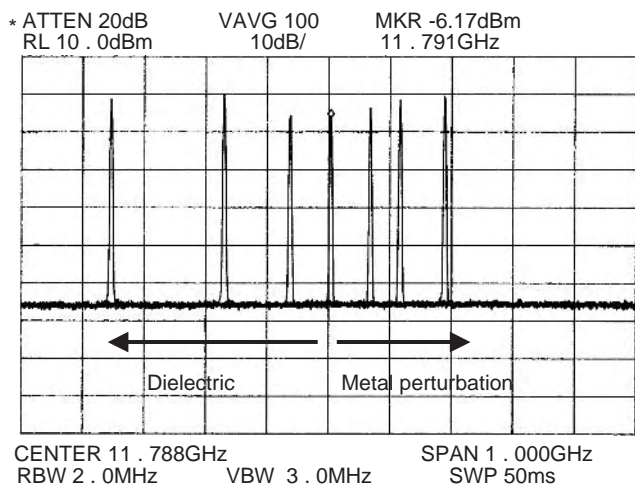


Figure 10. Mechanically micrometer-head-controlled DRO results with the dielectric and metal perturbation: (a) spectrum analyzer display of tuning the oscillation frequency; (b) measured oscillation frequencies versus PET-controlled voltages.

temperature stability, and sensitivity to acceleration or sudden movement (jolts, jerks, etc.).

As in other applications, the piezoelectric material can be used to actuate antennas [30,31]. In addition, the single-line PET phase shifter is easily expanded to a multi-line PET phase shifter, which will be particularly useful for simple and low-priced phased-array antenna systems [22,32]. The coplanar waveguide (CPW) line, instead of the microstrip line, can be also perturbed to be another type of PET phase shifter [33].

4. CONCLUSIONS

New piezoelectric transducer (PET)-controlled tunable microwave circuits have been successfully demonstrated. Theoretical results agreed well with measured data. A

new analog PET-controlled phase shifter using perturbed microstrip line showed the largest phase shift with low loss over ultrawide bandwidth up to 40 GHz. The new phase shifter should be helpful for beamsteering and beamforming of antenna arrays. In addition, new PET-tuned bandpass filter, ring resonator, one-dimensional (1D) photonic bandgap (PBG) resonator, and dielectric resonator oscillator (DRO) have been demonstrated with the largest tuning range to date. The proposed tuning method should have many applications in monolithic and hybrid microwave integrated circuits.

BIBLIOGRAPHY

1. J. Uher and W. J. R. Hofer, Tunable microwave and millimeter-wave band-pass filters, *IEEE Trans. Microwave Theory Tech.* **39**(4):643–653 (April 1991).
2. B. S. Virdee, Current techniques for tuning dielectric resonators, *Microwave J.* 130–138 (Oct. 1998).
3. G. Matthaei, L. Young, and E. M. T. Jones, *Microwave Filters, Impedance-Matching Networks, and Coupling Structures*, Artech House, Dedham, MA, 1980, Chap. 17.
4. M.-Y. Li and K. Chang, New tunable phase shifters using perturbed dielectric image lines, *IEEE Trans. Microwave Theory Tech.*, **46**(10):1520–1523 (Oct. 1998).
5. T. Shen, K. A. Zaki, C. Wang, and J. Deriso, Tunable dielectric resonators with dielectric tuning disks in cylindrical enclosures, *IEEE MTT-S Int. Microwave Symp. Digest*, Boston, 2000, pp. 1441–1444.
6. D. Nicholson, Ferrite tuned millimeter wave bandpass filters with high off-resonance isolation, *IEEE MTT-S Int. Microwave Symp. Digest*, 1988, pp. 867–870.
7. W. S. Ishak and K. W. Chang, Tunable microwave resonators using magnetostatic wave in YIG-films, *IEEE Trans. Microwave Theory Tech.* **34**:1383–1393 (Dec. 1986).
8. J. Uher, J. Bornemann, and F. Arndt, Magnetically tunable rectangular waveguide E-plane integrated circuit filters, *IEEE Trans. Microwave Theory Tech.* **36**:1014–1022 (June 1988).
9. F. A. Miranda, G. Subramanyam, F. W. V. Keuls, R. R. Romanofsky, J. D. Warner, and C. H. Mueller, Design and development of ferroelectric tunable microwave components for Ku- and K-band satellite communication systems, *IEEE Trans. Microwave Theory Tech.* **48**(7):1181–1189 (July 2000).
10. J. B. L. Rao, D. P. Patel, and V. Krichevsky, Voltage-controlled ferroelectric lens phased arrays, *IEEE Trans. Antenna Propag.* **47**(3):458–468 (March 1999).
11. K. Chang, *Microwave Ring Circuits and Antennas*, Wiley, New York, 1996, Chap. 4.
12. P. C. Kandpal and C. Ho, A broadband VCO using dielectric resonators, *IEEE MTT-S Int. Microwave Symp. Digest*, 1988, pp. 609–612.
13. J. Y. Lee and U.S. Hong, Voltage controlled dielectric resonator oscillator using three-terminal MESFET varactor, *Electron. Lett.* **30**(16):1320–1321 (Aug. 1994).
14. S. Lucyszyn and I. D. Robertson, Synthesis techniques for high performance octave bandwidth 180° analog phase shifters, *IEEE Trans. Microwave Theory Tech.* **40**(4):731–740 (April 1992).
15. A. S. Nagra and R. A. York, Distributed analog phase shifters with low insertion loss, *IEEE Trans. Microwave Theory Tech.* **47**(9):1705–1711 (Sept. 1999).

16. S.-S. Lee, A. H. Udupa, H. Erlig, H. Zhang, Y. Chang, D. H. Chang, D. Bhattacharya, B. Tsap, W. H. Steier, L. R. Dalton, and H. R. Fetterman, Demonstration of a photonically controlled RF phase shifter, *IEEE Microwave Guided Wave Lett.* **9**(9):357–359 (Sept. 1999).
17. G. Molin and J. Renpei, A study on the optical control of dielectric resonator stabilized FET oscillator, *Proc. Asia Pacific Microwave Conf.*, 1997, pp. 565–568.
18. H.-T. Kim, J.-H. Park, Y.-K. Kim, and Y. Kwon, Millimeter-wave micromachined tunable filters, *IEEE MTT-S Int. Microwave Symp. Digest*, Anaheim, CA, 1999, pp. 1235–1238.
19. A. Borgioli, Y. Liu, A. S. Nagra, and R. A. York, Low-loss distributed MEMS phase shifter, *IEEE Microwave Guided Wave Lett.* **10**(1):7–9 (Jan. 2000).
20. T.-Y. Yun and K. Chang, A low-loss time-delay phase shifter controlled by piezoelectric transducer to perturb microstrip line, *IEEE Microwave Guided Wave Lett.* **10**(3):96–98 (March 2000).
21. T.-Y. Yun and K. Chang, An electronically tunable photonic bandgap resonator controlled by piezoelectric transducer, *IEEE MTT-S Int. Microwave Symp. Digest*, Boston, June 2000, pp. 1445–1447.
22. T.-Y. Yun and K. Chang, A phased-array antenna using a multi-line phase shifter controlled by a piezoelectric transducer, *IEEE MTT-S Int. Microwave Symp. Digest*, Boston, June 2000, pp. 831–833.
23. R. C. Buchanan, ed., *Ceramic Materials for Electronics*, Marcel Dekker, New York, 1986, Chap. 3.
24. K. Chang and K. Klein, Dielectrically shielded microstrip (DSM) lines, *Electron. Lett.* **23**(10):535–537 (May 1987).
25. T.-Y. Yun and K. Chang, One-dimensional photonic bandgap resonators and varactor turned resonators, *IEEE MTT-S Int. Microwave Symp. Digest*, Anaheim, CA, 1999, pp. 1629–1632.
26. B. Bhat and S. K. Koul, Unified approach to solve a class of strip and microstrip-like transmission lines, *IEEE Trans. Microwave Theory Tech.* **30**(5):679–686 (May 1982).
27. A. K. Verma and R. Kumar, New empirical unified dispersion model for shielded-, suspended-, and composite-substrate microstrip line for microwave and mm-wave applications, *IEEE Trans. Microwave Theory Tech.* **46**(8):1187–1192 (Aug. 1998).
28. M. Kirschning and R. H. Jansen, Accurate model for effective dielectric constant of microstrip with validity up to millimeter-wave frequencies, *Electron. Lett.* **18**(6):272–273 (March 1982).
29. T. C. Edwards, *Foundations for Microstrip Circuit Design*, Wiley, New York, 1981, Chap. 8.
30. G. Washington, H. S. Yoon, M. Angelino, and W. H. Theunissen, Design, modeling, and optimization of mechanically reconfigurable aperture antennas, *IEEE Trans. Anten. Propag.* **50**(5):628–637 (May 2002).
31. P. R. Lawson and J. L. Yen, A piecewise deformable subreflector for compensation of cassegrain main reflector errors, *IEEE Trans. Anten. Propag.* **36**(10):1343–1350 (Oct. 1998).
32. S.-G. Kim and K. Chang, Independently controllable dual-feed dual-beam phased array using piezoelectric transducers, *IEEE Antenna and Wireless Propag. Lett.* **1**(3):81–83 (March 2002).
33. S.-G. Kim, T.-Y. Yun, and K. Chang, Time-dealy phase shifter controlled by piezoelectric transducers on coplanar waveguide, *IEEE Microwave Wireless Compon. Lett.* **13**(1):19–20 (Jan. 2003).

PIEZOELECTRICITY

YUKIO ITO
 KENJI UCHINO
 The Pennsylvania State
 University

Certain materials produce electrical charges on their surfaces as a consequence of applied mechanical stress. The induced charges are proportional to the mechanical stress. This is called the direct piezoelectric effect and was discovered by Jacques and Pierre Curie in 1880. Materials showing this phenomenon also conversely have a geometric strain proportional to an applied electric field. This is the converse piezoelectric effect. The root of the word “piezo” means “pressure”; hence the original meaning of the piezoelectricity implied “pressure electricity” [1,2].

Piezoelectric materials provide coupling between electrical and mechanical parameters. The materials used earliest for its piezoelectric properties was single-crystal quartz. Quartz crystal resonators for frequency control appear today at the heart of clocks and are also used in TVs and computers. Ferroelectric polycrystalline ceramics such as barium titanate and lead zirconate titanate exhibit piezoelectricity when electrically poled. Since these ceramics possess significant and stable piezoelectric effects, that is, high electromechanical coupling, they are capable of producing large strains/forces and hence are extensively used as transducers. Piezoelectric polymers, notably polyvinylidene difluoride and its copolymers with trifluoroethylene and piezoelectric composites combining a piezoelectric ceramic with a passive polymer, have been developed that offer a high potential. More recently, thin films of piezoelectric materials have received attention because of their potential utilization in microsensors, microtransducers, and microactuators.

Piezoelectricity is being extensively utilized in the fabrication of various devices such as transducers, actuators, surface acoustic wave devices, and frequency control. In this article we discuss the piezoelectric effect, a brief history of piezoelectricity followed by present-day piezoelectric materials that are used, and finally various potential applications of piezoelectric materials.

1. PIEZOELECTRICITY

1.1. Relationship between Crystal Symmetry and Properties

All crystals can be classified into 32 point groups according to their crystallographic symmetry. These point groups are divided into two classes; one has a center of symmetry, and another lacks it. There are 21 noncentrosymmetric point groups. Crystals belonging to 20 of these point groups exhibit piezoelectricity. The cubic class 432, although lacking a center of symmetry, does not permit piezoelectricity. Of these 20 point groups, there are 10 polar crystal classes containing a unique axis, along which an electric dipole moment is oriented in the unstrained condition.

Pyroelectric effect appears in any material that possesses a polar symmetry axis. As a result of this the material develops an electrical charge on the surface owing to change in magnitude of the dipole moment with changing temperature. Among the pyroelectric crystals whose spontaneous polarization are reorientable by application of an electric field of sufficient magnitude (not exceeding the breakdown limit of the crystal) are ferroelectrics [3,4]. Table 1 shows the crystallographic classification of the point groups.

1.2. Piezoelectric Coefficients

Materials are deformed by stresses and the resulting deformations are represented by strains ($\Delta L/L$). When the stress \mathbf{T} (force per unit area) causes a proportional strain \mathbf{S}

$$\mathbf{S} = \mathbf{s}\mathbf{T} \quad (1)$$

where all quantities are tensors; \mathbf{S} and \mathbf{T} are second-rank and \mathbf{s} is fourth-rank. Piezoelectricity creates additional strains by applied field \mathbf{E} . The piezoelectric equation is given by

$$\mathbf{S}_{ij} = \mathbf{s}_{ijkl}\mathbf{T}_{kl} + \mathbf{d}_{ijk}\mathbf{E}_k \quad (2)$$

where \mathbf{E} is the electric field and \mathbf{d} is the piezoelectric constant which is the third-rank tensor. This equation can be also expressed in a matrix form such as given for the case in a poled ceramics:

$$\begin{bmatrix} S_1 \\ S_2 \\ S_3 \\ S_4 \\ S_5 \\ S_6 \end{bmatrix} = \begin{bmatrix} s_{11} & s_{12} & s_{13} & & & \\ s_{12} & s_{11} & s_{13} & & & \\ s_{13} & s_{13} & s_{33} & & & \\ & & & s_{44} & & \\ & & & & s_{44} & \\ & & & & & 2(s_{11} - s_{12}) \end{bmatrix} \begin{bmatrix} T_1 \\ T_2 \\ T_3 \\ T_4 \\ T_5 \\ T_6 \end{bmatrix} + \begin{bmatrix} 0 & 0 & d_{31} \\ 0 & 0 & d_{31} \\ 0 & 0 & d_{33} \\ 0 & d_{15} & 0 \\ d_{15} & 0 & 0 \\ 0 & 0 & 0 \end{bmatrix} \begin{bmatrix} E_1 \\ E_2 \\ E_3 \end{bmatrix} \quad (3)$$

Another frequently used piezoelectric constant is g , which gives the electric field produced when a stress is applied ($\mathbf{E} = \mathbf{g}\mathbf{T}$). The \mathbf{g} constant is related to the \mathbf{d} constant

through the permittivity ϵ :

$$\mathbf{g} = \mathbf{d}/\epsilon \quad (4)$$

A measure of the effectiveness of the electromechanical energy conversion is the electromechanical coupling factor k which measures the fraction of the electrical energy converted to mechanical energy when an electric field is applied or vice versa when a material is stressed [5]. The relationship is in terms of k^2

$$k^2 = \frac{\text{electrical energy converted to mechanical energy}}{\text{input electrical energy}} \quad (5)$$

or

$$k^2 = \frac{\text{mechanical energy converted to electrical energy}}{\text{input mechanical energy}} \quad (6)$$

which can also be expressed by

$$k^2 = \mathbf{d}^2/(\epsilon \cdot \mathbf{s}) \quad (7)$$

k is always less than 1, because k^2 is below 1. Typical values of k are 0.10 for quartz, 0.4 for BaTiO₃ ceramic, 0.5–0.7 for PZT (lead zirconate-titanate) ceramic, and 0.1–0.3 for PVDF [poly(vinylidene difluoride)] polymer. Another important material parameter is the mechanical quality factor Q_m , which determines the frequency characteristics. The Q_m is given by

$$Q_m = 2\pi \times \frac{\text{energy stored over one cycle}}{\text{energy dissipated per cycle}} \quad (8)$$

2. HISTORY OF PIEZOELECTRICITY

As stated already the discovery of piezoelectricity in quartz (which is not ferroelectric) was done by Pierre and Jacques Curie in 1880. Ferroelectricity can provide the creation of useful piezoelectric materials. Rochelle salt was the first ferroelectric discovered in 1921. Until 1940 only two types of ferroelectrics were known, Rochelle salt and potassium dihydrogen phosphate and its isomorph. From 1940 to 1943, unusual dielectric properties such as the abnormally high dielectric constant of barium titanate BaTiO₃ were discovered independently by Wainer and Salmon, Ogawa, and Wul and Golman. After the discovery, compositional modifications for BaTiO₃ led to improvement in the temperature stability or the high-voltage output. Piezoelectric transducers based on BaTiO₃ ceramics were becoming well established in a number of device applications.

In the 1950s Jaffe and coworkers established the lead zirconate-lead titanate system (called PZT system) as suitable for inducing strong piezoelectric effects. The maximum piezoelectric response was found for PZT compositions near the morphotropic phase boundary, that is, the composition-dependent and temperature-independent

Table 1. Crystallographic Classification in Terms of Polarity and Centrosymmetry

Polarity	Symmetry	Crystal System										
		Cubic		Hexagonal		Tetragonal		Rhombohedral		Orthorhombic	Monoclinic	Triclinic
Nonpolar [22]	Centro [11]	<i>m3m</i>	<i>m3</i>	<i>6/mmm</i>	<i>6/m</i>	<i>4/mmm</i>	<i>4/m</i>	$\bar{3}m$	$\bar{3}$	<i>mmm</i>	<i>2/m</i>	
		432		622	$\bar{6}$	422	$\bar{4}$	$\bar{3}2$		222		
	Noncentro [21]	$\bar{4}3m$	23	$\bar{6}m2$	$\bar{6}$	$\bar{4}2m$	$\bar{4}$	32		222		
Polar (pyroelectric) [10]				<i>6mm</i>	6	<i>4mm</i>	4	3 <i>m</i>	3	<i>mm2</i>	<i>2m</i>	1

Inside the bold line are piezoelectrics.

rhombohedral–tetragonal phase change. Since then, the PZT system with various additives has become the dominant piezoelectric ceramics for potential applications. Other ferroelectric perovskite compounds were also extensively examined. The discovery of PZT solid solution systems was rapidly followed by its exploitation in a number of practical piezoelectric applications.

Kawai et al. discovered in 1969 that certain polymers, notably polyvinylidene difluoride, are piezoelectric when stretched during fabrication. Such piezoelectric polymers are also useful for some transducer applications. In 1978 Newnham et al. improved composite piezoelectric materials by combining a piezoelectric ceramic with a passive polymer whose properties can be tailored to the requirements of various piezoelectric devices.

There is another class of ceramic material which recently has become important; relaxor-type electrostrictors such as lead magnesium niobate (PMN), typically doped with 10% lead titanate (PT), which are potentially used for applications in piezoelectric actuator field. More recent breakthroughs in the growth of high quality large single crystal relaxor piezoelectric compositions have brought interest in these materials for wide applications ranging from high strain actuators to high frequency transducers for the medical ultrasound devices because of their superior electromechanical characteristics. More recently, thin films of piezoelectric materials such as zinc oxide (ZnO), or PZT have been extensively investigated and developed for use in microelectromechanical device applications.

3. PIEZOELECTRIC MATERIALS

This section summarizes the current status of piezoelectric materials: single crystal materials, piezoceramics, piezopolymers, piezocomposites, and piezofilms. Table 2

shows the material parameters of some representative piezoelectric materials described next [6,7].

3.1. Single Crystals

More recently, the piezoelectric ceramics have been widely used for a large number of applications. However, single crystal materials retain their utility, being essential for application fields such as frequency stabilized oscillators and surface acoustic devices. The most popular single-crystal piezoelectric materials are quartz, lithium niobate (LiNbO₃) and lithium tantalate (LiTaO₃). The single crystals are anisotropic, which gives different material properties depending on the cut of the materials and the direction of bulk or surface wave propagation.

Quartz is a well-known piezoelectric material. α -quartz belongs to triclinic crystal system with point group 32 and has a phase transition at 537°C to β type, which is not a piezoelectric. Quartz has the cut with a zero temperature coefficient. For instance, quartz oscillators using a thickness shear mode of AT-cut are extensively used for clock sources in computers, and frequency stabilized ones in TVs and VCRs (videocassette recorders). On the other hand, an ST-cut quartz substrate with *X*-propagation has a zero temperature coefficient for surface acoustic waves (SAWs) and so are used for SAW devices with high-stability frequencies. The other distinguishing characteristic of quartz is that it has an extremely high mechanical quality factor $Q_m > 10^5$.

Lithium niobate and lithium tantalate belong to an isomorphous crystal system and are composed of oxygen octahedron. The Curie temperatures of LiNbO₃ and LiTaO₃ are 1210 and 660°C, respectively. The crystal symmetry of the ferroelectric phase of these single crystals is 3 *m* and the polarization direction is along the *c* axis. These mate-

Table 2. Properties of Piezoelectric Materials

Parameter	Quartz	BaTiO ₃	PZT 4	PZT 5H	(Pb,Sm)TiO ₃	PVDF-TrFE
d_{33} (pC/N)	2.3	190	289	593	65	33
g_{33} (10 ⁻³ Vm/N)	57.8	12.6	26.1	19.7	42	380
k_t	0.09	0.38	0.51	0.50	0.50	0.30
k_p		0.33	0.58	0.65	0.03	
$\epsilon_{33}^T/\epsilon_0$	5	1700	1300	3400	175	6
Q_m	> 10 ⁵		500	65	900	3–10
T_c (°C)		120	328	193	355	

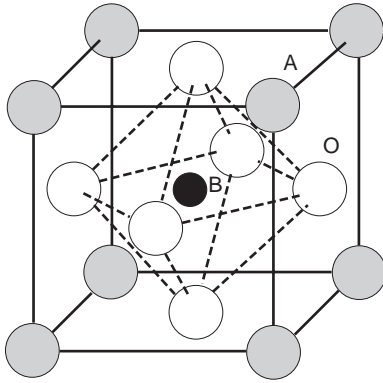


Figure 1. Perovskite structure ABO_3 . This ideal structure consists of a simple cubic unit cell with a large cation A on the corner, a smaller cation B in the body center, and oxygen O in the centers of the faces.

rials have high electromechanical coupling coefficients for surface acoustic waves. In addition, large single crystals can easily be obtained from their melt using the conventional Czochralski technique. Thus, both materials occupy very important positions in the surface acoustic wave device application field.

3.2. Ceramics

3.2.1. Perovskite Structure. Most of the piezoelectric ceramics have perovskite structure ABO_3 , as shown in Fig. 1. This ideal structure consists of a simple cubic unit cell with a large cation A on the corner, a smaller cation B in the body center, and oxygen O in the centers of the faces. The structure is a network of corner-linked oxygen octahedra surrounding B cations. Piezoelectric properties of perovskite-structure materials can be easily tailored depending on their applications by incorporating various cations in the perovskite structure.

3.2.2. Barium Titanate. Barium titanate ($BaTiO_3$) is one of the most thoroughly studied and most widely used piezoelectric materials. Figure 2 shows the temperature dependence of dielectric constants in $BaTiO_3$ demonstrating

the phase transition in $BaTiO_3$ single crystals. Three anomalies can be observed. The discontinuity at the Curie point (130°C) is due to a transition from a ferroelectric to a paraelectric phase. The other two discontinuities are accompanied with transitions from one ferroelectric phase to another. Above the Curie point the crystal structure is cubic and has no spontaneous dipole moments. At the Curie point the crystal becomes polar and the structure changes from a cubic to a tetragonal phase. The tetragonal axis is in the direction of dipole moment and thus along the spontaneous polarization. Just below the Curie temperature, the vector of the spontaneous polarization points in the $[001]$ direction (tetragonal phase), below 5°C it reorients in the $[011]$ (orthorhombic phase) and below -90°C in the $[111]$ (rhombohedral phase). The dielectric and piezoelectric properties of ferroelectric ceramics $BaTiO_3$ can be affected by its own stoichiometry, microstructure, and by dopants entering into the A and B site solution. Modified ceramic $BaTiO_3$ with dopants such as Pb or Ca ions have been used as commercial piezoelectric materials.

3.2.3. Lead Zirconate–Lead Titanate. Piezoelectric $Pb(Zr,Ti)O_3$ solid solutions (PZT) ceramics have been widely used because of their superior piezoelectric properties. The phase diagram of the PZT system ($PbZr_xTi_{1-x}O_3$) is shown in Fig. 3. The crystalline symmetry of this solid-solution system is determined by the Zr content. Lead titanate also has a tetragonal ferroelectric phase of perovskite structure. With increasing Zr content x , tetragonal distortion decreases and when $x > 0.52$ the structure changes from tetragonal $4mm$ phase to another ferroelectric phase of rhombohedral $3m$ symmetry. This transition is rather independent of temperature. The line dividing the two phases is called morphotropic phase boundary, that is, the change of symmetry occurs only as a function of composition. This composition is considered to have both phases. Figure 4 shows the dependence of several d constants on composition near the morphotropic phase boundary. The d constants have their highest values near the morphotropic phase boundary. This enhancement in piezoelectric effect is attributed to the increased ease of reorientation of the polarization under electric field. Doping the PZT material with donors or acceptors changes the

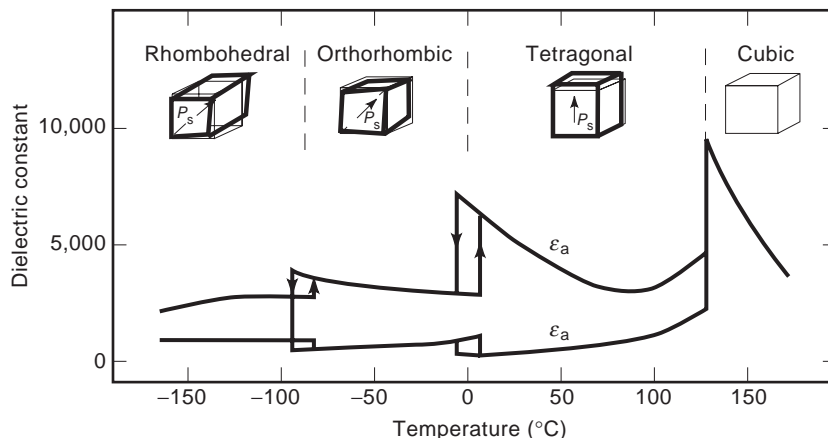


Figure 2. Dielectric constants of $BaTiO_3$ as a function of temperature. Three anomalies accompanied with phase transitions can be observed.

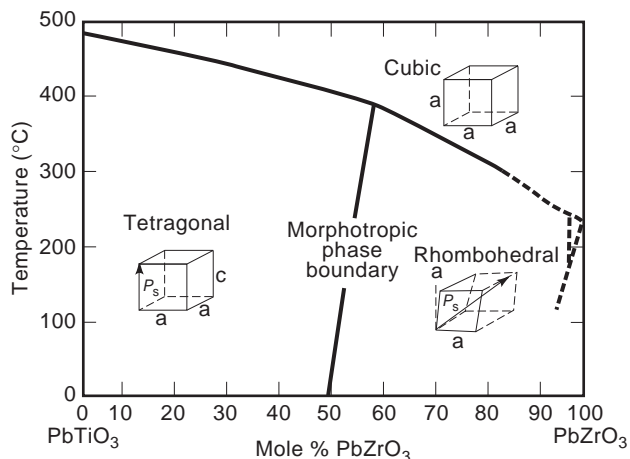


Figure 3. Phase diagram of the PZT system. The crystalline symmetry of this solid-solution system is determined by the Zr content. The line dividing the two, tetragonal and rhombohedral phases is called morphotropic phase boundary.

properties dramatically. Donor doping with ions such as Nb^{5+} or Ta^{5+} provides soft PZTs like PZT-5, because of the facility of a domain motion due to the resulting Pb vacancy. On the other hand, acceptor doping such as Fe^{3+} or Sc^{3+} leads to hard PZTs such as PZT-8, because oxygen vacancies will pin the domain-wall motion.

3.2.4. Lead Titanate. Lead titanate has a large crystal distortion. PbTiO_3 has tetragonal structure at room temperature with its tetragonality approximately equal to 1.063. The Curie temperature is 490°C . Densely sintered PbTiO_3 ceramics cannot be obtained easily, because they break up into a powder when cooled through the Curie temperature. This is due to the large spontaneous strain that occurs at the transition. Lead titanate ceramics modified by adding small amounts of additives exhibit a high piezoelectric anisotropy. Either $(\text{Pb}, \text{Sm})\text{TiO}_3$ [8] or $(\text{Pb}, \text{Ca})\text{TiO}_3$ [9] has extremely low planar coupling, that is,

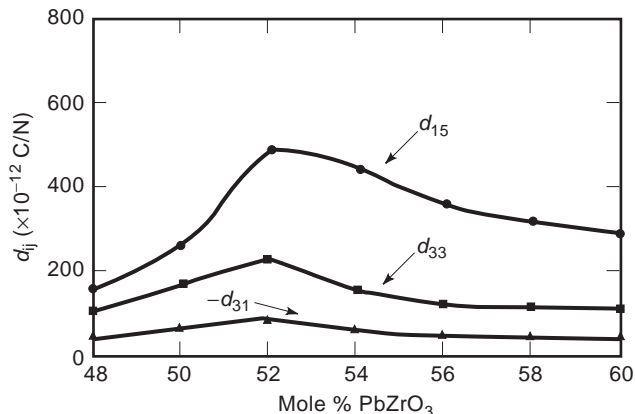


Figure 4. Several piezoelectric d strain coefficients versus composition near the morphotropic phase boundary for the PZT system. The d coefficients have their highest values near the morphotropic phase boundary.

large k_t/k_p ratio. Here, k_t and k_p are thickness-extensional and planar electromechanical coupling factors, respectively. $(\text{Pb}, \text{Nd})(\text{Ti}, \text{Mn}, \text{In})\text{O}_3$ ceramics with a zero temperature coefficient of surface acoustic wave delay have been developed as a superior substrate materials for SAW device applications [10].

3.3. Polymers

Poly(vinylidene difluoride), PVDF or PVF2, is piezoelectric when stretched during fabrication. Thin sheets of the cast polymer are then drawn, stretched, in the plane of the sheet in at least one direction, and frequently also in the perpendicular direction, to make the material into its microscopically polar phase. Crystallization from melt forms nonpolar α -phase, which can be converted into another polar β -phase by a uniaxial or biaxial drawing operation; these dipoles are then reoriented through electric poling. Large sheets can be manufactured and thermally formed into complex shapes. The copolymerization of vinylidene difluoride with trifluoroethylene (TrFE) results in random copolymer (PVDF-TrFE) with a stable, polar β phase. This polymer need not be stretched; it can be poled directly as formed. The thickness-mode coupling coefficient of 0.30 has been reported. Such piezoelectric polymers are used for directional microphones and ultrasonic hydrophones.

3.4. Composites

Piezocomposites composed of a piezoelectric ceramic and polymer are promising materials because of excellent and tailored properties. The geometry for two-phase composites can be classified according to the connectivity of each phase (1, 2, or 3 dimensionally) into 10 structures; 0-0, 0-1, 0-2, 0-3, 1-1, 1-2, 1-3, 2-2, 2-3 and 3-3 (11). A 1-3 piezocomposite or PZT-rod/polymer-matrix composite, is identified as a most promising candidate. The advantages of this composite are high coupling factor, low acoustic impedance, good matching to water or human tissue, mechanical flexibility, broad bandwidth in combination with low mechanical quality factor, and the possibility of making undiced arrays by only structuring the electrodes. The thickness-mode electromechanical coupling of the composite can exceed the k_t (0.40-0.50) of the constituent ceramic, almost approaching the value of the rod-mode electromechanical coupling, k_{33} (0.70 to 0.80) of that ceramic (12). Acoustic impedance is the square root of the product of its density and elastic stiffness. The acoustic match to tissue or water (1.5 Mrayls or $\text{kg m}^{-2} \text{s}^{-1}$) of the typical piezoceramics (20-30 Mrayls) is significantly improved by forming a composite structure, that is, by replacing heavy and stiff ceramic by light and soft polymer. Piezoelectric composite materials are especially useful for underwater sonar and medical diagnostic ultrasonic transducer applications.

3.5. Thin Films

Both zinc oxide (ZnO) and aluminium nitrate (AlN) are simple binary compounds with a Wurtzite-type structure, which can be sputter-deposited in a c -axis-oriented thin film on a variety of substrates. ZnO has large piezoelectric

coupling and its thin films are widely used in bulk acoustic and surface acoustic wave devices. The fabrication of highly c-axis oriented ZnO films has been extensively studied and developed. The performance of ZnO devices is, however, limited due to their small piezoelectric coupling (20–30%). PZT thin films are expected to exhibit higher piezoelectric properties. At present, the growth of PZT thin film is being carried out for use in microtransducers and microactuators.

3.6. Relaxor-Type Ferroelectric Materials

Relaxor ferroelectrics differ from normal ferroelectrics in terms of having broad phase transition from paraelectric to ferroelectric state, strong frequency dependence of dielectric constant (i.e., dielectric relaxation) and weak remanent polarization. Lead-based relaxor materials have complex disordered perovskite structures with a general formula $\text{Pb}(\text{B}_1, \text{B}_2)\text{O}_3$ ($\text{B}_1 = \text{Mg}^{2+}, \text{Zn}^{2+}, \text{Sc}^{3+}, \text{B}_2 = \text{Nb}^{5+}, \text{Ta}^{5+}, \text{W}^{6+}$). The B site cations are distributed randomly in the crystal. The characteristic of relaxors is a broad and frequency dispersive dielectric maximum. Relaxor-type electrostrictive materials such as lead magnesium niobate $\text{Pb}(\text{Mg}_{1/3}\text{Nb}_{2/3})\text{O}_3$ –lead titanate PbTiO_3 solid solution (PMN–PT) are very suitable for application in actuators. This relaxor ferroelectrics can also provide an induced piezoelectric effect. That is, the electromechanical coupling factor k_t varies with the applied dc bias field. As the DC bias field increases, the coupling increases and saturates. This behavior is reproducible. These materials would be applied for ultrasonic transducers that can be tunable by the bias field [13].

Single-crystal relaxor ferroelectrics have been developed that show very promising results in ultrasonic transducers and electromechanical actuators. Single crystals of $\text{Pb}(\text{Mg}_{1/3}\text{Nb}_{2/3})\text{O}_3$ (PMN), $\text{Pb}(\text{Zn}_{1/3}\text{Nb}_{2/3})\text{O}_3$ (PZN) and binary systems of these materials combined with PbTiO_3 (PMN–PT and PZN–PT) exhibit extremely large electromechanical coupling factors [14,15]. Large coupling coefficients and large piezoelectric constants have been found for these solid-solution crystals with morphotropic phase boundary compositions. PZN-8%PT single crystals were found to possess high k_{33} value of 0.94 for (001) crystal cuts. The k_{33} value of the conventional PZT ceramics is usually 0.70–0.80.

More recently, it was reported that these relaxor based ferroelectric single crystals also exhibit ultrahigh strain levels not available with current piezoelectric ceramics [16]. Pseudocubic (001)-oriented relaxor based rhombohedral crystals such as $(1-x)\text{PZN}-x\text{PT}$ ($x < 0.09$) and $(1-x)\text{PMN}-x\text{PT}$ ($x < 0.35$) were reported to have \mathbf{E} -field-induced strains up to 0.6% with negligible hysteresis. Ultrahigh strain levels more than 1.5%, nearly an order of magnitude higher than polycrystalline PZTs or electrostrictive PMN, could be achieved being related to an \mathbf{E} -field-induced phase transformation.

4. APPLICATIONS OF PIEZOELECTRIC MATERIALS

Piezoelectric materials can provide coupling between electrical and mechanical energy and thus have been exten-

sively used in a variety of electromechanical device applications. The direct piezoelectric effect is most obviously used in the generation of charge at high voltage such as for the spark ignition of gas in space heaters, cooking stoves, and cigarette lighters. Using the converse effect, mechanical small displacements and vibrations can be produced for actuators by applying a field. Acoustic and ultrasonic vibrations can be generated by an alternating field tuned at the mechanical resonance frequency of a piezoelectric device, and can be detected by amplifying the field generated by vibration incident on the material, which is usually used for ultrasonic transducers. The other important application field of piezoelectricity include the control of frequency. The application of piezoelectric materials ranges over many technology fields including ultrasonic transducers, actuators and ultrasonic motors, electronic components such as resonators, wave filters, delay lines, SAW devices and transformers, and high-voltage applications; gas ignitors, ultrasonic cleaning, and machining. Piezoelectric-based sensors, for instance, accelerometers, automobile knock sensors, vibration sensors, strain gages, and flow meters have been developed, because pressure and vibration can be directly sensed as electric signals through piezoelectric effect. Examples of these applications are given in the following sections.

4.1. Ultrasonic Transducers

One of the most important applications of piezoelectric materials is based on ultrasonic echo field [17,18]. Ultrasonic transducers convert electrical energy into mechanical form when generating an acoustic pulse and convert mechanical energy into an electrical signal when detecting its echo. Currently, piezoelectric transducers are being used in medical ultrasound for clinical applications ranging from diagnosis to therapy and surgery. They are also used for underwater detection, such as sonar and fish finding, and nondestructive testing.

The ultrasonic transducers often operate in a pulse-echo mode. The transducer converts electrical input into acoustic wave output. The transmitted waves propagate into a body, and echoes are generated which travel back to be received by the same transducer. These echoes vary in intensity according to the type of tissue or body structure, thereby creating images. An ultrasonic image represents the mechanical properties of the tissue, such as density and elasticity. We can recognize anatomical structures in an ultrasonic image since the organ boundaries and fluid-to-tissue interfaces are easily discerned. The ultrasonic imaging process can also be done in real time. This means we can follow rapidly moving structures such as the heart without motion distortion. In addition, ultrasound is one of the safest diagnostic imaging techniques. It does not use ionizing radiation like X rays and thus is routinely used for fetal and obstetrical imaging. Useful areas for ultrasonic imaging include cardiac structures, the vascular systems, the fetus, and abdominal organs such as liver and kidney. In brief, it is possible to see inside the human body by using a beam of ultrasound without breaking the skin.

There are various types of transducers used in ultrasonic imaging. Mechanical sector transducers consist of single, relatively large resonators and can provide images by mechanical scanning such as wobbling. Multiple-element array transducers permit discrete elements to be individually accessed by the imaging system and enable electronic focusing in the scanning plane to various adjustable penetration depths through the use of phase delays. Two basic types of array transducers are linear and phased (or sector). A linear array is a collection of elements arranged in one direction, producing a rectangular display. A curved linear (or convex) array is a modified linear array whose elements are arranged along an arc to permit an enlarged trapezoidal field of view. The elements of these linear type array transducers are excited sequentially group by group in a sweep of the beam in one direction. These linear array transducers are used for radiological and obstetrical examinations. On the other hand, in a phased-array transducer the acoustic beam is steered by signals that are applied to the elements with delays, creating a sector display. This transducer is useful for cardiology applications where positioning between the ribs is necessary.

Figure 5 shows the basic ultrasonic transducer geometry. The transducer is composed mainly of matching layers, piezoelectric material and backing [19]. One or more matching layers are used to increase sound transmissions into tissues. The backing is added to the rear of the transducer in order to damp the acoustic backwave and to reduce the pulse duration. Piezoelectric materials are used to generate and detect ultrasound. In general, broadband transducers should be used for medical ultrasonic imaging. The broad bandwidth response corresponds to a short pulse length, resulting in better axial resolution. Three factors are important in designing broad bandwidth transducers. The first is acoustic impedance matching, that is, effectively coupling acoustic energy to the body. The second is a high electromechanical coupling coefficient of the transducer. The third is electrical impedance matching,

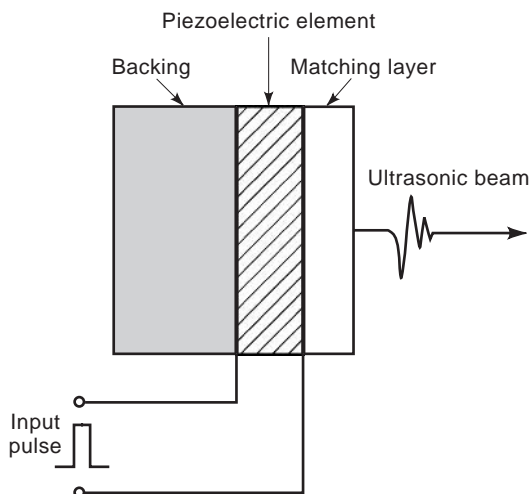


Figure 5. Prototype transducer geometry. The transducer is mainly composed of matching layer, piezoelectric material and backing.

Table 3. Comparison of Ultrasonic Transducer Materials

	PZT Ceramic	PVDF Polymer	PZT- Polymer Composite	ZnO Film
k_t	0.45–0.55	0.20–0.30	0.60–0.75	0.20–0.30
$Z(\text{Mrayls})$	20–30	1.5–4	4–20	35
$\epsilon_{33}^T/\epsilon_0$	200–5000	10	50–2500	10
$\tan\delta$ (%)	<1	1.5–5	<1	<1
Q_m	10–1000	5–10	2–50	10
ρ (g/cm^3)	5.5–8	1–2	2–5	3–6

that is, effectively coupling electrical energy from the driving electronics to the transducer across the frequency range of interest. These pulse echo transducers operate based on the thickness mode resonance of the piezoelectric thin plate. The thickness-mode coupling coefficient k_t is related to the efficiency of converting electric energy into acoustic and vice versa. Further, a low-planar-mode coupling coefficient, k_p , is beneficial for limiting energies being expended in non-productive lateral mode. A large dielectric constant is necessary to enable a good electrical impedance match to the system, especially with tiny piezoelectric sizes.

Table 3 compares the properties of ultrasonic transducer materials [7,20]. Ferroelectric ceramics, such as lead zirconate titanate and modified lead titanate, are today almost universally used as ultrasonic transducers. The success of ceramics is due to their very high electromechanical coupling coefficients. In particular, soft PZT ceramics such as PZT-5A and 5H type compositions are most widely used because of their exceedingly high coupling properties and because they can be relatively easily tailored, for instance, in the wide dielectric constant range. On the other hand, modified lead titanates such as samarium doped materials have high piezoelectric anisotropy: the planar coupling factor k_p is much less than the thickness coupling factor k_t . This absence of lateral coupling leads to reduced interference from spurious lateral resonances in longitudinal oscillators. This is very useful in high-frequency array transducer applications. One disadvantage to PZT and other lead-based ceramics is their large acoustic impedance (approximately 30 Mrayls) compared to body tissue (1.5 Mrayls). Single or multiple matching layers with intermediate impedances needed to be used in the case of PZT to improve acoustic matching.

On the other hand, piezoelectric polymers, such as poly(vinylidene)-difluoride-trifluoroethylene, have much lower acoustic impedance (4–5 Mrayls) than the ceramics and thus provide better matching with soft tissues. However, piezopolymers are less sensitive than the ceramics and they have relatively low dielectric constants, requiring large drive voltage and giving poor noise performance due to electrical impedance mismatching.

An alternative to ceramics and polymers is piezoelectric ceramic/polymer composites. Piezocomposites having 2–2 or 1–3 connectivity are commonly used in ultrasonic medical applications. These combine the low acoustic impedance advantage of polymers with the high sensitivity and low electrical impedance advantages of ceramics.

The design frequency of a transducer depends on the penetration depth imposed by the application. Resolution is improved with increasing frequency. Although a high-frequency transducer is capable of producing a high-resolution image, higher frequency acoustic energy is more readily attenuated by the body. A lower frequency transducer is used as a compromise when imaging deeper structures. Most medical ultrasound imaging systems operate in the frequency range from 2 to 10 MHz and can resolve objects approximately 0.2–1 mm in size. At 3.5 MHz, imaging to a depth of 10–20 cm is possible, while at 50 MHz, increased losses limit the depth to less than 1 cm. Higher-frequency transducers (10–50 MHz) are used for endoscope-based imaging and for catheter-based intravascular imaging. At higher frequencies over 100 MHz applications are used in the field of ultrasound microscopy. The operating frequency of the transducer is directly related to the thickness and velocity of sound in the piezoelectric materials employed. As frequency increases resonator thickness decreases. For a 3.5-MHz transducer, PZT ceramic thickness needs to be roughly 0.4 mm. Most conventional ceramic transducers, such as PZT, are limited to frequencies below nearly 80 MHz because of the difficulty of fabricating thinner devices [21]. For microscopic applications at frequencies over 100 MHz, corresponding to the thickness of less than 20 μm , piezoelectric thin-film transducers such as ZnO have to be used [22].

The design of ultrasonic transducers with piezoelectrics used in the medical field was mentioned above. Another major ultrasonic transducer application is the underwater sonar transducer employed as both acoustic source and hydrophone. Sonar (sound navigation and ranging) is used to explore the ocean and underwater objects. Hydrophones are underwater microphones for detecting sound in water and under hydrostatic pressure. The representative transducers widely used for high-power and low-frequency active sonar include the Tonpiliz and flextensional structures. The design of the Tonpiliz transducer typically involves head and tail masses that are configured for impedance matching and a central piezoceramic section, whose shape roughly resembles a mushroom [23]. This transducer is made from stacks of rings electroded on the flat surfaces and electrically connected in parallel and are electrically insulated for each other held together with a stress rod. On the other hand, the flextensional transducer uses a mechanical shell, generally made of metal such as steel or brass, to convert hydrostatic stress to a stress along one or more of the sensitive axes of a stack of piezoelectric ceramic plates or rings [24]. The flextensional transducers with different shapes of the outer shell have been designed to achieve an extremely high sensitivity.

4.2. Actuators and Motors

4.2.1. Actuators. Currently the other important applications of piezoelectric materials exist in actuator fields [25]. Actuators are defined as transducers capable of transferring input energy into a mechanical output energy. Using the converse piezoelectric effect, small displacement can be produced by applying a field to piezoelectric

materials. Vibrations can be generated by applying an alternating field. In advanced precision engineering, the demand for a variety of types of actuators that can adjust positions precisely (micropositioning devices), suppress noise vibrations (dampers), or drive objects dynamically (ultrasonic motors) exist. These devices are used in broad areas including optics, astronomy, fluid control, and precision machinery. For actuator applications, piezoelectric strain and electrostriction induced by an electric field are used. Electrostrictive materials such as lead magnesium niobate (PMN) ceramics are especially preferred because of their small degradation under severe operating conditions. The PMN is easily electrically poled when an electric field is applied around the transition temperature and depoled completely without any remanent polarization. This provides extraordinarily large apparent electrostriction though it is a secondary phenomenon of the electromechanical coupling. Figure 6 shows the longitudinal induced strain curve at room temperature in 0.9PMN–0.1PT [26]. The magnitude of the electrostriction is 10^{-3} , and this material has almost no hysteresis.

Figure 7 shows the design classification of ceramic actuators. Simple devices composed of a disk and multilayer type directly use the strain induced in a ceramic by the applied electric field. Complex devices do not use the induced strain directly but use the magnified displacement through a special magnification mechanism such as unimorph, bimorph, and moonie. The most popularly used multilayer and bimorph types have the following characteristics. The multilayer type does not show a large displacement (10 μm), but has advantages in generation force (1000 N), response speed (10 μs), lifetime (10^{11} cycles), and the electromechanical coupling factor k_{33} (0.70). The bimorph type exhibits a large displacement (300 μm), but shows disadvantages in generation force (1 N), response

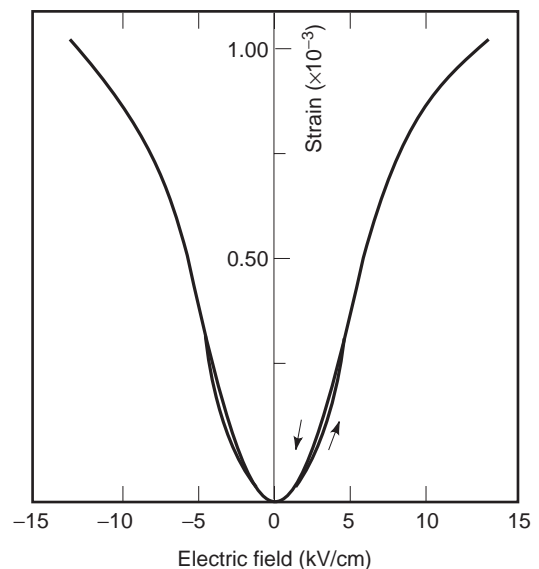


Figure 6. Longitudinal induced strain curve at room temperature in 0.9PMN–0.1PT as a function of electric field. The magnitude of the electrostriction is 10^{-3} and this has almost no hysteresis.

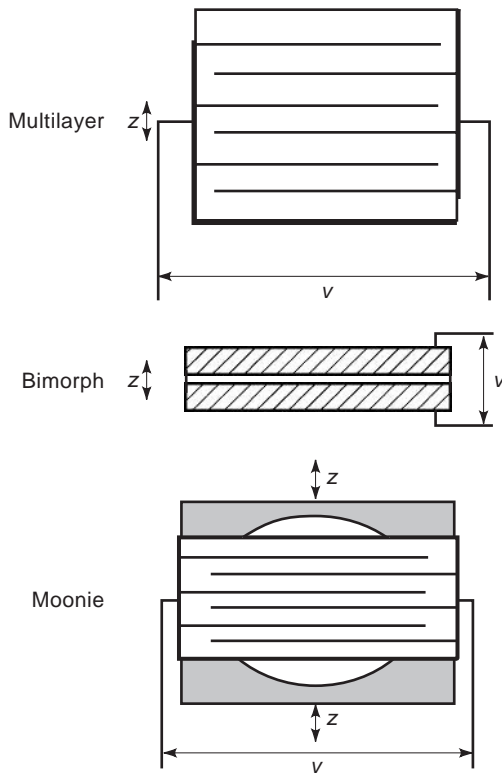


Figure 7. Structures of ceramic actuators. There are three representative types: multilayer, bimorph, and moonie types.

speed (1 ms), lifetime (10^8 cycles) and the electromechanical coupling factor k_{eff} (0.10). For instance, in a 0.65 PMN–0.35 PT multilayer actuator with 99 layers of 100- μm thick sheets ($2 \times 3 \times 10 \text{ mm}^3$), an 8.7 μm displacement is generated by a 100 V voltage, accompanied by a slight hysteresis. The transmit response of the induced displacement after the application of a rectangular voltage is as quick as 10 μs . In conclusion, the multilayer exhibits the field induced strain of 0.1% along the length.

Unimorph and bimorph devices are defined by the number of piezoelectric ceramic plates: only one ceramic plate is bonded onto an elastic shim, or two ceramic plates are bonded together simultaneously. The bimorph causes bending deformation because each piezoelectric plate bonded together produces extension or contraction under an electric field. In general, there are two types of piezoelectric bimorph: antiparallel polarization type and parallel polarization type, as shown in Fig. 8. Two poled piezoelectric plates with $t/2$ in thickness and L in length are bonded with their polarization directions opposite or parallel to each other. In cantilever bimorph configuration whose one end is clamped, the tip displacement δ_z under an applied voltage V is provided as follows:

$$\delta_z = 3/2 \cdot d_{31} (L^2/t^2) V \text{ (antiparallel type)} \quad (9)$$

$$\delta_z = 3d_{31} (L^2/t^2) V \text{ (parallel type)} \quad (10)$$

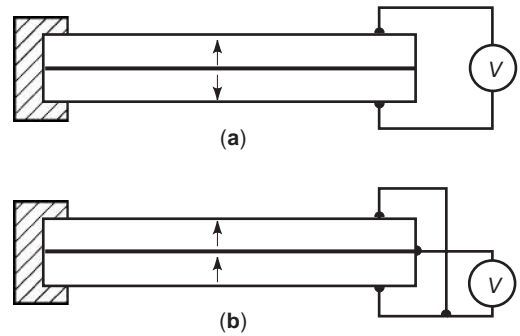


Figure 8. Two types of piezoelectric bimorphs: (a) antiparallel polarization type; (b) parallel polarization type.

The resonance frequency f_r for both types is given by

$$f_r = 0.16t/L^2 (\rho S_{11}^E)^{-1/2} \quad (11)$$

where ρ is density and S_{11}^E is elastic compliance. A metallic sheet (called a shim) is occasionally sandwiched between the two piezoelectric plates to increase the reliability, that is, the structure can be maintained even if the ceramics fracture. Using the bimorph structure, a large magnification of the displacement is easily obtainable. However, the disadvantages include a low response speed (1 kHz) and low generative force.

A composite actuator structure called moonie has been developed to amplify the small displacements induced in a piezoelectric ceramic. The moonie consists of a thin multilayer element and two metal plates with a narrow moon-shaped cavity bonded together. This device has intermediate characteristics between the conventional multilayer and bimorph actuators; this shows an order of magnitude larger displacement (100 μm) than the multilayer, and much larger generative force (100 N) with quicker response (100 μs) than the bimorph.

Some examples of applications of piezoelectric and electrostrictive actuators mentioned already are described next. The piezoelectric impact dot-matrix printer is the first mass-produced device using multilayer ceramic actuators. The advantage of the piezoelectric printer head compared to the conventional magnetic types are: low energy consumption, low heat generation, and fast printing speed. The longitudinal multilayer actuators do not exhibit a large displacement and thus a suitable displacement magnification mechanism is necessary. The displacement induced in a multilayer actuator pushes up the force point, and its displacement magnification is carried out through hinge levers so as to generate a large wire stroke. When the displacement in the piezoactuator is 8 μm , the wire stroke of 240 μm can be obtained, that is the magnification rate is 30 times.

Bimorph structures are commonly used for VCR head tracking actuators, because of their large displacements. An autotracking scan system uses the piezoelectric actuators so that the head follows the recording track even while driven at both still and quick modes. As can be anticipated, the bimorph drive is inevitably accompanied by

a torsional motion. To obtain a perfect parallel motion a special mechanism has to be employed. Piezoelectric bimorphs have also been used in phonograph pickup cartridges, and cantilever bimorphs with small masses attached to their free end can be used as accelerometers. Piezoelectric pumps for gas or liquid utilizing an alternating bending motion of bimorph have been developed for intravenous drip injection in hospitals and for medication dispensers in chemotherapy, chronic pain, and diabetes. Piezoelectric fans for cooling electronic circuits are made from a pair of bimorphs that are driven out of phase so as to blow effectively. Furthermore, piezobimorph-type camera shutters have been widely commercialized.

In optical control systems, lenses and mirrors require micropositioning and even the shapes of mirrors are adjusted to correct image distortions. For instance, a space qualified active mirror called articulating fold mirror utilizes six lead magnesium niobate (PMN) electrostrictive multilayer actuators to precisely position a mirror tip and tilt in order to correct the focusing aberration of the Hubble Space Telescope.

Piezoelectric actuators are also useful for vibration suppression systems of an automobile. An electronically controlled shock absorber was developed by Toyota. The piezoelectric sensors detecting road roughness is composed of 5 layers of 0.5 mm thick PZT disks. The actuator is made of 88 layers of 0.5 mm thick disks. Applying 500 V generates about 50 μm displacement, which is magnified by 40 times through a piston and plunger pin combination. This stroke pushes the change value of the damping force down, then opens the bypass oil route, leading to decrease in the flow resistance. This electronically controlled shock absorber has both controllability and comfortability simultaneously.

4.2.2. Ultrasonic Motors. An ultrasonic motor is an example of piezoelectric actuators using a resonant vibration. In ultrasonic motors linear motion is obtained from the elliptical vibration through frictional force. The motor basically consists of a high-frequency power supply, a vibrator, and a slider. The vibrator is composed of a piezoelectric driving component and an elastic vibrator part, and the slider is composed of an elastic moving part and a friction coat. The characteristics of the ultrasonic motors are low speed and high torque compared to the conventional electromagnetic motors with high speed and low torque [25,27].

The ultrasonic motors are classified into two types: a standing-wave type and a propagating-wave type. The standing wave is expressed by

$$V_s(x, t) = A \cos(kx) \cdot \cos(\omega t) \tag{12}$$

while the propagation wave is given by

$$\begin{aligned} V_p(x, t) &= A \cos(kx - \omega t) \\ &= A \cos(kx) \cdot \cos(\omega t) \\ &\quad + A \cos(kx - \pi/2) \cdot \cos(\omega t - \pi/2) \end{aligned} \tag{13}$$

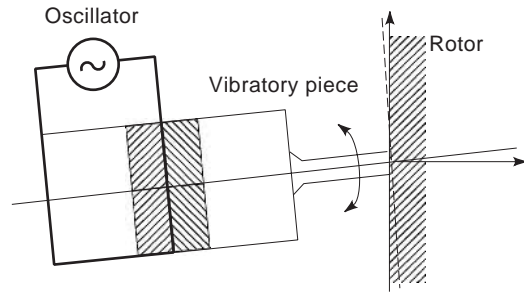


Figure 9. Vibratory coupler type ultrasonic motor. A vibratory piece is attached to a rotor or a slider with a slight cant angle.

A propagating wave can be generated by superimposing two standing waves whose phases differ by 90° to each other both in time and in space. The standing-wave type is sometimes known as a vibratory-coupler or a “woodpecker” type, where a vibratory piece is connected to a piezoelectric driver and the tip portion generates flat elliptic movement. Figure 9 shows a vibratory coupler type motor. A vibratory piece is attached to a rotor or a slider with a slight cant angle. The standing-wave type has high efficiency, up to 98% theoretical. However, a problem of this type is lack of control in both clockwise and counterclockwise directions. The principle of the propagation type is shown in Fig. 10. In the propagating-wave type, also called “surfing-type,” a surface particle of the elastic body draws an elliptic locus due to the coupling of longitudinal and transverse waves. This type generally requires two vibration sources to generate one propagating wave, leading to low efficiency (not more than 50%), but is controllable in both the rotational directions. An ultrasonic rotatory motor is successfully used in autofocusing cameras to produce precise rotational displacements. The advantages of this motor over the conventional electromagnetic motor are: silent drive (inaudible), thin motor design, and energy saving.

4.3. Resonators and Filters

When a piezoelectric body vibrates at its resonant frequency it absorbs considerably more energy than at other frequencies resulting in the fall of impedance. This phenomenon enables piezoelectric materials to be used as a

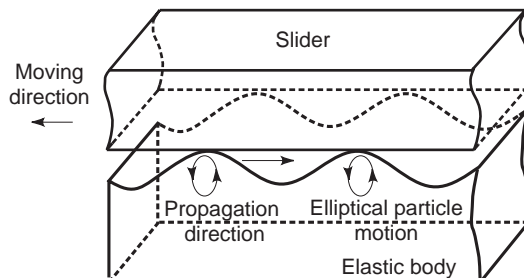


Figure 10. Principle of the propagating wave type ultrasonic motor. A surface particle of the elastic body draws an elliptic locus due to the coupling of longitudinal and transverse waves.

wave filter. A filter is required to pass a certain selected frequency band or to stop a given band. The bandwidth of a filter fabricated from a piezoelectric material is determined by the square of the coupling coefficient k , that is, nearly proportional to k^2 . Quartz crystals with very low k value of about 0.1 can pass very narrow frequency bands of approximate 1% of the center resonance frequency. On the other hand, PZT ceramics with a planar coupling coefficient of about 0.5 can easily pass a band of 10% of the center resonance frequency. The sharpness of the passband is dependent on the mechanical quality factor Q_m of the materials. Quartz has also a very high Q_m of about 10^6 which results in a sharp cutoff to the passband and well-defined frequency of the oscillator.

A simple resonator is a thin disk type, electroded on its plane faces and vibrating radially for applications in filters with a center frequency ranging from 200 kHz to 1 MHz and with a bandwidth of several percent of the center frequency. For a frequency of 455 kHz the disk diameter needs to be about 5.6 mm. However, if the required frequency is higher than 10 MHz, other modes of vibration such as the thickness extensional mode are exploited, because of its smaller-size disk. The trapped-energy type filters made from PZT ceramics have been widely used in the intermediate frequency range (at 10.7 MHz) for devices such as for FM radio receivers and transmitters. By employing the trapped-energy phenomena, the overtone frequencies are suppressed. The plate is partly covered with electrodes of a specific area and thickness. The fundamental frequency of the thickness mode beneath the electrode is less than that of the unelectroded portion, because of the extra inertia of the electrode mass. The longer wave characteristic of the electrode region cannot propagate in the unelectroded region. The higher-frequency overtones can propagate away into unelectroded region. This is known as trapped-energy principle. Figure 11 shows a schematic drawing of trapped-energy filter. In this structure the top electrode is split so that coupling between the two parts will only be efficient at resonance. More stable filters suitable for telecommunication systems have been made from single crystals such as quartz or LiTaO_3 .

4.4. SAW Devices

A surface acoustic wave (SAW; also called a Rayleigh wave) is composed of a coupling between longitudinal and shear waves in which the SAW energy is confined near the surface. An associated electrostatic wave exists

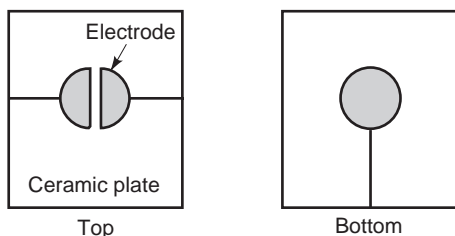


Figure 11. Trapped-energy-type filter. The top electrode is split so that coupling between two parts will be efficient only at resonance.

for a SAW on a piezoelectric substrate, which allows electroacoustic coupling via a transducer. The advantages of SAW technology are that the wave can be electroacoustically accessed and tapped at the substrate surface and its velocity is approximately 10^4 times slower than an electromagnetic wave. The SAW wavelength is on the same order of magnitude as line dimensions which can be photolithographically produced and the lengths for both short and long delays are achievable on a reasonable size substrates [28,29].

There are a very broad range of commercial system applications which include front-end and IF (intermediate frequency) filters, CATV (community antenna television) and VCR (video cassette recorder) components, synthesizers, analyzers, and navigators. In SAW transducers, finger electrodes provide the ability to sample or tap the wave and the electrode gap gives the relative delay. A SAW filter is composed of a minimum of two transducers. A schematic of a simple SAW bidirectional filter is shown in Fig. 12. A bidirectional transducer radiates energy equally from each side of the transducer. Energy that is not received is absorbed to eliminate spurious reflection.

Various materials are currently being used for SAW devices. The most popular single-crystal SAW materials are lithium niobate and lithium tantalate. The materials have different properties depending on the cut of the material and direction of propagation. The fundamental parameters considered when choosing a material for a given device applications are SAW velocity, temperature coefficients of delay (TCD), electromechanical coupling factor, and propagation loss. Surface acoustic waves can be generated and detected by spatially periodic, interdigital electrodes on the plane surface of a piezoelectric plate. A periodic electric field is produced when a radiofrequency (RF) source is connected to the electrode, thus permitting piezoelectric coupling to a traveling surface wave. If an RF source with a frequency f is applied to the electrode having periodicity d , energy conversion from an electrical to mechanical form will be maximum when

$$f = f_0 = V_s/d \tag{14}$$

V_s is the SAW velocity and f_0 is the center frequency of the device. SAW velocity is an important parameter determining the center frequency. Another important parameter for many applications is temperature sensitivity. For example, the temperature stability of the center frequency of

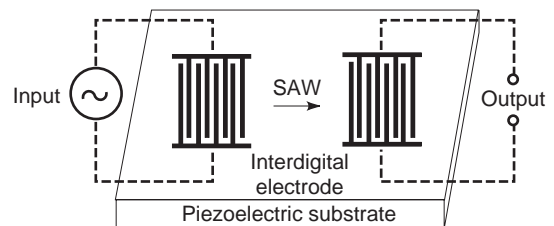


Figure 12. Typical SAW bidirectional filter consisting of two interdigital transducers. The input transducer generates surface acoustic waves in either direction and the output transducer converts the acoustic energy back to an electrical signal.

SAW bandpass filters is a direct function of temperature coefficient for the velocity and delay for the material used. The first-order temperature coefficient of delay is given by

$$(1/\tau) \cdot (d\tau/dT) = (1/L) \cdot (dL/dT) - (1/V_s) \cdot (dV_s/dT) \quad (15)$$

where $\tau = L/V_s$ is the delay time and L is the SAW propagation length. The surface wave coupling factor k_s^2 is defined in terms of the change in SAW velocity that occurs when the wave passes across a surface coated with a thin massless conductor, so that the piezoelectric field associated with the wave is effectively shorted-circuited. The coupling factor k_s^2 is expressed by

$$k_s^2 = 2(V_f - V_m)/V_f \quad (16)$$

where V_f is the free surface wave velocity and V_m is the velocity on the metallized surface. In actual SAW applications, the value of k_s^2 relates to the maximum bandwidth obtainable and the amount of signal loss between input and output, determining the fractional bandwidth versus minimum insertion loss for a given material and filter. Propagation loss is one of the major factors that determine the insertion loss of a device and is caused by wave scattering at crystalline defects and surface irregularities. Materials that show high electromechanical coupling factors combined with small temperature coefficients of delay are likely to be required. The free surface velocity V_0 of the material is a function of cut angle and propagation direction. The TCD is an indication of the frequency shift expected for a transducer due to a temperature change and is also a function of cut angle and propagation direction. The substrate is chosen based on the device design specifications and includes consideration of operating temperature, fractional bandwidth, and insertion loss.

Piezoelectric single crystals such as 128° -Y-X (128° -rotated-Y-cut and X-propagation)—LiNbO₃ and X- 112° -Y (X-cut and 112° -rotated-Y-propagation)—LiTaO₃ have been extensively employed as SAW substrates for applications in VIF (video intermediate frequency) filters. A *c*-axis-oriented ZnO thin film deposited on a fused quartz, glass, or sapphire substrate is also commercialized for SAW devices. Table 4 shows some important material parameters for some SAW materials.

Table 4. SAW Material Properties

	Material	Cut Propagation Direction	k^2 (%)	TCD (ppm/C)	V_0 (m/s)	ϵ_r
Single crystal	Quartz	ST-X	0.16	0	3158	4.5
	LiNbO ₃	128° -Y-X	5.5	-74	3960	35
	LiTaO ₃	X 112° -Y	0.75	-18	3290	42
	Li ₂ B ₄ O ₇	(110)-(001)	0.8	0	3467	9.5
Ceramic	PZT-In(Li _{3/5} W _{2/5})O ₃		1.0	10	2270	690
	(Pb,Nd)(Ti,Mn,In)O ₃		2.6	<1	2554	225
Thin film	ZnO/glass		0.64	-15	3150	8.5
	ZnO/Sapphire		1.0	-30	5000	8.5

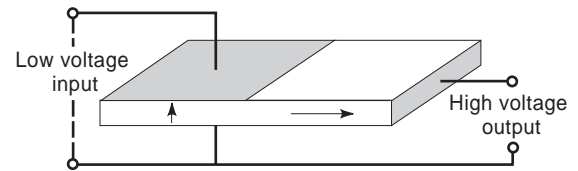


Figure 13. Fundamental Rosen-type structure of piezoelectric transformer. Two differently-poled parts coexist in one piezoelectric plate.

4.5. Delay Lines

A delay line can be formed from a slice of glass such as PbO- or K₂O-doped SiO₂ glass in which the velocity of sound is nearly independent of temperature. PZT ceramic transducers are soldered on two metallized edges of the slice of glass. The input transducer converts the electrical signal to a shear acoustic wave that travels through the slice. At the output transducer the wave is reconverted into an electrical signal delayed by the length of time taken to travel around the slice. Such delay lines are used in color TV sets to introduce a delay of approximately 64 μ s and are also employed in videotape recorders.

4.6. Piezoelectric Transformer

The transfer of vibration energy from one set of electrodes to another on a piezoelectric ceramic body can be used for voltage transformation. This device is called a piezoelectric transformer. Office automation equipment with liquid crystal displays have been successfully commercialized into such products as notebook type personal computers and car navigation systems. This equipment with a liquid crystal display requires a very thin, non-electromagnetic-noise transformer to start the glow of a fluorescent backlamp. This application has accelerated the development of piezoelectric transformers. Figure 13 shows a fundamental structure where two differently poled parts coexist in one piezoelectric plate. The plate has electrodes on half its major faces and on an edge, which is then poled in its thickness direction at one end and parallel to the long axis over most of its length. A low-voltage AC supply is applied to the large-area electrodes at a frequency that excites a length extensional mode resonance. A high-voltage output can then be taken from the small electrode and one of the larger electrodes. After the proposal by C. A. Rosen, piezoelectric transformers with several different structures

have been reported. A multilayer type transformer is proposed in order to increase the voltage rise ratio. The input part is of the multilayer structure with internal electrodes and the output electrodes are formed at the side surface of the rectangular plate. This transformer uses piezoelectric transverse mode for the input and output parts.

BIBLIOGRAPHY

1. B. Jaffe, W. Cook, and H. Jaffe, *Piezoelectric Ceramics*, Academic Press, London, 1971.
2. W. G. Cady, *Piezoelectricity*, McGraw-Hill, New York; rev. ed. by Dover Publications, 1964.
3. F. Jona and G. Shirane, *Ferroelectric Crystals*, Pergamon, London, 1962.
4. M. E. Lines and A. M. Glass, *Principles and Applications of Ferroelectric Materials*, Clarendon Press, Oxford, 1977.
5. *IEEE Standard on Piezoelectricity*, IEEE, New York, Inc., 1978.
6. Landold and Boernstein, *Numerical Data and Functional Relationships in Science and Technology: Crystal and Solid State Physics*, Vol. 11, Springer-Verlag, Berlin, 1979.
7. W. A. Smith, *Proc. SPIE Int. Symp.* **1733**:3–26 (1992).
8. H. Takeuchi et al., *J. Acoust. Soc. Am.* **7**:1114–1120 (1982).
9. Y. Yamashita et al., *Jpn. J. Appl. Phys.* **20**(Suppl. 20-4):183 (1981).
10. Y. Ito et al., *Appl. Phys. Lett.* **35**:595–597 (1979).
11. R. E. Newnham, D. P. Skinner, and L. E. Cross, *Mater. Res. Bull.* **13**:525 (1978).
12. W. A. Smith, *Proc. 1989 IEEE Ultrasonic Symp.*, 1989, p. 755.
13. H. Takeuchi et al., *Proc. IEEE 1990 Ultrasonic Symp.*, 1990, p. 697.
14. T. R. Shrout et al., *Ferroelectric Lett.* **12**:63 (1990).
15. J. Kuwata, K. Uchino, and S. Nomura, *Jpn. J. Appl. Phys.* **21**:1298 (1982).
16. S.-E. Park and T. R. Shout, Ultrahigh strain and piezoelectric behavior in relaxor based ferroelectric single crystals. *J. Appl. Phys.* **82**:1804–1811 (1997).
17. B. A. Auld, *Acoustic Fields and Waves in Solids*, 2nd ed., Krieger, Melbourne, 1990.
18. G. S. Kino, *Acoustic Waves: Device Imaging and Analog Signal Processing*, Prentice-Hall, Engelwood Cliffs, NJ, 1987.
19. C. S. Desilets, J. D. Fraser, and G. S. Kino, *IEEE Trans. Sonics Ultrason.*, **SU-25**:115 (1978).
20. T. R. Gururaja, *Am. Ceram. Soc. Bull.* **73**:50 (1994).
21. F. S. Foster, L. K. Ryan, and D. H. Turnbull, *IEEE Trans. Ultrason. Ferroelectr. Freq. Control* **38**:446 (1991).
22. Y. Ito et al., *IEEE Trans. Ultrason. Ferroelectr. Freq. Control* **42**:316 (1995).
23. D. F. McCammon and W. Thompson, Jr., The design of Tonpilz piezoelectric transducers using nonlinear goal programming, *J. Acoust. Soc. Am.* **68**:754–757 (1980).
24. K. D. Rolt, History of the flexensional electroacoustic transducer. *J. Acoust. Soc. Am.* **87**:1340–1349 (1990).
25. K. Uchino, *Piezoelectric Actuators and Ultrasonic Motors*, Kluwer, Boston, 1997.
26. L. E. Cross et al., *Ferroelectrics* **23**:187 (1980).
27. S. Ueha and Y. Tomikawa, *Ultrasonic Motors*, Clarendon Press, Oxford, 1993.
28. C. Campbell, *Surface Acoustic Wave Devices and Their Signal Processing Applications*, Academic Press, San Diego, 1989.
29. H. Matthews, *Surface Wave Filters*, Wiley-Interscience, New York, 1977.

PIN DIODES

ALY E. FATHY

University of Tennessee
Knoxville, Tennessee

ARYE ROSEN

Drexel University
Philadelphia, Pennsylvania

A PIN diode is a semiconductor device that operates at RF and microwave frequencies as a variable resistor in the forward direction. The resistance value of the PIN diode can be varied over a range of approximately 1 Ω –100 K Ω through the use of a DC or low-frequency control current. A unique feature of the PIN diode is its ability to control large amounts of RF power with relatively much lower DC levels.

The PIN diode is useful for leveling, limiting, and amplitude modulating an RF signal, when the control current is varied continuously. However, the device can be used for pulse modulating, attenuating, switching, and phase shifting of an RF signal if the control current is turned ON or OFF, or in discrete steps. In addition, the PIN's small size, weight, high switching speed, and minimized parasitic elements make it ideally suited for miniature, broadband RF signal applications.

1. PIN-DIODE MODEL

A PIN diode is a PN junction with a doping profile tailored so that an intrinsic layer I is sandwiched between the P region and the N region [1]. A model of a PIN diode chip is shown in Fig. 1. The chip is prepared with a wafer of almost pure intrinsic silicon, with high resistivity and long lifetime. A P region is then diffused into one diode surface and an N region is diffused into the other surface. Both regions are heavily doped, so we will call them P⁺ and N⁺, to indicate the heavy doping. The resulting intrinsic or I region of width W is sandwiched between P⁺- and N⁺-type regions. The width of the I-region is a function of the original thickness of the wafer, and its area A depends on how many small sections are defined across the wafer.

When a PIN diode is forward-biased, holes and electrons are injected from the P and N regions into the high-resistivity I region. These charges do not immediately recombine, and the average recombination time is called the *carrier lifetime* τ . Both τ and W in large part determine approximately the low-frequency limit of useful applications. The lifetime of PIN diode is determined by the design and is based on the required switching speed and is typically in the range of 5 ns to over 100 μ s [2,3].

The conductance of the diode is proportional to the stored charge, and the charge, in turn, is related to the

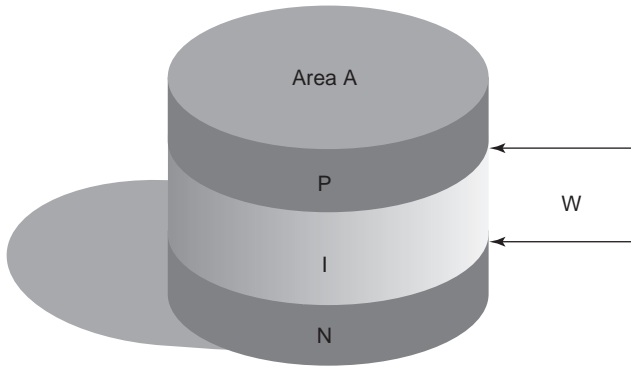


Figure 1. PIN-diode chip outline.

diode forward bias current I_F as follows [4,5]:

$$I_F = \frac{dQ}{dt} + \frac{Q}{\tau}$$

If the diode is biased only with a constant current, that is, in steady state, then the stored charge is constant and is equal to $Q = I_F \tau$. However, if the bias consists of both a constant current and a low-frequency RF, specifically, a time-varying signal, then the charge will be modulated, and the degree of modulation will depend on the AC and DC signal levels and frequency of operation as given by [4]

$$Q(\omega) = \frac{I_F \tau}{1 + j\omega\tau}$$

where ω is $2\pi f$ and f is the operating frequency. This charge frequency dependence is plotted in Fig. 2, and illustrates the fact that if the signal frequency is less than $f_c = 1/2\pi\tau$, then the signal modulation cannot be neglected; however, beyond that the modulation effect should decrease by about 6 dB/octave, and eventually disappears. In other words, at frequencies well below f_c , the PIN diode behaves as an ordinary PN junction diode, while in the vicinity of f_c , the diode will start to behave as a linear resistor with a small nonlinear component, and the signal will suffer from a measure of distortion. But, at frequencies beyond f_c , the diode appears essentially as a pure resistance controlled by a DC or a low-frequency control signal.

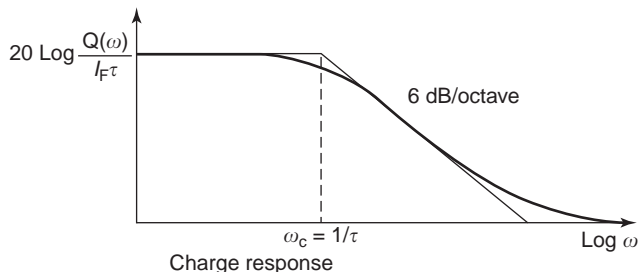


Figure 2. PIN diode charge response as function of frequency. (After [4].)

2. DETAILED PIN DIODE STRUCTURE

The ideal PIN structure will have a high-resistivity undoped I region. In practice, no silicon material is without impurities. A PIN diode consists of an extremely high-resistivity P or N region between low-resistivity highly doped P and N regions at its boundaries. For nomenclature, we will use the following notation: for heavily doped P and N materials we will use P^+ and N^+ , but for high-resistivity P and N material we will use the Greek notation π -type and ν -type, for P and N, respectively. Figure 3 shows a P^+ , ν , N^+ diode structure; the few impurity atoms of the I region will be ionized (assuming high-resistivity I layer), and the depletion region will extend through the P^+ and N^+ regions. For all practical purposes, the small penetration of the depletion region in the P^+ and N^+ regions can be neglected and the width of the depletion region will essentially be constant, equal to the I-region width, W_I . The same is true if the device is P^+ , π , N^+ ; however, the former structure is the most commonly manufactured one.

3. PUNCHTHROUGH VOLTAGE

Thus far, we have assumed that the I region has a very high resistivity, and that the depletion region extends to the P^+ and N^+ interfaces, even with no applied bias. Under these circumstances, the width of the I layer is almost constant and C_j is practically independent of the applied voltage. In other words, at zero voltage the depletion region has already extended through the I region. This type of device is called a *zero-punchthrough diode*, as the depletion region has punched through to the high-conductivity region even before bias was applied.

This is again, an ideal situation, the practical PIN diode with ionized impurity profiles is as shown in Fig. 4. At zero bias, a large portion, but not necessarily all, of the I region is depleted, and the width of the depletion region $W(0)$ is most likely less than the I-region width W . Applying a reverse bias, the depletion region spreads further, until it reaches the N^+ region (as shown in Fig. 4), and is called the *punchthrough voltage* V_{PT} .

The reverse bias potential required for punchthrough is given by [4,5]

$$V_{PT} = \frac{eN_D W^2}{2\epsilon_r \epsilon_0}$$

where N_D is the impurity concentration in the ν region. Obviously, if N_D equals zero (ideal case), then V_{PT} is zero.

V_{PT} can be used to measure the resistivity of the I region. Where the resistivity is related to the donor impurity as given by

$$\rho = \frac{1}{N_D e \mu_N}$$

where μ_N is the electron mobility, and combining the preceding two equations will result in the following expres-

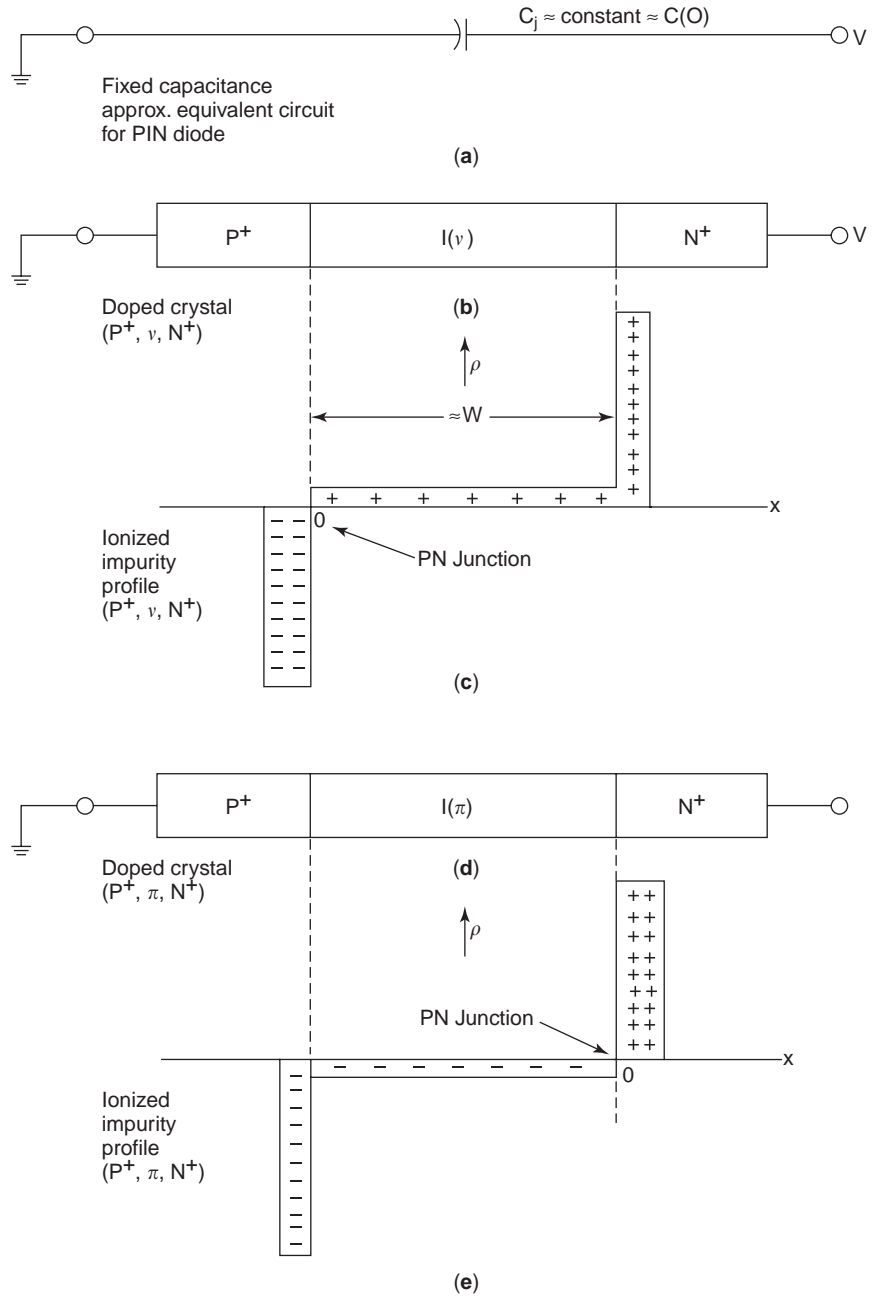


Figure 3. Profiles for the ν and π PIN types diodes. (After [4].)

sion that can be used to accurately estimate ρ [4,5]:

$$\rho = \frac{W^2}{2V_{PT}\epsilon_0\epsilon_r\mu_N} = \frac{(2.4 \times 10^8)W^2}{V_{PT}} (\Omega \cdot \text{cm})$$

where W unit is cm.

Example 1. A particular silicon diode has an I-region width of 0.0025 cm, and is found to have punchthrough voltage of 5 V. Evaluate its resistivity:

$$\rho = \frac{(2.4 \times 10^8)W^2}{V_{PT}} = \frac{(2.4 \times 10^8)(0.0025)^2}{5} = 300 \Omega \cdot \text{cm}$$

4. LOW-FREQUENCY EQUIVALENT-CIRCUIT MODEL

The equivalent circuit of a PIN diode depends on the operating frequency. At frequencies much lower than f_c , the equivalent circuit of just below the punchthrough case, is as shown in Fig. 5a, and the portions of the P^+ and the I regions, which were partially depleted, are represented by a depletion, or “swept”, region. While the remainder of the I region is unswept, and its overall characteristics are very similar to those of a normal PN junction diode.

At low frequencies (say, < 1 MHz), most of the current goes through the unswept capacitance C_{US} , while at higher frequencies (e.g., > 1 GHz), the current almost bypass it. And for all practical purposes, the total capacitance can

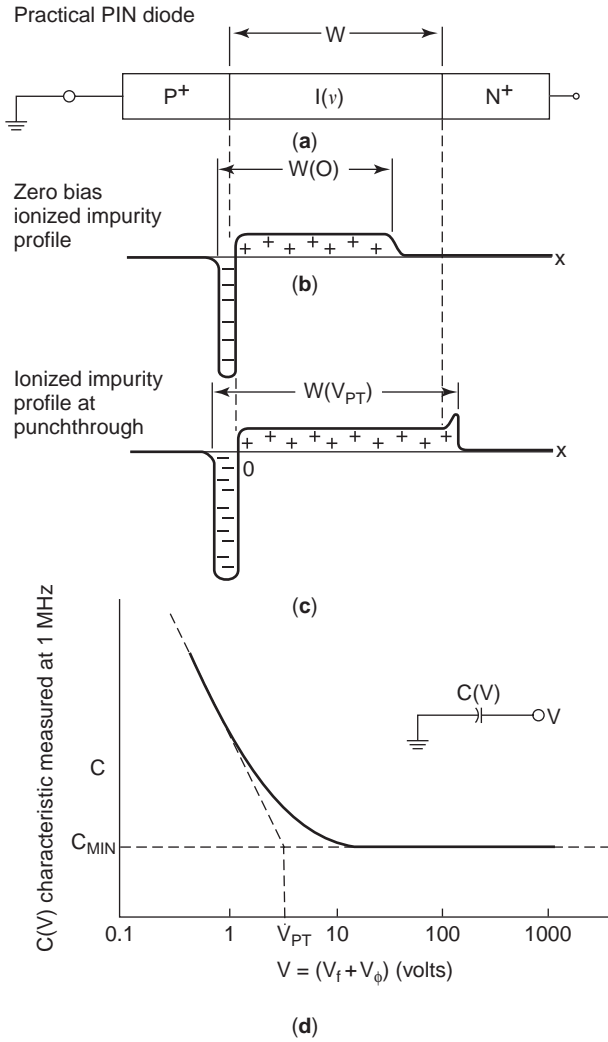


Figure 4. Practical PIN and reversed punchthrough characteristics. (After [4].)

be represented by the series combination of C_{SW} and C_{US} , which is approximately equal to C_j ; the full capacitance of the I region. To identify high and low frequencies, we define a frequency called the dielectric relaxation frequency f_R , given by [4,5]:

$$f_R = \frac{1}{2\pi R_{US} C_{US}}$$

where $R_{US} = \rho L/A$ and $C_{US} = \epsilon_0 \epsilon_r A/L$, where L is the width of the unswept region and A is its cross sectional area. Therefore

$$f_R = \frac{1}{2\pi \epsilon_0 \epsilon_r \rho} = \frac{153}{\rho(\Omega \cdot \text{cm})} \text{ GHz}$$

Usually an I layer has a resistivity of at least $100 \Omega \cdot \text{cm}$. A rule of thumb, is that for frequencies beyond $3f_R$ (also $> 10f_c$), the diode can be assumed to be a constant capacitance, that is, having constant depletion width W . Hence,

if we assume a $100 \Omega \cdot \text{cm}$ I layer, then for frequencies beyond 4.59 GHz, we need to use the microwave circuit model.

5. MICROWAVE EQUIVALENT CIRCUIT

The microwave equivalent circuit for the unpackaged PIN diode chip is shown in Fig. 6. In most applications the PIN diode is used as a switch; therefore, it is a better open circuit, for a lesser capacitance in the reverse-bias state. Also, the diode will have a better short circuit, for lower forward resistance, where decreasing R_F and R_R will lower the device insertion loss in the ON state. A figure of merit is generally used to relate to the PIN switching effectiveness. This is the switching cutoff frequency f_{CS} , expressed as follows:

$$f_{CS} = \frac{1}{2\pi c_J \sqrt{R_R R_F}}$$

In principle, the values of R_F and R_R can be evaluated and f_{CS} can be specified. The term *switching cutoff* is not intended to imply that a particular device can be used for designing a switching circuit at frequencies as high as f_{CS} . But it gives an upper limit as PIN diodes are typically used in a frequency range around $\frac{1}{100}$ th– $\frac{1}{50}$ th of f_{CS} . Meanwhile, in switching and phase shifting applications, the overall losses are proportional to the ratio of switching cutoff frequency to the operating frequency.

A more general representation of figure of merit for two impedance state switching devices has been proposed by Kurokawa and Schlosser [6], and the figure of merit is written as

$$Q = \frac{\sqrt{(r_1 - r_2)^2 + (x_1 - x_2)^2}}{\sqrt{r_1 r_2}}$$

where the impedances of the two states are $z_1 = r_1 + jx_1 = R_F$, and $z_2 = r_2 + jx_2 = R_R + 1/j\omega C_j$. Hence

$$Q = \frac{\sqrt{(R_F - R_R)^2 + (1/\omega C_j)^2}}{\sqrt{R_F R_R}} \approx \frac{1}{2\pi f C_j \sqrt{R_F R_R}}$$

when $|R_F - R_R| \ll 1/\omega C_j$, then this above expression can be simplified as

$$Q \approx f_{CS}/f$$

where f_{CS} is the switching cutoff frequency. Typical Q values are in the range of 100–200, and for f_{CS} are in the range of 350–800 GHz, respectively.

6. EVALUATION OF R_F

To determine the microwave properties of a diode when forward-biased, let us calculate the conductivity and

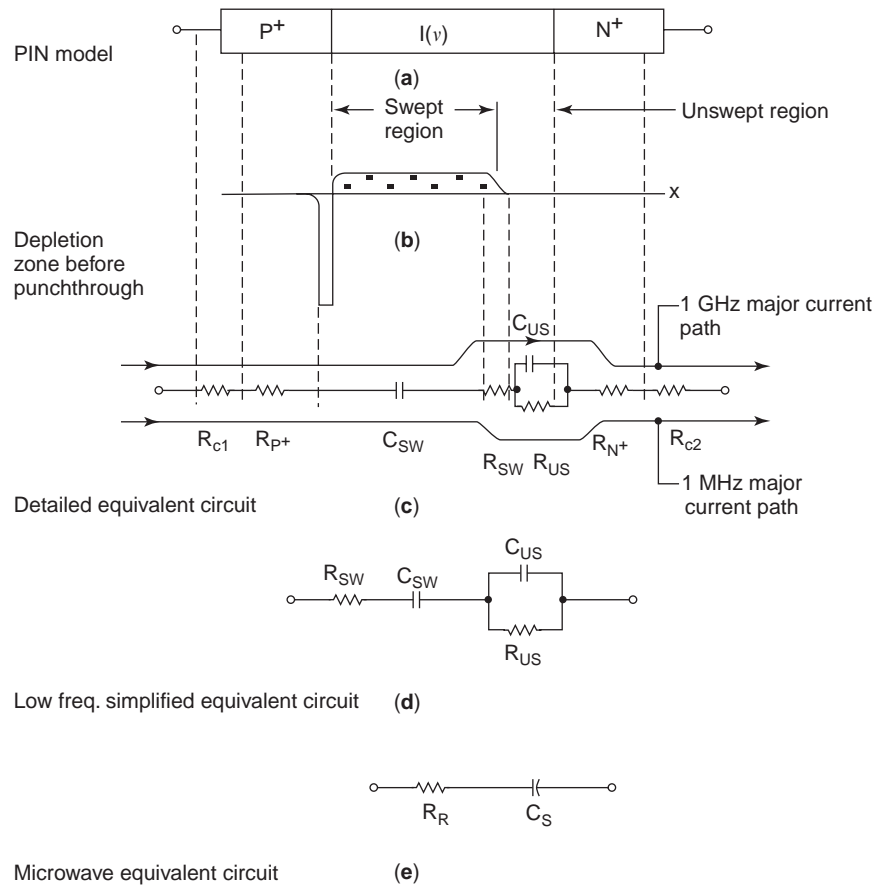


Figure 5. Reverse-bias PIN equivalent circuit: (a) PIN model; (b) depletion region before punchthrough; (c) detailed equivalent circuit; (d) equivalent circuit at low frequencies; (e) microwave equivalent circuit R_{C1} = contact resistance at left; R_{C2} = contact resistance at right; R_{P+} = semiconductor resistance of P⁺ region; R_{N+} = semiconductor resistance at N⁺ region; C_{SW} = capacitance of swept region; R_{US} = capacitance of the unswept region, R_{US} resistance of the unswept region; C_j junction capacitance = $C_{SW} + C_{US}$, $R_R = R_{C1} + R_{C2} + R_{P+} + R_{N+}$. (After [4].)

resistance of the I region under a forward-bias condition. We will first assume that the I region as a whole is electrically neutral (the injected carriers; $n=p$), and that the bias current injects both types of carrier, which recombine with one another in the I region after “long lifetime.” We will assume also that the average lifetime of these carriers before combining is sufficiently long to allow both the holes and the electrons to be uniformly distributed within the I-region.

Then, the conductivity of the I region is related to the ratio of the current density to the applied field strength $\sigma = J/E$, where J is the directed average rate of flow of electric charge. Hence the current J can be expressed as the sum of the current due to the two carriers in the I region and is given by

$$J = (ev_p p + ev_n n)E$$

where v_p and v_n are the average directed velocities of the n and p carriers, respectively, and where e , the magnitude of electron’s charge, is 1.6×10^{-19} C, and (p,n) are the respective injected hole and electron densities in the I region. Thus, the conductivity in terms of the mobility μ , which is defined as the average carrier velocity per unit of

applied electric field, and is given by

$$\sigma = e(\mu_p p + \mu_n n)$$

Hence, for a diode with thickness W and cross-sectional area A , its I-region resistance R_I is given by

$$R_I = \frac{W}{\sigma A} = \frac{W}{eA(\mu_p p + \mu_n n)}$$

Now, under the assumption of $n = p$, and $\tau_p = \tau_n$, the diode I region resistance is

$$R_I = \frac{W}{2eA\mu_{AP}p}$$

where $2\mu_{AP} = (\mu_p + \mu_n)$ is the ambipolar mobility [4], and is defined as the effective average of the hole and electron mobilities ($610 \text{ cm}^2/\text{V} \cdot \text{s}$ in silicon). But the stored charge, if the diode is injected, with fixed (i.e., constant) current is given by

$$Q_p = I_F \tau_p = I_F \tau = epAW$$

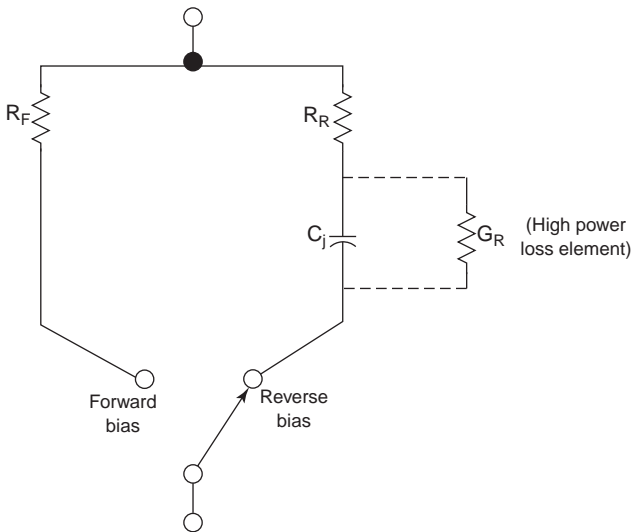


Figure 6. PIN diode chip equivalent circuit (C_j = reverse bias junction capacitance; R_F = forward-bias resistance; R_R = sum of semiconductor P^+ and N^+ resistances, and any contact resistance, i.e., $R_{C1} + R_{C2} + R_{P^+} + R_{N^+}$).

Then, the I-region resistance is [4]

$$R_I = \frac{W^2}{2\mu_{AP}\tau I_F}$$

Example 2. Find R_I for a silicon diode that has an I-region width of $W = 100 \mu\text{m}$, and a $4 \mu\text{s}$ τ lifetime that is injected by $I_F = 100 \text{ mA}$ in the forward bias.

Solution:

$$R_I = \frac{(100 \times 10^{-4})^2 \text{cm}^2}{\left(2 \times 610 \frac{\text{cm}^2}{\text{V} \cdot \text{s}}\right) \cdot (4 \times 10^{-6} \text{ s}) \cdot (100 \cdot 10^{-3} \text{ A})} = 0.21 \Omega$$

It is important to recognize that R_I does not depend on the cross-sectional area A , and is inversely proportional to the bias current I_F .

7. PRACTICAL RF RESISTANCE

The resistance R_I , which practically can be expressed by $R_I = K/I_F^x$ [7], governs the diode ON characteristics at RF frequencies, where R_I is the effective high-frequency resistance and I_F is the DC bias current in mA. The dependence of R_I on DC is similar in form to the dependence of the previously defined R_I on I_F in the low-frequency equivalent circuit; however, the constant K and the exponent x are different. Due to a variety of mechanisms that exist in the diode at RF frequencies, both K and x must be deter-

mined empirically. For a specific diode design, the exponent x is usually constant, very close to 1. Meanwhile, the constant K is highly dependent on the fabrication and process control, and its value can vary by as much as 3–1 from diode to diode. Fortunately, for switching or pulse operation, the variation of R_I between diodes at a given bias point is not significant since the diode is usually switched between a very high value and a very low value of resistance by the control current. For analog applications such as attenuating and modulating, the variation of R_I from unit to unit this could be troublesome.

8. R_R AND C_j REVERSE-BIASED CIRCUIT MODEL

At microwave frequencies, and under reverse bias, the I region is depleted of carriers and the PIN appears as an essentially constant capacitance to a microwave signal. Either series or parallel resistance can account for the presence of dissipative losses in the equivalent circuit (see Fig. 6). In a high-quality PIN diode, the I region has extremely high resistance, and most of the dissipation under RF occurs in the ohmic contacts (R_{C1} , R_{C2}), and in the resistance of P^+ and N^+ regions. Hence, a fixed resistance R_R is used to represent the overall losses.

Meanwhile, the I region is represented by a junction capacitance C_j , which is expressed approximately by the following simple parallel-plate capacitance formula

$$C_j \approx \frac{\epsilon_0 \epsilon_r \pi D^2}{4W}$$

where $\epsilon_0 = 8.85 \times 10^{-14} \text{ F/cm}$ is free-space permittivity, $\epsilon_r = 11.8$ equals the relative dielectric constant for silicon, D is the junction diameter, and W is the I region thickness.

9. EQUIVALENT CIRCUITS OF PACKAGED PIN DIODES

Packages typically introduce additional reactive elements in the form of package inductance L_p and package capacitance C_p . These elements are shown in Fig. 7.

Examples of these available packages, are given in Fig. 8, which shows typical HP PIN-diode packages, with package HP OUTLINE 15 having $L_p = 2.5 \text{ nH}$ and a C_p of 0.10 pF .

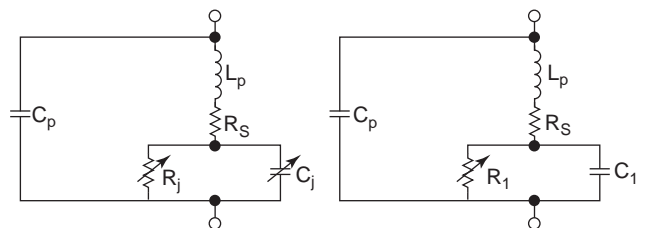
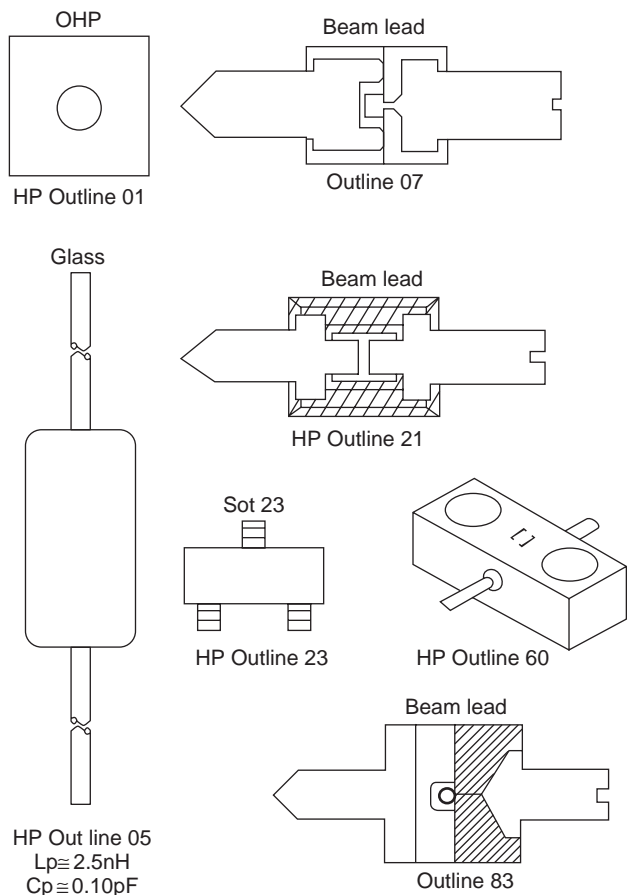


Figure 7. Equivalent circuits of PIN diodes: (a) low frequency; (b) high frequency.



Package outlines

Figure 8. Examples of HP various PIN packages.

10. PIN-DIODE APPLICATIONS

10.1. Design of Reflective SPST Switches

10.1.1. Ideal Case. The PIN diode is ideally suited for use in attenuating or switching of RF signals. In an ideal

case, when the diode is connected in series as shown in Fig. 9a, the attenuation will increase by increasing the RF resistance, which is controlled by the DC bias current. The opposite is true if the diode is connected in shunt as shown in Fig. 9b.

For switching applications, the bias will change abruptly between two states, high and low values. When the diode is ON and connected in series configuration, it should pass the RF signal with minimal loss, and when it's OFF it should isolate the RF signal from the load, by highly attenuating the RF signal.

Ideally the diode is assumed to be purely resistive at RF, and the attenuation for each circuit is given as

$$\alpha_{(series)} = 20 \log \left(1 + \frac{R_1}{2Z_0} \right)$$

$$\alpha_{(shunt)} = 20 \log \left(1 + \frac{Z_0}{2R_1} \right)$$

where $R_S = R_L = Z_0$ generator and load resistance respectively, and R_1 is the diode forward resistance at the specified DC bias current (i.e., $R_1 = R_F$).

In this ideal case, the attenuation does not depend on frequency and is a function of the ratio of the circuit characteristic impedance Z_0 and the diode resistance R_1 . The power dissipation in these types of switches is due partially to absorption, and partially to reflection, and they are classified as reflective switches.

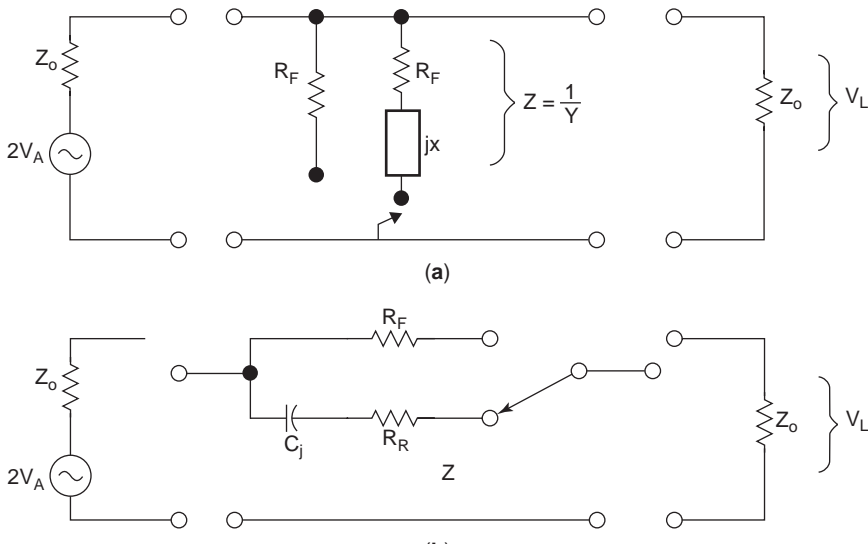


Figure 9. The diode is connected in shunt (a) and series (b), where the source and load impedances are equal to Z_0 .

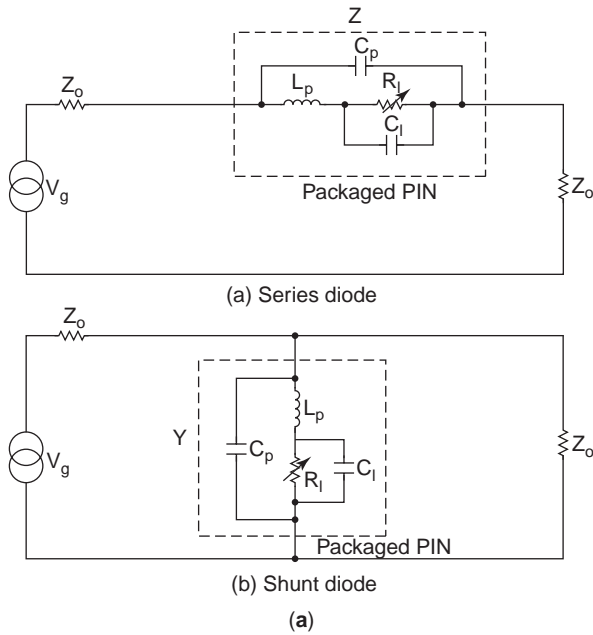


Figure 10. Packaged diodes used as reflective attenuators or switches.

switch in both series and shunt cases is

$$\alpha_{(\text{series})} = 20 \log(|1 + ZY_0/2|)$$

$$= 20 \log \left| 1 + RY_0 + \frac{(RY_0)^2}{4} + \frac{(XY_0)^2}{4} \right|$$

$$\alpha_{(\text{shunt})} = 20 \log(|1 + Z_0Y/2|)$$

$$= 20 \log \left| 1 + GZ_0 + \frac{(GZ_0)^2}{4} + \frac{(BZ_0)^2}{4} \right|$$

where the real device model is presented either by its impedance $(Z = R + jX)$ when connected in series, or by its admittance Y when connected in shunt where $(Y = G + jB)$.

In this practical case, it is obvious that the losses will be a function of frequency, and it is expected that the parasitic elements will degrade the performance quite significantly, and limit their operation at relatively higher frequency. However, some packages can be tailored to a

certain extent to extend the operating frequency range of these switches.

10.2. Design of Resonant SPST Switches

A packaged diode performance can be improved at high frequency by adding external reactance(s) to tune out the parasitic elements. These switches, called *resonant switches*, generally will be limited to <10% bandwidth. Where changing the state of the switch will be used to change the circuit topology from series resonance to parallel resonance. For example, when the switch is ON, it will have pure resistance (series resonance), and when the switch is OFF, it will have high resistance (parallel resonance).

For example, the circuit in Fig. 11a represents a diode connected in shunt. We externally add a shunt capacitance C_1 and a series inductance L_1 . When the diode is ON, it represents a pure resistance at microwave frequency, and L_1 and C_1 are adjusted to have parallel resonance based on L_1 and C_1 , and the points between A and B appear as high impedance. Meanwhile, when the diode is in the OFF state, it will present a capacitance C_j , and it will resonate with the inductance L_2 , and then at points A and B appear to have series resonance [8]. In both cases, if $L_1 = L_2$, then the resonant frequency is

$$f_0 \cong \frac{1}{2\pi\sqrt{L_1C_1}}$$

while in the ON state, there will be another series resonant frequency due to L_2 and C_1 , which will occur at about f_2 —that is, by appropriate design, it will be located approximately at $1.4f_0$.

11. MEASURING DIODE LIFETIME

A conventional method for measuring PIN-diode lifetime τ consists of injecting a known amount of charge Q_0 , into the I region and measuring the time τ_s required to extract it using a constant reverse-bias current. Figure 12 shows the equivalent circuit and charge–time profile. We first provide a forward-bias current I_F to flow for a long period of time (much longer than the expected lifetime) to store a charge Q_0 , which is given by $Q_0 = I_F\tau$. We then turn ON the switch S to provide a reverse current I_R , where the diode current I_D reverses direction and reaches a magnitude

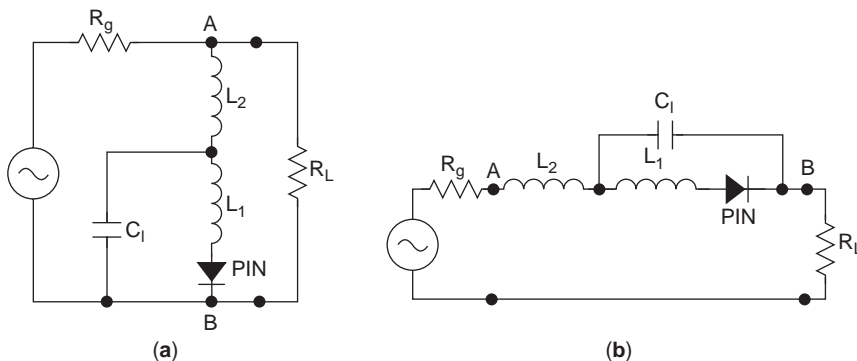


Figure 11. Resonant PIN switches realized by adding external parasitics L_1 , L_2 , and C_1 (After Ref. 8.)

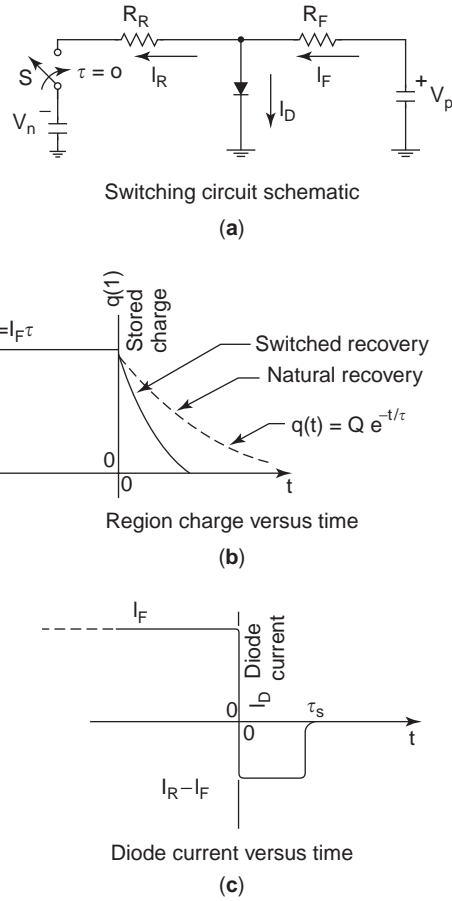


Figure 12. Evaluation of carrier lifetime (After [4].)

$(I_R - I_F)$, where $I_R > I_F$, by proper design of the circuit configuration. Due to the negative current, the stored energy Q_0 will be removed until it is completely depleted. Assuming that the discharge time τ_s is short compared to the lifetime ($\tau_s \ll \tau$), then the total charge time τ_s will be given by $Q_0 = I_F \cdot \tau = (I_R - I_F) \tau_s$, and the lifetime τ , will be found from [4,5]

$$\tau \approx \tau_s \left(\frac{I_R}{I_F} - 1 \right)$$

where $\tau_s \ll \tau$. Typical PIN diode lifetime may range from 0.1 to 100 μ s, which would require very fast switching speeds to satisfy the requirements that τ_s be small. In practice τ_s should be $\frac{1}{10}$ th of τ at most, which can be easily achieved with today's technology. It is imperative, however, that the experiment described above be repeated for different circuit settings to change the value of I_R and evaluate τ independent of τ_s .

12. PIN-DIODE POWER LIMITS

The maximum RF signal that a PIN diode can handle is limited by either the diode's breakdown voltage or its power dissipation capability. In most cases, power dissipation

capability sets limits on RF power-handling capability.

PIN diodes are usually operated in a reflective mode, and the amount of signal power that can be handled by a PIN diode in a circuit is usually much larger than the actual power dissipated in the diode. The ratio of the power dissipated in the diode to the incident power depends on the impedance of the diode relative to the circuit impedance, the number of diodes, and their relative interspacing.

Under forward bias, a PIN diode chip has an RF resistance of 1 Ω or less. Failure of the diode in this state will occur if the dissipative heating ($I^2 R_F$) is sufficient to cause the diode temperature to rise sufficiently to introduce metallurgical changes, and for silicon, as an example, it is about 1000°C. However, metal contacts at the silicon boundaries introduce failure mechanisms in the vicinity of 300–400°C.

Failure of a diode does not occur instantaneously when an overstress is applied unless the resulting temperature significantly exceeds 300°C. However, a mean lifetime can be expressed empirically based on the operating temperature and how close it is to the burnout temperature [4].

Since power handling can be many times greater than the power dissipated in the diode, the latter should be minimized and carefully controlled in high-power applications. The maximum power that a PIN diode can dissipate is given by [8,9]

$$P_{max} = \frac{T_{j(max)} - T_A}{\theta_{jc} + \theta_{jA}}$$

where

- $T_{j(max)}$ = maximum operating diode junction temperature
- T_A = ambient temperature
- θ_{jc} = thermal resistance—junction to case
- θ_{jA} = thermal resistance—case to ambient

The junction to diode is dictated by diode and package manufacture design, while the case to ambient is determined by how well the diode is thermally mounted. For a given diode, the maximum power dissipation limit can be obtained from its datasheet from the absolute maximum ratings. Designers can use a chart based on diode resistance to calculate a multiplier factor to evaluate the maximum power-handling capability of that device. For example, if the diode ON resistance is 1 Ω , and it is used in a series configuration, then the multiplying factor is 80 (as seen in Fig. 13), and if the maximum dissipated power is 1 W, then the RF power handling capability can be up to 80 W.

However, if the PIN operation is limited by reverse voltage breakdown, then we need to check the circuit performance under high voltage as shown below

$$P_A(max) = \frac{(V_{BR} - V_{bias})^2}{400} \text{ (Watts)}$$

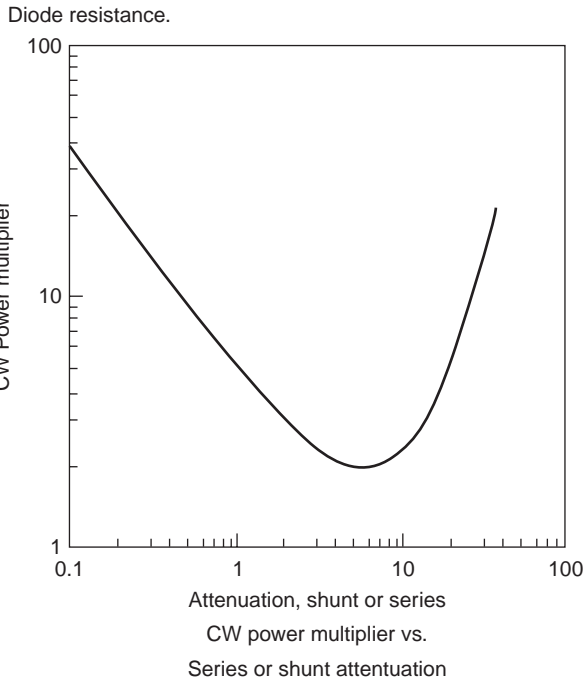
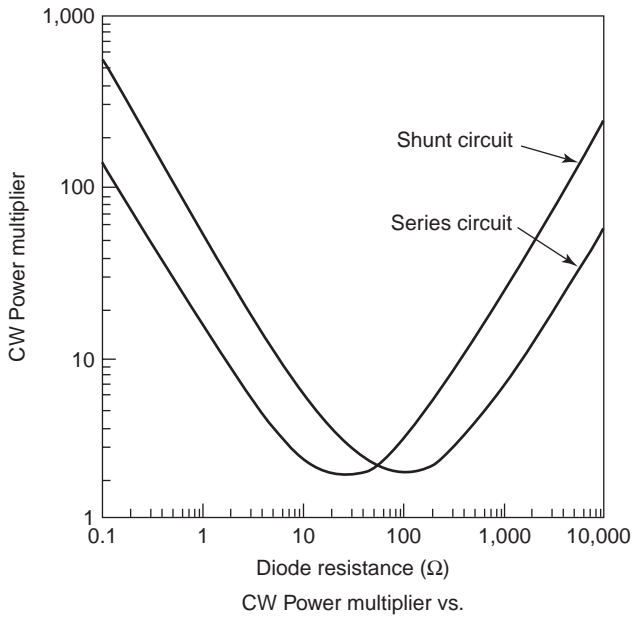


Figure 13. (a) Continuous-wave (CW) power multiplier versus diode resistance; CW multiplier versus series or shunt attenuation. (After Ref. 8.)

and for shunt circuit this is the same as

$$P_A(\text{max}) = \frac{(V_{BR} - T_{\text{bias}})^2}{100} \text{ (Watts)}$$

where V_{BR} is breakdown voltage and P_A can be optimized when we utilize devices with zero turn on voltages. However, in general, the maximum field E_{max} in Si at lower dopings is about 2.5×10^5 V/cm, which corresponds to a

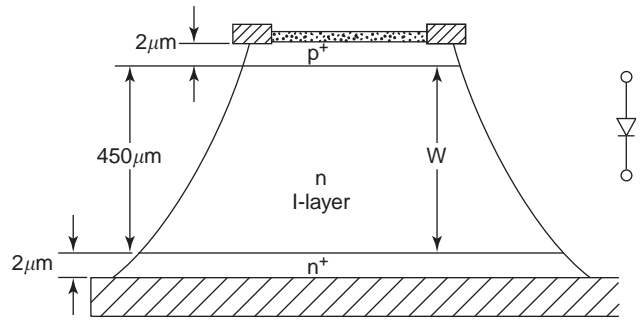


Figure 14. Vertical PIN diode structure.

breakdown voltage of [1]

$$V_{BR} \approx E_{\text{max}}W \approx 25W(\text{Volt})$$

where W is in micrometers.

13. DEVICE FABRICATION

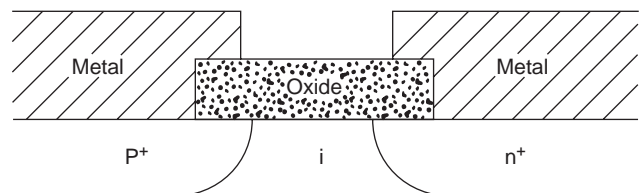
There are two distinct structures for PIN diodes, vertical or lateral (see Figs. 14, 15). There are various methods for diode fabrication. In the following, we will describe only two typical processes used in Si PIN fabrication: chemical vapor deposition (CVD) and ion implantation.

13.1. CVD Process

The PIN diodes are fabricated from v -type high-resistivity, (111)-oriented silicon crystal wafers with resistivity in the range of 1500–5000 $\Omega \cdot \text{cm}$ [10]. The wafer thickness is about 450 μm . Boron and phosphorus are diffused into opposite surfaces of the wafer from doped oxide layers. Diffusion depths of 1–2 μm for the $P^+ - v$ junction and 1–2 μm for the $N^+ - v$ junction are carefully permitted through extensive measurement testings.

Then a bimetal chrome–gold coating is sputter-deposited onto the silicon contact surfaces, followed by a gold plating 10 μm thick. A photoresist pattern of dots is then formed on the gold surface covering the N^+ layer, and the exposed gold is etched down to the chrome layer. The gold dots act as a mask layer, and the exposed chrome layer is removed by an aqueous etchant. Finally, the silicon surface is passivated with SiO_2 , Si_3N_4 by the sputtering technique, followed by a cured resin coating [10].

A cross section of PIN-diode structure is shown in Fig. 15, and the PIN-diode fabrication process is shown in Fig. 16.



The lateral PIN diode

Figure 15. Lateral PIN diode structure.

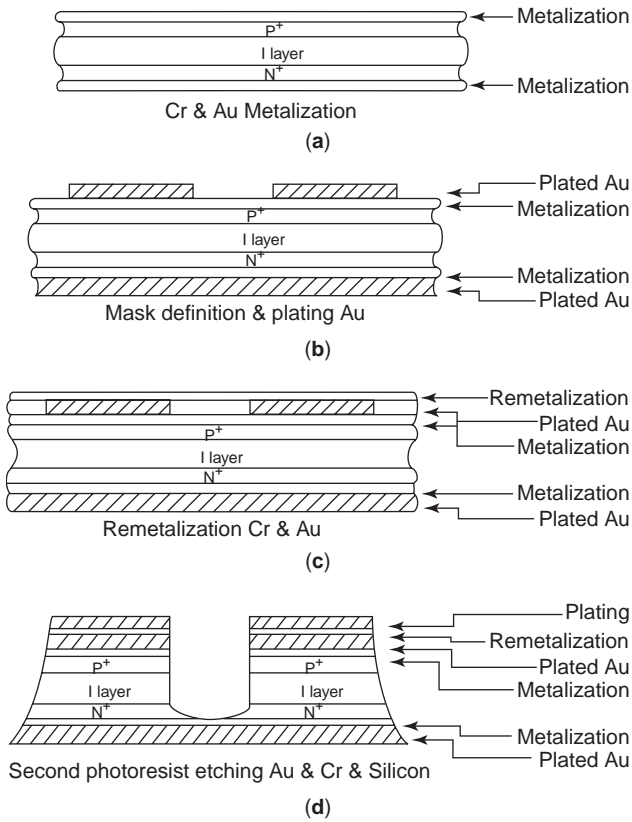


Figure 16. Step-by-step PIN-diode fabrication process. (After Ref. 10.)

13.2. Ion Implantation Process

Starting wafers are the same as those in the CVD process. Wafers are ion-implanted using a beam current of approximately 1 mA [10]. A $1 \times 10^{16} \text{ cm}^{-2}$ dose of B atoms impinges on one surface of the wafer at an implant energy of 150 keV, and the other side receives a $1 \times 10^{16} \text{ cm}^{-2}$ dose of P atoms at an implant energy of 150 keV. The sources are then driven for 15 minutes at 1200°C to form N⁺ and P⁺ contact layers. The concentration profile is shown in Fig. 17.

14. GaAs PIN DIODES

Undoped (100) liquid-encapsulated Chelchroski-grown GaAs substrate can be used to fabricate PIN diodes. In

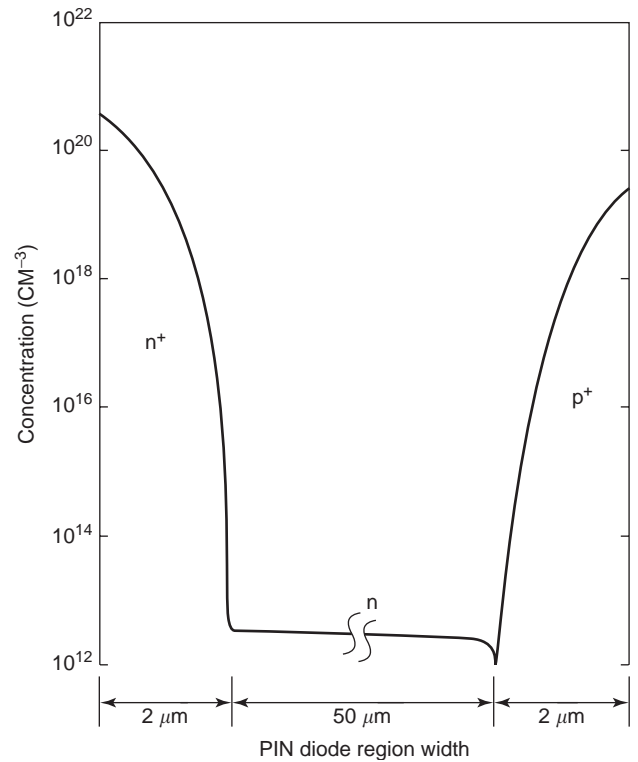


Figure 17. Concentration profile for a PIN diode. (After Ref. 10.)

the case of a vertical diode structure, A P⁺ layer and N⁺ layer are formed by ion implantation into the wafer of Be and Si, respectively, on top and bottom of the surface of the semiinsulating GaAs substrates (see Fig. 18). Then, wafers are annealed in the furnace under ASH₃/H₂ atmosphere. The N⁺ layer is formed first, followed by the P⁺ layer, as the Si implant in GaAs requires an annealing temperature for dose activation much higher than that for Be implantation [11]. Then, AuZn ohmic contacts are formed on the P side of the wafer using photolithography and liftoff. Finally, an AuGe–Ni–Au ohmic contact is formed on the back (v) of the wafer. The wafer is then diced for evaluation [11].

GaAs PIN diodes offer high switching speeds, high breakdown voltage, and a variable resistance with bias. In silicon, the electron and hole mobilities are almost the same.

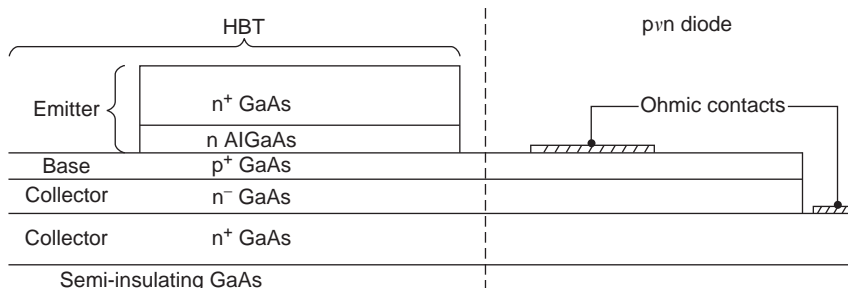


Figure 18. P-vN fabrication from HBT structure.

BIBLIOGRAPHY

1. S. M. Sze, *Physics of Semiconductor Devices*, Wiley-Interscience, 1981.
2. A. Rosen et al., Millimeter wave device technology, *IEEE Trans. Microwave Theory Tech.* **MTT-30** (1) (Jan. 1982).
3. A. Rosen et al., Silicon as a millimeter wave monolithically integrated substrate—a new look, *RCA Rev.* (Dec. 1981).
4. J. F. White, *Microwave Semiconductor Engineering*, Van Nostrand-Reinhold, New York, 1982.
5. H. A. Watson, *Microwave Semiconductor Devices and Their Circuit Applications*, McGraw-Hill, New York, 1969.
6. K. Kurokawa and W. O. Schlosser, Quality factor of switching diodes for digital modulation, *Proc. IEEE* **58**: 180–181, (Jan. 1970).
7. B. Doherty, Micronote Series 701, Microsomi.
8. *Applications of PIN Diodes*, Hewlett-Packard Application Note 922.
9. *Design with PIN Diodes*, MA-COM Application Note AG312.
10. A. Rosen and F. Zutavern, High power optically activated solid-state switches.
11. G. E. Ponchak, private communication.

POWER COMBINERS AND DIVIDERS

MAREK E. BIALKOWSKI
University of Queensland
(Australia) and National
University of Singapore

FENG-CHI E. TSAI
University of Queensland
Queensland, Australia

1. INTRODUCTION

Since the birth of radio in 1895, there has been a very rapid growth of radiocommunication technology. To obtain higher information transmission rates over larger distances, there has been a steady demand for using higher frequency bands and larger amounts of transmitted power. The most significant progress in these two directions took place during World War II and afterward. This led to the emergence and development of microwave (1–30 GHz frequency band) and millimeter wave (30–300 GHz frequency band) communication technologies. Key systems that operate now at microwave and millimeter-wave frequencies include terrestrial and satellite links, and radar. These systems use active and passive circuits, which fulfill a number of fundamental functions related to signal generation, modulation, launching, reception, and detection.

Prior to 1948, the year when the transistor was invented, the only semiconductor element that was used in microwave communication circuits was a crystal detector diode. At that time, microwave signal generation and amplification were dominated by vacuum tubes including magnetron, klystron, and traveling-wave tubes (TWTs) [1]. These devices still remain in use at kilowatt levels, where solid-state devices cannot yet compete. Since the late 1960s the situation with the dominance of microwave

power generation by tubes has changed dramatically. This was due to the introduction of microwave semiconductor devices such as the Gunn diode, avalanche diodes, and bipolar and field-effect transistors [1], which were able to produce considerable power levels and gain at microwave frequencies. With the invention and introduction of these new devices, there has been growing interest in developing techniques to obtain higher power levels by combining power from individual modules. The motivation for such techniques has been due to a number of reasons. For example, in the mid-1970s it became clear that the combination of even a modest number of IMPATT (impact avalanche transit-time) diodes could lead to the manufacture of a pulsed radar transmitter offering a significant reduction in size and weight, which required only tens of volts for its operation. This was in contrast to tubes that often required 1000 V supplies and a considerable warm-up time. Since the inception of the concept of power combining, in the late 1960s, many power-combining schemes have been tried and developed. These schemes often include the two tasks of power division and combination and therefore the terms *power combining* and *power dividing* often appear simultaneously.

Power-combining schemes involve different technologies and media. These range from metal waveguides and cavities, microstrip, and striplines for which the power is confined to a finite region. Alternatively, open space configurations are used. In that case, power is launched by a set of radiating elements, antennas, at the transmit side and is intercepted by another set of antennas at the receive side. The choice of technology and medium depends on the type of solid-state device involved in the power-combining scheme, operational frequency and bandwidth, and the type of application in which the combined power is required. The devices involved in power combining/dividing are known as *power combiners/dividers*. Because of their reciprocal character, the same circuits can alternatively be viewed as power combiners or power dividers. This designation depends on the nomination of their input and output ports. In most cases the configuration of power combiner/divider is fixed. However, there is a category of these devices whose configuration and operation is variable. These devices have a redundant number of input/output ports, only selected ones of which are activated at a given instance of time. This function is performed using various types of RF switches.

Power combining/dividing structures are the subject of this article. The presentation commences with an introduction of categories of power combiners followed by the fundamental characteristics of these structures. Methods of analysis and applications of power combiner/dividers are described next.

2. MICROWAVE AND MILLIMETER-WAVE POWER COMBINING TECHNIQUES

2.1. Power-Combining Principles

Power combining can be achieved in a variety of manners, but they can be generalized to two situations, shown in Fig. 1.

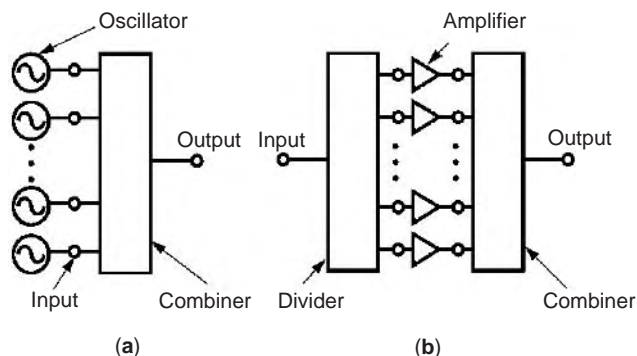


Figure 1. General configurations for power combining: (a) oscillators; (b) amplifiers.

In Fig. 1a, there are a number of individual oscillators, and the task is to combine them into a more powerful synchronized signal source. This is achieved via a suitable combining circuit. This circuit with some modifications can be used for injection-locked oscillators and reflection amplifiers. In that case, the output port is used as an input port for injection of an external signal.

Figure 1b shows a single low-power source that is split and applied to the inputs of amplifiers. In turn, the outputs of these amplifiers are combined into a common port to produce a more powerful source. In this case, both dividing and combining circuits are employed to obtain the function of power combining.

The proper functioning of a power combiner is related to the efficient utilization of individual oscillators or amplifiers that appear within its structure. First, the combined source has to function in a reliable manner. This means that it has to have stable and longlasting performance. The term *stability* may also refer to the purity of the frequency spectrum generated by the combined devices. The combining circuit should be able to synchronize individual sources and suppress any instability that can lead to multimode operation of multiple solid-state devices present in the combiner. Reliability is often associated with graceful degradation of performance of the combiner. It means that if one of the oscillators or amplifiers fails, the remaining devices should not be affected. Consequently, the power produced by the combiner should be only slightly reduced because of the absence of the failed unit. Graceful degradation has always been regarded as the most important aspect of the power-combining techniques in the competition of solid-state sources with tubes, for which failure is usually catastrophic. One additional aspect, in conjunction with graceful degradation, is feasibility of the “hot” replacement of a failed unit. A suitable provision in the power-combining/dividing structure is necessary to accomplish this task.

2.2. Classification of Power Combiners/Dividers

A systematic grouping of power combiners has been accomplished by Russell [2] and Chang and Sun [3]. As a result of this classification, three major categories of combiners have been introduced: chip-level, circuit-level, and

spatial-level. In addition to these three major groups, multiple-level and other types of combining schemes have also been identified [3]. This classification is not unique; however, it helps distinguish combiner/divider configurations in the context of their use. Chip-level combiners [4–7] can be viewed as a subcategory of circuit-level combiners. They utilize very small distances (a small fraction of a wavelength) between individual solid-state devices. As such, although they increase the generated power, they do not offer graceful degradation. This is because the failure of one chip usually leads to the destruction or prevention of operation of the remaining chips and thus to the catastrophic failure of the combined source. Other problems with this type of combiners concern low effective impedance and adverse thermal interactions. Standard circuit-level combiners utilize larger distances between individual solid-state devices and therefore they allow for the introduction of counter measures against a catastrophic failure of the combiner. Because of the marginal importance of chip-level combiners, Fig. 2 shows the reduced classification of combiners, which include only circuit-level and space-level combiner categories, with chip-level combiners omitted.

Circuit-type combiners [2,3] confine power within a finite region often enclosed by a conducting surface such as a cavity or a waveguide. Radiation into a free space is considered an undesired phenomenon due to power loss. In space-level combiners, power combining takes place in an unbounded [8] or partially bounded region [9]. In the latter case, the combining region often forms a space resonator. The combining process is accomplished using transmitting and receiving radiating elements (antennas). The relative dimensions, in terms of wavelength, of the spatial combiner structure are usually much larger than those of its circuit-type equivalent. Consequently, the quality factor that is achieved with space resonators is usually much larger than that obtained with circuit-type resonant cavities. Because of this feature, circuit-type combiners are employed at the lower end of microwave and millimeter-wave frequencies while the space-type combiners are aimed for use at the upper millimeter-wave frequency bands.

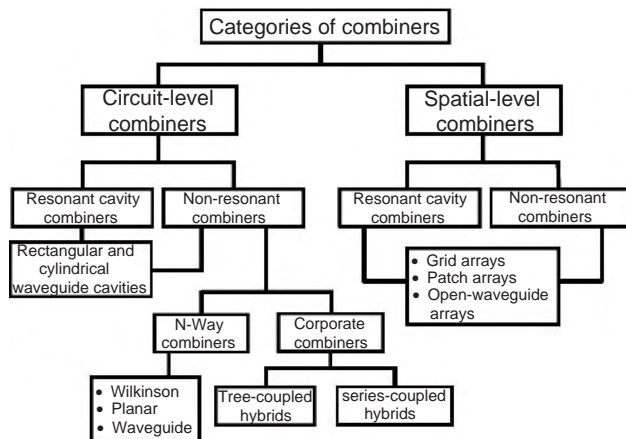


Figure 2. Categories of power combiners.

As shown in Fig. 2, circuit-level combiners are divided into resonant and nonresonant combiners. Resonant combiners use resonant cavities that exhibit a high quality factor Q and, as a result, feature small operational bandwidth. Because of this property, they serve the purpose of synchronizing multiple oscillators. Nonresonant combiners utilize structures with low quality factor and offer an increased operational bandwidth.

It has to be emphasized that similar-in-shape structures may appear in both resonant and nonresonant types of combiners [2,3]. For example, a cylindrical cavity with N coaxial ports including IMPATT or Gunn diode oscillators with a central port for power extraction is considered a resonant cavity combiner [10]. On the other hand, the same cylindrical cavity, but with peripheral coaxial probes and a central probe, can be considered a non-resonant, N -way radial combiner [11,12]. The difference lies in the Q factor that the cylindrical cavities provide [13]. The division into resonant and nonresonant cavity combiners may be less apparent for those structures for which it is difficult to identify whether they are resonant in operation. The proper identification of the Q factor may require solving an electromagnetic field problem to fully characterize a given structure. This is not always feasible.

Nonresonant combiners are generally divided into N -way and corporate-type combiners. Again, this classification is not unique and conforms to some earlier accepted terminology [2,3]. N -way combiners use a structure with N input ports and one output port. Corporate combiners use a tree of M -way combiners, where M is a small number, to create a combiner with a large number of input ports. The case of $M = 2$ leads to the binary-type corporate combiner. As has been indicated earlier, all the nonresonant combiners discussed here can also be regarded as power dividers. This is accomplished by designating input ports of an N -way combiner as output ports of a divider, and by renaming the common output port of the combiner to the input port of the N -way divider.

Similar to circuit-level combiners, spatial combiners can be divided into resonant (open-resonator cavity) and nonresonant structures [14]. Because of their similarities with Fabry–Perot cavity lasers [1], resonant-type spatial combiners using a space resonator with frontward and backward reflection mirrors are also termed *quasioptical power combiners* [9,14].

3. RESONANT AND NONRESONANT CAVITY COMBINERS/DIVIDERS

For the purpose of power combining and dividing, rectangular and cylindrical cavities are often used. Both resonant and nonresonant power combining structures can employ such cavities. As has been explained earlier, the identification of the resonant or nonresonant behavior can be distinguished by the quality factor that a given cavity structure offers. This factor depends on the method of launching and extracting the power and therefore on the cavity loading conditions. Resonant and nonresonant combiners/dividers using cavities are described in the following sections.

3.1. Rectangular Cavity Combiners/Dividers

The most popular configurations of rectangular cavities, which have been used for the purpose of power combining, are shown in Figure 3. The first structure, shown in Fig. 3a, is known as the *Kurokawa rectangular waveguide cavity combiner* [15,16]. It is considered as a resonant-type combiner. In this combiner, solid-state devices (IMPATT or Gunn diodes) operating as oscillators or amplifiers are connected to the lower coaxial lines. The upper coaxial lines are loaded with an absorber to stabilize the operation of the multiple-oscillator structure. They are also used to provide bias to solid-state devices. Please note that for the proper operation, pairs of coaxial lines are located close to waveguide walls, at the maximum of the magnetic field, and are spaced approximately at a half-waveguide wavelength along the waveguide. The waveguide short circuit is located a quarter-wavelength from the first adjacent coaxial pair. The bottom coaxial lines often include impedance-transforming circuits to obtain suitable impedance conditions for the proper operation of solid-state devices.

Figure 3b shows one variation of the basic Kurokawa combiner [17,18]. In this case, the bottom parts of the coaxial lines are removed and replaced by open-ended posts. In this configuration, solid-state devices are located in the gaps between the bottom waveguide floor and the tips of the posts. The rectangular waveguide in this configuration can be of a standard or oversized format.

Figure 3c shows a rectangular waveguide with coaxial probes [19]. In contrast to the Kurokawa-type combiner, individual amplifiers including active devices (diodes or

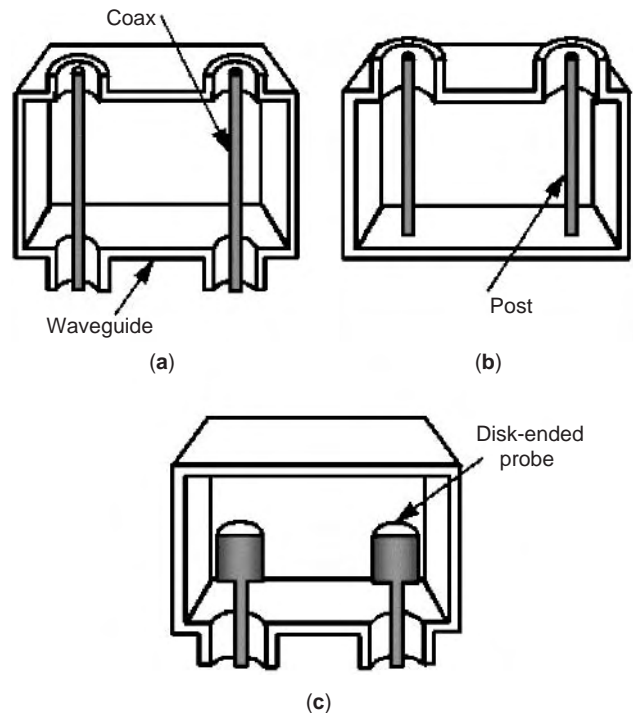


Figure 3. Rectangular waveguide cavity combiner/dividers: (a) cross-coupled coaxial lines; (b) posts; (c) disk-ended probes.

transistors) are connected externally to this structure via coaxial ports. These in turn couple power to the common rectangular cavity. Depending on the method of launching and extracting power, this basic configuration with some modifications can be used in ladder-type [19,20] and traveling-wave-type combiners/dividers [21]. In this case, coaxial probes or waveguide apertures can be used as combining ports. To combine power, reflection (single unit) and transmission (using dividing and combining units) configurations can be explored.

3.2. Cylindrical Cavity Combiners/Dividers

The principles of using cylindrical cavities for the purpose of power combining or dividing are analogous to those already presented for rectangular cavities. This is because both types belong to the same family of parallel-plate waveguides. The obvious differences are in the cross-sectional shapes, which consequently lead to their various uses. Figure 4 shows typical configurations of combiners/dividers that use a cylindrical cavity as a combining structure.

For the purpose of combining, it is usually assumed that the cavity operates in its TM_{0N0} mode whose field is constant with the cavity height and axially (azimuthally) symmetric. Power is extracted or launched by the centrally located probe (Figs. 4a–4c) or by the rectangular wave-

guide port (Fig. 4d). An important feature of the cylindrical cavity combiner/divider is that, since the mode of operation assumes fields azimuthally symmetric, in theory there is no minimum spacing between peripheral probes or coaxial lines. This is in contrast to the rectangular cavity combiner/divider in which the peripheral ports have to be spaced at half-waveguide wavelengths along the waveguide for proper operation.

3.3. Radial, Conical, and Hemispherical Cavity Combiners/Dividers

The cylindrical cavity with symmetrically located peripheral coaxial probes or lines and a single central coaxial probe, described above, can also be regarded as a radial cavity combiner/divider. This designation, instead of *cylindrical cavity combiner*, has been used in a number of references. Variations of this structure include shaping of the radial cavity and concern the use of different types of central and peripheral ports. Standard designs include a uniform-height radial cavity, which is fed by the central probe. However, some designs include a non-uniform-height cavity [29,30]. At the periphery, rectangular waveguide ports or coaxial probes are used. For the central port, full-waveguide-height coaxial probe [31,32] disk-ended [33,34], conical [35–37], or dielectric coated probes [38] are used. Similarly, peripheral probes can be formed by full-height coaxial probes [29,30], dielectric coated probes [37], conical probes [36], disk-ended probes [34], balun loops [39], continuous annular balun sections [35], or rectangular waveguide ports [33,38], instead of straight coaxial probes. Various configurations of radial cavity combiner/dividers are shown in Fig. 5.

Conical [2,3] and hemispherical cavity combiner/dividers [40,41], shown in Fig. 6, exhibit axial symmetry and utilize posts or coaxial probes for connecting solid-state sources or amplifiers. Posts or probes can also be used for signal launching and collecting.

4. NONRESONANT N-WAY COMBINERS

4.1. Cavity-Type Nonresonant N-way Combiners

N -way combiners form a single structure with N input ports and one output port. Some examples of these types of combiners have already been discussed and include radial, hemispherical, and conical cavities. In these structures, an azimuthally symmetric field is exploited in the power-combining/dividing process. In this case, the device operation is equivalent to N parallel transmission lines connected to one port. To support this mode of operation, input ports are excited in phase. Since in practice, the signals launched at the input ports may have different phases, dielectric beads or rods [40] of variable length or height may be used for tuning purposes to equalize the signal phases. An out-of-phase excitation of ports leads to the generation of higher-order modes that feature azimuthal (angular) dependence. To suppress higher-order asymmetric modes, slits [24,26] and resistive absorbers [24,25] are used. These components help increase the isolation between peripheral ports, which in turn improves

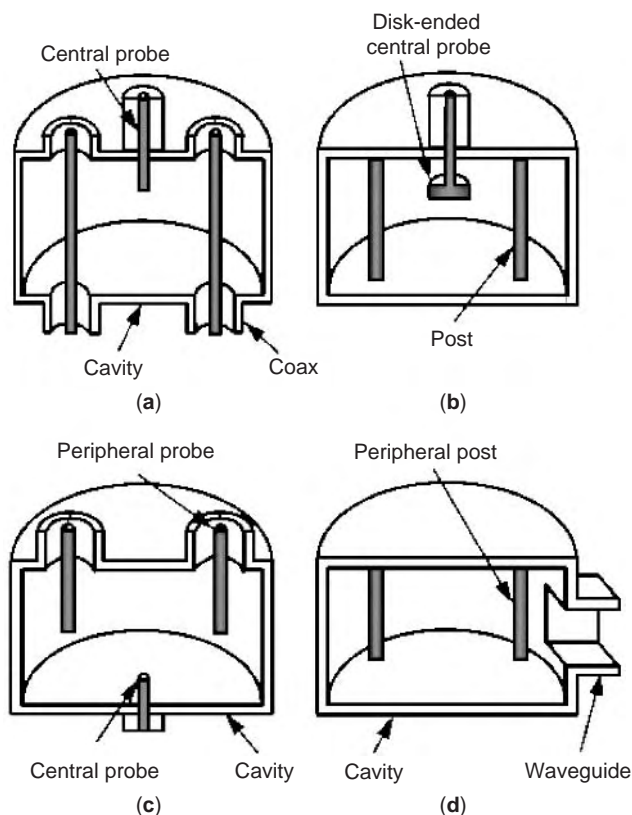


Figure 4. Cylindrical cavity combiner/divider configurations: (a) cross-coupled coaxial lines [10,12,22] and a central coaxial probe; (b) posts and disk-ended coaxial central probe [23,24]; (c) coaxial probes [25,26]; (d) posts and a waveguide aperture [27,28].

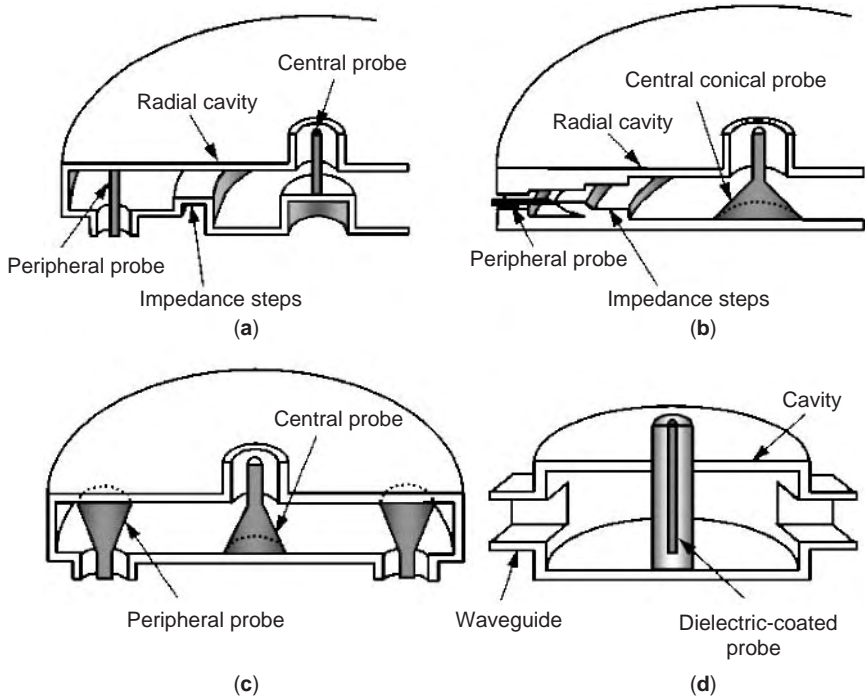


Figure 5. Various configurations of radial cavity combiners/dividers.

the graceful degradation performance of the combiner. This action is explained as follows.

In general, failure of a source, or an amplifier connected to a given port, results in a change of the load presented to this port. This new condition affects the performance of the remaining active devices. The extent of influencing the performance of other active devices depends on the isolation between the failed port and the remaining ports. Radially symmetric cavity combiners have a built-in isolation

that usually increases with the number of ports, and is equal to $1/N$ on average. This value may be considered insufficient in some applications, and this is why the resistive elements are introduced to increase isolation. When the slits or resistive vanes are located along the lines of the surface electric current of the dominant symmetric cavity mode, their effect on the fundamental mode is negligible. However, they cut lines of the currents that are associated with higher-order azimuthally varying

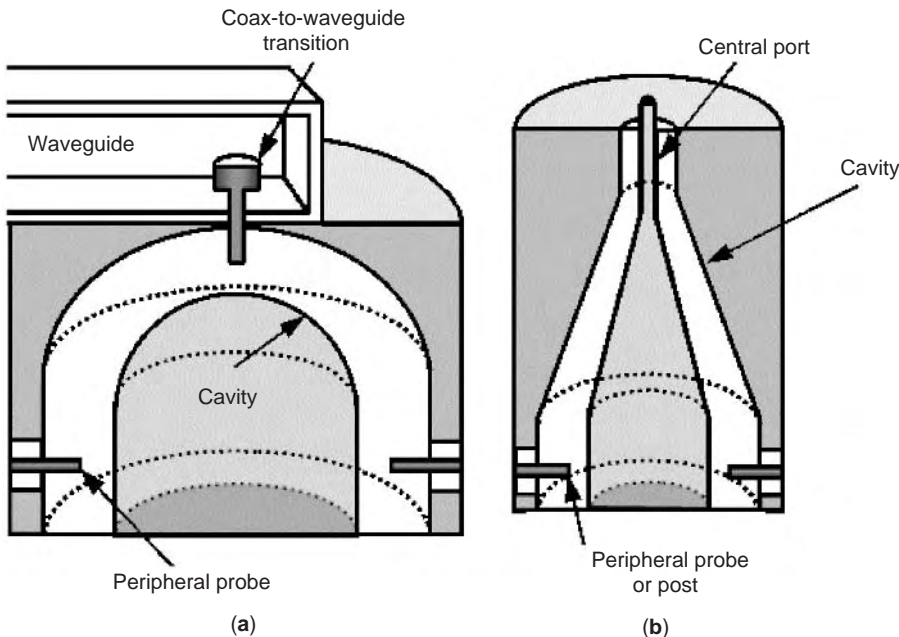


Figure 6. (a) Hemispherical and (b) conical cavity combiner/divider configurations.

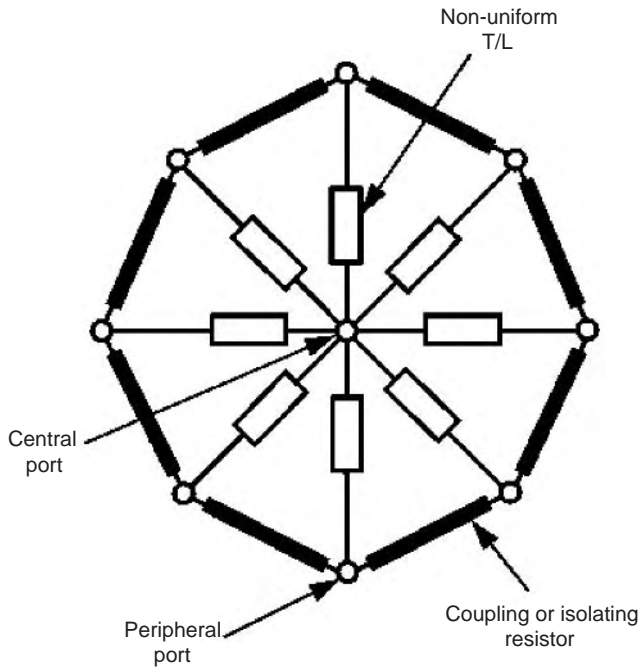


Figure 7. An equivalent circuit for a radial combiner under assumption of the dominant mode of operation.

fields. This results in absorption of higher-order modes and consequently improves the isolation between the peripheral ports.

An equivalent circuit for the radial (also hemispherical and conical) combiner under the condition of the dominant (symmetric, in-phase) mode of operation is shown in Fig. 7.

As can be seen in Fig. 7, a number of transmission lines of equal length (not necessarily quarter-wavelength), which meet at a common port, form this circuit. These lines are nonuniform as their characteristic impedance varies with distance. In this case, they operate as impedance tapers and provide suitable impedance transformation between the peripheral ports and the central port. This is to counter the parallel loading effect at the common port. The peripheral ends are connected via resistors. These resistors represent mutual coupling between the lines. These equivalent resistors may incorporate isolation resistors purposely introduced in the combiner.

4.2. Nonresonant Planar Radial-Line Combiners

Radial combiners do not necessarily have to be realized in waveguide. Their planar equivalents have also been investigated [42–47]. In these cases, a planar disk with a coaxial line at its center and N microstrip lines connected at its periphery form the combiner structure. A planar version of a radial combiner is shown in Fig. 8.

Depending on the design, nonuniform (tapered) or uniform (constant width) microstrip lines can be used to form this type of radial combiner. Additionally, resistors can be connected between the neighboring lines to improve isolation [42,43,46] and hence the graceful degradation performance of this device.

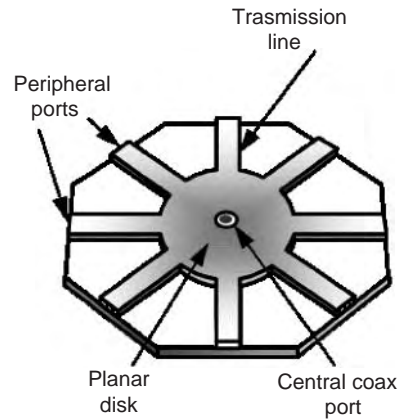


Figure 8. Planar version of a radial combiner with a coaxial central port and microstrip transmission lines connecting peripheral ports.

4.3. Wilkinson N -Way Combiners

Wilkinson's N -way combiner is one of the oldest power combining structures. It was introduced by Wilkinson in 1960 [48]. The device resembles in its concept the radial-line combiner and is synthesized using M sections of N uncoupled transmission lines of equal length with isolation resistors. A similar concept was also followed by Yee et al. [49]. The equivalent circuit of the N -way Wilkinson divider, which includes one-section transmission lines, is shown in Fig. 9. The difference, in comparison with an N -way radial-line combiner, is that in the present case the lines are uniform and are quarter-wavelength long. To meet the impedance matching conditions, the characteristic impedance of the lines is equal to $\sqrt{N} Z_0$, where Z_0 is the characteristic impedance of input and output transmission lines. Isolation between peripheral ports is improved using resistors between adjacent lines. Note that when N is greater than 2, the use of resistors in an N -way Wilkinson divider requires a crossover arrangement to effect connection between first and last output ports. The most well known version of the Wilkinson's divider is the two-way divider, as shown in Fig. 9b. It is used as a basic building block in a corporate-type combiner, which is discussed later.

Generalizations or variations of the standard Wilkinson divider were presented in Refs. 50–53. In particular, the synthesis of N -way dividers using M sections of N -wire uncoupled or coupled transmission lines was described in Ref. 50. To avoid multilayer construction of the standard Wilkinson N -way divider, for $N > 2$, new planar solutions concerning fork-type power dividers were presented in Ref. 51. Practical designs of four-way and seven-way dividers with isolation exceeding 20 dB between ports over a fractional bandwidth of 40% were demonstrated. The new structures presented in Ref. 52 feature an increased power-handling capability. The work in Ref. 53 concerns the design procedures for unequal power split-tee junctions.

4.4. Sectorial Radial Combiners

One problem with the N -way planar radial divider/combiner is that it uses hybrid (coaxial and planar) technology

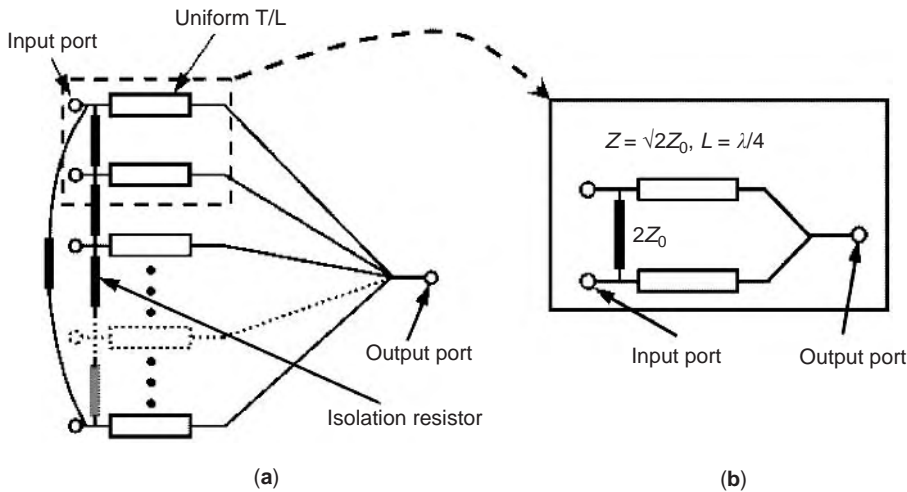


Figure 9. (a) An equivalent circuit of Wilkinson’s N -way power combiner; (b) its two-way version.

for its construction. This shortcoming can be avoided using a sectorial M -way planar combiner [54]. Variations of this structure are shown in Fig. 10.

Used as dividers, these structures can provide approximately equal power split with equal phase distribution. To increase the isolation between the peripheral ports, lumped resistors, as in the case of Wilkinson’s type combiner, can be used. In order to make output ports parallel as well as to provide equal phase division, exponential taper and purposely created holes can be used [55–57].

4.5. Corporate Combiners

Combiners with a large number of ports can be built using a tree of identical or similar hybrid devices with a small

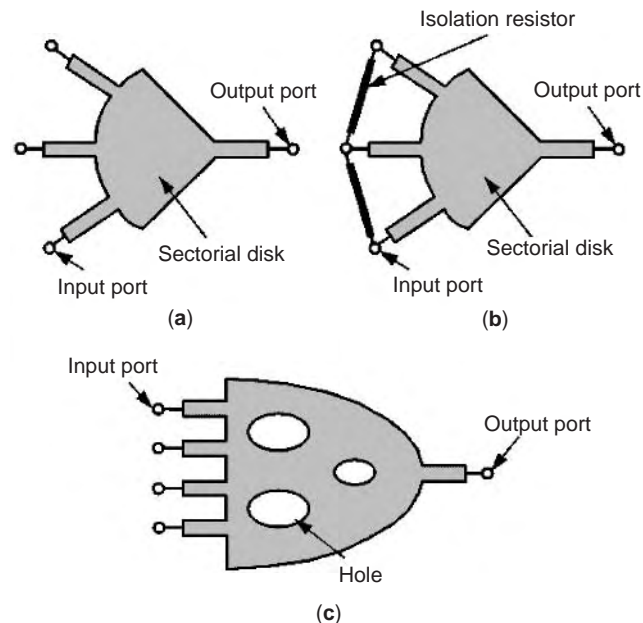


Figure 10. Sectorial planar combiners: (a) without isolation resistors; (b) with isolation resistors; (c) with holes for phase and amplitude equalization.

number of input/output ports. These combiners can include binary or generally M -ary basic building blocks. As a result, the number of input ports in such combiners is not arbitrary but given by 2^L or M^L , where L is the number of section in the longitudinal direction. Basic building blocks for the binary tree-type combiners are shown in Fig. 11.

These basic structures include the two-way Wilkinson’s combiner, the 3-dB quadrature hybrid and the rat-race hybrid [58]. Other possibilities include other types of couplers (e.g., coupled-line directional coupler) and the Gysel power combiner [52,59]. These hybrids can be built in waveguide or planar (e.g., microstrip) technologies. These structures have built-in isolation between their input ports, exceeding 20 dB, and feature an increased operational bandwidth, typically 20% or more.

The common property of the Wilkinson 3-dB quadrature and rat-race hybrids is that they can provide equal power division when they operate as dividers. Please note,

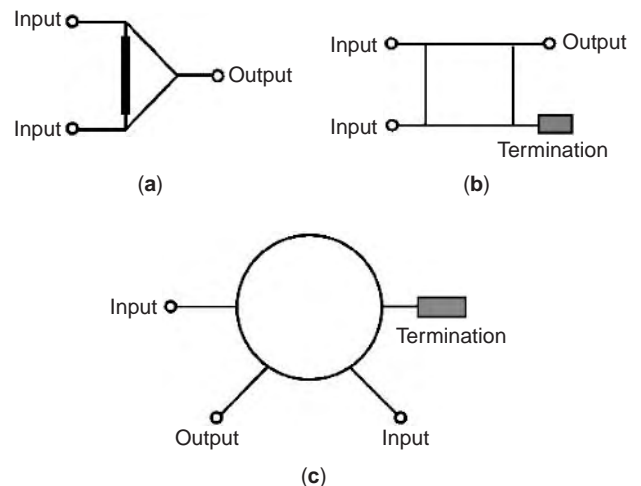


Figure 11. Basic blocks used in tree-type power combiners: (a) Wilkinson two-way divider; (b) 3-dB branchline coupler; (c) rat-race hybrid.

however, that alternative designs of these dividers can also offer unequal power division [53]. The differences between these building blocks concern the number of ports and phase relationships. The Wilkinson's hybrid is a three-port device and provides equal in-phase power split. The rat-race hybrid is a four-port device and is capable of in-phase and out-of-phase (180° phase difference) equal power split. The 3-dB branch coupler is a four-port device and provides equal power split with a 90° phase difference between its output ports. Because of the four-port arrangement, the subtracting port of the rat-race hybrid and the isolated port of the 3-dB coupler need be match-terminated prior to their use in the tree-type combiners.

Figure 12 shows examples of corporate (tree-type) combiners with two-way Wilkinson's combiners and 3-dB couplers. As can be seen in Fig. 12, assembling of the binary corporate structure using two-way Wilkinson or rat-race hybrids is straightforward. The use of the 3-dB coupler requires an extra care to account for the 90° phase difference in its output ports. This is accomplished using suitable connection arrangements, which compensate for 90° phase difference.

Major advantages of corporate combiners are that their designs are straightforward. Their disadvantages are due to losses. Heatsinking for isolation resistors also creates problems. Because each section includes quarter-wavelength transmission lines, the corporate combiner becomes less compact than the radial combiner does with a similar number of ports. As a result of losses and large size, corporate combiners with many branches can be inconvenient, especially at the lower end of microwave frequencies. An interesting discussion regarding the use of corporate and radial combiners has been presented in Refs. 59 and 39. The inconvenience of the corporate combiner due to its large dimension is diminished at upper microwave or millimeter-wave frequency bands, because its size is scaled. However, considerable conduction losses

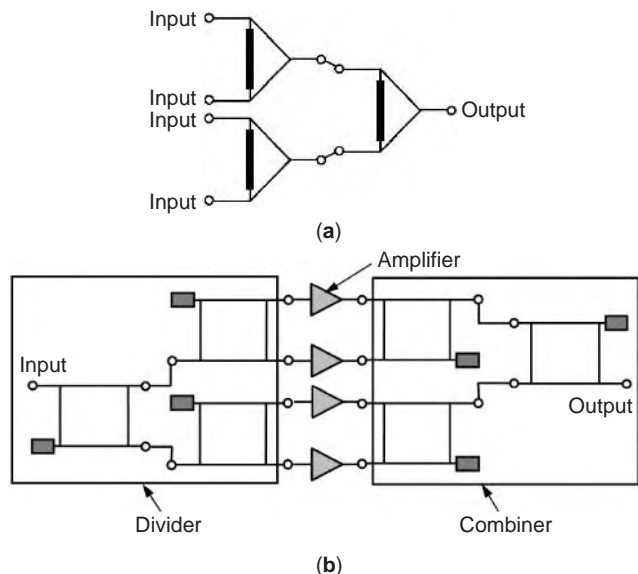


Figure 12. Typical configurations of corporate power combiners: (a) Wilkinson combiners; (b) 3-dB branchline couplers.

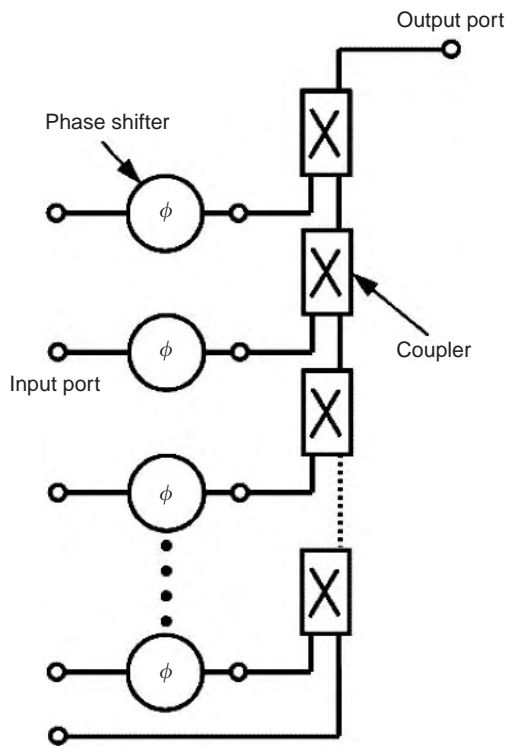


Figure 13. Chain-type combiner using couplers with unequal coupling coefficients.

occurring in these bands still restrict their use to only a few stages.

Similar to binary corporate combiners, M -ary corporate combiners can be built using M -way combiners [54]. However, they have not found many practical applications and therefore are not discussed here.

As shown in Fig. 13, combiners can also be built using hybrid circuits in the chain or serial configuration [2]. Using this approach, combiners with arbitrary number of input ports can be produced. These structures are easy to realize in practice. Usually, couplers with progressively increasing values of coupling are used in the chain. Because of the use of nonidentical couplers, phase shifters have to be included to compensate for unequal phases that can occur for input signals. As the phase equalization is not easy to accomplish at upper microwave frequencies, these circuits have not found wide acceptance at this particular frequency band.

4.6. Switchable Power Combiners

There a number of applications in which power division or combination have to be performed with regard to M selected ports of an N -port network (in which N is greater than M). Such a situation is met, for example, in a switched circular array antenna system for mobile satellite communication [60,61]. In this antenna system, only a few elements of a circular array facing a satellite need to be activated, while the remaining ones have to be deactivated. The function of activating and deactivating antenna elements is performed by a switched radial power

combiner/divider. The design and development of such a divider/combiner, which employs pin diodes as RF switches was described by Bialkowski and colleagues [60,62].

The concept of a switched radial divider/combiner for use with a mobile satellite circular antenna system is presented in Fig. 14. As seen in Fig. 14, the antenna array is formed by circular patches positioned on a truncated cone. These antenna elements are coupled via apertures to a switched radial divider/combiner. Beside RF switches, which activate and deactivate elements, 1-bit phase shifters are included to provide additional beams for this array. A switched radial divider with 14 output ports, with any three adjacent ports being active, was presented by Bialkowski et al. [60]. A device with eight total output ports, two of which were active, was described by Karmakar and Bialkowski [62]. A photograph of the fully developed 8-2-ON radial switch (including 1-bit phase shifters) is shown in Fig. 14b.

Another concept of switchable combiner is shown in Fig. 15. The device is a combination of a Wilkinson power combiner and a switching network. The combiner can operate in one-, two-, three-, and four-way modes, which means that up to four input signals can be combined to one output. In Fig. 15, the $\lambda/4$ transmission lines become open-ended stubs when they are turned off. The $\lambda/2$ lines are used to allow for obtaining an extra space required for incorporating multiple RF switches.

Characteristic impedances of transmission lines are optimized for minimum insertion loss and high return loss in all modes of operation.

5. SPATIAL POWER COMBINERS

5.1. General Considerations

Spatial combiners use arrays of radiating elements to combine power in an unbounded or partially bounded free space. The major difference with circuit-type combiners is that besides an active device and its biasing/impedance-matching circuit, an antenna is an integral part. Because of the integration of an active element with an antenna, spatial power combiners are often regarded as an extension of what is known as an *active-array antenna*. Different types of antennas, including dipoles, patch antennas, notch antennas, and open-ended waveguides, can be used to this purpose. This blending leads to a wide range of spatial combiner structures. Irrespective of the choice of particular antenna elements, they can be classified into one of the two types of configurations: *tile* or *tray*. In the tile configuration, which seems to be the most popular, active devices and antenna elements appear in one plane. The desired direction in which the radiated wave is produced is broadside direction. In the tray configuration active stages and radiating elements are supported by

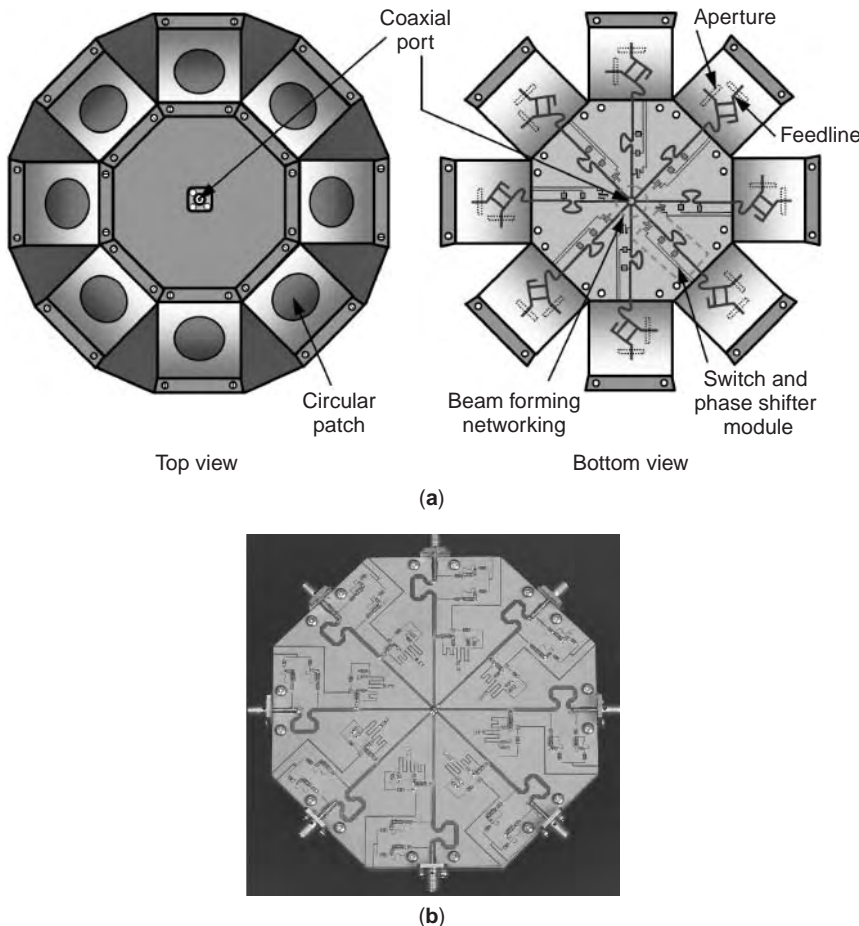


Figure 14. (a) Configuration of a switched circular array antenna (top and bottom views) showing the use of a switched radial divider/combiner; (b) photograph of a 8-2-ON radial divider combiner developed for use in a mobile satellite antenna system.

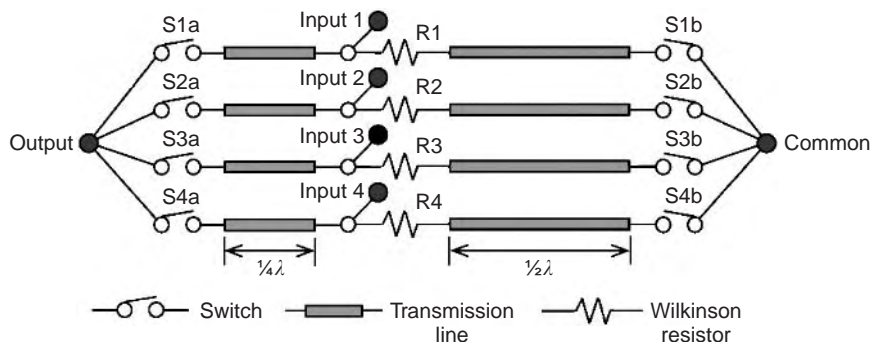


Figure 15. Configuration of a switchable power combiner divider utilizing a Wilkinson divider and a switching network.

separate ground planes that are stacked in vertical direction. In this configuration, antenna elements are chosen to radiate in an endfire direction. This configuration is also known as a *brick* configuration.

Similar to their circuit counterparts, spatial combiners can combine power due to individual oscillators or amplifiers. Thus the general principles for the combining schemes introduced earlier (in Fig. 1) also apply to this type of combiners. The difference is that now the combining has to take place in a given direction in space, which eventually can be collected by a horn antenna located in far- or near-field region of the active array. In the power-combining process dielectric lenses can also be used to focus the produced wave onto a power collecting antenna. When the active stages radiate in free space, the beam pointing at an undesired direction is considered as a loss in combining efficiency. This is a new aspect in comparison with the circuit-level combiners.

Most of the initially reported work on spatial combiners has been related to oscillators [63]. However, at subsequent stages work concerning amplifiers, frequency multipliers, detectors, mixers, and modulators were also developed [63]. Most of the more recent research work focusses on amplifiers instead of oscillators mainly because amplifiers do not need synchronization mechanism as do oscillators. Problems associated with synchronization relate mainly to the difficulties in maintaining oscillations, which are prone to electrical, thermal, and mechanical disturbances. In amplifier combiners, one (initial) source is required to be stable and to undergo an amplification process. This task is much easier to accomplish than synchronizing a multiple-source array.

Synchronizing of spatial oscillators, similar to their circuit counterparts, can be achieved using internal or external means. A preferable option is to use a high-*Q* resonator such as a spatial cavity resonator [64–68]. In contrast to a circuit-type cavity resonator, this resonator, in addition to its synchronizing role, has to enable power radiation in a desired direction. Because of this requirement, one of its mirrors usually has to be semitransparent. Signals reflected from the resonator’s walls (or mirrors) cause the self-injection of oscillators. Because of the high *Q* of the resonator, an electromagnetic field and consequently a signal having high spectral purity can be established. The resulting frequency of the spatially combined oscillators is closely related to the resonant

frequency of a field (mode) that can exist in the cavity. Note, however, that because the spatial cavity is partially enclosed, it can also support a continuous spectrum of modes. This is in contrast to the enclosed conducting cavities that exclusively support a discrete spectrum of modes. One inconvenience is that a spatial resonator occupies considerable volume, making the combiner’s design less compact. This disadvantage is of secondary importance at a millimeter frequency band due to a frequency scaling of the structure’s size. Frequency synchronization is also achieved internally through the self-signal injection in the combiner structure [69–72]. The mechanisms contributing to this phenomenon are due to mutual coupling of individual elements. This coupling can be accomplished by free-space or surface waves [69–74], resulting in the weak coupling mechanism, or via specially arranged transmission-line-type connecting circuits [75] or close spacing of active devices in grid-type combiners [76,77], which produce strong coupling between individual oscillators. If successfully accomplished, this synchronization approach makes the combiner’s design compact and low-profile. An alternative method for synchronizing individual oscillators is to inject an external high-purity signal [77,78]. An antenna can be used to illuminate the combiner array. Different mechanisms for synchronizing spatially combined oscillators are shown in Fig. 16.

The synchronization mechanism in the spatially combined oscillator array is not easy to explain. The general answer to this problem is given by Adler’s theory [79]. This theory provides general conditions for synchronization, which are related to the amplitudes and frequencies of the free-running oscillators and the injected signal. In particular, this theory provides the information on the locking (synchronization) bandwidth of the externally injected oscillator. The extension of this theory in relation to linear arrays of spatially combined oscillators has been presented [69–75]. The most recent contributions in this area are covered by Pogorzelski and colleagues [80,81].

The two parameters involved in the synchronization process are the frequency and the phase. Because of a large number of competing mechanisms whose parameters are not precisely known, the synchronization process may often be difficult to theoretically predict. The problem concerns a number of individual oscillators whose free-running frequencies may be different. These differences are due to various characteristics of individual solid-state

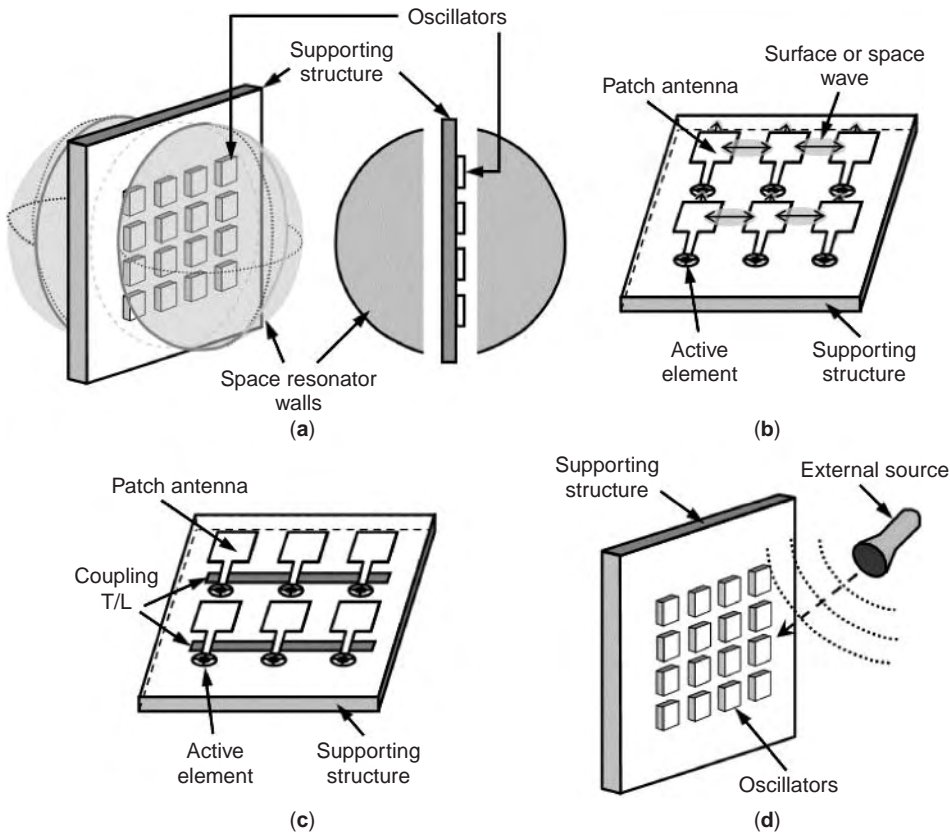


Figure 16. Methods of synchronizing spatially combined oscillators: (a) spatial resonator; (b) surface of space waves (weak coupling mechanism); (c) connecting transmission lines (strong coupling mechanism); (d) external source.

devices as well as the different environments they experience. Middle elements in the array observe similar environments. However, this is not the case for end elements in a finite-size array. Because of different environment and individual characteristics, the synchronized (in frequency) oscillators may feature different phases, which may generally have random values or can exhibit a progressive shift. Random phase differences lead to power-combining losses, as the signals, in a given direction, add out of phase. This phenomenon is similar to that observed in circuit-level combiners using N -way Wilkinson or radial combiners. On the other hand, the constructive (progressive) phase shift can result in an endfire beam launching or beam squint. These phenomena were explained in Refs. 72–74. It was shown that the phase shift could intentionally be controlled by end elements in the finite array [73,74]. It was also shown that by varying the free-running frequency of the oscillator at one end of the linear array, beam scan could be obtained. Larger scan angles could be obtained for strongly coupled arrays of elements.

The formation of the beam in the broadside direction usually improves with the use of a space resonator [71]. However, a comprehensive answer to the problem of synchronization of individual oscillators to achieve efficient directional combining is a challenging problem. Nevertheless, a number of relatively well synchronized spatial oscillators with good radiation characteristics have been demonstrated. Frequency tuning of such oscillators

using mechanical and electronic means has also been shown [63]. Features such as gradual degradation of spatially combined arrays have also been demonstrated [63].

The fundamental structures of spatially combined amplifiers are similar to those used in spatially combined oscillators. Their design often becomes less complicated than for oscillators. This is because the solid-state devices used in such amplifying arrays usually operate at their small-signal or linear amplification mode, for which characteristics are more feasible to obtain. However, coupling mechanisms due to surface or space waves and circuit connections still have to be taken into account to obtain a successful design. Reflection and transmission types of spatially combined amplifiers can be designed following a methodology similar to that already established for circuit-type combiners. The approach concerns the design of single-cell amplifiers. This design relies on knowledge of load conditions as presented by antenna elements that are connected to the input/output ports of individual amplifier modules. Assuming that various cells of the active array exhibit similar loading conditions due to the presence of other active stages, the task is to design and develop a single amplifier and replenish this design to form an array. Design of the entire combiner is facilitated when the individual cells are weakly coupled and the interactions with the remaining active cells can be neglected. This is often the practical case.

In contrast to spatially combined oscillators, the amplifier combiners require both the signal launching and combining devices (as shown in Fig. 1). These can be in the form of horn antennas or combinations of lenses and horns.

In general, these signal-launching/collecting devices require producing uniform illumination of individual amplifying cells while providing minimum insertion loss. The need for excitation uniformity is to have all the active stages equally contributing to the output port of the combiner. This condition is also required to obtain a large dynamic range of the entire amplifier combiner before saturation of individual active stages in the array can occur. Meeting the condition of uniformity of the active array and low insertion loss is a challenging task. This is explained as follows.

A uniform plane wave illuminating a planar active array is not so difficult to obtain by using a horn antenna located at a far-field zone. However, this arrangement suffers from considerable insertion losses due to spillover. In order to eliminate or reduce spillover losses, the horn should be located in the near field of the array. In order to meet the requirement of uniform amplitude illumination, a special type of horn (such as a hard horn) has to be

employed. However, because of near-field interactions between the array elements and the conducting walls a reduced operational bandwidth is usually obtained.

5.2. Classification of Spatial Power Combiners

The spatial combining structures can be classified in a variety of ways. One approach, which has already been introduced, is to group them in terms of tile and tray active-array configurations. An alternative grouping is in terms of resonant and nonresonant structures. However, as has already been indicated for circuit-level combiners, this classification may not be an easy task because estimation of the Q factor of a given structure can be difficult. A more convenient way is to classify spatial combiners in terms of their radiating elements. Using this approach, grid-type, patch (or slots), and open-ended rectangular waveguide types of power-combining structures can be introduced. These three types are shown in Fig. 17.

5.3. Grid Combiners

The grid-type combiner is one of very early structures introduced for the purpose of spatial power combining. The term *grid* was introduced as early as the 1960s [82,83] and

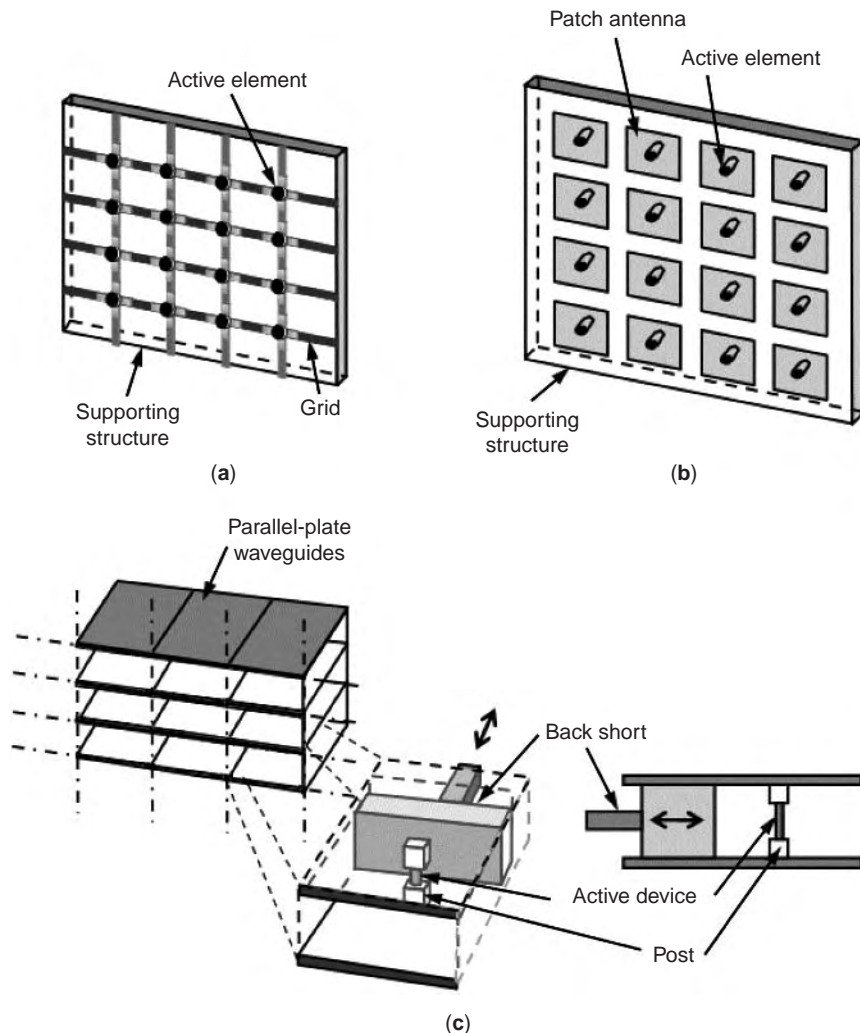


Figure 17. Basic configurations of spatial combiners: (a) grid structure; (b) microstrip patch antennas; (c) open-ended parallel-plate waveguides.

is related to wire antennas and selective periodic surfaces. The use of solid-state devices using grid structures was also reported at that time [84,85]. The first grid oscillators for quasioptical power combining were introduced in 1988 [86,87].

As shown in Fig. 17, the grid combiner is formed by an array of identical units that are called *cells*. Unit cells are densely spaced (approximately quarter-free-space-wavelength or less). This spacing creates a strong coupling mechanism between adjacent units. The vertical conducting strips in the grid structure act as dipole antennas. These can be fed by active elements such as diodes [86] or transistors [76,77,87]. The horizontal conducting strips or bars serve the purpose of biasing as well as heatsinking.

For the case of in-phase operation, which results in broadside radiation, the considerations of an infinite array are often reduced to that of a single cell. Assuming that the array operates in its dominant mode, as established by in-phase excitation of the identical unit cells, the structure can be regarded as an assembly of parallel rectangular waveguides with top and bottom walls formed by an electric conductor and sidewalls formed by magnetic conductors. In practice, the arrays are of finite size. However, an infinite array approach permits reasonable design rules.

As grid arrays are equivalent to densely packed dipoles, these arrays form inefficient radiators, as their equivalent radiation apertures are small, resulting in low directional gains. To obtain higher radiation efficiencies, antenna elements with a larger directional gain have to be used. This task can be accomplished with patch antennas that feature gain higher than that in dipole antennas. This statement concerns the situation when the active grid operates as an active planar array directly radiating in free space.

5.4. Spatial Combiners with Patch Antennas

One problem with grid-type combiners is that the design of the array has to be accomplished in a single step with all elements present, as there are almost no means for tuning or trimming. The available options for tuning include changing the bias conditions, use of transparent and non-transparent mirrors, and injection of an external signal. Consequently, the design has to be very predictable, as the design error can be costly. Although design of the passive grid structure can be accomplished in a very accurate and

repeatable manner, variations in performance of individual active devices may lead to design uncertainties in the active array.

Weakly coupled arrays of active patch antenna elements provide a better alternative to make the design more feasible. This is because single elements can be designed and tested before being assembled into the array. As has already been mentioned, a variety of antenna elements including different integration techniques with different types of active elements (diodes or transistors) can be used to this purpose. Figure 18 shows some typical arrangements that have already been explored.

As patch antennas and active devices take usually a larger space than do dipoles in grid arrays, special care has to be taken to minimize their dimensions to avoid undesired grating lobes or nulls in the radiation pattern, if the combiner operates as an active array radiating in free space. This requires minimization of the interelement spacing to a value smaller than one wavelength. As active devices require biasing lines and pads, which consume considerable space, this task may become a challenge. In some cases, a triangular lattice instead of the usual rectangular lattice may provide a solution to this problem [93].

Spatial oscillators or amplifiers integrated with patches can also be strongly coupled. This can be arranged using circuit connections between active elements [85]. To avoid multimode problems, resistors in transmission lines that connect adjacent active elements can be used [72].

Microstrip or patch antennas or printed dipoles in active arrays usually are arranged in the tile configuration. This is because these antennas radiate in the broadside direction. Depending on the layout, the resulting spatial power combiner can be of transmission or reflection type and the associated array is termed *transmitarray* or *reflectarray*, respectively. In the amplifier combiner, which uses the transmitarray configuration, an antenna positioned some distance from one side of the array launches an electromagnetic (EM) wave onto the active array. The array intercepts the incident wave, amplifies and phases (or delays) it by active delay circuitry, and then retransmits it. Another antenna located on the other side of the array intercepts and combines the amplified signal. For the reflectarray configuration a single antenna, for example, an orthomode horn capable of receiving dual-polarized

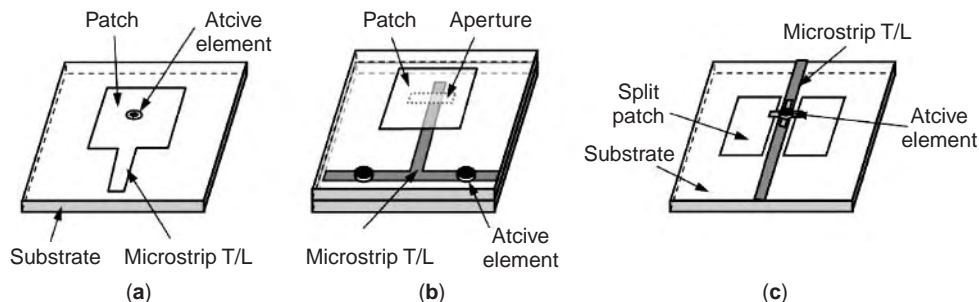


Figure 18. Different integration techniques used in spatially combined active array antennas: (a) Gunn or IMPATT diode beneath the patch [88,89]; (b) Gunn diode integrated with the feedline of the aperture coupled patch [90]; (c) FET transistor integrated with the patch [91,92].

signals, and appearing some distance away from one side of the array is used to both distribute and combine the signal.

5.5. Spatial Combiners Using Waveguides

Although spatial combiners with patch antennas seem to be more advantageous than grid-type combiners in terms of better integration with active elements and superior qualities for heatsinking, they still have a number of deficiencies. As with grids, they feature a limited tuning range and wide power output deviations. At millimeter-wave frequencies patch dimensions may become too small to accommodate an active device. In this case, patches can be replaced by waveguides [67], rectangular horns, or their equivalents such as notch antennas [94,95].

The use of open-ended parallel-plate waveguides for spatial power combining has been demonstrated [67,96]. In this case, each parallel-plate region consists of a number of equispaced Gunn diodes. The backshorts in the grooves are adjusted to provide the simultaneous frequency tuning. The parallel-plate guides are stacked in the vertical direction. This is equivalent to having a grooved mirror. For synchronization purposes, a spherical mirror with a waveguide aperture is positioned in the front of the grooved section, creating a Fabry–Perot resonator. The array of parallel-plate identical oscillators can be modeled in an analogous manner as the grid-type oscillator array, described earlier. For the dominant mode of operation (established by its symmetric arrangement and in-phase excitation), an infinite array of these oscillators is equivalent to an infinite array of unit cells having electric walls at the top and bottom walls and the magnetic walls on its sides. The difference with the planar grid is that this symmetry is enforced instead of being assumed. Perhaps because of this enforced mode of operation, the parallel-plate waveguide offers better stability in comparison with the planar grid.

A radial equivalent of the parallel-plate groove concept for the Fabry–Perot resonator operation has been presented [97]. In this case, instead of using parallel-plate regions, a circular groove was used to accommodate Gunn diodes to enable them to operate in an axially symmetric mode. As in the parallel-plate guide case, a ray-collimating window, which also served the purpose of frequency synchronization, was used. High combining efficiency close to 100% was obtained.

One very interesting alternative option to open-ended waveguides is a tapered-slot antenna, also known as a *notch antenna*, whose basic configuration is shown in Fig. 19.

This antenna is considered a planar equivalent of a horn antenna. Their variations include Vivaldi and antipodal antennas. Belonging to the class of traveling-type antennas, they feature an increased, often multiband, frequency operation. This is a significant advantage over the patch, which can barely obtain a 50% operational bandwidth. In contrast to the patch, which is used in the tile-type array, the notch antenna allows for the brick array construction, providing more space for inclusion of active devices. These are usually placed at the nonradiative end

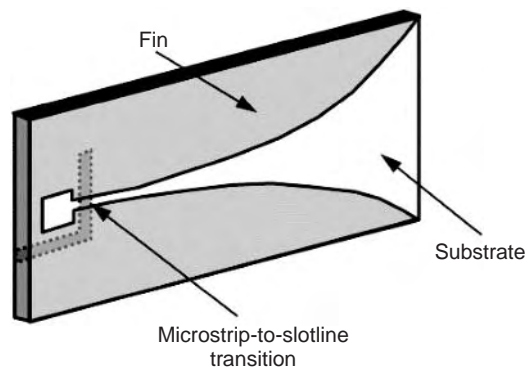


Figure 19. Configuration of a standard notch antenna fed by a microstrip coupled to the slot.

of the notch antenna. Examples of spatially combined oscillators and amplifiers using notch antennas have been presented in Refs. 95 and 98. Because of their large scope of operation, they are a suitable choice for broadband electronically tunable oscillators and multiband amplifiers. The use of tapered slot antennas to build the tray-type amplifier power combiner has been demonstrated [99]. The configuration of this amplifier is shown in Fig. 20.

It is worthwhile to note that tapered-slot antennas are not the only types of antennas that can be utilized in the tray-type power combiners. Other types of antenna elements that can be used in the tray-type power combiners are presented in Fig. 21.

Figure 21a shows quasi-Yagi antennas [100] as elements of tray power combiner. These elements feature an approximately 1-octave return loss bandwidth enabling a similar bandwidth for an entire combiner. Figure 21b shows a hybrid tray–tile combiner [101]. In this case, active stages are assembled using the tray configuration, while the coupling to pyramidal horns is achieved using passive patch arrays arranged in a tile configuration. Figure 21c shows a hybrid slab-beam combiner, with amplifiers positioned between focusing lenses [102].

6. ANALYSIS METHODS FOR POWER COMBINERS/DIVIDERS

Knowledge of equivalent-circuit parameters of power combiners/dividers is of paramount importance in their design process. This is often a nontrivial task, as it requires solving a three-dimensional electromagnetic field problem. In the past, many simplified methods were developed to tackle these complicated problems. Using these simplified methods, ample design rules for varieties of combiners/dividers were obtained. This situation has changed dramatically in the 1990s with a number of commercial, general-purpose electromagnetic (EM) field solvers being developed. Examples of commercial EM field software packages include IE3D of Zeland Software [103], Ansoft Ensemble [104], and High Frequency Structure Simulator [105], Agilent ADS [106], and CST Microwave Studio [107], to name just a few. In general, EM field solvers are based on integral or finite difference methods, in frequency or time do-

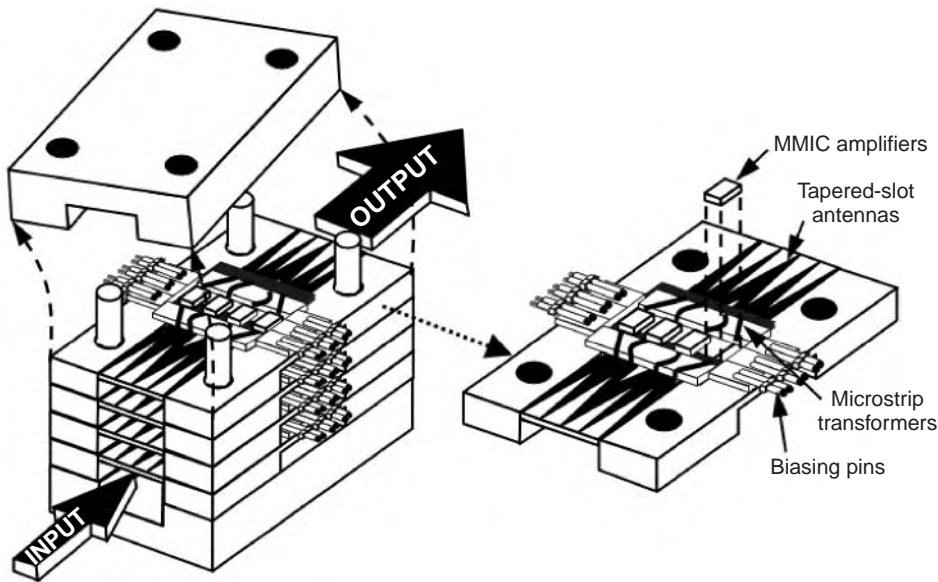


Figure 20. Configuration of a tray amplifier combiner using tapered-slot antennas.

main, and are capable of accurately analyzing arbitrarily shaped passive structures. Some of these software packages are also able to simultaneously analyze assemblies of passive and active devices in real time. One problem with the general-purpose EM field solvers is that they require large computing resources and long computational times. This may be inconvenient in cases when combining structures have to be optimized. This is because the optimization process usually requires much iteration time. Because of these shortcomings, it is advantageous to have alternative approximate ways for the analysis of combiners/dividers. In many cases, these methods can provide a relatively good approximation to the optimal design using less computing resources than the general-purpose commercial software. Nevertheless, the design process can be finalized using more accurate general-purpose software.

The following sections present examples of approximate methods for the analysis of selected power-combining/dividing structures, beginning with one-dimensional transmission-line-type combiners and then two- and three-dimensional structures.

6.1. Analysis of Transmission-Line-Type Combiners

As has been demonstrated earlier, a number of basic power-combining/dividing structures can be built using sections of transmission lines. For example, the Wilkinson power combiner/divider, 3-dB branchline coupler, and Gysel power combiner/divider can be built using microstrip or stripline transmission lines. The design equations for such structures using the transmission-line approach are straightforward and can be found in standard microwave books [58,108,109]; thus they are not repeated here. In practice, these simple design equations are not accurate enough as they neglect discontinuities in the form of tee junctions, mitered bends, and impedance steps, which real combining structures incorporate. To obtain a more accurate design, these discontinuities have to be taken into

account. Modern-day commercial software [103–107,110] not only provides this solution but also offers a necessary optimization before etching of the circuit takes place. This software can also take into account the presence of active devices in these structures [106].

6.2. Analysis of Planar Two-Dimensional Power-Combining Structures

Many planar power combiners cannot be represented by simple connections of transmission lines. Examples include microstrip planar circular disk combiners [45], sectorial dividers [54,55], and planar dividers with holes [56,57]. Also included in this list are combiners exploiting microstrip disk and annular ring-type couplers [111–113].

Analysis of these structures can be handled by a number of commercial software packages, which have been developed for the purpose of analyzing arbitrarily shaped 2- and 2.5D multilayer microstrip configurations. One example of such software is presented in Ref. 104. Full-wave analysis methods in real or spectral domains in association with the moment method can be employed to accomplish this task. The use of these software packages may lead to time-consuming computations due to their general-purpose nature.

For single-layer microstrip structures, an alternative boundary-element method can be used [112–114]. In this method, an arbitrarily shaped microstrip structure is modeled as a cavity, with top and bottom plates formed by a perfect electric conductor and their sidewalls formed by a perfect magnetic conductor. The electric field at the cavity's wall is assumed to be uniform with height but varying along the perimeter. In the combiner/divider, this cavity can incorporate a number of microstrip and coaxial ports. For coaxial ports, equivalent strips can be introduced to make the analysis approach uniform. To determine the equivalent circuit parameters, one of the ports is excited while the remaining ones are left open-circuited. At the excitation port the electric current is assumed to be

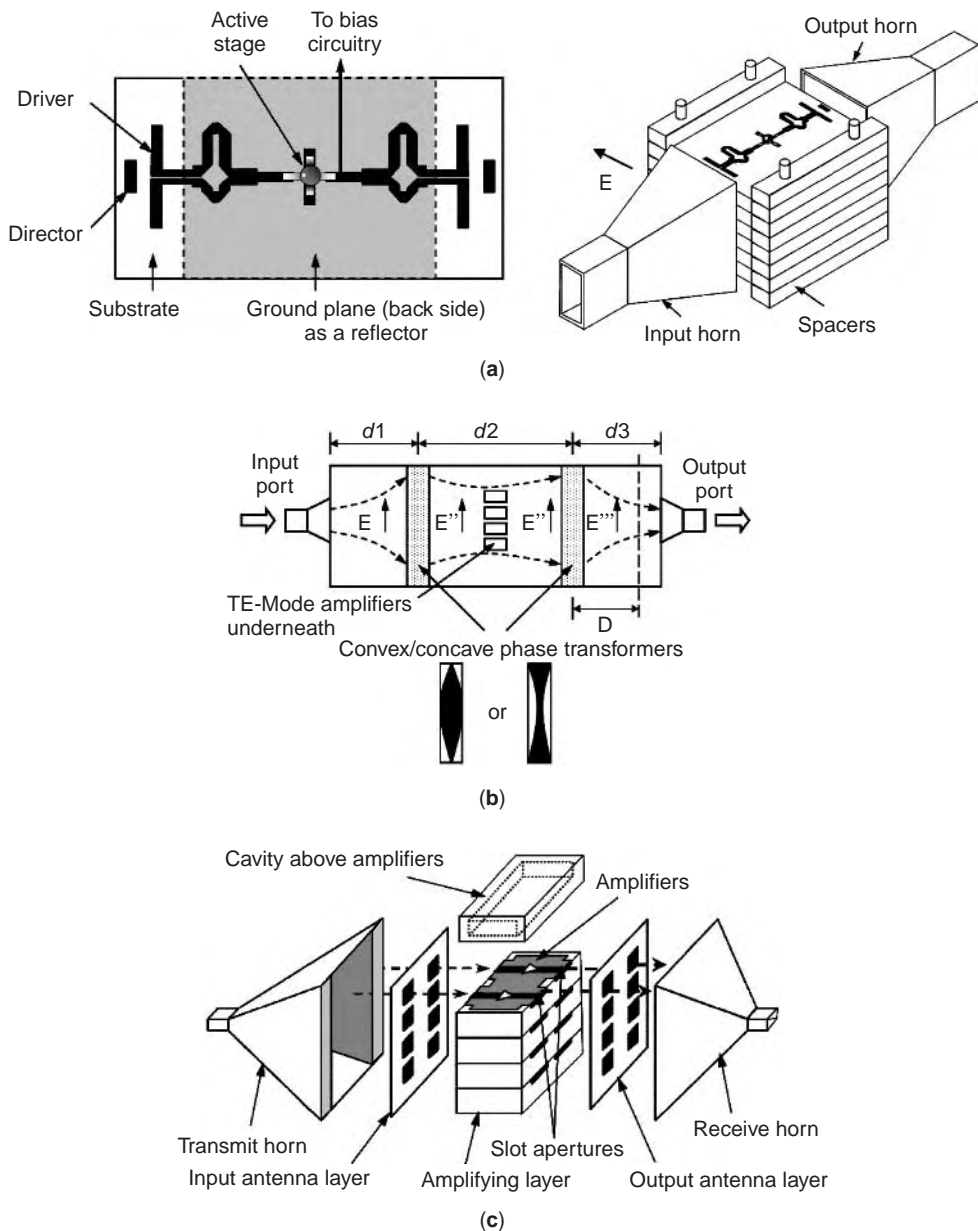


Figure 21. (a) Stacked-tray combiner including planar quasi-Yagi antennas; (b) waveguide-based aperture-coupled patch amplifier array; (c) hybrid slab-beam combiner.

known. The unknown is the electric field along the structure's perimeter, which has to be determined. As can be seen, using the magnetic wall model, a 2D problem is replaced by a 1D problem. This is in contrast to the usual full-wave analysis method in which the distribution of electric currents on an arbitrarily shaped conducting surface has to be determined to obtain equivalent parameters of planar single-layer circuits.

For an irregularly shaped microstrip structure, the wall surface is divided into a number of sections, each with a constant value of the electric field. Using field equations for a parallel-plate guide, a set of linear algebraic equations is generated that can be solved using standard methods. Having determined the electric field

distribution for the case of excitation of each single section of the boundary, an equivalent impedance matrix for the N port formed by N sections of the perimeter is determined [113,114]. For some regular microstrip structures, such as a circular disk or an annular ring, an alternative method of determining the impedance matrix of the equivalent N port can be employed. This time, the field in the cavity is expressed in terms of radial waves. The problem again reduces to a 1D problem, in which field expansion coefficients are determined. This alternative approach has been demonstrated in Refs. 45, 46, and 113.

One deficiency of the magnetic wall approach is the negligence of radiation. This leads to erroneous results at frequency points at which the structure becomes resonant

and radiating. Nevertheless, this approach generates reasonably accurate results for equivalent circuit parameters for many planar structures. The advantage of this approach is that these parameters are determined in a reasonably short time using an ordinary personal computer (PC), unlike general-purpose commercial software packages where the computational time becomes longer even using more powerful workstations.

6.3. Analysis of Waveguide and Cavity-Type Combiners

As has been shown in the preceding sections, many circuit-type power combining/dividing structures are formed by parallel-plate waveguides with coaxial probes or cylindrical posts perpendicular to the plates. Rectangular cavity, cylindrical, and radial cavities belong in this category.

Equivalent-circuit parameters of these structures can be derived assuming that rectangular waveguide entries, coaxial entries, or gaps in the posts form input/output ports of these structures. The usual assumption about these ports is that they support only single-mode operation. This includes the TEM mode for the coaxial line, the TE_{10} mode for the rectangular waveguide, and the TEM mode, having uniform dependence with height and axial symmetry, in the cylindrical gap in the post. Equivalent circuits of these structures, as viewed from their ports, can be determined by solving an electromagnetic field problem in which single ports are excited while the remaining ports are terminated. Depending on the chosen type of equivalent (admittance, impedance, or scattering matrix) parameters to be determined, a short circuit, an open circuit, or a match load is used as a termination. The choice depends on the configuration of the analyzed structure.

A major difficulty in finding a solution to this problem is due to arbitrarily positioned cylindrical posts and coaxial entries with respect to the walls of a rectangular or a cylindrical cavity, which do not allow for simple approximations. The analysis of these structures can be handled by a number of commercial software packages that have been developed for the purpose of analysis of arbitrarily shaped 3D passive structures such as the HFSS [105]. This approach is usually time-consuming, especially when the performance of these structures has to be optimized. This is why it is desirable to have approximate fast analyses. For this purpose, the problem can be simplified by assuming that the field in an adjacent cylindrical region containing a post or a coaxial probe (including the coaxial aperture) is axially symmetric. By making this assumption, the field in these cylindrical regions can be represented in terms of radial TM modes having only vertical component of the electric field and the azimuthal component of the magnetic field. These fields can generally vary in the vertical direction. The fields outside the cylindrical regions containing the probes or posts can be expressed as sums of waveguide modes. Special accelerating routines can be applied to achieve their fast convergence [115–117]. For a given excitation, the field within the combiner can be determined using, for example, a field-matching method. Using this approach, a number of elegant solutions to single or multiple probes in rectangular or radial guide have been presented in the microwave literature. The solutions

for rectangular waveguides include single and double coaxial probe [115,116], cylindrical posts and equivalent strip [117,118], and single and dual disk-ended probes [119]. Note that the problems of coaxially driven probes can also be solved in an alternative manner by replacing coaxial entries with equivalent gaps in post [119]. Excellent insights into the operation of a variety of coaxial-to-waveguide transitions with practical solutions have been presented in Ref. 120.

As in rectangular waveguide cavities, electromagnetic problems involving radial cavities with various types of posts and probes can be solved. Field-matching solutions for radial cavities with different types of probes were demonstrated in Refs. 34 and 38.

Radial or coaxial cavities with rectangular waveguide ports connected in their E or H plane were modeled in Refs. 121–123.

On the described basis of the analyses above, a number of computer programs have been developed. These programs can be run on any PC. They are able to determine equivalent-circuit parameters for a rectangular or radial cavity combiner with a moderate (<20) number of coaxial or waveguide ports at a single frequency point in a matter of seconds of central processing unit (CPU) time assuming at least a 100-MHz clock. Because of this feature, these programs are very useful in the analysis and design of many power-combining structures.

The developed analyses of parallel-plate type, rectangular, and radial cavity combiners with coaxial probes and cylindrical posts can also be useful in the design of conical and hemispherical cavity combiners. In this case, the design is divided into separate designs of central and peripheral probes. The design of the central probe is similar to the design of a good transition between a coaxial line and an infinite radial guide. The design of peripheral probes is equivalent to the design of probes in a rectangular waveguide with electric bottom and top walls and magnetic sidewalls. This design strategy was presented in Ref. 123.

6.4. Analysis of Spatial-Type Power Combining Structures

Similarly as for a circuit-type combiner, in order to obtain a predictable design of a space-type combiner it is important to know its equivalent circuit parameters as observed from the terminals of active devices. For example, knowledge of these parameters is necessary to obtain suitable impedance conditions for proper operation of active devices. Since some forms of space-level combiners represent active-array antennas, obtaining their radiation pattern through a suitable analysis is also of great importance. According to the classification presented in the preceding section, grids, arrays of patches, or assembly of open-ended waveguides have to be analyzed for characterizing these structures. Determining equivalent circuit parameters for such arrays is not a trivial task, usually due to a large number of elements, that require large computing resources. To ease the complexity of the problem, approximate and simplifying analyses can be applied to this purpose. In particular, these analyses may exploit symmetries

of power-combining structures to ease computational difficulties.

For large arrays of identical radiating elements with perfect symmetry in two planes, the analysis can often be confined to the unit cell problem. For example, this concept is explored in planar grid combiners, which is explained as follows. By assuming that the grid is infinite and active devices are matched and synchronized in magnitude, frequency, and phase, an identical environment is experienced by each one of these elements. Consequently, the analysis reduces to a single element cell. The unit cell often resembles the post or strip waveguide diode mounting structure that was initially analyzed in the 1970s [118]. The difference with the present case is that a perfect magnetic conductor, instead of an electric conductor, forms sidewalls of the equivalent rectangular waveguide. Using this equivalent-waveguide approach, grids including straight, bowtie, and double-vee strips can be analyzed [124,125].

For finite arrays, this approximate analysis can result in a relatively accurate equivalent circuit for elements in the center section of the array. This is because the elements in this section experience an environment similar to that in an infinite array. This is not the case for the end-array elements.

The absence of identical environment in a finite array makes the in-phase, unit cell analysis less accurate with respect to the array's radiation pattern. Because of the different neighboring environments, active elements may be out of phase. This results in effective combined power losses. Additionally, the progressive phase shift between adjacent elements that can unintentionally be established may result in an endfire operation of the array. To cause the elements to radiate in the broadside direction, the elements, particularly at the array's end, may require some means of tuning.

This example shows that for a finite-size grid array a strict EM field analysis is required to predict its real performance. This task can be accomplished with present-day software for the analysis of multilayer microstrip patch antennas such as those described in Refs. 104 and 105. This statement also applies to spatial combiners using patch antennas in so-called strong-coupled configurations.

For weakly coupled arrays of patches, the analysis of a single element may be sufficient for an ample design of the array. This is because impedance characteristics of the patch are only slightly affected by their placement in an array. However, the prediction of radiation performances of both weakly and strongly coupled patch arrays may still require a strict electromagnetic field analysis. For finite arrays, commercial software packages such as those described in Refs. 104 and 105 may be the best answer.

Spatial combiners with open-ended rectangular waveguides can be handled by approximate analyses, which have already been described for circuit-type rectangular waveguide combiners [123]. One extension, which is required in the present application, is to include open-space conditions at the apertures of these waveguides. An alternative way is to use commercial software packages, that are able to analyze three-dimensional open-ended waveguide diode mounting structures. The required tasks are

within the reach of the present day commercial packages using powerful workstations [126].

In order to accelerate the solution to the electromagnetic characterization of power-combining structures, it is advantageous to analytically preprocess a given problem or divide into smaller-scale problems that can be solved separately. The solution to the original problem is then found by connecting solutions of these smaller-scale electromagnetic problems into one solution. For example, spatial power combiners, including active stages and signal launching and collecting antennas, such as horn antennas, can be viewed as a cascade of waveguiding structures. These structures can be divided into sections, and each section can be modeled as a waveguide using a multimode approach. Such an approach has been applied to model the performance of conventional and special types of horn antennas and waveguide sections carrying the active stages of a power combiner. Examples of work in this field include Refs. 127 and 128.

7. APPLICATIONS

The preceding sections discussed the classification and analysis methods of various power-combining/dividing structures. This section discusses the application of circuit-level and space-level combiners to build powerful solid-state sources. Much of this discussion is concerned with the circuit-level power combining structures. The discussion concludes with examples of the most impressive circuit- and space-level combiners.

7.1. Solid-State Power Amplifiers (SSPAs) Using Circuit-Level Combiners

As can be gathered from the available literature concerning circuit-level power-combining capability of solid-state devices, the early structures dealt predominantly with two-terminal devices such as the Gunn or IMPATT diodes, whose outputs were combined to produce a more powerful source [2,3]. Waveguide cavities were used mainly as combining structures. The reason was that the early stage solid-state power combiners operated as oscillators. In this case, high- Q waveguide cavities were used for synchronization purposes.

Later developments in the field had seen the emergence of powerful three-terminal solid-state devices: transistors. These devices not only were able to produce a higher output level but also had higher DC-to-RF conversion efficiency, which was an extra advantage over their two-terminal counterparts. While the Gunn diode could achieve a few percent and the IMPATT diode could reach several percent, the transistor was able to achieve a 20–50%, DC-to-RF conversion rate.

As a three-terminal device, the transistor is better suited to planar rather than waveguide technology. Because of its likely broadband operation, the amplifier-mode rather than the oscillator mode of operation is preferred. Using the planar approach, cascaded amplifiers with tens of watts of output power can be built. However, even at this power level, these amplifiers require a good heatsink arrangement. This in turn requires a suitable substrate

with good thermal properties. Proper mounting of transistors including good-quality heatsinks is also necessary.

The cascade configuration has one advantage in that a large amplifying factor can be achieved using even a moderate number of amplifying stages. Its deficiency is that if one of the intermediate transistors fails, the entire amplifier may also record the failure. Thus this configuration does not exhibit graceful degradation. For to this reason, cascaded amplifiers are used in preamplification stages. A resilient strategy is required in the high-power stages to avoid catastrophic failure. Suitable power-combining techniques can be used to achieve this goal.

If one decides to continue with the planar technology to build the next amplifying stages, hybrid combiners are a good choice [39,130]. At the early stage of amplification process, two-way Wilkinson combiners can be used to build a corporate combining network [39]. This usually involves up to $N = 4$ individual modules. The configuration of Fig. 1b is employed in this process. A corporate divider splits the input signal into N ways. These in turn are input to N amplifying modules. A corporate combiner, identical to the divider, sums outputs of these amplifiers. As the next-size corporate combiner/divider handles $2^3 = 8$ amplifiers, it is often avoided because of its considerable size. It should be mentioned that some designers prefer to use 3-dB quadrature couplers instead of Wilkinson's dividers to build a corporate network [130] at this amplification stage.

Following this amplifying stage, the use of the corporate network faces some problems. This is due to the parasitics of isolating resistors [39] and general power losses that corporate networks incur. Dissipation of a considerable level of power in isolating resistors creates extra problems as well; thus, a preferable option is to share the failure between larger numbers of dissipating units. A waveguide radial divider/combiner and its like (hemispherical and conical combiners) provides a suitable solution [39,130]. The advantages of this device are a relatively large operational bandwidth (almost 1 octave), low insertion losses, good amplitude and phase balance as well as good isolation, which generally increase with the number of ports. Fine examples of radial divider/combiner employed in the last stages of solid-state transmitters have been demonstrated [33,39–42]. A 110-way radial divider/combiner was used in a 100-kW pulse L-band transmitter [39]. A 50-way radial divider/combiner was applied in a 22-kW pulse S-band transmitter [130]. A 20-way hemispherical divider/combiner was used in 60- and 80-Watt CW (continuous-wave) Ku-band SSPAs [40,41]. Similarly, a 30-way radial divider/combiner was employed in a 26-W CW X-band SSPA [42]. The design of a 60-GHz, 16-way power divider/combiner was presented in Ref. 33.

7.2. Solid-State Sources Using Space-Level Combiners

In Section 7.1 we showed that circuit-level combiners can offer the design of very reliable high-level power solid-state amplifiers at microwave frequencies and the lower end of millimeter waves. However, the extension of this type of combiner to upper millimeter-wave frequencies faces some difficulties. This is due to the tight manufac-

turing tolerances required at these frequency bands. For example, miniature coaxial probes are difficult to manufacture in some waveguide-type combiners. Other problems are associated with increased conductive and dielectric losses. For example, the quality factor for a resonant conductor cavity becomes low, making it less attractive for oscillator synchronization purposes.

The requirement for low conductive and dielectric losses demands that a new generation of millimeter-wave combiners should to a greater extent exploit a low-loss combining medium such as free space. At this frequency range, transversal dimensions of combining structures, in terms of multiples of wavelength, do not lead to a large physical size as is the case for their low-frequency counterparts. This means that a planar approach to building spatial combiners becomes a very feasible option. To reduce transversal dimensions, cascades of planar active stages can be explored [131]. However, at this stage of research, this solution has not found much success because of the reduced combining efficiency [131].

As mentioned earlier in this article, a lot of early work on spatial power combiners was concerned with oscillators. However, most of the more recent investigations concentrate on amplifiers. The reason is that amplifiers offer a larger instantaneous operational bandwidth. In addition, the amplifier design seems to be less critical, as compared to the oscillator, as knowledge of large-signal parameters of the solid-state device may be not necessary. The required small-signal parameters are easier to obtain from measurements or the manufacturer's data, making the design more feasible.

Although a large number of space-level combiners have been introduced, as summarized in three monographs [63,132,133], some of them have to be critically viewed. This is because the space-level combining concept is still in the exploration stage. For example, many of the structures presented are only low-cost prototypes. Often, they are formed by small-size arrays operating at the microwave frequency band.

Contrary to some expectations, spatial combiners may suffer from problems similar to those of their circuit-type counterparts. For example, in spatial resonators solid-state devices have to be properly spaced. Otherwise, a sudden drop in the combining efficiency is observed [65]. Patch oscillators with a strong coupling mechanism may suffer from the multimoding problem unless special configurations including resistive elements are used [75]. In addition, due to some undesired radiation mechanisms, spatial combiners face problems that have not been known for circuit-level combiners. For example, a random phase distribution in weakly or strongly coupled oscillators may be responsible for significant reduction in power-combining efficiency, while progressive phase shift can lead to an undesired beam squint [71,73–75] that effectively is regarded as power loss in the broadside direction.

The most impressive examples of spatial combiners, that have been accomplished so far concern structures with the largest number of passive or active elements. In this case, grid structures have a leading role. Examples include 100-element MESFET and HBT amplifiers or oscillators [77,134,135], a 464 element pin diode switch

[136], and a 4800 Schottky diode transmittance controller [136], to name only a few. Another example utilizing a large number of active stages involves a 137-element X-band amplifier reflectarray [137]. Other achievements in the field of space-level combining can be grouped in terms of the level of combined power and the frequency range in which a given level of power was reached. These include a 120-W X-band amplifier using the tray configuration of tapered-slot antennas [99], a 25-W Ka-band 45-element quasi-optical amplifier array using the tile configuration with through-plate coaxial transition [138] and a 5-W 37-GHz monolithic grid amplifier [139]. A 36-W V-band 272-element tray-type power combiner utilizing waveguide horns with focusing lenses, as described in Ref. 140, is a very impressive example with regard to the highest frequency of operation that has been achieved so far for space-level combiners.

Many of the above mentioned space-level combiners have been designed and developed with a considerable involvement of commercial companies. The interest and involvement of such institutions clearly indicates that the space-level power combining is not a purely academic research, but has a great potential to deliver new products to communication industries.

BIBLIOGRAPHY

1. S. Y. Liao, *Microwave Devices and Circuits*, 2nd ed., Prentice-Hall, Englewood Cliffs, NJ, 1985, pp. 167–168.
2. K. J. Russell, Microwave power combining techniques, *IEEE Trans. Microwave Theory Tech.*, **MTT-27**:472–478 (May 1979).
3. K. Chang, and C. Sun, Millimetre-wave power-combining techniques, *IEEE Trans. Microwave Theory Tech.* **MTT-31**:91–107 (Feb. 1983).
4. J. G. Josenhans, Diamond as an insulating heat sink for a series combination of IMPATT diodes, *Proc. IEEE* **56**:762–763 (1968).
5. C. T. Rucker et al., Symmetry experiments with four-mesa IMPATT-diodes, *IEEE Trans. Microwave Theory Tech.* **MTT-25**:75–76 (1977).
6. C. T. Rucker et al., Series-connected GaAs and Si diode chips: some new results, *Electron. Lett.* **13**(11):331–332 (1977).
7. C. T. Rucker et al., Multichip IMPATT power combining, a summary with new analytical and experimental results, *IEEE Trans. Microwave Theory Tech.* **MTT-27**:951–957 (1979).
8. D. Staiman, M. E. Breese, and W. T. Patton, New technique for combining solid-state sources, *IEEE J. Solid-State Circuits* **SC-3**:238–243 (1968).
9. J. C. Wiltse and J. W. Mink, Quasi-optical power combining of solid-state sources, *Microwave J.* 144–156 (1992).
10. R. S. Harp and H. L. Stover, Power combining of X-Band IMPATT circuit modules, *1973 IEEE-ISSCC Digest Tech. Papers*, 1973, Vol. XVI, pp. 118–119.
11. N. Okubo et al., A 6 GHz 80 W GaAs FET amplifier with TM-mode cavity power combiner, *1983 IEEE MTT-S Int. Microwave Symp. Digest*, 1983, pp. 276–278.
12. S. Nogi, M. Kojima, and K. Fukui, Wideband microwave power divider/combiner using conical-radial line, *1990 Asia-Pacific Microwave Conf. Proc.*, 1990, pp. 121–124.
13. R. Aston, Techniques for increasing the bandwidth of a TM₀₁₀-mode power combiner, *IEEE Trans. Microwave Theory Tech.* **MTT-27**:479–482 (1979).
14. J. A. Navarro, K. Chang, *Integrated Active Antennas and Spatial Power Combining*, Wiley Series in Microwave and Optical Engineering, Wiley, New York, 1996, Chapter 4.
15. K. Kurokawa and F. M. Magalhaes, An X-band 10-watt multiple-IMPATT oscillator, *Proc. IEEE* 102–103 (1971).
16. K. Kurokawa, The single-cavity multiple-device oscillator, *IEEE Trans. Microwave Theory Tech.* **MIT-19**:91–107 (1971).
17. K. Chang, and R. L. Ebert, W-Band power combiner design, *IEEE Trans. Microwave Theory Tech.* **MTT-28**:295–305 (1980).
18. K. Chang, W. F. Thrower, and G. M. Hayashibara, Millimeter-wave silicon IMPATT sources and combiners for 110–260 GHz range, *IEEE Trans. Microwave Theory Tech.* **MTT-29**:1278–1284 (1981).
19. K. Fukui et al., Ladder-type microwave power divider/combiners, *Electron. Commun. Jpn. Pt. 2* **74**(8):25–37 (1991).
20. A. Sanada, K. Fukui, and S. Nogi, A wideband microwave power divider/combiner with multiple-port double-ladder structure, *1992 Asia-Pacific Microwave Conf. Proc.*, Adelaide, 1992, pp. 885–888.
21. A. Sanada, K. Fukui, and S. Nogi, Traveling-wave microwave power divider composed of reflectionless dividing units, *IEEE Trans. Microwave Theory Tech.* **MTT-43**:4–20 (1995).
22. M. Dydyk, Efficient power combining, *IEEE Trans. Microwave Theory Tech.*, **MTT-28**:755–762 (1980).
23. C. A. Drubin et al., A 1 kW peak, 300 W avg IMPATT diode injection locked oscillator, *1982 MTT-S Int. Microwave Symp. Digest*, 1982, pp. 126–128.
24. S. Tanaka et al., Crucial factors in power combining by oversized cylindrical cavity multiple-device structures, *IEEE Trans. Microwave Theory Tech.* **MTT-37**:1755–1759 (1989).
25. H. Matsumara and H. Mizuno, Design of microwave power combiner with circular TM_{0m0} mode cavity, *Electron. Commun. Jpn. Pt. 2* **70**(9):1–10 (1987).
26. H. Matsumara, Analysis of a microwave power amplifier using a combiner/divider with circular cavities, *IEEE Trans. Microwave Theory Tech.* **MTT-38**:928–933 (1990).
27. K. Fukui and S. Nogi, Mode analytical study of cylindrical cavity power combiners, *IEEE Trans. Microwave Theory Tech.* **MTT-34**(9):943–951 (Sept. 1986).
28. S. Nogi and K. Fukui, TM_{0n0}- and TM_{m10}- mode oversized cylindrical cavity power combiners, *IEEE Trans. Microwave Theory Tech.* **MTT-35**:835–842 (1987).
29. G. W. Swift et al., A radial wave power combiner designed by broadband techniques, *15th European Microwave Conf. Proc.* 1985, pp. 973–978.
30. G. W. Swift and D. I. Stones, A comprehensive design technique for the radial wave power combiner, *1988 IEEE MTT-S Int. Microwave Symp. Digest*, 1988, pp. 279–281.
31. M. Oz, Wideband double-ridged 8-way radial combiner, *14th European Microwave Conf. Proc.*, Sept. 1984, pp. 317–322.
32. M. Oz et al., High efficiency, single-ridged, 16-way radial power combiner, *21st European Microwave Conf. Proc.* 1991, pp. 1029–1034.

33. T. Hsu, and M. D. Simonoutti, A wideband 60 GHz 16-way power divider/combiner, *1984 IEEE MTT-S Int. Microwave Symp. Digest* 1984, pp. 175–177.
34. M. E. Bialkowski, and V. P. Waris, Electromagnetic model of a planar radial-waveguide divider/combiner incorporating probes, *IEEE Trans. Microwave Theory Tech.* **41**:1126–1134 (1993).
35. A. Thompson, and J. V. Yelland, A sixty-way S-band radial waveguide, *14th European Microwave Conf. Proc.* 1984, pp. 335–340.
36. S. Nogi, M. Kojima, and K. Fukui, Wideband microwave power divider/combiner using conical-radial line, *1990 Asia-Pacific Microwave Conf. Proc.* 1990, pp. 121–124.
37. S. Nogi, F. Okazaki, and K. Fukui, A broadband conical-radial wave power divider/combiner, *1994 Asia-Pacific Microwave Conf. Proc.* 1994, pp. 507–510.
38. M. E. Bialkowski and V. P. Waris, Analysis of an N-way radial cavity divider with a coaxial central port and waveguide output ports, *IEEE Trans. Microwave Theory Tech.* **MTT-44**:2010–2016 (1996).
39. B. J. Sanders, Radial combiner runs circles around hybrids, *Microwaves* 55–58 (Nov. 1980).
40. P. J. Allen and J. B. Ness, A hemispherical radial power-waveguide divider/combiner for high power amplifiers, *IRECON 1987 Proc.*, Sydney, 1987, pp. 102–104.
41. P. Martin, P. J. Allen, and J. B. Ness, A 14 GHz 80 watt GaAs FET amplifier, *21st European Microwave Conf. Proc.* 1991, pp. 1465–1468.
42. E. Belohoubek et al., 30-way radial power combiner for miniature GaAs FET power amplifiers, *1986 IEEE MTT-S Int. Microwave Symp. Digest*, 1986, pp. 515–518.
43. A. Fathy and D. Kalokitis, Analysis and design of a 30-way radial combiner for Ku-band applications, *RCA Rev.* **47**: 487–508 (1986).
44. A. A. M. Saleh, Planar electrically symmetric n-way hybrid power dividers/combiners, *IEEE Trans. Microwave Theory Tech.* **MTT-28**:555–563 (1980).
45. M. D. Abouzahra and K. C. Gupta, Multiple-port power divider/combiner circuits using circular microstrip disk configurations, *IEEE Trans. Microwave Theory Tech.* **MTT-35**:1296–1302 (1987).
46. J. Goel, A K-band GaAs FET amplifier with 8.2-W output power, *IEEE Trans. Microwave Theory Tech.* **MTT-32**: 317–323 (1984).
47. M. Cohn, B. D. Geller, and J. M. Schellenberg, A 10 Watt broadband FET combiner/amplifier, *1979 IEEE MTT-S Int. Microwave Symp. Digest*, 1979, pp. 292–297.
48. E. J. Wilkinson, An N-way hybrid power divider, *IRE Trans. Microwave Theory Tech.* **MTT-8**:116–118 (1960).
49. H. Y. Yee, F. C. Chang, and N. F. Audeh, N-way TEM-mode broadband power dividers, *IEEE Trans. Microwave Theory Tech.* **MTT-18**:682–688 (1970).
50. N. Nagai, M. Maekawa, and K. Ono, Ne N-way power dividers, *IEEE Trans. Microwave Theory Tech.* **MTT-25**:1008–1012 (1977).
51. Z. Galani and S. J. Temple, A broadband planar N-way combiner/divider, *1977 IEEE MTT-S Int. Microwave Symp. Digest*, June 1977, pp. 499–502.
52. U. H. Gysel, A new N-way power divider/combiner suitable for high power applications, *1975 IEEE MTT-S Int. Microwave Symp. Digest*, June 1975, pp. 116–119.
53. L. I. Parad and R. L. Moynihan, Split-tee power divider, *IEEE Trans. Microwave Theory Tech.* **MTT-13**:91–95 (1965).
54. M. D. Abouzahra and K. C. Gupta, Multiport power divider-combiner circuits using circular-sector-shaped planar components, *IEEE Trans. Microwave Theory Tech.* **MTT-36**:1747–1751 (1988).
55. P. S. Kooi et al., A multi-way broadband sectorial power divider using exponential taper, *Proc. 1995 Asia-Pacific Microwave Conf. KAIST, Taejon, Korea, Oct. 9–13, 1995*, pp. 48–51.
56. Q.-C. Sun, K. W. Eccleston, and S. P. Yeo, The design of optimum planar power dividers/combiners for SSPA applications, *Proc. 1995 Asia-Pacific Microwave Conf.*, KAIST, Taejon, Korea, Oct 9–13, 1995, pp. 56–59.
57. K. W. Eccleston, Q.-C. Sun, and S. P. Yeo, Tapered microstripline power combiners with colinear input ports, *Microwave Opt. Technol. Lett.* (Aug. 1997).
58. E. A. Wolff and R. Kaul, *Microwave Engineering and Systems Applications*, Wiley, New York, 1988, Chapter 8.
59. S. J. Foti, R. P. Flam, and W. J. Scharpf, Jr, 60-way radial combiner uses no isolators, *Microwaves RF* 96–118 (July 1984).
60. M. E. Bialkowski, S. T. Jellett, and R. S. Varnes, Electronically steered antenna system for the Australian Mobilesat, *IEE Proc. Microwave Anten. Propag.* **143**:347–352 (1996).
61. N. C. Karmakar and M. E. Bialkowski, A compact switched-beam array antenna for mobile satellite communications, *Microwave Opt. Technol. Lett.* **21**:186–191 (1999).
62. N. C. Karmakar and M. E. Bialkowski, A beamforming network for a circular switched-beam phased array antenna, *IEEE Microwave Wireless Compon. Lett.* **11**:7–9 (2001).
63. J. A. Navarro and K. Chang, *Integrated Active Antennas and Spatial Power Combining*, Wiley, New York, 1996.
64. L. Wandinger and V. Nalbandian, Millimeter-wave power combining using quasi-optical techniques, *IEEE Trans. Microwave Theory Tech.* **MTT-31**:189–193 (1983).
65. J. W. Mink, Quasi-optical power combining of solid-state millimeter-wave sources, *IEEE Trans. Microwave Theory Tech.* **MTT-34**:273–278 (1986).
66. J. C. Wiltse and J. W. Mink, Quasi-optical power combining of solid-state sources, *Microwave J.* 144–150 (Feb. 1992).
67. S. Young and K. D. Stephan, Stabilisation and power combining of planar microwave oscillators with an open resonator, *1987 IEEE MTT-S Int. Microwave Symp. Digest*, 1987, pp. 185–188.
68. M. Nakayama et al., Quasi-optical resonator for millimeter and submillimeter wave solid-state sources, *1990 IEEE MTT-S Int. Microwave Symp. Digest*, 1990, pp. 1209–1212.
69. K. D. Stephan, Inter-injection-locked oscillators for power combining and phased arrays, *IEEE Trans. Microwave Theory Tech.* **MTT-34**:1017–1025 (1986).
70. K. D. Stephan, Analysis of inter-injection-locked oscillators for integrated phased arrays, *IEEE Trans. Anten. Propag.* **35**:771–781 (1987).
71. R. A. York and R. C. Compton, Quasi-optical for power combining using mutually synchronized oscillator arrays, *IEEE Trans. Microwave Theory Tech.* **MTT-39**:1000–1009 (1991).
72. R. A. York, Nonlinear analysis of phase relationships in quasi-optical oscillator arrays, *IEEE Trans. Microwave Theory Tech.* **MTT-41**:1799–1809 (1993).
73. P. Liao and R. A. York, Phase-shifterless beam-scanning using coupled-oscillators: Theory and experiment, *IEEE Trans. Microwave Theory Tech.* **MTT-41**:1810–1815 (1993).
74. P. Liao and R. A. York, A six-element beam-scanning array, *IEEE Microwave Guided Wave Lett.* **4**:20–22 (1994).

75. S. Nogi, J. Lin, and T. Itoh, Mode analysis and stabilisation of a spatial power combining array with strongly coupled oscillators, *IEEE Trans. Microwave Theory Tech.* **MTT-41**:1827–1837 (1993).
76. Z. B. Popovic et al., Bar-grid oscillators, *IEEE Trans. Microwave Theory Tech.* **MTT-38**:225–229 (1990).
77. Z. B. Popovic et al., A 100-MESFET planar grid oscillator, *IEEE Trans. Microwave Theory Tech.* **MTT-39**:193–200 (1991).
78. K. Chang, K. A. Hummer, and J. L. Klein, Experiments on injection locking of active antenna elements for active phased arrays and spatial power combiners, *IEEE Trans. Microwave Theory Tech.* **MTT-37**:1078–1084 (1989).
79. R. Adler, A study of locking phenomena in oscillators, *Proc. IRE Waves Electrons* 351–357 (June 1946).
80. R. J. Pogorzelski, P. F. Maccarini, and R. A. York, Continuum modeling of the dynamics of externally injection-locked coupled oscillator arrays, *IEEE Trans. Microwave Theory Tech.* **MTT-47**:471–478 (1999).
81. R. J. Pogorzelski, Two-dimensional array beam scanning via externally and mutually injection-locked coupled oscillators, *IEEE Trans. Anten. Propag.* **AP-49**:243–249 (Feb. 2001).
82. J. D. Kraus, A backward angle-fire array antenna, *IEEE Trans. Anten. Propag.* **12**:48–50 (1964).
83. C. Chen, Transmission of microwaves through perforated flat plates of finite thickness, *IEEE Trans. Microwave Theory Tech.* **MTT-37**:1078–1084 (1989).
84. W. C. Brown, Experiments in transportation of energy by microwave beam, *1964 IEEE MTT-S Int. Microwave Symp. Digest*, 1964, pp. 8–17.
85. C. Chen, The history of power transmission by radio waves, *IEEE Trans. Microwave Theory Tech.* **MTT-32**:1230–1242 (1984).
86. Z. B. Popovic and D. B. Rutledge, Diode grid oscillators, *Proc. 1988 IEEE Antennas Propagation Symp.*, 1988, pp. 442–445.
87. Z. B. Popovic, M. Kim, and D. B. Rutledge, Grid oscillators, *Int. J. Infrared Millimeter Waves* **9**:647–654 (1988).
88. H. J. Thomas, D. L. Fudge, and G. Morris, Gunn source integrated with microstrip patch, *Microwaves RF* **24**(2):87–91 (Feb. 1985).
89. M. Dydyk, Planar radial resonator oscillator, *1986 IEEE MTT-S Int. Microwave Symp. Digest*, 1986, pp. 167–168.
90. J. Lin and T. Itoh, Two-dimensional quasi-optical power combining arrays using strongly coupled oscillators, *IEEE Trans. Microwave Theory Tech.* **MTT-42**:734–741 (1994).
91. R. A. York, R. D. Martinez, and R. C. Compton, Active patch antenna element for array applications, *Electron. Lett.* **26**(7):494–495 (March 1990).
92. A. Balasubramaniyan and A. Mortazawi, Two-dimensional MESFET-based spatial power combiners, *IEEE Microwave Guided Wave Lett.* **3**:366–368 (1993).
93. A. W. Robinson and M. E. Bialkowski, Ku-band planar amplifier unit cell, *1995 Asia-Pacific Microwave Conf. Proc.*, Korea, Oct. 10–13, 1995, pp. 724–727.
94. S. Kawasaki and T. Itoh, Quasi-optical power planar arrays with FETs and slots, *IEEE Trans. Microwave Theory Tech.* **MTT-41**:1838–1844 (1993).
95. R. N. Simmons and R. Q. Lee, Spatial frequency multiplier with active linearly tapered slot antenna array, *1994 IEEE MTT-S Int. Microwave Symp. Digest*, 1994, pp. 1557–1560.
96. J. Bae et al., Millimeter and submillimeter wave quasi-optical oscillator with Gunn diodes, *IEEE Trans. Microwave Theory Tech.* **MTT-41**:1851–1854 (1993).
97. M. Sanagi et al., Fabry–Perot multiple-device oscillator using an axially symmetric mode, *Proc. 1994 Asia-Pacific Microwave Conf.*, Tokyo, 1994, pp. 859–862.
98. J. A. Navarro, Y. H. Shu, and K. Chang, Broadband electronically tunable planar active radiating elements and spatial power combiners using notch antennas, *IEEE Trans. Microwave Theory Tech.* **MTT-40**:323–328 (1992).
99. N. S. Cheng et al., A 120-W X-band spatially combined solid-state amplifier, *IEEE Trans. Microwave Theory Tech.* **MTT-47**:2557–2561 (1999).
100. M. E. Bialkowski and H. J. Song, Investigations into a power combining structure formed by uniplanar quasi-Yagi microstrip antennas, *Microwave Opt. Technol. Lett.* **27**:50–53 (2000).
101. A. B. Yakovlev, S. Oritz, M. Ozkar, A. Mortazawi, and M. B. Steer, A waveguide-based aperture-coupled patch amplifier array, full-wave system analysis and experimental evaluation, *IEEE Trans. Microwave Theory Tech.* **MTT-48**:2692–2699 (2000).
102. H. Hwang, G. P. Monahan, M. B. Steer, J. W. Mink, J. Harvey, A. Paollea, and F. K. Schwing, A dielectric slab waveguide with four planar power amplifiers, *1995 IEEE MTT-S Int. Microwave Symp. Digest*, May 1995, pp. 921–924.
103. IE3D, Zealand Software, Inc., Fremont, CA.
104. Ensemble, Ansoft Corp., Pittsburgh, PA.
105. High Frequency Structure Simulator (HFSS), Ansoft Corporation, Pittsburgh, PA.
106. Agilent ADS 2002, Agilent Technologies, Palo Alto, CA.
107. CST Microwave Studio, Computer Simulation Technology, Darmstadt, Germany.
108. D. M. Pozar, *Microwave Engineering*, Addison-Wesley, Reading MA, 1990.
109. S. Rosloniec, *Algorithms for Computer-Aided Design of Linear Microwave Circuits*, Artech House, Norwood, MA, 1990.
110. H. J. Song and M. E. Bialkowski, A multi-layer microstrip patch antenna sub-array design using CAD, *Microwave J.* **40**(3):22–34 (March 1997).
111. F. Tefiku and E. Yamashita, Improved analysis method for multiport microstrip annular-ring power-dividers, *IEEE Trans. Microwave Theory Tech.* **MTT-42**:376–382 (1994).
112. T. Kawai and I. Ohta, Planar-circuit-type 3 dB quadrature hybrids, *1994 IEEE MTT-S Int. Microwave Symp. Digest*, 1994, pp. 205–208.
113. M. E. Bialkowski and S. T. Jellett, A theoretical analysis of a planar elliptically shaped 3 dB quadrature coupler, *Microwave Optical Tech. Lett.* **8**:140–144 (1995).
114. T. Okoshi and T. Miyoshi, The planar circuits and approach to microwave integrated circuitry, *IEEE Trans. Microwave Theory Tech.* **MTT-20**:245–252 (1972).
115. A. G. Williamson, Analysis and modeling of a coaxial-line/rectangular waveguide junction, *Proc. IEE H* **129**:262–270 (1982).
116. M. E. Bialkowski, Modelling of a coaxial-waveguide power combining structure *IEEE Trans. Microwave Theory Tech.* **MTT-34**:937–942 (1986).
117. A. G. Williamson, Analysis and modeling of a single-post waveguide mounting structure, *Proc. IEE H* **129**:271–277 (1982).
118. R. L. Eisenhart and P. J. Khan, Theoretical and experimental analysis of a waveguide mounting structure, *IEEE Trans. Microwave Theory Tech.* **MTT-19**:706–719 (1971).

119. M. E. Bialkowski, Analysis of a coaxial-to-waveguide adaptor including a disc-ended probe and a tuning post, *IEEE Trans. Microwave Theory Tech.* **43**:344–349 (1995).
120. F. C. de Ronde, Ideal w.g. to coax transitions using a f.b.m. monopole, *1988 IEEE MTT-S Int. Microwave Symp. Digest*, 1988, pp. 591–593.
121. M. E. Bialkowski et al., Simplified mode-matching techniques for the analysis of coaxial-cavity-coupled radial e-plane power dividers, *IEEE Trans. Microwave Theory Tech.* **MTT-43**:1875–1880 (1995).
122. M. E. Bialkowski, V. P. Waris, and P. W. Davis, Field matching analysis of a hybrid structure including a radial cavity and h-plane coupled rectangular waveguides, *IEICE Trans. Electron.* (special issue on microwave and millimeter-wave technology) **E78-C(8)**:1146–1150 (Aug. 1995) (Japan).
123. V. Waris, *Field Matching Analyses of Radial Waveguide Power Combiners and Dividers*, Ph.D. thesis, Univ. Queensland, June 1997.
124. A. Pance and M. J. Wengler, Microwave modeling of 2-D active grid array antenna arrays, *IEEE Trans. Microwave Theory Tech.* **MTT-43**:1875–1880 (1995).
125. S. C. Bundy and Z. B. Popovic, Analysis of planar grid oscillators, *1994 IEEE MTT-S Int. Microwave Symp. Digest*, 1994, pp. 827–830.
126. P. W. Davis and M. E. Bialkowski, Performance of field matching and finite element methods on analyzing coaxial-to-waveguide transitions, *J. Electric. Electron. Eng.* (special issue on antennas) **15(1)**:23–29 (March 1995).
127. M. A. Ali et al., Analysis and measurement of hard horns for the excitation of quasi-optical amplifiers, *1998 IEEE MTT-S Int. Microwave Symp. Digest*, 1998, pp. 1469–1472.
128. M. B. Steer et al., Global modeling of spatially distributed microwave and millimeter-wave systems, *IEEE Trans. Microwave Theory Tech.* **MTT-47**:830–839 (1999).
129. W. Batty et al., Global coupled EM-electrical-thermal simulation and experimental validation for a spatial power combining MMIC array, *IEEE Trans. Microwave Theory Tech.* **MTT-50**:2820–2833 (2002).
130. M. Kumar et al., 22 kW next generation low cost s-band solid state transmitter for surveillance and air traffic control radars, *1995 IEEE MTT-S Int. Microwave Symp. Digest*, 1995, pp. 1601–1604.
131. W. A. Shiroma, B. L. Shaw, and Z. B. Popovic, Three dimensional power combiners, *1994 IEEE MTT-S Int. Microwave Symp. Digest*, 1994, pp. 831–834.
132. R. A. York and Z. B. Popovic, eds., *Active and Quasi-Optical Arrays for Solid-State Power Combining*, Wiley, New York, 1997.
133. A. Mortazawi, T. Itoh, and J. Harvey, eds., *Active Antennas and Quasi-Optical Arrays*. IEEE Press, Piscataway, NJ, 1999.
134. M. Kim et al., A 100-element HBT grid amplifier, *IEEE Trans. Microwave Theory Tech.* **MTT-41**:1762–1771 (1993).
135. K. D. Stephan, F. H. Spooner, and P. F. Goldsmith, Quasi-optical millimeter-wave hybrid and monolithic PIN diode switches, *IEEE Trans. Microwave Theory Tech.* **MTT-41**:1791–1798 (1993).
136. L. B. Sjogren et al., A monolithic diode array millimeter-wave beam transmittance controller, *IEEE Trans. Microwave Theory Tech.* **MTT-41**:1782–1790 (1993).
137. M. E. Bialkowski, A. W. Robinson, and H. J. Song, Design, development and testing of X-band amplifying reflectarrays, *IEEE Trans. Anten. Propag.* **AP-50**:1065–1076 (2002).
138. S. Ortiz et al., “A 25-Watt and 50-Watt Ka-Band quasi-optical amplifier”, *2000 IEEE MTT-S Int. Microwave Symp. Digest*, 2000, pp. 797–800.
139. B. Deckman et al., A 5-Watt, 37-GHz monolithic grid amplifier, *2000 IEEE MTT-S Int. Microwave Symp. Digest*, 2000, pp. 805–808.
140. J. J. Sowers et al., A 36-Watt V-band, solid-state source, *1999 IEEE MTT-S Int. Microwave Symp. Digest*, 1999, pp. 235–238.

PREAMPLIFIERS

J. F. DUQUE-CARRILLO
University of Extremadura
GUIDO TORELLI
University of Pavia

The essential task of sensors, detectors, and transducers is to convert the characteristics of the physical world (e.g., light, sound, pressure, displacement, temperature) into electrical signals, which are then suitably processed for the required application. Before being processed, these electrical signals must be conditioned by appropriate electronic circuitry.

Despite the improvements carried out in recent years, all sensors have a common characteristic: a weak signal delivered and a limiting noise level. Therefore, the front end of the sensor-associated electronic system must be an amplifier, usually called a *preamplifier*. Two main requirements must be satisfied for preamplifiers. First, they must raise the signal level adequately over a certain frequency range (linear amplification is very often requested). Second, they must contribute only a minimum amount of additional noise. Depending on the specific application, other features such as high linearity, large output swing, wide-band operation, and large output drive capability may be needed, but these requirements do not differ substantially from those of normal amplifiers. What is specifically important for preamplifiers is to optimize their noise performance. This is because, although the noise performance of a generic electronic system [which is made up of a preamplifier, signal conditioning and processing circuitry, and output interface (Fig. 1)] depends on the noise behavior of all these subsystems, in practice, in a well-designed system the noise performance is entirely dominated by the noise characteristics of the front-end circuit (preamplifier). This is true if the preamplifier gain is sufficiently high to allow the subsequent processing to be performed with negligible degradation in the signal-to-noise ratio. Hence, low-noise system design is focused mainly on low-noise preamplifier design.

1. BASIC CONCEPTS RELATED TO PREAMPLIFIERS

Some basic concepts useful in analyzing preamplifiers from the noise standpoint, namely, equivalent input noise,

119. M. E. Bialkowski, Analysis of a coaxial-to-waveguide adaptor including a disc-ended probe and a tuning post, *IEEE Trans. Microwave Theory Tech.* **43**:344–349 (1995).
120. F. C. de Ronde, Ideal w.g. to coax transitions using a f.b.m. monopole, *1988 IEEE MTT-S Int. Microwave Symp. Digest*, 1988, pp. 591–593.
121. M. E. Bialkowski et al., Simplified mode-matching techniques for the analysis of coaxial-cavity-coupled radial e-plane power dividers, *IEEE Trans. Microwave Theory Tech.* **MTT-43**:1875–1880 (1995).
122. M. E. Bialkowski, V. P. Waris, and P. W. Davis, Field matching analysis of a hybrid structure including a radial cavity and h-plane coupled rectangular waveguides, *IEICE Trans. Electron.* (special issue on microwave and millimeter-wave technology) **E78-C(8)**:1146–1150 (Aug. 1995) (Japan).
123. V. Waris, *Field Matching Analyses of Radial Waveguide Power Combiners and Dividers*, Ph.D. thesis, Univ. Queensland, June 1997.
124. A. Pance and M. J. Wengler, Microwave modeling of 2-D active grid array antenna arrays, *IEEE Trans. Microwave Theory Tech.* **MTT-43**:1875–1880 (1995).
125. S. C. Bundy and Z. B. Popovic, Analysis of planar grid oscillators, *1994 IEEE MTT-S Int. Microwave Symp. Digest*, 1994, pp. 827–830.
126. P. W. Davis and M. E. Bialkowski, Performance of field matching and finite element methods on analyzing coaxial-to-waveguide transitions, *J. Electric. Electron. Eng.* (special issue on antennas) **15(1)**:23–29 (March 1995).
127. M. A. Ali et al., Analysis and measurement of hard horns for the excitation of quasi-optical amplifiers, *1998 IEEE MTT-S Int. Microwave Symp. Digest*, 1998, pp. 1469–1472.
128. M. B. Steer et al., Global modeling of spatially distributed microwave and millimeter-wave systems, *IEEE Trans. Microwave Theory Tech.* **MTT-47**:830–839 (1999).
129. W. Batty et al., Global coupled EM-electrical-thermal simulation and experimental validation for a spatial power combining MMIC array, *IEEE Trans. Microwave Theory Tech.* **MTT-50**:2820–2833 (2002).
130. M. Kumar et al., 22 kW next generation low cost s-band solid state transmitter for surveillance and air traffic control radars, *1995 IEEE MTT-S Int. Microwave Symp. Digest*, 1995, pp. 1601–1604.
131. W. A. Shiroma, B. L. Shaw, and Z. B. Popovic, Three dimensional power combiners, *1994 IEEE MTT-S Int. Microwave Symp. Digest*, 1994, pp. 831–834.
132. R. A. York and Z. B. Popovic, eds., *Active and Quasi-Optical Arrays for Solid-State Power Combining*, Wiley, New York, 1997.
133. A. Mortazawi, T. Itoh, and J. Harvey, eds., *Active Antennas and Quasi-Optical Arrays*. IEEE Press, Piscataway, NJ, 1999.
134. M. Kim et al., A 100-element HBT grid amplifier, *IEEE Trans. Microwave Theory Tech.* **MTT-41**:1762–1771 (1993).
135. K. D. Stephan, F. H. Spooner, and P. F. Goldsmith, Quasi-optical millimeter-wave hybrid and monolithic PIN diode switches, *IEEE Trans. Microwave Theory Tech.* **MTT-41**:1791–1798 (1993).
136. L. B. Sjogren et al., A monolithic diode array millimeter-wave beam transmittance controller, *IEEE Trans. Microwave Theory Tech.* **MTT-41**:1782–1790 (1993).
137. M. E. Bialkowski, A. W. Robinson, and H. J. Song, Design, development and testing of X-band amplifying reflectarrays, *IEEE Trans. Anten. Propag.* **AP-50**:1065–1076 (2002).
138. S. Ortiz et al., “A 25-Watt and 50-Watt Ka-Band quasi-optical amplifier”, *2000 IEEE MTT-S Int. Microwave Symp. Digest*, 2000, pp. 797–800.
139. B. Deckman et al., A 5-Watt, 37-GHz monolithic grid amplifier, *2000 IEEE MTT-S Int. Microwave Symp. Digest*, 2000, pp. 805–808.
140. J. J. Sowers et al., A 36-Watt V-band, solid-state source, *1999 IEEE MTT-S Int. Microwave Symp. Digest*, 1999, pp. 235–238.

PREAMPLIFIERS

J. F. DUQUE-CARRILLO
University of Extremadura
GUIDO TORELLI
University of Pavia

The essential task of sensors, detectors, and transducers is to convert the characteristics of the physical world (e.g., light, sound, pressure, displacement, temperature) into electrical signals, which are then suitably processed for the required application. Before being processed, these electrical signals must be conditioned by appropriate electronic circuitry.

Despite the improvements carried out in recent years, all sensors have a common characteristic: a weak signal delivered and a limiting noise level. Therefore, the front end of the sensor-associated electronic system must be an amplifier, usually called a *preamplifier*. Two main requirements must be satisfied for preamplifiers. First, they must raise the signal level adequately over a certain frequency range (linear amplification is very often requested). Second, they must contribute only a minimum amount of additional noise. Depending on the specific application, other features such as high linearity, large output swing, wide-band operation, and large output drive capability may be needed, but these requirements do not differ substantially from those of normal amplifiers. What is specifically important for preamplifiers is to optimize their noise performance. This is because, although the noise performance of a generic electronic system [which is made up of a preamplifier, signal conditioning and processing circuitry, and output interface (Fig. 1)] depends on the noise behavior of all these subsystems, in practice, in a well-designed system the noise performance is entirely dominated by the noise characteristics of the front-end circuit (preamplifier). This is true if the preamplifier gain is sufficiently high to allow the subsequent processing to be performed with negligible degradation in the signal-to-noise ratio. Hence, low-noise system design is focused mainly on low-noise preamplifier design.

1. BASIC CONCEPTS RELATED TO PREAMPLIFIERS

Some basic concepts useful in analyzing preamplifiers from the noise standpoint, namely, equivalent input noise,

noise factor and noise figure, and noise matching, are introduced in this section.

1.1. Equivalent Input Noise

In the characterization of many nonideal electrical quantities, which are generated by a plurality of sources or mechanisms within a circuit, it is a common practice to replace all by one equivalent input source. This equivalent source has the same effect at the circuit output as the global effect of all the individual internal sources and, therefore, the circuit can be considered free of such mechanisms [1], which greatly simplifies circuit analysis and design. Offset voltage and noise are representative examples of what has been discussed.

A network, such as an amplifier, is made up of many components. Any electrical component has its own internal mechanisms of noise generation. As a result, the output of any real amplifier exhibits noise, which depends on factors such as internal noise sources, circuit topology, gain, and measurement bandwidth. The amplifier’s output noise power spectral density can be found by multiplying the noise power spectral density of each source by the squared module of its particular transfer function and then superposing all the individual noise contributions. This procedure must be followed for any frequency of interest.

Rather than by the noise measured at its output, an amplifier is best characterized by the minimum signal applied to its input, which is still detectable at the output of the signal processor. This signal may be conveniently regarded as equivalent to a virtual noise source located at the input. This is known as *equivalent input noise* or *input-referred noise* of the amplifier, and allows one to easily compare the total noise generated by the amplifier with the input signal. From the considerations above, the equivalent input noise power of an amplifier coincides with the output noise power divided by the squared module of the amplifier gain [2].

A similar idea is applied to the noise model of a generic sensor. Starting from its small-signal equivalent circuit, including all impedances and current/voltage signal generators, a noise equivalent circuit is derived by including the noise sources associated with resistances (or, better, with the real parts of impedances) and signal generators. From this equivalent noise circuit, an expression for small-signal gain and equivalent input noise is derived.

Figure 2a represents the equivalent noise circuit of a generic system consisting of a sensor and a preamplifier. The sensor is described by its signal voltage generator V_s , its internal series impedance Z_s , and a noise voltage generator $V_{n,s}$, which includes the contributions by all sensor noise sources. The preamplifier, having voltage gain A_v and input impedance Z_i , is represented from the noise point of view, by a noise voltage generator $V_{n,a}$ and a noise current generator $I_{n,a}$ placed in series and in parallel, respectively, with the input port. These noise generators, whose magnitude is specified in units of $V/(\text{Hz})^{1/2}$ and $A/(\text{Hz})^{1/2}$, respectively, are in general frequency-dependent, and are very often represented in terms of their mean-square voltage, $V_{n,a}^2 (V^2/\text{Hz})$, and mean-square current, $I_{n,a}^2 (A^2/\text{Hz})$. The two generators can be statistically correlated or not, depending on the specific case. For example, they are practically 100% correlated and totally uncorrelated, respectively, when modeling a metal oxide semiconductor (MOS) field-effect transistor or a bipolar junction transistor (BJT) in the midfrequency range [3]. When combining the effects of different noise sources, one must remember that noise is a random signal. Therefore, when summing two noise variables A_n and B_n , the result is $C_n^2 = A_n^2 + B_n^2 + 2 \text{Re}\{A_n^* B_n\}$, where $\text{Re}\{A_n^* B_n\}$ represents the real part of the cross-correlation spectrum of A_n and B_n . For ease of use, the correlation effect between two variables is very often expressed by using the so-called correlation coefficient γ , which is a normalized factor having a value between 0 (no correlation) and 1 (100% correlation). Using this approach, one has $C_n^2 = A_n^2 + B_n^2 + 2\gamma A_n B_n$.

Although the number of noise sources in Fig. 2a has been reduced to three, further simplifications are usually carried out to represent them just by one equivalent input noise voltage generator, $V_{n,eq}$, at the signal source location [2]. To derive an expression for the equivalent input noise, the total noise at the amplifier output, $V_{n,o}$, must be first derived. Assuming $V_{n,a}$ and $I_{n,a}$ to be statistically uncorrelated, one obtains:

$$V_{n,o}^2 = (V_{n,a}^2 + V_{n,s}^2) \cdot |A_v|^2 \cdot \left| \frac{Z_i}{Z_i + Z_s} \right|^2 + I_{n,a}^2 \cdot |A_v|^2 \cdot \left| \frac{Z_i \cdot Z_s}{Z_i + Z_s} \right|^2 \tag{1}$$

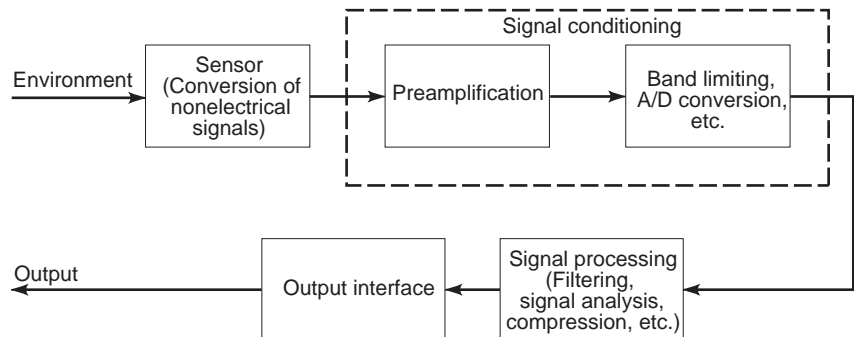


Figure 1. The electronic chain associated with a sensor includes a preamplifier, signal conditioning and processing circuitry, and output interface. The stages cascaded to the preamplifier may provide additional gain.

The system gain from the signal source location is

$$A'_v = A_v \frac{Z_i}{Z_i + Z_s} \tag{2}$$

Therefore, the equivalent input noise voltage, $V_{n,eq}$, which is equal to the total output noise divided by the squared module of the system gain, is given by

$$V_{n,eq}^2 = \frac{V_{n,o}^2}{|A'_v|^2} = V_{n,a}^2 + V_{n,s}^2 + I_{n,a}^2 \cdot |Z_s|^2 \tag{3}$$

After combining and reflecting all noise sources to the signal source location, the resulting equivalent circuit is as shown in Fig. 2b. The noise source $V_{n,eq}$ will generate exactly the output noise given by Eq. (1).

$V_{n,eq}^2$ can also be obtained from Fig. 2a by disconnecting the noiseless amplifier and evaluating the voltage across the noise generator $I_{n,a}$, which results Eq. (3). This operation corresponds to finding the equivalent dipole connected at the input of the noiseless amplifier (Thevenin theorem). In practice, the dipole in Fig. 2a constituted by

V_s , $V_{n,s}$, Z_s , $V_{n,a}$, and $I_{n,a}$, is exactly equivalent to the dipole in Fig. 2b constituted by V_s , $V_{n,eq}$, and Z_s .

Observe that, as indicated in Eq. (3), the equivalent input voltage noise does not depend on the amplifier gain and input impedance, although the effect of any noise generated at Z_i is implicit in $I_{n,a}$. However, $V_{n,eq}$ depends on the impedance of the signal source, as well as on the noise generated by the sensor (hence, the design approach for noise optimization will also depend on the kind of sensor impedance, that is resistive, capacitive, inductive, as will be shown below). Output noise will obviously depend on both the gain and the input impedance of the amplifier.

Following similar steps, an equivalent noise circuit of the system can also be derived in terms of an equivalent input noise current generator $I_{n,eq}$ (Fig. 2c)

$$I_{n,eq}^2 = I_{n,a}^2 + I_{n,s}^2 + \frac{V_{n,a}^2}{|Z_s|^2} \tag{4}$$

where $I_{n,s}^2 = V_{n,s}^2/|Z_s|^2$.

Either equivalent noise circuit can be used; however, it is generally more appropriate to characterize the system

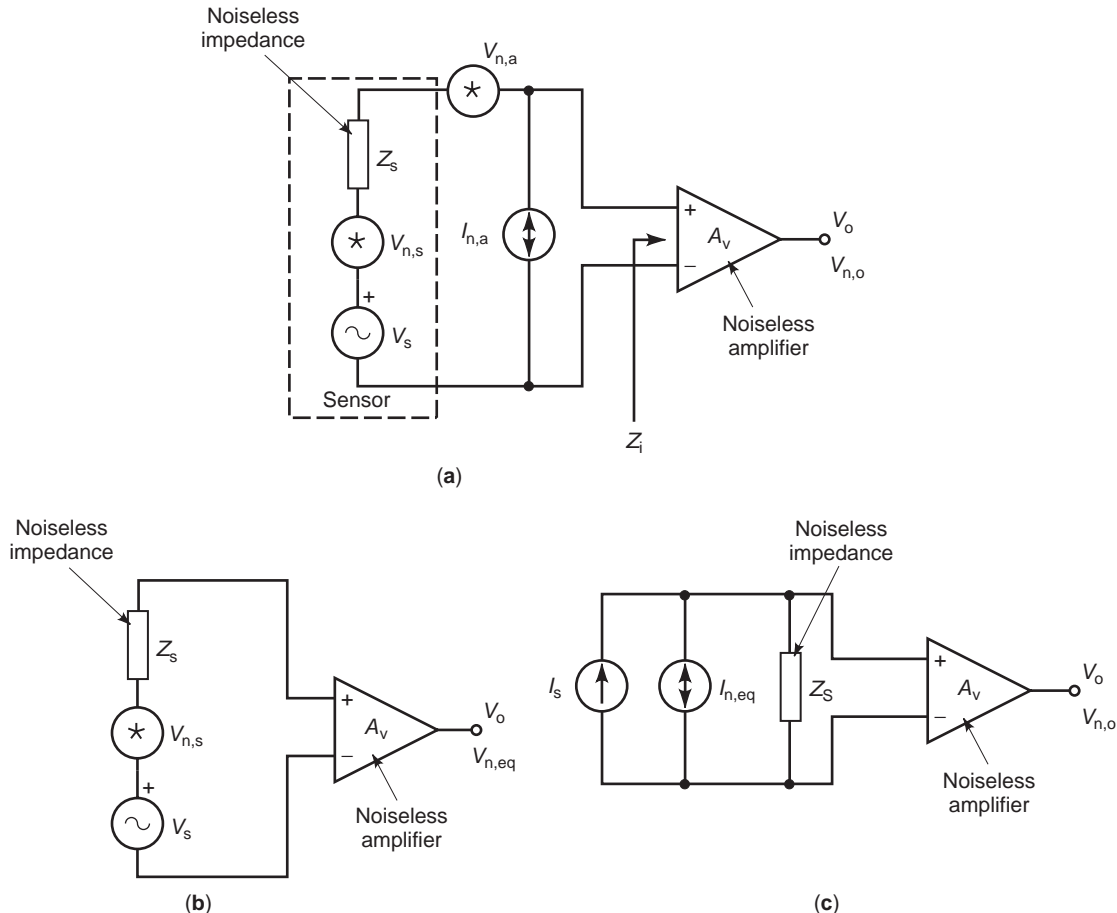


Figure 2. A generic system noise model (a) can be reduced to an equivalent circuit with an equivalent input noise voltage generator (b), or to an equivalent circuit with an equivalent input noise current generator (c).

noise in the same terms as the source signal (voltage or current).

If the amplifier noise voltage and current generators $V_{n,a}$ and $I_{n,a}$ are not statistically independent, as occurs when they contain some components arising from a common phenomenon, the scheme of Fig. 2b must include another noise voltage generator in series with $V_{n,eq}$. The power spectral density of this generator is a function of their correlation coefficient: $V_n^2 = 2\gamma|V_{n,a}I_{n,a}Z_s|$. In the same way, an additional noise current generator $I_n^2 = 2\gamma|V_{n,a}I_{n,a}/Z_s|$ has to be placed in parallel with $I_{n,eq}$ in the scheme of Fig. 2c.

1.2. Equivalent Input Noise in Cascaded Stages

Consider the network in Fig. 3, which consists of n cascaded stages having respective voltage gains $A_{v1}, A_{v2}, \dots, A_{vn}$ and equivalent input noise voltage sources $V_{n,eq1}, V_{n,eq2}, \dots, V_{n,eqn}$. It should be pointed out that a “stage” in this figure can be a complex circuit or even a single active device. Moreover, for each stage i ($i = 1, 2, \dots, n$), A_{vi} and $V_{n,eqi}$ are evaluated taking the value of input and output impedances into account. Assuming that noise sources of different stages are uncorrelated, as is the usual case, the total output noise power is

$$V_{n,o}^2 = V_{n,eq1}^2 \cdot |A_{v1}|^2 \cdot |A_{v2}|^2 \cdot \dots \cdot |A_{vn}|^2 + V_{n,eq2}^2 \cdot |A_{v2}|^2 \cdot \dots \cdot |A_{vn}|^2 + \dots + V_{n,eqn}^2 \cdot |A_{vn}|^2 \tag{5}$$

which corresponds to an equivalent input noise for the whole network equal to

$$V_{n,eq}^2 = \frac{V_{n,o}^2}{|A_{v1}|^2 \cdot |A_{v2}|^2 \cdot \dots \cdot |A_{vn}|^2} = V_{n,eq1}^2 + \frac{V_{n,eq2}^2}{|A_{v1}|^2} + \dots + \frac{V_{n,eqn}^2}{|A_{v1}|^2 \cdot |A_{v2}|^2 \cdot \dots \cdot |A_{vn-1}|^2} \tag{6}$$

From this equation, one concludes that the noise behavior of the whole network can be dominated by the first stage, provided that its voltage gain is large enough. In this case, in fact, noise contributions by the following stages can be neglected. The same conclusion also holds when considering current noise, obviously referring to the current gain rather than to the voltage gain of the stages.

1.3. Noise Factor and Noise Figure

Noise factor F is one of the most traditional parameters used to characterize the noise performance of an amplifier. It is defined as the ratio of the total available output noise power per unit bandwidth to the portion of that output noise power caused by the noise associated with the sensor, measured at the standard temperature of 290 K [4]. To emphasize that this parameter is a point function of frequency, the term “spot noise factor” may be used. Since the noise factor is a power ratio, it can be expressed in decibels. In this case, the ratio is referred to as noise figure (NF). Thus, taking Fig. 2 and Eq. (3) into account, we obtain

$$NF = 10 \cdot \log \frac{V_{n,o}^2}{V_{n,s}^2 \cdot |A_v'|^2} = 10 \cdot \log \frac{V_{n,eq}^2}{V_{n,s}^2} \tag{7}$$

An alternative expression for the noise figure can be derived from Eq. (7), obtaining

$$NF = 10 \cdot \log \frac{V_s^2 V_{n,o}^2}{V_{n,s}^2 \cdot (V_s^2 \cdot |A_v'|^2)} = 10 \cdot \log \frac{(V_s^2 / V_{n,s}^2)}{(V_o^2 / V_{n,o}^2)} = 10 \cdot \log \frac{(SNR)_i}{(SNR)_o} \tag{8}$$

where $(SNR)_i$ is the signal-to-noise ratio (SNR) available at the sensor output, and $(SNR)_o$ is the SNR at the output of the real (i.e., noisy) amplifier. This result indicates that NF accounts for the signal-to-noise power degradation caused by the preamplifier. Thus, for an ideal amplifier, which does not add any noise, the output signal-to-noise ratio is kept equal to its input counterpart, and $NF = 0$ dB. Alternatively, an NF of 3 dB means that half the output noise power is due to the amplifier.

As will be shown later, NF by itself is not always an appropriate figure of merit to characterize the noise performance of an amplifier. As stated above, NF is valid only to indicate how much noise is added by a preamplifier to a given input source resistance, and is therefore useful to compare noise behavior of different preamplifiers with a determined signal source. However, it is not a useful tool for predicting noise performance with an arbitrary source.

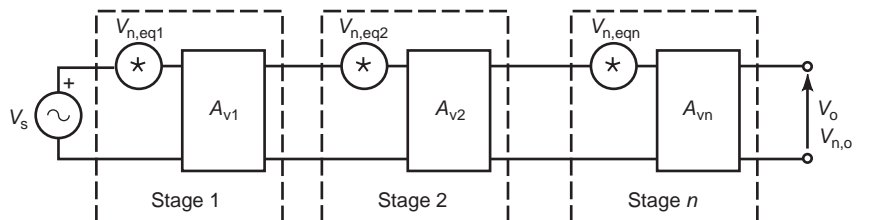


Figure 3. Schematics for evaluating the noise performance of an n -stage voltage amplifier.

1.4. Noise Matching

Let us now consider the particular case where the internal impedance of the signal source is a resistor R_s . This corresponds to one of the most frequently used types of sensors, which can be represented by a signal source generator V_s in series with its internal resistance and a thermal noise generator $V_{n,s}$, whose power spectral density is

$$V_{n,s}^2 = 4KTR_s \tag{9}$$

where K is Boltzmann's constant ($1.38 \times 10^{-23} \text{ W} \cdot \text{s/K}$) and T is the absolute temperature (K). According to Eq. (7), the noise figure for this resistive signal source is given by

$$\text{NF} = 10 \cdot \log \frac{4KTR_s + V_{n,a}^2 + I_{n,a}^2 R_s^2}{4KTR_s} \tag{10}$$

By differentiating this expression with respect to R_s , one obtains the so-called optimum source resistance, for which NF is minimum:

$$R_{\text{opt}} = \frac{V_{n,a}}{I_{n,a}} \tag{11}$$

From Eqs. (10) and (11), NF can be written as

$$\text{NF} = 10 \cdot \log \left[1 + \frac{V_{n,a} \cdot I_{n,a}}{4KT} \left(M + \frac{1}{M} \right) \right] \tag{12}$$

in which $M = R_s/R_{\text{opt}}$ is the matching factor. For a given $V_{n,a} \cdot I_{n,a}$ product, NF is minimum for $M = 1$.

The effect of the source resistance variation on NF for amplifiers having different values of the noise sources product $V_{n,a} \cdot I_{n,a}$, is illustrated in Fig. 4 [2, p. 46]. The minimum value of the noise figure, NF_{opt} , occurs at $R_s = R_{\text{opt}}$. As the product $V_{n,a} \cdot I_{n,a}$ increases, the noise figure also increases and is more sensitive to source resistance variations.

In the more general case where the correlation factor γ is different from zero, the optimum value F_{opt} of the noise factor corresponding to the optimum source resistance is easily calculated as

$$\begin{aligned} F_{\text{opt}} &= 1 + \frac{2 \cdot (1 + \gamma) \cdot I_{n,a}^2 \cdot R_{s,\text{opt}}^2}{V_{n,s}^2} \\ &= 1 + \frac{(1 + \gamma) \cdot I_{n,a} \cdot V_{n,a}}{2KT} \end{aligned} \tag{13}$$

F_{opt} defines the best performance obtainable when the source resistance can be selected to match R_{opt} . Equation (13) also clearly shows that, for any given source resistance and temperature, the best noise performance, obtained when perfect matching is achieved, depends on the product $V_{n,a} \cdot I_{n,a}$ of the amplifier [5,6].

Noise matching is based on the idea of modifying the amplifier equivalent input noise sources as seen at the

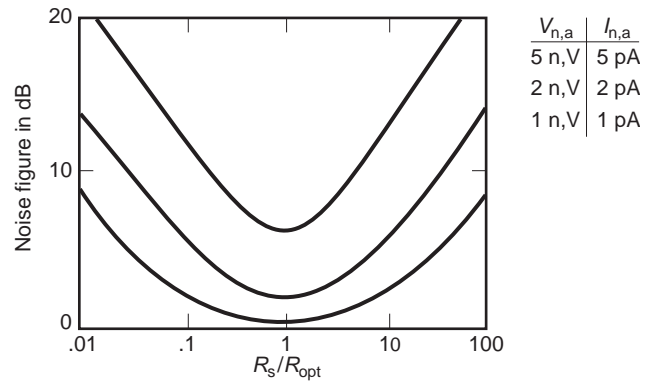


Figure 4. NF reaches its minimum value for $R_s = R_{\text{opt}}$. NF increases with increasing value of the product $V_{n,a} \cdot I_{n,a}$.

signal source location, to meet the condition $R_s = R_{\text{opt}}$, so as to minimize the total equivalent input noise [5]. This condition, which indicates that the preamplifier input stage is matched to the sensor, is considered as the essence of low-noise design. Of course, to keep the noise low, the rest of the amplifier must also be designed so that its noise contributions are low compared with those of the input stage.

A very simple and illustrative way to modify the amplifier equivalent input noise consists of coupling the sensor to the amplifier by means of a transformer with a primary-to-secondary turns ratio of $1 : N$ (Fig. 5 shows this for the case of a resistive sensor). The amplifier noise sources are reflected to the primary as $V'_{n,a} = V_{n,a}/N$ and $I'_{n,a} = NI_{n,a}$. The ratio of these reflected parameters is

$$R'_s = \frac{V'_{n,a}}{I'_{n,a}} = \frac{R_{\text{opt}}}{N^2} \tag{14}$$

Matching R'_s to R_s , one can derive the turns ratio required in the coupling transformer:

$$N = \sqrt{\frac{R_{\text{opt}}}{R_s}} \tag{15}$$

When this condition is met, the amplifier sees the optimum source resistance and, hence, the equivalent input

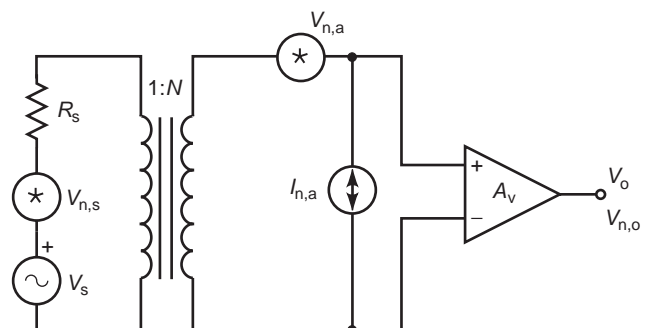


Figure 5. Noise matching by coupling transformer minimizes the total equivalent input noise.

noise is minimized. It has to be pointed out that a real transformer has its own internal noise sources and stray impedances, which have to be taken into account in an accurate low-noise design. Moreover, the use of a transformer requires a suitable shield to external electromagnetic fields, which can induce spurious currents in the transformer itself.

According to the results above, it appears that the noise figure NF can be alternatively improved by adding a series or shunt resistance to a given source resistance R_s (or, by correspondingly changing the sensor resistance), to make its final value equal to R_{opt} . However, due to the addition of an extra resistor, the signal-to-noise ratio gets worse. On the other hand, for $R_s = 0$, NF goes to infinity, although the actual output noise is less than that corresponding to any other value of source resistance, including R_{opt} . This contradictory situation arises from the fact that reducing NF improves the output SNR only if the SNR at the source remains constant. This condition is not met when matching is achieved by modifying the source resistance, but it is satisfied when using a coupling transformer. For the same reason, only when increasing sensor resistance increases the signal proportionally, should it be modified so as to match the amplifier optimum noise source resistance. When choosing or designing a preamplifier, the best noise performance is obtained by achieving the minimum equivalent input noise rather than the lowest noise figure.

Noise matching can also be achieved in the case of narrowband signal sources. By exploiting the resonance of a suitable LC group, the amplifier equivalent input noise as seen at the signal source location, can be optimized at the required center frequency. It is possible to follow this approach for both resistive and reactive narrowband sources [6].

Since transformers, as well as other coupling techniques using discrete components, are not compatible with solid-state circuits, noise matching for monolithic preamplifiers has to be obtained by appropriate choice of transistor sizes and bias conditions [7]. In particular, when $V_{n,a}$ is the dominant noise source of the preamplifier, noise matching can be obtained by using n input transistors connected in parallel rather than a single input transistor. Indeed, this technique reduces input noise voltage by a factor of \sqrt{n} and increases input noise current by the same factor, which from the noise standpoint, is equivalent to using a coupling transformer with a turns ratio of $1 : \sqrt{n}$ [5]. Similar techniques can also be adopted for discrete preamplifiers, even though much less flexibility is obviously available.

2. DESIGN CONSIDERATIONS FOR PREAMPLIFIERS

Designing or selecting a preamplifier for a specific application involves many specifications and choices. The procedure starts by considering sensor characteristics, such as signal source type, noise, impedance, and frequency response. As a function of that, the preamplifier must be designed so as to achieve the lowest value of equivalent input noise.

According to the discussion above, the ultimate limit of equivalent input noise is determined by the sensor impedance Z_s and the amplifier noise generators $V_{n,a}$ and $I_{n,a}$, where all these parameters may generally be frequency-dependent. Therefore, the signal source impedance and frequency range are decisive when choosing the type of preamplifier input device, as in a well-designed amplifier, noise performance is heavily affected by this element. To assist in this task, Fig. 6 [2, p. 210] can serve as a general guide. In this figure, the different ranges of source impedance values are covered by the different types of active or coupling devices. Low values of source resistance usually require the use of a coupling transformer for noise matching, while, for matching the highest source resistance range, the extremely low noise current $I_{n,a}$ of field-effect transistors is exploited.

With respect to the frequency range, in the simplest case of a resistive source, matching the amplifier optimum source resistance R_{opt} to the source resistance, minimizes the equivalent input noise at a given frequency. However, if the preamplifier must operate over a large frequency band, the designer's task is to minimize the noise integrated over this interval. Then, if the source impedance is reactive and/or the equivalent amplifier noise sources are functions of frequency, the use of a circuit simulator is often necessary to perform this integration over the whole bandwidth and optimize noise performance. With respect to this, it is important to note that the preamplifier bandwidth has to match, as much as possible, the signal spectrum needed in the specified application, since increasing the bandwidth increases the integrated output noise. Once the low and high amplifier cutoff frequencies of the preamplifier have been adjusted, the computer analysis may show that noise requirements are not fulfilled and, then, another operating point or different device sizes must be chosen. In extreme cases, different amplifiers or circuit topologies must be used.

Finally, needless to say, any noise injection from external source must be minimized. For example, in case electrical and/or magnetic shielding has to be provided against electromagnetic interference, power supply filtering can be required to ensure a quiet supply voltage, ground connections have to be carefully studied, and noise injection from digital sections has to be minimized. However, these considerations regard general system design, and are not specific to preamplifier design.

Next, the abovementioned design considerations are particularized for three types of source impedance (i.e., resistive, capacitive, and inductive), with emphasis on amplifiers for monolithic implementations. For this

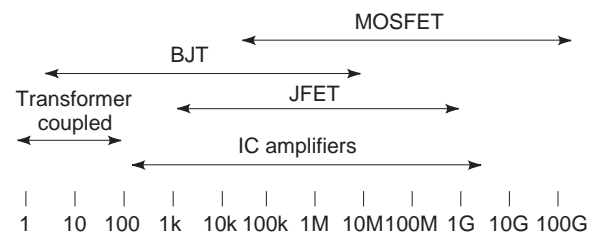


Figure 6. Guide for selection of input devices.

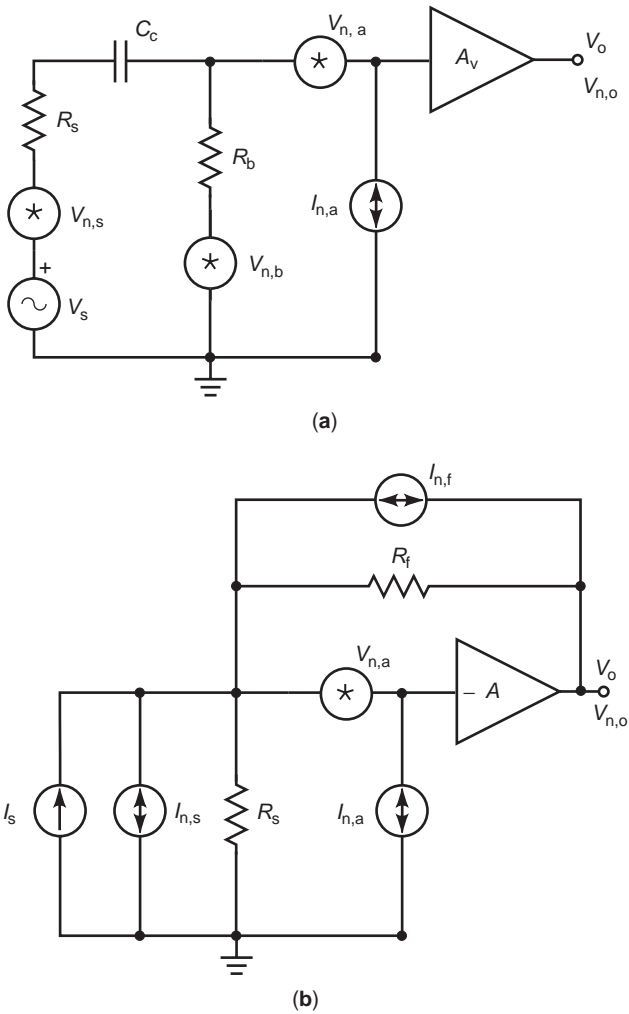


Figure 7. Preamplifiers with resistive sources: (a) voltage amplifier with coupling capacitor; (b) wideband transimpedance preamplifier.

reason, mainly bipolar and MOS transistors will be considered as amplifier devices.

2.1. Preamplifiers with Resistive Sources

The simplest type of source impedance is a resistance. Among sensors with this type of source impedance, some (i.e., voltaic sensors, such as thermocouples, thermopiles, infrared detectors, etc.) generate a voltage signal, while others (e.g., photoconductive detectors used in optoelectronic applications) produce a current signal. Figure 7 shows two generic preamplifiers with a resistive source (the noise sources, i.e., the resistor thermal noise generators and the equivalent amplifier input noise generators, are also included in both schemes). In Fig. 7a, a sensor voltage source is coupled to a voltage amplifier by means of a coupling capacitor C_c , while a resistor R_b is added for biasing the amplifier input device, which corresponds to a very usual situation. Instead, a resistive sensor, which provides a current signal, has been assumed in Fig. 7b. In this case, a transimpedance amplifier is used to amplify

the signal from the high-impedance source. The transimpedance gain of the amplifier V_o/I_s is determined by the feedback resistor R_f , provided that the loop gain is high enough.

Referring to the voltage amplifier in Fig. 7a, a highpass response is caused by the coupling capacitor C_c along with the equivalent series resistance of the input network. C_c must be chosen in such way that its reactance can be neglected in the frequency range of interest. Thus, the voltage gain in the input network is substantially independent of frequency. Moreover, the contribution of $I_{n,a}$ to the equivalent input noise voltage $V_{n,eq}^2$ [see Eq. (3)] yields results equal to $(I_{n,a}R_s)^2$.

Assuming a much higher amplifier input impedance than R_s and R_b , the equivalent input noise voltage of the system turns out to be

$$V_{n,eq}^2 \cong V_{n,s}^2 + V_{n,b}^2 \frac{R_s^2}{R_b^2} + V_{n,a}^2 \frac{(R_s + R_b)^2}{R_b^2} + I_{n,a}^2 \cdot R_s^2 + 2\gamma V_{n,a} I_{n,a} (R_s + R_b) \frac{R_s}{R_b} \tag{16}$$

In the remainder of this article, the generally accepted assumption that the amplifier noise is dominated by its input device will be adopted. In addition, single-ended input stages, which as a general rule allow the designer to minimize the noise contribution of the amplifier, will also be assumed.

First consider the case when the input transistor is a bipolar device. Neglecting $1/f$ noise and frequency-dependent terms in the frequency band of interest, the equivalent input noise sources can be approximated as [6]:

$$V_{n,a}^2 = 4KT r_b + \frac{2 \cdot (KT)^2}{qI_E} \tag{17a}$$

$$I_{n,a}^2 = 2qI_B = 2q \frac{I_C}{\beta} \tag{17b}$$

where r_b is the base resistance; q is the electron charge; I_E , I_B , and I_C are the DC emitter, base, and collector currents, respectively; and $\beta = I_C/I_B$ is the DC current gain. This operating region of the BJT is known as *short noise region* [2], since the shot noise mechanisms are the dominant ones. In this operating region, the correlation effects between the input voltage and current noise sources can usually be neglected ($\gamma \cong 0$). Here and in the following, it shall also be assumed that the noise contribution by the base resistance is negligible, as can be achieved with adequate layout, that is, by making r_b sufficiently small. The optimum noise resistance can be expressed as a function of the design parameters of the input transistor:

$$R_{opt} = \frac{V_{n,a}}{I_{n,a}} \cong \frac{KT}{qI_C} \sqrt{\beta} \tag{18}$$

The equivalent input noise of the system is minimum when the noise matching condition is fulfilled, that is, when R_{opt} as from Eq. (18) is made equal to the equivalent

resistance of the input network, $R_s || R_b$. This is achieved for the following biasing collector current:

$$I_{C,opt} = \frac{KT}{q} \frac{1}{(R_s || R_b)} \sqrt{\beta} \tag{19}$$

Obviously, the same result is achieved by differentiating $V_{n,eq}$ with respect to I_C for $V_{n,eq}$, as given by Eq. (16).

Replacing Eq. (19) into Eq. (16), the total equivalent input noise for the optimum biasing collector current can be derived:

$$V_{n,eq}^2 = 4KTR_s \left(1 + \frac{R_s}{R_b}\right) \cdot \left(1 + \frac{1}{\sqrt{\beta}}\right) \tag{20}$$

The first term, $4KTR_s(1 + R_s/R_b)$, is due to the thermal noise contribution of the source and biasing resistances, while the second term, $4KTR_s(1 + R_s/R_b)\beta^{-1/2}$, arises from the amplifier noise. It is apparent that the noise contributed by the amplifier is lower than the thermal noise by a factor of $\beta^{1/2}$. Also, the noise contribution of the biasing resistor can always be kept lower than that of R_s , by choosing $R_b > R_s$. Therefore, the noise performance of voltage amplifiers with bipolar input devices and resistive sources can be made to be dominated by the resistive source itself, if I_C can be chosen equal to $I_{C,opt}$. An alternative interpretation of Eq. (19) consists in considering the term $(1 + \beta^{-1/2})$ as the factor by which the preamplifier increases the thermal noise of the source and biasing resistances. In other words, this term is the lowest value of the optimum noise factor F_{opt} of a BJT working in the shot noise region used as the input device of an amplifier, which is obtained when the value of $I_{C,opt}$ corresponds to a sufficiently small collector current density [2].

Very similar conclusions are obtained when considering transimpedance amplifiers with resistive sources [3]—see Fig. 7b. Following the procedure above, one finds that the bias collector current of the input bipolar transistor for minimum noise is $I_{C,opt} = (KT/q)\beta^{1/2}/(R_s || R_f)$, and that the corresponding total equivalent input noise current is $I_{n,eq}^2 = [4KT/(R_s || R_f)] \cdot (1 + \beta^{-1/2})$. Again, in a well-designed bipolar preamplifier, noise performance can be made to be dominated by the resistive source, if R_f can be chosen sufficiently large. The choice of the feedback resistor R_f will result as the best tradeoff between noise, transimpedance gain, and bandwidth requirements.

Now refer to the case when an MOS transistor is used as the input device of the preamplifier in Fig. 7a. The equivalent input noise generators of an MOS device in the midfrequency range can be approximated as [3]

$$V_{n,a}^2 = \frac{8KT}{3g_m} + \frac{A_f}{WLf} \tag{21a}$$

$$I_{n,a}^2 = |j\omega C_{i1}|^2 V_{n,a}^2 \tag{21b}$$

where A_f is a suitable technology-dependent constant; W and L are the width and length, respectively, of the transistor; g_m is its transconductance; and C_{i1} , its input capacitance. As the noise voltage source is placed in series with

the signal source, the only way to minimize its contribution to the total equivalent input noise voltage $V_{n,eq}^2$ is to minimize the noise source itself. To reduce thermal noise, a large transistor transconductance must be used, which means a large aspect ratio and a large bias current. To reduce the $1/f$ term, a large gate area is required. The contribution of the noise current source to $V_{n,eq}^2$ is equal to $V_{n,a}^2[\omega(R_s || R_b)C_{i1}]^2$, and is, therefore, negligible with respect to $V_{n,a}^2$ in the frequency band of interest ($\omega < [(R_s || R_b)C_{i1}]^{-1}$).

When transimpedance amplifiers in MOS technology are considered, the contribution of the term $V_{n,a}^2$ to the total equivalent input noise current is given by $V_{n,a}^2/(R_s || R_f)^2$. This should be compared with the noise current $4KT/(R_s || R_f)$ contributed by the source and feedback resistances. Therefore, in the presence of a very large source resistance, the noise contribution of the amplifier can be made negligible provided that a sufficiently large feedback resistor is used. In this case, MOS amplifiers should be preferred to bipolar ones [3]. By contrast, in the case of a small source resistance, the source $V_{n,a}^2$ must be minimized to ensure low-noise performance of the preamplifier. This can be obtained with the same techniques as seen above for the case of the voltage amplifier. Again, the contribution due to the amplifier input current noise can be neglected in the frequency band of interest.

2.2. Preamplifiers for Optical Receivers

A very popular preamplifier application is for optical receivers. An optical receiver is a circuit able to detect and process a signal coming from an optical source. Basically, it is made up of an optical sensor followed by a preamplifier and a processing section. The optical sensor (photodetector), which in its simplest form, is a reversed-biased diode, converts the optical signal into an electrical current. The photodetector is modeled as a current source with an ideally infinite output resistance and a capacitance in parallel. As the input electrical signal can be very small (e.g., down to the nA range), it must be amplified with a preamplifier to a level suitable for the following processing. Therefore, low noise, high gain and, in many cases, high bandwidth and adequate dynamic range, are key amplifier requirements in this kind of application.

The basic principle of a preamplifier for optical receivers is to convert the current signal provided by the photodetector I_s into a voltage signal having a suitable amplitude. The most popular configuration consists of a transresistance amplifier, as illustrated schematically in Fig. 8a [8], where noise generators are not shown. The current I_s generated by the photodetector flows through the feedback resistor R_f , which, in turn, produces an amplifier output voltage $V_o = -I_s R_f$, provided that the loop gain is large enough. The required current-to-voltage conversion can also be achieved by feeding the signal current directly to a grounded resistor R_g (Fig. 8b) [9]. A suitable active stage is cascaded to provide decoupling between the input section and the following stages and, in this case, additional voltage gain. The choice of R_g results as a tradeoff between gain (V_o/I_s) and low thermal noise added to the signal current ($4KT/R_g$) on the one hand, and band-

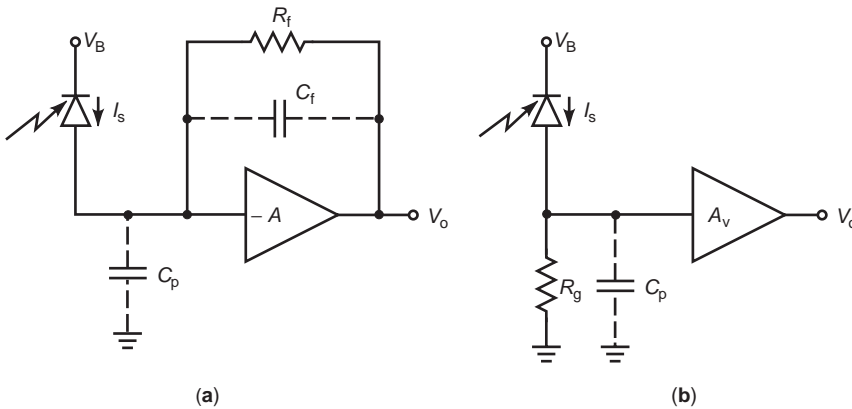


Figure 8. Preamplifiers for optical receivers. A transresistance preamplifier (a) is generally preferred to the use of a grounded resistor followed by an active stage (b).

width, which is limited to $1/(2\pi R_g C_p)$, on the other, where C_p includes the photodetector capacitance in parallel with the amplifier input capacitance. For this reason, an equalizer stage (substantially, a parallel group RC) is very often cascaded to the active stage when R_g has a large value [9]. The use of a large R_g also causes a limited input dynamic range, as the whole voltage signal $R_g I_s$, is applied to the input of the active stage.

The transresistance configuration of Fig. 8a provides the best tradeoff in terms of noise and gain on one hand and bandwidth on the other, and also gives no problems regarding input dynamic range. The achievable signal bandwidth (assuming that the amplifier has an ideal frequency behavior) is now equal to $1/[2\pi R_f(C_f + C_p/A)]$, where C_f is the parasitic capacitance around the amplifier ($C_f \ll C_p$). The actual bandwidth of the system is limited either by parasitic capacitances in the feedback network or by the bandwidth of the amplifier. The former is a common case in high-gain applications, when a large value of R_f is used, while the latter is more typical in lower-gain applications. In any case, attention must be paid to achieving frequency stability, as a closed-loop configuration is adopted. Neglecting the feedback parasitic capacitance, the equivalent input current noise of the system in the frequency band of interest is

$$I_{n,eq}^2 = 4 \frac{KT}{R_f} + I_{n,s}^2 + I_{n,d}^2 + I_{n,a}^2 + V_{n,a}^2 \left| \frac{1 + \omega R_f C_p}{R_f} \right| \tag{22}$$

where $I_{n,s}$ and $I_{n,d}$ account for shot noise of signal and dark currents of the photodetector, respectively. From this equation, one can observe that the contribution of $V_{n,a}$ to the total equivalent input noise increases at high frequencies, even though at low frequencies, it can be negligible if $V_{n,a}$ is sufficiently small (“noise gain peaking” effect [8]). However, at very high frequencies, the contribution of $V_{n,a}$ is limited by the ratio C_p/C_f and then rolls off due to the amplifier open-loop response.

2.3. Preamplifiers with Capacitive Sources

A capacitive sensor source can be modeled, in its useful frequency range, as a voltage source in series with a capacitor or as a current source in parallel with a capacitor (the case where the sensor signal is delivered in the form of a charge packet will be briefly addressed at the end of this section). The output signal of the sensor is taken either as the open-circuit voltage or the short-circuit current, respectively. Sensor capacitance and signal frequency depend on the application, and can vary by several orders of magnitude (from picofarad up to nanofarad and from hertz to megahertz ranges, respectively). Typical examples are capacitive antennas (e.g., for radio receivers), electret microphones, some piezoelectric sensors such as hydrophones, optical detectors, and so forth. In this section, wideband monolithic preamplifiers, specifically, will be considered. In the case of narrowband applications, noise optimization can be achieved by adding a suitable series or parallel inductance in the input network, using a technique very similar to that used for narrowband preamplifiers with inductive sources [6] (see the next section). The basic principle is to determine a proper resonance that ideally makes the effects of the amplifier input current or voltage noise source disappear at the frequency of interest, thereby minimizing the system equivalent input noise.

Two basic topologies of wideband preamplifiers for capacitive signal sources are depicted in Fig. 9, where the voltage source representation is used for the sensor, and equivalent input noise generators are also shown. Notice that, ideally, no noise is generated in the signal source, due to its reactive nature. In Fig. 9a, biasing resistor R_b has been included. This resistor must be large enough so that, in the frequency band of interest, the pole generated by the group $R_b C_c$ roughly cancels out the effects of the zero located in the origin, which arises due to C_c . Thus, the preamplifier gain is independent of frequency, as required in most wideband applications. This is a typical situation in preamplifiers for electret microphones, where, in the case of monolithic implementations, an active biasing resistor is generally used to avoid excessive silicon area occupation due to the large resistance value required [10,11]. Noise considerations for this topology are very

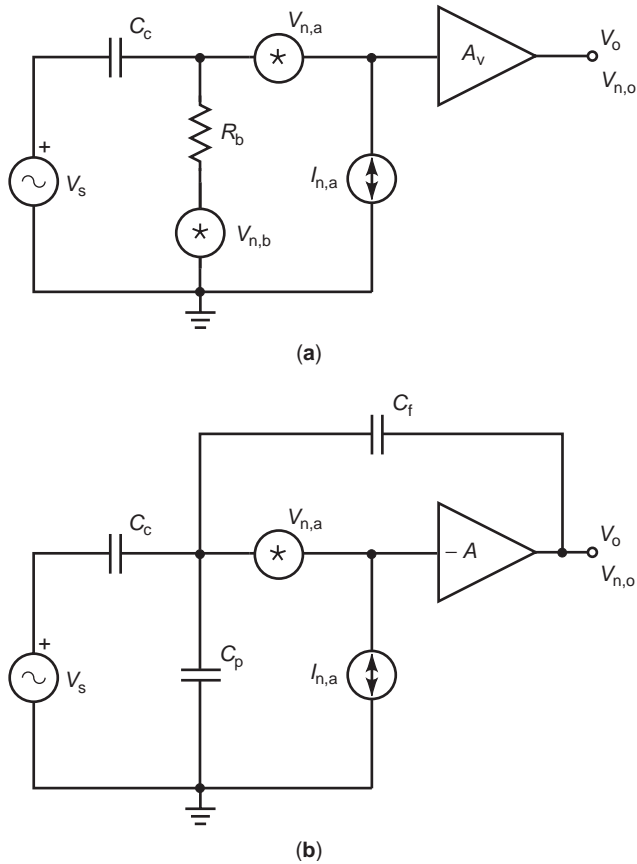


Figure 9. Preamplifier with capacitive sources: (a) voltage amplifier with biasing resistor; (b) voltage amplifier with capacitive feedback.

similar to those for voltage amplifiers with resistive sources, although in the present case the source resistance is assumed to be negligible, and obviously the dominant noise source is the amplifier.

In the capacitive feedback structure of Fig. 9b, no dc feedback or biasing elements has been drawn, although generally dc stabilization is required (this can be obtained, e.g., with a very large feedback resistor, and will be neglected in the following noise considerations). In this scheme, the feedback capacitor C_f sets the midfrequency voltage gain equal to $-C_s/C_f$. Also in this case, therefore, the gain is substantially independent of frequency. Moreover, it shows no dependence upon the parasitic capacitance C_p associated to the input line, which is very useful in applications requiring long cable connections between the sensor and the amplifier [12]. Choosing the best value of C_f derives from two contrasting requirements. On the one hand, a small capacitor C_f should be chosen, so that the minimum input signal must be amplified to a level adequate to drive the cascaded stages, while on the other hand, capacitor C_f should not be so small that the amplifier output saturates in the presence of the maximum allowed input signal.

Again, regardless of the application, the noise performance of the preamplifier is of paramount importance, as it generally determines the sensitivity of the overall sys-

tem. From Fig. 9b, the equivalent input noise voltage is

$$V_{n,eq}^2 = V_{n,a}^2 \left[\frac{C_f + C_s + C_p}{C_s} \right]^2 + I_{n,a}^2 \left| \frac{1}{j\omega C_s} \right|^2 + 2\gamma \left| V_{n,a} I_{n,a} \frac{1}{j\omega C_s} \right| \frac{C_f + C_s + C_p}{C_s} \quad (23)$$

For the best noise performance, the most straightforward choice is again the use of single-ended input stages, although fully differential amplifier solutions are also used for this kind of sensor [12,13]. As pointed out above, in this section we consider mainly bipolar and MOS input devices, as currently JFET circuits are used only in specific applications (e.g., in charge-sensitive amplifiers for nuclear physics experiments; see below). In the case of a bipolar input transistor, taking into account its equivalent input sources given in Eqs. (17) and neglecting the correlation factor γ , the total equivalent input noise turns out to be

$$V_{n,eq}^2 = 4KT \left(r_b + \frac{KT}{2qI_C} \right) \cdot \left(\frac{C_f + C_s + C_p}{C_s} \right)^2 + \left(\frac{2qI_C}{\beta} \right) \left| \frac{1}{j\omega C_s} \right|^2 \quad (24)$$

It is apparent that a small base resistance r_b and a high large current gain β are needed for low noise. Moreover, one can see that, for any given value of I_C , the base current shot noise contribution [second term in Eq. (24)] is dominant at low frequencies, while voltage noise [first term in Eq. (24)] dominates at high frequencies. To achieve noise minimization, noise matching must be achieved by a suitable choice of the collector bias current I_C . Indeed, increasing I_C has opposite effects on two noise contributions. The optimal value of I_C can be easily calculated by taking the derivative of Eq. (24) with respect to I_C , obtaining [3,7]

$$I_{C,opt} = \frac{KT}{q} \omega(C_s + C_p + C_f) \sqrt{\beta} \quad (25)$$

Notice that Eq. (25) is formally identical to Eq. (19): $\omega(C_s + C_p + C_f)$ represents the module of the admittance to the input network. As observed, $I_{C,opt}$ depends on the frequency. As a consequence, when required, wideband noise optimization with bipolar input stages is not possible. Obviously, when choosing the value of I_C , other features such as gain and operation speed must also be taken into account.

In the case of a MOS input transistor, using the noise sources in Eqs. (21), the equivalent input voltage noise source turns out to be

$$V_{n,eq}^2 = V_{n,a}^2 \left[\frac{C_f + C_s + C_p + C_i}{C_s} \right]^2 \quad (26)$$

where the term C_i results from the presence of the input noise current, taking also in account the 100% correlation existing between $V_{n,a}$ and $I_{n,a}$.

It should be emphasized that noise transfer gain does not depend on frequency. The term $V_{n,a}^2$ includes a flicker as well as a thermal component. Both these contributions should be reduced to a minimum to achieve low-noise performance. To reduce input-referred noise, capacitances C_p and C_f must be minimized, even though they are noiseless elements. As far as C_i is concerned, it is worth pointing out that its value is strictly related to the input transistor size. Changing its value has two opposite effects on noise performance. On one hand, increasing the aspect ratio W/L of the input device leads to a decrease in both flicker and thermal noise, as a result of the corresponding increase in its gate capacitance and transconductance, respectively. On the other, from Eq. (26), increasing C_i will also degrade noise performance. An optimized value of the input transistor capacitance and, hence, of its size, is therefore necessary, which is determined by taking the derivative of Eq. (26) with respect to C_i . The gate length should be set to the minimum to maximize amplifier performance in terms of thermal noise and gain–bandwidth product. Noise optimization results are different when flicker and thermal components are considered, as a consequence of the different dependence of their noise spectral density upon C_i . In the case of flicker noise, the best capacitance matching is obtained by setting $C_i = C_s + C_p + C_f$, while for thermal noise, the best value is $C_i = (C_s + C_p + C_f)/3$. When both flicker and thermal noise contributions are important, a tradeoff value of C_i is chosen, for example, the average of the two optimal values [3]. An analytical derivation of the optimum C_i value in the presence of both thermal and flicker series noise can be found in Ref. 14. A suitably large bias current is also required to maximize the transconductance of the input transistor and, hence, reduce its thermal noise. An n-channel input device also helps to this end. On the contrary, flicker noise is generally smaller for p-channel devices [15–17].

It has been shown [3] that, for a capacitive source, an MOS input device offers better noise performance than does a bipolar one. Obviously, a suitable design is needed to minimize noise contributions by the other components and following stages in the circuit (for the latter purpose, e.g., some gain should be introduced in the first stage of the amplifier). Depending on the application, high linearity, large load drive capability, and wide output dynamic range can also be required of the preamplifier, as these features are related mainly to an optimized design of its output stage. Moreover, due to the presence of the feedback loop, adequate frequency stability must be provided. Bipolar technology offers inherent advantages for such requirements; however, CMOS preamplifiers meeting all the specifications needed can be developed using adequate circuit design approaches. These include using a three-stage topology, a noninverting class A–B output stage, and suitable compensation techniques [3] and employing parasitic bipolar transistors [12]. When possible, CMOS technology is the preferred choice as it allows the designer to integrate the preamplifier together with the cascaded processing section at low cost.

BiCMOS technology has also been proposed to implement the preamplifier [3]. BiCMOS technology provides both CMOS and bipolar devices on the same chip. This

allows the designer to take advantage of the superior noise performance of a CMOS transistor used as the input device and, at the same time, to exploit the excellent features of bipolar transistors to achieve the other requirements with simpler circuits with respect to fully CMOS solutions. The main disadvantage of BiCMOS technology is its increased process complexity and, hence, its higher cost.

2.4. Charge-Sensitive Preamplifiers

In some very important applications using a capacitive source, the input signal is delivered as a charge packet Q_i . The signal source can be generally represented as a delta-like current source $Q_i\delta(t)$. Popular examples are detector systems for elementary particle physics experiments [18,19] and spectrophotometers and vision systems based on photodiodes operating in the storage mode [20]. The basic scheme (Fig. 10) is substantially the same as the previous one. The readout amplifier, generally referred to as a *charge-sensitive amplifier*, produces an output voltage step with an amplitude equal to $-Q_iC_f$ in response to an input charge packet Q_i ; DC stabilization is generally obtained either with a very large feedback resistor or with a feedback switch S_R , which is turned on during suitable reset time intervals.

These noise-matching considerations still apply (in particular, the relationships obtained for the optimal input capacitance of the amplifier). In these applications, noise performance is usually expressed in terms of equivalent noise charge (ENC). This is defined as the charge which the detector must deliver to the amplifier input in order to achieve unity signal-to-noise ratio at the output, and is usually expressed in electrons.

Detectors for nuclear physics experiments represent a very critical application of charge-sensitive amplifiers. Here, the amplifier is generally followed by a noise-shaping filter (or “pulseshaper”), which has the purpose of optimizing the overall signal-to-noise ratio of the detector system. This is required as, in general, electronic noise sets the limit to the accuracy of these systems. The best achievable value of ENC increases, with a substantially

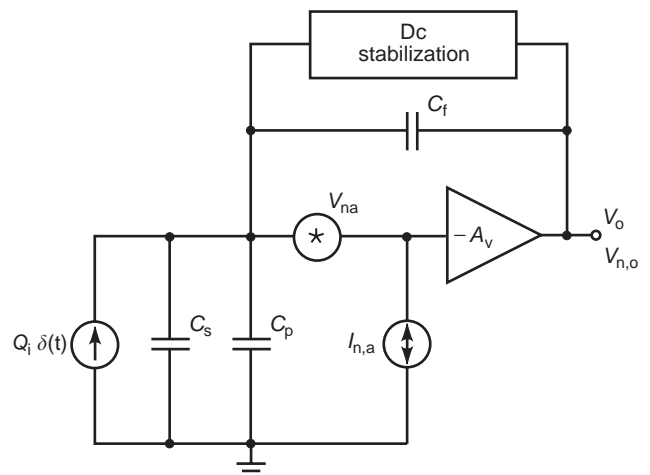


Figure 10. Basic scheme of a charge-sensitive preamplifier.

linear relationship, with increasing detector capacitance C_s (in fact, a larger C_s leads to a larger equivalent noise charge for the same equivalent input noise). The obtained values of ENC ranges from few electrons for $C_s < 1$ pF (pixel detectors), to hundreds of electrons for microstrip detectors (C_s in the order of several hundred or even more than 1000 pF).

In some applications, junction field-effect transistors (JFETs) are preferred in front-end electronics for ionization detectors of capacitive nature, mainly because they show better radiation tolerance with respect to MOS devices and much smaller input current as compared to BJTs [21,22]. Nevertheless, under particular operating conditions, such as very short shaping time (< 50 ns) and low-power constraints, BJTs can offer superior performance [23,24]. CMOS solutions have also been developed for readout electronics to exploit the capability of CMOS technology for very high integration density and low power consumption [3,25]. In fact, as a huge number of readout channels are needed in modern detector systems, small size and low power dissipation are also important requirements, which make the monolithic approach the most appealing solution. CMOS technology is very attractive, especially for detectors that are placed not very close to the radiation environment and use a pulse shaper with a very fast response (i.e., short peaking time), so that flicker noise is negligible with respect to thermal noise. A BiCMOS solution implementing a low-power high-gain transresistance amplifier has also been presented [26].

2.5. Preamplifiers for Inductive Sources

An inductive sensor source can be generally modeled as a current source in parallel with an inductance. An internal resistance can also be present, to account for the real part of the sensor impedance. Examples of inductive sensors include magnetic heads (e.g., for tape and video cassette recorders), inductive pickups, dynamic microphones, ferrite antennas, and so forth. The operation principle of such sensors is to convert the information, received in the form of an electromagnetic field, into an electrical signal by means of an inductive coil. In most cases, very weak signals are generated and, therefore, very severe noise specifications have to be met by the preamplifier. Obviously, the reactive elements in the circuit do not contribute any noise directly, however, their presence affects the noise behavior of the circuit.

Very different situations occur when narrowband and wideband applications are considered. A typical preamplifier topology for narrowband inductive signal sources is illustrated in Fig. 11, where equivalent input noise generators are also shown. L_p is the source inductance, R_s is the sensor resistance, R_b can be a biasing or a load resistor, and C_p is a shunt capacitance (including both parasitic and, in this case, added capacitances). C_c is a DC decoupling capacitor ($C_c \gg C_p$), and will be regarded as a short circuit in the frequency band of interest. The voltage signal at the amplifier input turns out to be equal to

$$V_i = \frac{I_s \cdot j\omega L_p R_T}{j\omega L_p + (1 - \omega^2 L_p C_p) R_T} \quad (27)$$

where $R_T = R_b || R_s$. The presence of the resonance due to the group $L_p C_p$ is apparent.

For this configuration, one can choose a suitable size of the shunt capacitance C_p to obtain the best noise matching [6]. In fact, the expression of the equivalent input noise current for the circuit in Fig. 11 is easily calculated as

$$I_{n,eq}^2 = I_{n,s}^2 + I_{n,b}^2 + I_{n,a}^2 + V_{n,a}^2 \left| \frac{1}{R_T} + \frac{1 - \omega^2 L_p C_p}{j\omega L_p} \right|^2 + 2\text{Re} \left\{ I_{n,a}^* V_{n,a} \left(\frac{1}{R_T} + \frac{1 - \omega^2 L_p C_p}{j\omega L_p} \right) \right\} \quad (28)$$

Each noise current source reflects unchanged to the input at any frequency. By contrast, the coefficient of the noise voltage contribution is frequency dependent, and turns out to be minimum at the resonant frequency $\omega_0 = 1/(L_p C_p)^{1/2}$. This behavior obviously derives from the large impedance shown by the parallel group $L_p C_p$ at the resonance frequency. Neglecting the correlation effect between $V_{n,a}$ and $I_{n,a}$, the resulting equivalent input noise current is given by $I_{n,eq}^2 = I_{n,s}^2 + I_{n,b}^2 + I_{n,a}^2 + V_{n,a}^2/R_T^2$. It should be pointed out that no reactive element appears in the expression for minimum noise.

Let us now turn our attention to wideband applications, where a flat response is required for the signal. The amplifier configuration in Fig. 11 can no longer be used, as the resonant group inherently provides narrowband signal response. To overcome this limitation, a constant transimpedance topology can be used, as shown in Fig. 12. The voltage across the group $L_p C_p$ is ideally maintained constant, regardless of signal amplitude and frequency, thereby preventing any resonance effect. The current I_s delivered by the sensor is injected into R_f , thus achieving the desired frequency-independent transfer gain: $V_o/I_s = -R_f$. The equivalent input noise current in this topology turns out to be

$$I_{n,eq}^2 = I_{n,s}^2 + I_{n,f}^2 + I_{n,a}^2 + V_{n,a}^2 \left| \frac{1}{R_s} + \frac{1}{R_f} + \frac{1 - \omega^2 L_p C_p}{j\omega L_p} \right|^2 + 2\text{Re} \left\{ I_{n,a}^* V_{n,a} \left(\frac{1}{R_s} + \frac{1}{R_f} + \frac{1 - \omega^2 L_p C_p}{j\omega L_p} \right) \right\} \quad (29)$$

The noise contributed by the amplifier is represented by the terms including $I_{n,a}$ and $V_{n,a}$. The use of a large inductance L_p reduces the contribution of $V_{n,a}^2$. This is especially true at low frequencies, where $\omega^2 L_p C_p \ll 1$. By contrast, at high frequencies, a small value of C_p helps to achieve low noise.

For practical cases, when very low noise is required, the term $I_{n,f}^2 = 4KT/R_f$ due to the feedback resistor can result too high, thus setting too large a noise floor to the structure. To reduce this contribution, a combined capacitive and resistive feedback configuration has been proposed, as shown in Fig. 13 [27]. The transimpedance gain of this structure is equal to $-[1 + j\omega(C_1 + C_2)R_f]/j\omega C_1$, which for the frequency range $\omega \gg 1/[(C_1 + C_2)R_f]$ can be approximated by $-R_f(C_1 + C_2)/C_1$ and, hence, achieves the

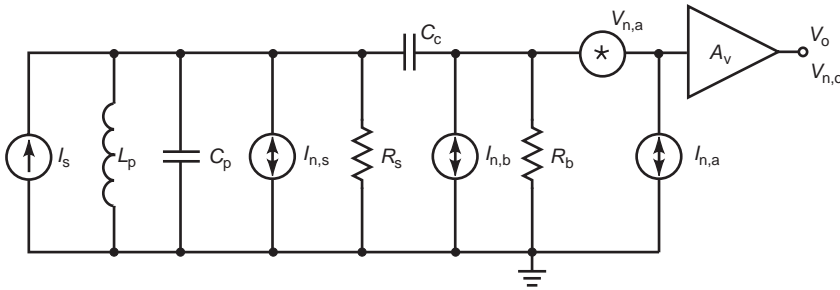


Figure 11. Basic topology of a preamplifier for a narrowband inductive source (shunt capacitance C_p includes both parasitic and, in this case, added capacitances).

required frequency independence. Obviously, a careful stability analysis is required when designing the amplifier for this feedback configuration. The input-referred noise current due to the feedback network turns out to be $I_{n,f}^2 [C_1 / (C_1 + C_2)]^2$, and is, therefore, reduced by a factor of $(1 + C_2 / C_1)^2$, with respect to the noise generated by the feedback resistor. To obtain a substantial noise reduction, C_2 is set much larger than C_1 and, hence, the reduction factor becomes $\sim (C_2 / C_1)^2$. In practice, to achieve any given transimpedance gain, we now use a resistor which is C_2 / C_1 times smaller than in the case of a conventional transimpedance topology using a purely resistive feedback. Its current noise $I_{n,f}^2$ is, therefore, larger by the same factor, however, its input-referred contribution is divided by a factor of $(C_2 / C_1)^2$ and, therefore, a substantial improvement (by a factor of C_2 / C_1) is achieved. It should be noted that with this assumption ($C_2 \gg C_1$), the resonance frequency in the input network is approximately equal to $\omega_{LC} = 1 / [L_p (C_p + C_1)]^{1/2}$.

When a bipolar input transistor is used in the amplifier, the correlation term in Eq. (29) can be neglected, and noise minimization requires a small base resistance r_b and a large current gain β . Moreover, as in the case of a capacitive signal source, the collector current I_C must be set to an optimal value, as a consequence of its opposite effects on input voltage and current noise components. Again, this optimal current is frequency dependent, and therefore noise optimization cannot be obtained in a wide

frequency range [3,27] leading to the choice of a tradeoff current for any given application.

When using CMOS technology, no noise contribution due to the gate current is present, thus removing the basic limiting factor to the noise performance in bipolar preamplifiers (i.e., the base shot noise component). As for the case of capacitive signal sources, it can be shown that noise optimization is achieved by suitably sizing the input transistor of the preamplifier. Again, the optimal size is different when considering flicker and thermal noise. Furthermore, as a consequence of the frequency dependence of the coefficient of $V_{n,a}^2$ in the expression of the total equivalent input noise current [see Eq. (29)], the optimal transistor size also depends on frequency, in contrast with the case of preamplifiers for capacitive sources. For frequencies much lower than the resonance frequency ω_{LC} , optimization is achieved by choosing an amplifier input capacitance $C_i \cong 1 / (\omega^2 L_p)$ for both flicker and thermal noise [3]. For $\omega > \omega_{LC}$, wideband noise optimization can be obtained by setting $C_i = \sim (C_p + C_1) / 3$ and $C_i = \sim (C_p + C_1)$ in the thermal and flicker noise domains, respectively. Both noise components must be taken into account when determining the input transistor size for any given application, which can be done by using numerical simulation.

Also in the case of wideband preamplifiers for inductive sources, a detailed noise analysis [3] shows that, in spite of the presence of a large flicker noise component, CMOS technology leads to better noise performance than does the

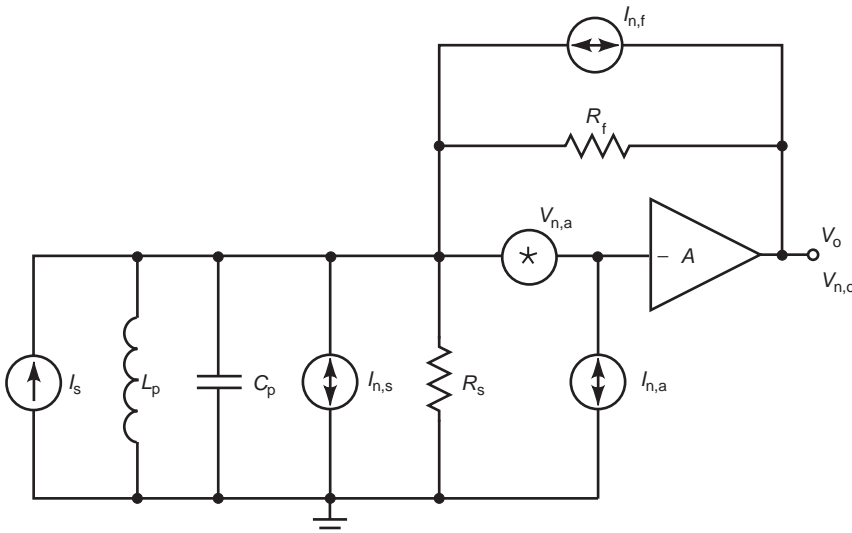


Figure 12. A transimpedance configuration for an inductive source ensures frequency-independent gain.

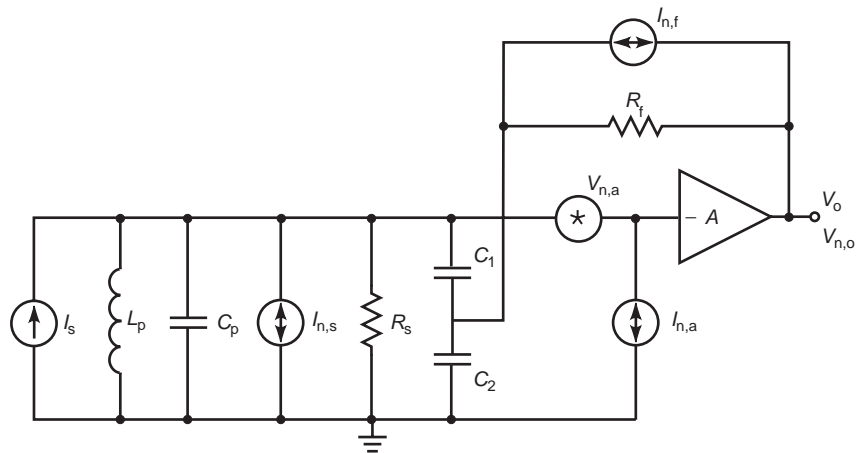


Figure 13. The use of a combined resistive and capacitive feedback in a transimpedance amplifier minimizes the noise contribution of the feedback network.

bipolar one. Again, BiCMOS technology has been proposed to exploit the advantages coming from integrating both CMOS and bipolar devices in the same chip, even though at an increased cost of the fabrication process.

BIBLIOGRAPHY

1. IRE Subcommittee 7.9 on Noise, Representation of noise in linear two ports, *Proc. IRE* **48**:69–74 (1960).
2. C. D. Motchenbacher and J. A. Connelly, *Low-Noise Electronic System Design*, Wiley, New York, 1993.
3. Z. Y. Chang and W. M. C. Sansen, *Low-Noise Wide-Band Amplifiers in Bipolar and CMOS Technologies*, Kluwer, Norwell, MA, 1991.
4. IRE Subcommittee on Noise, IRE standards on methods of measuring noise in linear two ports, 1959 (IRE Standard 59 IRE 20. S1), *Proc. IRE* **48**:60–68 (1960).
5. Y. Netzer, A new interpretation of noise reduction by matching, *Proc. IEEE* **62**:404–406 (1974).
6. Y. Netzer, The design of low-noise amplifiers, *Proc. IEEE* **69**:728–741 (1981).
7. M. Steyaert, Z. Y. Chang, and W. Sansen, Low-noise monolithic amplifier design: Bipolar versus CMOS, *Analog Integr. Circuits Signal Process.* **1**:9–19 (1991).
8. J. G. Greame, *Photodiode Amplifiers: Opamp Solutions*, McGraw-Hill, New York, 1996.
9. D. J. T. Heatley, Optical Receivers, in J. E. Franca and Y. Tsvividis, eds., *Design of Analog-Digital VLSI Circuits for Telecommunications and signal Processing*, 2nd ed., Prentice-Hall, Englewood Cliffs, NJ, 1994.
10. J. Silva-Martinez and J. Salcedo-Suñer, A CMOS preamplifier for electret microphones, *Proc. 1995 IEEE Int. Symp. Circuits Syst.*, 1995, Vol. 3, pp. 1868–1871.
11. J. F. Duque-Carrillo et al., VERDI: An acoustically programmable and adjustable CMOS mixed-mode signal processor for hearing aid applications, *IEEE J. Solid-State Circ.* **SC-31**:634–645 (1996).
12. B. Stefanelli et al., A very low-noise CMOS preamplifier for capacitive sensors, *IEEE J. Solid-State Circ.* **SC-28**:971–978 (1993).
13. A. C. Pluygers, A novel microphone preamplifier for use in hearing aids, *Analog Integr. Circuits Signal Process.* **3**:113–118 (1993).
14. L. Fasoli and M. Sampietro, Criteria for setting the width of CCD front end transistor to reach minimum pixel noise, *IEEE Trans. Electron. Devices* **ED-43**:1073–1076 (1996).
15. J.-C. Bertails, Low-frequency noise considerations for MOS amplifier design, *IEEE J. Solid-State Circ.* **SC-14**:773–776 (1979).
16. E. A. Vittoz, The design of high-performance analog circuits on digital CMOS chips, *IEEE J. Solid-State Circ.* **SC-20**:657–665 (1985).
17. K. R. Laker and W. Sansen, *Design of Analog Integrated Circuits and Systems*, McGraw-Hill, New York, 1994.
18. E. Gatti and P. F. Manfredi, Processing the signals from solid-state detectors in elementary particle physics, *La Rivista del Nuovo Cimento* **1**(series 3) (1986).
19. V. Radeka, Low-noise techniques in detectors, *Ann. Rev. Nucl. Part. Sci.* **38**:217–277 (1988).
20. A. Sartori et al., A 2-D photosensor array with integrated charge amplifier, *Sensors Actuators A Phys.* **46–47**:247–250 (1995).
21. G. Bertuccio and A. Pullia, A low noise silicon detector preamplifier system for room temperature X-ray spectroscopy, *Proc. Symp. Semicon. Room-Temperature Radiation Detector Appl. Mater. Res. Soc. Symp. Proc.*, 1993, Vol. 302, pp. 597–603.
22. G. Bertuccio, A. Pullia, and G. De Geronimo, Criteria of choice of the front-end transistor for low-noise preamplification of detector signals at sub-microsecond shaping times for X- and γ -ray spectroscopy, *Nucl. Instr. Meth. Phys. Res.* **A380**:301–307 (1996).
23. E. Gatti, A. Hrisoho, and P. F. Manfredi, Choice between FETs or bipolar transistors and optimization of their working points in low-noise preamplifiers for fast pulse processing: Theory and experimental results, *IEEE Trans. Nucl. Sci.* **30**:319–323 (1983).
24. G. Bertuccio, L. Fasoli, and M. Sampietro, Design criteria of low-power low-noise charge amplifiers in VLSI bipolar technology, *IEEE Trans. Nucl. Sci.* **44**:1708–1718 (1997).
25. I. Kipnis et al., A time-over-threshold machine: The readout integrated circuit for the BaBar silicon vertex tracker, *IEEE Trans. Nucl. Sci.* **44**:289–297 (1997).
26. J. Wulleman, A low-power high-gain transresistance BiCMOS pulse amplifier for capacitive detector readout, *IEEE J. Solid-State Circ.* **SC-32**:1181–1191 (1997).

27. Z. Y. Chang and W. Sansen, Stability and noise performance of constant transimpedance amplifier with inductive source, *IEEE Trans. Circ. Syst.* **CAS-35**:264–271 (1989).

PRINTED INDUCTORS

BAN-LEONG OOI
 DAO-XIAN XU
 National University of
 Singapore
 Singapore

1. INTRODUCTION

The surging demand of modern wireless silicon-based radiofrequency integrated circuits (RFICs) has placed great importance and interest in on-chip passive components. The design criteria for wireless mobile communication equipment, which include low cost, low supply voltage, low power dissipation, low noise, high frequency of operation, and low distortion, cannot be satisfactorily met in many cases without the use of on-chip monolithic silicon spiral inductors. These monolithic inductors allow significantly improved levels of performance in monolithic power amplifiers, low-noise amplifiers, upconversion-downconversion mixers, and low-phase-noise local oscillators. The on-chip inductor is able to resonate with any parasitic capacitance, thus allowing potentially higher frequency operation. It provides bias current with no significant dc drop, which incidentally improves linearity of the system. An added advantage of the on-chip inductor is that inductive degeneration can lead to simultaneous noise and power matching.

In order to reap these advantages, it becomes crucial for the circuit designer to be able to predict, design, optimize, and model accurately the characteristics of the on-chip inductor. Although there are several good textbooks [1–4] that present overviews of the printed inductors, except for Niknejad [5], few have delved indepth into the subject of spiral inductor analysis and characterization. It

is thus the objective of this article to provide a summarized description of the various methods of designing, modeling, and characterizing the on-chip spiral inductor. The emphasis is to present useful techniques of on-chip spiral inductor designing and modeling that complement information given in other handbooks or textbooks. Interested readers who require a good overview of printed inductors can refer to Refs. 1–5 for further details.

2. SPIRAL INDUCTOR DESIGN

The spiral inductor is the most common structure for implementing the on-chip inductor in many foundry processes, and a typical on-chip spiral inductor structure is shown in Fig. 1. A spiral structure is typically laid out using two or more of the top metal layers in most of the standard foundry process. The top metal layers are used primarily because this will help in minimizing the resistive coupling to the substrate and in turn, in reducing the loss of the overall spiral inductor. More than two metal layers can be utilized to increase the Q factor.

The quality factor (Q) of an inductor, which is defined as

$$Q = 2\pi \frac{\text{energy stored}}{\text{energy loss in one oscillation cycle}} \quad (1)$$

is a gauge of the effective magnetic energy storage capability of the inductor. Thus, a high quality factor is critical for a spiral inductor. For silicon-based RFICs, the spiral inductor suffers from performance limitations related to issues such as substrate injection through oxide, substrate coupling by ohmic and displacement current, lateral currents to nearby substrate taps, and skin effects [6]. This causes the Q of the inductor to be low (i.e., <10) at high frequencies. As a result, many high-speed RF components such as voltage-controlled oscillators (VCO) or high power amplifiers using on-chip inductors have limited performance compared to designs using off-chip components. The use of off-chip components adds complexity and cost to the design of these circuits, which has directly led to intense research aimed at improving the performance of

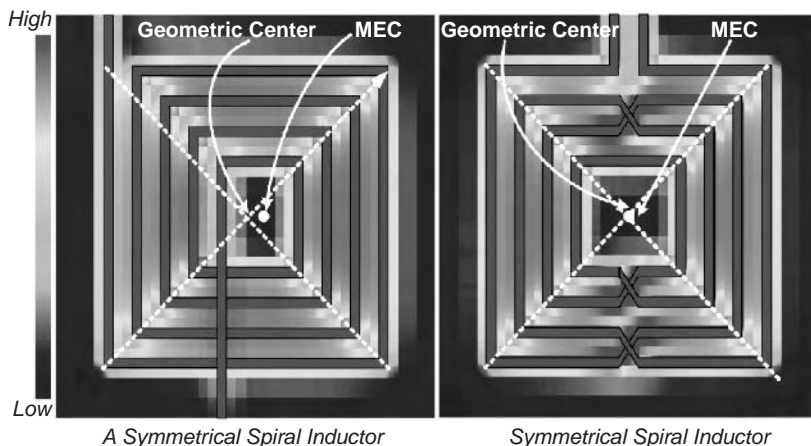


Figure 1. Magnetic field intensity comparison of symmetric and the asymmetrical spiral inductors.

on-chip spiral inductors. Significant efforts [7,8] have been expended with the aim of providing high- Q inductors for critical RF applications. These methods include (1) growing a high-resistivity silicon substrate with thicker metallization so as to mimic the low-loss semiinsulating GaAs substrate; (2) creating a bulk cavity in the silicon substrate under the inductor; (3) introducing patterned ground shield to reflect the electric field between the inductor and the substrate; (4) varying the inductor's geometry such as the shape, trace width, metal spacing, number of turns, number of metal layers, and topology; and finally (5) exciting the inductor in a differential manner.

Techniques 1–3 involve extra processing cost, whereas techniques 4 and 5 are adversely affected by both the non-uniform metal thickness and the parasitic capacitance effects. Of particular interest and worthy of mention under technique 4 is the design of the symmetric spiral inductor, which can give higher Q than can the asymmetric spiral inductor. Wrapping of the metal lines of the squared spiral inductor, as shown in Fig. 1, allows the flux from each turn to be added, thus increasing the inductance per unit length of the structure. From the comparison of the magnetic field intensity plot presented in Fig. 1, one can intuitively deduce that the “golden rule” of designing high- Q inductor [9] would be to reduce the number of overlaps in the inductor, ensure that the geometric center coincides with the magnetoelectric center (MEC), and force the current to loop in the same direction. The magneto-electric center corresponds to the point where both the magnetic and electric fields are a local minimum. With fewer overlaps, the electric coupling, which is counterproductive to Q , can be minimized. With the same loop current flows, and coincident MEC and geometric center, less magnetic field cancellation would result, thus leading to higher magnetic energy storage in the inductor.

3. SPIRAL INDUCTOR MODELING AND CHARACTERIZATION

An accurate model for the on-chip spiral inductor, which can efficiently represent its electrical performance for circuit simulation and optimization with other design components, is of great importance for silicon-based radiofrequency integrated circuit designers. Although the generic electromagnetic field solver such as Ansoft HFSS, or other partial-element equivalent-circuit (PEEC)-based solvers, can provide reasonable performance evaluation of the spiral inductor; these simulators are computationally intensive and time-consuming. Other techniques for analysis include the Greenhouse method [10], the Wheeler formula [11] and a “data-fitted monomial expression” [12]. A crude estimate (within 30%) for the inductance value of a spiral inductor provided by Lee [13] is given as

$$L = \mu_0 n^2 r \approx 1.2 \times 10^{-6} n^2 r \quad (2)$$

where n and r represent respectively the number of turns and radius of the spiral inductor and μ_0 is the permeability

of the semiconductor substrate. These techniques are either relatively inaccurate or not scalable over a wide range of layout dimensions and process parameters. For inductor design insights and optimization, a compact, physical lumped-element circuit model would be preferred as it could be easily integrated in any commercial computer-aided design software program such as Microwave Office, Agilent Advanced Design System (ADS), or Serenade from Ansoft.

Figure 2 reviews a typically adopted equivalent circuit used for spiral inductor modeling. In the model, L_s represents the spiral inductance whereas R_s is the metal series resistance whose behavior at high frequency is governed by the eddy-current effect and the skin effect. The series feedforward capacitance C_s , which accounts for the capacitance due to overlaps between the spiral and the center-tap underpass, is usually expressed as

$$C_s = \frac{nW^2 \epsilon_{\text{SiO}_2}}{t_{\text{SiO}_2}} \quad (3)$$

The parasitic C_{ox} , C_{si} , and R_{si} , which are respectively the oxide capacitance, substrate capacitance, and resistance, are computed from

$$C_{\text{ox}} = \frac{\epsilon_0 \epsilon_{\text{eff}}(\epsilon_{\text{SiO}_2}, h_1)}{F(h_1, W)} \quad (4)$$

$$C_{\text{si}} = \frac{\epsilon_0 \epsilon_{\text{eff}}(\epsilon_{\text{Si}}, h_2)}{F(h_2, W)} \quad (5)$$

$$R_{\text{si}} = \frac{2F(h_2, W)}{\sigma_{\text{si}}(1 + \sqrt{1 + 10h_2/W})} \quad (6)$$

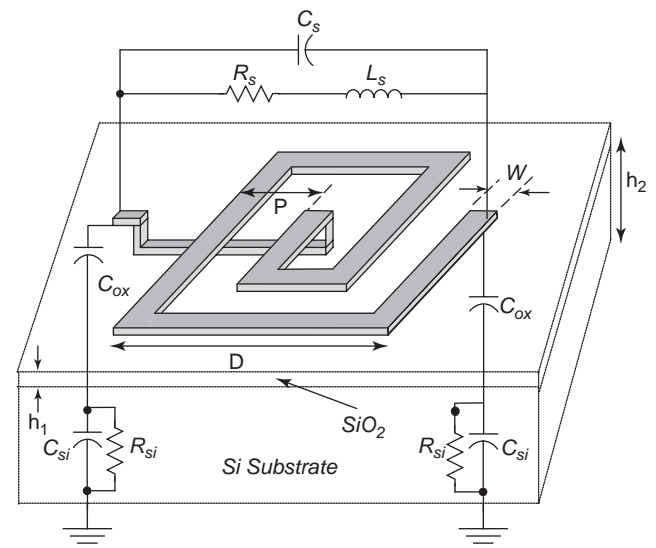


Figure 2. A typical equivalent circuit for spiral inductor.

where

$$F(h_2, W) = \begin{cases} \frac{1}{2\pi} \ln(8h/W + W/4h), & h/W \geq 1 \\ WW/h + 2.42 - 0.44h/W + (1 - h/W)^6, & h/W \leq 1 \end{cases} \quad (7)$$

$$\epsilon_{\text{eff}}(\epsilon, h) = \frac{(\epsilon + 1)}{2} + \frac{(\epsilon - 1)}{2\sqrt{1 + 10h/W}} \quad (8)$$

where n is the number of the overlaps, ϵ_{SiO_2} and t_{SiO_2} denote the dielectric constant and thickness of the oxide layer, ϵ_{Si} is the permittivity of the silicon substrate, and W is the spiral linewidth.

The equivalent circuit, as shown in Fig. 2, strongly lacks the frequency dependence of R_s and L_s as a result of current crowding in the conductor. The circuit also fails to describe the distributed characteristics of the inductor under high-frequency operation. Prominent effects such as eddy-current effect and skin effect are not incorporated in the model. An improved circuit model [14], which represents the eddy current as an electrical component, is shown in Fig. 3. The branch constituted by the series connection of L'_s , R'_s , and in parallel with R_s is taken as circuit elements contributing to the overall eddy-current loss. The voltage over R_s represents the total voltage effect of each induced eddy-current segment. Compared with the conventional spiral inductor model in Fig. 2, the new model has an added advantage. By circuit theory

$$\text{Re}(Z_{\text{in}}) = R_s - \frac{R_s^2(R_s + R'_s)}{(R_s + R'_s)^2 + \omega^2 L_s'^2} \quad (9)$$

$$\text{Im}(Z_{\text{in}})/\omega = L_s + \frac{R_s^2 L_s'}{(R_s + R'_s)^2 + \omega^2 L_s'^2} \quad (10)$$

where Z_{in} is the input impedance of the inductor, Eqs. (9) and (10) provide a frequency varying effect for both the resistance and inductance. This overcomes the limitation of the conventional circuit model in that it can only offer constant values for both resistance and inductance.

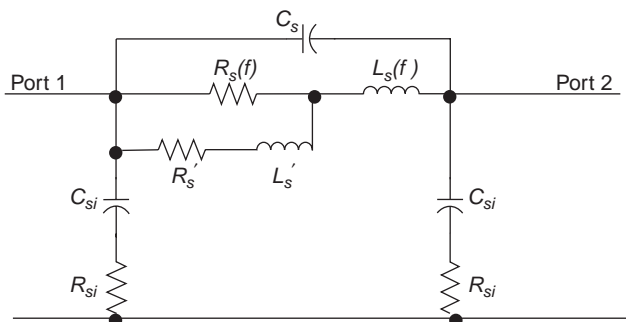


Figure 3. A modified circuit model for spiral inductor.

Figures 4a and 4b illustrate the accuracy of the improved circuit model (as in Fig. 3) over the conventional circuit model given in Fig. 2. The measured S parameters, which are indicated in blue, are taken from a sample inductor 1 of 1.75 turns, $10\ \mu\text{m}$ width (W), $15\ \mu\text{m}$ pitch (P), $100\ \mu\text{m}$ outer dimension (D), and $1.5\ \mu\text{m}$ metal thickness (h_2). As shown in the figure, the improved circuit model gives a better agreement than does the conventional circuit model.

Conventionally, the Q of a spiral inductor is experimentally evaluated by

$$Q = \frac{\text{Im}(1/Y_{11})}{\text{Re}(1/Y_{11})} \quad (11)$$

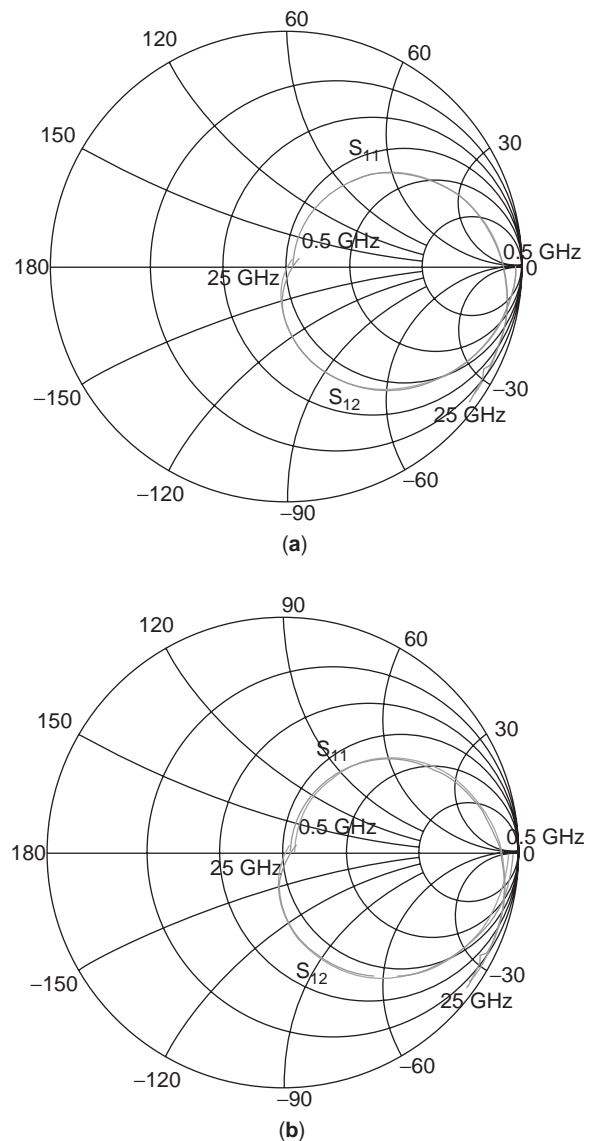


Figure 4. Comparison of two equivalent-circuit models for a typical spiral inductor: (a) measured S parameters (indicated in blue) versus new model (indicated in red); (b) measured S parameters (indicated in blue) versus old model (indicated in red). (This figure is available in full color at <http://www.mrw.interscience.wiley.com/erfme>.)

where Y_{11} is the Y parameter of the spiral inductor. With the presence of the equivalent-circuit model as in Fig. 2, a greater insight into the dependence of equivalent-circuit parameters on Q can be obtained. Yue and Wong [15] had expressed the Q of a typical spiral inductor as

$$Q = \left[\frac{\omega L_s}{R_s} \right] \left[\frac{R_p}{R_p + [(\omega L_s/R_s)^2 + 1]R_s} \right] \left[1 - \frac{R_s^2(C_s + C_p)}{L_s} - \omega^2 L_s(C_s + C_p) \right] \quad (12)$$

where

$$R_p = \frac{1}{\omega^2 C_{ox}^2 R_{si}} + \frac{R_{si}(C_{ox} + C_{si})^2}{C_{ox}^2} \quad (13)$$

and

$$C_p = C_{ox} \frac{1 + \omega^2(C_{ox} + C_{si})C_{si}R_{si}^2}{1 + \omega^2(C_{ox} + C_{si})R_{si}^2} \quad (14)$$

One can deduce from Eq. (12) that Q depends solely on three terms indicated by the enclosed square brackets. The term $\omega L_s/R_s$ represents the magnetic energy stored and the ohmic loss in the series resistance. The second term in Eq. (12) is the substrate loss factor, which accounts for the energy dissipated in the semiconducting silicon substrate. The last term is the self-resonance factor describing the reduction in Q due to a change in the peak electric energy with frequency and the vanishing of Q at the self-resonant frequency. This term is a strong function on the inherent capacitance of the spiral inductor. The self-resonant frequency is the upper bound for an inductor to be functional. The equivalent-circuit models as shown in Figs. 2 and 3 help facilitate a greater insight into the operation of the spiral inductor and provide meaningful hints in minimizing the induced loss, which is important for RFIC technology.

3.1. Resistance Calculation

Normally, one would expect multiple turns to be required for a spiral inductor to attain higher inductances. However, with more turns, the current on the trace will be non-uniformly distributed and the overall inductance will not be as high as one would expect. The concept of current redistribution in the metallic trace of the spiral inductor can be traced from two effects: the skin effect and the eddy-current effect. Conventionally, the series resistance R of the spiral inductor under skin effect often assumes the form

$$R = \frac{\rho l}{W\delta(1 - e^{-T/\delta})} \quad (15)$$

where ρ , W , and l represent respectively the resistivity, metal width, and total length of the spiral inductor. T and δ denote respectively the metal thickness and skin depth ($\delta = \sqrt{2/\omega\sigma\mu}$). For frequencies below 2 GHz, the skin effect

is relatively small in most process since the metallic trace thickness is typically less than or equal to the skin depth. For frequencies higher than 2 GHz, the series resistance increases as the skin effect becomes more prominent, and approaches an asymptote proportional to the square root of frequency. In contrast, current crowding, which is caused by the eddy currents in the metal traces of the spiral inductor, is a strong function of frequency. It causes the resistance to increase at a higher frequency. The eddy current, which has a significant effect on the inductance of the spiral inductor, manifests itself not only as a skin effect but also as a proximity effect. This major current crowding mechanism is generally missing in most of the inductor equivalent-circuit modeling and incorporation of these effects in spiral inductor modeling is thus the subject of this section.

The basic concept of current crowding lies in the current redistribution caused by the B -field variation on the adjacent turn. The B field can actually adopt a simplified expression given as

$$B(n) \approx \frac{B_0(n - M)}{(N - M)} = \frac{I_{ex}0.65\mu_0(n - M)}{P(N - M)} \quad (16)$$

where n is the index for the turn number, N is the total number of turns, B_0 is the field at the innermost turn (turn number N), M is the turn number where the field falls to zero and reverses direction, P is the turn pitch (refer to Fig. 5), and I_{ex} is the excitation current. Using

$$J = \begin{cases} J_0 e^{(z-T/2)/\delta}, & T/2 \geq z \geq 0 \\ J_0 e^{-(z+T/2)/\delta}, & 0 \geq z \geq -T/2 \end{cases} \quad (17)$$

where T is the metal trace thickness and applying the Faraday's law, the per unit length surface eddy current for the n th turn [16] becomes

$$\begin{aligned} |I_{eddy,n}| &= 2 \int_0^{T/2} \int_0^{W/2} \omega \sigma B(n) x e^{(z-T/2)/\delta} dx dz \\ &= 0.162 \omega \sigma W^2 I_{ex} \delta (1 - e^{-T/2\delta}) \frac{\mu_0 |n - M|}{P(N - M)} \end{aligned} \quad (18)$$

where δ refers to the skin depth. σ and μ are respectively the conductivity and permeability of the metallic trace. The power dissipated in the n th turn due to the eddy current is thus expressed as

$$\begin{aligned} P_{eddy,n} &= 4\sigma l_n \omega^2 B^2(n) \int_0^{T/2} \int_0^{W/2} x^2 e^{2(z-T/2)/\delta} dx dz \\ &= \frac{1}{12} \sigma l_n \omega^2 B^2(n) W^3 \delta (1 - e^{-T/\delta}) \end{aligned} \quad (19)$$

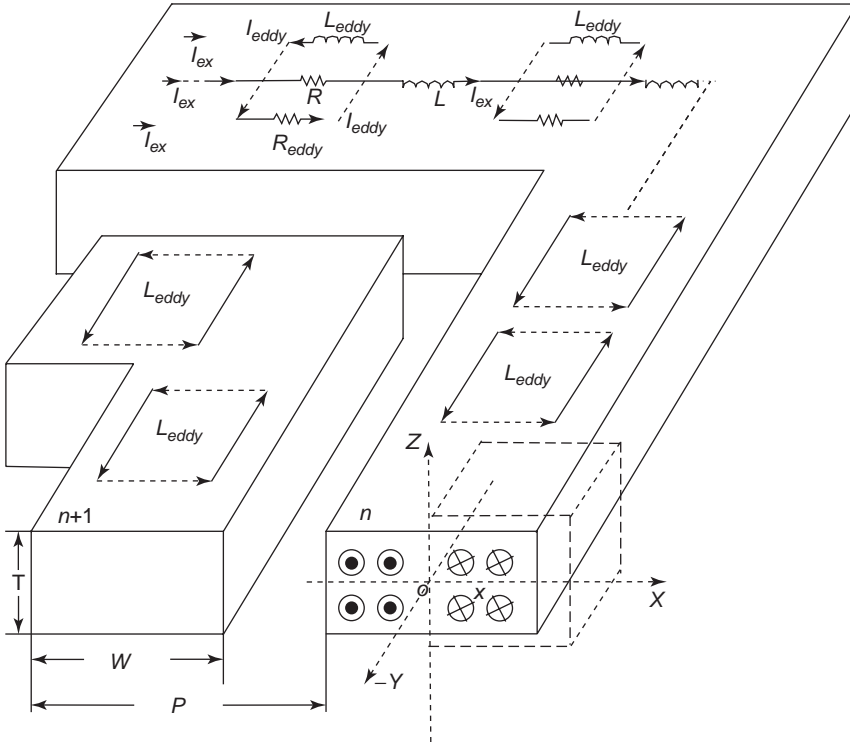


Figure 5. Simplified illustration of eddy-current effect.

where l_n is the length of the n th turn. Therefore, the total spiral resistance is given as

$$R_{\text{total}} = R_0 + \frac{0.05W^4T\sigma^{3/2}\mu_0^2}{\mu^{1/2}P^2(N-M)^2} \sum_{n=1}^N R_n(n-M)^2 \times \omega^{3/2}(1 - e^{-\sqrt{T^2\mu\sigma\omega/2}}) \quad (20)$$

where R_0 is the theoretical DC resistance of the inductor and is computed by $R_0 = \sum_n l_n / \sigma WT$. Here, $\sum_n l_n$ is total metal length of the spiral inductor. In order to obtain a rough review of the ω dependence on R_{total} at the various frequency ranges, through simplification of Eq. (20), we have

$$R_{\text{total}} = R_0 + 0.05W^4T\sigma^{3/2} \times \frac{\mu_0^2}{\mu^{1/2}P^2} \sum_{n=1}^N R_n \frac{(n-M)^2}{(N-M)^2} \omega^{3/2} \quad (21)$$

at high frequency,

$$R_{\text{total}} \approx R_0 + 0.035W^4T^2\sigma^2 \times \frac{\mu_0^2}{P^2} \sum_{n=1}^N R_n \frac{(n-M)^2}{(N-M)^2} \omega^2, \quad (22)$$

at low frequency

Figures 6a and 6b provide a comparison of the resistance values computed from Eqs. (20)–(22). The adopted

parameters for inductor 3 include 3.5 turns, 10 μm width, 11.5 μm pitch, 75 μm inner dimension (d), and 0.7 μm alumini-metal thickness whereas for inductor 4, the parameters include 2 turns, 6 μm width, 8 μm pitch, 75 μm inner dimension, and 1 μm copper metal thickness. In the figures, predicted curve 1 refers to Eq. (20), and predicted curve 2 refers to Eq. (21), whereas predicted curve 3 refers to Eq. (22). As illustrated in Fig. 6, Eq. (20) is relatively more accurate for the resistance simulation in the whole frequency domain. Equation (22) is valid when ω is very low and the skin depth δ is much larger than the metal thickness T . By comparing prediction curve 2 of inductor 4 with that of inductor 3, we conclude that Eq. (21) is valid only when ω is high enough that δ is much smaller than T .

3.2. Inductance Calculation by Partial Inductance Method

The total inductance of a spiral inductor can be separated into two aspects: self- and mutual inductance. Since an inductor is intended for storing magnetic energy only, an ideal expression of its inductance in terms of width, gap spacing, and length is essential in terms of equivalent-circuit modeling [16]. The eddy-current and skin effects will result in nonuniform current distributions in the metallic trace, thus forcing the inductance to be *current-dependent*. As a result, the self- and mutual inductances must be derived from a more fundamental electromotive definition

$$e = -\frac{d\phi}{dt} = -L \frac{di}{dt} \quad (23)$$

where e is the electromotive force induced by the change of magnetic flux ϕ in one closed loop. The concept of partial inductance, which involves the magnetic flux between a conductor and infinity, will be adopted in this section.

By ignoring the effect of the ground plane and the substrate, the width and thickness of the cross section are divided into infinitely thin, uniformly distributed segments as in Fig. 7. Using Eq. (23), the overall self-inductance caused by the magnetic flux in the N -filament system is approximated as

$$L_{\text{self}} \approx \frac{L_1 + \sum_{n=1}^N \left(\left[\frac{k_n}{\sum_{j=1}^N k_j} \right] \sum_{\substack{m=1 \\ m \neq n}}^N M_{mn} \right)}{N} \tag{24}$$

$$\approx \frac{\sum_{n=1}^N \left(k_n \sum_{\substack{m=1 \\ m \neq n}}^N M_{mn} \right)}{N \sum_{j=1}^N k_j}$$

where $N = M_1 N_1 = M_2 N_2 = \dots$ is the total number of filaments in each metallic trace, M_{mn} is the mutual inductance value between the m th and n th current filaments, L_1 is the self-inductance of a filament, and

$$i_n = \frac{k_n i_{\text{total}}}{\sum_{j=1}^N k_j} \tag{25}$$

Similarly, the mutual inductance between any two different traces with N filaments (see Fig. 7) is expressed as

$$L_{\text{mutual}} = \frac{1}{M_1 N_1} \sum_{n=1}^{M_2 N_2} \sum_{m=1}^{M_1 N_1} \left(\frac{k_n M'_{mn}}{\sum_{j=1}^N k_j} \right) \tag{26}$$

where M'_{mn} refers to the mutual inductance between the m th and n th current filaments in different conductors. The sum of each M' due to all the other parts in the metallic trace will provide an overall interparts mutual inductance of a spiral inductor. The mutual inductance is computed from

$$M_{mn} = 0.002\ell \left[\ln \left(\frac{\ell}{g} + \sqrt{1 + \frac{\ell^2}{g^2}} \right) - \sqrt{1 + \frac{g^2}{\ell^2}} + \frac{g}{\ell} \right] \tag{27}$$

$$\approx 0.002\ell \left(\ln \frac{2\ell}{g} - 1 + \frac{g}{\ell} - \frac{g^2}{4\ell^2} + \dots \right)$$

where ℓ is the length of the filaments, g is the geometric mean distance between the two filaments and is expressed

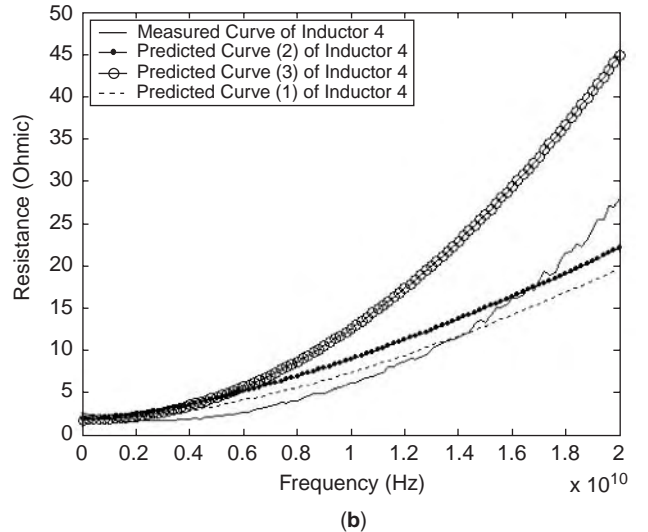
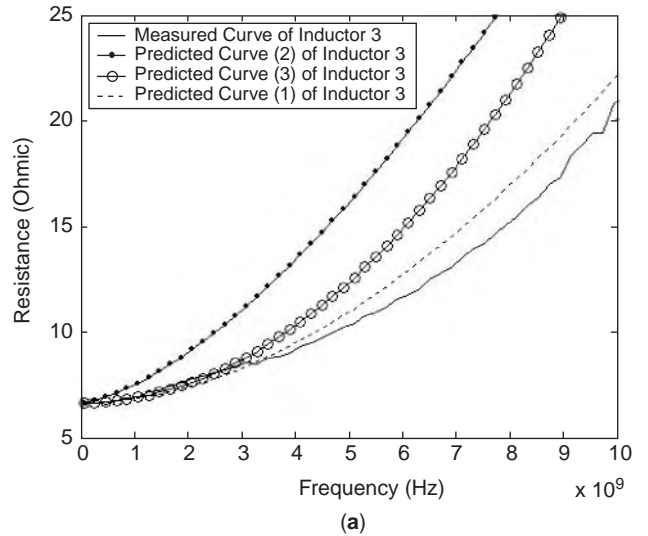


Figure 6. Resistance comparison for (a) inductor 3 and (b) inductor 4 after deembedding.

as

$$g = \lim_{N \rightarrow \infty} \left[\prod_{m=1}^N \left(\prod_{n=1}^N \sqrt{c^2 + \left[(m-n) \frac{b}{N} \right]^2} \right)^{1/n} \right]^{1/m}$$

where c and b are respectively the longitudinal length and separation distance of the cross section of two filaments.

Under the skin effect, the attenuation of the current density J_s as a function of distance z away from the surface can be represented by the function

$$J_s(z) = \begin{cases} J_0 e^{z/\delta}, & 0 \geq z \geq -T/2 \\ J_0 e^{-(z+T)/\delta}, & -T/2 \geq z \geq -T \end{cases} \tag{28}$$

where J_0 refers to the current density at the surface ($z = 0$) as indicated in Fig. 8. The current I can be obtained by

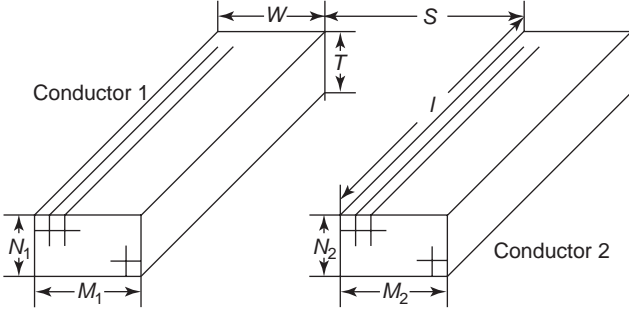


Figure 7. Cross section illustration of two conductors in parallel.

integrating J_s over the total cross-sectional area, yielding

$$\begin{aligned} I &= W \left(\int_{-T/2}^0 J_0 e^{z/\delta} dz + \int_{-T}^{-T/2} J_0 e^{-(z+T)/\delta} dz \right) \\ &= 2WJ_0\delta(1 - e^{-T/2\delta}) \end{aligned} \quad (29)$$

By dividing the cross section of the trace into smaller filaments as in Fig. 8, followed by setting $k_n = J_s$ ($z = -nT/N$) TW/N , and combining with Eqs. (24)–(26), the inductance calculation due to the current redistribution under the skin depth effect becomes

$$\begin{aligned} \frac{L_{\text{self}}^\beta}{L_{\text{self}}^\alpha} &= K_1 \\ &= \lim_{N \rightarrow \infty} \frac{T \sum_{n=1}^{N/2} e^{-Tn/(N\delta)} \sum_{\substack{m=1 \\ m \neq n}}^N \overline{M}_{mn}}{\delta(1 - e^{-T/2\delta}) \sum_{n=1}^N \sum_{\substack{m=1 \\ m \neq n}}^N \overline{M}_{mn}} \end{aligned} \quad (30)$$

and

$$\frac{L_{\text{mutual}}^\beta}{L_{\text{mutual}}^\alpha} = \lim_{N \rightarrow \infty} \frac{T \sum_{n=1}^{N/2} e^{-Tn/(N\delta)} \sum_{m=1}^N \overline{M}'_{mn}}{\delta(1 - e^{-T/2\delta}) \sum_{n=1}^N \sum_{m=1}^N \overline{M}_{mn}} \quad (31)$$

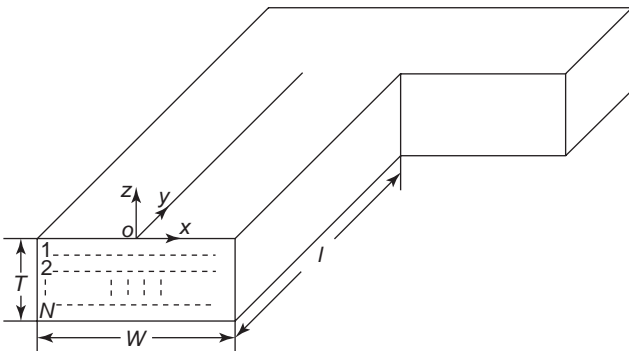


Figure 8. Segmentation method on the cross section of metallic trace under skin effect.

where the superscripts α and β represent respectively the conditions when the current is uniform and when it is under skin effect. \overline{M}_{mn} refers to the mutual inductance between the m th and n th filaments within the same trace, and \overline{M}'_{mn} denotes the mutual inductance between the m th and n th filaments of different traces. Since the distance between two filaments of different traces is much larger than a single filament thickness, we can approximate

$$\sum_n \overline{M}_{m1} = \sum_m \overline{M}'_{mn} = \dots = \sum_m \overline{M}'_{mn} \quad (32)$$

If the skin effect is considered alone, we have

$$L_{\text{mutual}}^\alpha \approx L_{\text{mutual}}^\beta \quad (33)$$

The eddy currents in the metallic trace of the spiral inductor are induced by the initial excitation current (see Fig. 5). Using Eqs. (16) and Faraday's and Ohm's law, an approximate expression to describe the eddy current is given as

$$J_{\text{eddy},n}(x) = \frac{0.65\omega\mu_0}{P} I_0 \sigma x \left(\frac{n-M}{N-M} \right) \quad (34)$$

From Fig. 9, one can observe that the eddy current effect on the overall self-inductance is neutralized as the currents on both sides of a metallic trace are in opposite directions. This, in turn, causes the overall magnetic field to be canceled. If we divide the cross section into infinite thin filaments along the x direction as in Fig. 9, we can achieve

$$\begin{aligned} L_{\text{self}}^\gamma &\propto \lim_{N, N' \rightarrow \infty} \sum_{n=1}^N \left(\sum_{\substack{m=1 \\ m \neq n}}^N \overline{M}_{mn} + \sum_{m'=1}^{N'} \overline{M}'_{m'n} \right) \\ &- \lim_{N, N' \rightarrow \infty} \sum_{n'=1}^{N'} \left(\sum_{m=1}^N \overline{M}_{mn'} + \sum_{\substack{m'=1 \\ m' \neq n'}}^{N'} \overline{M}'_{m'n'} \right) = 0 \end{aligned} \quad (35)$$

where the superscript γ represents the condition only under the eddy-current effect. This phenomenon also exists under the presence of skin effect, and Eq. (35) is valid under the incorporation of both skin depth and eddy-current effect.

While considering the mutual inductance between two different metallic traces caused by the eddy current, the total excitation current should be taken as I_0 . Using Eqs. (34) and (26) and setting $k_n = J_{\text{eddy}}[x = (nW/2N)]TW/2N$, we obtain

$$\frac{L_{\text{mutual}}^\gamma}{L_{\text{mutual}}^\alpha} = \frac{0.325\omega\mu_0 T \sigma W^2 K_2}{P} \left(\frac{n-M}{N-M} \right) \quad (36)$$

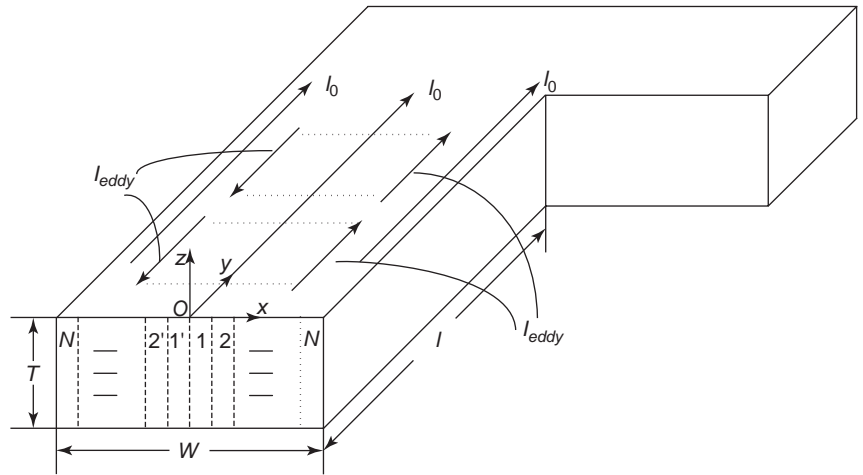


Figure 9. Segmentation method on the cross section of metallic trace with eddy current.

with

$$K_2 = \frac{\lim_{N, N' \rightarrow \infty} \sum_{n=1}^N \frac{n}{N} \left(\sum_{m=1}^N \overline{M'_{mn}} + \sum_{m'=1}^{N'} \overline{M'_{m'n'}} \right) - \lim_{N, N' \rightarrow \infty} \sum_{n'=1}^{N'} \frac{n'}{N'} \left(\sum_{m=1}^N \overline{M'_{mn'}} + \sum_{m'=1}^{N'} \overline{M'_{m'n'}} \right)}{\lim_{N, N' \rightarrow \infty} \sum_{n=1}^N \left(\sum_{m=1}^N \overline{M'_{mn}} + \sum_{m'=1}^{N'} \overline{M'_{m'n'}} \right) + \lim_{N, N' \rightarrow \infty} \sum_{n'=1}^{N'} \left(\sum_{m=1}^N \overline{M'_{mn'}} + \sum_{m'=1}^{N'} \overline{M'_{m'n'}} \right)} \quad (37)$$

But the eddy currents are in quadrature with the excitation current, and by first-order estimation [17–18], one may neglect the effect of eddy currents on the overall inductance calculation as the magnetic flux induced by the eddy currents within the metal trace provides no effective contribution to the initial magnetic field. In doing so, K_2 can be assumed as zero.

Figure 10 plots the weighting expression $e^{-kT/(N\delta)} \sum_{j=1}^N M_{kj} / \sum_{i=1}^{N/2} e^{-kT/(N\delta)} \sum_{j=1}^N M_{ij}$ versus k , where

$k = 1, 2, \dots, N$ is the filament number in Fig. 8 in a typical case with parameters $J_0 = 1 \text{ A/m}^2$, $T = 1 \mu\text{m}$, $W = 10 \mu\text{m}$, $N = 16$, and $l = 100 \mu\text{m}$. The weighting expression shows the self-inductance weightage of a filament over the total self-inductance of the single conductor. As shown in the diagram, under the skin effect, the self-inductance of each filament is nearly a constant and therefore, can be taken to be the same in subsequent computation in Section 3.3. Figure 11 shows a typical trend for K_1 found in Eq. (32)

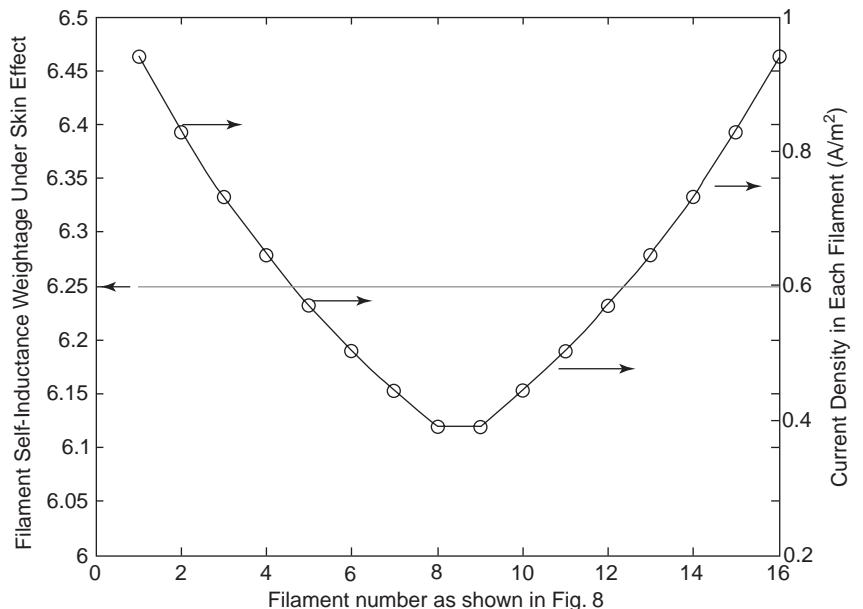


Figure 10. The self-inductance weightage and the current density under skin effect.

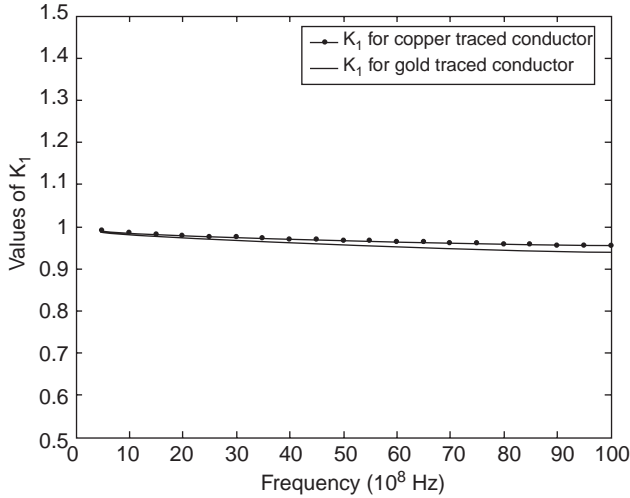


Figure 11. The characteristic change of K_1 .

for copper and gold trace spiral inductors of the same geometric parameters, namely, $T=1\ \mu\text{m}$, $W=10\ \mu\text{m}$, $N=16$, and $l=100\ \mu\text{m}$. As noted from the figure, K_1 in Eq. (32) can be taken as a constant to facilitate a faster computation for Eq. (32).

3.3. Frequency-Dependent Formulation for Inductance under the Skin Effect

The formulation for the series inductance as given in Section 3.2 has neglected the coupling effect of the series resistance. From the partitioning shown in Fig. 8, one can deduce that the specific skin effect complex internal impedance can be computed from the following expression

$$Y(\omega) = \sum_{n=1}^N \frac{1}{R_n + j\omega L} \quad (38)$$

where L is the self-inductance of each filament and is as given in Eq. (30). The value of L in Eq. (38) can be empirically taken as [21]

$$L = 0.002\ell_{\text{total}} \left[\ln\left(\frac{2\ell_{\text{total}}}{W+t}\right) + 0.5 - 0.00239 \right] \quad (39)$$

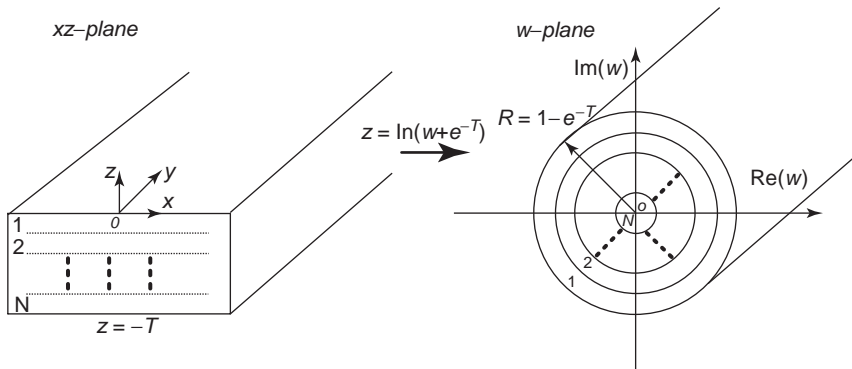


Figure 12. The conformal mapping from rectangular domain to circular domain.

where t is the thickness of each filament. To find R_n , the cross-section of the spiral inductor as in Fig. 8 is first mapped into a circle in the w plane using Ref. 19, and this transformation is expressed as

$$t = \ln(w + e^{-T}) \quad (40)$$

where

$$t = z + ix \quad (41)$$

With this transformation, each filament in Fig. 8 is subsequently mapped into a concentric ring within the circle as shown in Fig. 12. As a result of this, by borrowing the concept introduced by Gatous [20], R_n can be deduced to be

$$R_n = \frac{(4n-1)^2\pi}{64\sigma(1-e^{-T})^2} \quad (42)$$

The series term on the right-hand side of Eq. (38), evidently, may be considered as an equivalent circuit of parallel RL circuits as shown in Fig. 13. The specific skin effect complex internal impedance can thus be obtained by rearranging Eq. (38) to yield

$$R(\omega) + j\omega L_{\text{int}}(\omega) = \frac{1}{Y(\omega)} \quad (43)$$

where the resistive and reactive components on the surface of the metal are related by

$$R(\omega) = \frac{\sum_{n=1}^N \frac{R_n}{R_n^2 + \omega^2 L^2}}{\left(\sum_{n=1}^N \frac{R_n}{R_n^2 + \omega^2 L^2} \right)^2 + \omega^2 \left(\sum_{n=1}^N \frac{L}{R_n^2 + \omega^2 L^2} \right)^2} \quad (44)$$

$$L_{\text{int}}(\omega) = \frac{\sum_{n=1}^N \frac{L}{R_n^2 + \omega^2 L^2}}{\left(\sum_{n=1}^N \frac{R_n}{R_n^2 + \omega^2 L^2} \right)^2 + \omega^2 \left(\sum_{n=1}^N \frac{L}{R_n^2 + \omega^2 L^2} \right)^2} \quad (45)$$

It is clear here that when R_n equals zero, $R(\omega)$ would be zero whereas $L_{\text{int}}(\omega)$ would be equal to the parallel of all

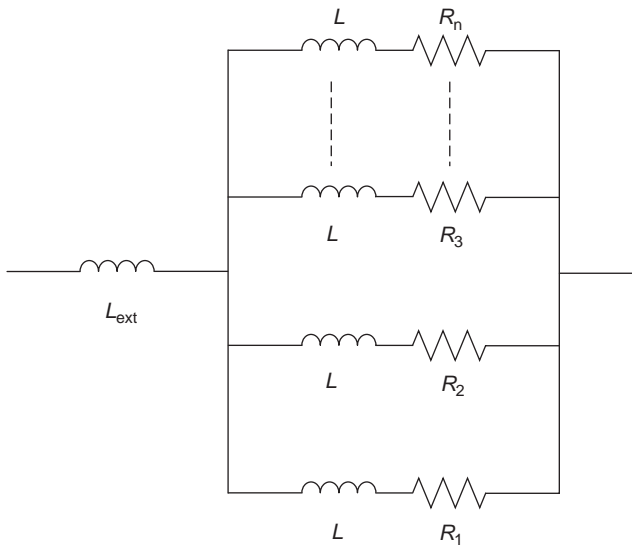


Figure 13. Equivalent circuit for the internal impedance in the metallic trace.

the self-inductance of the filament as given in Fig. 8. From Section 3.2, it is noted that this value of $L_{\text{int}}(\omega)$ will be a near constant under the effect when R_n equals zero. When the frequency is zero, Eqs. (44) and (45) are reduced to the well-known DC value. The DC inductance value is approximately given as [21]

$$L_{\text{DC}}^{\text{self}} = 0.002\ell_{\text{total}} \left[\ln \left(\frac{2\ell_{\text{total}}}{W+T} \right) + 0.5 - 0.00239 \right] \quad (46)$$

As the frequency increases, under the skin effect, the resistance $R(\omega)$ increases and the internal inductance $L_{\text{int}}(\omega)$ decreases to some limiting values depending on the geometry of the spiral inductor.

4. EXPERIMENTAL RESULTS AND DISCUSSION

From the discussion in Section 3.3, owing to the presence of the skin effect, the behavior of the theoretical inductance value of the spiral inductor is expected to be a decreasing function of frequency. However, in the measurement, the measured inductance is seriously affected by the presence of coupling capacitance C_s . For subsequent comparison in Fig. 14, we have subtracted from the measured data this capacitance's contribution through the following expression

$$L_s(f) = \frac{\text{imag}((-Y_{12} - j\omega C_s)^{-1})}{\omega} \quad (47)$$

where the value of C_s is attained by circuit optimizations and $\text{imag}(\cdot)$ denotes the imaginary part of the term enclosed in parentheses. In the circuit model shown in Fig. 3, $L_s(f)$ represents the theoretical frequency-dependent inductance of the spiral inductor. The simulated inductance $L_s(f)$ is computed by using the theoretical frequency-dependent inductance in Eqs. (30), (31), (45), and (46).

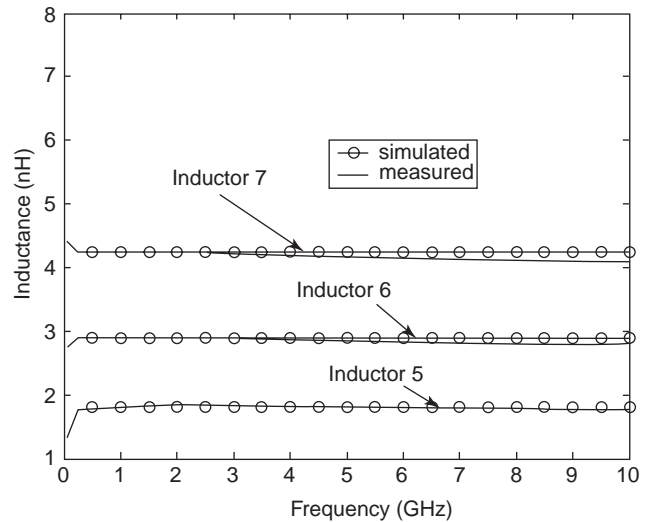


Figure 14. The measured and predicted inductances of spiral inductors.

To confirm that expression (47) can indeed predict the overall inductance behavior, we fabricated a series of circular copper-traced inductors. The layout parameters of the inductors include $6\ \mu\text{m}$ width, $2\ \mu\text{m}$ spacing, $1\ \mu\text{m}$ metal thickness, and $75\ \mu\text{m}$ inner dimension. The numbers of turns for inductors 5–7 are 3, 4, and 5, respectively. Figure 14 compares the measured inductance value and the simulated inductance from Eq. (47) for all the sample spiral inductors. The Cascade wafer probe and the HP8510 are used to measure the wafer containing the spiral inductors. Good agreement between the measured and predicted inductance values, especially for the domain below the resonance frequency of inductors, has been achieved in Fig. 14.

BIBLIOGRAPHY

1. D. J. Allstot, K. Choi, and J. Park, *Parasitic-Aware Optimization of CMOS RF Circuits*, Kluwer Academic Publishers, 2003.
2. I. D. Robertson and S. Lucyszyn, *RFIC and MMIC Design and Technology*, IEE Circuits, Devices and Systems Series 13, 2001.
3. I. J. Bahl, *Lumped Elements for RF and Microwave Circuits*, Artech House Pub., June 2003.
4. M. Golio, *The RF and Microwave Handbook*, CRC Press LLC, 2001.
5. A. M. Niknejad and R. G. Meyer, *Design, Simulation and Applications of Inductors and Transformers for Si RF ICs*, Kluwer Academic Publishers, Sept. 2000.
6. J. R. Long and M. A. Copeland, The modelling, characterization, and design of monolithic inductors for silicon RF IC's, *IEEE J. Solid-State Circ.* **32**:357–369 (March 1997).
7. C. P. Yue and S. S. Wong, On-chip spiral inductors with patterned ground shields for Si-based RF IC's, *IEEE J. Solid-State Circ.* **33**(5):743–752 (May 1998).

8. M. Danesh and J. R. Long, Differentially driven symmetric microstrip inductors, *IEEE Trans. Microwave Theory Tech.* **50**(1):332–341 (Jan. 2002).
9. B. L. Ooi and D. X. Xu, A comprehensive explanation on the high quality characteristics of symmetrical octagonal spiral inductor over non-symmetrical octagonal spiral inductor, *IEEE MTT-S Int. Microwave Symp. Digest*, 2003; *IEEE Radio Frequency Integrated Circuits (RFIC) Symp. Digest*, June 2003, pp. 259–262.
10. H. M. Greenhouse, Design of planar rectangular microelectronic inductors, *IEEE Trans. Parts, Hybrids, Pack.* **PH-10**:101–109 (June 1974).
11. H. A. Wheeler, Simple inductance formulas for radio coils, *Proc. IRE*, **16**(10):29–35 (1928).
12. S. S. Mohan, M. M. Hershenson, S. P. Boyd, and T. H. Lee, Simple accurate expressions for planar spiral inductances, *IEEE J. Solid-State Circ.* **34**(10):1419–1424 (Oct. 1999).
13. T. H. Lee, *The Design of CMOS Radio Frequency Integrated Circuits*, Oxford Univ. Press, Cambridge, UK, 1998.
14. B. L. Ooi, D. X. Xu, P. S. Kooi, and F. J. Lin, An improved prediction of series resistances in spiral inductor modeling with eddy current effect, *IEEE Trans. Microwave Theory Tech.* **50**(9):2202–2206 (Sept. 2002).
15. C. P. Yue and S. S. Wong, Physical modeling of spiral inductors on silicon, *IEEE Trans. Electron. Devices* **47**(3):560–568 (March 2000).
16. B. L. Ooi and D. X. Xu, Modified inductance calculation with current redistribution in spiral inductors, *IEE Proc. Microwave Anten. Propag.* **150**(6):445–450 (Dec. 2003).
17. W. B. Kuhn and N. M. Ibrahim, Analysis of current crowding effects in multi-turn spiral inductor, *IEEE Trans. Microwave Theory Tech.* **49**(1):31–38 (Jan. 2001).
18. B. L. Ooi, D. X. Xu, and L.-H. Guo, Efficient methods for inductance calculation with special emphasis on non-uniform current distributions, *Microwave Opt. Technol. Lett.* **40**(5):432–436 (Mar. 2004).
19. H. Kober, *Dictionary of Conformal Mapping*, Dover Publications, 1957, p. 86.
20. O. M. O. Gatous and J. Pissolato, Frequency-dependent skin-effect formulation for resistance and internal inductance of a solid cylindrical conductor, *IEE Proc. Microwave Anten. Propag.* **151**(3):212–216 (June 2004).
21. F. W. Grover, *Inductance Calculation*, Van Nostrand, New York, 1962.
- H. Ainspan, M. Soyuer, J. Plouchart, and J. Brughartz, A 6.25-GHz low DC power low-noise amplifier in SiGe, *Proc. CICC*, 1997, pp. 177–180.
- J. Y. C. Chang, A. A. Abidi, and M. Gaitan, Large suspended inductors on silicon and their use in a 2- μm CMOS RF amplifier, *IEEE Electron. Device Lett.* **4**:246–248 (May 1993).
- D. Lovelace, N. Camilleri, and G. Kannell, Silicon MMIC inductor modeling for high volume, low cost applications, *Microwave J.* **60**–71 (Aug. 1994).
- K. B. Ashby, I. A. Koullias, W. C. Finley, J. J. Bastek, and S. Moianian, High Q inductors for wireless applications in a complementary silicon bipolar process, *IEEE J. Solid-State Circ.* **31**(5):4–9 (1996).
- H. Heeb and A. E. Ruehli, Three-dimensional interconnect analysis using partial element equivalent circuits, *IEEE Trans. Circ. Syst. I: Fund. Theory Appl.* **39**(11):974–982 (Nov. 1992).
- K. Y. Su and J. T. Kuo, Analytical evaluation of inductance of spiral inductors using partial equivalent circuit (PEEC) techniques, *IEEE Antennas and Propagation Society International Symposium*, 2002, Vol. 1, 16–21, June 2002, pp. 364–367.
- P. Arcioni, R. Castello, L. Perregrini, E. Sacchi, and F. Svelto, An innovative modelization of loss mechanism in silicon integrated inductors, *IEEE Trans. Circ. Syst. II: Analog Digital Signal Process.* **46**(12):1453–1460 (Dec. 1999).
- N. M. Nguyen and R. G. Meyer, Si IC-compatible inductors and LC passive filters, *IEEE J. Solid-State Circ.* 1028–1031 (Aug. 1990).
- E. Mernyei, E. Darrer, M. Pardoen, and A. Sibrai, Reducing the substrate losses of RF integrated inductors, *IEEE Microwave Guided Wave Lett.* 300–301 (1998).
- A. E. Ruehli, Inductance calculations in a complex integrated circuit environment, *IBM J. Res. Devel.* **16**:470–481 (Sept. 1972).
- B. Mukherjee, L. Wang, and A. Pacelli, A practical approach to modeling skin effect in on-chip interconnects, *GLSVLSI'04*, Boston, MA, April 26–28, 2004.
- C. S. Sen and R. L. Wheeler, Skin effect models for transmission line structures using generic SPICE circuit simulators, *Proc. IEEE Topical Meeting on Electrical Performance of Electronic Packaging*, 1998, pp. 128–131.
- S. Kim and D. P. Neikrik, Compact equivalent circuit model for the skin effect, *IEEE Int. Microwave Symp. Digest*, 1996, pp. 1815–1818.

PULSE COMPRESSION

JENS BIEGERT
 JEAN-CLAUDE DIELS
 University of New Mexico
 Albuquerque, New Mexico

1. INTRODUCTION

The generation of ultrashort laser pulses is of tremendous interest because their attractive features—ultrabroadband spectra (nearing 1 octave) and ultrahigh intensity (terawatt range)—make them suitable for probing dynamic processes at never-before-accessed timescales and to study light-matter interaction at unprecedented intensity levels. Current techniques to generate the desired milli-

FURTHER READING

- S. Chaki, S. Aono, N. Andoh, Y. Sasaki, N. Tanino, and O. Ishihara, Experimental study on spiral inductors, *IEEE MTT-S Int. Microwave Symp. Digest*, June 1995, pp. 753–756.
- B. H. Park and P. E. Allen, Low-power, low-phase-noise CMOS voltage controlled oscillator with integrated LC resonator, *Proc. ISCAS'98*, Monterey, CA, June 1998, Vol. 4, pp. 421–424.
- A. Zolfaghari, A. Chan, and B. Razavi, Stacked inductors and transformers in CMOS technology, *IEEE J. Solid-State Circ.* **36**(4):620–628 (April 2001).
- Y. Papananos and Y. Kousoyannopoulos, Efficient utilization of on-chip inductors in silicon RF IC design using a novel CAD tool; the LNA paradigm, *Proc. ISCAS'98*, Monterey, CA, June 1998, Vol. 6, pp. 118–121.

joule-level femtosecond pulses are, however, rather complex and expensive [1,2]. The most common technique [3] is to use a femtosecond Ti:sapphire laser oscillator followed by one or more amplification stages. To avoid laser-induced damage during the amplification process, the pulse to be amplified is stretched in time, thus decreasing its intensity, and then amplified and afterward recompressed. The overall source therefore consists of a pump laser, an oscillator, a stretcher, amplifiers with their pump lasers (generally, frequency-doubled and q -switched neodymium based systems like Nd:YAG), and finally a compressor. A major drawback is that the complexity of these systems increases rapidly the shorter the amplified pulses have to be. For many applications, systems capable of producing pulses several 100 fs long are needed; the most sophisticated large-scale systems, however, are capable of producing 10-fs pulses in the low millijoule range.

Hence, one major objective of pulse compression through second harmonic generation is to design a cheaper, compact alternative to these large systems, with a simple Nd:YAG laser as source of energy. The Nd:YAG laser has been the workhorse of industrial applications for a couple of decades and may become the most economical source of femtosecond pulses as well. Pulses of 40–100 ps duration are routinely generated by mode-locked commercial Nd:YAG lasers, and the implementation of negative feedback has made it possible to decrease the pulse duration to 10 ps, and the pulse-to-pulse energy fluctuations to less than 1% [4]. After amplification, pulses of 10 ps duration and hundreds of millijoules energy are routinely generated at 1.064 μm . These picosecond pulses have sufficiently high peak intensity to be an ideal source for harmonic conversion through nonlinear optics.

Another very exciting possibility is to further reduce the already ultrashort (10-fs) pulses. The ultimate limit for propagating electromagnetic radiation is hereby half a cycle of the carrier electric field, which—at 800 nm—is 1.35 fs. Both cases, compression of long and ultrashort pulses, will be discussed.

A prerequisite for pulse compression is clearly the fact that the processes involved have to respond instantaneously on the timescale of the shortest optical pulse. Nonlinear crystals lend themselves nearly ideally to frequency conversion with ultrashort pulses because their nonlinearity is electronic and nonresonant. There appears to be no limit in the palette of frequencies that can be generated through nonlinear optics, from DC (optical rectification) to infrared (difference frequency generation and optical parametric generation and amplification), to visible, and to UV (sum frequency generation). The shorter the pulse, the higher the peak intensity for a given pulse energy (and thus the more efficient the nonlinear process). There is, however, an insidious problem that plagues nonlinear optics with ultrashort pulses—the velocity of a wave packet is not the same as that of the individual waves. In second-harmonic generation, even though the fundamental and second-harmonic waves are “phase-matched” (i.e., these waves propagate at the same wave velocity), the fundamental pulse propagates at a different velocity (in general faster) than the second harmonic pulse.

This effect, generally labeled *group velocity dispersion*, appears to be the nemesis of most frequency-mixing schemes. In general, because of group velocity dispersion, the second harmonic will propagate more slowly than the fundamental that feeds it. Therefore, the nonlinear interaction between two pulses of duration τ at frequencies ω_1 and ω_2 is limited to the walkoff distance $L = \tau / (v_{g1}^{-1} - v_{g2}^{-1})$, where v_{g1} and v_{g2} are the group velocities at their respective wavelengths. For instance, in type I interaction, the second harmonic of 800 nm radiation in BBO ($\beta\text{-BaB}_2\text{O}_4$) is delayed with respect to the fundamental by 194 fs/mm. Therefore, very thin (<1-mm) crystals are generally selected for all nonlinear mixing processes involving femtosecond pulses. It has been shown, however, that group velocity dispersion, combined with amplitude modulation associated with the depletion of the fundamental waves, can lead to efficient pulse compression [5,6]. Small amounts of compression was first demonstrated with subpicosecond pulses [7,8]. Subsequently, pulse compression through second-harmonic generation in very long (5–6-cm) KDP (KH_2PO_4) and KD*P (KD_2PO_4) crystals was predicted [6] and demonstrated [9]. It should be noted that a similar compression mechanism has been investigated in synchronously pumped optical parametric oscillators [10–13].

2. A SIMPLE MODEL OF PULSE COMPRESSION IN SECOND-HARMONIC GENERATION

Let us assume second-harmonic generation of two interacting fundamental waves with orthogonal polarizations (type II). Furthermore, assume the second harmonic, the group velocity (an extraordinary wave), to be intermediate between that of the ordinary (o) and extraordinary (e) fundamental waves. The second harmonic e wave is being generated by the nonlinear polarization $P_{e,\text{NL}} = \varepsilon_0 \chi^{(2)} E_o E_e$, where $E_j = \mathcal{E}_j \exp i(\omega t - k_j z)$ ($j = o, e$) are the electric fields of the ordinary and extraordinary fundamental waves and $\chi^{(2)}$ is the second-order nonlinear susceptibility. The wavevectors of the ordinary and extraordinary fundamental waves are $k_o = \omega n_o(\omega)/c$ and $k_e = \omega n_e(\omega)/c$ and for the second-harmonic wave $k_2 = \omega n_2(\omega_2)/c$, respectively; $n_o(\omega)$, $n_e(\omega)$ and $n_2(\omega_2)$ are the refractive indices of the nonlinear crystal. This nonlinear polarization generates a second-harmonic field as an extraordinary wave $E_2 = \mathcal{E}_2 \exp i(\omega_2 t - k_2 z)$ at the frequency $\omega_2 = 2\omega$. The propagating second harmonic will remain in phase with the second harmonic generated at any point z in the crystal, if momentum conservation (“phase matching”) is satisfied:

$$k_2 = k_o + k_e \quad (1)$$

This phase-matching condition is satisfied if the crystal orientation is chosen such that

$$n_2 = \frac{n_o + n_e}{2} \quad (2)$$

The phase-matching condition implies that the *phase velocities* are matched. After a propagation length L through the crystal, the phase delay of the second harmonic $L/v_{p,2}$ is equal to the sum of the phase delay of the two fundamentals $L/v_{p,o} + L/v_{p,e}$. The phase velocities are defined as

$$v_{p,2} = \frac{c}{n_e(\omega_2)} \quad v_{p,o} = \frac{c}{n_o(\omega)} \quad v_{p,e} = \frac{c}{n_e(\omega)} \quad (3)$$

The fact that the waves remain in phase does not necessarily imply that *pulses* simultaneously reach the end of the crystal. The three wavepackets propagate at the *group velocities* given by

$$\begin{aligned} \frac{1}{v_{g,2}} &= \frac{1}{c} \left[n_e(\omega_2) - \lambda \left. \frac{dn_e}{d\lambda} \right|_{\omega_2} \right] \\ \frac{1}{v_{g,o}} &= \frac{1}{c} \left[n_o(\omega) - \lambda \left. \frac{dn_o}{d\lambda} \right|_{\omega} \right] \\ \frac{1}{v_{g,e}} &= \frac{1}{c} \left[n_e(\omega) - \lambda \left. \frac{dn_e}{d\lambda} \right|_{\omega} \right]. \end{aligned} \quad (4)$$

If a fundamental pulse with an e and an o component enters the crystal, it will generate a second-harmonic pulse that will propagate at a different group velocity than either component of the fundamental. We have required that the velocity of the second harmonic is intermediate between that of the two fundamentals. Let us now consider the case where the fundamental e wave enters the crystal *delayed* with respect to the fundamental o wave. A second harmonic will be generated at the temporal overlap

between the two pulses, as sketched in Fig. 1a. In a frame of reference moving at the group velocity of the second harmonic, the two fundamental pulses will travel toward each other (since the faster e wave has been delayed). After some propagation distance, the overlap of the fundamentals increases, and so does the second harmonic (Fig. 1b). However, if the fundamental pulses are sufficiently intense as sketched in Figs. 1c and 1d, the growth of the second harmonic may be so rapid as to deplete the fundamentals. As a result, the spatial overlap of the two fundamentals remains small, as they move into each other (Fig. 1d). Crude order of magnitude estimates of the power required can be made by considering square fundamental pulses (temporal profile). Let us assume first that the group velocity of the second harmonic is exactly the average of the group velocities of the extraordinary and ordinary fundamentals. If, as in Fig. 1a, the two fundamental pulses are given a pre-delay, they will move across each other, in a frame of reference moving with the second harmonic, as they propagate through the crystal. One expects also that the second-harmonic pulse will be even longer than the fundamental. At perfect phase matching, the second harmonic generated after a distance z is given by [14]

$$\mathcal{E}_2(z) = \mathcal{E}(0) \tanh \frac{z}{L_{\text{sh}}} \quad (5)$$

where, at $z=0$, $\mathcal{E}_o = \mathcal{E}_e = \mathcal{E}$, and the characteristic distance L_{sh} is given by

$$\frac{1}{L_{\text{sh}}} = \frac{\omega \chi^{(2)}}{n_2 c} \mathcal{E} \quad (6)$$

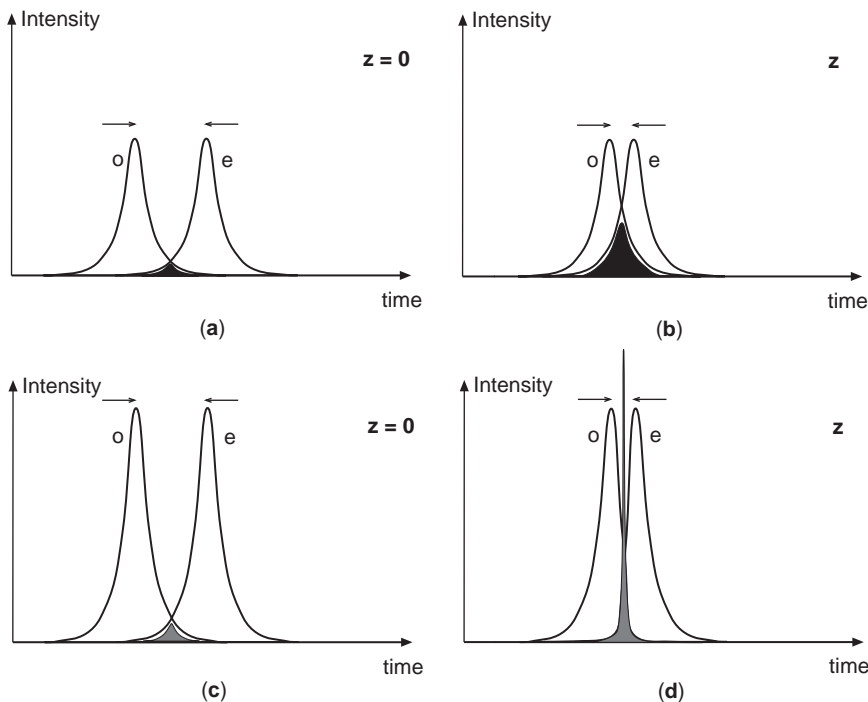


Figure 1. The three pulses are represented in a temporal frame of reference moving with the group velocity of the second harmonic. Initially, at $z=0$, the fundamental e is delayed with respect to the fundamental o wave [panels (a) and (c)]. For low input energies (a), the second harmonic will be broadened as the two fundamental pulses move into each other (b). For sufficiently high input energies (c), the overlap between the two fundamentals remains small because they are depleted by the upconversion process, and the second-harmonic pulse remains short (d).

For optimum production of a second-harmonic pulse of duration τ_{ov} , the fundamental pulses should move into each other by an overlap time τ_{ov} over the characteristic distance L_{sh} . The condition

$$\tau_{ov} = \frac{n_2 c}{\omega \chi^{(2)} \mathcal{E}} \left(\frac{1}{v_{g,e}} - \frac{1}{v_{g,o}} \right) \quad (7)$$

leads to an optimum intensity $I_0 = W_0/\tau_{ov}$ (where W_0 is the pulse energy density over the overlap time) for the fundamental pulses. The intensity I_0 of the fundamental square pulses is given by

$$I_{o,e} = \frac{\varepsilon_0 c n_{o,e} \mathcal{E}^2}{2} = \frac{0 c^3 n_{o,e} n_2^2}{2(\omega \chi^{(2)} \tau_{ov})^2} \left(\frac{1}{v_{g,e}} - \frac{1}{v_{g,o}} \right)^2 \quad (8)$$

3. APPLICABILITY TO VARIOUS WAVELENGTH RANGES

The basic requirement for pulse compression is that the group velocity of the second harmonic be intermediate in the group velocities of the o and e fundamentals. This allows, in a frame of reference that moves at the second-harmonic group velocity, the fundamental pulses to cross over each other. As mentioned above, this requirement is, unfortunately, satisfied only for conversion of near-infrared pulses [15] in KDP and KD*P crystals. It is, however, possible to control the relative group velocities while maintaining the phase matching condition, either by tilting an energy front with respect to the wavefront [16,17], or by using noncollinear interaction. It is particularly intriguing that large pulse compression can be achieved despite the following circumstances:

1. The crystal is longer than the minimum length over which all frequency components of the pulse spectrum remain in phase.
2. The shortest pulses that are generated are affected by group velocity dispersion (to all orders).

The first point can be explained by the fast depletion of the fundamental wave. It is this fast amplitude modulation that provides the frequency components that make the broad bandwidth for these short pulses. The exact conditions for compression are not easily met—in fact, pulse broadening rather than compression has also been predicted and observed [18]. The second point has never been completely addressed, because all models to date are based on Maxwell's equations in the time domain, where group velocity effects have to be treated by higher (higher than 1) order differential operators. We present here an approach in the frequency domain, where the dispersion is taken exactly into account to any order. It has been shown [15,19], as expected, that the influence of the higher-order terms is significant for femtosecond pulses and cannot be neglected.

4. GENERAL EQUATIONS AND NOTATIONS

Our model is based on a Fourier transformation of Maxwell's wave equations for a total electric field vector \mathbf{E} that is the sum of the second harmonic-field polarized as an e wave, and the fundamentals polarized as o and e waves [20]

$$\begin{aligned} & \left(\frac{\partial^2}{\partial x^2} + \frac{\partial^2}{\partial y^2} + \frac{\partial^2}{\partial z^2} - \frac{1}{c^2} \frac{\partial^2}{\partial t^2} \right) \mathbf{E}(x, y, z, t) \\ & = \mu_0 \frac{\partial^2}{\partial t^2} \mathbf{P}(x, y, z, t) \end{aligned} \quad (9)$$

where μ_0 is the magnetic permeability of free space. The source term of Eq. (9) contains the polarization \mathbf{P} , which is decomposed into two parts:

$$\mathbf{P} = \mathbf{P}^L + \mathbf{P}^{NL} \quad (10)$$

For the linearly polarized plane wave propagating along z , the wave equation reduces to

$$\left(\frac{\partial^2}{\partial z^2} - \frac{1}{c^2} \frac{\partial^2}{\partial t^2} \right) \mathbf{E}(z, t) = \mu_0 \frac{\partial^2}{\partial t^2} [\mathbf{P}^L + \mathbf{P}^{NL}] \quad (11)$$

Substituting for the Fourier transformed linear polarization $\tilde{\mathbf{P}}^L(\Omega, z) = \varepsilon_0 \chi(\Omega) \tilde{\mathbf{E}}(\Omega, z)$ in the Fourier transform of the propagation equation [Eq. (11)], we get

$$\begin{aligned} & \left[\frac{\partial}{\partial z} + i \frac{\Omega}{c} \sqrt{\varepsilon(\Omega)} \right] \left[\frac{\partial}{\partial z} - i \frac{\Omega}{c} \sqrt{\varepsilon(\Omega)} \right] \tilde{\mathbf{E}}(z, \Omega) \\ & = \mu_0 \Omega^2 \tilde{\mathbf{P}}^{NL}(\Omega, z) \end{aligned} \quad (12)$$

where we have introduced the dielectric constant

$$\varepsilon(\Omega) = [1 + \chi(\Omega)] \quad (13)$$

and the Fourier transform of the nonlinear polarization $\tilde{\mathbf{P}}^{NL}(\Omega, z)$. Let us substitute for the total field \mathbf{E} in the Fourier transform of Eq. (11)

$$\begin{aligned} \tilde{\mathbf{E}}(\Omega, z) & = \tilde{\mathbf{E}}_2(\Omega, z) + \tilde{\mathbf{E}}_o(\Omega, z) + \tilde{\mathbf{E}}_e(\Omega, z) \\ & = \frac{1}{2} \tilde{\mathcal{E}}_2[(\Omega - \omega_2), z] e^{-ik_2(\Omega - \omega_2)z} \hat{\mathbf{i}}_e \\ & \quad + \frac{1}{2} \tilde{\mathcal{E}}_o[(\Omega - \omega), z] e^{-ik_o(\Omega - \omega)z} \hat{\mathbf{i}}_o \\ & \quad + \frac{1}{2} \tilde{\mathcal{E}}_e[(\Omega - \omega), z] e^{-ik_e(\Omega - \omega)z} \hat{\mathbf{i}}_e + \text{c.c.} \end{aligned} \quad (14)$$

where $\hat{\mathbf{i}}_o$ and $\hat{\mathbf{i}}_e$ represent unit vectors along the ordinary and extraordinary directions of polarization, Ω is the frequency variable in the Fourier transform, and c.c. denotes complex conjugate.

In Eq. (14), the propagation constants $k_i(\Omega)$ are defined by

$$\begin{aligned} k_2(\Omega) &= \frac{\Omega}{c} \sqrt{\varepsilon_2(\Omega)} = \frac{\Omega}{c} n_2(\Omega) \\ k_o(\Omega) &= \frac{\Omega}{c} \sqrt{\varepsilon_o(\Omega)} = \frac{\Omega}{c} n_o(\Omega) \\ k_e(\Omega) &= \frac{\Omega}{c} \sqrt{\varepsilon_e(\Omega)} = \frac{\Omega}{c} n_e(\Omega) \end{aligned} \quad (15)$$

The Fourier transforms of the fundamental fields $\tilde{\mathbf{E}}_o$ and $\tilde{\mathbf{E}}_e$ are centered at $\Omega = \omega$, and the Fourier transform of the second-harmonic field $\tilde{\mathbf{E}}_2$ is centered at $\Omega = \omega_2 = 2\omega$.

To simplify the notation, we have introduced $\Delta\Omega$ as argument of the Fourier transforms of the envelopes:

$$\begin{aligned} \tilde{\mathcal{E}}_2(\Delta\Omega, z) &= \tilde{\mathcal{E}}_2(\Omega - 2\omega, z) \\ \tilde{\mathcal{E}}_o(\Delta\Omega, z) &= \tilde{\mathcal{E}}_o(\Omega - \omega, z) \\ \tilde{\mathcal{E}}_e(\Delta\Omega, z) &= \tilde{\mathcal{E}}_e(\Omega - \omega, z) \end{aligned} \quad (16)$$

After substitution of the fields [Eq. (14)], Eq. (12) thus leads to a system of three coupled differential equations for the evolution of each field $\tilde{\mathbf{E}}_o$, $\tilde{\mathbf{E}}_e$, and $\tilde{\mathbf{E}}_2$. For instance, the evolution of the second-harmonic field $\tilde{\mathbf{E}}_2(\Omega, z) = 1/2 \tilde{\mathcal{E}}_2(\Delta\Omega, z) \exp(-ik_2(\Delta\Omega)z) \hat{\mathbf{1}}_e$, is given by

$$\begin{aligned} \frac{\partial}{\partial z} \tilde{\mathcal{E}}_2(\Delta\Omega, z) &= i \frac{\mu_0}{k_2} (\omega + \Delta\Omega)^2 \tilde{\mathbf{P}}^{\text{NL}}(\Delta\Omega, z) e^{ik_2(\Delta\Omega)z} \\ &\quad - \frac{i}{2k_2} \frac{\partial^2}{\partial z^2} \tilde{\mathcal{E}}_2(\Delta\Omega, z) \end{aligned} \quad (17)$$

Note that there has been no slowly varying envelope approximation made in Eq. (17). The total nonlinear polarization, in the time domain, has contributions at the second harmonic and fundamental wavelength along the extraordinary direction, and one contribution at the fundamental wavelength along the ordinary wave:

$$\begin{aligned} \tilde{\mathbf{P}}^{\text{NL}}(t, z) &= \varepsilon_0 \chi^{(2)} \left[E_o(t, z) E_e(t, z) \hat{\mathbf{1}}_e \right. \\ &\quad \left. + E_2(t, z) E_o^*(t, z) \hat{\mathbf{1}}_e + E_2(t, z) E_e^*(t, z) \hat{\mathbf{1}}_o \right] \end{aligned} \quad (18)$$

It is straightforward to insert the total field [Eq. (14)] and the Fourier transform of the nonlinear polarization [Eq. (18)] — in which the products of time-dependent fields are replaced by convolutions and correlations — into the propagation equation [Eq. (12)]. The resulting system of three coupled equations, with one corresponding to the spectral

components around the second-harmonic frequency, and the other two corresponding to the ordinary and extraordinary components of the fundamental field is

$$\begin{aligned} \frac{\partial \tilde{\mathcal{E}}_2(\Delta\Omega, z)}{\partial z} &= -i \left(\frac{\omega_2 + \Delta\Omega}{4n_2 c \Delta\Omega} \right)^{(2)} \int_{-\infty}^{\infty} \tilde{\mathcal{E}}_o(\Delta\Omega', z) \tilde{\mathcal{E}}_e(\Delta\Omega - \Delta\Omega', z) \\ &\quad e^{-i[k_o(\Delta\Omega) + k_e(\Delta\Omega - \Delta\Omega) - k_2(\Delta\Omega)]z} d\Delta\Omega' \\ &\quad + \frac{i}{2k_2} \frac{\partial^2 \tilde{\mathcal{E}}_2(\Delta\Omega, z)}{\partial z^2} \end{aligned} \quad (19)$$

$$\begin{aligned} \frac{\partial \tilde{\mathcal{E}}_o(\Delta\Omega, z)}{\partial z} &= -i \frac{(\omega + \Delta\Omega)\chi^{(2)}}{4n_o c \Delta\Omega} \int_{-\infty}^{\infty} \tilde{\mathcal{E}}_2(\Delta\Omega', z) \tilde{\mathcal{E}}_e^*(\Delta\Omega' - \Delta\Omega, z) \\ &\quad e^{i[k_o(\Delta\Omega) + k_e(\Delta\Omega' - \Delta\Omega) - k_2(\Delta\Omega)]z} d\Delta\Omega' \\ &\quad + \frac{i}{2k_o} \frac{\partial^2 \tilde{\mathcal{E}}_o(\Delta\Omega, z)}{\partial z^2} \end{aligned} \quad (20)$$

$$\begin{aligned} \frac{\partial \tilde{\mathcal{E}}_e(\Delta\Omega, z)}{\partial z} &= -i \frac{(\omega + \Delta\Omega)\chi^{(2)}}{4n_e c \Delta\Omega} \int_{-\infty}^{\infty} \tilde{\mathcal{E}}_2(\Delta\Omega', z) \tilde{\mathcal{E}}_o^*(\Delta\Omega' - \Delta\Omega, z) \\ &\quad e^{i[k_e(\Delta\Omega) + k_o(\Delta\Omega' - \Delta\Omega) - k_2(\Delta\Omega)]z} d\Delta\Omega' \\ &\quad + \frac{i}{2k_e} \frac{\partial^2 \tilde{\mathcal{E}}_e(\Delta\Omega, z)}{\partial z^2} \end{aligned} \quad (21)$$

Note that $\Delta\Omega$ in Eq. (19) covers a 2 times broader bandwidth than $\Delta\Omega'$. Similarly, $\Delta\Omega'$ in Eqs. (20) and (21) cover 2 times the bandwidth of $\Delta\Omega$ in these equations. It is convenient to present the solutions in the time domain, in a frame of reference propagating with a group velocity v_{g_2} . The fields to be represented are given by

$$\begin{aligned} \tilde{\mathcal{E}}_2(t, z) &= \int_{-\infty}^{\infty} \tilde{\mathcal{E}}_2(\Delta\Omega, z) \exp \left\{ -i \left[k_2(\Delta\Omega) - k_2 - \frac{\Delta\Omega}{v_{g_2}} \right] z \right\} \\ &\quad e^{-i\Delta\Omega t} d\Delta\Omega \end{aligned} \quad (22)$$

$$\begin{aligned} \tilde{\mathcal{E}}_o(t, z) &= \int_{-\infty}^{\infty} \tilde{\mathcal{E}}_o(\Delta\Omega, z) \exp \left\{ -i \left[k_o(\Delta\Omega) - k_2 - \frac{\Delta\Omega}{v_{g_2}} \right] z \right\} \\ &\quad e^{-i\Delta\Omega t} d\Delta\Omega \end{aligned} \quad (23)$$

$$\begin{aligned} \tilde{\mathcal{E}}_e(t, z) &= \int_{-\infty}^{\infty} \tilde{\mathcal{E}}_e(\Delta\Omega, z) \exp \left\{ -i \left[k_e(\Delta\Omega) - k_2 - \frac{\Delta\Omega}{v_{g_2}} \right] z \right\} \\ &\quad e^{-i\Delta\Omega t} d\Delta\Omega \end{aligned} \quad (24)$$

The constant terms k_2 , k_o , and k_e are the leading terms of the Taylor expansions for the wavevectors $k_2(\Delta\Omega)$, $k_o(\Delta\Omega)$, and $k_e(\Delta\Omega)$, respectively. If we choose the frame of reference moving with the second-harmonic pulse, then

$$\frac{1}{v_{g_2}} = k_2'_{2\omega} \quad (25)$$

which can be calculated from Sellmeier's equations.

Equations (19)–(21) describe the nonlinear interaction accurately to all orders without any approximations. It would be desirable, however, to neglect the second derivatives of the electric fields in order to simplify the equations and to speed up the already involved numerics. In one of the worst case scenarios, namely, generation of a 3-fs second harmonic pulse, we have found that the maximum value for $\partial^2 \mathcal{E} / \partial z^2$ is 200 times smaller than $2k \partial \mathcal{E} / \partial z$, and can therefore be neglected. Hence, we conclude that for the pulse durations under investigation, the reduction to a system of first-order differential equations suffices. We would like to note that one possible improvement, however, would be to include the nonlinear refractive index \bar{n}_2 into the equations to correct for small variations due to the ultraintense fields that are involved. The phase shift $\ell \cdot \Delta k$ resulting from the nonlinear refractive index \bar{n}_2 in the worst-case scenario in Fig. 8a for compression of the e component fundamental to 2.5 fs can be estimated from the $\chi_{\text{int}}^{(3)}$ value given in Ref. 21, to be $\ell \cdot \Delta k = \ell \cdot 2\pi \cdot \bar{n}_2 \cdot I / \lambda = 0.09 < 1$. This value is, therefore, small enough not to contribute significantly to the equations.

5. COMPRESSION OF “LONG” PULSES

The following simulations are based on second-harmonic generation in KDP, where the full Sellmeier formulas have been used in the definition of the various k vectors that appear in the wave equations. As a result, our model takes into account *all* group velocity dispersion effects as they

affect the pulse propagation and the pulse conversion process. As an illustration of the simple analytical consideration in Section 2, we calculate the second harmonic generated by two step functions (temporal profile). Two step function fundamental pulses enter the crystal with no initial overlap (Fig. 2a).

The ordinary and the extraordinary fundamental intensities are chosen to be equal and the relative group velocities are also chosen to be equal but opposite in sign. A short pulse is generated after a distance of 1 cm, as shown in Fig. 2b. In agreement with the simple considerations of Section 2, the width of the generated second harmonic is determined by the depletion of the two fundamentals moving into each other. The situation is much more complex when the full frequency dependence of the k vectors is taken into account. Perfect phase matching exists only for a single-frequency component. Because of the frequency dependence of the wavevectors, there will be some transfer of energy back from the second harmonic to the fundamental. Figures 3 and 4 illustrate the propagation and harmonic generation of two fundamental pulses with a Gaussian temporal profile. The fundamental ordinary and extraordinary waves have respectively intensities of 1.4 and 1 GW/cm², with the extraordinary wave pre-delayed by 14 ps with respect to the ordinary wave. A three-dimensional representation of the propagation of the intensities of the three waves inside a 6-cm-long KDP crystal is shown in Fig. 3. The depleted fundamental and second harmonic waves are shown after a propagation distance of 6 cm in Figs. 4a and 4b. To assess the influence of group velocity dispersion and higher-order terms in the

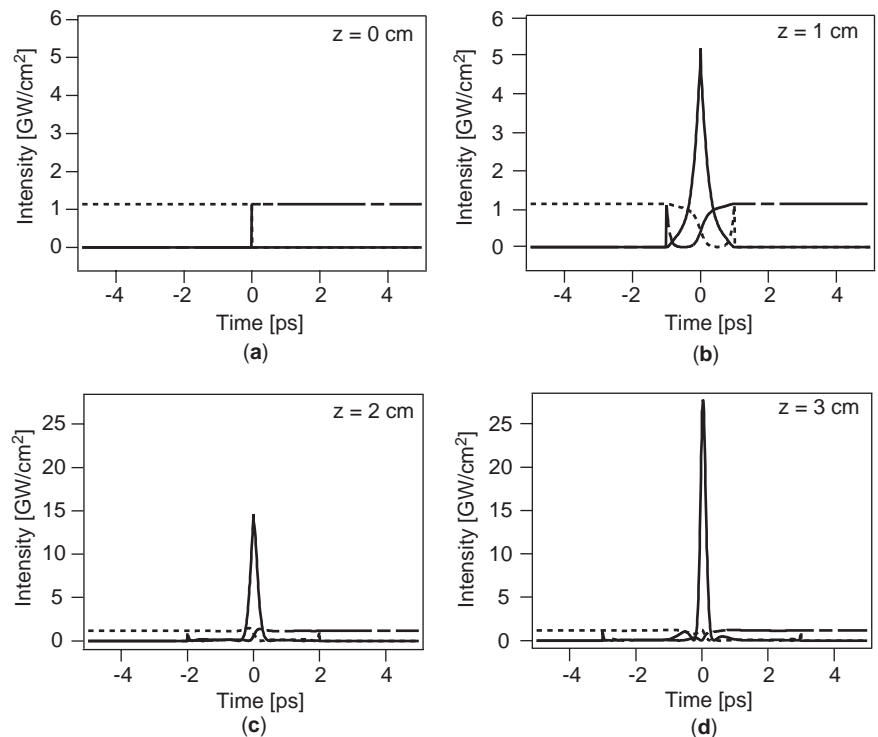


Figure 2. Square pulse second-harmonic generation. The dotted and dashed lines represent the ordinary and extraordinary fundamental intensities, respectively. The solid lines represent the extraordinary second-harmonic intensity. The successive plots are for $z = 0$ cm (a), $z = 1$ cm (b), $z = 2$ cm (c), and $z = 3$ cm (d). Note the different scales in intensity.

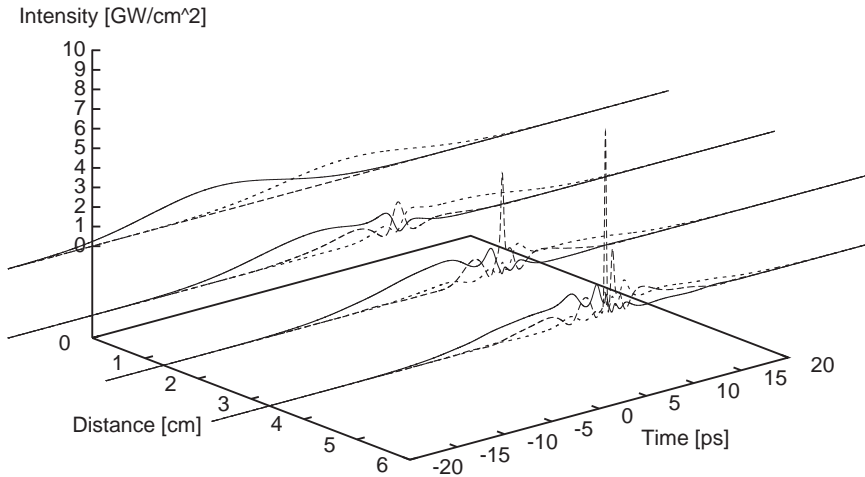


Figure 3. Three-dimensional representation of the propagation of the fundamental and the second-harmonic pulses.

expansion of the k vectors, the same calculation was performed in the approximation of constant group velocity at the various wavelengths. The results are shown in Figs. 4c and 4d. The parameters of the calculation were chosen for optimum pulse compression in the complete model. The very large difference in conversion efficiency in both cases clearly indicates that the higher-order terms in the expansion of the wavevector cannot be neglected. We have also carried out the experimental investigation of pulse compression. Our experimental arrangement is similar to the arrangement described in Ref. 10. The pump source is an active-passive mode-locked Nd:YAG laser controlled by

passive negative feedback with successive amplifier stages. In the described experiment, the system was adjusted to yield 14 ps pulses with pulse energies up to 150 mJ. The linearly polarized output beam passes through a half-wave plate that rotates its plane of polarization by 45° . The beam is then separated into two components by a polarizing beamsplitter, and each component is given a relative delay before being recombined at a second polarizing beamsplitter. The rotation of the waveplate enables one to control the ratio between the energies of both beams. The recombined pulses are sent as extraordinary and ordinary waves into the second-harmonic-generating crystal (6-cm-

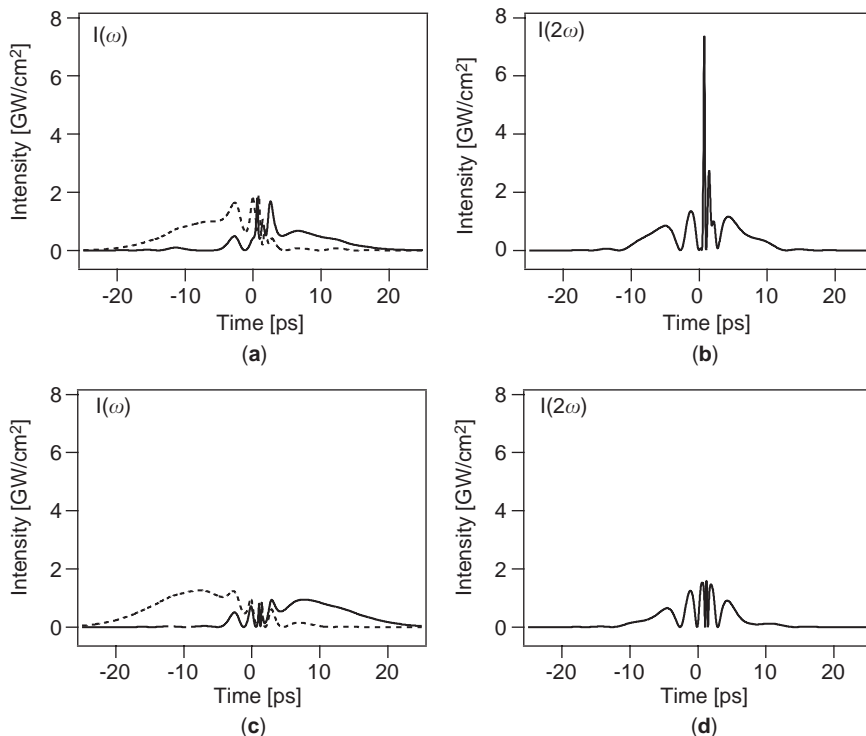


Figure 4. Results of the numerical simulation for pulse shapes of fundamental and second-harmonic pulses after propagation in 6-cm-long KDP crystal: (a) and (b) correspond to the exact calculation and (c) and (d), to the case of a linear approximation, neglecting group velocity dispersion.

long KDP). A portion of uniform intensity at the beam center is selected by a 9 mm apodized aperture positioned just before the crystal, giving a better than 95% top-hat transverse beam profile.

The duration of the compressed pulses at the second harmonic frequency was measured with a single-shot autocorrelator based on noncollinear second-harmonic generation in a 2 mm KDP type I crystal. An example of an autocorrelation trace of the second harmonic pulse, measured by a single-shot intensity autocorrelation, is shown in Fig. 5. The total power density of the 1.06- μm beam incident on the 6-cm-long KDP crystal was 2.6 GW/cm². The fundamental e beam was given a pre-delay of 10.5 ps with respect to the o wave. The intensity of the o pulse was 1.3 times that of the e pulse. The conversion efficiency was 14%. The width of the autocorrelation curve of the (green) compressed pulse is 480 fs, which corresponds to a sech^2 pulse of 309 fs duration. The compression factor is thus 45. The single-shot autocorrelator is a convenient diagnostic tool to optimize the laser. A trace such as in Fig. 5 is very sensitive to the quality of the optics used. For instance, the noise appearing on the right lobe of Fig. 5 is due to scratches on the filter (the autocorrelation should be exactly symmetric). In addition, the background is enhanced because of a contribution to the second harmonic from a non-uniform spatial beam structure.

The theoretical simulation led to a minimum compressed pulse duration of approximately 200 fs. The exact phase-matching condition for the central pulse wavelength was maintained for all numerical simulations. In the actual experiment, the shortest pulses are obtained after a slight retuning of the long frequency-doubling crystal. The two possible interpretations are that (1) the phase-matching condition is slightly different at high power than at low power, or (2) some dispersive effect of cascaded nonlinearities contribute to the pulse compression. Further simulations will be made in order to determine

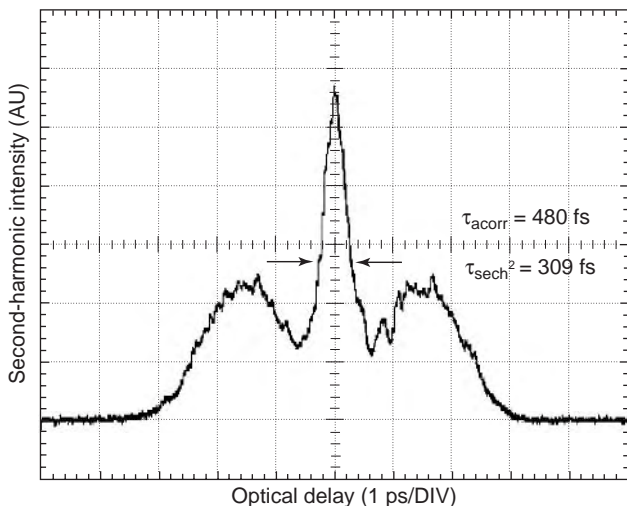


Figure 5. Single-shot autocorrelation trace of a compressed 532-nm pulse. The time delay on the horizontal axis is 1 ps/div. The autocorrelation intensity is plotted in arbitrary units.

whether, within our theoretical model, optimum compression indeed occurs at some detuning from the low-power phase-matching condition.

6. COMPRESSION OF ULTRASHORT PULSES

Pulse compression of a factor of ≥ 60 has been demonstrated for Nd:YAG laser picosecond pulses and second harmonic type II in KDP and KD*P [9,15]. The condition of second-harmonic group velocity intermediate between the ordinary and extraordinary fundamentals cannot in general be met at any wavelength, for any crystal. It is, however, possible to adjust the group velocity through a tilt of the energy front with respect to the phase front. Figure 6 illustrates the basic principle for a degenerate type I process. As shown in the lower part of the figure, the temporal overlap of the interacting waves decreases because of the higher velocity of the SH wave relative to the fundamental waves. Furthermore, the spatial overlap decreases as a result of spatial walkoff (ρ) of the fundamental wave. These two negative effects can, however, be used in conjunction with pulse front tilt to match the relative velocities of the two waves, as illustrated in the upper part of Fig. 6. Loosely speaking, as seen in the frame of reference of the SH wave, the lateral walkoff of the fundamental wave slows this wave down just to match the velocity of the SH wave.

For femtosecond pulses, it is not practical to generate a large energy tilt. For instance, an energy tilt of the order of 40° would be required for second-harmonic type II generation and compression in BBO of a 800-nm pulse of a Ti:Sapphire laser in collinear interaction [22]. A dispersive element such as a prism with a beam diameter: base length ratio of 20 (in the case of SF10 glass) would be needed to achieve the required energy front tilt of 40° .

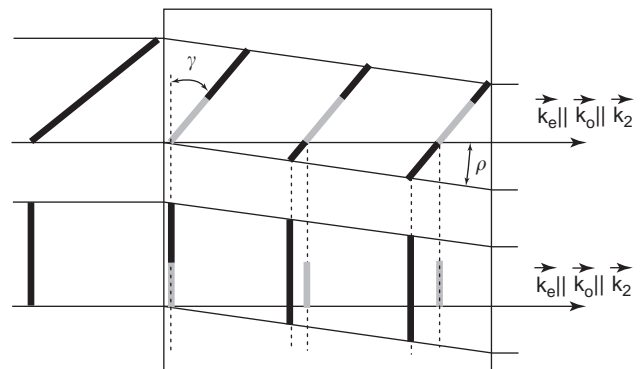


Figure 6. Shown is collinear degenerate type I interaction. For equal time intervals, the fundamental wave is illustrated as dark bars and the second-harmonic (SH) wave as gray bars. The gray bars are drawn with larger separation because of the typically higher velocity of the SH wave inside a crystal. The lower part shows temporal and lateral walkoff, whereas the upper part indicates how—for a given pulse front tilt—lateral walkoff can be used to adjust the relative velocities of the fundamental and SH waves to ensure overlap.

Table 1. Group Velocities for the *o*, *e*, and Second-Harmonic *e* Waves^a

Interaction	Fundamental (<i>o</i>) $v_{g,o}$ (10^8 m/s)	Second-Harmonic (<i>e</i>) $v_{g,2}$ (10^8 m/s)	Fundamental (<i>e</i>) $v_{g,e}$ (10^8 m/s)
Collinear	1.780	1.755	1.843
Noncollinear	1.798	1.905	1.934

^aValues are calculated for type II second-harmonic generation of 800-nm radiation for collinear and noncollinear (internal angle is 2°) interaction.

Dispersion in the glass would lead to large pulse broadening and phase modulation.

A better approach [22] is to use a noncollinear geometry; Table 1 shows how the group velocities of the participating waves can be changed from the collinear to the noncollinear case (here for an internal angle of 2°), leading to conditions for compression. The sketch of the interaction geometry in Fig. 7 shows that it is possible to obtain the respective group velocities through manipulation of the angles of incidence in the crystal and the energy tilt produced by a prism. Figure 7 pertains to the case of noncollinear interacting plane waves inside a 250- μm -long BBO crystal, cut for type II second-harmonic generation of laser pulses at 800 nm. Consistent with the one-dimensional approach used in the model [Eqs. (19)–(21)], the “energy-fronts” of all pulses should be aligned in the crystal. Since the interaction is noncollinear, the effect of energy front tilting from propagation under an angle through the air–crystal interface has to be precompensated to have zero energy front tilt inside the crystal. With the angle between the noncollinearly interacting fundamental beams set to $\theta = 2^\circ$ (internal angle; the external angle is $2\beta = 3.22^\circ$), the required pretilt angle can be achieved with a very thin prism (SF10) with a ratio of $a/b = 0.2$ for prism base length to beam diameter. The spatial chirp introduced by this thin prism is negligible compared to the value of $a/b = 20$ mentioned above.

The intensity profiles as function of interaction length in the case of the 10 fs fundamental with a 20-fs predelay

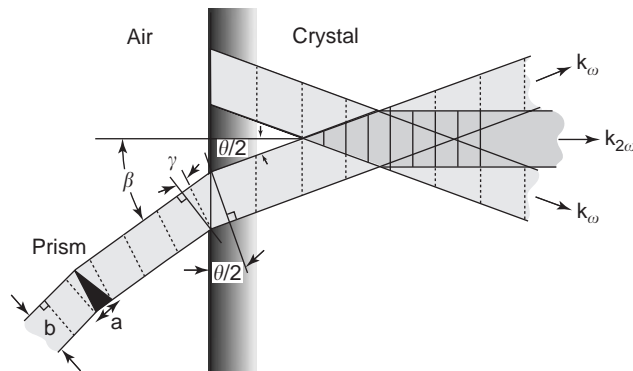


Figure 7. Experimental setup precompensating for the pulse front tilt that occurs from propagation through an interface under an angle $2\beta = 3.22^\circ$ (the pulse fronts are depicted as dotted lines). For the chosen type II SHG of 800-nm pulses $\theta = 2^\circ$, which is the angle between the incoming fundamental beams for noncollinear interaction. This requires a pulse front tilt of $\gamma = 0.62^\circ$ to precompensate for the propagation effect at the air–crystal interface. We also show that a very thin prism (SF10) can achieve γ with a ratio $a/b = 0.2$ for prism base length : beam diameter.

are shown in Figs. 8. It can be seen that the plots are not made exactly in the frame of reference of the second-harmonic wave that is indicated by the shift of the pulse in Fig. 8b with respect to the origin of the time axis. The group velocity difference between the fundamental waves relative to the second harmonic are also not exactly equal, which leads to several effects: The ordinary pulse is moving rapidly into the extraordinary pulse, causing strong modulation of the ordinary pulse, leading to the satellite in the extraordinary pulse. Furthermore, the strong energy exchange between the interacting waves and their imbalance in group velocities causes a rather pronounced satellite to appear only on the right side of the second-harmonic pulse profile instead of the expected smaller satellites on either side. Since the input parameters can be adjusted continuously in the experiment, it is conceivable that pulses without satellite could be generated by better symmetrization of the group velocities. Figure 8b shows a peak intensity of 9 GW/cm^2 for the 2.5-fs second harmonic for initial peak intensities for the fundamental pulses of roughly 13 GW/cm^2 . This indicates 70% conversion in intensity.

Furthermore, in order to more clearly understand the mechanisms involved, the simulations were performed for a broader range of input parameters: The fundamental input pulse duration was varied from 10 to 50 fs at the FWHM (full width at half-maximum) of the intensity profile. The more rapidly traveling *e* pulse was delayed with respect to the slower-traveling *o* pulse from 15 to 60 fs. Fundamental pulse energies were $400 \mu\text{J}$ each for the *o* and *e* pulses. The results are summarized through the contour plot of Fig. 9, showing the second-harmonic pulsewidth (FWHM) after an interaction length of $250 \mu\text{m}$ as a function of the input parameters mentioned above. The contour lines are separated on a logarithmic scale to base 10 in order to have a clearer picture of the range of pulsewidths. The emerging second-harmonic pulse shows widths ranging from about 2.5 to 34 fs. The shortest fundamental input pulses yield the shortest second-harmonic pulses as well. A 10-fs fundamental pulse, for instance, gives a second-harmonic pulse of about 2.5 fs for a pre-delay of 20 fs. The same result can be achieved for a pre-delay of 30 fs. This is a compression by a factor of 4. The longest calculated pulsewidth of 50 fs can yield a compressed second-harmonic of 10 fs, which has a compression factor of 5. If we were to draw a line in the contour plot, for which maximum compression can be achieved across the parameter range, it would roughly follow the gray dashed line in Fig. 9. Longer pulses therefore require a larger pre-delay to achieve maximum compression. It is clear that the overlap region of the *o* and *e* input pulses defines the initial second-harmonic pulsewidth. The strong energy exchange

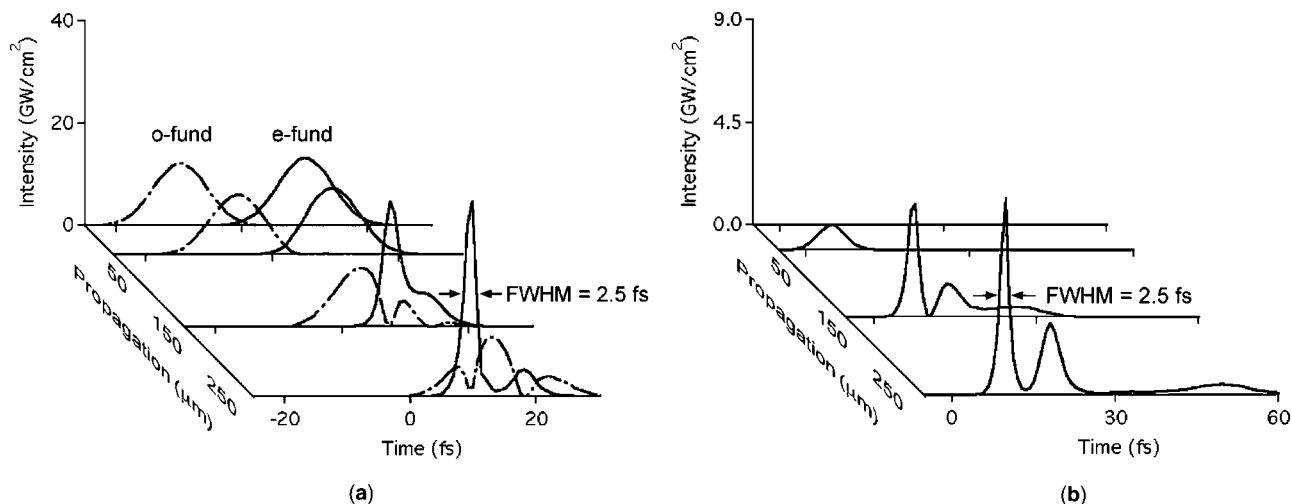


Figure 8. Fundamental (a) and second-harmonic waves (b) as they propagate and interact inside a 250- μm -long BBO crystal [note the different scales for (a) and (b)]. Group velocity mismatch leads to a compressed second-harmonic pulse with a FWHM of 2.5 fs (b). Furthermore, considerable pulse reshaping can be seen for the extraordinary fundamental in (a), leading to a shortened FWHM from 10 to 2.5 fs with a shoulder. Pulse energies were 400 μJ for each fundamental pulse, at a FWHM of 10 fs with a predelay of 20 fs.

between the interacting waves will finally determine the width of all participating pulses at the end of the interaction region.

7. CONCLUSION

The main conclusion of this work is that dispersion and phase-matching bandwidth do not set a fundamental limit to type II pulse compression in sum frequency generation as long as they are used in a controlled fashion. Amplitude modulation through fast depletion of the fundamental pulses provides the extra bandwidth required to generate ultrashort pulses. We have presented a theoretical model sufficient to describe the desired effects, pointed out its limitations, and compared it to existing models that do not use the full dispersion dependence. The model has been applied to compression of 14 ps to 310 fs pulses and has also been experimentally verified. Furthermore, compression of 10-fs ultrashort pulses down to 2.5 fs in the second harmonic and the fundamental wavelength has been predicted. In the ultrashort pulse case, the experimental requirements are rather modest, since a relatively long crystal can be used, and the energy tilt requires only a small-angle prism. We have chosen to illustrate the method by specific calculations applied to second-harmonic generation of 800 nm pulses in BBO. However, it can be applied to frequency mixing in various crystals. The same approach can also be applied to parametric generation, extending the compression method demonstrated by Umbrasas et al. [10]. In this work we exploit the properties of group velocity dispersion at the various wavelengths to achieve the desired compression, rather than select a particular orientation of a particular crystal (BBO) that has near-zero dispersion [23]. The latter technique leads to impressive results, but is limited to amplification and gen-

eration of wavelengths longer than 560 nm. Another method to generate ultrashort UV pulses would be conventional frequency doubling of an 800-nm pulse, followed by dispersion and phase modulation (chirping) through a gas-filled hollow fiber or capillary. The method described here

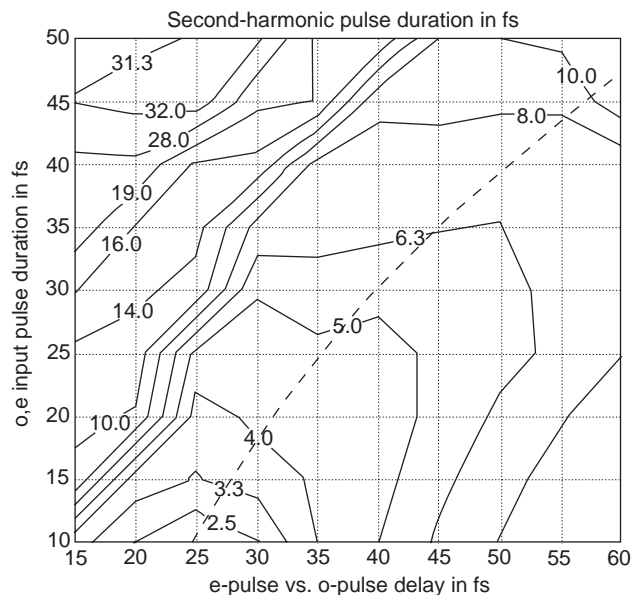


Figure 9. This contour map shows the pulse duration of the emerging second-harmonic signal as function of the o, e input pulse duration and the predelay between the o and e fundamental pulses. The results are calculated for type II second-harmonic generation of 800-nm pulses with single-pulse energies of 400 μJ and for an interaction length of 250 μm inside a BBO crystal. The angle between the noncollinearly interacting fundamental waves inside the crystal is 2°.

provides the same result in a single step, and allows for the compression of bandwidth-limited pulses.

Acknowledgment

This work was partially supported by NSF under grant ECS 0217882.

BIBLIOGRAPHY

1. S. Backus, J. Peatross, C. P. Huang, H. C. Kapteyn, and M. M. Murnane., Ti:sapphire amplifier producing millijoule-level, 21 fs pulses at 1 khz, *Opt. Lett.* **20**:2000–2002 (1995).
2. G. Steinmeyer, L. Gallmann, F. W. Helbing, and U. Keller, New directions in sub-10-fs optical pulse generation, *C. R. Acad. Sci. Paris* **IV** :1389–1406 (2001).
3. P. Maine, D. Strickland, P. Bado, M. Pessot, and G. Mourou, Generation of ultrahigh peak power pulses by chirped pulse amplification, *IEEE J. Quantum Electron.* **QE-24**:398–403 (1988).
4. V. Kubecek, S. Kumazaki, Y. Takagi, G. C. Reali, and K. Yoshihara, Actively and passively mode-locked Nd:YAP(YAlO₃) laser with negative feedback using CdSe and GaAs, *Jpn. J. Appl. Phys.* **30**:L1889–L1891 (1991).
5. Y. Wang and R. Dragila, Efficient conversion of picosecond laser pulses into second-harmonic frequency using group-velocity-dispersion, *Phys. Rev. A* **41**:5645–5649 (1990).
6. A. Stabinis, G. Valiulis, and E. A. Ibragimov, Effective sum frequency pulse compression in nonlinear crystals, *Opt. Commun.* **86**:301–306 (1991).
7. Y. Wang and B. Luther Davies, Frequency-doubling pulse compressor for picosecond high power neodymium laser pulses. *Opt. Lett.* **17**:1459–1461 (1992).
8. P. Heinz, A. Laubereau, A. Dubietis, and A. Piskarskas, Fiberless two-step parametric compression of sub-picosecond laser pulses, *Lithuanian Phys. Rev.* **33**:314–317 (1993).
9. A. Umbrasas, J. C. Diels, G. Valiulis, J. Jacob, and A. Piskarskas, Generation of femtosecond pulses through second harmonic compression of the output of a Nd:YAG laser, *Opt. Lett.* **20**:2228–2230 (1995).
10. A. Umbrasas, J. C. Diels, J. Jacob, and A. Piskarskas, Parametric oscillation and compression in KTP crystals, *Opt. Lett.* **19**:1753–1755 (1994).
11. J. D. V. Khaydarov, J. H. Andrews, and K. D. Singer, Pulse compression in a synchronously pumped optical parametric oscillator from group-velocity mismatch, *Opt. Lett.* **19**:831–833 (1994).
12. J. D. V. Khaydarov, J. H. Andrews, and K. D. Singer, 20-fold pulse compression in a synchronously pumped optical parametric oscillator, *Appl. Phys. Lett.* **65**:1614–1616 (1994).
13. L. Lefort, S. D. Butterworth, Y. P. Svirko, K. Puech, D. C. Hanna, and D. H. Jundt, Generation of fs pulses from order of magnitude pulse compression in a cw synchronously pumped optical parametric oscillator, *Proc. CLEO '98, San Francisco, USA*, OSA, 1998.
14. W. Koechner, *Solid-State Laser Engineering*, 2nd ed., Springer, Berlin–Heidelberg–New York, 1999.
15. J. Biegert, V. Kubecek, and J.-C. Diels, Pulse compression: Type II second harmonic pulse compression, in J. G. Webster, ed., *Wiley Encyclopedia of Electrical and Electronics Engineering*, Vol. 17, Wiley, New York, 1998.
16. A. Dubietis, G. Valiulis, G. Tamosauskas, R. Danielius, and A. Piskarskas, Nonlinear second-harmonic pulse compression with tilted pulses, *Opt. Lett.* **22**:1071–1073 (1997).
17. R. Danielius, A. Dubietis, and A. Piskarskas, Femtosecond high-contrast pulses from a parametric generator pumped by the self-compressed second harmonic of a nd:glass laser, *Opt. Lett.* **20**:2225–2227 (1995).
18. D. A. Guk and V. G. Dmitirev, Some characteristics of second harmonic generation under conditions of strong energy exchange between interacting waves, *Kvantovaya Elektron* **18**:106–110 (1990).
19. J. Biegert, V. Kubecek, and J.-C. Diels, Second harmonic pulse compression, in *Ultrafast Phenomena XI*, Springer-Verlag, 1998, New York, pp. 84–86.
20. J.-C. Diels and W. Rudolph, *Ultrashort Laser Pulse Phenomena*, Academic Press, Boston, 1995.
21. H. Tan, G. P. Banfi, and A. Tomaselli, Optical frequency mixing through cascaded second-order processes in β -barium borate. *Appl. Phys. Lett.*, **63**:2472–2471 (1993).
22. J. Biegert and J.-C. Diels, Compression of pulses of a few optical cycles through harmonic generation, *J. Opt. Soc. Am. B* **18**(8):1218–1226 (2001).
23. A. Shirakawa, I. Sakane, M. Takasala, and T. Kobayashi, Sub-5-fs pulse generation by pulse-front-matched noncollinear optical parametric amplification, *Appl. Phys. Lett.* **74**:2268–2270 (1999).

PULSE-SHAPING CIRCUITS

BRENT A. MYERS
DAVID B. CHESTER
Intersil Corporation

Digital communications systems such as wireless, optical, and wireline telecommunication networks have numerous well-known advantages over analog systems. These systems format binary data into discrete-time symbols, modulate the carrier using some form of digital modulation scheme (modulation in this simplified context includes symbol modulation and upconversion to a carrier frequency) to convert them to transmittable continuous-time signals, and transmit them over a channel. At the receiver the received signal is demodulated (demodulation includes both downconversion and symbol demodulation), symbol timing is recovered, and the received symbols are reformatted into a usable form. This process is shown in simplified form in Fig. 1.

The discrete-time symbols of a digital communication system are of duration T and are sequential; that is, they are orthogonal in time. To preserve the fixed time duration of symbols generated in the transmitter would require infinite bandwidth in the signal processing of the communication system and the communication channel. Finite bandwidth processing causes the symbols to spread in time. This causes the symbols to overlap in time and induces intersymbol interference (ISI).

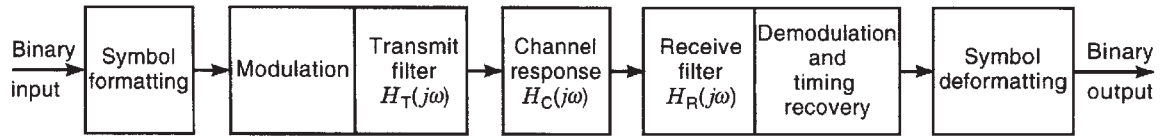


Figure 1. Simplified block diagram of a digital communication system.

As will be described in the next section, even when finite bandwidth signal processing is used in the communication system, the effects of ISI could be eliminated if ideal signal processing components (brickwall filters as an example) could be implemented. This is, of course, not possible. Pulse shaping is used in the implementation of digital communication systems to minimize ISI caused by nonideal channel characteristics and nonideal component implementations.

Pulseshaping is performed in the transmit and receive filters of a communication system. The most common class of filters used for pulseshaping are Nyquist filters [1–3]. This article gives an overview of the theoretical foundations of pulseshaping and describes some practical implementations of pulseshaping filters. The material in this article assumes that the communication channel can be modeled as a linear time-invariant filter with additive white Gaussian noise (AWGN). For more detailed and in-depth coverage of pulse shaping the reader is referred to Refs. 1–3.

1. THEORETICAL BACKGROUND

Ideal data symbols are of fixed duration T . The spectrum for such a symbol is of the form

$$H_s(j\omega) = \frac{\sin[T(\omega/2)]}{T(\omega/2)} \tag{1}$$

Thus such a symbol would require infinite bandwidth, which is, of course, impractical. Real communication channels are of fixed bandwidth W . The ideal bandlimited channel response [1] is

$$H_C(j\omega) = \begin{cases} 1, & |\omega| < W \\ 0, & |\omega| \geq W \end{cases} \tag{2}$$

The transmit filter, which is designed to shape the transmit symbols to meet the power spectrum constraints of the

channel, has an ideal frequency-domain response [1] of

$$H_T(j\omega) = \begin{cases} \pi/W, & |\omega| < W \\ 0, & |\omega| \geq W \end{cases} \tag{3}$$

The time-domain transmit filter response is therefore

$$h_T(t) = \frac{\sin(Wt)}{Wt} \tag{4}$$

This response is referred to as the pulseshape. $h_T(t)$ is the familiar sinc function, which has zero crossings at integer multiples of Wt except at $Wt = 0$, where it has a value of 1. If we assume a symbol sequence S_n and set $T = \pi/W$, then the pulse for each symbol is of the form shown in Fig. 2 for a single pulse and in Fig 3 for multiple pulses.

From Fig. 3 it is obvious that if symbols are sampled at times $t = nT$, where n is an integer, the effects of ISI are mitigated. This is because the contribution to the composite waveform is zero for all pulses except for the pulse corresponding to S_0 because they are all at a zero crossing point.

The problem is that to produce $h_T(t) = \sin(Wt)/Wt$ requires an ideal brickwall filter, which is impossible to implement. One could attempt to approximate the ideal filter, but this would not be cost-effective and would have other undesirable effects on the system such as making timing recovery difficult [1]. To address these problems, more practical pulseshapes have been developed.

The pulseshape at the input to the demodulator, $h_P(t)$, is the convolution of the transmit filter, the channel response, and the receive filter:

$$h_P(t) = h_T(t) * h_C(t) * h_R(t) \tag{5}$$

From our preceding discussions it is clear that to eliminate ISI, $h_P(t)$ should be forced to cross zero at nonzero integer multiples of T . This can be written as

$$h_P(kT) = \delta_k \tag{6}$$

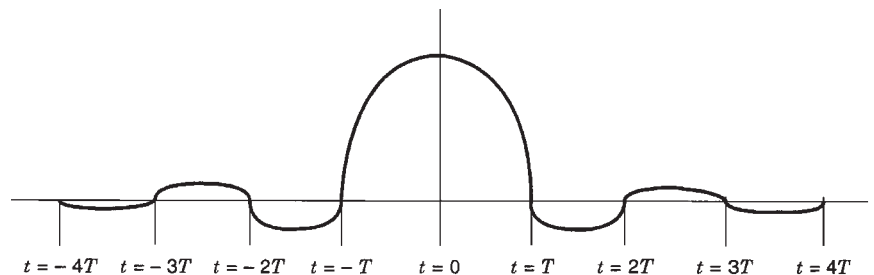


Figure 2. General form of a pulseshape for an ideally bandlimited symbol.

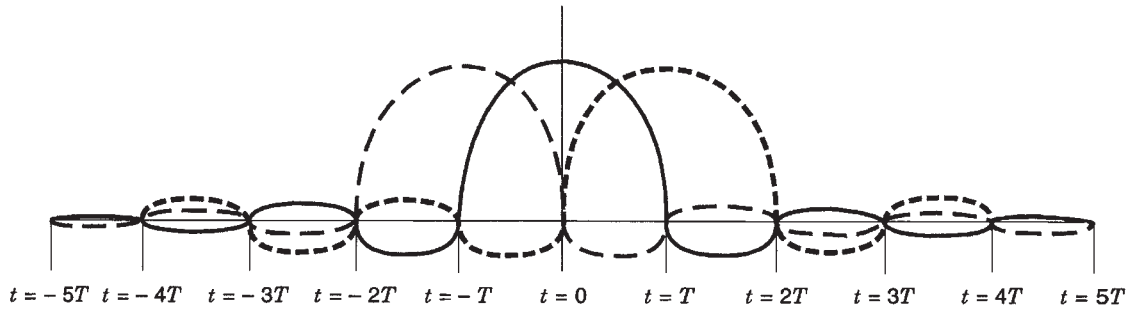


Figure 3. Multiple pulseshapes for an ideally bandlimited symbol.

The composite input to the demodulator is

$$R(t) = \sum_{n=-\infty}^{\infty} S_n h_P(t - nT) + N_R(t) \tag{7}$$

where $N_R(t)$ is the noise input at the demodulator:

$$N_R(t) = N(t) * h_R(t) \tag{8}$$

From Eq. (7) it can be seen that forcing the composite pulse to cross zero does not necessarily produce an optimal solution because it ignores the noise contribution. Joint optimizations are possible, but they are beyond the scope of this discussion. The reader is referred to Ref. 1 for in-depth coverage of this subject matter.

Taking the Fourier transform of Eq. (6) and applying the Nyquist sampling theorem, we get

$$\frac{1}{T} \sum_{n=-\infty}^{\infty} H_P \left(j\omega - n \frac{2\pi}{T} \right) = 1 \tag{9}$$

Equation (9) is referred to as the Nyquist criterion, and filter responses (pulses) that meet this criterion are referred to as Nyquist filters (pulses).

These filters require more than the ideal bandwidth defined in Eq. (3). While simplifying the system implementation, this additional bandwidth requirement costs additional spectrum and noise bandwidth at the receiver. The additional bandwidth is referred to as excess bandwidth and is usually expressed as a percentage of the ideal bandwidth:

$$B_{\text{excess}} = \left(\frac{B_{\text{actual}}}{B_{\text{ideal}}} - 1 \right) \times 100 \tag{10}$$

The actual pulseshape used in a particular application is highly dependent on the targeted channel characteristics. The most commonly used filters satisfying the Nyquist criterion for pulseshaping are raised-cosine filters. For this reason raised-cosine pulseshaping will be used in this article to describe implementations. Raised-cosine

filters are of the form

$$h_P(t) = \frac{\sin\left(\frac{\pi t}{T}\right)}{\pi t} \frac{\cos\left(\frac{\alpha \pi t}{T}\right)}{1 - \left(\frac{2\alpha t}{T}\right)^2} \tag{11}$$

$H_P(j\omega) =$

$$\begin{cases} T, & 0 \leq |\omega| \leq (1 - \alpha) \frac{\pi}{T} \\ \frac{T}{2} \left\{ 1 - \sin \left[\frac{T}{2\alpha} \left(|\omega| - \frac{\pi}{T} \right) \right] \right\}, & (1 - \alpha) \frac{\pi}{T} \leq |\omega| \leq (1 + \alpha) \frac{\pi}{T} \\ 0, & |\omega| > (1 + \alpha) \frac{\pi}{T} \end{cases} \tag{12}$$

where α controls the rate at which the energy rolls off. The smaller α is, the faster the rolloff. Note that for $\alpha = 0$,

$$h_P(t) = \frac{\sin\left(\frac{\pi t}{T}\right)}{\pi t} \tag{13}$$

which is the ideal pulseshape for a bandlimited channel.

In most actual implementations the raised-cosine filter is partitioned with part of the response implemented in the transmit filter and part implemented in the receive filter. The most common partitioning is to implement each as the square root of the raised-cosine filter. This is commonly referred to as a root-raised-cosine filter [1] and is given as

$$h_T(t) = h_R(t) = \frac{4\alpha \left(\cos\left((1 + \alpha) \frac{\pi t}{T} \right) + \frac{T \sin\left((1 + \alpha) \frac{\pi t}{T} \right)}{4\alpha t} \right)}{\pi \sqrt{T} \left[1 - \left(\frac{4\alpha t}{T} \right)^2 \right]} \tag{14}$$

and

$$H_T(j\omega) = H_R(j\omega) = \begin{cases} \sqrt{T}, & 0 \leq |\omega| \leq (1 - \alpha) \frac{\pi}{T} \\ \sqrt{\frac{T}{2} \left\{ 1 - \sin \left[\frac{T}{2\alpha} \left(|\omega| - \frac{\pi}{T} \right) \right] \right\}}, & (1 - \alpha) \frac{\pi}{T} \leq |\omega| \leq (1 + \alpha) \frac{\pi}{T} \\ 0, & |\omega| > (1 + \alpha) \frac{\pi}{T} \end{cases} \quad (15)$$

2. IMPLEMENTATION

In contemporary digital communication systems it is often not possible to achieve economically the required performance from analog pulse-shaping filters. Shaping filters are therefore implemented using a hybrid approach. The bulk of the shaping is done at baseband using finite impulse response (FIR) digital filters, which implement a truncated version of the pulse shape.

On the transmit side of a communication system data symbols are passed to an interpolating digital filter [4]. The impulse response of the digital filter typically spans multiple symbol times and is the convolution of the desired pulse-shaping response and precompensation for the rolloff frequency response of the subsequent digital-to-analog converter (DAC) if the rolloff is great enough to affect system performance. The output of the digital filter is passed to a DAC and a subsequent image-reject filter for conversion to continuous-time analog format. The output of the DAC in the spectral domain is the baseband spectrum and images of the baseband spectrum occurring within bands, which are bounded by integer multiples of one-half of the sampling rate f_s , all multiplied by a sinc function with nulls occurring at integer multiples of the sampling rate. In the case of lowpass signals the images are present near integer multiples of the sampling rate. In the time domain the output waveform is “stair-stepped.” The image-reject filter removes all of the spectral images and passes the baseband spectrum, thus “smoothing” or interpolating the time-domain waveform.

At the output of the image-reject filter, the shaped symbol pulses are in continuous-time analog format. They can then be up-converted to the desired radiofrequency (RF) for transmission. This process is shown in Fig. 4.

The operation at the receiver is the transpose of the transmit operation. The analog front end (AFE) of the

receiver translates the RF signal into a convertible pulse-train. The pulsetrain is then converted to a digital form via an analog-to-digital converter (ADC). The pulsetrain is filtered by a decimating FIR filter [4] with a root-raised-cosine response to complete the raised-cosine pulse-shaping operation. The receive process is shown in Fig. 5.

2.1. Digital Pulse-shaping Network

The actual design procedure for a pulse-shaping network is now presented. A transmit-side root-raised-cosine pulse-shaping network is described. The receive-side network will not be addressed since it is the network transpose of the transmit network.

Assume a digital data transmission system has a symbol period of T seconds, that is, every T seconds a new b_Q bit symbol is transmitted. In this description we assume $b_Q = 1$ for simplicity of illustration, although this is not necessary. Before transmission, it is necessary to shape each transmitted pulse. In this case a positive pulse-shape is transmitted for a bit value of zero. In addition to considering the desired pulse type, it is necessary to determine the length of the pulse relative to the symbol length and the resolution of the pulse or the number of bits used to compute the pulse values.

The interpolating FIR filter shown in Fig. 4 must be economically implementable and can therefore only approximate a desired pulse-shape, the root-raised cosine given by Eq. (14) in this case. The response is approximated by first determining the desired filter length. The filter length N is the product of the symbol interpolation factor L and the desired span M . The span is the number of symbol periods over which the shaping filter will operate.

The interpolation factor is selected to minimize the $\text{sinc}(x)$ distortion at the upper edge of the band of interest caused by the DAC and to simplify the implementation of the image-reject filter; the greatest consideration is the latter. As was mentioned previously, $\text{sinc}(x)$ distortion in the band of interest can be compensated for by putting a precompensation function $[1/\text{sinc}(x)]$ in the interpolating filter’s response. The higher the interpolation rate, the more distance there is between the band of interest and the first image in the spectral domain. The more distance there is, the simpler the image reject filter. Thus the interpolation factor becomes a tradeoff between the complexity of the digital interpolating filter and DAC speed, and the complexity of the image-reject filter. Typically, an interpolation factor of between 8 and 16 is a reasonable trade.

The span over which the impulse response is approximated depends on the amount of out-of-band energy that

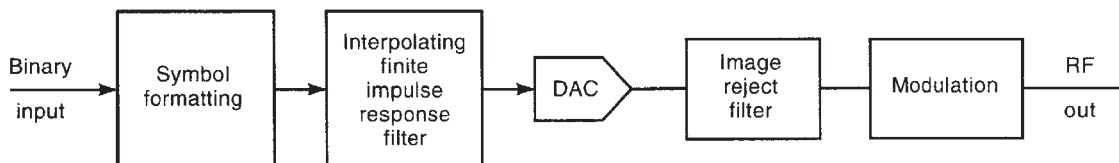


Figure 4. Pulse-shaping process in a digital transmitter.

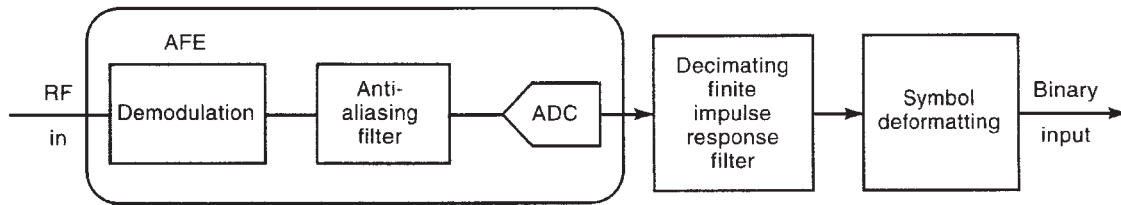


Figure 5. Pulseshaping process in a digital receiver.

can be tolerated. An ideal impulse response begins to approach zero after a number of time-domain sidelobes. However, the synthesized impulse is of finite duration. How closely the tails of the response approach zero is dependent on the length of time the impulse is approximated. Out-of-band energy is reduced as the span increases, so the tradeoff becomes filter order versus out-of-band energy due to time-domain sidelobe truncation. Typical values of the span factor are 4–16. A typical root-raised-cosine pulsedshaper would have an interpolation factor of 8 coupled with a span of 8 to yield a total filter length of 64.

2.2. Filter Coefficient Calculation

There are a number of possible methods for calculating the coefficients of the pulsedshaping filter. Two will be discussed here: the direct and optimal methods.

2.2.1. The Direct Method. An FIR digital filter is of the form

$$H(z) = \frac{Y(z)}{X(z)} = \sum_{n=0}^{N-1} a_n z^{-n} \tag{16}$$

The direct method samples the continuous-time impulse response at appropriate points in time to generate the filter coefficients a_n . Under the assumption of proper sampling

$$a_n = h(n) \stackrel{Z}{\Leftrightarrow} H(z) = \sum_{n=0}^{N-1} h(n) z^{-n} \cong H_D(z) \tag{17}$$

where $H_D(z)$ is the desired frequency-domain pulsedshape and $N-1$ is the filter order.

As stated previously, the total number of coefficients N is related to the span and interpolation factors by $N = LM$. Thus, continuing with the root-raised-cosine example, one would simply calculate N evenly spaced values using Eq. (14) to calculate the coefficients a_n . Since $h_T(t)$ is an even function about $t = 0$, it is necessary to shift $h_T(t)$ in time such that the sampled version of $h_T(t)$ [denoted by $h(n)$] is evenly symmetric around samples $(N-2)/2$ and $N/2$ to ensure a fully linear phase response [5]. Since there are L samples per symbol period T , $h_T(t)$ should be evaluated at integer multiples of T/L . This, along with the timeshift requirement, dictates that the discrete-time values neces-

sary to define $h_T(t)$ are given by

$$t(n) = \left(n + \frac{1}{2} - \frac{N}{2} \right) \frac{T}{L} \tag{18}$$

Substituting this into Eq. (14) gives the sampled version of $h_T(t)$,

$$h(n) = \frac{4\alpha \left(\cos \left((1 + \alpha) \frac{\pi t(n)}{T} \right) + \frac{T \sin \left((1 - \alpha) \frac{\pi t(n)}{T} \right)}{4\alpha t} \right)}{\pi \sqrt{T} \left[1 - \left(\frac{4\alpha t(n)}{T} \right)^2 \right]} \tag{19}$$

$n = 0, 1, \dots, N - 1$

This process is illustrated in Fig. 6 for a filter of length N equal to 64 and including $4\frac{1}{2}$ sidelobes on either side of the mainlobe of the root-raised-cosine function. Figure 7 shows the corresponding frequency-domain response of the pulsedshaping filter.

As is the case with any digital filter coefficient design method, once the floating-point coefficients are calculated, they must be converted to fixed-point format if the target digital filter is to be implemented in fixed-point arithmetic. Conversion of coefficients to fixed-point format can be as simple as truncation or rounding or can require sophisticated optimization processes. Let

$$a_n' = h'(n) = Q[h(n)] \tag{20}$$

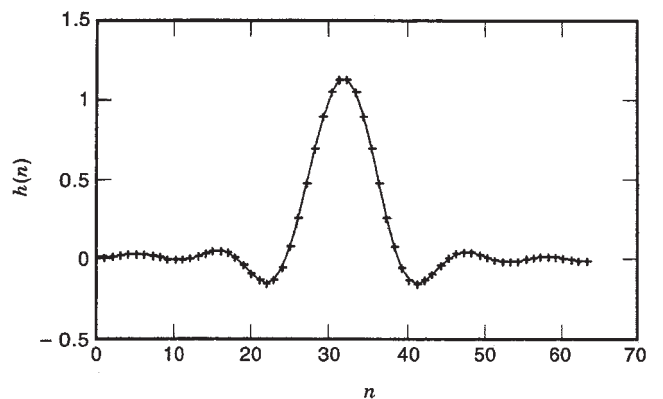


Figure 6. A discrete-time sampled root raised cosine.

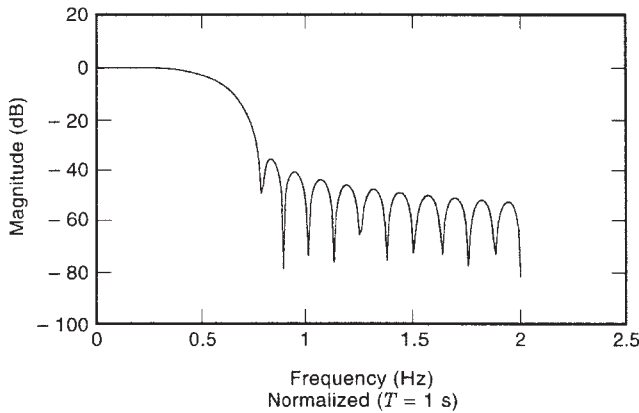


Figure 7. Frequency-domain response of the sampled root-raised cosine shown in Fig. 6.

be the quantized coefficients. The next step in the coefficient design process is to calculate the frequency response of the quantized filter coefficients and compare it with the desired frequency response to see if the filter is within acceptable error bounds. The frequency response of an FIR filter is found by evaluating the filter's z transform on the unit circle. That is, the magnitude frequency response of the quantized coefficients is given as

$$|H'(z)| = \left| \sum_{n=0}^{N-1} h'(n)z^{-n} \right|_{z=e^{j\omega}} \quad (21)$$

$H'(z)$ can be evaluated directly or by using a form of the DFT. If the filter's frequency response does not meet the required error bounds, then either the filter order N or the number of bits in the coefficient quantization must be increased and the appropriate steps in the coefficient design process must be repeated.

Coefficient quantization is not as straightforward as data quantization. The quantization of data words yields 6.02 dB of signal-to-noise ratio per bit. The number of bits required for coefficient quantization is a function of filter order and the frequency-response shape. A good rule of thumb for a worst-case metric [6] for the number of coefficient bits required is

$$b_C = \frac{(\text{required attenuation in dB})}{6.02} + \log_2 N \quad (22)$$

so that

$$\begin{aligned} \frac{(\text{required attenuation in dB})}{6.02} &\leq b_C \\ &\leq \frac{(\text{required attenuation in dB})}{6.02} + \log_2 N \end{aligned} \quad (23)$$

assuming no limiting roundoff error in the actual filter implementation. In most practical pulseshaping filter

implementations, the coefficient wordlength should be closer to the lower bound.

The floating-point coefficients (a_n) for the case $M=L=8$ are shown in matrix form. Each column represents samples in adjacent symbol periods. Since the impulse response spans eight symbol periods, there are eight corresponding columns.

$$a_n = \begin{bmatrix} -0.010 & -0.002 & 0.042 & -0.061 \\ -0.007 & -0.013 & 0.029 & 0.071 \\ 0 & -0.019 & -0.003 & 0.253 \\ 0.007 & -0.018 & -0.049 & 0.467 \\ 0.014 & -0.010 & -0.101 & 0.689 \\ 0.017 & 0.006 & -0.144 & 0.890 \\ 0.015 & 0.025 & -0.161 & 1.043 \\ 0.008 & 0.039 & -0.137 & 1.126 \\ 1.126 & -0.137 & 0.039 & 0.008 \\ 1.043 & -0.161 & 0.025 & 0.015 \\ 0.890 & -0.144 & 0.006 & 0.017 \\ 0.689 & -0.101 & -0.010 & 0.014 \\ 0.467 & -0.049 & -0.018 & 0.007 \\ 0.253 & -0.003 & -0.019 & 0 \\ 0.071 & 0.029 & -0.013 & -0.007 \\ -0.061 & 0.042 & -0.002 & -0.010 \end{bmatrix} \quad (24)$$

In converting the floating-point coefficients to fixed-point coefficients, maximum arithmetic efficiency can be obtained by scaling the fixed-point coefficients so that the maximum possible filter output is at the overflow threshold. Worst-case peak signals would occur for data patterns in which the maxima and minima of the impulse response overlap, or add (in the case of a negative pulse, the absolute value of the minima adds to the composite pulse). It turns out for the example here that an efficient peak value for the impulse response to take is 194 for a 9-bit integer two's-complement representation (maximum possible positive value of 255).

Scaling the matrix of the floating-point values to a peak value of 194 and rounding each coefficient to the nearest integer results in the coefficient set shown here, which

completes the synthesis of the pulse coefficients:

$$a_n' = \begin{bmatrix} -2 & 0 & 7 & -10 & 194 & -24 & 7 & 1 \\ -1 & -2 & 5 & 12 & 180 & -28 & 4 & 3 \\ 0 & -3 & 0 & 44 & 153 & -25 & 1 & 3 \\ 1 & -3 & -8 & 80 & 119 & -17 & -2 & 2 \\ 2 & -2 & -17 & 119 & 80 & -8 & -3 & 1 \\ 3 & 1 & -25 & 153 & 44 & 0 & -3 & 0 \\ 3 & 4 & -28 & 180 & 12 & 5 & -2 & -1 \\ 1 & 7 & -24 & 194 & -10 & 7 & 0 & -2 \end{bmatrix} \quad (25)$$

2.2.2. The Optimal Method. The optimal method requires an optimizing filter design program such as the Parks–McClellan program [5,7] but guarantees an optimum solution. To design the pulse-shaping filter coefficients using the optimal method, the EFF subroutine (EFF is the actual name of the subroutine in the published program) in the Parks–McClellan computer design program must be modified by inserting a floating-point, discrete-frequency version of the desired frequency-domain pulse-shape. The program is then executed with a desired filter order and the same iterative process of evaluating the frequency response of the quantized coefficient set as described previously for the direct method is followed until a set of coefficients is generated that is within the desired error bound. This method yields much more reliable results than the does direct method.

Even more sophisticated filter programs exist that optimize quantized coefficients. These programs allow designers to optimize the efficiency of a filter implementation.

2.3. Filter Hardware Implementation

The actual hardware realization of a pulse-shaping filter is highly dependent on symbol rates, filter order, process, and so on. Assuming symbol rates that allow implementations in state-of-the-art semiconductor processes, the filter would be implemented as some variation of a polyphase architecture [4].

Interpolation is the process of increasing the sampling rate while preserving the signal’s spectral content. The conceptual first step in interpolation is to insert $L - 1$ zero-valued samples between each valid input sample, expanding the sampling rate by L . This causes the original signal

spectrum to be repeated $L - 1$ times. This process is referred to as sample rate expansion. To complete the interpolation, the zero-valued input samples are converted to spectrally accurate approximations of the signal. This is equivalent to preserving the original signal spectrum. Thus, and again conceptually, the zero-stuffed input stream is filtered by a lowpass filter with a passband at the original spectral location and a passband gain of L . This filters out all the repeated spectra. This conceptual process is shown in Fig. 8.

In real implementations it would be a waste of storage and computational resources to store and multiply zero-valued data samples. For this reason, polyphase structures are used. A polyphase interpolator configures the standard N -tap filter structure into k phases of an $(N - 1)$ -element delay line. For example, an eighth-order ($N = 9$) FIR filter with $k = 3$ phases has three sets of three coefficients. The coefficients for the eighth-order filter are a_0, a_1, \dots, a_8 . The first polyphase taps the eight-element delay line at the input to the filter (a_0), after the third delay (a_3), and after the sixth delay (a_6). The second phase taps a_1, a_4 , and a_7 . The third phase taps a_2, a_5 , and a_8 . However, since all but every third element in the delay line would contain a zero-valued data sample, the delay line can be collapsed to a two-element delay line ($N/k - 1$ elements) with all phases using the same samples. The output of the interpolator is the commutated output of the three phases. Figure 9 illustrates the polyphase implementation of the nine-tap interpolator. Reference 4 details the efficient implementation of interpolation and decimation filters.

An interpolation filter can be implemented using standard multiply and accumulate elements, or in some cases it is most efficient to use table-lookup-based bit-slice filter methods [8]. The tradeoff is dependent on the number of bits required for the representation of a symbol. For low bit count, the bit-slice implementation is usually more efficient. As bit count increases, table sizes become unmanageable.

2.4. DAC

The DAC has the task of generating an analog output based on the digital input supplied by the FIR filter. The DAC must be linear to ensure that no unwanted spurious energy is generated. Several implementations are possible depending on the DAC resolution required. For relatively modest resolutions of 4–8 bits, simple binary-weighted current or charge-based approaches are possible. For higher resolutions, it may be desirable to use segmented approaches where each least significant bit (LSB) step has

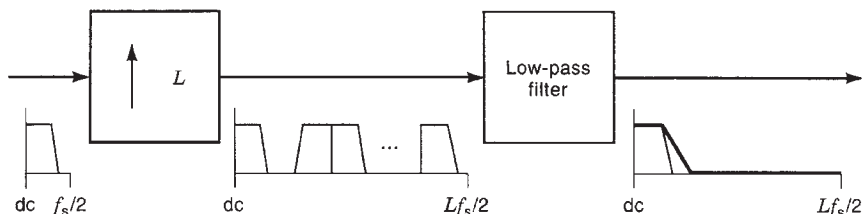


Figure 8. Illustration of the conceptual interpolation process.

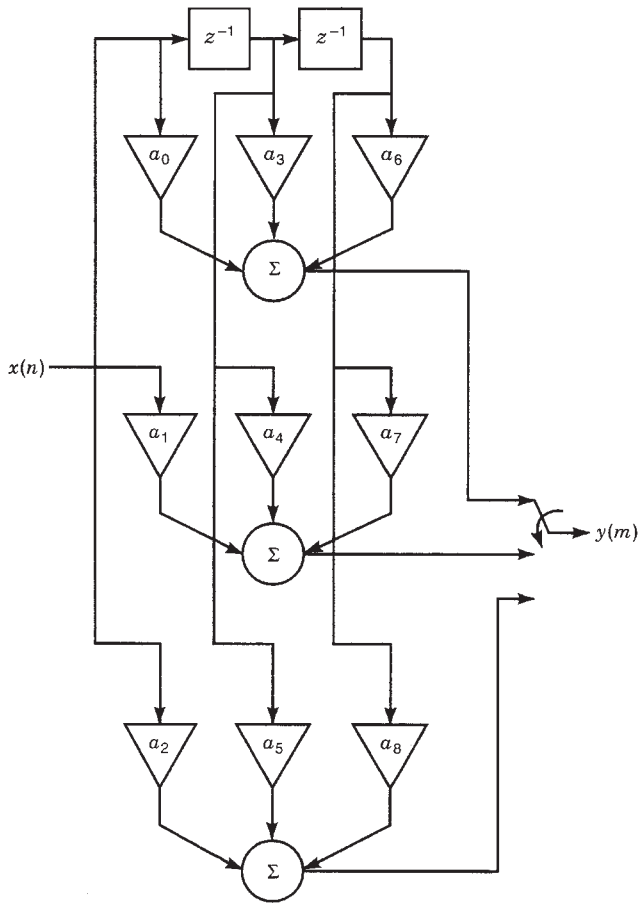


Figure 9. Polyphase implementation of an FIR interpolation filter.

a separate current- or charge-based generator. For example, a 5-bit segmented current-steered DAC would have 32 separate current sources feeding a common resistor to generate the desired output voltage. Sources are turned on or off depending on the value of the control word. This is opposed to a binary approach in which only five current sources are used scaled in binary fashion. For higher-bit resolutions, the binary approach can suffer from linearity errors due to mismatches at major carries. The advantage of a binary approach is smaller implementation area. For DACs of 9-bit resolution or higher, a combination of binary [for the most significant bits (MSBs)] and segmented (for the LSBs) is frequently used.

Standard DACs offer no image suppression, even if the DAC runs at a rate greater than the digital world update rate. Image suppression could be improved if the DAC could interpolate between successive word updates. Such a converter can be demonstrated, following up on the example begun for the pulse-shaping network. Suppose that specifications require that all spurious energy be at least 40 dB down with respect to the baseband level. This requires that all spectral images of the FIR filter be attenuated sufficiently to achieve this. Further suppose that the symbol rate is 128 kband. The update rate f_s of the digital filter is 1.024 MHz (because of the 1–8 interpolation factor from the preceding example), and hence the first

image replica will appear there. If the DAC were updated at the 1.024 MHz rate, then the amount of attenuation of the image due to rolloff would be only 17 dB. Consider an interpolating DAC operating at 5 times the digital update rate ($f_{s1} = 5.12$ MHz). The block diagram of an architecture suitable for monolithic integration accompanied by illustrative spectral plots is shown in Fig. 10. In this architecture, it is shown that interpolation can provide 20 dB of additional attenuation.

A simplified single-ended schematic of an interpolating DAC is shown in Fig. 11 [9]. ϕ_1 and ϕ_2 are nonoverlapping clocks operating at the interpolation frequency (5.12 MHz in the preceding example). The operational amplifiers are conventional fully differential folded cascade topologies. The input voltage reference is selected based on specific channel requirements and typically ranges from 250 mV to 1 V. It is usually supplied by an on-chip bandgap generator. The configuration is a cascaded charge redistribution DAC with the first stage an offset insensitive programmable amplifier to realize the four least significant bits [10]. Gain is determined by the sum of the binary-weighted capacitors at the input, dependent on the LSB word. The second stage is a modified second-order switched-capacitor biquad [11]. This stage has programmable gain to realize the four most significant bits of the DAC and acts as the summing point for the LSB portion. A straightforward charge transfer analysis yields the low-frequency output level as a function of the reference voltage V_{ref} and critical circuit capacitor values

$$V_{out} = \frac{C_3}{16C_3} \frac{V_{ref}}{C_1} (b_7C_12^{-4} + b_6C_12^{-3} + \dots + b_4C_12^{-1}) + \frac{V_{ref}}{C_7} (b_3C_72^{-4} \dots + b_0C_72^{-1}) \quad (26)$$

Here, b_0, b_1, \dots, b_7 represent the digital data (possible values of 0 or 1) with b_7 as the least significant bit. Since the DAC is fully differential, the sign bit is easily incorporated by cross-coupling the input connection to V_{ref} . Interpolation is accomplished by the fact that the final stage is really a switched-capacitor filter. DC–AC analysis is simplified by replacing the DAC capacitor array structure with an equivalent single-ended switched-capacitor network as shown in Fig. 12. Including the input offset voltages V_{off2}, V_{off3} for the operational amplifiers, the defining charge equations for this network are given by

$$[V_{o3}(n) - v_{off3}](1 + \alpha_2) + [V_{o2}(n) - v_{off3}]\alpha_6 = V_{o3}(n - 1) - v_{off3} \quad (27)$$

$$V_{o2}(n) - v_{off2} - \alpha_5v_{off2} - \alpha_3v_{off2} = [V_{in}(n - 1) - v_{off2}]\alpha_5 + [V_{o3}(n - 1) - v_{off2}]\alpha_3 + V_{o2}(n - 1) - v_{off2} \quad (28)$$

where V_{o2} and V_{o3} are outputs of amplifiers 2 and 3, respectively.

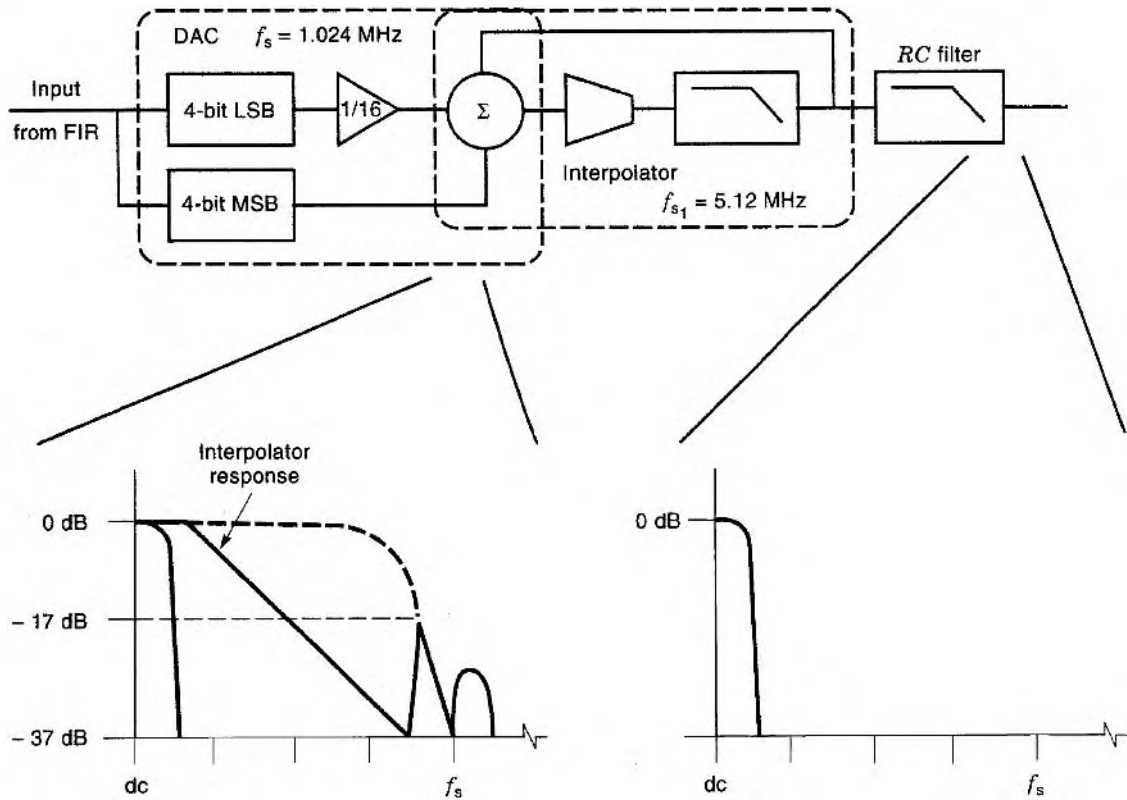


Figure 10. Digital-to-analog converter top-level block diagram.

Under steady-state conditions $n \rightarrow \infty$. With $V_{in}(n) = V_{in}(n - 1) = 0$, then

$$\begin{aligned} V_{o2}(n) &\rightarrow V_{o2}(n - 1) \rightarrow V_{o2}, \\ V_{o3}(n) &\rightarrow V_{o3}(n - 1) \rightarrow V_{o3} \end{aligned} \quad (29)$$

for the DAC

$$V_{o3} = 0 \quad (30)$$

$$V_{o2} = v_{off3} \left(1 + \frac{\alpha_2}{\alpha_6} \right) \quad (31)$$

where V_{o2} and V_{o3} are the DC offset voltage at the outputs of amplifiers 2 and 3, respectively. Under these conditions, solving Eqs. (27) and (28) yield the output offset voltages

where Eq. (31) is valid during high ϕ_1 . It is interesting to note that although the DAC output is a fully held signal over the 5.12 MHz clock period, it has no operational-amplifier-induced DC offset. This is simply due to the fact

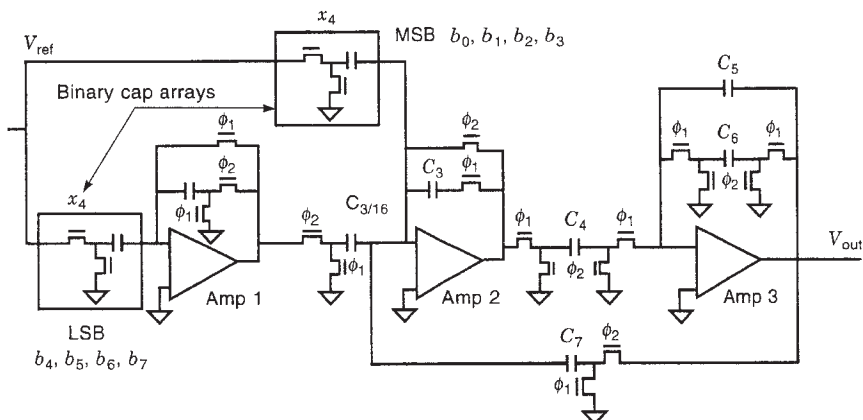


Figure 11. Simplified single-ended DAC schematic.

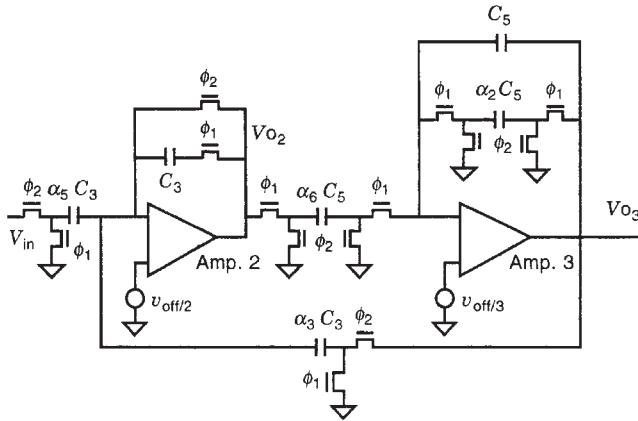


Figure 12. Interpolating filter.

that output offset at this point is due solely to amplifier 2, which has been nulled out.

Ignoring offset, Eqs. (27) and (28) may be transformed to the z domain, where the following transfer function may be derived:

$$\frac{V_{o3}(z)}{V_{in}(z)} = \frac{-\alpha_5\alpha_6}{1 + \alpha_2} \frac{z^{-1}}{1 - \frac{2 + \alpha_2 - \alpha_3\alpha_6}{1 + \alpha_2} z^{-1} + \frac{1}{1 + \alpha_2} z^{-2}} \quad (32)$$

This is the form of a second-order lowpass filter. Interpolation is accomplished by designing the filter such that little passband loss occurs at the digital filter's 3 dB point of 64 kHz. Setting specifications for the interpolating filter at no more than 0.3 dB loss at 100 kHz; then with a sampling frequency of 5.12 MHz, this leads to a desired transfer function of

$$H(z) = \frac{0.0910218z^{-1}}{1 - 1.4921346z^{-2} + 0.5831564z^{-2}} \quad (33)$$

Coefficient matching with Eq. (32) yields the necessary capacitor values. With 17 dB of loss due to the S/H effect and the loss at 1.024 MHz due to Eq. (33), the image at the DAC output is 37 dB lower. Hence, an additional 20 dB of image rejection is achieved with the use of interpolation techniques.

2.5. Image Filter

There are several techniques that are used to realize continuous-time monolithic filters. Standard active-filter techniques utilizing resistors and capacitors are the simplest approach but pole frequencies cannot be accurately placed due to typical process variations. If the image response is located very far away from the baseband spectrum, then accurate pole placement may not be necessary. In that case, the filter is simply designed such that the worst-case RC product leading to a high cutoff frequency is still sufficient to meet stopband energy requirements. Frequently, only first-order filters are required, but if the passive variation is significant enough, higher-order filters may be necessary to provide sufficient

attenuation. If a process has very linear components, such as thin-film resistors and double polysilicon or metal capacitors, it is possible to realize wide-dynamic-range filters with excellent linearity. Dynamic ranges over 93 dB are possible if linearity is a concern. If only diffuse resistors or depletion capacitors are available, then the corresponding voltage dependence of the passive devices reduces linearity considerably. In that case, interpolating DAC techniques may be desirable such that only a simple external RC filter is necessary for image filtering. Of course, linearity requirements must be considered to make a final decision.

Another technique that may be used includes MOSFET-C (metal oxide semiconductor field-effect transistor capacitance) filters [12], where MOSFET transistors operated in the linear region are used to replace resistors in active filters. Using special linearization techniques, MOSFET-C filters can achieve reasonable linearity (50–60 dB), and no special resistor material is required. However, MOSFET-C filters are limited in the frequency range that they can operate because of operational amplifier limitations and distributed parasitics [13]. They also require the use of tuning networks to ensure that the MOSFET devices stay in the linear region and close to the resistor values necessary to achieve the necessary time constants.

Finally, transconductance- C ($g_m - C$) networks can be used as image filters [14]. $g_m - C$ filters have the advantage of being able to achieve very high cutoff frequencies, typically in the 10–100 MHz area. These may be useful in cases where the data rate is very high and image frequencies may be close to baseband. Linearization techniques can achieve dynamic ranges in the area of 50–65 dB. $g_m - C$ filters have pole frequencies proportional to g_m/C , so stable transconductance networks are required to achieve stable pole locations. Usually, this implies some sort of tuning network to accurately set g_m for the desired cutoff.

3. SUMMARY

In this article an overview of the motivation, theory, and implementation of pulseshaping in digital communication systems has been presented. Digital communication systems transmit digital data as discrete-time symbols modulating a continuous-time waveform. Because actual communication channels are bandlimited, symbol times can overlap, inducing intersymbol interference. Pulse-shaping can reduce or eliminate intersymbol interference if it is closely matched to the characteristics of the channel.

A theoretical background for pulseshaping was established based on a channel that can be modeled as a linear time-invariant filter with additive white Gaussian noise. It was shown that for this type of channel a class of filters known as Nyquist filters are the most commonly used for pulseshaping, and the most popular filter in this class is the raised-cosine filter. Since the implementation of pulseshapers is commonly distributed between the transmit and receive sides of a communication system, an example

of the implementation of a transmit-side square root raised-cosine filter was presented.

The square-root-raised-cosine filter implementation presented was a hybrid analog–digital implementation, taking advantage of the strengths of both technologies.

BIBLIOGRAPHY

1. E. A. Lee and D. G. Messerschmitt, *Digital Communication*, 2nd ed., Kluwer Academic, Norwell, MA, 1994.
2. B. Sklar, *Digital Communications, Fundamentals and Applications*, Prentice-Hall, Englewood Cliffs, NJ, 1988.
3. R. E. Ziemer and R. L. Peterson, *Digital Communications and Spread Spectrum Systems*, Macmillan, New York, 1985.
4. R. E. Crochiere and L. R. Rabiner, *Multirate Digital Signal Processing*, Prentice-Hall, Englewood Cliffs, NJ, 1983.
5. L. R. Rabiner and B. Gold, *Theory and Application of Digital Signal Processing*, Prentice-Hall, Englewood Cliffs, NJ, 1975.
6. G. A. Mian and A. P. Nainer, On the performance of optimum linear phase low-pass FIR digital filters under impulse response coefficient quantization, *IEEE Trans. Acoust. Speech Signal Process.* **ASSP-29**:925–932 (1981).
7. T. W. Parks and McClellan, A program for the design of linear phase finite impulse response digital filters, *IEEE Trans. Audio Electroacoust.* **AU-20**:195–199 (1972).
8. F. J. Taylor, *Digital Filter Design Handbook*, Marcel Dekker, New York, 1983.
9. B. A. Myers et al., A frequency agile monolithic QPSK modulator with spectral filtering and 75 Ω differential line driver, *IEEE J. Solid-State Circ.* **33**:1394–1405 (1998).
10. R. Gregorian and G. Temes, *Analog MOS Integrated Circuits for Signal Processing*, Wiley, New York, 1986, pp. 414–416.
11. R. Gregorian, Switched capacitor filter design using cascaded sections, *IEEE Trans. Circ. Syst.* **CAS-27**:515–521 (1980).
12. Y. Tsvividis, M. Banu, and J. Khoury, Continuous-time MOS-FET-C filters in VLSI, *IEEE J. Solid-State Circ.* **SC21**:15–30 (1986).
13. J. Khoury and Y. Tsvividis, Analysis and compensation of high frequency effects in integrated MOSFET-C continuous-time filters, *IEEE Trans. Circ. Syst.* **CAS-34**:862–875 (1987).
14. K. Laker and W. Sansen, *Design of Analog Integrated Circuits and Systems*, McGraw-Hill, New York, 1994, pp. 652–657.

Q-FACTOR

DARKO KAJFEZ
University of Mississippi
University, Mississippi

1. INTRODUCTION

Figure 1 shows several one-port resonators. The lumped-element resonator in Fig. 1a is a simple parallel-resonant circuit, the resonant frequency of which is

$$\omega_0 = \frac{1}{\sqrt{LC}} \quad (1)$$

At this frequency, the absolute value of the input impedance reaches a maximum (admittance reaches a minimum). At other frequencies, the absolute value of impedance monotonically decays according to a well known bell-shaped curve in Fig. 2. In the elementary circuit theory, the Q factor of the parallel resonant circuit is defined as

$$Q_0 = \frac{\omega_0 C}{G_0} \quad (2)$$

which is a ratio of the susceptance (at the resonant frequency) to the conductance $G_0 = 1/R_0$ of the circuit. The larger the Q factor is, the narrower the bell-shaped curve, so the resonator can better discriminate between signals of different frequencies. Hence, the letter Q is used to denote a “quality” of the resonant circuit. The example in Fig. 2 is plotted in a normalized manner, for a resonator that has $Q = 1000$. In this example, the absolute value of impedance drops down to 16% when the operating frequency is only 0.3% away from the resonant frequency.

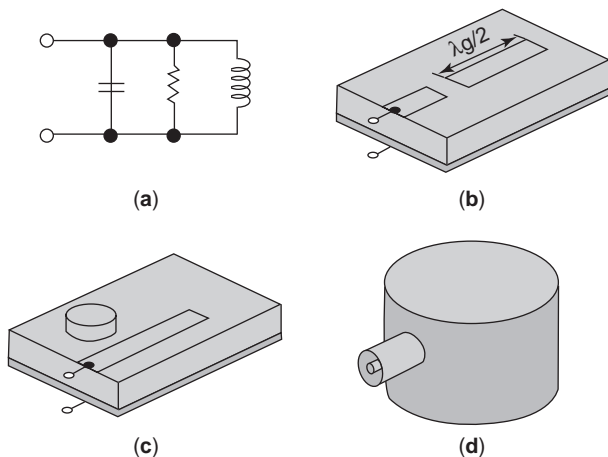


Figure 1. Resonators: (a) lumped element, (b) microstrip, (c) dielectric resonator, (d) cavity resonator.

At rf and microwave frequencies, the resonators are seldom built in the form of lumped inductances and capacitances. Instead, they consist of distributed circuits, such as a half-wavelength-long microstrip transmission line as shown in Fig. 1b. Much higher Q factors can be achieved by using dielectric resonators, which are integrated with microstrip circuits, as shown in Fig. 1c. For high power handling, it may be necessary to employ a hollow cylindrical or rectangular cavity, such as shown in Fig. 1d, in which the input is connected through a coaxial transmission line. In the vicinity of the resonant frequency of interest, each of these resonators has similar properties as the basic parallel resonant circuit, namely, their input impedance exhibits a bell-shaped resonant curve, and the width of the curve (or bandwidth) is inversely proportional to the Q factor. However, a lumped-circuit theory definition of Q factor given by (2) is not applicable for microwave resonators.

A more general definition of Q factor, valid for both lumped element resonators and for rf and microwave resonators, is formulated in terms of energy and power [1, p. 116]:

$$Q = \left[\frac{\omega W_{\max}}{P_d} \right]_{\omega = \omega_0} \quad (3)$$

where W_{\max} is the maximum (peak) energy stored in the resonator and P_d is the average power dissipated in the resonator. There are two types of energy stored in any resonator: electric energy W_e and magnetic energy W_m . For time-harmonic (sine and cosine) behavior of electromagnetic fields, the energy in the resonator fluctuates between the electric and magnetic types—when W_e is at maximum, W_m is zero and a quarter-period later W_e is zero and W_m is maximum, and so on. When the resonator is operating at its resonant frequency, the peak value of W_e is the same as the peak value of W_m .

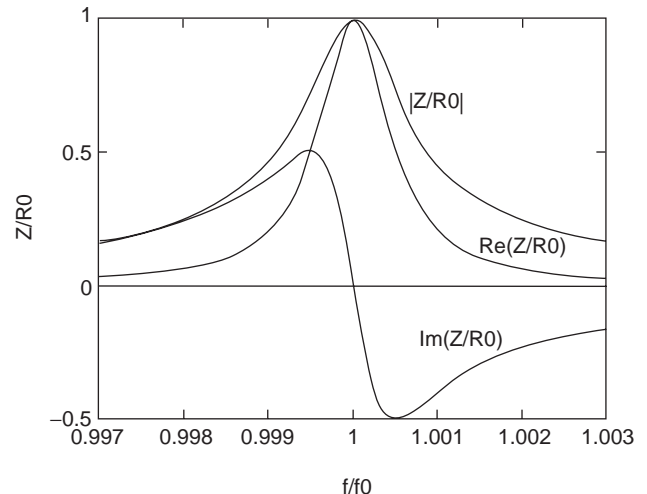


Figure 2. Normalized impedance of a parallel resonant circuit.

The lumped resonator from Fig. 1a has only one resonant frequency. This is in contrast to microwave resonators from Figs. 1b–1d, because each of them has an infinite number of resonant frequencies. To understand this, consider the half-wavelength microstrip resonator from Fig. 1b; when the frequency is twice as high as the first resonance, the length of the resonator becomes equal to one full wavelength. At that frequency, the input impedance again has a maximum, the peak of electric energy is equal to the peak of the magnetic energy, and one observes a second resonant frequency. For a still higher operating frequency, the point is reached where the length becomes equal to 1.5 wavelengths, thus becoming another resonance of the device. Each of these resonant frequencies is said to correspond to another resonant mode of operation. Likewise, the dielectric resonator from Fig. 1c as well as the hollow resonant cavity from Fig. 1d exhibit an infinite number of resonant modes, as the operating frequency grows higher and higher. At room temperature, the Q factors of the last two types of resonators may reach values higher than 10,000.

Resonators are the basic building blocks of RF filters and oscillators. The fundamental characteristics [2–4] that have to be specified for a resonator are (1) resonant frequency, (2) coupling coefficient, and (3) unloaded Q factor. Like any other circuit component, a resonator must be experimentally tested to determine its properties. Although some specialized instruments, called Q meters and *grid-dip meters*, were used in the past, the universal instrument for measuring the Q factor today is the automatic network analyzer.

By measuring a number of points on each side of the resonant frequency and by careful data processing, it is possible to determine the unloaded Q factors with an uncertainty smaller than 1%. Such accuracy is especially important in measuring the material properties of the samples that are inserted into a resonant cavity. By determining the difference in the cavity Q factor and its resonant frequency with and without the sample, one can accurately predict the complex permittivity and permeability of the sample and/or the surface resistivity of a conductor sample. For instance, by such a method one measures the surface resistance of high-temperature-superconductor samples [5].

2. LOADED, UNLOADED, AND EXTERNAL Q

To fully understand the operation of RF and microwave resonators of the types shown in Figs. 1c and 1d, a three-dimensional distribution of the electric and magnetic fields in the resonator should be determined by an analytical or a numerical procedure. It is then possible to integrate the stored energy over the volume of the resonator, and to determine the power dissipation in the resonator due to conductor losses and/or dielectric losses. These values substituted in (3) will provide the theoretical value of the Q factor of the resonator itself, the so-called unloaded Q factor.

For an experimental investigation of a resonator, it is convenient to study the resonant behavior with the use of

the equivalent circuit shown in Fig. 3a. It is assumed that the Q factor is larger than (at least) 100, and that the effect of other resonant modes is not noticeable within, say, 1% on each side of the resonant frequency under consideration. In other words, the treatment that follows is suitable for high- Q resonators.

Figure 3a shows the equivalent circuit, which is appropriate for all the distributed-element resonators from Fig. 1. The figure also contains an external Thevenin voltage source consisting of V_s and internal impedance R_c , which is equal to the characteristic impedance of the input transmission line. This source would represent the network analyzer, which is connected to input port 1 of the resonator. The transmission line of length l , located between input (port 1) and the location of the coupling (port 2), could be physically very short (e.g., just a length of one coaxial connector), but this length is seldom known very precisely.

Port 3 is the location of the resonator itself. The impedance $R_s + jX_s$ represents the transformation properties of the coupling mechanism. For a loop coupling, X_s is a positive reactance, and for a probe coupling, X_s is a negative reactance. The value of X_s can be considered to be constant in the frequency range of interest (say, 1% on each side of the resonant frequency). The susceptance B_0 of the

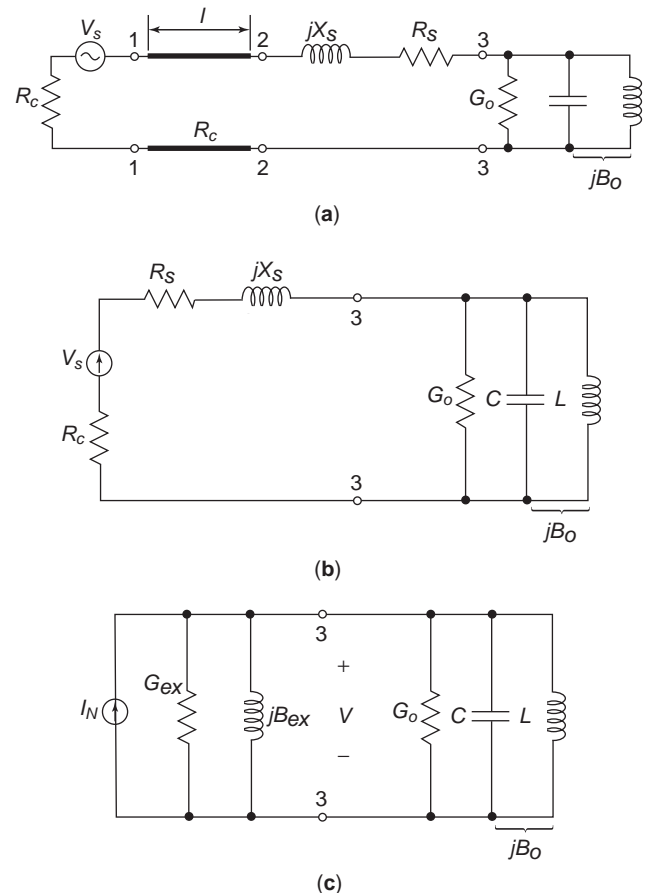


Figure 3. (a) The equivalent circuit of a one-port resonator; (b) Thevenin equivalent to the left of port 3; (c) Norton equivalent to the left of port 3.

resonator, represented by a parallel LC combination, is a function of frequency that varies hundreds or even thousands of times faster than X_s . The conductance G_0 represents the dissipation inside the resonator proper. The corresponding resistance is the inverse value, $R_0 = 1/G_0$.

Suppose that an observer can enter the resonator and look left and right from port 3 (see Fig. 3b). If the observer at port 3 now turns to the left (toward port 1), he/she sees the series combination of resistance R_s and the reactance X_s , and behind them a transmission line terminated in a Thevenin source. As the source impedance is equal to the characteristic impedance of the transmission line, the length of the transmission line does not change the impedance seen by the observer; any length of a transmission line, which is terminated in a matched load, has the same input impedance, equal to R_c .

Using elementary circuit theory rules, the external circuit that the observer saw, can now be replaced by a Norton's equivalent, consisting of a current source in parallel with an admittance, as shown in Fig. 3c. As a further simplification, impedance $R_c + R_s + jX_s$ was transformed into admittance $G_{ex} + jB_{ex}$, the external admittance felt by the resonator.

Now, the observer at port 3 can clearly see that the external circuit influences the resonator in two ways:

1. Susceptance B_{ex} is in parallel with B_0 and thus detunes the resonant frequency. However, this frequency shift is so small that it is of little consequence. The observer simply has to deal with a new, loaded resonator that has a slightly different resonant frequency, called *loaded resonant* frequency ω_L .
2. Conductance G_{ex} comes in parallel to G_0 , thus lowering the overall Q to a new value, called loaded Q , denoted Q_L . To find this value, consider the inverse of (3):

$$\left[\frac{P_d}{\omega W_{max}} \right]_{\omega=\omega_L} = \frac{P_0}{\omega_L W_{max}} + \frac{P_{ex}}{\omega_L W_{max}} \quad (4)$$

The dissipated power P_d consists of two parts: P_0 , the power dissipated in the unloaded resonator; and P_{ex} , the power dissipated in the external circuit. Each of the three terms in (4) is identified as a particular Q factor:

$$\frac{1}{Q_L} = \frac{1}{Q_0} + \frac{1}{Q_{ex}} \quad (5)$$

Q_L is the overall Q factor of the resonator and its external circuit. Q_0 is the unloaded Q factor of the unperturbed resonator, and Q_{ex} is the external Q factor.

The ratio of power dissipated in the external circuit to the power dissipated in the resonator is called coupling coefficient κ . In Fig. 3c, both G_0 and G_{ex} have common voltage V , so the ratio of powers is proportional to the ratio of conductances:

$$\kappa = \frac{V^2 G_{ex}}{V^2 G_0} = \frac{G_{ex}}{G_0} = \frac{Q_0}{Q_{ex}} \quad (6)$$

When an equal amount of power is dissipated in the external circuit as in the resonator itself, the coupling is said to be critical, and the coupling coefficient in this case is $\kappa = 1$. An undercritical coupling means that more power is dissipated in the resonator than in the external circuit, while an overcritical coupling means that more power is lost in the external circuit than in the resonator.

By eliminating Q_{ex} from (5) with the use of (6), one obtains the relationship between the unloaded and the loaded Q as follows:

$$Q_0 = Q_L(1 + \kappa) \quad (7)$$

As soon as one starts a measurement, the resonator is loaded by the external circuit (here the network analyzer), and the measurement will produce the loaded Q , namely, Q_L . The stronger the coupling one creates between the network analyzer and the resonator, the lower the value of the measured loaded Q . To find the unloaded Q , the measurement should be designed in such a way that it also provides the value of the coupling coefficient κ . Then, using Q_L and κ , one computes Q_0 from (7).

3. FREQUENTLY USED FORMULAS

The parallel resonant circuit in Fig. 4 is drawn in such a way that the lossless part of the circuit is to the right and the dissipative part is to the left of the observation port. The reactive part is described by the susceptance

$$B(\omega) = \omega_0 C \left(\frac{\omega}{\omega_0} - \frac{\omega_0}{\omega} \right) \quad (8)$$

where ω_0 is specified by L and C according to (1). This behavior is plotted in Fig. 5. At very low frequency B tends to negative infinity, and at very high frequency B tends to positive infinity. At resonant frequency ω_0 , the susceptance passes through zero. Taking the derivative of (8), one obtains the slope of the susceptance to be

$$\left. \frac{dB}{d\omega} \right|_{\omega=\omega_0} = 2C \quad (9)$$

In a narrow frequency range around $\omega = \omega_0$, the susceptance can be approximated by a straight line:

$$B(\omega) = \left. \frac{dB}{d\omega} \right|_{\omega=\omega_0} (\omega - \omega_0) \quad (10)$$

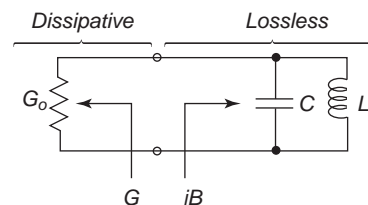


Figure 4. Conductance and susceptance of a parallel resonant circuit.

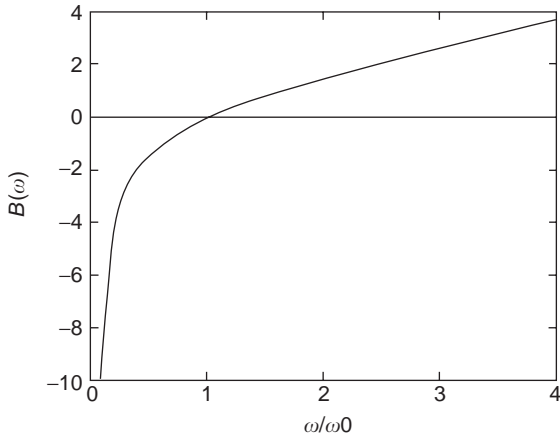


Figure 5. Susceptance of the circuit from Fig. 4.

The situation is shown in Fig. 6, which can be thought of as a zoomed region of Fig. 5. When the susceptance becomes equal to the conductance, the absolute value of the admittance is increased by a factor of $\sqrt{2}$, which corresponds to 3 dB. The two points on each side of ω_0 corresponding to a 3 dB increase are denoted ω_1 and ω_2 :

$$\left. \frac{dB}{d\omega} \right|_{\omega=\omega_0} (\omega_1 - \omega_0) = -G \tag{11}$$

$$\left. \frac{dB}{d\omega} \right|_{\omega=\omega_0} (\omega_2 - \omega_0) = G$$

By subtracting the two equations from each other, and by using (9) and (2), one obtains the 3 dB bandwidth:

$$BW = \omega_2 - \omega_1 = \frac{\omega_0}{Q_0} \tag{12}$$

Thus, the 3 dB bandwidth of an unloaded resonator is Q_0 times smaller than its resonant frequency! For example, an unloaded resonator with $Q_0 = 1000$, having its

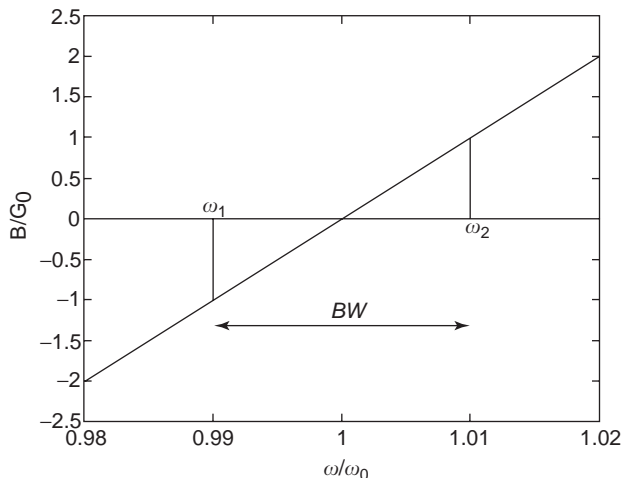


Figure 6. Linear approximation of susceptance in the vicinity of the resonant frequency.

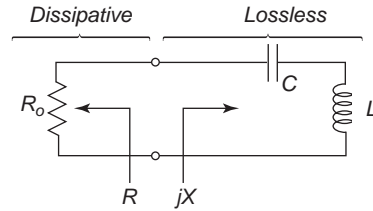


Figure 7. Resistance and reactance of a series-resonant circuit.

resonant frequency equal to 1 GHz, will display a bandwidth of 1 MHz. An additional external loading would lower the overall Q to a new value Q_L , so that the bandwidth of the loaded resonator is then given by modified (12) with Q_0 replaced by Q_L .

By eliminating C in (9) with the use of (2), one obtains the Q factor in terms of the susceptance slope as follows:

$$Q_0 = \left. \frac{\omega_0}{2G_0} \frac{dB}{d\omega} \right|_{\omega=\omega_0} \tag{13}$$

This expression is associated with the parallel resonant circuit in Fig. 4. For a series resonant circuit in Fig. 7, the Q factor is expressed in terms of the reactance slope:

$$Q_0 = \left. \frac{\omega_0}{2R_0} \frac{dX}{d\omega} \right|_{\omega=\omega_0} \tag{14}$$

The 3 dB bandwidth of the series resonant circuit is related to Q_0 by the same equation (12) as for the parallel resonant circuit.

As mentioned before, a distributed circuit has an infinite number of resonant frequencies, while a circuit consisting of lumped elements can have only a finite number of resonant frequencies. However, for a narrow vicinity of a particular resonant frequency ω_0 , either the susceptance or the reactance of a distributed circuit could be approximated by a straight line of the type shown in Fig. 6. For instance, when a resonator exhibits a parallel-type resonance, its susceptance may be approximated by (10). For the sake of simplicity, suppose that the resonator is lossless, and its external load will be a known conductance G_0 as shown in Fig. 8. Furthermore, suppose that the susceptance $B(\omega)$ can be determined by solving circuit equations and/or transmission-line equations for this particular resonator. Then, the loaded Q factor can be found by applying (13). Needless to say, each resonant mode will have a different value of Q factor.

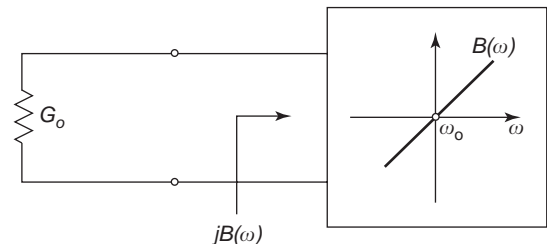


Figure 8. Microwave resonator and an external conductance.

Frequently, the resonator is created by using a half-wavelength section of microstrip transmission line open-circuited at both ends, or a quarter-wavelength coaxial line open-circuited at one end and short-circuited at the other. The propagation constant of a lossy transmission line is a complex number $\gamma = \alpha + j\beta$, where α is the attenuation constant [in nepers per meter (Np/m)] and β is the phase constant [in radians per meter (rad/m)]. When the attenuation is relatively small, the transmission line Q factor is defined as the ratio [1, p. 231]:

$$Q = \frac{\beta}{2\alpha} \tag{15}$$

Since Q is a dimensionless quantity, it is more convenient to specify the losses of a transmission line by its Q , rather than in terms of decibels (or nepers) per meter (or per 100 ft, as many manufacturers prefer to do). Typically, microstrip transmission lines have a Q factor of the order of 10^2 or more, and the solid-metal coaxial lines and waveguides of the order of 10^3 – 10^4 , depending on frequency, size of the cross section, and surface finishing.

4. TRANSMISSION-TYPE MEASUREMENT

Suppose that a manufacturer of the microstrip substrate wants to measure the Q factor of a transmission line fabricated from her material. She would probably create a half-wavelength resonator two-port, something like the one shown in Fig. 9a. Port A is the input, and port B is the output. The network analyzer is connected at both sides, and the transmission coefficient S_{21} is measured. The equivalent circuit of such a measurement is shown in Fig. 9b. For the sake of simplicity, the coupling loss resistors on the input and output sides have been ignored, and both reactances X_{s1} and X_{s2} are shown to be of capacitive nature.

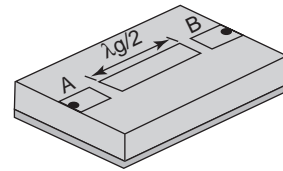
As before, one can change a Thevenin equivalent into a Norton equivalent, and obtain Fig. 9c. Suppose that the observer at port 3 (the resonator port) wears very special tinted glasses, tuned to the resonant frequency of the loaded resonator. He will not see any susceptances, because they cancel each other at that frequency. All that he will see is the three conductances shown in Fig. 9d. Since they are connected in parallel, the corresponding powers are proportional to the conductance values, and one can therefore define the input and output coupling coefficients as follows:

$$\kappa_1 = \frac{G_{ex1}}{G_0} = \frac{Q_0}{Q_{ex1}}; \quad \kappa_2 = \frac{G_{ex2}}{G_0} = \frac{Q_0}{Q_{ex2}} \tag{16}$$

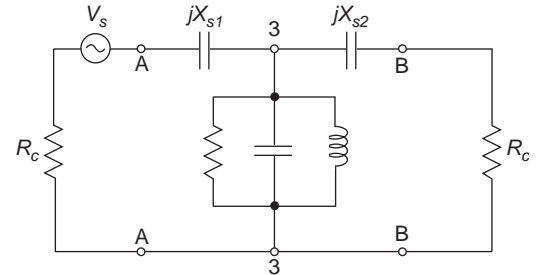
The overall coupling coefficient for this two-port resonator is the sum of the two:

$$\kappa = \kappa_1 + \kappa_2 \tag{17}$$

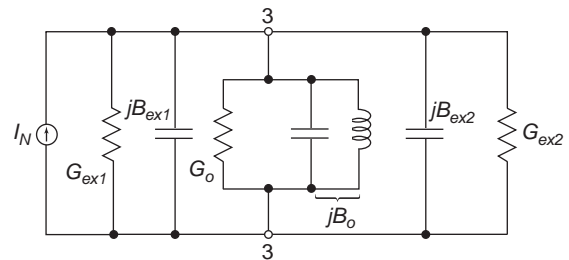
The magnitude of the forward transmission gain S_{21} displays the bell-shaped curve as a function of frequency, indicated in Fig. 10. The loaded Q of the system is



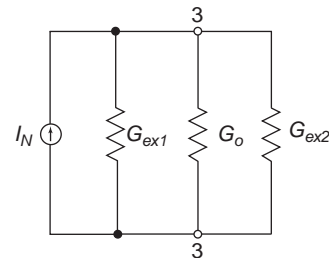
(a)



(b)



(c)



(d)

Figure 9. (a) Microstrip two-port resonator; (b) equivalent circuit of the resonator from Fig. 9a; (c) Norton's equivalent of the equivalent circuit from Fig. 9b; (d) equivalent circuit at the loaded resonant frequency.

inversely proportional to the difference between the 3 dB frequencies f_1 and f_2 at each side of the resonance:

$$Q_L = \frac{f_0}{f_2 - f_1} \tag{18}$$

Now that Q_L has been determined, one needs to find κ . That can be computed from magnitude S_{21} at the center frequency. It follows from Fig. 9d that the magnitude of S_{21} at the resonant frequency is

$$S_{21}(f_0) = \frac{2\sqrt{\kappa_1\kappa_2}}{1 + \kappa_1 + \kappa_2} \tag{19}$$

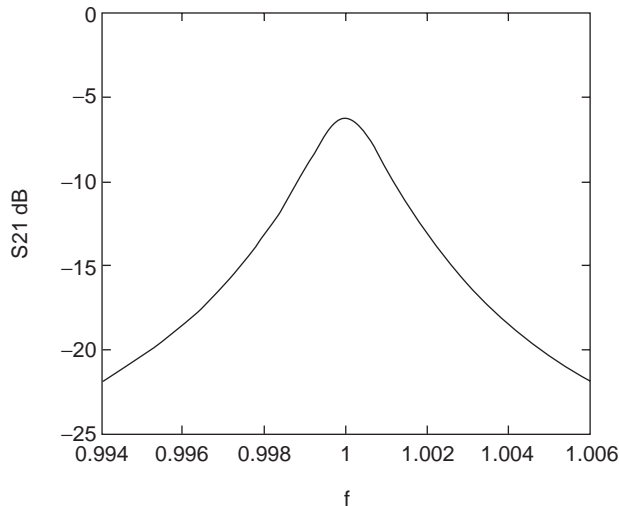


Figure 10. Forward transmission gain of the circuit from Fig. 9c.

Through a careful fabrication procedure, one can make the input and output airgaps equal to each other, so that

$$\kappa_1 = \kappa_2 \quad (20)$$

For such a symmetrical coupling, one obtains

$$\kappa = 2\kappa_1 = \frac{S_{21}(f_0)}{1 - S_{21}(f_0)} \quad (21)$$

and when this is substituted into (7), the unloaded Q can be computed as follows:

$$Q_0 = \frac{Q_L}{1 - S_{21}(f_0)} \quad (22)$$

This is the unloaded Q of the microstrip resonator, the number that the manufacturer of the substrate wanted to know.

Usually, the magnitude of $S_{21}(f_0)$ is expressed in decibels and called insertion loss α . Since S_{21} of a passive circuit is always smaller than unity, α is a negative number. Then, to compute $S_{21}(f_0)$, one uses the following expression:

$$S_{21}(f_0) = 10^{\alpha/20} \quad (23)$$

For the transmission-type measurement to be accurate, condition (20) must be satisfied, requiring that the input and output couplings equal each other. In this measurement, there is no possibility of verifying this equality; one must trust that the mechanical tolerances are tight enough to ensure equality. Another important factor to keep in mind is that the accuracy is seriously reduced when coupling is larger than critical. This happens because $S_{21}(f_0)$ approaches unity as the coupling strengthens. Therefore, the denominator of (22) becomes a difference of two almost equal numbers, so that even a small error in $S_{21}(f_0)$ will cause a large error in Q_0 (even though Q_L has been measured accurately). A detailed analysis of uncertainty in the transmission-type measurement can be found in Ref. 6.

5. REFLECTION-TYPE MEASUREMENT

For this measurement, the resonator needs only one accessible port. When the network analyzer is attached to this port, the equivalent circuit looks the same as shown in Fig. 3a. The measurement procedure is well documented in microwave measurement handbooks such as those by Ginzton [2], Sucher and Fox [3], or Matthaei et al. [4]. Although these books were written before the first network analyzer was produced, the principles involved remain unchanged. With few modifications, the reflection-type measurement can be performed with a network analyzer [7]. The beauty of this measurement is a perfect circle (so-called Q circle) that the measured reflection coefficient, plotted on a Smith chart, describes as a function of frequency.

Figure 11 shows a measured reflection coefficient S_{11} (a complex number) as function of frequency. The center of the Q circle is rotated by an angle θ with respect to the real axis of the Smith chart. Two particular circuit elements from Fig. 3a may cause this rotation: (1) the length of the transmission line l between the coupling loop and the reference position (input coaxial connector) rotates S_{11} by an angle $-2\beta l$, where β denotes the propagation constant of the line; then (2) the reactance X_s rotates (and also shrinks) the circle, as will be discussed in Section 7. Anyway, the rotation is of no importance for the determination of Q_L and κ . To determine the value of Q_L , it is necessary to identify three points on the Q circle. As shown in Fig. 11, the first of those points is center frequency f_L ($\cong f_0$). The other two frequencies, f_1 and f_2 , belong to the two points inclined by $\phi = 45^\circ$ on each side of the centerline. Then, the loaded Q is computed by (18).

To find the coupling coefficient, one has to measure the diameter d of the Q circle. Weakly coupled resonators will produce small Q circles and strongly coupled resonators, large ones. The equation for computing the coupling coefficient κ from the measured value of d is [7]

$$\kappa = \frac{1}{(2/d) - 1} \quad (24)$$

The unit of length for measuring d is the radius of the Smith chart. Thus, when $d = 1$, point f_L is located at the center of the Smith chart and the coupling coefficient is $\kappa = 1$ (critical coupling).

Thus, Ginzton's reflection-type measurement of Q is also a three-point method. In its original version, the Q circle was drawn by hand on the Smith chart point by point. The points were identified by their corresponding frequencies. To find the frequencies of $\phi = \pm 45^\circ$, it was necessary to graphically construct a linear scale for frequencies perpendicular to the $\phi = 0$ line, and then interpolate between the nearest measured points [2]. These constructions are nowadays performed numerically by the data processing procedures that are described in Section 8.

The reflection-type measurement can also be applied to transmission-type cavities [8]. In Fig. 12a, port 2 is terminated in a matched load R_c , and the reflection-type measurement is performed on reflection coefficient S_{11} . The measured results are denoted Q_{L1} and κ_{m1} . In

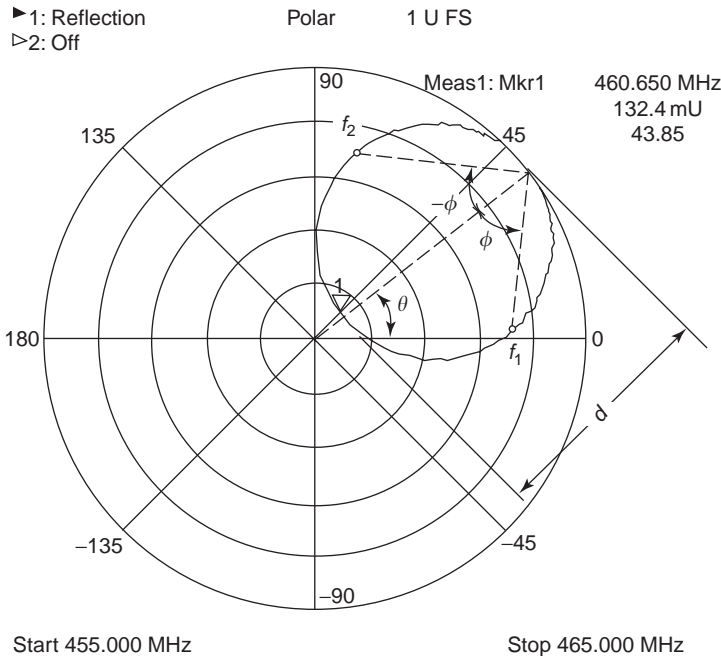


Figure 11. Network analyzer display of the Q-factor measurement by Ginzton's method.

Fig. 12b, port 1 is terminated in a matched load, and the reflection-type measurement is performed on reflection coefficient S_{22} . The results are Q_{L2} and κ_{m2} . In both measurements, the cavity is loaded by characteristic impedance at both ports, so values Q_{L1} and Q_{L2} should come out to be the same. Their difference provides information on how accurate the measurement is. The input and output coupling coefficients are then obtained as follows:

$$\kappa_1 = \kappa_{m1} \frac{1 + \kappa_{m2}}{1 - \kappa_{m1}\kappa_{m2}} \quad (25)$$

$$\kappa_2 = \kappa_{m2} \frac{1 + \kappa_{m1}}{1 - \kappa_{m1}\kappa_{m2}} \quad (26)$$

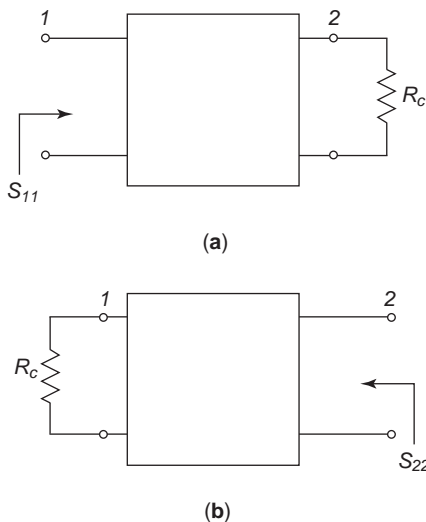


Figure 12. Reflection-type measurement of a transmission-type resonator: (a) measuring S_{11} , (b) measuring S_{22} .

Unlike the insertion loss procedure from Section 4, this procedure does not require the two coupling coefficients to be equal to each other. In fact, the procedure yields both values κ_1 and κ_2 , which can then be substituted in (17), and then the unloaded Q follows from (7).

6. REACTION-TYPE MEASUREMENT

When a dielectric resonator is mounted close to a microstrip transmission line so that it forms a two-port, it is possible to measure the Q factor by connecting the network analyzer to both ends of the microstrip (points A and B in Fig. 13). This configuration is called the *reaction-type measurement of Q factor*, and it was proposed by Podcameni et al. [9], and analyzed in more detail by Khanna and Garault [10].

The measured value of S_{11} , shown on the polar display of the network analyzer, also displays Q circles, and the stronger the coupling, the larger the diameter of the Q circle. Figure 14a shows several circles for couplings κ between 0.5 and 2. Also, the figure shows $\phi = \pm 45^\circ$ lines to read frequencies f_1 and f_2 for the determination of Q_L . Likewise, if the transmission coefficient S_{21} is observed on the polar display shown in Fig. 14b, the Q circles are clearly visible, but bunched toward the right-hand side. In both figures, all the circles are about half the size of those

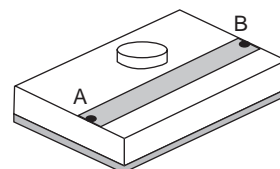


Figure 13. Two-port resonator suitable for the reaction-type measurement of Q .

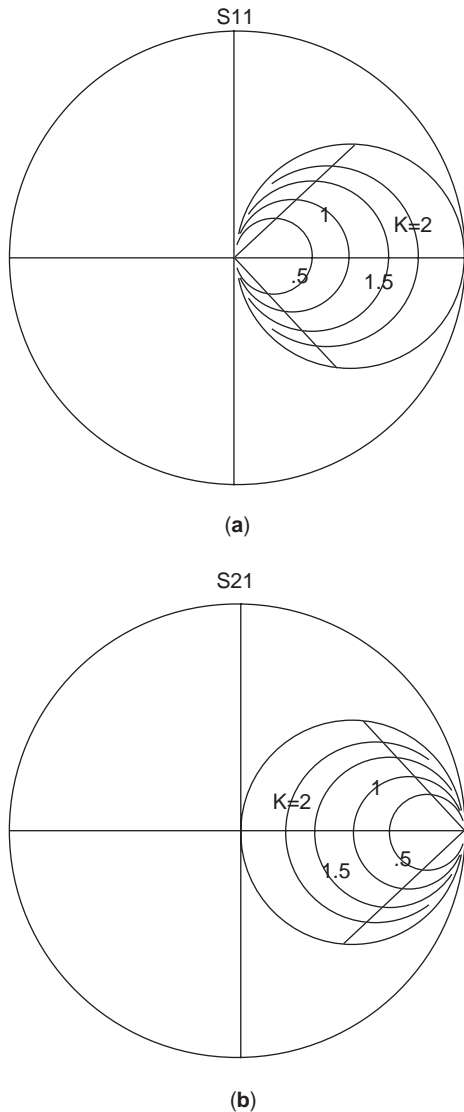


Figure 14. (a) Typical S_{11} circles in a reaction-type measurement; (b) typical S_{21} circles in a reaction-type measurement.

in the reflection-type measurement. For instance, the largest theoretically possible diameter of the Q circle for the reaction-type measurement is $d=1$ (for an infinitely strong coupling), and for the critical coupling, the diameter is $d=0.5$. Although the resolution of the measurement may be reduced because of the smaller circles, this is nevertheless a convenient procedure, because the resonator is mounted in exactly the same environment as will be used in a typical oscillator or filter design.

Reference 10 also describes a procedure for scalar reaction-type measurements, using only the amplitudes of S_{11} and S_{21} for determining the loaded and unloaded Q .

7. THE ROLE OF X_s

According to elementary circuit theory, the value of external susceptance G_{ex} , loading the resonator in Fig. 3c, is

given by

$$G_{ex} = \frac{R_c + R_s}{(R_c + R_s)^2 + X_s^2} \tag{27}$$

Therefore, the coupling coefficient, as defined by (6), becomes

$$\kappa = \frac{G_{ex}}{G_0} = \frac{R_0}{R_c} \cdot \frac{1 + \frac{R_s}{R_c}}{\left(1 + \frac{R_s}{R_c}\right)^2 + \left(\frac{X_s}{R_c}\right)^2} \tag{28}$$

If (X_s/R_c) and (R_s/R_c) are negligibly small quantities, then the coupling coefficient is simply

$$\kappa = \beta = \frac{R_0}{R_c} \tag{29}$$

The symbol β has traditionally been used to denote the coupling coefficient when the equivalent circuit does not contain the series reactance X_s [2-4,9,10]. For the full equivalent circuit, which also takes into account that reactance, it is safer to use a new symbol, κ , based on the definition of the coupling coefficient derived from a ratio of powers, as in (6). Furthermore, symbol β could be confused with the phase constant of the transmission line.

To demonstrate the influence of X_s on the Q -circle size and position, the reflection coefficient as "seen" by the network analyzer at port 1 in Fig. 3a has been computed for several values of X_s . For the sake of simplicity, the coupling losses were ignored ($R_s = 0$) and the length of the transmission line was set to zero. The characteristic impedance of the line was set to $R_c = 1$, and the resonator losses were represented by $R_0 = 1.5$. Four different values of X_s were shown: $X_s = 0, 0.5, 1, 2$. The resulting Q circles are shown in Fig. 15.

For the vanishing reactance, $\kappa = \beta = 1.5$, so that both definitions of the coupling coefficient give the same result. The Q circle is centered on the real axis, and its diameter is $d = 1.2$. The difference between the two definitions

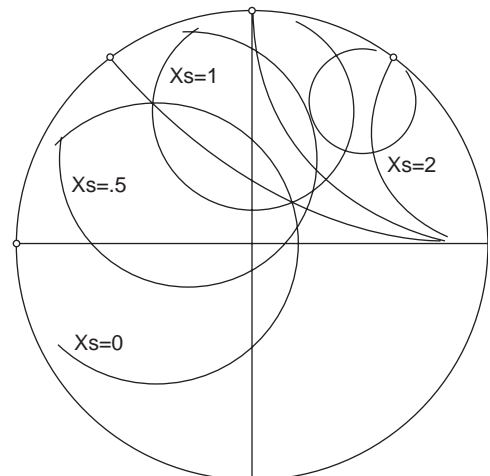


Figure 15. Input reflection coefficient for several different values of X_s in Fig. 3.

becomes noticeable for $X_s = 0.5$, because the Q circle is rotated, and its diameter is now only $d = 1.09$. For a large reactance, such as $X_s = 2$, the diameter shrinks further to $d = 0.461$, and the corresponding coupling coefficient is only $\kappa = 0.3$. If definition (29) were used, the coupling coefficient for all four cases would be equal to $\beta = 1.2$.

One has to keep in mind that port 1 is the only terminal that can be either measured or incorporated into an external circuit, such as an oscillator or a filter. Port 3 is simply not amenable to any measurement. There is no such thing as an observer who can sneak into the resonator, sit on port 3, and tell us how big X_s is. A practical answer to this dilemma is to accept the coupling coefficient such as predicted by size d of the measured Q circle. To avoid the apparently impossible task of finding the accurate value of X_s , one should allow the length of the transmission line to be increased by the amount needed to rotate the observed Q circle back to the real axis. At this new reference position (which were previously called “the detuned short position”), one may use the equivalent circuit without X_s . At the same time, one should be aware that the loaded resonant frequency f_L is theoretically different from the unloaded resonant frequency f_0 . This difference can be ignored for all practical purposes, at least within the first three digits of f_0 . For the high- Q resonators, the loaded resonant frequency f_L is practically identical with the unloaded resonant frequency f_0 . The relationship is expressed as follows [16]:

$$f_0 = f_L \left(1 - \frac{\kappa X_s}{2Q_0 R_c} \right) \quad (30)$$

As an example, for a critically coupled resonator with $Q_0 = 1000$, having a normalized value of coupling reactance $(X_s/R_c) = 1$, the two frequencies differ by 0.05%.

The role of coupling resistance R_s has a different effect. Specifically, R_s detaches the Q circle from the outer rim of the Smith chart. This fact is used in the curve-fitting procedure to estimate the severity of coupling losses.

8. CURVE-FITTING PROCEDURES

Common to all the measurement procedures described until now is the fact that one has to measure manually some S parameters at frequencies f_0 , f_1 , and f_2 and then compute the values of Q_L and κ . These procedures may commonly be called “three-point procedures.” They were all developed during the era of analog instrumentation.

Today’s network analyzers are all computer-controlled and therefore digital instruments. They can measure almost instantly up to 1601 frequency points and either store them, or deliver them to a file to be read by another computer. Data processing can then be used to determine the center and the diameter of the circle on the Smith chart; interpolate the exact position of frequency points f_0 , f_1 , and f_2 ; and utilize any appropriate equation for an accurate computation of Q_L and κ . The data processing is usually based on a curve-fitting procedure that attempts to fit the data to a circle on a complex plane [11–15].

Typically, 50 or more points of the measured scattering parameter S_{11} (or S_{21}) are used.

The circle on a complex plane can be described by a fractional linear function of real variable t as follows:

$$S_{11}(t) = \frac{a_1 t + a_2}{a_3 t + 1} \quad (31)$$

Variable t is the relative frequency detuning with respect to the loaded resonant frequency f_L defined as follows:

$$t = 2 \frac{f - f_L}{f_0} \quad (32)$$

Although (32) requires f_0 in the denominator, very little error is committed by using f_L instead. The loaded resonant frequency f_L is determined as the point closest to the center of the Smith chart. The weighted least-square curve fitting is then used to find the three complex coefficients a_1 – a_3 [14]. From the three coefficients, one can determine the needed parameters Q_L , κ , and Q_0 . For instance, if the coupling losses R_s are negligible, the loaded Q factor is

$$Q_L = \text{Im}(a_3) \quad (33)$$

and the diameter of the Q circle is

$$d = \left| a_2 - \frac{a_1}{a_3} \right| \quad (34)$$

With the use of (24) one can now compute the coupling κ , and then the unloaded Q follows from (7).

A side benefit of a curve-fitting procedure is the fact that there are many more measured data than needed for determining the three unknown coefficients. The problem is thus overdetermined, which allows the possibility of statistically estimating the standard deviations for all the quantities of interest [17]. Figure 16 shows a display of the software QZERO for Windows¹ with the best-fit circle and the estimated values for the loaded and unloaded Q factors, coupling, and the loaded resonant frequency. The estimated values are also accompanied by their uncertainties (standard deviations). It should be emphasized that these uncertainties describe only the random errors and not the systematic errors. The systematic errors of various models of network analyzers differ from each other, and they also depend on the frequency of operation. An analysis of systematic errors for the reflection-type curve fitting-method can be found in Ref. 18.

As mentioned in the previous section, the coupling losses (modeled by the presence of resistor R_s) can cause the Q circle to be detached from the perimeter of the Smith chart. Figure 17 shows the effect of coupling losses when

¹QZERO for Windows software, version 2.2, Vector Forum, Oxford, MS. Student version is distributed free to students and faculty at educational institutions by sending an e-mail message to eedarko@olemiss.edu. The full version may be obtained from Vector Forum via telephone at +1-662-234-4287.

Q Zero for windows (c) 2000 D. Kajfez

data file name = M415 .dac
 8/04/2003 16:01:15
 N= 51
 lossy coupling
 QL= 4585.7 ± 6.8
 Q0= 7500.7 ± 15.6

K= 0.635680 ± 0.00239
 KS= 0.004936
 FL= 3.38318777E+00

Plot 10
 Port 1 of 1

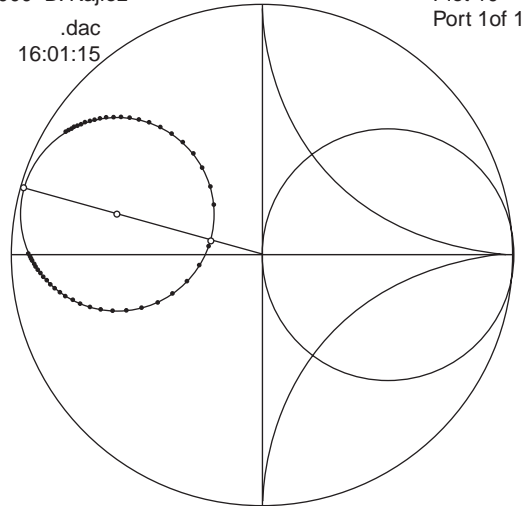


Figure 16. Measured data analyzed by the curve-fitting procedure.

$R_s = 0.04$, $X_s = 0.8$, $R_0 = 0.75$, and $R_c = 1$. Once the center and diameter d of the Q circle are known, it is possible to evaluate diameter d_2 of an auxiliary circle that is tangential to both the Q circle and the Smith chart perimeter. Diameter d_2 is now used to find the overall coupling coefficient κ , which includes also the coupling losses [17]:

$$\kappa = \frac{1}{\frac{d_2}{d} - 1} \quad (35)$$

For the special case when coupling losses are negligible, the auxiliary circle coincides with the perimeter of the Smith chart, so that $d_2 = 2$, and (35) becomes identical with (24).

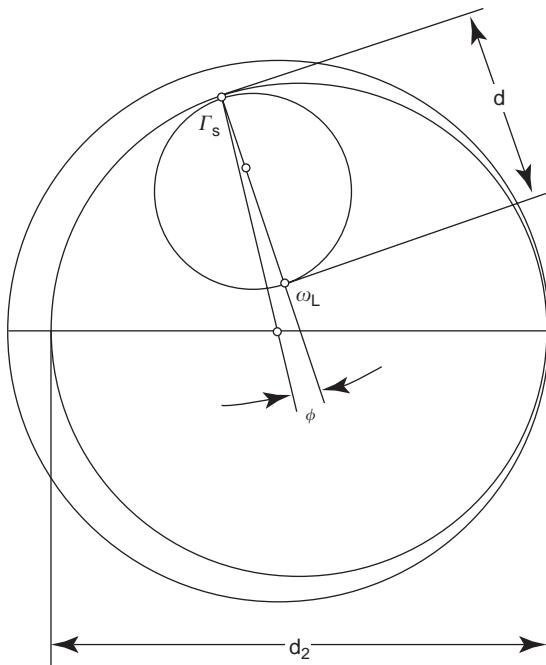


Figure 17. Q -circle in the presence of coupling losses.

For carefully manufactured resonators, the coupling losses should be small, of the order of $R_s/R_0 < 0.01$. The overall coupling coefficient of a reflection type resonator now consists of two parts:

$$\kappa = \kappa_c + \kappa_s \quad (36)$$

where κ_c is the coupling that describes the power loss in external resistance R_c , and κ_s describes the power loss in the resistance R_s of the coupling mechanism. The ratio of κ_s to κ_c is proportional to normalized coupling loss resistance

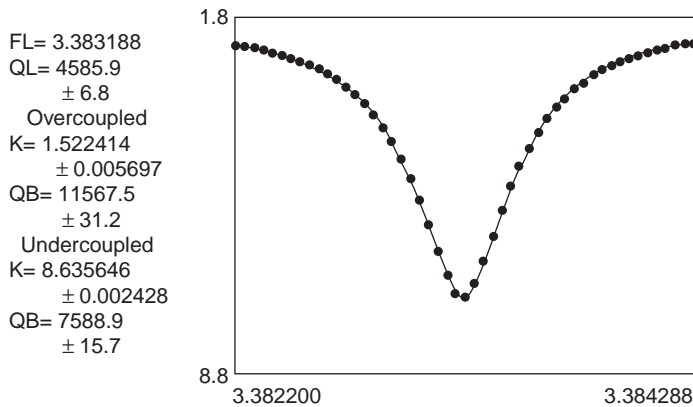
$$\frac{\kappa_s}{\kappa_c} = \frac{R_s}{R_c} \quad (37)$$

The value of $\kappa_s = 0.00493$ is also shown on the display of QZERO in Fig. 16. This number is clearly an approximation, and the program does not attempt to find its standard deviation. Nevertheless, the value may be of use to a design engineer who wants to compare several different versions of coupling to the same resonator. In the example shown, approximately 0.5% of the total power is dissipated in the resistance of the coupling loop.

When a vector network analyzer is not available, it is possible to use the measured data taken with a scalar network analyzer and perform the data fitting to a theoretical resonance curve. Program SCALARQ² is intended for processing the amplitude (but not the phase) of reflection coefficient S_{11} . The theory of operation can be found in Ref. 19. An example of the display obtained by SCALARQ can be seen in Fig. 18. This example utilizes the same input data as in Fig. 16, except that the phase information is ignored. The measured data points are shown by black dots, and a solid line shows the best-fit resonant curve $|S_{11}(f)|$. Since the phase of the reflection coefficient is not known, one cannot plot the results on a Smith chart. Thus, one cannot tell whether this reflection coefficient represents an overcoupled or an undercoupled case. There are

²The DOS program SCALARQ is incorporated with the book *Q Factor* [17].

13:58:38.18 89/14/98 Scalar Q (c)1998 D. Kajfez M415.DAC



<M>ARKER. &W, OR <E>ND ?

Figure 18. Curve-fitting procedure for scalar valued data.

two possible interpretations of the measured data, and the display of SCALARQ shows both of them. Another, independent, experiment must be performed in order to decide which of the two answers is correct. Except for this limitation, the accuracy of the results obtained by SCALARQ is of the same order as the one obtained by QZERO. The resulting $Q_0 = 7500.9$ for the undercoupled case agrees very well with the value $Q_0 = 7500.7$ obtained in Fig. 16.

BIBLIOGRAPHY

1. S. A. Schelkunoff, *Electromagnetic Waves*, Van Nostrand, New York, 1943.
2. E. L. Ginzton, *Microwave Measurements*, McGraw-Hill, New York, 1957, Chap. 9.
3. M. Sucher and J. Fox, eds., *Handbook of Microwave Measurements*, Polytechnic Press, New York, 1963, Chap. 7.
4. G. L. Matthaei, L. Young, and E. M. T. Jones, *Microwave Filters, Impedance-Matching Networks, and Coupling Structures*, McGraw-Hill, New York, 1964, Chap. 11.
5. J. Mazierska, Dielectric resonator as possible standard for characterization of high temperature superconducting films for microwave applications, *J. Supercond.* **10**(2):73–84 (1997).
6. D. Kajfez, S. Chebolu, M. R. Abdul-Gaffoor, and A. A. Kishk, Uncertainty analysis of the transmission-type measurement of Q-factor, *IEEE Trans. Microwave Theory Tech.* **47**(3): 367–371 (March 1999).
7. D. Kajfez and E. J. Hwan, Q-factor measurement with network analyzer, *IEEE Trans. Microwave Theory Tech.* **MTT-32**:666–670 (July 1984).
8. D. Kajfez, Reflection-type Q factor measurement of transmission-type cavities, *Proc. 2000 Asia-Pacific Microwave Conf.* Sidney, Dec. 2000, pp. 449–452.
9. A. Podcameni, L. F. M. Conrado, and M. M. Russo, Unloaded quality factor measurement for MIC dielectric resonator application, *Electron. Lett.* **17**:656–658 (1981).
10. A. P. S. Khanna and Y. Garault, Determination of loaded, unloaded and external quality factors of a dielectric resonator coupled to a microstrip line, *IEEE Trans. Microwave Theory Tech.* **MTT 31**:261–264 (March 1983).
11. W. P. Wheless and D. Kajfez, Microwave resonator circuit model from measured data fitting, *1986 IEEE MTT-S Symp. Digest*, Baltimore, June 1986, pp. 681–684.
12. M. C. Sanchez, E. Martin, and J. Zamarro, New vectorial automatic technique for characterisation of resonators, *IEE Proc. H.* **136**:145–150 (April 1989).
13. C. P. Hearn, P. G. Bartley, and E. S. Bradshaw, A modified Q-circle measurement procedure for greater accuracy, *Microwave J.* **36**:108–113 (Oct. 1993).
14. D. Kajfez, Linear fractional curve fitting for measurement of high Q factors, *IEEE Trans. Microwave Theory Tech.* **42**:1149–1153 (July 1994).
15. K. Leong and J. Mazierska, Precise measurements of the Q factor of dielectric resonators in the transmission mode—accounting for noise, crosstalk, delay of uncalibrated lines, coupling loss, and coupling reactance, *IEEE Trans. Microwave Theory Tech.* **50**(9):2115–2127 (Sept. 2002).
16. D. Kajfez, Correction for measured resonant frequency of unloaded cavity, *Electron. Lett.* **20**(2):81–82 (Jan. 19, 1984).
17. D. Kajfez, *Q Factor*, Vector Forum, Oxford, MS, 1994.
18. D. Kajfez, Random and systematic uncertainties of reflection-type Q-factor measurement with network analyzer, *IEEE Trans. Microwave Theory Tech.* **51**(2) (Feb. 2003).
19. D. Kajfez, Q factor measurement with a scalar network analyzer, *IEE Proc. Microwave Antenn. Propag.* **142**:369–372 (Oct. 1995).

FURTHER READING

- R. Beringer, Resonant cavities as microwave circuit elements, in C. G. Montgomery, R. H. Dicke, and E. M. Purcell, eds., *Principles of Microwave Circuits*, Dover, New York, 1965.
- E. Collin, *Foundations for Microwave Engineering*, McGraw-Hill, New York, 1966, Chap. 7.
- S. Ramo, J. R. Whinnery, and T. Van Duzer, *Fields and Waves in Communication Electronics*, Wiley, New York, 1965.
- D. F. Hanson, “Microwave Resonators,” in D. Kajfez and P. Guillon, eds., *Dielectric Resonators*, Noble Publishing, Atlanta, 1998.

Q-FACTOR MEASUREMENTS

ANDRE LUITEN
University of Western Australia
Nedlands, Australia

1. INTRODUCTION

This article presents a review of both traditional and modern methods of “ Q factor” measurement. Many of the techniques to be described were first developed in order to determine the Q factors of resonances falling in the microwave frequency domain. One thus finds that the language of the microwave engineer has become all pervasive in the field, although the reader should note that the basic principles are just as applicable to measuring the Q factors of radiofrequency, millimeter, infrared, and optical resonators. The article commences with a definition of the Q factor and a description of the experimental parameters that need to be measured so as to determine the Q factor of a resonance. The various methods for measuring these parameters will then be outlined, including the particular advantages and disadvantages of a technique, the equipment required for the measurement, and its potential for accuracy. Finally, some of the latest developments in the field of Q measurement will be presented.

Measurement of the Q factor involves measurement of the defining characteristics of a resonance. Electromagnetic resonance will be found in any device that is able to store oscillatory energy for a length of time that is long compared to the period of oscillation of the electromagnetic energy. The Q factor is a measure of the “quality” of the resonance in the sense that a high- Q -factor resonance is one in which the energy dissipation rate is low, or equivalently that the energy storage time is long.

Clearly the concept of energy storage requires that the device both prevent the escape of energy into the environment, as well as to minimize conversion of this electromagnetic energy into other forms of energy. Microwave resonators make use of two main methods to trap energy: (1) storage of the fields in a volume that is surrounded by conductive material and (2) storage inside a high-dielectric material by total internal reflection at the dielectric surface. Resonators using method 1 are termed *microwave cavities*; those using method 2 are termed *dielectric resonators*. It is also possible, of course, to build hybrid resonators that use both mechanisms to trap energy. Any electromagnetic field pattern that satisfies Maxwell’s equations in the resonator volume and satisfies the boundary conditions imposed by the resonator surfaces, is called a *normal mode* or *resonance* of the resonator [1].

For energy to enter and leave a resonator, there must be some electrical or magnetic pathway between the resonator and an external transmission line. This pathway is most commonly provided by either a magnetic loop probe or electric stub probe on the end of a coaxial transmission line that protrudes into a cavity resonator or a direct opening in the metallic wall between a cavity and a waveguide transmission line (iris coupling), or by placing a dielectric resonator in close proximity to a microstrip

conductor (evanescent field or reactive coupling). The number of coupling ports, as well as the type of coupling used on those ports, is used to further characterize microwave resonators. Resonators with a single port using probe or iris coupling are termed *reflection resonators*. Resonators with two or more ports using probe or iris coupling are termed *transmission resonators*. Two-port resonators making use of reactive coupling are termed *reactive* or *absorption resonators*.

Microwave resonators, and accurate Q measurements to characterize those resonators, are vitally important in microwave engineering and physics:

1. Filters can be constructed from resonators because of their selective behavior in the frequency domain. A filter is a device that can transmit or reflect a desired signal while rejecting other nearby unwanted signals.
2. Resonators are widely used as oscillator tank circuits as well as for the study of materials in high electromagnetic fields. Both of these applications arise because of the energy enhancement qualities of resonators.
3. Measurements of electrical conductivity can be performed by an accurate measurement of the Q factor of a microwave resonator that has been constructed of the material of interest [2,3]. This measurement technique has undergone a renaissance with great interest in measurements on high-temperature superconductors [4].
4. Microwave properties of materials can be measured by their impact on the Q factor and resonant frequency of a microwave resonance when they are loaded into a microwave resonator [1,5,6]. Highly sensitive measurements of the Q and resonant frequency are required to gain accurate material characterization. The dielectric loss and dielectric constants of fluids and gases have been reported by a number of workers using this method [7,8]. Magnetic and electrical properties of solids have also been reported [9–12].
5. Oscillators that have a high frequency stability in the short term require high- Q resonators: the best frequency stabilities ever reported are by a superconducting cavity microwave oscillator operating near 2 K with a Q factor around 10^{11} [13], and by a sapphire dielectric resonator oscillator at 6 K with a Q above 4×10^9 [14].

Microwave Q factors of interest range from a low value of 2 [15] up to 10^{11} for an electropolished superconducting cavity at cryogenic temperatures [13]. Coupling factors (see below) to these resonances can vary from 10^{-3} for extremely lightly coupled wavemeter resonators up to 10^3 for superconducting cavities at cryogenic temperatures. No single technique can be expected to operate over this full range and always give high-resolution and high-accuracy measurements. The desire to generate accurate measurements over this full range of interest has led to the large number of Q measurement methods reported here.

Many traditional methods for obtaining the Q factor have fallen from favor either because of improvements in technology or because the original cumbersome technique can now be circumvented. For example, one of the major reasons for devising time-domain Q -measuring techniques was to avoid difficulties arising from the typically poor frequency stability of microwave signal generators of the time. However, modern quartz-based synthesizer technology provides a frequency stability that is adequate to measure the Q factors of all except the very highest- Q resonators. A second example is found with the very rare use of traditional voltage standing-wave ratio (VSWR) measurement techniques in modern laboratories. These techniques are slow [16] and cumbersome as they require a device to be moved mechanically to perform measurements. Modern network analyzers can make equivalent measurements essentially instantaneously without the need for mechanical changes to the circuit. Nevertheless, traditional Q measurement techniques still have importance because of their simplicity, low-cost instrumentation, and instructional value. For these reasons they will be discussed below. For highly detailed instructions on performing these methods, the reader should refer to excellent descriptions in the classical texts [17,18].

2. DEFINITIONS

The letter Q was first used to describe the ratio of reactance to resistance of low-frequency inductors and capacitors [18]. The widespread technique of describing microwave resonators in terms of low-frequency circuit elements led to an association of the letter Q with the ratio of reactance to resistance in resonant circuits. A simple calculation [see Eq. (3)] shows that there is also a close relationship between Q and the time for energy to dissipate in such an equivalent circuit. This led to the incorrect but widespread belief that Q is the initial letter of the expression “quality factor” (abbreviated as Q factor), a term related to the length of time that a resonant circuit stores energy. The agreed modern definition of the Q factor of any general resonant circuit (including electronic, optical, and mechanical resonators) is [18] 2π multiplied by the ratio of stored energy to the energy dissipated per cycle or expressed symbolically

$$Q = \frac{2\pi U}{\Delta U} \tag{1}$$

where U is the total energy of the system and ΔU is the energy dissipated in a cycle. This equation can be solved to determine how the stored energy decays as a function of time. The energy dissipated in one cycle can be written as

$$\Delta U = \frac{\partial U}{\partial t} \frac{1}{f_0} \tag{2}$$

where f_0 is the resonant frequency. Substituting (2) into (1) the time dependence of U is found as

$$U(t) = U_0 e^{-(\omega_0/Q)t} \tag{3}$$

where U_0 is the initial energy of the resonant system and $\omega_0 \equiv 2\pi f_0$ is the angular resonant frequency. From a simple inspection of Eq. (3) another more practical definition of Q can be stated as: 2π times the number of cycles required for the energy in the system to decay to $1/e$ of some initial amount, or

$$Q = \frac{2\pi\tau}{T_0} \tag{4}$$

where τ is the time taken for the energy to decrease to $1/e$ of its value (conventionally called the *ringdown time*) and $T_0 \equiv 1/f_0$ is the resonant period. As will be seen below, direct use is made of expression (4) in determining Q factors with one of the time-domain measurement techniques. All other measurement techniques make use of the response of the resonator to forced oscillation. To understand these techniques, we will need to derive expressions that will describe the behavior of the resonator under the influence of an external field.

2.1. Microwave Resonators

A diagram of a transmission microwave resonator is given in Fig. 1a. The figure shows an empty metallic cavity where a coupling between the resonator and some external transmission lines is provided by small openings in the walls of the cavity. A general low-frequency analog to this microwave resonator, its coupling arrangement, and the external transmission lines is given by Fig. 1b. In general, such a resonant cavity has an infinite number of normal modes, each represented by a parallel LCR circuit [19]. The k th resonant frequency is given by the expression

$$(f_0)_k = \frac{1}{2\pi\sqrt{L_k C_k}} \tag{5}$$

and the unloaded Q of the k th resonance can be determined by substituting the energy dissipation provided by R_k and the energy storage provided by C_k and L_k into Eq. (1):

$$(Q_u)_k = R_k \sqrt{\frac{L_k}{C_k}} \tag{6}$$

The iris coupling has been modeled as a transformer of an arbitrary turns ratio [17,20]. X_{e1} and R_{e1} are the equivalent reactance and shunt resistance of the input coupling network and transmission line, respectively, while X_{e2} and R_{e2} are the equivalent parameters for the resonator output coupling network. R_s is the series impedance of the signal generator, and R_L is the equivalent load resistance of the equipment that is monitoring the resonator. Any measurement of the resonant system represented by Fig. 1b will yield a result that is a combination of the properties of the transmission line and the coupling mechanism as well as the resonator. However, under certain conditions it is possible to determine the Q of a particular mode while ignoring the influences of the load, the coupling mechanism, the transmission line, and other modes. In this case the external impedances can be transformed into the resonant circuit giving the circuit shown in Fig. 1c. This circuit is far more amenable to analysis and is the resonance model

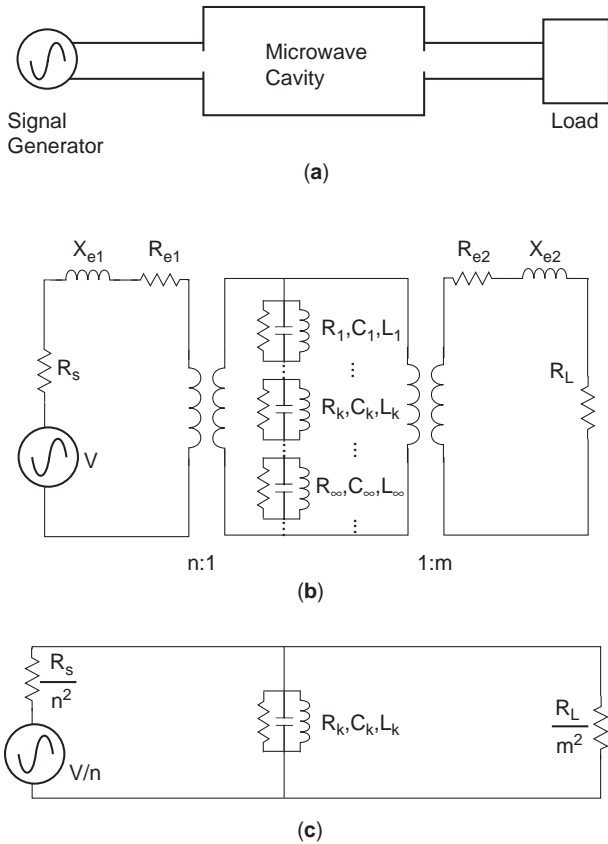


Figure 1. (a) A block diagram of a microwave cavity resonator with iris coupling on the input and output ports. The source and load are coupled to the cavity with waveguide transmission lines. (b) An equivalent LCR circuit for the microwave system in Fig. 1a. The infinite number of possible resonant modes of the cavity resonator is represented by an infinite series of LCR circuits: $(R_1, C_1, L_1), \dots, (R_k, C_k, L_k), \dots, (R_\infty, C_\infty, L_\infty)$. The input and output coupling networks have been modeled with a series loss (R_{e1}, R_{e2}) and series inductance (X_{e1}, X_{e2}) to factor in any losses or reactance of the coupling network. The source and load series impedance are denoted by R_s and R_L , respectively. The iris coupling has been modeled as a transformer of unknown turns ratio. (c) A simplified version of part (b) in which the traditional assumptions of Q-factor measurement have been made. The coupling reactance and loss are assumed to be zero. The source and load are assumed to be perfectly impedance-matched to the line impedance. All other resonances of the cavity are assumed to be sufficiently far from the resonance of interest that they can be safely ignored. The transformers have been eliminated by transforming the external components into an effective impedance that would be seen by the resonant circuit.

assumed by traditional measurement techniques as it greatly simplifies postmeasurement analysis (attempts were sometimes made to allow for coupling losses, i.e., $R_{e1} \neq 0$ [18]). These simplifications will lead to important errors if the resonator is strongly overcoupled, the Q of the resonance is relatively low, the generator or source is poorly matched to the transmission line or there is an excessive level of reactance in the coupling mechanism or transmission line. For the sake of a simple introduction, we will use the circuit shown in Fig. 1c and reserve discussion of the more complex situation until Section 4.2.

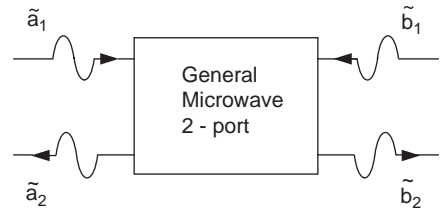


Figure 2. A diagram representing the scattering of microwave voltage waves by a general microwave two-port.

To describe how microwave radiation interacts with a resonator, we will use a scattering matrix formalism. Figure 2 shows a voltage wave \tilde{a}_1 incident on an arbitrary microwave two-port device. The wave is scattered by the two-port, some of its energy going into a reflected wave \tilde{a}_2 and part into a transmitted wave \tilde{b}_2 . We express all three waves as

$$A \exp(j\omega t + \beta z) \tag{7}$$

where ω is the applied angular microwave frequency, A is the voltage amplitude of the wave, β is the propagation constant, and z is the measurement position. We define the resonator scattering terms s_{11} and s_{21} as

$$s_{11} \equiv \frac{\tilde{a}_2}{\tilde{a}_1} \text{ and } s_{21} \equiv \frac{\tilde{b}_2}{\tilde{a}_1} \tag{8}$$

We can, of course, define equivalent parameters for port 2. By substituting Eq. (7) into Eq. (8) we note that s_{11} and s_{21} will depend on the measurement position. This leads to the difficulty that we need to specify the measurement plane each time we quote the resonator scattering parameters. Theoretically we could avoid this difficulty by always referring the measurement to some special preestablished measurement plane, such as the plane that is coincident with the coupling device. However, in practice, always taking measurements at some particular position could pose a great deal of difficulty. Instead we choose to define some special planes that have a well-defined measurable characteristic. If a measurement is made of s_{11} at a frequency that is far from the resonant frequency, we can always find a position on the line that responds as if there were a short circuit or an open circuit on the transmission line. These planes are termed the *detuned short* or *detuned open* positions [17,18,20]. From the *detuned short* position the equivalent low-frequency circuit shown in Fig. 1c is an accurate representation of the real microwave circuit (given that all the assumptions stated above still hold). Modern measurements can avoid this difficulty of determining the reference plane, as will be shown below. The scattering parameters at the *detuned short* position for the circuit shown in Fig. 1c have been calculated as [21,22]

$$s_{11}(\varepsilon) = \frac{\beta_1 - \beta_2 - 1 - jQ_u \varepsilon}{1 + \beta_1 + \beta_2 + jQ_u \varepsilon} \tag{9}$$

$$s_{21}(\varepsilon) \equiv s_{12}(\varepsilon) = \frac{2\sqrt{\beta_1 \beta_2}}{1 + \beta_1 + \beta_2 + jQ_u \varepsilon} \tag{10}$$

where $\varepsilon \equiv (f/f_0) - (f_0/f)$, f is the incident frequency, f_0 is the resonant frequency as defined in Eq. (5), Q_u is the unloaded Q of the resonator as defined in Eq. (6), and β_1 and β_2 are the coupling factors that are defined as the ratio of the internal resonant resistance to the external resistances when transformed into the resonant circuit

$$\beta_1 = \frac{n^2 R_k}{R_s} \quad \text{and} \quad \beta_2 = \frac{m^2 R_k}{R_L} \quad (11)$$

where n is the effective turns ratio of the input coupling mechanism and m is the effective turns ratio of the output coupling mechanism. If $\beta < 1$, a resonator is termed *undercoupled*; if $\beta > 1$, a resonator is termed *overcoupled*; and if $\beta = 1$, the resonator is critically coupled. Equation (9) also applies to single-port reflection resonators if β_2 is set to zero. We note also that the coupling factor represents the ratio of the power dissipated in the relevant external circuit to the power dissipated in the resonator.

It is useful to split expressions (9) and (10) into their real and imaginary parts as this will give us the in-phase response and quadrature phase response of the resonator, respectively. In other words, the real part of Eq. (9) gives us the portion of the reflected wave that is in phase with the incident signal, and the imaginary part will give the fraction of the reflected signal that is $\pi/2$ out of phase with the incident signal:

$$\text{Real}[s_{11}] = \frac{(1 + \beta_1 + \beta_2)(\beta_1 - \beta_2 - 1) - \varepsilon^2 Q_u^2}{(1 + \beta_1 + \beta_2)^2 + \varepsilon^2 Q_u^2} \quad (12)$$

$$\text{Imag}[s_{11}] = \frac{-2\beta_1 \varepsilon Q_u}{(1 + \beta_1 + \beta_2)^2 + \varepsilon^2 Q_u^2} \quad (13)$$

$$\text{Real}[s_{21}] = \frac{2\sqrt{\beta_1 \beta_2}(1 + \beta_1 + \beta_2)}{(1 + \beta_1 + \beta_2)^2 + \varepsilon^2 Q_u^2} \quad (14)$$

$$\text{Imag}[s_{21}] = \frac{-2\sqrt{\beta_1 \beta_2} \varepsilon Q_u}{(1 + \beta_1 + \beta_2)^2 + \varepsilon^2 Q_u^2} \quad (15)$$

An interesting and novel way of summarizing this information is by using a three-dimensional parametric plot of the resonator response as a function of frequency (see Fig. 3). If we make two-dimensional projections of this plot along the principal axes, we will see response curves that are more familiar to the microwave engineer. To display this, we have projected the three-dimensional plot onto the faces of the box in Fig. 3 and then rotated these faces into view. Viewing the curve that has been projected onto the plane perpendicular to the real axis, we see the imaginary response of the resonator (Fig. 3b); looking along the imaginary axis, we observe the real response of the resonator (Fig. 3c); and finally, looking parallel to the frequency axis, we observe a circle—which is termed the “ Q circle” of the resonator (Fig. 3d). This horizontal projection plane is more readily recognized as the Smith chart [23]. The Smith chart gives the magnitude of s_{11} by the distance that a plotted point is from the origin, while the phase of s_{11} (ϕ) is given by the angle that the line joining the point to the origin makes with the real axis. The most important

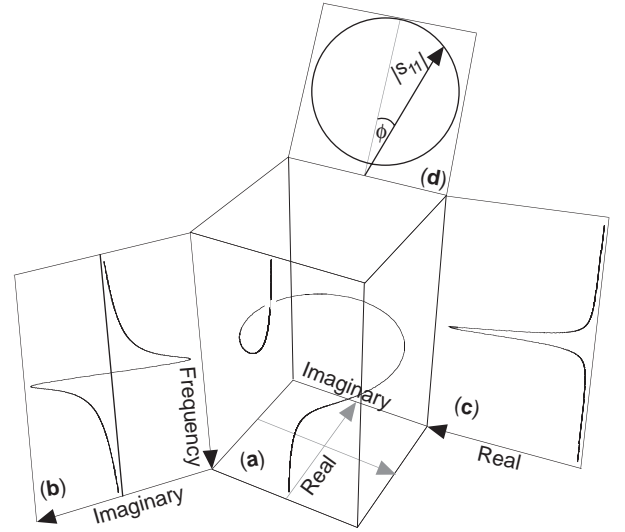


Figure 3. (a) A three-dimensional display of the scattering parameter s_{11} from a reflection resonator. The curve has been projected onto the faces of the box, and these faces have been rotated into view. (b) The imaginary (or quadrature phase) reflection response of the resonator. (c) The real (or in-phase) reflection response of the resonator. (d) The Q circle of the resonator on a Smith chart. The phase and magnitude of the reflection coefficient at a particular frequency are respectively given by the distance of a plotted point is from the origin and the angle it forms with the real axis.

advantage of this three-dimensional description of the resonator response is the clear demonstration of the intimate relationship that exists between the many descriptions of microwave resonators given in the literature: the real and imaginary components of the scattering matrix, the Smith chart, and the magnitude and phase of the response.

Q -factor measurements of two-port microwave resonators frequently employ measurements of the transmitted and reflected power as a function of frequency. In cases of moderate to high Q , the derived frequency variable ε defined above can be simplified with negligible error to

$$\varepsilon \approx \frac{2\Delta f}{f_0} \quad (16)$$

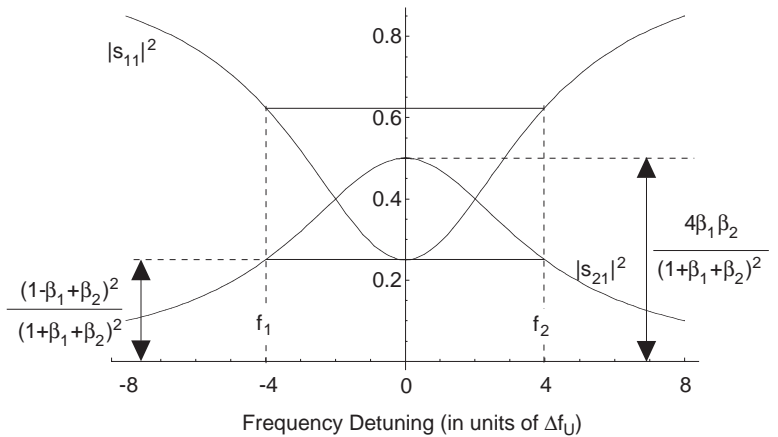
where we define a frequency detuning Δf as $\Delta f \equiv f - f_0$. The squared magnitude of s_{11} and s_{21} (which gives the reflected and transmitted power coefficients, respectively) can be derived from Eqs. (9) and (10) as follows:

$$|s_{11}(\Delta f)|^2 = \frac{(1 - \beta_1 + \beta_2)^2 + 4\left(\frac{Q_u \Delta f}{f_0}\right)^2}{(1 + \beta_1 + \beta_2)^2 + 4\left(\frac{Q_u \Delta f}{f_0}\right)^2} \quad (17)$$

$$|s_{21}(\Delta f)|^2 = \frac{4\beta_1 \beta_2}{(1 + \beta_1 + \beta_2)^2 + 4\left(\frac{Q_u \Delta f}{f_0}\right)^2} \quad (18)$$

Plots of these functions have been given in Fig. 4 together with some important limiting values. Throughout

Figure 4. The power reflection and transmission coefficients of a two-port resonator with $\beta_1=1$ and $\beta_2=2$. The loaded Q of the resonator is given by $Q_L=f_0/(f_2-f_1)$, where f_1 and f_2 are the points at which the power transmission coefficient is half the maximum power transmission, or the points where the power reflection coefficient is the average of the on- and off-resonance power reflection coefficients.



the rest of this article, we will assume that the approximation shown in Eq. (16) can always be made. For simplicity, the argument of the scattering parameter functions will henceforth be just the frequency detuning as shown above.

2.2. Loaded Q (Q_L), Unloaded Q (Q_U), and External Q (Q_E)

There are three distinct Q factors associated with the losses in a microwave circuit. The unloaded Q (Q_U) is the Q factor that would be measured as the electromagnetic coupling to the resonator tended to zero. Thus, it is associated with dissipation that occurs inside the resonator [R_k in Fig. 1c; see also Eq. (6)]. The external Q (Q_e) is the dissipation that occurs external to the resonator but is coupled into the resonance by the coupling to the external circuit (R_s and R_L in Fig. 1c). We can derive an expression for the external Q factors in the same way as we found the unloaded Q factor [Eq. (6)]:

$$Q_{e1} = \frac{R_s}{n^2} \sqrt{\frac{C}{L}} \quad \text{and} \quad Q_{e2} = \frac{R_L}{m^2} \sqrt{\frac{C}{L}} \quad (19)$$

The loaded Q (Q_L) is the Q factor actually measured by the experimenter. It includes the contributions of all losses in the circuit that provide a dissipation mechanism for the resonant energy (both internal and external to the resonant circuit). We can write the relationship between the loaded Q , the unloaded Q , and the external Q factors as follows:

$$\frac{1}{Q_L} = \frac{1}{Q_U} + \frac{1}{Q_{e1}} + \frac{1}{Q_{e2}} \quad (20)$$

Using the definitions of the coupling factors [Eq. (11)] and the definitions of the unloaded and external Q factors [Eqs. (6) and (19)], we can simplify Eq. (20) to

$$Q_u = (1 + \beta_1 + \beta_2)Q_L \quad (21)$$

2.3. Overview of Q-Factor Measurement Techniques

A simplification of some of the preceding expressions can be used to generate a few practical methods to measure the Q factor. From an examination of Eq. (17) we see that

the maximum power transmitted through the resonator occurs when the incident frequency is exactly equal to the resonant frequency. As we move away from the resonant frequency, the transmitted power falls as the square of the frequency detuning. Clearly an important measure of such a resonant feature would be its sharpness. We choose to measure the sharpness of the feature by the frequency difference between the two frequency points that transmit half the maximum power; that is, we need to find the two values of the frequency detuning Δf that satisfy the following equation:

$$|s_{21}(\Delta f)|^2 = \frac{1}{2} |s_{21}(0)|^2 \quad (22)$$

The solutions to this equation are

$$(\Delta f) = \pm \frac{1}{2} \frac{(1 + \beta_1 + \beta_2)f_0}{Q_U} = \pm \frac{1}{2} \frac{f_0}{Q_L} \quad (23)$$

Let us define a new parameter, Δf_L : the loaded half-bandwidth of the resonance that is equal to the positive solution of Eq. (23):

$$\Delta f_L = \frac{1}{2} \frac{f_0}{Q_L} \quad (24)$$

The analysis above suggests a method for measuring Q_L in transmission resonators. By measuring the resonant frequency, the maximum transmission power, and the two frequency points at which the transmitted power is down by half, we can directly calculate the loaded Q .

To derive the unloaded Q (Q_u) from this measurement, we will need to determine the coupling factors and use Eq. (21). A measurement of the scalar reflection coefficient on resonance and the scalar transmission coefficient on resonance yields the left-hand sides of Eqs. (17) and (18). Rearranging these equations, we can solve for the coupling coefficients in terms of the measured quantities

$$\beta_1 = \frac{(\Gamma_0 \pm 1)^2}{1 - \Gamma_0^2 - T_0^2} \quad \text{and} \quad \beta_2 = \frac{T_0^2}{1 - \Gamma_0^2 - T_0^2} \quad (25)$$

where we have defined the on-resonance values to be $\Gamma_0 = |s_{11}(0)|$ and $T_0 = |s_{21}(0)|$. Equation (17) can also be

applied to find the coupling coefficient of a one-port resonator by letting β_2 be equal to zero. Rearranging as with Eq. (25), we find

$$\beta_1 = \frac{1 \pm \Gamma_0}{1 \mp \Gamma_0} \quad (26)$$

It is not possible to determine which of the two possible solutions for β_1 shown in Eqs. (25) and (26) is, in fact, the actual one if we are limited to scalar measurements. To remove this ambiguity, it is necessary to either measure the phase shift on resonance [16], or to vary the physical coupling in a known way and then remeasure the scalar reflection coefficient [18,24]. If it is unnecessary to know the coupling factors individually but only for the purpose of determining the unloaded Q factor from the measured loaded Q factor, then one can use [22]

$$1 + \beta_1 + \beta_2 = \frac{2}{s_{11}(0) + s_{22}(0)} \quad (27)$$

If it is possible to measure the full complex character (a vector measurement) of the scattering parameters, then there are a large number of alternative methods to estimating the Q factor of a resonator. For simplicity, we will perform the following calculations for a one-port reflection resonator ($\beta_2 = 0$). Nonetheless, it should be noted that the equations that govern reflection, transmission, and reaction resonators are all essentially equivalent [25], and so most Q measurement techniques can be equally applied to all three types of resonator [25,26].

To commence, let us determine the relationship that exists between the real and imaginary components of s_{11} at an arbitrary frequency detuning that will allow us to directly determine the unloaded Q factor. Let us define an unloaded half-resonance bandwidth in the same way as we did for a loaded half-resonance bandwidth [Eq. (24)]:

$$\Delta f_U \equiv \frac{1}{2} \frac{f_0}{Q_U} \quad (28)$$

Substituting Δf_L and Δf_U into the real and imaginary parts of s_{11} [Eqs. (12) and (13)], we find the following relationships:

$$\text{Im}[s_{11}(\pm \Delta f_L)] = \mp \{1 + \text{Re}[s_{11}(\pm \Delta f_L)]\} \quad (29)$$

$$\text{Im}[s_{11}(\pm \Delta f_U)] = \mp \left\{ 1 - \sqrt{2 - (\text{Re}[s_{11}(\pm \Delta f_U)])^2} \right\} \quad (30)$$

If the frequency detuning is varied until one of these equations are satisfied, the value of the detuning will directly give the loaded or unloaded half-bandwidth. By backsubstitution into Eqs. (28) and (24), the unloaded and loaded Q may be found.

3. SOURCES OF Q MEASUREMENT ERRORS

We can divide measurement error into two categories: systematic and random. A systematic error yields a consistent result on a repeated measurement of a constant

quantity but with a value that differs from the true value. Such a measurement could have a high resolution but simultaneously a relatively poor accuracy. Random measurement errors (noise) result in a scattering of measurement values when making a repeated measurement of a constant quantity. If a measurement system is dominated by random noise, it is relatively easy to estimate its accuracy by making multiple measurements of a constant quantity and quoting some statistical measure of the measurement sequence. An improvement in the resolution of the measurement can also usually be made by averaging multiple measurements. An estimation of the accuracy of a system that is dominated by systematic errors is far more difficult. If one has another system with a known accuracy, it is possible to compare the measurement system with this second accurate system. If this is not possible because this new technique has accuracy superior to that of all other devices, or because such a reference system is not available, then the usual technique is to measure the same quantity with two or more completely independent techniques under varying conditions and quote the differences between the results.

3.1. Systematic Q Measurement Errors

Any Q estimation technique that samples the scattering parameters at a number of separate instants requires that we place conditions on the amplitude and frequency stability of the probing microwave source. Any drift in the source frequency during the measurement will result in distortions to the resonance curve shape and thus a consequent distortion of the loaded Q value. Of course, this becomes more serious as the Q factor becomes higher. Drifts in the amplitude of the source will give rise to distortions in the measured coupling factors, which will result in errors in the estimation of the unloaded Q . This effect will have higher significance as the relevant coupling factor becomes smaller. The relative error in the Q factor under these conditions depends on the order in which the measurements are taken as well as the particular values of the coupling and Q factors. However, for a worst-case estimate using a frequency drifting source, we can assume that the measurements are taken in ascending or descending frequency order and equally spaced; then the fractional error in estimation of Q_L will be

$$\frac{\Delta Q_L}{Q_L} = \pm \frac{tkQ_L}{f_0} \quad (31)$$

where t is the time required to sample the response between $+\Delta f_L$ and $-\Delta f_L$ and k is the frequency drift rate of the source in Hertz per second (Hz/s).

Drifts in the resonant frequency of the resonance during the measurement will also cause distortions to the measured Q values in much the same way as will drifts in the source frequency. This is especially important when the temperature coefficient of the resonator is large and the resonator Q factor is high. For example, in the case of a sapphire dielectric resonator at 77 K the fractional frequency temperature coefficient is around $10^{-5}/\text{K}$, while Q_L is around 5×10^7 [27]. Temperature drifts of the order

of 200 μK during the period of measurement will limit the accuracy of the Q -factor measurement to 10%.

Almost all non-time-domain Q measurements have traditionally relied on the ability to treat the resonance as a single resonance that is well described by an equivalent LCR network. In a situation where there are losses or reactance in the coupling network, a mismatch of the source or measurement equipment with the transmission lines, or interfering resonances in the resonator or in the external transmission lines, there will be distortions to the classic resonance shape with consequent errors in the measured Q factors. It is difficult to summarize all the errors induced by ignoring these effects since there are so many possibilities. The reader is best referred to a number of articles for examples of treatment of these issues [28–30]. However, as an example, if we consider the modern Q circle method (see below), it will give a Q_U that is 15% in error for each 1 dB of return loss that is ignored in the lines leading to a critically coupled resonator.

In resonators that are remote from the experimental apparatus, or in systems with poorly matched loads and sources, resonances can appear in the connecting transmission lines that cause distortions to the resonance shape. The best solution to this problem is to suppress these spurious resonances by using microwave isolators. To overcome high levels of coupling reactance or interfering resonances in the resonator itself, one must refer to some of the methods covered in the Section 4.2 [30].

If the resonator contains materials that have properties (either reactive or resistive) that are altered by the amplitude of the incident microwave fields, then one must consider the effects of nonlinear behavior in altering the measured Q factor [31,32]. For example, microwave resonators that have been loaded with ruby have even demonstrated negative Q factors [31]. Probing the resonance can also introduce other problems such as inducing temperature changes in the resonator that will displace the resonance feature, cause electrical breakdown, or otherwise modify the properties of the dielectric or conductive material in the cavity. For example, most superconducting cavities demonstrate a very strong Q dependence on power [3,33]. Under all these circumstances great care must be taken to ensure that correct results are obtained. One obvious method to test for nonlinear effects is to measure the Q factor over a range of incident powers and ensure that no change has occurred in its measured value. Alternatively, by making a Q measurement based on the points just near the center of resonance, one can attempt to reduce the effect of the nonlinearity [33].

Finally, any inaccuracies in the calibrations of the measuring instruments will lead to inaccuracies in the Q -factor measurement. For example, Sucher [18] has calculated the error in measurement of the Q of a transmission resonator from an error in the attenuation measurement (ΔA) of the half-power transmission points as follows:

$$\frac{\Delta Q_L}{Q_L} = -0.23\Delta A \quad (32)$$

Thus a 0.1-dB error in measurement leads to an inaccuracy of 2.3%.

3.2. Random Q Measurement Errors

Random noise in the Q -factor measurement apparatus will lead to random variations in a series of measurements of a constant resonance. Many of the mechanisms mentioned above as sources of systematic errors can also be sources of random errors if the property or mechanism exhibits fluctuations rather than just causing a fixed offset in the measurement result. For instance, frequency fluctuations (phase noise) of the microwave source will create an amplitude noise in the reflected or transmitted power. This will limit the experimenter's ability to identify a particular point on a resonance curve. For example, to measure the Q factor of an X-band dielectric resonator that is of order 10^5 to an accuracy of 1% requires that the position of the measured frequency points be known to better than 1 kHz. Such frequency stability is achieved only by quartz-based microwave frequency synthesizers.

All Q measurements are ultimately limited by the intrinsic noise of the amplitude or phase sensor in the analyzing instruments. The resulting fractional noise in the Q measurement is very dependent on the prevailing conditions of the measurement. For example, with weakly coupled resonators the effects of noise in the amplitude measurement will have a greatly magnified effect in producing inaccuracy in the Q measurement. For further details of the effects of noise, the reader is referred to the more recent literature on the subject [28,30].

4. SURVEY OF Q-FACTOR MEASUREMENT TECHNIQUES

To assist the reader, the multitude of Q measurement techniques have been classified into the categories shown in Fig. 5. A major distinction has been drawn between spatial and temporal techniques because of the very different technologies required for the two types of measurement. *Spatial* techniques rely on using a slotted-line device to measure the voltage standing-wave ratio (VSWR) in the incident microwave line. The VSWR gives a measure of the magnitude of the reflection coefficient of the resonator while the position of the voltage minima in the VSWR pattern gives a measure of the reflection phase.

The *temporal* classification includes Q measurements made using frequency- and time-domain techniques. *Frequency-domain* techniques rely on measuring the scalar or vector components of the scattering parameters as a function of frequency. Frequency domain measurements are the most commonly encountered of all Q -factor estimation techniques in modern times as they are both precise and easily implemented using modern equipment. *Time-domain* measurements rely on measuring the time response of a resonance excited by an impulse of energy. These techniques have the advantage of avoiding the need for high-quality signal sources, and can also be of use when high-speed Q -factor estimation is required. *Static frequency-domain* techniques include techniques that either rely on a stepwise measurement of the scattering parameters at a number of particular frequency points or could be performed with a continuously swept source as long as the swept frequency during a single measurement is much less than the bandwidth of the resonance. Within

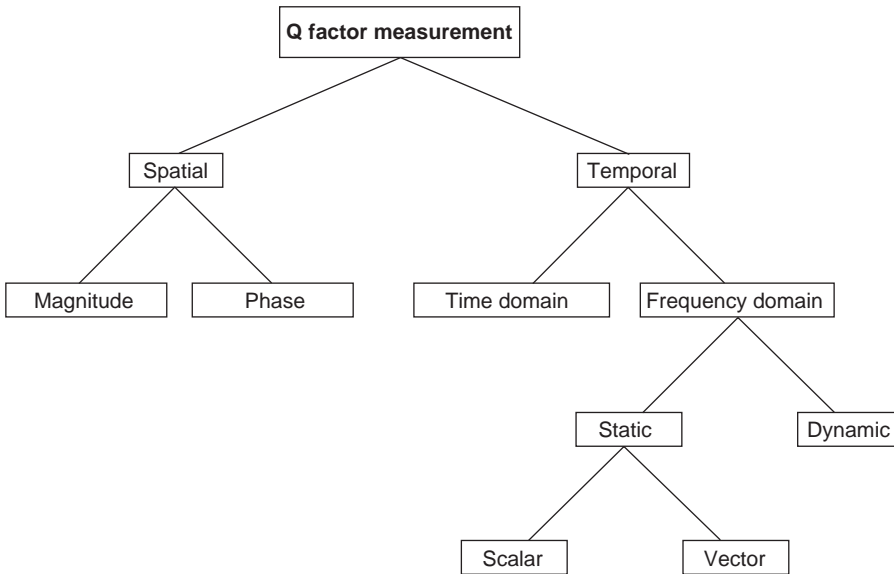


Figure 5. The very large number of different methods of Q measurement have been classified within this scheme to clarify the broad differences between the techniques. The headings of the following sections follow the classifications shown on this diagram.

these frequency-domain techniques the experimenter has the choice of measuring the scalar or full vector components of the scattering parameters depending on the available equipment. *Dynamic frequency-domain* measurements rely on measuring the response of a resonance to a frequency-modulated incident signal. These types of measurement are still quasistatic in the sense that the modulation frequency is much less than the resonance width.

4.1. Traditional Methods of Q Measurement

Below we present a number of measurement techniques that were traditionally used to estimate the Q factor. These techniques have fallen out of favor in more recent times because of the wide availability of network analyzers and quartz-based microwave synthesizers together with the inherently time-consuming nature of these approaches. Nonetheless, their instructional value and previous importance requires a quick review of the techniques. Indeed, as we will see later, some modern Q -factor measurements are simply modern implementations of these fundamental techniques.

4.1.1. Spatial Methods: Magnitude and Phase. If a measurement is made of the voltage along the incident line of the microwave resonator in Fig. 2, we would find a standing wave formed by the interference of the incoming and outgoing waves. The ratio of the minimum to maximum voltage as measured along this transmission line is termed the voltage standing-wave ratio (VSWR) and can be directly measured with a slotted-line device. The locations of the voltage minima (or maxima) in this pattern are determined by the phase of the reflected signal [17,18]. The amplitude of the VSWR is given by

$$\text{VSWR} = \frac{1 + |s_{11}|}{1 - |s_{11}|} \tag{33}$$

To compare s_{11} for under and overcoupled resonators, a plot of each is given on a Smith chart in Fig. 6 (as viewed from the *detuned short* position). One notes that $|s_{11}|$ (and hence the VSWR also) of an overcoupled resonator is large and relatively constant, although the reflection phase changes by 2π across the resonance. The undercoupled resonance demonstrates a relatively small phase variation, although the relative VSWR change is large. This knowledge arms the engineer with a technique for an accurate measurement of the Q using a slotted-line device whatever the coupling value. If a resonator is overcoupled, a measurement of the position of the voltage minima should be made; if the resonator is undercoupled, a measurement of the magnitude of the VSWR will yield the more accurate result.

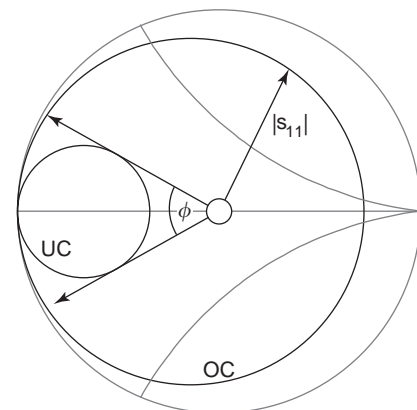


Figure 6. Smith chart plots of the s_{11} responses of an overcoupled (OC) and an undercoupled (UC) resonance. The reflection phase of the OC resonance changes by 2π across the resonance, while the reflection phase of the UC resonance reaches a maximum value of $\phi/2$ before returning to zero and then reaching a minimum value of $-\phi/2$ before once again returning to zero. However, the relative changes in magnitude of the reflection coefficient across resonance are much larger in the case of the undercoupled resonator.

Substitution of Eq. (9) into Eq. (33) yields the result that the VSWR on resonance is equal to $\beta_1^{\pm 1}$ for a one-port resonator. A measurement of the VSWR alone is unable to resolve the sign of the exponent, although an additional measurement can determine this (see below).

The VSWR at $\pm\Delta f_L$ and $\pm\Delta f_U$ for the undercoupled case can be calculated as a function of the VSWR on resonance (V_0) to be

$$V(\pm\Delta f_L) = \frac{\left| \frac{j+V_0}{1+V_0} + 1 \right|}{\left| \frac{j+V_0}{1+V_0} - 1 \right|} \quad \text{and} \quad V(\pm\Delta f_U) = \frac{\left| \frac{1-(1+j)V_0}{1+(1+j)V_0} + 1 \right|}{\left| \frac{1-(1+j)V_0}{1+(1+j)V_0} - 1 \right|} \quad (34)$$

Thus, if we measure V_0 , substitute it into equation above, and then measure the frequency detuning at which the VSWR is equal to the calculated value, we can immediately determine Q_U and Q_L .

For overcoupled resonators, the Q is accurately determined by measuring the position of the voltage minima (or maxima) as the resonant frequency is changed (for a tunable resonator), or as the incident signal frequency is changed. A plot of the position of the voltage minima for two single-port resonators ($\beta_1 = 0.6$ and 1.6) is given in Fig. 7 as a function of resonant frequency. The relatively large change in the position of the minima for overcoupled resonators is clearly visible. The points on the overcoupled resonator curve that are most easily identified experimentally occur where the minima shift is $\pm \pi/2$ (this is half the maximum shift). As the phase shift on reflection from the resonator is given by

$$\phi = \text{Arctan} \left[\frac{\text{Im}[s_{11}]}{\text{Re}[s_{11}]} \right] \quad (35)$$

it is clear that a phase shift of $\pm \pi/2$ occurs when the real part of s_{11} [Eq. (12)] is equal to zero. Solving this to find the $\pi/2$ frequency detuning points gives

$$\Delta f_{\pi/2} = \pm \frac{1}{2} \frac{f_0}{Q_U} \sqrt{\beta_1^2 - 1} \quad (36)$$

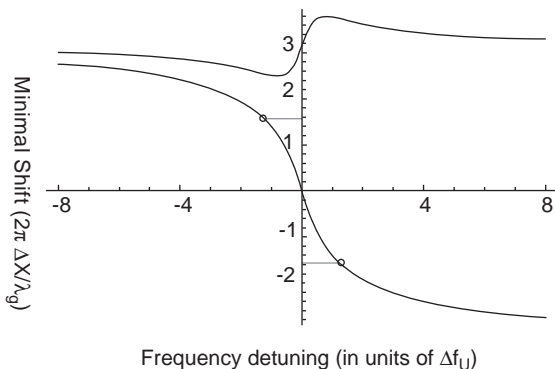


Figure 7. Calculated position shift (in radians) of the minima in the VSWR pattern as a function of resonant frequency for two resonances with $\beta_1 = 0.6$ (upper curve) and 1.6 (lower curve). The position shift is much larger for the overcoupled resonator, which is in accordance with our prediction from the Smith chart plot in Fig. 6.

Thus a measurement of the particular frequency detuning that gives a $\pi/2$ shift combined with a measurement of the on-resonance VSWR will yield the unloaded Q of the resonator.

Figure 7 also suggests a simple method to determine whether a resonator is under- or overcoupled. For undercoupled resonators the position of the minima is the same when the input signal is on resonance as well as when it is tuned far from resonance. This is not the case for overcoupled resonators. Thus, if the slotted-line probe is adjusted onto a voltage minimum at resonance, and then the resonant frequency is shifted so that it is far from resonance, only in the case of an undercoupled resonator will the probe still be at a voltage minimum.

4.1.2. Time-Domain Techniques

4.1.2.1. Decrement Method. The decrement method [17,18] is one of the older methods of measuring the Q factors of high- Q resonators. Before the advent of quartz-based microwave synthesizers, the frequency stability of the best Gunn oscillators and klystrons meant that measurements of Q factors higher than 10^4 – 10^5 would be inaccurate. To overcome this difficulty, a new method was developed that would excite the resonance with an impulse of energy and then directly monitor the dissipation of energy with time.

The technique requires a microwave oscillator whose output power can be switched on or off by an external signal driven by a pulse generator with a repetition rate much slower than the resonator ringdown time [see Eq. (4)]. This pulsed generator also triggers an oscilloscope that is monitoring the energy leaking from resonator from either the input or output port using a crystal detector. The power leaking from the resonator is proportional to the stored energy in the resonator. If the crystal detector has an accurate square law response (i.e., if its output voltage is proportional to the incident power), then the oscilloscope screen display is an accurate representation of Eq. (3) and the Q can be directly determined by measuring the time taken for the signal to drop by a factor of e . This time interval can then be substituted into Eq. (4) and the loaded Q determined.

Care must be taken to ensure that the microwave source frequency is resonant with the resonance under study and that the source output power is constant. To avoid this difficulty a method making use of a continuously swept source has been suggested [34]. In this case, the source is swept across the resonance, and when it becomes resonant, the increase in transmitted power is used to automatically trigger the oscilloscope and switch off the source.

Decrement techniques can be used to measure loaded Q factors near 10 GHz in the range upward from 10^3 (ring-down times longer than a fraction of a microsecond). However, inaccuracies enter the decrement techniques if the bandwidth of the power detector and/or the oscilloscope is inadequate to correctly capture the transient response of the resonator, and thus the technique is more often used for Q factors higher than 10^5 . The measured Q factor will also be in error if the response of the crystal detector is not accurately proportional to power.

Unfortunately, time-domain methods provide no information on the coupling and thus can only generate the loaded Q of a resonance. This difficulty may be overcome if it is possible to vary the coupling to the resonator. In this case the coupling can be made progressively smaller until the measured Q does not change with any further reduction in coupling. At this point the loaded Q will be equal to the unloaded Q to within the experimental resolution. The accuracy of the decrement techniques is directly proportional to the fractional error in the estimation of the ring-down time.

4.1.2.2. Fast-Sweep Decrement Method. The fast sweep decrement method [35] is a modification of the above-described method with three advantages: (1) the researcher can make use of more widely available continuous-wave (CW) sweep microwave generators rather than the pulsed generator required above, (2) the required frequency stability of the microwave source is much less stringent, and (3) no sophisticated electronics are required.

This measurement is suitable for a reflection resonator and requires a microwave detector to monitor the signal reflected from the resonator. The source is swept over a frequency range that is much wider than the bandwidth of the resonance with a sweep time that is much longer than the ringdown time of the resonator. The frequency sweep rate, however, is set such that the source sweeps across the resonance in a time that is much shorter than the ringdown time. An instant after the sweep has passed through the resonance, the detector mounted on the reflected port receives two signals: (1) the reflected off-resonance signal, which has a frequency corresponding to the instantaneous frequency of the source and (2) the signal leaking out from the resonator at the resonant frequency. The detector mixes these two signals, giving rise to a characteristic frequency chirp arising because the frequency difference between the instantaneous source frequency and the resonant frequency is time-dependent. The chirp has an exponential envelope that follows the decreasing strength of the leaking signal. From Ref. 35 we see that the envelope of the chirp has an exponential time constant that is twice as long as that seen in the normal decrement method

$$Q_L = \pi \tau_e f_0 \tag{37}$$

where τ_e is the time required for the signal envelope to decrease to $1/e$ of its amplitude. Clearly, a measurement of τ_e can yield Q_L via Eq. (37).

A colleague of the author [36] has developed a high-speed and reasonably precise Q measurement system based around the sweep decrement technique. A crystal detector is used to monitor the reflected power from the resonator under test. Two multimeters follow the AC and DC voltage outputs of this detector. The DC voltage is proportional to the microwave power incident on the resonator, while the AC voltage is proportional to the amplitude of the transient frequency chirp. The amplitude of the chirp is, in turn, proportional to both the incident power and the Q of the resonance. The ratio of the AC and DC voltages is thus proportional to the loaded Q factor of

the resonance, while the constant of proportionality can be determined by an initial calibration using one of the other techniques for measuring Q factors. This technique can then generate a measurement of the loaded Q after every sweep cycle, which is limited only by the requirement that the sweep time be long compared to the ringdown time of the resonance. The technique has been shown to give measurements with a resolution of around 5%, and more importantly can be used to monitor the Q factor when it is changing quickly.

4.1.3. Scalar Static Frequency-Domain Techniques

4.1.3.1. Half-Power Points Technique. Earlier in this article we outlined a method to determine the loaded Q based on a transmission measurement. To state this again, if we determine the particular frequency detuning at which the transmitted power has dropped to half of the on-resonance value, then substitution of this value into Eq. (23) will allow calculation of Q_L . This technique requires the accurate determination of the resonant frequency in order to calculate the correct value of Δf . However, determination of the exact resonant frequency by a measurement of the frequency dependence of the transmitted power is an inaccurate method since the transmitted power has only a weak frequency dependence near the center of resonance. Furthermore, the fractional error induced in the Q is highly sensitive to an error in the calculation of Δf arising from a misidentification of the resonant frequency (Δf_0):

$$\frac{\Delta Q_L}{Q_L} = \frac{\Delta f_0}{f_0} Q_L \tag{38}$$

Since we can measure source frequency differences very accurately using an electronic frequency counter, a much better method of measuring Q relies on measuring the two frequencies f_1 and f_2 at which the transmission power is down by half from the on-resonance value [17,18]:

$$f_1 - f_0 = \frac{1}{2} \frac{f_0}{Q_L} \quad \text{and} \quad f_2 - f_0 = -\frac{1}{2} \frac{f_0}{Q_L} \tag{39}$$

If we calculate the difference between these two equations, we obtain

$$f_1 - f_2 = \frac{f_0}{Q_L} \tag{40}$$

where we can determine Q_L without the need for an accurate determination of f_0 (see Fig. 4). An additional measurement of the on-resonance reflection and transmission coefficients [Eq. (25)] gives us the additional coupling information required to calculate Q_U .

Nonetheless it is important to note that an accurate measurement of the Q factor using this method relies on extremely accurate attenuation measurements [Eq. (32)]. An alternative microwave bridge method has also been proposed that can find the half transmission points very accurately [37].

4.1.3.2. Calibrated Attenuator Method. One of the difficulties of the half-power points technique is the necessity

for an accurately calibrated power detector. To avoid this difficulty, we can make use of a calibrated attenuator. This method relies on finding the maximum transmission point while there is 50% attenuator placed in the signal path between the microwave source and the detector. This attenuation is then removed and the source detuned to the two frequency points at which the original output voltage is regained on the detector. Once again the loaded Q is calculated using Eq. (40).

4.1.3.3. Reflected Power Technique. An alternative way to determine both Q_L and Q_U is through the use of reflected power measurements as a function of frequency. An initial measurement is made of the reflection coefficient on resonance so as to determine the coupling using Eq. (26). We can then modify Eq. (17) so as to determine the power reflected from a single-port resonator at the loaded half-bandwidth points $\pm\Delta f_L$ to obtain

$$|s_{11}(\pm\Delta f_L)|^2 = \frac{1 + \beta_1^2}{(1 + \beta_1)^2} \tag{41}$$

Substitution of the coupling into the right-hand side of Eq. (41) decides the expected reflection coefficient at the half-bandwidth points. Finally, adjustment of the source frequency to the two detunings that yield the expected reflection coefficient will determine the loaded bandwidth. From these values, together with the coupling coefficient determined earlier, we can clearly calculate Q_L and Q_U .

4.1.3.4. Straight-Line Methods. Several methods have been suggested for measuring the Q factor from a scalar reflection or transmission coefficient where transformed frequency coordinates are used so that the resonance shape appears to be linear [18,38,39]. This method lends itself to a manual graphical solution or to a simple least-squares fit on a computer. We can rearrange Eq. (17) for a one-port resonator [we can also do the same thing for the transmission coefficients (38)] to define a new variable:

$$\delta_U(\Delta f) \equiv \left(\frac{Q_U \Delta f}{f_0} \right) = \pm \sqrt{\frac{(1 + \beta_1)^2 |s_{11}(\Delta f)|^2 - (1 - \beta_1)^2}{1 - |s_{11}(\Delta f)|^2}} \tag{42}$$

If we have calculated β_1 from a measurement of the on-resonance reflection coefficient [see Eq. (25)], then for each measurement of s_{11} we can calculate a value for the variable δ_U [all values are known on the right-hand side of Eq. (42)]. If we plot these values of δ_U as a function of frequency detuning (Δf), we will find a straight line that has a slope equal to Q_U/f_0 . From the slope we can clearly generate the unloaded Q [39].

When implemented in a computer-based system, this technique has the potential for excellent high-accuracy measurements of the order of 0.01% for Q factors of the order of 10^4 [38]. This accuracy arises because the measurement scheme makes use only of reflection data that are in close proximity to the center of resonance, as well as

because it is possible to take many more measurements than there are free parameters to be determined. By limiting the measurement to small frequency detunings, there is a reduction in the effect of interference from other resonator and transmission-line modes. To achieve the accuracy reported, the researchers used nearly 1000 data points to characterize the resonance. This technique also has another advantage in that the degree of linearity of the plot is a measure of the level of interference from other modes. This provides an immediate indication as to the quality of the measurement.

A method similar to the one mentioned above has been suggested in connection with transmission measurements at 93 GHz [40,41]. One of the potential problems with the abovementioned method is finding the exact center of resonance. Any errors in this identification introduce a large error because Δf in Eq. (42) will be in error [see Eq. (38)]. If we define a new variable, m

$$m^2 \equiv \frac{|s_{21}(0)|^2}{|s_{21}(\Delta f)|^2} \tag{43}$$

then we can rewrite Eq. (18) as follows:

$$m^2 = 1 + 4 \left(\frac{Q_L \Delta f}{f_0} \right)^2 \tag{44}$$

If we measure the left-hand side of Eq. (43) at a known frequency detuning, we can immediately calculate Q_L from Eq. (44). However, any error in the measurement of the resonant frequency will introduce large errors. We would like to perform the calculation in a way that is insensitive to the exact value of the resonant frequency. If we measure m^2 at two frequency points on either side of the resonance, we can rewrite Eq. (44) as follows:

$$\begin{aligned} \Delta f_1 = f_1 - f_0 &= \frac{f_0}{2Q_L} \sqrt{m_1^2 - 1} \quad \text{and} \\ \Delta f_2 = f_2 - f_0 &= \frac{f_0}{2Q_L} \sqrt{m_2^2 - 1} \end{aligned} \tag{45}$$

If we take the difference of these two equations, we can derive a further equation to define Q which is dependent only on a frequency difference that can be measured very accurately:

$$Q_L(f_1, f_2) = \frac{f_0}{2(f_1 - f_2)} \left(\sqrt{m_1^2 - 1} + \sqrt{m_2^2 - 1} \right) \tag{46}$$

If we make N measurements of m^2 on either side of the resonant frequency, then we have N^2 pairs of m values. From each pair we can calculate a value for Q_L using Eq. (46). The variance of the ensemble of Q_L values is a measure of the closeness with which the data follow the theoretical resonance curve. If there is any systematic variation of Q_L as a function of frequency, this suggests the effects of interfering resonances. This method is therefore a very useful indicator of the “isolation” of the resonance [42].

4.1.3.5. Single-Frequency Techniques. As mentioned above, resonators and the resonator Q factor are commonly used to measure the electrical, optical, or magnetic properties of materials [43,44]. These measurements are usually undertaken by measuring the properties of a resonator before and after making some change to that resonator such as, for example, inserting a small sample into the resonator, changing the illumination level on a sample already in the resonator, or changing the resonator temperature. In these cases, we are more interested in a measurement of the change in Q rather than absolute measurement of the Q factor. A single-frequency measurement technique determines changes in the Q factor essentially instantaneously and doesn't require measurements in the time or frequency domain.

If the change we have made to the resonator is sufficiently small such that the electromagnetic field distribution near the coupling ports is unchanged, then we can expect that the effective coupling ratios m and n in Fig. 1 will also remain unchanged. Thus, if a change causes a modification to the losses in the resonator [R_k in Eqs. (6) and (11)], then the measured Q_u and coupling will change but the ratio of these two parameters will remain constant:

$$\frac{Q_u}{\beta_1} = \frac{R_s}{n^2} \sqrt{\frac{L_k}{C_k}} = C \quad (47)$$

where C is some constant. Thus a simple continuous measurement of the reflected power on resonance will determine any changes in the coupling and hence also from Eq. (47) any changes in Q_u . In more recent times these single-measurement techniques have been used to measure the properties of high-temperature superconducting films with high speed and precision [45].

4.1.3.6. Dual-Resonator Techniques. A novel method for determining all resonator parameters from a simultaneous measurement of two resonators has been described by a number of authors [46–48]. In these techniques the power transmission and/or reflection coefficient of a resonator are (is) plotted as a function of the transmission coefficient of a tunable reference resonator. The output plots are a function of the difference in resonant frequency of the two resonators and the ratio of their Q factors. Analytic expressions for the shapes of these curves have been derived in terms of the difference frequency and Q factor ratio, and these can be adjusted to fit experimentally derived measurements [46,48]. The accuracy of this method is similar to those of the other techniques reported here ($\sim 2\%$), although it is necessary to know the Q factor of the reference resonator in advance of these measurements using one of the other methods. The major advantage of the technique is that it is unnecessary to use calibrated power detectors, although the detectors must have a matched response. The second major advantage arises because any source frequency instability is suppressed as this is common to both resonator measurements. The quality of the measurement is determined by the stability of the reference resonator.

4.1.3.7. Integration Technique. If neither a frequency-stable source nor a calibrated power measuring device is available (meaning that accurate measurements of the half-power transmission points are impossible), then it is possible to use a so-called integration method [49]. Let us integrate the transmitted power coefficient [Eq. (18)] as a function of frequency to obtain the following expression

$$\int_{-\infty}^{\infty} P_{\text{inc}} |s_{21}|^2 d\Delta f = \frac{P_0 \pi f_0}{2Q_L} \quad (48)$$

where P_{inc} is the incident microwave power and P_0 is the power transmitted at the resonant frequency. This equation can be implemented experimentally if we use a microwave sweep oscillator to sweep the frequency over many loaded bandwidths and then use an analog integrator to integrate the output of a crystal detector monitoring the transmission port of the resonator. An additional measurement of the output voltage of the detector when the generator is on-resonance determines the only other unknown parameter so that Q_L can be determined. The integration method has also been proposed as an accurate method to determine the small changes in Q associated with determining losses in materials via resonator perturbation methods [50].

4.1.3.8. Numerical Methods. One of the earliest computer-based methods of measuring the Q factor was reported by Pandrangi et al. [51]. A computer directed a voltage-controlled oscillator (VCO) to step through the resonance curve of a transmission resonator at around 1 GHz. The incident and transmitted power were monitored by detectors that were in turn monitored by the computer. The power transmission coefficient was obtained by a division of these signals and a polynomial fitted to a smoothed version of these data. By differentiation of this polynomial, the inflection points of the resonance curve were found (see Fig. 8). To determine how the inflection points are related to the Q , we need to find when

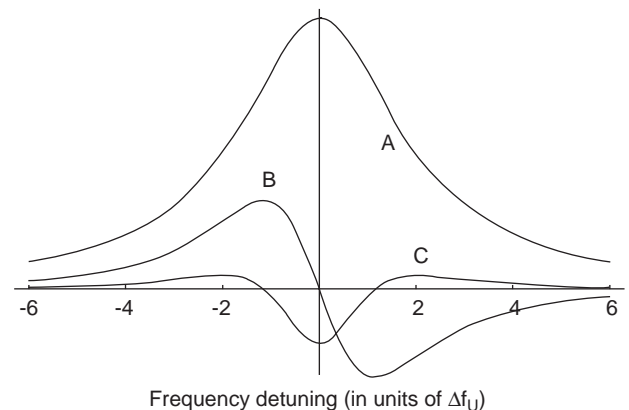


Figure 8. A plot of the frequency dependence of the power transmission coefficient (region A) as well as its first (region B) and second derivative (region C) with respect to frequency (arbitrary vertical scale). Note that the curve possesses two inflection points (points where the second derivative is equal to zero).

the second frequency derivative of Eq. (18) is equal to zero, specifically

$$\frac{\partial^2}{\partial \Delta f^2} \{|s_{21}(\Delta f_{\text{inf}})|^2\} = 0 \quad (49)$$

which has the following equation as its solution:

$$\Delta f_{\text{inf}} = \pm \frac{f_0}{2\sqrt{3}Q_L} \quad (50)$$

The experimental results were limited by frequency instability in the VCO to around 5%.

4.1.3.9. Oscillator Frequency Lock Technique. An interesting method for accurately measuring the phase as a function of frequency is presented by Linzer and Stokesberry [52]. In this case a klystron is frequency-locked to the center of a resonance by detection of the imaginary part of the reflection or transmission coefficient and then by controlling the frequency of the klystron to hold the imaginary response at zero. Adjustment of the feedback mechanism is then made so that the locking system is now partially sensitive to the real part of the reflection coefficient, and thus it will then lock at some distance from the center of resonance. The particular dependence of the oscillator frequency on this adjustment is determined by the loaded Q of the resonator, and hence a measurement of the frequency dependence of the oscillator on this adjustment allows determination of the loaded Q with a relatively high accuracy.

4.1.4. Vector Static Frequency-Domain Methods

4.1.4.1. Q Circles Method. If one measures both the phase and magnitude (or real and imaginary components) of s_{11} using either the VSWR method, a reflection bridge [53], or a network analyzer, then it is possible to plot s_{11} directly on a Smith chart. If plots of the loci of Eqs. (29) and (30) for all Δf_L and Δf_U are also placed on the chart, then the intersections of the s_{11} curve and these two solution sets give the loaded and unloaded half-bandwidths. This manual graphical solution method has been outlined in great detail by Ginzton [17].

4.1.4.2. Straight-Line Methods. If one can measure the real and imaginary components of s_{11} or s_{21} of a resonator separately, then one can plot the following ratios as a function of Δf for each of the different resonator types:

$$\frac{\text{Im}[s_{11}(\Delta f)]}{\text{Re}[s_{11}(\Delta f)]} \quad \text{[reaction (54)],}$$

$$\frac{\text{Im}[s_{21}(\Delta f)]}{\text{Re}[s_{21}(\Delta f)]} \quad \text{(transmission),}$$

$$\frac{\text{Im}[s_{11}(\Delta f)]}{\text{Re}[s_{11}(\Delta f)]} \quad \text{(reflection)}$$

All of these ratios yield a straight line with a slope of $2Q_L/f_0$. Clearly a simple measurement of the slope yields a value for Q_L .

4.1.5. Dynamic Frequency-Domain Techniques. There are two main dynamic frequency-domain techniques: the harmonic or inflection point technique and the intermodulation method. Both of these techniques rely on the fact that at two frequency points on either side of the resonant frequency there are points where the second derivative of the resonance curve is equal to zero [see Fig. 8 and Eqs. (48) and (49)]. It is important to note that the sweep rates (in Hz/s^1) for both of these techniques need to be much slower than $(f_0/Q_L)^2$ for the measurement to be accurate. In this sense the measurements are still quasistatic, although we have chosen to term them “dynamic” as the measurement is made at a frequency that differs from the sweep frequency.

4.1.5.1. Harmonic (Inflection Points) Technique. When a frequency-modulated (FM) signal is incident on a typical transmission or reflection resonance response (as shown in Fig. 4), it will result in an amplitude modulation of the transmitted or reflected signal because of the intrinsically dispersive nature of a resonance. If the frequency deviation is small, the magnitude of the resulting amplitude modulation (AM) will be proportional to the slope of the response curve at the average frequency of the incident signal. If the resonance response has a nonzero curvature, that is, if the second derivative is not zero, then the transmitted or reflected signal will also contain an AM component at the second harmonic of the modulating frequency. For example, a measurement of the second-harmonic AM amplitude when transmitted through a resonance will yield a curve that is proportional to curve C in Fig. 8 (the second frequency derivative of the resonance). Since extremely sensitive synchronous detection techniques exist (such as lockin amplifiers) this method can very accurately find the points for which there is no second-harmonic AM [17,18]. Using Eq. (50), this value can be easily converted to the loaded Q of the resonator.

4.1.5.2. Intermodulation Method. A potential problem arises in the previous method if the original FM signal is not completely free from higher-harmonic content, as is often the case. If the incident signal already contains some level of second-harmonic AM, then the measurement of the inflection points will be in error. To avoid this, it is possible to use a development of the method mentioned in Section 4.1.5.1 termed the *intermodulation method* [17,18]. If we simultaneously frequency-modulate an incident signal at two different frequencies, it is clear that we will generate AM components in the transmitted signal at the two fundamental FM frequencies. However, if there is any nonlinearity of the frequency dependence of the resonance response, then we will also generate AM components at the difference and sum frequency of the two modulating frequencies. We can set the detection system to be sensitive to one of these intermodulation components. Once again, when identification of the inflection points is completed, we can calculate Q_L using Eq. (50).

4.2. Modern Measurement Techniques

Because of advent of powerful personal computers for data analysis, combined with the wide availability of

microwave equipment with computer interfaces, many new techniques have been devised that allow the lifting of the restrictions that were previously placed on Q measurement. For example, accurate measurements can now be made in the presence of transmission-line or coupling reactance. An additional advantage of computer-aided measurement is that a large number of measurements that would be tedious to take manually, are easily made. The data averaging that occurs from using such large numbers of data samples gives improved immunity to random noise in the Q measurement. This section describes some of the latest methods and is divided into sections that highlight the major advantage of the technique.

4.2.1. Scalar High-Resolution Measurements. Kajfez [24] has developed a technique that uses a scalar network analyzer to measure the values of the reflection coefficient as a function of frequency. This technique takes into account moderate coupling losses and therefore allows the off-resonance reflection coefficient to differ from 1. When compared to vector curve-fitting methods, this technique, like all scalar techniques, suffers from the disadvantage that it is impossible to tell whether a resonator is over- or under-coupled. Nonetheless, its accuracy is comparable with vector methods ($\sim 0.2\%$).

Luiten et al. [55] have developed a new data averaging technique that eliminates the need for expensive network analyzers and relies only a measurement of the square of the magnitude of the reflection or transmission coefficient as a function of frequency. The acquired data are then fitted using a nonlinear algorithm to the expected shape of a completely general resonance [Eq. (17) or (18)]. The fitting mechanism is adaptive, which gives the program a robustness and an ability to “follow” the parameters of a resonance if these evolve during the measurement. This feature has been used to measure the temperature dependence of the thermal, electrical, and magnetic properties of TiO_2 and Al_2O_3 crystals [10]. The extreme frequency stability of the source in this case (fractional frequency stability $\sim 10^{-15}$) meant that the Q measurements had a resolution of 0.03% despite the loaded bandwidth being only 10 Hz.

4.2.2. Vector High-Resolution Measurements. Al Zoubi et al. [56] have developed a modern method that is essentially an update of the traditional VSWR-based techniques mentioned earlier in this article. This method is intended for accurate, automatic, and rapid measurements of resonators intended for integrated microwave circuit devices. It yields Q -factor measurements with 2–3% accuracy in just a few seconds of measurement time.

A simple modification to the Q -circle method has been suggested by Hearn et al. [57] to take into account losses in the coupling network. It can be shown that Eq. (30) is equivalent to the condition that the magnitude of the real and imaginary parts of the impedance of the resonator are equal. In cases where there is loss in the coupling mechanism or the transmission lines, a correction needs to be made; otherwise the estimated Q will be less than the true value. Hearn et al. have suggested a correction that reduces the errors of the traditional measurement by

around 80 times in the case of high coupling loss and small coupling. Unfortunately this correction cannot be implemented with a simple Smith chart overlay, although it is easily implemented in an automated measurement system.

Sanchez et al. [54] report an absorption resonator Q measurement system based on a computer-driven network analyzer. This system empirically removes the effects of any loss in the coupling network, or transmission lines, by rescaling the data by a factor obtained from the transmission coefficient far from resonance. A fit is performed to the Q circle from which the coupling and Q is found. The Q_U measurement error is around 1%.

Kajfez [58] has developed a method that uses a network analyzer combined with computer analysis to generate and fit Q circles [Figs. 3d and 6]. Instead of graphically finding the solutions, he uses a least-squares fitting routine to an expression that includes the effects of a frequency-independent line and coupling reactance as well as any losses in the coupling network. This technique avoids the ambiguity that exists between over- and under-coupled resonators in scalar techniques. The technique’s accuracy is estimated at around 0.1% when utilizing approximately 1000 data points. This technique is now available as a commercial software product.

In the presence of significant line inductance we find that instead of the ideal circle that should be seen in a plot of the real and imaginary components of the resonator impedance, we find a curve that is nearly circular but with a smaller diameter and that crosses over itself [59]. By finding the two frequencies corresponding to the cross over point as well as those corresponding to the maximum and minimum of the imaginary impedance component (the “critical points”), we can determine Q_U very accurately. These measurements are relatively easy using a modern network analyzer and will generate Q factors that have an accuracy of about 0.5%

4.2.3. Harmonic Power Ratiometry. A very interesting technique has been developed that is closely related to the dynamic frequency-domain techniques mentioned above and offers high speed and extreme precision as well as a very inexpensive measurement system in order to determine the loaded Q factor [60]. The basis of the technique is to lock the average frequency of a frequency-modulated (FM) microwave signal to the resonant frequency. The dispersion of the resonance generates amplitude modulation (AM) in the reflected or transmitted signals, but since the resonance is an even function about the resonant frequency, there will be power only in the even harmonics of the modulation frequency. The power ratio in two adjacent even harmonic orders is related to both the bandwidth of the resonance and the frequency deviation of the incident signal. The remarkable performance of synchronous detection methods allows a measurement precision of better than parts in 10^4 .

4.2.4. Measuring Resonance Parameters in the Presence of Other Resonances. Kajfez and Hwan [61] have developed an overlay for a network analyzer that takes into account the effects of inductance and loss in the coupling

and transmission network as well as the effects of any distant resonant modes. These effects are modeled as a frequency-dependent reactance in series with the mode of interest. The effect of this frequency-dependent series inductance is to cause the Q circle to develop distortions that make its apparent diameter smaller than it would otherwise be. If an accurate determination of the reference plane of the measurement is made, this technique can also generate the inductance of the coupling network.

Sauer et al. [62] have modeled the effects of reflections that exist in the lines between the measuring apparatus and the resonator under test. These reflections create subsidiary line resonances that distort the resonance shape and create errors in measurement of the Q factor. The model can accurately fit experimental data taken in the presence of interfering line resonances and thus yield a Q factor with an accuracy of $\sim 1\%$.

An extensive analysis and experimental procedure has been developed that allows for the accurate measurement of Q factors and coupling coefficients of two or more modes that are in extremely close proximity [19,63]. The process relies on developing an expression that fully represents the circuit shown in Fig. 1b with enough free parameters to represent all visible resonance curves in the data as well as an additional frequency-dependent term to represent any coupling reactance. The free parameters are then adjusted by a least-squares fitting procedure to the experimental data. Even in the situation where a double loop is visible on the Smith chart because two resonances are within a few bandwidths of each other, the accuracy of the Q measurement is maintained at around 2%.

4.2.5. Measuring the Q of Low- Q Resonators. Resonator measurements are generally made through transmission lines or coupling networks that have poorly understood characteristics. The interaction between these external networks causes distortions to the resonance and therefore to the apparent Q factor. This is an especially difficult problem when the Q factor of the resonator is low since the frequency dependence of the resonator impedance becomes comparable to that of the external circuit parameters. Kajfez and Wheless [64] have developed an expression for determining Q_U when it is measured through an arbitrary two-port. Using a similar approach, Drozd and Joines [15] have developed a general Q -factor measuring method based on the full s_{11} parameters as determined by a computer-driven network analyzer. The loaded Q is shown to be given by

$$Q_L = \frac{\omega_0}{2R_k} \left| \frac{dX_k}{d\omega} \right| \quad (51)$$

where X_k is the total reactance of the k th resonance and R_k is the total resistance of the k th resonance. The frequency derivative of the reactance is estimated from a number of measurements of s_{11} in the immediate neighborhood of center frequency of the resonance. Measuring near the center of resonance gives immunity from the influences of stray inductance in the transmission line and coupling mechanism. This method proves to be far more accurate than a measurement of the half-power points or of the

critical points, both of which are relatively distant from the resonant frequency. In addition, this method does not make the common assumption of Eq. (16), which can cause errors for the lowest Q values. As a result, this method yields accurate results even for Q factors of the order of 2.

4.2.6. Oscillator Phase Noise Determination. Fuchs [65] has made use of Leeson's [66] relation that in a microwave resonator-oscillator the loaded Q factor of the resonator translates the phase fluctuations of the oscillator components into frequency fluctuations for noise frequencies within the bandwidth of the resonance. By artificially introducing high levels of component phase noise, the oscillator frequency noise can easily prevail over the noise of the measurement system. A measurement of the spectrum of the oscillator phase noise will yield the loaded Q to an accuracy of around 10%.

4.2.7. Theoretical Q Estimates. Theoretical estimation of Q factors has always been extremely difficult for all except the simplest metallic cavities with a well-known surface resistance. A number of attempts have been made to model more complex hybrid dielectric resonators and estimate the Q factors on purely theoretical grounds [42,67,68]. These estimates have value in that they could allow an independent verification of the veracity of Q measurement techniques. Unfortunately, as the accuracy of these calculations is still only around 10%, their predictive power is not yet useful in selecting between the results of various measurement techniques.

Acknowledgment

The author would like to sincerely thank Tony Mann for a critical reading of the original manuscript. In addition, I would also like to thank all the personnel of the Frequency Standards and Metrology research group at the Physics School of UWA for providing an innovative and challenging workplace that has created the environment for this work. The interest of others has always been the strongest motivation for my work.

BIBLIOGRAPHY

1. H. B. G. Casimir, On the theory of electromagnetic waves in resonant cavities, *Philips Res. Rep.* **6**:162–182 (1951).
2. D. Kajfez and A. Gundavajhala, Measurement of material properties with a tunable resonant cavity, *Electron. Lett.* **29**(22):1936–1937 (1993).
3. C. M. Lyneis, *Experimental Studies of Microwave Properties of 8.6GHz Superconducting Niobium, Niobium-Tantalum, and Tantalum Cavities*, Ph.D. thesis, Dept. Physics, Stanford Univ., CA, 1974 (unpublished).
4. J. Ceremuga, J. Krupka, and T. Kosciuk, Resonant measurements of surface resistance of high- T_c superconducting films: How good or bad are they? *J. Supercond.* **8**(6):681–689 (1995).
5. J. J. Hinds and W. H. Hartwig, Materials-properties analyzers using superconducting resonators, *J. Appl. Phys.* **42**(1):170–179 (1971).
6. M. N. Afsar, J. R. Birch, and R. N. Clark, The measurement of the properties of materials, *Proc. IEEE* **74**(1):183–199 (1986).

7. G. Birnbaum and J. Franeau, Measurement of the dielectric constant and loss of solids and liquids by a cavity perturbation technique, *J. Appl. Phys.* **20**:817–818 (1949).
8. G. Johri, R. Ngoui, and J. Roberts, A study of experimental and theoretical shifts in a resonant microwave cavity loaded with polar and non-polar molecules in the gas phase, *J. Microwave Power Electromagn. Energy* **24**(4):227–235 (1989).
9. D. Grissom and W. H. Hartwig, Dielectric dissipation in NaCl and KCl below 4.2 K, *J. Appl. Phys.* **37**(13):4784–4789 (1966).
10. A. N. Luiten, M. E. Tobar, J. Krupka, R. Woode, E. I. Ivanov, and A. G. Mann, Microwave properties of a Rutile resonator between 2–10 K, *J. Phys. D:Appl. Phys.* **31**:1383–1391 (1998); J. G. Hartnett, A. N. Luiten, J. Krupka, M. E. Tobar, and P. Bilski, Influence of paramagnetic chromium ions in crystalline YAG at microwave frequencies, *Journal of Physics D (Applied Physics)*, **35**(13):1459–1466 (2002).
11. N. Klein, C. Zuccaro, U. Dähne, H. Schulz, N. Tellmann, A. Kutzner, A. G. Zaitsev, and R. Wördenweber, Dielectric properties of rutile and its use in high temperature superconducting resonators, *J. Appl. Phys.* **78**(11):6683–6686 (1995).
12. R. J. Deri, Dielectric measurements with helical resonators, *Rev. Sci. Instrum.* **57**(1):82–86 (1986).
13. S. R. Stein and J. P. Turneaure, Superconducting cavity stabilized oscillators with improved stability, *Proc. IEEE* **63**:1249–1250 (1975).
14. Chang, S. A. G. Mann, and A. N. Luiten, Improved cryogenic sapphire oscillator with exceptionally high frequency stability, *Electron. Lett.* **36**(5):480–481 (2000).
15. J. M. Drozd and W. T. Joines, Determining Q using S parameter data, *IEEE Trans. Microwave Theory Tech.* **MTT-44**(11) (1996).
16. J. R. Ashley and F. M. Palka, Reflection coefficient measurement of microwave resonator Q factors, *Microwave J.* **14**:35–39 (June 1971).
17. E. L. Ginzton, *Microwave Measurements*, McGraw-Hill; New York, 1957.
18. M. Sucher, Measurement of Q, in M. Sucher and J. Fox, eds., *Handbook of Microwave Measurements*, Vol. II, Wiley, New York, 1963, pp. 417–493.
19. W. P. Wheless and D. Kajfez, Experimental characterization of multimoded microwave resonators using automated network analyzer, *IEEE Trans. Microwave Theory Tech.* **MTT-35**(12) (1987).
20. K. Kurokawa, *An Introduction to the Theory of Microwave Circuits*, Academic Press; New York, 1969.
21. Z. Galani, M. J. Bianchini, R. C. Waterman, R. Dibiasi, R. W. Laton, and J. Bradford Cole, Analysis and design of a single resonator GaAs FET oscillator with noise degeneration, *IEEE Microwave Theory Tech.* **MTT-32**(12):1556–1565 (1984).
22. D. H. Han, Y. S. Kim, and M. Kwon, Two port cavity Q measurement using scattering parameters, *Rev. Sci. Instrum.* **67**(6):2179–2181 (1996).
23. P. H. Smith, *Electronic Applications of the Smith Chart in Waveguide, Circuit and Component Analysis*, McGraw-Hill; New York, 1969.
24. D. Kajfez, Q-factor measurement with a scalar network analyzer, *IEE Proc. Microwave Anten. Propag.* **142**(5):369–372 (1995).
25. M. C. Sanchez, E. Martin, and J. M. Zamarro, Unified and simplified treatment of techniques for characterizing transmission, reflection or absorption resonators, *IEE Proc.* **137**(4):209–212 (1990).
26. A. Khanna and Y. Garault, Determination of loaded, unloaded and external quality factors of a dielectric resonator coupled to a microstrip line, *IEEE Trans. Microwave Theory Tech.* **MTT-31**(3):261–264 (1983).
27. M. E. Tobar, E. I. Ivanov, R. Woode, and J. Searls, Low noise microwave oscillators based on high-Q temperature stabilized resonators, *Proc. 48th IEEE Int. Frequency Control Symp.*, 1994, pp. 433–440.
28. D. Kajfez, Random and systematic uncertainties of reflection-type Q-factor measurement with a network analyzer, *IEEE Trans. Microwave Theory Tech.* **51**(2):512–519 (2003).
29. D. Kajfez, S. Chebolu, M. R. Abdul-Gaffor, and A. A. Kishk, Uncertainty analysis of the transmission-type measurement of Q-factor, *IEEE Trans. Microwave Theory Tech.* **47**(3):367–371 (1999).
30. K. Leong and J. Mazierska, Precise measurements of the Q factor of dielectric resonators in the transmission mode-accounting for noise, cross-talk, delay of uncalibrated lines, coupling loss and coupling reactance, *IEEE Trans. Microwave Theory Tech.* **50**(9):2115–2127 (2002).
31. A. E. Siegman, *Microwave Solid State Masers*, McGraw-Hill; New York, 1964.
32. J. Petykiewicz, in *Wave Optics*, Kluwer Academic; Dordrecht, 1992, Chap. 10.14.
33. X. S. Rao, C. K. Ong, and Y. P. Feng, Q-factor measurement of nonlinear superconducting resonators, *Electron. Lett.* **36**(3):271–273 (2000).
34. A. I. Kocherzhin, M. P. Kukhtin, V. P. Lobachev, and N. S. Repalov, Device for measurement of high Q values by attenuation, *Instrum. Exp. Tech.* **31**(2):494–496 (1988).
35. H. J. Schmitt and H. Zimmer, Fast sweep measurements of relaxation times in superconducting cavities, *IEEE Trans. Microwave Theory Tech.* **MTT-14**:206–207 (1966).
36. A. G. Mann, Physics Dept., Univ. Western Australia, unpublished communication.
37. K. Watanabe and I. Takao, A bridge method for simultaneous measurements of coupling coefficient and loaded Q of a single ended cavity, *Rev. Sci. Instrum.* **44**(11):1625–1627 (1973).
38. K. D. McKinstry and C. E. Patton, Methods for determination of microwave cavity quality factors from equivalent circuit models, *Rev. Sci. Instrum.* **60**(3):439–443 (1989).
39. Z. Frait and C. E. Patton, Simple analytic method for microwave cavity Q determination, *Rev. Sci. Instrum.* **51**(8):1092–1094 (1980).
40. R. K. Mongia and R. K. Arora, Accurate measurement of the Q factor of an open resonator in the W frequency band range, *Rev. Sci. Instrum.* **63**:3877–3880 (1992).
41. R. K. Arora, S. Aditya, and X. Xu, Computer aided measurement of Q-factor with application to quasi-optical resonators, *IEEE Trans. Instrum. Meas.* **IM-40**(5):863–866 (1991).
42. R. K. Mongia, C. L. Larose, S. R. Mishra, and P. Bhartia, Accurate measurement of Q-factors of isolated dielectric resonators, *IEEE Trans. Microwave Theory Tech.* **MTT-42**(8):1463–1467 (1994).
43. V. Subramanian and J. Sobhanadri, New approach to measuring the Q-factor of a microwave cavity using the cavity perturbation technique, *Rev. Sci. Instrum.* **65**(2):453–455 (1994).
44. B. Tian and W. R. Tinga, Single-frequency relative Q measurements using perturbation theory, *IEEE Trans. Microwave Theory Tech.* **MTT-41**(11):1922–1927 (1993).
45. M. Jacob, J. Mazierska, K. Leong, and J. Krupka, Novel method for calculation and measurement of unloaded Q-factor of

- superconducting dielectric resonators, *IEEE MTT-S Digest* **3**:1993–1996 (2001).
46. G. Magerl and K. R. Richter, A novel method for cavity parameter measurement, *IEEE Trans. Instrum. Meas.* **IM-25**(2):145–151 (1976).
 47. G. Magerl, Fast measurement of cavity coupling coefficients, *IEEE Trans. Microwave Theory Tech.* **MTT-26**(3):223–224 (1978).
 48. I. Kneppo, Comparison method of measuring Q of microwave resonators, *IEEE Trans. Microwave Theory Tech.* **MTT-25**:423–426 (1977).
 49. I. Kneppo, Integration method of measuring Q of the microwave resonators, *IEEE Trans. Microwave Theory Tech.* **MTT-26**(2):131 (1978).
 50. J. C. Liu, H. C. Chou, J. C. Chung, and P. C. Lu, Accurate measurement of the Q factor for the cavity perturbation method, *Microwave Opt. Lett.* **13**(2):87–90 (1996).
 51. R. K. Pandrangi, S. S. Stuchly, and M. Barski, A digital system for measurement of resonant frequency and Q factor, *IEEE Trans. Instrum. Meas.* **IM-31**(1):18–21 (1982).
 52. M. Linzer and D. P. Stokesberry, A frequency lock method for the measurement of Q factors of reflection and transmission resonators, *IEEE Trans. Instrum. Meas.* **IM-22**(1):61–77 (1973).
 53. G. Ghosh, S. Sen, D. Dasgupta, and P. K. Saha, Method of measuring loaded Q-factor of single ended cavity resonators using reflection bridge, *Rev. Sci. Instrum.* **49**(3):378–379 (1978).
 54. M. C. Sanchez, E. Martin, and J. M. Zamarro, New vectorial automatic technique for characterization of resonators, *IEE Proc.* **136**(2):147–150 (1989).
 55. A. N. Luiten, A. G. Mann, and D. G. Blair, High resolution measurement of the temperature-dependence of the Q, coupling and resonant frequency of a microwave resonator, *Meas. Sci. Technol.* **7**:949–953 (1996).
 56. A. Y. Al Zoubi, N. A. Al Omari, and M. F. Alfaouri, A computer-assisted method for Q-factor measurement of dielectric resonators, *Meas. Sci. Technol.* **9**:109–112 (1998).
 57. C. P. Hearn, P. G. Bartley, and E. S. Bradshaw, A modified Q-circle measurement procedure for greater accuracy, *Microwave J.* **36**(10):108–111 (1993).
 58. D. Kajfez, Linear fractional curve fitting for measurement of high Q factors, *IEEE Trans. Microwave Theory Tech.* **MTT-42**(7):1149–1153 (1994).
 59. E. Y. Sun and S. H. Chao, Unloaded Q measurement—the critical points method, *IEEE Trans. Microwave Theory Tech.* **MTT-43**(8):1983–1986 (1995).
 60. B. Nebendahl, D. -N. Peligrad, M. Pozek, A. Dulcic, and M. Mehring, An AC method for the precise measurement of Q-factor and resonance frequency of a microwave cavity, *Rev. Sci. Instrum.* **72**(3):1876–1881 (2001).
 61. D. Kajfez and E. J. Hwan, Q-factor measurement with network analyzer, *IEEE Trans. Microwave Theory Tech.* **MTT-32**(7):666–670 (1984).
 62. B. Sauer, K. A. H. van Leeuwen, A. Mortazawi-M., and P. M. Koch, Precise calibration of a microwave cavity with a non-ideal waveguide system, *Rev. Sci. Instrum.* **62**(1):189–197 (1991).
 63. W. P. Wheless, A resonator de-embedding procedure, *IEEE Trans. Microwave Theory Tech.* **MTT-38**(4):864–869 (1989).
 64. D. Kajfez and W. P. Wheless, Invariant definitions of the unloaded Q factor, *IEEE Trans. Microwave Theory Tech.* **MTT-34**(7):840–841 (1986).
 65. M. Fuchs, Simple and accurate measurement of loaded Q factor of microwave oscillators using thermal noise injection, *Proc. 20th European Microwave Conf. 1990*, Vol. 1, pp. 512–516.
 66. D. B. Leeson, A simple model of feedback oscillator noise spectrum, *Proc. IEEE* **54**:329–330 (1966).
 67. J. Krupka, Computations of frequencies and intrinsic Q factors of TE_{0nm} modes of dielectric resonators, *IEEE Trans. Microwave Theory Tech.* **MTT-33**(1) (1985).
 68. C. Wang, B. Q. Gao, and C. P. Deng, Accurate study of Q factor of resonator by a finite difference time-domain method, *IEEE Trans. Microwave Theory Tech.* **MTT-43**(7):1524–1529 (1995).

FURTHER READING

D. Kajfez, *Q Factor*, Vector Forum, Oxford, MS, 1994.

QUADRATURE PHASE SHIFT KEYING (QPSK)

SERIOJA O. TATU
RENATO G. BOSISIO
École Polytechnique
Montreal, Quebec, Canada

1. INTRODUCTION

The various modulation techniques offered different solutions in terms of cost and received signal quality. Frequency modulation and phase modulation present certain immunity to noise, whereas amplitude modulation was simple to demodulate. More recently, however, digital modulation has gained in popularity.

Quadrature phase shift keying (QPSK) is a digital frequency modulation technique used for sending data over radio or cable networks. In QPSK modulation, a cosine carrier is varied in phase while keeping amplitude and frequency constant. The term “quadrature” implies that there are four possible phase values of the carrier in time. In QPSK modulation, information is conveyed through phase variations. In each time period, the phase can change only once. Since there are four possible phases, there are two bits of information conveyed within each timeslot.

Figure 1 shows a typical QPSK constellation in the complex plane and the bit pair associated with each possible signal phase value. The bits are mapped onto corresponding QPSK symbols using the Gray code. An important property of this code is that the adjacent symbols (phase states) differ by only one bit. In transmission systems corrupted by noise and interference, the most frequent errors are introduced by decision errors between adjacent states. In such cases, the Gray code is advantageous, particularly when QPSK systems are followed by single-error-correcting decoders.

Each QPSK symbol is represented by a complex number $I + jQ$, corresponding to the real-valued I and Q channels, respectively.

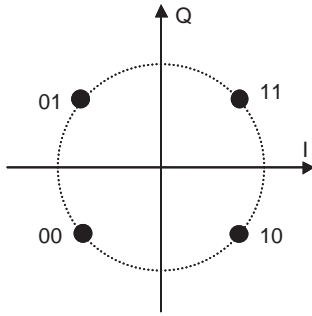


Figure 1. The QPSK constellation.

2. QPSK MODULATORS

2.1. QPSK Modulating Principle

Figure 2 shows a block diagram of the QPSK modulator [1]. The datastream is converted by a serial-to-parallel converter into two separate streams. One stream, $I(t)$, is in phase signal, and the other, $Q(t)$, is in quadrature signal, and each stream has a symbol rate equal to half the incoming bit rate. Both I and Q signals are separately applied to multipliers. The second input to the I multiplier is the carrier signal, $\cos(\omega t)$, and the second input to the Q multiplier is the quadrature carrier, the signal shifted by exactly 90° . The outputs of both multipliers are BPSK signals. The I and Q multiplier outputs are then added to give the QPSK signal, $S(t)$.

For an unfiltered QPSK signal, phase transitions occur instantaneously and the signal has a constant-amplitude envelope. According to this principle, the QPSK modulated signal $S(t)$ can be expressed as follows:

$$S(t) = I(t) \cdot \cos(\omega t) + Q(t) \cdot \cos\left(\omega t + \frac{\pi}{2}\right) \quad (1)$$

Each real signal, $I(t)$ or $Q(t)$, has two possible values. These values are $A/\sqrt{2}$ and $-(A/\sqrt{2})$, respectively, considering that the radius value in Fig. 1 is equal to A .

Therefore, for a QPSK-modulated signal, four possible phase values of $S(t)$ signal can be obtained: $\pi/4$, $3\pi/4$, $5\pi/4$, and $7\pi/4$. These values are expressed in the following four equations:

$$\begin{aligned} & \frac{A}{\sqrt{2}} \cdot \cos(\omega t) + \frac{A}{\sqrt{2}} \cdot \cos\left(\omega t + \frac{\pi}{2}\right) \\ &= A \cdot \left[\cos(\omega t) \cdot \cos\left(\frac{\pi}{4}\right) - \sin(\omega t) \cdot \sin\left(\frac{\pi}{4}\right) \right] \quad (2) \\ &= A \cdot \cos\left(\omega t + \frac{\pi}{4}\right) \end{aligned}$$

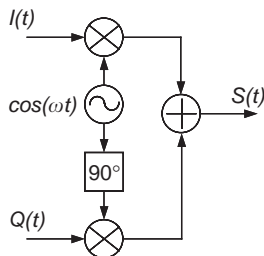


Figure 2. The QPSK modulating principle.

$$\begin{aligned} & -\frac{A}{\sqrt{2}} \cdot \cos(\omega t) + \frac{A}{\sqrt{2}} \cdot \cos\left(\omega t + \frac{\pi}{2}\right) \\ &= A \cdot \left[-\cos(\omega t) \cdot \cos\left(\frac{\pi}{4}\right) - \sin(\omega t) \cdot \sin\left(\frac{\pi}{4}\right) \right] \quad (3) \end{aligned}$$

$$= A \cdot \cos\left(\omega t + \frac{3\pi}{4}\right)$$

$$\begin{aligned} & -\frac{A}{\sqrt{2}} \cdot \cos(\omega t) - \frac{A}{\sqrt{2}} \cdot \cos\left(\omega t + \frac{\pi}{2}\right) \\ &= A \cdot \left[-\cos(\omega t) \cdot \cos\left(\frac{\pi}{4}\right) + \sin(\omega t) \cdot \sin\left(\frac{\pi}{4}\right) \right] \quad (4) \end{aligned}$$

$$= A \cdot \cos\left(\omega t + \frac{5\pi}{4}\right)$$

$$\begin{aligned} & \frac{A}{\sqrt{2}} \cdot \cos(\omega t) - \frac{A}{\sqrt{2}} \cdot \cos\left(\omega t + \frac{\pi}{2}\right) \\ &= A \cdot \left[\cos(\omega t) \cdot \cos\left(\frac{\pi}{4}\right) + \sin(\omega t) \cdot \sin\left(\frac{\pi}{4}\right) \right] \quad (5) \end{aligned}$$

$$= A \cdot \cos\left(\omega t + \frac{7\pi}{4}\right)$$

Figure 3 represents a typical phase variation of a QPSK modulated signal versus time. The simulation was performed using the proprietary Advanced Design System (ADS) simulator of Agilent Technologies. Typically, during simulations, a random bit generator is employed as a bit source, and such is the case here. Four possible phases can be clearly identified, as seen in this figure. In the case of the simulation presented in Fig. 3, the bit rate was set at 2 Mbps (1 Mbps on each channel I or Q).

Figure 4 shows the spectrum of an unfiltered QPSK signal, obtained using an ADS simulation having the same bit rate of 2 Mbps. The spectrum is centered on the carrier frequency. The baseband signals, $I(t)$ and $Q(t)$, and the QPSK signal at the modulator output were not filtered. Therefore, the resulting spectrum is a wideband signal.

Phase changes for filtered QPSK signals result in a varying envelope amplitude. The effects of the envelope fluctuation on the transmitter RF spectrum and the bit error rate (BER) performances are presented by Feher [1].

At the modulator the QPSK signal output is usually filtered to limit the radiated spectrum, then amplified, and finally transmitted to the receiver over the transmission channel.

The offset-keyed quadrature-phase shift-keyed (OQPSK) modulation is quite similar to the conventional or coincident QPSK modulation [1]. The difference lies in the data transitions between the I and Q streams as they enter in the multipliers. One of the serial-to-parallel converter output streams is then *offset* from the other by delaying with a half of the incoming bit duration. The I and Q datastreams can never be in transition simultaneously. The result is that only the 90° phase transition occurs in the modulator output signals. Similarly to the QPSK, the unfiltered OQPSK signal has a constant-amplitude envelope. However, for filtered OQPSK signals, the transmitted signal has an amplitude envelope variation of 3 dB

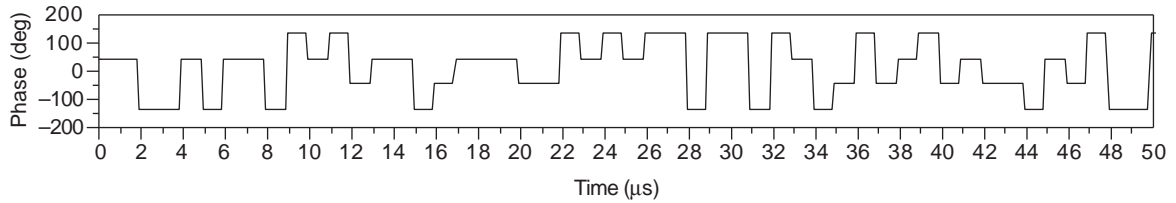


Figure 3. The phase of a QPSK-modulated signal using a random bit sequence.

(30%), as compared to the 100% amplitude envelope variation for conventional QPSK systems [1].

The design of coherent QPSK and OQPSK demodulators is a difficult task, particularly if very fast modem synchronization is required. To avoid the need of a complex carrier recovery circuit and to improve the synchronization speed of the demodulator, differential QPSK (DQPSK) demodulation may be employed instead of coherent demodulation [1].

2.2. Six-Port QPSK Modulator

In practice, especially at millimeter-wave frequencies, the mixers are costly components and difficult to fabricate. To avoid this problem, a different type of QPSK modulator, the six-port modulator, can be designed using power dividers and couplers [2].

The basic components of this QPSK modulator are the Wilkinson power divider and the 90° hybrid coupler. Figure 5 shows the Wilkinson power divider and the 90° hybrid coupler symbols.

The related *S* parameters of the Wilkinson power divider and of the 90° hybrid coupler, respectively, are as follows:

$$S = -\frac{1}{\sqrt{2}} \begin{bmatrix} 0 & j & j \\ j & 0 & 0 \\ j & 0 & 0 \end{bmatrix} \quad (6)$$

$$S = \frac{1}{\sqrt{2}} \begin{bmatrix} 0 & j & 1 & 0 \\ j & 0 & 0 & 1 \\ 1 & 0 & 0 & j \\ 0 & 1 & j & 0 \end{bmatrix} \quad (7)$$

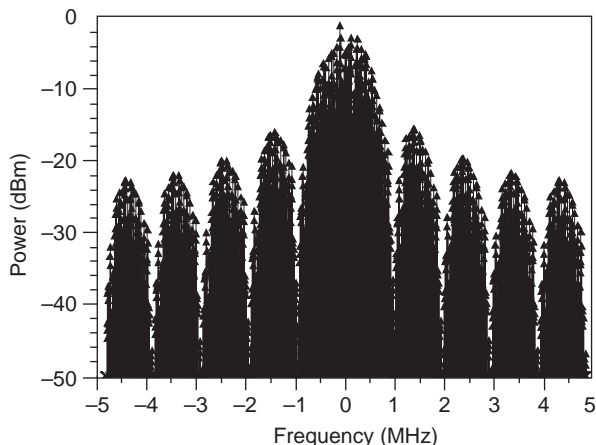


Figure 4. Simulated spectrum of an unfiltered QPSK signal.

In order to understand the six-port QPSK modulator principle, a basic circuit—the controlled phase shifter must be first presented. This circuit consists of a 90° hybrid coupler and two monoports having the reflection coefficient equal to Γ . Figure 6 shows the phase shifter block diagram.

The scattering parameters are used to express the circuit equations. For each monoport, the input and output reflected signals, *a* and *b*, are related by the equation $a_i = \Gamma \cdot b_i$, where $i = 2, 3$. Therefore, we obtain

$$\begin{bmatrix} b_1 \\ b_2 \\ b_3 \\ b_4 \end{bmatrix} = \frac{1}{\sqrt{2}} \begin{bmatrix} 0 & j & 1 & 0 \\ j & 0 & 0 & 1 \\ 1 & 0 & 0 & j \\ 0 & 1 & j & 0 \end{bmatrix} \cdot \begin{bmatrix} a_1 \\ \Gamma b_2 \\ \Gamma b_3 \\ a_4 \end{bmatrix} \quad (8)$$

and

$$b_1 = \frac{1}{\sqrt{2}} (j\Gamma b_2 + \Gamma b_3) \quad (9)$$

$$b_2 = \frac{1}{\sqrt{2}} (ja_1 + a_4) \quad (10)$$

$$b_3 = \frac{1}{\sqrt{2}} (a_1 + ja_4) \quad (11)$$

$$b_4 = \frac{1}{\sqrt{2}} (\Gamma b_2 + j\Gamma b_3) \quad (12)$$

The relationship between the output and the input signal can be obtained using the previous equations. The phase of the output signal *b*₄ depends of the phase of the reflection coefficient Γ :

$$b_4 = j\Gamma a_1 \quad (13)$$

Supposing that $\Gamma = \exp(j\phi)$, the output signal will be equal to

$$b_4 = ja_1 \exp(j\phi) \quad (14)$$

If a 50-Ω load is connected at the output port of this circuit, the reflected signal to the input port ($b_1 = j\Gamma a_4$) will be equal to zero because $a_4 = 0$. Therefore, the circuit will

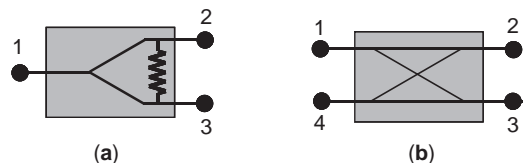


Figure 5. Wilkinson power divider (a) and the 90° hybrid coupler (b) symbols.

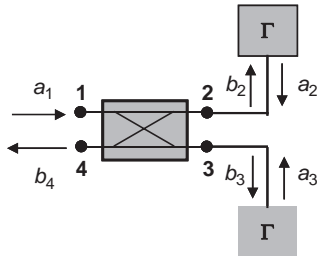


Figure 6. Phase shifter block diagram.

be a phase shifter having an excellent return loss to the input port.

Figure 7 shows the six-port modulator diagram according to relations (6) and (7). A 90° hybrid coupler, two controlled phase shifters, and a Wilkinson power combiner, compose the six-port QPSK modulator. This modulator circuit has six ports: an RF input port connected to the carrier generator, an RF output port that generates the modulated signal, and four control ports connected to monoports.

The signal values are specified on the diagram in Fig. 7. The output signal is a function of the input signal a , and of the monoports reflection coefficients Γ_1 and Γ_2 :

$$S(t) = \frac{a}{2} [j\Gamma_1(t) + \Gamma_2(t)] \quad (15)$$

During the modulation process, each reflection coefficient, $\Gamma_1(t)$ or $\Gamma_2(t)$, has two possible values. In this study, these values are -1 (equivalent to a short circuit) and $+1$ (equivalent to an open circuit). Table 1 shows the four states of the output QPSK modulated signal and related Γ values. In this table, four possible phase values of the RF signal can be clearly identified.

3. QPSK DEMODULATORS

3.1. QPSK Demodulating Principle

Figure 8 shows a block diagram of the QPSK demodulator. The demodulated signals $I(t)$ and $Q(t)$ are obtained using a

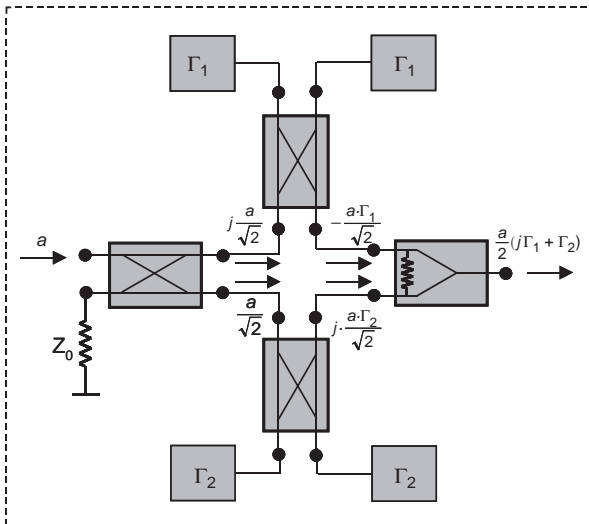


Figure 7. Block diagram of the six-port QPSK modulator.

Table 1. The Four States of Output QPSK-Modulated Signal and Related Γ Values

Γ_1	Γ_2	QPSK Signal
1	1	$\frac{a}{2}(1+j) = \frac{a}{\sqrt{2}} \exp(j\frac{\pi}{4})$
1	-1	$\frac{a}{2}(-1+j) = \frac{a}{\sqrt{2}} \exp(j\frac{3\pi}{4})$
-1	-1	$\frac{a}{2}(-1-j) = \frac{a}{\sqrt{2}} \exp(j\frac{5\pi}{4})$
-1	1	$\frac{a}{2}(1-j) = \frac{a}{\sqrt{2}} \exp(j\frac{7\pi}{4})$

reference signal, a 90° phase shifter, mixers, and lowpass filters.

The QPSK-modulated signal can be expressed as

$$S(t) = \text{Re}\{A \exp[j(\omega t + \varphi_i)]\} = A \cos(\omega t + \varphi_i) \quad (16)$$

where the phase variation during the time φ_i has four possible states, according to the QPSK constellation of Fig. 1:

$$\varphi_i = (2i - 1)\frac{\pi}{4}, \quad i = 1, 2, 3, 4 \quad (17)$$

The demodulation of QPSK signals requires coherent detection. Because the I and Q signals are in quadrature (orthogonal), the receiver is able to demodulate them independently of each other, operating effectively as two independent BPSK receivers.

The signal value to the I multiplier output can be expressed as

$$\begin{aligned} & A \cos(\omega t + \varphi_i) \cdot A \cos(\omega t) \\ &= \frac{A^2}{2} \cos(2\omega t + \varphi_i) + \frac{A^2}{2} \cos \varphi_i \end{aligned} \quad (18)$$

The signal value to the Q multiplier output is given by the equation

$$\begin{aligned} & A \cos(\omega t + \varphi_i) \cdot A \cos\left(\omega t + \frac{\pi}{2}\right) \\ &= -A^2 \cos(\omega t + \varphi_i) \cdot \sin(\omega t) \\ &= -\frac{A^2}{2} \cdot \sin(2\omega t + \varphi_i) + \frac{A^2}{2} \sin \varphi_i \end{aligned} \quad (19)$$

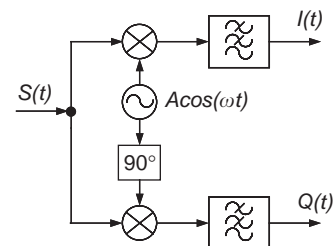


Figure 8. Block diagram of the QPSK demodulator.

Table 2. Specific Binary Outputs for Four Possible Input Symbols

φ_i	I	Q	Binary Output
$\frac{\pi}{4}$	C	C	11
$\frac{3\pi}{4}$	-C	C	01
$\frac{5\pi}{4}$	-C	-C	00
$\frac{7\pi}{4}$	C	-C	10

Finally, at the output of the lowpass filters we obtain the I/Q-demodulated signals:

$$I(T) = \int_0^T \left[\frac{A^2}{2} \cos(2\omega t + \varphi_i) + \frac{A^2}{2} \cos \varphi_i \right] dt \tag{20}$$

$$= \frac{A^2 T}{2} \cos \varphi_i$$

$$Q(T) = \int_0^T \left[-\frac{A^2}{2} \sin(2\omega t + \varphi_i) + \frac{A^2}{2} \sin \varphi_i \right] dt \tag{21}$$

$$= \frac{A^2 T}{2} \sin \varphi_i$$

where T is the symbol period and φ_i is the phase of the i th QPSK signal. The regenerated I and Q streams are then recombined in a parallel-to-serial converter to recover the original input datastream.

Table 2 lists the specific binary outputs in the case of the four possible input symbols, where the constant C is defined as $A^2 T / 2\sqrt{2}$. Comparison with the diagram presented in Fig. 1 shows that the correct binary data are recovered by the QPSK demodulator.

The OQPSK demodulator is identical to that used for coincident QPSK, except that the regenerated I datastream is delayed with half the incoming bit duration (if the Q datastream is delayed in the modulation process), so that when combined with the regenerated Q stream, the original input data stream is recreated. Details of encoding and decoding subsystems QPSK, OQPSK, and DQPSK are presented in Ref. 1.

A typically standard demodulator, the MAX 2701 circuit from the Maxim Company, is shown in Fig. 9. The circuit diagram follows the demodulator principle. This circuit uses differential amplifiers, mixers, and external bandpass and lowpass filters. This circuit operates excellently up to 2.45 GHz [3].

In practice, especially at millimeter-wave frequencies, the mixers are costly components, and are difficult to fabricate. To avoid this problem, a different type of QPSK demodulator, the six-port demodulator, will be presented in the next section.

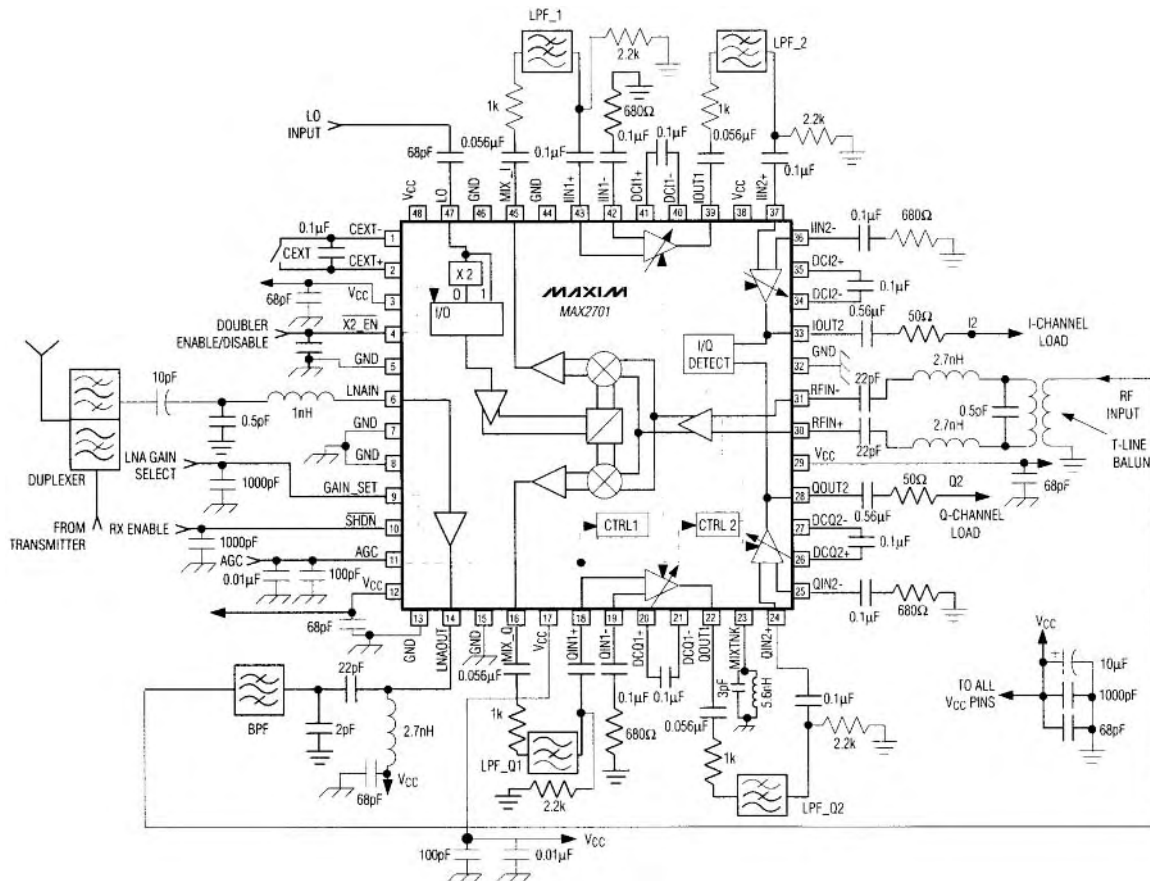


Figure 9. Diagram of a typically standard QPSK demodulator.

3.2. Six-Port QPSK Demodulator

3.2.1. Basic Theory. The six-port junction is a passive and linear microwave circuit composed of several couplers. The four six-port output signals are a function of two RF input signals. Complex impedance or phase measurements can be obtained by simple power or voltage magnitude measurements at the four output ports [4].

The six-port junction was first utilized as a low-cost alternative to a network analyzer. A number of six-ports were designed to perform measurements of reflection coefficients [5–7].

The six-port can also be designed to perform phase measurements between two input RF signals. If one of these signals is a reference signal, and the second one is an unknown RF signal, their phase difference can be measured. Therefore, a phase shift key (PSK) demodulator can be developed using direct-conversion architecture. Excellent demodulation results were obtained in direct-conversion receivers (DCRs) for QPSK modulation [8–12].

Figure 10 shows the complete diagram of the six-port phase discriminator, composed of a Wilkinson power divider and three 90° hybrid couplers. This junction is specially designed to perform phase measurements. The phase shift between the RF input signal and the RF reference signal can be obtained using power measurements to the six-port outputs.

The S matrix of the proposed six-port phase discriminator can be easily obtained using this figure and the S parameters of the Wilkinson power divider and the 90° hybrid coupler as presented in Eqs. (6) and (7). The S matrix of the six-port phase discriminator is

$$[S] = \frac{1}{2} \begin{bmatrix} 0 & 0 & 0 & 0 & -j & +j \\ 0 & 0 & 0 & 0 & +1 & +j \\ 0 & 0 & 0 & 0 & +1 & +1 \\ 0 & 0 & 0 & 0 & -j & -1 \\ -j & +1 & +1 & -j & 0 & 0 \\ +j & +j & +1 & -1 & 0 & 0 \end{bmatrix} \quad (22)$$

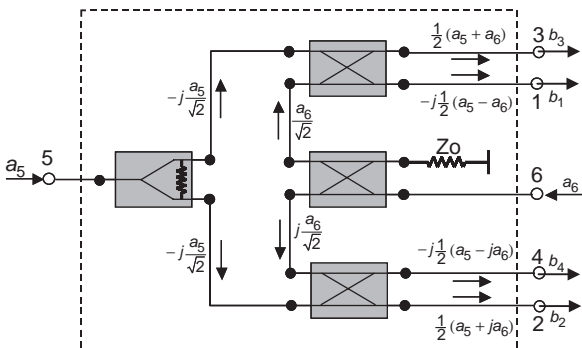


Figure 10. Block diagram of the six-port phase discriminator.

If the two input signals have the same amplitude a , the general equation of the six-port output signals is

$$b_i = a \cdot [S_{5i} \exp(j\theta_5) + S_{6i} \exp(j\theta_6)], \quad i = 1, 2, 3, 4 \quad (23)$$

$$b_i = \frac{a}{2} \exp(j\theta_5) \cdot \left\{ 1 - \exp \left[j \left(\theta_6 - \theta_5 - (i-1) \frac{\pi}{2} \right) \right] \right\}, \quad (24)$$

$$i = 1, 2, 3, 4$$

Each output power is proportional with $|b_i|^2$ and has a minimum value corresponding to a certain phase difference $\Delta\theta = \theta_6 - \theta_5$, according to Eq. (24).

Therefore, the six-port junction can be used directly to demodulate a QPSK signal, where each minimum corresponds to a different state of the input signal. The two RF signals have the same frequency, but a different phase: the reference phase θ_5 , for the local-oscillator (LO) signal and an unknown phase θ_6 , for the input PSK modulated signal.

If the phase of the reference signal is set at $\theta_5 = \pi/4$, the q_i points of the six-port junction are

$$q_i = \exp \left\{ j \left[\frac{\pi}{4} + (i-1) \frac{\pi}{2} \right] \right\}, \quad i = 1, 2, 3, 4 \quad (25)$$

where the q_i points represent the complex solution of the equations $b_i = 0$.

Four power detectors are connected to the six-port circuit outputs. The DC output voltage of an ideal power detector is proportional to the second power of the magnitude of the RF input signal:

$$V_i = K_i |b_i|^2, \quad i = 1, 2, 3, 4 \quad (26)$$

Assuming that four identical detectors $K_i = K$ are used, the theoretical DC output voltages are

$$V_i = K |a|^2 \left| \sin \left(\frac{\Delta\theta}{2} - (i-1) \frac{\pi}{4} \right) \right|^2, \quad i = 1, 2, 3, 4 \quad (27)$$

Each DC output voltage is periodical with 360° and shifted in phase with 90° multiples compared to the other DC output signals. The normalized output voltages can be obtained using Eq. (27):

$$v_i = \left| \sin \left(\frac{\Delta\theta}{2} - (i-1) \frac{\pi}{4} \right) \right|^2, \quad i = 1, 2, 3, 4 \quad (28)$$

Figure 11 shows the normalized output voltages as a function of phase difference between the two RF input

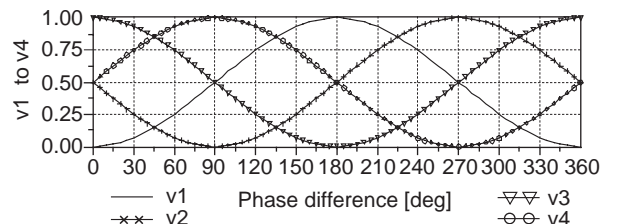


Figure 11. Normalized six-port DC output voltages versus the phase difference between the RF input signals.

signals. Each output voltage has a single maximum (or minimum) value corresponding to a 0° to 360° phase difference between the RF input signals.

In the I/Q complex plane a Γ vector can be defined using the four six-port DC output voltages:

$$\Gamma = [(V_3 - V_1) + j(V_4 - V_2)] \exp\left(j\frac{\pi}{4}\right) \quad (29)$$

The normalized Γ_n vector is obtained using the normalized six-port DC output voltages:

$$\Gamma_n = [(v_3 - v_1) + j(v_4 - v_2)] \exp\left(j\frac{\pi}{4}\right) \quad (30)$$

In the I/Q complex plane the Γ_n vector turns in a circle having the radius equal to one and the center in the origin. This Γ_n vector, always having the magnitude equal to one and the phase equal with the RF input signal phase θ_6 , represents the analog demodulated signal in the I/Q plane.

A QPSK modulated signal has four possible phase states: $\pi/4$, $3\pi/4$, $5\pi/4$ and $7\pi/4$, as presented in Fig. 1. The analog direct demodulated signal can be calculated using the six-port DC output voltage equations (28) and the Γ_n vector (30). The theoretical demodulation results are presented in Table 3.

This new approach allows for high-speed QPSK demodulation because the direct demodulated signal is obtained using only a linear combination of six-port DC output voltages. However, a reference signal must be obtained using a carrier recovery technique.

3.2.2. Examples of Six-Port Demodulators. Three six-port circuits operating in the Ka frequency band will be presented in this section: a hybrid circuit (MHMIC) and two MMIC (monolithic microwave integrated circuit) circuits.

As is known, the six-port junction is composed of three 90° hybrid couplers and a Wilkinson power divider. Four RF power detectors, connected to the six-port outputs, are also integrated on the same circuit.

Figure 12 shows a photograph of the distributed parameters MHMIC Ka-band six-port circuit, fabricated on a 250- μm ceramic substrate having a relative permittivity of 9.9. The RF power detectors are realized using Schottky diodes. The MHMIC six-port circuit size is 23 \times 23 mm [11].

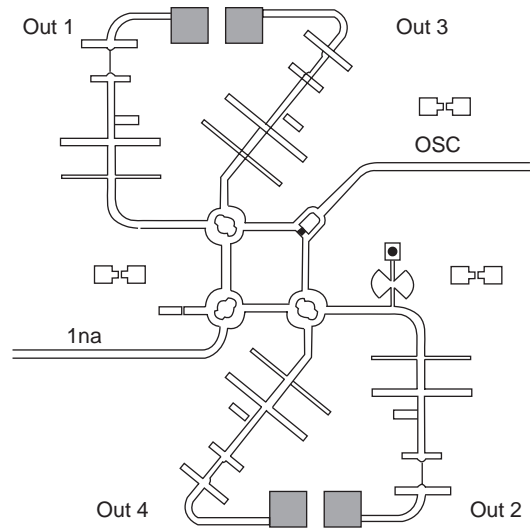


Figure 12. The MHMIC circuit (size 23 \times 23 mm).

Figure 13 shows a photograph of the distributed parameters MMIC six-port circuit fabricated on a 100- μm GaAs substrate, having a relative permittivity of 12.9. The RF power detectors are implemented using integrated Schottky diodes. Transitions to a coplanar line were used to the RF inputs. The size of the distributed parameters MMIC six-port circuit is 4 \times 4 mm [12].

A photograph of the second MMIC six-port circuit, fabricated on the same type of GaAs substrate, is presented in Fig. 14. Shunt capacitors connected to the ports were used in order to reduce the size of the 90° hybrid coupler. Therefore, the diameter of the 90° hybrid coupler becomes 600 μm , compared to 1300 μm in the first MMIC version. The matching networks are made using transmission lines and shunt capacitors. The size of the distributed and discrete parameters MMIC six-port circuit is 2 \times 3-mm [12].

Analog signal processing (ASP) was used to demodulate a QPSK signal according to Eqs (27)–(30). Comparative demodulation results for these six-port junctions, in the operating frequency band, are presented.

The six-port output signals are a function of six-port S parameters and input RF signals according to Eq. (23). Therefore, the QPSK-demodulated signal, represented by the Γ vector in the I/Q complex plane, is a function of the six-port S parameters in the operating frequency band, the input RF power to DC voltage conversion

Table 3. Theoretical Demodulation Results for QPSK Modulation Using a Six-Port Demodulator

Bits Tx	θ_6	v_1	v_2	v_3	v_4	$\Gamma_n(\text{Rx})$	Bits Rx
11	$\frac{\pi}{4}$	0	0.5	1	0.5	$\exp\left(j\frac{\pi}{4}\right)$	11
01	$\frac{3\pi}{4}$	0.5	0	0.5	1	$\exp\left(j\frac{3\pi}{4}\right)$	01
00	$\frac{5\pi}{4}$	1	0.5	0	0.5	$\exp\left(j\frac{5\pi}{4}\right)$	00
10	$\frac{7\pi}{4}$	0.5	1	0.5	0	$\exp\left(j\frac{7\pi}{4}\right)$	10

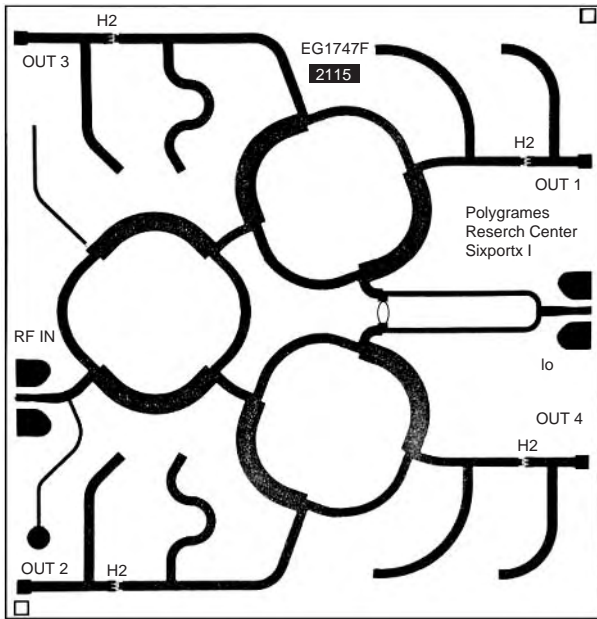


Figure 13. The first MMIC six-port (size 4 × 4 mm).

characteristic of the Schottky detector, and the input RF signal power.

Figure 15 shows the six-port DC output voltages versus the phase difference between the RF input signals for the MHMIC circuit. The LO power level and the RF input power level are -20 dBm.

The geometric representation of the Γ vector in the I/Q plane was obtained through Advanced Design System (ADS) simulations using a sweep of the phase difference between the RF input signals. The phase step was set at 5°.

Figure 16 shows the demodulation results for various input power levels, at the central frequency of 27 GHz (MHMIC circuit). The markers indicate the demodulation result corresponding to a QPSK modulation, having a phase error of the demodulated signal of less than 2°. Even if the RF levels are not equal, the Γ vector still turns on a circle. The reduced radii correspond to the decrease of the RF input power level. The DC offset is close to zero, as seen in this figure, because a differential approach was

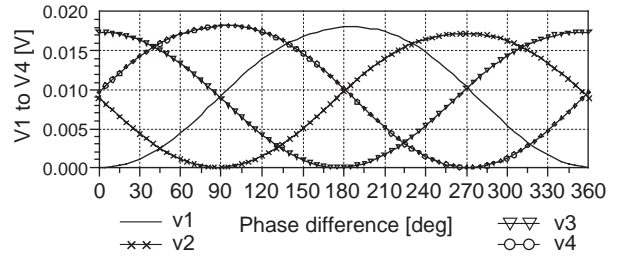


Figure 15. Six-port DC output voltages versus the phase difference between the RF input signals for the MHMIC circuit.

used in the Γ equation and all the detectors are almost identical.

Figure 17 shows the Γ vector using a sweep of the phase difference between the RF input signals, in the frequency band. The four states corresponding to the QPSK modulation can be clearly identified. This shows that the MHMIC circuit is an excellent direct demodulator and can be used for other PSK modulations, because the Γ vector turns practically on a circle, as presented in the theoretical part. Two MMIC circuits, fabricated at the *TriQuint Semiconductor Foundry* using 0.25 μm GaAs PHEMT technology, were also investigated using the same method.

The conversion result of the DC output voltage versus the RF input power in the case of the distributed parameters MMIC detector is nonlinear. Therefore, the shape of the six-port DC output voltages versus the phase difference between the RF input signals corresponding to the first MMIC circuit, presented in Fig. 18, are different compared to the theoretical result of Fig. 11. However, each output voltage has a single maximum value corresponding to a 360° phase difference sweep, which allows the direct demodulation of a BPSK or a QPSK signal. The geometric representation of Γ vector in the I/Q complex plane was obtained using ADS simulations. The phase step was set at 5°.

Figure 19 shows the simulated demodulation results corresponding to various input power levels at the central

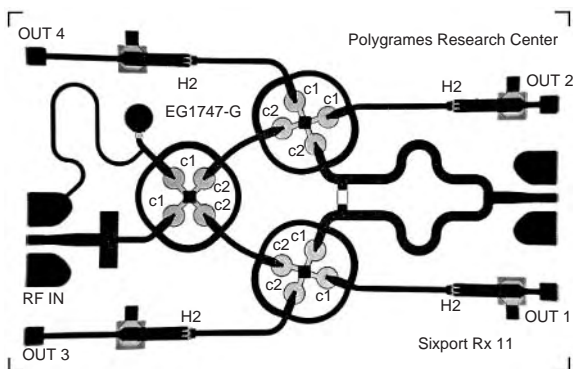


Figure 14. The second MMIC six-port (size 2 × 3 mm).

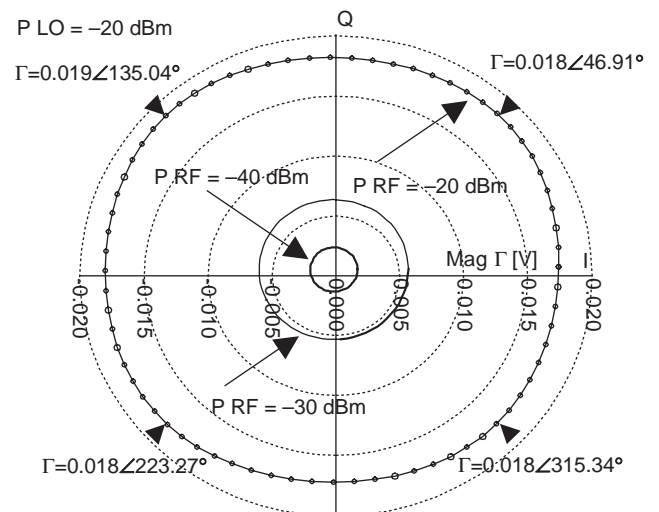


Figure 16. Demodulation results for various input power levels at the central frequency of 27 GHz (MHMIC circuit).

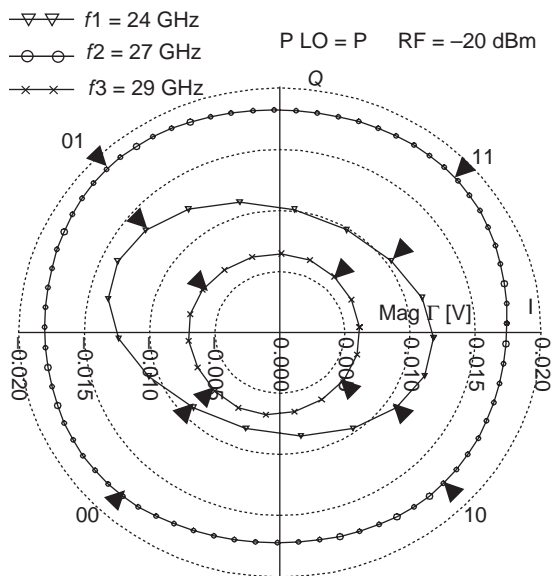


Figure 17. Demodulation results in the frequency band (MHMIC circuit).

frequency of 27 GHz. The dynamic range is reduced, compared to the MHMIC circuit, because the MMIC detector is not very sensitive for small RF input power levels. The markers indicate the demodulation result corresponding to a QPSK modulation, having a phase error of less than 2°. Even if the RF levels are not equal the Γ vector turns around the origin, and the DC offset is close to zero. The Γ shape is no longer a circle because of the nonlinearity of the RF power to DC voltage detector conversion. However, BPSK or QPSK signals can be demodulated with no need of the six-port calibration.

Figure 20 shows Γ vector as a function of the sweep of the phase difference between the RF input signals in the frequency band of 1 GHz. The four states corresponding to the QPSK modulation can be clearly identified in this figure.

The conversion result of the DC output voltage versus the RF input power corresponding to the second MMIC detector is not linear. Therefore, the shape of the six-port DC output voltages versus the phase difference between the RF input signals for the second MMIC circuit, presented in Fig. 21, are also different from the theoretical result of Fig. 11.

In the case of this MMIC implementation, the detector sensibility increases by using a higher load value, but the

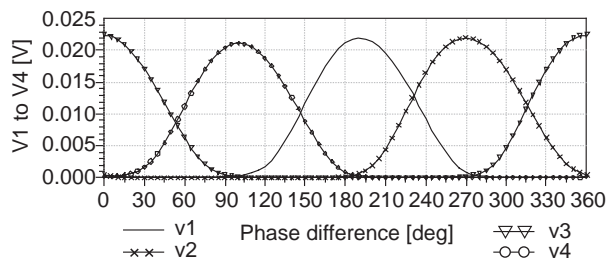


Figure 18. Six-port DC output voltages versus the phase difference between the RF input signals for the first MMIC circuit.

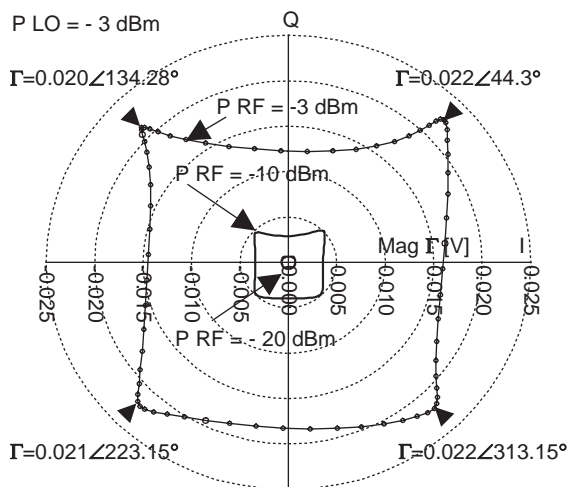


Figure 19. Demodulation results for various input power levels at the central frequency of 27 GHz (the first MMIC circuit).

linearity of the conversion result deteriorates. For this reason, a 1000 Ω load value was used for a greater sensitivity of the Schottky detector, instead of a 50 Ω load value, as used for the first MMIC circuit.

Figure 21 shows that each six-port DC output voltage has a single maximum value corresponding to a 360° phase difference sweep, which allows the direct demodulation of a BPSK or QPSK signal.

Figure 22 shows the simulated demodulation results corresponding to various input power levels, at the central frequency of 27 GHz. The markers indicate the demodulation result corresponding to a QPSK modulation, having a phase error of less than 1°. Even if the RF levels are not equal, the Γ vector turns around the origin. Therefore, the DC offset is close to zero. The Γ shape is no longer a circle because of the nonlinearity of the RF power to DC voltage

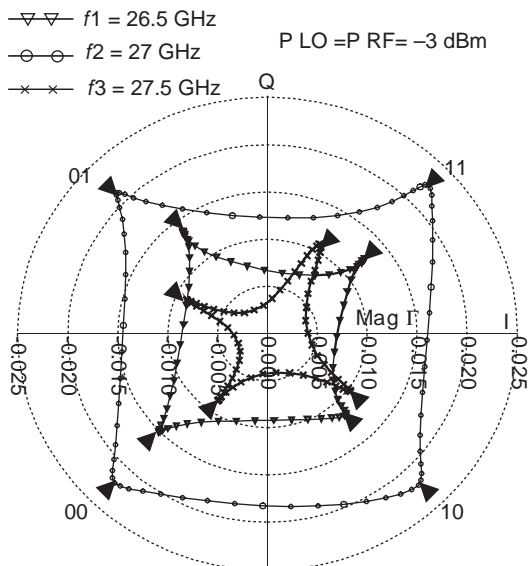


Figure 20. Demodulation results in the frequency band (the first MMIC circuit).

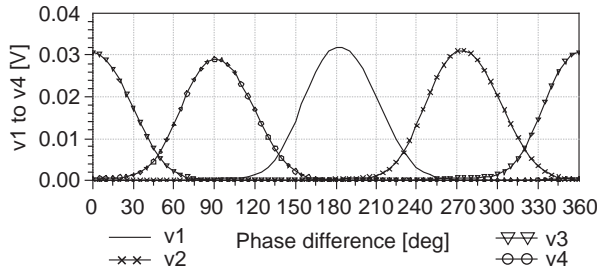


Figure 21. Six-port DC output voltages versus the phase difference between the RF input signals for the second MMIC circuit.

detector conversion. However, BPSK or QPSK signals can be demodulated with no need of the six-port calibration.

Figure 23 shows the Γ vector in function of the sweep of the phase difference between the RF input signals in the frequency band of 0.75 GHz. The four states corresponding to the QPSK modulation can be clearly identified in this figure.

In order to perform bit error rate (BER) measurements, baseband circuits were designed. To build up the baseband circuits, operational amplifiers, high-speed comparators and NAND logic circuits are used [11,12]. These circuits make up an analog to digital converter and generate output bits [a TTL (transistor–transistor logic) signal] using the analog vector Γ represented in the I/Q complex plane, as seen in Figs. 16,17,19,20,22, and 23.

In conclusion, analog signal processing (ASP) and a six-port circuit were used to directly demodulate a QPSK signal. This new approach allows a high-speed PSK demodulation because the direct demodulated signal (the Γ vector) is obtained using only a linear combination of the six-port DC output voltages. The DC offset is close to zero, due to the differential approach used in Γ equation.

The six-port calibration and the use of a digital signal processing (DSP) are not needed in the case of this application. Therefore, the bit rate is limited only by the speed of the baseband circuit, composed of operational amplifiers and comparators, and not by the speed of the DSP module.

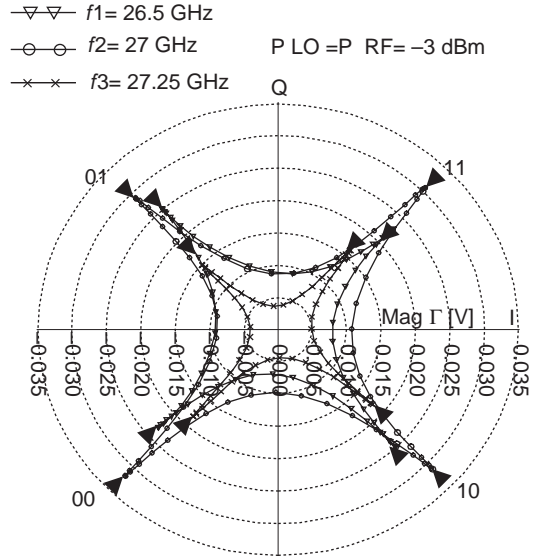


Figure 23. Demodulation results in the frequency band (the second MMIC circuit).

In the case of a general PSK modulation, RF power detectors having almost a linear conversion characteristic must be used. In particular, for BPSK or QPSK modulations, this condition can be avoided, due to the particular six-port architecture, as concluded in the case of the MMIC circuits.

The main advantages of the six-port direct-conversion receiver, compared to a standard one, are the low cost and high bit rate. This new QPSK demodulator avoids the use of mixers using a passive circuit, the six-port phase discriminator.

4. CARRIER RECOVERY

The design of the coherent carrier recovery circuit for the demodulation of QPSK signals is critical and involves several performance considerations and tradeoffs. Therefore, various carrier regeneration schemes have been developed and implemented.

Design of the coherent carrier recovery circuit has to be done considering various critical requirements. The effects of the input data rate and the signal to noise ratio variations on the overall performance of the system have to be considered, and system elements having broadband characteristics must be designed.

The following schemes are considered to implement the coherent carrier recovery in a QPSK demodulator: the Costas loop [13], the multiplication loop [14], and the reverse-modulation loop [15].

4.1. The Costas Loop

A block diagram of this carrier recovery method is presented in Fig. 24.

The input-modulated signal is split into two paths, which are mixed with the voltage-controlled oscillator (VCO) signal in the QPSK detector to produce the demodulated I and Q signals.

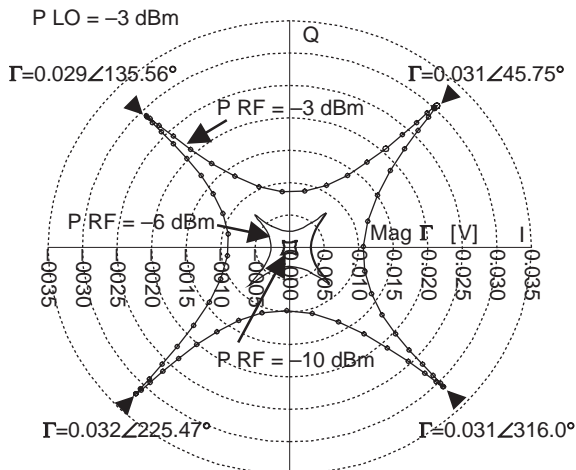


Figure 22. Demodulation results for various input power levels at the central frequency of 27 GHz (the second MMIC circuit).

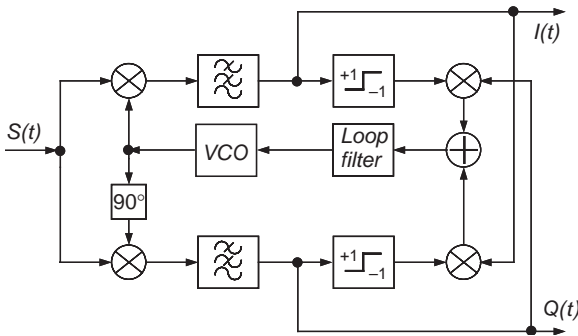


Figure 24. Block diagram of QPSK demodulator with the Costas loop.

The samples of the same I and Q datastreams are also amplified and filtered into the Costas arm filters. The arm filter outputs feed the Costas phase detectors, which generate an estimated phase error signal through a polarity loop. The corresponding output phase error signal feeds a loop filter or a phase-locked loop (PLL) circuit, which drives the VCO. The VCO replaces the local oscillator (LO) of the coherent detector.

4.2. The Multiplication Loop

A multiplication loop block diagram for QPSK carrier recovery is given in Fig. 25.

The input QPSK modulated signal is

$$S(t) = \text{Re}\{A \exp[j(\omega t + \varphi_i)]\} = A \cos(\omega t + \varphi_i) \tag{31}$$

where

$$\varphi_i = (2i - 1) \frac{\pi}{4}, \quad i = 1, 2, 3, 4 \tag{32}$$

during the time, for a QPSK modulated signal.

Considering the output of Fourth-order nonlinearity and assuming ideal quadrupling, by a trigonometric identity, we obtain

$$S^4(t) = [A \cos(\omega t + \varphi_i)]^4 = 3 \frac{A^4}{8} + \frac{A^4}{2} \cos[2(\omega t + \varphi_i)] + \frac{A^4}{8} \cos[4(\omega t + \varphi_i)] \tag{33}$$

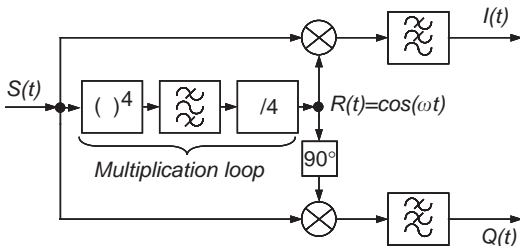


Figure 25. Block diagram of QPSK demodulator with the multiplication loop.

The filtered output contains the desired harmonic:

$$\begin{aligned} \cos[4(\omega t + \varphi_i)] &= \cos[4\omega t + (2i - 1)\pi] \\ &= \cos(4\omega t - \pi) = -\cos(4\omega t) \end{aligned} \tag{34}$$

Frequency division by 4 yields the desired coherent carrier component:

$$R(t) = \cos(\omega t) \tag{35}$$

4.3. The Reverse Modulation Loop

A remodulation technique for QPSK carrier recovery is shown in Fig. 26.

The input-modulated signal is split into two paths. The first path feeds the QPSK demodulator. The second one is delayed with a percentage of the bit period (τ); this signal represents the local oscillator signal of the QPSK modulator. The I and Q streams are also amplified and filtered. The filter outputs feed the phase detectors. The reverse-modulated signal feeds the loop filter circuit, which replaces the VCO (voltage-controlled oscillator) of the coherent demodulator.

For a high signal-to-noise ratio (SNR), the phase detector error characteristic has four stable lock points situated at 90° multiples. Therefore, the QPSK remodulator should exhibit a faster acquisition time compared to a conventional Costas loop [15].

A reverse-modulation loop (RML) using the six-port demodulator was proposed for Ka-band direct-conversion receivers [16].

The RML provides a rapid carrier recovery using the input QPSK-modulated signal. The proposed RML generates the reference signal using a QPSK modulator, controlled by output-demodulated signals, and avoids the need of a PLL circuit with VCO. For a 4-Mbps QPSK signal, the time delay is set at $0.1 \mu\text{s}$, which corresponds to 20% of a bit length.

Figure 27 shows the simulated QPSK signal spectrum and the carrier recovery signal spectrum corresponding to the same bit rate. It is seen that the signal level of the recovered signal is at least 30 dB above other spectral lines. The power level of the carrier-recovered signal is related to the power level of the input QPSK signal.

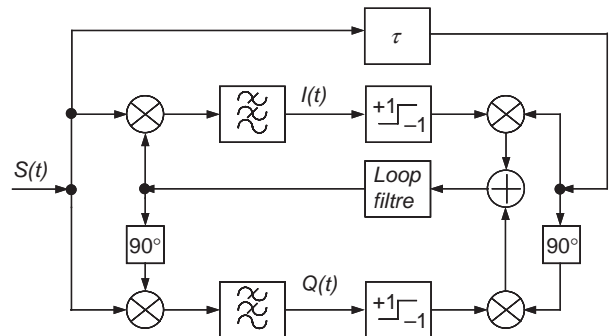


Figure 26. Block diagram of QPSK demodulator with the reverse modulation loop.

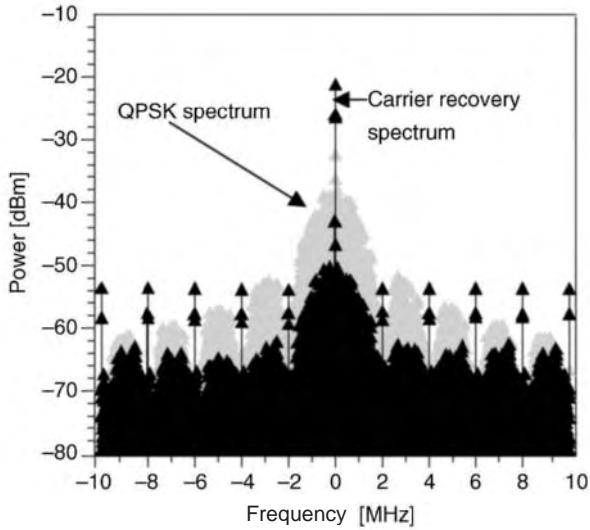
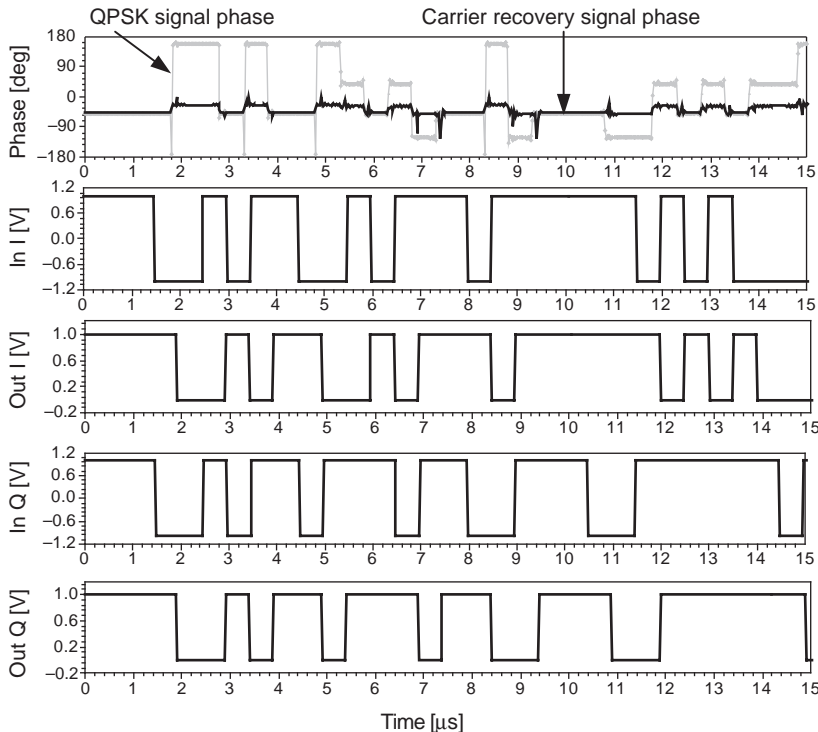


Figure 27. The QPSK and carrier recovery signal spectrum using a reverse modulation loop.

Therefore, the dynamic range of the QPSK six-port receiver increases [12].

Figure 28 shows demodulation results using a QPSK six-port demodulator with a carrier recovery circuit based on this reverse modulation loop. The phases of the input QPSK signal and carrier recovery signal, the pseudorandom bit sequence at the transmitter (labeled “In I” and “In Q” on the diagram) and the received bit sequence (“Out I” and “Out Q”) versus the time are presented.

The phase error of the recovered signal is about $\pm 20^\circ$, except for the glitches. These glitches produce spectral lines spaced at around 2 MHz, as seen in Fig. 27.



The I/Q bit sequence obtained at the six-port QPSK demodulator output shows excellent demodulation results. The time delay between output and input I/Q signals corresponds to the propagation time from transmitter to receiver.

5. PROBABILITY OF ERROR FOR QPSK

The probability of error for the QPSK signals can be derived using the equations of I and Q demodulated signals [Eqs. (20) and (21)] in the presence of noise. The presence of noise may cause an incorrect reception of symbols by the demodulator [17].

By symmetry, the error rates for all input symbols are equal, so it can be assumed that one of these symbols (e.g., $i = 2$) is received. According to Eqs. (16) and (17), this signal can be expressed by

$$\begin{aligned} S_2(t) &= \text{Re}\{A \exp[j \cdot (\omega t + \varphi_2)]\} \\ &= A \cos(\omega t + \varphi_2) \\ &= A \cos\left(\omega t + 3\frac{\pi}{4}\right) \end{aligned} \quad (36)$$

Then, considering the additive Gaussian noise having a power spectral density of $N_0/2$, the received signal is

$$\begin{aligned} S(t) + N(t) &= S_2(t) + N(t) \\ &= A \cos\left(\omega t + 3\frac{\pi}{4}\right) + N(t) \end{aligned} \quad (37)$$

Figure 28. RF signals phases and related IQ signals using a six-port QPSK demodulator.

According to Eqs. (20) and (21), the output filtered I and Q signals are

$$I(T) = -\frac{A^2T}{2\sqrt{2}} + N_0(T) = -\frac{E_S}{\sqrt{2}} + N_0(T) \tag{38}$$

$$Q(T) = \frac{A^2T}{2\sqrt{2}} + N_0(T) = \frac{E_S}{\sqrt{2}} + N_0(T) \tag{39}$$

where $E_S = (A^2T)/2$ is the symbol energy and $N_0(T)$ is the noise component of the output:

$$N_0(T) = \int_0^T N(t)A \cos \omega t dt \tag{40}$$

which represents a Gaussian random variable.

The variance of $N_0(T)$ can be calculated as follows:

$$\begin{aligned} \sigma^2 &= E\{N_0^2(T)\} \\ &= E\left\{ \int_{t=0}^T \int_{s=0}^T A^2 N(t)N(s) \cos \omega t \cos \omega s dt ds \right\} \tag{41} \\ &= \frac{A^2TN_0}{4} = \frac{E_S N_0}{2} \end{aligned}$$

The detection threshold for both detectors is zero, so the probability of a symbol error for I signal is

$$\begin{aligned} P_e^I &= P(I \geq 0) = P\left\{ N_0(T) \geq \frac{E_S}{\sqrt{2}} \right\} \\ &= \int_{E_S/\sqrt{2}}^{\infty} \frac{1}{\sigma\sqrt{2\pi}} \exp\left(-\frac{u^2}{2\sigma^2}\right) du \end{aligned} \tag{42}$$

By changing the variable $x = u/(\sigma\sqrt{2})$, the error probability becomes

$$P_e^I = \frac{1}{\sqrt{\pi}} \int_{E_S/2\sigma}^{\infty} \exp(-x^2) \cdot dx = \frac{1}{2} \operatorname{erfc}\left(\frac{E_S}{2\sigma}\right) \tag{43}$$

Using equation (41) it can be obtained that:

$$\frac{E_S}{2\sigma} = \sqrt{\frac{E_S}{2N_0}} \tag{44}$$

Because the symbol period T is twice the bit period, it can be concluded that $E_S = 2E_b$, where E_b is the bit energy. Therefore, the error probability will be

$$\begin{aligned} P_e^I &= \frac{1}{2} \operatorname{erfc}\left(\frac{E_S}{2\sigma}\right) = \frac{1}{2} \operatorname{erfc}\left(\sqrt{\frac{E_S}{2N_0}}\right) \\ &= \frac{1}{2} \operatorname{erfc}\left(\sqrt{\frac{E_b}{N_0}}\right) \end{aligned} \tag{45}$$

By symmetry, the probability of a symbol error for Q is

$$\begin{aligned} P_e^Q &= \frac{1}{2} \operatorname{erfc}\left(\frac{E_S}{2\sigma}\right) = \frac{1}{2} \operatorname{erfc}\left(\sqrt{\frac{E_S}{2N_0}}\right) \\ &= \frac{1}{2} \operatorname{erfc}\left(\sqrt{\frac{E_b}{N_0}}\right) \end{aligned} \tag{46}$$

Since the overall probability that a symbol is received correctly is the product of the probabilities that each arm operates correctly, the overall probability of error for a symbol is

$$\begin{aligned} P_e^{(S)} &= 1 - (1 - P_e^I) \cdot (1 - P_e^Q) = 2P_e^I \\ &- (P_e^I)^2 \approx 2P_e^I = \operatorname{erfc}\left(\sqrt{\frac{E_b}{N_0}}\right) \end{aligned} \tag{47}$$

In practice, the QPSK signal with Gray coding is used. We can then assume that a symbol error is most likely to cause only a single bit error. Since each symbol contains 2 bits, the bit error rate for the QPSK will be one half the symbol error rate:

$$P_e^{\text{QPSK(gray)}} = \frac{1}{2} \operatorname{erfc}\left(\sqrt{\frac{E_b}{N_0}}\right) \tag{48}$$

This equation (48) shows that the probability of error of a QPSK signal (Gray coded) is equivalent to the probability of error for a BPSK signal. Thus, using QPSK modulation it is possible to achieve twice the data rate of the BPSK modulation, with the same bandwidth and error rate. This fact has led to the extensive use of QPSK modulation in a wide variety of applications.

Figure 29 shows the theoretical bit error rate (BER) versus the E_b/N_0 ratio for a QPSK modulation, according to Eq. (48).

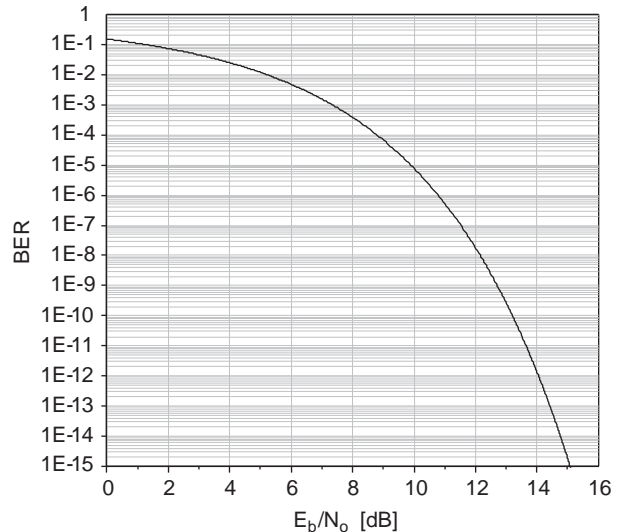


Figure 29. The theoretical bit error rate (BER) versus the E_b/N_0 ratio for a QPSK modulation.

Acknowledgments

The financial support of the National Science Engineering Research Council (NSERC) of Canada is gratefully accepted. The authors would like to acknowledge Emilia Moldovan, Zhiyan Song, Eric Marsan, Traian Antonescu, and the technical personnel of Poly-Grames Research Center of the “École Polytechnique de Montréal” for their valuable contributions to this article.

BIBLIOGRAPHY

1. K. Feher, *Wireless Digital Communications—Modulation and Spread Spectrum Applications*, Prentice-Hall, Englewood Cliffs, NJ, 1995.
2. E. Marsan, J. C. Schiel, G. Brehm, K. Wu, and R. G. Bosisio, High speed carrier recovery suitable for direct digital QPSKtransceivers, *Proc. RAWCON 2002 Conf.*, 2002, pp. 87–90.
3. J. C. Schiel, S. O. Tatu, K. Wu, R. G. Bosisio, Six-port direct digital receiver (SPDR) and standard direct digital receiver (SDR) results for modulation at high speeds, *Proc. IMS 2002 Conf.*, 2002, Vol. 2, pp. 931–934.
4. C. A. Hoer, The six-port coupler: A new approach to measuring voltage, current, power impedance and phase, *IEEE Trans. Instrum. Meas.* **21**(4): 466–470 (1972).
5. G. F. Engen, The six-port reflectometer: An alternative network analyzer, *IEEE Trans. Microwave Theory Tech.* **25**(12): 1075–1080 (1977).
6. G. F. Engen, An improved circuit for implementing the six-port technique of microwave measurements, *IEEE Trans. Microwave Theory Tech.* **25**(12): 1080–1083 (1977).
7. M. P. Weidman, A semi automated six port for measuring millimeter-wave power and complex reflection coefficient, *IEEE Trans. Microwave Theory Tech.* **25**(12): 1083–1086 (Dec. 1977).
8. J. Li, R. G. Bosisio, and K. Wu, Computer and measurement simulation of a new digital receiver operating directly at millimeter-wave frequencies, *IEEE Trans. Microwave Theory Tech.* **43**(12): 2766–2772 (1995).
9. M. Abe, N. Sasho, V. Brankovic, and D. Krupezevic, Direct conversion receiver MMICbased on six-port technology, *Proc. European Conf. Wireless Technology ECWT 2000*, 2000, pp. 139–142..
10. J. Hyryläinen and L. Bogod, Six port direct conversion receiver, *Proc. European Microwave Conf.* 1999, pp. 341–347.
11. S. O. Tatu, E. Moldovan, K. Wu, and R. G. Bosisio, A new direct millimeter-wave six-port receiver, *IEEE Trans. Microwave Theory and Tech.* **49**(12): 2517–2522 (2001).
12. S. O. Tatu, E. Moldovan, G. Brehm, K. Wu, and R. G. Bosisio, Ka band direct digital receiver, *IEEE Trans. Microwave Theory and Tech.* **50**(11): 2436–2442 (2002).
13. L. K. Simon and W. C. Lindsey, Optimum performance of suppressed carrier receivers with Costas loop tracking, *IEEE Trans. Commun.* **25**(2): 215–227 (1977).
14. C. J. Wolejsza and D. Chakraborty, TDMAmodem design criteria, *Comsat Tech. Rev.* **9**(2a) (1979).
15. C. L. Weber, Demodulator-remodulator coherent tracking receiver for QPSKand SQPSK, *IEEE Trans. Commun.* **28**(12): 1945–1953 (1980).
16. S. O. Tatu, E. Moldovan, K. Wu, and R. G. Bosisio, A rapid carrier recovery loop for direct conversion receivers, *Proc. RAWCON 2003, Conf.* 2003, pp. 159–162.
17. D. M. Pozar, *Microwave and RF Design of Wireless Systems*, Wiley, New York, 2001.

QUASI-OPTICAL CIRCUITS

WAYNE A. SHIROMA

MICHAEL P. DELISIO

University of Hawaii at Manoa

In contrast to conventional electronic circuits in which the input and output signals are voltages and currents, quasi-optical circuits have input and output signals that are electromagnetic beams. Quasioptical circuits use components typically associated with optics, such as lenses, mirrors, and polarizers, but are targeted toward the millimeter- and sub-millimeter-wave regimes of the electromagnetic spectrum between 30 GHz and a few terahertz. This article focuses on *active* quasioptical circuits used for generating, amplifying, and processing millimeter-wave beams.

Millimeter-wave systems offer a number of advantages over their microwave and optical counterparts. Compared with microwave systems, millimeter-wave systems have wider bandwidth and reduced size and weight. Compared with optical systems, millimeter waves have the advantage of penetrating smoke, fog, and dust. Millimeter-wave applications include high-resolution imaging systems, satellite crosslinks, automotive collision avoidance, indoor wireless communications, and identification tagging for tracking inventory.

These applications often exploit the atmospheric absorption characteristics of the millimeter-wave regime (Fig. 1). For example, the attenuation windows are used for long-range communications and radar systems, while the absorption peaks are used for short-range communication systems such as indoor wireless local-area networks and covert battlefield communications.

A major obstacle in developing millimeter-wave systems, however, is the limited power-handling capacity of semiconductor devices in this frequency range. Figure 2 [1] compares the average power of representative solid-state and vacuum electronic devices. While solid-state devices have the advantage of size, weight, reliability, manufacturability, and DC requirements, their power tends to fall off with a $1/f$ to $1/f^2$ frequency dependence.

To take advantage of the benefits of solid-state technology while at the same time meeting system specifications, the power from many individual devices must be added coherently. Although a variety of power combiners based on conventional circuit techniques have been developed [2] they have serious limitations at millimeter-wave frequencies where large numbers of devices must be combined and transmission losses are excessive.

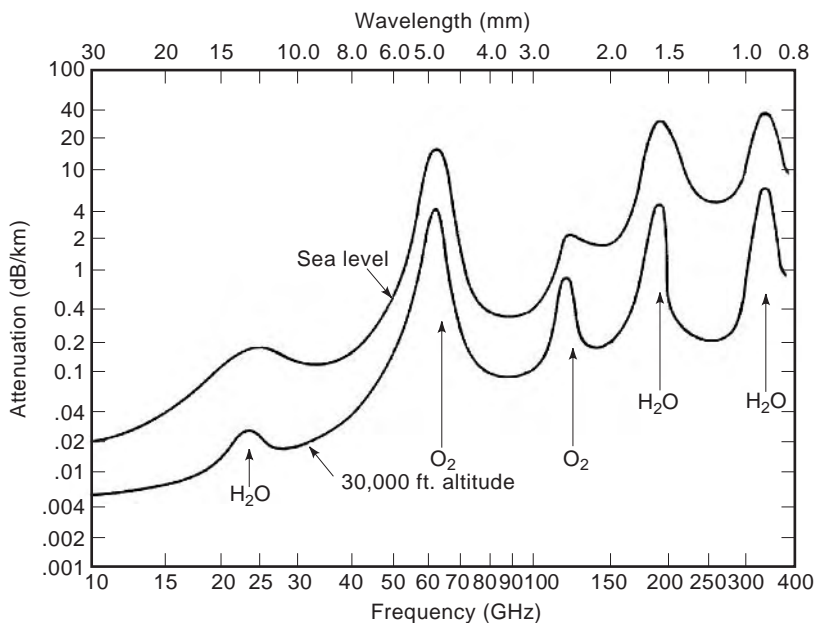


Figure 1. Atmospheric absorption of millimeter waves (horizontal propagation). Attenuation windows occur at 35, 94, 140, and 260 GHz. Absorption peaks occur at 21, 60, 119, and 183 GHz [1].

1. QUASIOPTICAL POWER COMBINING

To address this problem, research has concentrated on developing power combiners using quasioptical methods. Although active quasioptical techniques have a history dating back several decades, it was Mink's classical paper on quasioptical power combining [3] that provided the catalyst for the increased research activity in recent years. A quasioptical power combiner can be likened to a gas laser system, shown in Fig. 3. Even though each gas molecule contributes just a small portion of the total power in the

optical beam, the total power can be quite large. This combining scheme is efficient for two reasons: because of the dense packing of molecules in the system and because the combined power is guided in free space rather than by lossy metal walls.

In a quasioptical power combiner, an array of solid-state devices is distributed over a planar radiating structure and interacts directly with an electromagnetic beam. The spacing between devices scales with frequency: the higher the frequency, the closer the spacing, and therefore the more devices can be packed per unit area. As in the

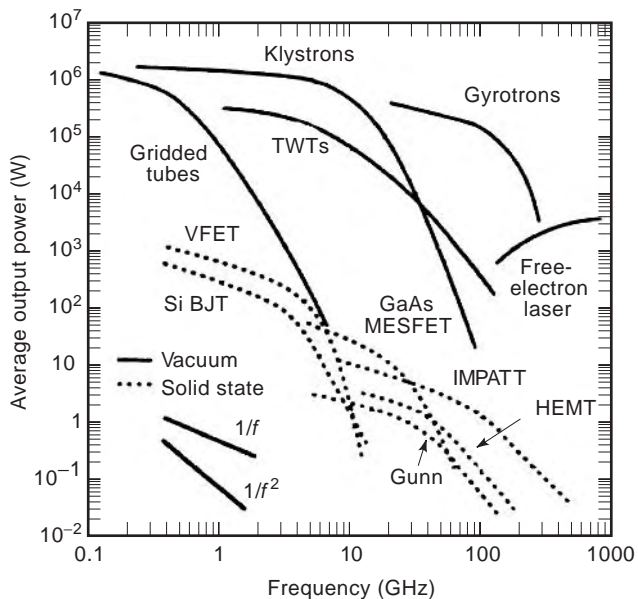


Figure 2. Power-handling capacity of solid-state and vacuum devices [1]. The Gunn and impact-ionization-avalanche-transit-time (IMPATT) devices are solid-state diodes. The silicon bipolar, metal-semiconductor field-effect transistor (MESFET), and high-electron-mobility transistor (HEMT) devices are transistors.

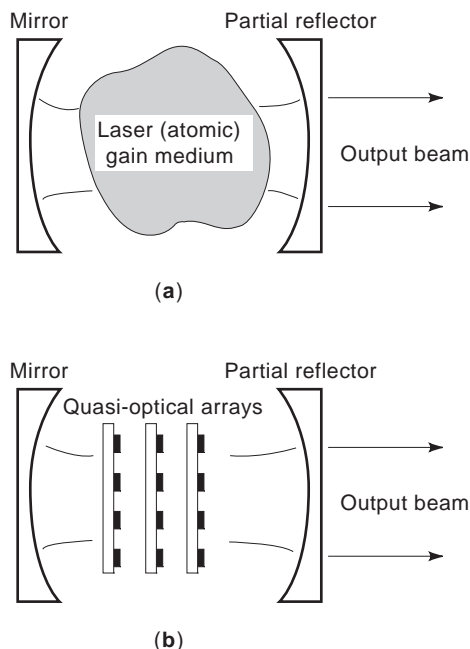


Figure 3. Analogy between a (a) gas laser and (b) quasioptical power combiner [1].

laser, the total output power can be substantial, even though the power from an individual device is small.

Since the publication of Mink's paper, quasioptical applications have evolved beyond just power generation to more functional circuits such as amplifiers, mixers, phase shifters, switches, frequency multipliers, modulators, and beamsteerers. All of these quasioptical circuits share the following advantages:

- The array's unit cell primarily determines the driving-point impedances seen by the active devices, while the output power scales with the total number of devices incorporated. This allows a designer to optimize for gain through the unit cell and to select the array size independently to meet the system power requirement. In many arrays already demonstrated, 100 low-power devices have been spatially power-combined.
- Quasioptical circuits are compact, lightweight, and amenable to monolithic integration. The antenna is an integral part of the circuit design, which reduces the size of the circuit-antenna module since the feedlines are eliminated. The biasing scheme is also simple, since often all of the devices in the array are biased in parallel.
- The noise from each unit cell is usually uncorrelated, so the noise figure for the array will be no worse than the noise figure of a single device, leading to a high signal-to-noise ratio at the receiver.
- The total output power is a result of combining a large number of devices. Therefore, the reliability of quasioptical components is high; a fraction of the devices can fail before the component fails, resulting in graceful degradation of the component.

Millimeter-wave power can be generated quasioptically in three basic ways: by direct conversion of direct current (DC) power to radiofrequency (RF) power with an oscillator array; by amplifying a low-power source with an amplifier array; or by cascading a low-frequency source with a frequency-multiplier array. Each of these techniques will be discussed in the following sections.

2. OSCILLATORS

An oscillator is essentially a device that converts DC power to RF power. In quasioptical architectures, the RF power must also be radiated efficiently into free space. Quasioptical oscillators can be divided into two categories: grid oscillators and coupled-oscillator arrays.

2.1. Grid Oscillators

In the grid approach, solid-state devices are embedded in a metal grating supported by a dielectric substrate (Fig. 4). The horizontal lines of the grid serve as DC bias lines, and the vertical lines as antennas. The mirror, substrate, and grid dimensions are chosen to resonate the devices at the oscillation frequency. The devices are typically spaced a small fraction of a wavelength apart. An oscillation is

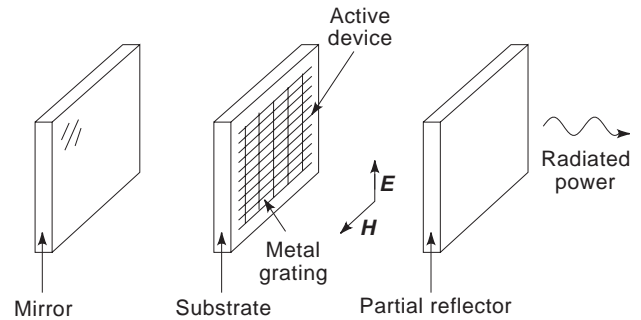


Figure 4. Schematic of a grid oscillator. The radiated power is combined in free space. (Courtesy of IEEE [10].)

triggered by any noise or transient on the DC bias. RF currents on the vertical leads cause an electromagnetic wave to be radiated away from the grid. Feedback from the mirror provides the injection-locking between devices, resulting in a single-frequency, self-locked oscillation.

Grid oscillators have been demonstrated at both microwave and millimeter-wave frequencies, up to 43 GHz [4–10]. Oscillators using up to 100 transistors have been developed, demonstrating the feasibility of large-scale power combining. Active grids can also be cascaded, as demonstrated in Ref. 11, where four transistor grids were placed in a cavity so that the final configuration resembled that of Fig. 3b. Other cascaded grids include a quasioptical voltage-controlled oscillator, which was composed of back-to-back transistor and tuning-diode arrays [12].

2.2. Coupled-Oscillator Arrays

In the grid approach, the oscillator can be interpreted as an active frequency-selective surface with the spacing between devices a small fraction of a wavelength apart. In contrast, in the coupled-oscillator array, each element is independent and contains a conventional planar antenna, and elements are not as closely spaced apart as they are in a grid. Mutual coupling between devices can be enforced using transmission-line interconnections, as shown in Fig. 5. A wide variety of coupled-oscillator arrays have been demonstrated in recent years [13–21], owing to the flexibility of this approach.

Electronic steering of the radiated beam, which is important for radar applications, can be accomplished by enforcing a prescribed phase shift between elements in the array. Typically this is done by associating a phase shifter with each oscillator element; the result is known as a phased array. Two types of steering techniques have been demonstrated in quasioptical oscillator arrays that do not require individual phase shifters for each antenna. In the first method, two coherent signals with a predetermined phase shift are injected into two opposite ends of the array [22]. The phase shift is divided equally along the chain. In the second method, the constant phase progression is established by detuning the frequencies of the end elements in the array [23]. When all of the oscillators are set to the same free-running frequency, the array is uniformly phased and a broadside beam results. When the frequencies of the end elements are slightly detuned from the

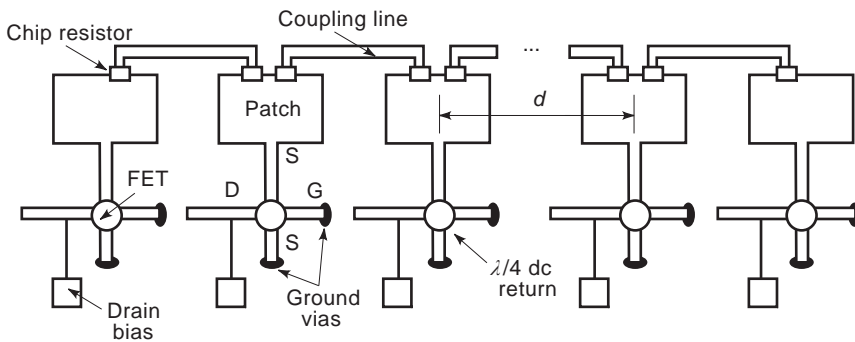


Figure 5. Coupled-oscillator array using patch antennas and field-effect transistors (FETs). (Courtesy of IEEE [24,53].)

others, a constant phase progression is established along the array. A scanning range from -15° to 30° from broad-side was reported for an X-band array [24].

3. AMPLIFIERS

Quasioptical amplifiers have been the object of considerable attention since their development in the early 1990s. Because of their immediate applicability to both military and industrial radar and communications systems, these amplifiers have been the focus of several coordinated academic, government, and industrial research efforts. Several possible amplifier configurations are illustrated in

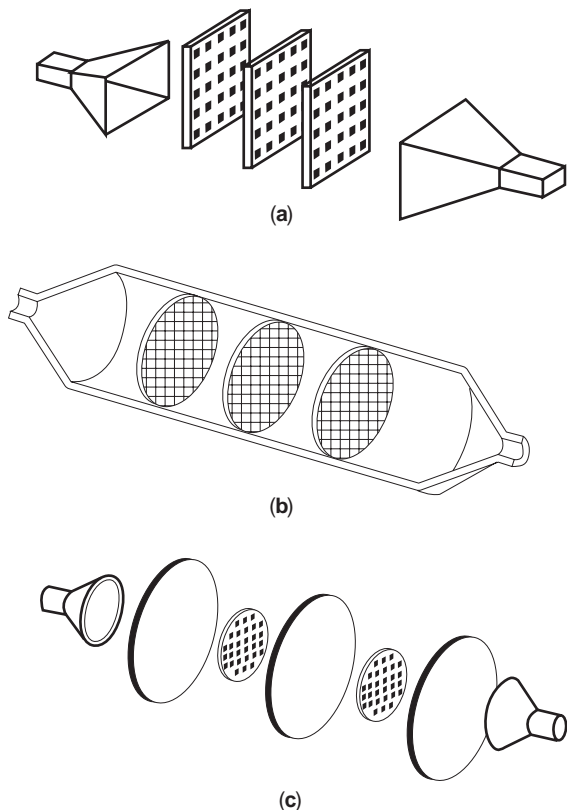


Figure 6. (a) Free-space, (b) waveguide, and (c) lens-focused quasioptical amplifier configurations [25]. Successful amplifiers have been demonstrated using all three configurations [1].

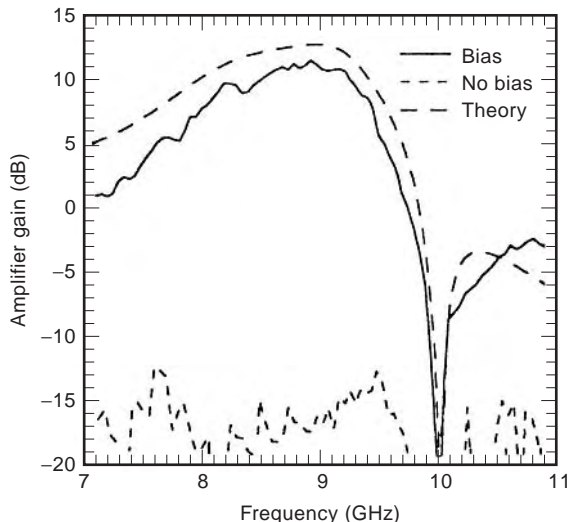
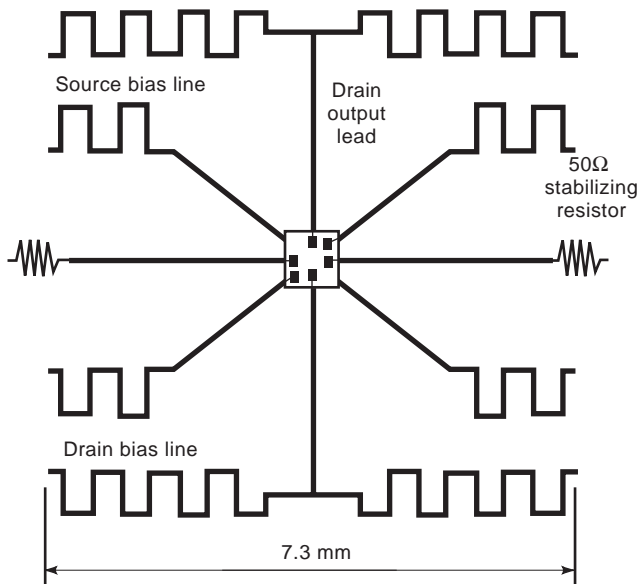


Figure 7. Unit cell and gain of a 100-element pHEMT grid amplifier [28]. This grid produced 3.7 W of saturated output power. (Courtesy of IEEE.)

Fig. 6 [25]. The amplifier arrays consist of many unit cells, each cell containing input and output antennas connected by an amplifier. The arrays are excited by an input microwave or millimeter-wave beam. The amplified output is reradiated into free space. The input and output beams are usually orthogonally polarized to provide isolation and thus reduce mutual coupling. Wire-grid polarizers are often used to help confine the signal path to the forward direction. Several amplifier arrays may be cascaded to increase the gain.

Quasioptical amplifiers are often labeled as being either *grid amplifiers* or *active arrays*. Grid amplifiers have smaller unit cells, typically less than $\lambda_0/4$. A differential transistor pair usually provides the gain. The input and output antennas are short dipoles that are strongly coupled because of the close spacing. Grid amplifiers are usually modeled by defining an equivalent waveguide unit cell based on symmetry and then developing a transmission-line equivalent circuit. Active arrays, on the other hand, have larger unit cells, usually near $\lambda_0/2$. Because of the larger cells, multitransistor MMIC: monolithic microwave integrated circuit amplifiers can be employed. More conventional resonant slot or patch antennas are often used.

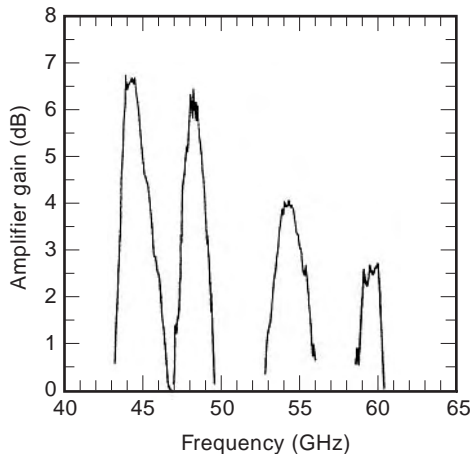
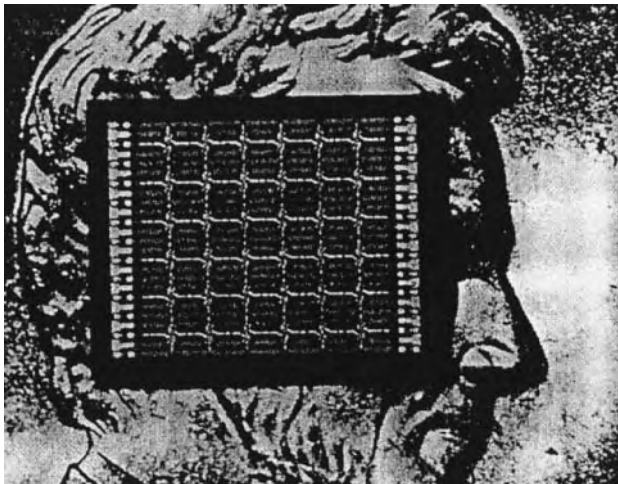


Figure 8. Photograph and gain of a 36-element pHEMT monolithic grid amplifier [30]. The unit cell size is 0.52mm. (Courtesy of IEEE.)

Modeling of active arrays is more straightforward because the larger cell reduces coupling between elements. At this point, both the grid amplifier and active-array approaches have been quite successful.

3.1. Grid Amplifiers

The first quasioptical amplifiers were grids developed in the early 1990s by Rutledge and coworkers at the California Institute of Technology [26,27]. A unit cell for a 100-element hybrid X-band array using pHEMT: pseudomorphic high-electron-mobility transistor transistors is shown in Fig. 7 [28]. A horizontally polarized input beam excites RF currents on the horizontal leads of the grid. These currents drive the gates of the transistor pair in the differential mode. The output currents are redirected along the vertical leads, producing a vertically polarized output beam. Thin meandering lines provide the transistor bias. These bias lines are intended to present a rather high impedance to the input wave. The peak gain is 12 dB at 9 GHz with a 15% 3 dB bandwidth. The minimum noise figure is 3 dB, which is less than 2 dB greater than the minimum noise figure available from a single HEMT. Finally, this 100-element grid provided 3.7 W of saturated output power.

Grid amplifiers are among the few successful monolithic millimeter-wave quasioptical amplifiers. A 36-element heterojunction bipolar transistor (HBT) grid produced 5 dB of gain at 40 GHz with a saturated output power of 670 mW [29]. Figure 8 shows a photograph of a 36-element pHEMT grid amplifier [30]. This amplifier could be tuned to operate at frequencies between 44 and 60 GHz by repositioning the external wire-grid polarizers. Continued efforts are underway to develop monolithic grids further.

3.2. Active Arrays

Active-array amplifiers have also been very successful. The approaches vary, but usually involve larger unit cells with more conventional antennas [31–39]. Amplifiers using back-to-back integrated horn antennas, patch

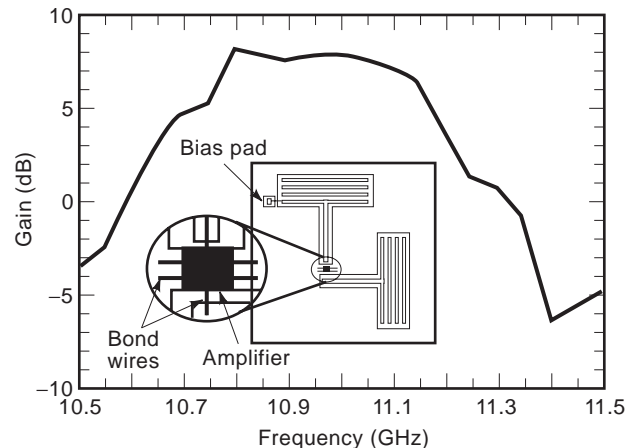


Figure 9. Unit cell and gain of a 16-element active array using folded slot antennas [1,32]. The folded slot antennas are designed to match to 50Ω.

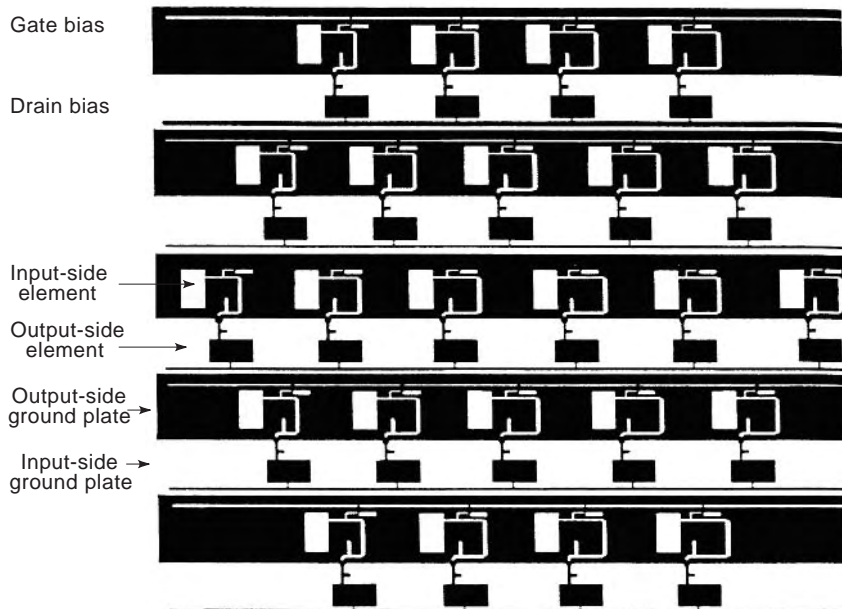


Figure 10. A 24-element lens-amplifier array using patch antennas [33]. The input and output patch antennas are on opposite sides of the dielectric substrate, isolated by interleaving ground strips [1].

antennas, slot antennas, and probe antennas have been demonstrated. Figure 9 illustrates an approach pursued by York and coworkers at the University of California at Santa Barbara [32]. Orthogonally polarized folded slot antennas are used to provide $50\ \Omega$ input and output feeds. A commercial HBT MMIC amplifier is used as a gain stage. Coplanar waveguide transmission lines connect the amplifier to the antennas. A 16-element array produced about an 8 dB gain at 11 GHz with a 5% bandwidth.

Another very successful approach is the lens–amplifier configuration developed by Popović and others at the University of Colorado [33]. Figure 10 shows the idea. Patch antennas are used at the input and output. The two antennas are on opposite sides of a dielectric substrate, isolated by interleaving ground strips. Gain is provided by a single transistor, although multistage amplifiers may also be used. Microstrip lines connect the antennas to the amplifier. Through careful selection of the electrical lengths of these microstrip lines, the array can be designed to focus a plane wave to a spot much like a lens. This particular array demonstrated a peak gain of 8 dB at 9.8 GHz. Other lens amplifiers have also been developed with considerable success [34], including bi-directional amplifiers that can be used for both transmission and reception [35].

Figure 11 illustrates yet another very promising approach developed by York and others [38]. MMIC amplifiers are integrated with tapered slot antennas forming an amplifier “card.” Several cards are stacked into a conventional metal waveguide to form the active array. This approach has been very successful with an X-band array; a 2×4 array has achieved 10 dB of gain over the entire waveguide band from 8 to 12 GHz. Furthermore, the array generated 20 W of output power.

Monolithic active-array amplifiers have also shown success in the millimeter-wave band. An array of 112 pHEMT amplifiers achieved a gain of 9 dB at 39 GHz with an output power of 630 mW [39]. Researchers are continuing to develop active-array technology for millimeter-wave applications.

4. FREQUENCY CONVERSION AND BEAM CONTROL ARRAYS

Quasioptical technology shows great promise for many other applications in addition to direct power generation and amplification. Quasioptical mixers, frequency

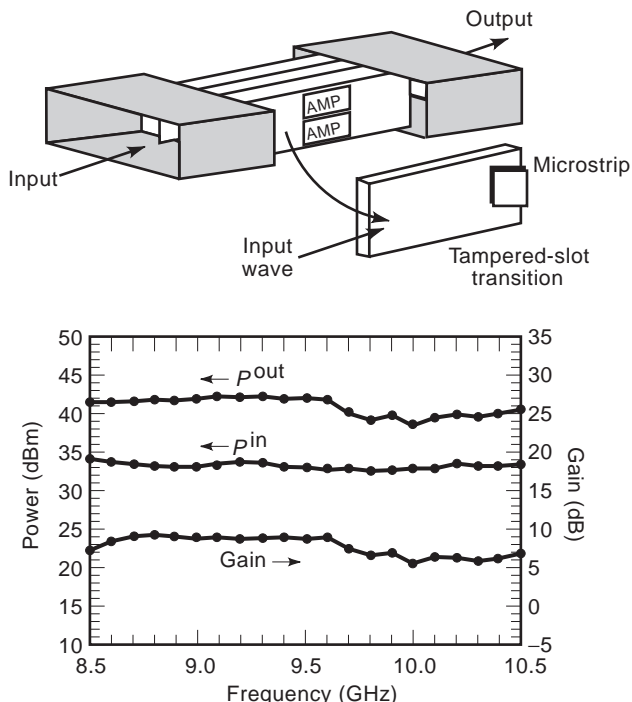


Figure 11. Configuration and gain of an eight element waveguide active array [38]. This array produced 20 W using eight high-power MMICs. (Courtesy of IEEE.)

multipliers, beam switches, and beamsteering components have been investigated. While these components are interesting alone, they are integral components in any quasi-optical transmitter or receiver.

4.1. Frequency Conversion Arrays

A quasi-optical grid periodically loaded with diodes will act as a nonlinear surface. When illuminated with an incident beam of radiation, the nonlinearities in the diode array will generate radiation not only at the fundamental frequency but at higher-order harmonics as well. Diode grids can therefore be used to generate very-high-frequency signals by multiplying a lower fundamental frequency. Luhmann and others at the University of California at Davis have demonstrated a 760-element doubler grid that generated 0.5 W at 66 GHz when illuminated with a 2.5 W input at 33 GHz [40]. This group has also reported a 5 W 99 GHz output tripler grid using 3100 diodes [41]. Multiplier grids have proved extremely successful at terahertz frequencies; a 144-element doubler produced 5.5 mW output at 1 THz [42,43]. This output power is almost two orders of magnitude more than that available using competing non-quasi-optical techniques. The terahertz doubler array is shown in Fig. 12. The success of these grids is a testament to the utility of quasi-optics.

Diode mixer grids have also been demonstrated. The local-oscillator (LO) and RF signals illuminate a diode grid quasi-optically. The intermediate-frequency (IF) signal is

the difference between the RF and LO frequencies. Due to the nature of quasi-optical arrays, the mixer’s conversion loss and noise figure are comparable to those of a single-diode microstrip mixer. On the other hand, the array’s power-handling capability increases with the number of elements, thereby increasing the dynamic range. A 100-element mixer grid [44] had a third-order intercept nearly 20 dB greater than that of a single-diode microstrip mixer. This feature makes quasi-optical receivers very attractive for high-dynamic-range wireless communications applications.

4.2. Beam Control Arrays

Diode grid arrays have also shown promise as beam-control arrays. Quasi-optical phase shifters [45,46] and switches [46–48] are among the many successful beam control components. Figure 13 shows a millimeter-wave monolithic p-i-n-diode switching array [48] developed by Stephan and others. The p-i-n diodes act as switches; depending on the DC diode bias, the array will either reflect or transmit an incident beam. This array switched a 94 GHz beam with an insertion loss of 4 dB and an isolation of 22 dB. An array of varactor diodes will behave in a similar way. By varying the varactor bias, and thus the junction capacitance, the phase of a quasi-optical beam can be shifted.

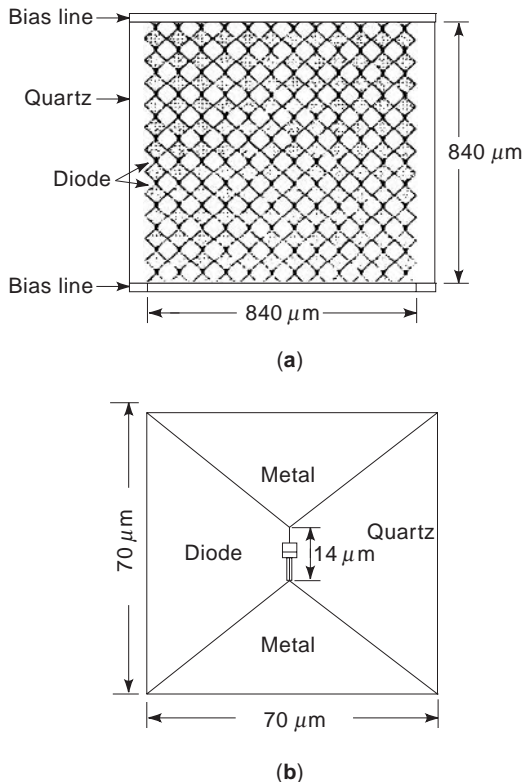


Figure 12. (a) A monolithic terahertz multiplier grid [42] and (b) unit cell detail. This grid produced 5.5 mW at 1 THz. (Courtesy of IEEE.)

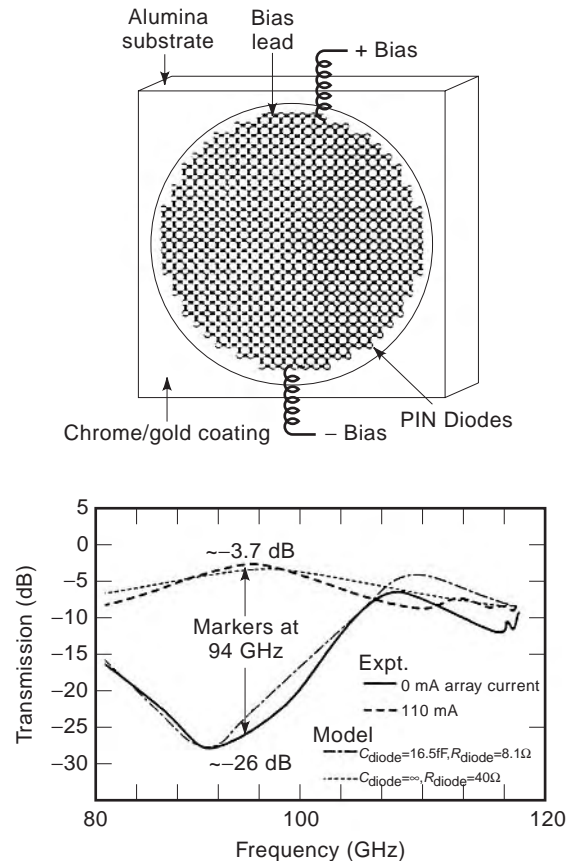


Figure 13. A p-i-n-diode switch array with measured and modeled transmission loss. (Courtesy of IEEE [48].)

One very intriguing application of quasioptical phase shifters is for beamsteering. Progressively shifting the phase of an incident beam across the surface of the quasioptical array will cause the beam to change directions. These quasioptical beamsteerers could one day replace the slow, heavy mechanical systems or the complicated phased-array systems used in many radar transmitters. One particularly promising approach is to use tiny microelectromechanical (MEMS) switches to provide the phase shift [49] without the parasitic losses associated with millimeter-wave diodes.

5. CHARACTERIZATION OF QUASIOPTICAL ARRAYS

Quasioptical components are both active circuits and antenna arrays. These components must be characterized with this unique property in mind. Researchers have developed several figures of merit useful for quasioptical characterization. Gouker [50] has attempted to standardize some of these figures. In this section, characterization of quasioptical oscillators and amplifiers will be discussed.

5.1. Oscillator Characterization

Consider the quasioptical oscillator or transmitter array illustrated in Fig. 14. This array, with active area A and directive gain G_t is located a distance R from a receiving horn antenna with directive gain G_h . The quasioptical array transmits a total power of P_t . λ_0 is free-space wavelength. The power received by the receiving horn antenna P_r will be given by the Friis transmission equation:

$$P_r = G_t P_t G_h \left(\frac{\lambda_0}{4\pi R} \right)^2 \tag{1}$$

G_h , R , and λ_0 are usually well-known quantities. This measurement directly reveals the array’s effective isotropic radiated power (EIRP), which is the product of the actual radiated power P_t and the array’s directive gain G_t :

$$\text{EIRP} = P_t G_t = \frac{P_r}{G_h} \left(\frac{4\pi R}{\lambda_0} \right)^2 \tag{2}$$

To compute the array’s total radiated power, the directive gain G_t must be computed from a complete measurement

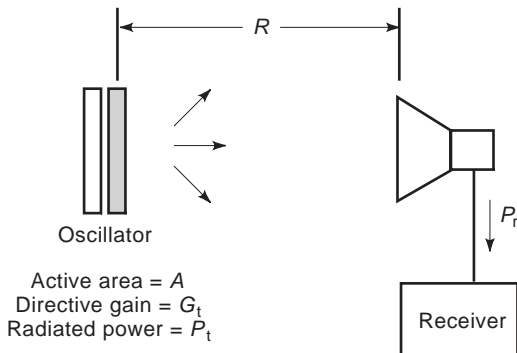


Figure 14. Measurement setup used to characterize a quasioptical oscillator.

of the array’s three-dimensional radiation pattern. Often, one can estimate the array’s the directive gain using the active area A :

$$G_t \approx \frac{4\pi A}{\lambda_0^2} \tag{3}$$

This approximation is most valid for larger arrays with dimensions of several wavelengths on a side. This gives an estimate of the radiated power from the measured EIRP.

5.2. Amplifier Characterization

Several techniques have been used to measure the gain of quasioptical amplifiers. One popular method is a far-field approach shown in Fig. 15. The first step is to calibrate the system. This is done with the two horn antennas copolarized, as shown in Fig. 15a. The calibrated power P_c is related to the transmitted power P_t using the Friis transmission equation

$$\frac{P_c}{P_t} = \left(\frac{G_h \lambda}{4\pi(2R)} \right)^2 \tag{4}$$

where G_h is the directive gain of the transmitting and receiving horn antennas and R is the distance between the amplifier and each horn. Then, the amplifier gain is measured using the setup shown in Fig. 15b. In this case, the received power is related to the transmitted power by

$$\frac{P_r}{P_t} = \frac{G_h A}{4\pi R^2} G \frac{G_h A}{4\pi R^2} \tag{5}$$

where G is the power gain of the amplifier and A is the physical area of the active array. This allows us to express the amplifier gain as

$$G = \frac{P_r}{P_c} \left(\frac{\lambda R}{2A} \right)^2 \tag{6}$$

This simple formula reveals that the gain of the amplifier can be computed from a relative power measurement and three well-known parameters.

Another method used to measure gain is the lens-focused approach shown in Fig. 16. This is a modified version of the quasioptical reflectometer reported by Gagnon [51]. The system is calibrated by placing an absorbing screen at the focal plane, as depicted in Fig 16a. The screen has an aperture cut in it, matching the physical area A of the amplifier. The gain is measured in the cross-polarized setup illustrated in Fig. 16b. For this method, the amplifier gain is simply the ratio of the power received from the grid P_r to the calibration power P_c .

A third method of measuring amplifiers involves placing the array in a large, overmoded waveguide [36,39]. Like the lens-focused approach, this method has the advantage of being very straightforward—the gain can be measured directly using a network analyzer. Care must be taken, however, to avoid exciting higher-order waveguide modes. Furthermore, the edges of the overmoded waveguide must be loaded with a dielectric in order to uniformly illuminate the array.

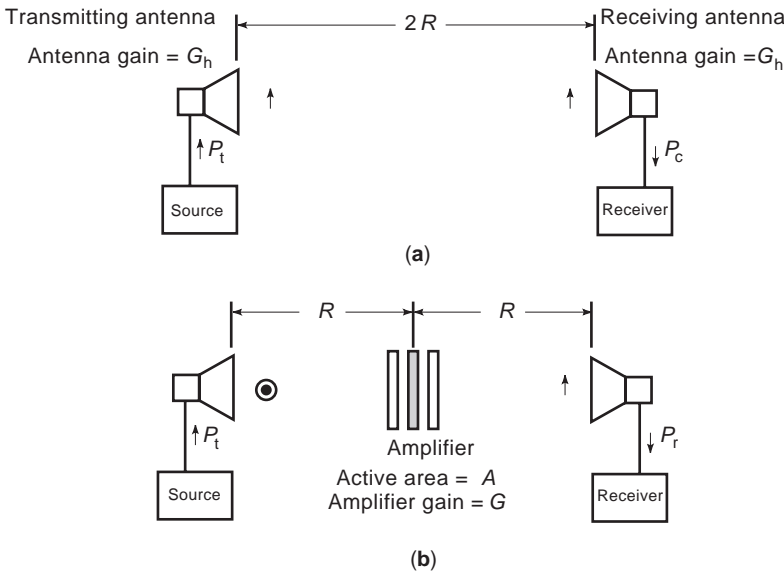


Figure 15. Far-field setup used to measure the gain of a quasioptical amplifier: (a) the calibration step is performed with the horns copolarized; (b) the measurement is performed with the horns cross-polarized [1].

At this point, it should be stressed that the far-field arrangement of Fig. 15 is not how a quasioptical amplifier is ultimately intended to be used—the high path losses between the grid and the horns would result in a very inefficient system. Instead, a quasioptical amplifier would be

employed in a system where the microwave beam is confined, such as in an overmoded waveguide or a lens-focused system like Fig. 16. Much of the diffraction losses are eliminated, possibly resulting in a system with appreciable flange-to-flange gain. On the other hand, the far-field method is simpler to set up in the laboratory, as there are no lenses to focus or align or metal waveguide to machine. Any of the methods should give similar results; the gain of a 100-element HBT grid amplifier was measured using both far-field and lens-focused approaches, with nearly identical results [28].

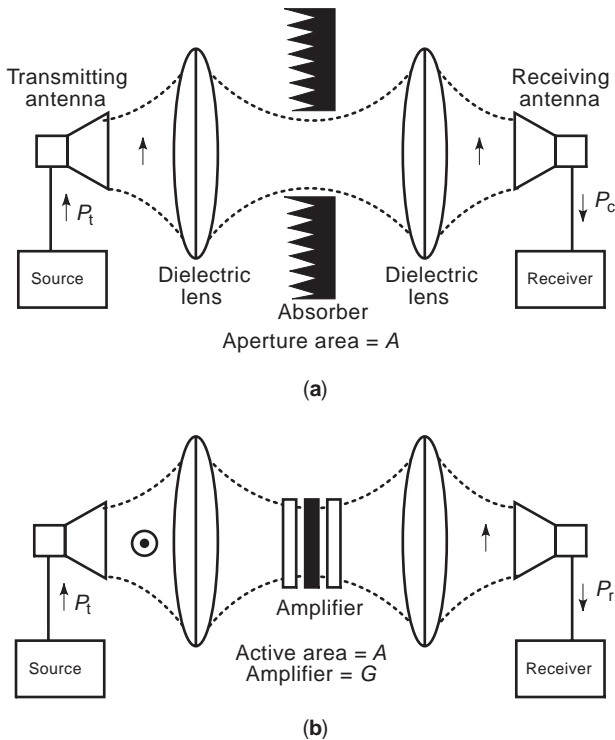


Figure 16. Lens-focused setup used for gain measurement. (a) The calibration step is performed with copolarized horns and an aperture cut into an absorbing screen. (b) The measurement is performed with the horns cross-polarized [1].

6. PASSIVE QUASIOPTICAL COMPONENTS

Passive components are used to characterize the active arrays described above, and are also necessary building blocks for quasioptical subsystems. Goldsmith [52] summarizes the extensive work on passive quasioptical devices, including their use in Gaussian beam waveguide systems. Frequency-dependent components include path-length modulators, polarization processing components, polarization transducers, hybrids, attenuators, power dividers, ferrite devices, absorbers, and calibration loads. Frequency-dependent components include planar frequency-selective surfaces and grids, perforated plates, interferometers, layered dielectrics, diffraction gratings, and resonators.

7. QUASIOPTICAL SUBSYSTEMS AND MODELING TECHNIQUES

One of the attractive features of the quasioptical approach is the ability to form systems by cascading surfaces that perform different analog signal processing functions, such as the transceiver front end shown in Fig. 17. Numerous

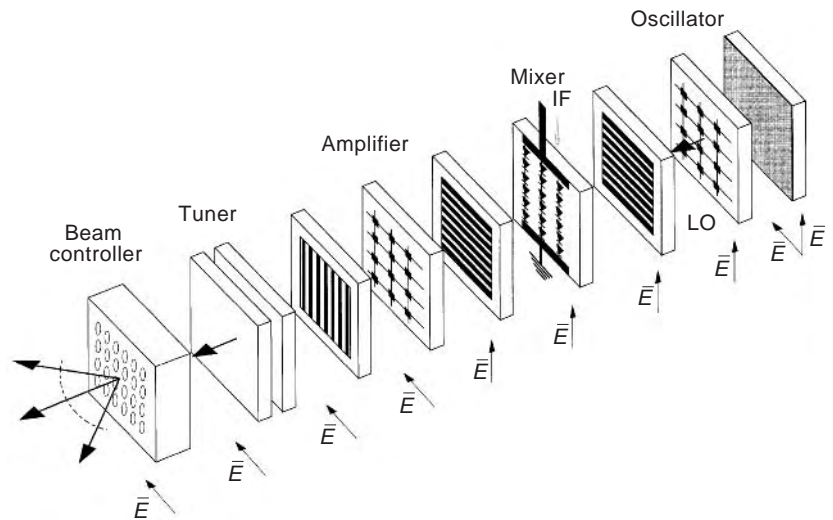


Figure 17. Quasi-optical transceiver front end consisting of cascaded quasi-optical arrays. (Figure courtesy of J. C. Chiao, University of Hawaii.)

individual components have already been developed, and a demonstration of an end-to-end quasi-optical subsystem could occur soon.

To characterize the various components that constitute a quasi-optical subsystem, one must understand the complicated interactions among the semiconductor devices, the antenna element, dielectric substrate, and the radiated and evanescent fields. Determining the driving-point impedance presented to the device at each feedpoint of the array is thus a nontrivial task. Further complications

arise from edge effects and the mutual coupling between array elements. One of the simplest techniques for making this problem more tractable is to assume an infinite array with identical cells. Based on symmetry, a unit cell can be defined with prescribed boundary conditions.

An example of a transmission-line model arising from this approximation is that of a diode-loaded grid shown in Fig. 18 [45]. The vertical metal leads of the grid are represented by a shunt inductor, and the substrate is represented by a section of transmission line whose characteristic impedance is equal to the wave impedance in the dielectric. A system such as the one in Fig. 17 can be characterized in a similar manner by cascading equivalent transmission-line models. For more complex array geometries, full-wave methods must be used to more accurately design these systems.

For a more detailed discussion of quasi-optical circuits, the interested reader is referred to Ref. 1.

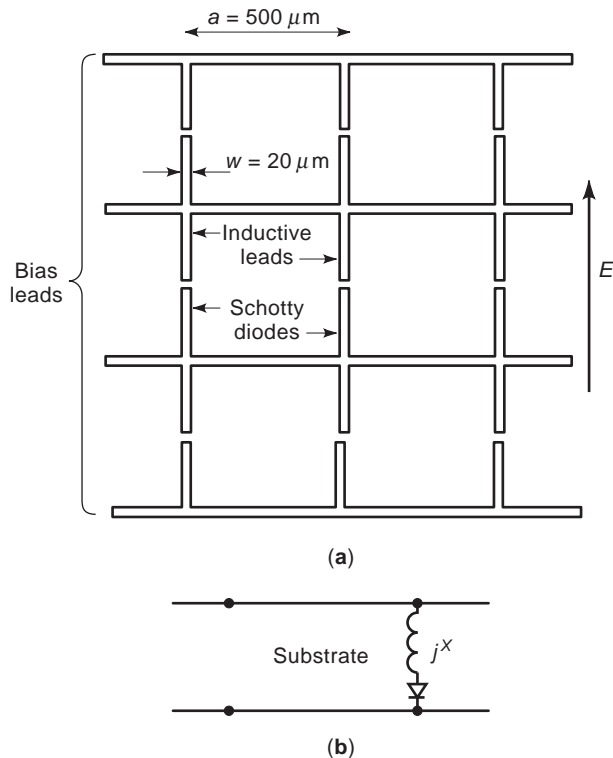


Figure 18. (a) Diode-loaded grid and (b) equivalent transmission-line model [45]. (Courtesy of IEEE.)

BIBLIOGRAPHY

1. R. A. York and Z. B. Popović, eds., *Active and Quasi-Optical Arrays for Solid-State Power Combining*, Wiley, New York, 1997.
2. K. Chang and C. Sun, Millimeter-wave power-combining techniques, *IEEE Trans. Microwave Theory Tech.* **MTT-31**: 91–107 (1983).
3. J. W. Mink, Quasi-optical power combining of solid-state millimeter-wave sources, *IEEE Trans. Microwave Theory Tech.* **34**:273–279 (1986).
4. Z. B. Popović et al., Bar-grid oscillators, *IEEE Trans. Microwave Theory Tech.* **38**:225–230 (1990).
5. Z. B. Popović et al., A 100-MESFET planar grid oscillator, *IEEE Trans. Microwave Theory Tech.* **39**:193–200 (1991).
6. R. M. Weikle, II et al., Planar MESFET grid oscillators using gate feedback, *IEEE Trans. Microwave Theory Tech.* **39**: 193–200 (1991).
7. J. B. Hacker et al., A 10-watt X-band grid oscillator, *IEEE MTT-S Int. Microwave Symp. Digest*, San Diego, CA, 1994, pp. 823–826.

8. S. C. Bundy and Z. B. Popović, A generalized analysis for grid oscillator design, *IEEE Trans. Microwave Theory Tech.* **42**:2486–2491 (1994).
9. P. Preventza, M. Matloubian, and D. B. Rutledge, A 43-GHz AlInAs/GaInAs/InP HEMT grid oscillator, *IEEE MTT-S Int. Microwave Symp. Digest*, Denver, CO, 1997, pp. 1057–1060.
10. W. A. Shiroma and Z. Popović, Analysis and optimization of grid oscillators, *IEEE Trans. Microwave Theory Tech.* **45**:2380–2386 (1997).
11. W. A. Shiroma, B. L. Shaw, and Z. B. Popović, A 100-transistor quadruple grid oscillator, *IEEE Microwave Guided-Wave Lett.* **4**:350–351 (1991).
12. T. Mader, S. Bundy, and Z. B. Popović, Quasi-optical VCOs, *IEEE Trans. Microwave Theory Tech.* **41**:1775–1781 (1993).
13. K. D. Stephan, Inter-injection-locked oscillators for power combining and phased arrays, *IEEE Trans. Microwave Theory Tech.* **34**:1017–1025 (1986).
14. R. A. York and R. C. Compton, Mode-locked oscillator arrays, *IEEE Microwave Guided-Wave Lett.* **1**:215–218 (1991).
15. J. Birkeland and T. Itoh, A 16 element quasi-optical FET oscillator power combining array with external injection locking, *IEEE Trans. Microwave Theory Tech.* **40**:475–481 (1992).
16. M. J. Vaughan and R. C. Compton, 28 GHz omni-directional quasi-optical transmitter array, *IEEE Trans. Microwave Theory Tech.* **43**:2507–2509 (1995).
17. A. Mortazawi and B. C. DeLoach, A nine-MESFET two-dimensional power combining array employing an extended resonance technique, *IEEE Microwave Guided-Wave Lett.* **3**:214–216 (1993).
18. R. A. York and R. C. Compton, Quasi-optical power combining using mutually synchronized oscillator arrays, *IEEE Trans. Microwave Theory Tech.* **39**:1000–1009 (1991).
19. R. A. York, Nonlinear analysis of phase relationships in quasi-optical oscillator arrays, *IEEE Trans. Microwave Theory Tech.* **41**:1799–1809 (1993).
20. J. Lin, S. T. Chew, and T. Itoh, A unilateral injection-locking type active phased array for beam scanning, *IEEE MTT-S Int. Microwave Symp. Digest*, San Diego, CA, 1994, pp. 1231–1234.
21. F. Poegel et al., Demonstration of an oscillating quasi-optical sab power combiner, *IEEE MTT-S Int. Microwave Symp. Digest*, Orlando, FL, 1995, pp. 917–920.
22. K. D. Stephan and W. A. Morgan, Analysis of inter-injection-locked oscillators for integrated phased arrays, *IEEE Trans. Anten. Propag.* **35**:771–781 (1987).
23. P. Liao and R. A. York, A new phase-shifterless beam scanning technique using arrays of coupled oscillators, *IEEE Trans. Microwave Theory Tech.* **41**:1810–1815 (1993).
24. P. Liao and R. A. York, A 1-watt X-band power-combining array using coupled VCOs, *IEEE MTT-S Int. Microwave Symp. Digest*, San Diego, CA, 1994, pp. 1235–1238.
25. M. Gouker, Spatial power combining, in R. A. York and Z. B. Popović, eds., *Active and Quasi-Optical Arrays for Solid-State Power Combining*, Wiley, New York, 1997, Chap. 2.
26. M. Kim et al., A grid amplifier, *IEEE Microwave Guided Wave Lett.* **1**:322–324 (1991).
27. M. Kim et al., A 100-element HBT grid amplifier, *IEEE Trans. Microwave Theory Tech.* **41**:1762–1771 (1993).
28. M. P. De Lisio et al., Modelling and performance of a 100-Element pHEMT grid amplifier, *IEEE Trans. Microwave Theory Tech.* **44**:2136–2144 (1996).
29. C.-M. Liu et al., Monolithic 40-GHz 670-mW HBT grid amplifier, *IEEE MTT-S Int. Microwave Symp. Digest*, San Francisco, CA, 1996, pp. 1123–1126.
30. M. P. De Lisio et al., A 44–60 GHz monolithic pHEMT grid amplifier, *IEEE MTT-S Int. Microwave Symp. Digest*, San Francisco, CA, 1996, pp. 1127–1130.
31. H. S. Tsai, M. J. W. Rodwell, and R. A. York, Planar amplifier array with improved bandwidth using folded-slots, *IEEE Microwave Guided Wave Lett.* **4**:112–114 (1994).
32. H. S. Tsai and R. A. York, Quasi-optical amplifier array using direct integration of MMICs and 50- Ω multi-slot antenna, *IEEE MTT-S Int. Microwave Symp. Digest*, Orlando, FL, 1995, pp. 593–596.
33. J. S. H. Schoenberg, S. C. Bundy, and Z. B. Popović, Two-level power combining using a lens amplifier, *IEEE Trans. Microwave Theory Tech.* **42**:2480–2485 (1994).
34. J. Schoenberg et al., Quasi-optical antenna array amplifiers, *IEEE MTT-S Int. Microwave Symp. Digest*, Orlando, FL, 1995, pp. 605–608.
35. S. Hollung, A. Cox, and Z. Popović, A bi-directional quasi-optical lens amplifier, *IEEE Trans. Microwave Theory Tech.* **45**:2352–2357 (1997).
36. T. Ivanov and A. Mortazawi, A two stage spatial amplifier with hard horn feeds, *IEEE Microwave Guided Wave Lett.* **6**:88–90 (1996).
37. C.-Y. Chi and G. M. Rebeiz, A quasi-optical amplifier, *IEEE Microwave Guided Wave Lett.* **3**:164–166 (1993).
38. N.-S. Cheng et al., 20 watt spatial power combiner in a waveguide, *IEEE MTT-S Int. Microwave Symp.*, Baltimore, MD, 1998, pp. 1457–1460.
39. E. A. Sovero et al., A Ka band monolithic quasi optic amplifier, *IEEE MTT-S Int. Microwave Symp.*, Baltimore, MD, 1998, pp. 1453–1456.
40. C. F. Jou et al., Millimeter-wave diode frequency doubler, *IEEE Trans. Microwave Theory Tech.* **36**:1507–1514 (1988).
41. H.-X. L. Liu et al., Monolithic quasi-optical frequency tripler array with 5-W output power at 99 GHz, *IEEE Electron. Devices Lett.* **14**:329–331 (1993).
42. A. Moussessian et al., A terahertz grid frequency doubler, *IEEE MTT-S Int. Microwave Symp. Digest*, Denver, CO, 1997, pp. 683–686.
43. D. S. Kurtz et al., Submillimeter-wave sideband generation using a planar diode array, *IEEE MTT-S Int. Microwave Symp.*, Baltimore, MD, 1998, pp. 1903–1906.
44. J. B. Hacker et al., A 100-element planar Schottky diode grid mixer, *IEEE Trans. Microwave Theory Tech.* **40**:557–562 (1992).
45. W. W. Lam et al., Millimeter-wave diode-grid phase shifters, *IEEE Trans. Microwave Theory Tech.* **36**:902–907 (1988).
46. L. B. Sjögren et al., Phased array operation of a diode grid impedance surface, *IEEE Trans. Microwave Theory Tech.* **42**:565–572 (1994).
47. X. H. Qin et al., Monolithic millimeter-wave beam control array, *IEEE MTT-S Int. Microwave Symp. Digest*, Orlando, FL, 1995, pp. 1669–1672.
48. K. D. Stephan, F. H. Spooner, and P. F. Goldsmith, Quasi-optical millimeter-wave hybrid and monolithic PIN-diode switches, *IEEE Trans. Microwave Theory Tech.* **41**:1791–1798 (1993).
49. J.-C. Chiao and D. B. Rutledge, Microswitch beam-steering grid, *17th Int. Conf. Infrared Millimeter Waves Digest*, Pasadena, CA, 1992, pp. 406–407.

50. M. A. Gouker, Toward standard figures-of-merit for spatial and quasi-optical power-combined arrays, *IEEE Trans. Microwave Theory Tech.* **43**:1614–1617 (1995).
51. D. R. Gagnon, Highly sensitive measurements with a lens-focused reflectometer, *IEEE Trans. Microwave Theory Tech.* **39**:2237–2240 (1991).
52. P. F. Goldsmith, *Quasioptical Systems*, IEEE Press, New York, 1998.
53. R. A. York, P. Liao, and J. J. Lyrch, Oscillator array dynamics with broadband N-port coupling networks, *IEEE Trans. Microwave Theory Tech.* **42**:2040–2045 (1994).

RADAR ALTIMETRY

R. KEITH RANEY
Johns Hopkins University
Laurel, Maryland

1. INTRODUCTION

Satellite-based radar altimetry over the world's oceans is the main theme of this article. Rather than measure the unknown clearance of the radar above potentially hazardous topography (which is one rationale for an aircraft radar altimeter, for example), satellite-based altimeters are designed to measure the height of the ocean's surface relative to an objective reference such as Earth's mean ellipsoid. Such sea surface height measurements have become essential for a wide variety of applications in oceanography, geodesy, geophysics, and climatology [1]. A satellite-based altimeter circles Earth in about 90 min, generating surface height measurements along its nadir track. These measurements accumulate, providing unique synoptic data that have revolutionized our knowledge and understanding of both global and local phenomena, from El Niño to bathymetry. A satellite-based radar altimeter also provides measurements of significant wave height and wind speed along its nadir track.

Although one might view these altimeters as relatively simple instruments, their phenomenal measurement accuracy and precision requires elegant microwave implementation and innovative signal processing. This article provides an overview of the applications that drive these requirements, and a description of the resulting state-of-the-art design concepts.

A nadir-viewing altimeter in a repeat-track orbit is constrained by a fundamental tradeoff between temporal coverage (revisit period D days) and spatial coverage (track separation at the equator W kilometers): $DW = \text{constant}$ for a given inclination and altitude. If more than one altimeter is under consideration, as either independent assets or a preplanned constellation, then the spacetime trade space is enlarged, and more measurement objectives may be satisfied. The limitations imposed by this constraint have motivated "multibeam" or "wide swath" altimeter concepts, although all such architectures imply a compromise on height measurement accuracy. The leading example of this genre is reviewed at the end of this article.

The sea surface height (SSH) measurement objectives of space-based altimeters can be grouped into three broad categories: large-scale dynamic sea surface topography, mesoscale oceanic features, and the cryosphere—near-polar sea ice and continental ice sheets. Satellite altimeters dedicated to determining the ocean's large-scale dynamic surface topography are characterized by absolute SSH measurement accuracy on the order of centimeters along tracks of more than 1000 km, and orbits that retrace their surface tracks every 10–20 days. In contrast,

mesoscale missions focus on SSH signals of less than ~ 300 km in length. This application requires measurement precision sufficient to sustain relative height measurements, and for geodetic data, relatively dense track-to-track spacing. Geosat is the leading example of this category, for both geodetic (nonrepeat) and mesoscale (exact-repeat) orbits. Observation of oceanic and polar ice sheets requires that the altimeter have robust range and spatial resolution, accuracy, and precision in response to the nonzero average surface slope in both the along-track and cross-track directions of the continental glaciers. Suitable orbits must have near-polar inclination, and multi-year relative accuracy. Cryosat is reviewed as the first example of this class of radar altimeter mission.

Radar altimeters must provide accurate and precise SSH measurements from a spacecraft whose roll and pitch attitudes are not known exactly. These requirements can be satisfied by the pulse-limited altimeter paradigm, which is characterized by (1) large time-bandwidth pulse modulation, (2) antenna directivity that illuminates a surface area larger than the spatially resolved footprint, and (3) extensive noncoherent (postdetection) waveform averaging. The design of the TOPEX altimeter is described as an example. Footprint resolution and measurement precision can be improved by combining coherent and increased incoherent processing, exemplified by the delay-Doppler altimeter, which borrows applicable techniques from synthetic aperture radar (SAR). The article closes with an overview of future developments and advanced mission concepts.

2. RADAR ALTIMETER SATELLITES

All satellite radar altimeters to date (Table 1) are incoherent pulse-limited instruments, as described in a later passage. Since 1973 height measurement accuracy has improved, due primarily to dedicated effort and increasing skill applied to estimation and correction of systematic errors. Performance also has benefited from improved on-board hardware and algorithms, and improved orbit determination. The Jason-1 altimeter represents the state of the art in absolute SSH measurement accuracy (as of the year 2003). Online access to descriptions of most of these radar altimeter missions may be found at the Website given in Ref. 2.

2.1. Orbits

An altimeter's SSH accuracy on large scales depends to first order on how well the height of the altimeter itself can be determined. Given the state of the art in satellite tracking systems, the dominant error in satellite (radial) position determination is uncertainty in knowledge of the gravity field (often expressed in terms of geoid height) [3]. At lower orbit altitudes, the higher-frequency components of the gravity field are enhanced. The impact can be significant. For example, gravity variations of about 400 km

Table 1. Summary of Satellite Radar Altimeters

Altimeter	Agency	Year	Orbit Repeat (days)	Inclination (degrees)	Altitude (km)	Equatorial Spacing (km)	Band	Propagation Measurements	Accuracy
Skylab (3)	NASA	1973	No	~48	435	—	Ku	None	50 m
GEOS-3	NASA	1975–1978	No	115	845	~60	Ku	None	50 cm
Seasat	NASA	1978	~17, 3	108	800	160, 800	Ku	H ₂ O	20 cm
Geosat	USN	1985–1989	~3, 17.05	108	800	~4, 160	Ku	None	10 cm
ERS-1	ESA	1991–1997	3, 35, 176	98.5	785	20–800	Ku	H ₂ O	7 cm
TOPEX ^a	NASA	1992–	9.916	66	1336	315	C, Ku	H ₂ O, e ⁻	2 cm
Poseidon ^a	CNES	1992–	9.916	66	1336	315	Ku	H ₂ O	5 cm
ERS-2	ESA	1995–	35	98.5	781	80	Ku	H ₂ O	7 cm
GFO	USN	1998–	17.05	108	800	160	Ku	H ₂ O	5 cm
RA-2	ESA	2002	35	98.5	800	80	S, Ku	H ₂ O, e ⁻	7 cm
Jason-1	CNES	2001	9.916	66	1336	315	C, Ku	H ₂ O, e ⁻	1.5 cm
Cryosat	ESA	(2004)	369	92	720	—	Ku	None	(5 cm)
Jason-2	CNES	(2007)	9.916	66	1336	315	C, Ku	H ₂ O, e ⁻	(1.5 cm)

^aTOPEX/Poseidon was a joint NASA/CNES mission on the same spacecraft.

wavelength are 100 times larger at an altitude of 500 km than they are at 1000 km. In general, the accuracy of precision orbit determination is better for higher altitudes.

Atmospheric drag is approximately 10 times greater at 800 km than at 1200 km [4]. For example, over one orbit at 1200 km altitude, drag imposes a 1-cm decay on the orbit radius. At 800 km altitude, the effect is 10 times greater, resulting in a 10-cm decay per orbit. Atmospheric drag increases significantly during periods of higher solar flare activity, the peaks of which occur approximately every eleven years.

Whereas a 10-cm decay in radius per orbit may not seem like much for a satellite at 800 km altitude, these decreases accumulate. Smaller orbit radii induce higher spacecraft velocities. Thus, orbit decay accelerates the satellite, shifting its ground track away from its exact-repeat path. An altimeter's repeat pattern can be maintained only by replacing the energy removed by drag forces. Active intervention is required, usually in the form of thruster firings of controlled strength, duration, and direction. Orbit maintenance maneuvers are required more frequently when the altimeter's orbit is subject to larger perturbations. A review of the orbit maintenance histories of radar altimeter satellites may be found in Ref. 5.

2.2. Review of Missions

The first satellite radar altimeter was the proof-of-concept S-193 instrument (General Electric) that flew on three Skylab missions. The objectives were to verify predicted waveform response to wind and waves, measure the radar cross section of the sea at vertical incidence, measure interpulse correlation properties, and observe the effect of off-nadir antenna orientation. Geos-3 (General Electric) provided the first geodetic and geophysical results of significance within the National Geodetic Satellite Program, including the first maps of sea-level variability and the marine geoid. Geos-3 and the S-193 altimeters used conventional pulse compression techniques.

The Seasat altimeter (Johns Hopkins University Applied Physics Laboratory) was the first to use full-deramp pulse compression, which opened the way for the very

small range resolution required for many oceanographic applications. The deramp technique (described below) has been adopted by all radar altimeters since then. Seasat was designed to measure global ocean topography and the marine geoid, as well as wave height and surface wind-speed. The Geosat (Johns Hopkins University Applied Physics Laboratory) altimeter's design was patterned closely after that of the Seasat altimeter. Geosat was a U.S. Navy military satellite whose primary mission was to map Earth's marine geoid to then-unprecedented accuracy (drifting orbit). Since their declassification in 1995, data from the first 18 month geodetic mission have become the backbone of the global bathymetric chart that is the industry standard [6,7]. Geosat's secondary mission was to observe dynamic oceanographic phenomena, for which it was maneuvered into an exact-repeat orbit (period 17.05 days) [8]. The Geosat follow-on (GFO) altimeter (E-Systems) is meant to replicate as much as possible the Geosat exact-repeat mission, leading toward an operational capability for the U.S. Navy. There has been no dedicated geodetic radar altimeter mission since Geosat, although a new mission known as "Abyss-Lite" is being actively promoted.

In the late 1980s, planning for satellite radar altimeter missions split into two themes, determined by the relative priority of their measurements. If the altimeter is the prime payload instrument, then the orbit and mission design can be optimized accordingly. This theme was initiated by TOPEX/Poseidon (T/P), a joint United States (NASA) and French (CNES) mission. TOPEX (Johns Hopkins University Applied Physics Laboratory) was designed to measure and map the dynamic ocean topography with sufficient accuracy to determine large-scale circulation patterns [1]. TOPEX' most famous contribution is early observation and near-real-time monitoring of El Niño events, whose height signature over the equatorial eastern Pacific ocean typically is an increase on the order of 10–20 cm with respect to the mean. Poseidon (Alcatel Espace), contributed by France, is a small proof-of-concept instrument that has a solid-state transmitter. Poseidon is the precursor of the Jason altimeters, and the SIRAL instrument aboard Cryosat. Cryosat (described

below) will be the first radar altimeter designed to observe polar and continental ice sheets from space.

The T/P orbit repeat period (9.916 days) was chosen carefully to satisfy adequate observation of the dominant aliased tidal constituents. All solar tidal constituents would be ambiguous with other height signals if the repeat period were an integral number of days (20). For T/P, the time of day for each subsequent observation slips by about 2 h. The T/P repeat pass footprint location accuracy is better than ± 1 km, a requirement that is bounded by the cross-track gradient of the oceanic geoid. The T/P instrument package includes a three-frequency radiometer to measure and compensate for propagation delays due to atmospheric moisture (H_2O). TOPEX is the first altimeter to use two frequencies to estimate and compensate for propagation delays imposed by ionospheric electrons (e^-). The Jason-1 altimeter (Alcatel Espace) [9] is designed to follow in the footsteps of TOPEX, figuratively and literally. Following the launch of Jason-1 into the T/P orbit, TOPEX was maneuvered into a “tandem” phasing so that the measurements of the two altimeters could be cross-calibrated. The follow-on mission Jason-2 will be identical to Jason-1, and may also include an experimental wide-swath ocean altimeter (outlined in the closing sections of this article).

If the altimeter is not the primary payload, then the resulting mission and orbit are likely to be determined by other requirements, which may compromise altimetry. The European Space Agency’s satellite altimeters (Selenia Spazio) on ERS-1 and ERS-2, as well as the advanced radar altimeter RA-2 [10] (Alenia Spazio) on ESA’s Envisat, are of second priority with respect to the other instruments on their respective spacecraft. Their sun-synchronous orbits are less than optimum for precision altimetry. The orbit of ERS-1 was adjusted during its mission to a long repeat period (176 days). That long repeat period generated a relatively dense surface sampling grid useful for estimating sea ice cover, geodesy, and bathymetry, but is less than optimum for most other applications.

3. GLOBAL DYNAMIC TOPOGRAPHY—ACCURACY

The principal objective of an oceanographic satellite radar altimeter designed to observe the dynamic sea surface topography over very large spatial scales is to measure the absolute height h_S of the sea surface (Fig. 1) with respect to the standard reference ellipsoid. The keyword here is *accuracy*: the mean bias error of the measurements with respect to an absolute reference. Height measurement accuracy depends, among other factors, upon the accuracy of accounting for variations in the speed of microwave propagation between the radar and the surface. The absolute SSH measurement problem is challenging because the geophysical signal is small, at most on the order of tens of centimeters, yet that signal has to be derived from a satellite altimeter at altitude of 1400 km or so, whose raw range measurement is subject to corrections as large as several tens of meters, and corrections for the geoid of many tens of meters. The accuracy of estimating the dynamic topographic signal is limited by the corrections

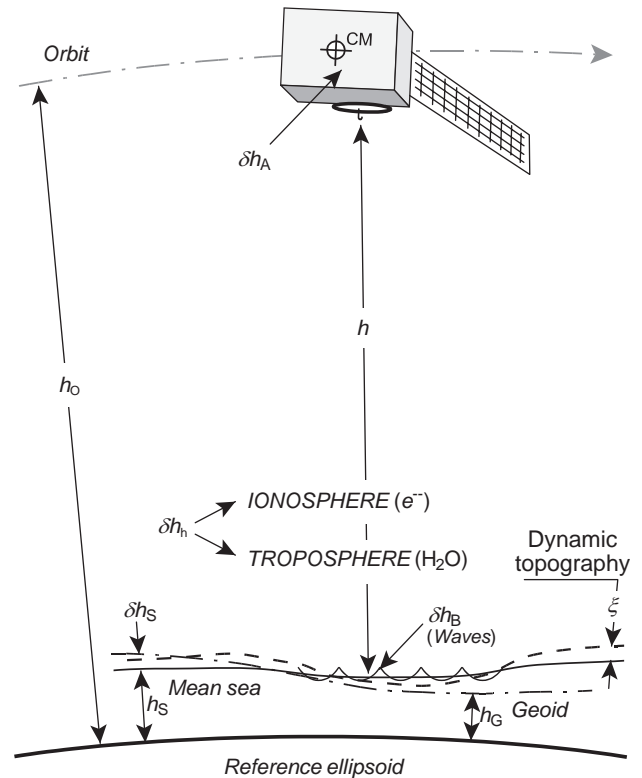


Figure 1. A satelliteborne radar altimeter measures the round-trip time delay of transmitted signals, from which is deduced the altimetric height h between the satellite’s orbit and the reflecting surface. For most geophysical interpretations, the altimetric height is converted to the surface’s height, which is described using the standard ellipsoid of Earth as the reference.

for variations in the speed of light (nominally c) and other perturbations, as well as the height accuracies of the orbit, marine geoid, tides, and atmospheric pressure. The implied errors have been reduced over the years, after considerable focused effort. State-of-the-art height accuracy (Jason-1) is better than 3 cm (10-day average) or 1.5 cm (1 month average computed with multi-orbit crossover data), which is a remarkable achievement.

The mean sea level, governed primarily by the marine geoid, differs from the reference ellipsoid by ± 50 m or more, approaching $+100$ m in parts of the Indian Sea. Often, the geophysical signal of interest is the dynamic topography ζ , defined as the distance between the marine geoid h_G and the physical sea surface, corrected for systematic offsets due to tides and atmospheric pressure, for example. The dynamic topography would be zero if the sea were at rest relative to Earth. The dynamic topography reflects small surface slopes associated with geostrophic currents, of which the Gulf Stream is a well-known example. Cross-stream surface slopes are proportional to the mean current flowrate; the resulting slope signals are indicative of large-scale oceanic circulation patterns.

3.1. The Altimeter’s Measurements

Whereas the objective is determination of the distance between the radar and the sea surface, the altimeter

actually measures round-trip delay t_T . The altimeter’s relative height h is derived from the measured time delay by $h = t_T c/2$, where c is the speed of light. At the accuracy required of an oceanographic altimeter, this deceptively simple proportionality must take into account the small but significant retardation of the radar’s microwaves as they propagate through the atmosphere and the ionosphere.

In addition to sea surface height, the satellite radar altimeter’s waveform supports two other oceanographic measurements: significant wave height (SWH) and surface windspeed (WS). Over a quasiflat sea, a pulse-limited altimeter’s idealized mean waveform is a step function whose risetime is equal to the compressed pulselength, and whose position on the time-delay axis is determined by the altimeter’s height (Fig. 2). If the sea surface is modulated by gravity waves, the altimetric depth of the surface increases, which reduces the slope of the waveform’s leading edge. Hence, SWH is proportional to the waveform risetime. If the sea surface is under stress from wind, the resulting fine-scale roughness decreases the power of the pulse reflected back to the altimeter. Hence, WS is inversely related to mean waveform power. In practice, the inflections of the idealized flat-surface response function waveform are softened by the pulse weighting, and the waveform plateau is attenuated over time by the weighting of the antenna pattern.

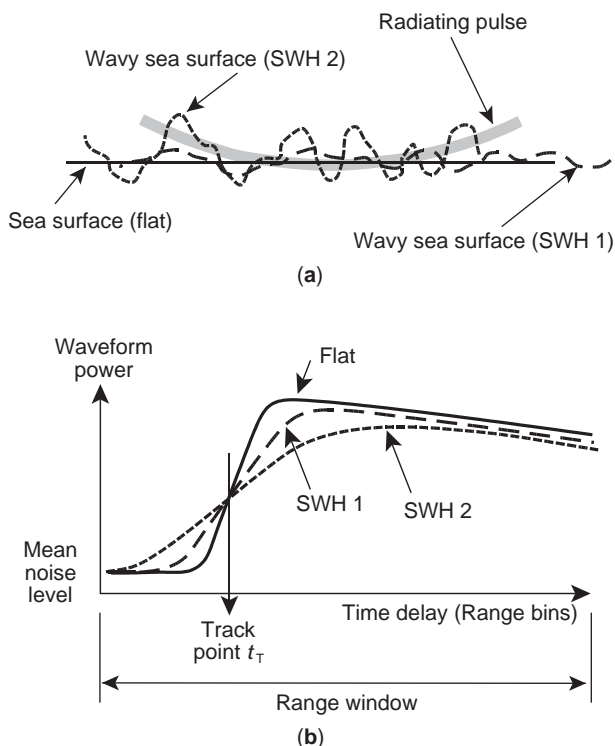


Figure 2. A pulse-limited altimeter’s radiated signal intersects the wavy surface of the ocean from above (a). The output (averaged) waveform is the altimeter’s response to the surface (b). Waveform (round-trip) time delay t_T and leading-edge slope indicate height above the surface and the large-scale roughness (SWH) of the surface, respectively.

To extract SWH and WS from waveform data, finely tuned algorithms have been developed and validated against *in situ* buoy measurements. For example, the TOPEX Ku-band altimeter measures SWH to within ± 0.5 m up to more than 5.0 m, and WS within ± 1.5 m/s up to more than 15 m/s. These figures correspond to averages over 1 second, or about 6 km along the subsatellite path of the altimeter’s footprint, which typically is 3–5 km wide, determined by mean sea state.

3.2. Height Error Budget

The ultimate accuracy of an altimeter depends critically on estimation and removal of the systematic errors inherent to the measurement. Once recovered from the altimetry data, sea surface height h_S is used to derive the signal ξ of the dynamic sea surface topography by

$$\xi = h_S - h_G - \delta h_S$$

in which the independent variables imply geophysical corrections: geoid determination (h_G), and Earth tides, oceanic tides, inverse barometer corrections and so on (δh_S).

An oceanographic altimeter collects radar ranging data that are reduced to sea surface height h_S according to

$$h_S = h_O - h - \delta h_A - \delta h_B - \delta h_h \tag{1}$$

where the last three terms on the right-hand side of Eq. (1) entail corrections to be derived from electromagnetic (EM) reflection and propagation phenomena. Orbit radial height (h_O) is determined through extensive instrumentation and analysis, with a net uncertainty. The magnitude of the uncorrected height errors, and the TOPEX postcompensation residual height uncertainties that remain in h_S , are summarized in Table 2.

3.2.1. Instrument Corrections δh_A . Height errors that arise in the altimeter and spacecraft environment may be driven close to zero by careful design and calibration [11,12]. Range delay has to be adjusted to account for the electronic distance from the antenna phase center, through the transmitter, receiver, and processor, to the

Table 2. TOPEX Height Accuracy

Uncertainty Source	Height Error	Residual Uncertainty (cm)
Instrument δh_A		
Noise	~25 cm	2
Waveform bias	~25 cm	3
Timing bias	~1 m	1
Surface interaction δh_B		
EM bias	~0.05 × SWH	2
Skewness	∝ SWH	1
Propagation δh_h		
Ionosphere	5–25 cm	1.3
Dry troposphere	~2.2 m	0.7
Wet troposphere	5–50 cm	1.2
Orbit h_O	(Large)	3.5
RSS error	>2.5 m	<5

satellite's center of mass. The required timing correction is a function of spacecraft attitude, temperature, and age, among other perturbations. The waveform leading-edge delay is tracked dynamically on-board, but not perfectly. After calibration and compensation, the combined equivalent distance root-sum-squared (RSS) uncertainty of TOPEX from all on-board sources is about 3.7 cm, less than two Ku-band wavelengths.

3.2.2. Surface Corrections δh_b . The radiated wave front impinges on the sea surface, and then is reflected. In the presence of waves, the mean EM surface sensed by the reflection deviates from the physical sea surface. The resulting height measurement bias occurs because ocean waves tend to reflect more strongly from their troughs than from their crests. Ocean waves also tend to be asymmetric in their height distribution, described by skewness. This causes the area of the reflecting surface that lies above the mean sea level to be larger than the area below. If scattering were simply proportional to area, this skewness would bias the height measurement. Both EM bias and skewness bias are reduced through empirically derived algorithms that depend on the local significant wave height.

3.2.3. Propagation Corrections δh_h . EM propagation is retarded by free electrons in the ionosphere, by the air mass of the troposphere, and by the water content of the troposphere. If uncorrected, the height measurement error from these three sources would be about 2.5 m, intolerable for oceanic radar altimetry. The largest error is due to the dry troposphere, but this contribution varies slowly over the planet, and is not problematic. It can be removed almost completely through application of standard models that depend simply on atmospheric pressure and Earth latitude.

Atmospheric water content may vary considerably with location. The resulting pathlength changes, if uncorrected, could imply the presence of large but false oceanic height signals. The only reliable way to counteract its effect is to measure the water content directly along the altimeter's propagation path. Atmospheric water content may be estimated rather well with radiometric techniques. TOPEX carries a three-frequency (18, 21, and 37 GHz) water-vapor radiometer (WVR) whose data are used to reduce the wet troposphere pathlength error to 1.2 cm [13].

The altimeter's radiation is delayed also by the total count of free electrons [i.e., total electron content (TEC)] found in the layer above about 70 km [14]. Depending on the solar cycle, solar illumination, and other parameters, the TEC varies widely, causing an apparent increase in pathlength up to 25 cm. The optical pathlength delay due to TEC depends on frequency f as f^{-2} . Hence, simultaneous altimeter heights h_1 and h_2 obtained at two different frequencies $f_1 > f_2$ can be combined as

$$h = \frac{f_1^2}{f_1^2 - f_2^2} h_1 - \frac{f_2^2}{f_1^2 - f_2^2} h_2$$

to offset the unwanted ionospheric delay error. The TOPEX altimeter operates at Ku band (13.6 GHz) and

C band (5.2 GHz), generating height estimates h_K and h_C , respectively. The TOPEX algorithm that corrects for the ionospheric pathlength delay is $h = 1.18h_K - 0.18h_C$.

3.2.4. Orbit Determination h_O . The dominant error in absolute height measurements from a radar altimeter is the uncertainty of the satellite's instantaneous radial distance from the reference ellipsoid. The perturbations on a satellite in low-Earth orbit, in order of importance, include: variations in the gravity field; radiation pressures; atmospheric pressure; tides, both oceanic and solid Earth; and the troposphere. Real-time observation of the satellite's orbital perturbations is subject to errors also, compounded by insufficient knowledge of the Earth's geoid, and location uncertainties for the tracking systems.

The principal methods used by T/P for precision orbit determination (POD) rely on its global positioning system (GPS) receivers and the "Doppler orbitography and radio-positioning integrated by satellite" (DORIS) data system. DORIS instantaneous navigation is better than 4 m on all axes, a tolerance that reduces to less than 5 cm (radial) after precision processing. T/P carries a set of optical retroreflectors (corner cubes) mounted around the circumference of the altimeter antenna. When within view of ground stations equipped with precision range measurement lasers, the corner cubes can be illuminated. The resulting laser ranging measurements are used to calibrate the onboard orbit determination systems.

The radial orbit determination error for TOPEX/Poseidon has been reduced to less than 3.5 cm when averaged (RSS) over its orbital repeat period [15]. The predominant errors have 2–3 cm peaks, concentrated at a once-per-orbit frequency. Orbit determination residuals can be reduced through analysis of height measurements at locations at which the ascending and descending satellite orbits cross. After removal of all geophysical signals and adjustment for changes in the orbit, the measured heights at each crossover point should be equal. Comparison of the actual crossover differentials helps refine the orbital models. For TOPEX, crossover analysis of many orbits over a period of 30 to 60 days reduces the residual to about 2 cm. At this level of precision, inaccuracies in Earth's tide and geoid models dominate the remaining error. Improvements in these models are expected to lead to 1 cm radial orbit accuracies for the Jason series of altimeters.

Such tight orbit determination is unlikely to be achieved in the near future for the radar altimeter satellites at 800 km altitudes. For example, the working objective for POD on GFO is 5 cm, based primarily on GPS tracking and dynamic modeling (although it was better than 7 cm only rarely during 1998–2002).

4. THEORETICAL FOUNDATIONS

Altimeters generally fall into one of two kinds, determined by their beamwidth and range resolution. Radar altimeters illuminate the surface through an antenna pattern of width β , which typically is less than a few degrees. As a part of the onboard processing, the received energy is

processed into resolved range shells. Beamwidth determines the width βh of the surface illuminated by the antenna. As it intersects the surface, each range of resolved length ρ also determines a surface area of width $2r_P$ [16]. Beam-limited radar altimeters are those for which $\beta h < 2r_P$. Conversely, $2r_P < \beta h$ for pulse-limited altimeters. The altimeters cited in Table 1 are all pulse-limited.

4.1. Pulse-Limited Altimeters

Figure 3 illustrates the pulse-limited condition. The height accuracy of a pulse-limited altimeter is much less sensitive to (small) angular pointing errors than is the case for a beam-limited altimeter.

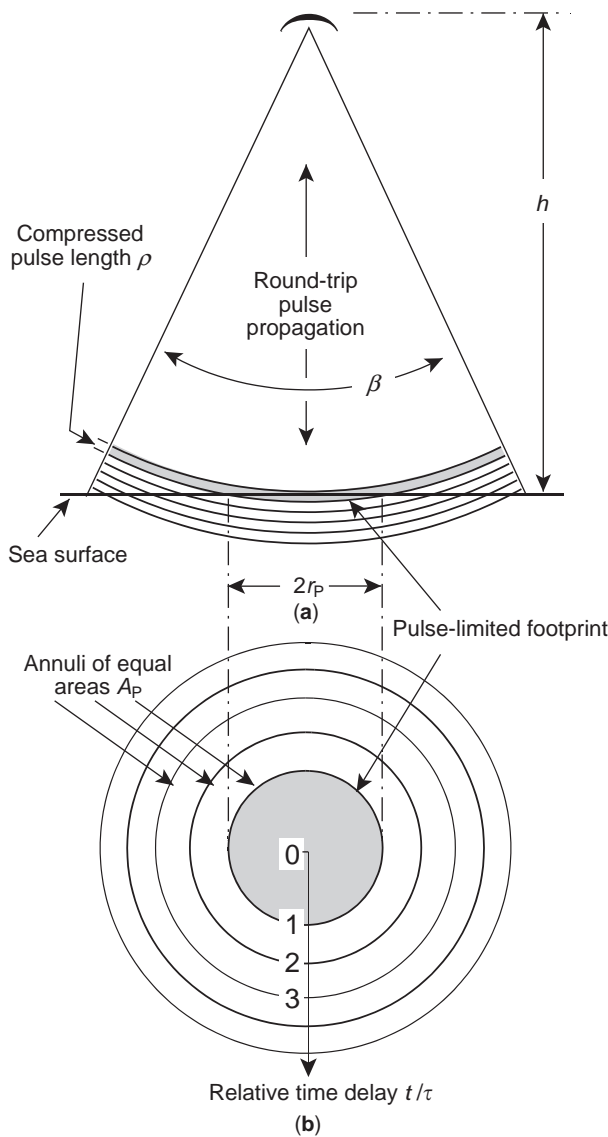


Figure 3. Elevation (a) and plan view (b) of a pulse-limited radar altimeter’s illumination geometry. The surface area simultaneously illuminated within the duration of the compressed radar pulseshift dominates the height measurement. This pulse-limited area expands for larger significant wave height (SWH).

The pulse-limited radius r_P of a quasiflat surface on Earth of mean radius R_E is

$$r_P = \sqrt{\frac{c\tau h}{\alpha_R}} \tag{2}$$

where $\alpha_R = (R_E + h)/R_E$ is a consequence of the spherical observation geometry. For typical satellite radar altimeters, the pulse-limited footprint over a quasiflat surface is on the order of 2 km in diameter. The pulse-limited area is

$$A_P = \pi r_P^2 = \frac{\pi c\tau h}{\alpha_R} \tag{3}$$

As the pulse continues to impinge on and spread over the surface, the resulting pulse-limited annuli all have areas equal to that of the initial pulse-limited footprint. Hence, the received power tends to maintain the level corresponding to the peak of the initial response. The pulse-limited areas expand in response to increasing large-scale surface roughness, which in the oceanographic context is expressed as significant wave height (SWH).

4.2. Radiometric Response

The classical single-pulse radar equation that describes the postprocessing peak power P is

$$P = \frac{P_T G^2(\theta) \lambda^2 C_R \sigma}{(4\pi)^3 h^4} \tag{4}$$

where σ is the effective radar cross section, P_T is the transmitted power, $G(\theta)$ is the one-way power gain of the antenna as a function of off-boresight angle, λ is radar wavelength, h is height, and the range pulse processing gain (compression ratio) is C_R . In the altimetry literature, the radar cross section usually is interpreted to mean $\sigma = \sigma^0 A_\sigma$, where σ^0 (sigma 0) is the normalized scattering coefficient (dimensionless) of the terrain and A_σ is the area of the resolved footprint. The peak power observed within a conventional radar altimeter, at the instant that the pulse-limited area at nadir is fully illuminated, is given from Eqs. (3) and (4) by

$$P_P = \frac{P_T G^2 \lambda^2 C_R \pi c \tau \sigma^0}{(4\pi)^3 h^3 \alpha_R} \tag{5}$$

The power described by Eq. (5) is proportional to compressed pulseshift τ and to the inverse cube of height h^{-3} .

4.3. Flat-Surface Response

Under reasonable conditions, the expected output $g(t)$ from any linear sensor is given by the convolution $g(t) = p(t) * s(t)$ of the sensor’s impulse response $p(t)$ over the distribution $s(t)$ that describes the input data source. A pulse-limited radar altimeter is an example of a linear system, but its response to input data takes on a special form due to the relatively strange geometry through which it views surface height variations. As a function of time, the

radiating pulse first strikes the surface, and then spreads out over it. The so-called *flat-surface response* is the altimetric counterpart to the generic impulse response function. It serves as the primary analytical basis for description of a radar altimeter’s waveform from a variety of surface topographies.

In the altimetry literature two closely related “flat surface” functions appear, denoted here as $p_I(t)$ and $p_F(t)$. The (idealized) flat surface response $p_I(t)$ was introduced originally [16] as a system function to account for the effects of antenna pattern, illumination geometry, and incoherent surface scattering. As an extension, Brown’s [17] flat-surface response $p_F(t)$ includes the impact of the compressed pulshape and signal processing as well as the functional dependencies captured in $p_I(t)$. Brown’s model is used most widely.

The difference between these two flat-surface functions is subtle but significant. The average input data distribution presented to a conventional radar altimeter is accurately modeled by $s(t) = p_I(t) * q(t)$, which is a convolution of the (idealized) flat-surface response $p_I(t)$ with the topographic distribution $q(t)$ of the surface. The resulting radar altimeter linear model is the convolution $g_A(t) = p_F(t) * q(t)$, where $p_F(t) = p(t) * p_I(t)$ is Brown’s flat-surface response function and $p(t)$ is the conventional linear system impulse response of the altimeter. The output $g_A(t)$ is known as the *altimeter waveform*, examples of which are sketched in Fig. 2.

The flat-surface response function (averaged) of a conventional satellite radar altimeter is

$$\begin{aligned}
 p_F(t) &= 0 && \frac{1}{\tau} \left[t - \frac{2h}{c} \right] \leq 0 \\
 &= \frac{t}{\tau} && 0 < \frac{1}{\tau} \left[t - \frac{2h}{c} \right] \leq 1 \\
 &= 1 && 1 < \frac{1}{\tau} \left[t - \frac{2h}{c} \right]
 \end{aligned} \tag{6}$$

under the simplifying condition of a perfectly rectangular compressed unity pulse of length τ . The defining characteristic of this response is that it is essentially a step function; following its linear rise over the duration of the compressed pulse, its maximum value is supported for many subsequent delay intervals. In practice, this waveform is attenuated in time, due primarily to weighting of the antenna pattern away from boresight. Also, the waveform itself is more rounded, as a consequence of the weighted shape of the compressed pulse produced by a realistic altimeter.

5. DERAMP ON RECEIVE

A satellite-based radar altimeter needs to measure the distance accurately, but only for an essentially planar surface, oriented orthogonally to the radar’s line of sight. Conservative design suggests that all radar resources should be concentrated near the reflection from that surface. Hence, ocean-viewing altimeters have a small range window that tracks the delay and strength of the surface

reflection. The ocean’s surface has a significant wave height of less than 20 m or so, and its radar backscatter coefficient spans 3–20 dB, to cite parameters used in the testing of the TOPEX altimeter. In practice, range gate delay and backscatter tracking are met with two servo-regulator feedback loops (Fig. 4). The first loop is a second-order height tracker consisting of range position (alpha tracker) and range rate (beta tracker). The second loop is the receiver gain control (AGC). Altimeter height measurement is given by the setting of the range delay coarse and fine values, corrected by the remaining height error measured from the waveform’s position in the tracker. Surface windspeed and significant wave height are derived from the AGC values and the waveform’s shape, respectively.

The precision of an individual height measurement is determined by range resolution. If a simple short pulse were transmitted, then the height resolution would equal the pulselength. The principal disadvantage of a short pulse is that it contains little energy. The inherent resolution of a pulse is inversely proportional to its bandwidth. Most radar altimeters use some form of modulation on the transmitted signal to maintain a large bandwidth within a longer pulse, thus increasing the transmitted energy at no loss of resolution. A well-established modulation technique used in many airborne radar altimeters is frequency-modulated continuous wave (FMCW), from which height is

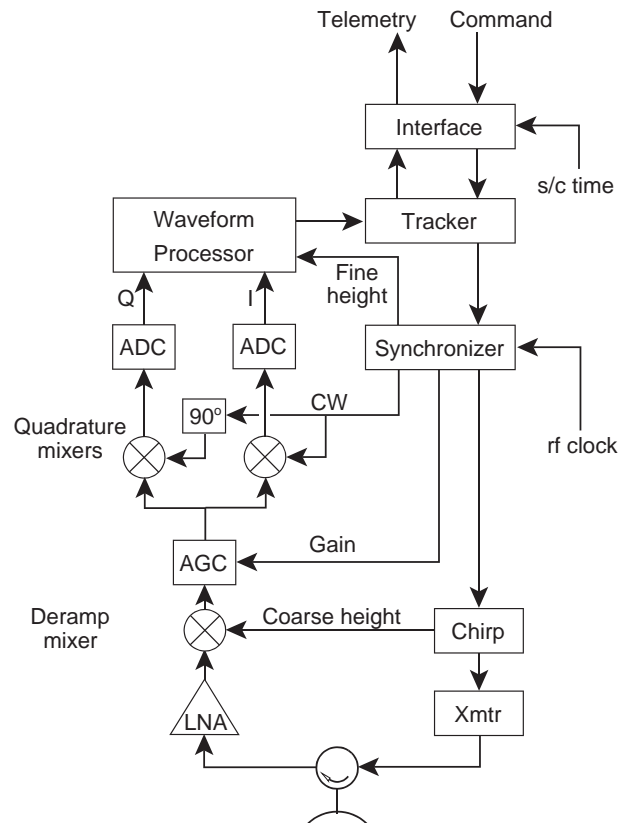


Figure 4. The functional diagram of a modern satellite altimeter is centered on the waveform tracker, whose outputs are (1) translated into science data to be returned via telemetry and (2) transformed into closed-loop timing and gain controls for the radar.

proportional to the frequency difference between the transmitted and received signals. An alternative approach is pulse compression, whereby a relatively long large time-bandwidth pulse is transmitted, and then processed (compressed) after reception to a simple short pulse of unity time-bandwidth.

Satellite-based radar altimeters use a different and specialized form of modulation and demodulation. The relatively distant and narrow range window typical of an ocean-viewing satellite radar altimeter is ideal for the full-deramp (stretch) technique [18], which was first applied to altimetry by MacArthur [19] in the Seasat altimeter. The defining feature of the full-deramp technique is that the transmitted pulselength is longer than the depth of the range window.

The full-deramp (dechirp) technique employs a transmitted chirp (linear FM signal) of duration T_P , bandwidth B_P , chirp rate k_P , and center frequency f_0 . For a pulse initiated at $t = 0$, the transmitted frequency is $f_0 + k_P t$, $t \in T_P$, as shown in Fig. 5. The bandwidth is $B_P = k_P T_P$, and the associated time-bandwidth product is $k_P T_P^2$. Pulse bandwidths and the time-bandwidth products for satellite radar altimeters are large, on the order of 300 MHz and 30,000, respectively. The compressed pulselength τ is given by the inverse bandwidth of the transmitted pulse, or alternatively, by the original pulselength T_P divided by the time-bandwidth product. Thus, a fully deramped altimeter's height resolution is

$$\tau = \frac{1}{k_P T_P} \text{ seconds or } \rho = \frac{c}{2k_P T_P} \text{ meters} \quad (7)$$

The altimeter tracking system anticipates the time t_0 when the reflected signals will arrive back at the radar; to meet them, another chirp is generated, at time $t_C \approx t_0$ and center frequency $f_0 - f_1$, where f_1 is to become the receiver's intermediate frequency (IF). (The deramp chirp

time t_C in general is slightly different from t_0 , as explained in the tracking discussion below.) The deramp chirp is mixed with the incoming signals, after which their difference frequencies are retained, to produce the set of deramped data signals shown in the figure.

The key to many characteristics unique to a radar altimeter lies in this deramp domain. The deramped signal from the m th individual scatterer at time delay t_m is a CW segment of length T_P and frequency

$$f_m = 2k_P(t_m - t_C), \quad t_m \in T_R \quad (8)$$

where T_R is the time spanned by the received signals. For a range window R_H meters deep, $T_R = 2R_H/c$. The IF bandwidth B_I is determined by the FM rate and the range window, $B_I = 2k_P R_H/c$. If the range depth of the scene is small, as is the case with radar altimeters meant to operate over the ocean, then the corresponding IF bandwidth is small, typically less than 5 MHz. Clearly, the full-deramp technique offers a considerable savings in system bandwidth at all subsequent stages, and at no cost in range resolution.

The deramped window duration $T_D \geq T_P + T_R$ must be larger than the pulse duration to accommodate the extra time induced by the range window timespan. The full-deramp technique works best when $T_P \gg T_R$, a condition that is very well satisfied for oceanographic altimeters for which T_R is less than 1% of T_P . *Alert:* There is a conceptual pitfall lurking in the deramped signal domain. Time and frequency reverse their customary roles. In this domain, time delay is no longer a measure of the radar range to reflectors. Rather, the signals' time duration T_P determines their compressed pulse resolution according to Eq. (7), and thus "time" behaves as a bandwidth. Conversely, each scatterer's round-trip time delay, relative to the trackpoint, is proportional after deramp to the CW frequency given by Eq. (8), relative to the IF center frequency. Thus "frequency" behaves as delay time, which is proportional to radar range.

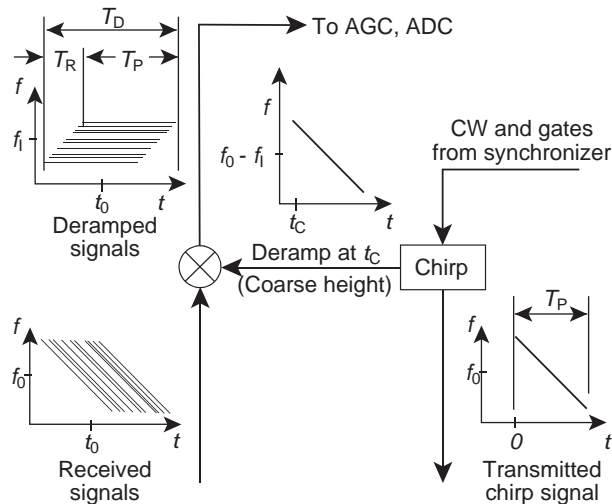


Figure 5. A long linearly frequency-modulated (chirp) pulse is transmitted (as in Fig. 4), followed by full-deramp demodulation on receive to produce a relatively narrowband set of CW data signals at intermediate frequency f_1 .

6. THE TOPEX DESIGN

The TOPEX Ku-band altimeter [11,12,19] illustrates the essential features of conventional space-based radar altimeters (Fig. 4). The TOPEX altimeter is controlled by a synchronizer whose inputs are derived from the tracker outputs, slaved to a master radiofrequency clock at 80 MHz. The tracker and synchronizer control the altimeter in all seven of its operational modes: test, calibrate, standby, coarse track acquisition, fine track acquisition, coarse-resolution track, and fine-resolution track. Table 3 lists values for selected TOPEX parameters.

In the fine-resolution track mode, the radar transmits a linear FM (chirp) pulse of length 102.4 μ s and bandwidth 320 MHz. The signal generator consists of a digital section that creates 40-MHz chirps at baseband, followed by RF sections that multiply and mix the signals to meet the final bandwidth and center frequency. The chirped pulses at 13.6 GHz are amplified in a traveling-wave tube (TWT) to

Table 3. TOPEX Chirp Parameter Values

Parameter	Symbol	Value	Units
Chirp rate	k_P	-3.125	MHz/ μ s
Pulse duration	T_P	102.4	μ s
Pulse bandwidth	B_P	320	Hz
Time \times bandwidth	—	32768	(Nil)
Pulse resolution	ρ	0.469	m
Pulse resolution	τ	3.125	ns
Carrier (Ku-band)	f_0	13.6	GHz
Carrier (C band)	f_0	5.2	GHz
IF frequency	f_1	500	MHz
IF bandwidth	B_I	3	MHz
Range timespan	T_R	400	ns
Deramp timespan	T_D	~ 103	μ s

20 W (peak), and transmitted at 4.5 kHz pulse repetition frequency (PRF) through an antenna 1.5 m in diameter.

The received pulses are amplified and then mixed with a delayed chirp signal, centered at 13.1 GHz to produce an ensemble of CW data signals spread over a band of ~ 3 MHz about an intermediate frequency of 500 MHz. The deramped data signals are further amplified, subject to gain control in the AGC attenuator, mixed down to in-phase and quadrature video, lowpass-filtered and digitized. At this stage, the lowpass filter has the effect of removing echoes from ranges that are well outside the desired range gate window. The signals are magnitude-squared, and summed to produce smoothed height waveforms. Extensive waveform averaging over statistically independent samples is essential to suppress the speckle noise that otherwise would dominate the waveforms. The smoothed waveforms are processed to extract the data of interest, and the tracking outputs are fed back to close the control loops of the radar.

The Ku-band and the C-band channels are time-multiplexed, which impacts system timing from the PRF to the processor.

6.1. Sampling and Waveform Processing

The mean amplitude of the deramped signals is normalized through an AGC amplifier. The receiver gain is set by the level observed in the waveform processor. Signal level is proportional to the scattering coefficient (σ_0) of the water's surface, which in turn is a function of surface windspeed. The normalized signals in the TOPEX altimeters are mixed down to in-phase (I) and quadrature (Q) video channels and passed through 625-kHz lowpass filters prior to analog-to-digital sampling at a 1.25 MHz rate. This produces a set of 128 complex samples uniformly spaced over the 103.2- μ s deramp interval T_D .

The tracker and synchronizer control the position of the altimeter height settings through two paths: coarse, and fine. The coarse height feedback depends on the deramp trigger t_C that is slaved to the 80 MHz clock, which has a period of 12.5 ns. Thus, choice of t_C is restricted to a set of discrete delays separated by 12.5 ns, corresponding to height intervals of 1.875 m each. The fine height feedback is exercised in the digitized deramp domain (Fig. 6). In the deramp domain, a small frequency shift is equivalent to a

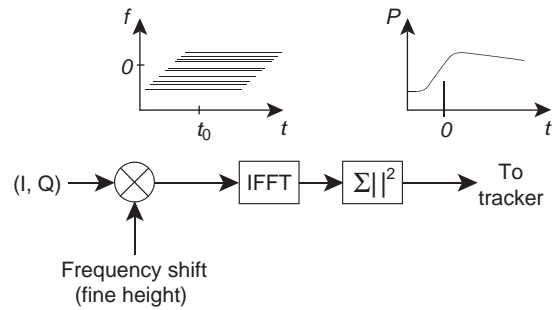


Figure 6. The waveform processor (see Fig. 4) of a pulse-limited radar altimeter performs three basic functions: (1) application of a frequency shift to effect the fine range delay correction, (2) an inverse FFT applied to each return to transform the CW signals into a power distribution as a function of altimetric height (relative to the trackpoint), and (3) summation over many of these individual power waveforms to form the averaged waveform that is sent to the tracker.

small time delay Δt . For a fine time shift interval $-12.5 \text{ ns} < \Delta t < 12.5 \text{ ns}$, the corresponding frequency shift is $k_P \Delta t$, bounded by $\pm 39.0625 \text{ kHz}$. The 25-ns fine time shift adjustment interval is large enough to accommodate anticipated range rates without having to reset the course height feedback selection within one waveform-processing cycle.

Following frequency shift, the data are inverse fast Fourier transformed (IFFT) and magnitude-squared detected. The IFFT converts CW to time shift (relative to the trackpoint), and compresses the data to its individual pulse resolution, 0.469 m. Each resulting waveform is a distribution of power across the bins within the range window (as suggested in Fig. 2).

As is true for most radars, the received waveform produced by an individual pulse is corrupted by speckle noise. Speckle is created by the coherent interference within a given echo between unresolved and competing elementary scatterers, and causes the signal's standard deviation to be large. (In the limit, the standard deviation equals the signal's mean value for an individual waveform drawn from a Gaussian ensemble). The standard deviation of the speckle can be reduced by summing (averaging) many statistically independent waveforms together. Statistical independence between sequential returns observed by a radar altimeter depends primarily on the radar pulse repetition rate (PRF), the antenna size, the spacecraft velocity, and sea surface conditions [20]. The pulse-to-pulse statistical independence threshold for TOPEX is about 2.5 kHz, yet its PRF = 4.5 kHz. The pulse rate above the threshold improves the additive SNR, but does not contribute to speckle reduction.

6.2. Tracking

The TOPEX Ku-band channel averages 228 pulses over a so-called track interval of about 50 ms to produce the smoothed waveforms delivered to the tracker at a 20 Hz rate. For each waveform, the range window (Fig. 2) is partitioned into 128 sample positions or bins, each of size equal to the radar's range resolution. Groups of bins are

organized into *tracking gates* of various sizes whose outputs are used to calculate the parameters that control the altimeter's feedback loops, and to provide the first-order science data from the instrument [21]. The tracking algorithm, based on an Intel 80186 microprocessor, iterates at the waveform input rate of 20 Hz. Each tracking gate is normalized so that its gain is inversely proportional to its width, which is the number of samples that it spans. The range width of each gate is a power of 2 times the intrinsic range resolution of the altimeter.

The noise gate estimates the mean noise level from samples 5–8, which occur well before the waveform begins to respond to surface reflections. The mid-point of the waveform's leading edge is tracked to keep it centered between samples 32 and 33. The AGC gate spans samples 17–48, which are centered on bin 32.5, the so-called *trackpoint*.

The output of the AGC gate is fed back to control the altimeter's gain loop. TOPEX is required to measure waveform power (proportional to σ_0) with an accuracy of ± 1 dB and a precision of ± 0.25 dB. In response to the waveform levels observed in the AGC gate, the receiver attenuator is adjusted in 1 dB steps. To meet the accuracy and precision requirements, from pulse to pulse the attenuator setting is dithered between neighboring steps. This has the effect of interpolating the mean AGC setting to an effective accuracy of less than 0.1 dB when averaged over all 228 input waveforms. Waveform power (σ_0) returned as science data is equal to the mean AGC level plus the AGC tracking gate level.

To summarize, the altimeter's measurements are: SSH—the position of the trackpoint, plus the trackpoint offset; SWH—proportional to the width of the waveform leading edge of the waveform; and WS—proportional to a function (empirically determined) of $1/(\text{waveform power})$, hence derived from the AGC setting.

7. GRAVITY AND BATHYMETRY—PRECISION

Radar altimetric data are the basis for state-of-the-art geodesy expressed through the ocean's surface, and consequently, global bathymetry. The principal objective of a geodetic satellite radar altimeter [22] is to measure the (along-track) slope of the sea surface caused by gravity deflections over spatial scales less than a few hundreds of kilometers (Fig. 7). Sea surface slope is derived by taking

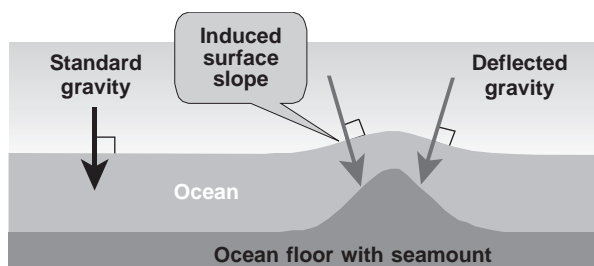


Figure 7. The ocean's bottom topography causes subtle variations in the local gravity field, which are expressed as small tilts in the ocean's surface. These are observable by satellite altimetry.

the difference between two neighboring height measurements, where the slope tangent equals "rise over run." The keyword for these measurements is *precision*: the standard deviation (noise) of the sea surface height measurement about its mean value. Height measurement precision is determined by the radar altimeter's postprocessing range resolution, and by the amount of averaging available for each estimate. Note that a precision measurement may still have poor accuracy, if its mean value is biased away from the correct value. When comparing two neighboring height measurements, any constant bias is canceled by differentiation as long as the error is the same for both measurements. The sea surface slope measurement problem is challenging because the desired slope signals are as small as 6 mm height differential (rise) for each 6-km along-track separation (run). Such a slope corresponds to one microradian of gravity deflection, or about a one milligal gravity anomaly.

In addition to height precision, geodetic altimetry requires smaller along-track resolution than does a conventional altimeter, and a suitable orbit. The altimeter's footprint resolution should be smaller than about 6 km, which corresponds to the minimum half-wavelength scale of the observable gravity anomaly spectrum. The orbit should not repeat for ~ 1.2 years, to yield an average ground track spacing of 6 km, again in respect of the anomaly spectrum. The orbit's inclination should be near $50\text{--}63^\circ$ (or $113\text{--}120^\circ$ retrograde) to resolve north and east slopes nearly equally, and to cover the lower latitudes where existing data are inadequate. Note that oceanographic radar altimeter missions (TOPEX/Poseidon, Jason-1, ERS1/2, Envisat, and Geosat ERM/GFO) normally are placed into exact-repeat orbits (10–35 days), and as a consequence have widely spaced (80–315-km) ground tracks. Such orbits cannot resolve the short-wavelength two-dimensional surface slopes required for useful bathymetry.

Since absolute height accuracy is not required, geodetic radar altimeters can be relatively basic instruments. They do not need to compensate for propagation delays; hence they need only one frequency, and they do not need a water-vapor radiometer. Indeed, such an instrument is preferred; it has been shown that efforts to correct for path delays usually add noise to slope estimates [23]. Geodetic measurements provided by the Geosat and ERS-1 (both single-frequency altimeters with no WVR) furnish the best resolution oceanic gravity from space to date. Their resulting bathymetric resolution is limited to about 25 km north-south, with poorer resolution of east-west slope components. These results reflect the less-than-optimum resolution, waveform precision, and orbit inclination of those two altimeters. Geodetic resolution at the ocean's surface can be no finer than about 6 km (half wavelength), a limit that is determined by the average depth of the ocean, which is about 4 km.

Gravity anomalies are caused by topographic relief on an interface between two volumes of differing mass density. In the deep ocean, sediments are thin, and the basaltic seafloor crust is internally flat-layered, and so gravity anomalies at the surface reflect the topography of the ocean floor. Conversely, at continental margins the

seafloor is nearly flat and sediments are generally thick. Beneath these sediments there may be basins or other geologic structures of interest. In such regions, surface slope signals are due primarily to topographic variations at the interface between crystalline rocks and their sedimentary overburden. The sediment–basement interface provides essential reconnaissance information for petroleum exploration. The correlation between slope and existing depth soundings readily distinguishes these two environments [24].

The slope signals required to estimate bathymetry are bandlimited (12–300 km full wavelength), as determined by fundamental physical principles. Hence, the height measurements of a geodetic altimeter need to maintain relative accuracy—precision—only over this relatively narrow band. Within this band, precision turns out to be the dominant limiting condition. Sea surface slope measurements are derivatives of the altimeter’s natural measurements, height. Taking derivatives eliminates constant and longwave height errors, but it amplifies noise at short wavelengths. Using a simple model in which height errors are assumed to be a Gaussian white-noise process over the geodetic band, the one-sigma slope error is about $1.8 \mu\text{rad}$ if the altimeter’s one-sigma height precision is 1 cm for a one-second averaged height value. Experience teaches that height precision degrades with increasing significant wave height (SWH). One of the factors that motivated the development of the delay–Doppler approach to radar altimetry was to improve measurement precision.

8. DELAY–DOPPLER

The delay–Doppler technique leads to better measurement precision, a smaller effective footprint at nadir, and increased tolerance of along-track surface gradients typical of continental ice sheets. The central innovation in the delay–Doppler concept [25,26] is that it combines the benefits of coherent and incoherent signal processing, rather than relying exclusively on incoherent averaging as is the case for all conventional satellite radar altimeters. The coherent processing stages, patterned after well-established methods developed for synthetic aperture imaging radar (SAR), allow much more of the instrument’s radiated power to be converted into height measurement data. One consequence of delay–Doppler signal processing is that less transmitted power is required than with a conventional altimeter. The delay–Doppler technique also enjoys the benefits of the pulse-limited range measurement geometry.

The coherent processing transforms groups of data into the Doppler frequency domain, where delay corrections are applied, analogous to SAR range curvature correction [27]. Doppler processing determines the size and location of the along-track footprint, which is (1) smaller than the pulse-limited diameter, (2) a constant of the system, and (3) relatively immune to surface topographic variations. Waveforms are incoherently summed corresponding to each surface position as the altimeter progresses along track. One direct result is that each height measurement from a delay–Doppler altimeter has more incoherent

averaging than is possible from a conventional radar altimeter.

The delay–Doppler technique exploits coherence between pulses, in contrast to the pulse-to-pulse incoherence that is the norm for conventional pulse-limited altimeters. Pulse-to-pulse coherence requires that the PRF be above the interpulse correlation threshold, rather than below it as is normal for conventional incoherent radar altimeters [20]. To assure correlation, the PRF must be high enough so that at least two pulses are emitted while the satellite’s forward motion equals the along-track aperture size of the altimeter’s antenna.

8.1. Delay–Doppler Domain

The objective of delay compensation is to remove the extra delay (Fig. 8) that is induced by the spherical curvature of the radar’s ranging wavefront as it impinges on the ocean’s surface. At each along-track angular offset θ_D from nadir, there is an extra range distance $\Delta h = h(\sec \theta_D - 1)$ due to range curvature. As it is received, the signal includes returns from scatterers at many different angles. Hence, the problem is multivalued; in the signal domain compensation for wavefront curvature is impossible. This is the situation for conventional incoherent radar altimeters. In the delay–Doppler altimeter, however, along-track coherent processing circumvents this dilemma. Transformation from the signal domain to the frequency (Doppler) domain reduces delay compensation to a single-valued problem: at each Doppler frequency f_D the extra range delay increment is unique, and known.

The delay increment, in terms of Doppler frequency f_D as its independent variable, is

$$\Delta h(f_D) \approx \alpha_R \frac{\lambda^2 h}{8V^2} f_D^2 \quad (9)$$

where V is the velocity of the spacecraft along its orbit. Recall that the deramped data in the range direction appear as constant (CW) frequencies. Each range delay increment translates into an equivalent CW frequency shift. These unwanted frequency shifts may be nullified by multiplying the data field by equal and opposite CW signals prior to the range IFFT, analogous to the fine tracking frequency shift of a conventional radar altimeter. The result is evident in Fig. 9, which compares the flat-surface response waveform (as it would appear in the delay–Doppler domain) before and after delay compensation.

8.2. Implementation

The delay–Doppler altimeter introduces additional along-track processing steps (Fig. 10) after the range deramp and before the range IFFT. The net effect of the extra processing is to transform the signal space from one to two dimensions. A Fourier transform is applied to these data in the along-track dimension, implemented in real time onboard as a set of parallel FFTs that span the range window width. Signals in the resulting two-dimensional deramp/Doppler domain are phase-shifted to eliminate the unwanted range.

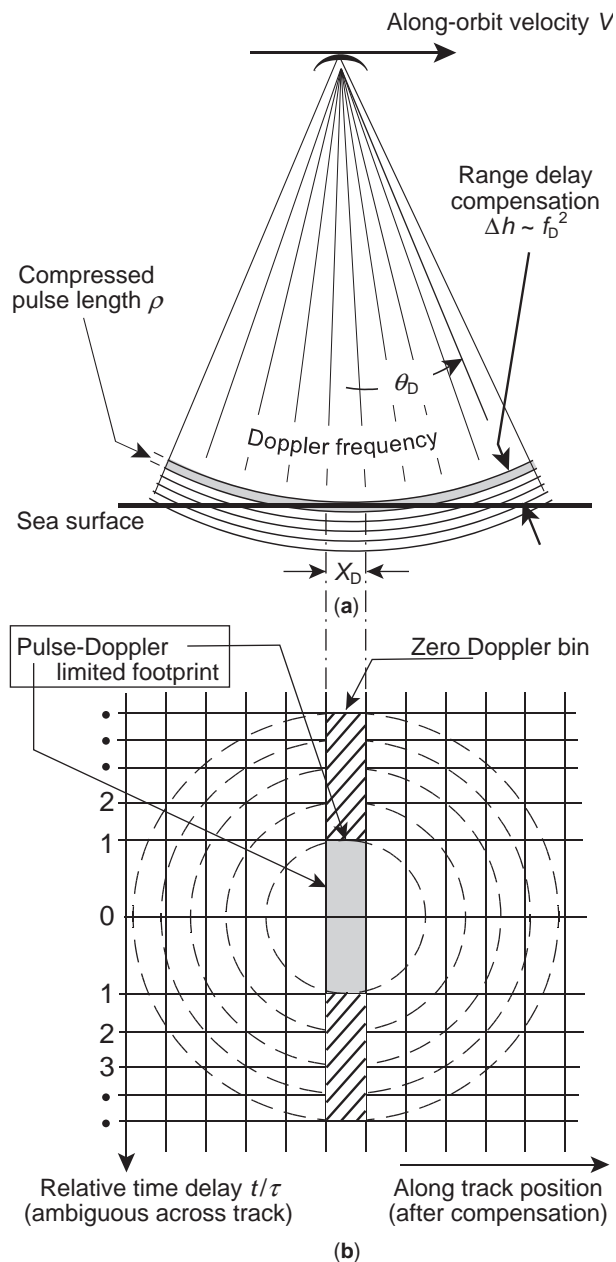


Figure 8. Elevation (a) and postcompensation plan view (b) of a delay/Doppler radar altimeter’s illumination geometry. The resolved along-track footprint X_D is Doppler-limited. The cross-track footprint is pulse-limited. Although the footprint is smaller than the pulse-limited area, more averaging is available at each Doppler bin position.

The delay correction phase functions are

$$\Phi(f_D, t) = \exp \left\{ +j2\pi k_P \frac{2}{c} \Delta h(f_D) t \right\} \quad (10)$$

which are CW signals whose frequency is matched to the delay increment given by Eq. (9). The data at this stage consist of an ensemble of two-dimensional CW signals. Frequency in the time-delay direction is proportional to (minimum) delay relative to the range trackpoint, and

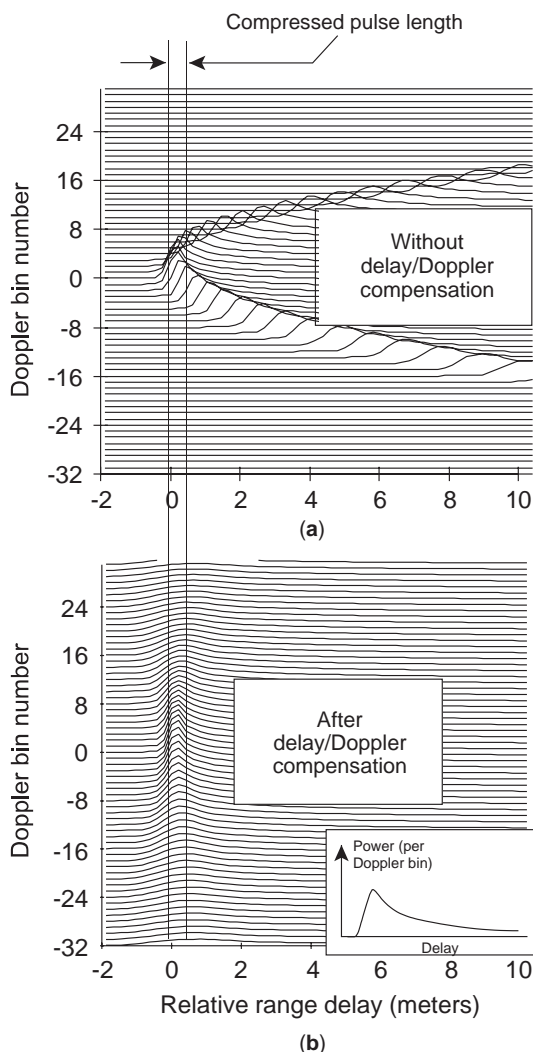


Figure 9. Simulated height waveforms, as they would appear in a compressed pulse (delay) and Doppler data array before (a) and after (b) curvature compensation, illustrate how delay/Doppler processing shifts more of the reflected energy into the pulse-limited region, thus improving the height estimates.

frequency in the along-track direction is proportional to the scatterer’s along-track position relative to the zero-Doppler position.

The remaining data processing is carried out in parallel, consisting of a range IFFT at each Doppler frequency bin, detection, and assignment of the height estimates to their respective along-track positions. The process is repeated over subsequent blocks of data, from which many statistically-independent waveforms are accumulated at each along-track position. As the altimeter passes over each scatterer, the corresponding height estimates move in sequence from the highest Doppler filter to each lower frequency filter, until the scatterer is out of sight. Thus, the final waveform at each along-track position is the average (incoherent sum, normalized) of estimates from all Doppler filters. If the Doppler filters are designed to span the along-track antenna beamwidth, then all along-track data contribute to the height estimates.

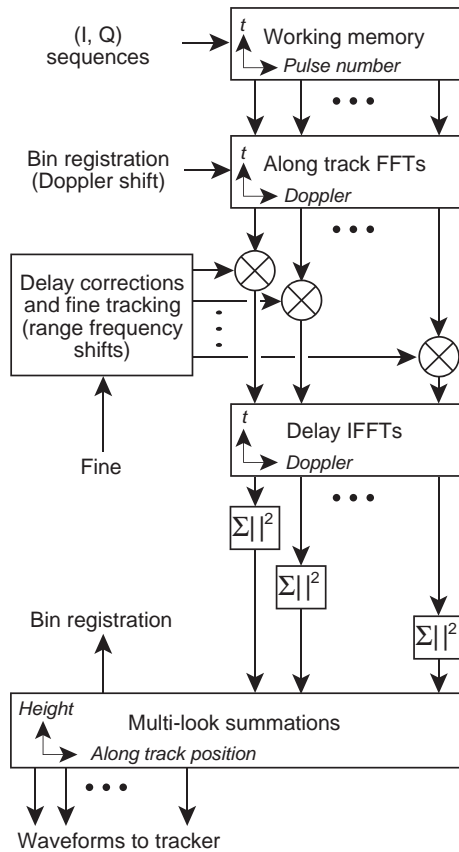


Figure 10. A delay/Doppler radar altimeter waveform processor (see Fig. 4) must be augmented with a cache memory to store the deramped returns from a sequence of transmitted pulses. FFTs are applied across these data to derive their Doppler frequency spectra, which then are corrected for curvature delay by phase multiplication.

8.3. Footprint

Delay–Doppler processing may be interpreted as an operation that flattens the radiating field in the along-track direction. In this transformed data space (Fig. 8b), the (x, y) cells have constant along-track length, but their cross-track widths decrease as the square root of delay time. The cross-track footprint is determined by the pulse-limited condition.

The along-track impulse response is set up by the Doppler filters. Along-track impulse position is determined by the zero-Doppler position for each burst of data. Along-track position can be adjusted by artificial Doppler shifts to maintain registration of subsequent Doppler bins, which is the along-track analog of the fine height adjustment in an incoherent radar altimeter.

Ideally, the along-track zero-Doppler position is equivalent to the geometric subsatellite point, nadir. The along-track location of the zero-Doppler plane is independent of satellite attitude, and also is independent of terrain slope. Thus, the height measurements at all Doppler frequencies can be located along track with respect to zero Doppler. In practice, the zero-Doppler bin location may not coincide with nadir. A vertical spacecraft velocity component adds

a Doppler shift to the signals. Vertical velocity and its implied Doppler error can be estimated. Offsetting Doppler shifts can be applied in response to a spacecraft vertical velocity component to assure registration of the Doppler bins with their corresponding along-track positions defined with respect to nadir.

8.4. Unfocused Condition

The foregoing is predicated on a simple isometry between Doppler frequency and along-track spatial position. This equivalence is valid for an along-track resolution that is comparable to or larger than the first Fresnel zone. In synthetic aperture radar parlance, this zone is known as the *unfocused SAR resolution*. Using the classic quarter-wavelength criterion, the radius a_0 of the first Fresnel zone is

$$a_0 = \sqrt{\frac{h\lambda}{2}}$$

which for a Ku-band altimeter leads to an along-track (unfocused) dimension of 180 m from an altitude of 800 km (or about 230 m from an altitude of 1334 km). As these quantities are less than the nominal delay–Doppler along-track cell size of 250 m, the processing task is trivial—no focusing is required. Focus operations would be required if the Fresnel radius were larger than the along-track cell dimension. If a smaller cell size is desired such as for altimetry over land, or if a very high satellite altitude or longer radar wavelength were chosen, then the along-track processor would have to incorporate phase matching to focus the data.

8.5. Incoherent Averaging

There are two stages in a delay-Doppler altimeter at which incoherent averaging takes place: within each Doppler bin and across neighboring bins. Detected returns from many pulses are averaged together to build the waveform within each bin. For a typical satellite altimeter, these waveforms would accumulate within each 250-m bin at about a 26 Hz rate. Subsequent averaging (incoherent integration) over adjacent waveforms typically extends over 0.1 s (or 1.0 s), during which time the antenna illumination pattern progresses in the along-track direction by an appreciable distance, approximately 0.6 km (or 6 km). *Alert:* the relative location of each delay–Doppler-derived height estimate is synchronized to coincide with the forward motion of the instrument, thus eliminating along-track elongation of the footprint, as is the case for a conventional altimeter. The result is that a delay–Doppler altimeter generates significantly more incoherent averaging than does a conventional altimeter, and at less compromise in along-track footprint size.

One immediate benefit is better measurement precision. Consider the case of height precision in the context of geodetic requirements. Figure 11 shows a plot of height precision *versus* SWH for a delay–Doppler altimeter (DDA) and a conventional radar altimeter (RA). The plot shows that the DDA meets the height precision requirement of 1 cm at 3 m SWH, a result that is consistent with

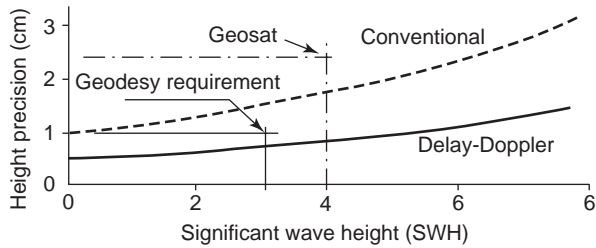


Figure 11. Height precision of a delay-Doppler radar altimeter (calculated for a Ku-band system in an 800-km Earth orbit) compared to that of a conventional altimeter, as a function of significant wave height. The requirements derived from state-of-the-art oceanic geodesy, and the nominal performance of the Geosat altimeter are included, for reference.

previous analyses [28]. The figure also shows that the DDA is about half as sensitive as an RA to increasing SWH. This is important for geodetic applications, as measurement precision degraded by larger significant wave heights is a major source of noise in Geosat surface slope estimates [7].

8.6. Flat-Surface Response

The customary concept of flat surface response applies only to the delay time dimension for a delay-Doppler altimeter. This means that the inherent delay/elevation ambiguity characteristic of pulse-limited altimeters is reduced from two spatial dimensions to only one dimension. The cross-track ambiguity that remains is suggested in Fig. 8, which shows that at any given Doppler frequency, there are two possible sources for reflections having a given (relative) time delay. These arise from either side of the minimum delay locus, which nominally is the subsatellite track. Of course, the point of first reflection (at zero relative delay time) may be to one side of the subsatellite track, as would be true in general when there is a nonzero cross-track terrain slope. The cross-track ambiguity and the delay/elevation ambiguity both may be at least partially resolved through application of other means such as the monopulse phase-sensing technique.

The flat-surface delay time response (after processing) of the delay-Doppler altimeter has the functional form

$$\begin{aligned}
 f_D(t) &= 0 & \frac{1}{\tau} \left[t - \frac{2h}{c} \right] &\leq 0 \\
 &= \sqrt{\frac{t}{\tau}} & 0 < \frac{1}{\tau} \left[t - \frac{2h}{c} \right] &\leq 1 \\
 &= \sqrt{\frac{t}{\tau}} - \sqrt{\frac{t}{\tau} - 1} & 1 < \frac{1}{\tau} \left[t - \frac{2h}{c} \right] &
 \end{aligned} \quad (11)$$

where τ is the compressed pulselength (Eq. (7)). The curve of Eq. (11) represents the (average) strength of the altimeter's response to illumination of a quasiflat surface as a function of time delay, just as in the conventional case. Note that the response to a flat surface for all regions $t < \tau$ have much less relative power for the delay-Doppler altimeter than for the conventional radar altimeter

described by Eq. (6). The cross-track (time-delay) width of $f_D(t)$ is approximately equal to τ .

8.7. Radiometric Response

The delay-Doppler altimeter can take advantage of reflections from the entire length of the antenna illumination pattern in the along-track direction to estimate the height of each resolved patch of subsatellite terrain. This implies that substantially more integration is possible than in a pulse-limited altimeter. Under the assumption that the dominant scattering mechanism is nonspecular, the integration gain is linear in power. It follows that the total power arising from each resolved cell is larger for the delay-Doppler altimeter than for a conventional pulse-limited altimeter, even though the postprocessing footprint size is smaller.

Height estimation for each resolved scattering cell benefits from integration as long as that cell is illuminated by the antenna pattern. For each scattering cell, the equivalent along-orbit integration is governed by the length βh of the antenna footprint, expanded by the orbital factor α_R . The along-orbit integration may be interpreted in terms of an equivalent along-track area A_D that contributes to the received signal power for a delay-Doppler altimeter on a single-pulse basis. The cross-track dimension is set by the pulse-limited condition. Thus

$$A_D = 2h\beta\sqrt{c\tau\alpha_R} \quad (12)$$

The postprocessing power of the delay-Doppler flat-surface response function is

$$P_D = \frac{P_T G^2(\theta) \lambda^2 C_R \sigma^0}{(4\pi)^3 h^{5/2}} 2\beta\sqrt{c\tau\alpha_R} \quad (13)$$

which has an $h^{-5/2}$ height dependence, and a square-root dependence on compressed pulselength. The height dependence in Eq. (13) is the geometric mean between (h^{-3}) for the pulse-limited case described by Eq. (5) and (h^{-2}) for the beam-limited case. Reduced sensitivity to compressed pulselength τ in comparison to the pulse-limited case may be helpful in system optimization.

From Eqs. (4) and (13), the relative power efficiency of the two altimeters is given by the ratio

$$\frac{P_D}{P_P} = \alpha_R \frac{A_D}{A_P}$$

in which it is assumed that all other factors (such as average transmitted power and antenna gain) are equal in the two cases. The areas A_D and A_P are given by Eqs. (3) and (12), respectively. To first order, the relative radiometric advantage of the delay-Doppler altimeter over the pulse-limited altimeter is given simply by the ratio of the equivalent areas over which the signals are integrated. For example, the delay-Doppler technique would require only about one-tenth of the transmitter power of TOPEX to support the same SNR performance, yet it yields waveforms with reduced speckle due to increased incoherent summation.

8.8. Cross-Track Interferometry

Pulse-limited radar altimeters work best over relatively mild topographic relief of mean slope zero, such as the ocean's surface. Over ice sheets or terrestrial surfaces, performance is degraded. Unwanted characteristics include footprint dilation over rougher terrain, height errors in proportion to surface mean slope, and the tendency of the footprint location to hop from one elevated region to another (without the control or knowledge of the data analyst). Beam-limited techniques, of which laser altimeters are extreme examples, circumvent these problems, but may imply their own set of disadvantages.

A major potential application of radar altimetry is to monitor the height of extensive ice sheets, as found in Greenland or Antarctica. Approximately 95% of these surfaces have slopes less than $\sim 3^\circ$, which is sufficient to trick a conventional altimeter into very large height errors. For example, an unknown one-degree slope would lead to a 120-m surface height error, which is unacceptable. Although the delay-Doppler technique helps overcome errors induced by surface slope components in the along-track direction, that is not sufficient.

Error due to an unknown cross-track slope component can be mitigated if its slope is known. Radar interferometry, as an adjunct to a delay-Doppler altimeter, can be used to measure such cross-track surface slopes. The phase monopulse technique uses this principle to estimate the angle of arrival of reflections from a tilted surface collected through two antennas separated in the cross-track direction of the altimeter (Fig. 12). In a radar altimeter that uses phase monopulse [29], a scatterer at cross-track distance Δy away from nadir precipitates a pathlength difference Δh , observable through the cross-channel differential phase. The cross-track phase monopulse technique can measure the presence of small (mean) cross-track surface slopes. Once measured, the slope data can be applied to recover accurate estimates of the height h of (gently) sloping surfaces. The cross-track phase monopulse technique complements the delay-Doppler technique, which is an along-track enhancement.

8.9. D2P Airborne Testbed

The first embodiment of the delay-Doppler altimeter combined with a phase monopulse cross-track receiver is the D2P radar developed at the Johns Hopkins University Applied Physics Laboratory [30]. The D2P is a coherent airborne radar altimeter that operates from 13.72 to 14.08 GHz (Ku band). The system transmits a linear FM chirp signal at 5 W peak power, with pulselengths ranging from 0.384 to 3.072 μs . The system uses two receiver channels and a pair of antenna arrays, separated by a 14.5-cm baseline, to provide for angle measurements in the cross-track direction. The system provides real-time display of the delay-Doppler spectrum and cross-track phase of a burst sequence (typically 16 consecutive pulses). The D2P system typically is installed into a P-3 research aircraft. More recent campaigns include flights to Greenland, Svalbard, and Antarctica, and over sea ice.

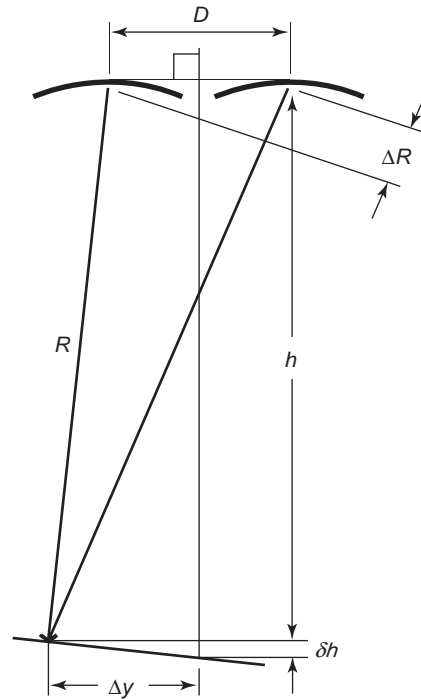


Figure 12. The cross-track (mean) surface slope can be estimated by a measurement of the phase difference between the same return observed through two separated antennas. The range difference ΔR is proportional to their phase difference, from which the slope-induced height correction δh can be calculated.

9. FUTURE DIRECTIONS

9.1. Cryosat

Cryosat [31] is the first satellite of the European Space Agency's Living Planet Programme to be realized in the framework of the Earth Explorer Opportunity Missions. The mission concept was selected in 1999 with launch anticipated in 2004. The Cryosat orbit will have high inclination (92°) and a long repeat period (369 days, with a 30-day subcycle), designed to provide dense interlocking coverage over the polar regions. Its aim is to study possible climate variability and trends by determining the variations in thickness of Earth's continental ice sheets and marine sea ice cover.

The Cryosat altimeter will be the first of its kind: SAR/Interferometric Radar ALtimeter (SIRAL), whose advanced modes are patterned after the D2P altimeter [32], and whose flight hardware has extensive Poseidon heritage. Unlike previous radar altimeter missions, Cryosat will downlink all altimetric data. These data will support three modes: conventional, interferometric, and synthetic aperture. The conventional (pulse-limited) mode will be used for open ocean (for calibration and sea surface height reference purposes) and the central continental ice sheets that are relatively level. The interferometric mode will be used for the more steeply sloping margins of the ice sheets. The synthetic aperture mode will be used primarily over sea ice, where its sharper spatial resolution and better precision will support

measurement of the freeboard for floating sea ice. These measurements can be inverted to estimate ice thickness.

9.2. WSOA

The wide-swath ocean altimeter (WSOA) [33] has been promoted by the Jet Propulsion Laboratory as a means to overcome the dominant timespace coverage dilemma that confronts ocean altimetry. The standard altimeter measurement geometry is strictly nadir-viewing; only one subsatellite height profile is gathered during each pass of the spacecraft. Whereas nadir heights can be very accurate, the surface heights of all regions between nadir tracks remain unobserved, and hence unknown. Many applications would prefer a substantially wider swath of simultaneous height measurements.

Several altimeters have been proposed over the years that would scan the surface below with a set of altimetric beams arrayed orthogonally to the subsatellite path. The goal is reasonable—to generate a wide swath of height measurements, rather than the single subsatellite line of data points typically available. However, there are problems with this general approach. The predominant difficulty is that the measurement is based on triangulation, rather than the much more robust (minimum) range measurement of nadir altimetry. Off-nadir triangulation is extremely sensitive to the satellite's roll angle error $\delta\theta$. Height accuracy within a beam-limited paradigm, at an off-nadir measurement angle θ , depends to first order on $h(\tan\theta \sec^2\theta)\delta\theta$, which increases rapidly from zero as the off-nadir angle is increased. In contrast, a pulse-limited nadir altimeter's height measurement accuracy is not degraded in response to small attitude errors at the spacecraft. The height accuracy requirements typical of oceanographic applications of a few centimeters cannot be met by a single-pass multibeam or wide-swath system given the state of the art of controlling or determining spacecraft (roll) attitude control.

The WSOA concept promises to overcome this roadblock by combining swaths from ascending and descending passes. The accurate nadir heights from one pass will be applied to remove systematic cross-track height errors in the intersecting swath. This approach is expected to provide useful height measurements across the swath for those oceanic features whose height signals are highly correlated over the time between the two passes, typically a few days.

The WSOA is designed to measure ocean surface height within a 200-km swath centered on the nadir track. In a suitable orbit, such an instrument could observe nearly all the ocean's surface with a spatial resolution of ~ 15 km. This WSOA is under negotiation as a demonstration instrument on the Jason-2 mission, post 2007.

9.3. WITTEX

WITTEX, named in honor of E. Witte, who in 1878 first discovered the geostrophic current equation, is an acronym for "water inclination topography and technology experiment." A WITTEX constellation would consist of three coplanar small-satellite radar altimeters [34,35]. The satellites would be spaced apart by several hundred kilome-

ters along their orbit. Earth rotation will cause their subsatellite tracks to be laterally separated. Along-orbit spacecraft spacing will determine the separation and temporal coverage of the resulting surface tracks. The measurements along each set of three near-parallel tracks occur within minutes of each other.

In principle, WITTEX data would support measurement of the cross-track surface gradient as well as the usual along-track gradient. Hence, two orthogonal components of the surface gradient could be observed, from which can be derived the two-dimensional geostrophic current. In practice, height biases will exist between the cross-track measurements. Even if small, such differential biases would compromise the track-to-track height comparisons. One means of offsetting these systematic errors is to cross-calibrate the respective altimeters. This is easily done, since the altimeters are in the same orbit plane. Their surface tracks cross each other at maximal latitudes. When these crossovers occur over the ocean, coincident height measurements from the different instruments can be cross-calibrated.

9.4. Dual-Use Altimetry

To date, the two themes of dynamic mesoscale ocean topography and geodesy have remained disjoint. Geodesy requires a nonrepeating orbit, whereas traditional oceanographic altimetry, including mesoscale observations, relies on exact-repeat orbits. More recent investigations suggest that the two objectives could be satisfied by one altimeter in a nonrepeating orbit, if adequate near-simultaneous ancillary data were available from a more conventional mission such as Jason. The feasibility of dual-use altimetry is a work in progress [36]. If verified, such a mission could be very appealing, since it would attract more potential users (and sponsors), and would require relatively low-cost space-based assets (single frequency, and no WVR, as long as the resolution and precision requirements imposed by geodesy were satisfied). Adoption of this paradigm would require users to think outside traditional boundaries.

Acknowledgment

This article was prepared under the support of a Johns Hopkins University Applied Physics Laboratory Stuart S. Janney Fellowship, for which the author is grateful.

BIBLIOGRAPHY

1. L.-L. Fu and A. Cazanave, *Satellite Altimetry and the Earth Sciences*, Academic Press, 2001.
2. URL/AVISO, <http://www.aviso.oceanobs.com/> (accessed July 2003).
3. V. L. Pisacane, Satellite techniques for determining the geopotential of sea surface elevations, *J. Geophys. Res.* **91**: 2365–2371 (1986).
4. M. E. Parke, R. H. Stewart, D. L. Farless, and D. E. Cartwright, On the choice of orbits for an altimetric satellite to study ocean circulation and tides, *J. Geophys. Res.* **92**: 11693–11707 (1987).

5. R. K. Raney, On orbit selection for ocean altimetry, *IEEE Trans. Geosci. Remote Sens.* (in press).
6. URL/Geodesy, <http://www.ngdc.noaa.gov/mgg/bathymetry/predicted/explore.HTML> (accessed July 2003).
7. D. T. Sandwell and W. H. F. Smith, Marine gravity anomaly from Geosat and ERS-1 satellite altimetry, *J. Geophys. Res.* **102**:10039–10054 (1997).
8. Special sections: Geosat science and altimeter technology, *Johns Hopkins APL Tech. Digest* **10**(4) (1989).
9. URL/Jason, http://www-aviso.cls.fr/html/missions/jason/welcome_uk.html (accessed July 2003).
10. URL/RA-2, <http://envisat.esa.int/instruments/tour-index/ra2/> (accessed July 2003).
11. P. C. Marth, J. R. Jensen, C. C. Kilgus, J. et al., Prelaunch performance of the NASA altimeter for the TOPEX/Poseidon Project, *IEEE Trans. Geosci. Remote Sens.* **31**:315–332 (1993).
12. A. R. Zieger, D. W. Hancock, G. S. Hayne, and C. L. Purdy, NASA radar altimeter for the TOPEX/Poseidon project, *Proc. IEEE* **79**:810–826 (1991).
13. S. J. Keihm, M. A. Janssen, and C. S. Ruf, TOPEX/Poseidon microwave radiometer (TMR) III: Wet tropospheric range correction and pre-launch error budget, *IEEE Trans. Geosci. Remote Sens.* **33**:147–161 (1995).
14. S. Musman, A. Drew, and B. Douglas, Ionospheric effects on Geosat altimeter observations, *J. Geophys. Res.* **95**:2965–2967 (1990).
15. D. B. Chelton, J. C. Ries, B. J. Haines, et al., Satellite altimetry, in L.-L. Fu and A. Cazanave, eds., *Satellite Altimetry and Earth Sciences*, International Geophysics Series, Academic Press, San Diego, 2001, pp. 1–122.
16. R. K. Moore and C. S. Williams, Jr., Radar return at near-vertical incidence, *Proc. IRE* **45**:228–238 (1957).
17. G. S. Brown, The average impulse response of a rough surface and its applications, *IEEE Anten. Propag.* **25**:67–74 (1977).
18. W. J. J. Caputi, Stretch: a time-transformation technique, *IEEE Trans. Aerospace Electron. Syst.* **AES-7**:269–278 (1971).
19. J. L. MacArthur, C. C. Kilgus, C. A. Twigg, and P. V. K. Brown, Evolution of the satellite radar altimeter, *Johns Hopkins APL Tech. Digest* **10**:405–413 (1989).
20. E. J. Walsh, Pulse-to-pulse correlation in satellite radar altimetry, *Radio Sci.* **17**:786–800 (1982).
21. D. B. Chelton, E. J. Walsh, and J. L. MacArthur, Pulse compression and sea-level tracking in satellite altimetry, *J. Atmosph. Oceanic Technol.* **6**:407–438 (1989).
22. D. T. Sandwell and W. H. F. Smith, Bathymetric estimation, in L.-L. Fu and A. Cazenave, eds., *Satellite Altimetry and Earth Sciences*, Academic Press, New York, 2001, pp. 441–457.
23. M. M. Yale, D. T. Sandwell, and W. H. F. Smith, Comparison of along-track resolution of stacked Geosat, ERS-1 and TOPEX satellite altimeters, *J. Geophys. Res.* **100**:15117–15127 (1995).
24. W. H. F. Smith and D. T. Sandwell, Global seafloor topography from satellite altimetry and ship depth soundings, *Science* **277**:1956–1961 (1997).
25. R. K. Raney, The delay Doppler radar altimeter, *IEEE Trans. Geosci. Remote Sens.* **36**:1578–1588 (1998).
26. R. K. Raney, *Delay Compensated Doppler Radar Altimeter*, U.S. Patent 5,736,957 (1998).
27. R. K. Raney, Radar fundamentals: technical perspective, in F. Henderson and A. Lewis, eds., *Principles and Applications of Imaging Radar, Manual of Remote Sensing*, 3 ed., Wiley-Interscience, New York, 1998, pp. 9–130.
28. J. R. Jensen and R. K. Raney, Delay Doppler radar altimeter: Better measurement precision, *Proc. IEEE Geoscience and Remote Sensing Symp. IGARSS'98*, Seattle, WA, 1998, pp. 2011–2013.
29. J. R. Jensen, Angle measurement with a phase monopulse radar altimeter, *IEEE Trans. Anten. Propag.* **47**:715–724 (1999).
30. URL/D2P, <http://fermi.jhuapl.edu/d2p>, Johns Hopkins Univ. Applied Physics Laboratory (accessed July 2003).
31. URL/CryoSat, <http://www.esa.int/export/esaLP/cryosat.html>, European Space Agency (accessed July 2003).
32. R. K. Raney and J. R. Jensen, An Airborne CryoSat Prototype: The D2P radar altimeter, *Proc. Int. Geoscience and Remote Sensing Symp. IGARSS02*, Toronto, IEEE, 2002.
33. URL/WSOA, http://ibib.grdl.noaa.gov/SAT/pubs/Jason2_paper.doc (accessed July 2003).
34. R. K. Raney and D. L. Porter, WITTEX: An innovative three-satellite radar altimeter concept, *IEEE Trans. Geosci. Remote Sens.* **39**:2387–2391 (2001).
35. URL/JHUAPL, <http://fermi.jhuapl.edu/> (accessed July 2003).
36. W. H. F. Smith and R. Scharoo, ftp://falcon.grdl.noaa.gov/pub/walter/combi_anim.gif, NOAA (accessed July 2003).

RADAR ANTENNAS

TIE JUN CUI
 WENG CHO CHEW
 FU-CHIARNG CHEN
 University of Illinois at
 Urbana—Champaign

Although the principle of radar has been known and advocated by many scientists since the early 1900s, it did not come into its own until its widespread development and application in World War II when the word *radar* was coined. Since then, the use of radar has expanded prodigiously. Important applications are found not only in numerous military problems but also in many public and commercial areas (e.g., civil air-traffic control, aircraft navigation, ship safety, spacecraft, ground detection, and remote sensing of the environment). It is even applied to law enforcement when police use radar to check the speed of cars.

The major types of radar are pulse radar, high-range-resolution radar, continuous-waveform (CW) radar, moving-target indication (MTI) radar, airborne radar, tracking radar, pulse Doppler radar, ground penetrating radar, synthetic aperture radar (SAR), and inverse SAR. Each of these radar types employs a different characteristic waveform, which is determined by the corresponding radar antenna and signal-processing method.

The radar antenna is an important component of radar. For different radar types, the requirement for antenna performances and functions is varied. Because the subject of radar antennas is very extensive, only selected types and performances of radar antennas are discussed in this

article. The reader should consult the bibliography for further details [1–5].

Radar antennas serve as transducers to couple electromagnetic (EM) energy into the atmosphere. A simple description of the antenna in a radar system is shown in Fig. 1. The functions of the antenna when transmitting are to concentrate the radiated energy from the transmitter into a shaped directive beam in a predetermined direction. When receiving, the antenna again forms a beam in a particular direction and collects the energy contained in the reflected target echo signals. Received energy is sent to the receiver via transmission lines. Therefore, the primary purpose of the antenna is to determine accurately the angular direction of the target in both transmit and receive modes. For this purpose, a highly directive beamwidth is required, not only to achieve accurate angular targets but also to resolve closely located targets. This important feature of radar antennas can be quantitatively expressed in terms of the beamwidth, gain, and sidelobes.

Generally, the functions of radar antennas can be classified into beamscanning and target tracking. Beamscanning fulfills the search or surveillance function of a radar. It requires that the narrow directive beam be scanned rapidly and repeatedly over the region where the detected target may appear. Target tracking, however, requires that the narrow beam follow the target once it has been detected. In some radar systems, particularly airborne radars, the antenna is designed to perform both searching and tracking functions.

The preceding functional description of radar antennas implies that a single antenna is used for both transmitting and receiving via the duplexer, a device that permits both transmission and reception of EM waves with the single antenna. This is true for most radar systems, but there are exceptions (e.g., the bistatic radars in which separate transmit and receive antennas are used). This article considers only the single antenna.

Radar antennas are mainly classified into two types: quasioptical antennas, which can be analyzed by optics methods like geometric optics and physical optics, and array antennas. In some cases, small antennas are used (e.g., in ground penetrating radars). Quasioptical antennas include reflector antennas and lens antennas. The former are still widely used for radar, whereas lens antennas, although still used in some communication and

military applications, are no longer used in modern radar systems. Therefore, because of limited space, we discuss only reflector antennas and array antennas.

1. BASIC PARAMETERS AND REQUIREMENTS

Consider a radar antenna located at the origin of a spherical coordinate system as shown in Fig. 2. The observation point is on a sphere having a very large radius R , which is located in the far field of the antenna. Assuming that the antenna is reciprocal, so that the transmit and receive patterns are identical. When the antenna is transmitting, its radiation efficiency is defined as

$$\eta = \frac{P_r}{P_0} \tag{1}$$

where P_0 is the total power consumed by the antenna, and P_r is the power radiated by the antenna. The later can be expressed by the radiation intensity $\Phi(\theta, \phi)$

$$P_r = \int_0^{2\pi} \int_0^\pi \Phi(\theta, \phi) \sin \theta d\theta d\phi \tag{2}$$

in which ϕ is the azimuth angle and θ is the elevation angle, as shown in Fig. 2. From Eq. (2), the average radiation intensity is easily obtained:

$$\langle \Phi \rangle = \frac{P_r}{4\pi} \text{ (watts/steradian)} \tag{3}$$

From Eqs. (1)–(3), we can define some basic parameters of an antenna. Directivity is a measure of the ability of the antenna to concentrate the radiated power in a particular direction. Thus it can be defined as the ratio of the achieved radiation intensity in the direction to the average:

$$D(\theta, \phi) = \frac{\Phi(\theta, \phi)}{\langle \Phi \rangle} \tag{4}$$

In practice, one is usually interested in the maximum directivity of the mainlobe.

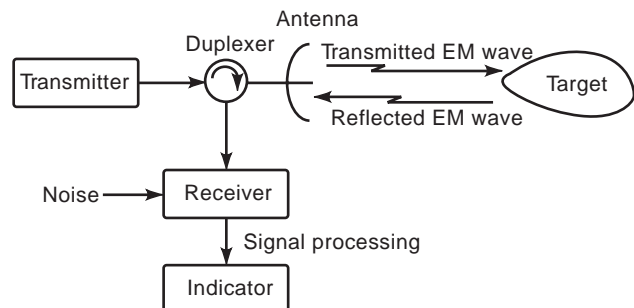


Figure 1. Basic elements in a radar system in which the antenna is an important part. It can be served as transmitting and receiving.

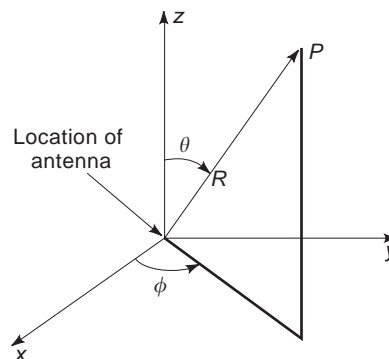


Figure 2. Spherical coordinate system. The azimuth angle ϕ and elevation angle θ are adopted by most antennas.

Gain is another important parameter of an antenna. It represents the ability to concentrate the power accepted by the antenna in a particular direction:

$$G(\theta, \phi) = \frac{\Phi(\theta, \phi)}{P_0/4\pi} = \eta D(\theta, \phi) \quad (5)$$

Thus antenna gain is always less than directivity except for a lossless and reflectionless antenna ($\eta = 1$). Again, the peak value of the gain, G_0 , is of more interest in practice.

The aperture of an antenna is its physical area projected on a plane perpendicular to the desired direction. If the antenna is lossless and the aperture of area A is uniformly illuminated with equiphase, the directivity is given by

$$D_0 = \frac{4\pi A}{\lambda^2} \quad (6)$$

which is the maximum available gain from an aperture A . Practical antennas are not uniformly illuminated, but they have a maximum in the center of the aperture and are less tapered toward the edges in order to reduce the sidelobes of the pattern. In this case, an effective aperture is defined from the directivity:

$$A_e(\theta, \phi) = \frac{\lambda^2}{4\pi} D(\theta, \phi) \quad (7)$$

The concept of effective aperture is very useful when considering the antenna in its receiving mode, which measures the effective absorption area of the antenna to an incident plane wave. Let A_e be the peak value of $A_e(\theta, \phi)$. Clearly, the effective aperture A_e is always less than the physical aperture A by a factor η_a

$$A_e = \eta_a A \quad (8)$$

which is usually called the aperture efficiency. From the definitions in Eqs. (6)–(8), we can see that the aperture efficiency measures only how effectively a given aperture is used, but does not involve the EM energy loss. Therefore, the efficiency of the antenna should be the multiplication of η_a and antenna losses η_L .

When the power radiation intensity $\Phi(\theta, \phi)$, the directivity $D(\theta, \phi)$, the gain $G(\theta, \phi)$, and the effective aperture $A_e(\theta, \phi)$ are normalized to their peak values, they will be identical and are called the antenna radiation pattern, which in fact represents the EM-energy distribution in three-dimensional (3D) angular space. There are several ways to plot the radiation pattern: rectangular or polar, voltage intensity or power density, absolute value or dB value, or power per unit solid angle. However, the 3D plots of radiation pattern require extensive data. Thus two-dimensional (2D) plots are usually adopted as a result of the ease in measurement and plotting. Generally, the two cuts of 3D plots in the principal elevation and azimuth planes are sufficient to describe the pattern performance of an antenna, which is much less costly.

Instead of azimuth and elevation, E - and H -plane patterns are usually used in actual radar antennas because the terms *azimuth* and *elevation* imply the Earth-based

reference coordinates, which are not applicable to some space-based systems like airborne and satellite.

The mainlobe of the radiation pattern is in the direction of maximum gain; all other lobes are called sidelobes. In addition to the peak gain of the main lobe, two other important features of an antenna pattern are the beamwidth of the mainlobe, which is usually specified at the half-power level (3 dB), and the maximum sidelobe level. The half-power beamwidth (HPBW) is usually a measure of the resolution of an antenna. Therefore, if two identical targets at the same range can be separated by the HPBW, they are said to be resolved in angle.

The beamwidth of an antenna is determined by the size of the antenna aperture as well as the amplitude and phase distributions across the aperture. For a given distribution, the half-power beamwidth in a particular plane is inversely proportional to the size of the aperture in that plane

$$\text{HPBW} = K \frac{\lambda}{L} \quad (9)$$

where L is the aperture dimension and K is a constant for the given distribution, which is known as the beamwidth factor. Accurate estimate of the beamwidth factor must take into account the aperture illumination function. However, $K = 70^\circ$ can give a rough estimate in most cases. For reflector-type antennas, a good estimation to K is given by [6]

$$K = 1.05238I + 55.9486 \text{ (deg)} \quad (10)$$

in which I is the absolute value of edge illumination in decibels.

From the half-power beamwidths in two orthogonal principle planes, one can obtain a practical formula for predicting the gain of a relatively lossless antenna

$$G_0 = \frac{C}{\theta_1 \theta_2} \quad (11)$$

where C is a unitless constant and θ_1 and θ_2 are HPBWs in degrees. The accurate value of C depends on the antenna efficiency, but the rough estimate can be taken from 26,000 to 35,000 [1,7].

Ideally, an antenna radiation pattern would consist of a single mainlobe and no sidelobes. However, for all practical radar antennas, it contains numerous sidelobes. These sidelobes can be a source of problems for the radar system. For example, a radar for detecting low-flying aircraft targets can receive strong ground or ocean echoes, which is called the clutter, through the sidelobes. This signal will interfere with the desired echoes coming from the low radar-cross-section targets through the mainlobe. Another fatal problem of the sidelobes is coming from jamming, which threatens most military radars. Therefore, it is often (but not always) desirable to design radar antennas with sidelobes as low as possible to minimize such problems. However, low sidelobes and high gain are competing requirements. Thus, the tradeoff between sidelobes level, gain, and beamwidth is an important consideration for designing radar antennas.

2. REFLECTOR RADAR ANTENNAS

Reflector antennas are one of the most important radar antennas and are widely used in practical radar systems. They provide an economical way to distribute energy over a large aperture area and produce shaped or pencil beams with high gain. In accordance with different demands, there are many types of reflector antennas with different shapes and feed systems.

2.1. Types of Reflectors

A wide variety of reflector antennas have been used in radar system. Figure 3 shows the most common reflector antennas.

2.1.1. Paraboloidal Reflector Antennas. The paraboloidal reflector antenna shown in Fig. 3a is a classical one with a round aperture. The theory and design of this kind have been well developed and discussed in the literature [1,5]. In this antenna, the feed is placed at the focus of the paraboloid. Then the spherical wave emerging from the feed strikes on the reflector and is transformed into a plane wave after reflection to form a pencil beam. Usually, the paraboloidal antenna provides a high gain and a minimum beamwidth with the simplest and smallest feed.

An important parameter for this paraboloid is the ratio of the focal length f to the aperture diameter D . For fixed aperture, when f increases, the reflector becomes flatter and introduces less distortion for polarization and off-axis beam. However, a narrow primary beam that leads to a larger feed is also required. For example, the size of the horn to feed a reflector of $f/D = 1.0$ is approximately four times that of $f/D = 0.25$. In general, most reflectors are chosen to have a ratio between 0.25 and 0.5.

Besides the round aperture, a variety of reflector outlines are also used in practice (2, 5). For example, an oblong shape is chosen when the azimuth and elevation beamwidths have different requirements.

2.1.2. Parabolic Cylinder Antennas. It is very common that only one of the azimuth and elevation beams must be steerable or shaped while the other is not. In this case, a parabolic cylinder reflector fed by a line source shown in Fig. 3b can meet the requirement at a modest cost. The line source feed may be a parallel-plate lens, a slotted waveguide, a phased array, and so on [1]. Of course, the parabolic cylinder antenna is not limited to these applications. It can even be applied when both patterns are fixed in shape (e.g., the AN/TPS-63).

Parabolic cylinders suffer from large blockage if they are symmetric; thus they are often built offset. Properly designed, however, a cylinder fed by an offset multiple-element line source can have excellent performance [8].

2.1.3. Shaped-Reflector Antennas. A good method of shaping the beam in one plane is using shaped reflectors [9], as shown in Fig. 3c, in which the surface itself is no longer a paraboloid. From Fig. 3c, each portion of the reflector is aimed in a different direction, making the analysis complicated. However, with modern computers, arbitrary beam shapes can be approximated accurately by direct integration of the reflected primary pattern.

A disadvantage of the shaped reflector is that its effective aperture is very small because a large fraction of its energy is radiated to a wide angle. However, it can reduce the blockage from the feed. In most shaped reflectors, the feed is usually placed outside the secondary beam. Then the blockage can be virtually eliminated even though the feed appears in front of the reflector, as shown in Fig. 3c.

Comparing shaped-reflector antennas with parabolic cylinder antennas, the shaped reflector is cheap and simple to construct. But it has less control over the beam shape because only the phase of the wave across the aperture is changed, whereas both phase and amplitude can be adjusted in the linear array for the parabolic cylinder.

2.1.4. Multiple-Beam Reflector Antennas. Very often the radar designer needs multiple beams to provide extended

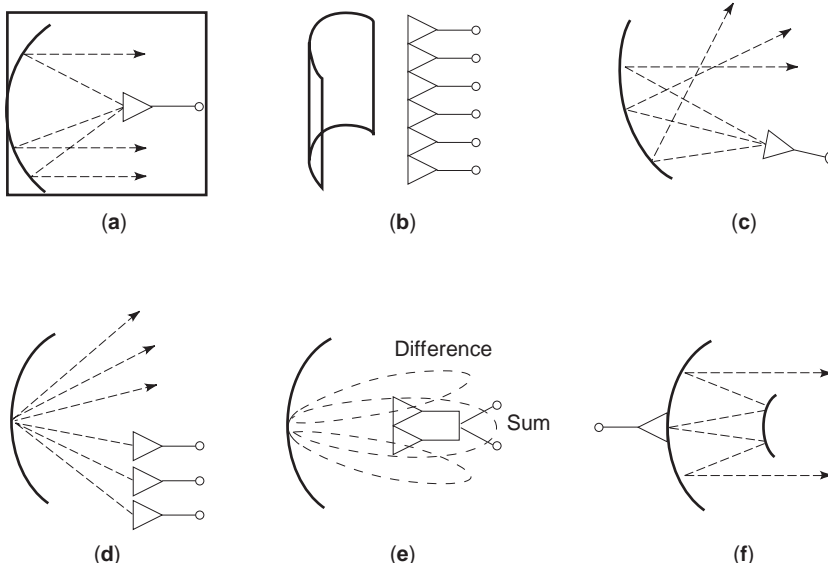


Figure 3. Common reflector antenna types: (a) paraboloid; (b) parabolic cylinder; (c) shaped reflector; (d) multiple beam; (e) monopulse; (f) Cassegrain.

coverage. This requirement can be achieved by using a reflector with multiple feeds [10], as shown in Fig. 3d. As we know, a feed at the focal point of a paraboloid forms a beam at the direction parallel to the focal axis. The feeds displaced from the focal point, however, will form additional beams at distinct angles from the axis with nearly full gain. Therefore, the coverage range of the radar can be increased. However, when the feed is off the focus, a distortion occurs on the antenna pattern. As the angular displacement increases, the beamwidth becomes larger, and additional sidelobes arise. The other limitation of this kind of antennas is that the extended feeds increase the blockage of the aperture.

2.1.5. Monopulse Reflector Antennas. An especially common multiple-beam radar antenna is the monopulse reflector illustrated in Fig. 3e. In fact, the illustration shows an amplitude comparison system, which is far more prevalent than the phase comparison system. In the amplitude system, the sum of the even-numbered source outputs fed by a single pulse forms a high-gain and low-sidelobe beam, and the difference forms a precise deep null at the peak value direction of sum pattern. The sum beam is used on bolt transmit and receive to detect the target, whereas the difference beams provide angle determination in both azimuth and elevation angles. Therefore, the monopulse reflector is normally used in tracking systems in which the antenna is removable and keeps the target near the null in difference pattern.

A tradeoff to design the monopulse radar antenna is the choice of feed size. The conflict arises between the goals of high sum-beam gain and large difference-beam slopes. For example, for a four-horn feed, the former requires a small overall horn size to reduce the blockage, whereas the latter requires large individual horns. Also, high difference sidelobes are required for tracking purpose in the design. To overcome these problems, many methods have been presented and several suggested configurations of the feed are given in Ref. 11.

2.1.6. Multiple-Reflector Antennas. Multiple-reflector systems can offer more degrees of flexibility by shaping the primary beam and then overcoming some of the shortcomings of single reflector. Figure 3f shows the most common type of multiple reflector, the Cassegrain antenna [12], in which the feed system is conveniently located behind the main reflector. In the Cassegrain system, the subreflector is a hyperboloid. The feed is placed at the left focus of the hyperboloid, and the paraboloid focus coincides with the right focus. From geometry optics, the spherical wave radiated by the feed and then reflected to the main reflector by the hyperboloid is equivalent to the one emerging directly from the right focus. Therefore, the wave reflected from the main reflector is also a plane wave that forms a pencil beam. A similar antenna to Cassegrain is the Gregorian antenna, which uses an ellipsoidal subreflector rather than a hyperboloidal one.

Aperture blockage can be very large for symmetric Cassegrain antennas, as illustrated in Fig. 3f. There are two ways to reduce blockage. The first method is to make the diameter of the subreflector equal to that of the feed,

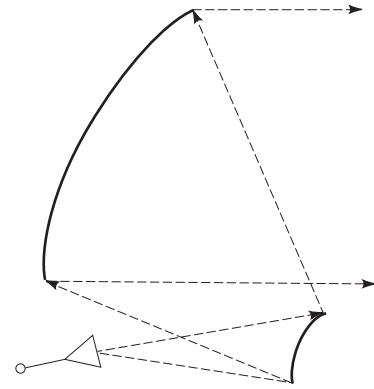


Figure 4. Offset dual reflector. The blockage of the subreflector can be virtually eliminated.

but the reduction is limited. The second method, which is generally used, is achieved by offsetting both the feed and subreflector. For example, Fig. 4 shows an offset dual reflector with blockage and supporting struts virtually eliminated. This antenna usually has very low sidelobes.

The geometry of the Cassegrain antenna is especially attractive for monopulse tracking radar because the radiofrequency (RF) plumbing can be placed behind the reflector to avoid blocking of the aperture. Also, the long runs of transmission line out to the feed at the focus of a conventional monopulse reflector are avoided. Therefore, the Cassegrain antennas usually have a low noise temperature.

2.2. Feeds for Reflector Antennas

In the previously discussed antennas, a spherical wave from the focus of the paraboloidal reflectors will be transferred into a plane wave to form a pencil beam at the transmit mode, while the incoming plane wave will be converted into spherical phase fronts centered at the focus on their receive mode. Thus the feeds for reflector antennas must be point-source radiators so that they can radiate spherical waves. Other requirements for reflector feeds include the proper illumination of the reflector with a prescribed amplitude distribution, a minimum spillover, and the correct polarization with no or minimum cross-polarization. These are the basic factors chosen to design a feed. For a different application of the antennas, other considerations must be included.

The most common feeds for reflector antennas are the flared waveguide horns, which are very suitable for microwave-frequency radar systems (L band and higher). At lower frequencies, dipole feeds, Yagi-Uda, or logperiodic feeds are sometimes used. For example, a linear array of dipoles can feed a parabolic cylinder reflector. Rectangular waveguide horns propagating the dominant TE_{01} mode are widely adopted because they meet the high-power and other requirements, although in some cases circular waveguide horns propagating TE_{11} mode have also been used. These single-mode horns provide just one linear polarization. When such additional requirements as polarization diversity, multiple beams, high beam efficiency, or ultra-low sidelobes are needed, the design for feeds becomes

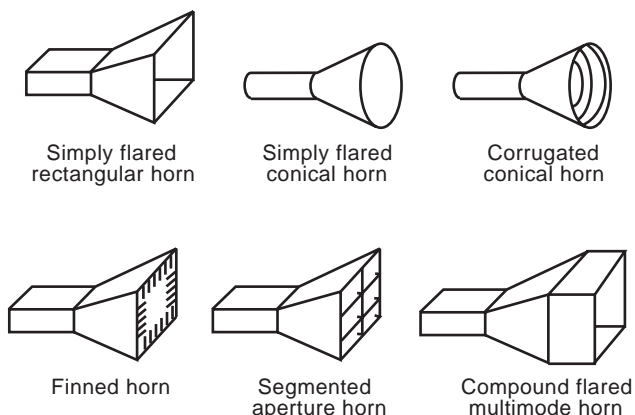


Figure 5. Various types of feeds used in radar antennas.

more complicated. In these cases, segmented horns, finned horns, multimode horns, and corrugated horns must be used. Figure 5 illustrates some of the types, which have been well studied [1,13].

In addition, the sitting of the feeds has also a great influence to the performance of the reflector antennas. Figure 6 shows several placement styles of the feeds.

2.3. Reflector Antennas Design and Analysis

The analysis and design of conventional paraboloidal reflectors are well developed [1,5] and not stated here. However, most of the rotating search radars require that the antenna patterns have a narrow azimuth beamwidth for angular resolution and a shaped elevation beam for multiple requirements, for example, the ARSR-3 radar for air-traffic control and the AN/TPN-19 for ground control. Thus, a shaped reflector is nearly always the practical choice. In this section, we will consider the analysis and design of such kinds of antennas.

2.3.1. Requirements. When a search radar works, small nearby targets like birds and insects may clutter the output of the radar because of the inverse fourth-power

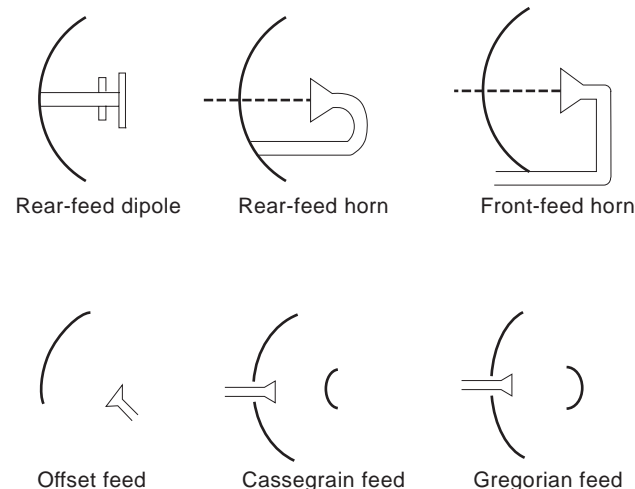


Figure 6. Various placements of the feeds in radar antennas.

variation of signal strength with range. For example, the radar that can detect a 1 m^2 target at 100 nmi can detect a 10^{-4} m^2 target at 10 nmi. [Nautical mile (nmi), where $1 \text{ nmi} = 1852 \text{ m}$ is usually used as the range unit.] To avoid the clutter, the receiver gain should be reduced at short range and increased at distant range so that the received signal from a target of constant size remains unchanged with range. The programmed control of the receiver gain to keep a constant echo signal strength is called sensitive time control (STC), which is an effective method of eliminating the radar echoes from unwanted objects. Therefore, STC is usual requirement for designing the search radar.

A typical range coverage requirement for the rotating search radars is shown in Fig. 7, which is an idealized simplification of the STC requirement [14]. It gives a relationship between the radar range, height, and elevation angle. From Fig. 7, at low elevation angles ($0.5\text{--}3.5^\circ$), the maximum range is the critical requirement. When the elevation angle increases ($3.5\text{--}9.5^\circ$), however, the height becomes the governing requirement. In this period, the corresponding pattern is a cosecant square. At high elevation angles ($9.5\text{--}30^\circ$), the STC is used.

The two-way coverage requirement shown in Fig. 7 is inconvenient for antenna design. It can be converted into a pattern requirement if we plot only the range against angle because the range is directly proportional to the pattern amplitude, as shown in Fig. 8 (the solid line).

2.3.2. Analysis. Antenna analysis is very important not only in analyzing a given antenna but also in antenna design. Because the accurate design is usually an iterative procedure, in each iterative cycle, an analysis is needed.

There are two methods to analyze a given antenna: current distribution method and aperture field method [5]. For shaped antennas, however, the first one is more suitable. From the magnetic field H radiated by the feed, one can get the induced current on the reflector surface

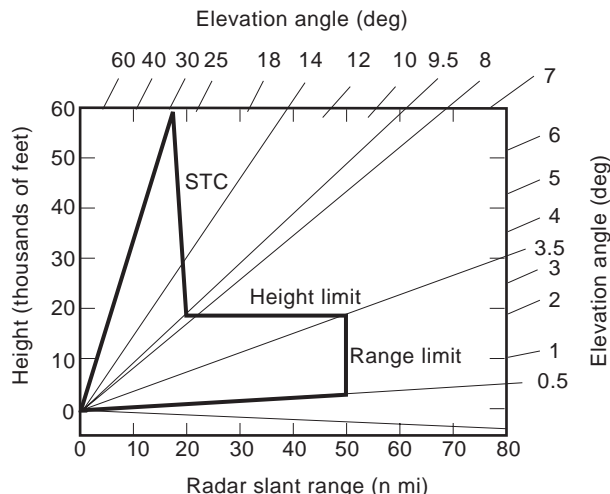


Figure 7. Typical two-way coverage requirement of the search radar, in which a relationship between the radar range, height, and elevation angle is given.

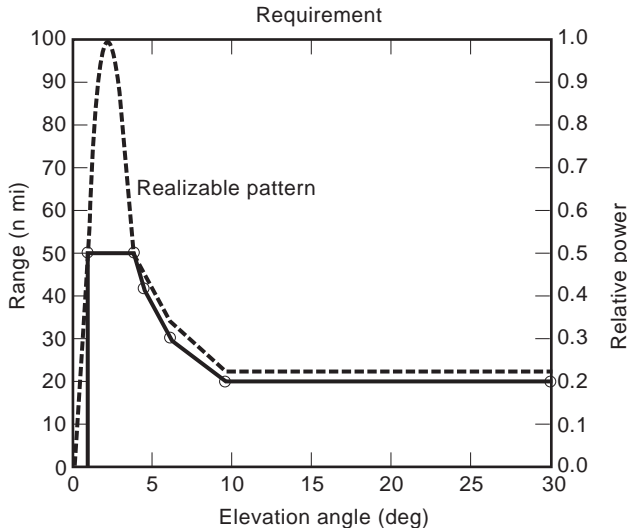


Figure 8. Coverage requirement (solid line) and realizable pattern (dashed line).

$\mathbf{J} = 2\hat{\mathbf{n}} \times \mathbf{H}$. Then the radiated fields by the reflector can be obtained by integration.

This type of accurate analysis is quite time-consuming. In practical design, the antenna pattern and gain are usually approximated in the first several iterative cycles. For rotating search radars, the antenna pattern can be obtained directly from the coverage requirement; however, the designer must realize that the range-angle plot represents the minimum range requirement. If some ripple is anticipated (normally about ± 1 dB), the design curve should be raised 1 dB in the height limit and STC coverage regions. For the range limit region, a reasonable situation is achieved by assuming that a section or several sections of the reflector are shaped so that the -3 dB points of the resulting pattern will coincide with the two corners of the range limit portion, as shown in Fig. 8 (dashed line), which is just the realizable elevation pattern of the antenna.

For the gain of shaped beam considered here, we assume that the azimuth and elevation power patterns are separable. Then, using the definition in Eq. (5), the maximum gain (in mainbeam direction) can be expressed as

$$G = \frac{4\pi}{\int \int f_{az}(\phi) f_{el}(\theta) d\phi d\theta} = \frac{4\pi}{\int f_{az}(\phi) d\phi \int f_{el}(\theta) d\theta} \quad (12)$$

where $f_{az}(\phi)$ and $f_{el}(\theta)$ are azimuth and elevation power patterns. For simplicity, the azimuth power pattern can be approximated by a Gaussian function: $f_{az}(\phi) = \exp[-2.7726(\phi/BWAZ)^2]$. Then

$$\int f_{az}(\phi) d\phi = 1.0645BWAZ \quad (13)$$

in which BWAZ is the azimuth half-power beamwidth. For the other integral in Eq. (12), it can be easily found from Fig. 8.

2.3.3. Design. For shaped-beam antennas, the shaping is generally in one plane (elevation), with a narrow pattern of conventional design in the orthogonal plane (azimuth). The parabolic cylinder antenna fed from a line source is convenient for obtaining independent control of the patterns. However, it is much more expensive and heavier than a reflector fed from a point source. In order to obtain a shaped beam, the antenna with a point source feed requires a reflector surface with double curvature. An easy but efficient way to do this is to use an offset paraboloidal antenna by adding several shaped sections. Each successive section points slightly higher than the preceding section, as shown in Fig. 9. Clearly, the projections of added sections are virtually missing the feed. So there is no feed blockage. The design of the added sections can be done iteratively by using a computer. However, the antenna's width and height can be directly approximated from the antenna patterns [14]

$$\text{Width} = \frac{65\lambda}{BWAZ} \quad (14)$$

$$\text{Height} = \frac{65\lambda}{BWEL} \frac{\int f_{el}(\theta) d\theta}{\Delta \int f_{el}(\theta) d\theta} \quad (15)$$

in which BWEL is the elevation half-power beamwidth, and $\Delta \int$ is the integral in the range-limit region.

2.4. Practical Considerations

In the analysis and design of radar antennas, some practical considerations must be taken into account because they can affect the performances of the antennas. There are a lot of practical details for different radar antennas, but here we consider only four common effects: feed support blockage, surface leakage, surface tolerance, and radomes.

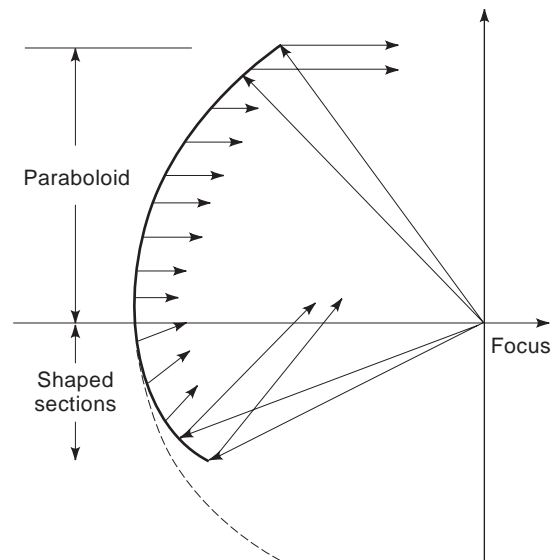


Figure 9. An example of shaped-beam antenna design.

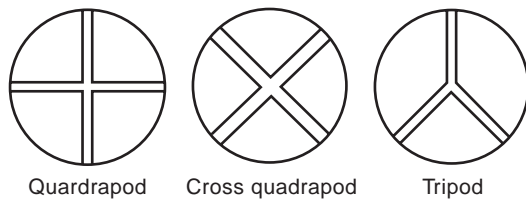


Figure 10. Some common feed supports used in radar antennas.

2.4.1. Feed Support Blockage. No matter whether the feed is placed in the front or rear, there is always blockage from the feed supports. In the case of Cassegrain or Gregorian, the blockage comes from the support of the subreflector. Like the blockage of feeds, the supports have two effects on the antenna's performance: they put a shadow in the desired distribution, and they scatter the intercepted power. Both effects can reduce the gain and increase the sidelobe level.

The effective size of the blockage may be larger than its projected area depending upon the material and polarization. For conducting supports, the effective size equals the actual dimension in the E plane, whereas the effective width becomes $W + \sqrt{0.5\lambda d}$ (where W and d are the width and thickness of a strut) in the H plane [15]. Therefore, the blockage of a strut of 0.125λ square in cross section will be three times larger when it is parallel to the E field than when it is parallel to the H field. In addition, various ways of sitting the supports have different effects. Figure 10 shows three common ways of supporting the feeds. Note that the tripod arrangement produces sidelobe ridges that are broader but 6 dB lower than those of the quadrapods [15]. The feed support blockage can be reduced by using a dielectric strut.

2.4.2. Surface Leakage. Many reflectors are designed with a tubular grid or wire mesh instead of a solid metal surface in order to reduce the wind resistance and the antenna's weight. To accomplish this, the opening area in the structure should be as large as possible. However, the openings lead to surface leakage, from which backlobe is produced. The larger the area of the opening is, the higher the backlobe is. Therefore, a suitable design of the surface structure is important to the antenna's performance. Figure 11 illustrates some of the common reflector surfaces, in which the gap S between conductors must be much smaller than a half-wavelength in the H plane so that the passage of EM energy will be below cutoff [14].

2.4.3. Surface Tolerance. Mechanical consideration to design reflector antennas is very important in a radar system. In most cases, it is even more difficult and complicated than the electrical design, especially for a high-performance radar. The surface tolerance is one important part of the mechanical design. The reflector surface must be smooth enough so that it remains within close tolerances of the ideal surface. Typically, the surface error must be less than $\lambda/28$.

The roughness of reflector surface can cause small phase error on the aperture. From the antenna tolerance

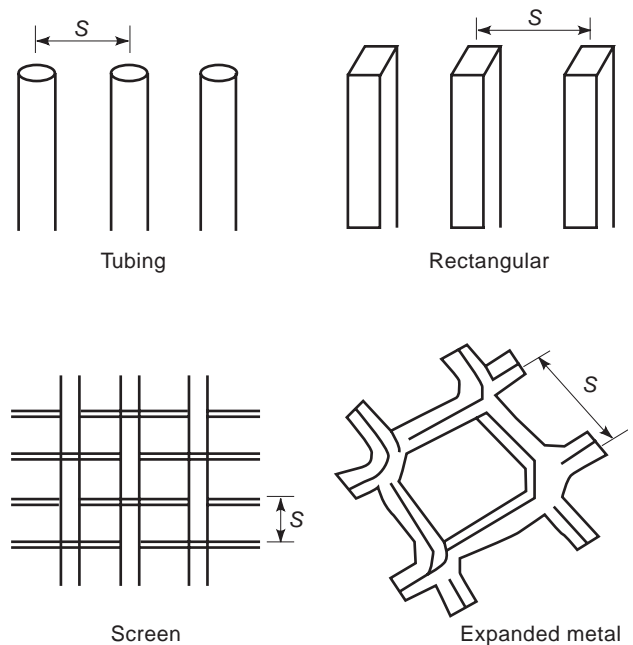


Figure 11. Common types of reflector surfaces that can reduce the wind resistance.

theory, the loss of gain due to phase error is approximated by

$$\frac{G_1}{G_0} \approx 1 - \bar{\delta}^2 \quad (16)$$

where G_1 and G_0 are gains with and without phase error, and $\bar{\delta}^2$ is the mean square phase error. From Eq. (16), one clearly sees that for 1 dB loss of gain the phase error $\sqrt{\bar{\delta}^2}$ must be less than 0.45 rad, which means the reflector surface error must be less than $\lambda/28$.

2.4.4. Radomes. Antennas for ground-based radars are often subjected to high winds, icing, and temperature extremes so they must be sheltered if they are to survive and perform under adverse weather conditions. The shelter to protect antennas is called a radome. Antennas mounted on aircraft must also be housed within a radome to offer protection from large aerodynamic loads. An ideal radome should be perfectly transparent to the RF radiation from (or to) the antenna but mechanically strong if they are to provide the necessary protection. These two requirements are usually competing, thus the design of radomes must be compromised [17].

The design of radomes for antennas can be divided into two separate classes, depending on whether the antenna is for airborne or ground-based (or ocean-based) applications. The airborne radome is characterized by smaller size than ground-based radomes because the antennas that can be carried in an aircraft are generally smaller. The airborne radome must be strong enough to form a part of the aircraft structure and usually it is designed to conform to the aerodynamic shape of the aircraft, missile, or space vehicle in which it is to operate. If the antenna scans inside the streamlined radome, the incident angle may be

varied around the normal direction. This will lead to great degradation of antenna performance.

A properly designed radome should distort the antenna pattern as little as possible. The presence of a radome can affect the gain, beamwidth, sidelobe level, beam direction, the voltage standing-wave ratio (VSWR), and antenna noise temperature. Sometimes in tracking radars, the change rate of the beam direction can be very important.

3. PHASED-ARRAY RADAR ANTENNAS

Besides reflectors, phased-array antennas are also important in radar systems. An attractive advantage of the phased-array antenna for radar applications is that it can steer a beam without having to move a large mechanical structure. For example, when a single radar simultaneously carries out the functions of surveillance and tracking, it must pause for an instant to confirm or disprove a possible alert as a surveillance radar, however, it is required to follow several targets by pointing at each of them successively without any loss of time as a tracking radar. In this case, a phased-array antenna is the best choice because it can steer the beams rapidly by means of electronic control.

The first large steerable directive phased-array antenna for the reception of trans-Atlantic shortwave communication was developed and installed by the Bell Telephone Laboratories in the late 1930s. However, it was limited because the beam was scanned by mechanically actuated phase shifters. A major advance in phased-array technology was made in the early 1950s with the replacement of the mechanically actuated phase shifters by electronic phase shifters, from which the scanning in one angular coordinate can be electronically controlled. The introduction of digitally switched phase shifters employing either ferrites or diodes in the early 1960s made a significant improvement in the practice use, in which a phased array could be electronically steered in two orthogonal angular coordinates. With the development of modern computer and solid-state microwave devices, multifunction phased-array antennas have been developed.

Array antennas can take many different forms for various applications. However, they always include some common components. Figure 12 shows a basic schematic of the phased-array antennas. Clearly, a phased-array system contains an element array composed of many similar radiating elements, a power splitter, the phase shifters, the transmitter and receiver, and a central computer. The radiating elements might be dipoles, open-ended waveguides (or small horns), slots cut in waveguide, printed-circuit patches, or any other type of antennas. On its transmission mode, the power splitter divides the energy from the transmitter to the various elements of the array via the phase shifters. Then the phases and amplitudes of the array can be controlled by the computer. Generally, the amplitude characteristic does not vary during scanning except for adaptive and optimum arrays. Therefore, one can adjust the phase and amplitude taper on array by using the phase distribution and the amplitude distribution to meet different uses.

3.1. Basic Characteristics

See ANTENNA ARRAYS for a detailed analysis of phased-array antennas. Here we give only some general characteristics important to the analysis and design of radar antennas.

For a general planar array, when the elements are spaced by a half-wavelength to avoid the generation of grating lobes, the number of the radiating elements N for a pencil beam can be approximated from the broadside beamwidth by [18]

$$N \approx \frac{10000}{\text{HPBW}^2} \text{ or } \text{HPBW} \approx \frac{100}{\sqrt{N}} \quad (17)$$

where HPBW is the 3 dB beamwidth (in degrees) of the antenna pattern. When the beam points in the broadside direction to the aperture, the corresponding antenna gain is

$$G_0 \approx N\pi\eta \quad (18)$$

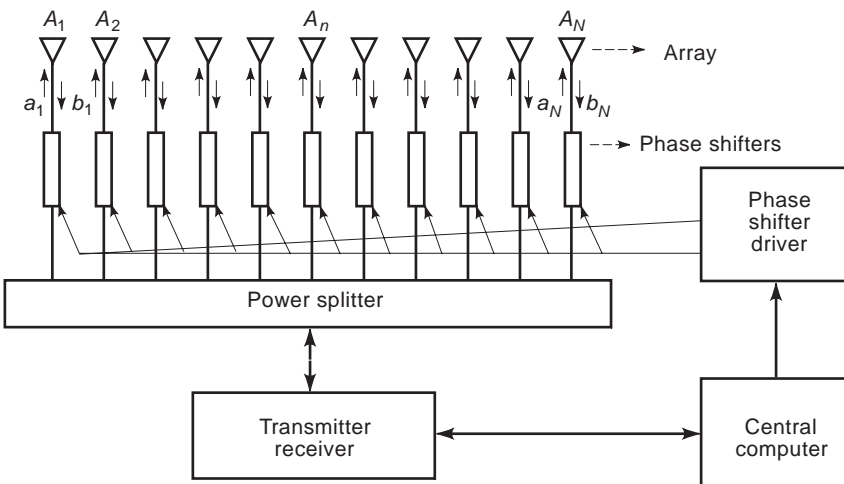


Figure 12. General structure of a phased array in which the phase shifter driver provides different phases to the array.

where η is the antenna efficiency, which accounts for antenna losses (η_L) and reduction in gain caused by weighting the elements with a nonuniform amplitude distribution (η_a).

When the antenna is scanning to an angle θ_0 , the scanned beamwidth is increased from the broadside beamwidth

$$\text{HPBW}(\theta_0) \approx \frac{\text{HPBW}}{\cos \theta_0} (\theta_0 \neq 90^\circ) \tag{19}$$

whereas the gain of the planar array is reduced to that of the projected aperture:

$$G_0(\theta_0) \approx N\pi\eta \cos \theta_0 \tag{20}$$

These characteristics can provide an easy way to estimate quickly when analyzing and designing array antennas.

3.2. Types of Arrays

The arrays used in radar systems can be classified by such different means as geometry and functions. This subsection will discuss several typical arrays.

3.2.1. Linear Arrays. The linear array generates a fan beam when the phase relationships are such that the radiation is perpendicular to the array. If the radiation is at some other angles, the antenna pattern is a cone-shaped beam. The broadside linear-array antenna may be used where broad coverage in one plane and a narrow beamwidth in the orthogonal plane are required. An active application of linear array is that it can act as the feed for a parabolic cylinder antenna, as discussed earlier.

3.2.2. Planar Arrays. The two-dimensional planar array is capable of steering the beams in two angular coordinates. It is probably the array of most interest in radar applications because of its versatility. Generally, a rectangular aperture can produce a fan-shaped beam, whereas a square or a circular aperture can generate a pencil beam. The array may also be made to produce simultaneously many search and or tracking beams with the same aperture. Most of arrays discussed later will be the planar arrays.

3.2.3. Conformal Arrays. Sometimes, a radar designer is required to place array elements on an arbitrary surface to achieve a directive beam with good sidelobe level and efficiency, which can be easily scanned electronically. For example, on an aircraft, arrays arranged along the nose, on the wings, or on the fuselage would be attractive options. In this case, a conformal array, which conforms to the geometry of a nonplanar surface, should be used [1].

In principle, the array on any surface can be made to radiate a beam in some given direction by applying the proper phase, amplitude, and polarization at each element. In practice, however, it is very difficult to control the beam shape and obtain low sidelobes from an arbitrary surface when the beam is electronically scanned. Further-

more, the mechanisms for feeding the elements and generation of the phase shifter command are also more complicated than those of a planar array. Therefore, the application of conformal array is possible only for some simple shapes like cylinder and cones.

Most of the work on conformal arrays has been with the cylinder because it has a geometry suitable for antennas that scan 360° in azimuth. Although it is of a relatively simple shape compared with others, the properties of the cylindrical array are not as suitable as those of planar array. In the cylindrical array, the radiation pattern cannot be separated into an element factor and an array factor as they can in the planar array. Considering the additional difficulties in the practical control, the conformal arrays are not widely used in the radar systems.

3.2.4. Thinned Arrays. Most array antennas have equal spacings between adjacent elements. In order to obtain a given beamwidth with considerably fewer elements, a thinned array has sometimes been considered. Generally, the shape of the main beam has little distortion after thinning. However, the average sidelobes are degraded in proportion to the number of elements removed. Figure 13 shows an example of thinned arrays, in which 77.5% of the elements are randomly removed from a regular grid [19].

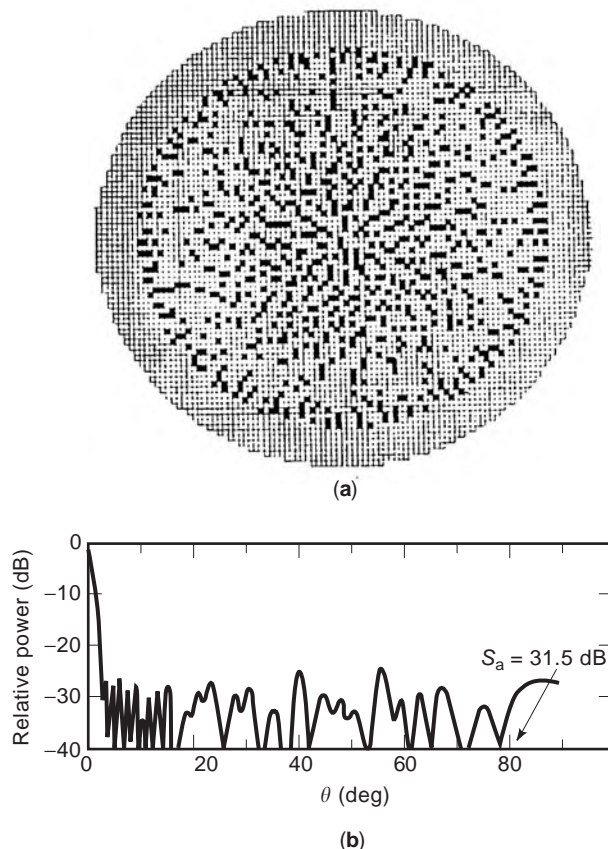


Figure 13. (a) Thinned array with a 4000-element grid containing 900 elements; (b) typical pattern for thinned array in which S_A is the average sidelobe level. (From Wiley [15, Figs. 5 and 6] courtesy of Bendix Radio Div., Bendix Corporation.)

Then the gain, which is caused by the actual element number, will drop by 6.5 dB, while almost 77.5% of the power is delivered to the sidelobes because the main beam is nearly unchanged.

Therefore, the design of a thinned array consists of selecting the size of the aperture to give the desired beamwidth, selecting the number of actual elements to give the desired gain, and arranging the element distribution to obtain some required properties of the sidelobes.

The thinned arrays have seen only limited applications in radar system because of the reduction in gain and the increases in sidelobes. Instead of thinning elements, the number of phase shifters can also be thinned, in which some of the phase shifters in the array can be used to adjust the phase of more than one element. A 50% saving of the phase shifters might be possible [20].

3.2.5. Phase-Scan Arrays. The beam of an antenna points to the direction perpendicular to the phase front. In phase-scan arrays, the phase front is adjusted by controlling the phase of each radiating element to steer the beam, as shown in Fig. 14a. The phase shifters are electronically actuated to perform rapid scanning and are adjusted in phase to a value between 0 and 2π rad. If the spacing between two adjacent elements is S , the incremental phase shift ψ will be $\psi = (2\pi/\lambda)S \sin \theta_0$, in which θ_0 is the scan angle. Because the phase shifters have phase shift that is virtually independent of frequency, the scan angle θ_0 is frequency-dependent.

3.2.6. Time-Delay-Scan Arrays. Phase scanning was seen to be frequency-sensitive. Time-delay scanning provides a way that is independent of frequency. Instead of the phase shifters, delay lines are used in the time-delay-scan arrays, as illustrated in Fig. 14b. For the spacing distance between two adjacent elements S , the incremental time delay from element to element is $t = (S/c) \sin \theta_0$, in which c is the velocity of propagation of wave and θ_0 is

again the scan angle. The time-delay circuits accompanied by all radiating elements are normally too cumbersome. A reasonable compromise solution is to share one time-delay network by a group of elements in which each element has its own phase shifter. However, this will cause a grating lobe problem.

3.2.7. Frequency-Scan Arrays. A change in frequency of an EM signal propagating along a transmission line produces a change in phase. This provides a simple way for obtaining the electronic phase shift, as shown in Fig. 14c. In this case, the incremental phase shift is

$$\psi = (2\pi/\lambda)l = (2\pi/\lambda)S \sin \theta_0 + 2\pi m \quad (21)$$

in which l is the length of line connecting adjacent elements. When the beam points broadside ($\theta_0 = 0$), Eq. (21) yields $m = l/\lambda_0$, where λ_0 is the wavelength corresponding to the beam position at broadside. Then the direction of beam pointing can be obtained from Eq. (21):

$$\sin \theta_0 = \frac{l}{S} \left(1 - \frac{\lambda}{\lambda_0} \right) \quad (22)$$

Comparing with other ways, the frequency-scanning system is relatively inexpensive and easy to implement. Frequency-scan arrays have been developed and used to provide elevation-angle scanning. Combined with the mechanical horizontal rotation, it served as 3D radars in the past.

3.2.8. Multiple-Beam-Forming Arrays. One of the properties of the phased array is the ability to generate multiple independent beams simultaneously from a single aperture. In principle, an N -element array can generate N independent beams. Multiple beams allow parallel operation and can obtain a higher data rate than a single beam. The multiple beams may be fixed in space, steered

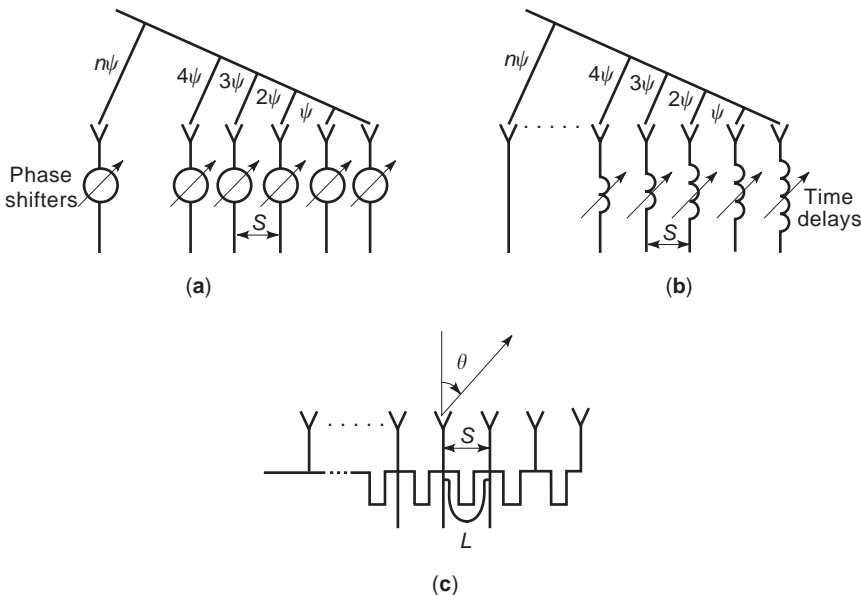


Figure 14. Scanning of arrays: (a) phase scan; (b) time-delay scan; (c) frequency scan.

independently, or steered as a group. In some applications, multiple beams are generated on receive and connected to separate receivers, whereas only one wide radiation pattern is needed on transmit so that it can cover all the received beams. Such multibeam systems have found application with mechanical rotation for 3D coverage.

3.2.9. Low-Sidelobe Arrays. A low sidelobe level is one of the most important requirements for the radar antennas, especially for military radars that may be threatened by the jamming. Therefore, the low sidelobe level has been and will be of great interests to radar designers. By modern technology, an ultralow sidelobe has been achieved in the Airborne Warning and Control System (AWACS) radar, which now supports sidelobe levels of more than 50 dB below the mainbeam peak [21]. However, as mentioned earlier, the low sidelobe and high gain are competing requirements. Thus the cost to achieve low sidelobe is a reduction in gain and an increase in beamwidth. Considering the practical implementation, the low sidelobes also require a high-tolerance control and a good environment free from obstructions that could increase the sidelobes so low-sidelobe antennas are usually expensive. In spite of these drawbacks, the trend toward low-sidelobe arrays has accelerated because low sidelobes provide an excellent deterrent to electronic countermeasures (ECM).

From the aperture theory, antenna sidelobes are related to the aperture amplitude distribution. For phased arrays, the amplitude taper is generally fixed and does not change. However, the amplitude of each radiating element can be controlled individually by the computer, which makes it possible to achieve very low sidelobes.

The relation between the antenna pattern and the aperture illumination has been studied extensively in many literatures. It has been shown that the far-field pattern is just the Fourier transform of the aperture distribution. Some typical illumination functions and their corresponding gains, sidelobes, and beamwidths can be found in Refs. 5 and 18. For low-sidelobe arrays, the Taylor illumination for the sum patterns and the Bayliss illumination, a derivative form of the Taylor illumination, for the difference patterns are usually chosen because they can provide low sidelobes at a minimum loss in gain. Note that the sidelobes predicted by the aperture illuminations are suitable for perfect phase and amplitude distributions (error-free). In practice, aperture illuminations must be chosen to provide peak sidelobes below the requirements to allow for errors. The effect of errors on the design will be mentioned next.

3.3. Practical Considerations

The array theory gives only the theoretical analysis and design of the phased arrays. For practical use in radar systems, a lot of details must be considered. In this subsection, some important considerations are addressed.

3.3.1. Phase Shifters. As already stated, there are three basic techniques to steer the beam electronically: frequency scanning, time-delay scanning, and phase scanning with phase shifters. In practice, the use of phase shifters

is the most popular technique, but many other techniques have been developed for a variety of phase shifters [22]. Generally, the phase shifters can be classified into two categories: reciprocal and nonreciprocal. For reciprocal phase shifters, the phase change does not depend on the direction of propagation. Therefore, it is not needed to switch the phase states between transmit and receive if the reciprocal phase shifters are used. For a nonreciprocal phase shifter, however, it is necessary to change the phase states between transmit and receive. Typically, it takes a few microseconds to switch the nonreciprocal phase shifters. During this period, the radar cannot detect targets.

A perfect phase shifter could change its phase rapidly; handle high power; require control signals of little power; be of low loss, light weight, small size, and reasonable cost; and have a long life. But in practice, no one device is universal enough to meet all the requirements. Various phase shifters possess these properties in varying degrees. Presently, three types of phase shifters are used in the phased-array antennas: the diode phasers, which are all reciprocal; the nonreciprocal ferrite phasers; and the reciprocal ferrite phasers. Each of the three types has its own advantage. The choice of phase shifters is highly dependent on the radar requirements.

3.3.2. Array Elements and Matching. Almost any type of radiating antenna element can be considered for an array antenna. In practice, the dipole, open-ended waveguide (or small horn) and slotted waveguide have found wide applications. Detailed descriptions of these antennas have been investigated in the standard textbooks [1,5]. However, note that the properties of a radiating element in an array is significantly different from its properties when in free space. For example, the radiation resistance of a half-wavelength dipole in free space is $73\ \Omega$, but when it is in an infinite array with half-wavelength spacing and a back screen of quarter-wave separation, it will be $153\ \Omega$ when the beam is broadside. The impedance also varies with scan angles.

The change of impedance with scan angle makes the matching of an array antenna difficult. There are conditions where an antenna that is well matched at broadside may have some angles at which most of the power is reflected. Unlike a conventional antenna, the mismatch of array antennas will affect both the level of the radiated power and the shape of the antenna pattern.

3.3.3. Mutual Coupling. If two radiating elements are widely separated, the energy coupled between them is small, and the influence of one to the other on the current excitation and pattern can be negligible. However, when the elements are placed closer, their coupling will increase. Generally, the strength of the coupling in a phased array is related to the distance between elements, the pattern of the elements, and the structure of the array. For example, the radiation pattern of a dipole has a null at $\theta = \pm 90^\circ$ and a peak value at $\theta = 0^\circ$. Thus, the dipoles in a straight line are loosely coupled, whereas the dipoles parallel to each other have a strong coupling.

For a phased array, the effect of coupling between elements is focused mainly on the pattern and impedance of

the element, which are usually called the active element pattern and the active element impedance. The exact analysis of coupling in practical arrays is rather complicated. A convenient way is to assume that the array is infinite in extent and has a uniform amplitude distribution and a linear phase taper from element to element. Under such an assumption, every element in the array has the same environment; thereby a significant simplification in the calculations can be made. It has been shown that the infinite-array model has a good prediction to the actual arrays. Even for a modest array that has fewer than 100 elements, the predicted results can also give reasonable agreement [23].

3.3.4. Errors in Arrays. As indicated in Section 3.2.9, the errors in the amplitude and phase of the current at individual elements of the array may cause distortion of the radiation pattern. Additional factors of the error include the missing or inoperative elements, rotation or translation of an element from its correct position, and variations in the individual element patterns. These errors can result in a decrease in gain, increase in sidelobes, and shift in the direction of the main beam.

When errors occur in the phase and amplitude of the aperture, the energy will be removed from the main beam and distributed to the sidelobes. If the errors are purely random, they will produce random effects on the main beam and all sidelobes. When the errors are correlated, the sidelobe energy will be lumped at discrete locations in the far field. Usually, the correlated errors provide higher sidelobes than do the random errors, but they are located at some certain directions only. Both of the correlated and random errors should be considered in the practical design of phased arrays [18,24].

3.4. Applications

In many cases, phased-array antennas have been of considerable interest in the radar systems because they have different properties from those of reflector antennas. Hence, a number of phased-array radar systems have been built for different uses [18,25]. Examples include the AN/SPS-33 radar for the purpose as aircraft surveillance from onboard ship; the AN/FPS-85 for satellite surveillance; the PAR and MSR for ballistic missile defense; the AN/SPY-1 and PATRIOT for air defense; the EAR (Electronically Agile Radar) for airborne bomber; the AN/TPN-19 and AN/TPS-32 used in aircraft landing systems; the AWACS and AN/TPS-70 for airborne warning and control systems; the MESAR as a multifunction electronically scanned adaptive radar; the AN/TPQ-37 Firefinder radar; the PAVE PAWS for providing early warning of ballistic missiles and performing satellite tracking; the COBRA DANE for tracking of ballistic missile; and the COBRA JUDY for collecting data on foreign ballistic missile tests [18,25].

Although the array antennas have many unique characteristics that make them candidates for use in radar systems, they are expensive. As technology advances, the costs can be reduced, particularly in the areas of phase shifters and drivers. In the meantime, the high demand for better performance with lower sidelobes and wider bandwidth

makes the costs high. In the future, the great potential for cost reduction may be the application of solid-state systems with a transmit/receive module at each element.

BIBLIOGRAPHY

1. R. C. Johnson and H. Jasik, eds., *Antennas Engineering Handbook*, 2nd ed., McGraw-Hill, New York, 1984.
2. M. I. Skolnik, ed., *Radar Handbook*, 2nd ed., McGraw-Hill, New York, 1990.
3. L. J. Cantafio, ed., *Space-Based Radar Handbook*, Artech House, Norwood, MA, 1989.
4. M. I. Skolnik, *Introduction to Radar Systems*, 2nd ed., McGraw-Hill, New York, 1980.
5. C. A. Balanis, *Antenna Theory Analysis and Design*, 2nd ed., Wiley, New York, 1997.
6. M. J. Komen, Use simple equations to calculate beam width, *Microwaves* **20**(13):61–63 (1981).
7. W. L. Stutzman and G. A. Thiele, *Antenna Theory and Design*, Wiley, New York, 1981.
8. R. L. Fante et al., A parabolic cylinder antenna with very low sidelobes, *IEEE Trans. Anten. Propag.* **AP-28**:53–59 (1980).
9. K. Aoki et al., Design method for an offset dual-shaped reflector antenna with high efficiency and an elliptical beam, *IEEE Proc. H. Microwave Anten. Propag.* **140**(2):121–128 (1993).
10. Y. T. Lo, On the beam deviation factor of a parabolic reflector, *IRE Trans. Anten. Propag.* **AP-8**:347–349 (1960).
11. P. W. Hannan and P. A. Loth, A monopulse antenna having independent optimization of the sum and difference modes, *IRE Int. Conv. Rev.*, Part 1, 1961, pp. 57–60.
12. C. Granet, Designing axially symmetric Cassegrain or Gregorian dual-reflector antennas from combinations of prescribed geometric parameters, *IEEE Anten. Propag. Magn.* **40**(2):76–82 (1998).
13. A. W. Love, *Electromagnetic Horn Antenna*, IEEE Press, New York, 1986.
14. H. E. Schrank, G. E. Evans, and D. Davis, Reflector antennas, in M. I. Skolnik, ed., *Radar Handbook*, 2nd ed., McGraw-Hill, New York, 1990.
15. C. L. Gray, Estimating the effect of feed support member blocking on aperture gain and sidelobe level, *Microwave J.* (3):88–91 (1964).
16. J. Ruze, Antenna tolerance theory—a review, *Proc. IEEE* **54**:633–640 (1966).
17. J. D. Walton, Jr., ed., *Radome Engineering Handbook*, Marcel Dekker, New York, 1970.
18. T. C. Cheston and J. Frank, Phased array radar antennas, in M. I. Skolnik, ed., *Radar Handbook*, 2nd ed., McGraw-Hill, New York, 1990.
19. R. E. Willey, Space tapering of linear and planar arrays, *IRE Trans. Anten. Propag.* **AP-10**:369–377 (1962).
20. N. Goto and D. K. Cheng, Phase shifter thinning and sidelobe reduction for large phased array, *IEEE Trans. Anten. Propag.* **AP-24**:139–143 (1976).
21. G. E. Evans and H. E. Schrank, Low sidelobe radar antennas, *Microwave J.* **26**(7):109–117 (1983).
22. M. R. Iravani and D. Maratukulam, Review of semiconductor-controlled (static) phase shifters for power systems applications, *IEEE Trans. Power Syst.* **9**:1833–1839 (1994).
23. J. Frank, *Phased Array Antenna Development*, Appl. Phys. Lab. Rep., Johns Hopkins Univ., TG 882, March 1967.

- 24. J. L. Allen, *The Theory of Array Antennas*, MIT Lincoln Lab. Rep. 323, July 1963.
- 25. P. E. Rawlinson and H. R. Ward, Radar antennas, in R. C. Johnson and H. Jasik, eds., *Antenna Engineering Handbook*, 2nd ed., McGraw-Hill, New York, 1984.

RADAR APPLICATIONS

GEORGE A. TSIHRINTZIS
 University of Piraeus
 Piraeus, Greece

1. INTRODUCTION

Radar (*radio detection and ranging*) systems attempt to infer information about remotely located objects from reflections of deliberately generated electromagnetic waves at radio frequencies. Typically, a radar system operates in the environment depicted in Fig. 1 and the information sought is *detection* of the presence of target objects in the midst of *clutter*, *recognition* (classification) of targets, and *estimation* of target parameters such as *range* (distance from the radar antenna), *bearing* (azimuth and

elevation), *orientation*, *velocity*, *acceleration*, or *backscattering cross section* (reflectivity) distribution.

Early radar systems could only scan the environment, to detect an aircraft when it appeared in their beam and to measure its range and bearing. The range resolution cell was determined by the length of the unmodulated transmitted pulse and was much larger than the aircraft. Thus, it was reasonable to model the aircraft as a point target and the system interference as white Gaussian thermal noise. Subsequently, the detection problem was reduced to that of detecting a point target in white Gaussian noise. Modern radar systems, however, are expected to perform the much more sophisticated tasks stated above for multiple targets simultaneously, at the finest possible target *resolution* and with the highest possible *accuracy*. Additionally, the domain of utilization of radar techniques has expanded beyond the traditional aircraft detection and ranging to applications such as estimation of the parameter (range, velocity, acceleration, and backscattering cross section) distribution of *spread* targets, aerial imaging, and ground or foliage penetrating radar imaging. To achieve their expanded tasks, modern radar systems combine high-quality hardware with sophisticated signal design and processing algorithm development and implementation based on statistical descriptions of both the target characteristics and the clutter distributions.

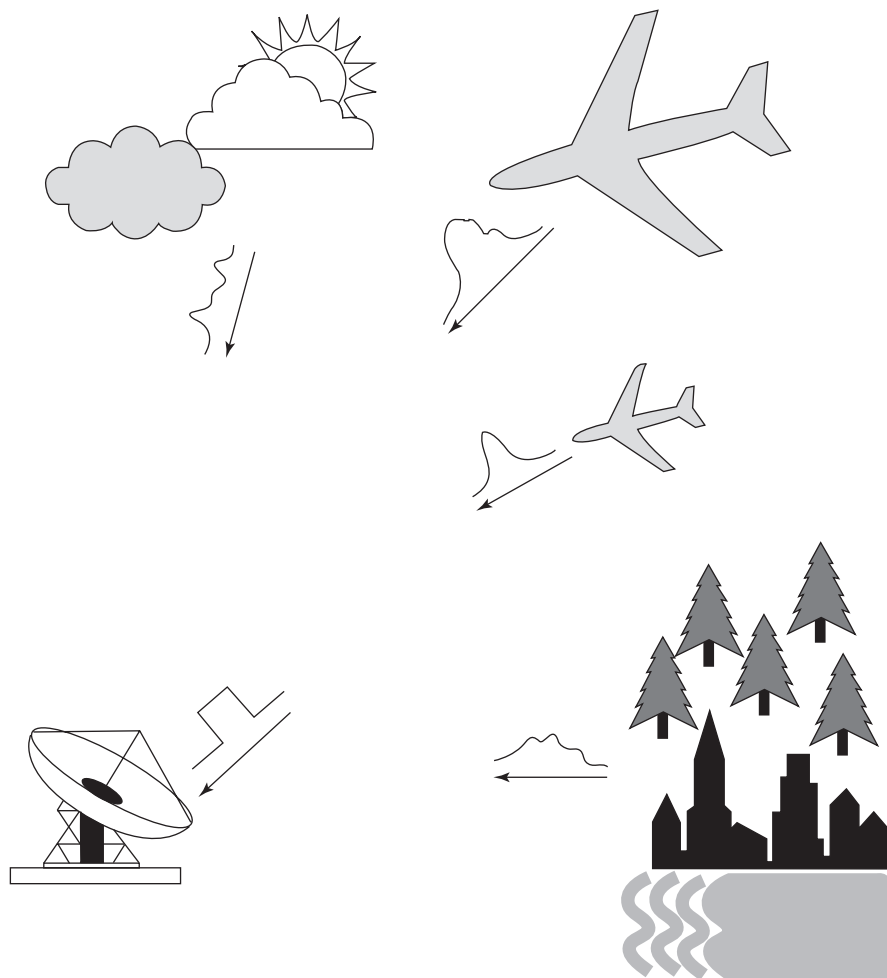


Figure 1. Typical environment in which a radar system needs to operate.

Applications of modern radar can be found in the military, the civilian, and the scientific regimes. Military applications include search and surveillance of enemy targets; navigation, control, and guidance of weapons; battlefield surveillance; and antiaircraft fire control. Among civilian applications, prominent are those in air, water, and land transportation, including aircraft navigation; collision avoidance with both other aircraft and terrain obstacles; detection and avoidance of weather disturbances and clean-air turbulence; altimetry; air traffic control; shore-based ship navigation; collision avoidance for ships and small boats; harbor and waterway traffic control; collision avoidance of land vehicles; tracking of vehicles; and traffic law enforcement, as well as space applications in detection and tracking of satellites and control of rendezvous and docking of space vehicles. Finally, scientific applications include remote sensing of Earth's environment from aircraft and satellites for planetary observation; weather radar for study and monitoring of precipitation, clouds, and major weather disturbances; ground mapping; ground-penetrating radar for detection of buried objects; foliage-penetrating radar for detection of hidden targets; and high-resolution imaging of objects and terrain via synthetic aperture imaging radars.

2. RADAR TARGET MEASUREMENT ELEMENTS

2.1. Point-Target Measurements

Assume that the radar antenna transmits the narrowband pulse

$$s_T(t) = u(t)e^{i2\pi f_0 t}, \quad 0 < t < T \tag{1}$$

where f_0 is the carrier frequency at which the radar operates and $u(t)$ is a pulse of duration T and bandwidth B smaller than the carrier frequency. Typical transmitted radar pulses are illustrated in Fig. 2. Specifically, Figs. 2a and 2c illustrate square pulses of duration $T = 10^{-2}$ ms modulating the amplitude of sinusoids of carrier frequency $f_0 = 0.25$ MHz and $f_0 = 1$ MHz, respectively. In Fig. 2d, a sinusoid of carrier frequency $f_0 = 1$ MHz is amplitude-modulated by a Gaussian rather than a square pulse of duration $T = 10^{-2}$ ms. Finally, in Fig. 2b, a sinusoid of carrier frequency $f_0 = 0.25$ MHz is frequency-modulated by a square pulse of duration $T = 10^{-2}$ ms with a rate of change of transmitted frequency $\beta = 1.5 \times 10^2 \text{ ms}^{-2}$. Signals, such as the linear frequency-modulated sinusoid in Fig. 2b, are also referred to as *chirps* and are used to increase the range resolution of the radar system.

The pulse illuminates a point target and is reflected back toward the antenna. Let Δ be the round-trip delay between the time at which the rising edge of the pulse leaves the radar antenna, is reflected by the target, and is received back at the antenna. Since the target is moving, this delay will be a function $\Delta(t)$ of time. Ignoring amplitude attenuation and constant phase shifts due to reflection, the received pulse will be

$$s_R(t) = u[t - D(t)]e^{i2\pi f_0 [t - \Delta(t)]} \tag{2}$$

The information about the target motion is contained in the round-trip delay $\Delta(t)$ as a function of time and the distortion it causes on the received pulse $s_R(t)$. The delay $\Delta(t)$ depends on the target position at the instant of reflection, which for a signal received at time t , occurs at

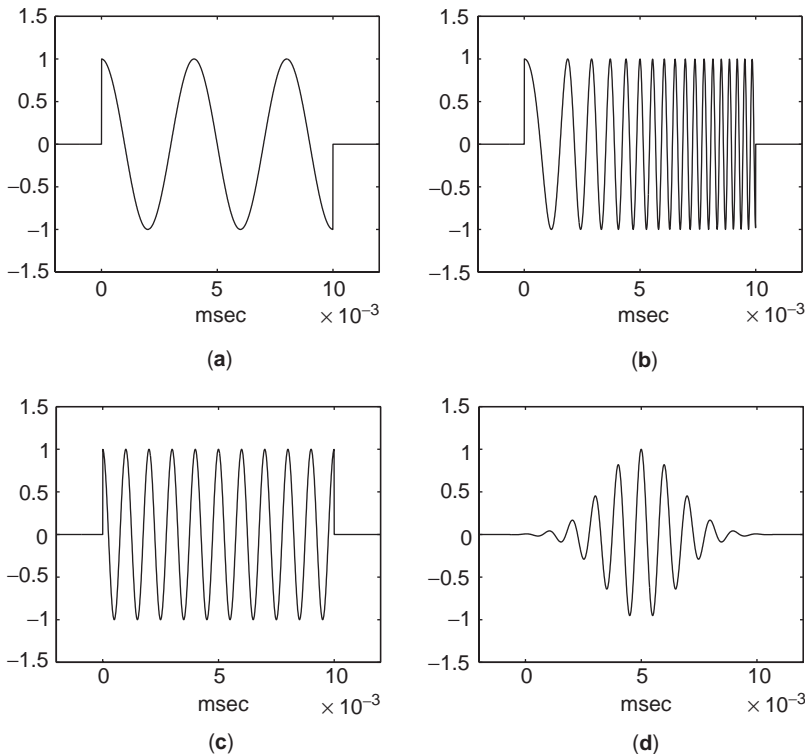


Figure 2. Typical transmitted radar pulses of various modulation formats.

time $t - [\Delta t/2]$. Thus

$$\Delta(t) = \frac{2}{c} R \left[t - \frac{\Delta(t)}{2} \right] \quad (3)$$

where $R(t)$ is the target *range*, that is, the distance from the radar antenna to the target, as a function of time.

If the target moves slowly enough for the delay $\Delta(t)$ to be approximately constant within the duration T of the illuminating pulse, then the target can be regarded as stationary. However, it is often the case that the target moves very fast in comparison with the pulse duration and different instants of the pulse are differently delayed. In the general case, the relation between the target motion, the round-trip delay, and the received pulse is too complicated to be tractable. Several simplifications can lead, however, to tractable mathematical relations. Assume that the delay $\Delta(t)$ is a smooth enough time function to be expandable into a Taylor series around the time instant $t_0 = \Delta(t=0) \equiv \Delta_0$ at which the leading pulse edge is received back at the receiver:

$$\begin{aligned} \Delta(t) = & \Delta_0 + \Delta_0^{(1)}(t - t_0) + \frac{\Delta_0^{(2)}}{2}(t - t_0)^2 \\ & + \frac{\Delta_0^{(3)}}{6}(t - t_0)^3 + \dots \end{aligned} \quad (4)$$

where $\Delta_0^{(k)} = (d^k \Delta / dt^k)(t_0)$ is the k^{th} derivative of the round-trip delay evaluated at the time instant t_0 .

Define now the target parameters of interest:

$$\begin{aligned} t_0 = \Delta_0 & \quad \text{delay coefficient} \\ v_0 = -f_0 \Delta_0^{(1)} & \quad \text{Doppler (velocity) coefficient} \\ \gamma_0 = -f_0 \frac{\Delta_0^{(2)}}{2} & \quad \text{acceleration coefficient} \\ \varepsilon_0 = -f_0 \frac{\Delta_0^{(3)}}{6} & \quad \text{hyperacceleration coefficient} \end{aligned}$$

and use Eqs. (3) and (4) to relate them to the target range and its derivatives. Algebraic manipulation gives the target parameters as the following functions of the range $R_0 = R(t_0/2)$ and its derivatives $R_0^{(k)} = (d^k / dt^k) R(t_0/2)$ at time $t_0/2$:

$$t_0 = \frac{2R_0}{c} \quad (5)$$

$$v_0 \approx -f_0 \frac{2R_0^{(1)}}{c} \quad (6)$$

$$\gamma_0 \approx -f_0 \frac{R_0^{(2)}}{c} \quad (7)$$

$$\varepsilon_0 \approx -f_0 \left[\frac{R_0^{(3)}}{3c} - \left(\frac{R_0^{(2)}}{c} \right)^2 \right] \quad (8)$$

The approximations in Eqs. (6)–(8) are valid simplifications for the practical cases of $R_0^{(1)} \ll c$ of the exact expressions in Ref. 16 (p. 59).

From Eq. (8), it is seen that even the simplified expression for the target hyperacceleration ε_0 is still a complicated function of target range derivatives. Higher order terms in Eq. (4) have coefficients that are nonmanageable functions of target range derivatives. Fortunately, practical radar systems need deal only with targets moving sufficiently smoothly for only the delay and Doppler and, occasionally, the acceleration coefficient (and, rather rarely, the hyperacceleration coefficient) to be significant in the expansion in Eq. (4). Additionally, only the delay term t_0 is significant in the complex envelope $u[t - D(t)]$, while the higher order terms affect only the phase in the exponential in Eq. (2); that is, the pulse received by the radar from a single target illuminated with the pulse of Eq. (1) is

$$s_R(t) \approx u(t - t_0) e^{i2\pi[f_0(t-t_0) + v_0(t-t_0) + \gamma_0(t-t_0)^2 + \varepsilon_0(t-t_0)^3]} \quad (9)$$

where t_0 , v_0 , γ_0 , and ε_0 are the target delay, Doppler (velocity), acceleration, and hyperacceleration parameters. Typical return pulses are shown in Fig. 3. The pulses are computed from Eq. (9) for various values of the parameters t_0 , v_0 , γ_0 , and ε_0 , assuming that the transmitted pulse was the pulse in Fig. 2a.

2.2. Matched-Filter Response to Received Pulse

The received pulse is processed through a bank of filters, each matched to a different set of values of the target parameters. The filter matched to the set of parameter values $(\tau, v, \gamma, \varepsilon)$ has impulse response

$$\begin{aligned} h(t; \tau, v, \gamma, \varepsilon) = & u^*(-t - \tau) e^{-i2\pi[f_0(-t-\tau) + v(-t-\tau) + \gamma(-t-\tau)^2 + \varepsilon(-t-\tau)^3]} \\ = & u^*(-t - \tau) e^{i2\pi[f_0(t+\tau) + v(t+\tau) - \gamma(t+\tau)^2 + \varepsilon(t+\tau)^3]} \end{aligned} \quad (10)$$

Assume now that the input to this matched filter is the received pulse in Eq. (9), multiplied by an unknown complex-valued amplitude $Ae^{i\delta}$ and corrupted by additive noise: $Ae^{i\delta} s_R(t) + n(t)$. The output of the filter will be

$$\begin{aligned} \eta_{\tau, v, \gamma, \varepsilon}(t) = & \int_0^{T_0} [Ae^{i\delta} s_R(\xi) + n(\xi)] h(t - \xi) d\xi \\ = & Ae^{i\delta} e^{i2\pi f_0(t+\tau-t_0)} \chi(t + \tau - t_0, v - v_0, \gamma - \gamma_0, \varepsilon - \varepsilon_0) \\ & + \int_0^{T_0} n(\xi) h(t - \xi) d\xi \end{aligned} \quad (11)$$

where T_0 is the time interval during which the radar is in receive mode (e.g., the time interval between two successive pulse transmissions). Equation (11) consists of two terms, a term due to noise and a signal term containing the *ambiguity function*

$$\begin{aligned} \chi(\tau, v, \gamma, \varepsilon) = & \int_{-\infty}^{\infty} u(\xi) u^* \\ & \times (\xi - \tau) e^{-i2\pi[v(\xi-\tau) + \gamma(\xi-\tau)^2 + \varepsilon(\xi-\tau)^3]} d\xi \end{aligned} \quad (12)$$

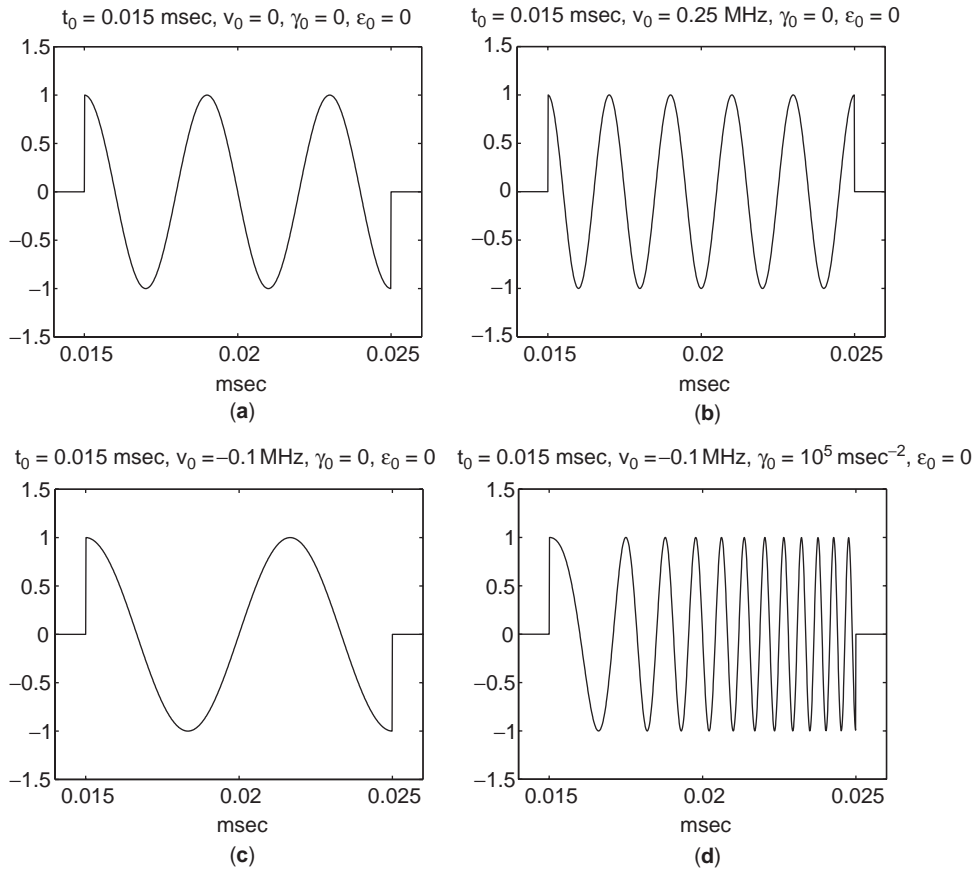


Figure 3. Typical radar return pulses. The pulses are computed from Eq. (9) for various values of the delay, Doppler, acceleration, and hyperacceleration parameters, assuming that the transmitted pulse was the pulse in Fig. 2a.

Clearly, the magnitude of the signal term at any time t is maximized if the filter parameters are selected equal to the target parameters, that is, if $\tau = t_0$, $v = v_0$, $\gamma = \gamma_0$, and $\varepsilon = \varepsilon_0$. Target *detection* can be performed by monitoring the matched-filter outputs at each instant t and examining whether they exceed a preset threshold. If the threshold is exceeded, then target detection is declared. If a target is thus detected, its parameters are subsequently *estimated* as the parameters of the matched filter that produces maximum output. A simplification to this target detection/estimation rule can be achieved by noticing that the matched-filter delay τ is not significant in that it corresponds only to a shift in the time instant of occurrence of the maximum of the matched-filter output. Indeed, a change in the round-trip delay t_0 changes only the time at which the maximum occurs. Thus, only a bank of matched filters need to be used, in which the delay τ is fixed to zero and the target range is estimated from the time instant of occurrence of the maximum of the matched-filter output. If, however, the other target parameters are significant, an entire bank of filters need to be used, with each filter matched to different target parameter values. In summary, the criterion for declaring target detection is

$$\max_{t,v,\gamma,\varepsilon} |\eta(t)| \geq \text{threshold} \quad (13)$$

and the set of values $(\hat{t}, \hat{v}, \hat{\gamma}, \hat{\varepsilon})$, which provide the maximum constitute the target parameter estimates. The threshold is set so as to keep the probability of a *false alarm* below a specified maximum tolerance. Since the complex amplitude $Ae^{i\delta}$ is unknown and varying, *constant false-alarm rate* (CFAR) techniques need to be utilized to adaptively set the threshold. Figure 4 depicts typical CFAR *receiver operating characteristics*, which have been experimentally computed for three different foliage-penetrating radar receivers (reprinted with permission from Ref. 10).

2.3. Distributed-Target Measurements

The theory of single-target measurements needs to be modified and extended if the radar is to operate at a resolution that is sufficiently high for the *spread* of one or more target parameters to exceed the corresponding resolution bin. Examples of such targets include the terrain, vegetation foliage, extended manmade objects such as buildings with more than one smooth surfaces, or even aircraft when the resolution bin is significantly smaller than its typical dimensions. In these cases, the pulse received at the radar antenna can be considered as the superposition of a small or large or even infinite number of reflections from individual scattering centers on the target.

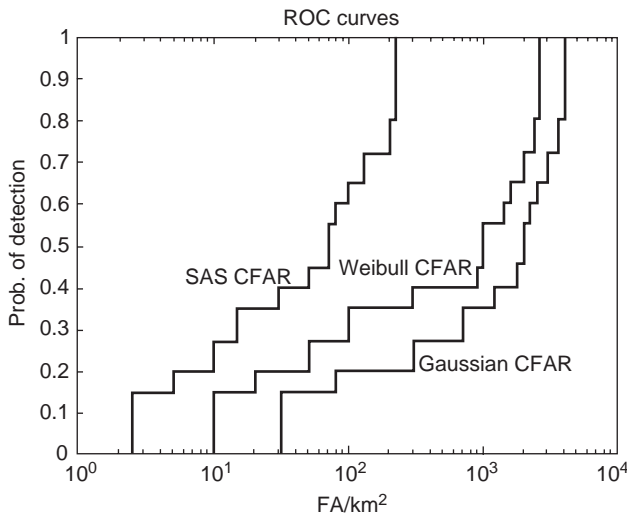


Figure 4. Typical CFAR radar receiver operating characteristics that have been computed experimentally for three different foliage-penetrating radar receivers (reprinted with permission from Ref. 10, © 1999 IEEE).

Serious difficulties in extending the theory of single-to multiple- (distributed-) target measurements arise if the scattering centers of the target are not stationary during illumination with the radar pulse or new ones emerge or several disappear as a result of target motion. Additionally, the target may be dispersive; that is, its significant scattering centers may vary with frequency, making the target behavior rather complex. For the theory of distributed-target measurements to remain tractable, the assumption needs to be made that the target is represented by a possibly infinite, yet fixed, set of scattering centers. Additionally, no dispersion can be allowed; that is, the scattering centers need to be frequency-independent.

With these assumptions in mind, consider a target consisting of N scattering centers illuminated with the pulse of Eq. (1). The reflected pulse measured at the radar antenna will be

$$s_R(t) = \sum_{n=1}^N A_n e^{i\delta_n} u(t - t_n) \times e^{2\pi i [f_0(t-t_n) + v_n(t-t_n) + \gamma_n(t-t_n)^2 + \varepsilon_n(t-t_n)^3]} \quad (14)$$

producing the signal part at the output of the matched filter of Eq. (10)

$$\eta_{\tau,v,\gamma,\varepsilon}(t) = \sum_{n=1}^N A_n e^{i\delta_n} \chi(t + \tau - t_n, v - v_n, \gamma - \gamma_n, \varepsilon - \varepsilon_n) \quad (15)$$

Under the assumptions of stationarity of the target scattering centers during illumination with the radar pulse and their independence, cross-terms in the signal part of the magnitude square of the matched-filter output will be

relatively small. Thus

$$|\eta_{\tau,v,\gamma,\varepsilon}(t)|^2 \approx \sum_{n=1}^N |A_n|^2 |\chi(t + \tau - t_n, v - v_n, \gamma - \gamma_n, \varepsilon - \varepsilon_n)|^2 \quad (16)$$

Considering the limit of $N \rightarrow \infty$ densely packed scattering centers, the magnitude square of the matched-filter output becomes

$$|\eta_{\tau,v,\gamma,\varepsilon}(t)|^2 = \iiint\limits_{v-v_0, \gamma-\gamma_0, \varepsilon-\varepsilon_0} |A(t_0, v_0, \gamma_0, \varepsilon_0)|^2 |\chi(t + \tau - t_0, v - v_0, \gamma - \gamma_0, \varepsilon - \varepsilon_0)|^2 dt_0 dv_0 d\gamma_0 d\varepsilon_0 \quad (17)$$

In Eq. (17), $|A(t_0, v_0, \gamma_0, \varepsilon_0)|^2$ is the target *backscattering cross-section distribution* as a function of the delay, Doppler (velocity), acceleration, and hyperacceleration parameters. Clearly, if the magnitude square of the ambiguity function consists of a single central spike with very narrow width, that is, if

$$|\chi|^2 \approx \delta(t + \tau - t_0, v - v_0, \gamma - \gamma_0, \varepsilon - \varepsilon_0) \quad (18)$$

then

$$|\eta_{\tau,v,\gamma,\varepsilon}(t)|^2 \approx |A(t + \tau, v, \gamma, \varepsilon)|^2 \quad (19)$$

In words, the matched-filter response represents (and measures) the target backscattering cross section for the particular values of delay, Doppler, acceleration, and hyperacceleration to which the filter is matched. Consequently, a bank of matched filters, each adjusted to a different delay, Doppler, acceleration, and hyperacceleration, yields the entire target cross-section distribution. A simplification can be obtained by considering only matched filters corresponding to delay $\tau=0$ in the bank and utilizing the entire matched-filter output for parameter distribution estimation.

3. SEARCH (SURVEILLANCE OR ACQUISITION), TRACKING, AND NAVIGATION RADAR

3.1. Search Radar

A *search* (also known as *surveillance* or *acquisition*) radar uses an efficient scan pattern to cover an angular sector with a narrow pencil beam in order to detect the presence of a suspected target. Typical scan patterns include the *helical* (Fig. 5a), the *Palmer* (Fig. 5b), the *spiral* (Fig. 5c), the *raster* (or *TV*) (Fig. 5d), and the *nodding* (Fig. 5e) patterns. In the *helical* pattern, the beam is continuously rotated in azimuth while it is simultaneously raised or lowered in elevation. The *Palmer* pattern consists of a rapid circular scan about the antenna axis, combined with a linear movement of the axis of rotation, and is suited to a search area which is larger in one dimension than the other. The *spiral* scan covers an angular search volume with circular symmetry. Both the Palmer and the spiral scans need to vary the scanning speed during the scan cycle for all parts of the scan volume to receive the same

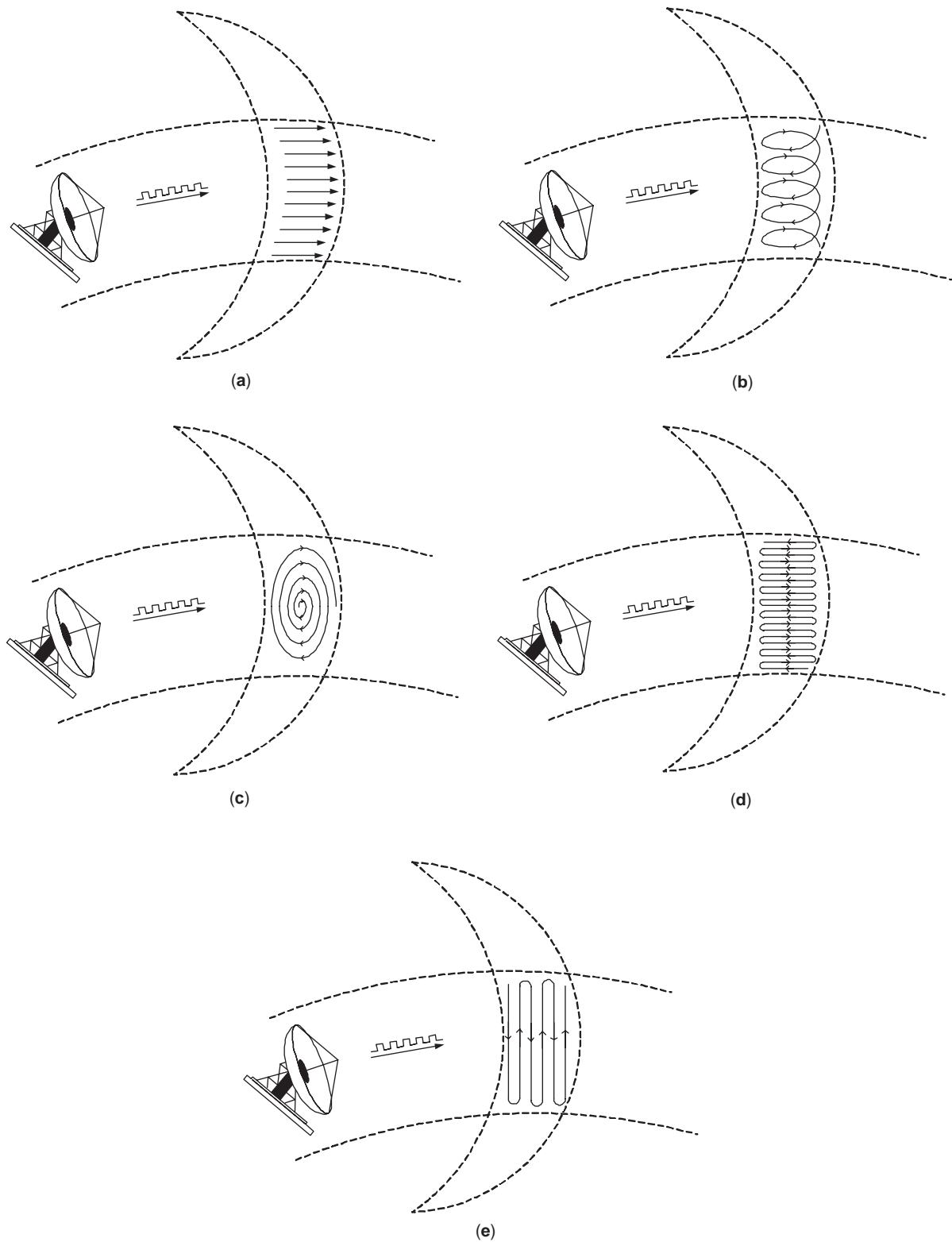


Figure 5. Depiction of the helical (a), Palmer (b), spiral (c), raster (d), and nodding (e) scan patterns of a surveillance radar.

energy. The *raster* scan is produced by oscillating the antenna beam fast in azimuth and slowly in elevation, while the *nodding* scan is produced by oscillating the antenna fast in elevation and slowly in azimuth. Both

the raster and the nodding scans cover a rectangular area, but can also be used to obtain hemispherical coverage. Hemispherical coverage can also be obtained by the helical pattern.

3.2. Tracking Radar

A *tracking* radar measures the coordinates of a target found by a search radar and provides data that can be used to determine the target path and predict its future position. All or part of the available data (range, elevation and azimuth angle, Doppler frequency shift, acceleration, and hyperacceleration) may be used in predicting future target position. Correspondingly, the radar may track in range, in angle, in Doppler, in acceleration, in hyperacceleration, or in any combination of those. Tracking radars either supply continuous tracking data on a particular target (*continuous tracking radar*) or supply sample data on one or more targets (*track-while-scan*) radar. The target parameters in a continuous tracking radar are tracked by a servocontrol loop activated by an error signal generated at the radar receiver. The information available from a tracking radar can either be displayed on a cathode-ray-tube (CRT) display for action by a human operator, or may be supplied to a digital computer and automatically processed to determine the target path and predict its probable future course. The latter is usually called *automatic detection and track* mode or *integrated automatic detection and track* mode when the outputs from more than one radars are automatically combined.

3.2.1. Sequential Lobing Radar. The difference between the target angular position and a reference direction, usually the antenna axis, is the *angular error*. The tracking radar attempts to position its antenna to make the tracking error zero and, thus, locate the target along the reference direction. One method used to obtain the direction and the magnitude of the angular error in one coordinate is to alternately switch the antenna beam between two positions. This is called *lobe switching*, or *sequential switching*, or *sequential lobing*. The difference in amplitude between the voltages in the two switched positions is a measure of the angular displacement of the target from the switching axis. The sign of the difference determines the direction that the antenna must be moved in order to align the switching axis with the direction of the target. Two additional positions are needed to obtain the angular error in the orthogonal coordinate. Thus, a two-dimensional sequentially lobing radar might consist of a cluster of four feed horns illuminating a single antenna, arranged so that the right-left up-down sectors are covered by successive antenna positions. Both transmission and reception are accomplished at each position.

3.2.2. Conical Scan Radar. Conical scan tracking radar uses continuous rotation of an offset antenna beam rather than discontinuous stepping between four discrete positions. The angle between the rotation and the antenna axes is called the *squint angle*. The echo signal is modulated at the frequency of the beam rotation. The phase of the modulation depends on the angle between the target and the rotation axis and can be used to locate the target and continuously position the rotation axis on it.

3.2.3. Monopulse Tracking Radar. The sequential lobing and conical scan tracking radars require a train of echo

pulses in order to extract the angular error signal. This echo train must contain no amplitude modulation components other than the modulation produced by the scanning, otherwise the tracking accuracy will be degraded. On the other hand, pulse-to-pulse amplitude modulations have no effect on tracking accuracy if the angular measurement is based on a single pulse rather than several. If two or more antenna beams are used simultaneously, it is possible to extract angular error information from a single pulse from the relative phase or the relative amplitude of the echo signal received in each beam. Tracking radars that derive angular error information from a single pulse are known as *simultaneous lobing* or *monopulse* radars. An example of a simultaneous lobing technique is *amplitude comparison monopulse*, in which the echoes received from two offset antenna beams are combined so that both the sum and the difference signals are obtained simultaneously. The sum signal provides range information, while the difference signal provides angular error information in one angular direction.

3.2.4. Track-While-Scan Radar. A search radar can obtain the track of a target by marking the coordinates of the target from scan to scan. Such a radar is called *track-while-scan* radar and either requires a human monitor to manually mark the target path or uses a digital computer to perform *automatic detection and tracking*. The automatic detection is achieved by quantization of the range into intervals equal to the range resolution. At each range bin, the detector integrates the number of pulses expected to be returned from a target as the antenna scans past and compares them with a threshold to indicate the presence or absence of a target. When a new detection is received, an attempt is first made to associate it with an existing track. When the detection is declared independent of existing tracks, the radar attempts to make a smooth estimate of the target's present position and velocity, as well as a predicted position and velocity. One method to achieve this is to use either the so-called α - β tracker or a Kalman filter that utilizes a dynamic model for the trajectory of a maneuvering target and the disturbance or uncertainty of the trajectory.

3.3. Navigation Radar

Navigation radar is used to provide the necessary data for piloting an aircraft from one position to another without any need for navigation information transmitted to the aircraft from a ground station. A self-contained aircraft navigation system utilizes a continuous-wave Doppler radar to measure the drift angle and true speed of the aircraft relative to Earth. The drift angle is the angle between the centerline (heading) of the aircraft and the horizontal direction (ground track). A navigation radar requires at least three noncoplanar beams to measure the vector velocity, that is, the speed and its direction, of the aircraft. Such a radar measures the vector velocity relative to the frame of reference of the antenna assembly. This vector velocity can be converted to a horizontal reference on the ground by determining the direction of the vertical and the aircraft heading by some auxiliary

means. Usually, the radar uses four beams that are initially disposed symmetrically about the aircraft axis, with two facing forward and two facing rearward. If the aircraft vector velocity is not in the direction of the aircraft heading, the two forward-facing beams will not read the same Doppler frequency. This Doppler difference can be fed in a servomechanism that will align the axes of the antennas with the ground track of the aircraft. The angular displacement of the antennas from the aircraft heading is the drift angle, and the magnitude of the Doppler frequency is a measure of the speed along the ground track. The uses of the two rearward beams are similar, but improves the accuracy considerably by reducing the errors caused by vertical motion of the aircraft and pitching movements of the antennas.

4. HIGH-RESOLUTION IMAGING RADAR

A *radar image* is a visual representation of the spatial microwave reflectivity distribution of a target illuminated by the electromagnetic radiation emitted by the radar. Equivalently, a radar image represents a collection of reflection coefficients assigned to an array partitioning the target space. Thus, a radar image is generated by the same physical mechanism that generates an optical image observed by a human observer, in which the optical reflectivity distribution is reconstructed. In humans, however, the aperture size of the imaging system is on the order of 10,000 wavelengths, orders of magnitude (in wavelengths) greater than the aperture size of the corresponding radar imaging systems. Since the resolution of an imaging system, namely, its ability to represent distinctly two closely spaced elements, is inversely related to its aperture size, radar imaging systems would appear primitive when compared to their optical counterparts and, whereas a single optical image is usually sufficient for target recognition, several radar images of the same target, corresponding to various viewing angles, are usually required. However, the usefulness of radar imaging systems is not undermined by their lower-resolution capabilities. Advantages of radar imaging systems over their optical counterparts include their day or night capability, since they supply their own illumination, or their all-weather capability, since radiowaves propagate through clouds and rain with only limited attenuation. Additionally, larger aperture sizes (and, thus, higher resolution) can be *synthesized* from the given physical aperture using techniques such as those described later in this article.

4.1. Direct-Imaging Radar

Direct imaging radar systematically scans a three-dimensional volume in angle and range with short pulses emitted from a pencil-beam antenna and range gating and displays the intensity of the received signals as a function of the spatial coordinates interrogated. The spatial resolution is established by the angular (beamwidth) and range (pulse duration) resolution of the sensor without subsequent processing. If range gating is not used, then range is not resolved and the radar image is a

two-dimensional projection of the reflectivity distribution along the radar line of sight. Direct imaging is the simplest form of radar imaging, requiring minimal data processing and allowing the target to be stationary. However, it requires very large aperture and subnanosecond pulses for a high degree of spatial resolution, while, as a result of beam widening, its cross-range resolution degrades as the range increases.

4.2. Synthetic Imaging Radar

Synthetic imaging radar attempts to overcome the limitations of direct imaging radar and create fine spatial resolution by synthetic means in which results from many observations of the target at different frequencies and illumination angles are coherently combined. The term “synthetic” here refers to the synthesis of resolution commensurate with short-pulse, large-aperture illumination from a number of elemental measurements of illumination with not-as-short pulses and not-as-large aperture.

4.2.1. Range Processing Radar. The first task of imaging radar involves discrimination on the basis of range. High resolution in the determination of range is achieved when the transmitted pulse duration T is narrowed down and the corresponding system bandwidth B is increased, so that the time-bandwidth product (TB) is constant. Maximum sensitivity is accomplished when the time-bandwidth product is set to unity, $TB = 1$. Thus, the required range resolution can be achieved when target reflections are measured over a band of frequencies. Any radar waveform that supports an extended bandwidth can be used; the specific type of waveform determines only the necessary implementation of the receiver for coherently processing the wideband signal.

In contrast to direct-imaging methods, in which all the spectral components of the signal must be present simultaneously, synthetic imaging methods require that the spectral components be present sequentially. In the simplest implementation of high range resolution by synthetic means, several narrowband measurements are made at discrete frequency increments. Such radars are called *stepped-frequency* systems and can be either *continuous-wave* (CW), at each frequency emitting an unmodulated sinusoid, or *pulsed*, amplitude-modulating each frequency sinusoid. Stepped-frequency continuous-wave systems are susceptible to aliased responses and transmitter coupling, shortcomings alleviated by pulsing the transmitter and time-gating the receiver as in a pulsed, stepped-frequency system. Although individual narrowband responses have insignificant resolution potential, the coherent combination of the responses provides the resolution allowed by the total bandwidth spanned. Alternatively, high range-resolution can be accomplished using *swept-frequency* (*linear FM*) systems and corresponding wideband receivers. Range resolution in swept-frequency systems is achieved by measuring the difference in instantaneous frequency between the instant of emission of the radar pulse by the transmitter and the instant of its reception back at the receiver.

4.2.2. Synthetic Aperture Processing Radar. High resolution in the cross-range direction can be obtained by scanning a focused beam across the object. If the aperture that forms the scanning beam is focused at the target plane, the minimum lateral extent of the focused spot is approximately

$$\Delta = \frac{\lambda R}{D} \quad (20)$$

where λ is the wavelength, R is the observation distance, and D is the aperture dimension. Resolution of two adjacent object points on a plane perpendicular to the line of sight of the radar is possible if their distance is greater than the spot dimension. Thus, for a fixed wavelength and observation distance, the resolution is increased by increasing the aperture size. High-resolution direct-imaging radars would, therefore, need to have physically large aperture.

Synthetic imaging radars synthesize equivalent large aperture for high-resolution cross-range imaging by sequentially stepping a sensor through small incremental distances and storing samples of the amplitudes of the corresponding received signals. The stored signals are coherently summed to produce signals equivalent to those that would be received by the corresponding large physical aperture. In effect, *synthetic aperture radars* (SARs) coherently process signals scattered from the same target for various viewing angles by utilizing relative motion between the sensor and the target. Depending on the type of relative motion between sensor and target, synthetic aperture radars can be linear, spotlight, or inverse.

Linear Synthetic Aperture Radar. In linear SAR, also called *stripmap* SAR, the radar sensor is moved along a linear path and images stationary targets in its line of sight. Linear SAR is widely used for mapping terrain features and ground-based objects from airborne platforms.

Spotlight Synthetic Aperture Radar. Spotlight SAR involves observing a target with the radar antenna fixed on it while the viewing angle is changed.

Inverse Synthetic Aperture Radar. Inverse SAR involves a stationary radar viewing targets rotating about an axis perpendicular to the line of sight.

4.2.3. Doppler Processing Radar. Spatial resolution in cross-range, that is, along an axis perpendicular to the radar line of sight, can be obtained if a target rotates relative to the radar sensor and the target reflections are Doppler-processed. This is possible since the Doppler frequency shift in waves reflected by a rotating target is proportional to the lateral offset of the reflector along an axis normal to the axis of rotation and the line of sight. Indeed, if d and R_0 ($R_0 \gg d$) are the distances of a reflecting point and the radar sensor, respectively, from the center of a target rotating at an angular velocity Ω , then the distance of the reflecting point from the radar sensor at time t is approximately

$$r(t) = R_0 - d \sin(\Omega t) \quad (21)$$

According to Eq. (6), the Doppler coefficient at time t in the received wave will be

$$v_0(t) = \frac{-2}{c} \frac{dr(t)}{dt} = \frac{2d\Omega}{c} \cos(\Omega t) \quad (22)$$

From Eq. (22), it is clear that the Doppler coefficient for every reflecting point in a target rotating with angular velocity Ω is a harmonic function of time, the amplitude of which is proportional to the instantaneous lateral distance of the reflecting point from the center of rotation. Doppler processing of the received signal for cross-range resolution can be done online by either a bank of contiguous filters or first sampling it and then analyzing it with Fourier transform processors of sufficiently high speed. Offline processing, on the other hand, can be performed by recording the received signal for later processing. In either case, the signal is usually frequency translated to retain only its complex envelope.

4.2.4. Holographic Processing Radar. Optical holography records the spatial distribution of the intensity of the interference of lightwaves diffracted by an object and a reference beam in a *hologram*. This overcomes the difficulty associated with lack of optical phase-sensitive storage media. Later, the hologram can be used to reconstruct the lightwaves associated with the original object by illumination with the reference beam used in the recording step. A holographic reconstruction allows a viewer the perception of a *virtual image* of the original object.

Microwave holography follows recording and reconstruction procedures analogous to optical holography. In microwave holography, the field amplitude scattered from an object coherently illuminated from a transmitter is mapped over a prescribed recording aperture by a coherent detector that is scanned over the aperture. The detected bipolar signal, representing the complex envelope of the time-varying field, is added to a bias level sufficient to make the resultant always positive. The resulting signal is used to produce a film transparency with an amplitude transmittance function that is real and positive. The area probed by the detector represents the hologram aperture, the reference signal for the coherent detector represents the reference beam, and the signal scattered from the object is the object beam. A variation, known as *scanned holography*, of the (conventional) procedure described above attempts to scan the transmitter and the receiver independently and offers some advantages in resolution.

5. WEATHER OBSERVATION RADAR

Radar is a powerful research instrument in meteorology and also for telecommunications at frequencies higher than 1 GHz, since it allows for the gathering of considerable quantities of data on the three-dimensional structure of the atmosphere in a flexible, efficient, and rapid manner. Radar applied to hydrometeor observation provides two types of information: (1) quantitative information on

the local distribution of the reflectivity and speed distribution in the scattering medium and (2) qualitative information on the small- and medium-scale structure of the targets, their evolution and movement, and other information heuristically extracted by expert analysts. This information can be used to describe atmospheric phenomena and study radiowave propagation, such as the provision of various statistics on precipitation and attenuation.

5.1. Precipitation Measurements

The most frequent quantitative application of the radar observation is to distinguish ice and liquid phases of precipitation. This task is particularly challenging in convective storms, where liquid water can exist at temperatures colder than 0 °C and ice can be found at temperatures warmer than 0 °C. Equally important and challenging is the task of quantifying rain, snow, or hail precipitation rates, where the difficulty lies in the dependence of the rates on detailed knowledge of the drop size distributions. Although radar techniques have practical limitations and their accuracy is highly suspect, they offer important advantages over conventional methods based on pluviometer array measurements—they allow for spatial continuity of the observations and improved access to the observation of the variability of the precipitation; and make it possible to observe the three-dimensional structure of the system generating the precipitation, as well as survey over a wide area from a single measurement point in real time; data acquisition, storage, and processing is simple. Radars capable of measuring multiple parameters (e.g., vertical and horizontal reflectivities and/or a spectrum of terminal velocities) in each resolution cell, in combination with satellites, rain gauges, and other instruments, may give the desired accuracy in measuring rainfall rates and discriminating rain from frozen precipitation.

5.2. Storm and Wind Observation

A pulsed Doppler radar can estimate the reflectivity and range velocity distribution inside a storm's shield of clouds. If a single beam is used, a three-dimensional picture of a storm typically requires 2–5 min of data collection time. This delay is imposed not only by antenna rotation limitations but also by the requirement for collection of a large number of radar echoes for reduction of the statistical uncertainty in the reflectivity and velocity estimates. Although the storm can change significantly during this period, with subsequent distortion of the reflectivity and velocity radar images, the returned estimates are considered highly valuable.

In practice, more significant than the reflectivity and velocity distributions are estimates of the rainfall rate and wind velocity. Doppler radar, however, measures the range velocity of hydrometeors rather than air, and often this differs significantly from the range component of wind. Nevertheless, since hydrometeors quickly respond to wind forces, their terminal velocities give negligible bias estimates of the range component of the wind.

5.3. Turbulence Measurement

The mean velocity and spectrum width measured by Doppler radar are weighted averages of point velocities. Therefore, they are sufficient to depict motion on scales larger than the resolution cell, but cannot infer the details of the flow inside the cell. Nevertheless, Doppler radar offers the possibility of measurement and study of turbulence on scales smaller than the resolution cell if a firm connection between the statistical and physical properties of the atmosphere and Doppler-derived measurements is established.

5.4. Clean-Air Observation

A radar designed to identify and track precipitating storms can also detect echoes from scatterers in fair weather. In such cases, the distribution of spatial reflectivity in clean air can be associated with meteorological phenomena such as turbulent layers, waves, and fronts, flying birds and insects, or atmospheric pollutants. Clean air echoes not related to any visible scatterers have been conclusively proved to emanate from refractive index irregularities.

Waves reflected by sharp, quasipermanent changes in the dielectric permittivity of the atmosphere form the coherent component in the echo received by the radar. Coherent echoes exist if the scattering medium does not time-modulate the amplitude or phase of the transmitted radar pulses, even though spatial variations may exist. Coherent echoes appear as peaked and narrow components in the Doppler spectrum. On the other hand, incoherent components are contained in the echo signal if time-varying (turbulent) scatter is present. Incoherent echoes demonstrate themselves as broad components in the Doppler spectrum.

6. LASER RADAR SYSTEMS

It is natural to attempt to extend radar techniques to the optical portion of the electromagnetic spectrum. The fact that optical wavelengths are orders of magnitude smaller than their radio counterparts allows for very fine resolution in the estimation of target parameters, such as angular position, range, and tangential and radial velocities. The first optical radar systems investigated used incoherent light from xenon or other flashlamps. With the invention of the *laser* (light amplification by stimulated emission of radiation), however, they were replaced by systems that employed coherent laser light. Such systems were initially called *lidar* (light detection and ranging) and, in more advanced, higher performance versions, *ladar* (laser detection and ranging) in complete analogy to radar.

The development of practical ladar systems followed a path similar to the development of radar systems: Reflectivity and backscattering cross-section data were collected and tabulated for a number of targets at available laser operating wavelengths; laser pointing could be accomplished by mounting the laser on existing radar platforms; the scan patterns of radar were employed in ladar systems

as well; the signal design and processing techniques of radar were also applicable to ladar systems.

When compared to radar, ladar systems exhibit advantages and disadvantages, both due to their use of very short wavelengths. On one hand, very short wavelengths result in very high information bandwidths and very fine resolution. Exploitation of the bandwidth can be achieved with today's advanced signal-processing techniques and hardware. Additionally, unlike the use of solid-state lasers in early ladars, which allowed only for signal envelope processing, today's ladars use gas lasers, which also allow for signal phase processing. On the other hand, however, very short wavelengths result in low power efficiency and high atmospheric propagation losses. As a result, ladar is preferable to microwave and millimeter-wave radar for long-range ground-to-space and space-to-space applications or short-range atmospheric applications, where the propagation loss penalty does not outweigh fine resolution.

6.1. Ladar Information Processing

A ladar measures a target's range, position, velocity, and motion by modulating its laser beam, detecting the reflected return, and processing the return signal to derive the desired information. Methods have been developed for amplitude, frequency, and phase modulation and for modulation by polarization. Laser radiation can be modulated both by direct action on coherent signals inside the laser during their generation (internal modulation) and through action on the radiated light outside the laser (external modulation). A number of electrooptical, acoustooptical, and mechanical beam modulation devices are available with different inherent modulation rates, yielding amplitude or frequency modulation of the transmitted beam.

Solid-state lasers cannot provide the necessary spectral purity to utilize phase processing of ladar signals. Gas lasers, such as helium–neon and carbon dioxide, however, have high spectral purity and can be modulated in amplitude or frequency with bandwidths of up to 525 MHz

(yielding a resolution of approximately one foot) with relatively low drive powers. Ladar signal processing techniques are similar to those used in microwave radar. In fact, the same circuits for signal-envelope processing may be employed in many cases. The use of ladar allows the exploitation of highly precise and unique methods for angle estimation and tracking.

7. GROUND/FOLIAGE-PENETRATING RADAR

In the recent years (as of 2003), an attempt has been made to use radar systems to detect and map "targets" buried under Earth's surface or obscured by foliage. Primarily, interest arises from a number of potential applications, such as detecting and locating unexploded ordnance in a battlefield, manmade objects in landfills, buried hazardous waste, subsurface plumes of refined hydrocarbons, or military equipment hidden in forest vegetation. The radar is either spaceborne, airborne, or ground-towed and possibly operates in SAR mode. In Fig. 6, a typical configuration is shown in which a ground-towed, ground-penetrating radar is utilized for excavation planning. The task of the radar in this application is to map (image) the location of buried pipes and discriminate them from other unwanted buried objects, such as rocks and small metal pieces (*volume clutter*).

A ground/foilage-penetrating radar needs to utilize *ultrawideband* (UWB) signals, containing both low- (for deeper penetration) and high- (for higher resolution) frequency components. This can be achieved in two ways: (1) by emission of very short in duration (and, subsequently, ultrawide in bandwidth) pulses or (2) by sequential emission of narrowband signals whose carrier frequency increases in steps, covering a wide frequency band.

Even though the perspective of ground/foilage-penetrating radar from initial tests has been encouraging, a number of difficulties have delayed the development of this technology. These include:

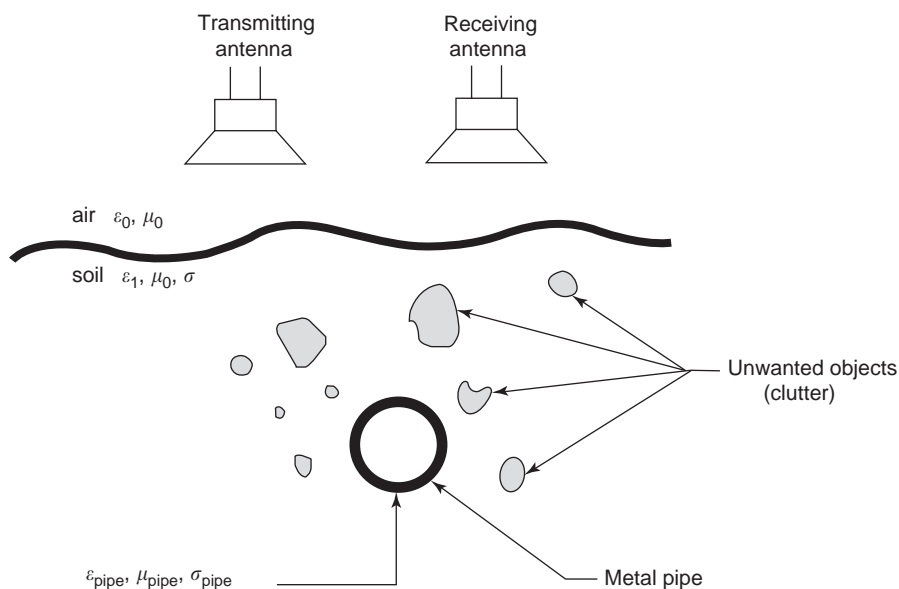


Figure 6. Typical configuration of a ground-towed, ground-penetrating radar utilized for excavation planning. The task of the radar in this application is to map (image) the location of buried pipes and discriminate them from other unwanted buried objects, such as rocks and small metal pieces, (*volume clutter*).

- High electromagnetic wave absorption, especially under moist soil conditions
- Random distributions of soil particles, such as rocks, that tend to scatter the electromagnetic energy, increase propagation losses, and reduce the image contrast
- High clay content to which water binds and, thus, dipolar relaxation loss mechanisms are encouraged
- Roughness of the air–soil interface that tends to increase backscattering that interferes with the penetrating radar signature

Similar factors affect the development of foliage-penetrating radar systems.

To date, the success of ground/foilage-penetrating radar surveys seems to be absolutely site-dependent. A thorough understanding of a site's geology, hydrology, and topography is of paramount importance. Before undertaking a radar survey, it is necessary to obtain as much information as possible about the physical characteristics of the specific site. If log-boring log or well-monitoring data are available, they should be analyzed to determine soil stratigraphy and hydrology. If such data are not available, it is prudent to gather representative soil samples.

The applications for radar in subsurface target detection seem to fall into two broad categories, depending on the scale of the system, target, terrain structures, and search volumes. The case of large scales is made if the targets sought are large relative to the average wavelength and the soil inhomogeneities. In this case, imaging would play a (secondary) role in reducing the number of false alarms of the detection procedure. If small targets, such as mines or weapons, are of interest, they would be hard to distinguish from clutter and the role of imaging would be enhanced. Thus, it is difficult or perhaps pointless to develop a single radar system for the detection of both large/deep and small/shallow targets. The wide frequency range requirement imposes stringent requirements in the range of both the electronics and the size of the relevant antennae and contributes to the delay of development of this significant radar application. However, ground/foilage-penetrating radar technologies are presently an area of significant research investigation.

8. CURRENT TRENDS

Besides research in ground/foilage penetrating radar technologies, significant research is also conducted in the development of *spacetime adaptive processing* (STAP) algorithms. STAP refers to multidimensional adaptive filtering algorithms that simultaneously combine the signals from the elements of an array antenna and the multiple pulses of a coherent radar waveform. STAP can improve the detection of low-velocity targets obscured by mainlobe clutter, detection of targets masked by sidelobe clutter, and detection in combined clutter and jamming environments.

Significant research is also conducted into the use of signal processing tools other than the traditional Fourier transform-based ones for target detection and recognition. Such tools are, for example, based on the theories of

wavelet-induced multiresolution analyses (WIMAs) of signals. A WIMA allows for the decomposition and simultaneous representation of a signal in time and scale and, therefore, is capable of processing signals at different scales. WIMA-based radar target detection and recognition have been actively researched.

BIBLIOGRAPHY

1. C. G. Bachman, *Laser Radar Systems and Techniques*, Artech House, Dedham, MA, 1979.
2. L. J. Battan, *Radar Observation of the Atmosphere*, Univ. Chicago Press, 1973.
3. P. Bello, Joint estimation of delay, Doppler, and Doppler rate, *IRE Trans. Inform. Theory* 330–341 June 1960.
4. W. G. Carrara, R. S. Goodman, and R. M. Majewski, *Spotlight Synthetic Aperture Radar: Signal Processing Algorithms*, Artech House, Norwood, MA, 1995.
5. I. Cindrich, N. K. Del Grande, S. Gowrinathan, P. B. Johnson, and J. Stanley, eds., *Aerial Surveillance Sensing Including Obscured and Underground Object Detection*, Vol. 2217, SPIE—The Society for Optical Engineering, Bellingham, WA, 1994.
6. N. K. Del Grande, I. Cindrich, and P. B. Johnson, eds., *Underground and Obscured Object Imaging and Detection*, Vol. 1942, SPIE—The Society for Optical Engineering, Bellingham, WA, 1993.
7. A. J. Devaney, R. Raghavan, H. Lev-Ari, E. Manolakos, and M. Kokar, *Automatic Target Detection and Recognition: A Wavelet Approach*, Final Report on ARPA Grant F49620-93-1-0490, 1995.
8. R. J. Doviak and D. S. Zrnić, *Doppler Radar and Weather Observations*, Academic Press, San Diego, CA, 1992.
9. A. K. Fung, *Microwave Scattering and Emission Models and Their Applications*, Artech House, Norwood, MA, 1994.
10. R. Kapoor, A. Banerjee, G. A. Tsihrintzis, and N. Nandhakumar, Detection of targets in heavy-tailed foliage clutter using an ultra-wideband (UWB) radar and alpha-stable clutter models, *IEEE Trans. Aerospace Electron. Syst.* **AES-35**: 819–834 (1999).
11. E. J. Kelly, The radar measurement of range, velocity, and acceleration, *IRE Trans. Milit. Electron.* 51–57 (April 1961).
12. E. J. Kelly and R. P. Wishner, Matched-filter theory for high-velocity, accelerating targets, *IEEE Trans. Milit. Electron.* 56–69 (Jan. 1965).
13. R. Meneghini and T. Kozu, *Spaceborne Weather Radar*, Artech House, Norwood, MA, 1990.
14. D. L. Mensa, *High Resolution Radar Cross-Section Imaging*, Artech House, Norwood, MA, 1991.
15. D. R. Rhodes, *Introduction to Monopulse*, McGraw Hill, New York, 1959.
16. A. W. Rihaczek, *Principles of High Resolution Radar*, Artech House, Norwood, MA, 1996.
17. A. W. Rihaczek and S. J. Heshkowitz, *Radar Resolution and Complex-Image Analysis*, Artech House, Norwood, MA, 1996.
18. H. R. Raemer, *Radar Systems Principles*, CRC Press, Boca Raton, FL, 1997.
19. H. Sauvageot, *Radar Meteorology*, Artech House, Norwood, MA, 1991.
20. S. M. Sherman, *Monopulse Principles and Techniques*, Artech House, Norwood, MA, 1984.

21. M. I. Skolnik, *Introduction to Radar Systems*, McGraw Hill, New York, 1980.
22. G. A. Tsihrintzis, P. M. Johansen, and A. J. Devaney, Buried object detection and location estimation from electromagnetic field measurements, *IEEE Trans. Anten. Propag.* **AP-47**: 1742–1744 (1999).
23. G. A. Tsihrintzis and C. L. Nikias, Evaluation of fractional, lower-order statistics-based detection algorithms on real radar sea-clutter data, *IEE Proc. F: Radar, Sonar, Navig.* **144**:29–37 (1997).
24. F. T. Ulaby and M. G. Dobson, *Handbook of Radar Scattering Statistics for Terrain*, Artech House, Norwood, MA, 1989.
25. J. Ward, *Space-Time Adaptive Processing for Airborne Radar*, MIT-Lincoln Laboratory Technical Report 1015, 1994.

RADAR CROSS-SECTION

DAVID C. JENN
Naval Postgraduate School

Radar cross section (RCS) is a measure of the magnitude of the scattered electromagnetic wave from a body relative to the magnitude of the wave incident on the body. To many people RCS is synonymous with stealth. Stealth technology has become an integral part of all military systems since it was first employed in the 1970s. However, RCS is just one aspect of stealth, the design philosophy that seeks to make a platform (such as an aircraft, ship, or ground vehicle) undetectable to a wide range of sensors. Such a platform is referred to as low-observable (LO). In addition to radar, the infrared, acoustic, and visible signatures must be controlled. In the past, the RCS has received the most attention because the detection range of radar is generally much greater than that of other sensors. Undetectability does not necessarily imply a very low signature, only that the target must be indiscernible against the background. In the visible region (wavelengths visible to the eye) stealth has been used since World War II in the form of camouflage.

A typical radar and target arrangement is shown in Fig. 1. The transmitter illuminates the target from a distance R_t . If the body is sufficiently far from the transmitting antenna, the incident spherical wavefront will be approximately planar across the target. The incident wave induces currents on the surface of the body, and even within its volume if the material is not a perfect electric conductor. The induced currents give rise to a scattered field, which is detected by the receiver at a distance R_r .

The arrangement shown in Fig. 1 is referred to as *bistatic*; the directions of the transmitter and receiver are different as viewed from the target. The *monostatic* case is more common; that is, the directions of the transmitter and receiver are the same as viewed from the target. For a truly monostatic radar the transmit and receive channels should use the same antenna. Frequently the radar will use separate antennas for transmit and receive, but they will be closely spaced on the same platform. This configuration is referred to as *quasimonostatic*, and can be considered as monostatic for the purpose of specifying the RCS of a distant target.

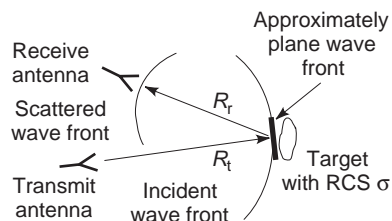


Figure 1. *Bistatic* RCS refers to an arrangement where the transmitting and receiving antennas are at different locations as viewed from the target. For the monostatic case the transmitting and receiving antennas are collocated.

static, and can be considered as monostatic for the purpose of specifying the RCS of a distant target. The majority of radars currently in use for both military and civilian applications are monostatic.

Most radars are designed to provide information on the target's location and velocity. Location is given in terms of the range (radial distance) from the radar along with direction. The range to the target is obtained by a time-delay measurement. An electromagnetic wave is transmitted in the direction of the target, and the round-trip travel time is converted to distance using the known velocity of propagation of the wave. The direction of the wave is obtained from antenna pointing. Velocity can be measured using the frequency shift due to the Doppler effect or two range measurements at closely spaced times to obtain the target's range rate. Any measurement of the target parameters assumes that the reflected wave is strong enough to be detected and processed by the radar. Search radars are specifically designed for this purpose. They are used to scan large volumes of space for targets at great distances (hundreds or even thousands of kilometers). Once a target has been detected it is handed over to a tracking radar. Modern multifunction radars are designed to perform both search and track functions.

Although both the search and track operations are more difficult for targets with low RCS, the primary objective of RCS reduction is to defeat search radars (i.e., avoid detection). The role of the RCS in the detection of a target is demonstrated by the basic form of the radar equation derived later. It shows that when all other radar system parameters are fixed, the maximum detection range of a target varies as the fourth root of RCS. Thus, by reducing the target RCS, the range at which it is first seen by the radar is also reduced.

The RCS of modern aircraft and ships has been significantly reduced, but in response to the lower cross sections, more sensitive radars have evolved. The RCS designer is at a disadvantage in this respect because a truly LO platform must be designed from the start. Stealth cannot simply be added on after all other design tradeoffs have been made. The entire design and test cycle of an aircraft can be a decade, and its operational life several decades. On the other hand, the radar designer may be able to significantly increase the capability of a radar by simply replacing a system component such as an antenna or signal processor. These are relatively minor changes and can be integrated into deployed radars in a

Table 1. Frequency Band Designations

Band Designation	Frequency Range
HF	3–30 MHz
VHF	30–300 MHz
UHF	300–1000 MHz
L	1–2 GHz
S	2–4 GHz
C	4–8 GHz
X	8–12 GHz
Ku	12–18 GHz
K	18–27 GHz
Ka	27–40 GHz
MM	40–300 GHz

couple of years, thereby decreasing the effectiveness of the LO platform for the rest of its operational lifetime.

The scattering properties of the target are only one of several considerations that enter into the selection of the operating frequency of a radar [1,2]. Others are size constraints, antenna gain and beamwidth, transmitter power, ambient noise, Doppler shift, and atmospheric attenuation. The frequency spectrum is divided into bands with letter designations as shown in Table 1. A few long-range ballistic missile defense radars operate in the 300-MHz region (UHF), but most others use frequencies greater than 1 GHz (L band and above). Devices at low frequencies are larger than similar devices at a higher frequency, and therefore the system’s components require more volume. Likewise the antenna must be larger at a low frequency than at a high frequency to achieve the same beam width and gain. Low frequencies are capable of handling more power because the applied voltages can be higher without causing breakdown. Finally, ambient noise is lowest in the 1–10 GHz range, and low-altitude atmospheric attenuation favors frequencies below 18 GHz.

The function of the radar also influences the choice of frequency. For instance, an airborne imaging radar must be compact and lightweight, but also have a narrow antenna beam for resolving scatters. These all favor a high frequency. On the other hand, a ground-based search radar must radiate high power to achieve a large detection range. In this case the larger and heavier equipment that is necessary for high-power operation is not a problem.

1. DEFINITION OF RADAR CROSS SECTION

Radar cross section is defined as [3]

$$\frac{\text{Power reflected towards receiver per unit solid angle}}{\text{Incident power density}/4\pi}$$

In general it is dependent on many parameters. They include

1. The size, shape, and material composition of the body
2. The frequency and polarization of the incident electromagnetic wave

3. The direction from which the wave illuminates the body, as well as that at which the observer is located (the angle at which the target is viewed is referred to as the *aspect angle*)

These factors are taken into consideration when a radar is designed to detect a specific target. On the other hand, if a vehicle is to face a radar with known specifications, the target can be designed with the radar’s performance in mind. For example, if an aircraft will be flying directly at a radar in most mission scenarios, then it will be wise to put extra effort into reducing the nose-on RCS, perhaps even at the expense of raising it at broadside aspect angles. Furthermore, if the frequency of the radar is known, then the RCS reduction effort need only concentrate on that frequency.

The conventional symbol for RCS is σ and it has units of square meters. As evident in Table 2, typical values of the RCS range from 0.0005 m² for insects to 100,000 m² for a large ship. The decibel unit is convenient when working with quantities that extend over several orders of magnitude. The RCS in decibels relative to a square meter (dBsm) is defined as

$$\sigma_{\text{dBsm}} = 10 \log_{10} \sigma$$

Implicit in the definition of RCS is the assumption that the frequency is fixed.

Mathematically the RCS is given by

$$\sigma(\theta, \phi, \theta_i, \phi_i) = \lim_{R_r \rightarrow \infty} 4\pi R_r^2 \frac{|\mathbf{E}_s(\theta, \phi)|^2}{|\mathbf{E}_i(\theta_i, \phi_i)|^2} \tag{1}$$

where

\mathbf{E}_i = plane-wave electric field intensity incident from the direction (θ_i, ϕ_i)

\mathbf{E}_s = scattered spherical wave electric field intensity observed from the direction (θ, ϕ)

R_r = distance from the target to the observer as shown in Fig. 1

At first glance it may appear that RCS is a function of range because of the R_r^2 in Eq. (1). However, the scattered field is a spherical wave whose electric field has a $1/R_r$ dependence, which, when squared, cancels the factor in the denominator. Hence RCS is a range-independent quantity.

Electromagnetic scattering and radiation problems can be formulated in either the time domain (TD) or the

Table 2. Typical Values of RCS

Target	RCS (m ²)
Insects	0.0005
Small birds	0.01
People	0.5
Cars (front)	5–10
Fighter aircraft nose on broadside	10–50
Bomber aircraft	500–1000
Ships	1000–100000

frequency domain (FD) [4,5]. In fact, the scattering body can be represented as a linear system with impulse and frequency responses. The RCS as a function of time is related to the RCS as a function of frequency by the Fourier transformation. There are advantages and disadvantages to working in each domain. Early radar systems operated over narrow frequency ranges, and the need to compare calculated and measured data dictated that calculations also be done in the frequency domain. Modern radars operate over wide frequency ranges, and in order to characterize their performance adequately, the target RCS must also be determined over the same wide range of frequencies. For a large, complex target, the calculation of the RCS at each frequency is potentially a time-consuming task. It may be more efficient to compute the target's response to a waveform in the time domain and then perform a Fourier transformation to obtain the RCS at many frequencies simultaneously. Thus the measurement or calculation of RCS can be performed by either of two procedures:

1. *Frequency Domain.* The received power is obtained as the target is rotated through a range of angles while a continuous wave (CW) fixed-frequency source is radiating. The frequency can be changed and another plot of RCS versus angle obtained, and so on. At any fixed angle the RCS from a large number of frequencies can be Fourier transformed to obtain the time-domain response of the target at that particular angle.
2. *Time Domain.* The received power as a function of time is obtained at each aspect angle of interest. The time histories are inverse Fourier transformed to yield the frequency response of the target at each angle. If the Fourier transform of the waveform and the impulse response of the radar system are known, then the target's frequency response can be converted to RCS.

There are several aspects of the RCS that enter into the design of an LO platform, and therefore the discussion of the RCS logically falls along similar lines. They include the following topics:

1. Electromagnetic (EM) scattering mechanisms and the physical aspects of scattering
2. Analytical and computational methods
3. Reduction methods
4. Measurement techniques

A brief overview of each of these four topics is given, followed by mathematically based discussions of RCS prediction and reduction.

2. BASIC SCATTERING CHARACTERISTICS OF BODIES

2.1. Frequency Regions

The scattering characteristics of a target are strongly dependent on the frequency of the incident wave. There

are three frequency regions in which the RCS of a target is distinctly different. They are referred to as the (1) low-frequency, (2) resonance, and (3) high-frequency regimes [6]. The labels are somewhat misleading in that low and high are defined relative to the size of the target when normalized to the incident wavelength, rather than to its physical size. If the target is smooth and it can be roughly described by a characteristic length L , then the three frequency regimes can be defined in terms of the quantity βL , where

$$\beta = 2\pi/\lambda \quad (2)$$

and λ is the wavelength.

Low-Frequency Region ($\beta L \ll 1$). At these frequencies the phase variation of the incident plane wave across the extent of the target is small. Thus the induced current on the body is approximately constant in amplitude and phase. The particular shape of the body is not a factor in the RCS pattern shape. For example, both a small sphere and a small cube have essentially isotropic (direction-independent) scattering patterns. In general, σ versus βL is smooth and varies as λ^{-4} . This region is also called the Rayleigh region.

Resonance Region ($\beta L \approx 1$). When βL is on the order of 1, the phase variation of the incident field across the body is significant and all parts contribute to the scattering pattern. A plot of σ versus βL is oscillatory. This region is also referred to as the Mie region.

High-Frequency Region ($\beta L \gg 1$). There are many cycles in the phase variation of the current across the body, and consequently the scattered field will be very angle-dependent. The peak scattering levels are primarily due to isolated points. For example, the peak scattering from large flat plates originates from specular points on the surface. (They are the mirrorlike reflection points for which the angle of reflection equals the angle of incidence.) A plot of σ versus βL is smooth in this region and may be independent of λ . This is also called the optical region.

The RCS of a sphere, which is plotted in Fig. 2, clearly illustrates the three frequency regions. The appropriate characteristic dimension of the sphere is its radius; therefore, let $L = a$. (One could argue that based on the previous discussion that $L = 2a$ should be used. However, the boundaries between the frequency regions are defined by orders of magnitude; they are not sharp. Hence either choice for L is acceptable. For a sphere quantities are generally normalized to the radius, and therefore $L = a$ is the most convenient choice.) For $\beta a < 1$, the curve is almost linear, but above 1 it begins to oscillate. This is the resonance region. The oscillations die out at higher values, and above $\beta a \leq 10$ the curve approaches a constant equal to πa^2 .

2.2. Polarization and the Scattering Matrix

In addition to frequency, polarization plays a major factor in determining the scattering characteristics of a body. Polarization refers to the orientation of the electric field vector. The incident wave polarization is determined by the orientation of the transmit antenna, while the receive

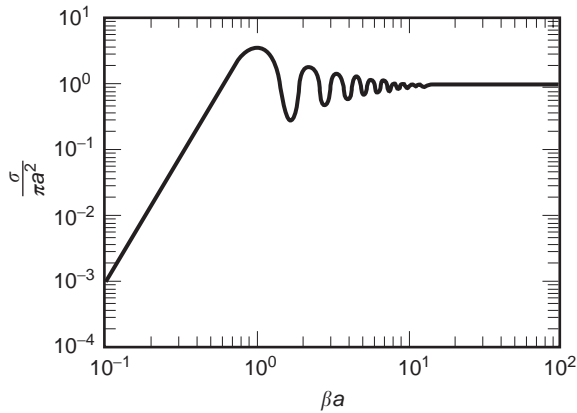


Figure 2. The RCS of a sphere illustrates the three frequency regions: (1) Rayleigh (linear region at low frequencies), (2) resonance (oscillatory region), and (3) optical (flat high frequency region).

antenna determines the receive polarization. If the antennas are linearly polarized and their electric field vectors are aligned, then the copolarized scattered field is measured. On the other hand, if linear transmit and receive antennas are orthogonal (electric field vectors crossed at 90°), then the cross-polarized component of the scattered field is sensed.

The copolarized scattered field is generally used, for several reasons. First, the copolarized scattered field component is usually much higher than the cross-polarized component. Second, for monostatic radars it is more efficient to use the same antenna for transmit and receive, and hence the transmit and receive polarizations are identical. However, measuring both components provides the most information available from the scattered field and may assist in target identification.

A polarization-specific RCS can be expressed as

$$\sigma_{qp} = \lim_{R_r \rightarrow \infty} 4\pi R_r^2 \frac{|\mathbf{E}_{sq}|^2}{|\mathbf{E}_{ip}|^2} \quad (3)$$

where p denotes the polarization of the incident wave and q the polarization of the receiver. Common polarization designations are defined with regard to a reference such as the ground or surface. They include horizontal and vertical (H and V); parallel and perpendicular (\parallel and \perp); rectangular (x and y). A scattering matrix relates the scattered field components to the incident field components:

$$\begin{bmatrix} \mathbf{E}_{s\theta} \\ \mathbf{E}_{s\phi} \end{bmatrix} = \begin{bmatrix} S_{\theta\theta} & S_{\theta\phi} \\ S_{\phi\theta} & S_{\phi\phi} \end{bmatrix} \begin{bmatrix} \mathbf{E}_{i\theta} \\ \mathbf{E}_{i\phi} \end{bmatrix} \quad (4)$$

The elements of the scattering matrix can be determined by computation or measurement.

The RCS of a cylinder illustrates the effect of polarization on scattering level and pattern shape. As shown in Fig. 3, a relatively strong copolarized RCS exists even for thin wires, whereas the cross-polarized RCS tends to zero.

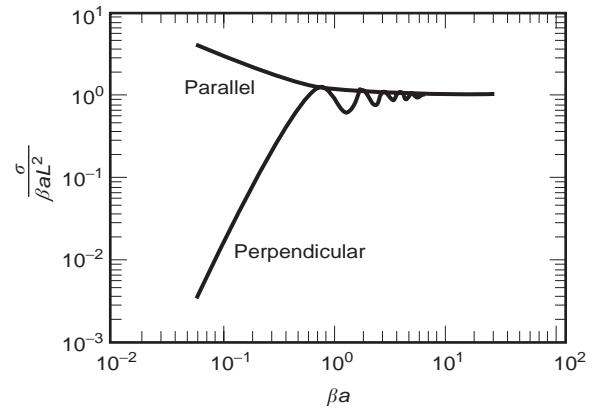


Figure 3. A cylinder illustrates how a target's RCS can depend on the incident wave polarization. At low frequencies the cylinder becomes a thin wire that is transparent to a perpendicularly polarized wave.

At high frequencies the cross sections for both polarizations asymptotically approach the same value.

2.3. Monostatic versus Bistatic RCS

The vast majority of radars currently in use are monostatic, because most systems must operate from a single platform. However, the monostatic RCS (backscatter) of electrically large smooth flat targets is very small unless the radar is positioned normal to the surface. Besides the normal, large cross sections are observed in the specular ($\theta = \theta_i$) and forward ($\theta = \theta_i + \pi$) scattering directions.

Bistatic radars have the transmit and receive antennas in two separate locations. Thus a bistatic radar with a receiver at either of these two locations would have the advantage of larger target RCS. However, there are also disadvantages such as reduced operational flexibility because of the restricted transmit–receive relationships, and maintaining a coherent reference for the transmitter and receiver.

3. SCATTERING MECHANISMS

The RCSs of targets encountered by most radars are complicated geometric shapes. There are a few exceptions such as weather balloons and buoys. However, simple shapes such as plates, spheres, cylinders, and wires are useful in studying the phenomenology of RCSs. Furthermore, complex shapes can be decomposed into basic geometric building blocks (primitives) that can be assembled to form a more complex shape. Figure 4 shows an aircraft represented by cylinders, plates, cones, and hemispheres. The RCS of the model in Fig. 4 is shown in Fig. 5. A collection of basic shapes gives an acceptable RCS estimate that can be used during the initial design stages of a platform. The locations and levels of the largest RCS lobes are of most concern at this stage of the design process. The accuracy of the RCS estimate at other angles depends on how the interactions between the various shapes are handled. These are more difficult to include, as will be seen later. Even when they are included, the agreement

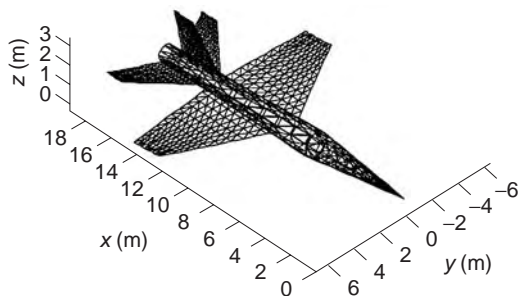


Figure 4. Simple geometric shapes such as plates, cylinders, and spheres can be used to build more complicated targets. The interaction between the individual parts is important in determining low-level RCS.

with the measured RCS may not be particularly good if the interactions are not modeled accurately. For an LO target more sophisticated numerical techniques must be used.

As evident from the pattern in Fig. 5, the RCS of a large, complex target is a rapidly varying function of angle. However, as complicated as it looks, isolated features of the pattern shape and level can be associated with the behavior of the currents induced in and on the scattering body. For example, the high narrow spikes result from mirrorlike specular reflections from large flat surfaces. Other lobes can be associated with surface waves, multiple reflections, diffraction, and so on. These so-called scattering mechanisms are depicted in Fig. 6.

The lines in the figure are ray representations for propagating waves. They denote the direction of power flow and are normal to the planes of constant phase.

For any particular aspect angle, frequency, and polarization, if one scattering mechanism dominates over all others, then it may be possible to express the total scattered field as a combination of scattered fields E_{s1} , E_{s2} , E_{s3} , ..., each due to a separate scattering mechanism:

$$E_s \approx E_{s1} + E_{s2} + E_{s3} + \dots$$

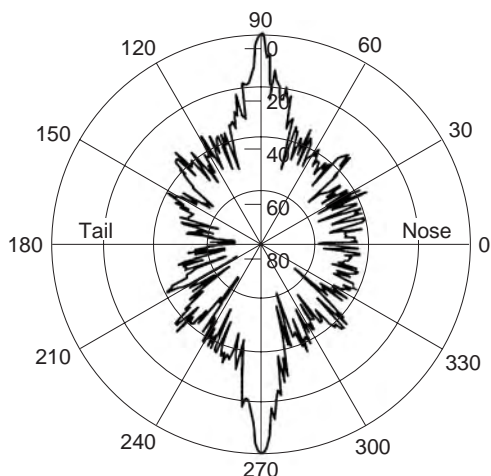


Figure 5. An azimuth plot of the RCS of the aircraft in Fig. 4 is shown. The two large lobes are due to the fuselage, which is modeled as a cylinder.

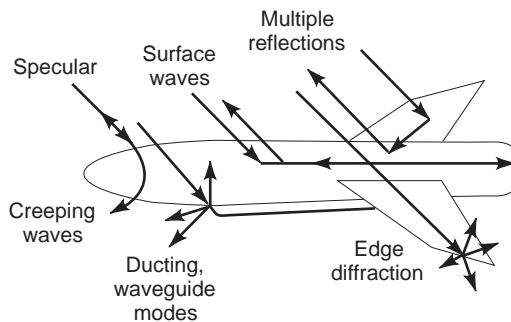


Figure 6. The total RCS of a target can often be decomposed into a sum of contributions from distinct scattering mechanisms. Some important mechanisms for electrically large targets are depicted in this figure.

and if one of these terms is much greater than all others, then

$$|E_s|^2 \approx |E_{s1}|^2 + |E_{s2}|^2 + |E_{s3}|^2 + \dots$$

It follows from Eq. (1) that the total RCS can be written as a sum of RCSs, each attributed to a separate scattering mechanism:

$$\sigma \approx \sigma_{s1} + \sigma_{s2} + \sigma_{s3} + \dots \tag{5}$$

Note that Eq. (5) is a convenient way of decomposing the scattered field for the purpose of assisting the RCS modeling and reduction efforts. First, if sufficiently accurate models exist for the individual scattering mechanisms, then Eq. (3) suggests that they can be combined under the appropriate circumstances to model their collective effects for a complex target. Second, since the largest terms in Eq. (3) correspond to the source of the most intense scattering, it may be possible to determine which scattering mechanism dominates, and thereby choose an appropriate reduction technique.

3.1. Reflection

This is the mechanism that yields the highest RCS peaks, but they are limited in number because Snell's law must be satisfied. When multiple surfaces are present, multiple reflections are possible. For instance, the incident plane wave could reflect off of the fuselage of an aircraft, hit a fin, and then return to the radar.

3.2. Diffraction

Diffracted fields are those scattered from discontinuities such as edges, corners, and vertices. The waves that are diffracted from these shapes are less intense than reflected waves, but they can emerge over a wide range of angles. At aspects requiring low RCS, the diffracted waves can be significant.

3.3. Surface Waves

The term *surface wave* refers to the current traveling along a body and includes several types of waves [7]. In general, the target acts as a transmission line, guiding the

wave along its surface. If the surface is a smooth closed shape such as a sphere, the wave can circulate around the body many times. Such waves are called *creeping* waves because they appear to creep around the back of a curved body. On curved bodies the surface wave continuously radiates. Radiating surface waves on flat bodies are usually called *leaky waves*. *Traveling waves* appear on slender bodies and along edges, and suffer little attenuation as they propagate [8]. If the surface is terminated with a discontinuity such as an edge, the traveling wave will be reflected back along the surface and radiate toward its origin.

3.4. Ducting

Also called waveguide modes, ducting occurs when a wave is trapped in a partially closed structure. An example is an air inlet cavity on a jet. Once the wave enters the cavity, many bounces can occur before a ray emerges. There are many paths that the ray can take, and therefore rays emerge at almost all angles. The result is a large, broad monostatic RCS lobe. An optical analogy of this is the glowing of a cat's eye when it is illuminated by a light.

3.5. Interactions

It is possible that these mechanisms will interact with each other. For example, a wave reflected from a flat surface can subsequently be diffracted from an edge or enter a cavity. For a complex target the interactions are not always obvious and the decomposition of the scattered field no longer makes sense.

4. PREDICTION METHODS

The analytical methods used to calculate RCSs are similar to those used in antenna analysis. A radar target is essentially acting as an antenna. The incident wave induces a current on the target, and the induced current radiates a field just as an antenna would. However, in the radar case it is called a scattered field as opposed to a radiated field. A good example is a reflector antenna or "satellite dish." The incident field from a feed horn excites currents on the reflector, which in turn give rise to a radiated field. In the radar analogy, the feed horn represents the radar's transmit antenna, while the reflector is the target. If the distribution of current is known for a target, then the currents can be used in the radiation integrals (Stratton–Chu integrals) to determine the scattered field. Once the scattered field is known, the RCS can be computed.

Of course, the problem is that the induced current on the target is unknown and generally very difficult to determine. An analytical solution is possible in only a few simple cases. In other cases it is feasible to solve Maxwell's equations or integral equations for the current numerically. These solutions are rigorous in that there are no assumptions or restrictions imposed. The only error in the solution is due to the numerical evaluation of the integral or differential equations. The alternative to a numerical solution is to take an intuitive guess at

the current, in which case the resulting RCS is only approximate.

Several methods of RCS prediction are described below. The classical solution techniques are not discussed in this list, because most are limited to one- or two-dimensional structures or simple three dimensional ones. The methods of interest here are those that can be applied to complex three-dimensional targets. The methods most commonly encountered are physical optics, microwave optics (ray tracing), the method of moments, and finite-difference methods.

4.1. Physical Optics

The physical optics (PO) approximation [9] provides a means of estimating the surface current induced on an arbitrary body. On the portions of the body that are directly illuminated by the incident field, the induced current is simply proportional to the incident magnetic field intensity. On the shadowed portion of the target the current is assumed to be zero. The current is then used in the radiation integrals to compute the scattered field far from the target.

PO is a high-frequency approximation that gives best results for electrically large bodies ($L \geq 10\lambda$). It is most accurate in the specular direction. Since PO assumes that the current abruptly decays to zero at a shadow boundary, the computed field values at angles far from the specular directions and in the shadow regions are inaccurate. Furthermore, surface waves are not included. PO can be used in either the time or the frequency domain. It can be supplemented by the physical theory of diffraction (PTD), which provides corrections to PO approximation that improve the accuracy of the current distribution near edges.

4.2. Microwave Optics

Microwave optics refers to a collection of ray-tracing methods that can be used to analyze electrically large targets of arbitrary shape. The rules for ray tracing in a simple medium (linear, homogeneous, and isotropic) are similar to reflection and refraction in optics. Geometric optics (GO) [10] is the classical theory of ray tracing used since the days of Newton. It provides a formula for computing the reflected and refracted fields. In addition, the geometric theory of diffraction (GTD) is used in conjunction with GO to include diffraction. Diffracted rays originate from the scattering of the incident wave at edges, corners, and vertices. The formulas are derived on the basis of infinite frequency ($\lambda \rightarrow \infty$), which implies an electrically large target. Ray optics is frequently used in situations that severely violate this restriction and still yields surprisingly good results. The major disadvantage of ray tracing is the bookkeeping required for a complex target. It is used primarily in the frequency domain.

4.3. Method of Moments

The method of moments (MM) is a technique used to solve an integral equation [11]. Integral equations are so named because the unknown quantity appears in an integrand.

In electromagnetics they are derived from Maxwell's equations and the boundary conditions. The unknown quantity can be a combination of volume or surface current (either electric or magnetic). The MM reduces the integral equations to a set of simultaneous linear equations that can be solved using standard matrix algebra. The size of the matrix involved depends on the size of the body; current computer capabilities allow bodies on the order of 10 or 20 wavelengths to be modeled.

Most MM formulations require a discretization (segmentation) of the body. Therefore, they are compatible with finite-element methods used in structural engineering, and the two are frequently used in tandem during the design of a platform. The MM can be used to solve both time- and frequency-domain integral equations.

4.4. Finite-Difference Methods

Finite differences are used to approximate the differential operators in Maxwell's equations in either the time or the frequency domain [5,6]. As with the MM technique, the target and surrounding space must be discretized. Maxwell's equations and the boundary conditions are enforced on the surface of the target and at the boundaries of the discretization cells. This method has found extensive use in computing the transient response of targets to various waveforms. Finite-difference methods do not require the large matrices that the MM does, because the solution is stepped in time throughout the scattering body.

5. REDUCTION OF RADAR CROSS SECTIONS

RCS reduction techniques are traditionally classified as geometric shaping, materials selection, and passive and active cancellation. The boundaries between these categories are not always distinct, and a reduction approach may draw on all of these simultaneously.

5.1. Shaping

Target shaping is the first step in RCS reduction. The first rule of shaping is to avoid presenting large flat surfaces to the radar. For large surfaces specular reflection is the dominant scattering mechanism. The direction of strongest reflection for a smooth surface is given by the law of reflection. Therefore, by examining the relationship between the direction of incidence and the surface normal, the direction of maximum scattering can be predicted. If a target is composed of several surfaces and one could visualize a plot of the normals of the surfaces, then it is expected that there would be few normals pointed in directions of low RCS.

It will be shown that the maximum monostatic RCS of a large flat surface occurs when the incident wave and observer are located normal to the surface. The maximum value is

$$\sigma_m = \frac{4\pi A^2}{\lambda^2} \quad (6)$$

where A is the area of the surface. Thus the RCS can be minimized by minimizing the area presented to the radar.

If it is not possible to tilt a large surface sufficiently, then it can be broken into a number of smaller surfaces, each tilted in a slightly different direction.

These approaches have led to rather unconventional aircraft shapes such as that of the F-117 Nighthawk (commonly referred to as the "Stealth Fighter") [12]. To date, shaping has not been applied extensively to ships and ground vehicles, although that is beginning to be done. Modern ship designs are making some concessions to RCS control, such as canting deckhouse walls and enclosing mast structures.

Another aspect of shaping is edge alignment. Once the specular reflections have been controlled, the contributions from edges (such as traveling waves and diffraction) may become important. Aligning edges is one way of maintaining low-RCS spatial sectors. For example, in plan form it is seen that the edges of the B2 bomber fall along only a couple of fixed angles.

The second rule of shaping is to avoid or hide retroreflectors. Retroreflectors are simple geometric structures that tend to redirect the incident radar wave back in the direction from which it arrives. Surfaces that meet at a 90° angle are strong retroreflectors, and therefore the angles between the tail rudder and elevator surfaces of a stealthy aircraft are always canted. New designs such as the tailless McDonnell Douglas X-36 have no vertical surfaces at all.

Cavities are another type of retroreflector. They have a very broad scattering pattern. Thus jet intakes are often located above the wing or else employ an electromagnetic screen to prevent penetration by the incident wave.

Obviously there is a limit to the degree of shaping that can be incorporated while simultaneously meeting other operational requirements. For example, extreme shaping applied to an aircraft degrades its aerodynamic performance and control characteristics. Another disadvantage of low-RCS shapes is that they have slim profiles, which reduces the useful enclosed volume relative to a conventional shape.

5.2. Materials and Coatings

Obviously the material composition of a body affects its RCS. For example, a metal plate has a higher RCS than a glass plate. Similarly, a plastic aircraft body has a lower RCS than one with a metal skin. The electrical characteristics of a material are defined by its constitutive parameters [13]:

1. Permittivity, $\varepsilon = \varepsilon_0 \varepsilon_r = \varepsilon' - j\varepsilon''$ (F/m)
2. Permeability, $\mu = \mu_0 \mu_r = \mu' - j\mu''$ (H/m)
3. Conductivity, σ_c (Ω/m)

where ε_0 and μ_0 are the permittivity and permeability of free space. The imaginary parts are associated with dissipation (attenuation) of the fields in the medium.

The permittivity determines the fundamental relationship between the electric field intensity \mathbf{E} and flux density \mathbf{D} . For the vast majority of materials that occur in nature

one can write

$$\mathbf{D} = \boldsymbol{\varepsilon} \mathbf{E} \quad (7)$$

where the boldface $\boldsymbol{\varepsilon}$ denotes a matrix. Expanding Eq. (7) and explicitly including the spatial and frequency dependences gives

$$\begin{bmatrix} D_x \\ D_y \\ D_z \end{bmatrix} = \begin{bmatrix} \varepsilon_{xx}(x, y, z, f) & \varepsilon_{xy}(x, y, z, f) & \varepsilon_{xz}(x, y, z, f) \\ \varepsilon_{yx}(x, y, z, f) & \varepsilon_{yy}(x, y, z, f) & \varepsilon_{yz}(x, y, z, f) \\ \varepsilon_{zx}(x, y, z, f) & \varepsilon_{zy}(x, y, z, f) & \varepsilon_{zz}(x, y, z, f) \end{bmatrix} \begin{bmatrix} E_x \\ E_y \\ E_z \end{bmatrix} \quad (8)$$

Likewise, the permeability determines the fundamental relationship between the magnetic field intensity \mathbf{H} and magnetic flux density \mathbf{B} , which for most materials can be written as

$$\mathbf{B} = \boldsymbol{\mu} \mathbf{H}$$

or

$$\begin{bmatrix} B_x \\ B_y \\ B_z \end{bmatrix} = \begin{bmatrix} \mu_{xx}(x, y, z, f) & \mu_{xy}(x, y, z, f) & \mu_{xz}(x, y, z, f) \\ \mu_{yx}(x, y, z, f) & \mu_{yy}(x, y, z, f) & \mu_{yz}(x, y, z, f) \\ \mu_{zx}(x, y, z, f) & \mu_{zy}(x, y, z, f) & \mu_{zz}(x, y, z, f) \end{bmatrix} \begin{bmatrix} H_x \\ H_y \\ H_z \end{bmatrix} \quad (9)$$

The following special cases occur frequently:

1. *Isotropic.* The diagonal components of the permittivity and permeability matrices are equal, and the off-diagonal elements are zero; that is, $\varepsilon_{pp} = \varepsilon_r \varepsilon_0$ and $\mu_{pp} = \mu_r \mu_0$; $\varepsilon_{pq} = 0$ and $\mu_{pq} = 0$ if $p \neq q$ ($p, q = x, y, \text{ or } z$).
2. *Nondispersive.* The constitutive parameters are independent of frequency. Most materials exhibit some dispersion (frequency dependence) if the frequency change is great enough. However, we define a nondispersive material as one whose ε_r and μ_r are sufficiently constant within the frequency band of the radar illuminating the material.
3. *Homogeneous.* The constitutive parameters are independent of location in the material. Almost all materials are inhomogeneous on a microscopic scale. For our purpose a homogeneous material is one that has a sufficiently small variation in ε_r and μ_r throughout its volume.

To examine the dependence of the RCS on the constitutive parameters, consider an infinite interface between free space and a half-space of material with ε_r and μ_r . The Fresnel reflection coefficient for a plane wave normally incident on the interface is

$$\Gamma = \frac{\eta - \eta_0}{\eta + \eta_0} \quad (10)$$

where the intrinsic impedances are defined by

$$\eta_0 = \sqrt{\frac{\mu_0}{\varepsilon_0}}$$

and

$$\eta = \sqrt{\frac{\mu_r \mu_0}{\varepsilon_r \varepsilon_0}} = \eta_0 \sqrt{\frac{\mu_r}{\varepsilon_r}}$$

From Eq. (1) the RCS is proportional to the square of the scattered electric field intensity. Since the scattered field intensity (in this case the reflected field) is proportional to Γ , it follows that $\sigma \propto |\Gamma|^2$. Thus the RCS will be reduced in direct proportion to the reduction in reflection coefficient squared. This is an ideal limit, because in practice the material thickness is finite, and there will likely be some reflection from its back face and scattering from its edges.

Unfortunately, in most applications the target materials cannot be selected solely on the basis of the electromagnetic properties ε_r and μ_r . Mechanical properties such as strength, weight, and thermal conductivity have a higher priority. In the drive to reduce weight and increase strength, composite materials have found widespread military and civilian application [14].

Composites are formed from multiple constitutive materials in a manner that yields a final product having desirable properties from each material. Graphite is an example of a composite that is used extensively in the aircraft industry. Although the primary motivation for the use of composites has been structural, the reflection from most composite materials is lower than that for conductors. However, the majority of the incident field that is not reflected from the composite's surface is transmitted through the material, and the transmitted field can potentially be scattered from internal metallic objects. The use of nonconductors also complicates other electrical design issues such as the grounding of electrical systems and lightning protection.

An absorbing layer is another example of the application of materials for RCS reduction. A layer of absorbing material is deposited on the surface of the target. As the incident wave propagates through the material, energy is extracted from the field and its intensity diminishes [15]. Thus a weaker field is reflected at the target surface, and the reflected wave is attenuated further as it travels back through the material. The circuit analog of this type of material is a resistor.

A material that performs the function just described is referred to as a radar absorbing material (RAM). High absorption is desired, yet the material thickness and weight must be minimized. Unfortunately, many materials with high loss also have high reflection coefficients. Thus there is significant reflection of the incident wave at the absorbing-layer face, and little energy enters the material where attenuation takes place.

There are some materials that possess more complicated or exotic electromagnetic properties that can potentially be exploited for RCS reduction. For example, since the ε_{pq} affect the velocity of propagation along the coordinate axes of the material, it may be possible to construct $\boldsymbol{\varepsilon}$ for a material so that the polarization of the scattered field is different from that of the incident field. Thus the polarization of a wave rotates as it propagates through the medium, and scattered energy is converted to a field component that the radar is not capable of sensing.

Another example is a spatially dispersive medium. The electric flux density depends on both the electric field intensity and the magnetic flux density. A *chiral* material [16] has the constitutive relationship

$$\mathbf{D} = \epsilon \mathbf{E} + j\zeta \mathbf{B}$$

This type of behavior is associated with materials that have a helical molecular structure. It is possible to produce this type of behavior artificially by dispersing small helical coils throughout a bulk material.

In the past, the reduction of RCSs has focused on treating each scattering source, or hotspot, individually. For instance, an absorbing layer might be installed to reduce scattering from a wing edge. The layer will reduce the edge scattering, but will also introduce new scattering sources at the perimeter. For a useful reduction method, the new scattering sources must be much weaker than those of the original edge. But as the scattering intensities of the sources become smaller, one quickly reaches the point where the new scattering sources introduced by the treatments are comparable to those being treated. At this level the interaction between scatterers becomes important, and this complicates the design and application of RCS treatments.

5.3. Cancellation Techniques

Cancellation refers to RCS reduction methods that are based on the introduction of a secondary scatterer whose scattered field is adjusted to cancel the reflection of the primary target [17,18]. The total field at the radar receiver is the vector sum of the fields scattered by the target and the cancellation element. Therefore, if the cancellation field can be made equal and opposite to the field scattered from the body at the angle, polarization, and frequency of interest, then destructive interference occurs. The secondary scatterer is referred to as the *cancellation element*, and its scattered field the *cancellation field*.

The cancellation element can be a detached body located near the original target, or an attached protrusion. Both are referred to as *parasitic* elements. The combination of the target with the scattering element is frequently called the *loaded body*. If the cancellation field is fixed, then the system is a *passive* one. On the other hand, if the system can respond to changes in the incident field, then it is an *active* one. A fair amount of information about the radar and the target is required for an active system: the threat radar frequency, its direction and polarization, and the target's RCS in the direction of the radar.

5.3.1. Passive Cancellation. Since the cancellation of the two fields is essentially a tuning method, this technique is only effective over a narrow frequency band and usually limited to a small spatial sector. If large parasitic elements are to be avoided, then the magnitude of RCS that can be canceled is small. Thus passive cancellation is usually used to supplement shaping and absorbers.

The most common cancellation elements are slots and wires. Two orthogonal elements are required to cancel an incident wave of arbitrary polarization. The elements can

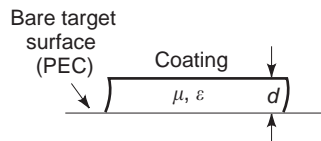


Figure 7. A Dallenbach layer is used to reduce the RCS of a conductor. The material electrical characteristics and thickness are chosen to provide a reflection coefficient of zero.

be increased in size or number so as to provide sufficient gain to cancel the RCS in the direction of interest.

Two examples of passive cancellation are the Salisbury screen and Dallenbach layer [19]. A Salisbury screen consists of a resistive film located a distance d in front of the target surface. The film resistivity is chosen so that the reflection from its surface is exactly canceled by the field that passes through the film, is reflected from the target, and then is transmitted back through the film.

The Dallenbach layer shown in Fig. 7 is similar to the RAM coating discussed earlier, except that the layer thickness is chosen to provide destructive interference between the fields scattered from the top of the layer and the boundary at the back of the layer, rather than absorption within it. Thus the top of the layer serves the same purpose as the resistive film does for the Salisbury screen.

5.3.2. Active Cancellation. Active cancellation (also known as adaptive cancellation) is the extension of passive cancellation to handle dynamic threat scenarios. In the context used here, it does not include *deception*, which comprises techniques of modifying and retransmitting a signal. For the present discussion, the source of RF energy is the radar's signal. Two levels of sophistication are considered:

1. *Fully Active.* The cancellation network receives, amplifies, and retransmits the threat signal in such a way that it is out of phase with the static (skin) RCS of the target. The transmitted signal amplitude, phase, frequency, and polarization can be adjusted to compensate for changing threat parameters.
2. *Semiactive.* No amplification of the incident signal energy is provided by the cancellation network, but adjustable devices in the network allow the reradiated signal to compensate for limited changes in the radar signal parameters.

The demands for a fully active system are almost always so severe as to make it difficult to implement. It requires amplifiers and antennas that cover the anticipated threat angles, frequencies, incident power densities, and polarizations. A knowledge of the radar's direction is required, as well as the target's own RCS. A semiactive system is not as complicated with regard to hardware, but the use of adjustable devices still requires bias lines, controller units, and a computer with the appropriate databases.

Because of the growing importance of low-level scattering sources (in particular, manufacturing-induced errors that differ from platform to platform), adaptive cancellation techniques are receiving increased attention. Adaptive cancelers have the ability to modify the amplitude and phase of the new scattering source to compensate for changes in the original scattering source that may occur with frequency or observation angle. In principle, adaptive techniques are capable of adjusting to changing physical and electrical conditions brought on by exposure to the environment. However, cancellation is most effective when there are a small number of coherent scattering sources rather than a large number of random sources.

5.3.3. Treatments for Surface Waves. Surface waves, and in particular traveling waves, present a special challenge as far as RCS reduction is concerned [6]. The target acts as a combination of antenna and transmission line, collecting incident energy and guiding it along the surface. As depicted in Fig. 8, when a discontinuity (such as a termination) is encountered, the surface wave is reflected. As it propagates in the reverse direction, it loses energy by radiation. A dielectric-coated ground plane can support a surface wave for incident plane waves having a component of \mathbf{E} normal to the surface; a magnetic-coated ground plane can support a surface wave for incident plane waves having a component of \mathbf{H} normal to the surface.

The most common technique for treating surface-wave reflections that arise from surface discontinuities is one borrowed from transmission line theory: the use of transformer sections. Typically a quarter-wave matching section is appended to the termination of the surface, and the surface characteristics of the matching section are chosen to allow the wave to continue propagating in the forward direction, thereby eliminating the reflected field.

6. SPECIAL STEALTH ISSUES

To achieve and maintain low observability requires careful design, manufacturing and maintenance procedures to a level that may seem trivial to the nonspecialist. Instances of bird droppings, loose screws, and pebbles kicked up from the takeoff roll having resulted in increased RCS have been reported [12]. Some special stealth-related issues are discussed below.

6.1. Integration of Sensors and Sensor RCS

Active sensors that transmit energy, such as microwave and laser radars, need to have a low probability of inter-

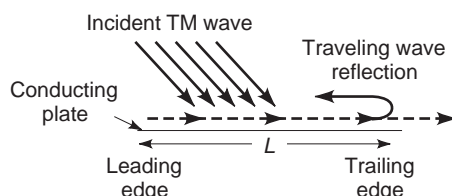


Figure 8. Traveling waves along a surface are treated using a transmission line matching method: the quarter-wave transformer.

cept (LPI). One aspect of LPI involves controlling the spatial distribution of radiation by using narrow antenna beams and low sidelobes. Another is to control the power distribution in the frequency spectrum, which is directly related to the transmitted waveform. For example, wide-bandwidth spread-spectrum pseudorandom waveforms distribute their power almost uniformly over a wide frequency band and hence appear like noise, making detection extremely difficult.

The RCSs of sensors installed on an LO platform, especially antennas in the radar frequency bands, are an area of concern. Unlike cavities, antennas cannot always be hidden from the radar's field of view without degrading the performance of the accompanying system. Ideally, if the incident wave frequency is in the operating band of the antenna (where the antenna is efficient), then its RCS is low because most of the incident wave is collected and appears at the antenna terminals.

The antenna scattering occurs when the frequency of the radar wave is outside the antenna's operating band. Large reflection sources may occur inside the antenna at frequencies out of its operating band, resulting in scattering characteristics similar to those of a cavity. Furthermore, if the antenna is composed of widely spaced (relative to wavelength) periodic elements, Bragg diffraction can occur. Bragg lobes are high-RCS spikes that result at multiple angles when the round trip path length differences between adjacent elements are an integer multiple of 2π . (This is similar to array grating lobes in the radiation case.)

The obvious antenna RCS reduction methods, such as adding lossy materials to attenuate out-of-band reflections, also decrease the antenna's gain in its operating band. The preferred approach is to incorporate a frequency-selective surface (FSS) into the design. An ideal FSS permits radiation in the antenna's frequency band to pass through unattenuated while all other frequencies are reflected or absorbed. FSS shielding has been applied to antennas on ship masts [20] and as missile radomes [21].

In the drive to reduce the number of low-level scattering sources, continuity of the platform external surface should be maintained. The number of apertures (openings) must be kept to a minimum. Apertures are needed for radar and communication antennas, which operate at microwave frequencies, and infrared and optical sensors. By integrating the infrared and optical sensors into the antennas, two or three apertures can be replaced by a single one.

6.2. Computational Advances

The need to predict the mutual interactions between many low-level scattering sources has fueled research in the area of computational electromagnetics (CEM). Numerical solutions of the rigorous equations of scattering from complex bodies have existed since the early 1960s. They involve reducing the electromagnetic equations to a set of simultaneous linear equations, which are solved by matrix methods. The dimension of the matrix increases as the size of the target measured in wavelengths increases (that is, all target dimensions are scaled by the

wavelength of the incident wave). It has only been in recent years that the dramatic increase in computer memory and speed has made this approach practicable for aircraft and ships. Even so, rigorous methods are still limited to low frequencies for targets that are physically large.

Approximate solutions have been developed based on the assumption that scattering is localized, so that interactions between distant parts of the structure can be neglected. The approximations have constantly been improved by adding higher-order corrections based on ever more detailed electromagnetic models as well as empirical data. Both the rigorous and the approximate computer models have incorporated geometry builders that can utilize computer-aided drawing (CAD) files generated by commercially available drawing programs. This capability allows for *concurrent engineering*—the ability to make a structural change and immediately assess its effect on the RCS.

6.3. Effect of Imperfections and Flaws

An important limitation in achieving low RCS is the imperfections introduced during the manufacture and assembly of the platform and the installation of its systems. Their effect on RCS performance depends on whether the imperfections are periodic or random in nature. Most error sources are nearly random, and their net effect on RCSs is to shift energy from the scattering mechanisms discussed previously to diffuse scattering. Diffuse surfaces reflect uniformly in all directions, independent of the angle of incidence; they are electrically rough surfaces. The magnitude of the diffuse scattering increases with the extent of the surface roughness (imperfection). Since diffuse scattering is not angle-dependent, shaping is not a practical way of reducing the RCS for it, and therefore very close tolerances must be maintained to keep the diffuse scattering to acceptable levels. Maintaining close tolerances is one of the primary cost drivers in the manufacture of LO platforms. Eventually a point is reached where the question must be asked: How much money is an additional RCS reduction of a few percent worth?

6.4. Maintenance and Testing

A second important cost driver is the maintenance of an LO platform. The natural elements, along with the harsh operating environment, stress and degrade the electrical and mechanical properties of materials. Special testing methods are required to determine if and when the RCS has been affected by exposure to the environment. So-called go-no-go tests compare a set of measured data from the platform under test with a reference dataset obtained from a known “clean” one of identical configuration. A significant deviation in the data sets would signify a correspondingly significant change in RCS. A test of this type does not require a high level of precision, and therefore can be conducted using portable test equipment. Data can be taken by probes located close to the platform surfaces, that is, in the near-field region of the scatterers.

If a platform fails the go-no-go check in the field, then it will be sent to a test and repair facility for further evaluation. Specialized facilities and repair techniques are required because of the uncommon materials involved and the exacting tolerances that must be satisfied. The integrity of localized repairs can be checked using hand-held reflection devices that verify local surface reflection characteristics.

6.5. Tradeoff between Stealth and Electronic Warfare

Low observability demands the most of technology and forces concessions in many other aspects of platform design and performance. At some point the burden of increasing stealth may become unacceptable. Electronic warfare (EW) techniques (now referred to as *electronic attack* and *electronic protect* in the United States) are a complement to low RCS. Common EW techniques currently in use around the world include jamming, decoys, and chaff [22]. The major disadvantage of EW is that the radar is aware of the target's presence. However, the radar is denied information on the target's range and velocity. Even though the radar is not completely disabled, a combination of EW and low RCS can cause the radar to lose lock, forcing it to reacquire a target repeatedly. This is a time-consuming process that ties up valuable radar resources. With all other factors constant, chaff, deception, and jamming are more effective for low-RCS targets than for conventional ones.

Some older platforms currently in the field are being retrofitted or upgraded to reduce the RCS and other signatures. All new aircraft, ships, and ground vehicles are incorporating some degree of stealth design and technology. However, it appears that the complete dominance of stealth in all aspects of design, as seen in the F-117, has been abandoned. Programs like the F-22, the Comanche helicopter, and the Euro-fighter are opting for a balance between stealth and other performance measures.

7. THE RADAR EQUATION

Consider the situation shown in Fig. 1 with the radar operating at a frequency f . The corresponding wavelength is $\lambda = c/f$, where $c \approx 2.998 \times 10^8$ m/s is the speed of light in free space. Define the following quantities:

- P_t = transmitter power delivered to the transmit antenna
- G_t = transmit antenna gain, a measure of how efficiently the antenna concentrates power in the direction of the target
- G_r = receive antenna gain
- A_{er} = effective area of the receive antenna, which can approach the physical area of the antenna aperture for a very efficient antenna

From antenna theory, antenna gain and effective area are related by

$$G_r = \frac{4\pi A_{er}}{\lambda^2} \quad (11)$$

The power scattered by the target that is delivered to the receive antenna terminals is given by

$$P_r \frac{P_t G_t}{4\pi R_t^2} \sigma \frac{1}{4\pi R_r^2} A_{er}$$

The first factor on the right-hand side is the power density incident on the target. Multiplying this factor by σ gives the fraction of incident power scattered in the direction of the receiver. The product of the first three factors represents the scattered power density at the receive antenna. Finally, multiplying by A_{er} gives the scattered power collected by the antenna.

Specializing to the monostatic case ($G_t = G_r \equiv G$ and $R_t = R_r \equiv R$) and using the relationship between effective area and gain give the result

$$P_r = \frac{P_t G^2 \sigma \lambda^2}{(4\pi)^3 R^4}$$

This form of the radar equation is too simple to be of practical use in predicting a radar's performance. However, two important features are evident. The first is the R^4 in the denominator, which is a disadvantage to the radar system designer, whose goal is to increase the detection range of the radar. The second is that the received power is linearly related to σ , which is a disadvantage to the RCS engineer.

If the minimum scattered power that the radar receiver can detect is P_m , then the corresponding maximum detection range is obtained by solving the radar equation for R :

$$R_m = \sqrt[4]{\frac{P_t G^2 \sigma \lambda^2}{(4\pi)^3 P_m}} \quad (12)$$

Therefore, to halve the maximum detection range requires that the RCS be reduced by a factor of $2^4 (= 16)$.

Finally, note that the radar equation was derived for a single-frequency wave. Typical radar waveforms, such as pulse trains, occupy a band of frequencies. The radar equation may have to be evaluated at several frequencies in the radar band if the quantities in the equation are not constant.

8. CALCULATION OF RADAR CROSS SECTION

RCS prediction methods can be broadly categorized as either rigorous or approximate. Rigorous methods are those that have been shown by mathematical proof to converge to the exact result under the appropriate conditions. However, in practice, there is always some small error present in the computed data due to the numerical evaluation of integrals, computer roundoff, and so on. Examples of rigorous methods are the finite-difference time domain (FDTD) technique and the MM.

Approximate formulations are based on assumptions and therefore are subject to limitations in their application and accuracy. Unlike the rigorous methods, even if there is no computational error, the approximate result

will not necessarily converge to the true result. If the approximation is a good one, then the error will not be significant for the problem under consideration. Examples of approximate methods are PO and microwave optics.

8.1. Phasors

Phasor notation is commonly used when working with time-harmonic fields. *Time-harmonic fields* are those that have a sinusoidal time variation of the form $\cos \omega t$, where $\omega = 2\pi f$. Since the sources and fields have the same time dependence, it can be factored out of all electromagnetic quantities and suppressed (i.e., dropped). When the calculations are completed, the time variation is reintroduced. Thus a time-varying quantity $\mathcal{E}(x, y, z, t)$ can be obtained from the phasor $\mathbf{E}(x, y, z)$ by multiplying the phasor by $e^{j\omega t}$ and taking the real part

$$\mathcal{E}(x, y, z, t) = \text{Re}[\mathbf{E}(x, y, z)e^{j\omega t}]$$

All quantities appearing throughout this article are phasors unless otherwise indicated.

8.2. Spherical and Plane Waves

Ideal spherical waves (i.e., waves for which the planes of constant phase are spheres) originate from point sources, which do not actually exist. However, for practical purposes, spherical wave behavior results if the observer is located "far enough" from an extended source as depicted in Fig. 1. Spherical waves have the phasor form

$$\mathbf{E}(r) = \mathbf{E}_0 \frac{e^{-j\beta r}}{r} \quad (13)$$

where r is the distance from the source. The vector constant \mathbf{E}_0 (which may have complex components) is determined by the amplitude, phase, and polarization of the extended source.

At great distances from the source ($r \rightarrow \infty$) the target only intercepts a small section of the spherical wavefront with a very large radius of curvature. Thus it appears that planes of constant phase exist over the extent of the target, and the electric field can be approximated by

$$\mathbf{E}(r) = \mathbf{E}_0 e^{-j\beta r}$$

where r is now the distance from the phase reference and \mathbf{E}_0 is determined from the intensity of the spherical wave at the target. If the source is at the origin of a spherical coordinate system, then \mathbf{E}_0 can only have $\hat{\theta}$ and $\hat{\phi}$ components in the far zone. (This would be the case for a radar antenna located at the origin.)

Both spherical and plane waves have the characteristics of a transverse electromagnetic (TEM) wave:

1. The electric and magnetic field vectors are perpendicular to each other and the direction of propagation.
2. The magnitudes of the electric and magnetic fields are related by the intrinsic impedance of free space.

Thus, if $\hat{\beta}$ is a unit vector in the direction of propagation, then

$$\mathbf{H} = \frac{\hat{\beta} \times \mathbf{E}}{\eta_0} \tag{14}$$

A plane wave of arbitrary polarization is given by the formula

$$\mathbf{E} = (E_{0\theta}\hat{\theta} + E_{0\phi}\hat{\phi})e^{-j\beta \cdot \mathbf{r}} \tag{15}$$

where \mathbf{r} is a position vector to the point x,y,z at which the field is to be evaluated:

$$\mathbf{r} = \hat{x}x + \hat{y}y + \hat{z}z$$

The corresponding magnetic field intensity for a plane wave propagating inward toward the origin ($\hat{\beta} = -\hat{\mathbf{r}}$) is

$$\mathbf{H} = -\frac{1}{\eta_0}(E_{0\theta}\hat{\phi} - E_{0\phi}\hat{\theta})e^{-j\beta \cdot \mathbf{r}} \tag{16}$$

The $\hat{\theta}$ component of the electric field is called *transverse magnetic to z* (TM_z) because the magnetic field vector associated with this component [$E_{0\theta}\hat{\phi}$ term in Eq. (16)] lies entirely in a plane transverse to the z axis. Similarly, the $\hat{\phi}$ component of the electric field is referred to as *transverse electric to z* (TE_z) because this component of the electric field [$E_{0\phi}\hat{\theta}$ term in Eq. (15)] lies entirely in a plane transverse to the z axis. Thus, for a TM_z-polarized plane wave $E_{0\phi} = 0$; for a TE_z-polarized plane wave $E_{0\theta} = 0$. Any arbitrary polarization can be expressed as a linear combination of the two. In a similar manner one could define TE_x, TM_y, and so on.

8.3. Radiation Integrals

Scattered fields are set up by a combination of electric and (in general) magnetic currents. Currents are induced such that the total fields satisfy the boundary conditions and Maxwell's equations. The radiation integrals provide a means of calculating the fields due to a prescribed set of currents. The radiation integrals, or Stratton–Chu integrals, are integral solutions to Maxwell's equations. They can be derived directly by taking the curl of Maxwell's first two equations, using the vector Green's theorem, and then integrating [23].

For RCS calculations, according to Eq. (1), only the scattered field far from the target is of interest, because $R \rightarrow \infty$. Consider a scattering body of volume V that is enclosed by a surface S as shown in Fig. 9. The standard convention is to denote observation point quantities by unprimed symbols, and source point quantities by primed symbols.

In the far zone, the following approximations are employed:

1. The vector from the origin to the observation point and the vector from any source point on S to the observation point are approximately parallel (\mathbf{R} parallel to \mathbf{r}).

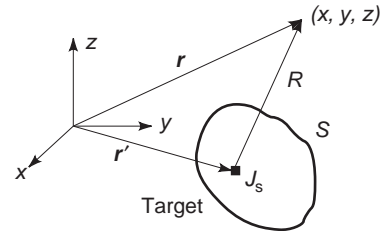


Figure 9. Current flows on the surface of a PEC. The total scattered field at the observation point is obtained by an integration of the current over the entire surface.

2. For large distances the difference in amplitude between a spherical wave emanating from the origin and one emanating from any point on the surface S is negligible ($1/R \approx 1/r$).

With these assumptions, the radiation integral for the electric field components tangential to a sphere of radius r centered at the origin can be expressed as

$$\begin{aligned} \mathbf{E}_{s\theta}(x,y,z) &= -\frac{j\beta\eta_0}{4\pi r} e^{-j\beta r} \iiint_V \left(\mathbf{J} \cdot \hat{\theta} + \frac{1}{\eta_0} \mathbf{M} \cdot \hat{\phi} \right) e^{-j\beta \hat{\mathbf{r}} \cdot \mathbf{r}'} \end{aligned} \tag{17a}$$

$$\begin{aligned} \mathbf{E}_{s\phi}(x,y,z) &= -\frac{j\beta\eta_0}{4\pi r} e^{-j\beta r} \iiint_V \left(\mathbf{J} \cdot \hat{\phi} - \frac{1}{\eta_0} \mathbf{M} \cdot \hat{\theta} \right) e^{-j\beta \hat{\mathbf{r}} \cdot \mathbf{r}'} \end{aligned} \tag{17b}$$

where \mathbf{J} (A/m²) and \mathbf{M} (V/m²) are the volume electric and magnetic currents, respectively. (Magnetic current is a fictitious quantity because isolated magnetic charge does not exist, but under some circumstances it is used as a matter of mathematical convenience.)

The use of volume current is advantageous for computing the scattered fields from highly inhomogeneous bodies. However, for most targets, it is more efficient to use a surface current formulation. As shown in Fig. 10, current flows on all interfaces between materials, as well as the external surface of the target. For surface currents, the

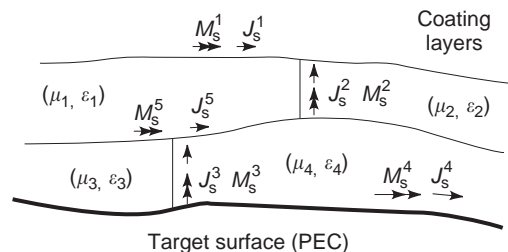


Figure 10. If a target is not a PEC, then volume currents may exist inside the target. The volume currents can be replaced by surface currents using the surface equivalence principle.

far-field form of the radiation integral becomes

$$\begin{aligned} \mathbf{E}_{s\theta}(x, y, z) &= -\frac{j\beta\eta_0}{4\pi r} e^{-j\beta r} \iint_S \left(\mathbf{J}_s \cdot \hat{\theta} + \frac{1}{\eta_0} \mathbf{M}_s \cdot \hat{\phi} \right) e^{-j\beta \hat{r} \cdot \mathbf{r}'} \quad (18a) \end{aligned}$$

$$\begin{aligned} \mathbf{E}_{s\phi}(x, y, z) &= -\frac{j\beta\eta_0}{4\pi r} e^{-j\beta r} \iint_S \left(\mathbf{J}_s \cdot \hat{\phi} - \frac{1}{\eta_0} \mathbf{M}_s \cdot \hat{\theta} \right) e^{-j\beta \hat{r} \cdot \mathbf{r}'} \quad (18b) \end{aligned}$$

where S includes all of the surfaces over which nonzero current exists. If the current is known, then the integrals in Eqs. (17) or (18) can be evaluated numerically.

If the scattering body is a perfect electrical conductor (PEC), then only electric current exists, and the surface of integration corresponds to a real physical surface. However, S in Eq. (18) need not exist; it can be a fictitious surface defined for convenience. The currents on the fictitious surface can be determined from the actual tangential electric and magnetic fields at every point on S . Thus

$$\mathbf{J}_S = \hat{\mathbf{n}} \times \mathbf{H} \quad (19a)$$

$$\mathbf{M}_S = \hat{\mathbf{n}} \times \mathbf{E} \quad (19b)$$

where $\hat{\mathbf{n}}$ is the unit vector normal to the surface. This is a consequence of the *equivalence principle* of electromagnetics [4].

8.4. Approximate Prediction Methods

Approximate prediction methods are used for a variety of reasons, but primarily because they are computationally less demanding, thereby allowing data to be generated more rapidly. This is an advantage in the early stages of design, when major tradeoff studies are being performed. Coarse approximations can be applied in the beginning, and then refined as the design progresses. Eventually it may be necessary to verify the performance of a specific design by a rigorous calculation.

At microwave frequencies, useful approximations should include scattering contributions from large surface areas, edges, surface waves, and interactions between and among surfaces and edges. There are two approaches to computing the RCS. One is based on estimating the induced currents and is referred to as a current-based approach: the PO approximation. The second is based on postulating relationships between the incident and scattered waves, or rays: GO. This is a ray-based approach.

PO and GO are used to calculate the scattered field from surfaces; the effects of the edges of surfaces are not

properly modeled or not included. Supplemental theories have been developed to allow for edge scattering. The PTD is the current-based method used in conjunction with PO. The GTD is a ray-based method for calculating diffracted fields. Both the current and ray approaches can be shown to yield identical results under the same conditions. Table 3 summarizes the two methods.

8.4.1. Physical Optics. A rigorous calculation of the currents \mathbf{J}_s and \mathbf{M}_s typically requires a great amount computational effort. The PO approximation is an estimate of the electric current that is accurate for a large, smooth PEC. The current is approximated by [9]

$$\mathbf{J}_s(x, y, z) = \begin{cases} 2\hat{\mathbf{n}}(x, y, z) \\ \quad \times \mathbf{H}_i(x, y, z) & \text{on the illuminated part of } S \\ 0 & \text{on the shadowed part of } S \end{cases} \quad (20)$$

where \mathbf{H}_i is the incident magnetic field intensity.

Equation (20) is explained by approximating the target surface in the vicinity of the point (x, y, z) by an infinite, flat surface. Assume that the incident wave is due to a source at a distance R and the electric field vector is parallel to the surface. By the method of images, the target can be removed and replaced by an equivalent scattering source at a distance R below the surface. To satisfy the boundary conditions (i.e., the tangential component of the total electric field must be zero) the electric field of the equivalent scattering source must be equal and opposite to that of the incident field. Because the two waves are propagating in opposite directions toward the surface, from Eq. (14) the magnetic field vectors will be oriented in the same direction; thus the factor of 2 in Eq. (20).

Perhaps the simplest application of the PO approximation is for a flat plate [6]. Let the plate be centered at the origin in the $z = 0$ plane and have dimensions of a in the x direction and b in the y direction. A plane wave of arbitrary polarization is incident at an angle θ_i . The PO approximation for the current is

$$\mathbf{J}_S \approx 2(\mathbf{J}_{0x}\hat{\mathbf{x}} + \mathbf{J}_{0y}\hat{\mathbf{y}}) \frac{e^{-j\beta \hat{\mathbf{r}}_i \cdot \mathbf{r}'}}{\eta_0} \quad (21)$$

where

$$J_{0x} = E_{0\theta} \cos \phi - E_{0\phi} \cos \theta \sin \phi$$

$$J_{0y} = E_{0\theta} \sin \phi + E_{0\phi} \cos \theta \cos \phi$$

and

$$-\hat{\mathbf{r}}_i \cdot \mathbf{r}' = u_i x + v_i y + w_i z$$

Table 3. Summary of Approximate Methods For RCS Prediction

Mechanism	Current-Based	Ray Optics-Based
Surface scattering	GO surface current—physical optics (PO)	Specular rays—geometric optics (GO)
Edge scattering	Fringe currents—physical theory of diffraction (PTD)	Diffracted rays—geometric theory of diffraction (GTD)
Surface waves	Interaction between fringe currents	Multiple diffractions between edges

The subscript “i” denotes incident wave quantities. The x , y , and direction cosines are defined by

$$u_i = \sin \theta_i \cos \phi_i \quad (22a)$$

$$v_i = \sin \theta_i \sin \phi_i \quad (22b)$$

$$w_i = \cos \theta_i \quad (22c)$$

Using Eq. (21) in (18a) and the fact that $z' = 0$ gives

$$\mathbf{E}_{s\theta} = \frac{-j\beta}{2\pi r} e^{-j\beta r} \hat{\boldsymbol{\theta}} \cdot (\mathbf{J}_{0x} \hat{\mathbf{x}} + \mathbf{J}_{0y} \hat{\mathbf{y}}) \int_{-a/2}^{a/2} \int_{-b/2}^{b/2} e^{j\beta(x'u_i + y'v_i)} e^{j\beta(x'u + y'v)} dx' dy' \quad (23)$$

For the monostatic RCS $u_i = u$ and $v_i = v$; therefore the exponents in the integrand can be combined. Furthermore, the x and y integrals can be separated, and both are of the form

$$\int_{-a/2}^{a/2} e^{j2\beta x'u} dx' = a \frac{\sin(\beta ua)}{\beta ua} \equiv a \operatorname{sinc}(\beta ua) \quad (24)$$

Now assume that a TM_z -polarized plane wave is incident ($E_{0\phi} = 0$) and the radar receive antenna is sensitive to the same polarization. Thus we use the notation $\sigma_{\theta\theta}$, where the first subscript denotes the polarization of the receiver and the second the polarization of the incident wave. Using Eqs. (23) and (24) in the definition of RCS yields

$$\sigma_{\theta\theta} = \frac{4\pi A^2}{\lambda^2} \operatorname{sinc}^2(\beta ua) \operatorname{sinc}^2(\beta vb) \cos^2 \theta \quad (25)$$

where $A = ab$ is the area of the plate.

The monostatic RCS of a square plate with $a = 5\lambda$ and $b = 2.5\lambda$ is shown in Fig. 11 for $\phi = 0^\circ$. The xz and yz planes are referred to as *principal planes*, because they are transverse to the plate edges. For comparison, the RCS obtained by a rigorous calculation of the current (MM) is also shown. (The MM result is converged and can therefore be considered exact.) The maxima of the $\operatorname{sinc}(\cdot)$

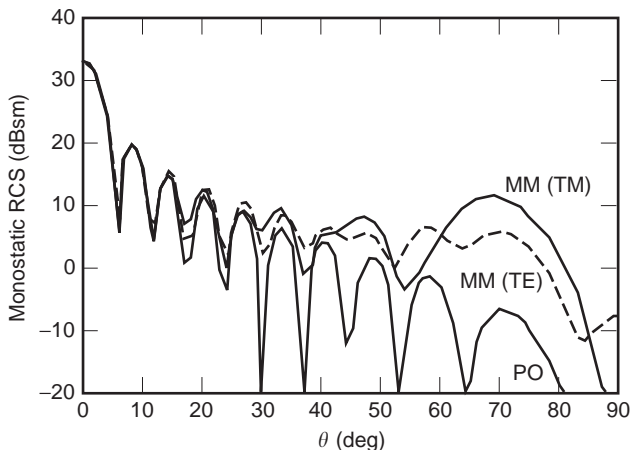


Figure 11. A comparison of the RCS of a plate with dimensions $a = 5\lambda$ and $b = 2.5\lambda$ in the plane $\phi = 0^\circ$. The approximate (PO) and rigorous (MM) methods are in close agreement in the region of the main lobe but disagree at wide angles.

functions in Eq. (25) occur at $\theta = \phi = 0^\circ$ and have values of 1. Thus the maximum value of the RCS is given by Eq. (6). As the dimensions of the plate in wavelengths increase, the width of the central lobe narrows. Note that the major difference between the two methods occurs at wide angles (near $\pm 90^\circ$). In this region the RCS is primarily determined by the current distribution near the plate edges, which is where the PO approximation fails.

8.4.2. Physical Theory of Diffraction. The PTD, also known as the method of edge waves (MEW), is a current-based approach to obtaining the edge scattered field [24]. The total current on a conductor with an edge can be decomposed into a PO component and a nonuniform (edge or fringe) component. If the fringe current is known, then the edge-scattered field can be computed by using this current in the radiation integral. The total field at an observation point is the sum of the PO and edge-scattered fields.

For a surface that is very large relative to the wavelength of the incident wave, the current distribution at a point near the edge is primarily determined by the local features of the geometry. If the edge is very long and the point under consideration is not close to the end of the edge, then the current is approximately the same as that for an infinitely long edge. Thus edge scattering can be considered a local phenomenon, and the current approximated by the current of the corresponding canonical scattering problem. (A canonical problem is one that has fundamentally the same geometry as the one under consideration, but whose solution is known.) If the total current can be determined for a canonical problem, in this case an infinite knife edge, then the PO component can be subtracted out and the result used as an estimate for the fringe current on a finite edge. The fringe currents are then used in the radiation integrals to obtain an edge-scattered field.

This approach has the advantage that the edge-scattered fields remain finite at shadow and reflection boundaries. However, the fringe currents extend a significant distance from the edge (a minimum of about 0.5λ), so that two-dimensional integrals must be evaluated. Michaeli has reduced the PTD fringe currents to filaments that flow along the body edge, thus reducing the integration to one dimension [25].

The electric and magnetic current filaments for a knife edge are given by

$$\begin{aligned} \mathbf{I}_e = & \frac{-2j}{\eta_0 \beta \sin^2 \gamma'} \frac{\sqrt{2} \sin(\phi'/2)}{\cos \phi' + \delta} [\sqrt{1 - \delta} - \sqrt{2} \cos(\phi'/2)] (\mathbf{E}_i)_{\tan} \\ & + \frac{2j}{\beta \sin \gamma' (\cos \phi' + \delta)} (\cot \gamma' \cos \phi' + \cos \phi \cot \gamma) \\ & + \sqrt{2} \cos(\phi'/2) \frac{\delta \cot \gamma' - \cot \gamma \cos \phi}{\sqrt{1 - \delta}} (\mathbf{H}_i)_{\tan} \end{aligned} \quad (26)$$

$$\mathbf{I}_m = \frac{2j\eta_0}{\beta \sin \gamma' \sin \gamma \cos \phi' + \delta} \left(1 - \frac{\sqrt{2} \cos(\phi'/2)}{\sqrt{1 - \delta}} \right) (\mathbf{H}_i)_{\tan} \quad (27)$$

where

$$\delta = \frac{\cos \gamma' \cos \gamma + \sin \gamma' \sin \gamma - \cos^2 \gamma'}{\sin^2 \gamma'}$$

The PTD is simple in principle, but can be inconvenient in practice. The currents in Eqs. (26) and (27) are a function of incidence angle, so for monostatic calculations the integrations must be performed again after each angle change. Another disadvantage is that modeling the fringe current interaction is difficult. On the plus side is that the edge-scattered field is simply added to the PO field. This is the major attraction of the PTD, since PO is so convenient and widely used.

8.4.3. Geometric Optics. GO is the theory of ray tracing that has been used for centuries to design systems of lenses such as telescopes. It works well at optical frequencies because the lens and mirror dimensions are much larger than a wavelength and thus the interaction of the wave with the lens becomes a localized phenomenon. The reflected ray appears to originate from a single point on the surface, called a specular or reflection point.

GO is the most basic theory that describes wave behavior on reflection or refraction at an interface between two materials [10]. GO is based on seven assumptions or postulates:

1. Waves are everywhere locally plane and TEM.
2. The wave direction is specified by the normal to the equiphase surfaces, that is, a ray. (Equiphase surfaces are also referred to as eikonal surfaces.)
3. Rays travel in straight lines in a homogeneous medium (Fermat's principle).
4. Polarization is constant along a ray.
5. At the reflection point, the reflected fields are linearly related to the incident fields by reflection coefficients.
6. Reflected rays satisfy the law of reflection.
7. Power in a tube of rays is conserved. The field strength is inversely proportional to the square root of the cross-sectional area of the flux tube.

Ray tubes are also called ray bundles or flux tubes. For a plane wave, all of the rays are parallel and therefore a bundle of rays has a constant cross section. However, for a spherical wave, a bundle of rays expands as the distance from the source increases. The power flowing through a slice of the bundle must be constant if the medium is lossless and power is conserved.

For the general scattering problem the incident wave front and scattering surface may have some curvature, as illustrated in Fig. 12. The local curvature at a point on a doubly curved surface, whether it is a wave front or target surface, can be expressed in terms of two principal radii of curvature. Let the incident wave front be characterized by the principal radii of curvature R_1^i and R_2^i . Similarly, let the scattering surface be characterized by the principal radii of curvature R_1^s and R_2^s . If these two sets of radii are

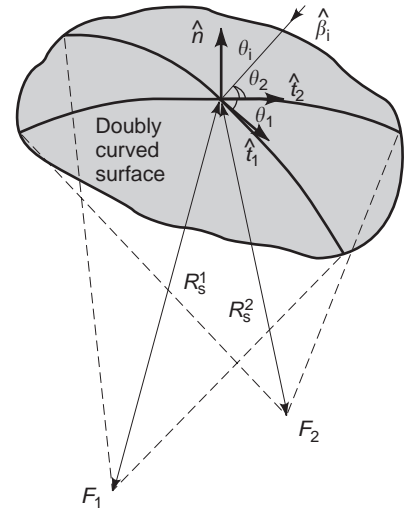


Figure 12. GO can be used to predict the reflected field from a doubly curved surface. The curvatures of the incident wave front and surface affect the curvature of the reflected wavefront.

known, then the radii of curvature of the reflected wavefront can be computed using the following equation

$$\frac{1}{R_{1,2}^r} = \frac{1}{2} \left(\frac{1}{R_1^i} + \frac{1}{R_2^i} \right) + \frac{1}{f_{1,2}} \quad (28)$$

where $f_{1,2}$ are the focal lengths in the two principal planes. (The focal length is another measure of curvature.) The focal lengths can be computed by [4]

$$\begin{aligned} \frac{1}{f_{1,2}} = \frac{1}{\cos \theta_i} & \left(\frac{\sin^2 \theta_2}{R_1^s} + \frac{\sin^2 \theta_1}{R_2^s} \right) \\ & \pm \left[\frac{1}{\cos^2 \theta_i} \left(\frac{\sin^2 \theta_2}{R_1^s} + \frac{\sin^2 \theta_1}{R_2^s} \right)^2 - \frac{4}{R_1^s R_2^s} \right]^{1/2} \end{aligned} \quad (29)$$

where the angles are given by

$$\theta_1 = \cos^{-1}(\hat{\mathbf{t}}_1 \cdot \hat{\boldsymbol{\beta}}_i) \quad (30a)$$

$$\theta_2 = \cos^{-1}(\hat{\mathbf{t}}_2 \cdot \hat{\boldsymbol{\beta}}_i) \quad (30b)$$

$$\theta_i = \cos^{-1}(\hat{\mathbf{n}} \cdot \hat{\boldsymbol{\beta}}_i) \quad (30c)$$

The vectors $\hat{\mathbf{t}}_1$ and $\hat{\mathbf{t}}_2$ are tangent to the surface at the reflection point and lie in principal planes 1 and 2, respectively.

The postulates allow the reflected field to be computed from the incident field at the reflection point by multiplying by a reflection coefficient. In matrix form

$$\mathbf{E}_r(s) = \mathbf{R} \cdot \mathbf{E}_i(s') \mathbf{A}(s) e^{-j\beta s} e^{j\phi_c} \quad (31)$$

where

$$\mathbf{E}_r(s) = \begin{bmatrix} E_{r\perp}(s) \\ E_{r\parallel}(s) \end{bmatrix} \quad (32)$$

$$\mathbf{E}_i(s') = \begin{bmatrix} E_{i\perp}(s') \\ E_{i\parallel}(s') \end{bmatrix} \quad (33)$$

and the reflection coefficient matrix is

$$\mathbf{R} = \begin{bmatrix} \Gamma_{\perp\perp} & \Gamma_{\perp\parallel} \\ \Gamma_{\parallel\perp} & \Gamma_{\parallel\parallel} \end{bmatrix} \quad (34)$$

The subscripts \parallel and \perp refer to a polarization where the electric field is parallel or perpendicular to the plane of incidence (the plane defined by the vectors $\hat{\mathbf{n}}$ and $\hat{\boldsymbol{\beta}}_i$).

The divergence and spreading factor for the reflected wave is

$$A(s) = \left(\frac{R_1^r R_2^r}{(R_1^r + s)(R_2^r + s)} \right)^{1/2} \quad (35)$$

The quantity s' is the distance from the source point S to the reflection point Q , and s is the distance along the reflected ray from the reflection point to the observation point P .

The last factor in Eq. (31) allows for phase transitions through caustics, which are points or lines at which the cross section of a ray tube is zero (and thus the power density is infinite); we have

$$\phi_c = \begin{cases} 0 & \text{if neither center of curvature lies between } Q \text{ and } P \\ \pi/2 & \text{if one center of curvature lies between } Q \text{ and } P \\ \pi & \text{if both centers of curvature lies between } Q \text{ and } P \end{cases} \quad (36)$$

A well-known formula for the RCS of a curved surface can be derived using the preceding formulas. The fact that for a plane wave $R_1^i = R_2^i = \infty$ and the observer is far from the target ($R_1^s, R_2^s \gg s$) yields the approximation

$$\sigma \approx \pi R_1^s R_2^s \quad (37)$$

Equation (37) has been widely applied to basic geometric shapes such as spheres and ellipsoids. Note that GO predicts zero field in shadow regions. That is, if the path between the source and observation points is blocked, then there is no received field.

8.4.4. Geometric Theory of Diffraction. GO provides a means of calculating the field reflected from a surface. The associated edge effects require a mathematical model for edge diffraction. The GTD is such a ray-based edge diffraction theory [26]. For the GTD, rays are hypothesized that obey diffraction laws similar to reflection laws. A diffraction coefficient is defined, which depends on the edge geometry and polarization of the incident wave. On diffraction, the scattered field is given by the incident field

times the diffraction coefficient. Furthermore, the diffracted wave follows prescribed straight-line paths in free space. The total field at an observation point is the vector sum of all the reflected and diffracted fields arriving at that point.

As first developed, the GTD had several shortcomings with regard to singularities in the field. Several modified versions of the GTD, such as the uniform theory of diffraction (UTD) [27] and the asymptotic theory of diffraction (ATD) [28], have eliminated the problems in many cases by introducing correction factors. In the following discussions GTD will refer to the collection of these diffraction theories.

The postulates of the GTD are similar to those of GO; only numbers 5 and 6 change:

5. At the diffraction point, the diffracted fields are linearly related to the incident fields by diffraction coefficients.
6. Diffracted rays emerge radially from the edge.

In addition, rays traversing a caustic encounter a phase advance of 90° ; an edge is always a caustic. At a focus there is a phase advance of 180° .

The behavior of diffracted rays from an infinite conducting wedge is illustrated in Fig. 13. The diffracted rays lie on the surface of a cone (referred to as the Keller cone) with its tip located at the diffraction point and axis along the edge. The cone half-angle γ is equal to the angle that the incident ray makes with the edge, γ' (a consequence of Fermat's principle). The coordinate variables (s, γ, ϕ) and (s', γ', ϕ') uniquely define the directions of diffraction (observation) and incidence (source), respectively.

In the light of postulate 5 the diffracted field from an edge can be written as

$$\mathbf{E}_d(s) = \mathbf{D} \cdot \mathbf{E}_i(s') A(s) e^{-j\beta s} \quad (38)$$

The vectors \mathbf{E}_d and \mathbf{E}_i have the same form as in Eqs. (32) and (33), except that parallel and perpendicular are defined relative to the edge rather than the plane of incidence. In Eq. (38) \mathbf{D} is a two-dimensional matrix of

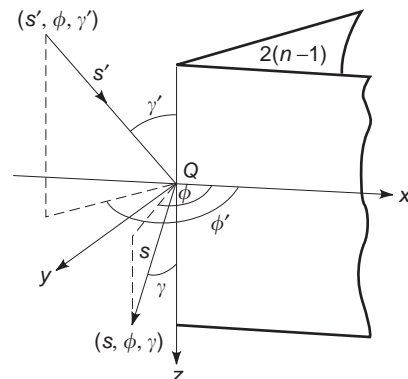


Figure 13. The GTD is used to predict edge diffracted fields. As long as the diffraction point is not near the end of the edge, the diffracted field is similar to that of an infinitely long edge.

diffraction coefficients

$$\mathbf{D} = \begin{bmatrix} D_{\perp\perp} & D_{\perp\parallel} \\ D_{\parallel\perp} & D_{\parallel\parallel} \end{bmatrix} \quad (39)$$

and the divergence and spreading factor is

$$A(s) = \left(\frac{\rho_c}{s(\rho_c + s)} \right)^{1/2} = \begin{cases} \frac{1}{\sqrt{s}}, & \text{plane waves} \\ \sqrt{\frac{s'}{s(s+s')}}}, & \text{spherical waves} \end{cases} \quad (40)$$

where ρ_c is the distance from the caustic.

The diffraction coefficients are derived from the appropriate canonical problem. The GO field is subtracted from the total scattered field. The difference is the diffracted field, which can be used to determine the elements of \mathbf{D} , given the known form of Eq. (36). For a knife edge the diffraction coefficients are

$$D_{\parallel,\perp} = \frac{e^{-j\pi/4}}{2\sqrt{2\pi\beta} \sin \gamma} \left(\frac{F(\beta\ell a(\phi^-))}{\cos \phi^-} \pm \frac{F(\beta\ell a(\phi^+))}{\cos \phi^+} \right) \quad (41)$$

where the transition function is

$$F(\xi) = j2|\sqrt{\xi}|e^{j\xi} \int_{|\sqrt{\xi}|}^{\infty} e^{-t^2} dt \quad (42)$$

with

$$\begin{aligned} \phi^\pm &= \phi \pm \phi' \\ \alpha(\phi^\pm) &= 2 \cos(\phi^\pm/2) \\ \ell &= \begin{cases} \frac{ss'}{s+s'} \sin^2 \gamma, & \text{spherical waves} \\ s \sin^2 \gamma, & \text{plane waves} \end{cases} \end{aligned} \quad (43)$$

In special cases where \mathbf{E}_d is tangent to the surface of a PEC, the surface diffracted ray is zero. For a rectangular plate, there will not be an interaction (higher-order diffraction) between the two parallel edges. In fact, there is an interaction between two edges of a parallel plate even when the electric field is parallel to the edge, and it is included by adding a slope diffraction term to Eq. (38)

$$\mathbf{E}_d(s) = \left(\mathbf{D} \cdot \mathbf{E}_i(\mathbf{Q}) + \mathbf{D}' \cdot \frac{\partial \mathbf{E}_i}{\partial n} \Big|_{\mathbf{Q}} \right) A(s) e^{-j\beta s} \quad (44)$$

where \mathbf{D}' is a matrix of slope diffraction coefficients.

8.5. Rigorous Methods

8.5.1. Method of Moments. The radiation integrals provide a means of calculating the scattered field from a target once the induced current on the surface is known. Except for the most simple shapes, the current distribu-

tion on the target is not known accurately. For electrically large bodies that are smooth and sufficiently flat, the PO approximation provides a good estimate at points far from discontinuities and shadow boundaries. By a discontinuity is meant any abrupt change in the surface contour or composition. Examples are edges, steps, cracks, and material joints.

In order to compute the current rigorously, an integral equation (IE) for the current can be formulated from Maxwell's equations and the boundary conditions. IEs have the unknown quantity in the integrand and possibly in other terms outside of the integral. In most problems of practical interest, the IE must be solved numerically using a computer. The most popular solution technique, called the *method of moments* (MM), consists in expanding the current into a series with unknown coefficients [11]. The expansion is inserted into the integral equation and a weighting process applied. The properties of the expansion functions are used to reduce the integral equation to a set of simultaneous linear equations that can be solved for the coefficients.

The *E*-field integral equation (EFIE) is the most commonly used. It can be derived by using the general form of the radiation integrals and placing the observation point on the surface of the body. [The general form of the radiation integrals does not make the assumption of a far-field observation point as in Eqs. (17) and (18).] If the target is a PEC, then $(\mathbf{E}_i + \mathbf{E}_s)_{\text{tan}} = 0$ on the surface. The incident field is known, and the radiation integrals give the scattered field in terms of the unknown surface current. Thus the following form of the EFIE is obtained:

$$\begin{aligned} \mathbf{E}_i(\mathbf{r})|_{\text{tan}} &= \iint_S (j\omega\mu_0 \mathbf{J}_s(\mathbf{r}') G(\mathbf{r}, \mathbf{r}')) \\ &\quad - \frac{j}{\omega\epsilon} [\nabla' \cdot \mathbf{J}_s(\mathbf{r}')][\nabla' G(\mathbf{r}')] \Big|_{\text{tan}} ds' \end{aligned} \quad (45)$$

where, as usual, primes denote source point quantities associated with the current and unprimed denotes observation point quantities. The free-space Green function is defined by

$$G(\mathbf{r}, \mathbf{r}') = \frac{e^{-j\beta R(\mathbf{r}, \mathbf{r}')}}{4\pi R(\mathbf{r}, \mathbf{r}')} \quad (46)$$

with

$$R(\mathbf{r}, \mathbf{r}') = \sqrt{(x-x')^2 + (y-y')^2 + (z-z')^2}$$

Equation (45) is reduced to a matrix equation using the MM. First the current is expanded into a series of basis functions $\{\mathbf{J}_n\}$ with unknown current coefficients $\{I_n\}$:

$$\mathbf{J}_s(\mathbf{r}') = \sum_{n=1}^N I_n \mathbf{J}_n(\mathbf{r}') \quad (47)$$

The basis functions are chosen to be mathematically convenient and adequately represent the current over

the surface. They are of two general types: (1) subdomain or (2) entire domain. In the subdomain case, each function is nonzero over only a part of the surface. On the other hand, each entire domain basis function is nonzero over the entire surface. Using a function of time as an analogy, it can be expressed as a series of sinusoids (Fourier series), which are an example of entire-domain basis functions. The time function could also be expressed as a series of steps (a “stair step” approximation), which is an example of subdomain basis functions.

Once the basis functions are chosen, Eq. (47) is inserted into Eq. (45) and a test is performed that involves multiplying by a set of weighting functions \mathbf{W}_n and integrating. Generally the complex conjugates of the basis functions are selected as the weighting functions (Galerkin’s method): $\mathbf{W}_n = \mathbf{J}_n^*$. This leads to N equations

$$V_m = \sum_{n=1}^N \iint_{S_m} Z_{mn} I_n, \quad m = 1, 2, \dots, N$$

which can be cast into the matrix form

$$\mathbf{V} = \mathbf{Z}\mathbf{I} \quad (48)$$

where

$$Z_{mn} = \iint_{S_m} \iint_{S_n} \{j\omega\mu_0 \mathbf{W}_m(\mathbf{r}) \cdot \mathbf{J}_n(\mathbf{r}') - \frac{j}{\omega\epsilon} [\nabla' \cdot \mathbf{J}_n(\mathbf{r}')] [\nabla' \cdot \mathbf{W}_m(\mathbf{r})] \} \times G(\mathbf{r}, \mathbf{r}') ds ds' \quad (49)$$

which is an impedance, and

$$V_m = \iint_{S_m} \mathbf{W}_m(\mathbf{r}) \cdot \mathbf{E}_i ds \quad (50)$$

which is a voltage. Thus Eq. (48) can be solved for \mathbf{I} , then used in Eq. (47), which in turn is used in the radiation integrals to obtain the scattered field.

A commonly encountered basis function is the triangular subdomain [29]. The surface of a target is represented by a collection of triangular facets. This type of subdomain has the flexibility to model curved surfaces with arbitrary edge contours. Each basis function is associated with an edge as shown in Fig. 14:

$$\mathbf{J}_n(\mathbf{r}') = \begin{cases} \frac{L_n \rho_n^+}{2A_n^+}, & \mathbf{r}' \text{ in } T_n^+ \\ \frac{L_n \rho_n^-}{2A_n^-}, & \mathbf{r}' \text{ in } T_n^- \end{cases} \quad (51)$$

The current at a point in a subdomain is the vector sum of the currents crossing all edges, weighted by the distance from the edge.

Using Eq. (51) in Eq. (49) gives

$$Z_{mn} = L_m \left(\frac{j\omega}{2} (A_{mn}^+ \cdot \rho_m^{c+} + A_{mn}^- \cdot \rho_m^{c-}) + \Phi_{mn}^- - \Phi_{mn}^+ \right)$$

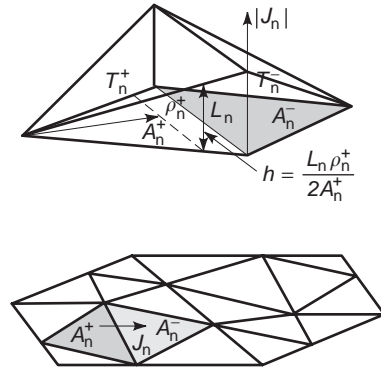


Figure 14. Any arbitrary-shaped surface can be represented by triangular facets. Triangular (rooftop) basis functions span each edge. The total current is a superposition of all of the basis functions at a point.

where

$$A_{mn}^\pm = \frac{\mu_0}{4\pi} \iint_{S_n} \mathbf{J}_n(\mathbf{r}') \frac{e^{-j\beta R_{mn}^\pm}}{R_{mn}^\pm} ds'$$

$$\Phi_{mn}^\pm = \frac{j}{4\pi\omega\epsilon_0} \iint_{S_n} \nabla' \cdot \mathbf{J}_n(\mathbf{r}') \frac{e^{-j\beta R_{mn}^\pm}}{R_{mn}^\pm} ds'$$

$$R_{mn}^\pm = |\mathbf{r}_{mn}^{c\pm} - \mathbf{r}'|$$

The excitation vector elements are

$$V_m = L_m (\mathbf{E}_m^+ \cdot \rho_m^{c+} + \mathbf{E}_m^- \cdot \rho_m^{c-})$$

where the electric field at the centroid of the facet is

$$\mathbf{E}_m^\pm = \mathbf{E}_i(\mathbf{r}_m^{c\pm})$$

These basis functions result in a linear approximation to the current over each facet. The rigorous result for the rectangular plate shown in Fig. 11 was computed using the method of moments.

There are a few instances when other basis functions may be more efficient than triangular subdomains. For example, consider a body of revolution (BoR), which is generated by rotating a plane curve around an axis. Included in this class are cylinders, cones, spheres, and ellipsoids. A hybrid basis function, that is, a combination of entire-domain and subdomain basis functions, is an efficient alternative to triangular facets [30]. In these cases overlapping triangular basis functions can be used to represent the current along the generating curve axis, while entire-domain complex exponentials are used in the azimuthal direction (around the circumference of the body). The result is a linear approximation to the current in the axial direction (from back to front) and a Fourier series representation for the current around the body. The major advantage of this approach is that each Fourier mode, which is actually a matrix whose size is determined by the number of subdomains along the axis, is independent of all other modes. Thus a large-matrix problem is decomposed into a series of smaller matrices, thereby

permitting larger bodies to be modeled for a given computer resource.

8.6. Hybrid Methods

Hybrid computation methods combine several prediction techniques in a single solution [31,32]. A hybrid solution decomposes a problem into subproblems, which are solved using different techniques. Generally the mutual effects (interaction between the subproblems) are included to some degree. For example, PO is known to give excellent results for large smooth surfaces away from edges and discontinuities. A hybrid approach might use PO on regions of the surface away from discontinuities and the MM near discontinuities. Larger problems can be modeled than with a pure MM approach, and more accuracy is achieved than using PO separately. The disadvantage is that each hybrid combination is tailored for a specific type of problem and therefore may not yield accurate results under all conditions.

One hybrid method that is used extensively in RCS calculation for large targets at high frequencies is the shooting and bouncing ray (SBR) technique [33]. It combines GO and PO, and can be supplemented by the PTD. Current distributions are determined from the trajectories of rays in a dense bundle. The current distributions can be used to:

1. Initiate secondary rays to evaluate multiple reflections
2. Compute PTD fringe currents for edge diffraction contributions
3. Compute the far scattered fields

Currently this technique is the most accurate and flexible for computing the RCSs of large complex targets such as aircraft with engine inlets and cockpits.

8.7. Surface Impedance Approximation

The *impedance boundary* is an approximate boundary condition that can be used to replace a surface composed of multiple materials and layers by a single surface. It was first proposed by Leontovich [34] and is frequently referred to as the Leontovich boundary condition. The concept is illustrated in Fig. 15, which shows the use of a surface current approach to calculate the scattered field from a target composed of several materials.

The possibility of surface currents flowing on all of the interfaces dramatically increases the mathematical and computational complexity of the problem over that of a single surface. In many cases it may be sufficient to replace the collection of surfaces with a single layer that has approximately the same external scattering properties as the combination of original surfaces. (For the RCS the fields inside the body are not of interest.) The same scattering properties for the original and equivalent problems are ensured if the boundary conditions on the tangential field components are the same. The required relationship between the electric and magnetic fields is referred to as a *surface impedance approximation*.

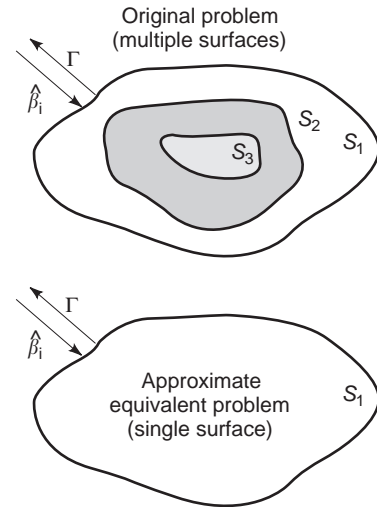


Figure 15. A complex multilayered target can be replaced by an equivalent target having the same surface contour but an equivalent surface impedance.

Mathematically it relates the tangential components of the electric and magnetic fields at every point on the surface:

$$\eta_s = \frac{|\mathbf{E}_{\text{tan}}|}{|\mathbf{H}_{\text{tan}}|} \quad (52)$$

where η_s is the surface impedance in ohms. In vector form

$$\eta_s \hat{\mathbf{n}} \times \mathbf{H} = \mathbf{E} - (\hat{\mathbf{n}} \cdot \mathbf{E}) \hat{\mathbf{n}} = \eta_s \mathbf{J}_s \quad (53)$$

There is a dual to this equation:

$$-\frac{1}{\eta_s} \hat{\mathbf{n}} \times \mathbf{E} = \mathbf{H} - (\hat{\mathbf{n}} \cdot \mathbf{H}) \hat{\mathbf{n}} = \frac{1}{\eta_s} \mathbf{M}_s \quad (54)$$

Comparing Eqs. (53) and (54) reveals that the surface impedance relates the electric and magnetic currents at every point on the surface:

$$\mathbf{M}_s = -\eta_s \hat{\mathbf{n}} \times \mathbf{J}_s \quad (55)$$

Note that $\eta_s = 0$ corresponds to a PEC, and the resulting reflection coefficient for a wave normally incident on the PEC is

$$\Gamma = \frac{\eta_s - \eta_0}{\eta_s + \eta_0} = -1 \quad (56)$$

The surface impedance approximation is most accurate when

1. The surface is electrically large and the incident wave is near normal incidence to the surface ($\theta_i \approx 0^\circ$).
2. The relative dielectric constant of the material is high ($\sqrt{\epsilon_r} \gg 1$).
3. The local radius of curvature of the surface is large compared to a wavelength.

Impedance boundary conditions can be used to derive integral equations (35) or to simplify an approximate solution. They are widely used in spite of the fact that they usually cannot be justified rigorously.

An estimate of the surface impedance can be obtained from the permittivities and permeabilities of the constituent materials. For layers, a transmission-line model can be used to compute the reflection coefficient at the outer surface, and then Eq. (56) solved for η_s . Using this approach, η_s is a function of the angle of incidence because the Fresnel reflection coefficients are angle-dependent. Generally an average value near normal incidence is used, because it is near the local normal that each region of the surface makes its greatest contribution to the RCS.

A second set of approximate boundary conditions are used to represent thin films [36]. They are the resistive sheet and conductive sheet boundary conditions, which provide a relationship between the currents on the surface and the tangential field components. A resistive sheet is an infinitely thin imperfect electric conductor (finite conductivity), and it does not support a magnetic current, namely

$$\mathbf{E}_{\text{tan}} = \mathbf{J}_s R_s \quad (57)$$

where R_s is the surface resistivity in ohms per square. The limiting cases are $R_s = 0$ for a PEC and $R_s = \infty$ for a perfectly transparent sheet. The reflection coefficient of the sheet is

$$\Gamma = \frac{-\eta_0}{2R_s + \eta_0} \quad (58)$$

Resistive films are an effective means of controlling the reflection coefficient of a surface. They consist of thin metallic deposits on low-dielectric films such as Mylar. A common example of a commercially available resistive film is window tinting of the type used for automobiles.

The dual of the resistive sheet is the *conductive sheet*, with the boundary condition

$$\mathbf{M}_s = -\frac{\mathbf{H}_{\text{tan}}}{G_s} \quad (59)$$

where G_s is the surface conductance. The conductive sheet does not support an electric current. A combination of resistive and conductive sheets can be viewed as an *impedance sheet*.

Figure 16 compares the RCSs of PEC and composite aircraft wings. The RCS of the composite wing is significantly reduced because more of the wave is transmitted and less reflected.

8.8. Rough Surfaces

Imperfections and errors in the assembly and manufacturing processes have a significant effect on the low-level RCS. The sources of errors are variations in the physical dimensions and electrical characteristics of the target materials. Most of the errors behave in a random fashion. Random deviations in the characteristics of a target result in an increase in diffuse scattering and a corresponding decrease in specular reflection.

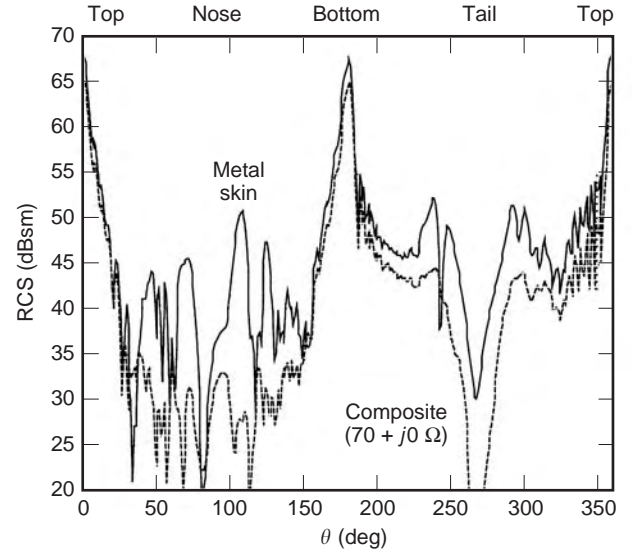


Figure 16. The RCS of a metal skin aircraft is compared to that of a composite aircraft. The monostatic RCS is lower for the composite aircraft because more of the incident field is scattered in the forward direction. The surface impedance approximation has been used.

The Rayleigh condition is the traditional criterion for a rough surface

$$\bar{h} \leq \frac{\lambda}{8 \sin \psi}$$

where \bar{h} is the average height of the irregularities and ψ the grazing angle. The surface impedance boundary condition can also be used to simulate surface irregularities [37].

The calculation of the RCS for targets with random characteristics can be performed using a Monte Carlo simulation (method of repeated trials) or by applying probability theory to the governing equations of electromagnetics. Both approaches start by writing the RCS in terms of the random variables of interest (for example, target dimensions). In the Monte Carlo method, the equations are computer-programmed and repeatedly executed using a different random seed each time. The average RCS and its standard deviation can be computed from the output data.

Another approach is to take the expected value of the RCS expression. If the probability density functions of the random variables are known, then the expectation operation results in an expression for the average RCS. Using this approach, the RCS of a “lumpy” surface with a correlation interval \bar{c} (the distance beyond which on average the surface deviations become independent) is given approximately by [6]

$$\sigma = \frac{4\pi A^2}{\lambda^2} \cos^2 \theta e^{-4\beta^2 \bar{c}^2} \left[P_0 + \frac{4\pi \bar{c}^2 \beta^2 \bar{\delta}^2}{A} \exp\left(\frac{c^2 \pi^2 \sin^2 \theta}{\lambda^2}\right) \right] \quad (60)$$

where $\bar{\delta}^2$ is the variance of the surface deviations (assumed small). P_0 is the error-free power pattern

normalized to A^2 . [Using a flat plate as an example, $P_0 = [\text{sinc}(\beta ua) \text{sinc}(\beta vb) \cos \theta]^2$.] The second term in the brackets of Eq. (60) represents a random noise that increases with the level of the error. A small correlation interval yields lower, more uniformly dispersed scattering than a large correlation interval.

9. MEASUREMENT OF RADAR CROSS SECTION

Measurements are a crucial step in the design and verification of an LO platform. In general, measured RCS data can serve three purposes:

1. To establish a target's RCS for design verification
2. For comparison with calculated RCS to evaluate numerical methods or the validity of approximations
3. As a diagnostic tool

Measurements are performed throughout the design of a stealthy platform. During the conceptual stage, scale models of candidate designs may be built and tested to verify that the RCS levels are close to those expected. At various stages in the development of the full-scale components (such as wings and antennas), measurements can be used to verify assembly tolerances, RCS treatments, and other manufacturing processes. Problem areas can be reworked and then checked again. Finally, if the target is not too large, a measurement can be made on the completed product. This step may serve as part of the official fulfillment of a contract.

Measurement facilities can be categorized by a variety of attributes that include physical characteristics, instrumentation capabilities, and data analysis and presentation modes. Table 4 summarizes some commonly used descriptors.

Most systems measure monostatic RCSs by using a fixed transmit/receive antenna and rotating the target. The traditional continuous wave (CW) measurement involves two steps. First, a calibration target of known RCS (typically a sphere) is placed in the chamber, and the

Table 4. RCS Measurement Facility Descriptors

System Descriptor	Categories
Physical Configuration	Indoor/outdoor
	Near field
	Far field
	Compact
Instrumentation	Tapered
	Time domain
	Frequency domain
Data analysis and presentation	Continuous wave (CW)
	Pulsed CW
	Fixed frequency/variable aspect
	Fixed aspect/frequency sweep
	Two-dimensional frequency Aspect
	Time-domain trace
	Target imaging
	Polar or rectangular plots

received power is recorded for reference. Next, the calibration target is replaced by the object with unknown RCS, and the power measured as the target is rotated. By comparing the received and reference powers, the RCS of the unknown target is obtained. In an analog system, the power difference drives the vertical (RCS) axis of a plotter, and the horizontal (angle) axis is slewed to the target mount. The final result is a plot of RCS versus aspect angle. The data obtained using the classical far-field CW RCS measurement of a rectangular plate are illustrated in Fig. 17.

For a true far-field measurement the target must be illuminated by a plane wave. This condition is never rigorously satisfied in practice, because the need for a directive transmit antenna usually results in a nonuniform-amplitude illumination of the target. Furthermore, the wave incident on the target is always spherical, not planar. Finally, because the system components are near the floor, ceiling, and walls, reflections from these surfaces affect the measurement.

Figure 17 illustrates the types of inaccuracies that can occur, such as sidelobe asymmetry and the existence of a noise floor. The noise floor sets a lower limit on the RCS that can be reliably measured. Measures of chamber performance are

1. Pattern symmetry in angle
2. Noise floor (noise level)
3. Quiet zone (linear extent of the region where the amplitude and phase of the incident wave are approximately plane)

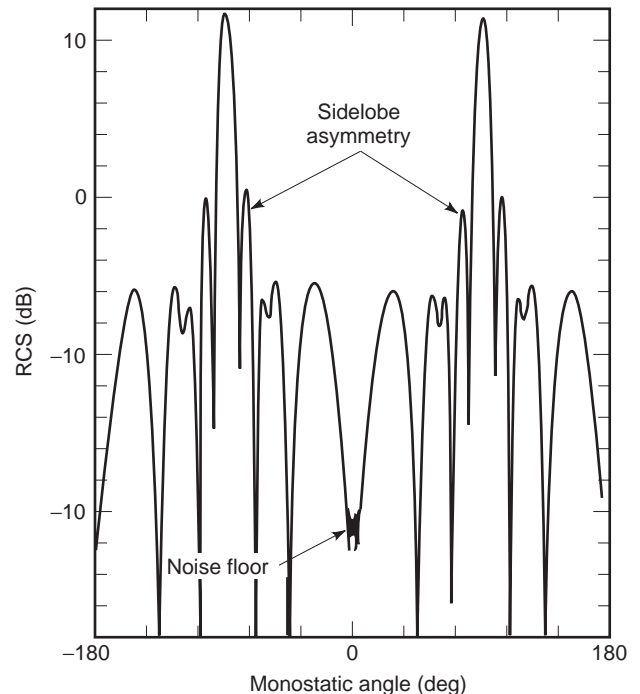


Figure 17. The measured RCS of a 16-in. square plate for a 2 GHz CW source. Errors in the measurement were more pronounced in older measurement systems. Background subtraction techniques can be used to reduce measurement errors.

4. Repeatability
5. Allowable target size and weight for the mount
6. Allowable range of target motion
7. Instrumentation capabilities
8. Data processing capabilities
9. Data presentation capabilities

The state-of-the-art instrumentation used in RCS measurement is essentially a programmable multimode radar. Data can be collected in either the time or the frequency domain and transformed back and forth between the two. In the time domain, gating can be employed to discard signals that do not correspond to the time delay of a scattered signal from the target's extent. Processing such as *windowing* can be performed on the raw data to enhance various characteristics and then see how they behave as a function of frequency or aspect. Data processing techniques can even generate high-resolution images that highlight scattering hot spots on the target.

9.1. Chamber Configurations

The majority of all RCS measurement facilities are completely enclosed (indoor ranges). This provides isolation from the external environment, which is desirable for both security and technical reasons. In an indoor chamber the interference from other RF sources is reduced or eliminated, and the temperature is controlled for increased instrumentation stability. The result is a more accurate and repeatable measurement than possible in an outdoor facility. The obvious limitation on an indoor chamber is the size of the building required for large targets.

Figure 18 shows two types of indoor chambers. The first is the standard far-field configuration. The separation of the antenna and target must be large enough so that the difference between an ideal plane wave and the actual spherical wave is negligible. The required distance is a function of target size and the frequency. If the distance is R and the target length L , as indicated in Fig. 19, the round-trip phase difference between rays to the edge and center is

$$2\beta\Delta_{\max} = 2\beta[\sqrt{R^2 + (L/2)^2} - R] \approx \frac{\pi L^2}{2R\lambda} \quad (61)$$

where the right-hand side holds for $R \gg L$. Based on the convention used for the definition of the far field of a radiating antenna, one may limit the round trip phase error to $\pi/8$, so that the minimum range becomes

$$R_{\min} = \frac{4L^2}{\lambda}$$

This limit turns out to be overly restrictive and is usually not adhered to in practice. Equation (61) assumes that all of the target surface contributes coherently to the total RCS, as will happen, for example, with a smooth plate. On the other hand, if the target is composed of many independent scatterers, the far-field distance is primarily determined by the distribution of dominant scatterers in space. Thus when the dominant scatterers are clustered, a much smaller range is acceptable [38].

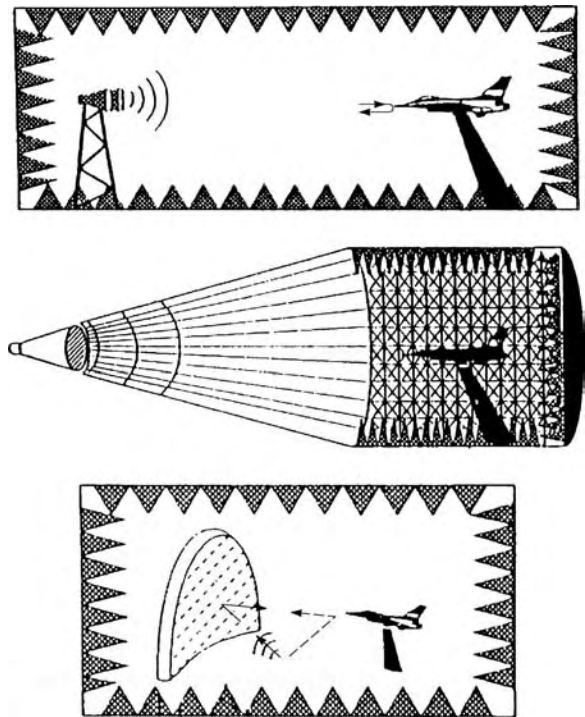


Figure 18. Common indoor chamber configurations include the conventional far-field range, the tapered chamber, and the compact range. The compact range is capable of handling physically large targets over a wide frequency range.

In addition to a plane phase front at the target, the amplitude of the incident wave across the target must be constant. The amplitude distribution is controlled by the antenna beamwidth and the ratio L/R . An isotropic antenna provides the flattest phase front, but also results in stronger illumination of the chamber walls and other obstacles. The transmitted power must also be higher if the antenna gain is low. Thus there is a tradeoff involved in determining the optimum antenna configuration.

The demands on chamber size required for accurate low-level RCS measurements have resulted in the

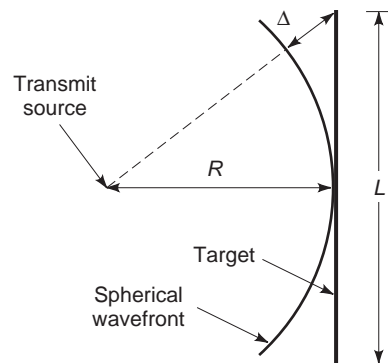


Figure 19. The incident spherical wave from the transmitter deviates from a plane wave. The deviation leads to an error in the measured RCS. To reduce the error the transmitter to target distance must be increased.

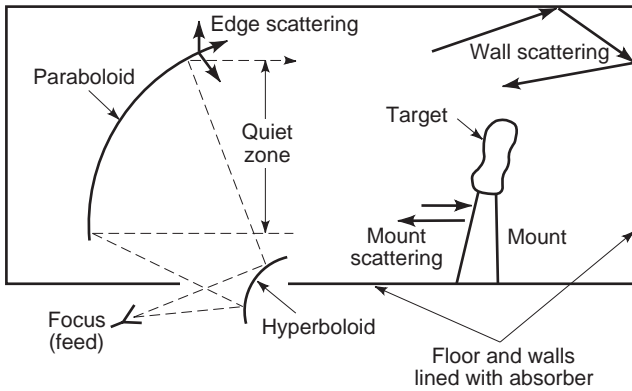


Figure 20. A compact range provides a uniform field over the target with shorter antenna-to-target distances than a conventional far-field range. Some sources of measurement error are illustrated.

development of *compact ranges*. The layout of a typical compact range is shown in Fig. 20. The parent reflector configuration is a Cassegrain, and the reflector surfaces have been arranged so that no blockage occurs. The antenna is located at the focus, and a plane-wave field is excited a short distance in front of the paraboloid. The total volume of a compact range is much less than that of a far-field configuration.

The compact range is not without its own problems, though. To obtain uniform amplitude over the target requires a shaped feed pattern or some subreflector shaping. Cross-polarization and edge diffraction can be significant. Since the target is close to the reflector edges, the effects of edge scattering are especially important at low RCS levels. Much effort has gone into the design of rolled or serrated edges that control the level and direction of edge diffraction.

9.2. Sources of Measurement Error

The received signal in a measurement is not entirely due to scattering from the target. It also includes noise introduced by the receiving system and extraneous scattered signals originating from the chamber walls and other obstacles. Furthermore, some of the transmit signal couples directly to the receive antenna. This leakage is strongest when a common antenna is used for both transmit and receive.

Chambers that are used to measure low-level RCSs must be carefully designed, maintained, and calibrated. Great care is taken to reduce the error signals in the vicinity of the target. The cross-sectional dimension of the chamber that is essentially free of extraneous signals and maintains the plane-wave phase and amplitude is called the *quiet zone*. It is usually specified in feet or meters. The quiet zone, frequency range of operation, and noise floor effectively characterize the chamber performance.

Measurement errors are mitigated using background subtraction. First a measurement is taken with the target absent. Ideally the received signal should be zero if the chamber walls are perfect absorbers and there is no leakage. In practice a nonzero signal is present due to the sources indicated in Fig. 20, and this value is stored as

a reference. Next, the measurement is repeated with the target present. The measured value includes the target's RCS as well as the error signals. If the interaction between the target and chamber is negligible, vector subtraction of the background signal should yield a close approximation to the isolated target's RCS.

The subtraction method requires that the characteristics of the measurement equipment remain stable during the calibration and measurement runs. If the power level or frequency drifts, the background reference is no longer valid and the difference is attributed to the target. Even small changes in phase caused by cable movement can affect low RCS measurements.

9.3. Target Mounts

A potential source of large measurement error is the target mount. If at all possible, the pedestal should be made of low-density material that does not scatter. Frequently the target is suspended and held in tension using thin polyester filaments similar to fishing line. For large, heavy targets that must be tilted and rotated there is no alternative but to use metal mounts. In this case special-shaped fixtures are used to shield the pedestal. Absorbing material can also be used in conjunction with shaping to reduce mount scattering.

9.4. Resolved RCS and Target Imaging

Returns from individual scattering elements on a complex target can be isolated or resolved. The strength of the return is plotted as a function of down range (y) and cross-range (x) in Fig. 21. If the cell size becomes small enough, a high-resolution two-dimensional image of the target can be constructed. As shown in Fig. 22, imaging clearly identifies the strongest scattering sources on a target.

Resolving the individual scattering sources on a target requires that accurate angle and range information be available as the returns are received. Range resolution is achieved by using a short pulse that only illuminates a small slice of the target. Knowledge of the time elapsed after the leading edge of the pulse hits the target is equivalent to knowledge of the downrange coordinate y .

One method of obtaining the crossrange value is by accurately pointing a narrow antenna beam. The beam is scanned over the entire solid angle of the target, thereby

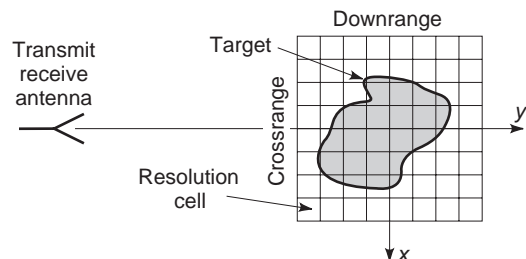


Figure 21. Radar images can be generated by plotting the intensity of the scattered field as a function of the target surface coordinates. The downrange size of the resolution cell is determined by the radar pulsewidth; the crossrange resolution is determined by the Doppler measurement capability of the radar.

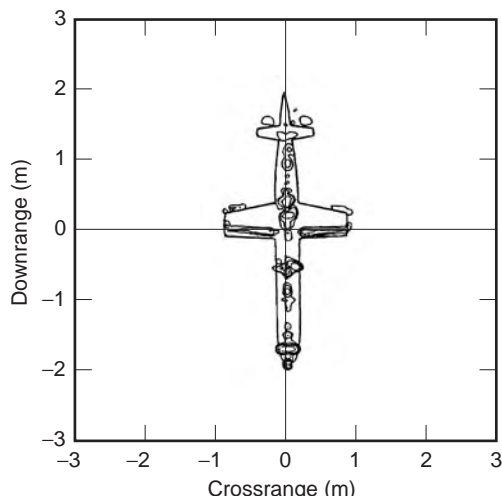


Figure 22. The radar image of the target can be used to determine where RCS treatments should be applied, as well as evaluate the effectiveness of RCS reduction methods.

providing angle data that can be processed along with the range data to construct an image. This approach is not efficient at microwave frequencies, however, because of the large antenna size needed for fine angle resolution. It is more practical at millimeter wavelengths and smaller, and is highly successful at laser wavelengths. A more practical method for obtaining crossrange exploits the Doppler shift [39]. The target is rotated at an angular velocity ω_r as shown in Fig. 23. Target surface points rotate with a linear velocity that depends on their distance from the center of rotation. The radial component of relative velocity (component along R) gives rise to a Doppler shift.

Referring to the coordinate system shown in Fig. 23, let R_0 be the range to the target's center of rotation along the y coordinate, and r the distance to a scattering point at a distance d from the center. Using the law of cosines, we obtain

$$r^2 = R_0^2 + d^2 - 2dR_0 \cos \phi$$

which simplifies to

$$r = R_0 \sqrt{1 - \frac{2d \sin \phi}{R_0}}$$

when $R_0 \gg d$. The first term under the square root is associated with the round-trip time delay to and from

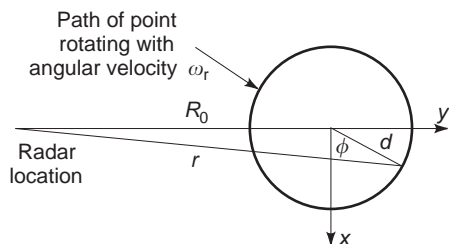


Figure 23. A point rotating on the surface of the target has a Doppler frequency shift. The frequency shift can be used to determine the cross-range coordinate.

the target center, and the second is the Doppler shift due to rotation. Since $\phi = \omega_r t$ (where ω_r is the rotation rate of the target), the Doppler frequency in hertz is

$$f_d = \frac{1}{2\pi} \frac{d}{dt} (-2\beta R_0 + 2\beta d \sin \omega t) = \frac{2\omega_r}{\lambda} x \quad (62)$$

This method of rotating the target to obtain crossrange information is the same principle used in inverse synthetic aperture radar (ISAR) method.

BIBLIOGRAPHY

1. M. Skolnik, *Introduction to Radar Systems*, 2nd ed., McGraw-Hill, New York, 1980.
2. B. Eddie, *Radars*, Prentice-Hall, Englewood Cliffs, NJ, 1993.
3. G. Ruck et al., *Radar Cross Section Handbook*, Plenum, New York, 1970.
4. C. Balanis, *Advanced Engineering Electromagnetics*, Harper & Row, San Francisco, 1982.
5. K. Kunz and R. Luebbers, *The Finite-Difference Time Domain Method for Electromagnetics*, CRC Press, Boca Raton, FL, 1993.
6. D. Jenn, *Radar and Laser Cross Section Engineering*, AIAA Education Series, Washington, DC, 1995.
7. A. Ishimaru, *Electromagnetic Wave Propagation and Scattering*, Prentice-Hall, Englewood Cliffs, NJ, 1991.
8. L. Peters, End-fire echo area of long, thin bodies, *IRE Trans. Anten. Propag.* 133 (Jan. 1958).
9. R. Harrington, *Time-Harmonic Electromagnetic Fields*, McGraw-Hill, New York, 1961.
10. J. Keller, Determination of reflected and transmitted fields by geometrical optics, *J. Opt. Soc. Am.* 40(1):48 (1950).
11. R. Harrington, *Field Computation by Moment Methods*, Macmillan, New York, 1961.
12. W. Streetman and J. Goodall, *Lockheed F-117A*, Motorbooks International, Osceola, WI, 1990.
13. D. Cheng, *Field and Wave Electromagnetics*, 2nd ed., McGraw-Hill, New York, 1989.
14. M. Schwartz, *Composite Materials Handbook*, 2nd ed., McGraw-Hill, New York, 1992.
15. V. Weston, Theory of absorbers in scattering, *IEEE Trans. Anten. Propag.* AP-11:578 (1963).
16. N. Engheta and D. Jaggard, Electromagnetic chirality and its applications, *IEEE Anten. Propag. Soc. Newslett.* 6 (Oct. 1968).
17. R. Harrington, Theory of loaded scatterers, *Proc. IEE Electron.* 111(4):617-623 (1964).
18. R. Harrington, The control of electromagnetic scattering by impedance loading, *Proc. IEEE* 53:993-1004 (1965).
19. E. Knott, J. Schaeffer, and M. Tuley, *Radar Cross Section*, Artech House, Norwood, MA, 1989.
20. *Navy Times* 4. (Jan. 12, 1998).
21. E. Pelton and B. Munk, A streamlined metallic radome, *IEEE Trans. Anten. Propag.* AP-22:799 (1974).
22. D. C. Schleher, *Introduction to Electronic Warfare*, Artech House, Norwood, MA, 1986.
23. S. Silver, *Microwave Antenna Theory and Design*, McGraw-Hill, New York, 1949.

24. P. Ufimtsev, *Method of Edge Waves in the Physical Theory of Diffraction*, transl. from Russian by USAF Systems Command, Foreign Technology Division, Sept. 7, 1971.
25. A. Michaeli, Equivalent edge currents for arbitrary aspects of observation, *IEEE Trans. Anten. Propag.* **AP-32**:252–258 (1984); corrections, **AP-33**(2) (1985).
26. J. Keller, Geometrical theory of diffraction, *J. Opt. Soc. Am.* **52**(2):116 (1962).
27. R. Kouyoumjian and P. Pathak, A uniform geometrical theory of diffraction for an edge in a perfectly conducting surface, *Proc. IEEE* **62**:1448 (1974).
28. J. Boersma and Y. Rahmat-Samii, Comparison of two leading theories of edge diffraction with the exact uniform asymptotic solution, *Radio Sci.* **15**(6):1179 (1980).
29. S. Rao, D. Wilton, and A. Glisson, Electromagnetic scattering by surfaces of arbitrary shape, *IEEE Trans. Anten. Propag.* **AP-30**:409 (1982).
30. L. Medgyesi-Mitschang and J. Putnam, Hybrid solutions for scattering from large bodies of revolution with material discontinuities and coatings, *IEEE Trans. Anten. Propag.* **AP-32**:717 (1984).
31. E. Ekelman and G. Thiele, A hybrid technique for combining the moment method treatment of wire antennas with the GTD for curved surfaces, *IEEE Trans. Anten. Propag.* **AP-28**:831 (1980).
32. T. J. Kim and G. Thiele, A hybrid diffraction technique—general theory and applications, *IEEE Trans. Anten. Propag.* **AP-30**:888–898 (1982).
33. H. Ling, K. Chou, and S. Lee, Shooting and bouncing rays: Calculating the RCS of an arbitrarily shaped cavity, *IEEE Trans. Anten. Propag.* **AP-37**:194 (1989).
34. T. Senior, Impedance boundary conditions for imperfectly conducting surfaces, *Appl. Sci. Res.* **8**(B):418 (1960).
35. L. Medgyesi-Mitschang and J. Putnam, Integral equation formulations for imperfectly conducting scatterers, *IEEE Trans. Anten. Propag.* **AP-33**:206 (1985).
36. T. Senior, Combined resistive and conductive sheets, *IEEE Trans. Anten. Propag.* **AP-33**:577 (1985).
37. T. Senior, Impedance boundary conditions for statistically rough surfaces, *Appl. Sci. Res.* **8**(B):437 (1960).
38. B. Welsh, A minimum range criterion for RCS measurements of a target dominated by point scatterers, *1984 AP-S/URSI Int. Symp.*, 1984, Vol. APS-17-3, p. 666.
39. D. Mensa, *High Resolution Radar Cross Section Imaging*, Artech House, Norwood, MA, 1981.
40. RCS *Measurement Capabilities at the Pacific Missile Test Center*, Radar Signature Branch, Pt. Mugu, CA.

RADAR EQUIPMENT

MARC RESSLER
 MATTHEW BENNETT
 TUAN TON
 LAM NGUYEN
 Army Research Laboratory

Modern radars operate at frequencies from megahertz to hundreds of gigahertz and at power levels from milliwatts to megawatts. This means that many RF hardware

components will vary greatly, whereas control and display systems will be functionally and physically similar. In recent years, the improvements in solid-state devices and the explosive growth in the capabilities of digital circuits and digital processors have provided new approaches to radar designs. Analog circuits, which tend to be smaller and have lower power consumption, are being replaced with digital circuits, which are more stable in the presence of varying temperature, vibration, and power supply voltages, while providing flexibility often unavailable in the analog domain.

1. RADAR FREQUENCIES

To provide some measure of security during World War II (WWII), letters were used to designate frequency bands instead of specifying frequencies. Although the electronic warfare community has adopted a sequentially lettered set of frequency bands, the original radar band designations were so commonly used that eventually a standard for letter designated radar bands (IEEE Std 521-1984) was developed. Table 1 [1] shows these bands and the actual frequency assignments designated for radar operation by the International Telecommunications Union (ITU) for North and South America (region 2). Note that no specifically assigned HF radar band exists and that the UHF radar band extends only to 1000 MHz, whereas the more common definition of UHF extends to 3000 MHz. The use of the millimeter designation is often applied to the frequencies above 40 GHz, thus including both the V and W bands.

The radar bands are grouped together with similar performance characteristics. The high-frequency (HF)

Table 1. Standard Radar-Frequency Letter Band Nomenclature

Band Designation	Nominal Frequency Range	Radar Frequency Ranges Based on ITU Assignments for Region 2
HF	3–30 MHz	None
VHF	30–300 MHz	138–144 MHz 216–225 MHz
UHF	300–1000 MHz	420–450 MHz 890–942 MHz
L	1000–2000 MHz	1215–1400 MHz
S	2000–4000 MHz	2300–2500 MHz 2700–3700 MHz
C	4000–8000 MHz	5250–5925 MHz
X	8000–12,000 MHz	8500–10,680 MHz
K _u	12–18 GHz	13.4–14.0 GHz 15.7–17.7 GHz
K	18–27 GHz	24.05–24.25 GHz
K _a	27–40 GHz	33.4–36.0 GHz
V	40–75 GHz	59–64 GHz
W	75–110 GHz	76–81 GHz 92–100 GHz
mm	110–300 GHz	126–142 GHz 144–149 GHz 231–235 GHz 238–248 GHz

Source: IEEE Std 521-1984, Copyright © 1984. IEEE. All rights reserved.

band requires physically large antennas but has negligible propagation losses and can take advantage of ionospheric bending at HF to support extended range, over-the-horizon (OTH) radars. The frequency of operation is usually adjusted to find the optimal propagation path to the desired target region of the globe as ionospheric conditions change. Very high frequency (VHF) and ultrahigh frequency (UHF) radars require parabolic reflectors that are too large to be practical and even Yagi antenna arrays are a few meters long, but propagation losses because of atmospheric and weather effects are still negligible, making VHF and UHF radars suitable for long-range surveillance. Two-way losses through 10–20 m of foliage (typical of what might be seen from an aircraft) are about 3–6 dB [2–4], making VHF and UHF bands suitable for finding targets masked by trees. Two-way losses in these bands for sandy soils may run as low as 1 dB/m in dry soils to over 30 dB/m in damp soils, and above 100 dB/m in soils with high clay content, making it possible to detect subterranean targets at shallow depths depending on soil type [5–7].

L band offers higher resolution with antenna reflectors approximately 10 m across, while propagation losses remain low [8]. S band and more notably C band are suitable for medium-range operations as atmospheric and weather losses climb, but this also means they are useful for weather measurements [9,10]. X band and K_u band can provide high resolution with meter-sized antennas but have noticeably more propagation losses, limiting their use to shorter ranges or clear-weather operation. K_a -band and higher suffer high atmospheric losses and extreme rain losses and backscatter but provide very high resolution with physically small antennas that may be used in short range applications such as radar fuzing and fire control systems. The water absorption lines at 22.2 and 185 GHz and the oxygen resonance lines at 60 and 120 GHz produce such high losses as to limit operations near these frequencies. Lower-loss “windows” in the atmospheric attenuation near 35 and 95 GHz provide the possibility of short-range operations but still at higher losses than K_u band.

To meet system requirements, the radar designer must pick a range of components and frequency band that will support the desired performance. The basic radar range equation is

$$R^4 = \frac{P_t G_t L_t}{4\pi} \times \frac{A_e L_r \sigma}{4\pi k T_0 B F_n \text{SNR}} \times L_p L_a \quad (1)$$

The first group of terms is related to the transmitter, the second to the receiver, and the third to other propagation effects, where

- R = maximum radar range
- P_t = average transmit power
- G_t = gain of transmit antenna
- L_t = losses from transmitter to antenna (e.g., circulators, duplexers, transmission lines)
- A_e = effective antenna aperture of receive antenna (aperture area times efficiency)
- L_r = losses in receive path, similar to those for the transmit chain

- σ = radar cross section of target
- k = Boltzmann’s constant
- T_0 = system reference temperature (typically 290 K)
- B = receiver bandwidth
- F_n = receiver noise figure
- SNR = signal-to-noise ratio required to meet detectability requirements (typically 12–15 dB)
- L_p = two-way antenna pattern losses
- L_a = two-way propagation losses (atmospheric, weather)

Note that there is no frequency-related term in Eq. (1). However, the effective aperture is related to the gain of the receive antenna by

$$G_r = \frac{4\pi A_e}{\lambda^2}$$

where λ is the wavelength. Thus, for a fixed aperture size, the gain increases with frequency. The choice of frequency is typically application-driven, but since the size of many RF components scale inversely with frequency (see Fig. 1), the radar designer may choose a particular frequency band based on size and weight constraints if radar performance will not be adversely affected. Atmospheric and transmission line losses generally increase with frequency, and receiver noise figures degrade. The designer can improve transmit and receive gain by using a higher-gain antenna, at the cost of a loss in area coverage and can increase signal-to-noise performance by using a narrower system bandwidth, or by effecting an equivalent bandwidth reduction with signal processing. Often the only choice left to the designer, to meet target detectability requirements, is to increase average power.

2. TYPES OF RADAR

There are a number of basic variations in radar system designs. We will examine the operation of different types and some of the hardware specific to particular types.

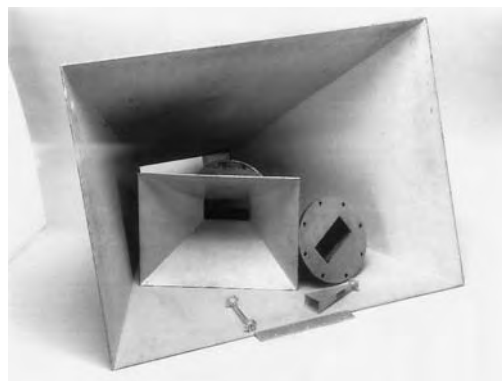


Figure 1. A 15-dB-gain L-band horn that contains the other items dwarfs the W-band waveguide and 25 dB gain horn sitting in front of an S-band coupler and 15 dB gain horn. (U.S. Army photo.)

2.1. Continuous-Wave Doppler Radar

The simplest of all radars, and by far the most common, is the continuous-wave (CW) Doppler radar. Its biggest advantage is also its biggest disadvantage [11]. By operating at a 100% duty cycle, it maximizes the use of the transmit power and eliminates issues of Doppler ambiguity, but the receiver is forced to operate while the transmitter is on and no range information is available (although modulating the carrier frequency can provide range information). For a medium-power, sensitive radar, two antennas are usually required to isolate the receiver from the large transmit signal and from the noise sidebands of the transmitter. Nearby fixed targets (clutter) can also have an impact on performance because they will also cause a large signal return that might overload the receiver. Most CW radars have homodyne (direct-conversion) receivers; that is, the local oscillator for the mixer is at the same frequency of the transmitter. Figure 2 shows a simplified block diagram of a CW radar. The return signal from the target is shifted in frequency because of the radial component of the velocity of the target with respect to the radar (i.e., that portion of the motion that is toward or away from the radar v_r). A sample of the transmit signal f_0 is used as the local oscillator signal. This signal is mixed with the return signal from the target and the difference between these signals is the Doppler shift f_d , which is fed to a frequency meter. The sum frequency out of the mixer is usually so far beyond the response of such a meter that filtering is not necessary, although it can be easily provided with a simple lowpass filter. The Doppler shift is

$$f_d = f_0 \frac{2v_r}{c} = \frac{2v_r}{\lambda} \quad (\text{for } v_r \ll c)$$

where the frequency is shifted up for approaching velocities and down for receding velocities. The factor of 2 is a result of the signal traveling both ways and can perhaps be more easily understood as a change in signal phase. If the target moves a half wavelength closer to the radar, the pathlength to the target and back changes by one wavelength.

The Doppler shift is in the human audible range for typical ground target speeds and operating frequencies in X band and K_u band, and a number of radars have been built. The basic output device of these radars is a set of headphones the operator wears. This is not as strange as it sounds because a trained operator can estimate velocity of the target. Other moving parts of the target (e.g., wheels, treads, propellers) provide secondary audible signatures so that the operator also can determine to what class the

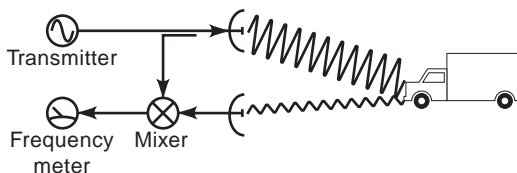


Figure 2. Block diagram for a simplified CW Doppler radar.

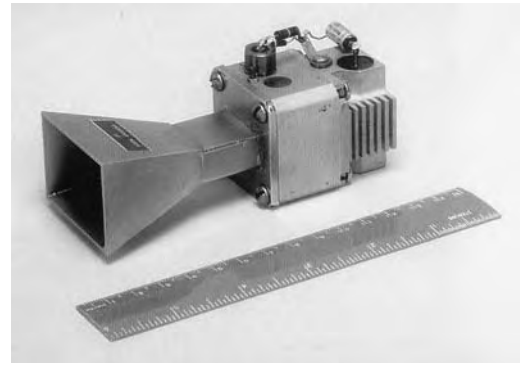


Figure 3. An X-band Doppler transceiver and mating horn antenna. Mechanical tuning coarsely sets frequency, whereas fine tuning and AFC can be provided by modulating the operating voltage. (U.S. Army photo.)

target belongs (such as wheeled vs. tracked vehicles or fixed wing vs. rotary wing aircraft) [12].

Small, low-power versions of CW Doppler radars are used as speed sensors (mostly well known in police radar applications), automatic door openers in warehouses and retail stores, intrusion detectors, vehicle detectors for traffic control, and proximity fuzes in rockets, bombs, and projectiles. In these applications, the range to the target is usually small, and the loss in sensitivity because of the use of a single antenna is acceptable. One of the parts that made designs of such radars simpler was the Microwave Associates (now M/A-COM) Gunnplexer Doppler transceiver (Fig. 3), which packs a transmitter, ferrite circulator, and mixer into a single module. A Gunn oscillator is the basic transmitter, which is coupled to a single antenna through the circulator. Transmitter power reflected back from the antenna port acts as the local oscillator into the single balanced mixer (an adjustable screw allows intentional standing-wave ratio (SWR) mismatch to force an adequate level of return signal). The addition of an antenna, frequency meter, and a direct-current (DC) power source completes the radar (Fig. 4).

2.2. Pulse Radar

The pulse radar is what most people think of when they think of radar, which is the acronym for radio detection and ranging. A short burst of microwave energy is transmitted toward the target, and the time t for the echo to return in microseconds is measured to determine the

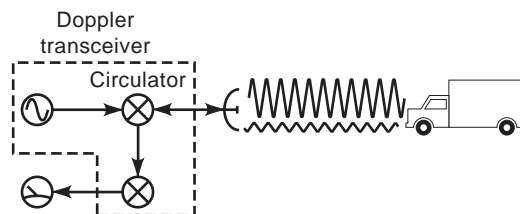


Figure 4. Block diagram for a simple single-antenna CW Doppler radar based on a Doppler transceiver.

range r to the target in meters where

$$r = c \frac{t}{2}$$

with the factor of 2 representing the path the signal takes to the target and back. The length of the pulse determines the capability of the radar to resolve two closely spaced targets, the basic limitation being that the echoes from the two targets will merge into a single return. At a pulsewidth of $t_w \mu s$, this merging occurs when the two targets are separated by approximately a distance r using the preceding formula. Decreasing the pulsewidth improves resolution capability at a cost of reduced average power levels.

The development in Britain of the magnetron (a pulsed power oscillator) during WWII made microwave pulse radar practical, and the magnetron [13] is still the most commonly used transmitter in pulse radars. It is capable of producing peak power levels of kilowatts through megawatts in compact packages (Figs. 5 and 6). A simplified block diagram of a magnetron-based pulse radar is shown in Fig. 7. The power supply/modulator provides the high-voltage pulse at the desired pulse repetition frequency (PRF) to drive the magnetron. The PRF is usually set to guarantee that there is enough time between pulses to receive a return from the farthest expected target range. The transmit/receive (T/R) switch, or duplexer, automatically connects the transmitter to the antenna, while effectively disconnecting the receiver from the antenna. The T/R switch in high-powered radars is often based on a gas-filled tube that conducts in the presence of the RF field [14], but in lower-powered sets, these functions may be assumed with circulators or positive-intrinsic-negative (pin) diode switches [15]. The receiver protector is typically a diode limiter that further restricts the voltage developed across the receiver input, whereas the transmitter is operating to protect sensitive low-noise preamplifiers in the receiver.

Referring again to the radar range equation, we note that the return signal for a fixed-size target varies as the fourth power of the range to the target. This means that a target at 1 km will be 80 dB stronger than that target at a range of 100 km. The sensitivity-time-control (STC) increases the gain of the receiver versus the time elapsed from when the pulse was transmitted (this is effectively

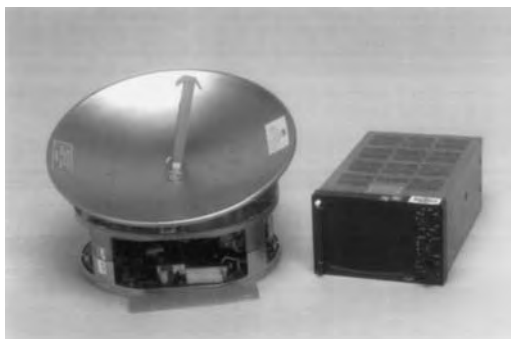


Figure 5. An X-band weather radar designed for aircraft use. The transmitter and receiver are located in the assembly behind the reflector, and the control electronics are located in the display unit. The transmitter is a 3 kW magnetron that is approximately 60 cm^3 . (U.S. Army photo.)

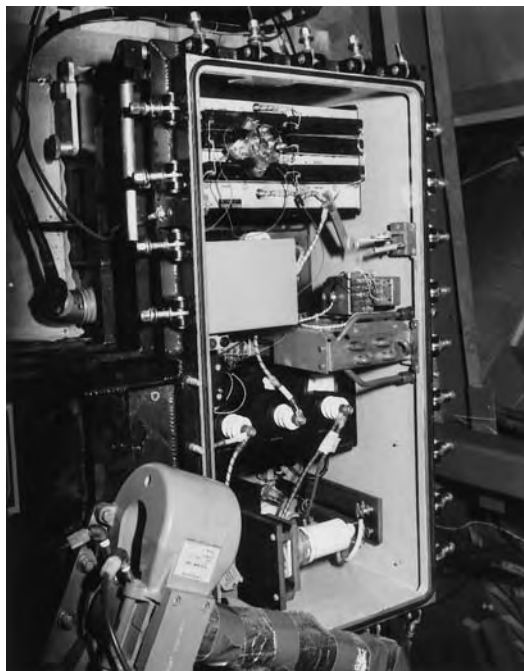


Figure 6. A 1 MW X-band magnetron transmitter. The power supply/modulator is in the upper left with its $20 \times 40\text{-cm}$ cover removed. The large rectangular device to the right of the water-cooled heat exchanger is the pulse-forming network. (U.S. Army photo.)

the range to a target) so that there is less change in signal dynamic range as the range to target varies [16], and allows choosing an analog-to-digital converter (ADC) with fewer bits to support the receiver output. R^4 correction will produce a constant radar cross-sectional output but will usually require controlling the gain of multiple stages of the receiver. However, the targets are often not the limiting factor in setting dynamic range limits. In ground-based radars, clutter (undesired wide area returns from natural or cultural objects) is usually larger than the desired targets, and the amount of clutter region illuminated by a radar beam increases as range increases; so in this case, an r^3 gain correction is a better choice. Weather radars, on the other hand, respond to the backscatter return from a volume of space, so a constant target return is best obtained with an r^2 correction. Figure 8 shows a combined receiver protector/STC module attached to the duplexer of a lowpower radar.

2.3. Moving-Target Detecting Radars

As mentioned in the previous paragraph, in a ground-based radar, a large region of high-strength undesired

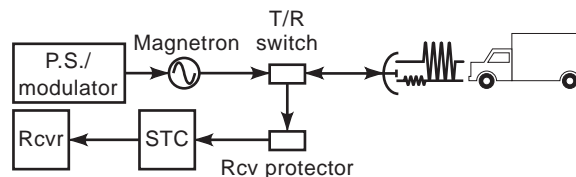


Figure 7. Block diagram of a magnetron-based pulse radar.

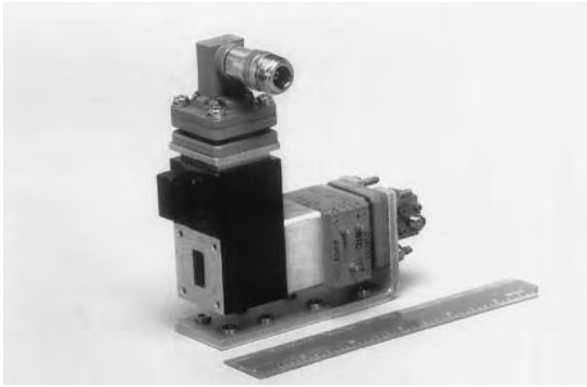


Figure 8. A 500-W K_u -band duplexer with a combined receiver protector/STC module attached. Antenna connection is made to the open waveguide connection on the left, and the transmitter is connected to the RF connector on the top. The receiver protector can be run in a self-rectifying mode or can be driven by an external DC signal. STC control range is about 30 to 40 dB. (U.S. Army photo.)

radar signals from fixed targets (clutter) masks the moving targets the radar is typically designed to detect. A moving-target indication (MTI) radar attempts to minimize the response from the clutter to enhance the signal-to-clutter ratio and improve target detectability. A simple block diagram of how this can be accomplished is shown in Fig. 9. A sample of the received signal is delayed by one pulse repetition interval (PRI—the inverse of PRF) and subtracted from the current input signal. This can be a rather long delay and was often provided by multiple reflections within a multifaceted bulk quartz delay line. Such long delays can also be provided by digital shift registers or memory circuits, in which the subtraction is provided after the ADC stage. The digital approach has the advantages of stability in time and temperature, whereas the analog approach reduces the dynamic range into the ADCs, relaxing the requirements for the number of bits required. Proper cancellation of the clutter requires being able to compensate for the delays and losses through the delayed path, and in this case the digital approach also has an advantage, as the analog approach typically requires constructing a circuit path that duplicates the attenuation of the delay line and the gain, delay, and nonlinearities of the delay-line amplifier chain to provide proper cancellation. As long as the radar has adequate stability, the fixed targets will maintain the same phase from pulse to pulse and will be canceled, whereas the moving targets will vary in phase, thus producing a time-varying output. However, realize that the moving targets must have a radial component of motion with respect to the radar location for this phase difference to occur.

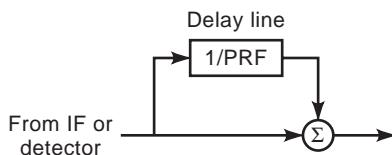


Figure 9. Block diagram of a simple one-pulse canceler.

Targets that move tangentially to the radar will be canceled, as if they were not moving, because no phase change is observed. Note also that a pulsed radar is basically a sampled data system, which leads to a similar problem if the target is moving at a rate such that its Doppler frequency is equivalent to the PRF, or a multiple thereof, because this is equivalent to sampling a signal a number of complete cycles later, and no phase difference will be observed from sample to sample. These target velocities are referred to as “blind speeds” because targets moving at these speeds will not be detected by an MTI radar [17].

Although magnetrons do not have pulse-to-pulse phase stability, they have reasonable short-term stability in frequency, and it is possible to synchronize the final receiver local oscillator (the coherent oscillator, or COHO) phase to that of the transmitter on each pulse (known as a coherent-on-receive system) and thus provide magnetron-based radars with an MTI mode of operation. Area MTI is another approach to clutter reduction, and one that does not require a coherent radar system in which a complete scan of the radar video is stored in memory and subtracted from the next scan. In a digital image, this operation is equivalent to a pixel-by-pixel subtraction and will mask small targets located over large areas of clutter (cities, forests) as the larger signal returns from the two samples of the clutter regions are subtracted from each other, leaving a small residue. Area MTI does have the advantage that tangentially moving targets are highlighted because they will have moved far enough between scans to appear in a different position on the screen.

Another approach to detecting moving targets is the pulse-Doppler radar: a coherent transmitter–receiver (Figs. 10 and 11) processes the received signals, not only into range bins but also into multiple Doppler bins. This processing is done most easily with a digital signal processor [18], providing the temporary storage for a group of pulse returns and typically a Fourier transform to provide the bank of filters. The quadrature mixer of Fig. 10 provides both in-phase (I) and quadrature (Q) outputs to a pair of ADCs to support complex fast Fourier transforms (FFTs). There are now purely digital approaches [19,20] that can provide I and Q outputs from a single, higher sample-rate ADC. The advantage of the digital approach is that there are no problems in balancing gain and phase in the two channels. Having both I and Q outputs allows

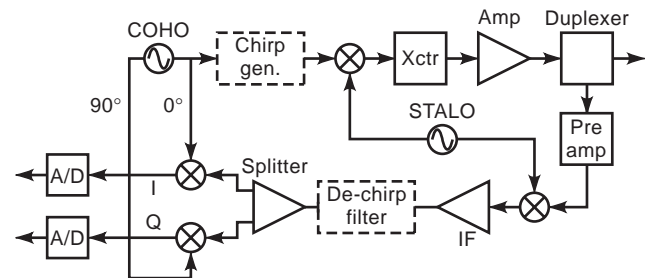


Figure 10. Block diagram of a coherent transceiver for use in pulse Doppler radar. The stable local oscillator (STALO) provides the translation frequency from RF to IF. Optional chirp modules are denoted by the dashed boxes.

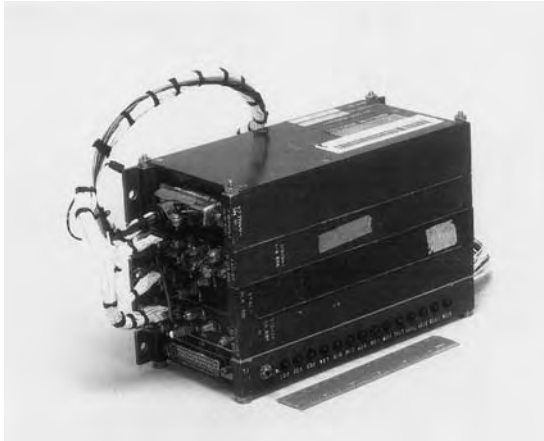


Figure 11. The Eaton/AIL G-199 K_u -band transceiver for the AN/TPS-74(V) modular radar. Various modules could be substituted to provide options for ground or airborne applications. This specific assembly contains modules for power supply, exciter, STALO, receiver, and antenna pedestal control.

sorting the Doppler bins into incoming (Doppler above the carrier frequency) and outgoing (Doppler below the carrier frequency) velocities. The zero frequency (DC) filter output is where the bulk of the clutter lies, and it is discarded. Motion of the clutter or the radar may spread the clutter energy into adjacent frequency bins, and they may be discarded as well, either automatically or under operator control. If the radar is on an airborne platform (Fig. 12), then returns from large clutter patches on the ground can be used to select the Doppler bin or bins that represent the clutter velocity in the direction of look [21]. As mentioned previously, the Doppler frequencies depend on the radial component of the target velocity. Dopplers that exceed the Nyquist criteria will be interpreted as having a direction opposite to their actual direction of travel, and blind



Figure 12. The electrically driven antenna of an F-16 equipped with one of Northrop Grumman's APG-66/68(V) family of coherent radars. The radar supports 25 air-to-air, air-to-ground, and mapping modes that provide target detection, acquisition, and tracking in both benign and hostile electromagnetic emissions environments. (Photo courtesy of Northrop Grumman Corporation.)



Figure 13. The Northrop Grumman ASR-12 is a modular, fully solid-state, S-band airport surveillance radar. It uses a moving-target detection scheme that combines adaptive Doppler filter and fine-scale clutter mapping to enhance the returns from tangential targets. (Photo courtesy of Northrop Grumman Corporation.)

speeds will again occur at multiples of the PRF. Increasing the PRF can eliminate this ambiguity in Doppler determination, at the cost of creating an ambiguity in range. Range ambiguity can occur when the PRF is high enough that a target return from a far-range target generated by an earlier pulse appears in the range processing time of the current pulse [22]. Dithering the PRF or switching between multiple PRFs can allow Doppler and range ambiguities to be resolved [17,23], but such an approach will not work with the simple fixed-delay MTI of Fig. 9. Modern air-traffic control radars (Fig. 13) use a combination of MTI techniques to improve detection of targets because aircraft often circle the airport as well as make direct approaches and departures.

Because we already have a coherent transceiver that allows us to recover the phase of the received signal, a number of improvements to the radar system performance are possible by modulating the transmitted waveform. This modulation increases the bandwidth of the transmitted signal, which, when processed in the receiver, provides improved resolution, while maintaining a longer pulsewidth to improve the average signal power. The disadvantage is that a long pulse limits the ability to detect targets close to the radar, in what is called the eclipsing zone, because returns from these targets will arrive at the receiver while the transmitter is still on. The most common modulation approach is to use linear FM, or chirp, modulation [24]. This can be provided simply with a surface acoustic wave (SAW) device in the transmit chain (Fig. 14) and a complementary compressive SAW device in the receiver intermediate frequency (IF), returning a signal with a pulsewidth equivalent to that of the modulation bandwidth. Alternately, high-speed synthesizers can provide the transmit modulation [25], while digital signal processors can provide the compressive function.

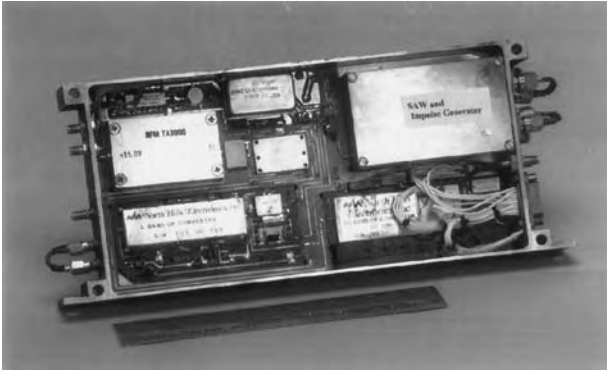


Figure 14. An exciter module from the AN/TPS-74(V) showing in the upper right the 60-MHz impulse generator and mating SAW chirp unit. For this unit, the 10 μ s transmit pulse was compressed to a 0.5 μ s pulse in the receiver for a 20:1 compression ratio. (U.S. Army photo.)

2.4. Synthetic Aperture Radar

Although we have now seen a way to improve the resolution in range, it would seem that the only way to improve the resolution in cross-range is to increase the size of the antenna system, narrowing the beamwidth of the radar. In synthetic aperture radar (SAR), cross-range resolution improvement is accomplished by moving an antenna in space [26], creating an effective aperture that is much larger than the physical antenna (Fig. 15). Returns from targets in the direction of motion of the radar are shifted up in frequency, whereas those behind the radar are shifted down in frequency, allowing the contributions from various points in the range swath to be separated. Typically, an SAR will also have a high resolution in range, requiring a large amount of frequency content in the transmitted waveform and thus a wide IF bandwidth and a high-speed ADC. If chirp modulation is used to generate the bandwidth, then by reproducing the slope of the modulating waveform in the receiver mixer (an approach called stretch processing), these bandwidths can be reduced [27]. Modern direct digital synthesizers (DDS) (Fig. 16) allow such flexibility in frequency control. In addition, they are able to compensate for distortions in amplitude and phase response because of the transmit-

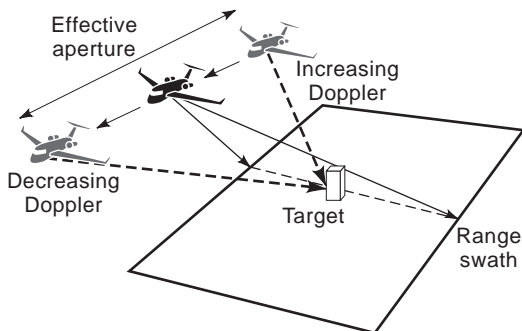


Figure 15. Synthetic aperture radar. As the antenna is moved, radar returns from all the surveillance areas are collected and stored to be later processed as if there was a single antenna the size of the aperture flown.

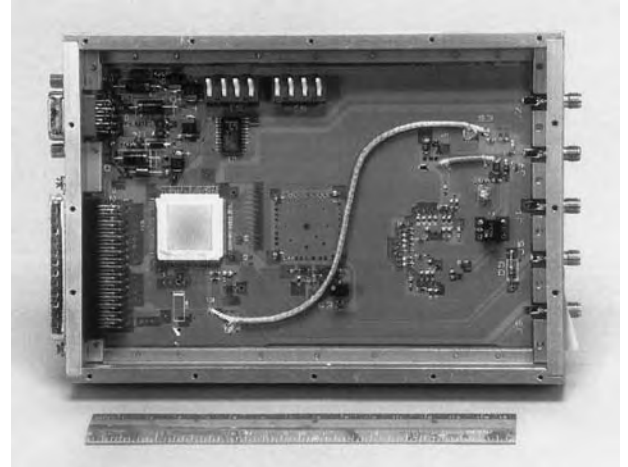


Figure 16. An experimental direct digital synthesizer. DDS technology has an advantage over other traditional waveform-generation techniques—it can arbitrarily create different waveforms in a small, lightweight, cost-effective package. The Sciteq DDS architecture is a double-accumulator GaAs linear frequency modulation synthesizer that allows input of the starting frequency and chirp rate and has a separate phase modulation port. Maximum output bandwidth is 230 MHz, with 24-bit frequency resolution, updated at a 2 ns rate, and spurious responses below -50 dBc. (U.S. Army photo.)

receive chain [28]. Combining the return signals from all the aperture positions usually requires a high-speed processor (Fig. 17) capable of processing a large number of two-dimensional FFTs, but the resulting imagery (Fig. 18) is almost photographic in clarity.

In SAR, there is the need to have relative motion between the radar and the target, but the motion does not need to be along straight line, nor does the antenna need to be oriented normal to the flight path. Some of the more

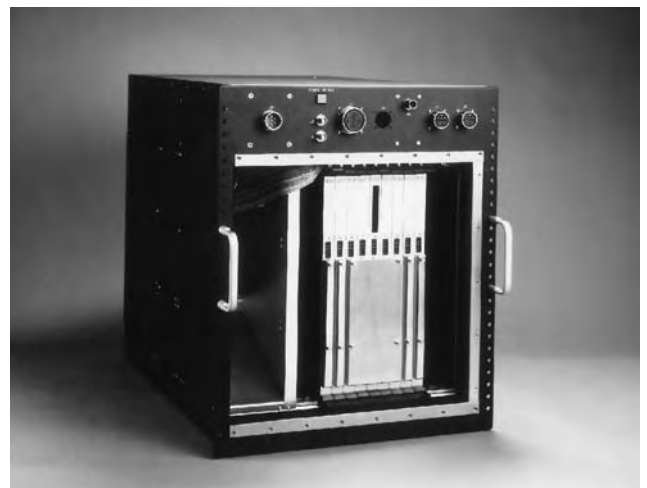


Figure 17. A large number of calculations are necessary to process SAR data. This radar signal processor, used in a Northrop Grumman SAR, consists of nine 9U VME cards, each containing 16 Intel i860 array processors. Each processor card has an aggregate rating of 1.28 Gflops. (Photo courtesy of Mercury Computer Systems, Inc.)

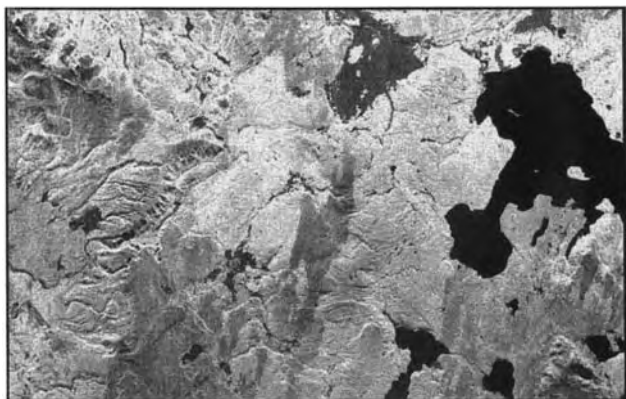


Figure 18. A NASA SAR image of Yellowstone National Park, Wyoming. The image was obtained using the L-band radar channel, with vertical transmit polarization and horizontal receive, on the shuttle's 39th orbit on October 2, 1994. The large dark feature at the right is Yellowstone Lake, which appears this way because the bulk of the transmit energy is forward-scattered off the relatively smooth lake surface.

common variations of SAR include spotlight SAR and inverse SAR (ISAR). In spotlight SAR [29] the antenna is continually pointed toward the area of interest, by rotating the antenna as the aperture is flown, or by flying an aperture in the shape of an arc [30]. This allows larger than normal apertures to be flown (thus improving resolution) as well as allowing use of higher-gain, narrower-beamwidth antennas. ISAR is typically viewed as having the radar fixed and the target moving; more generally, however, both can move as in the cases of airborne radars imaging ships. In ISAR, the motion of the maneuvering target is used to provide additional detail of the target for target recognition [31] and possibly allowing 3D reconstruction of the target. This implies that existing radars could gain from added signal processing capabilities, but the processing burden is high, as the path and maneuvering nature of the target is unknown and must also be extracted from the data to correctly focus the target [32].

2.5. Impulse Radar

An impulse radar is perhaps the simplest form of pulse radar. An extremely short pulse, or a single cycle of a sine wave, which has a very wide bandwidth, is radiated from an antenna that typically sets the useful radar bandwidth of the system [33,34]. The short pulsewidth provides an inherent high-range resolution capability. Most of these systems are denoted ultra wideband (UWB) radars because their bandwidth is greater than half their center frequency, and many of them operate in the VHF and/or UHF region to provide foliage or ground penetration capability. Because the frequency coverage and bandwidth can be provided by other means (such as chirp), the advantages that the impulse radar offer are the capability to detect close-in targets (as in ground contact radars) because of the small eclipsing zone and simple and highly efficient transmitters that are low in size and weight (Fig. 19).



Figure 19. The PowerSpectra BASS-02X is a bulk avalanche semiconductor switch activated by a semiconductor laser. Rise-times are about 150 ps with a falltime of approximately 2 ns. Peak output power is approximately 2 MW, and average power is approximately 1.5 W. Prime power is 28 VDC, and the unit weighs approximately 2 kg. (U.S. Army photo.)

2.6. Bistatic Radar

Some of the problems with radars are that they are active devices, and therefore susceptible to detection; they can have large, high-power transmitters that reduce their mobility; and they detect Doppler shifts only from the radial component of target velocities. One way to improve the situation is to separate the transmitter and to provide remote, receive-only radar systems (Fig. 20). Such systems are called bistatic radars, or more appropriately multi-static radars when multiple transmitters and receivers are used [35]. Forward-scattered energy from large regions is often much stronger than the backscattered energy and may give clues as to the texture or construction of the region. Existing radars (designed for other purposes) are often used as the transmit source, whereas smaller, cheaper receivers take advantage of the existing signals to provide simple low-cost radars at multiple sites, all serviced by the existing emitter. Bistatic radars have been used for semiautomatic missile guidance (the missile carries only the receiver, while the launching platform usually supports the transmitter), low-cost passive cueing of target angle of approach, examining heavenly bodies (from separate Earth locations or with an Earth receiver and a satellite transmitter) and providing simultaneous reception from multiple sites to develop three-dimensional models of ionospheric or atmospheric events [36].

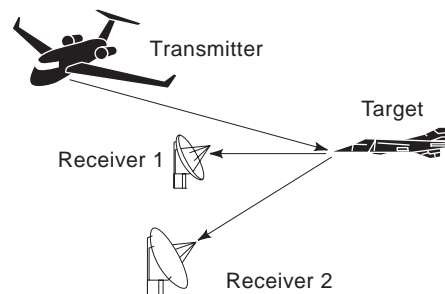


Figure 20. In a bistatic radar, the transmitter and receivers are physically separated, and multiple receivers are serviced by the same transmitter.

3. RADAR NOMENCLATURE

No standards exist for the identification of commercial radar systems, although many manufactures will number a series of products with a common name or common acronym descriptive of their purpose. The most common nomenclature system is the Joint Electronics Type Designation System (JTEDS, MIL-STD-196D, 1985), which is an outgrowth of the Joint Army-Navy Nomenclature System (AN System) and the Joint Communications-Electronics Nomenclature System developed during WWII in the United States. Although the JTEDS nomenclature scheme also covers units and subgroups of systems, it is best known for its distinctive sequence of the letters AN followed by a forward slash, followed by a three-letter indicator series, followed by a dash, and then followed by a sequence number and possibly suffixes designating variations in the design. The three indicator letters (Table 2) describe the type of installations, type of equipment, and purpose of the system. Radar systems will always have a middle letter P, although some systems with a P may not be radars because this equipment type also covers radar detectors, electronic recognition and identification (IFF) equipment, radar beacons, and pulse-type navigational aids. The system has been extended to include other English-speaking countries with blocks of sequence numbers being assigned to various countries. Canada is assigned sequence numbers 500–599 and 2500–2599, Australia has the block 2000–2099, New Zealand has 2100–2199, and the United Kingdom has 2200–2299. Thus the designator AN/APS-506 identifies a Canadian airborne search radar, whereas AN/PPS-15A is the first upgrade to a U.S. man-portable search radar.

The U.S. National Weather Service designates its radars as WSR (originally for Weather Service Radar, now

more commonly Weather Surveillance Radar) followed by a number, which is the last two digits of the year the radar was put into service. Thus the WSR-57 is a unit that was first placed into service in 1957. Later units had alphabetic suffixes designating the radar band in which they operated, such as WSR 74C and the WSR-74S. Most recently, the letter designator has been used for other purposes as well, as in the WSR-88D (the NEXRAD system radar) where the D designation stands for Doppler. The Federal Aviation Administration (FAA) has a series of radars for air-traffic control, which typically are designated by their task name acronyms and a sequence number. Examples of current equipment include the long range air route surveillance radars (ARSR-4) (Fig. 21), the terminal surface monitoring airport surveillance radars (ASR-9 and 11) and airport surface detection equipment (ASDE-3); the windshear products, which include the shared NEXRAD system and the terminal Doppler weather radar (TDWR); and the secondary surveillance radar designated as the precision runway monitor (PRM).

4. RADAR TARGETS

It is useful to have a set of standard radar targets that can be used to test, evaluate, or measure the performance of radar systems [37]. The most common of these are simple geometric shapes; their radar cross section (RCS) is easily calculable and have been extensively studied in the literature. The sphere is the best known of these targets, re-radiating uniformly in all directions, but it does not present a very large RCS for its physical size. A specular reflector, like the flat plate, presents a much larger cross section, especially at higher frequencies, but this larger return happens only over a small angular region, near the

Table 2. Equipment Indicators

Installation	Type of Equipment	Purpose
A—Piloted aircraft	A—Invisible light, heat radiation	A—Auxiliary assembly
B—Underwater mobile, submarine	C—Carrier	B—Bombing
D—Pilotless aircraft	D—Radiac	C—Communications
F—Ground, fixed	E—Laser	D—Direction finder
G—Ground, general	G—Telegraph/teletype	E—Ejection/release
K—Amphibious	I—Interphone/public address	G—Fire control/searchlight directing
M—Ground, mobile	K—Electromechanical/inertial wire	H—Recording/reproducing
P—Portable	L—Countermeasures	K—Computing
S—Water	M—Meteorological	M—Maintenance/test
T—Ground, transportable	N—Sound in air	N—Navigational
U—General utility	P—Radar	Q—Special/combined purposes
V—Ground, vehicular	Q—Sonar/underwater sound	R—Receiving/passive detecting
W—Surface and underwater combination	R—Radio	S—Detecting/range/bearing/search
Z—Airborne vehicle combination	S—Special/combinations of types	T—Transmitting
	T—Telephone (wire)	W—Automatic or remote control
	V—Visual/visible light	X—Identification and recognition
	W—Armament	Y—Surveillance and control
	X—Facsimile/television	
	Y—Data processing	

Note: Special suffix T is reserved for training, and suffixes X, Y, and Z are reserved for changes in voltage, phase, or frequency. (V) designates variable groupings of equipment and (P) designates units accepting plugins. (Xnn) designates developmental units with the second (and third) letter used to designate the developmental agency. Open () (called “bowlegs”) designate developmental equipment or generically indicate equipment families.

Source: Adapted from MIL-STD-196D, 1985.



Figure 21. The ARSR-4 is a long-range, three-dimensional, solid-state surveillance system. It was specifically designed as a joint-use radar for the FAA, the U.S. Air Force, and US Navy. The ARSR-4 detects all aircraft out to 463 km through all weather and clutter conditions as well as man-made interference. (Photo courtesy of Northrop Grumman Corporation.)

normal to the surface. Corner reflectors have a wider angle of acceptance, in at least one dimension, as does a cylinder. Figure 22 shows a number of radar targets and their approximate RCS, based on geometric optics. For these RCS values to be realistic, target dimensions need to be about 10λ . As target dimensions approach 1λ , or less, diffraction effects must be considered, and the target cross sections should be calculated using physical optics, uniform theory of diffraction, or computational electromagnetics [38].

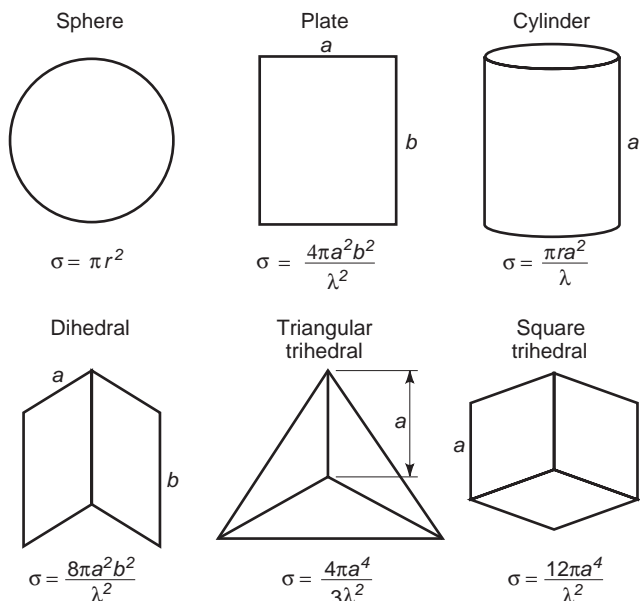


Figure 22. Common radar targets and their equivalent radar cross section σ , where r is the radius of the circular objects.



Figure 23. A motorized set of trihedrals provides a moving target for W band. Note the angle offset between the support arm and the trihedrals. This offset was designed so that the “flash” from the arm, as it becomes normal to the radar wave, will not occur at the same time as the peak of the trihedral response.

Although it is not the optimal solution [39], the triangular plate trihedral is the most commonly used specular target, having a reasonably wide angle of operation in both elevation and azimuth and having simple assembly requirements. The RCS of a 30-cm-radius sphere is 0.28 m^2 , whereas a triangular trihedral with sides 30 cm long has a maximum RCS 37.7 m^2 , at 10 GHz. These targets are usually placed a number of wavelengths above the ground to help reduce multipath interference and oriented to maximize target return in the expected direction of the radar.

These targets are useful for evaluating pulse radars, but for evaluating MTI and pulse Doppler radars, a moving target is needed. Figure 23 shows a simple approach to the problem, but one in which the radial velocity of the target varies over the angle swept by the motorized arm. Electronic simulators have the advantage that RCS and Doppler can be varied by simple choice of circuit parameters, and with the addition of a delay line, even the range to the target can appear to vary. This delay can allow the



Figure 24. A K_u -band electronic moving-target simulator. One horn receives the transmitted signal, which is mixed down with one STALO and mixed back up with another matched STALO. A discriminator circuit provides a visual indication of target Doppler frequency and direction. An attenuator provides control over the radar cross section of the return signal.

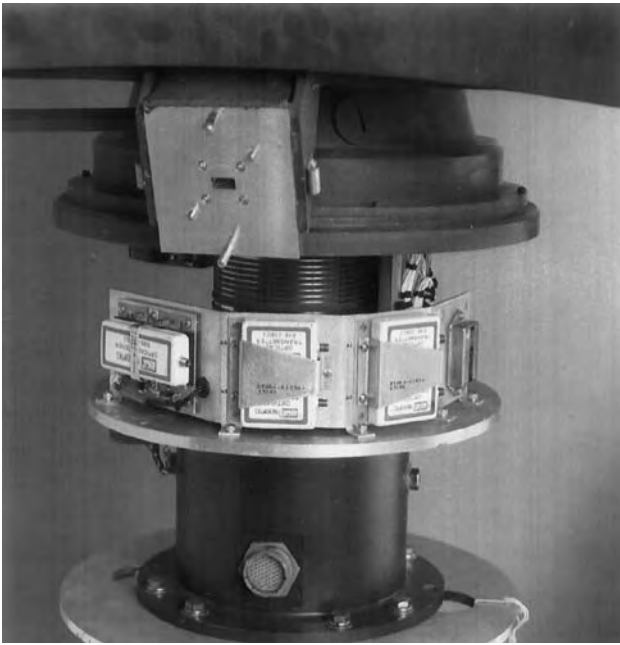


Figure 25. The slip ring assembly for the AN/TPS-74(V) showing the fiberoptic transceivers. Only DC power and digital signals pass through the slip rings.

target return to be placed in a range cell that differs from the one the simulator occupies, thus eliminating possible corruption of the signal because of the clutter return from the simulator itself. The target simulator is often a simple superhetrodyne receiver that uses a single sideband modulator to add the desired Doppler signal to the IF output, which is then upconverted back to the initial radar band with the same local oscillator chain. The choice of upper or lower sideband will, respectively, make the target appear

as either incoming or outgoing. The addition of an extremely long delay line can allow such an electronic simulator to be used in a laboratory setting while making targets appear as if they are kilometers away. A simpler, although less time and temperature stable, approach to designing a target simulator is shown in Fig. 24, in which the return frequency is simply shifted.

5. SCANNING THE SCENE

The typical surveillance radar antenna (Fig. 13) rotates through 360° of azimuth and possibly some amount of elevation. RF is usually supplied through a rotary joint for azimuth and through another rotary joint for elevation, or for limited angles, through flexible waveguide. For lower radar frequencies, the losses may be low enough, and for fixed installations, usually an abundance of transmitter power is available. But at higher frequencies, the losses and noise because of these feed mechanisms may be objectionable. One approach to avoid these losses, for lower-power mobile systems, is to mount the radar transceiver at the antenna (Fig. 25), or at least part of the RF assembly at the antenna. Figure 26 shows the large rotating antenna radomes of the E-2C. The larger, and perhaps more well-known, E-3 Sentry airborne warning and control system (AWACS) sports a similar 9.1-m-diameter rotodome, which rotates at 6rpm over a Boeing 707. However, vertical scanning and height finding are performed by electronic scanning techniques using ferrite phase-shifters. The phase shifters, phase control electronics, receiver protectors, and receiver preamplifiers are mounted on back of the antenna. A better view of an electronic elevation scan can be seen in the picture of the ARSR-4 antenna in Fig. 27. Many applications require much less than 360° coverage, and with the radar transceiver mounted at the



Figure 26. A pair of Northrop Grumman E-2C Hawkeyes are easily identified by their distinctive 7.3-m (24-ft)-diameter rotodomes, which contain both the low-side lobe radar antenna and the IFF antenna. A Lockheed Martin An/APS-145 radar system automatically detects, identifies, and tracks targets at ranges exceeding 300 mi. (U.S. Naval Institute collection.)

Figure 27. The view inside the radome of the ARSR-4, long-range L-band radar, exposes the phased array feed that supports up to nine simultaneous elevation beams that can be steered up to 30°. The reflector/feed assembly rotates mechanically through 360° azimuth. (Photo courtesy of Northrop Grumman Corporation.)

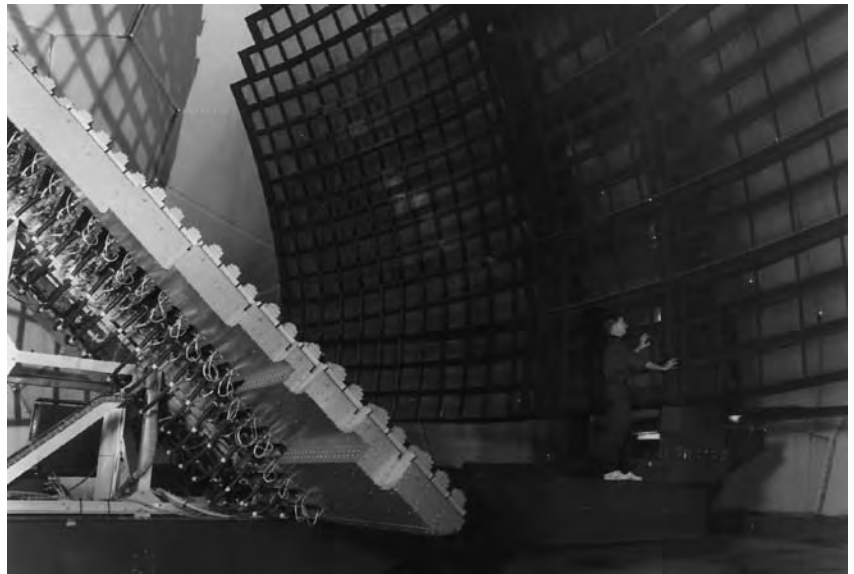


Figure 28. The Arleigh Burke (DDG-51) Aegis system is based on the AN/SPY-1D multifunction phased-array S-band radar. The SPY-1 antennas are the octagonal panels on the corners of the deckhouse. The inset in the upper left shows an antenna being installed in a deckhouse. (U.S. Naval Institute collection.)

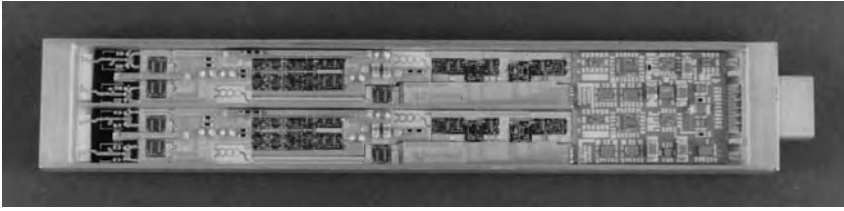


Figure 29. The Lockheed Sanders Mark IV microwave module is a two-channel MMIC T/R module that covers 6–18 GHz in a package of which its volume is less than 16 cm^3 (cubic centimeters). The module is 2.1 cm wide \times 11.9 cm long. (© Lockheed Martin Corporation 1991.)

antenna, often flexible cables can supply power and control signals. Another approach is shown in Fig. 5, in which azimuth scanning is provided by tilting the reflector left and right, while elevation is accomplished by moving the feed horn.

It is possible to provide 360° coverage and elevation control in a phased-array-based antenna system. The Aegis weapons system (Fig. 28) is based on the AN/SPY-ID multifunction phased-array S-band radar, which is able to perform search, track, and missile guidance functions simultaneously with a track capacity of over 100 targets. Four antenna panels, situated around the deckhouse, provide full 360° coverage. Each array has 4100 discrete elements and measures $3.65 \times 3.65 \text{ m}$. Output power is approximately 4 MW and is provided by a four-stage amplifier employing traveling-wave tubes (TWT) and cross-field amplifiers (CFAs). It is possible to build high-power solid-state radars while avoiding the need for high-power phase shifters to provide beamsteering. T/R modules allow the construction of large phased arrays in which the output of literally hundreds of low-power solid-state amplifiers are spatially combined. Common phase shifters and builtin RF switching in such modules means that beamsteering works the same on both transmit and receive. Figure 29 shows a 6–18 GHz dual-channel T/R module that uses a single vector modulator in each channel to provide phase and amplitude control for both the receive and transmit paths. Each channel also supports a vertical and horizontal antenna channel so that multiple polarizations can be used, including, with the addition of a 90° phase-shifter, circular polarization. A common serial digital control circuit runs both channels to minimize control lines and provides control over the T/R switches,

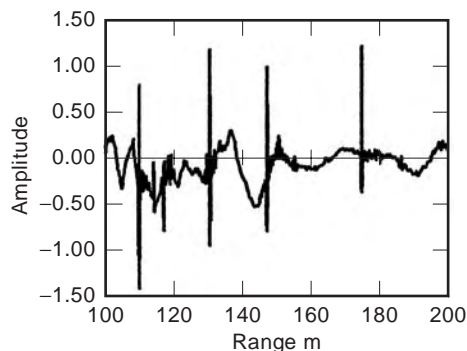


Figure 30. An A-scope display from a high-resolution impulse radar. The large spikes are the result of trihedral targets in the scene. The slower variations in the baseline value are due to the clutter return from the surrounding terrain.

the 5-bit phase shifters, and the 4-bit attenuators. The preamplifiers and output amplifiers both have nominal gains of 20 dB with typical noise figures of less than 8 dB and output powers of 26 dBm [40].

6. RADAR DISPLAYS

The original radar displays, developed during WWII, were assigned alphabetic designators (A, B, etc.) and were based on oscilloscope technology. Many of the display types were developed to satisfy special needs, typically to present additional information on the screen [41]. Displays can be broken into three general types: one-axis, two-axis, and plan view. In the A-scope (Fig. 30), the most common one-axis display, the amplitude of the radar return is plotted against radar range, which is usually derived from a linear time-based sweep circuit. The sweep circuit allows the operator to change the sweep speed to change the range coverage being displayed. Two-axis displays are based on an x - y oscilloscope and use intensity modulation to indicate the amplitude of the return signal. The most common two-axis display is the B-scope, in which azimuth position is plotted on the horizontal axis and range is plotted on the vertical axis. Elevation is the next most commonly used variable in a two-axis display. The problem with two-axis displays is the geometric distortion that results from plotting angular displacements on a linear axis. Plan displays solve this distortion problem by plotting in cylindrical coordinates, or sectors of cylindrical coordinates. The most common of these displays is the plan position indicator (PPI) or type P display. Early PPI displays rotated the deflection assembly of the CRT in synchronism with rotation of the radar antenna so that the range sweep started at the center of the CRT and moved out radially in the direction the antenna was currently pointing.

More recently, the large use of computers in radar processing has resulted in the use of computer-driven displays to generate synthetically plan view plots of radar data while adding both coordinate and cultural features on the same display (Fig. 31), virtually eliminating the need for plastic plotting boards for keeping track of targets. The explosive growth of the personal computer has led to a large number of computer-driven raster display systems. Monochrome, color, and LCD displays are typically available for small shipboard radar systems, whereas high-resolution color graphic displays are now being used in military and air traffic control radar systems. These displays (Fig. 32) allow the radar operator to overlay map information, weather data, satellite photos, target

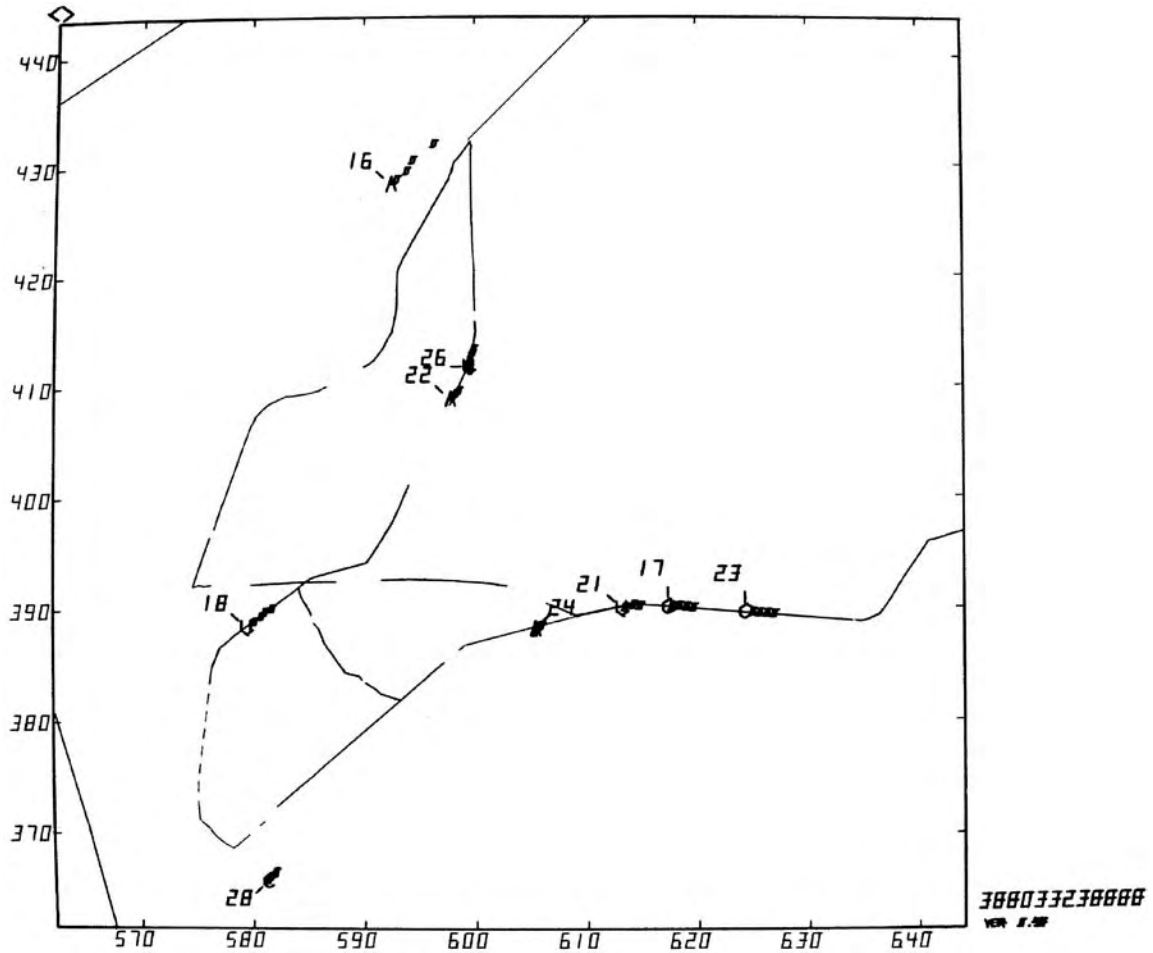


Figure 31. A computer-driven vector scope displays a plan view of an area registered to UTM map coordinates and includes digitized road networks over which radar targets can be plotted. Moving targets that are being automatically tracked are plotted as numbered symbols with “tails” that show a recent history of past locations.



Figure 32. A modern synthetic radar display that allows overlay of map data, weather data, air traffic controller to pilot datalinks, and IFF information to generate a powerful airspace management tool. (Photo courtesy of Northrop Grumman Corporation.)

identification indicators, as well as system status information on a single screen.

BIBLIOGRAPHY

1. Reprinted from IEEE Std 521-1984, *IEEE Standard Letter Designations for Radar Frequency Bands*, copyright 1984 by the Institute of Electrical and Electronics Engineers, Inc. The IEEE disclaims any responsibility or liability resulting from the placement and use in the described manner. Information is reprinted with the permission of the IEEE.
2. F. T. Ulaby, R. K. Moore, and A. K. Fung, *Microwave Sensing*, Artech House, Norwood, MA, 1981, Vol. 3, pp. 1868–1872, 1882–1884.
3. B. T. Binder et al., SAR foliage penetration phenomenology of tropical rain forest and northern U.S. forest, *Record IEEE 1995 Int. Radar Conf.*, 1995, pp.158–163.
4. M. A. Karam et al., A microwave scattering model for layered vegetation, *IEEE Trans. Geosci. Remote Sens.* **GRS-30**: 767–784 (1992).
5. M. I. Mirkin et al., Results on ground penetration SAR phenomenology from June 1993 Yuma experiment, *Record IEEE 1995 Int. Radar Conf.*, 1995, pp. 164–170.

6. B. C. Brock and W. E. Patitz, *Optimum Frequency for Ground-Penetrating Synthetic-Aperture Radar (GPSAR)*, Sandia National Laboratories, Report SAND93-0815, 1993.
7. B. Johnson et al., A research and development strategy for unexploded ordnance sensing, *MIT Lincoln Laboratory Project Report EMP-1*, April 1, 1996, pp. 33–37, 78.
8. Ref. 2, Vol. 1, pp. 256–343.
9. R. J. Doviak and D.S. Zrnic, *Doppler Radar and Weather Observations*, Academic Press, San Diego, 1983.
10. A. R. Holt, Some factors affecting the remote sensing of rain by polarisation diversity radar in the 3–35 GHz frequency range, *Radio Sci.* **19**:1399–1412 (1984).
11. F. E. Nathanson, *Radar Design Principles*, New York, McGraw-Hill, 1969, pp. 359–390.
12. *Operator's and Organization Maintenance Manual, Radar Sets*, TM-115840-298-12, HQ Dept. Army, June 1967, pp. 1–36.
13. A. F. Harvey, *Microwave Engineering*, Academic Press, London, 1963, pp. 545–554.
14. Ref. 13, pp. 889–937.
15. E. A. Wolff and R. Kaul, *Microwave Engineering and Systems Applications*, Wiley, New York, 1988, pp. 251–274, 315–332.
16. G. W. Stimson, *Introduction to Airborne Radar*, Hughes Aircraft Co., El Segundo, CA, 1983, p. 420.
17. Ref. 16, pp. 429–433.
18. J. S. Shreve, Digital Signal Processing, in M. I. Skolnik, ed., *Radar Handbook*, 1st ed., McGraw-Hill, New York, 1970.
19. M. Waters and B. R. Jarrett, Bandpass signal sampling and coherent detection, *IEEE Trans. Aerospace Electron. Syst.* **AES-18**:731–736 (1982).
20. W. Rice and K. H. Wu, Quadrature sampling with high dynamic range, *IEEE Trans. Aerospace Electron. Syst.* **AES-18**:736–739 (1982).
21. Ref. 16, pp. 371–386.
22. Ref. 16, pp. 403–414.
23. Ref. 12, pp. 391–404.
24. A. W. Rihaczek, *Principles of High-Resolution Radar*, McGraw-Hill, New York, 1969, pp. 226–286.
25. B-G. Goldberg, Linear Frequency Modulation—Theory and Practice, *RF Design* **16**:39–46 (1993).
26. J. C. Curlander and R. N. McDonough, *Synthetic Aperture Radar*, Wiley, New York, 1991.
27. D. A. Debell and T. S. Diviney, Use of IF sampling and stretch processing for a lower-cost mapping radar, *Proc. SPIE* **2747**:98–105 (1996).
28. A. Hill and J. Surber, Using Aliased-Imaging Techniques in DDS to generate RF signals, *RF Design* **16**(9):31–36 (1993).
29. C. V. Jakowatz Jr., et al., *Spotlight-Mode Synthetic Aperture Radar: A Signal Processing Approach*, Kluwer Academic Publishers, Boston, 1996.
30. M. Jin and M. Chen, Analysis and simulation for a spotlight-mode aircraft SAR in circular flight path, *Int. Geosci. Remote Sens. Symp.* **4**:1777–1780 (1993).
31. Musman, D. Kerr, and C. Bachmann, Automatic recognition of ISAR ship images, *IEEE Trans. Aerospace Electron. Syst.* **AES-32**:1392–1404 (1996).
32. B. D. Steinberg and D. L. Carlson, Production and use of synthetic aperture images of aircraft: Adaptive beamforming and 3-D stereo viewing, *Proc. SPIE*, **1630**:131–140 (1992).
33. H. L. Bertoni, L. Carin, and L. B. Felsen, eds., *Ultra-wide-band, Short-pulse Electromagnetics*, Plenum Press, New York, 1993.
34. L. Carin and L. B. Felsen, eds., *Ultra-wideband, Short-pulse Electromagnetics 2*, Plenum Press, New York, 1995.
35. N. J. Willis, *Bistatic Radar*, Artech House, Boston, 1991.
36. Wurman, S. Heckman, and D. Boccippio, A bistatic multiple-doppler network, *J. Appl. Meteorol.* **32**:1802–1814 (1993).
37. Ref. 2, Vol. 2, pp. 766–779.
38. R. Stone (ed.), *Radar Cross Sections of Complex Objects*, IEEE Press, New York, 1990.
39. Sarabandi and T.-C. Chiu, Optimum corner reflectors for calibration of imaging radars, *IEEE Trans. Anten. Propag.* **AP-44**:1348–1361 (1996).
40. Bugeau et al., Advanced MMIC T/R Module for 6 to 18 GHz multifunction arrays, *IEEE Microwave Millimeter-wave Monolithic Circuits Symp.*, 1992.
41. D. K. Barton and S. A. Leonov, eds., *Radar Technology Encyclopedia*, Artech House, Boston, 1997, pp. 140–145.

FURTHER READING

- M. I. Skolnik, *Introduction to Radar Systems*, 2nd ed., McGraw-Hill, New York, 1980 (the standard textbook).
- M. I. Skolnik, ed., *Radar Handbook*, 2nd ed., McGraw-Hill, New York, 1990 (with 25 chapters, each written by an expert in the field).

RADAR IMAGING

VICTOR C. CHEN
U.S. Naval Research Laboratory
Washington, DC

1. INTRODUCTION

Radar is an electromagnetic instrument used for the detection and location of targets, such as aircraft, ships, and ground vehicles. Radar transmits electromagnetic energy to a target and receives the reflected signal. From the received radar signal, target-related information such as location and velocity can be accurately measured. Compared to optical and infrared sensors, radar as a radiofrequency (RF) sensor can perform with high accuracy, at long distances, and under all weather conditions. Therefore, it has been widely used for civilian and military purposes. Radar is capable of detecting and imaging moving targets for wide-area surveillance, targeting information, and other military purposes. It is also capable of generating high-resolution maps for earth-resource mapping, terrain structure information, environment monitoring, and other civilian applications.

Radar imaging is an imaging method obtained by processing radar signals reflected from objects. The radar image of an object is the distribution of its reflectivity in the range and cross-range domain. The range is the dimension

6. B. C. Brock and W. E. Patitz, *Optimum Frequency for Ground-Penetrating Synthetic-Aperture Radar (GPSAR)*, Sandia National Laboratories, Report SAND93-0815, 1993.
7. B. Johnson et al., A research and development strategy for unexploded ordnance sensing, *MIT Lincoln Laboratory Project Report EMP-1*, April 1, 1996, pp. 33–37, 78.
8. Ref. 2, Vol. 1, pp. 256–343.
9. R. J. Doviak and D.S. Zrnic, *Doppler Radar and Weather Observations*, Academic Press, San Diego, 1983.
10. A. R. Holt, Some factors affecting the remote sensing of rain by polarisation diversity radar in the 3–35 GHz frequency range, *Radio Sci.* **19**:1399–1412 (1984).
11. F. E. Nathanson, *Radar Design Principles*, New York, McGraw-Hill, 1969, pp. 359–390.
12. *Operator's and Organization Maintenance Manual, Radar Sets*, TM-115840-298-12, HQ Dept. Army, June 1967, pp. 1–36.
13. A. F. Harvey, *Microwave Engineering*, Academic Press, London, 1963, pp. 545–554.
14. Ref. 13, pp. 889–937.
15. E. A. Wolff and R. Kaul, *Microwave Engineering and Systems Applications*, Wiley, New York, 1988, pp. 251–274, 315–332.
16. G. W. Stimson, *Introduction to Airborne Radar*, Hughes Aircraft Co., El Segundo, CA, 1983, p. 420.
17. Ref. 16, pp. 429–433.
18. J. S. Shreve, Digital Signal Processing, in M. I. Skolnik, ed., *Radar Handbook*, 1st ed., McGraw-Hill, New York, 1970.
19. M. Waters and B. R. Jarrett, Bandpass signal sampling and coherent detection, *IEEE Trans. Aerospace Electron. Syst.* **AES-18**:731–736 (1982).
20. W. Rice and K. H. Wu, Quadrature sampling with high dynamic range, *IEEE Trans. Aerospace Electron. Syst.* **AES-18**:736–739 (1982).
21. Ref. 16, pp. 371–386.
22. Ref. 16, pp. 403–414.
23. Ref. 12, pp. 391–404.
24. A. W. Rihaczek, *Principles of High-Resolution Radar*, McGraw-Hill, New York, 1969, pp. 226–286.
25. B-G. Goldberg, Linear Frequency Modulation—Theory and Practice, *RF Design* **16**:39–46 (1993).
26. J. C. Curlander and R. N. McDonough, *Synthetic Aperture Radar*, Wiley, New York, 1991.
27. D. A. Debell and T. S. Diviney, Use of IF sampling and stretch processing for a lower-cost mapping radar, *Proc. SPIE* **2747**:98–105 (1996).
28. A. Hill and J. Surber, Using Aliased-Imaging Techniques in DDS to generate RF signals, *RF Design* **16**(9):31–36 (1993).
29. C. V. Jakowatz Jr., et al., *Spotlight-Mode Synthetic Aperture Radar: A Signal Processing Approach*, Kluwer Academic Publishers, Boston, 1996.
30. M. Jin and M. Chen, Analysis and simulation for a spotlight-mode aircraft SAR in circular flight path, *Int. Geosci. Remote Sens. Symp.* **4**:1777–1780 (1993).
31. Musman, D. Kerr, and C. Bachmann, Automatic recognition of ISAR ship images, *IEEE Trans. Aerospace Electron. Syst.* **AES-32**:1392–1404 (1996).
32. B. D. Steinberg and D. L. Carlson, Production and use of synthetic aperture images of aircraft: Adaptive beamforming and 3-D stereo viewing, *Proc. SPIE*, **1630**:131–140 (1992).
33. H. L. Bertoni, L. Carin, and L. B. Felsen, eds., *Ultra-wide-band, Short-pulse Electromagnetics*, Plenum Press, New York, 1993.
34. L. Carin and L. B. Felsen, eds., *Ultra-wideband, Short-pulse Electromagnetics 2*, Plenum Press, New York, 1995.
35. N. J. Willis, *Bistatic Radar*, Artech House, Boston, 1991.
36. Wurman, S. Heckman, and D. Boccippio, A bistatic multiple-doppler network, *J. Appl. Meteorol.* **32**:1802–1814 (1993).
37. Ref. 2, Vol. 2, pp. 766–779.
38. R. Stone (ed.), *Radar Cross Sections of Complex Objects*, IEEE Press, New York, 1990.
39. Sarabandi and T.-C. Chiu, Optimum corner reflectors for calibration of imaging radars, *IEEE Trans. Anten. Propag.* **AP-44**:1348–1361 (1996).
40. Bugeau et al., Advanced MMIC T/R Module for 6 to 18 GHz multifunction arrays, *IEEE Microwave Millimeter-wave Monolithic Circuits Symp.*, 1992.
41. D. K. Barton and S. A. Leonov, eds., *Radar Technology Encyclopedia*, Artech House, Boston, 1997, pp. 140–145.

FURTHER READING

- M. I. Skolnik, *Introduction to Radar Systems*, 2nd ed., McGraw-Hill, New York, 1980 (the standard textbook).
- M. I. Skolnik, ed., *Radar Handbook*, 2nd ed., McGraw-Hill, New York, 1990 (with 25 chapters, each written by an expert in the field).

RADAR IMAGING

VICTOR C. CHEN
U.S. Naval Research Laboratory
Washington, DC

1. INTRODUCTION

Radar is an electromagnetic instrument used for the detection and location of targets, such as aircraft, ships, and ground vehicles. Radar transmits electromagnetic energy to a target and receives the reflected signal. From the received radar signal, target-related information such as location and velocity can be accurately measured. Compared to optical and infrared sensors, radar as a radiofrequency (RF) sensor can perform with high accuracy, at long distances, and under all weather conditions. Therefore, it has been widely used for civilian and military purposes. Radar is capable of detecting and imaging moving targets for wide-area surveillance, targeting information, and other military purposes. It is also capable of generating high-resolution maps for earth-resource mapping, terrain structure information, environment monitoring, and other civilian applications.

Radar imaging is an imaging method obtained by processing radar signals reflected from objects. The radar image of an object is the distribution of its reflectivity in the range and cross-range domain. The range is the dimension

along the radar line of sight (LoS) to the object, and the cross-range is the dimension transverse to the radar LoS. An important factor of the image quality is its resolution: the ability to separate closely spaced scatterers in range or in cross-range. The resolution along the radar LoS to the object is called *slant range* or *range resolution*. The resolution transverse to the radar LoS is called the *cross-range resolution*. The range resolution is inversely proportional to the bandwidth of the transmitted signal. High range resolution is obtained by using wide-bandwidth radar signal waveforms. High cross-range resolution requires a large aperture for the radar antenna.

A large aperture can be synthesized by using a small real antenna aperture mounted on a moving platform. The synthetic aperture technique was initially developed in the 1950s [1–3]. Such a radar system with a synthetic aperture is called the *synthetic aperture radar* (SAR). The first SAR was an airborne system. Later, in 1978 a spaceborne SAR system was built.

The most common modes in SAR are stripmap mode and spotlight mode. In stripmap mode, the antenna beam bears on a fixed direction relative to the moving direction of the platform as illustrated in Fig. 1a. When the platform moves, a strip of area is swept over. If the antenna direction is off the perpendicular of the flight path, it is referred to as *squinted stripmap SAR*. The stripmap mode can generate a wide-area map of the terrain. The length of the imaged area is determined by the length of the data collection; and the azimuth resolution in along-track direction is determined by its antenna beamwidth. It should be noted that after correction of range migrations, the “azimuth” is actually the “cross-range,” and the azimuth resolution becomes the cross-range resolution. The concept of spotlight synthetic aperture was proposed in 1980 [4]. In the spotlight mode, the antenna has narrower beamwidth and steers to the same small patch of an area as the physical aperture moves through the length of the synthetic aperture as shown in Fig. 1b. Spotlight SAR generates images of smaller scenes at finer resolution. The azimuth resolution is determined by the length of the data collection, and the size of the imaged area is determined by the antenna beamwidth. Another mode, called *inverse synthetic aperture radar* (ISAR), is similar

to spotlight SAR, but its data collection is different. In ISAR, the radar can be stationary and the target being imaged is moving. The relative motion between the radar and the target is the key to creating an image of the target. Unlike spotlight SAR, which moves around the target area in order to acquire the necessary angular data, ISAR collects multiple aspect data through the target’s movement.

In SAR and ISAR, a common approach for generating an image from collected data is a range–Doppler processor, which takes the Fourier transform along the azimuth direction in the range-compressed data. With the spotlight SAR and ISAR configuration, data are inherently distributed in a polar grid. To use the Fourier transform for generating a focused image, the processor must remap the polar formatted data onto a rectangular grid, called *polar formatting*. Other approaches of generating a focused image, such as the wavenumber approach [5,6], were also developed.

2. RADAR IMAGING GEOMETRY AND SYNTHETIC APERTURE

To produce a focused radar image, the processor in radar imaging systems should include motion compensation, interpolation, data formatting, Fourier transform, autofocus, and distortion correction. The focused image produced may be further used for feature extraction, image registration, image exploitation, and automatic target recognition.

2.1. Geometry

The geometry of airborne radar is shown in Fig. 2, where an aircraft is moving with a constant velocity V at height H and along a flight track parallel to the x axis. Assume that the origin of a coordinate system (x, y, z) is located at the center of the scene. The range between the flight path and the center of the scene is $R_s = (H^2 + y_0^2)^{1/2}$, where y_0 is the ground range to the center of the scene. Assume that the length of the synthetic aperture is L and that the azimuth resolution of the radar image is determined by the length of the synthetic aperture. When the platform

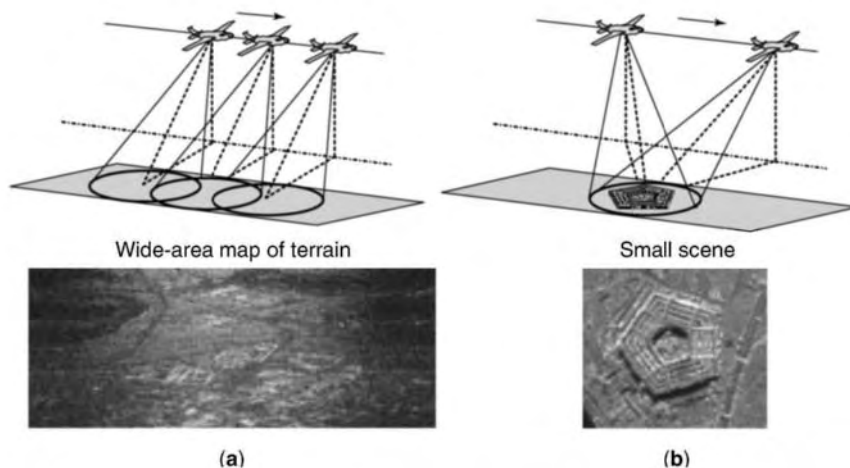


Figure 1. (a) Stripmap SAR; (b) spotlight SAR.

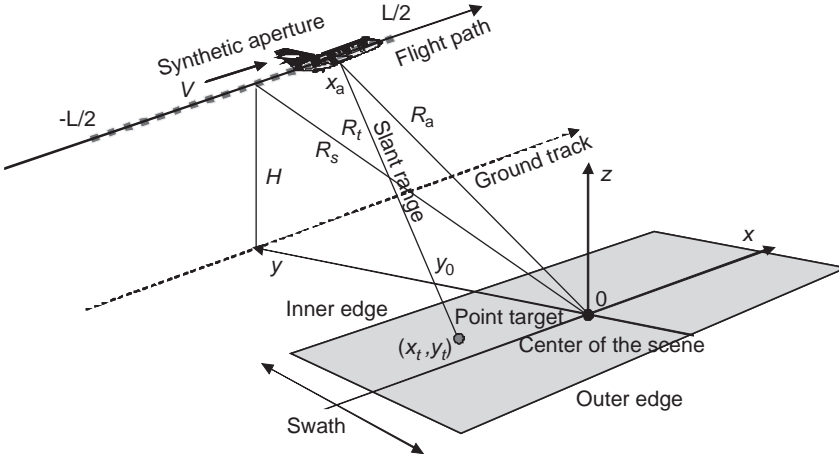


Figure 2. Geometry of airborne SAR.

moves, the radar antenna position x_a along the flight path varies. Thus, the distance from the antenna to the center of the scene R_a also varies. Assume a point target is located at $(x_t, y_t, z_t = 0)$ and the distance between the radar antenna and the point target is $R_t = [(x_a - x_t)^2 + y_t^2 + H^2]^{1/2}$, which also varies with x_a . In Fig. 2, the area being imaged is assumed to be two-dimensional. The limits on y are the inner and outer edges of the swath, and the limit on x is determined by the length of data collection.

2.2. Synthetic Aperture

Radar with a real aperture transmits signals and receives signals reflected from an object. The 3-dB-beamwidth β is determined by the length of the real aperture (D_{RA}) and the wavelength (λ): $\beta = \lambda/D_{RA}$. Assume a point scatterer at range R . For a small β , the azimuth resolution along the track is

$$\Delta A = 2R \tan \frac{\beta}{2} \cong R\beta = R \frac{\lambda}{D_{RA}}$$

To achieve a high azimuth resolution, it is necessary to either increase the physical aperture size or reduce the wavelength. For example, to achieve a desired along-track azimuth resolution of 1 m at a range of 50,000 m, a radar operating at 0.03 m of wavelength (X band) needs a physical aperture length

$$D_{RA} = \frac{\lambda}{\Delta A} R = \frac{0.03}{1} 50,000 = 1500 \text{ (m)}$$

which is too long to realize. Therefore, to achieve the same azimuth resolution without using an extremely large physical aperture, a synthetic aperture technique must be used. The synthetic technique moves a real aperture along a track to transmit and receive signals at each sample location and, then, coherently processes the received signals at all the sample locations to synthesize a large aperture.

For the stripmap mode, x indicates the position of the radar platform along the line of the track. The sampling interval Δx is determined by the platform velocity V and the pulse repetition frequency (PRF): $\Delta x = V/\text{PRF}$. The

maximum length of the synthetic aperture is determined by the length that the scatterer remains in the beamwidth of the real aperture. The effective length of the synthetic aperture D_{SA} is twice that of the physical aperture length $2D_{RA}$. Thus, the azimuth resolution of the synthetic aperture becomes

$$\Delta A_{SA} = R\beta_{SA} = R \frac{\lambda}{2D_{RA}} = R \frac{\lambda}{2R\lambda/D_{RA}} = \frac{D_{RA}}{2}$$

Thus, for the stripmap SAR, the azimuth resolution of the synthetic aperture is not dependent on the range and the wavelength. It is determined only by the physical aperture length D_{RA} . A smaller aperture offers better along-track resolution.

However, in the spotlight SAR, the radar antenna is steered to a small patch area when the radar platform is moving. Thus, longer real apertures can be used, and smaller beamwidth steers to a small area of interest. The azimuth resolution is proportional to the total slew angle covered, but not half of the physical extent of the real aperture used.

As mentioned earlier, the ‘‘azimuth resolution’’ used here is not quite exact because after correcting range migration, the ‘‘azimuth’’ is actually the ‘‘cross-range’’ [7].

3. STRIPMAP-MODE SAR IMAGING

In the stripmap-mode SAR, the radar antenna steering angle is at a fixed angle and the range to the center of the swath is kept constant. The most important aspect of the stripmap SAR is that the azimuth resolution is dependent only on the physical length of the real aperture and independent of the range and the frequency or wavelength. Thus, smaller physical aperture offers better azimuth resolution.

The imaging geometry of the stripmap SAR mode is shown in Fig. 2. The waveform usually used in high-resolution stripmap SAR is a linear FM chirp. Dechirp processing is performed on the radar receiver side. Some image formation algorithms, such as the range migration algorithm, do not require a chirp waveform and dechirp on

the receiver side. The received signal returned from a point scatterer can be expressed as a 2D convolution of the radar cross-section (RCS) with an impulse response function h . This impulse response function can be expressed as a 2D convolution of two impulse response functions: $h = h_1 \otimes h_2$, where h_1 is the impulse response function for azimuth compression and h_2 is the impulse response function for range compression [8]. To compensate for range migration, interpolation in the range–Doppler domain is used to straighten the curved point scatterer locus. Therefore, the RCS of the target can be reconstructed by two step correlations of the returned signal with two impulse response functions h_2 and h_1 .

Usually, SAR data $s(t,x)$ are arranged in a 2D matrix in the slant-range/along-track domain, called the (t,x) domain. Focusing of SAR data requires a 2D space-variant correlation algorithm. One method is 2D time-domain correlation, but its computational load is high. Other algorithms take advantage of the frequency-domain correlation. They are the range–Doppler algorithm, range migration algorithm, chirp-scale algorithm, and other variations of wavenumber-domain algorithms.

3.1. Range–Doppler Algorithm

The change of the time delay (slant range) from pulse to pulse is referred to as the “range migration.” To solve the problem of range migration in satellite SAR, a range–Doppler algorithm that processes SAR data into complex images was introduced by Wu in 1976 [9]. Since then, the range–Doppler algorithm has become a standard algorithm for satellite SAR. To handle satellite SAR geometries with squint, a secondary range compression algorithm was also proposed [8].

SAR data are usually arranged in the delay time t (or slant-range) and the along-track x (or azimuth), that is, (t,x) domain. However, the range–Doppler algorithm works in the slant range and the spatial azimuth frequency or Doppler domain, called the (t,k_x) domain, where k_x is the spatial frequency of the along-track x . To transform into the Doppler domain, the Fourier transform is taken in the along-track domain x . Then, in the (t,k_x) domain, the correction of the range migration is performed by using interpolation.

The spatial frequency k is also called the *wavenumber* and is equivalent to the number of times a wave has the same phase over the spatial domain. The wavenumber is defined by $k = \omega/c = 2\pi/\lambda$, where ω is the angular frequency and c is the speed of the wave propagation. If the radar radiation wave has an incident angle θ , the wavelength and wavenumbers k_x and k_y are related by [5]

$$\lambda = \frac{2\pi c}{\omega}; \quad k_x = \frac{2\pi}{\lambda} \sin \theta; \quad k_y = \frac{2\pi}{\lambda} \cos \theta; \quad \omega = \frac{c}{2} \sqrt{k_x^2 + k_y^2}$$

The range–Doppler algorithm can be summarized as follows:

1. *Range Migration Correction.* By taking a 1D Fourier transform of the range-compressed baseband data $s(t,x)$ in the along-track or x direction, the range–

Doppler data in the delay time t (or slant range) and spatial wavenumber k_x (or Doppler) can be obtained: $S(t, k_x) = FT_{1D}\{s(t, x)\}$. Range migration correction is performed by a k_x -dependent timeshift that requires a time-domain interpolation. Thus, the range migration correction function is a k_x -dependent linear phase function in the 2D Fourier domain (ω, k_x)

$$\exp\left\{j \frac{cR}{4} \cdot \frac{k_x^2}{\omega_0^2} \omega\right\}$$

where ω is the temporal frequency of the delay time t , R is the slant or across-track range, and ω_0 is the carrier angular frequency.

2. *Azimuth Compression.* Azimuth compression is performed by multiplying a phase compensation function

$$\exp\left\{jR \cdot \left(\sqrt{4 \frac{\omega_0^2}{c^2} - k_x^2} - 2 \frac{\omega_0}{c}\right)\right\} \\ \approx \exp\left\{-j \frac{cR}{4} \cdot \frac{k_x^2}{\omega_0}\right\}$$

to correct the spreading of the range-dependent loci.

The combined 2D range and azimuth correction function can be expressed by

$$\exp\left\{-j \frac{cR}{4} \cdot \frac{k_x^2}{\omega_0^2} (\omega_0 - \omega)\right\}$$

Compared with the optimal 2D correction function, the range–Doppler algorithm has a 2D phase aberration that causes defocusing when the squint angle or spatial Doppler wavenumber is large.

3.2. Range Migration Algorithm

The range migration algorithm (RMA) was originally from seismic signal processing [10,11] and is an important image formation method for stripmap SAR. It is also an important algorithm for spotlight SAR image formation [12,13].

The RMA works in the temporal frequency and spatial wavenumber (ω, k_x) domain by taking a 2D Fourier transform of the range-compressed data. Thus, the time delay becomes a phase shift, which is a linear function of ω and can be easily compensated by a phase operation. Therefore, range migration is no longer a problem in the (ω, k_x) domain. The algorithm uses a matched filter and a coordinate remapping called the *Stolt interpolation* to transform from coordinates (ω, k_x) into (k_r, k_x) , where

$$k_r = \sqrt{4k^2 - k_x^2}$$

is the spatial wavenumber in the slant range.

The RMA can be summarized as follows:

1. Transform the collected data $s(t, x)$ into the frequency domain by taking the 2D Fourier transform:

$$S(\omega, k_x) = \text{FT}_{2\text{D}}\{s(t, x)\}$$

2. Map the 2D transformed data from the (ω, k_x) domain to the (k_r, k_x) domain by Stolt interpolation. The Stolt interpolation is a k_x -dependent point-to-point mapping from ω to k_r :

$$k_r(\omega, k_x) = \sqrt{4\left(\frac{\omega + \omega_0}{c}\right)^2 - k_x^2} - 2\frac{\omega_0}{c}$$

3. Perform the 2D phase compression in the (k_r, k_x) domain: using $\exp[jR_S(\sqrt{k_r^2 - k_x^2} - k_r)]$ to compensate the range migration, where R_S is a fixed slant-range distance between the flight path and the center of the scene as shown in Fig. 2.
4. Take a 2D inverse Fourier transform to reconstruct the image.

The RMA can be used with waveforms other than chirp waveforms. It is also not necessary to dechirp on the receiver side. The RMA does not have the space-variant defocus and geometric distortion that other algorithms usually suffer from (such as the polar format algorithm). Thus, it can be used to form a fine-resolution image of a large terrain area and to image large scenes at short range. However, because scatterers located at different positions have different migration loci, the Stolt interpolation requires a long computation time.

3.3. Chirp-Scale Algorithm

The range–Doppler algorithm and wavenumber-domain algorithms need interpolation that makes the SAR image formation processing more complicated in design and becomes a large source of aliasing effects.

An algorithm called the *chirp-scale algorithm* (CSA), sometime called the *differential range deramp algorithm* [14–16], is an efficient image formation algorithm that eliminates interpolation procedure and still preserves phase information. It works in both the range–Doppler domain and the 2D spatial frequency domain. It can be used in the stripmap mode as well as the spotlight mode. This algorithm can handle large apertures and large squints, and has better phase and geometry accuracy than other algorithms.

The key to this algorithm is to use the linear FM property of the range chirp to differentially shift the range energy as a function of spatial azimuth frequency, and then to do the range cell migration correction (RCMC) in the 2D spatial frequency domain.

The CSA begins with data chirped in the range. First, it processes the collected data in order to compensate its phase to a line that is parallel to the flight path and crossing through the center of the scene. Then, the processed data are chirped in both azimuth and range. The CSA

transforms data to the two-dimensional spatial frequency domain. All the range cell migration trajectories are adjusted to match the reference trajectory of a scatterer at the selected reference range R_{ref}

$$\tau_{\text{ref}}(k_x) = \frac{2}{c} R_{\text{ref}} [1 + C(k_x)]$$

where

$$C(k_x) = \frac{1}{\sqrt{1 - [\lambda k_x / (2v)]^2}} - 1$$

is the curvature factor and v is the relative velocity between the reference scatterer and the radar. This procedure requires a linear scaling with a scale factor $[1 + C(k_x)]^{-1}$. Then, RCMC is performed by multiplying a phase function to each point. However, because only the shift and linear components are compensated, RCMC does not completely compensate for motion through resolution cells. However, the result is still satisfactory.

The CSA algorithm can be summarized as follows:

1. *Azimuth FFT*. Take FFT in the azimuth direction and transform the data from the (t, x) domain to the range–Doppler (t, k_x) domain, where the linear FM signal structure prior to range compression can be exploited.
2. *Chirp Scaling Operation*. Multiply by a function whose phase is chosen so that the range migration phase term of every scatterer is equalized to that of the reference range. After range focusing, the spatial loci of the resulting range curvatures are equalized.
3. *Range FFT*. The data are transformed to the 2D wavenumber (k_r, k_x) domain.
4. *2D Phase Compensation*. This procedure includes RCMC, range compression, and secondary range compression (SRC). The RCMC corrects the dominant range curvature effects, known as the “bulk RCMC”.
5. *Range Inverse FFT*. Transform the data back to the range–Doppler (t, k_x) domain.
6. *Azimuth Filter and Phase Residual*. In the range–Doppler domain, an azimuth frequency (k_x) -dependent bandpass filter is selected for weighting and look processing, and the Doppler centroid is adjusted over the range.
7. *Azimuth Inverse FFT*. Take inverse FFT in the azimuth direction. The focused complex image is obtained.

4. SPOTLIGHT MODE SAR IMAGING

Spotlight SAR [17,18] images objects in a small area or a target of interest as illustrated in Fig. 1b. In the spotlight SAR, the radar antenna is steered to the same small patch of area when the radar platform is moving; thus, its

footprint always stays over the same area of terrain. Since much longer real apertures are used, a smaller beamwidth and consequently a smaller footprint stays over a small area of interest. In spotlight SAR, the azimuth resolution is proportional to the total slew angle covered, and not half of the physical extent of the real aperture.

4.1. Image Formation in Spotlight SAR

The azimuth resolution in the spotlight SAR is proportional to the total effective rotation angle of the antenna

$$\Delta A = \frac{\lambda}{2\Delta\theta}$$

where $\Delta\theta$ is the total integrated angle.

The returned baseband signal from the scene center has zero Doppler frequency shift because there is no relative radial motion between the radar and the scene center after motion compensation to the scene center. While the translation is compensated, rotational motions between the radar and the scene center still remain. First, the signal is dechirped in both range and azimuth. Then, the data are transformed into the 2D wavenumber (k_r, k_x) domain.

However, in the (k_r, k_x) domain the data samples are not on a rectangular grid. They are on a ribbon-type polar grid. Because the Fourier transform is performed in a rectangular format, a 2D interpolation must be applied to remap the data from a polar grid to a rectangular grid. This is called *polar formatting*. After interpolation, the 2D sampling points are lined up on a uniform grid in both range and cross-range. Then, a matched filter can be applied to compensate for nonlinear phase shift and, therefore, a 2D Fourier transform can be used for both range and azimuth compression simultaneously. By taking a 2D inverse Fourier transform, the final image can be formed. If the scene of a target of interest is small, the small ribbon-type polar data are approximately rectangular. Thus, a 2D inverse Fourier transform can be directly applied without image defocus.

For spotlight SAR, either RMA or CSA can be directly applied without requiring motion compensation to the center of the scene.

4.2. Polar Formatting Algorithm

The polar formatting algorithm (PFA) is an image formation technique based on tomography. It was originally developed for spotlight SAR imaging [19,20], and has been

adapted for use in ISAR imaging [21]. In spotlight SAR and ISAR, the relative rotation between the radar and the object causes the collected data to be distributed in polar format. To obtain fine-resolution imagery using Fourier-based image formation, polar-to-rectangular remapping is required. PFA compensates the phase of the collected radar data to a fixed point at the center of the scene and, thus, the preprocessed data become dechirped in azimuth as well as in range.

The PFA involves reconstructing the spatial distribution of an object by applying the Fourier transform to a set of observations, where each is a projection of the object onto a line, taken over a series of aspect angles. A Fourier transform produces a line segment in the 3D Fourier space offset from the origin by the carrier frequency and at an angle determined by the angle of the radar LoS. As successive pulses are received and the aspect between the radar and the object changes, the line segment sweeps out a data surface in 3D Fourier space. Once the data surface is formed, an image of the object can be reconstructed by transforming the surface into the spatial domain using the inverse Fourier transform.

The implementation of the PFA involves measuring the target motion dynamics, estimating parameters for the data surface model, projecting the data surface onto a planar surface, interpolating the data into equally spaced samples, and performing the inverse Fourier transform. The image formed by the PFA is illustrated in Fig. 3. The comparison of imagery produced by the conventional method shown on the left side of the figure and the polar reformatting method shown on the right side of the figure and the improvement in the image quality can be seen. Polar reformatting can produce high-quality imagery even in conditions with significantly complex target motion.

4.3. Autofocus

If the relative motion between the radar and the target cannot be accurately estimated and compensated, the residual relative motion will induce phase errors. The phase error is the cause of image defocusing. *Autofocus* is a technique that estimates and compensates the phase errors in the range-compressed phase history data in order to achieve a well-focused image of the target. Most autofocus algorithms are space-invariant compensations that apply the same phase correction function to the whole data.

There are many autofocus algorithms available; two important ones are the phase gradient algorithm (PGA) and the prominent point processing (PPP) algorithm.

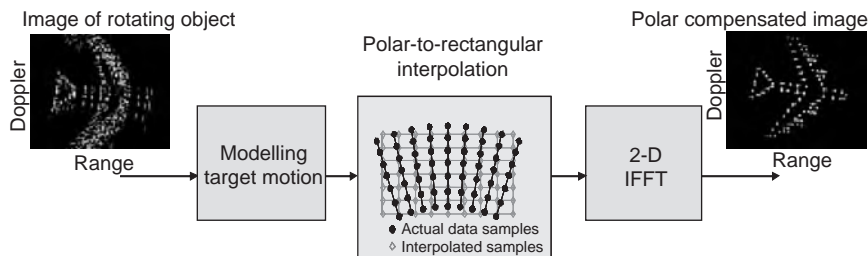


Figure 3. Radar image formed by polar formatting algorithm.

4.3.1. Phase Gradient Algorithm. The phase gradient autofocus (PGA) proposed by Wahl et al. [22] has been widely used in SAR systems. It was developed to make a robust estimation of the gradient of the phase error using the defocused SAR image data. The PGA is an iterative algorithm that allows robust and nonparametric estimation and exploits the redundancy of the phase error information contained in the degraded image. Because the performance of the PGA is independent of the content in a SAR scene, there is no need to require isolated pointlike reflections in the SAR scene as in other algorithms.

The PGA can be applied to a phase-degraded complex SAR image no matter how the image was formed. Because the complex image and phase history are a Fourier transform pair, the range-compressed phase-history-domain data can be obtained by taking a 1D Fourier transform in the azimuth direction.

To allow robust phase error estimation and image restoration, there are four critical processing steps in the PGA:

1. *Center (Circular) Shifting.* This procedure performs a circular shift on each row of the image in order to place the strongest scatterer of the row in the middle of the image.
2. *Windowing.* This consists of weighted windowing of each row of the image previously shifted. This operation allows one to preserve the width of the central image points and discard the others that do not contribute to the phase error estimation. Shifting and windowing together may achieve the highest signal-to-noise ratio in order to maximize the accuracy of the phase error estimation.
3. *Phase Gradient Estimation.* This is a linear, unbiased minimum variance estimate. The phase error estimate is obtained by integrating the estimated phase gradient. Before operating the phase correction on each row, it is necessary to remove the linear phase component from the estimated phase error to prevent any image shifting due to the phase correction.
4. *Iterative Phase Correction.* This procedure is applied iteratively to the image until the root-mean-square phase error becomes small enough or convergence is reached. Finally, all the estimated phase errors are summed together to give a total phase error, which is removed from the original image.

4.3.2. Prominent Point Processing. Prominent point processing (PPP), initially used in resolving moving target imaging in SAR [23], utilizes information from several prominent points to correct phase errors and convert non-uniform rotation into a uniform rotation.

In spotlight SAR, any motion compensation method must remove space-variant errors as well as space-invariant errors. Multiple PPP is the procedure that can remove both space-invariant and space-variant errors. In the multiple PPP, the first prominent point is used to remove translational motions and adjust frequency and phase of the returned signal so as to form a new image center. The

second prominent point corrects the phase error induced by nonuniform rotations. The third prominent point is used to measure the rotation rate and estimate the azimuth scale factor of the resulting image to achieve complete focusing.

Figure 4 is a block diagram of multiple PPP embedded in a spotlight SAR image formation. Instead of using sensors to measure motion dynamics, the first point corrects the space-invariant phase error induced by translation motion and, thus, a new image center is formed. The second point makes uniform rotation, and equalizes the gain of the sampling position in azimuth. The third point estimates the azimuth scale factor corresponding to the new sampling position in azimuth. Then, the PFA utilizes this information on accurate angular position to interpolate and generates fine-resolution and well-focused SAR images.

5. INVERSE SYNTHETIC APERTURE RADAR (ISAR) IMAGING

In spotlight SAR, the radar platform moves around the object being imaged to acquire the necessary angular data, while in ISAR, a stationary radar collects the angular data through the object's movement. Therefore, ISAR can be seen as a variation of SAR that images objects by coherently processing the returned radar data collected at different aspect angles.

The challenges in ISAR image formation stem from the unknown nature of the object's motion. An object being imaged is often engaged in complicated motions that combine translation and rotational motions. Thus, motion compensation must be applied to form a focused image of the object. Because the only available information is the radar-collected data themselves, the ISAR motion compensation is a data-driven process.

5.1. ISAR Motion Compensation

An ISAR image is formed by the Doppler shift at each range cell, obtained by taking the Fourier transform over the observation time interval. To use the Fourier transform properly, it is assumed that the frequency content of the analyzed signal is time-invariant. With this assumption, a long observation time provides high Doppler resolution. However, when the target moves, Doppler shifts are time-varying and the assumption of time-invariant Doppler frequency shifts is no longer valid. Thus, the Doppler spectrum becomes smeared, degrading the cross-range (formally called the *azimuth resolution*), and the radar image becomes blurred.

There are many motion compensation algorithms for solving the problem of Doppler smearing and image blurring [24,25]. Most methods are Fourier-based approaches. In order to apply the Fourier transform properly, during the imaging time scatterers must remain in their range cells and their Doppler frequency shifts must be constant.

Motion compensation algorithms typically consist of range alignment and Doppler tracking. The standard range alignment is accomplished by tracking the movement of a reference point in the range profile (such as a

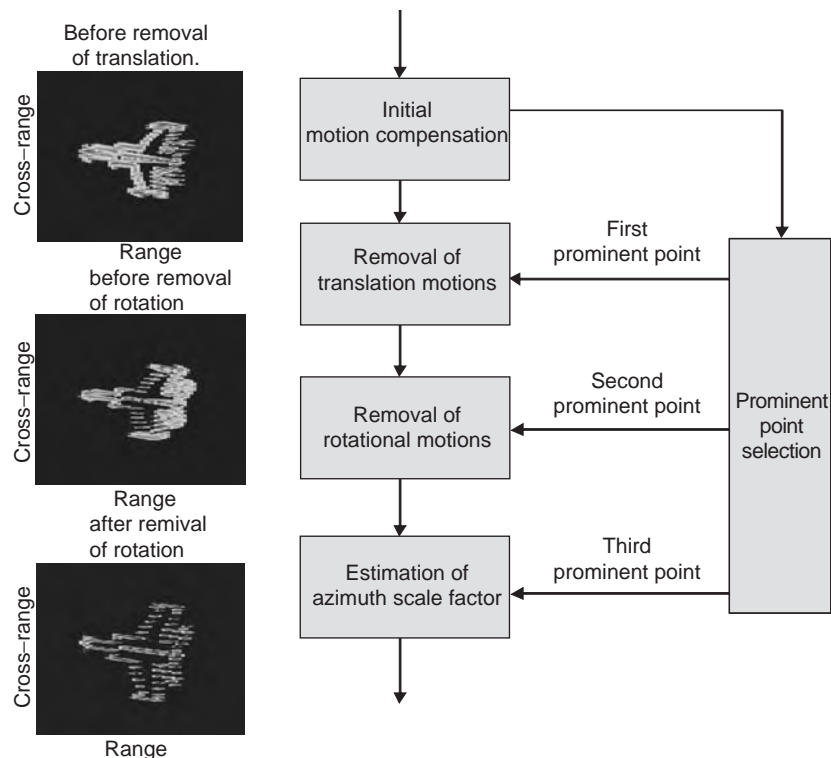


Figure 4. Block diagram of the multiple prominent point processing.

prominent peak or the centroid) across pulses and fitting it to a low-order polynomial [26]. This coarse range alignment allows a point scatterer to be sorted into the same range bin across all the pulses. However, the accuracy of the alignment is limited by the range resolution. The range alignment may not be sufficient to overcome the phase errors measured in terms of the radar wavelength. Consequently, Doppler tracking must be carried out in order to align the phase. There are many different schemes that perform Doppler tracking, including the subaperture approach [27,28], the cross-range centroid tracking approach [29], and PGA. These methods consider the Doppler shifts of the target as a whole, and apply the same correction vector to all the scatterers in the image. This is effective when translation motion is dominant.

From the radar received signal, if the target's range as a function of time is known exactly over the imaging time duration, then the extraneous range-dependent phase term can be removed by multiplying its conjugate with the received signal. This is referred to as *gross focusing* or *motion compensation*. Then, the image of the target can be formed simply by taking the inverse Fourier transform of the motion-compensated signal.

When the coherent processing interval is long or when the target exhibits fast maneuvers, the phase error due to the nonuniform rotational motion is seldom negligible and must also be properly compensated. One useful scheme to carry out this operation is to utilize the multiple PPP algorithm to track one or more point scatterers in the image in order to extract the motion parameters. Once the motion parameters are known, compensation of both translation and rotational motions can be achieved. The main

challenge in applying the multiple PPP algorithm is the selection of the prominent point scatterers. However, in practice, prominent point scatterers may be difficult to pinpoint or not available at all.

Time-frequency analysis is another attractive way to address the Doppler tracking issue in motion compensation [30,31]. Specifically, in Ref. 30 it was shown that by applying the time-frequency transform in place of the Fourier transform, the ISAR image can be effectively examined at each dwell-time instance, thus eliminating range drift and Doppler smearing. A time-frequency-based procedure for achieving both translation and rotational motion compensation can be found in Ref. 32, where an adaptive procedure extended from the adaptive spectrogram [33] is used to select and extract the phase of multiple prominent point scatterers on the target. The extracted phase is then coupled with the multiple PPP model to eliminate the undesirable motion errors in the original radar data. In this manner, the phase of the focused image is preserved and the Doppler resolution offered by the full coherent processing interval can be achieved.

5.2. ISAR Polar Formatting

The PFA for ISAR imaging is similar to that for spotlight SAR imaging. The main difference is that in ISAR processing the motion of the target provides the change in aspect necessary for Doppler processing, whereas in spotlight SAR the change in aspect comes from the motion of the radar. As a consequence of this difference, the aspect change between the radar and the target is both unknown and uncontrollable in ISAR imaging. Because the aspect

change defines the shape of the data surface, the rotation of the target must be determined before PFA can be used to process the data into imagery. Instead of modeling the target motion, ISAR PFA models the data surface directly and uses measurable scatterer motion quantities, such as range, Doppler, and translation acceleration, to estimate the data surface model parameters [21]. A quadratic data surface model may be used that requires few parameters but still allows compensation for the majority of the non-linear rotational motion in the target.

5.3. Time–Frequency-Based ISAR Image Formation

Conventional ISAR image formation is based on the Fourier transform and assumes that Doppler frequency shifts of scatterers are constant. However, when the Doppler spectrum is time-varying, Fourier-based images become blurred and, thus, time–frequency-based image formation should be used to generate clearer images of moving targets [30].

Figure 5a illustrates time–frequency-based image formation. Standard motion compensation is used prior to image formation. The Fourier-based image formation generates only one image frame from an $M \times N$ complex (in-phase and quadrature phase) dataset. The data consist of M time-series histories, each having length N . However, time–frequency-based image formation takes the time–frequency transform for each time series and generates an

$N \times N$ time–Doppler distribution. By combining the M time–Doppler distributions at M range cells, the $N \times M \times N$ time–range–Doppler cube $Q(r_m, f_n, t_n)$ can be formed as

$$Q(r_m, f_n, t_n) = \text{TF}\{G(r_m(n))\}$$

where TF denotes the time–frequency operation with respect to the variable n . At a particular time instant t_i , only one range–Doppler image frame $Q(r_m, f_n, t_n = t_i)$ can be extracted from the cube. There are a total of N image frames available, and every one represents a full range–Doppler image at a particular time instant. Therefore, by replacing the Fourier transform with the time–frequency transform, a 2D range–Doppler Fourier image frame becomes a 3D time–range–Doppler image cube. The integration of the N timeframes is equivalent to the Fourier image. By sampling the image cube in time, a time sequence of 2D range–Doppler images can be viewed. Each individual time-sampled frame from the cube provides not only a clear image with superior resolution but also temporal change properties from one time to another.

Figure 5b shows the conventional ISAR Fourier image of an aircraft using an X-band radar operating at 9000 MHz [31]. Because the target is maneuvering, the Fourier image of the target is still blurred even after applying the standard procedure for focusing. By using time–frequency-based image formation, because each scatterer has its own range and Doppler shift at each time instant,

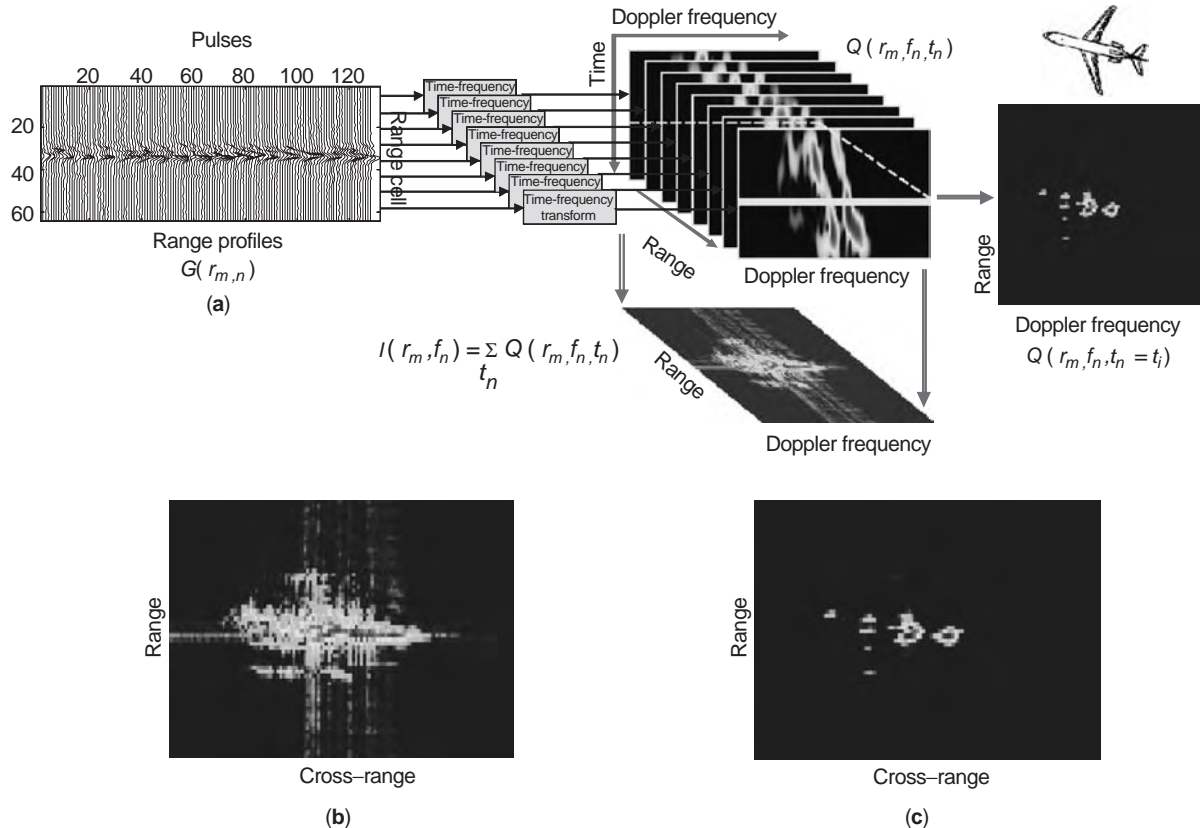


Figure 5. (a) Time–frequency-based image formation; (b) Fourier image; (c) time–frequency image.

without knowing any of the target's kinematic parameters and after resampling the data, a blurred Fourier image becomes a sequence of clear time–frequency images. Figure 5c shows one of these time–frequency images in which the nose, wingtips, fuselage, and engines of the aircraft can be seen very clearly. The blurred image due to target maneuvering can be refocused without applying sophisticated autofocus or motion compensation algorithms.

6. SAR IMAGING OF MOVING TARGETS

A SAR image is a high-resolution map of surface target areas and terrain in the range and cross-range domains. If there are moving targets in the scene, SAR cannot simultaneously produce clear images of both the stationary targets and moving targets. Usually, moving targets appear as defocused and spatially displaced objects superimposed on the SAR map. Therefore, how to detect and clearly image moving targets becomes an important issue.

Moving-target indication (MTI) is a function in SAR. With the MTI function, radar returns from terrain and stationary objects can be suppressed; only the returns from moving targets are used to reconstruct radar images. For focusing the image of detected moving targets, many algorithms that compensate the target's motion and perform phase correction can be used. Because of the additional Doppler shift caused by target motion, the detected and focused target is not necessarily located in its true location in the SAR scene. To relocate it, a multiple-aperture antenna array may be used in the SAR system.

When targets are moving, the motion-induced phase errors cause these images to be mislocated in the cross-range dimension and smeared in both the cross-range and the range domains.

Raney in [34] first discussed the issue of SAR imaging of moving targets. He proposed a simple frequency-domain technique for detecting moving targets in a single-aperture channel SAR. Because the detection requires clutter suppression, clutter cancellation approaches using multiple-antenna channels, such as the space-time adaptive processing, can also be used.

6.1. Multiple-Antenna SAR

Raney discussed the effect of motion parameters on the image of a moving target, specifically, the problem of image smearing and mislocating [34]. If we know the Doppler centroid and the Doppler rate exactly, then the velocity of the moving target can be calculated. However, the Doppler centroid and the Doppler rate of the moving target are determined not only by its velocity but also by its initial location, which we may not know. Therefore, the velocity of a moving target cannot be obtained, and the mislocating problem cannot be solved.

To estimate the target's velocities and reposition mislocated moving targets to their true locations, multiple-antenna systems, such as the interferometry, planar apertures, and antenna arrays, are required. Using multiple antennas with their independent receive channels, the so-called displaced phase center antenna technique or the

spacetime adaptive processing technique can be applied to suppress clutter.

The displaced phase center antenna (DPCA) technique was motivated by the two-pulse cancellation technique in moving-target indication [35]. Two side-looking antenna apertures are aligned along the flight track and normal to the radar LoS. The PRF of the transmitted signals is adjusted such that if a pulse is transmitted at the first aperture, the second aperture will transmit a pulse when it moves to the position where the first aperture was located and transmitted the previous pulse. With DPCA, targets that are buried in the clutter and cannot be detected using single-channel methods may be detectable.

DPCA uses only two antenna apertures. If multiple apertures are used, the radar receives a set of returns, each stamped by its time of arrival and its spatial location at the apertures. The multiaperture processing is referred to as a *space-time processing*. Space-time adaptive processing (STAP) is the one with adaptive spatial and temporal weights [36,37].

With multiple-antenna and space-time adaptive processing, SAR is able to detect moving targets and produce range and cross-range image of both stationary targets and moving targets.

6.2. Ground Moving-Target Indicator

The ground moving-target indicator (GMTI) is designed to reject radar returns from clutter, such as buildings and trees, and detect moving targets, such as tanks, trucks, and aircraft, that could otherwise be obscured. The difference in Doppler frequency shifts between moving targets and the clutter is used to suppress the clutter and detect moving targets. With the GMTI, slow moving targets can also be detected even if their Doppler shifts are very small.

Several multiple-antenna techniques are used to perform GMTI. The basic idea behind using multiple antennas is to have multiple phase centers. The radar compares the received data at the same place in space but at different times. When the radar platform moves, the phase center of each antenna passes through the same place but at a different time. This is called a *displaced phase center*. With displaced phase centers, the clutter will remain the same, but moving targets will change their locations.

In the GMTI radar system, instead of a single-antenna aperture, an antenna array is used. The antenna array may be either along the flight track such as the Joint Strategic Target Attack Radar System (Joint STARS) [38], which is an electronically scanned side-looking airborne radar, or a scanned planar array mounted on the nose of an airplane such as the AN/APY-6 radar [39]. Both the Joint STARS and the AN/APY-6 is a three-port interferometric radar. Compared with the conventional monopulse radar, the interferometric radar provides a low-sidelobe radiation pattern.

7. CONCLUDING REMARKS

After more than 20 years' accomplishments in theories, algorithms, and experiments, radar imaging becomes a well-developed technique and is widely used for civilian

and military purposes. However, many conventional synthetic aperture radar systems operate with a single antenna and a fixed polarization mode for both transmission and reception, and generate two-dimensional images.

Polarimetric SAR that utilizes combinations of antenna polarization for transmission and reception has been developed [40]. Polarimetry provides valuable information on identifying different scattering properties in SAR scenes. Polarimetric data are usually represented by a complex scattering matrix or covariance matrix. Combinations of the antenna polarization include horizontal transmit/horizontal receive (HH), horizontal transmit/vertical receive (HV), vertical transmit/horizontal receive (VH), and vertical transmit/vertical receive (VV). Any polarization can be obtained by a linear combination of a set of orthogonal polarizations.

The conventional SAR image is a two-dimensional depth (range) and width (cross-range) image without height. If height information can be obtained for each cell in the SAR image, then a three-dimensional image of the SAR scene can be generated. Similar to the optical stereo technique, a three-dimensional SAR image may be obtained by using two SAR images of the same scene recorded at different antenna locations, called the *interferometric* SAR. The interferometric SAR utilizes two receiving antenna apertures to record radar returns from scatterers at slightly different altitudes and generates topographic maps. The phase difference between the two receiving apertures is related to the height of a scatterer [41,42]. Height information can also be obtained in a single-antenna SAR flying along a curved flight path or by making two passes of a straight-line flight path at different altitudes. Polarimetric interferometry SAR proposed in Ref. 43 combines the polarimetric and the interferometric SAR that improves the signal-to-noise ratio in SAR image.

For imaging objects under tree canopy or buried in the ground, ultrawideband (UWB) foliage penetration (FOPEN) SAR and ground penetration radar (GPR) have been developed. UWB SAR operates at a low radiofrequency (20–1100 MHz) such that it can penetrate foliage for counter camouflage, concealment, and deception (CCD) and penetrate ground for the detection of buried objects [44,45].

Another advanced development in radar imaging is the bistatic SAR. “Bistatic” means that the transmitter and receiver of the radar are located in two different sites, which have the potential of countering vulnerability from electronic countermeasures. To form an image from a bistatic radar, image formation algorithms derived from the monostatic SAR must be modified to include the effects of motion in both the transmitter and the receiver. More sophisticated high-resolution bistatic image formation algorithms are under development [46,47].

BIBLIOGRAPHY

1. C. W. Sherwin, J. P. Ruina, and R. D. Rawcliffe, Some early developments in synthetic aperture radar systems, *IRE Trans. Military Electron.* **6**:111–115 (1962).
2. C. A. Wiley, Synthetic aperture radars, *IEEE Trans. Aerospace Electron. Syst.* **21**:440–443 (1985).
3. J. C. Curlander and R. N. McDonough, *Synthetic Aperture Radar: Systems and Signal Processing*, Wiley, New York, 1991.
4. J. L. Walker, Range-doppler imaging of rotating objects, *IEEE Trans. Aerospace Electron. Syst.* **16**(1):23–52 (1980).
5. C. Cafforio, C. Pratti, and F. Rocca, SAR data focussing using seismic migration techniques, *IEEE Trans. Aerospace Electron. Syst.* **27**:194–207 (1991).
6. M. Soumekh, *Fourier Array Imaging*, Prentice-Hall, Englewood Cliffs, NJ, 1994.
7. F. H. Wong and T. S. Yeo, New applications of nonlinear chirp scaling in SAR data processing, *IEEE Trans. Geosci. Remote Sens.* **39**(5):946–953 (2001).
8. M. Y. Jin and C. Wu, A SAR correlation algorithm which accommodates large-range migration, *IEEE Trans. Geosci. Remote Sens.* **22**:592–597 (1984).
9. C. Wu, A digital system to produce imagery from SAR, *Proc. AIAA Conf. Systems Design Driven by Sensors*, paper 76–968, 1976.
10. R. H. Stolt, Migration by Fourier transform, *Geophysics*, **43**(1):23–48 (1978).
11. J. Gazdag and P. Sguazzero, Migration of seismic data, *Proc. IEEE* **72**(10):1302–1315 (1984).
12. A. S. Milman, SAR imaging by ω -k migration, *Int. J. Remote Sens.* **14**(10):1965–1979 (1993).
13. C. Prati, A. M. Guarnieri, and F. Rocca, Spot mode SAR focusing with the technique, *Proc. Int. Symp. Geoscience and Remote Sensing*, 1991, pp. 631–634.
14. H. Runge and R. Bamler, A novel high precision SAR focussing algorithm based on chirp scaling, *Proc. Int. Symp. Geoscience and Remote Sensing*, 1992, Vol. 1, pp. 372–375.
15. I. Gunning, F. Wong, and R. K. Raney, A SAR processing algorithm with no interpolation, *Proc. Int. Symp. Geoscience and Remote Sensing*, 1992, Vol.1, pp. 376–379.
16. R. K. Raney, H. Runge, R. Bamler, I. G. Gunning, and F. H. Wong, Precision SAR processing using chirp scaling, *IEEE Trans. Geosci. Remote Sens.* **32**:786–799 (1994).
17. W. G. Carrara, R. S. Goodman, and R. M. Majewski, *Spotlight Synthetic Aperture Radar: Signal Processing Algorithms*, Artech House, Boston, 1995.
18. C. V. Jakowatz, D. E. Wahl, P. H. Eichel, D. C. Ghiglia, and P. A. Thompson, *Spotlight-Mode Synthetic Aperture Radar: A Signal Processing Approach*, Kluwer Academic, Boston, 1996.
19. J. L. Walker, W. Carrara, and I. Cindrich, *Optical Processing of Rotating-Object Radar Data Using a Polar Recording Format*, Technical Report RADC-TR-73-136, AD 526 738, Rome Air Development Center, Rome, NY, May 1973.
20. J. L. Walker, Range-Doppler imaging of rotating objects (Section IV), *IEEE Trans. Aerospace Electron. Syst.* **16**(1):23–52 (1980).
21. R. Lipps and D. Kerr, Polar reformatting for ISAR imaging, *Proc. 1998 IEEE Radar Conf.* 1998, pp. 275–280.
22. D. E. Wahl, P. H. Eichel, D. C. Ghiglia, and C. V. Jakowatz, Phase gradient autofocus—a robust tool for high resolution SAR phase correction, *IEEE Trans. Aerospace Electron. Syst.* **30**(3):827–835 (1994).
23. S. Werness, W. Carrara, L. Joyce, and D. Franczak, Moving target imaging algorithm for SAR data, *IEEE Trans. Aerospace Electron. Syst.* **26**(1):57–67 (1990).

24. D. R. Wehner, *High-Resolution Radar*, 2nd ed., Artech House, Norwood, MA, 1994.
25. J. S. Son, G. Thomas, and B. C. Flores, *Range-Doppler Radar Imaging and Motion Compensation*, Artech House, Norwood, MA, 2001.
26. C. C. Chen and H. C. Andrews, Target motion induced radar imaging, *IEEE Trans. Aerospace Electron. Syst.* **16**(1):1–14 (1980).
27. D. A. Ausherman, A. Kozma, J. L. Walker, H. M. Jones, and E. C. Poggio, Developments in radar imaging, *IEEE Trans. Aerospace and Electron. Syst.* **20**(4):363–400 (1984).
28. T. M. Calloway and G. W. Donohoe, Subaperture autofocus for synthetic aperture radar, *IEEE Trans. Aerospace Electron. Syst.* **30**(2):617–621 (1994).
29. T. Itoh, H. Sueda, and Y. Watanabe, Motion compensation for ISAR via centroid tracking, *IEEE Trans. Aerospace Electron. Syst.* **32**(3):1191–1197 (1996).
30. V. C. Chen and S. Qian, Joint time-frequency transform for radar range–Doppler imaging, *IEEE Trans. Aerospace Electron. Syst.* **34**(2):486–499 (1998).
31. V. C. Chen and H. Ling, *Time-Frequency Transforms for Radar Imaging and Signal Analysis*, Artech House, Norwood, MA, 2002.
32. Y. Wang, H. Ling, and V. C. Chen, ISAR motion compensation via adaptive joint time-frequency technique, *IEEE Trans. Aerospace Electron. Syst.* **34**(2):670–677 (1998).
33. S. Qian and D. Chen, *Introduction to Joint Time-Frequency Analysis—Methods and Applications*, Prentice-Hall, Englewood Cliffs, NJ, 1996.
34. R. K. Raney, Synthetic aperture imaging radar and moving targets, *IEEE Trans. Aerospace Electron. Syst.* **7**(3):499–505 (1971).
35. F. R. Dickey and M. M. Santa, *Final Report on Anti-Clutter Techniques*, General Electric Co., Heavy Military Electronics Dept., Report R65EMH37, Syracuse, NY, 1953.
36. L. E. Brennan and I. S. Reed, Theory of adaptive radar, *IEEE Trans. Aerospace Electron. Syst.* **9**(2):237–252 (1973).
37. L. E. Brennan, J. D. Mallett, and I. S. Reed, Adaptive array in airborne MTI radar, *IEEE Trans. Anten. Propag.* **24**(5): 607–615 (1976).
38. H. Shnitkin, Joint stars phased array radar antenna, *IEEE AES Syst. Mag.* 34–41 (Oct. 1994).
39. L. A. Gross, R. A. Guarino, and H. D. Holt, AN/APY-6 real time surveillance and targeting radar development, *Proc. RTO SET Symp. High Resolution Radar Techniques*, Spain, 1999, pp. 31.1–6.
40. F. T. Ulaby and C. Elachi, *Radar Polarimetry for Geoscience Applications*, Artech House, Norwood, MA, 1990.
41. R. Gens and J. L. V. Gendren, SAR interferometry—issues, techniques, applications, *Int. J. Remote Sens.* **17**:1803–1835 (1996).
42. M. D. Desai, Spotlight mode SAR stereo technique for height computation, *IEEE Trans. Image Process.* **6**(10):1400–1411 (1997).
43. S. R. Claude and K. P. Papathanassiou, Polarimetric SAR-interferometry, *IEEE Trans. Geosci. Remote Sens.* **36**(9): 1551–1565 (1998).
44. L. Happ, K. A. Kappra, M. A. Ressler, J. P. Sichina, K. Sturges, and F. Le, Low-frequency ultra-wideband synthetic aperture radar 1995 BOOMSAR tests, *Proc. 1996 IEEE Nat. Radar Conf.* 1996, pp. 54–59.
45. S. L. Earp, E. S. Hughes, T. J. Elkins, and R. Vickers, Ultra-wideband ground-penetrating radar for the detection of buried metallic mines, *IEEE AES Syst. Mag.* 30–34 (Sept. 1996).
46. J. H. G. Ender, Signal theoretical aspects of bistatic SAR, *Proc. Int. Symp. Geoscience and Remote Sensing*, 2003, Vol. 3, pp. 1438–1441.
47. A. M. Horne and G. Yates, Bistatic synthetic aperture radar, *Proc. Radar Conf. 2002*, Oct. 15–17, 2002, pp. 6–10.

RADAR POLARIMETRY

MARK A. SLETTEN
 Naval Research Laboratory
 Washington, DC
 DAVID J. McLAUGHLIN
 University of Massachusetts
 Amherst, Massachusetts

Radar polarimetry is the study of the vector nature of radar signals and how the relationships between the vector field components can be used to infer the geometry and composition of the illuminated surfaces and targets. In much the same way that a color photograph contains more information than a black-and-white image, polarimetric radar systems, those that measure the vector properties of the scattered radiation, provide much more information on the illuminated scene than do single polarization systems. The polarimetric properties of a radar target are intimately connected to the target's geometry. Spherically shaped targets, such as raindrops, respond to polarized electromagnetic radiation very differently than do the pointed corners of a building, the filamentary branches of a tree, or the waves on the ocean surface. Polarimetric radar systems quantify these differences and exploit them. For instance, polarimetry can be used to better discriminate between bursts of wind-blown rain and aircraft, between breaking water waves and submarine periscopes, and between forested and urban areas.

Polarization is a characteristic of all electromagnetic (EM) radiation. Any EM wave, regardless of which part of the spectrum it occupies, propagates through free space as a transverse wave. The electric and magnetic fields of the wave are directed perpendicular to one another and lie in a plane perpendicular to the direction of propagation. It is the direction of these fields and how they vary with time and space that define the *polarization state* of the wave. The phenomenon of polarization can be illustrated easily with polarized sunglasses. Polarized sunglasses are designed to preferentially attenuate light whose electric field is oriented horizontally, since this is the predominant polarization state of the reflected light that constitutes glare. When the glasses are oriented horizontally (as they are when they are worn), the light that passes through the lenses is essentially vertically polarized. If a second pair of glasses is placed in line with the first, little change in the transmitted light will occur until the second pair is rotated by 90°. The lenses then become cross-polarized, and the

view through the cascaded lenses goes dark as the second lens blocks the polarized light passed by the first.

Most common radar systems, such as those found on ships for navigation or those used by police to monitor automobile speeds, use a single antenna and thus a single polarization. These systems transmit a pulse with a polarization state determined by the antenna design. The pulse propagates out from the antenna, reflects off the target, and then propagates back to the antenna, where it is detected by the radar receiver. Although the target echo and the transmitted pulse may have different polarization states, due to changes incurred by the target's geometry or composition, only the component of the reflected echo that matches the antenna polarization will be collected. Were the target to alter the polarization state sufficiently, such that the reflected echo was orthogonal to the transmitted pulse, no echo would be detected by the radar. As in the case of the cross-polarized sunglasses, the target would be essentially invisible to this single-polarization radar. In contrast, polarimetric radar systems use multiple antennas and switches that allow a complete characterization of the reflected echo while allowing variation in the transmitted polarization as well. In fact, a fully polarimetric system can determine the echo for *any* combination of transmit and receive polarizations using only a small number (at most four) of judiciously chosen measurements.

Radar systems require more than multiple antennas and switches to operate polarimetrically. Another important aspect of a polarimetric radar system is *coherence*. Determination of the polarization state of an EM wave requires specification of both the relative magnitudes of the EM field components as well as their relative phases. A radar is coherent if it can measure the relative phase, as well as magnitude, of received echoes, and thus polarimetric radars must be coherent. (An exception to this rule is discussed in the last section of this article.) *Relative phase* indicates the timing of one EM wave component relative to another, specifying whether the vertically polarized component reaches its peak when the horizontal is near its minimum, for instance. This timing difference contains information on the structure and composition of the target.

Relative phase is also crucial if the response of a target to an arbitrary combination of transmit and receive polarizations is to be mathematically synthesized, rather than directly measured. This process is called *polarization synthesis*. From a small set of coherent measurements utilizing orthogonal polarizations (e.g., vertical and horizontal), polarization synthesis computes the radar cross section (RCS) of a given target for *any* desired combination of transmit and receive polarizations. No additional measurements of the target are needed. The results of polarization synthesis indicate which polarization combinations enhance the visibility of the target and which combinations reduce the backscatter from other, undesired objects (often referred to as *clutter*). In addition, a plot of the RCS as a function of the receive and transmit polarizations forms a *polarization signature*, which may indicate the basic geometry of the target.

Just how much can be learned about an object or a surface from its polarimetric properties is still an area of

active research, particularly in the remote sensing community. Airborne polarimetric radars are being investigated as tools for monitoring land use, classifying terrain, topographic mapping, and imaging of the ocean surface. The mathematical tools that aid in the analysis and interpretation of polarimetric data are under development as well. These tools allow decomposition of a complicated scene into simpler, canonical structures that indicate the nature of the predominant scattering centers.

The following sections describe radar polarimetry in more detail. In the next section, the basic mathematical framework of polarimetry is presented, including the representation of polarized EM fields and of the polarimetric response. Important aspects of polarimetric system design are then discussed, and the article concludes with a summary of current research topics.

1. MATHEMATICAL FOUNDATION

1.1. Representation of Polarized Electromagnetic Waves

1.1.1. Completely Polarized Waves. The polarization state of an EM wave is determined by the relative magnitudes and phases of its electric field components. Assume a plane EM wave is propagating along the z -axis of a right-handed coordinate system. The electric field lies in the x - y plane and can be expressed as

$$\mathbf{E} = E_x^\circ \cos(\omega t - kz + \alpha_x) \hat{\mathbf{x}} + E_y^\circ \cos(\omega t - kz + \alpha_y) \hat{\mathbf{y}} \quad (1)$$

where $\omega = 2\pi f$ is the radian frequency, $k = 2\pi/\lambda$ is the wave-number, λ is the wavelength, t is time, and $\hat{\mathbf{x}}$ and $\hat{\mathbf{y}}$ are unit vectors in the x and y directions, respectively. α_x and α_y are the phases of the x and y components, and the corresponding magnitudes are E_x° and E_y° .

The wave is said to be *linearly polarized* if $\alpha_x = \alpha_y = \alpha$. In this case, the two components are in phase with one another and Eq. (1) can be simplified to

$$\begin{aligned} \mathbf{E} &= \cos(\omega t - kz + \alpha) \cdot (E_x^\circ \hat{\mathbf{x}} + E_y^\circ \hat{\mathbf{y}}) \\ &= E^\circ \cos(\omega t - kz + \alpha) \cdot \hat{\mathbf{e}} \end{aligned} \quad (2)$$

where

$$E^\circ = \sqrt{(E_x^\circ)^2 + (E_y^\circ)^2} \quad (3)$$

$$\hat{\mathbf{e}} = \frac{E_x^\circ \hat{\mathbf{x}} + E_y^\circ \hat{\mathbf{y}}}{E^\circ} \quad (4)$$

In this case, the field is always parallel to the unit vector $\hat{\mathbf{e}}$, as illustrated in Fig. 1. As the magnitude and sign of the field vary with time and/or position, the tip of the field vector traces out a straight line parallel to $\hat{\mathbf{e}}$.

Elliptical polarization results when $\alpha_x \neq \alpha_y$. In this more general case, the two components are no longer in phase and the direction of the electric field is no longer constant. The tip of the electric field vector at any point in space (value of z) traces out an ellipse as time progresses. This can be illustrated by evaluating Eq. (1) at a

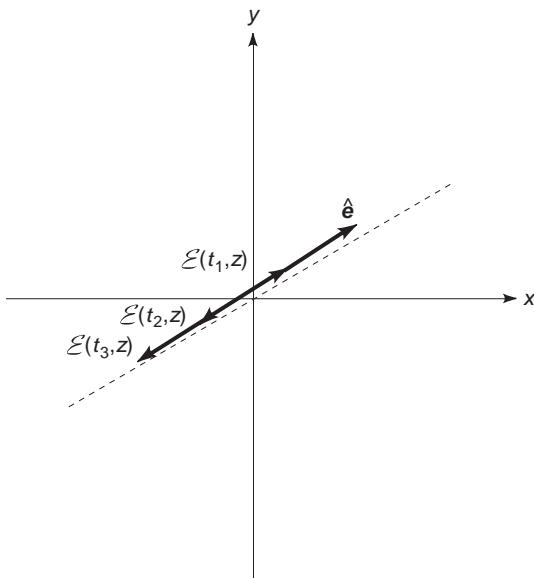


Figure 1. Electric field at three instants in time for a linearly polarized EM wave. The electric field vector is always parallel to a line defined by the vector $\hat{\mathbf{e}}$. The direction of $\hat{\mathbf{e}}$ depends on the relative magnitudes of the x and y components of the field.

particular value of z , for example, $z = 0$:

$$\mathbf{E}(z = 0) = E_x^{\circ} \cos(\omega t + \alpha_x) \hat{\mathbf{x}} + E_y^{\circ} \cos(\omega t + \alpha_y) \hat{\mathbf{y}} \quad (5)$$

This ellipse is illustrated in Fig. 2. The ellipse is characterized by its *orientation angle* ψ and *ellipticity angle* χ . In terms of the original x and y amplitudes and phases, ψ and χ are given by

$$\begin{aligned} \tan(2\psi) &= \tan(2\xi) \cdot \cos(\delta) \\ \sin(2\chi) &= \sin(2\xi) \cdot \sin(\delta) \end{aligned} \quad (6)$$

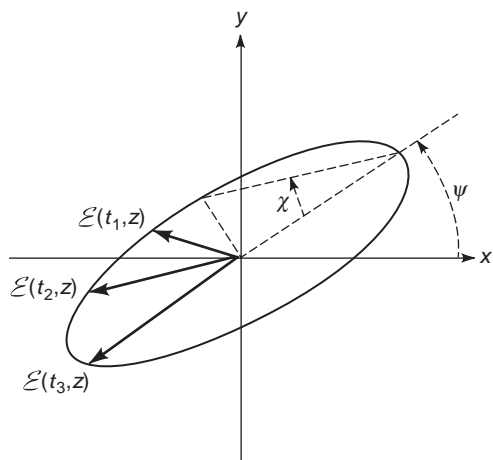


Figure 2. Electric field at three instants in time for an elliptically polarized EM wave. The tip of the electric field vector traces out an ellipse as time progresses. The ellipse is characterized by its orientation angle ψ and its ellipticity angle χ .

where

$$\tan(\xi) = \frac{E_y^{\circ}}{E_x^{\circ}} \quad (7)$$

and

$$\delta = \alpha_y - \alpha_x \quad (8)$$

Note that ψ is defined as the smallest angle between the x axis and the major axis of the ellipse. The ellipticity angle can be related to the major and minor axes of the ellipse, $2E_x^{\circ}$ and $2E_y^{\circ}$, respectively, through the expression

$$\tan(\chi) = \mp E_y^{\circ} / E_x^{\circ} \quad (9)$$

With these definitions, the limits of χ are $-45^{\circ} \leq \chi \leq 45^{\circ}$ while ψ spans the range $-90^{\circ} \leq \psi \leq 90^{\circ}$. The direction of rotation of the electric field vector about the ellipse is specified by the sign of χ . By IEEE convention, left-hand elliptical polarization is specified by $\chi > 0$, while right-hand rotation is denoted by $\chi < 0$. Note that if $|\chi| = 45^{\circ}$, the ellipse degenerates to a circle. This special case is referred to as *circular polarization*.

Vector notation is a convenient way to denote polarized fields. In vector exponential form, Eq. (1) can be written as

$$\mathbf{E} = \text{Re} \left\{ e^{-j(\omega t - kz + \alpha_y)} \begin{bmatrix} E_x^{\circ} e^{j\delta} \\ E_y^{\circ} \end{bmatrix} \right\} = \text{Re} \{ e^{-j(\omega t - kz + \alpha_y)} \mathbf{E} \} \quad (10)$$

where

$$\mathbf{E} = \begin{bmatrix} E_x^{\circ} e^{j\delta} \\ E_y^{\circ} \end{bmatrix} \equiv \begin{bmatrix} E_x \\ E_y \end{bmatrix} \quad (11)$$

completely defines the polarization state of the wave. When a polarized electromagnetic wave is expressed in the vector form of Eq. (11), the time harmonic factor $e^{-j(\omega t - kz)}$ is assumed. The phase factor $e^{-j\alpha_y}$ in Eq. (10) can be dropped, since the value of α_y depends on the arbitrary choice of a phase reference. The polarization state can be defined even more compactly by the complex polarization ratio, $P = E_y/E_x$. All aspects of a polarized wave (except for field strength) can be expressed in terms of this single, complex number [1a].

The *Stokes vector* is an alternative representation of polarized fields, defined in the following manner:

$$\mathbf{F} = \begin{bmatrix} |E_x|^2 + |E_y|^2 \\ |E_x|^2 - |E_y|^2 \\ 2 \text{Re}(E_x E_y^*) \\ 2 \text{Im}(E_x E_y^*) \end{bmatrix} = \begin{bmatrix} I_0 \\ Q \\ U \\ V \end{bmatrix} \quad (12)$$

[The Stokes vector is sometimes defined with the element V in the second position within the vector:

$$\mathbf{F} = \begin{bmatrix} |E_x|^2 + |E_y|^2 \\ 2 \operatorname{Im}(E_x E_y^*) \\ |E_x|^2 - |E_y|^2 \\ 2 \operatorname{Re}(E_x E_y^*) \end{bmatrix}$$

In addition, some authors define $V = 2 \operatorname{Im}(E_x^* E_y) = (-1) \cdot 2 \operatorname{Im}(E_x E_y^*)$.] While the representations in Eqs. (11) and (12) contain the same information about wave polarization in the case of a completely polarized wave, the Stokes vector has the advantage that all the vector elements are real-valued, and, as discussed in the following section, it can accommodate fields that are not completely polarized.

For completely polarized waves, it can be shown that $I_0^2 = Q^2 + U^2 + V^2$. This is the equation of a sphere of radius I_0 . Each polarization state can thus be mapped uniquely onto a point of a sphere, using the parameters Q, U, V as Cartesian coordinates. This graphical representation of wave polarization is referred to as the *Poincaré sphere* [1b].

1.1.2. Partial Polarization. Not all polarized EM waves can be adequately described using the representation of Eq. (11). The polarization state of natural EM waves, such as sunlight, is unpolarized, meaning that the polarization state varies randomly from one time instant to the next. Similarly, the polarization state of the radar backscatter from some surfaces, such as the sea surface or a wind-blown canopy of trees, may vary rapidly with time. The total radar backscatter in these cases is the vector sum of many individual echoes produced by many discrete scattering centers located within the radar footprint, each of which is moving and evolving. The net polarization state may be nearly linear at one instant, but elliptical only a few milliseconds later. Even if these surfaces could be frozen in time, the polarization state would still vary appreciably as the radar beam was moved about in space, since new scattering centers would enter the spot illuminated by the beam as others would exit. What is needed in these situations is a *statistical* measure of the polarization state of the wave. The Stokes vector can be adapted to these situations, in which the time and/or spatially varying fields are termed *partially polarized*.

For partially polarized waves, the ensemble averages of the Stokes vector elements, indicated by angular brackets $\langle \rangle$, are used. The Stokes vector becomes

$$\mathbf{F} = \begin{bmatrix} \langle |E_x|^2 + |E_y|^2 \rangle \\ \langle |E_x|^2 - |E_y|^2 \rangle \\ \langle 2 \operatorname{Re}(E_x E_y^*) \rangle \\ \langle 2 \operatorname{Im}(E_x E_y^*) \rangle \end{bmatrix} \quad (13)$$

The average may be over time with the radar directed at a single spot, over space if the surface is stationary, or over a mixture of time and space. The last two elements, U and V ,

indicate the degree of correlation between the x and y components. For a completely unpolarized wave, E_x and E_y are uncorrelated and thus $U = V = 0$.

1.1.3. Vertical and Horizontal Polarization. In most radar applications, it is more convenient to represent polarized waves in a spherical, rather than rectangular, coordinate system. Since the electric and magnetic fields that propagate in free space are transverse to the direction of propagation, and thus do not always lie in a convenient, fixed plane (such as the x - y plane assumed thus far), a spherical coordinate system is a more natural choice. This is illustrated in Fig. 3. The direction of propagation of the wave (formerly the \hat{z} direction) is denoted by the unit vector $\hat{\mathbf{k}}$, while the transverse coordinate unit vectors (formerly $\hat{\mathbf{x}}$ and $\hat{\mathbf{y}}$) are $\hat{\mathbf{v}}$ and $\hat{\mathbf{h}}$. The coordinate system $(\hat{\mathbf{k}}, \hat{\mathbf{v}}, \hat{\mathbf{h}})$ is defined such that it coincides with the standard spherical system $(\hat{\mathbf{r}}, \theta, \phi)$. The letters \mathbf{v} and \mathbf{h} refer to *vertical* and *horizontal* polarization, respectively, a reference to the fact that if the $\theta = 90^\circ$ plane is assumed to be Earth's surface (as it usually is), $\hat{\mathbf{v}}$ contains a vertically oriented component while $\hat{\mathbf{h}}$ lies in a horizontal plane. In this coordinate system, a spherical wave can be expressed as

$$\mathbf{E} = (E_v \hat{\mathbf{v}} + E_h \hat{\mathbf{h}}) \frac{e^{jk \cdot \mathbf{r}}}{r} \quad (14)$$

where $\mathbf{r} = r\hat{\mathbf{r}}$, and r is the distance from the coordinate system origin. Sufficiently far from the origin and over a small enough range of angles about the direction $\hat{\mathbf{k}}$, this

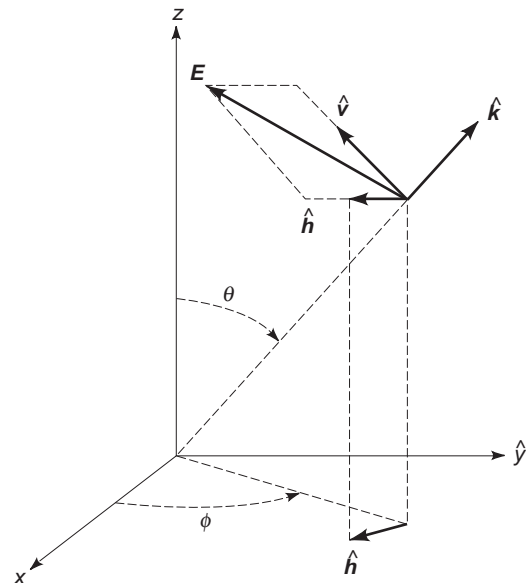


Figure 3. Diagram indicating the decomposition of the electric field $\mathbf{E}(t, z)$ into vertically and horizontally polarized components. The direction of propagation, denoted by the unit vector $\hat{\mathbf{k}}$, and the vertically and horizontally polarized unit vectors, $\hat{\mathbf{v}}$ and $\hat{\mathbf{h}}$, respectively, form a right-handed coordinate system coincident with the standard spherical coordinate system $(\hat{\mathbf{r}}, \theta, \phi)$. The terms “vertical” and “horizontal” arise from the fact that $\hat{\mathbf{h}}$ is always parallel to the horizontal ($\theta = 90^\circ$) plane while $\hat{\mathbf{v}}$ has a component in the vertical (\hat{z}) direction.

spherical wave can be considered to be a plane wave. All the expressions derived above for a plane wave propagating in the z direction are then still valid with the x and y subscripts interchanged with “ v ” and “ h ”, respectively. Note that with this transformation, the orientation angle, ψ , is defined relative to the vertical axis. Other authors use alternative conventions, however, that define ψ relative to the horizontal.

1.2. Representation of the Polarimetric Response

The previous section describes how the polarization state of an EM wave can be described mathematically. In this section, two formalisms are presented that describe how the polarization state of a wave is *altered* when it reflects off a target. The first, which applies to completely polarized waves, utilizes the *scattering matrix* to describe the target’s polarimetric properties. The second, which can be applied to completely or partially polarized targets, uses the *Mueller matrix* to describe the target. Both matrices describe the target’s polarimetric properties by quantifying how the polarization of the reflected wave is related to the polarization of the incident wave, and both are *complete* descriptions of the scattering properties of the illuminated scene or target. As shown in what follows, the response of the scene to any combination of transmit and receive polarizations can be computed from these matrices, without the need for additional measurements.

When using any representation of the polarimetric response, care must be taken that consistent source, target, and receiver coordinate systems are used. This article assumes the backscatter alignment (BSA) convention in which the incident and scattered wave unit vectors are identical. For a description of other conventions, see Refs. 1a, 1b, and 2. The notation used in this section closely matches that of Ref. 2.

1.2.1. Polarization Scattering Matrix. The scattering matrix is a 2×2 matrix relating the transmitted wave incident on a target \mathbf{E}^t to the reflected wave at the receiver \mathbf{E}^r :

$$\mathbf{E}^r = \frac{e^{jkr}}{r} \bar{\mathbf{S}} \mathbf{E}^t \quad (15)$$

where

$$\mathbf{E}^r = \begin{bmatrix} E_v^r \\ E_h^r \end{bmatrix}, \quad \mathbf{E}^t = \begin{bmatrix} E_v^t \\ E_h^t \end{bmatrix} \quad (16)$$

and

$$\bar{\mathbf{S}} = \begin{bmatrix} \bar{S}_{vv} & \bar{S}_{vh} \\ \bar{S}_{hv} & \bar{S}_{hh} \end{bmatrix} \quad (17)$$

is the scattering matrix. The elements of $\bar{\mathbf{S}}$ are complex, containing both magnitude and phase information, but in most cases the four magnitudes and phases are not independent. In the case of a monostatic radar in the absence of any nonreciprocal materials (e.g., ferromagnetics or

plasmas in a magnetic field), the reciprocity theorem forces $\bar{S}_{vh} = \bar{S}_{hv}$, and thus there are three independent magnitudes and two independent (relative) phases. Although not explicitly shown in Eq. (17), the elements of $\bar{\mathbf{S}}$ are in general functions of the radar frequency as well as the orientation of the target relative to the radar system.

The variation of the scattering matrix elements with target orientation is undesirable in terms of target recognition. The task of identifying an unknown target at an unknown aspect would be much simpler if the form of its scattering matrix were essentially independent of orientation. An eigenvalue analysis of the scattering matrix can partially achieve this goal while also providing physical insight into the scattering process. Through an eigenvalue analysis (e.g., see Ref. 1b), it can be shown that the scattering matrix can be diagonalized and represented by the following five independent parameters; m^2 , the maximum RCS of the target; ψ_t , the orientation angle; τ , the symmetry angle; ν , the bounce angle; and γ , the polarizability angle. With the exception of ψ_t , which is a direct measure of the target’s rotation angle, these parameters are independent of target rotations about the radar line of sight and are thus relatively invariant indicators of a target’s identity. (The parameter values will change, however, if the radar views the target from a different line of sight.) τ is a measure of the symmetry of the target, having a value of 0° for targets with a plane of symmetry and a value of $\pm 45^\circ$ for nonsymmetric objects, and is also the ellipticity angle of the eigenvectors. The bounce angle ν indicates the number of bounces involved in the target scattering, with a value of 0° corresponding to an odd number of bounces and a value of $\pm 90^\circ$ indicating an even number. Examples of odd bounce targets are spheres (one bounce) and trihedral corner reflectors (three bounces; see Example 1 below here), while the dihedral corner reflector is an even bounce scatterer (two bounces; see Example 2 here). The polarizability γ indicates the ability of the target to polarize incident radiation that is unpolarized, with 0° and 45° corresponding to complete and no polarizability, respectively. An example of a target with a high degree of polarizability is a long, thin wire, which tends to reflect only radiation polarized parallel to its axis. In contrast, a sphere exhibits $\gamma = 45^\circ$, since it has no preferred axis of symmetry. These five parameters are sometimes referred to as the Huynen parameters, in reference to their introduction by J. R. Huynen [3]. These parameters also describe the *null* and *maximum polarizations* for the target, those polarization states for which the RCS is zero and m^2 , respectively. When plotted on the Poincaré sphere, these polarization states define a characteristic structure called the *polarization fork* (see, e.g., Refs. 2 and 4).

In practice, the elements of the scattering matrix are generally obtained by recording the radar echoes from two pulses. First, the radar system transmits a pure vertically polarized wave

$$\mathbf{E}^t = E_v^t \begin{bmatrix} 1 \\ 0 \end{bmatrix}$$

and the receiver detects and records both the vertically and horizontally polarized echoes, E_{vv} and E_{hv} . From

Eqs. (15)–(17), \bar{S}_{vv} and \bar{S}_{hv} can then be calculated from

$$\bar{S}_{vv} = \frac{r}{e^{jkr}} \cdot \frac{E_{vv}}{E_v^t}, \quad \bar{S}_{hv} = \frac{r}{e^{jkr}} \cdot \frac{E_{hv}}{E_v^t} \quad (18)$$

Similarly, \bar{S}_{hh} and \bar{S}_{vh} are determined by transmitting a pure horizontally polarized pulse,

$$\mathbf{E}^t = E_h^t \begin{bmatrix} 0 \\ 1 \end{bmatrix}$$

and recording the vertically and horizontally polarized echoes E_{hh} and E_{vh} from which the remaining scattering matrix elements

$$\bar{S}_{hh} = \frac{r}{e^{jkr}} \cdot \frac{E_{hh}}{E_h^t}, \quad \bar{S}_{vh} = \frac{r}{e^{jkr}} \cdot \frac{E_{vh}}{E_h^t} \quad (19)$$

are obtained. Of course, two pulses of any two linearly independent polarization states could be used to determine the scattering matrix elements, since Eq. (15) defines four equations in four unknowns. But in general practice, pure vertically and horizontally polarized pulses are used.

Example 1 (Sphere). The simplest scattering matrix is that of sphere, given by

$$\bar{S}_{\text{sphere}} = A \begin{bmatrix} 1 & 0 \\ 0 & 1 \end{bmatrix} \quad (20)$$

where the constant A depends on the sphere’s size. This target does not alter the polarization state of the incident radiation, since $\bar{S}_{hv} = \bar{S}_{vh} = 0$, and responds identically to horizontally and vertically polarized radiation. Other objects with scattering matrices of the same form are large, flat surfaces at normal incidence and trihedral corner reflectors. The latter is a type of radar calibration target resembling the inside corner of a box. For these targets, the Huynen parameters τ , ν , and γ are equal to 0° , 0° , and 45° , respectively, while the orientation angle ψ_t is arbitrary.

Example 2 (Rotated Dihedral Corner Reflector). A dihedral corner reflector is a radar calibration target formed from two intersecting, perpendicular plates. The scattering matrix of this target with the seam rotated at an angle θ relative to the horizontal plane is

$$\bar{S}_{\text{dihedral}} = A \begin{bmatrix} \cos(2\theta) & \sin(2\theta) \\ \sin(2\theta) & -\cos(2\theta) \end{bmatrix} \quad (21)$$

where A depends on the size of the plates. The tendency of this target to depolarize (change the polarization state of) the incident radiation is strongly dependent on its orientation. At $\theta = 22.5^\circ$, vertically or horizontally polarized incident radiation will be rotated 45° after reflection, whereas at $\theta = 45^\circ$, the rotation is 90° . The Huynen parameters for the dihedral are $\psi_t = \theta$, $\tau = 0^\circ$, $\nu = 45^\circ$, and $\gamma = 45^\circ$.

Example 3 (Helix). The scattering matrix for a simple helix is

$$\bar{S}_{\text{helix}} = \frac{1}{2} \begin{bmatrix} -1 & \pm j \\ \pm j & 1 \end{bmatrix} \quad (22)$$

where the $+$ and $-$ signs refer to left- and right-handed helices, respectively. The factor $j = \sqrt{-1} = e^{j\pi/2}$ arises from the natural mode of oscillation for the helix, circular polarization, in which the relative phase between the vertical and horizontal components is $\pi/2$ radians (90°). The Huynen parameters τ and γ are $\pm 45^\circ$ and 0° , respectively, while ψ_t and ν are arbitrary.

1.2.2. Mueller Matrix. In the same way that the scattering matrix relates the EM fields incident on and reflected from a target, the Mueller matrix relates the incident and scattered Stokes vectors

$$\mathbf{F}^r = \frac{1}{r^2} \bar{\mathbf{L}} \mathbf{F}^t \quad (23)$$

where

$$\mathbf{F}^r = \begin{bmatrix} I_0^r \\ Q^r \\ U^r \\ V^r \end{bmatrix}, \quad \mathbf{F}^t = \begin{bmatrix} I_0^t \\ Q^t \\ U^t \\ V^t \end{bmatrix} \quad (24)$$

and $\bar{\mathbf{L}}$ is the 4×4 Mueller matrix. Unlike in the case of the scattering matrix, the Mueller matrix elements are real. (Note that a factor of $1/r^2$ is required, rather than $1/r$ as for the scattering matrix expression, since the Stokes vector elements are proportional to products of the field components.) As shown in Ref. 2, the Mueller matrix elements can be expressed in terms of the scattering matrix elements through

$$\bar{\mathbf{L}} = \mathbf{R} \bar{\mathbf{W}} \mathbf{R}^{-1} \quad (25)$$

where

$$\mathbf{R} = \begin{bmatrix} 1 & 1 & 0 & 0 \\ 1 & -1 & 0 & 0 \\ 0 & 0 & 1 & 1 \\ 0 & 0 & -i & i \end{bmatrix} \quad (26)$$

and

$$\bar{\mathbf{W}} = \begin{bmatrix} \bar{S}_{vv}^* \bar{S}_{vv} & \bar{S}_{vh}^* \bar{S}_{vh} & \bar{S}_{vh}^* \bar{S}_{vv} & \bar{S}_{vv}^* \bar{S}_{vh} \\ \bar{S}_{hv}^* \bar{S}_{hv} & \bar{S}_{hh}^* \bar{S}_{hh} & \bar{S}_{hh}^* \bar{S}_{hv} & \bar{S}_{hv}^* \bar{S}_{hh} \\ \bar{S}_{hv}^* \bar{S}_{vv} & \bar{S}_{hh}^* \bar{S}_{vh} & \bar{S}_{hh}^* \bar{S}_{vv} & \bar{S}_{hv}^* \bar{S}_{vh} \\ \bar{S}_{vv}^* \bar{S}_{hv} & \bar{S}_{vh}^* \bar{S}_{hh} & \bar{S}_{vh}^* \bar{S}_{hv} & \bar{S}_{vv}^* \bar{S}_{hh} \end{bmatrix} \quad (27)$$

This relationship between $\bar{\mathbf{L}}$ and $\bar{\mathbf{S}}$ is strictly valid only for completely polarized targets, since $\bar{\mathbf{S}}$ does not exist otherwise. Complex radar targets, such as wind-blown trees, exhibit time-varying polarization matrix elements, and no single scattering matrix can describe their polarization transformation properties. The elements of $\bar{\mathbf{S}}$ tend to be zero-mean quantities, and so averaging these terms is not an effective way to describe the average polarization scattering behavior of a target. This average behavior can be described by computing a time-averaged Mueller matrix, however. In practice, the average Mueller matrix is sometimes calculated by first computing the scattering matrix elements from each pair of a large number of alternating vertically and horizontally polarized transmit pulses, using Eqs. (18) and (19). Equations (26) and (27) are then used to compute individual Mueller matrices for each measurement. The final, averaged Mueller matrix is then calculated by averaging the individual matrix elements. This procedure is valid if the target or scene of interest can be considered to be stationary, and thus completely polarized, over the time period required to transmit a single pair of vertically and horizontally polarized pulses. As this interval can be as short as a fraction of a millisecond, this is a very reasonable assumption in many cases. A direct technique for computing the time-averaged Mueller matrix, without calculating a sequence of polarization scattering matrices, is described in Ref. 5.

Some authors use different names for the matrix $\bar{\mathbf{L}}$ defined using the BSA convention and that defined using the forwardscatter alignment (FSA) convention, referring to the former as the *Kennaugh matrix* and the latter as the *Mueller matrix* [1a]. While making this distinction avoids potential confusion, both are commonly referred to as the Mueller matrix.

1.2.3. Other Representations of the Polarimetric Response. In addition to the scattering and Mueller matrix formalisms, the polarimetric scattering properties of the target can also be expressed by the covariance matrix \mathbf{C} and the coherency (or density) matrix ρ . In terms of the scattering matrix elements, these matrices are given by

$$\mathbf{C} = \begin{bmatrix} S_{vv}S_{vv}^* & \sqrt{2}S_{vv}S_{vh}^* & S_{vv}S_{hh}^* \\ \sqrt{2}S_{vh}S_{vv}^* & 2S_{vh}S_{vh}^* & \sqrt{2}S_{vh}S_{hh}^* \\ S_{hh}S_{vv}^* & \sqrt{2}S_{hh}S_{vh}^* & S_{hh}S_{hh}^* \end{bmatrix} \quad (28)$$

$$\rho = \begin{bmatrix} aa^* & ab^* & ac^* \\ ba^* & bb^* & bc^* \\ ca^* & cb^* & cc^* \end{bmatrix} \quad (29)$$

where

$$a = \frac{S_{vv} + S_{hh}}{2}, \quad b = \frac{S_{vv} - S_{hh}}{2}, \quad c = S_{vh} = S_{hv} \quad (30)$$

(These expressions apply to the backscattering, reciprocal case. In the general bistatic case, both \mathbf{C} and ρ are 4×4 matrices.) As in the case of the Mueller matrix, these

matrices can be applied to the partially polarized case through averaging of the elements, and they contain the same information as do the scattering or Mueller matrices. Different aspects of polarimetry are expressed more compactly with one representation or the other, however. (See, e.g., Refs. 2 and 4.)

1.2.4. Polarization Synthesis. The scattering and Mueller matrices are complete representations of the polarimetric scattering properties of a target or surface in that the target response to any combination of transmit and receive polarizations can be computed from them. *Polarization synthesis* refers to the process of determining a target's response to an arbitrary combination of transmit and receive polarizations by way of the target's scattering or Mueller matrix, without actually transmitting and receiving these polarization states.

The equation describing polarization synthesis can be derived by starting with the definition of the (monostatic) RCS of a target

$$\sigma = 4\pi \lim_{r \rightarrow \infty} r^2 \left(\frac{\mathbf{E}^s \cdot \mathbf{E}^{s*}}{\mathbf{E}^t \cdot \mathbf{E}^{t*}} \right) = 4\pi \lim_{r \rightarrow \infty} r^2 \left(\frac{|\mathbf{E}^s|^2}{|\mathbf{E}^t|^2} \right) \quad (31)$$

where $|\mathbf{E}^s|^2$ is the electric field intensity scattered by the target, measured at the receiver, and $|\mathbf{E}^t|^2$ is the incident electric field intensity, measured at the target, and r is the distance between the radar antenna and the target. This expression states that the RCS is given by the power per unit solid angle incident on the antenna divided by the power per unit area incident on the target.

As it stands, this expression does not account for the polarization of the receive antenna. A system will measure this value of the RCS only if the receive antenna is designed to receive the polarization state of \mathbf{E}^s . Otherwise, only a fraction of the power incident on the antenna will be actually absorbed, and the measured RCS will be lower than that given by Eq. (31). This effect can be accounted for in the following way. The polarization of an antenna is defined by the unit vector \mathbf{p} , the polarization vector, given by

$$\mathbf{p} = \frac{\mathbf{E}}{|\mathbf{E}|} \quad (32)$$

where, by IEEE convention, \mathbf{E} is the far field radiated by the antenna when it is used to transmit. If a field \mathbf{E}^s impinges on a receive antenna having polarization \mathbf{p}^r , the effective field incident on the antenna is the projection of \mathbf{E}^s on \mathbf{p}^r , $\mathbf{p}^r \cdot \mathbf{E}^s$, and the effective field intensity is then $|\mathbf{p}^r \cdot \mathbf{E}^s|^2$. The expression for the cross section in this case is

$$\sigma_{rt} = 4\pi \lim_{r \rightarrow \infty} r^2 \left(\frac{|\mathbf{p}^r \cdot \mathbf{E}^s|^2}{|\mathbf{E}^t|^2} \right) \quad (33)$$

Noting that $\mathbf{E}^s = (e^{jkr}/r)\bar{\mathbf{S}}\mathbf{E}^t$ and making the substitution $\mathbf{p}^t = (\mathbf{E}^t/|\mathbf{E}^t|)$ produces the polarization synthesis equation:

$$\sigma_{rt} = (\mathbf{p}^r \cdot \bar{\mathbf{S}}\mathbf{p}^t)^2 \quad (34)$$

Once $\bar{\mathbf{S}}$ has been determined, the target RCS for *any* combination of transmit and receive polarizations can be computed from this expression. The unit vectors \mathbf{p}^r and \mathbf{p}^t corresponding to the desired transmit and receive polarizations are simply inserted. A similar expression using the Stokes vector and Mueller matrix representation can also be derived [2].

1.2.5. Polarization Response. The RCS values computed by Eq. (34) can be represented graphically by a surface termed the *polarization signature* or *polarization response* [6]. The term *signature* refers to the fact that these surfaces are distinctive and can be used to broadly classify targets. Two types of signatures are used: the co-polarized signature, in which the incident and scattered polarization states are assumed to be identical; and the cross-polarized signature, in which the incident and scattered states are assumed to be orthogonal. The signatures of some common targets are shown in Figs. 4–6.

Example 4 (Sphere). The co- and cross-polarized signatures of a sphere are shown in Figs. 4a and 4b, respectively. The signature consists of a plot of the target RCS versus the ellipticity and orientation angles χ and ψ of the incident and scattered radiation. Linearly polarized states lie along the $\chi = 0^\circ$ line, with vertical located at ($\chi = 0^\circ$, $\psi = \pm 90^\circ$) and horizontal located at ($\chi = 0^\circ$, $\psi = 0^\circ$). Left- and right-handed circular polarizations are located along the $\chi = \pm 45^\circ$ lines. The ridge in the copolarized surface along the $\chi = 0^\circ$ line indicates that the copolarized RCS of the sphere is maximized when the polarization is linear. The response vanishes when circular polarization is used. (For this reason, some operational radar systems use circular polarization when monitoring targets through rain. This choice of polarization reduces the clutter signal produced by raindrops, which are roughly spherical in shape.) In

contrast, the cross-polarized response is minimized by linear polarization and maximized when circular polarization is used. The surfaces in Fig. 4 are also the polarization signatures of a trihedral corner reflector and a flat plate at normal incidence, since these targets have the same normalized scattering matrices as the sphere [Eq. (20)].

Example 5 (Dihedral Corner Reflector). Figures 5a and 5b show the co- and cross-polarized responses, respectively, of a dihedral corner reflector with its seam oriented parallel to the horizontal plane. The copolarized RCS is maximum for vertical, horizontal, and circular polarizations, but vanishes for linear polarized radiation with an orientation angle $\psi = \pm 45^\circ$. Examination of the dihedral scattering matrix [Eq. (21)], shows that when the incident polarization state is linear with $\psi = \pm 45^\circ$, the scattered and incident polarization states are orthogonal. The copolarized response consequently vanishes, while the cross-polarized response (Fig. 5b), exhibits maxima at these points.

Example 6 (Helix). The co- and cross-polarized signatures of a left-handed helix are shown in Figs. 6a and 6b, respectively. The co-polarized RCS is maximized when left-hand circular polarization is used and vanishes for right-hand circular polarization. Unlike for the sphere or the dihedral corner reflector, the cross-polarized response of the helix never achieves a value of 1.

2. POLARIMETRIC RADAR DESIGN

A polarimetric radar, or polarimeter, measures the scattering matrix of a target by sequentially transmitting a pair of orthogonally polarized pulses toward the target and simultaneously measuring the co- and cross-polarized

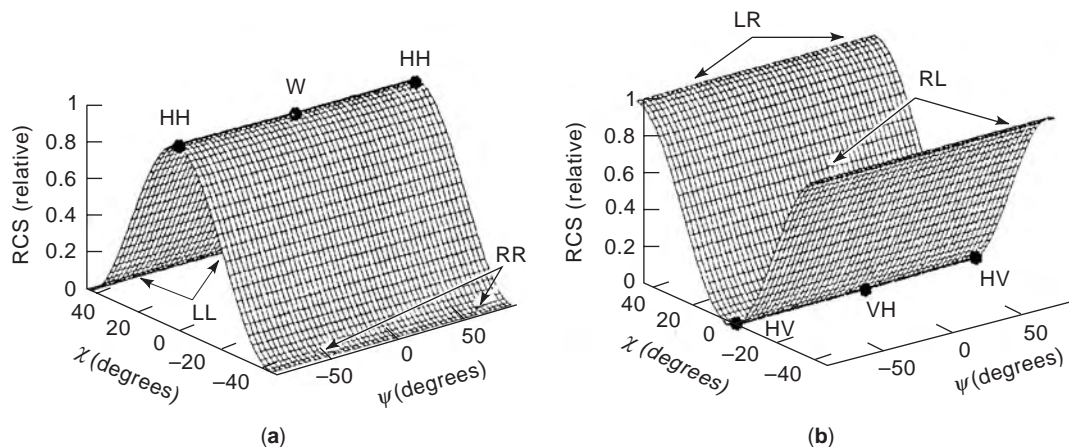


Figure 4. (a) Copolarized signature for a sphere. The surface is a plot of the normalized RCS of the sphere versus the orientation and ellipticity angles of the transmit and receive polarizations. The cross section is maximum for linearly polarized radiation, as indicated by the ridge in the surface for $\chi = 0$, and vanishes for left- and right-handed circular polarization ($\chi = \pm 45^\circ$). (b) Cross-polarized signature for the sphere. The cross-polarized signature is a plot of the normalized RCS of the sphere versus the orientation and ellipticity angles of the transmit polarization, assuming that the transmit and receive antennas are orthogonally polarized. The cross-polarized RCS vanishes for linear polarization and is maximized for left- and right-handed circular polarization.

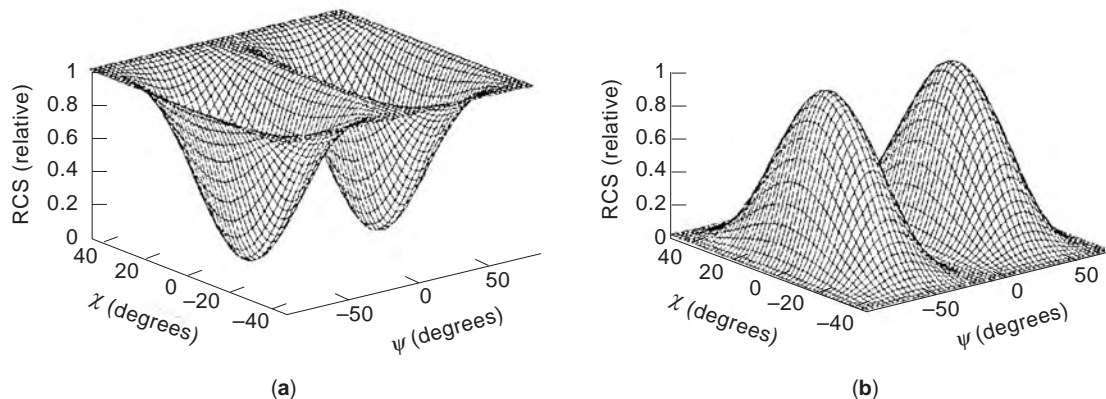


Figure 5. (a) Copolarized signature for a dihedral corner reflector with its seam oriented horizontally. The RCS is maximum for vertical, horizontal, and circular polarizations and vanishes for linear polarizations with $\psi = \pm 45^\circ$. (b) Cross-polarized signature for the dihedral corner reflector. The cross-polarized RCS is maximum for linear polarizations with $\psi = \pm 45^\circ$ and vanishes for vertical, horizontal, and circular polarizations.

components of the scattered wave. The need to transmit and receive multiple polarizations makes the design of a polarimetric radar more complicated than the design of a conventional, single polarization, radar system. A basic polarimeter is composed of a transmitter that generates microwave pulses at a specified carrier frequency, an antenna capable of transmitting and receiving two orthogonally polarized wave components and focusing these waves into a narrow angular beamwidth in space, switching circuitry that alternately routes the transmitted pulses between the two orthogonal ports of the antenna feed, a pair of receivers for detecting the signals received from the antenna, and a multichannel data acquisition system for recording the signals backscattered from the target.

As in conventional radar design, the most important design equation for radar polarimetry is the radar range equation

$$SNR = \frac{P_t G_t \sigma A}{(4\pi)^2 R^4 k T B F_n} \tag{35}$$

which gives the receiver signal-to-noise ratio (SNR) in terms of the peak transmitted power level P_t ; the antenna gain, $G_t = 4\pi/\theta^2$, where θ is the antenna's focusing beamwidth (assumed here to be equal in azimuth and elevation planes, as is the case for a pencil-beam antenna); the antenna's collecting area A , which typically ranges between 60% and 95% of its physical area, depending on the aperture illumination efficiency; the polarization-dependent radar cross section of the target σ ; the range between the radar antenna and the target R ; the bandwidth B and noise figure F_n of the receiver; Boltzmann's constant, $k = 1.38 \times 10^{-23}$ J/K; and the physical temperature of the receiver T , usually taken to be 290 K. Whereas reliable radar target detection can often be accomplished with a receiver SNR of 15 dB using a conventional radar [7], measuring the polarimetric response of a target typically requires SNR levels of 20 dB or higher [8]. A large part of polarimeter system design involves trading off the various parameters of Eq. (35) to achieve a specified level of SNR performance. Reference 2 describes some of the tradeoffs

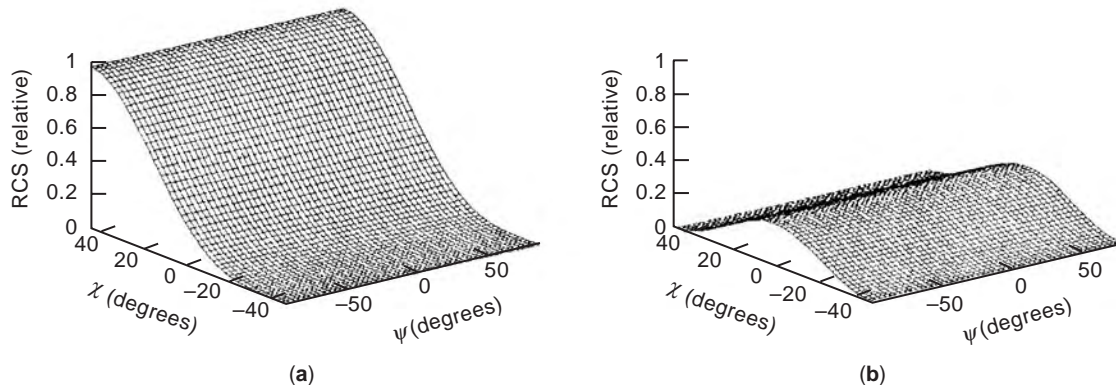


Figure 6. (a) Copolarized signature for a left-handed helix. The copolarized RCS is maximized by left-handed circular polarization and vanishes for right-handed circular polarization. (b) Cross-polarized signature of a left-handed helix. The cross-polarized response is maximized with linear polarizations, but the peak response is weaker than the maximum exhibited in the copolarized case.

involved in the design of a spaceborne imaging radar polarimeter having transmitted power level $P_t = 5$ kW, antenna gain $G_t = 10,000$ (40 dB), and surface area $A = 32$ m² (15 dB) that achieves an SNR level of 24 dB when viewing Earth's surface at 400 km range. Another example of a spaceborne imaging polarimeter is given in Ref. 9.

The operating wavelength of a polarimetric radar system is chosen as the result of a tradeoff among considerations such as the physical size of the antenna, peak transmitted power level, availability of components, cost, and for most remote sensing applications, the sensitivity of the surface backscatter coefficient [or normalized radar cross section (NRCS)] to environmental parameters. In general, radar systems operating at higher microwave frequencies have smaller antennas and larger peak transmitted power levels than do radars operating at lower microwave frequencies. The focusing gain and physical size of an antenna are related by the equation $A = \lambda^2 G_t / 4\pi$ (assuming 100% aperture efficiency), where wavelength λ is inversely related to the operating frequency f by the equation $\lambda = c/f$, where c is the speed of light. These equations reveal that larger antenna gains can be obtained for a given antenna size at higher frequencies than at lower frequencies. Conversely, a specified amount of focusing gain can be achieved with a smaller physical antenna size at a higher frequency than at a lower frequency. However, receiver SNR is proportional to the product of the focusing gain and the physical collecting area of the antenna. Therefore, increasing the operating frequency to reduce the physical size of an antenna while achieving a specified level of antenna gain results in reduced receiver SNR. This loss must be compensated by increasing the peak transmitted power level of the radar system. This tradeoff is particularly important in airborne and spaceborne radar system deployments where it is desirable to utilize small antennas.

At millimeter-wave frequencies and higher microwave frequencies (typically above X band), atmospheric attenuation becomes an important consideration, and the SNR in Eq. (35) must be multiplied by the term $\exp(-2\alpha R)$, where α , having units of nepers (napiers) per meter (Np/m), is the attenuation coefficient. Attenuation coefficients for propagation through the clear atmosphere and through rain are given in Ref. 10 for different frequencies. When scattering targets are small compared with the operating wavelength, such as raindrops observed with a millimeter-wave radar system, σ is a strong function of frequency and is given by the Rayleigh expression $\sigma = a/\lambda^4$, where the constant a depends on the shape of the target. The SNR in this case is given by the equation

$$\text{SNR} = \frac{P_t G_t^2 a \exp(-2\alpha R)}{(4\pi)^3 R^4 k T B F_n \lambda^2} \quad (36)$$

which reveals that increases in the operating frequency (decreases in wavelength) result in higher SNR levels relative to operating at a lower operating frequency. Reference 11 describes a dual-frequency polarimetric radar system developed for cloud profiling studies. The radar contains transmitters operating at 33 and 95 GHz that

share a common 1-m-diameter dielectric lens antenna. Because of the strong wavelength dependence in the backscatter coefficient from the raindrops, the 33-GHz channel of this radar requires 120 kW peak power level, whereas the 95-GHz channel requires only 1.5 kW peak power level to achieve the same SNR.

2.1. Transmitter Design Considerations

Polarimetric processing of radar data involves the coherent combination of scattered wave measurements corresponding to a pair of consecutive transmitted pulses. Phase-coherent transmitters are therefore used in most polarimetric radar designs. (A technique for measuring the time-averaged Mueller matrix directly that does not require a coherent transmitter is described in Ref. 5.) The master oscillator power amplifier (MOPA) transmitter configuration is commonly used in coherent transmitter design. In this configuration, a low-power (typically in the tens of milliwatts) microwave signal, derived from a microwave oscillator that is phase-locked to a stable crystal oscillator, is pulse-modulated using a pin diode switch and then amplified to achieve the required peak power level using a power amplifier. Solid-state field-effect transistor (FET) amplifiers are often used in lower frequency (X-band and below) microwave systems having power levels of several watts. Microwave power tube amplifiers [TWTs (traveling-wave tubes) and klystrons] are often used in higher-power and microwave frequency radar transmitters. Examples of polarimeter systems utilizing klystron amplifiers with peak power levels of 200 kW at S band and 1.5 kW at 95 GHz are described in Refs. 11 and 12, respectively. MOPA transmitters tend to be expensive, typically costing several tens to hundreds of thousands of dollars. These systems provide for highly flexible transmitted waveforms, however, and a variety of waveforms (pulsed, chirped, phase-coded) can be generated using a MOPA design.

Self-excited power oscillator tubes, such as the magnetron oscillator and the extended interaction oscillator (EIO), are also used in polarimeter transmitter designs. These devices often cost considerably less than MOPA transmitters, but they are typically limited to pulsed applications. These incoherent power oscillators typically exhibit frequency drift and pulse-to-pulse phase modulations, and frequency stabilization and coherent-on-receive circuits are required when these devices are used in polarimetric radar designs. Reference 11 gives an example of a high-power magnetron transmitter for a millimeter-wave polarimeter system.

2.2. Polarimeter Antennas

Polarimetric radar antennas must be capable of transmitting and receiving two orthogonally polarized waves. Any pair of orthogonal polarizations can be used, but vertical/horizontal linear and right/left circular are the most common. As in a conventional radar, the physical size of the antenna must be large enough to achieve the focusing beamwidth and directive gain specified by the system design and SNR budget, and the antenna sidelobes must be below some specified value. The antenna designs used in

radar polarimeters must also achieve high polarization purity. A typical specification requires the cross-polarized radiation, integrated across the antenna pattern, to be 30 dB below the copolarized signal level [8].

Many of the antennas used for conventional radar design can be used in polarimeter systems by adapting them for dual-polarization operation. A corrugated horn antenna equipped with an orthomode transducer (OMT) can be used for dual-linear polarization operation in applications requiring modest directive gain (up to 20 dB). Higher levels of directive gain can be achieved by using the corrugated horn to illuminate a parabolic reflector in either a prime-focus or Cassegrain configuration [13,14]. References 11 and 15 describe millimeter-wave polarimeter systems that use dielectric lens antennas. The antenna for the polarimetric radar flown on the space shuttle, the *Spaceborne Imaging Radar—C* (SIR-C), is a microstrip patch array with transmit/receive (T/R) modules distributed across the array surface [9]. The system operates simultaneously at L and C bands.

2.3. Polarization Switches

Single-pole double-throw (SPDT) switches are needed in the transmitter of a polarimetric radar to alternately route the transmitted signal between the two ports of the antenna. The switching is performed on a pulse-to-pulse basis, so the switches must be capable of toggling the high-power microwave-transmitted pulse between the two antenna ports at switching speeds of 0.1–1 ms or faster. For low-power (less than 10 W), short-range polarimeter designs, pin diode switches are often used. Higher-power applications (up to tens or hundreds of watts of peak transmitted power level) typically use ferrite switching circulators. Three circulators are typically used in the design, as described in Ref. 14. Off-the-shelf ferrite switching circulators capable of handling several tens of kilowatts are commonly available at L- through Ku-band microwave frequencies at a cost of several thousand dollars per circulator.

Many polarimeter designs require peak transmitter power levels that are too high for off-the-shelf ferrite switches. Reference 14 describes a high-power, 1-MW S-band polarimeter design that uses a ferrite switching circulator custom-made at a cost of \$75,000. Reference 11 describes a 33-GHz, 125-kW polarimeter that uses two separate transmitters to feed the antenna ports, rather than a single transmitter with a polarization switch.

2.4. Receiver and Data Acquisition

Two superheterodyne receiving channels are used in a polarimeter to detect the co- and cross-polarized components of the scattered wave. Current designs achieve dynamic ranges of up to 100 dB by using low-noise front-end amplifiers, matched filters, and wide-dynamic-range coherent detectors. Standard in-phase/quadrature demodulator circuits operate over a limited dynamic range, typically on the order of 30 dB. The wide-dynamic-range circuits used in many polarimeter receivers use logarithmic detectors for measuring signal amplitude and constant-phase limiters followed by in-phase/quadrature demodulators for

measuring signal phase. Examples of these detector circuits are given in Refs. 11 and 14. Data acquisition systems with six channels are required in polarimeters that utilize these wide-dynamic-range detectors.

2.5. Polarimeter Calibration

Calibration is an important aspect of polarimetric radar design that has received considerable attention in recent years. In order to determine the scattering or Mueller matrix of a target, accurate measurements of the relative magnitudes and phases of the EM fields constituting the target echo are needed. However, the estimates of these quantities that the radar system produces are inevitably contaminated by the system itself, due to component mismatch and/or a lack of polarization isolation. Without a proper calibration, the fixed biases (errors) in the measured magnitudes and phases introduced by the system cannot be differentiated from the true radar response of target. The objective of calibration is thus to determine the gain (magnitude and phase) of the four different measurement paths (vertical transmitter–vertical receiver; vertical transmitter–horizontal receiver; horizontal transmitter–horizontal receiver; and horizontal transmitter–vertical receiver) followed by the radar pulse during measurement of a target's scattering matrix, as well as to estimate the degree of cross-polarization distortion caused by the transmitting and receiving antennas. Once these calibration measurements are made, the contribution of the system to any target measurement can be determined and removed. One technique that is commonly used is to measure the polarimetric scattering behavior of three reference targets having known scattering matrices. The measurements so obtained provide enough information to uniquely determine the set of seven complex unknowns in the polarimeter distortion matrices required for polarimetrically calibrating the radar system [16]. Other calibration techniques have been developed that invoke assumptions about the observed targets, such as reciprocity and uncorrelated co- and cross-polarized scattering, to estimate the system distortion matrices directly, without relying on reference scattering targets [17]. A procedure for field calibration of bistatic polarimeter systems without using reference scattering targets has also been developed [18]. For a summary of polarimetric calibration procedures, see Ref. 19.

3. CURRENT RESEARCH

3.1. Radar Scattering Studies

Polarimetric radar measurements can often be used to determine the physical scattering mechanisms responsible for a radar echo. As discussed in a previous section, a sphere and a trihedral corner reflector are examples of “odd-bounce scatterers” that exhibit scattering matrices having elements S_{vv} and S_{hh} in phase with each other. A dihedral corner reflector, in contrast, is an example of an “even-bounce scatterer”, in which the S_{vv} and S_{hh} elements exhibit a 180° phase difference. In the case of the Mueller matrix, the elements L_{33} and L_{44} convey similar

information. A complex radar target dominated by a single-bounce scattering mechanism exhibits large positive values for elements L_{33} and L_{44} , whereas these elements are negative when the target is dominated by a double-bounce scattering mechanism. In contrast, the Mueller matrix of a target composed of a combination of even- and odd-bounce scatterers exhibits near-zero values for L_{33} and L_{44} [20].

The mechanisms responsible for radar backscatter from the sea surface are a topic of current investigations. McLaughlin et al. [13] describe measurements of ocean waves in the Chesapeake Bay performed at a 3° grazing angle using a high-range-resolution (1.5-m) X-band polarimetric radar. These measurements were conducted to determine the physical scattering mechanisms responsible for *sea spikes*, which are strong radar echoes with anomalous polarization characteristics that occur in low-grazing-angle radar backscatter from the ocean surface. Figure 7 shows a typical copolarization signature of the ocean surface echo in the absence of a sea spike. The plot exhibits maximum RCS at VV polarization, minimum RCS at HH polarization, and intermediate cross sections of approximately 0.25, corresponding to a level 6 dB below the VV peak, at right-hand and left-hand circular polarizations. The *coefficient of variation*, a measure of the polarization sensitivity of a scatterer, is defined as the ratio of minimum to maximum RCS in a polarization signature plot [6]. The coefficient of variation of this plot is 0.01 (-20 dB), indicating that the radar echo is highly polarized. The Mueller matrix (not shown) exhibited large values for L_{33} and L_{44} , meaning that a single-scattering mechanism, such as distributed *Bragg scattering*, dominates the radar echo from the ocean surface. Figure 8 shows a copolarization signature for a sea spike radar echo that occurred during the passage of a long ocean wave crest through the radar resolution cell. The sea spike echo exhibits polarimetric scattering characteristics that are substantially different from the ocean surface echo in the absence of sea spikes. Figure 8 exhibits RCS maxima at VV and HH polarizations as well as a large “pedestal”

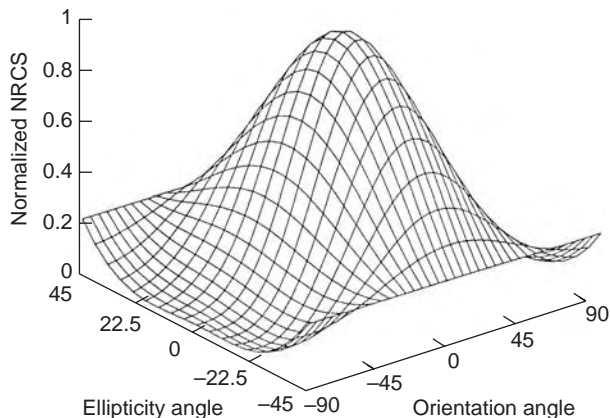


Figure 7. Copolarized signature of the sea surface in the absence of sea spikes. The high RCS at vertical polarization, the minimum at horizontal polarization, and the high degree of polarization (low pedestal) indicate a single, Bragg-like scattering mechanism.

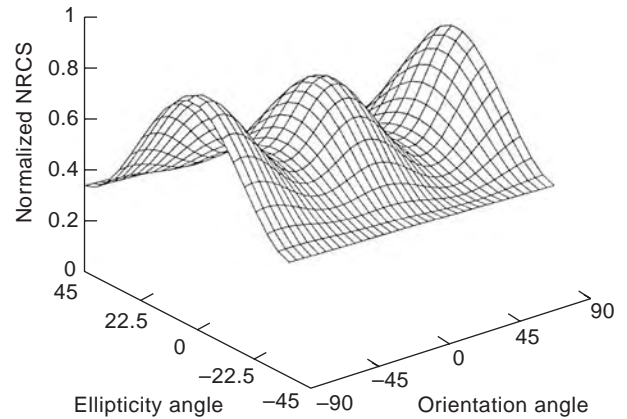


Figure 8. Copolarized signature of the sea surface in the presence of a sea spike. Peaks in the response at both vertical and horizontal polarizations and the low degree of polarization (high pedestal) indicate a mixture of scattering mechanisms.

corresponding to relatively high cross-section values at other copolarization states. The coefficient of variation for this plot is 0.3 (-5.2 dB), a relatively large value, meaning that the echo is weakly polarization-sensitive. The L_{33} and L_{44} Mueller matrix elements for this echo had small values indicating that no single scattering mechanism dominates the backscatter signal. One possible explanation for this observation is that a combination of Bragg resonant waves and non-Bragg scatterers, such as plumes generated at breaking wavecrests, combine to form the sea spike echo from the ocean surface.

Sletten et al. [21a,b] have also utilized a polarimetric radar to investigate sea spikes. In their experiments, an *ultrawideband*, polarimetric radar system was used to investigate the backscatter from breaking water waves generated in a laboratory wavetank. (The term *ultrawideband* refers to the ability of a radar to measure the backscatter from a target over a wide band of radar frequencies simultaneously.) Observed differences in the VV and HH responses as a function of radar frequency indicate that the strongest echoes (sea spikes) produced by the breakers are the result of a double-bounce scattering mechanism, arising from multiple scatter between the front face of the wave and a plume near its crest. In particular, the VV and HH frequency responses were found to be roughly complementary (i.e., HH high when VV is low, and vice versa), a result related to the 180° phase shift observed between S_{hh} and S_{vv} for double-bounce scatterers.

3.2. Image Classification

Another active area of research is image classification. In remote sensing, the objective of this research is to automatically separate different regions of an image into different classes, dependent on the type of terrain or land usage. For instance, classification schemes are under development to separate forested, urban, agricultural, and water-covered regions in remotely sensed imagery. In an ideal classification scheme, the signal characteristics that define each class can be uniquely associated with physical attributes of the scatterers in that class. Polarimetric

images are the best candidates for this type of processing, given the amount of information they provide on the scatterers in the scene. Signal polarization constitutes another dimension in which distinctions can be drawn between regions in an image. The same principle can be applied to the problem of detecting and classifying targets (as opposed to regions within an image) with a nonimaging radar. This is the situation encountered in some military applications.

Polarimetric target decomposition is one approach to classification. In this approach, the scattering, Mueller, or coherency matrix is considered to be a linear combination of several basis matrices, each of which represents a canonical target or a departure of the original matrix from the canonical target. In any radar image of a real surface, the signal for a given pixel is produced by several (perhaps many) scattering centers or objects within the illuminated scene. The total signal is a mixture of the echoes produced by each scattering center, and thus the polarimetric properties of that pixel are a mixture as well. In addition, motion of the scatterers (due to surface winds, e.g.) may cause variation in their scattering properties, resulting in partial polarization. Target decomposition techniques attempt to break the measured matrices down into their fundamental constituents or to extract the characteristics of the primary scattering centers from the background.

The application of polarimetric decomposition theories to radar problems began with the pioneering work of Huynen [22]. Huynen decomposed the coherency matrix into two components: a pure (i.e., completely polarized) target, and a mixed (partially polarized) state that was invariant to rotations of the radar system about the line of sight. The pure target is intended to represent the average, or dominant, target, and the mixed state is the residue or remainder. Enforcing rotational invariance on the residue ensures, at least to some degree, that the mixed state has no preferred axis of symmetry and is thus produced by the unpolarized noise in the measurement. Holm and Barnes [23] later determined that there are actually two other Huynen-like decompositions of the coherency matrix, which makes interpretation of the results somewhat ambiguous. Holm and Barnes also developed another decomposition method, referred to as the “natural” or “characteristic” decomposition, which breaks the coherency matrix into three components: a matrix representing a pure state that provides a measure of the average target; a mixed-state matrix, which indicates the variance of the target about its average; and an unpolarized component. This decomposition is based on an eigenvalue analysis of the coherency matrix and can thus be expected to produce statistically independent components. In a simulation, this method was successfully used to extract a rotating dihedral corner reflector embedded in polarization noise. Krogager and Czyz [24] have taken a different approach to the decomposition problem, concentrating instead on decomposition of the scattering matrix. In this technique, the scattering matrix is decomposed into three coherent (nonaveraged) components that can be physically interpreted as representing a sphere, a rotated dihedral corner reflector, and a helix. While these three matrices are not orthogonal (the dihedral component can also be attributed

to a pair of helices), the technique has physical appeal and may be a natural scheme for some applications. Freeman and Durden [25] have developed a three-component model comprising three mechanisms: volume scatter from a cloud of dipoles with random orientations, double-bounce scatter from two orthogonal surfaces with different dielectric constants, and a moderately rough surface modeled by Bragg scatter. A fit of this three-component model to imagery containing backscatter from a variety of vegetation and open water indicates that the model describes the actual scattering mechanisms well. Cloude and Pottier have summarized these and other decomposition techniques [26] and have introduced their own classification scheme based on an eigenvector decomposition of the coherency matrix [27]. The technique classifies pixels within an image through two parameters: the polarimetric entropy H , which is derived from the eigenvalues of the coherency matrix and that indicates the degree of polarization; and an angle α , which indicates the dominant scattering mechanism. α ranges from 0° to 90° , with low values indicating geometric optics and higher values indicating Bragg scattering and double-bounce mechanisms. The authors divide the H - α plane into different zones, each of which indicates a different class of scattering behavior. The scheme is unsupervised (i.e., does not require training data), and the results of its application to imagery containing a mixture of vegetation, urban buildings, and open water are promising.

Other approaches to polarimetric image classification exist as well. For instance, Lee et al. [28] have applied a Bayes maximum-likelihood classifier to the problem, including the effects of multiple-look averaging, while Yueh [30] conducted a similar investigation assuming single-look statistics. Lee et al. [29] have also combined the unsupervised decomposition scheme of Cloude and Pottier with a maximum-likelihood classifier based on the complex Wishart distribution for the polarimetric covariance matrix. Ferrazzoli et al. [31] have used a simplified scheme that considers the normalized RCS values for five polarization combinations (HH, VV, HV, circular copolarized, and circular cross-polarized) and three radar frequency bands (P, L, and C) to distinguish between forest, urban areas, and agricultural areas and to classify several types of crops. Fully polarimetric synthetic aperture radar (SAR) imagery has also been classified using algorithms based on neural nets (see, for instance, Ref. 32).

3.3. Contrast Enhancement

The scattering environment observed by a radar system is composed of many different targets that scatter incident electromagnetic energy. To the extent that the different scatterers or classes of scatterers have different polarization signatures, the echoes from one type of scatterer may be enhanced relative to the echoes from other scatterers by using a polarimetric radar. As discussed earlier in this article, knowledge of the polarization scattering matrix or Mueller matrix of a target allows one to calculate the transmitting and receiving polarizations that would result in maximum or minimum radar cross-section level [33]. It is also possible to simulate (synthesize) any desired

receive polarization in the signal processor of a polarimetric radar by forming a weighted linear combination of the signals received by the two receiving channels [34]. Similarly, it is possible to synthesize any arbitrary transmitting antenna polarization by forming a weighted linear combination of the received signals corresponding to two consecutive transmitted pulses. Therefore, the processor can synthesize the appropriate combination of transmitting and receiving antenna polarization states that maximize (or minimize) the echo from a given scatterer having a known polarization scattering matrix or Mueller matrix.

Figure 9 illustrates the concept of image contrast enhancement. Figures 9a, 9b, and 9c show SAR images of San Francisco, California processed using HH, VV, and VH=HV polarizations, respectively. The Golden Gate Bridge appears as a bright, vertical line in the middle third of the images, and Golden Gate Park is the wide, horizontal band that appears in the lower quadrant. A comparison of the three images shows that HH polarization maximizes the contrast between the developed, urban areas (recognized by a grid pattern formed by perpendicular streets) and Golden Gate Park, which contains mixed vegetation. VV polarization increases the relative RCS of the waves present on the surface of the Pacific Ocean, as seen by a comparison of Figs. 9a and 9b, while the image in Fig. 9c shows that maximum contrast between the land and water occurs for the HV(=VH) polarization combination. [The imaging polarimeter used to collect the data presented in Fig. 9, the NASA/JPL AIRSAR, was developed by the Jet Propulsion Laboratory (JPL). For more information on the system and its successors, see Refs. 2, 6, and 35].

For target detecting radars, it is desirable to enhance the radar echo from wanted targets, such as aircraft, while suppressing the echo from unwanted targets, such as terrain clutter. In certain imaging radar applications, it is desirable to enhance the echo from one type of terrain while suppressing the echo from other types of terrain. The limitations to contrast enhancement are (1) lack of a priori knowledge of the scattering matrix of the desired target and (2) similarity of polarimetric responses of the desired and undesired scattering targets. Research performed on the target detection problem, including techniques to adaptively estimate the scattering matrices of targets and clutter, is described in Refs. 36–38. Work in polarization-based suppression of bistatic clutter is described in Ref. 39. Several papers dealing with polarimetric contrast enhancement in imaging radars for terrain mapping are summarized in Ref. 2.

3.4. Meteorology

While Doppler (coherent) radar has become an indispensable tool for meteorologists, the current fleet of operational weather radars utilize a single polarization. Research has shown, however, that polarization-diverse radars can provide weather forecasters with additional information. For example, polarimetric radar systems can discriminate ice particles from water droplets, and can detect hail. Radar echoes from precipitation are complex and depend on the shape, size distribution, water-phase state, and type of hydrometeor responsible for scattering the incident energy [40]. Large raindrops assume a flat pancake shape as they achieve terminal falling velocity, and thus scatter horizontally polarized energy more effectively than vertically polarized energy. Hailstones, in contrast, have irregular shapes but tumble as they fall, and thus exhibit equal scattering cross sections at vertical and horizontal polarizations. Exploiting this observation, Aydin et al. [41] developed a technique for discriminating rain from hail echoes by computing the ratio of horizontal to vertical power levels received when a dual-polarization radar transmits pulses into storms. Accurate measurement of rainfall rate is another important and evolving issue in the meteorological community. The relationship between the radar reflectivity coefficient of rain and the rain rate is different for different types of rain. Seliga and Bringi [42] have shown that independent measurement of rain reflectivity at vertical and horizontal polarizations provides more accurate rainfall estimates than do single-polarization radar estimates. Polarization diverse radars can also provide information on clouds. Mead [5] has developed a lightweight 94-GHz radar for airborne cloud profiling studies, and has used this system to determine the height of the melting layer. The technique involves calculation of the ratio of cross-polarized to copolarized scattering when looking vertically into a layer of developing clouds.

3.5. Topographic Mapping

Schuler et al. [43,44] have developed a technique to extract topographic information from fully polarimetric radar imagery. The method extracts the azimuthal slope of the imaged terrain by determining the shift that this slope induces in the polarimetric response. Integration of the inferred slopes across the image, in conjunction with suitable tie points (integration constants), then yields the elevation profile. To illustrate the basic principle behind

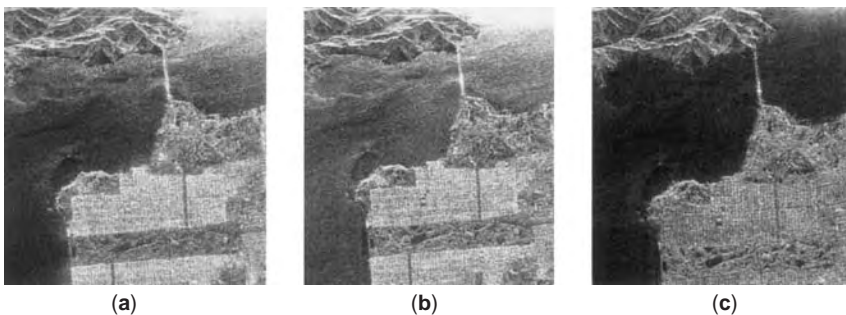


Figure 9. Synthetic aperture radar image of San Francisco, near Golden Gate Park, processed with three different polarization combinations: (a) HH polarization, showing the strongest contrast between urban and mixed vegetation areas; (b) VV polarization, which exhibits stronger backscatter from the areas covered by open water; and (c) HV = VH polarization, which maximizes the contrast between open water and land.

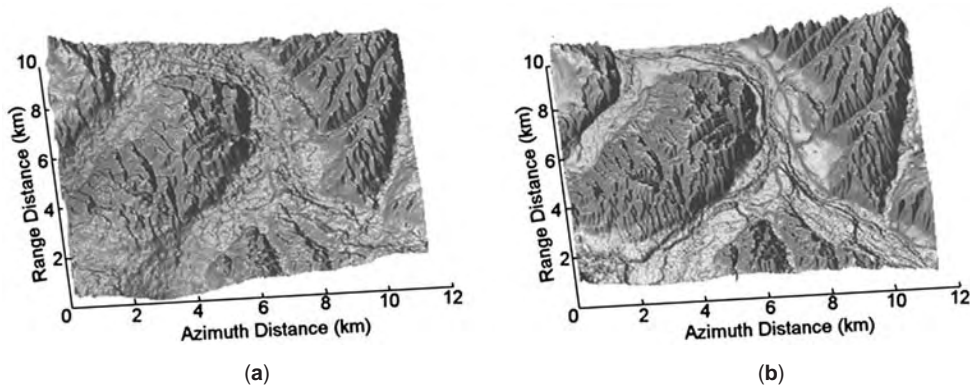


Figure 10. (a) Topographic map of Camp Roberts, CA produced from polarimetric SAR data collected by the JPL AIRSAR. The surface elevation is computed by integrating surface slopes derived from the polarimetric signature. Data from two orthogonal aircraft passes are used to reduce the number of required tie points to one. (b) Topographic map of the area in Fig. 10a produced using the JPL TOPSAR system. The RMS difference between the maps is 28 m.

the technique, assume that the scattering from the surface can be described by Bragg scatter, and thus has a scattering matrix (in the absence of any azimuthal tilts) of the form

$$\mathbf{S} = \begin{bmatrix} a & 0 \\ 0 & b \end{bmatrix} \quad (37)$$

where a and b are real and $b > a$. If the surface is tilted in the azimuthal plane by an angle δ , the scattering matrix becomes

$$\mathbf{S} = \begin{bmatrix} \cos \delta & -\sin \delta \\ \sin \delta & \cos \delta \end{bmatrix} \cdot \begin{bmatrix} a & 0 \\ 0 & b \end{bmatrix} \cdot \begin{bmatrix} \cos \delta & \sin \delta \\ -\sin \delta & \cos \delta \end{bmatrix} \quad (38)$$

which, after carrying out the matrix multiplication, can be expressed as

$$\mathbf{S} = \begin{bmatrix} a \cos^2 \delta + b \sin^2 \delta & (a - b) \cos \delta \sin \delta \\ (a - b) \cos \delta \sin \delta & a \sin^2 \delta + b \cos^2 \delta \end{bmatrix} \quad (39)$$

$$= \begin{bmatrix} S_{\delta(hh)} & S_{\delta(hv)} \\ S_{\delta(vh)} & S_{\delta(vv)} \end{bmatrix}$$

Tilting the surface introduces the off-diagonal terms $S_{\delta(hv)}$ and $S_{\delta(vh)}$ with $S_{\delta(hv)} = S_{\delta(vh)}$ from reciprocity. Solving this system of equations for δ produces the following expression:

$$\delta = \frac{1}{2} \tan^{-1} \left(\frac{2S_{\delta(vh)}}{S_{\delta(hh)} - S_{\delta(vv)}} \right) \quad (40)$$

Thus, the azimuthal slope of the surface can be derived from the elements of the measured scattering matrix. While Eq. (40) applies only to the case of Bragg scattering and cannot be applied in general, it illustrates the basic principle behind the method. A more general technique

for determining the shift in the polarimetric response, and thus the azimuthal slope, is discussed in Ref. 43.

Figure 10a shows an elevation map of the terrain near Camp Roberts, CA, derived from JPL AIRSAR data using this method [44]. For comparison, a digital elevation map (DEM) of the same area derived from data collected with the JPL TOPSAR system, an interferometric SAR designed to measure terrain topography, is displayed in Fig. 10b. The overall form of the two maps agrees very well, as do many of the details. The RMS elevation difference between the maps over the entire region is 28 m, while the maximum and minimum elevations in the scene are 300 and 180 m, respectively. The errors in the polarimetrically derived map are greatest in the river valleys, where more complex, manmade structures are present. In order to reduce the required number of tie points to one, data from two orthogonal aircraft passes have been used. The final elevation map is obtained as an iterative solution to the Poisson equation using curvature data derived from the two passes as inputs [43].

BIBLIOGRAPHY

1. (a) H. Mott, *Antennas for Radar and Communications—a Polarimetric Approach*, Wiley, New York, 1992; (b) J. L. Eaves, and E. K. Reedy, eds., *Principles of Modern Radar*, Van Nostrand Reinhold, New York, 1987, Chapter 20.
2. F. T. Ulaby and C. Elachi, eds., *Radar Polarimetry for Geoscience Applications*, Artech House, Boston, 1990.
3. J. R. Huynen, Measurement of the target scattering matrix, *Proc. IEEE* 936–946 (Aug. 1965).
4. W. M. Boerner, H. Mott, E. Luneberg, C. Livingstone, B. Brisco, R. Brown, and J. S. Patterson, in: R. A. Reyerson, ed., *The Manual of Remote Sensing*, 3rd ed., ASPRS Publishing, Bethesda, MD, 1997, Chapter 5.
5. J. B. Mead and R. E. McIntosh, Millimeter wave radars for remotely sensing clouds and precipitation, *Proc. IEEE* 82(12):1891–1906 (Dec. 1994).
6. J. J. van Zyl, H. A. Zebker, and C. Elachi, Imaging radar polarization signatures: theory and observation, *Radio Sci.* 22(4):529–543 (July–Aug 1987).

7. M. I. Skolnik, *Radar Handbook*, McGraw-Hill, New York, 1990.
8. P. C. Dubois, D. Evans, and J. van Zyl, Approach to derivation of SIR-C science requirements for calibration, *IEEE Trans. Geosci. Remote Sens.* **30**(6):1145–1149 (Nov. 1992).
9. B. L. Huneycutt, Spaceborne imaging radar-C instrument, *IEEE Trans. Geosci. Remote Sens.* **27**(2):164–169 (March 1989).
10. F. T. Ulaby, R. K. Moore, and A. K. Fung, *Microwave Remote Sensing, Active and Passive*, Vol. 2, Artech House, Norwood, MA, 1986.
11. S. P. Lohmeier, S. M. Sekelsky, J. M. Firda, G. A. Sadowy, and R. E. McIntosh, Classification of particles in stratiform clouds using the 33 and 95 GHz polarimetric cloud profiling radar system (CPRS), *IEEE Trans. Geosci. Remote Sens.* **35**(2):256–270 (March 1997).
12. D. J. McLaughlin et al., Fully polarimetric bistatic radar scattering behavior of forested hills, *IEEE Trans. Anten. Propag.* **50**(2):101–110 (Feb. 2002).
13. D. J. McLaughlin, N. Allan, E. Twarog, and D. B. Trizna, High resolution polarimetric radar scattering measurements of log grazing angle sea clutter, *IEEE J. Ocean. Eng.* **20**(3):166–178 (July 1995).
14. J. Metcalf et al., *An 11-cm Full-Matrix Polarimetric Radar for Meteorological Research*, USAF Phillips Laboratory Geophysics Directorate, Environmental Research Paper PL-TR-91-2167, No. 1088, June 1991.
15. A. L. Pazmany, R. E. McIntosh, R. D. Kelly, and G. Vali, An airborne 95 GHz dual-polarized radar for cloud studies, *IEEE Trans. Geosci. Remote Sens.* **32**(4):731–739 (July 1994).
16. R. M. Barnes, *Polarimetric Calibration Using In-Scene Reflectors*, Report TT-65, MIT Lincoln Lab., Lexington, MA, 1986.
17. J. J. van Zyl, Calibration of polarimetric images using only image parameters and trihedral corner reflector responses, *IEEE Trans. Geosci. Remote Sens.* **28**:337–348 (1990).
18. D. J. McLaughlin, Z. Ren, and Y. Wu, A bistatic polarimeter calibration technique, *IEEE Trans. Geosci. Remote Sens.* **33**(3):796–799 (May 1995).
19. A. Freeman, SAR calibration: An overview, *IEEE Trans. Geosci. Remote Sens.* **30**:1107–1121 (Nov. 1992).
20. J. J. VanZyl, Unsupervised classification of scattering behavior using radar polarimetry data, *IEEE Trans. Geosci. Remote Sens.* **27**(1) (Jan. 1989).
21. (a) M. A. Sletten and D. B. Trizna, An ultrawideband, polarimetric radar for the study of sea scatter, *IEEE Trans. Anten. Propag.* **42**(11) (Nov. 1994); (b) M. A. Sletten and J. Wu, Ultrawideband, polarimetric radar studies of breaking waves at low grazing angles, *Radio Sci.* **31**(1) (Jan.–Feb. 1996).
22. J. R. Huynen, Phenomenological theory of radar targets, in P. L. E. Uslenghi, ed., *Electromagnetic Scattering*, Academic Press, New York, 1978.
23. W. A. Holm and R. M. Barnes, On radar polarization mixed target state decomposition techniques, *Proc. 1988 IEEE Natl. Radar Conf.* 249–254.
24. E. Krogager and Z. H. Czyz, Properties of the sphere, diplane, helix decomposition, *Proc. 3rd Int. Workshop on Radar Polarimetry*, Nantes, France, March 21–23, 1995.
25. A. Freeman and S. Durden, A three component scattering model to describe polarimetric SAR data, *Radar Polarim. SPIE* **1748**:213–224 (1992).
26. S. R. Cloude and E. Pottier, A review of target decomposition theorems in radar polarimetry, *IEEE Trans. Geosci. Remote Sens.* **34**(2):498–518 (March 1996).
27. S. R. Cloude and E. Pottier, An entropy based classification scheme for land applications of polarimetric SAR, *IEEE Trans. Geosci. Remote Sens.* **35**(1):68–78 (Jan. 1997).
28. J. S. Lee, M. R. Grunes, and R. Kwok, Classification of multi-look polarimetric SAR imagery based on complex Wishart distribution, *Int. J. Remote Sens.* **15**(11):2299–2311 (July 20, 1994).
29. J. S. Lee, M. R. Grunes, T. L. Ainsworth, L. Du, D. L. Schuler, and S. R. Cloude, Unsupervised classification using polarimetric decomposition and the complex Wishart classifier, *IEEE Trans. Geosci. Remote Sens.* **37**(5):2249–2258 (Sept. 1999).
30. H. A. Yueh, A. A. Swartz, J. A. Kong, R. T. Shin, and L. M. Novak, Bayes classification of terrain cover using normalized polarimetric data, *J. Geophys. Res.* **93**(B12):15261–15267 (Dec. 10, 1988).
31. P. Ferrazzoli, S. Paloscia, P. Pampaloni, G. Schiavon, S. Sigismondi, and D. Solimimi, The potential of multifrequency polarimetric SAR in assessing agricultural and aboreal biomass, *IEEE Trans. Geosci. Remote Sens.* **35**(1):5–17 (Jan. 1997).
32. C.-T. Chen, K.-S. Chen, and J.-S. Lee, The use of fully polarimetric information for the fuzzy neural classification of SAR images, *IEEE Trans. Geosci. Remote Sens.* **41**(9):2089–2100 (Sept. 2003).
33. J. J. van Zyl, C. H. Papas, and C. Elachi, On the optimum polarizations of incoherently reflected waves, *IEEE Trans. Anten. Propag.* **AP-35**(7) (July 1987).
34. D. Guili, Polarization diversity in radars, *Proc. IEEE* **74**(2):245–286 (Feb. 1986).
35. H. A. Zebker, J. J. Van Zyl, S. L. Durden, and L. Norikane, Calibrated imaging radar polarimetry: technique, examples, and applications, *IEEE Trans. Geosci. Remote Sens.* **29**(6) (Nov. 1991).
36. V. C. Vannicula and S. Lis, Polarization vector signal processing for radar clutter suppression, in W. M. Boerner et al., eds., *Inverse Methods in Electromagnetic Imaging*, Reidel, Hingham, MA, 1985, Vol. 2, pp. 739–770.
37. G. A. Ioiannidis and D. E. Hammers, Optimum antenna polarizations for target discrimination in clutter, *IEEE Trans. Anten. Propag.* **AP-27**:357–363 (May 1979).
38. L. M. Novak, M. B. Sechtin, and M. J. Cardullo, Studies of target detection algorithms that use polarimetric radar data, *IEEE Trans. Aerospace Electron. Syst.* **25**(2) (1989).
39. D. J. McLaughlin and R. S. Raghavan, *A Study of Polarimetric Strategies for Suppressing Bistatic Clutter with Applications to Radar Detection*, USAF Rome Laboratory Contract F19628-93-k-0005, final report, June 1997.
40. M. Hall, ed., Special papers: Multiple parameter radar measurements of precipitation, *Radio Sci.* **19** (1984).
41. K. Aydin, T. Seliga, and V. Balaji, Remote sensing of hail with a dual linear polarization radar, *J. Clim. Appl. Meteorol.* **25**:1475–1484 (1986).
42. T. A. Seliga and V. N. Bringi, Potential use of radar differential reflectivity measurements at orthogonal polarizations for measuring precipitation, *J. Appl. Meteorol.* **15**:69–76 (1976).
43. D. L. Schuler et al., Topographic mapping using polarimetric SAR data, *Int. J. Remote Sens.* **19**(1):141–160 (1998).
44. D. L. Schuler et al., Terrain topography measurement using multipass polarimetric synthetic aperture radar data, *Radio Sci.* **35**(3):813–832 (2000).

RADAR REMOTE SENSING

JAKOB J. VAN ZYL
YUNJIN KIM
California Institute of
Technology
Pasadena, California

Radar remote sensing instruments acquire data useful for geophysical investigations by measuring electromagnetic interactions with natural objects. Examples of radar remote sensing instruments include synthetic aperture radars (SAR), scatterometers, altimeters, radar sounders, and meteorological radars such as cloud and rain radars. The main advantage of radar instruments is their ability to penetrate clouds, rain, tree canopies, and even dry soil surfaces depending on the operating frequencies. In addition, since a remote sensing radar is an active instrument, it can operate during day and night by providing its own illumination.

Imaging remote sensing radars such as SAR produce high-resolution (from submeter to few tens of meters) images of surfaces. The geophysical information can be derived from these high-resolution images by using proper postprocessing techniques. Scatterometers measure the backscattering cross section accurately in order to characterize surface properties such as roughness. Altimeters are used to obtain accurate surface height maps by measuring the round-trip time delay from a radar sensor to the surface. Radar sounders can image underground material variations by penetrating deeply into the ground. Unlike surveillance radars, remote sensing radars require accurate calibration in order for the data to be useful for scientific applications.

In this article, we start with the basic principles of remote sensing radars. Then, we discuss the details of imaging radars and their applications. We complete the remote sensing radar discussion by briefly examining nonimaging radars such as scatterometers, altimeters, radar sounders, and meteorological radars. We also provide extensive references for each type of radar for readers who need an in-depth description of a particular type.

1. RADAR PRINCIPLES

We start our discussion with the principles necessary to understand the radar remote sensing instruments that will be described in later in this article. For more detailed discussions, readers are referred to Refs. 1–3.

1.1. Radar Operation

A radar transmits an electromagnetic signal and receives and records the echo reflected from the illuminated terrain. Hence, a radar is an active remote sensing instrument since it provides its own illumination. The basic radar operation is illustrated by Fig. 1. A desired signal waveform, commonly a modulated pulse, is generated by a waveform generator. After proper frequency upconversion and high-power amplification, the radar signal is transmitted from an antenna. The reflected echo is received by

the antenna and is amplified and downconverted to video frequencies for digitization. The digitized data are either stored in a data recorder for later ground data processing or processed by an onboard data processor. Since remote sensing radars usually image large areas, they are commonly operated from either an airborne or a spaceborne platform.

1.2. Basic Principles of Radar Imaging

Imaging radars generate surface images very similar to visible and infrared images. However, the principle behind the image generation fundamentally varies between the two cases. Visible and infrared sensors use a lens or mirror system to project the radiation from the scene on a “two-dimensional array of detectors,” which could be an electronic array or a film using chemical processes. The two-dimensionality can also be achieved by using scanning systems. This imaging approach conserves the angular relationships between two targets and their images as shown in Fig. 2.

Imaging radars use the time delay between the echoes that are backscattered from different surface elements to separate them in the *range* (cross-track) dimension, the angular size (in the case of the real aperture radar), or the Doppler history (in the case of the synthetic aperture radar) to separate surface pixels in the *azimuth* (along-track) dimension. The imaging radar sensor uses an antenna that illuminates the surface to one side of the flight track. Usually, the antenna has a fan beam that illuminates a highly elongated elliptical shaped area on the surface as shown in Fig. 3. The illuminated area across the track defines the image *swath*. Within the illumination beam, the radar sensor transmits a very short effective pulse of electromagnetic energy. Echoes from surface points farther away along the cross-track coordinate will be received at proportionally later time (Fig. 3). Thus, by dividing the receive time in increments of equal time bins, one can subdivide the surface into a series of *range bins*. The width in the along-track direction of each range bin is equal to the antenna footprint along the track x_a . As the platform moves, the sets of range bins are covered sequentially, thus allowing strip mapping of the surface line by line. This is comparable to strip mapping with a push-broom imaging system using a line array in the visible and infrared part of the electromagnetic spectrum. The brightness associated with each image pixel in the radar image is proportional to the echo power contained within the corresponding time bin. As we will see later, the different types of imaging radars really differ in the way in which the azimuth resolution is achieved.

The *look angle* is defined as the angle between the vertical direction and the radar beam at the radar platform, while the *incidence angle* is defined as the angle between the vertical direction and the illuminating radar beam at the surface. When Earth surface curvature effects are neglected, the look angle is equal to the incidence angle at the surface when the surface is flat. In the case of spaceborne systems, surface curvature must be taken into account, which leads to an incidence angle that is always larger than the look angle [3] for flat surfaces. If

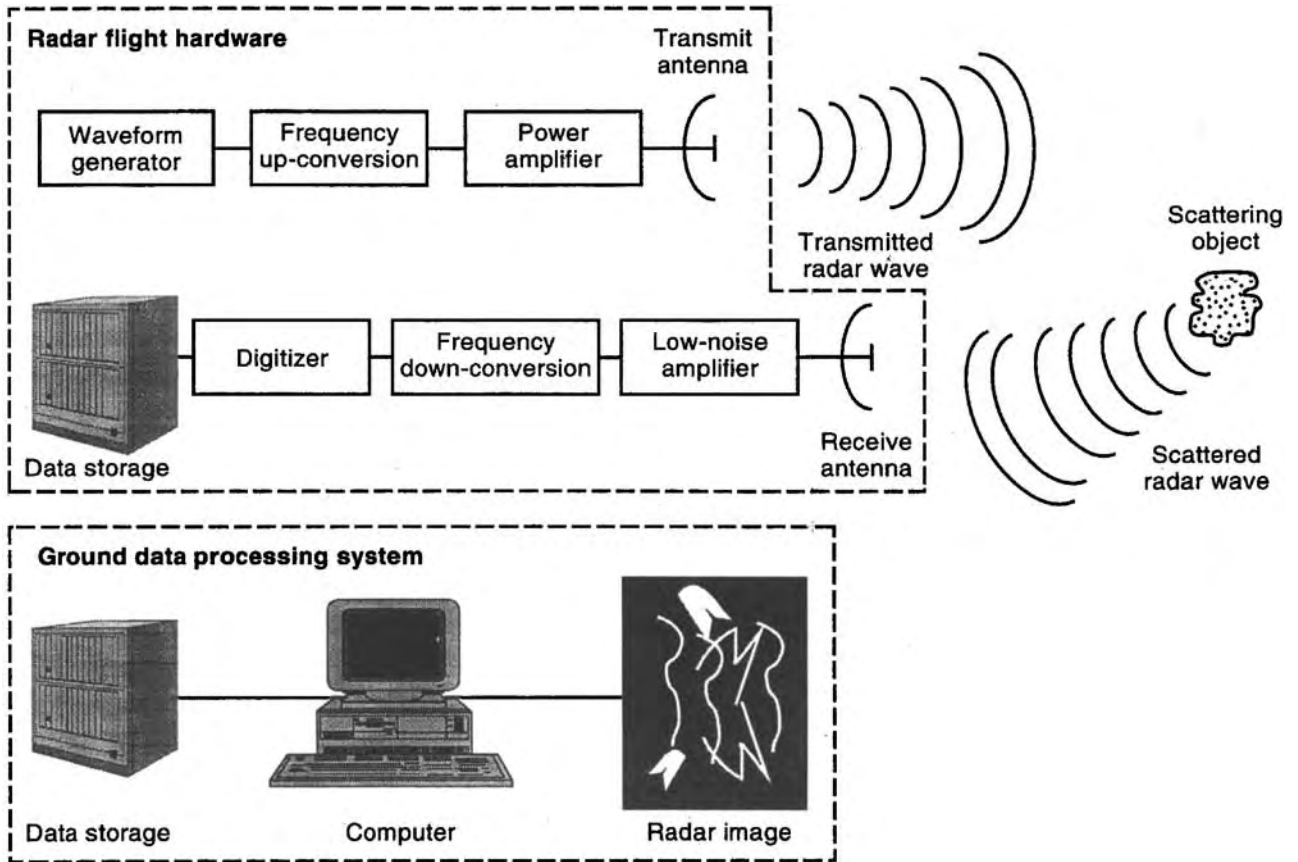


Figure 1. The basic components of a radar system. A pulse of energy is transmitted from the radar system antenna, and after a time delay an echo is received and recorded. The recorded radar echoes are later processed into images. The flight electronics are carried on the radar platform, either an aircraft or a spacecraft. Image processing is usually done in a ground facility.

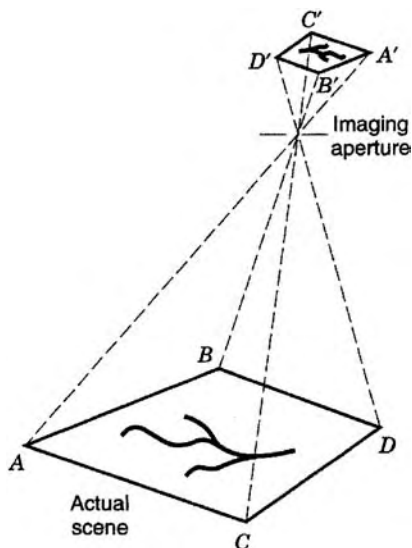


Figure 2. Optical imaging systems preserve the angular relationship between objects in the image.

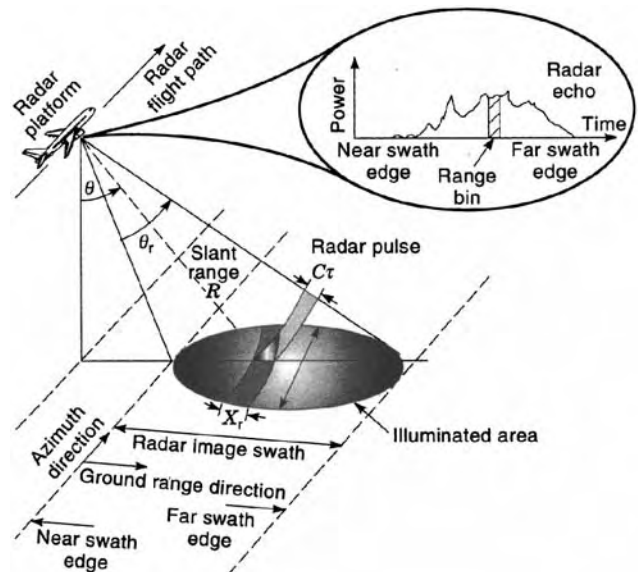


Figure 3. Radar imaging geometry and definition of terms.

topography is present, that is, if the surface is not flat, the local incidence angle may vary from radar image pixel to pixel.

1.3. Resolution

The *resolution* is defined as the surface separation between the two closest features that can still be resolved in the final image. First, consider two point targets that are separated in the range direction by x_r . The corresponding echoes will be separated by a time difference Δt equal to

$$\Delta t = 2x_r \frac{\sin \theta}{c} \tag{1}$$

where c is the speed of light and the factor 2 is included to account for the signal round-trip propagation. The angle θ in Eq. (1) is the incidence angle. The two features can be differentiated if the leading edge of the pulse returned from the second object is received later than the trailing edge of the pulse received from the first feature. Therefore, the smallest discriminable time difference in the radar receiver is equal to the pulse effective time length τ :

$$2x_r \frac{\sin \theta}{c} = \tau \Rightarrow x_r = \frac{c\tau}{2 \sin \theta} \tag{2}$$

In other words, the range resolution is equal to half the footprint of the radar pulse on the surface. Sometimes the effective pulse length is described in terms of the system bandwidth B . To a good approximation

$$\tau = \frac{1}{B} \tag{3}$$

The $\sin \theta$ term in the denominator of Eq. (2) means that the range resolution of an imaging radar will be a strong function of the look angle at which the radar is operated. To illustrate, a signal with a bandwidth $B = 20$ MHz (i.e., effective pulse length $\tau = 50$ ns) provides a range resolution of 22 m for $\theta = 20^\circ$, while a signal bandwidth $B = 50$ MHz ($\tau = 20$ ns) provides a range resolution of 4.3 m at $\theta = 45^\circ$.

In the azimuth direction, without further data processing, the resolution x_a is equal to the beam footprint on the surface that is defined by the azimuth beamwidth of the radar antenna θ_a given by

$$\theta_a = \frac{\lambda}{L} \tag{4}$$

from which it follows that

$$x_a = \frac{h\theta_a}{\cos \theta} = \frac{\lambda h}{L \cos \theta} \tag{5}$$

where L is the antenna length and h is the altitude of the radar above the surface being imaged. To illustrate, for $h = 800$ km, $\lambda = 23$ cm, $L = 12$ m, and $\theta = 20^\circ$, then $x_a = 16$ km. Even if λ is as short as 2 cm and h as low as 200 km, x_a will still be equal to about 360 m, which is considered to be a relatively low resolution, even for remote sensing. This has led to very limited use of the real

aperture technique for surface imaging, especially from space. Equation (5) is also directly applicable to optical imagers. However, because of the small value of λ (about $1 \mu\text{m}$), resolutions of a few meters can be achieved from orbital altitudes with an aperture only a few tens of centimeters in size.

When the radar antenna travels along the line of flight, two point targets, at different angles from the flight track, have different Doppler frequencies. Using this Doppler frequency spread, one can obtain a higher resolution in the along-track direction. As shown in the synthetic aperture radar section, the along-track resolution can be as small as the half of the antenna length in the along-track direction. This method is often called *Doppler beam sharpening*.

1.4. Radar Equation

One of the key factors that determine the quality of the radar imagery is the corresponding *signal-to-noise* ratio, commonly abbreviated SNR. This is the equivalent of the brightness of a scene being photographed with a camera versus the sensitivity of the film or detector. Here, we consider the effect of thermal noise on the sensitivity of radar imaging systems.

Let P_t be the sensor generated peak power transmitted out of the antenna. One function of the antenna is to focus the radiated energy into a small solid angle directed toward the area being imaged. This focusing effect is described by the antenna gain G , which is equal to the ratio of the total solid angle over the solid angle formed by the antenna beam

$$G = \frac{4\pi}{\theta_r \theta_a} = \frac{4\pi LW}{\lambda^2} = \frac{4\pi A}{\lambda^2} \tag{6}$$

where L is the antenna length in the flight track direction, W is the antenna length in the cross-track direction, and A is the antenna area. The radiated wave propagates spherically away from the antenna toward the surface. Thus the power density P_i per unit area incident on the illuminated surface is

$$P_i = \frac{P_t G}{4\pi R^2} \tag{7}$$

The backscattered power P_s from an illuminated surface area s is given by

$$P_s = P_i s \sigma_0 \tag{8}$$

where σ_0 is the surface *backscattering cross section*, which represents the efficiency of the surface in reemitting back toward the sensor some of the energy incident on it. It is similar to the surface albedo at visible wavelengths. The backscattered energy propagates spherically back toward the sensor. The power density P_c at the antenna is then

$$P_c = \frac{P_s}{4\pi R^2} \tag{9}$$

and the total received power is equal to the power intercepted by the antenna

$$P_r = P_c A \quad (10)$$

or

$$P_r = \frac{P_t G_t}{4\pi R^2} s \sigma_0 \frac{\lambda^2 G_r}{(4\pi R)^2} \quad (11)$$

In Eq. (11) we explicitly show that the transmit and receive antennas may have different gains. This is important for the more advanced SAR techniques such as polarimetry, where antennas with different polarizations may be used during transmission and reception.

In addition to the target echo, the received signal also contains noise that results from the fact that all objects at temperatures higher than absolute zero emit radiation across the whole electromagnetic spectrum. The noise component that is within the spectral bandwidth B of the sensor is passed through with the signal. The thermal noise power is given by

$$P_N = kTB \quad (12)$$

where k is Boltzmann's constant ($k = 1.38 \times 10^{-23} \text{ W}^{-1} \text{ Hz}^{-1} \text{ K}^{-1}$) and T is the total equivalent noise temperature. The resulting *signal to noise ratio* is then

$$\text{SNR} = \frac{P_r}{P_N} \quad (13)$$

One common way of characterizing an imaging radar sensor is to determine the surface backscatter cross section σ_N , which gives an $\text{SNR} = 1$. This is called the *noise equivalent backscatter cross section*. It defines the weakest surface return that can be detected, and therefore the range of surface units that can be imaged.

1.5. Backscattering Cross Section and Calibration Devices

The *normalized backscattering cross section* represents the reflectivity of an illuminated area in the backscattering direction. A higher backscattering cross section means that the area more strongly reflects the incidence radar signal. It is mathematically defined as

$$\sigma_0 = \lim_{R, A_i \rightarrow \infty} \left\{ \frac{4\pi R^2}{A_i} \frac{\langle E_s E_s^* \rangle}{E_i E_i^*} \right\} \quad (14)$$

where A_i is the illuminated area and E_s and E_i are the scattered and incident electric fields, respectively. In order to calibrate the radar data, active and/or passive calibration devices are commonly used.

By far the most commonly used passive calibration device is a trihedral corner reflector, which consists of three triangular panels bolted together to form right angles with respect to each other. The maximum radar cross section (RCS) of a trihedral corner reflector is given by

$$\text{RCS} = \frac{4\pi a^4}{3\lambda^2} \quad (15)$$

where a is the long-side triangle length of a trihedral corner reflector. This reflector has about 40° half-power beamwidth, which vendors the corner reflector response relatively insensitive to the position errors. In addition, these devices are easily deployed in the field, and since they require no power to operate, they can be used unattended in remote locations under most weather conditions.

1.6. Signal Modulation

A pulsed radar determines the range by measuring the round-trip time by transmitting a pulse signal. In designing the signal pattern for a radar sensor, there is usually a strong requirement to have as much energy as possible in each pulse in order to enhance the signal-to-noise ratio. This can be done by increasing the peak power or by using a longer pulse. However, particularly in the case of spaceborne sensors, the peak power is usually strongly limited by the available power devices. On the other hand, an increased pulse length (i.e., smaller bandwidth) leads to a lower range resolution [see Eq. (2)]. This dilemma is usually resolved by using *modulated* pulses that have the property of a wide bandwidth even when the pulse is very long. One such modulation scheme is the linear frequency modulation or chirp.

In a "chirp", the signal frequency within the pulse is linearly changed as a function of time. If the frequency were linearly changed from f_0 to $f_0 + \Delta f$, the effective bandwidth would be equal to

$$B = |(f_0 + \Delta f) - f_0| = |\Delta f| \quad (16)$$

which is independent of the pulse length. Thus a pulse with long duration (i.e., high energy) and wide bandwidth (i.e., high range resolution) can be constructed. The instantaneous frequency for such a signal is given by

$$f(t) = f_0 + \frac{B}{\tau'} t \quad \text{for} \quad -\frac{\tau'}{2} \leq t \leq \frac{\tau'}{2} \quad (17)$$

and the corresponding signal amplitude is

$$A(t) \sim \cos \left[\int f(t) dt \right] = \cos \left[f_0 t + \frac{B}{2\tau'} t^2 \right] \quad (18)$$

Note that the instantaneous frequency is the derivative of the instantaneous phase. A pulse signal such as Eq. (18) has a physical pulse length τ' and a bandwidth B . The product $\tau' B$ is known as the *time-bandwidth product* (TBP) of the radar system. In typical radar systems, TBPs of several hundred are used.

At first glance it may seem that using a pulse of the form of Eq. (18) cannot be used to separate targets that are closer than the projected physical length of the pulse. It is indeed true that the echoes from two neighboring targets that are separated in the range direction by much less than the physical length of the signal pulse will overlap in time. If the modulated pulse, and therefore the echoes, have a constant frequency, it will not be possible to resolve the two targets. However, if the frequency is modulated as described in Eq. (18), the echoes from the two targets will

have different frequencies at any instance of time and therefore can be separated by frequency filtering. In actual radar systems, a matched filter is used to *compress* the returns from the different targets. It can be shown [3] that the effective pulselength of the compressed pulse is as given by Eq. (3). Therefore, the achievable range resolution using a modulated pulse of the kind given by Eq. (18) is a function of the chirp bandwidth, and not the physical pulselength. In typical spaceborne and airborne SAR systems, physical pulselengths of several tens of microseconds are used, while bandwidths of several tens of megahertz are no longer uncommon for spaceborne systems, and several hundreds of megahertz are common in airborne systems.

2. REAL APERTURE RADAR

The real aperture imaging radar sensor uses an antenna that illuminates the surface to one side of the flight track. Usually, the antenna has a fan beam that illuminates a highly elongated elliptical shaped area on the surface as shown in Fig. 3. As mentioned before, the illuminated area across the track defines the image swath. For an antenna of width W operating at a wavelength λ , the beam angular width in the range plane is given by

$$\theta_r \approx \frac{\lambda}{W} \quad (19)$$

and the resulting surface footprint or swath S is given by

$$S \approx \frac{h\theta_r}{\cos^2 \theta} = \frac{\lambda h}{W \cos^2 \theta} \quad (20)$$

where h is the sensor height above the surface, θ is the angle from the center of the illumination beam to the vertical (known as the *look angle* at the center of the swath), and θ_r is assumed to be very small. To illustrate, for $\lambda = 27$ cm, $h = 800$ km, $\theta = 20^\circ$, and $W = 2.1$ m, the resulting swath width is 100 km.

As shown before, the main disadvantage of the real aperture radar technique is the relatively poor azimuth resolution that could be achieved from space. From aircraft altitudes, however, reasonable azimuth resolutions can be achieved if higher frequencies (typically at X band or higher) are used. For this reason, real aperture radars are not commonly used any more.

3. SYNTHETIC APERTURE RADAR

Synthetic aperture radar refers to a particular implementation of an imaging radar system that utilizes the movement of the radar platform and specialized signal processing to generate high-resolution images. Prior to the discovery of synthetic aperture radar principle imaging radars operated using the real aperture principle, and were known as *side-looking aperture radars* (SLARs).

Carl Wiley of the Goodyear Aircraft Corp, is generally credited as the first person to describe the use of Doppler frequency analysis of signals from a moving coherent

radar to improve along-track resolution. He noted that two targets at different along-track positions will be at different angles relative to the aircraft velocity vector, resulting in different Doppler frequencies. Therefore, targets can be separated in the along-track direction on the basis of their different Doppler frequencies. This technique was originally known as *Doppler beam sharpening*, but later became known as *synthetic aperture radar* (SAR). The reader interested in a discussion of the history of SAR, both airborne and spaceborne, is referred to an excellent discussion in Chap. 1 of Ref. 3.

In this section, we discuss the principles of radar imaging using synthetic aperture techniques, the resulting image projections, distortions, tonal properties, and environmental effects on the images. We have attempted to give simple explanations of the different imaging radar concepts. For more detailed mathematical analysis, the reader is referred to specialized texts such as Refs. 1–3.

3.1. Synthetic Aperture Radar Principle

As discussed in the previous section, a real aperture radar cannot achieve high azimuth resolution from an orbital platform. In order to achieve a high resolution from any altitude, the synthetic aperture technique is used. This technique uses successive radar echoes acquired at neighboring locations along the flight line to synthesize an equivalent very long antenna that provides a very narrow beamwidth and thus a high image resolution. In this section, we explain the synthetic aperture radar (SAR) using two different approaches, the synthetic array approach and the Doppler synthesis approach, which lead to the same results. We will also discuss uses of linear frequency modulation (chirp) as well as some limitations and degradation that are inherent to the SAR technique. Our discussion closely follows that of Ref. 1.

The range resolution and radar equation derived previously for a real aperture radar are still valid here. The main difference between real and synthetic aperture radars is in the way in which the azimuth resolution is achieved.

3.1.1. Synthetic Array Approach. The synthetic array approach explains the SAR technique by comparing it to a long array of antennas and the resulting increase in the resolution relative to the resolution achieved with one of the array elements. Let us consider a linear array of antennas consisting of N elements (Fig. 4). The contribution on the n th element to the total far-field electric field E in the direction β is proportional to

$$E_r \sim a_n e^{i\phi_n} e^{-ikd_n \sin \beta} \quad (21)$$

where a_n and ϕ_n are the amplitude and phase of the signal radiated from the n th element, d_n is the distance of the n th element to the array center, and $k = 2\pi/\lambda$. The total electric field is given by

$$E(\beta) \sim \sum_n a_n e^{i\phi_n} e^{-ikd_n \sin \beta} \quad (22)$$

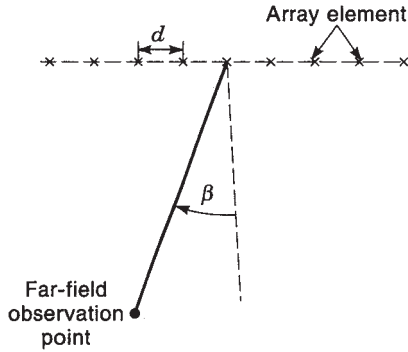


Figure 4. Geometry of a linear array of antenna elements.

If all the radiators are identical in amplitude and phase and are equally spaced with a separation d , then

$$E(\beta) \sim ae^{i\phi} \sum_n e^{-inkd \sin \beta} \quad (23)$$

This is the vector sum of N equal vectors separated by a phase $\Psi = kd \sin \beta$. The resulting vector shown in Eq. (23) has the following properties:

- For $\beta = 0 \Rightarrow \Psi = 0 \Rightarrow$ all vectors add together leading to a maximum for E .
- As β increases, the elementary vectors will spread and lead to a decrease in the magnitude of E .
- For β such that $N\Psi = 2\pi$, the vectors are spread all around a circle leading to a sum equal to zero.

Thus, the radiation pattern has a null for

$$Nkd \sin \beta = 2\pi \Rightarrow \beta = \sin^{-1} \frac{2\pi}{Nkd} = \sin^{-1} \frac{\lambda}{D} \quad (24)$$

where $D = Nd$ is the total physical length of the array.

From the discussion and equations above it is seen that an array of total length $D = Nd$ has a beamwidth equal to the one for a continuous antenna of physical size D . This is achieved by adding the signals from each element in the array coherently, namely, amplitude *and* phase. The fine structure of the antenna pattern depends on the exact spacing of the array. Close spacing of the array elements is required to avoid grating effects.

In a conventional array, the signals from the different elements are combined together with a network of waveguides or cables leading to a single transmitter and receiver. Another approach is to connect each element to its own transmitter and receiver. The signals are coherently recorded and added later using a separate processor. A third approach could be used if the scene is quasistatic. A single transmitter/receiver/antenna element can be moved from one array position to the next. At each location a signal is transmitted and the echo recorded coherently. The echoes are then added in a separate processor or computer. A stable oscillator is used as a reference to assure coherency as the single element moves along the array line. This last configuration is used in a SAR where a

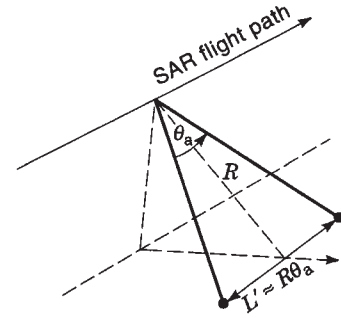


Figure 5. The width of the antenna beam in the azimuth direction defines the length of the synthetic aperture.

single antenna element serves to synthesize a large aperture.

Referring to Fig. 5, it is clear that if the antenna beam is equal to $\theta_a = \lambda/L$, the maximum possible synthetic aperture length that would allow us to observe a point is given by

$$L' = R\theta_a \quad (25)$$

This synthetic array will have a beamwidth θ_s equal to

$$\theta_s = \frac{\lambda}{2L'} = \frac{\lambda}{2R\theta_a} = \frac{L}{2R} \quad (26)$$

The factor 2 is included to account for the fact that the 3 dB (half-power) beamwidth is narrower in a radar configuration where the antenna pattern is involved twice, once each at transmission and reception. The corresponding surface along-track resolution of the synthetic array is

$$x_a = R\theta_s = \frac{L}{2} \quad (27)$$

This result shows that the azimuth (or along-track) surface resolution is equal to half the size of the physical antenna and is independent of the distance between the sensor and the surface. At first glance this result seems most unusual. It shows that a smaller antenna gives better resolution. This can be explained in the following way. The smaller the physical antenna is, the larger its footprint. This allows a longer observation time for each point on the surface; thus a longer array can be synthesized. This longer synthetic array allows for a finer synthetic beam and surface resolution. Similarly, if the range between the sensor and surface increases, the physical footprint increases, leading to a longer synthetic array and finer angular resolution that counterbalances the increase in the range.

As the synthetic array gets larger, it becomes necessary to compensate for the slight changes in geometry when a point is observed (Fig. 6). It should also be taken into account that the distance between the sensor and the target is variable depending on the position in the array. Thus, an additional phase shift needs to be added in the processor to the echo received at location x_i equal to

$$\phi_i = 2k(R_0 - R_i) = \frac{4\pi}{\lambda}(R_0 - R_i) \quad (28)$$

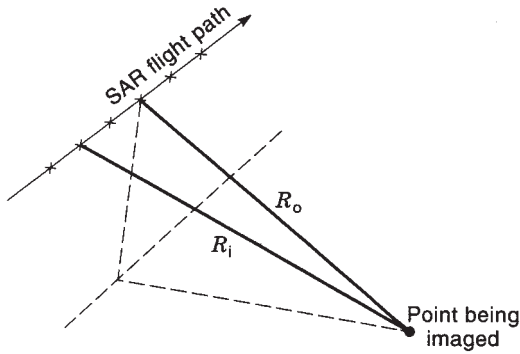


Figure 6. For large synthetic arrays, one has to compensate during ground processing for the change in geometry between the antenna elements and the point being imaged.

where R_0 is the range at closest approach to the point being imaged. In order to focus at a different point, a different set of phase shift corrections needs to be used. However, because this is done at a later time in the processor, optimum focusing can be achieved for each and every point in the scene. SAR imaging systems that fully apply these corrections are called *focused*.

In order to keep the processing simple, one can shorten the synthetic array length and use only a fraction of the maximum possible length. In addition, the same phase shift correction can be applied to all the echoes. This would lead to constructive addition if the partial array length is such that

$$\phi_i \leq \frac{\pi}{4}$$

or

$$2k \left\{ \sqrt{R^2 + \left(\frac{L'}{2}\right)^2} - R \right\} \leq \frac{\pi}{4} \tag{29}$$

For large ranges, this reduces to

$$L' \leq \sqrt{\frac{\lambda R}{2}} \tag{30}$$

and the achievable azimuth resolution is

$$x_a \geq \sqrt{2\lambda R} \tag{31}$$

This is called an *unfocused* SAR configuration where the azimuth resolution is somewhat degraded relative to the fully focused one, but still better than that of a real aperture radar. The advantage of the unfocused SAR is that the processing is fairly simple compared to that of a fully focused SAR.

To illustrate, for a 12-m antenna, with a wavelength of 3 cm, and a platform altitude of 800 km, the azimuth resolutions will be 6, 220, and 2000 m for the cases of a fully focused SAR, an unfocused SAR, or a real aperture radar, respectively.

3.1.2. Doppler Synthesis Approach. Another way to explain the synthetic aperture technique is to examine the

Doppler shifts of the radar signals. As the radar sensor moves relative to the target being illuminated, the back-scattered echo is shifted in frequency due to the Doppler effect. This Doppler frequency is equal to

$$f_d = 2 \frac{v}{c} f_0 \cos \Psi = 2 \frac{v}{\lambda} \sin \theta_t \tag{32}$$

where f_0 is the transmitted signal frequency, Ψ is the angle between the velocity vector $\vec{v} = v\hat{v}$ and the sensor-target line, and $\theta_t = \pi/2 - \Psi$. As the target moves through the beam, the angle θ_t varies from $+\theta_a/2$ to $-\theta_a/2$, where θ_a is the antenna azimuth beamwidth. Thus, a well-defined Doppler history is associated with every target. Figure 7 shows such a history for two neighboring targets P and P' located at the same range but at different azimuth positions. The Doppler shift varies from $+f_D$ to $-f_D$ where

$$f_D = 2 \frac{v}{\lambda} \sin \frac{\theta_a}{2} \tag{33}$$

When $\theta_a \ll 1$, Eq. (28) can be written as

$$f_D = 2 \frac{v}{\lambda} \frac{\theta_a}{2} = 2 \frac{v}{\lambda} \frac{\lambda}{2L} = \frac{v}{L} \tag{34}$$

The instantaneous Doppler shift is given by

$$f_D(t) = 2 \frac{v}{\lambda} \theta_t \approx 2 \frac{v^2 t}{\lambda h} \cos \theta \tag{35}$$

where $t = 0$ corresponds to the time when the target is exactly at 90° to the flight track. Thus, the Doppler histories for the two points P and P' will be identical except for a time displacement equal to

$$\Delta t = \frac{PP'}{v} \tag{36}$$

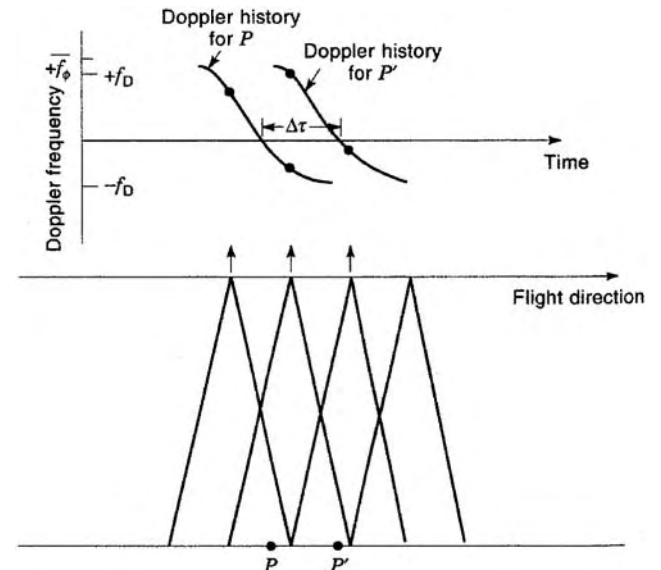


Figure 7. Doppler history for two targets separated in the azimuth direction.

It is this time displacement that allows the separation of the echoes from each of the targets.

The resolution along-track (azimuth resolution) x_a is equal to the smallest separation PP' that leads to a time separation Δt that is measurable with the imaging sensor. It can be shown that this time separation is equal to the inverse of the total Doppler bandwidth $B_D = 2f_D$. In a qualitative way, it can be stated that a large B_D gives a longer Doppler history that can be better matched to a template. This would allow a better determination of the zero Doppler crossing time. Thus, the azimuth resolution is given by

$$x_a = (PP')_{\min} = v\Delta t_{\min} = v\left(\frac{1}{2f_D}\right) = v\left(\frac{L}{2v}\right) = \frac{L}{2} \quad (37)$$

which is the same as the result derived using the synthetic array approach [see Eq. (27)].

As mentioned earlier, the imaging radar transmits a series of pulsed electromagnetic waves. Thus, the Doppler history from a point P is not measured continuously but is sampled on a repetitive basis. In order to get an accurate record of the Doppler history, the Nyquist sampling criterion requires that sampling occurs at least at twice the highest frequency in the Doppler shift. Thus, the pulse repetition frequency, usually abbreviated PRF, must be larger than

$$\text{PRF} \geq 2f_D = \frac{2v}{L} \quad (38)$$

In other terms, this equation means that at least one sample (i.e., one pulse) should be taken every time the sensor moves by half an antenna length. The corresponding aspect in the synthetic array approach is that the array elements should be close enough to each other to have a reasonably “filled” total aperture in order to avoid significant grating effects. To illustrate, for a spaceborne imaging system moving at a speed of 7 km/s and using an antenna 10 m in length, the corresponding minimum PRF is 1.4 kHz.

3.2. Signal Fading and Speckle

A close examination of a synthetic aperture radar image shows that the brightness variation is not smooth but has a granular texture called “speckle” (Fig. 8). Even for an imaged scene that has a constant backscatter property, the image will have statistical variations of the brightness on a pixel-by-pixel basis but with a constant mean over many pixels. This effect is identical to when a scene is observed optically under laser illumination. This is a result of the coherent nature (or very narrow spectral width) of the illuminating signal.

To explain this effect in a simple way, let us consider a scene that is completely “black” except for two identical bright targets separated by a distance d . The received signal V at the radar is given by

$$V = V_0 e^{-i2kr_1} + V_0 e^{-i2kr_2} \quad (39)$$

and assuming that $d \ll r_0$ (for spaceborne radars, the pixel size is typically on the order of tens of meters, while the

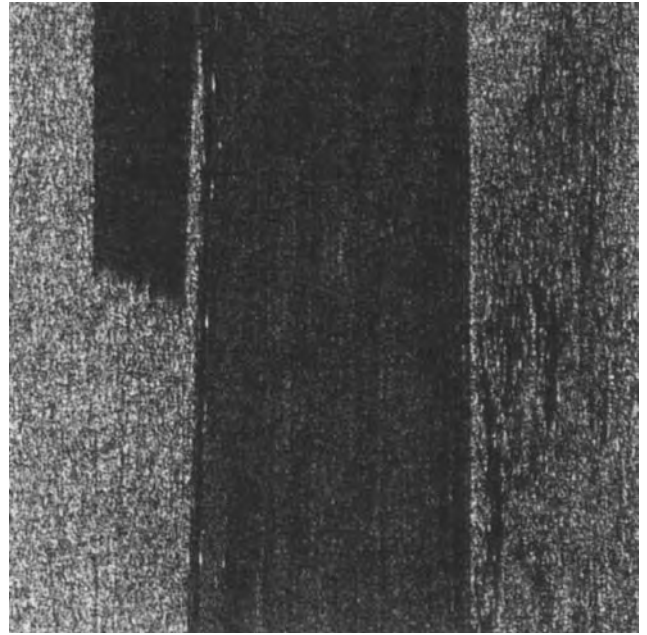


Figure 8. The granular texture shown in this image acquired by the NASA/JPL AIRSAR system is known as “speckle”. Speckle is a consequence of the coherent nature in which a synthetic aperture radar acquires images.

range is typically several hundred kilometers), then

$$\begin{aligned} V &= V_0 e^{-i2kr_0} (e^{-i2kd \sin \theta} + e^{+i2kd \sin \theta}) \\ \Rightarrow |V| &= 2|V_0 \cos(kd \sin \theta)| \end{aligned} \quad (40)$$

which shows that, depending on the exact location of the sensor, a significantly different signal value would be measured. If we now consider an image pixel that consists of a very large number of point targets, the resulting coherent superposition of all the patterns will lead to a “noiselike” signal. Rigorous mathematical analysis shows that the resulting signal has well-defined statistical properties [1–3]. The measured signal amplitude has a Rayleigh distribution, and the signal power has an exponential distribution. In order to narrow the width of these distributions (i.e., reduce the brightness fluctuations), successive signals or neighboring pixels can be averaged incoherently. This would lead to a more accurate radiometric measurement (and a more pleasing image) at the expense of degradation in the image resolution.

Another approach to reduce speckle is to combine images acquired at neighboring frequencies. In this case the exact interference patterns lead to independent signals but with the same statistical properties. Incoherent averaging would then result in a smoothing effect. In fact, this is the reason why a scene illuminated with white light does not show speckled image behavior.

In most imaging SARs, the smoothing is done by averaging the brightness of neighboring pixels in azimuth, or range, or both. The number of pixels averaged is called the number of *looks* N . It can be shown [1] that the signal standard deviation S_N is related to the mean

signal power \bar{P} by

$$S_N = \frac{1}{\sqrt{N}} \bar{P} \quad (41)$$

The larger the number of looks N , the better the quality of the image from the radiometric point of view. However, this degrades the spatial resolution of the image. It should be noted that for N larger than about 25, a large increase in N leads to only a small decrease in the signal fluctuation. This small improvement in the radiometric resolution should be traded off against the large increase in the spatial resolution. For example, if one were to average 10 resolution cells in a 4-look image, the speckle noise would be reduced to about 0.5 dB. At the same time, however, the image resolution would be reduced by an order of magnitude. Whether this loss in resolution is worth the reduction in speckle noise depends on both the aim of the investigation and the kind of scene imaged.

Figure 9 shows the effect of multilook averaging. The same image as Fig. 8, acquired by the NASA/JPL AIRSAR system is shown displayed at 1, 4, 16, and 32 looks, respectively. This figure clearly illustrates the smoothing effect, as well as the decrease in resolution resulting from the multilook process. In one early survey of geologists done by Ford [4], the results showed that even though the optimum number of looks depended on the scene type and resolution, the majority of the responses preferred 2-look images. However, this survey dealt with images that had rather poor resolution to begin with, and one may well find that with today's higher-resolution systems, analysts may be asking for a larger number of looks.

3.3. Ambiguities and Anomalies

Radar images could contain a number of anomalies that result from the way imaging radars generate the image. Some of these are similar to what is encountered in optical systems, such as blurring due to defocusing or scene motion, and some such as range and azimuth ambiguities are unique to radar systems. This section addresses the anomalies most commonly encountered in radar images.

As mentioned earlier (see Fig. 3), a radar images a surface by recording the echoes line by line with successive pulses. The leading edge of each echo corresponds to the near edge of the image scene, and the tail end of the echo corresponds to the far edge of the scene. The length of the echo (i.e., swath width of the scene covered) is determined by the antenna beamwidth and the size of the data window. The exact timing of the echo reception depends on the range between the sensor and the surface being imaged. If the timing of the pulses or the extent of the echo are such that the leading edge of one echo overlaps with the tail end of the previous one, then the far edge of the scene is folded over the near edge of the scene. This is called *range ambiguity*. Referring to Fig. 10, the temporal extent of the echo is equal to

$$T_e \approx 2 \frac{R}{c} \theta_r \tan \theta = 2 \frac{h\lambda}{cW} \frac{\sin \theta}{\cos^2 \theta} \quad (42)$$

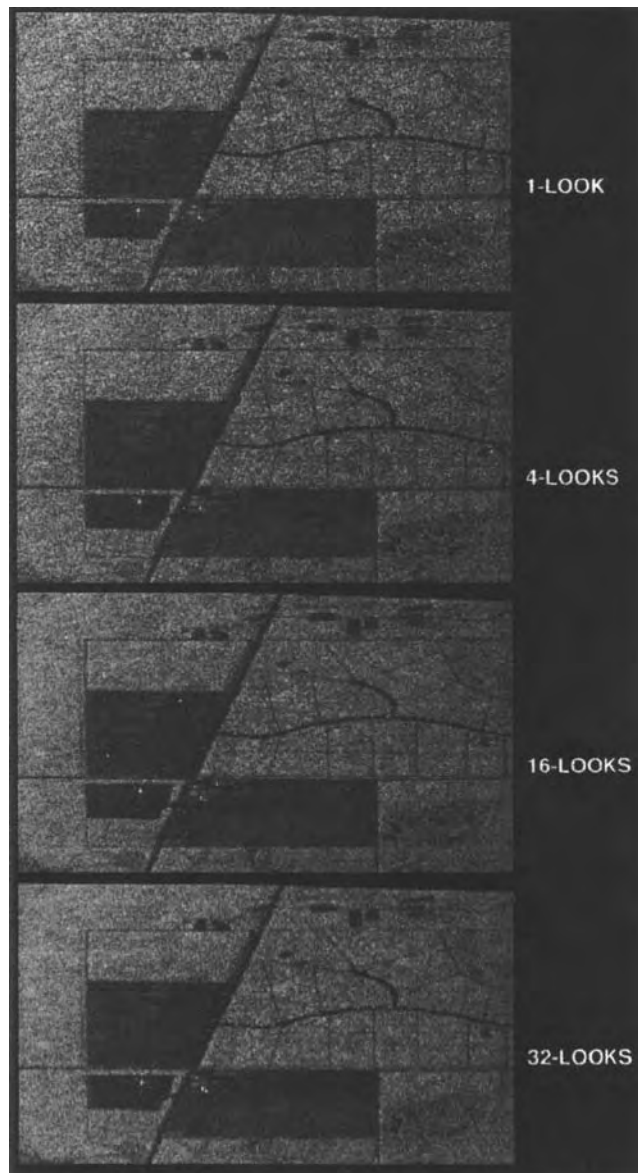


Figure 9. The effects of speckle can be reduced by incoherently averaging pixels in a radar image, a process known as *multilooking*. Shown in this figure is the same image, processed as a single look (the basic radar image), 4 looks, 16 looks, and 32 looks. Note the reduction in granular texture as the number of looks increase. Also note that as the number of looks increase, the resolution of the images decreases. Some features, such as those in the largest dark patch, may be completely masked by the speckle noise.

This time extent should be shorter than the time separating two pulses (i.e., $1/\text{PRF}$). Thus we must have

$$\text{PRF} < \frac{cW \cos^2 \theta}{2h\lambda \sin \theta} \quad (43)$$

In addition, the sensor parameters, specifically the PRF, should be selected such that the echo is completely within an interpulse period; that is, no echoes should be received during the time that a pulse is being transmitted.

Equation (43) gives an upper limit for the PRF. Another kind of ambiguity present in SAR imagery also results

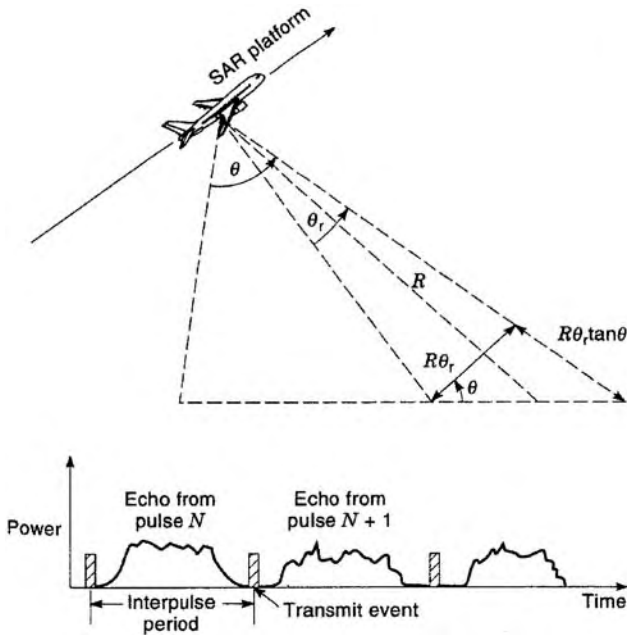


Figure 10. Temporal extent of radar echoes. If the timing of the pulses or the temporal extent of the echoes is such that the leading edge of one echo overlaps the trailing edge of the previous one, the far edge of the scene will be folded over the near edge, a phenomenon known as *range ambiguities*.

from the fact that the target’s return in the azimuth direction is sampled at the PRF. This means that the azimuth spectrum of the target return repeats itself in the frequency domain at multiples of the PRF. In general, the azimuth spectrum is not a bandlimited signal; instead, the spectrum is weighted by the antenna pattern in the azimuth direction. This means that parts of the azimuth spectrum may be aliased, and high-frequency data will actually appear in the low-frequency part of the spectrum. In actual images, these *azimuth ambiguities* appear as ghost images of a target repeated at some distance in the azimuth direction as shown in Fig. 11. To reduce the azimuth ambiguities, the PRF of a SAR has to exceed the lower limit given by Eq. (33).

In order to reduce both range and azimuth ambiguities, the PRF must therefore satisfy the conditions expressed by both Eq. (33) and Eq. (43). Therefore, we must insist that

$$\frac{cW \cos^2 \theta}{2h\lambda \sin \theta} > \frac{2v}{L} \tag{44}$$

from which we derive a lower limit for the antenna size as

$$LW > \frac{4vh\lambda \sin \theta}{c \cos^2 \theta} \tag{45}$$

Another type of artifact in radar images results when a very bright surface target is surrounded by a dark area. As the image is being formed, some spillover from the bright target, called sidelobes, although weak, could exceed the background and become visible as shown in Fig. 12. It should be pointed out that this type of artifact

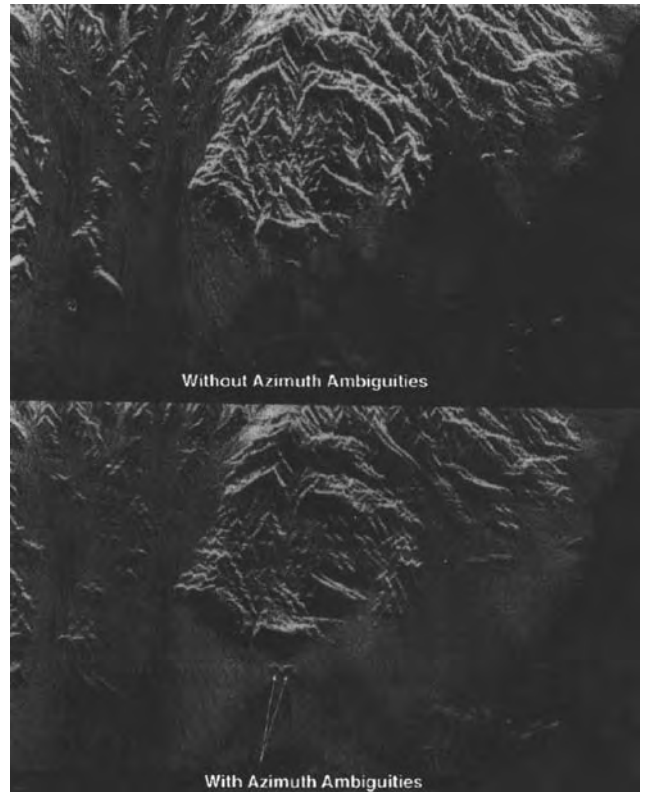


Figure 11. Azimuth ambiguities result when the radar pulse repetition frequency is too low to sample the azimuth spectrum of the data adequately. In that case, the edges of the azimuth spectrum fold over themselves, creating ghost images as shown in this figure. The top image was adequately sampled and processed, while the bottom one clearly shows the ghost images due to the azimuth ambiguities. The data were acquired with the NASA/JPL AIRSAR systems, and a portion of Death Valley in California is shown.

is not unique to radar systems. They are common in optical systems, where they are known as the *sidelobes* of the point spread function. The difference is that in optical systems, the sidelobe characteristics are determined by the characteristics of the imaging optics, namely, the hardware, whereas in the case of a SAR, the sidelobe characteristics are determined by the characteristics of the processing filters. In the radar case, the sidelobes may therefore be reduced by suitable weighting of the signal spectra during matched filter compression. The equivalent procedure in optical systems is through apodization of the telescope aperture.

The vast majority of these artifacts and ambiguities can be avoided with proper selection of the sensor’s and processor’s parameters. However, the interpreter should be aware of their occurrence because in some situations they might be difficult, if not impossible, to suppress.

3.4. Geometric Effects and Projections

The time delay/Doppler history basis of SAR image generation leads to an image projection different from that in the case of optical sensors. Even though at first look radar images seem very similar to optical images,

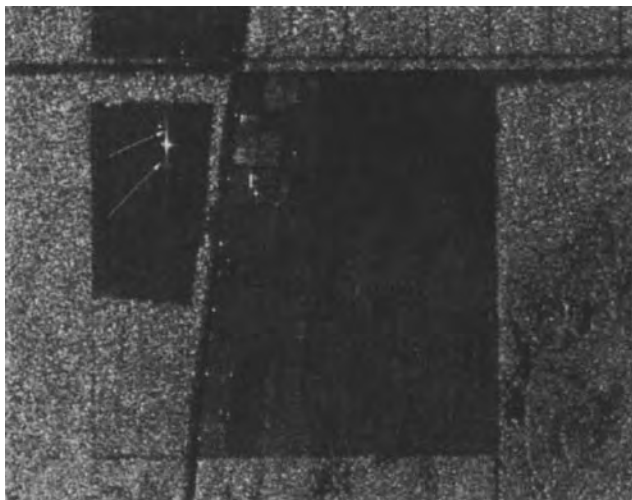


Figure 12. Sidelobes from the bright target, indicated by arrows in this image, mask out the return from the dark area surrounding the target. The characteristics of the sidelobes are determined mainly by the characteristics of the radar processing filters.

close examination quickly shows that geometric shapes and patterns are projected differently by the two sensors. This difference is particularly acute in rugged terrain. If the topography is known, a radar image can be reprojected into a format identical to an optical image, thus allowing image pixel registration. In extremely rugged terrain, however, the nature of the radar image projection leads to distortions that sometimes cannot be corrected.

In the radar image, two neighboring pixels in the range dimension correspond to two areas in the scene with slightly different range with respect to the sensor. This has the effect of projecting the scene in a cylindrical geometry on the image plane, which leads to distortions as shown in Fig. 13. Areas that slope toward the sensor appear shorter in the image, while areas that slope away from the sensor seem longer in the image than do horizontal areas. This effect is called *foreshortening*. In the extreme case where the slope is larger than the incidence angle, *layover* occurs. In this case, a hill would appear to be projected over the region in front of it. Layover cannot

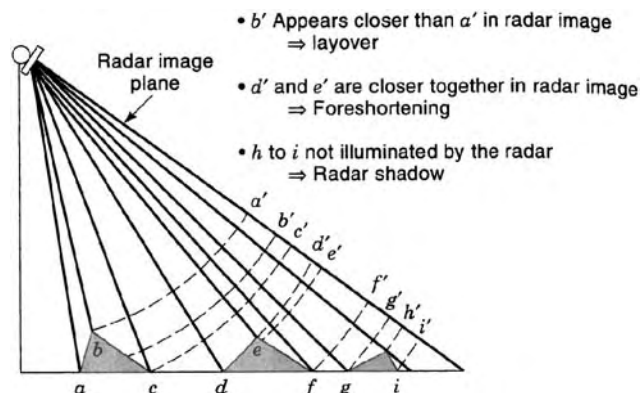


Figure 13. Radar images are cylindrical projections of the scene onto the image plane, leading to characteristic distortions. Refer to the text for more detailed discussions.

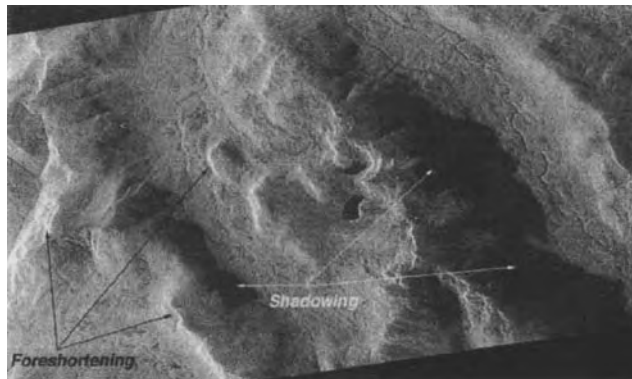


Figure 14. This NASA/JPL AIRSAR image shows examples of foreshortening and shadowing. Note that since the radar provides its own illumination, radar shadowing is a function of the radar look direction and does not depend on the sun angle. This image was illuminated from the left.

be corrected and can be avoided only by having an incidence angle at the surface larger than any expected surface slopes. When the slope facing away from the radar is steep enough such that the radar waves do not illuminate it, *shadowing* occurs and the area on that slope is not imaged. Note that in the radar images, shadowing is always away from the sensor flight line and is not dependent on the time of data acquisition or the sun angle in the sky. Shadowing can be beneficial for highlighting surface morphologic patterns. Figure 14 contains some examples of foreshortening and shadowing.

4. ADVANCED SAR TECHNIQUES

The field of synthetic aperture radar changed dramatically over the years, and especially since the early 1990s with the operational introduction of advanced radar techniques such as polarimetry and interferometry. While both of these techniques have been demonstrated much earlier, radar polarimetry became an operational research tool only with the introduction of the NASA/JPL AIRSAR system in the early 1980s, and reached a climax with the two SIR-C/X-SAR flights on board the space shuttle *Endeavour* in April and October 1994. Radar interferometry received a tremendous boost when the airborne TOPSAR system was introduced in 1991 by NASA/JPL, and further when data from the European Space Agency ERS-1 radar satellite became routinely available in 1991.

4.1. SAR Polarimetry

Electromagnetic wave propagation is a vector phenomenon; that is, all electromagnetic waves can be expressed as complex vectors. Plane electromagnetic waves can be represented by two-dimensional complex vectors. This is also the case for spherical waves when the observation point is sufficiently far removed from the source of the spherical wave. Therefore, if one observes a wave transmitted by a radar antenna when the wave is at a large distance from the antenna (in the far field of the antenna), the radiated electromagnetic wave can be adequately described by a

two-dimensional complex vector. If this radiated wave is now scattered by an object, and one observes this wave in the far field of the scatterer, the scattered wave can again be adequately described by a two-dimensional (2D) vector. In this abstract way, one can consider the scatterer as a mathematical operator that takes one 2D complex vector (the wave impinging on the object) and changes that into another 2D vector (the scattered wave). Mathematically, therefore, a scatterer can be characterized by a complex 2×2 scattering matrix

$$\mathbf{E}^{\text{sc}} = [\mathbf{S}]\mathbf{E}^{\text{tr}} \quad (46)$$

where \mathbf{E}^{tr} is the electric field vector that was transmitted by the radar antenna, $[\mathbf{S}]$ is the 2×2 complex scattering matrix that describes how the scatterer modified the incident electric field vector, and \mathbf{E}^{sc} is the electric field vector

that is incident on the radar receiving antenna. This scattering matrix is a function of the radar frequency and the viewing geometry. Once the complete scattering matrix is known and calibrated, one can synthesize the radar cross section for any arbitrary combination of transmit and receive polarizations. Figure 15 shows a number of such synthesized images for the San Francisco Bay area in California. The data were acquired with the NASA/JPL AIRSAR system.

The voltage measured by the radar system is the scalar product of the radar antenna polarization and the incident wave electric field:

$$V = \mathbf{p}^{\text{rec}} \cdot [\mathbf{S}]\mathbf{p}^{\text{tr}} \quad (47)$$

Here, \mathbf{p}^{tr} and \mathbf{p}^{rec} are the normalized polarization vectors describing the transmitting and receiving radar

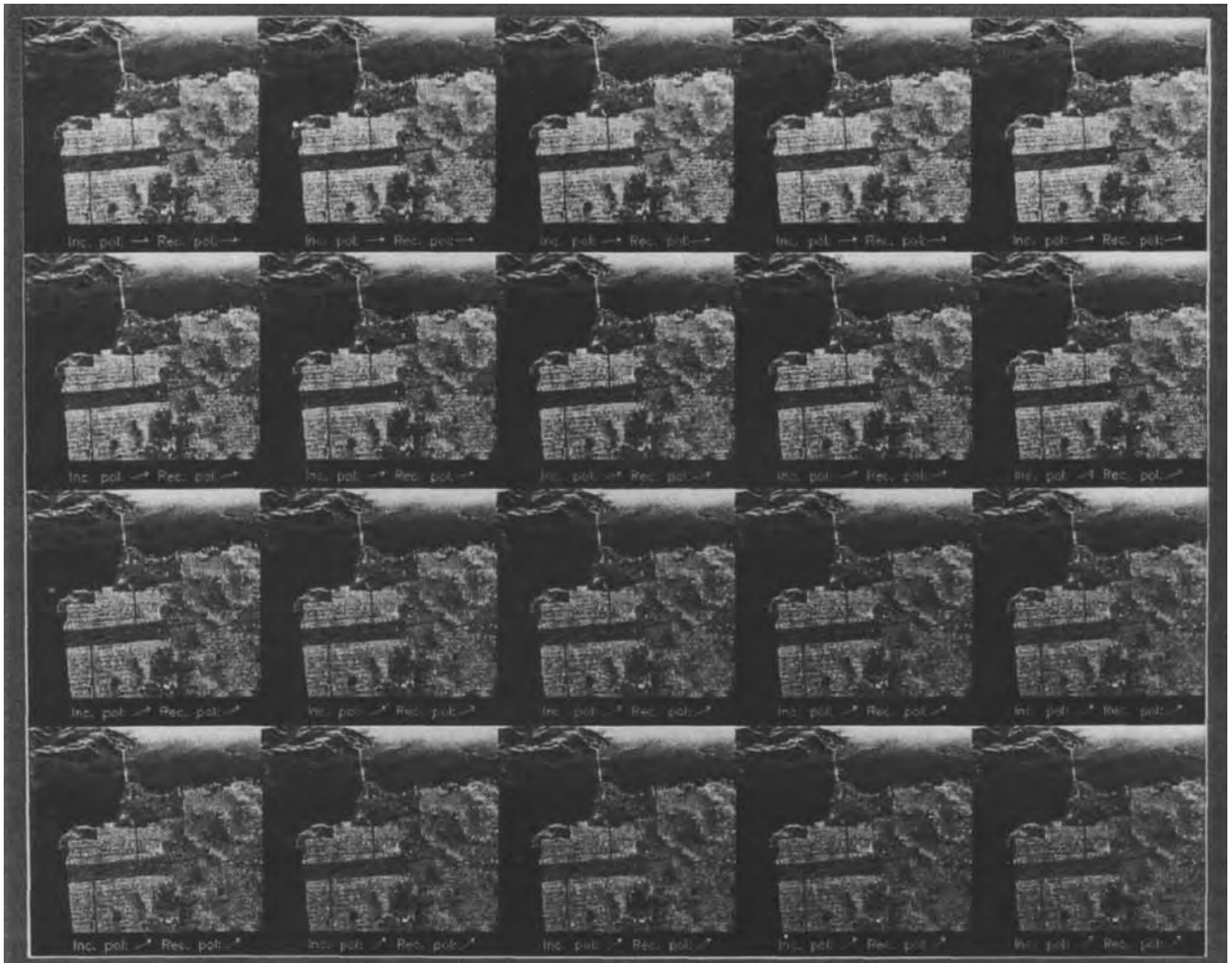


Figure 15. Radar polarimetry allows one to synthesize images at any polarization combination. This set of images of San Francisco, California, was synthesized from a single set of measurements acquired by the NASA/JPL AIRSAR system. Note the differential change in brightness between the city (the bright area) and Golden Gate Park, the dark rectangular area in the middle of the images. This differential change is due to difference in scattering mechanism. The city area is dominated by a double reflection from the streets to the buildings and back to the radar, while the park area exhibits much more diffuse scattering.

antennas. The power received by the radar is the magnitude of the voltage squared

$$P = VV^* = |\mathbf{p}^{\text{rec}} \cdot [\mathbf{S}]\mathbf{p}^{\text{rad}}|^2 \quad (48)$$

Expanding the expression inside the magnitude sign, it can be shown that the received power can also be written in terms of the scatterer covariance matrix as follows

$$P = VV^* = (\tilde{\mathbf{A}}\mathbf{T})(\tilde{\mathbf{T}}\mathbf{A})^* = \tilde{\mathbf{A}}\mathbf{T}\mathbf{T}^*\mathbf{A}^* = \mathbf{A} \cdot [\mathbf{C}]\mathbf{A}^*; [\mathbf{C}] = \tilde{\mathbf{T}}\tilde{\mathbf{T}}^* \quad (49)$$

where $\tilde{\mathbf{A}} = (p_h^{\text{rec}} p_h^{\text{rad}} p_v^{\text{rec}} p_v^{\text{rad}} p_h^{\text{rec}} p_h^{\text{rad}} p_v^{\text{rec}} p_v^{\text{rad}})$ represents the antenna polarization vector elements and $\tilde{\mathbf{T}} = (S_{hh} S_{hv} S_{vh} S_{vv})$ represents only the scatterer. The superscript * denotes complex conjugation. The covariance matrix characterization is particularly useful when analyzing multilook radar images, since the covariance matrix of a multilook pixel is simply the average covariance matrix of all the individual measurements contained in the multilook pixel. Equation (49) shows the covariance matrix to be a 4×4 complex matrix. In the case of radar backscatter, reciprocity dictates that $S_{hv} = S_{vh}$ and the covariance matrix can in general be written as a 3×3 complex matrix.

The typical implementation of a radar polarimeter involves transmitting a wave of one polarization and receiving echoes in two orthogonal polarizations simultaneously. This is followed by transmitting a wave with a second polarization, and again receiving echoes with both polarizations simultaneously. In this way, all four elements of the scattering matrix are measured. This implementation means that the transmitter is in slightly different positions when measuring the two columns of the scattering matrix, but this distance is typically small compared to a synthetic aperture, and therefore does not lead to a significant decorrelation of the signals. The NASA/JPL AIRSAR system pioneered this implementation for SAR systems [5], and the same implementation was used in the SIR-C part of the SIR-C/X-SAR radars [6].

The past few years (as of 2004) have seen relatively few advances in the development of hardware for polarimetric SAR systems; newer implementations are simply using more advanced technology to implement the same basic hardware configurations as in the initial systems. Significant advances were made, however, in the field of analysis and application of polarimetric SAR data.

4.1.1. Polarimetric SAR Calibration. Many of the advances made in analyzing polarimetric SAR data result directly from the greater availability of calibrated data. Unlike the case of single-channel radars, where only the radar cross section needs to be calibrated, polarimetric calibration usually involves four steps: crosstalk removal, phase calibration, channel imbalance compensation, and absolute radiometric calibration [7]. *Crosstalk removal* refers to correcting mostly the cross-polarized elements of the scattering matrix for the effects of system crosstalk that couples part of the copolarized returns into the cross-polarized channel. *Phase calibration* refers to correcting

the copolarized phase difference for uncompensated path-length differences in the transmit and receive chains, while *channel imbalance* refers to balancing the copolarized and cross-polarized returns for uncompensated gain differences in the two transmit and receive chains. Finally, absolute radiometric calibration involves using some kind of a reference calibration source to determine the overall system gain to relate received power levels to normalized radar cross section.

While most of the polarimetric calibration algorithms currently in use were published in 1990 and 1991 [7–11], several groups are still actively pursuing the study of improved calibration techniques and algorithms. The earlier algorithms are reviewed in Refs. 12 and 13, while Ref. 14 provides a comprehensive review of SAR calibration in general. Some of these earlier algorithms are now routinely used to calibrate polarimetric SAR data operationally, as, for example, in the NASA/JPL AIRSAR and SIR-C processors [15].

4.1.2. Example Applications of Polarimetric SAR Data.

The availability of calibrated polarimetric SAR data allowed research to move from the qualitative interpretation of SAR images to quantitative analysis of the data. This sparked significant progress in classification of polarimetric SAR images, lead to improved models of scattering by different types of terrain, and allowed the development of some algorithms to invert polarimetric SAR data for geophysical parameters, such as forest biomass, surface roughness, and soil moisture.

4.1.3. Classification of Earth Terrain. Many Earth science studies require information about the spatial distribution of landcover types, as well as the change in landcover and land use with time. In addition, it is increasingly recognized that the inversion of SAR data for geophysical parameters involves an initial step of segmenting the image into different terrain classes, followed by inversion using the algorithm appropriate for the particular terrain class. Polarimetric SAR systems, capable of providing high-resolution images under all weather conditions as well as during day or night, provide a valuable data source for classification of Earth terrain into different landcover types.

Two main approaches are used to classify images into landcover types: (1) maximum-likelihood classifiers based on Bayesian statistical analysis and (2) knowledge-based techniques designed to identify dominant scattering.

Some of the earlier studies in Bayesian classification focused on quantifying the increased accuracy gained from using all the polarimetric information. References 16 and 17 showed that the classification accuracy is significantly increased when the complete polarimetric information is used compared to that achieved with single-channel SAR data. These earlier classifiers assumed equal a priori probabilities for all classes, and modeled the SAR amplitudes as circular Gaussian distributions, which means that the textural variations in radar backscatter are not considered to be significant enough to be included in the classification scheme. Reference 18 extended the Bayesian classification to allow different a priori probabilities for different classes.

The method in that study [18] first classifies the image into classes assuming equal a priori probabilities, and then iteratively changes the a priori probabilities for subsequent classifications on the basis of the local results of previous classification runs. Significant improvement in classification accuracy is obtained with only a few iterations. More accurate results are obtained using a more rigorous maximum a posteriori (MAP) classifier where the a priori distribution of image classes is modeled as a Markov random field and the optimization of the image classes is done over the whole image instead of on a pixel-by-pixel basis [19]. In a subsequent work, the MAP classifier is extended to include the case of multifrequency polarimetric radar data [20]. The MAP classifier was used in Ref. 21 to map forest types in the Alaskan boreal forest. In this study, five vegetation types (white spruce, balsam poplar, black spruce, alder/willow shrubs, and bog/fen/nonforest) were separated with accuracies ranging from 62 to 90%, depending on which frequencies and polarizations are used.

Knowledge-based classifiers are implemented according to determination of dominant scattering mechanisms through an understanding of the physics of the scattering process as well as experience gained from extensive experimental measurements [22]. One of the earliest examples of such a knowledge-based classifier was published in 1989 [23]. In this unsupervised classification, knowledge of the physics of the scattering process was used to classify images into three classes: odd numbers of reflections, even numbers of reflections, and diffuse scattering. The odd and even numbers of reflection classes are separated on the basis of the copolarized phase difference, while the diffuse scattering class is identified according to high cross-polarized return and low correlation between the copolarized channels. While no direct attempt was made to identify each class with a particular terrain type, it was noted that in most cases the odd numbers of reflection class corresponded to bare surfaces or open water; even numbers of reflections usually indicated urban areas or sparse forests, sometimes with understory flooding present; while diffuse scattering is usually identified with vegetated areas. As such, all vegetated areas are lumped into one class, restricting the application of the results. Pierce et al. [22] extended this idea and developed a level 1 classifier that segments images into four classes: tall vegetation (trees), short vegetation, and urban and bare surfaces. First the urban areas are separated from the rest by using the L-band copolarized phase difference and the image texture at C band. Then areas containing tall vegetation are identified using the L-band cross-polarized return. Finally, the C-band cross-polarized return and the L-band texture are used to separate the areas containing short vegetation from those with bare surfaces. Accuracies better than 90% are reported for this classification scheme when applied to two different images acquired in Michigan. Another example of a knowledge-based classification is reported in by Hess et al. [24]. In this study, a decision-tree classifier is used to classify images of the Amazonian floodplain near Manaus, Brazil into five classes: water, clearing, macrophyte, nonflooded forest, and flooded forest based on polarimetric scattering properties. Accuracies better than 90% are reported.

4.1.4. Geophysical Parameter Estimation. One of the most active areas of research in polarimetric SAR involves estimating geophysical parameters directly from the radar data through model inversion. Space does not permit a full discussion of the most recent work here. Therefore, in this section only a brief summary of recent work will be provided, with emphasis on vegetated areas.

Many electromagnetic models exist to predict scattering from vegetated areas [25–34], and this remains an area of active research. Much of the work is aimed at estimating forest biomass [35–39]. Earlier works correlated polarimetric SAR backscatter with total aboveground biomass [35,36] and suggested that the backscatter saturates at a biomass level that scales with frequency, a result also predicted by theoretic models. This led some investigators to conclude that these saturation levels define the upper limits for accurate estimation of biomass [40], arguing for the use of low-frequency radars to monitor forest biomass [41].

More recent work suggests that some spectral gradients and polarization ratios do not saturate as quickly and may therefore be used to extend the range of biomass levels for which accurate inversions could be obtained [37]. Reference 41 showed that inversion results are most accurate for monospecies forests, and that accuracies decrease for less homogeneous forests. Those authors conclude that the accuracies of the radar estimates of biomass are likely to increase if structural differences between forest types are accounted for during the inversion of the radar data.

Such an integrated approach to retrieval of forest biophysical characteristics has been reported [42,43]. These studies first segment images into different forest structural types, and then use algorithms appropriate for each structural type in the inversion.

Furthermore, Dobson et al. [43] estimate the total biomass by first using the radar data to estimate tree basal area and height and crown biomass. The tree basal area and height are then used in allometric equations to estimate the trunk biomass. The total biomass, which is the sum of the trunk and crown biomass values, is shown to be accurately related to allometric total biomass levels up to 25 kg/m², while Kasischke et al. [44] estimate that biomass levels as high as 34–40 kg/m² could be estimated with an accuracy of 15–25% using multipolarization C-, L-, and P-band SAR data.

Research in retrieving geophysical parameters from nonvegetated areas is also an active research area, although not as many groups are involved. One of the earliest algorithms to infer soil moisture and surface roughness for bare surfaces was published in 1992 [45]. This algorithm uses polarization ratios to separate the effects of surface roughness and soil moisture on the radar backscatter, and an accuracy of 4% for soil moisture is reported. More recently, Dubois et al. [46] reported a slightly different algorithm, based only on the copolarized backscatters measured at L band. Their results, using data from scatterometers, airborne SARs, and spaceborne SARs (SIR-C), show an accuracy of 4.2% when inferring soil moisture over bare surfaces. Shi and Dozier [47] reported an algorithm to measure snow wetness and demonstrated accuracies of 2.5%.

4.2. SAR Interferometry

SAR interferometry refers to a class of techniques where additional information is extracted from SAR images that are acquired from different vantage points, or at different times. Various implementations allow different types of information to be extracted. For example, if two SAR images are acquired from slightly different viewing geometries, information about the topography of the surface can be inferred. On the other hand, if images are taken at slightly different times, a map of surface velocities can be produced. Finally, if sets of interferometric images are combined, subtle changes in the scene can be measured with extremely high accuracy.

In this section, we shall first discuss so-called cross-track interferometers used for the measurement of surface topography. This will be followed by a discussion of along-track interferometers used to measure surface velocity. The section ends with a discussion of differential interferometry used to measure surface changes and deformation.

4.2.1. Radar Interferometry for Measuring Topography.

SAR interferometry was first demonstrated by Graham [48], who demonstrated a pattern of nulls or interference fringes by vectorally adding the signals received from two SAR antennas: one physically situated above the other. Later, Zebker and Goldstein [49] demonstrated that these interference fringes can be formed after SAR processing of the individual images if both the amplitude and the phase of the radar images are preserved during the processing.

The basic principles of interferometry can be explained using the geometry shown in Fig. 16. Using the law of cosines on the triangle formed by the two antennas and the point being imaged, it follows that

$$(R + \delta R)^2 = R^2 + B^2 - 2BR \cos\left(\frac{\pi}{2} - \theta + \alpha\right) \quad (50)$$

where R is the slant range to the point being imaged from the reference antenna, δR is the pathlength difference

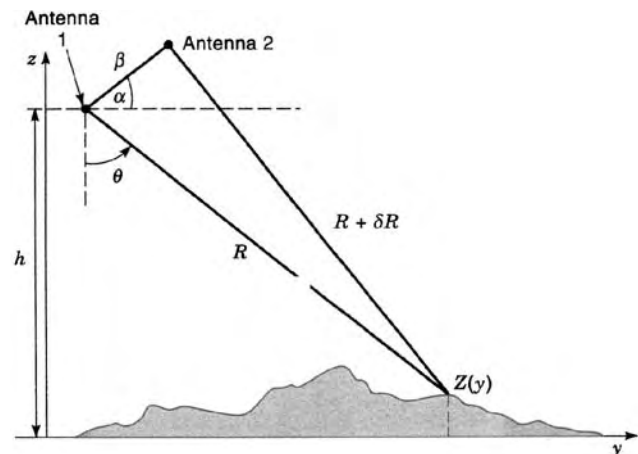


Figure 16. Basic interferometric radar geometry. The pathlength difference between the signals measured at each of the two antennas is a function of the elevation of the scatterer.

between the two antennas, B is the physical interferometric baseline length, θ is the look angle to the point being imaged, and α is the baseline tilt angle with respect to the horizontal.

From Eq. (50) it follows that we can solve for the pathlength difference δR . If we assume that $R \gg B$ (a very good assumption for most interferometers), one finds that

$$\delta R \approx -B \sin(\theta - \alpha) \quad (51)$$

The radar system does not measure the pathlength difference explicitly, however. Instead, what is measured is an interferometric phase difference that is related to the pathlength difference through

$$\phi = \frac{a2\pi}{\lambda} \quad \delta R = -\frac{a2\pi}{\lambda} B \sin(\theta - \alpha) \quad (52)$$

where $a = 1$ for the case where signals are transmitted out of one antenna and received through both at the same time, and $a = 2$ for the case where the signal is alternately transmitted and received through one of the two antennas only. The radar wavelength is denoted by λ .

From Fig. 16, it also follows that the elevation of the point being imaged is given by

$$z(y) = h - R \cos \theta \quad (53)$$

where h denotes the height of the imaging reference antenna above the reference plane with respect to which elevations are quoted. From Eq. (52) one can infer the actual radar look angle from the measured interferometric phase as

$$\theta = \alpha - \sin^{-1}\left(\frac{\lambda\phi}{a2\pi B}\right) \quad (54)$$

Using Eqs. (54) and (53), one can now express the inferred elevation in terms of system parameters and measurables as follows:

$$z(y) = h - R \cos\left(\alpha - \sin^{-1}\left(\frac{\lambda\phi}{a2\pi B}\right)\right) \quad (55)$$

This expression is the fundamental interferometric SAR equation for broadside imaging geometry.

SAR interferometers for the measurement of topography can be implemented in one of two ways. In the case of single-pass interferometry, the system is configured to measure the two images at the same time through two different antennas usually arranged one above the other. The physical separation of the antennas is referred to as the *baseline* of the interferometer. In the case of repeat-track interferometry, the two images are acquired by physically imaging the scene at two different times using two different viewing geometries.

So far most single-pass interferometers have been implemented using airborne SARs [49–51]. The Shuttle Radar Topography Mission (SRTM), a joint project between the United States National Imagery and Mapping Agency (NIMA) and the National Aeronautics and Space Administration (NASA), was the first spaceborne implementation of a single-pass interferometer [52]. Launched

in February 2000 from Cape Canaveral in Florida on the space shuttle *Endeavour*, SRTM used modified hardware from the C-band radar of the SIR-C system, with a 62-m-long boom and a second antenna to form a single-pass interferometer. The SRTM mission acquired digital topographic data of the globe between 60° north and south latitudes during one 11-day shuttle mission. The SRTM mission also acquired interferometric data using modified hardware from the X-band part of the SIR-C/X-SAR system in a collaboration between NASA and the Deutsches Zentrum für Luft und Raumfahrt (DLR) in Germany. The swaths of the X-band system, however, were not wide enough to provide global coverage during the mission.

The SRTM payload used the maximum resources that the space shuttle could offer with respect to energy use, flight duration, and payload mass, with the result that the mapping phase of the flight operations was limited to 159 orbits. With the 62-m-long mast, and the more than 13 tons of payload, SRTM was the largest structure ever flown in space. The C-band radar was operated in the SCANSAR mode, which allowed complete global coverage between 54° south latitude and 60° north latitude. All the SRTM data have been processed into digital elevation maps. Figure 17 shows a shaded relief map of the state of California derived from the SRTM data. Processed data and general information about the SRTM mission can be

found on the Web at <http://www.jpl.nasa.gov/srtm/> and at <http://srtm.usgs.gov/>. The vertical accuracy (90%) of the SRTM data is estimated to be about 7 m.

Most of the SAR interferometry research has gone into understanding the various error sources and how to correct their effects during and after processing. As a first step, careful motion compensation must be performed during processing to correct for the actual deviation of the aircraft platform from a straight trajectory [53]. As mentioned before, the single-look SAR processor must preserve both the amplitude and the phase of the images. After single-look processing, the images are carefully coregistered to maximize the correlation between the images. The so-called interferogram is formed by subtracting the phase in one image from that in the other on a pixel-by-pixel basis.

The interferometric SAR technique is better understood by briefly reviewing the difference between traditional and interferometric SAR processing. In traditional (noninterferometric) SAR processing, it is assumed that the imaged pixel is located at the intersection of the Doppler cone (centered on the velocity vector), the range sphere (centered at the antenna), and an assumed reference plane, as shown in Fig. 18. Since the Doppler cone has its apex at the center of the range sphere, and its axis of symmetry is aligned with the velocity vector, it follows



Figure 17. Shaded relief map of California derived from SRTM C-band radar interferometry measurements.

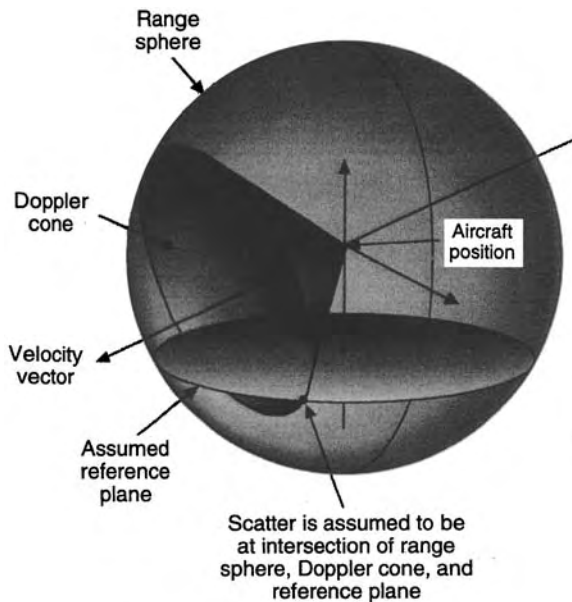


Figure 18. In traditional (noninterferometric) SAR processing, the scatterer is assumed to be located at the intersection of the Doppler cone, the range sphere, and some assumed reference plane.

that all points on the intersection of the Doppler cone and the range sphere lie in a plane orthogonal to the velocity vector.

The additional information provided by cross-track interferometry is that the imaged point also has to lie on the cone described by a constant phase, which means that one no longer has to assume an arbitrary reference plane. This cone of equal phase has its axis of symmetry aligned with the interferometer baseline and also has its apex at the center of the range sphere. It then follows that the imaged point lies at the intersection of the Doppler cone, the range sphere, and the equal phase cone, as shown in Fig. 19. It should be pointed out that in actual interferometric SAR processors, the two images acquired by the two interferometric antennas are actually processed individually using the traditional SAR processing assumptions. The resulting interferometric phase then represents the elevation with respect to the reference plane assumed during the SAR processing. This phase is then used to find the actual intersection of the range sphere, the Doppler cone, and the phase cone in three dimensions.

Once the images are processed and combined, the measure phase must be *unwrapped*. During this procedure, the measured phase, which varies only between 0° and 360° , must be unwrapped to retrieve the original phase by adding or subtracting multiples of 360° . The earliest phase unwrapping routine was published by Goldstein et al. [54]. In this algorithm, areas where the phase will be discontinuous as a result of layover or poor signal-to-noise ratios are identified by branchcuts, and the phase unwrapping routine is implemented such that branchcuts are not crossed when unwrapping the phases. Phase unwrapping remains one of the most active areas of research, and many algorithms remain under development.

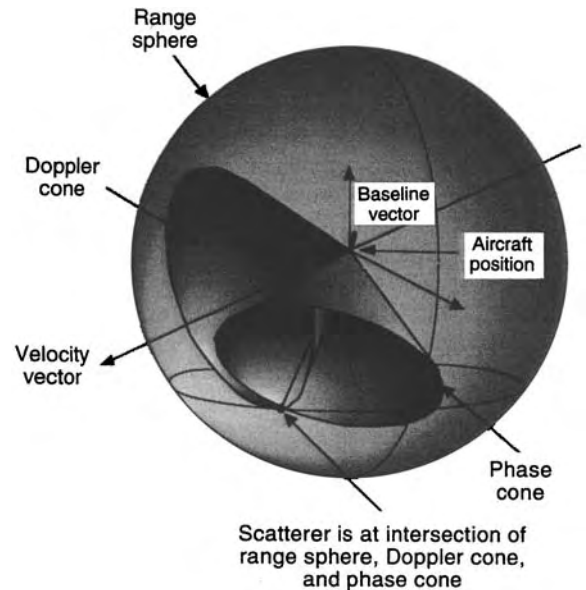


Figure 19. Interferometric radars acquire all the information required to reconstruct the position of a scatterer in three dimensions. The scatterer is located at the intersection of the Doppler cone, the range sphere, and the interferometric phase cone.

Even after the phases have been unwrapped, the absolute phase is still not known. This absolute phase is required to produce a height map that is calibrated in the absolute sense. One way to estimate this absolute phase is to use ground control points with known elevations in the scene. However, this human intervention severely limits the ease with which interferometry can be used operationally. Madsen et al. [53] reported a method by which the radar data themselves are used to estimate this absolute phase. The method breaks the radar bandwidth up into an upper and lower halves, and then uses the differential interferogram formed by subtracting the upper-half spectrum interferogram from the lower-half spectrum interferogram to form an equivalent low-frequency interferometer to estimate the absolute phase. Unfortunately, this algorithm is not robust enough in practice to fully automate interferometric processing. This is one area where significant research is needed if the full potential of automated SAR interferometry is to be realized.

Absolute phase determination is followed by height reconstruction. Once the elevations in the scene are known, the entire digital elevation map can be geometrically rectified. Madsen et al. [53] reported accuracies ranging between 2.2 m RMS for flat terrain and 5.5 m RMS for terrain with significant relief for the NASA/JPL TOPSAR interferometer.

An alternative way to form the interferometric baseline is to use a single-channel radar to image the same scene from slightly different viewing geometries. This technique, known as *repeat-track interferometry*, has been applied mostly to spaceborne data starting with data collected with the L-band SEASAT SAR [54–59]. Other investigators used data from the L-band SIR-B [60] the C-band ERS-1 radar [61,62], and more recently the L-band SIR-C

[63] and the X-band X-SAR [64]. Repeat-track interferometry has also been demonstrated using airborne SAR systems [65].

Two main problems limit the usefulness of repeat-track interferometry. The first is due to the fact that, unlike the case of single-pass interferometry, the baseline of the repeat-track interferometer is not known accurately enough to infer accurate elevation information from the interferogram. Zebker et al. [62] show how the baseline can be estimated using ground control points in the image. The second problem is due to differences in scattering and propagation that results from the fact that the two images forming the interferogram are acquired at different times. One result is temporal decorrelation, which is worst at the higher frequencies [58]. For example, C-band images of most vegetated areas decorrelate significantly over as short a time as one day. This problem more than any other limits the use of the current operational spaceborne single-channel SARs for topographic mapping, and led to proposals for dedicated interferometric SAR missions to map the entire globe [66,67].

4.2.2. Along-Track Interferometry. In some cases, the temporal change between interferometric images contains much information. One such case is the mapping of ocean surface movement. In this case, the interferometer is implemented in such a way that one antenna images the scene a short time before the second antenna does, preferably using the same viewing geometry. Goldstein and Zebker [68] described such an implementation in which one antenna is mounted forward of the other on the body of the NASA DC-8 aircraft. In a later work, Goldstein et al. [69] measured ocean currents with a velocity resolution of 5–10 m/s. Marom et al. [70,71] along-track interferometry used to estimate ocean surface current velocity and wavenumber spectra. This technique was also applied to the measurement of ship-generated internal wave velocities [72].

In addition to measuring ocean surface velocities, Carande [73] reports a dual-baseline implementation, implemented by alternately transmitting out of the front and aft antennas, to measure ocean coherence time. He estimated typical ocean coherence times for L band to be about 0.1 s. Shemer and Marom [74] proposed a method to measure ocean coherence time using only a model for the coherence time and one interferometric SAR observation.

4.2.3. Differential Interferometry. One of the most exciting applications of radar interferometry is implemented by subtracting two interferometric pairs separated in time from each other to form a so-called differential interferogram. In this way surface deformation can be measured with unprecedented accuracy. This technique was first demonstrated by Gabriel et al. [75] using SeaSat data to measure millimeter-scale ground motion in agricultural fields. Since then this technique has been applied to measure centimeter-meter-scale coseismic displacements [76–81] and measure centimeter-scale volcanic deflation [82]. The added information provided by high-spatial-resolution coseismic deformation maps was shown to provide

insight into the slip mechanism that would not be attainable from the seismic record [79,80].

Differential SAR interferometry has also led to spectacular applications in polar ice sheet research by providing information on ice deformation and surface topography at an unprecedented level of spatial details. Goldstein et al. [83] observed icestream motion and tidal flexure of the Rutford Glacier in Antarctica with a precision of 1 mm per day and summarized the key advantages of using SAR interferometry for glacier studies. Joughin [84] studied the separability of ice motion and surface topography in Greenland and compared the results with those from both radar and laser altimetry. Rignot et al. [85] estimated the precision of the SAR-derived velocities using a network of in situ velocities, and demonstrated, along with Joughin et al. [86], the practicality of using SAR interferometry across all the different melting regimes of the Greenland ice sheet. Large-scale applications of these techniques is expected to yield significant improvements in our knowledge of the dynamics, mass balance, and stability of the world's major ice masses.

One confusing factor in the identification of surface deformation in differential interferograms is due to changing atmospheric conditions. In observing Earth, radar signals propagate through the atmosphere, which introduces additional phase shifts that are not accounted for in the standard geometric equations describing radar interferometry. Spatially varying patterns of atmospheric water vapor change the local index of refraction, which, in turn, introduces spatially varying phase shifts to the individual interferograms. Since the two (or more) interferograms are acquired at different times, the temporal change in water vapor introduces a signal that could be on the same order of magnitude as that expected from surface deformation, as discussed by Goldstein [87]. Another limitation of the technique is temporal decorrelation. Changes in the surface properties may lead to complete decorrelation of the images and no detectable deformation signature [78].

4.2.4. Polarimetric Interferometry. In the preceding discussion on radar interferometry, it was assumed that only one polarization was transmitted, and only one polarization measured on reception of the radar waves. However, as mentioned before, electromagnetic wave propagation is by nature a vector phenomenon. Therefore, in order to capture the complete information about the scattering process, interferometric measurements should really be made in the full polarimetric implementation of a radar system. In this case, there are really three different measurements being made at the same time. First, there are the two polarimetric radar measurements at each end of the baseline, represented below by the two covariance matrices $[C_{11}]$ and $[C_{22}]$. Since the baseline is generally short compared to the distance to the scene, these two measurements can be expected to be nearly identical, except for the very small change in the angle of incidence from one end of the baseline to the other. (The exception, of course, is if the two measurements are made in the repeat-track implementation. In that case, temporal changes could cause the two covariance matrices to be quite different.) The third

measurement, of course, is the full vector interferogram as opposed to the scalar implementation described earlier.

The vector interferogram, which is the complex cross-correlation of the signal from one end of the baseline with that from the other end of the baseline, can be described as

$$V_1 V_2^* = \tilde{\mathbf{A}}_1 \mathbf{T}_1 \tilde{\mathbf{T}}_2^* \mathbf{A}_2^* = \mathbf{A}_1 \cdot [\mathbf{C}_{12}] \mathbf{A}_2^* \quad (56)$$

The correlation of the two signals after averaging is

$$\begin{aligned} \mu &= \frac{\langle V_1 V_2^* \rangle}{\sqrt{\langle V_1 V_1^* \rangle \langle V_2 V_2^* \rangle}} \\ &= \frac{\mathbf{A}_1 \cdot \langle [\mathbf{C}_{12}] \rangle \mathbf{A}_2^*}{\sqrt{(\mathbf{A}_1 \cdot \langle [\mathbf{C}_{11}] \rangle \mathbf{A}_1^*) (\mathbf{A}_2 \cdot \langle [\mathbf{C}_{22}] \rangle \mathbf{A}_2^*)}} \end{aligned} \quad (57)$$

where the angular brackets $\langle \rangle$ denote averaging. The interferometric phase is the phase angle of the numerator of [57]

$$\phi_{\text{int}} = \arg(\mathbf{A}_1 \cdot \langle [\mathbf{C}_{12}] \rangle \mathbf{A}_2^*) \quad (58)$$

Using this formulation, Cloude and Papathanassiou [88] showed, using repeat-track SIR-C interferometric data, that polarization diversity can be used successfully to optimize the correlation between images. They also showed significant differences in the measured elevation in forested areas when using polarization optimization. At present, polarimetric interferometry is a very active research area. Unfortunately, progress is hampered severely by lack of availability of well-calibrated data, as only a handful of radar systems have been upgraded to full polarimetric interferometry capability.

Current research is still only beginning to realize the full potential of radar interferometry. Because of the success of the SRTM mission, and some excellent fundamental research in the application of interferometric and differential interferometric radar data, the next few years will undoubtedly see an explosion in the interest and use of this type of remote sensing data.

5. NONIMAGING RADARS

5.1. Ocean Scatterometer

Scatterometers measure the surface backscattering cross section precisely in order to relate the measurement to geophysical quantities such as the ocean wind vector (both speed and direction) [89]. Spaceborne ocean scatterometers are capable of measuring global wind vectors over oceans for use in studies of upper ocean circulation, tropospheric dynamics, and air-sea interaction. Typical resolution of an ocean scatterometer is several tens of kilometers even though a higher-resolution scatterometer can provide useful information such as the coastal ocean wind vector. Since the backscattering cross section depends strongly on the surface roughness and the dielectric constant, a scatterometer can detect the electrical and geometric properties of a surface. As wind blows over the ocean surface, wind stress generates surface waves that

roughen the ocean surface. Since the dielectric constant of an ocean surface is very large at the microwave spectrum, the backscattering is related mainly to the surface roughness. Therefore, the backscattering cross section measured by an ocean scatterometer is sensitive to the windspeed via the surface roughness [90]. Since the surface roughness scale at the size of the radar wavelength strongly influences the backscattering cross section, the scatterometer wavelength should be at the centimeter scale in order to derive the surface windspeed. Specifically, the surface roughness size (Λ) responsible for backscattering is related to the radar wavelength λ as

$$\Lambda = \frac{\lambda}{2 \sin \theta} \quad (59)$$

where θ is the incidence angle. This wavelength Λ is also known as the *Bragg wavelength*, which represents a resonance scale presented in the scattering surface.

The received power must be calibrated to produce the accurate backscattering cross section using the radar equation. The noise power must be estimated and subtracted from the receive power during the calibration process. As discussed in Section 3.2, radar return measurements are contaminated by the speckle noise. In order to measure the backscattering cross section accurately, a large number of independent observations must be averaged [91]. This can be done in either the frequency or time domain. In scatterometry, a commonly adopted parameter for the backscattering cross section measurement accuracy is K_p defined as

$$K_p = \frac{\sqrt{\text{var}\{\sigma_0\}}}{\sigma_0} \quad (60)$$

which is the normalized standard deviation of the measured backscattering cross section [92]. To obtain an accurate measurement, K_p must be minimized.

Using the calibrated backscattering cross section, a geophysical model function must be developed to relate the backscattering cross section to the wind vector [93]. In general, a model function can be written as

$$\sigma_0 = F(\vec{U}) \quad (61)$$

for the given frequency, incidence angle, and polarization of a scatterometer. Here, \vec{U} denotes the wind vector (speed and direction). Because of the difficulty in deriving rigorous theoretical models, empirical models have been used for scatterometry applications. Figure 20 shows schematic model functions. As an example of a model function, Wentz and coworkers [94,95] have used SeaSat data to derive a Ku-band geophysical model function known as SASS-2.

It can be observed that σ_0 is a function of the radar azimuth angle (α) relative to the wind direction. A single σ_0 measurement is not sufficient to solve for both windspeed and direction. Figure 21 shows the double-sinusoidal relationship [93]. Thus, σ_0 is maximum at upwind ($\alpha=0$) and downwind ($\alpha=180$) directions while it is minimum near the crosswind direction ($\alpha=90$ and 270). As can be

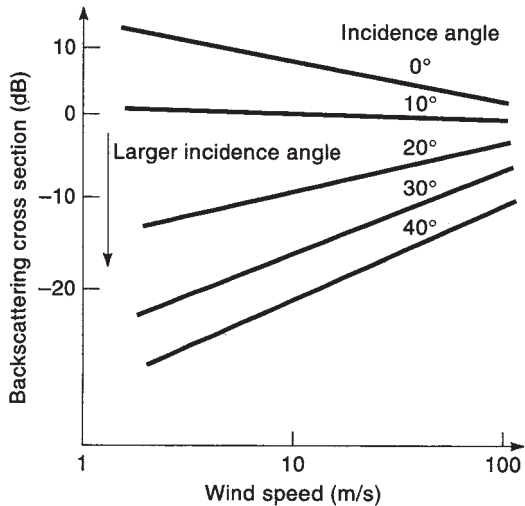


Figure 20. Schematic scatterometer model function. Using this geophysical model function, backscattering measurements are related to windspeed.

seen from Fig. 21, σ_0 in the upwind direction is slightly higher than one in the downwind direction. In principle, a unique wind vector can be determined as a result of this small asymmetry. However, extremely accurate measurements are required to detect this small difference. It is clear that more than one σ_0 measurement must be made at different azimuth angles to determine the wind direction. In order to explain the wind direction determination technique, we use a simple model given by

$$\sigma_0 = AU^\gamma(1 + a \cos \alpha + b \cos 2\alpha) \quad (62)$$

where A , a , b , and γ are empirically determined for the windspeed U measured at a reference altitude (usually at 19.5 m above the ocean surface). As can be seen from Eq. (62), two measurements provide the windspeed U and the wind direction with a fourfold ambiguity.

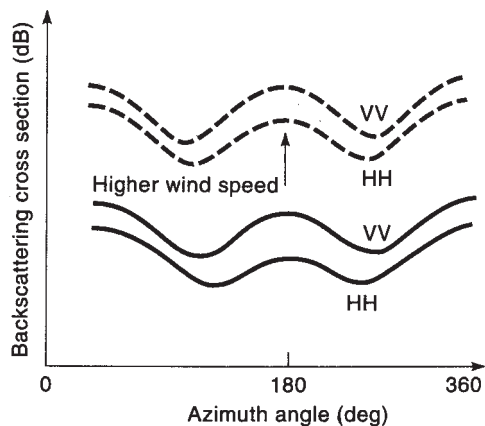


Figure 21. Backscattering cross section in terms of the radar azimuth angle relative to the wind direction. Note that σ_0 in the upwind direction is slightly higher than in the downwind direction.

Additional measurements must be used to remove the ambiguity. Otherwise, auxiliary meteorological information is required to select the correct wind direction from ambiguous vectors [96].

An ocean scatterometer must be designed to provide multiple azimuth measurements and wide-swath coverage. Two antenna types have been used for this purpose: multiple-fan beam and conically scanning spot beam [97]. For example, a multiple-fan beam with three antennas can measure backscattering cross sections at three different azimuth angles as shown in Fig. 22a. As a satellite moves, an ocean surface is observed by the forward-looking antenna, the center antenna, and the aft antenna. The narrow antenna pattern provides resolution in one dimension, and the Doppler and range filtering provides resolution in the wide antenna pattern direction. The advantage of the multiple-fan beam is that the multiple azimuth measurements are made at fixed optimal azimuth angles. The disadvantages are that the nadir gap and the measurements must be made at a wide range of incidence angles. A conically scanning antenna system with two beams can make maximum four azimuth measurements at fixed two incidence angles as shown in Fig. 22b. The advantages of the scanning antenna are that the geophysical model function should be limited to a narrow range of incidence angles and there is no nadir gap. The obvious disadvantage is that the antenna system must rotate continuously.

The hardware of a scatterometer is composed of three major components: RF, digital, and antenna subsystems. The functions of both RF and digital subsystems are similar to the imaging radar case. Typically, a scatterometer signal is amplified by TWTA (traveling-wave tube amplifier) consisting of a TWT (traveling wave tube) and the associated high-voltage power supply. A stable calibration noise source is used to calibrate the receiver gain. The digital subsystem accumulates many independent measurements in both frequency and time domains to minimize K_p and to reduce the data volume. The ground processing system should produce global ocean wind vectors in a timely manner for natural-hazard applications such as hurricane tracking. In addition, it is important to identify the data contaminated by ice, land, and rain.

Examples of a spaceborne scatterometer are SASS (Seasat-A Scatterometer System), ERS-1 [98,99], NSCAT, and SeaWinds. Their radar parameters are shown in Table 1.

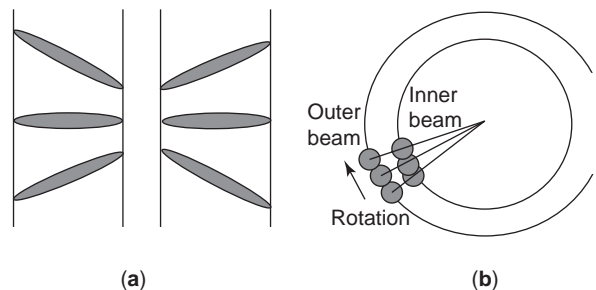


Figure 22. Two scatterometer antenna implementations: (a) multiple-fan beam; (b) conically scanning spot beam.

Table 1. Spaceborne Scatterometer Parameters

	SASS	ERS-1	NSCAT	SeaWinds
Frequency (GHz)	14.6	5.3	14	13.4
Spatial resolution (km)	50	50	25, 50	25
Swath width (km)	500	500	600	1800
Antenna type	Fan beam	Fan beam	Fan beam	Scanning spot beam
Number of antennas	4	3	6	1
Polarization	VV,HH	VV	VV,HH	VV,HH
Orbit altitude (km)	800	785	820	803

5.2. Ocean Altimeter

A radar altimeter [89] measures the distance between the sensor and the surface at the nadir direction to derive a topographic map of the surface. The primary application of a spaceborne ocean altimeter is to measure the sea surface elevation resulting from geostrophic ocean currents, which requires an accuracy of several centimeters. Long-term measurements of an ocean topography will contribute to the determination of the general circulation of the ocean and its variability. This allows us to study the role of oceans in the Earth climate system.

A radar altimeter transmits a short pulse to the nadir direction and measures the round-trip time (T) accurately. Hence, the distance (H) from the sensor to the surface can be calculated from

$$H = \frac{vT}{2} \tag{63}$$

where v is the speed of a radar wave in the propagating medium. The height error (δH) can be written in terms of the velocity error (δv) and the timing error (δT) as

$$\delta H = \frac{T\delta v}{2} + \frac{v\delta T}{2}. \tag{64}$$

The velocity error results from the refractive index variation due to ionosphere and atmosphere. A dual-frequency altimeter can be used to estimate the ionospheric effect, and a multiple-frequency radiometer may be used to estimate the atmospheric range delay. The timing error is related mainly to the finite signal bandwidth and the clock accuracy on the spacecraft. In addition, the small-scale roughness variation over the surface elevation causes an electromagnetic bias [100]. This bias is about 1% of the significant wave height (SWH). These errors must be estimated and corrected to achieve the required height accuracy. The location of a satellite must be known accurately since the distance is measured from an altimeter. Global positioning system (GPS) data and other satellite tracking techniques can be used for precision orbit determination.

The altimeter spatial resolution can be determined by either the radar beamwidth or the pulselength. If the beam footprint is smaller than the pulse footprint, the altimeter is called *beam-limited*. Otherwise, it is pulse-limited (see Fig. 23). The beam-limited footprint is given by

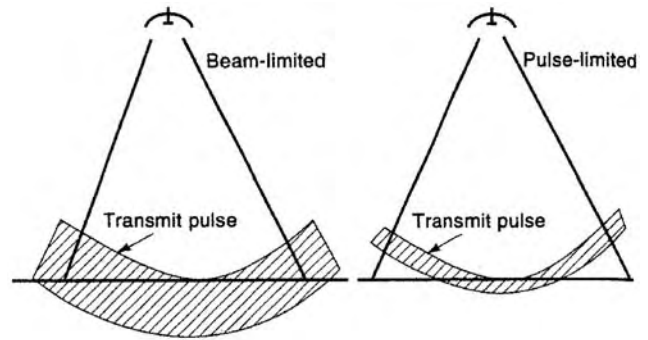


Figure 23. Beam-limited and pulse-limited altimeter footprints.

$\lambda h/L$, while the pulse-limited footprint is $2\sqrt{c\tau h}$. Here, h is the altitude, L is the antenna length, and τ is the pulselength. For a typical ocean altimeter, a long physical pulse is used to increase the signal-to-noise ratio. Then, a pulse compression technique is used to increase the range resolution. A “deramping” chirp technique is used for pulse compression. The deramping chirp is identical to the transmit chirp with a given time lag. The return signal and the deramping chirp are mixed together, and the difference frequency is processed to determine the range precisely.

The altimeter mean return waveform $W(t)$ [101,102] can be written as

$$W(t) = F(t)*q(t)*p(t) \tag{65}$$

where $F(t)$ is the flat surface impulse response, including radar antenna beamwidth and pointing angle effects, $q(t)$ is the surface height probability density function, and $p(t)$ is the radar system impulse response. Here, the symbol $*$ denotes the convolution operator. As illustrated in Fig. 24, the return pulseshape changes for different surface roughness. The antenna pointing angle is also important for waveform fitting. The half-power point on the waveform corresponds to the nadir mean sea level if the sea surface height distribution is Gaussian. In order to operate the altimeter electronics within the linear region of all receivers, an automatic gain control is implemented. An adaptive tracking unit attempts to track nadir mean sea level by keeping the half-power point in the tracking gate.

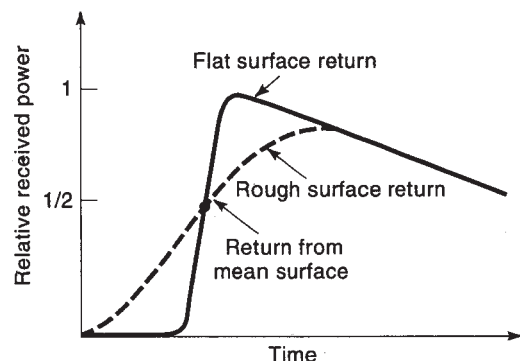


Figure 24. Altimeter return pulseshape for different surface roughnesses.

As an example of radar altimeters, we briefly describe the TOPEX radar altimeter [103]. The resulting RMS height accuracy of a single-pass TOPEX measurement is 4.7 cm [104]. This information is used to study the circulation of the world's oceans. The TOPEX altimeter is a dual-frequency (5.3- and 13.6-GHz) radar in order to retrieve the ionospheric delay of the radar signal. The TOPEX microwave radiometer measures sea surface emissivity at three frequencies (18, 21, and 37 GHz) to estimate the total water vapor content. The bandwidth and the pulsewidth of the TOPEX altimeter are 320 MHz and 102.4 μ s, respectively. The peak transmit power is 20 W. The antenna is a 1.5-m parabola with the 1.1° beamwidth at Ku band. In addition, the satellite carries a GPS receiver for precise satellite tracking. All these measurements are used to produce high-accuracy altimeter data. More recent research topics related to radar altimetry can be found in Ref. 104.

Conventional altimetry observations produced by the TOPEX altimeter provide high-precision ocean topography in the along-track direction. This allows the calculation of one geostrophic velocity component. However, knowledge of the two-dimensional velocity vector is required for an accurate estimate of important ocean characteristics such as the transport of mass, heat, freshwater, and chemicals. A new instrument using radar interferometry has been proposed to measure two-dimensional ocean topography. This instrument is known as the *wide-swath ocean altimeter* [105]. A three-satellite radar altimeter concept also has been proposed to observe the two-dimensional ocean surface gradient [106].

5.3. Radar Sounder

Radar sounders are used to image subsurface features by measuring reflections from dielectric constant discontinuities. For example, an ice sounding radar can measure the ice thickness by detecting the ice-ocean boundary [107]. In order to penetrate into subsurface, a long-wavelength radar is desired. Various radar sounding techniques are comprehensively summarized by Daniels et al. [108]. In order to image subsurface features, a radar signal must penetrate to the target depth with the satisfactory SNR. Like other radars, subsurface sounding radars should have an adequate bandwidth for sufficient resolution to detect buried objects or other dielectric discontinuity.

For a ground-penetrating radar [109], a probing antenna must be design for efficient coupling of electromagnetic radiation into the ground. The depth resolution can be obtained by using similar techniques described in the previous sections. However, the physical distance must be estimated from the slant range information and the real part of the medium refractive index. In order to enhance horizontal resolution, one can use the synthetic aperture technique. However, the matched filter construction is very difficult since the medium dielectric constant is usually inhomogeneous and unknown. The most important quantity to design a subsurface radar is the medium loss that determines the penetration depth. For a ground subsurface radar, it is advantageous to average many samples or increase effective pulselength to enhance

SNR. Polarimetric information is also important when buried objects are long and thin since strong backscattering is produced by a linearly polarized signal parallel to the long axis.

For an airborne [110] or a spaceborne radar sounder [111], subsurface returns must be separated from unwanted surface returns. Since a surface return is usually much stronger than a subsurface return, the radar must be designed for an extremely low sidelobe. A surface return can be an ambiguous signal if it is at the same range as a subsurface return (surface ambiguity). This problem becomes more serious as the altitude of a radar becomes higher or the antenna gain becomes lower. In addition, when the medium loss is large, radar must have a large dynamic range to detect a small subsurface return.

As an example of orbiting radar sounders, we will briefly describe the Apollo 17 lunar sounder radar [111]. The objectives of the sounder experiment were to detect subsurface geologic structures and to generate a lunar surface profile. Since lunar soil and rock exhibit less attenuation due to the absence of free water, one may expect deeper subsurface penetration compared with the observations on Earth. This sounder was operating at three frequencies (5, 15, and 150 MHz). This instrument was also used to generate a lunar surface profile using the strong surface return. In addition, galactic noise in the lunar environment was measured at the HF band.

5.4. Cloud Radar

Spaceborne cloud measurements to be accomplished by NASA's CloudSat mission [112,113] will answer a number of outstanding cloud-climate problems. The CloudSat measurements will evaluate quantitatively the representation of clouds and cloud processes in global atmospheric circulation models. The cloud profiling radar of the CloudSat will provide the global survey of the vertical structure of cloud systems at 500 m vertical resolution and 1.4 km horizontal resolution. Most meteorological radars [114] operate at centimeter wavelengths in order to avoid the significant attenuation by precipitation. However, cloud radars operate at millimeter wavelength since clouds cannot be observed easily by using conventional centimeter wavelength radars [115]. In order to minimize absorption, the radar frequency must be in the spectral windows whose center frequencies are 35, 100, and 150 GHz. The first millimeter-wave radar observations of clouds were done in the 35-GHz window [116]. Using the technology development at 94 GHz, the CloudSat radar operates at 94 GHz since higher radar reflectivity is expected at shorter wavelengths.

The cloud profiling radar of the CloudSat measures the power reflected from clouds as a function of distance from the radar. A minimum detectable cloud reflectivity is -26 dBZ. The radar is composed of RF electronics, digital electronics, high-power amplifier, and antenna subsystems. The CloudSat antenna diameter is a fixed 1.85-m-diameter reflector made from space-qualified composite graphite material to reduce mass. The antenna gain is higher than 63 dBi, and the sidelobes are less than -50 dB for angles larger than 7° from the boresight.

The low sidelobe level is important to eliminate the contamination from the surface reflection that is much stronger than the reflection from clouds. In order to minimize the loss, the quasioptical transmission line is used to feed the antenna instead of waveguides. The peak transmit power is 1.7 kW produced by EIK (extended-interaction klystron) and a high-voltage power supply. The thermal noise is reduced by averaging many samples of measured power and subtracting the estimated noise power. A higher PRF provides more samples to average; however, it increases the range ambiguity.

For a pulsed radar, the received power (P_r) can be written as

$$P_r = \frac{P_t G^2 \lambda^2 V}{(4\pi)^3 r^4} \eta e^{-2\alpha} \quad (66)$$

where P_t is the peak transmit power, G is the antenna gain, λ is the wavelength, V is the resolution volume, η is the volumetric radar cross section, and α is the one-way loss [117]. If the cloud particles are much smaller than the radar wavelength, using the Rayleigh scattering method, the radar reflectivity (Z) can be written as

$$Z = \frac{\eta \lambda^4}{\pi^5 |K|^2} \quad (67)$$

where $K = (n^2 - 1)/(n^2 + 2)$ and n is the complex refractive index of a particle. If cloud returns are measured coherently, the radial velocity (v_r) can be measured by using the Doppler frequency (f_d) as

$$v_r = \frac{f_d \lambda}{2} \quad (68)$$

Coherent radar measurements provide simultaneous radar reflectivity and radial velocity profiles in terms of altitude. More recent airborne cloud radars [118,119] can measure polarimetric reflectivity that can provide the additional information such as the linear depolarization ratio (LDR). Using these parameters, a cloud region classification (ice, cloud droplets, mixed-phase hydrometeors, rain, and insects) can be achieved [117]. If multi-wavelength measurements are made, it may be possible to estimate the drop size distribution.

5.5. Rain Radar

The accurate measurement of rainfall is an important factor in understanding the global water–energy cycle. Rain radars measure the rain reflectivity that can be used to estimate the parameters related to rainfall using inversion algorithms [120]. As an example of rain radars, one of the tropical rainfall measuring mission (TRMM) [121] instruments is a single-frequency (13.8-GHz), cross-track scanning radar for precipitation measurement. The satellite altitude is 350 km, and the scanning swath is 220 km. The range and surface horizontal resolutions are 250 m and 4 km, respectively. Using TRMM data, the rain profile can be estimated [120].

The operation frequency (13.8 GHz) is selected by considering both antenna size and attenuation. At this frequency, the antenna size does not have to be too large and the attenuation is small enough to measure rainfall near the surface. As an airborne rain radar, the National Aeronautics and Space Administration and the Jet Propulsion Laboratory developed an airborne rain-mapping radar (ARMAR) that flies on the NASA DC-8 aircraft [122]. The ARMAR operates with the TRMM frequency and geometry to understand the issues related to the TRMM rain radar.

Due to the downward-looking geometry, it is possible that surface clutter return may obscure return from precipitation. Even for an antenna looking off-nadir, the nadir return can be at the same range as precipitation. In order to overcome these difficulties, both antenna sidelobes and pulse compression sidelobes must be low (~ -60 dB relative to the peak return) enough to detect precipitation. In order to measure rain reflectivity accurately, it is necessary to calibrate the radar precisely. Radar measurements such as the reflectivity, the fall velocity, the horizontal–vertical polarization phase difference, and the differential reflectivity can be used to estimate rain rate and rain profile.

BIBLIOGRAPHY

1. C. Elachi, *Introduction to the Physics and Techniques of Remote Sensing*, Wiley, New York, 1987.
2. F. T. Ulaby, R. K. Moore, and A. K. Fung, *Microwave Remote Sensing: Active and Passive*, Vol. II: *Radar Remote Sensing and Surface Scattering and Emission Theory*, Artech House, Dedham, MA, 1982.
3. J. C. Curlander and R. N. McDonough, *Synthetic Aperture Radar Systems & Signal Processing*, Wiley, New York, 1991.
4. J. P. Ford, Resolution versus speckle relative to geologic interpretability of spaceborne radar images: A survey of user preferences, *IEEE Trans. Geosci. Remote Sens.* **GRS-20**: 434–444 (1982).
5. H. A. Zebker, J. J. van Zyl, and D. N. Held, Imaging radar polarimetry from wave synthesis, *J. Geophys. Res.* **92**: 683–701 (1987).
6. R. L. Jordan, B. L. Huneycutt, and M. Werner, The SIR-C/X-SAR synthetic aperture radar system, *IEEE Trans. Geosci. Remote Sens.* **GRS-33**:829–839 (1995).
7. J. J. van Zyl, A technique to calibrate polarimetric radar images using only image parameters and trihedral corner reflectors, *IEEE Trans. Geosci. Remote Sens.* **GRS-28**:337–348 (1990).
8. H. A. Zebker and Y. L. Lou, Phase calibration of imaging radar polarimeter Stokes matrices, *IEEE Trans. Geosci. Remote Sens.* **GRS-28**:246–252 (1990).
9. A. L. Gray, P. W. Vachon, C. E. Livingstone, and T. I. Lukowski, Synthetic aperture radar calibration using reference reflectors, *IEEE Trans. Geosci. Remote Sens.* **GRS-28**:374–383 (1990).
10. A. Freeman, Y. Shen, and C. L. Werner, Polarimetric SAR calibration experiment using active radar calibrators, *IEEE Trans. Geosci. Remote Sens.* **GRS-28**:224–240 (1990).

11. J. D. Klein and A. Freeman, Quadpolarisation SAR calibration using target reciprocity, *J. Electromagn. Waves Appl.* **5**:735–751 (1991).
12. H. A. Zebker, J. J. van Zyl, S. L. Durden, and L. Norikane, Calibrated imaging radar polarimetry: Technique, examples, and applications, *IEEE Trans. Geosci. Remote Sens.* **GRS-29**:942–961 (1991).
13. A. Freeman, J. J. van Zyl, J. D. Klein, H. A. Zebker, and Y. Shen, Calibration of Stokes and scattering matrix format polarimetric SAR data, *IEEE Trans. Geosci. Remote Sens.* **GRS-30**:531–539 (1992).
14. A. Freeman, SAR calibration: An overview, *IEEE Trans. Geosci. Remote Sens.* **GRS-30**:1107–1121 (1992).
15. A. Freeman, M. Alves, B. Chapman, J. Cruz, Y. Kim, S. Shaffer, J. Sun, E. Turner, and K. Sarabandi, SIR-C data quality and calibration results, *IEEE Trans. Geosci. Remote Sens.* **GRS-33**:848–857 (1995).
16. J. A. Kong, A. A. Swartz, H. A. Yueh, L. M. Novak, and R. T. Shin, Identification of Earth terrain cover using the optimum polarimetric classifier, *J. Electromagn. Waves Appl.* **2**:171–194 (1988).
17. H. H. Lim, A. A. Swartz, H. A. Yueh, J. A. Kong, R. T. Shin, and J. J. van Zyl, Classification of Earth terrain using polarimetric synthetic aperture radar images, *J. Geophys. Res.* **94**:7049–7057 (1989).
18. J. J. van Zyl and C. F. Burnette, Bayesian classification of polarimetric SAR images using adaptive *a-priori* probabilities, *Int. J. Remote Sens.* **13**:835–840 (1992).
19. E. Rignot and R. Chellappa, Segmentation of polarimetric synthetic aperture radar data, *IEEE Trans. Image Process.* **1**:281–300 (1992).
20. E. Rignot and R. Chellappa, Maximum *a-posteriori* classification of multifrequency, multilook, synthetic aperture radar intensity data, *J. Opt. Soc. Am. A* **10**:573–582 (1993).
21. E. J. M. Rignot, C. L. Williams, J. Way, and L. Viereck, Mapping of forest types in Alaskan boreal forests using SAR imagery, *IEEE Trans. Geosci. Remote Sens.* **GRS-32**:1051–1059 (1994).
22. L. E. Pierce, F. T. Ulaby, K. Sarabandi, and M. C. Dobson, Knowledge-based classification of polarimetric SAR images, *IEEE Trans. Geosci. Remote Sens.* **GRS-32**:1081–1086 (1994).
23. J. J. van Zyl, Unsupervised classification of scattering behavior using radar polarimetry data, *IEEE Trans. Geosci. Remote Sens.* **GRS-27**:36–45 (1989).
24. L. L. Hess, J. M. Melack, S. Filoso, and Y. Wang, Delineation of inundated area and vegetation along the Amazon floodplain with the SIR-C synthetic aperture radar, *IEEE Trans. Geosci. Remote Sens.* **GRS-33**:896–904 (1995).
25. R. H. Lang and J. S. Sidhu, Electromagnetic backscattering from a layer of vegetation, *IEEE Trans. Geosci. Remote Sens.* **GRS-21**:62–71 (1983).
26. J. A. Richards, G. Sun, and D. S. Simonett, L-band radar backscatter modeling of forest stands, *IEEE Trans. Geosci. Remote Sens.* **GRS-25**:487–498 (1987).
27. S. L. Durden, J. J. van Zyl, and H. A. Zebker, Modeling and observation of the radar polarization signature of forested areas, *IEEE Trans. Geosci. Remote Sens.* **GRS-27**:290–301 (1989).
28. F. T. Ulaby, K. Sarabandi, K. McDonald, M. Whitt, and M. C. Dobson, Michigan microwave canopy scattering model, *Int. J. Remote Sens.* **11**:1223–1253 (1990).
29. N. Chauhan and R. Lang, Radar modeling of a boreal forest, *IEEE Trans. Geosci. Remote Sens.* **GRS-29**:627–638 (1991).
30. G. Sun, D. S. Simonett, and A. H. Strahler, A radar backscatter model for discontinuous coniferous forest canopies, *IEEE Trans. Geosci. Remote Sens.* **GRS-29**:639–650 (1991).
31. S. H. Yueh, J. A. Kong, J. K. Rao, R. T. Shin, and T. LeToan, Branching model for vegetation, *IEEE Trans. Geosci. Remote Sens.* **GRS-30**:390–402 (1992).
32. Y. Wang, J. Day, and G. Sun, Santa Barbara microwave backscattering model for woodlands, *Int. J. Remote Sens.* **14**:1146–1154 (1993).
33. C. C. Hsu, H. C. Han, R. T. Shin, J. A. Kong, A. Beaudoin, and T. LeToan, Radiative transfer theory for polarimetric remote sensing of pine forest at P-band, *Int. J. Remote Sens.* **14**:2943–2954 (1994).
34. R. H. Lang, N. S. Chauhan, J. K. Ranson, and O. Kilic, Modeling P-band SAR returns from a red pine stand, *Remote Sensing Environ.* **47**:132–141 (1994).
35. M. C. Dobson, F. T. Ulaby, T. LeToan, A. Beaudoin, E. S. Kasischke, and N. Christensen, Dependence of radar backscatter on conifer forest biomass, *IEEE Trans. Geosci. Remote Sens.* **GRS-30**:412–415 (1992).
36. T. LeToan, A. Beaudoin, J. Riom, and D. Guyon, Relating forest biomass to SAR data, *IEEE Trans. Geosci. Remote Sens.* **GRS-30**:403–411 (1992).
37. K. J. Ranson and G. Sun, Mapping biomass of a northern forest using multifrequency SAR data, *IEEE Trans. Geosci. Remote Sens.* **GRS-32**:388–396 (1994).
38. A. Beaudoin, T. LeToan, S. Goze, A. Nezry, and A. Lopez, Retrieval of forest biomass from SAR data, *Int. J. Remote Sens.* **15**:2777–2796 (1994).
39. E. Rignot, J. Way, C. Williams, and L. Viereck, Radar estimates of aboveground biomass in boreal forests of interior Alaska, *IEEE Trans. Geosci. Remote Sens.* **GRS-32**:1117–1124 (1994).
40. M. L. Imhoff, Radar backscatter and biomass saturation: Ramifications for global biomass inventory, *IEEE Trans. Geosci. Remote Sens.* **GRS-33**:511–518 (1995).
41. E. J. Rignot, R. Zimmerman, and J. J. van Zyl, Spaceborne applications of P-band imaging radars for measuring forest biomass, *IEEE Trans. Geosci. Remote Sens.* **GRS-33**:1162–1169 (1995).
42. K. J. Ranson, S. Saatchi, and G. Sun, Boreal forest ecosystem characterization with SIR-C/XSAR, *IEEE Trans. Geosci. Remote Sens.* **GRS-33**:867–876 (1995).
43. M. C. Dobson, F. T. Ulaby, L. E. Pierce, T. L. Sharik, K. M. Bergen, J. Kellendorfer, J. R. Kendra, E. Li, Y. C. Lin, A. Nashashibi, K. Sarabandi, and P. Siqueira, Estimation of forest biophysical characteristics in northern Michigan with SIR-C/X-SAR, *IEEE Trans. Geosci. Remote Sens.* **GRS-33**:877–895 (1995).
44. E. S. Kasischke, N. L. Christensen, and L. L. Bourgeau-Chavez, Correlating radar backscatter with components of biomass in loblolly pine forests, *IEEE Trans. Geosci. Remote Sens.* **GRS-33**:643–659 (1995).
45. Y. Oh, K. Sarabandi, and F. T. Ulaby, An empirical model and an inversion technique for radar scattering from bare soil surfaces, *IEEE Trans. Geosci. Remote Sens.* **GRS-30**:370–381 (1992).
46. P. C. Dubois, J. J. van Zyl, and T. Engman, Measuring soil moisture with imaging radars, *IEEE Trans. Geosci. Remote Sens.* **GRS-33**:915–926 (1995).

47. J. Shi and J. Dozier, Inferring snow wetness using C-band data from SIR-C's polarimetric synthetic aperture radar, *IEEE Trans. Geosci. Remote Sens.* **GRS-33**:905–914 (1995).
48. L. C. Graham, Synthetic interferometer radar for topographic mapping, *Proc. IEEE* **62**:763–768 (1974).
49. H. Zebker and R. Goldstein, Topographic mapping from interferometric SAR observations, *J. Geophys. Res.* **91**:4993–4999 (1986).
50. H. A. Zebker, S. N. Madsen, J. Martin, K. B. Wheeler, T. Miller, Y. Lou, G. Alberti, S. Vettorella, and A. Cucci, The TOPSAR interferometric radar topographic mapping instrument, *IEEE Trans. Geosci. Remote Sens.* **GRS-30**:933–940 (1992).
51. N. P. Faller and E. H. Meier, First results with the airborne single-pass DO-SAR interferometer, *IEEE Trans. Geosci. Remote Sens.* **GRS-33**:1230–1237 (1995).
52. T. G. Farr and M. Kobrick, Shuttle radar topography mission produces a wealth of data, *Eos* **81**:583–585 (2000).
53. S. N. Madsen, H. A. Zebker, and J. Martin, Topographic mapping using radar interferometry: Processing techniques, *IEEE Trans. Geosci. Remote Sens.* **GRS-31**:246–256 (1993).
54. R. M. Goldstein, H. A. Zebker, and C. Werner, Satellite radar interferometry: Two-dimensional phase unwrapping, *Radio Sci.* **23**:713–720 (1998).
55. F. K. Li and R. M. Goldstein, Studies of multibaseline spaceborne interferometric synthetic aperture radars, *IEEE Trans. Geosci. Remote Sens.* **GRS-28**:88–97 (1990).
56. C. Prati and F. Rocca, Limits to the resolution of elevation maps from stereo SAR images, *Int. J. Remote Sens.* **11**:2215–2235 (1990).
57. C. Prati, F. Rocca, A. Moni Guarnieri, and E. Damonti, Seismic migration for SAR focussing: Interferometrical applications, *IEEE Trans. Geosci. Remote Sens.* **GRS-28**:627–640 (1990).
58. H. A. Zebker and J. Villasenor, Decorrelation in interferometric radar echoes, *IEEE Trans. Geosci. Remote Sens.* **GRS-30**:950–959 (1992).
59. C. Prati and F. Rocca, Improving slant range resolution with multiple SAR surveys, *IEEE Trans. Aerospace Electron. Syst.* **29**:135–144 (1993).
60. A. K. Gabriel and R. M. Goldstein, Crossed orbit interferometry: Theory and experimental results from SIR-B, *Int. J. Remote Sens.* **9**:857–872 (1988).
61. F. Gatelli, A. Monti-Guarnieri, F. Parizzi, P. Pasquali, C. Prati, and F. Rocca, The wavenumber shift in SAR interferometry, *IEEE Trans. Geosci. Remote Sens.* **GRS-32**:855–865 (1994).
62. H. A. Zebker, C. L. Werner, P. A. Rosen, and S. Hensley, Accuracy of topographic maps derived from ERS-1 interferometric radar, *IEEE Trans. Geosci. Remote Sens.* **GRS-32**:823–836 (1994).
63. E. R. Stofan, D. L. Evans, C. Schmillius, B. Holt, J. J. Plaut, J. van Zyl, S. D. Wall, and J. Way, Overview of results of spaceborne imaging radar-C, X-band synthetic aperture radar (SIR-C/X-SAR), *IEEE Trans. Geosci. Remote Sens.* **GRS-23**:817–828 (1995).
64. J. Moreira, M. Schwabish, G. Fornaro, R. Lanari, R. Bamler, D. Just, U. Steinbrecher, H. Breit, M. Eineder, G. Franceschetti, D. Guedtner, and H. Rinkel, X-SAR interferometry: First results, *IEEE Trans. Geosci. Remote Sens.* **GRS-33**:950–956 (1995).
65. A. L. Gray and P. J. Farris-Manning, Repeat-pass interferometry with airborne synthetic aperture radar, *IEEE Trans. Geosci. Remote Sens.* **GRS-31**:180–191 (1993).
66. A. Moccia and S. Vettorella, A tethered interferometric synthetic aperture radar (SAR) for a topographic mission, *IEEE Trans. Geosci. Remote Sens.* **GRS-31**:103–109 (1992).
67. H. A. Zebker, T. G. Farr, R. P. Salazar, and T. H. Dixon, Mapping the world's topography using radar interferometry: The TOPSAT mission, *Proc. IEEE* **82**:1774–1786 (1994).
68. R. M. Goldstein and H. A. Zebker, Interferometric radar measurements of ocean surface currents, *Nature* **328**:707–709 (1987).
69. R. M. Goldstein, T. P. Barnett, and H. A. Zebker, Remote sensing of ocean currents, *Science* **246**:1282–1285 (1989).
70. M. Marom, R. M. Goldstein, E. B. Thronton, and L. Shemer, Remote sensing of ocean wave spectra by interferometric synthetic aperture radar, *Nature* **345**:793–795 (1990).
71. M. Marom, L. Shemer, and E. B. Thronton, Energy density directional spectra of nearshore wave field measured by interferometric synthetic aperture radar, *J. Geophys. Res.* **96**:22125–22134 (1991).
72. D. R. Thompson and J. R. Jensen, Synthetic aperture radar interferometry applied to ship-generated internal waves in the 1989 Loch Linnhe experiment, *J. Geophys. Res.* **98**:10259–10269 (1993).
73. R. E. Carande, Estimating ocean coherence time using dual-baseline interferometric synthetic aperture radar, *IEEE Trans. Geosci. Remote Sens.* **GRS-32**:846–854 (1994).
74. L. Shemer and M. Marom, Estimates of ocean coherence time by interferometric SAR, *Int. J. Remote Sens.* **14**:3021–3029 (1993).
75. A. K. Gabriel, R. M. Goldstein, and H. A. Zebker, Mapping small elevation changes over large areas: Differential radar interferometry, *J. Geophys. Res.* **94**:9183–9191 (1989).
76. D. Massonnet, M. Rossi, C. Carmona, F. Adragna, G. Peltzer, K. Freigl, and T. Rabaute, The displacement field of the Landers earthquake mapped by radar interferometry, *Nature* **364**:138–142 (1993).
77. D. Massonnet, K. Freigl, M. Rossi, and F. Adragna, Radar interferometric mapping of deformation in the year after the Landers earthquake, *Nature* **369**:227–230 (1994).
78. H. A. Zebker, P. A. Rosen, R. M. Goldstein, A. Gabriel, and C. L. Werner, On the derivation of coseismic displacement fields using differential radar interferometry: The Landers earthquake, *J. Geophys. Res.* **99**:19617–19634 (1994).
79. G. Peltzer, K. Hudnut, and K. Feigl, Analysis of coseismic displacement gradients using radar interferometry: New insights into the Landers earthquake, *J. Geophys. Res.* **99**:21971–21981 (1994).
80. G. Peltzer and P. Rosen, Surface displacement of the 17 May 1993 Eureka Valley, California, earthquake observed by SAR interferometry, *Science* **268**:1333–1336 (1995).
81. D. Massonnet, P. Briole, and A. Arnaud, Deflation of Mount Etna monitored by spaceborne radar interferometry, *Nature* **375**:567–570 (1995).
82. D. Massonnet and K. Freigl, Satellite radar interferometric map of the coseismic deformation field of the M = 6.1 Eureka Valley, California earthquake of May 17, 1993, *Geophys. Res. Lett.* **22**:1541–1544 (1995).
83. R. M. Goldstein, H. Englehardt, B. Kamb, and R. M. Frolich, Satellite radar interferometry for monitoring ice sheet motion: Application to an antarctic ice stream, *Science* **262**:1525–1530 (1993).
84. I. R. Joughin, *Estimation of Ice-Sheet Topography and Motion Using Interferometric Synthetic Aperture Radar*, Ph.D. thesis, Univ. Washington, Seattle, 1995.

85. E. Rignot, K. Jezek, and H. G. Sohn, Ice flow dynamics of the Greenland Ice Sheet from SAR interferometry, *Geophys. Res. Lett.* **22**:575–578 (1995).
86. I. R. Joughin, D. P. Winebrenner, and M. A. Fahnestock, Observations of ice-sheet motion in Greenland using satellite radar interferometry, *Geophys. Res. Lett.* **22**:571–574 (1995).
87. R. M. Goldstein, Atmospheric limitations to repeat-track radar interferometry, *Geophys. Res. Lett.* **22**:2517–2520 (1995).
88. S. R. Cloude and K. P. Papathanassiou, Polarimetric SAR interferometry, *IEEE Trans. Geosci. Remote Sens.* **GRS-36**:1551–1565 (1998).
89. C. Elachi, *Spaceborne Radar Remote Sensing: Applications and Techniques*, IEEE Press, New York, 1988.
90. M. A. Donelan and W. J. Pierson, Radar scattering and equilibrium ranges in wind-generated waves with application to scatterometry, *J. Geophys. Res.* **92**:4971–5029 (1987).
91. W. J. Plant, The variance of the normalized radar cross section of the sea, *J. Geophys. Res.* **96**:20643–20654 (1991).
92. C. Y. Chi and F. K. Li, A comparative study of several wind estimation algorithms for spaceborne scatterometers, *IEEE Trans. Geosci. Remote Sens.* **26**:115–121 (1988).
93. F. M. Naderi, M. H. Freilich, and D. G. Long, Spaceborne radar measurement of wind velocity over the ocean—an overview of the NSCAT scatterometer system, *Proc. IEEE* **79**:850–866 (1991).
94. F. J. Wentz, S. Peteherych, and L. A. Thomas, A model function for ocean radar cross sections at 14.6 GHz, *J. Geophys. Res.* **89**:3689–3704 (1984).
95. F. J. Wentz, L. A. Mattox, and S. Peteherych, New algorithms for microwave measurements of ocean winds: Applications to SEASAT and the special sensor microwave imager, *J. Geophys. Res.* **91**:2289–2307 (1986).
96. M. G. Wurtele, P. M. Woiceshyn, S. Peteherych, M. Borowski, and W. S. Appleby, Wind direction alias removal studies of SEASAT scatterometer-derived wind fields, *J. Geophys. Res.* **87**:3365–3377 (1982).
97. M. W. Spencer, W. Tsai, and D. G. Long, High resolution measurements with a spaceborne pencil-beam scatterometer using combined range/Doppler discrimination techniques, *IEEE Trans. Geosci. Remote Sens.* **41**:567–581 (2003).
98. C. L. Rufenach, J. J. Bates, and S. Tosini, ERS-1 scatterometer measurements—Part I: The relationship between radar cross section and buoy wind in two oceanic regions, *IEEE Trans. Geosci. Remote Sens.* **36**:603–622 (1998).
99. C. L. Rufenach, ERS-1 scatterometer measurements—Part I: An algorithm for ocean-surface wind retrieval including light winds, *IEEE Trans. Geosci. Remote Sens.* **36**:623–635 (1998).
100. E. Rodriguez, Altimetry for non-Gaussian oceans: Height biases and estimation of parameters, *J. Geophys. Res.* **93**:14107–14120 (1988).
101. G. S. Brown, The average impulse response of a rough surface and its applications, *IEEE Trans. Antenn. Propag.* **AP-25**:67–74 (1977).
102. D. B. Chelton, E. J. Walsh, and J. L. MacArthur, Pulse compression and sea level tracking in satellite altimetry, *J. Atmos. Ocean. Technol.* **6**:407–438 (1989).
103. A. R. Zieger, D. W. Hancock, G. S. Hayne, and C. L. Purdy, NASA radar altimeter for the TOPEX/POSEIDON project, *Proc. IEEE* **79**:810–826 (1991).
104. TOPEX/POSEIDON; Geophysical evaluation, *J. Geophys. Res.* **99** (1994).
105. B. D. Pollard, E. Rodriguez, L. Villeux, T. Akins, P. Brown, A. Kitiyakara, and M. Zawadski, The wide swath ocean altimeter: Radar interferometry for global ocean mapping with centimetric accuracy, *Proc. IEEE Aerospace Conf.*, 2002.
106. R. K. Raney and D. L. Porter, WITTEX: An innovative three-satellite radar altimeter concept, *IEEE Trans. Geosci. Remote Sens.* **39**:2387–2391 (2001).
107. R. Bindshadler, P. Nornberger, D. Blankenship, T. Scambos, and R. Jacobel, Surface velocity and mass balance of ice streams D and E, West Antarctica, *J. Glaciol.* **42**:461–475 (1996).
108. D. J. Daniels, D. J. Gunton, and H. F. Scott, Introduction to subsurface radar, *IEE Proc.* **135F**:278–320 (1988).
109. ‘Special issue on ground penetrating radar,’ *J. Appl. Geophys.* **33** (1995).
110. T. S. Chuah, *Design and Development of a Coherent Radar Depth Sounder for Measurement of Greenland Ice Sheet Thickness*, Radar Systems and Remote Sensing Laboratory RSL Technical Report 10470-5, Univ. Kansas Center for Research, Inc., 1997.
111. L. J. Porcello, R. L. Jordan, J. S. Zelenka, G. F. Adams, R. J. Phillips, W. E. Brown, S. H. Ward, and P. L. Jackson, The Apollo lunar sounder radar system, *Proc. IEEE* **62**:769–783 (1974).
112. G. L. Stephens and D. G. Vane, The CloudSat mission, *Proc. IGARSS’03*, 2003.
113. E. Im, S. L. Durden, C. Wu, and The CloudSat radar team, development status of the cloud profiling radar for the CloudSat mission, *Proc. IGARSS’03*, 2003.
114. R. J. Doviak and D. S. Zrnicek, *Doppler Radar and Weather Observations*, Academic Press, Orlando, 1984.
115. R. M. Lhermitte, Cloud and precipitation remote sensing at 94 GHz, *IEEE Trans. Geosci. Remote Sens.* **26**:256–270 (1997).
116. P. V. Hobbs, N. T. Funk, R. R. Weiss, J. D. Locatelli, and K. R. Biswas, Evaluation of a 35 GHz radar for cloud physics research, *J. Atmos. Ocean. Tech.* **2**:35–48 (1985).
117. S. P. Lohmeier, S. M. Sekelsky, J. M. Firda, G. A. Sadowy, and R. E. McIntosh, Classification of particles in stratiform clouds using the 33 and 95 GHz polarimetric cloud profiling radar system (CPRS), *IEEE Trans. Geosci. Remote Sens.* **35**:256–270 (1997).
118. A. L. Pazmany, R. E. McIntosh, R. D. Kelly, and G. Vali, An airborne 95 GHz dual polarized radar for cloud studies, *IEEE Trans. Geosci. Remote Sens.* **32**:731–739 (1994).
119. G. A. Sadowy, R. E. McIntosh, S. J. Dinardo, S. L. Durden, W. N. Edelstein, F. K. Li, A. B. Tanner, W. J. Wilson, T. L. Schneider, and G. L. Stephens, The NASA DC-8 airborne cloud radar: Design and preliminary results, *Proc. IGARSS’97*, 1997.
120. Z. S. Haddad, E. A. Smith, C. D. Kummerow, T. Iguchi, M. R. Farrar, S. L. Durden, M. Alves, and W. S. Olson, The TRMM “Day-1” radar/radiometer combined rain-profiling algorithm, *J. Meteor. Soc. Japan* **75**:799–809 (1997).
121. J. Simpson, R. F. Adler, and G. R. North, A proposed tropical rainfall measuring mission (TRMM) satellite, *Bull. Am. Meteor. Soc.* **69**:278–295 (1988).
122. S. L. Durden, E. Im, F. K. Li, W. Ricketts, A. Tanner, and W. Wilson, ARMAR: An airborne rain-mapping radar, *J. Atmos. Ocean. Technol.* **11**:727–737 (1994).

RADAR REMOTE SENSING OF IRREGULAR STRATIFIED LAYERS

EZEKIEL BAHAR
University of Nebraska—
Lincoln
Lincoln, Nebraska

1. INTRODUCTION

A unified full-wave solution to scattering from irregular stratified media is adapted to sensing surface features with multiple scales of fluctuations. An overview of the full-wave approach with extensive reference to articles in the technical literature have been published in Volume 17 of the Wiley *Encyclopedia of Electrical and Electronics Engineering* [1]. The full-wave analysis leads to a set of generalized telegraphists' equations, which account for scattering due to fluctuations in the medium parameters (complex permittivity and permeability) as well as surface roughness. These medium and surface-height fluctuations are assumed to consist of a continuum of very-large-scale (compared to wavelength) to very-small-scale features. For purposes of illustration, only random rough-surface height fluctuations are considered here. Thus the composite rough surfaces are characterized by their surface height probability density functions, including their surface height spectral density functions. The surface height spectral density functions, which are the Fourier transforms of the surface height autocorrelation functions, are assumed to consist of a very broad spectrum of spatial components, corresponding to a wide range of correlation lengths. It is shown that the high- and low-frequency limiting forms of the original full-wave solutions [2] reduce to the physical optics solutions [3] and the small perturbation solution [4], respectively [5].

In general however, unlike the physical optics solutions for highly conducting surfaces, the full-wave solutions are polarization-dependent and, unlike the small-perturbation solution, the original full-wave solutions are not restricted by specific values of the mean-square heights of the rough surfaces. However, the original full-wave expressions, based on an iterative solution of the generalized telegraphists' equations, are restricted to rough surfaces with small to moderate mean-square slopes [2]. In order to apply rough-surface scattering theories to surfaces with multiple scales of roughness, two scale theories based on perturbation–physical optics hybrid approaches were introduced [6–8]. Thus patches of small-scale surfaces are assumed to ride on the large-scale surfaces, and the total cross section is expressed as a sum of a large-scale physical optics cross section and a slope-modulated small-scale surface cross section. Since the expressions for the small-scale surface cross sections are based on the small-perturbation solution, the Rayleigh parameters associated with the small-scale surface ($\beta = 4k_0^2 \langle h_s^2 \rangle$, where k_0 is the free-space wavenumber and $\langle h_s^2 \rangle$ is the mean-square height of the small-scale surface), are assumed to be significantly smaller than unity. Moreover, the results were shown to be

critically dependent on the choice of the Rayleigh parameters associated with the small-scale surface [8]. Since the superposition of a small-scale surface on a large-scale physical optics surface does not increase the power scattered by the rough surface, the results based on the summation of the two cross sections are restricted to very small fluctuations from the physical optics surface.

In this work the full-wave solutions are expressed in variational forms as a weighted sum of two cross sections [9]. Consistent with energy conservation, the contribution to the total cross section due to the surface with the larger-scale spectral components of the rough surface is reduced by a factor related to the characteristic function for the surface with the smaller-scale spectral components. The contributions to the total cross section due to the surface with the smaller-scale spectral components of the rough surface are modulated by the slopes of the surface with the larger-scale spectral components.

To avoid problems associated with ideal (step-type) filters, a smooth filtering scheme is introduced in order to separate the larger-scale (spatial) spectral components from the smaller-scale spectral components [10,11]. The variational parameter used to separate the larger-scale surface from the smaller-scale surface is associated with the mean-square height or slope of the larger- or smaller-scale surface. It may also be associated with the patch or pixel size associated with the smaller-scale surface [12].

Using the unified full-wave approach, this variational parameter associated with spectral splitting of the composite rough surface can be varied in a continuous manner. In one limit the entire rough-surface scatter cross section is given by the small-slope, original full-wave solution [2]. In the other limit the entire rough-surface cross section is given by the high-frequency limit of the full-wave solution (related to the physical optics solution). In these two limits no spectral decomposition of the rough surface is assumed. For the intermediate cases the variational parameter (related to the fraction of the mean-square heights or slopes of the larger-scale surface) is varied in a continuous manner. Thus, for example, $\langle h_1^2 \rangle / \langle h^2 \rangle$ or $\langle \sigma_1^2 \rangle / \langle \sigma^2 \rangle$ (where $\langle h_1^2 \rangle$ and $\langle \sigma_1^2 \rangle$ are the mean-square heights and slopes of the larger-scale surface while $\langle h^2 \rangle$ and $\langle \sigma^2 \rangle$ are the mean-square heights and slopes of the total rough surface) is varied continuously between zero and unity. It is shown that the total scatter cross section for the composite rough surface is stationary over a very broad range of the variational parameter. The criteria used to determine the stationarity of the results for the backscatter cross sections is related to the norm of the error over the full range of incident angles. The norm is related to the variational parameter [associated with the mean-square heights, slopes, or patch (pixel) size [12]]. Since the original full-wave solution is restricted by a specific value of the mean-square height and the mean-square slope of the rough surface, the results associated with the variational parameter [related to the fractional mean-square slope (σ_1^2 / σ^2)] are most revealing.

Since the slopes of the very-small-scale rough surface do not contribute to the cross section, the unified full-wave solutions can be applied without spectral truncation to Pearson–Moskovitz surfaces [8] or fractural surfaces.

Application of this work to remote sensing of soil moisture content is also of special interest. It is readily shown that for the physical optics limit or the small perturbation limit, the ratio of the backscatter cross sections for the vertically to horizontally polarized waves is independent of the surface roughness. Therefore, the extraction of information on moisture content from the measured data is relatively straightforward. However, in general this ratio cannot be assumed to be independent of surface roughness. In these cases it is necessary to determine the impact of surface slopes on the scatter cross sections in order to extract the data on moisture content. The full-wave approach can be applied to the remote sensing of manmade rough surfaces as well as naturally occurring surfaces. Contrary to results based on the small-perturbation approach, the unified full-wave solutions for the ratio of the backscatter cross section for vertically to horizontally polarized waves can be near unity, in agreement with experimental results.

2. FORMULATION OF THE PROBLEM

The rough interface that separates free space (with permittivity ϵ_0 and permeability μ_0) from a half-space characterized by its complex permittivity ϵ_1 and permeability μ_1 is given by

$$f(x_s, y_s, z_s) = y_s - h(x_s, z_s) = 0 \quad (1)$$

where $-L < x_s < L$ and $-l < z_s < l$ and $h(x_s, z_s) = h_0 = \text{const}$ for $|x| > L$ and $|z| > l$.

The electric field of the vertically or horizontally polarized plane wave incident in free space is given by

$$\vec{E}_i^P(x, y, z) = \vec{a}^P E_{i0}^P \exp(-i\vec{k}^i \cdot \vec{r}) \quad (2)$$

in which the superscript P, V (vertical) or H (horizontal) denotes the polarization of the wave. The unit vector \vec{a}^V is parallel to the plane of incidence and \vec{a}^H is perpendicular to the plane of incidence. The magnitude of the incident wave is E_{i0}^P , the wavevector \vec{k}_0^i for the incident wave in free space is parallel to the unit vector $\vec{a}^V x \vec{a}^H$, and \vec{r} is the position vector to the observation point. The unit vector normal to the mean plane of the rough surface $y = h_0$ is \vec{a}_y . Assuming $\exp(i\omega t)$ time excitations, the free-space wave-number is $k_0 = \omega \sqrt{\mu_0 \epsilon_0}$. The incident wavevector is in the direction of the unit vector \vec{n}^i .

$$\begin{aligned} \vec{k}_0^i = \vec{k}_0 \vec{n}^i = k_0 (\sin \theta_0^i \cos \phi^i \vec{a}_x \\ - \cos \theta_0^i \vec{a}_y + \sin \theta_0^i \sin \phi^i \vec{a}_z) \end{aligned} \quad (3)$$

in which θ_0^i is the elevation angle of incidence measured from the y axis and ϕ^i is the azimuth angle. The full-wave solution for the electromagnetic radiation fields diffusely scattered from the two-dimensionally rough surface is

given by

$$\begin{aligned} G_s^f = \left(\frac{k_0}{2\pi i} \right)^2 \int_{-L}^L \int_{-l}^l \int_{-\infty}^{\infty} \int_{-\infty}^{\infty} S(\vec{k}', \vec{k}^i) \exp(-i\vec{k}'_0 \cdot \vec{r}) \\ \times \exp(i\vec{v} \cdot \vec{r}_t) \frac{[\exp(iv'_y h) - \exp(iv'_y h_0)]}{v'_y} \\ \times dx_s dz_s \frac{dk'_{0y} dk'_{0z}}{k'_{0x}} G^i = G^f - G_D^f \end{aligned} \quad (4)$$

in which G_s^f and G^i are 2×1 column matrices whose elements are the vertically and horizontally polarized components of the diffusely scattered electric fields and the incident electric fields E_s^{Pf} and E_1^P ($P = V, H$), respectively. The integrations are over the surface variables x_s, z_s and the wavevector variables k'_{0y}, k'_{0z} for the radiation fields. The 2×2 scattering matrix $S(\vec{k}', \vec{k}^i)$ is given by

$$S(\vec{k}', \vec{k}^i) = 2 \cos \theta'_0 \cos \theta_0^i R(\vec{k}', \vec{k}^i) \quad (5)$$

in which the elements of the 2×2 matrix $R(\vec{k}', \vec{k}^i)$ are

$$\begin{aligned} R^{\text{HH}} = \\ \frac{[\mu_r C_1^i \cos(\phi' - \phi^i) - S_0' S_0^i] (1 - 1/\epsilon_r) + (1 - \mu_r) \cos(\phi' - \phi^i)}{(C_0' + \eta_r C_1^i)(C_0^i + \eta_r C_1^i)} \end{aligned} \quad (6)$$

$$\begin{aligned} R^{\text{VV}} = \\ \frac{[\epsilon_r C_1^i \cos(\phi' - \phi^i) - S_0' S_0^i] (1 - 1/\mu_r) + (1 - \epsilon_r) \cos(\phi' - \phi^i)}{(C_0' + C_1^i/\eta_r)(C_0^i + C_1^i/\eta_r)} \end{aligned} \quad (7)$$

$$R^{\text{HV}} = \frac{-n_r [(1 - 1/\mu_r) C_1^i - (1 - 1/\epsilon_r) C_1^i] \sin(\phi' - \phi^i)}{(C_0' + C_1^i/\eta_r)(C_0^i + \eta_r C_1^i)} \quad (8)$$

$$R^{\text{VH}} = \frac{n_r [(1 - 1/\epsilon_r) C_1^i - (1 - 1/\mu_r) C_1^i] \sin(\phi' - \phi^i)}{(C_0' + \eta_r C_1^i)(C_0^i + C_1^i/\eta_r)} \quad (9)$$

The scatter wavevector in the direction of the unit vector \vec{n}^i is

$$\vec{k}'_0 = \vec{k}_0 \vec{n}^i = k_0 (\sin \theta'_0 \cos \phi' \vec{a}_x + \cos \theta'_0 \vec{a}_y + \sin \phi' \vec{a}_z) \quad (10)$$

where θ'_0 and ϕ' are respectively the elevation angle and azimuth angle for the scattered wave. The relative complex permittivity and permeability are $\epsilon_r = \epsilon_1/\epsilon_0$, $\mu_r = \mu_1/\mu_0$, respectively. The relative refractive index and intrinsic impedance of medium 1 below the interface are $n_r = (\mu_r \epsilon_r)^{1/2}$ and $\eta_r = (\mu_r/\epsilon_r)^{1/2}$, respectively. The sines and cosines of the angles θ_0 and θ_1 above and below the rough interface (denoted by S_0, S_1 and C_0, C_1) are related through Snell's law.

The position vector to a point on the rough surface is

$$\begin{aligned} \vec{r}_s = x_s \vec{a}_x + h(x_s, z_s) \vec{a}_y + z_s \vec{a}_z \\ = \vec{r}_t + h(x_s, z_s) \vec{a}_y \end{aligned} \quad (11)$$

and \bar{r}_t is its projection of \bar{r}_s on the x, z plane. The vector \bar{v}' is given by

$$\bar{v}' = \bar{k}'_0 - \bar{k}^i_0 \quad (12)$$

For L and $l \rightarrow \infty$, G_D^f , the second term in Eq. (4) reduces to the specularly reflected plane wave from an infinite flat surface. For observation points in the far field $k_0 r \gg 1$, the wavevector variables in Eq. (4) can be integrated using the steepest-descent method, and the diffusely scattered fields reduce to

$$G_s^f = G_0 \int_{-l}^l \int_{-L}^L S(\bar{k}^f, \bar{k}^i) \exp(-i\bar{v} \cdot \bar{r}_t) \frac{[\exp(i\bar{v}_y h) - \exp(i\bar{v}_y h_0)]}{v_y} dx_s dz_s = G^f - G_D^f \quad (13)$$

in which

$$\begin{aligned} \bar{k}_0^f &= k_0 (\sin \theta_0^f \cos \phi^f \bar{a}_x + \cos \theta_0^f \bar{a}_y) \\ &+ \sin \theta_0^f \sin \phi^f \bar{a}_z = k_0 \bar{n}^f \end{aligned} \quad (14)$$

and

$$\bar{v} = \bar{k}_0^f - \bar{k}^i_0 \quad (15)$$

The coefficient G_0 in Eq. (13) is

$$G_0 = \frac{k_0^2 \exp(-ik_0 r)}{2\pi i r} \quad (16)$$

In Eq. (13), the elements of the scattering matrix $S(\bar{k}^f, \bar{k}^i)$ can be obtained from Eqs. (5)–(9) on replacing the angles in \bar{k}' by the corresponding angles in \bar{k}^f .

If the mean surface is normal to the unit vector \bar{n} as shown in Fig. 1, the solutions for the diffusely scattered fields are given by Eq. (13) or (4) except that the scattering matrices $S(\bar{k}^f, \bar{k}^i)$ or $S(\bar{k}', \bar{k}^i)$ are replaced by

$$D(\bar{k}^f, \bar{k}^i) = T^f S_n(\bar{k}^f, \bar{k}^i) T^i \quad (17)$$

in which S_n^{PQ} , the elements of the scattering matrix S_n , are obtained from S^{PQ} on replacing the cosines of the incident and scatter angles in the reference coordinate system with the cosines of the incident and scatter angles in the tilted coordinate system, $(-\bar{n}^i \cdot \bar{n})$ and $(\bar{n}^f \cdot \bar{n})$, respectively. Furthermore, $\cos(\phi^f - \phi^i)$ is replaced by the cosine of the angle between the planes of incidence and scatter in the tilted coordinate system:

$$\cos(\phi^{fn} - \phi^{in}) = \frac{(\bar{n}^i \times \bar{n}) \cdot (\bar{n}^f \times \bar{n})}{|\bar{n}^i \times \bar{n}| |\bar{n}^f \times \bar{n}|}$$

The sines of the angles are transformed in a similar manner. The 2×2 matrices T^i and T^f respectively relate the vertically and horizontally polarized incident and scattered fields in the reference coordinate system to the incident and scattered fields in the tilted coordinate system [13]. In addition, the differential surface element $dx_s dz_s$ is replaced by $dx_s dz_s / \bar{n} \cdot \bar{a}_y$, and $h(x_s, z_s)$ is measured normal to the mean surface. Thus the full-wave solutions are invariant to coordinate translations and rotations. They

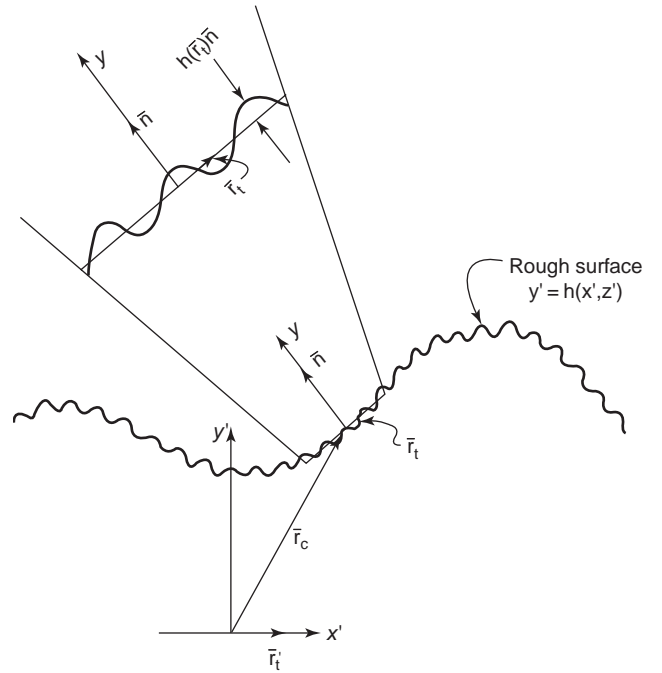


Figure 1. Arbitrarily oriented pixel on a rough surface.

intrinsically satisfy the reciprocity and duality relationships in electromagnetic theory.

3. FULL-WAVE SCATTER CROSS SECTIONS

Starting with the original full-wave solutions for the far fields in Eq. (13), the radar cross sections per unit area are expressed as follows

$$\langle \sigma_0^{PQ} \rangle = |S^{PQ}(\bar{k}^f, \bar{k}^i)|^2 Q(\bar{k}^f, \bar{k}^i) \quad (18)$$

in which $S^{PQ}(\bar{k}^f, \bar{k}^i)$ is the surface element scattering coefficient for incident waves in the direction \bar{n}^i and polarization $Q = V$ (vertical) or H (horizontal) and scatter waves in the direction \bar{n}^f and polarization $P = V$ or H and

$$Q(\bar{k}^f, \bar{k}^i) = \frac{k_0^4}{\pi \bar{v}_y^2} \int_{-2L}^{2L} \left(1 - \frac{|x_d|}{2L}\right) \left(1 - \frac{|z_d|}{2L}\right) \times [\chi_2(\bar{v}_y, -\bar{v}_y) - |\chi(\bar{v}_y)|^2] \exp(i\bar{v} \cdot \bar{r}_{dt}) d\bar{r}_{dt} \quad (19)$$

in which

$$\bar{r}_{dt} = (x_{s1} - x_{s2})\bar{a}_x + (z_{s1} - z_{s2})\bar{a}_z = x_d\bar{a}_x + z_d\bar{a}_z \quad (20)$$

and $d\bar{r}_{dt} = dx_d dz_d$.

For homogeneous isotropic random rough surfaces with Gaussian height probability density functions, the characteristic function $\chi(v_y)$ and the joint characteristic functions $\chi_2(v_y, -v_y)$ are given by

$$|\chi(v_y)|^2 = \exp[-v_y^2 \langle h^2 \rangle] \quad (21a)$$

and

$$\chi_2(v_y, -v_y) = \exp[-v_y^2 \langle h^2 \rangle (1 - R(r_d))] \quad (21b)$$

in which $v_y = \bar{v} \cdot \bar{a}_y$, $\langle h^2 \rangle$ is the mean-square height of the rough surface and $R(r_d)$ is the normalized surface height autocorrelation function, the Fourier transform of the surface height spectral density function $W(k)$. For homogeneous isotropic random rough surface the surface height autocorrelation function is a function of distance $r_d = (x_d^2 + z_d^2)^{1/2}$ only and $Q(\bar{k}^f, \bar{k}^i)$ can be expressed as follows for L and l much larger than the correlation lengths l_c :

$$Q(\bar{k}^f, \bar{k}^i) = \frac{2k_0^2}{v_y^2} \int_0^\infty (\chi_2(v_y, -v_y) - |\chi(v_y)|^2) \quad (22)$$

$$J_0(v_{xz} r_d) r_d dr_d$$

where J_0 is the Bessel function of order zero and

$$v_{xz} = (v_x^2 + v_z^2)^{1/2} = (v^2 - v_y^2)^{1/2} \quad (23)$$

It should be noted that $Q(\bar{k}^f, \bar{k}^i)$ remains finite as $v_y \rightarrow 0$ (backscatter at grazing angles).

4. DECOMPOSITION OF RANDOM ROUGH SURFACES INTO TWO SURFACES

Since the original full-wave solutions were derived iteratively for rough surfaces with small to moderate slopes, the corresponding expressions for the radar cross sections [Eq. (18)] are restricted to random rough surfaces with moderate to small slopes. In order to apply the full-wave solutions to rough surfaces with larger slopes, the surface is regarded as a superposition of a larger-scale surface consisting primarily of the larger-scale spatial components of the surface height spectral density function and a smaller-scale surface consisting primarily of the smaller-scale spatial components of the surface height spectral density function $W(k)$. To avoid problems associated with ideal (step-type) filters, a smooth decomposition procedure into larger and smaller scale surfaces is adopted [10,11]. To illustrate the smooth decomposition procedure, two cases are considered here. Assume first that the surface height autocorrelation function $\langle h^2 \rangle R(r_d)$ and its Fourier transform, the surface height spectral density function $W(k)$ are Gaussian:

$$\begin{aligned} W(k) &= \frac{\langle h^2 \rangle}{4\pi^2} \int_{-\infty}^{\infty} R(r_d) \exp(-i\bar{k} \cdot \bar{r}_d) d\bar{r}_d \\ &= \frac{\langle h^2 \rangle l_c^2}{4\pi} \exp\left(-\frac{k^2 l_c^2}{4}\right) \end{aligned} \quad (24)$$

where $\bar{r}_d = x_d \bar{a}_x + z_d \bar{a}_z$, $r_d = (x_d^2 + z_d^2)^{1/2}$, $\bar{k} = k_x \bar{a}_x + k_z \bar{a}_z$, and $k = (k_x^2 + k_z^2)^{1/2}$. The corresponding expression for the larger-scale surface is

$$\begin{aligned} W_1(k) &= \frac{\langle h_1^2 \rangle}{4\pi^2} \int_{-\infty}^{\infty} R_1(r_d) \exp(-i\bar{k} \cdot \bar{r}_d) d\bar{r}_d \\ &= \frac{\langle h_1^2 \rangle l_{cl}^2}{4\pi} \exp\left(-\frac{k^2 l_{cl}^2}{4}\right) \end{aligned} \quad (25)$$

Thus the surface height spectral density function for the smaller scale surface is

$$W_s(k) = W(k) - W_1(k) \quad (26)$$

Since $W_s(k=0) = 0$, the autocorrelation length l_{cl} and the mean-space height $\langle h_1^2 \rangle$ of the larger-scale surface are related to the autocorrelation length l_c and mean-square height $\langle h^2 \rangle$ of the total surface as follows:

$$\langle h_1^2 \rangle l_{cl}^2 = \langle h^2 \rangle l_c^2 \quad (27)$$

As a result, $l_{cl}^2 = \langle h^2 \rangle l_c^2 / \langle h_1^2 \rangle \geq l_c^2$, since $\langle h_1^2 \rangle \leq \langle h^2 \rangle$. Thus $W_s(k)$ is positive for all values of k and it peaks at k_m , where

$$k_m^2 = \frac{8 \ln(l_{cl}/l_c)}{l_{cl}^2 - l_c^2} \quad (28)$$

The corresponding surface height autocorrelation function for the smaller-scale surface is

$$\begin{aligned} \langle h_s^2 \rangle R_s(x_d) &= \langle h^2 \rangle \exp\left[-\left(\frac{r_d}{l_c}\right)^2\right] \\ &\quad - \langle h_1^2 \rangle \exp\left[-\left(\frac{r_d}{l_{cl}}\right)^2\right] \end{aligned} \quad (29)$$

where $\langle h_s^2 \rangle = \langle h^2 \rangle - \langle h_1^2 \rangle$ and $R_s(0) = 1$. The normalized autocorrelation function $R_s(r_0) = 0$ for

$$\begin{aligned} r_0^2 &= \ln\left[\frac{\langle h^2 \rangle}{\langle h_1^2 \rangle}\right] \frac{l_c^2 l_{cl}^2}{(l_{cl}^2 - l_c^2)} \\ &= \ln\left(\frac{l_{cl}}{l_c}\right)^2 \left(\frac{l_c^2 l_{cl}^2}{(l_{cl}^2 - l_c^2)}\right) \end{aligned} \quad (30)$$

Thus for $r_d < r_0$, $R(r_d) > 0$ and for $r_d > r_0$, $R(r_d) < 0$. The mean-square slope for Gaussian random rough surfaces is

$$\sigma^2 = \frac{4\langle h^2 \rangle}{l_c^2} \quad (31a)$$

The mean-square slope of the large-scale surface is

$$\sigma_1^2 = \frac{4\langle h_1^2 \rangle}{l_{cl}^2} \quad (31b)$$

and

$$\frac{\sigma_1^2}{\sigma^2} = \frac{\langle h_1^2 \rangle l_c^2}{\langle h^2 \rangle l_{cl}^2} = \left(\frac{\langle h_1^2 \rangle}{\langle h^2 \rangle}\right)^2 = \left(\frac{l_c}{l_{cl}}\right)^4 \quad (32)$$

The ratio of the mean-square height of the larger- or smaller-scale surface to the mean-square height of the total surface can be varied in a continuous manner between

zero and one, and the spectral decomposition between the two surfaces is smooth.

A more complex illustration of a composite rough surface that is considered here is a superposition of Pearson–Moskowitz-type sea surfaces. The spectral density function for such a rough surface is given by

$$W(k) = W_1(k) + W_2(k) = \frac{2}{\pi} \left[\frac{B_1 k^4}{(k^2 + \kappa_1^2)^4} + \frac{B_2 k^4}{(k^2 + \kappa_2^2)^4} \right] \quad (33)$$

in which the parameters $\kappa_i = 1/(335.2V_i^4)^{1/2} \text{cm}^{-1}$ and V is the windspeed in meters per second. For $k = \kappa_i$, $W_i(k) = (B_i/8\pi\kappa_i^4)$ is maximum. It is assumed here that $\kappa_2 > \kappa_1$. In this case the smooth decomposition is achieved by choosing the spectral density function for the smaller-scale surface as follows

$$W_s(k) = \frac{2}{\pi} \frac{(B_1 + B_2)k^4}{(k^2 + \kappa_s^2)^4} \quad (34)$$

where $\kappa_s \geq \kappa_2$. Thus, for $k \gg \kappa_s$

$$W(k) \approx W_s(k) \rightarrow \frac{2(B_1 + B_2)}{\pi k^4} \quad (35)$$

The corresponding expression for the larger-scale surface height spectral density function is

$$W_1(k) = W(k) - W_s(k) \quad (36)$$

and $W_1(k) > 0$ for all values of k . Furthermore, for $k \gg \kappa_s$

$$W_1(k) \rightarrow \frac{8[B_1(\kappa_s^2 - \kappa_1^2) + B_2(\kappa_s^2 - \kappa_2^2)]}{\pi k^6} \quad (37)$$

The corresponding surface height autocorrelation functions are Fourier transforms of $W(k)$, $W_s(k)$, and $W_1(k)$:

$$\langle h_i^2 \rangle R_i(r_d) = \frac{\pi}{2} \int_{-\infty}^{\infty} W_i(k) e^{i\vec{k} \cdot \vec{r}_d} k dk$$

They can be expressed in terms of modified Bessel functions [12,14]. The mean-square height of the total surface is

$$\langle h^2 \rangle = \frac{B_1}{6\kappa_1^2} + \frac{B_2}{6\kappa_2^2} = \langle h_1^2 \rangle + \langle h_2^2 \rangle \quad (38)$$

The mean-square height of the smaller-scale surface is

$$\langle h_s^2 \rangle = \frac{B_1 + B_2}{6\kappa_s^2} \quad (39)$$

and the mean-square slope of the larger scale surface is

$$\sigma_1^2 = \frac{\pi}{2} \int_{-\infty}^{\infty} W_1(k) k^3 dk = B_1 \ln \left(\frac{\kappa_s}{\kappa_1} \right) + B_2 \ln \left(\frac{\kappa_s}{\kappa_2} \right) \quad (40)$$

To evaluate the mean-square slope of Pearson–Moskowitz-type random rough surfaces, it is necessary to truncate the upper limit of the surface height spectral density function [8]. However, no such truncation is needed here to evaluate the mean-square slope of the larger-scale surface since $W_1(k)$ decreases as $1/k^6$ for $k \gg \kappa_s$. Evaluation of the full-wave solutions for the scatter cross sections does not involve the slopes of the smaller-scale (capillary) surface. This could also have a significant positive impact on the study of scattering from fracture-type random rough surfaces.

4.1. Application of the Unified Full-Wave Approach to Two-Scale Models

Using the decomposition scheme illustrated in Section 3, the composite random rough surface is expressed as

$$h(x_s, z_s) = h_1(x_s, z_s) + h_s(x_s, z_s) \quad (41)$$

in which the total h , larger-scale h_1 , and smaller-scale h_s , random rough surface heights are characterized statistically through their individual surface height spectral density functions. On applying the unified full-wave approach to two-scale models of composite random rough surfaces, it is shown that the total scatter cross sections (per unit area) $\langle \sigma^{\text{PQ}} \rangle$ can be expressed as follows in terms of a weighted sum of two cross sections [9]

$$\langle \sigma^{\text{PQ}} \rangle = \langle \sigma_s^{\text{PQ}} \rangle + |\chi_s| \langle \sigma_1^{\text{PQ}} \rangle \quad (42)$$

in which $\langle \sigma_s^{\text{PQ}} \rangle$ is the normalized scatter cross section associated with the small-scale surface (tilt-modulated by the slopes of the larger-scale surface). This cross section is given by the statistical average of $D^{\text{PQ}}(\vec{k}^f, \vec{k}^i) Q_s(\vec{k}^f, \vec{k}^i)$ over the slopes of the larger-scale surface, characterized by its probability diversity function

$$p(h_x, h_z) = p \left(\frac{\partial h_1}{\partial x}, \frac{\partial h_1}{\partial z} \right)$$

The unit vector normal to the tilted smaller scale surface is

$$\begin{aligned} \vec{n} &= \frac{-h_x \vec{a}'_x + \vec{a}'_y - h_z \vec{a}'_z}{(1 + h_x^2 + h_z^2)^{1/2}} \\ &= \sin \Omega \cos \tau \vec{a}'_x + \cos \Omega \cos \tau \vec{a}'_y + \sin \tau \vec{a}'_z \end{aligned}$$

in which Ω and τ are tilt angles in and perpendicular to the plane of incidence, thus

$$\langle \sigma_s^{\text{PQ}} \rangle = \langle D^{\text{PQ}}(\bar{\mathbf{k}}^f, \bar{\mathbf{k}}^i) Q_s(\bar{\mathbf{k}}^f, \bar{\mathbf{k}}^i) \rangle \quad (43)$$

in which D^{PQ} , (the slope-dependent surface element scattering coefficient) is the PQ ($P, Q = V, H$) element of the scattering matrix $D(\bar{\mathbf{k}}^f, \bar{\mathbf{k}}^i)$ given by Eq. (17) and $Q(\bar{\mathbf{k}}^f, \bar{\mathbf{k}}^i)$ is the slope-modulated version of Eq. (22)

$$Q_s(\bar{\mathbf{k}}^f, \bar{\mathbf{k}}^i) = \frac{2k_0^2(1+h_x^2+h_z^2)}{v_y^2} \times \int_0^\infty [\chi_{2s}(v_y, v_y) - \chi_s(v_y)] \cdot J_0(v_{xy}r_d) r_d dr_d \quad (44)$$

where $v_y = \bar{\mathbf{v}} \cdot \bar{\mathbf{n}}$ and $v_{xz} = (v_x^2 + v_z^2)^{1/2} = (v^2 - v_y^2)^{1/2}$. Furthermore, $\chi_{2s}(v_y, -v_y)$ and $\chi_s(v_y)$ are the joint characteristic function and characteristic function for the smaller-scale surface. The second term in Eq. (42) is the contribution from the larger scatter scale surface. This contribution is equal to the physical optics scatter cross sections associated with the larger-scale surface $\langle \sigma_1^{\text{PQ}} \rangle$, weighted down by the magnitude squared of the smaller-scale surface characteristic function. It can be shown that

$$\langle \sigma_1^{\text{PQ}} \rangle = |D_s^{\text{PQ}}(\bar{\mathbf{k}}^f, \bar{\mathbf{k}}^i)|^2 Q_1(\bar{\mathbf{k}}^f, \bar{\mathbf{k}}^i) \quad (45)$$

where $D_s^{\text{PQ}}(\bar{\mathbf{k}}^f, \bar{\mathbf{k}}^i)$ is the value of surface element scattering coefficient evaluated at the specular point where the unit vector normal to the surface is given by

$$\bar{\mathbf{n}}_s = \frac{\bar{\mathbf{v}}}{v} \quad (46)$$

Furthermore

$$Q_1(\bar{\mathbf{k}}^f, \bar{\mathbf{k}}^i) = \frac{2k_0}{\bar{v}_y} \int_0^\infty [\chi_{2l}(v'_{ys} - v'_y) - |\chi_1(v'_y)|^2] \times x J_0(v'_{xz}r_d) r_d dr_d \quad (47)$$

where $\chi_{2l}(v'_y, -v'_y)$ and $\chi_1(v'_y)$ are the joint characteristic function and the characteristic function for the larger-scale surface and $v'_y = \bar{\mathbf{v}} \cdot \bar{\mathbf{a}}'$, $v'_{xz} = (v'^2 - v_y'^2)^{1/2}$ and $\bar{\mathbf{a}}'$ is normal to the mean plane (see Fig. 1).

Since h_l and h_s can be chosen such that the variational parameters $\langle h_l^2 \rangle / \langle h^2 \rangle = 1 - \langle h_s^2 \rangle / \langle h^2 \rangle = n$ or $\sigma_l^2 / \sigma^2 = n$ can be varied between zero and one. The corresponding expressions for the total cross sections can be evaluated as functions of the variational parameters n . Denoting these quantities with the subscript n , the norm of the error over the range of backscatter angles θ_0^i is defined as follows

$$E_{n+\Delta n/2}^{\text{PQ}} = \sum_1 \frac{\langle \sigma_{n+\Delta n}^{\text{PQ}}(\theta_0^i) \rangle - \langle \sigma_n^{\text{PQ}}(\theta_0^i) \rangle}{\langle \sigma_{n+\Delta n}^{\text{PQ}}(\theta_0^i) \rangle + \langle \sigma_n^{\text{PQ}}(\theta_0^i) \rangle} \frac{2}{\Delta n}$$

in which

$$\Delta_n = \begin{cases} \frac{\langle h_l^2 \rangle_{n+\Delta n} - \langle h_l^2 \rangle_n}{\langle h_l^2 \rangle} \\ \text{or} \\ \frac{[\langle \sigma_l^2 \rangle_{n+\Delta n} - \langle \sigma_l^2 \rangle_n]}{\sigma_l^2} \end{cases}$$

The variational parameter could also be related to the smaller-scale surface patch size [12].

The cross sections $\sigma_n^{\text{PQ}}(\theta_0^i)$ are stationary over a wide range of the variational parameter (related to the mean-square heights or slopes of the larger-scale surface). The final cross sections are evaluated for n where the norm of the error is minimum.

5. CONCLUDING REMARKS

In this article a comprehensive procedure is presented for applying a unified full-wave approach to evaluate the radar cross sections of random rough surfaces, based on a variational two-scale model.

This variational approach is based on the intrinsic properties of the full-wave solution. In the low-frequency limit, when the wavelength of electromagnetic waves incident on the rough surfaces is very large compared to the scales of roughness of the surface, the full-wave solution reduces to the polarization-dependent small-perturbation solution. In the high-frequency limit, when the wavelength is much smaller than the scales of roughness of the surface, the full-wave solution reduces to the physical optics solution (associated with specular point scattering).

In the case of most natural land or sea surfaces, the scales of roughness consist of a continuum of very small to very larger scales of roughness. In these cases it becomes difficult to distinguish between surfaces with the larger scales and smaller scales of roughness. Furthermore, the hybrid perturbation-physical optics, two-scale approaches were restricted by the value of the Rayleigh parameter $\beta = 4k_0^2 \langle h_s^2 \rangle$ (associated with the small-scale surface) and the results were shown to be very sensitive to the selection of the spatial wavenumber k_d where spectral splitting is assumed to occur [8]. One reason for this is that the total cross section was assumed to be a simple sum of two cross sections instead of (42).

Several features distinguish the full-wave results (based on the two-scale model) from the familiar two-scale approach. A smooth decomposition of the surface height spectral density function is adopted rather than a step-type decomposition associated with the wavenumber k_d . The variational parameter associated with the fractional mean-square heights or slopes of the larger-scale surface, can be varied between one and zero in a continuous manner. In one limit, the full-wave solution reduces to the original full wave solution [2]. In the other limit, the full-wave solution reduces to the physical optics solution (associated with specular point scattering and the Fresnel reflection coefficients). For highly conducting surfaces, these physical optics solutions are polarization-independent. For the intermediate cases (associated with the

variational parameters between one and zero) the full-wave solutions for the total radar cross sections are expressed as weighted sums of two cross sections [9]. Thus, when the contributions from the smaller-scale rough surface increases, the corresponding contribution from the larger-scale spectral components of the surface decreases. The stationarity of the results (based on the unified full-wave approach) over a broad range of variational parameters corresponds to a broad minimum in the norm of the error (as defined in the previous section). The value of the total radar cross section obtained in this manner is relatively insensitive to changes in the variational parameter. The results obtained using the familiar hybrid perturbation–physical optics approach are very sensitive to changes in k_d (where spectral splitting occurs).

BIBLIOGRAPHY

1. E. Bahar, Radar remote sensing of irregular stratified media, in J. G. Webster, ed., *Wiley Encyclopedia of Electrical and Electronic Engineering*, Vol. 17, Wiley, New York, 1999, pp. 635–654.
2. E. Bahar and G. G. Rajan, Depolarization and scattering of electromagnetic waves by irregular boundaries for arbitrary incident and scatter angles—full wave solutions, *IEEE Trans. Anten. Propag.* **AP-27**(2):214–225 (1979).
3. P. Beckmann and A. Spizzichino, *The Scattering of Electromagnetic Waves from Rough Surfaces*, Macmillan, New York, 1963.
4. S. O. Rice, Reflection of electromagnetic waves from a slightly rough surface, *Commun. Pure Appl. Math.* **4**:352–378 (1951).
5. E. Bahar and B. S. Lee, Full wave solutions for rough surface bistatic radar cross sections: Comparison with small perturbation, physical optics, numerical, and experimental results, *Radio Sci.* **29**(2):407–429 (1994).
6. J. W. Wright, A new model for sea clutter, *IEEE Trans. Anten. Propag.* **AP-16**(2):217–223 (1968).
7. D. E. Barrick and W. H. Peake, A review of scattering from surfaces with different roughness scales, *Radio Sci.* **3**(8):865–868 (1968).
8. G. S. Brown, Backscattering from a Gaussian-distributed perfectly conducting rough surface, *IEEE Trans. Anten. Propag.* **AP-28**:943–946 (1978).
9. E. Bahar, Scattering cross sections for composite random surfaces—full wave analysis, *Radio Sci.* **16**(6):1327–1335 (1981).
10. E. Bahar and R. D. Kubik, Tilt modulation of high resolution radar backscatter cross sections: Unified full wave approach, *IEEE Trans. Geosci. Remote Sens.* **31**:1229–1242 (Sept. 1993).
11. E. Bahar and R. D. Kubik, Simulation of high resolution radar polarimetric images—Unified full wave approach, *Int. J. Remote Sens.* **14**(15):2829–2845 (1993).
12. E. Bahar and X. Zhang, A new unified full wave approach to evaluate the scatter cross sections of composite random rough surfaces, *IEEE Trans. Geosci. Remote Sens.* **34**(4):973–980 (1996).
13. E. Bahar, Full wave solutions for the depolarization of the scattered radiation fields by rough surfaces of arbitrary slope, *IEEE Trans. Anten. Propag.* **AP-29**(3):443–454 (1981).
14. M. Abramowitz and I. A. Stegun, *Handbook of Mathematical Functions with Graphs Formulas and Mathematical Tables*, National Bureau of Standards, Applied Mathematical Series, Vol. 55, 1964.

RADAR SIGNAL DETECTION

MINSHENG WANG
Texas Instruments Incorporated
ANDREW K. CHAN
Texas A & M University

Each day, we constantly make decisions. Given certain hypotheses, information is selected on which to base each decision, and under certain conditions, we may need to determine the reliability of the information. Such is the case in radar signal detection—a returned signal is received, and we have to decide whether a target is present or absent. If there were no noise or interference, the decision could be made with complete confidence. However, in reality, the received signal is usually heavily corrupted by environmental noise, interference, and noise from the radar system itself, and so on. In order to make a reliable decision, the noise and unwanted signals have to be suppressed with a so-called matched filter before a decision can be made.

Owing to the existence of noise and interference, radar signal detection has to be treated as a statistical problem, regardless of whether the signal under detection is deterministic. This statistical formalism of radar signal detection theory can be applied to all types of radar signals without restriction. To understand radar signal detection, noise has to be described quantitatively. A time-limited deterministic signal can be described as a time series, and a periodic deterministic signal can be represented as a Fourier series. In contrast, noise cannot be represented as a deterministic function in the time or frequency domains. In other words, we cannot predict a noise-contaminated radar signal with absolute certainty. However, with available noise information such as the expectation, the power, or even the probability distribution of noise, we can select a criterion on which to base our decision.

1. BASIC CONCEPTS AND CRITERIA

1.1. Concepts of Signal-to-Noise Ratio and Matched Filter

The signal-to-noise ratio (SNR) in radar and communication systems is defined as

$$\text{SNR} = \frac{(\text{signal power})}{(\text{noise variance})} \quad (1)$$

The maximum output SNR, the most frequently used criterion for radar detection, is defined as the ratio of the maximum instantaneous output signal power to the output noise power. The input SNR is a major limiting factor for radar detection performance.

For a fixed input SNR, a linear time-invariant filter whose frequency response function maximizes the output SNR is called a *matched filter*. Matched filtering transforms the raw radar data into a form that is suitable for (1) generating the optimal decision for detection, (2) estimating the target parameters with a minimal RMS error, or

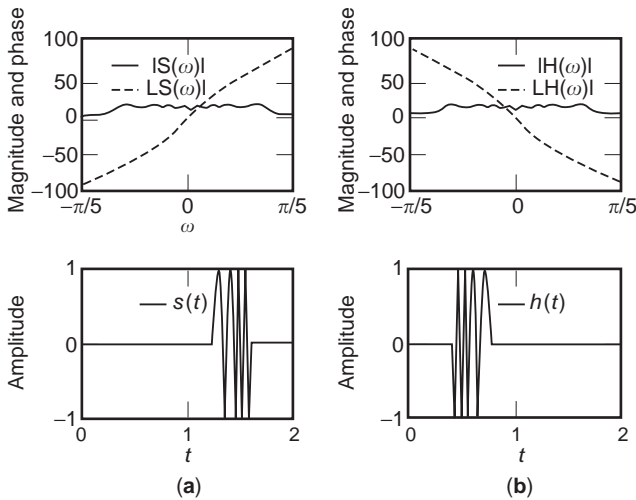


Figure 1. (a) Signal $s(t)$ and (b) matched-filter $h(t)$ relations. Phase in units of degrees. The phase from $H(\omega)$ is the negative of that from $S(\omega)$, while $h(t)$ is the time reversal of $s(t)$.

(3) obtaining the maximum resolving power for a group of targets. The characteristics of matched filters can be described by either a frequency-domain transfer function or a time-domain impulse response function, each related to the other by the Fourier transform. In the frequency domain, the matched-filter transfer function $H(\omega)$ is the complex conjugate of the spectrum of the signal. Thus, in general terms

$$H(\omega) = kS^*(\omega)e^{-j\omega T} \tag{2}$$

where $S(\omega)$ is the spectrum of the input signal $s(t)$ and T is a delay constant required to make the filter physically realizable. The normalizing factor k and the delay constant are generally ignored in formulating the underlying significant relationship. This simplification yields

$$H(\omega) = S^*(\omega) \tag{3}$$

Equation (3) reveals that the bandwidth of the receiver must be the same as that of the signal. This is under-

standable, because if the bandwidth of the receiver is wide compared with that occupied by the signal energy, extraneous noise may be introduced into the excess bandwidth, which lowers the output signal-to-noise ratio. On the other hand, if the receiver bandwidth is narrower than the signal bandwidth, the noise energy is reduced along with part of the signal energy. The result is again a lowered SNR. When the receiver bandwidth is identical to the signal bandwidth as in the case of the matched filter, the output SNR is maximized. The conjugate in Eqs. (2) and (3) allows the phases of $S(\omega)$ and $H(\omega)$ to cancel each other out, and leaves the output signal spectrum a linear phase, $e^{-j\omega T}$, which results in a peak at the time instant T in the output.

The corresponding time-domain relationship between the signal to be detected and the matched filter is obtained from the inverse Fourier transform of $H(\omega)$. This leads to the result that the impulse response of a matched filter is a replica of the time inverse of the known signal function. Thus, if $h(t)$ represents the matched-filter impulse response, the relationship equivalent to Eq. (2) is given by

$$h(t) = ks(T - t) \tag{4}$$

As before, k and T can be ignored to yield the basic relationship

$$h(t) = s(-t) \tag{5}$$

Figure 1 illustrates the relationship given by Eqs. (3) and (5), where $s(t)$ is a pulsed linear frequency-modulated (LFM) signal with the form

$$s(t) = \begin{cases} \sin[2\pi(t - 1.2)^2], & t \in [1.2, 1.6] \\ 0, & \text{otherwise} \end{cases} \tag{6}$$

The phase from $H(\omega)$ is the negative of that from $S(\omega)$, while $h(t)$ is the time reversal of the $s(t)$.

Figure 2a shows a received signal, which is the signal $s(t)$ of Eq. (6) corrupted by a 6 dB Gaussian noise; that is, the input SNR is -6 dB. It is difficult to detect the

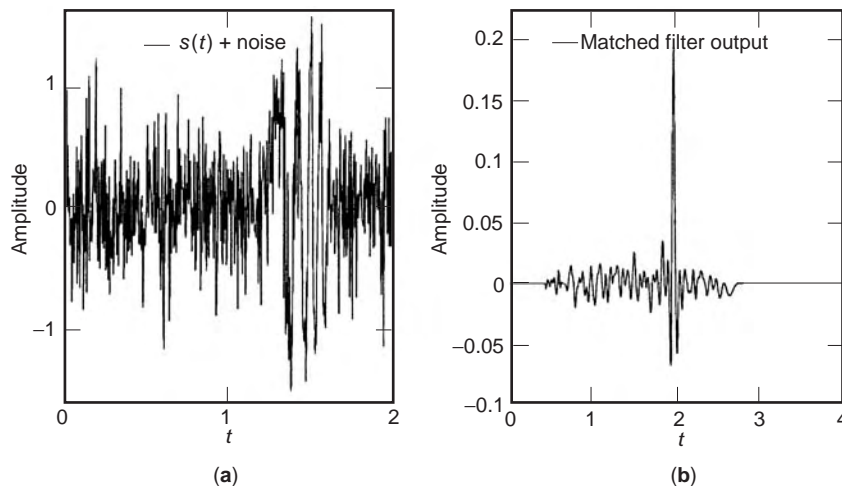


Figure 2. (a) Signal corrupted by noise by (b) the matched-filter output. The peak in the matched-filter output indicates the existence of the signal.

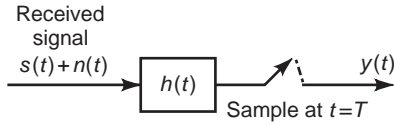


Figure 3. Block diagram of a matched filter.

existence of the signal $s(t)$ from this figure. However, after the received signal is processed by the matched filter, the detector output peak in Fig. 2b clearly indicates the existence of the signal.

The output from the matched filter, as shown in Fig. 3, is the convolution between the received signal and the matched filter impulse response:

$$\begin{aligned}
 y(t) &= \int_0^t [s(\tau) + n(\tau)]h(t - \tau) d\tau \\
 &= \int_0^t [s(\tau) + n(\tau)]s(T - t + \tau) d\tau
 \end{aligned}
 \tag{7}$$

Sampling $y(t)$ at $t = T$ yields the maximum output signal value, that is

$$\begin{aligned}
 y(t)_{\max} &= y(T) = \int_0^T [s(\tau) + n(\tau)]s(\tau) d\tau \\
 &= E_s + \int_0^T n(\tau)s(\tau) d\tau
 \end{aligned}
 \tag{8}$$

where E_s represents the signal energy. It can be easily verified that the expectation of $y(t)_{\max}$ is E_s , because the second term in Eq. (8) represents the noise whose mean is zero. This can be easily seen from Fig. 2b in which the maximum signal energy occurs at $t = T = 2$, and the maximum value is close to the expectation of $E_s = 0.18$ in this experiment. A detailed analysis of the matched filter will be given in Section 2.

Equation (7) describes the output of the matched filter as the cross-correlation between the received signal and a replica of the transmitted signal. This implies that the matched filter can be replaced by a cross-correlation that performs the same mathematical operation, as shown in Fig. 4. The received signal is multiplied by a delayed replica of the transmitted signal $s(t - t_1)$, and the product is passed through a lowpass filter. The cross-correlation

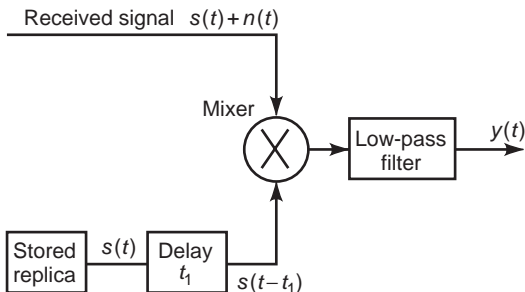


Figure 4. Block diagram of a cross-correlation, which is another implementation of the matched filter.

tests for the presence of a target at only one time: t_1 . Targets at other time delays, or ranges, may be found by varying t_1 . However, this requires a longer search time. The search time can be reduced by adding parallel channels, each containing a delay line corresponding to a particular value of t_1 , as well as a multiplier and a lowpass filter.

Since the cross-correlation and the matched filter are equivalent mathematically, the choice of which one to use in a particular radar application is determined by the practicality of implementation. The matched filter, or an approximation, has been generally preferred in the vast majority of applications.

1.2. Decision Criteria for Radar Signal Detection

The statistical detection problem consists of examining the received radar waveform $r(t)$ in a resolution cell to determine which of the following two hypotheses is true. The first hypothesis H_1 asserts that a target is present, and the received signal contains the target signature and noise. The second hypothesis H_0 states that the target is absent and only noise is present in the received signal. The problem can be compactly stated as

$$H_1: r(t) = s(t) + n(t) \tag{9}$$

$$H_0: r(t) = n(t)$$

The conditional probability density function completely describes the received signal statistically in both cases:

$$\begin{aligned}
 p(r|H_1) &= \text{conditional probability density function with} \\
 &\quad \text{target present}
 \end{aligned}
 \tag{10}$$

$$\begin{aligned}
 p(r|H_0) &= \text{conditional probability density function with} \\
 &\quad \text{target absent}
 \end{aligned}$$

For reasons of simplicity, r is assumed to be a single sampled point of the received radar signal. The extension from a single sampled point to multiple sampled points is straightforward. The likelihood ratio is defined as

$$\Lambda(r) = \frac{p(r|H_1)}{p(r|H_0)} \tag{11}$$

The likelihood ratio $\Lambda(r)$ is also called the likelihood statistic. It is a random variable since it is a function of the random variable r . The *maximum likelihood (ML) decision criterion*, which chooses the hypothesis that most likely causes the observed signal, is

$$\begin{aligned}
 &H_1 \\
 \Lambda(r) &\geq 1 \\
 &H_0
 \end{aligned}
 \tag{12}$$

This expression means that H_1 is selected if $\Lambda(r)$ is greater than 1; otherwise H_0 is selected. It can be seen that the ML criterion is a very simple decision criterion.

To describe the detection performance better, the probabilities of detection and false alarm are used in radar detection. The probability of detection refers to the probability of asserting the presence of a target when the target is indeed present

$$P_d = \int_{R_0}^{\infty} p(r|H_1) dr \quad (13)$$

where R_0 is the decision boundary. The proper value of the boundary R_0 depends on the criterion of decision. The probability of false alarm is the probability of asserting the presence of a target when the target is actually absent:

$$P_{fa} = \int_{R_0}^{\infty} p(r|H_0) dr \quad (14)$$

A sketch of the two density functions is shown in Fig. 5, where P_d and P_{fa} are, respectively, shown by the vertically and the horizontally hatched areas. If the observed value r is large, we would be confident in picking H_1 . If r is small, we would pick H_0 , as shown in Fig. 5.

Obviously, a decision rule should be selected to maximize P_d while restricting the P_{fa} . The simplest rule in this class, which is extensively used in radar detection, is the *Neyman–Pearson criterion*. This criterion specifies a decision boundary that maximizes the probability of detection (P_d) while maintaining a fixed probability of false alarm P_{fa} . The detection problem under the Neyman–Pearson criterion can be formulated as follows:

$$\text{Maximum: } P_d = \int_{R_0}^{\infty} p(r|H_1) dr \quad (15)$$

$$\text{Under constraint: } P_{fa} = \int_{R_0}^{\infty} p(r|H_0) dr = \alpha$$

The optimum decision region can be found by using the calculus of extrema and forming the objective function

$$J = P_d + \eta(\alpha - P_{fa}) \quad (16)$$

where η is a Lagrange multiplier. This can be written as

$$J = \eta\alpha + \int_{R_0}^{\infty} [p(r|H_1) - \eta p(r|H_0)] dr \quad (17)$$

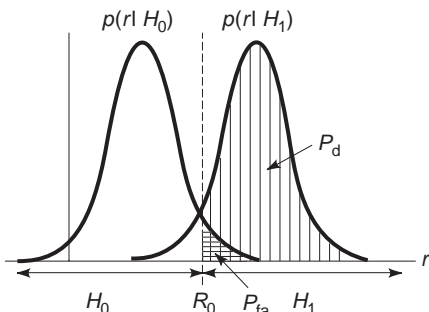


Figure 5. Probability of false alarm P_{fa} and probability of detection P_d , which are function of the threshold R_0 .

The integration interval in Eq. (17) is related to choosing the hypothesis H_1 , as illustrated in Fig. 5. It is clear that J and hence P_d are maximized by choosing the hypothesis H_1 when

$$p(r|H_1) - \eta p(r|H_0) > 0 \quad (18)$$

and by choosing the hypothesis H_0 when

$$p(r|H_1) - \eta p(r|H_0) < 0 \quad (19)$$

To this end, the decision rule based on the Neyman–Pearson criterion is

$$\begin{aligned} &H_1 \\ \Lambda(r) &\geq \eta \\ &H_0 \end{aligned} \quad (20)$$

and η is determined by the required false-alarm probability α . In radar detection, the choice of α is based on operational considerations, that is, the need to keep the false-alarm rate within acceptable bounds (e.g., a few false alarms per second). A typical value of α for radar detection is 10^{-6} .

Other popular criteria are the *Bayes criterion* and the *minimum error probability (MEP) criterion*. The Bayes criterion minimizes the average cost of the decision. Symbols denoted by C_{00} , C_{01} , C_{10} , and C_{11} represent the costs for a correct miss (no target is declared when no target is present), a false dismissal (no target is declared when a target is present), a false alarm, and a correct detection, respectively. Also denoted are the a priori probabilities $P(H_0)$ and $P(H_1)$ by P_0 and P_1 , respectively. The Bayes rule makes the likelihood ratio test

$$\begin{aligned} &H_1 \\ \Lambda(r) &\geq \eta \\ &H_0 \end{aligned} \quad (21)$$

where $\eta = [P_0(C_{10} - C_{00})]/[P_1(C_{01} - C_{11})]$. If we select the cost of an error to be 1 and the cost of a correct decision to be 0, $C_{01} = C_{10} = 1$, and $C_{00} = C_{11} = 0$. In this case, minimizing the average cost is equivalent to minimizing the probability of error. Therefore, the MEP rule is the same as expression Eq. (21), but with $\eta = P_0/P_1$. If the a priori probabilities are equal, that is, $P_0 = P_1$, the MEP rule coincides with the ML rule with $\eta = 1$.

1.3. Implementation of Decision Criteria

Let us suppose that the observed signal r has the following Gaussian distribution conditional probability density functions

$$p(r|H_0) = \frac{1}{\sqrt{2\pi}\sigma} e^{-r^2/(2\sigma^2)} \quad (22)$$

$$p(r|H_1) = \frac{1}{\sqrt{2\pi}\sigma} e^{-(r-\mu)^2/(2\sigma^2)} \quad (23)$$

where μ denotes the mean of the received signal value and σ^2 represents the noise variance. The likelihood ratio

test is therefore

$$\Lambda(r) = \frac{e^{(r-\mu)^2/(2\sigma^2)} H_1}{e^{r^2/(2\sigma^2)} H_0} \geq \eta \quad (24)$$

After taking the logarithm of both sides, the criterion becomes

$$R_0 \geq \frac{\sigma^2}{\mu} \ln \eta + \frac{\mu}{2} \quad (25)$$

In Eq. (25) it is seen that the likelihood ratio test, in which $\Lambda(r)$ of Eq. (24) is compared with a threshold η , is transformed into a comparison of the observable r with the threshold in Eq. (25), which is a function of η . As an example, supposing $P(H_0)$ and $P(H_1)$ are known, with $P(H_0)/P(H_1) = 2$, then the decision rules are choose H_1 if

For the maximum likelihood ($\eta = 1$): $R_0 > \frac{\mu}{2}$ (26)

For the minimum error probability ($\eta = 2$): $R_0 > \frac{\mu}{2} + \frac{\sigma^2 \ln 2}{\mu}$ (27)

Since the a priori probability of H_0 is twice that of H_1 , the MEP rule requires a larger value of R_0 for the selection of H_0 than the ML, in which this information is not used. The MEP scheme therefore yields a better decision rule in this case.

For a Neyman–Pearson criterion, suppose a value of $P_{fa} = 10^{-4}$ can be tolerated. The threshold η is determined from

$$P_{fa} = 10^{-4} = \int_{R_0}^{\infty} \frac{1}{\sqrt{2\pi}\sigma} e^{-x^2/(2\sigma^2)} dx \quad (28)$$

to be $\eta = 3.72 \sigma$. So H_1 is chosen if for the Neyman–Pearson rule ($P_{fa} = 10^{-4}$),

$$R_0 > 3.72\sigma \quad (29)$$

A typical illustration of these thresholds for this example’s three decision criteria is given in Fig. 6. An important observation is that these criteria employ the likelihood ratio test. In other words, the test is performed by simply processing the received data to yield the likelihood ratio and then comparing it with the threshold, which depends upon the criterion used. Thus, in practical situations where the a priori probabilities and the cost may vary, only the threshold changes, and the computation of the likelihood ratio is not affected.

As observed previously, in radar detection it is very hard to define the Bayes cost C_{ij} ; moreover, it is also practically impossible to define or evaluate the a priori probabilities P_0 and P_1 , that is, the probabilities that, in a given resolution interval, a target is present or absent. These are the main reason why the Bayes and minimum error probability criteria cannot be used in radar detection. In contrast, for the same reason, the Neyman–Pearson

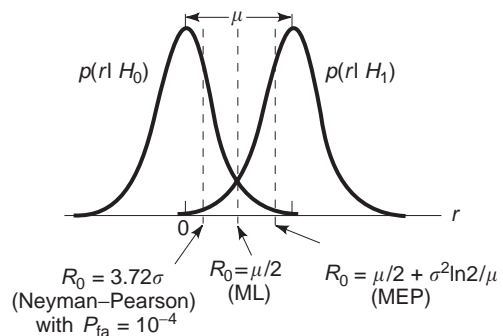


Figure 6. Decision thresholds for different decision criteria.

criterion is particularly well suited to radar detection, owing to its concept of the “ P_{fa} threshold” fixed a priori, while P_d is maximized.

1.4. Receiver Operating Characteristic

A graph showing the probability of detection, P_d , versus the probability of false alarm, P_{fa} , with the threshold as a parameter is referred to as a receiver operating characteristic (ROC) curve. We note that the ROC depends on the conditional density function of the observed signal under each hypothesis, that is, $p(r|H_i)$, $i = 0,1$, and not on the assigned costs, or a priori probabilities.

Suppose that the observed signal r has the probability density functions of Eqs. (22) and (23). Varying the threshold R_0 , P_d of Eq. (13), and P_{fa} of Eq. (14) produces the corresponding ROC curves for $\sigma = 1$ and $\mu = 1,2,3$ as shown in Fig. 7.

The two extreme points on the ROC for $P_{fa} = P_d = 1$ and $P_{fa} = P_d = 0$ are easily verified. P_d of Eq. (13) may be rewritten as a function of the likelihood ratio $\Lambda(r)$ as

$$P_d = \int_{\eta}^{\infty} p_{\Lambda}(\lambda|H_1) d\lambda \quad (30)$$

where η is threshold of the likelihood ratio just as R_0 is the threshold of the observed signal, and $p_{\Lambda}(\lambda|H_1)$ in Eq. (30) is the conditional probability density function of the variable Λ . Similarly, P_{fa} of Eq. (14) is rewritten as

$$P_{fa} = \int_{\eta}^{\infty} p_{\Lambda}(\lambda|H_0) d\lambda \quad (31)$$

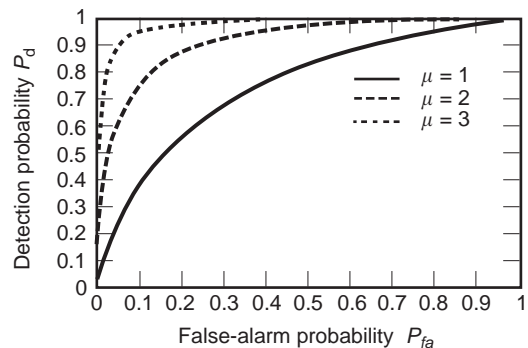


Figure 7. ROC curves for different values of μ .

Since Λ is a ratio of two nonnegative quantities, it takes on values from 0 to ∞ . When the threshold η is 0, the hypothesis H_1 is always true and thus $P_{fa} = P_d = 1$. When the threshold η is ∞ , the hypothesis H_0 is always true and thus $P_{fa} = P_d = 0$. These are clearly depicted in Fig. 7.

Of course, ROC curves may be drawn for any hypothesis test involving a threshold, but the ROC curves have particularly useful properties for the likelihood ratio test. One is the fact that the slope of the ROC at a particular point on the curve represents the threshold value of the likelihood ratio η . Taking the derivative of Eqs. (30) and (31) with respect to η we have

$$\frac{dP_d}{d\eta} = -p_{\Lambda}(\eta|H_1) \quad (32)$$

and

$$\frac{dP_{fa}}{d\eta} = -p_{\Lambda}(\eta|H_0) \quad (33)$$

Also,

$$\begin{aligned} P_d &= \int_{R_0}^{\infty} \Lambda(r)p(r|H_0) dr \\ &= \int_{\eta}^{\infty} \lambda p_{\Lambda}(\lambda|H_0) d\lambda \end{aligned} \quad (34)$$

Taking the derivative of Eq. (34) with respect to η , we obtain

$$\frac{dP_d}{d\eta} = -\eta p_{\Lambda}(\eta|H_0) \quad (35)$$

Combining Eqs. (32), (33), and (35), the slope of the ROC curve obtained is

$$\frac{dP_d}{dP_{fa}} = \frac{p_{\Lambda}(\eta|H_1)}{p_{\Lambda}(\eta|H_0)} = \eta \quad (36)$$

In the Neyman–Pearson criterion, the slope of the ROC curve at a particular point represents the likelihood ratio threshold η of achieving P_d and P_{fa} at that point. In the Bayes criterion, the threshold η is determined by a priori probabilities and the costs. Consequently, P_d and P_{fa} are determined on the point of the ROC at which the tangent has a slope of η .

Since the ROC curves are always concave and facing downward, it is possible to determine an “optimum” value (the knee) for P_{fa} , such that a small decrease of its value causes a fast decrease of P_d , while any increase has a very small effect (the saturation zone, where the rate of change is nearly 0.)

Finally, we note that the most important part of the ROC curve is the upper left-hand (northwest) corner. This is the so-called high-performance corner, where a high-detection probability occurs with a low false-alarm probability. This part of the plot could be stretched out by the use of appropriate (such as logarithmic) scales.

2. ANALYSIS OF A MATCHED FILTER

2.1. Derivation of the Matched Filter

The matched filter achieves the maximum output SNR, which is

$$\frac{S}{N} = \frac{\text{(maximum instantaneous output signal power)}}{\text{(output noise power)}} \quad (37)$$

Consider a signal $s(t)$ with the spectrum $S(f)$ and finite energy

$$E_s = \int_{-\infty}^{\infty} |s(t)|^2 dt = \int_{-\infty}^{\infty} |S(f)|^2 df \quad (38)$$

For the input signal $s(t)$ and the filter with transfer function $H(f)$, the instantaneous power of the output signal $y(t)$ is

$$|y(t)|^2 = \left| \int_{-\infty}^{\infty} S(f)H(f)e^{j2\pi ft} df \right|^2 \quad (39)$$

For white noise with a two-sided noise power spectral density $N_0/2$, the output power spectral density is $|H(f)|^2 N_0/2$. Therefore, the noise power at the filter output is

$$\sigma^2 = \frac{N_0}{2} \int_{-\infty}^{\infty} |H(f)|^2 df \quad (40)$$

Using Eqs. (39) and (40) in Eq. (37) leads to the following

$$\frac{S}{N} = \frac{\left| \int_{-\infty}^{\infty} S(f)H(f)e^{j2\pi fT} df \right|^2}{(N_0/2) \int_{-\infty}^{\infty} |H(f)|^2 df} \quad (41)$$

where T denotes the time at which the maximum value of $|y(t)|^2$ occurs.

Using Schwarz' inequality

$$\left| \int_{-\infty}^{\infty} f(x)g(x) dx \right|^2 \leq \int_{-\infty}^{\infty} |f(x)|^2 dx \int_{-\infty}^{\infty} |g(x)|^2 dx \quad (42)$$

we obtain

$$\frac{S}{N} \leq \frac{\int_{-\infty}^{\infty} |S(f)|^2 df \int_{-\infty}^{\infty} |H(f)|^2 df}{(N_0/2) \int_{-\infty}^{\infty} |H(f)|^2 df} \quad (43)$$

It follows that the signal-to-noise ratio will be a maximum when

$$H(f) = kS^*(f)e^{-j2\pi fT} \quad (44)$$

yielding the requirement of the matched filter. From discussions above it is evident that the maximum

signal-to-noise ratio can be expressed as

$$\text{SNR}|_{\max} = \frac{2E_s}{N_0} \tag{45}$$

Equation (45) indicates that the detection capability of a particular signal depends only on its energy content, and not on the time structure of the signal. However, it is necessary to process the signal through a matched filter to obtain this condition in practice. We note that E_s/N_0 is defined as the input SNR, and it is clear from Eq. (45) that the maximum output SNR for the matched filter is twice that of the input SNR if the noise is white.

In general case, when the noise is nonwhite (colored noise), the derivation of the matched filter can be carried out in a similar way. If the power spectral density of the nonwhite noise is $N(f)$, then Eq. (40) is written as

$$\sigma^2 = \int_{-\infty}^{\infty} N(f)|H(f)|^2 df \tag{46}$$

Therefore, by multiplying and dividing the integrand of the numerator of Eq. (41) by $\sqrt{N(f)}$ and using Eq. (46)

$$\begin{aligned} \frac{S}{N} &= \frac{\left| \int_{-\infty}^{\infty} \frac{S(f)}{\sqrt{N(f)}} H(f) \sqrt{N(f)} e^{j2\pi fT} df \right|^2}{\int_{-\infty}^{\infty} N(f) |H(f)|^2 df} \\ &\leq \frac{\int_{-\infty}^{\infty} |S(f)|^2 / N(f) df \int_{-\infty}^{\infty} |H(f)|^2 / N(f) df}{\int_{-\infty}^{\infty} |H(f)|^2 N(f) df} \\ &= \int_{-\infty}^{\infty} |S(f)|^2 / N(f) df \end{aligned} \tag{47}$$

and the maximum is achieved when

$$H(f) = \frac{kS^*(f)e^{-j2\pi fT}}{N(f)} \tag{48}$$

The conjugate is not needed in the denominator because $N(f)$ is always real (and nonnegative). If the noise is white—that is, if $N(f)$ is a constant over the band of $H(f)$ —then Eq. (48) is the same as Eq. (44) for the white noise. The matched filter for nonwhite noise can be interpreted as the cascade of two filters. The first one, whose transfer function is $1/\sqrt{N(f)}$, is the “whitening” filter. This filter makes the noise spectrum flat (white). The second one is matched to the signal filtered by the whitening filter, that is, to the whitening signal with the spectrum $S(f)/\sqrt{N(f)}$.

We note that it is not necessary that the noise be Gaussian for Eq. (45) to hold, but only that its power spectral density be flat over the frequency band of interest. To summarize, the matched filter maximizes the output SNR over all probability densities, provided the power spectral density (PSD) is a constant. In the event that the noise PSD is nonwhite (colored noise), the matched

impulse response corresponds to the modified signal spectrum $S^*(f)e^{-j2\pi fT}/\sqrt{N(f)}$ rather than simply $S^*(f)e^{-j2\pi fT}$.

2.2. Justification of the Signal-to-Noise Ratio Criterion

We derived the matched filter under the criterion of maximizing the output SNR. We remark here that the matched filter can also be derived under the likelihood ratio criterion [1]. In this section, we want to justify the maximum output SNR criterion, and more specifically derive the relationship between the output SNR and the system performance in terms of the probability of error.

The total probability of error for a radar receiver consists of the false-alarm probability P_{fa} and the false-dismissal probability P_{fd} . A false dismissal declares no target when a target is present:

$$P_{fd} = \int_{-\infty}^{R_0} p(r|H_1) dr \tag{49}$$

For equal a priori probabilities $P(H_0) = P(H_1) = \frac{1}{2}$, the total probability of error is

$$\begin{aligned} P_e &= \frac{1}{2}(P_{fd} + P_{fa}) \\ &= \frac{1}{2} + \frac{1}{2} \int_{-\infty}^{R_0} [p(r|H_1) - p(r|H_0)] dr \end{aligned} \tag{50}$$

Supposing $p(r|H_i)$, $i = 0,1$ is a Gaussian distribution that is given by Eqs. (22) and (23), P_e can be expressed as

$$\begin{aligned} P_e &= \frac{1}{2} - \frac{1}{2} \left(\frac{1}{\sqrt{\pi}} \int^{(\mu-R_0)/\sqrt{2\sigma}} e^{-r^2} dr + \frac{1}{\sqrt{\pi}} \int_0^{R_0/\sqrt{2\sigma}} e^{-r^2} dr \right) \\ &= \frac{1}{2} - \frac{1}{4} \left[\text{erf} \left(\frac{\mu - R_0}{\sqrt{2\sigma}} \right) + \text{erf} \left(\frac{R_0}{\sqrt{2\sigma}} \right) \right] \end{aligned} \tag{51}$$

where

$$\text{erf}(x) = \frac{2}{\pi} \int_0^x e^{-r^2} dr \tag{52}$$

is the error function. The minimum of P_e occurs when $R_0 = \mu/2$, and

$$P_e|_{\min} = \frac{1}{2} \text{erfc} \left(\frac{\mu/2}{\sqrt{2\sigma}} \right) \tag{53}$$

where

$$\text{erfc}(x) = 1 - \text{erf}(x) = \frac{2}{\sqrt{\pi}} \int_x^{\infty} e^{-r^2} dr \tag{54}$$

is the complementary error function. Recalling that μ is the expectation of the matched filter output at time T under the H_1 hypothesis

$$\mu = E[y(T)|H_1] = E \left[\int_0^T [s(\tau) + n(\tau)]s(\tau) d\tau \right] = E_s \tag{55}$$

and

$$E[y(T)|H_0] = E\left[\int_0^T n(\tau)s(\tau) d\tau\right] = 0 \quad (56)$$

Defining σ^2 to be the variance of $y(T)$ under the H_0 or H_1 hypotheses, it is given that

$$\begin{aligned} \sigma^2 &= \text{Var}[y(T)|H_1] = \text{Var}[y(T)|H_0] \\ &= \int_0^T \int_0^T E[n(t)n(\tau)]s(t)s(\tau) dt d\tau \\ &= \frac{N_0}{2} \int_0^T \int_0^T \delta(t-\tau)s(t)s(\tau) dt d\tau \\ &= \frac{1}{2} E_s N_0 \end{aligned} \quad (57)$$

The application of Eqs. (55) and (57) to Eq. (53) leads to the following minimum probability of error:

$$\begin{aligned} P_{e|\min} &= \frac{1}{2} \text{erfc}\left(\sqrt{\frac{E_s}{4N_0}}\right) \\ &= \frac{1}{2} \text{erfc}\left(\sqrt{\frac{\text{SNR}|_{\max}}{8}}\right) \end{aligned} \quad (58)$$

It is clear from Eq. (58) that $P_{e|\min}$ is inversely proportional to $\text{SNR}|_{\max}$, because $\text{erfc}(x)$ is a monotonic decreasing function. In other words, a lower probability of error means a higher output SNR, and requires a higher input SNR. Figure 8 shows the relationship between $P_{e|\min}$ and $\text{SNR}|_{\max}$. This curve should be shifted to the left by 3 dB if it is plotted with respect to the input SNR, since $\text{SNR}|_{\max}$ is twice the input SNR. For example, a 10^{-5} error probability corresponds to an output SNR of 18.6 dB, and 15.6 dB of input SNR is required. Therefore, it is justifiable to use the signal-to-noise ratio criterion in radar detection.

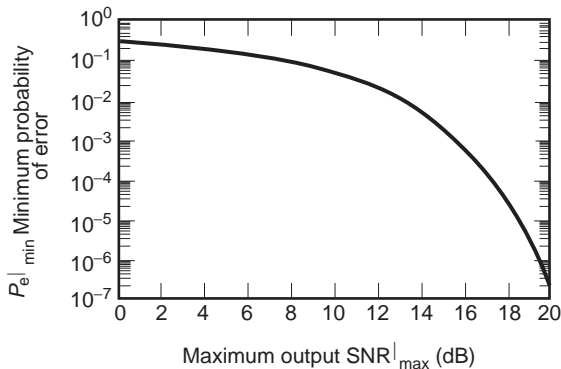


Figure 8. Minimum error probability $P_{e|\min}$ versus maximum output signal-to-noise ratio $\text{SNR}|_{\max}$.

3. NONCOHERENT DETECTIONS

A received radar signal is a *bandpass* random process because it is modulated on a carrier. Radar detection is classified into coherent and noncoherent detections depending upon whether the carrier phase at the receiver is available. Specifically, the matched filter and the cross-correlation discussed previously are coherent because they require the knowledge of the carrier phase. The envelope and all the other nonlinear detections are noncoherent due to their ignorance of the phase information in the received signal. To understand the nonlinear detections, we introduce the representations of bandpass signals and bandpass processes.

3.1. Representation of Bandpass Signals

The concept of a bandpass signal is a generalization of the concept of monochromatic signals. A bandpass signal is a signal $x(t)$ whose spectrum $X(f)$ is nonzero for frequencies in a usually small neighborhood of some high frequency f_0 , that is

$$X(f) = 0 \text{ for } |f - f_0| \geq W \quad (59)$$

where the frequency f_0 is referred to as the central frequency (carrier frequency) of the bandpass signal. A radar signal that is modulated on a carrier is a bandpass signal. It is assumed that the bandpass signal is real-valued. Figure 9a illustrates the spectrum of a bandpass

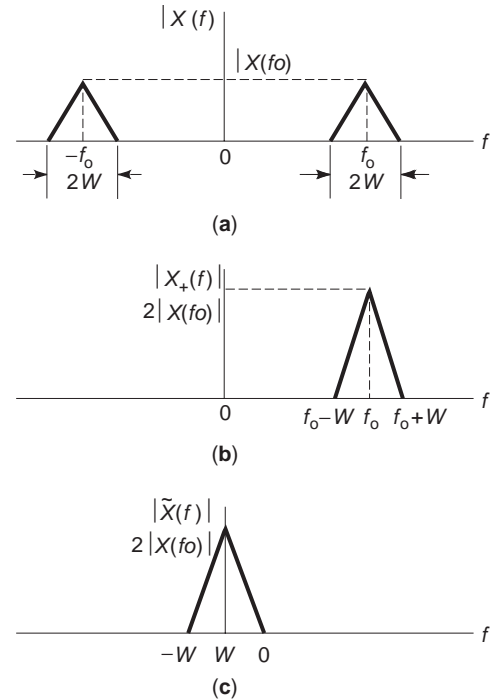


Figure 9. (a) Amplitude spectrum of a bandpass signal $x(t)$; (b) amplitude spectrum of pre-envelope $x_+(t)$; (c) amplitude spectrum of complex envelope $\tilde{x}(t)$. The spectrum of $x_+(t)$ is twice the positive spectrum of $x(t)$, and the spectrum $\tilde{x}(t)$ is a lowpass version of that $x_+(t)$.

signal $x(t)$. A real-valued bandpass signal $x(t)$ can be represented as the real part of a complex signal $x_+(t)$, called the *preenvelope* or *analytic signal* of $x(t)$, where

$$x_+(t) = x(t) + j\hat{x}(t) \tag{60}$$

and

$$\hat{x}(t) = \frac{1}{\pi} \int_{-\infty}^{\infty} \frac{x(\tau)}{t - \tau} d\tau \tag{61}$$

is the Hilbert transform of $x(t)$. The spectrum of the preenvelope signal is readily found from the Fourier transform of Eq. (60) to be

$$X_+(f) = X(f) + X(f) \operatorname{sgn}(f) = \begin{cases} 2X(f), & f > 0 \\ X(0), & f = 0 \\ 0, & f \leq 0 \end{cases} \tag{62}$$

The spectrum of the preenvelope signal is obtained by deleting the negative frequencies from $X(f)$ and multiplying the positive frequencies in $X(f)$ by 2, as illustrated in Fig. 9b.

The spectrum of the *complex envelope* is obtained by shifting $X_+(f)$ to the left by f_0 , that is

$$\tilde{X}(f) = X_+(f + f_0) \tag{63}$$

and

$$\tilde{x}(t) = x_+(t) e^{-j2\pi f_0 t} \tag{64}$$

The amplitude spectrum of $\tilde{x}(t)$ is illustrated in Fig. 9c.

It is clear that $\tilde{x}(t)$ is a lowpass signal, meaning that its frequency components are located around the zero frequency. $\tilde{x}(t)$ is the lowpass representation of the bandpass signal $x(t)$. In general, $\tilde{x}(t)$ is a complex signal having $x_c(t)$ and $x_s(t)$ as its real and imaginary parts

$$\tilde{x}(t) = x_c(t) + jx_s(t) \tag{65}$$

where $x_c(t)$ and $x_s(t)$ are lowpass signals, respectively, and are called the *in-phase* and *quadrature* components of the bandpass signal $x(t)$. Notice that $x(t)$ is the real part

of $x_+(t)$. Using Eq. (65), we obtain

$$x(t) = \operatorname{Re} [\tilde{x}(t) e^{j2\pi f_0 t}] \tag{66} = x_c(t) \cos(2\pi f_0 t) - x_s(t) \sin(2\pi f_0 t)$$

This is the *canonical representation* for a bandpass signal in terms of the in-phase component $x_c(t)$ and quadrature component $x_s(t)$ of the complex envelope associated with the signal.

The complex envelop can be employed to find the outputs of bandpass systems driven by bandpass signals. Accordingly, by analyzing the complex envelope representation of a bandpass signal, we may develop the complex lowpass representation of the bandpass system by retaining the positive-frequency half of the transfer function $H(f)$, and shift it to the left by f_0 . Let $\tilde{H}(f)$ denote the transfer function of the complex lowpass system so defined. The analysis of the bandpass system with transfer function $H(f)$ driven by the bandpass signal with spectrum $X(f)$, as depicted in Fig. 10a, is replaced by an equivalent but simpler analysis of a complex lowpass system with transfer function $\tilde{H}(f)$ driven by a complex lowpass input with spectrum $\tilde{X}(f)$, as shown in Fig. 10b. The complex lowpass output $\tilde{y}(t)$ is obtained from the inverse Fourier transform of $\tilde{Y}(f)$. Having determined $\tilde{y}(t)$, we may find the desired bandpass output $y(t)$ simply by using the relation

$$y(t) = \operatorname{Re} [\tilde{y}(t) e^{j2\pi f_0 t}] \tag{67}$$

The bandpass to lowpass transformation is also true for bandpass random processes. $X(t)$ is a bandpass process if its power spectral density $S_x(f) = 0$ for $|f - f_0| \geq W$. $X(t)$ can be represented by its in-phase component $X_c(t)$ and quadrature component $X_s(t)$ in the same way that a bandpass signal does. Specifically

$$X(t) = X_c(t) \cos(2\pi f_0 t) - X_s(t) \sin(2\pi f_0 t) \tag{68}$$

where $X_c(t)$ and $X_s(t)$ are two lowpass processes representing the real and imaginary parts of the complex envelope process $\tilde{X}(t)$ respectively. $X(t)$ can be found from the complex envelope process $\tilde{X}(t)$ by

$$X(t) = \operatorname{Re} [\tilde{X}(t) e^{j2\pi f_0 t}] \tag{69}$$

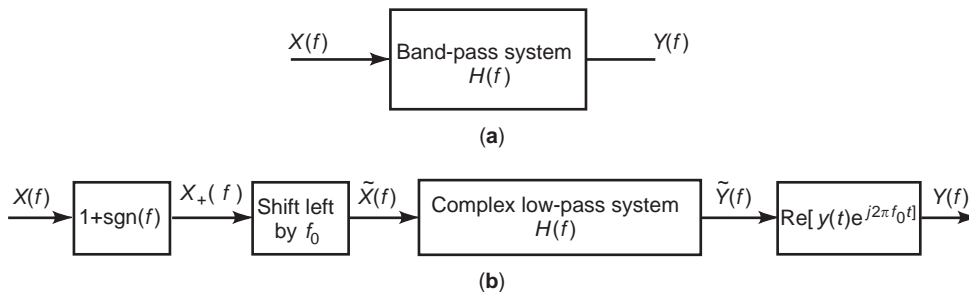


Figure 10. (a) Bandpass description and (b) complex envelope description of a system. Complex envelope description simplifies the analysis of a bandpass signal.

3.2. Envelope Detection and Square-Law Detection

The matched filter is the optimal detection for an exactly known signal (i.e., phase, amplitude, and Doppler frequency are known) in a background of white noise. However, both the matched filter and the cross-correlation need to generate a synchronous reference, which is difficult to realize. In a typical radar application, the range between the target and the radar represents a very large number of transmitted signal wavelengths. This makes specifying the phase of the return signal extremely difficult, and we usually assume that the signal phase of the return signal is a random variable uniformly distributed over an angle of 2π rad. The matched-filter detection is often used to set a standard of performance, as it represents the optimal detection when all signal parameters are exactly known.

The synchronization problem in the matched-filter detection is obviated in a practical system by employing an envelope detection. The envelope $V(t)$ of a bandpass signal $x(t)$ is given by

$$V(t) = \sqrt{x_s^2(t) + x_c^2(t)} \quad (70)$$

The complex envelope $\tilde{x}(t)$ can be represented more compactly as

$$\tilde{x}(t) = V(t)e^{j\theta(t)} \quad (71)$$

where

$$\theta(t) = \arctan \frac{x_s(t)}{x_c(t)} \quad (72)$$

The procedure for obtaining the envelope is shown in Fig. 11, which is the extraction of the in-phase and quadrature components and the derivation of the envelope from them. Specifically, the multiplication of $x(t)$ by $2 \cos(2\pi f_0 t)$ in the in-phase channel yields

$$\begin{aligned} 2x(t) \cos(2\pi f_0 t) &= 2 \cos(2\pi f_0 t) [x_c(t) \cos(2\pi f_0 t) \\ &\quad - x_s(t) \sin(2\pi f_0 t)] \\ &= x_c(t) + x_c(t) \cos(4\pi f_0 t) \\ &\quad - x_s(t) \sin(4\pi f_0 t) \end{aligned} \quad (73)$$

The mixing operation produces two images besides the expected lowpass component. The product $2x(t) \cos(2\pi f_0 t)$ is passed through an ideal lowpass filter (the integrator in Fig. 11), which rejects the images and leaves $x_c(t)$. Similar operations in the quadrature channel produce $x_s(t)$. The square sum of the quadrature components yields the envelope $V(t)$.

Removing the square-root operation from Fig. 11 yields the square-law detection. A detailed performance analysis of these detections is given in Section 4.

The envelop can be extracted alternatively by passing the bandpass signal $x(t)$ through a rectified and a lowpass filter, as illustrated in Fig. 12. Such a description can

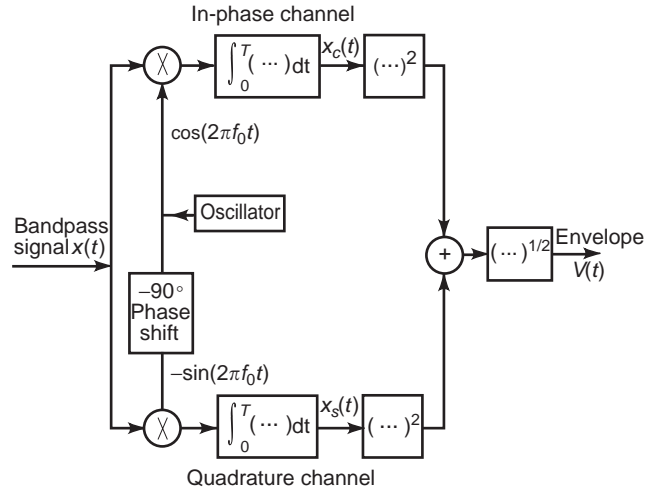


Figure 11. Block diagram of the envelope detection.

sometimes simplify the analysis and is easier to implement physically because the various rectifiers are readily available from the diodes and the transistors. The output of the full-wave linear rectifier is proportional to the magnitude of its input, while the output of the full-wave square-law (quadratic) rectifier is proportional to the squared magnitude of its input. The half-wave rectifier, of course, gives only the positive portion of its input. Fig. 13 shows these transfer characteristics. Referring to Fig. 12, we may write

$$V(t) = \text{Env}[x(t)] = \text{LF}[|x(t)|] \quad (74)$$

where LF indicates the low-frequency portion. Also, considering the full-wave quadratic rectifier in place of the full-wave linear rectifier, we may write

$$V^2(t) = \text{LF}[x^2(t)] \quad (75)$$

The band-pass signal $x(t)$ in Eqs. (74) and (75) has the following form:

$$x(t) = V(t) \cos[2\pi f_0 t + \theta(t)] \quad (76)$$

Then in the case of the square-law rectifier, we have

$$\begin{aligned} x^2(t) &= V^2(t) \cos^2[2\pi f_0 t + \theta(t)] \\ &= \frac{1}{2} V^2(t) + \frac{1}{2} V^2(t) \cos[4\pi f_0 t + 2\theta(t)] \end{aligned} \quad (77)$$

Since the envelope $V(t)$ is slowly varying compared to the carrier frequency f_0 , the first term in Eq. (77) is concentrated around zero frequency. The fact that the term is the square of the envelop means that the bandwidth will be somewhat greater than that of $V(t)$. The second term in Eq. (77) will be concentrated around $2f_0$ with a bandwidth

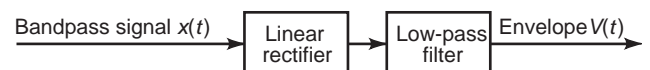


Figure 12. Envelope detection with a linear rectifier.

that depends on both the envelop square $V^2(t)$ and the phase modulation $\theta(t)$. In most cases of interest, the bandwidth of the total modulation will be small enough compared to f_0 so that the lowpass filter following the rectifier will easily separate the low-frequency portion of Eq. (77).

In the case of the full-wave linear rectifier, we may write

$$\begin{aligned}
 |x(t)| &= V(t) |\cos[2\pi f_0 t + \theta(t)]| \\
 &\approx \frac{2V(t)}{\pi} \left\{ 1 + \frac{2}{3} \cos[4\pi f_0 t + 2\theta(t)] \right. \\
 &\quad \left. - \frac{2}{15} \cos[8\pi f_0 t + 4\theta(t)] + \dots \right\}
 \end{aligned}
 \tag{78}$$

The lowpass filter will remove all of the terms in the curly bracket except for the first term. Thus, if the bandwidth of $V(t)$ is not too large, a very good approximation of the envelope can be obtained. A similar analysis can be carried out to show that the half-wave linear and the half-wave quadratic rectifiers extract the envelope $V(t)$.

We note that the envelope detection is referred to as a linear detection, due to its transfer characteristic stipulating that the output is proportional to the input when the input is positive, as illustrated in Fig. 13a. The operation of the envelope detection, however, is of course highly nonlinear, and as a result the output consists of a DC term proportional to the envelope, plus an infinite number of harmonics of the input at $2f_0$, $4f_0$, and so on. It is for this reason that the envelope detection must be passed through a lowpass filter, thus eliminating the unwanted harmonics. Similar comments apply to the square-law detection.

3.3. Justification of the Noncoherent Detections

The justification of the envelope and the square-law detections by the likelihood ratio criterion is given in

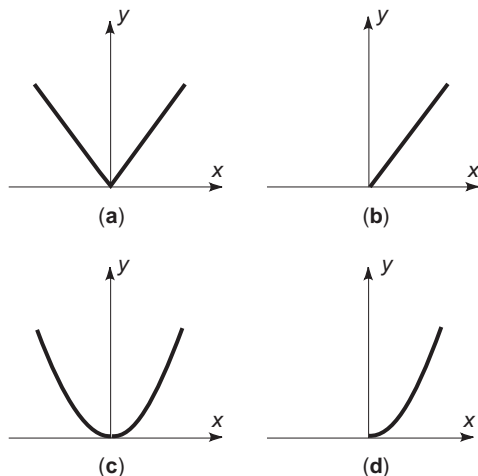


Figure 13. Various rectifier characteristics for (a) full-wave linear rectifier, (b) half-wave linear rectifier, (c) full-wave square-law (quadratic) rectifier, and (d) half-wave square-law (quadrature) rectifier.

this subsection. The radar detection process may include downconversion of the carrier frequency to a more manageable intermediate frequency (IF). This step, however, is irrelevant to the results we are going to obtain and is therefore omitted. Consider the signal to be a carrier pulse of the form

$$s(t) = \begin{cases} A \cos(2\pi f_0 t + \theta), & 0 \leq t \leq T \\ 0, & \text{otherwise} \end{cases}
 \tag{79}$$

The two hypotheses are

$$\begin{aligned}
 H_1 : r(t) &= s(t) + n(t) = A \cos(2\pi f_0 t + \theta) + n(t) \\
 H_0 : r(t) &= n(t)
 \end{aligned}
 \tag{80}$$

for $0 \leq t \leq T$, and $n(t)$ is a Gaussian white-noise process with two-sided spectral density $N_0/2$.

The detection problem described by Eq. (79) consists of examining the received waveform $r(t)$ and determining whether it consists of a signal plus noise or noise alone. The optimal detection, as described previously, forms the likelihood ratio which is compared against a threshold.

The sampling bandwidth B , which is the reciprocal of the sampling interval, must be sufficiently large to pass along essentially all of the signal energy, which will be the case if $B \geq 1/T$. In this case, by the sampling theorem we know that the number of samples k is given by $k = 2BT$. Given these conditions, the likelihood ratio can be written as

$$\begin{aligned}
 \Lambda(r) &= \frac{\exp\left(-\frac{1}{2\sigma^2} \sum_{i=1}^{2BT} [r(t_i) - s(t_i)]^2\right)}{\exp\left(-\frac{1}{2\sigma^2} \sum_{i=1}^{2BT} r^2(t_i)\right)} \\
 &= \exp\left(\frac{1}{2\sigma^2} \sum_{i=1}^{2BT} [2r(t_i)s(t_i) - s^2(t_i)]\right)
 \end{aligned}
 \tag{81}$$

where the noise variance σ^2 is $(N_0/2)2B = N_0B$. Recall from the sampling theorem [2,3] that for any two band-limited functions $u(t)$ and $v(t)$ we can write

$$\begin{aligned}
 &\int_{-\infty}^{\infty} u(t)v(t) dt \\
 &= \sum_n \sum_m u\left(\frac{n}{2B}\right)v\left(\frac{m}{2B}\right) \int_{-\infty}^{\infty} \frac{\sin 2\pi B(t - n/2B)}{2\pi B(t - n/2B)} \\
 &\quad \frac{\sin 2\pi B(t - m/2B)}{2\pi B(t - m/2B)} dt \\
 &= \frac{1}{2B} \sum_{n=-\infty}^{\infty} u\left(\frac{n}{2B}\right)v\left(\frac{n}{2B}\right)
 \end{aligned}
 \tag{82}$$

Applying this to Eq. (81), we have

$$\begin{aligned}\Lambda(r) &= \exp\left(\frac{1}{N_0} \int_0^T [2r(t)s(t) - s^2(t)] dt\right) \\ &= \exp\left(\frac{1}{N_0} \int_0^T [2r(t)A \cos(2\pi f_0 t + \theta) \right. \\ &\quad \left. - A^2 \cos^2(2\pi f_0 t + \theta)] dt\right)\end{aligned}\quad (83)$$

Because the signal is of finite duration, the approximation in passing from the discrete to the continuous representation improves as B is allowed to become very large.

In the noncoherent case, θ in Eq. (83) is unknown. Since no auxiliary information about θ is available, it is reasonable to assume θ to be uniformly distributed over 2π rad. An average likelihood ratio is

$$\begin{aligned}\Lambda(r)_{\text{av}} &= \int_0^{2\pi} \Lambda(r)p(\theta) d\theta \\ &= \frac{\exp(-A^2 T/2N_0)}{2\pi} \int_0^{2\pi} \\ &\quad \left[\exp\left(-\frac{2A}{N_0} \int_0^T r(t) \cos(2\pi f_0 t + \theta) dt\right) \right]\end{aligned}\quad (84)$$

The exponent in the integrand can be written as

$$\begin{aligned}-\frac{2A}{N_0} \int_0^T r(t) \cos(2\pi f_0 t + \theta) dt \\ = -\frac{2A}{N_0} X_c \cos \theta + \frac{2A}{N_0} X_s \sin \theta\end{aligned}\quad (85)$$

where

$$X_c = \int_0^T r(t) \cos(2\pi f_0 t) dt, \quad X_s = \int_0^T r(t) \sin(2\pi f_0 t) dt \quad (86)$$

and Eq. (84) becomes

$$\begin{aligned}\Lambda(r)_{\text{av}} &= \exp\left(-\frac{A^2 T}{2N_0}\right) \int_0^{2\pi} \exp\left(-\frac{2A}{N_0} (X_c \cos \theta - X_s \sin \theta)\right) \frac{d\theta}{2\pi} \\ &= \exp\left(-\frac{A^2 T}{2N_0}\right) I_0\left(\frac{2AV}{N_0}\right)\end{aligned}\quad (87)$$

where $V = \sqrt{X_c^2 + X_s^2}$ and I_0 is the modified Bessel function of order zero. The likelihood ratio test is therefore

$$\ln \left[I_0\left(\frac{2AV}{N_0}\right) \right] \underset{H_0}{\overset{H_1}{\geq}} (E_s/N_0)\eta \quad (88)$$

where the signal energy $E_s = A^2 T/2$. Thus the natural logarithm of the modified Bessel function I_0 is the optimum noncoherent detection characteristic. For a large SNR, the likelihood ratio test can be approximated as

$$\ln \left[I_0\left(\frac{2AV}{N_0}\right) \right] \underset{H_0}{\overset{H_1}{\approx}} \frac{2AV}{N_0} \geq (E_s/N_0)\eta \quad (89)$$

and for a small SNR

$$\ln \left[I_0\left(\frac{2AV}{N_0}\right) \right] \underset{H_0}{\overset{H_1}{\approx}} \frac{A^2 V^2}{2N_0^2} \geq (E_s/N_0)\eta \quad (90)$$

The implementation of the likelihood ratio test of Eq. (89) has been shown in Fig. 11, where the in-phase and the quadrature channels generate the x_c and x_s in Eq. (86), respectively. Summation of the square of x_c and x_s yields the square-law detection of Eq. (90). Taking the square root in addition to the square-law detection yields the envelope detection of Eq. (89).

4. PERFORMANCE ANALYSIS OF COHERENT AND NONCOHERENT DETECTIONS

4.1. Detection Probability Analysis

From the mean and the variances given by Eqs. (55)–(57), the false-alarm probability P_{fa} for the coherent detection is determined by

$$\begin{aligned}P_{\text{fa}} &= \int_{R_0}^{\infty} \frac{1}{\sqrt{\pi E_s N_0}} \exp(-x^2/E_s N_0) dx \\ &= \frac{1}{\sqrt{\pi}} \int_{R_0/\sqrt{E_s N_0}}^{\infty} e^{-x^2} dx \\ &= \frac{1}{2} \operatorname{erfc}\left(\frac{R_0}{\sqrt{E_s N_0}}\right)\end{aligned}\quad (91)$$

The detection probability P_d is given by

$$\begin{aligned}P_d &= \int_{R_0}^{\infty} \frac{1}{\sqrt{\pi E_s N_0}} \exp(-(x-E_s)^2/E_s N_0) dx \\ &= \frac{1}{\sqrt{\pi}} \int_{(R_0-E_s)/\sqrt{E_s N_0}}^{\infty} e^{-x^2} dx \\ &= \frac{1}{2} \operatorname{erfc}\left(\frac{R_0-E_s}{\sqrt{E_s N_0}}\right)\end{aligned}\quad (92)$$

For the noncoherent detection, the in-phase and the quadrature components from Eq. (86) are

$$\begin{aligned}
 X_c &= \int_0^T r(t) \cos(2\pi f_0 t) dt = \int_0^T A \cos(2\pi f_0 t + \theta) \cos(2\pi f_0 t) dt \\
 &+ \int_0^T n(t) \cos(2\pi f_0 t) dt = \frac{AT}{2} \cos \theta \\
 &+ \int_0^T n(t) \cos(2\pi f_0 t) dt \\
 X_s &= \frac{AT}{2} \sin \theta + \int_0^T n(t) \cos(2\pi f_0 t) dt \tag{93}
 \end{aligned}$$

For white Gaussian noise with two-sided spectral density $N_0/2$, we have the following quantities:

$$\begin{aligned}
 E[X_c] &= \frac{AT}{2} \cos \theta \\
 E[X_s] &= \frac{AT}{2} \sin \theta \\
 \text{Var}[X_c] &= \text{Var}[X_s] \tag{94} \\
 &= E \left[\int_0^T \int_0^T n(s)n(t) \cos(2\pi f_0 t) \cos(2\pi f_0 s) dt ds \right] \\
 &= \frac{N_0 T}{4}
 \end{aligned}$$

and therefore the joint probability density functions can be written as

$$\begin{aligned}
 p_1(X_c, X_s | \theta) &= \frac{1}{\pi N_0 T / 2} \\
 &\exp \left(- \frac{(X_c - AT \cos \theta / 2)^2 + (X_s - AT \sin \theta / 2)^2}{N_0 T / 2} \right) \tag{95} \\
 p_0(X_c, X_s) &= \frac{1}{\pi N_0 T / 2} \exp \left(- \frac{X_c^2 + X_s^2}{N_0 T / 2} \right)
 \end{aligned}$$

under the H_1 and H_0 hypotheses, respectively. The averaged joint probability density function of $p_1(X_c, X_s | \theta)$ is

$$\begin{aligned}
 p_{1,av}(X_c, X_s | \theta) &= \int_0^{2\pi} \frac{1}{2\pi} p_1(X_c, X_s | \theta) d\theta \\
 &= \int_0^{2\pi} \frac{1}{2\pi} \frac{1}{\pi N_0 T / 2} \\
 &\exp \left(- \frac{X_c^2 + X_s^2 - AT(\cos \theta)X_c - AT(\sin \theta)X_s + A^2 T^2 / 4}{N_0 T / 2} \right) d\theta \\
 &= \frac{1}{\pi N_0 T / 2} \exp \left(- \frac{X_c^2 + X_s^2 + A^2 T^2 / 4}{N_0 T / 2} \right) \\
 &I_0 \left(\frac{2\sqrt{A^2 T^2 (X_c^2 + X_s^2) / 4}}{N_0 T / 2} \right) \tag{96}
 \end{aligned}$$

For an envelope ($V = \sqrt{X_c^2 + X_s^2}$) detection, let $X_c = V \cos \theta$, $X_s = V \sin \theta$, then $dX_c dX_s = V dV d\theta$. We have

$$\begin{aligned}
 p_{1,av}(V) &= \int_0^{2\pi} p_{1,av}(V, \theta) d\theta \\
 &= \int_0^{2\pi} \frac{V}{\pi N_0 T / 2} \exp \left(- \frac{V^2 + A^2 T^2 / 4}{N_0 T / 2} \right) I_0 \left(\frac{2AV}{N_0} \right) d\theta \\
 &= \frac{4V}{N_0 T} \exp \left(- \frac{V^2 + A^2 T^2 / 4}{N_0 T / 2} \right) I_0 \left(\frac{2AV}{N_0} \right) \tag{97}
 \end{aligned}$$

which is a Rice distribution.

Under the H_0 hypothesis, we substitute $A = 0$ and use $I_0(0) = 1$ in Eq. (97) to obtain the following Rayleigh distribution:

$$p_0(V) = \frac{4V}{N_0 T} \exp \left(- \frac{V^2}{N_0 T / 2} \right) \tag{98}$$

The threshold R_0 is therefore determined from the false-alarm probability P_{fa} using

$$P_{fa} = \int_{R_0}^{\infty} \frac{4V}{N_0 T} \exp \left(- \frac{V^2}{N_0 T / 2} \right) dV = \exp \left(- \frac{R_0^2}{N_0 T / 2} \right) \tag{99}$$

as

$$R_0 = \sqrt{-\frac{N_0 T}{2} \ln P_{fa}} \tag{100}$$

And the detection probability P_d is given by

$$P_d = \int_{R_0}^{\infty} \frac{4V}{N_0 T} \exp \left(- \frac{V^2 + A^2 T^2 / 4}{N_0 T / 2} \right) I_0 \left(\frac{2AV}{N_0} \right) dV \tag{101}$$

This can be put into a more convenient dimensionless form with the changing of variable $x = V / \sqrt{N_0 T / 4}$ from which

$$P_d = \int_{(-2 \ln P_{fa})^{1/2}}^{\infty} x \exp \left(- \frac{x^2 + \alpha^2}{2} \right) I_0(\alpha x) dx \tag{102}$$

where

$$\alpha^2 = A^2 T / N_0 = 2E_s / N_0 \tag{103}$$

For a square-law ($Z = X_c^2 + X_s^2$) detection, let $X_c = \sqrt{Z} \cos \theta$, $X_s = \sqrt{Z} \sin \theta$; then $dX_c dX_s = \frac{1}{2} dZ d\theta$. From Eq. (96) we have

$$\begin{aligned}
 p_{1,av}(Z) &= \int_0^{2\pi} \frac{1}{\pi N_0 T} \exp \left(- \frac{Z + A^2 T^2 / 4}{N_0 T / 2} \right) I_0 \left(\frac{\sqrt{A^2 T^2 Z}}{N_0 T / 2} \right) d\theta \\
 &= \frac{2}{N_0 T} \exp \left(- \frac{Z + A^2 T^2 / 4}{N_0 T / 2} \right) I_0 \left(\frac{\sqrt{A^2 T^2 Z}}{N_0 T / 2} \right) \tag{104}
 \end{aligned}$$

which is a noncentral χ^2 distribution. Under H_0 , we have the following central χ^2 distribution:

$$p_0(Z) = \frac{2}{N_0 T} \exp\left(-\frac{Z}{N_0 T/2}\right) \quad (105)$$

The threshold R_0 can be determined from the false-alarm probability P_{fa} , which is given by

$$\begin{aligned} P_{\text{fa}} &= \int_{R_0}^{\infty} \frac{2}{N_0 T} \exp\left(-\frac{Z}{N_0 T/2}\right) dZ \\ &= \exp\left(-\frac{R_0}{N_0 T/2}\right) \end{aligned} \quad (106)$$

to be

$$R_0 = -\frac{N_0 T}{2} \ln P_{\text{fa}} \quad (107)$$

The detection probability P_d is given by

$$\begin{aligned} P_d &= \int_{R_0}^{\infty} \frac{2}{N_0 T} \exp\left(-\frac{Z + A^2 T^2/4}{N_0 T/2}\right) \\ &\quad \times I_0\left(\frac{\sqrt{A^2 T^2 Z}}{N_0 T/2}\right) dZ \end{aligned} \quad (108)$$

Changing the variable $x = Z/N_0 T/4$ in Eq. (108) yields a more convenient dimensionless form

$$P_d = \int_{-2 \ln P_{\text{fa}}}^{\infty} \frac{1}{2} \exp\left(-\frac{x + \alpha^2}{2}\right) I_0(\alpha \sqrt{x}) dx \quad (109)$$

where α is given by Eq. (103). Changing the variable $y = \sqrt{x}$ in Eq. (109) leads to the interesting result that P_d is identical to that given by Eq. (102) for the envelope detection. Note that the difference between the envelope and the square-law detector concerns the presence or absence of the square-root operation. Supposing for a square-law detection that an observation value is greater than R_0 of Eq. (107); then the square root of this value must be greater than R_0 of Eq. (100) for the envelope detection. Therefore, the square-law detection and the envelope detection bear the same detection characteristics.

The P_d 's in Eqs. (92), (102), and (109) show explicitly that the detection probabilities depend only on P_{fa} and the signal-to-noise ratio E_s/N_0 . Note that, in addition to P_{fa} , the detection threshold R_0 depends on the received signal energy in the coherent case of Eq. (91), but only on the noise and the integration time in the noncoherent case of Eqs. (100) and (107), which is somewhat more convenient.

A comparison of coherent and noncoherent detections is presented in Fig. 14 in terms of the value of P_d that can be achieved for a given value of P_{fa} as a function of signal-to-noise ratio E_s/N_0 . We note the following: (1) For small values of E_s/N_0 (say, less than 3 dB) for any given value of P_{fa} , noncoherent detection requires 2–3 dB more SNR than that required by coherent detection in order to achieve the

same value of detection and (2) for large values of E_s/N_0 (say, greater than 10 dB) the difference in SNR required by the two schemes is less than approximately 1 dB, and it is clear that with further increase E_s/N_0 , the difference eventually becomes negligible.

4.2. Output Signal-to-Noise Analysis

To evaluate the detection performance, we can compare output SNRs of different schemes other than the detection probabilities we used in the last section. Recall that the SNR is the ratio between the signal power and the noise variance. The signal power is the square of the mean of the detection statistic under H_1 . Thus only the mean and the variance are required to compute the SNR. In contrast, the detection probability requires full knowledge of the probability density function, which may not be available sometimes. Therefore the output SNR, which is easier to obtain, is also used to evaluate the detection performance. Of course the detection-probability-based performance evaluation, if it is available, is more accurate than the SNR-based evaluation. In this section, the output SNR will be used to compare the detection performance between the matched filter and the square-law detection.

The matched filter output Y for an input signal $A \cos(2\pi f_0 t)$ can be written as

$$Y = \int_0^T [A \cos(2\pi f_0 t) + n(t)] \cos(2\pi f_0 t) dt \quad (110)$$

The bandpass noise $n(t)$ can be expressed in the form

$$n(t) = n_c(t) \cos(2\pi f_0 t) + n_s(t) \sin(2\pi f_0 t) \quad (111)$$

Hence

$$\begin{aligned} Y &= \frac{AT}{2} + \int_0^T [n_c(t) \cos(2\pi f_0 t) + n_s(t) \sin(2\pi f_0 t)] \cos(2\pi f_0 t) dt \\ &= \frac{AT}{2} + \frac{n_c(t)T}{2} \end{aligned} \quad (112)$$

Equation (112) indicates that the quadrature noise $n_s(t) \sin(2\pi f_0 t)$ has been rejected by the lowpass filter from the output. The first term in Eq. (112) is the signal component with output signal power $A^2 T^2/4$, while the second term represents the in-phase noise component with output noise power $E[n_c^2(t)]T^2/4$. Using Ref. 2

$$E[n_c^2(t)] = E[n_s^2(t)] = E[n^2(t)] = \sigma^2 \quad (113)$$

we obtain the output SNR

$$\text{SNR}_{\text{out}} = \frac{A^2}{\sigma^2} \quad (114)$$

The input signal power is $A^2/2$ and the input noise power is $E[n^2(t)] = \sigma^2$. The input SNR is therefore

$$\text{SNR}_{\text{in}} = \frac{A^2}{2\sigma^2} \quad (115)$$

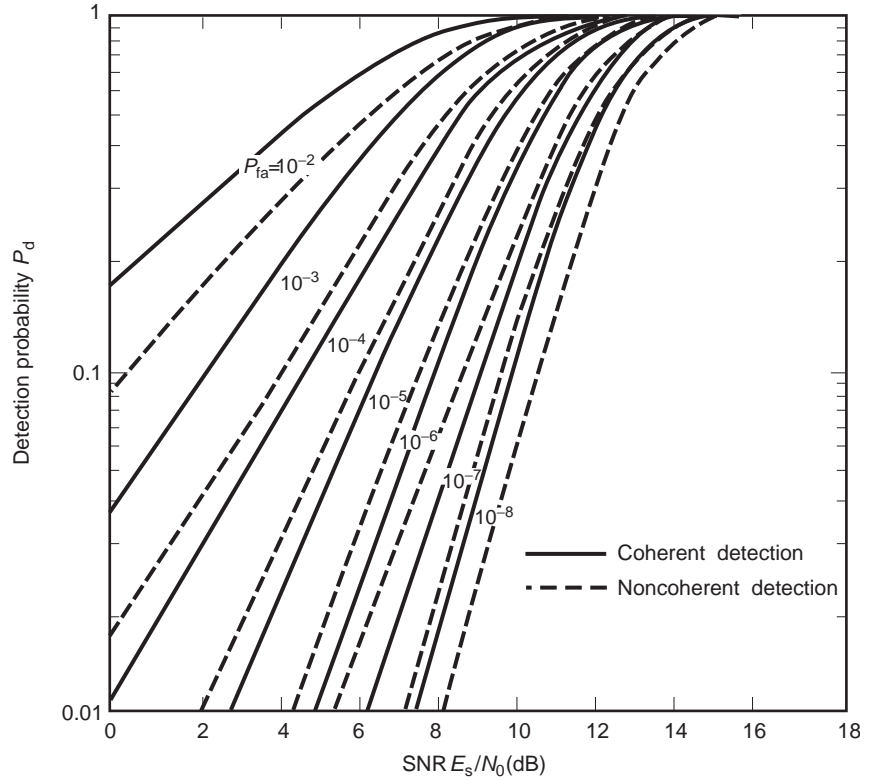


Figure 14. Detection probability for coherent and noncoherent detection.

and we have the following relationship between the input and output SNRs for coherent detection:

$$\text{SNR}_{\text{out}} = 2\text{SNR}_{\text{in}} \quad (116)$$

It is clear that coherent detection gives a 3 dB improvement in SNR. The reason for this improvement is that the multiplier and lowpass filter in Eq. (110) eliminate the quadrature noise component $n_s(t) \sin(2\pi f_0 t)$.

On the other hand, in the noncoherent case both the in-phase and the quadrature noise components come into play. To analyze the square-law detection easily, we use the equivalent scheme of Fig. 12 with the square-law rectifier characteristic of $y = x^2$, as shown in Fig. 13c, replacing the linear rectifier. The output Z of a square-law detection for the following received signal

$$A \cos(2\pi f_0 t) + n_c(t) \cos(2\pi f_0 t) + n_s(t) \sin(2\pi f_0 t) \quad (117)$$

can be written as [4]

$$Z = \frac{T}{2} [A^2 + 2An_c(t) + n_c^2(t) + n_s^2(t)] \quad (118)$$

This output can be regarded as composed of three terms. The first term, $A^2T/2$, is the desired output signal component with output signal power $(A^2T/2)^2$. The second term, $ATn_c(t)$, represents the carrier-noise component with the associated output noise power $A^2T^2\sigma^2$. The third term, $\frac{1}{2}[n_c^2(t) + n_s^2(t)]$, is the self-noise component. The associated

noise power is

$$\begin{aligned} & \frac{T^2}{4} E\{[n_c^2(t) + n_s^2(t)]^2\} - \frac{T^2}{4} \{E[n_c^2(t) + n_s^2(t)]\}^2 \\ &= \frac{T^2}{2} \{E[n_c^4(t) + \{E[n_c^2(t)]\}^2] - T^2\{E[n_c^2(t)]\}^2\} \\ &= T^2\sigma^4 \end{aligned} \quad (119)$$

where $E[n^4(t)] = 3\{E[n^2(t)]\}^2 = 3\sigma^4$ has been used in the last step. With these results, we can write the output SNR as

$$\text{SNR}_{\text{out}} = \frac{A^4/(4\sigma^4)}{A^2/\sigma^2 + 1} = \frac{\text{SNR}_{\text{in}}^2}{2\text{SNR}_{\text{in}} + 1} \quad (120)$$

If the input SNR is much larger than 1, the output SNR is approximately equal to $\frac{1}{2}\text{SNR}_{\text{in}}$, with the square-law detection thus causing a 3 dB reduction in signal-to-noise ratio. For input signal-to-noise ratios that are much less than 1, 2SNR_{in} is negligible compared with 1, and Eq. (120) shows that SNR_{out} is now equal to SNR_{in}^2 . In this case, the square-law detection causes a very serious degradation of the signal-to-noise ratio.

The relationship between SNR_{out} and SNR_{in} for the matched filter and the square-law detection is shown in Fig. 15. It is clear from both Fig. 14 and Fig. 15 that the noncoherent detection is inferior to the coherent detection for low input signal-to-noise ratios and approximates the coherent detection for high input signal-to-noise ratios

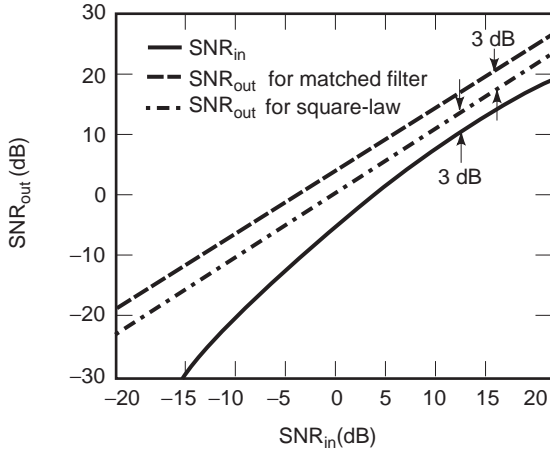


Figure 15. Output signal-to-noise ratios for the matched filter and the square-law detection.

in the detection probability and the output signal-to-noise ratio.

5. DETECTION OF THE LINEAR FREQUENCY-MODULATED SIGNAL

In the previous sections, we have considered the detection of the narrowband signal such as the single-frequency sinusoidal pulses given by Eq. (79). The product of time duration T and bandwidth B is essentially 1. There is an inherent conflict between long-range detection and high-range-resolution capability for such signals. Because the received signal energy E_s attenuates rapidly as the range increases, the long range requires large transmitted signal amplitudes in order to have a sufficiently large value of E_s/N_0 for reliable detection and range estimation. But all radar systems have a limitation on the peak transmitted signal power, which imposes an upper limit on the transmitted signal amplitude. Of course, the required value of E_s can also be obtained by maintaining the transmitted signal amplitude at some maximum value A and increasing the signal duration T . In this case the signal bandwidth B , which is approximately $1/T$, is small. But since the signal bandwidth B is inversely proportional to the range resolution [5], then achieving the required E_s by increasing T reduces B , thereby degrading range resolution capability.

On the other hand, if B can be increased essentially independently of T , there is no such conflict. This is why modern radar systems employ large time-bandwidth product (BT) signals. In the radar system, the earliest and most widely used large BT signal is the linear frequency-modulated (LFM) signal [1,3]. In addition to providing a solution to the long-range-high-resolution problem, the LFM signal is also a form of Doppler-invariant waveform [3].

We note that in military communication systems, a large time-bandwidth product signal is referred to as a spread-spectrum signal [2]. It provides resistance to jamming and has a low interception probability because the signal is transmitted at low power. Among various

spread-spectrum signals, the direct-sequence spread-spectrum (DSSS) signal, where the transmitted signal is modulated by a pseudorandom sequence, is used in code-division multiple-access (CDMA) communications [6]. The frequency-hopped spread spectrum (FHSS) is another widely used spread-spectrum signal in modern communication systems [2,7].

5.1. Wigner-Ville Distribution and Ambiguity Function of an LFM Signal

For an LFM signal, the analytic form is

$$s(t) = \begin{cases} \exp\left[j\left(2\pi f_0 t + \frac{m}{2}t^2\right)\right], & 0 \leq t \leq T \\ 0, & \text{otherwise} \end{cases} \quad (121)$$

The instantaneous frequency in Eq. (121) is

$$f_i(t) = f_0 + mt \quad (122)$$

which has an initial frequency f_0 and increases at a frequency rate m . Since an LFM signal is a nonstationary signal, the best way to describe it is through such distribution functions as the Wigner-Ville distribution (WVD) and the ambiguity function (AF). The WVD of a signal $s(t)$ is defined as

$$\text{WVD}(t, f) = \int_{-\infty}^{\infty} s(t + \tau/2)s^*(t - \tau/2)e^{-j2\pi f\tau} d\tau \quad (123)$$

WVD is the Fourier transform (with respect to the delay τ) of the signal's correlation function. It relates the time and the instantaneous frequency of a signal. Substituting the LFM signal of Eq. (121) into this definition yields [15]

$$\text{WVD}(t, f) = \begin{cases} 2(T - 2|t - T/2|)\text{sinc}\{(T - 2|t - T/2|)[f - f_i(t)]\} & 0 \leq t \leq T \\ 0, & \text{otherwise} \end{cases} \quad (124)$$

where $f_i(t)$ is given in Eq. (122) and the sine function is defined as

$$\text{sinc}(t) = \begin{cases} \sin(\pi t)/(\pi t) & t \neq 0 \\ 1 & t = 0 \end{cases}$$

Figure 16 shows the WVD for an LFM signal with $f_0 = 20$, $m = 12$, and $T = 2$. It is seen from the WVD that the instantaneous frequency linearly increases with the time in accordance with Eq. (122), whereas this relationship is not observable from the spectrum of the signal, which is also shown at the top of Fig. 16.

The ambiguity function (AF) is defined as

$$\text{AF}(\tau, \zeta) = \int_{-\infty}^{\infty} s(t + \tau/2)s^*(t - \tau/2)e^{-j2\pi\zeta\tau} dt \quad (125)$$

where ζ and τ denote the frequency shift and the delay, respectively. AF is the Fourier transform (with respect to the time t) of the signal's correlation function, and it

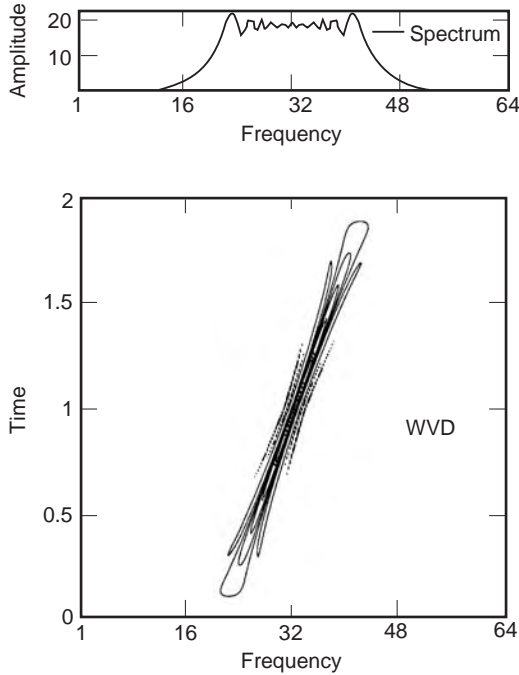


Figure 16. Spectrum (top) and WVD (bottom) of an LFM signal.

relates the delay and the Doppler frequency (or frequency shift). Note that the AF and the WVD form a two-dimensional (2D) Fourier pair, that is

$$\begin{aligned} \tau \xrightarrow{\mathcal{F}} f \quad \xi \xrightarrow{\mathcal{F}^{-1}} t \quad [\text{AF}(\tau, \xi)] &= \int_{-\infty}^{\infty} \int_{-\infty}^{\infty} \text{AF}(\tau, \xi) e^{j2\pi\xi t} e^{-j2\pi f \tau} d\xi d\tau \\ &= \text{WVD}(t, f) \end{aligned} \quad (126)$$

where \mathcal{F} and \mathcal{F}^{-1} denote the Fourier and its inverse operators, respectively. Applying Parseval's theorem $\int u(t)v^*(t) dt = \int U(f)V^*(f) df$ to Eq. (125), we obtain

$$\text{AF}(\tau, \xi) = \int_{-\infty}^{\infty} S^*(f)S(f + \xi)e^{j2\pi f \tau} df \quad (127)$$

The AF can therefore be regarded as the matched-filter output with a different delay τ and frequency shift ξ .

The AF has proved to be an important tool in analyzing and constructing radar signals by relating range and velocity resolutions. By constructing signals having a particular ambiguity function, desired performance characteristics are achieved. For example, the magnitude AF of the LFM signal in Eq. (121) is

$$|\text{AF}(\tau, \xi)| = \begin{cases} (T - |\tau|)\text{sinc}[(T - |\tau|)(\xi - m\tau)], & |\tau| \leq T \\ 0, & \text{otherwise} \end{cases} \quad (128)$$

which is shown in Fig. 17 for the same LFM signal in Fig. 16. The AF is symmetric about the origin $\tau = \xi = 0$, and the greatest value appears above the origin. The time delay τ is related to the range, and the frequency shift ξ is related to the Doppler shift. Thus AF describes the range-

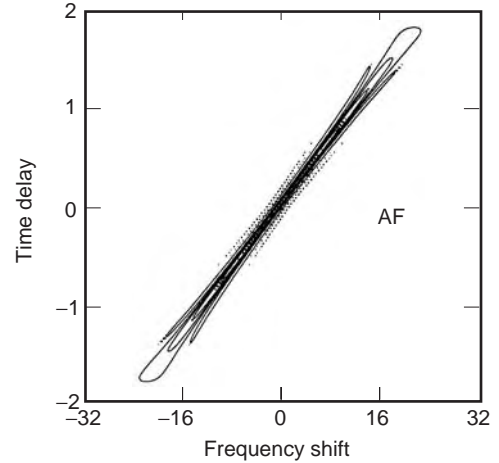


Figure 17. Ambiguity function of the LFM signal. The AF is symmetric about the origin, and its greatest value appears above the origin.

Doppler ambiguity of the transmitted signal. An ideal radar signal is the one whose AF is a thumbtack function because it leaves the least ambiguity in resolving the range and Doppler shift.

5.2. Detection of Multiple LFM Signals

The matched-filter detection is the optimal detection if all of the signal information (phase, initial frequency, and frequency rate) is available. However, these parameters are difficult to specify because accurate values of the range, the velocity, and the acceleration of a target are not available. Noncoherent detection is thus preferred. Next, we are going to consider the noncoherent detection of multiple LFM signals in a noise background.

For multiple LFM signal detection, it is often the case that the frequency rate is the only parameter of interest in practice [8]. In other words, the frequency rates distinguish different LFM signals. Such a scenario occurs in the radar detection of a small, fast-moving missile launched from a relatively slow-moving aircraft. Multiple LFM signals can be detected by locating maxima in the frequency rate in many applications.

5.2.1. AF of Multiple LFM Signals. The input signal to be analyzed is modeled by a linear sum of 2 (may be extended to more than 2) LFM signals with frequency rates m_0 and m_1 as given by

$$r(t) = \sum_{i=0}^1 \exp \left[j \left(\omega_i t + \frac{1}{2} m_i t^2 \right) \right] \quad (129)$$

Here ω_i represent the carrier (or the initial) frequency, which is proportional to the velocity of the target, and the frequency rate m_i is proportional to the acceleration. The AF defined by

$$\text{AF}_r(\tau, \omega) = \int_{-\infty}^{\infty} r(t + \tau/2)r^*(t - \tau/2)e^{-j\omega t} dt \quad (130)$$

is computed for the signal $r(t)$ of Eq. (129) to yield

$$\begin{aligned} \text{AF}_r(\tau, \omega) = & \delta(\omega - m_0\tau)e^{j\omega_0\tau} + \delta(\omega - m_1\tau)e^{j\omega_1\tau} \\ & + \exp\left[j\left(\frac{\omega_0 + \omega_1}{2}\tau + \frac{m_0 - m_1}{8}\tau^2\right)\right] Q_1 \\ & + \exp\left[j\left(\frac{\omega_0 + \omega_1}{2}\tau + \frac{m_1 - m_0}{8}\tau^2\right)\right] Q_2 \end{aligned} \quad (131)$$

where

$$\begin{aligned} Q_1 = & \exp\left(-j\frac{[-2\omega + (m_0 + m_1)r + 2\omega_0 - 2\omega_1]^2}{8(m_0 - m_1)}\right) \int_{-\infty}^{\infty} \\ & \exp\left[j\frac{m_0 - m_1}{2}\left(t + \frac{-2\omega + (m_0 + m_1)r + 2\omega_0 - 2\omega_1}{2(m_0 - m_1)}\right)^2\right] dt \\ Q_2 = & \exp\left(-j\frac{[-2\omega + (m_0 + m_1)r + 2\omega_1 - 2\omega_0]^2}{8(m_1 - m_0)}\right) \int_{-\infty}^{\infty} \\ & \exp\left[j\frac{m_1 - m_0}{2}\left(t + \frac{-2\omega + (m_0 + m_1)r + 2\omega_1 - 2\omega_0}{2(m_1 - m_0)}\right)^2\right] dt \end{aligned}$$

The last two terms of Eq. (131) are interference terms generated by the two LFM components in the signal $r(t)$, due to the nonlinearity of the AF. Using the following identity

$$\int_{-\infty}^{\infty} e^{-jmt^2} dt = \sqrt{\frac{\pi}{m}} \exp\left(-j\frac{\pi}{4}\right), \quad m > 0 \quad (132)$$

Q_1 and Q_2 are combined to give

$$\begin{aligned} \text{AF}_r(\tau, \omega) = & \delta(\omega - m_0\tau)e^{j\omega_0\tau} + \delta(\omega - m_1\tau)e^{j\omega_1\tau} + 2\sqrt{\frac{2\pi}{m_0 - m_1}} \\ & \times \exp\left[j\left(\frac{\omega(\omega_0 - \omega_1) + \omega_1 m_0\tau - \omega_0 m_1\tau}{m_0 - m_1}\right)\right] \\ \text{Re}\left\{ \exp\left[j\left(\frac{m_0 m_1 \tau^2 + \omega^2 + (\omega_0 - \omega_1)^2 - \omega(m_0 + m_1)\tau}{2(m_0 - m_1)} - \frac{\pi}{4}\right)\right] \right\} \end{aligned} \quad (133)$$

Figure 18(a) shows the AF [Eq. (133)] of a signal composed of two LFM signals that may represent two targets with different velocities and accelerations. Although there is cross-term interference, we can identify the two straight lines representing the bicomponent signal in Fig. 18a. However, the two LFM signals are not obvious if they are corrupted by noise. Figure 18b is identical to Fig. 18a except that the two signals are corrupted by Gaussian white noise with SNR = -6 dB.

5.2.2. Detecting Multiple LFM Signals using Radon Ambiguity Transform. Recall that the radon transform [9], commonly used for the reconstruction of images in computer tomography, is defined by

$$R_{s,\phi}\{f(x,y)\} = \int_{-\infty}^{\infty} \int_{-\infty}^{\infty} f(x,y) \delta(x \sin \phi + y \cos \phi - s) dx dy \quad (134)$$

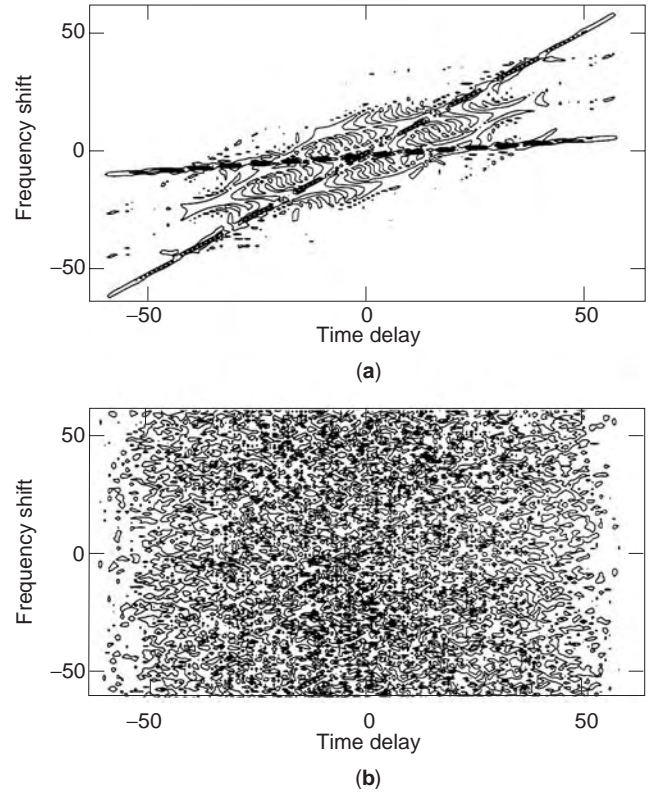


Figure 18. The ambiguity functions of bicomponent LFM signal (a) without noise, and (b) with the additive white Gaussian noise (SNR = -6 dB).

for $-\infty < s < \infty$ and $-\pi/2 < \phi < \pi/2$, where the δ function specifies the direction of integration. The parameter s represents the shifted location of the origin. Equation (134) actually represents the sum of the values of $f(x,y)$ along the line that makes an angle ϕ with the x axis and is located at a distance s from the origin. The Radon-Wigner transform [9,10] is a special case when $f(x,y)$ in Eq. (134) takes the WVD of a multicomponent LFM signal. The WVD of a bicomponent signal is graphically drawn in Fig. 19a. The Radon-Wigner transform of Fig. 19a should produce two maxima in the resulting α - ω plane. Figure 19b is the AF of the same signal in Fig. 19a. The AF is the 2D Fourier transform of the WVD; thus they share the same angles of α_0 and α_1 as shown in the WVD. However, the initial frequencies shown in Fig. 19a have disappeared in Fig. 19b, since they have been mapped into the phase of the AF. This also explains why the AFs of the two chirps pass through the origin in the τ - ζ plane. Thus, by applying the Radon transform to the *phase-free* ambiguity function, detection of multicomponent signals can be reduced from the 2D search problem in the Radon-Wigner transform to a 1D search problem. The advantage of the ambiguity function over the WVD has been shown in the kernel design for the time-frequency analysis [11]. This work can be extended to the detection of multicomponent signals [12].

Since all directions of interest pass through the origin of the ambiguity plane, the Radon transform with parameter s set to 0 is applied to the phase-free ambiguity

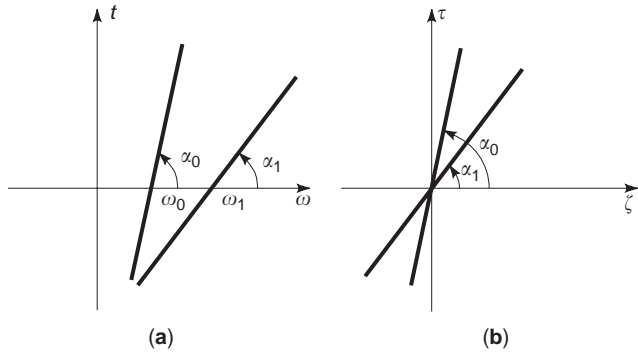


Figure 19. (a) The WVD of a bicomponent signal; (b) the AF of the bicomponent signal.

function of Eq. (133). We essentially compute the line integral along a straight line with its direction specified by the δ function $\delta(\xi - m\tau)$ in the ambiguity plane. Therefore the detection statistic can be formed by the so-called Radon ambiguity transform [12] as

$$\begin{aligned} \eta(m) &= \int_{-\infty}^{\infty} \int_{-\infty}^{\infty} |\text{AF}_r(\tau, \zeta)| \delta(\zeta - m\tau) d\tau d\zeta \\ &= \int_{-\infty}^{\infty} |\text{AF}_r(\tau, m\tau)| d\tau \end{aligned} \tag{135}$$

Since the infinite in Eq. (135) usually diverge, it is necessary to first remove the constant term from the integrand. Specifically, for $m \neq m_i$ ($i = 0, 1$) and assuming $m_0 - m_1 > 0$, we have from Eq. (133)

$$\begin{aligned} &|\text{AF}_r(\tau, m\tau)| \\ &= \left| 2\sqrt{\frac{2\pi}{m_0 - m_1}} \cos(a_m \tau^2 + b) \right| \\ &= 4\sqrt{\frac{2}{\pi(m_0 - m_1)}} \left(1 + \sum_{n=1}^{\infty} \frac{2(-1)^{n-1}}{(2n)^2 - 1} \right. \\ &\quad \left. \times \cos(2na_m \tau^2 + 2nb) \right) \end{aligned} \tag{136}$$

with

$$\begin{aligned} a_m &= \frac{m_0 m_1 + m^2 - m(m_0 + m_1)}{2(m_0 - m_1)}, \\ b &= \frac{(\omega_0 - \omega_1)^2}{2(m_0 - m_1)} - \frac{\pi}{4} \end{aligned} \tag{137}$$

Removing the constant from Eq. (136) and substituting it into Eq. (135) yield

$$\begin{aligned} \eta(m) &= 4\sqrt{\frac{2}{a_m(m_0 - m_1)}} \sum_{n=1}^{\infty} \frac{2(-1)^{n-1}}{(2n)^2 - 1} \sqrt{\frac{1}{n}} \\ &\quad \times \sin\left(2nb + \frac{\pi}{4}\right) \end{aligned} \tag{138}$$

For $m \neq m_0$ or m_1 (i.e., $a_m \neq 0$), it is clear that $\eta(m)$ is finite. By Eqs. (137) and (138), we have $\eta(m) \rightarrow \infty$ as $m \rightarrow m_0$ or $m \rightarrow m_1$. Therefore, by calculating $\eta(m)$ and comparing it to a preset threshold, the multicomponent signals can be detected.

5.2.3. Finite-Length Signal. Now we consider a bicomponent finite-length signal as given by

$$r(t) = \begin{cases} \frac{1}{\sqrt{T}} \exp\left[j\left(\omega_0 t + \frac{1}{2}m_0 t^2\right)\right] \\ + \frac{1}{\sqrt{T}} \exp\left[j\left(\omega_1 t + \frac{1}{2}m_1 t^2\right)\right] & \text{for } |t| \leq \frac{T}{2} \\ 0 & \text{for } |t| > \frac{T}{2} \end{cases} \tag{139}$$

with the assumption that $\omega_0 = \omega_1$ and $m_0 > m_1$ for simplicity purposes. The modulus of the ambiguity function of $r(t)$ for $\omega = m\tau$ can be calculated by making use of the following integral

$$\int e^{j(px^2 + 2qx)} dx = \sqrt{\frac{\pi}{2p}} e^{-jq^2/p} \left[C\left(\frac{px+q}{\sqrt{p}}\right) + jS\left(\frac{px+q}{\sqrt{p}}\right) \right] \tag{140}$$

to yield

$$\begin{aligned} &|\text{AF}_r(\tau, m\tau)| \\ &= \begin{cases} \frac{2 \sin\left((T - |\tau|)\frac{\tau}{2}(m - m_0)\right)}{T\tau(m - m_0)} + \frac{2 \sin\left((T - |\tau|)\frac{\tau}{2}(m - m_1)\right)}{T\tau(m - m_1)} \\ + \frac{2}{T} \sqrt{\frac{\pi}{m_0 - m_1}} \times \{ [C(X_0) + C(X_1)] \cos(a_m \tau^2) \\ + [S(X_0) + S(X_1)] \sin(a_m \tau^2) \} & \text{for } |\tau| \leq T \\ 0 & \text{for } |\tau| > T \end{cases} \end{aligned} \tag{141}$$

where

$$C(x) = \int_0^x \cos\left(\frac{\pi t^2}{2}\right) dt, \quad S(x) = \int_0^x \sin\left(\frac{\pi t^2}{2}\right) dt$$

are the Fresnel integrals, and

$$\begin{aligned} X_0 &= \sqrt{\frac{m_0 - m_1}{8}} \left(T + \frac{2(-m + m_1)}{m_0 - m_1} \tau \right) \\ X_1 &= \sqrt{\frac{m_0 - m_1}{8}} \left(T + \frac{2(m - m_0)}{m_0 - m_1} \tau \right) \end{aligned}$$

while a_m in Eq. (141) is defined by Eq. (137). For $|\tau| \leq T$, the first two terms in Eq. (141) represent the auto terms of the signal, while the rest express the cross-terms. Figure 20 shows the integral of Eq. (141) over τ , that is,

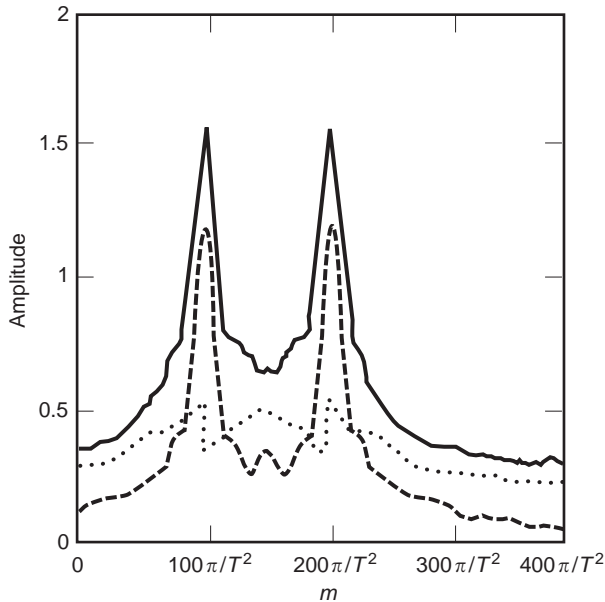


Figure 20. The $\eta(m)$ of two equal-amplitude LFM signal with $T = 40$, $m_0 = 200\pi/T^2$, $m_1 = 100\pi/T^2$. Solid line: $\eta(m)$. Dashed line: auto terms only. Dotted line: cross-terms only. The two peaks indicate the existence of the equal-amplitude \angle FM signals.

$\eta(m)$, for two LFM signals with equal amplitudes. Also shown in Fig. 20 are the integrals of the auto terms and cross-terms of Eq. (141).

5.2.4. Output Signal-to-Noise Ratio Analysis. The output SNR of the statistics η in Eq. (135) can be analyzed by making use of the following quantities [12]

$$E(\eta|H_0) = N_0$$

$$E(\eta|H_1) = A + N_0$$

$$\text{Var}(\eta|H_0) = N_0^2$$

$$\text{Var}(\eta|H_1) = 2AN_0 + N_0^2$$

to find

$$\text{SNR}_{\text{out}} = \frac{A^2}{2AN_0 + N_0^2} = \frac{\text{SNR}_{\text{in}}^2}{2\text{SNR}_{\text{in}} + 1} \quad (142)$$

It is seen from Eq. (142) that there is a 3 dB loss in SNR between the input and the output when the input SNR is high, and the output SNR degrades severely when the input SNR is low, illustrating a typical nonlinear detection characteristic.

6. CONCLUSION

We have presented the techniques of radar signal detection, as well as the related performance analyses. The following conclusions can be drawn:

- Among various detection criteria, the Neyman–Pearson criterion is particularly well suited to radar

detection, owing to its concepts of a priori fixed P_{fa} and maximized P_{d} .

- The coherent detection, in the form of a matched filter or a cross-correlation, is the optimal detection for an exactly known signal (i.e., phase, amplitude, and Doppler frequency are known) in a background of white noise.
- In a typical radar application, the range between the target and the radar represents a very large number of transmitted signal wavelengths. This makes specifying the phase of the return signal extremely difficult, and a noncoherent detection has to be used.
- The noncoherent detection is inferior to the coherent detection for low input signal-to-noise ratios and approximates the coherent detection for high input signal-to-noise ratios.
- There is an inherent conflict between long-range detection and high-range-resolution capability for the unity time-bandwidth signal. Large time-bandwidth signals such as an LFM signal do not have such a conflict.
- Large time-bandwidth signals can be described by the ambiguity function or the Wigner–Ville distribution. The Radon ambiguity transform can be used to detect multiple LFM signals.

BIBLIOGRAPHY

1. C. E. Cook and M. Bernfeld, *Radar Signals: An Introduction to Theory and Application*, Academic Press, New York, 1967.
2. J. G. Proakis and M. Salehi, *Communication Systems Engineering*, Prentice-Hall, Englewood Cliffs, NJ, 1994.
3. J. Minkoff, *Signals, Noise, and Active Sensors*, Wiley, New York, 1992.
4. J. Brown and E. V. D. Glazier, *Signal Analysis*, Reinhold, New York, 1964.
5. D. L. Mensa, *High Resolution Radar Cross-Section Imaging*, Artech House, Norwood, MA, 1991.
6. A. J. Viterbi, *Principles of Spread Spectrum Communication*, Addison-Wesley, Reading, MA, 1995.
7. J. G. Proakis, *Digital Communications*, McGraw-Hill, New York, 1995.
8. P. M. Djuric and S. Kay, Parameter estimation of chirp signals, *IEEE Trans. Acoust. Speech Signal Process.* **AASP-38**:2118–2126 (1990).
9. J. C. Wood and D. T. Barry, Tomographic time-frequency analysis and its application toward time varying filtering and adaptive kernel design for multicomponent linear-FM signals, *IEEE Trans. Signal Process.* **42**:2094–2104 (1994).
10. J. C. Wood and D. T. Barry, Radon transformation of time-frequency distributions for analysis of multicomponent signals, *IEEE Trans. Signal Process.* **42**:3166–3177 (1994).
11. B. Ristic and B. Boashash, Kernel design for time-frequency signal analysis using the radon transform, *IEEE Trans. Signal Process.* **41**:1996–2008 (1993).
12. M. Wang, A. K. Chan, and C. K. Chui, Linear frequency modulated signal detection using the radon-ambiguity transform, *IEEE Trans. Signal Process.*, **46**:571–586 (1998).

FURTHER READING

- M. Barkat, *Signal Detection and Estimation*, Artech House, Norwood, MA, 1991.
- B. Bouachache, Time-frequency signal analysis, in S. Haykin, ed., *Advances in Spectral Estimation and Array Processing*, Prentice-Hall, Englewood Cliffs, NJ, 1991, Vol. 1, Chap. 9, pp. 418–517.
- J. V. DiFranco and W. L. Rubin, *Radar Detection*, Prentice-Hall, Englewood Cliffs, NJ, 1968.
- J. L. Eaves and E. K. Reedy, eds., *Principles of Modern Radar*, Van Nostrand-Reinhold, New York, 1987.
- G. Galati, ed., *Advanced Radar Techniques and Systems*, Peter Peregrinus, Stevenage, UK, 1993.
- H. V. Poor, *An Introduction to Signal Detection and Estimation*, Springer, New York, 1988.
- D. C. Schleher, *MTI and Pulsed Doppler Radar*, Artech House, Norwood, MA, 1991.
- H. Urkowitz, *Signal Theory and Random Processes*, Artech House, Norwood, MA, 1983.

RADAR SIGNAL PROCESSING

WEI YE
TAT SOON YEO
National University of
Singapore

1. FUNDAMENTALS OF RADAR SIGNAL PROCESSING

The capability of radar in acquiring information about targets and environments has been greatly improved over the decades, not only owing to the advent of sophisticated hardware, but also the development of advanced signal processing techniques. Conventional radar is used mainly for detection, localization, and tracking of targets. High-resolution imaging radar can provide more information such as target size, shape, and image and hence can be used for target recognition, which is desired by modern radar. Signal processing plays a key role in most modern radar operations. *Radar signal processing* commonly refers to the techniques that are used to extract desired information about a target from the received signals. Such information usually includes target presence and the position, velocity, trajectory, and image of the target.

According to their objectives, the signal processing techniques can be divided into two categories. The techniques in the first category are used mainly to enhance the useful signal and suppress interference, thus enabling the radar to work satisfactorily in less-than-ideal environments. The techniques in the second category are developed to improve the resolving capability of radar, thus enabling the radar to extract complex information, such as target size and shape.

1.1. Signal Enhancement and Interference Suppression

Extraction of desired information from radar echoes is not an easy task under most circumstances, since the wanted signal has to compete with unwanted signals, such as noise, clutter, and external interference. Noise includes thermal noise and other noise-like disturbances and errors introduced into the receiving channels of radar. It is normally modeled as a Gaussian random process with a uniform power spectrum (white). Clutter is the echo from targets of no interest. For example, if the target of interest is an aircraft, the echoes from the ground, clouds, and rain will produce clutter. Unlike that of noise, the spectrum of clutter is not uniform and is determined by the Doppler frequency and strength of the clutter source. External interference can be generated either by hostile jamming devices or other microwave equipment operating nearby. Radars usually operate in such a combined environment. Different techniques are required to suppress noise, clutter, and jamming since they have different properties.

We first consider coping with noise. In order to ensure reliable detection and processing, it is desirable to maximize the signal-to-noise ratio (SNR). The optimum filter that achieves the maximum SNR is the *matched filter*. The matched filter is widely used in radar systems and is often considered part of the radar receiver, because the intermediate-frequency (IF) amplifier in the radar receiver is normally designed as the matched filter. The matched filter is also an important element in pulse compression. The theory of matched filter is discussed in detail in another article in this encyclopedia, RADAR SIGNAL DETECTION. This article briefly introduces the concept of matched filter.

Denote the input signal and its Fourier transform by $s(t)$ and $S(\omega)$, respectively. The input noise is assumed to be white and stationary. Its spectral density in watts/hertz is $N_0/2$. The frequency response of the matched filter is [1]

$$H(\omega) = kS^*(\omega) \exp(-j\omega t_0) \quad (1)$$

where the asterisk denotes the complex conjugate, k is a gain constant, and t_0 is a time delay that makes the filter physically realizable. The impulse response of the matched filter is the inverse Fourier transform of Eq. (1), which is

$$h(t) = ks(t_0 - t) \quad (2)$$

So the impulse response is the image or time inverse of the input signal.

The SNR used here is defined as the ratio of the peak instantaneous signal power and the average noise power. It is maximized at the output of the matched filter as $\text{SNR}_{\max} = 2E/N_0$, where E is the signal energy. It is an interesting fact that the output SNR is independent of the waveform shape of the input signal.

Clutter reduction is also a major concern for many radar applications. Moving-target indication (MTI) is an important technique that can discriminate moving targets from fixed or slowly moving clutter. MTI is based on the phenomenon that the target moving with finite radial

velocity produces a Doppler frequency whereas the fixed target does not. So the difference in Doppler frequency can be utilized to filter out the fixed clutter.

For radars operating in military environment, antijamming capability is a crucial performance indicator. In this case, the technique of frequency-domain filtering is ineffective, since the interfering signal usually has similar Doppler properties as the desired signal. However, a jamming source is confined to within a certain spatial angle and is usually not in the same direction as the target. So it can be removed by spatial filtering. The technique of spatial filtering is known as *beamforming*. By combining the signals of individual elements of a phased-array antenna, it can synthesize a beam pattern whose mainlobe points to the desired target and a very low sidelobe points to the jamming source.

However, no practical techniques can completely suppress these unwanted signals. The residual interference will lead to a higher false-alarm rate when a fixed threshold is used to decide the presence of a target. Having too many false alarms is unacceptable for the radar detector. Moreover, it also increases the computational load of subsequent data processors. Therefore, a device is needed to control the threshold adaptively in order to maintain an approximately constant false-alarm rate (CFAR).

1.2. Improvement of Resolving Capability

Radar has two main tasks: detection and information extraction. Early radar only has the capability to extract simple target information, such as range, angle, and velocity. Modern radar is able to acquire complicated information such as target size, shape, and image. This is largely a result of the advancement of radar signal processing. Extracting such information requires the radar to have high resolution in one or two (or even three) dimensions.

Range resolution is the ability of radar to distinguish adjacent targets in range direction. If the radar transmits a short pulse of single frequency, range resolution is decided by the pulse duration T . In this case, two scatterers adjacent in range can be distinguished by the radar if their echoes are separated in time delay by more than the pulsewidth. So the range resolution is

$$\rho_r = cT/2 \quad (3)$$

where c is the speed of light and the factor 2 is introduced by the two-way time delay.

Thus, the shorter the pulse, the finer the range resolution. However, a very short pulse carries little energy, and it is impractical, if not impossible, to generate short pulses of very large amplitudes. Hence, a detection range would be shortened, due to fixed SNR requirement of the receiver. To overcome this drawback, high-resolution radars usually adopt long-duration, wideband, coded pulses, which can be compressed to very short pulses after reception by an operation called *pulse compression*.

High range resolution makes it possible for the radar to acquire information on target size and shape. On the other hand, if the target image is needed, the radar must have

high resolution in the azimuth direction as well. For conventional radar, this corresponds to the angular resolution, which is actually the antenna beamwidth, because the radar can distinguish two scatterers in the azimuth only if their angular separation is greater than the antenna beamwidth. The beamwidth is decided by the ratio of the signal wavelength to the aperture size of the antenna. The larger the aperture, the sharper the beam.

However, it is usually impractical to increase the aperture size of a real antenna to a great extent. For instance, assuming a signal wavelength of 3 cm, a whopping 300 m antenna aperture is needed in order to resolve two targets located 1 m apart at a range of 10 km. The synthetic aperture radar (SAR) is developed to overcome this limitation. In SAR, the radar is installed on a moving platform, such as an aircraft or a satellite. The radar transmits and receives a series of pulses while moving with the platform. This is equivalent to obtaining discrete samples of a long aperture. The long antenna aperture can be synthesized by a coherent summation of these samples after proper phase adjustment. Thus, SAR achieves high resolution in azimuth in a practical way. It presents the image of the target by resolving the backscattering intensity of each small range-azimuth cell.

1.3. Radar Signal Processor

In a radar system, the device that performs the operations of radar signal processing is termed the *radar signal processor*. The radar signal processor is sometimes considered part of the radar receiver in early days. In modern radars, it incorporates more and more important functions and is usually considered a separate subsystem due to its significance.

Figure 1a shows the block diagram of the receiving and processing channel of the radar system. The receiver accepts radiofrequency (RF) signals from the antenna and downconverts then to an intermediate frequency. The signals are then amplified, converted to videofrequency (baseband), and sent to the analog-to-digital converter (ADC). The digital samples of the signals are the input to the signal processor. Finally, the output of the signal processor goes to the data processor and display devices.

Figure 1b gives an inside view of the radar signal processor, which encompasses all major functions of radar signal processing. The configurations of practical signal processors may vary according to the main function of radar. A typical signal processor usually does not contain all the components depicted in the block diagram, and may not incorporate them in the given order.

1.4. Coherent Signal Processing

Most functions of the radar signal processor require coherent processing, which means that both signal amplitudes and phases are utilized. Noncoherent processing only uses signal amplitudes. A device called *synchronous detector* or *phase-sensitive detector*, as shown in Fig. 2, obtains coherent video signals. It consists of two orthogonal channels denoted by I (in-phase) and Q (quadrature), which correspond to the real and imaginary part of a signal, respectively.

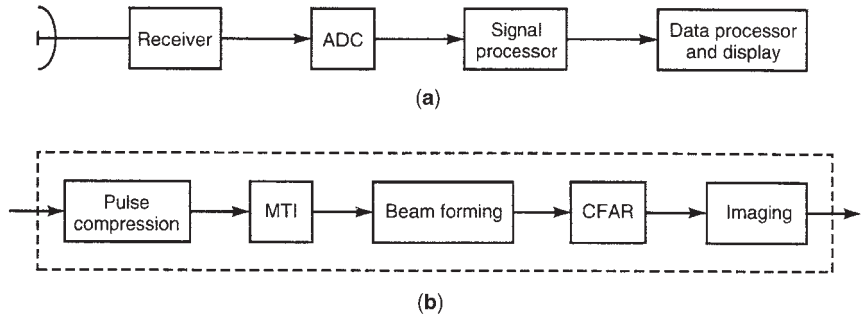


Figure 1. (a) Position of the radar signal processor in the receiving and processing channel of a radar system; (b) An inside view of the radar signal processor. The configurations vary in practical processors.

The input is usually an IF signal, which has the general form of

$$s(t) = A(t) \cos[2\pi f_c t + \phi(t)] \quad (4)$$

where $A(t)$ is the amplitude or envelope, f_c is the IF frequency, and $\phi(t)$ is the phase. It is mixed with the following orthogonal signals in the two channels:

$$r_1(t) = \cos 2\pi f_c t, \quad r_Q(t) = \sin 2\pi f_c t \quad (5)$$

The output of the multiplier in the I channel is

$$s(t)r_1(t) = \left(\frac{1}{2}\right)A(t) \cos[2\pi(2f_c t + \phi(t))] + (1/2)A(t) \cos \phi(t) \quad (6)$$

The first term has a doubled frequency and is thus removed by the subsequent lowpass filter (LPF). The final output of the I channel is

$$I(t) = \left(\frac{1}{2}\right)A(t) \cos \phi(t) \quad (7)$$

Similarly, the output of the Q channel is

$$Q(t) = \left(\frac{1}{2}\right)A(t) \sin \phi(t) \quad (8)$$

The complex video signal can be reconstructed as

$$v(t) = 2[I(t) + jQ(t)] = A(t) \exp[j\phi(t)] \quad (9)$$

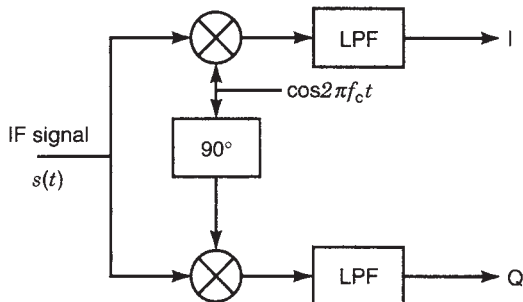


Figure 2. The synchronous detector consists of two orthogonal channels, corresponding to the real and imaginary parts of a signal. Its output is a complex video signal.

This complex signal is the so-called *complex envelope* of $s(t)$. It contains the information of the amplitude as well as the phase.

2. MOVING-TARGET INDICATION

Discrimination of moving targets from strong, fixed clutter is necessary for many radar applications, for example, air surveillance and air-traffic control. The MTI achieves this goal by means of the Doppler effect generated by a moving target. The transmitted signal is a series of pulses with a pulse repetition frequency (PRF) f_r . The Doppler frequency f_D of a moving target will introduce a varying phase term into the received signal. The total phase of the received signal becomes

$$\phi(t) = 2\pi f_D t + \phi_0 \quad (10)$$

where ϕ_0 is the initial phase. The output video signals of the synchronous detector are

$$x_I(t) = A(t) \cos(2\pi f_D t + \phi_0) \quad (11)$$

$$x_Q(t) = A(t) \sin(2\pi f_D t + \phi_0) \quad (12)$$

In the frequency domain, their spectra are centered at $\pm f_D$. On the other hand, a fixed target has zero Doppler frequency. The different spectral locations makes it possible to separate moving targets from fixed clutter.

The I or Q components or both can be used in the MTI process. If only one channel is used, the signal of a moving target may be lost in some special cases. For example, a moving target generating a Doppler frequency f_D that equals half the sampling frequency may not be detected if the samples happened to fall at the zero crossings. Using both I and Q channels can overcome this problem. In this case, the signals of I and Q are fed into two separate MTI filters.

2.1. Delay-Line Cancelers

The delay-line canceler is a widely used form of MTI. Since the video signal of a fixed target does not vary from pulse to pulse, it can be subtracted using adjacent pulses. The *single canceler* is the simplest implementation of the MTI. Figure 3 shows its structure. The delay line therein introduces a delayed time that exactly equals one interpulse period, which is the reciprocal of the PRF, that is,

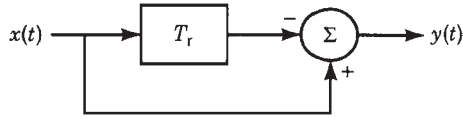


Figure 3. The single canceler utilizes only two pulses. The delay time T_r exactly equals one interpulse period.

$T_r = 1/f_r$. The single canceler utilizes only two pulses, and the output signal is

$$y(t) = x(t) - x(t - T_r) \quad (13)$$

The frequency response of a single canceler can be obtained via the Fourier transform of Eq. (13)

$$Y(\omega) = X(\omega) - X(\omega) \exp(-j\omega T_r) \quad (14)$$

where $\omega = 2\pi f_D$, since the frequency of the video signal is actually its Doppler frequency, as shown in Eqs. (11) and (12). So the frequency response of the single canceler is

$$H(\omega) = Y(\omega)/X(\omega) = 1 - \exp(-j\omega T_r) \quad (15)$$

The magnitude of the frequency response is

$$|H(\omega)| = 2 \sin(\omega T_r/2) = 2 \sin(\pi f_D/f_r) \quad (16)$$

Figure 4 shows the filtering mechanism of the delay-line canceler. The solid line is the magnitude of the frequency response of the single canceler. It forms notches at the zero Doppler frequency and the integer multiples of f_r . The moving target whose Doppler frequency is not zero will pass the filter.

The spectrum of completely fixed clutter is an impulse at zero Doppler frequency and can be removed by the single canceler. However, practical ground clutter usually has a finite spectrum due to the slow motion of clutter scatterers, for example, the trees swaying in the wind. The common model of the ground clutter is the Gaussian-shaped power spectrum centered on zero Doppler frequency, as depicted in Fig. 4. It can be seen that the notches of the single canceler are not wide enough to remove most of the clutter spectrum. An improved solution is to use a double canceler.

A *double canceler* is formed by cascading two single cancelers and utilizes three signal pulses, as shown in Fig. 5a. The frequency response of the double canceler is

$$\begin{aligned} H(\omega) &= [1 - \exp(-j\omega T_r)]^2 \\ &= 1 - 2 \exp(-j\omega T_r) + \exp(-2j\omega T_r) \end{aligned} \quad (17)$$

The magnitude of the frequency response, depicted by the dashed line in Fig. 4, is

$$|H(\omega)| = 4 \sin^2(\omega T_r/2) = 4 \sin^2(\pi f_D/f_r) \quad (18)$$

Compared with the single canceler, the double canceler provides broader rejection notch and thus removes more

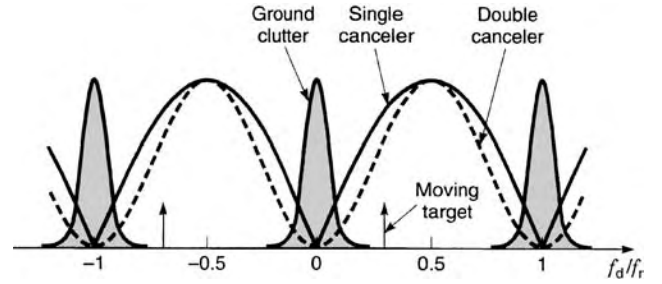


Figure 4. The solid line is the frequency responses of the single canceler. It has rejection notches at zero Doppler frequency and nf_r , where n is an integer. The double canceler, shown as the dashed line, provides broader notches and thus removes more clutter. Blind speed occurs when the Doppler frequency of the target equals nf_r .

clutter. The second equation of Eq. (17) indicates that the double canceler can be implemented by a transversal filter, or finite impulse response (FIR) filter, as shown in Fig. 5b.

It is also possible to construct a triple or multiple canceler using similar methods. One advantage of the delay-line canceler is that it is able to process all target and clutter echoes, regardless of range.

2.2. Performance of Moving-Target Indicator

Many indicators have been used to describe MTI performance. Among them, the MTI improvement factor is the most widely used. Other indicators used are clutter attenuation, MTI gain, subclutter visibility, cancellation ratio, and clutter visibility ratio.

2.2.1. MTI Improvement Factor. This is defined [2] as “the signal-to-clutter ratio at the output (s_o/c_o) of the clutter filter divided by the signal-to-clutter ratio at the input (s_i/c_i) of the clutter filter, averaged uniformly over all target radial velocities of interest.” The improvement factor accounts for both clutter attenuation and target gain. It

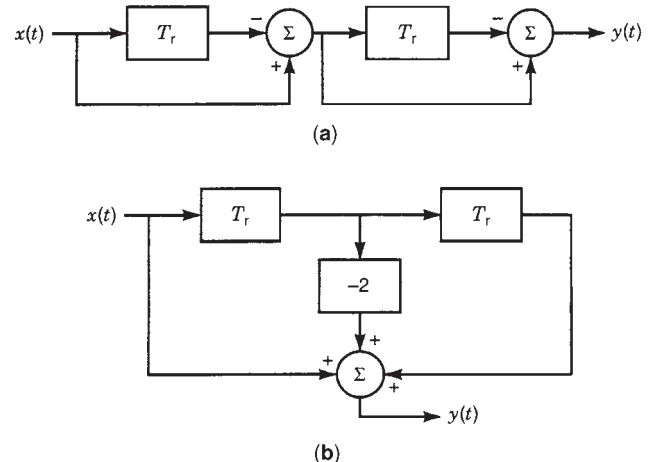


Figure 5. (a) Double canceler is constructed by cascading by two single cancelers. An equivalent implementation is shown in (b), which is a transversal filter, or FIR filter.

can be expressed mathematically as

$$I = \frac{\overline{(s_o/c_o)}}{\overline{(s_i/c_i)}} \quad (19)$$

For the clutter with a zero-mean Gaussian-shaped spectrum, the improvement factors of the single canceler and the double canceler are given, respectively, as [3]

$$I_1 \approx 2(f_r/2\pi\sigma_c)^2 \quad (20)$$

$$I_2 \approx 2(f_r/2\pi\sigma_c)^4 \quad (21)$$

where σ_c is the standard deviation of the clutter power spectrum.

2.2.2. Clutter Attenuation. The ratio of clutter power at the input of the MTI to the power of residual clutter at the output.

2.2.3. MTI Gain. The ratio of signal power at the output of the MTI to signal power at the input, averaged over all target radial velocities of interest.

From the definitions of the improvement factor, the clutter attenuation, and the MTI gain, the relationship between them can be expressed by

$$I = \frac{\overline{(s_o/c_o)}}{\overline{(s_i/c_i)}} = \frac{\overline{(s_o)}}{\overline{(s_i)}} \frac{c_i}{c_o} = GCA \quad (22)$$

where G is the MTI gain and CA is the clutter attenuation.

2.2.4. Subclutter Visibility. This is defined [2] as the ratio by which the target echo power may be weaker than the coincident clutter echo power and still be detected with specified detection and false-alarm probabilities. Target and clutter powers are measured on a single pulse return, and all target radial velocities are assumed equally likely. Subclutter visibility measures the capability of the MTI to detect moving target in the presence of clutter. For example, 20 dB of subclutter visibility means that the moving target can be detected even though the clutter echo power is 100 times the target echo power.

2.3. Other Moving-Target Indicators

2.3.1. Blind Speed and Staggered-PRF MTI. As shown in Fig. 4, the frequency responses of the single and double canceler have periodic nulls at multiples of PRF f_r . If the moving target produces a Doppler frequency that exactly equals f_r , or multiples of f_r , its echo will also be canceled by the MTI. In other words, radar is not able to detect a target moving at one of these radial velocities. So such a speed is named a blind speed.

Blind speed is actually an inherent phenomenon of pulsed radars in which a sinusoidal signal with the Doppler frequency f_D is discretely sampled at the frequency f_r . In the case that $f_D = nf_r$, the sampling occurs at the same point in each corresponding Doppler cycle. Then the moving target looks as if it is stationary.

The problem of blind speed can be alleviated by staggering the PRF, because a speed that is blind at one PRF is generally not blind at another PRF. In this case, the interpulse period of the transmitted signal is changed from pulse to pulse. Time delay in the MTI canceler is also changed correspondingly. This type of MTI is called staggered-PRF MTI. It has a much higher first blind speed than that of the conventional MTI.

In staggered-PRF MTI, the ratio of interpulse periods is usually expressed by a set of prime integers, which has no common divisor other than 1. If N interpulse periods are staggered by $d_1: d_2: \dots : d_N$, the increase of the first blind speed V can be expressed by

$$\frac{V}{V_B} = \frac{d_1 + d_2 + \dots + d_N}{N} \quad (23)$$

where V_B is the blind speed corresponding to the average interpulse periods.

2.3.2. Moving-Target Detector. The moving-target detector (MTD) is an enhanced version of traditional MTI. The basic structure of a MTD is a MTI precanceler followed by a Doppler filterbank. The Doppler filterbank performs the Doppler filtering or Doppler frequency analysis and is typically implemented by the fast Fourier transform (FFT). A Doppler filterbank using N -pulse FFT divides the whole frequency band into N parts, which are processed separately.

The Doppler filterbank provides the following advantages: (1) the SNR is improved since the signal in a certain filter competes only with interference that can pass the filter, (2) the Doppler frequency of a target can be measured to a high accuracy, (3) moving clutter with a nonzero mean of Doppler shift can be rejected by separately adjusting the threshold of each filter, and (4) a clutter map can be generated using the output from the filterbanks.

2.3.3. Adaptive MTI. The adaptive MTI is able to adaptively shift its rejection notch to the location of the clutter spectrum. It is very useful for canceling moving clutter, whose Doppler frequency is not zero. An example of adaptive MTI implementation is the time-averaged-clutter coherent airborne radar (TACCAR) [4]. A phase-error circuit estimates the phase change of clutter signals between pulses, which is caused by its Doppler frequency. The averaged estimate of phase error is used to control the coherent oscillator (COHO) to produce a phase-shifted reference signal for mixing with the return signal. This is equivalent to shifting the Doppler center of the moving clutter to zero. Then a conventional MTI can be used to cancel the clutter. Other implementation methods of adaptive MTI includes changing the weights of the MTI filter and using modern spectral estimation method.

2.3.4. Airborne MTI. The airborne MTI (AMTI) refers to the MTI techniques utilized by a moving radar. The relative motion between radar and fixed clutter displaces the Doppler spectrum of clutter from zero. Thus, the adaptive MTI is one of the AMTI techniques. Another adverse

effect of platform motion is the loss of signal correlation between adjacent pulses, because the illuminated area is slightly displaced from one pulse to the next. The effects of platform motion can be mitigated by physically or electrically displacing the antenna phase center along the plane of the aperture. This technique is called displaced phase center antenna (DPCA).

A relatively new technique is named spacetime adaptive processing (STAP). It simultaneously cancels clutter in angle (space) and Doppler (time) domain. For example, the clutter coming from the antenna mainlobe is spread out in Doppler frequency due to platform motion and is not easy to be canceled in the Doppler domain. The STAP technique can effectively resolve the clutter within the beam width into angle Doppler cells. Targets can be detected in cells that are not occupied by clutter.

3. BEAM FORMING

The radar often encounters jamming interference in the military environment. The jamming source usually occupies the same frequency band as the desired signal and is difficult to eliminate by frequency filtering. Fortunately, the spatial location of jamming source is usually different from that of the target. Spatial filtering can thus be used to separate them in the space domain.

Spatial filtering in radar is achieved by forming a specific radar antenna beam pattern. A narrow mainlobe means good selectivity, and low sidelobes means strong rejection capability. However, producing an antenna with very low sidelobes in all directions is difficult to achieve in practice. High-power interfering signals can still come into the receiver through sidelobes and degrade the desired signal. Furthermore, the direction of jamming source may change with time. The beamforming technique deals with this problem. It is able to adaptively form an antenna beam pattern with a very low sidelobe in the direction of the interference.

Beam forming utilizes array antennas and considers only signal reception. The array elements are discrete spatial samples over the entire antenna aperture. The signals received by each element are weighted and summed to form the array output. When the weights of array elements can be adaptively adjusted, it is called *adaptive beamforming*.

3.1. Linear Array Model and Classical Beamforming

An ideal linear array consists of identical, omnidirectional, equispaced sensors that are located along a straight line. Figure 6 shows a linear array beamformer for processing narrowband signals. At time instant k , each sensor samples the arriving signal. The output of the beamformer is calculated as

$$y(k) = \sum_{n=1}^N w_n^* x_n(k) \quad (24)$$

where $x_n(k)$ is the input signal of sensor n at time k . For the convenience of notation, a complex conjugate is applied to the weight w_n . Equation (24) can be rewritten in

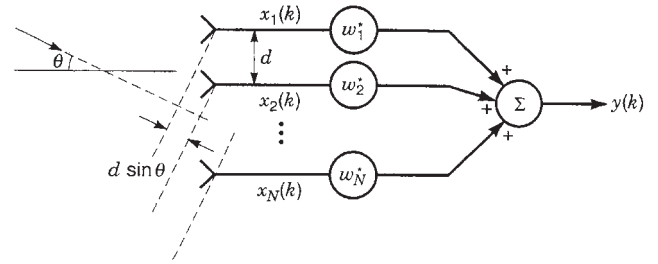


Figure 6. In the linear array model for processing narrowband signals, the signals received by each element are weighted and summed to form the array output.

the following vector form

$$y(k) = \mathbf{w}^H \mathbf{x}(k) \quad (25)$$

where \mathbf{w} and \mathbf{x} are N -dimensional column vectors and H denotes the transposed conjugate.

The array receives plane waves from a target if it is located in the far field. Assume that the signal has a carrier frequency f and comes from direction θ , which is defined as the angle of incidence with respect to the broadside of the array. If two adjacent array elements are separated by a distance d , the signals they received have a phase difference of

$$\phi(\theta, f) = 2\pi(f/c)d \sin \theta \quad (26)$$

where c is the speed of light. In the following analysis, we assume a fixed carrier frequency f . So $\phi(\theta, f)$ is simply denoted by $\phi(\theta)$. At time instant k , if the signal received by the first element is $A(k)\exp[j\phi_1(k)]$, that received by the n th element is $A(k)\exp[j(\phi_1(k) - (n-1)\phi(\theta))]$.

If the first element is used as reference, which means the phase of its signal, $\phi_1(k)$, is set to zero, then the phase of each array element can be written as

$$\mathbf{d}(\theta) = (1, \exp[j\phi(\theta)], \dots, \exp[j(N-1)\phi(\theta)])^H \quad (27)$$

This vector is termed the steering vector, which is also known as the direction vector, array manifold, or array response vector. The output of the beamformer can be expressed as

$$y(k) = \mathbf{w}^H \mathbf{x}(k) = A(k) \mathbf{w}^H \mathbf{d}(\theta) \quad (28)$$

The normalized output is denoted by

$$r(\theta) = \mathbf{w}^H \mathbf{d}(\theta) \quad (29)$$

where $r(\theta)$ is called the beamformer response. The square of $r(\theta)$ is defined as the beam pattern.

In classical beamforming, the objective is to approximate the ideal response that is unity in a desired direction and zero elsewhere. The classical beamformer, also known as the conventional beamformer, is used to receive a desired signal coming from a known direction θ_0 . The solution is to choose the weight as $\mathbf{w} = \mathbf{d}(\theta_0)$. From Eq. (29) the

beamformer response is

$$r(\theta) = \sum_{n=0}^{N-1} \exp\{-jn[\phi(\theta) - \phi(\theta_0)]\} \tag{30}$$

$$= S_N\{[\phi(\theta) - \phi(\theta_0)]/2\}$$

where $S_N(x)$ is defined as

$$S_N(x) = N \sin(Nx)/(N \sin x) \tag{31}$$

and is called the periodic sinc function. The peak of the response is located at angle θ_0 . So the mainlobe of the beam points to θ_0 . It is also said that the beam is steered to θ_0 . In practice, amplitude tapering or weighting is usually used to control the sidelobe levels. As $r(\theta)$ is the summation of the phase-shifted output of each element, the beamformer is also termed a *phased array*.

3.2. Adaptive Beamforming

3.2.1. Multiple Sidelobe Canceler. As stated earlier, strong jamming sources usually come into the receiver through antenna sidelobes. It is thus desirable to form a beam pattern with nulls in the directions of the jamming sources. The multiple sidelobe canceler (MSC) is the earliest beamformer that achieves this goal. An MSC consists of a main antenna and one or more auxiliary antennas, as shown in Fig. 7. The mainlobe of the main antenna points to the target of interest. Interfering signals are assumed to enter through its sidelobes. It is assumed that the auxiliary antennas only receive interfering signals and noise. The weight of each element can be adaptively adjusted to produce an output that estimates the interfering signals in the main channel. Subtracting the output from the main channel by this estimate effectively cancels the interference in the main channel.

Denote the signal in the main channel by y_m , the input of auxiliary antennas by \mathbf{x}_a , and the weight vector by \mathbf{w} . The output of the auxiliary array is $y_a = \mathbf{w}^H \mathbf{x}_a$. Since y_a is assumed not to contain the target signal, successful cancellation of interference is equivalent to minimization the

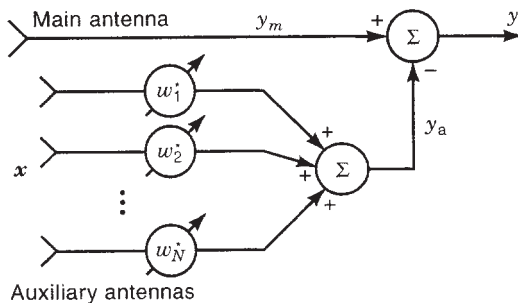


Figure 7. The multiple sidelobe canceler consists of a main antenna and an auxiliary adaptive beamformer. The latter estimates the interference in the main channel, which is then subtracted from the main channel.

overall output power $E[|y_m - y_a|^2]$:

$$P_{\min} = \min_w E(|y_m - \mathbf{w}^H \mathbf{x}_a|^2) \tag{32}$$

The weight that satisfies this equation is called the optimum weight, which is given by [5]

$$\mathbf{w}_{\text{opt}} = \mathbf{R}_a^{-1} \mathbf{p}_{\text{am}} \tag{33}$$

where $\mathbf{R}_a = E[\mathbf{x}_a \mathbf{x}_a^H]$ is the covariance matrix of input data in auxiliary antennas, and $\mathbf{p}_{\text{am}} = E[\mathbf{x}_a y_m^*]$ is the cross-correlation vector of \mathbf{x}_a and y_m .

One should notice the assumption that the target signal is absent in the auxiliary antennas. This is necessary. Otherwise, it will cause cancellation of target signal in the final output. However, the MSC can still work well with slight signal loss if the target signal in the auxiliary antennas is very small.

3.2.2. Linearly Constrained Adaptive Beamforming. Another popular class of adaptive beamforming techniques is the linearly constrained adaptive beamforming. It prevents the loss of desired signal by imposing linear constraints on the weights. Equation (29) shows that the beamformer response to a signal from direction θ is $\mathbf{w}^H \mathbf{d}(\theta)$. If the direction of interest is θ_0 , the constraint can be expressed as $\mathbf{w}^H \mathbf{d}(\theta_0) = f$, where f is constant. It ensures that the desired signal from angle θ_0 will pass the beamformer with response f . Thus, minimizing the overall output power, $E[|y|^2] = \mathbf{w}^H \mathbf{R}_x \mathbf{w}$, will minimize the output produced by interference and noise from directions other than θ_0 . The linearly constrained beamforming can be expressed as

$$\min_w \mathbf{w}^H \mathbf{R}_x \mathbf{w} \text{ subject to } \mathbf{w}^H \mathbf{d}(\theta_0) = f \tag{34}$$

The solution of the optimum weight is

$$\mathbf{w} = f^* \frac{\mathbf{R}_x^{-1} \mathbf{d}(\theta_0)}{\mathbf{d}^H(\theta_0) \mathbf{R}_x^{-1} \mathbf{d}(\theta_0)} \tag{35}$$

When $f=1$, the beamformer is also termed the minimum variance distortionless response (MVDR) beamformer. There is only one constraint on \mathbf{w} in Eq. (34). In fact, multiple constraints can also be used to add more control on the beam former response [6].

The generalized sidelobe canceler (GSC) [7] is an alternative approach to the linearly constrained adaptive beamforming. It converts the constrained optimization of Eq. (34) to unconstrained optimization by separating out the constraint. Figure 8 shows the structure of the GSC. The upper or main branch is a classical beamformer, which has a fixed weight \mathbf{w}_c . The weight \mathbf{w}_c is chosen so that the response of the main beamformer satisfies the constraint in Eq. (34). So the desired signal from angle θ_0 will pass the main beam former with desired response f . Interference and noise will produce some output determined by \mathbf{w}_c . The lower branch is an adaptive beamformer, which is used to estimate the output produced by

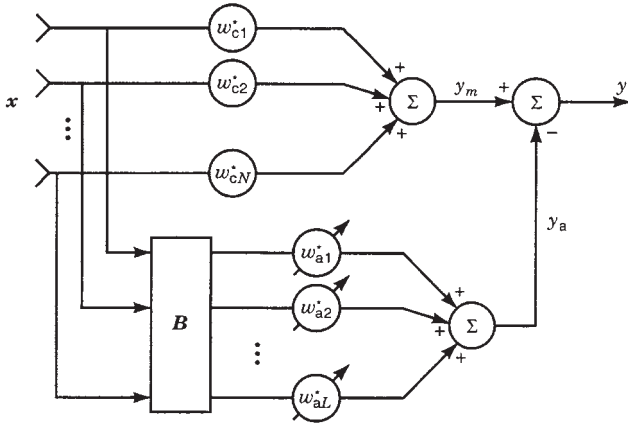


Figure 8. The upper channel of the generalized sidelobe canceler is a classical beamformer, which has a constant response to the desired signal. The lower channel is an adaptive beamformer. It estimates the interference in the upper channel, which is then subtracted from the upper channel. The blocking matrix B blocks desired signal and thus prevent signal cancellation.

interference and noise in the main beamformer. The estimate is then subtracted from the main branch to cancel the interference and noise in the final output. This is similar to that in the MSC. The difference is that there is a preprocessing matrix B in the lower branch of the GSC. The purpose of B is to block the desired signal and thus to prevent signal cancellation in the final output. So B is named the blocking matrix. For an array that is not pre-steered, B needs to satisfy $d^H(\theta_0)B = 0$. The columns of B are linearly independent, and the number of columns L should be less than the number of array elements.

The overall output of the GSC is $y = y_m - y_a$, where y_m and y_a are the output of the upper and lower beamformers, respectively. Since y_a does not contain the desired signal, cancellation of interference and noise is again equivalent to minimize the overall output power

$$\min_{w_a} E[|y_m - y_a|^2] \quad (36)$$

The solution to the unconstrained optimization is

$$w_a = (B^H R_x B)^{-1} B^H R_x w_c \quad (37)$$

where $R_x = E[\mathbf{x}\mathbf{x}^H]$ is the covariance matrix of input data.

Besides the MSC and the GSC, there are some other criteria for constructing an adaptive beam former, such as using a reference signal or maximizing the SNR.

3.2.3. Adaptive Algorithms. Calculation of the optimum weights for the adaptive beam formers discussed before requires knowledge of second-order statistics, especially the covariance of the input signal. Such information is normally not available and needs to be estimated from received data. The optimum weights are usually estimated and adjusted by adaptive algorithms.

It can be proved that the adaptive beamforming problem is equivalent to the adaptive filtering. So the many adaptive algorithms developed for adaptive filtering can

be utilized for adaptive beamforming. One popular class of adaptive algorithms is based on the gradient, for example, the widely used least-mean-square (LMS) algorithm. Another important class is based on the least-square estimation, such as the sample matrix inversion (SMI) and the recursive least square (RLS) algorithm. There is a separate article in this encyclopedia, RADAR SIGNAL DETECTION, that discusses the adaptive filtering technique. For details of these adaptive algorithms, please refer to that article.

4. CONSTANT FALSE-ALARM RATE

A radar detector makes decision of target presence or absence from the echo of each resolution cell. If the echo is stronger than a prespecified threshold, the decision of target presence is made. Otherwise, it declares no target. The basic parameters of a radar detector are the probability of false alarm and the probability of detection. The article RADAR SIGNAL DETECTION in this encyclopedia discusses basic theories of radar detection. This article focuses on an advanced technique for the detector to maintain approximately constant false-alarm rate (CFAR).

4.1. CFAR Principles

We first investigate the principles of CFAR in the background of Gaussian interference. In this case, the interfering signals in both channels of I and Q, denoted by x and y respectively, are Gaussian processes with zero mean and variance (power) of σ^2 . This is a common model for noise and many types of clutter. A linear envelope detector produces the signal envelope or magnitude, $r = \sqrt{x^2 + y^2}$, which is used for target detection. The r has a Rayleigh probability density function (pdf) as

$$p(r) \frac{r}{\sigma^2} \exp\left(-\frac{r^2}{2\sigma^2}\right) \quad (38)$$

The mean value of r is

$$E[r] = \sigma\sqrt{\pi/2} \quad (39)$$

The false-alarm probability P_{FA} for a given threshold r_t can be calculated as

$$P_{FA} = \int_{r_t}^{\infty} p(r) dr = \exp(-r_t^2/2\sigma^2) \quad (40)$$

The P_{FA} is extremely sensitive to the changes of interference power σ^2 . For example, doubling the interference power can increase the value of P_{FA} from 10^{-8} to 10^{-4} . Hence, it is necessary to maintain approximately constant false-alarm rate in order to ensure that the radar works well when the intensity of interference changes. This can be achieved by adaptively adjusting the threshold according to the interference power. An equivalent method is to normalize the interference signal so that its pdf will be independent of its power σ^2 .

Normalization of the Gaussian processes x and y is done by computing x/σ and y/σ . Correspondingly, the normalized envelope is

$$r_N = \sqrt{(x/\sigma)^2 + (y/\sigma)^2} = r/\sigma \tag{41}$$

Its pdf becomes

$$\begin{aligned} p(r_N) &= p(r = \sigma r_N) / |dr_N/dr| \\ &= r_N \exp(-r_N^2/2) \end{aligned} \tag{42}$$

The false-alarm probability is

$$P_{FA} = \int_{q_t}^{\infty} p(r_N) dr_N = \exp(-r_t^2/2) \tag{43}$$

It can be seen that the new false-alarm probability is independent of the interference power σ^2 . This is the desired property of CFAR. Therefore, if σ can be estimated from the received signals, the normalization process r/σ will produce the constant false-alarm rate. From Eq. (39), we know that an estimate of σ can be obtained by estimating the mean value of r .

An alternative method is to use a square-law envelope detector. The magnitude squared of the envelope is produced, denoted by $q = r^2$, and used for deciding the presence of the target. The pdf of q can be calculated from Eq. (38) as

$$\begin{aligned} p(q) &= p(r = \sqrt{q}) / |dq/dr| \\ &= \frac{1}{2\sigma^2} \exp\left(\frac{-q}{2\sigma^2}\right) \end{aligned} \tag{44}$$

The mean value of q is

$$E[q] = 2\sigma^2 \tag{45}$$

Normalization of q can be done as

$$q_N = r_N^2 = r^2/\sigma^2 = q/\sigma^2 \tag{46}$$

The pdf of the normalized variable q_N is

$$\begin{aligned} p(q_N) &= p(q = \sigma^2 q_N) / |dq_N/dq| \\ &= \exp(-q_N/2)/2 \end{aligned} \tag{47}$$

In this case, the false-alarm probability for a preset threshold q_t is

$$P_{FA} = \int_{q_t}^{\infty} p(q_N) dq_N = \exp(-q_t/2) \tag{48}$$

The false-alarm probability is independent of σ^2 . So the CFAR property is achieved by the normalization of q/σ^2 . Equation (45) indicates that an estimate of σ^2 can be obtained by estimating the mean value of q .

The CFAR principle in the presence of Gaussian interference has been discussed for the linear and square-law envelope detectors. For non-Gaussian interference, its envelope cannot be represented by the Rayleigh pdf model. Specific models, such as the lognormal or the Weibull distribution must be used according to the environment and application. In such cases, the CFAR can still be achieved by proper normalization of the interference signal. The CFAR processing protects the radar detector from excessive numbers of false alarms. The cost is that the probability of detection will be slightly reduced compared with similar cases of thermal-noise-only environment.

4.2. Cell-Averaging CFAR

As analyzed before, for Gaussian interference, the normalization factor can be obtained by estimating the mean value of the signal output from the envelope detector. One basic approach of CFAR is to estimate the mean value by averaging the signals of a set of reference cells around the cell under test. This technique is called cell-averaging CFAR (CA-CFAR). The reference cells can be either in range, angle, or Doppler frequency. The basic assumption in CA-CFAR is that the interference is statistically homogeneous over the reference cells and the cell under test.

Figure 9 shows the structure of the CA-CFAR processor that uses reference cells in range. The envelope detector can have either a linear characteristic that produces the envelope r or a square-law characteristic that produces the magnitude squared of envelope q . The received signals from the reference cells are averaged to produce an estimate of their mean value. The immediate neighbors of the test cell are sometimes discarded in case a strong target signal extended into them. The signal of the test cell is then normalized by dividing it by the estimated mean and multiplying it with a scaling constant k . We know from Eqs. (39) and (45) that $k = \sqrt{\pi}/2$ for the linear detector

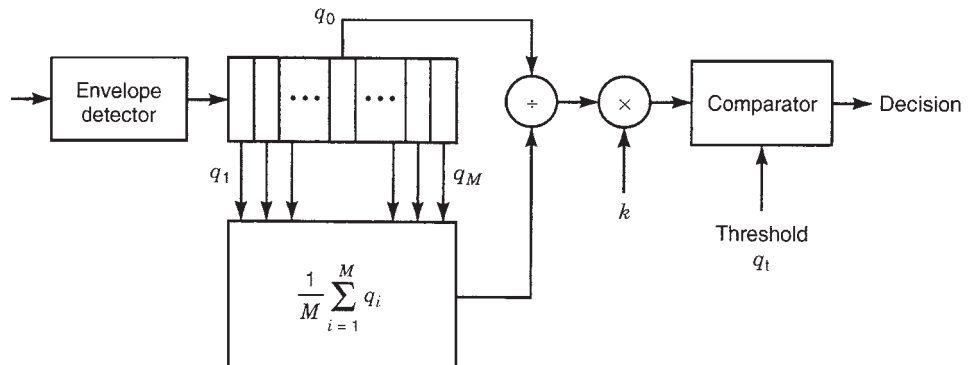


Figure 9. A number of reference cells around the cell under test are used to estimate the interference power in the cell-averaging CFAR processor. The estimate is used to normalize the signal, which is equivalent to adaptively adjusting the threshold.

and $k=2$ for the square-law detector. Finally the normalized envelope of the test cell is compared with a preset threshold to decide if a target is present.

The CA-CFAR principle is applicable to both linear and square-law detection. The analysis that follows is developed for square-law detection without loss of generality. Denote the magnitude squared of envelope of the test cell by q_0 , and that of the reference cells by $q_i (i=1, \dots, M)$. These random variables are statistically independent and have the same probability density function in a homogeneous environment as given in Eq. (44). Their joint density function is

$$p(q_0, \dots, q_M) = \prod_{i=0}^M \frac{1}{2\sigma^2} \exp\left(\frac{-q_i}{2\sigma^2}\right) \quad (49)$$

Denote the sum of the M reference cells by $q_M = \sum q_i$. The normalization of q_0 is

$$q_{0N} = kMq_0/q_M = 2Mq_0/q_M \quad (50)$$

q_{0N} is then compared with a threshold q_t , and the target-present decision is made when

$$q_{0N} > q_t \quad (51)$$

In practice, only a limited number of reference cells M can be utilized to estimate the mean value. Intuitively, the performance of CA-CFAR must be dependent on M . Substituting Eq. (50) into Eq. (51), we get

$$q_0/q_M > q_t/(2M) \quad (52)$$

For random variables $q_i (i=1, \dots, M)$ having the density function given by Eq. (49), the ratio q_0/q_M , called f variate, is known to have the following pdf [8]:

$$p(f) = M/(1+f)^{M+1}, \quad 0 \leq f < \infty \quad (53)$$

The false-alarm probability can then be calculated as

$$P_{FA} = \int_{q_t/2M}^{\infty} p(f)df = \left(1 + \frac{q_t}{2M}\right)^{-M} \quad (54)$$

It can be seen from Eq. (54) that the CFAR property can be achieved even for small values of M , since the false-alarm probability is independent of the interference power σ^2 . Equation (54) approximates the ideal performance when M is very large such that

$$\lim_{M \rightarrow \infty} \left(1 + \frac{q_t}{2M}\right)^{-M} = \exp(-q_t/2) \quad (55)$$

For a limited number of reference cells, higher signal-to-noise ratio is needed to achieve the required false-alarm probability and detection probability. This is referred to as the CFAR loss.

For Swerling I and II targets, one can find the detection probability using similar methods. The signals of a Swerling I or II target in I and Q channels are also modeled as a

zero-mean Gaussian process with a variance of σ_s^2 . The overall variance is thus $\sigma_s^2 + \sigma^2$ when the target is present. Denote the signal-to-noise ratio by $\text{SNR} = \sigma_s^2/\sigma^2$. A similar analysis shows the detection probability P_d is

$$P_d = \left(1 + \frac{q_t}{2M(1+\text{SNR})}\right)^{-M} \quad (56)$$

and

$$\lim_{M \rightarrow \infty} P_d = \exp\left(-\frac{q_t}{2(1+\text{SNR})}\right) \quad (57)$$

For given P_{FA} and P_d , the SNR for M reference cells, denoted by SNR_M , can be derived from Eqs. (54) and (56). On the other hand, the SNR for $M \rightarrow \infty$, denoted by SNR_∞ , can be obtained from Eqs. (55) and (57). The CFAR loss is defined as the ratio of SNR_M and SNR_∞ . It is a function of P_{FA} , P_d , and M . It has been shown [9] that for large M , the CFAR loss can be approximated by $P_{FA}^{-1/2M}$.

4.3. Ordered-Statistics CFAR

The CA-CFAR does not work well for nonhomogeneous interference. One example is when there are interfering targets in the reference cells. Another case is when the background clutter varies dramatically along either range or azimuth or both. Cell averaging can no longer produce the correct estimate, which results in the loss of detection performance. The ordered-statistics CFAR (OS-CFAR) has been proven to have better performance in such environments.

In the OS-CFAR, the threshold is determined by multiplying one of the ranked cell by a scaling factor. Assume that the reference cells have the signals of $q_i (i=1, \dots, M)$ after the envelope detector. They are ranked as $q_1 \leq q_2 \leq \dots \leq q_K \leq \dots \leq q_M$. The variable K is the rank of the cell to be used for calculating the threshold, which is

$$q_t = \alpha q_K \quad (58)$$

The scaling factor α provides a mechanism to control the false-alarm probability.

4.4. Clutter-Map CFAR

The clutter-map CFAR is an effective approach for dealing with nonhomogeneous interference. It utilizes the statistics of past observations on the test cell itself rather than that of the reference cells. It assumes that the statistics of the test cell do not change during the observations so that time averaging can be performed. In fact, the average of previous observations on each cell produces a clutter map—an estimate of clutter power in each corresponding cell.

The principle of clutter-map CFAR is similar to that of the CA-CFAR. The basic analysis of CA-CFAR is applicable to clutter-map CFAR. In clutter-map CFAR processing, the M reference samples are obtained from M scans on the test cell. They are averaged in the same way as that in CA-CFAR to produce an estimate of the interference power. Further processing is also similar to CA-CFAR. In a new

scan, if the target-present decision is made, the power estimate will not be updated. Otherwise, the new sample is used to compute a new average.

A simplified implementation is to store only the estimate by previous samples, denoted by \hat{p}_{n-1} from previous $n - 1$ scans, and updates the estimate with the new sample q_n :

$$\hat{p}_n = (1 - w)\hat{p}_{n-1} + wq_n \tag{59}$$

This is actually an exponential smoothing, since

$$\hat{p}_n = w \sum_{i=0}^{\infty} (1 - w)^i q_{n-i} \tag{60}$$

The value of w determines the length of the exponential window. In practice, the length of the window should be chosen to commensurate with the rate of change of the interference power.

5. PULSE COMPRESSION

Pulse compression is a technique that obtains high range resolution while maintaining good detection range. Signals used for pulse compression should have large bandwidth. There are two approaches to increase the bandwidth: frequency modulation (FM) and phase coding. The device that performs the pulse compression is the matched filter.

5.1. Frequency Modulation Waveforms

The linear FM signal is the earliest pulse compression waveform. Techniques for linear FM pulse compression are well developed and widely used. Another relatively new technique adopts the stepped-frequency waveforms.

5.1.1. Principles of Linear FM Pulse Compression. The linear FM signal, whose carrier frequency varies linearly during the pulse, is the most widely used waveform. It is also known as the *chirp* signal and can be expressed by

$$s_i(t) = A \cos(2\pi f_0 t + \pi \mu t^2), \tag{61}$$

$$-T/2 \leq t \leq T/2$$

where f_0 is the carrier frequency. The constant μ is called the chirp rate. The instantaneous frequency of the signal is $f_i = f_0 + \mu t$, which starts at $f_0 - \mu T/2$ and ends at $f_0 + \mu T/2$. The signal bandwidth is $B = \mu T$.

It can be shown [10] that the matched filter for the linear FM pulse compression can be expressed as

$$h(t) = \sqrt{j\mu} \exp[j2\pi(f_0 t - \mu t^2/2)] \tag{62}$$

The $h(t)$ has an inverse chirp rate as compared with the input signal. The output of the matched filter is

$$s_0(t) = \int_{-\infty}^{\infty} s_i(\tau)h(t - \tau) d\tau$$

$$= \sqrt{j\mu} \int_{-T/2}^{T/2} \exp\{j2\pi[f_0 \tau + \mu \tau^2/2 + f_0(t - \tau) - \mu(t - \tau)^2/2]\} d\tau$$

$$= \sqrt{j\mu T^2} \frac{\sin(\pi \mu T t)}{\pi \mu T t} \exp[j2\pi(f_0 t - \mu t^2/2)] \tag{63}$$

The envelope of the output signal is a sinc function:

$$e_o(t) = \sqrt{\mu T^2} \frac{\sin(\pi \mu T t)}{\pi \mu T t} \tag{64}$$

For the sinc function, the peak-null pulsewidth is defined as the distance from the peak to the first null. For $\sin x/x$, the first null occurs at $x = \pi$. So the width of the compressed pulse is

$$T' = \frac{1}{\mu T} = \frac{1}{B} \tag{65}$$

It equals the reciprocal of the signal bandwidth. The pulse compression ratio is defined as the ratio of the pulsewidth before and after the pulse compression processing. From Eq. (65), we have

$$D = T/T' = TB \tag{66}$$

Therefore, the pulse compression ratio is equal to the time-bandwidth product of the signal.

From Eq. (3), the range resolution after pulse compression is

$$\rho_r = \frac{cT'}{2} = \frac{c}{2B} \tag{67}$$

It should be noted that the peak-null pulsewidth corresponds to the mainlobe width at -4 dB (power) points. Another definition of pulsewidth is the mainlobe width at -3 dB, which is called half-power pulsewidth and can be expressed as K_w/B , where K_w is a constant factor. For the sinc function, $K_w = 0.866$.

It is well known that the sinc function has high sidelobes. To reduce sidelobes, one approach is to apply weighting in the compression filter. It can greatly reduce the sidelobes at the cost of mainlobe broadening. Table 1 lists some popular weighting functions with the corresponding peak sidelobe levels and mainlobe width at -3 dB. Another approach to reduce the sidelobes is to use nonlinear FM waveforms. In this case, the spectrum of the transmitted signal is weighted, which also provides low sidelobes in the compressed pulse.

Table 1. Properties of Weighting Functions

Weighting Function	Peak Sidelobe Level (dB)	Mainlobe Width at -3 dB, K_w/B
Rectangular	-13.26	$0.886/B$
Hanning	-31.5	$1.42/B$
Hamming	-42.5	$1.32/B$
Taylor, $\bar{n} = 5$	-35	$1.19/B$
Taylor, $\bar{n} = 6$	-40	$1.25/B$
Dolph-Chebyshev	-40	$1.20/B$

5.1.2. Implementation of Linear FM Pulse Compression.

The commonly used analog devices for linear FM pulse compression are the dispersive delay lines, in which the signal delay is dependent on its frequency. The most popular one is the surface acoustic wave (SAW) device. The electrical signal is converted into a surface wave at the input, which propagates through the medium at acoustic speed. The dispersive property of the device achieves the matched filtering. At the output the wave is converted back to the electrical signal. Another type of ultrasonic device is the bulk acoustic wave device, which is less energy-efficient than the SAW device. These ultrasonic devices can process signals with bandwidth greater than 1000 MHz [10].

Linear FM pulse compression can also be implemented by digital methods. The received signal is sampled by an ADC and transformed into the frequency domain via FFT. The matched filtering is performed in the frequency domain by multiplying the signal spectrum with the frequency response of the matched filter. The result is then transformed back into the time domain.

A third technique is called stretch processing, which can process signals with very large time-bandwidth products. Figure 10 shows its principle. Echoes from a set of scatterers are linear FM signals whose starting points correspond to the ranges of each scatterer. They are mixed with a reference signal, which is also a linear FM with the

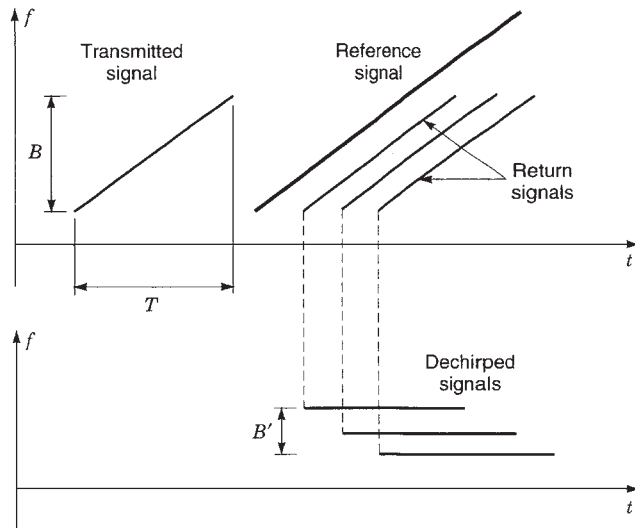


Figure 10. The stretch processing can reduce the signal bandwidth by dechirping the return signal. The dechirped signal is then digitized and transformed by an FFT, which accomplishes pulse compression.

same chirp rate as that of the transmitted signal. The mixing (dechirping) process removes the frequency modulation of the received signal. Each dechirped signal has a constant frequency that corresponds to its range. An ADC then samples these dechirped signals. Finally, a frequency analysis by FFT distinguishes each scatterer in the range. The stretch processing is also widely used in high-resolution radars.

5.1.3. Stepped-Frequency Waveforms. In this pulse compression technique, the radar transmits a burst of narrowband pulses, and the carrier frequency changes discretely from pulse to pulse by a stepsize Δf . Compared with the linear FM waveform, the stepped-frequency waveforms can be regarded as discrete modulation in frequency. If there are N pulses in a burst, the overall bandwidth of the transmitted signal is $B = N\Delta f$.

Each received pulse is then downconverted to baseband, and a pair of I and Q samples is collected in a desired range gate. The length of the range gate is determined by Δf , which is $r = c/(2\Delta f)$. The ensemble of I and Q samples represent results that the received signal within the desired range gate is discretely sampled in the frequency domain over the bandwidth B . There is a condition to be satisfied. That is, the duration of the baseband response of each pulse should extend the whole desired range gate. This is ensured if $T_p \geq 1/\Delta f$, where T_p is the duration of each pulse.

Pulse compression is accomplished by applying the inverse discrete Fourier transform on the N pairs of I and Q samples. The result is a high-resolution range profile with N complex samples over the desired range gate. The length of the range profile is r , and the resolution is

$$\rho_r = \frac{c}{2B} = \frac{c}{2N\Delta f} \quad (68)$$

Pulse compression using the stepped frequency avoids the requirements of wide instantaneous bandwidth and high sampling rates. However, transmitting multiple pulses require relatively long time. When there is large motion between the radar and the target, the motion-induced phase errors between pulses must be compensated before the pulse compression can be performed.

5.2. Phase-Coded Waveforms

The phase-coded signal is a constant-amplitude sinusoid that is divided into N equal segments. The phase of the sine wave in each segment is selected according to given code sequence. If the phase is set at either 0 or π , it is called *binary*, or biphase, coding. If the code sequence contains more than two values, it is called *polyphase coding*.

The pulse compression principle can be demonstrated by correlation processing, which is equivalent to matched filtering. Consider a binary-coded signal with N segments. Denote the value of the k th segment by a_k , which is either 1 or -1. The aperiodic autocorrelation function of this waveform can be written as

$$\Phi(m) = \sum_{k=1}^N a_k a_{k+m}, \quad -(N-1) \leq m \leq N-1 \quad (69)$$

If $m = 0$, then $a_k a_{k+m} = 1$ for each segment k , and the summation equals N . When $m \neq 0$, the value of the autocorrelation function is much smaller than N . Thus the correlation processing produces a narrow pulse, whose mainlobe locates at $m = 0$ with the amplitude of N . The regions where $m \neq 0$ are sidelobes. A well-designed code sequence can produce a pulse with very low sidelobes.

The Barker codes are the binary codes that have the lowest peak sidelobe. The aperiodic autocorrelation of Barker codes has the value of either 0 or 1 for $m \neq 0$, and hence the peak sidelobe is 1. With respect to the mainlobe, the peak sidelobe level is $\frac{1}{13}$, or -22.3 dB. However, no Barker codes whose length is greater than 13 have been found. The pulse compression ratio for Barker codes is limited to the maximum value of 13. So it is important to find longer sequences with good sidelobe properties.

The minimum peak sidelobe codes are the binary sequences that attain the lowest peak sidelobes for a given length. Of course, the Barker codes belong to this class of codes. Codes with length of 14–48 have been found [11]. For example, for length 48, the best peak sidelobe that can be achieved is 3, which is -24.1 dB with respect to the mainlobe. Other types of long binary codes are random and pseudorandom codes, in which the phase value of 0 or π are chosen in a random or essentially random manner, each with a probability of 0.5.

All binary codes have the common weakness that they are quite sensitive to the Doppler shift in the received signal. Their performance degrades significantly for large Doppler frequencies. The polyphase codes exhibit better Doppler tolerance and have relatively good sidelobe characteristics. Frank codes and P4 codes are commonly used polyphase codes. They can be thought of as discrete approximations to the linear FM waveform.

The two devices to implement the phase-coded pulse compression are the all-range compressor and cross correlator. The former is suitable for signals with varying delays, and works well for all target range. The latter is usually used when the target range is approximately known.

6. HIGH-RESOLUTION RADAR IMAGING

A radar image is the spatial distribution of microwave reflectivity corresponding to the object. Besides high range resolution, an imaging radar also requires a high azimuth resolution. It thus requires a large antenna aperture in azimuth direction. To avoid practical difficulties in constructing a large antenna, the synthetic aperture technique is developed.

6.1. Principles of Synthetic Aperture Techniques

The azimuth resolution of a real antenna is discussed first. Consider the linear array model of Fig. 6. For simplicity, we assumed that there is no beamsteering and uniform weighting is applied to each array element, that is, $\mathbf{w} = [1, 1, \dots, 1]^T$. Similar to Eq. (30), the array response

can be found as

$$r(\theta) = \sum_{n=0}^{N-1} \exp[-jn\phi(\theta)] \tag{70}$$

$$= N \frac{\sin[N\pi(d/\lambda) \sin \theta]}{N \sin[\pi(d/\lambda) \sin \theta]}$$

where $\lambda = c/f$ is the wavelength. The $r(\theta)$ is also periodic sinc function similar to Eq. (31). The peak of its mainlobe is at $\theta = 0$. Its first null occurs when $\sin \theta = \lambda/(Nd)$, where $Nd = D$ is the entire array aperture. When D is very large, $\sin \theta$ is very small, and $\sin \theta \approx \theta$. So the first null occurs at $\theta = \lambda/D$. The peak-null beamwidth, the distance from the peak to the first null, is thus

$$\beta_\theta = \lambda/D \tag{71}$$

Although the result is derived from the array antenna, it is applicable to continuous-aperture antennas. The azimuth resolution of a real antenna at range R is $R\lambda/D$.

Synthesizing a large antenna aperture can be achieved by mounting a small-aperture antenna on a moving platform. The antenna transmits and receives signals while the platform moves. The received data can then be used to synthesize a large aperture. Such a system is called synthetic aperture radar (SAR).

Figure 11 shows two common operating modes of SAR: strip map and spotlight. In stripmap SAR, the antenna beam is fixed relative to the flight path. The moving antenna sweeps out a strip of terrain that is parallel to the flight path. In spotlight SAR, the beam is steered to continuously illuminate a relatively small patch of terrain. There is another widely used mode that is called inverse synthetic aperture radar (ISAR). In ISAR, the radar is usually stationary (although it can also be moving), and the target being imaged is moving. After motion compensation, the relative motion between the radar and the target is similar to that of the spotlight SAR.

The azimuth resolution of SAR can be derived from Fig. 12 by finding the synthetic-array response. The cross-range (azimuth) direction, denoted by x , is defined in the

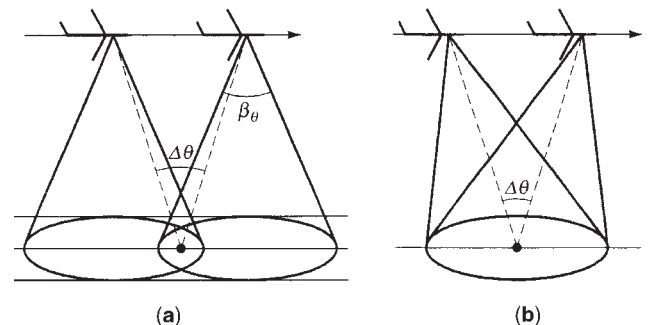


Figure 11. (a) Stripmap-mode SAR. Its resolution is limited by the antenna beamwidth β_θ due to the fixed antenna pointing. (b) Spotlight-mode SAR. The antenna tracks a small imaging area. Its resolution can be very high, but imaging area is limited by antenna beamwidth.

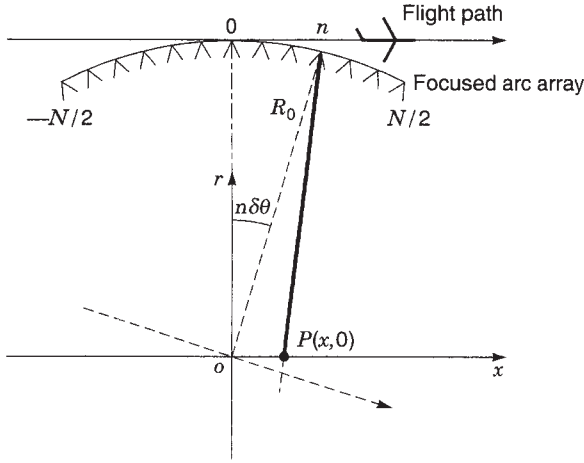


Figure 12. The cross-range resolution of SAR can be derived from this array model. It is compensated to an arc array in the focused SAR processing.

flight direction. SAR processing can be of focused or unfocused type. In focused processing, the phases of the signals are compensated so that each array element receives a signal from the origin O with the same phase. It is equivalent to transforming the linear array into an arc array. The unfocused processing does not perform such phase compensation and has a low resolution. The cross-range resolution is derived here only for focused processing.

The movement of the radar along the arc path introduces a relative rotation between the radar and the target. The observing angle from radar to the origin O will change an amount of $\delta\theta$ between two adjacent elements. Assume that there are N elements in all, and the central element is the reference. The n th element has an observing angle of $n\delta\theta$ ($-N/2 \leq n \leq N/2$).

Denote the distance from the origin to each element on the arc array by R_0 . Since only the cross-range resolution is of interest, we consider a point P at $(x, 0)$. It is in the far field with respect to the real antenna and $x \ll R_0$. So the distance from P to the n th element is

$$R_n(x) \approx R_0 - x \sin n\delta\theta \quad (72)$$

The phase of the signal caused by the two-way time delay is

$$\phi_n(x) = \frac{4\pi}{\lambda} R_n(x) \approx \frac{4\pi}{\lambda} R_0 - \frac{4\pi}{\lambda} x \sin n\delta\theta \quad (73)$$

The first term in Eq. (73) is a constant phase and can be removed. The term $n\delta\theta$ is usually very small, and thus $n\delta\theta \approx n\delta\theta$. So the array response is

$$\begin{aligned} r(x) &\approx \sum_{n=-N/2}^{N/2} \exp\left(-j \frac{4\pi}{\lambda} x n \delta\theta\right) \\ &= N \frac{\sin[(2\pi/\lambda)N\delta\theta x]}{(2\pi/\lambda)N\delta\theta x} \end{aligned} \quad (74)$$

It is a sinc function. The peak is at $x = 0$, and the first null occurs at $(2\pi/\lambda)N\delta\theta x = \pi$. So the cross-range resolution

measured by the peak-null beamwidth is

$$\rho_x = \frac{\lambda}{2\Delta\theta} \quad (75)$$

where $\Delta\theta = N\delta\theta$ is the total integration angle. The cross-range resolution expressed by Eq. (75) is applicable to strip-map SAR, spotlight SAR, and ISAR. It can also be expressed by the synthetic aperture length L since $\Delta\theta = L/R_0$. Thus

$$\rho_x = \frac{\lambda R_0}{2L} \quad (76)$$

In stripmap SAR, the synthetic aperture length L and the integration angle $\Delta\theta$ are limited by the beamwidth of the real antenna β_θ due to the fixed beamsteering. As shown in Fig. 11, the maximum value of $\Delta\theta = \beta_\theta$, which is expressed by Eq. (71). Therefore, the maximum cross-range resolution in stripmap SAR is

$$\rho_{x \max} = \frac{\lambda}{2(\lambda/D)} = \frac{D}{2} \quad (77)$$

where D is the aperture length of the real antenna.

6.2. Stripmap SAR Image Formation

The most common method for stripmap SAR image formation is the range-Doppler (RD) algorithm. Consider the geometry of data collection shown in Fig. 13, where r denotes the slant range and x denotes the cross-range. Assume that the transmitted pulse is

$$s_t(t) = a(t) \exp\{j[\omega t - \phi(t)]\} \quad (78)$$

where $a(t)$ is a rectangular window of unity amplitude over the pulse duration, and $\phi(t)$ represents the phase modulation. The distance from the radar to a target at $x = 0$ varies according to

$$R(x, r) = \sqrt{r^2 + x^2} \approx r + x^2/(2r) \quad (79)$$

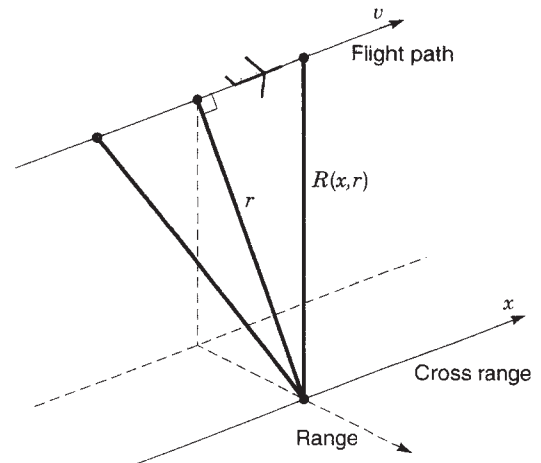


Figure 13. Data collection geometry of the stripmap SAR.

The received signal from this point after demodulation is

$$s_r(t, x, r) = \sigma a [t - 2R(x, r)/c] \exp(-j\{4\pi R(x, r)/\lambda + \phi[t - 2R(x, r)/c]\}) \quad (80)$$

where σ is the radar cross section of the target. The change of antenna gain is assumed to be small and can be omitted. The normalized form of Eq. (80) is the impulse response:

$$h(t, x, r) = a [t - 2\Delta R(x, r)/c] \exp(-j\{4\pi\Delta R(x, r)/\lambda + \phi[t - 2\Delta R(x, r)/c]\}) \quad (81)$$

where

$$\Delta R(x, r) = R(x, r) - r \approx x^2/(2r) \quad (82)$$

which is the well-known range migration (RM). RM can be neglected if β_θ is small. It is also omitted in the unfocused processing. In the focused processing, the integration of the signal must be along the curved locus, or the curved locus must be straightened (RM-compensated) before integration.

The return signal from an extended target $\sigma(x, r)$ is

$$s_r(x, r) = \sigma(x, r) \otimes h(x, r) \quad (83)$$

where \otimes denotes a two-dimensional convolution. It can be shown (12) that Eq. (83) can be expressed by

$$s_r(x, r) = [\sigma(x, r) \otimes h_1(x, r)] \otimes h_2(x, r) \quad (84)$$

where

$$h_1(x, r) = \delta(r - \Delta R(x, r)) \exp[-j4\pi\Delta R(x, r)/\lambda] \quad (85)$$

$$h_2(x, r) = (2/cv)\delta(x)a(r) \exp[-j\phi(r)] \quad (86)$$

where v is the along-track speed of the radar and $\delta(x)$ is Dirac's delta function. It can be seen that the received signal is obtained by sequentially convolving $\sigma(x, r)$ with two impulse response h_1 and h_2 . Therefore $\sigma(x, r)$ can be reconstructed by sequentially correlating the return signal $s_r(x, r)$ with h_2 and h_1 . Equation (86) shows that h_2 is actually a one-dimensional (1D) function of range r , and has the same waveform as the transmitted pulse. Correlation of $s_r(x, r)$ with h_2 is thus the conventional pulse compression in range.

The h_1 is a 2D function, due to the RM effect. The RM compensation is usually implemented by an interpolation in the range-Doppler domain, which straightens the curved locus. The signal is then compressed in azimuth after the correction [12–14]. To further reduce the phase errors, a technique called secondary range compression [13–15] can be adopted.

Besides the RD algorithm, two wavenumber domain algorithms have also been developed for SAR processing: the range migration algorithm (RMA) [16] and the chirp scaling algorithm (CSA) [17]. Denote the Fourier transform of $h(t, x, r)$ by $H(\omega, k_x, k_r)$, where k_x and k_r are spatial frequencies and are usually called x and r wavenumbers; ω is the temporal frequency, and $k_r = 2\omega/c$.

The RMA first transforms the received data $s_r(x, t)$ to $S_r(k_x, \omega)$ by a 2D Fourier transform. Then it maps the data from the $k_x - \omega$ domain to the $k_x - k_r$ domain by a process called Stolt interpolation. A 2-D phase compensation is performed in this domain, which corrects the range migration effect. The image is finally constructed by a 2D inverse Fourier transform.

The RMA is capable of imaging a large terrain area with fine resolutions. Its drawback is that the Stolt interpolation is time consuming. Figure 14 shows an example of SAR image processed by the RMA. The raw data were collected by ESAR-2, and made available by German Aerospace Research Establishment (DLR). The image resolution is about 3 m in range and 0.2 m in azimuth.

The difficulty of RM correction is that scatterers located at different positions have different migration loci, and thus a large amount of computational effort is need. On the other hand, with its unique procedures, the chirp scaling algorithm is able to adjust all the different loci to the same trajectory in the 2D spatial-frequency domain



Figure 14. An example of an ESAR-2 stripmap SAR image. It is processed by the range-migration algorithm. [The ESAR-2 data were made available by courtesy of the German Aerospace Research Establishment (DLR).]

without much computational effort. Then the range-migration correction can be easily performed by a phase multiplication to each point.

The CSA requires only FFTs and complex multiplies. No interpolation is needed. So it is computationally efficient. However, it has been shown (18) that the CSA implements only the shift and linear components of the Stolt mapping. So the RM compensation is not complete. Nonetheless, such approximate compensation can produce satisfactory results for most applications.

6.3. Image Formation in Spotlight SAR and ISAR

The spotlight SAR and ISAR are developed mainly for imaging a small terrain or target with high resolutions. To take the advantage of the small imaging area, spotlight SAR and ISAR systems usually adopt the linear FM signal and the stretch processing technique described earlier. Stretch processing can largely reduce the analog signal bandwidth, and thus requires low AD sampling rates, and small storage memory.

Recall the principles of stretch processing depicted in Fig. 10. Here the reference signal for dechirping (mixing) process is chosen to be the replica of the return signal from the center of the scene being imaged. The return signals from the scene center after mixing have zero Doppler frequency, which means that there is no relative radial motion between the radar and the scene center. So it is also referred to as motion compensation with respect to the scene center. While this procedure compensates the translational motion, it retains the rotational motion between the radar and the scene center, which forms an ideal arc synthetic array.

It can be shown [18] that the motion compensation dechirpes received signals in both range and azimuth directions and transforms the data into the $k_r - k_x$ domain. As discussed earlier, this is the two-dimensional spatial-frequency (wave-number) domain. Thus, the image can be constructed by a 2D inverse Fourier transform. The question is that the data samples in the $k_r - k_x$ domain are not located on a rectangular grid. Rather, they are on the polar coordinates. The data support is a ribbon whose size is determined by the transmitted bandwidth B and the integration angle $\Delta\theta$, as shown in Fig. 15.

For a small scene size, if the values of B and $\Delta\theta$ are small, which means low resolutions in range and azimuth, the small ribbon can be directly approximated by a rectangle. Then the 2D inverse Fourier transform can be performed by two 1D inverse FFTs in range and azimuth. This method is referred to as a rectangular format algorithm. A scatterer can be well focused by this algorithm if it does not move through resolution cells during the whole observation. For large scene size and high resolutions, the scatterer's motion through resolution cells will cause image defocus. So the data must be stored in the polar format. Since the Fourier transform does not have fast algorithms in polar format, a 2D interpolation is needed to map the data from polar to rectangular grid. Finally the image can be constructed via two 1D inverse FFTs. This method is called polar format algorithm.

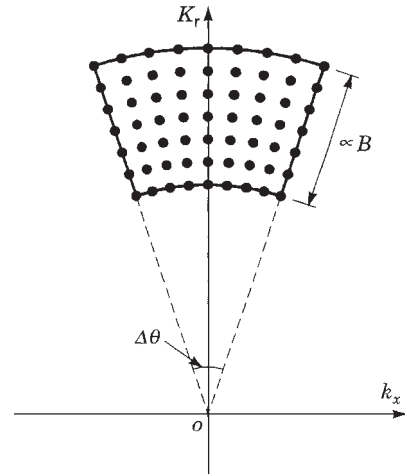


Figure 15. Support area of spotlight SAR signals after motion compensation to the scene center. Its size is determined by the signal bandwidth and the integration angle. Data samples are located on the polar format.

The range-migration algorithm and the chirp scaling algorithm discussed in the preceding section can be utilized for spotlight SAR image formation. They do not require motion compensation to the scene center. Another method known as convolution backprojection algorithm, which is widely used in computer-aided tomography (CT), can also be used for spotlight SAR image formation, since the geometry of data collection in spotlight SAR is very similar to that in CT [19].

6.4. Autofocus Techniques

Even in a well-design SAR system, it is still difficult to measure the relative motion between the radar and the target with high accuracy over the whole synthetic aperture. The case is even worse in ISAR because the target is usually non-cooperative. In such cases, phase errors will be introduced to the received signals. Such phase errors are space-invariant, which means all the range bins have the same phase error during one observation. Autofocus is a useful technique to estimate and remove the space-invariant phase errors.

Many autofocus algorithm have been presented, such as the map drift (MD) algorithm [18], the dominant scatterer algorithm (DSA) [20], the phase gradient autofocus (PGA) algorithm [21], and the weighted least-square (WLS) algorithm [22].

Autofocus usually begins in the range-compressed phase history domain, where the data are compressed in range but not compressed in azimuth. Suppose the strongest scatterer in the n th range bin has the Doppler frequency f_n and the initial phase $\psi_{0,n}$. Other smaller scatterers are treated as clutter. So the phase of the signal at range bin n and aperture position m is

$$\Phi_n(m) = 2\pi f_n m + \psi_{0,n} + \phi_n(m) \quad (87)$$

where $\phi_n(m)$ is the phase fluctuation caused by clutter. Clutter is commonly assumed independent from range bin

to range bin. When corrupted by a phase error $\gamma(m)$, Eq. (87) becomes

$$\Phi_n(m) = \gamma(m) + 2\pi f_n m + \psi_{0,n} + \phi_n(m), \quad (88)$$

$$n = 1, 2, \dots, N$$

where N is the number of range bins. $\gamma(m)$ is the same for all range bins, since it is space-invariant.

Autofocus is carried out in two steps: estimation and correction. The challenge is the estimation of $\gamma(m)$. Once the estimate $\hat{\gamma}(m)$ is obtained, correction can be done by multiplying the range-compressed phase history data by $\exp[-j\hat{\gamma}(m)]$.

The WLS algorithm is an optimal estimation of $\gamma(m)$ in the sense that it minimizes the variance of the residual phase error. It is capable of estimating and removing all kinds of phase errors, no matter if they are of low order, high order, or entirely random. The first step in the WLS algorithm is to shift the strongest scatterer in each range bin to the center of the image, thus removing its Doppler frequency offset. The initial phase $\psi_{0,n}$ is a constant and can also be removed by proper processing. Then Eq. (88) becomes

$$\Phi_n(m) = \gamma(m) + \phi_n(m), \quad n = 1, 2, \dots, N \quad (89)$$

The task is to estimate the error $\gamma(m)$ from Eq. (89). Since $\phi_n(m)$ causes estimation errors, the objective of the WLS estimation is to minimize the variance of the estimation error. Rewriting Eq. (89) using vector notations, we have

$$\Phi(m) = \mathbf{H}_\gamma(m) + \phi(m) \quad (90)$$

where $\Phi(m) = [\Phi_1(m), \Phi_2(m), \dots, \Phi_N(m)]^T$, $\phi(m) = [\phi_1(m), \phi_2(m), \dots, \phi_N(m)]^T$ and $\mathbf{H} = [1, 1, \dots, 1]^T$.

Denote the variance of the phase term $\phi_n(m)$ by σ_n^2 . The covariance matrix of $\phi(m)$ is

$$\mathbf{R} = \text{diag}[\sigma_1^2, \sigma_2^2, \dots, \sigma_n^2] \quad (91)$$

The weighted least-square estimate of $\gamma(m)$ is

$$\hat{\gamma}_{\text{wls}}(m) = (\mathbf{H}^T \mathbf{R}^{-1} \mathbf{H})^{-1} \mathbf{H}^T \mathbf{R}^{-1} \Phi(m) \quad (92)$$

Figure 16 shows a real ISAR image of an aircraft that is auto-focused by the WLS algorithm. The image resolution is approximately 0.4×0.4 m.

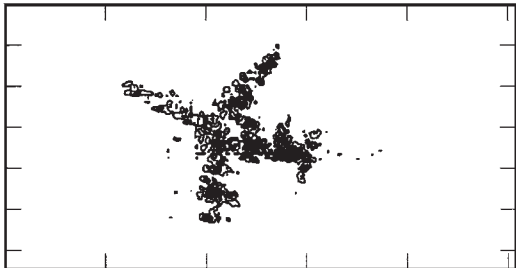


Figure 16. A real ISAR image of an aircraft. It is autofocused by the WLS algorithm.

The PGA is a widely used algorithm in SAR community. It has an iterative procedure for phase error correction. The first step is the same as that in the WLS algorithm, that is, moving the strongest scatterer of each range bin to the image center. The second step is the windowing of each shifted image. The window is centered on the strongest scatterer. Windowing increases the SNR by preserving the width of dominant blur while discarding scatterers that cannot contribute to the phase error estimation.

The next step is to estimate the phase error, or rather, the phase gradient or phase difference. Denote the range-compressed phase history data by $g_n(m) = |g_n(m)| \exp\{j[\gamma(m) + \phi_n(m)]\}$, where $\phi_n(m)$ is the phase fluctuation caused by the clutter within the window. A linear unbiased minimum variance estimate of the gradient of the phase error is

$$\hat{\gamma}(m) = \frac{\sum_n \text{Im}[g_n^*(m) \{\dot{g}_n(m)\}]}{\sum_n |g_n(m)|^2} \quad (93)$$

Another estimate of the phase difference is

$$\Delta\hat{\gamma}(m) = \angle \left[\sum_n g_n(m+1) g_n^*(m) \right] \quad (94)$$

where \angle denotes the angle of the complex quantity computed on $[-\pi, \pi]$. This is a maximum likelihood estimate.

The estimated phase gradient or phase difference is integrated to obtain the estimate of phase error $\hat{\gamma}(m)$. It is used for correction after removing any bias and linear component. Then the PGA goes back to its first step and adopts a narrower window. The process is repeated until the image is well focused.

7. SUMMARY

This article has discussed major techniques of radar signal processing. These techniques can be divided into two categories. The first category includes the techniques for suppressing interference and enhancing the useful signal. They ensure reliable detection and processing, and are listed as follows:

- *Matched Filter.* It is the optimum filter that achieves the maximum SNR.
- *MTI.* It discriminates moving target from fixed clutter by Doppler filtering.
- *Beamforming.* It mitigates against jamming sources by spatial filtering.
- *CFAR.* It maintains a constant false-alarm rate even if the clutter intensity varies.

The techniques in the second category are developed mainly for improving the resolving capability of radar. They enable radar to acquire complex information like target size, shape, and image:

- *Pulse Compression.* It achieves high resolution in range direction without sacrificing the detection range.

- *Radar Imaging*. The synthetic aperture radar is developed to attain high resolution in azimuth direction. The signal processing techniques in SAR are discussed in some details, including methods for image formation, motion compensation, and autofocus.

It is foreseeable that radar will advance with the advancement of signal processing techniques and hardware technology. It will be more robust when working in less-than-ideal environments and have stronger capability for acquiring complex information.

BIBLIOGRAPHY

1. M. I. Skolnik, *Introduction to Radar Systems*, 2nd ed., McGraw-Hill, New York, 1980.
2. J. Radatz, *The IEEE Standard Dictionary of Electrical and Electronics Terms*, 6th ed., IEEE, New York, 1997.
3. D. K. Barton and S. A. Leonov, *Radar Technology Encyclopedia*, Artech House, Boston, 1997.
4. M. I. Skolnik, *Radar Handbook*, 2nd ed., McGraw-Hill, New York, 1990.
5. S. Haykin and A. Steinhardt, *Adaptive Radar Detection and Estimation*, Wiley, New York, 1992.
6. B. D. Van Veen and K. M. Buckley, Beamforming: A versatile approach to spatial filtering, *IEEE Acoust. Speech Signal Process. Mag.* **5**(2):4–24 (1988).
7. L. J. Griffiths and C. W. Jim, An alternative approach to linearly constrained adaptive beamforming, *IEEE Trans. Anten. Propag.* **30**:27–34 (1982).
8. R. Nitzberg, *Adaptive Signal Processing for Radar*, Artech House, Boston, 1992.
9. N. Levanon, *Radar Principles*, Wiley, New York, 1988.
10. D. R. Wehner, *High-Resolution Radar*, 2nd ed., Artech House, Boston, 1995.
11. F. E. Nathanson, *Radar Design Principles*, 2nd ed., McGraw-Hill, New York, 1990.
12. C. Wu, K. Y. Liu, and M. Y. Jin, Modeling and a correlation algorithm for spaceborne SAR signals, *IEEE Trans. Aerospace Electron. Syst.* **18**:563–575 (1982).
13. M. Y. Jin and C. Wu, A SAR correlation algorithm which accommodates large range migration, *IEEE Trans. Geosci. Remote Sens.* **22**:592–597 (1984).
14. R. Bamler, A comparison of range-doppler and wavenumber domain SAR focusing algorithms, *IEEE Trans. Geosci. Remote Sens.* **30**:706–713 (1992).
15. F. H. Wong and I. G. Cumming, Error sensitivities of a secondary range compression algorithm for processing squinted satellite SAR data, *Proc. IEEE Geosci. Remote Sens. Symp. (IGARSS'89)*, Vancouver, 1989, pp. 1702–1706.
16. C. Cafforio, C. Prati, and F. Rocca, SAR data focusing using seismic migration techniques, *IEEE Trans. Aerospace Electron. Syst.* **27**:194–207 (1991).
17. R. K. Raney et al., Precision SAR processing using chirp scaling, *IEEE Trans. Geosci. Remote Sens.* **32**:786–799 (1994).
18. W. G. Carrara, R. S. Goodman, and R. M. Majewski, *Spotlight Synthetic Aperture Radar: Signal Processing Algorithms*, Artech House, Boston, 1995.
19. C. V. Jakowatz, Jr. et al., *Spotlight-Mode Synthetic Aperture Radar: A Signal Processing Approach*, Kluwer Academic, Boston, 1996.
20. C. C. Chen and H. C. Andrews, Target-motion-induced radar imaging, *IEEE Trans. Aerospace Electron. Syst.* **16**:2–14 (1980).
21. D. E. Wahl et al., Phase gradient autofocus—a robust tool for high resolution SAR phase correction, *IEEE Trans. Aerospace Electron. Syst.* **30**:827–835 (1994).
22. W. Ye, T. S. Yeo, and Z. Bao, Weighted least square estimation of phase errors for SAR/ISAR autofocus, *IEEE Trans. Geosci. Remote Sens.* **37**:2487–2494 (1999).

RADAR TARGET RECOGNITION

KIE B. EOM
The George Washington
University
Washington, DC

1. INTRODUCTION

Recent (as of 2003) advances in radar provides sufficient resolution and enough information to recognize tactical targets from radar returns [21]. For target recognition applications, different types of radar, such as synthetic aperture radar (SAR), millimeter-wave (MMW) real aperture radar (RAR), and interferometric synthetic aperture radar (IFSAR), have been explored [1–4]. Modern radar system also provides extensive data including fully polarimetric and Doppler channels [14,26,32], but there still are many challenges for target recognition using radar returns [16,17]. This is because special characteristics of radar and recent advances of radar technology make the recognition of targets difficult. For example, the radar profile changes drastically for the small change in viewing angle, and the recent development of stealth technology significantly alters the radar signature. In radar target recognition, many different approaches for different radar types are suggested, and are discussed in this article.

Synthetic aperture radar provides high resolutions for both range and azimuth directions, and have been used widely for target recognition applications. Since SAR is an imaging radar, it can provide detailed images of target area with cloud-penetrating characteristics. When its fully polarimetric data is utilized, targets can be recognized with high accuracy. The SAR target recognition is typically done in multiple stages [18]. The first stage of a typical SAR target recognition algorithm is a prescreener, where regions of interest are located in this stage. Constant false-alarm rate (CFAR) detection algorithm is often used in the first stage. The second stage may be a discriminator, where natural clutter false alarms are rejected. In this stage, textural features are extracted from the target-size windows applied to the neighborhood of pixels located by CFAR detection. The third stage is typically a classifier, where the targets are classified and manmade discretely are rejected. Extensive studies in statistical pattern recognition have been done, and many different pattern classifiers are used in target recognition applications.

For SAR target recognition, spatial matched filters have been investigated [18] for the recognition of ground vehicles. Novak's [18] spatial matched filter approach in target recognition is explained in later sections.

Although SAR technology provides many advantages over real aperture radar (RAR), there are many applications where RAR is important. The azimuth resolution of SAR is much better than that of RAR, but it is typically based on the assumption that the movement of the radar is at constant speed and direction in SAR processing. When the radar is moving at rapidly changing speed and trajectory, as in the case of the radar mounted at fighter airplanes or self-guidance weapons, the assumptions for SAR processing are not correct. Millimeter-wave (MMW) RAR represents the next generation of military smart sensors for detection, tracking, and surveillance because of its high-range resolution, which is critical in target recognition [6]. The MMW RAR technology is sufficiently advanced, and the range resolution of MMW radar is sufficiently high to discriminate tactical targets at a distance of several kilometers [31]. The target recognition by hierarchical modeling of high-range resolution (HRR) millimeter-wave (MMW) radar signatures is discussed in this article.

The artificial neural network (ANN) has been widely used in target recognition. The use of ANN in radar target recognition is also discussed in this article. ANNs are used as pattern classifiers, feature extractors, model adaptation, fuzzy classification, and in other applications in radar target classification. Feedforward neural networks have been used as pattern classifiers after the training with known target samples. The learning algorithm of neural networks provides a powerful tool for adaptation of the classifier to input vectors [24]. A self-organizing feature map has been used as a feature extractor [27] for radar target recognition. In combination with Kohonen's learning vector quantizer (LVQ) for supervised classification, it has been applied to the recognition of ground vehicles from MMW HRR radar signatures [27]. Perlovsky et al. [19] suggested that the model-based neural network to include a priori information to an ANN. This approach can reduce the search space of the neural network by incorporating a priori information to the adaptability of an ANN. The fuzzy neural network (FNN) approach [25] is also suggested to classify targets that may belong to more than one class. The advances in neural network approaches can potentially improve the performance of target recognition algorithms further. There are many approaches to incorporate information from many different sources for radar target recognition. By fusing the information from more than one sensor, the accuracy of radar target recognition may be improved. Two approaches in utilizing information from multiple sensors are discussed in this article. Interferometric synthetic aperture radar (IFSAR) provides elevation information, in addition to two-dimensional radar image, by processing interference between radar returns received by two different antennas. By processing IFSAR image and fusing to SAR of visual images, the accuracy of the target recognition can be improved substantially. The approach of combining IFSAR and visual images using the image registration approach is

discussed in this article. There are statistical approaches in data fusion, and Bayesian data fusion approaches are used in radar target recognition [13]. In this approach, features from polarimetric SAR images are fused to improve the recognition accuracy.

Radar target recognition is a complex problem, and no single algorithm performs better than other algorithms with different types and modes of radar. In this article, different approaches for radar target recognition is discussed in terms of radar types and approaches.

2. HIERARCHICAL MODELING APPROACH FOR NONCOOPERATIVE TARGET RECOGNITION

The target recognition using hierarchical modeling of MMW RAR radar signatures is considered in Ref. 10, and the algorithm is tested with MMW radar data from non-cooperative target identification (NCTI) database. In radar target recognition problems, the targets may be shifted and scaled from the trained data. The change in viewing angle results scale change in radar signature, and the change in azimuth angle change results shifting in radar signature. Therefore, a classifier using features extracted from the radar signatures should classify targets reliably even when radar signatures are shifted or scaled. In general, parameters of time-series models such as ARMA (autoregressive moving-average) are not scale-invariant [20,22]. Thus, the classification of scaled targets with model parameter features can result in poor classification accuracy. There are a few approaches to make a classifier more reliable to shifting and scaling. For example, the use of scale-invariant features or a training with scaled samples can make a classifier more robust to scaling.

Hierarchical ARMA modeling approach is briefly discussed as follows. Suppose that a continuous signal $x(t)$ is a training sample. The classifier need to classify scaled signal of $x(t)$ correctly as the same class as $x(t)$. The scaled signal of $x(t)$ is given by

$$y_x(t) = \frac{1}{\alpha} x(\alpha t) \quad (1)$$

One approach to achieve this is to train a classifier with features extracted from scaled signals of $x(t)$. For example, different features at m different scales are extracted from scaled signals $y_{x_1}(t), y_{x_2}(t), \dots, y_{x_m}(t)$, then the classifier is trained with these multiscale features. If the number of scales included in the training is large enough, the classifier will classify signals having large scale changes.

However, there are at least two potential problems with this approach if the signal is a discrete signal $\{x(i), i = 1, \dots, N\}$: (1) the original signal is defined only at discrete points—the signal at the finer scale is not defined at certain points; and (2) feature extraction is performed multiple times with a single training sample, and the computational complexity increases linearly as the number of scales increases. These difficulties can be solved by the hierarchical modeling approach. The hierarchical modeling approach presented in this section extracts multiscale features without adding much computational complexity.

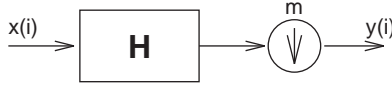


Figure 1. A decimation filter.

A discrete signal can be scaled to a coarser scale or a finer scale by decimation filtering or interpolation, respectively [7,8,11,12]. We will first consider the decimation filtering of a signal, and its effect to the statistical model, and then we will consider the scaling to a finer scale as a modeling process. A decimation filter is defined as a local averaging (FIR filtering) followed by a downsampling process as shown in Fig. 1 [29,35]. If the downsampling rate is m , the decimation-filtered signal represents the signal at the scale reduced by a factor of m .

Let H be a FIR filter of length r and \downarrow be the downsampling operator of factor m :

$$H(\delta) = \sum_{k=0}^{r-1} h_k \delta^k, \quad \text{where } \delta \text{ is a unit delay operator} \quad (2)$$

$$(\downarrow x)(i) = x(mi) \quad (3)$$

Suppose that a signal at a coarser scale $y_m(i)$ is obtained by decimation filtering of the original signal $x(i)$:

$$y_m(i) = H(\delta)x(im), \quad i = 1, \dots, N/m \quad (4)$$

Suppose that the signal $\{x(i), i = 1, \dots, N\}$ follows an ARMA(p, q) model

$$x(i) = \sum_{j=1}^p \alpha_j x(i-j) + \sum_{j=0}^q b_j w(j), \quad i = 1, \dots, N \quad (5)$$

where $\{w(i)\}$ is a zero mean white-noise sequence with variance σ_w^2 and the a_j and b_j terms are real coefficients. Equation (5) can be rewritten as

$$A_p(\delta)x(i) = B_q(\delta)w(i), \quad i = 1, \dots, N \quad (6)$$

where

$$A_p(\delta) = 1 - a_1\delta^1 - a_2\delta^2 - \dots - a_p\delta^p, \quad (7)$$

$$B_q(\delta) = 1 + b_1\delta^1 + b_2\delta^2 + \dots + b_q\delta^q$$

and δ is the unit delay operator, and we assume that the roots of $A_p(\delta)$ and $B_q(\delta)$ lie inside of the unit circle for stability and invertability of the model.

To find features at coarser scale, the model at a coarser scale should be considered. The following theorem summarizes the results on the modeling of a decimation-filtered ARMA process.

Theorem 1. The decimation-filtered process $\{y_m(i)\}$ defined in (4) follows an ARMA(p, q^*) model, where the order of AR polynomial is p and the order of the MA polynomial is $q^* = [(p(m-1) + r + q - 1)/m]$, and the model parameters can be obtained from the model parameters of $x(i)$

$$C_p(\delta)y_m(i) = D_{q^*}(\delta)v(i) \quad (8)$$

where

$$C_p(\delta) = 1 - c_1\delta^1 - c_2\delta^2 - \dots - c_p\delta^p \quad (9)$$

$$D_{q^*}(\delta) = 1 + d_1\delta^1 + d_2\delta^2 - \dots + d_{q^*}\delta^{q^*},$$

Also the AR polynomial $C_p(\delta)$ of aggregated data satisfies the following relation:

$$\begin{aligned} C_p(\delta) &= 1 - c_1\delta^1 - \dots - c_p\delta^p \\ &= (1 - r_1^m\delta)(1 - r_2^m\delta) \dots (1 - r_p^m\delta) \end{aligned} \quad (10)$$

where r_1, \dots, r_p are roots of $A_p(\delta)$.

The proof can be found in Ref. 10.

The ARMA model parameters are shift-invariant because the model's parameters depend only on mean and correlations. Power spectral density can be estimated by using ARMA model parameters, and is also shift-invariant and provides features that are intuitively appealing. For example, spectral peaks or notches represents presence or absence of a frequency component in the signal. For radar signal classification, ARMA power spectrum features at multiple scales are used. Power spectral density of an ARMA process can be estimated by an extended least-squares (ELS) method.

Suppose that $x(i)$ is an ARMA(p, q) process and $w(i)$ is the input white sequence with variance σ^2 as defined in Eq. (5). Let $R_{xx}(k)$ be the autocorrelation functions of $x(i)$, and $R_{xw}(k)$ be the cross-correlation between $x(i)$ and $w(i)$. The Yule-Walker equation for the ARMA process $x(i)$ is given by the following equation:

$$R_{xx}(k) = \begin{cases} \sum_{i=1}^p a_i R_{xx}(k-i) + \sum_{i=1}^q b_i R_{xw}(k-i), & k = 0, \dots, q \\ \sum_{i=1}^p a_i R_{xx}(k-i), & k > q \end{cases} \quad (11)$$

The AR (autoregressive) parameters are estimated by solving these Yule-Walker equations. By using the estimated AR parameters, MA (moving-average) component of $x(i)$ can be obtained by filtering AR component from $x(i)$:

$$\hat{x}_{\text{ma}}(i) = x(i) - \sum_{k=1}^p \hat{a}_k x(i-k) \quad (12)$$

The power spectral density of the ARMA process $x(t)$ is estimated from the correlations of $x_{\text{ma}}(t)$ and the AR parameters estimated by Yule-Walker equations. The ELS power spectrum estimation algorithm is summarized below.

ELS Spectrum Estimation Algorithm

Step 1. Compute sample correlations $R_{xx}(k)$ for $k = 0, \dots, p+q$:

$$\hat{R}_{xx}(k) = \frac{1}{N-k} \sum_{i=1}^{N-k} x(i)x(i+k) \quad (13)$$

Step 2. Estimate AR parameters a_1, \dots, a_p by

$$\begin{bmatrix} \hat{a}_1 \\ \vdots \\ \hat{a}_p \end{bmatrix} = \begin{bmatrix} R_{xx}(q) & \cdots & R_{xx}(q+1-p) \\ \vdots & \ddots & \vdots \\ R_{xx}(q+p-1) & \cdots & R_{xx}(q) \end{bmatrix}^{-1} \begin{bmatrix} R_{xx}(q+1) \\ \vdots \\ R_{xx}(q+p) \end{bmatrix} \quad (14)$$

Step 3. Compute the sample correlation of MA component $x_{\text{ma}}(i)$, which is obtained by removing AR component:

$$\begin{aligned} \hat{R}_{\text{ma}}(k) &= R_{xx}(k) - \sum_{j=1}^p a_j R_{xx}(k-j) - \sum_{j=1}^p a_j R_{xx}(k+j) \\ &+ \sum_{j=1}^p \sum_{l=1}^p a_j a_l R_{xx}(k-j+l), \quad k=0, \dots, q \end{aligned} \quad (15)$$

Step 4. Compute the ARMA power spectrum:

$$S_{xx}(\omega) = \frac{R_{\text{ma}}(0) + 2 \sum_{k=1}^q R_{\text{ma}}(k) \cos(\omega k)}{\|1 - \sum_{k=1}^p \hat{a}_k e^{-j\omega k}\|^2} \quad (16)$$

For each training sample $x(i)$, the models at the other scales (both coarser and finer scales) are obtained by the hierarchical modeling approach presented in this section. The model at a coarser scale is obtained using Theorem 1. The AR polynomial is obtained by Eq. (10), and the correlation of the signal at the coarse scale is obtained with a proper choice of smoothing filter H , such as the Gaussian filter. Thus, the spectral density of the signal at a coarser scale is obtained by the ELS algorithm. The model at a finer scale is obtained by the approach explained in the next step sequence. The AR polynomial of the signal at a finer scale are obtained under a no-hidden-periodicity assumption [34,35]. The correlation function at a finer scale is obtained by disaggregation [10], and the ARMA spectrum at a finer scale is obtained by the ELS estimation algorithm. The multiscale feature extraction algorithm is summarized below.

Multiscale Spectral Feature Extraction Algorithm

Step 1. Each radar return is normalized to zero mean and unit variance by

$$\bar{x}(i) = \frac{x(i) - \hat{m}}{\hat{\sigma}} \quad (17)$$

where \hat{m} and $\hat{\sigma}^2$ are sample mean and sample variances of $x(i)$. M K -dimensional features from M scales (including coarser and finer scales) are ob-

tained from the normalized radar returns by the following procedure.

Step 2. For each training sample, the AR parameters and correlations are estimated by the ELS algorithm. For $k=0,1,\dots,K-1$, the power spectrum is estimated at $\omega = \pi k/K$. The logarithm of the power spectral density forms a K -dimensional feature vector.

Step 3. At each coarser scale, a feature vector is obtained by estimating the power spectrum using the ELS method with model parameters obtained by the hierarchical modeling approach. The logarithm of the power spectral density forms a K -dimensional feature vector at a coarser scale. Feature vectors at multiple scales are obtained by repeating this step at coarser scales.

Step 4. At each finer scale, a feature vector is obtained by estimating the power spectrum using the ELS method with model parameters obtained by the hierarchical modeling approach. This is repeated for other finer scales, and multiple K -dimensional feature vectors are obtained from the logarithm of the power spectral density.

Classification is done by a minimum-distance classifier with multiple prototypes. In this approach, each training sample generates M prototypes corresponding to M scales. Therefore, if there are N training signals for each class, then NM prototypes will be available for each class. Let us assume that there are N_k prototypes $\mathbf{z}_k^1, \dots, \mathbf{z}_k^{N_k}$ in the class $k \in \{1, \dots, K\}$. For a test pattern \mathbf{x} , the distance to the class k is defined by

$$D_k = \min\{d(\mathbf{x}, \mathbf{z}_k^l)\} \quad (18)$$

where the intersample distance $d(\mathbf{x}, \mathbf{z})$ is the Euclidian distance between \mathbf{x} and \mathbf{z} . The distance D_i is the smallest of the distances between \mathbf{x} and each prototype of the class k . The test pattern \mathbf{x} is classified by the minimum-distance decision rule: \mathbf{x} is classified into class k if $D_k < D_i$ for all $i \neq k$.

In Ref. 10, the hierarchical model-based features are tested with NCTI data. Figure 2 shows a typical NCTI radar signature, and estimated power spectral density. In Ref. 10, about 95% of classification accuracy is reported with 5000 MMW RAR radar signatures.

3. NEURAL NETWORKS APPROACHES

Neural networks have been widely used in radar target recognition applications [19,24,25,27]. A good survey on the use of neural networks in target recognition can be found in Ref. 24. Neural network approaches have been popular because they have many promising qualities in target recognition applications. Neural networks have the capability for adaptation to additional targets and environments. The existence of powerful learning algorithms is one of the main strengths of the neural network approach [24]. They also offer techniques for selecting, developing, clustering, and compressing features into a

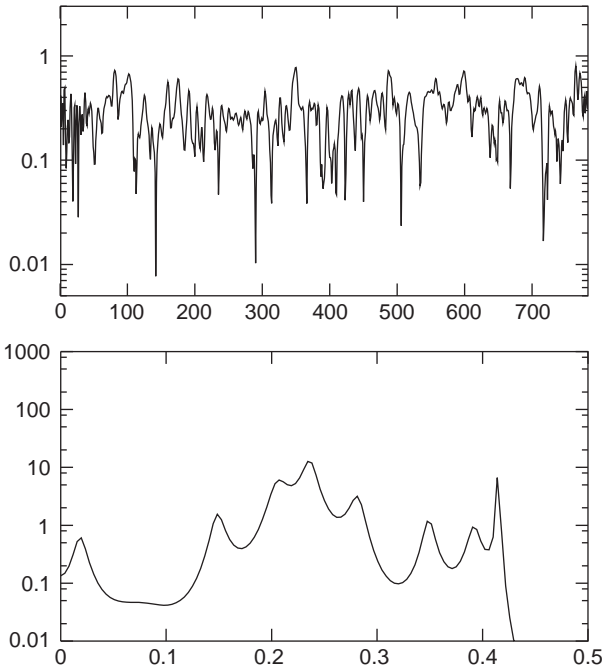


Figure 2. A HRR radar signature from NCTI database and its power spectrum estimated by hierarchical modeling.

useful set, and provide automatic knowledge acquisition and integration techniques for target recognition systems.

Feedforward neural networks have been used as pattern classifiers for target recognition [23]. Let x_i be the multidimensional feature vector extracted from a radar image, and let S be the index set of the target patterns:

$$S = \{i | i \in \text{target pattern}\} \quad (19)$$

The optimum receiver [23] defined by

$$R_s(x_1, \dots, x_N) = \sum_{i \in S} x_i \quad (20)$$

can be implemented as a neural network

$$y_s = \Theta \left(\sum_i W_{Si} x_i - T \right) \quad (21)$$

where T is the threshold and $\Theta(x)$ is the Heaviside step function. Roth [23] showed that detection of target patterns out of a set of P of patterns can be handled by the feedforward neural network presented above.

Neural networks have been also used as a feature extractor for target recognition. Kohonen's self-organizing map (SOM) and learning vector quantizer (LVQ) have been used in the two-stage target recognition approach [27]. SOM is based on unsupervised competitive learning where only one output node, or one per local group of nodes at a time, gives the active response to the current input signal, clusters input vectors into preselected C classes by adapting connection weights to nodes in the network, and is used as a feature extractor [27]. At each

iteration of the SOM algorithm, the best matching node c is selected by

$$c = \operatorname{argmin}\{\|x - m_i\|\} \quad (22)$$

where x is the current input vector and $\{m_1, \dots, m_C\}$ is the set of nodes (cluster centers). Then each node m_i located in the neighborhood of the node c is adapted by the learning rule

$$m_i(t+1) = m_i(t) + \eta_i(t)[x(t) - m_i(t)] \quad (23)$$

where the gain $\eta_i(t)$ can be a simple monotonically decreasing function of time or a Gaussian gain function defined by

$$\eta_i(t) = \alpha(t) \exp \frac{-\|r_c - r_i\|^2}{2\sigma^2(t)} \quad (24)$$

The learning rate $\alpha(t)$ and the kernel width $\sigma(t)$ are monotonically decreasing functions, and their exact forms are not critical. LVQ is used as a supervised classifier of the features extracted by SOM [27]. Stewart et al. [27], reported greater than 94% accuracy in the target recognition experiment with MMW data having five types of ground vehicles.

The model-based neural network (MBNN) was introduced [19] to combine a priori knowledge of models of data with adaptivity to changing data properties. Both learning and adaptation of the MBNN is done by iterative estimation of association weights and model parameters. Different statistical models for different physical processes, background clutter, outlier, target pixels, and other elements are also introduced in Ref. 19. This approach has a potential for improving target recognition performances by allowing the inclusion of a priori information in addition to the adaptability of a neural network.

Fuzzy neural networks are also used in radar target recognition. Fuzzy ARTMAP and EMAP neural networks are suggested [25] for radar target recognition. The fuzzy neural network allows one to make soft decisions in classifying a target, and each input vector can belong to more than one class. The fuzzy association between the input vector and the classified target can potentially improve the performance and the complexity of the adaptation.

4. EXPLOITATION OF ELEVATION DATA FROM IFSAR

IFSAR is a technique to generate high-resolution Digital Elevation Map (DEM) based on the phase difference in SAR signals received by two spatially separated antennas [36]. There are drawbacks in height maps derived from IFSAR data: The data are noisy and the spatial resolution is far inferior to that of visual data. The spatial resolution is further degraded by the noise removal step. Figure 3 shows a height map produced by a real IFSAR. A typical IFSAR elevation image is noisy and needs to be filtered before it can be used reliably. Also, there are regions with "no data," resulting either from the fact that the original scene was not on a rectangular grid or from radar geometry effects that cause some points not to be mapped.

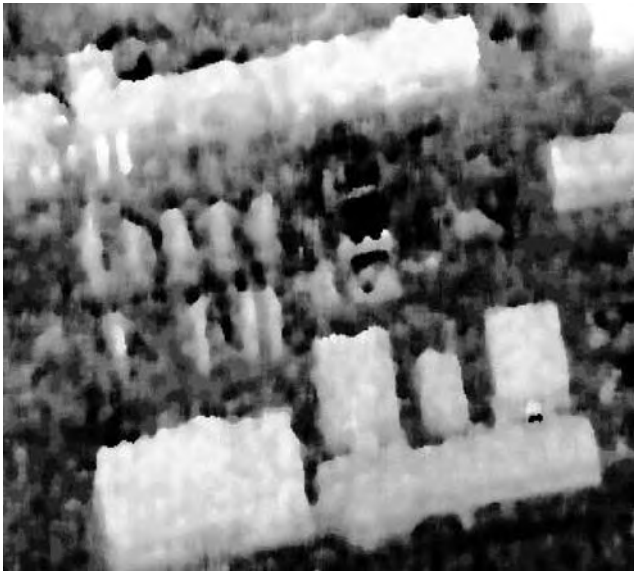


Figure 3. An IFSAR image.

Interpolation and nonlinear filtering techniques are used to filter the elevation data.

Positioning of IFSAR and visual data allows for the fusion of clues from both sensors for target recognition. It is needed to overcome various difficulties resulting from the limitations of the sensor. For example, building detection requires the extraction and grouping of features such as lines, corners, and building tops to form buildings [9]. The features extracted from visual data usually include many unwanted (spurious) edges and lines that do not correspond to buildings. The grouping stage requires complex and computationally intensive operations. Further, the height of a building is typically estimated by extracting shadows and sun angle when available, and is not reliable when the shadows are cast on adjacent buildings. Another drawback of methods based exclusively on visual data lies in their sensitivity to imaging conditions.

IFSAR elevation data can be used in conjunction with visual data to overcome the abovementioned difficulties. Current IFSAR technology provides sufficient elevation resolution to discriminate building regions from surrounding clutter. These building regions are not well defined from a visual image when the buildings have the same intensity level as their surrounding background. Similarly, a building having different colors may be wrongly segmented into several buildings. IFSAR data are not affected by color variations in buildings and therefore are better for building detection.

Figure 4 shows a visual image and edges detected by the Canny operator for the area shown in Fig. 3. The left portion of Fig. 4 shows a building with two different roof colors and roof structures on many buildings. Many spurious edges not corresponding to the building appear in the edge map shown on the right of Fig. 4. Using the IFSAR elevation map shown in Fig. 3, buildings and ground regions are labeled using a two-class classifier. The IFSAR and visual images are registered. Figure 5 shows the

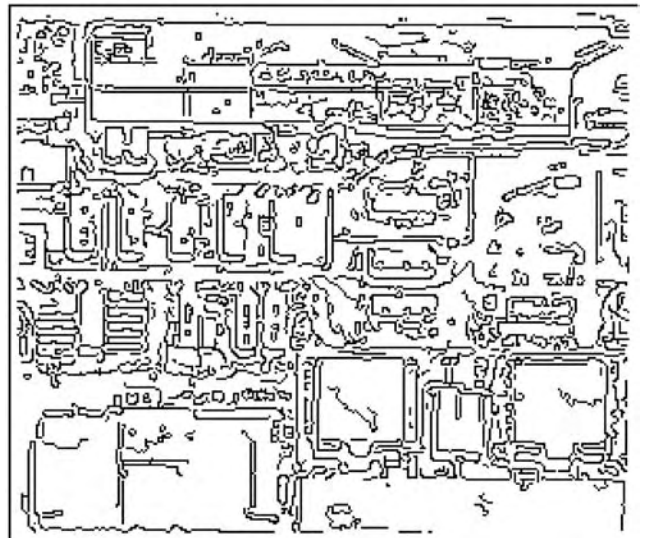
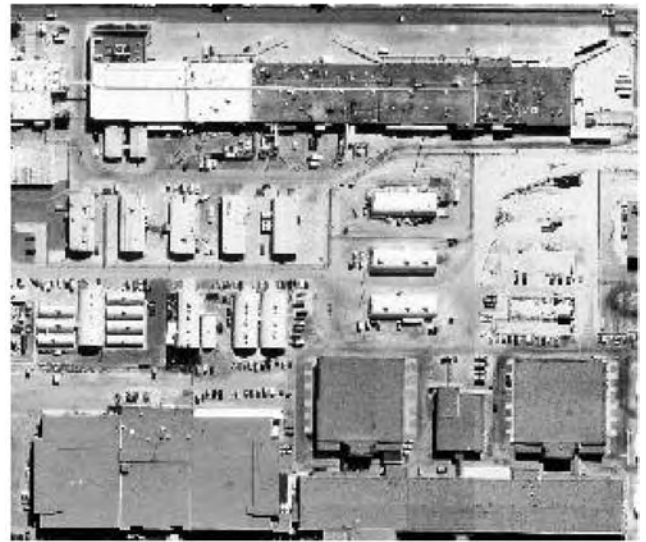


Figure 4. Visual image and edges detected by the Canny operator.

result of registration of a visual image and the segmented elevation image. Features corresponding to roads, parked cars, trees, and other objects are suppressed from the visual images using the segmented buildings derived from the IFSAR image.

The location and the directions of edges in the segmented image are estimated, and are used to locate edges of buildings in the visual image. In the visual image, an edge pixel corresponding to each edge pixel in the registered height image is searched in the direction perpendicular to the estimated direction in the height image. If an edge is found within a small neighborhood, the edge pixel is accepted as a valid edge of a building. If such a pixel is not found in the neighborhood, the edge is not accepted. Figure 6 shows the refined edges obtained by searching in the neighborhoods of height edges. Most of building edges in the height image are found while the unwanted edges are removed.

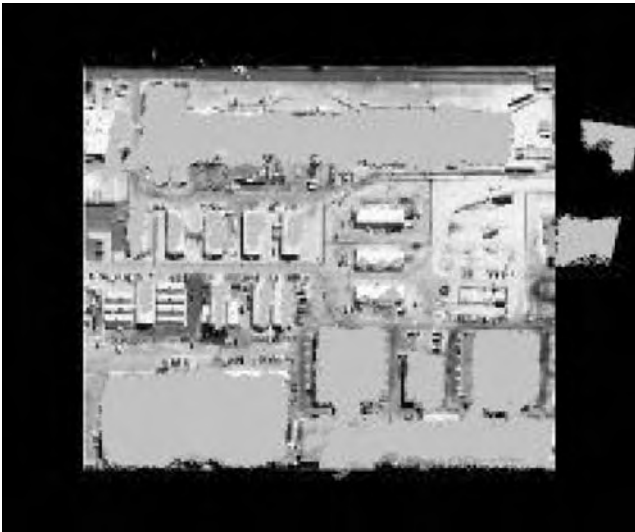


Figure 5. Buildings segmented from the IFSAR image overlaid to visual image.

5. SPATIAL MATCHED-FILTER CLASSIFIERS FOR SAR

A typical target recognition using SAR is done in multiple stages, and is illustrated by the block diagram in Fig. 7. In



Figure 6. Edges Refined using IFSAR result.

the first stage, a CFAR detector prescreens by locating potential targets on the basis of radar amplitude. Since a single target may produce multiple detections, the CFAR detections are clustered (grouped together). Then a region of interest (RoI) around the centroid of each cluster is passed to the next stage of the algorithm for further processing.

The second stage takes each RoI as its input and analyzes it. The goal of this discrimination stage is to reject natural clutter false alarms while accepting real targets. This stage consists of three steps: (1) determining the position and orientation of the detected object, (2) computing simple texture features, and (3) combining the features into a discrimination statistic that measures how “target-like” the detection object is.

The third stage is classification, where a 2D pattern-matching algorithm is used to (1) reject clutter false alarms caused by manmade clutter discretely (buildings, bridges, etc.) and (2) classify the remaining detected objects. Those detected objects that pass the second stage are matched against stored reference templates of targets. If none of the matches exceeds a minimum required score, the detected object is classified as clutter; otherwise, the detected object is assigned to the class with the highest match score.

Matched filters are investigated in [18] as pattern-matching classifiers in target recognition system shown in Fig. 7. They are the synthetic discriminant function (SDF), the minimum average correlation energy (MACE) filter, the quadratic distance correlation classifier (QDCC), and the shift-invariant 2D pattern-matching classifier. The basic structures of the SDF and the MACE filter are characterized in the frequency domain by

$$H = AX(X^\dagger AX)^{-1}U \quad (25)$$

where H denotes the DFT of the spatial matched filter. The matrix X is composed of a set of target training vectors obtained by taking the DFT of the target training images. The vector U represents a set of constraints imposed on the values of the correlation peaks obtained when the training vectors are run through the spatial matched filter. The matrix A represents a positive definite weighting matrix. A is an identity matrix for SDF, and is the inverse of the following matrix D

$$D = \sum_{i=1}^N \text{diag}[|X_i(1)|^2, |X_i(2)|^2, \dots, |X_i(p)|^2] \quad (26)$$

where N is the number of training images and p is the dimension of the training vectors.

In the QDCC, the DFT of the spatial matched filter is expressed by

$$H = S^{-1}(m_1 - m_2) \quad (27)$$

where m_1 and m_2 are means of the DFTs of the training images for classes 1 and 2, respectively. S is a diagonal matrix defined by

$$S = \frac{1}{N} \left[\sum_{i=1}^N (X_i - M_1)^\dagger (X_i - M_1) + \sum_{i=1}^N (Y_i - M_1)^\dagger (Y_i - M_1) \right] \quad (28)$$

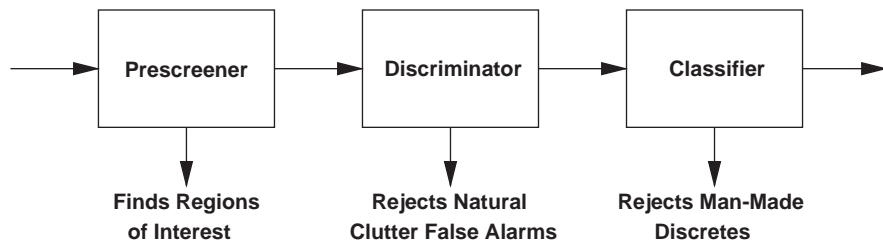


Figure 7. Block diagram of a typical base-line target recognition system (adapted from Novak [17]).

where M_1 and M_2 are matrices with elements of m_1 and m_2 placed on the main diagonal and X_i and Y_i are i th training vectors from classes 1 and 2, respectively.

In the shift-invariant 2D pattern matching classifier, the correlation scores are calculated by

$$\rho_i = \max\{\text{DFT}^{-1}[R_i \times T^*]\} \quad (29)$$

where T is the DFT of the decibel-normalized test image and R_i is the i th reference template.

Novak et al. [18] did extensive experiment with the high-resolution (1 ft \times 1 ft) fully polarimetric SAR data. In the four-class classification experiment using four types of spatial matched filter classifiers, it is reported that all targets are correctly classified [18].

6. MULTISENSOR FUSION

There has been research on multisensor fusion for target recognition [28]. Some of the motivating factors of such research are increased target illumination, increased coverage, and increased information for recognition. Significant improvement in target recognition performance has been reported [13] when multiple radar sources were utilized using sensor fusion approaches. Tenney and Sandell [30] developed a theory for obtaining the distributed Bayesian decision rules. Chair and Varshney [5] presented an optimal fusion structure given that detectors are independently designed. The target recognition using multiple sensors is formulated as a two-stage decision problem in Ref. 13. A typical radar target recognition approach using data fusion is illustrated in Fig. 8. After the prescreening, Single-source classifications are performed first; then the fusion of decisions is performed.

The data fusion problem is treated as an m -hypothesis problem with individual source decisions being the observations. The decision rule for m hypothesis is written as

$$\text{Decide } w_i \text{ if } g_i(u) > g_j(u) \text{ for all } j \neq i \quad (30)$$

For Bayes' rule, $g_i(u)$ is an a posteriori probability:

$$g_i(u) = p(w_i | u) \quad (31)$$

Since the a priori probability and the distribution of features cannot be estimated accurately, a heuristic function is used [13]. It is a direct extension of Bayesian approach introduced by Chair and Varshney [5], and the function $g_i(\cdot)$ is generalized to include the full threshold range

$$g_i(u) = \log \frac{P_1}{P_0} + \sum_{\Omega_1} \log \frac{P_i^d}{P_i^f} + \sum_{\Omega_0} \log \frac{1 - P_i^d}{1 - P_i^f} \quad (32)$$

where P_0 and P_1 are prior probabilities, Ω_1 and Ω_0 are the sets of all i such that $\{g_i(u) \geq T_i\}$ and $\{g_i(u) < T_i\}$ respectively, where T_i is the individual source threshold for partitioning decision regions, and the probabilities P_i^f and P_i^d are false-alarm rates and probabilities of detections of each local sensor. The probabilities P_i^f and P_i^d are defined by the cumulative distribution function (cdf) for each decision statistic. In practice, the cdf is quantized and estimated from training on the individual sensor's classifier error probabilities. In a distributed scenario, the weighting can be computed at each sensor and transmitted to the fusion center where they will be summed and compared to the decision threshold. In Ref. 13, the data fusion approach is applied to multiple polarimetric channels of a SAR image, and substantially improved classification performance is reported.

7. SUMMARY

In radar target recognition, different types of radar are employed for different applications. Each radar system has different characteristics, and target recognition approaches using different radar are discussed.

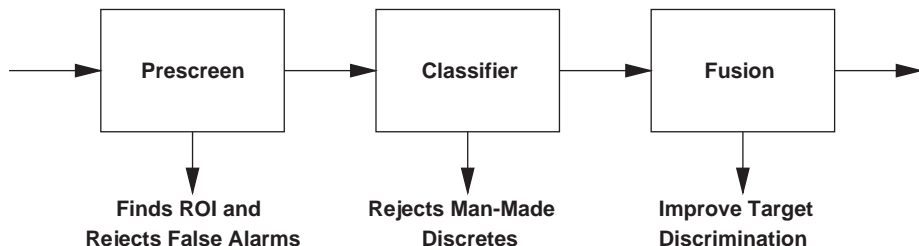


Figure 8. A typical data fusion approach for target recognition (adapted from Hauter et al. [13]).

BIBLIOGRAPHY

1. J. S. Baras and S. I. Wolk, Model-based automatic target recognition from high-range-resolution radar returns, *SPIE Proc.* **2234**:57–66 (1994).
2. M. Basseville, A. Benveniste, and A. S. Willsky, Multiscale autoregressive processes, Part I & II, *IEEE Trans. Signal Process.* **40**:1915–1954 (1992).
3. B. Bhanu, Automatic target recognition: State of the art survey, *IEEE Trans. Aerospace Electron. Syst.* **22**(4):364–379 (1986).
4. V. Cantoni, L. Lombardi, L. Cinque, S. Levisaldi, and C. Guerra, Recognizing 2D objects by a multi-resolution approach, *Proc. Int. Conf. Pattern Recognition*, Jerusalem, Israel, Oct. 1994, Vol. 3, pp. 310–316.
5. Z. Chair and P. K. Varshney, Optimal data fusion in multiple sensor detection systems, *IEEE Trans. Aerospace Electron. Syst.* **22**(1):98–101 (1986).
6. N. C. Currie, R. D. Hayes, and R. N. Trebits, *Millimeter-Wave Radar Clutter*, Artech House, 1992.
7. I. Daubechies, The wavelet transform, time-frequency localization and signal analysis, *IEEE Trans. Inform. Theory* **36**:961–1005 (1990).
8. D. M. Dunn, W. H. Williams, and T. L. DeChaine, Aggregate versus subaggregate models in local area forecasting, *J. Am. Stat. Assoc.* **71**:68–71 (1976).
9. R. Chellappa, Q. Zhang, C. Shekhar, P. Burlina, and K. Eom, On the positioning of multisensor imagery for exploitation and target recognition, *Proc. IEEE.* **85**(1):120–138 (Jan. 1997).
10. K. B. Eom and R. Chellappa, Non-cooperative target classification using hierarchical modeling of high range resolution radar signatures, *IEEE Trans. Signal Process.* **45**(9):2318–2327 (Sept. 1997).
11. J. Geweke, Temporal aggregation in the multiple regression model, *Econometrica* **46**:643–662 (1978).
12. C. W. J. Granger and M. J. Morris, Time series modeling and interpretation, *J. Roy. Stat. Soc. A*-**139**:246–257 (1976).
13. A. Hauter, K. C. Chang, and S. Karp, Polarimetric fusion for synthetic aperture radar target classification, *Pattern Recogn.* **30**(5):769–775 (1997).
14. S. Kingsley and S. Quegan, *Understanding Radar Systems*, McGraw-Hill, 1992.
15. D. C. McKee, C. Bandera, S. Ghosal, and P. J. Rauss, Model-based automatic target recognition using hierarchical foveal machine vision, *SPIE Proc.* **2755**:70–79 (1996).
16. R. A. Mitchell and R. Dewall, Overview of high range resolution radar target identification, *Proc. Automatic Target Recognition Working Group Conf.*, Monterey, CA, Nov. 1994.
17. L. M. Novak, A comparison of 1-D and 2-D algorithms for radar target classification, *Proc. IEEE Int. Conf. Systems Engineering*, Aug. 1991.
18. L. M. Novak, Radar target identification using spatial matched filters, *Pattern Recogn.* **27**(4):607–617 (1994).
19. L. I. Perlovsky, W. H. Schoendorf, B. J. Burdick, and D. M. Tye, Model-based neural network for target detection in SAR images, *IEEE Trans. Image Process.* **6**(1):203–216 (1997).
20. F. A. Pino, P. A. Morettin, and R. P. Mentz, Modelling and forecasting linear combinations of time series, *Int. Stat. Rev.* **55**:295–313 (1987).
21. A. W. Rihaczek and S. J. Hershkowitz, *Radar Resolution and Complex-Image Analysis*, Artech House, 1996.
22. O. Rioul, A discrete-time multiresolution theory, *IEEE Trans. Acoust. Speech Signal Process.* **41**:2591–2606 (1993).
23. M. W. Roth, Neural networks for extraction of weak targets in high clutter environments, *IEEE Trans. Syst. Man Cyber.* **19**(5):1210–1217 (1989).
24. M. W. Roth, Survey of neural network technology for automatic target recognition, *IEEE Trans. Neural Networks* **1**(1):28–43 (1990).
25. M. A. Rubin, Application of fuzzy ARTMAP and ART-EMAP to automatic target recognition using radar range profiles, *Neural Networks* **8**(7-8):1109–1116 (1995).
26. M. L. Skolink, *Introduction to Radar Systems*, McGraw-Hill, 1980.
27. C. Stewart, Y. C. Lu, and V. Larson, A neural clustering approach for high resolution radar target classification, *Pattern Recogn.* **27**(4):503–513 (1994).
28. N. S. Subotic, B. J. Thelen, J. D. Gorman, and M. F. Reiley, Multiresolution detection of coherent radar targets, *IEEE Trans. Image Process.* **6**(1):21–35 (1997).
29. L. G. Telser, Discrete samples and moving sums in stationary stochastic processes, *J. Am. Stat. Assoc.* **62**:484–499 (1967).
30. R. R. Tenney and N. R. Sandell, Detection with distributed sensors, *IEEE Trans. Aerospace Electron. Syst.* **17**:501–510 (1981).
31. J. D. Wald, D. B. Krig, and T. DePersia, ATR: Problems and possibilities for the IU community, *Proc. ARPA Image Understanding Workshop*, Jan. 1992, pp. 255–264.
32. D. R. Wehner, *High Resolution Radar*, Artech House, 1987.
33. W. Wei, The effect of temporal aggregation of parameter estimation in distributed lag model, *J. Econometr.* **8**:237–246 (1978).
34. W. W. S. Wei and D. O. Stram, Disaggregation of time series models, *J. Roy. Stat. Soc. B*-**52**:453–467 (1990).
35. M. A. Wincek and G. C. Reinsel, An exact likelihood estimation procedure for regression ARMA time series models with possibly non-consecutive data, *J. Roy. Stat. Soc. B*-**48**:303–313 (1986).
36. H. A. Zebker and R. M. Goldstein, Topographic mapping from interferometric synthetic aperture radar observations, *J. Geophys. Res.* **91**(B5):4993–4999 (1986).

RADAR TRACKING

JOSEPH A. BRUDER
Air Force Research Laboratory

Radar tracking is the ability to determine the position and velocity vector of a target at any particular instant in time, to predict its position in the future, and to distinguish the desired target from other targets and clutter. For a typical radar, the direction from the radar antenna (or antennas) to the target is generally determined in the polar coordinates of range (distance), azimuth (horizontal) angle, and possibly vertical angle. For a sophisticated coherent radar, tracking targets in Doppler frequency space may also be required. Thus radar tracking can be one dimensional (range, angle, or Doppler), two-dimensional (range and

azimuth angle), three-dimensional (range, azimuth angle, and elevation angle), or four-dimensional (range, azimuth angle, elevation angle, and Doppler). For some systems, radar information is converted to Cartesian coordinates, and the tracking functions are performed in coordinates such as latitude, longitude, and height.

Target tracking is necessary for a number of reasons. In order to direct a weapon such as a missile or a projectile to a target, the range, future range, and angles from the radar to the target must be determined by the radar. By knowing the position of the target relative to that of the missile, the guidance computer can direct the missile to the target. Aircraft controllers must know an aircraft's location relative to other aircraft in the vicinity, and by tracking the positions of all the aircraft in their assigned sectors, they can control the spacing of the aircraft to ensure flight safety.

1. EXAMPLES OF RADAR TRACKERS

A police radar can determine the speed of the vehicle in the field of view of the radar by measuring the Doppler frequency of the return (echo) signal from the vehicle because the Doppler frequency is directly proportional to the vehicle's velocity. Most police radars must track the Doppler frequency over a given period of time to ensure measurement. A missile guidance radar must continually track the target's range, azimuth angle, and elevation angle in order to predict the future target position; thus, it is an example of a three-dimensional tracker. An airborne radar such as the APG-70 in the F15-E aircraft utilizes Doppler processing for clutter rejection, as well as range, azimuth angle, and elevation for target-tracking purposes, and is thus an example of a four-dimensional tracking radar. A phased-array radar must be capable of maintaining track simultaneously on multiple targets, while still scanning its field of regard for new targets.

2. HISTORY OF RADAR TRACKING

In the early days of radar, range and angle-tracking functions were performed manually. Using a device such as a track ball, the operator could keep the crosshairs positioned on the range and azimuth angle of a detected target viewed on a display such as a plan position indicator (PPI) display. The PPI display, such as that shown in Fig. 1, provides a two-dimensional display of range and azimuth angle for a radar with an azimuth-scanning antenna. Targets result in blips on the display where the brightness (and size) of the blips are related to the amplitude of the target echoes at the receiver. The output of the track ball can provide readout of the target range and azimuth angle or provide the required range and angle information to weapons systems for targeting purposes. Although this was a satisfactory technique for tracking slow-moving targets such as ships, it is certainly a tedious process.

To aid in the tracking of ships and aircraft, a rate-aided device was added to some systems. With rate-aided tracking, the operator needed to make only fine adjustments to

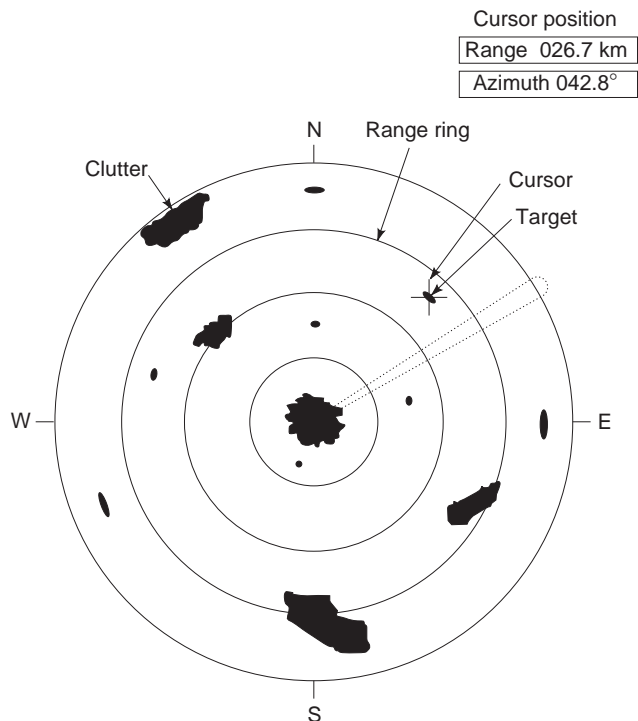


Figure 1. PPI radar display showing targets and clutter.

account for changes of the target range and angle rates with respect to the radar. With this configuration, the radar operators were better able to track faster-moving objects such as aircraft. Still, this tracking function required the constant attention of the radar operator.

Automated target tracking evolved as a necessary tool to allow the radar operator to perform the tracking function efficiently. After range and angle trackers are locked onto the target, the tracker then senses any error between the current target position and that predicted by the tracker and automatically and continuously adjusts the tracker functions either on a pulse-to-pulse or scan-to-scan basis. As a result, automatic radar tracking can maintain target track more accurately than a human operator and can better follow fast maneuvering targets.

3. TRACKING BASICS

For automatic target tracking, a sequential procedure must be used to acquire the target and initiate track. The three steps are target detection, target acquisition, and target track.

3.1. Target Detection

In order for the received echo signal from the target to be detected by the radar, the receive signal strength in that particular range cell must be stronger than the residual noise in the radar and other interfering signals in that range cell. For a target separated from clutter, the primary interfering source is receiver noise. Although it is desired to declare a target's presence with high probability, it is also necessary to keep the probability of false

alarm (declaring a target detection when no target is present) as low as possible. The two values are tied closely together: for a given signal-to-noise (SNR), lowering the detection threshold to increase the probability of detection threshold also increases the probability of false alarm. Depending on the target detection criteria, a SNR of 8–15 dB is generally required to keep the probability of detection reasonably high, while keeping the probability of false alarms at or below 10^{-6} . Probability of detection vs. false alarm curves are available in Blake [1] and a number of other sources.

In many cases, the single-pulse SNR may be below the threshold, but the SNR can be improved by integrating a number of pulses. For coherent operation, the SNR improvement is directly proportional to n , the number of pulses coherently integrated. For noncoherent operation, the SNR improvement for small n , is usually near $n^{0.8}$ in practical radar systems where $n < 20$. Most real targets are composed of complex reflecting surfaces; the scattering contributions of these separate reflecting surfaces tend to add and subtract vectorially to the overall radar cross section (RCS) of the target. The fluctuations in RCS caused by these surfaces will affect the probability of detection and false alarm. Swerling [2] has derived the probability of detection and false-alarm curves for both slowly varying and rapidly varying target RCS fluctuations. For these cases, the required SNR required can be obtained from this set of curves.

3.2. Target Acquisition

Target acquisition for tracking can be done either manually or automatically. For manual target acquisition, the operator needs to point the radar antenna (or an angle cursor) on the azimuth angle to the target and designate the desired target range. Alternately, the operator could use a lightpen if available to designate the target azimuth angle and range to the tracker. When the particular target is within the acquisition limits of the tracker, the acquisition process can be initiated to lock the tracker up on the target range and azimuth.

For automatic target acquisition, the tracker must have either a designated philosophy for selecting the target for track acquisition, or the tracker must have sufficient capability of tracking all the targets satisfying the track initiation criteria. For example, for a radar altimeter, the track would be initiated on the closest radar returns to the radar. For a scanning surveillance radar, the tracker would need to have sufficient capability to track all the targets satisfying the track criteria.

4. RANGE TRACK

When the target has been acquired by the tracker, the tracker must determine not only the range and angular positions but also the velocity vector of the target, and it must determine the velocity components in range and angle in order to maintain track on the target. This is especially important in order to maintain track during conditions of track fade or during momentary passage of other targets or clutter returns. Target trackers differ in

complexity and include (1) dedicated single target trackers, (2) track-while-scan target trackers, and (3) multiple target trackers. For scan-to-scan and multiple target trackers, association algorithms are required to keep track of the targets, especially during crossing target events.

4.1. Dedicated Range Trackers

Dedicated target trackers generally use radars with antennas that spotlight the desired target with the antenna beam and keep the antenna beam spotlighted on the target during the entire tracking process. This type of tracker is generally used with weapon systems that require continuously updated position information on the target. This is a relatively simple type of tracker and will be used to explain the principles of tracking. The tracking process will be described as composed of the following process: range tracking, angle tracking, and Doppler tracking.

For a radar system, the range from the radar to a target is precisely determined from the time delay between the transmission of the radar signal and the receipt of the radar echo from the target arriving back at the radar's receive antenna. The range (R) from the radar antenna to the target is then given by

$$R = \frac{c\tau}{2}$$

where

c = speed of light (2.997×10^8 m/s)

τ = delay time between transmit and receive target echo

Because radar signals travel at the speed of light, the range to the target is approximately 150 m for each microsecond of time delay between the time the radar signal is transmitted and when the return echo signal reflected from the target arrives at the receiver.

4.1.1. Range Tracking with an FMCW Radar. The simplest type of radar used for range tracking is that of frequency-modulated carrier wave (commonly referred to as an FMCW) radar. One of the prime advantages of using an FMCW radar is that, for a given signal-to-noise ratio, the average transmit power is much less than the peak power required for a pulse-type radar. Transmit signal frequency is generally swept linearly over a period of time, such as shown in Fig. 2. This signal is transmitted toward the target and returns with a time delay (τ). By comparing

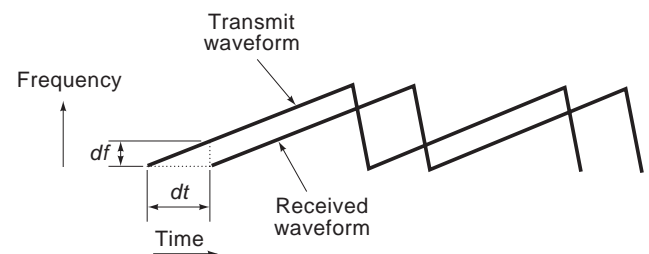


Figure 2. FMCW transmit and receive waveforms.

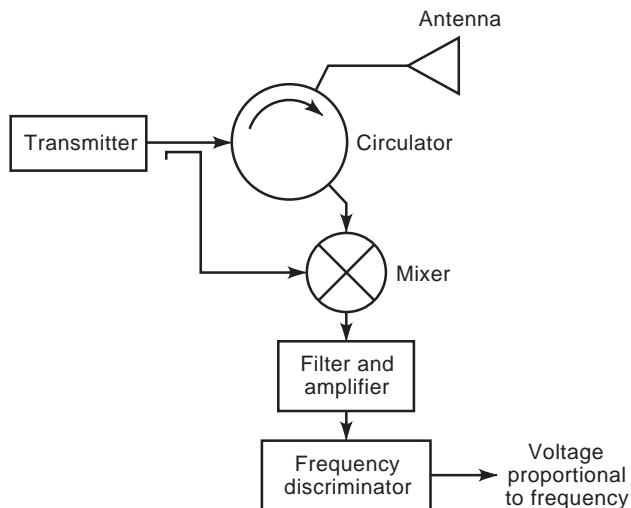


Figure 3. Typical FMCW circuit.

the frequency of the received signal with that currently being generated by the transmitter, the time delay (and hence the range) can be determined from the equation

$$R = \frac{c\tau}{2} = \frac{c\Delta f}{2} \left(\frac{dt}{df} \right)$$

where

- Δf = difference frequency between the received signal and the transmit signal
- df/dt = rate of change in frequency versus time for the transmit signal

The circuitry for a FMCW ranging system is rather simple, as shown in Fig. 3. The transmitter is coupled to the antenna through a circulator, for example, to isolate the transmit signal from the receiver input. Transmit signal is reflected by the target, received by the antenna, and then mixed with the current transmit signal. The mixed signal is then amplified, filtered to remove the radiofrequency (RF) transmitter and receive signal components, and coupled to a frequency discriminator circuit. The frequency discriminator provides an output voltage that is proportional to the input frequency. Thus the output signal is proportional to the range to the target.

For a moving target, the frequency of the returns from the target are not only affected by the range to the target but also by the target velocity with respect to the radar. In

order to separate frequency change effects resulting from range from those resulting from target velocity, an up/down ramp waveform, such as that shown in Fig. 4 can be used. The frequency change caused by velocity essentially moves the entire receive frequency up or down, and by averaging the frequency difference between the up frequency and down frequency portions of the waveform, both the range and the target velocity can be determined from the following equations. The range is determined from the average of the frequency differences during the positive frequency ramp and the negative frequency ramp, thus

$$R = \frac{c \left(\frac{\tau_p + \tau_n}{2} \right)}{2} = \frac{c(\Delta f_p + \Delta f_n)}{4} \left(\frac{dt}{df} \right)$$

The velocity of the target relative to that of the radar is a function of the frequency difference between the positive ramp portion and the negative ramp portion. The velocity of the target in the direction toward the radar (positive Doppler frequency) is then

$$v = \frac{\lambda f}{2} = \frac{\lambda(\Delta f_n - \Delta f_p)}{4}$$

where λ is the wavelength of the transmit frequency.

Range tracking using an FMCW radar can be accomplished simply by averaging the output voltage from the frequency discriminator, which is proportional to the time delay between the transmit and receive signals, and hence is proportional to the target range. Extreme linearity and slope calibration of the frequency sweep is required for accurate range determination. For example, a 1% error in the linearity of the linearity or slope, can have an equivalent error in the range determination.

4.1.2. Range Tracking with Pulsed Radar. For pulsed radar, the target range is measured from the time delay (τ) between transmit pulse and received echo from the target. Figure 5 shows the basic configuration of a range tracker used with pulsed radar. The “heart” of a range tracker is the time discriminator that enables the tracker to determine the time difference between the range reference (estimated delay time) and the actual range of the target return. The range error (ϵ_r) is normally bipolar and proportional to the range (or time) difference between the estimated range and measured range. The range error is then input to a range and velocity estimator (and possibly acceleration estimator) circuit. The function of the range

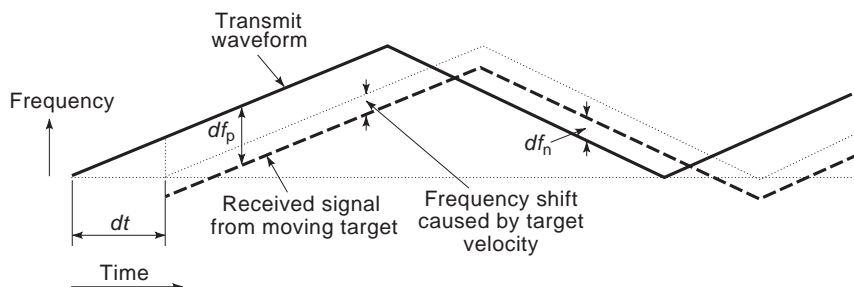


Figure 4. FMCW waveform for resolving target range from velocity.

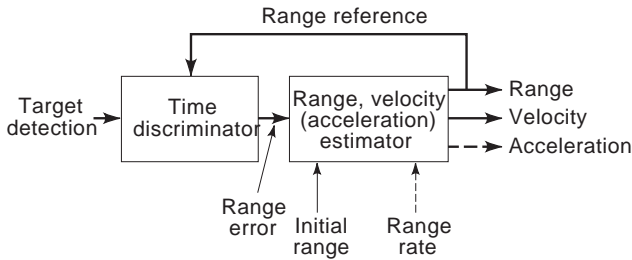


Figure 5. Basic pulsed radar range tracker.

error output is to drive estimated range to the measured range. In most cases, an initial range (and possibly range rate) in the general vicinity of the target range must be input to the range, velocity estimator circuit in order to enable it to acquire the target.

There are three basic classes of range trackers, which will be designated as analog, digital, and computer tracker range trackers. The most common analog-type tracker range trackers. The most common analog-type tracker circuit uses early and early-late gates, such as those shown in Fig. 6. The detected target video is input to both early and late gates. During the early gate time, the portion of the video signal existing during that time period is fed through to an integrator circuit, which integrates the signal energy during that time period. The late gate likewise feeds the video signal during the late gate time period to a second integrator. The outputs of the two integrators are compared in a difference circuit. If there is more video energy in one of the integrators, an error signal proportional to the difference is generated. The polarity of the error signal depends on which integrator output is greater. The error voltage then is provided to the range servo loop circuit, which generates voltages proportional to the estimated range, velocity, and possibly acceleration. The range voltage (estimated range) drives the timing generator, which generates the early and late gate times dependent upon the range voltage. If more video energy is in the late gate time, the error voltage causes the range voltage to increase so that the partition between the early and late gates moves out in range and becomes aligned on the centroid of the video pulse. In order for the range tracker to initially acquire track, the early-late gates must be positioned so that a significant portion of

the target video energy appears in the early or late gate times. An operator can accomplish this by observing a radar display and setting the initial range into the track circuit.

The range tracking accuracy of the range tracker is dependent upon the signal-to-noise power ratio (SNR) of the signal compared to the noise in the early and late gate time periods. According to Barton [3], the standard deviation of the range error (σ_{r1}) on a single pulse basis is given by

$$(\sigma_{r1}) = \frac{1}{2B\sqrt{\text{SNR}}} \text{ for } (B\tau_o \geq 1)$$

where

B = receiver frequency bandwidth
 τ_o = pulsewidth

Normally, the servo loop integrates a number of pulses to provide smoothing of the range voltage, which reduces the effects of noise jitter on the range determination. For noncoherent operation, the range error is effectively reduced by $1/n$, the number of pulses integrated. The resulting range error is then given by

$$\sigma_r = \frac{1}{2B\sqrt{f_r t_o (\text{SNR})}}$$

where

f_r = pulse repetition frequency
 t_o = observation time

Digital range trackers can be implemented using a number of techniques. In most cases, the range information (estimated range) is stored in a digital counter and is updated (up- or downcounted) depending on the actual range compared to the estimated range. An early-late gate discriminator, such as that shown for the analog range tracker can be used, and the error voltage then drives the up/down count. A simpler method for accomplishing the discrimination function is shown in Fig. 7. For this case, a range window is positioned about the radar video, and the video voltage is sampled at equal increments across the

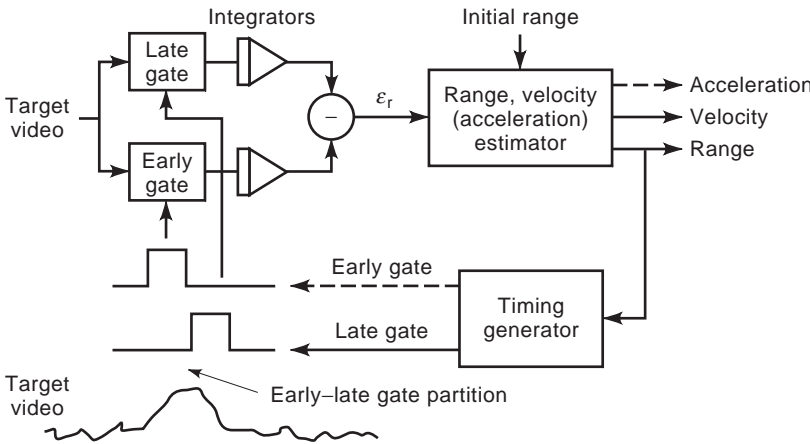


Figure 6. Analog early-late gate range tracker.

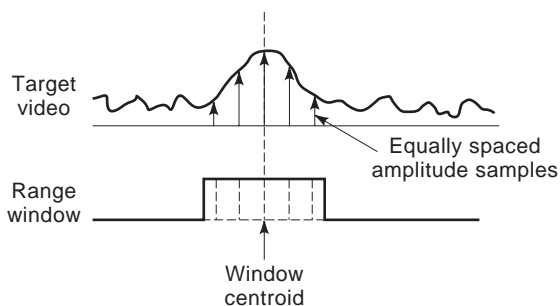


Figure 7. Digital range track sampler.

pulse. It should be noted that the digital discriminator of Fig. 7 requires that the signal be passed through an approximately matched filter prior to sampling, if the SNR is to be optimized. The split-gate tracker performs the matched filter function by averaging over the gates, and hence can be preceded by an IF amplifier with wider bandwidth. The digital circuit then drives the center of the range window to the centroid of the target video signal by equalizing the voltages in the early and late sample times. Three samples are required, as a minimum, for this type of discriminator: an early sample, a late sample, and an on-target sample. When the tracker is centered on the target, the on-target sample voltage is maximized, thus indicating that a true target is being tracked, rather than noise. Again, the range window must initially be set to the approximate target range or caused to slew automatically until a target is detected.

The analog and digital trackers described earlier are intended primarily for range tracking a single target, and in most cases the radar antenna is boresighted on the target either manually or by using an angle tracker. Tracking circuits, either analog or digital, can be designed to track targets using continuously scanning antennas. For this case, the target returns are received only by the radar during the time when the antenna beam scans by the target, and the tracker must use prediction algorithms to estimate the position of the target on the next scan. If multiple targets are to be tracked, then individual analog or digital tracking circuits must be used for each target tracked. In most cases where multiple targets are to be tracked, especially in scanning-type radars, the tracking functions are performed in a computer using specialized tracking algorithms. Because track-while-scan tracking normally involves angle tracking as well as range tracking, the discussion on multiple target computer tracking will be deferred.

5. ANGLE TRACKING

Angle tracking can differ depending on the application. For dedicated target-tracking radars, the antenna is kept boresighted on the target by the angle-tracking circuits and the antenna servo. With a continuously scanning antenna, the centroid of the target returns is measured each time the radar scans by the target, and uses an estimator to predict the position of the target on the next scan. For multifunction or phased-array radars, the target track is updated each time the antenna is scanned to the target location. Because track-while-scan and multitarget trackers normally require range (and possible Doppler tracking), the angle tracking described in this section is limited to a single target, boresighted angle tracking systems. The most common types of on-boresight trackers use conical scan, sequential lobe, or monopulse angle-sensing techniques.

5.1. Conical Scan Angle Trackers

Conical scan is the simplest angle-sensing technique in that only a single receiver channel is required. As shown in Fig. 8, the antenna beam is squinted off the antenna rotational axis. The squinted antenna beam is rotated about the antenna boresight by either rotating the antenna or nutating an offset feed. If the target is located on the antenna boresight, the target video signal maintains a constant amplitude as the antenna rotates. However, if the target moves off boresight, the target video signal will have a sinusoidal amplitude variation given by

$$E_t = E_0[1 + K_s \varepsilon \cos(\omega_s t + \phi)]$$

where

- E_0 = average magnitude of received signal
- ε = angular distance of target from boresight
- K_s = antenna error slope
- ω_s = antenna rotator scan frequency
- ϕ = phase angle of the return modulation relative to the scan rotation

In order to determine the transverse (azimuth) and elevation angle error components, the equation can be rewritten in the form

$$E_t = E_0[1 + K_s \varepsilon_t \cos \omega_s t + K_s \varepsilon_e \cos \omega_s t]$$

where

- ε_t = transverse (azimuth) angle error component
- ε_e = elevation angle error component

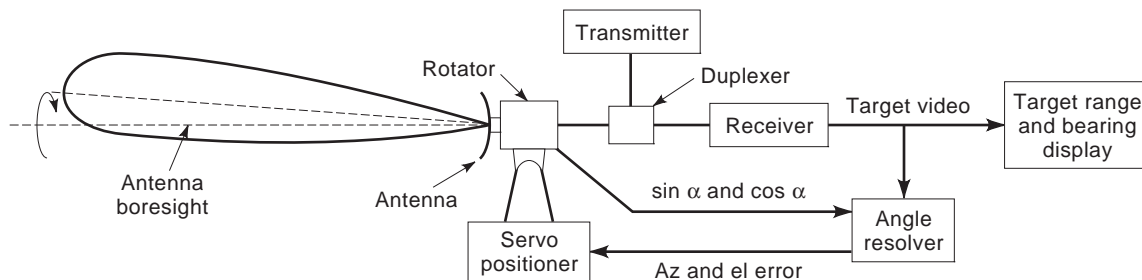


Figure 8. Conical scan radar.

By using the preceding equation, the angle resolver can determine the azimuth and elevation error components of the target direction from boresight. These angle error components are then coupled into the azimuth and elevation inputs of the antenna servo positioner, which then drives the antenna boresight onto the target direction. Although this is conceivably the easiest angle-sensing technique, it is susceptible to tracking errors produced by amplitude fluctuations of the target. Also, for military applications, because the conical scan modulation can be detected, modulation jammers can drive the antenna off the target.

5.2. Sequential Lobe

Sequential lobe angle sensing is similar to that of conical scan, except that the beam is switched electronically between beam positions. For dual-axis (azimuth and elevation) angle sensing, generally four beam positions are used (up, down, left, right). By comparing the amplitude of the received signals in the upper and lower beams, and knowing the shape of the antenna beams, the angular elevation angle of the target from the antenna boresight can be determined. A similar technique can be used for azimuth angle sensing. The technique can either use a single receiver channel or separate receivers for azimuth and elevation angle sensing. The advantage of the technique is that the switching of the beams can be accomplished on a pulse-to-pulse basis, thus making it less vulnerable to target radar cross-sectioned fluctuations. It, however, still has a vulnerability to modulation-type jammers.

“Lobe on receive only” (LORO) is a variation of sequential lobe sensing. With this technique, the transmitter either uses a separate transmit horn on boresight or transmits simultaneously through all four horns. The sequential lobing is accomplished only on receive, through sequential sampling of the signals in the four horns. The advantage of LORO is that modulation jammers cannot detect the sequential modulation pattern of the receivers.

5.3. Monopulse

Monopulse sensing provides the ability to determine the angle of arrival in a single pulse by simultaneously processing the signals in multiple receive beams. Figure 9

shows an example of a four-horn monopulse configuration for dual-plane (elevation and azimuth) angle sensing. The four-horn configuration shown in Fig. 9 is useful for a description of the basic process, but practical radars built since the 1960s have used more complex feed systems to optimize the sum gain, difference error slopes, and sidelobes of all channels. Amplitude-type monopulse uses simultaneous antenna beams squinted at angles off the elevation and azimuth boresights. The relative amplitude of receive signals determines the angular distance of the target off the boresight. Another type of monopulse, referred to as phase-sensing monopulse, uses separate receive apertures spaced a short distance apart, but with the beams pointed parallel with the antenna boresight. For this type of monopulse sensing, the phase difference between the receive signals determines the angular distance of the target from boresight. The monopulse feed, such as shown in Fig. 9, is normally used either to illuminate a paraboloidal reflector directly or to illuminate a subreflector for a Cassegrain-type antenna. The monopulse feed is normally attached directly to a Σ and Δ comparator. The Σ and Δ comparator combines the received signals in the four beams to form a Σ signal, a Δ_{AZ} signal, and a Δ_{EL} signal. According to Rhodes (4), amplitude sensing and phase sensing are equivalent and can be converted to Σ and Δ sensing. Within the 3 dB beamwidth of the Σ pattern of the monopulse antenna, the function Δ/Σ is approximately linear. The target azimuth angle θ off the azimuth boresight and the elevation angle β off the elevation boresight can be determined from

$$\theta \approx K \frac{|\Delta_{AZ}|}{|\Sigma|} \cos \phi_{AZ}$$

$$\beta \approx K \frac{|\Delta_{EL}|}{|\Sigma|} \cos \phi_{EL}$$

K = antenna slope (a function of the squint angle of the beams)

ϕ_{AZ} = phase angle of the Δ_{AZ} signal relative to the Σ signal

ϕ_{EL} = phase angle of the Δ_{EL} signal relative to the Σ signal

For a pointlike target (target extent \ll less than the antenna beamwidth), the phase angle between the Σ and

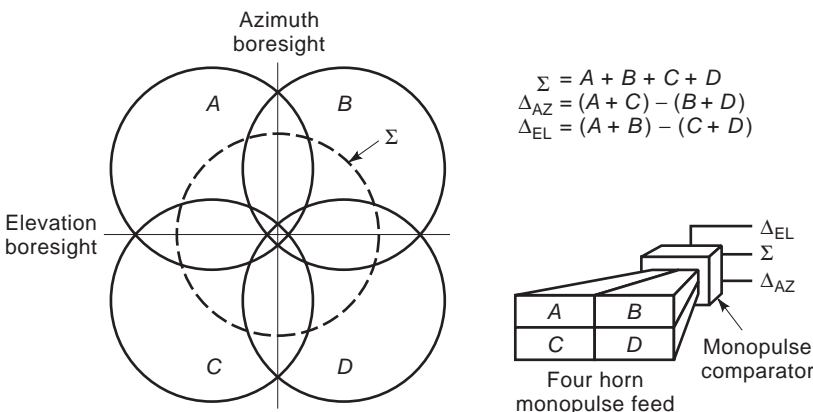


Figure 9. Four-horn monopulse antenna beam patterns.

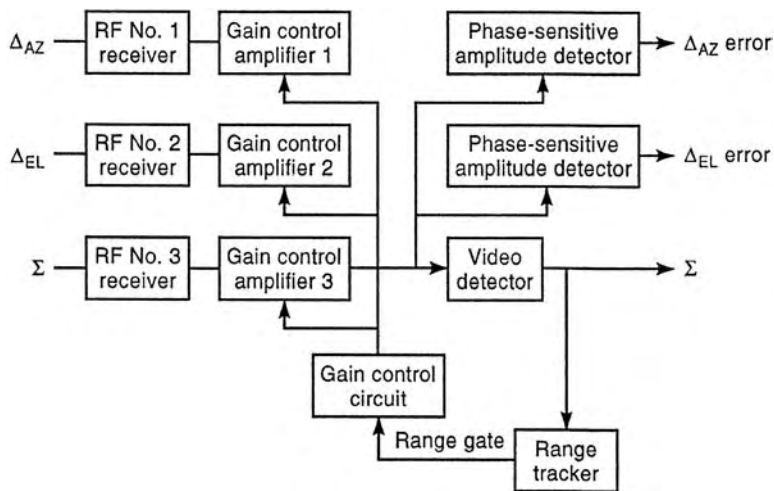


Figure 10. Three-channel monopulse circuit.

Δ signals is normally either 0° or 180° , depending on which side of the boresight the target is located.

A typical configuration for a three-channel monopulse receiver is shown in Fig. 10. The Σ and Δ signals, after down-conversion to IF, are amplified in gain-controlled amplifiers. The Δ IF outputs from the gain-controlled amplifiers are input to amplitude-sensitive phase detectors, along with the Σ IF outputs. The phase-sensitive amplitude detector provides a video output signal proportional to the amplitude of the Σ signal and the cosine of the phase angle between the Δ signal and the Σ signal. In order to maintain a constant number of volts per degree for the output phase amplitude phase detectors, the gain of the receivers must be maintained to provide a constant output signal level at the range of the target. To do this, the sum signal is detected to provide a Σ video signal to a range tracker circuit, which then locks the range onto the target. The output video signal is then sampled at the range of the target, and this is then used to form the gain control voltage in the three receiver channels. This Σ signal normalization maintains the desired number of output volts per degree from the Δ channel receivers. Close tolerances on gain and phase track of the three

gain control amplifiers are required to provide the integrity of the angle error calibration.

Figure 11 shows an example of a two-channel monopulse receiver. The Σ , Δ_{AZ} , and Δ_{EL} microwave signals out of the monopulse comparator are switched in a RF commutator so that on receive pulse 1, $\Sigma + \Delta_{AZ}$, and $\Sigma - \Delta_{AZ}$ signals are in receiver channels 1 and 2, respectively. On the second receive pulse, $\Sigma + \Delta_{EL}$, and $\Sigma - \Delta_{EL}$ are coupled in to receive channels 1 and 2. On the third receive pulses, the Δ polarities are switched, so that the $\Sigma - \Delta_{AZ}$, and $\Sigma + \Delta_{AZ}$ signals are input to channels 1 and 2 on the third pulse, and the $\Sigma - \Delta_{EL}$, and $\Sigma + \Delta_{EL}$ signals are in channels 1 and 2 on the fourth pulse. The receive signals in channels 1 and 2 are down-converted from RF to intermediate frequency (IF), amplified in gain-controlled amplifiers and subsequently converted to video. The decommutator circuit then uses the difference in the video outputs to form the Δ_{AZ} error and the Δ_{EL} error signals. The error signals are then coupled into the antenna servo to maintain the antenna boresight on the tracked target.

In order for the angle circuit to maintain a constant number of volts per degree for the angle error output, the gain of the receivers must be maintained to provide a

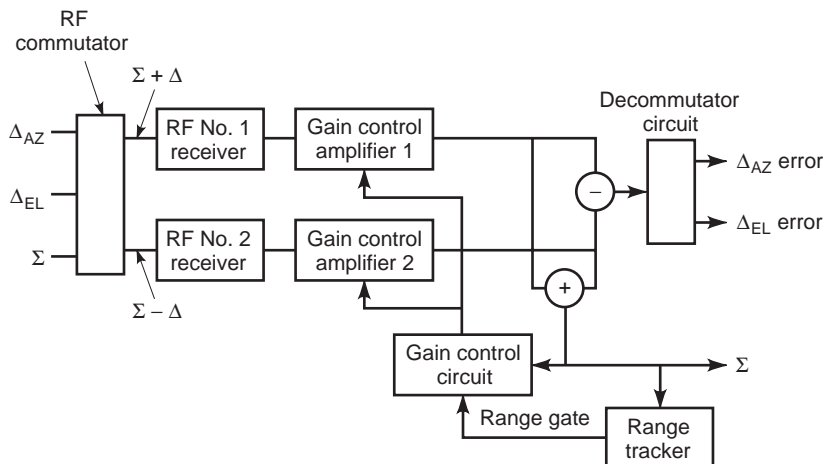


Figure 11. Two-channel monopulse circuit.

constant (on the average) output signal level at the target range. In order to accomplish this, the sum of the video receive signals is provided to a range tracker circuit, which then determines the range to the tracked target. The output video signal is then sampled at the range of the target, and this is then used to form the gain control voltage to both the receiver channels, in order to maintain relatively constant target output levels in the receivers.

The advantage of the two-channel receiver is that it eliminates the need for a third receiver channel, and that it eliminates any zero drift in the phase-sensitive amplitude detectors. This is at the expense of 3 dB less efficiency (as compared to the three-channel configuration), and potential sensitivity to target amplitude fluctuation if the two channel gains are not identical. The disadvantage is that the angle error is only determined on alternate pulses, and any noise or differential losses in the switching process will tend to degrade the accuracy and precision of track. Thus, some sacrifice in tracking precision will be suffered in comparison to a full three-channel monopulse angle tracker.

5.4. Angle Error Sources

The accurate determination of the angle to the target is influenced by a number of factors including radar-dependent errors, target-dependent errors, and propagation effects. Radar-dependent errors include the effects of thermal noise, antenna misalignment and cross coupling errors, and radar instrumentation error sources. The angular errors resulting from thermal noise can be quantified and are primarily dependent upon the signal-to-noise ratio. For a conical scan radar, the variance in the angle determination is given by

$$\sigma_t = \frac{1.4\theta_c}{K_s \sqrt{B\tau(\text{SNR})(f_r/\beta_n)}}, \text{ for SNR} > 4$$

where

- K_s = conical scan angle error slope
- θ_c = antenna 3 dB bandwidth
- SNR = signal-to-noise power ratio
- f_r = pulse repetition frequency
- β_n = servo bandwidth
- B = receiver bandwidth
- τ = pulsewidth

For a monopulse angle tracker, the variance is given by

$$\sigma_t = \frac{\theta_m}{K_m \sqrt{B\tau(\text{SNR})(f_r/\beta_n)}}, \text{ for } B\tau > 1$$

where

- K_m = monopulse error slope
- θ_m = antenna 3 dB Σ beamwidth

Glint is one of the most significant target dependent, angle error sources for complex targets such as aircraft and

ships. Complex targets consist of multiple scatterers separated in angle and range. Rather small variations in target aspect angle can change the phase relationship of the separate scatterers, resulting in large variations of the amplitude and indicated angle to target. Depending on the extent of the scatterers and their phase relationships, the indicated angle to the target can actually be outside the physical dimensions of the target. In order to understand the phenomena, the slope of the phase front resulting from two isolated point targets is given by Dunn and Howard [5] as

$$\delta' = \frac{L \cos \psi}{2} \left[\frac{1 - a^2}{1 + 2^2 + 2a \cos(\phi + \frac{2\pi L}{\lambda} \sin \psi)} \right]$$

where

- a = relative amplitude of the one scatterer to the stronger scatterer
- L = lateral distance separating the two scatterers
- ϕ = relative phase of the two scatterers
- ψ = angle between the perpendicular bisector of the scatterers and direction to the radar

If ψ is set equal to zero, then

$$\delta' = \frac{L}{2} \left[\frac{1 - a^2}{1 + a^2 + 2a \cos \phi} \right]$$

The preceding equation has been plotted in Fig. 12 for $a = 0.9$. As can be seen from the plot, when the relative phase angle between the two scatterers approaches 180° , the indicated angular position is outside the directions to the two scatterers.

Propagation effects such as multipath and ducting can also affect the angular indication, especially for elevation angle sensing. Multipath is a severe problem for low angle tracking of targets, where the multipath return from the terrain is in the main beam (or possibly even the sidelobes) of the antenna. Multipath contributions can be both from

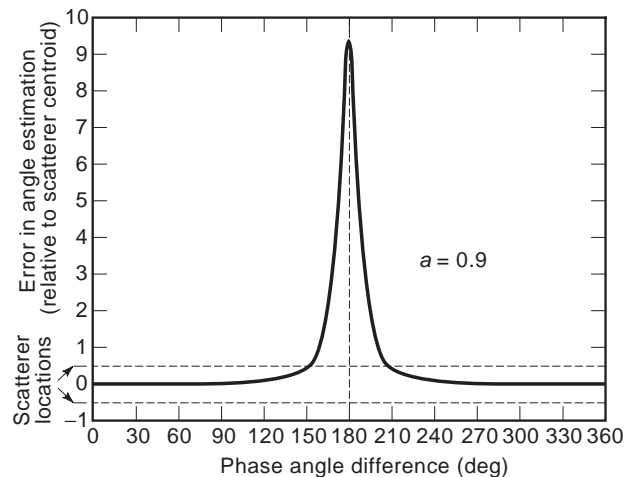


Figure 12. Phase front warpage caused by two scatterers.

specular and diffuse reflections from the terrain, and their contributions are a function of the surface roughness. For specular reflections, the return signals can be expressed as

$$E = A_t f(\theta_t) + A_r \rho_o f(-\theta_r) e^{-j\alpha}$$

where

- A_t = free-space target amplitude at the antenna
- A_r = free-space multipath (target image) amplitude at the antenna
- $f(\theta_t)$ = antenna voltage gain in the direction of the target
- $f(-\theta_r)$ = antenna voltage gain in the direction of the multipath return
- ρ_o = magnitude of the reflection coefficient
- α = relative phase angle between the direct and the multipath return

In a sense, the angular errors caused multipath effects are similar to those associated with the two-point scatterer situation.

6. DOPPLER TRACKING

Tracking targets in a clutter background is one of the major problems for radar trackers. Fortunately, terrain clutter generally has a narrow specular extent. If the target is moving, the Doppler frequency of its return is normally outside that of the terrain clutter. Doppler filtering can then be used to reject clutter, while keeping the target returns. The simplest type of Doppler filtering is obtained by using moving-target indication (MTI) processing. More advanced Doppler processing enables the determination of the Doppler frequency (and hence the radial velocity) of the target. MTI or Doppler filtering must be applied to both sum and difference channels of a monopulse tracker, and in conical scan or lobing radar must be able to cancel the modulation induced on the clutter by scanning.

6.1. MTI Processing

For a ground-based radar system, MTI processing provides the capability to reject clutter by filtering out the returns whose spectral content is close to the pulse repetition frequency (PRF) of the radar. This is accomplished by comparing the phase and amplitude of the target returns on successive pulse intervals. Coherent radar operation is normally used for MTI processing, however, coherent on-receive MTI processing can be used with noncoherent radars to provide most of the benefits achieved with coherent radar processing. In MTI processing, if the phase and amplitude of the returns stay constant over two, three, or more pulse intervals, then the returns are assumed to be associated with clutter and are rejected. The phase (and possibly the amplitude) of moving target returns will change on a pulse-to-pulse basis and are not rejected by the MTI filtering. MTI-filtered target returns can then be tracked by range and angle tracking circuits.

6.2. Doppler Filtering

Full Doppler tracking requires coherent radar operation and can improve the tracking ability of the radar using narrow filter bandwidths, thus increasing the sensitivity of the radar. The Doppler filtering can also enable the determination of the actual Doppler frequency of the radar returns, thus providing an exact determination of the target radial velocity. In addition, for airborne radars, the Doppler frequencies of the clutter returns are a function of the aircraft velocity and the aspect angles to the clutter patch. Thus MTI processing cannot be used for clutter rejection with airborne radars.

Continuous-wave (CW) radar provides the ability to track a moving target while rejecting clutter. Normally, separate transmit and receive antennas are used for CW tracking radars. An example of a Doppler phase-locked loop, a simplified version of that shown by Morris [6], is given in Fig. 13. The Σ signal input is mixed down to the center frequency (f_2) of the narrow bandpass filter. The input to the Σ signal mixer is derived from a combination of the output of the phase-locked oscillator (PLO), which is then mixed with the IF local-oscillator (IF LO) frequency to provide the IF signal necessary to mix the Σ signal down to frequency f_2 . Any increase or decrease in the Doppler frequency (f_D) will cause the PLO output frequency to change in order to maintain the input to the bandpass filter at frequency f_2 . The Δ_{AZ} and Δ_{EL} signals are also mixed down to frequency f_2 . The Δ_{AZ} and Δ_{EL} signals are narrowband filtered, and used to derive the Δ_{AZ} error and Δ_{EL} error signals.

For a high PRF pulsed Doppler radar, a narrow pass-band filter is normally used to limit the receive spectrum to $f_0 \pm PRF/2$. This has the effect of converting the pulsed signal to CW, at which time the CW Doppler tracking configuration described earlier can be used for the Doppler and angle tracking. If range tracking of the signal is also required, the signal must first be sampled at the range of the target prior to narrowband filtering. A minimum of two adjacent range cell samplers, each followed by narrowband Doppler filter, are required to accomplish range tracking. In this case, the range samplers act as early and

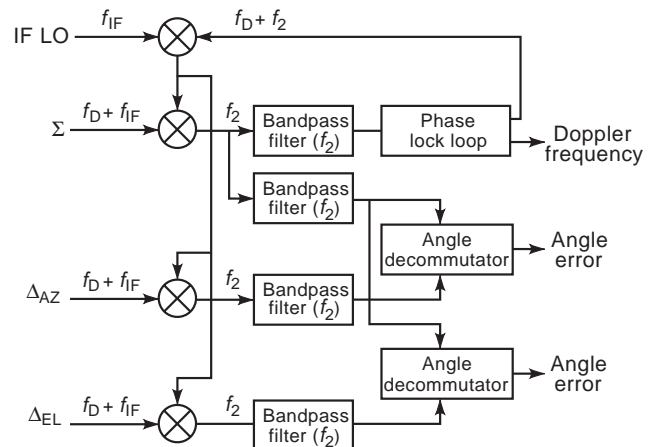


Figure 13. Doppler phase-locked loop.

late gate samplers, and by comparing the output Doppler amplitudes, the range tracker can keep the received pulses centered between the two range samplers. Acquisition with a pulsed Doppler tracker can be a complicated process. In order for the Doppler tracker to acquire the target, both the range and Doppler frequency must be established in order to provide the Doppler output signals required for tracking. Thus, unless the range and the Doppler frequency is known (and normally they are not), a search process both in range and Doppler frequency must be initiated to find the target and initiate track. Other configurations exist for Doppler filter trackers. Barton [3] describes a technique using narrowband filters offset above and below from a center frequency. By comparing the amplitudes out of the high- and low-frequency narrowband filters, an estimate of the Doppler frequency can be obtained on a single-pulse basis.

6.3. Digital Doppler Processing

With the advent of high-speed digital processors, the Doppler frequencies can be computed directly. For this type of processing, the receive signals are normally converted to I and Q digital format using high-speed analog to digital converters. The range-sampled I and Q signals can be stored for a selected number of pulse repetition intervals (PRI), and input to fast Fourier transform (FFT) computational routines. The FFT computes the detected amplitude versus Doppler frequency for each sampled range. Tracking algorithms can then use the detected targets out of the FFT processor to establish the range track, and subsequently angle and Doppler track.

7. RADAR AMBIGUITIES

Generally radars are classified as low-, medium-, or high-PRF radars. For low PRF radars, all the target (and clutter) returns are received prior to transmission of the next radar pulse. With high PRF radars, the Doppler frequencies of all the target (and clutter) signals are less than that of the radar PRF. Low PRF radars, which are unambiguous in range, are generally ambiguous in Doppler, whereas high PRF radars are normally highly ambiguous in range. Medium PRF radars can be ambiguous in both range and Doppler.

7.1. Range Ambiguities and Eclipsing

Figure 14 shows receive signals over several PRI. The returns from target 1 occur within the same PRI as the transmit pulse that initiated the target returns, and so target 1 range is unambiguous. The returns from target 2 occur at the same times when other transmit pulses are being generated. Because receiver returns are normally disabled during the transmit pulse times to prevent receiver saturation (and possibly burnout), target 2 returns are eclipsed, and not detected in the receiver. The returns from target 3 are from a range exceeding the unambiguous range, so that the returns in the current PRI are associated with pulses transmitted several pulses

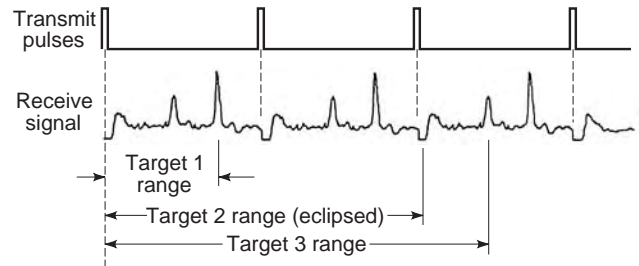


Figure 14. Range ambiguities and eclipsing.

earlier. Thus, from the radar display, the returns from target 3 appear to be from a much closer range.

Range eclipsing occurs quite frequently in high PRF radars because of the relatively high transmit time duty factors. Even on medium PRF radars eclipsing must be avoided for reliable target detection. Eclipsing can be avoided by changing the PRF when the radar determines that the tracked target range is approaching an eclipse situation. An alternate solution is to switch between two or more PRI, so that the target will be visible in the PRIs in which it is not eclipsed.

Clutter returns with delay times exceeding the PRI (second-time around returns) can cause serious problems to an MTI radar. This is because many MTI radars employ pulse-to-pulse stagger to avoid blind ranges. With PRF-staggered MTI radar, second time around clutter returns are not canceled because the apparent range changes from pulse to pulse. In general, range ambiguities need be resolved, especially for medium- and high-PRF radars. Even for relatively low PRF radar, such as the AN/MPS-36 instrumentation tracking radar with a 320-Hz PRF (unambiguous range of 253 nm), the radar when its return is augmented by a transponder can track missiles many thousands of miles. A number of methods are available for resolving range ambiguities. One method is to use a form of PRF stagger in which the transmission time is varied on a pulse-to-pulse basis. The only receive pulses that align on a pulse-to-pulse basis are those corresponding to the destagger associated with that specific number of PRI. Another method is to apply intrapulse coding on the transmit pulse in which the coding is changed on a pulse-to-pulse basis. On receipt, receive signals can then be associated with the particular transmit pulse responsible for the target returns.

7.2. Doppler Ambiguities and Blind Speeds

Figure 15 illustrates receive signals (in frequency space) for a pulsed coherent radar. The spectral content of the clutter returns are centered about the PRF frequency lines denoted by $f_0 \pm n_{PRF}$. Target 1 has a Doppler frequency that is less than the PRF, and so its Doppler can be determined unambiguously. Target 2 Doppler frequency is at a multiple of the PRF, and because the clutter returns are normally much higher than those of the target, it is highly unlikely that the target will be detected. In fact, most coherent radars intentionally reject frequencies around the $f_0 \pm n_{PRF}$ frequencies, specifically to reject clutter. Target speeds associated with Doppler frequencies

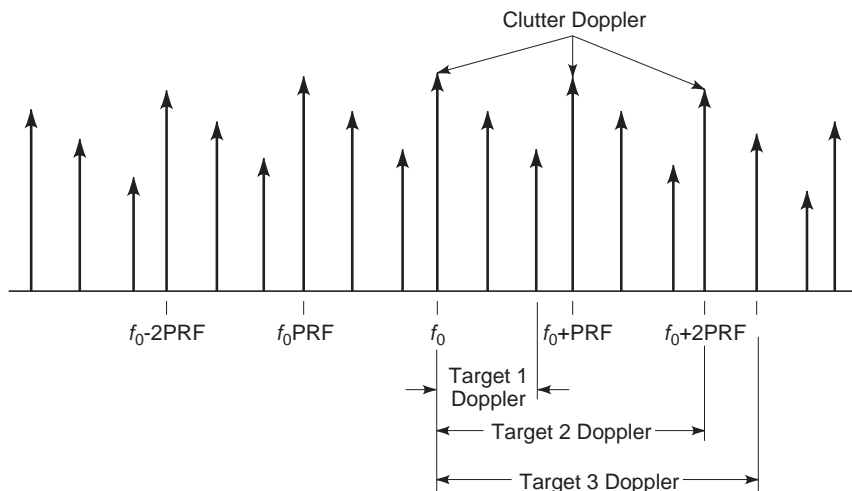


Figure 15. Doppler ambiguity and blind speeds.

of $f_0 \pm nPRF$ are referred to as blind speeds. Target 3 Doppler frequency exceeds that of the PRF so that the actual Doppler frequency cannot be determined from the receive spectrum.

Blind speeds can be avoided by several methods. Many coherent MTI radars avoid blind speeds by varying the PRF on a pulse-to-pulse basis. By appropriately selecting a number of different PRFs, and switching PRFs on a pulse-to-pulse basis, blind speeds can be avoided over a large range of target velocities. However, as noted previously, second-time-around clutter returns will pose a problem to this type of processing. Most Doppler radars require a constant PRF during the coherent processing interval (CPI). Doppler radars can avoid blind speeds by switching to a different PRF when it notes that it is approaching a blind speed. Alternately, the radar could transmit groups of pulses at different PRFs so that at most only one group would be at the blind speed.

Resolving Doppler ambiguities can be accomplished by several techniques. If the radar is tracking the target range, the range rate determination is generally accurate enough to enable determination of which PRF multiple the target Doppler is located. If two or more groups of Doppler PRFs are used, the ambiguity can often be resolved from the measured Doppler frequencies resulting from the multiple PRFs.

7.2.1. Multiple-Target Tracking. In many cases there is a need to track multiple targets simultaneously. Continuously scanning surveillance radars, such as the FAA’s ASR-9 airport surveillance radars, must track all the targets (airplanes) within their coverage regime. This tracking must be performed on a scan-to-scan basis, and thus this type of tracking is commonly referred to as track-while-scan processing. Phased-array radars are also multiple target trackers, because they normally interleave switched-beam locations to track a number of targets, with scanning for new targets, as well as performing other possible functions. With these radars, the targets (or aircraft) are only viewed for a number of pulses on a scan-to-scan (or look-to-look) basis.

Most modern scan-to-scan (or look-to-look) radars use computers for multiple target tracking. Because the aircraft positions typically change on a look-to-look basis, tracking algorithms must be derived to predict the estimated target positions on the next scan, based on previous scans. The accuracy of these predicted positions is limited by the maneuver capabilities of the targets being tracked, so that the predicted positions are only estimates of their actual positions. Association algorithms must then be used to determine (1) if detected target is associated with an established track, (2) which established target track the target should be associated with, and (3) to determine if a new track should be established, if no track association is made.

Figure 16 shows a typical flow diagram for a multiple target tracker. The raw target position information, such as range and azimuth angle (and possibly elevation angle or height), is derived in the radar. Most multiple target tracker associative algorithms prefer to track in rectangular coordinates (R_N, R_E, R_V) rather than polar coordinates so that the conversion must be made from polar coordinates. If North is assumed to be at zero degrees, then

$$R_N = R \cos \theta \cos \beta$$

$$R_E = R \sin \theta \cos \beta$$

$$R_V = R \sin \beta$$

where

R = range

θ = azimuth angle

β = elevation angle

The current target position (R_C) is then

$$R_C = \sqrt{(R_N)^2 + (R_E)^2 + (R_V)^2}$$

After the coordinate transformations are performed on the incoming radar target data, present target detections are

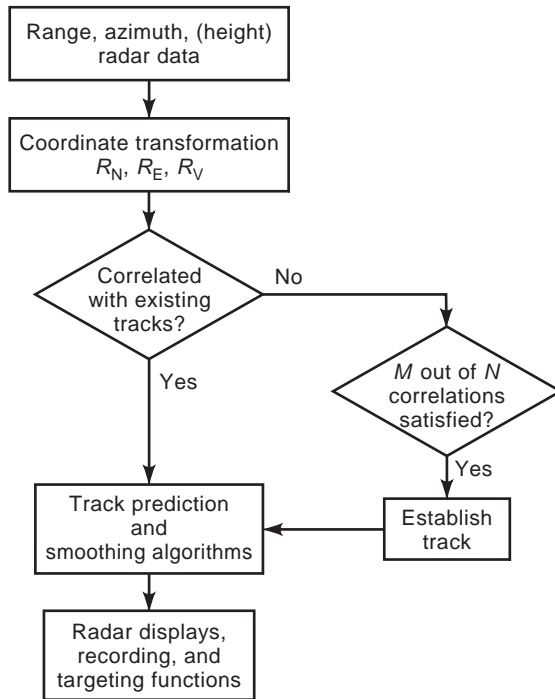


Figure 16. Multiple target tracking.

then compared in association algorithms to determine if the target data are associated with established target tracks. For the FAA airport surveillance radars, the radar target detections are also associated with the secondary (beacon) radar target reports. The beacon returns also include aircraft identification and reported aircraft height. The combined associations are then used to update the target tracks and predict the aircraft locations on the next scan using the track prediction and smoothing algorithms. If the target detection is not associated with any of the present target tracks, then the position information is considered for the establishment of a new target track. In order to establish a new target track, generally the target must be associated with m on n of the previous scans in order to establish a new track. After the m out of n association is made, a new track is established, and the past position information on those target detections is used to predict the target location on the next scan. Target tracks are generally dropped after a certain number of successive target track associations are missed. The information on established target tracks is then routed to radar displays and possibly to weapons systems.

7.3. Smoothing and Prediction Algorithms

Radar measurements of target positions and velocities are often imprecise as a result of a number of factors, such as signal-to-noise ratio, target RCS fluctuations, multipath, and clutter contamination. Various algorithms can be used for the track smoothing and prediction to mitigate the effects of scan-to-scan position and velocity measurement errors, and thus to improve the accuracy of tracking. Kalman filters [7] are probably the best-known smoothing and prediction algorithms. Alpha, beta (α, β or α, β, γ) trackers are a subset of the Kalman filters and are the simplest

because they use precomputed fixed gains. The $\alpha, \beta, \tilde{\alpha}$ equations applied to position and velocity smoothing are

$$\hat{R}_C = \hat{R}_{PC} + \alpha(R_C - \hat{R}_{PC})$$

$$\hat{R}_C = \hat{R}_C + \beta \frac{(R_C - \hat{R}_{PC})}{T}$$

$$\hat{R}_C = \hat{R}_{PC} + \gamma \frac{(\hat{R}_C - \hat{R}_{PC})}{T}$$

and for prediction are

$$\hat{R}_{P(C+1)} = \hat{R}_C + \hat{R}_C T + (T^2/2)\hat{R}_C$$

$$\hat{R}_{P(C+1)} = \hat{R}_C + \hat{R}_C T$$

$$\hat{R}_{P(C+1)} = \hat{R}_C$$

where

T = sampling period

R_C = measured position

\hat{R}_C = smoothed estimate of current position

\hat{R}_{PC} = predicted position at the time of the measurement

$\hat{R}_{P(C+1)}$ = predicted position T s later

\hat{R}_C = smoothed estimate of current velocity

\hat{R}_{PC} = predicted velocity at the time of measurement

$\hat{R}_{P(C+1)}$ = predicted velocity T s later

\hat{R}_C = smoothed current acceleration

$\hat{R}_{P(C+1)}$ = predicted acceleration T s later

T = time between measurements

The precomputed fixed gains α, β, γ can vary between zero and one, with values toward one giving the greatest emphasis toward the current measurements, whereas values toward zero provide the greatest smoothing. Benedict and Bordner [8] analyzed the gains for an α, β for track-while scan application and determined the optimal selection for this application as

$$\beta = \alpha^2 / (2 - \alpha)$$

The performance of the α, β, γ trackers are limited by the selection of the fixed gains, which may not be optimal for all situations. Bar-Shalom and Li [9] discusses the use of Bayesian data association techniques, as well as multiple model estimators for providing superior performance for multitarget tracking.

BIBLIOGRAPHY

1. L. V. Blake, Prediction of radar range, in M. I. Skolnik, ed., *Radar Handbook*, McGraw-Hill, New York, 1990, chap. 2.
2. P. Swerling, Probability of detection for fluctuating targets, *IRE Trans.* **IT-6**:269–308 (1960).
3. D. K. Barton, *Radar System Analysis*, Prentice-Hall, Englewood Cliffs, NJ, 1964.

4. D. R. Rhodes, *Introduction to Monopulse*, McGraw-Hill, New York, 1959, p. 41; reprint, Artech House, Norwood, MA, 1980.
5. J. H. Dunn and D. D. Howard, Radar target amplitude, angle, and Doppler scintillation from analysis of the echo signal propagating through space, *IEEE Trans. Microwave Theory Tech.* **MTT-16**:715–728 (1968).
6. G. V. Morris, Doppler frequency tracking, in J. L. Eaves and E. K. Reedy, eds., *Principles of Modern Radar*, Van Nostrand Reinhold, New York, 1987, Chap. 19.
7. R. E. Kalman, New results in linear filtering and prediction theory, *ASME Trans.* **83D**:95–108 (1961).
8. T. R. Benedict and G. W. Bordner, Synthesis of an optimal set of track-while-scan smoothing equations, *IRE Trans. Autom. Control* **AC-7**:27–32 (1962).
9. Y. Bar-Shalom and Xiao-Rong Li, *Multitarget-Multisensor Tracking: Principles and Techniques*, Yaakov Bar-Shalom, Storrs, CT, 1995.

RADIATION EFFECTS

JAMES R. SCHWANK
 FRED W. SEXTON
 PAUL E. DODD
 MARTY R. SHANEYFELT
 Sandia National Laboratories
 Albuquerque, New Mexico

Significant damage can occur to semiconductor devices exposed to ionizing and other types of radiation. In the last three to four decades, considerable work has been performed investigating the effects of radiation on semiconductor devices. Some of the earlier work investigating these effects focused on radiation-induced damage in minority-carrier devices (e.g., bipolar transistors) caused by displacement damage and on transient radiation effects caused by high-dose-rate pulses of ionizing irradiation. Displacement damage occurs as a high-energy particle; for example, a proton or neutron collides with an atom in a material. The high-energy particle can knock an atom from its lattice site to an interstitial site, creating a vacancy/interstitial pair. This results in the creation of deep and shallow trap sites in the material that can compensate majority carriers, cause carrier removal, and act as generation, recombination, and trapping centers. Displacement effects are important primarily for minority-carrier and optoelectronic devices. A high-dose-rate pulse of ionizing radiation will generate many electron–hole pairs in a short period of time. Photocurrents will be generated that may cause temporary loss of stored information or disrupt functional operation of an IC (dose rate upset). In some cases, permanent damage to a device results.

In 1964, Hughes and Giroux [1] found that MOS devices were very sensitive to ionizing irradiation. Prior to this work, it was commonly believed that ionizing irradiation would have little effect on MOS devices. Since the initial work by Hughes and Giroux, a large amount of work has been performed investigating the mechanisms for ionizing radiation effects in MOS devices and methods

for hardening MOS devices to ionizing irradiation. Total-dose ionization degradation can occur as energetic particles (e.g., protons, electrons, X rays, gamma rays) ionize atoms in the material, creating electron–hole pairs. Ionizing radiation can induce significant charge buildup in oxides (e.g., the gate oxide of a MOS transistor or the field oxide of a MOS or bipolar IC), causing large threshold voltage shifts, and decreases in carrier mobility and bipolar transistor gain. This can result in large increases in the static power supply of an IC, degradation in timing, and potential loss of functionality. Total-dose ionizing radiation often results in permanent or long-term degradation. There are many potential environments that can expose devices to ionizing irradiation (e.g., space environments).

In addition to causing total-dose ionization degradation and displacement damage, energetic particles, such as protons, alpha particles, and heavy ions associated with space environments, can also cause single-event effects (SEEs). As a single high-energy particle (e.g., energetic heavy ion, proton, alpha particle, or neutron) strikes a material, it generates a dense plasma of electron–hole pairs along the path of the particle, which can trigger a variety of SEEs. Single-event effects are classified into two types: *soft errors*, which cause no permanent damage and may be correctable, and *hard errors*, which result in permanent damage to the device. A single-event upset (SEU) is an example of a soft error, where only the logic state of the circuit is changed. SEUs were first observed in space in 1975 [2]. Soft errors can be corrected by reloading the original information into a memory element or by restarting an algorithm in a CPU. If the error rate caused by single-event upsets is too high, performance degradation and even system failure can result. Hard errors are observed in circuits where high electric fields are present across insulating layers, such as nonvolatile memories, thin gate oxides, and capacitors used in analog technologies. For example, permanent damage can be induced by energy deposition in a small region of the dielectric after the passage of a high-energy particle. This effect is termed *single-event gate rupture* (SEGR). Protons and heavy ions may also trigger high-current conditions that can result in permanent circuit failure. Examples of this type of hard error are single-event latchup (SEL) in silicon controlled rectifiers (SCRs) and CMOS and bipolar ICs, single-event snapback (SESB) in nMOS devices, and single-event burn-out (SEB) in power transistors.

The early studies of radiation effects on electronic devices were funded primarily through military programs. Government funding constituted a significant fraction of the funding for advanced semiconductor device development, and government agencies had some influence on the course of device development. Consequently, the major focus was on investigating the effects of and hardening devices to radiation from nuclear radiation environments and on improving device performance to displacement, total-dose ionization, and high-dose-rate pulse effects. Single-event effects were relatively unimportant because devices were relatively simple and operated at high voltage levels. Hardening devices to SEE was relatively straightforward. Many commercial semiconductor suppliers

worked with government laboratories to manufacture radiation-hardened devices.

Today, the emphasis of radiation effects studies has changed dramatically. With the end of the cold war, government funding spent on nuclear radiation effects studies has dropped substantially. Commercial IC development is rapidly progressing, and government funding constitutes only a small fraction of that spent on advanced semiconductor development. As such, individual government agencies have little influence on the course of commercial IC development. Only a few commercial IC suppliers are willing to work with government laboratories to manufacture radiation-hardened devices.

Meanwhile, the number of commercial and military space programs has increased dramatically. The complexity of ICs in space systems (both commercial and military) is rapidly advancing. As a result, more emphasis is now placed on single-event effects. As dimensions of integrated circuits (ICs) continue to shrink and power supply levels are decreased, less radiation-induced charge is required to upset electronics, and present-day ICs are becoming more susceptible to single-event effects. Single-event effects are no longer a problem just for devices in space systems. Naturally occurring terrestrial radiation can also induce single-event upsets on Earth and in low-altitude aircraft. As electronic technologies continue to advance, radiation-induced effects on IC reliability are becoming increasingly important even for commercial electronics used on Earth.

The reduction in government funding and the number of suppliers of radiation-hardened devices has also increased the use of nonhardened commercial off-the-shelf (COTS) components in space systems. For COTS devices, the total-dose irradiation margin between device failure and system requirements can be small. This makes methods for ensuring device hardness in space environments based on laboratory measurements increasingly important. A larger fraction of government funding is now spent on developing techniques for improving hardness assurance test guidelines.

Because of the changing emphasis of radiation effect studies, we focus the following discussion on those effects pertinent to space and terrestrial radiation environments, namely, single-event and total-dose ionization effects. Emphasis is placed on those effects relevant to MOS transistors and ICs. MOS devices constitute a major portion of the electronics of nearly all modern space systems. The material covers radiation effects in both commercial and hardened devices. Although we focus on MOS technology, special issues relevant to other types of devices, for example, low-dose-rate effects in bipolar technologies and single-event upset in GaAs ICs, are also discussed.

To place the discussion of radiation effects in its proper context, we first give an overview of the space and terrestrial radiation environments. Single-event effects are covered in Section 2, which begins with a discussion of the charge collection mechanisms that are the basis for all single-event effects. Circuit issues relevant to single-event effects, including both soft and hard errors, are then presented. The final topic is total-dose ionization effects. The mechanisms for total-dose effects are first reviewed, followed by a discussion of charge buildup in ICs. We close

with a review of present methods for improving total-dose hardness.

1. SPACE AND TERRESTRIAL RADIATION ENVIRONMENTS

The particle flux of the natural radiation environment varies widely in composition from Earth's surface to the interplanetary environment of space probes. In the space environment, only protons and heavy ions have sufficient mass and energy to cause soft errors, while both protons and electrons contribute to total-dose damage. In the terrestrial environment, cosmic rays and secondary-particle showers cause upsets in ground-based electronics and in aircraft electronics. A detailed understanding of the radiation environment is necessary in order to estimate device reliability and, ultimately, the useful lifetime of a system.

In this section we describe the radiation environment in more detail, including a description of the dependence of the particle flux on energy, spacecraft altitude, inclination, and shielding. Understanding these dependencies and building accurate models of the environment experienced by spacecraft is important for error rate predictions. We also discuss the influence of the near-Earth environment on terrestrial and low-altitude radiation environments.

1.1. Definition of Terms

Before proceeding, it is important to define a few commonly used terms to describe space and terrestrial radiation environments. As a particle passes through a material, it loses energy by collisions with the electrons (electronic stopping) and nuclei (nuclear stopping) of the target material [3]. The rate of energy loss per unit pathlength dE/dx , from both mechanisms is called the *total stopping power* and is expressed in units of ergs/cm. Mass stopping power is the energy loss per unit mass per area $1/\rho dE/dx$, where ρ is the density of the target material. In SEE studies, we normally consider the amount of energy transferred per unit pathlength to a given material, where linear energy transfer (LET) is given in units of $\text{MeV mg}^{-1} \text{cm}^2$ (or $\text{MeV} \cdot \text{cm}^2/\text{mg}$). LET considers only the energy deposited along or near the particle's path, while stopping power considers all energy lost to the material. This distinction is important when considering energy deposition and collection on a microscopic scale, where track structure may be important. In most cases, however, mass stopping power is used to estimate LET, and the terms will be used synonymously in the remaining text. The dependence of LET on energy has a peak, which, in silicon, is roughly equal to the atomic number of the ion. A carbon atom, for example, has a peak LET of about $6 \text{ MeV} \cdot \text{cm}^2/\text{mg}$, and LET decreases on either side of this peak. The energy at which the peak occurs (known as the *Bragg peak*) increases with the mass of the ion.

In many environments, particle flux is isotropic and may strike a system from any direction. Here it is defined as the number of particles per square meter per second impinging on a unit sphere from all directions. When flux is anisotropic, it is defined as the number of particles (#) passing through the center of a sphere from a unit solid

angle. This measure has units of $\#/m^2 \cdot \text{steradian} \cdot s$, and is, by definition, 4π smaller than the isotropic flux. Fluence is simply the flux integrated over time and is given in units of $\#/m^2$ or $\#/m^2 \cdot \text{steradian}$ for isotropic or anisotropic fluence, respectively.

Total-dose ionizing radiation is normally specified in either units of rad or gray (Gy); $1 \text{ rad} = 100 \text{ Gy}$. A rad is equal to 100 ergs of energy deposited per gram of material. The energy deposited must be specified for the material of interest. For example, for a MOS transistor, total dose is measured in units of rad(Si) or rad(SiO_2). For a space satellite, the dose rate can vary over a wide range, from less than 10^{-6} to mid- 10^{-3} rad(Si)/s. For a 5-year space mission, these dose rates correspond to a total-dose range of less than 1 krad(Si) to more than 5 Mrad(Si).

1.2. Natural Space Radiation Environment

The natural space radiation environment consists of a steady-state component and a transient component. The former consists of energetic charged particles trapped within Earth's radiation belts, the solar wind, and very energetic galactic cosmic rays that originate outside our solar system. The environment changes over a period of years as it is moderated by solar activity and by precession of Earth's magnetic field with respect to Earth's axis of rotation. The transient environment is influenced primarily by energetic solar events, such as coronal mass ejections (CMEs), solar flares, and solar storms. This section discusses the major factors from the steady-state and

transient environments that influence the performance of integrated circuits and semiconductor devices in space.

1.2.1. Earth's Radiation Belts. Energetic charged particles in the near-Earth environment are trapped in Earth's magnetic field-forming regions that have been called the *van Allen radiation belts* after James van Allen, who designed the first instruments to measure and analyze Earth's radiation belts [4]. The structure of Earth's magnetic field, the magnetosphere, defines the shape of the radiation belts, which, to first order, can be described as a series of concentric shells of decreasing magnetic flux with increasing altitude. Each shell (called *L shells*) is given as a dimensionless number in units of Earth radii ($R_e = 6371 \text{ km}$). Because the magnetic field lines in a dipole field converge at the north and south magnetic poles, the distance between L shells decreases at polar latitudes, while the shells extend farthest at the magnetic equator, which is tilted 11° from Earth's geographic equator. A more detailed description of Earth's magnetosphere and its effect on the radiation environment can be found in Ref. 4.

The radiation belts, depicted in Fig. 1, begin at an altitude of about 1000 km at the magnetic equator. The most abundant particles are electrons and protons; however, some low-energy heavy ions are also found. The distribution of trapped protons with energy greater than 10 MeV consists of one region that peaks at about 5000 km and extends to about 18,000 km (3.8 Earth radii). Higher energies are confined to lower L shell, so, for example, the

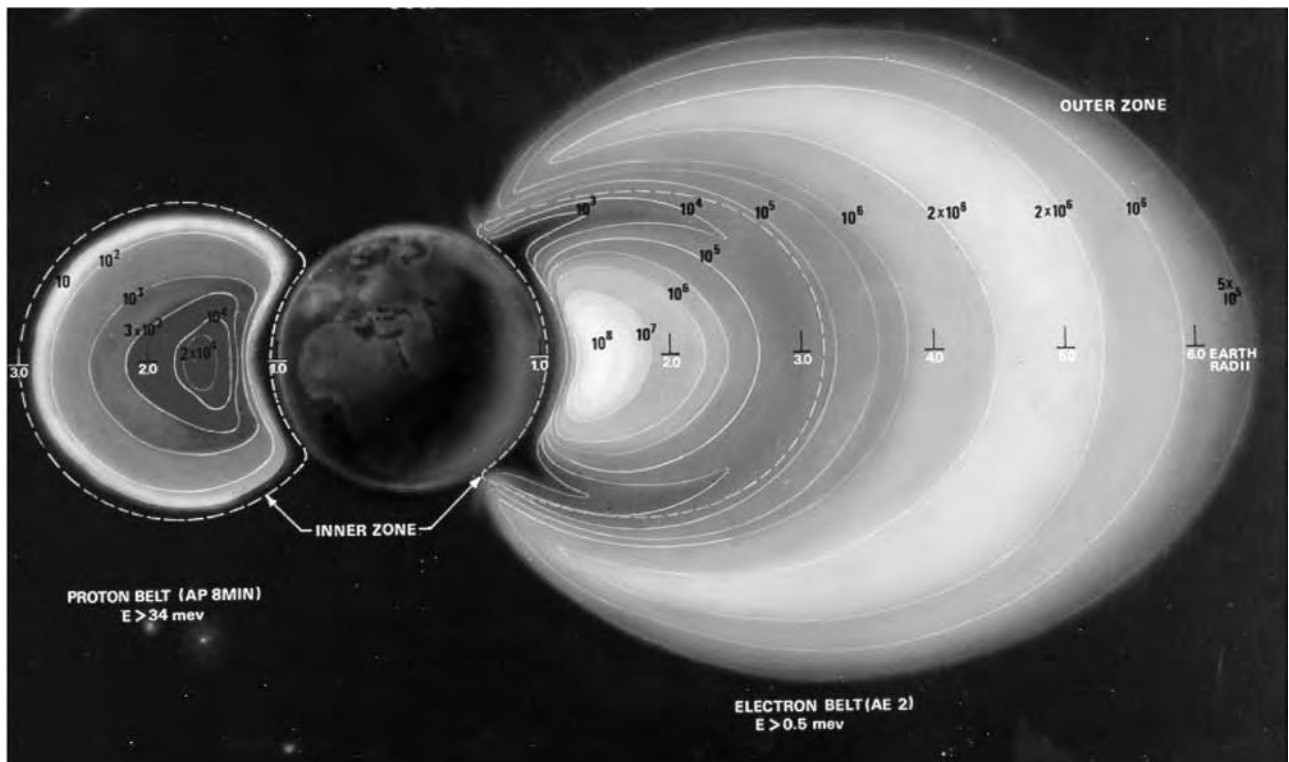


Figure 1. Density of the van Allen radiation belts formed by Earth's magnetosphere. The proton belt has a single peak at about 1.5 R_e , and the electron belt is double peaked at 1.4 R_e and 4.9 R_e . Note that the belts are actually toroidal but are separated here for clarity.

>400 MeV distribution extends only from $L=1.2-2$. Normal intensities for proton flux are on the order of $10^6/\text{cm}^2 \cdot \text{s}$. The electron belts are divided into *inner* and *outer* radiation belts. The inner belt peaks at approximately 4000 km, and extends to about 9600 km (2.8 Earth radii), while the outer belt ranges from 11,500 km to about 70,000 km (12 Earth radii). In low-Earth orbit (LEO), spacecraft encounter both inner-belt electrons and protons, while in geosynchronous orbit (GEO), about 35,775 km, primarily outer-belt electrons are encountered. The most intense total-dose radiation environment is encountered at half geosynchronous orbit, about 17,500 km.

1.2.2. The South Atlantic Anomaly. Above the Atlantic Ocean off the South American coast the magnetosphere dips toward Earth, causing a region of increased proton flux, called the *South Atlantic anomaly* (SAA). This region extends as low as 500 km. The proton flux of particles with energy greater than 30 MeV is 10^4 times more intense at 1000 km in the SAA than at comparable altitudes over other regions of Earth. At higher altitudes the magnetosphere is more uniform and the proton flux depends only on L shell.

1.2.3. Galactic Cosmic Rays. Galactic cosmic rays (GCRs) originate outside the solar system and propagate throughout all space. The relative composition of the GCR flux is highly dependent on the ion species, as shown in Fig. 2 [5]. Its composition is roughly 85% protons, 14% alpha particles, and 1% heavy nuclei, and spans more than 11 orders of magnitude in flux. Note that there are four orders of magnitude difference in the intensity of iron; the most abundant are high-LET heavy ion and protons. The flux for each species peaks at energies of 100–1000 MeV/nucleon, then tails off to energies as high as 100 GeV/nucleon [6]. At these energies it is virtually impossible to shield circuits from heavy-ion strikes. The galactic cosmic ray flux provides a steady background radiation on the order of tens of particles/ $\text{cm}^2 \cdot \text{s}$ that, because of their high

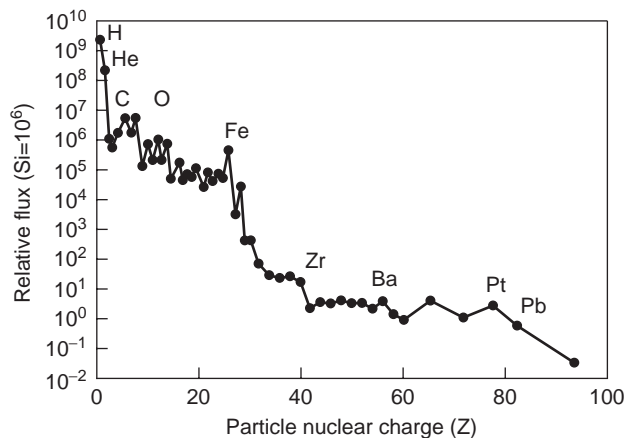


Figure 2. Galactic cosmic ray particle spectrum as a function of mass. Protons and helium ions are the most abundant elements, but there are a significant number of heavier elements up to Fe. Because of their high LET, even the low flux of ions heavier than Fe must be considered [5].

LET, must be considered in spacecraft system design to ensure survival.

1.2.4. Solar Flares. Solar flares contain high fluxes of protons, electrons, and some energetic heavy ions, and generally last from hours to days [7]. Because these fluxes are orders of magnitude higher than the steady-state flux of the radiation belts and the GCR flux, peak error rates in satellites are dominated by solar protons and heavy ions. Proton fluence during a large flare can exceed 10^{10} protons/ cm^2 , and can have energies greater than 100 MeV. Depending on the energy spectrum of a given flare, solar protons can extend to altitudes as low as 5 Earth radii. Flares can also inject energetic particles into Earth's radiation belts, some of which are trapped and form new radiation belts persisting for months [8]. Early researchers thought that large flares were anomalous events. It is now known, however, that the fluence distribution of flares forms a continuum that is well described by an extreme value distribution [9], which predicts a 10% chance per year of a large flare during the 7 active years of the 11-year solar cycle.

Coronal mass ejections (CMEs) are solar events in the Sun's chromosphere that eject large quantities of highly ionized gas into interplanetary space and have an associated magnetic bubble [10]. When this magnetic bubble hits Earth's magnetosphere, the resulting shock can accelerate charge particles into the radiation belts. For large CME, the magnetosphere can be significantly perturbed, reducing the magnetic shielding experienced by satellites. Magnetic storms are perturbations of the magnetosphere, and can persist for hours to days after a large transient and are associated with CMEs, flares, and changes in the embedded solar magnetic field. The solar wind is a steady stream of protons, electrons, doubly ionized helium, and a small quantity of heavier ions that emanate from the sun's outer atmosphere and permeate throughout the solar system and beyond [11]. While the solar wind has an average variation that follows solar activity, it can change by orders of magnitude in a period of hours during CMEs and flares. Electrons dominate the total-dose contribution from the solar wind. However, their energies are in the eV-keV range and are easily stopped by thin shields. CMEs and the solar wind do not contribute significantly to total dose or SEE in spacecraft systems. However, they can cause significant charging on exposed dielectric surfaces. After a critical charge is reached, these insulators can destructively discharge. Dielectric charging must be considered in overall system design.

1.2.5. Dependencies. In Earth orbit, the contribution of the GCR and solar flare fluxes to the total particle flux depends on solar activity. The galactic component, for example, is affected by the screening effect of the solar wind; as solar activity decreases, the galactic component increases. On the other hand, the interplanetary and flare components increase with solar activity, since they are composed primarily of particles originating in the Sun. The change in the integral LET spectra (total flux of particles with LET greater than or equal to a given LET) as a

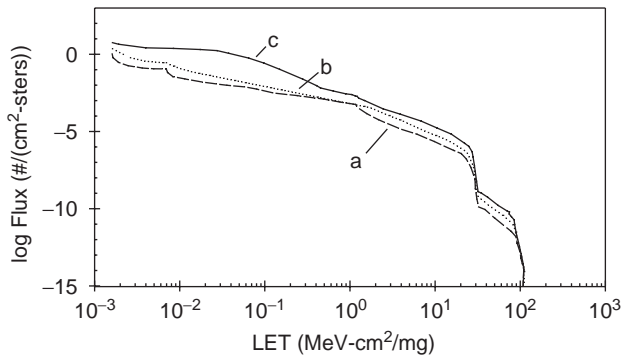


Figure 3. The integral LET spectra under (a) solar maximum conditions, (b) solar minimum conditions, and (c) Adam's 10% worst-case environment. Integral LET curves give the flux for all particles with a given LET or less [14].

function of solar activity is shown in Fig. 3 for a spacecraft in geosynchronous orbit. These particular curves were calculated for 25 mils of aluminum. The lowest intensity (curve *a*) occurs at solar maximum excluding solar flares. This represents the absolute minimum at geosynchronous orbit. The environment at solar minimum (curve *b*) describes the environment for approximately 40% of the time. This is the pure galactic cosmic ray spectrum. If we add solar flares to this, the 90% environment results (curve *c*). Alternatively, we say that the environment is more severe than curve *c* only 10% of the time. This curve, called "Adams' 90% worst-case environment," has been used quite frequently to represent the space environment in error rate calculations [12]. With the development of improved solar flare models, however, the solar minimum environment with a separate model for solar flares is now considered the best estimate of the worst-case environment [13].

Earth's magnetosphere screens out particles below a specific energy determined by the particle's magnetic rigidity, defined as the momentum per unit charge, and the local field strength. The magnetic field deflects particles with lower rigidity and prevents their further penetration. Near the equator the Earth magnetic field screens all but the most energetic ions, while at the poles the particle flux is not significantly attenuated.

The penetration range of cosmic rays in a material depends on their energy. Therefore, the skin of a spacecraft and electronic boxes provides some degree of shielding to electronic components. The degree to which a spectrum is affected by shielding depends on the hardness of the spectrum. Additional shielding may prove effective against low-energy components, but is relatively ineffective in reducing hard components such as high-energy protons and the galactic cosmic ray spectrum. For example, the GCR spectrum is only marginally reduced for aluminum thicknesses in the 2–10-g/cm² range (300 mils to 1.45 in. thicknesses). Only when shielding is on the order of 50–100 g/cm² is appreciable attenuation of this spectrum realized [14]. Spacecraft walls are normally about 100 mils thick, and more recent honeycomb construction to reduce weight provides even less shielding.

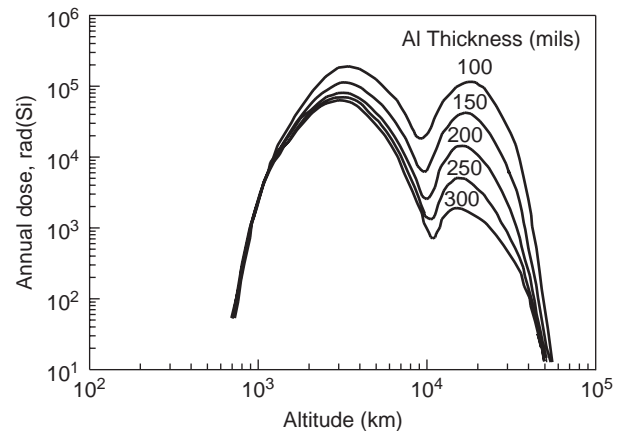


Figure 4. Annual ionizing dose accumulated as a function of altitude with shielding thickness of 100–300 mils of aluminum.

The combined contribution of trapped electrons, protons, and solar flare protons to ionizing dose accumulated to a spacecraft is shown in Fig. 4 as a function of altitude and aluminum shielding thickness. Two peaks are evident; the first, at 3000 km, is due primarily to trapped protons, while the second peak, at 17,500 km, is due to trapped electrons. As shielding thickness increases from 100 to 300 mils, the first peak decreases a factor of 3, while the second peak decreases more than 60 fold. This clearly illustrates the effectiveness of shielding against electrons, and the difficulty of shielding against high-energy protons. As an example of how this information is useful for ensuring survival of a space-based system, consider the annual dose accumulated to a system in three different orbits with 100 mils of aluminum shielding. A spacecraft in a low-Earth orbit of 800 km will receive an annual dose of only 300 rad(Si), while a spacecraft in geosynchronous orbit at 35,000 km will receive about 10 krad(Si) per year and a system in half-geosynchronous orbit, 17,500 km, will receive a dose in excess of 100 krad(Si) per year. For a 10-year design lifetime these three systems require electronics that can survive doses of 3, 100, and 1000 krad(Si), respectively. Clearly, the design issues for a low-Earth orbit are much more tractable than those for a system in the middle of the radiation belts.

1.3. The Terrestrial Radiation Environment

As they interact with Earth's upper atmosphere, galactic cosmic rays produce a shower of secondary particles that includes protons, neutrons, pions, muons, electrons, and photons. The density of secondaries is highly dependent on altitude, latitude, longitude, and the variation of the primary GCR flux with solar activity. It peaks at an altitude of about 15 km, just above commercial airplane altitudes, and decreases at lower altitudes due to absorption and thermalization processes that remove secondaries [15]. The neutron flux in the energy range 1–10 MeV has a maximum at an altitude of 18.3 km [60 kft (kilofeet)], but is significant as low as 9 km (30 kft). Taber and Normand [16] have shown a strong correlation between the upset

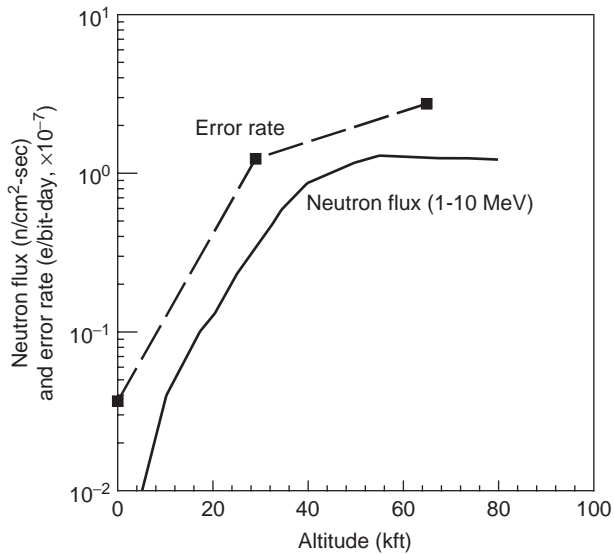


Figure 5. Single-event upsets measured in a 16-kbit SRAM as a function of aircraft altitude and neutron flux. The interaction of galactic cosmic rays with the upper atmosphere generates secondary showers of energetic nucleons whose flux peaks at about 60 kft. SEU in avionics are well correlated with the neutron flux of the secondary showers [16].

rate observed in a 64,000-bit memory and measured neutron flux as a function of altitude, as shown in Fig. 5. Note that the error rate has been scaled by a factor of 10^7 to plot on the same graph. Similar correlations have been demonstrated as a function of latitude. Secondary protons have been considered as a possible cause for in-flight SEUs; however, their latitude dependence doesn't correlate with the measured data.

SEUs are also being observed at ground level, and their frequency and distribution are consistent with terrestrial cosmic rays. Ziegler [15] showed that the frequency of errors in large computer memory systems, for example, scales linearly with altitude of the city in which they are located. In a test of both SRAM and DRAM (static and dynamic random access memory)-based systems, a 13x increase in error rate was observed as altitude increased from sea level to 10,000 ft (Leadville, CO). Similarly, error rate decreased as concrete absorber thickness increased. More recently, Lage et al. [17] showed that terrestrial cosmic ray induced SEUs present a lower limit to system error rates after other sources of bit errors, such as package alphas, have been considered.

Terrestrial cosmic ray induced upset poses a significant challenge to the reliability of future systems. Although error detection and correction (EDAC) techniques are successful for mitigating upsets in memory systems, the possibility that new upset mechanisms will surface with next-generation technologies, such as logic upsets, cannot be discounted. Also, new materials being used for improved performance in advanced IC technologies can introduce new sources of particle flux. Solder bump interconnects in flip-chip packaging can be a source of alpha particles if high-purity lead is not used. The effect of

technology and design changes on SEU is now a first-order consideration for next-generation ICs.

2. SINGLE-EVENT EFFECTS

The field of single-event effects (SEE) deals with the response of semiconductor devices and ICs to the passage of a single energetic atomic particle, such as a highly accelerated proton, or a heavily ionized iron nucleus. There are a wide variety of effects, but the classic one, termed *single-event upset* (SEU), describes the corruption of information stored in solid-state memory devices. As an energetic charged particle transits the semiconductor material it deposits energy to the lattice atoms, generating a dense plasma of free electrons and holes as the lattice atoms are ionized (holes are the absence of an electron, and act electrically like a positively charged particle). When this excess charge is collected across a high-field region, such as a p-n junction in a semiconductor device, a current pulse results that the device can interpret as a valid signal. For memory devices, this event can change stored information. For complex ICs, such as microprocessors, it can result in improper execution of a program, and even in the processor locking up.

SEU was first observed experimentally in 1975, when Binder et al. [2] attributed bit-flips in bipolar *J-K* flip-flops in a communication satellite to galactic cosmic rays. A few years later, May and Woods [18] observed upsets in dynamic random access memories (DRAMs) caused by alpha particles from the decay of radioactive material in ceramic packages. That same year, Pickel and Blandford [19] reported soft errors in NMOS DRAMs in space. Proton- and neutron-induced upsets were observed by Guenzer and coworkers in 1979 [20]. Since that time, upsets have been observed in many satellite systems and are a major design consideration for any space-based system.

Single-event effects have traditionally been a concern only for semiconductors that are used in space environments, where devices can be exposed to a high flux of radiation. The continuing decrease of feature size in ICs and the commensurate decrease in charge representing information has led to an increased SEU sensitivity. The universality of this trend was noted by Petersen and Marshall [21], who observed a power-law dependence of critical charge to upset as a function of technology feature size for a wide variety of technologies (Fig. 6). At technology scaling levels of $0.5\mu\text{m}$ and below, they predicted that critical charge would decrease to less than 5 fC (Femto-coulombs). In fact, upsets due to terrestrial cosmic rays are now being observed in large memory systems at sea level [22], and in avionics systems at altitudes from 30 to 60 kft [23]. Johnston [24] noted that data from submicrometer IC technologies suggest this trend may not continue unabated, as chip manufacturers try to reduce alpha-particle sensitivity. However, it is now known that many manufacturers are in fact already below the alpha-particle threshold for upset and error rates are continuing to increase in today's advanced low-voltage technologies.

The field of SEE encompasses a wide range of disciplines including high-energy physics, cosmic ray physics,

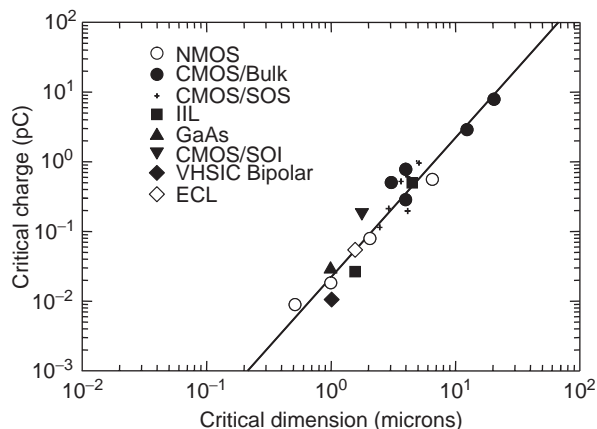


Figure 6. Critical charge as a function of critical dimensions for various technologies. Historically, power-law dependence has been observed [21].

solid-state physics, electrical engineering, IC processing, circuit design and analysis, system architecture, and computer modeling. Despite the breadth of overlap with many areas of research, a working knowledge of the important effects can be obtained by mastery of a few concepts from these diverse areas.

2.1. See Mechanisms: Charge Deposition

There are two primary methods by which ionizing radiation releases charge in a semiconductor device: direct ionization by the incident particle itself, and ionization by secondary particles created by nuclear reactions between the incident particle and the struck device. Both mechanisms can lead to integrated circuit malfunction.

2.1.1. Direct Ionization. When an energetic charged particle passes through a semiconductor material it frees electron-hole pairs along its path as it loses energy. When all its energy is lost, the particle comes to rest in the semiconductor, having traveled a total pathlength referred to as the particle's *range*. We frequently use the term *linear energy transfer* (LET) to describe the energy loss per unit path length of a particle as it passes through a material. LET has units of $\text{MeV} \cdot \text{cm}^2/\text{mg}$, because the energy loss per unit pathlength (in MeV/cm) is normalized by the density of the target material (in mg/cm^3), so that LET may be quoted roughly independent of the target. We can easily relate the LET of a particle to its charge deposition per unit pathlength. In silicon, an LET of $97 \text{ MeV} \cdot \text{cm}^2/\text{mg}$ corresponds to a charge deposition of $1 \text{ pC}/\mu\text{m}$. This conversion factor of about 100 is handy to keep in mind to convert between LET and charge deposition. Direct ionization is the primary charge deposition mechanism for upsets caused by heavy ions, where we define a heavy ion as any ion with $Z \geq 2$ (i.e., particles other than protons, electrons, neutrons, or pions). Lighter particles such as protons seldom produce enough charge by direct ionization to cause upsets in memory circuits.

2.1.2. Indirect Ionization. Although direct ionization by light particles rarely produces enough charge to cause

upsets, this does not mean that we can ignore these particles. Protons and neutrons can both produce significant upset rates due to indirect mechanisms. As a high-energy proton or neutron enters the semiconductor lattice, it may undergo an inelastic collision with a target nucleus. Any one of several nuclear reactions may occur, including (1) elastic collisions that produce Si recoils; (2) the emission of alpha (α) or gamma (γ) particles and the recoil of a daughter nucleus (e.g., Si emits α -particle and a recoiling Mg nucleus); and (3) spallation reactions, in which the target nucleus is broken into two fragments (e.g., Si breaks into C and O ions), each of which can recoil. Any of these reaction products can now deposit energy along their paths by direct ionization. Because these particles are much heavier than the original proton or neutron, they deposit higher charge densities as they travel and therefore may be capable of causing an SEU. Once a nuclear reaction has occurred, the charge deposition by secondary charged particles is the same as from a directly ionizing heavy-ion strike.

2.2. See Mechanisms: Charge Collection

The dense plasma of electrons and holes that are generated along the track of a heavy-ion strike are collected through a variety of mechanisms. Considering charge collection in the semiconductor itself, these processes include drift collection in high electric field regions, and diffusive charge collection outside field regions. These processes are illustrated in Fig. 7a. Charge carriers that are generated in the initial depletion region are separated by the existing electric field and are rapidly collected. Holes are swept to the p-type side of the junction, and electrons are swept to the n-type side of the junction, resulting in a current pulse. The charge plasma surrounding the ion track can be dense enough to perturb the initial electric field lines of the junction, so that it reaches well beyond the extent of the original depletion region of the p-n junction into the more lightly doped side of the junction. As equilibrium is re-established, the extended field collapses sweeping additional charge into the junction where it is collected. This is the field funnel process first explained by Hsieh et al. [25] using 2D simulation, and subsequently described analytically by McLean and Oldham [26]. Dodd et al. [27] provided a graphic depiction of this process using 3D modeling. These prompt charge collection processes occur in tens to hundreds of picoseconds depending on doping levels in the substrate. These times are faster than circuit response times in present technologies.

Outside the high-field regions of the junction and the field funnel, charge is collected by diffusive processes that are driven by concentration gradients in quasineutral regions of the semiconductor as described by Kirkpatrick [28] for single-event upset. This process occurs later in time, and can extend to as long as 10 ns, which is on the order of the circuit response time or slower. The shape of the charge collection transient can be a first-order concern for determining upset sensitivity, depending on the technology and circuit design. This is discussed further in the next section.

In some IC technologies, parasitic three-layer n-p-n and p-n-p structures are formed that can be sources of

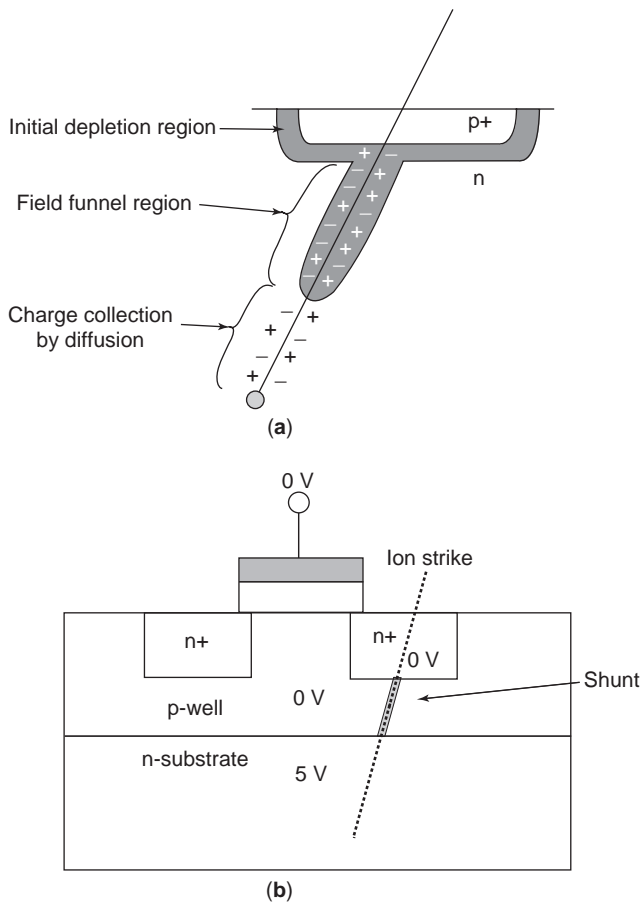


Figure 7. Charge collection mechanisms include photocurrent collection due to (a) drift in the depletion and field funnel regions and diffusive charge collection and (b) charge collection when regions of like doping are connected by a plasma shunt.

shunt current or bipolar amplification when charge is generated in the base region. In the first case, a heavy-ion strike can connect regions of similar doping that are separated by a region of opposite doping, as seen in Fig. 7b. A charge can flow between like regions when a potential difference exists. This *shunt* effect was observed by Hauser et al. [29], in CMOS test structures and by Sexton et al. [30] in pass-gate transistors in a CMOS technology. Bipolar amplification can significantly reduce the SEU hardness of some technologies. It has been shown to be especially important for partially depleted silicon-on-insulator (SOI) transistors [31,32] and GaAs MESFET [33–35] transistors as a heavy-ion strike liberates carriers in the body region of an SOI transistor or in the substrate of a GaAs transistor below the active region of the device. While minority carriers recombine quickly, the lifetime of majority carriers can be very long. Majority carriers that don't recombine can drift toward the source region and lower the source-to-body potential, which can cause the injection of minority carriers from the source into the body. This process can greatly increase the amount of charge collection. Another mechanism that can reduce the SEU hardness of GaAs ICs is carrier-induced channel modulation or the backchannel turnon mechanism [36–38]. This mechanism arises from excess holes located

in low-field regions below the active channel region that tend to “backgate” the channel. Near pinchoff, small modulations of the fields in the channel can give rise to large increases in channel conduction. These charge amplification mechanisms lead to very low LET thresholds ($<1 \text{ MeV} \cdot \text{cm}^2/\text{mg}$) and very high saturation upset cross sections ($>10^{-5} \text{ cm}^2/\text{bit}$) in GaAs ICs, resulting in very high upset rates in space environments [39].

A technique that has been suggested to reduce charge amplification in GaAs ICs is to grow the active transistor regions on top of a low-temperature (LT)-grown buffer layer [40]. The lifetime of carriers in LT GaAs layers is extremely short. This will reduce the time that holes (majority carriers) remain in the substrate and substantially reduce the charge collected via both the bipolar amplification and channel modulation mechanisms.

The region from which charge is collected is referred to as the *sensitive volume* (SV). As the discussion above indicates, multiple mechanisms can contribute to charge collection, making it difficult to clearly define a SV. Additionally, circuits that are sensitive to the rate at which charge is collected will have a SV that varies with circuit operation. In spite of these complexities, the SV concept is widely used because of the intuitive insight it gives to the underlying physical processes, and is useful as a mathematical construct in error rate prediction methodologies (discussed in Section 2.9.).

2.3. Single-Event Upset (SEU)

The sensitivity of an IC to single-event upset is expressed as the ratio of number of upsets to the total particle fluence, that is, $\# \text{ upsets}/\# \text{ (particles/cm}^2\text{)}$. Because this term has units of cm^2 , it is referred to as the *error cross section*. Experimental cross section data are normally plotted as a function of LET, for particles striking the IC normal to the surface. Two key parameters are determined from cross section curves: the threshold LET for upset L_0 and the saturation cross section σ_{sat} . The threshold LET is a measure of the minimum LET required to upset the most sensitive region of the chip, while the saturation cross section should equal the total area of the sensitive regions of the chip. These parameters are used to estimate the error rate for a given IC in a specific environment. In Fig. 8 we show an ideal and a measured cross section curve for a typical commercial memory chip. The ideal cross-sectional curve (dashed line) is a step function with a well-defined threshold and saturation cross section. Below threshold no cell upsets, while above threshold all sensitive cells upset. For a real device, however, there is a distribution of thresholds due to variation of charge collection across a cell and cell-to-cell variation in sensitivity, resulting in a smoothly increasing cross section with LET. As LET increases, more regions of the device are sensitive to upset. The measured cross section increases until all sensitive regions upset and the cross section curve saturates. Also shown in Fig. 8 is a fit to the data based on the Weibull distribution function (solid line), which is often used in reliability estimation techniques.

Cross-section curves are sometimes plotted as a function of linear charge deposited (LCD) with x-axis units of

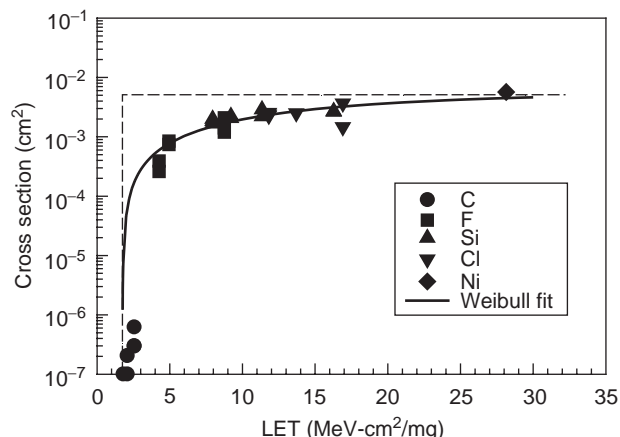


Figure 8. A typical upset cross-sectional curve is compared to an ideal curve. The ideal curve has an abrupt threshold and a well-defined saturation cross section, whereas measured curves show a gradual threshold and an ambiguous saturation cross section.

pC/μm (for silicon, 1 MeV·cm²/mg is equivalent to 0.0104 pC/μm). Measured upset curves such as this are taken over a range of LET, where LET is increased by using higher Z ions (for C to Ni ions used here, LET ranged from 2.5 to 28 MeV·cm²/mg). LET is also varied by increasing the angle of the ion strike relative to the surface normal, thereby increasing the pathlength through the SV and increasing the amount of charge deposited in the SV. This results in a higher “effective LET,” which is given by

$$L_{\text{eff}} = L_0 \cos(\theta) \tag{1}$$

where L_0 is the ion LET at normal incidence and θ is angle of incidence relative to the surface normal. The effective LET approximation has been used extensively in the past for large-geometry devices that have large, flat sensitive volumes. It breaks down, however, as device geometries shrink and the dimensions of the SV are nearly equal. In this case, a more involved correction for angle of incidence is required [41].

Dynamic circuits, such as a dynamic RAM (DRAM) cell, depend on charge storage on a circuit node or in a region of silicon for proper operation. For a DRAM, the amount of charge necessary for proper circuit operation is a function of the sensitivity of the sense amplifiers, the memory cell capacitance, and the bitline capacitance. A 1-transistor DRAM memory cell is shown schematically in Fig. 9. Information is stored on capacitor C_{cell} , which is written and refreshed through the access transistor. When the cell is subsequently accessed by turning this transistor on, the bitline is pulled down and the complement state of the cell is sensed on the bitline. The critical charge representing a bit of information on capacitor C_{cell} can be as small as 0.1–0.5 pC. This is equivalent to only 5×10^5 to 3×10^6 electrons. If an ion strike results in charge collection to the memory node on the same order of magnitude as the original charge on the node, a bit error will occur. In subsequent refresh cycles the error will be maintained, since the new state of the memory cell appears to be valid information. The primary consideration for dynamic circuits

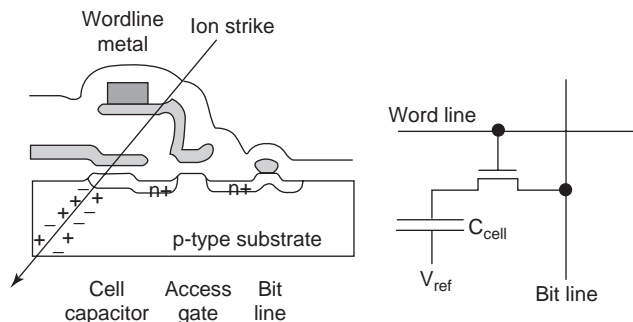


Figure 9. Circuit schematic of a one-transistor DRAM memory cell. Information is stored as charge on the capacitor C_{cell} and is accessed through the single transistor.

like this is whether the collected charge exceeds the critical charge required to represent a logic state on the memory node. If the critical charge is exceeded, an upset occurs. Massengill [42] discusses DRAM upset in more depth.

In static circuits, such as a CMOS static RAM (SRAM) or D-latch, upset is controlled by the rate at which charge is collected. A schematic diagram of a 6-transistor (6T) memory cell is shown in Fig. 10. Each series connection of n- and p-channel transistors forms an inverter whose input is the common gate, and whose output is the common drain. When the output of each inverter is coupled to the input of the other inverter, a bistable memory element is formed. In this diagram feedback resistors are shown in the cross-coupling links. Feedback resistors (R_{FB}) are used to slow the response of the circuit to the ion strike [43], thereby hardening the memory to upset, but there is a commensurate performance penalty. Following an ion

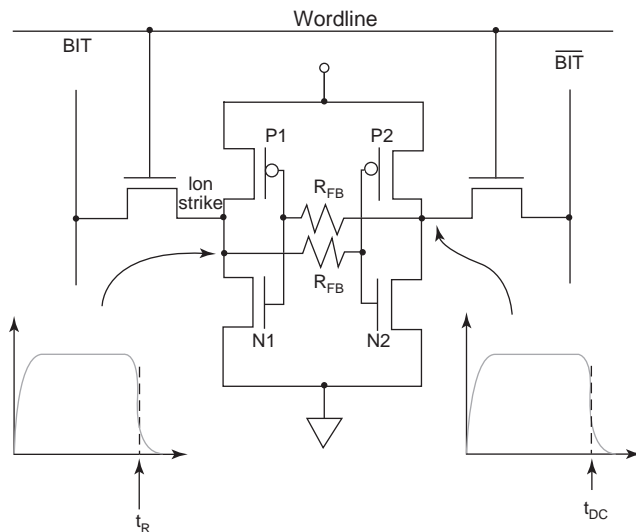


Figure 10. Logic diagram and circuit schematic for a 6-transistor CMOS SRAM memory cell. The cross-coupled inverters form a bistable memory element. Each inverter is composed of a series-connected n- and p-channel transistor. The voltage transients following a heavy-ion strike to an OFF-biased p drain are shown. Feedback resistors R_{F} are inserted in the cross-coupling links to reduce SEU sensitivity [43].

strike to the off-biased drain of transistor P1 (labeled “ion strike” in the figure), a current spike is observed on the drain node of the inverter formed by transistors N1 and P1. If charge is collected by the drain of P1 faster than it is removed by the unstruck n-channel transistor N1 (called the *restoring transistor*), the node voltage will rise to a diode drop above V_{DD} (see the lower left waveform in Fig. 10) and an upset may occur.

Whether an upset occurs depends on the competing processes of removing excess charge at the struck node, and changing the state of the opposing inverter of the memory cell [43]. The time required for the struck node to recover to one-half the voltage swing at the node is defined as the recovery time t_R . The time required to switch the opposing inverter formed by transistors N2 and P2 is defined as the decoupling time t_{DC} (see the lower right waveform in Fig. 10). Upset will occur in this analysis if t_R is greater than t_{DC} . Memory cells can be hardened to SEU by adding feedback resistors in the cross-coupling link between inverters (shown as R_{FB} in the figure). This effectively increases t_{DC} , and gives the cell more time to remove excess charge before responding to the transient.

As packing density increases, the charge deposited by a single ion strike can be collected by the sensitive volumes of more than one memory cell and multiple bits are upset. Zoutendyk et al. [44] first observed this phenomena experimentally, called *multiple-bit upset* (MBU), and it has since been measured in many different technologies. MBU has also been observed in closely spaced trench capacitor storage cells used in advanced DRAMs. In this case upset was attributed to a shunt connecting two adjacent storage regions [45]. Most error detection and correction (EDAC) implementations are able to detect and correct one bit upset in a single word and can detect two bit upsets without correction in a word. If a memory chip is laid out such that multiple bits in a single word are topographically adjacent, MBU can defeat these EDAC schemes. More complex EDAC approaches can be applied, but these require additional bits of memory and much more error correction overhead. The better approach is to ensure at the chip design level that logical bits in a word are not located physically close to each other.

2.4. Single-Event Transients (SETs)

An area that is becoming increasingly important is the propagation of single-event transients (SETs) in digital logic circuits. SETs are momentary voltage or current disturbances that, although they don't cause an upset in the circuit actually struck by an energetic particle, are propagated through subsequent circuitry and eventually cause an SEU. The problem here is that as circuit speeds rise, the probability that a momentary glitch will be clocked as valid data and propagated through subsequent circuitry increases. For example, even particles well below the upset threshold can cause a momentary flip in the state of an SRAM cell. Consider the case where this memory cell is actually a digital latch circuit in a microprocessor. If this latch value is accessed immediately after an ion strike and the value is clocked down the line, it matters little that the struck latch eventually returns to its original state,

because the corrupt value has already been passed on to the next stage of the circuit. These types of errors are likely to become a pervasive problem as clock speeds continue to increase, and will be difficult to protect against, especially in commercial microprocessors where speed is paramount. It has been predicted that for circuits built in technologies below $0.35\mu\text{m}$, propagated SETs will be a major single-event failure mode [46].

2.5. Single-Event Functional Interrupt (SEFI)

Single-event functional interrupts are a complex failure mode whereby a particle strike triggers an IC test mode, a reset mode, or some other mode that causes the IC to temporarily lose functionality [47]. As devices become increasingly complex, they may be more likely to exhibit SEFIs. For example, synchronous DRAMs are very complicated ICs that incorporate built-in self-test (BIST) modes and self-repairing boot sequences that remap nonfunctional bits in the memory with redundant bits on the chip. An ion strike to a SDRAM with such circuits may initiate a BIST mode, cause a chip reset to occur, or throw the IC into an idle state [48]. These events can have serious consequences on system operation, sometimes requiring device reset to clear the condition [49].

2.6. Hard Errors

2.6.1. Single-Event Latchup (SEL). The single most important effect that designers of space-based systems must consider is catastrophic damage resulting from single-event latchup. Latchup is a high current condition that results from thyristor [also known as a *silicon controlled rectifier*, (SCR)] action in four-layer p-n-p-n structures. Because four-layer p-n-p-n structures do not occur in standard SOI ICs, SOI ICs are latchup-immune. Latchup creates a low-resistance path from power supply to ground in CMOS ICs, which are vulnerable to this failure condition because of the complementary structure required for this technology [50]. As shown in Fig. 11, a pair of coupled parasitic bipolar transistors are associated with the p-well structure. A vertical n-p-n transistor is formed from the n-type substrate, p-well, and n-channel source, while the p-well, n-type substrate, and p-channel source form a lateral p-n-p transistor. The lumped-parameter equivalent circuit is shown on the right-hand side of the figure.

Latchup is triggered in SCR structures by excess current in the base of the lateral p-n-p transistor. When sufficient current flows in the substrate (across R_S), the emitter base junction of the p-n-p transistor is forward-biased and injects a large current into the p-well. This current induces a voltage drop in the p-well (across R_W) which turns on the vertical n-p-n transistor. As the n-p-n transistor turns on, it reinforces the initial current in the substrate and a regenerative condition exists which results in high current and low resistance. The holding voltage for latchup is on the order of 1 V. Latchup is triggered on the order of hundreds of nanoseconds, and destructive burnout occurs on the order of hundreds of microseconds [51]. The threshold for latchup decreases with increasing temperature and power supply voltage [52,53]. Latchup

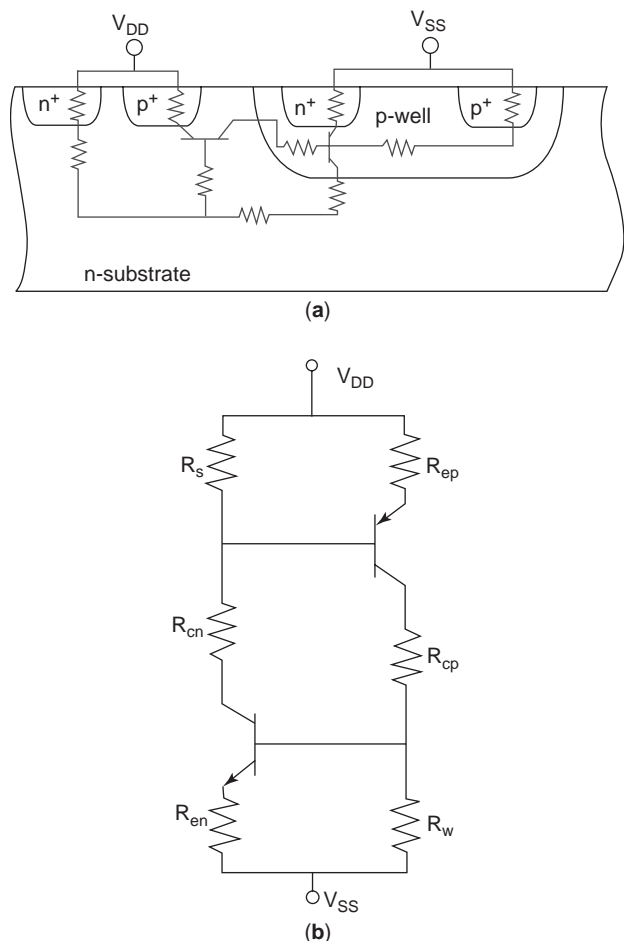


Figure 11. Cross section of a CMOS technology showing (a) the vertical n-p-n lateral p-n-p transistors formed in this p-well technology and (b) a circuit schematic indicating how the parasitic elements are electrically connected [50].

susceptibility in advanced technologies is addressed by Johnston [52,54].

During SEL measurements, latchup cross section is calculated in the same manner as upset cross section, that is, the number of upsets divided by the fluence to latchup, and is plotted as cross section versus LET.

2.6.2. Single-Event Gate Rupture (SEGR). Another major consideration for designers is a catastrophic failure known as *single-event gate rupture* (SEGR) [55,56]. This effect can occur under conditions of high field, such as during a write or clear operation in a nonvolatile SRAM or E²PROM [electrically erasable programmable read-only memory (also abbreviated EEPROM)]. It has become a concern for advanced technologies as oxide thicknesses scale below 10 nm and oxide fields increase above 5 MV/cm [57]. As a heavy ion passes through the dielectric, a highly conductive plasma path is formed, which allows the capacitor formed by this structure to discharge. If sufficient energy is stored on the capacitor as a result of high electric fields, excessive heating during discharge can create a thermal runaway condition [55]. Temperatures can be high enough

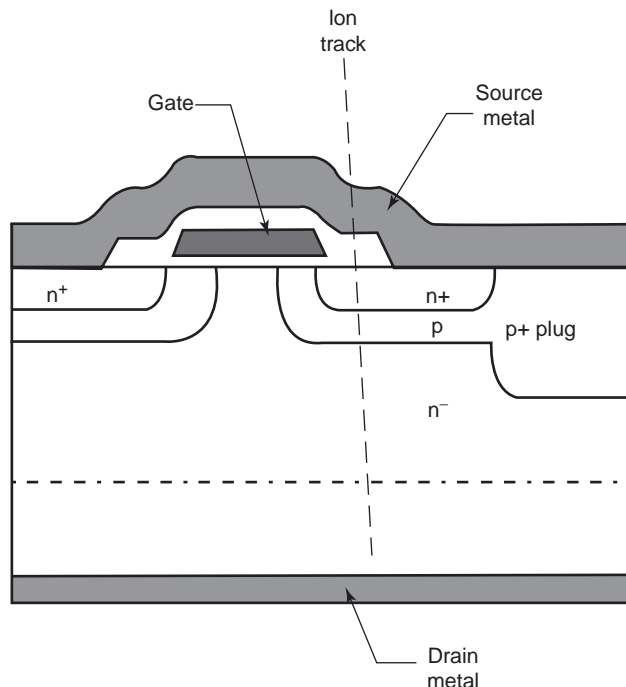


Figure 12. Cross section of a typical power MOSFET structure.

to cause the dielectric to melt and the overlying conductive layers to evaporate.

In a power MOSFET, the requirement for a standoff voltage on the order of 100s of volts is satisfied by dropping this potential over the thickness of the silicon substrate. A typical cross section of a power MOSFET is shown in Fig. 12. In normal operation, the MOSFET gate induces a channel between the source and drain regions. Current flows from the source to the drain near the surface, then is collected in the heavily doped substrate. The lightly doped epi layer doping and thickness determine the ON resistance of the device. As a heavy ion passes through the substrate, the large bias on the drain is electrically coupled into the oxide electric field, resulting in gate rupture at voltages well below the rated standoff voltage. This mechanism is described in detail by Brews et al. [58]. Figure 13 shows the set of V_{GS} and V_{DS} biases that result in SEGR as a function of various heavy ions for a power MOSFET rated to 70 V with a 50-nm gate oxide. The data cover an LET range from 3 MeV · cm²/mg for F to 82 MeV · cm²/mg for Au. The control data shown in the graph (open circles and dashed line) denote nominal rupture voltages with no heavy-ion exposure, which are -40 and 73 V for V_{GS} and V_{DS} , respectively. During exposure to heavy ions, however, the V_{GS} at which SEGR occurs decreases as V_{DS} increases. An empirical equation that fits this dependence has been developed by Wheatley et al. [56]:

$$V_{GS} = 0.84 \left(1 - \exp \frac{-L}{17} \right) \times V_{DS} - \frac{50}{1 + L/50} \quad (2)$$

where V_{GS} is the gate bias at which rupture occurs, V_{DS} is drain-source voltage, and L is the incident ion LET. This

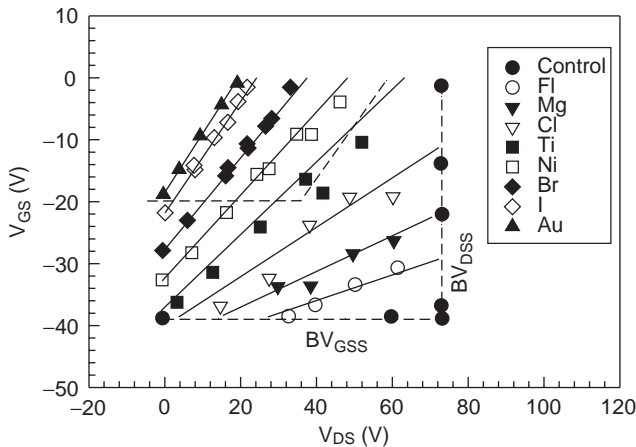


Figure 13. Dependence of single-event gate rupture as a function of drain–source bias, gate–source bias, and ion species. Breakdown voltages without ion irradiation are shown as a dashed curve (control), and the manufacturer’s suggested derating in space is shown by the dotted curve [56].

equation correctly fits the observed trend of decreasing V_{GS} with increasing V_{DS} and LET. The first term describes the coupling of drain bias from the substrate into the gate, while the second term accounts for the effect of the ion passing through the oxide itself. Fits to this equation are shown as solid lines in Fig. 13. Each line denotes the safe operating range for this part as a function of heavy ion. Note that the safe operating range decreases for increasingly heavy ions (higher LET). The manufacturer’s recommended derating for SEGR is shown as a dotted line in Fig. 13. This represents a 50% decrease in maximum V_{GS} and V_{DS} to account for SEGR.

The industry trend toward increasing electric fields as oxide thickness and feature size scale down in advanced technologies raises the concern that SEGR may be a limiting factor for integrated circuits (ICs) in space applications. It has been suggested that, as devices scale to 0.25 μm and below, SEGR by Fe ions will occur, leading to a large increase in catastrophic failures in space hardware. Sexton et al. [57] found that as oxide thickness decreased below 10 nm, the increasing breakdown strength of the oxides resulted in a higher-than-expected gate voltage for rupture, contrary to earlier predictions. Their results suggest that advanced technologies will be more SEGR-resistant at a given electric field than expected. They caution, however, that SEGR will continue to be a significant concern for devices that operate with gate oxide electric field above 5 MV/cm. Massengill also found that in highly scaled (ultrathin) gate oxides and in alternate high- k dielectrics SEGR should not be a limiting factor in advanced technologies [59]. Although there can be considerable variation in the voltage to hard breakdown for different dielectrics, for all the dielectrics investigated by Massengill [59], the breakdown voltages were above the power supply voltages that will be seen in future highly scaled commercial technologies as suggested by the SIA National Technology Roadmap for Semiconductors. As such, it does not appear that SEGR will be a significant problem for highly scaled commercial technologies.

2.6.3. Single-Event Burnout (SEB). Destructive failure resulting from heavy-ion exposure is observed in bipolar power transistors and in power MOSFETS [60–62]. In this phenomenon, the excess current generated by the passage of a heavy ion triggers a secondary photocurrent that overheats the device and causes catastrophic failure. In power MOSFETS, a parasitic n-p-n bipolar transistor exists between the epi layer (collector), the p-type body (base), and the n-type source (emitter) (see Fig. 12). When a heavy ion passes through this parasitic transistor, excess current is generated in the base region. Excess hole current flows toward the body contact, raising the local potential along the base–emitter junction. If sufficient current flows to raise this potential to the turnon voltage of this junction, the base–emitter junction becomes forward-biased, turning on the n-p-n transistor. Following turnon, the transistor enters a second breakdown condition where thermal runaway reinforces the mechanism caused by avalanching at the epi–substrate junction. This condition has been called current-induced avalanche (CIA) [63]. If the external circuit can provide sufficient current, local overheating in a portion of the device will occur, destroying the device. There is a definite threshold voltage required for burnout to occur, and this is often well below the normal breakdown voltage for the device. Fischer [62] has measured failure threshold voltages ranging from 22 to 90% of the rated breakdown voltage for devices from several manufacturers.

2.6.4. Snapback. Snapback is a high current, low resistance condition that occurs only in n-channel transistors. It has an IV characteristic that is similar to latchup exhibiting a negative-resistance region, and a low-resistance region. Like latchup, it can be triggered by external stimuli that inject sufficient current into the p-channel regions well to cause the n source to become forward-biased. Snapback initiation has been observed by avalanche induced breakdown at the n drain [64], by excess photocurrents generated during moderate dose rate gamma irradiation [64], and by heavy-ion strikes to sensitive n-drain or p-channel regions [65].

A significant difference between latchup and snapback is that the holding voltage is on the order of several volts depending on channel length and doping levels, much higher than the 1 V holding voltage seen in latchup. Snapback can be sustained only when the load circuit on the n-channel device can provide sufficient holding current. For CMOS ICs, the load devices are p-channel transistors. Since holding current is on the order of milliamps, snapback is normally observed in output buffers and internal bus drivers. Although latchup is not a concern for SOI technologies, snapback (also known as single-transistor latch) can be a significant problem for SOI technologies, especially those using wide-gate partially depleted transistors [66].

2.7. Proton-Induced Effects

Because of the small stopping power for protons, insufficient charge is generated to induce SEE at current levels of sensitivity. Interaction of a proton with the

semiconductor lattice can generate secondary particles with higher LET that can cause SEE [67]. Elastic scattering of target nuclei, for example, can deposit enough energy to cause soft errors. Of more importance is the contribution to upset from inelastic scattering events, where the incident proton reacts with the target nucleus. About one of every 10^5 protons will experience an inelastic collision with the target lattice. As the composite nucleus decays, it can emit alpha particles and lower-energy protons. In addition, the daughter nucleus can recoil with enough energy to cause upset through direct ionization. The composite nucleus can also decay through a spallation reaction, where the compound nucleus breaks up into two heavy fragments, both of which recoil and deposit energy. Researchers have observed proton-induced upset, latchup, and burnout. To date, no instance of SEGR has been attributed to protons.

2.8. SEU Mitigation

Depending on the application, a low rate of SEU is acceptable in systems. EDAC circuitry and software are often included to handle these errors [68,69]. Some examples of EDAC include use of parity bits, Reed–Solomon encoding, and Hamming codes. If errors occur too frequently, however, the error-handling architecture of a system may be overwhelmed and system failure can result. In mission-critical applications, such as circuitry for a satellite attitude control system, SEU hardened devices must be used to reduce the probability of system failure.

Special design and fabrication techniques are available to harden circuitry to SEU. Circuit design techniques include increasing the size of transistors to remove excess charge faster [70] and use of redundant circuits and voting logic to determine the correct state [71]. Feedback resistors and capacitance can be added to internal nodes of memory cell to reduce sensitivity to transients [72]. All these techniques incur some degree of performance penalty. Increased size carries a density penalty, and adding redundant circuitry increases chip power and reduces functional density. Use of feedback resistors and capacitors reduce the speed of the device.

A more direct approach to SEU mitigation centers on reducing the amount of charge collected following a heavy-

ion strike. A prime example of this approach is the use of silicon-on-insulator (SOI) substrates. The SEU tolerance of a nonhardened SRAM design can be increased by fabricating the design in a SOI-based technology. Figure 14 is a cross section of a SOI transistor. The active silicon channel region is built on top of an insulating layer (buried oxide) instead of a silicon substrate. Because SOI/MOS transistors are fabricated on an insulating layer, the amount of p-n junction area and the sensitive volume are greatly reduced, potentially making SOI/MOS ICs superior to bulk silicon ICs for single-event upset. Also, because there are no possible parasitic bipolar transistors between n- and p-channel transistors, and consequently, no four-layer structures, it is impossible to latchup SOI-based technologies. However, to take full advantage of SOI technology, steps must be taken to reduce or mitigate parasitic effects (e.g., floating effects). SOI transistors operate in two modes: partially depleted and fully depleted. *Partially depleted transistors* are defined as transistors where the silicon thickness is greater than the maximum depletion width formed by the conducting channel. In *fully depleted transistors*, the conducting channel and depletion region extend throughout the thickness of the silicon layer. The presence of a floating-body region of nondepleted silicon between the edge of the depletion region and the silicon/buried oxide interface in a partially depleted technology provides a place where excess charge can build up. As a result, the SEU hardness of SOI transistors can be reduced by bipolar amplification, similar to that for GaAs ICs. A common method for reducing bipolar amplification in SOI transistors is to use body ties, which can provide a convenient means to connect the body region to a voltage reference (e.g., normally a transistor source diffusion) [73–76]. Thus, the body tie connects the floating body region of a partially depleted transistor to a fixed potential. This can provide an efficient path for majority carriers liberated in the body region to drift out of the body region, greatly reducing bipolar amplification. For the same technology generation and equivalent device structure, by using body ties, hardened partially depleted SOI ICs can be fabricated that have LET thresholds considerably higher than hardened bulk-silicon ICs. In a fully depleted technology, excess charge is more readily swept out by the high fields in the channel region, and the effects of bipolar amplification are significantly reduced.

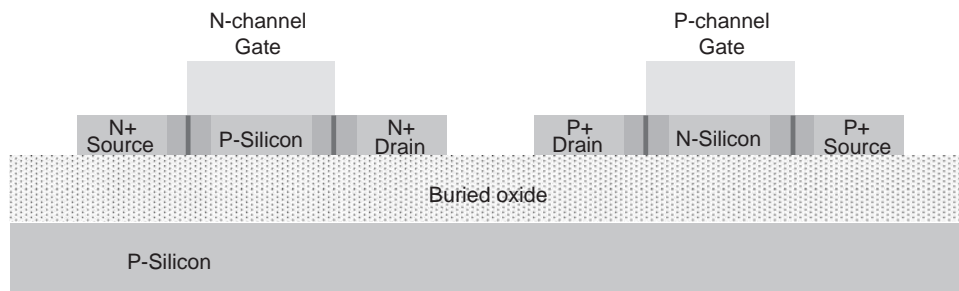


Figure 14. Cross section of a SOI transistor. The active silicon channel is built on top of an insulating oxide leading to a lower sensitive charge collection volume and reduced p-n junction area. These properties make SOI ICs superior to bulk silicon ICs for single-event upset and high-dose-rate pulsed-irradiation hardness.

2.9. Error Rate Prediction

Error rate predictions are based on an estimation of the particle flux that is expected for a given part during its lifetime and a measurement of the SEE sensitivity of the part. The environment has been discussed earlier. Part sensitivity is often described in terms of its critical charge Q_C , defined as the minimum collected charge necessary to upset a circuit. (Note that for simplicity it is assumed that collected charge and deposited charge are equal. When this condition does not apply, other corrections are required.) For dynamic circuits this concept is easily applied because the collected charge negates the stored charge at a node. However, in the case of CMOS latches and memory cells, a critical charge is more difficult to define since these circuits are sensitive to the rate at which charge is collected, and charge collection is modulated by the circuit response. Here critical charge can be estimated by considering the response of the circuit and integrating only charge collected during the time that the circuit is vulnerable to upset. This approach was taken by Dodd and Sexton [77], who clearly demonstrated the need to differentiate between deposited and collected charge. See Ref. 78 for an excellent review of various error rate prediction methodologies that have been used and recommended approaches.

For error rate calculations, the problem is one of determining the probability of any ion, from the full spectrum of ions available, with a given LET or greater passing through the SV at any angle such that it deposits sufficient energy to cause upset. Because flux is isotropic, we must consider all possible pathlengths, and the longer the path through the sensitive volume the more energy (charge) is deposited. In other words, with longer pathlength, ions with lower LET can cause upset. Mathematically, error rate is determined from

$$R(E_C) = A_p \int \Phi[L_t(s, E_C)] f(s) ds \quad (3)$$

where the integration is performed over the distribution of all pathlengths s through the SV. In this equation A_p is the average projected area of the SV, Φ is the LET spectrum for a given environment, L_t is the threshold LET for any path s and Q_C , and $f(s)$ is the distribution of pathlengths through the SV.

This form of the error rate calculation has the following underlying assumptions: (1) the shape of the SV is assumed to be described by an RPP, (2) ion LET is constant through the SV, (3) track structure can be ignored, (4) charge collection by diffusion from outside the SV can be ignored, (5) the SV is augmented by a funnel length that is invariant with ion LET or energy, (6) all charge generated within the SV is collected, and (7) there is a sharp threshold for upset. Because the measured cross section curve is not a step function but has a gradual rise from an onset threshold, current practice is to integrally weight the error rate based on the measured data. Mathematically this is described by

$$R = \int R(E) f(E) dE \quad (4)$$

where the integral is performed from the measured onset threshold to saturation and $f(E)$ is a probability density function that describes the experimental data.

Error rate calculations using Eqs. (3) and (4) are readily performed using an error rate code, such as CREME96 [79], or a commercially available software package called SPACERAD [80]. Both of these codes include the latest environment models, and can include shielding models. The latter also includes utilities that take into account discontinuities that arise in the dataset due to the geometry of the SV as described by Connell et al. [81].

Error rate calculations from proton-induced upset proceeds along a different path. Here the measured sensitivity of a part is given as a function of particle energy, so the error rate is simply the integral of error cross section over the fluence of particles with energy sufficient to cause upset. Mathematically this is given by

$$R(E) = \int_0^\infty \sigma(E) \Phi(E) dE \quad (5)$$

where $\sigma(E)$ is the error cross section and $\Phi(E)$ is the proton spectrum of the environment. Note that no pathlength calculation involving and assumed RPP is required, because the nuclear reaction of the proton in the SV is assumed to be isotropic and independent of angle. Further, the statistics of the proton interaction are included in the $\sigma(E)$ data. For further information, the reader is referred to Ref. 82.

2.10. Terrestrial Single-Event Effects

The occurrence of soft errors in terrestrial microelectronics manifested itself shortly after the first observations of SEU in space [83]. This watershed paper from authors at Intel found a significant error rate in DRAMs as integration density increased to 16,000 and 64,000, spurring a flurry of terrestrial SEU-related work in the late 1970s [84]. The primary cause of soft errors at the ground level was quickly diagnosed as alpha-particle contaminants in packaging materials [83]. For example, according to Ziegler, the Intel problem was traced to a new LSI (large-scale integration) ceramic packaging plant that had just been built downstream from the tailings of an abandoned uranium mine [85]. Radioactive contaminants in the water used by the factory were contaminating the ceramic packages they manufactured. By using low-activity materials for IC fabrication and on-chip shielding coatings [85,86], the terrestrial soft-error problem essentially disappeared for several years. Occasionally, changes in suppliers or procedures have caused semiconductor manufacturers temporary but considerable headaches due to raised radioactive contaminant levels in materials such as nitric and phosphoric acid [85,87]. The march toward higher integration densities has made soft-error concerns a continual design consideration for advanced DRAM and SRAM development since the early 1980s. A particular area of concern is flip-chip packaging technologies that place a source of alpha particles (Pb-Sn solder bumps) right on the die itself, where they cannot be shielded by coating layers

[88]. Elimination of materials rich in ¹⁰B, such as borophosphosilicate glass (BPSG) dielectric layers, has been shown to reduce the thermal neutron soft-error rate (SER) by several orders of magnitude [89,90].

Even in the absence of on-chip sources of radiation, recent studies have conclusively proved that terrestrial cosmic rays (primarily neutrons) are a significant source of soft errors in both DRAMs and SRAMs [91,93]. Upsets have been observed both at ground level and in aircraft and have been convincingly correlated to the altitude and latitude variation of the neutron flux [91,93,94]. Lage et al. have shown that even without alpha particles, a baseline of cosmic ray upsets still exists for high-density SRAMs [92]. O’Gorman has shown that neutron upsets disappear for DRAMs placed 200 m underground in a salt mine, while they increase dramatically for systems operated above 10,000 ft in Leadville, CO [91]. In addition to SEU observed in memories used in large computer systems and aircraft, upsets have been observed in SRAMs used in implantable medical devices such as cardiac defibrillators [95].

Figure 15 shows the measured cosmic ray neutron soft error rate (SER) versus power supply voltage in several generations of SRAMs from a variety of vendors [96]. Terrestrial soft-error failure rate specifications are usually given in terms of FIT rates, where FIT = failure in time = 1 error in 10⁹ device hours. In this figure, SER is reported in FIT/Mbit of memory to allow comparison between memories of different sizes. For reference, an uncorrected SER of 1000/Mbit would lead to 1 error every 3 weeks in a system with 256 Mbytes of memory. From this figure, it is clear that low-voltage SRAMs exhibit unacceptably high SER without error correction, and that different IC technologies can have SER varying by two orders of magnitude at a given voltage. Because of the high SER that exists in many modern memory technologies, error detection and correction (EDAC) is often built into memories to reduce FIT rates [97].

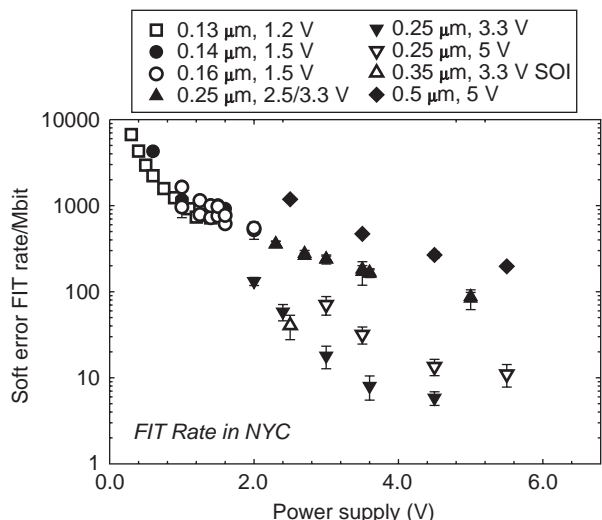


Figure 15. Terrestrial soft error failure rate as a function of power supply voltage for SRAMs manufactured in several different technologies by several vendors.

Destructive single-event effects can also occur in ground-based systems. For example, neutron-induced single-event burnout has caused destructive failures in large-area, high-voltage power diodes used for railroad applications in Europe [98]. It has been experimentally demonstrated that significant neutron-induced latchup rates can occur in high-density SRAMs at ground level [96]. For example, the ground-level neutron-induced latchup FIT rate of a 0.25-μm, 3.3-V 4-Mbit SRAM is shown in Fig. 16. At the maximum rated voltage (3.6 V) at room temperature the latchup FIT rate is 336 FIT/Mbit. At this FIT rate, a 256-Mbyte system using these SRAMs could experience 0.0165 latchups per day, or about 1 latchup every 60 days. Even worse, at this part’s maximum permitted operating temperature of 85°C, the ground-level latchup FIT rate rises to 566 FIT/Mbit at 3.6 V, or nearly one latchup per month in a 256-Mbyte system! These SRAMs exhibited latchup even at 1.5 V, and indeed at 85°C the latchup rate is still more than 100 FIT/Mbit at this voltage. It is also important to note that latchup can’t be circumvented using error correction.

Revelations such as these have significant implications for manufacturers of commercial memory chips and computer systems because systems can’t realistically be shielded against incident neutrons. Meeting specified failure rates is expected to be a significant challenge for commercial semiconductor manufacturers. A typical specification is to maintain a FIT rate less than 1000 [92]. A complicating factor is that since FIT rates are often specified *per device*, meeting a constant FIT rate specification actually requires reducing the error rate *per bit* as the number of bits per device is increased.

It has been suggested that because manufacturers of commercial microelectronics for terrestrial applications have had to deal with alpha-particle-induced upsets from packaging materials, commercial parts will by design remain hard to at least the alpha-particle threshold [99]. Indeed, there is historical evidence supporting this view as data from more than 10 years of microprocessor evolution show a constant upset threshold just above the threshold for alpha-particle upset [99]. However, it is also

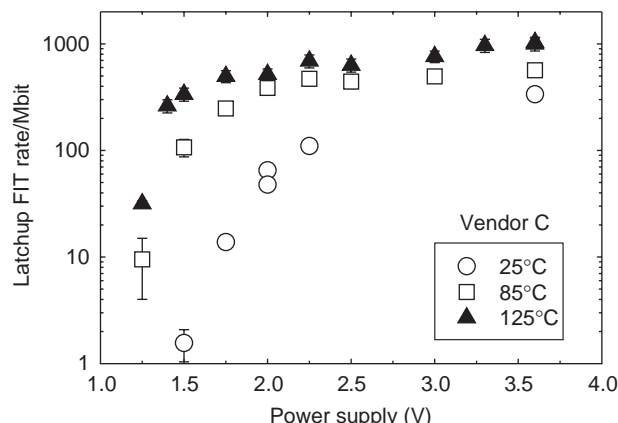


Figure 16. Terrestrial neutron-induced latchup failure rate in 0.25-μm, 3.3-V 4-Mbit SRAM as a function of power supply voltage and operating temperature.

known that many manufacturers have specific soft-error-driven design rules for placement of devices relative to on-chip solder bumps and/or use hardened circuit designs for I/O circuitry that must be in the vicinity of such on-chip alpha sources [100]. This clearly implies that many devices being manufactured are in fact already below the alpha-particle threshold for upset.

Many of the techniques traditionally used in the radiation effects community to SEU-harden devices are of such a nature that they are unlikely to be adopted by commercial manufacturers. They tend to consume more power, reduce manufacturability, and severely impact IC performance or integration density. Commercial DRAMs have generally exhibited a fairly constant SEU performance because DRAM manufacturers have intentionally maintained the unit cell capacitance through the use of clever modifications to the storage cell [97,101]. The nodal capacitance for SRAMs, however, has been steadily shrinking [92]. To counteract increased terrestrial soft-error rates, manufacturers may find it necessary to explicitly add capacitance to high-density SRAMs. Lage et al. have predicted that this will be necessary for the 4-Mbit generation of SRAMs and beyond [92]. Design-hardened circuits are useful for critical logic paths or circuitry, but because of area penalties will likely not be adopted on a large scale except as a last resort. The use of error-correcting memory architectures is already becoming more common again, and this trend will likely continue. Mitigating soft errors in high-speed digital logic circuits will be especially challenging. Fault-tolerant systems are routinely used in aircraft mechanical systems and seem a natural choice for preventing neutron-induced SEU in avionics [102]. SOI is a possible solution to the terrestrial SEU problem, although, as noted previously, SOI is not automatically upset immune.

3. TOTAL-DOSE IONIZATION EFFECTS: MOS DEVICES

Electronic devices in satellite systems orbiting Earth can be exposed to very high flux levels of ionizing radiation. Ionizing radiation can cause significant degradation and permanent failure of electronic components. In the natural space environment, both electrons and protons can contribute to total-dose ionizing radiation-induced degradation. Manmade systems, including high-energy particle accelerators and some types of IC processing equipment (e.g., X ray lithography radiation sources and scanning electron microscopes) can also expose electronics to high ionizing radiation levels.

MOS devices are particularly susceptible to ionizing radiation damage. The harsh radiation environment of space has long been known to cause significant radiation-induced degradation of MOS devices [1]. Radiation-induced charge buildup in gate, field, and SOI buried oxides can all contribute to device degradation. Much of the early work investigating the mechanisms for total-dose effects in MOS devices focused on gate oxides. Moreover, much of this work focused on device response at short times after a pulse of ionizing radiation. Gate oxides were relatively thick, and radiation-induced charge buildup in

gate oxides was a major contributor to device degradation in ionizing radiation environments. Although a good part of the work identifying the mechanisms for device degradation was gained by examining device response at short times after a pulse of ionizing radiation, the same mechanisms to a large degree also govern device response in low-dose-rate space environments. In more contemporary devices, as gate oxides are becoming extremely thin, radiation-induced charge buildup in field oxides and SOI buried oxides dominates device degradation in ionizing radiation environments. As will be discussed below, radiation-induced charge buildup in oxides rapidly decreases with oxide thickness, making standard thermal gate oxides of advanced technologies very hard to ionizing radiation.

There is still some controversy over the details for the mechanisms for radiation-induced charge buildup in oxides, especially in nontraditional oxides such as the base oxides of bipolar devices, which can lead to enhanced low-dose-rate sensitivity (ELDRS) effects in bipolar devices. Nevertheless, identification of the general mechanisms for radiation-induced charge buildup in oxides has been vital for the development of reliable qualification test guidelines for MOS devices. The development of reliable qualification test guidelines is still an active area of investigation and continues to benefit from improvements in our knowledge of the mechanisms for radiation effects.

In this section, we review the mechanisms for radiation-induced charge buildup in MOS oxides. The effects of charge buildup in gate, field, and SOI buried oxides on IC performance are described. Mechanisms for the time-dependent buildup and neutralization of radiation-induced charge leading to different failure levels and mechanisms in different radiation environments are highlighted. Techniques for reducing radiation-induced charge (device hardening) are also discussed.

3.1. Basic Mechanisms: Gate Oxides

As a MOS oxide is exposed to high-energy ionizing radiation, electron-hole pairs will be created uniformly throughout the oxide. The carriers generated by ionizing irradiation induce buildup of charge in the oxide, which leads to device degradation. Figure 17 [103] is a schematic band diagram of a MOS capacitor under positive gate bias and depicts the mechanisms by which ionizing irradiation induces charge buildup in an oxide. Under a positively applied bias as shown in Fig. 17, unrecombined radiation-generated holes will transport to the Si/SiO₂ interface. A fraction of these holes will be trapped near the interface, creating a positive oxide-trapped charge. As a result of the hole transport and trapping process, hydrogen is liberated in the oxide which can drift to the Si/SiO₂ interface to form interface traps. The total threshold voltage shift ΔV_{th} for a transistor is given by the sum of the threshold voltage shifts due to interface trap and oxide-trapped charge. Therefore

$$\Delta V_{th} = \Delta V_{ot} + \Delta V_{it} \quad (6)$$

where ΔV_{ot} and ΔV_{it} are the threshold voltage shift due to oxide-trapped and interface trap charge, respectively. The

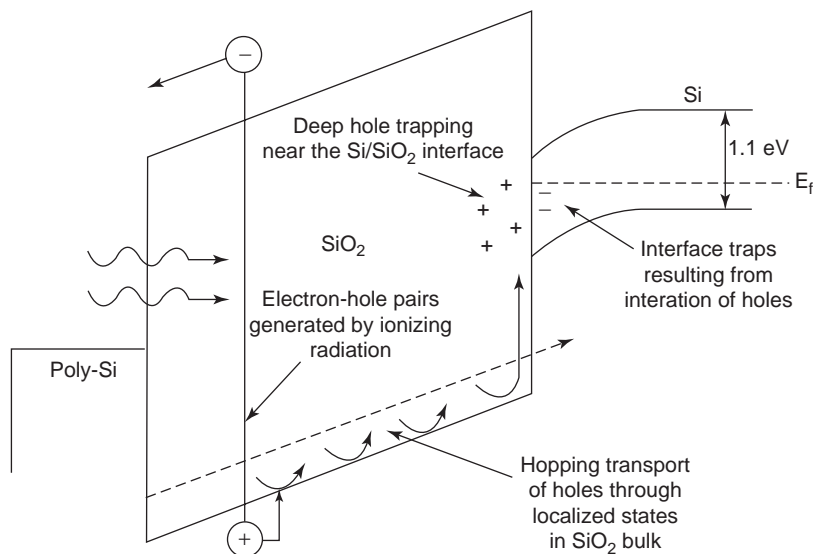


Figure 17. Schematic band diagram of a MOS capacitor under positive bias illustrating the mechanisms for radiation-induced charge buildup. Positive oxide-trapped charge occurs as holes are trapped in the oxide, and interface trap buildup results from the release of hydrogen during the hole transport and trapping process [103].

mechanisms for these charge components are now discussed in detail.

3.1.1. Charge Yield. If an electric field exists across the oxide of an MOS transistor, once released, electrons in the conduction band and holes in the valence band will immediately begin to transport in opposite directions. Electrons are extremely mobile in silicon dioxide and are normally swept out of silicon dioxide in picoseconds [104,105]. However, even before the electrons can leave the oxide, some fraction of the electrons will recombine with holes in the oxide valence band. This is referred to as *initial recombination*. The fraction of holes that do not recombine is referred to as the *charge yield*. The amount of initial recombination is highly dependent on the electric field in the oxide and the energy and type of incident particle [103,106]. In general, strongly ionizing particles form dense columns of charge where the recombination rate is relatively high. On the other hand, weakly ionizing particles generate relatively isolated charge pairs, and the recombination rate is lower [103].

3.1.2. Oxide-Trapped Charge. Under positive bias, holes that escape initial recombination will transport toward the Si/SiO₂ interface at a rate much slower than electrons. Holes are believed to transport through the Si/SiO₂ by polaron hopping through localized states in the oxide [107,108]. The time that it takes holes to hop through the oxide is dependent on temperature, electric field, and oxide thickness [107–110].

As the holes reach the vicinity of the Si/SiO₂ interface, some fraction of the holes will become trapped in the oxide near the Si/SiO₂ interface. This trapped charge results in a positive-charge buildup in the oxide and is referred to as *oxide-trapped charge*. The positive charge buildup causes a negative oxide-trapped charge threshold-voltage shift that can be calculated from

$$\Delta V_{ot} = -\frac{1}{C_{ox}t_{ox}} \int_0^{t_{ox}} \rho(x) x dx \quad (7)$$

where C_{ox} is the oxide capacitance, t_{ox} is the oxide thickness, and $\rho(x)$ is the spatial distribution of the net charged oxide traps in the oxide. For standard thermal oxides, most of the trapped holes are located close to the Si/SiO₂ interfaces [111]. For SOI buried oxides and other specially processed oxides, hole traps are often distributed throughout the bulk of the oxide [112–116].

The microscopic nature of several oxide trap point defects in thermally grown oxides has been identified by electron paramagnetic resonance experiments [117,118]. The most important of these is called the E' center. At least nine variations of the E' center have been detected. Most E' centers are characterized by an unpaired electron highly localized on a silicon atom bonded to three oxygen atoms. The chemical notation for the generic E' center is given by $\uparrow\text{Si}\equiv\text{O}_3$ or $\cdot\text{Si}\equiv\text{O}_3$.

Once holes are trapped, they can be neutralized by electron tunneling from the silicon [119–122] and by the thermal emission of electrons from the oxide valence band [120,123–125]. In addition to the neutralization of oxide traps by electron tunneling or thermal emission, oxide trap charge also can be compensated as electrons are trapped at electron trap sites associated with the trapped holes. Oxide-trapped charge neutralization can occur over very long periods of time, from seconds to years. In some cases, the rate of oxide-trapped charge neutralization can be relatively large, whereas, for some technologies little or no oxide-trapped charge neutralization has been observed. The rate of neutralization by thermal emission of electrons is dependent on temperature. The rate of neutralization by electron tunneling is dependent on the spatial distance of the oxide traps from the Si/SiO₂ interface and the electric field in the oxide. For neutralization to occur by electron tunneling, the traps must be located very close to the Si/SiO₂ interface. Therefore, the rate of oxide-trapped charge neutralization is highly dependent on the spatial and energy distribution of traps in the oxide.

Combining the effects of hole trapping and neutralization, we note that the amount of oxide trapped charge

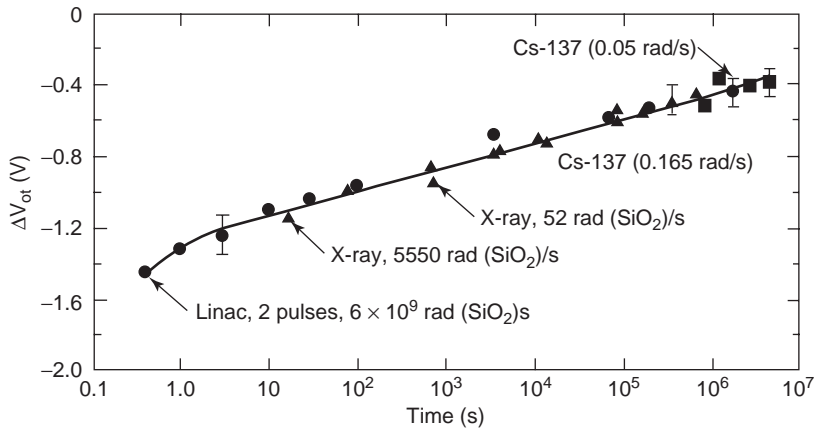


Figure 18. Neutralization of oxide-trapped charge occurs after irradiation, leading to a logarithmic decrease in the magnitude of ΔV_{ot} with time [126].

and its associated threshold voltage shift (ΔV_{ot}) are time-dependent. For short times after a pulse of irradiation, little neutralization of trapped charge occurs and the magnitude of ΔV_{ot} can be very large. Long times after a pulse of irradiation, considerably more neutralization can occur and the magnitude of ΔV_{ot} may be small. Similarly, for devices exposed to ionizing irradiation in space, where the dose rate is very low, neutralization of oxide-trapped charge can occur constantly during irradiation and ΔV_{ot} may always be small. The time dependence for trapped-hole neutralization at room temperature is illustrated in Fig. 18 [126] where the voltage shift due to oxide trap charge ΔV_{ot} is plotted versus time for hardened n-channel polysilicon gate transistors irradiated to 100 krad(SiO_2) at dose rates from 6×10^9 to 0.05 rad(SiO_2)/s and then annealed at room temperature. The bias during irradiation and anneal was 6V, and the gate oxide thickness of the transistors was 60 nm. The largest voltage shift (~ -1.45 V) was for short times after the highest-dose-rate irradiation. For the lowest-dose-rate irradiation [0.05 rad(SiO_2)/s], the maximum voltage shift was approximately -0.4 V and occurred after irradiating transistors to 100 krad(SiO_2). During anneal, the decrease in ΔV_{ot} follows a logarithmic time dependence. Note that at each dose rate, ΔV_{ot} falls on the same straight line. Thus, the rate at which ΔV_{ot} is neutralized is dose-rate-independent.

The fraction of holes that is trapped and the rate of neutralization are dependent on processing conditions. The percent of trapped holes can vary from a few percent for specially processed hardened oxides to 100% for commercial oxides. One processing step that can significantly affect the amount of radiation-induced oxide-trapped charge is the temperature of processing steps after gate oxide deposition [127]. Figure 19 illustrates the effect of anneal temperature on oxide-trapped charge buildup. Plotted is ΔV_{ot} versus anneal temperature for polysilicon gate capacitors with an oxide thickness of 46 nm irradiated to 1 Mrad(SiO_2). ΔV_{ot} was measured shortly after irradiation. For temperatures above 850°C , increasing anneal temperature results in a large increase in ΔV_{ot} . The large increase in ΔV_{ot} with increasing temperature is due to the outdiffusion of oxygen from the oxide during the anneal, creating oxide traps [128].

3.1.3. Interface Traps. As holes are trapped near the Si/ SiO_2 interface and as holes transport to the interface, H^+ ions are released in the oxide. Under a positive bias as shown in Fig. 17, these hydrogen ions can drift to the Si/ SiO_2 interface. Once the H^+ ions reach the interface, they can react to form interface traps [129–135]. Density functional theory calculations [136–138] suggest that interface traps are created by the direct interaction of protons at the Si/ SiO_2 interface via the simple reaction



where $\text{H} - \text{Si} \equiv \text{Si}$ denotes a silicon atom bonded to one hydrogen atom and backbonded to three silicon atoms and $\cdot\text{Si}^+ \equiv \text{Si}$ denotes a silicon ion with a dangling bond (interface trap). With a positively applied bias, the positively charged trivalent interface trap $\cdot\text{Si}^+ \equiv \text{Si}$ will be rapidly transformed to a negatively charged site as it captures electrons from the silicon inversion layer [136]. The microscopic structure of the radiation-induced interface trap has been identified by electron paramagnetic resonance measurements as the P_b center [118]. A P_b center is

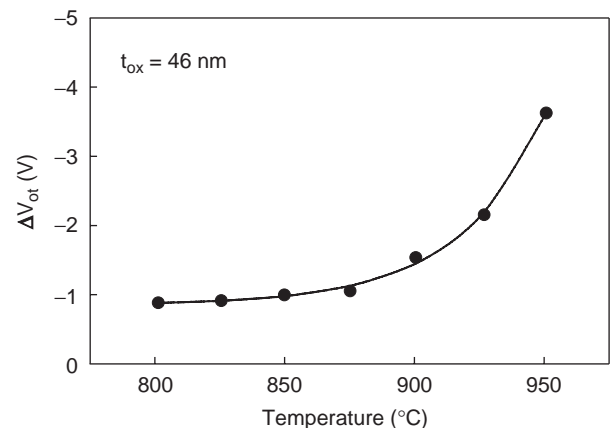


Figure 19. The increase in radiation-induced, oxide-trapped charge voltage shift with the annealing temperature after gate deposition during device fabrication. Processing temperatures above 850°C increase the amount of radiation-induced, oxide-trapped charge [127].

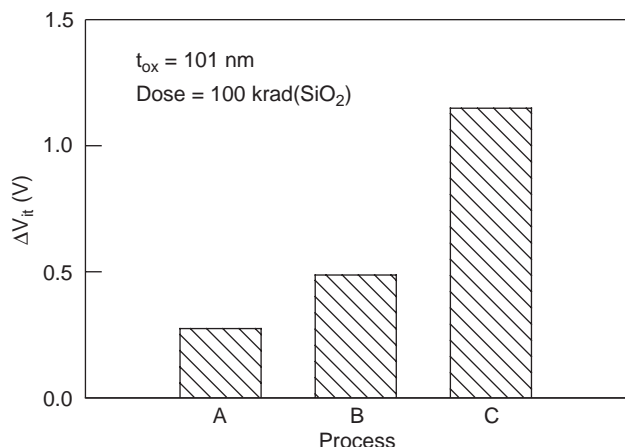


Figure 20. Effect of the amount of hydrogen used in the ambient gases of high-temperature anneals and oxidations following gate deposition during device fabrication on radiation-induced interface trap charge. Capacitors fabricated using process A were processed using the least amount of hydrogen, and capacitors fabricated using process C were processed using the maximum amount of hydrogen. Increasing the amount of hydrogen increases the amount of radiation-induced interface traps [139].

a trivalent silicon defect site similar to the E' center except that the P_b center is backbonded by three silicon atoms.

The magnitude of interface-trap buildup depends on the amount of hydrogen used in ambient gases for anneals and oxidations following gate deposition [139]. Figure 20 is a plot of threshold voltage shift due to interface traps ΔV_{it} for capacitors fabricated using anneals in ambients containing varying amounts of hydrogen. The capacitors fabricated using process A were processed using the least amount of hydrogen and the capacitors fabricated using process C were fabricated using the greatest amount of hydrogen. The capacitors had an oxide thickness of 101 nm and were irradiated to 100 krad(SiO₂). The capacitors fabricated using the greatest amount of hydrogen resulted in the largest radiation-induced interface trap charge voltage shifts.

Interface traps at the Si/SiO₂ interface are amphoteric and can act as either donor or acceptor traps. Traps in the upper half of the bandgap typically act as acceptors; thus, if the Fermi-level at the interface is above the trap energy level, the trap accepts an electron from the silicon and is negatively charged. Acceptor traps are most important for n-channel transistors. Thus, for n-channel transistors, interface traps are predominantly negatively charged. Interface traps in the lower half of the bandgap typically act as donors; that is, if the Fermi level at the interface is below the trap energy level, the trap donates an electron to the silicon, and is positively charged. Donor interface traps are most important for p-channel transistors. Thus, for p-channel transistors, interface traps are predominantly positively charged. If the Fermi level is near midgap, acceptor traps in the upper half of the bandgap will be empty, donor traps in the lower half of the bandgap will be filled, and the net interface trap charge will be close to zero. Because interface traps are located at the

Si/SiO₂ interface, they can rapidly respond to changes in applied bias.

The voltage shift due to interface trap charge is given by

$$\Delta V_{it} = \frac{-qN_{it}}{C_{ox}} \quad (9)$$

where q is the charge of an electron and N_{it} is the number of charged interface traps. Because interface traps for n-channel transistors are predominantly negatively charged, ΔV_{it} will be positive for n-channel transistors. Similarly, interface traps for p-channel transistors are predominantly positively charged and ΔV_{it} will be negative for p-channel transistors.

The rate of buildup of interface trap charge depends on the kinetics of hydrogen transport and interaction in the oxide and at the interface. This causes the buildup of interface traps to occur over long periods of time (compared to that of oxide-trapped charge buildup). The saturation of interface trap buildup can take thousands of seconds to occur. Figure 21 indicates the slow buildup of interface traps following pulses of ionizing irradiation [135]. Plotted is the radiation-induced increase in the density of interface traps ΔD_{it} for capacitors irradiated to 75 krad(Si) using a 10-MeV electron linear accelerator (LINAC) at dose rates from 1.3×10^7 to 1.4×10^9 rad(Si)/s. Capacitors were irradiated using short 10- μ s pulses with a repetition rate of 4 Hz. The dose rate is determined from the total dose divided by the total irradiation time. At the highest dose rate, the buildup follows an approximate linear-with-log time response from 3 to 3000 s. Interface trap buildup does not begin to saturate until more than 10^5 s after irradiation. Unlike oxide-trapped charge, interface traps do not undergo neutralization or anneal at room temperature. Thus, the maximum amount of interface trap buildup will occur after interface trap buildup has saturated, specifically, $> 10^5$ s for these capacitors. Some interface trap annealing at 100°C has been reported by several workers [140–142]. However, higher temperatures are normally

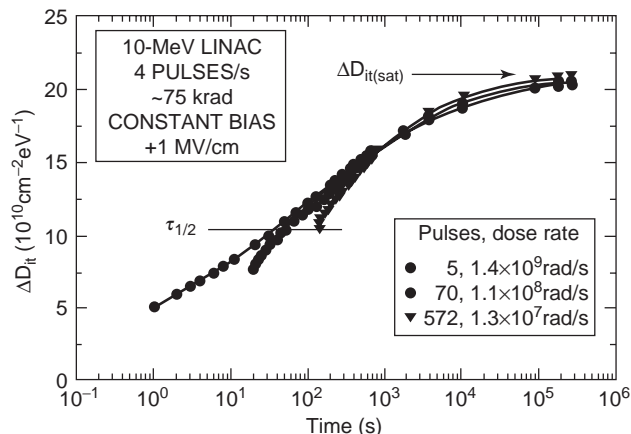


Figure 21. The increase in the density of interface traps following pulses of ionizing radiation. The buildup of interface traps does not saturate until more than 10^5 s after irradiation for these devices [135].

required to observe significant interface trap annealing [143,144].

In addition to causing a change in threshold voltage, a buildup of radiation-induced interface traps also can cause a decrease in carrier mobility. The degradation in carrier mobility μ with interface trap charge buildup follows the general relationship [145]

$$\mu = \frac{\mu_0}{1 + \alpha \Delta N_{it}} \quad (10)$$

where μ_0 is the preirradiation mobility and α is a constant. This equation is valid under most conditions, except for short times (<0.1 s) after a pulse of irradiation [146]. At short times after irradiation (~ 0.01 s), there can be a significant concentration of oxide-trapped charge close to the Si/SiO₂ interface, which can affect, and in some cases dominate, the degradation in mobility. As electrons tunnel from the silicon into the oxide, neutralizing oxide charge close to the interface, the importance of charged hole traps on mobility becomes decreasingly important.

3.1.4. Border Traps. Some oxide traps can be located close enough to the interface that they can exchange charge with the silicon on the time frames of an electrical measurement. These oxide traps will act electrically like interface traps, but are in fact, oxide traps. Oxide traps close to the interface that act electrically like interface traps are called *border traps* [147]. For an oxide trap to behave like a border trap, it must be within ~ 3 nm of the Si/SiO₂ or gate/SiO₂ interface [103,147]. Note that all oxide traps are likely to act as border traps for oxide thickness less than 6 nm (gate oxides of advanced IC technologies).

3.1.5. Effect of Oxide Thickness. A key process condition that has a very large effect on gate oxide hardness is oxide thickness. Fortunately, as the thickness of the gate oxide decreases, radiation hardness improves. The threshold voltage shifts due to oxide-trapped charge and interface trap charge decrease with slightly less than a t_{ox}^2 thickness dependence ($t_{ox}^{1.5}$ to $t_{ox}^{1.8}$). Because of the improvement in hardness with decreasing thickness, gate oxides in advanced commercial technologies can be extremely radiation-hard. The basic mechanisms of radiation effects for ultrathin oxides are different from those for moderately thick gate oxides. Ultrathin oxides are those in which oxide trap charge can be neutralized by electrons tunneling from either the gate or the Si/SiO₂ interface. Because a relatively higher number of the oxide traps will be accessible to electron tunneling, there will also be a relatively higher number of oxide traps that can act as border traps [147]. In fact, for very thin oxides (<6 nm), there may be no “bulklike” traps, and all traps in the oxide have the potential to function as border traps. Thus, for ultrathin oxides, it is possible to have no net positive radiation-induced oxide trap charge, and all traps may function electrically like interface traps (either true interface traps or border traps).

3.1.6. Alternate Gate Dielectrics. Silicon dioxide has been the primary gate insulator since MOS ICs were first developed. To achieve the drive currents required by advances in IC technology, SiO₂ gates are becoming extremely thin. They will soon reach a point where electron tunneling will cause prohibitively large increases in power consumption. To circumvent this problem, alternate gate dielectrics with high dielectric constants (also referred to as “high- k ” dielectrics) are being explored. With a high-dielectric-constant gate material a much thicker dielectric can be used to obtain the equivalent capacitance of much thinner SiO₂ gates. For these thicker high dielectric constant insulators, electron tunneling is reduced and oxide trap charge may be more significant.

At the present time, there is extremely little information on the radiation hardness of the dielectrics under consideration for replacing SiO₂. Because the dielectric gates will be physically thicker and deposited or grown using different techniques, it is possible that these dielectrics could trap significantly more charge than thinner thermally grown SiO₂ gates. As a result, the radiation-induced charge trapping in the gate insulator may once again affect IC radiation hardness. Two alternate dielectrics that have been explored are hafnium oxide, HfO₂ [148] and stacked Al₂O₃ and oxynitride gate dielectrics [149]. The hole-trapping efficiency for HfO₂ gate dielectrics has been determined to be around $\sim 28\%$, which is much larger than that for high-quality gate oxides. For stacked Al₂O₃ and oxynitride gate dielectrics, the oxide-trapped charge voltage shift has been shown to have approximately a t_{ox}^4 thickness dependence and is somewhat larger than that for high-quality gate oxides, and there is negligible interface trap buildup [149]. For gate insulator thicknesses of interest to advanced IC technologies, the threshold voltage shifts in these dielectrics should not be a major concern.

Another alternative dielectric that has been explored is reoxidized nitrided oxides (RNOs) [150–155]. Nitrided oxides can be fabricated by several different methods. One of the most straightforward methods is to anneal a thermal oxide in an ammonia (NH₃) ambient. An ammonia anneal results in a large concentration of nitrogen throughout the dielectric with peak concentrations at both interfaces. The primary difference between thermal and RNO dielectrics in ionizing radiation environments is the nearly total lack of interface trap buildup for RNO dielectrics [156]. Thick gate insulator RNO dielectrics (37 nm) have been fabricated in which there is no measurable interface trap buildup for transistors irradiated to total doses in excess of 50 Mrad(Si) [156]. This makes RNO gates attractive for space applications. The amount of oxide-trapped charge buildup in RNO dielectrics has also been shown to be less than that for comparable thermal oxides [156].

3.1.7. Total Threshold Voltage Shift. For a n-channel transistor, ΔV_{it} is positive and ΔV_{ot} is negative. Therefore, ΔV_{it} and ΔV_{ot} compensate each other as seen in Eq. (6). Because the timescales for ΔV_{it} buildup and ΔV_{ot} buildup and neutralization are different, the amount of compensation, and hence, ΔV_{th} , is time-dependent. For short times after a pulse of irradiation, ΔV_{ot} will dominate the

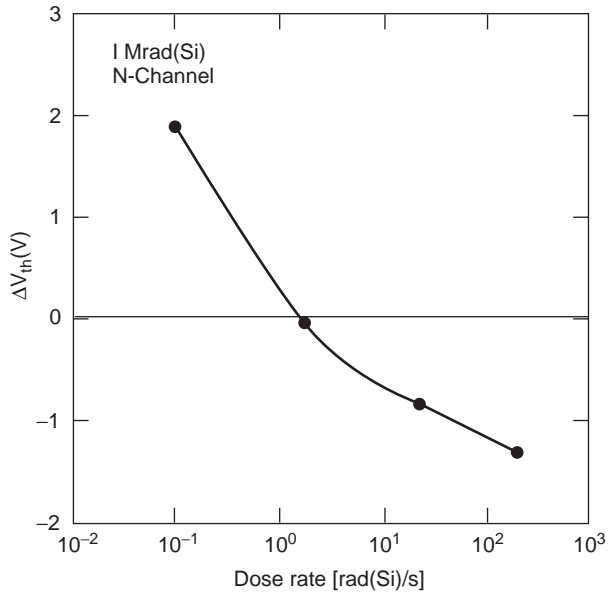


Figure 22. Radiation-induced, n-channel transistor threshold voltage shift versus dose rate of the radiation source. At high dose rates (short times), the threshold voltage shift is dominated by oxide-trapped charge and the threshold voltage shift is negative. At low dose rates (long times), the threshold voltage is dominated by interface trap charge and the threshold-voltage shift is positive [157,158].

threshold voltage shift and ΔV_{th} will be large and negative. For long times after a pulse of irradiation or for low-dose-rate exposures (e.g., space), ΔV_{it} may dominate the threshold voltage shift and ΔV_{th} may be large and positive. For p-channel transistors both ΔV_{ot} and ΔV_{it} are negative, they add together, and the radiation-induced threshold voltage shift is always negative. Figure 22 illustrates the change in ΔV_{th} with time (dose rate) for n-channel transistors [157,158]. Plotted is ΔV_{th} versus dose rate for transistors irradiated to 1 Mrad(Si). For low-dose-rate exposures (long times), interface trap buildup dominates and ΔV_{th} is large and positive. For higher dose rate exposures (shorter times), oxide-trapped charge dominates and ΔV_{th} is large and negative.

As illustrated in Figure 22, the radiation-induced threshold voltage shift for n-channel transistors can be either positive or negative. As the radiation dose is increased, the magnitude of the threshold voltage shift will increase negatively. This will result in a dramatic increase in the OFF-state leakage current (drain-to-source current I_{DS} measured at zero gate-to-source voltage V_{GS}) of individual transistors and a large increase in the static power supply current I_{DD} of an IC. If the increase in I_{DD} is high enough, functional failure can occur [159].

At low dose rates, the threshold voltage can be dominated by interface-trap charge. If this is the case, the threshold voltage can be large and positive. (Oxide-trapped charge can dominate the electrical response even at low dose rates for some technologies [160].) A large positive threshold voltage shift will decrease transistor drive. Coupled with a decrease in carrier mobility caused by the increase in number of charged interface

traps, the decrease in transistor drive will cause a degradation in IC timing parameters and potentially cause IC functional failure.

Neutralization of oxide-trapped charge and the buildup of interface trap charge with time will also affect IC electrical performance with time. Short times after a pulse of radiation, the magnitude of the threshold voltage shift of a n-channel transistor will be at its maximum value, causing the largest increase in I_{DS} and concomitantly the static power current of an IC (I_{DD}) will be at its maximum value. The threshold voltage will shift positively as oxide-trapped charge is neutralized. This will cause a decrease in I_{DS} at $V_{GS} = 0$ V. Thus, an IC that fails I_{DD} specifications shortly after a pulse of irradiation may pass I_{DD} specifications at longer times. However, as oxide-trapped charge continues to be neutralized (either at long times after a pulse of irradiation or during low-dose-rate exposure) and interface traps continue to build up, at some point transistor response may begin to be dominated by interface trap charge and ICs may begin to fail as a result of timing related issues. The change in n-channel transistor threshold voltage from negative to positive with time after irradiation is often referred to as the *rebound effect* [161]. To summarize, initially after a pulse of irradiation ICs may fail as a result of high leakage currents, moderate times after irradiation (or for moderate dose rate exposures) ICs may pass all specifications, and long times after irradiation (or for low-dose-rate exposures) ICs may fail because of timing related issues. The change in IC parametric and functional behavior with time makes it difficult to predict or assess IC failure in low-dose-rate satellite environments from moderate dose rate laboratory measurements.

3.2. Field Oxides

Even though the radiation hardness of commercial gate oxides may improve as the IC industry tends toward ultrathin oxides, field oxides of advanced commercial technologies will still be relatively thick and can be very soft to ionizing radiation. A relatively small dose in a field oxide [~ 10 krad(Si) for many commercial devices] can induce sufficient charge trapping to cause field-oxide-induced IC failure. As such, radiation-induced charge buildup in field oxides is the main cause of IC failure in many advanced commercial technologies.

Field oxides are much thicker than gate oxides. Typical field oxide thicknesses are in the range of 100–1000 nm. Unlike gate oxides, which are routinely grown by thermal oxidation, field oxides are produced using a wide variety of deposition techniques. The trapping properties in field oxides may be poorly controlled and can be considerably different from those for a gate oxide.

Two common types of field oxide isolation used today are local oxidation of silicon (LOCOS) and shallow-trench isolation (STI). LOCOS isolation has been used for many years. More recently, commercial IC suppliers have replaced LOCOS isolation with STI for advanced submicron technologies. Figure 23a [162] shows the cross section of an n-channel transistor with LOCOS isolation illustrating positive charge buildup in the bird's beak regions. Similar charge buildup will occur for STI as illustrated in Fig. 23b

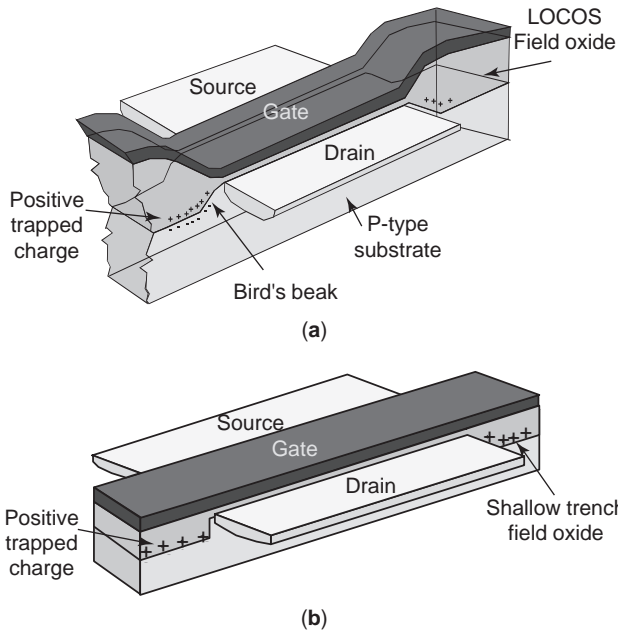


Figure 23. Two common types of field oxide isolation: (a) LOCOS and (b) shallow-trench isolation [162]. Positive charge buildup in the oxides can invert the underlying p-type surfaces.

[162]. As positive radiation-induced charge builds up in the field oxide overlying a p-type surface, it can invert the surface forming an n-type region underneath the field oxide. As the surface inverts, conducting paths can be generated that will greatly increase the leakage current. One leakage path occurs at the edge of the gate oxide transistor between the source and drain. Another leakage path could occur between the n-type source and drain regions of a transistor and the n well of adjacent p-channel transistors. These two leakage paths will cause an increase static power supply current of an IC. Because radiation-induced charge buildup in field oxides is predominantly positive, its effect is usually most important for n-channel transistors.

The field oxide forms a parasitic field oxide transistor in parallel with the gate oxide transistor. For example, at the edges of the gate transistor the gate polysilicon extends over the field oxide region as shown in Fig. 23. The parasitic field oxide transistor consists of the gate polysilicon, a portion of the field oxide, and the source and drain of the gate transistor. The effect of the excess leakage current from a parasitic field oxide transistor on the gate oxide transistor is illustrated in Fig. 24 [163]. Plotted in Fig. 24 are the drain-to-source leakage current versus gate-to-source voltage curves for an n-channel gate oxide transistor with (combined curve) and without field oxide leakage and for a parasitic field oxide transistor. Because of the large thickness of the field oxide, the preirradiation threshold voltage of the parasitic field oxide transistor is relatively large, but as positive radiation-induced charge builds up in the field oxide, it can cause a very large negative threshold voltage shift of the parasitic field oxide transistor. If the threshold voltage shift of the parasitic field oxide transistor is large enough (as depicted in

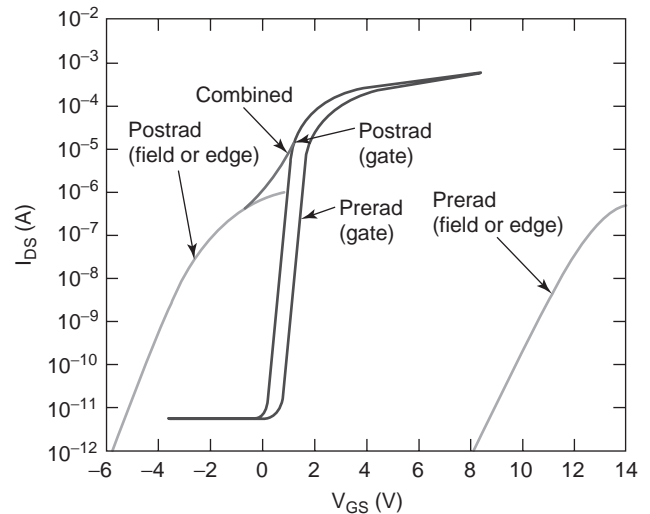


Figure 24. Buildup of radiation-induced positive charge in a field oxide can cause large negative shifts in the threshold voltage of the parasitic field oxide transistor. If the shift is large enough, as shown in the figure, the parasitic field oxide leakage current will add to the leakage current of the gate oxide transistor [163]. (This figure is available in full color at <http://www.mrw.interscience.wiley.com/erfme>.)

Fig. 24), it will cause an OFF-state leakage current (gate voltage at zero volts) to flow, which can significantly add to the drain-to-source current of the gate oxide transistor. Hence, the field-oxide leakage prevents the gate oxide transistor from being completely turned off. This will greatly add to the static supply leakage current of an IC and might cause functional failure.

The amount of field oxide leakage depends greatly on IC process and topography. For example, for STI the topography of the shallow-trench and process conditions inherently lead to variations in the trench sidewall insulator thickness between the silicon trench and overlying conductors (e.g., polysilicon). This is especially pronounced at the top corner of the trench. At the top corner, the shallow insulator thickness can result in very high fields across the insulator. These high fields in trench corner regions have been shown to severely limit the radiation hardness [162]. As the magnitude of the electric field across the trench corner increases, the magnitude of the threshold-voltage shift of the parasitic field oxide transistor increases [162].

Several methods can be employed to improve the radiation hardness of field oxides. Increasing the doping level underneath the bird's beak region of LOCOS isolation or along the sidewall of STI, will increase the preirradiation threshold voltage of the parasitic field oxide transistor and increase the amount of radiation-induced charge required to invert the underlying p-type surfaces. For STI, process techniques that increase the insulator thickness around trench corners and using n⁺ pullback regions have been successfully used to improve the radiation hardness of STI ICs [162].

3.3. SOI Buried Oxides

The total-dose hardness of an SOI transistor depends on the radiation hardness of three oxides: (1) gate, (2) field

oxide or sidewall isolation, and (3) buried oxide. The mechanisms for the radiation-induced degradation of the gate oxide of a MOS/SOI transistor are identical to the mechanisms for the gate oxide of a MOS transistor fabricated on a bulk silicon substrate as discussed above. Most present-day SOI circuits use LOCOS or STI for transistor isolation. The radiation hardness of these oxides was discussed above. Some mesa-isolated SOI technologies include sidewall oxides. A sidewall oxide exists as the gate oxide extends over the edges of the silicon island and forms a parasitic transistor in parallel with the top transistor. In some cases, the sidewall oxide is less radiation-tolerant than the top oxide and can greatly increase the transistor leakage current. The sidewall-oxide-induced leakage forms a shoulder in the MOS transistor I/V curve and is similar to that caused by a parasitic field oxide transistor for a bulk silicon MOS transistor (see Fig. 24). Sidewall leakage can be eliminated by proper processing of the sidewalls [164–167]. For example, heavily doping the sidewall by selective implantation can be used to increase the threshold voltage of the parasitic sidewall transistor, reducing its importance to the radiation response [164,165].

The biggest difference between the total-dose response of SOI and bulk silicon technologies is radiation-induced charge buildup in the buried oxide of SOI transistors. As SOI buried oxides are exposed to ionizing radiation, radiation-induced charge will become trapped in the buried oxide. This radiation-induced trapped charge is predominantly positively charged. As illustrated in Fig. 23a, this charge buildup in the buried oxide can invert the backchannel interface forming a leakage path between the source and drain of the top-gate transistor. For simplicity, the charge buildup as illustrated in Fig. 25a is shown to be located close to the buried oxide/backchannel interface. However, in general, charge will be trapped throughout the buried oxide. Inversion of the backchannel interface can lead to large increases in leakage current of a partially depleted transistor. Because the top-gate transistor is electrically coupled to backgate transistor in a fully depleted

transistor, radiation-induced charge buildup in the buried oxide of a fully depleted transistor will cause a decrease in the threshold voltage of the top-gate transistor.

A simple method for quantifying the amount of radiation-induced charge buildup in the buried oxide is to measure the threshold voltage of the backgate transistor. The backgate transistor consists of the source and drain of the top-gate transistor, the buried oxide is the gate dielectric, and the substrate acts as the gate contact. The bias configuration for measuring the backgate I/V characteristics are shown in Fig. 25b. The bias configuration and measurement conditions are identical to those for measuring the top-gate I/V characteristics except that the gate bias is applied to the substrate. Typical I/V curves for the backgate transistor are shown in Fig. 26a. The transistors were irradiated with ^{60}Co gamma rays in the OFF ($V_{\text{GS}} = V_{\text{S}} = 0$ V; $V_{\text{DS}} = 5$ V) bias condition. As noted in the figure, positive charge buildup in the buried oxide can cause large negative shifts in the backgate transistor I/V curves. As the radiation-induced charge buildup becomes sufficiently large to cause an increase in the leakage current at zero backgate bias, the top-gate leakage current will begin to increase as illustrated in Fig. 26b. This leakage current resulting from radiation-induced charge buildup in the buried oxide will prevent the top gate from being completely turned off. If it is large enough, it can cause parametric and potentially functional failure.

The radiation response of buried oxides has been found to be highly dependent on the fabrication process [168,169]. Two common methods for fabricating SOI substrates are separation by implanted oxygen (SIMOX) and by wafer bonding. SIMOX substrates are formed by implanting a silicon substrate with oxygen ions to very high fluence levels and then annealing the substrate at very high temperatures (e.g., 1350°C) to form the buried oxide. Bonded SOI substrates are formed by growing an oxide on the surface of one wafer and then bonding the wafer to a second substrate. There are numerous methods for producing the thin top silicon layer of the SOI substrate. Common to all bonded wafer processes is a high-temperature bond-strengthening anneal (e.g., 1100°C). The high-temperature anneals used to fabricate SOI substrates (both SIMOX and bonded) cause oxygen to outdiffuse from the buried oxide, leaving behind numerous oxide defects. These defects can lead to radiation-induced trapped charge [170]. It is natural to expect that the high-fluence implants used to fabricate SIMOX substrates (and some bonded oxide substrates) may cause numerous implant-related defects throughout the buried oxide. Previous work [169,171–174,188–192] has shown that up to 100% of the radiation-generated holes are trapped in the bulk of the oxide at deep trap sites close to their point of origin. Once trapped, some of the holes are slowly neutralized by electrons by thermal detrapping at room temperature [169,171–174]. In addition to hole trapping, electrons are also trapped throughout the bulk of the buried oxide [169]. Most of the trapped electrons are thermally detrapped within < 1 s after a pulse of radiation. After the electrons are detrapped, the resultant charge is due to a high concentration of trapped holes causing large negative threshold-voltage shifts of the buried oxide.

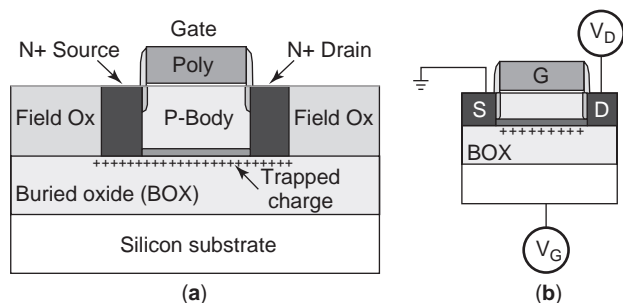


Figure 25. (a) Cross section of a partially depleted SOI transistor illustrating radiation-induced charge buildup in the buried oxide and inversion of the backchannel interface. For simplicity, radiation-induced charge buildup in the buried oxide is depicted as a sheet of charge close to the backchannel interface, whereas in general positive charge is trapped throughout the buried oxide. (b) Bias configuration for measuring the backchannel threshold voltage. This measurement is useful for quantifying the net amount of positive charge in the buried oxide.

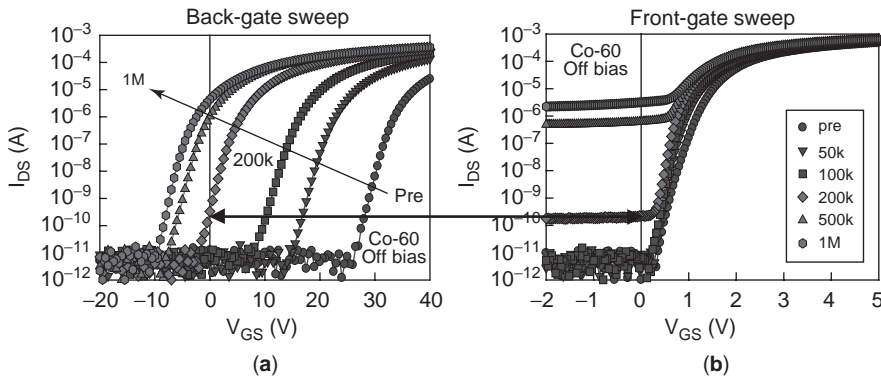


Figure 26. Gate voltage versus drain current I/V curves for (a) the backgate transistor and (b) top-gate transistor. Positive charge buildup in the buried oxide can cause large negative shifts in the backgate transistor threshold voltage and if large enough, as depicted in the figure, can cause large increases in the top-gate leakage current. (This figure is available in full color at <http://www.mrw.interscience.wiley.com/erfme>.)

Several techniques have been proposed to mitigate the effects of radiation-induced charge trapping in the buried oxide on transistor performance. These techniques can be grouped into two general categories: techniques that reduce the amount of net positive radiation-induced trapped charge and techniques that reduce the effects of radiation-induced trapped charge on transistor performance. One technique that has been proposed to reduce the amount of net radiation-induced positive trapped charge is to implant the oxide with silicon [175,176].

A transistor structure that reduces the effect of radiation-induced charge trapped in the buried oxide on transistor performance is the body-under-source field-effect transistor (BUSFET) [177]. The BUSFET is similar to a standard SOI transistor except that the source penetrates only partially through the top silicon layer. (If the drain also penetrates only partially through the top silicon layer, there could be a large decrease in dose rate and single-event upset hardness due to additional junction area.) As radiation-induced charge is trapped in the buried oxide, the charge will invert the backchannel interface. However, because the source penetrates only partially through the buried oxide, the inverted layer cannot form a conducting path between the source and the drain and no increase in top-gate transistor leakage current will occur.

3.4. Hardness Assurance Issues

Radiation test guidelines have been written with the intent to ensure device functionality in space environments. One such guideline in the United States is MIL-STD 883, Method 1019 [178]. Knowledge of the basic mechanisms of radiation effects has led to considerable improvements in the test methods [178,179]. For example, the latest Method 1019 test guideline consists of a two-part test to ensure that a device will function within acceptable, bounded limits during its lifetime. The first part of the test is a laboratory irradiation at a dose rate between 50 to 300 rad(Si)/s to the specification requirement. As long as the laboratory dose rate is greater than the expected space dose rate, this test will ensure that the threshold voltage shift of gate or field oxide transistors will be more negative for the laboratory irradiation than in space. Thus, this part of the test bounds the contribution of oxide trap charge. The second part of the test is a 100°C, 1-week “rebound” test following an additional irradiation to 50% of the specification requirement. As long as the rebound

anneal does not anneal interface trap charge, this test will ensure that the threshold-voltage shift will be more positive than in space, and, thus, provide an effective way to test for interface-trap-related failures. Two other issues that can affect the reliability of hardness assurance testing are preirradiation elevated temperature stress effects and the optimum laboratory radiation source for qualifying devices in space radiation environments.

3.4.1. Preirradiation Elevated Temperature Stress (Burn-In) Effects. To improve system reliability, devices are often exposed to elevated temperature anneals (e.g., burnin anneal) prior to system assembly. These anneals increase the cost of devices. To reduce the cost of radiation characterization, devices used for radiation tests seldom have been subjected to reliability screens. Thus, devices used for radiation characterization are rarely exposed to the same elevated temperature anneals as those used in space systems.

Shaneyfelt et al. [180,181] showed that preirradiation elevated temperature stresses (PETSS) can affect device hardness. Examples of the effects of preirradiation elevated temperature anneals are illustrated in Fig. 27, which plots the “standby” power supply leakage current I_{DD} of

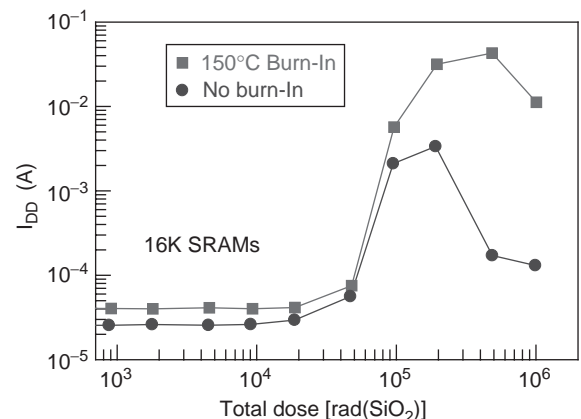


Figure 27. Standby power supply leakage current versus total dose for 16K SRAMs subjected to and not subjected to a preirradiation 150°C, 1-week elevated temperature stress. The devices exposed to a typical burn-in test show increased radiation-induced degradation [180]. (This figure is available in full color at <http://www.mrw.interscience.wiley.com/erfme>.)

16,000 SRAMs with and without a preirradiation 150°C, one-week anneal, and irradiated with 10-keV X rays with a 5-V power supply voltage in a checkerboard pattern [180]. The ICs were measured in a checkerboard complement pattern. For the ICs not subjected to a preirradiation anneal, the maximum IC leakage current is approximately 3.5 mA and occurs at a total dose of 200 krad(SiO₂). For the ICs subjected to a preirradiation anneal, the maximum IC leakage current is approximately 45 mA and occurs at a 500 krad(SiO₂). The maximum IC leakage current for the ICs subjected to a preirradiation elevated temperature stress is more than an order of magnitude higher than for the ICs not subjected to an elevated temperature stress. Further, after irradiating to a total dose of 500 krad(SiO₂), the IC leakage current for the ICs subjected to a preirradiation temperature stress is more than two orders of magnitude higher than for the ICs not subjected to a preirradiation elevated temperature stress. Hence, these data show that PETS can significantly affect IC radiation hardness.

The effect of preirradiation elevated temperature stresses on IC radiation response is clearly a concern for hardness assurance testing. Note that when we refer to elevated temperature stresses, we are not limiting ourselves to those used for burnin and other reliability tests. High-temperature process steps used in device packaging, during system assembly and use, and elsewhere also could have large impacts on IC radiation response [181]. Preirradiation elevated temperature stresses have been addressed in the U.S. military test guideline MIL-STD-883, Method 1019. For each technology, one should determine if the devices are susceptible to PETS effects. Unless the technology has been shown not to exhibit PETS effects, radiation characterization must be performed on devices subjected to all elevated-temperature-biased stresses required by reliability qualification, packaging, or system requirements. This is especially true for technologies where IC failure is dominated by radiation-induced increases in leakage current. Otherwise, the amount of radiation-induced degradation may be severely underestimated.

3.4.2. Optimum Laboratory Radiation Sources for Hardness Assurance Testing. In space, electronic devices can be exposed to high fluences of electrons and protons. In the laboratory, however, ⁶⁰Co gamma- and X-ray sources are more cost-effective for routine evaluation of the radiation hardness of electronic devices for space environments. X-ray sources can operate at higher dose rates than most ⁶⁰Co sources and can be used to irradiate individual die at the wafer level. Because of these properties, X-ray sources are often used for process development and control [159]. Cobalt-60 gamma sources are normally used for hardness assurance testing. For example, the present MIL-STD-883, Method 1019 test guideline used for qualifying devices for space applications requires devices to be irradiated using moderate-dose-rate ⁶⁰Co sources [178]. Some work has been performed comparing the differences in total dose degradation for X-ray and ⁶⁰Co irradiations. In some cases good correlation between ⁶⁰Co and X-ray radiation-induced degradation was observed [182]; however, in other cases large differences were observed [183,184]. These re-

sults indicate that for some technologies, ⁶⁰Co and X-ray irradiations may produce considerably different results.

The justification for using ⁶⁰Co gamma sources for hardness assurance testing is based primarily on historical practice rather than on technical grounds. This leads to an obvious question: For technologies where X-ray and ⁶⁰Co irradiations cause different amounts of device degradation, which radiation source is best suited for simulating energetic electrons or protons? Work in 2001 [185] comparing the radiation-induced response of pMOSFET dosimeters showed that the radiation-induced response for high-energy protons (60–200 MeV) was only 65–85% of the ⁶⁰Co radiation-induced response. This result raises concern that ⁶⁰Co radiation sources may not be the best radiation source for simulating device response in proton-rich space environments. In this section, we will concentrate on differences between ⁶⁰Co and low-energy X-ray radiation sources, the two most popular types of laboratory radiation sources for characterizing the radiation hardness of ICs for space environments.

Figure 28 shows the ratio of the backgate transistor threshold voltage shift for X-ray and proton irradiations and the ratio for ⁶⁰Co gamma and proton irradiations for transistors irradiated in the 0 V and transmission gate (or pass gate) (TG) bias configurations [184]. The X-ray and proton data were taken at a dose rate of 270 rad(SiO₂)/s, and the ⁶⁰Co gamma data were taken at a dose rate of 50 rad(SiO₂)/s. X-ray data taken at 270 and 50 rad(SiO₂)/s showed no noticeable differences in backgate threshold voltage shift for the different dose rates for devices irradiated to total doses up to 500 krad(SiO₂). Hence, the fact that the data were taken at somewhat different dose rates should not affect the conclusions. Within experimental uncertainties, the X-ray and proton radiation-induced backgate threshold voltage shifts are nearly equal for all total dose levels and bias conditions examined. However, the ratio of ⁶⁰Co gamma and proton backgate threshold shifts varies widely, especially for low total doses. The fact that there is agreement in the backgate threshold voltage shifts at high total doses is not surprising. At this point, the threshold voltage shift is significant and therefore the

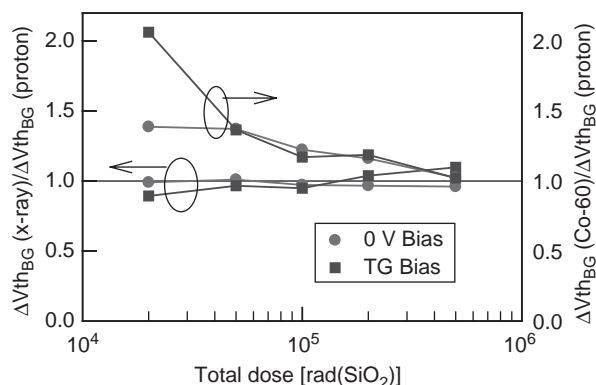


Figure 28. Ratio of X-ray to 41.4-MeV proton and ⁶⁰Co gamma to 41.4-MeV proton radiation-induced backgate threshold voltage shifts as a function of total dose for SOI transistors. Transistors were irradiated with either a 0-V or TG bias configuration [184]. (This figure is available in full color at <http://www.mrw.interscience.wiley.com/erfme>.)

internal field in the oxide is also significant. Thus, a low-field condition in the oxide is no longer satisfied. Note that this is due to the size of the threshold voltage shift, not the total dose. Devices that shift more or less with dose will therefore reach this point at different dose levels. Thus, for this proton energy, total dose levels, and devices, X-ray irradiations much better simulate proton radiation-induced degradation than do ^{60}Co gamma irradiations. Good correlation between X-ray and proton-radiation-induced degradation has been observed for proton energies between 20 and 200 MeV and in the radiation-induced degradation of field oxides in bulk silicon technologies [184]. As a result, for SOI and bulk silicon transistors, laboratory X-ray irradiations may more closely simulate proton-rich environments such as low-Earth orbits (at least in the energy range of 20–200 MeV) than do laboratory ^{60}Co gamma irradiations. This contradicts the commonly accepted tenet that ^{60}Co gamma sources should be used for all hardness assurance qualification. The better match between X-ray and proton-radiation-induced damage was suggested to be a closer match of the initial charge yield between 10-keV X-rays and protons at low electric fields [184]. This does not preclude the use of ^{60}Co gamma radiation sources for device qualification in proton-rich environments. Cobalt 60 gamma radiation sources may overestimate the total-dose degradation and, therefore, are a more conservative radiation source.

Because the charge yield for ^{60}Co gamma rays more closely matches the charge yield for electrons with energies relevant to the space environment, ^{60}Co gamma irradiation better simulates the radiation-induced degradation of SOI devices in electron-rich space environments than does X-ray irradiation [186]. Thus, to simulate total-dose degradation in electron-rich environments such as geosynchronous orbits, ^{60}Co gamma sources are probably still the optimum laboratory radiation source for device qualification.

4. TOTAL-DOSE IONIZATION EFFECTS: BIPOLAR AND III-V DEVICES

4.1. Bipolar Devices: Enhanced Low-Dose-Rate Sensitivity

Since the early 1990s, it has been known that some types of bipolar devices exhibit enhanced low-dose-rate sensitivity (ELDRS) at low electric fields [187–193]. This means that the amount of total-dose degradation in bipolar transistors and ICs that is observed at a given total dose is greater at low dose rates than high dose rates. In general, the degradation results from the buildup of radiation induced charge in the field oxides used to isolate the base and emitter contacts and recombination centers that are created at the Si/SiO₂ interface. ELDRS in n-p-n transistors has been attributed primarily to increased positive oxide trap charge buildup in the isolation oxide overlying the base-emitter junction [193,194]. This charge enhances the surface recombination rate in the p-base region. On the other hand, lateral and substrate p-n-p transistors are primarily affected by increased interface trap charge buildup in the thick isolation oxide over the emitter-base region [192,195]. In most cases, ELDRS effects have

been shown to be more important for lateral or substrate p-n-p transistors than for n-p-n transistors [190]. In fact, Johnston and coworkers [190] showed that the relative damage at low dose rates ($< 0.01 \text{ rad}(\text{SiO}_2)/\text{s}$) for junction-isolated linear processes could be greater than a factor of 2 larger in linear bipolar circuits dominated by p-n-p transistor response than in those dominated by n-p-n transistor response. A data compendium of bipolar linear circuits that exhibit ELDRS can be found in Ref. 196.

ELDRS is illustrated in Fig. 29, which is a plot of the input bias current for LM111 voltage comparators versus total dose for dose rates of 50, 0.1, and 0.01 $\text{rad}(\text{SiO}_2)/\text{s}$ [197]. The voltage comparators were irradiated with all pins short-circuited. As observed in Fig. 29, voltage comparators irradiated at low dose rates have a much larger increase in input bias current than voltage comparators irradiated at high dose rates. This ELDRS effect can cause failure of ICs in satellite environments not observed in standard laboratory testing. As such, ELDRS severely complicates hardness assurance testing for space environments.

Developing an accelerated hardness assurance test method to estimate the “true” low-dose-rate effects in bipolar devices remains a very challenging issue facing the radiation effects community [198,199]. Unfortunately, high-dose-rate irradiation followed by room-temperature annealing, which can accurately estimate the radiation response of CMOS devices at low dose rates [200,201], does not accurately estimate the low-dose-rate response of many types of bipolar devices [187,191]. In MOS devices this is referred to as *time-dependent effects*, not a “true” low-dose-rate effect. Time dependent effects also exist in bipolar devices and must not be confused with a “true” low-dose-rate effect. This has made it difficult to develop a quick and accurate total-dose hardness assurance test method for predicting the radiation response of bipolar devices with the potential to exhibit ELDRS effects. Currently, the most promising rapid screen involves the use of an elevated temperature irradiation at relatively low dose rates ($\leq 1 \text{ rad}(\text{SiO}_2)/\text{s}$) [202,203]. However, the optimum irradiation temperature for this procedure varies from

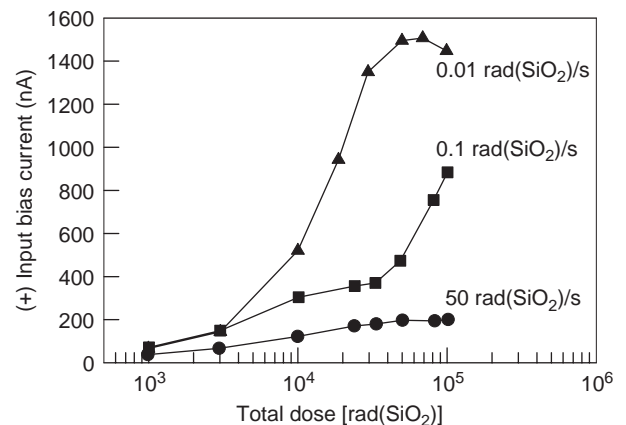


Figure 29. Input bias current versus dose for LM111 voltage comparators irradiated at dose rates of 50, 0.1, and 0.01 $\text{rad}(\text{SiO}_2)/\text{s}$ [197].

technology to technology [196,203], and does not always bound the low-dose-rate response, and the required dose rate is significantly lower than the current dose rate range [50–300 rad(SiO₂)/s] used for qualifying CMOS technologies. As a result, manufacturers do not have a reliable laboratory test guideline for timely assessment of the radiation hardness of their bipolar technologies. Nevertheless, test procedures have been added to the MIL-STD-883, Test Method 1019 for testing bipolar linear devices that require the use of either low dose rate or elevated-temperature irradiations [204].

On a positive note, researchers have shown that final chip passivation layers can have a major impact on the total-dose hardness of bipolar linear technologies [205]. It is found that devices fabricated without passivation layers do not exhibit ELDRS or preirradiation elevated temperature stress (PETS) sensitivity, while devices from the same production lot fabricated with either oxide/nitride or doped-glass passivation layers are sensitive to ELDRS and PETS. It was also shown that removing the passivation layers on devices that exhibit ELDRS could mitigate ELDRS and PETS effects. While this is obviously not a practical solution to the ELDRS and PETS problems for ICs to be used in space systems, it does appear to indicate that ELDRS and PETS effects are probably not intrinsic to many bipolar process technologies prior to deposition of the final passivation layer. In addition, ELDRS and PETS effects do not appear to be inherently related to circuit design or layout, but are related to mechanical stress effects, hydrogen in the device, or a combination of the two. It appears that mechanical stress induced by the passivation layers might play a critical role in determining the radiation response of bipolar linear ICs. Passivation layers can easily alter mechanical stress in the die. The introduction of thermal cycles and moisture after fabrication has been shown to further impact the film stress [206,207]. These two facts are consistent with both changes in radiation response between unpassivated and passivated devices at high dose rates, and the observation of PETS sensitivity in passivated devices. These results suggest that proper engineering of the final chip passivation layer might eliminate ELDRS and PETS effects in bipolar integrated circuits.

4.2. III–V Devices

These devices are inherently hard to ionizing irradiation. Previous works have shown that GaAs devices can be irradiated with gamma rays to levels in excess of 100 Mrad (GaAs) without significant degradation [208,209]. III–V devices have also been shown to very hard to proton irradiation [210]. Protons interact through ionization effects and can cause displacement damage. Displacement damage can reduce the lifetime of minority carriers and can cause carrier removal. Because GaAs devices are predominantly majority-carrier devices, and the channel regions have relatively high dopant concentrations, neither of these mechanisms cause significant degradation of GaAs devices.

5. SUMMARY AND CONCLUSIONS

The harsh environment of space and manmade systems can cause significant degradation to electronics, which can lead to system failure. The types of degradation range from permanent failure due to total-dose ionizing irradiation and single-event hard errors to temporary loss of information due to single-event upsets. The mechanisms for degradation and failure levels are dependent on many factors, including device type, system design and application, and radiation environment.

As IC technologies continue to advance, they are becoming more susceptible to terrestrial-radiation-induced effects. Terrestrial irradiation can cause single-event upsets in advanced IC technologies, reducing IC reliability. Methods for hardening ICs to single-event effects have been known for a long time. However, most of these techniques require the implementation of circuit and/or device changes that degrade IC electrical performance and/or yield and are not suitable for high-performance commercial devices. Thus, new techniques or other IC technologies (e.g., SOI) will be required to reduce the effects of terrestrial irradiation on IC reliability.

IC response to ionizing radiation has a complex time dependence. The time dependence of oxide-trapped charge buildup and neutralization and the buildup of interface traps makes it difficult to ensure device hardness in space environments based on laboratory measurements. Considerable work has been performed to improve radiation hardness assurance test guidelines, and test guidelines are now available that take into account time-dependent radiation-induced charge buildup. Still, more work needs to be performed to better understand the mechanisms for charge buildup and device degradation to further improve hardness assurance test guidelines, especially for device types that may exhibit nonstandard MOS radiation-induced behavior (e.g., bipolar devices).

Acknowledgments

The authors gratefully acknowledge many useful discussions with their colleagues, especially Dan Fleetwood, Peter Winokur, and Gerald Hash. Sandia is a multiprogram laboratory operated by Sandia Corporation, a Lockheed Martin Company, for the United States Department of Energy's National Nuclear Security Administration under Contract DE-AC04-94AL85000.

BIBLIOGRAPHY

1. H. L. Hughes and R. A. Giroux, *Electronics* **37**:58 (1964).
2. D. Binder, E. C. Smith, and A. B. Holman, *IEEE Trans. Nucl. Sci.* **NS-2**(6):2675-2690 (1975).
3. J. F. Ziegler, in J. F. Ziegler, ed., *The Stopping and Ranges of Ions in Matter*, Pergamon Press, New York, 1980, Vol. 6.
4. J. Barth, in N. Van Vanno, ed., *IEEE Nuclear and Space Radiation Effects Conf. Short Course*, July 1997.
5. R. A. Mewaldt, *Proceedings of Interplanetary Particle Environment*, in J. Feynman and S. Gabriel, eds., Pasadena, CA, March 16, 1987, pp. 121–132; available as JPL Publication 88–28, April 15, 1988.

6. J. H. Adams, Jr., R. Silberberg, and C. H. Tsao, *NRL Memorandum Report 4506*, Aug. 25, 1981.
7. J. Feynman and S. B. Gabriel, *IEEE Trans. Nucl. Sci.* **NS-43**(2):344–352 (1996).
8. M. S. Gussenhoven, E. G. Mullen, and D. H. Brautigam, *IEEE Trans. Nucl. Sci.* **NS-43**(2):353–368 (1996).
9. M. A. Xapsos, G. P. Summers, P. Shapiro, and E. A. Burke, *IEEE Trans. Nucl. Sci.* **NS-43**(6):2772–2777 (1996).
10. D. V. Rheames, *Rev. Geophys.* (Suppl.) **33**:585 (1995).
11. J. M. Nash, Solar Wind, *Time*, pp. 54–55, September 9, 1996.
12. J. H. Adams, Jr., *IEEE Trans. Nucl. Sci.* **NS-29**(6):2095–2100 (1982).
13. E. L. Petersen, *IEEE Trans Nucl. Sci.* **NS-43**(6):2805–2813 (1996).
14. J. H. Adams, Jr., *IEEE Trans. Nucl. Sci.* **NS-30**(6):4475–4480 (1983).
15. J. F. Ziegler, *IBM J. Res. Devel.* **40**(1):19–39 (1996).
16. A. Taber and E. Normand, *IEEE Trans. Nucl. Sci.* **NS-40**:120 (1993).
17. C. Lage, D. Durnett, T. McNelly, K. Baker, A. Bormann, D. Dreier, and V. Soorholtz, *Proc. IEDM* 821–824 (1993).
18. T. C. May and M. H. Woods, *IEEE Trans. Electron. Devices* **ED-26**:2–9 (1978).
19. J. C. Pickel and J. T. Blandford, Jr., *IEEE Trans Nucl. Sci.* **NS-25**(6):1166–1171 (1978).
20. C. S. Guenzer, E. A. Wolicki, and R. G. Allas, *IEEE Trans Nucl. Sci.* **NS-26**(6):5048 (1979).
21. E. L. Petersen and P. W. Marshall, *J. Radiat. Effects: Res. Eng.* **6**(2):1–23 (1988).
22. E. Normand, *IEEE Trans. Nucl. Sci.* **NS-43**(6):2742–2750 (1996).
23. E. Normand, *IEEE Trans. Nucl. Sci.* **NS-43**(2):461–474 (1996).
24. A. Johnston, *Proc. 4th European Conf. Radiations and Their Effects on Devices and Systems*, Cannes, France, Sept. 15–19, 1997.
25. C. M. Hsieh, P. C. Murley, and R. R. O'Brien, *IEEE Electron. Device Lett.* **EDL-2**(4):103–105 (1981).
26. F. B. McLean and T. R. Oldham, *IEEE Trans Nucl. Sci.* **NS-29**(6):2018–2023 (1982); T. R. Oldham and F. B. McLean, *IEEE Trans Nucl. Sci.* **NS-30**(6):4493–4500 (1983).
27. P. E. Dodd, F. W. Sexton, and P. S. Winokur, *IEEE Trans Nucl. Sci.* **NS-41**(6):2005–2017 (1994).
28. S. Kirkpatrick, *IEEE Trans. Electron. Devices* **ED-21**(11):742–753 (1979).
29. J. R. Hauser, S. E. Diehl-Nagle, A. R. Knudson, and A. B. Campbell, *IEEE Trans Nucl. Sci.* **NS-32**(6):4115–4121 (1985).
30. F. W. Sexton, R. K. Treece, K. J. Hass, K. L. Hughes, G. L. Hash, C. L. Axness, S. P. Buchner, and K. Kang, *IEEE Trans Nucl. Sci.* **NS-37**(6):1861–1868 (1990).
31. L. W. Massengill, D. V. Kerns, Jr., S. E. Kerns, and M. L. Alles, *IEEE Electron. Device Lett.* **11**(2):98–99 (Feb. 1990).
32. C. Brisset, P. Dollfus, O. Musseau, J.-L. Leray, and P. Hesto, *IEEE Trans. Nucl. Sci.* **41**(6):2297–2303 (Dec. 1994).
33. A. Campbell, A. Knudson, D. McMorrow, W. Anderson, J. Roussos, S. Espy, S. Buchner, K. Kang, D. Kerns, and S. Kerns, *IEEE Trans. Nucl. Sci.* **NS-36**:2292 (1989).
34. T. R. Weatherford, D. McMorrow, W. R. Curtice, A. B. Campbell, and A. R. Knudson, *1993 IEEE Int. Reliability Physics Symp. Proc.*, p. 357.
35. J. R. Schwank, F. W. Sexton, T. R. Weatherford, D. McMorrow, A. R. Knudson, and J. S. Melinger, *IEEE Trans. Nucl. Sci.* **42**(6):1585 (Dec. 1995).
36. D. McMorrow, J. S. Melinger, A. R. Knudson, A. B. Campbell, T. Weatherford, and L. H. Tran, *IEEE Trans. Nucl. Sci.* **NS-39**:1657 (1992).
37. T. R. Weatherford, D. McMorrow, W. R. Curtice, A. R. Knudson, and A. B. Campbell, *IEEE Trans. Nucl. Sci.* **NS-40**:1867 (1993).
38. D. McMorrow, T. Weatherford, A. R. Knudson, L. H. Tran, J. S. Melinger, and A. B. Campbell, *IEEE Trans. Nucl. Sci.* **NS-40**:1858 (1993).
39. B. W. Hughlock, G. S. LaRue, and A. H. Johnston, *IEEE Trans. Nucl. Sci.* **37**(6):1894 (Dec. 1990).
40. D. McMorrow, T. R. Weatherford, W. R. Curtice, A. R. Knudson, S. Buchner, J. S. Melinger, L. H. Tran, and A. B. Campbell, *IEEE Trans. Nucl. Sci.* **42**(6):1837 (Dec. 1995).
41. L. W. Connell, F. W. Sexton, and A. K. Prinja, *IEEE Trans Nucl. Sci.* **NS-42**(6):2026–2034 (1995).
42. L. W. Massengill, *IEEE Trans Nucl. Sci.* **NS-32**(2):577–593 (1996).
43. H. T. Weaver, C. L. Axness, J. D. McBrayer, J. S. Browning, J. S. Fu, A. Ochoa, Jr., and R. Koga, *IEEE Trans Nucl. Sci.* **NS-43**(6):1281–1286 (1987).
44. J. A. Zoutendyk, L. D. Edmonds, and L. S. Smith, *IEEE Trans Nucl. Sci.* **NS-36**(6):2267–2274 (1989).
45. J. S. Chern, P. Yang, P. Pattnaik, and J. A. Seitchik, *IEEE Trans. Electron. Devices* **ED-33**(6):822–834 (1996).
46. D. G. Mavis and P. H. Eaton, *Mission Research Corporation Technical Report P8111.29*, Sept. 1998.
47. R. Koga, S. H. Penzin, K. B. Crawford, and W. R. Crain, *Proc. 4th RADECS*, 1997, pp. 311–318.
48. R. Koga, S. H. Crain, P. Yu, and K. B. Crawford, *2001 IEEE Radiation Effects Data Workshop Record*, 2001, pp. 182–189.
49. R. Koga, P. Yu, K. B. Crawford, S. H. Crain, and V. T. Tran, *2001 IEEE Radiation Effects Data Workshop Record*, 2001, pp. 6–13.
50. B. L. Gregory and B. D. Shafer, *IEEE Trans Nucl. Sci.* **NS-30**(6):293 (1979).
51. F. N. Coppage and D. C. Evans, *IEEE Trans Nucl. Sci.* **NS-24**(6):2226 (1977).
52. A. H. Johnston and B. W. Hughlock, *IEEE Trans Nucl. Sci.* **NS-37**(6):1886–1893 (1990).
53. P. E. Dodd, M. R. Shaneyfelt, J. R. Schwank, and G. L. Hash, Neutron-induced latchup in SRAMs at ground level, *2003 IEEE Int. Reliability Physics Symp. Proc.*, 41st Annual (in press).
54. A. H. Johnston, *IEEE Trans Nucl. Sci.* **NS-43**(2):505–521 (1996).
55. T. F. Wrobel, *IEEE Trans Nucl. Sci.* **NS-34**(6):1262–1268 (1987).
56. C. F. Wheatley, J. L. Titus, and D. I. Burton, *IEEE Trans Nucl. Sci.* **NS-41**(6):2152–2159 (1994).
57. F. W. Sexton, D. M. Fleetwood, M. R. Shaneyfelt, P. E. Dodd, and G. L. Hash, *IEEE Trans Nucl. Sci.* **NS-44**(6):2345–2352 (1997).
58. J. R. Brews, M. Allenspach, R. D. Schrimpf, K. F. Galloway, J. L. Titus, and C. F. Wheatley, *IEEE Trans. Nucl. Sci.* **NS-40**(6):1959–1966 (1993).
59. L. W. Massengill, B. K. Choi, D. M. Fleetwood, R. D. Schrimpf, K. F. Galloway, M. R. Shaneyfelt, T. L. Meisenheimer, P. E. Dodd, J. R. Schwank, Y. M. Lee, R. S. Johnson, and G.

- Lucovsky, *IEEE Trans. Nucl. Sci.* **48**(6):1904–1912 (Dec. 2001).
60. J. H. Hohl and K. F. Galloway, *IEEE Trans Nucl. Sci.* **NS-34**(6):1275–1280 (1987).
 61. A. E. Waskiewicz, J. W. Groninger, V. H. Strahan, and D. M. Long, *IEEE Trans Nucl. Sci.* **NS-33**(6):1710–1713 (1986).
 62. T. A. Fischer, *IEEE Trans. Nucl. Sci.* **NS-34**(6):1786–1791 (1987).
 63. T. F. Wrobel, F. N. Coppage, G. L. Hash, A. J. Smith, *IEEE Trans Nucl. Sci.* **NS-32**(6):3991–3995 (1985).
 64. A. Ochoa, Jr., F. W. Sexton, T. F. Wrobel, G. L. Hash, and R. J. Sokel, *IEEE Trans. Nucl. Sci.* **NS-30**(6):4127–4134 (1983).
 65. R. Koga and W. A. Kolasinski, *IEEE Trans Nucl. Sci.* **NS-36**(6):2367–2374 (1989).
 66. P. E. Dodd, M. R. Shaneyfelt, J. R. Schwank, G. L. Hash, B. L. Draper, and P. S. Winokur, *IEEE Trans. Nucl. Sci.* **47**(6):2165–2174 (Dec. 2000).
 67. E. L. Petersen, *IEEE Trans. Nucl. Sci.* **NS-28**(6):3981–3686 (1981).
 68. C. L. Chen and M. Y. Hsiao, *IBM J. Res. Devel.* **28**(2):124–134 (1984).
 69. S. Karp and M. K. Gilbert, *IEEE Trans. Aerospace Electronic Syst.* **29**(2):310–316 (1993).
 70. A. E. Giddings, F. W. Hewlett, R. K. Trek, D. K. Nichols, L. S. Smith, and J. A. Zoutendyk, *IEEE Trans. Nucl. Sci.* **NS-32**(6):4159–4163 (1985).
 71. L. R. Rockett, Jr., *IEEE Trans Nucl. Sci.* **NS-35**(6):1682–1687 (1988).
 72. F. W. Sexton, R. K. Treece, K. J. Hass, K. L. Hughes, G. L. Hash, C. L. Axness, S. P. Buchner, and K. Kang, *IEEE Trans. Nucl. Sci.* **NS-37**(6):1861–1868 (1990).
 73. G. E. Davis, L. R. Hite, T. G. W. Blake, C.-E. Chen, H. W. Lam, and R. DeMoyer, Jr., *IEEE Trans. Nucl. Sci.* **32**(6):4432–4437 (Dec. 1985).
 74. L. W. Massengill, D. V. Kerns, Jr., S. E. Kerns, and M. L. Alles, *IEEE Electron. Device Lett.* **11**(2):98–99 (Feb. 1990).
 75. L. R. Hite, H. Lu, T. W. Houston, D. S. Hurta, and W. E. Bailey, *IEEE Trans. Nucl. Sci.* **39**(6):2121–2125 (Dec. 1992).
 76. S. E. Kerns, L. W. Massengill, D. V. Kerns, Jr.; M. L. Alles, T. W. Houston, H. Lu, and L. R. Hite, *IEEE Trans. Nucl. Sci.* **36**(6):2305–2310 (Dec. 1989).
 77. P. E. Dodd and F. W. Sexton, *IEEE Trans. Nucl. Sci.* **NS-42**(6):1764–1771 (1995).
 78. J. C. Pickel, *IEEE Trans. Nucl. Sci.* **NS-43**(2):483–495 (1996).
 79. A. J. Tylka, J. H. Adams, Jr. P. R. Boberg, B. Brownstein, W. F. Dietrich, E. O. Flueckiger, E. L. Petersen, M. A. Shea, D. F. Smart, and E. C. Smith, *IEEE Trans. Nucl. Sci.* **NS-44**(6):2150–2160 (1997).
 80. SPACERAD is a trademark of the Space Radiation Associates, 1430 Willamette Street, Suite 1, Eugene, OR 97401, USA.
 81. L. W. Connell, P. J. McDaniel, A. K. Prinja, and F. W. Sexton, *IEEE Trans. Nucl. Sci.* **NS-42**(2):73–82 (1995).
 82. E. L. Petersen, *IEEE Trans Nucl. Sci.* **NS-43**(2):496–304 (1996).
 83. T. C. May and M. H. Woods, *IEEE Trans. Electron. Devices* **26**(1):2–9 (1979).
 84. See numerous papers in the 1978–1980 proceedings of the IEEE International Reliability Physics Symposium.
 85. J. F. Ziegler, H. W. Curtis, H. P. Muhlfeld, C. J. Montrose, B. Chin, M. Nicewicz, C. A. Russell, W. Y. Yang, L. B. Freeman, P. Hosier, L. E. LaFave, J. L. Walsh, J. M. Orro, G. J. Unger, J. M. Ross, T. J. O’Gorman, B. Messina, T. D. Sullivan, A. J. Sykes, H. Yourke, T. A. Enger, V. Tolat, T. S. Scott, A. H. Taber, R. J. Sussman, W. A. Klein, and C. W. Wahaus, *IBM J. Res. Devel.* **40**(1):3–18 (1996).
 86. T. C. May, *IEEE Trans. Compon. Hybrids, Mfg. Technol.* **2**(4):377–387 (1979).
 87. Z. Hasnain and A. Ditali, *Proc. IEEE Int. Reliability Physics Symp.* 1992, pp. 276–280.
 88. Y. Tosaka, S. Satoh, T. Itakura, H. Ehara, T. Ueda, G. Woffinden, and S. A. Wender, *IEEE Trans. Electron. Devices* **45**(7):1453–1458 (1998).
 89. R. C. Baumann and E. B. Smith, *Microelectron. Reliabil.* **41**:211–218 (2001).
 90. H. Kobayashi, K. Shiraishi, H. Tsuchiya, M. Motoyoshi, H. Usuki, Y. Nagai, K. Takahisa, T. Yoshiie, Y. Sakurai, and T. Ishizaki, *IEDM Tech. Digest* 2002, pp. 337–340.
 91. T. J. O’Gorman, *IEEE Trans. Electron. Devices* **41**(4):553–557 (1994).
 92. C. Lage, D. Burnett, T. McNelly, K. Baker, A. Bormann, D. Dreier, and V. Soorholtz, *IEDM Tech. Digest* 1993, pp. 821–824.
 93. E. Normand, *IEEE Trans. Nucl. Sci.* **43**(6):2742–2750 (1996).
 94. E. Normand, *IEEE Trans. Nucl. Sci.* **43**(2):461–474 (1996).
 95. P. D. Bradley and E. Normand, *IEEE Trans. Nucl. Sci.* **45**(6):2929–2940 (1998).
 96. P. E. Dodd, M. R. Shaneyfelt, J. R. Schwank, and G. L. Hash, *Proc. Int. Reliability Physics Symp.*, 2003.
 97. R. Baumann, *IEDM Tech. Digest* 2002, pp. 329–332.
 98. E. Normand, J. L. Wert, D. L. Oberg, P. P. Majewski, P. Voss, and S. A. Wender, *IEEE Trans. Nucl. Sci.* **44**(6):2358–2366 (1997).
 99. A. H. Johnston, *IEEE Trans. Nucl. Sci.* **45**(3):1339–1354 (1998).
 100. Private communication, numerous U.S. semiconductor and computer manufacturers.
 101. L. W. Massengill, *IEEE Trans. Nucl. Sci.* **43**(2):576–593 (1996).
 102. A. H. Taber and E. Normand, *DNA Technical Report DNA-TR-94-123*, 1995.
 103. F. B. McLean, H. E. Boesch, Jr., and T. R. Oldham, in T. P. Ma and P. V. Dressendorfer, eds., *Ionizing Radiation Effects in MOS Devices and Circuits*, Wiley, New York, 1989, pp. 87–192.
 104. R. C. Hughes, *Appl. Phys. Lett.* **26**(8):436–438 (1975).
 105. R. C. Hughes, *Phys. Rev. Lett.* **30**(26):1333–1336 (1973).
 106. M. R. Shaneyfelt, D. M. Fleetwood, J. R. Schwank, and K. L. Hughes, *IEEE Trans. Nucl. Sci.* **38**(6):1187–1194 (Dec. 1991).
 107. F. B. McLean and G. A. Ausman, Jr., *Phys. Rev. B.* **15**(2):1052–1061 (1977).
 108. F. B. McLean, G. A. Ausman, Jr., H. E. Boesch, Jr., and J. M. McGarrity, *J. Appl. Phys.* **47**(4):1529–1532 (1976).
 109. H. E. Boesch, Jr., J. M. McGarrity, and F. B. McLean, *IEEE Trans. Nucl. Sci.* **NS-25**(3):1012–1016 (1978).
 110. H. E. Boesch, Jr., F. B. McLean, J. M. McGarrity, and P. S. Winokur, *IEEE Trans. Nucl. Sci.* **NS-25**(6):1239–1245 (1978).

111. P. M. Lenahan and P. V. Dressendorfer, *J. Appl. Phys.* **55**(10):3495–3499 (1984).
112. H. E. Boesch, Jr., T. L. Taylor, L. R. Hite, and W. E. Bailey, *IEEE Trans. Nucl. Sci.* **NS-37**(6):1982–1989 (1990).
113. C. A. Pennise and H. E. Boesch, Jr., *IEEE Trans. Nucl. Sci.* **NS-37**(6):1990–1994 (1990).
114. H. E. Boesch, Jr., T. L. Taylor, and G. A. Brown, *IEEE Trans. Nucl. Sci.* **NS-38**(6):1234–1239 (1991).
115. C. A. Pennise and H. E. Boesch, Jr., *IEEE Trans. Nucl. Sci.* **NS-38**(6):1240–1246 (1991).
116. R. E. Stahlbush, G. J. Campisi, J. B. McKitterick, W. P. Maszara, P. Roitman, and G. A. Brown, *IEEE Trans. Nucl. Sci.* **NS-39**(6):2086–2097 (1992).
117. P. M. Lenahan and P. V. Dressendorfer, *IEEE Trans. Nucl. Sci.* **NS-29**(6):1459–1461 (1982).
118. P. M. Lenahan and P. V. Dressendorfer, *IEEE Trans. Nucl. Sci.* **NS-30**(6):4602–4604 (1983).
119. T. R. Oldham, A. J. Lelis, and F. B. McLean, *IEEE Trans. Nucl. Sci.* **NS-33**(6):1203–1209 (1986).
120. P. J. McWhorter, S. L. Miller, and W. M. Miller, *IEEE Trans. Nucl. Sci.* **NS-37**(6):1682–1689 (1990).
121. S. Manzini and A. Modelli, in J. F. Verweij and D. R. Wolters, eds., *Insulating Films on Semiconductors*, North-Holland, Elsevier Science, 1983, pp. 112–115.
122. M. Schmidt and K. Koster, Jr., *Phys. Stat. Solid. B* **174**(1):53–66 (1992).
123. G. F. Derbenwick and H. H. Sanders, *IEEE Trans. Nucl. Sci.* **NS-24**(6):2244–2247 (1977).
124. P. J. McWhorter, S. L. Miller, and T. A. Dellin, *J. Appl. Phys.* **68**(4):1902–1909 (1990).
125. B. Ballard and G. Barbottin, *Instabilities in Silicon Devices*, Vol. 2, Elsevier Science, New York, 1989, p. 32.
126. D. M. Fleetwood, P. S. Winokur, and J. R. Schwank, *IEEE Trans. Nucl. Sci.* **NS-35**(6):1497–1505 (1988).
127. J. R. Schwank and D. M. Fleetwood, *Appl. Phys. Lett.* **53**(9):770–772 (1988).
128. W. L. Warren, M. R. Shaneyfelt, D. M. Fleetwood, J. R. Schwank, P. S. Winokur, R. A. B. Devine, and D. Mathiot, *IEEE Trans. Nucl. Sci.* **NS-41**(6):1817–1827 (1994).
129. C. M. Svensson, in S. T. Pantelides, ed., *The Physics of SiO₂ and Its Interfaces*, Pergamon Press, Elmsford, 1978, pp. 328–332.
130. F. B. McLean, *IEEE Trans. Nucl. Sci.* **NS-27**(6):1651–1657 (1980).
131. N. S. Saks, R. B. Klein, and D. L. Griscom, *IEEE Trans. Nucl. Sci.* **NS-35**(6):1234–1240 (1988).
132. N. S. Saks and D. B. Brown, *IEEE Trans. Nucl. Sci.* **NS-37**(6):1624–1631 (1990).
133. N. S. Saks and R. W. Rendell, *IEEE Trans. Nucl. Sci.* **NS-39**(6):2220–2228 (1992).
134. M. R. Shaneyfelt, J. R. Schwank, D. M. Fleetwood, P. S. Winokur, K. L. Hughes, and F. W. Sexton, *IEEE Trans. Nucl. Sci.* **NS-37**(6):1632–1639 (1990).
135. M. R. Shaneyfelt, J. R. Schwank, D. M. Fleetwood, P. S. Winokur, K. L. Hughes, G. L. Hash, and M. P. Connors, *IEEE Trans. Nucl. Sci.* **NS-39**(6):2244–2251 (1992).
136. D. M. Fleetwood, *Microelectronics Reliability*, manuscript in preparation.
137. S. N. Rashkeev, D. M. Fleetwood, R. D. Schrimpf, and S. T. Pantelides, *Phys. Rev. Lett.* **87**(16):165506/1–4 (Oct. 2001).
138. S. N. Rashkeev, D. M. Fleetwood, R. D. Schrimpf, and S. T. Pantelides, *IEEE Trans. Nucl. Sci.* **48**(6):2086–2092 (Dec. 2001).
139. J. R. Schwank, D. M. Fleetwood, P. S. Winokur, P. V. Dressendorfer, D. C. Turpin, and D. T. Sanders, *IEEE Trans. Nucl. Sci.* **NS-34**(6):1152–1158 (1987).
140. N. S. Saks, D. B. Brown, and R. W. Rendell, *IEEE Trans. Nucl. Sci.* **38**(6):1130–1139 (Dec. 1991).
141. P. S. Winokur, H. E. Boesch, Jr., J. M. McGarrity, and F. B. McLean, *J. Appl. Phys.* **50**(5):3492–3495 (May 1979).
142. D. M. Fleetwood, P. V. Dressendorfer, and D. C. Turpin, *IEEE Trans. Nucl. Sci.* **34**(6):1178–1183 (Dec. 1987).
143. A. J. Lelis, T. R. Oldham, and W. M. DeLancey, *IEEE Trans. Nucl. Sci.* **38**(6):1590–1597 (Dec. 1991).
144. D. M. Fleetwood, F. V. Thome, S. S. Tsao, P. V. Dressendorfer, V. J. Dandini, and J. R. Schwank, *IEEE Trans. Nucl. Sci.* **35**(5):1099–1112 (Oct. 1988).
145. F. W. Sexton and J. R. Schwank, *IEEE Trans. Nucl. Sci.* **NS-32**(6):3975–3981 (1985).
146. F. B. McLean and H. E. Boesch, Jr., *IEEE Trans. Nucl. Sci.* **NS-36**(6):1772–1783 (1989).
147. D. M. Fleetwood, *IEEE Trans. Nucl. Sci.* **NS-39**(2):269–271 (1992).
148. J. A. Felix, D. M. Fleetwood, R. D. Schrimpf, J. G. Hong, G. Lucovsky, J. R. Schwank, and M. R. Shaneyfelt, *IEEE Trans. Nucl. Sci.* **49**(6):3191–3196 (Dec. 2002).
149. J. A. Felix, M. R. Shaneyfelt, D. M. Fleetwood, J. R. Schwank, R. D. Schrimpf, P. E. Dodd, E. P. Gusev, and C. D'Emic, *IEEE Trans. Nucl. Sci.* (in press).
150. T. Hori, H. Iwasaki, and K. Tsuji, *IEEE Trans. Electron. Devices* **36**(2):340–350 (Feb. 1989).
151. L. Manchanda, G. R. Weber, Y. O. Kim, L. C. Feldman, N. Moryia, B. E. Weir, R. C. Kistler, M. L. Green, and D. Brasen, *Microelectron. Eng.* **22**(1–4):69–72 (Aug. 1993).
152. T. Hori, Y. Naito, H. Iwasaki, and H. Esaki, *IEEE Electron. Devices Lett.* **7**(12):669–671 (Dec. 1986).
153. H. Fukuda, T. Arakawa, and S. Ohno, *IEEE Trans. Electron. Devices* **39**(1):127–133 (Jan. 1992).
154. T. Hori, *IEEE Trans. Electron. Devices* **37**(9):2058–2069 (Sept. 1990).
155. T. Hori, S. Akamatsu, and Y. Odake, *IEEE Trans. Electron. Devices* **36**(1):118–126 (Jan. 1992).
156. G. L. Dunn and P. W. Wyatt, *IEEE Trans. Nucl. Sci.* **36**(6):2161–2168 (Dec. 1989).
157. P. S. Winokur, F. W. Sexton, J. R. Schwank, D. M. Fleetwood, P. V. Dressendorfer, T. F. Wrobel, and D. C. Turpin, *IEEE Trans. Nucl. Sci.* **NS-33**(6):1343–1351 (1986).
158. J. R. Schwank, in L. W. Massengill, ed., *1994 IEEE Nuclear and Space Radiation Effects Conf. Short Course*, 1994, p. II–62.
159. M. R. Shaneyfelt, K. L. Hughes, J. R. Schwank, F. W. Sexton, D. M. Fleetwood, and P. S. Winokur, *IEEE Trans. Nucl. Sci.* **38**(6):1598–1605 (Dec. 1991).
160. D. M. Fleetwood, P. S. Winokur, and T. L. Meisenheimer, *IEEE Trans. Nucl. Sci.* **NS-38**(6):1552–1559 (1991).
161. J. R. Schwank, P. S. Winokur, P. J. McWhorter, F. W. Sexton, P. V. Dressendorfer, and D. C. Turpin, *IEEE Trans. Nucl. Sci.* **NS-31**(6):1434–1438 (1984).
162. M. R. Shaneyfelt, P. E. Dodd, B. L. Draper, and R. S. Flores, *IEEE Trans. Nucl. Sci.* **45**(6):2584–2592 (Dec. 1998).
163. T. R. Oldham et al., *IEEE Trans. Nucl. Sci.* **34**(6):1184–1189 (Dec. 1987).

164. R. A. Kjar and J. Peel, *IEEE Trans. Nucl. Sci.* **21**(6):2081 (Dec. 1974).
165. L. S. Napoli, R. K. Smeltzer, J. L. Yeh, and W. F. Heagerty, *IEEE Trans. Nucl. Sci.* **29**(6):1707–1711 (Dec. 1982).
166. S. S. Tsao, D. M. Fleetwood, and H. T. Weaver, *IEEE Trans. Nucl. Sci.* **34**(6):1686–1691 (Dec. 1987).
167. D. M. Fleetwood, S. S. Tsao, and P. S. Winokur, *IEEE Trans. Nucl. Sci.* **35**(6):1361–1367 (Dec. 1988).
168. H. E. Boesch, Jr. and T. L. Taylor, *IEEE Trans. Nucl. Sci.* **39**(6):2103–2113 (Dec. 1992).
169. H. E. Boesch, Jr., T. L. Taylor, L. R. Hite, and W. E. Bailey, *IEEE Trans. Nucl. Sci.* **37**(6):1982–1989 (Dec. 1990).
170. W. L. Warren, M. R. Shaneyfelt, J. R. Schwank, D. M. Fleetwood, P. S. Winokur, R. A. B. Devine, W. P. Maszara, and J. B. McKitterick, *IEEE Trans. Nucl. Sci.* **40**(6):1755–1764 (Dec. 1993).
171. C. A. Pennise and H. E. Boesch, Jr., Determination of the charge-trapping characteristics of buried oxides using a 10-keV X-ray source, *IEEE Trans. Nucl. Sci.* **37**(6):1990–1994 (Dec. 1990).
172. H. E. Boesch, Jr., T. L. Taylor, and G. A. Brown, *IEEE Trans. Nucl. Sci.* **38**(6):1234–1239 (Dec. 1991).
173. C. A. Pennise and H. E. Boesch, Jr., *IEEE Trans. Nucl. Sci.* **38**(6):1240–1246 (Dec. 1991).
174. R. E. Stahlbush, G. J. Campisi, J. B. McKitterick, W. P. Maszara, P. Roitman, and G. A. Brown, *IEEE Trans. Nucl. Sci.* **39**(6):2086–2097 (Dec. 1992).
175. H. Hughes and P. McMarr, U.S. Patent 5, 795, 813 (1996).
176. B. J. Mrstik, H. L. Hughes, P. J. McMarr, R. K. Lawrence, D. I. Ma, I. P. Isaacson, and R. A. Walker, *IEEE Trans. Nucl. Sci.* **47**(6):2189–2195 (Dec. 2000).
177. J. R. Schwank, M. R. Shaneyfelt, B. L. Draper, and P. E. Dodd, *IEEE Trans. Nucl. Sci.* **46**(6):1809–1816 (Dec. 1999).
178. D. M. Fleetwood, P. S. Winokur, L. C. Riewe, and R. L. Pease, *IEEE Trans. Nucl. Sci.* **NS-36**:1963 (1989).
179. D. M. Fleetwood, P. S. Winokur, C. E. Barnes, and D. C. Shaw, *Radiat. Phys. Chem.* **43**:129 (1994).
180. M. R. Shaneyfelt, D. M. Fleetwood, J. R. Schwank, T. L. Meisenheimer, and P. S. Winokur, Effects of burn-in on radiation hardness, *IEEE Trans. Nucl. Sci.* **41**(6):2550–2559 (Dec. 1994).
181. M. R. Shaneyfelt, P. S. Winokur, D. M. Fleetwood, J. R. Schwank, and R. A. Reber, Jr., *IEEE Trans. Nucl. Sci.* **43**(3):865–872 (June 1996).
182. D. M. Fleetwood, P. S. Winokur, R. W. Beegle, P. V. Dressendorfer, and B. L. Draper, *IEEE Trans. Nucl. Sci.* **32**(6):4369–4375 (Dec. 1985).
183. D. M. Fleetwood, S. S. Tsao, and P. S. Winokur, *IEEE Trans. Nucl. Sci.* **35**(6):1361–1367 (Dec. 1988).
184. J. R. Schwank, M. R. Shaneyfelt, P. E. Dodd, V. Ferlet-Cavrois, R. A. Loemker, P. S. Winokur, D. M. Fleetwood, P. Paillet, J.-L. Leray, B. L. Draper, S. C. Witzczak, and L. C. Riewe, *IEEE Trans. Nucl. Sci.* **47**(6):2175–2182 (Dec. 2000).
185. R. L. Pease, M. Simons, and P. Marshall, *IEEE Trans. Nucl. Sci.* **48**(3):908–912 (June 2001).
186. P. Paillet, J. R. Schwank, M. R. Shaneyfelt, V. Ferlet-Cavrois, and O. Flament, *IEEE Trans. Nucl. Sci.* (in press).
187. E. W. Enlow, R. L. Pease, W. E. Combs, R. D. Schrimpf, and R. N. Nowlin, *IEEE Trans. Nucl. Sci.* **38**:1342 (1991).
188. R. N. Nowlin, D. M. Fleetwood, R. D. Schrimpf, R. L. Pease, and W. E. Combs, *IEEE Trans. Nucl. Sci.* **40**:1686–1693 (1993).
189. A. Wei, S. L. Kosier, R. D. Schrimpf, D. M. Fleetwood, and W. Combs, *Appl. Phys. Lett.* **65**:1918–20 (1994).
190. A. H. Johnston, G. W. Swift, and B. G. Rax, *IEEE Trans. Nucl. Sci.* **41**:2427 (1994).
191. D. M. Fleetwood, S. L. Kosier, R. N. Nowlin, R. D. Schrimpf, R. A. Reber, Jr., M. DeLaus, P. S. Winokur, A. Wei, W. E. Combs, and R. L. Pease, *IEEE Trans. Nucl. Sci.* **41**:1871–1883 (1994).
192. S. McClure, R. Pease, W. Will, and G. Perry, *IEEE Trans. Nucl. Sci.* **43**:2544 (1994).
193. S. C. Witzczak, R. C. Lacoce, D. C. Mayer, D. M. Fleetwood, R. D. Schrimpf, and K. F. Galloway, *IEEE Trans. Nucl. Sci.* **45**:2339 (1998).
194. D. M. Fleetwood, L. C. Riewe, J. R. Schwank, S. C. Witzczak, and R. D. Schrimpf, *IEEE Trans. Nucl. Sci.* **43**:2537–2546 (1996).
195. D. M. Schmidt, D. M. Fleetwood, R. D. Schrimpf, R. L. Pease, R. J. Graves, G. H. Johnson, K. F. Galloway, and W. E. Combs, *IEEE Trans. Nucl. Sci.* **42**:1541–1549 (1995).
196. R. L. Pease, S. McClure, A. H. Johnston, J. Gorelick, El Segundo, T. L. Turflinger, M. Gehlhausen, J. Krieg, T. Carriere, Astrium, Velizy, and M. Shaneyfelt, *Workshop Record of the 2001 IEEE Radiation Effects Data Workshop*, Vancouver, Canada, July 2001, pp. 127–133.
197. M. R. Shaneyfelt, J. R. Schwank, S. C. Witzczak, D. M. Fleetwood, R. L. Pease, P. S. Winokur, L. C. Riewe, and G. L. Hash, *IEEE Trans. Nucl. Sci.* **47**(6):2539–2545 (Dec. 2000).
198. R. L. Pease, L. M. Cohn, D. M. Fleetwood, M. A. Gehlhausen, T. L. Turflinger, D. B. Brown, and A. H. Johnston, *IEEE Trans. Nucl. Sci.* **44**:1981 (1997).
199. R. L. Pease, J. Krieg, M. Gehlhausen, D. Platteter, and J. Black, *IEEE Trans. Nucl. Sci.* **45**:2665 (1998).
200. J. R. Schwank, P. S. Winokur, P. J. McWhorter, F. W. Sexton, P. V. Dressendorfer, and D. C. Turpin, *IEEE Trans. Nucl. Sci.* **31**:1434 (1984).
201. D. M. Fleetwood, P. S. Winokur, L. C. Riewe, and R. L. Pease, *IEEE Trans. Nucl. Sci.* **36**:1963 (1989).
202. A. H. Johnston, C. I. Lee, and B. G. Rax, *IEEE Trans. Nucl. Sci.* **43**:3049 (1996).
203. T. Carriere, R. Ecoffet, and P. Poirot, *IEEE Trans. Nucl. Sci.* **47**:2350 (Dec. 2000).
204. MIL-STD-883D, Test Method 1019.6, *Ionizing Radiation (Total Dose) Test Procedure*, Defense Electronics Supply Center (DESC), Dayton, OH.
205. M. R. Shaneyfelt, R. L. Pease, J. R. Schwank, M. C. Maher, G. L. Hash, D. M. Fleetwood, P. E. Dodd, C. A. Reber, S. C. Witzczak, L. C. Riewe, H. P. Hjalmarson, J. C. Banks, B. L. Doyle, and J. A. Knapp, *IEEE Trans. Nucl. Sci.* **49**:3171 (2002).
206. G. Carlotti, L. Doucet, M. Dupeux, *J. Vacuum Sci. Technol. B* **14**:3460 (1996).
207. T. H. Wu and R. S. Rosler, *Solid State Technology* **35**:65 (1992).
208. J. K. Notthoff, *IEEE Trans. Nucl. Sci.* **32**(6):4061 (Dec. 1985).
209. M. A. Listvan, P. J. Vold, and D. K. Arch, *IEEE Trans. Nucl. Sci.* **34**(6):1664 (Dec. 1987).
210. G. L. Hash, J. R. Schwank, M. R. Shaneyfelt, C. E. Sandoval, M. P. Connors, T. J. Sheridan, F. W. Sexton, E. M. Shayton, and J. A. Heise, *IEEE Trans. Nucl. Sci.* **41**(6):2259–2266 (Dec. 1994).

FURTHER READING

- T. P. Ma and P. V. Dressendorfer, eds., *Ionizing Radiation Effects in MOS Devices and Circuits*, John Wiley, New York, 1989.
- December issues of the *IEEE Trans. Nucl. Sci.*
- D. M. Fleetwood and R. Gaillard, eds., *IEEE Trans. Nucl. Sci.* **NS-43**(2) (April 1996).
- J. F. Ziegler and G. R. Srinivasan, eds., *IBM J. Res. Devel.* **40**(1) (1996).
- D. B. Brown, ed., *IEEE Nuclear and Space Radiation Effects Conf. Short Course*, July 1991.
- F. W. Sexton, ed., *IEEE Nuclear and Space Radiation Effects Conf. Short Course*, July 1992.
- A. H. Johnston, ed., *IEEE Nuclear and Space Radiation Effects Conf. Short Course*, July 1993.
- L. W. Massengill, ed., *IEEE Nuclear and Space Radiation Effects Conf. Short Course*, July 1994.
- J. R. Schwank, ed., *IEEE Nuclear and Space Radiation Effects Conf. Short Course*, July 1995.
- R. L. Pease, ed., *IEEE Nuclear and Space Radiation Effects Conf. Short Course*, July 1996.
- N. Van Vonno, ed., *IEEE Nuclear and Space Radiation Effects Conf. Short Course*, July 1997.
- J. C. Pickel, ed., *IEEE Nuclear and Space Radiation Effects Conf. Short Course*, July 1998.
- D. M. Fleetwood, ed., *IEEE Nuclear and Space Radiation Effects Conf. Short Course*, July 1999.
- L. Cohn, ed., *IEEE Nuclear and Space Radiation Effects Conf. Short Course*, July 2000.
- P. E. Dodd, ed., *IEEE Nuclear and Space Radiation Effects Conf. Short Course*, July 2001.
- P. V. Dressendorfer, ed., *IEEE Nuclear and Space Radiation Effects Conf. Short Course*, July 2002.

RADIATION MONITORING

CLINTON L. LINGREN
 DANIEL WEIS
 GEORGE L. BLEHER
 DONALD P. GIEGLER
 Individual Consultants

With the nuclear age came a need to monitor radiation levels for the protection of workers and the population, and monitoring instruments to fill this need were first developed for projects in government and university laboratories.

Early radiation monitors built in the 1950s were based on vacuum-tube electronics, which were then modified to use industrialized components that would withstand the environment of nuclear power plants. The cumbersome vacuum-tube instruments generated a lot of heat and required large, forced-air-cooled cabinets for housing readouts in the reactor control room.

During the late 1950s and early 1960s, vacuum tube-based electronics were replaced with transistor-based,

solid-state electronics that reduced the required space for the control-room instruments. Each radiation detector had its own channel of electronics, including signal-conditioning circuitry, control-room readout, and associated power supplies. For a typical channel, the detector with a small amount of signal-conditioning electronics was located at the point of detection and the balance of the channel was mounted in or near the reactor control room. These analog-based, radiation-monitoring systems required a separate indicating system for each detection channel in the control room, and they had separate signal, high-voltage, low-voltage, and control-logic cables for each channel between the control room and the detector. This resulted in miles of multiconductor and shielded cabling in a typical plant to provide the required radiation indication at the control room.

In the late 1970s and early 1980s distributed microprocessors were developed, replacing the early analog systems with digital logic. These new microprocessor-based monitoring systems replaced the miles of multiconductor cables with single twisted-pair cables in a loop or star interconnecting configuration and replaced analog indicating instruments with a computer display.

Radiation is always around us and we are constantly being bombarded by radiation of subatomic particles and electromagnetic rays. Sources of the radiation from above us include our sun and solar system as well as the rest of the vast universe of space; and sources of radiation surrounding us include the soil and rocks in the earth and plants, animals, and people that are near us, as well as materials derived from those. Radiation includes both *ionizing* radiation in the form of X rays, gamma rays, alpha particles, beta particles, neutrons, protons, cosmic rays, and so on, and *nonionizing* radiation in the form of the lower-energy portion of the electromagnetic spectrum, including electrical power in our homes, radio and video waves broadcast via cable or transmitted by air, visible light, and infrared energy emitted by bodies according to their temperature.

Radiation monitoring is concerned with measuring and monitoring ionizing radiation. Little is known about the harmful effects of ionizing radiation at levels that are typically encountered in our environment (natural background levels). Effects of high doses of ionizing radiation have been documented as result of such incidents as the atomic bombs dropped on Japan, the atomic accident at Chernobyl, and observation of the effects of therapeutic uses of radiation. It is generally assumed that all radiation is harmful and that people should receive the minimum radiation exposure for what needs to be accomplished. Naturally occurring radiation at historically typical background levels serves as the reference from which allowable additional radiation-exposure limits are set. Medical diagnostic radiation is the primary source of increased radiation over background for most people.

Radiation dose levels that cause death immediately or within a few weeks are well established. Radiation induced malignant tumors have been noted since the earliest use of X rays and other forms of ionizing radiation. Hypothetical increased risks forecasts for low-level radiation doses are based on linear or quadratic extrapolation of

FURTHER READING

- T. P. Ma and P. V. Dressendorfer, eds., *Ionizing Radiation Effects in MOS Devices and Circuits*, John Wiley, New York, 1989.
- December issues of the *IEEE Trans. Nucl. Sci.*
- D. M. Fleetwood and R. Gaillard, eds., *IEEE Trans. Nucl. Sci.* **NS-43**(2) (April 1996).
- J. F. Ziegler and G. R. Srinivasan, eds., *IBM J. Res. Devel.* **40**(1) (1996).
- D. B. Brown, ed., *IEEE Nuclear and Space Radiation Effects Conf. Short Course*, July 1991.
- F. W. Sexton, ed., *IEEE Nuclear and Space Radiation Effects Conf. Short Course*, July 1992.
- A. H. Johnston, ed., *IEEE Nuclear and Space Radiation Effects Conf. Short Course*, July 1993.
- L. W. Massengill, ed., *IEEE Nuclear and Space Radiation Effects Conf. Short Course*, July 1994.
- J. R. Schwank, ed., *IEEE Nuclear and Space Radiation Effects Conf. Short Course*, July 1995.
- R. L. Pease, ed., *IEEE Nuclear and Space Radiation Effects Conf. Short Course*, July 1996.
- N. Van Vonno, ed., *IEEE Nuclear and Space Radiation Effects Conf. Short Course*, July 1997.
- J. C. Pickel, ed., *IEEE Nuclear and Space Radiation Effects Conf. Short Course*, July 1998.
- D. M. Fleetwood, ed., *IEEE Nuclear and Space Radiation Effects Conf. Short Course*, July 1999.
- L. Cohn, ed., *IEEE Nuclear and Space Radiation Effects Conf. Short Course*, July 2000.
- P. E. Dodd, ed., *IEEE Nuclear and Space Radiation Effects Conf. Short Course*, July 2001.
- P. V. Dressendorfer, ed., *IEEE Nuclear and Space Radiation Effects Conf. Short Course*, July 2002.

RADIATION MONITORING

CLINTON L. LINGREN
 DANIEL WEIS
 GEORGE L. BLEHER
 DONALD P. GIEGLER
 Individual Consultants

With the nuclear age came a need to monitor radiation levels for the protection of workers and the population, and monitoring instruments to fill this need were first developed for projects in government and university laboratories.

Early radiation monitors built in the 1950s were based on vacuum-tube electronics, which were then modified to use industrialized components that would withstand the environment of nuclear power plants. The cumbersome vacuum-tube instruments generated a lot of heat and required large, forced-air-cooled cabinets for housing readouts in the reactor control room.

During the late 1950s and early 1960s, vacuum tube-based electronics were replaced with transistor-based,

solid-state electronics that reduced the required space for the control-room instruments. Each radiation detector had its own channel of electronics, including signal-conditioning circuitry, control-room readout, and associated power supplies. For a typical channel, the detector with a small amount of signal-conditioning electronics was located at the point of detection and the balance of the channel was mounted in or near the reactor control room. These analog-based, radiation-monitoring systems required a separate indicating system for each detection channel in the control room, and they had separate signal, high-voltage, low-voltage, and control-logic cables for each channel between the control room and the detector. This resulted in miles of multiconductor and shielded cabling in a typical plant to provide the required radiation indication at the control room.

In the late 1970s and early 1980s distributed microprocessors were developed, replacing the early analog systems with digital logic. These new microprocessor-based monitoring systems replaced the miles of multiconductor cables with single twisted-pair cables in a loop or star interconnecting configuration and replaced analog indicating instruments with a computer display.

Radiation is always around us and we are constantly being bombarded by radiation of subatomic particles and electromagnetic rays. Sources of the radiation from above us include our sun and solar system as well as the rest of the vast universe of space; and sources of radiation surrounding us include the soil and rocks in the earth and plants, animals, and people that are near us, as well as materials derived from those. Radiation includes both *ionizing* radiation in the form of X rays, gamma rays, alpha particles, beta particles, neutrons, protons, cosmic rays, and so on, and *nonionizing* radiation in the form of the lower-energy portion of the electromagnetic spectrum, including electrical power in our homes, radio and video waves broadcast via cable or transmitted by air, visible light, and infrared energy emitted by bodies according to their temperature.

Radiation monitoring is concerned with measuring and monitoring ionizing radiation. Little is known about the harmful effects of ionizing radiation at levels that are typically encountered in our environment (natural background levels). Effects of high doses of ionizing radiation have been documented as result of such incidents as the atomic bombs dropped on Japan, the atomic accident at Chernobyl, and observation of the effects of therapeutic uses of radiation. It is generally assumed that all radiation is harmful and that people should receive the minimum radiation exposure for what needs to be accomplished. Naturally occurring radiation at historically typical background levels serves as the reference from which allowable additional radiation-exposure limits are set. Medical diagnostic radiation is the primary source of increased radiation over background for most people.

Radiation dose levels that cause death immediately or within a few weeks are well established. Radiation induced malignant tumors have been noted since the earliest use of X rays and other forms of ionizing radiation. Hypothetical increased risks forecasts for low-level radiation doses are based on linear or quadratic extrapolation of

limited data where relatively large populations received very high doses. However, studies have not yet validated those models, and risk from low-level radiation may be lower than is generally postulated.

Background radiation levels are different at different places on Earth, due to elevation, the makeup of the soil, and related factors. For example, background radiation in Denver, Colorado is about twice that of San Diego, due primarily to the higher elevation with less air mass to absorb radiation from space, such as cosmic rays. People are typically exposed to higher background radiation in masonry buildings than in wood structures because of naturally occurring radioactivity in the materials in cement, brick, or rock. The human body contains radioactivity in the form of naturally occurring potassium-40, carbon-14, and other radioactive isotopes. According to current government regulations, if a laboratory animal were injected with the amount of radioactivity in an average person's body, it would be considered radioactive (see Further Reading list).

Commonly encountered radioactive objects include glow-in-the-dark radium watch dials made during the first half of the twentieth century, thorium oxide coated gas-lamp mantles, smoke detectors containing about 1 microcurie of americium-241, fluorescent lamp starters containing a minute amount of krypton-85, porcelain tooth caps colored with metal oxides that contain uranium to give an improved reflective appearance, radon gas in tightly built homes over radium-containing soil or rock and in water supplies, and potassium-containing fertilizers. Although these may give off ionizing radiation at levels that would require careful accountability in a laboratory or industrial environment under state or federal regulations, they are seldom considered hazardous and are not required to be monitored.

In today's society there are areas where the use of ionizing radiation that must be monitored according to state or federal government regulations to ensure that radiation does not pose a hazard to personnel or to the environment: areas include radiation for instructional use in schools and universities, medicine, industrial gauging, sterilization of medical supplies or food, mining and milling of radioactive ores, steel mills, space flights, fusion facilities, and nuclear reactors.

The use of radiation sources at schools and universities may range from simple isotopic sources for demonstration purposes that are small enough to be exempt from regulations to fully operational nuclear test reactors where reactor physics is taught and isotopic sources are produced.

The use of ionizing radiation in medicine includes electron beams, X-ray sources, and gamma-ray sources for transmission imaging or for therapy and gamma-ray sources tagged to pharmaceuticals and injected into the patient for determining organ function in nuclear medicine. The types of sources include isotopic sources, X-ray tubes, and linear accelerators. X-ray tubes and linear accelerators generate ionizing radiation only when power is properly applied; however, isotopic sources always emit radiation as a result of the natural decay of the radioactive isotope. The physicians or medical technologists are responsible for properly administering radiation to patients;

they use radiation monitoring devices to ensure that source strengths and photo energies are proper. Those who handle the isotopic sources should not be exposed inadvertently and receive doses above allowable limits.

Many industries use radiation sources for making routine measurements, such as material density, fill height of beverage containers, or material thickness. Radiation is also used to sterilize some medical supplies after the packaging is sealed. A typical radiation source is cobalt-60 with a half-life of just over 5.3 years and a photon energy of just over a million electronvolts; a typical sterilization dose is a million rads. Some foods are also exposed to gamma radiation to kill bacteria and prevent spoilage. Some seeds or bulbs are irradiated with lower doses to enhance growth and increase production. Some gemstones are irradiated to enhance color and brilliance. These industries and radiation facilities use radiation monitoring to calibrate and control exposure doses and to monitor personnel exposure.

Increased incidence of lung cancer among underground miners exposed to radon and radon daughters in their occupations has been demonstrated in epidemiological studies of the inhalation of radon gas and its effects on the lung epithelium. Efficient control of radon and radon daughters in underground mines has been difficult. It is the role of radiation monitoring to identify radiation exposure and assist in its control in underground mines (both uranium mines and non-uranium mines) where radon gases may be present.

The need for radiation monitoring in steelmills is fairly recent and is the result of 49 known incidents since 1973 where companies have inadvertently melted shielded radioactive sources, typically cobalt-60 or cesium-137. These incidents have not caused worker injuries but have resulted in economic harm to the companies with costs typically ranging from \$5 million to \$25 million per accidental melt of a radioactive source. These costs include loss of the melt, facility decontamination, and shutdown of steel production. The sources, generally, had been lost from licensees that had used them for industrial applications. It is also important to identify radioactively contaminated scrap, such as metal activated in a nuclear facility or contaminated in a melt from a lost source. To find a shielded source in a carload or truckload of scrap poses is very difficult.

Radiation monitors and detectors are placed on spacecraft for several purposes. Measuring secondary emissions, induced by the absorption of protons or neutrons, from the surface of planets or moons can identify the elements on the surface of the planets or moons. Monitoring the levels of radiation impinging on the spacecraft can provide information for predicting effects on the materials in the spacecraft and can be used to turn off sensitive electronic components during times of unexpectedly high-radiation exposure where radiation damage occurs when the components are powered.

Atomic fusion is another source of radiation; fusion combines light elements to create elements of greater atomic weight, neutrons, and excess energy, neutrons are eventually absorbed by the surrounding materials, typically resulting in radioactive isotopes. Radiation monitoring is required to measure levels of radiation during

facility operation as well as radiation levels from neutron activation.

In the fission process in nuclear test reactors and nuclear power reactors, heavy atoms, such as uranium-235, absorb a neutron and split into fission products that include gamma rays, neutrons, alpha particles, beta particles, and lighter elements that are typically radioactive. Radioactive materials result from the fission process, as well as from activation from absorption of neutrons or other atomic particles. Radiation monitoring in nuclear power plants is discussed in detail later in this article.

Any of the facilities discussed prior that has one or more licensable radiation sources must have instruments that can measure the radiation from the source(s) and must provide personnel monitoring devices, such as film badges, ring badges, or thermoluminescent dosimeters (TLDs), to monitor the dose that personnel receive who work where they may be exposed to radiation from the source(s) that exceeds 10% of federally established limits. A personnel dosimeter badge is worn only by the individual to whom it is issued and, when not being worn, it is stored where it will not be exposed to radiation. This badge provides a record of radiation exposure for evaluating potential adverse effects and for ensuring that no worker exceeds established limits, such as the annual total body effective dose equivalent limit of 5 rem. Federally established limits in the United States of America can be found in the US Code of Federal Regulations, 10 CFR 20.

1. RADIATION MONITORING IN NUCLEAR POWER PLANTS

Radiation-monitoring (RM) systems are installed in nuclear power plants to satisfy U.S. Nuclear Regulatory Commission (USNRC) regulations and plant operating license requirements. The objective of those requirements is to protect both personnel and the environment from the effects of ionizing radiation. An installed system measures, displays, and records the presence and level of radiation and alerts plant personnel to excessive levels of radioactivity, and control actions are initiated automatically for required functions when levels exceed their limits.

Monitoring radiation in nuclear power plants is often divided into categories according to application. Typical categories include area monitoring [1] for determining radiation levels in areas where personnel may be working or may have a need to enter; process monitoring [2,3] for determining radiation levels in processes in the plant; effluent monitoring [4] for determining amounts of radiation leaving the plant through any pathway; and perimeter monitoring for identifying any increase in radiation level at the perimeter of a plant. Both process monitors and effluent monitors can be further separated in two categories according to whether they monitor a gaseous stream or a liquid stream. The instruments can be grouped according to the design as area γ -ray monitors, liquid monitors, and atmospheric gaseous, particulate, or iodine monitors.

A typical radiation-monitoring instrument has many functions to perform: it may detect, display, and record levels of radiation in the plant and provide alarms when

selected radiation levels are exceeded; it may monitor process flow lines for detecting radioactive leakage; it may monitor effluent for recording radioactivity levels and inhibiting excessive releases from the plant; it may provide signals for control functions in other systems; it may provide samples for analysis for complying with USNRC Regulatory Guide 1.21; and it may provide postaccident monitoring in accordance with the requirements of NUREG 0737.

Electrical equipment in nuclear power plants is separated into safety categories according to the functions performed in order to establish quality requirements for procurement, installation, operation, and maintenance. The typical categories are *safety-related* and *non-safety-related*. The safety-related category implies that the equipment is essential to ensure the integrity of the reactor-coolant pressure boundary, the capability to shut down the reactor and maintain it in a safe shutdown condition, or the capability to prevent or mitigate the consequences of accidents that could result in potentially major offsite exposures to the public. Safety-related equipment has the highest quality requirements and must not cease to perform its functions when any single credible failure occurs with the equipment. Other categories are introduced for postaccident monitoring equipment that must operate following a design basis accident. (The *design basis accident* for a nuclear power plant is the worst credible accident postulated for the plant for the purpose of evaluating risks and potential hazards associated with siting the plant.)

Most radiation-monitoring instrumentation is typically classed as nonsafety related, with some specific instruments identified either as safety-related or as postaccident monitors [5] that may have quality requirements similar to safety-related equipment. Requirements for safety-related equipment typically include demonstrated performance under normal and extreme service conditions and installation of redundant channels that are powered from redundant, safety-related power sources. Each channel may also be required to have demonstrated capability of performing its function under design basis service conditions following a design basis earthquake.

The USNRC has established the Standard Review Plan (SRP) [6] as a guide for reviewing designs of nuclear power plants against requirements, including a review of radiation-monitoring systems. An owner of a nuclear power plant provides a safety analysis review to respond to all points of the SRP. The installed RM system must meet the commitments made in the final safety analysis review and the requirements of documents referenced therein.

2. SYSTEM OVERVIEW

A nuclear power plant must have radiation monitors installed at strategic locations throughout the plant for monitoring radiation levels in order to meet regulatory requirements. In addition, laboratory instruments are used for analyzing collected samples of liquids or gases, and portable or handheld instruments are used for making surveys. Chemistry or health physics group members typically observe and record continuous radiation-monitor

channels, but they typically rely on collecting and analyzing samples of effluents for final determination of the off-site dose, and likewise they rely on portable instruments for confirming radiation levels where people are working. Effluent samples are analyzed in laboratory instruments that measure ionizing radiation with excellent energy resolution for identifying the radioactive isotopes contained in the samples. These analyzers typically employ cryogenically cooled germanium detectors.

The descriptions of radiation-monitoring instruments contained herein relate to instruments installed in nuclear power plants for continuous monitoring and do not include laboratory or handheld instruments. The installed systems typically monitor magnitudes of radiation and initiate alarms when radiation levels approach established setpoints; however, because of the need to operate continuously in the plant environment, the energy resolution of the detectors is much poorer than what is available with laboratory instruments.

Analog RM systems usually have a detector installed at each location where radiation levels are to be monitored with a small amount of signal-conditioning electronics, and the detectors are connected by long instrumentation cables to a cabinet at the reactor control room in which are installed signal-conditioning electronics, alarms, readout devices, and power supplies associated with each detector.

Digital RM systems are typically distributed computer systems that include a microcomputer and required power supplies located at or near each detector location, and a communication cable connects that location to a central computer at the control room and at a health physics office or other location where the information is to be used. The communication cable is usually a simple twisted-shielded pair cable.

Typical locations in a pressurized-water reactor (PWR) nuclear power plant where area monitors may be installed include the control room, radiochemical laboratory, hot machine shop, sampling room, reactor-building personnel access, refueling bridge, in-core instrumentation area, fuel storage area, auxiliary-building-demineralizer area, waste-gas-decay-tank area, drumming area, waste-hold-up-tank area, charging-pump area, turbine-building area, and main steam lines.

Typical monitoring points for gaseous process monitors include reactor-building-containment area for airborne gaseous and particulate monitoring, radioactive-waste-disposal-area vent, waste-gas header, fuel-handling-area vent, and control room for airborne gaseous and particulate monitoring. Monitoring points for liquid process monitors may include chemical- and volume-control-system-letdown line, radioactive-waste-condensate return, component cooling water, normal-sample-laboratory isolation, and main steam lines.

Gaseous effluent monitoring may be performed in the plant vent stack, in the condenser air ejector, and in the containment purge stack. Liquid-effluent monitors are typically installed in the radioactive-waste discharge line, in the neutralization sump discharge line, in the turbine plant area sump, and in the steam-generator blowdown. The locations listed above are typical for a PWR plant but may be different in each plant.

3. SOURCES OF RADIOACTIVE MATERIAL

The primary sources of radioactive material in light-water-cooled nuclear power plants are the fission process in the reactor core and neutron activation. The fission process, the splitting of uranium atoms, emits neutrons, γ rays, and β particles directly and creates radioactive elements in the fuel-pellet regions. Those radioactive materials then decay primarily by emission of γ and β radiation.

Neutron activation occurs whenever any atom absorbs one of the neutrons that is emitted from a splitting uranium atom. The absorbing atom gains atomic weight, thus becoming a new isotope of the same element, which may be unstable or radioactive and decay to a more stable state by emitting radiation. Neutron activation creates radioactive material in the fuel-pellet region; in the reactor-coolant region; in support structures, reactor vessel, and piping; and in the regions surrounding the reactor vessel, including the air in that vicinity. In addition to neutron activation, some atoms may be activated by particle radiation emitted from fission products or from neutron-activated elements.

The plant is designed to keep radioactive material contained; however, if systems become unsealed, some radioactive material may leak into the coolant through the fuel cladding, then from the reactor coolant through the pressure boundary or from coolant purification and radioactive-waste processing systems into secondary systems. It is this leakage that radiation-monitoring systems are expected to detect during normal reactor operation. γ rays and β particles are the forms of radiation that are most readily detected.

The concentration and quantities of radioactive material in various regions of the plant depend on the balance among production, leakage, and removal of individual isotopes. In the fuel-pellet region, production processes include fission-product production directly from fissioning uranium atoms, parent-fission-product decay, and neutron activation. Removal processes include decay, neutron activation, and leakage through cladding defects into the coolant. In the coolant region, production processes include (1) leakage of fission and activation products from the fuel-pellet region and from fuel cladding and core structures, (2) parent decay in the coolant, and (3) neutron activation in the coolant materials. Removal is by decay, by coolant purification, by feed and bleed operations, and by leakage. The most abundant isotopes in the coolant are radioactive noble gases (^{85}Kr , ^{133}Xe , and ^{135}Xe during normal operation) and radioactive halogens (in particular ^{131}I).

Neutron activation leads to two isotopes of particular interest, ^{16}N and ^{14}C . ^{16}N is produced by a neutron-proton reaction with ^{16}O and decays by higher-energy γ -ray decay with decay energies of 6.1 and 7.1 MeV. The half-life of ^{16}N is 7.3 s. While there is substantial decay of ^{16}N as it exits from the core and passes through the turbine, it must still be considered in the design of the turbine shielding for boiling-water reactors (BWRs). The detection of ^{16}N in the secondary side of PWRs may be used to monitor changes in steam generator leakage. ^{14}C is produced by neutron activation of ^{17}O and ^{14}N .

The principal generation of tritium (^3H) is from fission and neutron interaction with boron, lithium, and deuterium. The main leakage source is fission tritium released through fuel-cladding defects. Tritium produced in the coolant contributes directly to the tritium inventory, while tritium produced in control element assemblies contributes only by leakage and corrosion.

Activation and corrosion of reactor core support structures produce corrosion products, forming a radioactive material commonly referred to as *radioactive crud*. Corrosion product constituents are typically ^{60}Co , ^{58}Co , ^{54}Mn , ^{51}Cr , ^{59}Fe , and ^{95}Zr .

3.1. Leakage Sources

Any system containing radioactive materials in liquid form is a potential source of radioactive leakage, and radioactive leakage into the reactor-containment area comes from the reactor-coolant system and coolant purification systems. Leakage from systems containing potentially radioactive liquids is collected and processed by liquid radioactive-waste systems. Noble gases that are dissolved in liquid leakage may go out of solution and into the local atmosphere.

Radioactive material can be released into effluents from secondary systems due to leakage. For PWRs, the amount of release depends on reactor-coolant radioactive material concentrations, reactor-coolant leakage rate, primary to secondary leakage rate, steam-generator blowdown rate, and secondary-system leakage rates. Abnormal leakage from the fuel region to the reactor coolant is commonly detected by monitoring the reactor-coolant-system (RCS) letdown stream, either continuously or on a sampling basis.

In PWRs, reactor coolant remains liquid under pressurization in a primary coolant loop and transfers its heat through a heat exchanger to a secondary coolant loop that is converted to steam in the steam generator. The secondary system is typically monitored on steam generator blowdown, component-cooling-water, and liquid-radioactive-waste-processing systems to check for leakage from primary to secondary coolant loops.

In BWRs, reactor coolant is converted directly to steam for use in the steam turbine. γ radiation levels external to the main steam lines are monitored to detect increased levels of radiation in the reactor coolant that may indicate problems such as significant fuel-cladding failure. A fuel-cladding failure would allow fission products, particularly noble gases, to be transported to the steam lines, which could cause the radiation level external to the steam lines to be well above normal background levels.

In both PWRs and BWRs, condenser exhaust is monitored.

3.2. Reactor-Coolant-System Leakage Detection

An increase in reactor-coolant-system leakage rate in a nuclear power plant of 1 gal/min must be identifiable within 1 h. USNRC Regulatory Guide 1.45, *Reactor Coolant Pressure Boundary Leakage Detection System*, outlines the means required for monitoring RCS leakage and indicates that this function must be provided also following

a design basis earthquake. Three required means of monitoring leakage rate are (1) sump level and flow monitoring, (2) airborne-particulate radioactivity monitoring, and (3) either monitoring condensate flow rate from air coolers or monitoring airborne-gaseous radioactivity.

The sump flow rate and airborne-particulate channels are found to be capable of indicating an increase in RCS leakage of 1 gal/min within 1 h under most operating conditions. However, airborne-gaseous monitoring was found to have a much longer response time. This shortcoming was identified generically in a USNRC staff memorandum and is mainly due to the long half-life of ^{133}Xe , the major noble gas in the RCS, and the background radiation level from ^{41}Ar , which is created by neutron activation of air around the reactor vessel. Most RM systems use gross energy measurement methods for RCS leakage detection. Potential leakage-detection improvements using spectral capabilities of new γ -ray sensitive detectors for particulate and gaseous monitoring have been predicted, which might allow specific isotopes to be measured and separated from background radiation.

3.3. Liquid Effluent

Liquid-waste systems in a nuclear power plant collect and process radioactive liquid wastes generated during plant operation and reduce their radioactivity and chemical concentrations to levels of clean water acceptable for being discharged to the environment or recycled in the plant. Radioactivity removed from the liquids is concentrated in filters, ion exchange resins, and evaporator bottoms, and these concentrated wastes are sent to a radioactive-waste solidification system for packaging and eventual shipment to an approved offsite disposal location. If the water is to be recycled to the reactor-coolant system, it must meet the water-purity requirements for reactor coolant. If the liquid is to be discharged, the activity level must be consistent with the discharge criteria of the U.S. *Code of Federal Regulations*, 10CFR20. These liquids normally pass through liquid radiation monitors prior to being recycled or discharged.

4. UNITS OF MEASURE IMPORTANT TO RADIATION MONITORING

Becquerel	The becquerel (Bq) was adopted in 1975 as unit of measure of activity, which is the measure of the rate of decay of a radioisotopic source. 1 Bq is one disintegration per second.
Curie	The curie (Ci) is a measure of the activity or number of disintegrations per second of a radioactive source. It was originally an estimate of the activity of 1 g of pure radium-226. 1 Ci is 3.7×10^{10} disintegrations per second (Bq).
Gray	The gray (Gy) is a measure of absorbed dose. 1 Gy is 1 joule per kilogram, or 100 rad.
Rad	The rad is a measure of absorbed dose in units of energy per unit mass of the absorbing material. 1 rad is 100 ergs per gram. The magnitude of dose will depend on material

properties as well as on the radiation source. Air is typically used as the basis of measurement. When water is substituted for air, the absorbed dose is nearly the same because the atomic number of water is nearly the same as for air.

Rem	The rem is used to measure the effect of radiation on living organisms and was derived from the words <i>radiation equivalent in man</i> and is equal to the absorbed dose times a quality factor, Q . For γ rays and β particles, $Q=1$ and 1 rem is equal to 1 rad. For charged particles, Q is much larger than 1.
Roentgen	The roentgen (R) is a measure of γ -ray exposure in terms of the charge due to ionization by the exposing radiation in a unit of mass of the material. 1 roentgen is 1 electrostatic unit of charge in 1 cubic centimeter of air at standard temperature and pressure.
Sievert	The sievert (Sv) is a measure of the effect of radiation on living organisms and is equal to 100 rem.

5. TYPICAL DETECTORS AND MONITOR TYPES

5.1. Area Radiation Monitors

Area radiation monitors continuously measure radiation levels at various locations within nuclear power plants including reactor-containment-building work areas and fuel-storage facilities for ensuring personnel safety. Area monitors have historically used Geiger-Muller (GM) tubes, ionization chambers, or scintillation crystals coupled to photomultiplier (PM) tubes, depending on the manufacturer and the sensitivity or range requirements. A block diagram of a typical GM-tube-based area monitor is shown in Fig. 1.

In a GM tube [7] an avalanche breakdown occurs in the gas in the tube each time ionizing radiation is detected and then self-extinguishes. The magnitude of the resulting signal (an electronic pulse) is independent of the number of original ion pairs that initiated the process and therefore independent of the energy of the detected ionizing radiation. The electronics in a GM-tube-based area monitor senses these pulses and converts them to a signal that is proportional to their rate of occurrence. However, present-day GM-tube monitoring systems use energy-compensated GM tubes for which the number of counts detected is nearly proportional to the total energy absorbed.

Thin-walled GM tubes used for area monitors are normally energy compensated for a linear response or $\pm 20\%$ or better for γ -ray energies of 60 keV–1.25 MeV. The filter is designed to attenuate the lower-energy γ rays below approximately 100 keV and to increase the responses of higher-energy γ rays by the effect of the high- Z material used for the filter. This energy-compensation effect is due to the complex contribution of primary photon transmission or attenuation and secondary-particle production or attenuation at various depths in the GM-tube wall or outer energy filter [8].

In an ionization chamber [9] ionizing radiation is absorbed in the gas in the chamber, and the number of electron-ion pairs thus created is proportional to the energy of the absorbed radiation. The bias voltage on the ionization chamber sweeps the charge carriers to the electrodes, causing an electrical current to flow, and external circuitry typically measures the magnitude of the current from this ionization process. The current output signal from an ionization-chamber-based area monitor is proportional to the energy of the radiation absorbed in the gas in the chamber in the γ -ray flux field. These area radiation monitors are often calibrated in units of R/h.

When ionizing radiation is absorbed in a scintillator, a light pulse is produced. In turn the light pulse is converted into an electrical pulse in a PM tube that is optically coupled to the scintillator. Over a broad range of energies, the amplitude of the electrical pulse is proportional to the energy of the absorbed radiation. In a scintillator-based area monitor the output signal is proportional to the number of absorbed-radiation events in the detector and independent of energy if the electronics just counts events and provides a count-rate output signal. If the current from the PM tube is measured, the signal will be proportional to the energy of the absorbed radiation.

A typical pulse-counting area monitoring may have a range from 1 to 100,000 counts per minute. A typical ionization-chamber-based area monitor may have a range from 10^{-10} to 10^{-3} A, corresponding to a range from 1 to 10,000,000 rad/h. This high range may be used for applications such as postaccident monitoring inside containment.

5.2. Process Monitors

Process monitors provide information about radiation levels within the nuclear power plant's liquid, steam, and gaseous processing and storage systems. Liquid monitors may have the detectors mounted in the liquid or steam line or may have them mounted offline with a sample

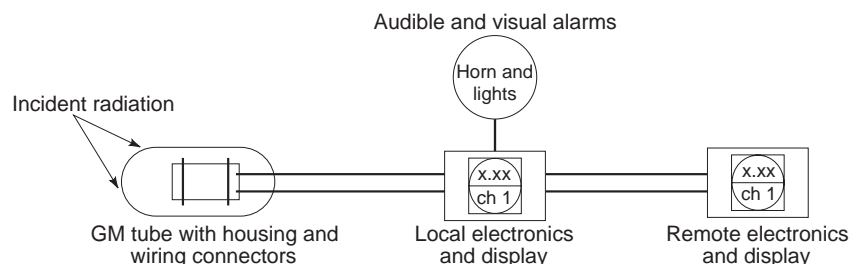


Figure 1. Typical block diagram of an area radiation monitor.

stream taken from the main line and flowing through the detector sample chamber. Gaseous monitors too can have the detectors mounted in the stream or in a sample chamber. If the monitor is in a sample chamber, the gas to be monitored, which could be from a duct or from an open area such as the control room, passes through that sample chamber.

Process monitors typically measure radiation levels that are far below normal background levels, and, as a result, the detectors must be shielded from all external sources of radiation.

5.3. Effluent Monitors

Effluent monitors are similar to process monitors except that they monitor liquid or gaseous streams that leave the nuclear power plant boundary and may transport radioactivity.

The monitors described below are applicable to both process and effluent monitors according to the application to which they are dedicated.

5.3.1. Airborne Monitors

5.3.1.1. Off-Line Particulate and Noble-Gas β -Particle Scintillation Detectors. The β -particle sensitive particulate and noble-gas monitors incorporate plastic scintillators coupled to PM tubes. The gas-detector assemblies are of similar construction. These detectors use similar entrance windows, plastic scintillators, light pipes, and PM tubes. A typical particulate detector is built up from a plastic scintillator coupled to a PM tube and a 0.001-in.-thick aluminum entrance window used for β -particle detectors.

During original prototype evaluation, detectors are tested with solid β -particle sources to obtain a high signal-to-noise ratio when setting the discrimination level. Without changing the detector's alignment, responses are then obtained for calibrated solid or gaseous β -particle sources. The solid alignment sources are serialized and kept for future use. These sources are used for aligning production detectors and prototype detectors prior to isotopic calibration. After alignment of a production monitor to the same counting efficiency as the prototype detector that uses the same solid source, the production and prototype monitors have nearly identical responses to radioactive gases in the sample chamber or to activity on the filter.

After a monitor has been calibrated at a factory and shipped to a customer, corrections to the calibration may be required to account for atmospheric pressure affects because the response of the detector to β -particle radiation in the sample chamber is determined, not only by the total activity in the sample chamber, but also by self-absorption in the sample gas, which changes with gas pressure.

5.3.1.2. High-Temperature, Inline, Noble-Gas, β -Particle Scintillation Detectors. These detectors are designed to operate at high temperatures and to be installed directly into an airduct. The detector assemblies are similar to the off-line β -particle scintillation detectors with the following exceptions.

A thin (0.007-in.-thick) CaF_2 (Eu) crystal or a high-temperature plastic scintillator (0.010 in. thick) and a quartz light pipe are used in place of the plastic scintillator with a Lucite light pipe, and a high-temperature PM tube is used. These detectors use the same 0.001-in.-thick aluminum entrance window as do the other β -particle detectors. Prototype detectors are aligned using the same methods described for the offline β -particle scintillator. After alignment, a prototype detector is installed into a test fixture to simulate the geometry of the intended installation.

5.3.1.3. Iodine Detectors. Detectors used for the iodine channels normally consist of a 2-in.-diameter by 2-in.-long sodium iodide crystal with a 2-in.-diameter photomultiplier tube. The detectors are typically specified to have a maximum resolution of 8% for a 662 keV cesium-137 photopeak and may be supplied with an americium-241 pulser for pulse height stabilization.

The electronics associated with a typical iodine channel has an energy-window discriminator with adjustable lower and upper thresholds. When the amplitude of a pulse signal from the detector lies between the lower and upper thresholds, the signal is counted as a valid event. The typical output is the number of events per unit time that fall within the energy window.

Since each detector has its own resolution and the system is operating as a single-channel analyzer, each detector's response will be unique. The response from a calibrated simulated iodine-131 source (barium-133) for each detector may be used when calculating the individual detector's expected responses for iodine-131. Upon completing the alignment of the iodine channel as a single-channel analyzer on the 356 keV photons of barium-133, the window will need to be readjusted to be centered on the 364 keV photons of iodine-131.

A typical pulse height stabilizer consists of a small sodium iodide crystal. The doped crystal provides a constant source of γ -ray equivalent energy (GEE) in the form of light pulses. The light pulses are detected by the PM tube and converted to an electrical pulse by the PM tube and the preamplifier. The GEE is produced from an americium-241 5 MEV α -particle decay in the pulser crystal. These high-energy light pulsers are attenuated to an equivalent light energy of a 3 MEV γ -ray decay at the time the pulser crystal is imbedded into the mother crystal.

A typical preamplifier may contain three window circuits as shown in Fig. 1. One window is used to monitor the americium-241 stabilization signal from the detector, one is used to monitor the iodine peak, and one is used to monitor the background level at energies just above the iodine window. By monitoring the known stabilization source, compensation can be made for instabilities, such as from temperature variations in the gain of the PM tube and preamplifier. The background window can be used for active background subtraction.

5.3.1.4. Particulate, Iodine, and Noble-Gas Monitor. Often the measurement of airborne-particulate radiation, radioactive iodine, and radioactive noble gas is combined

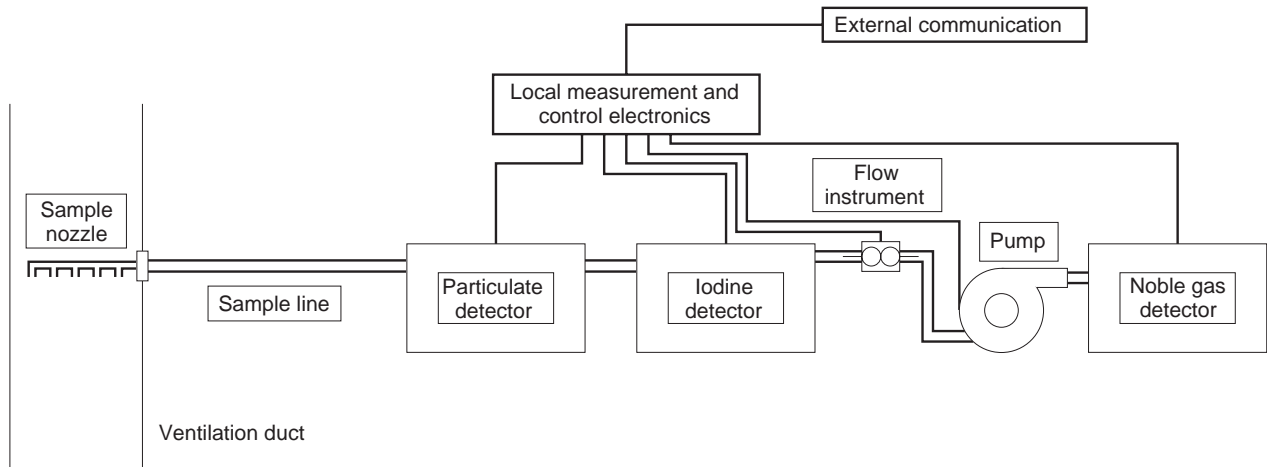


Figure 2. Block diagram of an airborne-particulate, iodine, and noble-gas monitor.

into a single instrument for such applications as airborne containment-building or vent-stack monitoring. A typical block diagram for such an instrument is shown in Fig. 2.

5.3.1.5. Typical Postaccident-Effluent, Wide-Range, Gas Monitor. A stack gas monitor typically is mounted near the nuclear power plant vent stack and receives a sample of the gas in the stack, which has been collected with isokinetic nozzles mounted in the stack. A normal-range monitor would be constructed as described previously and may cover a range of about five decades. A wide-range gas monitor may cover a range of about 12 decades through the use of multiple detectors.

An isokinetic nozzle is used to sample the air in the stack because, by keeping the velocity of the air entering the nozzle the same as the velocity of the gas bypassing the nozzle, a more representative sample of gas should be obtained for analysis in the monitor.

The low-range detector may be a β -particle scintillator and the preceding description applies. The mid- and high-range detectors may be solid-state detectors of a material such as cadmium telluride.

5.4. Liquid Monitors

Liquid monitors typically employ a sodium iodide scintillator coupled to a PM tube to measure γ radiation in the liquid stream. The liquid monitor may be mounted in-line with the stream to be monitored, or a sample stream may be extracted from the main stream and routed through a sample chamber into which the detector of the offline liquid monitor is mounted.

An in-line liquid monitor typically is bolted directly into the liquid line with flanges on each end of the section of pipe that passes through the monitor. The monitor consists of a section of inline pipe, a detector mounted adjacent to the pipe, and lead shielding surrounding the pipe and detector to prevent radiation from the surrounding area from entering the detector.

An off-line liquid monitor typically has a sample chamber into which the detector is inserted, and liquid enters and leaves the sample chamber through small-diameter

pipes. Lead shielding surrounds the sample chamber and detector to prevent radiation from the area around the monitor from entering the detector.

The volume of water near the detector in a liquid monitor causes Compton scattering of the radioactivity in the liquid so that the signal seen by the detector includes not only the primary γ -ray energies but even more lower-energy signals from scattering of the primary photons. Therefore, there is typically no effort to distinguish specific energies of radiation in a liquid monitor.

5.5. Perimeter Monitors

Many nuclear power plants put radiation monitors around the perimeter of the plant site to measure dose levels at the site boundary. Communication with these monitors is often achieved by telephone lines or radio transmission. Perimeter monitors are typically high-sensitivity area monitors. At least one vendor has provided large-diameter, high-pressure ionization chambers and another vendor offers energy-compensated GM tubes. Typically requirements include an on-scale reading at normal background levels, a wide range for detecting significant radiation releases, and battery backup to avoid loss of data during a power outage.

6. MONITOR-PERFORMANCE PARAMETERS

In order for the monitors in the RM system to perform their required functions, they must operate within specific bounds of range, sensitivity, accuracy, and response time. The range is usually described in terms of the smallest and greatest magnitudes of activity or concentration for which the output signal is a valid representation and the radiation energies that may be included in the measurement. Sensitivity is a statement of how the output signal responds to a change in the measured variable. Accuracy is a measure of the uncertainty in the output signal. And response time is a measure of the length of time required for the output signal to change as a result of a change in the measured variable.

6.1. Range and Sensitivity

The range of an instrument may be limited on the low end by noise or by instrument precision and accuracy or it may be established by the scale and levels set for the output signal. The upper end of the range may be limited by the linearity or saturation characteristics of the detector or instrument.

The scales of most radiation monitors are logarithmic, and the span of an individual radiation channel is typically 5 decades. A decade is a factor of 10, so that a scale from 1 to 100,000 is 5 decades. The American National Standards Institute (ANSI) Standard N42.18 Section 5.4.2 recommends that the span be at least four decades above the minimum detectable level (MDL). Spans of more than six decades often require the use of multiple channels with overlapping ranges. Guidance for selecting the ranges for specific monitors is provided in ANSI N42.18 and ANSI/ANS-6.8.2 for effluent monitors, in ANSI/ANS-6.8.1 for area monitors, and in Regulatory Guide 1.97 for postaccident monitors.

For monitors that measure the concentration of radioactivity in gases or liquids, range and sensitivity are normally specified for a certain isotope or a distribution of isotopes as opposed to being specified over an interval of radiation energies. For monitors that measure dose rate, range, and sensitivity are normally specified over an interval of radiation energies.

Sensitivity is normally determined by the characteristics of the detector. For monitors that measure dose rate, the sensitivity is often given as the ratio of the change in output signal to the change in radiation level that caused the signal to change, for example, for an ionization chamber, sensitivity is normally given in units of (A)/(R/h) or for a GM-tube-based area monitor, the sensitivity is usually given in units of (cpm)/(R/h), where cpm is counts per minute. For monitors that measure concentrations of radioactivity, the sensitivity is normally stated as the minimum detectable signal, which is a function of the detector characteristics, the effectiveness of radiation shielding, and the magnitude of background radiation.

6.1.1. Direct Measuring Instruments. A radioactive material concentration estimate A for a direct measurement is given by

$$A = \frac{y - \text{Bkg}}{R_d}$$

where y is the detector response to the concentration A plus the background, Bkg is the detector response to background, and R_d is the detector response per unit of concentration. A direct measurement is, for example, measurement of a gas or liquid volume in a fixed geometry. Typical units for y and Bkg are counts per minute, and typical units for R_d are counts per minute per $\mu\text{Ci}/\text{cm}^3$.

The uncertainty in the concentration estimate due to counting statistics alone depends on the magnitudes of the total count and of the background count during some fixed time. The uncertainty due to counting statistics is then

translated into an uncertainty in the concentration estimate by dividing by detector response.

The maximum sensitivity represents the lowest concentration of a specific radionuclide that can be measured at a given confidence level in a stated time (at a given flowrate, where applicable) under specific background radiation conditions (see ANSI 42.18, Section 5.3.1.4). The maximum sensitivity is commonly termed *minimum detectable level* (MDL) and is defined in terms of the uncertainty in interferences (termed *background* in radiation detection) and the response of the radiation detector:

$$\text{MDL} = \frac{C_L s_b}{R_d}$$

where C_L is the confidence level desired in the measurement (unitless) and s_b is the background uncertainty in units of the detector output (e.g., counts per minute).

A MDL that is termed *minimum detectable concentration* (MDC) is based on ANSI N42.18:

$$\text{MDC} = \frac{2s_b}{R_d}$$

Another MDL is termed *lower limit of detection* (LLD) [10].

$$\text{LLD} = \frac{4.66s_b}{R_d}$$

6.1.2. Indirect Measuring Instruments. Radiation monitors that view a medium through which a sample has been drawn (e.g., particulate channels that monitor the radiation buildup on a filter) have additional characteristics for the establishment of range.

Detector response is stated in terms of output per unit of activity deposited on the filter medium. The quantity of activity on the filter for isotopes with half-lives much longer than the sample collection time is the product of concentration A times sample flowrate f times the sample collection time T . Then the concentration estimate becomes

$$A = \frac{y - \text{Bkg}}{R_i f T}$$

where R_i is the detector output per unit activity on the filter [e.g., (counts per minute)/ μCi]. Then

$$\text{MDC} = \frac{2s_b}{R_i f T}$$

and

$$\text{LLD} = \frac{4.66s_b}{R_i f T}$$

A specification of sensitivity also establishes the level above which the setpoint value should be established. Set points should be well above MDLs in order to avoid spurious alarm/trip outputs due to statistical fluctuations in the measurement. See ANSI/ANS-HPSSC-6.8.2, Section 4.4.8.

Ambient background radiation is specified in order to determine the quantity of shielding required around the radiation detector, and this specified ambient level should be greater than the levels expected during plant operation. Detector-assembly performance can be stated in terms of detector response per unit background radiation for a specified isotope.

6.1.3. β -Particle Detectors for Airborne-Radiation Monitoring. Airborne effluent is frequently monitored by drawing a sample from the effluent stream into a lead-shielded sample chamber. The sample chamber is viewed by a detector with a thin (around 0.010 in.), predominantly β -particle-sensitive detector, since nearly all noble gases emit 1 β particle per disintegration.

β particles that are in excess of several hundred keV will lose about 100 keV for entrance normal to the detector face. The lower discriminator must be set above noise in the detection system. The upper discriminator needs to be open ended or set above 500 keV due to the high-energy tail of the energy distribution deposited by the β particles. This energy straggling for β particles results from infrequent, large-angle scattering by which the β particle can lose up to one half of its initial energy [11].

The decays per disintegration are the first factor in determining the response of a detector. The isotopic distribution of radioactive elements during normal reactor operation is significantly different from that postulated for accident releases. The use of a β -particle-sensitive detector has the advantage that the number of β particles per disintegration changes little from normal operation releases to the release postulated under accident conditions. γ -ray-sensitive detectors are at a disadvantage because the number of γ rays released per disintegration rises dramatically from normal operation to postulated initial-accident conditions and drops as noble gases decay. The element seen in normal operation is predominately ^{133}Xe , which undergoes γ -ray decay about 35% of the time. Initial-accident noble gas yields around 2 γ rays per disintegration.

6.2. Over-Range Condition

An RM instrument should operate over its range within the required accuracy, and when radiation levels are significantly above the range (above full scale), the instrument must survive and continue to present an appropriate readout. When an instrument is in an over-range condition, it is important that the instrument output not fall below full scale with input levels up to 100 times greater than full scale.

Count-rate circuits are typically limited in their maximum counting rates by the resolving time required to distinguish two consecutive input pulses. That resolving time is sometimes referred to as *deadtime*, and if a second pulse occurs during the deadtime, it is missed and not counted. This is sometimes referred to as count-rate loss due to pulse pileup. If count-rate loss gets so severe that the output actually decreases while the input is still increasing, the condition is called *foldover*. Radiation emission from radioactive atoms is a random process and has a

Poisson statistical distribution. The resolving time of most count-rise instruments is equal to or greater than the width of the incoming pulse. As the input rate increases, the count-rate loss will increase until the output goes into saturation or even foldover. In some instruments, very high input rates have been able to freeze the circuit and cause the output rate to go toward zero. Such instruments are sometimes referred to as “paralyzable” and those that overcome this failing as “nonparalyzable.”

The instrument output count rate n can be calculated, as shown by Evans [12], from the input rate N and the instrument dead time p , during which the circuitry cannot respond to a second input pulse, by the equation

$$n = Ne^{-Np}$$

A useful method for estimating count-rate loss for a system that obeys Poisson statistics is to use the following approximation: when the output count rate is $A\%$ (any value below 10%) of the frequency represented by the inverse of the dead time, $1/p$, the instrument has a count-rate loss of approximately $A\%$.

Many design methods have been used to eliminate or reduce the effects of foldover and prevent the output of an instrument from going below full scale when the input levels are above full scale.

6.3. Accuracy

The definition of accuracy from ANSI Standard N42.18 is “The degree of agreement [of the observed value] with the true [or correct] value of the quantity being measured.” Accuracy cannot be adjusted nor otherwise affected by calibration. It is a performance specification against which a channel is tested. For channels with multiple components, the individual accuracies are combined as part of the overall accuracy.

Accuracies, for monitors measuring concentration-related quantities, are normally specified for a certain isotope or a distribution of isotopes as opposed to radiation energies. Accuracies for monitors measuring dose rate are normally specified over an interval of radiation energies.

ANSI Standard N42.18, Section 5.4.4, provides a guideline that the instrument error for effluent monitors should not exceed $\pm 20\%$ of reading over the upper 80% of its dynamic range.

6.4. Response Time

For safety-related equipment, system response times used in safety analyses include the response times of the individual subsystems performing the protective function. This typically consists of instrument response time and mechanical system response time. The system response time must be allocated among the subsystems.

For a radiation monitoring channel, the response time depends on the initial radiation levels, the increase in radiation level as a function of time, and the channel setpoint.

ANSI Standard N42.18 recommends that radiation-monitoring-channel response time be inversely proportional to the final count or exposure rate. This characteristic

RADIO BROADCAST STUDIO EQUIPMENT

WALT LOWERY
Symetrix, Inc.

comes naturally with analog count-rate circuits. The time constant is typically established by a resistance and a capacitance in the feedback path of an operational amplifier, and for logarithmic circuits the resistance is typically the forward resistance of a diode at its current operating point. A factor of 10 increase in count rate will typically make the time response a factor of 10 faster. And, in these type circuits, if the change in input activity is a step function, the time response will be strictly a function of the end point and will not be affected by the starting point. Digital circuits, including software algorithms, are typically designed to emulate the time response of their analog counterparts. Thus fast response times can be provided at high radiation levels and longer response times at lower levels. Both types of circuits usually offer the ability to adjust the time constant to match requirements of the application.

Slow response times are needed to provide stable, smoothed outputs at the low end of the range. ANSI Standard N18.42 recommends that response times at low radiation levels should be long enough to maintain background readings within the required accuracy.

BIBLIOGRAPHY

1. ANSI/ANS Publication HPSSC-6.8.1-1981, *Location and Design Criteria for Area Radiation Monitoring Systems for Light Water Nuclear Reactors*.
2. ANSI/ISA S65.03-1962, ANSI Standard *Standard for Light Water Reactor Coolant Pressure Boundary Leak Detection*.
3. USNRC Regulatory Guide 1.45, *Reactor Coolant Pressure Boundary Leakage Station Systems*.
4. American National Standards Institute Standard ANSI N42-18, *Specification and Performance at On-Site Instrumentation for Continuously Monitoring Radiation in Effluents*.
5. The requirements for postaccident monitoring equipment are outlined in USNRC Regulatory Guide 1.97, Revision 3, and NUREG 0737.
6. USNRC NUREG 0800, *Standard Review Plan*, Sects. 11.5, 12.3, and 12.4.
7. G. F. Knoll, *Radiation Detection and Measurement*, Wiley, New York, 1979, Chap. 7.
8. D. J. Allard and A. M. Chabot, The N-16 gamma radiation response of Geiger-Mueller tubes, *Health Phys. Soc. Annu. Meet.*, Washington, DC, 1991.
9. G. F. Knoll, *Radiation Detection and Measurement*, Wiley, New York, Chap. 5.
10. USRCC NUREG/CR-4007, *Lower Limit of Detection: Definition and Elaboration of a Proposed Position for Radiological Effluent and Environmental Measurement*, 1984.
11. N. Tsoulfanidis, *Measurement and Detection of Radiation*, Hemisphere Publishers, New York, 1983, Chap. 13.
12. R. D. Evans, *The Atomic Nucleus*. New York: McGraw-Hill, 1955, p. 785.

FURTHER READING

N. P. Alazraki and F. S. Mishkin, eds., *Fundamentals of Nuclear Medicine*, Soc. Nuclear Medicine, New York.

The quality of a broadcast station's only distributed product, its sound, is determined by the events taking place in the studio. The best source material and the best air talent will produce only marginal results when burdened by inadequate equipment. Even in television, audio can no longer be treated as a secondary technology. State-of-the-art equipment, properly used in the studio, equates to ratings and translates to revenue for the station.

This article describes the equipment and operation of audio facilities used in radio and television studios. First is an overview of typical studio layout and a discussion of the major components used in an audio facility. This article provides the novice engineer with guidance for the design and construction of a studio suited for the station's needs. We also make the leap to digital audio equipment and investigate the new terms and standards destined to change studio operations forever.

Broadcast studios now take advantage of digital audio source material, digital audio processing equipment, and now digital consoles. A major manufacturer recently introduced a digital studio-transmitter link (STL) system that operates without data compression. Just as compact disks (CDs) killed vinyl disks as the standard source material for radio broadcasters over an alarmingly short period of time, digital broadcast equipment is poised to eclipse analog studio systems. We have the potential to reduce the radio studio to a touch-screen computer operation, but the trend in the industry remains loyal to familiar function and feel. Broadcasters prefer their digital equipment to emulate the friendly analog devices that they have used for decades.

1. TYPICAL RADIO STUDIO LAYOUTS

Many stations in active markets have suffered as a result of changes in formats and managers and engineers who have left a crazy quilt of analog and digital equipment. The results have handicapped each station's ability to survive in a competitive market. Programming needs, available space, and creativity of former engineers often dictated the design of a studio. Design du jour, accompanied by galloping changes in technology, leaves many studios ripe for redesign and rebuilding.

The station's current format should dictate the main design parameters. The operational concepts will be much different for a music format than for a news/talk operation. It is possible to catalog radio station studios under a few general categories.

1.1. Music Formats

Studios built for music formats remain the most common, particularly in smaller markets. The basic configuration consists of an audio console, two or more CD players, and multiple cart players all arranged on a U- or L-shaped desk. Other associated equipment might include audio

routing, transmitter remote control, and telephone interface equipment. Careful design places all equipment within arm's reach of the operator. This configuration handles the rather simple programming needs nicely. The announcer on duty mixes and switches audio, reads announcements, plays music from CD players, plays commercials from digital cart players, and switches news and network programming from a satellite receiver.

Some stations transfer music from CD to analog, or digital, cart, making the studio an all-cart operation. In this situation the studio contains four to six cart playback decks and no CD players. Having all program material on cart makes the operation more "idiotproof." The operator needs only to talk, push plastic boxes into slots, and push-buttons.

Going one step further, some stations retrieve their program material from digital audio storage systems. Commercials and music are stored digitally on a hard drive, retrieved when required, converted back to analog audio, and fed to the console. This eliminates the physical handling of any audio storage medium. The operator controls each audio event with keyboard and mouse.

Music formats require positions for one operator and possibly an announcement booth for the newscaster. With the popularity of the zoo format, many large-market stations designed their studios for two or three on-air personalities. One member of the team operates the console, one juggles phone calls and pulls music and spots, and the third handles news. The studio layout varies with the duties handled by each member of the team.

1.2. News/Talk Formats

All-news stations serve up information from live in-studio talent and short-duration feeds from a large number of sources. Here the board operator functions as an engineer rather than on-air talent. Small studios orbit the central control room allowing eye contact between the board operator and on-air talent. The console provides more of a switching function than audio mixing. Live news or talk programs dictate a larger number of console inputs than the typical disk-jockey operation. Digital audio storage systems help this format flow smoothly because the operator is busy enough without the mechanics of handling carts.

Technology now allows replacement of the audio console with a computerized audio switching system. Hard-disk audio storage systems use multiple computers linked to a central network server through a local-area network (LAN). Each studio retains access to all stored program material. The operator sees the log displayed on the screen and can shift events around, control audio source equipment, adjust levels, and even read copy and tags directly from the screen.

Talk formats require a studio for the show host and the on-air guests. A large round table with the microphone booms mounted in the center allows the host and any guests working room plus affords eye contact between them. The show producer operates the mixing console and telephone hybrids in the control room. If not located

in an adjacent room, the show's call screener also shares the space in the control room.

Large-market budgets afford lots of labor power and first-class equipment. A visit to a small-market talk show may reveal the show host running all the control room equipment while talking with callers. The station's telephone receptionist works frantically screening calls and shuttling caller names on yellow sticky notes to the frenzied show host.

1.3. The Production Studio

A separate studio provides an area for commercial production work and transfer of music to a cart or a digital audio storage system. The production studio provides access to CD players, a digital audio workstation, cart recorders, equalization, patch panels, reel-to-reel recorders, and possibly turntables. The production studio provides more flexibility and handles a wider variety of audio media than the on-air studio.

The 4-, 8-, and 16-track consoles and multitrack recorders found in major market production facilities often intimidate the typical disk jockey accustomed only to segueing music and commercials. These consoles feature submaster mixing busses, allowing the mix down of multiple tracks of music, voice tracks, and sound effects, producing complex spots and promos. Special effects and equalization, not needed in the main studios, remain standard fare in production.

Production directors are enthusiastic about digital workstations because they allow editing without razor blades and splicing tape. Digital workstations bring to audio production the speed and versatility that word processing brought to typing. Workstations allow editing of individual tracks, a feat impossible with multitrack reel-to-reel tape editing.

Because all material produced in this studio will eventually be played on the air, the quality of the equipment should be equal to, if not better than, that used in the main studio. Smaller-market stations erroneously tend to scrimp on equipment for the production room. Using hand-me-down and cast-off equipment in the production studio hampers the potential success of the station.

2. TYPICAL TELEVISION STUDIO LAYOUT

Audio for television stations can be challenging because of the need for many types of audio mixes. Multichannel TV sound (MTS) requires a stereo program feed to the transmitter, on-camera talent needs a monitor mix, programs with a studio audience require a mono public address (PA) mix, and talk and news programs must have a mix-minus for telephone hybrids and possibly a mix in a different language for a second audio program (SAP) channel.

The Grand Alliance advanced television (ATV) threatens to make life even more interesting. As the motion picture format 5.1-channel comes to television, the audio engineer must deal with left channel, center channel, right channel, two surround channels, and a low-frequency effects (LFE) channel. The first five audio channels offer full 20 kHz bandwidth. The LFE channel provides

response from 3 to 125 Hz. All this arrives as digitally compressed audio in the Dolby AC-3 format.

Audio monitoring of the preview channel is accomplished through the mixer solo function. If a remote truck is involved, an interruptible foldback (IFB) system requires a program audio feed plus audio cues to the talent at the truck. The console to handle all this requires a design specifically for these complex tasks. The TV audio operator mixes audio and nothing else.

An audio routing switcher tied to the video switcher assumes some of the workload. The audio switcher operates in sync with the video source, leaving level correction adjustments to the station's audio processing chain.

3. STUDIO PLANNING

3.1. Technical Basics

Analog audio signals consist of complex mixtures of altering currents of different frequencies at different powers. In broadcasting, the decibel (dB) serves as one unit for measuring audio power. We measure the power with VU (volume units) meters, marked in decibels, on our equipment. What is a decibel? The decibel is one-tenth of the logarithm of the ratio of two powers.

The VU meter shows a "0" reading, but it is not on the left end of the scale; it's to the right of center. On a VU meter, "0" does not mean zero or none. These volume units are referenced to the 1 mW of power produced by a 1 kHz audio tone across a 600 Ω load. This combination of audio power (1 mW) and load value (600 Ω) creates 0.775 V of audio and is represented by the "0" on the VU meter.

The designation dBm identifies all readings referenced above or below this power level. A signal of -3 dBm contains half of the energy of a signal measured at 0 dBm. A signal of +3 dBm is twice as loud as the 0 dBm signal. A signal of +10 dBm is 100 times as powerful.

Decibel values identified as dBu (decibels-unterminated) indicate an audio voltage of 0.775 V across an open circuit. Decibels measured in dBv (decibels-volts) are also measured across an open circuit but are referenced to 1.0 V. Because the circuit lacks the traditional 600 Ω load, these are simple measurements of an audio voltage, not power. Modern analog equipment no longer uses 600 Ω impedance-matching circuits; most references to decibels now carry the dBu or dBv notation.

Occasionally the 0 dBm output level on a console drives the input meter on a recorder to +4 dBm. 0 dBm still equals 0 dBm, but equipment manufacturers often calibrate their equipment to provide an output level of +4 dBm, or +8 dBm, when the output VU meter indicates 0 dBm. Engineers always standardize operating levels of all equipment in the station. This allows them to patch any output into any input without operating level problems.

Signal levels of 0, +4, and +8 dBm are all valid operating levels. Each station may use a different level, but an engineer will calibrate all the equipment in the station to one of these three "standard" operating levels. Someone bringing in equipment from outside the facility may find it necessary to recalibrate to the signal level used

throughout the facility. Digital audio equipment presents another level-matching challenge. Headroom meters, not VU meters, monitor digital inputs. A headroom meter indicates how close the input signal comes to clipping the analog-to-digital converter circuit. A 0 dBm signal fed to a digital recorder with 18 dB of headroom will appear on the headroom meter at -18 dB. You will find headroom meters referencing a decibel value identified as dBfs (decibels referenced to full scale).

3.2. Analog Equipment

An analog VU meter operates like the speedometer in a car, which directly shows the speed at which the car is traveling as a stated value. A headroom speedometer would show how much faster the car can go in relation to the speed limit. In this example, we will assume a speed limit of 60 mph (37 km/h). When the headroom speedometer shows -10 mph (-6 km/h), a conventional speedometer would show a speed of 50 mph (31 km/h). The headroom speedometer displays that there are 10 mph (6 km/h) to go before reaching the 60 mph (37 km/h) speed limit.

Analog circuits tolerate operation with the levels driven in the red above 0 dBm on their VU meters. 0 dBm is not the clip point. An analog circuit clips when the audio signal exceeds the voltage potential of the power supply. A sine wave then flattens on the peaks when the input signal reaches a level higher than the power supply voltage. This condition results in audio distortion.

Typically analog audio equipment clips around +24 dBu. If the manufacturer calibrated the VU meter to an output of +4 dBu ("0" on the meters equals an output of +4 dBu), the equipment is said to have 20 dB of headroom. Input audio reading an average value of 0 dB could contain audio peaks 20 dB higher without clipping and distorting as it passes through the equipment. It is easy to understand why analog equipment with 20 dB of headroom forgives trespasses into the red above 0 dB on the VU meter.

3.3. Digital Equipment

Digital equipment inputs demand closer attention. When a digital recorder, with a headroom meter, is driven above "0," the digital audio clips and the recording will contain irreparable distortion, clicks, or pops. Digital audio clips at the analog-to-digital converter (ADC). Digital clipping occurs when the analog input signal drives the ADC past its maximum output capability. The converter is outputting all 1s and can no longer digitally reproduce the rising analog input. Good digital recording practice maintains peaks of -6 dBfs.

3.4. Balancing Input and Output

Professional analog broadcast equipment features balanced inputs and outputs. A balanced audio output consists of two wires that carry the analog audio voltage to the next device. Neither of these wires connect to ground. Only the cable shield, which protects the audio from electrical noise and hum, is grounded. A balanced circuit can

be run over properly shielded audio cables several hundred feet long.

The 230 V electrical circuit to an electric stove is similar. Two wires carry 230 V between them. Anyone who connects either wire to ground, may not live to tell about the resulting sparks. Although the low voltages associated with balanced audio do not represent any danger, grounding either side will short-circuit half the audio voltage to ground. Balanced outputs should not be directly connected to unbalanced audio inputs.

When wiring balanced analog audio, care should be taken to connect the high, or plus (+), terminals. Connect the low, or negative (-), terminals only to similarly marked terminals. If 3-pin XLR connectors are used, pin 2 is always high (+). Pin 3 is always low (-). Pin 1 of an XLR connector is ground. When $\frac{1}{4}$ -in. tip-ring-sleeve (TRS) plugs are used, the tip is high (+), the ring is low (-), and the sleeve is ground. Failure to follow the rules of polarity will result in out-of-phase audio. Stereo audio, wired out of phase, results in an audio dead spot centered in front of the speakers. Listeners with monaural radios hear only the difference between left channel and right channel if out-of-phase audio is fed to the transmitter.

In 1984, a Baltimore, Maryland, FM station once operated for 2 days with its audio out of phase. It went unnoticed by those listening in stereo; no one at the station detected anything wrong. But a bedside monaural clock radio reproduced nothing but a left minus right signal. Mono listeners assumed that the station was off the air; they heard only high-frequency spitting noises and muffled mumbling.

An unbalanced audio circuit consists of a single conductor and grounded shield. Consumer electronic equipment uses unbalanced audio circuits easily identified by the single-pin, RCA phono plugs found on the connecting cables. An unbalanced circuit carries half the power of a balanced circuit. It is more subject to hum and noise. Unbalanced circuits cannot support long runs of cable for this reason.

An unbalanced circuit is similar to the 115-V wiring in a house. One wire delivers 115-V to the lights, the second wire in the lamp cord is ground. It can carry only half the voltage of a balanced, 230-V circuit. Connecting an unbalanced output directly to a balanced input will not damage the equipment, but the input level will be too low. A matching interface box is needed to convert the unbalanced output to a balanced one and boost the signal level.

Bridging audio input circuits present no load to the source audio. Bridging inputs abandon the traditional 600- Ω , power-matching input circuits found on older equipment. Without a load, no power transfer takes place. These bridging circuits simply transfer an audio voltage from output to input. A bridging input handles a wider variety of input sources than possible when everything terminated with a 600 Ω load. If an output requires a 600 Ω termination, a 620 Ω resistor tied across the input terminals provides a perfect match.

In the days of tube equipment, both inputs and outputs used transformers. Tubes could not drive 600 Ω loads directly; solid state equipment could. Audio equipment manufacturers slandered the transformer with rumors of poor

performance as they removed them during the transition to solid-state design. Good transformers are expensive; manufacturers looked for ways to cut their costs and the audio transformer became a casualty.

Some applications still require the physical isolation that only a transformer can provide. Any time that audio equipment connects to a phone line, a transformer blocks the 48 V “telco battery” from entering the equipment. Unusually long audio cable runs operate best, with lower noise, when a transformer isolates the equipment on each end. The audio transformer provides best common-mode rejection (CMMR) of electrical noise included into long cable runs. Transformers still provide input termination on many high-end microphone preamplifiers. The transformer provides the required 150 Ω load for the microphone and isolates the preamp from the phantom voltage required to power condenser microphones. Common mode rejection of noise becomes even more important when dealing with the extremely low-level output signals of dynamic microphones.

3.5. Where to Begin (Step 1)

Planning a new studio, or rebuilding an old one, begins with a layout on paper or computer screen of all the required audio sources and feeds. The console inputs offer a good place to start. Working from a list of all possible sources, the engineer assigns them priorities according to how often and how quickly the operator must put them on the air. This determines the number of mixing channels needed and how many switched inputs each mixer requires.

All frequently used audio sources should be assigned to individual console mixers. Keeping input switching and patching required of the operator to a minimum avoids errors and dead air. A console with two or three more inputs and mixers than absolutely necessary provides insurance against obsolescence and frequent studio rewiring jobs.

Accepted engineering practice runs all line-level inputs through patch panels on their way to console inputs. This allows the engineer to reroute special program audio and patching around any problems that may develop. The exception to the rule is microphone-level audio. Directly wiring microphone outputs to the console input terminals remains the best option. Microphone input positions seldom change, and the extra wiring through patch panel jacks invites noise problems. A possible exception is the television studio where the program must allow transfer from set to set.

Part of proper planning for a new console ensures that levels from all sources will be compatible with the input levels required by the console. If not properly matched, the operating positions of the potentiometers will be different for each mixer, making it difficult for the operator to run the board properly. The operator may open the pot a fraction of a turn and drive the meters to the pin or may not get enough gain even with the control fully open. Either situation results in a poor audio mix with possible distortion and noise problems. Normal operation sets rotary attenuators at the 2 o'clock position and slider attenuators at a 70% position.

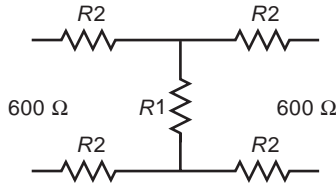


Figure 1. The H-pad resistive network reduces levels and matches impedances in balanced analog audio circuits.

All studio sources should be adjusted to operate within their normal output range. Interface amplifiers (matching boxes) should be used to boost low-level audio sources to the +4 dB levels required for most consoles. If the source signal overloads the console input, an H-pad will drop it to gain a proper match.

An H-pad is a simple network of five resistors arranged in the shape of an H laid on its side. The resistors convert some of the audio energy into heat, which drops the audio level by a predictable amount. At the same time, the H-pad maintains the impedance of the circuit. Pads of 10 dB or greater also correct impedance mismatches. Figure 1 illustrates the schematic of the resistive H-pad.

Pads are essential when connecting two audio transformers directly together. If an output transformer directly feeds an input transformer, the output transformer sees a changing inductive load. The frequency response of the system suffers. With an H-pad between them, the output transformer sees a linear resistive load. The H-pad may be mounted inside the equipment or at the studio punch blocks. Table 1 shows resistor values for commonly needed 600 Ω H-pads.

The worksheets in Figs. 2 and 3 offer an example of the starting point for designing a studio. Figure 2 illustrates wiring to the console inputs; Fig. 3 designates the wiring path of the console outputs. Preparing customized worksheets for each studio saves false starts and wiring errors. Any computer spreadsheet program accommodates the

Table 1. Typical H-Pad Values

Loss (dB)	R1 (Ω)	R2 (Ω)
1	5100	18
3	1800	51
6	820	100
8	560	130
10	430	160
12	330	180
14	240	200
16	200	220
18	150	240
20	120	240
22	100	270
24	75	270
26	62	270
28	47	270
30	39	270
32	30	300
34	24	300
36	18	300
38	15	300
40	12	300

task easily. Computer drafting programs offer another option for perfecting studio wiring prior to pulling cable.

The studio outlined in these worksheets is one of two in a station. A second studio serves as the production room. Patch panels route all audio. Outputs of both studios appear at the patch panel in the main studio as well as the production studio. If technical problems take the control room offline, the station can originate the program from the production console.

3.6. Buying Equipment

Preparation of a shopping list and cost estimate for new equipment follows the design of the studio on paper. The major components (console, cart players, professional CD players, and furniture) should be chosen early in the planning stage so that budget cuts will not compromise their quality. Price increases, sales tax, and shipping costs should be allowed for, and hidden “handling” or drop-shipment charges should be scrutinized.

Each engineer should maintain a working relationship with a reputable broadcast equipment dealer. Absolute bottom-dollar may not be the best deal. There is no saving in paying \$15 less for a CD player that fails to arrive in time to make the on-air date for the new studio. Experienced broadcast equipment salespeople offer their best deals and service to customers with whom they do regular business.

The shopping list should arrive at the dealer at least a week before the cost estimate is needed in order to allow the dealer time to research and work up a quotation. Engineers who demand quotations on short notice seldom get serious attention by dealers. Competition in the broadcast supply business ensures that pricing between reputable dealers will vary by only a few percentage points.

Competitive bids should be limited to two. Time is more valuable than chasing nickels and dimes. If the regular dealer does not offer an item required for the project, ask for a recommendation for a source. A salesperson will know all good suppliers and sometimes offer to get equipment not in the suppliers’ normal line for the best customers. This extra service can be worth a lot more than a few dollars when considering the big picture.

4. AUDIO CONSOLES

4.1. Radio Consoles

Centered in the radio studio, in front of the disk jockey, sits the on-air audio console. An 8–12 mixer analog console typifies this unit. Smaller mixing consoles find their way into news editing rooms and production studios.

The number of mixing channels limits the number of audio events that can occur simultaneously or in rapid succession. The station format dictates its requirements. Although an operator-assisted easy listening or satellite-based format may be able to use a four or five channel console, it would be out of the question for a fast-paced contemporary or rock program. These smaller consoles may not offer an audition bus or switchable inputs. The lack of multiple switched inputs requires one mixer for

Studio Wiring Plan			
Audio Source	Input Jacks, Patch Panel #1	Output Jacks, Patch Panel #1	Console Inputs
Microphone #1			Mixer 1
Microphone #2			Mixer 2
CD #1	Jacks 1 & 2	Jacks 25 & 26	Mixer 3
CD #2	Jacks 3 & 4	Jacks 27 & 28	Mixer 4
Cart #1	Jacks 5 & 6	Jacks 29 & 30	Mixer 5
Cart #2	Jacks 7 & 8	Jacks 31 & 32	Mixer 6
Cart #3	Jacks 9 & 10	Jacks 33 & 34	Mixer 7
Satellite #1	Jacks 11 & 12	Jacks 35 & 36	Mixer 8
Satellite #2	Jacks 13 & 14	Jacks 37 & 38	Mixer 9
Reel-to-reel	Jacks 15 & 16	Jacks 39 & 40	Mixer 10
Phone hybrid	Jacks 17 & 18	Jacks 41 & 42	Mixer 11
EAS receiver	Jacks 19 & 20	Jacks 43 & 44	Mixer 12
Production studio	Jacks 21 & 22	Jacks 45 & 46	Mixer 13
Spare	Jacks 23 & 24	Jacks 47 & 48	Mixer 14

Figure 2. Careful planning of the console inputs prevents delays and rework during the installation process.

Studio Wiring Plan			
	Input Jack, Patch Panel #2	Output Jack, Patch Panel #2	
Program output	Jacks 1 & 2	Jacks 25 & 26	AGC amplifier input
AGC amplifier out	Jacks 3 & 4	Jacks 27 & 28	Limiter input
Limiter output	Jacks 5 & 6	Jacks 29 & 30	STL transmitter
Spare	Jacks 7 & 8	Jacks 31 & 32	Spare
Audition output	Jacks 9 & 10	Jacks 33 & 34	Reel-to-reel
Spare	Jacks 11 & 12	Jacks 35 & 36	Prod. console in
Mono output	Jacks 13 & 14	Jacks 37 & 38	Office monitor
Mix-minus output	Jacks 15 & 16	Jacks 39 & 40	Telephone hybrid
Spare	Jacks 17 & 18	Jacks 41 & 42	Spare
Prod. console out	Jacks 19 & 20	Jacks 43 & 44	Spare
Spare	Jacks 21 & 22	Jacks 45 & 46	Spare
Spare	Jacks 23 & 24	Jacks 47 & 48	Spare

Figure 3. This example of studio wiring of the console shows the versatility afforded by patch panels. Should the main console fail, patch cords can feed the production studio to the on-air processing and the transmitter.

each audio source. External switchers can provide extra flexibility when required.

The console found in most control rooms offers 10 or more mixers. The most common variety features rotary attenuators. Heavy on-air use begs for step attenuators because they require only occasional cleaning in order to maintain silent operation. These attenuators use make-before-break switches to move through a series of resistive pads. The step between the contacts results in uniform 2 or 3 dB steps throughout the entire range of 20 or more steps. Their rugged construction offers smooth, quiet, dependable operation, but with large size and rotary design as limiting factors. Program audio passes directly through the attenuator, but a switch routes the audio into the console cue bus as the attenuator reaches its fully counter-clockwise position.

Wear and buildup of dirt plague attenuators that depend on sliding a contact over a resistive element. The resistive element consists of either carbon, conductive plastic, or metal film. Normal wear changes the element's resistance, and buildup of worn-off carbon may cause erratic resistive changes in the contact between the slider and the element. Noise and uneven tracking between stereo channels results with age.

Noisy pots present a major problem when the program audio routes directly through the potentiometer. In the case of a voltage-controlled amplifier (VCA) design, audio does not pass through the control. With the VCA design, only a sample DC control voltage passes through the potentiometer. This voltage controls the gain of an amplifier, which carries the program audio. Figure 4 offers a schematic of a VCA control circuit.

VCA console design solves the problem of audible noise from defective attenuators, but the noisy attenuator will affect the accuracy of the control voltage. The audio passing through the VCA-controlled circuit will become erratic and nonlinear as the noisy control moves through its range. Replacement of the defective attenuator prevents clumsy-sounding crossfades and stereo channel dropouts. This console design allows for the use of cheaper rotary or straight-line (slider) attenuators. As with any amplifier with VCA introduces some thermal noise and distortion. A good console has an overall distortion figure of 0.05% or less. The noise floor should be less than -90 dBm.

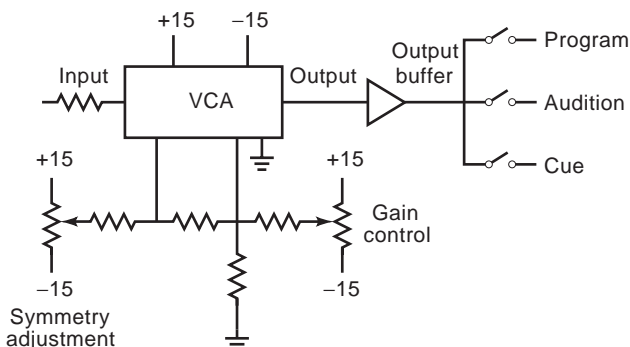


Figure 4. The VCA allows gain control via an adjustable DC voltage. This circuit is typical of those found in VCA-controlled audio mixers.

Modular design consoles offer the engineer major advantages. Removing and swapping modules make troubleshooting easy. The layout of the console allows easy changes to keep up with station format undulations. The positioning of blank panels created dividers, neatly grouping sources together. Custom panels accommodate special functions such as reel-to-reel recorder control or telephone line selection. Extra space left in the main rack offers expansion with additional mixers as the station's needs grow. These benefits justify the extra investment in a modular console.

For on-air use, a cue channel allows the operator to receive cue audio from remotes and networks and to preview program material. Even if carts deliver all program material, a cue channel is essential. It serves as a valuable troubleshooting tool for the station engineer.

In the early days of radio, all program material was live, and the audition channel served as the cue channel. Levels were set, and program material was previewed using the audition channel. Today the audition channel records network feeds for later use while the program audio travels the program channels. The audition channel can monitor the audio quality and set levels of remote feeds using the studio monitor system.

Some consoles allow audio from the mixers to feed the program and audition channels simultaneously. This allows recording of on-air programming using the audition channel. In talk formats using fixed-time-delay systems, the audition channel mixes the real-time program audio and feeds it to the delay. The output of the delay is brought back into the console on the program channel, which then feeds the delayed program to the transmitter.

4.2. Television Audio Consoles

The requirements of TV audio are compounded because more live audio sources come into play (as opposed to radio, where most program material is recorded). In television installations, additional monitoring requirements mean multiple output mixes. Television consoles include mono input modules for microphones, telephone hybrids, and other mono sources. The inputs offer a gain control or switch to allow stepping between microphone and line-level input. These modules include a pan pot to allow left-right positioning of the apparent audio source. A mode switch may replace the pan pot, enabling selection of normal stereo, left channel only, right channel only, a mono mix, or reversed channels. A cue channel feed plus a solo button permit stereo monitoring of a single audio source in the control-room monitors. Audio sweetening requirements make equalization on each module a popular option.

The ability to create multiple audio feeds by using sub-master mixing buses represents the major departure from radio consoles. The operator assigns mixer outputs to sub-master buses, and these submasters in turn create the master mix. This allows us to create several mix-minus feeds for special monitoring requirements.

4.3. Console Features and Options

A growing list of optional equipment available on audio consoles serve both radio and television audio mixing.

These make them more user-friendly. Clocks and timers put timing functions in the immediate field of vision of the board operator. The timer resets to zero anytime that a new channel is selected so the operator will know how long a CD or cart has been running.

A mix-minus, program audio minus the caller's voice, feeds console to the telephone hybrid and then down the line to the caller. If program audio, including the caller's voice, were fed to the phone hybrid, a feedback path would exist. Figure 5 illustrates a block diagram of a mix-minus circuit for telephone hybrid. This example demonstrates that not all console inputs must route to the mix-minus bus. Note that only input 1 and input 2 (announcer microphones) connect to program, audition, and mix-minus circuits.

If the studio contains multiple phone hybrids, a mix-minus feed for each hybrid is required so that callers will be able to hear each other's comments. In a television studio, a mix-minus feed provides on-air monitoring for talent on a live set. This feed includes program audio minus the talent's microphone preventing acoustic feedback while allowing the talent to hear program material and cues.

Consoles designed for radio production and television contain prefader processing patch points. These route the audio source compressors, equalizers, or other signal-processing devices before arriving at the mixing bus. These processing loops provide convenient connection points for microphone processing units.

Monitor amplifiers may be external or built into the console. Power and space limitations restrict built-in monitor amps to less than 10 W. Many engineers prefer to drive studio monitors with external, higher-power amplifiers. The stereo monitor system should contain a stereo/mono switch. This allows the operator to check out-of-phase program material and misaligned tapes. A single-pole, single-throw switch wired between left and right

channels at the monitor gain control accomplishes this function. At some stations, the control room monitors routinely operate in the mono mode. This immediately alerts station personnel to out-of-phase conditions.

A well-designed console offers switchable input levels and impedance matching on each input module. This handy feature allows easy transfer of input sources to different mixers, allowing for future changes in the studio. An input amplifier could then be used for either microphone or line-level audio. A second best system would have interchangeable mixer input amplifiers, which an engineer could shuffle between positions in the console mainframe.

Going one step further, some consoles offer programmable presets for input configuration. The engineer first stores pre-programmed console input settings in memory, then tells the console which program is planned for use. All the input sources automatically switch to the proper mixer. Fast and accurate setups result.

Professional consoles feature balanced, bridging inputs. Bridging audio input circuits used in modern consoles handle a wider variety of input sources than possible when everything was designed with 600Ω, +4 dBm terminations. A bridging input provides a 10 kΩ or greater termination impedance, which provides no load to the source equipment. If an output requires a 600Ω termination, a 620Ω resistor tied across the input provides proper matching.

Remote start contacts for cart machines and other program sources became standard equipment in the 1980s. They allow the operator to start the equipment by simply turning on the appropriate channel. Some console manufacturers provide more flexibility by using logic circuits, which allow the mixer to be turned on by pushing the Start button on the cart player. When the cart machine recues, the mixer automatically turns off. Automatic disabling of this logic when the input selector is switched to another input source eliminates the annoyance of having a cart machine start when the mixer is turned on for an auxiliary function.

Console manufacturers offer consoles with a choice of conventional analog VU meters or light-emitting diode (LED) bar-graph metering. LED metering provides multiple color visual monitoring of root-mean square (RMS) audio voltage plus peak values. One model shows left, right and peaks on a single display. LED displays may make operators less likely to run a board with the meters buried in the red.

Multitrack recorders and digital workstations in the broadcast production environment require consoles with more than a single pair of left and right outputs. Four and eight channel consoles assist in producing award-winning production. Channel assignment switches route the audio to the proper bus. Pan pots then shift it between left and right. Equalizers on each mixer allow adjustments to each audio source. Such production consoles resemble those once found only in recording studios.

Alert engineers realize that digital technology arrived to the audio console industry in the mid-1990s. The basic operating rules still apply to these new boards. The only exception is that they pass along a digital signal rather

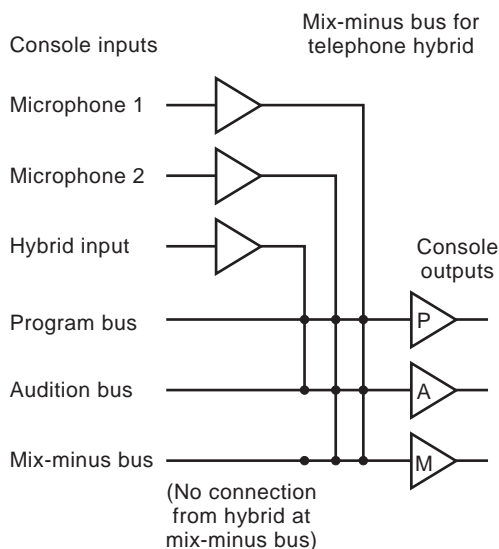


Figure 5. Broadcast consoles used with telephone hybrids require a mix-minus bus to feed the send input of the telephone hybrid. The mix-minus allows the caller to hear the talk show host's voice (microphone 1 and microphone 2) but prevents the caller's audio from being fed back into the hybrid.

than analog. As of this writing, many digital consoles remain in the prototype stage.

5. AUDIO DISTRIBUTION AND ROUTING

5.1. Patch Panels

There are three basic types of patch panels, or jack fields. The tip/sleeve $\frac{1}{4}$ -in. jack size is the oldest type, consisting of one conductor and one shield. This obsolete design dates back to the early days of radio. The tip/sleeve patch panel requires four single-plug cords to patch a balanced stereo connection.

The tip/ring/sleeve $\frac{1}{4}$ -in. panel remains the most popular patch panel for radio. It offers two shielded conductors per cable. A pair of single-plug cords will complete a stereo circuit. Dual-plug cable assemblies allow the convenience of patching a stereo source with a single cable.

The most useful $\frac{1}{4}$ -in. patch panel design includes dual rows of 24 jacks. This configuration allows stereo pair spacing. These panels usually group their jacks in pairs with wider spacing between stereo pairs. This spacing technique, when used with a dual-plug patch cord, makes it impossible to cross-patch an audio source. Cross-patching occurs when the user inserts the first single patch cord in one audio feed and the second patch cord in the adjacent audio feed on the patch panel. The dual plug will align only in paired jacks; cross-patching becomes impossible with these types of patch panels and dual plug cords.

Patch panel jack numbering uses the following convention: the jack in the top, left corner is identified as jack 1. Counting across and to the right, the last jack on the top row becomes jack 24. Jack 25 falls below jack 1 and is the first jack on the bottom row, starting on the left. Jack 48 is located on the bottom row at the right end and below jack 24. Although patch panels may contain more, or fewer, than 48 jacks, this numbering system remains the standard for identifying individual jacks.

The $\frac{1}{4}$ -in. patch panels also come in single rows of 26 jacks or dual rows of 52 jacks. These panels have standard spacing between all jacks and allow an additional stereo circuit on the 26-jack version and two additional stereo circuits on the 52 jack, dual-row model.

Special configurations of the $\frac{1}{4}$ -in. jack field can create very useful designs. One version offers three rows of 26 jacks for a total of 78 jacks on the panel. The wiring scheme of the two lower rows create a conventional dual-row patch panel. Wiring the top row directly to the circuits of the middle row of jacks allows monitoring these equipment output circuits by patching between the top row jacks and the monitor amplifier inputs. Inserting a plug into the top-row jacks does not interrupt the normal audio path through the patch panel.

Another custom item is a patch panel with special jacks that not only switch the conductors but also the shield when a patch cord is inserted. The patching of microphone circuits requires this seldom-used configuration.

One arrangement features patch panels built into a 19-in. (48-cm) rack mount chassis. The entire assembly mounts into the equipment rack just like the equipment that it connects. The jacks appear on the front of the rack,

and the rear termination points on the rear offer easy access to equipment wiring from the back of the rack. There remains a misconception that this design provides protection from radiofrequency interference (RFI). However, the phenolic bay fronts provide no shielding of the jacks, and some manufacturers even wire these designs with unshielded wire.

Rapidly making its way out of the recording studio and into broadcasting is the bantam or tiny-telephone jack field. These 0.175-in.-diameter plugs and jacks feature the tip/ring/sleeve configuration. The bantam patch panel consumes about half the space that a similar $\frac{1}{4}$ -in. jack panel would require in an equipment rack. The 96 jacks fit in a $1\frac{3}{4} \times 19$ -in. (4.45 \times 48-cm) rack space. Television facilities discovered bantam jack fields years ago.

5.1.1. Patch Panel Wiring and Termination. The jacks used in an audio patch panel have, for each circuit, a set of contacts that make contact when no plug is inserted in the jack. The circuit connection opens when the user inserts a plug. This allows for “normaling.” An audio source wired to a pair of these jacks passes automatically to the pair of jacks associated with an input that it normally feeds. Proper procedure wires all outputs to the top row of jacks in a dual-row patch panel, and the “normals” connect them to the bottom row of jacks. When not interrupted by the insertion of a patch cord, outputs feed to the proper inputs directly below, which are their normal connections. Figure 6 illustrates several methods of wiring patch panel normals.

Short jumpers between the rows usually make the connection for the normals between upper and lower rows of jacks. The jumpers can be brought rear terminations. If the normals route through a termination, the engineer can determine whether the circuit is normaled. Changes in normaling then can be made without removing the patch panel and unsoldering the jumpers.

When situations require the board operator to reroute the output of a cart player normaled to console input 3 to input 6, the operator first inserts a pair of cords in the top row of jacks associated with the cart machine’s output. This interrupts the audio path going to mixer input 3 by breaking the normal circuit. The operator then inserts the other ends of the patch cords in the jacks on the lower row associated with inputs for mixer 6. This breaks the normal circuit from the audio device normally feeding mixer 6 and puts the output audio from the cart player into the console input for mixer 6. Inserting a plug into a patch panel with conventional normal wiring breaks the circuit.

If the engineer wants the ability to monitor equipment outputs at the patch panel, half-normaling or top-row bridging wiring design meets the need. Half-normaling wiring connects the jumpers of the top row of jacks directly to their jack arms. The normaling contacts of the top-row jacks are not connected. This means that the circuit between the top-row jacks and the bottom-row jacks is broken only by inserting a plug into the lower-row jacks. This allows high-impedance monitoring, or metering, across the circuits without interrupting the audio connection.

Experienced engineers never connect patch panel jacks directly to equipment inputs and outputs. Termination

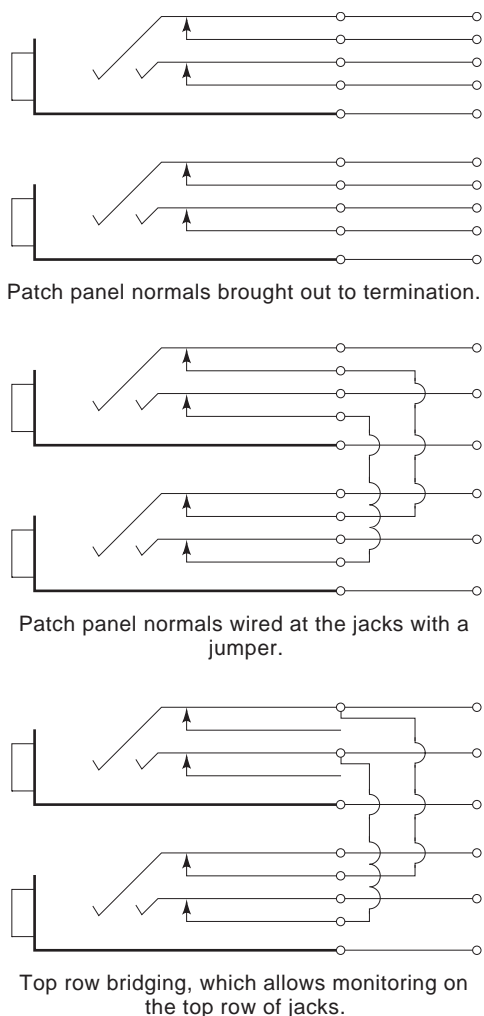


Figure 6. Audio patch panels are wired with either (1) all connections brought out to punch blocks, (2) the normals connected by jumpers at the jacks, or (3) the top jacks bridged to allow monitoring of the audio outputs wired to the top row of jacks.

blocks speed patch panel installation and offer flexibility when making wiring changes. Accepted practice mounts patch panel termination blocks in individual equipment racks, in a group in each studio, or in a central point in the engineering area. Short jumpers between connections on the termination blocks complete the links between inputs and outputs. This allows wiring changes at a convenient, easy-to-reach location without pulling new wire between equipment. Terminations used including solder-type “Christmas trees,” wire wrap, type 66 telephone punch blocks, or the newer types of punch blocks designed for stranded copper wire.

Christmas trees remain popular with engineers who trust only solder connections. They still serve well in remote trucks because of vibration concerns. Otherwise, they are obsolete.

Most engineers have switched to punch-type terminations. A specifically designed tool “punches” insulated wire into a slotted connector. The wire insulation strips away as the wire pinches into the connection. The process

eliminates the soldering task associated with Christmas tree blocks. The “66” block accommodates 22-gauge solid wire used in telephone service. Using only solid 22 wire ensures dependable connections. Stranded wire generally works although the strands may flatten out, preventing dependable removal of the insulation. Some strands may also break in the punchdown process. Solid conductor wire should be used for best results.

5.2. Audio Routing Switchers

The audio routing switcher offers an alternative to patch panels. This unit accomplishes the same function by switching the audio with relays or solid state switches rather than by plugs and jacks.

The system eliminates patch cords, can often be operated by remote control, and may often route audio to more than one feed at a time. Some of the more elaborate systems feature computer control. The increased flexibility of a routing switcher provides the only practical solution when many audio sources must be switched frequently such as in a busy TV control room.

Failure of the relays or cross-point switches in routing switchers adds some cause for concern. What happens when there is a power interruption? Latching-type relays hold their connections if power fails. Powering the routing switcher through an uninterruptible power supply presents another choice for fail-safe operation.

Size determines the cost of a routing switcher. A stereo switcher with 12 inputs and 12 outputs contains 288 cross-points (12 inputs × 12 outputs × 2 audio channels = 288). If the switcher is visualized as two side-by-side matrices of 12 horizontal lines (inputs) intersected by 12 vertical lines (outputs), each intersection becomes a possible connection point. One matrix represents left-channel audio; the other represents the right channel.

In a television station, engineers must decide whether individual switchers handle left, right, mono, SAP, or if one large system routes all signals and audio. With the larger system approach, mono sources connect directly into left and right channels. The switcher may correct channel reversals and create mono mixes. A switcher with sufficient cross-points to handle all switching tasks requires a larger investment than several smaller ones assigned to individual channels. The station considering the new ATV format is looking at a major investment in routing for the system’s six channels of audio.

5.3. Distribution Amplifiers

When distributing audio to a number of locations on a continuous basis (without switching), a distribution amplifier (DA) proves invaluable. Sending a console’s output to several recorder and other studios or routing a satellite receiver’s feed to all studios ensure the distribution amplifier an important role in audio routing. A DA eliminates the need for constant patching and switching of various pieces of equipment. A DA becomes the only practical solution when audio must be fed in multiple directions on a constant basis.

The typical DA provides six to eight stereo outputs for each channel. Although there may be no input level

adjustment, economical units should provide individual output trim pots. Modular distribution systems offer more versatility and avoid wasted, unused outputs. One model offers four stereo inputs, which can be assignable to any of its 14 stereo outputs by the use of jumpers. Popular DA options include metering, input level adjustment, audio compression, loss-of-signal alarms, and redundant power supplies.

6. STUDIO MONITORS

The control room audio monitoring system provides the first line of defense in spotting equipment failures and problems. For that reason, professional monitor speakers should be selected.

In choosing monitors, room size dictates cabinet size. In a large studio, invest in monitors with 12-in. woofers, 5-in. (13-cm) midrange cones and horn or dome tweeters. Size limits small studios to a model with 5- or 6-in. (13- or 15-cm) woofers. Current speaker technology offers amazingly good sound quality from small cabinets. The designer should look for low distortion and flat response.

A meticulous studio designer will consider background noise sources, reverberation time of the room, interaction from walls and ceiling, and room equalization. Doing this properly means testing the control room with a real-time analyzer and positioning the monitors for best results. This is seldom practical.

When mounting the monitors on walls, suspension mounts, preferably with vibration-isolating components, should be used. Each monitor should be positioned an equal distance from the operator's normal position. Sound-proofing material should be used on as much of the flat wall surfaces in the room as possible.

In small studios, "near-field" monitoring provides the best solution. The monitors should be positioned in a triangular arrangement with equal distances between the monitors and the ears of the operator. Near-field monitoring ensures that the monitors will be close enough to the listener that the direct audio from the speakers will overpower reflections and any undesirable acoustics of the room. Mounting solutions include a shelf, or wall brackets, above the console, suspension from the ceiling, or floor stands behind the console but directly in front of the operator. Near-field monitors should be positioned at, or just above, ear level.

The power amplifier becomes another vital consideration. Space and power requirements limit audio console internal monitor amplifiers to 10 W or less. Noise and distortion specifications may not be as good as those of stand-alone amplifiers.

Matching the power amplifier with the requirements of the monitors means another task in studio design. Pushing a low-power amplifier to provide adequate listening levels can cause audio waveform clipping with distortion on peaks. Operating in this manner could damage the speakers. A better choice would be to operate a more powerful amplifier in a conservative manner.

To prevent DJs from blowing the speaker voice coils with too much power, fast-blowing fuses should be in-

stalled in the lines. The engineer needs to experiment with fuse values and listening levels to find the proper combination.

Just as important as amplifier power is the wiring between amplifier and monitors. At least 16 AWG, should be used for low-power amplifier and speaker combinations. Heavier wire, up to 12 AWG should be used for combinations above 100 W or long runs of speaker wire. The cables from the amplifier, out of the rack, across the ceiling, and then down to the monitors may eat up 50 ft (15 m) of wire even in a small studio. Audio purists insist that the wire-length for both speakers remain equal.

7. AUDIO SOURCES

7.1. Compact-Disk Players

The CD player commonly provides the audio source of choice in radio. CD technology encodes audio as digital bits recorded as etched holes on the surface of the disk. A transparent plastic coating protects the surface so that only an accumulation of dirt or scratches affect the playback quality. The bits are read by a laser beam focused on the spinning disk. Because nothing but the laser beam touches the disk, there is no wear.

Selecting the best equipment that the station can afford represents the most cost-effective choice. Several manufacturers build CD players designed specifically for broadcast and professional use. If the station that must use semiprofessional players should remember that they were designed for use in a living room a few hours a week. These consumer-grade machines will not last indefinitely when run in a radio station 24 hours a day.

A station using semiprofessional players should keep two spare (meaning new, unopened, in the box) players in the station for quick replacement of a failed machine. No attempt should be made to repair a failed consumer-grade machine. They can be replaced with less trouble and expense than making repairs.

The output level and impedance of semiprofessional CD players are not the same as broadcast quality ones. If the console inputs require +4 dB levels and present 600 Ω loads, a matching interface should be used. These matching boxes convert the -20 dB, high-impedance, unbalanced output of the consumer-grade CD player to a +4 dB, 600 Ω , balanced source. Consumer-grade equipment can be difficult to cue and slow to start; the engineer should evaluate units carefully before committing to purchasing a quantity.

7.2. Turntables

Turntables still find work in some radio stations, but their importance has greatly diminished. Some unique source material remains available only on vinyl; the owner of one broadcast equipment manufacturing firm still sells 40 to 50 phono preamplifiers a month.

Turntables come in two flavors: the idler wheel design and direct drive. The once-common broadcast turntable used a motor which turned at 1800 rpm driving an idler wheel. The idler wheel in turn drove a large hub at the

center of the platter. This design minimized wow and flutter caused by fluctuations in motor speed. The use of a heavy platter achieved further speed stability. Rapid starts necessary for tight cueing required a heavy, powerful motor.

The direct-drive turntable became more popular because of its reduced noise, wow, and flutter. There is no idler wheel to replace or bearings to lubricate; the platter is the rotor of these slow-turning electronic motors. The speed control circuits of direct-drive turntables constantly monitor and adjust their speed, keeping it more accurate than if left to line voltage and frequency. Further contributing to the demise of the rim-drive tables, the speed control function made precise speed enhancement of music possible. Circuit repairs may be a problem because of the minimal documentation provided with most direct-drive turntables.

No real broadcast tone arms remain; all current models are designed for consumer use. They track well and adjust easily but some prove difficult to cue and are not very rugged. A professional tone arm can be adjusted once and then left alone except for occasional testing. When installing a tone arm, the template from the turntable manufacturer should be used and the instructions supplied with the arm followed. The tracking weight is specified by the cartridge manufacturer.

The choice of the phono cartridge depends on the audio quality required. Rugged, less-expensive models give the longest life in on-air use. Moving up to more expensive but less rugged models gains better separation and high-frequency response. Consumer-grade phono cartridges should be avoided.

The turntable's preamplifier is easily neglected because it is never seen after installation. The important specifications of noise, frequency response, and separation need consideration. More expensive models offer filtering, high-frequency cut or boost, and adjustable cartridge loading.

Another pressing concern for the engineer is the pre-amp's resistance to radio frequency interference if the studio is co-located with the transmitter. The RF easily makes itself known in these high-gain amplifiers.

7.3. Microphones

No serious program director ever leaves the choice of the studio microphone to chance. Dynamic microphones remain the most popular for studio use. They are rugged, dependable, and affordable.

Condenser microphones crept out of the recording studios into FM stations during the 1970s and 1980s. Condensers yield flatter frequency response but cost more. Ribbon microphones were the industry standard in the 1960s years ago but are traded only by collectors today.

Wireless microphones provide the advantage of mobility at radio remotes and for television use. The wireless systems use either a miniature lavalier mike and belt-pack transmitter or a handheld design with the transmitter in the microphone case. Television news crews value the extra directional characteristics of shotgun microphones in situations when the sound professional cannot get close to the on-camera person. TV studio sets use

the shotgun mike on a boom to keep the microphone off-camera.

7.4. Audio Cart Machines

Since the 1950s, continuous-loop tape cartridge (cart machines) have proved invaluable for playing commercials, jingles, and music. Even stations that rely on digital audio storage system keep a few cart machines around as a backup system.

A mono machine uses two tracks, the upper track for program material and the lower for cueing. Stereo versions use three audio tracks on the endless loop of tape. Two of the tracks record stereo audio: the third carries cue tones. Trading recorded carts between mono and stereo players will not work because the tracks do not line up.

A brief 1000 Hz tone is recorded on the cue track at the beginning of the cart recording process. When the cart recorder is in the record mode, pushing the Start button generates the 1000 Hz "stop" tone and begins the recording process. After the tape loop cycles through the cart and returns to the starting point, the playback head detects the 1000 Hz stop tone and stops the tape at the beginning of the recorded program material.

Deluxe machines offer secondary and tertiary tones for cueing and starting the next tape. The secondary, or aux tone, is at 150 Hz tone and customarily triggers the next event in the program sequence of automation systems. The tertiary tone is a 8 kHz tone and triggers a cue light to warn air talent as the program material nears its end. The operator manually inserts the secondary and tertiary tones while recording the cart.

Although still a dependable and reasonably good storage medium for commercials and music, digital audio storage systems bulldozed the cart machine out of the radio business. In addition, while cart machines ruled the studio, their manufacturers failed to standardize on a single type of motor. As a result, when sales volumes fell, the price of all those custom motors rose at a logarithmic rate. Cart machine prices rocketed as the price of hard drives fell.

7.5. Reel-to-Reel Tape Recorders

The reel-to-reel recorder still remains a workhorse in some stations because of its simplicity and durability. Tape also provides an economical means for storing longer program material without filling the hard drive of the station's digital audio storage system.

Reel-to-reel recorders operate by mixing the incoming audio with a high-frequency AC bias signal of fixed level and frequency. This combined signal magnetizes the tiny ferric oxide particles attached to the plastic tape as it moves past the record head. During playback, the play head converts the magnetic fields stored on the recorded tape to an audio voltage sonically equal to the signal originally recorded.

The bias signal ensures that the record head creates a magnetic field sufficient to penetrate the ferric oxide portion of the audio tape fully. The frequency of the bias signal must be supersonic and typically is at least 5 times the frequency of the highest audiofrequency recorded on the

tape. The bias signal may be optimized for a particular audiotape by adjusting the bias level to produce minimum harmonic distortion when recording and reproducing a sine wave at a frequency in the range of 2–3 kHz. The operator’s manual for the reel-to-reel recorder will contain instruction for optimization of the bias signal.

During playback, an equalization curve applied in the playback preamplifier ensures that the reproduced audio produces a mirror image of the audio previously recorded. The equalization curve corrects inaccuracies related to the electrical characteristics of the record head, playback head, and speed of the tape as it moves past the heads. Both low-frequency and high-frequency compensation perfect the playback process.

Alignment of both the record and playback heads provide job security for the station engineer. Both heads must remain exactly perpendicular to the tape as it moves past the heads. Incorrect azimuth (side-to-side) alignment causes poor high-frequency reproduction. Stereo recorders exhibit a loss of stereo separation when allowed to drift out of perfect 90° azimuth alignment. Improper zenith (front-to-back tilt) also contributes to the high-frequency reproduction problem.

Professional machines include a third head in the tape recording process. An erase head uses the bias signal to clear any previously recorded audio from the tape during the recording process. If damaged, or not properly aligned, the erase head will leave remnants of audio beneath the new recording. In extreme cases, the old recording makes itself heard during silent, or low-level, portions of the new recording.

In the radio station control room, the reel-to-reel records news feeds from networks and reporters in the field. FM stations record music requests and contests winners on a reel-to-reel for delayed playback. Some program material arrives in the station on reel-to-reel tape. A two-track stereo deck with speeds of 7½ IPS (inches per second) and 15 IPS fills the requirements of most control rooms.

Tape reels constantly turn in the typical production studio. Tape edit points, marked with a grease pencil, are cut with a razor blade and edited in a splicing block. Tape containing unwanted audio is discarded, and the two edit points are then spliced together. Words can be cut out and loose cues tightened using this methods. This works well with mono or two-track stereo formats. When editing with a multitrack machine, the operator should remember that all tracks are cut on the tape as the audio is edited.

When producing commercials with multitrack machines, the operator records elements of the production on different tracks and then mixes all tracks to a single stereo mix as the finished product records to cart. A multitrack recorder makes adding tags or reading copy into “doughnut” tapes much easier. The stereo music bed or agency tape is recorded on two tracks, and a third track contains the local copy. If the announcer makes a mistake, only the voice track must be recorded.

Multitrack recorders have a selective synchronization feature that switches the record heads of the tracks not in the record mode to the playback amplifier in order to synchronize playback with recording. Without this feature the timing between playback and the recorded audio on

different tracks will be off by an amount equal to the distance between the record head and the playback head.

The favorite tape speeds for production work are 15 IPS = 38.1 cm/s and 30 IPS = 76.2 cm/s. Faster tape speeds generate the widest possible bandwidth and best audio quality. Faster speeds make cut and splice editing easier because the audio spreads over a greater distance on the tape.

7.6. Telephone Hybrids

During the 1990s, talk radio and TV talk shows moved to a position as a dominant format leader. This challenged station engineers to get the caller’s voice from the telephone to the transmitter. The clash between old and new technologies made the job difficult.

The telephone system between the telephone company’s central office and the home, or business, remains largely the same as it was at the turn of the century. We still depend on a pair of copper wires to transfer voices from one place to another. This part of the dialup telephone network still operates as a two-wire system.

Both the voice being transmitted and the voice being received mingle back and forth on the same pair of wires. A telephone hybrid converts the two-wire system into a four-wire system which separates the caller’s voice from that of the talk show host. Figure 7 shows the theory behind a telephone hybrid.

In this example, the core of the hybrid consists of two transformers, each having a single primary winding and two secondary windings. The talk show host’s voice, the transmit audio, feeds to the phone line from the primary of T1 and through secondary 1 of T1. The caller’s voice, the

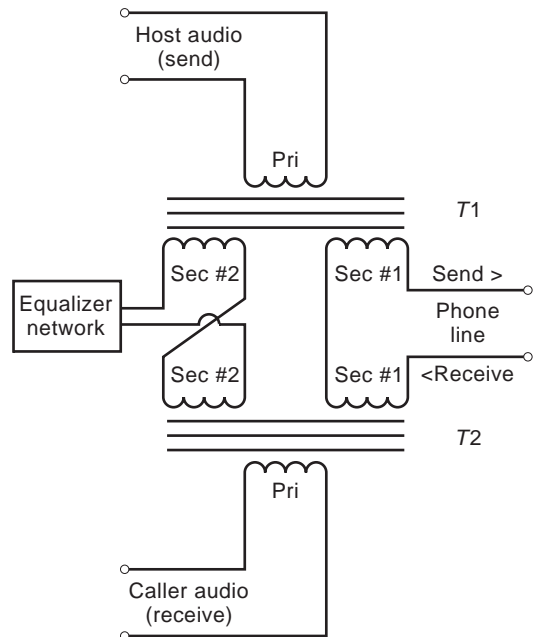


Figure 7. The telephone hybrid circuit converts the two-wire telephone line into a four-wire circuit. The hybrid creates individual send and receive audio connections separating the caller’s voice from that of the host.

receive audio, travels from the phone line through secondary 1 of T2, then to the primary winding of T2. Note that the transmit audio also passes, in series, through secondary 1 of T2. This means that the transmit audio appears in T2.

Note what is happening with secondary 2 on both T1 and T2; they are wired out-of-phase in relation to the first secondary windings. Although the transmit audio is introduced into T2 because secondaries 1 of both transformers are wired in series, the transmit audio is canceled out by the out-of-phase wiring of secondaries 2. This leaves, in theory, only the receive audio, the caller's voice, on the primary of T2.

If the phoneline exhibited a perfect 900 Ω resistive load, a 900 Ω resistor at the location of the equalization network would produce a perfect match. Telephone lines do not represent a perfect world. Capacitance creeps into the mix because the phone company uses miles of 22-gauge twisted pair to connect to its central office. That much twisted wire forms a nice capacitor. The resistance of the circuit varies with the length of all that 22-gauge wire running back to the phone company. Loading coils, used in the telephone circuits to flatten frequency response, add the inductance.

We connect our hybrid to what amounts to an *RCL* network when we plug into the phoneline. The null created by the out-of-phase circuit created by the 2 secondaries no longer matches the amount of transmit audio induced into T2 through its 1 secondary. A tunable equalization network wired between the 2 secondaries compensates for the electrical characteristics of the phone line circuit. When improperly tuned, audible amounts of out-of-phase host audio mixes with the caller's voice making the host sound "hollow," as if the show were taking place at the bottom of a large metal trash can. Our hybrid circuit may cascade into feedback in extreme cases of mismatch.

An analog phone hybrid requires tuning for best performance on each phone line to which it will connect. The process involves transmitting pink noise during a call to an outside phone number and then tuning the equalization network for a minimum level of pink noise at the hybrid's caller output. Digital phone hybrids accomplish this task with a short pink noise burst at the beginning of each phonecall. The result is perfect separation of host and caller audio with excellent-sounding talk show audio.

Integrated hybrid systems include multiple hybrids and call switching functions in a single unit. This approach removes the challenge of building a talk show phone system from scratch with equipment from different manufacturers. The multiple hybrid system also handles the requirement of multiple mix-minus feeds. The installation time saved justifies any additional cost of the combined phone hybrid and call handling system.

7.7. Broadcast Delay Units

Radio talk shows can be hazardous to a station's liability insurance. The spontaneity of a good talk show ensure that callers can, and will, say anything. This prompts the need for a system that allows time to "pull the plug"

before certain words, or accusations, pass through the transmitter.

Before digital technology accomplished this task with no moving parts, there was tape. Tape delay systems employed a special cart machine with an erase head. A 10-s cart was inserted in the recorder. Real-time audio was recorded on the tape. It took the 10 s for the tape to loop through the cart before reaching the playback head. The output audio emerged from the recorder 10 s after it was recorded, allowing time for the talk show producer to interrupt the delayed audio containing profanity.

Simple digital delays perform this task without the worries of moving parts and broken tape. The device simply converts audio to a digital signal, records it in memory, and then plays it back 10 s later. The talk show producer mixes the program in the console's audition channel, which feeds the input of the digital delay. The output of the delay routes to the program channel of the console and to the transmitter.

If things go wrong, the producer turns off the mixer carrying the delayed audio to the program channel and inserts fill music and has the option of switching the show host from the audition channel to the program channel after dropping the caller. The host then resumes the program in real time.

Both tape delay and fixed-time digital delays pose the problem of transition in and out of delay. If the show host simply starts talking at the beginning of the program, words won't exit the delay system until 10 s later. Meanwhile, the audience is treated to 10 s of silence. Most stations overcome this by playing a 10 s recorded introduction to the show on the program channel as the show host begins talking on the audition channel. The host's voice exits the delay precisely as the recorded message ends. If timed properly, the transition is seamless.

A better approach to the problem of keeping talk show audio respectable is the digital delay unit that gradually builds the delay at the start of the program. This delay digitally records the real-time audio into memory. While it is building the delay time, it plays back the program audio slightly more slowly than it is being recorded. This process gradually fills the memory until the delay time reaches the maximum. After the memory fills, this delay operates just like the fixed-time delay; the audio appears at the output 10 s after it is received at the input.

If a caller says something offensive, the host pushes a dump button that erases all, or part, of the audio in memory. Because the profanity is stored in memory, it disappears when the dump button is pushed. The program now is on the air in real time and the delay begins the process of rebuilding the delay time again. After about a minute the host has enough delay in memory to begin taking callers on the air again.

This type of delay allows easy return to real time at the end of talk program. A few minutes before the show ends, the producer puts the delay in the exit mode. Now the delay records the program, but it plays back slightly faster than it is recording. This eventually depletes the audio stored in memory and the program returns to real time. The best of these delays features a relay bypass that takes the delay off-line when it is not in delay, or if it fails.

7.8. Audio Remote Systems

One of the most profitable activities for a radio station is the commercial remote. This consists of packing off one or two of the on-air staff with a van full of prizes, amps, speakers, and a microphone to a remote location. The primary concern is to transmit the voices of the talent from the site back to the radio station with reasonable quality. The dialup telephone network provides a cheap and easy solution.

The output of a simple microphone mixer, or small audio console, connected to a telephone line coupler provides the basis for the most elementary remote system. The person doing the remote calls the station, is connected to the control room console via the station's telephone hybrid, and monitors the off-air signal for his cues. This system is easy to set up and operate, but the dialup phone system limits the audio quality. Our telephone system, designed only to transmit voice from one telephone to another, limits the bandwidth to a range of 300–3200 Hz. The talent at the remote site *sounds* as if they are on the telephone.

7.9. Telephone Frequency Extenders

The problem with using the dial-up telephone system for delivering broadcast audio is the limited frequency response. The fact that the telephone system rolls off all audio below 300 Hz costs 2.5 octaves of audio on the low end (50–300 Hz). This tends to product the “tinny” characteristic that makes unprocessed, dialup telephone remotes sound bad when compared with the full-spectrum audio of regular programming. There is a solution.

Analog telephone frequency extenders trick the telephone system into passing audio with a bandwidth of 50–2900 Hz. An encoder–decoder process shifts audio frequencies upward by 250 Hz, sends the up-shifted audio over the phone line, and then returns the audio to its normal frequencies on the receive end. The encoder travels to the location of the remote broadcast and serves the double duty of shifting the audio up by 250 Hz plus connecting the remote mixer to the dial-up telephone network. Most include telephone touchpads for dialing.

The encoder converts 50 Hz audio upward by 250 Hz to a frequency of 300 Hz. Audio at its natural frequency of 2950 Hz exits the encoder at a frequency of 3200 Hz, which barely squeezes through the limited bandwidth of the phone system. The output of the frequency extender encoder sounds quite strange. Even the lowest baritone voice sounds very high-pitched. Obviously, reverse treatment is required on the receiving end.

The frequency extender system's decoder shifts the audio, which it receives down by 250 Hz, restoring it to the original frequencies. The analog frequency extension process delivers an audio bandwidth of 50–2950 Hz. The result is very pleasing voice transmission over a dialup telephone circuit. The process sacrifices one-seventh of an octave between 2950 and 3200 Hz, but it restores 2.5 octaves between 50 and 300 Hz.

The system suffers from two disadvantages. Analog frequency extension is a one-way system. When the remote is out of the range of the broadcast station's signal, a second

telephone line is required for talk-back and cueing. Compatible equipment is required on each end. A station in New York cannot send frequency-extended audio to a station in Los Angeles unless both have identical equipment.

7.10. Digital Audio Codecs

The computer age brings another means of transferring high-fidelity audio from one point to another. We can now digitize the source audio, apply data compression techniques, and send the audio over telephone lines via modems. Because computer modems operate bidirectionally, we also pick up the benefit of two-way audio communication over a single phone line.

In a nutshell, these digital audio codecs (coder/decoder) consist of a computer sound card, a modem, and data compression software bundled into a single package. The modem is designed for Switched 56, integrated services digital network (ISDN), or dialup lines. Switched 56 service provides data transfer at a rate of 56 kilobits per second (kbps). ISDN doubles the speed to 128 kbps.

Dialup lines limit data transfer to less than 53 kbps and will vary from line to line with weather and with telephone traffic conditions. A 28.8 kbps computer modem does not always connect at a speed of 28.8 kbps. Switched 56 and ISDN service are consistent. The tradeoff for less audio bandwidth brings the ease of connection to any existing telephone line without extra line charges and construction delays. For a 4-h commercial remote, the use of a dialup line is a moot point. Coverage of a week-long special event may justify the expense of an ISDN line.

Systems designed for Switched 56 lines provide a 7.0 kHz, bidirectional audio circuit. ISDN service doubles the bandwidth to 15 kHz or allows stereo 7.5 kHz audio transmission. Improvements in modem speed and technology now challenge these premium services with bidirectional audio bandwidth of up to 10 kHz over dialup telephone lines. The program audio bandwidth capability depends not only on the bandwidth of the telephone circuit, but on the data compression algorithm used in the codec.

The audio compression (data reduction) algorithms most frequently employed with Switched 56 and ISDN lines include ISO MPEG Layer II [International Standards Organization (ISO), Moving Pictures Experts Group (MPEG)], ISO MPEG Layer III, apt-X, Musicam USA, or the international telephone standard ITU G.722 (formerly CCITT G.722). The rules of compatibility dictate that the codec on each end of the telephone line use the same algorithm. MPEG Layer III will operate with a Layer II device, but performance is limited to Layer II levels. MPEG is not compatible with ITU G.722. Likewise, apt-X talks only with apt-X. Musicam USA will converse with MPEG Layer II.

G.722 introduces a minimal delay, making it the most popular algorithm for talk shows and live remotes. Stations often find themselves using their top-of-the-line codecs in the “plain-vanilla” G.722 mode. A further discussion on audio compression algorithms is contained in Section 8.

7.11. POTS Codecs

The compression algorithms discussed above were designed for use on Switched 56 or ISDN lines, which have a guaranteed data rate of 56 kbps or 64/128 kbps. Standard analog telephone lines (POTS, or plain old telephone service) provide varying data rates depending on line quality. Telephone modems, such as the one in your computer, are designed to scale the transmitted and received data rate accordingly. This sliding data rate makes it very difficult to use compression algorithms, which were designed for specific transmission speeds.

New technologies have emerged that permit the transmission of compressed audio over POTS, thus delivering a bandwidth much higher than the normal 3 kHz signal normally available. POTS codecs use high-speed modems (33.6 kbps as of this writing) and compression rates in the 12:1 range to deliver audio bandwidths varying from 5 to 10 kHz, depending on the connection speed of the modems.

There is an important difference between audio sent by POTS codecs and audio sent via computer or the Internet. Computers use asynchronous modems, which means that they send a packet of information, wait for confirmation that the packet was received, then go on to the next packet. For one-way delivery of audio that has been stored at a site, this method of transmission is not a problem. However, asynchronous modems must use a buffer to reconstruct the audio. This creates a delay large enough that two-way communication with the studio is simply not possible over the single telephone line used for the remote. For “real-time” bidirectional remotes, most POTS codecs use synchronous modems. With a synchronous modem, a bit is transmitted, and without waiting for verification of receipt, the modem goes on to the next bit. This constant data stream in both directions results in audio that is delayed only by the compression algorithm used. The modems go through a complex “handshaking” process to determine the best data rate for transmission in order to minimize errors caused by lost bits.

There are four companies producing POTS codecs, and each company uses a different approach to audio compression. One company uses ITU G.728 compression, also known as code excited linear prediction (CELP). Two other manufacturers use modifications of the MPEG Layer III algorithm; however, their systems are not compatible with one another. The fourth uses a proprietary compression algorithm designed specifically for the slower connect speed of POTS. All four companies’ codecs are designed to scale transmit speeds and bandwidths according to line quality; however, the range of connection speeds varies with the manufacturer. Before buying a POTS codec, the designer should try to get a pair of demonstration units to determine whether they will work for the station’s application. Remember, two codecs are needed, both from the same manufacturer.

8. DIGITAL AUDIO SYSTEMS

8.1. The Standards

The Audio Engineering Society and European Broadcasting Union (AES/EBU) standards provide a benchmark for

digital inputs and outputs. Fortunately, these standards provide a common denominator found on all professional equipment. AES/EBU, also known as AES3, created a balanced system that can transmit digital stereo audio up to 100 m over a single shielded, twisted-pair wire.

AES/EBU calls for internal transformer coupling, with DC blocking capacitors, on both input and output circuits. The circuit is designed for shielded audio cable with an impedance of 110 Ω. The digital input protocol must match the digital output of the source. AES3 ensures that any two pieces of equipment using this standard will work together. Copies of AES3—1992 are available, for a fee, from the Audio Engineering Society in New York; the phone number is (212) 661-8528.

The AES3—1992 standard specifies a nominal signal voltage between 2 and 7 V measured across a 110 Ω terminating resistor. An earlier standard (1985) allowed a 2–10 V range. No compatibility problems exist between the 1985 and 1992 standards.

AES3 specifies connections using the familiar XLR three-pin audio connectors. Pins 2 and 3 carry the digital signal. Pin 1 is ground. This convention is exactly the same as used in wiring XLR connectors for microphone or balanced line-level audio. The connectors remain the same but the wire does not.

Miniature broadcast audio cable (Belden 8451 or West Penn 291) does not meet the impedance specification. Digital audio is actually computer data that run at a rate of 64 Hz times the sample rate. Digital audio, sampling at a rate of 48 kHz, becomes a data stream running at 3.072 Mbps (64 Hz × 48 kHz = 3.072 MHz). Cable capacitance can rapidly degrade the 3 MHz signal. Low-capacitance digital audio cable will do a satisfactory job of transferring the digital audio signal for the AES3-specified distance of 100 m (328 ft).

The need to transport digital audio farther than 100 m (328 ft) resulted in a new standard using unbalanced coaxial cable. AES-3id—1995 allows transmission of a 1 V digital audio signal up to 1000 m (3280 ft). Considering the 3 MHz frequency of digital audio, 75 Ω coaxial cable make a lot of sense. No knowledgeable engineer would suggest conducting a 3 MHz RF signal over twisted-pair audio cable. AES-3id calls for RG6A/U, or RG59B/U, cable and BNC connectors.

Television and video production facilities rapidly embraced this new standard. AES-3id not only allows for longer cable lengths, but also permits them to use 75 Ω cable, terminated with BNC connectors, for both video and digital audio signals. Copies of AES-3id—1995 are available for a fee from the Audio Engineering Society in New York. The Society’s phone number is (212) 661-8528.

Sony and Phillips developed a standard for consumer-grade equipment. S/P DIF (Sony/Phillips Digital Interface Format) defines an unbalanced digital connection. S/P DIF and AES3 signals do not mix in all cases. An AES/EBU input will accept a S/P DIF output, but a S/P DIF input will not accept an AES/EBU output without an interface to correct the differences in the data formats and wiring. Only equipment with AES3 inputs and outputs should be used.

S/P DIF specifies the old RCA phono pin connector; 75 Ω coax works well as the conductor. The problem of yet another connector and cable type in the studio proves reason enough to standardize on AES3 digital equipment in the station.

The AES/EBU (AES3) standard supports 16, 20, or 24 bit quantization formats. The 20 bit audio sounds better than 16 bit; 24 bit offers improved performance over a 20 bit digital signal. When audio is digitized, sine waves are changed into vertical samples based on time. They also get sampled horizontally based on amplitude. Amplitude resolution is determined by the quantization format, the bit rate. Each bit communicates 6 dB of amplitude information.

In theory, the 16 bit audio of a CD can communicate up to 96 dB of amplitude change (6 dB × 16 bits = 96 dB). The 24 bit digital audio can reproduce a theoretical dynamic range of 144 dB (6 dB × 24 bits = 144 dB). In the real world, digital audio equipment achieves performance less than theoretically possible. The 16 bit audio typically renders 90 dB of dynamic range due to the limitations of the analog-to-digital converters and digital-to-analog converters.

An increase in dynamic range means a lower noise floor. Note the 48 dB reduction in the noise floor when comparing 16 bit digital audio with a 24 bit signal. Assuming a clip level of +24 dBu, 16 bit digital audio equipment can theoretically reproduce a minimum signal level of -72 dBu. Twenty bit digital audio has the potential of reproducing a minimum signal of -120 dBu. Figure 8 illustrates the difference in possible dynamic range between 24, 20, and 16 bit digital audio.

AES3 standardizes sample rates of 32.0, 44.1, and 48.0 kHz. The digital recording process limits the maxi-

imum recordable audio frequency to one-half the sample rate. Each cycle of a sine wave must be sampled at least twice during a cycle. If not sampled once during its positive peak and once on its negative peak, the sound cannot be accurately sampled and converted to digital audio.

A sample rate of 44.1 kHz permits audio bandwidth up to 22 kHz. The sample rate of 48.0 kHz pushes the upper limit to 24 kHz. Equipment using a 32 kHz sample rate chokes off the audio at 16 kHz but consumes less bandwidth and/or hard-disk space.

Today the existence of three sample rates hinders digital broadcasting. Compact disks came out of the gate with the sample rate of 44.1 kHz. This single-standard sample rate crossed all brand names and entrenched itself as *the* sample rate for CD work. Recording studios adopted the sample rate of 48.0 kHz in an effort to achieve better fidelity. Digital audio workstation and digital audio storage equipment manufacturers shifted downward to 32.0 kHz to conserve disk space because FM radio passes only 15 kHz of audio bandwidth.

No manufacturers of digital broadcast equipment currently exhibit any interest in trying to develop a standard sample rate frequency. They support all three sample rates, driving up the cost of digital equipment. The issue of sample rate frequency remains as another roadblock slowing the progress of the digital output of a CD player from directly reaching the FM digital exciter.

As digital audio consoles approach the threshold of the control room, the engineer wishing to “go digital” in the studio has a problem. The digital audio of different sample rates cannot be combined even though all the sources adhere to the AES/EBU standard. Somewhere in the studio system sample rate conversion must take place. The 44.1 kHz sample rate of the CD must switch to the 48.0 kHz sample rate of the console, which must convert to the 32 kHz sample rate of the digital STL.

One console manufacturer offers input modules that match the sample rate of input audio to that of the console. Its solution to the problem is sample rate conversion on each input. A standard sample rate for all broadcast applications offers a better solution, but that has not yet happened. Careful planning during equipment selection remains the best defense for minimizing potential problems.

Even after the sample rate problem has been addressed, one more problem surfaces when a digital console arrives in the on-air studio. When mixing two digital audio sources of the same sample rate, their clocks must be synchronized. If one digital audio source runs at 48,000.00 Hz and is mixed with a second signal running at 48,000.02 Hz, and the internal clocks run separately, digital “train wrecks” occur.

The results pollute the combined audio with clicks and pops. A digital master clock provides a workable solution. A single timing signal connected to all digital audio equipment in the station synchronizes everything in frequency as well as phase.

This plan works when all digital equipment in the studio offers clock input connections. However, not all digital equipment is designed with this feature. Older digital equipment featured a “word clock,” which ran at the

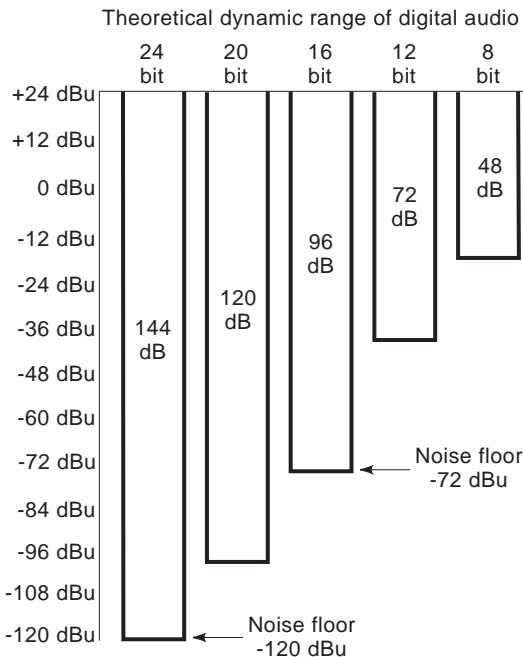


Figure 8. Higher quantization rates (bit rates) result in a wider dynamic range for digital audio. 24 bit audio provides a theoretical dynamic range of 144 dB for a 48 dB lower noise floor over 16 bit audio. This also means a 48 dB lower noise floor.

sample rate. Newer equipment locks internal clocks together with the AES standard digital audio reference signal (DARS), which is an AES3 digital signal without audio. The digital equipment manuals must be checked to verify which systems will operate in a facility.

Three more pieces of the AES/EBU puzzle remain. The first bit of the digital signal indicates whether the output signal originates from consumer-grade equipment or professional gear. If the first bit of the first 8 bit word is a 0, the source audio is from consumer equipment. Professional equipment identifies itself as such with a 1. Many professional recorders will not accept a signal from semi-professional equipment.

Digital audio may also include a consumer copyright protection bit. The serial copy management system (SCMS) prevents illegal digital copying. Digital audio also includes a parity checksum for the channel status data. The cyclic redundancy check (CRC) error light on the recorder may indicate a problem with the recording configuration.

Unfortunately the engineer will need a digital audio analyzer to identify these situations correctly. The fixes require a means of real-time editing of the channel status bits or reprogramming of the equipment.

System designers greatly increase the storage capacity of hard disks by using the bit rate reduction techniques of ISO MPEG, Audio Processing Technology's apt-X, Musicam, the international telephone ITU G.722 standard, Dolby's AC-2 or AC-3. Without bit rate reduction, 1 min of stereo audio consumes about 10 MB (megabytes) of hard-drive space. With a 4:1 bit rate reduction the same 10 MB could store 4 minutes of audio.

Early algorithms accomplished bit rate reduction by transmitting only the difference between samples. These systems gained a 2:1 reduction in digital data, but were nondestructive. The algorithm restored the original audio signal when decoded.

Lossy bit rate reduction discards bits not needed because the human ear would not hear the sound reproduced by the bit when played back. The sound would be either too low in volume to be heard, or covered up by a louder sound. The data-compressed information reproduces an audio signal almost indistinguishable from the original to the critical ear. This destructive process changes the source audio forever. After the data are compressed, the exact original audio can never be recovered. Huge gains in storage space and transmission bandwidth requirements justify the use of these algorithms.

The MPEG compression algorithm is the audio portion of a video compression system standardized by the ISO. The facts that (1) it is accepted worldwide and (2) it is attached to a video compression scheme ensure that it will be here for a long time. MPEG offers three levels of signal quality identified as Audio Layers I, II, and III. The complexity of the system, including hardware, rises and the quality of the audio improves with each advancing layer. Audio Layer I provides transparent 20 kHz audio quality at a compression ratio of 4:1. Audio Layer II achieves the same results but at a ratio of 6:1. Audio Layer III operates as high as 24:1.

Musicam USA's compression system is compatible with MPEG Audio Layer II. Musicam chops the 20 kHz audio

spectrum into bands of 750 kHz. It then discards any unnecessary bits in each band. The Musicam system represents a compromise between transparent re-creation of compressed audio and complexity of the processing algorithm. Processing delays increase with complexity of any system's algorithm.

Bit rate reduction serves to allow digitized audio transmission over limited bandwidth media. Early digital STL systems use bit rate reduction to squeeze two channels of 15 kHz audio and remote control data into the 500 kHz bandwidths of the 950 MHz spectrum. Remember that bit rate reduction algorithms throw away part of the digitized audio, preventing further audio processing. All audio compression and limiting must happen before the program audio passes through a digital STL that uses bit rate reduction. Two digital STL systems that do not use audio compression algorithms were introduced in 1997. These solve the problem of bit rate reduction and should become the systems of choice.

T1 digital telephone systems offer enough bandwidth to allow uncompressed audio to reach the transmitter. A T1 STL system offers flexibility in the location of audio processors. Multiband compression may be applied at the studio, and final limiting accomplished at the transmitter site. T1 systems also solve the problem of the congested 950 MHz spectrum.

Technology changes rapidly. An engineer should carefully study current technology as applied to the products available before making an investment in digital equipment.

8.2. Digital Audio Storage Systems

Digital audio storage offers the most rapidly developing technology in the broadcast audio field. Its acceptance by the industry became apparent in 1995; both Ampex and 3M announced their exit from the magnetic tape business. The magnitude of this development becomes evident after considering that Ampex pioneered magnetic tape recording in the United States. Working with development money provided by Bing Crosby, it perfected the process that was first used on Crosby's radio show. Digital recording media now include magnetic tape, hard drives, high-density floppy disks and magneto-optical (MO) disks.

Designed for the consumer market, the rotating head digital audio tape (DAT) machine became widely accepted by broadcasters. This format uses a rotating head much like a videocassette recorder (VCR), and records on a cartridge tape. DAT cartridges offer recording times of 60, 90, and 120 minutes. The cartridge design prevents razor blade editing. Professional models feature fast cueing, instant starts, remote control, and time-code compatibility. DAT machines offer broadcasters the ability to record live events, concerts, and network feeds in the digital domain without increasing noise and sacrificing dynamic range.

Stations using multitrack consoles for production work may take advantage of eight-track DAT recorders. Like their smaller cousins, the eight-track models use a rotating head but record on VHS videotape cartridges. These DAT recorders excel in recording live concerts and storing multitrack production work.

Smaller facilities may opt for the digital cart machines coming on the market. These record to super-high-density floppy disks, minidisks, or MO disks. They offer the advantages of low-noise digital audio reproduction and the elimination of head alignment woes and maintenance associated with analog cart machines. But it leaves the disk jockey still sorting and slamming plastic devices into slots and pushing start buttons.

Note, however, that there is still a need for human intervention for trouble shooting and problem solving.

If a station is planning a transition to “digital,” why handle the storage medium at all? Digital audio storage systems using hard drives as the storage medium threaten to oust cart machines and carts of all types from the control room. Hard-drive systems now offer the capability to store and play all the station’s commercial library plus its program material. Multiple hard drives provide the necessary “crash protection.” The systems can automatically record network feeds for delayed broadcast, eliminating the need for reel-to-reel recorders. One large system offers simultaneous access to program audio by seven studios.

8.3. Digital Editing and Workstations

The digital audio workstation benefits the broadcast station with faster and more creative production, using a process quite similar to the way word processors edit written text. Digital workstation systems store multiple audio tracks on hard disk and allow editing in random access memory (RAM). Two or more analog input channels (through A/D converters) and direct digital inputs receive the incoming audio. Options allow analog or digital outputs. They allow editing tracks individually and produce a finished product by using keyboard and scrub wheel rather than grease pencil and razor blade. The audio waveform of each track crawls across a screen allowing visual as well as audible cueing and editing.

To produce a spot with a digital audio workstation, the operator records the audio tracks and music beds in the system memory, commands the workstation to move component sounds, adjusts timing, edits tracks, and finally completes a stereo mix. Unlike razor-blade editing with analog tape, the software process preserves the original material. Correcting mistakes and editing experiments become child’s play with the Undo key found on most editors.

Workstation editors most closely emulating the operation of a reel-to-reel recorder get production work flowing quickly with minimal training time. An accurate scrub wheel operation speeds the work of a producer tightening loose voice tracks and other tricky edits. Scrub audio sounds exactly like that heard when manually rocking tape back and forth across the playback head of an analog tape deck.

A good display shows the audio waveform of all tracks on the screen simultaneously. Most editors show a vertical cursor line that moves across a stationary audio waveform as the editor reproduces the audio. This display mode consumes fewer computer resources than a system that shows the audio waveform crawling across a stationary cursor

because the screen is not continually requiring refreshment. Some audio producers favor a display that depicts the waveform moving across a stationary cursor as the screen more accurately represents the operation of a reel-to-reel machine where the tape travels left to right across the stationary playback head.

Creative engineers can assemble a two-track audio workstation with a Pentium PC, a good sound card, and editing software. The system should include as large a hard drive as possible; the source material plus overhead consumes about 12 MB/min for stereo audio. A 1-MB drive handles most two-track production tasks. The more elaborate systems include mixing capabilities providing an all-in-one approach for production work.

9. AUDIO PROCESSING EQUIPMENT

9.1. Compressors

All the hype whirling about concerning the on-air processing market simply clouds the central issue of reducing dynamic range of the source material. The difference between the loudest sound and the quietest equals the dynamic range. Audio compressors take large, rapidly rising audio voltages and make medium-sized, slowly rising audio voltages. The goal remains simple: reducing the dynamic range and increase the average modulation level of the transmitter.

The industry complicated matters when, in the 1960s, one engineer found a way to crank the average modulation level up 3 dB higher than the station across town. The resulting “modulation wars” in the AM band trashed audio quality and drove listeners to FM. Then Mike Dorrrough showed us how to crunch FM audio without sounding quite as bad. Bob Orban next combined the stereo generator with Dorrrough’s multiband limiter and other than doing all this digitally, not much has happened since.

If the output of a CD player were connected directly to the audio inputs of a transmitter, the wide dynamic range would prevent the average modulation from reaching more than 50–60%. The station would disappear from the band among those processing their audio by today’s aggressive standards. An AM station operating this way would sacrifice a part of its coverage area. An audio compressor reduces the dynamic range to a more practical spread and holds the modulation level at a much higher value.

Here is how it works. A threshold control defines the point where the compressor starts to attack a rising audio voltage. If the compressor’s threshold control instructs it to attack a voltage at -20 dB, the compressor will attempt to hold down a rising audio signal after it rises above the -20 dB level. A signal below -20 dB will pass through the compressor unscathed.

After the audio passes the threshold (-20 dB), the ratio control instructs the compressor how serious it is about restricting the level of the audio voltage. A 5 : 1 ratio limits an audio signal that has risen 5 dB to an increase of only 1 dB at the compressor output. Using this example, an input signal of -20 dB would appear at the compressor output at -20 dB; no compression would take place. An input

signal of -15 dB (5 dB higher) would show up at the output at a level of -19 dB (1 dB higher).

Low ratios induce less compression for any given input above the threshold. When the user increases the ratio, the compressor aggressively attacks the dynamic range of the source material. The threshold presents more of a “brickwall” to the incoming audio as the operator dials in ratios of 10:1 and higher. Premium-quality compressors offer two thresholds with an independent ratio control attached to each threshold.

This type of compressor moderately squeezes a rising signal of low level as it crosses the first threshold level. Should the signal continue to rise above the second threshold, more aggressive compression attacks the signal. A compression ratio of 20:1 used above the second threshold provides the peak-limiting required to properly modulate a transmitter.

The compressor’s “knee” is the point where the incoming audio signal rises above the threshold and the compression action begins. A “hard-knee” compressor engages the compression precisely at the exact threshold value with the exact ratio. A good ear hears the full amount of processing kick in as the signal rises above the threshold. If the compressor smoothes the transition with a gradual, rounded transition point at the threshold, the processing action engages slowly over about a 6 dB range. The transition into processing is less apparent as the compressor begins to act on the rising audio signal. This describes a “soft-knee” compressor. The old tube-type compressors, the UREI LA-2 for example, remain popular because of the smooth transition through their soft knee.

Release time determines how quickly the compressor releases the compression when a falling voltage drops below the threshold. A slow release time may measure 2.5 s or longer. A fast release time, measured in milliseconds, will release as each low-frequency waveform decays. A high compression ratio coupled with fast release time may result in too much of a good thing.

When more aggressive compression hammers the dynamic range, the normal soft passages in music disappear and the normal voice migrates to a stream of shouted commands. Overcompressed audio becomes irritating over a period of time. Some musical notes can actually be lost. If guitar notes and the beats of a kick drum arrive at the input of a compressor at the same time, the compression required to tame the kick drum will drop the level of the guitar so much that some notes will not be heard.

In the AM modulation wars of the 1960s, Mike Dorrrough recognized this deficiency and split the audio spectrum into three bands. In the discriminate audio processor, the Dorrrough DAP, Dorrrough assigned each band its own compressor. The combined outputs of the compressors reassembled the complete audio spectrum while gaining independent compression for each band. Now the kick drum’s compressor could be stomping 12 dB of compression while the guitar’s band may only receive 3 dB of compression. The listeners no longer missed the rhythm guitar. Thus was born multiband compression.

This all sounds easy. Figuring out the frequencies included in each band made things more complicated. The proper crossover frequencies, the points on the audio

spectrum where bass becomes midrange and midrange becomes treble were elusive and depended on the program material. The crossover frequencies for the relatively narrow AM spectrum were not correct for the 15 kHz FM spectrum.

Also, that each band required different attack and release times. The much shorter waveforms of high frequencies require faster attack than the long waveforms of bass frequencies. Improper attack and release times for adjacent bands results in inconsistent processing in each of the three bands. Release times set too short for the low band will overcompress the bass notes. When the release time for the high-frequency band is set too long, the highs disappear and the station will sound “muddy.”

9.2. Limiters

A peak limiter fits in the program chain just ahead of the transmitter, the stereo generator for FM. The limiter provides a brick wall for any overshoots that the compressor misses. Its sole purpose is to prevent overmodulation of the transmitter.

Limiters used for U.S. FM broadcast include the 75 μ s preemphasis curve that boosts the high frequencies. Other countries may use different preemphasis curves; check the government’s broadcast specifications. FM limiters operate symmetrically; positive and negative peaks receive equal limiting. AM limiters operate asymmetrically. They clamp their negative peaks at 100% modulation while allowing positive peaks to shoot upward to 125%. This maximizes the modulation and output power of the AM transmitter. AM limiters also include the National Radio Standards Committee (NRSC) preemphasis curve and 10 kHz lowpass filter. C-QUAM, AM stereo processing, usually requires an optional circuit board.

Most engineers locate the peak limiter at the transmitter site, feeding its input from the STL output. They leave the multiband compressor at the studio. Leaving the compressor at the studio end also enhances the modulation of a 950 mHz radiolink.

9.3. AGC/Levelers

A novice may confuse an automatic gain control (AGC) amplifier with a compressor. The AGC/leveler is not an audio-processing device. It will not reduce the dynamic range or limit loud audio peaks. The AGC amplifier ensures that the compressor and limiter receive constant input levels.

The AGC operates similarly to a compressor when a signal above its target output range appears at the input. In this case, the AGC amplifier gently pulls the signal level down to the target output level. It is operating like a compressor set with a 2:1 ratio and a slow, 2 min release time.

The AGC amplifier reacts differently when the input signal falls below the target output level. Now it turns up the gain of the low-level signal, bringing it slowly up to the target output range. Compressors cannot accomplish this level correction function.

Changing input levels to a compressor or limiter subjects the program audio to varying amounts of

compression. Audio from a loud source may receive too much compression, creating distortion. If the output of a low-level source is not corrected, it receives little or no compression and sounds weak and thin. Sudden changes in the station’s audio processing irritate listeners.

AGC/levelers provide a safety net for sloppy board operation, the times when the meters remain buried in the red for minutes at a time. Stations employing walkaway operations, where no one sits at the console correcting levels as the automation system switches between sources, benefit greatly from the processing consistency created by an AGC amplifier.

9.4. Equalization

Engineers work nights in anguish maintaining audiofrequency response as “flat” or linear as possible. Program directors toil overtime in anguish producing a “signature” sound for the station. The two professionals butt heads at the equalizer. In the audio processing chain, creative use of an equalizer gives character to the station’s audio. In production, an equalizer routinely cleans hum and hiss from noisy tapes. The production director also creates special effects and unique voice tracks with the help of his or her equalizer.

Low frequencies can be boosted to produce a heavy “thumping” bass and the upper mid-range can be boosted to add brightness. Enhancement of the highs and lows with an equalizer satisfies the desire to make a station sound better to the average nontechnical listener than the competition. Table 2 matches the audio ranges and qualities with the knobs on the equalizer.

Equalizers come in two types. The best known, the graphic equalizer, divides the audio spectrum into a series of bands represented by rotary or slider controls on the front panel. The operator adjusts the controls to affect gain in each particular band. The graphic equalizer with slider controls creates a visual picture of the frequency response curve that is being produced. Nontechnical people find it easy to use because of this design. Nine out of ten program directors prefer a graphic equalizer in the station’s processing chain to tailor the on-air sound.

The parametric equalizer provides more versatility in the hands of a trained operator. A specific frequency can be dialed in with a parametric equalizer for elimination or boosting. A graphic equalizer does not allow this frequency-specific accuracy. The parametric equalizer also allows the adjustment of filter bandwidth or selectivity. A narrow bandwidth can “notch out” a hum or buzz. A wide band-

width produces broad curve to boost or cut an entire band of frequencies. The typical parametric equalizer offers three or four sections covering the entire audio spectrum. Parametrics are considered valuable tools in the production studio.

9.5. Microphone Processors

Stations spend thousands of dollars for processing equipment to compress and equalize their music program material. The studio microphone often suffers from processing neglect although it deserves major attention. Compression, equalization, and “de-essing” of the studio microphone give the on-air talent a chance of competing with the professionally produced program material played on the air. A good microphone processor elevates the local disk jockey closer to the voice quality level of professional voice talent.

Compression reduces the dynamic range of the natural voice, providing more power and punch by raising its average energy; it becomes louder. The added power prevents the voice from being buried by song introductions and music beds. The equalizer provides a means of boosting regions of the voice spectrum that lack natural presence. Male DJs always want a generous boost of low-frequency energy. A “muddy” voice benefits from a boost in “brightness” from the equalizer’s upper midrange (around 2.5 kHz). The de-esser reduces annoying, lisping, spitting “s” sounds. Sibillance problems show up at frequencies between 6 and 7 kHz. The de-esser monitors the energy level in this range and kicks in additional compression to reduce sibillance problems. When adjusted properly, the de-esser will take the edge off a sibillance problem without punishment to the high-end frequency response. A de-esser circuit requires fast attack and release timing and a narrow (less than 0.5 octave) bandwidth.

The properly adjusted combination of 3 dB of compression, a one-octave, 6 dB boost at 125 Hz, and a two-octave, 3 dB boost at around 2.5 kHz from the equalizer can convert any voice to an acceptable quality. Table 3 provides some direction for equalizer adjustments.

Without voice processing on the studio microphone, the station may find itself overprocessing its music while stretching to achieve a suitable amount of processing for the on-air voices. The addition of a microphone processor provides a more balanced processing mix from on-air voices and produced program material. Suddenly the local announcers no longer sound “wimpy” compared with network announcers and production studio voices.

9.6. Noise Reduction Systems

Noise reduction systems minimize source noise from analog audio tape, vinyl records, and remote program unit (RPU) radio links. Dolby and dual-ended systems record encoded audio on tape and decode it to reproduce the original audio with a lower level of system noise.

Audio “companding” (compression/expanding) systems provide another option. During the recording process, the dynamic range of the program material is severely compressed, keeping it further above the noise floor of the recording medium. The process reverses during playback

Table 2. Audio Qualities and their Frequencies

Quality	Audio Frequency Range (Hz)
Subbass	15–65
Bass	65–256
Voice	256–2,048
Upper vocal	2,048–3,750
Presence	3,750–5,000
Sibillance	6,000–7,000
Brilliance	6,500–15,000

Table 3. Vocal Qualities and Frequencies

Audio Frequency Range	Descriptive Quality
75–200 Hz	Rumble, heaviness
200–300 Hz	Bassiness, bigness
400–600 Hz	Warmth, chesty
600–1,000 Hz	Volume, loudness
2–4 kHz	Clarity
3 kHz	Presence, nasal
5–8 kHz	Enunciation, brightness
6–7 kHz	Sibilance
10 kHz +	Mouth and air noise

when the recorded audio is expanded restoring the normal dynamic range. These dual-ended systems provide benefit in audio tape recording but require identical equipment on each end of the record/reproduce process.

Dolby and companding noise reduction systems hide noise. Single-ended systems provide freedom from the encode/decode process by “painting over” noise. These frequency-sensitive gating devices eliminate all audio in certain bands when the signal falls below a fixed threshold. The theory of operation assumes that anything below the threshold must be noise and should be eliminated. Single-ended systems offer a better solution than cutting the frequencies associated with tape hiss with an equalizer. The equalizer also eliminates desirable program material in that spectrum. The noise reduction unit attenuates a part of the audio spectrum only when no significant program material appears in that band.

9.7. Effects Generators

Digital effects generators enable production directors to produce the special effects of phasing, flanging, and echo for creative production. Several effects devices allow easy pitch changes of voice and music for special effects and to compensate for speed adjustments made to time tapes perfectly to 30 or 60 s. When tape speed varies more than 2% or 3%, pitch correction restores normal tone to the voice.

When using reverberation in program material, the amount mixed in should be 20 dB down from normal program level. Otherwise, the effect will be too distracting. When used with compression or limiting, it should be mixed back into the audio chain at the limiter output. This prevents the percentage of the mix from varying with the operation of the compressor/limiter.

10. SUMMARY

This article attempts to describe the state of the art in equipment and standards of engineering practice. A review of previous work on the subject of studio audio for the National Association of Broadcasters, starkly depicted the vast changes in the hardware realm in just 5 short years. Broadcasting technology now provides a digital signal path from the audio source to the transmitter.

The standards, which have served well since the infancy of broadcasting, now fall to new technology.

Digital AES/EBU (AES-3) interface supersedes the “standard” 600 Ω , +4 dB connection between audio equipment. Long-familiar hardware—punch blocks, screw barrier strips, and XLR connectors—make way for DB25s, fiber optic cable, and ISDN.

The broadcast engineer can now build a studio using source material from digital audio storage devices mixed on a totally digital console. The console could become a touch-screen controlled computer. The all-digital processing system has arrived. Some stations have already replaced their 950-mHz STLs with T1 carrier systems. A digital STL that uses no data compression was introduced in 1997. Equalized program telephone lines are on the way out, and 111C repeat coils are obsolete. Digital stereo generators arrived several years ago; an engineer can now buy a digital FM exciter.

Retooling to provide the new technology in hardware challenges the equipment industry. New names are emerging and some of the industry leaders are fading from vogue as they fall behind the pace of changing technology. Pressure will be on broadcast engineers also to educate themselves in order to provide competitive product to their listeners and viewers.

Acknowledgments

Special thanks go to Elaine Jones and Lynn Distler of Comrex Corporation, Dave Burns of Harris Corporation's Broadcast Division, and Daniel Queen of the Audio Engineering Society for their contributions, clarifications, and assistance in the preparation of this article.

AC-2 is a registered trademark of Dolby Laboratories.

AC-3 is a registered trademark of Dolby Laboratories.

apt-X is a registered trademark of Audio Processing Technology.

C-QUAM is a registered trademark of Motorola.

Dolby is a registered trademark of Dolby Laboratories.

Musicam is a registered trademark of Musicam USA.

Optimod is a registered trademark of AKG Acoustics.

Orban is Bob's last name, and a registered trademark of AKG Acoustics.

Pentium is a registered trademark of Intel.

BIBLIOGRAPHY

1. D. Eger (chairman), *AES3–1992 (ANSI S4.40-1992)*. New York: Audio Engineering Society, Inc., 1992.
2. R. Finger (chairman), *AES-3id–1995*. New York: Audio Engineering Society, Inc., 1995.
3. R. Chinn, *Symetrix 601 Owner's Manual*, Symetrix, Inc., Lynnwood, WA, 1992.
4. W. Lowery, Studio audio, in *NAB Engineering Handbook*, 8th ed. National Association of Broadcasters, Washington, DC, 1992.

FURTHER READING

- H. Ennes, *AM-FM Broadcasting*, Howard W. Sams, New York, Co., 1974.

C. Meyer and J. Watkinson, *The Book: An Engineer's Guide to Digital Transmission*, NVISION, Nevada City, CA, 1997.

G. Mendenhall, *Maintaining a 100% Digital Path from the Studio to the 'On-Air' Signal*, Harris Corporation, Broadcast Division, Quincy, IL, 1995.

J. Noah, Performing QC on digital audio, *Broadcast Eng.* (Intertec Publishing, Overland Park, KS) **38**(4):92 (April 1996).

S. Pizzi, Understanding audio data compression, *Broadcast Eng.* (Intertec Publishing, Overland Park, KS) **38**(5):52 (May 1996).

T. Skelton, Audio for the wide screen, *Broadcast Eng.* (Intertec Publishing, Overland Park, KS) **38**(2):88 (Feb. 1996).

Technical staff, *A Primer: Digital Aural Studio to Transmitter Links*. TFT, Inc., Santa Clara, CA, 1994.

Anonymous, About digital audio codecs, in *Product Summary*, Comrex Corp., Acton, MA, 1997.

RADIO DIRECTION FINDING

RICHARD L. JOHNSON
 JACKIE E. HIPP
 WILLIAM M. SHERRILL
 Southwest Research Institute
 San Antonio, Texas

Radio direction finding is the technique of measuring radiowave angle of arrival (AoA), as illustrated in Fig. 1. A transmitting antenna radiates radio energy toward the direction finding site. At distances greater than several wavelengths from the transmitting antenna, the radiowave can be represented as a plane wave, with linear contours of constant phase perpendicular to the direction of propagation. Ideally, the radiated energy propagates along the most direct path from the transmitter to the receiver. The receiving system is conventionally called a *direction finder* (DF). Figure 1 shows AoA expressed in terms of an *azimuth* component in the horizontal (x-y) plane and an *elevation* component measured in the vertical plane, relative to the horizon.

A direction finder employs one or more antennas in a DF array, used to detect the incoming radiowave. The out-

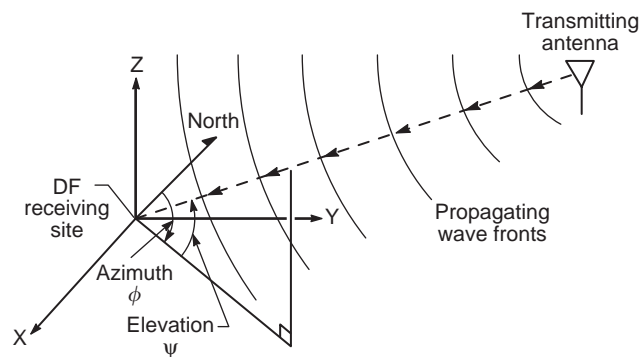


Figure 1. Radiowave received at a direction-finding site. Contours of constant amplitude propagate radially from the transmitting antenna, and the angle of arrival is characterized by azimuth and elevation.

put of each antenna is applied to a radio receiver, and this signal is sampled and supplied to a DF computer processor for determining AoA. The DF processor may either (1) determine the direction of energy flow toward the direction finder, (2) measure the direction of maximum rate of phase change across the DF array, or (3) estimate the velocity vector, normal to the plane-wave fronts. A well-known example of a simple DF system, which is still in use, is a rotatable loop antenna connected to a radio receiver as shown in Fig. 2. AoA is measured by determining the direction of energy flow toward the DF antenna. This is accomplished by rotating the loop for minimum audible output as indicated by the headphones, and thereby placing the null response of the loop on the AoA of the received signal. Thus, the direction to the transmitter is indicated by the broadside angle of the loop. The loop also has a null response on the reciprocal bearing, 180° from the true AoA. This problem of ambiguity can be resolved with an auxiliary "sense antenna."

The advent of radiocommunication in the late 1890s launched the development of DF techniques for navigation and radio transmitter location. Radio navigation and radio location are complementary technologies exploiting a common methodology. For example, signals received at sea from known shore-based radio beacons are used for navigation by *triangulation* to fix the position of a ship (Fig. 3a). Conversely, a network of two or more direction finders at known locations can be used to locate a radio transmitter by triangulation as shown in Fig. 3b.

For location applications, the DF network result is the observed *line of bearing* (LoB) or *bearing* to the transmitter. A LoB is expressed either as the *true bearing*, specifically, an angle measured clockwise from true north, or as a *relative bearing*, which is measured clockwise from a reference direction such as the heading of a mobile DF platform (ship, aircraft, vehicle). True bearings are generally used to locate a radio transmitter on a map.

A major factor affecting DF system performance is the process of *confirming* that each reported bearing is associated with the correct signal. Since there may be many signals on the air with overlapping frequencies, confirmation is sometimes a very difficult task. Often the achievable accuracy of a DF network is determined by the

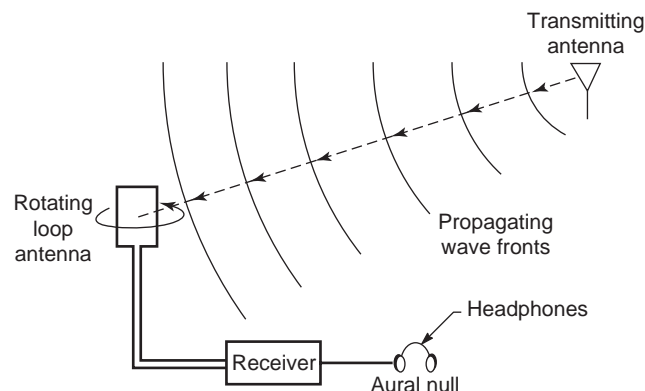


Figure 2. Rotating simple loop antenna direction-finding system. The headphones are used to detect when the AoA is broadside to the loop and the received signal is minimum.

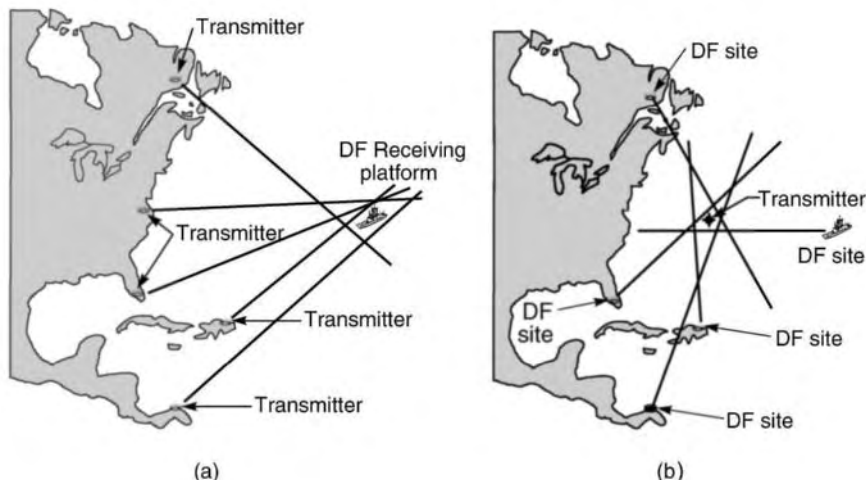


Figure 3. Similarities between radio navigation and DF radio location technology: (a) shipboard navigation technique using five radio beacons for position fixing; (b) radio transmitter location technique with five DF sites.

reliability with which each bearing is confirmed to be associated with the correct signal.

Operational DF measurements are always subject to error, and minimizing DF error is a major consideration in direction finder system design. DF error may be divided into three categories:

1. *Site error* is caused by reradiating structures and ground-plane characteristics at the DF antenna site that distort the arriving wavefronts into nonplanar configurations. Under these conditions the estimated AoA will vary depending on the location of the DF antenna array in the wavefield.
2. *Measurement error* may be caused by imperfections in the DF system instrumentation but is more frequently dominated by perturbed conditions in the received wavefield. Multipath propagation and co-channel interference create a multicomponent wavefield and are common sources of error in DF algorithms that are based on a single-plane-wave model. Multipath occurs when the signal arrives at the DF site via two or more propagation paths. Co-channel interference is caused by other on-the-air signals transmitted at frequencies that overlap the signal of interest.

3. *Propagation error*, the most fundamental source of error, is introduced by the propagation medium, which may deviate the radiowave off the most direct path to the DF receiver. At best, the DF system accurately measures AoA as received at the DF site, and the estimated bearing may not indicate the “true” direction to the transmitter. Propagation error, which is beyond the control of the DF system engineer, imposes a fundamental limit to achievable DF accuracy.

Conventional shipboard DF operations in the high frequency band (2–30 MHz) illustrate all of these DF errors in a single situation (Fig. 4). Signals experience multipath propagation through the ionosphere. Also, the ionosphere introduces propagation error by deviating each of the arriving propagation modes out of the great-circle plane. A conventional single-plane-wave DF algorithm produces DF error by treating the superimposed ionospheric modes as a single plane wave. Finally, the ship’s superstructure introduces additional site error by reradiating the incident waves into the DF array, thus creating a second and more complex source of multipath.

This brief introduction has provided an overview of the science and technology of radio direction finding. For a

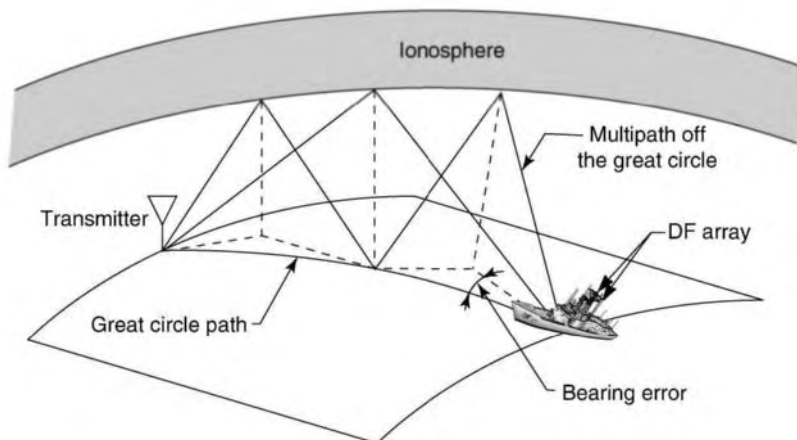


Figure 4. Shipboard direction-finding scenario illustrating sources of bearing errors. An error will result because the radio wave is not traveling on a direct path from the transmitter. The presence of multiple signal paths will induce a measurement error due to wave interference, and the metallic structure of the ship will cause errors due to reflections near the receiving antenna.

more thorough overview of the field, the interested reader is referred to Refs. 1–3. An extensive bibliography of direction finding literature is provided in Ref. 4. The following sections discuss various approaches to DF system design. Conventional DF design techniques based on the assumption of a single incident plane-wave signal are considered. The impact of operational conditions on conventional DF system performance is emphasized along with important methods for mitigating site error. Also, modern design techniques are described that are based on the decomposition of multicomponent wavefields. These latter DF techniques are generally referred to as *superresolution methods*. Finally, current trends in DF research are surveyed and performance benefits are assessed.

1. APPLIED DIRECTION-FINDING TECHNOLOGY

A radio direction finding system performs both time and spatial sampling of the field distribution and processes the samples to estimate AoA. A DF system acquires spatial samples through a combination of individual antenna placements and/or antenna patterns. The local description of any spatial field distribution may be estimated from either a set of spatially separated samples or a set of spatial derivatives at a single point in space.

A local description of a field at an arbitrary point \mathbf{r} in a Cartesian coordinate system may be developed by considering a monochromatic plane wave propagating in free space as

$$x(t, \mathbf{r}) = B \exp[j2\pi(f_0 t + \mathbf{k}_0 \cdot \mathbf{r}) + \gamma] \quad (1)$$

where $\mathbf{r} = (r_x, r_y, r_z)$ is the spatial coordinate, B is signal amplitude, f_0 is the frequency of the wave, $\mathbf{k}_0 = \mathbf{v}f_0/|\mathbf{v}|^2$ is the wavenumber that is a function of the scalar frequency and \mathbf{v} is the vector velocity of propagation (typically assumed to be the speed of light in free space), and γ is a random phase that is uniformly distributed over $[0, 2\pi]$. The AoA information is contained in the $2\pi\mathbf{k}_0 \cdot \mathbf{r}$ phase term and is given as

$$\begin{aligned} 2\pi\mathbf{k}_0 \cdot \mathbf{r} &= \beta(r_x \cos \varphi \cos \psi + r_y \sin \varphi \cos \psi + r_z \sin \psi) \\ \beta &= 2\pi|\mathbf{k}_0| = 2\pi/\lambda_0 \\ \lambda_0 &= \text{wavelength} \\ \varphi &= \text{azimuth AoA} \\ \psi &= \text{elevation AoA} \end{aligned} \quad (2)$$

If it is assumed that there are M antennas in the array, then a simultaneous sampling of the output at each antenna may be expressed as a column vector $\mathbf{X}(t, \mathbf{r}) = [x_1, \dots, x_M]^T$, where the superscript T denotes the transpose operation. The vector \mathbf{X} is known as an *array snapshot*. If the AoA term in Eq. (1) is separated, then the array snapshot for a single incident signal may be characterized as

$$\mathbf{X}(t, \mathbf{r}) = \mathbf{A}(\mathbf{r})s(t) + \mathbf{N}(t) \quad (3)$$

where $s(t) = B \exp(j2\pi f_0 t + \gamma)$ is the time-varying part of the signal, and the thermal noise in each of the M receiving channels is represented by $\mathbf{N}(t) = [n_1, \dots, n_M]^T$. $\mathbf{A}(\mathbf{r})$ is an $M \times 1$ column vector that represents the antenna array response for a signal arriving from an arbitrary direction (φ, ψ) as

$$\begin{aligned} \mathbf{A}(\mathbf{r}) &= [a_1, \dots, a_M]^T \\ a_i &= \exp(j2\pi\mathbf{k}_0 \cdot \mathbf{r}_i) \end{aligned} \quad (4)$$

for an array of isotropic antennas. The column vector given by Eq. (4) is referred to as the *array-steering vector*. The collection of all array steering vectors as a function of AoA, polarization, and frequency is referred to as the *array manifold*.

Two examples of wavefield sampling are shown in Fig. 5. Figure 5a illustrates an aerial view looking down on the surface of Earth at a single plane wave propagating across a circular array of eight antennas. In this case, the amplitude term B in Eq. (1) is constant throughout the space. The phase term $2\pi(f_0 t + \mathbf{k}_0 \cdot \mathbf{r}) + \gamma$ is illustrated for constant contours of $n\pi$ as a function of \mathbf{r} . The contours plot as parallel straight lines, and AoA is orthogonal to the contours of constant phase. In the example plot of Fig. 5b, it is assumed that four signals are propagating across an interferometer array of seven antennas. Signals of equal amplitude are assumed to be arriving from azimuth and elevation AoAs of $(45^\circ, 15^\circ)$, $(50^\circ, 30^\circ)$, $(60^\circ, 45^\circ)$, and $(45^\circ, 50^\circ)$, respectively. In this case, the amplitude of the composite signal is not constant but varies with \mathbf{r} . The dark contours illustrate those regions where the composite amplitude exceeds a normalized threshold of 0.95 units. The thin lines are contours of constant phase showing a somewhat distorted pattern. Clearly, the antenna array is not able to adequately sample all the features of the spatial interference pattern, and a plane-wave solution will incur multipath error; decomposing the wavefield into its individual components is required for a complete DF solution.

The processing objective of radio direction finding is to determine a unique AoA that is consistent with the set of data measured on the array. The key to this process is a knowledge of the array manifold *that includes site effects of the operational environment*. In the most general form, the bearing estimation process requires an iterative comparison between the observed data and the array manifold for every possible combination of polarization and AoA.

The remainder of this section describes DF techniques that progress from simple closed-form solutions (where stringent constraints apply to the antenna patterns, array geometry, local scattering environment, and number of simultaneous signals), to more general calibration-based DF processing algorithms, and finally to DF methods that decompose multisignal wavefields.

1.1. Single-Plane-Wave Direction Finding

1.1.1. Direction Finding in the Absence of Site Effects. Traditional DF techniques assume a single uniform plane wave incident on the DF antenna array. These DF techniques require noninvasive electromagnetic field measurements across a region in space in which the wavefront must maintain its properties as a uniform plane wave.

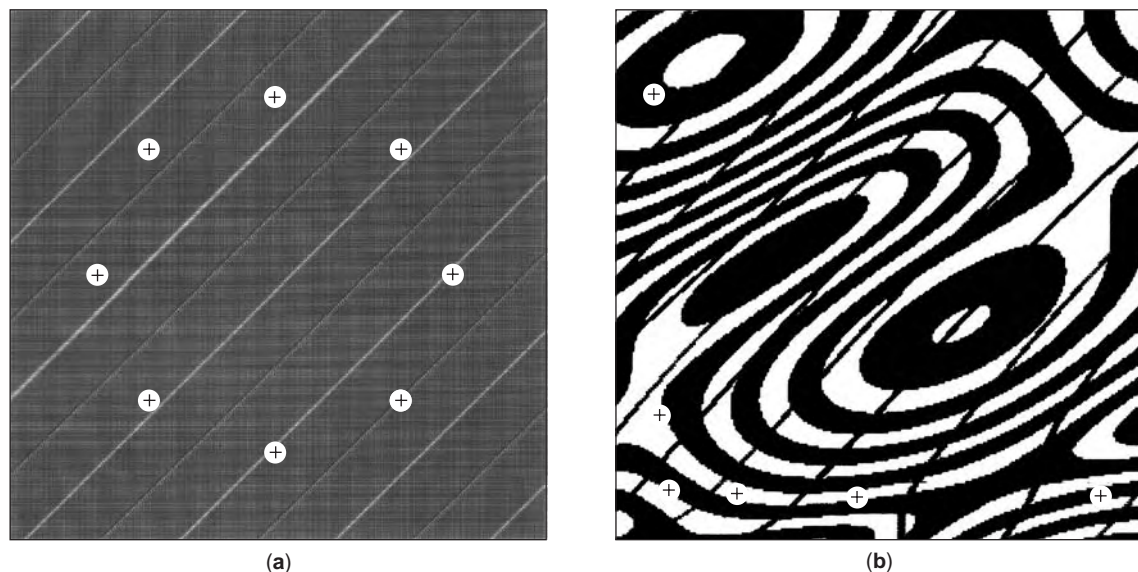


Figure 5. Contrasting single and multiple plane-wave fields incident on DF arrays: (a) single plane wave incident on a circular array of antennas—amplitude is everywhere constant and contours of constant phase are parallel straight lines; (b) multiple plane waves incident on orthogonal baseline interferometer array—contours of constant amplitude and phase are distorted. (Contour plot provided by D. N. Travers.)

This requirement imposes stringent constraints on the installation site, on the selection of the antenna elements, on the array geometry, and in some cases on the class of signals against which the system can operate. The requirement that the system be noninvasive demands that (1) no antenna element within the array perturbs the response characteristics of any other antenna element (i.e., mutual coupling must be negligible) and (2) the array of antennas must be installed in a region that is sufficiently separated from structures that would disturb the planarity property of the propagating wave. The selection of array geometry, choice of antenna elements, and site selection are all design factors that influence the simplicity of the DF process and system performance for various signal conditions [signal-to-noise ratio (SNR), polarization, elevation, etc.].

If the noninvasive constraints are satisfied and simple antenna elements are deployed in a favorable array geometry, then the characteristic response of the system (array manifold) may be analytically predicted as a function of AoA and polarization. In this case, AOA may be calculated by closed-form analytic solution, thus avoiding the more general requirement for an iterative search. For example, solution of Eq. (2) for phase measurements made among identical elements in a circularly disposed antenna array (CDAA) produces an estimate of AoA using a closed-form arctangent solution. Many CDAA closed-form processing techniques relax the mutual coupling constraint among the antenna elements, provided array rotational symmetry is preserved.

Table 1 lists eleven examples of traditional DF systems that are based on the assumption of a single uniform plane wave incident on the antenna array. The table summarizes antenna array configuration, basis for AoA determination, and primary advantages and disadvantages, and

provides literature references to more detailed descriptions. Table 2 illustrates the corresponding antenna array geometries and analytic processing algorithms associated with the eleven examples of Table 1. DF results are derived from solutions of Eqs. (1) and (2) with appropriate modifications to account for antenna patterns and array geometry.

Under more general conditions, it may not be possible or desirable to impose the restrictive design constraints that are essential for traditional DF techniques. Under more general installation conditions, arbitrary and diverse antenna elements that experience mutual coupling are installed in irregular array geometries (sometimes dictated by the site) on a location that distorts the characteristics of the incident uniform plane wave. Under these conditions, the DF process must be generalized to determine AoA by performing an iterative comparison between the observed response vector and the array manifold. Further, calibration measurements to determine installed antenna response patterns are required to characterize the array manifold as a function of AoA, frequency, and polarization. DF calibration and its application to iterative DF processing are discussed in the next section.

1.1.2. DF under Conditions of Site Interaction. The previous discussion focused on DF systems that were isolated from electrically conducting structures, and each antenna element within the array was excited by a single, uniform plane wave. However, an incident wave induces currents on conducting structures in the vicinity of the array, and these induced currents become sources of secondary radiation that also couple into the DF antennas. In the presence of conducting structures, DF antennas experience phase and amplitude perturbations that distort their ideal

Table 1. Examples of Traditional DF Systems

DF System	Typical Array Description ^a	Basis of Operation	Primary Advantages	Primary Limitations	Ref.
Rotatable loop	Single, rotatable loop	Determines orientation of horizontal component of curl of electric field vector	Simple processing, small antenna size	Polarization error	5
Crossed loops	Orthogonal pair of fixed, horizontal-axis loops				
Rotatable H-Adcock	Pair of identical, vertical electric dipoles, differentially connected	Responds to horizontal spatial derivatives of vertical electric field vector	Avoids polarization error by responding only to vertical polarization	Reduced sensitivity over loop	6
Four-element Adcock array	Four element, mast-mounted array of vertical electric dipoles, differential connection of diametrically opposite element pairs				
Spinning spaced loop	Coaxial pair of identical loops, differentially connected	Responds to horizontal spatial derivatives of horizontal magnetic field vector	Responsive to all polarizations, without polarization error	Reduced sensitivity over loop	7,8
Fixed, crossed spaced loop	Four, cross-spaced loops				
Phase-sampled linear interferometer	Two linear arrays of identical antenna elements	Measures phase gradient	Reduced noise-induced DF error	Requires large, clear site	9
Phase-sampled pseudo-doppler	CDAA of linear monopoles or dipoles		Phase-only process	Sensitive to phase errors	10
Willenweber	CDAA of multiple vertical elements in presence of cylindrical reflecting screen	Develops high-gain, rotating-beam pattern	High sensitivity, good interference rejection	Requires large, clear site.	11
Amplitude mode	CDAA of identical antenna elements	Develops various orders of spatial derivatives in horizontal plane	Higher-order patterns tend to be less sensitive to site interaction	Higher-order patterns are less sensitive to low-level signals	12
Phase mode	CDAA of identical antenna elements	Develops various orders of spatial derivatives in horizontal plane	DF processing reduces to measuring a phase difference	Directly sensitive to phase errors	12

^aSee Table 2 for array geometry.

patterns. If one assumes ideal array patterns, these distortions result in erroneous DF estimates. To the extent that the structures remain stationary, the distorted antenna patterns and the erroneous DF estimates are repeatable functions of the incident signal AoA, polarization, and frequency. This repeatable characteristic provides the basis for using calibration measurements to improve DF performance under conditions of stationary site interaction.

Calibration measurements to accommodate site interaction can be performed at either of two levels: (1) measurement of AoA error correction values or (2) measurement of installed antenna response patterns. The application and effectiveness of these two basic approach-

es for DF operation in the presence of site interaction are the focus of the following paragraphs. Under either scenario, the basic procedure for performing the calibration is to record the appropriate measurement from the *installed* DF system while exposing it to a controlled (calibration) incident plane wave under every appropriate combination of signal parameter (i.e., azimuth, elevation, polarization, and/or frequency).

1.1.2.1. Calibration for AoA Error Correction. For a low degree of residual site interaction with the DF antennas, moderate pattern distortion and moderate DF error exist. In this case, calibration for AoA error correction is effective. One conventional approach for reducing AoA er-

Table 2. Traditional DF Array Geometries and Algorithms


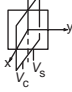
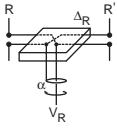
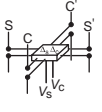
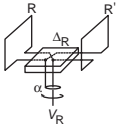
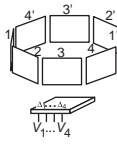
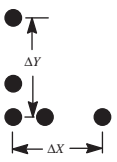


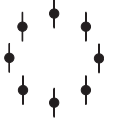

DF System	Typical Array Configuration	DF Algorithm (ϕ = Azimuth AoA, Ψ = Elevation AoA)
Rotatable loop		Operator monitors both the loop response V_R and the loop orientation α while rotating the loop to identify the response null from a vertical polarization response pattern described by $V_R(\alpha) \propto \sin(\phi - \alpha)$
Crossed simple-loops		$\phi = \tan^{-1} \frac{V_S}{V_C}$
Rotatable H-Adcock		Operator monitors both the H-Adcock response V_R and the azimuth orientation α of the H-Adcock array while rotating the array to identify the response null from a response pattern described by $V_R(\alpha) \propto \sin(\phi - \alpha)$
Four-element Adcock array		$\phi = \tan^{-1} \frac{V_S}{V_C}$
Spinning spaced loop		Operator monitors both the spaced-loop response V_R and the orientation α of the spaced-loop array while rotating the array to identify the stable response null from a response pattern described by $V_R(\alpha) \propto [E_H \sin \Psi \sin(\phi - \alpha) - E_V \cos(\phi - \alpha)] \cos \Psi \sin(\phi - \alpha)$ where E_V and E_H are respectively the vertically and horizontally polarized components of the incident electric field
Fixed, cross-spaced loop (four-spaced loops illustrated)		$A_0 = (V_1 + V_2 + V_3 + V_4)/4$ $A_2 = (V_1 - V_3)/2$ $B_2 = (V_2 - V_4)/2$ $D = \pm(A_2^2 + B_2^2 - A_0^2)^{1/2}$ $S_2 = (A_2 D + B_2 A_0)/(A_0^2 + D^2)$ $C_2 = -(A_2 A_0 - B_2 D)/(A_0^2 + D^2)$ $\phi = 1/2 \tan^{-1}(S_2/C_2)$
Phase-sampled linear interferometer		Use unambiguous phase measurements from short baselines to resolve the ambiguities in the phases $\Delta\Phi_x$ and $\Delta\Phi_y$ measured across the two long baselines ΔX and ΔY ; use the resolved phase measurements $\Delta\Phi_x$ and $\Delta\Phi_y$ to estimate the azimuth and elevation AoA
Phase-sampled pseudodoppler		Resolve the ambiguous phase measurements to assure that phase differences between adjacent elements remain less than 180° in magnitude; compute the Fourier series coefficients A_1 and B_1 for the first harmonic of the resolved phase progression around the circle; solve for the azimuth AoA: $\phi = \tan^{-1}(B_1/A_1)$
Wullenweber		Develop a pair of rotating high-gain beams to produce (1) a rotating-beam pattern having a deep pattern null in the steering direction and (2) a rotating-beam pattern having a high-gain pattern maximum in the steering direction
Amplitude mode		Combine every individual response v_n from CDAA element located at orientation α_n to develop responses proportional to the sine/cosine Fourier series coefficients A_m and B_m for the m th harmonic of the directional response around the array:

Table 2. (Continued).

DF System	Typical Array Configuration	DF Algorithm (ϕ = Azimuth AoA, Ψ = Elevation AoA)
Phase mode		$A_m = \sum v_n \cos(m\alpha_n)$ $B_m = \sum v_n \sin(m\alpha_n)$ <p>Calculate the unambiguous azimuth AoA using two adjacent modes:</p> $\phi = \tan^{-1} \left(\frac{B_{m+1}}{A_{m+1}} \right) - \tan^{-1} \left(\frac{B_m}{A_m} \right) \text{ for } m \geq 0$ <p>In the absence of intrinsic polarization error, an ambiguous AoA may be calculated from a single mode as</p> $\phi = \frac{1}{m} \tan^{-1} \left(\frac{B_m}{A_m} \right) + \frac{\pi}{m}, \quad i = 0, 1, \dots, m \text{ for } m > 0.$ <p>Develop response proportional to the exponential Fourier series coefficients a_m for the mth harmonic of the directional response around the array:</p> $a_m = \sum v_n e^{-jm\alpha_n}$ <p>The azimuth AoA is estimated as the phase difference between the responses of two adjacent phase mode responses:</p> $\phi = \Phi(a_m) - \Phi(a_{m-1})$

rors in DF performance is to start with a carefully controlled site in which the DF array is removed as far as practical from perturbing structures. To the extent that this objective can be achieved, AoA errors due to site interaction are minimized. In this situation, a reasonably good AoA approximation is obtained using the single plane wave assumption, and residual AoA error due to site interaction is reduced through a calibration correction curve.

A primary criterion for AoA error correction to be effective is that the curve of corrected bearing versus observed bearing (i.e., the uncorrected AoA estimated by the DF system) is single valued. Figure 6 shows two calibration correction curves illustrating both moderate and severe AoA error. The calibration curve of Fig. 6a shows a moderate case of site interaction and a corresponding single valued AoA correction curve. The calibration curve of Fig. 6b illustrates the impact of severe site interaction and displays reentrant regions. There are two intervals in which one value of observed bearing estimated by the DF system is associated with more than one corrected bearing. Calibration for AoA errors is not effective in reentrant regions, and DF based on an experimentally determined array manifold is generally necessary.

1.1.2.2. Calibration of Antenna Responses. DF is a process that requires a priori knowledge of the installed array steering-vectors. Conventional DF system development assumes a carefully controlled array of antennas having response patterns that are closely approximated by ideal predictions. When the DF array is installed on an adverse

site, antenna patterns can suffer severe distortion from nearby conducting structures. In such cases, required knowledge of the installed array steering vectors must be obtained by measuring antenna responses and storing this information in an array manifold consisting of antenna patterns versus frequency, AoA, and polarization. For ship and aircraft platforms, the installed array steering-vectors may be measured by repeatedly turning the platform in circles to expose the antennas to all possible AoAs from a far-field calibration station transmitting a wide range of signal frequencies. As an alternative, array manifolds have been obtained by performing calibrationlike measurements of antenna responses from scale-model arrays installed on highly detailed miniature models of the platform.

1.1.2.3. Iterative Search DF Techniques. The essential process of any iterative search DF technique is to select the AoA of the calibrated array steering-vector that *best* agrees with the measured array response to the unknown signal. The primary difference between DF iterative search schemes is the criterion for obtaining *best* agreement. A commonly used procedure for iteratively comparing observed array response to the calibrated array response vectors is a beamsteering process that acts as an equivalent bank of matched filters. In this case, *best* agreement is defined in a least-mean-squared error sense.

A digital beamformer may be viewed as a matched filter that processes the observed antenna response to produce a single (scalar) response that is maximum when the preferred direction of the beamformer *best* agrees with

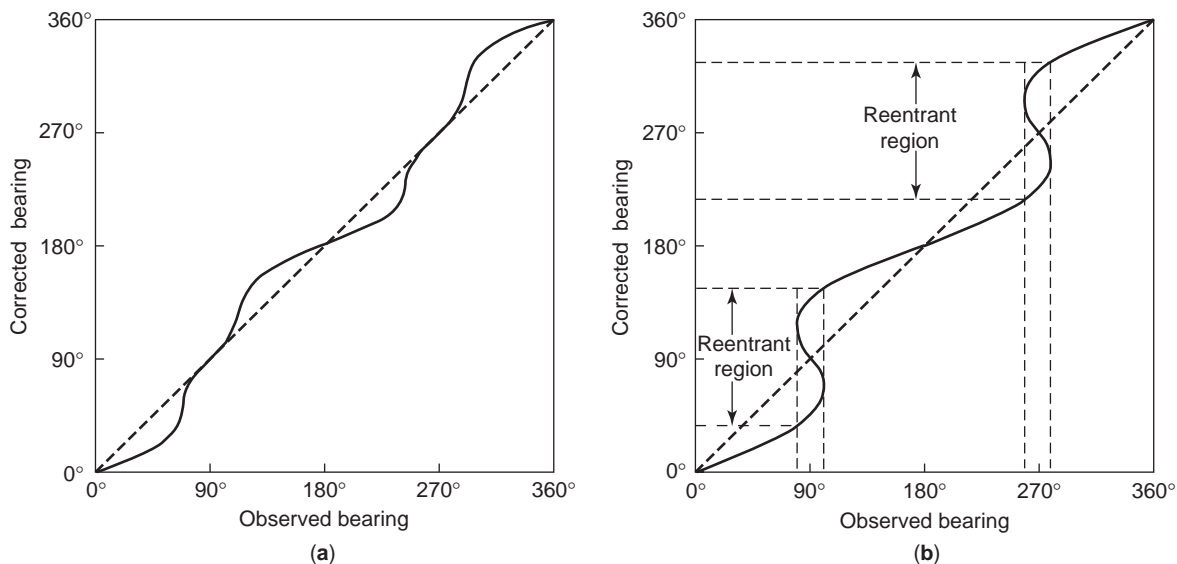


Figure 6. Moderate and severe site interaction AoA calibration curves: (a) moderate site interaction having AoA errors that are correctable; (b) severe site interaction having reentrant regions in which AoA error correction is ambiguous.

the AoA of the signal. Beamsteering DF iteratively processes an observed response vector through a progression of matched filters (viz., array steering vectors), each of which represents a different AoA. Under the constraint of a normalized input vector (i.e., unit norm), the output level of the filter is maximum when excited by a vector that matches the filter parameters. Or, stated another way, maximum output is obtained from the filter whose steering vector AoA *best* agrees with the bearing of the observed signal. In this manner, the process scans (or steers) a simulated beam over all possible AoAs, searching for the steering direction that maximizes the beamformer response.

The beam steered iterative process may be characterized mathematically by considering an array manifold of L steering vectors for a particular frequency. The array manifold is the set of array steering vectors \mathbf{A}_i for $i = 1, L$. This implies that the DF system was calibrated at L bearings in the interval $[0^\circ, 360^\circ]$. If $\hat{\mathbf{X}}$ denotes the observed array response vector for a signal of interest, then the output y_i of each matched filter is given as

$$y_i = |\mathbf{A}_i^H \hat{\mathbf{X}}|, \quad i = 1, L \tag{5}$$

where H denotes the Hermitian or conjugate transpose operation. The *best* AoA estimate is obtained when y_i is a maximum. A typical plot of y is shown in Fig. 7. In this illustration, $L = 25$, and the AoA estimate is 195° corresponding to the maximum value associated with the array steering vector at y_{14} . This process results in an AoA estimate that is *best* in a least squared (vector match) error sense.

Three areas of particular importance that impact the performance of DF systems which are based on iterative search techniques are (1) antenna array design, (2) adequacy of calibration, and (3) polarization effects. Antenna

array design critically influences the pattern of the steerable beam. The characteristics of the steerable beam are determined by the geometry of the array, the intrinsic element patterns, and the number of antennas in the array. Of primary concern in the design of the steerable beam pattern is the beamwidth of the mainlobe and relative level of the sidelobes.

Beamsteering DF system performance is also controlled by the accuracy and completeness of the calibration process used to characterize the array manifold. To obtain robust maxima in the matched-filtering process, the array manifold should be acquired at high SNR to

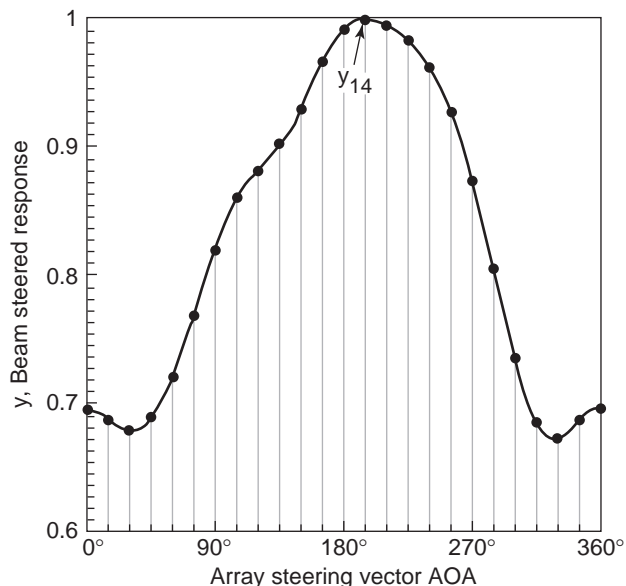


Figure 7. Beamsteered iterative search indicating a maximum when steering angle matches AoA of arriving signal.

minimize the possibility of contaminated data. The calibration data must be measured in AoA increments that permit accurate interpolation.

The array manifold varies not only with AoA but also with signal polarization. Under arbitrary polarization conditions, the steering vector must be adjusted to match the polarization *and* the AoA of the incident signal. For arbitrary polarization applications, the array manifold at each steering direction must consist of a *pair* of steering vectors for two different polarizations, for instance, $\mathbf{A}_V(\varphi, \psi)$ and $\mathbf{A}_H(\varphi, \psi)$ for vertical and horizontal polarization. The additional maximization step required by the polarization extension of beamsteering DF at each bearing is to maximize the beamformer response over all possible linear combinations of $\mathbf{A}_V(\varphi, \psi)$ and $\mathbf{A}_H(\varphi, \psi)$. The matched filter thus becomes a digital beamformer that processes the observed antenna response producing a single (scalar) response that is maximum when the steered direction of the beamformer matches the AoA of the received signal.

1.2. DF Error Mitigation

There are a number of sources of error in radio direction finding, and an exhaustive discussion is well beyond the scope of this survey; however, there are three categories common to all DF systems: (1) site errors, (2) measurement errors, and (3) propagation errors. These are considered in the following discussion.

1.2.1. Site Errors. The antenna array is generally designed to operate on a site that is clear of obstructions and reradiating structures. As discussed in the previous section, array calibration is generally used to mitigate site error in those cases where the DF antenna must operate in a cluttered environment. The concern in this section is selecting a site that least perturbs the incident signal.

Generally, DF systems are deployed on level, unobstructed terrain where the ground dielectric constant and conductivity are reasonably uniform within 10–20 wavelengths of the antenna array. Abrupt discontinuities in the electrical properties of the terrain such as nearby rivers, lakes, or coastlines should be avoided. Also, DF sites in the vicinity of rock or mineral outcroppings are undesirable. Abrupt changes in terrain topology such as nearby mountains, high cliffs, or deep ravines should be avoided.

In addition to selection of natural features, proximity to manmade reradiating structures should also be considered. The DF site should be clear of aboveground conductors such as utility lines and wire fences. The site should not have buried conductors beneath the antenna array such as pipelines or utility distribution lines. The site should be clear of tall structures such as buildings, bridges, or water towers.

It is rarely possible to achieve all of these conditions at a DF site. Generally, there are a number of other antennas deployed at a DF site, as well as buildings and facilities that support other signal intelligence-gathering activities. In practice, the DF system engineer attempts to locate the antenna array on a site that contains the *fewest* perturbing factors.

1.2.2. Measurement Errors. Leaving aside instrumental accuracy and resolution determined by SNR, significant DF measurement errors are caused by multipath and co-channel wave interference, which corrupt the planarity of an incident wavefront. Two approaches for mitigating measurement errors are (1) acquire data under favorable conditions and exclude corrupted data, and (2) extract the desired signal from the interference.

The first class of techniques includes wavefront tests that determine whether a single plane wave is present or if the wavefield is corrupted by interference. A test that has been used in CDAA systems is to compare the array scan of amplitude versus azimuth with an ideal sum or difference array response [1]. In the case of the sumbeam response, one tests for a symmetric mainlobe having an expected width depending on frequency. When this condition is satisfied, it is assumed that a single plane wave is present and the bearing data are accepted; otherwise, the bearing data are rejected. Another test which has been used successfully in interferometer systems is that of a linear phase progression across the array [12]. If the wavefield consists of a single planewave, then the relative phase between separated antennas is linearly dependent on distance. In the presence of wave interference, this condition is seldom satisfied.

The second class of techniques includes Fourier analysis [fast Fourier transform (FFT)] methods that decompose the received signal into highly resolved spectral bins. In many cases, interference due to other on-the-air signals may be separated from the desired signal through a difference in spectral occupancy. In this situation, accurate DF results may be obtained by DF processing each spectral bin occupied by the signal of interest and ignoring the spectral bins corrupted by the interfering signal. Another approach is to use the superresolution techniques described in the next section. These techniques decompose the wavefield into its constituent components and permit accurate DF for each component of the wavefield.

1.2.3. Propagation Errors. DF error caused by propagation off the great-circle path is essentially beyond the control of the system designer. In this case, the signal arrives at the antenna array from a direction that is not on the direct path to the transmitter. An example is a cellular telephone signal, propagating in a dense urban environment, received after reflection from several buildings. The received AoA may be considerably different from the true bearing to the transmitter. Another example is the refractive error introduced by the ionosphere on HF ionospheric paths [3].

The essential approach to minimize the effect of off-path DF errors is to perform DF on the first arriving signal. One method for implementing this technique is to acquire data on the leading edge of the waveform after a signal OFF-to-ON transition and before the multipath components arrive. Another alternative is to decompose the complex wavefield and identify the first arriving signal through cepstral delay analysis [13]. In both implementations, the intent is to estimate AoA for the first arriving signal on the premise that it will most nearly represent the true bearing to the transmitter.

A technique that has been developed to mitigate off-path errors for HF skywave signals is that of elevation angle discrimination. This technique is based on the premise that signals arriving at higher elevation angles spend more time in the ionosphere and are therefore more prone to off-path refraction than are signals arriving at lower elevation angles. In those cases where multipath propagation is present, the mode arriving at the lower elevation angle produces an azimuth estimate closer to the great circle bearing than a higher angle mode. This situation is almost always true in practice. The limiting case is a surface wave with a simultaneous skywave component over a path at sea. The surface wave invariably produces a more accurate bearing estimate.

1.3. Superresolution Direction-Finding Methods

DF techniques described in the previous section were concerned primarily with system response to a single-component wavefield. In contrast, the problem considered in this section is that of decomposing a multicomponent wavefield. Superresolution methods are particularly attractive for solving the multicomponent problem since the wavefield is generally undersampled in the spatial domain; that is, the dimensions of the antenna array are small relative to the scale of the spatial interference pattern.

An important building block used in superresolution spectrum analysis is the spatial covariance matrix. If the vector \mathbf{X} denotes an array snapshot at time t_0 , then $\mathbf{X}(t_0, \mathbf{r}) = [x(t_0, \mathbf{r}_1), x(t_0, \mathbf{r}_2), \dots, x(t_0, \mathbf{r}_M)]^T$ and for M antennas, the spatial covariance matrix is given as

$$\mathbf{R} = \begin{bmatrix} R(\mathbf{r}_1, \mathbf{r}_1) & R(\mathbf{r}_1, \mathbf{r}_2) & \cdots & R(\mathbf{r}_1, \mathbf{r}_M) \\ R(\mathbf{r}_2, \mathbf{r}_1) & R(\mathbf{r}_2, \mathbf{r}_2) & \cdots & R(\mathbf{r}_2, \mathbf{r}_M) \\ \vdots & \vdots & \ddots & \vdots \\ R(\mathbf{r}_M, \mathbf{r}_1) & R(\mathbf{r}_M, \mathbf{r}_2) & \cdots & R(\mathbf{r}_M, \mathbf{r}_M) \end{bmatrix} \quad (6)$$

$$= E\{\mathbf{X}(t, \mathbf{r})\mathbf{X}^H(t, \mathbf{r})\}$$

where \mathbf{H} is the Hermitian operator and $E\{\cdot\}$ denotes statistical expectation. Each matrix element $R(\mathbf{r}_i, \mathbf{r}_j)$ is the averaged product of the output of the antenna located at point \mathbf{r}_i times the conjugated output of the antenna located at point \mathbf{r}_j .

1.3.1. Subspace-Based Superresolution. A large volume of work has been presented since the early 1980s on superresolution techniques that are based on an eigendecomposition of the spatial covariance matrix. Many modern algorithms have their origin in the early work of Pisarenko [14], which was revived and expanded by Schmidt [15]. Schmidt's *multiple-signal classification* (MUSIC) algorithm is the most widely cited superresolution technique in the present day literature. It has been the springboard for a seemingly endless flow of methods that are variations of the original approach. In this treatise, the original MUSIC algorithm is considered; however, for

an extensive survey of MUSIC-related techniques, the reader is referred to Krim and Viberg [16].

The initial step in the MUSIC algorithm is to solve the following eigenequation

$$\mathbf{R}\mathbf{E} = \lambda\mathbf{E} \quad (7)$$

where \mathbf{R} is the $M \times M$ spatial covariance matrix, λ is an arbitrary eigenvalue, and \mathbf{E} is an arbitrary eigenvector. This formulation implicitly assumes that the noise background is uncorrelated white Gaussian noise. The M eigenvalues may be ordered such that $\lambda_M \geq \lambda_{M-1} \geq \dots \geq \lambda_1$. The corresponding eigenvectors are arranged to form the matrix \mathbf{R}_E :

$$\mathbf{R}_E = [\mathbf{E}_M, \mathbf{E}_{M-1}, \dots, \mathbf{E}_1] \quad (8)$$

A threshold value is determined such that the eigenvalues greater than the threshold are assumed to be associated with eigenvectors residing in the signal subspace. Likewise, eigenvalues that are smaller than the threshold produce eigenvectors that are assumed to be in the noise subspace. If the spatial covariance matrix were $M \times M$ and there were d signals in the wavefield, then the resulting eigenvector matrix would be partitioned such that the first d columns are vectors spanning the signal subspace, and the rightmost $p = (M - d)$ columns are vectors spanning the noise subspace. If the matrix partition corresponding to noise were denoted \mathbf{R}_p , then the MUSIC spectrum would be given by

$$P = (\mathbf{A}^H \mathbf{R}_p \mathbf{R}_p^H \mathbf{A})^{-1} \quad (9)$$

where \mathbf{A} is the $M \times 1$ array-steering vector defined in the previous section. AoA is determined using an approach similar to the technique described in Section 1.1.2.3. A scalar value P is computed using Eq. (9) for each array steering vector \mathbf{A} , and AoA is given by the array steering vector that maximizes P . If multiple signals were present in the incident wavefield, then the MUSIC spectrum would exhibit multiple peaks. This is illustrated in the next section.

1.3.2. Multisignal DF Example. The MUSIC algorithm is capable of simultaneous DF on multiple incident signals. To illustrate the capability, a linear antenna array geometry is considered with two interfering signals incident on the array [17]. The antennas were deployed in a nine-element minimum redundancy array configuration and this provided an equivalent 30-element filled array measurement. The plot of Fig. 8 shows the results obtained for one signal on array endfire at 180° and a second signal at 61° off array boresight at 151° . The signal at 151° also produced a peak at 209° due to the inherent bearing ambiguity present in a linear array. The effect of the end fire grating lobe of the antenna array is evidenced by the relatively broad peak about 180° . The signal arriving at a bearing removed from the endfire condition produced the more robust peaks observed at 151° and 209° . Although the MUSIC algorithm was able to provide DF results for

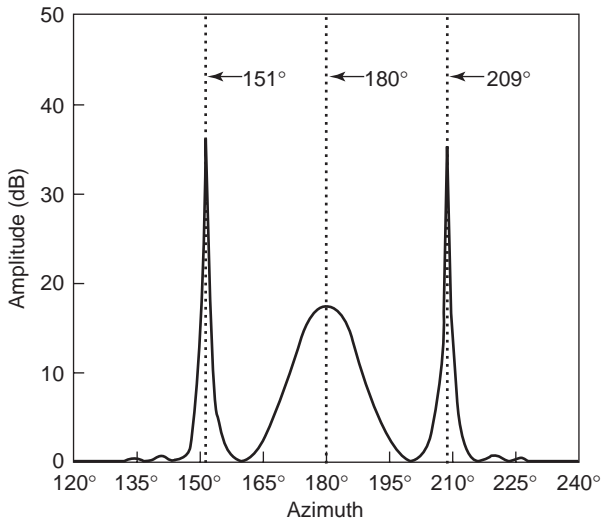


Figure 8. Two signals incident on a linear antenna array resolved using the MUSIC superresolution algorithm. The signals are received from azimuths of 151° and 180° , and the peak at 209° is an ambiguity. The peak at 180° is somewhat smeared because the AoA of the signal is aligned with the longitudinal axis of the array (or endfire).

both signals, these data clearly indicated that angular resolution becomes poorer for signals arriving from directions near array endfire.

A situation in which the MUSIC algorithm was unable to correctly resolve the two signals is shown in Fig. 9. In this case, the AoA separation of the two signals was 4° , and the AoAs were near array endfire, 160° and 164° respectively. The image solutions were evident at 196° and 200° azimuth. Because the AoAs were close together and near array endfire, the MUSIC algorithm as not able to

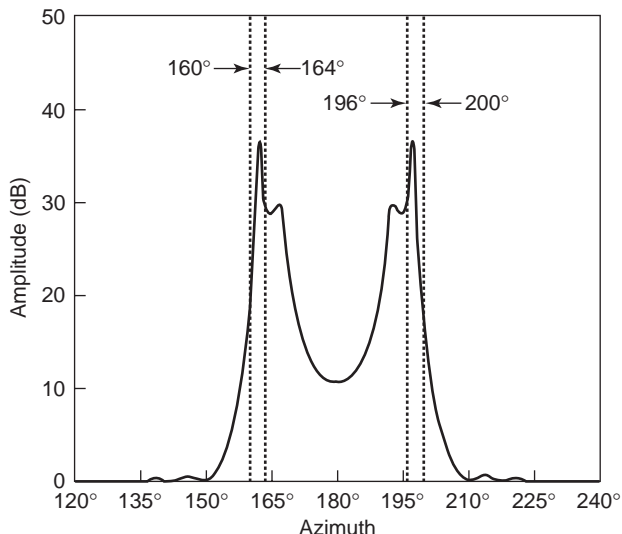


Figure 9. Two unresolved signals arriving from azimuths of 160° and 164° on a linear antenna array. The peaks at 196° and 200° are due to ambiguities in the array. In this case the effective aperture of the array was too small to resolve an AoA separation of 4° . A possible solution would be to lengthen the array by adding more antennas.

resolve the two signals. Two peaks were evident in the MUSIC spectrum; however, neither one indicated an AoA correctly associated with an arriving signal. Improved AoA resolution can be realized for signals arriving on or near the boresight of the array (i.e., orthogonal to the array).

1.3.3. Superresolution Implementation Issues. One of the primary difficulties encountered in the implementation of the superresolution techniques is the requirement for a precise characterization of the antenna array response (viz., array manifold). In general, the array manifold must be known for all frequencies, polarizations, and AoAs. In practice, an array deployed on highly conducting soil and on a site free of interacting structures, may be characterized mathematically using ideal antenna responses [17]. However, for antenna arrays deployed on shipboard, airborne, satellite, or other cluttered sites, a mathematical characterization is generally not possible and the array manifold must be determined by calibration using a transmitter at known locations. Because of the highly robust nature of the superresolution techniques, the array calibration must be done in sufficiently close increments of AoA, frequency, polarization, and elevation as to avoid significant interpolation error. These issues were discussed in the previous section relating to array calibration.

Another source of difficulty is detecting the number of signals in the wavefield. One rule of thumb is based on the relative magnitudes of the eigenvalues. Larger eigenvalues are associated with signals and smaller eigenvalues are associated with noise. This process works reasonably well in high-SNR situations, but it is unreliable for low SNR. It has been shown that underestimation of the number of signals results in poor AoA performance [18], and for this reason, system designers generally try to overestimate the number of signals; however, overestimation may be a problem in low-SNR situations because the eigenbased techniques tend to produce extraneous peaks corresponding to the number of estimated signals. A number of techniques for signal detection have been developed and one which continues to be used as a baseline for performance comparisons is the minimum-description-length (MDL) criterion developed by Wax and Kailath [19].

Coherent signal interference causes a difficulty in the application of superresolution technology. The spatial covariance analysis proceeds on the assumption that the matrix elements are a function of the separation between antennas and are not dependent on the location of the antennas within the wavefield. If the signals are incoherent, then the spatial interference pattern will move relative to the antenna array, and the elements of the spatial covariance matrix will depend only on the relative separation between antennas. However, if the signals are coherent, then the spatial interference pattern will be fixed in space and the elements of the spatial covariance matrix will depend on both separation and location of the antennas. In this case, the analysis will fail. To overcome the difficulty caused by coherent interference, Shan et al. [20] have proposed a technique of *spatial smoothing*, which partitions the antenna array into identical subsets and averages

several covariance matrices of reduced size. This effectively moves the array relative to the interference pattern.

In general, the eigendecomposition part of the computation is not a significant burden, but the search for the AoA solution may be computationally intense. In particular, one must perform the matrix multiplication within Eq. (9) for each array steering vector leading to a solution. For an azimuth-only solution, the task is greatly simplified and the computational burden generally depends on the number of antennas in the array. In the case of 2D azimuth-and-elevation AoA solutions, a number of numerical search techniques have been applied, and they all encounter the well-known difficulties of dependence on starting point, convergence to local maxima, and other variables.

It should also be noted that the superresolution techniques require a separate radio receiver connected to each antenna to permit simultaneous sampling of the array. For this reason, superresolution implementations are frequently called N -channel systems. Multiple matched receiver channels are a major cost driver in the implementation of superresolution methods. Generally, the system designer must evaluate hardware cost versus the expected performance improvement as compared with a more conventional DF architecture consisting of a reference receiver connected to one antenna and another receiver that sequences through all the antennas in the array.

2. TRENDS IN DF RESEARCH

Two primary areas of research in the science and technology of radio direction finding are (1) efforts to improve DF system performance in the presence of reradiating structures and (2) investigations to improve the performance of the superresolution wavefield decomposition techniques. The discussion in this section focuses on a representative subset of the many important research efforts under way.

2.1. Ongoing Developments in Array Calibration Technology

Array manifold errors arise from differences between the overall system response (including site interactions, antenna elements, interfacing networks, cabling, characteristic impedances vs. frequency, etc.) and the model from which the array manifold was derived. Errors in the array manifold generally cause DF performance degradation that equals or exceeds degradations caused by measurement errors. Array manifolds are frequently based on the model of ideal array geometry, perfect channel amplitude/phase match, complete interelement isolation, and absence of site interaction. To the extent that these assumptions are valid, the array manifold can usually be generated analytically. When these simplifying assumptions do not apply, a conventional procedure has been to generate the array manifold through exhaustive calibration measurements with the installed array responding to cooperative transmitters, a procedure that can be expensive and/or impractical.

Because DF performance is critically dependent on the array manifold, the development of efficient methods for

accurately and completely characterizing the array manifold is a topic of active investigation. These investigations typically begin with an initial estimate of the array manifold and an assumed underlying relationship between the installed responses of the array and the initial array manifold characterization. The objective is to minimize the quantity and difficulty of controlled measurements required to accurately characterize the *installed* patterns as a function of azimuth, elevation, polarization, and/or frequency of interest. The initial array manifold characterization is analytically estimated and is assumed to be correct except for discrete, unknown factors that account for (1) antenna mutual coupling, as was done by Friedlander and Weiss [21], (2) directionally independent amplitude and phase errors, and (3) perturbations in the location of each antenna element, as proposed by Weiss and Friedlander [22].

Many research efforts seek to use a bootstrapping technique to develop a *calibrated* array manifold. In this approach, system responses are measured using signals of opportunity, and the initial estimate of the array manifold is adaptively modified to agree with the measured data. These developments usually exploit various constraints on array geometry, nature of modeling error for generating the initial array manifold estimate, knowledge and distribution of AoAs, the statistical nature of the incident signal temporal characteristics, and other factors. Constraints on knowledge of *calibration* signal AoA range from requiring complete knowledge to a complete lack of knowledge, in which case the signal AoA and the array manifold correction factors must be jointly estimated from multiple measurements of responses to the unknown signals. In a related approach, Gustafsson et al. [23] characterize the statistical distribution of the random differences between the initial model and the installed system response, and use this information as a basis for developing linear transformations (through weighting factors) to estimate system responses and reduce modeling errors.

2.2. Research in Superresolution Direction-Finding Techniques

2.2.1. Detection of the Number of Signals. Since eigen DF processing is dependent on an accurate estimate of the number of signals present, research is continuing to define more effective estimation techniques. Two techniques of hypothesis testing for signal detection using eigenvalues were developed by Wax and Kailath [19] and are called the Akaike information criterion (AIC) and MDL methods. One of the difficulties encountered in the application of these two techniques is that performance tends to degrade rapidly as the noise background departs from the white Gaussian assumption. In a more recent work, Chen et al. [24] have proposed a technique called the *canonical correlation test* (CCT) method, which is designed to work well in unknown colored noise and does not require a subjective threshold setting. Also, Wu and Wong [25] have developed an algorithm called *parametric detection* (PARADE), and they contend that the performance of their method is better than that of the CCT approach, particularly in the presence of correlated signals.

It has been observed that the performance of the AIC and MDL criteria tends to degrade in the presence of coherent or highly correlated signals. Ma and Teng [26] report a technique to detect the number of coherent signals through the use of a modified spatial smoothing scheme called *weighted subspace smoothing* (WSS). The authors suggest that the WSS technique provides significant performance improvement over the conventional MDL method in the presence of highly correlated or coherent signals.

Another difficulty in the application of the AIC and MDL criteria is that the performance tends to degrade significantly for short data records or in the small-sample case. This problem has been considered recently by Shah and Tufts [27], who propose a nonparametric procedure designed to improve performance for short data records with moderate-to-high SNRs. The authors contend that the AIC and MDL criteria do not provide flexible control over the false-alarm rate while their method permits a choice of false-alarm rate and corresponding probability of error. In a related work, Zhu et al. [28] develop two new criteria based on information theoretic and eigendecomposition methods and an assumed noise covariance structure. The development results in modified AIC and MDL criteria which the authors claim to show significant performance improvement over the conventional AIC and MDL methods in the case of small-sample populations.

2.2.1.1. Real-Time Subspace-Based Implementations.

Two difficulties routinely encountered in a DF operational scenario are (1) tracking radio transmitters that are in motion and (2) the continual appearance and disappearance of radio transmissions. In both cases, there is a difficulty in realizing real-time adaptive responses with the eigenbased techniques since the averaging operation is used to estimate the spatial covariance matrix. Averaging is necessary to obtain wide-sense stationarity and to achieve statistical stability. In a real-time signal environment, it is highly desirable to update the estimate of the number of signals present and corresponding AoAs with each new snapshot of array data.

A class of fast subspace-tracking (FST) algorithms has been recently developed by Rabideau [29]. The techniques require on the order of $O(Md)$ operations per update (where M is the number of antennas and d is the number of estimated signals). This is contrasted with the $O(M^2d)$ operations required in eigendecomposition methods. The author also implements a rank-adaptive version of the approach called RAFST which tracks changes in the number of signals present in the wavefield.

Another tracking technique, developed by MacInnes and Vaccaro [30], requires $O(M^2)$ operations per update. The authors also propose a scheme for detecting a change in the number of signal sources using each new array snapshot. The authors contend that the new algorithm is capable of tracking rapidly changing AoAs, and that the response is virtually identical to that obtained through the use of a complete eigendecomposition at each timestep. Moreover, the technique is able to accurately track appearing and disappearing sources.

Zha [31] has proposed the use of newly developed fast subspace decomposition methods that exploit the redundancy in large antenna arrays to reduce the computational burden of estimating AoA. The computational complexity is $O(Md) + O(d^3)$ per data vector update.

Another technique proposed to achieve real-time implementation has been developed by performing only linear operations on the data. It is called *subspace method without eigendecomposition* (SWEDE). The technique was developed by Eriksson et al. [32] and is computationally simpler than the exact implementations of the eigenbased methods and is also more robust to assumptions regarding noise spatial correlation. The authors assert that the approach is computationally more efficient than the approximate fast eigendecomposition algorithms, and that the computational complexity of the method is $O(Md^2)$.

2.2.1.2. Coherent Signal Analysis. The problem of correlated signals has been attacked primarily through the application of spatial smoothing as suggested by Shan et al. [20]. In the presence of coherent signals, the primary difficulty arises from the fact that the spatial covariance matrix is not statistically stationary in the wide sense; that is, the terms in the matrix depend on antenna *location* as well as *spatial separation*. Spatial smoothing is a process whereby the array is partitioned into smaller subarrays, and the resulting covariance matrices from the subarrays are averaged. The resulting averaged covariance matrix effectively *decorrelates* the coherent signals. There are a number of research efforts in progress designed to improve on the spatial smoothing approach.

A technique has been proposed by Li et al. [33] to estimate AoA for coherent signal components without the use of spatial smoothing and eigendecomposition. The authors have developed a new method for 2D spatial spectrum estimation of coherent signals using a rectangular planar array, and the method works in the presence of unknown noise environments. The authors claim that the performance of the proposed technique is similar to that of spatial smoothing in the presence of spatially white noise and provides improved performance in spatially colored noise environments.

In another approach, Delis and Papadopoulos [34] propose an enhanced forward/backward spatial filtering method that provides improved performance over spatial smoothing techniques. The authors contend that their enhanced spatial filtering approach requires the same number of antenna elements as the spatial smoothing methods, and it achieves improved performance.

An improved spatial smoothing technique has been proposed by Du and Kirilin [35]. Two problems with the spatial smoothing method are that it reduces the effective aperture of the array and does not take into account the cross-correlation between the subarrays. The authors propose an averaging technique that utilizes the correlations between the subarrays to produce a more statistically stable estimate of the averaged covariance matrix. The authors suggest that the technique provides improved performance when the subarrays are small compared to the size of the overall array.

3. OPERATIONAL ISSUES

All direction-finding operations proceed on the axiomatic assumption that the bearing measured is confirmed on the signal of interest. The advance of DF technology has produced DF systems with the *potential* for excellent operational performance. Experience shows that this potential may never be realized in practice unless equal consideration is given to explicit *confirmation* that the AoA reported is on the signal of interest. Traditionally, DF confirmation has been the responsibility of the DF operator, while DF system engineers have concentrated on bearing accuracy, sensitivity, and response time. The growing speed and complexity of communications signals plus the need to control DF operating costs strongly favor automatic, unmanned DF operations where automatic DF confirmation then becomes crucial for success. A review of DF confirmation techniques is beyond the scope of this article. However, DF confirmation processing is rapidly becoming an integral and indispensable part of DF system engineering. As a result, DF processing choices are increasingly concerned with the acquisition of signal parameter data *directly tied to the corresponding DF measurement* to confirm that the bearing is associated with the signal of interest.

BIBLIOGRAPHY

- P. J. D. Gething, *Radio Direction Finding and Superresolution*, Peter Peregrinus, London, 1991.
- H. H. Jenkins, *Small-Aperture Direction-Finding*, Artech House, Norwood, MA, 1991.
- L. F. McNamara, *The Ionosphere: Communications, Surveillance, and Direction Finding*, Krieger, Malabar, FL, 1991.
- D. N. Travers, ed., *Abstracts on Radio Direction Finding*, 2nd ed., Southwest Research Institute, San Antonio, TX, 1996.
- R. E. Franks, Direction-finding antennas, in Y. T. Lo and S. W. Lee, eds., *Antenna Handbook: Theory, Applications, and Design*, Van Nostrand Reinhold, New York, 1988, pp. 25-4-25-9.
- D. N. Travers, Characteristics of electrically small-spaced loop antennas, *IEEE Trans. Anten. Propag.* **13**(4):639-641 (1965).
- J. E. Hipp, Experimental comparisons of sky wave DF algorithms using a small circular array of loop antennas, *4th Int. Conf. HF Radio Systems and Techniques*, London, 1988, pp. 215-220.
- H. D. Kennedy and W. Wharton, Direction-finding antennas and systems, in H. Jasik, ed., *Antenna Eng. Handbook*, McGraw-Hill, New York, 1961, pp. 39-16-39-18.
- J. E. Hipp, *Adaptive Doppler DF System*, U.S. Patent 5,321,410 (1994).
- R. M. Wundt, Wullenweber arrays, *Signal Processing Arrays; Proc. 12th Symp.* Dusseldorf, 1966.
- D. E. N. Davies, Circular arrays, in A. W. Rudge, K. Milne, A. D. Olver, and P. Knight, eds., *The Handbook of Antenna Design*, London: Peter Peregrinus, London, 1986, pp. 999-1003.
- W. M. Sherrill, D. N. Travers, and P. E. Martin, *Phase Linear Interferometer System and Method*, U.S. Patent 4,387,376 (1983).
- R. L. Johnson, Q. R. Black, and A. G. Sonstebly, HF multipath passive single site radio location, *IEEE Trans. Aerospace Electron. Syst.* **30**(2):462-470 (1994).
- V. F. Pisarenko, The retrieval of harmonics from a covariance function, *Geophys. J. Roy. Astronom. Soc.* **33**:347-366 (1973).
- R. O. Schmidt, Multiple emitter location and signal parameter estimation, *IEEE Trans. Anten. Propag.* **AP-34**(3):276-280 (1986).
- H. Krim and M. Viberg, Two decades of array signal processing research, *IEEE Signal Process. Mag.* **13**(4):67-94 (1996).
- R. L. Johnson, An experimental investigation of three eigen DF techniques, *IEEE Trans. Aerospace Electron. Syst.* **28**(3):852-860 (1992).
- R. L. Johnson, Eigenvector matrix partition and radio direction finding performance, *IEEE Trans. Anten. Propag.* **AP-34**(4) (1986).
- M. Wax and T. Kailath, Detection of signals by information theoretic criteria, *IEEE Trans. Acoust. Speech Signal Process.* **ASSP-33**:387-392 (1985).
- T. J. Shan, M. Wax, and T. Kailath, Spatio temporal spectral analysis by eigenstructure methods, *IEEE Trans. Acoust. Speech Signal Process.* **ASSP-32**(4):817-827 (1984).
- B. Friedlander and A. J. Weiss, Direction finding in the presence of mutual coupling, *IEEE Trans. Anten. Propag.* **39**(3):273-284 (1991).
- A. J. Weiss and B. Friedlander, Array shape calibration using eigenstructure methods, *Signal Process.* **22**(3):251-258 (1991).
- K. Gustafsson, F. McCarthy, and A. Paulraj, Mitigation of wing flexure induced errors for airborne direction-finding applications, *IEEE Trans. Signal Process.* **44**(2):296-304 (1996).
- W. Chen, J. P. Reilly, and K. M. Wong, Detection of the number of signals in noise with banded covariance matrices, *IEE Proc. Radar Sonar Navig.* **143**(5):289-294 (1996).
- Q. Wu and K. M. Wong, Determination of the number of signals in unknown noise environments—PARADE, *IEEE Trans. Signal Process.* **43**(1):362-365 (1995).
- C.-W. Ma and C.-C. Teng, Detection of coherent signals using weighted subspace smoothing, *IEEE Trans. Anten. Propag.* **44**(2):179-187 (1996).
- A. A. Shah and D. W. Tufts, Determination of the dimension of a signal subspace from short data records, *IEEE Trans. Signal Process.* **42**(9):2531-2535 (1994).
- Z. Zhu, S. Haykin, and X. Huang, Estimating the number of signals using reference noise samples, *IEEE Trans. Aerospace Electron. Syst.* **27**(3):575-579 (1991).
- D. J. Rabideau, Fast rank adaptive subspace tracking and applications, *IEEE Trans. Signal Process.* **44**(9):2229-2244 (1996).
- C. S. MacInnes and R. J. Vaccaro, Tracking direction-of-arrival with invariant subspace updating, *IEEE Trans. Signal Process.* **50**:137-150 (1996).
- H. Zha, Fast algorithms for direction-of-arrival finding using large ESPRIT arrays, *Signal Process.* **48**:111-121 (1996).
- A. Eriksson, P. Stocia, and T. Soderstrom, On-line subspace algorithms for tracking moving sources, *IEEE Trans. Signal Process.* **42**(9):2319-2329 (1994).
- P. Li, J. Sun, and B. Yu, Two-dimensional spatial-spectrum estimation of coherent signals without spatial smoothing and eigendecomposition, *IEE Proc. Radar Sonar Navig.* **143**(5):295-299 (1996).
- A. Delis and G. Papadopoulos, Enhanced forward/backward spatial filtering method for DOA estimation of narrowband coherent sources, *IEE Proc. Radar Sonar Navig.* **143**(1) (1996).
- W. Du and R. L. Kirilin, Improved spatial smoothing techniques for DOA estimation of coherent signals, *IEEE Trans. Signal Process.* **39**(5):1208-1210 (1991).

RADIO-FREQUENCY IDENTIFICATION SYSTEMS (RFID)

HITOSHI HAYASHI
Nippon Telegraph and
Telephone Corporation
Yokosuka, Kanagawa, Japan

1. INTRODUCTION

There has been increased use of automatic identification–data collection (AIDC) systems for a variety of applications in many industrial and commercial fields. These technologies include [1]

- Barcodes (including two-dimensional symbols)
- Magnetic stripes
- Optical character recognition (OCR)
- Biometrics
- Smart cards
- Radiofrequency identification (RFID)

RFID technologies have become increasingly popular for use in AIDC systems. *Radiofrequency identification* (RFID) is the commonly used term for equipment that transmits and receives its unique identification data through wireless radiofrequency channels [2]. Although the most widely recognized AIDC applications are barcodes (designed in the 1970s), RFID has additional characteristics that are impossible to achieve with barcodes.

Table 1 compares the characteristics of RFIDs and barcodes. The most significant advantage of RFIDs is the noncontact, non-line-of-sight characteristics, where barcode technologies would be useless. This has made RFIDs indispensable for a wide range of AIDC applications that would not be possible otherwise.

Table 1. Characteristics of RFIDs Compared to Barcodes.

Characteristics	Explanation
Noncontact and non-line-of-sight data transfer	RFID tags can be read by noncontact and non-line-of-sight data transfer using wireless communications
Omnidirectional	They are relatively omnidirectional and readable from almost all directions
Potentially greater amount of data	Potentially greater amount of data can be carried.
Unique identification codes for individual items	Unique identification codes are allocated for individual items
Stable operation even in harsh environments	They work even in various environmental conditions, such as snow, fog, ice, or dust, by adaptively using packages.
Potentially rewritable	Data are rewritable during the product manufacturing stages or lifetime, if read/write type memory is used
Readable even when RFID tags are moving	High-speed read processing can be done even when they are in motion
Relatively long communication range ^a	They can provide long-range communications, especially when active tags are used.
Secured	Encryption can be applied to achieve high-level security
Good anticollision	Multiple tag reading can be done simultaneously
Copies/reproductions	Illegal copies or reproductions are difficult
Longlived/reusable	RFID tags are long-lived and reusable under normal conditions.

^aThey are sensitive to regulatory and environmental constraints.

2. RFID TAGS

Generally, an RFID system is composed of RFID readers and tags. Every object to be identified, such as people and animals, in the RFID system is physically labeled with an RFID tag. The tag carries a unique identification code, and the RFID reader reads and writes the identification codes stored by the RFID tags, which are also called IC tags or RF tags. The working of RFID systems and their features depend mainly on the type of RFID tags used. These tags can be classified in several ways, as shown in Fig. 1.

2.1. IC Chip

One optional characteristic of RFID tags is whether they contain an integrated circuit (IC) chip [3]. Chip type tags contain an IC chip, whereas chipless tags do not. Chipless tags are less expensive to make and are adequate for use in antitheft systems in retail stores. However, to enable an RFID reader to identify manufactured items from around the world, the RFID tags must have sufficient memory to contain an identification code large enough to identify a massive number of objects.

An electronic product code (EPC) concept was proposed by EPC Global Inc., which is the organization that sets the standards for RFID [4]. The EPC is a unique number that identifies a specific item in the supply chain. Each tag can store 96 bits of data, which is sufficient to include the manufacturer's name, the product name, and a tremendous number of unique identification codes that can be assigned to each product.

There are three components in IC chips:

1. RF analog front-end circuits
2. Digital circuits for data processing
3. Memory for data storage

The RF analog front end provides an interface between the antenna and the other functional blocks of the RFID tag

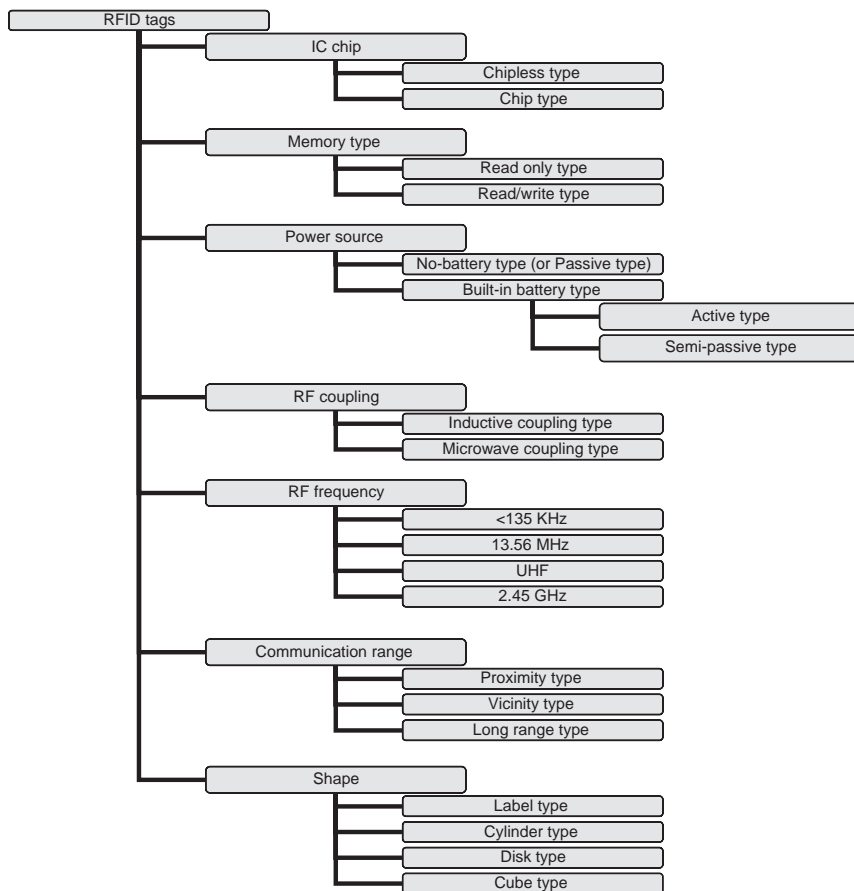


Figure 1. Classification of RFID tags.

such as the power supply, biasing, clock recovery, and data processing. We generally use flip-chip mounting technology to combine the IC chip with the antenna.

Alien Technology, a manufacturer of EPC tags, has developed a new chipmaking technology called *fluidic self-assembly* (FSA) to make miniaturized IC chips [5]. This process allows us to package ICs for assembly into EPC tags at extremely high speeds, which is important for the economical production of EPC tags.

For next-generation ultraminiaturized IC chips, Usami et al. unveiled a prototype called a “μ chip” [6]. The chip is only 0.3 mm² and can hold 128 bits of data. This has also

been authorized by the Ubiquitous ID Center, the organization that sets the standards for RFIDs in Asia [7].

2.2. Memory Type

Another classification of RFID tag is based on its memory type: read-only or read/write. Every RFID tag has an electronically programmed memory with a unique identification code. A “read only” tag has a read-only memory that stores an identification code recorded at the time of manufacturing or when allocated to an object. This is very promising for low cost applications, and can essentially

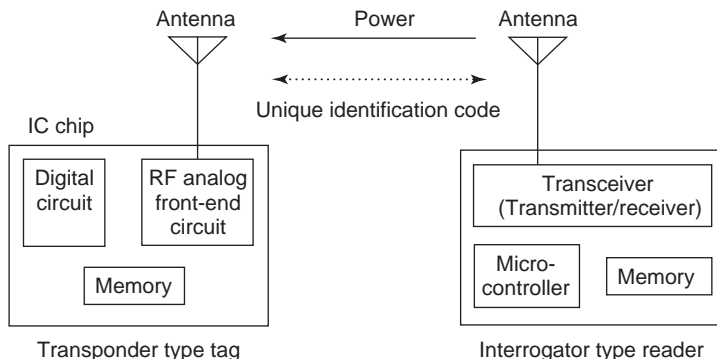


Figure 2. RFID system using transponder-type tags.

Table 2. Comparison between Passive and Active Tags

	Passive Type	Active Type
Communication range ^a	Short	Long
Function	Single	Multiple (adaptive with sensors)
Cost	Low	High
Reliability	Medium	High
Size	Small	Medium
Lifetime	Unlimited	Limited

^aSubject to regulatory and environmental constraints.

provide the same functions as read/write type tags in combination with well-designed networked distributed databases. Auto-ID Labs is currently studying a network infrastructure that will support the efficient and robust collection and delivery of information stored by RFID tags [8]. Read/write tags can have their memories changed or written over many times, and can therefore offer more functions than read only type tags.

2.3. Power Source

Most distinguished classifications of RFID tags are of either the passive, semipassive, or active type [3]. The difference between passive, semipassive, and active-type tags is in the power source and the transmitter. Passive tags have no on-tag power source and no active transmitter. Semipassive tags have an on-tag power source, but no active transmitter. Active tags have both an on-tag power source and an active transmitter. At present, passive tags are the most common.

2.3.1. Passive Tags. Typical RFID systems that use passive tags are made up of a transponder (transmitter/re-sponder)-type tag and an interrogator-type reader.

Figure 2 shows an RFID system using transponder type tags. The interrogator-type reader typically contains a transceiver (transmitter/receiver), a microcontroller, a memory, and a coupling element to connect with the transponder type tag (antenna). The transponder type tag is activated only when it is within the interrogation zone of an interrogator-type reader. The power required to activate the tag is supplied to it from a reader through an antenna.

Passive-type tags are widely used because they are small and very cheap. For example, they are extensively used in applications such as the automatic verification of tickets and gate management. Passive tags are attached to retail merchandise, particularly items that are small,

light, and expensive, such as game software and DVDs, to discourage shoplifting. If the item has not been paid for, an alarm sensor-activated will ring when the object passes through the entrance/exit gate.

2.3.2. Active Tags. Typical RFID systems that use active tags are made up of a transmitter-type tag and a receiver-type reader, or a transponder-type tag, and an interrogator-type reader.

Transmitter-type tags have transmitters only. They do not have receivers, and can periodically transmit their unique identification code, which is dependent on the presence of a receiver-type reader.

Transponder-type tags are activated only when they are within the interrogation zone of an interrogator-type reader. When compared to transmitter-type tags, the transponder-type tag has good anticollision or multiple-reading performance.

The most popular uses for active-type tags are in remote keyless entry systems. Identification of active-type tags is rapid and reliable, and is preferred for these applications. The long-communication-distance capability of active-type tags has made them attractive for locating applications as well.

2.3.3. Comparison between Passive and Active Tags.

Table 2 compares passive and active tags.

Passive-type tags are much lighter, less expensive, and durable than active tags, offering a virtually unlimited operational lifetime. The tradeoff is that they have shorter communication ranges than do active tags.

2.4. RF Coupling and RF Frequency

RFID tags are roughly classified by inductive or microwave coupling between antennas. In general, the configuration and size of the antenna depend on the RF frequency and desired gain, which determine the communication range.

Loop antennas or coils are used mainly for inductive coupling for near-field antennas. On the other hand, dipole antennas and microstrip patch antennas are used mainly as microwave coupling for far-field antennas. Microstrip patch antennas are fabricated on dielectrics with a conductive ground plane underneath. These are typically made using etched thin metal plates or printed conductive lines.

Active integrated antenna (AIA) technology, in which the passive and active components are integrated with the antennas to enable a variety of electrical functions, is also a promising future technology for RFID tags [9,10].

Table 3. General Electrical Characteristics of RFID Tags, Based on Representative RF Frequencies

RF Frequency	RF Coupling	Electromagnetic Interference	Influence of Water or Moisture	Communication Range ^a
<135 kHz	Inductive coupling	High	Very low	Short
13.56 MHz	Inductive coupling	Low	Low	Medium
UHF	Microwave coupling	Low	Medium	Long
2.45 GHz	Microwave coupling	Medium	High	Long

^aSubject to regulatory and environmental constraints.

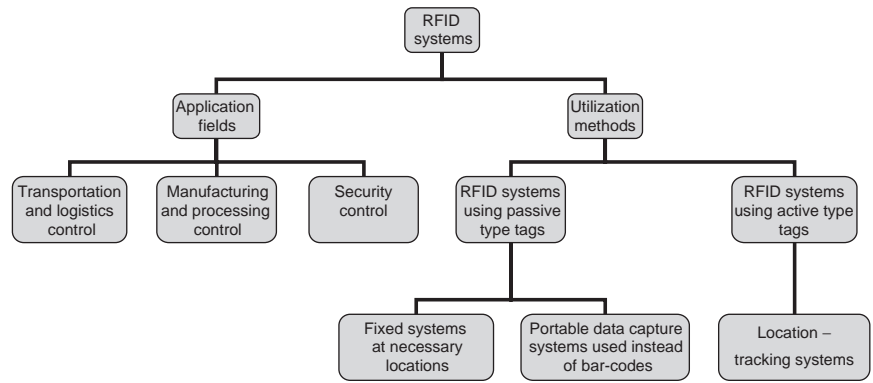


Figure 3. Classifications of RFID systems.

Table 3 shows the general electrical characteristics of RFID tags, based on representative RF frequencies. The allocated frequency and limited power, which influence the communication range, are set by the radio regulations of each country. We have to select an RF frequency that considers the radio regulations and the RFID applications.

2.5. Communication Range

An RFID tag is also classified by its communication range: proximity type, vicinity type, or long-range type. The communication range of proximity type tags is less than several centimeters, while the communication range of long-range tags is more than one meter.

2.6. Shape

RFID tags come in a wide variety of sizes and shapes, such as the label type, cylinder type, disk type, and cube type. We also have to select encapsulating materials within various environmental constraints and with consideration of RFID applications.

3. RFID SYSTEMS

We can roughly classify RFID systems as shown in Fig. 3.

3.1. Application Fields

RFID systems can be a common and useful tool for transportation and logistics, manufacturing and processing, and security control. Figure 4 shows the various applications for these systems.

3.2. Utilization Methods

RFID systems can roughly be grouped into three categories, using the utilization methods:

- Fixed systems at necessary locations (e.g., entrances/exits to detect theft in retail stores)
- Portable data capture systems used instead of bar-codes
- Location-tracking systems

In general, passive tags are used for fixed systems and portable data capture systems, while active tags are used for location-tracking systems.

Location-tracking systems generally rely on triangulation from the time of arrival (ToA) or received signal strength (RSS) [11,12].

3.2.1. ToA Location-Tracking Systems. The best known example of a location-tracking system that uses ToA is the global positioning system (GPS) [13,14]. Current GPSs have been miniaturized to such an extent that they can be

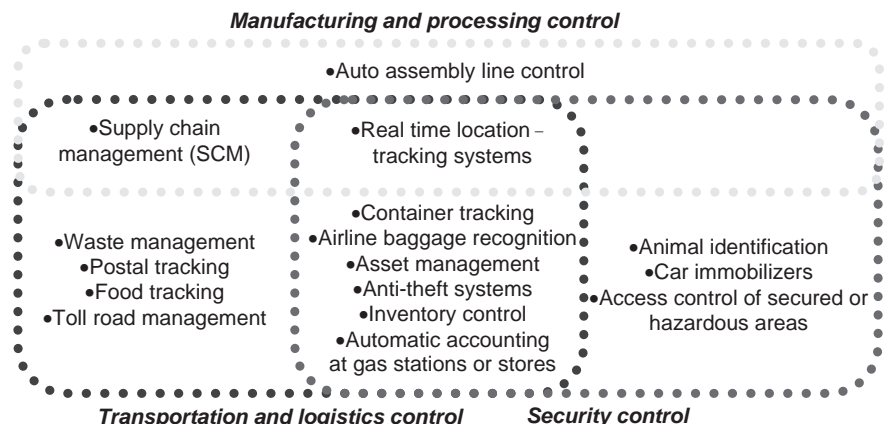


Figure 4. Various applications for RFID systems.

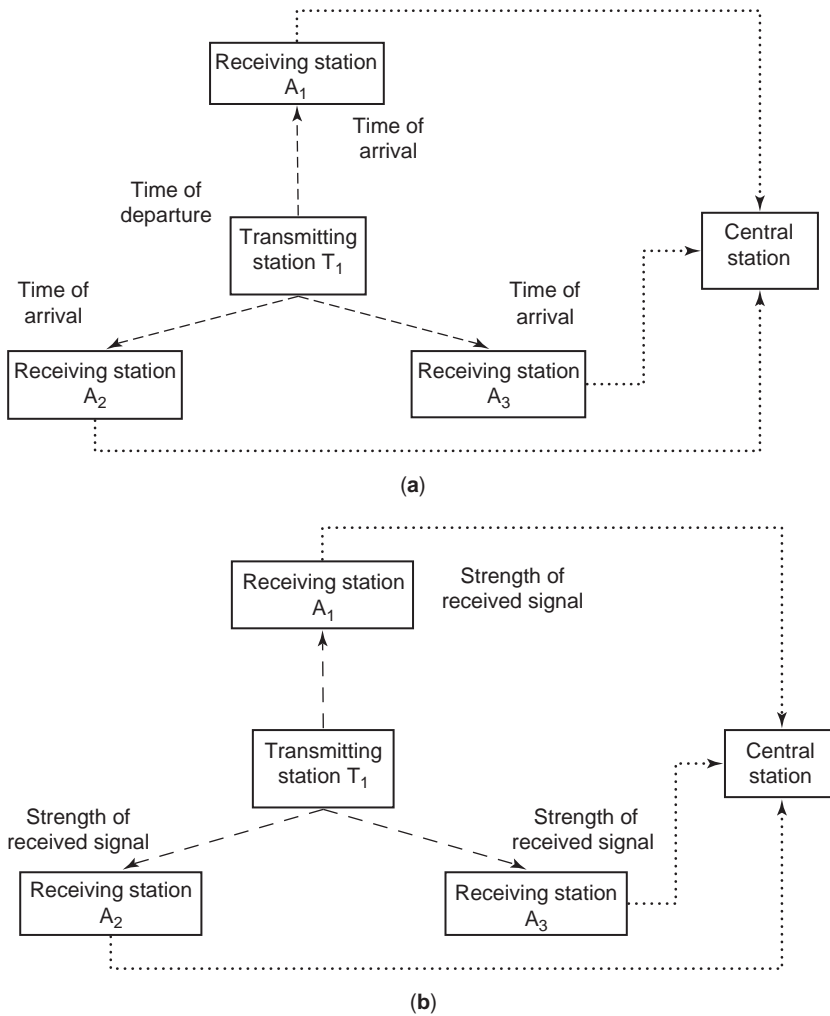


Figure 5. ToA (a) and RSS (b) location-tracking systems.

installed in watches or cellular phones. A ToA location-tracking system is shown in Fig. 5a. It includes a transmitting station T_1 , three or more receiving stations A_1 – A_3 , and a central station that communicates with the receiving stations. The transmitting station transmits a signal, containing its identification code and the current time (i.e., departure time) at predetermined time intervals, using radiowaves. Every time a receiving station receives a signal from a transmitting station, the received signal and the ToA with its identification code are transmitted to a central station. The central station calculates the distance between the transmitting station and each receiving station, based on information provided by the receiving stations, and then estimates the position of the transmitting station. More precisely, the central station determines the signal propagation time from the departure time and the ToA, and calculates the distance between the transmitting station and each receiving station by multiplying the propagation time by the propagation speed of the radiowaves. Then, the central station can estimate the position of the transmitting station by triangulation, relative to the receiving stations.

3.2.2. RSS Location-Tracking Systems. Figure 5b shows an RSS location-tracking system. This system includes a

transmitting station T_1 and three or more receiving stations A_1 – A_3 . The transmitting station generates and transmits radio signals during the positioning operation. Each receiving station reports the measured RSS to the central station. The central station calculates the distance between the transmitting station and each receiving station from the RSS, and then estimates the position of the transmitting station, based on its relative position to each receiving station.

3.2.3. Indoor Location-Tracking Systems. Although GPSs may be effective outdoors, they are unsuitable indoors. In GPSs, while it is possible to request an object's position by measuring the arrival time of the signal from a reference point over a wide outdoor area, large positioning errors can be expected in indoor environments. Even if a position is estimated using RSS information, in many cases the relationship between the distance and RSS does not follow the Friis transmission formula, expressed by

$$L = 20 \times \log_{10} \left(\frac{4\pi d}{\lambda} \right) \quad (1)$$

where L denotes the propagation loss, d the distance, and λ the wavelength [15,16].

The Friis transmission formula does not work for indoor propagation because the receiving station may be blocked from line-of-sight transmission, or local fluctuations in RSS may occur as a result of the influence of reflected waves.

Shimizu et al. proposed a location-tracking system that introduces a corrected Friis transmission formula that takes the environmental influences into consideration [2,12,17]. They also developed a prototype asset management system using active-type tags, in which an RMS position estimation error of 2.3 m was obtained in the test room ($\sim 200 \text{ m}^2$).

4. CONCLUSION

In the near future, every object will likely be connected to the Internet by unique identification codes, through RFID systems. Furthermore, the integration of sensing and actuating technology could also provide new ubiquitous applications. However, to increase the popularity of RFIDs, the following three problems must be solved:

- *Reduction in Cost of RFID Tags.* At present, RFID tags are much more expensive than barcodes. Therefore, we must reduce their cost.
- *Differences in Radio Regulations between Countries.* Radio regulations for RFID applications are different for each country, and this interferes with worldwide (global) use.
- *Protection of individual privacy.* Since RFID systems can be used to track and identify individuals after they have purchased items with RFID tags, there are profound privacy implications to be considered. One possible solution for this problem is to use "kill" technology. All EPC RFID tag specifications include a requirement that the tag will be deactivated when it receives a "kill command" [18]. This would allow a company to render the RFID tag useless after the sale and help assuage some of the privacy concerns related to the use of RFID systems.

BIBLIOGRAPHY

1. K. Finkenzerler, *RFID Handbook*, Wiley, Chichester, UK, 2003.
2. M. Shimizu, H. Hayashi, and M. Umehira, Ubiquitous applications using RFID tags, *NTT Rev.* **14**(5):22–26 (Sept. 2002).
3. T. A. Scharfeld, *An Analysis of the Fundamental Constraints on Low Cost Passive Radio Frequency Identification System Design*, M.S. thesis, Massachusetts Institute of Technology, 2001.
4. EPC Global Inc. (no date), homepage (online), EPC Global Inc. <http://www.epcglobalinc.org/> (May 13, 2004).
5. Alien Technology (no date), homepage (online), Alien Technology, <http://www.alientechnology.com/> (May 13, 2004).
6. M. Usami, A. Sato, K. Sameshima, K. Watanabe, H. Yoshigi, and R. Imura, Powder LSI: An ultra small RF identification chip for individual recognition applications, *Digest Tech. Papers of 2003 IEEE Int. Solid-State Circuits Conf. (ISSCC)*, Feb. 2003, Vol. 1, pp. 398–399.
7. Ubiquitous ID Center (no date), homepage (online), Ubiquitous ID Center, <http://uidcenter.org/> (May 13, 2004).
8. Auto-ID Labs (no date), homepage (online), Auto-ID Labs, <http://www.autoidlabs.org/> (May 8, 2004).
9. B. Strassner and K. Chang, Integrated antenna system for wireless RFID tag in monitoring oil drill pipe, *Proc. IEEE Antennas and Propagation Society Int. Symp.*, June 2003, Vol. 1, pp. 208–211.
10. K. Chang, R. A. York, P. S. Hall, and T. Itoh, Active integrated antennas, *IEEE Trans. Microwave Theory Tech.* **50**:937–944 (March 2002).
11. T. A. Scharfeld and M. Shimizu, A flexible and low-cost object identification and location system, *Proc. 6th Int. Symp. Wireless Personal Multimedia Communications (WPMC)*, MA9-4, Oct. 2003, Vol. 1, pp. 196–200.
12. H. Hayashi, T. Tsubaki, T. Ogawa, and M. Shimizu, Asset tracking system using long-life active RFID tags, *NTT Tech. Rev.* **1**(9):19–26 (Dec. 2003).
13. G. Lachapelle, B. Townsend, H. Gehue, and M. E. Cannon, GPS versus Loran-C for vehicular navigation in urban and mountainous areas, *Proc. IEEE-IEE Vehicle Navigation and Information Systems Conf.*, Ottawa, Canada, Oct. 1993, pp. 456–459.
14. P. Enge and P. Misra, *Proc. IEEE* (special issue on global positioning system) **87**(1):3–15 (Jan. 1999).
15. H. T. Friis, A note on a simple transmission formula, *Proc. IRE* **34**:254–256 (May 1946).
16. S. Drabowitch, A. Papiernik, H. Griffiths, J. Encinas, and B. L. Smith, *Modern Antennas*, Chapman & Hall, London, 1998.
17. T. Tsubaki, H. Hayashi, and M. Shimizu, Asset tracking system using RFID tags, *Proc. 6th Int. Symp. Wireless Personal Multimedia Communications (WPMC)*, WA16-1, Oct. 2003, Vol. 3, pp. 492–495.
18. MIT Auto-ID Center (no date), Hearing on RFID and privacy, testimony of Kevin Ashton (online), MIT Auto-ID Center, http://archive.epcglobalinc.org/privacy_hearing.asp (May 12, 2004).

FURTHER READING

- J. R. Tuttle, Traditional and emerging technologies and applications in the radio frequency identification (RFID) industry, *1997 Radio Frequency Integrated Circuits Symposium Digest*, Denver, June 1997, pp. 5–8.
- K. V. S. Rao, An overview of backscattered radio frequency identification system (RFID), *1999 Asia Pacific Microwave Conf. Digest*, Singapore, Nov. 1999, Vol. 3, pp. 746–749.
- M. Kossel, H. Bebedickter, and W. Baechtold, An active tagging system using circular polarization modulation, *1999 IEEE MTT-S Digest*, Anaheim, CA, June 1999, Vol. 4, pp. 1595–1598.
- J. Hightower and G. Borriello, Location systems for ubiquitous computing, *IEEE Comput. Mag.* **34**(8):57–66 (Aug. 2001).
- J. Werb and C. Lanzl, Designing a positioning system for finding things and people indoors, *IEEE Spectrum* **35**(9):71–78 (Sept. 1998).
- P. Bahl and V. N. Padmanabhan, RADAR: An in-building RF-based user location and tracking system, *Proc. IEEE INFOCOM 2000*, March 2000, Vol. 2, pp. 775–784.

RADIO-FREQUENCY INTEGRATED CIRCUITS

M. CHONGCHEAWCHAMNAN
Mahanakorn University of
Technology
Bangkok, Thailand

U. KARACAOGLU
INTEL Corp., ICG Wireless
Networking Group—WPD
San Diego, California

I. D. ROBERTSON
University of Leeds, Leeds
United Kingdom

1. INTRODUCTION

For many years III–V semiconductors were essential to realize monolithic microwave integrated circuits (MMICs). The late 1990s, however, saw a dramatic change of emphasis with silicon becoming the material of choice for microwave wireless transceivers because of the importance of analogue-digital integration and low cost [1]. The 1990s have been dubbed “the silicon radio decade” [2]. The vast majority of consumer wireless application are in the sub-6 GHz range, including cellular mobile systems, GPS, wireless LANs, RFID, and Bluetooth™ systems. Silicon technology is able to satisfy the noise figure requirements for these applications, and in many cases the power and efficiency requirements as well. These silicon RF integrated circuits are widely referred to as RFICs, and the historic distinction between “RF” and “microwave” has been lost. In the sub 6 GHz region, GaAs technology has been relegated to a few niche areas such as switches and high efficiency power amplifiers. Silicon technology offers much higher levels of integration, including mixed-mode and digital circuitry on the same chip. This latter requirement has led to the development of advanced BiCMOS processes, which produce RF bipolar and low power digital CMOS devices on the same chip, and to widespread interest in RF CMOS, which has less process steps and less mask levels, meaning lower costs.

Even at higher frequencies, Silicon heterojunction devices have started to challenge the dominance of GaAs. However, whereas GaAs provides a semi-insulating substrate ideal for microwave interconnects, silicon does not, and both the designer and process engineer have to address major difficulties at such high frequencies. High-

resistivity substrates, “3D” MMICs [3] and micromachining [4] are just some of the approaches that can be used to combat the substrate loss problem.

The design of an RFIC transceiver is very different from established RF design for a number of reasons:

1. The high level of integration means that interconnects are short and “50 Ω ” design concepts are mostly used only at the LNA input and PA output.
2. The substrate loss and coupling mean that layout techniques such as matching, guard rings, and isolation trenches have to be employed. Cross-chip coupling is a major issue and difficult to simulate, sometimes making it necessary to go through several design iterations.
3. The close integration of digital and analog functions, and techniques such as zero or near-zero IF architectures, mean that a wide range of CAD tools must be integrated into a single design environment.

The RF design, at transistor level and with much layout interaction, may be concurrent with digital design using hardware description languages such as Verilog™ and VHDL. In between, high-speed digital-analogue converters need detailed mixed-signal design. All these parts of the transceiver end up on the same mask, and the CAD environment must provide a seamless integration of the design. The design of fully integrated RFIC transceivers is so complex, and the design cycle so short, that intellectual property (IP) transfer and partnerships between design houses, foundries and consumer product manufacturing companies have become an important business strategy.

2. DEVICE TECHNOLOGY

2.1. Bipolar Transistors

For many years the bipolar device was the only available microwave device in silicon. In virtually all silicon technologies a planar device, fabricated by ion implantation, is used. To optimize the high-frequency performance the device structure must highly advanced, as exemplified by the double polysilicon device shown in Fig. 1. This structure gives higher transition frequencies, higher power gain, lower noise operation, better heat dissipation, simpler matching, and higher integration levels [5].

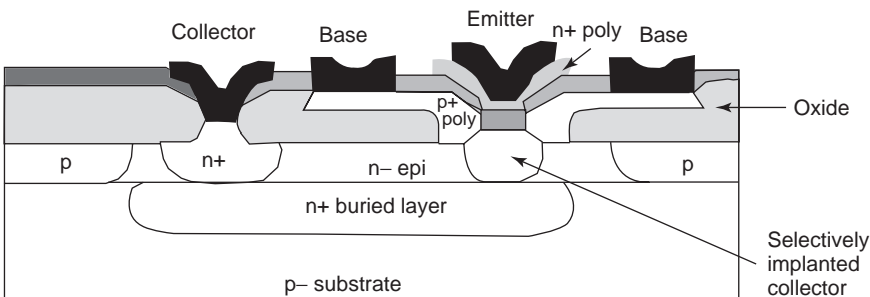


Figure 1. Double-polysilicon npn transistor in cross section.

Often, base resistance is high in bipolar devices, which means that their noise figure is higher than FETs and the f_{max} is reduced. With careful device design, this problem can be overcome to some extent. However, generally, the BJT has a number of parameters that eventually conflict when trying to optimize the device for high performance. Advanced silicon BJT technology, such as that in the Philips QUBiC4 BiCMOS process, is typically capable of $f_t \sim 40$ GHz and f_{max} of 90 GHz [5]. To improve the device much beyond that, it is necessary to change the structure and employ a heterojunction.

2.2. SiGe HBTs

Like the III–V HBTs, the SiGe HBT is based on having a wider bandgap in the emitter than in the base, as shown in Fig. 2. SiGe has a lower bandgap than does silicon, but Ge and Si have different lattice constants, so there is a limit to the maximum concentration of Ge that can be used. Up to that limit, the strain can be accommodated in the layer. The current gain increases dramatically with the difference in barrier height for electrons and holes, but this is traded off with other device parameters in order to achieve an optimum device. The following advantages are provided by the difference in bandgaps:

1. Improved emitter injection efficiency
2. Reduced base transit time
3. Higher output resistance
4. Reduced charge storage in the emitter

Broadly speaking, a key advantage is that the base can be much more highly doped than a standard BJT, and this means a thin base (5–10 nm) can be used without the penalty of a high base resistance. The thin base then leads to a much shorter transit time. The Philips QUBiC4G process (the SiGe equivalent of QUBiC4) achieves 75 GHz f_t and 110 GHz f_{max} . Experimental results have shown that f_t and f_{max} of >160 GHz can be achieved with quite modest lithography. Good noise figures and power efficiencies have also been reported, but it should be remembered that these good results may not be available from the same device structure as a result of the various tradeoffs.

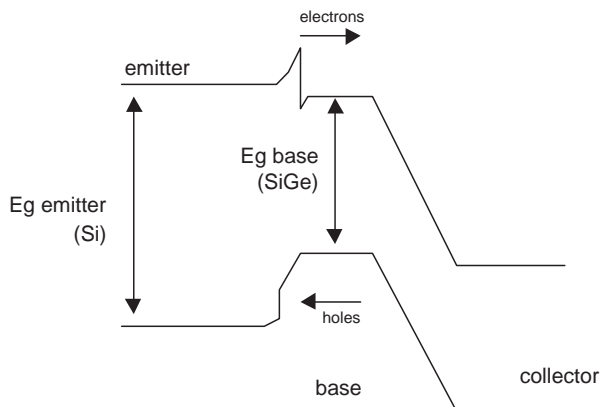


Figure 2. Basic SiGe HBT band diagram.

2.3. RF CMOS

CMOS technology is the foundation of the computer technology revolution. In logic gates the devices have much lower power consumption than do other technologies, and so microprocessors and memory use CMOS exclusively. For a system-on-chip radio solution there has been much interest in BiCMOS, with RF/analog functions in bipolar technology and DSP and other techniques, in CMOS.

However, the process complexity is high, and very many mask levels are needed. For lower cost it is preferable to realize the RF functions in CMOS and dispense with the need for bipolar devices. Already the Pentium™ can clock at >3 GHz and contains more than 50 million transistors.

To integrate RF electronics with these computing components is the ideal way to realize a single-chip communication transceiver. Techniques such as software radio and direct-conversion architectures have assisted with this. To fabricate the LNA, power amplifier, and oscillator on chip requires high-performance microwave devices; performance cannot be compromised. “RF CMOS” is the technology optimized for this combination of RF and base-band circuitry. It seems to dominate all applications in the low-GHz range. Figure 3 shows the photograph and Fig. 4 the layout of an Intel RFIC transceiver on 0.18 μm TSMC (Taiwan Semiconductor Manufacturing Corporation) CMOS technology. This IEEE 802.11a (5 GHz band) transceiver employs a direct-conversion architecture and includes an internal synthesizer. This is Intel’s first RFIC used in a WLAN product.

The outlook for RF CMOS is extremely promising. CMOS processes have become very advanced, with deep submicrometer devices and multiple levels of interconnect metals and dielectrics, as shown in the SEM photograph of the interconnect stack in Fig. 5 [6]. Functional blocks such

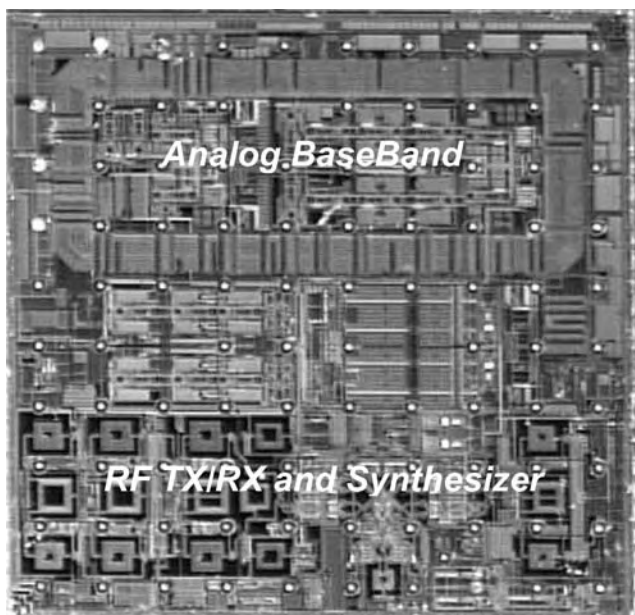


Figure 3. Microphotograph of Intel’s 802.11a RFIC transceiver. (Courtesy of and copyright Intel Corporation.)

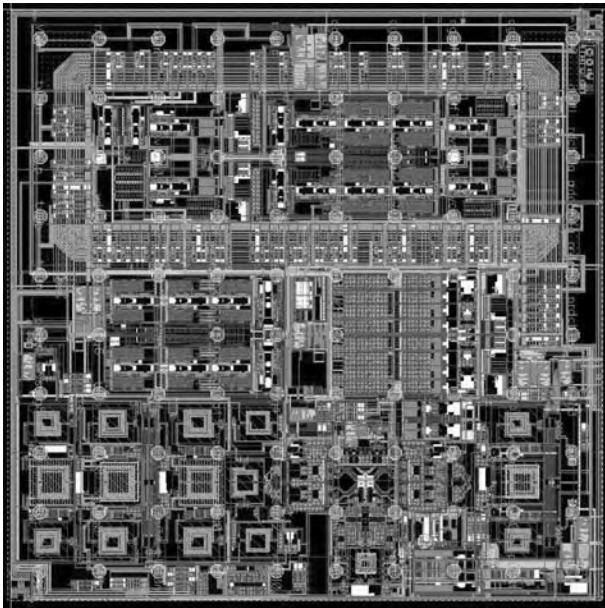


Figure 4. Layout of Intel's 802.11a RFIC transceiver. (Courtesy of and copyright Intel Corporation.)

an ALU (arithmetic logic unit) have been demonstrated at >10 GHz, and yet transistor scaling will continue for some years; Fig. 6 shows a cross section of the Intel TeraHertz transistor [7]. Intel's predictions are for > 1 billion

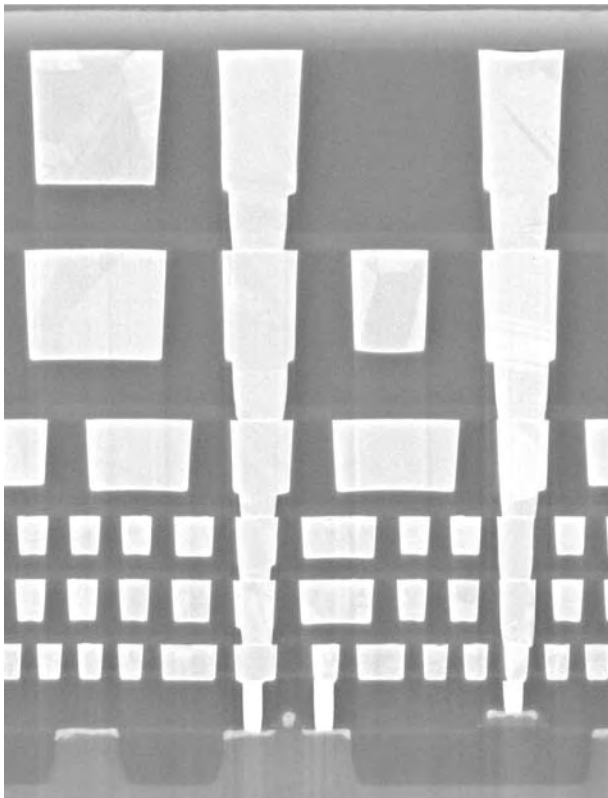


Figure 5. Interconnect stack in the Intel 130-nm P860 technology [6]. (Courtesy of and copyright Intel Corporation.)

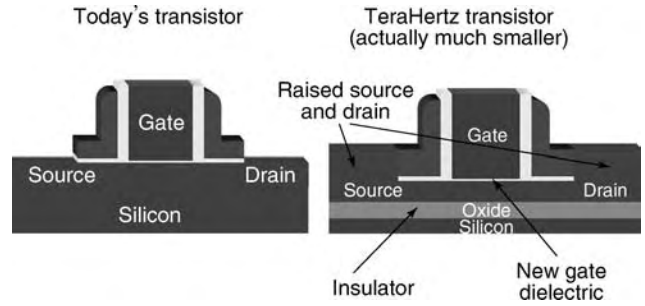


Figure 6. Intel TeraHertz transistor [7]. (Courtesy of and copyright Intel Corporation.)

transistors per chip and 45-nm technology by 2007, as illustrated in Fig. 7. This fantastic technological feat is the product of huge investment in research and development right across the range of process steps, guided by the industry roadmap for silicon [8]. EUV (extreme ultraviolet) lithography is a cornerstone in achieving 10 nm feature size. Power consumption, and therefore heat, is seen as the limiting factor.

There are three classes of the RF CMOS process:

1. Bulk CMOS
2. Bulk CMOS with RF technology enhancements
3. Silicon on Insulator (SOI)

“Bulk” CMOS is standard CMOS, as used in digital circuits, where the device is formed in the surface of the semiconductor wafer by implantation. This technology has been developed worldwide at massive cost to produce <0.1 μm feature size on 300-mm wafers. Even at the 0.18-μm technology node, CMOS can achieve 150 GHz f_{max} [9] with careful layout optimization. The F_{min} of the NMOS device is typically 1 dB at 2.45 GHz. This is poor compared to GaAs devices and SiGe ones, but is adequate for most wireless applications. Since the selling price of a complete Bluetooth transceiver is expected to be \$3 in 2005, bulk CMOS is preferred as it is the lowest-cost solution. The problem with standard bulk CMOS is that the substrate is not insulating; passive components have

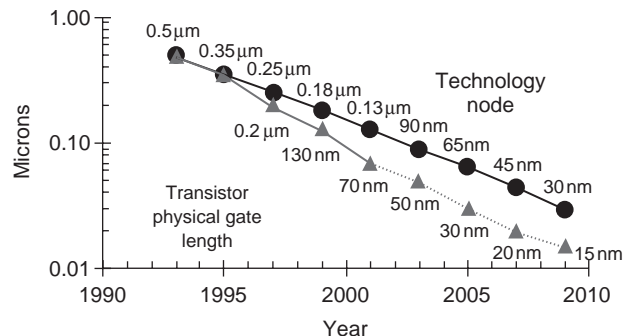


Figure 7. CMOS technology development [7]. (Courtesy of and copyright Intel Corporation.)

very poor performance, and coupling through the substrate can be serious. Techniques such as guard-rings and deep-trench isolation around individual building blocks are needed.

The RF technology enhancements used in some RF CMOS processes include extrathick metals, MIM capacitors, and a higher substrate resistivity. These enhancements ease some of the design challenges but lead to extra mask levels and more process steps. The added cost may not be acceptable for the \$3 radio transceiver.

SOI technology uses either a bonded-wafer approach or a thin silicon implanted oxide (SIMOX) technology to fabricate transistors that are isolated from the substrate. This greatly eases the coupling problems and improves the transistor performance by reducing key parasitic elements. Again, the added process complexity must be considered.

2.4. Silicon Heterojunction Field-Effect Devices

As in GaAs HEMTs, in silicon the field-effect device can be improved by using a heterostructure to create a thin channel of carriers that are separated from their donor/acceptor atoms. The SiGe HFET uses this approach, with either a Schottky gate junction or a gate oxide—the HMOST (heterojunction MOS transistor) device. “HCMOS” (Heterojunction CMOS) technology produces both NMOS and PMOS devices. HCMOS is necessary to realize low-power-consumption digital circuits.

For a given feature size, the SiGe device has approximately 2.5 times the f_v/f_{\max} of a standard silicon device. In the research lab, values over 100 GHz have been achieved, and predictions of >400 GHz have been made from simulations. The enhanced performance can be used to relax the fabrication requirements as well (e.g., use a 0.35- μm SiGe device that has approximately the same performance as a 0.13- μm standard device but much lower mask costs).

3. PASSIVE COMPONENTS

3.1. Resistors

There are numerous ways to implement a resistor in silicon technology. The resistors in integrated circuit technology deviate significantly from the ideal resistor. It is the parasitic capacitance, mainly from the substrate capacitance, which is the key parasitic element that restricts the maximum operating frequency of the resistor. Furthermore, linearity in the resistor and its temperature and process variations are other important factors that affect the design.

Among the techniques to realize resistors in silicon technology, the diffusion resistor is commonly used in standard bipolar technology and can be found in MOS technology. The resistors are formed by diffusing p^+ into an n well, or vice versa. Silicide technology can be used in this technique to reduce the sheet resistivity. Since the resistor structure fundamentally consists of n- and p-type material forming a diode junction, so the resistor’s voltage coefficient is relatively large [10].

Polysilicon resistors are extensively used in digital and analogue CMOS technology nowadays and are highly suitable for RF applications as they have low parasitic capacitance leading to higher frequency of operation. There are two types of polysilicon resistors: salicided and non-salicided structures. Compared with the salicided resistor, the nonsalicided resistor needs an additional mask to prevent a silicide layer forming during the salicidation process. The salicided resistor has a lower resistivity (5–10 Ω/square) than the nonsalicided one (100 Ω/square). Both resistors are commonly used in integrated circuit design because of their small temperature and voltage coefficients. Typically, the temperature coefficients of p^+ - and n^+ -doped resistors, depending on the technology used, are within $\pm 0.1\%/^\circ\text{C}$ and their variations to process are usually within $\pm 20\%$ [11].

The n-well resistor, however, offers the highest resistivity value and hence helps achieve a small die design, but its large temperature and voltage dependence limit it to certain applications, such as in pullup or pulldown resistors. For applications that need high precision and very small resistance values, a metal sheet can be deposited for the resistors. The desired resistance of such resistors can be calculated using the metal sheet resistivity. Alternatively, a small resistor can be obtained using the p^+ and n^+ source–drain region (3–5 Ω/square).

A given resistor type is typically defined by its sheet resistivity in ohms per square (Ω/square). We can determine the value of a resistor from its layout by counting the number of squares of the resistor and multiplying this with the Ω/square value. When the resistor has to be meandered for some specific layout, it has been suggested [12] that the squares at the corners contribute to the area by a factor of only 0.56. The resistor width should also be carefully chosen, especially in high-power and high-frequency applications, since this will relate to the maximum power handling and maximum operating frequency.

3.2. Capacitors

There are several roles for capacitors in RFIC design, including coupling AC signals, bypassing the low-frequency signals to ground, and controlling the operating frequency. Most silicon -based RFIC designs typically implement capacitors in the form of a parallel-plate capacitor. This structure is composed of two separated electrodes of area A , sandwiching a thin dielectric material of dielectric constant ϵ . The two electrodes are separated by a distance d . The capacitance value of this plate capacitor depending on the dielectric in use is given by $C = \epsilon A/d$. In standard silicon technology, there are several forms of the parallel-plate capacitor; for instance, poly–poly capacitor, polydiffusion capacitor and metal–insulator–metal (MIM) capacitor. Other techniques, such as the MOS capacitor, or an active-device-based voltage-dependent capacitor are also sometimes used.

The poly–poly capacitor is a parallel-plate structure in which polysilicon plates form both electrodes and a thin oxide is grown between them. A nitride layer can be used to obtain higher capacitance values. A metal–poly capacitor uses a metal plate as the top plate rather than the

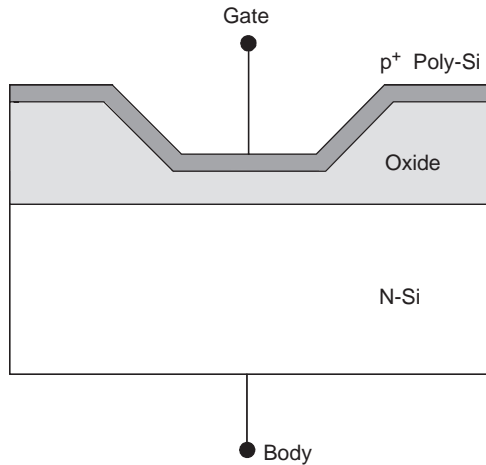


Figure 8. MOS capacitor.

polysilicon. The benefit of this change is that it minimizes the series parasitic resistance resulting from the electrode. For a polydiffusion capacitor, a highly-doped n^+ implant is applied at the specified area and then the gate oxide layer is grown on top. The fabrication of polydiffusion capacitors uses only the standard process steps. For RF circuit designs that mostly require low-parasitic capacitors, the metal–insulator–metal (MIM) capacitor with a well-controlled thin dielectric is best. However, they are only provided by some commercial foundries.

The MOS capacitor, shown in Fig. 8, is perhaps the most commonly used monolithic capacitor. The top plate is a heavily doped p^+ polysilicon layer; the dielectric layer is formed from silicon oxide, and the bottom plate is the n -type silicon. Here, the top- and the bottom-plate electrodes are referred to as the *gate* (G) and the *body* (B), respectively. The capacitance of the MOS structure depends on the voltage dropped across these two terminals (v_{GB}). According to the bias voltage, the MOS capacitance operates in three regimes: (1) accumulation, (2) depletion, and (3) inversion. Nikenejad has described its operation in more detail [13].

The MOS transistor can be used as a capacitor by connecting the source to the drain terminal for one plate and the gate terminal for the other plate. This capacitor can be used as a varactor in a voltage-controlled oscillator by changing from a low capacitance at low junction voltage to a high capacitance as the voltage exceeds the threshold voltage (v_{th}).

3.3. Inductors

The need for a single-chip solution, ease of system integration, and a low-cost design inevitably require an RFIC chip that needs a minimum number of off-chip components. Realizing a high-performance on-chip inductor is, however, one of the biggest challenges for RF engineers [14–16]. Apart from the main inductor design target, which is its inductance value L , two more parameters of the inductor critically affect the design of RFICs: the quality factor (Q) and the self-resonant frequency (f_{sr}), which are figures of merit defining how close it is to an ideal inductor. The Q factor represents the loss mechanisms in the

on-chip inductor, while the self-resonant frequency defines the inductor’s maximum useful operating frequency. Although there are other parameters, such as maximum power handling, Q and f_{sr} are the most important two parameters discussed here.

RFIC designers using a monolithic inductor struggle with low substrate resistivity in silicon, which is usually less than $20 \Omega \cdot \text{cm}$. As the single-chip solution with a high level of integration is demanded for future wireless communication, a standard heavily doped silicon substrate leading to low substrate resistivity is needed for easing the interface with low-frequency circuitry. The low substrate resistivity means that current is electrically and magnetically induced beneath the circuit and this limits the Q and f_{sr} of the inductor. This notoriously well-known conflict is unavoidable for Si-based RFICs unless some special techniques for enhancing the performance such as MEMS technology [17] or silicon-on-insulator (SOI) [18] are used with an increased cost. The details of these improved inductor technologies will be described later.

Figure 9 shows a simplified electrical model relating to the physical form of a square-type spiral on-chip inductor. This model is applicable not only to the square geometry but also other geometries such as circular and octagonal. The self-inductance of this spiral inductor is denoted by L . The series resistor R represents the loss mechanisms in the inductor. These are metallization, skin effect, and the eddy-current loss. The inductor Q at low frequency is limited mainly by the series resistance, which can be reduced by using stacked metals or increased metal thickness, by employing some smoother shapes such as octagonal or circular shapes rather than square, or by choosing a high-conductivity metal such as copper. In Fig. 9, C_p represents the capacitive element between the spiral turns and C_{ox} and C_{sub} are the oxide and substrate capacitances, respectively. These three capacitances contribute to f_{sr} and Q . Note that R_{sub} is the substrate resistance contribution, which also limits both Q and f_{sr} .

Many techniques are used to enhance planar spiral inductors. However, some of the techniques proposed in GaAs technology, for example, multilevel metallization, using copper, do not significantly enhance Si-based

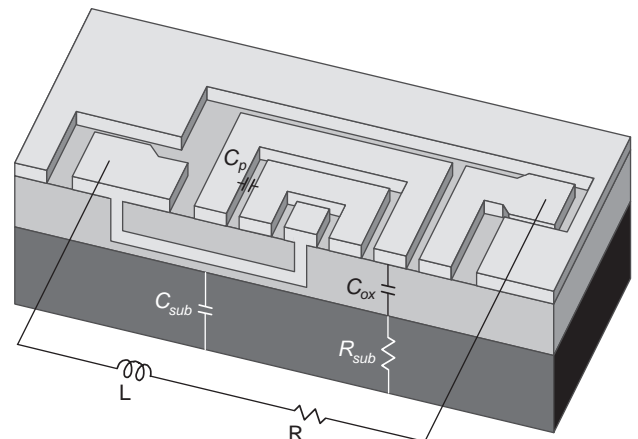


Figure 9. A first-order lumped model of a planar spiral inductor.

inductor performance since the substrate conductivity is the key contribution to degradation of the inductor. The achievable Q of spiral on-chip inductors in standard silicon processes is usually less than 15. Reducing the substrate loss can be achieved by short-circuiting or isolating the low-resistivity substrate from the circuit. Short-circuiting the substrate current is achieved using the patterned ground-shield technique [19], which is shown in Fig. 10a. The slots in the ground-shield plane are designed such that the induced loop ground current is reduced. The inductor Q at 1–2 GHz is increased by up to 33%, but f_{sr} is decreased due to the substrate capacitance increase. A high- Q inductor isolated from the substrate can be achieved by inserting a high-resistivity substrate such as sapphire material between the circuit and the low-resistivity substrate. A 5.5-nH spiral inductor, with a Q of 25 was realized in this way [18] with the drawback of increased process complexity. MEMS technology has been extensively used for improved inductors, including applying a bulk micromachining technique to remove the

underlying silicon substrate, surfacing micromachining, or using an electromechanical process. Note that these techniques need some special processing, and hence the cost of fabrication will increase. An inductor using this special technology to realize a suspended form is shown in Fig. 10b. The peak Q of this fully CMOS-compatible MEMS-based 1.32-nH inductor is 70 at 6 GHz [17]. “Self-assembly” techniques have been investigated by a number of researchers in order to realize inductors that are lifted up off the substrate [20,21].

3.4. Other Passive Components

Many passive components apart from the aforementioned components can be implemented for RFICs [22–24]. Resonators are used in many circuit blocks, such as voltage-controlled oscillators and RF bandpass filters, and can be realized in many forms. The simplest form is a tank circuit consisting of a parallel inductor and a capacitor. The capacitor is often a parasitic component in an active device. Transformers have been used on Si-based RFICs and applied to low-noise amplifier design and other circuit blocks. Other passive components, such as a balun and hybrid combiner, are also readily used and have shown feasibility in certain applications. Since these component topologies rely on a spiral inductor form, the key factor limiting their performance is, however, still the high substrate loss in silicon.

4. CAD

This section reviews the different CAD packages that are available and describes how they are used in conjunction with various models in the RFIC design process. A wide range of different component models can be used; the choice depends on the level of component characterization that has been carried out and on the specific CAD package that is available. For RFIC design a fully integrated CAD workstation that has an integrated layout library is essential. The key companies in the RFIC CAD business are listed in Table 1. A wide range of software is available. When mixed-signal design and DSP is integrated with RF circuitry for a single-chip radio solution, the design framework will have to integrate everything from VHDL (very high speed integrated circuit hardware description language) synthesis to transistor-level RF design tools.

4.1. System Block Diagram Simulation

Such is the complexity of many designs that individual circuits have to be treated as blackboxes with some kind of describing function. This enables complex subsystems, such as complete transmitters and receivers, to be designed at a high level. Since systems are becoming increasingly complex, and as digital signal processing becomes closely integrated with RF/microwave hardware, system-level and mixed-signal simulation is becoming more important and is receiving a great deal of attention. Note that where pseudorandom baseband signals and high-frequency carriers are present simultaneously, there may be *huge* numbers of sample points to be calculated; the “modulation domain” analysis in ADSTM addresses this problem.

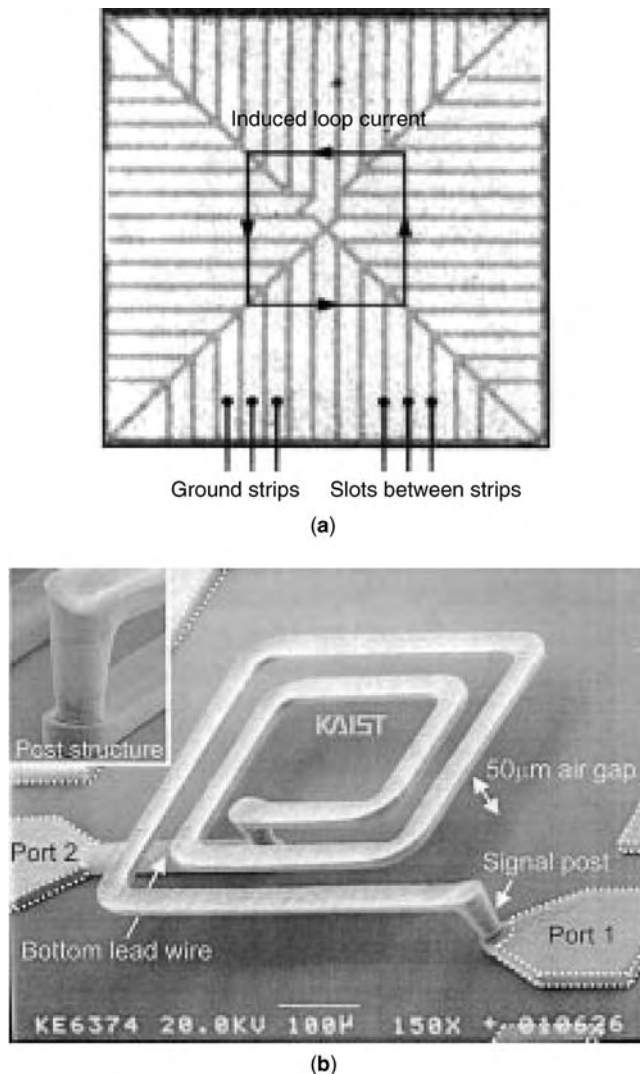


Figure 10. (a) Patterned ground shield [19]; (b) micromachined on-chip inductor [17]. (Copyright IEEE, used with permission.)

Table 1. A Selection of Commercial Simulators

Company	Product ^a	Type
Agilent	ADS	RF linear, nonlinear and system design suite
Ansoft	Momentum	3D planar EM simulator for passives
	Serenade	Integrated RF design environment
	Harmonica	Harmonic balance nonlinear
	Symphony	System-level RF design
Cadence	Ensemble	3D planar EM simulator
	Analog Design Environment	RFIC design suite
	AMS	Mixed-signal design
Mentor Graphics	SpectreRF	Nonlinear transistor-level simulation
	RF Architect/RF Layout	Board-level design linking to ADS
	ADMS	Mixed-signal simulation
Silvaco	EldoRF	Transistor-level RFIC design
	Athena, Atlas	Physical-level device simulation
	SmartSpice, Celebrity	SPICE-based VLSI design and layout
	UTMOST	Device model parameter extraction

^aAll trademarks are acknowledged.

4.2. Simulator Customization

Fierce competition requires that designs work first time to reduce time to market. Since successful RFIC design relies heavily on the accuracy of the available models for active and passive components, it is vital that manufacturers offer extensive model libraries and design information. The extent to which a process has been characterized and carefully developed into a fixed production process is often more important to a customer than the ultimate performance achievable. The characterization and process definition task, from the first RFOV (RF on water) testing of a new device up to the official release of a model library and design manual, may take many man-years. The model library is the fruit of a great deal of labor, and while it represents only a small part of the manufacturer's modeling and design information, the model library is the basis of all the customer's design work.

In a fully integrated CAD package there is seamless integration of the schematic (e.g., see Fig. 11) and parameterized layout. In order to achieve this level of design integration for ICs, the simulator must be customized to the foundry with suitable technology files, models, and parameterized layout library elements. In this way the layout and schematic can be linked together; a change made in the layout window will automatically result in a change of the parameters in the schematic. For example, if you edit the length of a track in the layout editor and then pass the new length information to the schematic, the simulation can be rerun directly. This transfer of information directly between the layout and the schematic/simulation is called backannotation. It should be noted, however, that despite all the apparent sophistication of such a CAD suite, it is as important as ever that the designer be aware of the nature and limitations of the models that he/she is using.

5. AMPLIFIERS

5.1. Low-Noise Amplifiers

The low-noise amplifier (LNA) is, perhaps, the most essential building block for a modern wireless receiver

since it must be able to receive an extremely small incoming signal from the front-end antenna from within a hostile atmosphere (both noise and interference signals) and, subsequently, boost the received signal while maintaining the signal quality. In order to achieve this, a good LNA must amplify the amplitude of an input signal while, ideally, no extra unwanted noise is added to the output signal of the LNA. The figure of merit most often used is the noise figure (NF). Besides NF, gain, and linearity, RF designers must consider the input and output impedances to ensure that no unnecessary mismatch loss occurs at the antenna-LNA interface. Furthermore, with the demand for low-cost, high-performance, and small-size portable communication terminals, various low-complexity receiver architectures, such as a homodyne receiver and a low-IF receiver, have been proposed to fulfill these design goals. However, new problems of these architectures have emerged. Hence, the subsystems supporting these proposed architectures must have enhanced features to counteract these new problems, such as LO and DC offset leakage in a homodyne receiver. Therefore, apart from an LNA's aforementioned conventional design parameters such as gain or NF, the LNA designer must be concerned with other design parameters, such as high reverse isolation of the LNA to prevent leakage of LO power from the mixer back to the antenna [25,26].

Designing LNAs in silicon technology is more problematic than in GaAs technology because of the low-resistivity substrate material, which contributes to substrate loss, eddy-current loss, and substrate capacitance. As discussed in Section 3, realization of high- Q and high-self-resonant frequency inductors on a standard silicon technology requires a laborious effort to achieve success. A low- Q inductor creates more dissipation loss and, hence, directly degrades the noise performance of the LNA. The substrate noise and coupling are other major problems in silicon technology. To suppress these, the differential topology is commonly used rather than the single-ended design because of its high common-mode noise rejection, although there are power consumption and circuit size tradeoffs [27].

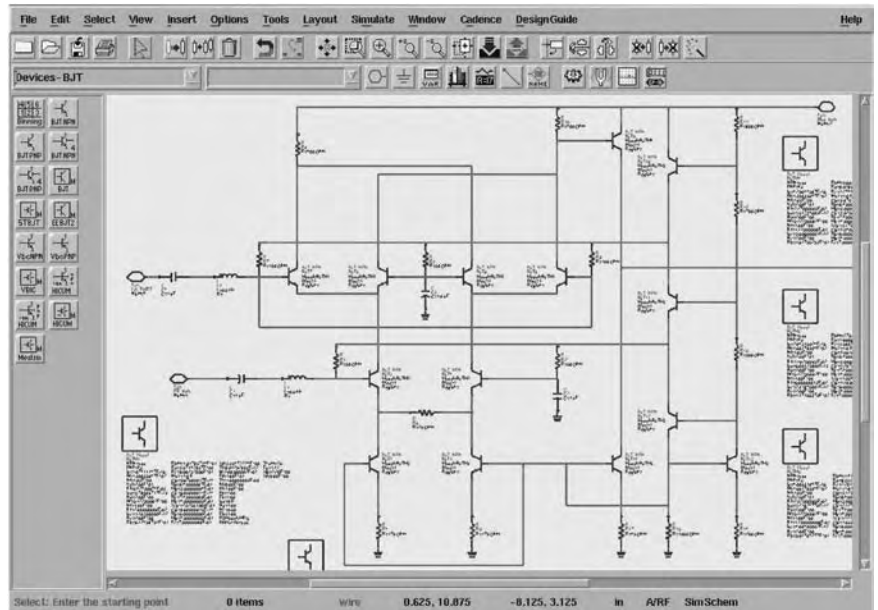


Figure 11. Gilbert cell mixer schematic in ADS™.

Among the numerous techniques used to implement the LNA for wireless applications nowadays with standard silicon technology, the common-emitter (for bipolar transistor) or common-source (for field-effect transistor) devices with inductive series feedback, as shown in Fig. 12a, are typically used to achieve a high gain, low noise, and simple design [28]. The topology comprises the operational bandwidth; the series feedback inductor L_E increases the input resistance by the amount of $R_i = \omega_T L_E$, where ω_T is the unity-gain frequency. This equation shows that the input impedance on the Smith chart of this common-source or common-emitter inductive series feedback topology can move to the 50-Ω region without the noise tradeoff, leading to simultaneous noise and power matching. Also, the input reactance, mostly in capacitive form, can be canceled by using a series inductor to resonate it out. This will simplify the design task efficiently. Nevertheless, the designed LNA has narrow bandwidth due to the input matching structure. Furthermore, in practice, the noise figure of the LNA is increased because of the finite Q inductor. The advantage of using this feedback is high linearity and good temperature dependence of gain

and input impedance so that the bias of this topology need not be accurate. Input-output isolation performance is a problem for this topology as the feedback capacitance and Miller capacitance dominate, especially at high frequency.

Figure 12b shows the emerging LNA architecture for Si-based application, namely, the “transformer feedback LNA” [29]. In this technique a portion of power from the drain terminal is magnetically coupled to the source terminal, which gives negative feedback. The amount of feedback is determined by the transformer’s coupling factor k , where the invert wiring arrangement mainly determines the mechanism of negative feedback. This feedback neutralizes the transistor by canceling the Miller capacitance, which, in turn, improves the reverse isolation. The minimum noise figure of this transformer feedback LNA is theoretically equal to the minimum noise figure of the device due to its inherent source degeneration property (L_{11}). Since a single transistor is required, this LNA topology is suitable for low-voltage applications. The right-hand side of Fig. 13 shows a chip microphotograph of a 5-GHz transformer feedback LNA designed on 0.18-μm CMOS technology [29].

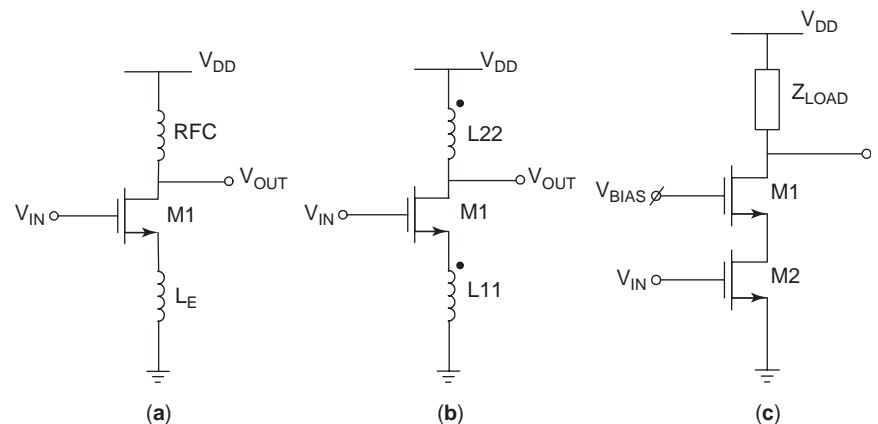


Figure 12. Three LNA topologies suited for silicon RFICs: (a) source degeneration; (b) transformer feedback; (c) cascode.

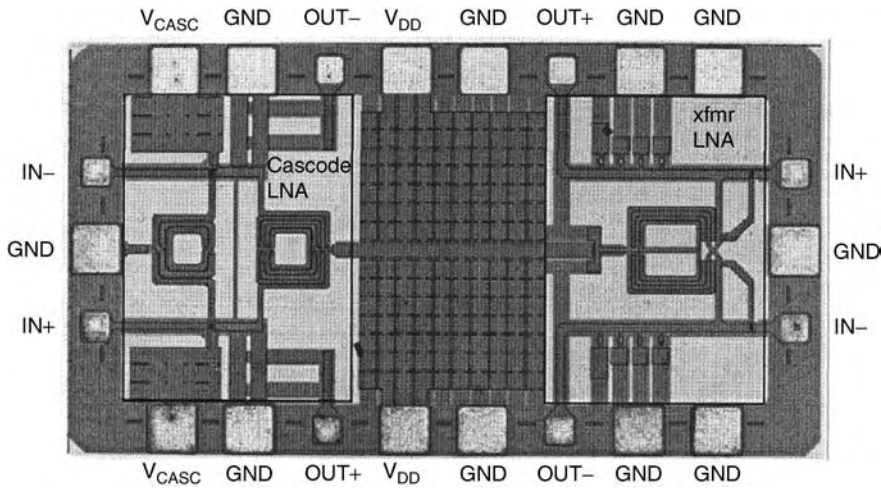


Figure 13. A 0.18- μm CMOS chip microphotograph of a 1-V 5-GHz transformer feedback LNA [29] (Copyright IEEE, used with permission.)

As shown in Fig. 12c, the cascode LNA architecture uses a series connection of a common-emitter (CE)/common-base (CB) or common-source (CS)/common-gate (CG) transistor pair. It eliminates the Miller multiplication of the feedback parasitic capacitance of the CE (CS) transistor. Then, the cascode LNA is almost unilateral; that is, low reverse transmission coefficient (S_{12}) is achieved, and this will simplify the amplifier design task for input-output matching. Although noise can be added from the CB (CG) stage, the noise figure of the cascode LNA is not significantly higher than the source/emitter degeneration transistor if the front-end CE (CS) of the cascode has sufficiently high gain. Since the front end is CE (CS), the source/emitter degeneration technique can also usually be applied to obtain simultaneous noise-power matching. There is, seemingly, a need for more headroom voltage for the cascode design due to the extra CB (CG) stage. Oscillation can possibly occur, especially at the second stage if the gate of the second stage is not small-signal-grounded. The microphotograph of a 5-GHz cascode LNA on 0.18- μm CMOS technology is shown in the left half of Fig. 13.

5.2. Power Amplifiers

The power amplifier (PA) is one of the most crucial RF front-end parts of a wireless transceiver. The PA's main function is to boost the signal power up to a specific power level that can transmit to the receiver at a desired distance. Small size, low cost, low voltage, and long battery life are needed for portable terminals; hence, a high-efficiency, high-power, and low-voltage-operated PA using a cheap IC technology such as silicon technology is required. In addition, a high-linearity PA is increasingly important to support multichannel and multiuser wireless communication technologies, for example, wideband code-division multiple-access (WCDMA) standards. PA design with cheap silicon technology seems to face the same problem as the LNA does. It is the poor passive component performance that is the main bottleneck. Loss in Si-based passive components used for matching networks or bias chokes causes low achievable power, low power gain, and increased power consumption, and ultimately, reduces the

power efficiency significantly. Sometimes, the off-chip component solution, particularly for the output matching network, is used to realize a high-performance PA, but this is not as desirable as the low-cost single-chip concept. Another problem in a fully integrated PA design, especially in CMOS technology, is the low breakdown voltages, source-drain, drain-gate, and drain-substrate, resulting in a low-power device. Higher output power can be achieved using an impedance transformer, but the low-performance passive components in standard silicon technology pose a challenge. Chip-level combining of small devices to achieve high power faces the notorious problem of low substrate resistivity. Fortunately, there is one promising technique worthy of mention, namely, the distributed active transformer (DAT). The DAT uses magnetic coupling of the output power from each push-pull transistor cell. Fig. 14 shows the microphotograph of a DAT-based >1-W PA chip using standard CMOS technology [30,31].

As mentioned before, silicon technology is preferred for wireless technology nowadays because of its relatively low cost compared with GaAs. However, silicon RFIC designers have to struggle with the low substrate resistivity,

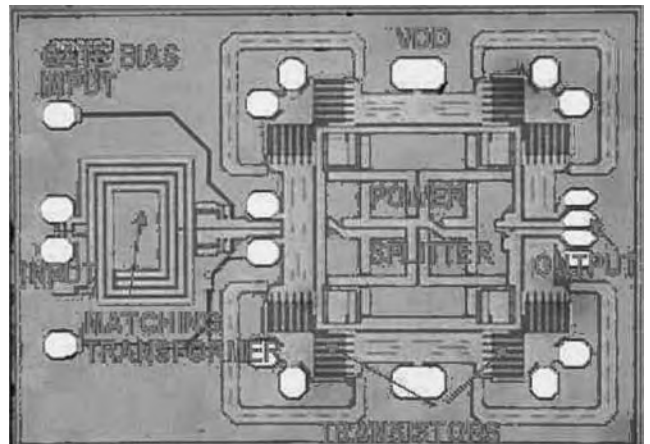


Figure 14. Chip microphotograph of DAT-based 1-W fully integrated PA on CMOS [30]. (Copyright IEEE, used with permission.)

giving many problems to solve. However, silicon has excellent thermal conductivity, 3 times that of GaAs. This makes the silicon-based PA more suitable for high-power application. Besides PA output power, the other crucial PA performance properties (linearity and efficiency) and enhancement techniques will be briefly discussed.

Efficiency is the most important PA design issue. Traditionally, the approaches to improve PA efficiency are achieved by controlling the DC biasing point, for instance, classes A, AB, B, and C. Among these, the most classical approach, class A, is the amplifier that provides the lowest maximum power efficiency but highest linearity [32]. As mentioned above, the derivative techniques of class A, such as classes B, AB, C, use a smaller bias current so that average biasing current is decreased. The power efficiency of these amplifier classes is significantly improved, but the distortion increases since the active devices are not conducting throughout the cycle. Therefore, these PA classes inevitably require an RF bandpass filter at the transistor output to eliminate the nonlinear generated harmonic distortion.

The class E PA [33] is intentionally designed such that the transistor is operated like a switch. The switch waveform and its duty cycle are controlled by the drive level and the biasing point at the transistor input. The output voltage and the output current waveform timings are designed such that no DC power dissipation occurs in the device. The PA is highly nonlinear since the output waveform is square-wave-like, and, as in classes B and C, a bandpass filter is needed to eliminate the harmonic distortion. Class F PA design [33] allows an increase in power efficiency by adding odd harmonics to flatten the output voltage waveform. This will allow more peak output power and then the efficiency increases.

The Doherty amplifier is very suitable for modern wireless applications, such as in multiuser multi-channel communication systems that need a power control scheme or in a high-capacity communication system that needs a high linearity transmitter—for example, orthogonal frequency-division multiplex (OFDM) systems. This technique tunes the output impedance of the main amplifier actively by employing a high-efficiency auxiliary amplifier. The feasibility of the CMOS-based Doherty amplifier was demonstrated [34] using a lumped-element approach to reduce loss and minimize the die area, and therefore the fabrication cost.

So far, all the aforementioned techniques to boost power efficiency trade off the PA linearity. There are various emerging wireless communication standards such as CDMA that transmit the information via the carrier envelopes. These standards impose very strict specifications on PA linearity. In order to meet these, linearization techniques are applied to the PA designs [35]. There are many proposed PA linearization techniques but only a few that are suitable for on-chip integration. Feedforward, although offering high performance in terms of intermodulation distortion and wide bandwidth, seems to be inappropriate for IC applications. The main reasons are its complexity and the sensitivity of the distortion reduction performance. The feedback technique has been used for ICs but has many disadvantages, such as narrow

bandwidth, potential instability, lower gain, and lower power, and hence is not so attractive for PA applications. Perhaps, the most successful linearization technique nowadays is the predistortion technique. The input signal is predistorted such that the predistorted input signal will cancel out the distortion generated from the nonlinear mechanisms in PA active devices. The predistortion technique is the most frequently used linearization technique especially in portable communication units because of its simplicity, compact size, low power consumption, good distortion reduction performance, and low cost. The simplest predistortion block is realized by using a diode, which is a standard device in silicon technology. Increasingly, the predistortion block is implemented at baseband using digital signal processing, which is widely used in wireless communication nowadays. The technology solution for a high-efficiency and high-linearity RFIC PA seems to be a high-efficiency PA with the digital predistortion technique [36].

The “linear amplification using nonlinear components” (LINC) technique is another technique that is gaining in popularity as the need for linear transmitters increases with the introduction of wideband systems using advanced modulation schemes. The LINC concept is based on the fact that a highly nonlinear amplifier can still deal with phase modulation. The amplitude modulation of the signal is replaced with a pair of constant-amplitude phase-modulated signals that are then independently amplified by two high-efficiency amplifiers, such as class C ones. The outputs are power combined to reconstruct the original input signal waveform. The LINC concept needs a signal processing part to generate the phase-modulated waveform pair, this being referred to as the signal component separator (SCS). In practice, the efficiency is reduced by combining loss and phase/gain mismatch has a significant impact on the nonlinear distortion reduction performance. Adaptive signal processing needs to be employed to eliminate this phase-gain mismatch. Figure 15 shows the microphotograph of a BiCMOS SCS chip with integrated mismatch control circuitry [37].

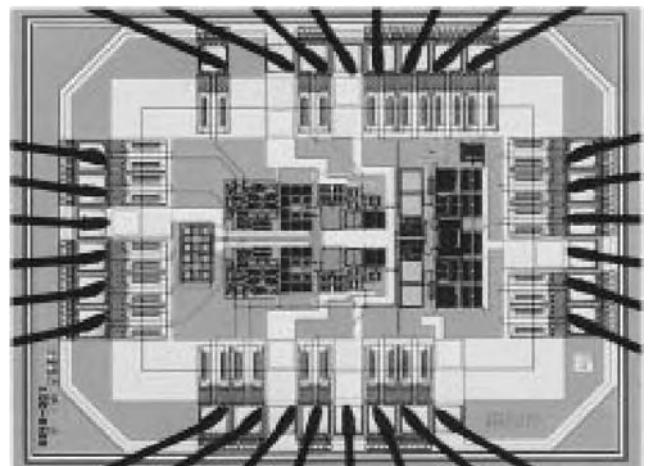


Figure 15. A chip microphotograph of BiCMOS SCS chip for 200-MHz IF LINC transmitter [37]. (Copyright IEEE, used with permission.)

6. OSCILLATORS

The oscillator is an essential component for all RF transmitters and receivers. Virtually all modern applications employ frequency synthesis in order to achieve good frequency stability and low phase noise. The voltage-controlled oscillator (VCO) is the key RF component in a phase-locked loop (PLL) frequency synthesizer. There are two classes of oscillator circuit, namely, feedback and negative-resistance oscillators. A feedback oscillator consists of an amplifier and a resonant circuit that couples the output signal back into the input. A negative-resistance oscillator consists of a negative-resistance circuit coupled to a resonator. In fact, the two types are quite similar because feedback is used to create the negative resistance, anyway. The ring oscillator is clearly a feedback oscillator, but since it does not use a high-*Q* resonator (e.g., LC type), its phase noise is fairly poor.

There are various kinds of resonators in general use at RF, including *LC* tuned circuits, cavity resonators, dielectric resonators, YIG resonators, and superconductive resonators. Few of them, however, can be integrated onto RFICs. A varactor-tuned oscillator can easily be realized using a resonator consisting of a varactor diode and an inductor or transmission line. The low-*Q* factor of such a resonator means that the phase noise is poor, and this approach is used only for noncritical applications or for externally phase-locked oscillators. For better phase noise performance the most common technique is to employ an off-chip resonator, a bond-wire inductor [38,39], or MEMS technology [40,41].

While the classic Colpitts oscillator is widely used in hybrid RF circuits, most RFIC oscillators are based on a differential pair, cross-coupled to provide positive feedback. This topology is simple and gives reliable startup. The differential oscillator rejects unwanted common-mode signals such as substrate and PSU (power supply unit) rail noise. The tank circuit consists of a pair of inductors with the capacitor *C* as shown in the NMOS-only version in Fig. 16a, realized with a pair of varactor diodes connected cathode to cathode with the tuning bias applied at the cathodes. For increased tuning range, additional switchable capacitors might be incorporated for band selection. It is widely known that the tank energy must be maximized to improve phase noise. A detailed analysis and procedures for optimum design of these *LC* VCOs has been presented by Ham and Hajimiri [42]. The complementary version of Fig. 16b gives some improvement in phase noise; however, the novel noise-shifting differential Colpitts VCO in Fig. 16c, designed with careful consideration of the optimum waveforms, gives the best performance [43]. For image rejection and direct conversion applications, a pair of quadrature outputs can be generated by coupling two such circuits together via the tank circuits [43,44].

6.1. Negative-Resistance Oscillators

Most microwave oscillator designs employ the negative resistance approach. Consider the circuit shown in Fig. 17, where Γ_R and Γ_T are the reflection coefficients of the resonator and the transistor, respectively. The oscillation

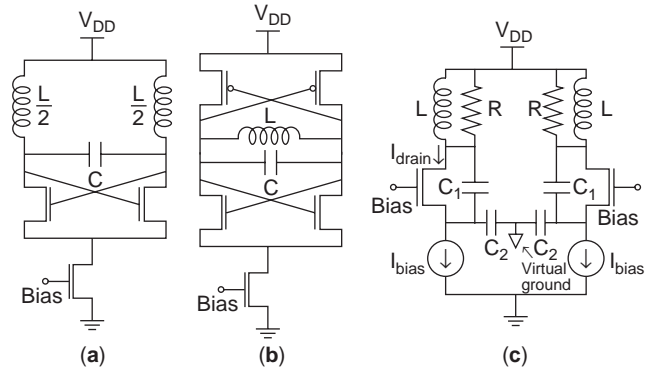


Figure 16. VCO circuits: (a) NMOS-only; (b) complementary; (c) differential Colpitts, [43]. (Copyright IEEE, used with permission.)

condition of a negative resistance oscillator can be stated as $\Gamma_R \Gamma_T = 1$. This expression implies that, at the frequency of oscillation, the return loss of the resonator has to be equal to the return gain of the active block, and the sum of the arguments of Γ_T and Γ_R has to be an integral multiple of 360° . A return gain means that a negative resistance must be present at the input terminal of the active device. Note that the oscillation frequency is not necessarily the same value as the resonant frequency of the resonator, provided the criterion above is satisfied. For oscillations to begin, the magnitude of the negative resistance must be bigger than the value determined from this small-signal condition. Because of the excess negative resistance in the circuit, the oscillation will grow in amplitude until the negative resistance is reduced in value, by nonlinear effects, to a steady-state value. In practice, the negative resistance is created by applying feedback to transistors.

In the case of the bipolar transistor (BJT or HBT), the device is often connected in common-base configuration with an inductive feedback element, as shown in Fig. 18a, and the negative resistance is developed at the emitter terminal. In the case of the FET the device can be in common-gate configuration with an inductive feedback element or in common-source configuration with a capacitive feedback element, as shown in Figs. 18b–d. The circuits provide feedback by circulating the output current

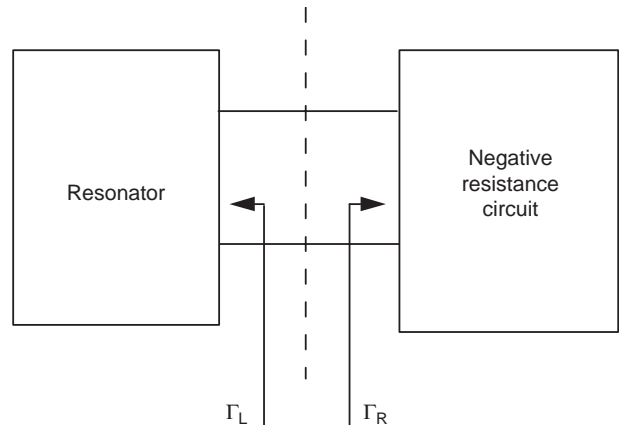


Figure 17. Negative-resistance oscillator.

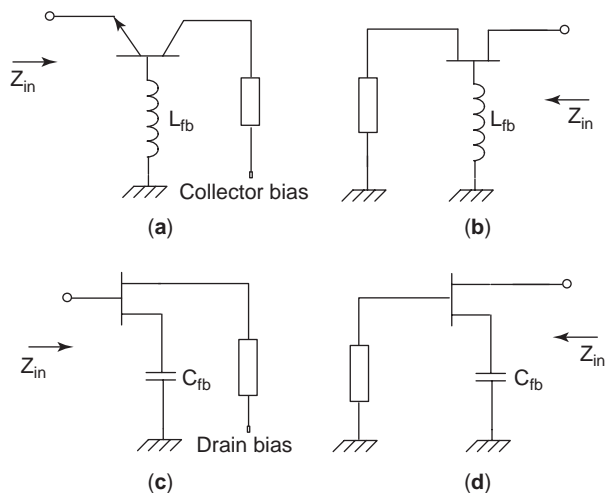


Figure 18. Negative-resistance oscillator topologies: (a) bipolar transistor in common-base FET; (b) common-gate FET (c); common-source FET (d).

through the feedback element in such a way that the voltage developed across the feedback element becomes part of the input signal.

6.2. Phase Noise

The various device technologies cannot be compared thoroughly without discussing phase noise. In active devices, low-frequency noise is dominated by trapping effects from defects in the bulk, at junctions, and at the surface. This contribution is known as flicker noise. The power spectral density (PSD) of flicker noise is inversely proportional to frequency, and meets the thermal (Johnson) and shot noise “floor” at a frequency called the “ $1/f$ corner frequency.” Above the $1/f$ corner frequency, thermal noise and shot noise dominate.

Flicker noise is particularly serious in nonlinear circuits, because the low-frequency noise can be upconverted to RF via the nonlinear mechanisms. In an oscillator, the noise will appear as sidebands on the RF, and these sidebands will interfere with the information signal(s). It should be noted, however, that this flicker noise limit is approached only when a very high factor is used in the oscillator, or when frequency synthesis is used.

FET devices have much higher $1/f$ corner frequencies than do bipolar devices, because current flow is lateral, in the plane of the interfaces that cause flicker noise. Typically FETs (including silicon) have corner frequencies >10 MHz, whereas bipolar devices have corner frequencies <1 kHz. For wireless applications—especially direct-conversion transceivers—low-phase-noise synthesized oscillators are of absolutely key importance, giving yet more challenges to the RF CMOS designer. More recent results have indicated that CMOS devices incorporating SiGe and with a buried channel have improved phase noise.

Relatively recently it has been shown that the waveform within the oscillator circuit has a dramatic effect on the phase noise, and the impulse sensitivity function (ISF) has been introduced to quantify this phenomenon [45].

6.3. Frequency Synthesis

Frequency synthesizers are one of the most challenging and crucial subsystems for a wireless system, especially for 3G, W-CDMA, WLAN, and future generations of wireless networks. The main challenges in the design of a frequency synthesizer are to achieve low phase noise with high frequency resolution, fast switching speed, low power consumption, small size, and low cost. The frequency synthesizer includes three main components: the reference oscillator, the VCO, and the phase-locked loop (PLL). Since the early 1990s PLLs and VCOs have begun to be integrated with the rest of the wireless system on the same silicon IC for reduced cost, size, and improved reproducibility of design.

Because of the increasing number of wireless users using the same band, and operating at progressively higher data rates, both interference and signal-to-noise-ratio have become key considerations in system design. Phase noise and spurious emissions contribute significantly to both of these issues and are largely dependent on PLL performance. Minimizing phase noise and spurs of the frequency synthesizer while staying within power consumption, size, and cost constraints is one of the main challenges for RF design engineers. Because of all these challenges and requirements, several different techniques are used to implement the PLL section of a transceiver. This section describes the existing PLL technologies and how emerging PLL technologies are making this challenge more manageable.

6.3.1. Direct Digital Synthesis. Direct digital synthesis, as shown in Fig. 19, uses a lookup table to store the sine wave values, and an accumulator driven by a clock simply steps continuously through the values. The signal is converted by a DAC, and filtered to reduce spurious signals resulting from the quantization. It is a very powerful technique with many advantages; for example, very fast phase-continuous frequency switching is possible. Commercial products have become extremely sophisticated, incorporating tremendous programmability and additional functions such as modulation. However, although DDS is moving into the RF range, generally a PLL solution will have lower chip area and power consumption. A DDS source can be integrated into a PLL as a hybrid solution offering many advantages.

6.3.2. Direct Synthesis. For completeness, direct synthesis should not be forgotten; in this method a plethora of signals is created from a single-crystal reference, and then these are multiplied together (with mixers) and divided into various combinations to generate other frequencies. The required frequency is set by using switches to select the desired combination for multiplication and division. However, the multiplicity of sources, mixers, and dividers means that this approach requires large chip space and high DC power consumption, so it has a limited applicability to RFICs.

6.3.3. Integer- N Synthesis. Integer- N or divide-by- N synthesis is the classic form of a digital PLL. A number

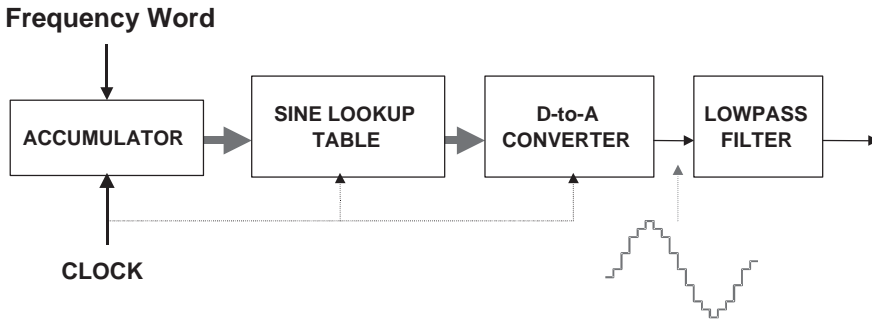


Figure 19. Simplified direct digital synthesizer block diagram.

of well-known texts describe their principles and optimum design procedures [46–48]. Referring to Fig. 20, the basic building blocks are as follows:

- Reference counter ($\div R$)
- Phase detector
- Loop filter
- Prescaler and programmable counter ($\div N$)
- VCO

6.3.3.1. Reference Counter. The most stable frequency references are usually high-frequency sources using crystal resonators, which operate in the MHz regime. However, in the basic PLL the reference frequency applied to the phase detector determines the minimum-frequency step-size. Thus, in order to provide reasonable frequency resolution, the crystal reference is first divided down by the reference counter; $F_r F_x / R$. With the basic PLL, with integer division in the feedback loop, F_r is the smallest frequency step that can be achieved at the output—it determines the frequency resolution. However, using a very small F_r is not a practical proposition, because then the reference signal is effectively multiplied up many, many times in frequency, degrading phase noise considerably; for a division ratio of N , the reference signal phase noise is in principle increased by $20 \log N$. For a 10-MHz crystal, divided by 1000 to give a 10 kHz resolution, the degradation is a whopping 60 dB.

6.3.3.2. Phase Detector. The phase detector compares the reference frequency signal to the divided VCO feedback, and generates an error signal that is passed through the loop filter and controls the VCO. For a high reference

frequency, a mixer might be used to multiply the two signals—the output is then a DC level when the two signals are the same frequency but out of phase. More often, digital circuits are used such as the J–K flip-flop, the exclusive-OR gate and the digital phase frequency detector. The phase frequency detector (PFD) is most widely used since it gives a monotonic output when the phase difference exceeds $\pm 2\pi$ —namely, when the frequencies are different. This means that it can pull the VCO into lock more effectively when switching frequency.

6.3.3.3. Loop Filter. The loop filter is required to filter noise from transitions at the phase detector output. However, if its bandwidth is too low (a large time constant), then the PLL will take a long time to switch from one frequency to another. Many systems use schemes such as dynamic channel allocation and frequency hopping, and fast switching is required. However, if the loop bandwidth is too large, there will be overshoot and problems with spurious signals. In general, when determining the bandwidth of the loop filter, the PLL designer must achieve a tradeoff between phase noise, switching speed, and spurious signal suppression. The loop filter can be active or passive. Passive filters are mainly resistor–capacitor networks that connect directly between the phase detector and VCO, but are mostly suitable only for narrowband applications. Active loops allow the synthesizer to generate large tuning voltage levels and are more suitable for wideband applications since a wide VCO tuning voltage range is needed.

6.3.3.4. Prescaler and Feedback Counter. A programmable counter (frequency divider) is required in order to vary the output frequency. However, programmable counters

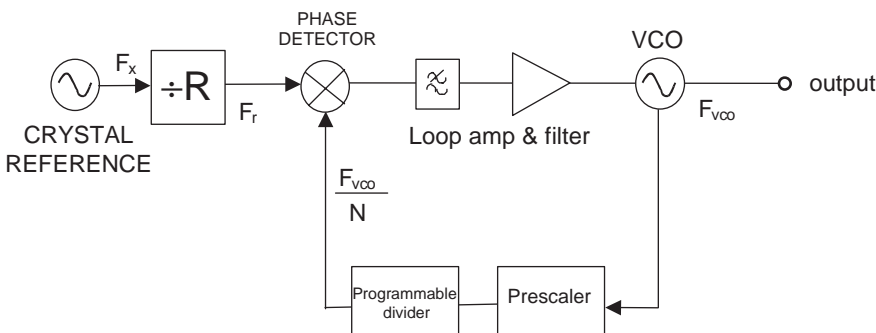


Figure 20. Integer- N PLL block diagram.

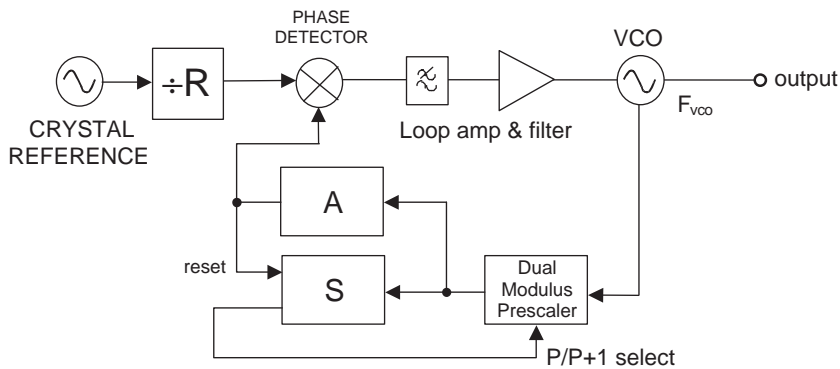


Figure 21. Dual-modulus PLL.

are fairly complex circuits, and cannot operate at very high frequency. A prescaler is a simpler circuit giving a fixed division ratio but able to operate at GHz frequencies. However, a simple prescaler ($\div P$) increases the minimum frequency step to $P \times F_R$. A dual-modulus prescaler can ease this problem at the expense of added complexity. As shown in Fig. 21, with the dual-modulus prescaler the feedback counter alternately divides by P and $P + 1$. This is achieved using the combination of a programmable counter (A) and a second counter, often called the swallow counter (S). At first the prescaler is set to $P + 1$; the swallow counter counts up to S and then sets the prescaler to P . Throughout, the programmable counter is counting and, when it reaches the value A , it resets the swallow counter. This means that the prescaler divides by $P + 1$ for S pulses, and by P for $(A - S)$ pulses, giving an aggregate division ratio (N) of $A \times P + S$. Dual-modulus prescalers and also multimodulus prescalers, have been widely adopted.

A dual-modulus system can be used as single modulus by simply setting the S value to 0. Most PLLs have two pairs of moduli, which can be statically selected via the programming interface. For example, the prescaler might be configurable as either 32/33 or 64/65. In a product, the various counters would have wide programming ranges to enable use in a wide variety of applications.

6.3.3.5. Speedup Mechanisms. In most cases, the loop filter must be designed to meet certain phase noise and spurious signal specifications, and this does not provide sufficient switching speed. Various speedup mechanisms can be used. One such method is to “pretune” the VCO to the desired new frequency. This puts the VCO close to the required frequency and the system near to locking. Other methods include various schemes to “tweak” the loop filter—for example, switch elements in or out temporarily, or charge up capacitors actively.

6.3.4. Fractional- N Synthesis. Integer PLLs, like that in Fig. 20, were the first digital implementation of frequency synthesis, and this traditional technique is still widely used in wireless applications. One of the main limitations of integer- N PLLs is that the VCO frequency cannot be varied in steps smaller than that of the divided reference (F_r). Integer- N is restricting when small frequency step size and low phase noise are required. Demand for faster

switching and lower phase noise in the local oscillator (LO) of wireless communication systems has led to dramatically increased interest in fractional- N synthesis. This was originally developed in the early 1970s by Hewlett-Packard and Racal, and was then known as the “digi-phase” technique. The fractional- N architecture allows frequency resolution that is a fractional (not integer) proportion of the reference frequency F_r . Therefore F_r can be higher than the stepsize and N can be reduced to improve phase noise.

The fractional- N architecture is shown in simplified form in Fig. 22. The dual-modulus prescaler PLL and fractional- N synthesizer look very similar at first sight—the difference becomes clear when looking at the signals in the time domain. In the dual-modulus prescaler, the switching between $N/N + 1$ takes place within a *single period* of F_r ; there is no phase error between the divided VCO signal and the reference, and the VCO output is rock-steady in the locked state. Therefore, everything is well behaved, but the division is integer and the frequency resolution is equal to F_r .

In the fractional- N PLL, for every group of F periods of F_r , the divider is set to N for a certain number of cycles, and $N + 1$ for the other K cycles. This gives an average division ratio of $N + K/F$ [47]. With programmable counters, a variable *fractional* divisor is achieved. The key is the *phase accumulation register* or *fractional accumulator*, which counts up to a set number F of F_r cycles in steps of K . This can only hold numbers from 0 to $F - 1$; every time the counter overflows, the divide number is changed for that F_r cycle to $N + 1$ (sometimes people refer to this as a *pulse removal process*—the result is the same). After the total of F pulses, everything is reset to the beginning. This is illustrated in Fig. 22b for $N = 3$, $F = 9$, and $K = 5$, giving a division ratio of $3\frac{5}{9}$. The upper trace is the F_r signal, for nine cycles, with the accumulator value indicated above it. The middle trace is the VCO signal, which has 32 pulses for the nine F_r pulses because the average divisor is $3\frac{5}{9} = \frac{32}{9}$. The lower trace is the signal from the counter that feeds the PFD. As can be seen, the average phase error is zero, but there are dynamic errors between the divided VCO signal and F_r . This leads to high levels of unwanted spurs called *fractional spurs*, which can be very large. To correct this, one method, as shown in Fig. 22a, is for the phase accumulation register to feed a DAC that generates an equal but opposite error signal and injects it

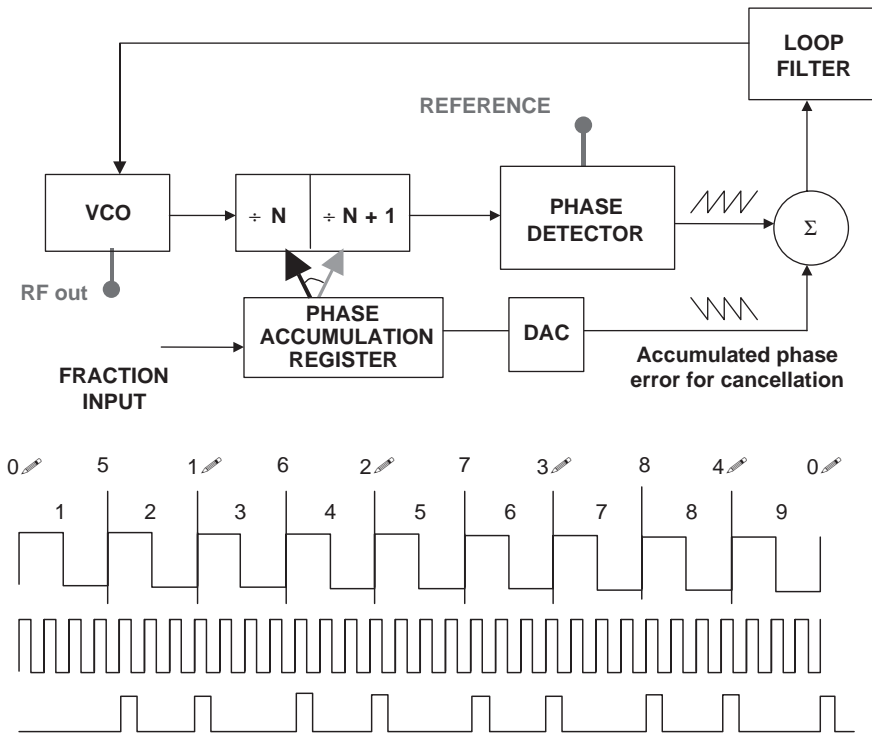


Figure 22. Fractional- N synthesis: (a) block diagram; (b) division process for $N = 3$, $F = 9$, $K = 5$.

at the PFD output. A very important technique is the use of a high-order sigma-delta modulator [49], which effectively dithers the $N/N + 1$ switching process so that the spurs spread out considerably and look like harmless high-frequency noise that is removed by the loop filter.

6.3.5. Summary. Integer- N synthesis is still popular despite some challenges. Most importantly, a small frequency stepsize requires a large division ratio, which compromises phase noise. Furthermore, if F_r is set equal to the desired channel spacing, reference spurs will occur exactly in band in the nearby channels. Integer- N requires the use of complex multiloop designs to achieve fine resolution without using a large division ratio with its associated high phase noise. Fractional- N synthesis is gaining in popularity as it offers significant potential improvement in phase noise performance due to the reduction in division ratio (N). The reference frequency can be set higher, and then the loop bandwidth increased for fast switching speed. Relatively new techniques, such as the use of sigma-delta modulators, can reduce the unwanted spurs to acceptable levels. Combinations of techniques, (i.e., hybrid approaches) and new techniques such as the antijitter circuit [50] are likely to be of increased interest as a way of improving performance even further.

7. MIXERS AND MODULATORS

Mixers and modulators on RFICs are almost always based on the Gilbert cell [51,52], shown in Fig. 23 for bipolar technology. T_1 to T_4 form the double-balanced mixer core; these four devices provide the commutating action, switching the RF input through four paths in current

mode. The double-balanced core ensures high port isolations and cancellation of even-order spurious products. T_5 and T_6 are the RF input gain stage and perform a voltage-to-current conversion. This stage may be linearized using either series feedback, for example, emitter degeneration, by adding an auxiliary feedback device in parallel, or by employing multi- \tanh cells or the micromixer [53–56]. The LO and RF signals are both fed into the mixer with balanced drive; the RF preamplifier can provide single-ended to balanced conversion, with low output impedance emitter follower output stages to drive the mixer. The balanced LO signal can be directly generated with a suitable push-pull oscillator. In CMOS form, especially for low-IF and

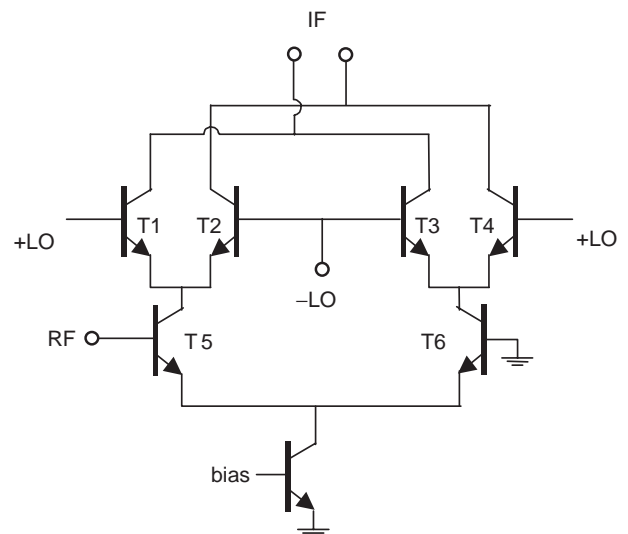


Figure 23. BJT Gilbert cell mixer.

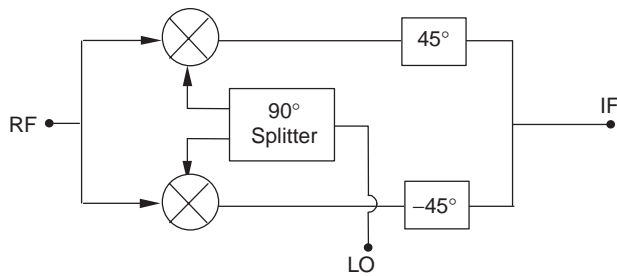


Figure 24. Hartley-type mixer.

direct-conversion receivers, phase noise is crucial problem, and must be optimized by careful design [57].

7.1. Resistive FET Mixers

High-linearity CMOS mixers with low $1/f$ noise can be realized using the time-varying channel resistance in an unbiased FET fed with an LO signal at the gate. Without drain bias, the channel resistance acts as a very linear time-varying resistor and the devices do not conduct any LO current component. This results in a mixer with low intermodulation and flicker noise. Other advantages of this mixer include low DC power consumption and natural separation of LO and RF/IF ports. Both single-balanced and double-balanced resistive mixers have been demonstrated [58,59]. The disadvantage is that the insertion loss, compared to the gain of the active mixer, requires high LNA gain in the receiver, which may cause stability problems and increase DC power consumption.

7.2. Image Rejection Mixers and Single-Sideband Upconverters

Rejection of the image signal is a major challenge in integrated superheterodyne receivers. Using off-chip filtering is possible but greatly complicates the packaging of the chip. The phasing-type image rejection mixer introduced by Hartley is widely used. It consists of a pair of mixers that are fed with identical RF input signals but a phase quadrature LO, as shown in Fig. 24. The upper or lower sideband is canceled by quadrature combining the two IF signals. To achieve the required wideband 90° phase difference at high IFs, polyphase RC filters are widely employed. Adaptive tuning of the amplitude and phase balance can be used for optimum image rejection. Often, the Weaver architecture is used in order to simplify the

design of the 90° phase shift circuitry. For low-IF frequencies, for example, for voice or low-data-rate systems, the 90° combining can be performed digitally after A-to-D conversion; however, the A-to-D converters must then have enough dynamic range to preserve the wanted signal information in the presence of a strong image signal. In many current systems this is impractical, when the image is perhaps 50 dB above the wanted signal in the extreme case. The direct-conversion receiver discussed in Section 9 is a better solution since there is no image; the mixer is then a demodulator, converting the input RF directly to baseband. Quadrature mixing is required in order to preserve the baseband information when modulation schemes such as QPSK and m -QAM are used because the information in the upper and lower sidebands is not identical. In direct-conversion receivers second-order intermodulation can be a major issue, and the even-harmonic quadrature mixer using antiparallel Schottky diodes has been proposed as a solution [60].

For image rejection upconverters, the principle is the same, but the circuit is usually called a *phasing-type single-sideband modulator*. The RF input signals and the modulating signals are fed in phase quadrature while the mixer outputs are combined with an in-phase combiner as shown in Fig. 25. As shown, the single-sideband modulator produces only the lower sideband. If the modulating frequency's 0 and 90° signals are switched, then the upper sideband is produced. For digital modulation, the SSB upconverter becomes the IQ modulator and the IF signals are at baseband. The IQ (vector) modulator is a powerful technique for generating an RF signal with a range of complex modulation schemes, such as QPSK, m -QAM, OFDM, and CDMA. Significant digital processing power and fast D-to-A converters are required in order to incorporate functions such as frequency shifting, linearization, and spectral shaping.

8. FILTERS

The RF filter is one of the key building blocks in wireless communication transceivers. The function of the RF filter is to eliminate undesired signals, including thermal noise, interference, image signals, harmonic distortion, and signal leakage. The background theory for the synthesis of RF filters is well established, but the realization of on-chip Si-based RF filters is still a research topic. Numerous RF designers involved in developing fully-integrated

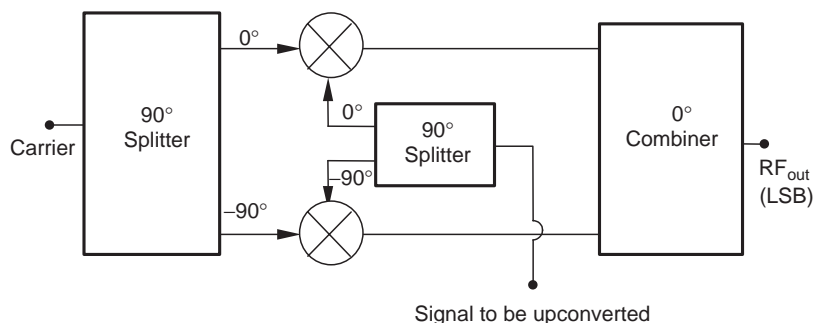


Figure 25. Single-sideband modulator block diagram.

transceiver chips become frustrated when trying to design a high-performance on-chip RF filter; passive components simply do not have sufficiently high enough Q factor, and active filters pose other problems. Often the problem is avoided by adopting other solutions, for example, by employing an image rejection mixer to reject image channels rather than attempting to realize an image filter.

There are, at present, three main approaches for on-chip RF filter design based on silicon technology. Their pros and cons will be briefly discussed in the following subsections.

8.1. Purely Passive Filters

The frequency response of passive filters is determined by the quality of the passive components that are used. The on-chip capacitor is not too problematic, but designing a low-loss on-chip inductor with standard silicon technology is difficult, as has been discussed already. The low- Q factor inductor significantly increases the passband insertion loss and also degrades the sharpness of the cutoff. The increased loss at the front-end receiver chain means increased receiver noise and hence degraded BER, while poor response sharpness limits the capability to reject the out-of-band unwanted signals and ultimately degrades the BER or robustness of the system. Usually, the achievable Q of spiral inductors on standard silicon technology is less than 15. Applying a lightly doped substrate, using insulator material, or MEMS technology effectively enhances the filter's Q , but fabrication is more expensive and may cause integration problems. Using bondwire inductors [61] to substitute planar spiral inductors is another solution but has not yet been proved practical in mass production. Consequently, purely passive RF bandpass filters seem to be an unattractive solution for silicon technology.

8.2. Inductorless Active Filters

Because of the large size and low Q of planar on-chip spiral inductors, active inductors realized by using two transistors with a feedback network have been widely studied. Figure 26 shows some topologies for single-ended active inductors in a CMOS process [62] using n- and p-type

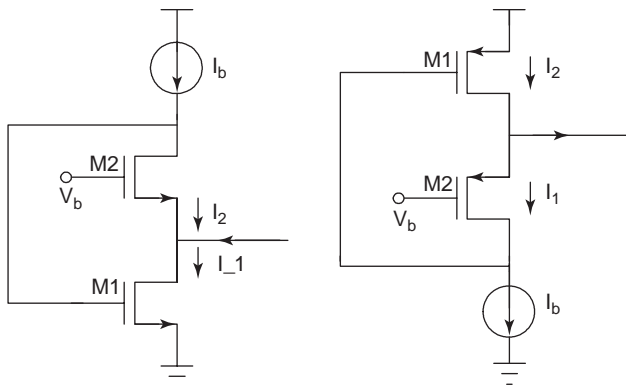


Figure 26. Some examples of single-ended CMOS active inductor.

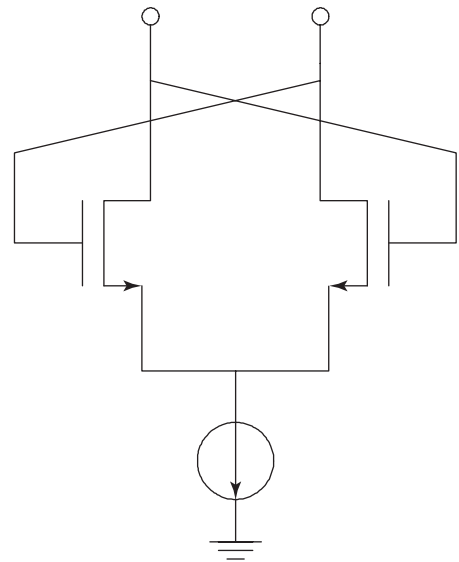


Figure 27. Differential CMOS active inductor.

transistors. To deal with substrate noise and coupling interference, these active inductors are usually realized in a differential form. The operating frequency of active inductors of the type shown in Fig. 26 increases as the unity-gain frequency of M_1 and M_2 increases. This can be accomplished by choosing small devices or applying larger bias current I_b . Of course, this leads to a dynamic range and power consumption degradation. The Q factor of such active inductors is usually less than unity, so for active filters some Q -enhancing schemes are necessary. The effect of low quality factor can be modeled as a series resistance; therefore, a negative series resistance is simply added to this positive resistance in the active inductor, contributing to a net zero resistance, which, in turn, increases Q dramatically [63,64]. Figure 27 shows a technique for synthesis of the negative resistance in differential form, which is often used [65]. One distinct benefit obtained from this inductorless active filter is the compact size since no planar inductors are used. Despite this, the inductorless active filter is still in doubt for its feasibility in RFIC applications. There are lots of disadvantages in this approach, and the major concern is its spurious-free dynamic range quantified by noise and intermodulation distortion, which is too poor for real-life wireless applications. The development of inductorless active filter techniques for Si-based RF applications is still in its infancy.

8.3. Active LC Filters

This technique was proposed as a compromise between circuit size and obtained dynamic range [65–68]. To achieve high dynamic range, a planar spiral inductor is used, rather than an active inductor in the previous subsection. The Q of the spiral inductor is enhanced by applying a Q -enhancement scheme such as a negative-resistance circuit. Another Q -enhancement technique [69], shown in Fig. 28, uses the negative mutual resistance, which negates the inherent parasitic resistance in the spiral inductor.

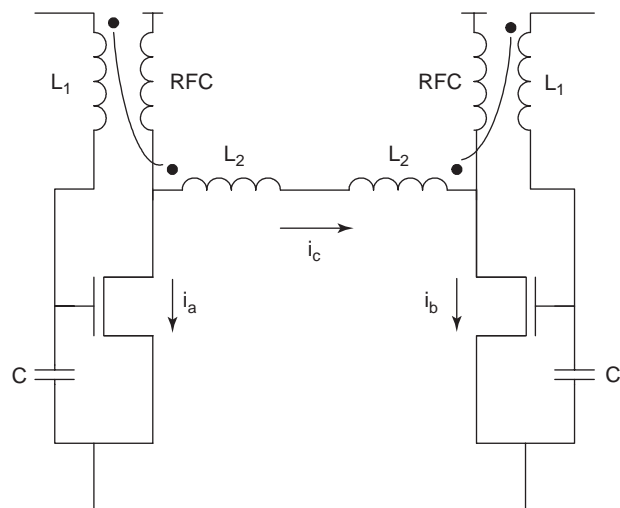


Figure 28. *Q*-enhanced resonator using mutual resistor scheme [69]. (Copyright IEEE, used with permission.)

The frequency response of this type of filter is affected by the frequency dependence of the synthetic negative resistance. Hence, this filter topology is limited to narrow-band applications. A balanced structure is preferred to a single-ended design, especially in silicon technology, since it has more immunity to the substrate coupling, substrate bounce, and noise from the supply lines, which are major problems. In addition, the balanced topology yields a high linearity since all even-order distortion is theoretically eliminated [70]. Automatic frequency and *Q* tuning techniques are essential for this active *LC* filter [68] because of the effects of tolerance, environmental variation, and the interacting effect of *Q* and frequency. Consequently, the power consumption, noise, and linearity of this filter are also determined by this automatic tuning circuit. The spurious free dynamic range is usually insufficient for wireless receivers but suits some wireless transmitter applications [68].

9. TRANSCEIVERS

The wireless market is highly competitive, and a single-chip solution [71–81] using Si technology is essential in order to achieve lowest possible cost. Unfortunately, it is highly challenging to design an integrated single-chip transceiver on silicon. It is well known that the digital CMOS process uses a heavily doped substrate to minimize the problem of latchup and substrate coupling, but this heavily doped substrate is not desirable for high-performance RF circuits. This conflict seems to be more problematic in a wireless receiver design since the sensitivity of the receiver must be sufficient to pick up extremely small received signals. In addition, to support multifunction applications, a multiband multimode wireless transceiver is needed to reduce cost [81]. The chip microphotograph in Fig. 29, which is a highly integrated quadband wireless transceiver designed on BiCMOS technology, exemplifies modern transceiver design. A wireless transceiver is composed of two main parts: a transmitter

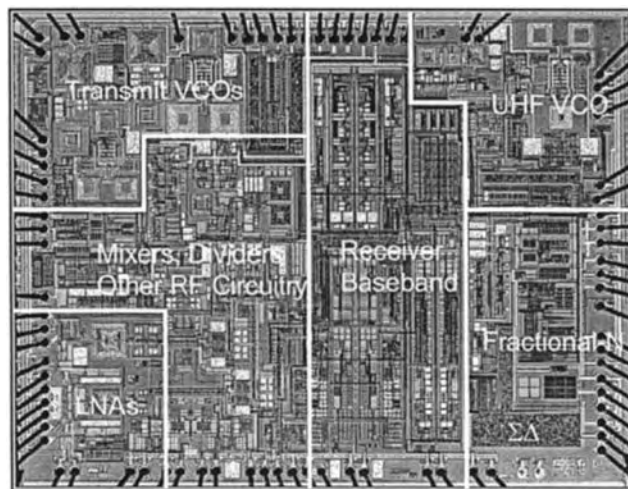


Figure 29. A chip microphotograph of BiCMOS-based quadband homodyne transceiver [81]. (Copyright IEEE, used with permission.)

and a receiver. These two subsystems will now be discussed individually in detail.

9.1. Transmitters

Figure 30(a) shows a double-conversion superheterodyne transmitter. The topology has two mixer stages and needs an IF filter to suppress the in-band noise from the IF gain block. The dynamic range and power control of the transmitter can be determined by controlling a variable-gain amplifier at the IF or RF stage. This leads to a high dynamic range but high design complexity due to the additional passive and active components needed. Compared with its companion, a direct-conversion transmitter, the finished design has a large chip area, leading to high chip cost, which is unacceptable for low-cost applications.

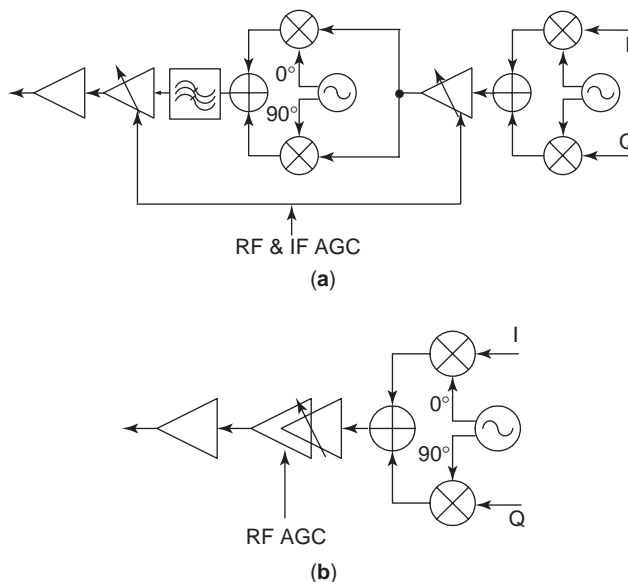


Figure 30. Wireless transmitter architectures: (a) double conversion; (b) direct conversion.

The most suitable single-chip and highly integrated solution for a wireless transmitter is perhaps the direct-carrier modulation or direct-conversion transmitter architecture, which is shown in Fig. 30b. Compared with its companion, the double-conversion transmitter, it evidently needs less circuit components by directly modulating baseband signals onto the RF carrier. Another benefit obtained is an increase in the versatility of the transmitter since the advances in high-speed digital technology and software radio techniques support the possibility of a multimode transmitter. Furthermore, numerous techniques for improving the transmitter performance, such as efficiency enhancement, linearization, and adaptive modulation, are highly feasible in the digital domain. However, care should be taken especially with I/Q phase and gain mismatch, VCO pulling, remodulation, and the dynamic range of the design [71].

The mismatch in phase and gain causes degradation in the transmitted signal quality, usually quantified in terms of error vector magnitude (EVM). Large EVM results in more spreading of the transmitted spectrum and degrades the signal-to-noise ratio. The VCO pulling and remodulation increase phase noise in the VCO and hence degrade the transmitted signal quality. Designing a VCO operating at double or quadruple of the LO is one of the solutions to eliminate this impairment. The high dynamic range of this transmitter is achieved only by adding amplifier gain stages at RF since there is no IF circuitry. For silicon technology, where the substrate loss is substantial, this may result in high power consumption being required for the direct-conversion transmitter, which is not suitable for specific applications that need high-dynamic-range transmitters.

Transmitters for wireless standards that use constant envelope modulation schemes [e.g., Gaussian minimum-shift keying (GMSK)] do not need such stringent dynamic range and linearity performance. The translation loop transmitter [71] is a candidate that is suitable for low-complexity transmitter designs as it has no need for the expensive SAW IF filter. The operation of this transmitter is similar to that of a standard PLL. Low complexity designs can be realized, but this architecture is limited to constant envelope modulation schemes only.

9.2. Receivers

Although various receiver architectures have been implemented for an integrated solution, none of them is the definitive approach for a particular wireless communication standard. The designers must reach a compromise based on cost, system complexity, and their own experience. In addition, all the existing receiver architectures have their advantages and disadvantages for a specific application. Therefore, in this subsection, each individual receiver architecture is discussed briefly.

The heterodyne receiver, shown in Fig 31a, has a long history in wireless communication systems, ranging from HF (high-frequency) to millimeter-wave bands and has been successfully used in various forms, whether with discrete components, hybrid circuits, or integrated circuits. The system downconverts the received RF signal to a low-frequency band, namely, the IF (intermediate frequency),

and the signal is then filtered and subsequently demodulated with low-frequency circuitry. The desired communication channel is selected by the frequency synthesizer (LO_1) such that the down-converting signal is fixed at a single IF. The key to the success of this architecture basically stems from its excellent selectivity by using a very high- Q IF filter to select channels. This high- Q IF filter offers the capability to eliminate nearby and out-of-band interference, and a high-selectivity and high-sensitivity receiver is achievable. Nevertheless, a Si-based single-chip solution for a heterodyne receiver has been hindered by the need for a high- Q filter. The design and realization of a high- Q IF filter on standard silicon ICs is still a research challenge. The simple approach to solve this is to employ an off-chip high- Q filter, normally a SAW filter. However, these are expensive, and furthermore the impedance interface of the on-chip mixer and IF amplifier must be set to $50\ \Omega$ for the SAW filter, and increased power consumption is inevitable. Consequently, this configuration seems unsuitable for applications that need low cost, low DC power, and small size, which are the major RFIC research issues nowadays.

The homodyne receiver, presently more often called the *zero-IF* or *direct-conversion receiver*, was, in fact, invented before its derivative, the heterodyne receiver. The homodyne structure is depicted in Fig. 31b. It is evident that this architecture has less components than the first since the received signal from the antenna is directly downconverted to baseband. The image problem is also eliminated as the IF is zero. However, it suffers other problems as a result of downconverting the received signal to DC. Because of the limited reverse-isolation performance of the LNA, LO leakage through the RF port of the mixer can be radiated to the atmosphere. Also, this LO leakage power can be reflected back into the receiver and then mixes with itself to produce an undesirable DC offset due to the mismatch of the antenna. Another homodyne receiver impairment is the second-order harmonic distortion effect from the second-order nonlinearity of the mixer. This problem seems to be more severe than the DC offset from LO leakage, which is static, since the modulating received signal is demodulated to DC via the second-order nonlinearity and then produces a time-varying DC offset. Furthermore, some channel conditions such as multipath fading and handset mobility can produce this dynamic DC offset. Consequently, the demodulated I/Q constellation is dynamically perturbed by this DC offset, and hence the receiver's BER will be considerably deteriorated unless the modulation signal is not sensitive to DC offsets. The flicker noise in active devices, especially in CMOS, also creates a DC offset by the down conversion mechanism.

Numerous techniques are used to control the DC offset problem. Cancellation of a static DC offset can be achieved by measuring the offset during the idle time intervals, but this is usable solely for time-division duplex systems, not for the frequency-division duplex mode. A time-varying DC offset is alleviated by choosing the subharmonic diode mixer with the drawback of high conversion loss. With careful design techniques, the homodyne receiver is well suited for wireless applications in which the low cost and long battery life are main targets.

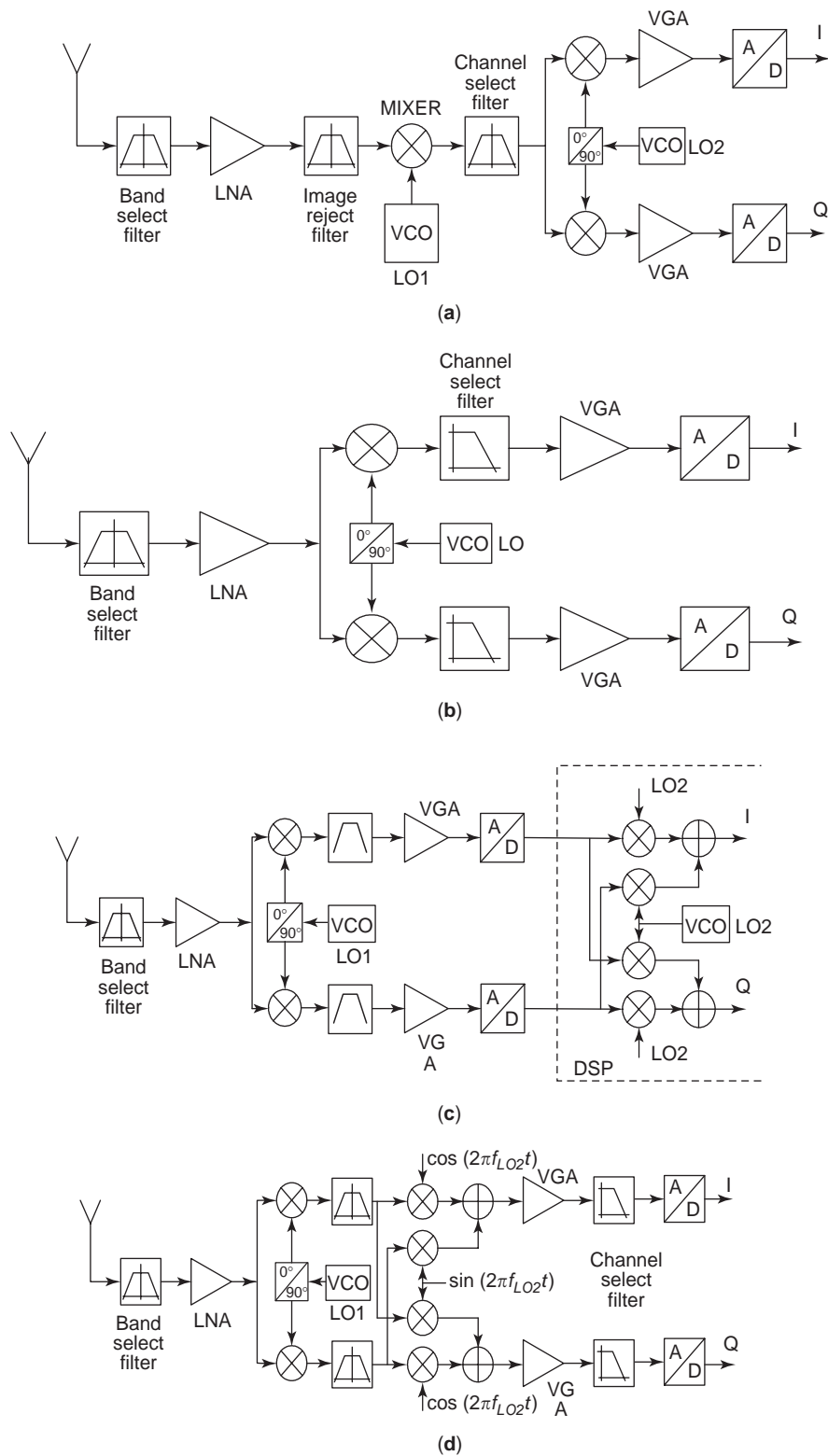


Figure 31. Some wireless receiver architectures: (a) heterodyne; (b) homodyne; (c) low IF; (d) wideband IF.

With the advance of digital CMOS technology, the low-IF receiver architecture, as shown in Fig. 31c, has been proposed. By selecting the IF low enough, the second downconversion can be performed in the digital domain. The IF must be chosen to be low in order to relax the ADC requirement. The advantage over the conventional het-

erodyne receiver is the low complexity, and the DC offset problem of the homodyne receiver does not exist. In principle, it achieves an integrated solution with minimal off-chip components. The digital (often software) downconversion step can incorporate techniques to achieve near-perfect quadrature for image rejection using a

Weaver-type topology. The phase and gain mismatch between the *I* and *Q* channel mixers can be adaptively tuned with complex algorithms [80]. However, the image signal is still present in the ADCs, and so the receiver topology is not suited when the image signal is much stronger than the desired RF signal, because of the ADC dynamic range problem.

Figure 31d shows the wideband IF receiver with double conversion. The LNA is followed by a quadrature down-conversion mixer to an IF, and this quadrature mixer will also suppress the image channels. However, the image rejection capability relies again on the *I-Q* phase/gain mismatch. There is no problem of LO leakage or DC offset unlike the homodyne receiver.

With the emerging digital technology leading to the development of high-speed digital circuitry, the second downconversion and the following filters can be implemented in the digital domain. The main disadvantage of this system is the large power consumption of the high-speed analog-to-digital converters (ADCs) and digital processing circuitry. So, there are trade offs, but this architecture inevitably finds application in wideband wireless communication, such as the 3G (third-generation) mobile systems.

10. CHIP-PACKAGE INTEGRATION

Virtually all RFICs require off-chip components, especially for power supply decoupling, and often components from a mix of semiconductor technologies must be combined in order to realize a product with the desired functionality and performance. Many microwave and millimeter-wave applications require certain key GaAs or InP components in order to achieve low noise, high power efficiency, and so on. Thus the chip(s) and package must be designed in a

coherent fashion for optimum results, and the system-in/on-package (SoP or SiP) approach has been widely adopted. Here, various ICs and high-*Q* passive components can be integrated, as shown conceptually in Fig. 32. Three main technologies are used for these multichip modules: MCM-L (laminate); MCM-C (ceramic), and MCM-D (deposited).

MCM-L technology uses copper on large fiberglass-reinforced or PTFE-based boards. In mass production, 18 × 24 in. panel sizes are common and costs per circuit are very low. Multilayer boards are produced by laminating different layers together. Vias can be produced by mechanical punching or laser machining. Using PTFE-based materials, this technology has been used to over 60 GHz.

In MCM-C technology, ceramic materials in tape or paste form are used to build up a multilayer substrate and metal pastes are deposited using screen printing. LTCC (low temperature cofired ceramic) technology has the advantage over MCM-L that SMT (surface mount technology) resistors and capacitors are already manufactured using the same sort of process. Therefore, embedded passive components can be fabricated in the module, which reduces component count and costs. Also, LTCC substrates offer a stable mechanical base for chip-on-board (CoB) assembly and offer better thermal properties than the organic materials of MCM-L technology.

MCM-D technology uses sputtering and evaporation of metals and spin coating of dielectrics. The metal deposition equipment used is relatively expensive, and the substrate must be in a vacuum. In mass production, the need to wait for the chamber pressure to drop down, and the limited substrate size, are significant drawbacks. However, thin-film technology gives the best pattern definition and the highest performance if suitable materials are used.

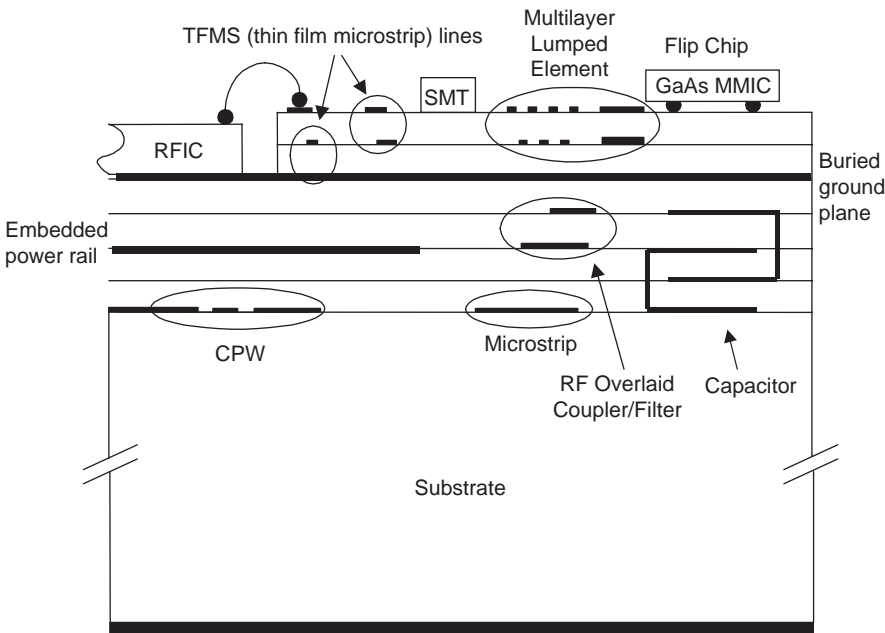


Figure 32. Conceptual system-in-package using a multilayer substrate [82].

Acknowledgments

Professor Robertson would like to acknowledge the support of the Engineering and Physical Sciences Research Council (EPSRC) as part of the *Continuing Education in Electronic Systems Integration*. Master's Training Package (Grant nr GR/N31122/01). See www.ceesi.ac.uk for details of the scheme and the academic partners.

M. Chongcheawchamnan would like to acknowledge the assistance of his project students and his colleague Sarayut Srisathit for their help in preparing this manuscript.

BIBLIOGRAPHY

- I. D. Robertson and S. Lucyszyn, *RFIC and MMIC Design and Technology*, IEE, 2001.
- J. Sevenhans, F. Op't Eynde, and P. Reusens, The silicon radio decade, *IEEE Trans. Microwave Theory Tech.* **50**(1): 235-244 (Jan. 2002).
- K. Nishikawa, I. Toyoda, K. Kamogawa, and T. Tokumitsu, Three-dimensional silicon MMICs operating up to K-band, *IEEE Trans. Microwave Theory Tech.*, **46**(5): 677-684 (May 1998).
- M. Rebeiz, *RF MEMS: Theory, Design, and Technology*, Wiley, New York, Feb. 2003.
- D. Szymd, R. Brock, N. Bell, S. Harker, G. Patrizi, J. Fraser, and R. Dondero, QUBiC4: A silicon RF-BiCMOS technology for wireless communication ICs, *Proc. 2001 BIPOLAR/BiCMOS Circuits and Technology Meeting* (Cat. 01CH37212), IEEE, 2001, pp. 60-63.
- S. Thompson, M. Alavi, M. Hussein, P. Jacob, C. Kenyon, P. Moon, M. Prince, S. Sivakumar, S. Tyagi, and M. Bohr, 130 nm logic technology featuring 60 nm transistors, low-K dielectrics, and Cu interconnects, *Intel Technolo. J.* (issue on semiconductor technology and manufacturing) **6**(2) (May 16, 2002).
- G. Marcyk and R. Chau, *New transistors for 2005 and beyond*, Nov. 26, 2001, <http://www.intel.com/research/silicon/micron.htm>.
- <http://public.itrs.net>.
- L. F. Tiemeijer, H. M. J. Boots, R. J. Havens, A. J. Scholten, P. H. W. de Vreede, P. H. Woerlee, A. Heringa, and D. B. M. Klaassen, A record high 150 GHz f_{max} realized at 0.18 μm gate length in an industrial RF-CMOS technology, *Int. Electron Devices Meeting Tech. Digest* (Cat. 01CH37224), IEEE, 2001, pp. 10.4.1-10.4.4.
- P. R. Gray and R. G. Meyer, *Analysis and Design of Analog Integrated Circuits*, 3rd ed., Wiley, Canada, 1993.
- B. Razavi, *Design of Analog CMOS Integrated Circuits*, pre-view ed., McGraw-Hill, New York, 2000.
- T. H. Lee, *The Design of CMOS Radio-Frequency Integrated Circuits*, Cambridge Univ. Press, 1998.
- A. Nikenejad, *Analysis, Simulation and Applications of Passive Devices on Conductive Substrates*, Ph.D. dissertation, Univ. California at Berkeley, 2000.
- J.-F. Luy, K. M. Strohm, et al., Si/SiGe MMIC's, *IEEE Trans. Microwave Theory Tech.* **43**(4) (April 1995).
- R. L. Bunch, D. I. Sanderson, and S. Rayman, Quality factor and inductance in differential IC implementation, *IEEE Microwave Mag.* 82-89 (June 2002).
- P. Russer, Si and SiGe millimeter-wave integrated circuits, *IEEE Trans. Microwave Theory Tech.* **46**(5): 590-603 (May 1998).
- J. B. Yoon, Y. S. Choi, B. Kim, Y. Eo, and E. Yoon, CMOS-compatible surface-micromachined suspended-spiral inductors for multi-GHz silicon RF ICs, *IEEE Electron Device Lett.* **23**(10): 591-593 (Oct. 2002).
- D. Kelly, and F. Wright, Improvements to performance of spiral inductors on insulators, *IEEE Int. Microwave Symp. Digest*, Vol. 1, June 2-7, 2002, pp. 541-543.
- C.P. Yue and S. S. Wong, On-chip spiral inductors with patterned ground shields for Si-based RF ICs, *IEEE J. Solid-State Circ.* **33**(5): 743-752 (May 1998).
- G. W. Dahlmann, E. M. Yeatman, P. Young, I. D. Robertson, and S. Lucyszyn, Fabrication, RF characteristics and mechanical stability of self-assembled 3D microwave inductors, *Sensors Actuators A-Physical* **A97-98**: 215-220 (April 1, 2002).
- V. M. Lubecke, B. Barber, E. Chan, D. Lopez, M. E. Gross, and P. Gammel, Self-assembling MEMS variable and fixed RF inductors, *IEEE Trans. Microwave Theory Tech.*, **49**(11) (Nov. 2001).
- D. C. Laney, L. E. Larson, et al., Microwave transformers, inductors, and transmission lines implemented in an Si/SiGe HBT process, *IEEE Trans. Microwave Theory Tech.* **49**(8) (Aug. 2001).
- J. N. Burghartz, M. Soyuer, et al., Integrated RF components in a SiGe bipolar technology, *IEEE J. Solid-State Circ.* **32**(9): 1440-1445 (Sept. 1997).
- R. C. Frye, S. Kapur, and R. C. Melville, A 2-GHz quadrature hybrid implemented in CMOS technology, *IEEE J. Solid-State Circ.* **38**(3): 550-555 (March 2003).
- A. Springer, L. Maurer, and R. Weigel, RF system concepts for highly integrated RFICs for W-CDMA mobile radio terminals, *IEEE Trans. Microwave Theory Tech.* **50**(1): 254-267 (Jan 2002).
- J. R. Long, A low-voltage 5.1-5.8 GHz image-reject downconverter RF IC, *IEEE J. Solid-State Circ.* **35**(9) (Sept. 2000).
- R. Gotzfried, F. Beibwanger, et al., RFIC's for mobile communication systems using SiGe bipolar technology, *IEEE Trans. Microwave Theory Tech.* **46** (5): 661-668 (May 1998).
- R. G. Meyer and W. D. Mack, A 1 GHz BiCMOS RF front-end IC, *IEEE J. Solid-State Circ.* **29**(3): 350-355 (March 1994).
- D. J. Cassan and J. R. Long, A 1-V transformer-feedback low-noise amplifier for 5 GHz wireless LAN in 0.18- μm CMOS, *IEEE J. Solid-State Circ.* **38**(3): 427-435 (March 2003).
- I. Aoki, S. D. Kee, D. B. Rutledge, and A. Hajimiri, Fully integrated CMOS power amplifier design using the distributed active-transformer architecture, *IEEE J. Solid-State Circ.* **37**(3): 371-383 (March 2002).
- www.chic.caltech.edu.
- U. Erben, M. Wahl, A. Schiippen, and H. Schumacher, Class-A SiGe HBT power amplifiers at C-band frequencies, *IEEE Microwave Guided Wave Lett.* **5**(12): 435-436 (Dec. 1995).
- S. Cripps, *Advanced Techniques in RF Power Amplifier Design*, Artech House, London, 2002.
- C. Tongchoi, M. Chongcheawchamnan, and A. Worapishet, Lumped element based Doherty power amplifier topology in CMOS process, *Int. Symp. Circuits and Systems (ISCAS2003)*, Bangkok, Thailand, 2003.
- P. B. Kennington, *High-Linearity RF Amplifier Design*, Artech House, London, 2001.
- S. Kusunoki, K. Yamamoto, et al., Power-amplifier module with digital adaptive predistortion for cellular phones, *IEEE*

- Trans. Microwave Theory Tech.* **50**(12): 2979–2985 (Dec. 2002).
37. B. Shi and L. Sundstrom, A 200-MHz IF BiCMOS signal component separator for linear LINC transmitters, *IEEE J. Solid-State Circ.* **35**(7): 987–993 (July 2000).
 38. J. Craninckx and M. Steyaert, *Wireless CMOS Frequency Synthesizer Design*, Kluwer Academic Publishers, 1998.
 39. Y. Koo, H. Huh, Y. Cho, J. Lee, J. Park, K. Lee, D. K. Jeong, and W. Kim, A fully integrated CMOS frequency synthesizer with charge-averaging charge pump and dual-path loop filter for PCS- and cellular-CDMA wireless systems, *IEEE J. Solid-State Circ.* **37**(5): 536–542 (May 2002).
 40. A. Dec and K. Suyama, Micromachined electro-mechanically tunable capacitors and their applications to RF IC's, *IEEE Trans. Microwave Theory Tech.* **46**(12): 2587–2596 (Dec. 1998).
 41. A. Dec and K. Suyama, A 1.9-GHz CMOS VCO with micro-machined electromechanically tunable capacitors, *IEEE J. Solid-State Circ.* **35**(8): 1231–1237 (Aug. 2000).
 42. D. Ham and A. Hajimiri, Concepts and methods in optimization of integrated LC VCOs, *IEEE J. Solid-State Circ.* **36**(6): 896–909 (June 2001).
 43. R. Aparicio and A. Hajimiri, A noise-shifting differential Colpitts VCO, *IEEE J. Solid-State Circ.* **37**(12): 1728–1736 (Dec. 2002).
 44. P. Andreani, A. Bonfanti, L. Romano, and C. Samori, Analysis and design of a 1.8-GHz CMOS LC quadrature VCO, *IEEE J. Solid-State Circ.* **37**(12): 1737–1747 (Dec. 2002).
 45. A. Hajimiri and T. H. Lee, A general theory of phase noise in electrical oscillators, *IEEE J. Solid-State Circ.* **33**(2): 179–194 (Feb. 1998).
 46. R. E. Best, *Phase-Locked Loops: Design Simulation and Applications*, McGraw-Hill, New York, 1997.
 47. www.ti.com, Technical Brief SWRA029, Fractional/Integer-N PLL Basics, 1999.
 48. www.analog.com/library/analogDialogue/archives.html, Analogue Dialogue, *Phase Locked Loops for High-Frequency Receivers and Transmitters*, Vol. 33, 1999.
 49. B. De Muer and M. S. J. Steyaert, A CMOS monolithic $\Sigma\Delta$ -controlled fractional-N frequency synthesizer for DCS-1800, *IEEE J. Solid State Circ.* **37**(7): 835–844 (July 2002).
 50. M. J. Underhill, The adiabatic anti-jitter circuit, *Proc. Joint Meeting of the European Frequency and Time Forum and IEEE Int. Frequency Control Symp.* 1999, Vol. 2, pp. 611–614.
 51. B. Gilbert, A precise four-quadrant multiplier with subnanosecond response, *IEEE J. Solid-State Circ.* **3**(4): 365–373 (Dec. 1968).
 52. B. Gilbert and R. Baines, Fundamentals of active mixers, *Appl. Microwave Wireless* **7**(1): 10,12,14,21,22,24,27 (1995).
 53. B. Gilbert, The multi-tanh principle: A tutorial overview, *IEEE J. Solid-State Circ.* **33**(1): 2–17 (Jan. 1998).
 54. B. Gilbert, The MICROMIXER: A highly linear variant of the Gilbert mixer using a bisymmetric Class-AB input stage, *IEEE J. Solid-State Circ.* **32**(9): 1412–1423 (Sept. 1997).
 55. C. C. Meng, S. S. Lu, M. H. Chiang, and H. C. Chen, DC to 8 GHz 11 dB gain Gilbert micromixer using GaInP/GaAs HBT technology, *Electron. Lett.* **39**(8): 637–638 (April 17, 2003).
 56. H. C. Chen, C. C. Meng, and S. S. Lu, 2.4 GHz CMOS double balanced Gilbert cell micromixer, *Microwave Opt. Technol. Lett.* **28**(4): 251–253 (Feb. 20, 2001).
 57. A. Manstretta, R. Castello, and F. Svelto, Low 1/f noise CMOS active mixers for direct conversion, *IEEE Trans. Circ. Syst. II: Analog Digital Signal Process.* **48**(9): 846–850 (Sept. 2001).
 58. V. Geffroy, G. De Astis, and E. Bergeault, RF mixers using standard digital CMOS 0.35 μm process, *2001 IEEE MTT-S Int. Microwave Symp. Digest* (Cat. 01CH37157), Part Vol. 1, 2001, pp. 83–86.
 59. P. Gould, C. Zelle, and J. Lin, A CMOS resistive ring mixer MMICs for GSM 900 and DCS 1800 base station applications, *2000 IEEE MTT-S Int. Microwave Symp. Digest* (Cat. 00CH37017), Part Vol. 1, 2000, pp. 521–524.
 60. K. Kawakami, K. Tajima, M. Shimozawa, K. Itoh, N. Kasai, and A. Iida, Fully monolithic integrated even harmonic quadrature ring mixer with an active matched 90 degree power divider for direct conversion receivers, *IEEE MTT-S Int. Microwave Symp. Digest*, 1997, II, pp. 657–660.
 61. M. A. I. Mostafa, J. Schlang, and S. Lazar, On-chip RF filters using bond wire inductors, *Proc. ASIC/SOC Conf. 14th Annual IEEE Int.*, 2001, pp. 98–102.
 62. Y. Wu, M. Ismail, and H. Olsson, A novel CMOS fully differential inductorless RF bandpass filter, *Proc. IEEE Int. Symp. Circuits and Systems*, May 28–31, 2000, Vol. IV, pp. 149–152.
 63. S. Hara, T. Tokumitsu, T. Tanaka, and M. Aikawa, Broad-band monolithic microwave active inductor and its application to miniaturized wide-band amplifiers, *IEEE Trans Microwave Theory Tech.*, **36**(12): 1920–1924 (Dec. 1988).
 64. S. Lucyszyn and I. D. Robertson, Monolithic narrow band filter using ultra high-Q tunable active inductors, *IEEE Trans. Microwave Theory Tech.* **MTT-42**(12): 2617–2622 (Dec. 1994).
 65. D. Li and Y. Tsvividis, Active LC filters on silicon, *IEE Proc. Circ. Device Syst.* **147**(1): 49–56 (Feb. 2000).
 66. U. Karacaoglu and I. D. Robertson, MMIC active bandpass filter using varactor-tuned negative resistance elements, *IEEE Trans. MTT* **43**(12): 556–563 (Dec. 1995).
 67. S. Pipilos, Y. P. Tsvividis, J. Fenk, and Y. Papananos, A Si 1.8 GHz RLC filter with tunable center frequency and quality factor, *IEEE J. Solid-State Circ.*, **31**(10): 1517–1525 (Oct. 1996).
 68. D. Li and Y. Tsvividis, Design techniques for automatically tuned integrated gigahertz-range active LC filters, *IEEE J. Solid-State Circ.* **37**(8): 967–977 (Aug. 2002).
 69. T. Soorapanth and S. S. Wong, A 0 dB IL 2140.30 MHz bandpass filter utilizing Q-enhanced spiral inductors in standard CMOS, *IEEE J. Solid-State Circ.* **37**(5): 579–586 (May 2002).
 70. W. B. Kuhn, N. K. Yanduru, and A. S. Wyszynski, Q-enhanced LC bandpass filters for integrated wireless applications, *IEEE Trans. Microwave Theory Tech.* **46**(12): 2577–2586 (Dec. 1998).
 71. A. Loke and F. Ali, Direct conversion radio for digital mobile phones-design issues, status, and trends, *IEEE Trans. Microwave Theory Tech.* **50**(11): 2422–2435 (Nov. 2002).
 72. H. Darabi, S. Khorrarn, et al., A 2.4 GHz CMOS transceiver for Bluetooth, *IEEE J. Solid-State Circ.* **36**(12): 2016–2024 (Dec. 2001).
 73. J. Ryyanen, K. Kivekas, J. Jussila, L. Sumanen, A. Parsinen, and K. A. I. Halonen, A single chip multimode receiver for GSM900, DCS1800, PCS1900, and WCDMA, *IEEE J. Solid-State Circ.* **38**(4): 594–602 (April 2003).
 74. D. Manstretta, M. Brandolini, and F. Svelto, Second-order intermodulation mechanisms in CMOS downconverters, *IEEE J. Solid-State Circ.* **38**(3): 394–406 (March, 2003).
 75. L. Sheng, J. C. Jensen, and L. E. Larson, A wide-bandwidth Si/SiGe HBT direct conversion sub-harmonic mixer/downconverter, *IEEE J. Solid-State Circ.* **35**(9): 1329–1337 (Sept. 2000).

76. M. A. Copeland, S. P. Voinigescu, D. Marchesan, P. Popescu, and M. C. Maliepaard, 5 GHz SiGe HBT monolithic radio transceiver with tunable filtering, *IEEE J. Solid-State Circ.* **48**(2): 170–181 (Feb. 2000).
77. J. Jussila, J. Ryyanen, K. Kivekas, L. Sumanen, A. Parsinen, and K. A. I. Halonen, A 22 mA 3.0-dB NF direct conversion receiver for 3G WCDMA *IEEE J. Solid-State Circ.* **36**(12): (Dec. 2001).
78. M. Zargari, D. K. Su, et al., A 5 GHz CMOS transceiver for IEEE 802.11a wireless LAN systems, *IEEE J. Solid-State Circ.* **36**(12) (Dec. 2001).
79. H. Komurasaki, T. Sano, et al, A 1.8 V operation RF CMOS transceiver for 2.4 GHz-band GFSK applications, *IEEE J. Solid-State Circ.* **38**(5): 817–825 (May 2003).
80. S. Wu and B. Razavi, A 900-MHz/1.8-GHz CMOS receiver for dual-band applications, *IEEE J. Solid-State Circ.* **33**(12): 2178–2184 (Dec. 1998).
81. R. Magoon, A. Molnar, J. Zachan, G. Hatcher, and W. Rhee, A single-chip quad-band (850/900/1800/1900 MHz) direct conversion GSM/GPRS RF transceiver with integrated VCOs and fractional-N synthesizer, *IEEE J. Solid-State Circ.* **37**(12): 1710–1720 (Dec. 2002).
82. C. Y. Ng, *Microwave Mixers and Modulators Using Multilayer Technology*, Ph.D. thesis, Univ. Surrey, 2003

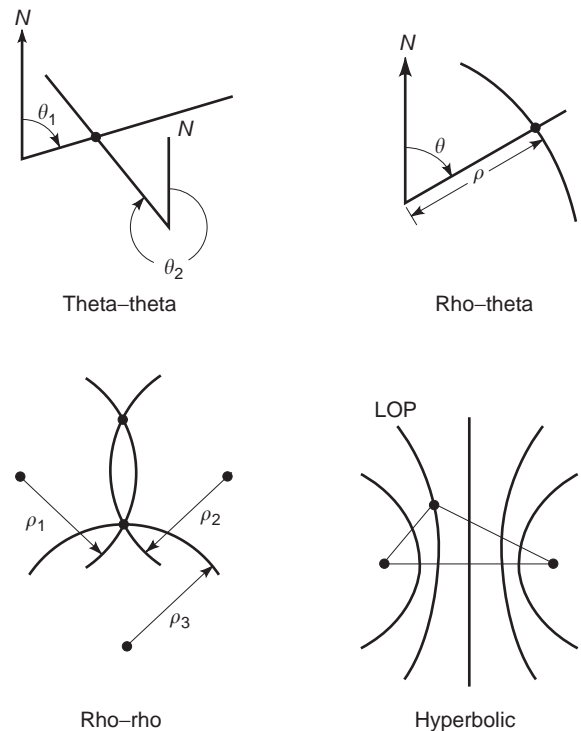


Figure 1. Geometric relationship of different radio navigation schemes.

RADIO NAVIGATION

GERALD BENDIXEN
Rockwell Collins, Inc.

A key function of navigation is the estimation of current position of a vessel. The reception of radio signals from transmitters whose location is known is a common means of implementing the position estimation functions. Several different schemes have been developed. They can be classified according to the means of determining a position from radio signals. Figure 1 provides the geometric relationships for the different schemes.

A theta–theta system determines the position by the vessel's bearing with respect to two transmitters. This scheme is not common in aviation due to its low accuracy when compared with other available systems.

Rho–theta system use radio signals to determine distance and bearing with respect to the transmitter. This scheme has been in common use in aviation for many years. Most of the airspace can be flown using this basic means of navigation. Errors in bearing measurement will result in position errors that depend on the distance from the station.

Rho–rho systems are based on distance measuring equipment (DME) that determines the position of an aircraft using two or more distance values. When only two distance values are available, there is potentially an ambiguity of position. This ambiguity is usually resolved by using the last computed position to determine the most reasonable position. The position accuracy of the rho–rho solution is dependent upon the accuracy of the measured

distance and the bearing angles to the stations. If the aircraft is close to the line through two stations, the error in the position solution using only those two stations becomes large.

Hyperbolic systems measure the time delay of signals simultaneously transmitted from three or more stations. The locus of all points that have a constant delay of signals from two stations is hyperbolic in shape and is called a line of position (LoP). The intersection of two LOP determine a unique position.

The accuracy of each navigation scheme is dependent on the particular implementation. The following sections describe the characteristics of the different equipment.

1. DME CHARACTERISTICS

Distance measuring equipment (DME) is a transponder system combining both airborne and ground equipment to provide distance information. The distance information may be used by other equipment or provided on an indicator to the pilot. In addition, the DME may provide ground speed information. Data from DME is used for both rho–rho and rho–theta navigation systems (see Fig. 2).

The major units of the airborne DME equipment are a receiver–transmitter together with an antenna. In addition, a control unit and distance display may be provided in the airborne equipment. The ground-based equipment is a transponder consisting of a receiver–transmitter and an antenna.

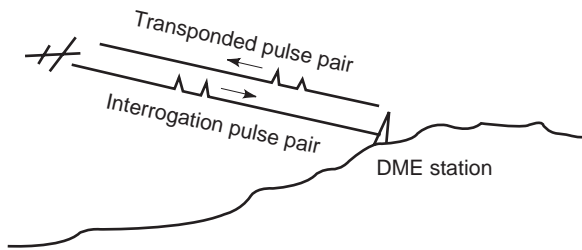


Figure 2. DME operation.

The DME ground-based facility is usually part of a VOR/DME, ILS/DME, VORTAC, or TACAN facility. A VOR/DME station is a VHF omnidirectional station combined with the DME. An ILS/DME facility is an instrument landing system with DME. TACAN is a military navigation system providing both azimuth and distance information. A VORTAC is a VOR facility together with TACAN equipment.

DME ground stations are capable of handling approximately 100 aircraft simultaneously. If more than 100 aircraft interrogate the ground station, the ground station reduces its sensitivity and replies to the 100 strongest interrogations. Most airborne DME units will operate down to a 50% reply efficiency, so operation is continued even when the ground stations does not respond to all interrogations.

The ground station continually transmits a 2700 pulse pair per second squitter signal. At 30s intervals, the ground station transmits a 1350 pulse pair per second signal that encodes the station identifier in Morse code. When interrogated by an airborne DME pulse pair, the ground station replaces the squitter pulse pair with a pulse pair 50 μs after interrogation.

The airborne equipment operates in two modes, search and track. In the search mode, the airborne equipment transmits 90 or more pulse pairs per second. The transmission rate is randomly shifted to prevent possible confusion effects due to another airborne DME transmitter. After each pulse pair is transmitted, the receiver equipment waits for a reply pulse pair that arrives with a consistent delay after the transmission. If such a reply is found, the airborne DME switches to the track mode and tracks the regular delays of the replies. In the track mode the airborne equipment reduces the interrogation rate to 20 or fewer pulse pairs per second. The reduction in the interrogation rate allows more airborne units to be serviced by the ground-based DME facility.

The airborne equipment converts the time duration between the transmission of the interrogation pulse pair and the reception of the reply pulse pair into distance. Because the speed of the radio signal is a known constant, the distance from the DME facility can be determined. To be more precise

Distance in nm

$$= (\text{Time duration in microseconds} - 50 \text{ ms}) / 12.359 \text{ ms/nm}$$

The airborne DME unit has memory that handles the situation when the reception of the DME reply is momentarily interrupted. The equipment uses the memory to

remain in the track mode and provide distance data during the reply interruption. The memory allows the DME to provide distance information for up to 10s after loss of reception.

It is common for airborne DME units to handle up to five DME ground facilities simultaneously by multiplexing the receiver-transmitter circuits. This allows the equipment to simultaneously provide distance information for up to five DME nav aids.

The airborne DME transmits and receives on one of 252 channels. There are 126 X and 126 Y channels. The transmit and receive frequencies of any one channel are separated by 63MHz. In the first 63 X channels, the ground-to-air frequency is 63MHz below the air-to-ground frequency. For X channels 64 through 126, the ground-to-air frequency is 63MHz above the air-to-ground frequency. For Y channels the situation is reversed. The ground-to-air frequency of the first 63 Y channels is 63MHz above the air-to-ground frequency. Channels 64Y to 126Y, the ground-to-air frequency is 63MHz below the air-to-ground frequency. The 252 ground-to-air frequencies are each whole MHz frequencies from 962 to 1213 MHz. The air-to-ground frequencies are each whole MHz frequencies from 1025 to 1150 MHz.

The duration between each pulse of the pulse pair transmitted by the airborne equipment and that of the ground equipment is different for X and Y channels. The table below shows the pulse spacing.

	Air-to-ground	Ground-to-air	
X-channel		12 μs	12 μs
Y-channel		36 μs	30 μs

Most DME channels are paired with a VHF frequency allocated to VOR or ILS. That is, for each VOR or ILS frequency there is an assigned DME channel for use when DME equipment is part of the nav aid facility. The X channels are paired with VHF frequencies in 100kHz increments (108.00, 108.10, 108.20, etc.). The Y channels are paired with VHF frequencies in 100kHz increments but offset by 50 kHz (108.05, 108.15, 108.25, etc.). The table below shows the DME channel pairing with VHF frequencies.

DME Channels	Assignment	VHF Frequencies
1–16	Unpaired	134.4–135.9 MHz
17–56		
Even channels with ILS	ILS and VOR	108.00–112.00 MHz
Odd channels with VOR		
60–69	Unpaired	133.3–134.2 MHz
57–59, 70–126	VOR	112.00–117.9 MHz

DME operation requires that the aircraft and the ground facility be in a direct line-of-sight connection. Terrain and the curvature of the earth limit the range. The formula below provides an approximate limit on the

range of DME equipment due to earth curvature with an assumption that the ground station antenna is about 16 ft. above the surface.

$$\text{DME range limit (nm)} = 1.23\sqrt{\text{aircraft altitude (ft)} + 4}$$

The DME provides the slant range distance from the aircraft to the DME navaid facility. If the DME range is large compared with the aircraft altitude the slant range is essentially the same as the ground distance. Navigation equipment that uses the DME range data can remove the effect of the aircraft altitude by incorporating in the calculation both the measured aircraft altitude and the elevation of the navaid as retrieved from the navigation database.

The accuracy of DME range measurement is dependent on the range, environmental conditions, and the equipment being used. A nominal 95% accuracy is about 0.1 nm at shorter ranges. For longer ranges the accuracy degrades due to atmospheric conditions and lower signal-to-noise ratio.

2. VOR EQUIPMENT CHARACTERISTICS

VHF omnidirectional range (VOR) equipment consists of a ground station (transmitter) and an airborne receiver. The VOR ground station continuously transmits a signal that may be used by all aircraft within reception range of the signal. Using the VOR signal, the receiver determines the bearing from the ground station to the receiver. VOR stations are often colocated with other navigational aids such as DME and TACAN stations. The frequency of VOR stations ranges from 108.00 to 117.95 MHz.

There are two types of VOR transmitters: Doppler VOR and conventional VOR. Doppler VOR has limited usage. The details of conventional VOR follow.

The transmitted signal from the VOR station consists of a VHF carrier and a 9960 Hz subcarrier. The VHF carrier is amplitude modulated by a variable 30 Hz signal whose phase is dependent upon the bearing with respect to the ground station. The 9960 subcarrier is frequency modulated by a 30 Hz reference signal. The subcarrier is modulated between 10440 and 9480 Hz (see Fig. 3).

Figure 4 illustrates the phase-bearing relationship of the two components of the VOR signal. At 0° bearing, the phase of the variable signal is the same as the phase of the reference signal. At 90° bearing from the ground station, the variable signal is 90° out of phase with respect to the reference signal. The phase difference between the two signals is proportional to bearing from the ground station to the receiver.

The phase difference between the variable signal and the reference signal is used by the receiver to determine the bearing from the ground station to the receiver. Essentially, the receiver separates the subcarrier from the VHF carrier, detects the phase of the 30 Hz signal in each and then determines the phase relationship.

In a conical area above the VOR station, the phase difference between the two signals cannot be detected reliably. This area is called the VOR cone of confusion.

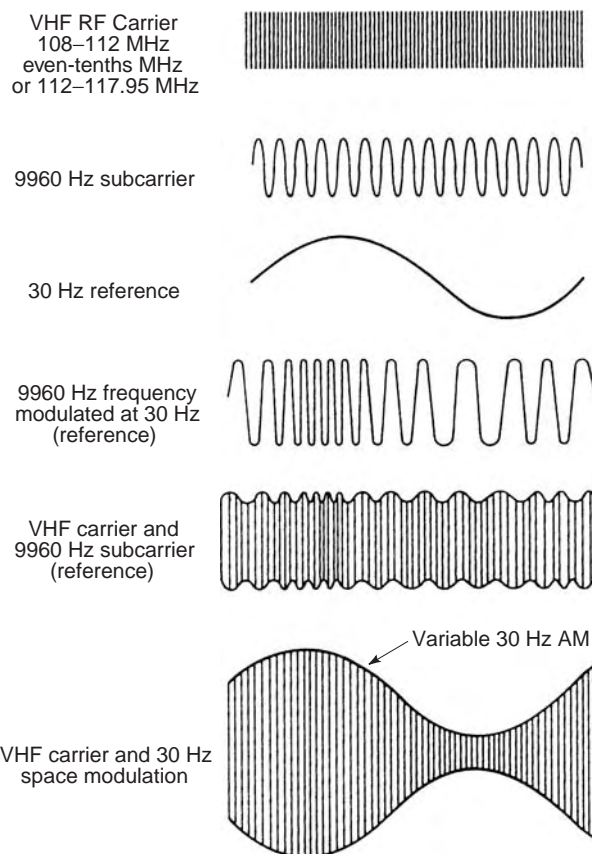


Figure 3. Components of VOR signal.

Receivers have monitors that detect this condition and provide alerts to the pilot that the signal is unreliable.

In general, the VOR ground-station antenna is physically aligned so that the VOR signal indicates 0° bearing when the receiver is magnetically north of the ground station. That is, in general, the VOR bearing from the ground station to the receiver is the same as the magnetic bearing to the receiver. However, Earth's magnetic field is constantly changing. In Europe and the United States there are regions where the magnetic north is changing 1° every 7 years. Therefore even if the VOR signal was aligned with magnetic north at one instant in time, after some period of time there can be a significant difference. When the difference becomes too large (2° or so), the VOR antenna is usually realigned.

The accuracy of VOR signals is degraded by range and terrain. Generally, the VOR signal error is less than 1°. As the range from the VOR station is increased, the VOR signal bearing often oscillates around the true bearing. This effect is known as scalloping.

There are several types of VOR indicators that are in common use. Most of the indicators provide bearing as a rotating arrow pointing to the bearing angle on an azimuth card. The azimuth card is slaved to the heading sensor so that the current heading is at the top directly under the lubber line. The indicators often include a distance indication that is connected to the DME.

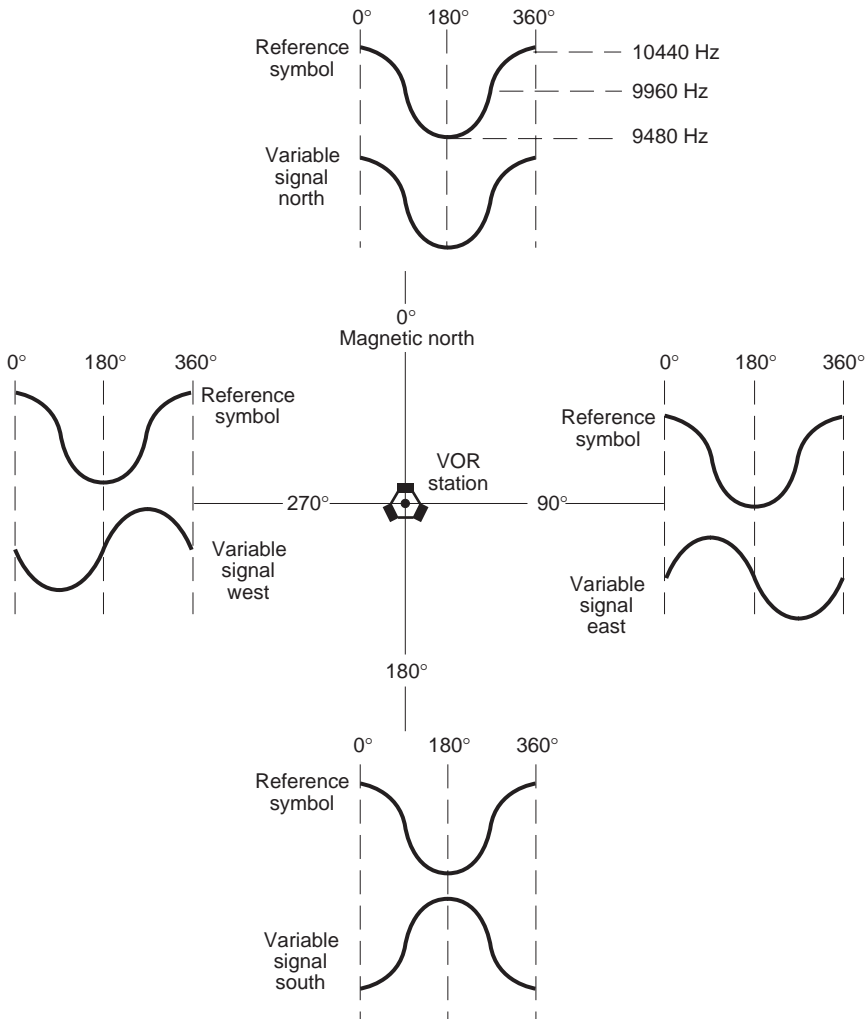


Figure 4. Phase relationship of VOR signal.

3. ILS CHARACTERISTICS

An instrument landing system (ILS) consists of ground-based transmitters and airborne equipment that provides lateral, along-track, and vertical guidance. The lateral signal is provided by a localizer transmitter and the vertical signal is provided by the glideslope transmitter. The airborne ILS receiver is capable of receiving and processing both the localizer and the glideslope signals. The along-track information is provided by marker beacons (transmitter located along the descent path that provide a narrow vertical radio signal) or distance measuring equipment (DME). The marker beacon receiver can be part of the ILS receiver or it can be a separate receiver (see Fig. 5).

The localizer beam is almost always aligned to guide the aircraft directly over the runway threshold. In certain

situations, only a localizer signal is provided and no electronic glideslope signal is provided. In some localizer-only situations, the localizer signal is not aligned to the runway but instead provides guidance to some location from which the pilot has other means to complete the landing.

In some cases, the ILS DME transponder delay is adjusted so that the sensed DME distance is zero at the runway threshold instead of at the DME antenna. Such DMEs are known as biased DMEs and the bias is indicated on the approach chart. There are two general arrangements of biased DMEs (see Fig. 6). In one case the DME antenna is located at the glideslope antenna and adjusted to read zero at the corresponding runway threshold. In the other case, the DME antenna is located midway between the two runway thresholds at opposite ends of the runway. In this case the single DME will support approaches from either direction and will read zero at both runway thresholds.

The localizer signal is transmitted on assigned frequencies between 108.1 and 111.95 MHz. As shown in Fig. 5, the localizer antenna is usually located past the far end of the runway very near the extended runway centerline. The signal pattern are two main lobes on each side of the centerline. The left lobe is predominantly modulated at

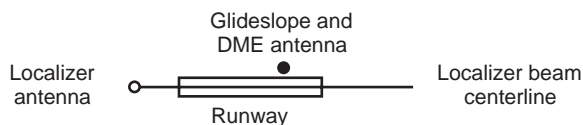


Figure 5. Common layout of ILS facility.

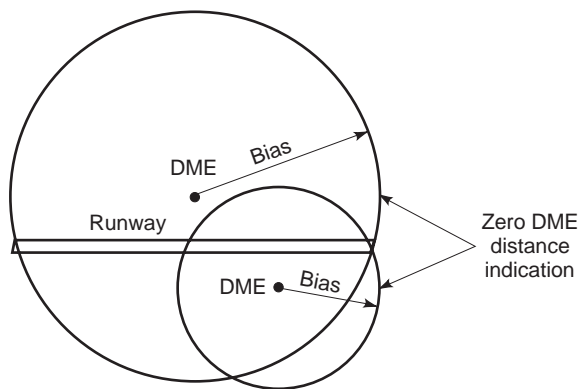


Figure 6. Biased DME antenna situations.

90 Hz and the right lobe is predominately modulated at 150 Hz. Along the center line, the two modulated signals are equal (see Fig. 7).

The localizer signal also extends backwards and is called the back course. This signal can be used for guidance but the modulation convention is reversed. There is no glideslope signal provided on the backcourse region. When flying the backcourse, either the equipment must reverse the localizer indications or the pilot must recognize and fly the reversed indications.

The glideslope signal is transmitted on assigned frequencies between 328.6 and 335.4 MHz. The glideslope antenna is located on the side of the approach end of the runway. The glideslope signal consists of two main lobes on each side of the desired glideslope path. The glideslope descent angle is usually 3°. To provide obstacle clearance or to reduce noise, steeper glideslope paths are used. The upper glideslope lobe is predominantly modulated at 90 Hz and the lower lobe is predominantly modulated at 150 Hz (see Fig. 8).

Marker beacon signals are transmitted at 75 MHz and are modulated at 400, 1300, or 3000 Hz. The transmitters are located along the descent path of to the runway. Figure 9 shows the general arrangement of the beacons. When the aircraft passes over the beacons, the marker beacon receiver detects the signal and provides an indication to the pilot of the passage. The exact location of the marker beacons is given on the approach procedure chart. Inner marker beacons are installed at runways with category II and category III operations.

In typical operation, the pilot maneuvers the aircraft to cross the localizer signal centerline. At this time, the localizer receiver provides an indication that the localizer signal is being received and provides a lateral deviation indication showing the aircraft displacement from the centerline. Using the lateral deviation indication, the

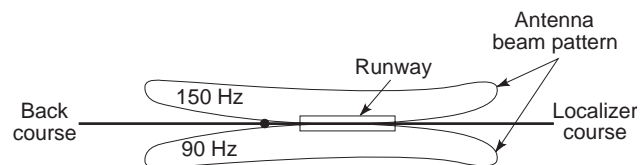


Figure 7. Localizer antenna lobe patterns.

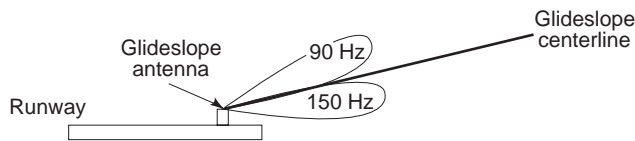


Figure 8. Glideslope antenna lobe patterns.

pilot steers to the localizer centerline until the glideslope receiver indicates reception of the glideslope signal. At that time the pilot has both lateral and vertical indications to guide the aircraft on the desired glideslope path. The marker beacons or DME indications provide along-track indications of the progress of the descent.

4. ADF NAVIGATION

The automatic direction finder (ADF) is the oldest and most widely used radio navigation system. The ADF system consists of a ground-based transmitter and an airborne receiver. The ADF system provides an indication of the bearing of the station from the aircraft centerline. The ADF receiver is capable of receiving AM signals from 190 to 1750 kHz. The transmitter can be either commercial AM broadcast stations or nondirectional beacons (NDB) that are installed expressly for radio navigation.

An omnidirectional antenna is used to receive the signal to aid in tuning the receiver. The ADF receiver determined the bearing of the station using the directional sensitivity of loop antenna. The loop antenna may be physically rotated to determine the bearing to the signal or the bearing may be determined using electronic sensing of the signal strength from more than one loop.

5. LONG-RANGE NAVIGATION (LORAN)

Low-frequency long-range navigation (LORAN) was first developed for military applications during World War II. Since then it has evolved into today's LORAN-C system that is also used for civil applications. Marine applications were the first to appear, followed by aviation applications.

The LORAN system consists of a group or chain of transmitting stations and a receiver. Within each chain there is one master station and several slave stations identified by a single letter. Associated with each chain is a unique group repetition interval (GRI) that identifies

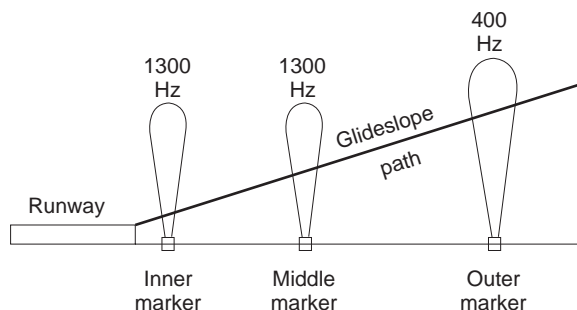


Figure 9. Marker beacon locations.

the chain. A single chain provides navigation coverage for several hundred miles from the master station. The frequencies of transmitted signal are between 90 and 110 kHz. The pulse patterns of the transmitters are different allowing the receiver to separate the received signals.

Within each chain, each station simultaneously transmits a pulse at the specified GRI. Each station has an assigned pulse pattern that allows the receiver to distinguish between the different signals. By determining the time differences between the set of received pulses, the receiver can determine the difference in distance from each transmitting station. If three or more signals are received, the receiver can determine the best estimate of the location of the receiver. The accuracy of the LORAN position estimate depends on the position of the receiver with respect to the location of stations providing signals. The nominal accuracy of the LORAN system is 0.25 nm when within the groundwave range.

To improve accuracy, LORAN receivers compensate for the differences in velocity of the ground wave when the signal is propagating over land rather than water.

6. GLOBAL POSITIONING SYSTEM (GPS)

The space segment of the global positioning system (GPS) consists of a set of orbiting satellite transmitters that provide two L-band, 1575.42 MHz (L1) and 1227.6 MHz (L2) signals. The two frequencies allow the appropriately equipped user to correct for errors due to ionospheric refraction. Civil receivers use only the L1 signal. The basic satellite configuration is a set of 24 satellites in 6 orbital planes.

The signals provided by the satellites are modulated with two pseudo-random-noise (PRN) codes: a coarse/acquisition (C/A) signal and a precise (P) signal. The P code component of the signal allows higher-precision ranging and information necessary to decode the signal that has restricted distribution.

The airborne GPS receiver receives the L1 signal of all satellites in view and by the use of correlation techniques can detect the unique C/A code for each satellite. The C/A code has a chipping rate of 1.023 MHz and a length of 1023 bits so it repeats every millisecond. By use of signals from four or more satellites, the receiver can determine the time reference and the range to each satellite and hence estimate the receiver position.

To deny the accuracy of GPS to unfriendly forces, the satellite signals are intentionally degraded using a concept known as selective availability (SA). This technique degrades to L1 signal characteristics to the extent that navigation accuracy is about 100 m (95%).

7. MICROWAVE LANDING SYSTEM (MLS)

Microwave landing systems consist of an azimuth and elevation microwave transmitters, a conventional DME transponder, and the airborne receivers. The azimuth transmitter provides coverage for 40° to each side of the

centerline. The elevation transmitter provides coverage up to 15° of elevation.

Microwave landing transmitters operate on one of 200 assigned frequencies between 5.031 and 5.1907 GHz. The azimuth transmitter provides a narrowbeam signal that sweeps the azimuth coverage area ($\pm 40^\circ$) at a rapid rate. By detecting the timing between the reception of the microwave signal, the receiver can determine the azimuth angle from the centerline. A preamble microwave signal is transmitted from a broadbeam antenna to indicate the beginning of the azimuth sweep. Various information is digitally encoded in the preamble signal. The elevation function is provided in the same manner as the azimuth function. High sweep rates provide about 40 samples per second for azimuth and elevation.

RADIO NOISE

ROGER DALKE

Institute for Telecommunication
Sciences

Radio noise can be defined as unwanted and unavoidable electromagnetic fluctuations that tend to obscure the information content of a desired radio signal. In a radio receiver, the noise disturbances are fluctuating voltages and currents that alter the desired signal's original frequency, amplitude, or phase in some unpredictable, unwanted manner. In early radios, much of the "noise" stemmed from the quality of the equipment; for example, poor contacts and unreliable connections, sensitivity to mechanical vibrations, and unstable detectors and amplifiers all contributed to the degradation of the radio signal. Over the years, there was steady progress in improving transmitters and receivers and greatly reducing or completely eliminating these and other noise sources. It was soon realized, however, that all sources of noise could not be totally eliminated and that a fundamental residual noise remained as a lower limit. This article focuses on such noise emanating from both natural sources and human activities that affect the performance of *narrowband* radiofrequency (RF) communications systems.

Typically radio noise is divided into two components—internal or *receiver* noise (that is, intrinsic noise generated by the receiving system components) and external or *environmental* radio noise (noise collected by the receiving system antenna). Receiver noise is largely due to natural processes such as *thermal noise*, arising from the motion of thermally agitated free electrons in resistors, and *shot noise*, resulting from current fluctuations superimposed on the steady current flow in both vacuum tubes and solid-state devices. Environmental noise is an intrinsic part of a wireless communications channel and consists of *natural radio noise* (i.e., noise originating from natural sources such as atmospheric noise and sky noise), and *unintentional* RF emissions due to human activity, which are

commonly referred to as *man-made* noise. Atmospheric noise is largely due to lightning and related phenomena, such as precipitation static. *Sky noise* is a generic term used to describe noise from a variety of terrestrial and extraterrestrial sources, such as cosmic noise and absorption of radio waves in Earth's atmosphere due to rain, water vapor, and oxygen. Intentional RF emissions that result in adjacent- and cochannel radio interference, including inter-modulation and jamming, are not covered in this article.

While such noise cannot be completely eliminated, understanding the character of radio noise allows engineers and system designers to evaluate radio system performance and devise means to lessen the adverse effects. The most important design parameter used to characterize noise performance is the predetection signal-to-noise ratio (SNR), and hence, noise power is generally the most significant parameter in relating the interference potential of noise to system performance. Noise power calculations must include noise generated in all components of the receiving system as well as the radio channel. This is usually accomplished by determining a single parameter, the *operating system noise factor*, which is essentially the ratio of the receiving system predetection noise power referenced to the terminals of an equivalent loss-less receiving antenna and the noise power available from a resistor at standard temperature (288 K).

In this article, important sources of receiver noise are described and the concept of receiver noise factor is developed. The noise factor concept is then extended to cover the entire radio receiving system, including the receiving antenna and environmental noise. This is followed by a description of important environmental noise sources.

1. RECEIVER NOISE AND NOISE FACTOR

The two most important receiver noise sources, used as noise standards and for noise characterization, are thermal and shot noise. Thermal noise is characterized as the spontaneous fluctuations in voltage across a resistor due to the random motion of thermally agitated electrons. Thermal noise is always present in any radio system and often establishes the lower limit of signal detection. Shot noise, on the other hand, originates in a flow of discrete charges not in equilibrium where the mean-square noise current is proportional to the product of elementary charge, the average current, and the bandwidth or $2eIb$ [1]. The cathode-to-anode stream of a temperature-saturated thermionic diode is an example of a pure shot noise generator. Shot noise currents in semiconductors such as diodes and transistors are due to the diffusion of charge carriers in p-n junctions.

Since thermal and shot noise may be described as being the sum of a very large number of random, short-lived disturbances, it follows from the central limit theorem that the processes are Gaussian. More precisely, observed voltages are white Gaussian noise. It was shown experimentally by Johnson [2] and theoretically by Nyquist [3] that the mean thermal noise power density available from a resistor is simply kT , where

$k = 1.38 \times 10^{-23} \text{ W Hz}^{-1} \text{ K}^{-1}$ is Boltzmann's constant and T is the absolute temperature of the resistor. The characterization as white noise is an approximation valid for typical narrowband RF communication systems operating at or near the standard ambient temperature $T_0 = 288 \text{ K}$. When quantum mechanical considerations are included, the mean power density kT is replaced by the more accurate expression obtained by Max Planck [4]

$$\frac{h\nu}{e^{h\nu/kT} - 1} \text{ (W/Hz)} \quad (1)$$

where $h = 6.626176 \times 10^{-34} \text{ J/Hz}$ is Planck's constant and ν represents frequency. Clearly, the flat power spectral density approximation is inaccurate when high frequencies are combined with cryogenic temperatures. Such systems are beyond the scope of this article.

Since both thermal and shot noise constitute white Gaussian noise sources, the properties of the noise voltage they deliver to an output circuit are indistinguishable. The significant difference is that thermal noise is proportional to temperature and shot noise is proportional to the average current. Hence, an equivalent noise temperature T_e can be used to characterize the noise of a device with thermal sources at temperature T and shot noise sources with mean power dw_s in an incremental bandwidth $d\nu$ as follows:

$$kT_e = kT + \frac{dw_s}{d\nu} \quad (2)$$

Solid-state shot noise sources such as noise diodes are commonly used in noise measurements. To achieve the required precision in T_e , these devices are calibrated against a primary standard. Noise diodes are commonly characterized in terms of excess noise ratio defined as

$$N_R = 10 \log_{10} \left(\frac{T_e}{T_0} - 1 \right) \text{ (dB)} \quad (3)$$

Thermal noise generated within or passing through a band-limited receiver circuit is colored and perhaps amplified. Since thermal noise power is independent of frequency over the bandwidth of most narrowband RF communication systems, it is useful to define a *noise-equivalent bandwidth* b_0 . When a resistor is attached to the input terminals of a linear receiver with gain $g(\nu)$, the total noise power available to the receiver w_a in the system band can be expressed in terms of the noise equivalent bandwidth as follows:

$$w_a = kT \int_0^\infty \frac{g(\nu)}{g_0} d\nu = kTb_0 \quad (4)$$

where g_0 is the nominal gain in the system bandwidth.

1.1. Statistical Characterization of Narrowband White Gaussian Noise

If the receiver input termination is a resistor, the receiver output noise voltage is a random function of time whose

behavior can only be described statistically. For a typical RF communication system, the signal is narrowband with respect to a central radiofrequency ν_c and the output noise voltage $V(t)$ can be written as

$$V(t) = \text{Re}\{v(t)e^{j2\pi\nu_c t}\} = E(t) \cos(2\pi\nu_c t - \Phi(t)) \quad (5)$$

where $v(t)$ is the complex baseband representation, $E(t)$ is the amplitude, and $\Phi(t)$ is the phase. In this representation, $v(t)$ is a complex random process and the pair $(E(t), \Phi(t))$ are two associated real random processes. When the observed voltages are white Gaussian noise, their baseband representations are 0-mean complex Gaussian processes with a flat power spectral density. This means that the co- and quad phases of v are independent and Gaussian distributed with 0 means and identical variances. It also means that voltages at different times are independent—a statement that must be emended by the fact that the receiver is narrowband, so that the actual observed power spectral density is proportional to the power spectrum of the receiver.

For these complex Gaussian processes, it is also true that the resulting amplitude and phase are independent of each other and that the phase is uniformly distributed over the complete circle. The amplitude is then *Rayleigh distributed*. In terms of the *instantaneous noise power* (which is proportional to the square of the amplitude), the cumulative distribution function (more precisely, the exceedance distribution function) is

$$\Pr\{\text{noise power} > w > 0\} = e^{-w/w_o} \quad (6)$$

where w_o is the average output noise power. This average equals the total area under the power spectral density curve and is equal to the sum of the mean power of the input noise amplified by the receiver and the mean noise power added by the receiver w_r or

$$w_o = g_o k T b_o + w_r \quad (7)$$

where T is the temperature of the resistor connected to the input terminals.

To obtain this result, the receiver noise is assumed to be Gaussian and white, as would be the case when thermal and shot noise are dominant. More generally, Eq. (7) is valid for any random processes. If the receiver noise is not Gaussian, however, the instantaneous power distribution would not be Rayleigh, as given in Eq. (6). The white Gaussian thermal noise assumption is reasonable for most narrowband RF receivers. In general, however, w_r will depend on frequency.

In noise calculations, it is important to define clearly what is meant by gain. There are many possible definitions of gain. Assuming that a signal generator is connected to the receiver input terminals and a power meter is connected to the receiver output terminals, an obvious choice would be to use the ratio of the input and output powers, or so-called *power gain*. Clearly, power gain depends on the impedance of both the signal generator as well as the impedance of the power meter, and hence a

noise characterization based merely on power gain is ambiguous. To circumvent this difficulty, the gain used in noise calculations is usually taken to be the *available power gain* [5], defined as the ratio of the available power from the receiver to the available power from a signal generator connected to the receiver input terminals so that any mismatch losses are included. With this definition, the gain does not depend on the receiver load; however, it does depend on the impedance of the signal generator.

In determining noise performance, the signal generator is often matched to the receiver so that the maximum power is delivered to the receiver. This is a reasonable choice for most RF applications, where signal generators, connecting cables, the loads, and so on are usually 50 Ω devices, or they are matched waveguide interfaces. It should also be noted that when there is a complete match at the input and output, the available gain and the power gain are equal.

1.2. The Receiver Noise Factor

In radio engineering it is desirable to have a simple, yet unambiguous method of characterizing the noise properties of a radio receiver. For this purpose, the concept of noise factor was developed and defined. There are a variety of ways to define noise factor. The basic idea is to relate the available noise power at the input of an active or passive two-port linear network to the noise power available at its output terminals. Assume that a CW signal generator is connected and matched to the input terminals of a receiver. Let w_g be the available signal generator power, w_1 be the signal power available at the load, and w_o be the available noise power at the load; the International Radio Consultative Committee (CCIR) [6] definition of noise factor is given as follows: The noise factor f_r of a radio receiver is defined to be the ratio of the available CW signal-to-reference noise power w_g/kT_0b_o at the terminals of the signal generator to the corresponding total signal-to-noise power ratio w_1/w_o available to the load of the linear portion of the receiver with the CW signal tuned to the maximum response of the receiver bandpass characteristic and with the signal generator output impedance at the reference temperature T_0 :

$$f_r = \frac{w_g/kT_0b_o}{w_1/w_o} = \frac{w_g}{w_1} \frac{w_o}{kT_0b_o} \quad (8)$$

The ratio w_1/w_g is simply the maximum available power gain and hence,

$$f_r = \frac{w_o}{g_o k T_0 b_o} \quad (9)$$

If it is assumed that the receiver bandwidth is very narrow $b_o \rightarrow d\nu$ so that the receiver noise is constant over the bandwidth, Eq. (9) gives the spot noise factor

$$f_s(\nu) = \frac{dw_o}{g(\nu)kT_0} \quad (10)$$

which is essentially a single-frequency value based on a unit bandwidth. It should be noted that the noise factor is simply the available output noise power referred to the input terminals (i.e., divided by the nominal gain) in units of kT_0b (i.e., the noise power available from a resistor at standard temperature).

The spot noise factor as given in Eq. (10) is equivalent to the Institute of Radio Engineers (IRE) definition [7]. In practice, for narrowband linear receivers, the weighted average spot noise factor over the system bandwidth \bar{f} is the quantity commonly used to characterize receiver noise performance

$$\bar{f} = \frac{\int_0^\infty f_s(v)g(v)dv}{\int_0^\infty g(v)dv} = \frac{w_0}{kT_0 \int_0^\infty g(v)dv} = \frac{w_0}{kT_0g_0b_0} \quad (11)$$

which is precisely f_r defined previously.

1.3. Noise Factor for a Passive Two-Port Linear Network

Communications receivers use transmission lines, attenuators, and other devices that can be generally classified as passive two-port linear networks. It is important to consider the effects of such devices operating in tandem with the actual receiver to characterize properly the noise performance of the receiving system.

The spot noise factor of a linear two-port network is obtained by calculating the power density ratio given in Eq. (10) when a resistor at reference temperature T_0 is connected to the input terminals of the network. If the network is at the ambient temperature T_0 , the available output noise power density is just kT_0 . If the network temperature is $T_n \neq T_0$, a correction arising from the temperature difference $T_0 - T_n$ must be included; hence

$$\frac{dw_0}{dv} = kT_n + gk(T_0 - T_n) \quad (12)$$

where g is the available gain. From Eq. (10), the spot noise factor is

$$f_s = 1 + \frac{T_n}{T_0} (1/g - 1) = 1 + \frac{T_n}{T_0} (\ell - 1) \quad (13)$$

where $\ell = 1/g$ is the available loss factor. Note that the spot noise factor depends on the input resistance used to determine the available gain (or loss).

1.4. Noise Factor for Cascaded Linear Networks

The noise factor for a linear receiving system can be calculated from the noise factors for its individual components. Understanding the relationship between the system noise factor and the noise factors for various components is important in system design since it shows which components contribute most significantly to the noise factor.

Assume that two networks are connected together: network a with spot noise factor f_a and gain g_a , and network b

with spot noise factor f_b and gain g_b . Further assume that a resistor is connected to the input of network a and the entire system is at temperature T_0 . The power density available at the output of network b is equal to the sum of the power density available at the input of network b scaled by g_b and the available noise power density due only to network b or

$$\frac{dw_0}{dv} = f_a g_a g_b kT_0 + (f_b - 1)g_b kT_0 \quad (14)$$

Using Eq. (10), the spot noise factor for two cascaded networks is

$$f_{ab} = f_a + \frac{f_b - 1}{g_a} \quad (15)$$

which is the result originally obtained by Friis [8]. Spot noise factors will usually vary somewhat across the band of an actual network and, for a particular system, the effects of nonuniform noise and gain may require additional consideration. As described previously, the weighted average spot noise factor is often used to characterize the receiving system.

This analysis is readily extended to several linear networks in cascade. For example, if network c is connected to the output terminals of network b , the system noise factor is

$$\begin{aligned} f_{abc} &= f_{ab} + (f_c - 1)/g_{ab} \\ &= f_a + (f_b - 1)/g_a + (f_c - 1)/g_a g_b \end{aligned} \quad (16)$$

and so on for additional networks. This result shows that if network a has a high gain, its noise factor will be the most important in determining the overall noise factor for the system. High-gain low-noise amplifiers are often used to reduce the noise factor in receiving systems.

1.5. Noise Factor for the Linear Portion of a Receiving System

In addition to the actual receiver, a typical radio receiving system is composed of an antenna, transmission lines, and other circuits, all of which contribute noise and must be included in the analysis of the system noise performance. Of particular importance for wireless systems is the receiving antenna, which collects environmental noise. By using the results of the previous sections, the noise factor can be extended to characterize any specified portion of an operating system at any specified set of input terminals. For a radio receiving system, the most useful reference point for noise factor calculations is the input to the terminals of an equivalent loss-free receiving antenna [6]. This reference point provides an appropriate and unique measure of the performance of the entire receiving system.

Typically, the linear portion of a receiving system can be divided into a series of cascaded two-port networks, as shown in Fig. 1. The receiving antenna is modeled as an equivalent loss-free antenna connected to an antenna circuit network. A section of transmission line connects the

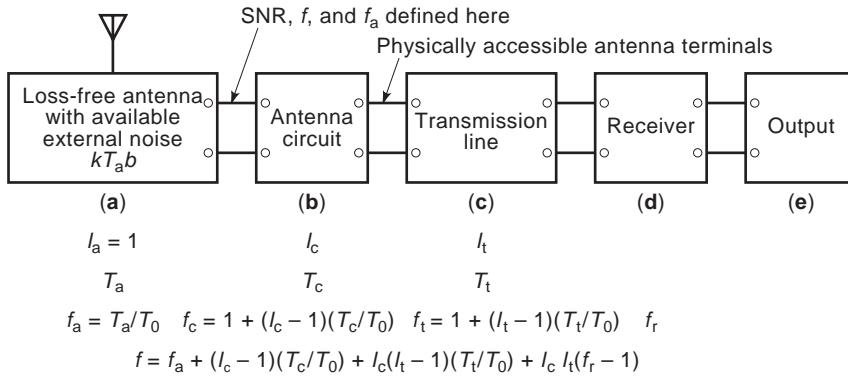


Figure 1. The receiving system and its operating noise factor, f .

antenna to the receiver. Using Eq. (16), the noise factor for the receiving system is

$$f = f_a + \frac{f_c - 1}{g_a} + \frac{f_t - 1}{g_a g_c} + \frac{f_r - 1}{g_a g_c g_t} \quad (17)$$

where f_a , f_c , and f_t are the spot noise factors; and g_a , g_c , and g_t are the gains of the antenna, antenna circuit, and transmission line, respectively; and f_r is the spot noise factor of the receiver.

The external noise power in the band $d\nu$ that is available at the terminals of the loss-free receiving antenna can be expressed as $kT_a d\nu$, where T_a is the noise temperature of the radiation resistance of the receiving antenna at the center frequency of the receiver. The antenna noise factor f_a is equal to the ratio T_a/T_0 . Since the antenna circuit and transmission line are passive two-port networks, the spot noise factor can be expressed as

$$f = T_a/T_0 + (l_c - 1)T_c/T_0 + l_c(l_t - 1)T_t/T_0 + l_c l_t(f_r - 1) \quad (18)$$

where the gains have been replaced by the corresponding loss factors. Strictly speaking, this result is meaningful for narrowband systems where the noise factors do not vary significantly over the operating frequency range. It should be understood that all of the spot noise factors and loss factors are determined with generator impedances that are the same as those in the actual receiving system. Also, the formula for cascaded networks is applicable regardless of the degree of match or mismatch between the output impedance of one network and the input impedance of the following network. The magnitudes of these mismatch losses do influence the values of the spot noise factors and loss factors and will thus affect the noise factor.

The quantity of interest for finite bandwidth systems is the weighted average spot noise factor, which is often referred to as the operating noise factor f_{op} [6]. The operating noise factor can be expressed in terms of the weighted average noise factors of the receiving system components as follows

$$f_{op} = \bar{f}_a + \bar{f}_{ct} - 1 + (b_r/b)(g_r/g_o)(\bar{f}_r - 1) \quad (19)$$

where, denoting the overall system gain at frequency ν as $g(\nu)$, the weighted average antenna noise factor is

$$\bar{f}_a = \frac{\int_0^\infty T_a(\nu)g(\nu) d\nu}{T_0 \int_0^\infty g(\nu) d\nu} \quad (20)$$

\bar{f}_{ct} is the weighted average combined noise factor of the antenna circuit and transmission-line network

$$\bar{f}_{ct} = \frac{\int_0^\infty f_{ct}(\nu)g(\nu) d\nu}{\int_0^\infty g(\nu) d\nu} \quad (21)$$

b is the equivalent bandwidth of the system, b_r is the equivalent bandwidth of the receiver, g_o is the nominal gain of the system, g_r is the maximum gain of the receiver, and \bar{f}_r is the weighted average receiver noise factor, as given in Eq. (11) and using the receiver gain function.

To apply the foregoing results, noise factors for the receiver, related electronic components, and an equivalent loss-less antenna must be determined. Using the definitions given in the previous sections, measurement methods can be readily devised and implemented to calculate accurately noise factors for receivers and other electronic components (see, for example, Ref. 9). The determination of the antenna noise factor is, in general, much more difficult. For RF communication systems, the antenna noise factor is often a nonstationary random process that varies with time, frequency, geographic location, and receiving antenna characteristics. As a consequence, researchers have spent many years measuring and compiling statistics that can be used to estimate the antenna noise factor for various environmental noise sources. In the case of man-made noise, not only is there a fast time dependence over fractions of an hour to days, but there is also a relatively slow time dependence based on advances in technology. Significant changes in the background noise for a particular environment may occur within a few years, and as a consequence published data can become outdated. Antenna noise factors based on published noise statistics are described in the following sections.

So far in this article, lowercase letters have been used to represent noise factors, gains, and bandwidths. In noise

analysis, it is common to express these quantities as decibels and to use uppercase letters to denote that the quantity is in decibels. Also, when given in decibels, the noise factor is usually referred to as *noise figure*; for example, the antenna noise figure is

$$F_a = 10 \log_{10} f_a \text{ (dB)} \quad (22)$$

and in decibels, the notations for gain and bandwidth are

$$G = 10 \log_{10} g \text{ (dB)}; B = 10 \log_{10} b \text{ (dB/Hz)} \quad (23)$$

This notation and terminology is used in the following sections.

2. ENVIRONMENTAL NOISE AND ANTENNA NOISE FIGURE

Environmental noise emanates from both natural and man-made sources and is collected by the receiving system antenna. The determination of noise parameters, such as the antenna noise figure F_a , requires careful measurement programs that must account for temporal, spatial, and frequency variations of the particular noise source. In this section, some of the more important sources of environmental noise are described. The statistical data presented are based on many years of measurements of natural and man-made noise over the entire radio spectrum.

2.1. F_a for Blackbody Radiation

All objects at temperatures above absolute zero radiate energy in the form of electromagnetic waves. A blackbody is a perfect absorber and a perfect radiator of electromagnetic energy. It absorbs all incident radiation at all wavelengths, and the radiation from it is a function of only temperature and wavelength. Although the concept of a blackbody is an idealization, it can be used to estimate the radio noise emitted by a variety of objects. For example, the cosmic background, thought to be the lingering echo of the creation of the universe, is equivalent to radiation from a blackbody at 2.7 K.

The *brightness* β of radiation from a blackbody radiator at temperature T and frequency ν is given by Planck's radiation law [10]:

$$\beta = \frac{2h\nu^3}{c^2(e^{h\nu/kT} - 1)} \text{ (W m}^{-2} \text{ Hz}^{-1} \text{ sr}^{-1}) \quad (24)$$

where $c = 2.99792458 \times 10^8$ (m/s) is the speed of light in free space. For typical radio frequencies and standard temperatures, where, $h\nu \ll kT$, this reduces to the Rayleigh-Jeans approximation

$$\beta \cong \frac{2kT}{\lambda^2} \quad (25)$$

where λ is the free-space wavelength. As in the case of thermal noise in a resistor, the radiation power is directly proportional to temperature.

The power received by an antenna from an incremental blackbody of area dA at temperature T in bandwidth $d\nu$ is

$$dw = \frac{1}{2} \beta \frac{\lambda^2}{4\pi} \gamma(\Omega) d\Omega d\nu \cong \frac{kT}{4\pi} \gamma(\Omega) d\Omega d\nu \quad (26)$$

where $d\Omega$ is the element of solid angle subtended at the receiver by dA and $\gamma(\Omega)$ is the directive gain of the antenna. Note that the antenna only collects half the power since only a single polarization is received. The total power collected when the blackbody radiation at temperature T is received from all directions is

$$w = kT d\nu \left(\frac{1}{4\pi} \int_{4\pi} \gamma(\Omega) d\Omega \right) = kT d\nu \quad (27)$$

which is the same as the total power available from a resistor at temperature T . Hence, the antenna temperature is simply T and $f_a = T/T_0$ independent of the antenna gain.

2.2. F_a for Common Natural and Man-Made Radio Noise Sources

Both natural and man-made radio noise have been measured and carefully studied by many scientists and engineers in the latter half of the twentieth century. The results of these efforts have been published in various journals, conference proceedings, and reports and recommendations of radio engineering organizations, such as the International Telecommunication Union (ITU) [11–14]. In this article, statistical data from these studies are presented for what are considered to be some of the more important environmental radio noise sources. For a more detailed treatment of these and other sources of radio noise, the reader is referred to the references.

The antenna noise figure F_a for background natural radio noise from 1 Hz to 1 THz is illustrated in Fig. 2 [15]. These data show that natural radio noise depends strongly on frequency over the radio spectrum (nominally 3 kHz–300 GHz). In addition, several noise sources are nonstationary in time and space (e.g., atmospheric, sun, rain). Of particular interest for communications systems operating at or below about 30 MHz is atmospheric noise, where F_a is random and is characterized by its statistics. Atmospheric noise is also non-Gaussian. The other noise sources shown in this figure are essentially Gaussian.

For RF systems operating at frequencies of several hundred megahertz and below, man-made noise is an important source of radio noise. Like atmospheric noise, man-made noise is both nonstationary and non-Gaussian. Figure 3 [16] shows the median antenna noise figure F_{am} for man-made noise in four environments and galactic noise as compared with the expected daytime and nighttime levels for atmospheric noise. Man-made noise is strongly dependent on frequency and, in general, the F_{am} curves have a slope of -27.7 dB/decade of frequency.

Figure 4 [15] shows the details of natural radio noise over the frequency range of 100 MHz–100 GHz. The estimated median business-area man-made noise has also been included. The $E(90^\circ)$ curve shows sky noise measured with a narrowbeam antenna at zenith. The water

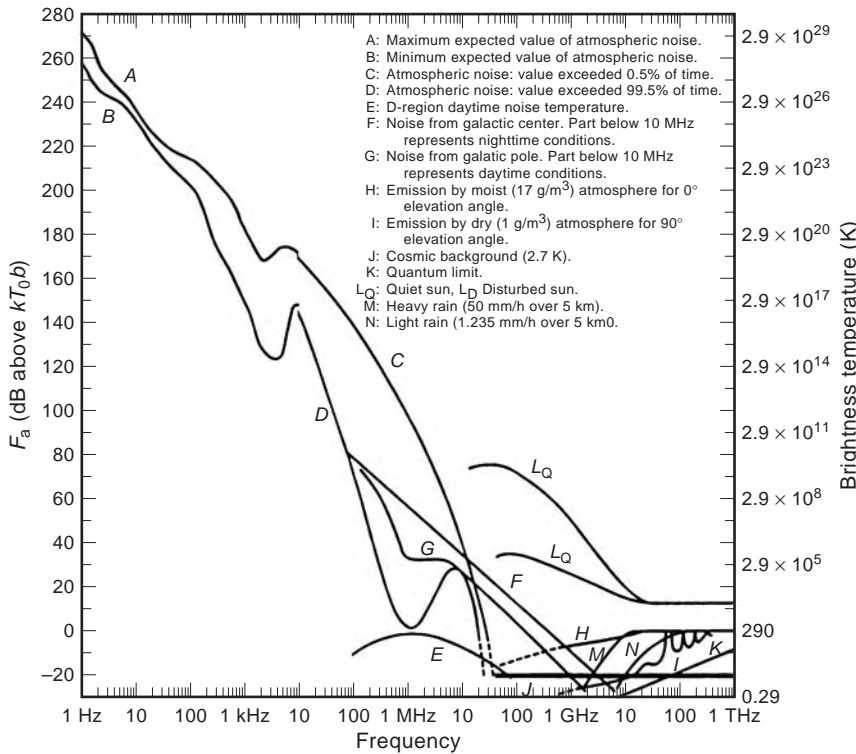


Figure 2. Natural radio noise (1 Hz-1 THz) [15].

and oxygen absorption bands are clearly visible. The $E(0^\circ)$ curve is sky noise with a narrowbeam antenna directed along Earth’s surface.

It was shown that when an antenna receives blackbody radiation at a uniform temperature from all directions, F_a does not depend on the receiving antenna gain. For most environmental noise sources, however, F_a does depend on the antenna gain and on several other factors. Appropriate corrections must be applied when the radio system-receiving antenna differs significantly from that used to measure the noise.

Curves L_D , L_Q , F , H , and M in Fig. 2 all refer to very narrowbeam antennas pointing directly at the source. Noise from such sources (sun, atmospheric gasses, the Earth surface) are also expressed in terms of brightness temperature. These curves can be used to calculate the

antenna temperature of a particular receiving antenna by integrating Eq. (25) in terms of temperature over the region occupied by the noise source

$$T_a = \frac{\gamma_0}{4\pi} \int_{\text{sources}} T(\Omega)p(\Omega) d\Omega \quad (28)$$

where γ_0 is the gain and $p(\Omega)$ is the pattern of the receiving antenna; that is, $\gamma(\Omega) = \gamma_0 p(\Omega)$. For example, the sun has a beamwidth of about $\frac{1}{2}^\circ$. If a receiving antenna with gain γ_0 is aimed at the sun and the pattern is essentially constant over the intersection with the sun’s beam, the antenna temperature is

$$T_a = \frac{\gamma_0}{4\pi} \int_{\text{Sun}} T(\Omega)p(\Omega) d\Omega \cong \gamma_0 T_s \left(\frac{\pi}{1440} \right)^2 \quad (29)$$

where T_s is the brightness temperature of the sun at the desired frequency.

In Fig. 4, there are two curves associated with galactic noise. Curve B is for an omnidirectional antenna, while curve C is for an infinitely narrow beam aimed toward the galactic center. Because of the relative motion of the earth and galaxy, galactic noise is not constant in time. A more accurate determination of galactic noise for other types of antennas can be obtained by using published radio sky data, which gives the brightness temperature as a function of position in the sky. Such data are available in CCIR Report 720-2 [14], which contains maps of the brightness temperature of the radio sky at 408 MHz and an approximate expression for the frequency dependence of the temperature.

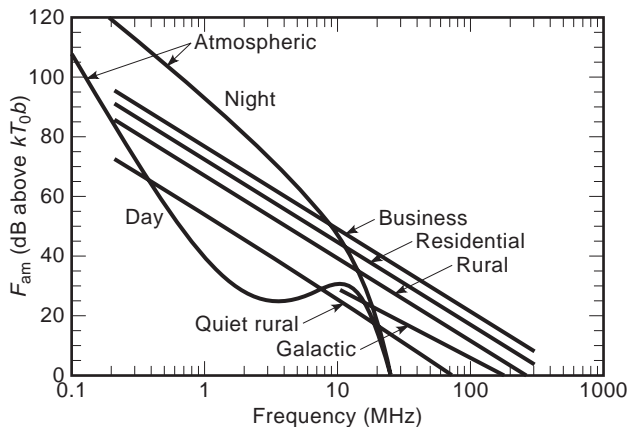


Figure 3. Median values of F_a [16].

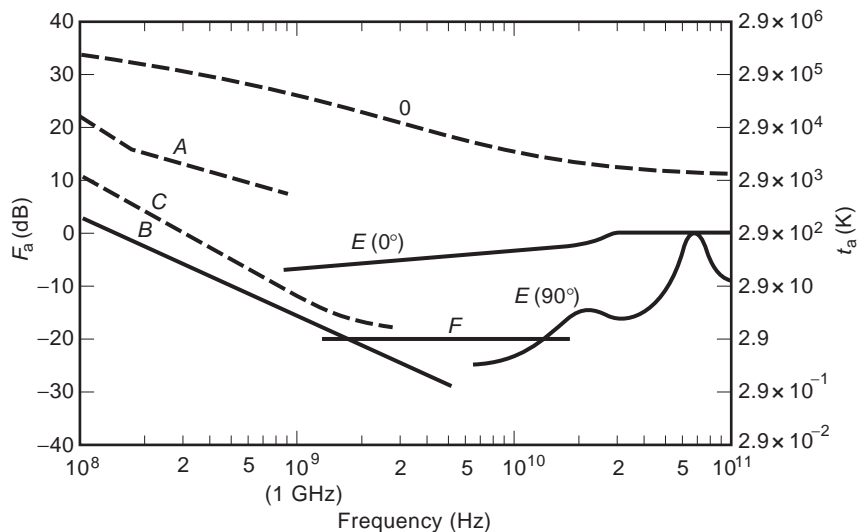


Figure 4. F_a versus frequency (100 MHz–100 GHz), where A = estimated median business area man-made noise, B = galactic noise, C = galactic noise (toward galactic center with infinitely narrow beamwidth), D = quiet sun ($\frac{1}{2}^\circ$ beamwidth directed at sun), E = sky noise due to oxygen and water vapor (very narrow beam antenna); upper curve 0° elevation angle, lower curve 90° elevation angle, F = cosmic background, 2.7 K [15].

2.3. Atmospheric and Man-Made Noise

The most significant sources of environmental radio noise at frequencies below 1 GHz are man-made and atmospheric. For these sources, the noise data were measured with a grounded electrically short monopole antenna. Since this type of noise most probably arrives at the receiver at relatively low elevation angles and from random directions, such an azimuthally omnidirectional antenna is well suited for noise measurements. Predicting the antenna noise figure for other types of receiving antennas requires an assessment of the differences between the ideal short monopole antenna and the desired receiving antenna. Factors that should be considered are antenna efficiency, directivity, polarization, and height above the ground.

The direction of arrival for both atmospheric and man-made noise has been shown to be nonuniform, varying by as much as 10 dB with direction [17]. Since the noise is nonstationary, predicting F_a for high-gain antennas would likely be arduous if worst-case estimates based on the measured data do not provide sufficient accuracy. For azimuthally symmetric antennas such as a half-wave dipole, a correction factor based on the ratio of the desired antenna gain to the reference antenna gain can be applied to obtain the appropriate value for F_a .

Since these noise processes are nonstationary, the usual design parameter, SNR, is random and the underlying statistics of the noise process as a function of time and geographic location must be understood to assess radio performance properly. These characteristics are discussed in more detail in the following sections.

Another important consideration is that both atmospheric and man-made noise are non-Gaussian. Typically, communication system performance is calculated on the basis of Gaussian noise. A more detailed analysis incorporating the statistics of the actual non-Gaussian noise process may be required in radio design and performance evaluations. Several publications listed in the references provide information regarding the impulsive nature of these noise sources and its effect on radio receivers.

2.3.1. Statistics of F_a for Atmospheric Noise. Atmospheric noise is an important consideration for wireless communication systems operating below 30 MHz. The main source of atmospheric noise is lightning. The electromagnetic energy emitted by electrical storms couples into the Earth–ionosphere waveguide, and hence, local noise levels can be significantly influenced by distant thunderstorms. Because of ionospheric interactions, overall atmospheric noise levels are greater at night, as shown in Fig. 3.

In Fig. 2, curves A , B , C , and D represent the expected range of F_a at the surface of the earth. These data are of the average background, taking into account all times of day, seasons, and the entire surface of Earth. Curves A and B give the maximum and minimum values of F_a from 1 Hz to 10 kHz. In this frequency range, there is very little seasonal, diurnal, or geographic variation. Note that the variation of F_a begins to increase significantly at about 100 Hz. This is due to the variability of the Earth–ionosphere waveguide cutoff. Curves C and D give the atmospheric noise from 10 kHz to about 30 MHz, above which the noise levels are quite low. Curve C is the value of F_a exceeded 0.5% of the time, and curve D is the value of F_a exceeded 99.5% of the time. These results are derived from background atmospheric noise and do not include effects of “nearby” electrical storms. A compilation of measurements showing the peak field strength for 1 mile distant lightning as a function of frequency is given in Fig. 5 [18].

The variability of F_a , particularly in the medium-frequency (MF) and high-frequency (HF) communication bands (300 kHz–30 MHz), is so large that the bounds given in Fig. 2 alone cannot be used to obtain a useful characterization of radio system performance. It is important, therefore, to know how F_a and other noise statistics vary with time and location. Starting in 1957, the average power levels and other relevant statistics were measured on a worldwide basis using a network of 15 stations. These measurements spanned 13 kHz–20 MHz and considered both the time of day and the season. The results of several years of measurements were published in the National Bureau of Standards (NBS) Technical Note Series 18 [19].

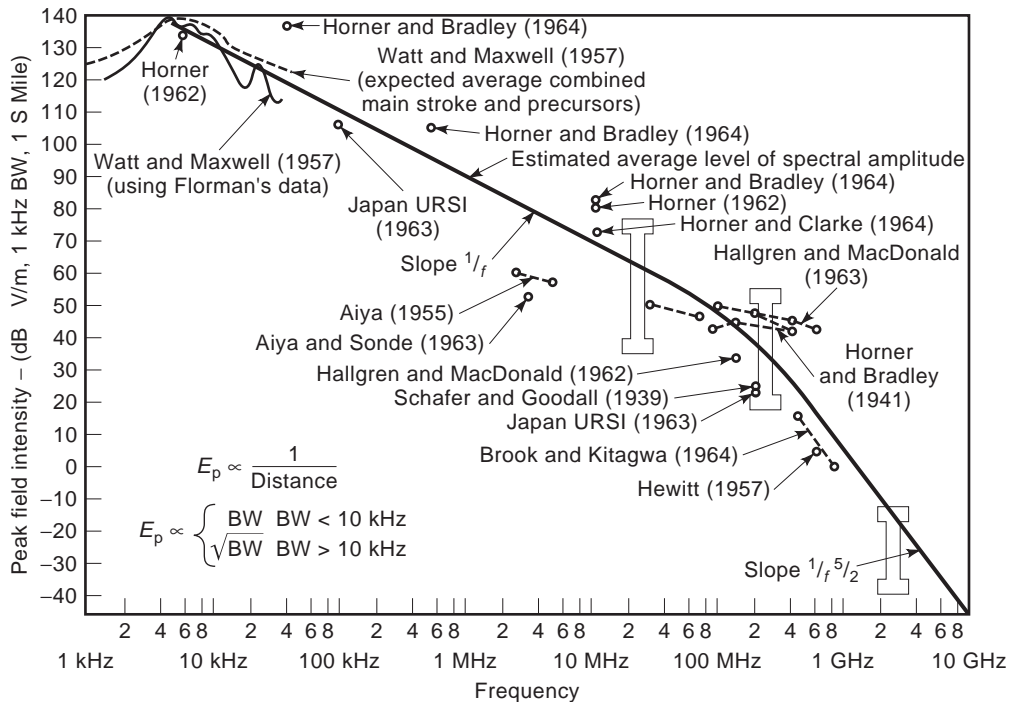


Figure 5. Lightning emission peak field strength, 1 mile distant. (Reprinted from p. 369 of Ref. 18, by permission, © 1982 IEEE.)

and later published in CCIR Report 332 [12]. A numerical representation of the data contained in Report 332 is also available [20].

The published data give, for each frequency, location, season, and time of day (measured in 4-h increments), the month-hour median value of F_a along with values exceed 10% (upper decile, D_u) and 90% (lower decile, D_l) of the time. As an example of these data, Fig. 6 shows worldwide values for the median antenna noise figure F_{am} in the winter between 0000 and 0400 local time. The median noise figure at other frequencies, D_u , D_l , and related statistics are obtained using the curves shown in Fig. 7.

The statistical distribution of F_a and hence the radio system SNR is readily obtained from the published data. For a given season and measurement time block (4 h) it has been shown that F_a is adequately represented by two lognormal distributions [21], one above the median value and one below. As an example, the distribution of F_a for 3 MHz at Boulder, Colorado in the winter at 0000–0400 can be determined using the data from Figs. 6 and 7. First, the 1 MHz value of F_{am} at the geographic location of interest is obtained from Fig. 6 and corrected to 3 MHz using Fig. 7. Then D_u and D_l as well as their standard deviations are obtained from Fig. 7. Using normal probability paper, these three points define the two intersecting lines that give the two desired lognormal distributions. The resulting distribution is shown in Fig. 8. Hence, if a radio system is operating at 3 MHz, the system performance can be conveniently specified in terms of the percent of time that the required SNR will be available at a particular geographic location, season, and time.

2.3.2. Statistics of F_a for Man-Made Noise. In 1974, Spaulding and Disney [22] presented results from many years of measurements of man-made radio noise. They devised methods for estimating the noise power and noise amplitude statistics that are important in the design of radio systems. These methods are described in the CCIR reports [13] and have been widely used by industry. Figure 3 summarizes these results in terms of the median antenna noise figure F_{am} . As with atmospheric noise, man-made noise is both nonstationary and non-Gaussian and is a significant source of radio noise for frequencies below a few hundred megahertz. The antenna noise figure F_a varies both in time and location. The noise level depends on the type and extent of human activities, which are conveniently classified into four man-made noise environments [13] described in Table 1.

The within-the-hour time variability of F_a is commonly described by two log-normal distributions [21], as described previously for atmospheric noise. Values of D_u and D_l are given in CCIR Report 258 as a function of frequency and environment. More recently, Spaulding and Stewart [21] have analyzed the data used to obtain these decile values and have found that it is appropriate to use the values $D_u = 9.7$ dB and $D_l = 7$ dB, independent of environmental category and frequency. Other proposed noise models described in Report 258 include a simple Gaussian model that does not describe the skewness observed in measured noise data and a more complex χ^2 model.

As an example, the distributions of F_a using $D_u = 9.7$ dB and $D_l = 7$ dB at 137 MHz for business, residential, rural, and quiet rural noise environments are shown in Fig. 9. These data include the contribution of Galactic

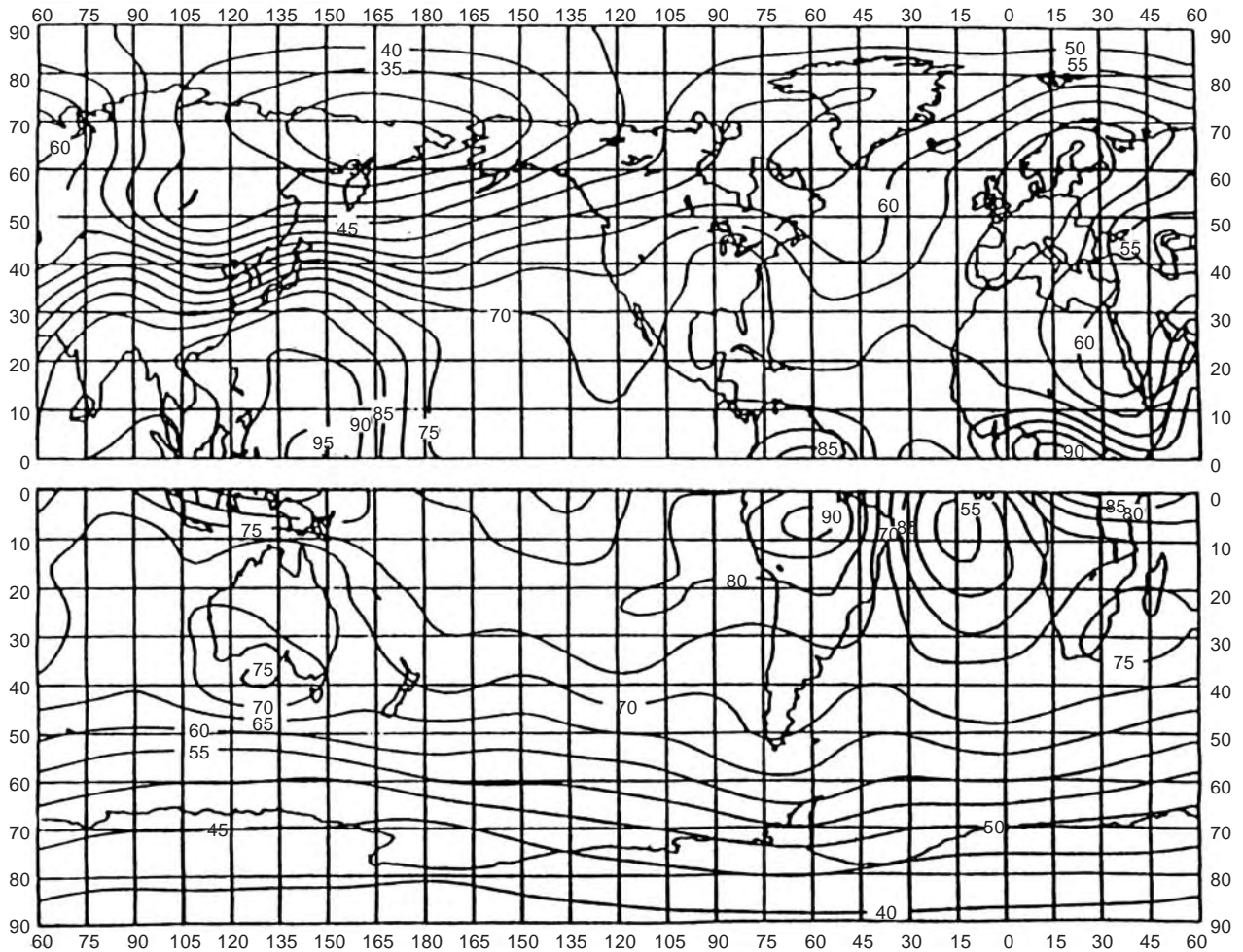


Figure 6. Expected values of atmospheric radio noise, F_{am} (dB above kT_0b at 1 MHz) (winter 0000–0400 LT) (12).

noise, which is only significant in the quiet rural noise environment.

Location variability is also an important consideration when characterizing F_a . The usual assumption [22] is that F_{am} is the noise figure exceeded 50% of the time at 50% of the locations. Hence, the time distribution of F_a as shown in Fig. 9 is the noise power exceeded at 50% of the locations for a particular environment. If it is assumed that the location variability is Gaussian, then the value \tilde{F}_a that is exceeded at other than 50% of locations is obtained from

$$\tilde{F}_a = F_a + \sqrt{2}\sigma_L \operatorname{erfc}^{-1} \left[\frac{\% \text{ locations}}{50} \right] \quad (30)$$

where erfc^{-1} is the inverse complementary error function and σ_L is the standard deviation of the location distribution.

The location variability in terms of the standard deviation σ_L of the median value as a function of frequency and environment is given in Table 2 [13]. As may be expected, σ_L for the business environment is much larger than either the residential or rural environment.

3. APPLICABILITY OF PUBLISHED MAN-MADE NOISE STATISTICS TO CONTEMPORARY ENVIRONMENTS

The man-made noise statistics presented are largely based on measurements that were made many years ago in North America by Spaulding and Disney [22]. More recently, Spaulding has warned that the CCIR data may now be inaccurate due to technological advances [23]. This is largely based on the fact that emissions from newer automobile ignition systems, a major contributor to man-made noise in urban areas, have decreased dramatically over the years. After reviewing more recent measurements and trend analyses, Spaulding concluded [23] that in the business environment “at 100 MHz in the 1970’s time-frame, F_{am} was on the order of 20 dB but now is probably approximately 20 dB less.” This conclusion, however, is not based on a comprehensive set of noise measurements as would be necessary to update the previous survey described in Ref. 23.

While the improvements in automobile ignition systems have likely affected the noise levels in business and residential environments, emissions from gap discharge and corona in power transmission and distribution lines have probably not decreased with time. Figure 10 [22]

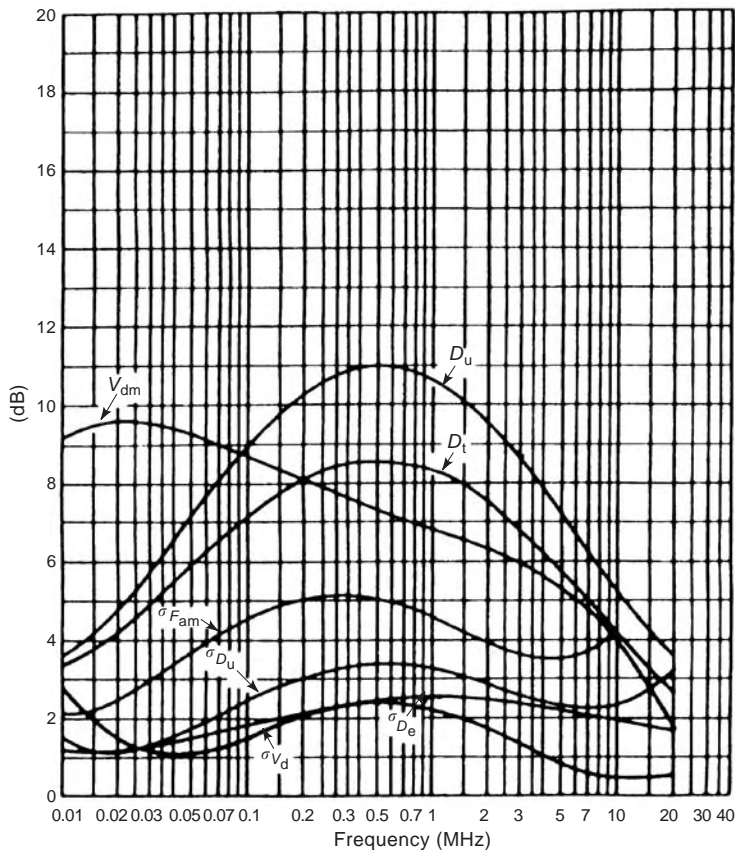
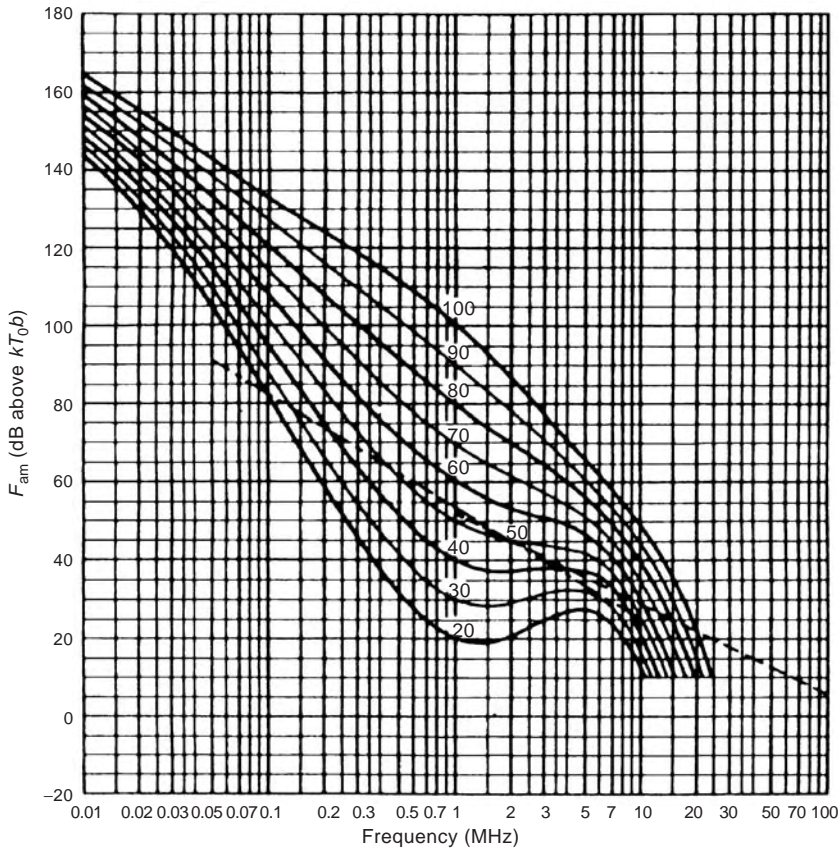


Figure 7. (a) Variation of radio noise with frequency (winter; 000–0400 LT) (12). ——— Expected values of atmospheric noise. - - - - - Expected values of galactic noise. (b) Data on noise variability and character (winter; 000–0400 LT) (12). $\sigma_{F_{am}}$: standard deviation of values of F_{am} . D_u : ratio of upper decile to median value, F_{am} . σ_{D_u} : standard deviation of values of D_u . D_t : Ratio of median value, F_{am} , to lower decile. σ_{D_t} : standard deviation of values of D_t . V_{dm} : expected value of median deviation of average voltage. The values shown are for a bandwidth of 200 Hz. σ_{V_d} : standard deviation of V_d [12].

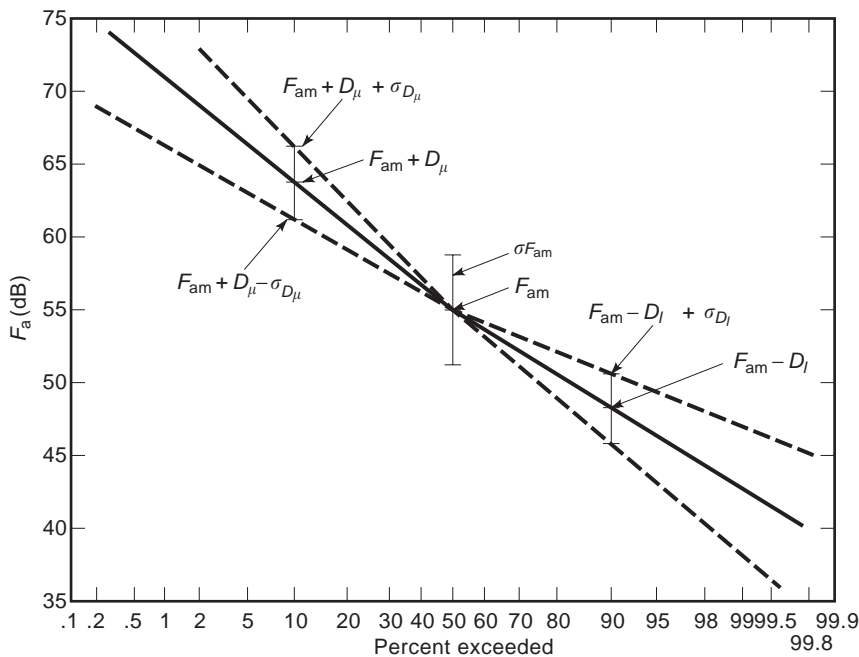


Figure 8. The distribution of F_a values for atmospheric radio noise at Boulder, Colorado, 3 MHz, for the winter season, 0000–0400 hours [21].

shows F_{am} under, and one-quarter mile from, a 115 kV line in rural Wyoming. It is interesting to note that the noise measured one-quarter mile from the power line is about the same as that predicted for a rural environment. A possible conclusion is that if power and distribution lines are the primary noise source in rural environments, rural man-made noise is not likely to have decreased. However, one would not expect noise in an urban environment to be less (than rural), as would be the case with the estimated 20 dB reduction in F_{am} .

Another factor that could significantly affect the level and character of man-made radio noise is the proliferation of electronic devices (e.g., computers, electronic switching devices, microwave ovens) that are unintentional RF emitters. Such devices have become ubiquitous in business, residential, and rural environments and could affect both the magnitude of the noise power as well as its frequency dependence.

The man-made noise data presented in the previous sections are applicable to North America; the validity of extension to other parts of the world cannot be determined precisely. CCIR Report 258 describes very high frequency (VHF) measurements made in business and residential

areas of the United Kingdom where the noise power was found to be some 10 dB below that shown in Fig. 3 [16]. This is attributed to differences in patterns of utilization of electric and mechanical appliances and regulation of interference. The report also states that, due to such differences, the noise statistics should be used with caution. It should be noted, however, that if an overall 10 dB reduction in urban noise can be justified, the man-made noise environments near 100 MHz would be bounded by what are now classified as rural (worst) and quiet rural (best) environments, as shown in Fig. 3.

Relatively recent noise measurements at 137 MHz [24] show that the statistics of man-made noise are significantly different from what is predicted by CCIR Report 258. For example, Fig. 11 shows the median, mean, and peak (exceeded 0.01% of the time) values of F_a measured over a 24-h period in a business environment. Diurnal variations corresponding to human activity are clearly

Table 1. CCIR Report 258 Definitions of Man-Made Noise Environments

Environment	Characteristics
Business	Areas where predominant usage is for any type of business
Residential	Areas used predominantly for single or multiple family dwellings (at least five single-family units per hectare), no large or busy highways
Rural	Areas where dwelling density is no more than one every two hectares
Quiet Rural	No definition given

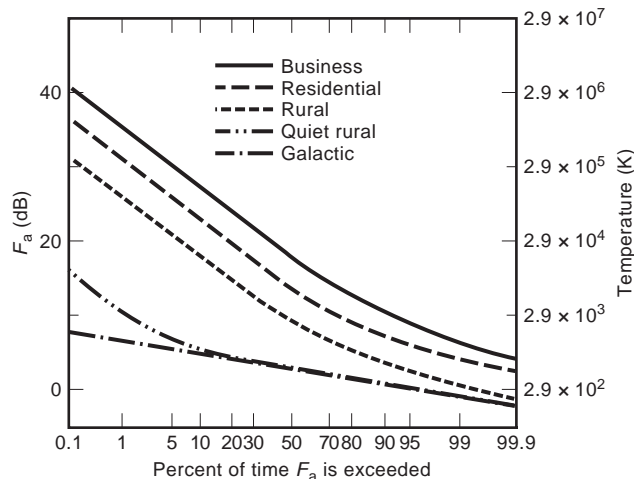


Figure 9. Distribution of F_a for man-made and galactic noise.

Table 2. Location Variability in Terms of the Standard Deviation for Various Environments

Frequency (MHz)	σ_L Business	σ_L Residential	σ_L Rural
0.25	6.1	3.5	3.9
0.50	8.2	4.3	4.4
1.00	2.3	2.5	7.1
2.50	9.1	8.1	8.0
5.00	6.1	5.5	7.7
10.00	4.2	2.9	4.0
20.00	4.9	4.7	4.5
48.00	7.1	4.0	3.2
102.00	8.8	2.7	3.8
250.00	3.8	2.9	2.3

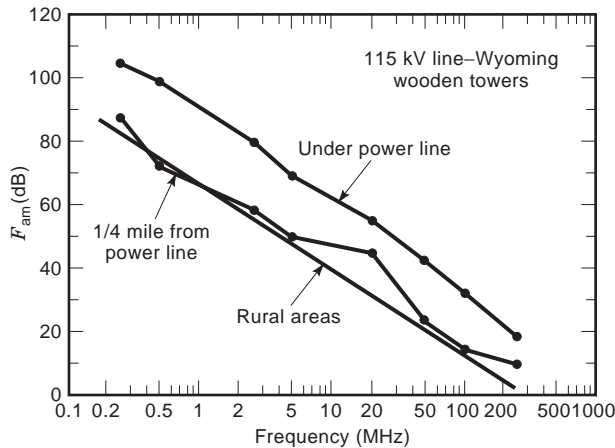


Figure 10. Power line noise measurements near a 115-kV line in rural Wyoming [22].

evident. The relatively steady within-the-hour values of the mean power (F_a) are not consistent with the predicted within-the-hour distribution of F_a for a business environment (see Fig. 9). Figure 12 shows the distribution of F_a measured at six urban sites plotted on normal probability paper. The distribution at a particular site was obtained by collecting statistics measured within two-minute intervals spaced about an hour apart from hours of continuous

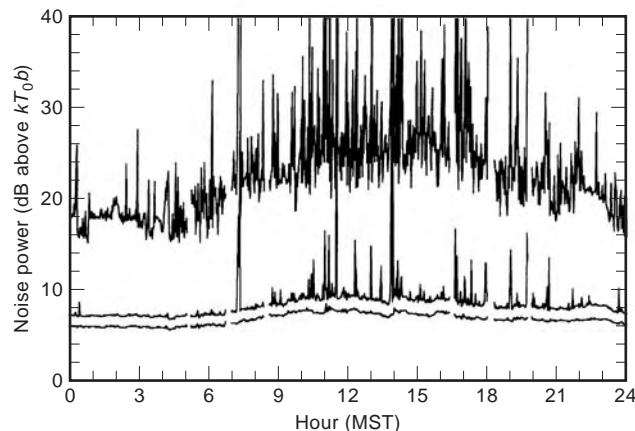


Figure 11. Median, mean, and peak noise power near an office park [24].

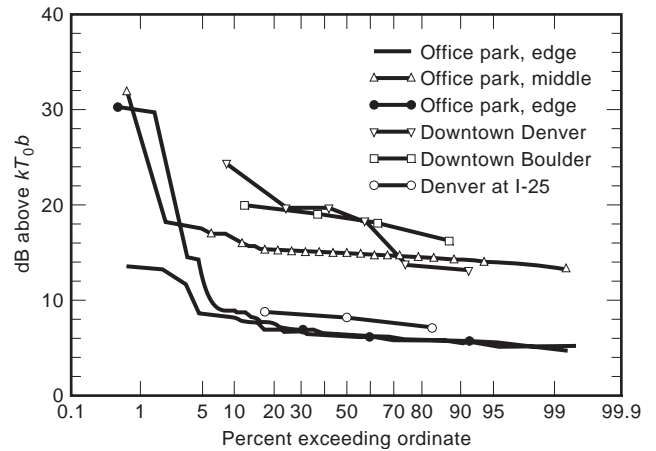


Figure 12. Power averages from measurements at six urban sites [24].

measurements made at that particular location. Hence, the results should correspond to the hour-to-hour time variability, which, for the most part, is relatively low at most of the locations. Location variations however are quite large, exceeding 12 dB in some cases. More importantly, these measurements show that there are business environments (down-town urban areas) where F_{am} is still nearly 20 dB.

In summary, the 137 MHz measurements demonstrate that important changes have occurred in both the level and character of man-made noise since the comprehensive noise survey described by Spaulding and Disney [22]. While these measurements can only be considered as a “spot check,” they do show that standard methods used to predict man-made radio noise are probably outdated. It is concluded that additional comprehensive man-made noise measurements at RF frequencies into the ultra-high-frequency (UHF) band will be necessary to provide radio system designers and engineers with the required tools to effectively design modern radio systems.

BIBLIOGRAPHY

1. W. R. Bennett, *Electrical Noise*, McGraw-Hill, New York, 1960, Chap. 5.
2. J. B. Johnson, Thermal agitation of electricity in conductors, *Phys. Rev.* **32**:97–109 (1928).
3. H. Nyquist, Thermal agitation of electric charge in conductors, *Phys. Rev.* **32**:110–113 (1928).
4. C. Kittel and H. Kroemer, *Thermal Physics*, Freeman, San Francisco, CA, 1980, p. 91.
5. R. Pettai, *Noise in Receiving Systems*, Wiley, New York, 1984, Chap. 7.
6. CCIR, *Operating Noise-Threshold of a Radio Receiving System*, CCIR Rep. 413, Geneva, Switzerland: International Telecommunications Union, 1966.
7. IRE standards on electron tubes: Definition of terms, 1957, *Proc. IRE* **45**:983–1010 (1975).
8. H. T. Friis, Noise figures of radio receivers, *Proc. IRE* **32**: 419–422 (1944).
9. R. Pettai, *Noise in Receiving Systems*, Wiley, New York, 1984, Chap. 11.

10. J. D. Kraus, *Radio Astronomy*, Cygnus-Quasar, Powell, OH, 1986, Chap. 3.
11. CCIR, *Worldwide Minimum External Noise Levels, 0.1 Hz to 100 GHz*, Rep. 670, International Telecommunications Union, Geneva, Switzerland, 1990.
12. CCIR, *Characteristics and Applications of Atmospheric Radio Noise Data*, Rep. 332-3, International Telecommunications Union, Geneva, Switzerland, 1986.
13. CCIR, *Man-Made Radio Noise*, Rep. 258-5, International Telecommunications Union, Geneva, Switzerland, 1990.
14. CCIR, *Radio Emission from Natural Sources in the Frequency Range above about 50 MHz*, Rep. 720-2, International Telecommunications Union, Geneva, Switzerland, 1986.
15. A. D. Spaulding, *The Natural and Man-Made Noise Environment in Personnel Communications Services Bands*, U.S. Dept. Commerce, NTIA Rep. 96-330 (revised), Boulder, CO, May 1997.
16. R. Achatz et al., *Man-Made Noise in the 136–138-MHz VHF Meteorological Satellite Band*, U.S. Dept. Commerce, NTIA Rep. 98-355, Boulder, CO, Sept. 1998.
17. H. Volland, *CRC Handbook of Atmospheric*, CRC Press, Boca Raton, FL, 1982, p. 294.
18. T. H. Shumpert, M. A. Honnel, and G. K. Lott, Jr., Measured spectral amplitude of lightning sferics in the HF, VHF, and UHF bands, *IEEE Trans. Electromagn. Compat.* **EMC-24**: 368–369 (1982).
19. National Bureau of Standards, *Quarterly Radio Noise Data*, Tech. Note 18 (1–32), U.S. Dept. Commerce, Washington, DC, 1959–1966.
20. D. L. Lucas and J. D. Harper, *A Numerical Representation of CCIR Report 332: High Frequency (3–30 Mc/s) Atmosphere-Radio Data*, NBS Tech. Note 318, U.S. Dept. Commerce, Washington, DC, 1965.
21. A. D. Spaulding and F. G. Stewart, *An Updated Noise Model for Use in IONCAP*, U.S. Dept. Commerce, NTIA Report 87-212, Boulder, CO, May 1997.
22. A. D. Spaulding and R. T. Disney, *Man-Made Radio Noise Part 1: Estimates for Business, Residential, and Rural Areas*, U.S. Dept. Commerce, OT Rep., 74-38, Boulder, CO, June 1974.
23. A. D. Spaulding, The roadway natural and man-made noise environment, *IVHS J.* **2**:175–211 (1995).
24. R. Dalke et al., Measurement and analysis of man-made noise in VHF and UHF bands, *1977 Wireless Commun. Conf.*, Boulder, CO, Aug. 11–13, 1977, pp. 229–233.

RADIO ON FIBER SYSTEMS (RoF SYSTEMS)

SHOZO KOMAKI
KATSUTOSHI TSUKAMOTO
Osaka University
Osaka, Japan

1. INTRODUCTION

Trends of user needs in communications are reflected in the advances in (1) wireless communications that enable us to use small and high-spectrum-efficient personal handy terminals (cellular phones) that employ a microcellular

architecture [1,2] and (2) global and seamless communication networking that enable international roaming and wide-area handover capability. Both types of advances are directed toward the same destination in terms of user demands; however, they are diametrically opposed from the viewpoint of technological feasibility. For example, handover among a large number of microcells poses many problems, and a huge number of base stations are required to make microcellular communication more global.

To solve these technical problems, it has been proposed that microcells in wide areas are connected by radio-on-fiber (RoF) links, where RF signals are transported through optically connected links, in the same way as in radio-air-interfaced space transmission [3–24]. One more user demand in multimedia communication has motivated the development of broadband service. To prepare wide-band service to the home, the fibers-to-the-home (FTTH) system has been implemented. Wireless mobile broadband service is easily implemented on the fiber-to-the-curb (FTTC) facility. These two systems, FTTH and FTTC, are collectively termed as the *fiber-to-the-air* (FTTA) system. The RoF systems are also applicable to the home networks, especially in the wireless home network system backbone.

In Section 2 of this article, the basic configuration and devices for RoF system are described. Section 3 discusses the performance calculations and designing method. Section 4 describes various application examples, such as communications, electrooptical sampling (EOS), and radioastronomy. Finally, in Section 5, networking of RF signals on fiber networks collectively referred to as the “Radio Highway” including wavelength-division multiplexing (WDM), optical time-division multiple access (optical TDMA), and optical code-division multiple access (optical CDMA), are described.

2. BASIC CONFIGURATIONS

The basic configuration of the RoF link is shown in Fig. 1. RF signals from different wireless services are accessed by the same base station and are then concentrated in the base station antenna. The received RF signals are converted to the optical signal by using an electrical-to-optical signal converter (E/O). Thereafter the optical signal is transmitted to the central control station (CCS) through the optical fiber, and converted to the RF signal by an optical-to-electrical (O/E) converter, usually by means of a photodiode. The converted RF signal is divided into the radio signals from each wireless service by using the appropriate bandpass filters.

The RoF link is implemented to the mobile systems as shown in Fig. 2, and has following advantages over the conventional microcellular base stations:

1. Use of base station equipment is versatile for various new types of service because the base station does not need to be replaced even if new service is installed.
2. Allowance for user concentration to a specific area is high because the control station equipment and

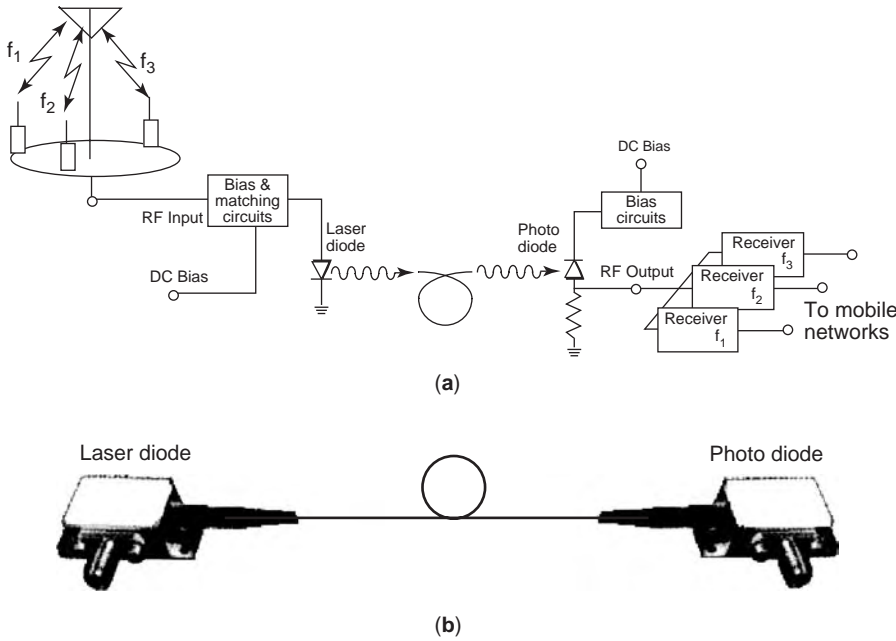


Figure 1. Basic configuration of RoF link: (a) block diagram; (b) photograph.

spectrum resource will be used in the user-concentrated area by switching the central equipment to the appropriate cell(s).

3. Base station operation/maintenance cost is low, because no complicated equipment is required, such as frequency-synthesized transceivers, modems, base-band circuits, and control circuits for frequency assignment.
4. Handover among cells is easy because the control station can observe all the cell signals simultaneously and instantaneous switching to the better signal is available at the control station.

3. DEVICES FOR RoF LINKS

The following components are required to realize the RoF link: (1) a light source, (2) an optical modulator, (3) an optical amplifier, and (4) a photodetector. The E/O converter consists of devices (1) and (2), and the O/E converter consists of device (4). Device (3) is installed in the relay nodes to compensate the fiber loss. In the simplest case of direct modulation, one laser diode (LD). One photodetector (PD), and one fiber can effect an RoF link. The LD, which current is directly modulated by the received RF signals, is used for the light source, and generates an intensity

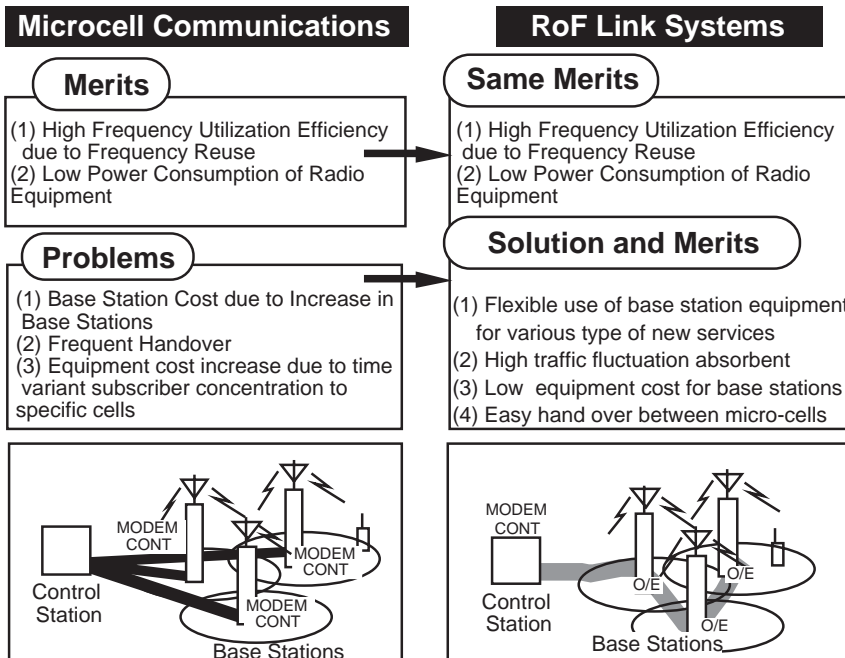


Figure 2. Microcell systems and RoF link solutions.

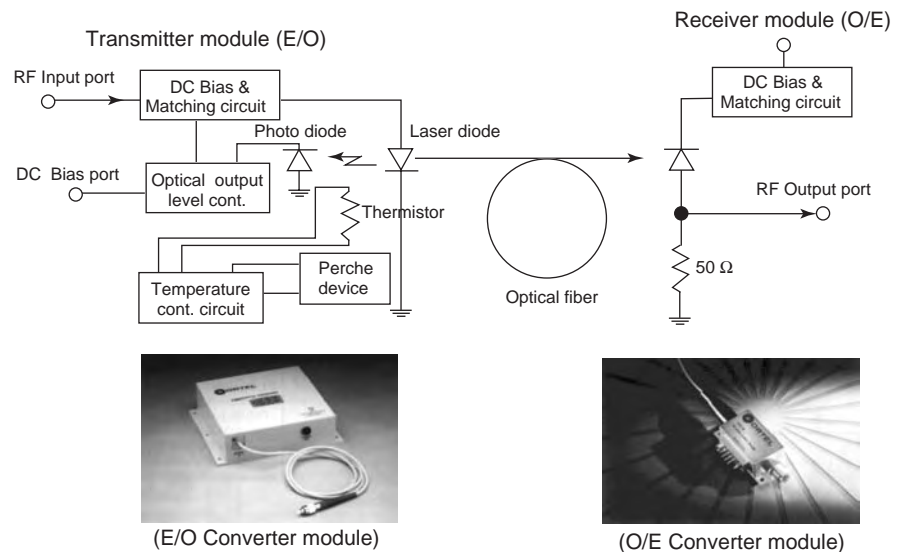


Figure 3. RoF link application (direct modulation).

modulated optical signal. A pin (positive–intrinsic–negative) photodiode (pin PD) is used for the O/E converter, and it converts the optical intensity to diode current in which the RF signals are included. So, in the minimum case, only two diodes can realize the RoF link. Several of these devices are described in the following paragraphs.

3.1. Light Source

Compactness and high output power are required in the same way as in the conventional digital transmission system, and 1.3 or 1.55 μm wavelength is selected for low loss and low dispersion capability of fiber. In case of direct-intensity modulation, modulation bandwidth, linearity, and high quantum efficiency of mobility are required for LD operation. The Fabry–Perot (FP) LD is used for low RF frequency range (< 1 GHz) because of cost considerations. If the range exceeds 1 GHz, a *distributed-feedback* (DFB) LD is used because of the modulation linearity and the optical spectrum coherency under the high-speed transition of diode current. Figure 3 shows the typical configuration of the direct-modulation RoF system in commercial use. In this model, the PD located at the transmitter side monitors LD output power, and optical output power of LD is controlled to maintain the constant level. Also, the *Peltier device* controls the LD temperature to maintain the temperature constant. This model can handle less than 8 GHz, and the link loss from RF input to RF output is about 20–30 dB [25].

3.2. External Modulator

In case of RF ranges beyond 10 GHz, external modulation is usually used. Figure 4 shows examples of the Mach–Zehnder (MZ) external modulator [26]. The MZ modulator is fabricated on the lithium niobium oxide (LiNbO_3) substrate and performs coplanar-type phase modulators, and thus is also called as LN modulator. In this modulator, the phase of two branches are modulated by the electrooptic characteristics of the substrate, and phase change of each branch is converted intensity change in the combined

output optical power. In the figure, two operation schemes of suppressed carrier double-sideband modulation (SC-DSB) and single-sideband modulation (SSB) are illustrated. In the latter case, bandwidth of the modulated optical fiber is narrow, so the optical fiber dispersion is not sensitive and LN modulation is suitable for high-RF signal transmission. The LN modulator requires high RF voltage $V\pi$ to achieve high-intensity change. In the normal case, $V\pi$ exists at several volts and with the driver fabrication, it is slightly difficult to match the 50 Ω impedance in the wide band. Also, the LN modulator characteristics depend on polarization, so polarization adjustment equipment at the input of LN modulator is required.

Another type of external modulation device is the *electroabsorption modulator* (EAM), shown in Fig. 5 [27–29]. This modulator utilizes a photodiode that is biased by DC + RF signals and operates as the optical attenuator and throughpath according with the bias voltage and optical wavelength. So it works as an optical intensity modulator. It is free from polarization and thus does not require a polarization controller even if the EAM is installed at the remote site. Also, as the EAM is a diode in structure, it works as a photodetector when it is appropriately biased. In EAM, RF signal matching is achieved by the stub-matching scheme and this widens the RF bandwidth and enhances modulation efficiency.

3.3. Optical Amplifier

There are no differences between digital transmission and RoF transmission from the viewpoint of optical amplifiers. Linearity and the noise factor (NF) are more sensitive for the RoF case. For the optical amplifier, there are several types, such as the rare-earth metal-doped fiber amplifier, the Raman amplifier, and the semiconductor optical amplifier (SOA). In the first category, the erbium-doped fiber amplifier (EDFA), the thulium-doped fiber amplifier (TDFA), and the praseodymium-doped fiber amplifier (PDFA) are used depending on the signal wavelength, 1.53–1.62 μm , 1.45–1.50 μm , and 1.3 μm , respectively. The Raman amplifier in the second category can amplify any

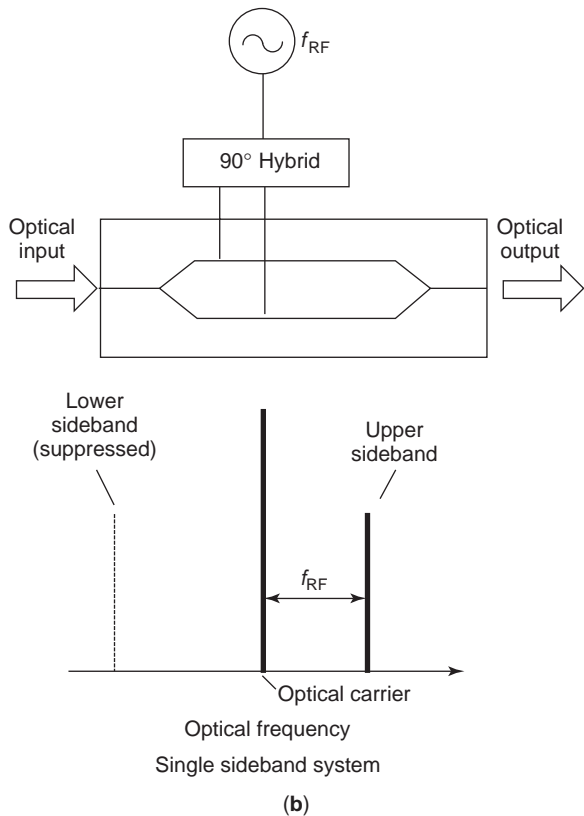
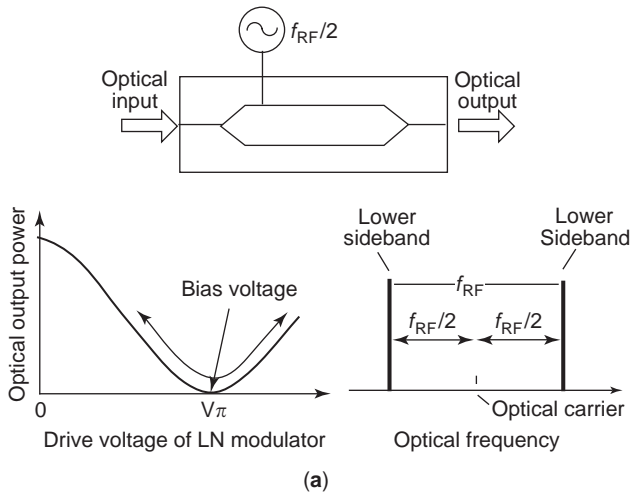


Figure 4. Configurations of Mach-Zehnder-type external modulations: (a) suppressed carrier system; (b) single-sideband system.

wavelength and can undoped normal fiber; however, it is necessary to improve the excited light power efficiency. The final SOA category has the advantage of compact size and power efficiency; however it has a drawback of polarization dependency and spontaneous-emission noise penalty. In the wavelength band 1.55 μm (C band), EDFA is generally used because of the linearity and low-noise features. Figure 6 shows an example EDFA block diagram. Typical performance of this amplifier is as follows: output power +13 dBm, power gain 30 dB, and noise figure less than 10 dB [30].

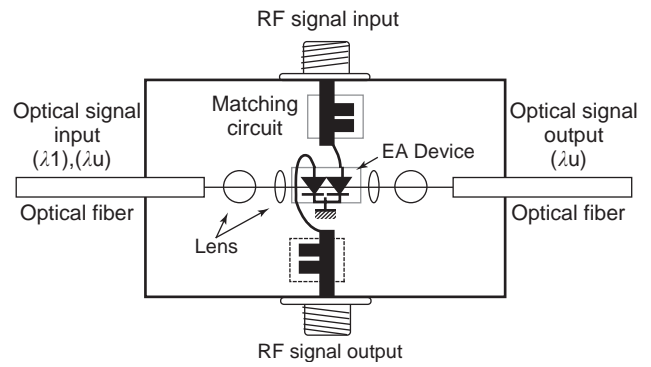


Figure 5. Electroabsorption external modulator (EAM) and detector.

3.4. Photodetector

The pin photodiode (pin PD) is more widely used than the avalanche photodetector (APD), because of the noise floor requirement and linearity. For frequency bands exceeding 10 GHz, the uni-directional-traveling carrier PD (UTC-PD) is used to achieve high maximum output power in the region of high-frequency band [31].

Figure 7 shows the structure and the output power of the pin PD and UTC-PD. From Fig. 7a, a hole in the pin PD deteriorates the response speed of photodetection because of the low mobility of hole and carrier accumulation. In contrast, the UTC-PD works on only high-mobility electron drift, and the light absorption layer is different from the intrinsic layer; this results in high-speed response, and the output power increases in the high-RF-frequency range. A comparison of output power levels is illustrated in Fig. 7b. For the forward link, the detected RF signal should be amplified by the RF stage, because the high transmission power from the antenna to air is required. Thus the detected power level should be high enough to avoid post-RF amplification. The UTC-PD can generate a detected power level of more than 0 dBm, without post-RF amplification. So, the UTC-PD is applicable for short-range wireless communication systems, such as wireless LAN (local-area network) applications.

To reduce the post-RF amplification, a phototransistor using a metal semiconductor field-effect transistor (MESFET) shows promising potential as a device suitable for high functional applications such as a mixer, an oscillator, or an amplifier, which is controlled by optical signals. Active-array applications are now under development. The High-electron-mobility FET (HEMT) is also applicable to photodetection, and has low noise performance; however, the absorption layer is too thin for HEMT, and some structure modification will be necessary for the photoabsorption layer. The EAM described in Section 3.2 can be also applicable to the photo detection by tuning DC bias voltage and/or wavelength.

4. RoF LINK PERFORMANCE AND DEGRADATION FACTORS

This section describes RoF link degradation factors, the process of performance calculation, and some numerical

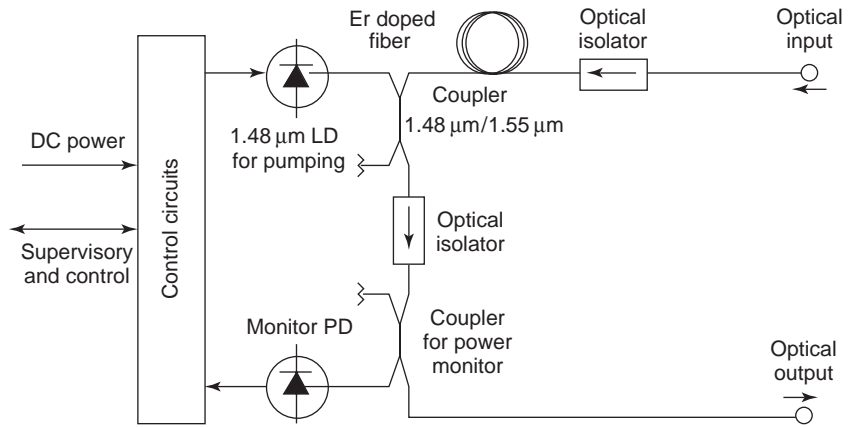
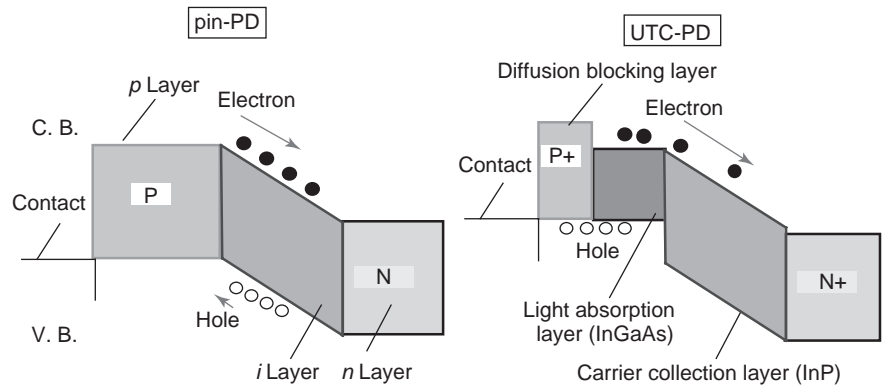


Figure 6. Typical configuration of EDFA amplifier.



(a)

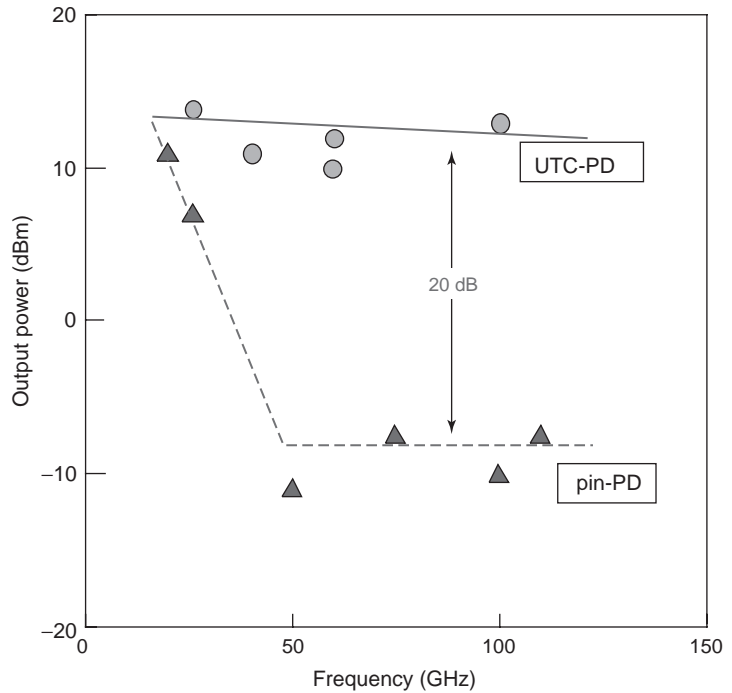


Figure 7. (a) Comparison of pin-PD and UTC-PD structures; (b) output powers.

results of the carrier-to-noise and distortion power ratio (CNDP). Several factors are involved: (1) detected RF signal power, (2) thermal noise, (3) shot noise, (4) relative intensity noise (RIN), and (5) intermodulation distortion (IMD).

4.1. Detected RF Signal Power

Detected RF signal power varies with respect to the received optical signal level, PD responsivity, and the optical modulation index (OMI). Detected RF power is proportional to m^2 and I_{ph}^2 , where m and I_{ph} are the optical modulation index and detected optical current, respectively. I_{ph} is determined by the optical received power, PD responsivity, and matching circuit configuration of PD. RoF RF-to-RF link loss is proportional to the square of optical loss. Detected RF signal power strongly depends on the matching circuit of the post-PD section, and bandpass operation can enhance the detected signal power level [24].

4.2. Thermal Noise

Thermal noise is white Gaussian noise, at the PD, and is proportional to the absolute temperature T , the Boltzmann constant k_B , and signal bandwidth BW. Also, optical amplifier noise (i.e., spontaneous emission) can be assumed to be the white Gaussian noise depending on the amplifier gain, and is treated as an index of the total noise factor (NF) increase.

4.3. Shot Noise

Shot noise is the noise component that is proportional to the input optical power, produced at PD. More recent RoF links utilize pin PD, so shot noise is lower than that associated with the use of the avalanche photodiode (APD). Also, the more recent RoF systems are applied for wide-bandwidth (e.g., 10-MHz) applications, so shot noise power is usually lower than that of thermal noise and can be disregarded in the normal system.

4.4. Relative Intensity Noise (RIN)

The noise component produced at the LD is proportional to the LD diode current, that is, proportional to the optical output power; this type of noise is called *relative intensity noise* (RIN). Usually, RIN is comparable to or greater than the thermal noise, when the LD output power is high. RIN depends on RF frequency and increases when the RF frequency is high. In the normal case, RIN values range between -120 and -150 dB/Hz.

4.5. Intermodulation Distortion

Intermodulation distortion occurs as a result of the nonlinearity of the RoF link, which results mainly from the nonlinearity of the modulator because high power driving is required. The optical modulation index (OMI) is used to indicate the modulation depth of the optical intensity. This parameter is normally defined by the ratio of the maximum envelope to peak-to-peak modulation depth. When OMI is small, the intermodulation distortion is low because the linear part of the optical modulator is used.

From the viewpoint of detected RF output power level, high OMI is desirable to maximize the RF output power. As a result, optimum OMI values occur when the CNDP is maximized.

Because of the intermodulation, multiple harmonic signals are generated. In wideband applications such as CATV systems, multioctave intermodulation should be considered. Second-harmonic and third-order intermodulation is taken into account; *second-order harmonics* is defined by composite second-order (CSO) and *third-order intermodulation* is defined by *composite third-order beats* (CTBs). In the mobile wireless application, bandwidth is narrow compared with the carrier frequency, so the second-order distortion can be filtered out at the RF stage, and third-order intermodulation (IM3) noise is dominant. Third-order distortion components are measured by the parameter of IM3. When the number of carriers becomes large, the intermodulation power increases because the number of intermodulation products also increases.

In case of the IM3 treatment, one example of the output power level of various components is shown in Fig. 8 according to the input RF power level of the RoF link. Desired RF output power increases both linearly and proportionally at input RF power levels less than -5 dBm. For higher levels, output power is gradually saturated. Signal power of third-order components increases in proportion to the cube of the input RF power, and as a result the IM3, defined by the ratio of third-order intermodulation component power and the fundamental output power, increases in proportion to the square of the input RF power. The intercept point as shown in Fig. 8 normally reflects this performance, as in the microwave amplifier case. The output power at the 1 dB gain compression is also used as the measure of RoF link. In the RoF link, the spurious-free dynamic range (SFDR) measure is also used to indicate system performance. SFDR is correlated with the system noise floor, which factors in radio system bandwidth and other properties, and this value is a measure of the allowable fade margin for radio signals.

4.6. Numerical Considerations for Carrier-to-Noise and Distortion Power Ratio

This section presents an example numerical calculation of a real RoF link applied for a mobile link. Deterioration factors and the overall configuration are shown in Fig. 9. There exist two main deterioration factors: (1) intermodulation among the RF carriers, as described in Section 4.5, and (2) time-varying frequency selectivity in received signal level, which is caused by the multipath fading and delay spread. In actual mobile communication systems, distances between mobile stations and a base station are not the same for each mobile station, and moreover multipath fading occurs in the propagation path. So the levels of signals received from every mobile stations differ, and these received signal levels fluctuating with time. This frequency selectivity-intermodulation problem is more severe in case of reverse link, in which transmission power control is not implemented. In the design of the nonlinearity degradation, received signal level variation due to multipath fading should be taken into consideration

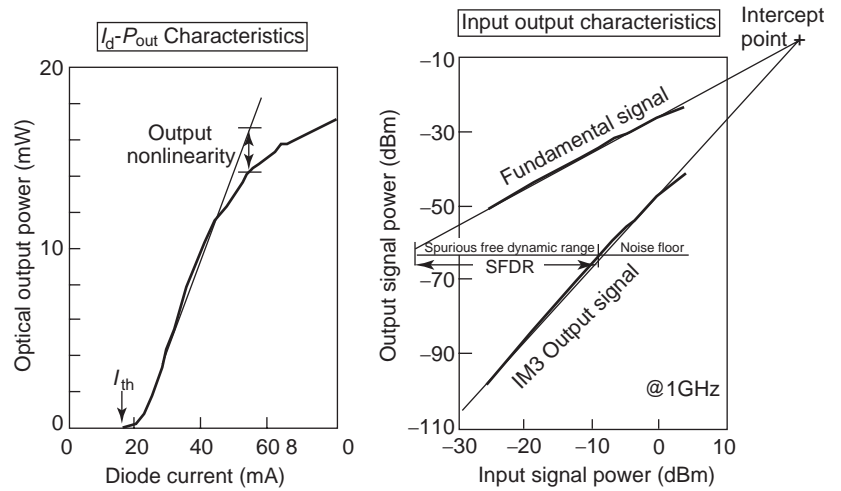


Figure 8. Fundamental characteristics of RoF link.

[14,15]. In this article, we assume that every received signal from the mobile station has the Rayleigh distribution of the same average power, and that all these signals are statistically independent of each other. Letting the received signal levels from the i th mobile station be denoted by r_i , the probability density function of r_i is shown as

$$p(r_i) = \frac{r_i}{\sigma^2} \exp - \frac{r_i^2}{2\sigma^2} \quad (1)$$

where σ^2 is the received signal average power. The received signal r is

$$r = \sum_i r_i \cos \omega_i t \quad (2)$$

where ω_i is the carrier frequency of the i th mobile station. The received RF signal is converted to the optical signal by E/O. E/O has nonlinear characteristics, and this nonlinearity causes the undesired intermodulation among r_i . The optical signal is reconverted to the RF signal by the photodetector. The signal-to-noise and distortion power ratio (CNDP) of the detected signal is shown by the following equation [4]

$$\frac{C}{N + D} = \frac{\frac{1}{2} m^2 I_{ph}^2}{(RIN I_{ph}^2 + 2eI_{ph} + \langle I_{th}^2 \rangle + \sigma_{IM}^2) BW} \quad (3)$$

where m , I_{ph} , RIN , e , I_{th}^2 , σ_{IM}^2 , and BW are optical modulation index, detected signal photocurrent, relative

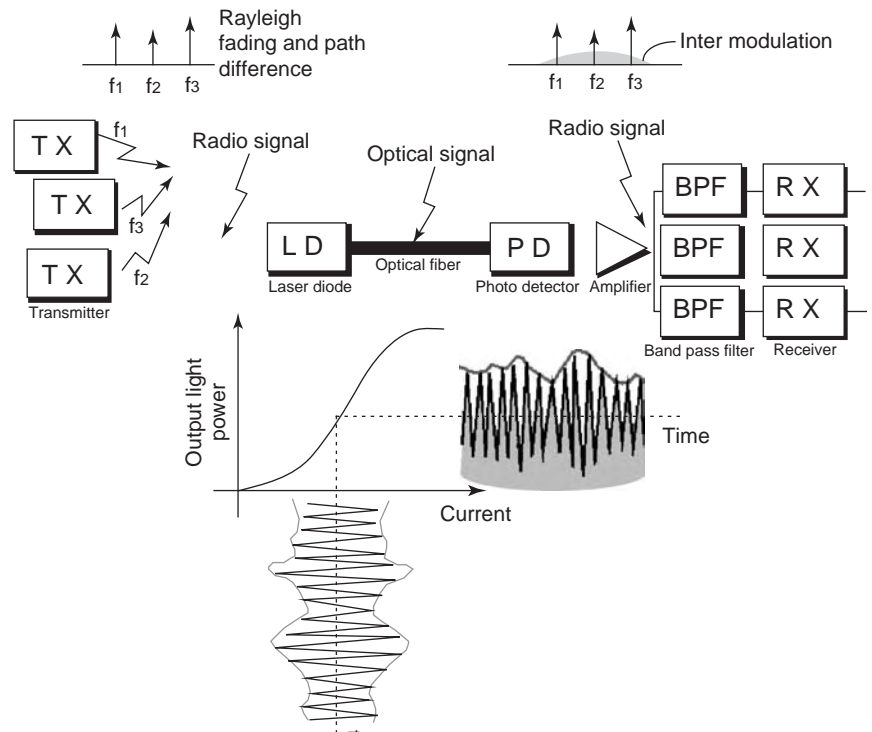


Figure 9. Degradation factors of RoF link.

intensity noise, electron charge, equivalent input noise-current variances, equivalent intermodulation spectrum density, and signal bandwidth, respectively. The output signal of the nonlinear device is denoted by the following equation

$$P = P_0 \left[1 + a_1 \sum_i r_i \cos \omega_i t + a_2 \left(\sum_i r_i \cos \omega_i t \right)^2 + a_3 \left(\sum_i r_i \cos \omega_i t \right)^3 + \dots \right] \quad (4)$$

where a_1 , a_2 , and a_3 are the nonlinear coefficients of the desired signal, second-order signal, and third-order signal respectively. For narrowband transmission as in mobile communications, latest factor that interferes with the desired signal is the third intermodulation as denoted in the previous section, and the intermodulation noise is shown in the following equation, where the radio signal consists of three tones, r_1 , r_2 , and r_3

$$\sigma_{IM}^2 BW = \frac{1}{2} \left(\frac{3}{2} a_3 r_1 r_2 r_3 \right)^2 I_{ph} \quad (5)$$

where the signal that experiences interference is the intermediate tone, signal r_2 . In this analysis, if tones r_i are Rayleigh distributed as shown in Eq. (1), then the average CNDR is calculated by the following equation:

$$\left\langle \frac{C}{N+D} \right\rangle = \int \dots \int_0^\infty \frac{C}{N+D} \times p(r_1)p(r_2) \dots p(r_m) \times dr_1 dr_2 \dots dr_m \quad (6)$$

Figure 10 shows the calculated examples of average CNDR $C/(N+D)$. The results shows the existence of an optimum OMI with a value that depends on the number of carriers.

5. APPLICATION EXAMPLE OF RoF LINK

The RoF link is applied for various application areas, such as (1) the hybrid fiber-coaxial (HFC) system in CATV services; (2) mobile communications, (3) broadband access networks, termed the *fiber-to-the-air* (FTTA) system, (4) electrooptic sampling (EOS), and (5) radioastronomy.

5.1. CATV Applications

Figure 11 shows the hybrid fiber-coaxial (HFC) system for most general application examples. In the conventional CATV system, cable loss and distribution power loss are very large, so a large number of line amplifiers is required to compensate these losses. When the core part of the CATV link is replaced by the RoF link, the cost of line amplifiers and the operation bandwidth are improved because the number of line amplifiers is reduced. In the CATV, 92 AM TV channels exist between 91.25 and 643.25 MHz, so the second-order harmonics CSO should

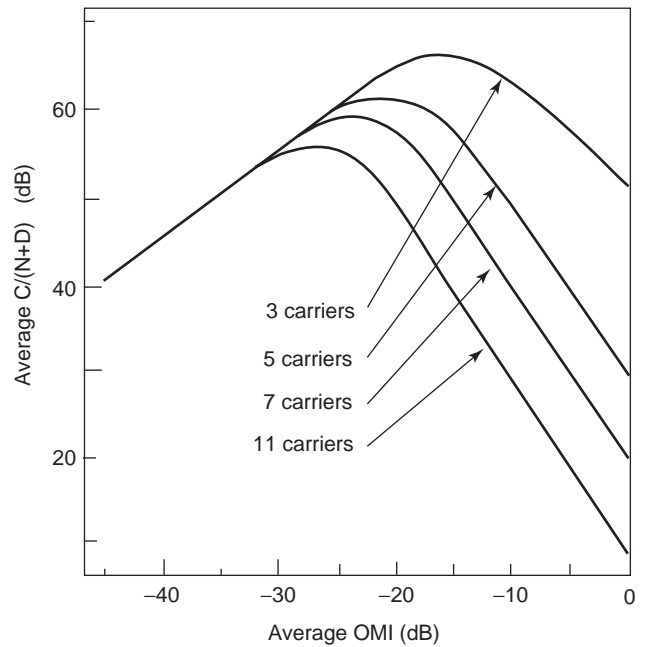


Figure 10. Calculated carrier-to-noise and distortion power ratio of RoF link [bandwidth 300 kHz per carrier; optical power -3.0 dBm; third nonlinearity 0.01; fiber loss 2 dB; noise power 4.0×10^{-22} W/Hz; photodetector sensibility 0.8 A/W (amperes per watt)].

be considered, and the required value will be more than 60 dBc.

5.2. Mobile Applications

In this section, we described several applications such as indoor wireless and mobile base station links for shadowing areas.

Figure 12 shows one of RoF link application for the mobile service shadowing area extension. In this application, a remote base station named “canister” is installed in the shadowing region of the main service area and the RoF link is used between canisters and a main mobile base station [9]. Many similar examples have been reported for

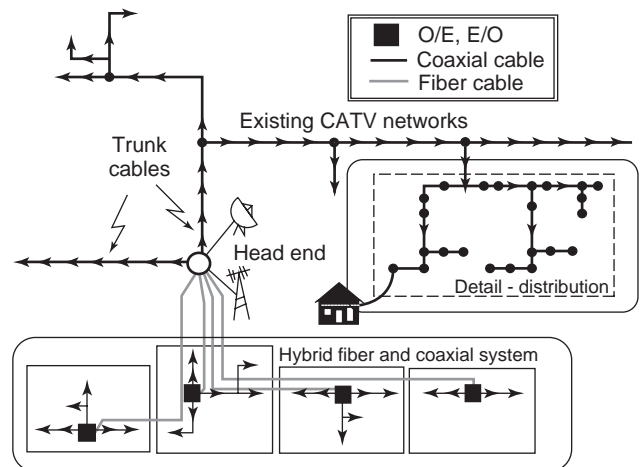


Figure 11. Hybrid fiber-coaxial link (HFC).

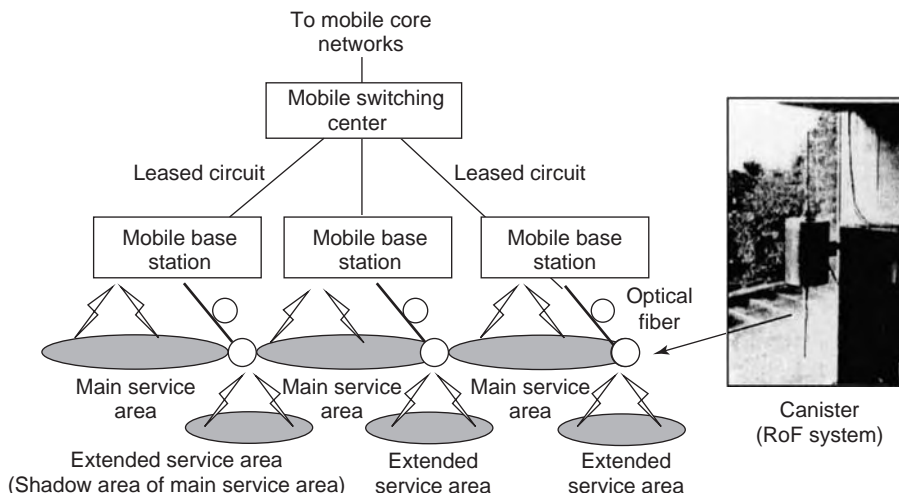


Figure 12. RoF link application for mobile communication system.

shadowing area extensions such as department stores and underground shopping mall parking lots. In some case, both ends are open air, and received RF signals are transmitted through fiber and reemitted to the shadowing area and vice versa. In these applications, the optical fiber length can be reduced; however, the spurious and noise emission to the open air should be strongly protected. In another case, the heterodyning method is applied and IF signal and reference signals for local oscillators are transmitted through fiber to reduce the cost of LD. When the system margin of fiber loss is large, an optical star coupler is used to broadcast one central station signal to several base stations. This configuration enables several base stations to be installed on a single fiber with bus connections, and reduces the cost of both fiber installation and equipment. Downlink signals from one LD are easier to broadcast; however, in the uplink stream, beat noise among the base station LDs is generated because of the optical wavelength difference of LDs and it impairs the detected RF signals. So LD wavelength control is required for uplink design if the bus link configuration is used.

Figure 13 shows another application example of indoor wireless LAN and cordless phone transmission. A 1.9-GHz

digital cordless phone and a 2.4-GHz wireless LAN signal are combined and transmitted from the central station and reemitted at the remote station. In this application, an unmodulated optical source with varying wavelength is supplied from the central stations and is modulated by the upstream RF signal by an electroabsorption (diode) module (EAM) as described in Section 3.2 of this article. So any well-designed remote station can be operated without DC power supply.

Figure 14 shows the intelligent transport system (ITS) application of an RoF link. In this application, several wireless services are frequency-shifted and lined queued up in the higher-frequency band at the central station, and transmitted to the roadside antenna and received by the vehicle. In the vehicle, required service is tuned out from the received signal. In this application, multiple roadside antennas are fed by the same signal, so they can operate as one macrocell and complicated handover is not required, even if a different roadside antenna is selected. So the microcellular system such as the personal handy-phone system (PHS) and Digital European Cordless Telephone (DECT) can be available in a high-speed vehicle, in the same way as are macrocell mobile systems.

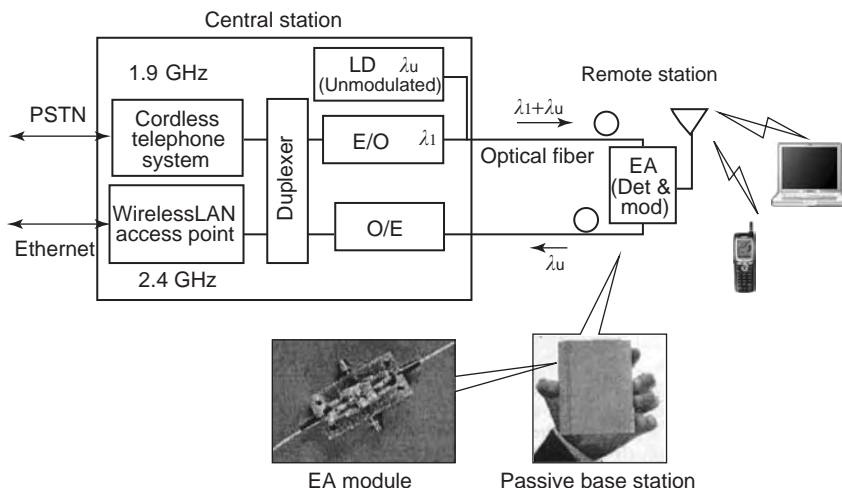


Figure 13. RoF application example for indoor wireless systems.

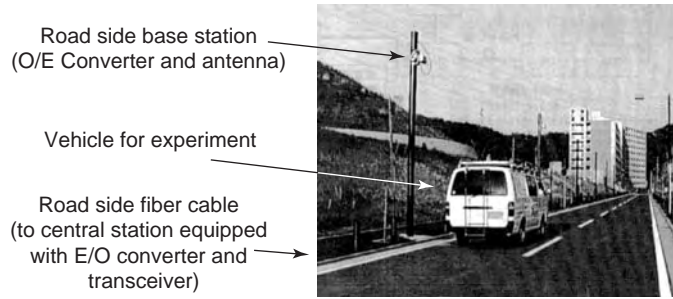
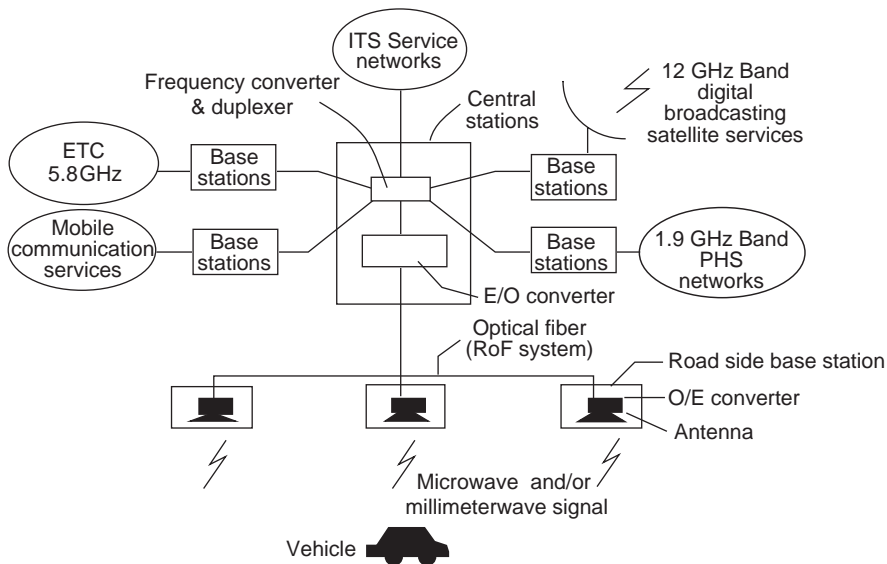


Figure 14. RoF link application example for ITS systems. (ETC=electrical tool correction system.)

5.3. Broadband Wireless Access Networks (BWA)

To realize the broadband service, the fiber infrastructure is considered to be one of the possible solutions. Using these fiber infrastructures, broadband wireless access, termed the *fiber-to-the-air system* (FTTA), is considered to be another available solution, and using the same infrastructure, the system can serve mobile broadband services, such as hotspot and mega and giga air services. Fig. 15 shows an example of a developed FTFTA system. In this system, a 27.7-GHz millimeter-wave 16-level quadrature amplitude-modulated signal (16-QAM), with a speed of 622 Mbps (megabits per second), is implemented and the RF signal is converted to an optical signal, and transmitted to the remote antenna units through passive star networks. From the remote antenna unit, the millimeter-wave signal is emitted to the home customer premise unit. Customers can extract their information from the 622-Mbps stream. For upstream service, data size for each customer is small, so a 40-Mbps frequency shift keying signal (FSK) with the 29.26-GHz carrier frequency is emitted from the customer premise unit. This signal is downconverted to the 615-MHz IF signal by mixing with a 29.875-GHz local signal that is supplied from the central control station. The converted optical signal is carried to the central station through passive star fiber networks. Using this configuration, the remote antenna unit does not require the installation of a millimeter-wave carrier oscillator, whose frequency, in the wide temperature range

experienced by an outdoor remote antenna unit, is expensive to stabilize.

5.4. Other Applications

As the speed of electronic device rapidly increases, scaling down progresses at the same time. Under this condition, on-wafer high-frequency and high-speed performance measurement is required to reduce the cost of fabrication. Conventional coaxial cable test probes interfere with device performance because the probe and cable are not sufficiently compact in size and their frequency-dependent conductor causes errors in performance test results. For a compact and conductorless test probe, electrooptic sampling (EOS), using the optical fiber probe and electrooptic conversion sensor, is one possible solution for this requirement. Figure 16 shows various applications for electrical field, DC voltage level, and radio emission test probe. More recently, > 200-GHz and 0.1–0.3-ps-pulse test probes have been developed. For the electrooptic device, LiTaO₃, KTP (Potassium Titanyl Phosphate), CdSe, and ZnTe are used.

Another RoF application is radioastronomy, such as in the Atacama (Chilean desert) Large Millimeter/submillimeter Array (ALMA). In this application, an array of large antennas is concentrated in central measurement equipment, and an RoF link is used for millimeter and submillimeter signal transmission between the antennas and the central measurement station, to reduce the signal loss and

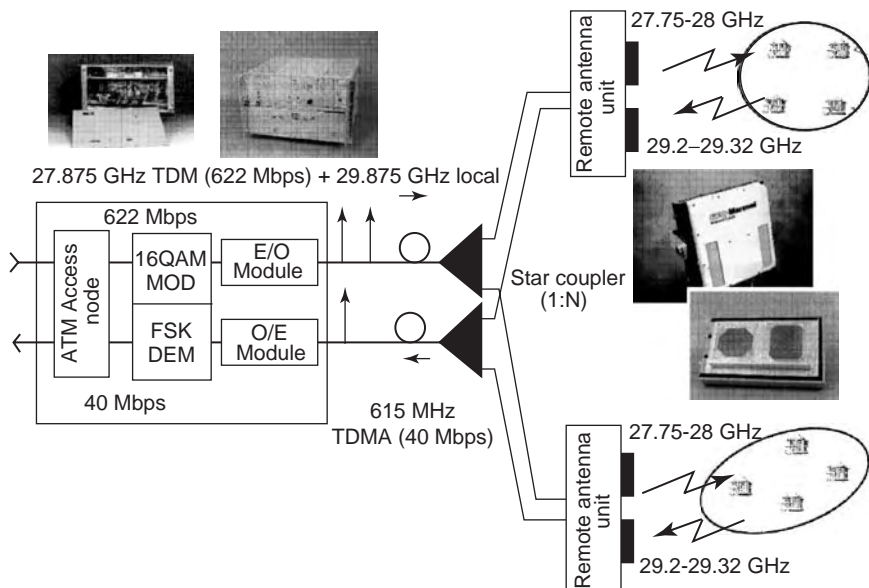


Figure 15. RoF link application example for FTTH systems.

to extend the frequency band. In this measurement, fiber length calibration among the antennas is required to maintain the coherence of received signals. Calibration methods are presented on the ALMA Website [32].

6. NETWORKING OF RoF SYSTEMS

6.1. Introduction to the RoF Networks (Radio Highway)

Figure 17 shows RoF networks where routing functions of the radio signals are developed and routing to various remote stations are conducted depending on their radio format, such as radiofrequency (RF) or modulation format. These RoF networkings are called the “Radio Highway” [3].

There are various types of networking configurations and optic multiplexing schemes, such as wavelength-division multiplexing (WDM), optic time-division multiple ac-

cess (optical TDMA), optical code-division multiple access (optical CDMA), and the chirp multiple transform (CMT) method.

The same as for the optical multiplexing and access methods, there are various access methods at the RF stage, such as subcarrier multiplexing (SCM), TDMA at RF stage, and CDMA at RF stage. These RF-stage access methods can be used in combinations of optic-stage multiple-access methods, independently and simultaneously. For example, optic WDM and optic CDM can be used simultaneously and have certain advantages such as channel number extension and networking flexibility. The simultaneous use of optic CDM and RF CDMA also enables seamless connection of RF and photonics. Conventional SCM with optic WDM is one of the combination solutions. A comprehensive description of all combinations would be elaborate and beyond the scope of this article, so some typical examples are described as follows.

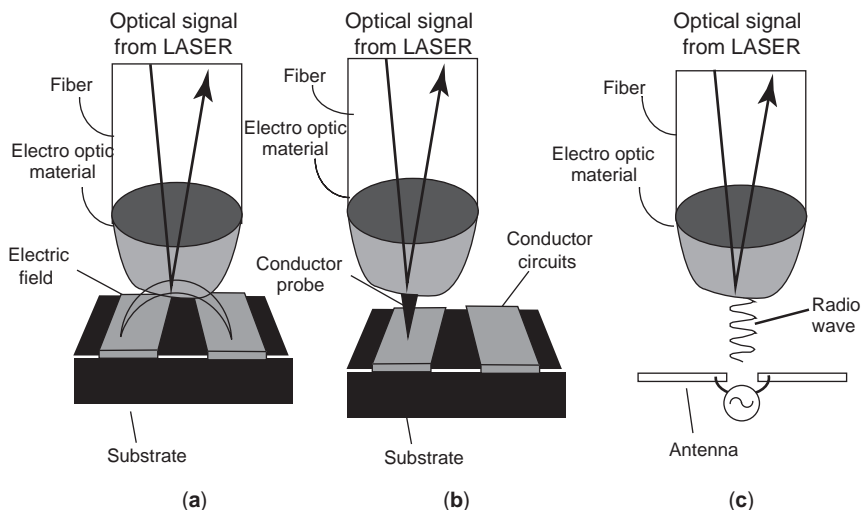


Figure 16. RoF applications for electrooptical sampling (EOS): (a) electric field test; (b) electric voltage; (c) electromagnetic waves.

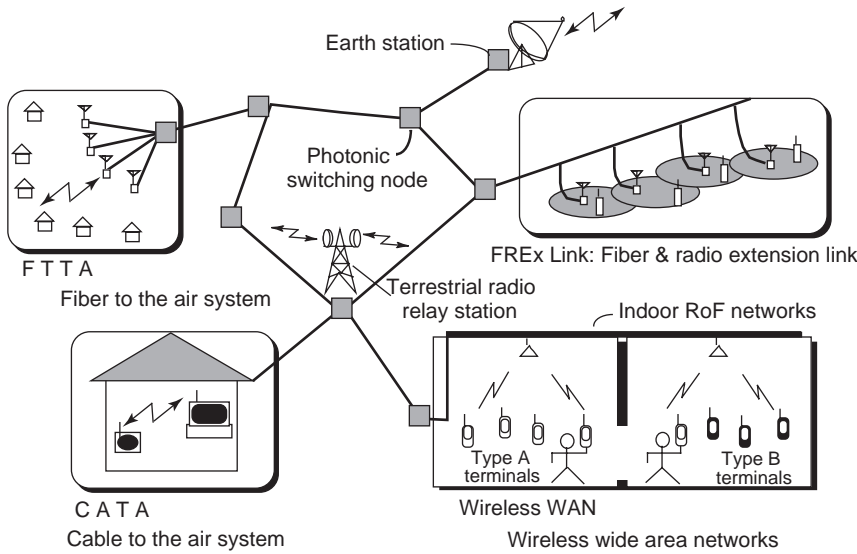


Figure 17. Networking of RoF systems (radio Highway networks).

6.1.1. Optic Wavelength-Division Multiplexing (WDM).

Extensive research on optic networks, such as dense wavelength-division multiplexing (DWDM) and wavelength routing technologies, are rapidly progressing to develop high-speed core networks, such as long line and metro networks. These technologies are applied mainly to the high-capacity baseband transmission, and these WDM technologies are applicable to the RoF link and RoF networks, after some discussion of the design of its signal-to-noise quality.

Figure 18 shows some example WDM applications to RoF systems. Figure 18a illustrates point-to-point bulk transmission on a wavelength-varying signal, in which one fiber and optical amplifier are used for multiple radio base stations (RBSs) that have different wavelengths. All the wavelengths are amplified periodically and transmitted to one destination. The photonic wavelength switch at the central station can reroute the specific RBS signal that has a specific wavelength to the different central stations. This application is used for multiple wireless services operating on single photonic networks.

Other applications are shown in Figs. 18b and 18c. In the Fig. 18c, every wavelength is assigned to every radio signal from one of sector antenna of the RBS. This configuration is suitable for single fiber-RBS applications. Also, different wavelengths can be assigned to forward and reverse links as shown in Fig. 18b.

The next configuration is shown in Fig. 18d. Different wavelengths are assigned for the different RF frequencies at the RBS, and different wireless service is transferred to the different central stations.

6.2. Optical TDMA Operation

For baseband pulse operation, optical TDMA is very easy; however, for RoF formats, TDMA necessitates consideration of, natural bandpass sampling. Pulse amplitude modulation (PAM) systems show promise in realizing RoF type optical TDMA systems, where multiplexing of

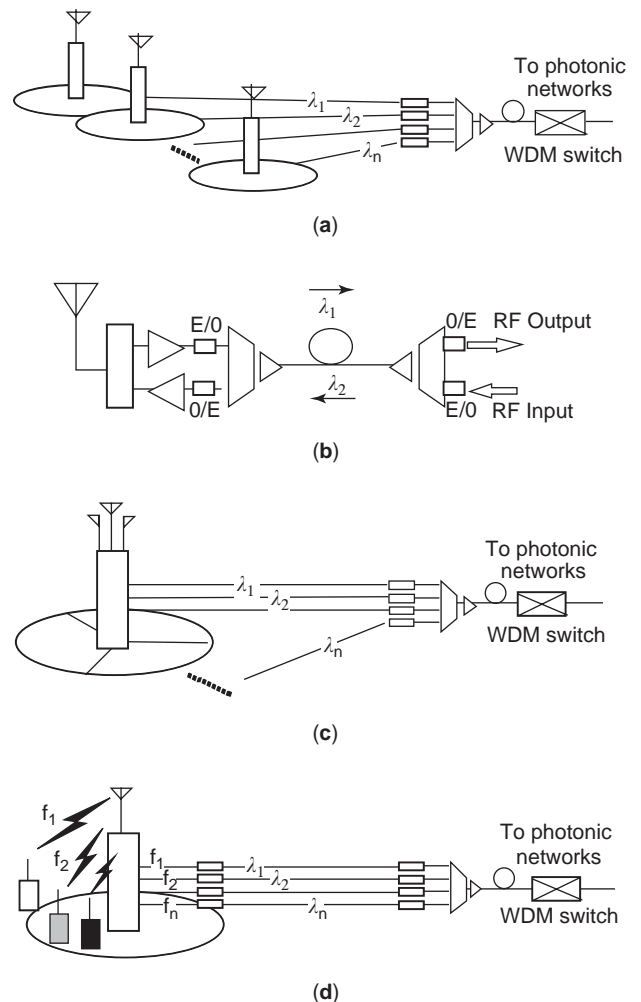


Figure 18. RoF networking example configurations using WDM: wavelengths assigned to (a) radio base stations; (b) duplexing; (c) sectors/diversity; (d) radio service/frequency bands.

several signals is achieved by interleaving the samples of the every RBS signal. According to the Nyquist sampling theorem, the signal whose highest frequency spectrum component is f_M is determined and regenerated at regular intervals separated by times $T_s \leq \frac{1}{2}f_M$; that is, the signal has to be periodically sampled every T_s seconds. T_s and $f_s = \frac{1}{T_s}$ are referred to as *sampling interval* and *sampling frequency*, respectively. If this theory is applied to the sampling of radio signals whose highest frequency spectrum component is in the low or medium gigahertz range, then, ultra-high-speed sampling such as twice the RF frequency is required. The radio signals are fortunately bandlimited in general, so natural bandpass sampling is applicable. Let the bandwidth of radio signal be B_{RF} and you can find that the required condition about sampling interval can be reduced to $\frac{1}{2}B_{RF}$. Such a sampling technique is referred as natural bandpass sampling or simply bandpass sampling [33]. Natural sampling is the window multiplication on RF signals, and bandpass filtering of received signal can reproduce the original signal.

Figure 19 shows the configuration of optical TDMA for upstream networks. In the system, the RF signal received by the RBS is intensity modulated to an optical signal and then switched by the photonic switch and multiplexed to one fiber and rerouted at the optical time switch in accordance with the optical digital header attached to the natural sampled RF signal. Asynchronous optical TDMA can be available when the optical signal bandwidth is sufficiently wider than the RF signal bandwidth. The synchronous mode in the downlink is better than the asynchronous mode, because the synchronous TDM is simple and synchronization is easy. One example of this application will be in the use of ITS roadside antennas, in which several broadband services such as videostreams from the central stations, and several low-speed asynchro-

nous TDMA wireless service streams from vehicles to central stations are operated.

6.3. Optical CDMA Operation

The optical CDMA method is suitable for the uplink of fiber-optic radio networks because it does not require any time synchronization among RBSs. There are various types of optical CDMA methods, such as the fiber delay line, the optical phase mask, and coherent optical phase modulation type [18–23]. In the method using fiber delay lines, encoding and decoding are performed by the sum of delayed optical pulses in the time domain. In the method using optical phase masks, spectral encoding and decoding are performed by phase modulation in the optical template mask. However, these methods have no flexibility in assigning code sequences. On the other hand, the direct optical switching CDMA (DOS-CDMA) scheme, using the optical ON/OFF switching by spread-spectrum code, has flexibility in terms of code assignment. Figure 20 shows the configuration of DOS-CDMA. Each radio signal received by each RBS antenna is transmitted to the central control station (CCS) by analog optical PAM formats, and the multiple accesses among many RBSs are performed by codes that differ from each other. Regeneration of radio signal is based on the bandpass natural sampling theory described earlier in the article. At a RBS, received radio signals are converted into optical intensity-modulated (IM) signals by modulating LD current directly, and are sampled by the optical switch (OSW), which is driven by a certain spread-spectrum code sequence. The output signal of the OSW is transmitted to a receiver through optical fiber. At the receiver, many spread-spectrum signals from many RBSs are received simultaneously. At the receiver, an optical polarity-reversed correlator (OPRC) is used to

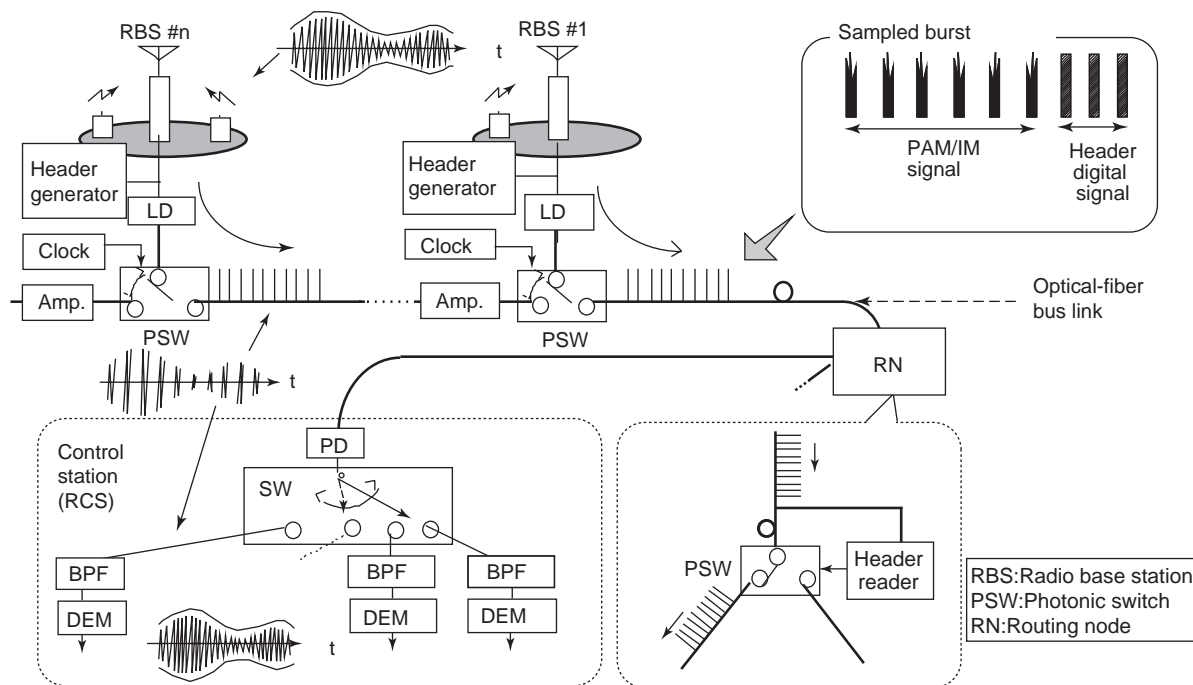


Figure 19. RoF networking example configurations using optic TDMA.

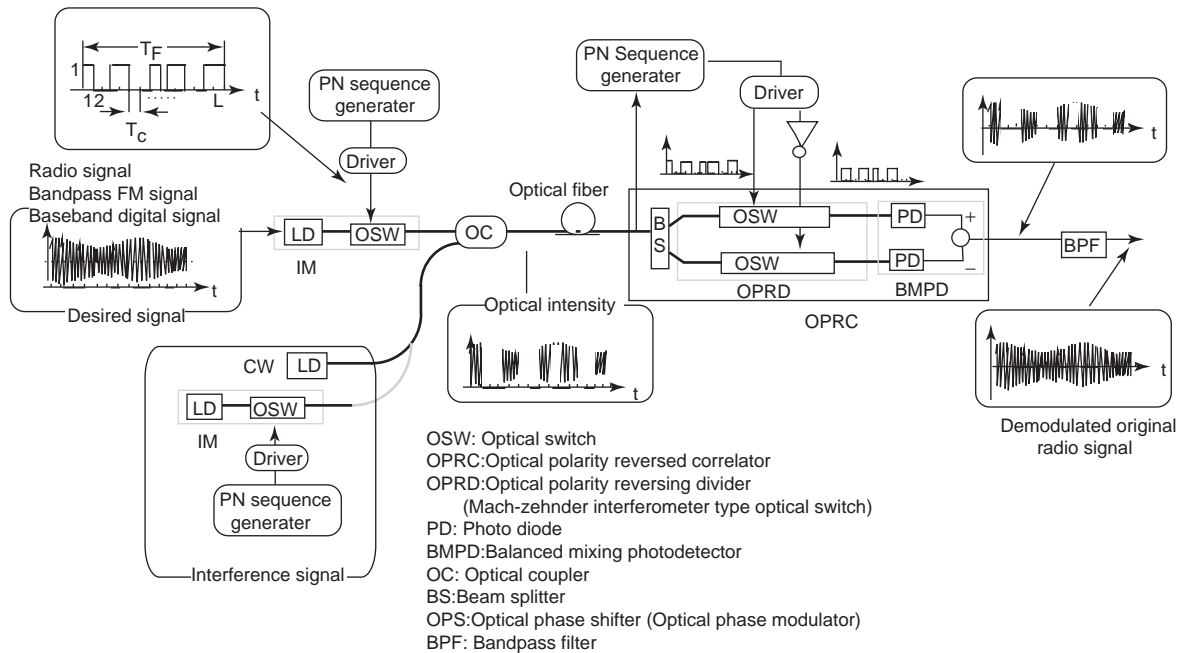


Figure 20. RoF networking example configuration using optic CDMA.

extract the desired signal. At the OPRC, the received signal is split into two signals. It is assumed that the despreading CDMA code, matched with the desired RBS, is regenerated at the RBS by using the retiming code generator such as the retiming block and the code synchronization block. The OPRC is driven by this code and polarity-reversed code, and two optical signals are derived from each branch; then the two RF signals are detected and subtracted. An optical signal from the desired RBS is correlated at the upper branch, and there is no output from the lower branch. From the undesired RBS, the optical signal is uncorrelated in two branches, and random signals are extracted from two branches. So the subtraction and averaging of two signals produces zero output response, and the uncorrelated signals from undesired RBSs are suppressed. As a result, only the desired RF signal is extracted from the mixture of optical signals from many base stations. This CDMA can be used in combination with WDM because the optical spectrum is not as wide in case of natural bandpass sampling and spectrum spreading.

7. SUMMARY

In this article, RoF technologies such as basic configurations, devices, performance design, and application examples are described. Section 6 describes the future trends of RoF networking, named "Radio Highway" technologies.

BIBLIOGRAPHY

1. D. C. Cox, W. S. Gifford, and H. Shervy, Low-power digital radio as a ubiquitous subscriber loop, *IEEE Commun. Mag.* **29**(3):92–95 (March 1991).
2. D. C. Cox, A radio system proposal for wide spread low-power tetherless communications, *IEEE Trans. Commun.* **39**(2):324–335 (Feb. 1991).
3. S. Komaki, K. Tsukamoto, S. Hara, and N. Morinaga, Proposal fiber and radio extension link for future personal communications, *Microwave Opt. Technol. Lett.* **6**(1):55–60 (Jan. 1993).
4. W. I. Way, Subcarrier multiplexed light wave system design considerations for subscriber loop applications, *IEEE J. Lightwave Technol.* **7**(11):1806–1818 (Nov. 1989).
5. J. Namiki, M. Shibutani, W. Doman, T. Kanai, and K. Emura, Optical feeder basic system design for microcellular mobile radio, *IEICE Trans. Commun.* **E76-B**(9):1069–1077 (Sept. 1993).
6. H. Ogawa, Microwave and millimeter-wave fiber optic technologies for subcarrier transmission systems, *IEICE Trans. Commun.* **E76-B**(9):1078–1090 (Sept. 1993).
7. W. I. Way, R. Olshansky, and K. Sato, eds., Application of RF and microwave subcarriers to optical fiber transmission in presence in recent and future broadband networks, *IEEE J. Select. Areas Commun.* **8**(7) (Sept. 1990).
8. A. J. Cooper, Fiber/radio for the provision of cordless/mobile telephony services in the access network, *Electron. Lett.* **26**(24):2054–2056 (Nov. 1990).
9. T. S. Chu and M. J. Gans, Fiber optic microcellular radio, *Proc. IEEE Vehicular Technology Conf.*, May 1991, pp. 339–344.
10. S. Komaki, and E. Ogawa, Trends of fiber-optic microcellular radio communication networks, *IEICE Trans. Electron.* **E79-C**(1):98–104 (Jan. 1996).
11. H. Harada, S. Kajiyama, K. Tsukamoto, and S. Komaki, TDM intercell connection fiber-optic bus link for personal radio communication systems, *IEICE Trans. Commun.* **E78-B**(9):1287–1294 (Sept. 1995).
12. W. C. Kwong, P. A. Perrier, and P. R. Prucnal, Performance comparison of asynchronous and synchronous code-division

- multiple-access techniques for fiber-optic local area networks, *IEEE Trans. Commun.* **39**(11):1625–1634 (Nov. 1991).
13. H. Otsuka, O. Kagami, S. Aikawa, and H. Takanashi, 256-QAM subcarrier transmission for broadband distribution networks, *Proc. IEEE Globecom*, Nov. 1991, pp. 51.6.1–51.6.6.
 14. H. Mizuguti, S. Komaki, and N. Morinaga, *Performance Analysis of Fiber Optic Link for Microcellular Mobile Communication Systems*, Technical Report of IEICE Japan, RCS91-50, Nov. 1991.
 15. T. Okuno, H. Mizuguti, S. Komaki, and N. Morinaga, An analysis of relationship between the performance of microcell optical link and the number of carriers, *Proc. Japanese Natl. Conf. IEICE*, paper B-425, March 1992.
 16. Y. Shoji, K. Tsukamoto, and S. Komaki, Proposal of the Radio Highway networks using asynchronous time division multiple access, *IEICE Trans. Commun.* **E79-B**(3):308–315 (March 1996).
 17. Y. Shoji, K. Tsukamoto, and S. Komaki, Proposal of chirp multiplexing transform/intensity modulation/direct detection system for Radio Highway networks, *IEICE Trans. Fundam.* **E81-A**(7):1396–1405 (July 1998).
 18. P. R. Prucnal, M. A. Santoro, and T. R. Fan, Spread spectrum fiber-optic local area network using optical processing, *IEEE J. Lightwave Technol.* **LT-4**(5):547–554 (May 1986).
 19. J. A. Salehi, A. M. Weiner, and J. P. Heritage, Coherent ultrashort light pulse code-division multiple access communication systems, *IEEE J. Lightwave Technol.* **7**(3):478–491 (March 1990).
 20. A. S. Holmes and R. R. A. Syms, A optical CDMA using quasisprime codes, *IEEE J. Lightwave Technol.* **LT-10**(2):279–286 (Feb. 1992).
 21. S. J. Park, K. Tsukamoto, and S. Komaki, Proposal of direct optical switching CDMA for cable-to-the-air system and its performance analysis, *IEICE Trans. Commun.* **E81-B**(6):1188–1196 (June 1998).
 22. S. J. Park, K. Tsukamoto, and S. Komaki, Polarity-reversing type photonic receiving scheme for optical CDMA signal in Radio Highway, *IEICE Trans. Electron.* **E81-C**(3):462–467 (March 1998).
 23. S. Kajiya, K. Tsukamoto, and S. Komaki, Proposal of fiber-optic radio highway networks using CDMA method, *IEICE Trans. Electron.* **E79-C**(1):111–117 (Jan. 1996).
 24. H. Al-Raweshidy, *Radio over Fiber Technologies for mobile Communications Networks*, Artech House, London, 2002.
 25. (Online) <http://www.ortel.com/>; <http://www.anacomsystems.com/>.
 26. (Online) http://www.socnb.com/techbox/hproduct_e/ln.html.
 27. (Online) <http://www.alcatel.com/optronics>.
 28. (Online) <http://www.cyoptycs.com/>.
 29. (Online) <http://www.oki.com/en/press/2002/z01117e.html>.
 30. (Online) <http://www.fujikura.co.jp/>.
 31. T. Ishibashi et al., Uni-traveling-carrier photodiodes, *Tech. Digest of Ultrafast Electron and Optoelectron.* **13**:83–87 (1997).
 32. (Online) <http://www.alma.nrao.edu/>.
 33. H. Taub and D. L. Schilling, *Principles of Communication Systems*, McGraw-Hill International Editions, Electrical and Electronic Engineering Series, 1986.

RADIO RECEPTION

ZORAN ZVONAR
Analog Devices
Wilmington, Massachusetts

Since the early introduction of radio, the significance and number of applications of radio services have constantly grown. From sophisticated satellite and microwave links that provide worldwide communication infrastructure, mobile radio and personal communication services (PCS) that are providing seamless communication capabilities, all the way to consumer products like cordless phones, wireless toy communicators or garage door openers, radio services have changed everyday life in a manner that could have not been predicted decades ago. The growing sophistication of systems and usages is closely related to the technical understanding necessary for putting radio systems into operation. Challenges in radio system design have grown tremendously because of the overcrowding of radio spectrum. The need for coordinating radio services has been identified early, and International Telecommunication Union (ITU) has established necessary regulations. The effective spectrum management is essential to maximizing the benefits that can be obtained from the radio spectrum [1]. After restructuring of the ITU in 1993, these problems have been the focus of ITU Radiocommunication Sector.

Radio systems operate in different radio frequency bands as shown in Table 1 [2]. This influences the characteristics of the radio channel. The signal propagation path may vary from a clear line of sight to being severely obstructed by buildings, mountains, and other environmental effects. Since radio channels are random in nature, understanding of the radio propagation phenomena and consequently their modeling play a major role in the prediction of the radio reception quality, which, in turn, enables efficient design of wireless systems. Large-scale propagation models characterize signal strength over long distances, while small-signal models describe the rapid fluctuation of the received signal over very short distances or short time duration.

Radio reception is influenced by different factors, summarized in Table 2. Radio propagation influences radiolink design, with path-loss models and statistics of large-scale fading as the major elements of a power budget. In addition to the power budget, radiolink design includes geographic positioning of transmitter and receiver, frequency planning, radiolink control schemes, and handover schemes. Requirements for the type of radio service, quality of service, coverage, and availability of the radiolink provide an additional set of parameters that influence radio link design. On the other hand, fading affects factors such as the radio receiver design, selection of modulation and coding scheme, techniques for fading compensation, synchronization circuits, and design of radio front-end. Selection of the appropriate receiver techniques determines the radio sensitivity which is an integral part of the power budget. Results of radiolink and radio receiver design are a part of wireless network design. Network ar-

Table 1. Summary of Frequency Bands for Operating Radio Systems

Frequency Band	Frequency Range	Mode of Radio Propagation	Radio Services	Major Characteristics
Very low frequency (VLF)	3–30 kHz	Ionospheric	Navigation, long-distance radio telegraphy	Small bandwidth, large antennas
Low frequency (LF), medium frequency (MF)	30–300 kHz, 300 kHz–3 MHz	Ground-wave ionospheric	Navigation, AM broadcasting, aeronautical, maritime communication	Quite large antennas, high power transmitters
High frequency (HF)	3–30 MHz	Ionospheric	Amateur radio, broadcasting, aeronautical maritime communication	High variability of channel conditions
Very high frequency (VHF), ultrahigh frequency (UHF)	30–300 MHz, 300 MHz–3 GHz	Direct waves, ground-reflected waves	Radio and television broadcasting, land mobile radio, paging, GPS	Relatively small antennas, considerable bandwidth
Superhigh frequency (SHF)	3–30 GHz	Direct waves	Satellite, radars, short-range communications, microwave terrestrial links	High losses, directional antennas
Extrahigh frequency (EHF)	30–300 GHz	Direct wave	Very short range communication, satellite-to-satellite links	Enormous bandwidths, rain absorption

chitecture, interfaces, and control are closely related to radio reception, which defines the physical layer of the network [4].

1. RADIOLINK DESIGN

1.1. Power Budget

The power budget (link budget) is the starting point for a radiocommunication link design. Major factors influencing the power budget are shown in Fig. 1. These factors include transmitting and receiving antenna gains G_T and G_R , path loss L_p (which depends on operating frequency, environment and type of radio service), fading margin M_F , interference margin M_I , and radio receiver sensitivity RS .

Transmitting antenna gain (usually specified as the gain relative to isotropic radiator) and receiving antenna gain are dependent on the carrier frequency and physical size of the antenna. For a given radio system, selection of the equipment determines antenna gains. Additional sources of signal loss at the antenna may include noise due to protective cover, pointing loss, feeder loss and antenna efficiency, described as the ratio of the effective aperture to the physical aperture of the antenna [5].

Link budget analysis of the radio system defines the maximum acceptable path loss

$$L_p \text{ (dB)} = P_T \text{ (dBm)} + G_T \text{ (dBi)} + G_R \text{ (dBi)} - M_F \text{ (dB)} - M_I \text{ (dB)} - RS \text{ (dBm)}$$

which can be used to estimate the coverage area of the system by determining the maximum transmitter–receiver distance.

The relationship between path loss and coverage area is crucial for the design of a radio system. Other sources of signal loss in radio propagation are caused by environmental effects such as rain, clouds, and fog.

The fading margin determines the outage probability of the system due to large-scale and/or small-scale fading. In a similar way, the interference margin can be built into the link budget to maintain desired performance in the presence of the interference, regardless of the interference mechanism, such as adjacent-channel interference (ACI), cochannel interference (CCI) in cellular systems, and intermodulation distortion (IMD) products created by the large interfering signals. The amount of margin depends on the required quality of service. It is expressed in terms

Table 2. Radio System Design Elements Relevant for Radio Reception

Radio Propagation	Radiolink Design	Radio Receiver Design	Radio Network Design
Large-scale fading	Requirements	Modulation	Architecture
Path loss	Radio services	Multiple access	Interfaces
Shadowing	Quality of service	Coding	Network control
	Coverage/range	Antifading techniques	
Small-scale fading (multipath fading)	Design	Interference suppression	
Delay spread	Power budget		
Coherence time	TX/RX allocation	Synchronization	
	Link control	Receiver hw design	

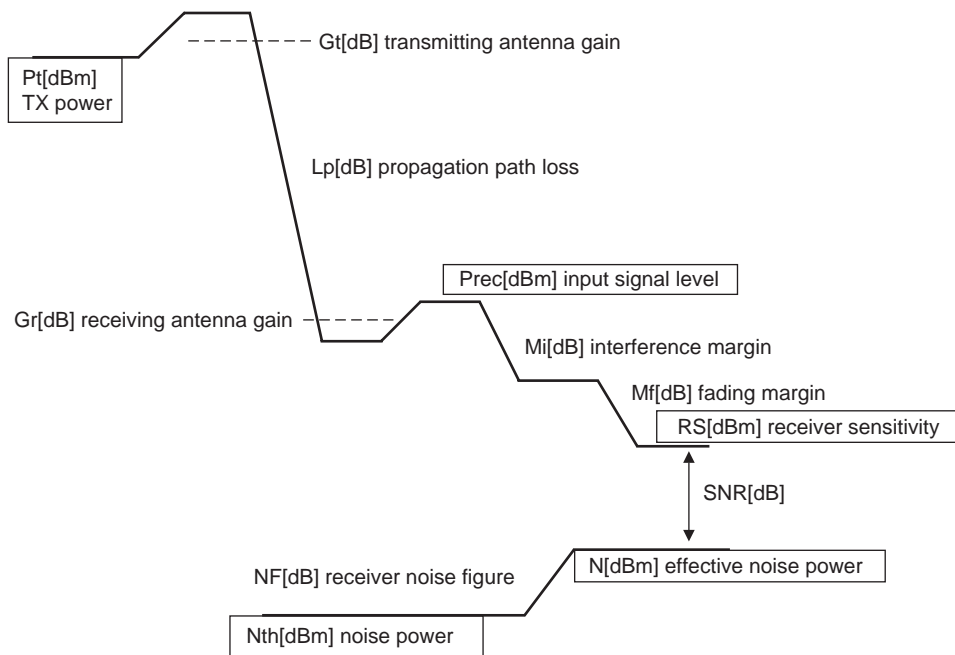


Figure 1. Power budget for radio-link design.

of signal-to-noise ratio (SNR) for analog systems or bit error rate (BER) for digital systems, and availability of the link, which is the measure of long-term link utility stated on an average basis, usually on the annual basis.

Radio receiver sensitivity describes the ability of the radio receiver to detect weak signals, and is derived from the performance objectives of the given radio service. Sensitivity specification includes the impact of techniques that are an integral part of radio reception at the detection level, such as diversity, coding, interleaving, as well as the impact of radio receiver such as noise figure and noise bandwidth.

1.2. Frequency Planning

Frequency planning is a part of link control and is essential part of radiolink design. Since the radio spectrum is the limited resource, coexistence of different services will be practically impossible without the planning procedure. It is effective way to optimize spectrum usage, enhance channel capacity, and reduce different types of interference.

Some of the benefits of frequency planning will be illustrated on the example of the mobile radio services. Frequency planning for mobile radio includes channel numbering, channel grouping into subsets, cell planning, and channel assignment. It controls ACI by channel separation, which provides adequate isolation, and CCI by selection of frequency reuse pattern. Frequency planning can be efficiently combined with cell sectorization to improve the system capacity. Different tradeoffs are involved in frequency planning based on targeted channel capacity and signal-to-interference ratio (SIR). The most popular OMNI frequency plan in mobile radio is $N = 7$ plan, which allows for ACI. This plan is outperformed by the $N = 9$ plan with respect to SIR, but the drawback is the reduced channel capacity. Detailed analysis of various frequency

plans can be found in Ref. 21. Besides the impact on technical parameters of the system, frequency planning greatly influences radio system growth and economics.

2. LARGE-SCALE VARIATIONS: PATH LOSS

The prediction of the path loss is the most important step in the radio system planning process since it determines radio coverage. Prediction models could include only finite number of parameters that can influence radio propagation, and often factors such as environment (effects of buildings, manmade obstacles, vegetation) as well as multipath fading are treated separately.

Three major mechanisms of radio propagation are reflection, diffraction, and scattering. Rather than focusing on the details of radiowave propagation, which are covered in Ref. 6, the models for large-scale path-loss prediction will be summarized indicating critical parameters that are influencing radio reception.

The free-space propagation model is applicable when there is unobstructed line-of-sight path between the transmitter and the receiver. This scenario is typical for satellite systems and microwave radio links. The path loss is given by

$$L_{\text{free space}}(\text{dB}) = -10 \log(G_T(\text{dB})) - 10 \log(G_R(\text{dB})) + 20 \log(f(\text{Hz})) + 20 \log(d(\text{m})) - 147.6$$

where G_T and G_R are transmitter and receiver antenna gains, f is the carrier frequency, and d is the distance between the transmitter and receiver. Free-space path loss has inverse square law dependence with the distance so received power is reduced by 6 dB when the range is doubled (20 dB/decade decay with distance). In the same manner path loss increases with the increase of carrier frequency. While increasing the antenna gains may com-

pensate for the loss due to high operating frequency in point-to-point links, in mobile radio links this is not possible due to required omnidirectional coverage. The equation for free-space path loss is only valid when distance d is in the far-field of the transmitting antenna.

In practical radio channels free-space model conditions do not apply and further corrections to the path loss have to be accounted. A simple but practical scenario includes the direct path and ground-reflected path between transmitter and receiver. This model has been found to be accurate for path-loss prediction over distances of several kilometres for mobile radio systems and for the line-of-sight microwave links. Assuming that transmitter and receiver antenna heights h_T, h_R are much smaller than the distance, path loss is given by

$$L_{\text{ground reflection}}(\text{dB}) = 40 \log(d(\text{m})) - 10 \log(G_T(\text{dB})) - 10 \log(G_R(\text{dB})) - 20 \log(h_T(\text{m})) - 20 \log(h_R(\text{m}))$$

In this case path loss is independent from carrier frequency; however, the inverse fourth power-law decay is observed when increasing distance. For distances that are larger than few tens of kilometres, the Earth curvature should be taken into account and the values of the reflection coefficient should be modified [2]. Also of importance is dependence of the reflection coefficient on polarization and materials of the reflected surface [2,3].

The diffraction mechanism allows the radiolink to be maintained even when receiver is in the obstructed area, shadowed by the object. Huygens' principle could be used to explain the diffraction [2]. For practical applications Fresnel zones should be considered [4]. The simple knife-edge diffraction model is often used to calculate signal attenuation. Objects within Fresnel zones may cause diffraction loss, which is the function of the dimensionless Fresnel–Kirchhoff diffraction parameter

$$v = h \sqrt{\frac{2(d_1 + d_2)}{\lambda d_1 d_2}}$$

The geometry of knife-edge diffraction is depicted in Fig. 2. Diffraction loss can be translated into path loss relative to free-space loss, and it is given by nomograms or by approximations which are expressed as

$$L(v)(\text{dB}) = \begin{cases} 20 \log(0.5 - 0.62v) & -0.8 < v < 0 \\ 20 \log[0.5 \exp(-0.95v)] & 0 < v < 1 \\ 20 \log \left[0.4 - \sqrt{0.1184 - (0.38 - 0.1v)^2} \right] & 1 < v < 2.4 \\ 20 \log \left(\frac{0.225}{v} \right) & v > 2.4 \end{cases}$$

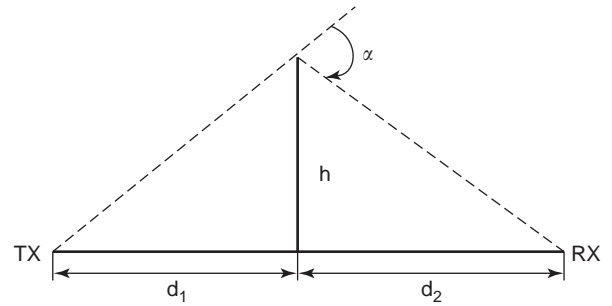


Figure 2. Knife-edge diffraction geometry.

In cases where there are more than one objects affecting the radio propagation, multiple knife-edge models should be introduced. Various approximate solutions have been presented, with different levels of accuracy. They have been compared by Parsons [2].

2.1. Path-Loss Prediction Models

Prediction models have evolved extensively in UHF/VHF bands addressing the growing importance of mobile radio services. Most models provide the prediction of the median path loss, the loss that is not exceeded at 50% of locations and for 50% of the time [2]. Knowledge of the radio signal statistics further allows estimation of the signal variability and prediction of the area where specified signal strength is achieved for a given percentage of location. Path-loss models differ in applicability to different terrain profiles and cover different level of details, from general to very specific scenarios. Most of the models are empirical, based on the interpretation of the measured data in the particular area by fitting curves or analytical expressions. The advantage of this approach is that it takes into account the variety of propagation factors through actual field measurements. However, the models are strictly applicable only to the environments characterized in measurements, and additional measurements are necessary in different frequency bands and on different locations to provide correction factors. Some of the commonly used models for outdoor and indoor environments will be discussed in subsequent sections. For more detailed comparison, the reader is referred to Refs. 2 and 3.

2.1.1. Outdoor Prediction Models. The significance of two models has been established in practice in VHF/UHF band: the Hata model and the Walfisch–Ikegami model [8]. Both models are empirical, derived from experimental data, and are extensively used in commercial computer-aided prediction tools. In general usage and accuracy of models depends on the propagation environment: Hata's model provides good accuracy in urban and suburban environments, the Walfisch–Ikegami model is widely used for dense urban environments and microcells. Extensions to both models are provided by The European Co-operative for Scientific and Technical research (COST) to cover the PCS band [9].

The Hata model, based on measurements of Okumura, has established empirical mathematical formulas for the path loss and considerably enhanced practical value of the

Okumura method [2]. It is restricted for the following range of parameters: frequency f 150–1000 MHz, height of the base station antenna h_{te} 30–200 m, height of the mobile unit antenna h_{re} 1–10 m, and distance d 1–20 km. The standard formula for basic transmission loss in urban area is

$$L_{urban}(dB) = 69.55 + 26.16 \log(f(\text{MHz})) - 13.82 \log(h_{te}(\text{m})) - a(h_{re}) + (44.9 - 6.55 \log(h_{te}(\text{m}))) \log(d(\text{km}))$$

where f is the carrier frequency, h_{te} is the effective transmitter antenna height, h_{re} is the effective receiver antenna height, d is the distance, and $a(h_{re})$ is the correction factor for effective receiver antenna height, which is a function of cell size. The correction factor for mobile antenna height for a small to medium-sized city (urban area) is computed as

$$a(h_{re})(dB) = (1.1 \log(f(\text{MHz})) - 0.7)h_{re}(\text{m}) - (1.56 \log(f(\text{MHz})) - 0.8)$$

and for a large city (dense urban area) as

$$a(h_{re})(dB) = \begin{cases} 8.29(\log(1.54h_{re}(\text{m})))^2 - 1.1, & f_c \leq 300\text{MHz} \\ 3.2(\log(11.75h_{re}(\text{m})))^2 - 4.97, & f_c \geq 300\text{MHz} \end{cases}$$

Suburban area path loss can be calculated using the modified equation

$$L_{suburban}(dB) = L_{urban}(dB) - 2 \left(\frac{\log(f(\text{MHz}))}{28} \right)^2 - 5.4$$

and path loss in open rural areas is given by

$$L_{rural}(dB) = L_{urban}(dB) - 4.78(\log(f(\text{MHz})))^2 - 18.33 \log(f(\text{MHz})) - 40.98$$

The Hata model is well suited for large cell mobile systems, but not for the PCS cells with the radius on the order of 1 km. The COST analysis of several measurements conducted in European cities for PCS band have resulted in an extended range of parameters for Hata's model to include the 1800 MHz frequency band [9]. The COST-231 proposed model for path loss is given by

$$L_{urban}(dB) = 46.3 + 33.9 \log(f(\text{MHz})) - 13.82 \log(h_{te}(\text{m})) - a(h_{re}) + (44.9 - 6.55 \log(h_{te}(\text{m}))) \log(d(\text{km})) + C_M$$

where all parameters are defined for the original Hata's formula and

$$C_M = \begin{cases} 0\text{dB}, & \text{for medium-sized city and suburban areas} \\ 3\text{dB}, & \text{for dense urban area} \end{cases}$$

COST-231-Hata's model is valid for scenarios with base station heights larger than rooftops in the vicinity of the base station. This is the case in large cells and small cells (maximum range 1–3 km), and path loss is determined largely by diffraction and scattering at rooftops in the vicinity of the mobile unit. Main rays propagate in this case above the rooftops. In practical situations it is not recommended to extend the range of validity on base station heights below the roof tops, as in the micro cell scenario. Wave propagation in micro cells (maximum range 0.5–1 km) is determined by diffraction and scattering around buildings, and main rays propagate in street canyons. These phenomena are further addressed by the Walfish-Ikegami model.

The approach of the Walfish-Ikegami model is restricted to radio paths that are obstructed by buildings and is not applicable if a line-of-sight path exists between the transmitter and receiver antennas within a street canyon. Few parameters are introduced to describe the character of the dense urban environment as depicted in Figs. 3 and 4: heights of buildings, widths of roads, building separation, and road orientation with respect to the direct radio path.

However, the model still considers only characteristic values and there is no consideration of the topographical database of the buildings. The models can be applied even when no data on the urban parameters are available by using the default values, which increases the prediction error. For a line-of-sight case in a street canyon the path loss is equal to

$$L_b(dB) = 42.6 + 26 \log(d(\text{km})) + 20 \log(f(\text{MHz})),$$

for $d \geq 20$ m

where the first constant in formula is determined so L_b is equal to free-space loss for 20 m. Otherwise the model is composed by three terms and restricted by the

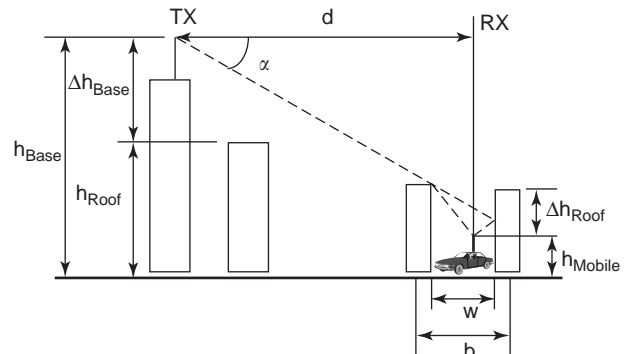


Figure 3. Parameters used in Walfish-Ikegami model.

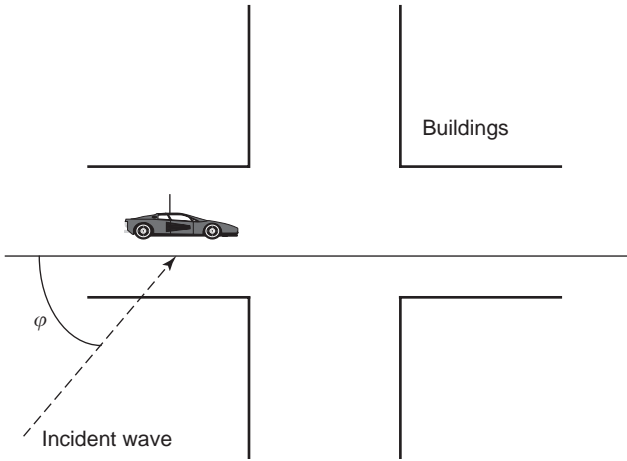


Figure 4. Definition of the street orientation in Walfish-Ikegami model.

free-space loss

$$L_b(\text{dB}) = \begin{cases} L_0 + L_{rts} + L_{msd} \\ L_0 \end{cases} \quad \text{for } L_{rts} + L_{msd} \leq 0$$

The free-space loss is given by

$$L_0(\text{dB}) = 32.4 + 20 \log(d(\text{km})) + 20 \log(f(\text{MHz}))$$

the rooftop-to-street diffraction and scatter loss is

$$L_{rts}(\text{dB}) = -16.9 - 10 \log(w(\text{m})) + 10 \log(f(\text{MHz})) \\ + 20 \log(\Delta h_{\text{mobile}}(\text{m})) + L_{\text{ori}}$$

where

$$L_{\text{ori}}(\text{dB}) = \begin{cases} -10 + 0.354\varphi^\circ & \text{for } 0 \leq \varphi < 35^\circ \\ 2.5 + 0.075(\varphi^\circ - 35) & \text{for } 35 \leq \varphi < 55^\circ \\ 4.0 - 0.114(\varphi^\circ - 55) & \text{for } 55 \leq \varphi \leq 90^\circ \end{cases}$$

and

$$\Delta h_{\text{mobile}} = h_{\text{roof}} - h_{\text{mobile}} \\ \Delta h_{\text{base}} = h_{\text{base}} - h_{\text{roof}}$$

The multiscreen diffraction loss

$$L_{\text{msd}}(\text{dB}) = L_{\text{bsh}} + k_a + k_d \log(d(\text{km})) + k_f \log(f(\text{MHz})) \\ - 9 \log(b(\text{m}))$$

consists of a number of terms:

$$L_{\text{bsh}}(\text{dB}) = \begin{cases} -18 \log(1 + \Delta h_{\text{base}}(\text{m})) & h_{\text{base}} > h_{\text{roof}} \\ 0 & h_{\text{base}} \leq h_{\text{roof}} \end{cases}$$

with

$$k_a(\text{dB}) = \begin{cases} 54 & h_{\text{base}} > h_{\text{roof}} \\ 54 - 0.8 \Delta h_{\text{base}}(\text{m}) & d \geq 0.5 \text{ km and } h_{\text{base}} \leq h_{\text{roof}} \\ 54 - \frac{0.8 \Delta h_{\text{base}}(\text{m})d(\text{km})}{0.5} & d \leq 0.5 \text{ km and } h_{\text{base}} \leq h_{\text{roof}} \end{cases}$$

representing the increase of path loss for base station antennas below the roof tops of the adjacent buildings,

$$k_d[\text{dB}] = \begin{cases} 18 & h_{\text{base}} > h_{\text{roof}} \\ 18 - 15 \frac{\Delta h_{\text{base}}}{h_{\text{roof}}} & h_{\text{base}} \leq h_{\text{roof}} \end{cases}$$

controlling the dependence of the multi-screen diffraction loss versus distance and

$$k_f(\text{dB}) = -4 + \begin{cases} 0.7 \left(\frac{f[\text{MHz}]}{925 - 1} \right) & \text{for urban and suburban areas} \\ 1.5 \left(\frac{f[\text{MHz}]}{925 - 1} \right) & \text{for dense urban area} \end{cases}$$

controlling the dependence of the multiscreen diffraction loss versus radiofrequency.

The COST-231-Walfish-Ikegami model is restricted to the following range of parameters: frequency f 800–2000 MHz, height of the base-station antenna h_{base} 4–50 m, height of mobile unit antenna h_{mobile} 1–3 m, and distance d 0.02–5 km. If the data on the structure of buildings and roads are unknown, the default values may be used: for b 20–50 m, $w = b/2$, h_{roof} 3 m times the number of floors plus the roof height, roof height is 3 m for pitched, 0 m for flat, and $\varphi = 90^\circ$.

The COST-Walfish-Ikegami model has been verified for frequencies in the 900 and 1800 MHz band and radio pathlengths from about 100 m to 3 km [9]. The path loss has very steep decay versus the height of the base-station antenna when the latter is close to the height of adjacent buildings and this case generally results in large prediction errors. Prediction errors are larger when $h_{\text{base}} \approx h_{\text{roof}}$. The performance of the model is poor for $h_{\text{base}} \ll h_{\text{roof}}$ because it does not consider waveguiding in the street canyons and diffraction at corners. For good performance of small-cell area coverage, the base-station antenna should be installed several meters (≥ 4 m) above the maximum rooftops of adjacent buildings within a radius of few hundred meters (e.g., 150 m). The prediction error may be quite large for microcells, which requires detailed knowledge of streets and buildings [9].

2.1.2. Indoor Prediction Models. Progress of personal communication services has established the need for accurate models that can support path-loss prediction inside and into the buildings. The major characteristics of indoor

radio channel are much smaller distances than in outdoor cases and higher variability of the environment. Building floorplan, construction materials, and building type greatly influence propagation characteristics. Partition losses at the same floor and partition losses between floors have been extensively measured and categorized [3].

For radio transmission originating outdoors, path loss due to signal penetration into the building should be considered. A number of factors have been found to influence penetration loss, including signal frequency, antenna pattern, and antenna position. Typical values for penetration loss measured in the 900-MHz band are on the order of 12 dB, with 6 dB lower loss when the building front (Facade) had windows [3].

Losses within buildings and penetration losses can be combined in the model characterizing propagation into the building [8]

$$L(\text{dB}) = L_{\text{mean}}(\text{dB}) + 10n \log(d(\text{m})) + kF(\text{dB}) \\ + pW_I(\text{dB}) + W_E(\text{dB})$$

where L_{mean} is the mean path loss from the transmitter to the building, n is the power exponent of the distance dependence, d is the distance into the building, k is the number of floors between transmitter and receiver, F is the floor loss factor, p is the number of interior walls between transmitter and receiver, W_I is the internal wall loss factor, and W_E is the external wall loss. For in-building path loss L_{mean} becomes path loss at 1 m distance from the transmitter antenna and W_E is not used. The wall loss factor depends on the construction materials and varies from 0.4 to 29 dB in the 900-MHz band.

Analysis of the experiments carried out in UK in the 900-MHz band in a typical office building with several floors resulted in the path-loss model

$$L(\text{dB}) = L_0(\text{dB}) + 10n \log(d(\text{m})) + kF$$

where L_0 is the path loss at 1 m distance from the transmitter antenna, n is the distance power-law coefficient, d is the vertical range in the building, k is the number of floors considered, and F attenuation per floor is measured in decibels. At 900 MHz n was approximately 4, $L_0 = 30$ dB, and F was 5.4 dB per floor [8].

More recent advanced methods for coverage prediction within buildings rely on site-specific propagation models and databases that support the ray-tracing method for deterministically modeling of the propagation environment. As three-dimensional building models and databases become widespread, deterministic methods may prevail for determining the path loss in a wide range of operating conditions [3].

2.2. Coverage Prediction Using Path-Loss Models

Propagation loss models can establish median path loss as a function of the distance between the transmitter and the receiver. Both theoretical and empirical models indicate that received signal power decreases logarithmically with distance with a slope of $10n$ dB per decade. The value of

the n ranges from 2 for a free-space propagation to larger values for obstructed paths (e.g., 3–5 for urban mobile radio, 4–6 for obstructed indoor propagation). However, this model does not consider different clutters, which may result in different signal levels for the same distance. The value of the path loss at a particular location is a random variable with a lognormal distribution (Gaussian when measured in dB units) about the mean value, which is distance-dependent. Lognormal statistics describes the shadowing effect at different locations. In practice values of the exponent n and standard deviation of the lognormal fading are determined from measured data. Shadowing is often referred to as a *long-term fading*.

The random effects of shadowing cause the signal level at certain locations to be lower than the specified level. Therefore it is useful to compute the coverage area with a certain radius, in particular the percentage of the area with a received signal equal or greater than the specified level. Tradeoff between the percentage of coverage (for a given exponent loss n and shadowing variance) and the amount of fading margin is an important element of the power budget. Details on the coverage computation procedure can be found in Refs. 3 and 4.

3. EFFECTS OF ENVIRONMENT

In addition to large-scale path loss, different attenuation factors due to the environment may influence the power budget. Additional signal attenuation may be the result of natural phenomena or artificially created environmental conditions.

3.1. Weather Effects

For microwave radio with line-of-sight paths different weather-related effects may contribute to fading and path loss. Examples include absorption and scattering by snow, hail, fog, and rain. Dry snow does not have significant effect on frequencies below 30 GHz; however, wet snow may cause larger attenuation. In general, this attenuation is not of concern. However, degradation of antenna characteristics due to snow and ice buildup on the surface may influence antenna directivity, and precautions may be taken by using protective radomes. For different types of antennas, attenuation loss due to accumulated ice is 2–7 dB. Another effect of snow is that it may affect the reflection coefficient, and in most cases, depending on the type of snow reflection coefficients, is close to 1 [7].

3.2. Molecular Absorption

The absorption from oxygen and water vapor in the atmosphere is an additional factor that has to be considered at certain frequencies. The atmosphere extends to an altitude of approximately 20 km, yet it represents a path-loss source that cannot be neglected.

Specific attenuation (given in dB/km) is calculated in Ref. 8, including local maxima of attenuation occur at frequencies around 22 GHz for the water vapor and 60 and 120 GHz for the oxygen. The respective values are around

0.2 dB/km for water vapor and around 15 and 2 dB/km for oxygen. However, system comparisons indicate that water vapor attenuation is far less important than rain attenuation even in the frequency range of ~ 20 GHz.

3.3. Rain Attenuation

One factor that is important when considering rain attenuation is polarization-related loss due to nonspherical shape of raindrops. The horizontally polarized waves experience larger attenuation than do vertically polarized ones. This can also result in a cross-polarization effect, which may be harmful for microwave systems using channel planning based on different polarizations. The frequency-related attenuation depends on the drop size distribution, and is not considered significant for the signals below 11 GHz for locations with rain climate similar to northern hemisphere. For tropical areas critical frequency is as low as 5 GHz.

Rain attenuation statistics prediction is based on rain rate data, which depends on rainfall microstructure. The ITU-R model is based on rain rate $R_{0.01\%}$ exceeded for 0.01% of the time with an integration time of 1 min. This information can be obtained from local measurements and in the case that measurements are not available from ITU-R reports. The specific attenuation is calculated as $\gamma_R = k R^\alpha$, where R is the rain rate in mm/hour, and k, α are regression coefficients that are a function of frequency and polarization [11]

$$k = \frac{k_H + k_V + (k_H - k_V) \cos^2(\theta) \cos(2\tau)}{2}$$

$$\alpha = \frac{k_H \alpha_H + k_V \alpha_V + (k_H \alpha_H - k_V \alpha_V) \cos^2(\theta) \cos(2\tau)}{2k}$$

where θ is the path elevation angle and τ is the polarization tilt angle relative to horizontal, $\tau = 45^\circ$ for circular polarization, and other parameters are as given in a Table 3. The effective pathlength in this case is calculated by multiplying the actual pathlength L with a reduction factor

$$r = \frac{1}{(1 + L/L_0)}$$

where

$$L_0 = 35 \exp(-0.015 R_{0.01\%})$$

Path attenuation exceeding the 0.01% of the time is estimated by

$$A_{0.01}(\text{dB}) = \gamma_R r L$$

Table 3. Parameters for Regression Coefficients Calculation

Frequency (GHz)	k_H	k_V	α_H	α_V
2	0.000154	0.000138	0.963	0.923
6	0.00175	0.00155	1.308	1.265
10	0.0101	0.00887	1.276	1.264
15	0.0367	0.0335	1.154	1.128

3.4. Attenuation Due to Clouds and Fog

In Earth-space radiocommunication systems for frequencies higher than 10 GHz the attenuation due to clouds may be important factor affecting system performance. The mechanism of attenuation is well understood since clouds and fog consist of small droplets and it is possible to express attenuation in terms of total water content per unit volume [12] as

$$\gamma(\text{dB/km}) = K_1[(\text{dB/km})(\text{g/m}^3)]M(\text{g/m}^3)$$

where γ is specific attenuation within the cloud, K_1 is the specific attenuation coefficient, and M is the liquid water content of the cloud or the fog. The typical water content is about 0.05 g/m^3 for medium fog with visibility ~ 300 m and 0.5 g/m^3 for thick fog with visibility ~ 50 m. The specific attenuation coefficient for the frequencies up to 1000 GHz is given by

$$K_1 = \frac{0.189f[\text{GHz}]}{\varepsilon''(1 + \eta^2)} (\text{dB km}^{-1} \text{ g}^{-1} \text{ m}^{-3})$$

where

$$\eta = \frac{2 + \varepsilon'}{\varepsilon''}$$

and complex dielectric permittivity of water is

$$\varepsilon''(f) = \frac{f(\varepsilon_0 - \varepsilon_1)}{f_p [1 + (f/f_p)^2]} + \frac{f(\varepsilon_1 - \varepsilon_2)}{f_s [1 + (f/f_s)^2]}$$

$$\varepsilon'(f) = \frac{\varepsilon_0 - \varepsilon_1}{[1 + (f/f_p)^2]} + \frac{\varepsilon_1 - \varepsilon_2}{[1 + (f/f_s)^2]} + \varepsilon_2$$

where $\varepsilon_0 = 77.6 + 103.3(\theta - 1)$, $\varepsilon_1 = 5.48$, $\varepsilon_2 = 3.51$ and $\theta = 300/T$, where T is temperature in kelvins. The principal and secondary relaxation frequencies are given by

$$f_p(\text{GHz}) = 20.09 - 142(\theta - 1) + 294(\theta - 1)^2$$

$$f_s[\text{GHz}] = 590 - 1500(\theta - 1)$$

Attenuation due to fog becomes significant at frequencies around 100 GHz with specific attenuation of 0.4 dB/km for medium fog, and 4 dB/km for thick fog.

3.5. Foliage

The leaves of maple, oak, hickory, and similar trees can cause additional signal loss in the frequency range above 400 MHz. In the winter leaves fall and received signal is generally stronger than in the summer. Various factors contribute to this type of loss, including operating frequency, type of leaves, height of the trees, and thickness of the foliage. In general, design practice is to add about 10 dB of allowance in the forest area in addition to predicted path loss [7].

In tropical rainforest areas leaves do not fall and their shape is different, producing different attenuation. Major studies carried out in the 50–800-MHz band indicate that loss increases linearly in log scale from 35 dB/decade at

50 MHz up to 40 dB/decade at 800 MHz. The foliage loss is approximately proportional to the operating frequency raised to fourth power, which is a good approximation for horizontal polarization. Vertical polarization experienced greater loss in general by 8–25 dB at 50 MHz and 1–2 dB at 800 MHz. For a transmitting antenna over tree-tops and a receiving antenna located in the trees, a delay spread of 0.2 μ s has been reported due to foliage [7].

3.6. Constructions

Although path-loss models tend to capture differences between buildup and rural areas, few specific conditions should be emphasized. Street orientation has the channel effect on the received-signal strength. For a mobile unit closer to the base station in the range of 1–2 mi, the difference between signal strengths in the case when the street is parallel to the base station and when it is perpendicular to it is about 10 dB. This phenomenon diminishes for distances over 5 mi.

A mobile receiver moving into a tunnel experiences a signal loss that is dependent on the frequency and the transmitter/receiver positioning. Experiments carried out for the transmitter at the entrance of the tunnel and the mobile receiver moving through the tunnel show that at 300 m inside the tunnel \sim 4 dB loss is observed at 1 GHz. Attenuation at lower frequencies was much higher, approaching 20 dB at 400 MHz [7]. Results from a study in New York have established inverse-law dependence of path loss versus the distance with an inverse law from 4 at 900 MHz reducing to 2 at 2400 MHz. Above this level, the frequency loss is less than in free space, indicating some sort of guiding mechanism.

The underpass effect results in a signal drop between 5 to 10 dB when a mobile receiver drives through. The period of the attenuation depends on vehicle speed. In cellular radio this type of effect usually does not affect the voice channel.

4. SMALL-SCALE VARIATIONS: MULTIPATH FADING

Small-scale *fading* (also referred as *fast fading*, *short-term fading*, or simply *fading*) describes the fluctuations of the received radio signal over a short period of time or a short travel distance. Substantial variations of the signal amplitude are caused mainly by local multipath propagation. Multiple replicas of the signal combine at the receiver antenna in different ways depending on the time of arrival and the phase of individual components, resulting in fluctuations that are fast compared to longer-term variation in mean signal level (shadowing). These fluctuations are seen in the received signal as large changes of amplitude over a small interval of time, random frequency modulation due to Doppler shifts on different multipath arrivals, and possible time dispersion due to different propagation delays of multipath components. Although fading is a basically spatial phenomenon, it is experienced as temporal phenomenon by a radio receiver moving through the multipath field. The motion of surrounding objects (reflectors, scatterers) also impacts fading characteristics in the case of a static transmitter/receiver pair, and/or when it

is comparable to the speed of the mobile. Fast fading is observed over a distance of \sim 0.5 l, with fades of depth \sim 20 dB frequent and larger fades of $>$ 30 dB less frequent, but not uncommon [4].

In practice there is no clear border between slow and fast fading. It is commonly assumed that in the areas where multipath occurs, radio signal consists of a local mean value that is constant over a small area, but varies slowly as the receiver moves, and a fast fading component superimposed on the slowly varying signal.

In mobile radiocommunications multipath fading occurs in urban areas where the height of the mobile antenna is much lower than that of the surrounding buildings and there is no line-of-sight path between the transmitter and the receiver. Propagation is determined mainly by scattering and diffraction around the buildings. In fixed radiolinks where the line-of-sight propagation exists, multipath propagation is caused by reflection from the ground or surrounding objects.

Besides multipath propagation, other factors may influence the fading characteristics. Relative motion between the transmitter and the receiver in mobile and low-Earth orbit satellite communications results in a phase change due to the difference in pathlengths, which can be observed as a Doppler frequency shift in each propagation path as illustrated in Fig. 5. The phase change is given by

$$\Delta\phi = \frac{2\pi\Delta l}{\lambda} = \frac{2\pi v\Delta t}{\lambda} \cos\theta$$

and the corresponding frequency shift is

$$f_d = \frac{1}{2\pi} \frac{\Delta\phi}{\Delta t} = \frac{v}{\lambda} \cos\theta$$

where v is the speed of the mobile unit. If mobile unit is moving toward the transmitter, positive Doppler shift results in increase of the received signal frequency, and if it is moving away from the transmitter, a negative Doppler shift results in decrease of the received-signal frequency. The angle between the incoming wave and the direction of

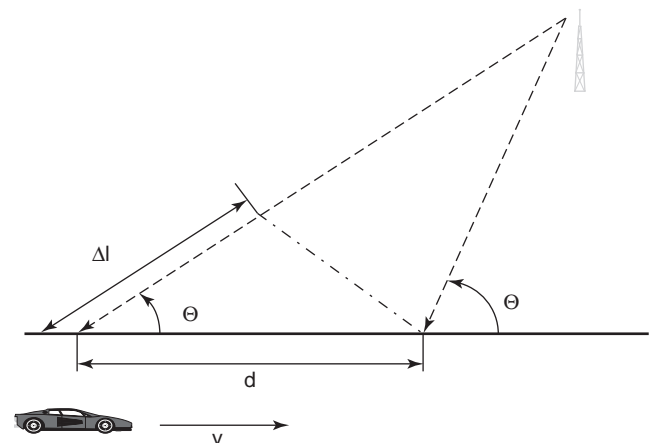


Figure 5. Geometry for illustration of Doppler effect.

motion determines the maximum rate of phase change that occurs when the waves are coming directly behind or ahead the mobile.

While characteristics of a fading channel are consequences of physical propagation phenomena, their impact on the received radio signal depends on the transmitted signal characteristics as well, primarily on the bandwidth of the transmitted signal. This relationship will be addressed in more detail in the following section.

4.1. Statistical Characterization of Multipath Fading Channels

Two major characteristics of a multipath fading channel can be observed by transmitting a short pulse (ideally impulse):

1. *Time spread* (dispersion) of the channel, resulting in more than one received pulse. Pulses differ with respect to differ in time of arrival, amplitude, and phase.
2. *Time variation*; the structure of multipath varies with time, and the same sounding experiment will produce different number of echoes with different arrival times, amplitudes, and phases if repeated at a different time.

Consequently a multipath fading channel is characterized in statistical terms. The impulse response of the time-varying multipath channel is represented by time-varying linear filter $h(\tau, t)$, where the variable t represents time of transmission and τ represents the channel multipath delay for a fixed value of t . Thus $h(\tau, t)$ represents the response of the channel at time t due to the impulse applied at time $t - \tau$. When the received signal contains discrete multipath components, the equivalent complex baseband impulse response model is given by

$$h(\tau, t) = \sum_n \alpha_n(t) \exp(-j2\pi f_c \tau_n(t)) \delta[\tau - \tau_n(t)]$$

where $\alpha_n(t)$ is the attenuation factor for the n th path, $\tau_n(t)$ is the propagation delay for the n th path, and f_c is the signal carrier frequency.

Statistical characterization of the fading channel is detailed in Ref. 15. In summary, channel impulse response $h(\tau, t)$ can be represented as a zero-mean complex-valued Gaussian process, so that its envelope at any time instant is Rayleigh distributed and the phase is uniform [16]. When a strong signal component (fixed scatterer, strong reflection) exists, $h(\tau, t)$ does not have a zero mean and the statistics of the channel is Rician [17]. Regardless of the probability distribution, a wide-sense stationary channel is characterized by two functions: *multipath intensity profile* and *power delay profile* of the channel, which give the average output power of the channel as a function of the time delay τ . The multipath spread T_m of the channel represents a range of values of τ over which the power delay profile is essentially nonzero.

In practice, power delay profiles are found by averaging instantaneous power delay profile measurements over a

local area to determine an average small-scale power delay profile. A typical spatial separation for sampling the channel is a quarter of a wavelength, over receiver movements no greater than 6 m in outdoor channels and no greater than 2 m in indoor channels [1]. Several statistical parameters quantify the delay characteristics of the channel. The *mean excess delay* is the first moment of the power delay profile

$$\tau_{\text{mean}} = \frac{\sum_n \alpha_n^2 \tau_n}{\sum_n \alpha_n^2}$$

and RMS delay spread is the square root of the second central moment of the power delay profile

$$\sigma_\tau = \sqrt{\overline{\tau^2} - \tau_{\text{mean}}^2}$$

where

$$\overline{\tau^2} = \frac{\sum_n \alpha_n^2 \tau_n^2}{\sum_n \alpha_n^2}$$

All delays are measured relative to the first detectable signal arriving at the receiver at $\tau_0 = 0$. Relative amplitudes of multipath components are also used in computations. Typical values of RMS delay spread are on the order of microseconds for outdoor mobile radio channels and nanoseconds for indoor radio channels [3].

The *maximum excess delay* is defined as $\tau_X - \tau_0$, where τ_X is the maximum delay at which the multipath component is X dB lower than the strongest multipath arrival, which is not necessarily at τ_0 . It is important to note that all parameters highly depend on the noise threshold in the power delay profile, which is used to differentiate multipath components and thermal noise.

The Fourier transform of the power delay profile determines frequency coherence properties of the channel. The inverse of the multipath spread

$$(\Delta f)_c = \frac{1}{T_m}$$

is a measure of the *coherence bandwidth* of the channel. Effectively, two signal components separated in frequency by more than a coherence bandwidth will be affected differently by a channel; that is, they will fade independently. Coherence bandwidth is practically quantified by a level of frequency correlation function and the RMS delay spread. For example, for a correlation function above 0.9 the coherence bandwidth is approximately [3]

$$(\Delta f)_c \approx \frac{1}{50 \sigma_\tau}$$

Time variations of the channel can be described by the *Doppler power spectrum* of the channel, which gives the signal intensity as a function of a Doppler frequency. The range of Doppler frequency over which the Doppler power spectrum is essentially nonzero is called the

Doppler spread B_d of the channel. It measures the spectral broadening caused by the time variations. The inverse of the Doppler spread

$$(\Delta t)_c \approx \frac{1}{B_d}$$

is the *coherence time* of the channel, and defines the time interval over which the characteristics of the channel can be regarded as constant. If the signal components are separated in time by more than the duration of coherence time, they can be regarded as independent.

However, B_d is not uniquely defined. On the other hand, if a purely sinusoidal tone of frequency f_c is transmitted over a channel, the received signal is within $[f_0 - f_d, f_0 + f_d]$, where f_d is the Doppler shift, showing that spectral broadening depends on the velocity of the mobile unit as well. A commonly used relationship describing the coherence time is given by [3]

$$(\Delta t)_c = \frac{0.423}{f_d}$$

The scattering function of the fading channel, representing power density as a two-dimensional function of delay and Doppler frequency, and different correlation functions of the channel are related via different Fourier transform pairs [15].

In the case of a Rayleigh fading channel, two important statistical parameters may clarify design choices of diversity techniques and error control codes:

1. The *level-crossing rate*, defined as the expected value of the rate at which the envelope of the Rayleigh fading process crosses a specified level in a positive-going direction [3]. The number of level crossings per second is given by

$$N_R = \sqrt{2\pi} f_d \rho e^{-\rho^2}$$

where f_d is the maximum Doppler frequency and $\rho = R/R_m$ is the normalized value of the specified level R by the local RMS amplitude of the fading envelope. For example, in the 900-MHz band with vehicle speed of 48 kmph (1000 mi/h), the maximum value is 39 crossings per second.

2. The *average fade duration*, defined as the average period of time for which the received signal is below a given level R . For Rayleigh fading, it is given by

$$\bar{\tau} = \frac{e^{\rho^2} - 1}{\rho f_d \sqrt{2\pi}}$$

showing the dependence on mobile (unit) speed. For a given fading margin, determined in a power budget, it is important to evaluate the rate at which the received signal falls below a certain level and the average time during which it remains below that level. These parameters directly translate into a

SNR reduction during the fade that can be used for the prediction of the radio performance.

4.2. Channel Classification

The impact of the fading channel on the received signal depends on the signal characteristics such as signal bandwidth and signal duration. The relationship between signal characteristics and channel parameters will serve as the criterion for channel classification. Let us consider digital communication system with signaling interval T .

For a signaling interval T much larger than the multipath spread of the channel, $T \gg T_m$, channel introduces a negligible amount of intersymbol interference. On the other hand, for a bandwidth of a signaling pulse $W \approx 1/T$, the previous relationship implies that the signal bandwidth is much smaller than the coherence bandwidth of the channel, resulting in *frequency-nonselective* or *frequency-related flat* fading. This implies that amplitude attenuation and phase shift introduced by channel are the same for all signal components and consequently spectral characteristics of the transmitted signal are preserved at the receiver. Channel distortion is simply a multiplicative random process. In this case multipath components of the signal cannot be resolved. This case is typical for narrowband communication signals. Flat fading may result in deep fades.

In a case where the signaling interval is smaller than the multipath spread of the channel, consecutive transmitted symbols interfere with each other at the receiver, producing intersymbol interference. In this case the signaling bandwidth W is larger than the coherence bandwidth of the channel, and different signal frequencies are subject to different gains and phase shifts. This type of channel is referred to as the *frequency-selective* channel. Frequency-selective channels are typical for wideband communication systems such as time-division multiple-access systems or spread-spectrum systems.

For a signaling interval T smaller than the coherence time of the channel, $T \ll (\Delta t)_c$, channel characteristics can be regarded as fixed during the symbol interval. In the frequency domain, the signaling bandwidth is much larger than the Doppler spread of the channel. This condition corresponds to a *slowly fading channel*. However, the rate of change of the channel depends on both signaling bandwidth and the velocity of the transmitter or the receiver.

For a signaling interval larger than the coherence time, channel impulse response changes within the duration of the symbol. This results in spectral broadening, which in turn leads to signal distortion since the signal bandwidth is smaller than the Doppler spread of the channel. This type of fading is referred to as *fast fading* or *time-selective fading*.

It should be pointed out that there is a slight inconsistency in terminology. The term *fast fading* is used to describe *multipath fading*, which is fast compared to shadowing effects [3]. On the other hand, multipath fading is characterized as *fast fading* when the signaling interval is larger than the coherence time of the channel [15]. Although it might be somewhat confusing, the

precise meaning of the term can be deduced from the context in which it is used.

For a physical channel with a given multipath delay spread and Doppler spread, different scenarios may arise depending on the signal design. A slow fading condition is desirable from the standpoint of receiver design since it allows coherent reception; synchronization circuits are able to track changes of the signal. It is important to note that even in situations characterized as slowly fading, that is, for which $B_d T \ll 1$, receiver performance may be significantly affected by channel fluctuations via non-perfect synchronization. The amount of degradation depends on the exact value of $B_d T$.

If signal bandwidth W cannot be selected independently of the signaling interval T , for a given fading rapidity, the system may be subject to frequency-selective or frequency-nonselective fading. Slow frequency-nonselective fading introduces constant multiplicative distortion and no ISI (intersymbol interference). Both coherent and non-coherent receivers can be employed. In the case of slow frequency-selective fading, equalization techniques should be used to compensate for ISI and equalizer operation is possible because of slow variations of the fading. In the case when signal bandwidth can be selected independently of signaling interval (as in spread-spectrum systems due to bandwidth expansion), one can simultaneously achieve no-ISI and slow fading conditions.

In the case of fast fading and frequency-nonselective channels, noncoherent reception techniques may be employed. On the other hand, fast frequency-selective fading presents a serious obstacle for a communication system.

The product $B_d T_m$ is called the *spread factor* of the channel and has a fixed value for a given physical channel. For underspread channels, $B_d T_m < 1$, the system can be designed to achieve the condition of negligible ISI and slow fading. For digital systems an optimal data rate can be derived to satisfy conditions for slow frequency-nonselective fading [13]

$$R = \frac{1}{T} = \sqrt{\frac{B_d}{T_m}}$$

For overspread channels signal design choices are more restricted and noncoherent reception is generally used.

4.3. Statistical Models for Fading Channels

While path-loss models play a crucial role in the power budget, determining the range and coverage zone of the radio system, statistical models for small-scale fading play an important role in receiver design and evaluation. Performance in the presence of fading is one of the major factors influencing the receiver sensitivity. Few major fading models for different radio scenarios will be summarized in this section.

With the advances in multiinput/multioutput wireless systems and spacetime coding, temporal characterization of the fading channels has been extended to cover spacetime propagation effects as well. Details on spacetime channel models can be found in Ref. 29.

4.3.1. Jake's Model. *Jake's model* of a Rayleigh fading path is based on scattering and is one of the most widely used models for a fading channel. It effectively models a frequency-nonselective fading channel with a Doppler spectrum of the form

$$S(f) = \frac{K}{\pi f_d \sqrt{1 - \left(\frac{f - f_c}{f_d}\right)^2}}$$

where K is a constant that depends on polarization (for detailed model derivation, see Ref. 12), f_c is the signal frequency, and $f_d = v/\lambda$ is the maximum Doppler shift, where v is the speed of vehicle and λ is the signal wavelength. This type of Doppler spectrum can be simulated using a model with $N_0 = 8$ sinusoids where in-phase and quadrature components of the fading signal are given by

$$x_c(t) = 2 \sum_{n=1}^{N_0} \cos(\beta_n) \cos(\omega_n t) + \sqrt{2} \cos \alpha \cos(\omega_d t)$$

$$x_s(t) = 2 \sum_{n=1}^{N_0} \sin(\beta_n) \cos(\omega_n t) + \sqrt{2} \sin \alpha \cos(\omega_d t)$$

and Doppler shift is given by $\omega_d = 2\pi f_d$, frequencies of the sinusoids are $\omega_n = \omega_d \cos(2\pi n/N)$, $N_0 = (N/2 - 1)/2$, and phases $\beta_n = \pi n/N_0$ and $\alpha = \pi/4$. This model shows excellent agreement with Rayleigh distribution, the autocorrelation Bessel function, and the Doppler spectrum [12]. This technique can be extended to generate up to N_0 independent fading signals, which is of importance for tapped-delay-line fading channel models for frequency-selective fading.

4.3.2. Tapped-Delay-Line Model for Outdoor Mobile Systems. Tapped-delay line models are commonly used to specify mobile radio channels. The structure of the model is straightforward, and measurements for a particular frequency band and geographic environment are used to develop model parameters. The model is specified in terms of number of multipath arrivals (usually fixed), relative delays, relative power of multipath components, and Doppler spectrum for each component. For a given radio standard these parameters may vary widely not only with different measurements but also with different signal characteristics considered.

As an example of the tapped-delay-line model, a wide-band propagation model for the GSM (global system for mobile communications) digital cellular standard is summarized. Discrete number of taps (6 and 12) is determined by their time delay and their average power, amplitudes of each tap are Rayleigh-distributed and varying according to a Doppler spectrum $S(f)$ [19]. Two types of Doppler spectrum are defined: *classical*, to be used in all except one case

$$S(f) = \frac{A}{\sqrt{\left(1 - \frac{f}{f_d}\right)^2}} \text{ for } f \in [-f_d, f_d]$$

where $f_d = v/\lambda$ is the maximum Doppler shift, and *Rician*, which is the sum of a classical Doppler spectrum and one direct path

$$S(f) = \frac{0.41}{2\pi f_d \sqrt{\left(1 - \frac{f}{f_d}\right)^2}} + 0.91\delta(f - 0.7f_d) \text{ for } f \in [-f_d, f_d]$$

Depending on the environment, few typical cases are specified: rural area, hilly terrain, and typical urban environment. Six tap models are summarized in Table 4.

4.3.3. Rumlmer Fading Model for Fixed Microwave Systems. This is a three-path model developed for a line-of-sight microwave radio channels is based on channel measurements on a typical link in a 6-GHz band. Since the differential delay of two multipath components is small, the channel transfer function is given by

$$H(f) = \alpha[1 - \beta \exp(-j2\pi(f - f_{\min})\tau_0)]$$

where α is the overall attenuation, β is a shape parameter resulting from multipath propagation, f_{\min} is the frequency of the fade minimum, and τ_0 is the relative time delay between the direct and multipath components. By fitting the model to the measurement data parameter, α is modeled as lognormally distributed, while distribution for β is given as $(1 - \beta)^{2.3}$. Two random variables are statistically independent. For $\beta > 0.5$, the mean of $-20 \log \alpha$ is

Table 4. Tapped-Delay Fading Channel Models for GSM Mobile Radio

Tap Number	Relative Time (μ s)	Average Relative Power (dB)	Doppler Spectrum
<i>a. Typical Case for Rural Area (RA) x, with x-speed of Mobile (km/h)</i>			
1	0.0	0	Rice
2	0.1	-4	Class
3	0.2	-8	Class
4	0.3	-12	Class
5	0.4	-16	Class
6	0.5	-20	Class
<i>b. Typical case for Hilly Terrain (HT) x</i>			
1	0.0	0	Class
2	0.1	-1.5	Class
3	0.3	-4.5	Class
4	0.5	-7.5	Class
5	15.0	-8.0	Class
6	17.2	-17.7	Class
<i>c. Typical Case for Urban Area (TU) x</i>			
1	0.0	-3.0	Class
2	0.2	0	Class
3	0.5	-2.0	Class
4	1.6	-6.0	Class
5	2.3	-8.0	Class
6	5.0	-10.0	Class

Source: Ref. 19.

25 dB, with a standard deviation of 5 dB. For smaller values of β , the mean decreases to 15 dB. The delay parameter was estimated to be $\tau_0 = 6.3$ ns.

4.3.4. Saleh-Valenzuela Indoor Statistical Model. This model is based on statistical modeling of the measurements of indoor propagation with a multipath resolution of 5 ns. The maximum reported multipath delay spread was on the order of 100–200 ns within rooms in the building and 300 ns in hallways. This model is based on multipath components arriving in clusters. Amplitudes of the components are independently Rayleigh distributed, with variance that decays exponentially with the cluster delay as well as with excess delay within a cluster. The difference from the tapped-delay-line model is that clusters and multipath components within the cluster are modeled as Poisson arrival processes with different rates and exponentially distributed interarrival time [3].

4.4. Effects of Fading on System Performance

Analog radio systems are relatively narrowband, even for high-capacity microwave links, and the major factor contributing to the degradation of system performance is the fading depth [8]. Therefore, a flat fading margin should be provided to ensure robust performance. This margin defines the additional loss that can be tolerated before the system SNR reaches an unacceptable level.

For a digital system, BER (bit error rate) is the performance measure and it should be specified for particular fading condition. Important note is that performance degradation of the digital signal is not graceful as in the analog one. For a narrowband system, performance may be specified in terms of flat-fading margin. For wideband systems, effects of frequency selectivity are more emphasized and use of equalization techniques and/or other forms of diversity are necessary to ensure desired performance. In that case, the fading margin may not be specified explicitly, but the receiver sensitivity may be specified for fading conditions, and will include the effects of fading countermeasures.

5. MANMADE NOISE AND INTERFERENCE

Radio systems are limited by either noise or interference. Characteristics of the noise greatly influence radio receiver design; however, most of the radio systems nowadays are interference-limited because of coexistence with other radio systems and/or multiple-access schemes employed. Interference level in the radio system is dependent on frequency, time, spatial location, and signal separation. Some of the major interference mechanisms for radio systems will be described in this section.

5.1. Impulse Noise

The nature and characteristics of noise are important for the radio reception in two ways. Understanding the noise phenomena leads to more efficient system design. Characterizing noise is crucial in performance prediction of any radio system since it directly affects the receiver

sensitivity. Radio systems are subject to different noise sources. Effects of thermal noise and receiver noise are well understood and are described by noise density and noise figure. This type of noise is characterized as Gaussian. Atmospheric noise has nonflat spectral density and decreases rapidly with frequency. Galactic noise is due to energy radiation from stars and planets; however, it is usually below the level of thermal noise.

The type of noise referred to as manmade noise is impulsive in nature and is generated by radiation of various types of electrical equipment such as vehicle ignition systems, alternator, power lines, neon lights, industrial noise from current switches, and from various domestic appliances. This type of noise can significantly affect the performance of a radio system. Its spectral characteristics are very irregular, and it also varies in level with location and time. Impulsive noise may be viewed as a combination of successive impulses, with random amplitudes and random time spacing. Different parameters have been established to qualitatively describe this type of noise, including mean or average voltage, peak voltage, amplitude probability distribution, pulse height distribution, level-crossing rate, and pulse duration distribution [2].

The median value of manmade noise power is given as a function of frequency up to 200 MHz by [10]

$$F_{\text{am}} = c - d \log(f(\text{MHz}))$$

where c and d take values from Table 5. In the frequency range 200–900 MHz the relationship is given by

$$F_{\text{am}} = 44.3 - 12.3 \log(f(\text{MHz}))$$

As mentioned earlier, ignition impulses from motor vehicles produce the significant component of manmade noise, in particular in the VHF band. Noise amplitude distribution in this case can be determined by

$$A[\text{dB}(\mu\text{V}/\text{MHz})] = 106 + 10 \log V(\text{vehicles}/\text{km}^2) - 28 \log(f(\text{MHz}))$$

where V is the traffic density.

Predicting the performance of the receiver in the presence of impulse noise is extremely difficult compared to relatively straightforward methods for Gaussian noise. Different techniques are presented in Ref. 2.

Table 5. Parameters for Calculation of Impulse Noise Median

Environmental Category	c	d
Business	76.8	27.7
Residential	72.5	27.7
Rural	67.2	27.7
Quiet rural	53.6	28.6

5.2. Cochannel Interference

Cochannel interference (CCI) is the consequence of better spectrum utilization. It is generated in a scenario where two or more communication signals are assigned to the same frequency and operate at the same time. CCI may be caused by a number of scenarios depending on the radio service: bad route planning for microwave radiolinks, failure to carry out coordination procedures for the same type of service, cross-polarization degradation in cross-polar frequency plan, cochannel interference due to frequency reuse in mobile radio systems, and cochannel interference due to multiple-access methods such as CDMA.

In any case, the result of cochannel interference is the presence of the same-type modulated signal at the receiver input, which may be lower than (in cellular TDMA and microwave systems) or on the same level as (in satellite and cellular CDMA systems) the desired signal. In most cases cochannel interference can be avoided by careful system planning. This will reduce the cochannel interference to an acceptable level such that system performance is not significantly degraded. Technical measures include proper cell design for cellular systems, including cell sectorization, power control techniques, and the use of orthogonal codes on the forward link in CDMA cellular systems (note that orthogonal codes in a CDMA system can be used only to eliminate intracell interference, the interference from neighboring cells will still be present). In the case when planning methods fail to reduce the amount of interference, a solution may be found in more sophisticated receiver design using interference suppression techniques.

5.3. Adjacent-Channel Interference

Adjacent-channel interference is the result of closely spaced radio channels in frequency, where the spectral content of the adjacent channels is spilling into the bandwidth of the desired channel. Factors determining the level of the interference are signal power and spectral distribution, power, and spectral distribution of the interfering signal intercepted by the receiver and distance dependence of the transmission losses between interfering transmitter and the desired signal receiver. ACI can be somewhat controlled by tight filtering; however, limiting factors are spectral utilization of the system and, on the other hand, the finite slope that can be achieved for filtering functions. Another way to improve adjacent channel performance is to design spectrally efficient modulation techniques that have largely concentrated power in a limited bandwidth with good rolloff properties, which in turn requires more elaborated demodulation schemes. Adjacent-channel interference in cellular systems can also be avoided by careful frequency planning, to ensure that adjacent channels are not used within the same cell or in the neighboring cells.

5.4. Near-Far Interference

Near-far interference in a radio system occurs when two different signals arrive at the receiver input with largely different power levels and may be interpreted as a special

form of cochannel interference. This may be the result of difference in distance of different transmitters from the same receiver, or in some cases fading conditions on the link, so that a closer transmitter may have lower power at the receiver when subjected to a deep fade. A consequence of the near-far problem is the performance degradation for weaker-signal reception. Although the near-far problem is general for radio reception, it is especially critical in direct-sequence CDMA systems where all signals are present at the receiver input, and may significantly reduce the capacity of a CDMA system. Countermeasures for the near-far problem include tight power control, which should ensure that all signals arrive to the receiver with the power level required for desired operation. Another possibility for cellular systems is to develop a frequency management plan that can greatly reduce the possibility of the near-far problem. Specific techniques for radio design include multiuser detection techniques [22].

6. RADIO RECEIVER DESIGN

The radio receiver consists of a channel interface followed by the demodulation component [23]. Channel interface of the radio receiver is characterized by the receiver selectivity and its ability to process both desired and undesired (interfering) signals. In order to achieve specified performance, the radio receiver must be designed to operate in the presence of noise, fading, and interference.

6.1. Basic Radio Receiver Parameters

Radio receiver sensitivity determines the input level of the weak radio signal that can be processed by a radio receiver to meet performance requirements. For analog receivers, performance measure is given in terms of required SNR, usually specified at the input to the detection circuit. For digital systems the performance measure is given in terms of BER or other parameters that can be derived from the BER requirement, depending on the type of radio service. The detection algorithm includes coding, interleaving, equalization, diversity, and other signal processing functions used to improve radio reception.

Receiver sensitivity is usually expressed by minimum detectable signal level for a required SNR, which includes the knowledge of the system bandwidth and is defined as

$$\begin{aligned} \text{RS(dBm)} = & -174 \text{ dBm} + 10 \log(\text{NF(dB)}) \\ & + 10 \log(\text{BW(Hz)}) + \text{SNR(dB)} \end{aligned}$$

where NF is the overall system noise figure referred to the input of the receiver and BW is the system noise bandwidth. For digital systems, the system requirement is commonly given in terms of energy per bit–noise density ratio E_b/N_0 . The relation between E_b/N_0 and SNR is given by $E_b/N_0 = \text{SNR} \cdot \text{BW} \cdot T$, where T is the bit duration [23]. Depending on the particular radio system and targeted operating environment, performance measure of the system (SNR or BER) can be evaluated under either fading or static conditions. In the first case the fading margin is derived from the statistics of the large-scale signal variation

such as lognormal fading. Small-scale signal variations are accounted for implicitly during BER evaluation. When BER of the system is specified under static conditions, the fading margin is derived from combined statistics of both large-scale and small-scale variation. The fading margin effectively defines the increase in SNR required to preserve the same BER as in the static case.

Radio sensitivity specifies the lowest detectable signal level at the radio input; however, both desired and unwanted signals may be present at the radio receiver input at high levels, and it is important to specify the performance for undesired response rejection. The unwanted strong signal may reduce a nearby weak (desired) signal, resulting in radio desensitization. The desensitization level is specified for a 1-dB weak-signal reduction and is a consequence of radio front-end saturation.

Another factor that may severely limit the performance of a radio receiver is intermodulation distortion (IMD), where unwanted strong signals produce a number of intermodulation products due to receiver front-end nonlinearities. IMD products, particularly third-order products, may fall directly in the bandwidth of the desired signal. To limit the level of the IMD products, the receiver is required to have a high intercept point in a particular order.

Dynamic range (DR) of the receiver is defined as the range of input signals that a radio receiver can process. Different factors may be taken into account depending on the radio service; however, the most common, the spurious-free dynamic range (SFDR), is defined as

$$\text{SFDR(dB)} = \frac{2}{3}(\text{IIP3(dBm)} - \text{RS(dBm)})$$

where IIP3 is the third-order input intercept point.

6.2. Modulation and Coding

Choice of the modulation method for radiocommunication depends on many factors. In all cases the goal of the radio receiver design is to achieve the required quality of the output signal (voice, video, data) using minimum SNR or E_b/N_0 . For power-limited systems, where bandwidth is not of concern (e.g., space communication links) noncoherent M -ary frequency shift keying (FSK) can be used to reduce the required E_b/N_0 for a given BER, at the expense of bandwidth expansion. For a bandwidth-limited system (as in most of the modern radio systems) spectrally efficient, coherent modulation schemes such as phase shift keying (PSK) or quadrature amplitude modulation (QAM) can be used at the expense of increasing required E_b/N_0 as the spectral efficiency increases [5]. However, additional requirements for the modulation format in radio communications such as robustness to fading, interference, and nonlinear distortions, motivated development of constant-envelope or near constant-envelope modulation such as offset quadrature phase shift keying (OQPSK) and minimum shift keying (MSK). Different forms of such modulation formats can be found in wireless systems [3]. Inherent resistance of a modulation method to the interference can be measured by determining required SIR for a specified BER. Performance functions for digital

modulations in the presence of interference are presented for various types and statistical characteristics of interferers in Ref. 23. Further advances in signaling methods for radio channels include the application of coded modulation techniques [15].

Additional performance gain can be obtained by using coding techniques at the expense of introducing redundancy to the transmitted digital signal. Channel coding protects the signal from the effects of noise, fading, and/or interference. Functions of channel codes are error detection and forward error correction. Both block and convolutional codes have been applied in radiocommunications [15]. Lately, there has been increasing attention to space-time codes [29] and turbo codes [30].

6.3. Diversity Reception for Fading Channels

Diversity reception techniques are used to reduce the effect of fading by exploiting the random nature of the radio channel. Independent or highly uncorrelated signal paths, known as *diversity channels*, are used to improve quality of the received signal. The concept of diversity is relatively simple—if one diversity channel is subject to a deep fade, another channel with a higher signal level can be selected or appropriate combining techniques can be applied to increase the signal level. The probability of all diversity channels being simultaneously below a given level is much less than the probability of any one of them being below that level. Therefore, a combination of different diversity channels will be subject to fewer severe fading conditions compared to any individual channel.

Diversity techniques may address different types of signal fluctuations. Large-scale fading is caused by shadowing due to variations in the propagation profile (hills, mountains) and the surrounding objects (buildings). To reduce the effect of the long-term fading, two geographically separated antennas may be used (for transmission or for reception), and the stronger signal may be selected. This type of diversity, known as *macroscopic diversity*, is often used in shortwave radio systems to reduce the ionospheric effects and in cellular systems to improve the performance of the forward link (where the mobile unit is selecting to receive signal from a base station that is not covered by the shadow) or of the reverse link (where signals from two base stations may be combined). The selective combining techniques is the most usual approach for macroscopic diversity [7].

Small-scale fading caused by multipath propagation in the vicinity of the receiver results in deep and rapid signal fluctuations. They occur over very short distances of a few wavelengths, and microscopic diversity techniques are employed to reduce the deep fades of the received signal. Different methods may be used to derive the diversity branches (channels).

Space diversity methods use physically separated antennas that can provide signals with low correlations. Typically, a separation of a few wavelengths is sufficient to obtain independently fading channels. Antenna separation is also dependent on antenna height, and can be reduced as the signal frequency increases. This type of diversity is widely used in microwave radiolinks and in

cellular radio, particularly for base-station reception. For base stations in mobile radio, the recommended ratio between antenna height and antenna separation is about 11, suggesting about 9 ft of antenna separation for a 100-ft antenna in the 900-MHz band [7]. Antenna diversity at the mobile unit can be achieved with an antenna separation as low as 17.5% of the signal wavelength. Practical antenna separation for microwave links is on the order 150–200 signal wavelengths. Receiver configuration for space diversity is relatively simple. The number of branches is selectable, and no extra bandwidth or power is needed to achieve diversity, making the space diversity one of the most popular schemes [4].

Frequency diversity relies on the diversity channels being separated (in frequency) by more than the coherence bandwidth of the channel, so the signal replicas will have very little correlation. Typical values used for mobile radio in 900-MHz band exceed 50 kHz in urban areas and 300 kHz in suburban areas [7]. This technique is often applied in microwave links, where diversity frequencies are available as the backup frequencies in the case of deep fading. Beside the requirements for additional bandwidth, a disadvantage of frequency diversity is the need for multiple receivers at different frequencies.

Polarization diversity is based on the fact that horizontal and vertical polarization signal components fade independently and may be combined (selected) at the receiver. This technique is used primarily for microwave links, where channel conditions vary slowly in time, although it has been increasingly considered for base-station reception in mobile radios. Two differently polarized antennas may be at the same place, hence there is no separation requirement as in space diversity. The drawback of the technique is the 3 dB power reduction at the transmitter since the power must be split between differently polarized antennas. Also, only two diversity branches are available in polarization diversity [7].

Angle diversity may be used at high operating frequencies (over 10 GHz) by pointing directional antennas in different directions at the receiver site. It is used predominantly by mobile units in cellular radio, since most of the multipath is created by local scatterers. Directive antennas also help in reducing the Doppler spread for each diversity branch.

Time diversity relies on transmitting the same signal at different times, so these signals fade at independent instances, so the fading characteristics will be changed and signals will be uncorrelated. The two transmissions should be separated by more than the coherence time of the channel. This diversity method is effective in applications where the fading mechanism is not related to the movement of the receiver. However, this method fails in the scenario where the mobile unit may remain still at the given location, which is the subject of deep fade, and the repeated signal components are highly correlated. While this method requires more spectrum and large buffer memory to store different signal replicas, the advantage is in simple implementation.

Interleaving is the technique used to obtain time diversity effect in modern digital communication systems. The function of the interleaver is to spread transmitted

bits in time so that a block of bits is not subject to a deep fade at the same time. This helps randomize burst errors and aid channel-coding techniques in reducing the overall BER [3].

The path diversity technique relies on receiver capability to resolve different multipath components in the time domain and subsequently combine them. This type of diversity is also referred to as the *implicit diversity* as opposed to other techniques that explicitly define diversity channels, since multipath diversity channels are obtained after signal reception. Adaptive equalizers and the RAKE receiver [15] are receiver techniques that provide path diversity, and are very effective in frequency-selective channels. Diversity gain depends largely on the delay profile of the channel.

Diversity techniques are usually applied at the receiver side, although some of the implementation complexity can be moved to a transmitter. For example, the base station in the mobile radio scenario may use the antenna that can provide better path propagation to a mobile unit at a specific location. Transmitter diversity allows the receiver to obtain diversity gain while operating as a standard non-diversity receiver [4,31].

Once the diversity channels are created, it remains to be decided how are they going to be combined in order to utilize the diversity effect. While macrodiversity schemes use almost exclusively selection combining, microdiversity schemes may employ one of the combining techniques outlined below. The methods of linear combining are derived from different optimization criteria, different levels of information available at the receiver, and different complexity constraints.

Selective combining simply selects the diversity branch with the highest signal level. This type of combining is easy to implement; additional requirements are antenna switch and monitoring circuitry. While in selective combining only one branch is used for subsequent signal processing and others are discarded, maximal ratio combining performs coherent combining of all diversity channels. This is the optimal method because it provides the maximal signal-to-noise ratio for signal detection. The weights applied to different diversity branches are proportional to the SNRs in each branch, and can be obtained by utilizing either pilot signals or sophisticated channel estimation techniques. When variable weighting is not available at the receiver, equal-gain combining may be utilized by coherently summing the signals from different diversity branches without weighting. This method still allows the receiver to exploit all diversity channels. Performance of equal-gain combining is better than selection combining and worse than maximal ratio combining, thus representing a viable technique as a tradeoff between performance and complexity. Performance improvement obtained by different combining schemes is summarized in Table 6.

Diversity reception may be interpreted as the simple case of coding, namely, repetitive coding, since the information is simply repeated on each diversity channel. Better spectrum utilization can be achieved by employing more sophisticated coding techniques for fading channels, in particular concatenated coding [15].

Table 6. SNR Improvements (in dB) for BER of 1% Relative to Single-Channel Reception: Comparison of Various Diversity Combining Schemes

Diversity Branches	Selection	Maximal Ratio	Equal Gain
2	10.0	11.5	10.8
4	16.0	19.0	18.0
6	18.0	22.0	21.5

Source: Ref. 20.

6.4. Interference Suppression Techniques

Every radio system operates in the presence of some form of interference. Regardless of the origin of interference (intentional or unintentional), some form of interference suppression must be employed in order to preserve system performance. Because of the increased number of services, most of the radio systems in operation are interference-limited rather than noise-limited. For power budget calculation, in addition to radio sensitivity, which is a function of the noise bandwidth of the receiver and the required SNR, the interference margin should be specified. Alternatively, the signal-to-interference ratio should be specified to satisfy required BER. Depending on the type of interference (CCI, ACI), different requirements may be imposed on the receiver.

Different approaches may be pursued to improve the efficiency of a radio system, such as reducing the channel spacing (increasing ACI), narrowband and wideband system overlay (creating narrowband cochannel interference to the wideband system), smaller cell design in mobile radio (increasing CCI), and overlapping footprints of the satellites.

With respect to the signal observation methods, interference suppression techniques could be broadly divided into *multichannel techniques*, where multiple sensors (antenna array) are employed for signal reception and *single-channel techniques*, where only one antenna is employed [25]. In a multichannel scenario, spatial filtering techniques may be realized via adaptive antenna arrays, relying on the different spatial distribution of the interfering signals. Single-channel techniques rely purely on temporal processing, usually using adaptive filtering. The most promising path for the modern receiver design is to incorporate spatiotemporal processing, efficiently combining capabilities of antenna arrays and temporal signal processing [26].

Spatial processing for interference signal suppression can be carried out using different techniques, including directional antennas, tilted beams, and height adjustment. However, adaptive antenna arrays with capability of adaptive beamforming have shown great potential for congested radio environments. Different algorithms and optimization criteria for adaptive beamforming are presented in Ref. 27.

Single-channel interference suppression techniques can be applied both in cases of spread-spectrum signaling and conventional techniques. Although all forms of spread-spectrum signals (direct sequence, frequency hopping, time hopping) provide certain interference

margin due to their inherent processing gain, additional techniques can be applied to further improve performance. Depending on the nature of interfering signal, different interference suppression algorithms have been developed. For narrowband interference rejection in direct sequence systems solutions include adaptive notch filters, decision feedback techniques, adaptive analog-to-digital conversion, and other nonlinear techniques. In the case of CDMA signals, where interference has the same characteristics as the desired signal, multiuser detection techniques are developed either in decentralized form (detection of single user of interest) or in centralized form (joint detection of all active users) [22]. Special techniques have been analyzed for frequency-hopping systems as well [25].

In non-spread-spectrum systems different techniques have been developed to cope with CCI, ACI, and ISI. Adaptive equalization techniques were shown to be efficient in combatting all three types of interference. Other methods include self-optimizing or blind receivers (based on different techniques such as constant modulus, higher-order statistics, probabilistic approaches etc.), neural network receivers, and other nonlinear techniques [25].

Most of the abovementioned interference suppression algorithms are performed in baseband. In addition to this different practical interference suppression schemes are developed at RF/IF stages of the receivers [28].

6.5. Signal Losses in Radio Receiver

Because of the inherent complexity of the radio receiver, a number of signal loss sources are associated with receiver design. Bandlimiting loss in transmitter and receiver is the result of finite-bandwidth usage, usually restricted by the radio regulations. Intersymbol interference in which received digital symbols overlap with each other may result from different effects: bandlimited operation, physical multipath radio propagation, and usage of partial response modulation formats. Local oscillator phase noise results in the phase jitter in the receiver and consequently degrades the performance of the detection algorithm. Nonlinear distortions in radio equipment include AM/AM and AM/PM conversion, limiter loss, and intermodulation distortion. AM/PM conversion produces phase variations in the signal, mostly after nonlinear amplification. Signal sidelobe growth is another effect that can produce excessive interference despite tight filtering at the transmitter. Hardlimiting stages in the receiver may cause suppression of weak-signal components in the presence of stronger ones. Intermodulation products are the result of multiple signals interacting in a nonlinear device and create additional noise source, which contributes to total noise level. Also, receiver operation can be largely affected by several imperfections associated with demodulation, such as imperfections of the synchronization circuits that are producing noisy estimates of received-signal parameters necessary for the detection process and finite numeric precision effects associated with programmable of fixed logic implementation of the demodulation functions.

BIBLIOGRAPHY

1. *National Spectrum Management*, Rec. ITU-R SM.1047, 1994.
2. D. Parsons, *The Mobile Radio Propagation Channel*, Wiley, New York, 1992.
3. T. Rappaport, *Wireless Communications Principles and Practices*, Prentice-Hall PTR, Upper Saddle River, NJ, 1996.
4. S. Sampei, *Applications of Digital Wireless Technologies to Global Wireless Communications*, Prentice-Hall PTR, Upper Saddle River, NJ, 1997.
5. B. Sklar, *Digital Communications*, NJ, Prentice-Hall, Englewood Cliffs, 1988.
6. J. Wait, Radiowave propagation, in J. G. Webster, ed., *Wiley Encyclopedia of Electrical and Electronics Engineering*, Wiley, New York, 1999.
7. W. Lee, *Mobile Communications Design Fundamentals*, 2nd ed., Wiley, New York, 1993.
8. J. Doble, *Introduction to Radio Propagation for Fixed and Mobile Communications*, Artech House, Boston, MA, 1996.
9. COST 231, *Urban Transmission Loss Models for Mobile Radio in the 900- and 1800-MHz band*, COST231 TD(90) 119, Rev. 2, The Hague, Sept. 1991.
10. *Radio Noise*, Rec. ITU-R, PI.372-6, 1994.
11. *Specific Attenuation Model for Rain for Use in Prediction Methods*, Rec. ITU-R, PN. 833-1, 1992.
12. *Attenuation Due to Fog and Clouds*, Rec. ITU-R PN. 840-1, 1992-1994.
13. S. Stein, Fading channel issues in system engineering, *IEEE J. Select. Areas Commun.* 5(2):68-89 (1987).
14. R. Steele, *Mobile Radio Communications*, Pentech Press, London, 1992.
15. J. Proakis, *Digital Communications*, 3rd ed., McGraw-Hill, New York, 1995.
16. C. Lewis, Rayleigh channels, in J. G. Webster, ed., *Wiley Encyclopedia of Electrical and Electronics Engineering*, Wiley, New York, 1999.
17. H. Bertoni, Rician channels, in J. G. Webster, ed., *Wiley Encyclopedia of Electrical and Electronics Engineering*, Wiley, New York, 1999.
18. W. Jakes, ed., *Microwave Mobile Communications*, An IEEE Press Classic Reissue, IEEE Press, Piscataway, NJ, 1993.
19. TS-GSM 05.05, *Digital Cellular Telecommunications System (Phase 2), Radio Transmission and Reception (GSM 05.05)*, ETSI, Sophia Antipolis, 1995.
20. V. Garg and J. Wilkes, *Wireless and Personal Communications Systems*, Prentice-Hall PTR, Upper Saddle River, NJ, 1996.
21. S. Faruque, *Cellular Mobile Systems Engineering*, Artech House, Boston, MA, 1996.
22. A. Duel-Hallen, J. Holtzman, and Z. Zvonar, Multiuser detection in CDMA systems, *IEEE Pers. Commun. Mag.* 2(2):46-58, (1995).
23. *Performance Functions for Digital Modulation Systems in an Interference Environment*, Rec. ITU-R SM. 1235, 1997.
24. *General Principles and Methods for Sharing between Radio Services*, Rec. ITU-R SM. 1132, 1995.
25. J. Laster and J. Reed, Interference rejection in digital wireless communications, *IEEE Signal Process. Mag.* 14(3):37-62 (1997).
26. A. Paulraj and C. Papadias, Space-time processing for wireless communications, *IEEE Signal Process. Mag.* 14(6):49-83 (1997).

27. R. Monzingo and T. Miller, *Introduction to Adaptive Arrays*, Wiley, New York, 1980.
28. *The Application of Interference Cancellers in the Fixed Satellite Service*, Rec. 734, 1992.
29. A. Paulraj, R. Nabar, and D. Gore, *Introduction to Space-Time Wireless Communications*, Cambridge Univ. Press, Cambridge, UK, 2003.
30. L. Hanzo, T. Liew, and B. Yeap, *Turbo Coding, Turbo Equalization and Space-Time Coding for Transmission over Fading Channels*, Wiley, New York, 2002.
31. A. Hottinen, O. Tirkkosen, and R. Wichman, *Multiantenna Transceiver Techniques for 3G and Beyond*, Wiley, New York, 2003.

RADIOMETRY

IAN A. GLOVER
University of Bradford
Bradford, West Yorkshire,
United Kingdom

Radiometry is concerned with the measurement, analysis, and interpretation of radiant electromagnetic energy. The simplest and most common measurement, made using an instrument called a *radiometer*, is of received electromagnetic power in a given frequency band. Some instruments, however, analyze the received energy's spectral distribution (spectroradiometers), its polarization (polarimeters), or its angular distribution in space (imaging radiometers). The usual objective of radiometric measurements is the inference from them of the physical and/or chemical state of the material from, or through which, the received electromagnetic energy has been emitted, reflected, or transmitted. Radiometry is therefore a branch of remote sensing and could be considered to include radar. In practice, however, the term *radiometry* is usually used to describe the measurement and characterization of naturally occurring radiation, or (unlike radar) scattered radiation originating as a narrowband signal. The former, called *passive radiometry*, deals principally with self-emitted thermal radiation and reflected radiation of solar origin. The latter, called *active radiometry*, relies on artificial illumination. Figure 1 illustrates these different types of radiometer. Active radiometers are sometimes called *scatterometers*.

Since all radiometers depend for their operation on the measurement of one or more parameters of electromagnetic radiation, a brief review of such radiation follows.

1. ELECTROMAGNETIC RADIATION

Whenever charges accelerate (other than those carried by electrons in stable orbits around the nuclei of atoms), or a subatomic particle in an atom makes a transition to a lower energy level, electromagnetic energy is radiated. This energy propagates as a disturbance of the electric and magnetic fields existing in space. An electromagnetic

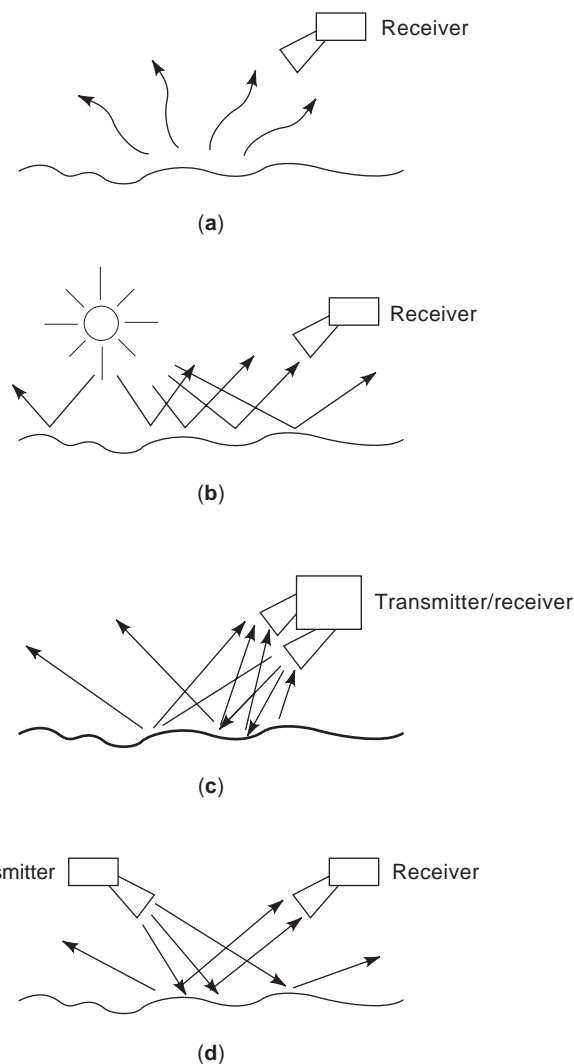


Figure 1. Passive and active radiometry: (a) passive measurements of self-emitted thermal radiation; (b) passive measurements of scattered solar radiation; (c) active (scatterometer) measurements employing monostatic geometry; (d) active (scatterometer) measurements employing bistatic geometry.

wave propagating in an isotropic, homogeneous medium has, sufficiently far from its source, an electric field vector \mathbf{E} , magnetic field vector \mathbf{B} , and unit vector pointing in the direction of wave propagation \mathbf{u} , which are mutually perpendicular. Furthermore, the wavefront has a curvature that is sufficiently small for it to be considered locally plane. (In a truly plane wave \mathbf{E} and \mathbf{B} would be constant with respect to position in any plane normal to the direction of propagation.)

For radiation of a single frequency (said to be *monochromatic*), \mathbf{E} and \mathbf{B} will vary sinusoidally with time and space. The amplitude (V/m) of such a wave is the peak value of its electric field strength, and its cyclical frequency f (Hz) is the number of oscillations (or cycles) that the electric field completes, at a given point in space, in one second. [The radian frequency ω (rad/s) is the phase advance in radians, at a given point in space, that the wave

27. R. Monzingo and T. Miller, *Introduction to Adaptive Arrays*, Wiley, New York, 1980.
28. *The Application of Interference Cancellers in the Fixed Satellite Service*, Rec. 734, 1992.
29. A. Paulraj, R. Nabar, and D. Gore, *Introduction to Space-Time Wireless Communications*, Cambridge Univ. Press, Cambridge, UK, 2003.
30. L. Hanzo, T. Liew, and B. Yeap, *Turbo Coding, Turbo Equalization and Space-Time Coding for Transmission over Fading Channels*, Wiley, New York, 2002.
31. A. Hottinen, O. Tirkkosen, and R. Wichman, *Multiantenna Transceiver Techniques for 3G and Beyond*, Wiley, New York, 2003.

RADIOMETRY

IAN A. GLOVER
University of Bradford
Bradford, West Yorkshire,
United Kingdom

Radiometry is concerned with the measurement, analysis, and interpretation of radiant electromagnetic energy. The simplest and most common measurement, made using an instrument called a *radiometer*, is of received electromagnetic power in a given frequency band. Some instruments, however, analyze the received energy's spectral distribution (spectroradiometers), its polarization (polarimeters), or its angular distribution in space (imaging radiometers). The usual objective of radiometric measurements is the inference from them of the physical and/or chemical state of the material from, or through which, the received electromagnetic energy has been emitted, reflected, or transmitted. Radiometry is therefore a branch of remote sensing and could be considered to include radar. In practice, however, the term *radiometry* is usually used to describe the measurement and characterization of naturally occurring radiation, or (unlike radar) scattered radiation originating as a narrowband signal. The former, called *passive radiometry*, deals principally with self-emitted thermal radiation and reflected radiation of solar origin. The latter, called *active radiometry*, relies on artificial illumination. Figure 1 illustrates these different types of radiometer. Active radiometers are sometimes called *scatterometers*.

Since all radiometers depend for their operation on the measurement of one or more parameters of electromagnetic radiation, a brief review of such radiation follows.

1. ELECTROMAGNETIC RADIATION

Whenever charges accelerate (other than those carried by electrons in stable orbits around the nuclei of atoms), or a subatomic particle in an atom makes a transition to a lower energy level, electromagnetic energy is radiated. This energy propagates as a disturbance of the electric and magnetic fields existing in space. An electromagnetic

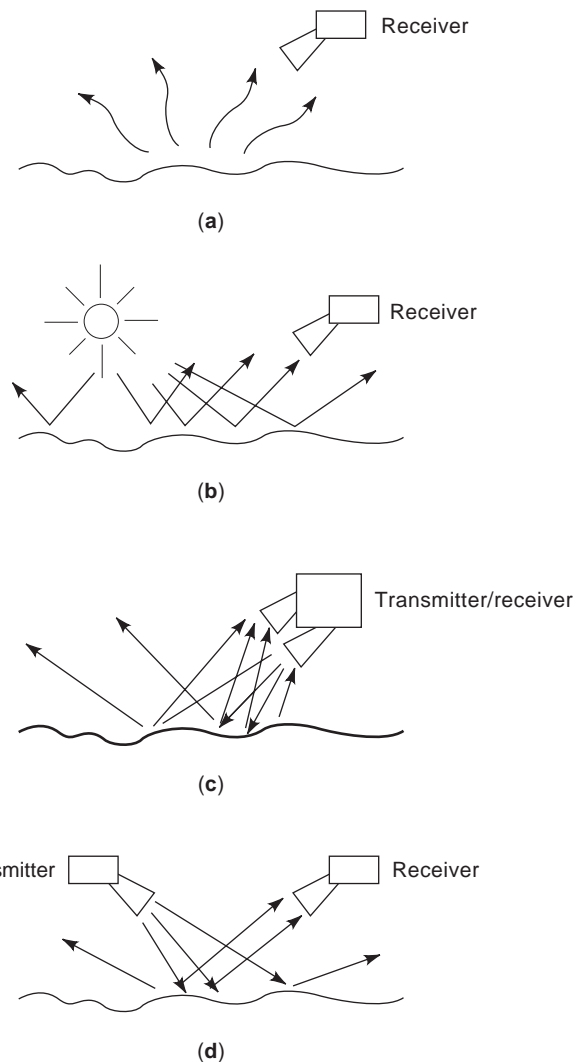


Figure 1. Passive and active radiometry: (a) passive measurements of self-emitted thermal radiation; (b) passive measurements of scattered solar radiation; (c) active (scatterometer) measurements employing monostatic geometry; (d) active (scatterometer) measurements employing bistatic geometry.

wave propagating in an isotropic, homogeneous medium has, sufficiently far from its source, an electric field vector \mathbf{E} , magnetic field vector \mathbf{B} , and unit vector pointing in the direction of wave propagation \mathbf{u} , which are mutually perpendicular. Furthermore, the wavefront has a curvature that is sufficiently small for it to be considered locally plane. (In a truly plane wave \mathbf{E} and \mathbf{B} would be constant with respect to position in any plane normal to the direction of propagation.)

For radiation of a single frequency (said to be *monochromatic*), \mathbf{E} and \mathbf{B} will vary sinusoidally with time and space. The amplitude (V/m) of such a wave is the peak value of its electric field strength, and its cyclical frequency f (Hz) is the number of oscillations (or cycles) that the electric field completes, at a given point in space, in one second. [The radian frequency ω (rad/s) is the phase advance in radians, at a given point in space, that the wave

makes in one second and is related to cyclical frequency by $\omega = 2\pi f$.] The phase constant β (rad/m) is the phase advance in radians that the wave makes, at a given instant of time, over one meter of space in the direction of propagation and is related to wavelength λ by $\beta = 2\pi/\lambda$. ($1/\lambda$ and β are therefore the spatial equivalent of cyclical and radiant frequency, respectively.)

Radiation of nonzero bandwidth has an amplitude at a point in space that fluctuates over time as the phase relationships between the constituent (and elemental) monochromatic waves change. The timescale over which this amplitude fluctuation occurs is related to the bandwidth Δf of the radiation and is characterized by a coherence time Δt . *Coherence time* is defined as the maximum timeshift for which the field of the original and timeshifted waves (at a given point in space) are correlated. An equivalent quantity, coherence length Δl , is defined (for a given instant in time) as the maximum spatial shift for which the fields of original and shifted waves are correlated. For quantitative work the term *correlated* must be interpreted as a correlation value greater than some specified fraction of its maximum. For consistent definitions of bandwidth, coherence length, and coherence time, these quantities are related by

$$\Delta l = c\Delta t = \frac{c}{\Delta f} \quad (1)$$

If the tip of the \mathbf{E} vector, representing a wave at a single point in space, traces out an elliptical curve, the wave is said to be (fully) polarized. If the curve traced out is random, the wave is said to be unpolarized. A wave with an \mathbf{E} vector locus that can be resolved into a deterministic component and a random component is said to be partially polarized. A fully polarized wave having a polarization ellipse with an axial ratio of 1.0 or ∞ is said to be circularly, or linearly, polarized, respectively. A linearly polarized wave therefore has an \mathbf{E} vector that traces out a straight line and that, in an isotropic medium, remains in a fixed plane as the wave propagates forward.

The concepts of coherence and polarization are not entirely unrelated since a wave observed on a timescale that is short with respect to its coherence time is always fully polarized. As the observation time increases, the polarization of the wave may gradually change; however, the changes appear random on a timescale large with respect to the wave's coherence time. A wave will remain fully polarized even when observed on a timescale much longer than its coherence time if energy is radiated in one polarization only.

In passive radiometry the received electromagnetic radiation is usually incoherent, spread across a wide band of frequencies, and unpolarized. The useful measurable quantities in this case are power density (W/m^2), radiation intensity (W/sr), power spectral density (W/Hz), and angular/spatial radiation distribution. In radiometry the first three of these quantities are generally referred to as *irradiance* (E), *radiant intensity* (I), and *radiant spectral flux* (Φ_f), respectively. In some applications, however (e.g., microwave radiometry), different terminologies are also often used (see Table 1).

2. DEFINITIONS OF RADIOMETRIC QUANTITIES

The commonly used radiometric quantities are as follows:

- Radiant energy Q (J)—the quantity of electromagnetic energy in a specified region of space or associated with a specified process
- Radiant flux Φ (W)—radiant energy per unit time crossing a specified surface
- Radiant density w (J/m^3)—radiant energy per unit volume
- Radiant flux density E or M (W/m^2)—radiant flux per unit area normal to a specified direction
- Irradiance E (W/m^2)—radiant flux density arriving at a specified surface
- Radiant exitance (or emittance) M (W/m^2)—radiant flux density leaving a specified surface
- Radiant intensity I (W/sr)—radiant flux per unit solid angle in a specified direction
- Radiance L ($\text{W sr}^{-1} \text{m}^{-2}$)—radiant intensity in a specified direction per unit projected area of the source normal to the specified direction

Radiation consisting of electromagnetic power distributed over a continuum of frequencies has infinitesimally small power at any single frequency. Each of the preceding quantities can be characterized at a single frequency, however, by considering the quantity to be measured within a small bandwidth Δf (centered on frequency f), dividing by Δf , and taking the limit as $\Delta f \rightarrow 0$. The result is a spectral density having those units of the original quantity per hertz. (An obvious variation on this definition uses radian frequency instead of cyclical frequency.) At optical frequencies spectral densities are usually expressed as quantities per meter of wavelength rather than per hertz of frequency. A spectral density is typically indicated by preceding the quantity with the word *spectral* and adding a subscript f , ω , or λ to the appropriate symbol. Spectral irradiance, for example, can be expressed in any of the following ways:

$$E_f(f) = \lim_{\Delta f \rightarrow 0} \left[\frac{\text{power density contained in frequency band } f - \frac{\Delta f}{2} \text{ to } f + \frac{\Delta f}{2}}{\Delta f} \right] \quad (2)$$

$$E_\omega(\omega) = \lim_{\Delta \omega \rightarrow 0} \left[\frac{\text{power density contained in frequency band } \omega - \frac{\Delta \omega}{2} \text{ to } \omega + \frac{\Delta \omega}{2}}{\Delta \omega} \right] \quad (3)$$

Table 1. Radiometric and Photometric Quantities

Quantity	Symbol	SI Unit	Other Common Units	Defining Equation	Comments
Radiant energy	Q_e	J	erg, kWh		Electromagnetic energy
Radiant flux	Φ_e	W	erg/s	$\Phi_e = \frac{dQ_e}{dt}$	Electromagnetic power
Radiant density	w_e	J/m ³	erg/cm ³	$w_e = \frac{dQ_e}{dV}$	Energy density
Irradiance	E_e	W/m ²	W/cm ²	$E_e = \frac{d\Phi_e}{dA}$	Power density (also called <i>radiant flux density</i>)
Radiant excitance	M_e	W/m ²	W/cm ²	$M_e = \frac{d\Phi_e}{dA}$	Power density (also called <i>emittance</i> and <i>radiant flux density</i>)
Radiant intensity	I_e	W/sr		$I_e = \frac{d\Phi_e}{d\Omega}$	Angular concentration of power (also called <i>radiation intensity</i>)
Radiance	L_e	W sr ⁻¹ m ⁻²	W sr ⁻¹ cm ⁻²	$L_e = \frac{dI_e}{(dA \cos \psi)}$	Angular concentration of power per unit projected area of source (also called <i>radiometric brightness</i> , especially in microwave applications)
Luminous energy	Q_v	lm s (talbot)	lm h	$\Phi_v = K_m \int_{0.36\mu m}^{0.83\mu m} \Phi_{e,\lambda}(\lambda) V(\lambda) d\lambda$	Photopic definition; scotopic definition uses primed versions of K_m and $V(\lambda)$.
Luminous flux	Φ_v	lm (lumen)		$\Phi_v = \frac{dQ_v}{dt}$	
Luminous density	w_v	lm s m ⁻³		$w_v = \frac{dQ_v}{dV}$	
Illuminance	E_v	lx (lux)	fc, ph	$E_v = \frac{d\Phi_v}{dA}$	1 lux (lx) = 1 lm/m ² 1 foot-candle (fc) = 1 lm/ft ² 1 phot (ph) = 1 lm/cm ² Also called <i>illumination</i>
Luminous excitance	M_v	lx		$M_v = \frac{d\Phi_v}{dA}$	Also called <i>luminous emittance</i>
Luminous intensity	I_v	cd (candela)		$I_v = \frac{d\Phi_v}{d\Omega}$	1 candela (cd) = 1 lm/sr
Luminance	L_v	cd/m ² (nit, nt)	sb, L, fL, asb	$L_v = \frac{dI_v}{(dA \cos \psi)}$	1 stilb (sb) = 1 cd/cm ² 1 lambert (L) = 1 cd/(π cm ²) 1 foot lambert (fL) = 1 cd/(π ft ²) 1 apostilb (asb) = 1 cd/(π m ²) Also called <i>photometric brightness</i>

$$E_\lambda(\lambda) = \lim_{\Delta\lambda \rightarrow 0} \left[\frac{\text{power density contained in wave band } \lambda - \frac{\Delta\lambda}{2} \text{ to } \lambda + \frac{\Delta\lambda}{2}}{\Delta\lambda} \right] \quad (4)$$

The relationship between these various expressions is summarized by

$$E_f(f) = E_\omega\left(\frac{\omega}{2\pi}\right) 2\pi = E_\lambda\left(\frac{c}{\lambda}\right) \frac{c}{f^2} \quad (5)$$

Spectral densities may be a function of frequency and, if so, may be measured by a spectroradiometer to yield information about the source of the radiation, material through which it has passed, or a surface from which it has been reflected. Often, however, spectral densities are constant with frequency (at least over the frequency band of interest). In this case they are referred to as white and are characterized by a single value.

2.1. Related Photometric/Luminous Quantities

Radiometric quantities relate to objective measures of energy and power carried by electromagnetic radiation of any

wavelength. Photometric (or luminous) quantities relate to the subjective visual impact that these quantities have on an observer [1]. In practice, photometric quantities are usually measured objectively but in such a way as to reflect the visual sensation experienced by a normal human observer. This is achieved by using detectors that mimic the response of the human eye/brain system and is called physical photometry. The definition of photometric quantities therefore involves the visual response of a (hypothetical) standard observer [2]. In fact, two standard responses, $V(\lambda)$ and $V'(\lambda)$, called the *photopic* and *scotopic spectral luminous efficiencies*, are defined (Fig. 2). These responses correspond closely to those of human observers under conditions of high (nominally daytime) and low (nominally nighttime) illumination, respectively. (The principal reason for the difference in these two responses is that different types of retinal receptors dominate under the two conditions; cones in the former case and rods in the latter case.)

Spectral luminous efficiencies are used to define a photometric/luminous quantity corresponding to each radiometric quantity, the same symbol usually being used for both. When confusion between the two is possible, the radiometric version is identified using a subscript e and the luminous version using a subscript v . For photopic vision, luminous flux Φ_v , for example, is related to the radiometric

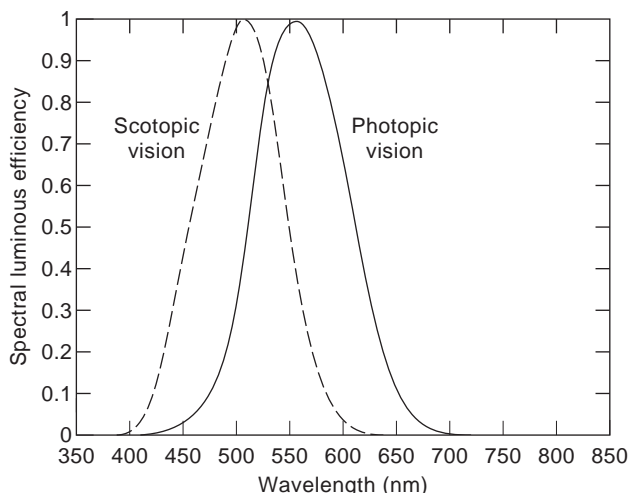


Figure 2. Spectral luminous efficiencies: photopic $V(\lambda)$ and scotopic $V(\lambda)$.

quantity, radiant spectral flux $\Phi_{e,\lambda}(\lambda)$, by

$$\Phi_v = K_m \int_0^\infty \Phi_{e,\lambda}(\lambda) V(\lambda) d\lambda \quad (6)$$

[Note that since $V(\lambda)$ is zero outside the range 0.36–0.83 μm , the limits of the integral in Eq. (6) can be replaced with these values.] The coefficient K_m (= 683.002 lm/W) in Eq. (6) is a conversion factor that changes radiometric units of watts (represented by the integral) into photometric units of lumens (lm). The scotopic version of Eq. (6) has identical form but is distinguished by primes added to Φ_v , $V(\lambda)$, and K_m . The value of K'_m is 1700.06 lm/W (rods, which are more sensitive than cones, dominate vision under conditions of poor illumination). The curves $K(\lambda) = K_m V(\lambda)$ and $K'(\lambda) = K'_m V'(\lambda)$, called the *photopic* and *scotopic spectral luminous efficiencies* (Fig. 3), intersect at a wavelength of 0.555 μm (540×10^{12} Hz), for which $V(\lambda)$ is

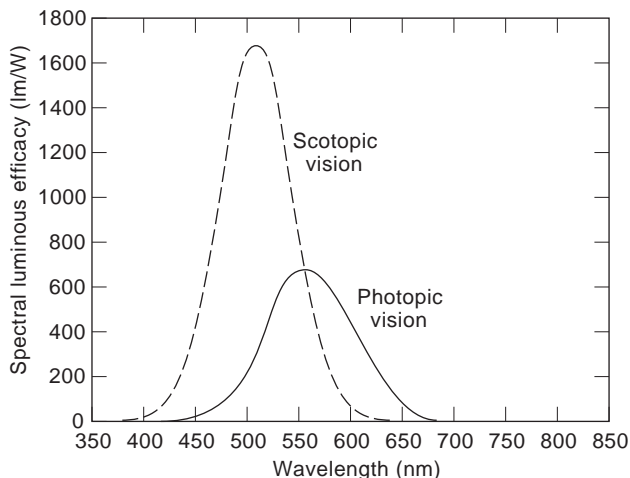


Figure 3. Spectral luminous efficacies: photopic $K(\lambda)$ and scotopic $K'(\lambda)$.

a maximum (unity). At this frequency, therefore, the luminous efficiency is 683 lm/W under all illumination conditions. At other frequencies the luminous efficiency is illumination-dependent. The wavelength of maximum visual response for scotopic vision is 0.507 μm .

Table 1 summarizes the radiometric and the corresponding photometric quantities.

2.2. Photon Flux

At optical and quasioptical frequencies, the interaction of electromagnetic fields with matter cannot always be explained in terms of smoothly varying field quantities, and recourse must be made to quantum theory. In this description electromagnetic fields are made up of discrete, quantized packets of energy called *photons*. The energy Q (joules) carried by each packet or quanta is related to the radiation's frequency by $Q = hf$ (J), where $h = 6.626 \times 10^{-34}$ (J · s), is Planck's constant. The probability that the energy carried by a photon will be transferred to a material particle (in a detector, for example) at some specific time and location is proportional to the irradiance (power density) at that time and location. In applications where individual photons may be detected, electromagnetic power is often referred to as a *photon flux*.

3. BLACKBODY RADIATION AND EMISSIVITY

A body that absorbs all electromagnetic radiation falling on it (converting the incident radiant energy to thermal energy) and that would therefore appear black at optical frequencies is called a *blackbody*. Such a body, in thermal equilibrium with its surroundings, must supply precisely as much energy back to, as it receives from, these surroundings. In the absence, of conduction and convection the energy transfer mechanism is limited to thermal radiation. The thermal radiant energy emitted by a body can never, therefore, be greater than that emitted by a blackbody of the same size, shape, and physical temperature. The degree of blackness of a body is quantified by its surface emissivity, defined as follows.

Emissivity, ϵ —ratio of spectral radiant exitance at the surface of a body to the spectral radiant exitance at the surface of a blackbody with the same physical temperature

The maximum value of emissivity, corresponding to that of a blackbody, is therefore unity and the minimum value, corresponding to a surface that reflects all radiant energy falling on it, is zero. A body with an emissivity that is independent of frequency, but less than unity, is called a *graybody*. Many natural materials have emissivities that are frequency-dependent, however, and this dependence, if measured radiometrically, can yield useful information about the material's composition and physical state.

The reflecting, transmitting, and absorbing properties of a material's surface, which can also be inferred from

radiometric measurements, are quantified as follows:

Reflectance, ρ —ratio of reflected to incident spectral radiant flux at a surface

Transmittance, τ —ratio of transmitted to incident spectral radiant flux at a surface

Absorptance, α —ratio of absorbed to incident spectral radiant flux at a surface

It is clear that

$$\rho + \tau + \alpha = 1 \tag{7}$$

The surface of a blackbody has an absorptance of unity and, therefore, a reflectance and transmittance of zero. More generally, for any opaque ($\tau = 0$) material, $\rho = 1 - \alpha$ and emissivity is numerically equal to absorptance (i.e., $\varepsilon = \alpha$).

A good model of a blackbody is the surface represented by a small hole drilled in a hollow cavity. Provided that the reflectance of the interior surface of the cavity is not too close to unity, then any radiant energy falling on to the hole is reflected a sufficient number of times inside the cavity for it to be fully absorbed before it can reemerge.

The spectral radiant excitation $M_f(f)$ of a blackbody (Fig. 4), is given by Planck's law [3]:

$$M_f(f) = \frac{2\pi h}{c^2} \frac{f^3}{\exp(hf/kT) - 1} \tag{8}$$

For optical frequencies, where it is traditional to express spectral quantities on a per meter of wavelength, rather than a per hertz of frequency, basis Eq. (8) can be written as

$$M_\lambda(\lambda) = \frac{2\pi hc^2}{\lambda^5} \frac{1}{\exp(hc/\lambda kT) - 1} \tag{9}$$

For $hf \ll kT$, which is appropriate for microwave radiometry at all commonly encountered temperatures, Eq. (8)

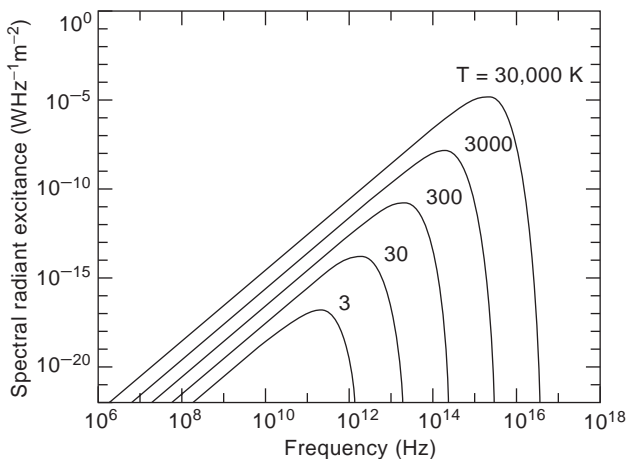


Figure 4. Planck's law for blackbody radiation.

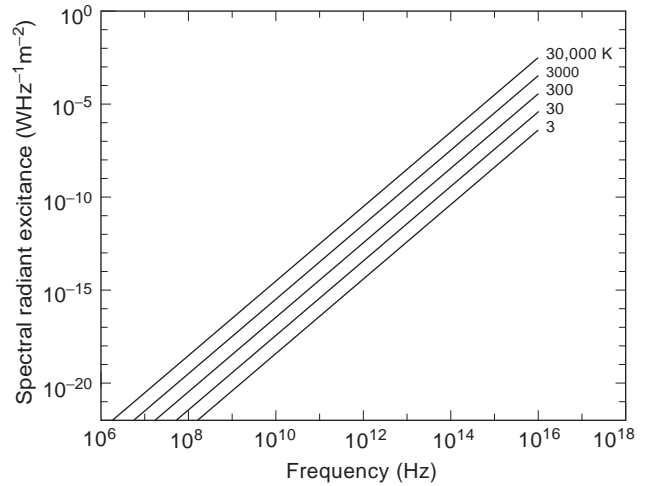


Figure 5. Rayleigh-Jeans approximation for blackbody radiation.

reduces to the Rayleigh-Jeans approximation (Fig. 5):

$$M_f(f) = \frac{2\pi}{c^2} kT f^2 \tag{10}$$

[The Rayleigh-Jeans version of Eq. (9) is $M_\lambda(\lambda) = 2\pi ckT/\lambda^4$.] The spectral radiant excitation of a body with emissivity < 1.0 is therefore given by

$$M_f(f) = \varepsilon(f) \frac{2\pi}{c^2} kT f^2 \tag{11}$$

3.1. Lambert's Law and Lambertian Radiators

Lambert's cosine law is that the radiant intensity from a blackbody surface is proportional to $\cos \psi$, where ψ is the angle between the direction of observation and the surface normal. Any surface (irrespective of its emissivity) that has this distribution of radiant intensity is said to be *Lambertian*. The radiance of such a surface (viz., radiant intensity per unit projected area) is independent of ψ . The spectral radiant excitation of an arbitrary surface is related to its spectral radiance by

$$M_f(f) = \int_0^{2\pi} \int_0^{\pi/2} L_f(\psi, f) \cos \psi \sin \psi \, d\psi \, d\gamma \tag{12}$$

which, for a Lambertian surface, reduces to

$$M_f(f) = L_f(f) \pi \tag{13}$$

The spectral radiance of a blackbody surface is therefore given by

$$L_f(f) = \frac{2h}{c^2} \frac{f^3}{\exp(hf/kT) - 1} \tag{14}$$

which for $kT \gg hf$ gives the Rayleigh–Jeans approximation

$$L_f(f) = \frac{2kT}{c^2} f^2 = \frac{2kT}{\lambda^2} \quad (15)$$

3.2. Radiometric Brightness and Antenna Temperatures

Consider a lossless antenna (i.e., one having an ohmic efficiency of 100%) with effective aperture area $A_e(\theta, \phi)$ receiving radiant energy from a surface S (Fig. 6). If a surface element of area dS (m²) lies at a distance R (m) from the antenna in the direction (θ, ϕ) , then the spectral radiant flux density arriving at the antenna due to this element is

$$dE_f = \frac{I_f(\theta, \phi)}{R^2} = \frac{L_f(\theta, \phi) dS \cos \psi}{R^2} \quad (16)$$

The power spectral density (or spectral radiant flux) received by the antenna is therefore

$$d\Phi_f = 0.5 A_e(\theta, \phi) dE_f = \frac{0.5 A_e(\theta, \phi) L_f(\theta, \phi) dS \cos \psi}{R^2} \quad (17)$$

(The factor of 0.5 accounts for the fact that the antenna will be polarization-matched to only half of the randomly polarized incident energy.) The quantity $dS (\cos \psi)/R^2$ in Eq. (17) can be identified as the solid angle $d\Omega$ subtended by the surface element at the antenna (Fig. 7). The power spectral density available at the antenna output terminals can therefore be expressed as either a surface, or a solid angle, integral:

$$\begin{aligned} \Phi_f &= 0.5 \int_S \int \frac{A_e(\theta, \phi) L_f(\theta, \phi) \cos \psi dS}{R^2} \\ &= 0.5 \int_{\Omega} \int A_e(\theta, \phi) L_f(\theta, \phi) d\Omega \end{aligned} \quad (18)$$

The power, or radiant flux, received within a band of frequencies f_{\min} to f_{\max} is then given by

$$\Phi = \int_{f_{\min}}^{f_{\max}} \Phi_f(f) df \quad (19)$$

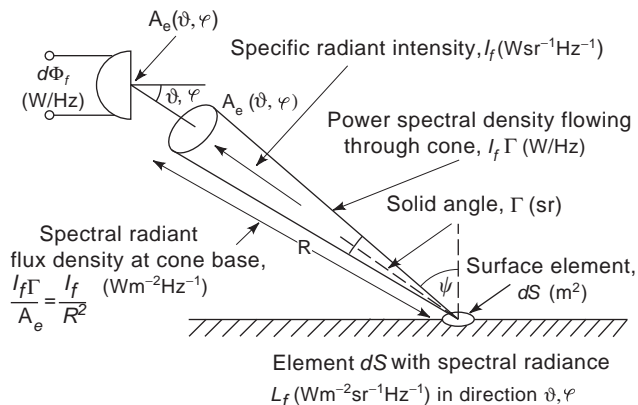


Figure 6. Spectral irradiance at radiometer antenna aperture due to radiating surface element dS .

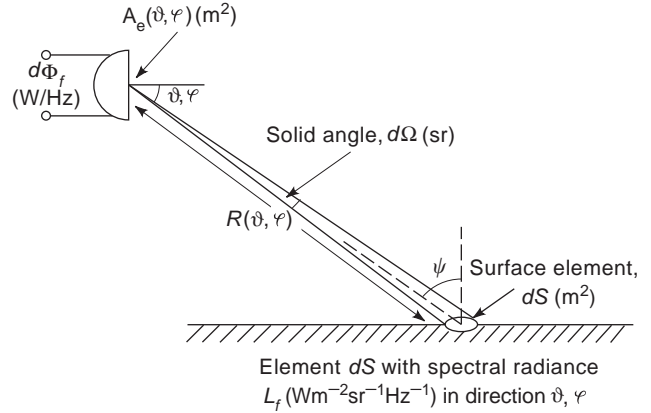


Figure 7. Solid angle subtended at radiometer antenna aperture by radiating surface element dS .

Since Eq. (18) is a power spectral density, an antenna aperture temperature T_a may be defined such that the noise power measured by a noiseless radiometer (i.e., one that has a noise figure of 0 dB), with a lossless antenna, is $kT_a B_N$ (where B_N is the radiometer noise bandwidth and k is Boltzmann's constant). For small B_N , such that $\Phi_f(f)$ can be considered white, $T_a = \Phi/kB_N = \Phi_f/k$ and

$$T_a = \frac{0.5}{k} \int_{\Omega} \int A_e(\theta, \phi) L_f(\theta, \phi) d\Omega \quad (20)$$

In a lossless antenna, effective area is related to antenna directivity by $A_e(\theta, \phi) = D(\theta, \phi) \lambda^2 / 4\pi$ [4], where $D(\theta, \phi)$ is the antenna directivity pattern. Equation (20) may therefore be written as

$$T_a = \frac{0.5 \lambda^2}{k 4\pi} \int_{\Omega} \int D(\theta, \phi) L_f(\theta, \phi) d\Omega \quad (21)$$

The quantity $(0.5 \lambda^2/k) L_f(\theta, \phi)$ is usually referred to as a *radiometric brightness temperature* $T_B(\theta, \phi)$, allowing Eq. (21) to be written as

$$T_a = \frac{1}{4\pi} \int_{\Omega} \int D(\theta, \phi) T_B(\theta, \phi) d\Omega \quad (22)$$

(In microwave radiometry the term *brightness* is often used as a synonym for spectral radiance.) The radiometric brightness temperature of a body is related to the body's physical temperature T by the body's emissivity:

$$T_B(\theta, \phi) = \varepsilon(\theta, \phi) T(\theta, \phi) \quad (23)$$

[The emissivity's dependence on ψ is not shown explicitly in Eq. (23) but is implied in its θ, ϕ dependence. The frequency dependence is suppressed only for clarity.] The first step in conventional radiometer data analysis usually requires that the radiometric brightness temperature of a particular region be estimated from a measurement of an antenna noise temperature T_A , defined by

$$T_A = \frac{\Phi_R}{kB_N} \quad (24)$$

where Φ_R is the power supplied to the radiometer by the antenna. If the antenna has nonzero ohmic loss, the measured antenna noise temperature will comprise an attenuated aperture temperature (the aperture temperature is the temperature measured by a lossless antenna) and a thermal contribution from the physical antenna structure itself. For an antenna with ohmic (or radiation) efficiency, η_Ω (expressed as a per unit, not percent, quantity), and physical structure temperature T_s the measured antenna noise temperature will be

$$T_A = \eta_\Omega T_a + (1 - \eta_\Omega) T_s \quad (25)$$

If the antenna loss is sufficiently small, then $T_a \cong T_A$. Equation (22) shows, however, that the antenna aperture temperature is a weighted average of the observed brightness temperature in which the weighting function is the antenna directivity pattern. If the antenna has a radiation pattern with low sidelobes and a beamwidth that is narrow with respect to the angular rate of change of brightness temperature, then T_a gives the required brightness temperature, in the direction of the mainlobe, directly. For an imaging radiometer (which scans a beam over some solid angle, e.g., to form an image), with a beam that is not sufficiently narrow, deconvolution of the antenna pattern from the resulting image may be necessary.

Since antenna directivity and gain are related [4] by $G(\theta, \phi) = \eta_\Omega D(\theta, \phi)$, then Eqs. (22) and (25) can be combined and written as

$$T_A = \frac{1}{4\pi} \int_{4\pi} G(\theta, \phi) T_B(\theta, \phi) d\Omega + (1 - \eta_\Omega) T_s \quad (26)$$

In the absence of significant atmospheric effects (losses and scattering), Eq. (26) shows that an adequate knowledge of antenna ohmic efficiency and antenna gain pattern will allow the brightness temperature of a surface (with a spatial resolution determined by the antenna beamwidth) to be found from a measurement of antenna noise temperature. (The noise figure of the radiometer must be considered, of course, when making this measurement [5].)

3.3. Atmospheric Loss and Scattering

If atmospheric effects cannot be neglected, then the brightness temperature inferred from Eq. (26) must be interpreted as an apparent brightness temperature since it will comprise a contribution from the target surface plus a contribution from the thermal emission of the atmosphere itself. Furthermore, the thermal radiation from each source (i.e., each surface element of the target and each volume element of the atmosphere) will be attenuated by the loss associated with the intervening atmosphere. Since atmospheric thermal emission is essentially isotropic, half of the thermal energy from each element is radiated upward (called *upwelling radiation*) and half is radiated downward (called *downwelling radiation*). For a downward-pointing radiometer (such as might be used in planetary surface remote sensing applications), downwelling radiation may be reflected by the ground back into the

antenna's mainlobe. The contribution of this ground-scattered radiation will depend on the ground reflectance and the integrated specific attenuation along the ground-reflected path to the radiometer. An upward-pointing radiometer (such as might be used in terrestrial atmospheric remote sensing applications) observes downwelling radiation from the atmosphere directly. The contribution from ground-scattered downwelling radiation, and ground thermal emission, will now be coupled into the antenna through its downward-pointing side- or backlobes. The significance of this radiation will depend on the gain of these lower hemisphere lobes and the brightness temperature of the region within the antenna's mainlobe. (If a microwave radiometer with high antenna gain is pointed at high elevation angle into a clear sky, well away from any discrete sources of radiation, then the brightness temperature observed by its mainlobe may be as low as a few degrees kelvin. Radiation emitted by, or reflected from, the ground may, under these conditions, be a very significant source of measurement error.)

The preceding description assumes that the atmosphere is an absorbing, but nonscattering, medium. For an atmosphere filled with scattering particles, or more general scattering inhomogeneities, this simplified description is inadequate. (The operating wavelength, and the physical size and composition of inhomogeneities, will determine whether they act as significant scatterers or not [6].) In this case more rigorous theories must be used to account for, and interpret, observed radiometric measurements [7].

4. APPLICATIONS

The most important application of radiometry lies in remote sensing of the earth's surface and its atmosphere [8]. Polar ice mapping, for example, is possible using passive microwave radiometers located on Earth-orbiting platforms. Microwave radiometry is especially useful for ice mapping because the contrast in emissivity between ice and water is particularly large at microwave frequencies. Furthermore, since passive microwave radiometry depends on self-emitted thermal radiation, and since Earth's atmosphere is essentially transparent at the microwave frequencies used, then data collection does not rely on solar illumination or the absence of cloud cover. (A requirement for solar illumination is particularly problematic in the polar regions, of course, due to the absence of the sun in winter.) Knowledge of annual, and longer-term, changes in the extent of the polar ice shelves is important in the field of climatology generally and to more recent concerns about possible climate change in particular.

Other surface materials (e.g., water/rock/sand) can be discriminated using microwave radiometers, and soil moisture mapping is also possible [9]. Radiometer measurements applied in this area are of obvious interest in climatology, agriculture, and environmental science. Processes of desertification, like changes in the polar ice cover, are of concern in the context of global warming.

A rather different application of microwave radiometry concerns the development of the worldwide satellite

communications network. Since a material's thermal emission and absorption are directly related, a brightness temperature measured at a given frequency can be used to infer the attenuation that an electromagnetic wave of that frequency would experience when propagating along the path observed. Ground-based, upward-pointing microwave radiometers can therefore be used to estimate the expected statistics of Earth-space signal attenuation for use in the design of microwave satellite communication systems [10]. The dominant mechanism resulting in large attenuation is the presence of precipitation along the path. Measurements of this type can, therefore, also be used in conjunction with appropriate signal attenuation/rain rate models to estimate rainfall intensity statistics for hydrological applications. (In more recent years, however, the use of meteorological radar has probably become the preferred rainfall remote sensing tool.)

Active microwave radiometry can, like its passive variant, operate independently of solar illumination and is immune to cloud cover (and, depending on frequency, other meteorological phenomena that may make the atmosphere opaque). Downward-pointing scatterometers, for example, can be used to map surface wind velocities by measuring the effective reflectance of the ocean surface. The technique used in this application depends on the fact that the received signal for a nadir pointing, monostatic scatterometer decreases as the wind speed increases and the water surface becomes rough. This is due to the tendency of the reflected energy to be scattered in many directions by the rough surface, rather than reflected, specularly, back along the illuminating path. The apparent reflectance of the ocean surface can therefore be used as a measure of wind-speed. Other reflectance measurements, using forward- and side-looking radiometer beams, allow wind velocity to be inferred since the reflecting facets of the waves have a preferred orientation that depends on wind direction.

Downward-pointing, millimeter-wave, spectroradiometer observations of brightness temperature around the absorption/emission lines of a homogeneously mixed atmospheric constituent can be used to estimate the vertical temperature profile of the atmosphere. Oxygen, which has a cluster of closely spaced resonance lines around 60 GHz, is often used for this purpose [11]. The basic principle of such temperature measurements is as follows. The brightness temperature observed at any given frequency represents a weighted mean taken over the observed path. The weighting factor at a particular altitude depends on the density of the oxygen at that altitude and on the attenuation of the intervening atmosphere. Thus at high altitudes (near the radiometer) the contribution to total brightness will be small because the density of the gas is low. At low altitudes (far from the radiometer) the contribution to total brightness will also be low because the intervening atmosphere will greatly attenuate this contribution. The observed brightness temperature will therefore be dominated by a region of the atmosphere at some intermediate height. If measurements are made across a band of frequencies coincident with the skirt of an atmospheric constituent's absorption band where atmospheric attenuation changes rapidly with frequency, then the height from which the dominant contribution arises also

changes with frequency. In this way a brightness temperature-frequency profile can be transformed to a brightness temperature versus altitude profile.

In a related area, microwave radiometry has been applied in the estimation, using zenith pointing radiometers, of integrated atmospheric water content (both liquid and gaseous phases). The large specific, and latent, heats of water mean that mapping of this quantity is important in understanding the global energy balance. If spectroradiometer measurements are made across a significant band of frequencies close to the water vapor absorption line at 22 GHz, then the water vapor's density profile can be inferred. The technique here is essentially the same as that described previously in the context of temperature profiling using the 60 GHz oxygen absorption line(s). The temperature profile is first estimated (using the oxygen line, e.g.), and the brightness temperature-frequency profile in the skirt region of the water vapor's absorption line is transformed to a brightness temperature-altitude profile. The water vapor's density at a given altitude is then inferred from the brightness at that altitude. Similar measurement can be used to find vertical profiles of many other atmospheric constituents with applications to environmental monitoring and pollution control.

Infrared radiometry (especially at 4 and 11 μm) can be used for ocean surface temperature mapping with obvious applications to meteorology and climatology. In practice, both these frequencies, and at least one other intermediate frequency, are usually required in order to correct for errors introduced by atmospheric water vapor and scattering by atmospheric aerosols. Multifrequency measurements can yield data with accuracies of 1 K.

Chlorophyll, the dominant pigmentation in most species of plants, has absorption lines close to 440 and 650 nm corresponding to the blue and red parts of the visible spectrum, thus giving vegetation its predominantly green color. (In fact, there are two distinct varieties of chlorophyll, blue-green and yellow-green, which both have absorption lines located about 10 nm either side of these frequencies [11].) In the near-infrared region, however, absorption by chlorophyll is very low and reflectance correspondingly high. Infrared and visible reflectance measurements can, together, yield information about the photosynthetic capacity of selected areas of the biosphere [12]. The presence of pigmentation other than chlorophyll can also be detected by spectroradiometric measurements and used to discriminate between different plant species. Furthermore, water absorption lines at 1.45 and 1.95 μm allow the water content of plant material to be estimated from infrared measurements. High-resolution, multiband, visible, and infrared radiance measurements can thus be used to assess the quantity, variety, health, and photosynthetic vigor of much of Earth's surface vegetation.

Visible multiband measurements of radiance can also be used to gather information about the phytoplankton of the oceans' surface layers. A particular problem associated with these measurements is that upwelling radiation originating in the intervening atmosphere must generally be accounted for. One solution relies on the fact that the oceans do not contribute to upwelling radiance in the red part of the spectrum. Measurements in the red region of

the spectrum over the oceans can therefore be used to estimate atmospheric upwelling radiance, which in turn can be used to infer atmospheric contributions at other wavelengths.

BIBLIOGRAPHY

1. C. J. Bartleson and F. Grum, eds., Academic Press, *Visual Measurements*, Orlando, London, 1984.
2. International Commission on Illumination, *The Basis of Physical Photometry*, Publication CIE 18.2 (TC-1.2), Commission Internationale de L'Eclairage, Paris, 1983.
3. F. T. Ulaby, R. K. Moore, and A. K. Fung, *Microwave Remote Sensing—Fundamentals and Radiometry*, Addison-Wesley, Reading, MA, 1981.
4. W. L. Stutzman and G. A. Thiele, *Antenna Theory and Design*, Wiley, New York, 1998.
5. N. Skou, *Microwave Radiometer Systems: Design and Analysis*, Artech House, Norwood, MA, 1989.
6. L. P. Bayvel and A. R. Jones, *Electromagnetic Scattering and Its Applications*, Applied Science Publishers, London, 1981.
7. G. Brussaard and P. A. Watson, *Atmospheric Modelling and Millimetre Wave Propagation*, Chapman & Hall, London, 1995.
8. C. Elachi, *Introduction to the Physics and Techniques of Remote Sensing*, Wiley, New York, 1987.
9. T. J. Jackson, Passive microwave remote sensing system for soil moisture: Some supporting research, *IEEE Trans. Geosci. Remote Sens.* **27**:225–235 (1989).
10. J. Thirlwell and R. G. Howell, OTS and radiometric slant-path measurements at Martlesham Heath (UK), *Annales des Telecommunications (France)* **36**:15–23 (1981).
11. E. Schanda, *Physical Fundamentals of Remote Sensing*, Springer-Verlag, New York, 1986.
12. P. J. Sellers, Canopy reflectance, photosynthesis and transpiration, *Int. J. Remote Sens.* **6**:1335–1372 (1985).

RADIOTELEMETRY

HAIPING TSOU
KAR-MING CHEUNG
California Institute of
Technology

Radiotelemetry, by definition, is the science and technology of automatically measuring and transmitting data by radio from remote sources, as from space vehicles, to receiving stations for recording and analysis. It involves preparing of data generated at remote sources, transmitting data through radio channels, and processing data at the receiving stations. Behind these three tasks, how to convey the information in a reliable and timely manner through a communication link is the most fundamental problem in this field.

There are many ways to define a communication link, depending on where the link starts and ends. Customarily,

a communication link is the transmission path through which information-bearing waveform flows from one point to another. A generic link includes the modulator, the transmitter, the channel, the receiver, and the demodulator. Another popular view of a link is to include error correction coding and encoding as part of the link because, as we see in a later discussion, link performance is a function of both modulation and coding. Yet, for a communication system that uses data compression, one might want to take an end-to-end view and include the error propagative effect of data compression in link design and analysis, because the error propagative property affects the integrity and throughput of the link. In the following sections, we briefly discuss some important elements of a communication link: data compression, forward error correction coding, modulation, demodulation, and synchronization. However, before moving on to these individual topics, we first discuss a higher level consideration of the overall link reliability, namely, the link budget analysis.

The main objective of link budget analysis is to maximize the data return for a communication link subject to (1) the available communication resources and (2) the required data quality. Power and bandwidth are the two primary resources in communication, and data quality is usually expressed in terms of the frequency of errors in the received data, that is, the bit error rate (BER). To design a communication system, the first step is to understand what the available resources are. Whether a system is power-limited (e.g., deep-space communications) or bandwidth-limited (e.g., near-Earth satellite communications) determines the available options for modulation and error correction coding schemes.

1. COMMUNICATION LINK BUDGET ANALYSIS

The link budget is a balance sheet of the gains and losses in decibels (dB) of various parameters in the communication path. Many of these parameters are statistical or time-varying or both. The required BER is a direct function of the bit signal-to-noise ratio (SNR), denoted as E_b/N_0 , which in turn is a function of the modulation and error-correction coding used. Because of the statistical nature (uncertainty) of these parameters, a safety margin M is built in to guarantee the transmission data quality at any given time.

To put link budget analysis into perspective, more parameters need to be defined and they are given as follows. To begin with, the total received signal-power-to-noise-power-spectral-density ratio, P_T/N_0 , which encompasses all the power gains and losses in the communication path, is conveniently expressed as [1]

$$\frac{P_T}{N_0} = \frac{\text{EIRP}(G/T)}{kL_sL_0} \quad (1)$$

where EIRP is the effective isotropic radiated power of the spacecraft, G/T is the receiver sensitivity of the ground system, k is Boltzmann's constant, $L_s = (4\pi d/\lambda)^2$ is the space loss where d is the distance between the transmitter and receiver, λ is the wavelength, and L_0 denotes all other

losses and degradation factors not specifically addressed in this equation. Note that all gains and losses are statistical quantities. Then, let R_s be the symbol rate and R_c be the code rate expressed as the ratio of the number of information bits in a code word to the number of coded bits in a codeword. The data rate or bit rate, denoted as R_b , is related to the symbol and code rates via $R_b = R_s R_c$. The bit SNR is written as

$$\frac{E_b}{N_0} = \frac{P_T/N_0}{R_s R_c} \quad (2)$$

Finally, let $(E_b/N_0)_{\text{req}}$ be the required E_b/N_0 to guarantee a certain BER. To ensure a reliable link, the constraining dependency is expressed in dB as follows:

$$\left(\frac{E_b}{N_0}\right)_{\text{req}} + M \leq \frac{P_T}{N_0} - R_s - R_c \quad (3)$$

The essence of link-budget analysis is to determine how much link margin M is required and this, in turn, is determined by how well the statistics of various link parameters are known. If M is too small, one might get a large data return but the data might have frequent errors. If M is too large, one might get continuous clean data but the throughput might be low. The analyst needs to make the right tradeoff on quantity versus quality, depending on the requirements and objectives of the service the link supports. Also, in an operational scenario, one usually starts out with a large M (a conservative approach) for a newly deployed system, and gradually reduces M (an aggressive approach) as more experience and confidence accumulates.

2. DATA COMPRESSION

In the midst of the Information Age, when new data—texts, images, sensor data, and many other forms of knowledge—are generated at a lightning pace, how these data are efficiently communicated and/or archived becomes increasingly important. Data obtained directly from sources usually contains much redundancy, and data compression is the process of applying “pressure” to remove the redundancy. The processes of compression and decompression add complexity to the overall system. The main issue in the use of data compression is the tradeoff between the efficiency of data handling and the complexity of signal processing to retrieve the information.

In the English language, letters such as “a” and “e” are used more frequently than “y” and “z,” and words like “and” and “the” are much more often than “data” and “compression”. For images and sensor data, the differences between adjacent samples are small rather than large. This nonuniform frequency distribution of data associated with most information sources allows one to assign shorter bit patterns to represent the more frequent elements from the source and longer bit patterns to represent the less frequent elements from the source. This is the simplest view of data compression.

Data compression is broadly classified in two categories: lossless and lossy compression. Lossless compression

denotes compression in which the decompressed or reconstructed data exactly match the original. Lossy compression represents compression methods where some degradation of quality is tolerable if a more compact but approximate representation is achieved. Next, we give brief surveys on text compression (lossless) and image compression (lossless and lossy). However, the compression of audio, video, and facsimile is beyond the scope of this article. Interested readers are encouraged to consult specialized books and technical journals in these areas.

Textual data is probably the first area where people applied compression. In 1832 Samuel Morse developed a code using dots, dashes, and spaces to represent letters, numbers, and punctuation for telegraph transmission. Each dot or dash is delimited by a space. A dot and a space take the same time. A dash is three times longer. Morse assigned fewer time units to more commonly occurring letters (e.g., “e” is a dot), and more time units to ones (e.g., “q” is dash–dash–dot–dash) that rarely occur. Today, most popular text compression schemes are different variations of the Lempel–Ziv (LZ) scheme developed in 1977 [2] and 1978 [3]. LZ schemes use a dictionary approach. Dictionary coding operates by replacing groups of consecutive characters with indices in some dictionary. It exploits the frequent reoccurrence of certain exact patterns that are very typical of textual data. Other than compressing text, LZ schemes are reasonably good at compressing images and other sources. LZ schemes are generally considered universal compression algorithms. The UNIX command “compress” and the modem standard V42.bis are examples of applications using LZ schemes.

Image compression and other waveform compression is lossless or lossy. For scientific and medical applications that demand further processing and analysis, one might prefer lossless compression to ensure data accuracy. In other applications, such as image database, electronic photography, and desktop publishing, where transmission and storage bandwidths are limited, lossy compression is usually employed to reduce the data size at the expense of image quality.

Lossless image compression consists of two steps: modeling and coding. A predictive model predicts a pixel value based on a previously transmitted one, and compares it with the current value. The error value is coded instead of the original pixel value. On the receiver side, because the errors and the predictive scheme are known, the receiver recovers the value of the original pixel. An example of lossless image compression is the Rice code used in space and satellite communications.

Lossy image compression involves an irreversible quantization step that causes distortion between the original and the reconstructed image. Popular techniques in lossy image compression include differential pulse-code modulation (DPCM), transform coding, subband coding, vector quantization, and some hybrid techniques. The Joint Photographic Expert Group (JPEG) established an international standard on still image compression that uses the discrete cosine transform along with scalar quantization and entropy coding. Currently, JPEG encoder and decoder chips are available from many semiconductor manufacturers.

3. FORWARD ERROR CORRECTION CODING

In 1948, the landmark paper “A mathematical theory of communication” [4] by Claude Shannon provided a mathematical framework for analyzing communication, the process of sending information from one point to another through a noisy media, by using the concept of entropy. He provided an existence proof showing that communication systems can be made arbitrarily reliable as long as the fraction of redundant signals in the signal stream exceeds a certain value, which is a function of the signal and noise statistics. The process of introducing redundancy in the signal stream to combat noise, so that retransmission is not needed, is called forward error correction coding. Shannon did not show how this could be done in his famous theorem. Later on, much research effort has yielded a variety of interesting theoretical and practical results in this area.

Because redundant signals are deliberately introduced in the signal stream as error correction coding, bandwidth expansion is expected. Encoding and decoding processes inevitably also add complexity to the overall system. However, it can be shown that, with a proper choice of coding scheme, the resulting E_b/N_0 can be considerably lower compared with an uncoded system. Thus error-correction coding allows one to trade power for bandwidth and complexity. In this article, the application of two popular error correction coding schemes, block codes and convolutional codes are explained, without providing the detailed performance analysis of these codes. Other more advanced coding schemes, like trellis codes and turbo codes, are not covered here. Interested readers are encouraged to consult specialized books and technical journals in this field.

In block coding, a block of k bits is encoded into a block of n bits, where $n > k$. There are 2^k codewords in a code space of 2^n . The code rate R_c , which is the ratio k/n , is a measure of the amount of added redundancy. The minimum distance d_{\min} , which is the Hamming distance between two closest code words, is a measure of the error correction capability of the code. It can be shown that $d_{\min} \leq n - k + 1$ (Singleton bound). For bounded-distance decoding, the number of errors t that the code can correct is related to d_{\min} by

$$2t + 1 \leq d_{\min} \quad (4)$$

In convolutional coding, sequences of k information bits long are encoded as continuous sequences using a kK -stage shift register, where K is called the constraint length. n output sequences are produced, each of which is generated by a selected set of combinations of these K input sequences. The n output sequences are multiplexed into a single-bit stream for transmission. Similar to a block code, the ratio k/n is a measure of the redundancy of the convolutional code. The minimum distance d_{free} between two closest code sequences, is a measure of the error correction capability of the code.

The most popular block code used today is the class of Reed–Solomon (RS) codes. RS codes are maximum-distance-separable codes that achieve maximum error

correction capability in the bounded-distance decoding sense. Well-known encoding and decoding algorithms exist that are reliable in software and hardware. RS codes are flexible. Long, powerful RS codes exist for demanding applications, and short RS codes for simple applications. Deep-space communications use the (255,223) RS code as the outer code of the concatenated coding system. This code is block-interleaved and is used in conjunction with an inner convolutional code to provide reliable communications between the spacecraft and the ground stations. The concatenated coding system is designed to combat the additive white Gaussian noise of the deep-space communication links. Simpler RS codes are used in compact disks (CD), a mass-marketed consumer product. The coding system used, called the cross-interleaved Reed–Solomon code (CIRC), is composed of two RS codes with (n,k) values (32,28) and (28,24). In between the two encoders are sets of delay lines which scramble the datastream. The CIRC coding system is designed to correct the burstlike errors, typical of a CD channel.

The most popular decoding scheme for convolutional codes is the Viterbi algorithm. The complexity of Viterbi decoding grows exponentially with the constraint length of the code, which is the number of memory elements in the encoder shift register. As mentioned earlier, convolutional codes are used in deep space communications. In the past, short constraint-length codes (7 or 9) are used because of the limitations in hardware technologies. Today, long constraint-length Viterbi decoders (up to 15) are designed and built. Convolutional codes are also popular in satellite communications and wireless communications. Presently, only short constraint-length convolutional codes are used in these areas.

4. INTERACTION BETWEEN DATA COMPRESSION AND ERROR CONTROL IN A COMMUNICATION SYSTEM

This section addresses the interaction between data compression and error control (containment/detection/correction) processes, two indispensable building blocks in modern digital communication systems. Data compression conserves transmission and storage bandwidth by removing redundancy in the source data. Error correction introduces controlled redundancy to the data to eliminate channel errors. A combination of both techniques ensures efficient and reliable transmission of information from one point to another. The famous separation principle indicates that data compression and error control processes can be completely separated, that is, the task of transmitting the output of a source through a channel can be separated without loss into the task of forming a binary representation of the source output and the task of sending a binary sequence through the channel. This is not quite true in practice, however. In evaluating an end-to-end communication system, we have to consider effects, like instrument failures, adverse weather conditions, synchronization loss, and other unpredictable phenomena in the communication system and the channel. The error control process cannot handle all possible kinds of errors. Thus the effect of error propagation should be considered

when evaluating a data compression scheme in a communication system.

There are two issues to be dealt with: how to prevent errors from occurring and, if errors occur, how to contain the errors. The former issue can be dealt with easily (at least in the conceptual sense) by using higher transmission power or more powerful error correction coding techniques on the channel and better fault-tolerance techniques on various system components. The second issue of how to contain errors is more intricate and has commonly been overlooked. There are mainly two approaches (or a combination of both) to deal with the problem. The first approach is to add extra redundancy to the compressed data to detect and confine errors. Some simple ways are adding a delimiter pattern at regular intervals and forcing fixed block-size transmission by appending filling 0s, and so on. These techniques reduce compression performance. The second approach is to choose data compression schemes that are less susceptible to error propagation. These schemes usually transmit the compressed data in fixed block size or inherently have delimiter patterns in their compressed data streams. We illustrate the interaction between data compression and error correction coding with an example in a later section.

5. MODULATION AND DEMODULATION

5.1. Modulation

Modulation is the process of transforming signals into waveforms suitable for transmission through a certain type of medium or channel. For example, when transmitting electronic signals through free space with an antenna that converts electronic signals into electromagnetic (EM) waves, the physical dimensions of the antenna aperture are at least of the same order of the wavelength of the EM wave. Therefore, a baseband signal has to modulate a sinusoidal signal at radiofrequency (RF), called the carrier, before transmitting it by antennas of reasonable size.

The typical modulation procedure for digital signal transmission starts with a baseband pulse-code modulation (PCM), which converts the analog signal into a binary datastream. Depending on the subsequent RF modulation schemes, this binary datastream is fed into different devices. For example, fixed-length blocks of the binary data are used to determine the instantaneous frequencies of the carrier for a frequency-shift-keyed (FSK) system. On the other hand, the binary data drive a pulse generator whose output modulates the subcarrier (if used) and the RF carrier in a typical phase-shift-keyed (PSK) system. There are several different binary data formats [5]. For example, non-return-to-zero (NRZ) and biphase (also known as the Manchester code) are the ones more commonly used. In some applications, pulseshapes other than the square pulse are selected to represent a binary digit in the datastream. The choice of a particular data format and pulseshape is determined by several factors, for example, considerations of bandwidth efficiency, inherent synchronization features, and the noise immunity of each data format.

PSK modulation has been widely adopted for deep-space communications mainly because it is a very efficient

type of modulation in bit error performance and the resulting signal has a constant envelope that allows the power amplifier to achieve the maximum efficiency by operating at the saturation point. In general, a communication system using the PSK modulation is designed to have a multiple phase-shift-keyed (MPSK) signal of which the number of phasor states, denoted by M , is any power of 2. The increased BER with M for MPSK signals, however, prevents its use when M is large. Furthermore, because of the ease of being decomposed into two orthogonal channels for further signal processing, the MPSK modulated signals commonly used for radiotelemetry are limited to the cases where $M = 4$ or lower, namely, the binary phase shift keying (BPSK), the quadrature phase shift keying (QPSK) or its variations, such as offset QPSK, unbalanced QPSK, and pulseshaped QPSK. For some applications, the quadrature amplitude shift keying (QAM) modulation is used to allow multilevel signals transmitted on either one or both of the mutually orthogonal channels.

It is possible to include subcarrier(s) for BPSK modulation. The purpose of using subcarrier(s) is to separate data sidebands of different signals and the carrier so that they do not interfere with each other. Whether or not to use subcarrier(s) depends on the mission design. For example, a subcarrier is preferred when a residual carrier component is preserved for spacecraft navigation or certain radio science experiments. On the contrary, it may not be a good idea to keep a subcarrier when transmission power is weak or the bandwidth efficiency becomes a major concern. Two types of subcarriers, the sine wave and the square wave, are commonly used. The sine-wave subcarrier along with the phase-modulated carrier produces fast-decaying data sidebands and, therefore, is recommended for near-Earth space missions where the interference caused by the power spillover to the adjacent frequency bands is the major concern [6]. The same recommendation also suggests using the square-wave subcarrier for deep-space missions because of the ease of generating a square wave onboard spacecraft and the relatively less stringent bandwidth allocation for this type of mission.

A phase-modulated (PM) telemetry signal is represented mathematically by

$$S_T(t) = \sqrt{2P_T} \sin\left(\omega_c t + \sum_{i=1}^N m_i S_i(t)\right) \quad (5)$$

where P_T is the total power of the received signal, ω_c is the carrier frequency, m_i is the modulation index associated with the i th data source, and

$$S_i(t) = \begin{cases} \sum_{k=-\infty}^{\infty} d_{k,i} P_i(t - kT), \\ \text{for PCM/PM (without subcarrier)} \\ \left[\sum_{k=-\infty}^{\infty} d_{k,i} P_i(t - kT) \right] \sin(\omega_{sc} t), \\ \text{for PCM/PSK/PM with a sine - wave subcarrier} \\ \left[\sum_{k=-\infty}^{\infty} d_{k,i} P_i(t - kT) \right] \text{sgn}[\sin(\omega_{sc} t)], \\ \text{for PCM/PSK/PM with a square - wave subcarrier} \end{cases} \quad (6)$$

represents either a normalized baseband waveform (with $d_{k,i} = \pm 1$) or a normalized BPSK modulated subcarrier waveform (at the frequency ω_{sc_i}). $P_i(t)$ is the pulse function of unit power and T is the reciprocal of the symbol rate. Note that, when more than one data sources are included [that is, $N > 1$ in Eq. (5)], only one data source output is allowed to directly modulate the carrier, denoted by its processing order as PCM/PM, and the rest must be put on subcarrier(s) before modulating the carrier, similarly denoted as PCM/PSK/PM in Eq. (6). An exception of this single PCM/PM rule is the code division multiplexing, in which multiple data sources are put directly on the carrier and remain distinguishable because of the unique code sequence (for example, pseudorandom codes or Walsh-Hadamard codes) used by each of them.

Typically, a deep-space downlink signal (i.e., a signal sent from spacecraft to Earth) consists of two or more data sources of which, besides the telemetry signal, a ranging signal is included for spacecraft navigational purpose [7]. For example, a mathematical expression of a downlink signal consisting of a sinusoidal ranging signal at the frequency ω_1 and a binary telemetry signal of NRZ format, $d(t)$, which is modulated onto a square-wave subcarrier, is given by

$$\begin{aligned}
 S_T(t) &= \sqrt{2P_T} \sin\{\omega_c t + m_1 \sin(\omega_1 t) \\
 &\quad + m_2 d(t) \operatorname{sgn}[\sin(\omega_{sc} t + \theta_{sc})] + \theta_c\} \\
 &= \sqrt{2P_T} \left\{ \begin{aligned}
 &J_0(m_1) \cos(m_2) \sin(\omega_c t + \theta_c) \\
 &+ d(t) J_0(m_1) \sin(m_2) \operatorname{sgn}[\sin(\omega_{sc} t + \theta_{sc})] \cos(\omega_c t + \omega_c) \\
 &+ \cos(m_2) \left[\sum_{n=1}^{\infty} 2J_{2n}(m_1) \cos(2n\omega_1 t) \right] \sin(\omega_c t + \theta_c) \\
 &+ \cos(m_2) \left\{ \sum_{n=0}^{\infty} 2J_{2n+1}(m_1) \sin[(2n+1)\omega_1 t] \right\} \cos(\omega_c t + \theta_c) \\
 &+ d(t) \sin(m_2) \left[\sum_{n=1}^{\infty} 2J_{2n}(m_1) \cos(2n\omega_1 t) \right] \\
 &\operatorname{sgn}[\sin(\omega_{sc} t + \theta_{sc})] \cos(\omega_c t + \theta_c) \\
 &- d(t) \sin(m_2) \left\{ \sum_{n=0}^{\infty} 2J_{2n+1}(m_1) \sin[(2n+1)\omega_1 t] \right\} \\
 &\operatorname{sgn}[\sin(\omega_{sc} t + \theta_{sc})] \sin(\omega_c t + \theta_c)
 \end{aligned} \right\} \quad (7)
 \end{aligned}$$

where $J_n(\cdot)$ is the n th-order Bessel function and θ_c and θ_{sc} are random carrier and subcarrier phases, respectively, each uniformly distributed over 0 to 2π . The first term in this expression is the residual carrier component, which is fully suppressed if the data modulation index m_2 equals $\pi/2$. The second term is the desired data-bearing component containing the telemetry information that needs to be demodulated. The third and the fourth terms contain

the ranging information to be extracted separately, and the rest are from inter-modulation of telemetry and ranging signals. Typically, on one hand, the ranging modulation index m_1 chosen is small (around $\frac{1}{2}$ or smaller) so that the power consumption by this ranging signal is relatively small. On the other hand, the data modulation index selected is large (close to its upper limit $\pi/2$) to ensure that only sufficient power goes to the residual carrier component and the rest of power is allocated solely for telemetry data transmission. The strategy of optimizing modulation indices for efficient power allocation is discussed in Ref. 8.

A QPSK phase-modulated telemetry signal is usually treated as a combination of two orthogonal BPSK signals. Mathematically, a general QPSK (or, more specifically, an unbalanced QPSK) signal takes the form

$$\begin{aligned}
 S_T(t) &= \sqrt{\alpha P_T} \sin\left(\omega_c t + \sum_{i=1}^M m_{c,i} S_{c,i}(t)\right) \\
 &\quad + \sqrt{(1-\alpha)P_T} \cos\left(\omega_c t + \sum_{i=1}^N m_{s,i} S_{s,i}(t)\right) \quad (8)
 \end{aligned}$$

where α is the percentage of transmitted power in one of the two channels. When only one binary signal of NRZ format is transmitted on each channel, that is, $M = N = 1$, with the modulation indices $m_{s,1} = m_{c,1} = \pi/2$, the QPSK signal is rewritten as

$$\begin{aligned}
 S_T(t) &= \sqrt{\alpha P_T} S_{c,i}(t) \cos(\omega_c t) \\
 &\quad - \sqrt{(1-\alpha)P_T} S_{s,i}(t) \sin(\omega_c t) \quad (9)
 \end{aligned}$$

a combination of two BPSK signals on two orthogonal basis functions. As long as the orthogonality is maintained, these two BPSK signals do not interfere with each other and the bandwidth efficiency, measured as how many bits of information transmitted over a unit bandwidth, of a QPSK signal is twice that of a BPSK signal [5]. Several variants of QPSK modulation, including the offset QPSK (OQPSK) and the minimum shift keying (MSK), are also commonly used in near-Earth space missions. A detailed description of these modulation schemes is not covered here.

5.2. Demodulation

Demodulation is the process of transforming received waveforms back into their original state by reversing the modulation procedure. After traveling through various types of media or channels, the received waveform is corrupted in many ways. For example, it is corrupted by receiver's internally generated noise which is typically modeled as an additive white Gaussian noise (AWGN), or externally introduced interference, such as multipath, fading. Hence, for demodulation, it is important to correctly estimate the vital parameters in the transmitted signal from the corrupted waveform and apply the locally generated reference signals to remove the modulation. The following simple example illustrates how an AWGN

corrupted BPSK signal is demodulated. The received signal is given by

$$r(t) = \sqrt{2P_T} \sin \left(\omega_c(t + \tau) + \left(\frac{\pi}{2} \right) \sum_{k=1}^{\infty} d_k P(t + \tau - kT) + \theta \right) + n(t) \quad (10)$$

where τ is the random propagation delay, θ is a uniformly distributed (over 0 to 2π) carrier phase, and $n(t)$ is a noise modeled as an AWGN with a two-sided power spectral density level at $N_0/2$ W/Hz. For the signal of NRZ format, the phase-modulated signal is equivalent to the product of the carrier and the baseband binary data waveforms, which is rewritten as

$$r(t) = \sqrt{2P_T} \left[\sum_{k=1}^{\infty} d_k P(t + \tau - kT) \right] \cos(\omega_c t + \theta_c) + n(t) \quad (11)$$

where $\theta_c = (\theta + \omega_c \tau)_{\text{mod } 2\pi}$ is the total carrier phase. To demodulate the carrier, the receiver needs to generate a local reference, say, $\sqrt{2} \cos(\omega_c t + \hat{\theta}_c)$, where $\hat{\theta}_c$ is an estimate of θ_c . A lowpass filtered version of the product of the local carrier reference and the received signal becomes

$$r'(t) = \sqrt{P_T} \left[\sum_{k=1}^{\infty} d_k P(t + \tau - kT) \right] \cos(\phi_c) + n'(t) \quad (12)$$

where $\phi_c = \theta_c - \hat{\theta}_c$ is the phase error between the actual and the estimated carrier phases. For constant or at least slowly varying ϕ_c , the factor $\cos(\phi_c)$ represents a signal amplitude attenuation, which is inevitably translated into degradation in bit error performance. To make a decision on each of the transmitted bits, say, the i th bit d_i , the resulting signal $r'(t)$ is sent to a matched filter whose operation is mainly to form a product of the input signal and a local replica of the pulse function followed by an integrate-and-dump (I&D) operation. The accurate timing estimate $\hat{\tau}$ is very important in this matched filter operation because an error renders integrating across 2 bits, which reduces the detected symbol (for coded system) or bit (for uncoded system) energy when adjacent bits are of opposite polarities and results in a higher probability of decision error.

Additional signal power degradation due to imperfect subcarrier synchronization, similar to the carrier case given here, is expected when a subcarrier is used. The power degradation resulting from each of the carrier, subcarrier, and symbol tracking operations is discussed later.

6. SYNCHRONIZATION

The process of estimating the phase and timing parameters from the incoming noise-corrupted signal and using this information to keep the locally generated reference signal aligned with these estimates and, therefore, with the incoming signal is called synchronization.

As indicated previously, coherent reception and demodulation require phase information about the carrier and subcarrier (if used) and also symbol timing information. This information must be provided and updated for coherent receivers all the time because they are usually time-varying with the changing characteristics of the channel. Therefore, individual tracking loops which continuously update their estimates of specific parameters are required to track and provide the needed information for a coherent receiver.

Although the tracking of carrier, subcarrier, and symbol timing are individually discussed in following, one should keep in mind that, strictly speaking, all these loops are effectively coupled together in the sense that no one achieves lock without help from others, except for residual carrier tracking in which a carrier tone is separately tracked. However, in practice, each loop's performance is usually analyzed independently to keep the problem manageable.

It is also important to know that all the tracking loops discussed later are motivated by the maximum a posteriori (MAP) estimation, which suggests only the open-loop structure of a one-shot estimator. The closed-loop structure derived by differentiating the likelihood function and equating the resulting loop feedback signal (also known as the error signal) to zero is only motivated by the MAP estimation [8].

6.1. Carrier Tracking

6.1.1. BPSK. The most commonly used device to track the phase of a sinusoidal signal, for example, the residual carrier component in Eq. (7), is the phase-locked loop (PLL). The PLL is composed of a phase detector, a loop filter, and a voltage-controlled oscillator (VCO) or, in a digital PLL design, a numerically controlled oscillator (NCO). The lowpass component of the phase detector output is a periodic function (of period 2π) of the phase error ϕ_c , which is called the S curve of the loop. A stable lock point exists at $\phi_c = 0$, one of the zero-crossing points where the S curve has a positive slope. The phase error for the first-order PLL, which has its loop filter implemented as a constant gain, is a Tikhonov distributed random variable and its probability density function (pdf) is given by [5]

$$p(\phi_c) = \frac{\exp[\rho_{\phi_c} \cos(\phi_c)]}{2\pi I_0(\rho_{\phi_c})} \quad |\phi_c| \leq \pi \quad (13)$$

where $I_k(\cdot)$ denotes the modified Bessel function of order k and $\rho_{\phi_c} = (\sigma_{\phi_c}^2)^{-1}$ is the loop SNR defined as the reciprocal of the phase error variance in radian². The loop SNR for the first-order PLL is expressed by

$$\rho_{\phi_c} = \frac{P_c}{N_0 B_L} \quad (14)$$

where B_L is the loop bandwidth. The detailed description of a PLL is discussed in another article in this encyclopedia and is not to be repeated here.

For the suppressed carrier in which no discrete carrier component appears in its spectrum, the carrier phase, embedded in the data-bearing component as the second term of Eq. (7), must be tracked by the Costas loop. The Costas loop is a phase-tracking loop whose functionality is similar to that of a PLL. Except for the same feedback path consisting of a loop filter and an NCO, a Costas loop has a double-arm loop structure, denoted, respectively, as the in-phase (I) and quadrature (Q) arms, with a phase detector and a lowpass arm filter in each. The incoming signal is first mixed with each of the two locally generated reference signals 90° apart, that is, $\sqrt{2} \sin(\omega_c t + \hat{\theta}_c)$ and $\sqrt{2} \cos(\omega_c t + \hat{\theta}_c)$, at the corresponding phase detector and then passed through the arm filter. Although the lowpass arm filter is either a passive RC-type filter or an active filter, it turns out that a matched filter (that is, an active filter) is the optimal design. The output of the two arm filters are multiplied, which effectively removes the data modulation, to form the loop feedback signal before it is fed into the loop filter. Because of this multiplication, a Costas loop is actually tracking twice the error phase. Accordingly, the Costas loop has two equally stable lock points at $\phi_c = 0$ and $\phi_c = \pi$, each corresponding to a zero-crossing point in the S curve (of period π) where the slope is positive. These dual lock point inevitably introduce phase ambiguity such that the demodulated data has inverted polarity if the loop locks at $\phi_c = \pi$. This 180° phase ambiguity is resolved in several ways. For example, a known sequence pattern is inserted in the transmitted symbol stream from time to time so that the inverted polarity is detected by examining the received sequence pattern. However, the most efficient method is employing a differential encoding scheme in the transmitted data so that the information is kept in the relative phase between adjacent symbols instead of in the absolute phase of each symbol [5]. On the receiver side, a corresponding differential decoding scheme is applied to extract the relative phase (or the transmitted information) after the symbol decision. A small penalty in terms of error performance exists for this differential encoding/decoding scheme because one incorrect symbol decision creates two consecutive errors in the relative phase.

The phase error for the first-order Costas loop with I&D arm fitters is similarly found as a Tikhonov distributed random variable and its pdf is given by

$$p(\phi_c) = \frac{\exp\left[\frac{\rho_{\phi_c}}{4} \cos(2\phi_c)\right]}{\pi I_0\left(\frac{\rho_{\phi_c}}{4}\right)} \quad |\phi_c| \leq \frac{\pi}{2} \quad (15)$$

and the associated loop SNR is given by

$$\rho_{\phi_c} = \frac{P_d}{N_0 B_L} \left(1 + \frac{1}{2E_s/N_0}\right)^{-1} \quad (16)$$

where $E_s/N_0 = P_d T/N_0$ is the symbol SNR. Note that the term in the parentheses is usually called the squaring loss, which results from the signal-noise product in the

loop feedback signal. At low symbol SNR, the squaring loss is significant.

As discussed previously, transmitted power is allocated to the residual carrier component and data-bearing component by the choice of the modulation index for the telemetry data. It has been proved that a fully suppressed carrier is the best way to maximize data throughput [9]. However, if a residual carrier component is desired for purposes other than communications, it is always a dilemma to set this modulation index because, on one hand, sufficient power must be given to the residual carrier so that it is successfully tracked by a PLL, and, on the other hand, the power allocated for data transmission should be kept as high as possible to maximize data throughput. Because the residual carrier and data sidebands are coherently related, a hybrid loop [10] that consists of the phase-locked loop and Costas loop structures is used to exploit this coherence and thereby improve carrier phase tracking in this scenario. This technique is also known as sideband aiding because it utilizes the power in the data-bearing component as the second term Eq. (7) to help residual carrier tracking.

In the hybrid loop, both error signals from the single-arm PLL structure and the double-arm Costas loop structure are weighted and added together to form an effective loop feedback signal. As a result, there are usually dual lock points for the hybrid loop, that is, $\phi_c = 0$ and $\phi_c = \pi$ and similar to those of a Costas loop. Yet, these two lock points generally are not equiprobable. It can be shown that [11] the lock point at $\phi_c = \pi$ vanishes when the modulation index is smaller than a threshold as a function of the symbol SNR.

With a given modulation index, an optimal relative weight between the PLL and Costas loop portion is derived to minimize the hybrid loop tracking jitter. Because the relative tracking performance between a PLL and Costas loop is determined by the relative power allocation and the additional squaring loss incurred in the Costas loop, it is not surprising to find that the optimal weight is a function of the modulation index and the symbol SNR.

6.1.2. QPSK. The carrier tracking of a QPSK signal is usually done by a generalized Costas loop motivated by MAP estimation theory. There are basically two variants of this generalized Costas loop: the polarity type known as the crossover Costas loop for high-SNR scenarios and the squaring type or low-SNR scenarios [7]. In the crossover loop, two products are formed by multiplying the hard-limited version of one arm-filter output with the other arm filter output before they are combined as the loop error feedback. The phase error for the first-order crossover Costas loop is a Tikhonov distributed random variable with pdf given by

$$p(\phi_c) = \frac{2 \exp\left[\frac{\rho_{\phi_c}}{16} \cos(4\phi_c)\right]}{\pi I_0\left(\frac{\rho_{\phi_c}}{16}\right)} \quad |\phi_c| \leq \frac{\pi}{4} \quad (17)$$

The associated loop SNR for this first-order crossover loop is

$$\rho_{\phi_c} = \frac{P_d}{N_0 B_L} \left\{ \frac{\left[\operatorname{erf}\left(\sqrt{\frac{E_s}{2N_0}}\right) - \sqrt{\frac{2}{\pi}} \left(\frac{E_s}{N_0}\right) \exp\left(-\frac{E_s}{2N_0}\right) \right]^2}{1 + \frac{E_s}{N_0} - \left[\sqrt{\frac{2}{\pi}} \exp\left(-\frac{E_s}{2N_0}\right) + \sqrt{\frac{E_s}{N_0}} \operatorname{erf}\left(\sqrt{\frac{E_s}{2N_0}}\right) \right]^2} \right\} \quad (18)$$

where the error function $\operatorname{erf}(\cdot)$ and its complimentary $\operatorname{erfc}(\cdot)$ are defined as

$$\operatorname{erf}(x) = 1 - \operatorname{erfc}(x) = \frac{2}{\sqrt{\pi}} \int_0^x e^{-x^2} dx$$

Note that, similar to Eq. (16) of the Costas loop, the term in the braces in Eq. (18) is the squaring loss of the crossover Costas loop. The squaring-type loop has a different squaring loss which is smaller than that of its polarity-type sibling in low SNR region. More details about the crossover Costas loop can be found in Ref. 13. Another alternative in tracking a QPSK signal is to use the demod-remod quadriphase tracking loop, which can be viewed as a fourth-power loop with a multiplication done at the IF level [7].

6.2. Subcarrier Tracking

Subcarrier tracking is almost identical to suppressed carrier tracking for BPSK signals because there is no residual tone left for the binary-phase-shift-keyed subcarrier. The Costas loop is used here to remove the data modulation and a squaring loss associated with this process is inevitable. However, depending on the use of a sine-wave or square-wave subcarrier, tracking performance is quite different. For the sine-wave subcarrier, there is no difference between its tracking and that of a suppressed carrier. On the contrary, additional improvement in the square-wave subcarrier tracking is realized by using a time-domain windowing function on the quadrature arm [13]. In this case, the windowing function around the midphase transition of the Q-arm reference signal is treated as an approximation of the time-domain derivative of its I-arm counterpart. According to the derivation of the MAP estimation, which implies the existence of an optimal open-loop structure when one of I-arm and Q-arm reference signals is the derivative of the other, the resulting loop SNR is greatly improved by shrinking the window size. The first-order loop SNR is given by

$$\rho_{\phi_{sc}} = \left(\frac{2}{\pi}\right)^2 \frac{P_d}{N_0 B_L} \left(\frac{1}{W_{sc}}\right) \left(1 + \frac{1}{2E_s/N_0}\right)^{-1} \quad (19)$$

where W_{sc} is the quadrature window size (between 0 and 1) relative to a subcarrier cycle. It is clear that the loop SNR is inversely proportional to the window size. However, using a small window inevitably reduces the loop's pullin range and raises the issue of loop stability. A reasonable window size of one-quarter or one-eighth is usually used to provide a 6–9 dB improvement in loop SNR.

No such improvement from quadrature windowing is realized for a sine-wave Costas loop of which the I-arm and Q-arm reference signals are two sine functions separated by 90° and, therefore, have the derivative relationship between them as suggested by the MAP estimation. Applying a quadrature window in this case actually destroys the derivative relationship and renders inferior loop performance.

6.3. Symbol Timing Tracking

Symbol synchronization has a direct impact on the data detection process because inaccurate symbol timing reduces the probability of making a correct decision. Although a separate channel may be used to send timing signals for synchronization, to extract the synchronization information directly from the data-bearing signal has the advantage that no additional power and frequency spectrum are required. Of course, to successfully extract symbol timing information from the transmitted symbol stream relies on the presence of adequate symbol transitions (zero crossings).

The data transition tracking loop (DTTL) is widely used for symbol synchronization. Similar to the Costas loop, DTTL has a double-arm loop structure with a hard decision followed by a transition detector in its in-phase arm and a delay in its quadrature arm to keep signals on both arms properly aligned. It is important to note that the term “in phase” refers to an operation synchronous with the timing of the received symbols and, therefore, the I-arm phase detector becomes a matched filter integrating from one symbol epoch to the next. The Q-arm phase detector performs another integration within a window, which is of a size W_{sym} (between 0 and 1) relative to the symbol interval and centered at the symbol epoch, causing the midpoint of the Q-arm integration interval offset by a half-symbol from its I-arm counterpart. Similar to square-wave subcarrier tracking, the time-domain windowing function on the quadrature arm improves the tracking performance but inevitably raises the issue of loop stability at the same time [5].

The DTTL has a single stable lock point at $\phi_{sym} = 0$. The phase error for the first-order DTTL is a Tikhonov distributed random variable and its pdf is given by

$$p(\phi_{sym}) = \frac{\exp(\rho_{\phi_{sym}} \cos(\phi_{sym}))}{2\pi I_0(\rho_{\phi_{sym}})} |\phi_{sym}| \leq \pi \quad (20)$$

with the corresponding loop SNR given as

$$\rho_{\phi_{\text{sym}}} = \frac{1}{(2\pi)^2} \frac{P_d}{N_0 B_L} \left(\frac{1}{W_{\text{sym}}} \right) \left\{ \frac{\left[\operatorname{erf} \left(\sqrt{\frac{E_s}{N_0}} \right) - \frac{W_{\text{sym}}}{2} \sqrt{\frac{1}{\pi}} \left(\frac{E_s}{N_0} \right) \exp \left(-\frac{E_s}{N_0} \right) \right]^2}{1 + \frac{W_{\text{sym}}}{2} \left(\frac{E_s}{N_0} \right) - \frac{W_{\text{sym}}}{2}} \right\} \left\{ \left[\sqrt{\frac{1}{\pi}} \exp \left(-\frac{E_s}{N_0} \right) + \sqrt{\frac{E_s}{N_0}} \operatorname{erf} \left(\sqrt{\frac{E_s}{N_0}} \right) \right]^2 \right\} \quad (21)$$

7. SYMBOL SNR DEGRADATION

Symbol SNR degradation is the direct cause of poor bit error performance and is translated into the telemetry system loss as seen in the next section when the receiver performs a hard decision on each demodulated symbol. When no hard decision is performed by the receiver, symbol SNR degradation directly affects decoder performance because the demodulated symbols, called soft symbols, are fed to the decoder without going through a hard-decision device.

Because of the difficulty of analyzing the coupled-carrier, subcarrier, and symbol-tracking loops, SNR degradation of the demodulated symbol (for a coded system) or bit (for an uncoded system) caused by imperfectly synchronized references is usually approximated as a product of degradation factors of the individual loops; each factor is derived on the basis of assuming perfect tracking in other loops. The overall degradation, conditioned on the corresponding phase errors, for the telemetry signal given in Eq. (7) is expressed by

$$\begin{aligned} D_{\text{SNR}}(\phi_c, \phi_{\text{sc}}, \phi_{\text{sym}}) &= D_c(\phi_c) D_{\text{sc}}(\phi_{\text{sc}}) D_{\text{sym}}(\phi_{\text{sym}}) \\ &= [\cos(\phi_c)]^2 \left[1 - \frac{2}{\pi} |\phi_{\text{sc}}| \right]^2 \left[1 - \frac{|\phi_{\text{sym}}|}{\pi} + \frac{\phi_{\text{sym}}^2}{2\pi^2} \right] \end{aligned} \quad (22)$$

Where $D_c(\phi_c)$, $D_{\text{sc}}(\phi_{\text{sc}})$ and $D_{\text{sym}}(\phi_{\text{sym}})$ are the degradation factors for the imperfect carrier, subcarrier, and symbol (or bit) synchronization, respectively. Hence, the averaged symbol (or bit) SNR degradation due to imperfect synchronization becomes

$$\overline{(D_{\text{SNR}})}_{\text{dB}} = \overline{(D_c)}_{\text{dB}} + \overline{(D_{\text{sc}})}_{\text{dB}} + \overline{(D_{\text{sym}})}_{\text{dB}} \quad (23)$$

where $\overline{D_c}$, $\overline{D_{\text{sc}}}$ and $\overline{D_{\text{sym}}}$ are the averaged power degradation factors obtained by averaging over the corresponding Tikhonov distributed phase errors.

In addition to the degradation caused by imperfect synchronization, it is also important to know that there are other sources of SNR degradation, for example, the

intermodulation terms and possible interference from the ranging signal found in Eq. (7), and the subcarrier and symbol waveform distortion introduced by the bandlimited channel.

8. BIT ERROR PERFORMANCE (UNCODED SYSTEM) AND TELEMETRY SYSTEM LOSS

Telemetry information is extracted from the demodulated data stream by a symbol decision process. For binary signals, it is typically a hard-limiting decision on an AWGN corrupted, antipodal, random variable. For an uncoded system, the bit (or symbol) error probability of a BPSK signal is well known as

$$P_b = \int_{-\pi}^{\pi} \frac{1}{2} \operatorname{erfc} \left[\sqrt{\frac{E_b}{N_0}} \cos(\phi_c) \right] p(\phi_c) d\phi_c \quad (24)$$

where $p(\phi_c)$, is the pdf of the carrier phase error given in Eq. (13), when the carrier is tracked by a PLL so that no phase ambiguity exists. However, with a fixed-loop SNR, an irreducible error probability exists no matter how large the bit SNR. This irreducible error probability is characterized solely by the carrier tracking loop SNR and, for a given loop bandwidth, is reduced only by allocating more power to the residual carrier component, which serves no purpose in transmitting telemetry except being tracked by PLL.

For suppressed carrier tracking of a BPSK signal by the Costas loop, the phase ambiguity exists and must be resolved. The bit error probability for a special case of perfect phase ambiguity resolution (say, by other means, such as a periodically inserted known sync pattern) is given by

$$P_b = \int_{-\pi/2}^{\pi/2} \frac{1}{2} \operatorname{erfc} \left[\sqrt{\frac{E_b}{N_0}} \cos(\phi_c) \right] p(\phi_c) d\phi_c \quad (25)$$

where $p(\phi_c)$ is the pdf in Eq. (15).

If a differential coding scheme is utilized to resolve the phase ambiguity, the biterror probability becomes [7]

$$\begin{aligned} P_b &= \int_{-\pi/2}^{\pi/2} \operatorname{erfc} \left[\sqrt{\frac{E_b}{N_0}} \cos(\phi_c) \right] \\ &\left\{ 1 - \frac{1}{2} \operatorname{erfc} \left[\sqrt{\frac{E_b}{N_0}} \cos(\phi_c) \right] \right\} p(\phi_c) d\phi_c \end{aligned} \quad (26)$$

where $p(\phi_c)$ is the pdf in Eq. (15). No irreducible error probability exists in the suppressed carrier tracking because the tracking loop SNR for a fixed loop bandwidth and bit duration product increases with the bit SNR. So far, only the impact of bit error probability from carrier tracking has been discussed, and one can find the SNR degradation from imperfect carrier tracking, that is, $\cos^2(\phi_c)$ appears repeatedly in Eqs. (24)–(26). When the overall impact of bit-error performance from all levels

of imperfect tracking, including carrier, subcarrier, and symbol, is considered, the bit error probability becomes a threefold integration involving the overall symbol SNR degradation given in Eq. (22). For example

$$P_b = \int_{-\pi}^{\pi} \int_{-\pi/2}^{\pi/2} \int_{-\pi/2}^{\pi/2} \frac{1}{2} \operatorname{erfc} \left[\sqrt{\frac{E_b}{N_0} D_{\text{SNR}}(\phi_c, \phi_{\text{sc}}, \phi_{\text{sym}})} \right] p(\phi_c) p(\phi_{\text{sc}}) p(\phi_{\text{sym}}) d\phi_c d\phi_{\text{sc}} d\phi_{\text{sym}} \quad (27)$$

where $p(\phi_{\text{sc}})$ and $p(\phi_{\text{sym}})$ are Tikhonov distributed pdf's of subcarrier and symbol phase errors, respectively. In fact, $p(\phi_{\text{sc}})$ takes the form of Eq. (15) of the Costas loop and $p(\phi_{\text{sym}})$ is given by Eq. (20). Note that the product of pdf's of individual phase errors is used in lieu of the hard-to-establish joint pdf from the coupled loops. For QPSK signals, the biterror probability is given by [7]

$$P_b = \int_{-\pi/4}^{\pi/4} \left(\frac{1}{4} \operatorname{erfc} \left\{ \sqrt{\frac{E_b}{N_0}} [\cos(\phi_c) - \sin(\phi_c)] \right\} + \frac{1}{4} \operatorname{erfc} \left\{ \sqrt{\frac{E_b}{N_0}} [\cos(\phi_c) + \sin(\phi_c)] \right\} \right) p(\phi_c) d\phi_c \quad (28)$$

where $p(\phi_c)$ is the pdf in Eq. (17).

The telemetry system loss is defined as a loss factor $L \geq 0$ dB, which represents the amount of additional bit SNR required for a lossy system to meet the same bit error performance of a perfectly synchronized system. For example, the bit error probability for a perfectly synchronized BPSK or QPSK system is given by

$$P_b = \frac{1}{2} \operatorname{erfc} \left(\sqrt{\frac{E_b}{N_0}} \right) \quad (29)$$

and, therefore, the required bit SNR for this ideal system at a given bit error probability p_b^* is expressed by

$$\left(\frac{E_b}{N_0} \right)^* = [\operatorname{erfc}^{-1}(2P_b^*)]^2 \quad (30)$$

The lossy system with a system loss L needs L times as much bit energy, namely, $E_b/N_0 = L(E_b/N_0)^*$, to achieve the same biterror probability or, in other words, to compensate for the loss incurred within.

9. ADVANCED TOPICS

9.1. Antenna Arraying

With recent space missions moving toward high data rate and low transmitting power operations, combining signals from several antennas to improve the effective SNR becomes the only viable option when the existing technologies of building larger single-aperture antenna and

lowering the system noise temperature are pushed to their limits.

Three arraying techniques [14] are briefly discussed here: symbol-stream combining, baseband combining and full spectrum combining, each combining signals at a different stage of signal processing.

For symbol-stream combining, each participating antenna performs carrier, subcarrier, and symbol synchronization individually. Then the symbols at each receiver output are combined, with the appropriate weights, to form the final symbols for detection or decoding. This scheme has the advantage of a small combining loss. It is also suitable for real-time combining from intercontinental antenna sites because combining is performed at a relatively low processing rate, that is, the symbol rate. The disadvantage is that each antenna needs a full set of receiver hardware and must lock on the signal individually.

In baseband combining, each antenna needs to lock on and remove the (residual) carrier by itself. Then the resulting baseband signals, including the data-modulated subcarrier, are combined for further synchronization and demodulation. The advantage of this scheme is that less hardware is required because only a single set of subcarrier and symbol tracking devices is needed to process the combined signal. The disadvantage is that each antenna still must lock on, at least, the carrier, individually.

In full spectrum combining, signals are combined at an intermediate frequency (IF). Before they are combined, the relative time delay and phase difference must be properly estimated and compensated for so that signals are coherently combined. Then the resulting IF signal is directed to a single receiver for further synchronization and demodulation. The advantage of this scheme is that only one of the participating antennas must lock on the combined IF signal, which allows including smaller antennas in this arraying scheme even though they cannot lock on the signal. The disadvantage is the very large transmission or recoding bandwidth required to carry the IF signals through the networked antenna sites for combination.

Besides the above-discussed arraying techniques, a scheme called the carrier arraying, which employs coupled carrier tracking devices from participating antennas should be mentioned here. This scheme by itself does not combine the signals and, thus, must be operated with symbol-stream or baseband combining to array the telemetry. In a carrier array scenario, a large master antenna generally locks on the signal by itself and then helps other smaller antennas to track by estimating and removing the signal dynamics in their input.

9.2. Buffered Telemetry Processing

The Deep Space Communications Complex (DSCC) Galileo Telemetry (DGT) is developed and implemented by the Jet Propulsion Laboratory to support the Galileo S-Band Mission. Many advanced technologies have been developed for this mission to cope with the failure to fully deploy the high-gain antenna of the Galileo spacecraft, making itself a showcase of future signal processing

technologies in the radiotelemetry field. In the following, selected key features of the DGT and the technologies behind these features are briefly described to illustrate the concept of buffered telemetry processing in which telemetry is recorded, processed, and reprocessed to minimize data loss in space missions operated with low link margins.

DGT is composed of four major subsystems, the full-spectrum recorder (FSR), the full-spectrum combiner (FSC), the buffered telemetry demodulator (BTD), the feedback concatenated decoder (FCD), and other control functions to coordinate the operations of these subsystems. Except for the FSR, the rest of the DGT is implemented in software and can be run on general-purpose workstations, which allows greater flexibility of signal processing without expensive custom-made hardware.

The FSR downconverts the RF signal to IF for digitization and then further open-loop downconverts each data sideband to the baseband, individually and coherently, before it is sampled and recorded. This significantly reduces the required bandwidth for transmission through the intercontinental antenna network because the processing rate is linked to the symbol rate, instead of the much higher subcarrier frequency.

The recorded signals (residual carrier and data sidebands centered at the first four harmonics of the square-wave subcarrier) are kept for the Galileo S-Band Mission) from arrayed antennas are combined by the FSC, which estimates and adjusts the time delay and phase for each recorded sideband coherently to a reference point chosen as the center of the Earth, and then combines the time- and phase-aligned signals from arrayed antennas to form an enhanced signal. The combined telemetry is archived and transferred to the BTD on request for synchronization and demodulation.

The BTD, known as the software receiver, is the signal processing core of DGT, which provides acquisition, synchronization, demodulation, and miscellaneous monitoring functions through its carrier, subcarrier, symbol-tracking loops and associated lock indicators [15]. In the BTD, the individually combined data sidebands are processed coherently and then are synthesized to form an equivalent signal as if it were a single signal processed by a regular receiver. The end product of the BTD is a demodulated soft symbol stream that is written to a file and transferred to the FCD on request for decoding and decompression.

Because the FSR/FSC combined data are recorded on tape, the BTD is actually designed to be able to work on any segment of data offline in either direction, forward or backward in time. In fact, with the availability of multiple CPU workstations, simultaneous BTD sessions are initiated on different segments of data. For example, one session is dedicated to process real-time samples forward (in time) while the others reprocess other recorded segments as needed. Then the soft symbol streams from these simultaneous sessions are merged into a single stream because each of them is properly time tagged. By taking advantage of the flexibility in software implementation, many noncausal signal processing techniques can be performed to process or reprocess the data to further

enhance the quality of the telemetry. One important feature of the BTD is the so-called gap closure processing [16], which greatly reduces possible data loss due to receiver acquisition, resynchronization, and loss of lock.

The need to reprocess a segment of sampled data arises from the failure of the BTD to maintain the in-lock status in any of its tracking loops or the failure of the FCD to properly decode the soft symbols. A segment of sampled data on which the telemetry cannot be extracted reliably is called a gap, and the processing of a gap to extract any valid information not available when that segment of samples was first processed is called gapclosure processing. Gaps caused by acquisition are found in the beginning of each pass or at instants when the receiver drops out of lock, whereas gaps generated by cycle slips in one of the loops occur randomly in a pass. Along with its demodulation efforts, the BTD tracks its internal states, including the lock indicators, the symbol SNR estimates, and the state variables inside the loop filter and the NCO for all three loops. These state variables are recorded at fixed intervals as checkpoints and, with them, a software receiver is easily restored to its state at checkpoint immediately before or after a gap. By estimating the parameters of a phase process in a region near a restored checkpoint where the phase tracking was successfully carried out, gap closure processing can start from this checkpoint and move into the gap. Two configurations, one for closed loop and the other for open loop, are used here. The closedloop configuration needs to initiate the loop filter with phase parameters estimates in a particular way, so that, when the loop is closed and starts to track at the checkpoint, the loop virtually starts immediately with steady state tracking. For a relatively stable phase process and a gap of small size, an openloop configuration is applied by using an estimated phase profile as the reference without resorting to a loop operation. Both configurations are applied to gap closure processing in either direction, forward or backward in time, because the buffered data can be processed in either order. This is especially useful when a gap occurs at the beginning of a track so that all the available checkpoint information is from the region behind this gap.

Another useful feature of BTD is its capability of seamless tracking through symbol rate changes. The reason for changing the symbol rate during a pass is to take advantage of the changing G/T figure as the elevation angle of an antenna changes in a pass. With a higher elevation angle, an antenna has a higher G/T figure and supports a higher symbol rate when the symbol SNR is fixed. The software implementation of BTD handles symbol rate changes without dropping a lock on symbol timing, as long as the rate changes follow a set of specific rules and their schedule is roughly known in advance.

The FCD is a subsystem that performs error correction decoding and data decompression in the DGT. Implemented in software on a multiprocessor workstation, it employs a feedback mechanism that passes intermediate decoding information from the outer code of the concatenated code to the inner code to facilitate multipass decoding which achieves a final bit error rate of 10^{-7} at a 0.65 dB bit SNR. The architecture and the detailed operations of the FCD are described in the next section.

9.3. Advanced Source and Channel Coding for Space Applications

In this section, we use the Galileo S-Band Mission again as an example to illustrate the application of advanced source and channel coding schemes to enhance telemetry return (17). First, using the integer cosine transform (ICT) for lossy image compression is briefly explained. Then, an advanced error correction coding scheme used to protect the heavily edited and compressed data is discussed, followed by a discussion of the interaction between data compression and error control (containment/detection/correction) processes.

9.3.1. Galileo's Image Compression Scheme. Galileo image compression is a block-based lossy image-compression algorithm that uses an 8×8 ICT. The ICT was first proposed in 1989 [18], and was streamlined and generalized a few years later [19,20]. It is an integral approximation of the popular discrete cosine transform (DCT), which is regarded as one of the best transform techniques in image coding. Its independence from the source data and the availability of fast transform algorithms make the DCT an attractive candidate for many practical image processing applications. In fact, the ISO/CCITT standards for image processing in both still-image and video transmissions include the two-dimensional DCT as a standard processing component in many applications.

The elements in an ICT matrix are small integers with sign and magnitude patterns resembling those of the DCT matrix. Besides, the rows of the ICT matrix are orthogonal. The integral property eliminates real multiplication and real addition operations, thus greatly reducing computational complexity. The orthogonality property ensures that the inverse ICT has the same transform structure as the ICT. Notice that the ICT matrix is required only to be orthogonal, but not orthonormal. However, any orthogonal matrix may be made orthonormal by multiplying it by an appropriate diagonal matrix. This operation is incorporated in the quantization (dequantization) stage of the compression (decompression), thus sparing the ICT (inverse ICT) from floating-point operations and, at the same time, preserving the same transform structure as in the floating-point DCT (inverse DCT). The relationship between the ICT and DCT guarantees efficient energy packing and allows the use of fast DCT techniques for the ICT. The ICT matrix used in the Galileo mission is given as follows:

$$\begin{bmatrix} 1 & 1 & 1 & 1 & 1 & 1 & 1 & 1 \\ 5 & 3 & 2 & 1 & -1 & -2 & -2 & -5 \\ 3 & 1 & -1 & -3 & -3 & -1 & 1 & 3 \\ 3 & -1 & -5 & -2 & 2 & 5 & 1 & -3 \\ 1 & -1 & -1 & 1 & 1 & -1 & -1 & 1 \\ 2 & -5 & 1 & 3 & -3 & -1 & 5 & -2 \\ 1 & -3 & 3 & -1 & -1 & 3 & -3 & 1 \\ 1 & -2 & 3 & -5 & 5 & -3 & 2 & -1 \end{bmatrix}$$

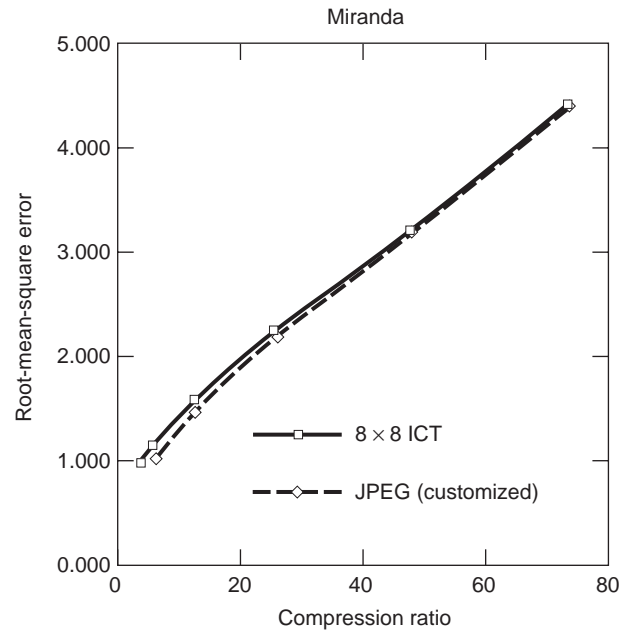


Figure 1. Rate distortion performance of ICT.

Figure 1 shows the rate distortion performance of the ICT scheme compared with the JPEG scheme. Simulation results indicate that the difference in performance between the use of floating-point DCT and the ICT is insignificant.

9.3.2. Galileo's Error Correction Coding Scheme. The Galileo error-correction coding scheme uses a $(255, k)$ variable redundancy RS code as the outer code and a $(14, \frac{1}{4})$ -long constraint-length convolutional code as the inner code. The RS codewords are interleaved to depth 8 in a frame. The redundancy profile of the Reed–Solomon codes is $(94, 10, 30, 10, 60, 10, 30, 10)$. The staggered redundancy profile was designed to facilitate the novel feedback concatenated decoding strategy [21,22]. This strategy allows multiple passes of channel symbols through the decoder. During each pass, the decoder uses the decoding information from the RS outer code to facilitate the Viterbi decoding of the inner code in a progressively refined manner. The FCD is implemented in software on a multiprocessor workstation. The code is expected to operate at a bit signal-to-noise ratio of 0.65 dB at a bit error rate of 10^{-7} . Figure 2 shows a schematic of the FCD architecture. In this article, only the implementation and operational aspects of the FCD task are discussed. The FCD novel node/frame synchronization scheme is discussed in Ref. 23, and its code selection and performance analysis are discussed in detail in Ref. 24.

9.3.2.1. The $(255, k)$ Variable-Redundancy Reed–Solomon Code. All RS codes for the Galileo mission use the same representation of the finite field $\text{GF}(256)$. Precisely, $\text{GF}(256)$ is the set of elements

$$\text{GF}(256) = \{0, a^0, a^1, a^2, \dots, a^{254}\} \quad (31)$$

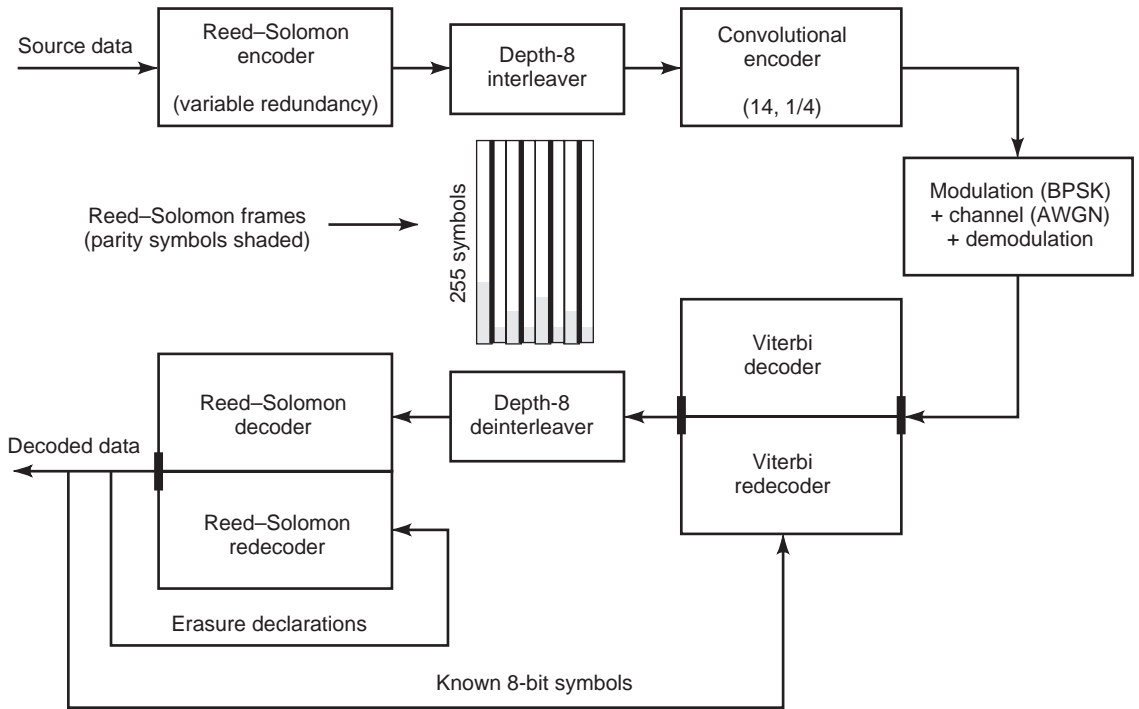


Figure 2. Schematic of the FCD.

where a , by definition, is a root of the primitive polynomial

$$p(x) = x^8 + x^7 + x^2 + x + 1 \quad (32)$$

[i.e., $p(a) = 0$].

In the encoding/decoding process, each power of a is represented as a distinct nonzero 8-bit pattern. The zero byte is the zero element in $GF(256)$. The basis for $GF(256)$ is descending powers of a . Note that this is the conventional representation, not Berlekamp's dual basis (25). The RS generator polynomial is defined as

$$g(x) = \prod_{i=0}^{n-k-1} (x - \alpha^{\beta(i+L)}) = \sum_{i=0}^{n-k} g_i x^i \quad (33)$$

where n denotes the codeword length in bytes, k denotes the number of information bytes, and α^β is a primitive element of $GF(256)$. The parameter b is chosen in some applications to minimize the bit-serial encoding complexity. Because the Galileo RS encoders are implemented in software, there is little advantage in preferring a particular value of b . The parameter L is chosen so that the coefficients of $g(x)$ are symmetrical. This reduces the number of Galois field multiplications in encoding by nearly a factor of 2.

The Galileo mission utilizes four distinct RS codes. We define $RS(n, k)$ as an RS code which accepts k data bytes as input and produces n bytes as a code word, where $n > k$. An $RS(n, k)$ code corrects t errors and s erasures if $2t + s \leq n - k$. These codes are referred to as $RS(255, 161)$, $RS(255, 195)$, $RS(255, 225)$, $RS(255, 245)$. Specifically, the parameters b

and L of these four codes are as follows:

- $RS(255, 161)$ $b = 1, L = 81$
- $RS(255, 195)$ $b = 1, L = 98$
- $RS(255, 225)$ $b = 1, L = 113$
- $RS(255, 245)$ $b = 1, L = 123$

These RS codes, being interleaved to depth 8, are arranged in a transfer frame as shown in Fig. 2. The RS decoders use a time-domain Euclid algorithm to correct errors and erasures. The details of the decoding algorithm are discussed in Ref. 26.

9.3.2.2. The $(14, \frac{1}{4})$ Convolutional Code and Its Parallel Viterbi Decoder. The $(14, \frac{1}{4})$ convolutional code used for the Galileo mission is the concatenation of a software $(11, \frac{1}{2})$ code and an existing hardware $(7, \frac{1}{2})$ code. The choice of convolution code is constrained by the existing $(7, \frac{1}{2})$ code, which is hardwired in the Galileo Telemetry Modulation Unit (TMU), and by the processing speed of the ground FCD. The generator polynomials of the $(11, \frac{1}{2})$ code and the $(7, \frac{1}{2})$ code in octal are (3403, 2423) and (133, 171), respectively. The generator polynomials of the equivalent $(14, \frac{1}{4})$ code are (26042, 36575, 25715, 16723).

The Viterbi decoder for the $(14, \frac{1}{4})$ code is implemented in software in a multiprocessor workstation with shared memory architecture. The use of a software decoder is possible because of the slow downlink data rate of the Galileo S-Band Mission. The advantages of a software-based decoder are that the development cost is low and it allows the flexibility to perform feedback concatenated decoding. We examined two different approaches to

parallelize the Viterbi algorithm: (1) state-parallel decomposition in which each processor is equally loaded to compute the add-compare-select operations per bit and (2) round-robin frame decoding that exploits the multiple processors by running several complete but independent decoders for several frames in parallel. Our early prototypes indicate that the first approach requires a substantial amount of interprocessor synchronization and communication and this greatly reduces the decoding speed. The second approach requires much less synchronization and communication because each processor is now an entity independent of the others. The performance scaling is nearly perfect. We chose the round-robin approach for the FCD Viterbi decoder. The details of the FCD software Viterbi decoder implementation are described in Ref. 27.

9.3.2.3. Redecoding. Redecoding, as shown in Fig. 2, uses information fed back from codewords successfully decoded by the RS decoder to improve the performance of Viterbi decoding. A correctly decoded RS bit forces the add-compare-select operation at each state to select the path that corresponds to the correct bit. Thus the Viterbi decoder is constrained to follow only paths consistent with known symbols from previously decoded RS codewords. The Viterbi decoder is much less likely to choose a long erroneous path because any path under consideration is pinned to coincide with the correct path at the locations of the known symbols. Each RS frame is decoded with four feedback passes. In the first pass, only the first code word RS(255,161) is decoded. In the second pass, the fifth codeword RS(255,195) is decoded. In the third pass, the third and seventh codewords RS(255,225) are decoded, and finally, in the fourth pass, the second, fourth, sixth, and eighth codewords RS(255,245) are decoded. During each pass, the decoder uses the decoding information from the Reed-Solomon outer code to facilitate Viterbi decoding of the inner code in a progressively refined manner. The details of the FCD redecoding analysis are given in Ref. 24.

9.3.3. Interaction between Data Compression and Error Control Processes. Packet loss and other uncorrectable errors in a compressed datastream cause error propagation, and the way the error propagates depends on the compression scheme. To maximize the scientific objectives with the limited transmission power of the low-gain antenna used in the Galileo S-Band Mission, most of the data (image and nonimage) are expected to be heavily edited and compressed. These valuable compressed data must be safeguarded against catastrophic error propagation caused by packet loss and other unforeseeable errors.

The ICT scheme for solid-state imaging (SSI) data is equipped with a simple but effective error containment strategy. The idea is to insert synchronization markers and counters at regular intervals to delimit uncompressed data into independent blocks so that, in case of packet loss and other anomalies, the decompressor searches for the next available synchronization marker and continues to decompress the rest of the data. In this case, the interval chosen is eight lines of uncompressed data. The error containment strategy guarantees that error propagation

does not go beyond the compressed code block where errors reside. Other options to prevent error propagation are also considered, but these options usually result in great onboard implementation complexity or excessive downlink overhead. For example, a self-synchronizing feature in Huffman code may be used to contain errors, but it is difficult to implement. A packetizing scheme with varying packet sizes may also be used to contain errors (by matching packet boundaries and the compressed data block boundary), but the packet headers introduce excessive downlink overhead in SSI data.

The SSI ICT error containment scheme works as follows. On the compression side, every eight lines of data are compressed into a variable-length, compressed data block. The dc (steady-state bias) value is reset to zero at the start of each compressed data block, thus making every block independent of the others. A 25-bit synchronization marker and a 7-bit modulo counter are inserted at the beginning of every compressed data block. The sync marker is chosen to minimize the probability of false acquisition in a bursty channel environment. The 25-bit synchronization marker pattern is 024AAAAB in hex. Simulation results indicate that this synchronization marker gives a probability of false acquisition of less than 10^{-8} . The decompression scheme consists of two program modules, the SSI ICT decompression module and the error detection/sync module. The SSI ICT decompression module reconstructs the data from the compressed datastream, and the error detection/sync module checks the prefix condition of the Huffman codes to detect any anomaly. When an anomaly is detected, a synchronization marker search is initiated to find the next available one. Decompression resumes from there on, and the reconstructed blocks are realigned by using the modulo counter. The corrupted portion of the data is flagged and reported.

The downlink overhead of the SSI ICT error containment scheme is a function of compression ratio (CR) and image width W. It is measured by the percentage of sync data (sync marker and counter) compared to the compressed data and is given by following equation:

$$\frac{4 \times CR}{8 \times W}$$

For example, an 800×800 SSI image has the following overhead as a function of the compression ratio:

Compression Ratio	Overhead
2	0.00125
4	0.00250
8	0.00500
16	0.01000

9.3.4. Multiple Spacecraft Support. Traditionally, every spacecraft is supported by one of the ground antennas for its uplink and downlink. This dedication requires efficient scheduling of the resources on the ground, including hardware, software, and personnel. With more and more

concurrent missions, the need for multiple spacecraft support by a single ground antenna to alleviate the scheduling problem becomes evident. For example, several proposed future missions to Mars by various joint efforts of international space agencies will place more than a dozen spacecraft, including orbiters, landers, and rovers, on or around Mars in the next 10 years. For these missions, it is highly possible that more than one spacecraft will come within the same beam width of a single ground antenna, and it constitutes the opportunity to communicate with them by using this single antenna with a considerable amount of operational cost saving over multiple antennas. In multiple spacecraft support, a telecommand uplink from a single ground antenna will be shared by the supported spacecraft, and multiple telemetry downlinks originated from these spacecraft will also have to be established by a single ground antenna.

Several options have been studied to support this multiple spacecraft scenario [28]. The most straightforward (and the most inefficient) option is to carefully assign different subcarrier frequencies to the supported spacecraft, allowing sufficient guard band to accommodate Doppler effects and tolerating some degree of spectrum overlapping in data sidebands in exchange for more simultaneous support. This method requires very tedious planning and is extremely inflexible when facing a dynamic scenario.

Another option is to redesign the spacecraft transponder so that the coherent turnaround ratio (TAR), which specifies the uplink to downlink carrier frequency ratio, is programmable. Each supported spacecraft receives its unique TAR from the uplink commands. As a result, different spacecraft will be instructed to use different downlink carrier frequencies because their TARs are distinct. Currently, a new digital transponder, known as the *small transponder modem* developed by the Jet Propulsion Laboratory, has such a built-in feature.

The third option is to use code-division multiple-access (CDMA) techniques similar to those used in commercial mobile cellular systems. CDMA offers far more simultaneous support than that of the previous two options. However, to support various types of spacecraft, the power dissimilarity problem between weak rover and strong orbiter signals has to be properly solved to avoid severe performance degradation for weaker signals. This option may be the best choice when more and more multiple spacecraft support scenarios emerge in the future.

BIBLIOGRAPHY

1. B. Sklar, *Digital Communications: Fundamentals and Applications*, Prentice-Hall, Englewood Cliffs, NJ, 1988.
2. J. Ziv and A. Lempel, A universal algorithm for sequential data compression, *IEEE Trans. Inform. Theory* **IT-23**:337–343 (1977).
3. J. Ziv and A. Lempel, Compression of individual sequences by variable rate coding, *IEEE Trans. Inform. Theory* **IT-24**:530–536 (1978).
4. C. E. Shannon, A mathematical theory of communication, *M. D. Comput.* **14**(4):306–317 (1997).
5. W. C. Lindsey and M. K. Simon, *Telecommunication System Engineering*, Prentice-Hall, Englewood Cliffs, NJ, 1973.
6. International Consultative Committee for Space Data Systems, CCSDS, *Recommendations for Space Data System Standards, Radio Frequency and Modulation Systems, part I, Earth Stations Spacecraft*, CCSDS 401.0-B, Blue Book, 1994.
7. J. H. Yuen, *Deep Space Telecommunications Systems Engineering*, Plenum, New York, 1983.
8. T. M. Nguyen, Technique to select the optimum modulation indices for suppression of undesired signals for simultaneous range and data operations, *IEEE Trans. Electromagn. Compat.* **32**:7–19 (1990).
9. M. K. Simon and S. Million, *Residual versus Suppressed Carrier Coherent Communications*, TDA Progress Rep. 42-127: July–Sept. 1996, Jet Propulsion Laboratory, Pasadena, CA, Nov. 15, 1996.
10. H. Tsou, M. K. Simon, and S. M. Hinedi, Closed loop carrier phase synchronization techniques motivated by likelihood functions, *1994 IEEE Int. Conf. Commun. Conf. Rec.* 1994, Vol. 2, pp. 934–939.
11. M. K. Simon et al., The performance of a coherent residual carrier PSK system using hybrid carrier phase synchronization, *1996 IEEE Int. Conf. Commun. Conf. Rec.* 1996, Vol. 2, pp. 1275–1280.
12. J. K. Holmes, *Coherent Spread Spectrum Systems*, Wiley, New York, 1982.
13. W. J. Hurd and S. Aquirre, A method to dramatically improve subcarrier tracking, *IEEE Trans. Commun.* **COM-36**:238–243 (1988).
14. A. Mileant and S. M. Hinedi, *Overview of Arraying Techniques in the Deep Space Network*, TDA Progress Rep. 42-104, Oct.–Dec. 1990, Jet Propulsion Laboratory, Pasadena, CA, 1991.
15. H. Tsou et al., A functional description of the buffered telemetry demodulator for the Galileo mission to Jupiter, *1994 IEEE Int. Conf. Commun. Conf. Rec.* 1994, Vol. 2, pp. 923–928.
16. H. Tsou et al., The recovery of buffered telemetry data for future low cost space missions, *1995 IEEE Int. Conf. Commun. Conf. Rec.* 1995, Vol. 2, pp. 919–923.
17. K. Cheung et al., Enhancing the Galileo data return using advanced source and channel coding, *NASA Technol. 2004 Conf.*, Washington, DC, Sept. 1994.
18. W. Cham, Development of integer cosine transform by the principle of dyadic symmetry, *IEE Proc. (Part I)* **136**:276, 282 (1989).
19. K. Cheung, F. Pollara, and M. Shahshahani, *Integer cosine transform for image compression*, TDA Progress Rep. 42-105, Jan.–March 1991, Jet Propulsion Laboratory, Pasadena, CA, 1991.
20. K. Cheung and K. Tong, Proposed data compression schemes for the Galileo S-band contingency mission, *Proc. NASA Space Earth Sci. Data Compression Workshop*, Snowbird, UT, 1993.
21. E. Paaske, Improved decoding for a concatenated coding system recommended by CCSDS, *IEEE Trans. Commun.* **COM-38**:1138–1144 (1990).
22. O. Collins and M. Hizlan, Determinate-state convolutional codes, TDA Progress Rep. 42-107: July–Sept. 1991, Jet Propulsion Laboratory, Pasadena, CA, 1991.
23. J. Statman et al., Decoder synchronization for deep space missions, TDA Progress Rep. 42-116, Oct.–Dec. 1993, Jet Propulsion Laboratory, Pasadena, CA, 1994.

24. S. Dolinar and M. Belongie, Enhanced decoding for the Galileo low-gain antenna mission, *Proc. 1994 IEEE Int. Symp. Inform. Theory*, Trondheim, Norway, 1994.
25. E. Berlekamp, Bit-serial Reed–Solomon encoder, *IEEE Trans. Inform. Theory* **28** (1982).
26. R. McEliece, The decoding of Reed–Solomon codes, TDA Progress Rep. 42-95, July–Sept. 1988, Jet Propulsion Laboratory, Pasadena, CA, 1988.
27. T. Chauvin and K. Cheung, A parallel Viterbi decoder for shared memory architecture, *SIAM Conf. Parallel Signal/Image Process. Multiprocess Syst.*, Seattle, WA, Aug. 1993.
28. H. Tsou et al., Description of communication system options for single-aperture multiple-link (SAML) mission support, TDA Progress Rep. 42-127: July–Sept. 1996, Jet Propulsion Laboratory, Pasadena, CA, 1996.

RADIOWAVE PROPAGATION CONCEPTS

CURT A. LEVIS
The Ohio State University

An advantage of electronic communication is that an artificial link (e.g., transmission line, cable, or waveguide) is not necessarily required between the signal source and the receiver. Indeed, the term “wireless” is used in many parts of the world in preference to “radio,” and even in the United States “wireless” is often used to describe commercial personal communication by radio. Although radiowaves also propagate in waveguides, cables, and transmission lines, the term “radiowave propagation” is used generally, and specifically in this article, for signal travel between a source and a receiver without guidance by such artificial devices. Examples of such systems are radio and television broadcasting, radio point-to-point communication, radar, radio navigation, and remote sensing.

The concept of radiowave propagation allows division of the total system problem into three separate parts: the transmitter or signal source, the receiver, and propagation. Thus propagation is defined as what happens between the source and the receiver. For this concept to be valid, the distances must be such that far-field criteria for

the antennas are satisfied; this allows separating antenna effects from propagation effects. In radar two propagation paths are involved: from the transmitter to the target and from the target to the receiver.

Much has been learned about radiowave propagation since Hertz first demonstrated wireless transmission from one room to another. Now radiowave propagation is considered a moderately mature science, yet new understanding continues to emerge. This article presents an overview of radiowave propagation concepts. More detailed information will be found in articles on specific topics in radiowave propagation.

1. THE INFLUENCE OF FREQUENCY AND ENVIRONMENT

1.1. Frequency

The spectrum of useful electromagnetic waves covers an extraordinarily wide range of frequencies from as low as 70 Hz to X rays at approximately 10 EHz (10^{19} Hz). For convenience, the lower part of the spectrum has been divided into frequency bands as shown in Table 1. The VLF to SHF band designations have been adopted as an international standard. The others are commonly used, but not all authors adhere to those definitions. Because the propagation behavior of radio waves does not change abruptly with frequency, the band designations are often used somewhat loosely with respect to radiowave propagation. For example, a system operating in the range 200–500 MHz might be described as a UHF system. In the microwave region of the spectrum, frequency bands are often denoted by letter codes originally applied to radar systems. These are given in Table 2.

1.2. Environment

The most important environmental influences on terrestrial propagation are those of the troposphere, the ionosphere, and the ground. The troposphere is the lower region of the atmosphere where ionization is too small to affect radio waves appreciably. Tropospheric effects are caused by refractive index variations, absorption of energy by atmospheric gases, and absorption and scattering by precipitation. The ionosphere is the region of the

Table 1. Frequency Band Designations

Band Designation	Abbreviation	Frequency Range	Free-Space Wavelength Range
Ultralow frequency	ULF	< 3 Hz	> 100 Mm
Extremely low frequency	ELF	3 Hz–3 kHz	100 Mm–100 km
Very low frequency	VLF	3–30 kHz	100–10 km
Low frequency	LF	30–300 kHz	10–1 km
Medium frequency	MF	300 kHz–3 MHz	1 km–100 m
High frequency	HF	3–30 MHz	100–10 m
Very high frequency	VHF	30–300 MHz	10–1 m
Ultrahigh frequency	UHF	300 MHz–3 GHz	1 m–10 cm
Super high frequency	SHF	3–30 GHz	10–1 cm
Extremely high frequency	EHF	30–300 GHz	1 cm–1 mm
Submillimeter		300 GHz–1 THz	1 mm–300 μ m

Source: *The New IEEE Standard Dictionary of Electrical and Electronics Terms*, 5th ed. © The Institute of Electrical and Electronics Engineers, 1993, Ref. 1, with modifications by the author. By permission of the IEEE.

Table 2. Standard Radar Frequency-Band Nomenclature

Band Designation	Frequency Range	Approx. Free-Space Wavelength Range
HF	3–30 MHz	100–10 m
VHF	30–300 MHz	10–1 m
UHF	300 MHz–1 GHz	1 m–30 cm
L	1–2 GHz	30–15 cm
S	2–4 GHz	15–7.5 cm
C	4–8 GHz	7.5–3.75 cm
X	8–12 GHz	3.75–2.5 cm
K _n	12–18 GHz	2.5–1.67 cm
K	18–27 GHz	1.67–1.11 cm
K _a	27–40 GHz	1.11 cm–7.5 mm
V	40–75 GHz	7.5–4 mm
W	75–110 GHz	4–2.73 mm
Millimeter(mm) ^a	110–300 GHz	2.73–1 mm
Submillimeter	300 GHz–3 THz	1 mm–100 μm

^aThe mm designation is sometimes used for the entire frequency range 40 GHz to 300 GHz when general information for this range is to be conveyed.

Source: *The New IEEE Standard Dictionary of Electrical and Electronics Terms*, 5th ed. © The Institute of Electrical and Electronics Engineers, 1993, Ref. 2, with modifications by the author. By permission of the IEEE.

atmosphere where free electrons produced by ionization strongly affect radio waves in the frequency ranges below about 30 MHz to 50 MHz. The lower altitudinal limit of the ionosphere is in the range of 60 km to 70 km. The term ground designates the surface of the earth, including bodies of water. Local structures, such as buildings, may also have important effects.

1.3. Interaction of Frequency and Environment

The effect of the environment depends greatly on the system frequency. For example, in frequency ranges below about 30 MHz, the ionosphere is likely to be of prime importance. At VHF and UHF, under certain meteorological conditions, tropospheric layering may form “ducts” that guide waves very efficiently in one frequency band, but not in another. The system frequency is also important with respect to the ground. At microwave frequencies, the wavelength and depth of penetration into the ground are on the order of centimeters; thus the dielectric constant and conductivity at the very surface are important, and even intuitively smooth ground may need to be considered rough if its vertical variations are not small compared to wavelength. In contrast, at VLF the penetration depth is many hundreds of meters; therefore the dielectric constant and conductivity far below the visible surface are important, and the ground may appear smooth even in mountainous areas. As these examples show, it is important to characterize the environment by parametric values appropriate to the system frequency.

The system design also influences the extent to which the environment affects signal propagation. For example, in many satellite communication system calculations the effects of the ground are neglected because the ground station antennas are highly directive and pointed upward. Thus little energy hits the ground on Earth-to-space

transmission, and little of the energy impinging on the ground is received by the antenna on the space-to-Earth path.

The effects of the troposphere, ionosphere, and ground vary with frequency and also with geographic location. In addition, the troposphere and ionosphere vary in time. This variability adds complexity to predicting signal propagation. In many cases, such predictions are limited to statistical estimates.

1.4. Noise Considerations

System performance depends on signal strength and also on noise that corrupts the signal. Depending on the system frequency, significant external noise sources may be impulses due to lightning propagated via the ionosphere, emissions from astronomical sources (e.g., the sun, radio stars), or the “blackbody” noise emanating from the transmission medium.

2. PROPAGATION MECHANISMS AND MODELS

An exact solution of the radiowave propagation problem entails solving Maxwell’s equations in the presence of the source and the environment. Such calculations are beyond the state of the art. Instead, approximations based on physical processes are used. For example, the reception of two rays from the transmitter might be considered, one directly and the other via reflection by the ground. Such physically based, mathematical or empirical approximations for calculating signal strength are called propagation models [3]. The term “propagation mechanism” is used here for the physical processes that lead to relatively simple propagation models.

In principle, all of the propagation mechanisms discussed later might be considered in every application, but generally one or a few account sufficiently well for the system performance, so that the others are neglected. However, the specific application must be kept in mind. For example, a very small interfering signal may be objectionable, and thus an interference calculation may require including a propagation mechanism that would otherwise be unimportant.

2.1. Direct Propagation

The simplest propagation mechanism is direct propagation in which the signal travels from the emitter to the receiver unaffected by any propagation medium, except possibly for attenuation and mild refraction. When attenuation and refraction are absent, propagation occurs as in free space. Direct propagation takes the form of a spherical wave, which can be approximated locally at the receiver as a plane wave.

Although free-space propagation is a highly idealized approximation, it has important applications. Many radars and many satellite communication systems operating in the UHF to C-band frequency range have antennas sufficiently directive to exclude ground effects, and at these frequencies atmospheric effects may generally be neglected. In these cases, the free-space model is applicable. For

satellite communications at higher frequencies, atmospheric effects become important, but the direct propagation model is still applicable when attenuation and refractive effects are included. Predictions are very much more complicated if the refractive index is inhomogeneous and time-varying.

In general, the direct propagation model applies when the emitter and receiver are in plain view with respect to one another, provided the effects of other propagation mechanisms are negligible. This situation is most frequently encountered in the atmosphere at UHF to SHF with systems utilizing highly directive antennas.

2.2. Terrain Reflections

When antennas are not highly directional, signals may travel directly from the emitter to the receiver and also by reflection from the ground. In this case, both paths must be considered in evaluating the system performance. Typical examples are ground-to-air, air-to-ground, and air-to-air communication at UHF. In air-to-air communication, the size limitation of aircraft antennas makes it impossible to use highly directive antennas in this frequency range, so that it is not possible to keep the signal from reaching the ground. In practical ground-to-air and air-to-ground communication, the ground station antenna is situated somewhat above the ground and is not sufficiently directive to discriminate against the ground-reflected ray. Thus the propagation model for these systems must include both the direct and the ground-reflection mechanisms.

2.3. Ducting

The effects of gravity and meteorological conditions make atmospheric density and humidity functions of altitude. Though the resulting variations of the refractive index are small, significant bending of the signal path in the vertical plane can occur. This refraction may be sufficiently strong to guide the wave along the Earth's surface, a behavior called ducting. Tropospheric ducts are most commonly observed at VHF and UHF. They may also exist at higher frequencies, but the more directional antennas employed at these frequencies are less likely to couple efficiently into a duct. Ducting is much more common at some geographic locations than others because it is closely related to meteorological phenomena. Although ducting is a fairly reliable means of communication in some locations, it is generally more likely to be a source of potential interference.

2.4. Terrain Diffraction

When the emitter and receiver are not within plain view of each other at VHF and higher frequencies, diffraction is an appropriate propagation mechanism. When the intervening terrain is hilly or mountainous, the diffracting obstacles are often modeled as cylinders or even as vertical half planes ("knife-edge" diffraction). Diffraction by a conducting sphere is the most common model for relatively flat terrain. More detailed computational models are becoming

increasingly available as a result of increased computer power, more theoretical insights, and better algorithms.

2.5. Ground Wave

When antennas operate near (in terms of wavelength) and on the ground, it is found that the direct and ground-reflected waves cancel almost completely. In this case, however, it is found that a wave can be excited that travels along the surface and decreases rapidly with altitude. Since efficient transmitting antennas at MF and lower frequencies are necessarily large structures because the wavelength is long, they are generally on or near the ground, and ground-wave propagation is important at these frequencies. It is the dominant mechanism for local standard AM broadcast reception in the 540 kHz–1.7 MHz band. It is also dominant at LF and VLF for relatively short distances.

2.6. Tropospheric Scatter

The troposphere is never truly homogeneous, as common experience with weather indicates. In fact, variations over a wide range of dimensional scales are ever present. These variations can be used to advantage when very reliable wireless point-to-point communications are needed over a path of hundreds of kilometers. When very strong signals are beamed at an atmospheric region within the line of sight of both stations, the relatively small signal scattered out of the beam toward the receiving station may, nevertheless, be sufficient to enable communication at rates on the order of 5 megabits per second over 150–400 km distances at UHF. This technique is useful for communication with communities in arctic regions, where other forms of communication (e.g., satellite communications, ionospheric reflection) are less reliable.

2.7. Ionospheric Reflection

In the upper LF, MF, and HF bands, signals give the appearance of traveling in rays that are reflected by the ionosphere above and by the ground below, resulting in a series of "hops." Actually, the rays are bent rather than sharply reflected in the ionosphere, but the effect is essentially the same. Signal transmission by this means is very efficient, and great distances are spanned with modest power and equipment. For these reasons the "short-wave" bands, as they are often called popularly, are utilized for broadcasting, point-to-point communications, and amateur use, and portions of this band of the radio frequency spectrum have become exceedingly crowded.

2.8. Waveguide Modes

Ray theory requires that the medium vary slowly with respect to wavelength. Thus it fails for radiowave propagation at frequencies lower than about 100 kHz because the corresponding wavelengths no longer meet the requirement that they be much smaller than the Earth-ionosphere distance. Instead, at VLF and ELF the Earth-ionospheric space is modeled as a concentrically spherical waveguide with the ground as the lower boundary and the ionosphere as the upper. In the ELF and lower VLF bands

only one, or at most a few, modes need to be considered. The number of modes and therefore the computational difficulty increases with frequency. Calculations in the LF frequency band are especially laborious, and a combination of ray and mode theory is often used.

2.9. Ionospheric Scatter

Signals with a frequency too high to be reflected coherently from the ionosphere may, nevertheless, still be affected by it. One possible effect is the scattering of small amounts of energy out of the beam by local irregularities. This is analogous to the scattering by local irregularities of the troposphere, as discussed previously. Ionospheric scattering is most pronounced in the frequency range immediately above that which supports coherent ionospheric reflections. Ionospheric D-region scatter systems have been operated successfully in the VHF band over 1000–2000 km distances with a bandwidth on the order of 100 Hz.

2.10. Meteor Scatter

Meteors are popularly considered rare phenomena, perhaps because our daytime habits and increasingly urbanized existence allow many of us to see them only rarely. Actually, visually observable meteors are not rare by any means, but those too small to observe visually are even more abundant. The number of meteors of a given mass entering the atmosphere approximates an inverse exponential function of the mass. As these meteors enter the atmosphere, they heat and ionize the gas around them, forming trails of ionization. Where this ionization is substantially more intense than that of the ambient ionosphere, the trails reflect signals of a higher frequency than normally reflected from the ionosphere. Meteor-scatter communication systems are operated successfully in the VHF band. Because suitably oriented trails are not always present, such systems must store the information to be transmitted between the occurrence of suitable trails and transmit the information in bursts when such trails are present. This limits the average data rate. Also, a means must be provided for sensing the occurrence of suitable trails. Usually each station continually transmits a pilot signal, and the other station is assured that a trail exists when it receives that signal.

2.11. Whistlers

Electromagnetic signals in the ELF/VLF frequency range can propagate through the ionosphere in a peculiar mode in which they closely follow the lines of the earth's magnetic field. It is not easy to launch artificial waves with such very long wavelengths, but lightning generates electromagnetic energy in this frequency range quite effectively. Lightning-generated signals travel along Earth's magnetic field lines, often going out to a distance of several Earth radii, and so are guided to the antipode, that is the point on the opposite hemisphere where the field line terminates. Part of the signal may be reflected from the antipode along the same field line to the point of origin and may be reflected there again, and so forth. The frequency

components of the signal are dispersed in the travel, so that the frequency at the receiver changes with time. When amplified, the resulting audio has a sound reminiscent of whistling; hence the name of the propagation mechanism. Although not useful for information transmission, this propagation mechanism is utilized to obtain information about the upper ionosphere. The same propagation mechanism, but using much stronger artificial magnetic fields, has been investigated for communicating at much higher frequencies through the much denser ion sheath that forms around space vehicles as they reenter the atmosphere.

2.12. Nonatmospheric Propagation

The propagation mechanisms discussed so far are those commonly encountered with electromagnetic signal propagation through space or the earth's atmosphere. A different environment prevails when signals propagate through the ocean, through the earth's crust, or through some planetary atmospheres. In the ocean, only signals at ELF or in the visible-light frequency band penetrate to substantial depths. Propagation to substantial depths through the ground also presents difficulties. Nevertheless, radar systems for locating objects, such as water and gas lines at typical shallow depths, are quite successful.

3. TRANSMISSION LOSS

The most significant question relating to propagation for a radar or telecommunication system is the adequacy of the received signal level. The ratio, usually expressed in decibels (dB), between the power at some point in the transmitting system and a corresponding point in the receiving system is called a loss. Although time delay or phase shift may also be important parameters in some systems, loss is a universal and primary consideration because it relates directly to signal strength. In many cases, the loss varies randomly in time or with location. Then statistical parameters relating to the loss are often the quantities of interest, for example, the median loss.

Several types of losses are defined; see Fig. 1. The usual symbol for loss is L , although A (for attenuation) is also used, and subscripts denote the specific loss under consideration. The loss definitions below follow, with some emendations, those in "The concept of transmission loss for radio links," Recommendation ITU-R P.341-4, of the International Telecommunication Union [4].

3.1. Total Loss

The total loss (L_t or A_t) of a link is the ratio between the power supplied by the transmitter and the power supplied to the corresponding receiver under real installation, propagation, and operational conditions. Note: it is necessary to specify the points at which these powers are determined.

3.2. System Loss

System loss (L_s or A_s) is the ratio of the RF power input to the transmitting antenna terminals and the resultant RF

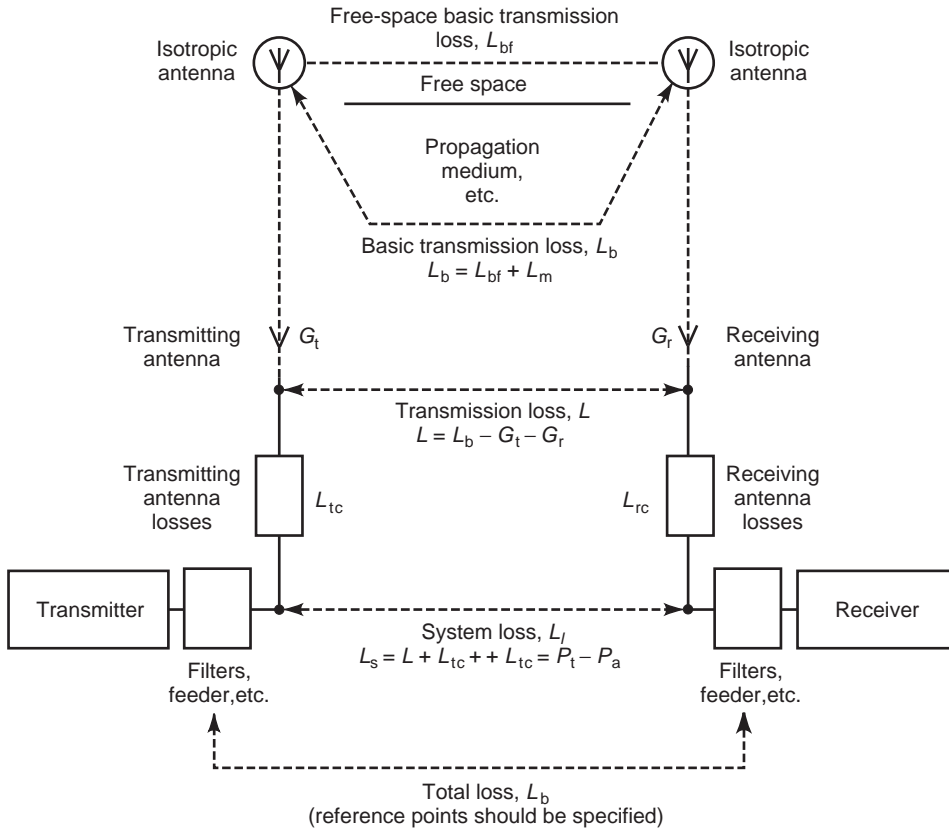


Figure 1. Definitions of losses. [Adapted from “The concept of transmission loss for radio links” (Recommendation ITU-R P.341-4), © International Telecommunication Union, 1996, Ref. 4. By permission.]

power available at the receiving antenna terminals. It is expressed in decibels by

$$L_s = 10 \log(p_t/p_a) = P_t - P_a \quad (1)$$

where P_t denotes the RF power input to the transmitter antenna terminals, P_a the available power at the receiving antenna terminals, both measured in the same units, and P_t , P_a are the corresponding power relative to a common reference level (e.g., 1 W) in decibels. Because the system loss is referred to the antenna terminals, it excludes all losses in feeder lines but includes all losses associated with the antenna, for example, antenna-grounding losses, dielectric losses in the antenna, antenna loading-coil losses, and antenna-terminating resistor losses, if applicable.

3.3. Transmission Loss

Transmission loss (L or A) is defined as the ratio between the power radiated by the transmitting antenna and the power that would be available at the receiving antenna terminals if this antenna were lossless but its radiation diagram, that is, its directional and polarization characteristics, were unchanged. In Fig. 1 the antenna losses L_{tc} and L_{rc} for transmitting and receiving, respectively, are defined as $10 \log(R'/R)$, where R' is the resistive component of the impedance of the designated antenna and R is its radiation resistance.

3.4. Basic Transmission Loss

Basic transmission loss, denoted by L_b or A_i , is the transmission loss that would occur if the antennas were replaced by hypothetical isotropic antennas with the same polarizations in the direction of propagation as the real antennas. The propagation path is retained, but the effects of obstacles close to the antennas are disregarded. The symbols G_t and G_r in Fig. 1 denote the directivity gains of the antennas for the polarization and direction of propagation being considered. The basic transmission loss is the ratio of the equivalent isotropic radiated power (EIRP) of the transmitter system to the available power from a hypothetical isotropic, lossless receiving antenna with the same polarization as that of the real antenna in the propagation direction.

3.5. Free-Space Basic Transmission Loss

The free-space basic transmission loss (L_{bf} or A_0) is the transmission loss that would occur if the antennas were replaced with hypothetical isotropic antennas, matched in polarization for maximum power transfer and located in an unbounded, lossless, homogeneous, isotropic environment, retaining the distance between antennas. Free-space basic transmission loss is a function only of the ratio of the distance d between transmitter and receiver to the wavelength λ . It is given in decibels by

$$L_{bf} = 20 \log\left(\frac{4\pi d}{\lambda}\right) \quad (2)$$

where d and λ are measured in the same units.

3.6. Loss Relative to Free Space

Loss relative to free space (L_m or A_m) is defined as the difference between the basic transmission loss and the free-space basic transmission loss in decibels:

$$L_m = L_b - L_{bf} \quad (3)$$

Loss relative to free space may be divided into losses of different types, for example, extinction loss, diffraction loss, wave interference loss, reflection loss, polarization-coupling loss, aperture-to-medium coupling loss. Because these losses are directly connected with propagation mechanisms, the end result of propagation studies is frequently presented in the form of loss relative to free space.

3.6.1. Extinction Loss. Extinction is the total attenuation due to absorption of signal power in the propagation medium and scattering of power out of the beam by the medium. In the troposphere at X band and higher frequencies, oxygen, water vapor, and precipitation absorb power from a propagating wave. Precipitation also scatters power out of the beam in the frequency range where particle or droplet size is not small compared to the wavelength. In the ionosphere, absorption is caused primarily by collision between electrons and neutral molecules. In ground-wave propagation, currents in the ground cause absorption losses.

3.6.2. Diffraction Loss. On a propagation path using diffraction by terrain features or by the spherical Earth, only a fraction of the power is scattered in a direction useful to the receiver. The resulting decrease in useful power density is considered a diffraction loss.

3.6.3. Wave Interference Loss. When several rays combine to produce the effective received wave, interference may cause a signal decrease relative to that of the ray directly received. This effect can be characterized as a wave interference loss, although this terminology is not encountered frequently in practice. Of course, signals may also be enhanced by interference, resulting in a negative wave interference loss.

3.6.4. Reflection Loss. Several phenomena result in reflection loss. If reflection from the ground occurs at a non-grazing incidence, the amplitude of the effective plane-wave reflection coefficient of the interface is less than unity, resulting in a reflection loss in the reflected ray. If the surface is rough on a scale comparable to the wavelength, energy is reflected in a range of angles about the specular, resulting in an effective specular reflection coefficient less than unity, and hence a reflection loss in the specular direction. If the reflecting surface is curved, the defocusing (or focusing) effect of the curvature decreases (or enhances) the reflected power density in the propagation direction of interest, resulting in a positive (or negative) reflection loss. The concave curvature of the ionosphere, as seen from the ground, causes focusing. The convex curvature of the Earth surface, as seen from above, causes defocusing.

3.6.5. Polarization-Coupling Loss. In an isotropic medium, polarization-coupling loss occurs when the receiving and transmitting antenna polarizations are not matched for optimum power transfer. This situation arises most frequently when interfering signals are being considered.

In an anisotropic medium, such as the ionosphere, plane waves of arbitrary polarization are split into two rays of characteristic polarizations. These rays propagate with generally different attenuations and phase shifts, and they recombine into a single plane wave when emerging from the medium or even within the medium. Polarization-coupling loss occurs when the transmitted wave polarization does not match that of a desired characteristic mode and when the receiving antenna does not match the polarization of the wave received.

3.6.6. Aperture-to-Medium Coupling Loss (Antenna-Gain Degradation). For some propagation mechanisms under certain conditions, the free-space directivity gain of the antennas is not realized. Then the directivity gain is said to be degraded, and the resulting signal loss is termed an aperture-to-medium coupling loss. As an example, in tropospheric scatter propagation a highly directive antenna is used to illuminate a region of the turbulent troposphere that is visible from both transmitter and receiver. The receiver utilizes a highly directive antenna to receive the signal scattered from the illuminated region. The part of the region within both the transmitting antenna beam and the receiving antenna beam is called the common volume. Increasing the directivity of each antenna increases the signal level, but the increase is not proportional to the directivity increase because the narrower beams reduce the common volume. Thus the full free-space directivity of the antennas is not realized. The loss in directivity, when considered an antenna effect, is called antenna-gain degradation; when considered as a propagation effect, it is called antenna-to-medium coupling loss. It is most pronounced for antennas with very high directivity.

Acknowledgment

By permission. Responsibility for selection and modification of this material rests solely with the author and not the ITU. The *ITU-R Recommendations* may be obtained from International Telecommunication Union, General Secretariat of Sales and Marketing Service, Place des Nations CH 1211 GENEVA 20 (Switzerland), Telephone: +41 22 730 61 41 (English)/+41 22 730 61 42 (French), Telex: 421 000 uit ch/Fax: +41 22 730 5194, X.400: S=Sales; P=itu; C=ch, Internet: *Sales@itu.int*.

BIBLIOGRAPHY

1. *The New IEEE Standard Dictionary of Electrical and Electronics Terms*, 5th ed. (IEEE Standard 100-1992), IEEE, New York, 1993, pp. 1062–1063.
2. Ref 1, p. 1053.
3. Ref 1, p. 1018.
4. The concept of transmission loss for radio links (Recommendation ITU-R P.341-4), in *ITU-R Recommendations 1995 P*, International Telecommunication Union, Geneva, 1996, pp. 6–11.

FURTHER READING

The P (propagation) series of the Recommendations of the Radio Sector (ITU-R) of the International Telecommunication Union (ITU) is a very authoritative source, for example, Ref. 4. The Recommendations include propagation models, definitions, and other technical material relating to radiowave propagation adopted and updated at International Radiocommunication Assemblies. [Before 1994, what is now ITU-R was called the International Radio Consultative Committee (CCIR) of the ITU, and its publications included Reports and Recommendations. Volume 5 dealt with propagation in nonionized media and Volume 6 with ionized media.]

An excellent, concise, yet fairly complete text for the mature reader is M. P. M. Hall, L. W. Barclay, and M. T. Hewitt, eds., *Propagation of Radiowaves*, IEE, London, 1996.

Much current research in radiowave propagation is published in *Radio Science*.

RADIOWAVE PROPAGATION GROUND EFFECTS

DAVID A. HILL
National Institute of Standards
and Technology

Radiowave propagation plays an important role in modern communication, radar, and navigation systems. The mathematical theory of radiowave propagation is based on Maxwell's equations [1], which were formulated by James Clerk Maxwell in the 1860s [2]. The first free-space radiowave transmission experiments between a pair of antennas were performed by Heinrich Hertz in the 1880s [3]. In

1897 Marconi first patented a wireless telegraphy system based on long-distance, radiowave propagation.

1. RADIOFREQUENCY SPECTRUM

Table 1 summarizes the frequency range, propagation characteristics, and applications of the letter-designated bands of the radiofrequency spectrum. The lower and upper bounds of the radiofrequency spectrum in Table 1 are somewhat arbitrary, but the indicated frequency range, 3 Hz–300 GHz, encompasses the portion of the electromagnetic spectrum for which conventional antennas are used to transmit and receive radiowaves. Some of the characteristics of the individual bands are as follows.

1.1. Extremely Low Frequency

Because free-space, extremely low-frequency (ELF) wavelengths are extremely long (greater than 100 km), antennas are very inefficient radiators because they are electrically small. The other major disadvantage of ELF is lack of bandwidth for information transmission. Despite these disadvantages, ELF is useful for worldwide communication with submarines because the long wavelengths have a useful penetration depth (also called skin depth) of several tens of meters in seawater. In addition, the earth and the ionosphere support a low-attenuation waveguide mode at ELF [4] so that a wave, once launched, will propagate around the world with little loss of intensity. The ionosphere is the part of the upper atmosphere where sufficient ionization exists to affect radiowave propagation, and these effects are covered thoroughly in Ref. 5. The earth-ionosphere waveguide can actually support cavity modes with resonances [6] in the ELF range, and these resonances (called Schumann resonances) further enhance the field strength worldwide. Unfortunately,

Table 1. The Radiofrequency Spectrum

Frequency Range	Band	Characteristics	Applications
3 Hz–3 kHz	ELF	Long wavelength; inefficient antennas; Earth-ionosphere waveguide; penetration of ground and seawater	Submarine communications; underground mine communications; geophysics
3–30 kHz	VLF	Large transmitting antennas; Earth-ionosphere waveguide	Long-range communication; navigation, and time-frequency dissemination; geophysics
30–300 kHz	LF	Earth-ionosphere waveguide; high atmospheric noise	Navigational beacons
300 kHz–3 MHz	MF	Ground wave; ionospheric reflections (at night)	AM broadcasting; maritime communications
3–30 MHz	HF	Long-distance ionospheric propagation; maximum usable frequency	Maritime and aeronautical communications; citizens band and amateur radio
30–300 MHz	VHF	Line-of-sight propagation; ionosphere scatter; meteor scatter	Television and FM broadcasting; air-traffic control; navigation
300 MHz–3 GHz	UHF	Line-of-sight propagation	Television broadcast; radar; satellite communication; mobile communication; global positioning system
3–30 GHz	SHF	Line-of-sight propagation; atmospheric absorption	Radar; satellite communication; microwave links
30–300 GHz	EHF	Line-of-sight propagation; severe atmospheric absorption	Radar; secure communication; satellite links

these resonances also enhance the competing atmospheric noise caused by thunderstorms.

ELF waves have an even larger skin depth (typically greater than 100 m) in ground or rock (which have lower electrical conductivities than sea water) and have been found useful for communication to and within underground mines [7]. Because of this ability to penetrate rock, ELF waves have also been used in direction-finding applications for location of miners trapped in underground mines [8].

1.2. Very Low Frequency

The free-space wavelengths at very low frequency (VLF) are still very long (10–100 km), and this generally dictates the use of large vertical transmitting antennas with large ground systems to reduce ground current losses. Smaller antennas, such as vertical whips, loops, and grounded horizontal wires, can be used for receiving. VLF antennas and propagation are thoroughly covered in Ref. 9.

Even though the bandwidth is limited, VLF systems are useful for long-range reliable communications, long-range dissemination of standards for frequency and time, long-range navigation (including the U.S. Navy Omega system), and geophysical probing of the ground and the ionosphere. For short ranges, VLF propagates predominantly by the ground wave. For long ranges, the reflections from the ionosphere become important, and multiple reflections between Earth and the ionosphere can be described by Earth–ionosphere waveguide modes [9].

1.3. Low Frequency

The low frequency (LF) band is also characterized by low attenuation of ground wave propagation and Earth–ionosphere waveguide propagation. Thus the LF band is useful for long-range communication and for marine and aeronautical radio navigation beacons. The LORAN-C navigation system is based on the arrival time of a ground-wave pulse with a carrier frequency of approximately 100 kHz so that later-arriving ionospheric reflections do not affect the system. The wavelengths are long enough (1–10 km) that large transmitting antennas are needed.

1.4. Medium Frequency

The most popular use of the medium-frequency (MF) band is AM broadcasting, which uses the frequency range from 535 to 1705 kHz. The propagation mode is generally vertically polarized ground wave, although ionospheric reflections (sky wave) can extend the range at night. Maritime communications is another application.

1.5. High Frequency

In the high-frequency (HF) band, ionospheric reflections provide the possibility of long-distance communications. The maximum usable frequency (MUF) for ionospheric reflection generally occurs in the upper part of the HF band, but the MUF is a complicated function of the incidence angle and the state of the ionosphere [5]. HF appli-

cations include maritime, aeronautical, amateur, and citizens band communications.

1.6. Very High Frequency

At frequencies above 30 MHz, propagation is predominantly by line of sight with some refraction (bending) caused by the atmosphere. However, in some cases ionospheric reflections can occur at frequencies up to 60 MHz. Scattering from ionized meteor trails (which can be up to 25 km in length) can be used for meteor burst communications [10]. Very high frequency (VHF) applications include television and FM radio broadcasting and air traffic control and navigation.

1.7. Ultrahigh Frequency

Ultrahigh-frequency (UHF) propagation is essentially by line of sight with some atmospheric refraction and some scattering by ionospheric irregularities. Applications include UHF television broadcasting, various radars, satellite communications, and personal communications [11]. The global positioning system (GPS) uses transmitting satellites in the UHF band.

1.8. Superhigh Frequency

Superhigh frequency (SHF) propagation is primarily line of sight, and atmospheric absorption becomes significant, particularly above 10 GHz. A water vapor absorption line exists at approximately 21 GHz, and rain absorption and scattering increase with frequency throughout the band. SHF applications include radar, satellite communication, and microwave links.

1.9. Extremely High Frequency

The extremely high-frequency (EHF) band is also called the millimeter-wave spectrum since the wavelength ranges from 1 to 10 mm. Atmospheric absorption becomes extreme in this band. An oxygen absorption band is centered at approximately 60 GHz, and numerous absorption peaks due to oxygen and water vapor occur above 100 GHz. Rain attenuation is significant throughout the entire EHF band. Satellite-to-satellite links are not affected by atmospheric absorption, and secure short-range communication systems take advantage of high attenuation to limit propagation range.

2. LINE-OF-SIGHT PROPAGATION

Line of sight is the dominant mode of propagation for elevated antennas and high frequencies, as indicated Table 1. The mathematical description of line-of-sight propagation is most easily obtained by considering simple antennas in a free-space environment. In this section two classical cases are discussed. First a Hertzian dipole source is considered to illustrate radiation of a spherical wave. Then transmission between a pair of antennas is analyzed to derive the classical expression for basic free-space transmission loss.

2.1. Radiation from a Hertzian Dipole

This article covers only steady-state, time-harmonic sources and fields [12] with time variation $\exp(j\omega t)$, where the angular frequency $\omega = 2\pi f$ and f is the radio frequency. The time dependence is suppressed in the equations. The basic source is a current I extending over an incremental length l . This elementary dipole source is called a Hertzian dipole and has a moment Il . If the dipole is directed along the z axis, as shown in Fig. 1, the radiated electric field has two components, E_θ and E_r , and the radiated magnetic field has only a single component H_ϕ . The expressions for these field components can be derived from scalar and vector potentials [12]

$$E_\theta = \frac{Il\eta_0}{4\pi} e^{-jk_0 r} \left(\frac{jk_0}{r} + \frac{1}{r^2} + \frac{1}{jk_0 r^3} \right) \sin \theta \quad (1)$$

$$E_r = \frac{Il\eta_0}{2\pi} e^{-jk_0 r} \left(\frac{1}{r^2} + \frac{1}{jk_0 r^3} \right) \cos \theta \quad (2)$$

and

$$H_\phi = \frac{Il}{4\pi} e^{-jk_0 r} \left(\frac{jk_0}{r} + \frac{1}{r^2} \right) \sin \theta \quad (3)$$

where the free-space wave number $k_0 = \omega \sqrt{\mu_0 \epsilon_0}$ the free-space impedance $\eta_0 = \sqrt{\mu_0 / \epsilon_0}$, μ_0 is the magnetic permeability of free space, and ϵ_0 is the dielectric permittivity of free space. The equations for radiation by the dual source (a magnetic dipole or small loop) are given in Ref. 12.

Very close ($k_0 r \ll 1$) to the Hertzian dipole, the electric field is dominated by the r^{-3} inverse cube term, and Eqs. (1) and (2) can be approximated by

$$E_\theta \approx \frac{Il \sin \theta}{4\pi j \omega \epsilon_0 r^3} \quad \text{and} \quad E_r \approx \frac{Il \cos \theta}{2\pi j \omega \epsilon_0 r^3} \quad (4)$$

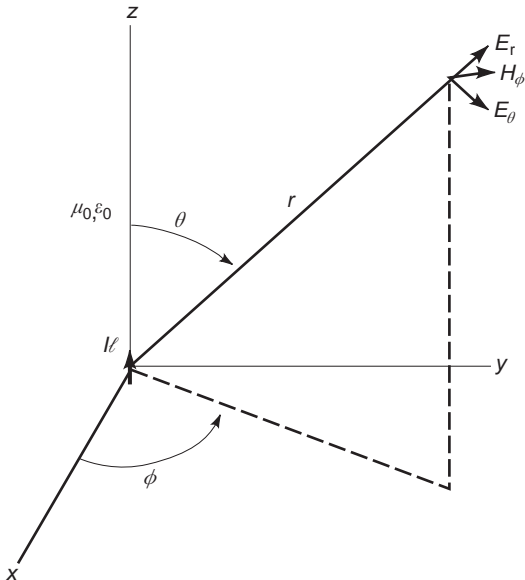


Figure 1. Geometry for radiation from a short electric dipole.

Equation (4) gives the electric field components of charges $\pm Il/j\omega$ separated by a distance l . The magnetic field of an electric dipole has no quasistatic term. At intermediate distances ($k_0 r \approx 1$), the inverse-square terms dominate Eqs. (1)–(3), and the field is called the induction field.

For most practical applications, such as communications or radar, the far fields are of interest. At large distances ($k_0 r \gg 1$), the inverse-distance terms dominate Eqs. (1) and Eq. (3), and the fields are approximated by

$$H_\phi \approx \frac{jk_0 Il}{4\pi r} e^{-jk_0 r} \sin \theta \quad \text{and} \quad E_\theta \approx \eta_0 H_\phi \quad (5)$$

Even though Eq. (5) applies to a Hertzian dipole, it illustrates the more general far-field properties that the electric and magnetic fields are related by the free-space impedance and they are orthogonal to each other and to the radial direction of propagation. Hence the radial electric field E_r in Eq. (2) has no inverse-distance term.

The power density of the electromagnetic field is called the Poynting vector \mathbf{S} and can be written

$$\mathbf{S} = \mathbf{E} \times \mathbf{H}^* \quad (6)$$

where boldface denotes vectors and $*$ denotes complex conjugate. The far-field expression for \mathbf{S} can be obtained by substituting Eq. (5) into Eq. (6)

$$\mathbf{S} \approx \hat{\mathbf{r}} \eta_0 \left(\frac{k_0 |I| l \sin \theta}{4\pi r} \right)^2 \quad (7)$$

where $\hat{\mathbf{r}}$ is the unit vector in the radial direction. The $\sin^2 \theta$ factor in Eq. (7) is specific to the radiation pattern of a Hertzian dipole, but the inverse-square dependence applies to the far field of any radiator. The total radiated power P can be obtained by integrating Eq. (7) over a far-field sphere [12]:

$$P = \int_0^{2\pi} d\phi \int_0^\pi d\theta r^2 \sin \theta \hat{\mathbf{r}} \cdot \mathbf{S} \quad (8)$$

$$= \frac{\eta_0 (k_0 |I| l)^2}{6\pi}$$

The result for the total radiated power in Eq. (8) is independent of the radius r at which the integration is evaluated, but the evaluation is simplest in the far field, where \mathbf{S} can be approximated by Eq. (7).

2.2. Free-Space Transmission Loss

Now consider free-space transmission between a pair of antennas in the far fields of each other. The received power P_r can be written [13]

$$P_r = \frac{P_t G_t G_r}{(2k_0 D)^2} = \frac{P_t G_t G_r \lambda_0^2}{(4\pi D)^2} \quad (9)$$

where P_t is the transmitted power, G_t is the gain of the transmitting antenna, G_r is the gain of the receiving antenna, D is the separation distance between the antennas,

and the free-space wavelength $\lambda_0 = 2\pi/k_0$. The D^{-2} factor represents the inverse-square dependence of the radiated power density available at the receiving antenna.

The antenna and propagation effects can be separated by writing Eq. (9) in the following form:

$$\frac{P_r}{P_t} = G_t G_r \left(\frac{\lambda_0}{4\pi D} \right)^2 \quad (10)$$

The squared factor on the right side of Eq. (10) is dimensionless and does not involve the antenna gains. The reciprocal is called the free-space transmission loss L_0 and is usually expressed in decibels:

$$\begin{aligned} L_0 &= 10 \log_{10} \left(\frac{4\pi D}{\lambda_0} \right)^2 \text{ dB} \\ &= 20 \log_{10} \left(\frac{4\pi D}{\lambda_0} \right) \text{ dB} \end{aligned} \quad (11)$$

Normally the antenna gains and the power ratio in Eq. (10) are also expressed in decibels.

3. REFLECTION FROM A PLANAR INTERFACE

3.1. Plane-Wave Incidence

Radiowaves are often reflected from smooth, flat surfaces, such as building walls or ground. When the reflecting surface is not a perfect conductor, part of the radio energy penetrates the surface, and part of the energy is reflected. Reflection of a plane wave from a uniform half-space with a planar interface can be analyzed exactly by matching boundary conditions at the interface, and the derived reflection coefficients can then be used in other practical applications.

Consider the idealized geometry in Fig. 2. A free-space plane wave propagating at an angle θ_0 to the surface normal is incident on a half-space with permittivity ϵ , electrical conductivity σ , and permeability μ . The angle of reflection θ_r equals the angle of incidence, $\theta_r = \theta_0$. The reflection coefficient depends on the polarization of the incident field.

For horizontal polarization (electric field perpendicular to the plane of incidence), the reflection coefficient Γ_h is given by [1]

$$\Gamma_h = \frac{\mu k_0 \cos \theta_0 - \mu_0 \sqrt{k^2 - k_0^2 \sin^2 \theta_0}}{\mu k_0 \cos \theta_0 + \mu_0 \sqrt{k^2 - k_0^2 \sin^2 \theta_0}} \quad (12)$$

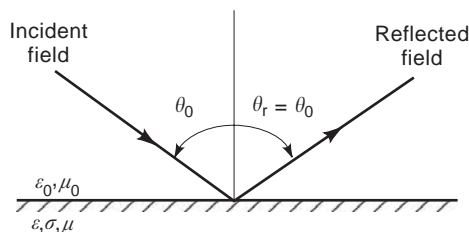


Figure 2. Geometry for plane-wave reflection from a homogeneous half space.

where $k = \omega \sqrt{\mu(\epsilon - j\sigma/\omega)}$. For vertical polarization (electric field parallel to the plane of incidence), the reflection coefficient Γ_v is

$$\Gamma_v = \frac{\mu_0 k^2 \cos \theta_0 - \mu k_0 \sqrt{k^2 - k_0^2 \sin^2 \theta_0}}{\mu_0 k^2 \cos \theta_0 + \mu k_0 \sqrt{k^2 - k_0^2 \sin^2 \theta_0}} \quad (13)$$

The reflection coefficients in Eqs. (12) and (13) apply to both the reflected electric and magnetic fields. The power reflection coefficients are obtained by taking the squares of the magnitudes of the field reflection coefficients, $|\Gamma_v|^2$ and $|\Gamma_h|^2$. In general, the reflection coefficients in Eqs. (12) and (13) are complex because k is complex. Thus the reflected field undergoes phase shift as well as reduction in amplitude. In the limiting case of grazing incidence ($\theta_0 = \pi/2$), both Γ_h and Γ_v equal -1 .

For the common case where the reflecting medium is non-magnetic ($\mu = \mu_0$), the reflection coefficients in Eqs. (12) and (13) simplify to

$$\Gamma_h = \frac{\cos \theta_0 - \sqrt{(k/k_0)^2 - \sin^2 \theta_0}}{\cos \theta_0 + \sqrt{(k/k_0)^2 - \sin^2 \theta_0}} \quad (14)$$

and

$$\Gamma_v = \frac{(k/k_0)^2 \cos \theta_0 - \sqrt{(k/k_0)^2 - \sin^2 \theta_0}}{(k/k_0)^2 \cos \theta_0 + \sqrt{(k/k_0)^2 - \sin^2 \theta_0}} \quad (15)$$

For the further simplification to a dielectric ($\sigma = 0$) reflecting medium, Eqs. (14) and Eq. (15) reduce to

$$\Gamma_h = \frac{\cos \theta_0 - \sqrt{\epsilon_r - \sin^2 \theta_0}}{\cos \theta_0 + \sqrt{\epsilon_r - \sin^2 \theta_0}} \quad (16)$$

and

$$\Gamma_v = \frac{\epsilon_r \cos \theta_0 - \sqrt{\epsilon_r - \sin^2 \theta_0}}{\epsilon_r \cos \theta_0 + \sqrt{\epsilon_r - \sin^2 \theta_0}} \quad (17)$$

where $\epsilon_r = \epsilon/\epsilon_0$.

As incidence angle θ_0 varies from 0 (normal incidence) to $\pi/2$ (grazing incidence), Γ_h varies smoothly from $(1 - \sqrt{\epsilon_r})/(1 + \sqrt{\epsilon_r})$ to -1 . However, for vertical polarization, the reflection coefficient Γ_v equals 0 at the Brewster angle, $\theta_B = \tan^{-1}(\sqrt{\epsilon_r})$. At this angle, all of the incident energy is refracted into the dielectric. An examination of Eq. (15) reveals that the presence of nonzero conductivity σ (which yields a complex k) prevents Γ_v from going to zero. However, if the imaginary part of k is small, there is nevertheless a pseudo-Brewster angle [14], where $|\Gamma_v|$ goes through a minimum.

3.2. Dipole Sources

Consider now a vertical electric dipole source located at a height h over a reflecting half space, as in Fig. 3. In the far

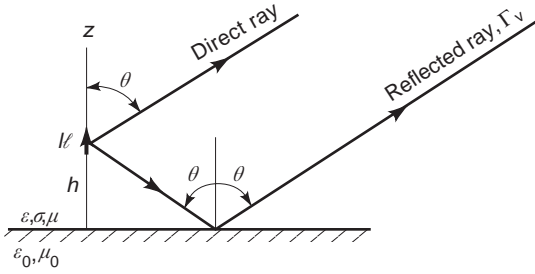


Figure 3. Far-field radiation from a vertical electric dipole over a homogeneous half-space. The reflection coefficient Γ_v is a function of the incidence angle θ .

field the electric field has only a θ component E_θ , which can be written as the sum of a direct and a reflected ray:

$$E_\theta = \frac{j\omega\mu_0 Il \sin \theta}{4\pi r} e^{-jk_0 r} \times (e^{jk_0 h \cos \theta} + \Gamma_v e^{-jk_0 h \cos \theta}) \quad (18)$$

where Γ_v is given by Eq. (13). For the special case of a perfectly conducting ground plane ($\sigma = \infty$), the reflection coefficient equals 1, and Eq. (18) reduces to

$$E_\theta|_{\sigma=\infty} = \frac{j\omega\mu_0 Il \sin \theta}{2\pi r} e^{-jk_0 r} \cos(k_0 h \cos \theta) \quad (19)$$

Equation (19) has a maximum at the interface, $\theta = \pi/2$.

The dual case of a vertical magnetic dipole source is shown in Fig. 4. The source is a small loop of area A and current I , and the loop axis is in the vertical direction. The electric field is horizontally polarized, and in the far field the ϕ component E_ϕ is

$$E_\phi = \frac{\eta_0 k_0^2 IA \sin \theta}{4\pi r} e^{-jk_0 r} \times (e^{jk_0 h \cos \theta} + \Gamma_h e^{-jk_0 h \cos \theta}) \quad (20)$$

where Γ_h is given by Eq. (12). For the special case of a perfectly conducting ground plane ($\sigma = \infty$), the reflection coefficient equals -1 , and Eq. (20) reduces to

$$E_\phi|_{\sigma=\infty} = \frac{j\eta_0 k_0^2 IA \sin \theta}{2\pi r} e^{-jk_0 r} \sin(k_0 h \cos \theta) \quad (21)$$

Equation (21) has a null at the interface, $\theta = \pi/2$.

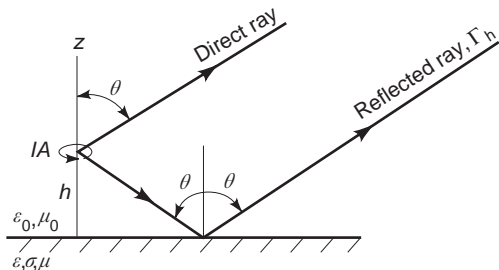


Figure 4. Far-field radiation from a vertical magnetic dipole over a homogeneous half space. The reflection coefficient Γ_h applies to horizontal polarization.

For realistic (finite) ground parameters, the reflection coefficients for both vertical polarization Γ_v and horizontal polarization Γ_h equal -1 at grazing incidence ($\theta = \pi/2$). Hence the direct and reflected rays cancel in Eqs. (18) and (20), and the electric field is 0:

$$E_\theta|_{\theta=\pi/2} = 0 \quad \text{and} \quad E_\phi|_{\theta=\pi/2} = 0 \quad (22)$$

In reality, only the space wave (the inverse-distance field that occurs for $\theta > 0$) is 0 at the interface. The ground wave is the dominant field component near the interface, and it will be discussed in detail later. It has a more rapid decay with distance, but it does not equal 0 at the interface.

4. PLANE-WAVE REFRACTION

4.1. Dielectric Medium

Consider a plane wave incident on a dielectric half-space, as in Fig. 5. For simplicity, the dielectric is taken to be lossless ($\sigma = 0$) and nonmagnetic ($\mu = \mu_0$). The incident field propagates at an angle θ_0 to the normal, and the transmitted field is refracted at an angle θ_t to the normal. The angle of refraction is determined by requiring that the phases of the refracted field and the incident field maintain the same relationship at all points along the interface. This requirement is met if the tangential wave numbers in the two media are equal: $k_0 \sin \theta_0 = k \sin \theta_t$. For the case of a dielectric medium, this reduces to

$$\frac{\sin \theta_t}{\sin \theta_0} = \sqrt{\frac{\epsilon_0}{\epsilon}} \quad \text{or} \quad \theta_t = \sin^{-1} \left(\frac{\sin \theta_0}{n} \right) \quad (23)$$

where $n = \sqrt{\epsilon/\epsilon_0} = \sqrt{\epsilon_r}$ is the refractive index. Equation (23) is called Snell's law (14). As with the reflection coefficient, the transmission coefficient depends on the polarization of the incident field.

For horizontal polarization (electric field perpendicular to the plane of incidence), the electric field transmission

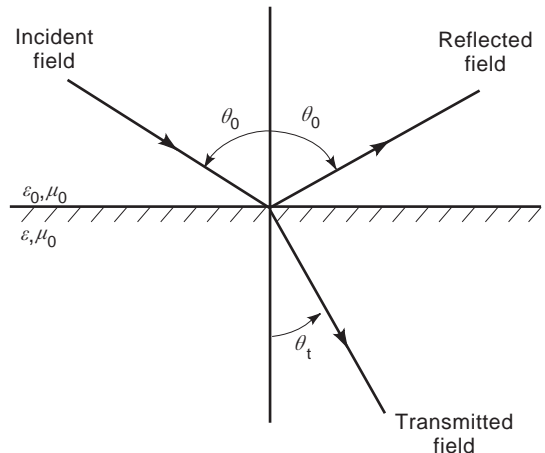


Figure 5. Reflection from and refraction into a dielectric half-space. The diffraction angle θ_t is determined from Snell's law.

coefficient T_h is given [1]

$$T_h = \frac{2 \cos \theta_0}{\cos \theta_0 + \sqrt{\epsilon_r - \sin^2 \theta_0}} \quad (24)$$

For vertical polarization (electric field parallel to the plane of incidence), the electric field transmission coefficient T_v is given by [1]

$$T_v = \frac{2\sqrt{\epsilon_r} \cos \theta_0}{\epsilon_r \cos \theta_0 + \sqrt{\epsilon_r - \sin^2 \theta_0}} \quad (25)$$

The magnetic field transmission coefficients are obtained by multiplying the electric field transmission coefficients in Eqs. (24) and (25) by $\sqrt{\epsilon_r}$.

4.2. Lossy Medium

Transmission into a lossy medium at oblique incidence is complicated by the fact that the planes of constant phase do not coincide with the planes of constant amplitude. Such a transmitted field is called an inhomogeneous plane wave [1]. To simplify the mathematics, the case of normal incidence, as shown in Fig. 6, will be considered.

For normal incidence the electric field is transverse to the z direction. The incident electric field E^i in the free-space region ($z > 0$) has unit amplitude:

$$E^i = \exp(jk_0z) \quad (26)$$

The reflected electric field E^r in the free-space region is

$$E^r = \Gamma_h|_{\theta_0=0} \exp(-jk_0z) \quad (27)$$

where Γ_h is given by Eq. (12). The transmitted electric field E^t in the lossy medium ($z < 0$) is

$$E^t = T \exp(jkz), \text{ where } k = \omega\sqrt{\mu(\epsilon - j\sigma/\omega)} \quad (28)$$

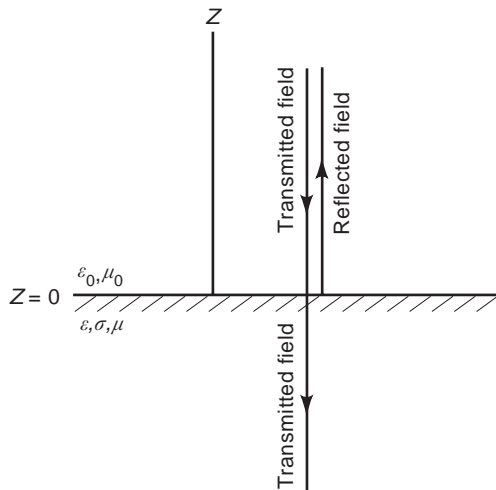


Figure 6. Reflection from and transmission into a lossy half-space for normal incidence.

The transmission coefficient T is given by

$$T = \frac{2\mu k_0}{\mu k_0 + \mu_0 k} \quad (29)$$

Equation (29) can be written compactly in terms of impedances:

$$T = \frac{2\eta}{\eta + \eta_0} \quad (30)$$

where η_0 is the free-space impedance and $\eta = \sqrt{\mu/(\epsilon - j\sigma/\omega)}$ is the impedance of the lossy medium. In general, T is complex, and the transmitted field undergoes both phase shift and reduction in amplitude.

As the transmitted field propagates into the lossy medium, it undergoes further attenuation and phase delay, as indicated by Eq. (28). The attenuation and phase shift can be isolated by normalizing the field to the value at the interface

$$\frac{E^t}{T} = \exp[\text{Im}(k)d] \exp[-j\text{Re}(k)d] \quad (31)$$

where Re indicates real part, Im indicates imaginary part, and $d = -z$ is the depth in the medium. The first exponential factor on the right side of Eq. (31) represents attenuation, and the second factor represents phase shift.

The skin depth δ is defined as the distance over which the amplitude of the field decreases to $1/e$ times its initial value. The expression for δ is

$$\delta = \frac{-1}{\text{Im}(k)} = \sqrt{\frac{2}{\sqrt{a^2 + b^2} - a}}, \text{ where } a = \omega^2\mu\epsilon \text{ and } b = \omega\mu\sigma \quad (32)$$

For a lossless medium ($\sigma = b = 0$), the skin depth δ is ∞ (no attenuation).

For the case where conduction currents dominate displacement currents ($\sigma \gg \omega\epsilon$), Eq. (32) simplifies to

$$\delta \approx \sqrt{\frac{2}{\omega\mu\sigma}} = \sqrt{\frac{1}{\pi f \mu\sigma}} \quad (33)$$

Equation (33) applies to high-conductivity metals, such as copper, and to soil and rock at low frequencies.

5. THROUGH-THE-EARTH PROPAGATION

The antenna and propagation issues are similar for subsurface communications [7] and geophysical probing of Earth [15]. Both applications require transmission of electromagnetic waves through Earth, and both face the problem of high attenuation. To penetrate Earth to depths of 100 m or more, it is necessary to employ frequencies below about 3 kHz (ELF). The reason for this is that the skin depth is proportional to $1/\sqrt{f}$, as indicated in Eq. (33). Although plane-wave propagation as discussed in the previous section gives valid results for distant sources, it does

not give valid quantitative results for the typical case where the transmitting antenna is located at or below the air–Earth interface. So this section will deal with the fields of surface or buried antennas.

At frequencies below 3 kHz, the free-space wavelength is greater than 100 km. Consequently, ELF antennas are electrically small even though they could be physically large. The methods and antennas used in geophysical probing are too varied to give a complete description. However, if we limit the applications to deep, subsurface probing and to through-Earth communication, then the most useful antennas are of two types: wire-loop antennas and straight-wire antennas grounded at the ends.

5.1. Fields of Loop Antennas

Loop antennas are commonly used in geophysical sounding and subsurface communications, and they have the advantage that no grounding is required. In geophysical sounding, loop antennas transmit a time-varying magnetic field into the earth, and eddy currents are excited in conducting bodies. These eddy currents generate a secondary magnetic field that can be received by a second loop antenna. In mine communications, transmitting loops can be used either at or below the Earth surface. Horizontal transmitting loops are typically a large, single turn of wire laid out on ground Earth. Various shapes, such as circular or rectangular, are used depending on the application. When the loop dimensions are small compared with the skin depth in Earth and the observer distance, the horizontal loop radiates as a vertical magnetic dipole.

A circular loop of radius a located at the earth surface ($z = 0$) is shown in Fig. 7. The earth conductivity is σ , and the magnetic permeability of both the air and Earth is μ_0 . For the low frequencies considered here, displacement currents are negligible, and the fields are independent of permittivity. This is called the quasistatic approximation and is obtained by setting the free-space wave number k_0 equal to 0. The wavenumber in Earth is approximated by $k \approx \sqrt{\omega\mu_0\sigma/j}$, where the square root is taken so that the imaginary part is negative.

When the circular loop carries a uniform current I , the nonzero field components are H_z , H_ρ , and E_ϕ . The vertical

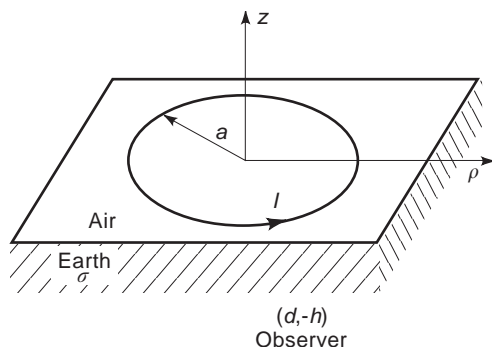


Figure 7. Circular loop on a conducting half-space with a subsurface observer.

magnetic field H_z in Earth ($z < 0$) is of primary interest for downlink communication between horizontal loops. At a depth h and a horizontal distance d , H_z is given by [16]

$$H_z = \frac{IA}{2\pi h^3} Q \quad (34)$$

where

$$Q = \int_0^\infty \frac{g^3 e^{-\sqrt{g^2 + jH^2}}}{g + \sqrt{g^2 + jH^2}} J_0(gD) \frac{2J_1(ga/h)}{ga/h} dg \quad (35)$$

$H = \sqrt{\omega\mu_0\sigma h}$, $D = d/h$, and J_0 and J_1 are the zero- and first-order Bessel functions [17]. The integration variable g is a normalized wavenumber; so the integration in Eq. (35) can be interpreted as the result of a superposition of all the waves that the loop antenna transmits into Earth. The exponential factor is consistent with skin depth attenuation because for small g it is given by $|\exp(-\sqrt{jH^2})| = \exp(-h/\delta)$, where δ is given by Eq. (33).

When $a/h \ll 1$, the factor $2J_1(ga/h)/(ga/h)$ approaches 1 over the significant range of g . In that case the dependence on a enters only on through the loop area $A (= \pi a^2)$, and the loop radiates like a magnetic dipole of moment IA . If the loop is buried at a depth h and the observer is located at the surface (as in uplink communications), the result for H_z is identical.

For the special case of $H = a/h = 0$, the quantity Q reduces to the following result for a static magnetic dipole:

$$Q \Big|_{H=a/h=0} = \frac{2 - D^2}{2(1 + D^2)^{5/2}} \quad (36)$$

If, in addition, $D = 0$, then $Q = 1$. Thus Q is the vertical magnetic field normalized to the on-axis magnetic field of a static magnetic dipole. For $D = 0$, both H_ρ and E_ϕ are 0.

In general, the integration in Eq. (35) must be performed numerically. The infinite upper limit presents no practical difficulty because of the exponential decay for large g . Figure 8 shows the normalized vertical magnetic field magnitude $|Q|$ on the loop axis ($D = 0$) as a function of normalized depth H for a magnetic dipole source ($a/h = 0$). For large values of H , the field strength decays exponentially just as a plane wave does. For geophysical probing, vertical sounding [18] is accomplished by varying the frequency, and low frequencies are required to obtain information on earth conductivity at great depth.

In mine communication [7] and source location [8], the off-axis ($D > 0$) field is of interest. Figure 9 shows the dependence of the vertical magnetic field strength on normalized horizontal distance D . For the static case ($H = 0$), there is a null at $D = \sqrt{2}$, as shown in Eq. (36), and that null can be useful in source location [8]. For nonzero values of H , Q is complex, and the null is filled in.

The magnetic field results in Figs. 8 and 9 are actually valid for small loops of any shape that can be represented by a magnetic dipole. When the loop dimensions are large, the field depends strongly on shape. The theory has been developed for loops of arbitrary shape in a conducting medium that is homogeneous or layered [19]. Results for a loop of nonzero radius are shown in Fig. 10 for the static

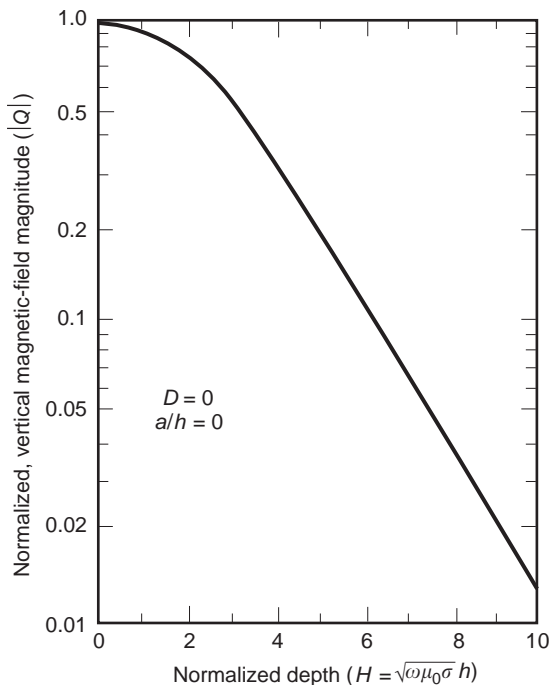


Figure 8. Magnitude of the normalized vertical magnetic field of a small circular loop ($a = 0$) as a function of the normalized depth H on the axis ($D = 0$), (From Ref. 16.)

case ($H = 0$). As the loop radius is increased, the vertical magnetic field is reduced on the axis ($D = 0$), but is increased at the larger horizontal distances. A similar behavior occurs for nonzero values of H .

Also, similar results have been calculated for rectangular loops [19].

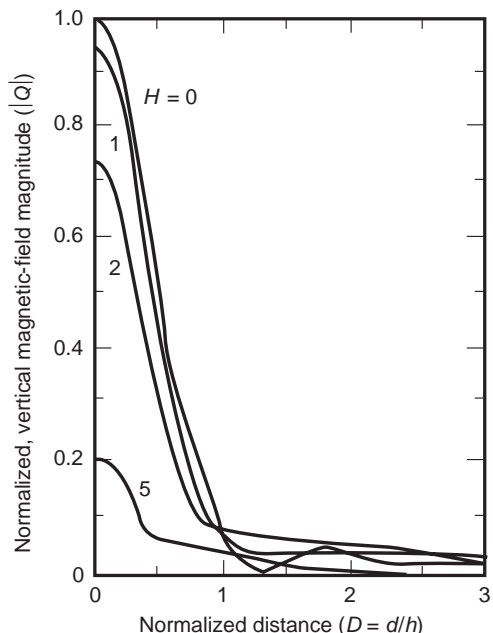


Figure 9. Magnitude of the normalized vertical magnetic field of a small circular loop ($a = 0$) as a function of the normalized horizontal distance D . (From Ref. 16.)

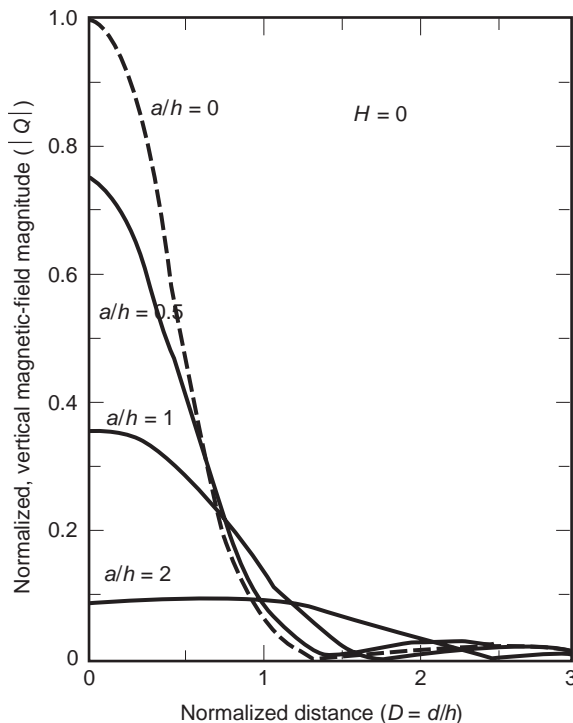


Figure 10. Magnitude of the normalized vertical magnetic field of a circular loop of radius a as a function of normalized distance D . (From Ref. 16.)

5.2. Fields of Grounded Wire Antennas

Grounded wire antennas are the other antenna type commonly used to transmit fields through Earth. In addition to geophysical sounding, these antennas are used for uplink and downlink communications in mines and for ELF communications with submarines [4]. A typical configuration is shown in Fig. 11. The antenna is of length $2l$, and the current I is assumed to be constant over the length of the antenna. This assumption is valid for insulated antennas grounded at the ends when the length of the antenna is much less than a free-space wavelength [20]. Because of the use of low frequencies, displacement currents are neglected in air and in the earth. The earth has conductivity σ and permeability μ_0 .

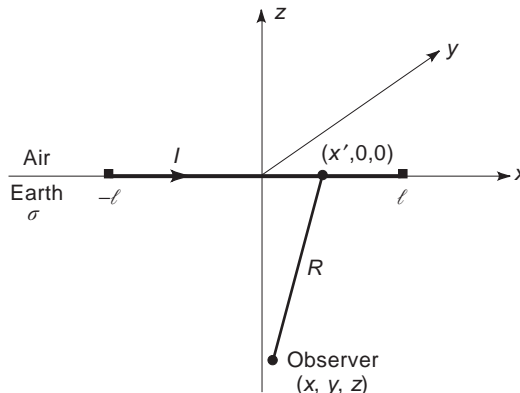


Figure 11. Electric line source on a conducting half space with a subsurface observer.

The subsurface electric and magnetic fields are both of interest in mine communication and in probing of geophysical features. In mine communication, the subsurface magnetic field is received with a loop antenna, or the subsurface electric field is received with a grounded wire antenna.

First consider the fields produced by an incremental current source of length dx' located at x' , as shown in Fig. 11. Because of the quasistatic approximation, the Sommerfeld integral forms for an incremental source of current moment $I dx'$ can be greatly simplified [21]. As a result, the magnetic field components are

$$dH_x = \frac{Idx'}{2\pi\gamma^2} \left(\frac{\partial^4 N}{\partial x \partial y \partial z^2} - \frac{\partial^3 P}{\partial x \partial y \partial z} \right) \quad (37)$$

$$dH_y = \frac{Idx'}{2\pi\gamma^2} \left(\frac{\partial^3 P}{\partial z^3} + \frac{\partial^3 P}{\partial x^2 \partial z} + \frac{\partial^4 N}{\partial z^2 \partial y^2} \right) \quad (38)$$

and

$$dH_z = \frac{Idx'}{2\pi\gamma^2} \left(\frac{\partial^4 N}{\partial y \partial z^3} - \gamma^2 \frac{\partial^2 N}{\partial y \partial z} - \frac{\partial^3 P}{\partial y \partial z^2} \right) \quad (39)$$

where $N = I_0[(\gamma/2)(R+z)]K_0[(\gamma/2)(R-z)]$, $P = R^{-1} \exp(-\gamma R)$, $R = \sqrt{(x-x')^2 + y^2 + z^2}$, $\gamma = \sqrt{j\omega\mu_0\sigma}$, and I_0 and K_0 are modified Bessel functions [17]. Similarly, the electric field components are

$$dE_x = \frac{-Idx'}{2\pi\sigma} \left(\frac{\partial^2 P}{\partial z^2} + \frac{\partial^3 N}{\partial y^2 \partial z} \right) \quad (40)$$

$$dE_y = \frac{Idx'}{2\pi\sigma} \frac{\partial^3 N}{\partial y \partial x \partial z} \quad (41)$$

and

$$dE_z = \frac{Idx'}{2\pi\sigma} \frac{\partial^2 P}{\partial x \partial z} \quad (42)$$

Although all six field components are, in general, nonzero, the dominant field components of interest are H_y , H_z , and E_x . These are the only nonzero components for a line source of infinite length, and all other field components vanish in the plane $x=0$, even for a line source of finite length. To obtain the fields of the entire line source, Eqs. (38)–(40) must be integrated over the range of x' from $-l$ to l . For normalization purposes, it is convenient to write the fields in the following forms:

$$H_y = \frac{I}{2\pi h} A(H, Y, X, L) \quad (43)$$

$$H_z = \frac{I}{2\pi h} B(H, Y, X, L) \quad (44)$$

and

$$E_x = \frac{-j\omega\mu_0 I}{2\pi} F(H, Y, X, L) \quad (45)$$

where $H = \sqrt{\omega\mu_0\sigma h}$, $Y = y/h$, $X = x/h$, $L = l/h$, and $h = -z$. The normalized quantities A , B , F , H , Y , X , and L are dimensionless. The specific forms for the normalized fields are

$$A(H, Y, X, L) = \frac{h}{\gamma^2} \int_{-l}^l \left(\frac{\partial^3 P}{\partial z^3} + \frac{\partial^3 P}{\partial x^2 \partial z} + \frac{\partial^4 N}{\partial z^2 \partial y^2} \right) dx' \quad (46)$$

$$B(H, Y, X, L) = \frac{h}{\gamma^2} \int_{-l}^l \left(\frac{\partial^4 N}{\partial y \partial z^3} - \gamma^2 \frac{\partial^2 N}{\partial y \partial z} - \frac{\partial^3 P}{\partial y \partial z^2} \right) dx' \quad (47)$$

and

$$F(H, Y, X, L) = \frac{1}{\gamma^2} \int_{-l}^l \left(\frac{\partial^2 P}{\partial z^2} + \frac{\partial^3 N}{\partial y^2 \partial z} \right) dx' \quad (48)$$

The integral forms in Eqs. (46)–(48) simplify for both the low-frequency (small H) and high-frequency (large H) cases [21], but numerical integration is required in general. Typical numerical results for $H=2$ are shown in Figs. 12–14. Although A , B , and F are complex for $H>0$, only the magnitudes are plotted. The phases are relatively constant as a function of L . For very small values of L , the fields are essentially those of a short dipole and are proportional to L , as indicated by Eqs. (38)–(40). For large L ,

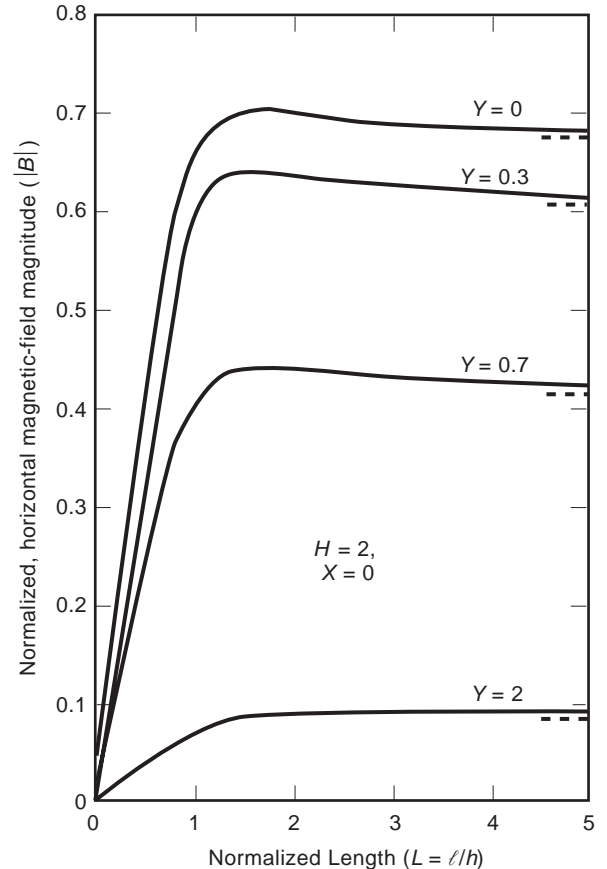


Figure 12. Magnitude of the normalized horizontal magnetic field as a function of the normalized line length L . The dashed lines indicate the limit, $L = \infty$. From Ref. 16.

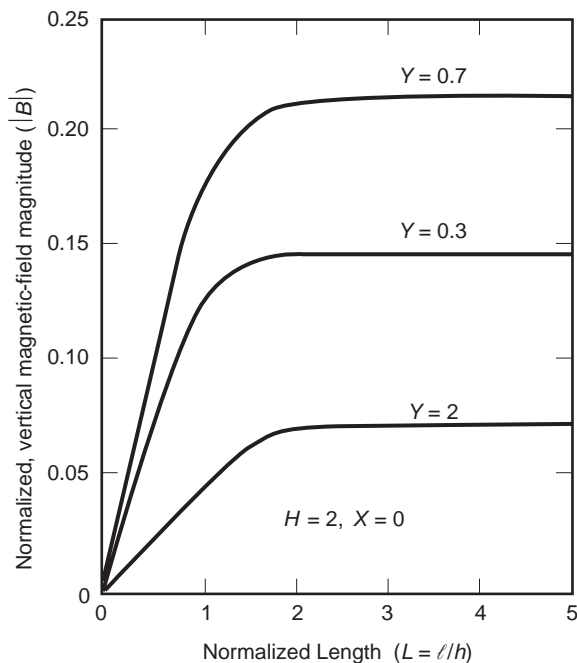


Figure 13. Magnitude of the normalized vertical magnetic field as a function of the normalized line length L . (From Ref. 16.)

the field components eventually reach those of an infinite line source [22]. The limits for large L are shown for the horizontal magnetic field as dashed lines in Fig. 12. In some geophysical applications, it is desirable to make the grounded wire long enough to simulate an infinitely long line source. An examination of Figs. 11–14 and other calculations [21] shows that this is approximately achieved

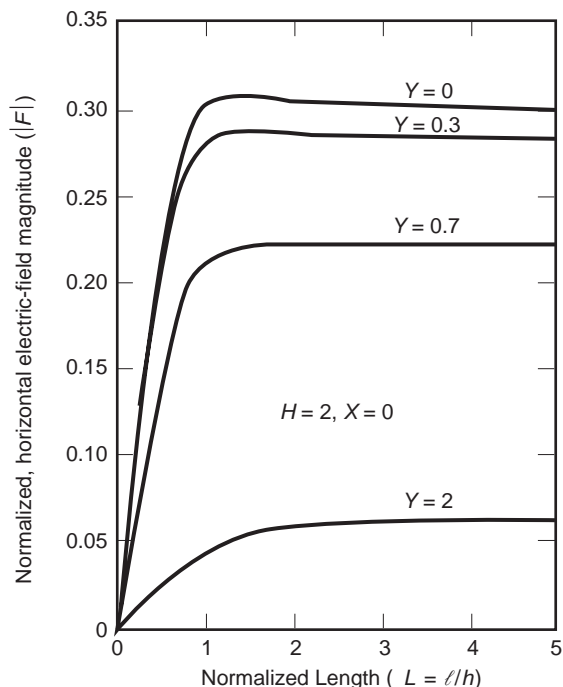


Figure 14. Magnitude of the normalized horizontal electric field as a function of the normalized line length L . (From Ref. 16.)

for L greater than ~ 2 . This means that the antenna length $2l$ should be at least 4 times the depth h of interest in a particular geophysical application.

Straight, grounded wires are also used to excite broadband, transient fields in Earth. To illustrate the dispersive nature of Earth, it is useful to examine the frequency dependence of the subsurface electric fields. The frequency dependence of all three components of the electric field has been analyzed [23], but only the dominant component E_x , will be considered here. Equations (45) and (48) can be recast in the following equivalent form

$$E_x = \frac{-I}{2\pi\sigma h^2} E_{xn}(W, L, X, Y) \tag{49}$$

where

$$E_{xn} = h^2 \int_{-l}^l \left(\frac{\partial^2 P}{\partial z^2} + \frac{\partial^3 N}{\partial y^2 \partial x} \right) dx' \tag{50}$$

and $W = \omega\mu_0\sigma h^2$. Equations (49) and (50) are consistent with Eqs. (45) and (48), but here the frequency dependence is explicitly displayed through the dimensionless frequency parameter W .

Some numerical results for $|E_{xn}|$ as a function of W are shown in Fig. 15. As W approaches 0, E_{xn} approaches the dc result E_{xn}^{dc} , which is obtained from the gradient of a scalar potential [23]

$$E_{xn}^{dc} = (L - X)R_1^{-3} + (L + X)R_2^{-3} \tag{51}$$

where

$$R_1 = \sqrt{(X - L)^2 + Y^2 + 1} \quad \text{and} \tag{52}$$

$$R_2 = \sqrt{(X + L)^2 + Y^2 + 1}$$

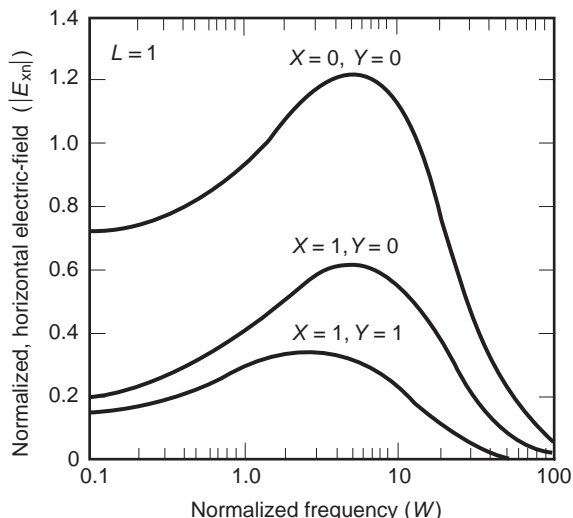


Figure 15. Magnitude of the normalized horizontal electric field of a horizontal line source as a function of the normalized frequency W .

When W becomes large, $|E_{xn}|$ decreases exponentially because the skin depth becomes small.

Straight, grounded wire antennas are also used underground. For example, long wire antennas have been laid out in mine tunnels for uplink transmission. The surface fields of such antennas have been computed for the general case where the antenna is not parallel to the air–earth interface [24] to model cases where either the tunnel or the Earth surface is not level.

6. GROUND-WAVE PROPAGATION

When both the transmitting and receiving antennas are located on the ground, the direct and reflected waves cancel. Consequently, the inverse-distance space wave is 0 as indicated in Eq. (22). In this case the ground wave is the dominant field component, and it can be calculated for either a flat-Earth model or a curved-earth model.

6.1. Flat-Earth Model

The flat-Earth model is useful for analyzing propagation along flat surfaces [25] or curved surfaces with very large radii of curvature (such as Earth). Consider a vertical electric dipole (VED) source located at an impedance surface, as shown in Fig. 16. The air region has free-space permittivity ϵ_0 , and free-space permeability μ_0 is assumed everywhere. The non-zero field components are E_z , and E_ρ , and H_ϕ .

For propagation analysis, Earth can be characterized by a surface impedance Z_s under fairly general conditions. The surface impedance is the ratio of the horizontal electric and magnetic fields at the earth surface: $Z_s = -(\mathbf{E}_\rho/H_\phi)|_{z=0}$. For the two-layer model shown in Fig. 16, the surface impedance for grazing incidence (as in ground-wave propagation) is given by [26]

$$Z_s = Z_1 Q \quad (53)$$

where

$$Z_1 = \eta_1 \sqrt{1 - \frac{\eta_1^2}{\eta_0^2}} \quad (54)$$

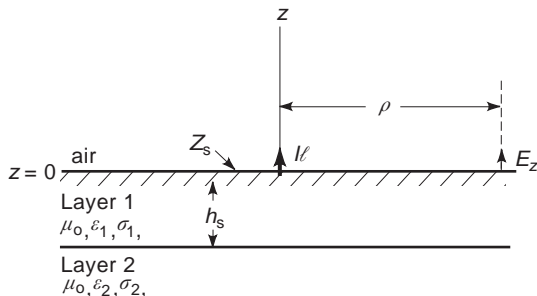


Figure 16. Vertical electric dipole source at the surface of a two-layer half-space. The surface impedance Z_s depends on the properties of both layers.

$$Q = \frac{(u_2/u_1) + (\gamma_2^2/\gamma_1^2) \tanh u_1 h_1}{(\gamma_2^2/\gamma_1^2) + (u_2/u_1) \tanh u_1 h_1} \quad (55)$$

$$\eta_1 = \sqrt{\frac{\mu_0}{\epsilon_1 - j\sigma_1/\omega}}, \quad u_1 = \sqrt{\gamma_1^2 + k_0^2}, \quad u_2 = \sqrt{\gamma_2^2 + k_0^2}, \quad \gamma_1^2 = j\omega\mu_0(\sigma_1 + j\omega\epsilon_1)$$

and $\gamma_2^2 = j\omega\mu_0(\sigma_2 + j\omega\epsilon_2)$. The layer thickness h_1 and the layer constitutive parameters are defined in Fig. 16. Q is a correction factor to account for the layering, and $Q = 1$ for a homogeneous earth. For any passive Earth model, the real part of the surface impedance must be nonnegative: $\text{Re}(Z_s) \geq 0$. For a homogeneous Earth, the phase of Z_s ranges from 0 to $\pi/4$. For a layered Earth, the phase of Z_s can range from $-\pi/2$ to $\pi/2$.

At large distances from the source ($k_0\rho \gg 1$), the dominant vertical electric field component E_z can be written [26]

$$E_z = \frac{-j\omega\mu_0 I l}{2\pi\rho} e^{-jk_0\rho} F(p) \quad (56)$$

where

$$F(p) = 1 - j\sqrt{\pi p} e^{-p} \text{erfc}(j\sqrt{p}) \quad (57)$$

$p = (-jk_0\rho/2)\Delta^2$, $\Delta = Z_s/\eta_0$, and erfc is the complementary error function (17). The function $F(p)$ is called the Sommerfeld attenuation function and is actually a correction to the field of a vertical electric dipole located at the surface of a perfectly conducting plane. The quantity p is dimensionless and called the numerical distance. For $|p| \ll 1$, we obtain $F(p) \approx 1$.

For large numerical distance ($|p| \gg 1$), the asymptotic form of F depends on the phase of p [26]:

$$F(p) \approx -\frac{1}{2p}, \quad -3\pi/2 \leq \text{phase}(p) \leq 0 \quad (58)$$

or

$$F(p) \approx -2j\sqrt{\pi p} e^{-p} - \frac{1}{2p}, \quad 0 < \text{phase}(p) \leq \pi/2 \quad (59)$$

The first term on the right side of Eq. (59) corresponds to a trapped surface wave [26] that can occur when the surface impedance is highly inductive (phase of $\Delta > \pi/4$). It does not occur for a homogeneous Earth, as indicated in Eq. (58). If Eq. (58) is substituted into Eq. (56), the following result is obtained for the electric field:

$$E_z \approx \frac{\eta_0 I l}{2\pi\rho^2 \Delta^2} e^{-jk_0\rho} \quad (60)$$

The ρ^{-2} dependence of the field in Eq. (60) is characteristic of a lateral wave that requires an interface to support it. A similar analysis is possible for horizontal polarization as produced by a horizontal electric dipole or vertical magnetic dipole source [26], but it is of less interest for

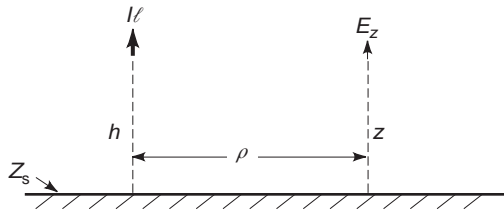


Figure 17. Elevated source and observer for propagation over a flat surface with surface impedance Z_s .

ground-wave propagation because it decays more rapidly with distance than vertical polarization.

If the height of either the transmitting dipole or the observer is raised above the interface, the field is increased by a factor called the height-gain function G [26]. Consider the case shown in Fig. 17, where both the source and observer are elevated. Then the electric field can be approximately written

$$E_z = \frac{-j\omega\mu_0 l l}{2\pi\rho} e^{-jk_0\rho} F(\rho) G(h) G(z) \quad (61)$$

where

$$G(h) = 1 + jk_0\Delta h \quad \text{and} \quad G(z) = 1 + jk_0\Delta z \quad (62)$$

By reciprocity, the height-gain function G is the same for the source and observer. Equation (62) is valid only for small heights ($k_0|\Delta|h \ll 1$).

6.2. Spherical Earth

The spherical-Earth model is used to account for diffraction loss that occurs for ground-wave propagation into the shadow region. The mathematical theory is complicated, but it has been well developed [26] and has been used to generate extensive numerical results for field strength as a function of distance, frequency, and Earth surface properties [27–29]. For short paths, the flat-Earth and spherical-Earth models give similar results, but for long paths the spherical-Earth model must be used for accurate predictions.

The geometry for a radial electric dipole source located at the surface of a sphere of radius a is shown in Fig. 18. The surface is characterized by a surface impedance Z_s , which can be determined by Eqs. (53)–(55) for a layered Earth. The non-zero field components are E_r , E_θ , and H_ϕ . The radial electric field E_r is the component of most interest, and its value at the surface ($r = a$) is

$$E_r = \frac{-j\omega\mu_0 l l}{2\pi d} e^{-jk_0 d} W \quad (63)$$

where d is the arc distance along the surface and W is the spherical-Earth attenuation function. It is a correction to the field of a vertical electric dipole on a perfectly conducting plane in the same manner as F for the flat Earth in Eq. (56). For large $k_0 a$ and $k_0 d$, W can be written as the classical residue series [25]

$$W = \sqrt{\frac{\pi x}{j}} \sum_{s=1}^{\infty} \frac{\exp(-jx t_s)}{t_s - q^2} \quad (64)$$

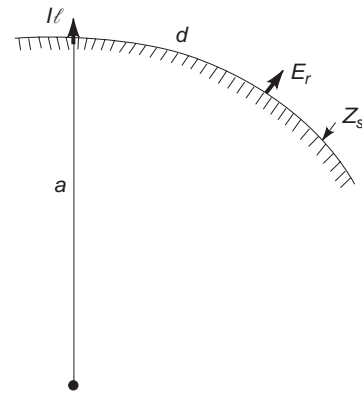


Figure 18. Vertical electric dipole source at the surface of a spherical earth with a surface impedance Z_s .

where $x = (k_0 a/2)^{1/3}(d/a)$, $q = -j(k_0 a/2)^{1/3}\Delta$, and $\Delta = Z_s/\eta_0$. The roots t_s satisfy the equation

$$w_1'(t_s) - q w_1(t_s) = 0 \quad (65)$$

where w_1 is an Airy function and w_1' is the derivative with respect to the argument. The Airy function w_1 is defined by

$$w_1(t) = \sqrt{\pi} [Bi(t) - jAi(t)] \quad (66)$$

where Ai and Bi are the Airy functions defined by Miller [30]. A systematic method for determining the roots of Eq. (65) has been presented for arbitrary values of the magnitude and phase of q [27].

The residue series in Eq. (64) is valid for any value of x , but converges slowly for small values of x . Two alternative methods are available for the calculation of W for small x . The power series in $x^{1/2}$ is most useful for small $|q|$, and the small-curvature expansion is most useful for large $|q|$.

The power series representation for W is given by (27,31)

$$W = \sum_{m=0}^{\infty} A_m (e^{j\pi/4} q x^{1/2})^m \quad (67)$$

where

$$A_0 = 1, \quad A_1 = -j\pi^{1/2}, \quad A_2 = -2$$

$$A_3 = j\pi^{1/2} \left(1 + \frac{1}{4q^3}\right), \quad A_4 = \frac{4}{3} \left(1 + \frac{1}{2q^3}\right)$$

$$A_5 = -\frac{j\pi^{1/2}}{2} \left(1 + \frac{3}{4q^3}\right), \quad A_6 = -\frac{8}{15} \left(1 + \frac{1}{q^3} + \frac{7}{32q^6}\right)$$

$$A_7 = \frac{j\pi^{1/2}}{6} \left(1 + \frac{5}{4q^3} + \frac{1}{2q^6}\right), \quad A_8 = \frac{16}{105} \left(1 + \frac{3}{2q^3} + \frac{27}{32q^6}\right)$$

$$A_9 = \frac{-j\pi^{1/2}}{24} \left(1 + \frac{7}{4q^3} + \frac{5}{4q^6} + \frac{21}{64q^9}\right)$$

and

$$A_{10} = - \left(\frac{32}{945} + \frac{64}{945q^3} + \frac{11}{189q^6} + \frac{7}{270q^9} \right)$$

In the numerical results to follow, the series has been truncated at $m = 10$ because higher-order coefficients A_m are not available in the literature.

The small-curvature expansion for W is given by [31,32]

$$W = F(p) + \frac{1}{4q^3} [1 - j\sqrt{\pi p} - (1 + 2p)F(p)] + \frac{1}{4q^6} \left[1 - j\sqrt{\pi p}(1 - p) - 2p + \frac{5p^2}{6} + \left(\frac{p^2}{2} - 1 \right) F(p) \right] \tag{68}$$

where $p = jxq^2 = -jk_0d\Delta^2/2$ and the flat-earth attenuation function $F(p)$ is given by Eq. (57). When the radius a approaches ∞ (zero curvature), q approaches ∞ , and W approaches F . An additional term in Eq. (68) proportional to q^{-9} has been obtained [31], but numerical results [27] indicate that it adds little improvement.

To illustrate the range of applicability of the various methods for computing W , a specific example for propagation at a frequency of 10 MHz is considered. The effective Earth radius a is taken to be 4/3 times the actual Earth radius of 6368 km in order to account for normal atmospheric refraction [33]. The magnitude of the normalized surface impedance $|\Delta| = 0.1$; this yields a value of 9.62 for the magnitude of q . For the phase of Δ , two values, 30° and 75° , are considered. The 30° value (phase of $q = -60^\circ$) lies in the range encountered for a typical homogeneous earth. The 75° value (phase of $q = -15^\circ$) lies in the highly inductive region, where a trapped surface wave is important. Numerical results for the magnitude of W as a function of distance are shown in Fig. 19, where the computations were carried out by four different methods. The oscillations in the vicinity of $d = 10$ km for the phase $(\Delta) = 75^\circ$ curve are due to interference between the trapped surface wave and the usual ground wave.

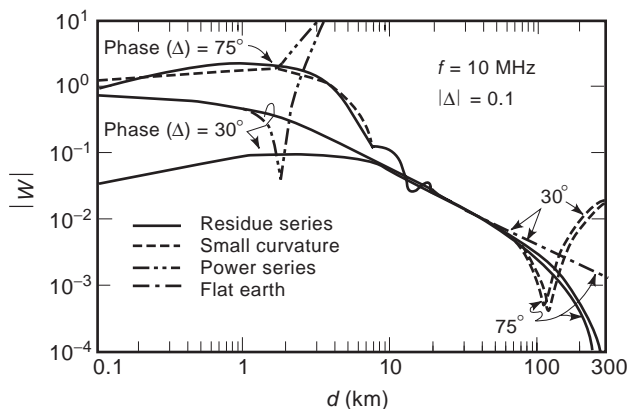


Figure 19. Magnitude of the spherical-Earth attenuation function as computed by various methods. (Results are shown outside their regions of validity for comparison purposes.) (From Ref. 27.)

Although the curve for phase $(\Delta) = 75^\circ$ contains more structure than that for phase $(\Delta) = 30^\circ$, the range of validity of the various computational methods depends only weakly on the phase of Δ . For graphical accuracy in Fig. 19, the different methods have the following ranges of validity. The residue series calculation from Eq. (64) using 50 terms is valid for d greater than about 10 km ($x > 0.11$). This value of d or x can always be decreased by increasing the number of terms. The small-curvature formula in Eq. (68) is valid for d less than ~ 50 km ($x < 0.57$). The power series in Eq. (67) is valid for d less than ~ 1 km ($x < 0.011$). The flat-Earth approximation in Eq. (57), which is the first term in Eq. (68), is valid for d less than ~ 15 km ($x < 0.17$). The characteristic of the flat-Earth approximation for large d is an algebraic decay (d^{-2}) as opposed to the correct exponential decay of the first term of the residue series. The small-curvature formula is far superior to the power series in this example because of the large value of $|q| = 9.62$.

Further calculations (27,34) reveal the following general criteria for the method of calculation. The residue series is most useful for $x > 0.2$ regardless of the magnitude of q . For $|x| < 0.2$, the power series is better for $|q| < 1$, and the small-curvature formula is better for $|q| > 1$. The phase of q does not have to be considered in deciding which method of calculation to use for W .

The magnitude of W as a function of d is shown in Fig. 20 for a larger value of $|\Delta| = 0.2$ and for numerous values of phase (Δ) . The results for $0^\circ \leq \text{phase } (\Delta) \leq 45^\circ$ show the expected smooth decay of the ground wave, but the trapped surface wave has a dominant effect for phase $(\Delta) > 45^\circ$. The root t_0 for the trapped surface wave, also called the Elliott mode [35], has the following asymptotic expansion [27] for large $|q|$:

$$t_0 \sim q^2 + \frac{1}{2q} + \frac{1}{8q^4} + \frac{5}{32q^7} + \frac{11}{32q^{10}} + \frac{539}{512q^{13}} - j2q^2 \exp \left(-\frac{4}{3}q^3 - 1 - \frac{7}{12q^3} - \frac{31}{48q^6} - \frac{397}{288q^9} \right) \tag{69}$$

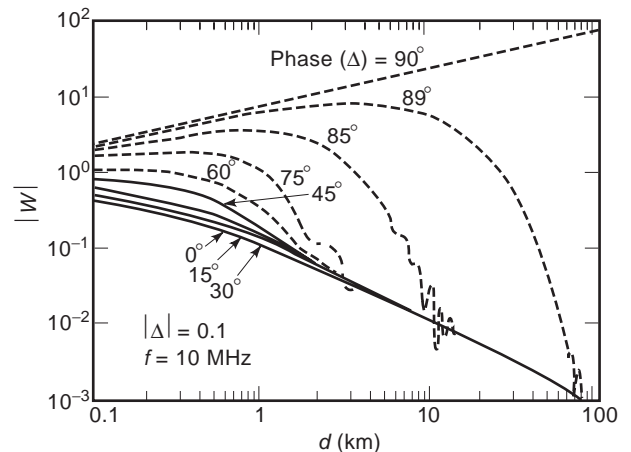


Figure 20. Magnitude of the spherical-Earth attenuation function for different values of the phase of the surface impedance. (From Ref. 27.)

Part of the reason for interest in inductive surface impedances is in modeling propagation over a layer of sea ice on the ocean [29].

The residue series in Eq. (64) can be generalized to the case of an elevated source and an elevated observer. For a source height of h_0 and an observer height of h , W takes the following form [28,29]

$$W = \sqrt{\frac{\pi x}{j}} \sum_{s=1}^{\infty} \frac{\exp(-jxt_s)}{t_s - q^2} G_s(y_0) G_s(y) \quad (70)$$

where

$$G_s(y) = \frac{w(t_s - y)}{w(t_s)} \quad (71)$$

$y_0 = k_0 h_0 (2/k_0 a)^{1/3}$, and $y = k_0 h (2/k_0 a)^{1/3}$. Since G_s depends on t_s , it is a function of s . G_s as given by Eq. (71) can be expanded in a power series in y [28,29]:

$$G_s(y) = 1 - qy + \frac{t_s}{2} y^2 - \frac{1 + t_s q}{6} y^3 + \dots \quad (72)$$

For low heights and small values of s , G_s can be approximated by the first two terms in Eq. (72):

$$G_s \approx 1 - qy = 1 + jk_0 \Delta h \quad (73)$$

G_s as approximated by Eq. (73) is independent of s and is equal to the height-gain function for the flat-Earth model in Eq. (62).

7. VARIABLE TERRAIN

Although the flat-Earth and spherical-Earth models are useful for analyzing ground-wave propagation, many propagation paths involve variable terrain where the ground properties or surface height vary along the path. The analysis of such paths usually requires approximate or numerical methods [36–39].

7.1. Mixed Path

Mixed-path theory has been developed to analyze smooth terrain that has a change in the Earth properties (conductivity and permittivity) between the source and the receiver. The mathematical theory has been developed for both a flat Earth [40] and a spherical Earth [41] but only the more general spherical-Earth model will be considered here.

The geometry for a two-section path is shown in Fig. 21. Propagation along a three-section path [41] has also been analyzed, but will not be covered here. As in the previous section, the radial electric field E_r is normalized to the case of a flat, perfectly conducting plane.

$$E_r = \frac{-j\omega\mu_0 I l}{2\pi d} e^{-jk_0 d} W'(x, q, q_1) \quad (74)$$

where W' is the mixed-path attenuation function, $q = -j(k_0/a)^{1/3} \Delta$, $q_1 = -j(k_0/a)^{1/3} \Delta_1$, $\Delta = Z_s/\eta_0$, $\Delta_1 = Z_{s1}/\eta_0$,

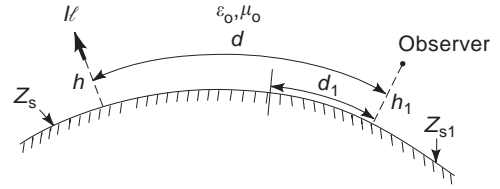


Figure 21. Propagation along a spherical Earth with a change in surface impedance from Z_s to Z_{s1} .

and a is the Earth radius. Consider first the case, where the source and observer are located at the surface ($h = h_1 = 0$). In this case, the following form of W' is most useful [42,43]

$$W'(x, q, q_1) = W(x, q) + \sqrt{\frac{x}{j\pi}} (q_1 - q) \int_0^{x_1} \frac{W(x - \hat{x}, q) W(\hat{x}, q_1)}{\sqrt{\hat{x}(\hat{x} - x)}} d\hat{x}, d_1 > 0 \quad (75)$$

where

$$W(x, q) = \sqrt{\frac{\pi x}{j}} \sum_{s=1}^{\infty} \frac{\exp(-jxt_s)}{t_s - q^2} \quad (76)$$

$x = (k_0 a/2)^{1/3} (d/a)$, and $x_1 = (k_0 a/2)^{1/3} (d_1/a)$. The spherical-Earth attenuation function in Eq. (76) is the same as that for the uniform path in Eq. (64), but the arguments are shown explicitly for use in Eq. (75). The square-root singularity in Eq. (75) is integrable, and its numerical evaluation [42] presents no difficulty. A useful alternative to Eq. (75) can be obtained by reciprocity [41]:

$$W'(x, q, q_1) = W(x, q_1) + \sqrt{\frac{x}{j\pi}} (q - q_1) \int_0^{x-x_1} \frac{W(x - \hat{x}, q_1) W(\hat{x}, q)}{\sqrt{\hat{x}(\hat{x} - x)}} d\hat{x} \quad (77)$$

Equations (75) and (77) have been used to calculate W' for a variety of paths and parameters [42]. Results for $|W'|$ are shown in Fig. 22 for propagation along a land-to-sea path for various lengths of the land section. The frequency is 10 MHz, the land constants are $\epsilon/\epsilon_0 = 15$ and $\sigma = 0.01$ S/m, and the sea constants are $\epsilon_1/\epsilon_0 = 80$ and $\sigma_1 = 4$ S/m. The increase in field strength that occurs in crossing the land-sea boundary has been called the recovery effect, and it has been observed experimentally by Millington [43]. A similar drop in phase has been calculated [42] and observed experimentally by Pressey et al. [44]. In Fig. 23, the length of the land section is fixed at 5 km, and the frequency is varied from 1 to 30 MHz. The recovery effect is most prominent at 30 MHz because the attenuation over land is so rapid at that frequency.

When either height, h or h_1 , is nonzero, Eqs. (75) and (77) are still valid, but W needs to be modified by the

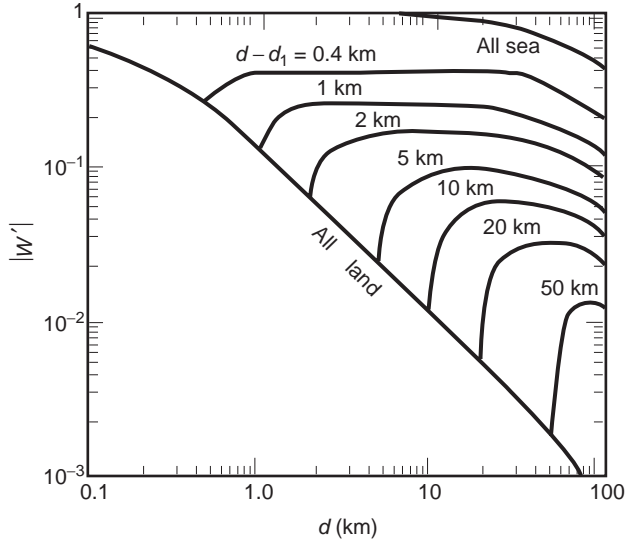


Figure 22. Magnitude of the attenuation function for a land-to-sea path for various lengths of the land section. Parameters: $f = 10$ MHz, $h = h_1 = 0$, $\epsilon/\epsilon_0 = 15$, $\sigma = 10^{-2}$ S/m, $\epsilon_1/\epsilon_0 = 80$, and $\sigma_1 = 4$ S/m. (From Ref. 42.)

appropriate height-gain function

$$W(x, q) = \sqrt{\frac{\pi x}{j}} \sum_{s=1}^{\infty} \frac{\exp(-jxt_s)}{t_s - q^2} \frac{w_1(t_s - y)}{w_1(t_s)}, \quad (78)$$

where $y = (2/k_0 a)^{1/3} k_0 h$

and

$$W(x, q_1) = \sqrt{\frac{\pi x}{j}} \sum_{s=1}^{\infty} \frac{\exp(-jxt_s)}{t_s - q_1^2} \frac{w_1(t_s - y)}{w_1(t_s)}, \quad (79)$$

where $y_1 = (2/k_0 a)^{1/3} k_0 h_1$

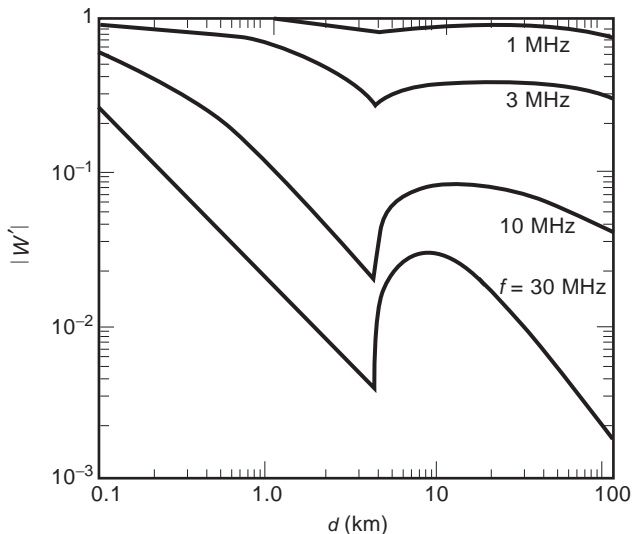


Figure 23. Magnitude of the attenuation function for a land-to-sea path for various frequencies. Parameters: $d - d_1 = 5$ km, $h = h_1 = 0$, $\epsilon/\epsilon_0 = 15$, $\sigma = 10^{-2}$ S/m, $\epsilon_1/\epsilon_0 = 80$, and $\sigma_1 = 4$ S/m. (From Ref. 42.)

It is possible to cast the integral forms of Eqs. (75) and (77) into a modal sum of the following form [42]

$$W'(x, q, q_1) = \sqrt{\frac{\pi x}{j}} (q_1 - q) \sum_{s=1}^{\infty} \sum_{t=1}^{\infty} \frac{\exp[-j(x - x_1)t_s - jx_1 t_r^{(1)}]}{(t_r^{(1)} - t_s)(t_s - q^2)(t_r^{(1)} - q_1^2)} \frac{w_1(t_s - y)}{w_1(t_s)} \frac{w_1(t_r^{(1)} - y_b)}{w_1(t_r^{(1)})} \quad (80)$$

where the roots $t_r^{(1)}$ satisfy the mode equation that is similar to Eq. (65):

$$w_1'(t_r^{(1)}) - q_1 w_1(t_r^{(1)}) = 0 \quad (81)$$

The double summation in Eq. (80) converges slowly when either x_1 , or $x - x_1$ is small, but the roots t_s and $t_r^{(1)}$ can be computed rapidly (27).

Results for $|W'|$ are shown in Fig. 24 for propagation along a land-to-sea path for various observer heights. The length of the land section is 10 km. As many as 600 roots, t_s and $t_r^{(1)}$, were used in computing the results [42] in Fig. 24. A good confirmation of the validity of the numerical results in Fig. 24 as computed by Eq. (80) is that the curve for $h_1 = 0$ agrees with the corresponding curve in Fig. 22 as computed by Eq. (75). As the observer height h_1 is increased, the recovery effect decreases in magnitude and begins at a range beyond the land-sea boundary.

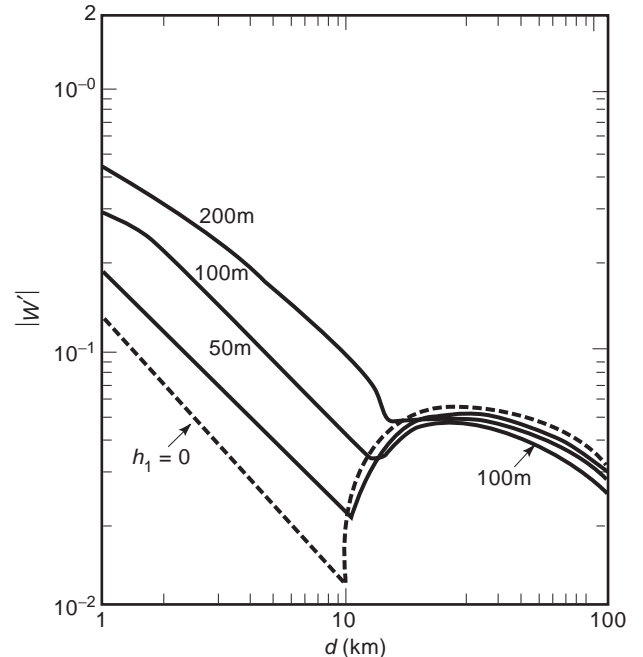


Figure 24. Magnitude of the attenuation function for a land-to-sea path for various observer heights. Parameters: $f = 10$ MHz, $d - d_1 = 10$ km, $h = 0$, $\epsilon/\epsilon_0 = 15$, $\sigma = 10^{-2}$ S/m, $\epsilon_1/\epsilon_0 = 80$, and $\sigma_1 = 4$ S/m. (From Ref. 42.)

7.2. Irregular Terrain

For many propagation paths, the ground parameters and terrain height vary as a function of position along the path. Analytical methods are not general enough to handle such variations, but the integral equation approach [45,46] has been found useful for ground-wave propagation over irregular, inhomogeneous terrain. Ott's program WAGNER has been thoroughly tested and used on a wide variety of paths [47], and Hill has generalized it to allow for an anisotropic layer over a homogeneous Earth [48]. The anisotropic layer is intended to model a forest layer, snowcover, or a layered Earth.

The general terrain model is shown in Fig. 25. The terrain height y , the slab thickness D , and the slab and ground constitutive parameters are functions of the horizontal distance ξ from the vertical electric dipole source. The terrain is represented by a normalized surface impedance Δ (referred to the top of the slab), which is a function of the slab and ground parameters and is thus a function of ξ . The problem is first solved by considering the case where the source and observer are located at the surface ($h_a = h_r = 0$). The vertical electric field E_y is normalized to the field of a vertical electric dipole on a conducting plane

$$E_y = \frac{-j\omega\mu_0 I l}{2\pi x} e^{-jk_0 x} f(x) \quad (82)$$

where $f(x)$ is the attenuation to be determined from the integral equation. The integral equation is [47,48]

$$f(x) = F(x, 0) - \sqrt{\frac{jk_0}{2\pi}} \int_0^x f(\xi) e^{-jk_0 \phi(x, \xi)} \left(y'(\xi) F(x, \xi) - \frac{y(x) - y(\xi)}{x - \xi} + [\Delta(\xi) - \Delta_a] F(x, \xi) \right) \frac{\sqrt{x}}{\sqrt{\xi(x - \xi)}} d\xi \quad (83)$$

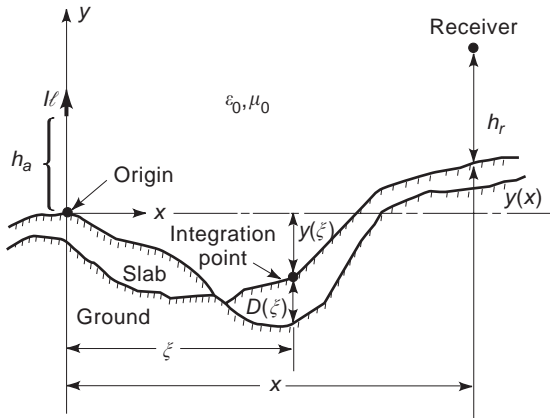


Figure 25. Geometry for the integral equation solution of propagation over irregular, inhomogeneous terrain. The slab and ground parameters can vary as a function of x , but are constant in y .

where

$$\phi(x, \xi) = \frac{[y(x) - y(\xi)]^2}{2x(x - \xi)} + \frac{y^2(\xi)}{2\xi} - \frac{y^2(x)}{2x}$$

$$F(x, \xi) = 1 - j\sqrt{\pi p} e^{-u} \operatorname{erfc}(j\sqrt{u})$$

$$p = -jk_0 \Delta^2(\xi)(x - \xi)/2, \quad u = p \left(1 - \frac{y(x) - y(\xi)}{\Delta(\xi)(x - \xi)} \right)^2$$

and $y'(\xi)$ is the slope $dy/d\xi$. The normalized surface impedance $\Delta(\xi)$ is a function of the slab and ground parameters [48]

$$\Delta(\xi) = \Delta_1 \frac{\Delta_2 + \Delta_1 \tanh(v_0 D)}{\Delta_1 + \Delta_2 \tanh(v_0 D)} \quad (84)$$

where

$$\Delta_1 = \frac{\sqrt{\varepsilon_{hc} - \kappa}}{\varepsilon_{hc}}, \quad \Delta_2 = \frac{\sqrt{\varepsilon_{gc} - 1}}{\varepsilon_{gc}}, \quad v_0 = jk_0 \sqrt{\varepsilon_{hc} - \kappa}$$

$$\varepsilon_{hc} = \varepsilon_h + \sigma_h / (j\omega\varepsilon_0), \quad \varepsilon_{gc} = \varepsilon_g + \sigma_g / (j\omega\varepsilon_0),$$

$$\varepsilon_{vc} = \varepsilon_v + \sigma_v / (j\omega\varepsilon_0), \quad \kappa = \varepsilon_{hc} / \varepsilon_{vc}$$

σ_v and ε_v are the vertical conductivity and relative permittivity of the slab, σ_h and ε_h are the horizontal conductivity and relative permittivity of the slab, and σ_g and ε_g are the conductivity and permittivity of the ground. The ground and the slab have free-space permeability μ_0 . The normalized surface impedance Δ_a is evaluated at the source.

Before discussing the numerical solution of Eq. (83), it is useful to examine the special case of a uniform path: $y(\xi) = y(x) = y'(\xi) = 0$ and $\Delta(\xi) = \Delta_a$. Thus the integrand is 0, and $f(x)$ is

$$f(x) = F(x, 0) = 1 - j\sqrt{\pi p_a} e^{-p_a} \operatorname{erfc}(j\sqrt{p_a}) \quad (85)$$

where $p_a = -jk_0 \Delta_a^2 x^2 / 2$. Equation (85) agrees with the flat-earth result in Eq. (56). When either y or Δ varies along the path, the integral equation must be solved numerically. A forward-stepping solution [49] in x is used to obtain values of f at discrete values of x along the path. Since Eq. (83) is a Volterra integral equation of the second kind, the value of $f(x)$ depends only on the previously computed values of $f(\xi)$ for $\xi < x$. Physically this means that backscatter is neglected.

To account for nonzero source and receiver heights, h_a and h_r , an attenuation function f_h is determined by use of height-gain functions G_s for a slab medium [48]:

$$f_h(x) = f(x) G_s(h_a) G_s(h_r) \quad (86)$$

The source and receiver can be located either in air (positive height) or in the slab (negative height). For the source or receiver in air, the height-gain function is

$$G_s(h) = 1 + jk_0 \Delta h, \quad h \geq 0 \quad (87)$$

where Δ is evaluated at the appropriate source or receiver location. For the source or receiver in the slab, the height-gain function is

$$G_s(h) = \frac{1}{\epsilon_{vc}} \frac{e^{v_0 z} + R e^{-v_0(2D+h)}}{1 + R e^{-2v_0 D}}, \quad -D < h < 0 \quad (88)$$

where $R = (\Delta_1 - \Delta_2) / (\Delta_1 + \Delta_2)$. The limit of G_s as h approaches 0 from above is 1:

$$G_s(0^+) = 1 \quad (89)$$

The limit of G_s as h approaches 0 from below is

$$G_s(0^-) = 1/\epsilon_{vc} \quad (90)$$

This is a consequence of the continuity of normal current flow.

The numerical solution of Eq. (83) has been thoroughly studied, and comparisons with experimental results have been shown [47,48]. Also, a comparison with an approximate analysis for propagation from a forest to a clearing has been made. This comparison provides an independent check because the approximate solution uses a Kirchhoff integration over the vertical aperture above the forest-clearing boundary [48] in contrast to the integral equation

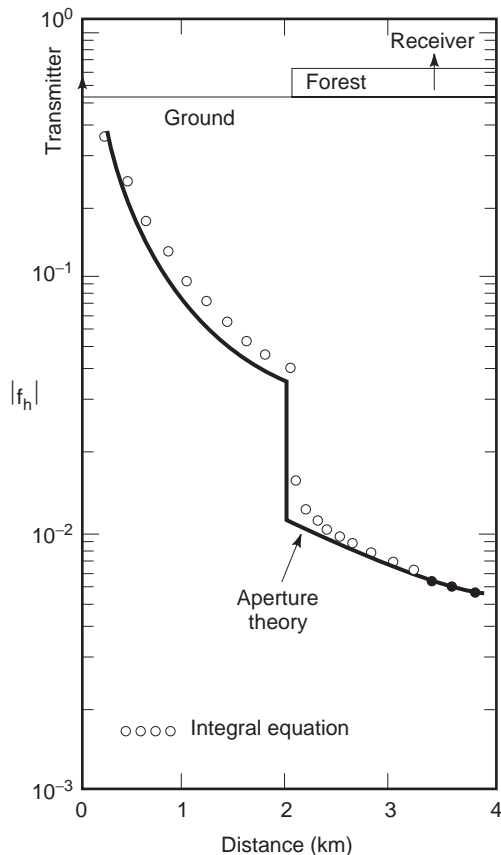


Figure 26. Propagation from a clearing to a forest at a frequency of 10 MHz. (From Ref. 48.)

solution, which integrates over the terrain surface. The numerical comparison for $|f_h|$ is shown in Fig. 26. The frequency is 10 MHz, the ground parameters are $\sigma_g = 10^{-2}$ S/m and $\epsilon_g = 10$, and the slab parameters are $D = 10$ m, $\sigma_h = 10^{-4}$ S/m, $\epsilon_h = 1.1$, $\sigma_v = 2.5 \times 10^{-4}$, and $\epsilon_v = 1.25$. Both the source and receiver are located at a height of 10^+ m. The approximate aperture theory shows a non-physical jump for the receiver at the forest boundary, but the more accurate integral equation solution smooths out the jump. Away from the boundary the two solutions agree well.

For typical terrain profiles and moderate path lengths (less than 100 km), the numerical solution of Eq. (83) is reasonably accurate and efficient for frequencies up to about 10 MHz. At higher frequencies the numerical solution can become unstable and predict a nonphysical oscillatory field strength as a function of distance. Also, the computer run time, which is roughly proportional to frequency squared, can become large. To improve the stability at higher frequencies, Ott [50] has modified the integral equation and computer code and has obtained stable numerical results for frequencies up to about 100 MHz.

7.3. Knife-Edge Diffraction

At high frequencies where the wavelength is small compared to terrain features and other obstacles such as buildings, knife-edge diffraction models [51] can provide useful field predictions. The simplest model is based on a single knife edge, as shown in Fig. 27. If the Kirchhoff approximation that the field in the semiinfinite aperture above the knife edge is equal to the incident field is made, then the aperture integration can be approximated with the following result for the diffracted field E_d at the receiver location R [14]:

$$E_d = E_0 F(v) = E_0 \frac{1+j}{2} \int_v^\infty \exp(-j\pi t^2/2) dt, \quad (91)$$

$$\text{where } v = h \sqrt{\frac{2(d_1 + d_2)}{\lambda_0 d_1 d_2}}$$

E_0 is the free-space field in the absence of the knife edge and $F(v)$ is the complex Fresnel integral. When the knife edge extends above the line connecting S and R (as in Fig. 27), h and v are positive. In this case, $|F| < 1/2$. When the top of the knife edge is below the line connecting S and R , h and v are negative. In this case, $|F| > 1/2$. As v approaches $-\infty$, $|F|$ approaches 1 in an oscillatory manner. The diffraction gain (in decibels) due to the presence of the

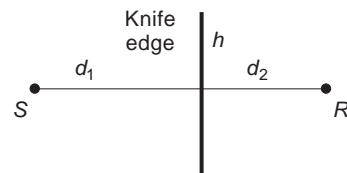


Figure 27. Geometry for diffraction by single knife edge.

knife edge is

$$G_d = 20 \log_{10} |F(v)| \quad (92)$$

To avoid computation of the Fresnel integral in Eq. (92), Lee [51] has provided simple approximations for F . The geometric theory of diffraction [52] provides a more rigorous high-frequency method for analyzing diffraction from knife edges and wedges, and it predicts results that depend on the polarization of the incident field.

A number of extensions to the single knife-edge model in Fig. 27 have been studied. The knife edge can be replaced by a rounded diffracting obstacle [53,54], which is a better model for broad-terrain features in some cases. Multiple knife edges [55–57] can be used to model paths with multiple diffracting obstacles. Vogler's analysis [58] is valid for an arbitrary number of knife edges, and his computer code will handle up to 10 knife edges.

BIBLIOGRAPHY

1. J. A. Stratton, *Electromagnetic Theory*, McGraw-Hill, New York, 1941.
2. R. S. Elliot, *Electromagnetics: History, Theory, and Applications*, IEEE Press, New York, 1993.
3. J. H. Bryant, *Heinrich Hertz: The Beginning of Microwaves*, IEEE Press, New York, 1988.
4. M. L. Burrows, *ELF Communications Antennas*, IEE/Peter Peregrinus, Stevenage, UK, 1978.
5. K. Davies, *Ionospheric Radio*, IEE/Peter Peregrinus, London, UK, 1989.
6. P. V. Bliokh, A. P. Nicholaenko, and Y. F. Fillippov (transl. by S. Chomet), *Schumann Resonances in the Earth-Ionosphere Cavity*, IEE/Peter Peregrinus, Stevenage, UK, 1980.
7. J. N. Murphy and H. E. Parkinson, Underground mine communications, *Proc. IEEE*, **66**:26–50 (1978).
8. J. R. Wait, Electromagnetic induction technique for locating a buried source, *IEEE Trans. Geosci. Electron.*, **9**:95–98 (1971).
9. A. D. Watt, *VLF Radio Engineering*, Pergamon Press, Oxford, UK, 1967.
10. D. L. Schilling, ed., *Meteor Burst Communications, Theory and Practice*, Wiley, New York, 1993.
11. K. Siwiak, *Radiowave Propagation and Antennas for Personal Communications*, Artech House, Norwood, MA, 1995.
12. R. F. Harrington, *Time-Harmonic Electromagnetic Fields*, McGraw-Hill, New York, 1961.
13. C. H. Liu and D. J. Fang, Propagation, in Y. T. Lo and S. W. Lee, eds., *Antenna Handbook: Theory, Applications, and Design*, Van Nostrand-Reinhold, New York, 1988, Chap. 29.
14. E. C. Jordan and K. G. Balmain, *Electromagnetic Waves and Radiating Systems*, Prentice-Hall, Englewood Cliffs, NJ, 1968.
15. G. V. Keller and F. C. Frischnect, *Electrical Methods in Geophysical Prospecting*, Pergamon Press, Oxford, UK, 1966.
16. D. A. Hill, Antennas for geophysical applications, in Y. T. Lo and S. W. Lee, eds., *Antenna Handbook: Theory, Applications, and Design*, Van Nostrand-Reinhold, New York, 1988, Chap. 23.
17. M. Abramowitz and I. A. Stegun, *Handbook of Mathematical Functions*, National Bureau of Standards, AMS 55, Washington, DC, 1968.
18. A. A. Kaufman and G. V. Keller, *Frequency and Transient Sounding*, Elsevier, Amsterdam, 1983.
19. J. R. Wait and D. A. Hill, Fields of a horizontal loop of arbitrary shape buried in a two-layer loop, *Rad. Sci.* **15**:903–912 (1980).
20. E. D. Sunde, *Earth Conduction Effects in Transmission Systems*, Van Nostrand, New York, 1949.
21. D. A. Hill and J. R. Wait, Subsurface electromagnetic fields of a grounded cable of finite length, *Can. J. Phys.* **51**:1534–1540 (1973).
22. J. R. Wait and K. P. Spies, Subsurface electromagnetic field of a line source on a conducting half-space, *Rad. Sci.* **6**:781–786 (1971).
23. D. A. Hill and J. R. Wait, Subsurface electric fields of a grounded cable of finite length for both frequency and time domain, *Pure Appl. Geophys.* **111**:2324–2332 (1973).
24. D. A. Hill, Electromagnetic surface fields of an inclined buried cable of finite length, *J. Appl. Phys.* **44**:5275–5279 (1973).
25. A. Banos, *Dipole Radiation in the Presence of a Conducting Half-Space*, Pergamon, New York, 1966.
26. J. R. Wait, Electromagnetic surface waves, in J. A. Saxton, ed., *Advances in Radio Research*, Academic Press, London, 1964, pp. 157–217.
27. D. A. Hill and J. R. Wait, Ground wave attenuation function for a spherical earth with arbitrary surface impedance, *Rad. Sci.* **15**:637–643 (1980).
28. D. A. Hill and J. R. Wait, Excitation of the HF surface wave by vertical and horizontal antennas, *Rad. Sci.* **14**:767–780 (1979).
29. D. A. Hill and J. R. Wait, HF radio wave transmission over sea ice and remote sensing possibilities, *IEEE Trans. Geosci. Remote Sens.* **19**:204–209 (1981).
30. J. C. P. Miller, *The Airy Integral*, Cambridge Univ. Press, Cambridge, UK, 1946.
31. H. Bremmer, Applications of operational calculus to ground-wave propagation, particularly for long waves, *IRE Trans. Anten. Propag.* **6**:267–272 (1958).
32. J. R. Wait, Radiation from a vertical antenna over a curved stratified ground, *Natl. Bur. Stand. J. Res.* **56**:237–244 (1956).
33. H. Bremmer, *Terrestrial Radio Waves*, Elsevier, New York, 1949.
34. K. P. Spies and J. R. Wait, On the calculation of antenna patterns for an inhomogeneous spherical earth, *Rad. Sci.* **11**:1361–1378 (1967).
35. R. S. Elliott, Spherical surface wave antennas, *IRE Trans. Anten. Propag.* **4**:422–428 (1956).
36. G. A. Hufford, A. G. Longley, and W. A. Kissick, *A Guide to the Use of the ITS Irregular Terrain Model in the Area Prediction Mode*, National Telecommunications and Information Administration Report 82-100, April 1982.
37. N. DeMinco, *Ground-wave Analysis Model for MF Broadcast Systems*, National Telecommunications and Information Administration Report 86-203, Sept. 1986.
38. N. DeMinco, *Automated Performance Analysis Model for Ground-wave Communication Systems*, National Telecommunications and Information Administration Report 86-209, 1986.
39. T. S. M. Maclean and Z. Wu, *Radiowave Propagation over Ground*, Chapman & Hall, London, 1993.
40. J. R. Wait, Mixed path ground-wave propagation: 1. Short distances, *J. Res. Natl. Bur. Stand.* **57**:1–15 (1956).

41. J. R. Wait, On the theory of mixed-path ground-wave propagation on a spherical earth, *J. Res. Natl. Bur. Stand.* **65D**:401–410 (1961).
42. D. A. Hill and J. R. Wait, HF ground wave propagation over mixed land, sea, and sea-ice paths, *IEEE Trans. Geosci. Remote Sens.* **19**:210–216 (1981).
43. G. Millington, Ground wave propagation over an inhomogeneous smooth earth, Part 1, *Proc. Inst. Electric. Eng.* **96**:53–64 (1949).
44. B. G. Pressey, G. E. Ashwell, and C. S. Fowler, Change of phase of a low-frequency wave propagated across a coast line, *Proc. Inst. Electric. Eng.* **103B**:527–541 (1956).
45. G. A. Hufford, An integral equation approach to the problem of wave propagation over an irregular terrain, *Quart. J. Appl. Math.* **9**:391–404 (1952).
46. R. H. Ott and L. A. Berry, An alternative integral equation for propagation over irregular terrain, *Rad. Sci.* **5**:767–771 (1970).
47. R. H. Ott, L. E. Vogler, and G. A. Hufford, *Ground Wave Propagation over Irregular, Inhomogeneous Terrain*, National Telecommunications and Information Administration Report 79-20, 1979.
48. D. A. Hill, *HF Ground Wave Propagation over Forested and Built-up Terrain*, National Telecommunications Administration Report 82-114, Dec. 1982.
49. C. Wagner, On the numerical solution of Volterra integral equations, *J. Math. Phys.* **32**:289–401 (1953).
50. R. H. Ott, RING: an integral equation for HF-VHF radio wave propagation over irregular, inhomogeneous terrain, *Rad. Sci.* **27**:867–882 (1992).
51. W. C. Y. Lee, *Mobile Cellular Telecommunications*, McGraw-Hill, New York, 1995.
52. G. L. James, *Geometrical Theory of Diffraction for Electromagnetic Waves*, Peter Peregrinus, Stevenage, UK, 1976.
53. J. R. Wait and A. M. Conda, Diffraction of electromagnetic waves by smooth obstacles for grazing angles, *J. Res. Natl. Bur. Stand.* **63D**:181–197 (1959).
54. L. E. Vogler, Radio wave diffraction by a rounded obstacle, *Rad. Sci.* **20**:582–590 (1985).
55. J. Epstein and D. W. Peterson, An experimental study of wave propagation at 850 Mc, *Proc. IRE* **41**:595–611 (1953).
56. G. Millington, R. Hewitt, and F. S. Immirizi, Double knife-edge diffraction in field-strength predictions, *Proc. IEE Monogr.* **507E**:419–429 (1962).
57. J. Deygout, Multiple knife-edge diffraction of microwaves, *IEEE Trans. Anten. Propag.* **14**:480–489 (1966).
58. L. E. Vogler, An attenuation function for multiple knife-edge diffraction, *Rad. Sci.* **17**:1541–1546 (1982).

RADIOWAVE PROPAGATION IN MULTIPATH CHANNELS

R. D. KOILPILLAI
Ericsson, Inc.

With the rapid growth in wireless communications, there is considerable interest in radiofrequency (RF) propagation and RF channel modeling in the 400 MHz–2 GHz

band, where multipath propagation is a characteristic property. The topic of RF signal propagation and the factors that affect the RF signals have been extensively studied since the late 1960s [1–3]. This article presents a comprehensive overview of the RF signal variations related to propagation in multipath fading channels. The diverse phenomena that cause signal variations are described via mathematical models. The different types of fading and their salient features are discussed in detail. The goal of this article is to provide a mathematical and an engineering-oriented treatment of multipath fading, thereby providing the reader with the necessary tools and the information to understand the different RF propagative issues and how they impact wireless communications.

The different propagative effects are classified in two major categories as shown in Fig. 1:

- Small-scale effects
- Large-scale effects

The small-scale effects are those caused by multipath propagation, the phenomenon by which the transmitted signal reaches the receiver via multiple paths. The received signal is a superposition of the different multipath signals, which add constructively or destructively, thereby producing signal fluctuations. The variations of the signal level are typically produced by movement over short distances (10–20 times the wavelength λ of the RF carrier) during which the mean signal level remains constant. The different types of fading and their mathematical characterization and modeling are discussed in the following sections.

On the other hand, large-scale effects are those caused by variations in the distance between transmitter and receiver, which are manifested in the form of path loss, and by environmental factors, such as terrain, which produce lognormal shadowing about the local mean signal level. These issues are also discussed in detail.

A schematic of a communication system is shown in Fig. 2. The term “channel” is used to imply different portions of the communication link. Two terms used in this article, namely, the propagative channel and the baseband channel need to be defined. The propagation channel is the physical medium that supports RF propagation between the transmitting and receiving antennas. This includes the objects that cause the multipath and time dispersion. This channel is time-varying. The baseband equivalent channel consists of a complex-valued baseband representation of the channel. If the nonlinearities in the IF/RF stages of both transmitter and receiver are neglected, then the baseband channel can also be represented by a linear, time-varying channel model, which includes the appropriate models for the propagation channel.

1. BASIC DEFINITIONS

1.1. Static Channels

The simplest type of communication channel is a static channel, in which the only signal impairment caused by

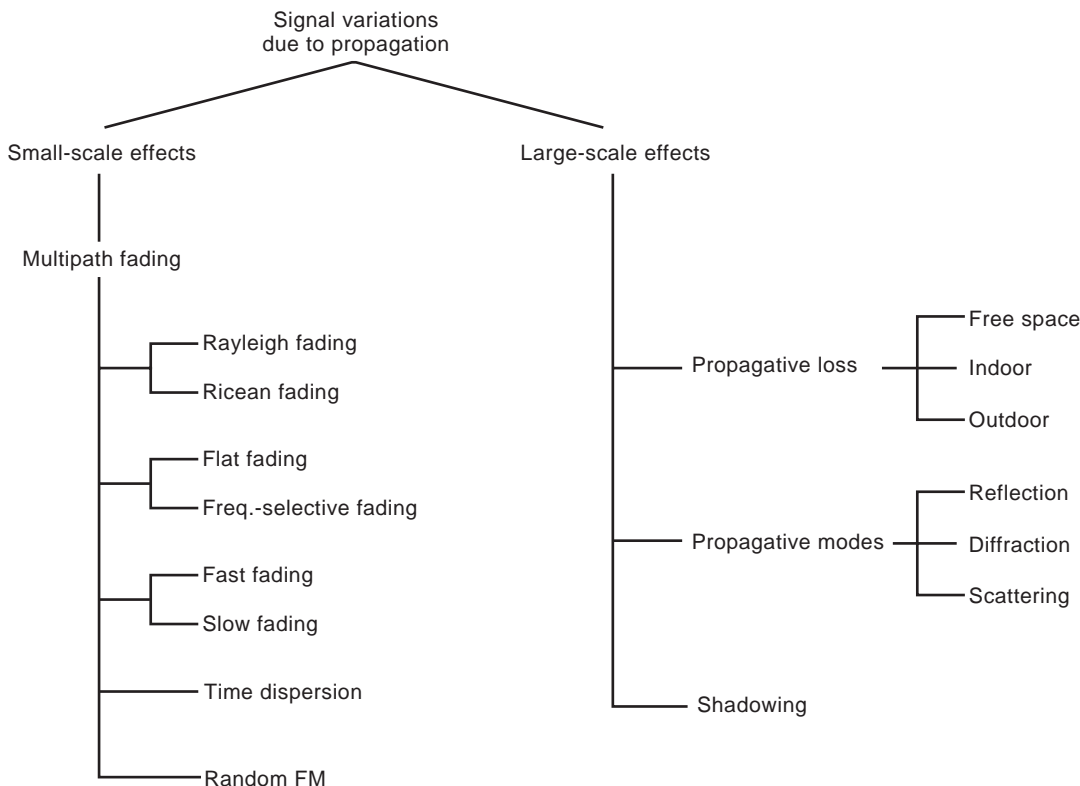


Figure 1. Classification of the small-scale effects and the large-scale effects that cause signal variability in an RF environment.

the channel is additive white Gaussian noise (AWGN). The noise is assumed to have a flat, power spectral density and is uncorrelated in time. These characteristics are typical of the thermal noise generated in communication equipment.

The AWGN channel is widely used to evaluate the performance of communication systems [4] (modulation, coding, etc.). In RF communications, a static environment is unlikely, except in a few situations when there is a dominant line-of-sight (LoS) component between the transmitter and receiver, and there is essentially no multipath, such as in microwave LoS links and in microcells. In practice, the AGWN channel serves the useful role of providing performance bounds for RF communication channels because the practical channels (typically Rayleigh and Ricean) always produce signal impairments more severe than the AGWN channel.

1.2. Fading Channels

Some of the commonly encountered communication channels, such as that encountered in wireline communications over telephone networks, can be characterized as AWGN channels that have a linear time-invariant (LTI) filter channel model. However, this representation does not apply to radio frequency (RF) channels because their transmission characteristics change with time and hence require statistical characterization using *linear, time-varying channel models*. Typically RF channels are characterized by the following time-varying phenomena:

1. Multipath propagation and signal fading
2. Multipath time dispersion
3. Doppler shift

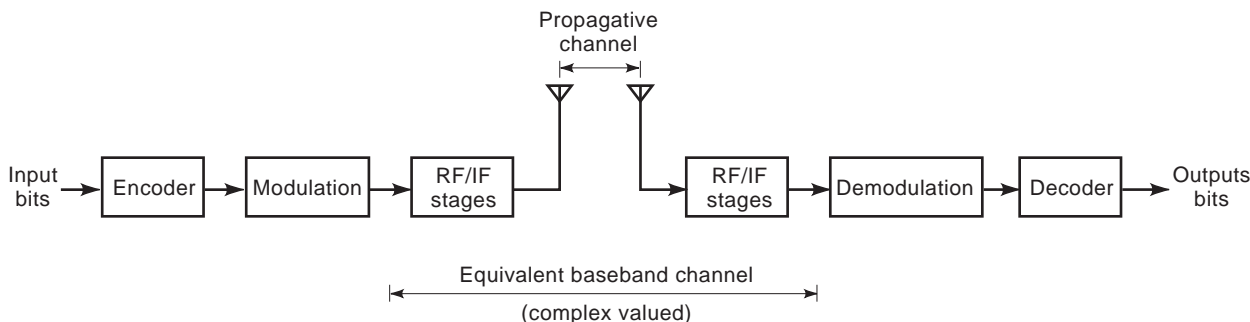


Figure 2. Definition of propagative channel and baseband channel.

4. Random frequency/phase modulation
5. Shadowing

In this article, these salient features of RF fading channels and their statistical characterization are described. Some examples of RF channels that fall in this category are

- Mobile cellular channels
- Mobile satellite channels
- Channels with ionospheric and tropospheric propagation

1.2.1. Multipath and Time Dispersion. *Multipath* is the phenomenon by which a transmitted signal reaches a receiver via multiple propagative paths, each of which has an associated propagative delay. For instance, in Fig. 3, the signal from the base station to the mobile station has three paths with propagative delays τ_1 , τ_2 , and τ_3 , respectively. One of them is the direct line-of-sight path between the transmitter and receiver (with delay τ_1). The other two paths (with delays τ_2 and τ_2) are caused by scatterers/reflectors. If a narrow pulse is transmitted in this channel (with $\tau_1 \neq \tau_2 \neq \tau_3$), then three copies of the pulse are received, as shown in Fig. 4. Channels exhibiting this property are called *time-dispersive*.

1.2.2. Doppler Spread. Another distinctive characteristic of radio channels is the time variation of the channel. This can be caused by mobility of transmitter or receiver or a change in the propagative environment (change in the scatterers). The received signal $x(t)$ in this time-varying multipath channel can be expressed as

$$x(t) = \sum_n \alpha_n(t) s[t - \tau_n(t)] \quad (1)$$

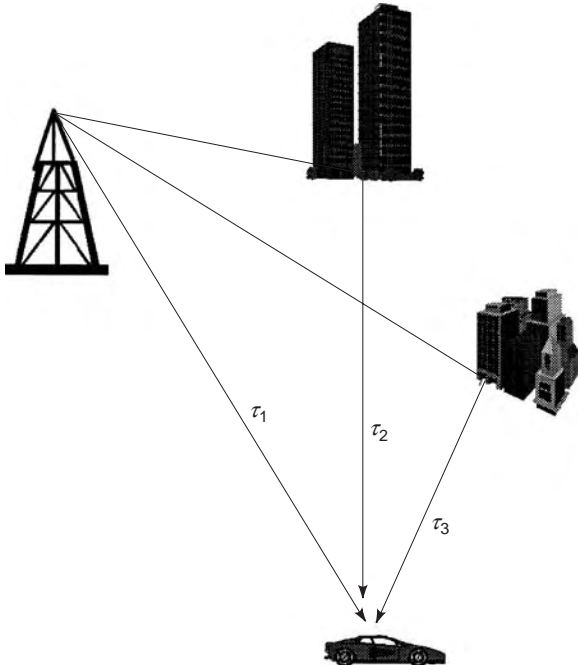


Figure 3. An example of multipath propagation due to multiple scatterers.

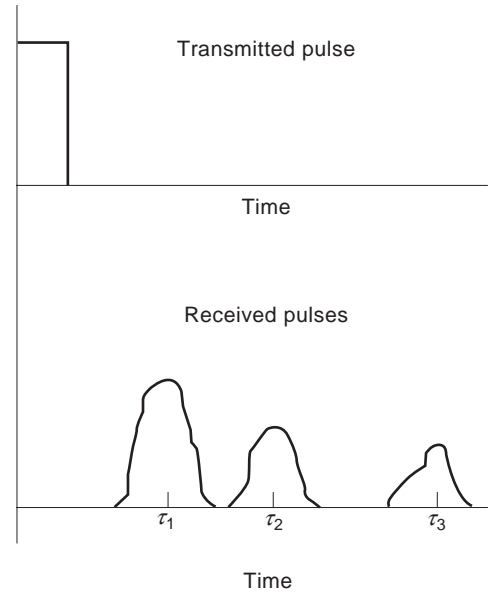


Figure 4. Effect of time dispersion due to multipath propagation.

where $s(t)$ is the modulated signal, $\alpha_n(t)$ and $\tau_n(t)$ are the attenuation factor and the propagative delay, respectively, for the signal received via the n th path. The modulated signal $s(t)$ is typically represented as [4]

$$s(t) = m(t) \cos[2\pi f_c t + \theta(t)] = \text{Re}[u(t)e^{j2\pi f_c t}] \quad (2)$$

with carrier frequency f_c , and $u(t) = m(t) \cos \theta(t) - jm(t) \sin \theta(t)$. Substituting Eq. (2) in Eq. (1), the signal received $x(t)$ is given by

$$x(t) = \text{Re} \left(\left\{ \sum_n \alpha_n(t) e^{-j2\pi f_c \tau_n(t)} u[t - \tau_n(t)] \right\} e^{j2\pi f_c t} \right) \quad (3)$$

The corresponding baseband (complex) signal $r(t)$ and the equivalent baseband channel $c(\tau; t)$ are given by

$$r(t) = \sum_n \alpha_n(t) e^{-j2\pi f_c \tau_n(t)} u[t - \tau_n(t)] \quad (4)$$

$$c(\tau; t) = \sum_n \alpha_n(t) e^{-j2\pi f_c \tau_n(t)} \delta[t - \tau_n(t)] \quad (5)$$

Consider the transmission of an unmodulated carrier $s(t) = A \cos 2\pi f_c t$. Then, using Eq. (4), with $u(t) = 1$, the received signal is given by

$$r(t) = \left[A \sum_n \alpha_n(t) e^{-j2\pi f_c \tau_n(t)} \right] \quad (6)$$

which also represents the response of the channel to a complex exponential $e^{j2\pi f_c t}$. Even though $s(t)$ is a monochromatic signal, the output of the channel $r(t)$ contains many different frequency components, which are generated as a result of the time variations of the channel response. The range of frequencies over which the spectrum of $r(t)$ is nonzero is called the *Doppler frequency*

spread (B_d) of the channel, which yields a measure that is directly proportional to the rate of variations of the channel response.

1.2.3. Signal Fading. In Eq. (5), $c(\tau;t)$ is the time-varying (complex-valued) channel impulse response (CIR) and is the discrete multipath channel model, wherein τ represents the time dispersion and t denotes the time index for the variations as a function of time. The CIR $c(\tau;t)$ can be viewed as the superposition of phasors, each with a time-varying gain/amplitude $\alpha_n(t)$ and a time-varying phase $\phi_n(t) = -2\pi f_c \tau_n(t)$. With random variations in $\alpha_n(t)$ and $\phi_n(t)$ (caused by the time-varying multipath), these phasors can add constructively or destructively. The *fading phenomenon*, which results in signal amplitude becoming very small, is caused by instantaneous destructive combining of the phasors. An important observation is that a small change in $\tau_n(t)$ produces a significant phase change (i.e., a 2π change occurs if $\tau_n(t)$ changes by $1/f_c$). Using the central-limit theorem, $r(t)$ can be modeled as a complex-valued Gaussian random process [4], which implies that $c(\tau;t)$ is also a complex-valued Gaussian random process in the t variable. This random amplitude variation is a fundamental characteristic of multipath channels, and hence its understanding is crucial to the use of these channels. In *Rayleigh fading* channels, $c(\tau;t)$ is modeled as zero-mean, and corresponds to the case when there are random variations in the scattering environment (usually caused by the movement of the transmitter or receiver) and there is no line-of-sight (LoS) path. In *Ricean fading* channels, $c(\tau;t)$ is nonzero mean because of the presence of a LoS component or because of fixed scatterers. Typically Rayleigh fading channels are encountered in all cellular and land-mobile radiocommunications, whereas Ricean fading channels are encountered in mobile satellite communications. A detailed characterization of these channels is presented in the subsequent sections.

In some cases, it is more suitable to have a continuous multipath model. In this case, the received signal $x(t)$ is given by

$$x(t) = \int_{-\infty}^{\infty} c(\tau;t)s(t-\tau) d\tau \quad (7)$$

which is similar to Eq. (1) with the summation replaced by an integral. This model is typically used in tropospheric scatter and ionospheric propagation. In the sequel, we focus on the discrete model for multipath channels, which is typical for most terrestrial RF channels.

1.2.4. Fading in a Mobile Communication Environment. If the transmitter and receiver were stationary and all the scatterers were fixed, then the signal fading variations, described in the previous section, would not be observed. In mobile communications (such as cellular), the receiver or transmitter is usually moving. So the scattering environment is constantly changing. A typical fading signal envelope (characterized by Rayleigh fading) for a mobile receiver using a carrier frequency $f_c = 1.9$ GHz and moving at 100 km/h, is shown in Fig. 5. It can be seen that

the signal envelope can vary as much as 40 dB (30 dB below and 10 dB above) relative to the rms value.

A spatial viewpoint of multipath fading is very useful. Consider a stationary transmitter and fixed scatterers. The signals from the scatterers can be visualized as forming a spatial standing wave pattern with peaks (points in space where the multipath signals add constructively) and troughs (where the signals add destructively). The spatial separation between troughs and peaks is roughly $\lambda/2$, where λ is the wavelength of the carrier. If a mobile receiver were to move through this spatial standing wave pattern, then it experiences the signal fading every time the receiver has moved by $\lambda/2$. In Fig. 5, the x axis is the time in seconds. As the receiver moves, it can experience multiple signal fades per second.

Example 1. Consider a mobile station moving at 100 km/h and communicating at a carrier frequency of 1.9 GHz. The corresponding wavelength $\lambda = 0.15$ m. Because the vehicle is moving at 100 km/h ($= 27.77$ m/s), the vehicle covers a distance corresponding to 176λ in 1 s. Hence, the envelope of signal received by the mobile can experience as many as 350 signal fades per second, as shown in Fig. 5. The extent of signal impairment depends on the extent of signal amplitude reduction, known as the *depth of the fade*. This is quantified via the level crossing rate and the duration of fades discussed in a subsequent section.

1.2.5. Shadowing. *Shadowing* is the term that refers to the long-term variations in the local mean of the received signal power at a distance d from the transmitter. These variations are typically caused by the terrain, buildings, foliage, and other obstructions in the signal path. If the instantaneous power of the signal received at the receiver is averaged to remove the effect of fast fading, the local mean signal level Ω' at that particular distance d from the transmitter is obtained. The local mean remains constant over a small distance (of the order of multiples of the wavelength of the RF carrier). The local mean Ω' is a

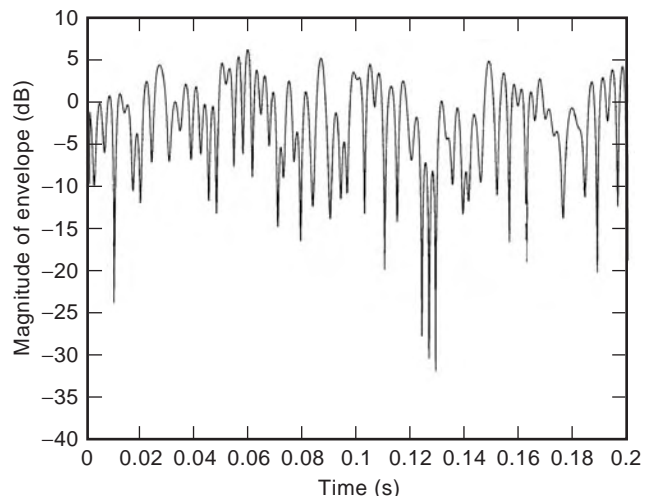


Figure 5. Typical envelope variations in Rayleigh fading at a vehicle speed of 100 km/h and carrier frequency 1.9 GHz. The RMS value of the signal envelope is 0 dB.

random variable because of the signal level variations caused by the terrain and other environmental factors. Through empirical studies, the RV Ω has been characterized by the log-normal distribution (see the next section) with a standard deviation in the typical range of 6–9 dB.

2. FADING DISTRIBUTIONS

The two most commonly encountered types of fading environments are

1. Rayleigh fading
2. Ricean fading

In this section, the statistical properties of Rayleigh and Ricean fading are described. This mathematical framework is very useful in providing tools for analyzing and simulating the performance of communications over fading channels and also for providing insight into the design of robust communication systems in a fading environment (see Ref. 16). Ricean fading covers a very broad spectrum of environments from static AWGN channels on the one end to Rayleigh fading channels on the other. So, it represents an entire family of fading channels. However, because Rayleigh channels are the most frequently encountered environment in wireless (mobile) communications, it forms an important class for study. Both Rayleigh and Ricean distributions refer to the statistics of the received signal's envelope.

3. RICE DISTRIBUTION

Let X and Y be two independent Gaussian random variables (RVs) with means m_1 and m_2 , respectively, and common variance σ^2 . Then the RV V , defined as $V \triangleq \sqrt{X^2 + Y^2}$, is distributed according to *Ricean distribution* [8], whose pdf is given by

$$f_V(v) = \begin{cases} \frac{v}{\sigma^2} I_0\left(\frac{sv}{\sigma^2}\right) e^{-(v^2 + s^2)/2\sigma^2} & v > 0 \\ 0 & v \leq 0 \end{cases} \quad (8)$$

where $s^2 = m_1^2 + m_2^2$ and I_0 is the zeroth-order modified Bessel function of the first kind given by

$$I_0(x) = \frac{1}{2\pi} \int_0^{2\pi} e^{x \cos u} du = \frac{1}{2\pi} \int_{-\pi}^{\pi} e^{x \cos u} du \quad (9)$$

It can be verified that the RV $\hat{V} = V^2$ has a noncentral chi-square distribution whose noncentrality parameter is s^2 . The cdf of a Ricean RV V is given by (4)

$$F_V(v) = \Pr(v \leq V) = \int_0^v f_V(v) dv = 1 - Q\left(\frac{s}{\sigma}, \frac{v}{\sigma}\right) \quad (10)$$

where Q is the generalized Q function defined as

$$Q(a, b) = e^{-\frac{a^2 + b^2}{2}} \sum_{k=0}^{\infty} \left(\frac{a}{b}\right)^k I_k(ab), \quad b > a > 0$$

and $I_k(x)$ is the k th-order modified Bessel function of the first kind.

Ricean fading is typically encountered in environments where there is a dominant, nonfading signal component (i.e., a line-of-sight path between transmitter and receiver, and this causes the nonzero mean of X and Y). This is commonly true in mobile satellite channels. The signal received can be modeled as the superposition of the scattered multipath signals (with random angles of arrival) and the line-of-sight signal. The effects of the scattered signals depends on their strength relative to the strength of the nonfaded signal, which is characterized by the parameter called *Ricean factor* K , defined as $K \triangleq s^2/2\sigma^2$. It is quite common to specify the Rice factor in decibels, $K_{\text{dB}} \triangleq 10 \log_{10} K$ dB. As mentioned previously, the Ricean distribution spans a broad spectrum of fading environments, including the following special cases:

- $K \rightarrow 0$ ($\Rightarrow s^2 \sim 0$) \Rightarrow Rayleigh fading channel
- $K \gg 1$ ($\Rightarrow s^2 \gg \sigma^2$) \Rightarrow static channel (no fading)

A plot of the Ricean pdf for different values of the Ricean factor K is given in Fig. 6. As the value of K increases, the mean (and also the variance) of V increases. In practice, this implies that the LOS signal component is stronger relative to the scattered signal components, and as a result the magnitude of signal fades is reduced. Figure 7 shows segments of Rayleigh and Ricean fading for different values of K . For $K=10$, in Fig. 7 the fade depth is typically ≤ 10 dB, whereas for $K=1$, signal fades of up to 30 dB are observed.

3.1. Rayleigh Distribution

As shown in the preceding section, the Rayleigh distribution is a special case of the Rice distribution ($K \rightarrow 0$ dB). The Rayleigh distribution can also be derived independently from the central chi-square distribution, as shown herein. Let X and Y be two independent identically distributed (i.i.d.) zeromean Gaussian RVs with variance σ^2 .

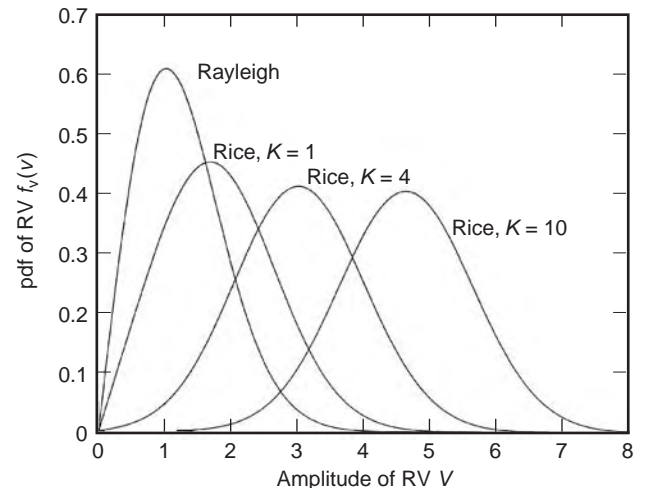


Figure 6. Plot of the Rayleigh pdf and the Ricean pdf for different values of the Rice factor $K=1, 4$, and 10 .

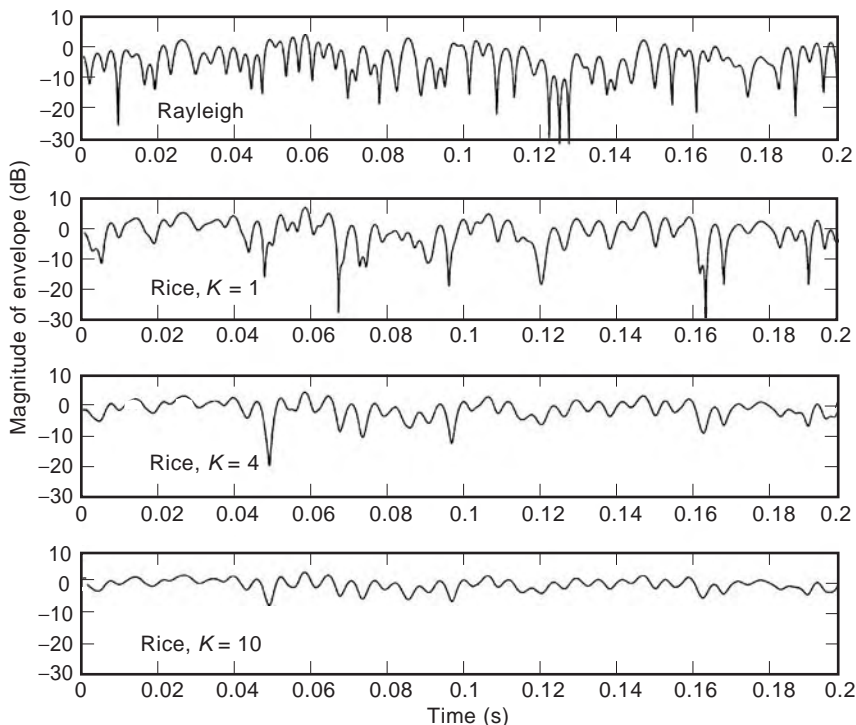


Figure 7. Plot of a typical segment of Rayleigh and Ricean fading waveforms.

Then the RV V defined as $V \triangleq \sqrt{X^2 + Y^2}$, is distributed according to the *Rayleigh distribution*, whose pdf is given by

$$f_V(v) = \begin{cases} \frac{v}{\sigma^2} e^{-\frac{v^2}{2\sigma^2}} & v \geq 0 \\ 0 & v < 0 \end{cases} \quad (11)$$

A brief derivation of the pdf $f_V(v)$ is given in the Appendix. Equation (11) can be obtained from Eq. (8) by setting $s^2 = 0$. It can also be shown that the RV $\hat{V} = V^2$ has a central chi-square distribution. The cdf of V is given by

$$\begin{aligned} F_V(v) &= Pr(v \leq V) = \int_0^v f_V(v) dv \\ &= 1 - e^{-\frac{v^2}{2\sigma^2}}, v \geq 0 \end{aligned} \quad (12)$$

The mean and variance of V are given by

$$E[V] = \sqrt{\frac{\pi}{2}} \sigma$$

and

$$E[V^2] = 2\sigma^2$$

and the higher order moments of V can be obtained from the expression [4]

$$E[V^k] = (2\sigma^2)^{k/2} \Gamma\left(1 + \frac{k}{2}\right)$$

3.2. Nakagami Distribution

The Nakagami- m distribution [5] was designed to fit empirical data and in some cases provides a better match than Rayleigh or Rice distributions. Hence, it is frequently used to characterize the statistical fluctuations of signals transmitted over multipath fading channels. An RV V with *Nakagami- m distribution* has a pdf given by

$$f_V(v) = \frac{2}{\Gamma(m)} \left(\frac{m}{\Omega}\right)^m v^{2m-1} e^{-\frac{mv^2}{\Omega}}, m \geq \frac{1}{2} \quad (13)$$

where $\Omega = E[V^2]$, $\Gamma(m)$ is the gamma function, and the parameter m is called the fading figure, defined as

$$m \triangleq \frac{\Omega^2}{E[(V^2 - \Omega)^2]}, m \geq \frac{1}{2}$$

The following are special cases of the Nakagami- m distribution:

- $m = 1$; the Nakagami- m distribution reduces to the Rayleigh pdf.
- $m = 1/2$; $f_V(v)$ is the one-sided Gaussian pdf (more severe than Rayleigh fading).
- $m \rightarrow \infty$; it is a static channel (no fading).
- The Nakagami- m distribution also provides a close approximation of the Rice distribution with the following relationship between the Rice factor K and the

Nakagami parameter m :

$$m = \frac{(K+1)^2}{(2K+1)}$$

Because of its versatility in modeling a wide range of fading conditions and its analytical tractability, the Nakagami- m distribution is widely used.

3.3. Lognormal Distribution

The variations in the local mean of the signal power received in a fading environment is referred to as shadowing. These variations are caused by terrain and other environmental factors. Shadowing is characterized via the lognormal distribution, as defined herein. An RV Ω' is said to have a log-normal distribution if its pdf is given by

$$f(\Omega) = \frac{1}{2\pi\sigma_\Omega} e^{-(\Omega-\mu)^2/2\sigma_\Omega^2} \quad (14)$$

where

$$\Omega = 20 \log_{10} \Omega'$$

$$\mu = E[\Omega]$$

and

$$\sigma_\Omega^2 = E[\Omega^2] - \mu^2$$

4. CHARACTERIZATION OF RAYLEIGH FADING

Extensive measurements of the envelope variations of signals have been carried out in the 100–2000 MHz frequency band, which covers commercial cellular, public safety, and special mobile radio applications. The measured data confirm that the envelope of the received signal is Rayleigh distributed when measured over short distances ($\sim 10\lambda$ – 20λ) over which the mean signal level is constant. In this section, the key results of the mathematical model of Rayleigh fading channels and their characterization are presented. For a complete derivation of the results, the reader is referred to Refs. 1–3. Herein, the model proposed in Ref. 1 is considered.

4.1. Mathematical Model for Rayleigh Fading

In Fig. 8, the X – Y plane is assumed to be the horizontal ground plane. Consider a mobile receiver moving with velocity v along the X axis. The model [1] is that the signal received consists of a number of horizontally traveling plane waves each with random amplitude (but equal on average) and random angle of arrival. The phases of the waves are uniformly distributed in $[0, 2\pi]$ and are assumed to be statistically independent of the amplitudes.

Let the angle of the n th incoming wave be α_n with respect to the X -axis. We assume a fixed transmitter with a vertically polarized antenna and a mobile receiver with a whip/monopole antenna. The vehicular motion introduces

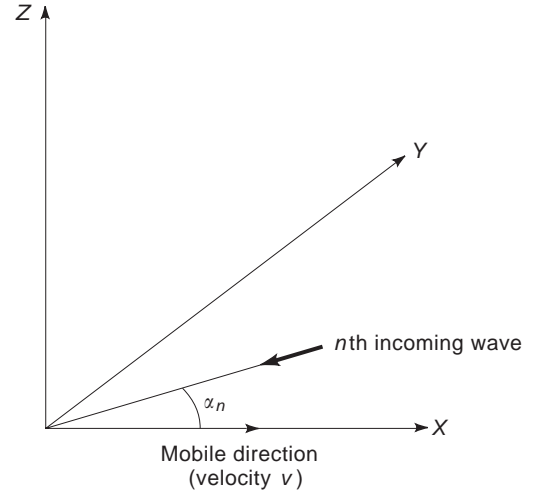


Figure 8. Reference figure for deriving the mathematical model for Rayleigh fading.

a Doppler shift given by

$$f_n = \frac{v}{\lambda} \cos \alpha_n (\text{Hz}) \quad (15)$$

where v is the velocity in m/s and λ is the wavelength (in meters) of the transmitted carrier signal. From Eq. (15), the maximum Doppler shift is given by $f_{n,\text{max}} = v/\lambda$ Hz.

The electric and magnetic field components received at the mobile receiver are E_z , H_x , and H_y respectively. Next, the expressions for E_z are derived. The superposition of the different waves is expressed as

$$E_z = E_0 \sum_{n=1}^N C_n \cos(2\pi f_c t + \theta_n) \quad (16)$$

where $\theta_n = 2\pi f_n t + \phi_n$, where f_c is the carrier frequency, f_n is the Doppler shift, $E_0 C_n$ is the amplitude of the n th wave, and ϕ_n are the random phase angles uniformly distributed in $[0, 2\pi]$. The C_n are normalized such that $(\sum_{n=1}^N C_n^2) = 1$, where $\langle \rangle$ indicates the ensemble average. For large N , using the central limit theorem, the field components E_z , H_x , and H_y can be approximated by Gaussian random processes. The following derivation assumes that the mean power of the signal is constant with time, which is typically the case as the mobile receiver traverses short distances (i.e., the shadowing is a constant). Equation (16) can be expressed as

$$E_z = T_c(t) \cos 2\pi f_c t - T_s(t) \sin 2\pi f_c t \quad (17)$$

where

$$T_c(t) = E_0 \sum_{n=1}^N C_n \cos(2\pi f_n t + \phi_n) \quad (18)$$

$$T_s(t) = E_0 \sum_{n=1}^N C_n \sin(2\pi f_n t + \phi_n)$$

Both $T_c(t)$ and $T_s(t)$ are Gaussian random processes. The corresponding RVs T_c and T_s have zero mean and equal variance given by

$$\langle T_c^2 \rangle = \langle T_s^2 \rangle = E_0^2/2$$

and the ensemble average is evaluated over α_n , ϕ_n , and C_n . The Gaussian RVs T_c and T_s are uncorrelated and hence independent. Their common variance is $E_0^2/2$. The envelope of E_z is given by

$$|E_z| = V \triangleq \sqrt{T_c^2 + T_s^2} \quad (19)$$

Using the results from the section on Rayleigh distribution, V is a Rayleigh distributed random variable, whose pdf is given by Eq. (11).

4.2. Power Spectrum of Rayleigh Fading

If the transmitted signal is a sinusoid of frequency f_c , the instantaneous frequency of the received signal arriving at angle α is given by [using Eq. (15)]

$$f(\alpha) = f_c + f_m \cos \alpha \quad (20)$$

where f_m is the maximum Doppler frequency. Hence

$$\cos \alpha = \left(\frac{f - f_c}{f_m} \right)$$

and

$$\sin \alpha = \sqrt{1 - \left(\frac{f - f_c}{f_m} \right)^2} \quad (21)$$

Assuming a large number of scatterers and that the mobile receiver has a vertical whip antenna, then the total incoming power is uniform as a function of the incident angle α . Using the derivation in Refs. 1 and 3, the power spectrum of the electric field is given by

$$S_{E_z}(f) = \begin{cases} \frac{3b}{2\pi f_m} \frac{1}{\sqrt{1 - \left(\frac{f - f_c}{f_m} \right)^2}}, & |f - f_c| \leq f_m \\ 0 & |f - f_c| > f_m \end{cases} \quad (22)$$

where b is a scale factor denoting the mean power received by an isotropic antenna. A normalized plot of the power spectrum is shown in Fig. 9. The peak of the power spectrum occurs at $\pm f_m$. The power spectra for the magnetic field components are given in Ref. 1.

4.3. Envelope Correlation for Rayleigh Fading

An important result obtained by using the power spectrum $S_{E_z}(f)$ is the envelope correlation $R_{TT}(\tau) = \langle T(t)T^*(t + \tau) \rangle$ where $T(t) = T_c(t) + jT_s(t)$ is the baseband representation of the E -field components given by Eq. (18) and the envelope correlation is expressed as a function of

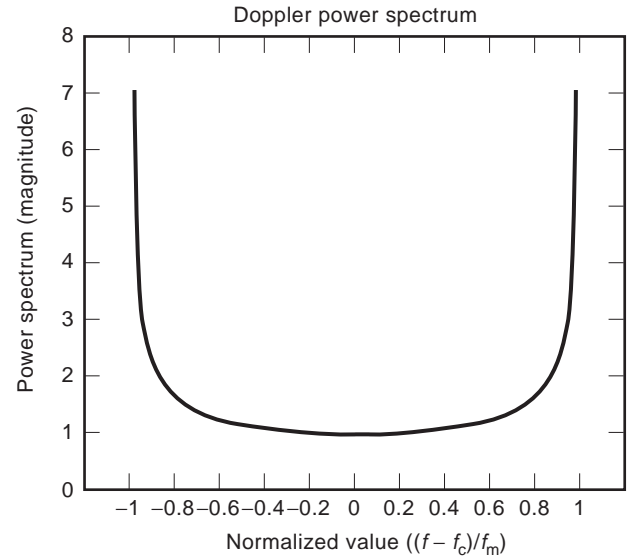


Figure 9. Power spectrum of the received E -field in a Rayleigh fading environment.

the time separation τ . Using the Fourier relationship

$$\begin{aligned} R_{TT}(\tau) &= \int_{f_c - f_m}^{f_c + f_m} S_{E_z}(f) e^{-j2\pi(f - f_c)\tau} df \\ &= \int_{f_c - f_m}^{f_c + f_m} \frac{3b}{2\pi f_m} \frac{e^{j2\pi(f - f_c)t}}{\sqrt{1 - \left(\frac{f - f_c}{f_m} \right)^2}} df \end{aligned} \quad (23)$$

it can be shown that

$$\begin{aligned} R_{TT}(\tau) &= \langle T_c(t)T_c(t + \tau) \rangle + \langle T_s(t)T_s(t + \tau) \rangle \\ &= \int_{f_c - f_m}^{f_c + f_m} \frac{3b}{2\pi f_m} \frac{1}{\sqrt{1 - \left(\frac{f - f_c}{f_m} \right)^2}} \cos(2\pi(f - f_c)t) df \end{aligned} \quad (24)$$

From Ref. 20, we have the result

$$\int_0^1 \frac{1}{\sqrt{1 - x^2}} \cos(ax) dx = \pi/2 J_0(a)$$

where J_0 is the zeroth-order Bessel function of the first kind. Using this result, we obtain

$$R_{TT}(\tau) = 1.5b J_0(2\pi f_m \tau) \quad (25)$$

This shows that the envelope of a Rayleigh faded signal has a Bessel autocorrelation function, which plays an important part in designing effective error correcting coding and interleaving techniques for Rayleigh fading channels.

4.4. Rayleigh Fading Statistics

Two statistical properties that help characterize Rayleigh fading are

1. The level crossing rate (LCR)
2. The duration of fades

The derivation of these two parameters is based on the work of Rice [1,7,8].

4.4.1. Level Crossing Rate. The level crossing rate (LCR) is defined as the expected rate at which the Rayleigh fading envelope $V(t)$, normalized to the local rms signal level, crosses a specified level (V_{ref} in a positive direction. Figure 10 depicts a typical envelope variation that has three crossings of the level V_{ref} in the duration of T seconds. The LCR N_V , the number of level crossings per second is given by [1]

$$N_V = \int_0^\infty \dot{v}p(V, \dot{v}) d\dot{v} = \sqrt{2\pi}f_m\rho e^{-\rho^2} \tag{26}$$

where \dot{v} is the rate of change (the time derivative) of the envelope $V(t)$, $p(V, \dot{v})$ is the joint pdf of v and \dot{v} at a specified value of V , and $\rho = V/V_{\text{rms}}$ is the normalized value of the envelope. It can be verified that the peak value of N_V occurs at $\rho = -3$ dB.

Example 2. Consider a signal with carrier frequency of 1.9 GHz and a receiver moving at a velocity of 100 km/ph. The corresponding value of the Doppler frequency $f_m = 176$ Hz. At a normalized value of $\rho = 0$ dB, using Eq. (26), we obtain the value $N_V = 162$ crossings/s. Hence the LCR gives a characterization of the fluctuation rate of the signal envelope.

4.4.2. Duration of Fades. The duration of fades is the expected value of the time at which the signal level is below a specified value V_{ref} . In Fig. 10, consider a time interval T (seconds), and let τ_i be the duration of the i th fade below the level V_{ref} . Then

$$P[v \leq V] = \frac{1}{T} \sum_i \tau_i \tag{27}$$

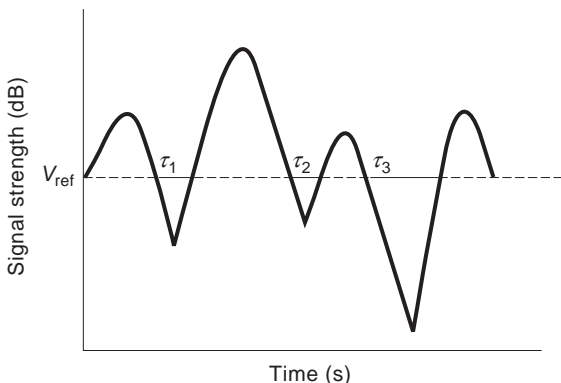


Figure 10. A method to compute the level crossing rate and fade duration for Rayleigh fading.

Using the expression for the pdf of V , we have

$$P[v \leq V] = \int_0^V p(v) dv = 1 - e^{-\rho^2} \tag{28}$$

where $\rho = V/V_{\text{rms}}$. Using Eqs. (27) and (28), we obtain the expression for \bar{T}_{fade} , the average duration of a fade below $v = V$ (as given in Ref. 1)

$$\bar{T}_{\text{fade}} = \frac{1}{TN_V} \sum_i \tau_i = \frac{1}{\sqrt{2\pi}} \frac{[e^{\rho^2} - 1]}{\rho f_m} \tag{29}$$

Example 2Cont. Consider the same example as in the preceding section. For the same parameters, using Eq. (29), the average duration of a fade 20 dB below the RMS value of the envelope $\rho = 1.43$ ms.

4.4.3. Observations Based on Fading Statistics.

- $N_V \propto f_m$ and $\bar{T}_{\text{fade}} \propto 1/f_m$
- At low Doppler frequency, the LCR is low, and hence the duration of fades is long. This observation is helpful in choosing diversity and error correction schemes over fading channels.
- The value of \bar{T}_{fade} yields an estimate of the number of symbols that may be lost because of a fade (burstiness of errors caused by fading).

In particular, if a mobile communication system is designed with a specified fade margin, then the performance of the receiver can be estimated by using the parameters f_m , ρ , and \bar{T}_{fade} to relate the instantaneous signal-to-noise ratio (SNR) to the instantaneous bit error rate (BER).

4.4.4. Random Frequency/Phase Modulation. The baseband representation of the E -field components, as given in Eq. (18), can be expressed as

$$T(t) = T_c(t) + jT_s(t) = A(t)e^{j\phi(t)} \tag{30}$$

where $T_c(t)$ is the in-phase component and $T_s(t)$ is the quadrature component. The effect of the multipath fading channel is represented by $T(t)$, which is a complex-valued, multiplicative scaling of the transmitted signal. The time-varying nature of $T_c(t)$ and $T_s(t)$ manifests itself as a random phase modulation of $\theta(t)$. In FM receivers, the effect of $T(t)$ produces a baseband noise component, which can be evaluated [1]. The baseband noise is characterized by the frequency deviation it produces. It is interesting to note that the frequency deviation (and hence, the rms value of the baseband noise) depends on the depth of the fade. As the signal envelope V experiences deep fades, the frequency deviation of the random FM increases proportionally. The effect of $T(t)$ can also be viewed as random phase rotation given by $\arctan [T_s(t)/T_c(t)]$. Hence, multipath fading causes impairments of the received signal that have the characteristics of random FM and random phase shifts.

5. SIMULATION OF RAYLEIGH FADING

In the preceding sections, the power spectrum and the envelope correlation of a Rayleigh faded signal have been discussed. Using these results, two methods are obtained for generating Rayleigh fading:

1. the stochastic filtered noise approach [9,10]
2. the Jakes method (deterministic) [1]

Both methods are easily modified to generate Ricean fading. Let $T(t) = T_c(t) + jT_s(t)$ be the complex baseband representation of Rayleigh fading. The main requirements on T_c and T_s for generating Rayleigh fading are that

- They have a Gaussian pdf.
- They be zero mean and have equal variance (typically normalized to 0.5, such that the variance of $T(t)$ is unity.
- T_c and T_s must be uncorrelated.
- The autocorrelation of $T(t)$ must satisfy the condition in Eq. (25); This condition also implies that the power spectrum closely approximates Eq. (22).

5.1. Filtered Noise Approach

The method for implementing the stochastic filtered noise approach is shown in Fig. 11. The steps are as follows:

1. Generate two independent Gaussian (white) noise sources.
2. Each of the sequence of random variables (samples of the noise) is filtered by a baseband Doppler filter whose frequency response is given by $\sqrt{S_{E_z}(f)}$.
3. The output of the Doppler filters yields the in-phase and quadrature components of the Rayleigh fading signal.

It can be verified that the output signal $T_c + jT_s$ has a Rayleigh envelope with the time correlation specified by the maximum Doppler frequency f_m . The filtering in step 2 can be done in the frequency domain via FFT. The steps for using the FFT for the filtering are outlined in Ref. 9.

5.2. Jakes' Method

In this section, the Jakes (deterministic) approach for generating Rayleigh fading is discussed (Fig. 12). The main advantage of this method over the stochastic

method is that segments of time-correlated fading can be generated without having to generate the fading in between the desired segments, as is typically the case when simulating the performance of time-division multiple-access (TDMA) signals.

The details of the model (Fig. 12) are as follows:

- There are N_0 oscillators with frequencies given by

$$f_n = f_m \cos\left(\frac{2\pi n}{N}\right), \quad n = 1, 2, \dots, N_0 \quad (31)$$

and one oscillator with frequency f_m , where f_m is the maximum Doppler frequency. The total number of oscillators is $(N_0 + 1)$, where $N_0 = \frac{1}{2}(N/2 - 1)$. The parameter N is chosen such that T_c and T_s are Gaussian and the power spectrum of $T(t) = T_c(t) + jT_s(t)$ closely approximates the condition in Eq. (22). In Ref. 1, it is shown that a good approximation is obtained for $N > 34$ ($\Rightarrow N_0 \geq 8$).

- In Fig. 12, the phases α and $\beta_n, n = 1, 2, \dots, N_0$ are chosen such that the probability distribution of the resultant phase ($\arg[T(t)]$) is close to a uniform distribution in $[0, 2\pi]$. These phases are introduced by the respective multipliers $2 \cos \beta_n$ and $2 \sin \beta_n$. The uniform distribution of $\arg[T(t)]$ is ensured if

$$\langle T_c^2 \rangle = \langle T_s^2 \rangle$$

and

$$\langle T_c T_s \rangle = 0 \quad (32)$$

Choices of values that satisfy Eq. (32) are

$$\alpha = 0$$

$$\beta_n = \frac{\pi n}{N_0 + 1}$$

$$\text{Scale 1} = \frac{1}{\sqrt{2N_0}}$$

$$\text{Scale 2} = \frac{1}{\sqrt{2(N_0 + 1)}}$$

Other choices are also possible:

- The oscillator phases ϕ_n in Fig. 12 are randomly chosen in the range $[0, 2\pi]$. The purpose of ϕ_n is to provide

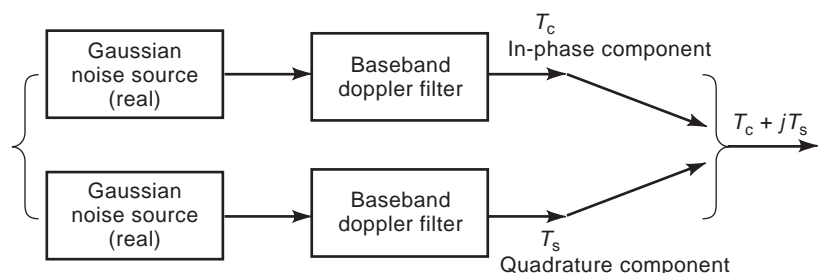


Figure 11. Stochastic filtered noise method for generating Rayleigh fading.

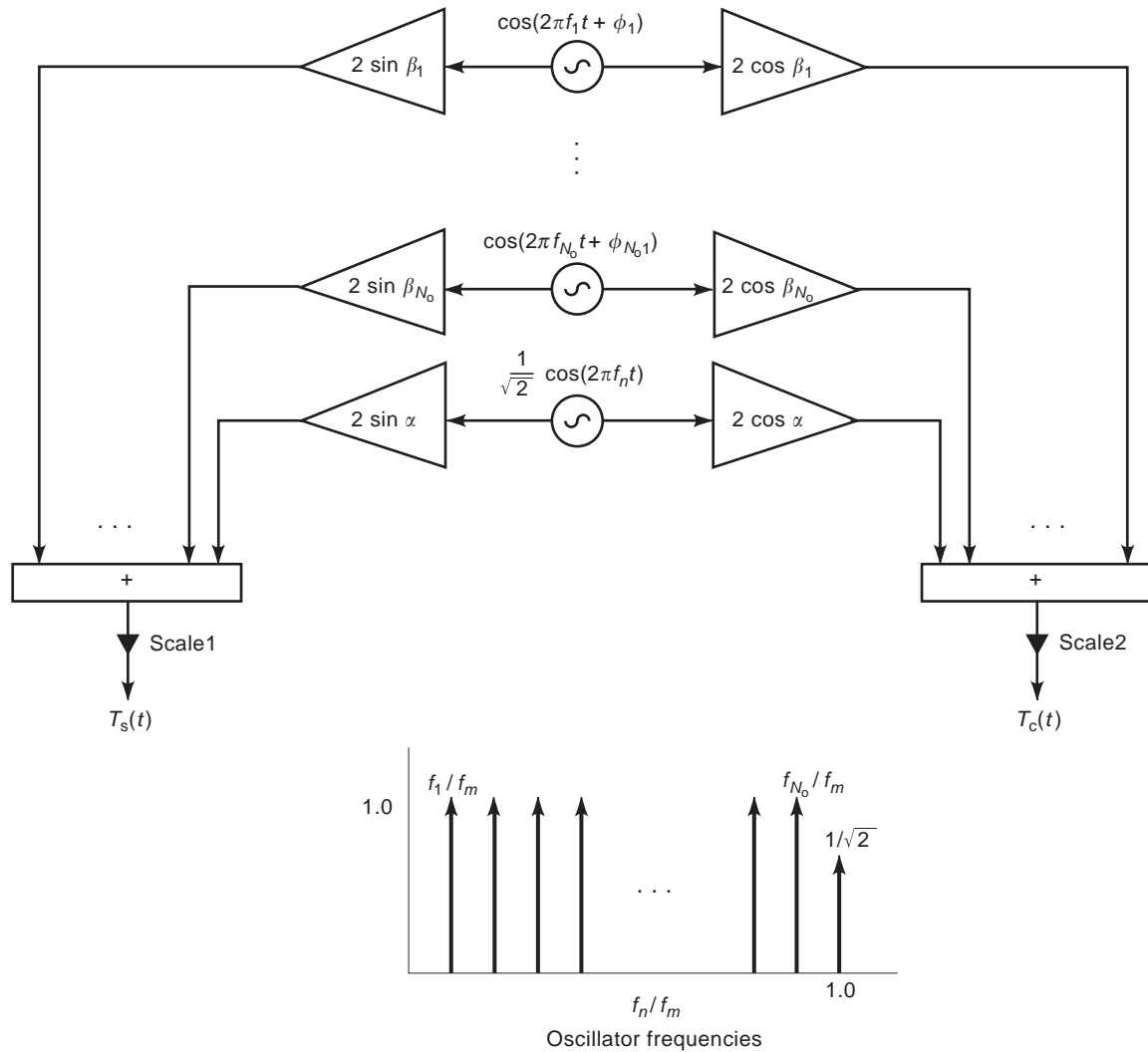


Figure 12. Jakes' method for generating Rayleigh fading.

a means of randomly initializing the fading waveform generator. They do not affect the statistical properties of $T_c(t)$ and $T_s(t)$.

5.3. Generating Multiple Uncorrelated Fading Waveforms

In many practical applications, it is necessary to generate multiple uncorrelated Rayleigh fading waveforms. In Ref. 1, a method of modifying Fig. 12 to generate multiple uncorrelated fading is mentioned. However, it has been observed [11] that the method in Ref. 1 produces waveforms with nonzero correlation when more than two waveforms are generated. An attractive and computationally efficient alternative is presented in [11] based on the Walsh-Hadamard transform. Using this method, the multiple fading waveforms are guaranteed to be uncorrelated.

6. CHARACTERIZATION OF MULTIPATH CHANNELS

Consider the equivalent, complex-valued, lowpass impulse response of a time-varying multipath channel $c(\tau;t)$ as

given by Eq. (5), where $c(\tau;t)$ is a zero-mean, complex-valued Gaussian random process in the variable t . Assume that $c(\tau;t)$ is wide-sense stationary (WSS). Then the autocorrelation of $c(\tau;t)$ is given by

$$\phi_c(\tau_1, \tau_2; \Delta t) = \frac{1}{2} E[c(\tau_1; t)c^*(\tau_2; t + \Delta t)] \tag{33}$$

Assuming uncorrelated scattering, that is, that the scattering/multipath signal at delay τ_1 given by $c(\tau_1;t)$ is uncorrelated to the signal at delay τ_2 given by $c(\tau_2;t)$; hence

$$\phi_c(\tau_1, \tau_2; \Delta t) = \phi_c(\tau_1; \Delta t)\delta(\tau_1 - \tau_2) \tag{34}$$

When $\Delta t = 0$, $\phi_c(\tau, 0) = \phi_c(\tau)$, which is called the *multipath intensity profile*, or the *power-delay profile*. There are different experimental methods for measuring the power-delay profile of a channel such as direct pulse measurement, spread spectrum sliding correlator measurement, and frequency-domain channel sounding [10]. A typical power-delay profile is given in Fig. 14. The range of τ over which

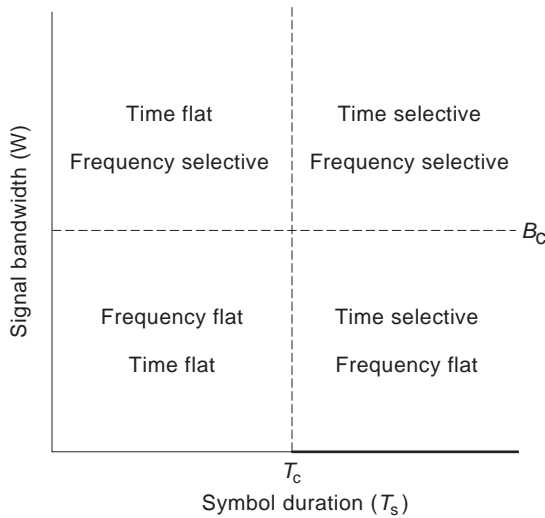


Figure 13. A typical power-delay profile and the method of sampling the power delay profile to generate a tapped-delay-line model.

$\phi_c(\tau)$ is nonzero is called the *multipath spread* of the channel τ_m .

6.1. Time Parameters

6.1.1. Time-Dispersion Parameters. The mean excess delay, RMS delay spread, and the excess delay spread are channel parameters that are obtained from the power-delay profile $\phi_c(\tau)$:

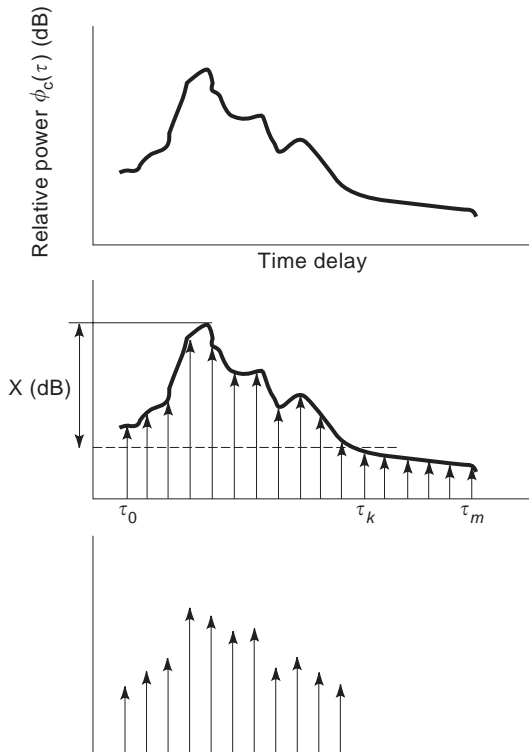


Figure 14. Classification of multipath fading channels.

- The *mean excess delay* of the power-delay profile is given by

$$\bar{\tau} = \frac{\sum_k \phi_c(\tau_k) \tau_k}{\sum_k \phi_c(\tau_k)} \quad (35)$$

- where $\phi_c(\tau_k)$ is the strength of the multipath component with delay τ_k (obtained from the power-delay profile). Typically the τ_k are measured relative to the first arriving multipath signal.
- The *RMS delay spread* is defined as $\sigma_\tau = \sqrt{\tau^2 - (\bar{\tau})^2}$, where τ^2 is given by

$$\tau^2 = \frac{\sum_k \phi_c(\tau_k) \tau_k^2}{\sum_k \phi_c(\tau_k)} \quad (36)$$

- Suppose that τ_0 is the first arriving multipath and τ_K is the delay beyond which the power drops below X dB of the maximum strength multipath component, then, $(\tau_K - \tau_0)$ is called the maximum excess delay (X dB).

In practice, the value of $\bar{\tau}$, τ^2 and σ_τ depend on the value of the threshold for detecting the presence of a signal component.

6.1.2. Coherence Bandwidth. The coherence bandwidth B_c is an important parameter in time-dispersive channels. B_c can be viewed as the range of frequencies over which there is a strong envelope correlation. There is, however, more than one formal definition of B_c . In Ref. 4, the coherence bandwidth is defined as the reciprocal of the multipath spread of the channel τ_m :

$$B_c \approx \frac{1}{\tau_m} \quad (37)$$

A more widely used engineering definition of B_c is given in Refs. 1, 7, 10, and 12. Wherein the coherence bandwidth is defined as the bandwidth over which the frequency correlation is > 0.5 . In Ref. 12 it is shown that to satisfy this condition,

$$B_c \approx \frac{1}{2\pi\sigma_\tau} \approx \frac{1}{6\sigma_\tau} \quad (38)$$

where σ_τ is the rms delay spread given by Eq. (36). Another interpretation of B_c is as follows. If two sinusoids with frequency separation $> B_c$ are transmitted through this channel, then they are affected differently. For modulated signals, if B_c is smaller than the BW of the signal (W), then the channel is said to be *frequency-selective*. If B_c is greater than the BW of the signal, the channel is said to be *frequency-nonselective*.

6.1.3. Coherence Time. The RMS delay spread (σ_τ) and the coherence BW (B_c) describe the time-dispersive nature of the channel. Analogously, the Doppler spread (B_D) and

the coherence time (T_c) describe the time-varying nature of the channel in a local area (small-scale region). The Doppler spread B_D , is defined as the range of frequencies over which the Doppler spectrum is nonzero. In Ref. 4, the coherence time is defined as

$$T_c \approx \frac{1}{B_D} \quad (39)$$

Coherence time is a measure of the length of time over which the channel impulse response is essentially constant. Alternatively, the coherence time can be viewed as the length of time over which two received signals have a strong potential for envelope correlation. Just as coherence BW has a statistical definition, coherence time T_c can be defined [12] as the time over which the time correlation function is ≥ 0.5 . In Ref. 12 it is shown that

$$T_c \approx \frac{9}{16\pi f_m} \quad (40)$$

where f_m is the maximum Doppler frequency.

6.2. Channel Classification

Multipath fading channels are classified on the basis of the way the channel appears to the transmitted signal. The coherence bandwidth B_c and the coherence time T_c , two of the main properties that influence the effect of the channel on the transmitted signal, are classified as follows:

- If the BW of the transmitted signal (W) is smaller than the coherence BW (B_c), then the fading channel appears as *frequency-nonselective* or *frequency flat*. This implies that all the frequencies of the transmitted signal experience the same channel effects. If $W = B_c$, then it is classified as a frequency-selective fading channel.
- If the duration of the received waveform [a symbol duration (T_s) for digital transmission] is less than the coherence time, then the channel is said to be *time flat*. Otherwise, it is classified as time-selective.

Based on these definitions, we have the classification depicted in Fig. 13.

6.3. A Tapped-Delay-Line Channel Model

In addition to providing channel information such as the RMS delay spread, the power-delay profile $\phi_c(\tau)$, also provides a means for modeling the channel using a tapped-delay-line (FIR) model. From Eq. (5), $\alpha_n(t)$ is the amplitude/gain coefficient for a path arriving with delay $\tau_n(t)$. A typical power-delay profile is shown in Fig. 14, which in the second figure, is uniformly sampled into equal delay bins. In general, the different bins contain a number of received signals (corresponding to different paths) whose times of arrival lie within the particular delay bin. These signals are represented by an impulse at the center of each delay bin that has an amplitude with the appropriate

statistical distribution (Rayleigh, Ricean, etc.). In deriving this model, two assumptions are made:

- There are sufficient number of rays clustered together in each delay bin.
- The statistical distribution of the envelope is known.

The rate of sampling the power-delay profile is affected by the time resolution desired and also the bandwidth of the transmitted signal. The next step after sampling the power-delay profile is to use a threshold (say, X dB below the peak of the power-delay profile), and using the threshold to truncate those samples below the threshold. This model can be implemented by using a tapped-delay line or FIR model, thereby allowing us to model arbitrary channel.

7. LARGE-SCALE EFFECTS

Understanding and characterizing the effects of the RF propagative channel are essential to designing RF communication systems. A wide range of channel conditions are encountered in RF communications, all the way from LOS channels to severely obstructed channels. Further, the channel may also be time-varying. Hence modeling is based on statistical and experimental information. This has continued to be an area of extensive research and measurement, since the early 1970s [1,7,10,16–20]. In this section, the two main components of signal variability due to the large-scale effects of RF propagation, namely, path loss and shadowing, are discussed.

7.1. Radio Signal Propagation

The salient features of RF propagation are briefly described in this section. For a detailed treatment of this subject, the reader is referred to Refs. 7 and 10. The three basic propagative mechanisms, illustrated in Fig. 15, are reflection, diffraction, and scattering. Together, these three modes enable us to estimate the signal level received by a transmitter for a given RF propagative channel.

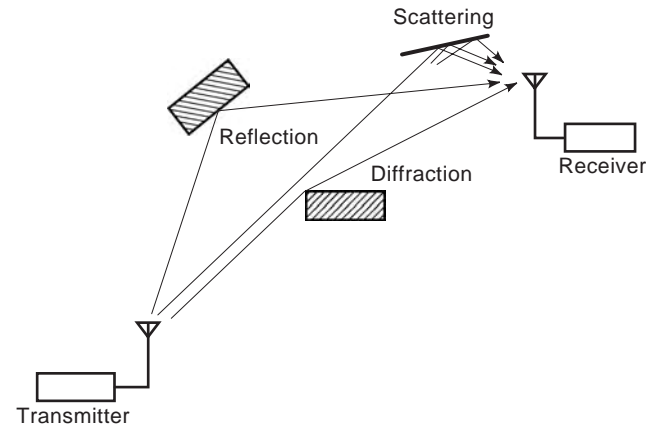


Figure 15. The different modes of RF signal propagation, reflection, diffraction, and scattering.

- *Reflection.* This occurs when a radiowave propagating in one medium is incident on another medium that has different electrical properties and a part of the energy is reflected back into the first medium, depending on the specific electrical properties of the second medium. If the second medium is a perfect conductor, all of the incident energy is reflected. If the second medium is a dielectric, then the energy is only partially reflected. The reflection coefficient is a function of the medium's properties, the signal frequency, and the angle of incidence. Reflections of RF signals typically occur from objects in the propagative path whose size is larger than the wavelength (λ) of the RF carrier, such as buildings and walls. In the case of cellular/PCS signals at 1.9 GHz, the wavelength $\lambda = 15 \text{ cm} \approx 6 \text{ in.}$ Hence, a variety of objects act as reflectors. Signals are also reflected from the ground. A model commonly used to characterize RF channels is the two-ray ground reflection model [10].
- *Diffraction.* This can be viewed as the “bending” of RF signals around an obstruction, as shown in Fig. 15. Diffraction occurs when the obstruction between the transmitter and receiver has sharp edges. As explained by Huygen's principle, when a wavefront impinges on an obstruction, then secondary wavelets are produced, which give rise to bending of waves around the obstruction. The field strength of the diffracted wave in the shadowed region is the vector sum of the electric field components of the secondary wavelets. The knife-edge diffraction model [10] can be used to characterize the diffraction caused by a single object, such as building in the path of an RF signal.
- *Scattering.* This occurs when the RF signal is incident on a surface that has a certain degree of “roughness” [7,10]. Scattering in an RF channel is commonly caused by objects, such as buildings. The *critical height* $h_c = \lambda/8 \sin \theta_i$, where θ_i is the angle of incidence. This implies that the maximum to minimum level of the surface must be greater than h_c .

7.2. Propagative Path-Loss Models

7.2.1. Free-Space Propagative Loss. When there is a LoS path between the transmitter and receiver, the free-space propagation model can be used to predict the signal strength. Such conditions occur in some satellite and terrestrial microwave communication links. Suppose that the distance between the transmitter and receiver is d meters, where d is in the far field. Then the free-space model (based on the Friis formula) gives

$$P_r(d) = \frac{P_t G_t G_r \lambda^2}{(4\pi)^2 L} \frac{1}{d^2} \quad (41)$$

where P_t and P_r are the transmitting and receiving power, respectively, with transmitting antenna gain G_t , receiving antenna gain G_r , and λ is the wavelength of the carrier. The term L represents the losses in the system ($L \geq 1$). The path loss L_p is the difference between the transmitting and

receiving power values expressed in decibels:

$$L_p(\text{dB}) = 10 \log_{10} \frac{P_t}{P_r} = 10 \log_{10} \left[\frac{(4\pi)^2 L}{P_t G_t G_r \lambda^2} \right] + 20 \log d \quad (42)$$

As the signal propagative distance d increases, the received power decreases at 20 dB/decade, as seen from Eq. (42). Another commonly used method to compute the signal power received $P_r(d)$ is by measuring it relative to the received power $P_r(d_0)$ at a reference point (distance d_0 from the transmitter) as given by

$$P_r(d) = P_r(d_0) \left(\frac{d_0}{d} \right)^2, \quad d \geq d_0 \quad (43)$$

7.2.2. Outdoor Propagative Loss. In dealing with non-LoS environments, which is typical of most RF communication links, such as cellular/PCS, we need appropriate models for computing the propagative path loss (because the criteria for free-space propagation are not met). This topic has been very extensively studied. Detailed information can be found in Refs. 7, 10, 12, and 16. Computation path loss is of particular interest to communication systems designers. Because the actual RF communication environments encountered in practice are so numerous, a unified theoretical/analytical framework for estimating path loss is not feasible. Most system designers resort to empirical approaches and semianalytical methods, which have been validated by experimental/measured data, to estimate the path loss. The work of Okamura and Hata [13] is very widely used for path loss estimation. Okamura's work is based purely on measured data, and Hata provided the empirical model to fit that data. The advantage of using empirical models and curve fitting to measured data is that it accounts for both known and unknown sources of path loss. On the other hand, the disadvantage is that the validity of the empirical model, derived from a set of data, is not guaranteed for a different environment.

Let d be the distance between the transmitter and receiver. Both theoretical and measurement-based models show that the average path loss $[L_p(d)]$ increases directly proportional to d^n , where n is called the path-loss exponent. Typically $n \geq 2$, as summarized in the Table 1. By contrast, in free space, $N=2$. The path loss $L_p(d)$ is given by

$$L_p(d) \propto d^n \quad (44)$$

$$L_p(d) = L_p(d_0) + 10n \log_{10} \left(\frac{d}{d_0} \right) \quad (45)$$

Table 1. Path-Loss Exponents for Different Environments

Environment	Path-Loss Exponent n
Free space	2
Urban cellular	2.7–4.0
In-building (non-LoS)	3.0–6.0
Shadowed urban cellular	4.0–6.0

The reference point d_0 is chosen such that $L_p(d_0)$ can be computed using the free-space path-loss model.

7.2.3. Hata and COST-231 Models. This is one of the most widely used models for estimating path loss in RF communication channels. Based on extensive measured data, Okamura generated sets of curves that characterize the median attenuation (50th percentile) $L_{p,50}$, for a wide range of environments [range of carrier frequency (f_c), effective height of transmitting antenna ($h_{t,\text{eff}}$), and distance d from transmitter]. Hata [12] provided an empirical formulation from Okamura's data, which shows good agreement (between the model and the measured data) for $f_c \leq 1.5$ GHz. An extension of Hata's model for frequencies up to 2 GHz is provided in Ref. 14. The Hata model and COST-231 models are given below:

Hata model:

$$L_{p,50} = 69.55 + 26.16 \log_{10} f_c - 13.82 \log_{10} h_{t,\text{eff}} - a(h_{r,\text{eff}}) + (44.9 - 6.55 \log_{10} h_{t,\text{eff}}) \log_{10} d \quad (46)$$

COST-231 model:

$$L_{p,50} = 46.3 + 33.9 \log_{10} f_c - 13.82 \log_{10} h_{t,\text{eff}} - a(h_{r,\text{eff}}) + (44.9 - 6.55 \log_{10} h_{t,\text{eff}}) \log_{10} d + C_M \quad (47)$$

where $h_{r,\text{eff}}$ is the effective height of the receiving antenna, $a(h_{r,\text{eff}})$, is a correction factor based on $h_{r,\text{eff}}$, and C_M is a correction factor based on the propagative environment. The details regarding $a(h_{r,\text{eff}})$, and C_M are provided in Ref. 10. The range of values for which the Hata and COST-231 models are valid are summarized in Table 2.

The Hata model has a correction factor for rural environments. In general, the Hata model and the COST-231 model provide an example of the path loss computation in a outdoor, non-LOS environment. A variation, called the COST231-Walfish-Ikegami model can be used for transmitting antennas above or below rooftops and is accurate for $d > 20$ m. A number of models similar to these discussed in this section are also used in practice. So, the choice of path-loss models must take into account all aspects of the propagative environment, including transmission frequency, distance of transmission, polarization, antenna heights, surface refractivity, terrain irregularity, foliage, climate, ground conductivity, and ground dielectric constant [10].

Table 2. Range of Validity of Hata and COST-231 Models

Parameter	Range of Validity	
	Hata	COST-231
Carrier frequency f_c	150–1500 MHz	1500–2000 MHz
Effective transmit height $h_{t,\text{eff}}$	30–200 m	30–200 m
Effective receive height $h_{r,\text{eff}}$	1–10 m	1–10 m
Distance d from transmitter	≥ 1 km	1–20 km
Correction factors	$a(h_{r,\text{eff}})$	$a(h_{r,\text{eff}}), C_M$

7.2.4. Indoor Propagative Loss. An increasing number of wireless communications applications are designed for indoor environments. Hence, there is considerable interest in indoor propagation and in models for it. Although the characteristics of indoor propagation vary slowly (quasi-static behavior [15]) as compared with outdoor propagation, a key difference is that propagation within a building is strongly influenced by a number of factors, such as building type, layout, construction material (amount of metal used), types of partitions, and height and placement of antennas. As a result, the variability in signal propagation and hence the path loss is quite significant. The model best suited for characterizing path loss in indoor propagation is similar to that for lognormal shadowing. The path loss at a distance d from the transmitter is given by

$$L_p(d) = \left[L_p(d_0) + 10n \log_{10} \left(\frac{d}{d_0} \right) + \Omega \right] (\text{dB}) \quad (48)$$

where Ω is a normal RV with standard deviation σ and n is the path loss exponent. It was reported in Ref. 15 that the typical range of n is 3–4. A comprehensive list of the typical values of n and σ for a variety of indoor environments is provided in Ref. 10.

7.3. Shadowing

As discussed earlier, shadowing is caused by terrain and other environmental factors, such as foliage. The effect of shadowing causes the variations in the mean of the received signal. Let $\hat{L}_p(d)$ denote the path loss (including the effect of shadowing) at a specified distance from the transmitter. Based on extensive measurements, it has been verified that $\hat{L}_p(d)$ can be characterized as a random variable with a lognormal distribution about the mean value. When expressed in dB, the RV perturbing the local mean value of the path loss is a normal RV, as given by

$$\hat{L}_p(d) = [L_p(d) + \Omega] (\text{dB}) \quad (49)$$

where $L_p(d)$ is given by one of the path-loss models in the preceding section and Ω is a normal RV with standard deviation σ . The RV Ω is obtained from the lognormal RV Ω' , whose pdf is given earlier. Equation (49) describes the path loss for a specified value of d but with different values of shadowing/obstructions between the transmitter and receiver. In practice, the path loss exponent n and the standard deviation σ , are used to characterize any environment. In most cases, n and σ can be calculated from measurements.

7.4. A Practical Design Model

The goal of this section is to provide a framework for combining the various results in this article relating to small-scale signal variations and large-scale signal variations into a set of relevant parameters that may be used by communication systems designers for link budget calculations. The components of the different effects and their impact on the link budget are shown pictorially in Fig. 16.

Predicting the expected mean received signal power is an important step in designing a communication link and

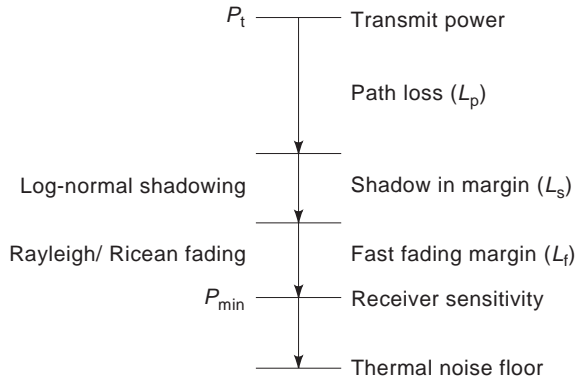


Figure 16. Different components of link budget—propagative loss, shadowing margin, and fading margin.

in estimating the coverage area for a specific transmitter. In Fig. 16, P_t is the transmitted signal power and P_{\min} is the minimum signal strength that must be received for the receiver to operate satisfactorily, that is, the signal strength to produce the minimum carrier-to-noise ratio (C/N) needed for acceptable communications. This is called *receiver sensitivity* and is expressed in dBm. There are three margins, one for each of the following practical effects:

- Propagative path loss
- Small-scale effects—fading margin
- Large-scale effects—shadowing margin

In the previous section, the methods of determining the path loss L_p for different environments were presented. The large-scale effect due to shadowing is modeled as a lognormal random variable. Hence, a shadowing margin L_s must be included in the link budget (Fig. 16). The small-scale effects, characterized by Rayleigh/Ricean fading, cause significant amplitude variations. Hence a fading margin L_f is also included in the link budget. From Fig. 16, the total transmitted power is given by

$$P_t = P_{\min} + L_f + L_s + L_p \quad (50)$$

The path loss L_p is deterministic (based on the distance between the transmitter and receiver), whereas the fading and shadowing are probabilistic. The amount of margin must be judiciously chosen so that the net margin is minimized but still meets the minimum signal strength requirements. If the amount of losses exceeds the margin of a communication system, then an *outage* occurs, which implies that the communication link cannot be used until the channel conditions improve. This summarizes the tradeoffs that must be handled by the designers of communication systems.

8. CONCLUSION

A comprehensive overview of the RF signal variations related to propagation in multipath fading channels has been presented. The diverse phenomena that cause signal

variations are described via mathematical models. The different types of fading and their salient features are discussed in detail. This article provides a mathematical and an engineering-oriented treatment of multipath fading, thereby providing the reader with the necessary tools and the information to understand the different RF propagative issues and the way they affect wireless communication.

9. APPENDIX: DERIVATION OF RAYLEIGH PDF

Let X and Y be two independent identically distributed (i.i.d.) zero-mean Gaussian RVs with variance σ^2 . Because X and Y are independent, their joint pdf is the product of their marginal pdf's:

$$F_{X,Y}(x,y) = \frac{1}{2\pi\sigma^2} e^{-\frac{x^2+y^2}{2\sigma^2}} \quad (A.1)$$

Using a change of variables, $V \triangleq \sqrt{X^2 + Y^2}$ and $\phi \triangleq \tan^{-1}(Y/X)$, the joint pdf $f_{V,\Theta}(v, \theta)$ is given by

$$F_{V,\Theta}(v, \theta) = \frac{f_{X,Y}(x,y)}{|\det \mathbf{J}(x,y)|} = \frac{v}{2\pi\sigma^2} e^{-\frac{v^2}{2\sigma^2}} \quad (A.2)$$

where $\mathbf{J}(x,y)$ is the Jacobian matrix for the transformation of variables. From Eq. (A.2), we obtain the marginal pdf of V and Θ as

$$f_{\Theta}(\theta) = \int_0^{\infty} f_{V,\Theta}(v, \theta) dv = \frac{1}{2\pi} \quad (A.3)$$

$$f_V(v) = \begin{cases} \frac{v}{\sigma^2} e^{-\frac{v^2}{2\sigma^2}} & v \geq 0 \\ 0 & v < 0 \end{cases} \quad (A.4)$$

Hence, Θ is uniformly distributed, and V is Rayleigh distributed.

BIBLIOGRAPHY

1. W. C. Jakes, *Microwave Mobile Communications*, Wiley, New York, 1974.
2. R. H. Clarke, A statistical theory of mobile-radio reception, *Bell Syst. Tech. J.* **47**:957–1000 (1968).
3. M. J. Gans, A power-spectral theory of propagation in the mobile-radio environment, *IEEE Trans. Vehic. Technol.* **VT-21**:27–38 (1972).
4. J. G. Proakis, *Digital Communication*, 3rd ed., McGraw-Hill, New York, 1995.
5. M. Nakagami, The m distribution: A general formula of intensity distribution of rapid fading, in W. G. Hoffman, ed., *Statistical Methods in Radio Wave Propagation*, Pergamon, New York, 1960, pp. 3–36.
6. I. S. Gradshteyn and I. M. Ryzhik, *Table of Integrals, Series, and Products*, Academic Press, Orlando, FL, 1980.
7. W. C. Y. Lee, *Mobile Communications Engineering*, McGraw-Hill, New York, 1982.
8. S. O. Rice, Statistical properties of a sine wave plus random noise, *Bell Syst. Tech. J.* **27**:109–157 (1948).

9. J. I. Smith, A computer generated multipath fading simulation for mobile radio, *IEEE Trans. Vehic. Technol.* **VT-24**:39–40 (1975).
10. T. S. Rappaport, *Wireless Communications: Principles and Practice*, IEEE Press, New York, 1996.
11. P. Dent, G. E. Bottomley, and T. Croft, Jakes' fading model revisited, *Electron. Lett.* **29**:1162–1163 (1993).
12. R. Steele, *Mobile Radio Communications*, IEEE Press, New York, 1995.
13. M. Hata, Empirical formula for propagation loss in land mobile radio services, *IEEE Trans. Vehic. Technol.* **VT-29**:317–325 (1980).
14. COST 231, Urban Transmission Loss Models for Mobile Radio in the 900- and 1800-MHz Bands, COST 231 TD(90) 119, Revision 2, The Hague, Sept. 1991.
15. A. Saleh and R. A. Valenzuela, A statistical model for indoor multipath propagation, *IEEE J. Select. Areas Commun.* **SAC-5**:128–137 (1987).
16. G. L. Stüber, *Principles of Mobile Communications*, Kluwer, Boston, 1996.
17. G. A. Arredondo and J. I. Smith, Voice and data transmission in a mobile radio channel at 850 MHz, *IEEE Trans. Vehic. Technol.* **VT-26**:88–93 (1977).
18. C. Loo and N. Secord, Computer models for fading channels with applications to digital transmission, *IEEE Trans. Vehic. Technol.* **VT-40**:700–707 (1991).
19. G. A. Arredondo, W. H. Chriss, and E. H. Walker, A multipath fading simulator for mobile radio, *IEEE Trans. Vehic. Technol.* **VT-22**:241–244 (1973).
20. GSM Series 03.30.

RECONFIGURABLE ANTENNAS

JENNIFER T. BERNHARD
 University of Illinois at
 Urbana—Champaign
 Urbana, Illinois

1. INTRODUCTION

The idea of antenna reconfiguration is not a recent one. Indeed, it is already more than two decades old (as of 2004). However, we are coming into an era where new functionality in antennas is not a novelty but rather a requirement to enable future communication and sensing systems. For instance, current planar phased-array technology is fundamentally limited in both scan angle and frequency bandwidth as a result of the limitations of the individual array elements. As another example, simple single antennas deployed on portable wireless data devices are usually minimally functional and limit noise immunity, battery life, and, ultimately, data throughput. Both of these cases illustrate the fact that limited antenna functionality could have a significant impact on performance of high-speed communication links in the future. One approach to expand system capability to meet new challenges is to develop reconfigurable antennas and apertures. Ideally, new communication systems can then

leverage this broad antenna functionality to take advantage of emerging techniques in wideband microwave circuits and signal processing, resulting in more efficient, secure, and cost-effective high-performance communication and sensing systems.

1.1. What Constitutes Reconfigurability?

Reconfigurability, when used in the context of antennas, is the capacity to change an individual radiator's fundamental operating characteristics through electrical, mechanical, or other means. Under this definition, then, the traditional phasing of signals between elements in an array to achieve beamforming and beamsteering does not make the antenna "reconfigurable," since the antenna's basic operating characteristics remain unchanged in this case [1,2].

Ideally, reconfigurable antennas should be able to alter their fundamental characteristics—their operating frequencies, impedance bandwidths, polarizations, and radiation patterns—independently to accommodate changing operating requirements (see ANTENNA PARAMETERS and ANTENNA THEORY articles for details on these fundamental characteristics). However, the development of these antennas poses significant challenges to both antenna and system designers. These challenges lie not only in obtaining the desired levels of antenna functionality but also in integrating this functionality into complete systems to arrive at efficient and cost-effective solutions. As in many cases of technology development, the majority of the system cost will come not from the antenna but the surrounding technologies that enable reconfigurability.

1.2. Overview

The goal of this article is to provide examples of the kinds of reconfigurable antennas that have been developed to date, in the hope that these examples may provide a foundation for new innovations in the future. While the reference list (Bibliography and Further Reading Sections) is extensive, it is by no means exhaustive. Rather, the selections chosen for discussion represent a cross section of the current state of the art. A firm grounding in basic antenna theory and design, found in the ANTENNA THEORY article, is desirable to understand fully all of the reconfigurable antennas' behaviors, capabilities, and shortcomings.

1.3. Organization

The sections are organized according to antenna capabilities rather than according their method of reconfigurability. Section 2 discusses frequency/bandwidth reconfigurable antennas, Section 3 describes polarization reconfigurable antennas, and Section 4 presents single-antenna elements with radiation pattern reconfigurability. In many cases, reconfigurable antennas possess more than one property that can change, but not independently. This happens, for example, when changes in operating frequency are coupled with changes in radiation patterns that cannot be avoided. In these cases, this behavior coupling is noted and the antennas are grouped according to their dominant characteristics. In contrast, Section 5

addresses radiating apertures that can change in more than one operating dimension in controlled, independent ways—that is, changes in the fundamental operating characteristics are largely decoupled. Section 6 offers a discussion of some supporting technologies that must be fully realized before reconfigurable antennas can proliferate. These technologies include reliable, mass-manufacturable RF MEMS switches, noninterfering switch and control bias networks, and expanded signal processing and feedback algorithms that exploit this new antenna functionality. Finally, Section 7 outlines the significant impact that reconfigurable antennas may have on future communication systems.

2. FREQUENCY RECONFIGURABILITY

Frequency reconfigurability is by far the area of antenna reconfigurability that has seen the most development to date. In many cases, changes in the operating frequency of an antenna have been referred to as “tuning,” since many changes to the antenna’s physical or electrical configuration produce relatively small variations within a frequency band around the antenna’s nominal operating point. These kinds of tuning techniques are most often applied to “resonant” antennas. Resonant antennas typically possess dimensions comparable to a half-wavelength (or integer multiples thereof) at the operating frequency. They also have commensurately narrow impedance bandwidths defined by the frequencies where the antenna’s input voltage standing-wave ratio (VSWR) is less than 2 (or a value of S_{11} less than -9.6 dB). Resonant antennas usually have impedance bandwidths less than 10%, and more commonly 1–2%. Therefore, for these antennas, tuning is most often achieved by discrete or continuous changes to their electrical lengths.

The following subsections are organized according to the degree to which the operating frequency and/or the impedance bandwidth of the antenna can be reconfigured.

2.1. Continuous Frequency Reconfigurability

The development of the first frequency-tunable antennas gained attention through a groundbreaking paper in 1982 [3]. In this work, wideband operation of a resonant, inherently narrowband structure, the rectangular microstrip patch antenna, was achieved using varactors (variable-capacitance devices) to vary the structure’s effective electrical length and, as a result, its operating frequency. Researchers have since applied the concept to frequency tuning for other microstrip, wire, and slot antennas [e.g., 4–11], including some that use ferrite substrate material [6] and substrates with embedded frequency-selective surfaces [11] and others that use optically variable capacitors or other optical tuning means [8,9].

Larger but continuous frequency shifts have been achieved with physical rather than electrical changes in antenna structure. One of these was first demonstrated in 1998, where a piezoelectric actuator system was employed to vary the spacing between a microstrip antenna and a parasitic radiator to change the operating frequency of the

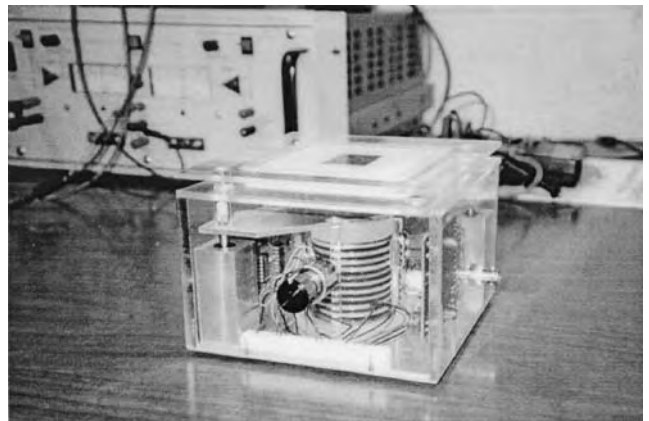


Figure 1. Mechanically actuated reconfigurable microstrip antenna with a parasitic radiator for continuous frequency tuning [14] (© IEEE 2001).

antenna [12–14]. A photograph of the prototype antenna is presented in Fig. 1. While normally possessing a very narrow impedance bandwidth (1%), controlled movement of the parasitic element, which changed the spacing s , delivered an effective bandwidth of about 9% as shown in Fig. 2. The bandwidth and gain of the structure also changed as a function of parasitic element spacing, but these changes were directly coupled to the changes in operating frequency.

Continuous frequency changes have also been demonstrated in a magnetically actuated out-of-plane microstrip antenna [15] that uses a micromachining process called *plastic deformation magnetic assembly* (PDMA) [16]. In this work, a microstrip antenna designed for operation around 26 GHz was covered with a thin layer of magnetic material and released from the substrate. Application of an external DC magnetic field causes plastic deformation of the antenna at the boundary point where it is attached to the microstrip feedline, resulting in a patch positioned at an angle over the substrate. A photograph of one prototype is given in Fig. 3. Small changes of the angle at which the structure resides results in changes in operating frequency that preserve radiation characteristics,

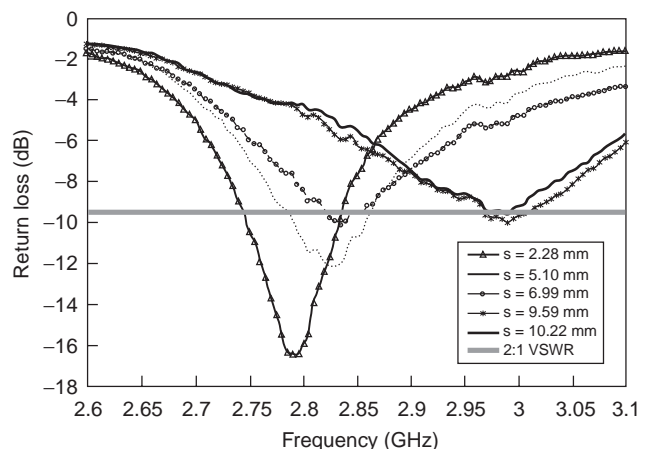


Figure 2. Measured return loss data versus frequency over a range of values of parasitic element spacing s [14] (© IEEE 2001).

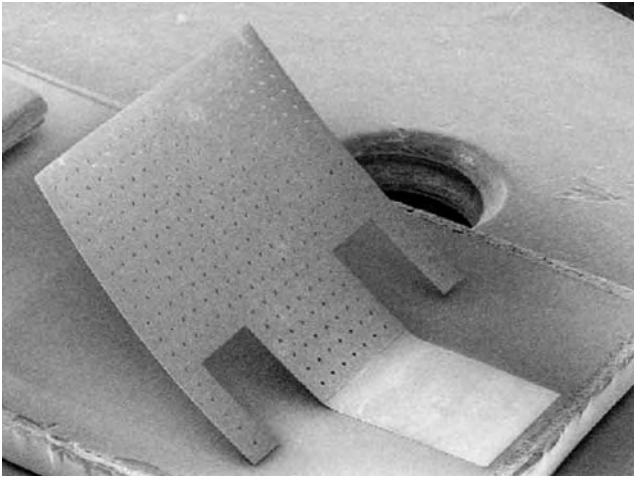


Figure 3. Photograph of a magnetically actuated out-of-plane frequency reconfigurable microstrip antenna [15] (© 2003 IEEE).

while larger angles result in frequency shifts accompanied by significant changes in the antenna’s radiation pattern. In particular, as the elevation angle between the patch and the horizontal substrate increases beyond 45°, the antenna’s radiation is more characteristic of a horn antenna, and changes toward the pattern of a monopole antenna as the angle approaches 90° [15].

2.2. Switched Multiple-Frequency Reconfiguration

Another approach to frequency reconfiguration is the use of switched connections that result in operation at two or more discrete frequency bands. Typically, the switching in these designs is enabled with diodes, FET switches, or proposed RF MEMS devices.

Using solid-state devices, one group has investigated the switchable operation of radiating slots [17]. In this approach, control of bias across a number of PIN diode switches changes the resonant frequency of a radiating slot structure by changing its apparent electrical length [17]. The structure, depicted in Fig. 4, has four switches (S1-S4) placed in positions along the slot to produce operating bands with a VSWR less than 2:1 in four separate bands. The researchers found that it was critical to strongly reverse bias switches in the OFF state to ensure appropriate impedance matching in the four bands [17]. Measured results demonstrate the discrete operating bands between 550 and 900 MHz (Fig. 5) and also indicate that the radiation characteristics of the antenna are essentially independent of the tuning [17].

While this approach to tuning works well as lower frequencies, the losses and parasitics inherent in solid-state switches limit their use as the frequency of operation increases. For operation at higher frequencies, a number of researchers have proposed the use of RF MEMS switches rather than diodes or FETs to achieve apparent changes in an antenna’s length or size. For instance, researchers have demonstrated a patch antenna integrated with RF MEMS actuators, shown in Fig. 6 [18]. These actuators are used to create capacitances at the edges of the patch that change the apparent electrical length of the patch. Exper-

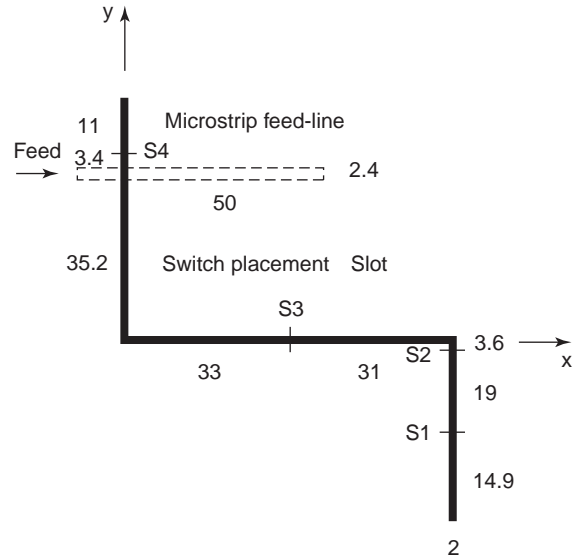


Figure 4. Planar reconfigurable VHF slot antenna with microstrip feedline after [17]; all units are in millimeters and switch positions are denoted with S1-S4 (© IEEE 2001).

imental results, provided in Fig. 7, indicate that this configuration shifts the operating frequency by about 1.6% (from 25 to 24.6 GHz) without significant changes in any other operating parameter. In other examples, Gupta et al. proposed the use of switches to change the electrical length of rectangular slot ring antennas [19], Ali and Wahid proposed switched lengths in a Yagi antenna [20], Weedon et al. proposed a two-dimensional grid of switchable patches to form large or small microstrip radiators [21,22], and Vinoy and Varadan proposed switched fractal antennas [23]. In prototype tests using ideal short and open circuits, all of these antennas succeed in maintaining radiating properties while switching their operating frequencies. Interestingly, an analysis of a two-dimensional array of filamentary microstrip dipoles interconnected by lossy MEMS switches indicates that the array-antenna

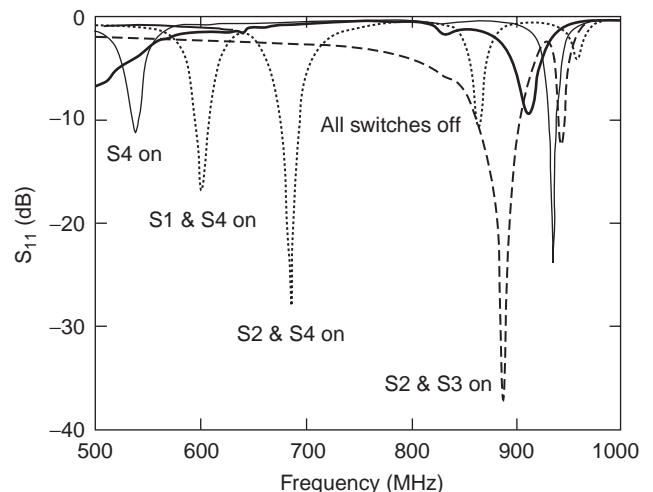


Figure 5. Measured return loss of the reconfigurable VHF slot antenna for various switch states [17] (© 2001 IEEE).

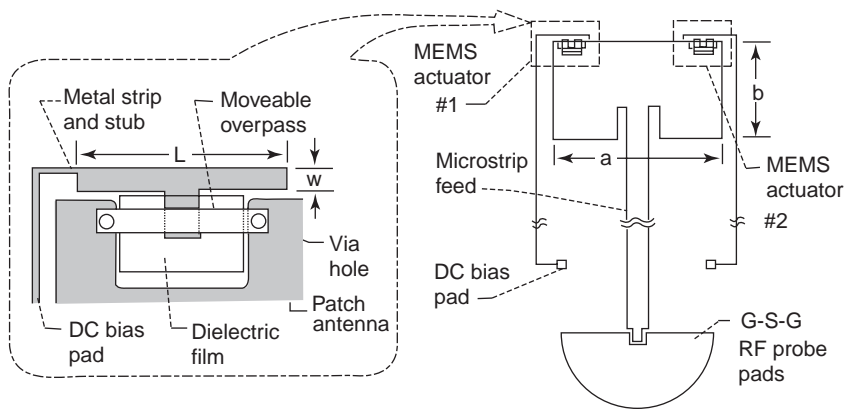


Figure 6. Frequency reconfigurable patch antenna element with two independent MEMS actuators, $L = 580 \mu\text{m}$, $W = 50 \mu\text{m}$, $a = 2600 \mu\text{m}$, $b = 1500 \mu\text{m}$ [18] (© IEEE 2001).

gain and the aperture efficiency remain much higher with frequency than in an array of fixed dipoles [2].

Another approach to switched-frequency reconfigurability is to combine a number of different antennas designed for different frequencies in a single structure and then use switches or other mechanisms to control the operating frequency. One example of this approach is a stacked reconfigurable antenna [24,25]. In this structure, two relatively broad frequency bands (each with approximately 40% bandwidth relative to their nominal operating frequencies) are alternately achieved in the 2–4 and 8–10 GHz frequency bands. The basic antenna structure

consists of a microstrip bowtie with a mixed dielectric substrate. Polarization variability at each feedpoint is supported by orthogonal placement of two balanced bowtie elements that can be driven to produce linear, elliptical, or circular polarization. Array operation in the lower band requires that the upper-band elements be disconnected via switches below the ground plane. In this stacked configuration, the upper-band elements act as floating parasitic elements for the lower-band elements, slightly broadening the impedance bandwidth. Operation of the upper-band elements requires that the lower-band elements be grounded via switches. In this configuration, the lower-band elements act as the ground plane for the upper-band elements [24,25].

Another example of a multiple-antenna-switched system is the reconfigurable leaky-wave/patch microstrip aperture [26]. This radiating system can operate over a range of frequencies and is shown in Fig. 8. The leaky-wave structures operating between 8 and 10 GHz are arrayed so that they provide high gain and moderate bandwidth and can be frequency-scanned about the elevation angle with gain up to 12 dB [26]. Figure 9 demonstrates the effect of frequency scanning in the leaky-mode array. Additionally, the ends of each of several leaky-wave apertures can be segmented into several smaller patch antenna apertures operating at discrete frequencies between 4 and 8 GHz through activation of switched connections.

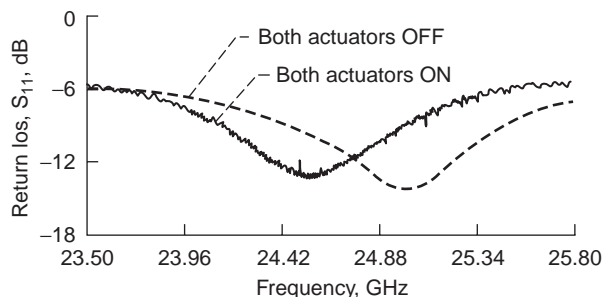


Figure 7. Measured return loss demonstrating switched frequency reconfigurability with integrated MEMS actuators [18] (© IEEE 2001).

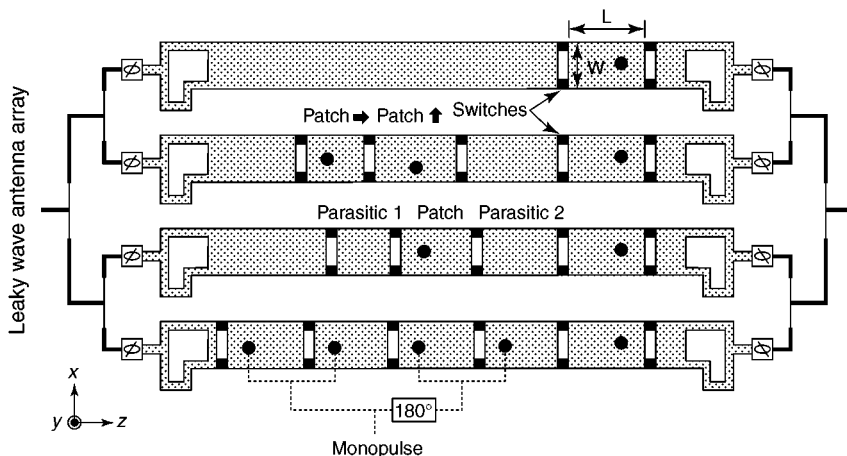


Figure 8. Schematic of reconfigurable leaky-wave/patch aperture array [26] (© IEEE 2002).

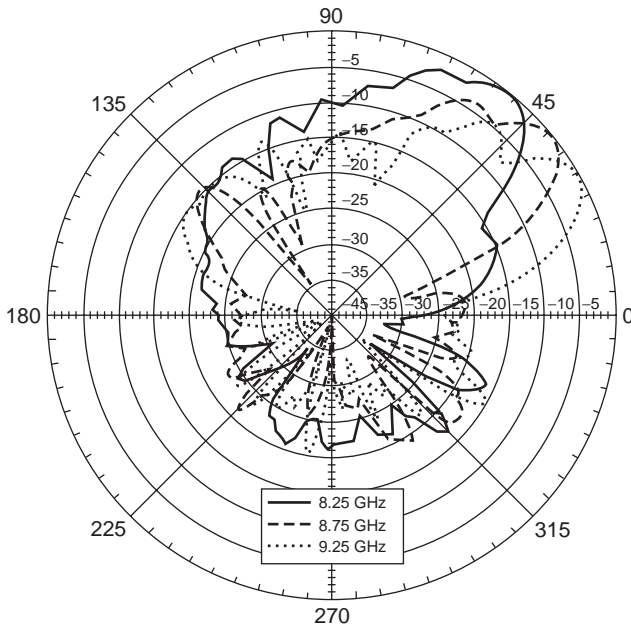


Figure 9. Measured frequency scanning using the leaky-wave structure of the reconfigurable array [26] (© IEEE 2002).

The patch antennas provide broadside radiation pattern coverage and moderate gain [26].

3. POLARIZATION RECONFIGURABILITY

Several antennas have also been developed that have reconfigurable polarization characteristics. From a design standpoint, this kind of reconfigurability can be more difficult to achieve than frequency reconfigurability, since the structure of the antenna has to change in ways that alter the way current flows on the antenna without affecting the operating frequency. Polarization reconfiguration could be useful for achieving more reliable wireless connections by adjusting to changing environmental

conditions, in effect, acting as a form of switched antenna diversity.

One example of such a polarization-agile antenna is the “patch antenna with switchable slots,” or PASS antenna [27]. The broader concept of the PASS has also been applied to achieve switched dual-band frequency reconfigurability as well [28]. In general, the PASS antenna consists of a microstrip antenna with one or more slots cut out of the copper patch, shown in Fig. 10 [27]. A switch (either solid-state or RF MEMS) is inserted in the center of the slot to control the behavior of currents on the patch. When the switch is open, currents must flow around the slot. When the switch is closed, the current can follow the shorter path created by the closed switch. Polarization reconfigurability is achieved by including two orthogonal slots on the surface of the patch. As demonstrated in the measurements provided in Fig. 11, alternate activation of the switches yields either right-hand or left-hand circular polarization. Others patch antennas with switchable circular polarization, using switches in the feed excitation slots rather than the surface of the patch, have also been proposed for active read/write microwave tagging systems [29].

Another polarization reconfigurable antenna, this one using a MEMS actuator, is shown in Fig. 12 [30]. In this design, the MEMS actuator is located within a simple microstrip patch antenna designed to support two orthogonal modes when excited in the corner. The actuator consists of a movable metal strip suspended over a metal stub. When the strip is suspended above the stub, the antenna has a circularly polarized radiation pattern (measurements shown in Fig. 13 [30]). Using electrostatic actuation, the metal strip can be lowered to create an antenna with dual linear polarization.

4. RADIATION PATTERN RECONFIGURABILITY

A diverse set of designs has emerged to date to deliver radiation pattern reconfigurability while maintaining other operating characteristics. This section is organized

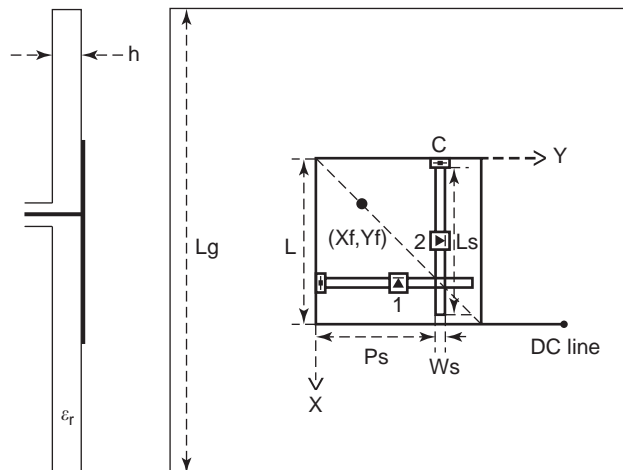


Figure 10. Geometry of a patch antenna with switchable slots (PASS) for RHCP/LHCP diversity [27] (© IEEE 2002).

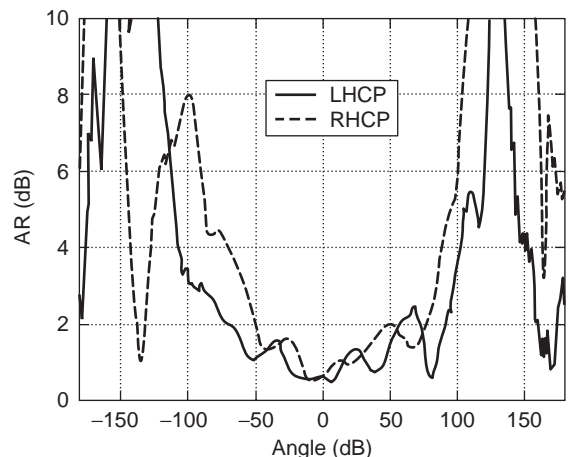


Figure 11. Measured axial ratio of the patch antenna with switchable slots in the xz plane [27] (© IEEE 2002).

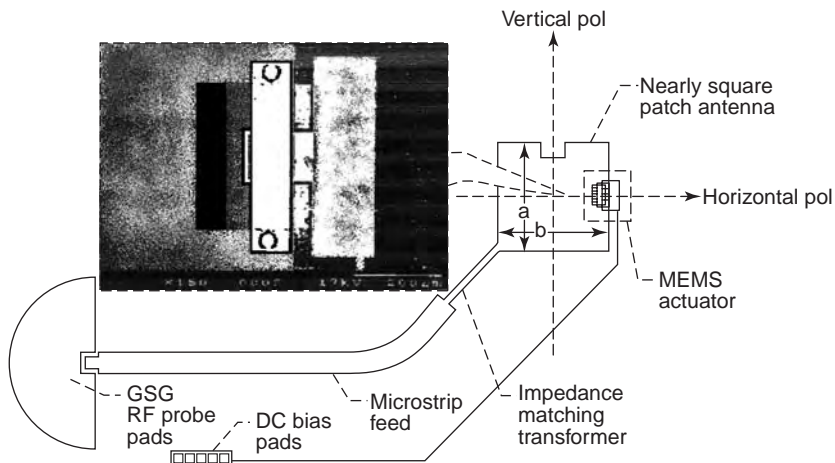


Figure 12. Polarization reconfigurable patch antenna element with integrated MEMS actuator, with $a = 1500 \mu\text{m}$, $b = 1492 \mu\text{m}$; inset shows photomicrograph of the MEMS actuator [30] (© IEEE 2002).

according to basic antenna type, since the mechanism for radiation pattern configuration relies heavily on specific antenna design.

4.1. Pattern Reconfigurable Microstrip Antennas

The ability to change radiation patterns on microstrip antennas while maintaining operating frequency is one of the most challenging areas of antenna reconfigurability. This is because the significant changes in the antenna structure necessary to produce changes in radiation characteristics are usually closely coupled to the input impedance of the antenna. Manipulation of an antenna's radiation pattern can be used to avoid intentional or non-intentional jamming sources, to act as a switched pattern diversity system, and to direct signals only toward intended users [31].

One research group has developed radiation reconfigurable microstrip antennas that maintain their

frequency and bandwidth characteristics [31]. The basic antenna structure consists of a single-turn square spiral antenna, shown in Fig. 14, which exhibits a broadside radiation pattern in its fundamental state. To enable reconfiguration, the antenna is equipped with two switches (either solid-state or RF MEMS) – one between the spiral and ground (shown on the left of Fig. 14) and a second that opens a small gap in the spiral arm (shown on the right of Fig. 14). When both switches are activated, this

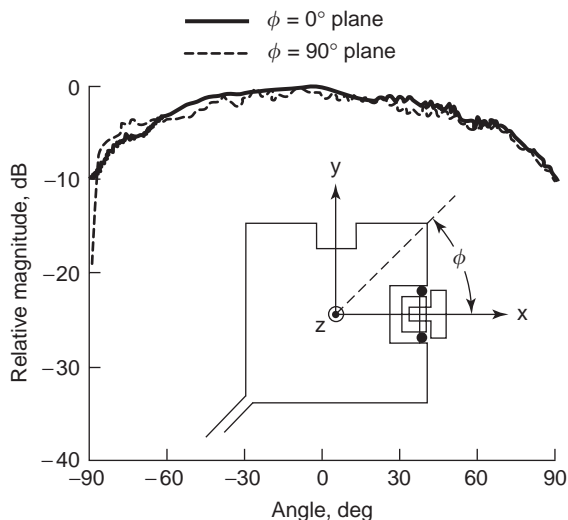


Figure 13. Measured circularly polarized radiation patterns of a MEMS-actuated polarization reconfigurable antenna [30] (© IEEE 2002).

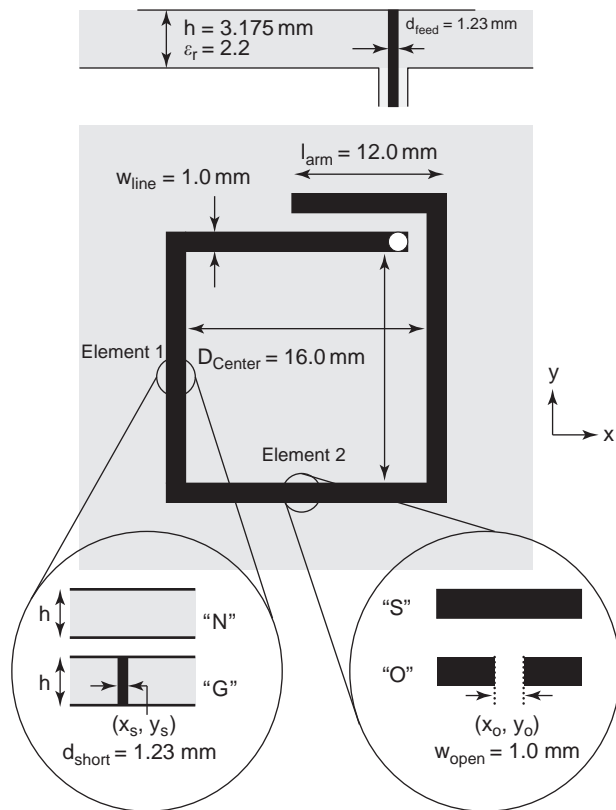


Figure 14. Radiation pattern and frequency reconfigurable square spiral microstrip antenna showing switch placements necessary for reconfiguration [31] (© IEEE 2003).

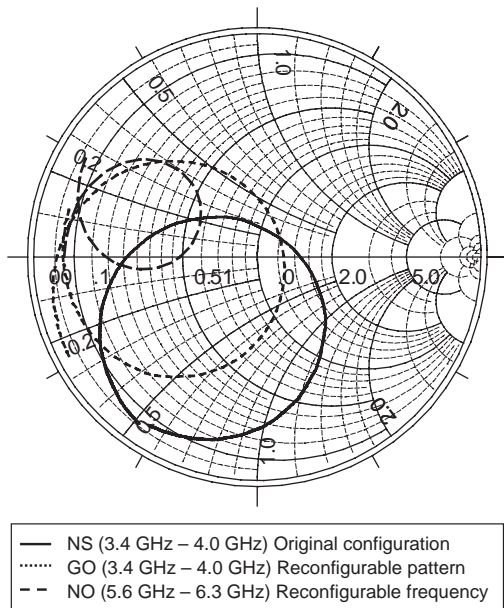


Figure 15. Measured input impedance of the original configuration (NS), the reconfigured radiation pattern (GO), and the reconfigured frequency (NO) [31] (© IEEE 2003).

configuration (called GO) maintains a shared 2:1 VSWR bandwidth of 50 MHz with the original configuration (called NS) operating at 3.7 GHz (see Fig. 15) while providing a 45° tilt from broadside in radiation pattern (Fig. 16). Additionally, with activation of only the second switch, the NO configuration provides a broadside radiation pattern at a higher operating frequency of 6.0 GHz [31]. This antenna and its variations are being considered for implementation in phased arrays [32] as well as implemented as a single element on portable computers to improve data communication link reliability and noise immunity [33].

4.2. Pattern Reconfigurable Reflector Antennas

Clarricoats and his colleagues were some of the first to demonstrate radiation pattern reconfigurability with aperture antennas by actively changing the structure of a mesh reflector [34,35]. Initially, changes in the reflector shape were achieved by manually adjusting each meshed region of interest [34]. Later, the process of reconfiguration was achieved by implementing computer-controlled stepper motors to pull strings attached to specific points on the reflector mesh [35].

A related, but more compact and accurate approach to reflector antenna pattern reconfigurability changes the shape of the subreflector in satellite applications [36]. The main reflector of this system has a fixed shape. The subreflector is made with a thin flexible material such that it deforms by movement of a set of piezoelectric linear point actuators attached on its back surface. When the subreflector is deformed, the electromagnetic field illuminating the main reflector can be changed, leading to a different far-field radiation pattern. During the design process, actuation points are successively added to the structure by

using an iterative electromagnetic finite-element algorithm to determine where the errors between the desired and actual subreflector shape is greatest [36].

Changes in reflector behavior have also been demonstrated using high-impedance surfaces (see the FREQUENCY-SELECTIVE SURFACES article for more information) [37,38]. High-impedance surfaces are created using a lattice of small resonant elements. This lattice produces high surface impedance near the resonant frequency of the elements, creating, in effect, an artificial ground plane. By inserting varactors between the resonant elements, the resonant frequency is tuned and the phase of a signal reflected from the surface is changed. Electronic control of the applied voltage across the varactors in the surface then allows reconfigurable beamshaping and beamsteering [37,38].

4.3. Pattern Reconfigurable Horn-Related Structures

A MEMS planar antenna was developed in 1999 that also uses mechanical changes in antenna structure to achieve reconfigurable radiation patterns [39]. Shown in Fig. 17, the basic antenna consists of a coplanar strip transmission line feed into a planar vee-shaped structure. Rotational hinges fixed to the substrate material hold the interior points of each arm in place. Each arm of the vee is movable by pulling or pushing by MEMS actuators, resulting in lateral movement of the arms. This lateral movement is then used to change the antenna's beam direction and/or the beamshape. Operating at 17.5 GHz, this antenna achieved *E*-plane beamsteering by rotating both arms by the same angle while maintaining a vee angle of 75° . Measured results shown in Fig. 18 show directional shifts of 30° and 48° for 30° and 45° positions of the vee, respectively [39]. Additionally, by moving the arms in opposite directions to change the vee angle, the antenna's beamshape could be changed as depicted in measured results provided in Fig. 19 [39].

Another group has implemented a flared planar dipole antenna with a tuned high-impedance surface to achieve beamsteering in the elevation plane [40]. The horizontally polarized antenna couples energy into leaky transverse waves on a tunable textured ground plane, shown in Fig. 20. The mechanically tunable surface, shown in more detail in Fig. 21, consists of a high-impedance ground plane and a tuning layer [40]. The tangential wavevector of the leaky waves is changed according to the change created in the surface resonant frequency by moving the tuning layer relative to the ground plane. Measured results on this design, shown in Fig. 22, indicate that beamsteering of at least 45° is possible [40].

4.4. Pattern Reconfigurable Array Structures

Other novel approaches to beamsteering have been developed by a research group at Texas A&M University [41]. Rather than employing conventional ferrite or solid-state phase shifters, these techniques steer beams through perturbations in propagation constants in a number of different transmission-line and antenna configurations. One of these is a movable grating antenna array fed by a dielectric image line (waveguide) that operates at

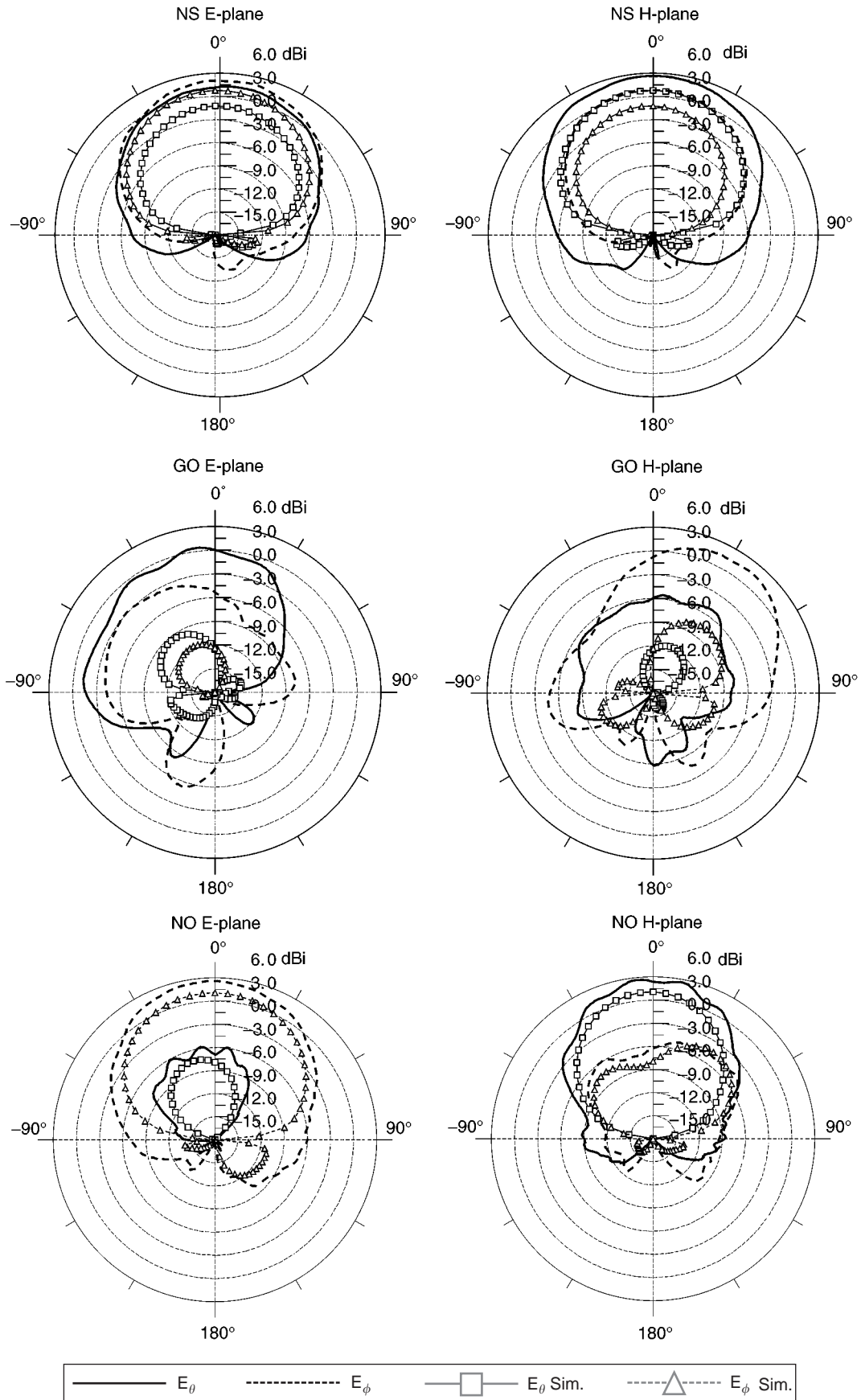


Figure 16. Measured and simulated gain (dBi) in the E plane (xz plane) and H plane (yz plane) for the three configurations of the antenna shown in Fig. 14 [31] (© IEEE 2003).

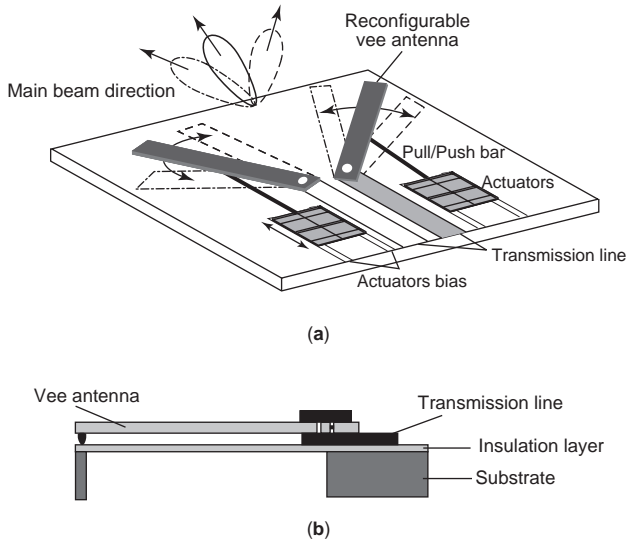


Figure 17. Concept (a) and cross section (b) of a MEMS reconfigurable vee antenna [39] (© IEEE 1999).

millimeter-wave frequencies, shown in Fig. 23 [41]. This leaky-wave antenna is essentially a dielectric waveguide with periodically placed conducting strips that form a grating above it. The widths of the strips on a thin, movable grating film placed over the dielectric image line are designed to gradually perturb the propagation constant along the line. Physical shifts of the grating film change the apparent grating spacings and result in a scanned beam [41]. In general, the antenna produces a fan-shaped beam, illustrated in Figs. 24 and 25, which is highly directional in one plane but very broad in the other. As indicated in Fig. 26, scan angles of up to 53° have been demonstrated with this design at 35 GHz, with lower scan angles achievable over an operating band between 30 and 40 GHz [41].

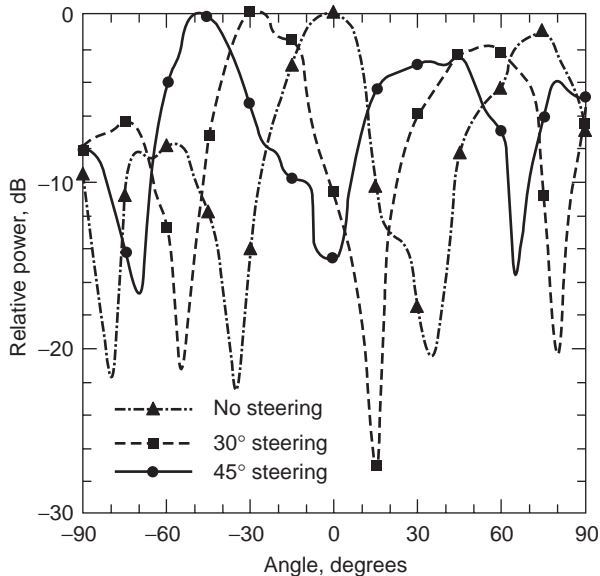


Figure 18. Measured *E*-plane beamsteering patterns for a 17.5 GHz 75° vee antenna [39] (© IEEE 1999).

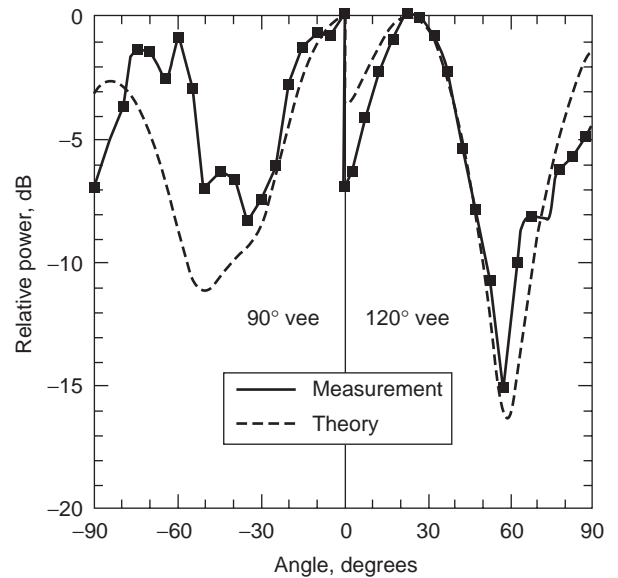


Figure 19. Measured and theoretical *E*-plane patterns (in halves) for 90° and 120° vee antennas [39] (© IEEE 1999).

5. RECONFIGURABLE APERTURES

Instead of reconfiguring a specific antenna, the two reconfigurable apertures discussed here take a unique

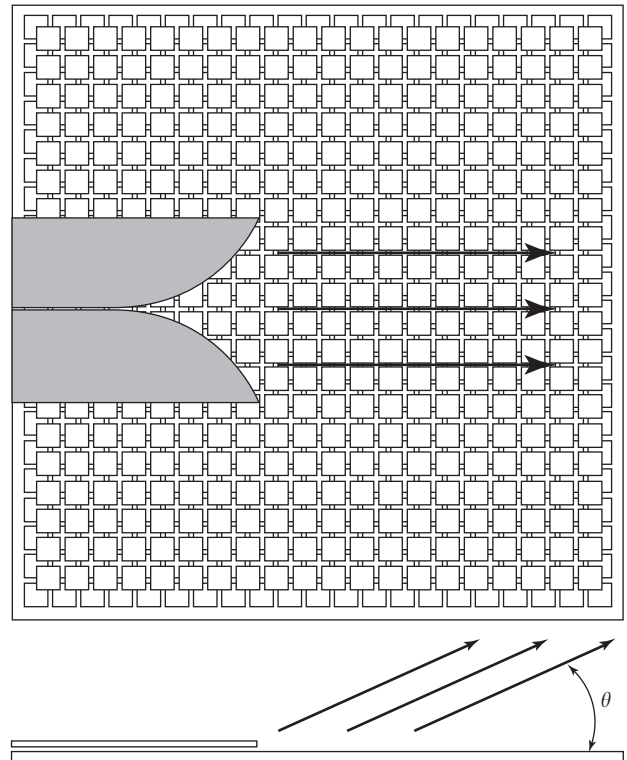


Figure 20. A reconfigurable antenna using horizontally polarized flared notch that couples energy into leaky modes on a tunable impedance surface; by tuning the surface resonant frequency (using a mechanically tunable surface impedance) with respect to the excitation frequency, the radiated beam is steered in the elevation plane [40] (© IEEE 2002).

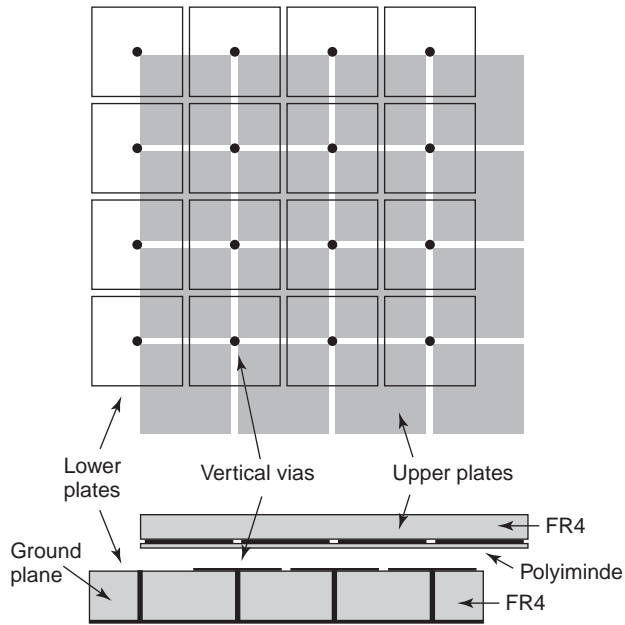


Figure 21. A detailed diagram of a mechanically tunable impedance surface created using two printed-circuit boards: a high-impedance ground plane and a separate tuning layer; the resonant frequency of the surface is tuned through movement of the tuning layer across the stationary high-impedance surface, which varies the capacitance between overlapping plates [40] (© IEEE 2002).

approach—creating whatever antenna is necessary to achieve specific frequency, bandwidth, polarization, and radiation characteristics. The first is an antenna that uses hundreds or thousands of FET or other switches to connect small nonresonant conductive pads that create a large antenna aperture [42]. A conceptual drawing of the aperture is provided in Fig. 27. To achieve any specified performance goal, a genetic search algorithm determines the combination of switch states across the aperture. For each pass through the genetic algorithm, a finite-difference time-domain electromagnetic simulation is used to evaluate candidate designs. In general, narrowband configurations achieve more gain than do wideband configurations, and high-frequency operation degrades as a result of the pad density and the solid-state switch capacitance [42].

Another antenna aperture concept, developed by researchers at the Sarnoff Corporation, uses semiconductor plasmas to form antenna structures [43]. Figure 28 highlights the difference between this approach and that of the previous aperture [42]. This “pixel” approach to a reconfigurable aperture relies on high-conductivity plasma islands that are formed and controlled by injected DC currents into high-resistivity silicon-based diode structures. A detailed description of the structure, including the plasma injection driver configuration, is shown in Fig. 29. While there are still many technical issues to be addressed with this design (including the challenge of creating the necessary carrier densities in the silicon), this approach possesses several unique and attractive features, one of which is that when turned off, the aperture possesses an extremely low radar cross section. In

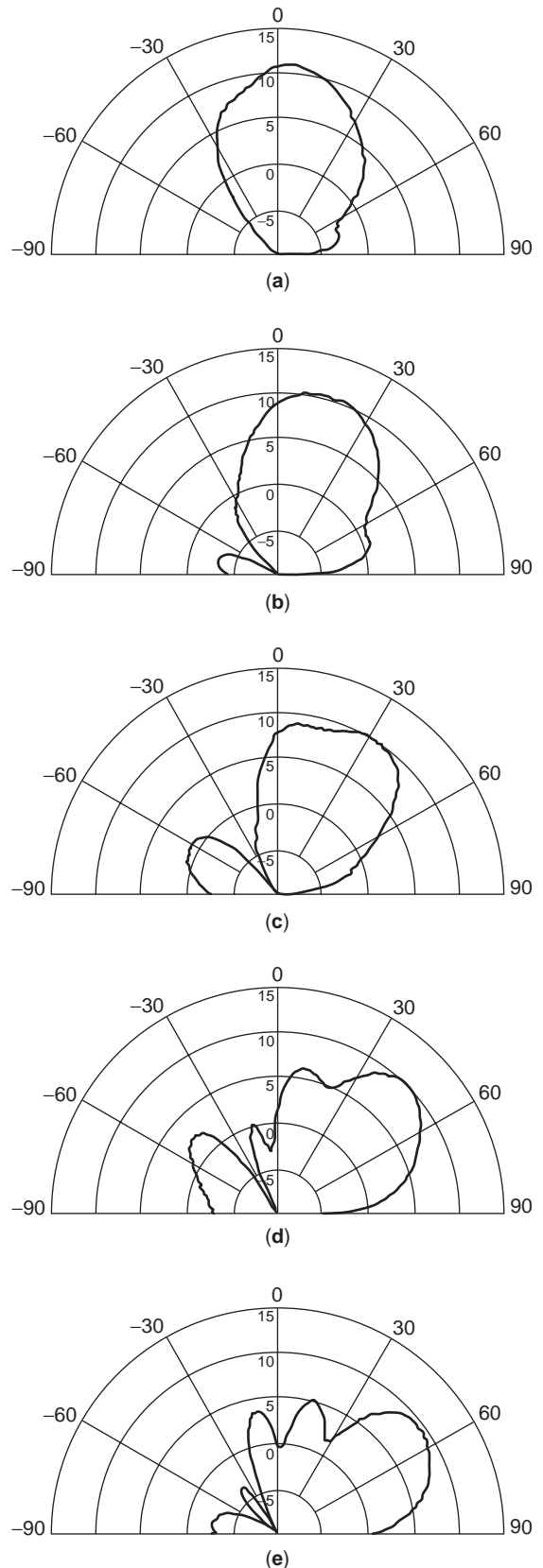


Figure 22. (a–e) Measured radiation patterns for five different positions of the tuning plate at a frequency of 2.5 GHz; each successive plot depicts a change in the relative position of the tuning plate by 63.5 μm [40] (© IEEE 2002).

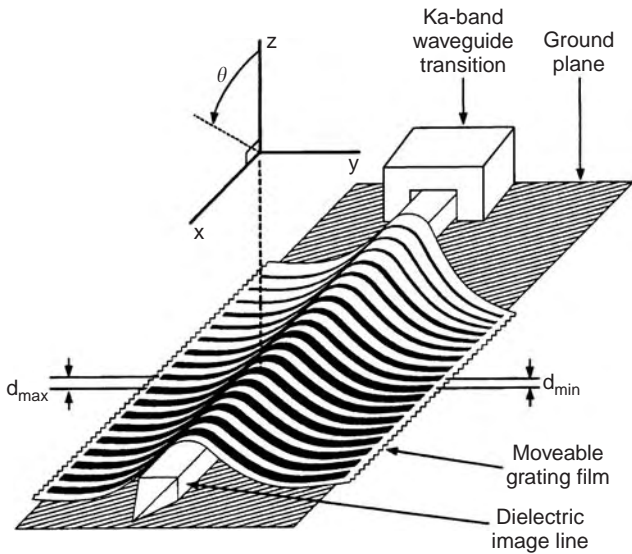


Figure 23. A movable grating antenna array fed by a dielectric image line, capable of beam scanning at millimeter-wave frequencies [41] (© IEEE 2002).

addition to forming specific antenna structures, it can also be used to reconfigure holograms for holographic antennas that promise to deliver performance comparable to traditional phased arrays without the need for expensive phase shifters [43].

6. ENABLING RECONFIGURABILITY

While research and development of reconfigurable antenna and aperture designs has seen tremendous growth since the 1990s, their deployment in real applications

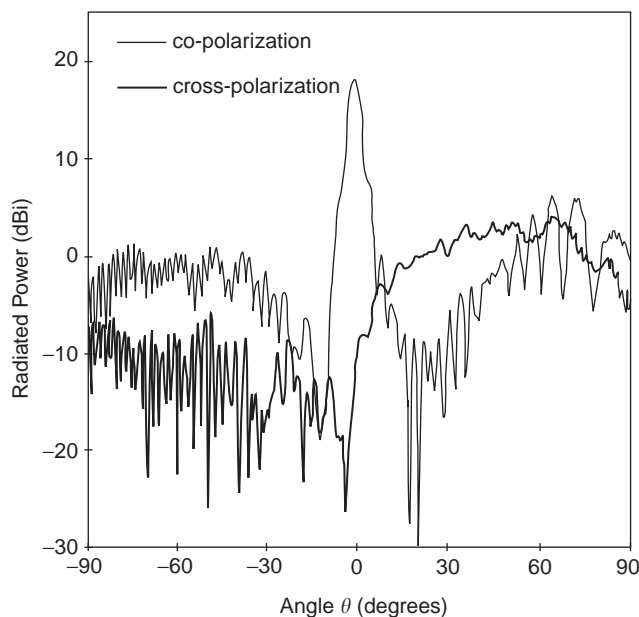


Figure 24. *xz*-plane co- and cross-polarization patterns at 35 GHz for a grating spacing of 7.8 mm [41] (© IEEE 2002).

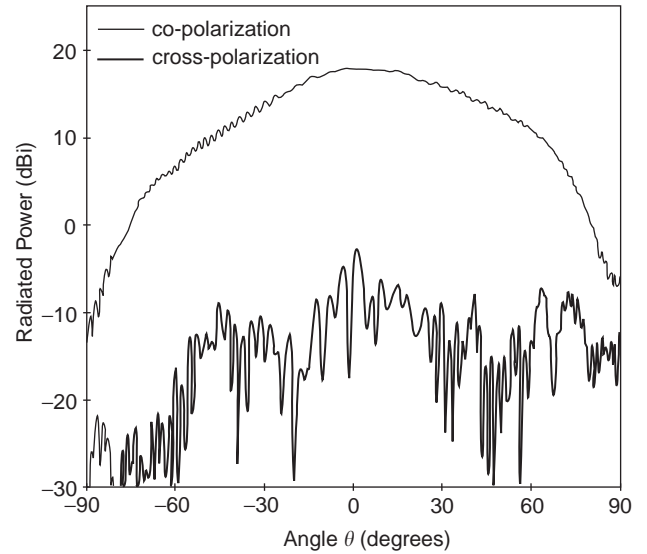


Figure 25. *yz*-plane co- and cross-polarization patterns at 35 GHz for a grating spacing of 7.8 mm [41] (© IEEE 2002).

will take much longer. This is due to the fact that there are several technological barriers that must be overcome to make reconfigurability both practical and affordable. The first issue is the device that makes the antenna reconfigurable, whether it is electrical, magnetic, or mechanical. While there have been continual advances in the development of RF MEMS switches and other devices, they still suffer from a number of drawbacks that prevent their deployment in actual systems. Some of these include power-handling capability, response time, high-frequency behavior, and packaging/integration strategies. While these drawbacks will be addressed in the near future, antenna designers must wait or develop reconfigurable structures in the meantime that use more mature

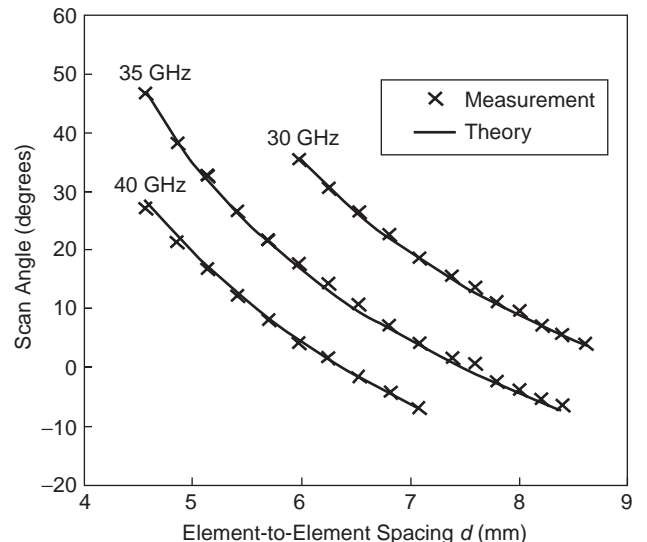


Figure 26. Measured and calculated beam scanning capabilities along the θ direction at 30, 35, and 40 GHz [41] (© IEEE 2002).

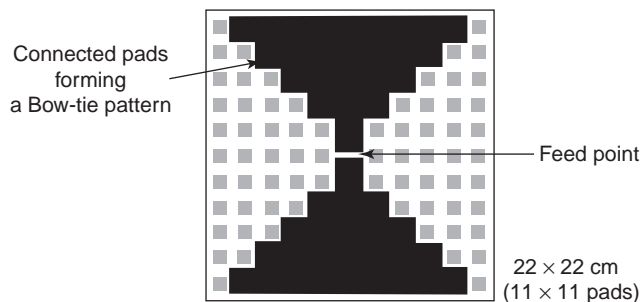


Figure 27. Conceptual architecture of a switched reconfigurable aperture; certain switches are closed (gray area) to form a bowtie structure [42] (© IEEE 2002).

technologies. (Interested readers are referred to the Further Reading list as well as the MICROELECTROMECHANICAL DEVICES article for a more complete picture of the evolution and the state of the art of enabling RF MEMS.)

The second issue is the actuation of the devices. Most reconfigurable antenna designers will acknowledge that the greatest engineering challenge for these antennas lies not in the design of the antenna but rather in the physical control infrastructure for the devices [42]. This barrier is particularly acute for reconfigurable designs that rely on hundreds or thousands of switches. A popular choice for overcoming this situation is some kind of optical signaling

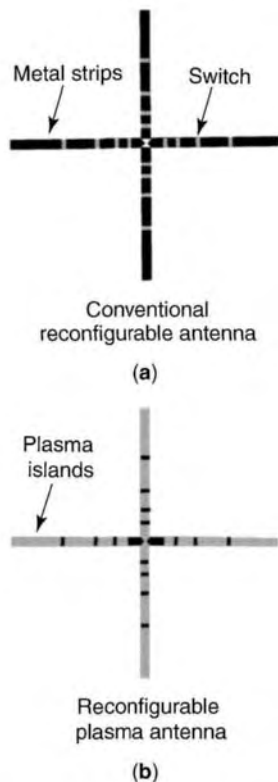


Figure 28. Reconfigurable dipoles made of (a) metal strips connected/isolated using MEMS or pin switches or (b) plasma islands activated or deactivated to establish conductive antennas [43] (© IEEE 2003).

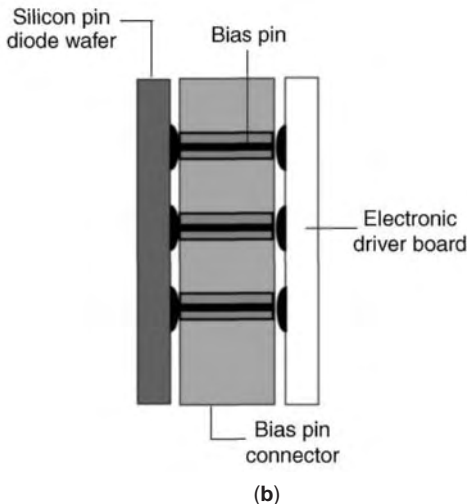
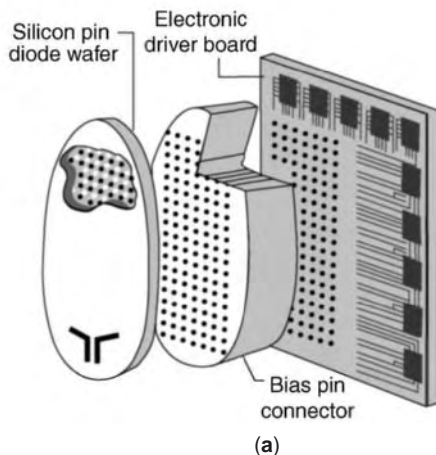


Figure 29. Depiction of a reconfigurable plasma grid structure: (a) grid structure is fabricated on top of the silicon wafer using silicon pin devices with an integrated feed, DC, and control circuitry; (b) cross section of the plasma grid structure showing the layer interconnection [43] (© IEEE 2003).

and control that does not interfere with normal antenna operation [9,42], but this approach will not work for all applications.

Finally, the most serious barrier to adoption of reconfigurable antennas may lie in the areas of signal processing and control. Without links back to system-level performance requirements and measures, antenna reconfigurability may be ignored or underutilized. It is imperative that members of the reconfigurable antenna community collaborate with researchers and developers in signal processing and control so that future systems can reach their full potential.

7. FUTURE OUTLOOK

New multifunction reconfigurable antennas have the potential to dramatically reduce the number and size of large array-based antenna systems, improve system efficiency, and decrease system cost and weight. They also have the potential to revolutionize the way we think about antennas, antenna systems, and their roles in national

defense, communications, and sensing. The age of the reconfigurable antenna is just beginning. With the requisite development of supporting technology and interactions with system designers, antenna reconfigurability promises to provide not only dramatic improvements in current system performance but also new degrees of freedom that will enable future systems with capabilities that previously were considered impossible.

BIBLIOGRAPHY

1. J. T. Bernhard, Reconfigurable antennas and apertures: State-of-the-art and future outlook, *Proc. SPIE Conf. Smart Electronics, MEMS, BioMEMS, and Nanotechnol.* **5055**:1–9 (2003).
2. E. R. Brown, On the gain of a reconfigurable-aperture antenna, *IEEE Trans. Anten Propag.* **49**:1357–1362 (Oct. 2001).
3. P. Bhartia and I. J. Bahl, Frequency agile microstrip antennas, *Microwave J.* **25**:67–70 (Oct. 1982).
4. M. P. Purchine, J. T. Aberle, and C. R. Birtcher, A tunable L-band circular microstrip patch antenna, *Microwave J.* **36**:80–88 (Oct. 1993).
5. P. M. Haskins, P. S. Hall, and J. S. Dachele, Active patch antenna element with diode tuning, *Electron. Lett.* **27**:1846–1848 (Sept. 26, 1991).
6. P. Rainville and F. Harackiewicz, Magnetic tuning of a microstrip patch antenna fabricated on a ferrite film, *IEEE Microwave Guided Wave Lett.* **2**:483–485 (Dec. 1992).
7. B. A. Cetiner, L. Jofre, and F. De Flaviis, Reconfigurable miniature multielement antenna for wireless networking, *Proc. 2001 Asia-Pacific Microwave Conf.*, 2001, Vol. 2, pp. 705–708.
8. M. L. VanBlaricum and C. J. Swann, Photonic systems for antenna control, *Proc. URSI Int. Symp. Signals, Systems, and Electronics*, 1995, Vol. 1, pp. 287–290.
9. M. L. VanBlaricum, A brief history of photonic antenna reconfiguration, *Proc. Int. Topical Meeting on Microwave Photonics*, 2000, Vol. 1, pp. 9–12.
10. S. Kawasaki and T. Itoh, A slot antenna with electronically tunable length, *Proc. IEEE/URSI Int. Symp. Antennas and Propagation*, 1991, Vol. 1, pp. 130–133.
11. Y. Erdemli, K. Sertel, R. Gilbert, D. Wright, and J. Volakis, Frequency-selective surfaces to enhance performance of broad-band reconfigurable arrays, *IEEE Trans. Anten. Propag.*, **50**:1716–1724 (Dec. 2002).
12. E. Kiely, G. Washington, and J. T. Bernhard, Design and development of smart microstrip patch antennas, *Smart Mater. Struct.* **7**:792–800 (Dec. 1998).
13. E. Kiely, G. Washington, and J. T. Bernhard, Design, actuation, and control of active patch antennas, *Proc. SPIE-Int. Soc. Opt. Eng.* **3328**:147–155 (1998).
14. J. T. Bernhard, E. Kiely, and G. Washington, A smart mechanically-actuated two-layer electromagnetically coupled microstrip antenna with variable frequency, bandwidth, and antenna gain, *IEEE Trans. Anten. Propag.* **49**:597–601 (April 2001).
15. J.-C. Langer, J. Zou, C. Liu, and J. T. Bernhard, Reconfigurable out-of-plane microstrip patch antenna using MEMS/plastic deformation magnetic actuation, *IEEE Microwave Wireless Compon. Lett.* **13**:120–122 (March 2003).
16. J. Zou, J. Chen, C. Liu, and J. E. Schutt-Aine, Plastic deformation magnetic assembly (PDMA) of out-of-plane microstructures: Technology development and application, *IEEE J. Microelectromech. Syst.* **10**:302–309 (June 2001).
17. D. Peroulis, K. Sarabandi, and L. P. B. Katehi, A planar VHF reconfigurable slot antenna, *Proc. IEEE/URSI Antennas and Propagation Society Int. Symp.*, 2001, Vol. 1, pp. 154–157.
18. R. Simons, D. Chun, and L. P. B. Katehi, Reconfigurable array antenna using microelectromechanical systems (MEMS) actuators, *Proc. IEEE/URSI Antennas and Propagation Society Int. Symp.*, 2001, Vol. 3, pp. 674–677.
19. K. C. Gupta, J. Li, R. Ramadoss, and C. Wang, Design of frequency-reconfigurable slot ring antennas, *Proc. IEEE/URSI Int. Symp. Antennas and Propagation*, 2000, Vol. 1, p. 326.
20. M. A. Ali and P. Wahid, A reconfigurable Yagi array for wireless applications, *Proc. IEEE/URSI Int. Symp. Antennas and Propagation*, 2002, Vol. 1, pp. 466–468.
21. W. H. Weedon, W. J. Payne, and G. M. Rebeiz, MEMS-switched reconfigurable antennas, *Proc. IEEE/URSI Int. Symp. Antennas and Propagation*, 2001, Vol. 3, pp. 654–657.
22. W. Weedon, W. Payne, G. Rebeiz, J. Herd, and M. Champion, MEMS-switched reconfigurable multi-band antenna: Design and modeling, *Proc. 1999 Allerton Antenna Applications Symp.*, 1999, Vol. 1, pp. 203–231.
23. K. Vinoy and V. Varadan, Design of reconfigurable fractal antennas and RF-MEMS for space-based systems, *Smart Mater. Struct.* **10**:1211–1223 (Dec. 2001).
24. J. T. Bernhard, N. Chen, R. Clark, M. Feng, C. Liu, P. Mayes, E. Michielssen, R. Wang, and L. G. Chorosinski, Electronically reconfigurable and mechanically conformal apertures using low-voltage MEMS and flexible membranes for space-based radar applications, *Proc. SPIE Smart Electron. MEMS* **4334**:129–136 (2001).
25. J. T. Bernhard, R. Wang, R. Clark, and P. Mayes, Stacked reconfigurable antenna elements for space based radar applications, *Proc. IEEE/URSI Antennas and Propagation Society Int. Symp.*, 2001, Vol. 1, pp. 158–161.
26. J. Sor, C.-C. Chang, Y. Qian, and T. Itoh, A reconfigurable leaky-wave/patch microstrip aperture for phased-array applications, *IEEE Trans. Microwave Theory Tech.* **50**:1877–1884 (Aug. 2002).
27. F. Yang and Y. Rahmat-Samii, A reconfigurable patch antenna using switchable slots for circular polarization diversity, *IEEE Microwave Wireless Compon. Lett.* **12**:96–98 (March 2002).
28. F. Yang and Y. Rahmat-Samii, Patch antenna with switchable slot (PASS): dual frequency operation, *Microwave Opt. Technol. Lett.* **31**:165–168 (Nov. 2001).
29. M. Boti, L. Dussopt, and J.-M. Laheurte, Circularly polarized antenna with switchable polarization sense, *Electron. Lett.* **36**:1518–1519 (Aug. 2000).
30. R. N. Simons, D. Chun, and L. P. B. Katehi, Polarization reconfigurable patch antenna using microelectromechanical systems (MEMS) actuators, *Proc. IEEE/URSI Int. Symp. Antennas and Propagation*, 2002, Vol. 1, pp. 6–9.
31. G. H. Huff, J. Feng, S. Zhang, and J. T. Bernhard, A novel radiation pattern and frequency reconfigurable single turn square spiral microstrip antenna, *IEEE Microwave Wireless Compon. Lett.* **13**:57–59 (Feb. 2003).
32. G. H. Huff, J. Feng, S. Zhang, and J. T. Bernhard, Behavior of pattern and/or frequency reconfigurable antennas in small arrays, *Proc. 2003 IEEE/URSI Int. Symp. Antennas and Propagation*, URSI, 2003, p. 151.
33. G. Huff, S. Zhang, J. Feng, and J. T. Bernhard, Performance and packaging issues of novel reconfigurable antennas in

- laptop computers, *Proc. IEEE/URSI Int. Symp. Antennas and Propagation*, URSI, 2002, p. 178.
34. P. J. B. Clarricoats and H. Zhou, The design and performance of a reconfigurable mesh reflector antenna, *IEE 7th Int. Conf. Antennas and Propagation*, 1991, Vol. 1, 322–325.
 35. P. J. B. Clarricoats, H. Zhou, and A. Monk, Electronically controlled reconfigurable reflector antenna, *Proc. IEEE Int. Symp. Antennas and Propagation*, 1991, Vol. 1, pp. 179–181.
 36. G. Washington, H.-S. Yoon, M. Angelino, and W. H. Theunissen, Design, modeling, and optimization of mechanically reconfigurable aperture antennas, *IEEE Trans. Anten. Propag.* **50**:628–637 (May 2002).
 37. D. Sievenpiper, J. Schaffner, R. Loo, G. Tangonan, S. Ontiveros, and R. Harold, A tunable impedance surface performing as a reconfigurable beam steering reflector, *IEEE Trans. Anten. Propag.* **50**:384–390 (March 2002).
 38. D. Sievenpiper and J. Schaffner, Beam steering microwave reflector based on electrically tunable impedance surface, *Electron. Lett.* **38**:1237–1238 (Oct. 2002).
 39. J.-C. Chiao, F. Yiton, M. C. Iao, M. DeLisio, and L.-Y. Lin, MEMS reconfigurable vee antenna, *IEEE MTT-S Int. Microwave Symp. Digest*, 1999, Vol. 4, pp. 1515–1518.
 40. D. Sievenpiper, J. Schaffner, J. J. Lee, and S. Livingston, A steerable leaky wave antenna using a tunable impedance ground plane, *IEEE Anten. Wireless Propag. Lett.* **1**:179–182 (2002).
 41. K. Chang, M. Li, T.-Y. Yun, and C. T. Rodenbeck, Novel low-cost beam steering techniques, *IEEE Trans. Anten. Propag.* **50**:618–627 (May 2002).
 42. L. N. Pringle, P. G. Friederich, S. P. Blalock, G. N. Kiesel, P. H. Harms, D. R. Denison, E. J. Kuster, T. L. Fountain, and G. S. Smith, GTRI reconfigurable aperture design, *Proc. IEEE Int. Symp. Antennas and Propagation*, 2002, Vol. 1, pp. 473–476.
 43. A. Fathy, A. Rosen, H. Owen, F. McGinty, D. McGee, G. Taylor, R. Amantea, P. Swain, S. Perlow, and M. El Sherbiny, Silicon-based reconfigurable antennas—concepts, analysis, implementation, and feasibility, *IEEE Trans. Microwave Theory Tech.* **51**:1650–1661 (June 2003).
- L. P. B. Katehi, J. F. Harvey, and E. Brown, MEMS and Si micro-machined circuits for high-frequency applications, *IEEE Trans. Microwave Theory Tech.* **50**(3):858–866 (March 2002).
- S. C. Shen, D. Becher, D. Caruth, and M. Feng, Development of broadband low-voltage RF MEMS switches, *2001 GaAs MAN-TECH Conf. Digest*, 2001, pp. 81–84.

RECTIFYING ANTENNAS (RECTENNAS)

BERND H. STRASSNER II
 Sandia National Laboratories
 Albuquerque, New Mexico
 KAI CHANG
 Texas A&M University
 College Station, Texas

1. INTRODUCTION

Rectifying antennas, commonly referred to as *rectennas*, are integral parts of microwave power transmission or wireless power transmission (WPT) systems. In WPT systems, RF power is transmitted from one location and captured at another location. The term *rectenna* consists of parts of the words “rectifier” and “antenna” since its function is to absorb incoming radio frequency (RF) energy and convert this energy to usable DC power.

Rectennas have been used in numerous space–space, ground–space, and ground–ground WPT demonstrations. However, these demonstrations have remained only studies into the feasibility of WPT. These “feasibility” studies and consequently many of the modern-day advances in rectenna technology have stemmed from Peter E. Glaser’s concept of space solar power (SSP) [1]. In an operational SSP system, a solar power satellite (SPS) would collect the sun’s solar power and convert it to microwave power. The satellite would then transmit the microwave energy to rectenna arrays positioned on Earth’s surface. These rectenna arrays, proposed to be several miles in diameter, would then capture the RF power and convert it to DC energy. Most of the world’s energy comes from the consumption of fossil fuels. These combustible fuels are limited resources that produce harmful byproducts when consumed. The idea of SSP providing readily available clean and continuous power for our future energy needs has generated widespread interest, especially in the United States and Japan.

Other advanced concepts for WPT include the ground–space application of powering aircraft and high-altitude platforms remotely using microwaves emitted from Earth’s surface. Several of the efforts in remotely powering aircraft are described in detail in Section 5. WPT can also be useful in several ground–ground applications including supplying power to remote locations such as islands where the infrastructure to generate power is either absent or not cost effective to build. However, the primary future use for WPT is seen in a myriad of space–space applications. These include supplying power to space

FURTHER READING

- D. Becher, R. Chang, M. Hattendorf, and M. Feng, Reliability study of low-voltage RF MEMS switches, *2002 GaAs MAN-TECH Conf. Digest*, 2002, pp. 93–96.
- E. R. Brown, RF-MEMS switches for reconfigurable integrated circuits, *IEEE Trans. Microwave Theory Tech.* **46**(11):1868–1880 (Nov. 1998).
- C. Bozler, R. Drangmeister, S. Duffy, M. Gouker, J. Knecht, L. Kushner, R. Parr, S. Rabe, and L. Travis, MEMS micro-switch arrays for reconfigurable distributed microwave components, *Proc. IEEE/URSI Int. Symp. Antennas and Propagation*, 2000, Vol. 2, pp. 587–591.
- H. Yoon, Y. Sha, P. Sharma, K. Vinoy, V. K. Varadan, and V. V. Varadan, Micromachined systems for RF and microwave antenna applications, *Proc. SPIE Smart Electron. MEMS* **4334**:156–163 (March 2001).
- K. A. Jose, H. Yoon, K. Vinoy, P. Sharma, V. K. Varadan, and V. Varadan, Low voltage tunable capacitors for RF MEM filters and antenna applications, *Proc. IEEE/URSI Int. Symp. Antennas and Propagation*, 2001, Vol. 3, pp. 670–673.

- laptop computers, *Proc. IEEE/URSI Int. Symp. Antennas and Propagation*, URSI, 2002, p. 178.
34. P. J. B. Clarricoats and H. Zhou, The design and performance of a reconfigurable mesh reflector antenna, *IEE 7th Int. Conf. Antennas and Propagation*, 1991, Vol. 1, 322–325.
 35. P. J. B. Clarricoats, H. Zhou, and A. Monk, Electronically controlled reconfigurable reflector antenna, *Proc. IEEE Int. Symp. Antennas and Propagation*, 1991, Vol. 1, pp. 179–181.
 36. G. Washington, H.-S. Yoon, M. Angelino, and W. H. Theunissen, Design, modeling, and optimization of mechanically reconfigurable aperture antennas, *IEEE Trans. Anten. Propag.* **50**:628–637 (May 2002).
 37. D. Sievenpiper, J. Schaffner, R. Loo, G. Tangonan, S. Ontiveros, and R. Harold, A tunable impedance surface performing as a reconfigurable beam steering reflector, *IEEE Trans. Anten. Propag.* **50**:384–390 (March 2002).
 38. D. Sievenpiper and J. Schaffner, Beam steering microwave reflector based on electrically tunable impedance surface, *Electron. Lett.* **38**:1237–1238 (Oct. 2002).
 39. J.-C. Chiao, F. Yiton, M. C. Iao, M. DeLisio, and L.-Y. Lin, MEMS reconfigurable vee antenna, *IEEE MTT-S Int. Microwave Symp. Digest*, 1999, Vol. 4, pp. 1515–1518.
 40. D. Sievenpiper, J. Schaffner, J. J. Lee, and S. Livingston, A steerable leaky wave antenna using a tunable impedance ground plane, *IEEE Anten. Wireless Propag. Lett.* **1**:179–182 (2002).
 41. K. Chang, M. Li, T.-Y. Yun, and C. T. Rodenbeck, Novel low-cost beam steering techniques, *IEEE Trans. Anten. Propag.* **50**:618–627 (May 2002).
 42. L. N. Pringle, P. G. Friederich, S. P. Blalock, G. N. Kiesel, P. H. Harms, D. R. Denison, E. J. Kuster, T. L. Fountain, and G. S. Smith, GTRI reconfigurable aperture design, *Proc. IEEE Int. Symp. Antennas and Propagation*, 2002, Vol. 1, pp. 473–476.
 43. A. Fathy, A. Rosen, H. Owen, F. McGinty, D. McGee, G. Taylor, R. Amantea, P. Swain, S. Perlow, and M. El Sherbiny, Silicon-based reconfigurable antennas—concepts, analysis, implementation, and feasibility, *IEEE Trans. Microwave Theory Tech.* **51**:1650–1661 (June 2003).
- L. P. B. Katehi, J. F. Harvey, and E. Brown, MEMS and Si micro-machined circuits for high-frequency applications, *IEEE Trans. Microwave Theory Tech.* **50**(3):858–866 (March 2002).
- S. C. Shen, D. Becher, D. Caruth, and M. Feng, Development of broadband low-voltage RF MEMS switches, *2001 GaAs MAN-TECH Conf. Digest*, 2001, pp. 81–84.

RECTIFYING ANTENNAS (RECTENNAS)

BERND H. STRASSNER II
 Sandia National Laboratories
 Albuquerque, New Mexico
 KAI CHANG
 Texas A&M University
 College Station, Texas

1. INTRODUCTION

Rectifying antennas, commonly referred to as *rectennas*, are integral parts of microwave power transmission or wireless power transmission (WPT) systems. In WPT systems, RF power is transmitted from one location and captured at another location. The term *rectenna* consists of parts of the words “rectifier” and “antenna” since its function is to absorb incoming radio frequency (RF) energy and convert this energy to usable DC power.

Rectennas have been used in numerous space–space, ground–space, and ground–ground WPT demonstrations. However, these demonstrations have remained only studies into the feasibility of WPT. These “feasibility” studies and consequently many of the modern-day advances in rectenna technology have stemmed from Peter E. Glaser’s concept of space solar power (SSP) [1]. In an operational SSP system, a solar power satellite (SPS) would collect the sun’s solar power and convert it to microwave power. The satellite would then transmit the microwave energy to rectenna arrays positioned on Earth’s surface. These rectenna arrays, proposed to be several miles in diameter, would then capture the RF power and convert it to DC energy. Most of the world’s energy comes from the consumption of fossil fuels. These combustible fuels are limited resources that produce harmful byproducts when consumed. The idea of SSP providing readily available clean and continuous power for our future energy needs has generated widespread interest, especially in the United States and Japan.

Other advanced concepts for WPT include the ground–space application of powering aircraft and high-altitude platforms remotely using microwaves emitted from Earth’s surface. Several of the efforts in remotely powering aircraft are described in detail in Section 5. WPT can also be useful in several ground–ground applications including supplying power to remote locations such as islands where the infrastructure to generate power is either absent or not cost effective to build. However, the primary future use for WPT is seen in a myriad of space–space applications. These include supplying power to space

FURTHER READING

- D. Becher, R. Chang, M. Hattendorf, and M. Feng, Reliability study of low-voltage RF MEMS switches, *2002 GaAs MAN-TECH Conf. Digest*, 2002, pp. 93–96.
- E. R. Brown, RF-MEMS switches for reconfigurable integrated circuits, *IEEE Trans. Microwave Theory Tech.* **46**(11):1868–1880 (Nov. 1998).
- C. Bozler, R. Drangmeister, S. Duffy, M. Gouker, J. Knecht, L. Kushner, R. Parr, S. Rabe, and L. Travis, MEMS micro-switch arrays for reconfigurable distributed microwave components, *Proc. IEEE/URSI Int. Symp. Antennas and Propagation*, 2000, Vol. 2, pp. 587–591.
- H. Yoon, Y. Sha, P. Sharma, K. Vinoy, V. K. Varadan, and V. V. Varadan, Micromachined systems for RF and microwave antenna applications, *Proc. SPIE Smart Electron. MEMS* **4334**:156–163 (March 2001).
- K. A. Jose, H. Yoon, K. Vinoy, P. Sharma, V. K. Varadan, and V. Varadan, Low voltage tunable capacitors for RF MEM filters and antenna applications, *Proc. IEEE/URSI Int. Symp. Antennas and Propagation*, 2001, Vol. 3, pp. 670–673.

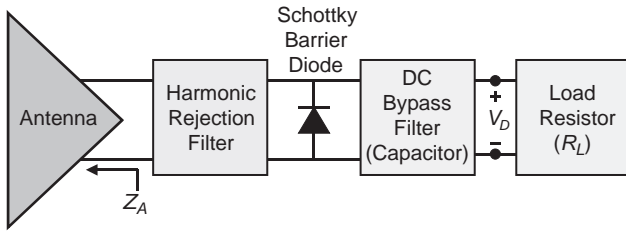


Figure 1. Schematic of the rectenna circuit.

colonies and space shuttles from nuclear powered satellites. This will enable space explorers to obtain the necessary power needed, at locations far from Earth, to further explore the depths of space.

2. RECTENNA OPERATION OVERVIEW

A schematic of the basic rectenna is illustrated in Fig. 1. A photo of an actual rectenna is shown in Fig. 2 to depict the corresponding rectenna components etched on a printed substrate. An antenna is used to capture the incident RF energy at frequency f . This energy is then passed through the harmonic rejection filter with minimal loss and on to the Schottky diode, where the RF energy is rectified to form DC power. The DC energy is then passed through the DC bypass filter to appear as the voltage V_D across the load resistor R_L . The remaining energies at the various harmonic frequencies $2f, 3f, \dots$ created from the Schottky diode's nonlinear process are reflected back to the diode by both the harmonic rejection filter and the DC bypass filter. This "trapping effect" results in additional mixing of the harmonic frequencies and ultimately in the generation of more DC power. The harmonic rejection filter also keeps

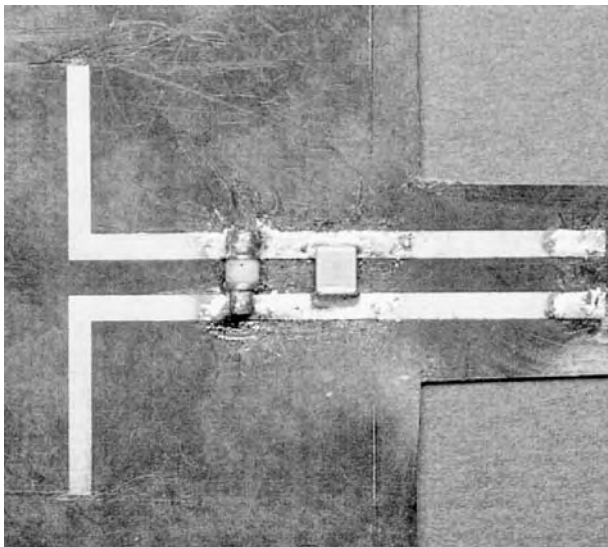


Figure 2. Photograph of a rectenna. A linear polarized dipole is used to absorb the incoming microwave energy. Copper strips (not seen) are etched on the substrate's backside between the dipole and the diode to form the harmonic rejection filter. A chip capacitor forms the DC bypass filter. The load resistor is not shown [2].

unwanted harmonic energy from reradiating into free space via the antenna. If allowed to reradiate, this harmonic energy could interfere with various electronic devices in close proximity to the rectenna that are operating in the same frequency band. In past designs, lowpass filters have been used to suppress the harmonic energy with very low loss. However, in more recent designs, bandstop filters have been used in order to provide much greater harmonic suppression while maintaining the low loss in the passband. In addition, the harmonic rejection filter is designed to match the real part of the diode's impedance to the antenna's input impedance Z_A . The DC bypass filter also serves two additional purposes: (1) it tunes out the reactance of the Schottky diode based on the DC bypass filter's position in the rectenna circuit, and (2) it blocks any RF signals from reaching the resistive load. This allows the DC voltage across the load resistor to be level with minimal amplitude versus time variation.

3. DESIGN THEORY

In designing a highly efficient rectenna, careful consideration must be given to choosing the proper diode, the type of transmission line to distribute the power between the rectenna's various components, the type of antenna, the spacing between the diode and the DC bypass filter (capacitor), and the resistance value of the load. The first component to consider is the nonlinear Schottky diode since the design of the other rectenna parts depends directly on the diode's performance.

The diode conversion efficiency (η_D) is key in determining the rectenna's performance and is based on the diode's equivalent circuit diagramed in Fig. 3. The diode efficiency is defined as the following ratio:

$$\eta_D = \frac{\text{DC output power}}{\text{RF power incident on diode}} \quad (1)$$

A diode model described by Yoo and Chang [3] is used to predict the Schottky diode's behavior. The model is a function of the diode's electrical parameters and the microwave circuit losses at the fundamental frequency of operation. Harmonic effects are not included because the

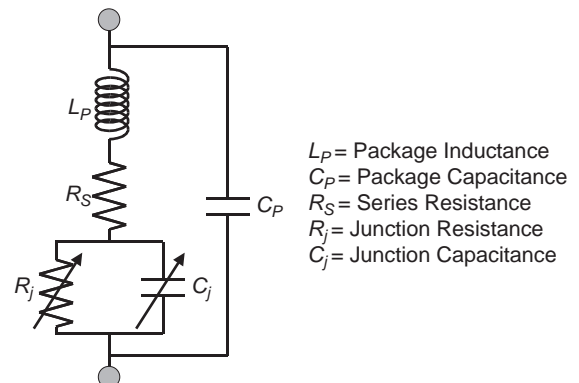


Figure 3. Schottky diode equivalent circuit.

major portion of the RF power is converted to DC, and the remaining RF power is considered to be predominantly at the fundamental frequency f . This also helps to keep the model simple. The package parasitics L_P and C_P are also neglected since, in most cases, where electrically small flip chip or beam lead diodes are used, their effects are negligible. The RF-to-DC conversion efficiency is described by [2,3]

$$\eta_D = \frac{1}{A+B} \quad (2)$$

where the low-frequency denominator asymptote is

$$A = 1 + \frac{R_L}{\pi R_S} \left(1 + \frac{V_{bi}}{V_D}\right)^2 \left[\theta_{on} \left(1 + \frac{1}{2 \cos^2 \theta_{on}}\right) - \frac{3}{2} \tan \theta_{on} \right] + \frac{R_L}{\pi R_S} \left(1 + \frac{V_{bi}}{V_D}\right) \frac{V_{bi}}{V_D} (\tan \theta_{on} - \theta_{on}) \quad (3)$$

and the high-frequency term is

$$B = \frac{R_S R_L C_j^2 \omega^2}{2\pi} \left(1 + \frac{V_{bi}}{V_D}\right) \left(\frac{\pi - \theta_{on}}{\cos^2 \theta_{on}} + \tan \theta_{on}\right) \quad (4)$$

where R_S is the diode's series resistance and ω is the angular frequency ($2\pi f$), V_{bi} is the forward-bias turnon voltage of the diode, and V_D is the self-bias voltage due to rectification across the terminals of the diode. The variable θ_{on} refers to the forward-bias turnon angle of the diode [3]. It is represented by

$$\tan \theta_{on} - \theta_{on} = \frac{\pi R_S}{R_L \left(1 + \frac{V_{bi}}{V_D}\right)} \quad (5)$$

Equation (5) is a transcendental equation and can be solved iteratively. The diode's abrupt junction capacitance C_j is

$$C_j = C_{j0} \sqrt{\frac{V_{bi}}{V_{bi} + |V_D|}} \quad (6)$$

where C_{j0} is the diode's zero bias junction capacitance. To keep the diode from exhibiting avalanche breakdown, the self-rectifying voltage V_D should be less than or equal to half of the breakdown voltage V_B . Given this limitation and Eqs. (2)–(6), selection of the proper diode can be based on its diode parameters R_S , V_{bi} , V_B , and C_{j0} . The diode voltage V_D should be chosen very close to $V_B/2$ for the best possible RF-to-DC conversion efficiency [4].

The diode's input impedance is defined as [2]

$$Z_D = \frac{\pi R_S}{D + jE} \quad (7)$$

where

$$D = \cos \theta_{on} \left(\frac{\theta_{on}}{\cos \theta_{on}} - \sin \theta_{on}\right) \quad (8)$$

and

$$E = \omega R_S C_j \left(\frac{\pi - \theta_{on}}{\cos \theta_{on}} + \sin \theta_{on}\right) \quad (9)$$

The real part of the diode's impedance from Eq. (7) is generally on the order of a couple hundred ohms. This resistance value determines the type of transmission line to use in order for the diode to achieve high RF-to-DC conversion efficiency. By choosing a transmission line with a characteristic impedance equal to the diode's real impedance, RF mismatch at the diode is eliminated. If mismatch is present, the RF-to-DC conversion efficiency suffers. A commonly used transmission line that can be designed to have characteristic impedances on the order of several hundred ohms is the coplanar stripline (CPS). CPS is composed of two parallel strips that, when constructed properly, can propagate energy from one location to another with very low loss.

The imaginary part of the diode impedance that results from Eq. (7) is tuned out using the length of transmission line between the diode and the DC bypass filter (chip capacitor). The capacitor acts electrically as a short to RF energy. Therefore, the combination of the capacitor and the length of transmission line between the diode and capacitor form a short-circuited tuning stub. The CPS has a topology that is readily suited to construct the short-circuited tuning stub. This tuning stub's length is adjusted by changing the capacitor's placement on the CPS. With the tuning stub counteracting the diode's reactance and the characteristic impedance of the CPS matching the real impedance of the diode, the RF energy that is incident on the diode will ideally see no reflection or mismatch across the terminals of the diode.

A technique described by Strassner and Chang [4] and shown in Fig. 4 utilizes a microstrip to CPS balun to determine the distance between the diode and the capacitor in conjunction with various source powers and load resistances. In addition, this technique provides a direct approach for experimentally determining the diode's RF-to-DC conversion efficiency versus the microwave power incident on the diode. In essence, this circuit provides a way to design the rectifier portion of the rectenna. Microwave energy is inputted into the microstrip line. The electromagnetic fields are then rotated in the transition region in order to match the microstrip line to the CPS. Once the energy strikes the diode, DC power is formed and passed to the load. The various harmonic energies strike the

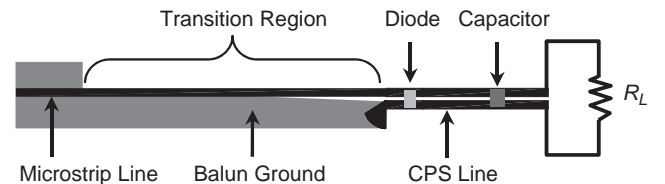


Figure 4. Circuit designed for the direct determination of a diode's RF-to-DC conversion efficiency. The black traces are etched on the top of the substrate, and the gray area is etched on the backside of the substrate [4].

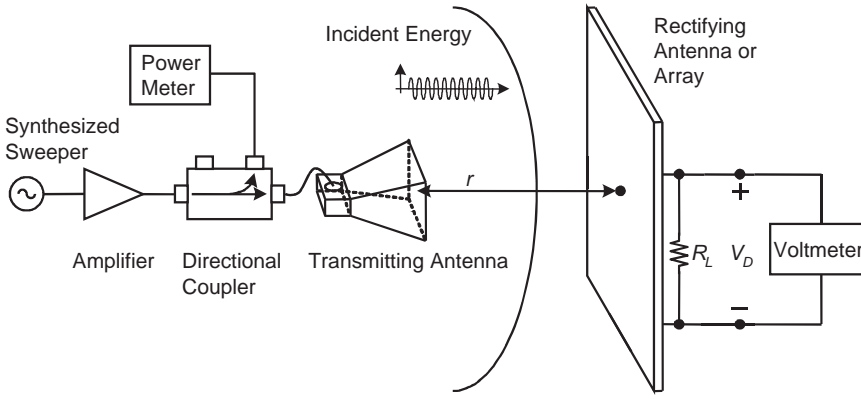


Figure 5. Rectenna measurement setup.

capacitor and are returned to the diode for further mixing. The distance between the capacitor and R_L can be arbitrary since only DC energy is propagated between the two. Likewise, the distance between the harmonic rejection filter and diode is arbitrary since both are matched to the characteristic impedance of the CPS. This direct measurement approach has the advantage over the model of including the effects of the higher order harmonics.

The final rectenna component is the *antenna*. The impedance Z_A looking into the terminals of the antenna must be purely real and must match the characteristic impedance of the transmission line that connects it to the harmonic rejection filter. Selection of the antenna is based on the necessary polarization, gain, and bandwidth as well as how the antenna is to be connected to the rest of rectenna circuitry. As far as printed rectennas are concerned, the ones that have achieved the highest efficiencies have used dipole antennas etched on thin substrates. These types of antennas are easily fed using CPS. A reflecting plane is normally placed approximately a $\lambda/4$ behind the dipole antenna in order to focus the antenna's energy in one direction. Since air acts as the dielectric between the dipole and the reflecting ground plane, the antenna can achieve close to 100% radiating efficiency. Having such a high radiation efficiency is key in achieving the best possible rectenna efficiency.

In many of the most recent designs where dipoles and CPS transmission lines are used, columns of parallel-cascaded rectennas are joined in series to produce large DC powers at the output of the array. In such cases, the rectennas on each column produce DC currents that are summed at the end of that column. Likewise, the DC voltages of each column are summed, resulting in the voltage V_A across the load resistor R_A . This array load resistor is defined by

$$R_A = R_L \frac{N_x}{N_y} \quad (10)$$

where N_x is the number of columns in the array, N_y is the number of rectennas in each column, and R_L is the optimal load resistance for each individual rectenna. The diodes are connected in parallel in each column, and the columns are connected in series.

Array spacing is governed both by the DC-pass filter placement and the effective areas of each individual

rectenna. The capacitors (DC-pass filters) not only optimize DC conversion but also isolate the array elements. Proper capacitor placement will enable each rectenna to capture energy with negligible reactance. Under this state of zero reactance, the array is perfectly matched.

4. FREE-SPACE MEASUREMENT

To obtain the rectenna's RF-to-DC conversion efficiency using the free-space measurement shown in Fig. 5, Eq. (1) or the diode efficiency is rewritten incorporating the Friis transmission equation as

$$\eta_D = \frac{\left(\frac{V_D^2}{R_L}\right)}{P_t G_t G_r \left(\frac{\lambda_0}{4\pi r}\right)^2} \quad (11)$$

where P_t and G_t are the transmitted power and transmitter gain, respectively, G_r is the gain of the rectenna's antenna, r is the distance between the transmitter and the rectenna, and λ_0 is the free-space wavelength at the fundamental frequency. The calculated free-space efficiency curves using Eqs. (2)–(6) should predict the directly measured diode efficiency using the balun circuit and the free-space measurement based on Eq. (11).

For determining a rectenna array's efficiency, in which multiple rectennas are combined together, the rectenna's antenna gain G_r in Eq. (11) is replaced by $4\pi A_e/(\lambda_0^2)$. The effective area of the array A_e is a physically measured quantity and corresponds to the rectenna array's total surface area exposed to the incident microwave energy. V_D is replaced by V_A , and R_L is replaced by R_A . V_A and R_A represent the array's output voltage and output load resistor, respectively.

The setup for obtaining the free-space measurement is presented in Fig. 5. In order to achieve uniform illumination across the rectenna array's surface, the transmitting horn antenna must be located far away from the rectenna array. However, this produces unwanted spillover effects where a significant portion of the transmitted energy misses the rectenna array's surface. To avoid these spillover effects, transmitting antennas are designed with low sidelobes and positioned close to rectenna array. At such

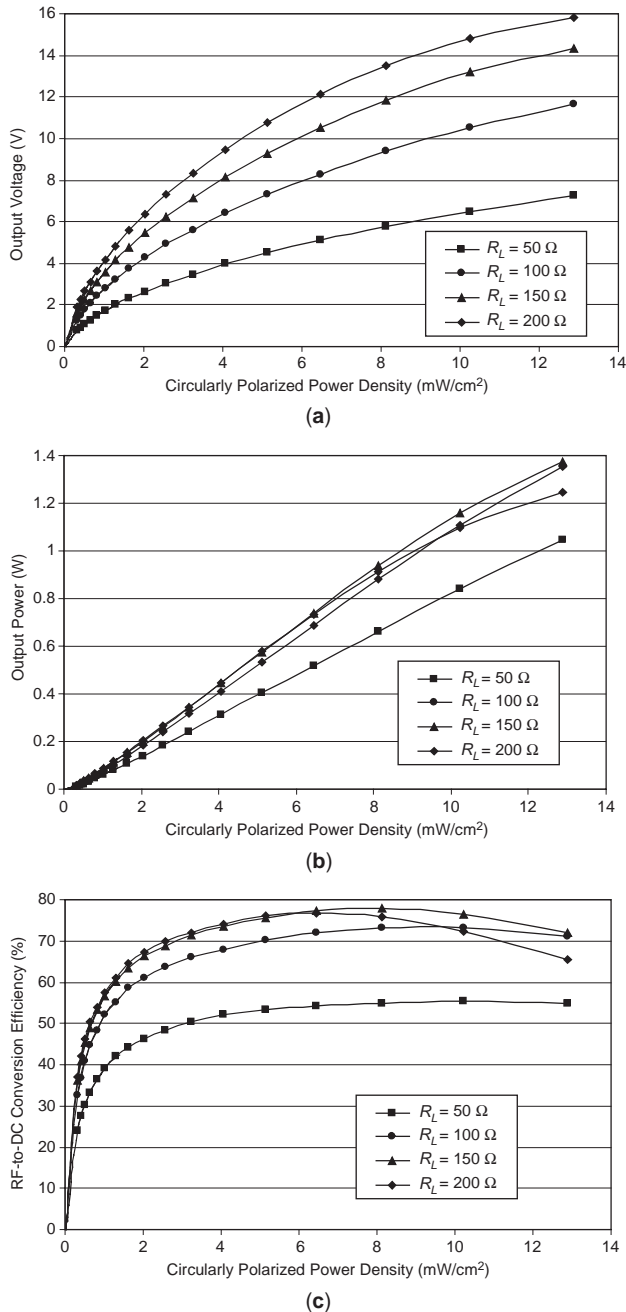


Figure 6. Rectenna array CP measured performance: (a) rectified voltage; (b) output power; (c) RF-to-DC conversion efficiency for various degrees of resistive loading.

close distances, the beamshape of the transmitting antenna’s gain is not constant over the rectenna array’s receiving aperture. Thus, each rectenna element in the array must be tuned specifically for its corresponding incident power density.

Typical plots of a rectenna array’s voltage across the load resistor, power at the load, and RF-to-DC conversion efficiency are shown in Fig. 6. These plots correspond to a 5.8 GHz circularly polarized rectenna designed by Strassner and Chang [5]. Figure 6a shows that as the load resistance R_L is increased, the voltage V_D will also increase.

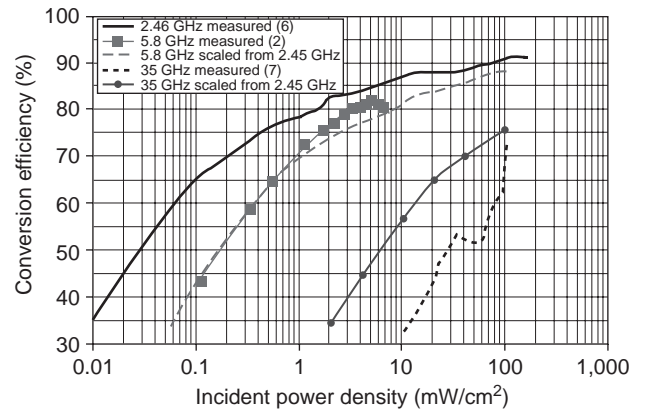


Figure 7. State-of-the-art rectenna efficiencies. (This figure is available in full color at <http://www.mrw.interscience.wiley.com/erfme>.)

This occurs in order to keep the DC output power constant as a function of V_D^2/R_L . Figure 6b illustrates the constant power versus load. As the load resistance decreases to 100Ω , the DC output power will start to decrease. This degradation is due in part to the mismatch between the lower load resistances and the CPS characteristic impedance. The poor performance when $R_L = 100 \Omega$ is also noticeable in the RF-to-DC efficiency plot in Fig. 6c. The rectenna yields excellent RF-to-DC conversion efficiency over a wide range of load resistances and incident power density levels. The peak efficiency moves to lower power densities as the load resistance is increased.

The chart in Fig. 7 shows the best efficiencies that have been achieved since the early 1960s for the frequencies 2.45 GHz [6], 5.8 GHz [2], and 35 GHz [7]. The plot illustrates how the efficiency degrades as the operating frequency increases. Predicting the conversion efficiency of higher frequencies from measured data gathered at 2.45 GHz works reasonably well. This scaling prediction is based on the effective area differences at the various frequencies. During scaling, the antenna gain is held constant at 6.4 dB. This gain is typical for a linearly polarized dipole antenna located $\lambda/4$ over a ground plane. The main limitations on increasing the RF-to-DC conversion efficiency lie in the device physics of the Schottky diode.

5. HISTORY AND APPLICATIONS OF THE RECTENNA

The first recorded demonstration of WPT occurred in 1888 when Heinrich Hertz used parabolic reflectors and half-wavelength dipoles to transmit and receive microwave power at a frequency of 500 MHz [8]. To generate the microwave energy, the opposite halves of the dipoles were charged to a high voltage until an arc occurred across the gap. This arcing released capacitive stored energy setting up oscillations along the dipole. The dipole then radiated a portion of the oscillating energy in the form of microwaves. This accomplishment by Hertz was vital to the experimental validation of Maxwell’s equations with regards to electromagnetic energy propagating in free space. Hertz’ approach was strictly scientific. He knew that the lack of efficient and continuous source power in his design, coupled with the fact that no device existed that could convert

RF energy to DC power efficiently, prevented it from being useful in any practical sense.

The concept of efficient WPT began in 1898 at Colorado Springs, CO when Nikola Tesla used energy at a frequency of 150 kHz to successfully power 200 lightbulbs. The RF energy was generated from large oscillators, now referred to as “Tesla coils,” and propagated over a distance of 26 miles to the lightbulbs [9]. Even given this outstanding accomplishment for its time, many people remained skeptical of the ability of such technology to achieve profitability. In the 1920s and 1930s, Japanese [10] and U.S. researchers [11] considered the feasibility of WPT but again came up against technological limitations. The crucial development that ultimately enabled WPT to become a useful technology was the development of high-power, high-efficiency microwave tubes by the Raytheon Company, Waltham, MA in the 1950s [12].

On May 22, 1963, William C. Brown and others at the Spencer Laboratory of the Raytheon Company in Burlington, MA gave a demonstration of the first complete WPT system to a group of United States Air Force officials who had sponsored the development of the aforementioned high power microwave tubes [13]. In this demonstration, DC power was converted into 400 W of microwave power with an assumed efficiency of 50% at 2.45 GHz. This microwave energy was then fed to a horn that illuminated an ellipsoidal reflector 2.8 m in diameter. The reflector then bounced the microwave energy to the reflector’s focal point 7.4 m away where a diagonal horn was located to collect the reflected energy. The efficiency of the transmission and collection of the microwave energy between the two horns was 52%. After being collected by the diagonal horn, the microwave energy was converted back to DC using a thermionic diode with a very narrow gap between the cathode and anode at an efficiency of 50%. By multiplying the three efficiencies together, the overall DC-to-DC efficiency was found to be 13%.

Riding the success of Raytheon’s DC-to-DC conversion experiment, the United States Air Force expressed further interests in the ability of powering certain aircraft using WPT. On October 28, 1964 at Raytheon’s Spencer Laboratory, a public demonstration of the tethered microwave powered helicopter shown in Fig. 8 was given [14]. The demonstration was aired internationally on Walter Cronkite’s *CBS News Program* and proved that WPT could potentially be used to power communication or surveillance aircraft flying at high altitudes indefinitely. The helicopter experiment also introduced a new microwave device termed the “rectenna.” The rectennas used in the helicopter experiment consisted simply of packaged Schottky diodes connected end to end. The leads of the diodes formed the dipole antennas and the diode rectified the captured energy. During the experiment, the helicopter flew to an altitude of 18 m above the transmitter. The helicopter weighed 2.3 kg, had a rotor diameter of 1.76 m, and had an excess lift capability of 0.7 kg. It flew for 10 h at an altitude of 14.7 m. A magnetron was used to generate the necessary microwave energy at 2.45 GHz. The rectenna array’s area covered 0.37 m², and the DC output power of the rectenna array supplied to the electric motor was 270 W. The success of the tethered helicopter experiment

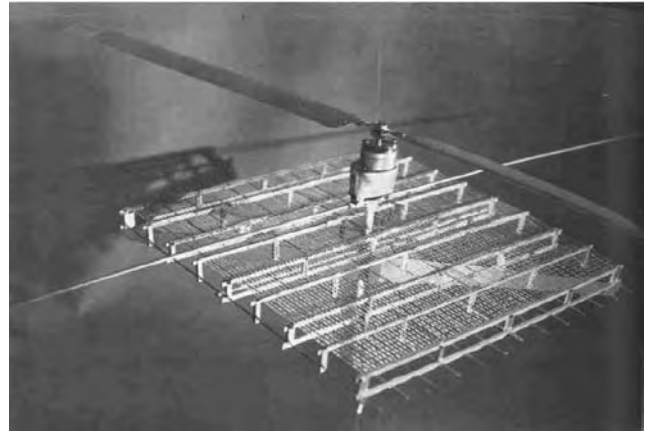


Figure 8. Air Force-Raytheon sponsored demonstration of microwave-powered helicopter was made to public media in October 1964.

prompted the Air Force to develop other tethered aircraft that could use microwave power to not only power the aircraft but also to change its pitch, yaw, roll, and position.

After a several-year lull in WPT, Brown gave a demonstration of the lightweight rectenna array to Werner von Braun and his staff at NASA MSFC in October 1968. The rectenna array had a power output: mass ratio of 1 kW/kg. This ratio represented an improvement of 3 over its predecessors. In the demonstration, a 3-ft parabolic antenna was illuminated with 200 W of microwave power at 2.45 GHz. The parabolic antenna reflected the energy to a rectenna array with an electric motor attached to a propeller to serve as the rectenna array’s load. When the rectenna array was placed in the beam from the parabolic antenna, the propeller spun impressively. Although the experiment was a simple one, it showed von Braun and his colleagues the merits of WPT. This in turn led to NASA funding WPT with the goal of improving the overall DC-to-DC efficiency.

In 1970 at NASA MSFC, Brown and his colleagues at Raytheon gained further support from NASA by demonstrating an overall DC-to-DC conversion of 26.6% [15]. For this experiment a new rectenna array design was developed that used four rectifying diodes in a bridge rectifier design. The system had a DC-to-microwave power efficiency of 65% and a radiated microwave power-to-DC conversion efficiency of 40.8%. This experiment also featured a “beam riding” capability in which a portion of the rectenna array’s output power was used to power a motor that kept the rectenna array in the beam of the transmitting antenna. The rectenna array was mounted on wheels to allow the movement of the array when the beam was steered. The array moved in an arc to maintain broadside orientation with the transmitting antenna’s beam.

Between 1970 and 1975, overall system efficiencies improved based on improvements in the pattern of the transmitting antenna. It had been discovered that if power were to be transmitted over long distances with any efficiency, a large transmitting antenna with negligible sidelobes would be needed. To meet this requirement, a dual-mode horn design was used to emit a Gaussian beam

with negligible sidelobes. Improvements in rectenna design also contributed to rises in overall efficiencies. Closer rectenna spacing in various patterns allowed for better collection of the power incident upon the rectenna array. Using the dual-mode horn, an efficiency of 60.2%, corresponding to the DC power at the rectenna array's output to the microwave power in the throat of the horn, was obtained. Had the dual band horn been available in the previous demonstrations in which reflector antennas were used, the efficiencies would have been about 1.5 times higher [8].

On March 4, 1975 at Raytheon, a demonstration of an overall DC-to-DC efficiency of $54.18\% \pm 0.94\%$ was given and certified by the Jet Propulsion Laboratory (JPL) Quality Assurance Department [16]. The certification was used to remove any doubts among the scientific and engineering communities. The demonstration was the culmination of a 5-year effort that had started in 1970 under the directorate of NASA MSFC and had focused on improving the overall DC-to-DC efficiency from 13% to 54%. The setup of the demonstration is shown in Fig. 9. A dual-mode horn emitted a Gaussian-shaped beam with negligible sidelobes at 2.446 GHz. Nearly all of the beam's energy was intercepted and absorbed by the rectenna array. The rectenna array then converted the microwave energy to DC power. The power density within the beam varies by a factor of 50 from the center of the beam to its edges, and the 199 rectenna array elements are matched in accordance to the power density of the beam at their corresponding positions. The breakdown of the 54.18% overall efficiency is 68.9% for the DC-to-microwave power conversion, 95% for the aperture-to-aperture transfer, and 82.4% for the beam collection and rectification. The DC output power was 495 W. The high rectenna efficiency is possible because of the gallium arsenide rectifier diodes used. These diodes are more efficient and can handle more power than their silicon predecessors.

In 1975, the transfer of microwave power to a rectenna array creating 30 kW of DC power at a distance of 1.54 km was demonstrated in the Mojave Desert at the JPL's Gold-

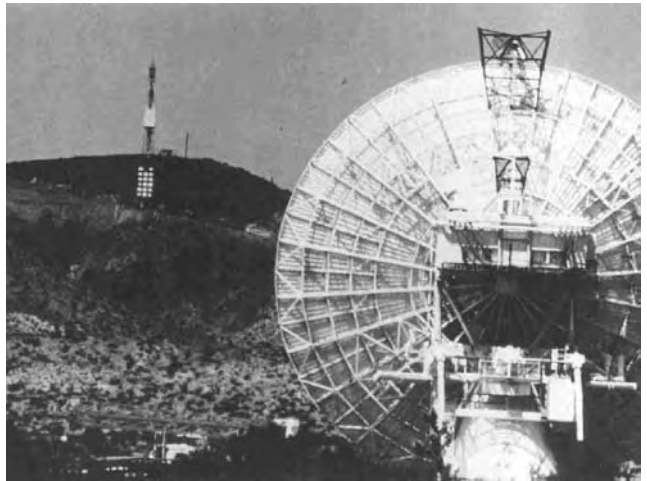


Figure 10. Demonstration of beamed power over one-mile distance at the JPL Goldstone facility in the Mojave Desert.

stone Facility [17]. The experiment set new records for WPT distance and the amount of power being transmitted. These new milestones proved the validity of WPT and its use in important applications. The demonstration setup is shown in Fig. 10. A high-powered klystron sends microwave energy at 2.388 GHz to the 25-m transmitting antenna seen in the foreground. This large antenna illuminates a 3.6×7.2 -m rectenna array located in the background a mile away. The rectenna array consists of 17 panels, each with 270 rectennas for a total of 4590 rectenna elements over the entire array. Of the microwave power intercepted by the rectenna array, 84% was converted into a DC power level of over 30 kW. Directly below the rectenna array is a bank of lights with two lights fed by each rectenna array panel. This rectenna array setup proved to be extremely robust surviving a lightning strike and years of use. The Goldstone demonstration was performed by Raytheon under contract from JPL.

After the Goldstone demonstration, attention shifted from the creation of full-WPT systems to improvements in rectenna design, especially with regard to RF-to-DC conversion efficiency and weight. The highest conversion efficiency was achieved by Brown at Raytheon in 1977 [18]. Brown used a GaAs-Pt Schottky barrier diode and aluminum bar dipole and transmission lines to achieve 90.6% conversion efficiency at 2.45 GHz and an input microwave power level of 8 W. In 1982, Brown and James Trimer developed the first printed thin-film rectenna. The printed rectenna operated at 2.45 GHz with 85% conversion efficiency. This rectenna was revolutionary in that it weighed 10 times less than any of its predecessors operating in the same frequency range [19]. Since the development of this rectenna, almost all rectennas have been printed using photolithographic etching techniques since they have the advantages of being lightweight and extremely easy to fabricate.

During the 1980s, the epicenter for WPT related research shifted from the United States to Japan. Japan saw SSP as a way to meet the energy needs of their nation given their limited natural resources and their ever-increasing reliance on nuclear energy. In 1983, Japan

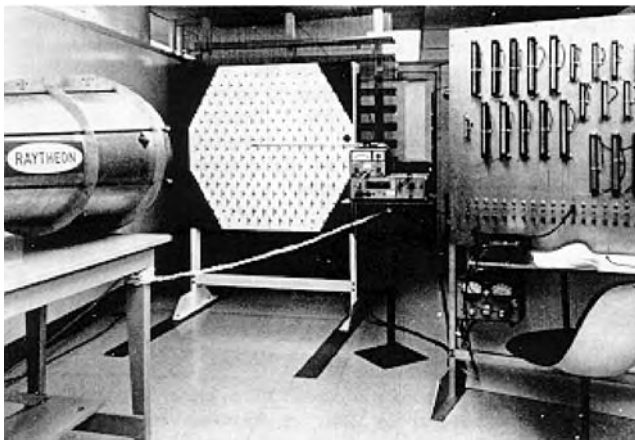


Figure 9. An overall system efficiency of $54.18\% \pm 0.94\%$ was obtained at the Raytheon Company with the demonstration setup shown. The DC power output was 495 W, and the frequency was 2.446 GHz.

conducted their *microwave ionosphere nonlinear interaction* experiment (MINIX) rocket experiment [20]. It was the first WPT experiment in the ionosphere. In the experiment, 830 W was transmitted from one rocket to another rocket. In the MINIX experiment, Langmuir waves and electron cyclotron harmonic waves were observed and then modeled using nonlinear wave-particle interaction theory.

In 1980, a program to develop a long endurance high altitude platform called the *stationary high-altitude relay program* (SHARP) was proposed in Canada [21]. The platform was to be the first unmanned, fuelless, lightweight airplane that would be powered remotely by microwaves enabling it to stay afloat for long periods of time. On September 17, 1987, the $\frac{1}{8}$ -scale prototype SHARP with a wingspan of 4.5 m seen in Fig. 11 flew on beamed microwave power for 20 min at an altitude of 150 m. A microwave beam, consisting of 10 kW of source power at 2.45 GHz, was transmitted by a parabolic dish antenna with a 4.5 m diameter. Two 5-kW magnetrons generated the source power. The parabolic antenna tracked the airplane that flew inside a 50° cone. The power density at the airplane was 400 W/m^2 . The rectenna array was made to be dual-polarized by using two overlaid linear dipole rectenna arrays that were orthogonal to each other. The rectenna array used HP 2835 silicon Schottky diodes with a power-handling capability of 1 W and a RF-to-DC conversion efficiency of 70%. The rectenna received enough microwave energy to generate 150 W of DC power to the electric motor in order to lift and fly the 4.1-kg airplane.

In 1991, ARCO Power Technologies, Inc., Washington, DC, developed a rectenna element with 72% conversion efficiency at 35 GHz [22]. This frequency shift from the traditional 2.45 GHz to 35 GHz resulted in much smaller aperture areas. However, the components necessary for generating high power at 35 GHz are inefficient and expensive. Because of the disadvantages noted at 35 GHz, a new operating frequency or 5.8 GHz was investigated. The 5.8 GHz frequency has small component sizes and greater

transmission ranges than does the 2.45 GHz. In 1992, the first C-band rectenna yielded 80% conversion efficiency [23]. These efficiencies were measured in a waveguide simulator with an input power level of approximately 700 mW per element. This rectenna used a printed dipole that fed a quad bridge of silicon Schottky diodes.

A project similar to SHARP was one carried out in Japan in the early 1990s. The Japanese program, called *microwave lifted airplane experiment* (MILAX), involved team members from Kyoto University, Kobe University, Communications Research Laboratory, Nissan Motor Co. Ltd., Fuji Heavy Industries Ltd., and Toshiba Co. [24]. The MILAX fuel-free airplane is composed of balsa wood in order to keep its weight under 4 kg, and its wingspan was 2.5 m. The MILAX flew successfully for 40 s at an altitude of about 15 m covering a distance of 400 m over a straight course. The frequency used in the MILAX experiment was 2.411 GHz. The MILAX active phase array transmitter was composed of five-stage gallium arsenic (GaAs) semiconductor amplifiers, 4-bit digital phase shifters, and circular microstrip antennas. The transmitter was divided into 96 subarrays, each consisting of three antennas, one phase shifter, and one GaAs amplifier. Each subarray could supply 13 W of microwave output power, resulting in a total system radiation capability of 1.25 kW. The microwave power beam was radiated toward the MILAX airplane by an active phased-array antenna. At a distance of 15 m, the transmitter provided a power density of 200 W/m^2 . The transmitter was installed on the roof of an automobile as seen in Fig. 12. Six rectenna subarrays, each consisting of 20 rectennas, were installed on the bottom of the MILAX airplane. Each rectenna used a microstrip circular patch antenna to receive the incoming microwave energy. The circular patch antennas had the advantage of being nonresonant at the integer multiple harmonic frequencies of 2.411 GHz. This gave the circular patches the capability of suppressing the harmonic energy arising from the Schottky diodes from reradiation without additional harmonic suppression filters. However, these patch antennas had radiating efficiencies lower than those

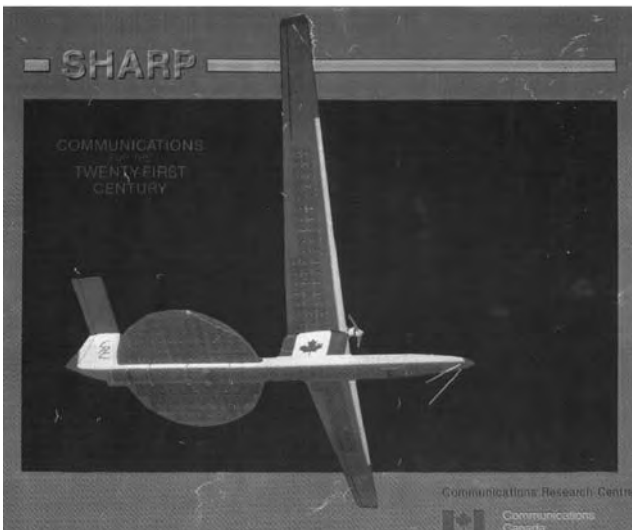


Figure 11. Unmanned aircraft for the SHARP project.



Figure 12. Application of microwave power transmission to microwave-driven airplane (MILAX fuel-free flight experiment).

of dipole antennas. The diodes used are eight HP5082-2350 Schottky diodes in 2-series/4-parallel combination. The power handling capability for the rectenna array was 1 W per element, and the microwave-to-DC conversion efficiency was about 52%.

In 1993, Japan launched the International Space Year—microwave power transmission in space (ISY-METS) experiment to show WPT in space for the first time [25]. From a rocket, 800 W of 2.45 GHz microwave energy was transmitted using microstrip array antennas mounted on four deployed paddles. The rectenna array was placed on a second rocket to receive and convert the incoming microwave energy to DC power. The rectenna array was developed by McSpadden and Chang at Texas A&M University, College Station, TX. It used an orthogonally placed pair of three dipole antennas to achieve dual polarization. This orthogonal layout was similar to the one used in the SHARP project.

In the years 1995–1997, NASA conducted its “fresh-look study” to look at how recent technological advances could serve SSP with regard to United States interests. The study caused NASA to mobilize funding to research institutions, and one of their goals was improvements in rectenna capability. One such advancement occurred in 1998 when McSpadden and Chang developed a printed dipole rectenna, similar to the ones used in the ISY-METS experiment, that achieved 82% conversion efficiency at 5.8 GHz [2]. The rectenna used a MA/COM 40150-119 Schottky diode for rectification on a CPS layout and is shown in Fig. 2.

Since the late 1990s, researchers have looked into the designing of dual and circularly polarized (CP) rectennas, especially for SSP systems. Energy that is transmitted from space to Earth or vice versa undergoes Faraday rotation. This rotation detrimentally affects linearly polarized systems. However, dual and circularly polarized systems are not affected since the broadside alignment of the transmitting and receiving antennas can be arbitrary. Dual and circular polarization enables the receiving and/or transmitting antennas to be rotated without changing the rectenna’s output voltage.

In 2000, a group at JPL was able to operate a 50-V dual-polarized rectenna array composed of 9 patch antennas and 18 diodes to around 52% RF-to-DC conversion at 8.51 GHz [26]. The array was designed to produce high voltages (>50 V) in order to drive electrical actuators. Stacked patches, each with two slot-coupled feed points, were used to achieve the dual polarization.

In 2001, the University of Colorado, Boulder, CO published two novel rectenna arrays for power collection over large bandwidths [27]. Both of these arrays operated from 4.5 to 8 GHz and from 8.5 to 15 GHz. The first is a grid rectenna array, and the second is a spiral rectenna shown in Fig. 13. The grid array had a maximum conversion efficiency of 35% at 5.7 GHz for an incident power density of 7.78 mW/cm^2 of circular polarized energy. The spiral array used alternating RHCP and LHCP spirals to achieve a maximum conversion efficiency of 45% at 10.7 GHz for 1.56 mW/cm^2 . The lower efficiencies are due to the relatively low gain of the radiating elements since both arrays have radiators that are electrically large.

In 2002, a linearly polarized dual-frequency rectenna designed in a CPS layout and operating at both 2.45 and 5.8 GHz was developed by Suh and Chang at Texas A&M University [28]. To resonate at the two frequencies, slight modifications to the traditional dipole structure were made as shown in Fig. 14. The rectenna was placed 17 mm above a metal reflecting ground plane to focus the antennas’ energy in one direction. The rectenna used a MA/COM MA4E1317 Schottky diode and a chip capacitor to achieve 84.4% and 82.7% at 2.45 GHz and 5.8 GHz, respectively. A combination of CPS lowpass and bandstop filters were used to suppress higher-order harmonic energy from reradiating into free space.

In 1999 NASA started its SSP exploratory research and technology (SERT) study. In 2002, as a result of the study, Strassner and Chang developed the printed CP rectenna array shown in Fig. 15 [5]. The array provides 78% RF-to-DC conversion for an incident power density of 8 mW/cm^2

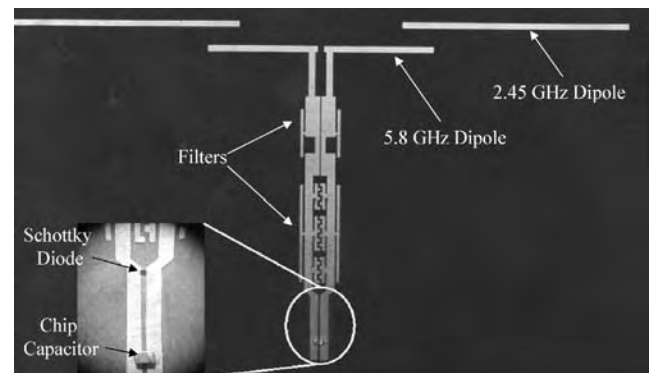


Figure 14. Dual frequency rectenna operating at 2.45 and 5.8 GHz.

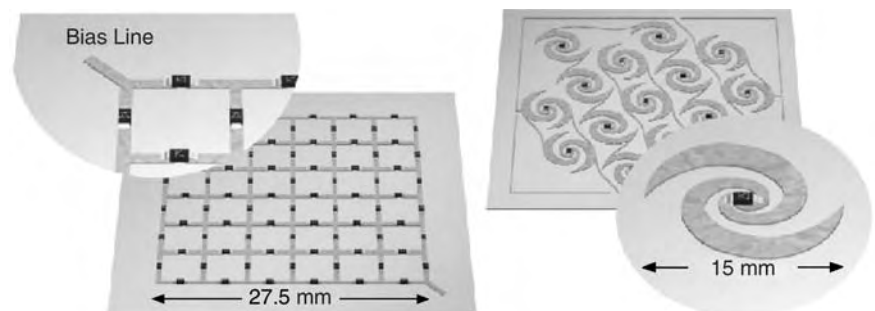


Figure 13. The grid and spiral rectenna arrays. The latter has alternating RHCP and LHCP elements while the former one half cycle of both polarizations equally. The black rectangles are Schottky diodes.

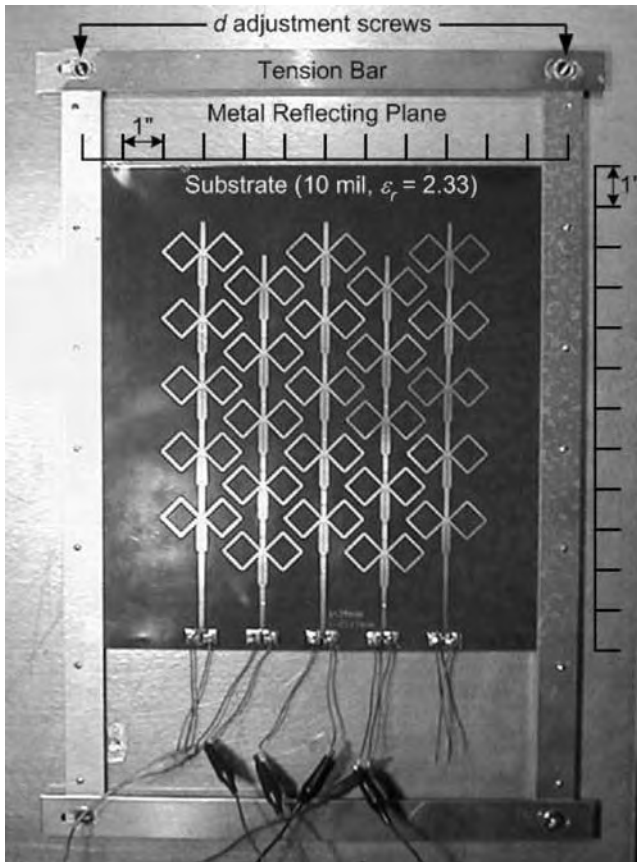


Figure 15. A 5.61-GHz circularly polarized printed rectenna array with over 78% efficiency.

at 5.61 GHz. The rectenna uses a folded dipole antenna called a *dual rhombic loop antenna* (DRLA), which has the advantages of being circularly polarized, having higher gain than a traditional dipole antenna and being easily implemented into a CPS circuit. In comparison with a traditional dipole antenna, the DRLA's gain of 10.7 dBi gives it the advantage of reducing the number of rectenna elements necessary to cover the same receiving area over the array's surface. This reduction means fewer diodes and capacitors leading to great cost benefits especially in the case of large arrays. For low-power-density applications, a modified version of this array in which 4 DRLAs are tied to each diode (4×1) was demonstrated at the World Space Congress 2002 in Houston, TX. The demonstration featured an 18×4 array of these 4×1 DRLA rectennas with each individual 4×1 rectenna having a standalone RF-to-DC conversion efficiency of 82% [29].

6. CONCLUSIONS

All the aforementioned rectenna research has led to the acquisition of highly efficient RF-to-DC conversion capabilities. Not only have the antennas improved, but so too have the rectifying circuits. Improvements in the device physics of the Schottky diode and rectenna fabrication will enable better RF-to-DC conversion efficiencies. Only time will tell whether these improvements and advances in solar cell technology can lead to the development of a fully

operational SSP system. SSP will most likely be the primary driver for future rectenna research. A renewable energy source with no harmful byproducts promises to be one of the most important quests of the new millennium. Imagine Japan, a country with very few natural resources, as the new global supplier of energy. Finding a clean, renewable energy source should be a primary focus for the entire global community, and SSP, with rectennas as one of its core components, could be a solution to the problem.

BIBLIOGRAPHY

1. P. Glaser, Power from the sun: Its future, *Sci. Mag.* **162**(3856):857–861 (Nov. 1968).
2. J. O. McSpadden, L. Fan, and K. Chang, Design and experiments of a high-conversion-efficiency 5.8-GHz rectenna, *IEEE Trans. Microwave Theory Tech.* **46**(12):2053–2060 (Dec. 1998).
3. T. Yoo and K. Chang, Theoretical and experimental development of 10 and 35 GHz rectennas, *IEEE Trans. Microwave Theory Tech.* **40**(6):1259–1266 (June 1992).
4. B. Strassner and K. Chang, 5.8-GHz circularly polarized rectifying antenna for wireless microwave power transmission, *IEEE Trans. Microwave Theory Tech.* **50**(8):1870–1876 (Aug. 2002).
5. B. Strassner and K. Chang, Highly efficient C-band circularly polarized rectifying antenna array for wireless microwave power transmission, *IEEE Trans. Antenn. Propag.* **51**(6):1347–1356 (June 2003).
6. W. C. Brown, *Electronic and Mechanical Improvement of the Receiving Terminal of a Free-Space Microwave Power Transmission System*, Raytheon Co., Wayland, MA, Technical Report PT-4964, NASA Report CR-135194, Aug. 1977.
7. P. Koert, J. Cha, and M. Macina, 35 and 94 GHz rectifying antenna systems, *SPS 91—Power from Space Digest*, Paris, Aug. 1991, pp. 541–547.
8. W. C. Brown, The early history of wireless power transmission, *Proc. Space Studies Inst. Space Manufacturing*, Princeton, NJ, May 8–11, 1997.
9. M. Cheney, *Tesla Man Out of Time*, Prentice-Hall, Englewood Cliffs, NJ, 1981.
10. H. Yagi and S. Uda, On the feasibility of power transmission by electric waves, *Proc. 3rd Pan-Pacific Sci. Congress*, Vol. 2, Tokyo, 1926, pp. 1305–1313.
11. Electric light without current, *Lit. Digest*, **112**(3):30 (Jan. 1932).
12. W. C. Brown, The history of power transmission by radio waves, *IEEE Trans. Microwave Theory Tech.* **32**(9):1230–1242 (Sept. 1984).
13. W. C. Brown, Experiments in the transportation of energy by microwave beam, *1964 IEEE Int. Record*, Vol. XII, Part 2, pp. 8–18.
14. W. C. Brown, J. R. Mims, and M. I. Heenan, An experimental microwave powered helicopter, *1965 IEEE Int. Record*, Vol. 13, Part 5, pp. 225–235.
15. W. C. Brown, *Free Space Microwave Power Transmission System Study*, final report on first phase of MSFC Contract NAS-8-25374, dated Dec. 10 1969–Dec. 10, 1971.
16. R. M. Dickinson and W. C. Brown, *Radiated Microwave Power Transmission System Efficiency Measurements*, Technical Memo 33-727, JPL (Jet Propulsion Lab., Calif. Inst. Technology), Pasadena, CA, March 15, 1975.

17. R. M. Dickinson, *Evaluation of a Microwave High Power Reception-Conversion Array for Wireless Power Transmission*, Technical Memo. 33-741, JPL, Pasadena, CA, Sept. 1, 1975.
18. W. C. Brown, *Electronic and Mechanical Improvement of the Receiving Terminal of a Free-Space Microwave Power Transmission System*, Raytheon Co., Wayland, MA, Technical Report PT-4964, NASA Report CR-135194, Aug. 1977.
19. W. C. Brown and J. F. Triner, Experimental thin-film, etched-circuit rectenna, *IEEE MTT-S Int. Microwave Symp. Digest*, Dallas, TX, June 1982, pp. 185–187.
20. H. Matsumoto, H. Hirata, Y. Hashino, and N. Shinohara, Theoretical analysis of nonlinear interaction of intense electromagnetic wave and plasma waves in the ionosphere, *Electron. Commun. Jpn. Pt. 3* **78**(11):104–114 (1995).
21. J. Schlesak, A. Alden, and T. Ohno, SHARP rectenna and low altitude flight trials, paper presented at IEEE Global Telecommunications Conf., New Orleans, Dec. 2–5, 1985.
22. P. Koert, J. Cha, and M. Macina, 35 and 94 GHz rectifying antenna systems, *SPS 91—Power from Space Digest*, Paris, France, pp. 541–547, Aug. 1991.
23. S. S. Bharj, R. Camisa, S. Grober, F. Wozniak, and E. Pendleton, High efficiency C-band 1000 element rectenna array for microwave powered applications, *IEEE MTT-S Int. Microwave Symp. Digest*, Albuquerque, NM, June 1992, pp. 301–303.
24. Y. Fujino, T. Ito, N. Kaya, H. Matsumoto, K. Kawabata, H. Sawada, and T. Onodera, A rectenna for MILAX, *Proc. 1st Wireless Power Transmission Conf.*, Texas, Feb. 1993, pp. 273–277.
25. N. Kaya, H. Matsumoto, and R. Akiba, Rocket experiment METS: Microwave transmission in space, *Space Power* **11**:267–274 (1992).
26. L. W. Epp, A. R. Khan, H. K. Smith, and R. P. Smith, A compact dual-polarized 8.51-GHz rectenna for high-voltage (50 V) actuator applications, *IEEE Trans. Microwave Theory Tech.* **48**(1):111–120 (Jan. 2000).
27. J. Hagerty and Z. Popović, An experimental and theoretical characterization of a broadband arbitrarily-polarized rectenna array, *IEEE MTT-S Int. Microwave Symp. Digest*, Phoenix, AZ, May 2001, pp. 1855–1858.
28. Y. H. Suh and K. Chang, A high-efficiency dual-frequency rectenna for 2.45- and 5.8-GHz wireless power transmission, *IEEE Trans. Microwave Theory Tech.* **50**: 1784–1789 (July 2002).
29. B. Strassner and K. Chang, 5.8 GHz circularly polarized dual rhombic loop traveling wave rectifying antenna for low power density wireless power transmission applications, *IEEE Trans. Microwave Theory Tech.* **51**(5):1548–1553 (May 2003).

REFLECTARRAY ANTENNA

JOHN HUANG
 Jet Propulsion Laboratory
 Pasadena, California

1. INTRODUCTION

The reflectarray antenna consists of a flat or slightly curved reflecting surface and an illuminating feed as

shown in Fig. 1. On the reflecting surface, there are many isolated elements (e.g., open-ended waveguides, printed patches, dipoles, or rings) without any power division transmission lines. The feed antenna illuminates these isolated elements, which are designed to scatter the incident field with electrical phases, which are required to form a planar phase front in the far-field distance. This operation is similar in concept to the use of a parabolic reflector that naturally reflects and forms a planar phase front when a feed is placed at its focal point. Thus the term “flat reflector” is sometimes used to describe the reflectarray, which utilizes technologies of both reflector and array. As shown in Fig. 2, there are several methods for reflectarray elements to achieve a planar phase front. For example, one is to use identical microstrip patches with different-length phase-delay lines attached to enable them to compensate for the phase delays over the different paths from the illuminating feed. Another method employs variable-size patches, dipoles, or rings to provide the elements with different scattering impedances and, thus, different phases to compensate for the different feed path delays. In the third method, for circular polarization only, the reflectarray has all identical circularly polarized elements but with different angular rotations to compensate for the feed pathlength differences.

To achieve low reflecting surface profile and low antenna mass, reflectarrays using printed microstrip elements have been developed. These reflectarrays combine some of the best features of the traditional parabolic reflector antenna and the microstrip array technology. Similar to a parabolic reflector, the reflectarray can achieve very good efficiency (>50%) for very large aperture since no power divider is needed and thus very little resistive insertion loss is encountered here. On the other hand, very similar to an array antenna, the reflectarray can have its main-beam designed to tilt at a large angle (>50°) from its broadside direction. Low-loss electronic phase shifters can be implanted into the elements for wide-angle electronic beam scanning. With this beam-scanning capability of the reflectarray, the complicated high-loss beamforming network and high-cost transmit/receive (T/R) amplifier modules of a conventional phased array are no longer needed. One significant advantage of the printed reflectarray is that, when a large aperture (e.g., 10-m) spacecraft antenna requires a deployment mechanism, the flat structure of the reflectarray allows a much simpler and more reliable folding or inflation mechanism than does the curved surface of a parabolic reflector. The flat reflecting surface of the reflectarray also lends itself for flush mounting onto an existing flat structure without adding significant mass and volume to the overall system structure. The reflectarray, which is in the form of a printed microstrip antenna, can be fabricated with a simple and low-cost etching process, especially when produced in large quantities. Another major feature of the reflectarray is that, with more than hundreds or thousands of elements in a general reflectarray having phase adjustment capability, it can achieve very accurate contour beamshape with a phase synthesis technique. With all these capabilities, there is one distinct disadvantage associated with the reflectarray antenna. This is its inherent narrow bandwidth, which

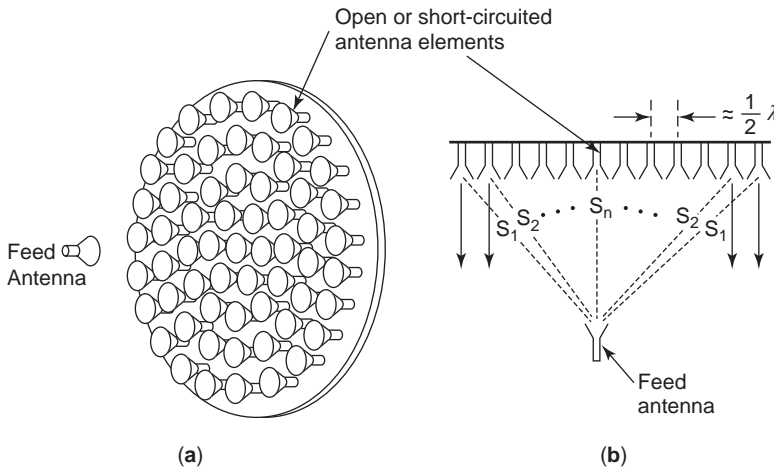


Figure 1. Configuration of a reflectarray antenna: three- (a) and two-dimensional (b) views.

generally cannot exceed much beyond 10%. This narrow-bandwidth behavior is discussed further in Section 4. Although the reflectarray has narrow bandwidth, due to its multitude of capabilities, the development, research, and application of the printed reflectarray antenna seem to be potentially boundless in the future.

2. REVIEW OF DEVELOPMENT HISTORY

The reflectarray antenna concept, shown in Fig. 1, was first demonstrated during the early 1960s [1]. Open-ended waveguide elements with variable-length waveguides were used to demonstrate the capability of achieving cophasal reradiated far-field beams. During this early time, since most wireless operations were done at relatively low microwave frequencies, the large-waveguide reflectarrays resulted in very bulky and heavy antennas. In addition, the efficiencies of these reflectarrays were not studied and optimized. More than 10 years later (in the mid-1970s), the very ingenious concept of “spiraphase” reflectarray was developed [2], where switching diodes were used in an eight-arm spiral or dipole element of a circularly polarized

reflectarray to electronically scan its mainbeam to large angles from the broadside direction. This is possible because, by angularly rotating a circularly polarized radiating element, its propagating electrical phase will also change by an appropriate amount proportional to the amount of rotation. However, because of the thick spiral cavity and large electronic components, the spiraphase reflectarray was still relatively bulky and heavy. Its aperture efficiency was still relatively poor. Thus, no continued development effort was followed. It should be noted here that, in order to ensure good efficiency for the reflectarray, the intricate relations between the element beamwidth, element spacing, and focal length/diameter (f/D) ratio must be well designed; otherwise, a large backscattered component field or a mismatched surface impedance would result.

Following the introduction of the printable microstrip antennas, the technologies of reflectarray and microstrip radiators were combined, and a typical configuration is illustrated in Fig. 3. Various printed microstrip reflectarray antennas were developed in the late 1980s and early 1990s for the purpose of achieving reduced antenna size

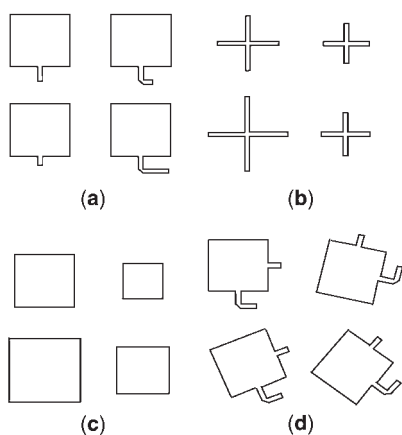


Figure 2. Various reflectarray elements: (a) identical patches with variable-length phase delay lines; (b) variable-size dipoles; (c) variable-size patches; (d) variable angular rotations.

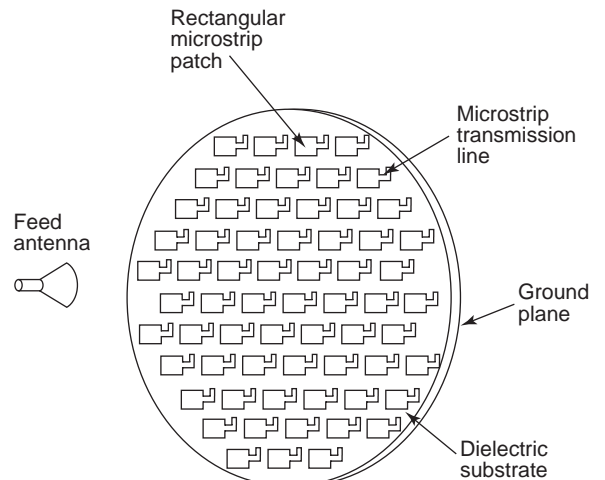


Figure 3. Microstrip reflectarray with identical patches but different-length phase delay lines.

and mass. These printed reflectarrays came in various forms as shown in Fig. 2 and are all with flat low-profile and low-mass reflecting surfaces. The ones that used identical patch elements with different-length phase-delay lines [3–8] have elements similar to those shown in Fig. 2a. The phase-delay lines, having lengths in the order of half-wavelength long or less, are used to compensate for the phase differences of different pathlengths from the illuminating feed. The second approach, shown in Fig. 2b, used elements that are made of printed dipoles with variable dipole lengths [9]. Different dipole lengths will yield different scattering impedances, which then provide the different phases needed to compensate for the different pathlength delays. Similarly, microstrip patches with variable patch sizes [10], shown in Fig. 2c, were also developed. Circularly polarized microstrip patches with identical size but variable angular rotations [11,12], shown in Fig. 2d, were designed to form a cophasal far-field reflectarray beam. In addition to those shown in Fig. 2, several other reflectarray or equivalent developments during the 1990s are worth mentioning here. Printed variable-length dipole elements were used to form a frequency scanned grating-reflector antenna with an offset feed [13]. Printed annular rings of variable diameters arranged in Fresnel-zone configuration were also used to focus the beam [14]. In the 1996 Phased Array Conference, a 94-GHz monolithic reflectarray [15], using one-bit pin (positive–intrinsic–negative) diode phase shifters, was reported to achieve wide-angle ($\pm 45^\circ$) electronic beam scanning. In the same conference, a 35-GHz reflectarray, using waveguide/dielectric elements with 3-bit ferrite phase shifters [16], was also reported to achieve $\pm 25^\circ$ beam scanning. One technique proposed [11], although not yet developed, is worth mentioning here. By using the angular rotation technique with circularly polarized elements, miniature or micromachined motors could be placed under each element to achieve wide-angle beam scanning without the need of T/R modules and phase shifters. For application in the spacecraft area, a deployable and low-mass one-meter diameter inflatable reflectarray antenna [17] at the X-band frequency was developed. Another unique spacecraft application of the reflectarray was conceived [18] and developed [19] by using its many elements, with a numerical phase synthesis technique, to form a uniquely shaped contour beam. From all these developments, it can be seen that, at the end of twentieth century, reflectarray antenna technology has sufficiently matured and has had a variety of possible applications throughout the microwave and millimeter-wave spectra.

In early 2000, the development of reflectarray mushroomed, and several performance improvement techniques are worth mentioning here. One used multilayer stacked patches to improve the reflectarray bandwidth from a few percent to more than 10% [20]. As an extension to the 1-m X-band inflatable reflectarray mentioned above, a 3-m Ka-band inflatable reflectarray consisting of 200,000 elements was also developed [21], which is currently known as the “electrically largest reflectarray.” An amplifying reflectarray was developed [22] for each element of the reflectarray to amplify the transmitted signal and, thus, achieved very high overall radiated power. In

order to achieve good antenna efficiency, the most critical segment of the reflectarray design is its elements. The element performance was optimized by using the genetic algorithm (GA) method [23]. The reflectarray using sub-reflector and array feed configuration to achieve fine beam scanning was also studied [24]. To combat the shortcomings of narrow-bandwidth, dual-band multilayer reflectarrays using annular rings [25] and crossed dipoles [26] are also being developed. Another development that is worth mentioning here is a folded reflectarray configuration [27], where two reflecting surfaces are used to reduce the overall antenna profile due the feed height of a conventional reflectarray.

3. ANALYSIS AND DESIGN PROCEDURES

The design and analysis of a reflectarray can be separated into four essential steps, which are discussed separately below.

3.1. Element Characterization

The most important and critical segment of the reflectarray design is its element characterization. If the element design is not optimized, it will not scatter the signal from the feed effectively to form an efficient far-field beam. Its beamwidth must correlate correctly with the reflectarray's f/D ratio to accommodate all incident angles from the feed. Its phase change versus element change (patch size, delay line length, etc.) must be calibrated correctly. One very popular technique for calibrating the phase is to use the infinite-array approach [10,28] to include local mutual coupling effect due to surrounding elements. It is not feasible for the current computer technology to have a complete rigorous solution to include all the mutual coupling effect of all elements since the reflectarray generally consists of too many elements. The infinite array approach can be done by using the method-of-moment technique [10,28] or equivalently done by a finite-difference time-domain (FDTD) analysis on a unit cell of a single element [29]. Mathematical waveguide simulator, which simulates the infinite-array approach, can also be adapted by using the commercial software HFSS (high-frequency structure simulator; a finite-element technique) to achieve the element phase information. All these techniques are used to derive the phase change–element change curve, which is generally an “S”-shaped curve with nonlinear relationship as illustrated in Fig. 4. The antenna designer should minimize the slope at the center of the curve to ensure that the phase change will not be overly sensitive to the element change. If the curve is too steep, the element change or fabrication tolerance may become an issue, in particular at high microwave frequencies.

3.2. Required Phase Delay

The pathlengths from the feed to all elements are all different, and this variation leads to different phase delays. To compensate for these phase delays, the elements must have corresponding phase advancements designed in according to a unique “S” curve similar to that shown in

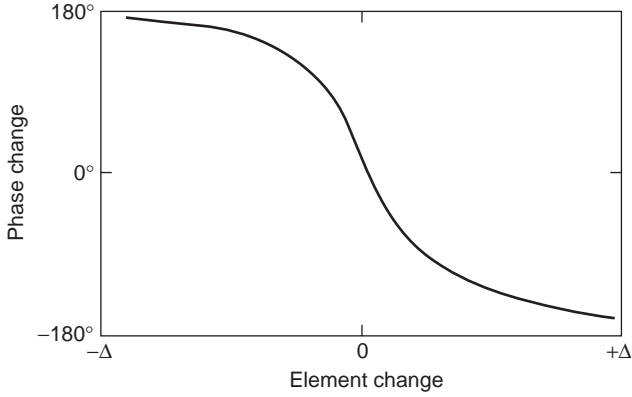


Figure 4. A typical “S” curve of a reflectarray element phase-change versus element-change.

Fig. 4. The following two equations give examples of how the compensating phase is calculated for each element of a reflectarray with a broadside-directed beam. The differential pathlength for each element is given as

$$\Delta L_{m,n} = L_{m,n} - L_{0,0} \quad (1)$$

where $L_{m,n}$ is the distance between the feed and the m th element, which can be obtained by using simple geometry. $L_{0,0}$ is the distance between the feed and a reference point on the reflectarray surface, such as the centerpoint. $\Delta L_{m,n}$ is thus the differential feed pathlength for the m th element. To achieve a collimated radiation, the phase advancement $\Delta\Phi_{mn}$ needed for the m th element is given by

$$\Delta\Phi_{mn} \text{ in degrees} = \left(\frac{\Delta L_{m,n}}{\lambda_0} - \text{integer of } \frac{\Delta L_{m,n}}{\lambda_0} \right) \times 360 \quad (2)$$

This equation indicates that the compensating phase can be repeated every 360° and the portion that is an integer multiple of a wavelength or 360° can be deleted.

3.3. Pattern Calculation

With all elements’ compensating phases known, the far-field radiation patterns can be calculated by the conventional array theory, where the radiation of all elements are summed together as follows. Consider a planar array consisting of $M \times N$ elements that are nonuniformly illuminated by a low-gain feed at position vector \vec{r}_f . Let the desired beam direction be specified by unit vector \hat{u}_0 . Then the far-field of the reflectarray in the \hat{u} direction will be of the form

$$E(\hat{u}) = \sum_{m=1}^M \sum_{n=1}^N F(\vec{r}_{mn} \cdot \vec{r}_f) \cdot A(\vec{r}_{mn} \cdot \hat{u}_0) \cdot A(\hat{u} \cdot \hat{u}_0) \cdot \exp[jk(|\vec{r}_{mn} - \vec{r}_f| + \vec{r}_{mn} \cdot \hat{u}) + j\alpha_{mn}] \quad (3)$$

where F is the feed pattern function, A is the reflectarray element pattern function, \vec{r}_{mn} is the position vector of the m th element, and α_{mn} is the required compensating phase of the m th element calculated by Eq. (2). The $\cos^q \theta$

factor is used for both F and A functions with no azimuth (ϕ) dependence.

3.4. Reflectarray Geometry Design

Determination of the geometry of a reflectarray basically consists in determining its f/D ratio, which is governed by its desired aperture efficiency. The aperture efficiency (η_a) can be defined as the product of the illumination (η_i) and spillover (η_s) efficiencies: $\eta_a = \eta_i \times \eta_s$. By integrating the pattern function of Eq. (3), the illumination efficiency for a center-fed reflectarray can be obtained in a closed form [30] as given by

$$\eta_i = \frac{[(1 + \cos^{q+1} \theta_e)/(q+1)] + [(1 - \cos^q \theta_e)/q]^2}{2 \tan^2 \theta_e [(1 - \cos^{2q+1} \theta_e)/(2q+1)]} \quad (4)$$

and the spillover efficiency is given by

$$\eta_s = 1 - \cos^{2q+1} \theta_e \quad (5)$$

where q is the exponent of the feed pattern function represented by $\cos^q \theta$ and θ_e is half of the subtend angle from the feed to the reflectarray aperture. The reflectarray element is approximated by cosine function. Equations (4) and (5) are calculated by assuming a circular aperture only for demonstration of the design procedures. Similar closed-form equations can be easily obtained for square, rectangular, or elliptical apertures by performing proper integrations. To give an example of how Eqs. (4) and (5) can be utilized to optimize a reflectarray design, Fig. 5 shows the calculated curve of spillover and illumination efficiencies versus the feed pattern factor q (feed beamwidth) for a 0.5-m 32-GHz reflectarray with a fixed f/D ratio of 1.0 ($\theta_e = 26.6^\circ$). It demonstrates that the maximum aperture efficiency is achieved at $q = 10.5$ or when the feed has a -3 dB beamwidth of 29° . Another curve, shown in Fig. 6, gives aperture efficiency as a function of f/D ratio for

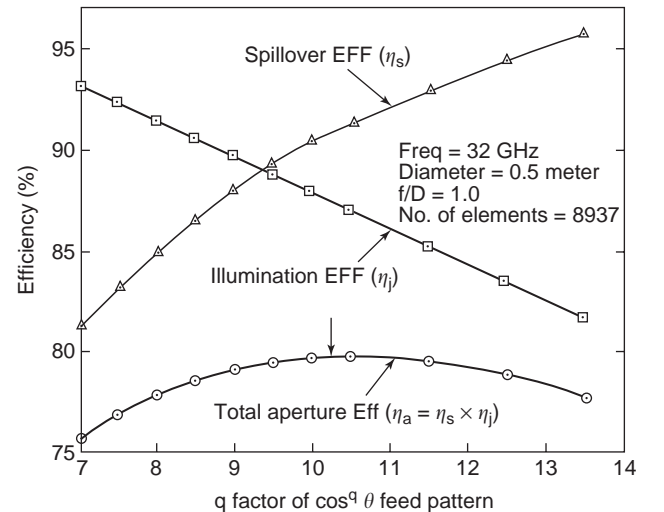


Figure 5. Spillover and illumination efficiencies versus feed pattern shape.

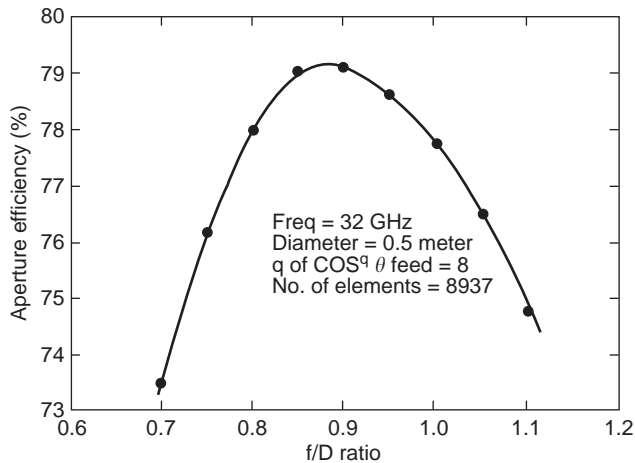


Figure 6. Aperture efficiency versus f/D ratio.

the same 0.5-m 32-GHz reflectarray when the feed beamwidth is fixed at 33.4° with $q=8$. In this case, the maximum aperture efficiency is achieved when the f/D ratio is 0.87. It can be seen that curves derived from Eqs. (4) and (5) are essential in obtaining an optimum efficiency design. The preceding discussion has been limited to the center-fed reflectarray. Offset reflectarray can also be optimally designed by using equations similar to Eqs. (4) and (5).

4. BANDWIDTH

The bandwidth performance of a reflectarray [11] is no match for that of a parabolic reflector, where infinite bandwidth theoretically exists. The bandwidth of a printed microstrip reflectarray is limited primarily by two factors: (1) the narrow bandwidth of the microstrip patch elements on the reflectarray surface and (2) the differential spatial phase delay. The microstrip patch element generally has a bandwidth of about 3–5%. To achieve wider bandwidth for a conventional microstrip array, techniques such as using thick substrate for the patch, stacking multiple patches, and using sequentially rotated subarray elements have been employed. More than 15% bandwidths have been reported. The second reflectarray limiting factor, the differential spatial phase delay, can be best explained by referring to Fig. 7, where the differential spatial phase delay, ΔS , is the phase difference between the two paths, S_1 and S_2 , from the feed to the reflectarray elements. This ΔS can be many multiples of the wavelength (λ) at the center operating frequency. It can be expressed as $\Delta S = (N + d)\lambda$, where N is an integer and d is a fractional number of a free-space wavelength λ . At each element location, d is compensated by an appropriate phase delay achieved by the reflectarray element design (achieved by variable patch size, variable phase-delay line length, etc.). As frequency changes, the factor $(N + d)\lambda$ becomes $(N + d)(\lambda + \Delta\lambda)$. Since the design and the compensating phase for each element is fixed for the center frequency, a frequency excursion error will occur in the reradiated phase front. The amount of phase change in each path when compared to a reference path, say, S_1 , is $(N + d)\Delta\lambda$, which can constitute

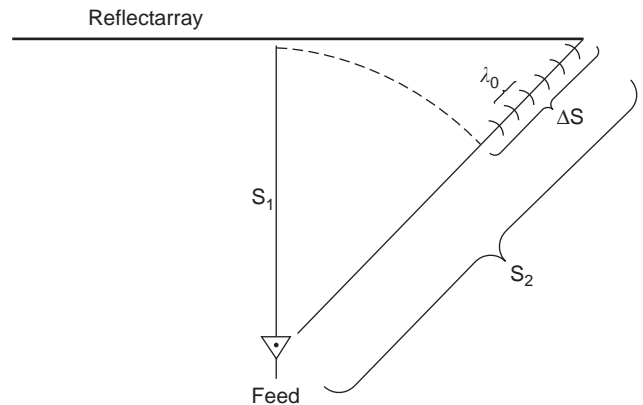


Figure 7. Differential spatial phase delay of reflectarray.

a significant portion of a wavelength or 360° . To reduce the amount of frequency excursion error, the integer number N must be reduced. Several methods can be used to reduce N :

1. Design the reflectarray with a larger f/D ratio and hence minimize the difference between paths S_1 and S_2 .
2. Simply avoid the use of a reflectarray with a large electrical diameter. The effects of f/D ratio and diameter on bandwidth performance were given in Figs. 5 and 6.
3. Reduce frequency excursion error by using time-delay lines or partial time-delay lines instead of the phase delays. In other words, when using the phase-delay line technique (not the variable-patch-size technique), instead of using $d\Delta\lambda$ for the delay-line length, $(N + d)\Delta\lambda$ could be used for the delay line. Certainly, additional line insertion loss and needed real estate for the lines are issues to be encountered.
4. Increase the bandwidth by using, instead of a complete flat reflectarray surface, a concavely curved reflectarray with piecewise flat surfaces. This curved reflectarray will remain advantageous over a curved parabolic reflector; for instance, its beam can be scanned to large angles with a phase shifter inserted into each element, and, for a space-deployable antenna, the piecewise flat surfaces in some cases can be folded more easily into a smaller stowed volume.

In order to mitigate the bandwidth problem, a recent (as of 2003) technique of using multilayer stacked-patch elements [20] has not only increased the element bandwidth but also reduced the effect of differential spatial phase delay. As a net result, the bandwidth has increased from a few percent to more than 10%. Multiband techniques can also be applied to the reflectarray. Recently, two dual-band techniques have been developed for the X- and Ka-band frequencies: (1) use of a double layer with two different-size rings and variable angular rotations [25] and (2) use of a double layer with X-band crossed dipoles over Ka-band patches [26]. To summarize, although the narrow-bandwidth characteristic is the primary shortcoming of a



Figure 8. A 3-m Ka-band inflatable reflectarray (the shining structure in front of the aperture is the surface flatness measurement device).

reflectarray, several techniques can be employed to improve bandwidth performance.

5. APPLICATIONS AND RECENT DEVELOPMENTS

In addition to those possible reflectarray applications mentioned in Sections 1 and 2, it is appropriate to present some details of several important applications and recent developments here. One is a Ka-band circularly polarized inflatable reflectarray [21] with a 3-m-diameter aperture developed by the Jet Propulsion Laboratory (JPL) for NASA's future spacecraft communication antenna application. As shown in Fig. 8, the antenna uses a torus-shaped (doughnut-shaped) inflatable tube to support and



Figure 10. Ku-band reflectarray with shaped contour beam capability (courtesy of Professor Dave Pozar, Univ. Massachusetts). (This figure is available in full color at <http://www.mrw.interscience.wiley.com/erfme>.)

tension a 3-m thin-membrane reflectarray surface. This circularly polarized reflectarray, having approximately 200,000 elements using the variable-angular-rotation technique [11,12], is considered electrically the largest reflectarray ever built. The reflectarray, which has a “natural” flat surface, retains its required surface tolerance [0.3 mm RMS (root mean square) in this case] by the inflatable structure much more easily than would a “non-natural” parabolic surface, particularly for long space flight. The design of this inflatable antenna was later improved, equipping the antenna with rigidizable inflatable tubes [21,31] in order to survive the hazardous space

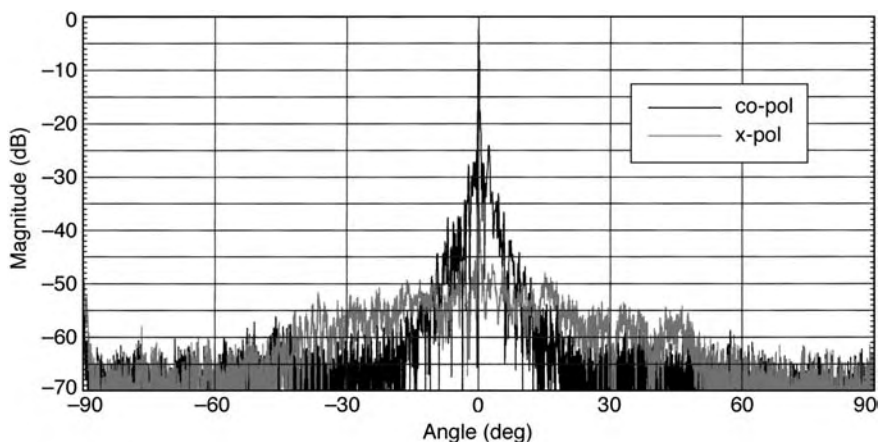


Figure 9. Measured radiation pattern of the 3-m Ka-band inflatable reflectarray.

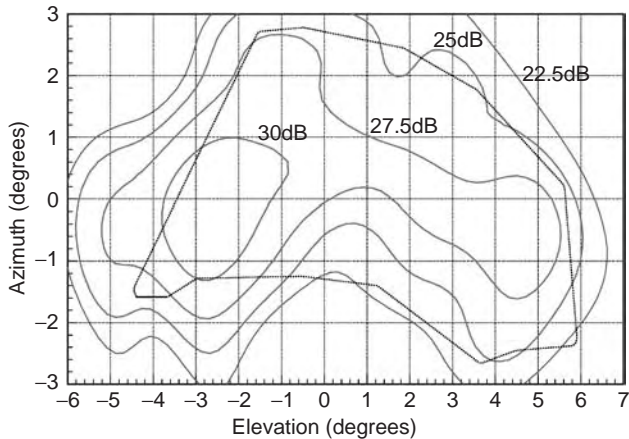


Figure 11. A measured contour beam plot of the reflectarray shown in Fig. 10. (This figure is available in full color at <http://www.mrw.interscience.wiley.com/erfme>.)

environment, such as bombardment by space debris and strenuous thermal effects (induced by solar flares, UV, radiation, etc). This reflectarray achieved an aperture efficiency of 30% with room for improvement and excellent far-field pattern shape with average sidelobe and cross-polarization levels below -40 dB as shown in Fig. 9. A second important development of the reflectarray is the achievement of a shaped contour beam by using the phase synthesis technique. This reflectarray, shown in Fig. 10, was developed by the University of Massachusetts [19] for a commercial application to provide Earth contour beam coverage. A typical calculated contour beam of this antenna, using the phase synthesis technique, is plotted in Fig. 11. Since a reflectarray generally has many thousands of elements, it has many degrees of freedom in design to provide an accurate and uniquely required contour beam. A third important development is a dual-frequency reflectarray, where the two frequencies are widely sepa-

rated, such as the X and Ka bands. The developed prototype antenna, shown in Fig. 12, is circularly polarized and uses variable-angular-rotation annular rings [25]. It was developed by the Texas A&M University for JPL/NASA's future space communication application. This antenna, with a diameter of 0.5 m, uses a multilayer configuration in which the X-band annular rings are placed above the Ka-band rings and serve as a frequency-selective surface to allow the Ka-band signal to pass through. The measured results indicate that there is only minimal impact on X-band performance, due to the presence of the Ka-band elements. The measured radiation patterns of the Ka-band reflectarray both without and with the X-band layer are shown in Figs. 13 and 14, respectively. There is no significant difference between the two patterns. However, the measured Ka-band gain of the dual-frequency dual-layer antenna is about 1.0 dB lower than that of the Ka-band alone antenna. The purely Ka-band reflectarray (Fig. 13) has a measured aperture efficiency of 50%, while the dual-frequency dual-layer antenna has a Ka-band efficiency of about 40%. In other words, the X-band annular rings did somewhat impact Ka-band performance. Efforts need to be carried out in the future to minimize this impact. One more recent development that is worth mentioning is a reflectarray having a rectangular aperture intended for the NASA/JPL wide-swath ocean altimeter (WSOA) radar application. This reflectarray uses variable-size patches as elements. The required rectangular aperture, as shown in Fig. 15, consists of five flat subapertures connected together to form a curved reflectarray [32]. The curving of the long dimension of the rectangular surface is to minimize the incident angles from the feed for the end elements and thus to optimize the radiation efficiency for all elements. The radiation efficiency here indicates the measure of amount of energy of each element that is reradiated in the desired mainbeam direction. The advantage of using reflectarray with flat subapertures is to allow mechanical folding of the flat panels into a compact structure for

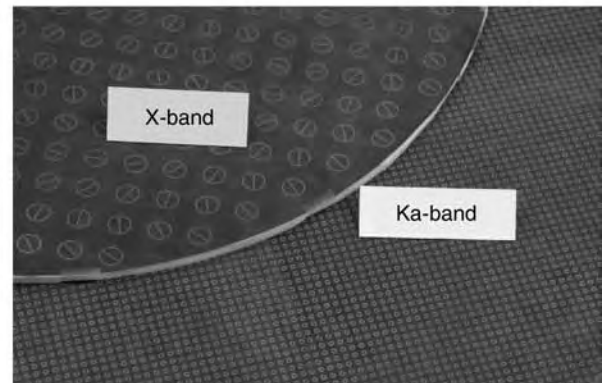
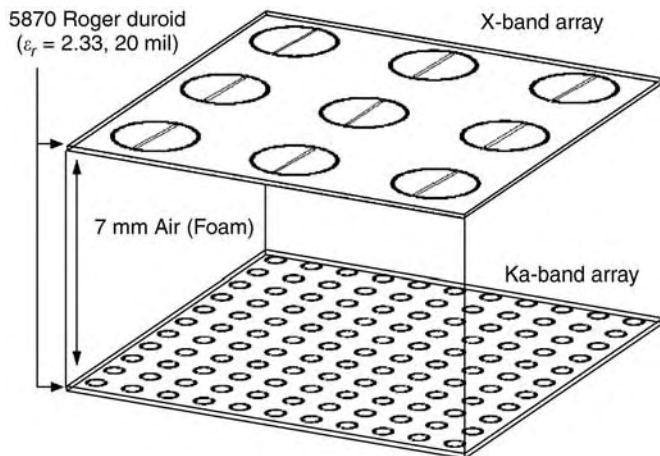


Figure 12. Sketch and photo of the X/Ka dual-band two-layer reflectarray antenna using annular ring elements. (This figure is available in full color at <http://www.mrw.interscience.wiley.com/erfme>.)

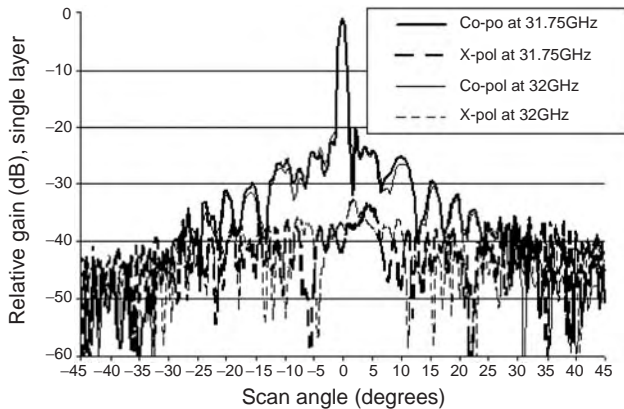


Figure 13. Measured radiation pattern of the single-layer Ka-band reflectarray.

spacecraft launch vehicle stowage. Preliminary test data indicate that this reflectarray is functioning properly, and some minor improvements are currently being carried out.

6. SUMMARY

The reflectarray antenna has come a long way. However, its development and application had not been widely adapted until the early 1990s, when the printable microstrip reflectarray was introduced. Except for its narrow-bandwidth characteristic, the reflectarray has many advantages over a parabolic reflector antenna type. The mainbeam of a reflectarray can be designed to tilt to a large angle from its broadside direction. Phase shifters can be implanted into the elements for wide-angle electronic beam scanning. For large-aperture spacecraft antenna applications, the reflectarray's flat surface allows the antenna to be constructed as an inflatable structure with relative ease in maintaining its surface tolerance in comparison to a curved parabolic surface. Its flat surface also can be made of multiple flat panels for ease in folding into a more compact structure for launch vehicle stowage. Very accurate beam shape can be achieved with phase synthesis technique for Earth contour beam coverage

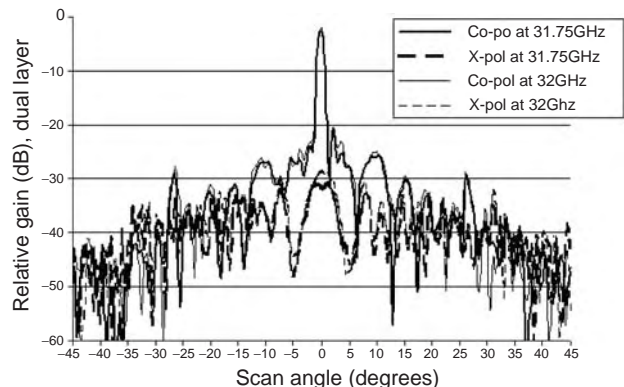


Figure 14. Measured Ka-band radiation pattern of the two-layer X/Ka dual-band reflectarray.

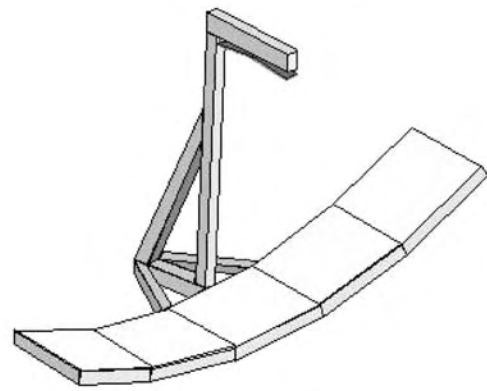


Figure 15. Drawing and photo of the piecewise flat reflectarray for space application.

applications. Due to these multitudes of capabilities, the door has just opened for the development, research, and application of printed reflectarray antennas. Two major areas that need further improvement in performance are the reflectarray's bandwidth and radiation efficiency.

Acknowledgment

Portions of the research activities described in these article were carried out by the Jet Propulsion Laboratory, California Institute of Technology, under contract with the National Aeronautics and Space Administration.

BIBLIOGRAPHY

1. D. G. Berry, R. G. Malech, and W. A. Kennedy, The reflectarray antenna, *IEEE Trans. Anten. Propag.* **AP-11**:645–651 (Nov. 1963).
2. H. R. Phelan, Spiralphase reflectarray for multitarget radar, *Microwave J.* **20**:67–73 (July 1977).
3. R. E. Munson and H. Haddad, *Microstrip Reflectarray for Satellite Communication and RCS Enhancement and Reduction*, US Patent 4,684,952 (Aug. 1987).
4. J. Huang, Microstrip reflectarray, *Proc. IEEE AP-S/URSI Symp.*, London, Canada, June 1991, pp. 612–615.
5. T. A. Metzler, *Design and Analysis of a Microstrip Reflectarray*, Ph.D. dissertation, Univ. Massachusetts, Sept. 1992.

6. Y. Zhang, K. L. Wu, C. Wu, and J. Litva, Microstrip reflectarray: Full-wave analysis and design scheme, *Proc. IEEE AP-S/URSI Symp.*, Ann Arbor, MI, June 1993, pp. 1386–1389.
7. R. D. Javor, X. D. Wu, and K. Chang, Beam steering of a microstrip flat reflectarray antenna, *Proc. IEEE AP-S/URSI Symp.*, Seattle, June 1994, pp. 956–959.
8. D. C. Chang and M. C. Huang, Multiple polarization microstrip reflectarray antenna with high efficiency and low cross-polarization, *IEEE Trans. Anten. Propag.* **43**:829–834 (Aug. 1995).
9. A. Kelkar, FLAPS: Conformal phased reflecting surfaces, *Proc. IEEE Natl. Radar Conf.*, Los Angeles, March 1991, pp. 58–62.
10. D. M. Pozar and T. A. Metzler, Analysis of a reflectarray antenna using microstrip patches of variable size, *Electron. Lett.* **65**:657–658 (April 1993).
11. J. Huang, Bandwidth study of microstrip reflectarray and a novel phased reflectarray concept, *Proc. IEEE AP-S/URSI Symp.*, Newport Beach, CA, June 1995, pp. 582–585.
12. J. Huang and R. J. Pogorzelski, A Ka-band microstrip reflectarray with elements having variable rotation angles, *IEEE Trans. Anten. Propag.* **46**:650–656 (May 1998).
13. F. S. Johansson, A new planar grating-reflector antenna, *IEEE Trans. Anten. Propag.* **38**:1491–1495 (Sept. 1990).
14. Y. T. Gao and S. K. Barton, Phase correcting zonal reflector incorporating rings, *IEEE Trans. Anten. Propag.* **43**:350–355 (April 1995).
15. J. M. Colin, Phased array radars in France: present and future, *Proc. IEEE Symp. Phased Array System and Technology*, Boston, Oct. 1996, pp. 458–462.
16. A. A. Tolkahev, V. V. Denisenko, A. V. Shishlov, and A. G. Shubov, High-gain antenna system for millimeter-wave radars with combined electrical and mechanical beam steering, *Proc. IEEE Symp. Phased Array System and Technology*, Boston, Oct. 1996, pp. 266–271.
17. J. Huang and A. Fera, A 1-m X-band inflatable reflectarray antenna, *Microwave Opt. Technol. Lett.* **20**:97–99 (Jan. 1999).
18. J. Huang, Capabilities of printed reflectarray antennas, *Proc. IEEE Symp. Phased Array System and Technology*, Boston, Oct. 1996, pp.131–134.
19. D. M. Pozar, S. D. Targonski, and R. Pokuls, A shaped-beam microstrip patch reflectarray, *IEEE Trans. Anten. Propag.* **47**:1167–1173 (July 1999).
20. J. A. Encinar, Design of two-layer printed reflectarray using patches of variable size, *IEEE Trans. Anten. Propag.* **49**:1403–1410 (Oct. 2001).
21. J. Huang, V. A. Fera, and H. Fang, Improvement of the three-meter Ka-band inflatable reflectarray antenna, *Proc. IEEE AP-S/URSI Symp.*, Boston, July 2001, pp. 122–125.
22. M. Bialkowski, A. W. Robinson, and H. J. Song, Design, development, and testing of X-band amplifying reflectarrays, *IEEE Trans. Anten. Propag.* **50**:1065–1076 (Aug. 2002).
23. R. E. Zich, M. Mussetta, M. Tovaglieri, P. Pirinoli, and M. Orefice, Genetic optimization of microstrip reflectarrays, *Proc. IEEE AP-S/URSI Symp.*, San Antonio, TX, June 2002, pp. III-128–III-131.
24. B. Khayatian and Y. Rahmat-Samii, Characterizing reflectarray antenna radiation performance, *Proc. IEEE AP-S/URSI Symp.*, Columbus, OH, June 2003 (in press).
25. C. Han, B. Strassner, K. Chang, and J. Huang, A dual-frequency 7/32 GHz reflectarray antenna, *Progress in Electromagnetics Research Symp.* (PIERS), Honolulu, Oct. 2003 (in press).
26. M. Zawadzki and J. Huang, A dual-band reflectarray for X- and Ka-bands, *PIERS Symp.*, Honolulu, Oct. 2003 (in press).
27. W. Menzel, D. Pilz, and M. Al-Tikriti, Millimeter-wave folded reflector antennas with high gain, low-loss, and low profile, (feature article), *IEEE Anten. Propag. Mag.* **44**(3):24–29 (June 2002).
28. D. Pozar, S. D. Targonski, and H. D. Syrigos, Design of millimeter wave microstrip reflectarrays, *IEEE Trans. Anten. Propag.* **45**:287–296 (Feb. 1997).
29. E. Girard, R. Moulinet, R. Gillard, and H. Legay, An FDTD optimization of a circularly polarized reflectarray unit cell, *Proc. IEEE AP-S/URSI Symp.*, San Antonio, TX, June 2002, pp. III-136–III-139.
30. J. Huang, *Analysis of a Microstrip Reflectarray Antenna for Microspacecraft Applications*, JPL TDA Progress Report 42-120, Feb. 15, 1995.
31. H. Fang, M. Lou, J. Huang, L. M. Hsia, and G. Kerdanyan, An inflatable/self-rigidizable structure for the reflectarray antenna, *Proc. 10th European Electromagnetic Structure Conf.*, Munich, Germany, Oct. 2001.
32. R. Hodges and M. Zawadzki, *Wide Swath Ocean Altimeter Antenna Electrical Subsystem—Preliminary Design Review*, JPL internal document, Jan. 2003.

REFLECTOMETERS, TIME-DOMAIN

ANDREW RUSEK
Oakland University
Rochester, Michigan

1. INTRODUCTION

Time-domain reflectometry is a measurement technique applied to determine the location, type, and quantitative character of discontinuities distributed in signal transmission channels such as computer or telephone networks, printed circuit boards, or other systems where signal delays are observed. Testing such systems, called *devices under test* (DUT), with TDR involves use of a fast pulse generator along with a *sampling oscilloscope* [11] and test fixture. Signals generated by the pulse generator are sent through the test fixture to the DUT. The most popular testing signal generated in broadband TDR systems is a steplike voltage. The signals are registered at the input to the *test fixture* by means of a sampling oscilloscope with coherent sampling, time transformation, and a track-and-hold vertical deflection system. Such a device allows the display of very small levels of reflected signals on the top of high levels of applied signals with minimal distortion.

TDR techniques can be enhanced when not only the input terminals of the DUT but also the output terminals are accessible by the oscilloscope. Measurements made from the output terminals, often called time-domain transmission (TDT) tests, include propagation delay and a pulse transmission function. Transmission tests can also

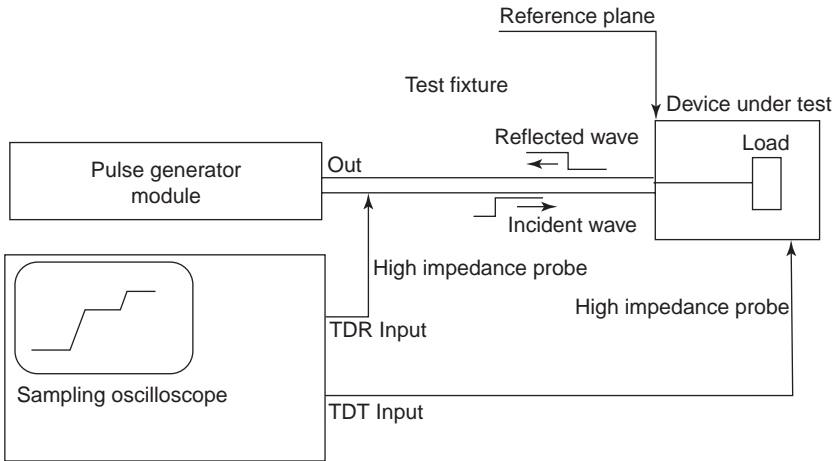


Figure 1. Block diagram of a time-domain reflectometer with time-domain transmission.

show the effects of mutual coupling between adjacent transmission channels, such as printed circuit board (PCB) traces.

In the article, the TDR measurement techniques are described, including basic properties and limitations of a real system such as finite risetime of the pulses, smooth transitions, small overshoots, jitter, and noise. Major examples demonstrated here include tests of the following:

- Resistance
- Capacitance
- Inductance
- Transmission-line characteristic impedance
- Inserted discontinuities of inductive, capacitive, and mixed types
- Differential and common-mode transmission-line impedances

In addition, effects of *transmission-line losses* and processes for correcting TDR test channel distortions are described. SPICE simulations are frequently used in conjunction with TDR measurements to enhance identification of characteristics related to the discontinuities [10,14,15]. The results of PSPICE simulations, included here to illustrate the normalization processes, are based on a demonstration version of this program [16]. The last part of the article demonstrates practical applications of TDR/TDT systems [3,4,16,17].

1.1. Applications of Time-Domain Reflectometry/ Time-Domain Transmission

TDR/TDT systems have found use in both electrical and nonelectrical areas. The following list includes a number of the most popular applications [1,9,12]:

1. Conductor length and return loss determination
2. Finding short and open connections in cables
3. Location of bad splices, loose connectors, and crimps
4. Location of moisture and water in cables
5. Measurement of cable parameters, such as characteristic impedance, losses, and propagation velocity
6. Determining signal integrity, and performing failure analysis of printed circuit boards used in high-speed digital and analog circuits
7. Evaluation of microstrip connections
8. Computer network cable tests
9. Characterization of integrated circuit packages
10. Sensing liquid levels

2. TIME-DOMAIN REFLECTOMETRY PRINCIPLES

2.1. Basic TDR/TDT Systems

A functional block diagram of a TDR/TDT is shown in Fig. 1. The step generator signal is transmitted through a test fixture such as transmission line (Fig. 2), and is finally

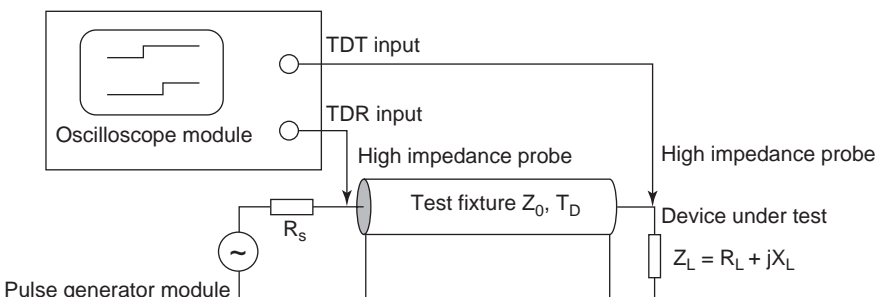


Figure 2. Impedance tests with a 50-Ω transmission-line test fixture.

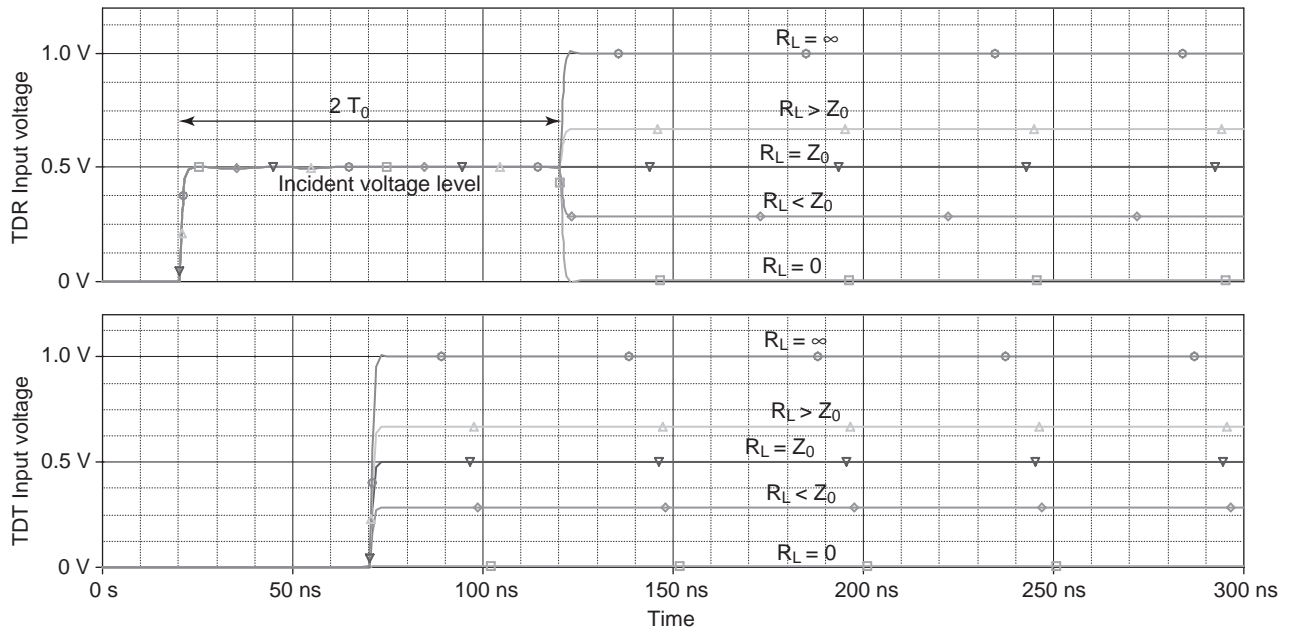


Figure 3. Displays demonstrating TDR and TDT input voltages for various resistances connected to a 50-Ω line test fixture. (This figure is available in full color at <http://www.mrw.interscience.wiley.com/erfme>.)

applied to the device or system under test (DUT). The test fixture impedance is usually matched to that of the generator. If the DUT impedance is not equal to the characteristic impedance of the transmission line of the test fixture, part of the incident voltage is reflected from the DUT. The reflected signal, which is delayed in relation to the incident voltage, appears as a step change on top of the

incident wave. The location of the impedance discontinuity d can be calculated from the transit time measured from the reflection and the reference point, marked from the front edge of the incident voltage signal

$$d = \frac{v_p \cdot t_d}{2} \tag{1}$$

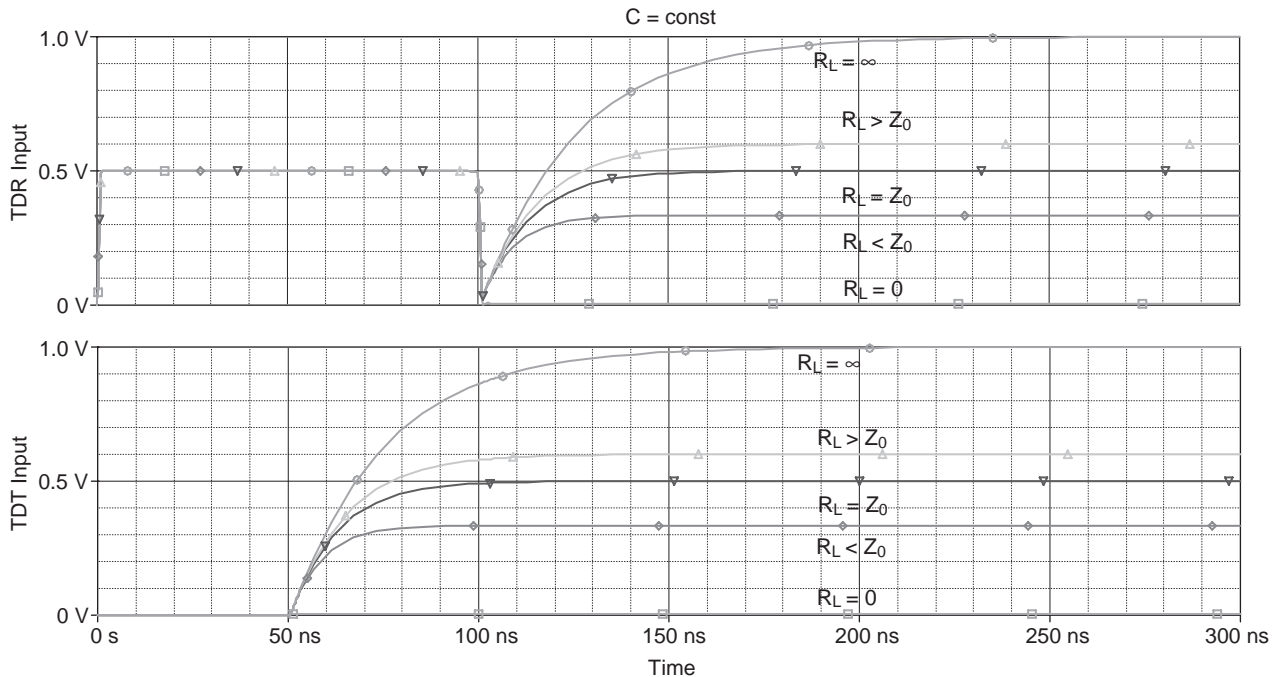


Figure 4. TDR input and TDT input voltages for parallel $R_L C$ loads of the 50-Ω transmission-line test fixture. (This figure is available in full color at <http://www.mrw.interscience.wiley.com/erfme>.)

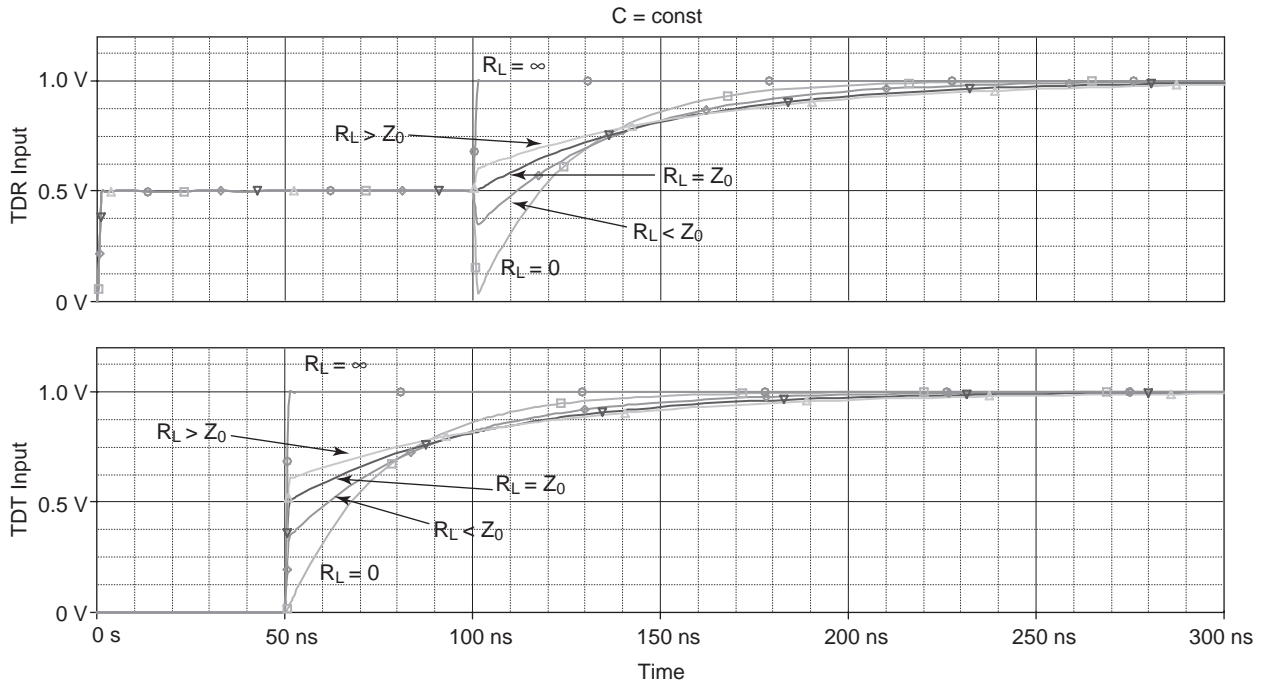


Figure 5. TDR input and TDT input voltages for series $R_L C$ loads of the 50- Ω transmission-line test fixture. (This figure is available in full color at <http://www.mrw.interscience.wiley.com/erfme>.)

where v_p is a wave propagation velocity and t_d is the transit time.

Figure 3 shows the voltages observed in a TDR/TDT system when the transmission line of the test fixture is matched to the source and the signals are reflected from pure resistive loads. The voltage amplitude reflected from the DUT, divided by the amplitude of the incident wave, determines the reflection coefficient at the load ρ_L . When an unknown resistance is connected to the source-matched transmission line, the value of the resistance

can be calculated as follows:

$$Z_L = Z_0 \left(\frac{1 + \rho_L}{1 - \rho_L} \right) \tag{2}$$

This equation is applied in the TDR/TDT internal processor to calculate the load parameters [15,16] (see also PSPICE simulations of differential TDR/TDT, Figs. 15 and 17). Figures 4–7 illustrate the voltage waveforms when the load of the test fixture (transmission line) is a

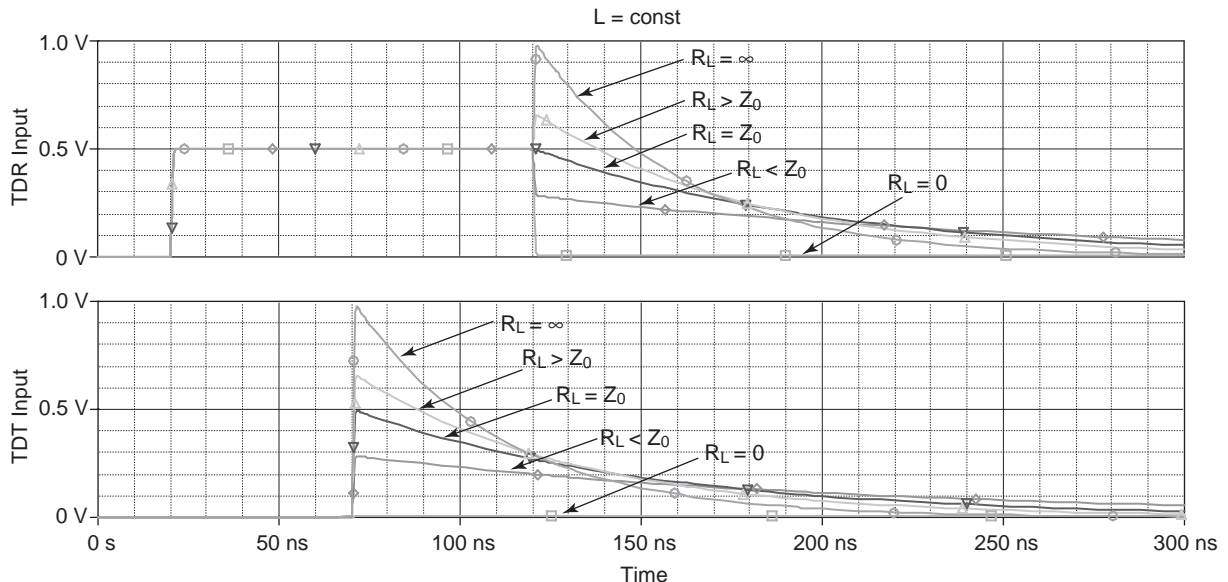


Figure 6. TDR input and TDT input voltages for parallel $R_L L$ loads of the 50- Ω transmission-line test fixture. (This figure is available in full color at <http://www.mrw.interscience.wiley.com/erfme>.)

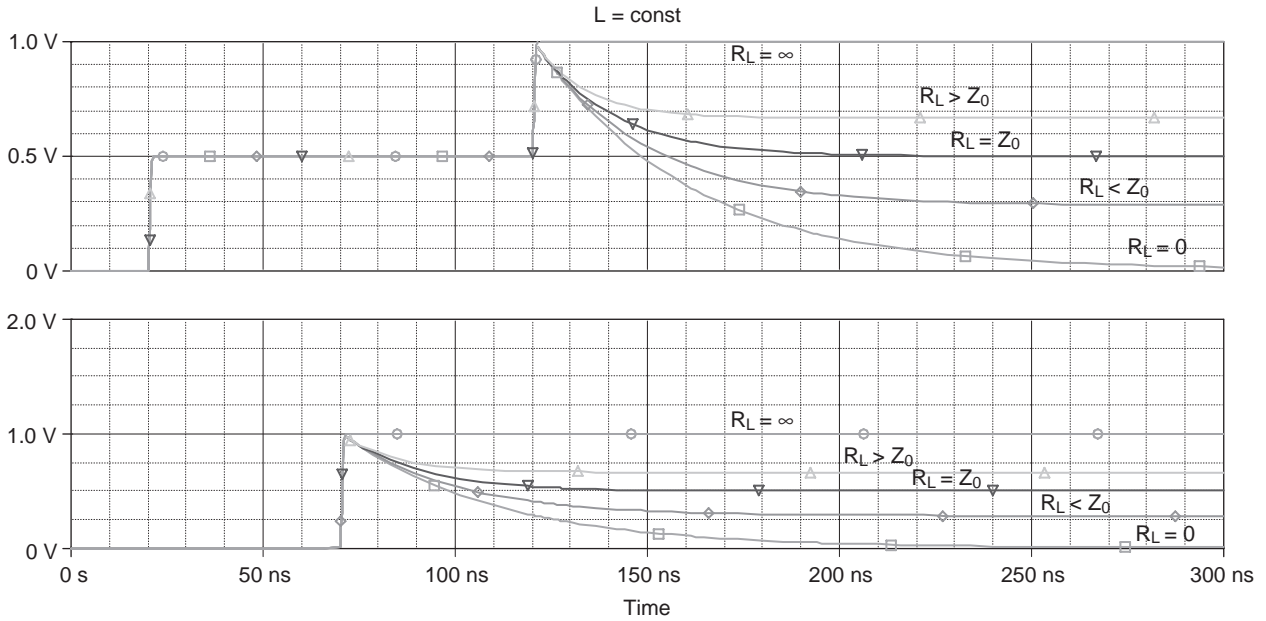


Figure 7. TDR input and TDT input voltages for series $R_L L$ loads of the 50- Ω transmission-line test fixture. (This figure is available in full color at <http://www.mrw.interscience.wiley.com/erfme>.)

combination of either resistance and capacitance, or resistance and inductance. In all cases shown, the load resistance is varied and either C or L is maintained constant. From steady-state voltage levels following the reflection, as well as from the shapes of the waves themselves, which reveal the time constant, it is possible to identify the character of the load and the values of unknown components. With this information, the parameters of the equivalent circuits representing the load can be evaluated from the equations listed in Table 1.

The waves that have been presented so far show the behavior of short transmission lines in which the losses, which are due largely to the skin effect, are negligible. In longer transmission lines the distributed losses distort the signals traveling along the lines. Examples of transmitted and reflected waves in a short terminated transmission line are shown in Fig. 8. For comparison, a lossless case is included. From these waveforms, it is possible to determine changes of the transmission-line resistance over the length of the cable.

Practical transmission channels in PCBs with packages of the integrated circuits may have longer connecting leads inserted between some sections of transmission lines or larger conductive surfaces shunting the signal. The TDR/TDT tests for such cases can be modeled as shown in Fig. 9. Two examples of the waveforms in these circuits are illustrated in Figs. 10 and 11.

2.2. Sources of Error

Three major sources of error are encountered in TDR/TDT tests:

1. Cables and connectors of the test fixture [2,6,7].
2. Oscilloscope

3. Test generator

Cables and connectors connecting the generator with the tested device introduce their own *reflections*, in addition to the reflections caused by the tested device (DUT). They also introduce distributed losses, which increase at higher frequencies. This reduces the speed of transition of generator pulses.

Oscilloscopes introduce two types of error. One is caused by bandwidth limitation, which leads to the “smoothing” of fast voltage transitions. The other type of

Table 1. Parameters of Equivalent Circuits Representing Load in Basic TDR/TDT Systems

Voltage Level for $t \rightarrow \infty$	Circuit Time Constant
For parallel connection of R_L and C_L	
$V_{in}(\infty) = \frac{R_L}{R_L + R_S} V_{source}$	$\tau = \frac{R_L \cdot R_S}{R_L + R_S} C_L$
For series connection of R_L and C_L	
$V_{in}(\infty) = V_{source}$	$\tau = (R_L + R_S) C_L$
For parallel connection of R_L and L_L	
$V_{in}(\infty) = 0$	$\tau = \frac{L_L(R_S + R_L)}{R_S \cdot R_L}$
For series connection of R_L and L_L	
$V_{in}(\infty) = \frac{R_L}{R_L + R_S} V_{source}$	$\tau = \frac{L_L}{R_S + R_L}$

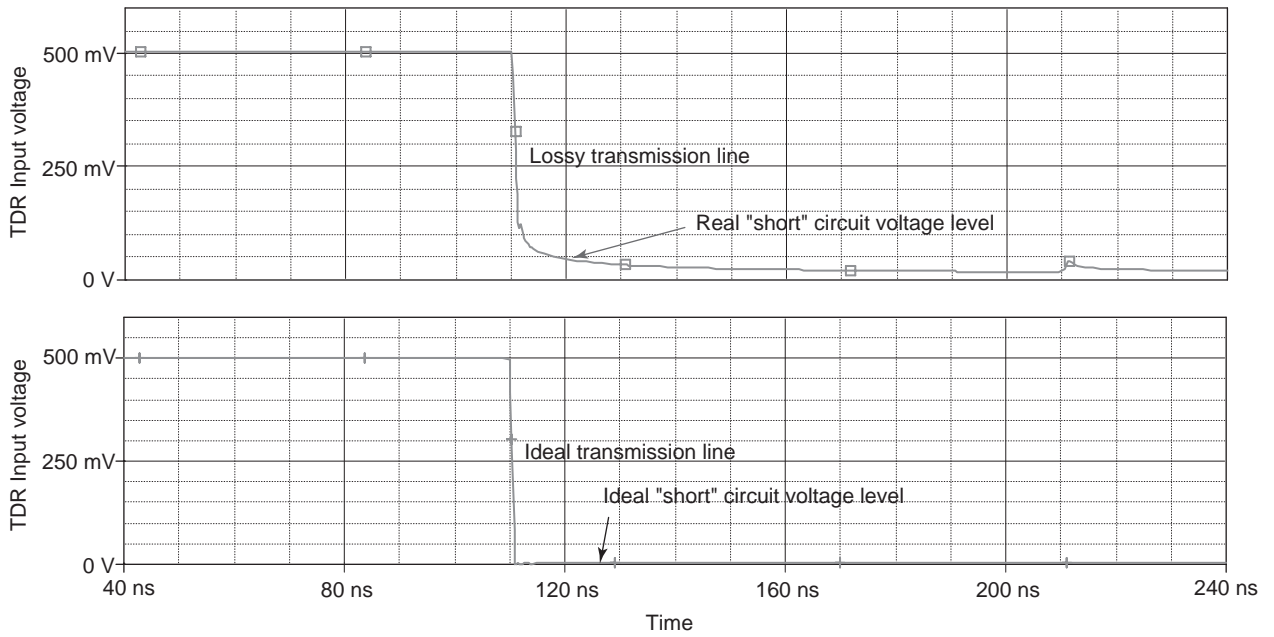


Figure 8. Reflected waves in short-ended transmission lines: (a) real transmission line; (b) ideal transmission line. (This figure is available in full color at <http://www.mrw.interscience.wiley.com/erfme>.)

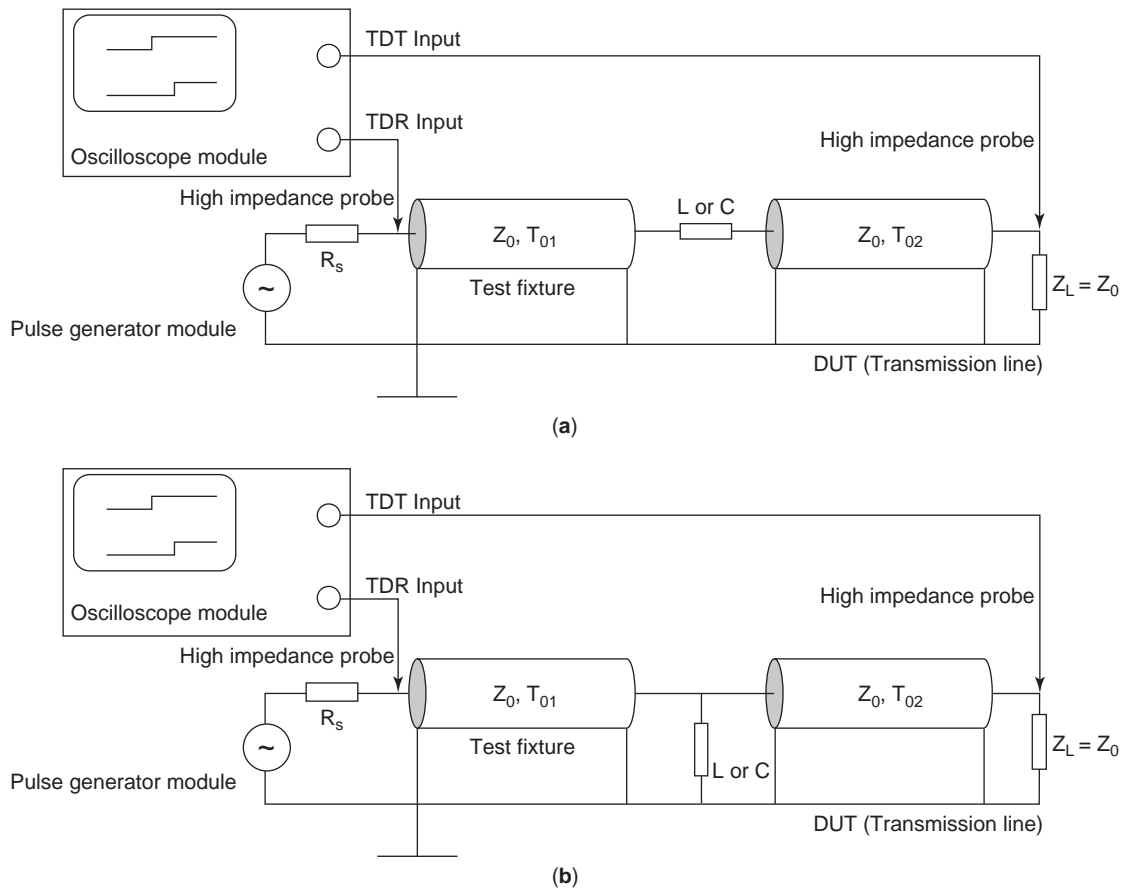


Figure 9. TDR/TDT tests of inserted reactance with a 50- Ω transmission-line test fixture: (a) series resistance; (b) parallel reactance.

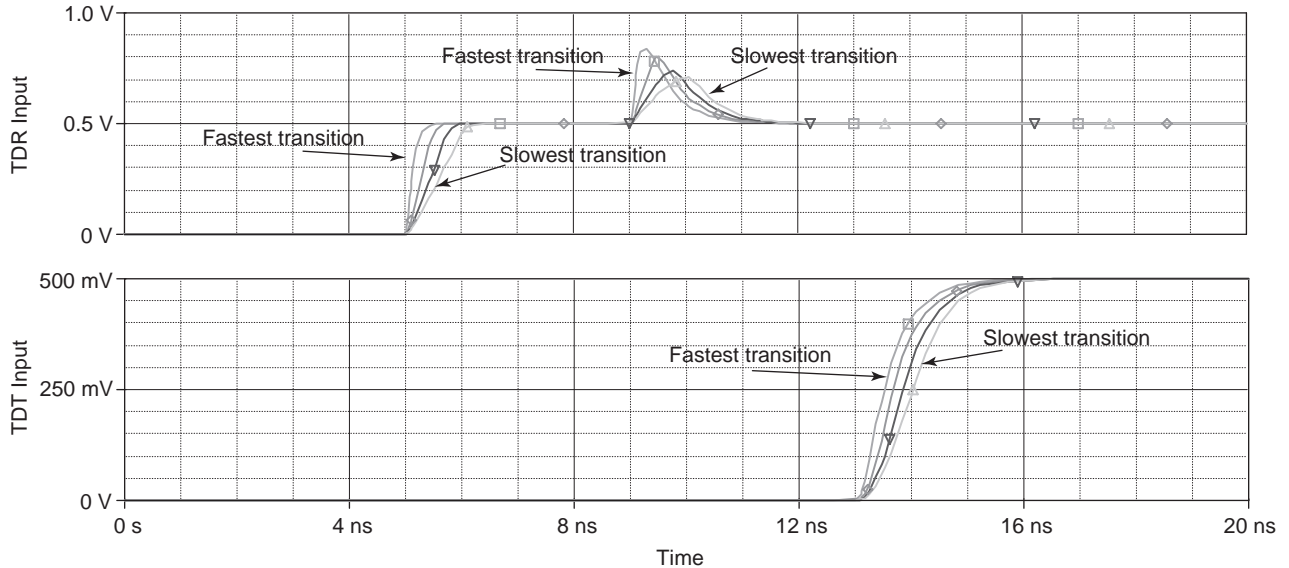


Figure 10. TDR and TDT input voltages for the system with an inductor inserted between transmission lines. Risetime of the input pulses is varied to show the distortion levels. (This figure is available in full color at <http://www.mrw.interscience.wiley.com/erfme>.)

errors includes coupling of the trigger channel into signal channel, interchannel interference, and input circuit mismatches to the test fixture [2,6,7].

Real testing pulses of TDR/TDT pulse generators have finite risetimes, and their top parts are not ideally flat. Some generators may produce pulses with overshoots. Associated with both the sampling oscilloscope and the generator are the errors caused by both jitter and noise. All these distortions limit TDR/TDT system resolution and make the observed waves more difficult to analyze, especially when the TDR/TDT system is used to test closely located small discontinuities of the transmission channel.

2.3. Corrections of Measurement Errors

Error correction can be effectively performed using internal signal processors built into modern TDR/TDT systems. One of the simplest methods of error correction is waveform subtraction. The method could be used to minimize errors common to both the tested device and the reference, such as trigger and *channel crosstalk errors*, and reflections from the test fixture and connectors. In the process of measurement, the common reference device is connected to the end of the test fixture. The test results in terms of the TDR input voltage are stored and the reflected part of this wave is computed. This reflected wave is then

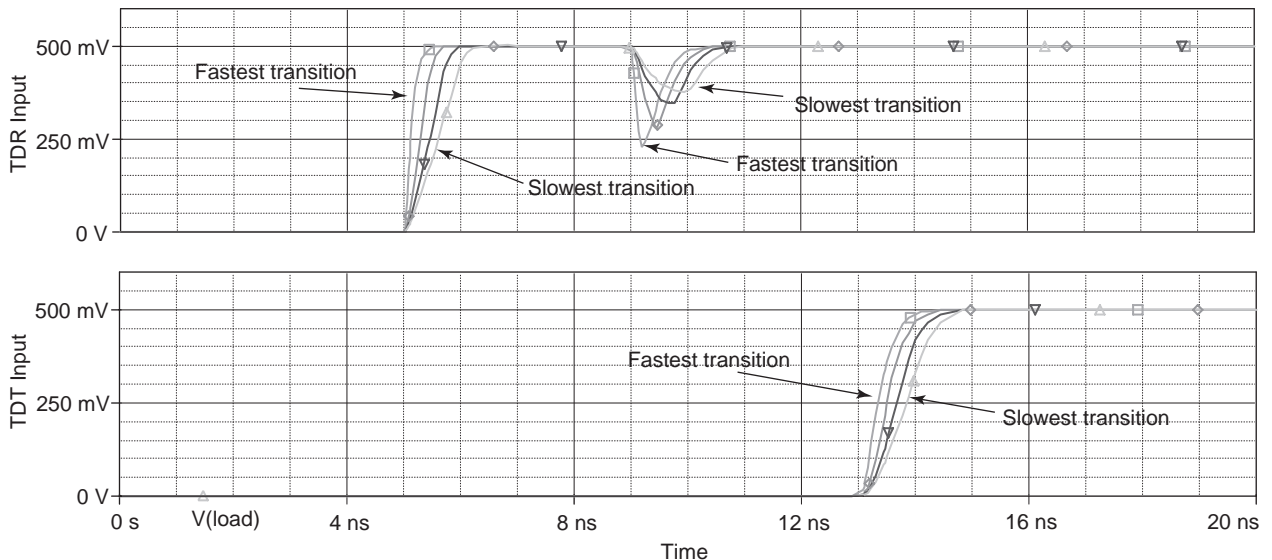


Figure 11. TDR and TDT input voltages for the system with a capacitor connected to the ground between transmission lines. Risetime of the input pulses is varied to show the distortion levels. (This figure is available in full color at <http://www.mrw.interscience.wiley.com/erfme>.)

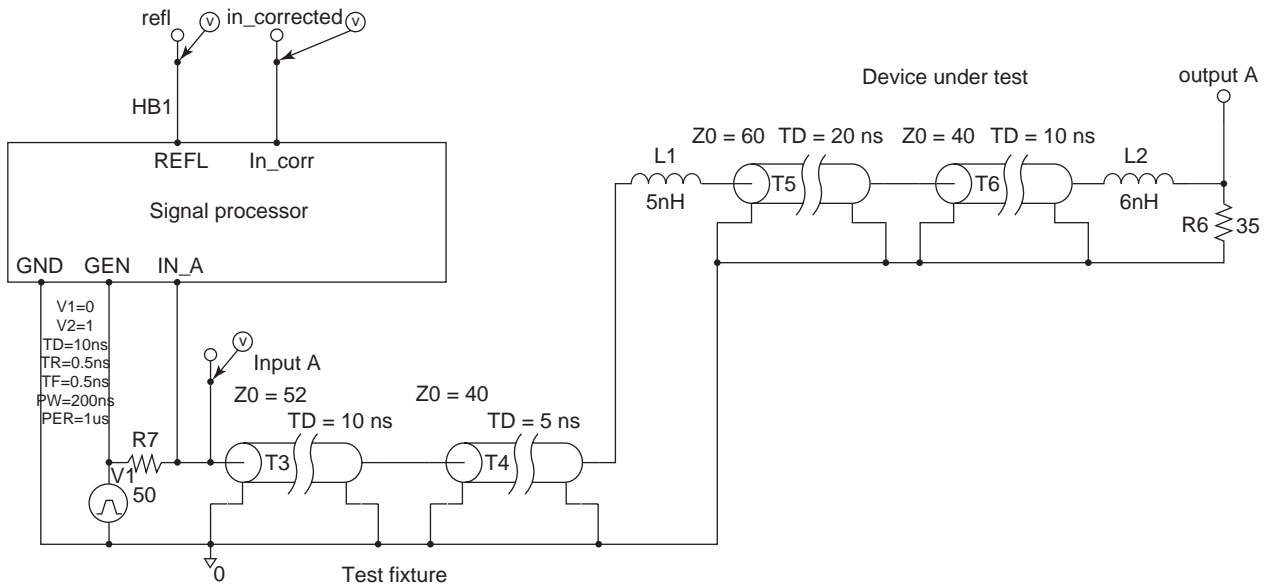


Figure 12. Simulated TDR/TDT system with imperfect test fixture.

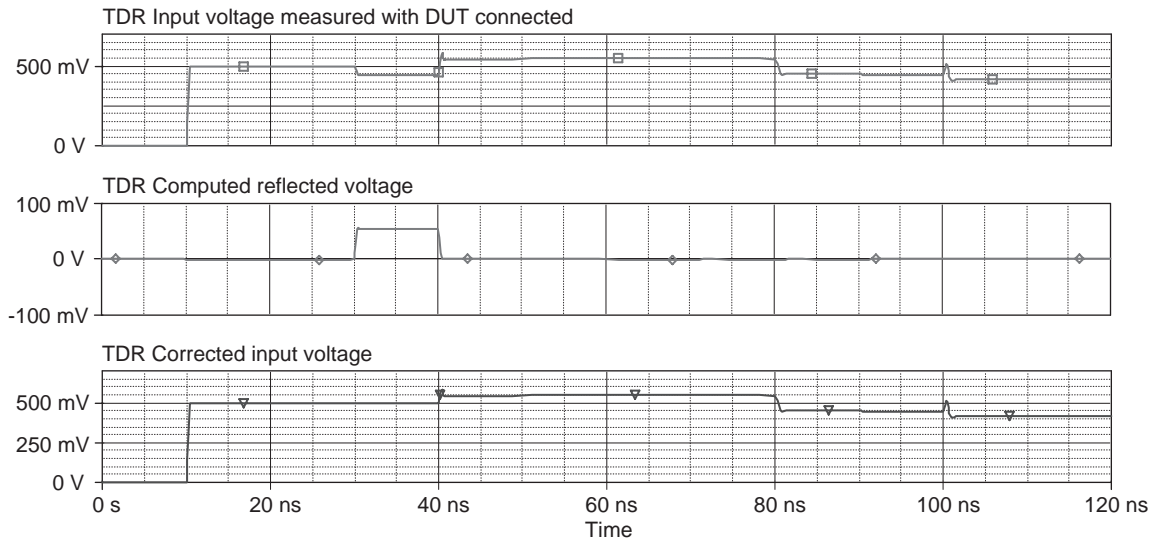


Figure 13. SPICE simulation results showing the effects of an imperfect test fixture and correction of its effect by subtraction. (This figure is available in full color at <http://www.mrw.interscience.wiley.com/erfme>.)

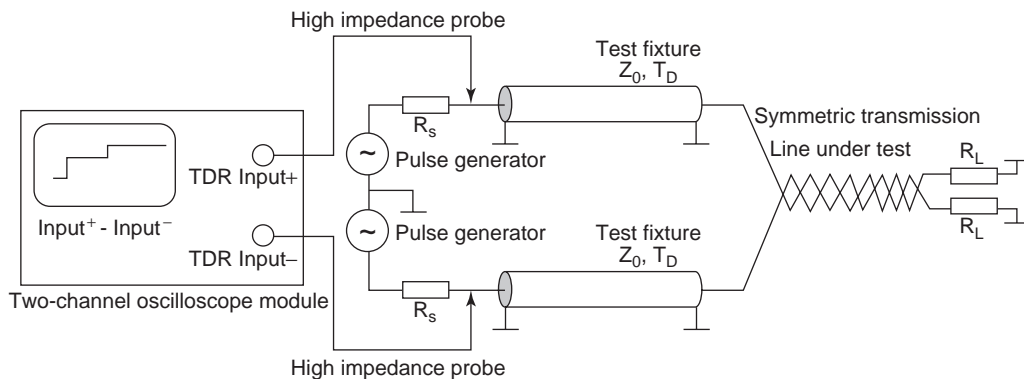


Figure 14. Differential impedance tests with a 50- Ω transmission-line test fixture.

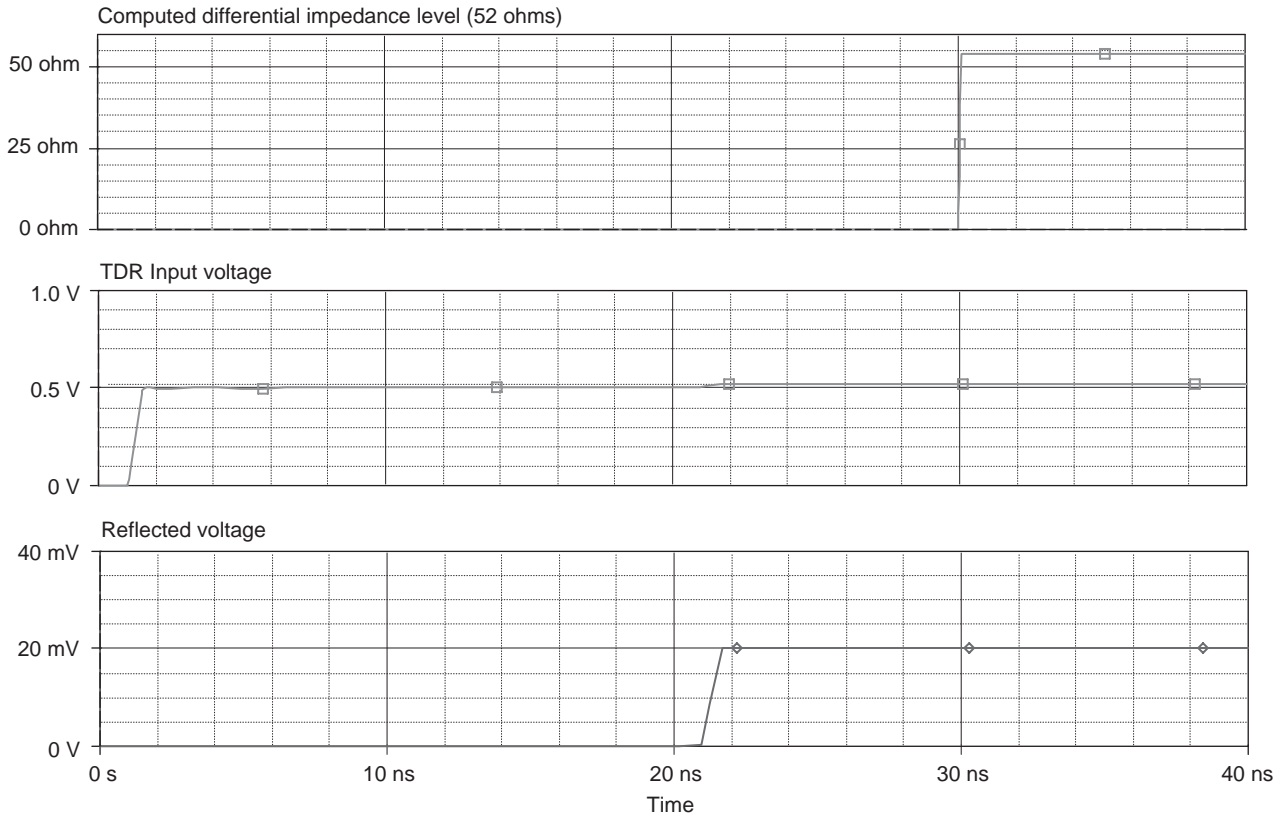


Figure 15. DTDR input, reflected voltages, and calculator output illustrating differential impedance measurement. (This figure is available in full color at <http://www.mrw.interscience.wiley.com/erfme>.)

subtracted from the input voltage obtained in the second phase of the measurements when the DUT is connected. The results of this procedure are limited to the specific risetime of the system. For instance, faster pulses reveal more discontinuities, which may not be important in particular applications.

The waveform subtraction method is illustrated by means of PSPICE simulations (PSPICE is a PC version

of SPICE). Figures 12 and 13 show the process of compensation for errors introduced by the test fixture composed of two transmission-line sections, T3 and T4. The characteristic impedances of these lines are 52 and 40 Ω, respectively. The device under test (DUT) is a connection of two transmission lines, two inductances and one resistor (L1, T5, T6, L2, and R6). Initially, the matching resistor (50 Ω) is connected to the end of the test fixture. Then,

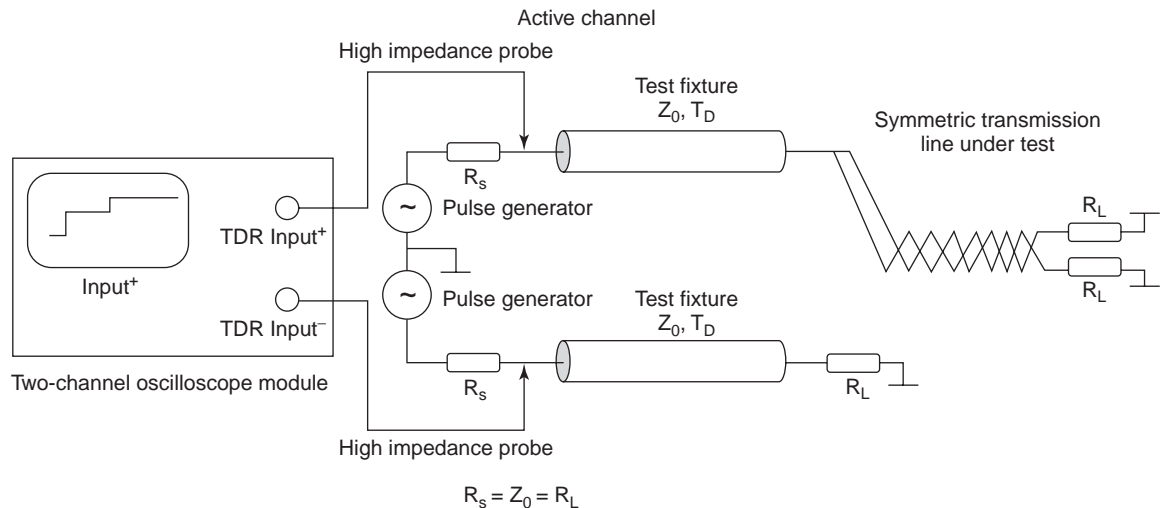


Figure 16. Single-channel measurement of a common-mode impedance with a 50-Ω transmission-line test fixture.

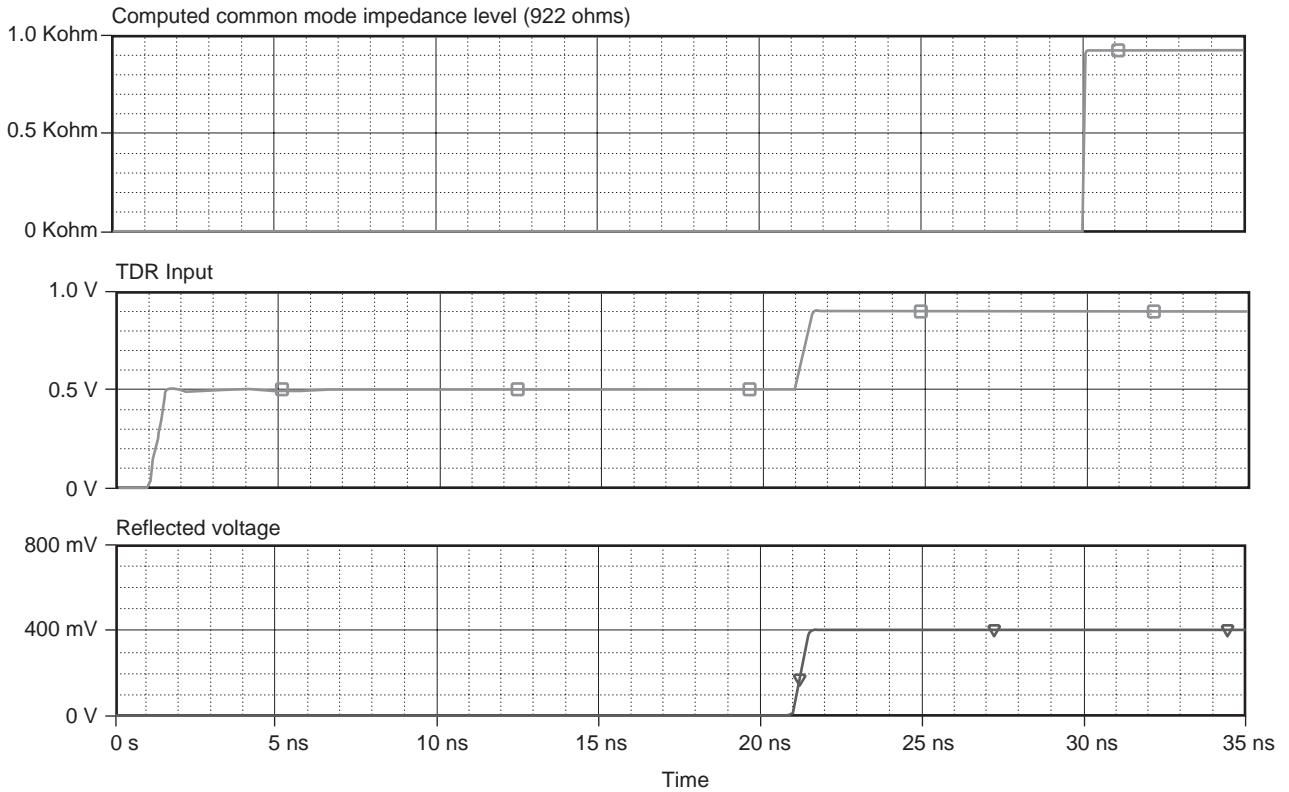


Figure 17. TDR measurement of common-mode impedance of symmetric transmission line. (This figure is available in full color at <http://www.mrw.interscience.wiley.com/erfme>.)

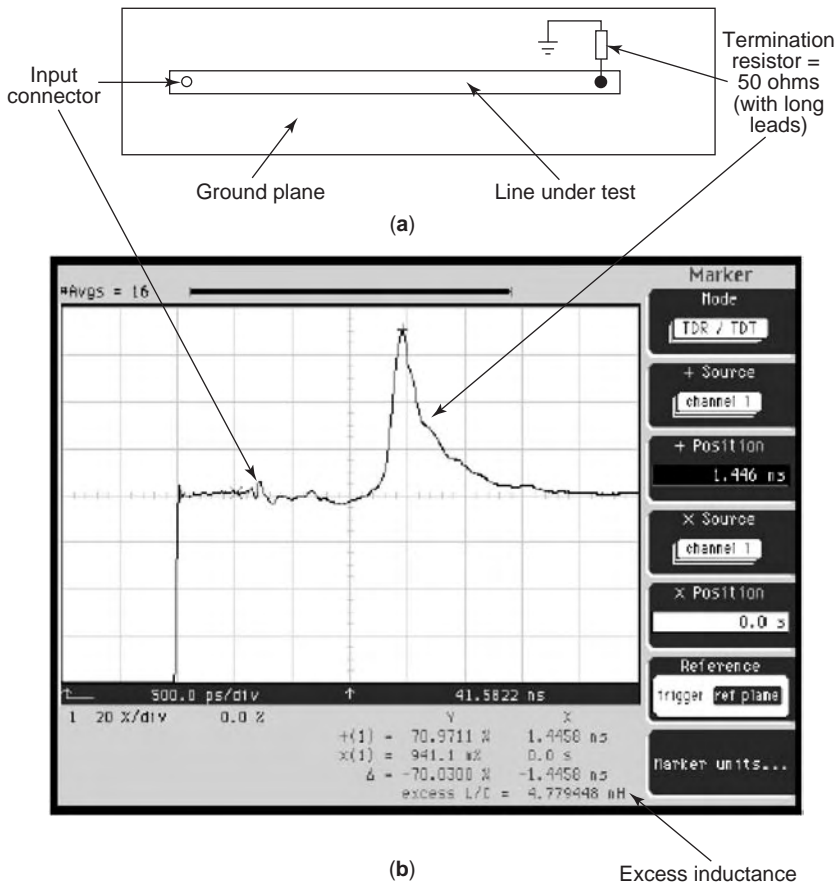


Figure 18. Effects due to termination resistor leads: (a) microstrip; (b) expanded TDR waveform (reprinted with permission of Agilent Technologies). (This figure is available in full color at <http://www.mrw.interscience.wiley.com/erfme>.)

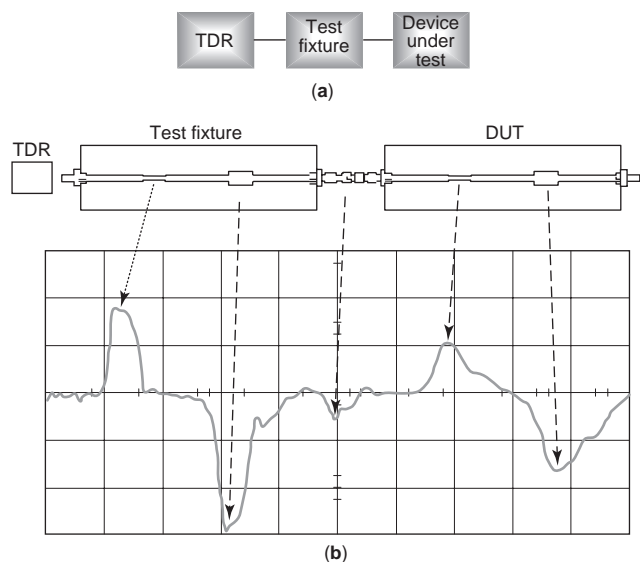


Figure 19. TDR measurements with the DUT at the end of imperfect test fixture: (a) block diagram; (b) unnormalized measurement results showing the effects of the test fixture (reprinted with permission of Agilent Technologies).

the calculated reflected waves are subtracted from the results of final tests while the DUT is connected. In the simulations, the calculations are performed in a parallel manner so the 50-Ω tests are done internally, inside the processing box. When the test fixture reflections can be isolated in time from the DUT reflections, it is possible to process the latter signals by windowing and creating corresponding impedance profiles [16]. It is still necessary to calibrate the test fixture with the reference device connected to the end of the test fixture as in the waveform subtraction method described earlier.

A significant reduction of the TDR/TDT system errors caused by the pulse generator speed limits can be achieved in a TDR/TDT system that takes advantage of digital signal processing called *normalization* [3,4]. The normalization process refers the measurement results to a test signal with a predefined risetime [5]. The measurement results are enhanced by digital filtering to boost high-frequency components of the processed signals. In this way,

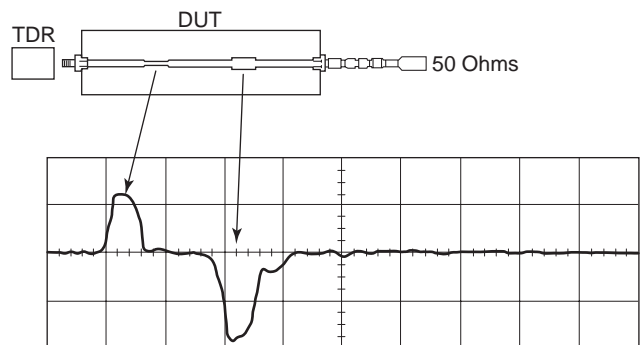


Figure 20. The unnormalized response of the DUT, measured without the test fixture (to demonstrate the results of normalization) (reprinted with permission of Agilent Technologies).

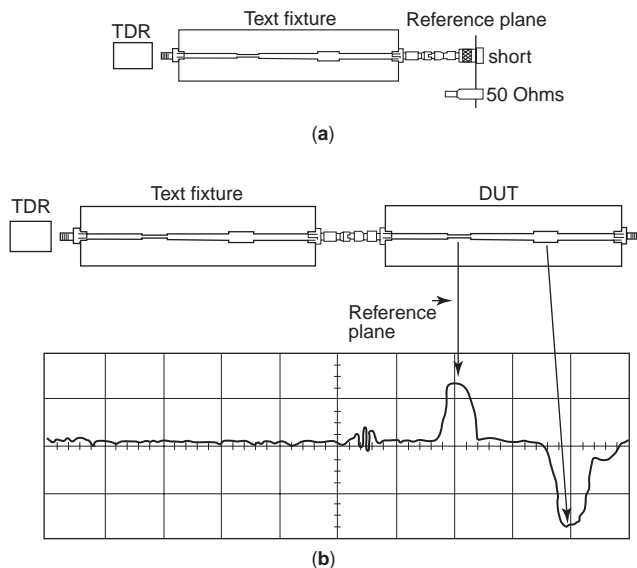


Figure 21. Normalized calibration that uses a short, then a 50-Ω termination to define a reference plane and generate a digital signature (filter): (a) circuit with the test fixture; (b) corrected measurements (reprinted with permission of Agilent Technologies).

the results of measurements can be enhanced as if the tests were performed in a faster TDR/TDT system [7].

2.4. TDR/TDT System Limitations

Most high-frequency TDR/TDT systems have been designed to investigate circuits whose impedance levels are close to 50 Ω. According to Ref. 2, 50-Ω systems are sufficiently accurate (<0.5% error) to measure load resistances or transmission-line characteristic impedances above 10 Ω. Testing changes of impedances or impedance profiling along the transmission channel, the lowest limit is 30 Ω to maintain errors below 1% [13].

The effects of the finite risetime of the TDR/TDT system limit the spatial resolution of the TDR measurements. The minimum distance that separates two consecutive discontinuities can be expressed as

$$\Delta d = \frac{c}{\sqrt{\epsilon_r}} \frac{t_r}{4} \tag{3}$$

where t_r is the system risetime, c is the open-space wave velocity, and ϵ_r is the relative dielectric constant of the transmission-line dielectric [3]. For instance, if the risetime is 20 ps and the relative dielectric constant is 2, then the minimum distance between two consecutive discontinuities is about 1 mm. This expression must be modified when the *jitter* is present in the measurement system. The jitter error has the same effect as if the equivalent risetime of the system had increased, thus reducing the spatial resolution.

System noise reduces the ability of TDR to detect small reflection amplitudes. Oscilloscope noise can reach the level of one division corresponding to maximum sensitivity of the scope (about 1 mV per division). Assuming that

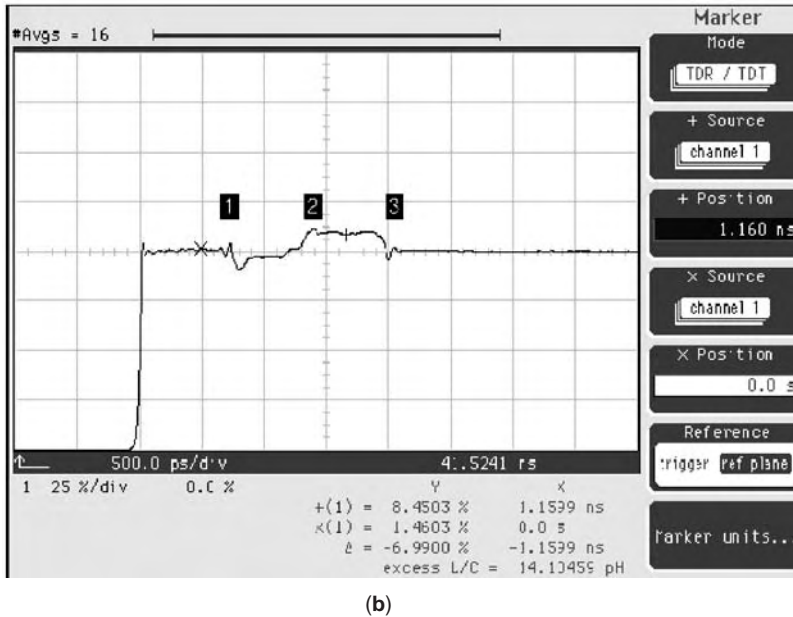
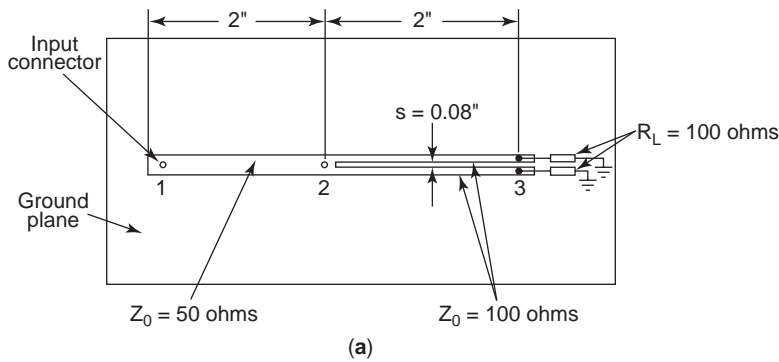


Figure 22. Example of the crosstalk in a hybrid power divider: (a) microstrip circuit; (b) expanded TDR waveforms (reprinted with permission of Agilent Technologies).

the incident pulse observed has an amplitude of 100 mV, reflection coefficients as small as 0.01 can be registered without major corruption caused by the noise. Better results can be achieved when analog smoothing or digital filtering is applied.

2.5. Differential Time-Domain Reflectometry

Differential time-domain reflectometry (DTDR) and reflectometers have been used to investigate symmetric transmission channels or lines such as *twisted-pair* or *slotted striplines* [8,14]. In DTDR systems, two pulses of opposite polarity are generated and applied to the tested symmetric DUT. Figure 14 shows a general block diagram for such a system. The *differential-mode impedance* can be determined from the reflections related to the differential input voltage, as shown in Fig. 15. The basic calculations are performed by the system processor, based on Eq. (2), and the results are displayed. *Common-mode impedance* can be also measured by using a single channel of the DTDR system (Fig. 16). The results obtained from Eq. (2) are multiplied by 2 if both transmission-line conductors are tested, as shown in Fig. 17. A drawback of differential TDR systems is that they require good pulse alignment.

The errors introduced by misalignment can be reduced by means of normalization processes [8].

3. EXAMPLES OF TDR/TDT TESTS AND TDR/TDT APPLICATIONS

3.1. TDR/TDT Test Examples

The following examples demonstrate the results of practical tests performed by a TDR/TDT measurement system [3,4]. Figure 18 shows the reflections observed when a long-lead resistor is connected to the end of a 50-Ω microstrip test fixture. The results from the measurement are displayed below the waveform. For example, the inductance of the resistor leads is 4.779448 nH, as the display shows. The next group of figures (Figs. 19–21) illustrate the process of normalization for a complex DUT. The test fixture was purposely selected to show the effectiveness of the normalization processes. The presence of the test fixture, which is normally used to delay unknown reflections with respect to the front of the test pulse, introduces visible signal distortions. The corrected measurements are shown in the last figure of this group. Normalization corrects for the effects of the test fixture and enhances the

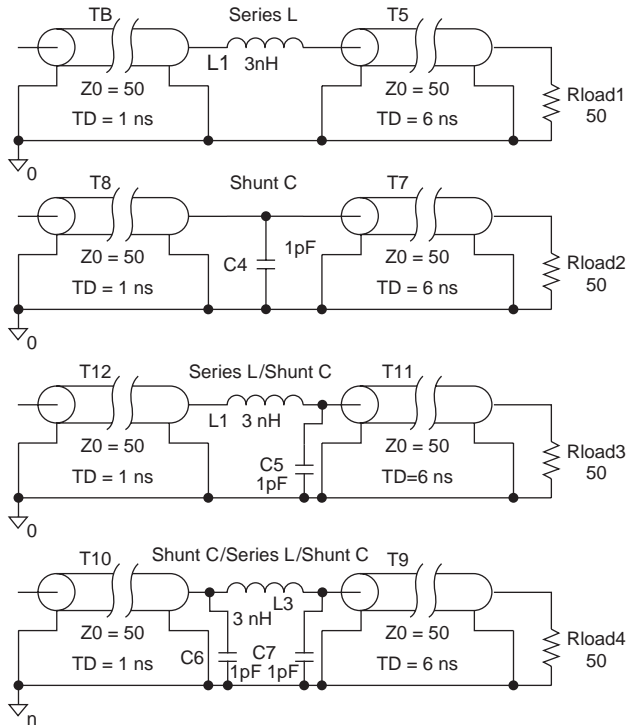


Figure 23. Typical examples of discontinuities represented in terms of lumped components.

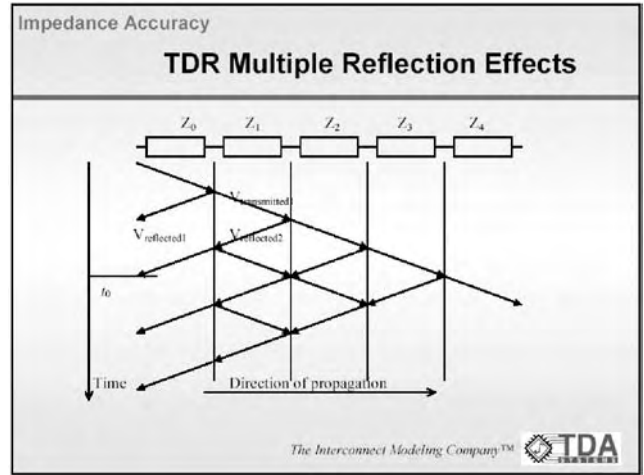


Figure 25. Bounced diagram for a cascade of transmission lines with different impedances (reproduced with permission of TDA Systems).

final reflections by shaping the reflections from the tested load as if faster testing pulses had been applied.

Figure 22 portrays the results from tests involving a hybrid power divider. The interaction between the two transmission-line branches introduces a crosstalk signal at point 2 of the tested board. The first reflection (point 1),

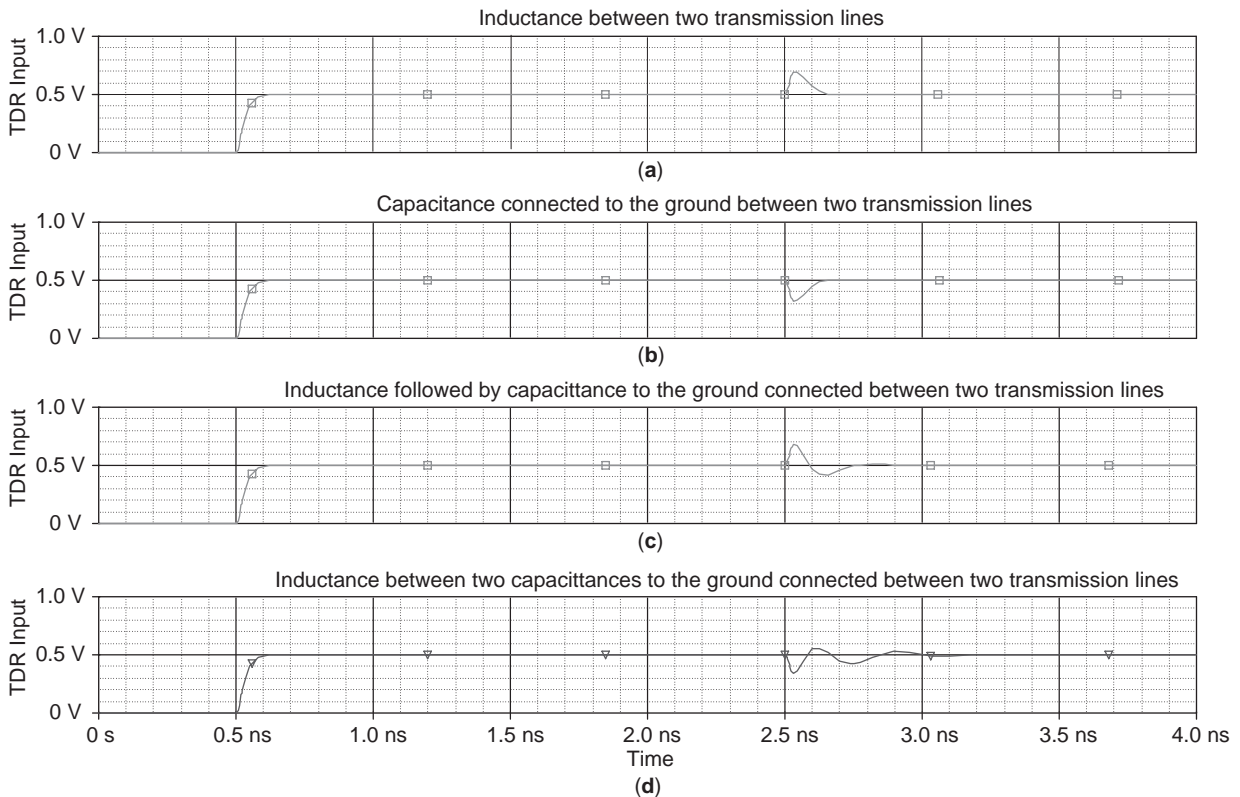


Figure 24. TDR input voltages observed in the circuit with two transmission lines and a reactance circuit inserted between them: (a) inductance between two transmission lines; (b) capacitance connected to the ground between two transmission lines; (c) inductance between two capacitances to the ground connected between two transmission lines. (This figure is available in full color at <http://www.mrw.interscience.wiley.com/erfme>.)

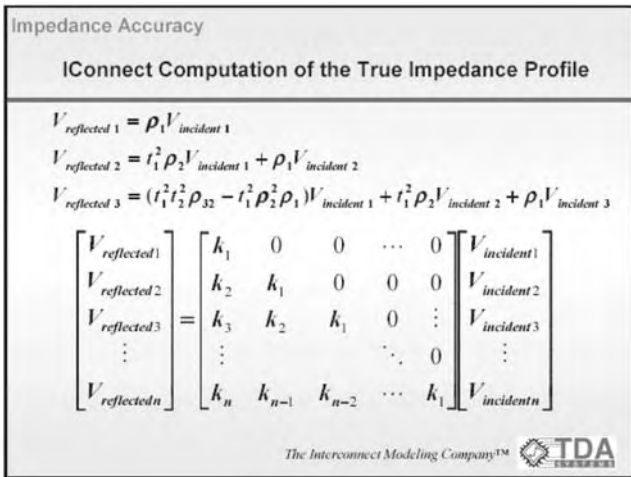


Figure 26. Expressions used to calculate the “true impedance profile” from the “raw impedance profile” using TDR input voltage levels (reproduced with permission of TDA Systems).

with its level below the centerline of the scope screen, suggests that the initial, single section of the transmission line has a characteristic impedance greater than the impedance of the test fixture. The end terminations of the hybrid power divider introduce very small reflections due to lead inductances of the two resistors.

3.2. Application of TDR/TDT to Investigate Signal Integrity of High-Speed Circuits

Recently, increased data rates in communication and computer systems, often reaching subnanosecond switching

speed, have created a need to introduce several gigabit standards and relate to them measurement methods. Conducting traces of the printed circuits, packaging connections, board connectors, and the connection of shorter or longer cables can degrade the *signal integrity* of the systems due to reflections, crosstalk, radiation, and losses in conductors and dielectrics. Application of the TDR/TDT measurement technique, combined with effective computer modeling, can help test the signal integrity of such systems during the initial design of circuit interconnections [16,17]. Figure 23 shows the composition for typical discontinuities connected between two sections of transmission lines, and Fig. 24 presents the corresponding TDR responses, which serve as basic signatures to help identify the types of discontinuities, find their structure, and, finally, determine the values of equivalent components.

In many practical systems, the TDR images are very complex because of the effects of *multiple reflections* caused by many discontinuities within the signal transmission channels. In such cases, hardware measurements can be enhanced by means of a computational method known as the *inverse scattering algorithm*, which was developed by TDA Systems Company [16,17]. To use such a technique, the *raw profile* of impedance is calculated from the input voltage data. Then the incident wave is computed from a reference TDR signal when a well-defined termination such as a short or open circuit is connected instead of the tested lines. The *true impedance profile* is then computed on the basis of the inverse scattering algorithm.

If a signal transmission forms a cascade of short sections of transmission lines of different impedances, the true impedance profile can be calculated from Eq. (2) by

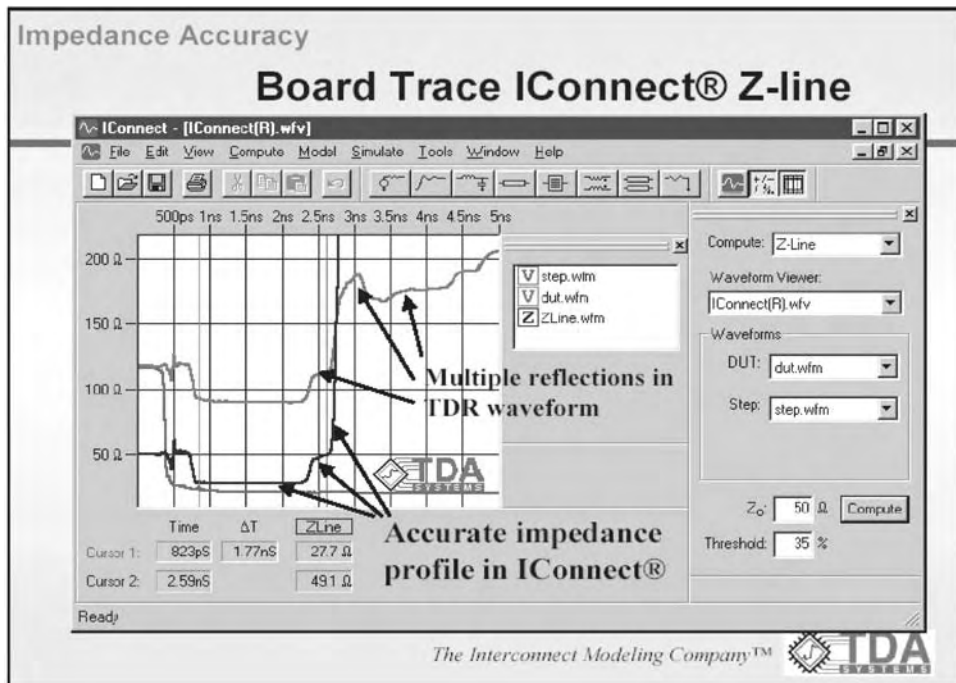


Figure 27. IConnect software application applied to determine the “true impedance profile” from the TDR voltages (reproduced with permission of TDA Systems).

applying it to section junctions. A sequence of bouncing waves is assembled, and from the observed voltage levels, the reflection coefficients are calculated at each junction. Then Eq. (2) can be directly applied to find corresponding line impedances. Such processes are illustrated by means of Figs. 25–27. The reflections can be compared with simulation to increase the accuracy of the final modeling.

4. SUMMARY

This article has described the basic theory behind time-domain reflectometry. In addition, several practical aspects such as reflections and their analysis for resistive and nonresistive loads terminating transmission lines have been demonstrated. Both asymmetric and symmetric transmission-line TDR parameter tests have been also covered. Several practical oscilloscope displays have been included to illustrate normalization processes, which have been additionally reinforced by simulations. Finally, software-enhanced high-speed interconnect modeling was briefly discussed.

BIBLIOGRAPHY

1. TDR Measurement of IEEE Implementation, homepage. (online): <http://www.zayante.com/html/documentation/TDR%20Measurement%20whit>.
2. N. G. Paulter, An assessment on the accuracy of time-domain reflectometry for measuring the characteristic impedance of transmission lines, *IEEE Trans. Instrum. Meas.* **50**(5):300–303 (Oct. 2001).
3. Agilent Technologies, *Time Domain Reflectometry Theory*, Application Note 1304-2.
4. Agilent Technologies, *Evaluating Microstrip with Time-Domain Reflectometry*, Application Note 1304-1.
5. Agilent Technologies, *Improving TDR/TDT Measurement Using Normalization*, Application Note 1304-5.
6. Hewlett-Packard, *Advanced TDR Techniques*, Application Note AN 62-3.
7. Agilent Technologies, *Faster Risetime for TDR Measurements*, Product Note 86100-4.
8. Agilent Technologies, *Differential Impedance Measurement with Time Domain Reflectometry*, Application Note 1382-5.
9. Tektronix Corporation, *Users Manual of 1S2 Sampling Unit*, Section 2.
10. D. J. Dasher, Measuring parasitic capacitance and inductance using TDR, *Hewlett-Packard J.* 83–96 (April 1996).
11. Agilent Technologies, *Agilent 86100B Wide-Band Oscilloscope*, Technical Specifications.
12. Hewlett-Packard, *Characterizing IC Packages with TDR/TDT and the UTP-3000 Test Fixture*, Application Note 1210-5.
13. P. Ferrari and G. Angenieux, Calibration of a time-domain network analyzer: A new approach, *IEEE Trans. Instrum. Meas.* **49**(1):178–187 (Feb. 2000).
14. Hewlett-Packard, *TDR Techniques for Differential Systems*, Application Note 62-2.
15. PSPICE 9.1, homepage (online), OrCad: <http://www.orcadpcb.com>.
16. *Signal Integrity Modeling of Gigabit Backplanes, Cables and Connectors Using TDR*, TDA Application Note, 2002 (online), TDA Systems: <http://www.tdasystems.com>.

17. D. Smolyansky and S. D. Corey, High-speed digital interconnect modeling from TDR measurements, *High-Performance System Design Conf., DesignCon 2000* (online), TDA Systems: <http://www.tdasystems.com>.

REFLECTOR ANTENNAS (PARABOLIC ANTENNAS, DISH ANTENNAS)

MARCO A. B. TERADA
New Mexico State University
Las Cruces, New Mexico

1. INTRODUCTION

Reflector antennas have been of significant importance for decades for several areas of electrical engineering, ranging from telecommunications and radars to deep-space exploration and radio astronomy. This is due to the high-gain characteristic of reflector antennas, typically above 30 dBi over wide frequency bandwidths, as well as its feasibility to accommodate high levels of power. If we extend the concept of a reflector antenna to a reflecting mirror and the human eye viewed as the feed antenna operating in receiving mode, reflector antennas have been known for centuries. Optical astronomers have long been using reflecting mirrors in telescopes in order to enhance the visibility of stars, planets, and other celestial bodies.

The basic principle of operation of a parabolic reflector is that all rays emanating radially from a point source located at the focal point are reflected as a concentrated bundle of parallel rays, which can propagate for very long distances without excessive attenuation. Conversely, incident rays parallel to the axis of symmetry of the paraboloid are all reflected toward its focal point, which concentrates the received signal in a single point. In that case, if the human eye or camera is placed a little bit behind the reflector focal point, an image with enhanced luminosity and definition is formed (see Fig. 1).

However, reflector antennas are wideband devices by nature, not being limited only to operate in frequencies covered by the spectrum of visible light. Radio telescopes, for example, search for celestial radio sources in a wide range of frequencies (e.g., 300 MHz–40 GHz). In this case, the radio sources and corresponding frequencies are

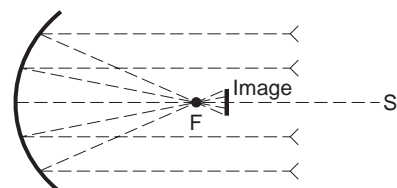


Figure 1. Basic principle of operation of a parabolic reflecting mirror. The paraboloid surface is formed by rotating the parabolic curve with respect to its axis of symmetry (s axis).

marked on charts according to their physical locations in the sky, forming maps similar to the ones elaborated by optical astronomers. Feed antennas are employed to receive the signals from the celestial radio sources at different bandwidths. The Very Large Array (VLA) in New Mexico for example, is an array of 27 shaped 25-m dual reflector antennas widely used in radioastronomy (see Fig. 2). Another example is the Green Bank Radio Telescope, the largest steerable reflector antenna in the world, discussed in certain detail in Section 3.3.

One of the first reflector antennas operating at radio-frequencies was built by Hertz in 1888, and consisted on a sheet of zinc of about 2×1.2 m, molded as a parabolic cylinder and illuminated by a dipole feed [1]. Since then, reflector antenna technology have gradually evolved toward the modern state of art known today for the purpose of improving electrical performance and/or simplifying the mechanical structure (see Fig. 3). The most basic form is the single axisymmetric parabolic reflector shown in Fig. 3a, which is still in widespread use primarily at low frequencies and for low-cost applications. Large reflectors frequently use an axisymmetric dual reflector system with a parabolic main reflector as shown in Fig. 3b. The sub-reflectors are hyperbolic (Cassegrain system) or elliptical (Gregorian system). These systems offer a shorter transmission line (or waveguide) run to the feed antenna and are often used as Earth terminal antennas in satellite communication networks.

Axisymmetric single and dual reflectors suffer from aperture blockage due to the presence of feed/subreflector and supporting mechanical structures in front of the main reflector aperture. This problem is solved by using an offset system with a main reflector that is a section of a paraboloid of revolution, as shown in Figs. 3c and 3d. Design and construction of offset reflectors are more elaborated than their symmetric counterparts.

Remarkable technological advancements were achieved during World War II, as reflectors were widely

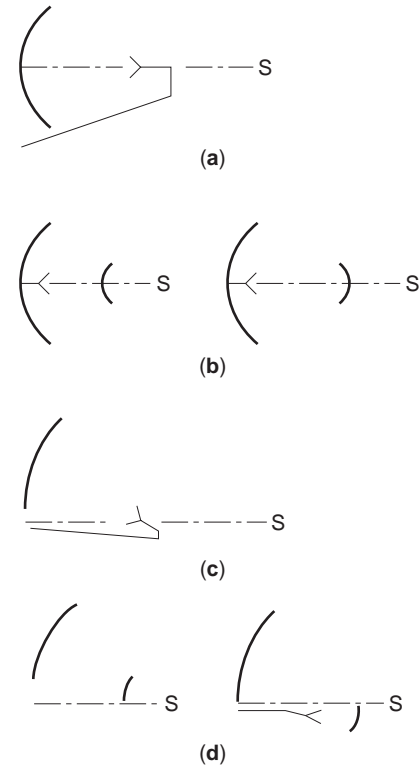


Figure 3. The evolution of reflector antenna systems: (a) single axisymmetric reflector; (b) dual axisymmetric reflector; (c) single offset reflector; (d) dual offset reflector. The main reflectors are parabolic.

employed in radar and communication systems [2]. However, it was only with the proliferation of digital computers in the late 1960s that most accurate analysis and synthesis algorithms were developed, especially the ones related to the configurations in Figs. 3c and 3d; see [3–7] for further information. Closed-form analysis algorithms are generally only applied to symmetric reflectors [4,8].



Figure 2. The *Very Large Array* (VLA) in New Mexico is a radiotelescope consisting of 27 shaped 25-m dual-reflector antennas. (Courtesy of the National Radio Astronomy Observatory—NRAO/AUI/NSF).

In addition, substantial improvements on the electrical performance of both axisymmetric and offset dual reflector configurations were obtained with shaping algorithms, an effort possible only with efficient numerical processing combined with a solid knowledge of differential geometry and electromagnetics [5,9,10]. The axisymmetric, dual shaped reflector was introduced in the 1970s [9] and is popular for large Earth station antennas. The offset, dual shaped reflector has a demonstrated aperture efficiency of 84.9% [11] and has been enjoying an increase in popularity. As a consequence, the analysis and design of reflector antennas are now a specialized and unique area in applied electromagnetics, responsible for many distinguished positions in industry and academics.

For the past few decades (as of 2003), reflector antennas have been applied mostly to the areas of satellite communications and wireless networks, deep-space exploration, and electronics defense. Besides specific designs applied to unique purposes, such as radiotelescopes and spacecrafts, reflector antennas are currently also being produced on a very large scale for commercial wireless applications, supporting the globalization process through engineering projects of aggregated values of more than hundreds of billions of dollars. The large international satellite operators, for example, such as Intelsat and Panamsat, allow many developing countries to have proper communication links to the rest of the world. Thus reflector antennas also have an important social impact, connecting people throughout the world, even the ones located in extremely remote areas of Earth, such as Indian tribes, exploration sites, and ships and vessels. In particular, VSAT (very-small-aperture-terminal) systems are proliferating in the world, connecting together branches of large corporations, such as chains of super markets, banks, and car manufacturers. The VSAT market is expected to grow at a rate of 20% per year [12].

Other examples of substantial social and economical impacts are the satellite-based broadband communication systems, such as the Hughes Spaceway and Intelsat Wild Blue in which well-defined multibeam coverage is required, and DTH (direct-to-home) satellite TV systems, such as Dish Network/Echostar and others, which employ small offset parabolic antennas to receive the satellite signals at our homes. As we can see, reflector antennas are present in our lives as major gateways for the exchange of information and also, in a more discrete profile, in defense systems responsible for sustaining our physical integrity and welfare. Reflector antennas can therefore be considered one of the most successful electrical devices of all times, especially due to their significant importance in many modern engineering systems and applications, such as wireless communications, satellite TV, and electronics defense, as well as in the exploration of our galaxy and beyond.

2. THE PARABOLIC REFLECTOR ANTENNA AND OTHER SINGLE-REFLECTOR SYSTEMS

2.1. Preliminary Considerations and Geometry

Single-reflector systems, such as the parabolic reflector antenna, consist of a reflecting surface illuminated by a

feed antenna, usually a horn. It is necessary to know the radiation characteristics of the feed antenna in order to evaluate correctly the electrical performance of the reflector system. A more in-depth discussion is presented in Section 5. In the next few sections we employ simple analytical models to describe the radiation properties of feed antennas. Once the feed pattern is known, the total radiation pattern of the reflector system can be obtained using the techniques described in Section 4, in combination with the geometric properties of the reflector itself, which is the main subject of this and following sections.

The general geometry of a parabolic reflector is shown in Fig. 4, and all associate symbols are listed in Table 1. Note that Fig. 4 is a cross-sectional view of the three-dimensional paraboloid. If a full rotation is performed with $H=0$ with respect to the axis of symmetry (s axis) in Fig. 4, an axisymmetric paraboloid of diameter D_p is formed. The offset reflector is generated from a subsection of the axisymmetric paraboloid. We limit our analytical analysis presented next to axisymmetric and offset parabolic reflectors with a circular projected diameter. However, other projected shapes, such as the elliptical one, are also used in practice with some extension, especially as Earth station antennas in communication links with synchronous satellites. An effort is made to discuss this and other types of reflector antennas.

2.2. Basic Equations

First we consider the axisymmetric parabolic reflector, which is obtained from Fig. 4 for $H=0$ and $\Psi_f=0^\circ$ (i.e., the feed antenna mainbeam peak is aimed at the reflector apex, point A). For this particular case, D_p is the diameter of the projected aperture and the aperture plane is the $x_f y_f$ plane, in which we define polar coordinates (ρ_f, ϕ_f) . Furthermore we associate the spherical coordinates (r_f, θ_f, ϕ_f) to the rectangular system $x_f y_f z_f$ shown in Fig. 4. The parabolic curve can then be expressed in any ϕ_f as

$$r_f = \frac{2F}{1 + \cos \theta_f} = F \sec^2 \frac{\theta_f}{2} \tag{1}$$

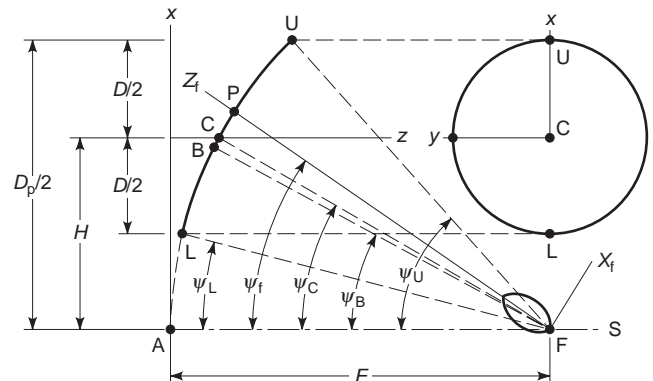


Figure 4. Geometry for the axisymmetric ($H=0$) and offset parabolic reflector. See Table 1 for definitions of parameters.

Table 1. Definitions of Symbols for Single Configuration

Symbols	Definitions
D	Diameter of the projected aperture of the parabolic main reflector ($D = D_p$ for an axisymmetric paraboloid)
D_p	Diameter of the projected aperture of the parent paraboloid
H	Offset of reflector center ($H = 0$ for an axisymmetric paraboloid)
F	Paraboloid focal length
Point F	Focal point
Point A	Apex of the parent paraboloid
Point B	Point on main reflector that bisects subtended angle viewed from focal point
Point C	Point on main reflector that projects to the center of the projected aperture
Point P	Point on main reflector corresponding to the ray arising from the peak of the feed pattern
ψ_f	Angle of feed antenna pattern peak relative to reflector axis of symmetry (s); the feed is directed toward point P
ψ_B	Value of ψ_f that bisects the reflector subtended angle (i.e., feed is aimed at point B)
ψ_C	Value of ψ_f when the feed is aimed at the reflector point C corresponding to the aperture center
$(\psi_U - \psi_L)$	Angle subtended by the parabolic main reflector as viewed from the focal point

or

$$F - r_f \cos^2 \frac{\theta_f}{2} = 0 \quad (2)$$

and the projection of r_f onto the aperture plane is

$$\rho_f = r_f \sin \theta_f = 2F \tan \theta_f \quad (3)$$

which yields $\rho_f = 0$ at the reflector apex ($\theta_f = 0^\circ$), and $\rho_f = D_p/2$ at the reflector edge ($\theta_f = \psi_0 = \psi_L = \psi_U$).

The axisymmetric paraboloid is completely specified in terms of its diameter D_p and curvature rate F/D_p . The greater is F/D_p , the flatter is the reflector. Common values are usually between 0.25 and 1.0. At the reflector edge, Eq. (3) becomes $D_p/2 = 2F \tan \psi_0$, which yields

$$\psi_0 = 2 \tan^{-1} \left(\frac{1}{4 \frac{F}{D_p}} \right) \quad (4)$$

The unit vector \hat{n} , normal to the parabolic surface, can be found by normalizing the gradient of Eq. (2) and is given by

$$\hat{n} = -\hat{r}_f \cos \frac{\theta_f}{2} + \hat{\theta}_f \sin \frac{\theta_f}{2} \quad (5)$$

The angle α_i between the surface normal, given by Eq. (5), and an incident ray coming from the focal point can then be calculated from

$$\cos \alpha_i = -\hat{r}_f \cdot \hat{n} = \cos \frac{\theta_f}{2} \quad (6)$$

Finally, the angle α_r between the correspondent reflected ray and surface normal can be determined by enforcing Snell's law on the reflector surface: $\alpha_r = \alpha_i$. Thus

$$\cos \alpha_r = \cos \frac{\theta_f}{2} = \hat{z} \cdot \hat{n} \quad (7)$$

where $\hat{z} = -\hat{r}_f \cos \theta_f + \hat{\theta}_f \sin \theta_f$. Equation (7) shows that *all rays coming from the focal point F are reflected by the parabolic surface as a collimated beam parallel to the z*

axis, which is coincident with the s axis for the axisymmetric reflector. Thus the total pathlength from all rays coming from the focal point F to the aperture plane is given by

$$r_f + r_f \cos \theta_f = r_f(1 + \cos \theta_f) = 2F \quad (8)$$

where Eq. (1) was employed in the derivation. Equation (8) shows that the total pathlength is constant, and we conclude that the phase distribution of a wave coming from a point source located at the focal point of a parabolic reflector will be constant across the aperture plane after reflection. This result yields another very important property of parabolic reflectors, namely, that *a parabolic reflector illuminated by a feed antenna with a unique phase center located at the focal point produces a uniform phase distribution across the aperture plane*. As already seen, the beam is also collimated, forming a section of a plane wave. Nevertheless, the amplitude distribution is not uniform, reaching a maximum at the center of the projected aperture and decreasing toward the edges of the axisymmetric paraboloid.

These basic properties make the parabolic reflector so widely used as reflector antennas. Although herein derived for the axisymmetric paraboloid, they are also valid for the offset case (i.e., $H \neq 0$ in Fig. 4). Offset reflectors offer significantly reduced aperture blockage, as the feed is not directly in front of the reflector, although still located at the focal point F , yielding higher gains when compared to axisymmetric reflectors of similar aperture sizes. From Fig. 4 we see that the feed needs to be tilted by an angle ψ_f in order to direct its pattern toward the offset reflector; otherwise large spillover (i.e., feed radiation missing the reflector) and associated gain loss are introduced. In many systems, the feed pointing angle ψ_f is set equal to the angle that bisects the reflector ψ_B , or to the angle pointed toward the center of the projected aperture ψ_C . The influence of the feed pointing angle ψ_f on the electrical characteristics of offset parabolic reflector antennas is discussed in Section 2.4. The angles shown in Fig. 4 are obtained from the following relations

$$\psi_L = 2 \tan^{-1} \left(\frac{4H - D_p}{4F} \right) \quad (9)$$

$$\psi_U = 2 \tan^{-1} \left[\frac{1}{4 \left(\frac{F}{D_p} \right)} \right] \quad (10)$$

$$\psi_B = \frac{\psi_L + \psi_U}{2} \quad (11)$$

$$\psi_C = 2 \tan^{-1} \left(\frac{H}{2F} \right) \quad (12)$$

with

$$D_p = D + 2H \quad (13)$$

As we see, there are many parameters necessary to specify completely a parabolic reflector antenna. However, before we design reflector systems, it is necessary to study a few of their characteristics and properties. This knowledge is essential for selecting appropriate configurations for specific applications. Long-distance and frequency reuse communication systems, for example, require antennas with high gain and low cross-polarization. Reflector antennas are particularly suitable for such applications due to their high gain. However, an in-depth understanding of their depolarization characteristics is necessary, in order to achieve designs that guarantee a suitable isolation between orthogonally polarized channels in frequency reuse systems. This and other properties that are almost exclusive to reflector antennas are discussed in the next section.

2.3. Cross-Polarization, Beam Squint, and Beam Deviation

2.3.1. Cross-Polarization. Polarization is a basic characteristic of an electromagnetic wave and describes the motion of the electric field vector at a fixed point in space as a function of time. The polarization of an antenna is the polarization of its radiated wave when operating in the transmitting mode. Generally, the polarization of any antenna system can be decomposed into two orthogonal components in the far field, referred to as *copolarization* and *cross-polarization*, respectively. In the particular case of reflector antenna systems, the copolarization is usually taken to be the one presented by the feed antenna employed to illuminate the reflector. As a consequence, the cross-polarization is orthogonal to the feed antenna main polarization. This agrees with Ludwig's third definition of cross-polarization [13] and is the one employed here. *Cross-polarization level* (XPOL) is defined quantitatively as the ratio of the peak in the cross-polarized radiation pattern to the peak value of the copolarized pattern (i.e., the mainbeam peak), usually expressed in decibels.

As mentioned previously, reflector antennas cannot be properly evaluated without first describing the feed antenna. A detailed discussion about modeling feeds is presented in Section 5. Here we employ an analytical model that, despite its simplicity, approximates reasonably well the copolar radiation properties of feeds usually encountered in practice, such as conical corrugated horns. The radiation pattern \vec{E}_f of an idealized balanced feed (i.e., the primary radiation is symmetric in ϕ_f) with a fixed phase

center can be described by [3]

$$\vec{E}_f = \frac{e^{-jkr_f}}{r_f} C(\theta_f) [\hat{\theta}_f \cos \phi_f - \hat{\phi}_f \sin \phi_f] \quad (14)$$

where k is the free-space wavenumber $2\pi/\lambda$ and

$$C(\theta_f) = G_0 10^{(FT/20)(\theta_f/\theta_{f0})^2} \quad (15)$$

where FT is the feed taper in decibels at $\theta_f = \theta_{f0}$ and the gain normalization constant G_0 is found by numerical integration of Eq. (15); see [for further details. We first examine the axisymmetric reflector of Table 2 using a balanced feed as described by Eq. (14), which is purely linearly polarized (LP) along the x axis, with the Gaussian pattern of Eq. (15) yielding a 10 dB beamwidth of 70° ; specifically, $FT = 10$ and $\theta_{f0} = 35^\circ$. A y_f -polarized feed pattern can be obtained from Eq. (14) by replacing the argument ϕ_f with $(\phi_f - \pi/2)$. In addition, a circularly polarized feed is obtained by combining the x_f -polarized pattern in Eq. (14) with a y_f -polarized pattern that is in phase quadrature (i.e., multiplied by a factor of j). The physical optics portion of the commercial code GRASP (general reflector antenna synthesis package) is used to compute the radiation patterns [14][14]. The physical optics formulation applied to the analysis of reflector antennas is discussed in Section 2.4.

For the axisymmetric configuration of Table 2, the computed level of XPOL displayed in Fig. 5 is very low; i.e., maximum of -65.35 dB below the main beam peak of 48.62 dBi. Typically, the feed assembly and supports, although not taken into account by the computer simulations, will create more XPOL than this. Although illustrated for a particular case, this is a general result (9), and we conclude that reflector-induced XPOL in axisymmetric reflectors illuminated by balanced feeds is often negligible. In addition, according to Fig. 5, the XPOL peaks are all located in the 45° planes.

Cross-polarization behavior of offset reflectors is illustrated with a derivative of the 171λ axisymmetric parent reflector of Table 2. The portion of the upper half of the axisymmetric reflector is retained such that the offset reflector of a 85.5λ projected aperture diameter is just fully offset (i.e., the bottom of the reflector just touches its axis of symmetry). If the feed remains pointed at the apex of the parent paraboloid (i.e., $\psi_f = 0^\circ$), negligible XPOL is generated [15]. However, this leads to large spillover and associated gain loss. Therefore, in practice the feed is tilted to direct its pattern toward the reflector, resulting in the introduction of high XPOL.

The offset configuration of Table 2 is not symmetric about the yz plane, and therefore XPOL is not canceled in this plane as in the axisymmetric case. In fact, it is exactly in the yz plane that the peak XPOL levels occur. However, reflector symmetry is still present about the xz plane, and no substantial XPOL occurs in that plane. These results are demonstrated using the GRASP code for the offset reflector example with the XPOL contour plot shown in Fig. 6, for which the feed has a pointing angle of $\psi_f = \psi_B = 39.81^\circ$, computed according to Eq. (11). The feed again has

Table 2. Axisymmetric and Offset Parabolic Reflector Configurations

Property	Axisymmetric	Offset
	<i>Reflector Configuration</i>	
Shape	Parabolic	Parabolic
Projected diameter D , (λ)	171	85.5
Parent reflector diameter D_p , (λ)	171	171
F/D_p	0.3	0.3
Offset of reflector center H , (λ)	0	42.75
	<i>Feed Configuration (On Focus)</i>	
Polarization	Linear (x_r)	Linear (x_r)
Pattern shape	Gaussian; Eqs. (14), (15)	Gaussian; Eqs. (14), (15)
Gain G_b , (dBi)	14.04	14.04
10-dB beamwidth (deg)	70	70
Feed angle ψ_b (deg)	0	39.81

the pattern given by Eqs. (14) and (15), with a 10 dB beamwidth of 70° . The computed peak XPOL is -22.4 dB relative to the copolarized beam maximum of 47.39 dBi. Figure 6 indicates that the copolarized pattern is still symmetric, and the XPOL peaks are located at the copolar -6 dB contour line.

This example is typical of single offset reflectors and shows that single offset paraboloids illuminated by conventional feeds are limited by XPOL performance [9]. It is worth noting that cross-polarization arises as a result of the reflector curvature and the tilting of the feed. A planar reflector for instance does not depolarize an incident field coming in a direction perpendicular to the reflector. Thus we note that XPOL reduces as the reflector curvature rate F/D_p increases. However, this reduction is not significant in offset reflectors because of the substantial feed tilting normally encountered in practice [15]. A XPOL level of about -22 dB is often unacceptably high [3,7]. In Section

3.2 we discuss procedures to reduce XPOL in offset parabolic reflectors. Next we discuss an important property of parabolic reflector antennas, inherently related to cross-polarization.

2.3.2. Beam Squint. As we have seen, offset reflectors offer significantly reduced aperture blockage but introduce high XPOL when illuminated by a LP feed. On the other hand, offset parabolic reflectors fed by a circularly polarized (CP) feed presenting a balanced radiation pattern do not have substantial XPOL. However, beam squint does occur [9,16]; that is, the mainbeam peak squints off of the reflector axis in the plane perpendicular to the plane of symmetry (i.e., beam squint occurs in the yz plane of Fig. 4). The beam squints to opposite sides depending on the sense of CP. Beam squint can be a major problem in satellite and deep-space communications if not carefully

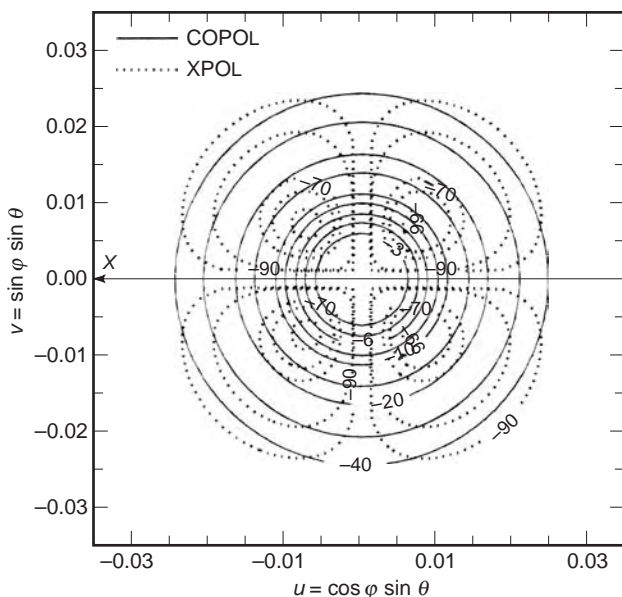


Figure 5. Contour plots in decibels of the computed co- and cross-polarized patterns of the 171λ -diameter axisymmetric parabolic reflector specified in Table 2.

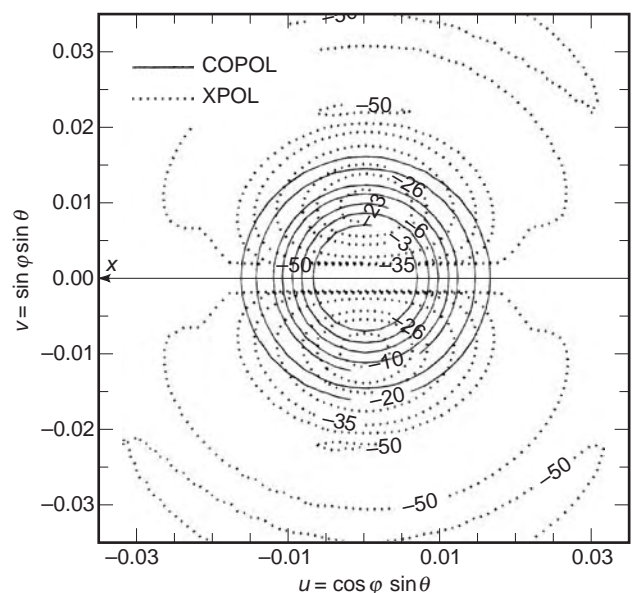


Figure 6. Contour plots in decibels of the computed co- and cross-polarized patterns of the 85.5λ -diameter just fully offset parabolic reflector specified in Table 2.

taken into account. A practical formula for the prediction of the beam squint angle θ_S in offset parabolic reflectors with on-focus CP feeds is [16]

$$\theta_S = \mp \sin^{-1} \left(\frac{\sin \psi_f}{2Fk} \right) \quad (16)$$

where F is the focal distance and k is the free space wave-number $2\pi/\lambda$. A negative θ_S means that the beam is squinted toward the left (left-hand CP feed), and conversely, a positive θ_S indicates a squint to the right (right-hand CP feed). Equation (16) shows that the amount of squinting is inversely proportional to the focal distance F ; that is, longer focal length reflectors experience less beam squint. If the feed is displaced from the focal point, an equation similar to Eq. (16) is derived as in Ref. 17. In offset parabolic configurations illuminated by off-focus CP feeds, beam squint occurs simultaneously with an effect called *beam deviation*, treated in the next section. Because of sense reversal encountered on reflection from the main reflector, the sense of the far-field radiation is opposite that of the feed [18]. For example, a right-hand circularly polarized (RHCP) feed produces a left-hand circularly polarized (LHCP) radiation in the reflector far field, as illustrated next.

We consider as an example a just fully offset configuration with a diameter $D=18.8\lambda$, $F/D_p=0.25$, and $H=9.4\lambda$, illuminated by a CP feed with a pattern of 10 dB beamwidth of 70° . This geometry was selected because it is used in VSAT applications at 18.5 GHz and measured data are available [3,9]. Figure 7 shows copolarized pattern cuts computed by GRASP [14] in the xz plane with opposite sense CP feeds. For the RHCP main-beam case (the feed is LHCP) the squint is to the left as observed in Fig. 7. Conversely, the LHCP mainbeam squints to the right. From Fig. 7 we note that the angle

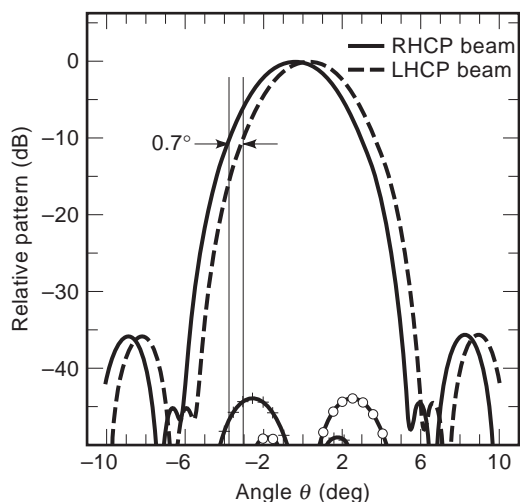


Figure 7. Computed RHCP and LHCP far-field patterns of a $18.8\text{-}\lambda$ just fully offset parabolic reflector. Note the beam squint effect. The LHCP (ooo) and RHCP (+++) cross-polarized patterns are associated with the RHCP and LHCP beams, respectively.

between the two beams (total beam separation) is 0.700° , which is in agreement with the value of 0.686° from Eq. (16). The reported measured value [3,9] is 0.750° . Finally, Fig. 7 also shows that circular XPOL is low (maximum of 42.71 dB below the gain of 33.88 dBi for any of the feed polarizations). The absence of reflector-induced circular XPOL in offset paraboloids with on-focus feeds is a general result, not limited to just fully offset paraboloids (17).

Although circular XPOL is low, there are a substantial number of LP cross-polarized fields present at any given instant of time, in both the aperture distribution and far-field pattern of the offset reflector [19]. This, in conjunction with the fact that the orthogonal components of the incident field are not in phase, which is the case of circularly polarized feed antenna, are the two necessary and sufficient conditions to generate beam squint [17]. We now present a brief explanation of the beam squint generation mechanism.

The electric field components on the left side of the reflector ($y > 0$ in Fig. 4) always lead or lag in phase relative to the ones on the right side, depending on whether the primary field is LHCP or RHCP [19]. This leads to a phase slope condition across the aperture, which squints the mainbeam to the left (negative angles in Fig. 7) or to the right (positive angles in Fig. 7). In order to illustrate the process, consider any two points in the projected aperture of the offset paraboloid that are equidistant from the reflector plane of symmetry. If the feed is LHCP, the electric field at those points rotates counterclockwise (RHCP mainbeam), as shown by Fig. 8. Thus, the electric field vector to the left is leading the one to the right, and as a final result (considering the influence of all points), the beam squints to the right (the view in Fig. 8). This is equivalent to a negative θ_S in Eq. (16), or to a squint to the left in the yz plane of the reflector coordinate system (negative angles in Fig. 7).

2.3.3. Beam Deviation. When a feed is laterally displaced from the focal point of a reflector, either axisymmetric or offset, the pattern mainbeam is scanned to the opposite side of the reflector axis. This is referred to as *beam deviation*, and arises from a tipping of the aperture field phase plane relative to the reflector aperture plane.

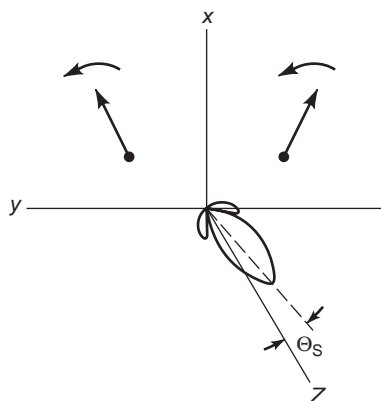


Figure 8. Beam squint generation mechanism.

The mainbeam direction determined on the basis of these considerations is herein referred to as the *reference axis*, which is tilted from the reflector axis (i.e., the z axis in Fig. 4) according to the amount of feed displacement. Note that for an axisymmetric configuration, the reflector and reference axes intersect at the apex of the parent paraboloid (point A in Fig. 4). If a CP feed is displaced from the focal point of an axisymmetric or offset paraboloid, both beam squint and deviation are present at the same time. Thus the amount of beam squint should be added to the reference axis in order to determine accurately the final position of the mainbeam.

For a feed displacement δ_f along the positive y_f direction as shown in Fig. 4, the reference axis is tilted in the direction opposite that of the reflector axis by an angle θ_D , computed according to

$$\theta_D = [\text{BDF}] \tan^{-1} \left(\frac{\delta_f}{F} \right) \quad (17)$$

where [BDF] is the beam deviation factor, which can be approximately determined for small feed displacements δ_f , in axisymmetric and offset paraboloids, by [3,20]

$$[\text{BDF}] = \frac{1 + 0.36 \left[4 \frac{F}{(D_p - 2H)} \right]^{-2}}{1 + \left[4 \frac{F}{(D_p - 2H)} \right]^{-2}} \quad (18)$$

The nonuniform aperture phase distribution introduced by the feed displacement is responsible for the beam deviation, as already commented, but also lead to pattern deterioration, which include beam broadening and null filling. These effects increase as δ_f becomes larger, resulting in substantial gain loss. Nevertheless, scanning of the beam by feed displacement is a technique widely used in practice, especially when it is difficult or impossible to move the reflector itself.

2.3.4. Summary of Main Results. There are a large number of possible reflector geometries, feed types, locations, and polarizations. Representative configurations were examined in the previous sections to provide specific values as well as general conclusions. The many possible configurations employing a parabolic reflector are summarized in Table 3 together with XPOL, beam squint, and beam deviation effects. Table 3 shows that unbalanced feeds (i.e., the primary radiation pattern is not symmetric) usually generate substantial XPOL independent of the feed polarization or reflector configuration. Beam squint normally occurs with circularly polarized feeds, except for small reflector antennas (i.e., $D < 12\lambda$ and $F/D_p < 0.25$), where it can also be present with a linearly polarized illumination [21]. Also, displacing the feed from the focal point normally generates XPOL and beam deviation. Table 3 presents a complete overview of the various depolarization and beam-pointing properties of single-parabolic-reflector antennas, which is of fundamental importance for designing effective reflector configurations.

2.4. Design and Manufacturing of Axisymmetric and Offset Parabolic Reflector Antennas

Design of reflector antennas presents a challenge to the antenna engineer, especially since so many parameters are available for adjustment. The main purpose of this section is to present a complete procedure to design axisymmetric and offset reflectors, as well as provide some insights on the basic tradeoffs inherent to the process.

Within this context, we start by examining the influence of feed-pointing angle, ψ_f , on gain (G), sidelobe level (SLL), and cross-polarization (XPOL) of offset reflectors having $H > D/2$ (i.e., general offset reflectors). Feed-pointing angle is a parameter of significant influence on the electrical behavior of reflector antennas, providing many insights on XPOL behavior. Scattering from supporting structure (struts) is not included, but for an offset configuration it is typically negligible. An offset reflector is

Table 3. Polarization and Beam-Pointing Characteristics of Single Parabolic Reflectors

Reflector Geometry	Location	Feed Type	Polarization	Cross-Polarization	Beam Squint
Axisymmetric	Onfocus	Balanced	Linear	No	No
		Unbalanced	Circular	No	No
	Offfocus ^a	Balanced	Linear	Yes	No
			Circular	Yes	No
		Unbalanced	Linear	Yes	Yes
			Circular	Yes	Yes
Offset ($\psi_f > 0^\circ$)	Onfocus	Balanced	Linear	Yes	No ^b
		Unbalanced	Circular	No ^b	Yes
	Offfocus ^a	Balanced	Linear	Yes	Yes
			Circular	Yes	Yes
		Unbalanced	Linear	Yes	No ^b
			Circular	Yes	Yes

^aBeam deviation also occurs; see Section 2.3.3.

^bExcept for small reflector antennas (i.e., $D < 12\lambda$ and $F/D_p < 0.25$); see Ref. 21 for further details.

chosen with a diameter $D = 85.5\lambda$, $F/D_p = 0.3$, and offset distance $H = 5D/8$, corresponding to a geometry that is popular in VSAT applications. The balanced feed pattern employed to illuminate the reflector is x_f -polarized, as modeled by Eqs. (14) and (15), with a 10 dB beamwidth of 70° .

Figure 9 shows G , SLL, and XPOL computed by GRASP [14] as the feed pointing angle, ψ_f , is varied for the selected configuration. We note from Fig. 9 that the gain curve has a broad peak, and the sidelobe level is not sensitive to feed pointing, except at very small angles ($\psi_f < 30^\circ$). Only the near-in sidelobes were considered in this analysis, and therefore spillover from the feed, which is particularly high for $\psi_f < 40^\circ$ and $\psi_f > 60^\circ$, was not included in Fig. 9. XPOL, however, decreases with decreasing ψ_f . Although illustrated for a particular case example, this is a generic and important result, showing that *in the limiting case where the feed is pointed at the apex of the parent paraboloid* (i.e., $\psi_f = 0^\circ$), *negligible XPOL is generated* [15]. However, this leads to large spillover and associated gain loss. Therefore, in practice the feed is tilted to direct its pattern toward the reflector, which introduces high cross-polarization. For approximate designs, as is often sufficient in practice, the feed can be aimed within the range $40^\circ \leq \psi_f \leq 60^\circ$ in order to keep spillover losses (and consequent gain loss) reasonable. For the particular configuration herein considered, peak gain operation is achieved with $\psi_f = 47^\circ$, which yields $G = 47.52$ dBi.

A classical design scenario has now emerged. The feed-pointing angle ψ_f is reduced until desirable cross-polarization performance is achieved or until gain is reduced as far as can be accepted. If, on the other hand, SLL is a critical parameter, then ψ_f can be optimized to yield nearly the lowest SLL over a practical range of angles, with only small reductions in G and XPOL [15]. This is discussed in more detail in the procedure for designing parabolic antennas, presented next.

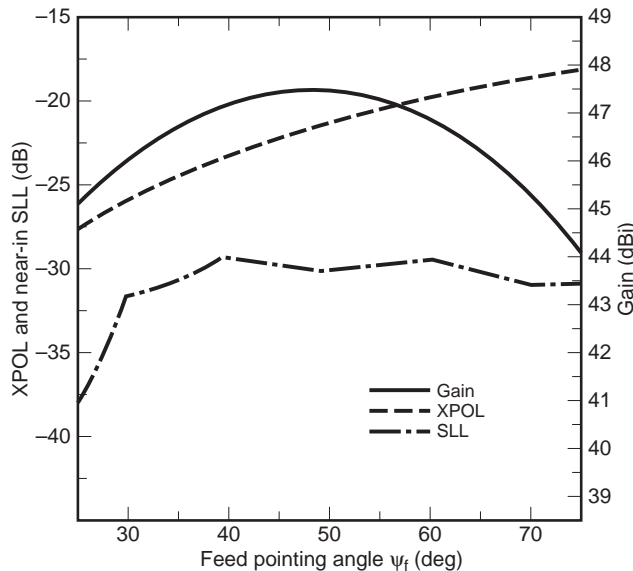


Figure 9. Gain G , sidelobe level (SLL), and cross-polarization level (XPOL) as a function of the feed-pointing angle ψ_f for an offset parabolic reflector with a 85.5λ diameter.

After the considerations discussed previously, we now have a reasonable understanding of the basic concepts of reflector antennas. The following steps are similar to those outlined in [22] and summarize a procedure to design axisymmetric ($H = 0$) and offset reflector antennas.

1. *Determination of Reflector Diameter.* The following equation is very useful to estimate a value of D to achieve a required gain G [20]

$$g_{[\text{not in dB}]} = \epsilon_{\text{ap}} \frac{4\pi A_p}{\lambda^2} = \epsilon_{\text{ap}} \left(\frac{\pi D}{\lambda} \right)^2 \quad (19)$$

where A_p is the physical area of the antenna aperture and ϵ_{ap} is the *aperture efficiency*, typically 0.65 (65%) for many parabolic reflector systems used in practice. Note that $G = 10 \log g$ [dB].

2. *Determination of Offset Distance.* The offset distance H controls the amount of blockage caused by the feed and supporting structure on the reflector projected aperture. Many reflectors nowadays are just fully offset paraboloids ($H = D/2$); that is, the bottom of the reflector just touches its axis of symmetry. This configuration avoids the blockage from the feed supporting structure (struts) and waveguide, although part of the feed aperture is still directly in front of the reflector. Nevertheless, the total blockage area is still significantly smaller than the one presented by axisymmetric configurations ($H = 0$). Values of H larger than $D/2$ can overcome blockage but also increase the total volume occupied by the reflector, which in some cases is not recommended. In addition, the manufacturing process and associated adjustments become more difficult as H increases.
3. *Selection of Reflector Curvature.* Values usually encountered in practice for the reflector curvature, F/D_p , are between 0.25 and 1.0, where D_p is given by Eq. (13). Higher values ease the manufacturing process (i.e., the reflector is flatter), but require a narrower feed pattern to illuminate the reflector, which results in larger feed antennas. A typical value nowadays is $(F/D_p) = 0.3$ which yields a compact design.
4. *Determination of Feed Pattern.* An important parameter for determining the necessary feed pattern is the *reflector illumination* RI, which in dB is given by

$$\text{RI} = 20 \log \left[\cos^2 \left(\frac{\theta_f + \psi_f}{2} \right) \right] + 20 \log(\cos^q \theta_f) \quad (20)$$

where the first term on the right-side is normally referred to as *spherical spreading loss*, and accounts for the power spreading due to spherical propagation of the wave between the focal point and the parabolic reflector surface. The second term in the right side of Eq. (20) is the normalized feed pattern in decibels of

$$C(\theta_f) = \cos^q \theta_f \quad (21)$$

which is a pattern model widely used in practice with Eq. (14), as an alternate to the one given by

Eq. (15). The main advantage of Eq. (21) over Eq. (15) is that the directivity of the feed, or its gain if ohmic losses are not taken into account, can be found analytically in closed form with [4]

$$g_{f[\text{not in dB}]} = 4q + 2 \quad (22)$$

where g_f is the gain of the balanced feed modeled by Eqs. (14) and (21). The parameter q can be obtained from Eq. (20) for a required reflector illumination (RI) in decibels at a direction θ_f as

$$q = \frac{\frac{\text{RI}}{20} - \log \left[\cos^2 \left(\frac{\theta_f + \psi_f}{2} \right) \right]}{\log(\cos \theta_f)} \quad (23)$$

An usual value for RI at the reflector edges, often referred to as *edge illumination* (EI), is -11 dB and assures optimal gain performance for axisymmetric paraboloids ($\psi_f = 0^\circ$ and $\theta_f = \psi_L = \psi_U$) [20].

In offset reflectors, $\psi_L \neq \psi_U$, but a specified value of EI at both edges can still be obtained by solving for ψ_f the equation formed by imposing that $q(\theta_f + \psi_f = \psi_L) = q(\theta_f + \psi_f = \psi_U)$, which yields $q(\theta_f = \psi_L - \psi_f) = q(\theta_f = \psi_U - \psi_f)$. Once ψ_f is determined, the parameter q can be calculated directly from Eq. (23) for the specified value of RI (i.e., EI), at either $\theta_f + \psi_f = \psi_L$ or $\theta_f + \psi_f = \psi_U$, since they now should yield the same result. Under this condition, the edge illumination is called *balanced*, and yields near-minimum side-lobe levels over practical ranges of feed pointing, with only small penalties in gain and cross-polarization [15]. A graphical technique to determine ψ_f for the same condition was introduced in [15], and is especially indicated when only measured feed patterns are available.

In practice, however, it is common to find offset systems employing $\psi_f = \psi_B$, Eq. (11), or $\psi_f = \psi_C$, Eq. (12). For either case the edge illumination is in general unbalanced. As a consequence, different values of q are obtained with Eq. (23), depending whether $\theta_f + \psi_f = \psi_L$ or $\theta_f + \psi_f = \psi_U$. A simple arithmetic mean can then be taken to specify the required feed pattern. Although approximate, this simple procedure yields reasonably good results in practice and is well suited for our purposes.

Once the parameter q is determined, Eqs. (22) and (19) can be used to estimate the aperture diameter, or area, of the required feed antenna. A typical value of $\epsilon_{\text{ap}} = 0.55$ (55%) can be used for feed horns. A more exact approach is available when the feed antenna is an open-ended rectangular waveguide of wide and narrow dimensions a and b , or an open-ended circular waveguide of radius a . For those cases, the waveguide dimensions can be determined from Eq. (22) respectively with $g_f = 32ab/\pi\lambda^2$ ($\epsilon_{\text{ap}} \approx 0.81$) or $g_f = 10.5\pi a^2/\lambda^2$ ($\epsilon_{\text{ap}} \approx 0.84$). If the result indicates a feed antenna with an aperture considered too large, a higher value of RI (i.e., EI at the reflector edges) should be employed to avoid unnecessary blockage. For an offset reflector, a larger value of H can also be tried and the whole procedure needs to be repeated.



Figure 10. Just fully offset parabolic reflector antenna built and tested for satellite TV reception at C band. (Courtesy of Carlos Muller, Univ. Brasilia.)

The aforementioned design procedure was successfully employed to obtain the preliminary design of a 1.6 m just fully offset paraboloid, built and tested for satellite TV reception at the C band (see Fig. 10). Nevertheless, the use of a suitable computer code before the manufacturing process is highly recommended to confirm the electrical performance of the reflector system. Techniques often implemented in numerical codes for the analysis of reflector antennas are discussed in Section 4.

As a final note, we mention that surface distortions from ideal parabolic shapes are normally introduced in any manufacturing process. Random reflector surface errors can be accounted for by modifying Eq. (19), such as to include a *random surface error efficiency*, ϵ_{rs} [20]:

$$g_{[\text{not in dB}]} = \epsilon_{\text{ap}} \epsilon_{\text{rs}} \left(\frac{\pi D}{\lambda} \right)^2 \quad (24)$$

where the total aperture efficiency became the product ($\epsilon_{\text{ap}} \epsilon_{\text{rs}}$):

$$\epsilon_{\text{rs}} = e^{-(2\beta\delta_s)^2} \quad (25)$$

The parameter δ_s is the root-mean-square (RMS) surface deviation and is approximately one-third of the peak-to-peak error [20]. Detailed information on other efficiency factors left in ϵ_{ap} can be found in the literature [20]. Mass production of reflectors using presses and molds to shape glass fibers and other components normally yield $\delta_s \approx 0.01\lambda$ ($\epsilon_{\text{rs}} = 0.98$ or 98%). Errors larger than that can cause significant gain loss and pattern deterioration due to the introduction of phase errors. Machined metal reflectors are very accurate and have $\delta_s \approx 0.04\text{--}0.5$ mm for a very large band of operating frequencies (from Ku band

down to S band). In fact, reflector antennas are wideband devices by nature, limited at the upper frequencies by the smoothness of the reflector surface and at the lower ones by the reflector electrical size. The operating bandwidth of a reflector antenna in practice is normally set by the bandwidth of the feed antenna employed to illuminate the reflector. Reflector antennas are normally fabricated from aluminum, graphite or carbon-fiber-reinforced plastic (CFRP) and glass fibers or glass-fiber-reinforced plastic (GFRP). Although herein illustrated for parabolic reflectors, random surface errors occur in any type of reflector antenna, such as the ones discussed next.

2.5. Other Single-Reflector Systems

A few other types of parabolic reflectors can also be obtained from Fig. 4, including offset configurations. The *parabolic cylinder*, for example, is generated by displacing the parabolic curve along the y -axis. This yields a focal line in contrast to the focal point of the parabolic reflector. A feedline or a linear array of feed antennas must be placed along the focal line for proper illumination of the reflector. Another example is the *parabolic torus*, formed by rotating the parabolic curve with respect to an axis perpendicular to the s axis of Fig. 4. The axis of revolution is in general placed at a distance from the apex greater than F and is confined to the plane shown by Fig. 4. Thus the parabolic torus possess a focal arc and can be visualized as a curved parabolic cylinder. Multiple feeds are normally employed to illuminate different sections of the reflector, producing independent beams with a single reflector antenna, a configuration widely used in satellite communications.

An example of a reflector antenna not generated by a parabolic curve is the spherical reflector, which is a section of a sphere. The Arecibo Observatory, located in Puerto Rico, employs an axisymmetric spherical main reflector with a diameter of 305 m for radio astronomy, ionospheric research and radar investigation of celestial bodies. A line feed is used because parallel rays coming from space are reflected along the reflector axis [23]. This is in contrast to the parabolic cylinder where the focal line is perpendicular to the reflector axis of symmetry. However, the spherical reflector possesses not only a focal line but also a focal region where feeds can be placed [24]. Dual offset shaped reflectors have also been proposed as feed systems, in order to correct the nonuniform phase distribution characteristic of spherical reflectors [23]. Dual- and multiple-reflector systems are treated in the next section.

3. MULTIPLE-REFLECTOR ANTENNA SYSTEMS

3.1. Cassegrain, Gregorian, and Multiple-Reflector Systems

Dual-reflector systems, such as the ones in Figs. 2b and 2d, can be formed by adding to the parabolic reflectors previously studied, a hyperbolic reflector (Cassegrain system) or an elliptical reflector (Gregorian system). Hyperbolic and elliptical reflectors have two focal points, F_1 and F_2 , and are normally referred to as *subreflectors* because of

their smaller size when compared to the parabolic main reflector.

It is known [3,25] that any ray coming from one of the focal points, say, F_2 , is reflected by an ellipsoid surface towards the other focal point, F_1 . For the hyperbolic surface, the reflection occurs such that the reflected ray appears to come from F_1 . Thus, any circular cone of rays (i.e., a section of a spherical wave) emanating from F_2 and directed to an elliptical, or hyperbolic, subreflector will then be reflected as another circular cone of rays with vertex at the other focal point F_1 . Furthermore, if F_1 is coincident with the paraboloid focal point F , and the feed is located at F_2 , a perfect circular cone of rays originated at F_1 will illuminate the paraboloid. Because of the parabola reflecting property, a section of a plane wave will then appear at the paraboloid aperture plane.

There are a few basic advantages of dual configurations over single ones; for instance, they provide a shorter waveguide run to the feed antenna. In addition, dual configurations present lower noise when used as satellite–Earth terminals. This is due to the limited noise introduced by the feed spillover beyond the subreflector, given that it is now directed to cold sky rather than hot earth (ground) as in the single-reflector case. Many satellite communication networks employ dual configurations as Earth terminal antennas. Finally, the inclusion of the subreflector introduces another degree of freedom, which can be used to enhance electrical performance, such as by canceling XPOL in offset systems, and/or prescribing the main aperture amplitude and phase distributions in dual shaped reflectors.

Within this context, dual shaped reflectors can be used to illuminate larger reflectors, such as the Arecibo (Puerto Rico) spherical reflector [23], forming a multiple-reflector system. In this case, they are shaped to correct the phase aberration characteristic of spherical reflectors. They can also be used to enhance the scanning properties of spherical reflectors [26].

A multiple-reflector system can also be formed with a parabolic main reflector, which is illuminated by a sequence of hyperboloids and/or ellipsoids employed as subreflectors. The subreflectors must be properly arranged such that a spherical wave is formed after each reflection. It can be shown [27] that such a multiple-reflector system is always equivalent to a single parabolic reflector, normally referred to as the *equivalent paraboloid*. This concept also applies to Cassegrain and Gregorian systems [25,27], and is especially useful to determine the conditions for canceling XPOL in offset systems, as discussed next.

3.2. Conditions for Minimizing Cross-Polarization in Offset Cassegrain and Gregorian Systems

The Cassegrain and Gregorian offset configurations of Fig. 3d can be optimized to cancel reflector-induced XPOL. We focus our discussion on the Gregorian system, but all main results presented here are also valid for the Cassegrain system [3,24,25]. Although less compact, the Gregorian configuration has been increasingly used in practical applications, especially as it allows the main reflector to have a

just fully offset geometry (i.e., the bottom of the main reflector just touches its axis of symmetry). Cost-effective designs often require that an existing single offset reflector mold be used to construct the main reflector of a dual configuration. However, many such existing molds in industry are for just fully offset geometries, which justifies the recent preference for Gregorian configurations. In order to upgrade an existing mold to a dual offset Cassegrain system, a main reflector other than just fully offset is required to avoid blockage. This is due to the fact that the hyperbolic subreflector, in contrast to the elliptical one, is located above the axis of symmetry of the parent main reflector, as shown by Fig. 3d. In addition, the Gregorian configuration allows the main reflector to be used also as a single-focused configuration without the need of removing the subreflector; see Section 3.3 for further details. Nevertheless, Cassegrain configurations have also been widely used in many practical systems, and all conditions for minimizing XPOL herein discussed also apply to them.

The general geometry of a dual offset Gregorian configuration is shown in Fig. 11, and the symbols are defined in Table 4. Although not shown in Fig. 11, the main reflector projected aperture is circular, such as the one in Fig. 4. The subreflector employed in a Gregorian offset design is a section of a parent ellipsoid described by the expression

$$\frac{(x_S - c)^2}{(f_S + c)^2} + \frac{y_S^2 + z_S^2}{(f_S + c)^2 - c^2} = 1 \quad (26)$$

where all variables and coordinates are as defined in Fig. 11 and Table 4. It is worth mentioning that the projections of the subreflector onto the $y_S z_S$ and $x_S y_S$ planes are ellipses.

As mentioned above, the geometry of Fig. 11 is equivalent to a single parabolic system. Furthermore, we saw previously that if the feed-pointing angle, ψ_f , is coincident with the reflector axis of symmetry, no substantial XPOL is generated. This condition can be satisfied for the equivalent single paraboloid, provided the original dual configuration of Fig. 11 satisfies the following relation [28]

$$\tan \alpha = \frac{|e^2 - 1| \sin \beta}{(1 + e^2) \cos \beta - 2e} \quad (27)$$

where e is the subreflector eccentricity ($0 < e < 1$ for an ellipsoid and $e > 1$ for a hyperboloid), $e = c/(f_S + c)$. Equation (27) is generally referred to as *Mizugutch condition* and has the following alternate form known as *Dragone condition* [25,27]

$$\tan \frac{\alpha}{2} = \frac{e + 1}{|e - 1|} \tan \frac{\beta}{2} \quad (28)$$

where the term $(e + 1)/(|e - 1|)$ is normally referred to as the *subreflector magnification*, M . Rusch et al. [25] gave a condition based on the same equivalent paraboloid concept that simultaneously minimize XPOL and spillover loss (i.e., feed radiation missing the subreflector)

$$\tan \frac{\beta}{2} = \left(\frac{e - 1}{e + 1} \right)^2 \tan \left(\frac{\beta + \psi_c}{2} \right) \quad (29)$$

where ψ_c is the angle subtended to the center of the main reflector and is given by Eq. (12). The Rusch condition, Eq. (29), can be applied only to dual systems employing a parabolic main reflector with a circular projected aperture, in contrast to Mizugutch or Dragone conditions,

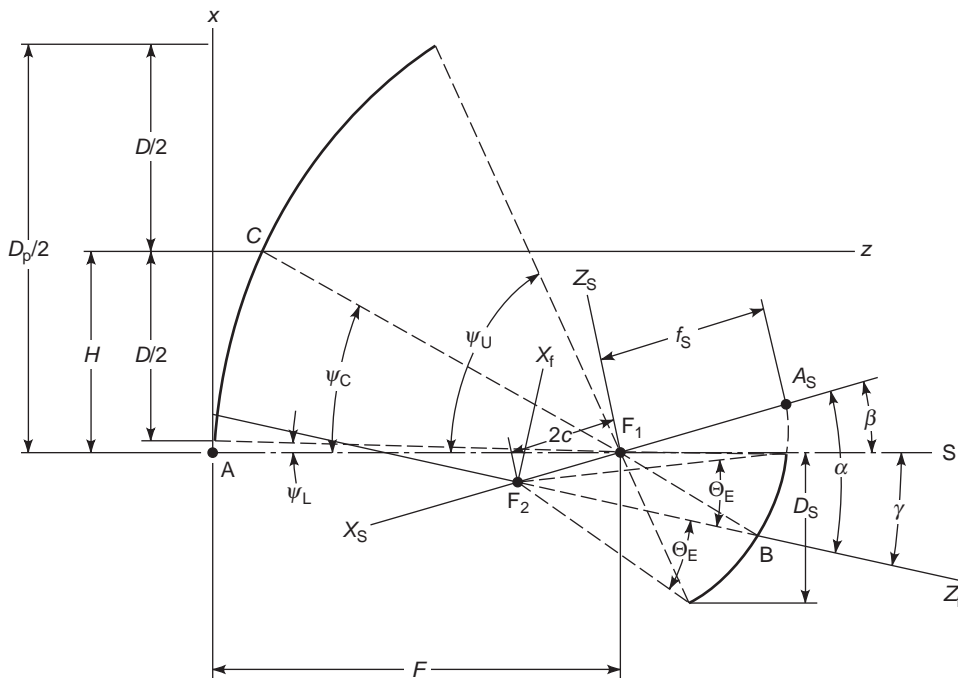


Figure 11. General geometry of the dual offset Gregorian reflector antenna. The symbols are defined in Table 4.

Table 4. Definitions of Symbols for Dual Configuration

Symbols	Definitions
D	Diameter of the projected aperture of the parabolic main reflector
D_p	Diameter of the projected aperture of the parent paraboloid
H	Offset of reflector center
F	Paraboloid focal length
Point F_1	Common focal point of the parabolic main reflector and ellipsoidal subreflector
Point F_2	Ellipsoid focal point; feed antenna location
Point A	Apex of the parent paraboloid
Point A_S	Apex of the ellipsoidal subreflector
Point B	Point on subreflector which bisects subtended angle viewed from F_2 ; point B also results from the intersection of the ray coming from point C on the main reflector and the feed axis (z_f)
Point C	Point on main reflector that projects to the center of the circular projected aperture
ψ_C	Angle of feed antenna pattern peak after reflecting on the subreflector relative to the main reflector axis of symmetry (s)
$(\psi_U - \psi_L)$	Angle subtended by the parabolic main reflector as viewed from the focal point F_1
D_S	Height of the ellipsoidal subreflector
e	Subreflector eccentricity ($0 < e < 1$ for an ellipsoid)
c	Half of the ellipsoid interfocal distance
f_S	Distance between a focal point and the closest ellipsoid apex
α	Feed pointing angle measured relative to the ellipsoid axis of symmetry (x_S)
β	Angle between the ellipsoid and parent paraboloid axes of symmetry (x_S and s , respectively)
γ	Angle between the main reflector and feed axes (s and z_f)
θ_E	Half of the angle subtended by the subreflector as viewed from the feed antenna location (ellipsoid focal point F_2)

Eqs. (27) and (28), which can be applied to reduce XPOL of systems with arbitrary projected apertures. Although more restrictive, the Rusch condition, in addition to XPOL, also minimizes spillover loss, given that the resulting equivalent paraboloid is constrained to be always axisymmetric [25]. This yields the feed axis of the original dual configuration pointing in the direction that bisects the subreflector subtended angle, as shown in Fig. 11. Enforcement of Mizugutch or Dragone conditions in general does not result in an axisymmetric equivalent paraboloid, which may lead to high spillover loss even though XPOL is kept to a minimum. In fact, the result in the Rusch condition, Eq. (29), can be visualized as the one particular solution of Eq. (27) or (28) that yields an axisymmetric equivalent paraboloid with $\psi_f = 0^\circ$, thus simultaneously minimizing XPOL and spillover loss.

It is important to note that Eqs. (27)–(29) are effective to reduce only the reflector-induced XPOL. A simple worst case model for predicting the influence of feed XPOL in reflector systems is [7]

$$\text{XPOL}_S = \text{XPOL}_F + \text{XPOL}_R \quad (30)$$

where XPOL_S , XPOL_F , and XPOL_R are respectively the cross polarization levels of the total system, the feed, and the reflector(s). XPOL here is expressed as a field ratio (not in decibels, using the $10^{\text{value in dB}/20}$ transformation). The simple result in Eq. (30) shows that either the feed or the reflector XPOL can dominate the system XPOL. Since dual offset configurations satisfying any of the conditions in Eqs. (27)–(29) yield low reflector XPOL, system XPOL is usually limited by feed XPOL. We use, as an example, a low cross-polarized dual offset Gregorian reflector antenna, employing a just fully parabolic main reflector with a 2.4-m diameter. When a feed XPOL value of -32 dB is

included, the system XPOL computed by GRASP [14] increases from -48.19 to -31.75 dB. Equation (30) yields -30.75 dB, which is in good agreement for such a simple formula. In addition, Eq. (30) can also be used to predict a feed XPOL level required to attend a given specification of system XPOL.

A clever way to minimize feed XPOL in synchronous satellite reflector systems is by using a *dual-gridded* reflector [29], normally made of carbon-fiber-reinforced plastic (CFRP). In this configuration, the parabolic reflector consists of two almost completely superimposed shells, such that the respective focal points fall in different locations to be fed by different feed antennas. Each shell reflects only one type of linear polarization. In a single *dual-gridded* configuration, the phase center of each one of the feeds is placed at the focal point of the parabolic shell that reflects the corresponding feed polarization. Thus the XPOL of the feed generating one type of polarization will be reflected only by the shell with a different focal point. This causes the XPOL beam to scan off boresight, as seen in Section 2.3.3. With the proper choice of orientations for the two shells, the XPOL beams generated by both feeds are steered off Earth coverage while the COPOL beams are kept at the desired locations.

As an illustration of using the minimum XPOL conditions expressed in Eqs. (27)–(29), we consider the offset parabolic system discussed next.

3.3. The Green Bank Radio Telescope

The Green Bank (Radio) Telescope (GBT) is the largest fully steerable radio telescope in the world (see Fig. 12). Its offset design provides a clear 100-m-diameter projected aperture. The GBT structure can be pointed to view the

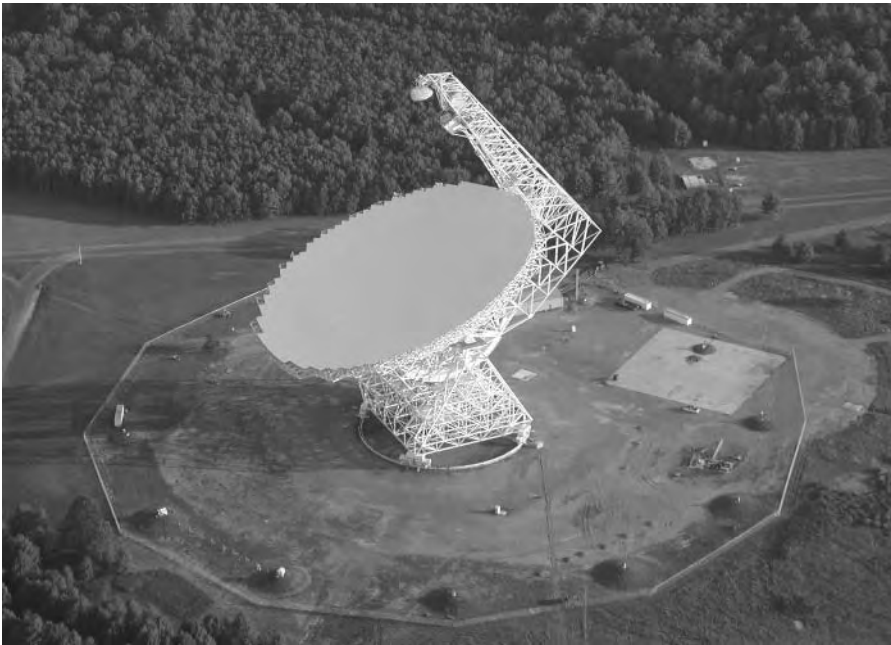


Figure 12. The Green Bank Radio Telescope reflector antenna. The 100-m main reflector consists of 2000 solid panels. The structure can be pointed to view the entire sky down to a 5° elevation angle, and is the largest fully steerable radio telescope in the world. (Courtesy of the National Radio Astronomy Observatory—NRAO/AUI/NSF.)

entire sky down to a 5° elevation angle using a wheel-and-track mechanical design. The reflecting surface consists of 2000 solid panels that can be positioned using actuators behind the panels. A laser-ranging system is used to determine the positions of the panels, adjusting surface accuracy with closed-loop control.

The GBT is connected to radiometers that can receive signals in several frequency bands. From 290 to 1230 MHz, the GBT operates as a single offset reflector using a feed assembly aimed directly at the main reflector. From 1 to 45 GHz, it operates as a Gregorian dual offset reflector using the feeds in the receiver room that are aimed at the ellipsoidal subreflector. The Gregorian con-

figuration has the focal points in the area between the subreflector and the main reflector, allowing the subreflector to remain fixed even when the telescope operates in the single offset reflector mode. This is not possible with a Cassegrain configuration [30].

We start by examining the GBT single offset configuration, with the characteristics listed in Table 5, employing the codes GRASP [14] and PRAC [7]. Further information on the parabolic reflector analysis code (PRAC) are presented in Section 4.2. The performance values, also listed in Table 5, were computed at 15 GHz in the plane normal to the plane of symmetry (i.e., the yz plane of Fig. 4). Note that both codes yield very similar results for this

Table 5. GBT Single-Offset-Reflector Configuration and Computed Performance Values

a. Main Reflector Configuration		
Shape	Offset paraboloid	
Projected diameter D	100 m	
Parent reference Diameter D_p	208 m	
Focal length F	60 m	
Offset of reflector center H	54 m	
b. Feed Configuration (On Focus)		
Computation	PRAC	GRASP
Polarization	Linear (x_f) cosine ^{4,58} ; Eqs. (14), (21)	Linear (x_f)
Pattern shape		Gaussian; Eqs. (14), (15)
Gain G_f (dBi)	13.08	13.14
10-dB beamwidth, degrees (deg)	77.92	77.92
Feed angle (ψ_f), degrees (deg)	42.77	42.77
System performance gain G (dBi)	82.87	82.79
Cross-polarization level (XPOL) (dB)	-21.54	-21.56
Sidelobe level (SLL) (dB)	-26.72	-27.21
Aperture efficiency ϵ_{ap} (%)	78.48	77.05

Table 6. GBT Dual Offset Reflector Configuration and Computed Performance Values

a. Reflector Configuration Values		
Main Reflector Configuration	Subreflector Configuration	
Shape: offset paraboloid	Shape: offset ellipsoid	
Projected diameter D , 100 m	Projected height D_S , 7.55 m	
Parent reference diameter D_p , 208 m	Parameter c of ellipse, 5.9855 m	
Focal length F , 60 m	Parameter f_S of ellipse, 5.3542 m	
Offset of reflector center H , 54 m	Eccentricity e 0.5278	
Angle (β), 5.58°	Angle (β), 5.58°	
b. Computed Performance Values		
Feed Configuration (On Focus)	GRASP	System Performance (GRASP)
Polarization	Linear (x_f)	Gain G 82.83 dBi
Pattern shape	Gaussian; Eqs. (14), (15)	Cross-polarization level (XPOL) -43.01 dB
Gain G_f	21.31 dBi	Sidelobe level (SLL) -22.56 dB
10-dB beamwidth	30°	Aperture efficiency ϵ_{ap} 77.76%
Angle (α)	17.91°	
Angle (γ)	12.33°	

geometry. We note from Table 5 that gain is 82.87 dBi and XPOL is -21.54 dB (61.33 dBi), as computed by PRAC.

In order to lower XPOL, we upgrade the GBT single offset system of Table 5 to a low cross-polarized dual offset Gregorian antenna according to Eq. (29). Design parameters, such as the desired subreflector size, were obtained from [1]. The resulting configuration is listed in Table 6 and agrees with [30]. New dual configurations employing the same GBT offset main reflector of Table 5 can be obtained using different design parameters, such as a new subreflector size or feed configuration, as discussed in [31].

Table 6 also presents the performance values at 15 GHz computed with GRASP in the same plane considered for the single offset configuration discussed previously. We note that XPOL is now -43.01 dB, more than 20 dB lower than the XPOL of the single configuration in Table 5. However, a feed antenna with high XPOL will likely degrade the total system XPOL performance, as addressed in the previous section.

4. ANALYSIS METHODS AND EVALUATION

4.1. Geometric and Physical Optics Formulations

In both geometric optics (GO) and physical optics (PO) formulations, the ultimate goal is to determine equivalent currents that can then be integrated to obtain the far-field patterns, a process well described in the literature on aperture antennas [20]. Here we focus on the assumptions and approximations inherent to each of these formulations, as well as on their intrinsic differences.

The GO technique yields the aperture fields assuming that Snell's law is satisfied on reflection. The far-field patterns can then be calculated using a Fourier transform directly, which is equivalent to obtaining equivalent currents and then integrating as described later in this section. With the use of image theory, it is necessary to know only the electric field distribution over the reflector pro-

jected aperture \mathbf{E}_r , which is computed from the incident electric field \mathbf{E}_i (i.e., the feed radiation), with [20]

$$\mathbf{E}_r = 2(\hat{n} \cdot \mathbf{E}_i)\hat{n} - \mathbf{E}_i \quad (31)$$

where \hat{n} is the unit vector normal to the surface; see Eq. (5). Equation (31) assumes that at the point of reflection the reflector is planar and perfectly conducting. In addition, the incident wave from the feed antenna is treated locally as a plane wave. These same assumptions are also used by the PO technique to determine the surface currents, \mathbf{J}_s , over the reflector as follows

$$\mathbf{J}_s = 2\hat{n} \times \mathbf{H}_i \quad (32)$$

where \mathbf{H}_i is the incident magnetic field from the feed antenna, and can be computed from Eq. (14), recalling that in the far-field $\mathbf{H} = (\hat{r} \times \mathbf{E})/\eta$ (where η is the free-space characteristic impedance). The PO approximation assumes that currents exist only over the side of the reflector directly illuminated by the feed antenna.

The far-field pattern can then be determined by summing up the individual contributions of each current point over the surface, taking into account the different amplitudes and phases due to the excitation and spatial location. Antenna theory shows that a unitary point source of current radiates a spherical wave, which is normally referred to as the *free-space Green function* ($e^{-jkr}/4\pi r$); see [20] for further details. In the limit, as the current distribution becomes continuous, such as the one given by Eq. (32), the weighted sum of spherical waves becomes an integral, yielding the radiated patterns.

Note that the integration process for obtaining the patterns is the same of the one employed by the GO technique, given that once the aperture distribution is determined from Eq. (31), equivalent currents can then be obtained and integrated over the reflector aperture. This process is equivalent to computing the Fourier

transform of the aperture distribution given in Eq. (31). One difference between GO and PO is that PO currents are determined over the reflector *curved* surface and the GO equivalent currents, over the *planar* projected aperture; the latter are already in a format more appropriate for integration through a Fourier transform. However, the use of a Jacobian transformation [3,4] maps the PO currents over the reflector curved surface to the planar aperture, yielding the possibility of also using Fourier transforms for performing the integration. Analytical integration is possible only for arbitrary symmetric reflectors [4,8], and numerical techniques are normally required to evaluate offset reflectors, as discussed in the next section.

The PO formulation is generally considered more accurate than GO to evaluate offset reflectors, especially if XPOL assessment is of main concern. However, pattern accuracy as determined from both techniques degrade beyond the mainbeam and near-in sidelobes. The pattern in the far-out region is dominated by diffraction effects, especially scattering from the reflector and/or subreflector edges. This is accounted for by augmenting GO with the use of the geometrical theory of diffraction (GTD) or augmenting PO with edge currents through the physical theory of diffraction (PTD); see [20] and [32] for further details. However, the near-in pattern region is, most of the time, the region of interest when analyzing high-gain antennas such as the reflector antennas considered here.

4.2. Numerical Implementation and Accuracy Evaluation

In this section we discuss one of many possible numerical implementations of the PO formulation addressed above; see [4] for alternate procedures. Reflector surface currents are computed from Eq. (32) for the balanced feed model given by Eqs. (14) and (21). A set of coordinate transformations, rotations, and translations is necessary in order to describe the far-field patterns as a function of the reflector local coordinate system $\{xyz\}$, given that the feed pattern is described as a function of the feed local coordinate system $\{x_f y_f z_f\}$. Although not shown, Eulerian angles [33] are employed for generality, and we mention that a solid background on geometry and vector calculus is normally required for the analysis of reflector antennas.

The procedure employs a Jacobian transformation, as discussed previously, and evaluates numerically the following integral [4] using a numerical procedure based on the Gauss–Zirniké integration method [34]

$$\vec{E}(\vec{r}) = -j \frac{\eta}{2\lambda} \frac{e^{-jkR}}{R} (\vec{I} - \hat{r}\hat{r}) \cdot \int_{s'} \int \vec{J}(\vec{r}') J_{\Sigma} e^{jk\hat{r} \cdot \vec{r}'} ds' \quad (33)$$

where $\hat{r} \cdot \vec{a}$ is shorthand for $\hat{r}(\hat{r} \cdot \vec{a})$, and $(\vec{I} - \hat{r}\hat{r})$ is included to remove the radial component (far-field approximation) [4]. The unit dyad \vec{I} is equal to the identity matrix for our purposes, and the Jacobian transformation, J_{Σ} [4,33], is employed to allow the integral to be evaluated over the reflector planar projected aperture s' . However, the currents are still defined over the reflector curved surface. In addition, the Jacobi–Bessel method [33] is used to express part of the kernel in Eq. (33) as a sum over a set of

orthogonal functions defined on the antenna aperture. Within this context, numerical integration is necessary only to evaluate the coefficients of the series expansion, which employs the modified Jacobi polynomials in the radial direction and a Fourier series in the circumferential direction.

The aforementioned procedure was implemented in the code PRAC (parabolic reflector analysis code) [7]. PRAC is a user-friendly code developed by the author to analyze axisymmetric and offset parabolic reflectors, and yields the co- and cross-polarized radiated fields with high accuracy and efficiency. PRAC is currently being used by many universities and major industries worldwide, and an academic version of the code is distributed with [20].

In order to evaluate the accuracy of the code, we select as a baseline configuration for analysis a just fully offset paraboloid with a diameter $D = 85.5\lambda$, $F/D_p = 0.3$, and offset distance $H = 42.75\lambda$. The reflector illumination is modeled by the balanced feed described by Eqs. (14) and (21), with a 10 dB beamwidth of 78° ($q = 4.57$ yielding a feed gain of 13.07 dBi). The offset reflector choice corresponds to a 1.8-m-diameter VSAT Earth terminal antenna operating at 14.25 GHz, similar to the one shown in Fig. 13.

Figure 14 shows the computed co- and cross-polarized patterns and measured data for the example offset parabolic reflector in the plane normal to the plane of symmetry (i.e., the yz plane). XPOL is expected to be maximum at

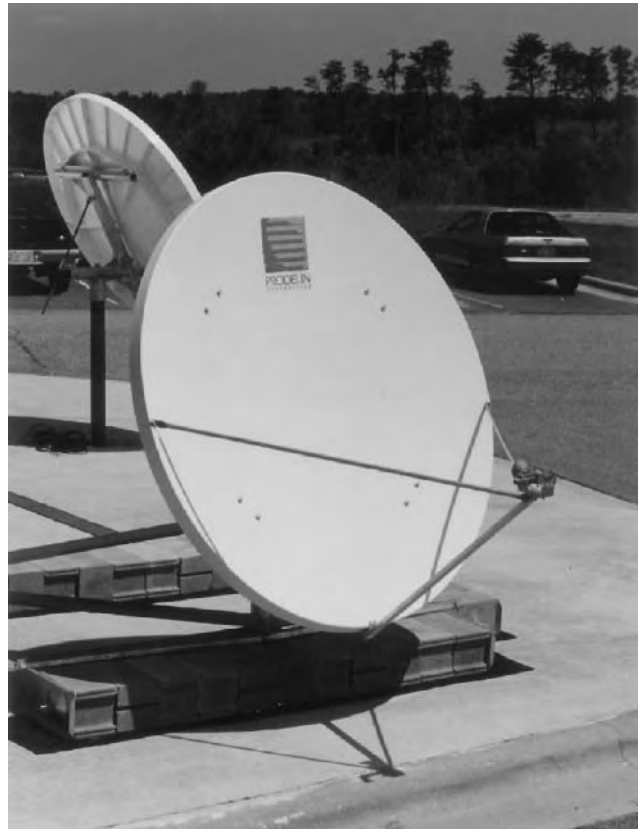


Figure 13. Just fully offset parabolic reflector antenna with a projected aperture diameter of 1.8 m (courtesy of Nick Moldovan, Prodelin Corp.).

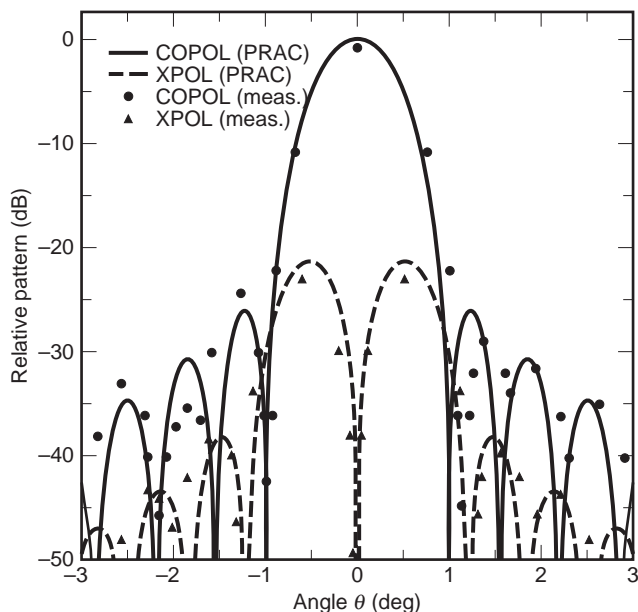


Figure 14. Computed and measured radiation patterns at 14.25 GHz of a 1.8-m single-offset parabolic reflector antenna.

this plane, as discussed in Section 2.3.1. We note from Fig. 14 that the results obtained with PRAC are in good agreement with the measured data. The measured gain of 46.78 dBi is about 0.8 dB below the computed gain of 47.60 dBi due to losses and system imbalances. System XPOL is also a little overestimated by the computer simulations for this example. In fact, the measured system XPOL is -22.00 dB, whereas PRAC yields -21.27 dB. Nevertheless, PRAC yields a valuable estimate on how the reflector system behaves electrically, showing the necessity of a numerical evaluation previous to the manufacturing process. It is worth mentioning that analysis of this same baseline configuration with the physical optics portion of GRASP [14], yielded almost identical results [7], with the exact same locations for the nulls and peak side lobes and XPOL lobes, confirming the accuracy of PRAC and PO analysis for evaluating offset reflectors.

As final notes on the analysis of reflector antennas, we mention that the lower integration limit in Eq. (33) can be set such that to account for an equivalent circular area of blockage, normally caused by the feed and supporting structure in axisymmetric reflectors. In addition, the integral in Eq. (33) can also be evaluated over areas s' other than the circular, in order to analyze reflectors with projected apertures such as the elliptical one. Reflectors with elliptical apertures present a far-field pattern with a mainbeam that is narrower in the plane containing the major axis of the ellipse, and are used in practice to transmit signals to synchronous satellites. The main advantage is a more compact design, when compared to the full circular aperture, offering less resistance to wind and saving material during the manufacturing process. The lower gain (i.e., wider beam) in the plane containing the minor axis of the ellipse does not degrade system performance for this particular application, given that only a single belt

of synchronous satellites exists and therefore beam resolution is required only in one plane. Finally, both GO and PO formulations can also be used to evaluate dual- and multiple-reflector systems. The simplest procedure is to first determine the radiation pattern of the system formed by the feed antenna and subreflector, and then use this result as the incident field on the next subreflector or main reflector. It is also common to employ GO for the subreflector analysis and then PO in the final step to evaluate the main reflector for better accuracy. This combination saves computer time as GO analysis is generally faster than PO [20].

5. FEED ANTENNAS

Feed antennas for reflector configurations are normally horn antennas (sectoral, pyramidal, conical corrugated, etc.), although wire antennas and others are also encountered in practice. The sectoral horn, for instance, is used for illuminating reflectors with elliptical projected apertures, which were discussed previously. In addition, it is also common to have an array of horns or other type of feed antennas illuminating shaped reflectors or large reflectors, such as radiotelescopes. This is because the array yields better control on the phase distribution employed to illuminate the reflector, enhancing beam contour and beam-scanning performance. Equation (17) can be used to set the initial positions for the feed antennas [3]. A contoured beam is required to illuminate properly an specified region of Earth, as seen from a satellite, and can be accomplished with the shaping of the reflector or with the use of a feed array; see also Section 6 for more details. An example of a multifeed array illuminating a parabolic reflector for contoured beam applications is the Intelsat-9 series of C-band and Ku-band satellites, built by Space Systems/Loral (see Fig. 15). The transmit feed array has more than 100 feed horns and is located on the Earth deck tower, facing the largest reflector shown in Fig. 15, which is a parabolic reflector with a superquadric projected aperture. Feed horns, as well as the remaining parts of the feed chain (polarizer, orthomode transducer, diplexer, etc.), can be manufactured with very good precision and electrical performance from aluminum, magnesium, titanium, graphite, or carbon-fiber-reinforced plastic (CFRP), glass fiber reinforced plastic (GRFP) and other materials.

We start by discussing analytical models that approximately describe the electrical behavior of feed antennas usually encountered in practice. It is not our intention to analyze feed antennas completely, but rather present simple analytical models that can be useful to antenna engineers as a first approximation to real feed patterns or more sophisticated models available in the literature [35]. The simplest model is the balanced feed given by Eq. (14), normally used with Eq. (15) or (21). Balanced radiation patterns can be obtained in practice with the use of multimode horns, like the Potter horn, and hybridmode horns, such as the conical corrugated ones [24,35]. An alternate version of Eq. (14) can be obtained for feeds presenting different pattern cuts in the E plane ($\phi_f = 0^\circ$) and H plane ($\phi_f = 90^\circ$). The feed patterns in these two planes are

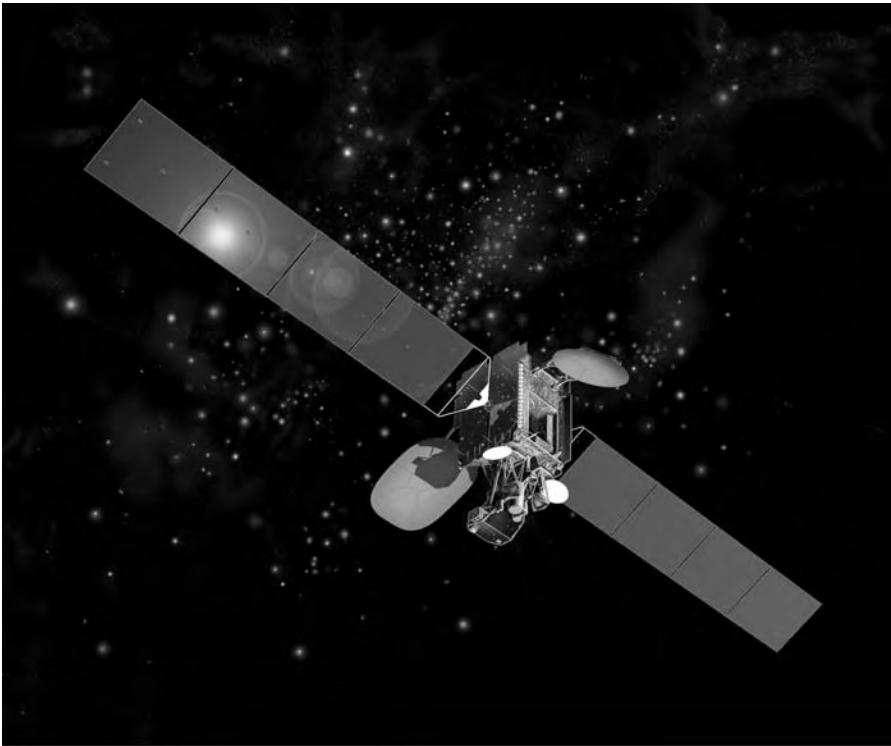


Figure 15. Intelsat-9 series of seven C-band and Ku-band satellites. The transmit feed array contains more than 100 feed horns and is located on the Earth-deck tower, facing the largest reflector shown in the figure. (Courtesy of Space/Systems Loral and Intelsat.)

usually all that is known. As in Eq. (14), we assume that the feed is purely linearly polarized in the x_f direction, yielding [3]

$$\mathbf{E}_f = \frac{e^{-jkr_f}}{r_f} [\hat{\theta}_f C_E(\theta_f) \cos \phi_f - \hat{\phi}_f C_H(\theta_f) \sin \phi_f] \quad (34)$$

where $C_E(\theta_f)$ and $C_H(\theta_f)$ denote the feed pattern cuts in the E and H planes, respectively. A y_f -polarized feed pattern, as well as circularly polarized ones, can be obtained from Eq. (34) introducing the modifications already suggested in Section 2.3.1. Note that Eq. (34) reduces to Eq. (14) for $C_E(\theta_f) = C_H(\theta_f) = C(\theta_f)$, yielding a balanced illumination.

As discussed in Section 2.3.4, balanced feeds yield improved performance when illuminating reflector systems. A type of balanced feed antenna widely used in practice is the corrugated conical horn, also often referred to as the *scalar horn*. Corrugated conical horns present a phase center that is reasonably stable with frequency [24,35], in addition to a copolarized pattern that is nearly balanced for practical purposes and can be well modeled by Eqs. (14) and (15) or (21).

The main purpose of using corrugations is to obtain the same boundary conditions around the inside of the horn. For corrugation depths of a quarter wavelength, the short circuit at the bottom is transformed to an open circuit at the top of the corrugation, yielding boundary conditions that appear to be more uniform as the number of corrugations per wavelength increase [20]. This yields a symmetric radiation pattern down to as low as -25 dB over a

reasonably wide operational bandwidth, typically of 1.6:1 or more.

The cross-polarized pattern, however, may contain peaks in the 45° planes [35]. As discussed in Section 3, and approximately modeled by Eq. (30), feed XPOL peaks appear in the far-field patterns of dual reflector systems, even with the enforcement of the conditions given by Eqs. (27)–(29). In order to minimize feed XPOL, a careful design and construction process must be performed. The corrugation depths must be set properly to achieve resonance, taking into account all dimensions related to the corrugations as well as the general geometry of the horn [24]. The process has been successfully accomplished in practice, often also employing sections of tapered and/or dual-depth corrugations, yielding horns presenting balanced copolar patterns and XPOL levels below -35 dB over practical operational bandwidths [24,36].

6. ADVANCED TOPICS AND RESEARCH

6.1. Reflector Antenna Upgrading

Reflector antenna designs have evolved through several configurations in order to increase performance and/or reduce structural complexity. Electrical parameters that are of prime interest are aperture efficiency, sidelobe level (SLL), and, more recently, cross-polarization level (XPOL). All topics discussed here apply to the various types of reflectors addressed previously. However, the offset configuration is the one most likely to retain in the near future the largest percentage of the reflector antenna market.

We first focus our attention on XPOL. Reflector antennas presenting low XPOL performance (e.g., $\text{XPOL} \leq -35 \text{ dB}$) are necessary for frequency reuse applications, in which an overlap of orthogonally polarized channels is permitted. Many efforts are being conducted to develop these kinds of antennas for mass production [7,37]. Dual offset reflectors can be designed for low-cost construction, provided that specific manufacturing constraints are carefully taken into account [7], an effort that can be achieved only with the increased interest of industry. Single offset systems illuminated by a matched feed [24] or a feed with a lens [37] can also be designed to satisfy stringent requirements on XPOL, yielding very compact designs. In the latter case, the lens is designed such that it replaces the subreflector, and in both cases bandwidth performance is not obtained as easily as with the dual-reflector configuration. Research continues to be conducted within the area, yielding innovative solutions that provide satisfactory XPOL performance while attending practical manufacturing specifications. Cost-effective solutions normally require that attendance of a particular specification, such as low XPOL, be achieved with minimal capital outlay, which implies on using the maximum amount of infrastructure and technology already implemented. In particular, as mentioned previously, there is a tendency to employ existing molds for the main reflector, a concept referred to as *reflector upgrading* [7].

Within this context, existing single offset reflector molds are normally used to construct the main reflector of a dual configuration. However, many such molds are for just fully offset geometries, which in general produce a dual reflector configuration that is Gregorian with the feed axis z_f intersecting the main reflector (see Fig. 11). The same problem may also occur in certain Gregorian configurations even when the main reflector is not just fully offset. The final design should provide suitable clearance between the bottom of the main reflector and the feed axis in order to access the feed antenna with a straight section of waveguide, thus reducing the complexity and cost of the manufacturing process. This setup is achieved by rotating the parent ellipsoid (i.e., the conical surface from where the subreflector is generated) until the desired clearance is obtained. The rotation is performed in a way such that the feed remains pointed toward the intersection of the new subreflector and the ray coming from the center of the main reflector, thus avoiding the introduction of spillover and phase errors.

The non-conventional design obtained after the rotation of the parent ellipsoid may present a XPOL degradation due to the fact that the minimum XPOL conditions, Eqs. (27)–(29), are no longer satisfied. A simple solution to this problem is to alter the value of the subreflector eccentricity, while keeping all orientation angles constant. In general, eccentricity values greater than the one employed before the rotation will reduce system XPOL [7], yielding a low cross-polarized dual offset Gregorian antenna that has adequate clearance between the feed axis and the bottom of the main reflector. In addition, the resulting configuration has the ability to operate with either a linearly polarized (LP) or a circularly polarized (CP) feed over a wide bandwidth without the need of being repositioned

(no substantial beam squint). Conversely, subreflector rotation can also be utilized with CP feeds to achieve beam scanning through beam squint, given the introduction of linear XPOL in a controlled way [38]. The process keeps the reflector system focused at all times, avoiding pattern degradations and sustaining broad operational bandwidth.

Compact designs for reflector systems is also a subject that has been investigated for years. It is desirable, for example, to upgrade a main reflector with a subreflector that is as small as possible. In addition, with the spreading of satellite TV at Ku band (see Figs. 16 and 17) employing single offset systems for reception, there is now widespread interest to minimize the size of the reflector while maintaining a required gain performance. This is only possible by increasing aperture efficiency through the reduction of diffraction effects and feed blockage. High-performance feeds are also necessary, especially if they are located close to the reflector, such as in a very compact design, requiring a complete near-field analysis. Finally, microelectronics technology is integrating both low- and high-frequency hardware to the feed system. It is common nowadays to find feeds that already include low-noise amplifiers, downconverters, and other electrical devices in a single unit.

6.2. Shaped, Deployable, and Frequency-Selective Reflector Surfaces

Reflector antennas can be shaped to improve gain and aperture efficiency. The basic concept is to shape the subreflector of a dual-reflector system to obtain the desired amplitude distribution at the main reflector projected aperture, normally nearly uniform for maximizing gain, and then shape the main reflector to recover the uniform phase distribution that was disturbed by shaping the subreflector. Resulting aperture efficiencies are usually in the range of 70–80%, although higher values have been reported for dual shaped offset systems [11]. The fundamental tradeoff that antenna designers must face, in this case, is the achievement of such efficiencies while still achieving satisfactory sidelobe levels.

Another topic certain to continue receiving attention in the future is the shaping of single-reflector systems for contoured beam applications. A contoured beam is necessary to illuminate efficiently from a satellite specific regions of Earth. This avoids unnecessary coverage of regions outside the satellite main service area. Reflector shapes for contoured beam and high-gain applications, especially for the offset case, are normally obtained numerically through elaborated synthesis and optimization processes [3–5,9,10,39], which include the feed antenna or array. Also important is the mathematical and numerical modeling of the surfaces to yield results possible to be implemented in practice [40]. Research has been conducted comparing the electrical performance of the following three configurations: (1) shaped reflector with a single feed, (2) parabolic reflector with a feed array, and (3) shaped reflector with a small feed array (hybrid configuration). Preliminary results indicate that the electrical performance (mainly gain and isolation) peaks for the first

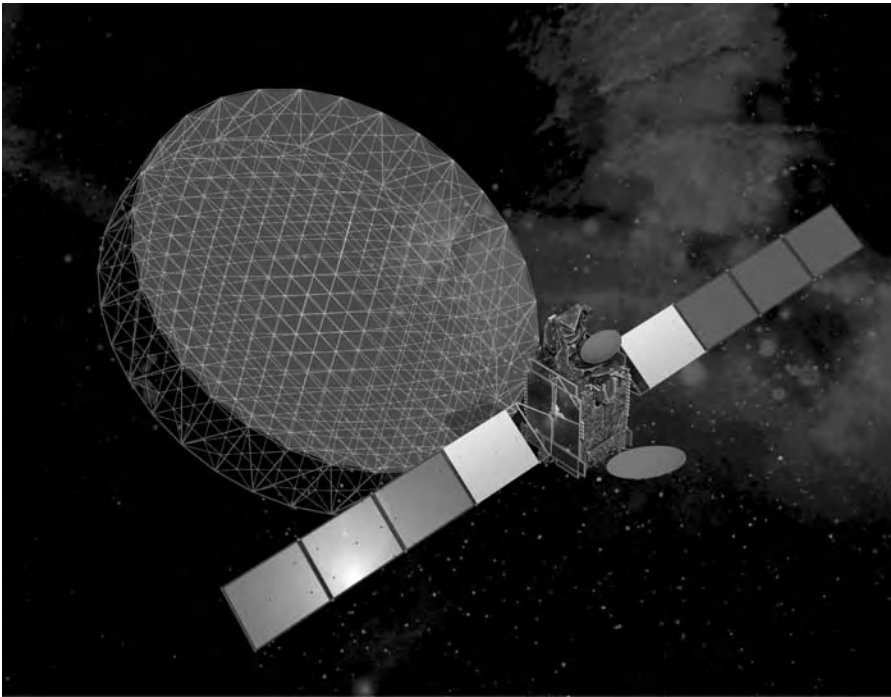


Figure 16. The MBSat satellite owned by Mobile Broadcasting Corporation (MBCO) of Japan and SK Telecom of Korea employs an unfurlable 12-m S-band reflector and two Ku-band reflectors to provide Japan and South Korea separately with over 50 channels of CD-quality audio and TV-quality video, traffic, and emergency information; newspaper and magazine content; games; and other services. (Courtesy of Space/Systems Loral.)

two configurations, with the hybrid one falling between them. In particular, state-of-the-art space technology employs a single receive/transmit feed illuminating a shaped reflector, nowadays a configuration with similar electrical performance to the parabolic reflector illuminated by a large feed array but with a quicker production time. The iPSTAR-1 satellite, for example, employs three Ku-band shaped reflectors on the Earth deck tower, in addition to the multibeam Ku-band and Ka-band deployable reflectors on the east and west panels, (see Fig. 18). Most shaped reflectors are fabricated from carbon-fiber-rein-

forced plastic (CFRP) using graphite molds, although other materials can also be used; see Section 2.4.

Reconfigurable shapes, deployable reflectors, and polarization- or frequency-selective surfaces require an in-depth study of electrical and magnetic materials, showing that reflector antenna engineering is currently impossible without large interdisciplinary activities. Frequency-sensitive surfaces, for example, reflect only radiation in specific frequency bandwidths [1]. A four-frequency reflector system has been used for the ESA/NASA Cassini mission to Titan, the largest moon of Saturn [1]. The subreflector

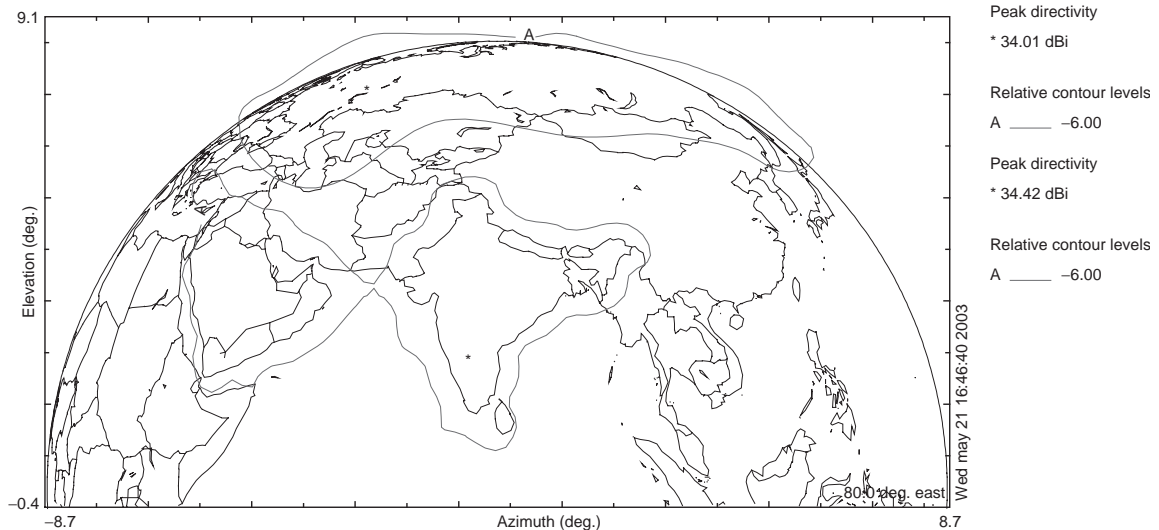


Figure 17. Reflector antenna 6-dB contours for Russia and India/Middle East coverages for a geosynchronous Ku-band satellite positioned at an orbital location of 80° east. (This figure is available in full color at <http://www.mrw.interscience.wiley.com/erfme>.)

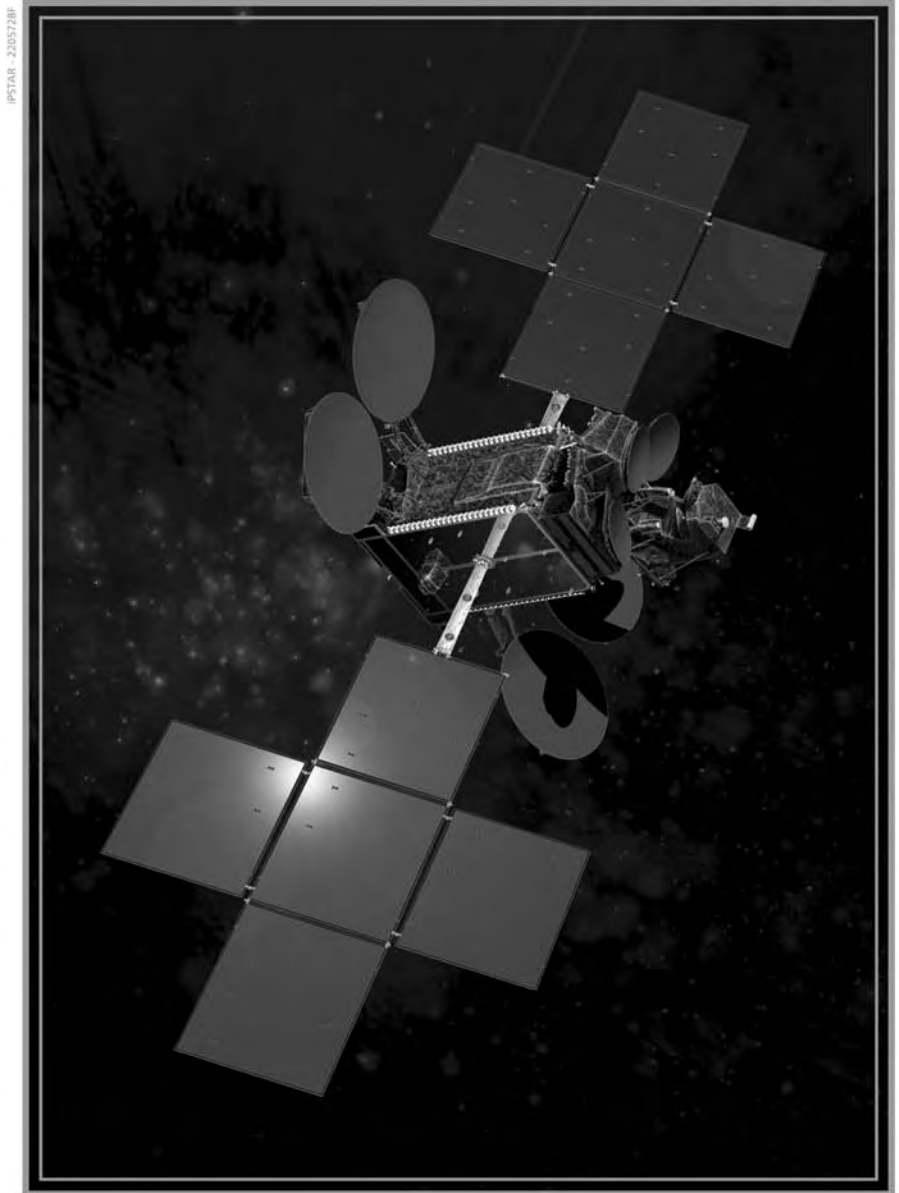


Figure 18. The iPSTAR-1 broadband satellite, owned by Shin Satellite Plc of Thailand, uses seven reflectors to generate 84 Ku-band spot beams, three Ku-band shaped beams, and 16 Ka-band spot beams, to provide direct-to-desktop last-mile services, including multimedia and data communication to customers in Asia, India, and Australia (courtesy of Space/Systems Loral).

carried by the Voyager spacecraft is another example, being transparent to radiation at S band and reflecting at X band. The subreflector was manufactured with X-band resonant aluminum crosses etched on a Mylar sheet, yielding reflecting and transmitting losses lower than 0.1 dB [1]. Geometries other than crosses can be obtained through the optimization techniques presented in the Section 6.4.

In particular, reflectors that can be deployed in space deserve distinct attention. The classical solution is the so-called umbrella reflector [1], which works well for axisymmetric and offset configurations. An idea that seems promising for the offset case is a configuration that opens similarly to a manual fan. An alternative to the classical umbrella configuration is an unfurlable configuration that

becomes self-sustained after deployment, such as the 12-m S-band meshed reflector antenna used in the MBSat satellite; see Fig. 16 for details. In addition, inflatable reflectors have also been investigated, with the successful construction and testing of a few prototypes.

6.3. Reflector Antenna Isolation

Isolation is one of the most important parameters related to reflector antennas in wireless communication networks, assessing the level of interference between multiple antenna beams within the same system or different systems. The multiple beams may be generated by the same or different reflector antennas. Isolation is normally accounted and optimized at the reflector antenna level [41].

Table 7. Definitions of Symbols for Transmit Isolation

$g_d(x_d)$	Gain of the transmit antenna serving the desired coverage at any and all points x_d within coverage “ d ”
$g_i(x_d)$	Gain of the transmit antenna serving the interfering coverage “ i ” with the same frequency and sense of polarization as the desired coverage “ d ” and at any and all points x_d within coverage “ d ”
$g_{\min,i}$	Minimum coverage gain of the transmit antenna serving the interfering coverage “ i ”
$g_{\min,d}$	Minimum coverage gain of the transmit antenna serving the desired coverage “ d ”
$EIRP_{\min,d}$	Minimum coverage $EIRP$ of the transmit antenna serving the desired coverage “ d ”
$EIRP_{\min,i}$	Minimum coverage $EIRP$ of the transmit antenna serving the interfering coverage “ i ”

Worst-case figures combined with error margins and tolerances are then employed to assess and optimize system level performance. We start by presenting procedures to evaluate beam-to-beam and composite isolation in wireless networks. The procedures are then implemented at an antenna level for a case example of a multibeam satellite network. It is worthy mentioning that the transmit isolation is always assessed over the *desired* beam(s), whereas the receive isolation over the *interfering* beam(s).

6.3.1. Transmit Beam-to-Beam Isolation. The *transmit isolation* between two cell coverages (i.e., physical area or space illuminated by the beams) is defined as the power ratio between the copolar pattern of the desired coverage “ d ” and the copolar or crosspolar pattern of the interfering coverage “ i ” at any point “ x_d ” within coverage “ d .” The transmit isolation between the two coverages is referred to here as “[$I_{TX}(x_d)$] $_{di}$ ” and defined by the following equation:

$$[I_{TX}(x_d)]_{di} = 10 \log_{10} \left(\frac{g_d(x_d) g_{\min,i} EIRP_{\min,d}}{g_i(x_d) g_{\min,d} EIRP_{\min,i}} \right) \quad (35)$$

where all symbols are as defined in Table 7.

6.3.2. Receive Beam-to-Beam Isolation. The receive isolation between two cell coverages is defined as the power ratio between the copolar pattern of the interfering coverage “ i ” and the copolar or cross-polar pattern of the desired coverage “ d ” at each point x_i within coverage “ i .” The receive isolation between the two coverages is referred to here as “[$I_{RX}(x_i)$] $_{di}$ ” and defined by the following equation

$$[I_{RX}(x_i)]_{di} = 10 \log_{10} \left(\frac{g_i(x_i) g_{\min,d} S_{\max,d}}{g_d(x_i) g_{\min,i} S_{\max,i}} \right) \quad (36)$$

where all symbols are as defined in Table 8.

Table 8. Definitions of Symbols for Receive Isolation

$g_i(x_i)$	Gain of the receive antenna serving the interfering coverage “ i ” with the same frequency and sense of polarization as the desired coverage “ d ” at the X% worst-case point “ x_i ” within coverage “ i .”
$g_d(x_i)$	Gain of the receive antenna serving the desired coverage “ d ” at the X% worst-case point “ x_i ” within coverage “ i .”
$g_{\min,d}$	Minimum coverage gain of the receive antenna serving the desired coverage “ d ”
$g_{\min,i}$	Minimum coverage gain of the receive antenna serving the interfering coverage “ i ”
$S_{\max,d}$	Maximum coverage power flux density within the desired coverage “ d ”
$S_{\max,i}$	Maximum coverage power flux density within the interfering coverage “ i ”.

6.3.3. Transmit Composite Isolation. The isolation between a desired cell coverage “ d ” and all other interfering cell coverages “ i ” is referred to here as the *composite transmit isolation* [$I_{TX}(x_d)$] $_d$ and defined as

$$[I_{TX}(x_d)]_d = 10 \log_{10} \left[\frac{1}{\sum_{d(d) \neq d(i)} \left(\frac{g_d(x_d) g_{\min,i} EIRP_{\min,d}}{g_i(x_d) g_{\min,d} EIRP_{\min,i}} \right)^{-1}} \right] \quad (37)$$

where all symbols are as defined in Table 7.

6.3.4. Receive Composite Isolation. The isolation between a desired cell coverage “ d ” and all other interfering cell coverages “ i ” is referred to here as the *composite receive isolation* [$I_{RX}(x_i^+)$] $_d$ and defined as

$$[I_{RX}(x_i^+)]_d = 10 \log_{10} \left[\frac{1}{\sum_{d(d) \neq d(i)} \left(\frac{g_i(x_i) g_{\min,d} S_{\max,d}}{g_d(x_i) g_{\min,i} S_{\max,i}} \right)^{-1}} \right] \quad (38)$$

where x_i^+ denotes a set of points x_i at the interfering coverages “ i ” ($i \neq d$) and all other symbols are as defined in Table 8. Note that the sum includes the desired receiving beam at multiple interfering locations resulting in the set of locations x_i^+ , in which each element accounts from the contribution from one interfering receiving beam at a location x_i within the interferer. The locations x_i are different within each interferer and in practice are the points resulting in the worst-case within X% of the area within each interferer. [$I_{RX}(x_i^+)$] $_d$ is an array where each element is the composite isolation of the desired receiving beam over X% of the total aggregated interfering coverage area. For each element the set x_i^+ is different.

Table 9. Transmit Isolation for 80°E*India Coverage*

Beam-to-beam C/I (dB)
 Carrier (beam): indiane_TX; interferer (beam): russia_TX
 Evaluated over polygon: India coverage
 Percentage of area: 90% 95% 100%
 Worst-case C/I (dB): 28.89 27.71 21.35

Composite C/I (dB)

Carrier (beam): indiane_TX
 Evaluated over polygon: India coverage
 Percentage of area: 90% 95% 100%
 Worst-case C/I (dB): 28.89 27.71 21.35

Middle East (me) Coverage

Beam-to-beam C/I (dB)
 Carrier (beam): indiane_TX; interferer (beam): russia_TX
 Evaluated over polygon: me coverage
 Percentage of area: 90% 95% 100%
 Worst-case C/I (dB): 25.52 23.64 20.72

Composite C/I (dB)

Carrier (beam): indiane_TX
 Evaluated over polygon: me coverage
 Percentage of area: 90% 95% 100%
 Worst-case C/I (dB): 25.52 23.64 20.72

Russia Coverage

Beam-to-beam C/I (dB)
 Carrier (beam): russia_TX; interferer (beam): indiane_TX
 Evaluated over polygon: Russia coverage
 Percentage of area: 90% 95% 100%
 Worst-case C/I (dB): 27.11 24.98 11.84

Composite C/I (dB)

Carrier (beam): russia_TX
 Evaluated over polygon: Russia coverage
 Percentage of area: 90% 95% 100%
 Worst-case C/I (dB): 27.11 24.98 11.84

6.3.5. Numerical Results. In this section the beam-to-beam and composite isolation are computed for a synchronous multibeam satellite positioned at an orbital location of 80° east. The reflector antenna 6-dB numerical contours for the Russia and India/Middle East coverages are shown in Fig. 17. Note that the India/Middle East beam is actually a single antenna beam, for which the isolation is computed separately for the India and Middle East coverages. Specific Earth station positions and XPOL isolation are omitted for simplicity. In addition, the input power and the flux density over different beams are assumed to be uniform.

The results for the transmit isolation are listed in Table 9. Note that the isolation values normally used are the ones computed based on 90% of the coverage areas (e.g., 28.89 dB for the India coverage). Nevertheless, the overall worst-case situations need to be assessed on a case-by-case basis, mostly with respect to their physical location, before a design is deemed completed. Similarly the receive isolation results are listed in Table 10. The beam-to-beam receive isolation needs to be assessed within each interfering coverage area, contrarily to the transmit case, which is always computed within the desired coverage area, as shown in the previous sections. In practice, the isolation tables are normally presented with detailed coverage plots showing the areas of non-compliance. Furthermore the isolation is also computed or estimated from the real measured patterns at various stages of manufacturing and integration, such as beam-forming network (BFN), array or feed antenna sniffing, near-field tests before and after environmental tests (vibration, hot and cold conditions), reflector system on mockup structure in CATR (compact antenna testing range), and reflector system on real structure in CATR after environmental tests (vibration and thermal vacuum); see Fig. 19.



Figure 19. Intelsat-9 satellite during system tests in the *compact antenna testing range* (CATR), an indoor antenna measurement range that directly measures the far-field patterns of an antenna either by itself or on the satellite (courtesy of Space/Systems Loral and Intelsat).

Table 10. Receive Isolation for 80.00 E

<i>India/Middle_East_rx</i>			
Beam-to-beam receive <i>C/I</i> (dB)			
Carrier (beam): indiam_e_RX; interferer (beam): russia_RX			
Evaluated over interferer polygon: Russia coverage			
Percentage of area: 90% 95% 100%			
Worst-case <i>C/I</i> (dB): 27.07 25.69 8.75			
Composite receive <i>C/I</i> (dB)			
Carrier (beam): indiam_e_RX			
Evaluated over interferer polygon(s): Russia coverage			
Percentage of area: 90% 95% 100%			
Worst-case <i>C/I</i> (dB): 27.07 25.69 8.75			
<i>Russia_RX:</i>			
Beam-to-beam receive <i>C/I</i> (dB)			
Carrier (beam): russia_RX; interferer (beam): indiam_e_RX			
Evaluated over interferer polygon: India coverage			
Percentage of area: 90% 95% 100%			
Worst-case <i>C/I</i> (dB): 28.64 25.50 13.35			
Beam-to-beam receive <i>C/I</i> (dB)			
Carrier (beam): russia_RX; interferer (beam): indiam_e_RX			
Evaluated over interferer polygon: me coverage			
Percentage of area: 90% 95% 100%			
Worst-case <i>C/I</i> (dB): 25.89 24.27 19.97			
Composite receive <i>C/I</i> (dB)			
Carrier (beam): russia_RX			
Evaluated over interferer polygon(s): India coverage, me coverage,			
Percentage of area: 90% 95% 100%			
Worst-case <i>C/I</i> (dB): 24.04 21.83 12.50			

6.4. Neural Networks and Genetic Algorithms Applied to the Synthesis of Reflector Antennas

As we have seen, reflector antenna applications range from very specific and unique systems, such as deployable reflectors and radiotelescopes (see Section 3.3), as well as large-scale production for commercial wireless networks, like earth terminals in VSAT networks and small receiving antennas for satellite TV. In addition, reflector antennas are also used in radar systems and other devices directly related to electronic warfare and defense. Because of the wide range of applications and commercial importance, it is essential to have reliable alternate algorithms to design effective reflector configurations. Analytical and numerical tools currently used with applied electromagnetics and appear to work well for the synthesis of reflector antennas, although relatively mature to other areas such as controls and signal processing, are neural networks and genetic algorithms [42–46].

The basic concept of using neural networks for designing reflector antennas is to first relate a few radiation patterns, or other parameter of interest, directly to the reflector geometries that generated them according to a previously selected analysis algorithm. The process is normally referred to as “training” the neural network. Once the training is completed, the desired radiation pattern is employed as the input parameter, such that the neural network yields as a result the corresponding reflector

geometry. Finally, the selected analysis technique is used on the resulting geometry to validate the process. This type of synthesis has been successfully implemented to determine reflector shapes for contoured beam applications [42]. Reflector antenna synthesis based on neural networks is normally very fast because analysis techniques are required only for the training of the network. Also currently under investigation is the effectiveness of using neural networks at a real-time level to reduce XPOL, noise, and interferences in single offset systems.

Genetic algorithms (GAs), on the other hand, rely on an optimization search to elect a suitable design. The initial set of configurations, referred to as the basis *population*, is formed by relating random designs to chromosomes, each one formed by a sequence of binary numbers that define the corresponding reflector geometry. A figure of merit is then assigned to each chromosome; these figures increase as the electrical performance of the configuration is closer to the desired one. Chromosomes with the highest figures of merit are elected to cross with the remaining ones, a process called *crossover* [43–45]. In addition, the best chromosomes (i.e., the ones with the highest figures of merit) are often duplicated before crossover, eliminating the worst ones, a procedure referred to as *natural selection* [43–45]. After the crossover is completed, a few binary numbers in a subset of chromosomes can be randomly altered, simulating the process of *mutation* in biological evolution. All figures of merit are then recomputed, and the whole process is repeated if the desired performance has not been achieved.

The aforementioned procedure is a basic description of a genetic algorithm, although variants are often encountered in practice [43–45]. A major advantage of GAs over other optimization techniques is that once the process has converged, more than one configuration attaining the desired performance is often encountered. It is also common to find configurations that are very different than classical solutions and could not be easily conceived through straightforward reasoning. Practical manufacturing constraints can then be considered for choosing the most adequate reflector antenna configuration.

Acknowledgments

The author is deeply grateful to Nick Moldovan (Prodelin Corporation), Bryan Lee, and Gert Van Omering (Space Systems/Loral), as well as to their institutions from providing many illustrations and photographs reprinted in this work. The author likewise thanks Intelsat and NRAO/AUI/NSF.

BIBLIOGRAPHY

1. W. V. T. Rusch, The current state of the reflector antenna art—entering the 1990’s, *Proc. IEEE* **80**:113–126 (1992).
2. S. Silver, ed., *Microwave Antenna Theory and Design*, McGraw-Hill, New York, 1949.
3. Y. Rahmat-Samii, Reflector antennas, in Y. T. Lo and S. W. Lee, eds., *Antenna Handbook*, Van Nostrand Reinhold, New York, 1988.

4. C. Scott, *Modern Methods of Reflector Antenna Design*, Artech House, Boston, 1990.
5. P. S. Kildal, Synthesis of multireflector antennas by kinematic and dynamic ray tracing, *IEEE Trans. Anten. Propag.* **38**:1587–1599 (1990).
6. K. W. Brown, Y. H. Lee, and A. Prata, Jr., A systematic design procedure for classical offset dual reflector antennas with optimal electrical performance, *IEEE Antennas Propagation Soc. Symp. Digest*, Ann Arbor, MI, 1993, pp. 772–775.
7. M. A. B. Terada and W. L. Stutzman, Computer-aided design of reflector antennas, *Microwave J.* **38**(8):64–73 (1995).
8. W. V. T. Rusch and P. D. Potter, *Analysis of Reflector Antennas*, Academic Press, New York, 1970.
9. A. W. Love, ed., *Reflector Antennas*, IEEE Press, New York, 1978.
10. B. S. Westcott, *Shaped Reflector Antenna Design*, Wiley, London, 1983.
11. A. G. Cha, Preliminary announcement of an 85 percent efficient reflector antenna, *IEEE Trans. Anten. Propag.* **31**:341–342 (1983).
12. A. H. Rana, J. McCoskey, and W. Check, VSAT technology, trends, and applications, *Proc. IEEE* **78**:1087–1095 (1990).
13. A. C. Ludwig, The definition of cross polarization, *IEEE Trans. Anten. Propag.* **21**:116–119 (1973).
14. TICRA Eng., *GRASP-Single and Dual Reflector Antenna Program Package*, Copenhagen, Denmark.
15. M. A. B. Terada and W. L. Stutzman, Design of offset-parabolic-reflector antennas for low cross-pol and low sidelobes, *IEEE Anten. Propag. Mag.* **35**(6):46–49 (1993).
16. A. W. Rudge and N. A. Adatia, Beam squint in circularly polarized offset parabolic reflector antennas, *Electron. Lett.* **11**:513–515 (1975).
17. D. W. Duan and Y. Rahmat-Samii, Beam squint determination in conic-section reflector antennas with circularly polarized feeds, *IEEE Trans. Anten. Propag.* **39**:612–619 (1991).
18. W. L. Stutzman, *Polarization of Electromagnetic Systems*, Artech House, Boston, 1993.
19. M. A. B. Terada and W. L. Stutzman, Cross polarization and beam squint in single and dual offset reflector antennas, *Electromagn. J.* **16**:633–650 (1996).
20. W. L. Stutzman and G. A. Thiele, *Antenna Theory and Design*, 2nd ed., Wiley, New York, 1997.
21. A. G. P. Boswell and R. W. Ashton, Beam squint in a linearly polarized offset parabolic reflector, *Electron. Lett.* **12**:596–597 (1976).
22. M. A. B. Terada, Educational procedure for designing and teaching reflector antennas in electrical engineering programs, paper presented 2002 American Soc. Engineering Education, Gulf-Southwest Annual Conf., Univ. Louisiana at Lafayette, March 20–22, 2002.
23. P. S. Kildal, Diffraction analysis of a proposed dual-reflector feed for the spherical reflector of the Arecibo observatory, *Radio Sci.* **24**:601–617 (1989).
24. A. W. Rudge, K. Milne, A. D. Olver, and P. Knight, eds., *The Handbook of Antenna Design*, Peter Peregrinus, London, 1982.
25. W. V. T. Rusch, A. Prata, Jr., Y. Rahmat-Samii, and R. A. Shore, Derivation and application of the equivalent paraboloid for classical offset Cassegrain and Gregorian antennas, *IEEE Trans. Anten. Propag.* **38**:1141–1149 (1990).
26. B. Shen and W.L. Stutzman, A scanning tri-reflector antenna with a moving flat mirror, *IEEE Trans. Anten. Propag.* **43**:270–276 (1995).
27. C. Dragone, Offset multireflector antennas with perfect pattern symmetry and polarization discrimination, *Bell Syst. Tech. J.* **57**:2663–2684 (1978).
28. Y. Mizugutch, M. Akagawa, and H. Yokoi, Offset dual reflector antenna, *IEEE Antennas Propagation Soc. Symp. Digest*, Amherst, MA, 1976, pp. 2–5.
29. T. Kitsuregawa, ed., *Satellite Communication Antennas*, Artech House, Boston, 1990.
30. S. Srikanth, Comparison of spillover loss of offset Gregorian and Cassegrain antennas, *IEEE Antennas Propagation Soc. Symp. Digest*, London, Canada, 1991, pp. 444–447.
31. M. A. B. Terada and W. L. Stutzman, Computer-aided design of reflector antennas: The Green Bank radio telescope, *IEEE Trans. Microwave Theory Tech.* **46**:250–253 (1998).
32. P. H. Pathak, Techniques for high-frequency problems, in Y. T. Lo and S. W. Lee, eds., *Antenna Handbook*, Van Nostrand Reinhold, New York, 1988.
33. Y. Rahmat-Samii and V. Galindo-Israel, Shaped reflector antenna analysis using the Jacobi-Bessel series, *IEEE Trans. Anten. Propag.* **28**:425–435 (1980).
34. W. L. Stutzman, S. W. Gilmore, and S. H. Stewart, Numerical evaluation of radiation integrals for reflector antenna analysis including a new measure of accuracy, *IEEE Trans. Anten. Propag.* **36**:1018–1023 (1988).
35. P. J. B. Clarricoats and A. D. Olver, *Corrugated Horns for Microwave Antennas*, Peter Peregrinus, London, 1984.
36. S. Ghosh, E. Kuhn, and A. Prata, Simplified high-performance dual-banded feed comprising a dual-depth corrugated launcher and a conventional horn, *Electron. Lett.* **20**:532–533 (1984).
37. E. Lier and S.A. Skyttemyr, A shaped single reflector offset antenna with low cross polarization fed by a lens horn, *IEEE Trans. Anten. Propag.* **42**:478–483 (1994).
38. M. Terada, Novel beam scanning technique for circularly-polarized reflector antennas, *IEEE Antennas Propagation Soc. Symp. Digest*, Columbus, OH, June 2003.
39. TICRA Eng., *POS—Physical Optics Shaping Code*, Copenhagen, Denmark.
40. J. R. Bergmann, R. C. Brown, P. J. B. Clarricoats, and Z. Hay, Synthesis of shaped-beam reflector antennas patterns, *IEE Proc.* **135**(H):48–53 (1988).
41. H.-H. Viskum and K. Tjonneland, A study on the isolation capability of multibeam reflector antennas, *IEEE Antennas Propagation Soc. Symp. Digest*, Newport Beach, CA, 1995, pp. 136–139.
42. G. Washington, Aperture antenna shape prediction by feed-forward neural networks, *IEEE Trans. Anten. Propag.* **45**:683–688 (1997).
43. D. S. Weile and E. Michielssen, Genetic algorithm optimization applied to electromagnetics: a review, *IEEE Trans. Anten. Propag.* **45**:343–353 (1997).
44. Y. Rahmat-Samii and E. Michielssen, *Electromagnetic Optimization by Genetic Algorithms*, Wiley, New York, 1999.
45. D. Correia, A. Soares, and M. Terada, Optimization of gain, impedance and bandwidth in Yagi-Uda antennas using genetic algorithm, *1999 SBMO/IEEE MTT-S, AP-S and LEOS Int. Microwave and Optoelectronics Conf.*, Rio de Janeiro, Aug. 9–12, 1999.
46. C. Christodoulou and M. Georgiopoulos, *Applications of Neural Networks in Electromagnetics*, Artech House, Boston, 2001.

REFRACTION AND ATTENUATION IN TROPOSPHERE

JEREMY E. ALLNUTT
Virginia Tech/Northern Virginia
Center
Falls Church, Virginia

Electromagnetic energy, often referred to in communications as *the signal* and traced in diagrams as a *ray*, travels at the speed of light c when in a vacuum, whether in the form of X-rays, visible light, or a radiowave. The value of c is 3×10^8 m/s. When the signal passes through a medium that is not a vacuum, it travels more slowly. The ratio between c and the speed in the medium v is the *refractive index* of the medium, denoted by $n = c/v$. The refractive index of a medium does not just affect the speed of electromagnetic energy flowing through it; it can also cause the magnitude of the signal to fluctuate over time periods on the order of a second or longer, due to variations in the refractive index within the medium. These signal fluctuations, called *scintillations*, are usually small and approximately symmetric about the average level of the signal, although this is not always so in severe scintillations. Where two dissimilar media form a common boundary, the different refractive indices of the media will cause the signal direction to diverge from its path if the incident direction is not normal to the boundary. This is called *refraction*, and the incident and refracted directions either side of the boundary are given by Snell's law (e.g., see Ref. 1).

The average refractive index of a medium is called the *bulk* refractive index, and it affects the average direction of the electromagnetic energy. Most media are not completely homogeneous, however; small volumes of different refractive indices will exist within the larger scale of the medium. These variations, which can exist over dimensions as small as a few centimeters in the troposphere, are termed the *small-scale* refractive index variations of the medium. They are like bubbles of air in a glass of soda. In the troposphere, the mixing of the small-scale "bubbles" within the larger scale of the medium can be caused by convection currents, due to heating of the air by the ground, or by turbulent effects in wind shear aloft. These variations give rise to the scintillations noted above.

In addition to changing the direction of travel of an electromagnetic signal and/or causing scintillations, a medium can both extract energy from a signal passing through it and alter the orientation sense of the electric vector (the polarization) of the signal as it passes through. The loss of energy is called *attenuation*, and the change in polarization sense is generally referred to as *depolarization*. In general, the longer the path through a medium is, the greater will be its effect on the electromagnetic signal passing through it. For this reason, paths through the atmosphere at low elevation angles will have greater ray bending, scintillation, attenuation, and depolarization than paths at high elevation angles.

1. REFRACTIVE EFFECTS

1.1. Bulk Refractive Effects

In still air, the atmosphere assumes a spherically stratified form with layers of generally decreasing refractive index lying one above the other. The refractive index of a given portion of the atmosphere will therefore vary far more quickly with change in height than with change in horizontal position. For this reason, an electromagnetic signal (a ray) leaving Earth's surface at an elevation angle of $< 90^\circ$ will bend away from the normal to the surface (see Fig. 1a). The curvature will be contained in one plane, the projection of which onto Earth's surface is the azimuth direction. If r is the radius of curvature of the ray [2], then

$$\frac{1}{r} = -\frac{\cos \theta}{n} \frac{dn}{dh} \quad (1)$$

where

θ = angle of the ray path to the horizontal at the point considered

n = refractive index of the atmosphere

dn/dh = vertical gradient of refractive index at a height h above Earth's surface

The minus sign indicates that the refractive index decreases with increasing altitude. For terrestrial radio systems, the elevation angle θ will be almost zero and, since the refractive index is almost unity, Eq. (1) will reduce to the approximate form

$$\frac{1}{r} = -\frac{dn}{dh} \quad (2)$$

If the radius of Earth is a , the difference in curvature between the ray path and the curvature of Earth along the terrestrial link is given by

$$\frac{1}{a} - \frac{1}{r} = \frac{1}{a} + \frac{dn}{dh} = \frac{1}{ka} = \frac{1}{R_e} \quad (3)$$

Here R_e is Earth's effective radius given by the product ka , where k is the effective Earth radius factor. The effective radius of Earth is often used in ray-tracing diagrams of the vertical profiles of terrestrial radio systems, because it allows for the average ray bending along the path (see Figs. 1b, 1c). Ray bending on satellite-to-ground paths may cause signal loss due to the spreading of the antenna beam. This effect, and that of elevation-angle-of-arrival variations, are negligible at elevation angles above about 3° and will be significant only for large antennas (diameter > 100 wavelengths).

The atmosphere has a *dry* and a *wet* refractive index component, the former due to the gases in the atmosphere (principally nitrogen and oxygen), and the latter due to the water vapor that is taken up into the atmosphere. Combining the two components together into a composite refractive index n gives

$$n - 1 = \frac{77.6}{T} \left(P + 4810 \frac{e}{T} \right) \times 10^{-6} \quad (4)$$

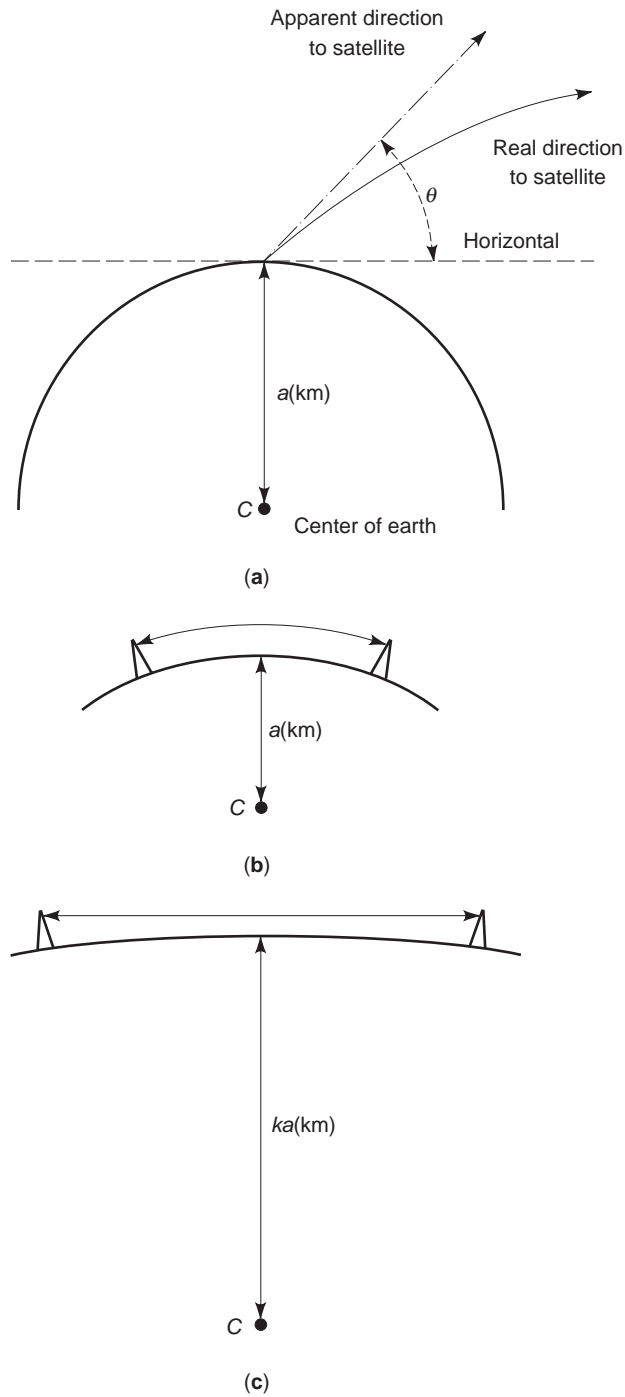


Figure 1. (a) Apparent and real directions to an Earth satellite, illustration of methods of ray tracing; (b) real radius and a curved ray path; (c) effective radius and a geometric ray path.

where

- P = atmospheric pressure (hPa)
- T = absolute temperature (K)
- e = water vapor pressure (hPa)

The hectopascal (hPa) is the same as a millibar.

The water vapor pressure e can be related to the relative humidity by [3]

$$e = \frac{He_s}{100} \tag{5}$$

and

$$e_s = a \exp\left(\frac{bt}{t+c}\right) \tag{6}$$

where

- H = relative humidity (%)
- t = temperature ($^{\circ}\text{C}$)
- e_s = saturation vapor pressure (hPa) at the temperature t

and the coefficients a , b , and c are as follows:

For water:

- $a = 6.1121$
- $b = 17.502$
- $c = 240.97$

For ice:

- $a = 6.1115$
- $b = 22.452$
- $c = 272.55$

The vapor pressure e is related to the water vapor density ρ (g/m^3) by [3]

$$e = \frac{\rho T}{216.7} \text{ (hPa)} \tag{7}$$

The refractive index of air is so close to unity that Eq. (4) is often rewritten as

$$n = 1 + 10^{-6} N \tag{8}$$

where N is the *refractivity* of the atmosphere and is given by $(77.6/T)(P + 4810e/T)$, with the same units as in Eq. (4).

1.1.1. Refractivity Profile. The refractivity profile is described by a mean refractive index gradient, which generally decreases exponentially with increasing altitude. A reference standard atmosphere for calculating the refractive index as a function of height $n(h)$ is given by [3]

$$n(h) = 1 + 10^{-6} N_0 \exp\left(\frac{-h}{h_0}\right) \tag{9}$$

where

- h = height above mean sea level (km)
- h_0 = reference altitude = 7.35 km
- N_0 = average value of atmospheric refractivity at mean sea level = 315

Rewriting Eq. (9) in terms of the refractivity, we have

$$N(h) = N_0 \exp \frac{-h}{h_0} \tag{10}$$

The rate of change of the refractivity profile with height dN/dh can be related to the parameter k used earlier. Sample values are given below [4]:

dN/dh (N/km)	k
157	$\frac{1}{2}$
0	1
-40	$\frac{4}{3}$
-157	∞
-200	-3.65

From this table above, it is clear that, when dN/dh is less than -157, the radius of curvature of Earth is greater than the radius of curvature of a signal that is initially propagating horizontal to the surface of Earth. The signal will therefore propagate beyond what would normally be the local horizon. This is a form of anomalous propagation, and the mechanism is referred to as *ducting*.

1.1.2. Refractive Ducts. Ducting is defined as occurring when a radio ray originating close to Earth’s surface is sufficiently refracted that it is either bent back toward the Earth surface or travels along a path that is parallel to the surface. Ducts are formed when layers of air having a relatively high refractive index are above layers with a relatively low refractive index. This *inversion* of the normal exponentially decaying refractive index profile with height is rare and leads to anomalous propagation conditions. Anomalous propagation, and the enhanced signal levels it causes at unlikely distances from the transmitter, is key to the estimation of potential interference between terrestrial systems caused by ducts. A signal will become trapped in a duct if the initial direction of the transmission (the angle of incidence) is very close to that of the horizontal refractive index boundaries of the duct. Typically, the angle of incidence of the signal, as it meets the boundary between the inversion layer and the atmosphere above, has to be smaller for thinner ducts. Typical values for a refractivity gradient of -300 N/km are [2] as

follows:

Critical Angle of Incidence (deg)	Duct Thickness (m)
0.1	10
0.14	20
0.22	50

Frequency also plays a part in the ducting. The higher the frequency, the smaller the duct thickness consistent with trapping. For the same -300 N/km profile assumed above, the minimum trapping frequency for a surface duct increases from approximately 2-2.5 GHz to 4-10 GHz to 25 GHz as the duct thickness changes from 40 to 30 m to 20 to 10 m, to 5 m, respectively [2]. The necessary condition for ducting to occur at a given elevation angle is given by [5]

$$\theta < \theta_c \tag{11}$$

where θ is the elevation angle and θ_c is the critical elevation angle above which ducting will not occur. The critical angle is given by

$$\theta_c = (2|\Delta M|)^{1/2} \text{ (mrad)} \tag{12}$$

where M is the modified refractivity (and $M = N + 10^6 h/a$, with h the height above the ground and a the radius of Earth), and ΔM is the change in M across the ducting layer. As an example, for θ_c to equal 1° , the required ΔM is 152.3.

Assuming a surface duct 50 m in height, the M lapse shown above corresponds to a refractivity gradient of 840 N-units/km. Refractivity gradients of this magnitude are extremely rare, and so ducting is normally limited to terrestrial radio systems or satellite-to-ground paths where the elevation angle is below 1° . The latter condition is not expected in commercial system used because it leads to poor propagation, but may have military applications in some situations.

1.1.3. Signal Delay. A signal propagating in the atmosphere will travel at a speed that is less than the speed of light in a vacuum. If a ranging system is being employed, such as the Global Positioning System (GPS), which ignores the true speed of the signal through the atmosphere, an error will be made in calculating the range. There will be two components of range error (here, range *delay*, since the signal will arrive later than expected). These are the range delay Δ_d due to dry air and the range delay Δ_w due to the moisture in the air. Typical values [6] are given in the table below for a path that exits the atmosphere to a satellite where the refractive index of the atmosphere is assumed to be unity. The range error values have been increased by 2% from those in Ref. 5 to allow for the additional atmosphere encountered from the 80 km height used in Ref. 5 for the target. Regression analyses [7] have shown that these typical range errors can be reduced in practice by 25% by incorporating site latitude, height above sea level, and time of day within the calculation

procedure:

Initial Elevation Angle (deg)	Elevation Angle Error (mdeg)	Range Error (m)
0	595	106
5	159	25.5
50	13.4	3.2

1.2. Small-Scale Refractive Effects

The air is rarely still; differential heating and cooling effects within the atmosphere induce wind currents from balmy breezes to tornado-force hurricanes and tropical cyclones. The resultant turbulence in the troposphere will cause small-scale changes in the refractive index. These in turn will lead to relatively rapid variations in the amplitude, phase, and angle of arrival of a signal [8]. The effect on the signal is usually described by one of the following observations:

1. The log amplitude χ (dB), which equals the ratio of the instantaneous amplitude of the observed signal to its mean amplitude
2. The scintillation variance of σ_χ^2 in dB² or the intensity σ_χ in dB_{rms}, which are the variance and root mean square of the log amplitude χ , respectively [8]

On terrestrial paths, the turbulence occurs in the *boundary layer*—the part of the troposphere that is next to the surface of Earth. In general, the signal fluctuations due to turbulence on terrestrial paths are neither performance- nor availability-limiting, the major propagation impairments being multipath (due to multiple atmospheric rays and ground reflections) and (for systems operating at frequencies above about 10 GHz) rain attenuation. On Earth-space paths, the primary cause of major tropospheric scintillations is cumulus clouds on warm, humid days. The attendant air entrainment process caused by the convective activity within the cloud structure induces turbulence; the more humid and hot the conditions are, the more severe the scintillations become. Similarly, the lower the elevation angle, the larger the amplitudes of both signal enhancements and degradations become. In most systems, tropospheric scintillation will affect the performance of only the link and not its availability [9]. At elevation angles below about 5°, however, low-angle fading effects become evident [10,11], and they can be system-limiting (i.e. cause a link outage). Figure 2 illustrates the general concept of performance and availability thresholds for digital communication systems [12].

1.3. Prediction of Tropospheric Scintillation

In most systems, it is the probable signal degradation that is required for the link budget analysis (signal enhancements being of relevance only for potential front-end amplifier saturation or for likely interference to other systems). The currently accepted modeling procedure to

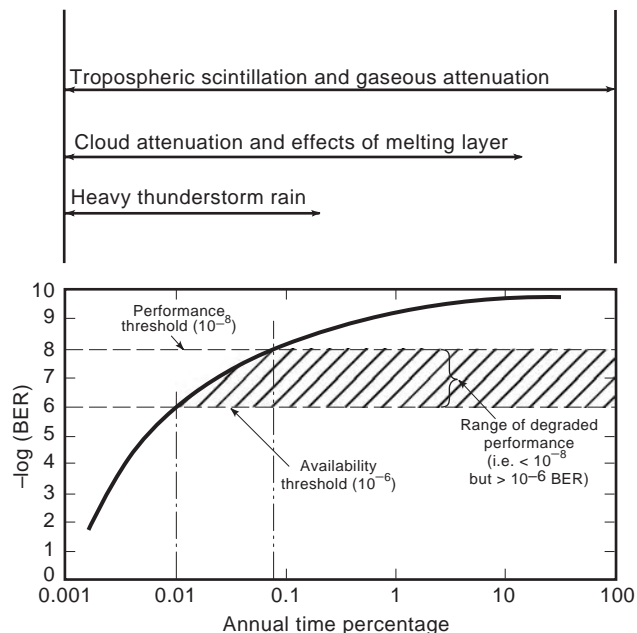


Figure 2. Example of annual statistics of bit error ratio (BER) versus time percentage for a given link.

calculate the effective signal reduction due to tropospheric scintillations on an Earth-space path [13] uses the wet term of the refractivity at ground level as the input parameter to predict the scintillation variance. The step-by-step procedure from Ref. 13 is given below for elevation angles $\geq 4^\circ$:

Parameters required for the method include: t = the average surface ambient temperature (°C) at the site for a period of one month or longer; H = average surface relative humidity (%) at the site for a period of one month or longer; f = frequency (GHz), where $4 \text{ GHz} \leq f \leq 20 \text{ GHz}$; θ = path elevation angle, where $\theta \geq 4^\circ$; D = physical diameter (m) of the Earth station antenna; and η = antenna efficiency; if unknown, $\eta = 0.5$ is a conservative estimate.

- Step 1. For the value of t , calculate the saturation water vapor pressure e_s (kPa), as specified in Ref. 3.
- Step 2. Compute the wet term of the radio refractivity N_{wet} , corresponding to e_s , t , and H as given in Ref. 3.
- Step 3. Calculate the standard deviation of the signal amplitude σ_{ref} used as a reference:

$$\sigma_{\text{ref}} = (3.6 \times 10^{-3}) + (10^{-4} \times N_{\text{wet}}) \text{ dB}$$

- Step 4. Calculate the effective pathlength L according to

$$L = (2h_L) / \sqrt{[\sin^2 \theta + 2.35 \times 10^{-4}]^{1/2} + \sin \theta} \text{ m}$$

where h_L is the height of the turbulent layer; the value of $h_L = 1000 \text{ m}$

Step 5. Estimate the effective antenna diameter D_{eff} from the geometric diameter D and the antenna efficiency η :

$$D_{\text{eff}} = (\eta)^{1/2} D \quad \text{m}$$

Step 6. Calculate the antenna averaging factor from

$$g(x) = \left\{ \left[3.86(x^2 + 1)^{11/12} \right] \times \sin\left(\frac{11}{6} \arctan \frac{1}{x}\right) - 7.08x^{5/6} \right\}^{1/2}$$

with

$$x = 1.22(D_{\text{eff}})^2 \frac{f}{L}$$

where f is the carrier frequency in GHz

Step 7. Calculate the standard deviation of the signal for the considered period and propagation path:

$$\sigma = \sigma_{\text{ref}}(f)^{7/12} \frac{g(x)}{(\sin \theta)^{1.2}}$$

Step 8. Calculate the time percentage factor $a(p)$ from the time percentage p of concern in the range $0.01 < p \leq 50$:

$$a(p) = -0.061(\log_{10} p)^3 + 0.072(\log_{10} p)^2 - 1.71 \log_{10} p + 3.0$$

Step 9. Calculate the scintillation fade depth for the time percentage p by

$$A_s(p) = a(p)\sigma \quad \text{dB}$$

This procedure has been found to accurately predict frequencies at least up to 30 GHz, although it tends to underpredict slightly at all frequencies in the hot, humid summer months. At higher frequencies (>30 GHz) it is expected that the same $f^{7/12}$ scaling law will apply as shown in step 7 above, although this anticipated result has not been tested experimentally. The fading portion of the tropospheric scintillation A_s is seldom significant for Earth-space paths at elevation angles above 20° for the frequency bands currently in operation (4–30 GHz). As the elevation angle decreases, or the frequency band increases, tropospheric scintillation fading becomes more significant. For example, at 11 GHz, A_s is less than 0.5 dB for 0.01% of an average year at elevation angles on the order of 30° . For the same frequency, A_s approaches 3 dB at elevation angles of 3.2° (11). These values of A_s are for non-raining periods and so will affect the performance of the system.

2. GASEOUS ABSORPTION

When a molecule or atom is nonsymmetric in its structure, it will have a preferred orientation if placed in an electric

field. Such molecules or atoms are said to be *polar*. Polar molecules or atoms cause far more loss to a radio signal than nonpolar molecules or atoms, since the application of an external field causes the polar molecules or atoms to reorient themselves. The reorientation (or relaxation) of the dipoles will remove energy from the applied field and cause heating of the medium. This is the principle of a microwave oven. The major constituents of the troposphere, oxygen and nitrogen, are electrically nonpolar, and so no absorption due to electric dipole resonance will take place. Oxygen, however, is a paramagnetic molecule with a permanent magnetic moment that causes resonant absorption at particular frequencies. Water and water vapor, which both contain two oxygen atoms, are therefore polar molecules, and so absorption occurs as a result of resonance at critical frequencies.

2.1. Oxygen and Water Vapor Resonance Lines

The specific gaseous attenuation γ (dB/km) is given by

$$\gamma = \gamma_o + \gamma_w \quad (\text{dB/km}) \quad (13)$$

where γ_o and γ_w are the specific attenuations (dB/km) due to dry air (essentially oxygen) and water vapor, respectively. The specific attenuation needs to be multiplied by the length of the path over which it operates to arrive at total path attenuation. On terrestrial paths, this is simply the distance between the transmitter and receiver L (km), and the path attenuation A (dB) is given by

$$A = \gamma L = (\gamma_o + \gamma_w)L \quad (\text{dB}) \quad (14)$$

For Earth-space paths, the situation is not so straightforward, since the density and make up of the atmosphere change rapidly with height. The value of L used must be able to take account of the density and other variations along the link through the atmosphere.

Figure 3, abstracted from Fig. 3 of Ref. 14, gives the total zenith gaseous attenuation at frequencies up to 1 THz (10^{12} Hz) for two conditions: a standard atmosphere and a dry atmosphere. A standard atmosphere is defined

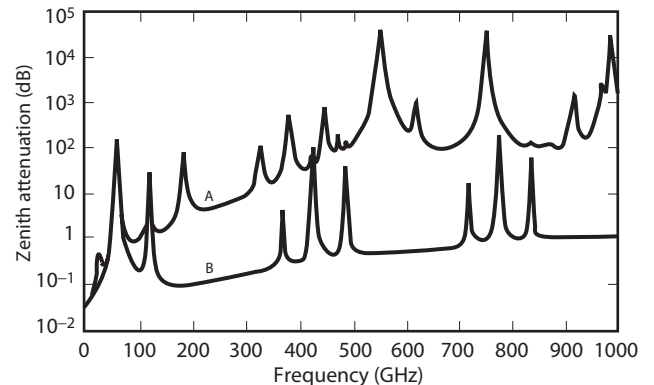


Figure 3. Zenith attenuation due to atmospheric gases (from Fig. 3 of Ref. 14). Curve A: standard atmosphere (7.5 g/m^3); curve B: dry atmosphere. (© ITU; reproduced with permission.)

as having the following surface characteristics: pressure 1013 hPa, temperature 15°C, and water vapor density 7.5 g/m³. In general, the dry atmosphere curve in Fig. 3 shows the resonance absorption lines of oxygen, while the standard atmosphere curve is a summation of the resonance absorption lines of water vapor and oxygen. A software code (in Matlab) that calculates the total gaseous attenuation in a line-by-line fashion up to a frequency of 1 THz is available from the Radiocommunication Bureau of the ITU in Geneva.

For nonzenith paths, it is necessary to know not only the specific attenuation at each point in the link but also the length of the path that has this specific attenuation. To derive the incremental pathlengths, ray bending through the atmosphere must be considered (see Fig. 1a). A full procedure to accomplish this is given in Ref. 14. In this procedure, formulae are given for the precise calculation of γ_o and γ_w , and the total zenith attenuation is calculated from

$$A_z = \gamma_o h_o + \gamma_w h_w \quad (\text{dB}) \quad (15)$$

where h_o is the equivalent height of the dry gaseous absorption and h_w is the equivalent height of the water vapor absorption. Typical values of h_o and h_w are 6 km and 2.1 km (during rainy conditions), respectively. For elevation angles between 10° and 90°, a cosecant law gives the total gaseous attenuation A , namely

$$A = \frac{A_z}{\sin \varphi} \quad (\text{dB}) \quad (16)$$

where φ is the elevation angle. For elevation angles below 10°, a more accurate formula that takes account of the real length of the atmospheric path is required [14]. For most Earth-space systems, gaseous absorption is not significant compared with the other impairments. It also changes very little with time and so is usually relatively easy to factor into a system design.

3. RAIN ATTENUATION

Attenuation due to rain is made up of two components: absorption and scattering. Absorption takes place when the incident signal energy is transformed into mechanical energy, thereby heating the raindrop. Scattering occurs when the incident signal is redirected away from the desired propagation path without energy loss to the raindrop. The relative importance of scattering and absorption is a function of the complex index of refraction of the raindrop and the size of the raindrop relative to the wavelength of the signal [15]. The significance of the scattered component generally increases with both the signal frequency and the size of the raindrop. In general, attenuation due to rain increases with increasing signal frequency for a given rain rate. Typical annual cumulative statistics for frequencies of 12, 18.7, 39.6, and 49.5 GHz on paths at an elevation angle of approximately 38° in Europe are shown in Fig. 4 (some data were extracted from Ref. 16). These curves show a monotonic increase in attenuation

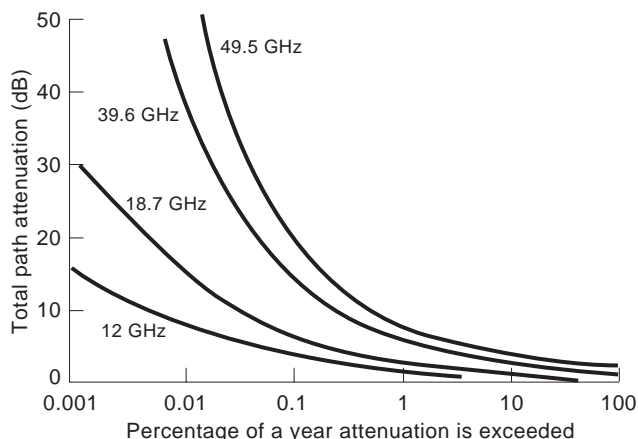


Figure 4. Average annual cumulative statistics of total path attenuation at an elevation angle of about 38° in Europe (some data extracted from Ref. 16).

with decreasing time percentage, which is typical of temperate climates. There is evidence, however, that in tropical, high-rain-rate regions there is a saturation effect in the attenuation and rainfall rate statistics at low time percentages, leading to a breakpoint in the cumulative statistics [17]. This and other features of high-rain-rate regions make the accurate prediction of attenuation due to rain very difficult for those locations.

Rain rarely consists of a homogeneous collection of raindrops falling at a constant rate. The size, shape, temperature, and fall velocities usually vary in a dynamic manner along the path. To calculate the attenuation of a radio signal passing through rain it is necessary to invoke a drop-size distribution and to integrate the attenuation contributions of the various raindrops along the path through the rain. The characteristics of rain vary so much in space and time that it is necessary to resort to empirical methods that employ statistical averaging. The accepted approach is to use a power-law representation based on the rainfall rate R (usually a rainfall rate measured at a point on the ground close to the communications link). The specific attenuation γ (dB/km) in rain is related to the rainfall rate R (mm/h) by the power law relationship

$$\gamma = kR^\alpha \quad (\text{dB/km}) \quad (17)$$

where k and α are regression coefficients [18] that take account of absorption and scattering.

3.1. Prediction of Attenuation

Rain attenuation prediction models fall into two classes: (1) those that attempt to analyze the physics of the process and model the constituents of storm cells and so on and (2) those that use empirical approaches with simplified assumptions. To date, those that use empirical methods have demonstrated the most consistent accuracy on a global basis (although, with the strong emphasis currently on the development of accurate, worldwide climatic parameter maps, a physical modeling approach should eventually prevail). For empirical methods, the key to

the prediction process is the development of a procedure that enables the user to move seamlessly from point rainfall rate on the ground to average rainfall rate along the path at any elevation angle. This approach is described below, abstracting directly from the current ITU-R prediction procedure for calculating rain attenuation on a satellite-to-ground path, as set out in Ref. 13:

The following parameters are required: $R_{0.01}$ = point rainfall rate for the location for 0.01% of an average year (mm/h); h_s = height above mean sea level of the Earth station (km); θ = elevation angle; f = frequency (GHz). The geometry is illustrated in Fig. 5. The method is applicable up to at least 30 GHz.

Step 1. Calculate the effective rain height h_R for the latitude of the station ϕ :

$$h_R \text{ (km)} = \begin{cases} 5 - 0.075(\phi - 23) & \text{for } \phi > 23^\circ \text{ Northern Hemisphere} \\ 5 & \text{for } 0^\circ \leq \phi \leq 23^\circ \text{ Northern Hemisphere} \\ 5 & \text{for } 0^\circ \geq \phi \geq -23^\circ \text{ Southern Hemisphere} \\ 5 + 0.1(\phi + 21) & \text{for } -71^\circ \leq \phi < -21^\circ \text{ Southern Hemisphere} \\ 0 & \text{for } \phi < -71^\circ \text{ Southern Hemisphere} \end{cases}$$

Step 2. For $\theta \geq 5^\circ$ compute the length of the slant path L_s below the rain height from

$$L_s = \frac{h_R - h_s}{\sin \theta} \quad \text{km}$$

For $\theta < 5^\circ$, the following formula is used:

$$L_s = [2(h_R - h_s) / \{[\sin^2 \theta + 2(h_R - h_s) / 8500]^{1/2} + \sin \theta\}] \quad \text{km}$$

Step 3. Calculate the horizontal projection L_G of the length of the slant path from

$$L_G = L_s \cos \theta \quad \text{km}$$

Step 4. Obtain the rain intensity $R_{0.01}$ exceeded for 0.01% of an average year at the site.

Step 5. Calculate the reduction factor $r_{0.01}$ for 0.01% of the time for $R_{0.01} \leq 100$ mm/h

$$r_{0.01} = \frac{1}{1 + L_G/L_0}$$

where $L_0 = 35 \exp(-0.015 R_{0.01})$ and, for $R_{0.01} > 100$ mm/h, use the value 100 mm/h in place of $R_{0.01}$.

Step 6. Obtain the specific attenuation, γ_R , using the frequency dependent regression coefficients k and α [18] by using

$$\gamma_R = k(R_{0.01})^\alpha \quad \text{dB/km}$$

Step 7. The predicted attenuation exceeded for 0.01% of an

average year is obtained from

$$A_{0.01} = \gamma_R L_s r_{0.01} \quad \text{dB}$$

Step 8. The estimated attenuation to be exceeded for other percentages of an average year, in the range 0.001–1%, is determined from the attenuation exceeded for 0.01% of an average year by using

$$\frac{A_p}{A_{0.01}} = 0.12p^{-(0.546 + 0.043 \log p)}$$

Note that the variability of the weather from year to year will cause this prediction method to vary similarly. Average accuracy better than about 35% should not be expected for any given year.

4. DEPOLARIZATION

The *polarization* sense of a wave usually refers to the preferred orientation of the electric vector. A perfectly polarized wave will have no component of its electric field in the orthogonal sense. There are only two states for a perfectly polarized wave: linear and circular. For linear polarization, it is common to use vertical and horizontal as the two orthogonal (linear) reference axes. For circular polarization, right-hand circular polarization (RHCP) and left-hand circular polarization (LHCP) are the two orthogonal (circular) reference senses. Depolarization from one reference polarization sense to the other occurs when

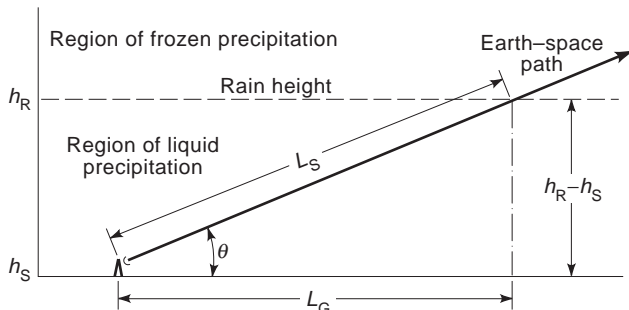


Figure 5. Schematic presentation of in Earth-space path (from Fig. 1 in Ref. 13). (© ITU; reproduced with permission.)

the signal passes through an anisotropic medium and the polarization sense of the signal is not aligned with the principal axes of the medium. Rain can be such a medium.

Raindrops exist in a dynamic medium: the atmosphere. When the drops are very small, surface tension forces (which strive to keep the drop perfectly spherical) far exceed the aerodynamic forces on the raindrop (which seek to shape the drop to conform with the external pressures). Under these conditions, the raindrops remain spherical and the rain medium appears symmetric to the signal. No signal depolarization therefore results. As the drops become larger, however, through coalescence with other drops on collision in the rain medium, the surface tension forces can no longer keep the drops spherical. The drops distort into elliptical shapes and so exhibit preferred orientation directions along the major and minor axes of the ellipsoid. Differential attenuation and phase shift will occur on component signals propagating along these axes and will result in signal depolarization. The degree of depolarization measured is called the *cross-polarization discrimination* (XPD) and is defined as

$$\text{XPD} = 20 \log_{10} \frac{E_{\text{co}}}{E_{\text{cross}}} \quad (\text{dB}) \quad (18)$$

where E_{co} is the field measured in the wanted (copolarized) polarization and E_{cross} is the field measured in the unwanted (cross-polarized) polarization. If the differential attenuation (α , nepers) and differential phase (β , radians) caused by a medium are known, XPD can be calculated from

$$\text{XPD} = 20 \log_{10} \left| \frac{e^{-(\alpha+j\beta)} + 1}{e^{-(\alpha+j\beta)} - 1} \right| \quad (\text{dB}) \quad (19)$$

Generally α and β are not known, and it is usual to model XPD against rain attenuation.

4.1. Prediction of Cross-Polarization Discrimination

The most often used prediction method for calculating XPD is that in the ITU-R Recommendation 618 [13]. The procedure is abstracted directly below:

The following parameters are needed: A_p , the rain attenuation (dB) exceeded for the required percentage of time p for the path in question; τ = tilt angle of the linearly polarized electric field with respect to the horizontal (for circular polarization, use $\tau = 45^\circ$); f = frequency (GHz); θ = path elevation angle (degrees). The method is applicable to frequencies between 8 and 35 GHz.

Step 1. Calculate the frequency-dependent term

$$C_f = 30 \log(f) \quad \text{for } 8 \leq f \leq 35 \text{ GHz}$$

Step 2. Calculate the rain-attenuation-dependent term

$$C_A = V(f) \log A_p$$

where

$$V(f) = 12.8f^{0.19} \quad \text{for } 8 \leq f \leq 20 \text{ GHz}$$

$$V(f) = 22.6 \quad \text{for } 20 < f \leq 35 \text{ GHz}$$

Step 3. Calculate the polarization improvement factor

$$C_\tau = -10 \log[1 - 0.484(1 + \cos 4\tau)]$$

The improvement factor $C_\tau = 0$ for $\tau = 45^\circ$ (which is equivalent to circular polarization) and reaches a maximum value of 15 dB for linearly polarized signals with $\tau = 0^\circ$ or 90° .

Step 4. Calculate the elevation-angle-dependent term

$$C_\theta = -40 \log(\cos \theta) \quad \text{for } \theta \leq 60^\circ$$

Step 5. Calculate the canting-angle-dependent term

$$C_\sigma = 0.0052\sigma^2$$

where σ is the effective standard deviation of the raindrop canting angle distribution, expressed in degrees; σ takes the value 0° , 5° , 10° , and 15° for 1%, 0.1%, and 0.01%, and 0.001% of the time, respectively.

Step 6. Calculate the rain XPD not exceeded for $p\%$ of the time:

$$\text{XPD}_{\text{rain}} = C_f - C_A + C_\tau + C_\theta + C_\sigma \quad \text{dB}$$

Step 7. Calculate the ice-crystal-dependent term

$$C_{\text{ice}} = \text{XPD}_{\text{rain}} \times \frac{0.3 + 0.1 \log p}{2} \quad \text{dB}$$

Step 8. Calculate the XPD not exceeded for $p\%$ of the time, including the effects of ice crystals:

$$\text{XPD}_p = \text{XPD}_{\text{rain}} - C_{\text{ice}} \quad \text{dB}$$

For frequencies below 8 GHz, the following scaling formula can be used for $4 \leq f_1, f_2 \leq 30$ GHz:

$$\text{XPD}_2 = \text{XPD}_1 - 20 \log \frac{f_2 [1 - 0.484(1 + \cos 4\tau_2)]^{1/2}}{f_1 [1 - 0.484(1 + \cos 4\tau_1)]^{1/2}}$$

The component for ice depolarization C_{ice} in the preceding formulation is known to underestimate the degree of ice crystal depolarization encountered on low-elevation-angle paths.

Depolarization can be system-limiting in the lower frequency bands, where rain attenuation is not significant (e.g., in the C band, which is the 6/4-GHz uplink/downlink pair for many satellite systems). As the frequency goes up, however, the amount of depolarization observed per decibel of attenuation becomes less and less until, by Ka band (the 30/20 GHz uplink-downlink pair), depolarization is rarely system-limiting. In analog systems, an XPD margin

of 12 dB is usually required to operate successfully. In digital systems, this margin can be reduced because of the possibility of adding coding to the signal. When two satellite links share the same transponder, but are using opposite polarizations (this is referred to as *polarization frequency reuse*), depolarization caused by ice crystals can be a problem. This is because the unwanted (depolarized) component of one link caused by the ice crystals entering the channel of the wanted signal in the satellite transponder without any attenuation having occurred.

5. ATTENUATION DUE TO CLOUDS AND FOG

Fog or mist is essentially supersaturated air in which some of the water has precipitated out to form small droplets of water, usually ≤ 0.1 mm in diameter [19]. Fog is formed mainly from two processes—radiation and advection [6]—and rarely extends more than 100 m above the ground. For this reason, fog is usually ignored in satellite-to-ground links design for frequencies below about 100 GHz. Clouds, however, are much more complicated.

Several models are available for the prediction of cloud attenuation [19–23], but there remain two major difficulties in turning these into link design tools: (1) an accurate cumulative distribution of the vertical and horizontal extent, on a global basis, of those clouds that contribute to slant path attenuation; and (2) separating this attenuation contribution from that due to rain formed in some of the cloud processes. Many measurements of rain attenuation implicitly include attenuation due to clouds. Understanding, and accurately predicting, the contribution of clouds to path attenuation is a key element in the modeling of the proposed V-band (50/40 GHz) satellite services. Of equal importance will be the development of modeling procedures that can predict the combined effects of all the attenuating phenomena on an Earth–space link [24,25].

6. ATTENUATION EFFECTS ON INFRARED AND VISIBLE LIGHT

The far infrared (~ 1 THz), infrared (~ 10 THz), and visible (~ 100 THz) portions of the electromagnetic spectrum have been utilized for many applications. Figure 3 shows that, for a dry atmosphere, the total zenith attenuation is only about 1 dB at 1 THz. This value of zenith attenuation is fairly constant for frequencies through visible light (100 THz). A “window” in the standard atmosphere exists around 890 GHz, the frequency of HCN masers, but the zenith attenuation at this frequency is still two orders of magnitude higher than that in the dry atmosphere (i.e., 100 dB vs. 1 dB total zenith attenuation). For all three frequency ranges, the key attenuating elements in the atmosphere are aerosols, usually cloud and fog droplets. Thick fog (liquid water density ≈ 0.5 g/m³) will cut visibility to 50 m (19). Most free-space laser links are therefore short-range (< 1 km) unless extraordinary powers are contemplated, such as the ~ 1 MW chemical oxygen iodine laser (COIL) planned for missile interception. At such huge power levels, though, the almost instantaneous heating process caused by the passage of the beam through the

atmosphere will modify the constituents along the path, thereby altering the transmission characteristics significantly.

BIBLIOGRAPHY

1. J. Powers, *An Introduction to Fiber Optic Systems*, 2nd ed., Irwin, Homewood, IL, 1997, Chap. 2, Sec. 2.2.
2. Effects of tropospheric refraction on radiowave propagation, Rec. ITU-R P.834-2, *ITU-R Recommendations, Propagation in Ionized and Non-ionized Media*, 1997.
3. The radio refractive index: Its formula and refractivity data, Rec. ITU-R P.453-6, *ITU-R Recommendations, Propagation in Ionized and Non-ionized Media*, 1997.
4. M. P. M. Hall and C. M. Comer, Statistics of tropospheric radio-refractive index soundings taken over a three year period in the UK, *Proc. IEE* **116**:685–690 (1969).
5. H. T. Dougherty and B. A. Hart, Recent progress in duct propagation predictions, *IEEE Trans. Anten. Propag.* **27**: 542–548 (1979).
6. W. L. Flock, *Propagation Effects on Satellite Systems at Frequencies below 10 GHz*, NASA Reference Publication 1108, 1983.
7. E. E. Altshuler, Tropospheric range-error corrections for the Global Positioning System, *IEEE Trans. Anten. Propag.* **46**:643–649 (1998).
8. D. Vanhoenacker-Janvier, Review of tropospheric scintillation measurements and prediction techniques, *CLIMPARA'98, Proc. URSI Commission F Open Symp. on Climatic Parameters in Radiowave Propagation Prediction*, Ottawa, Canada, 1998, pp. 93–98.
9. E. T. Salonen, J. K. Tervonen, and W. J. Vogel, Scintillation effects on total fade distribution for earth–satellite links, *IEEE Trans. Anten. Propag.* **44**:23–27 (1996).
10. J. L. Strickland, R. L. Olsen, and H. L. Werstiuk, Measurement of low-angle fading in the Canadian Arctic, *Ann. Telecommun.* **32**:530–535 (1977).
11. D. L. Bryant, Low elevation angle 11 GHz beacon measurements at Goonhilly earth station, *BT Technol. J.* **10**(4):68–75 (1992).
12. J. E. Allnutt and A. W. Dissanayake, The combination of attenuating phenomena in prediction procedures for 10–50 GHz satellite-to-ground paths, *CLIMPARA'98, Proc. URSI Commission F Open Symp. Climatic Parameters Radiowave Propagation Prediction*, Ottawa, Canada, 1998, pp. 183–190.
13. Propagation data and prediction methods required for the design of earth–space telecommunications systems, Rec. ITU-R P.618-5, *ITU-R Recommendations, Propagation in Ionized and Non-ionized Media*, 1997.
14. Attenuation by atmospheric gases, Rec. ITU-R P.676-3, *ITU-R Recommendations, Propagation in Ionized and Non-ionized Media*, 1997.
15. G. Brussaard, *Radiometry: A Useful Tool?* ESA publication SP-1071, 1985.
16. R. Polonio and C. Riva, ITALSAT propagation experiment at 18.7, 39.6, and 49.5 GHz at Spino D'Adda: Three years of CPA statistics, *IEEE Trans. Anten. Propag.* **46**(5):631–642 (1998).
17. G. H. Bryant, The structure of tropical rain from attenuation and rain exceedences, *Proc. ISAP'92*, Sapporo, Japan, 1992, pp. 877–880.

18. Specific attenuation model for rain for use in prediction methods, Rec. ITU-R P.838, *ITU-R Recommendations, Propagation in Ionized and Non-ionized Media*, 1992.
19. Attenuation due to clouds and fog, Rec. ITU-R P.840-2, *ITU-R Recommendations, Propagation in Ionized and Non-ionized Media*, 1997.
20. D. S. Slobin, Microwave noise temperature and attenuation of clouds: Statistics of these effects at various sites in the United States, Alaska, and Hawaii, *Radio Sci.* **17**:1443–1454 (1987).
21. E. E. Altshuler and R. A. Marr, Cloud attenuation at millimeter wavelengths, *IEEE Trans. Anten. Propag.* **37**:1473–1479 (1989).
22. F. Dintelmann and G. Ortgies, A semi-empirical model for cloud attenuation prediction, *Electron. Lett.* **25**:1487–1488 (1989).
23. E. Salonen, Prediction models of atmospheric gases and clouds for slant path attenuation, *Proc. Olympus Utilization Conf.*, Seville, Spain, 1993, pp. 615–622.
24. G. Feldhake, Estimating the attenuation due to combined atmospheric effects on modern earth–space paths, *IEEE Anten. Propag. Mag.* **39**:26–34 (1997).
25. A. W. Dissanayake, J. E. Allnut, and F. Haidara, A prediction model that combines rain attenuation and other propagation impairments along earth–space paths, *IEEE Trans. Anten. Propag.* **45**:1546–1558 (1997).

RESONANT TUNNELING DIODES

KOICHI MAEZAWA
Nagoya University
Nagoya, Japan

1. INTRODUCTION

Recent (as of 2003) progress in epitaxial growth technology has made it possible to fabricate thin structures where quantum effects emerge. In these thin structures, the wavelike nature of electrons dominates the current–voltage characteristics. Electrons can penetrate barriers (tunneling), interfere, and create standing waves. A resonant tunneling diode (RTD) exploits such effects. RTDs are characterized by unique current–voltage characteristics showing negative differential resistance (NDR). They consist of extremely thin semiconductor heterolayers with thicknesses of 1 to 10 nm.

Figure 1 shows an example of the RTD structure along with the conduction band diagram. The structure consists of wide-bandgap and narrow-bandgap semiconductors. Typically, it is made of GaAs/Al_xGa_{1-x}As system on GaAs substrate or In_{0.53}Ga_{0.47}As/In_{0.52}Al_{0.48}As system on InP substrate; the GaAs and In_{0.53}Ga_{0.47}As are narrow-bandgap semiconductors, and the Al_xGa_{1-x}As and In_{0.52}Al_{0.48}As are wide-bandgap ones. This structure is grown by molecular-beam epitaxy (MBE) or metallorganic chemical vapor deposition (MOCVD), which can grow epitaxial layer with one-monolayer precision.

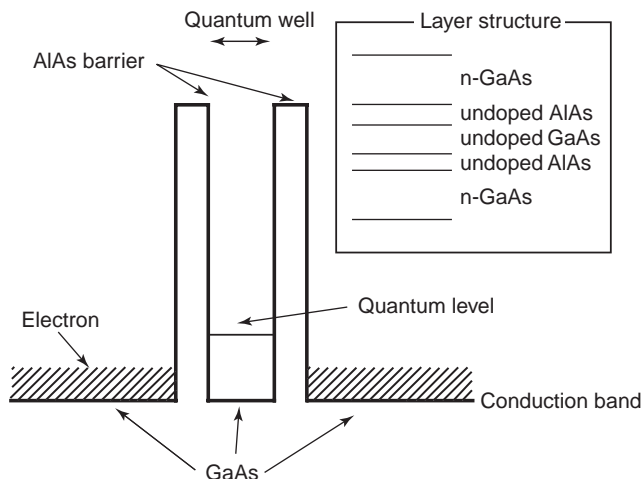


Figure 1. An example of the RTD structure with its conduction band diagram. This structure contains a quantum well, which is formed when a narrow-bandgap layer is sandwiched between two wide-bandgap layers.

This structure contains a quantum well, which is formed when a narrow-bandgap layer (well) is sandwiched by two wide-bandgap layers (barriers). In the well, the energy of electrons is quantized due to the wavelike nature of electrons. (The wavelength must be such that half the wavelength (or an integer multiple) matches the thickness of the quantum well, because the electron wave is fixed at the barriers.) Electrons having an energy equal to the quantized energy levels can pass through the barriers, while those that don't have an extremely small chance of passing through. Consequently, unique current–voltage characteristics having NDR are obtained with this structure. An example of such characteristics is shown in Fig. 2. (In this figure, the anomalous steplike structures shown in the negative differential resistance region are due to the spurious effect arising from oscillation within the measuring system.)

RTDs are attracting much attention because of their potential for high-speed operation as well as for high functionality due to the NDR. RTDs with 712 GHz oscillation [1] and 1.5 ps switching [2] have already been reported, and several functional RTD-based circuits [3], which include an oscillator, a mixer, multiple-valued logic, and a neuronlike weighted-sum function [4], have also been reported. These functions reduce the number of devices used, leading to lower power dissipation. Another advantage, one of the most important ones, is that RTDs can operate at room temperature. This differentiates RTDs from most other quantum effect devices, which can operate at only cryogenic temperatures. Thus RTDs are regarded as most practical quantum effect devices for ultra-high-speed analog and digital applications in the near future.

2. OPERATING MECHANISM

The operating mechanism of RTDs is explained here for a simple double-barrier RTD, although there are many

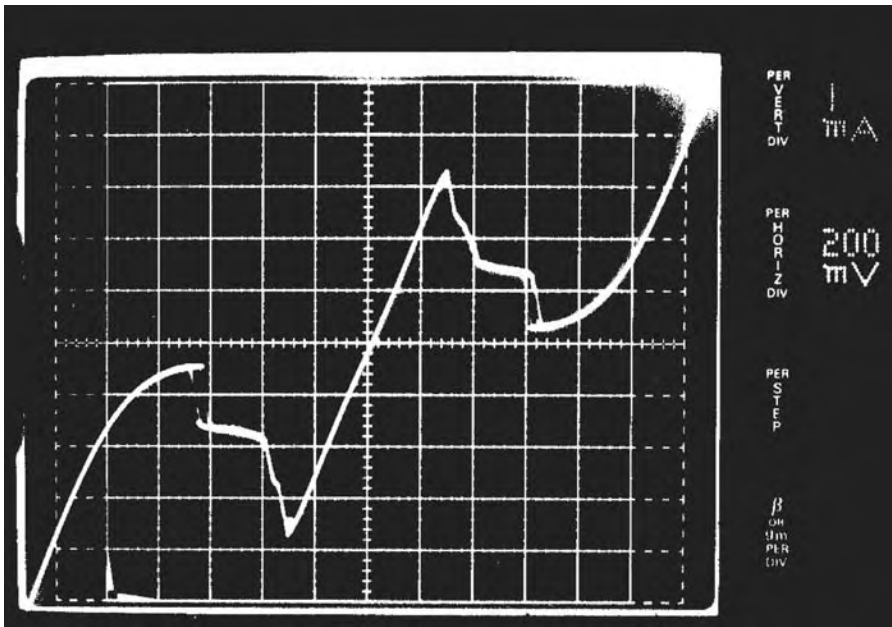


Figure 2. Current-voltage curve of the RTD. This curve is characterized by the NDR.

variations of the structure. Figure 3 shows a conduction band diagram of the RTD for various applied voltages along with current-voltage characteristics. For simplicity, it is assumed that the quantum well has only one subband, which has a minimum energy of E_0 . The current-voltage characteristics can be explained by the energy and momentum conservation through tunneling, as follows.

The z direction is set perpendicular to the wafer surface. This ensures that the translational symmetry in the xy plane holds during tunneling. Hence, the x and y components of the momentum, k_x and k_y , must be conserved at the tunneling, assuming where is no scattering. This indicates that the kinetic energy for z -directional motion and for motion perpendicular to the z direction must be conserved independently. Thus the electrons in the

emitter can go through the barrier into the well if the z component of the momentum k_z has a special value expressed as

$$k_{z0} = \frac{\sqrt{2m^*(E_0 - E_C)}}{\hbar} \tag{1}$$

where E_C is the energy of the conduction band edge of the emitter, m^* the electron effective mass, and \hbar Planck's constant divided by 2π . The current is proportional to the number of electrons having momentum k_{z0} of the above-mentioned value. This can be easily understood from Fig. 4, which illustrates the Fermi sphere for the degenerately doped emitter. Initially, the number of electrons

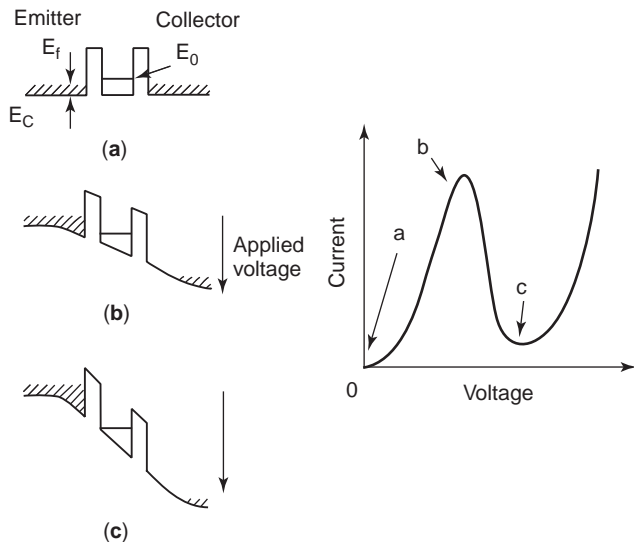


Figure 3. Conduction band diagram of the RTD for various applied voltages with current-voltage characteristics.

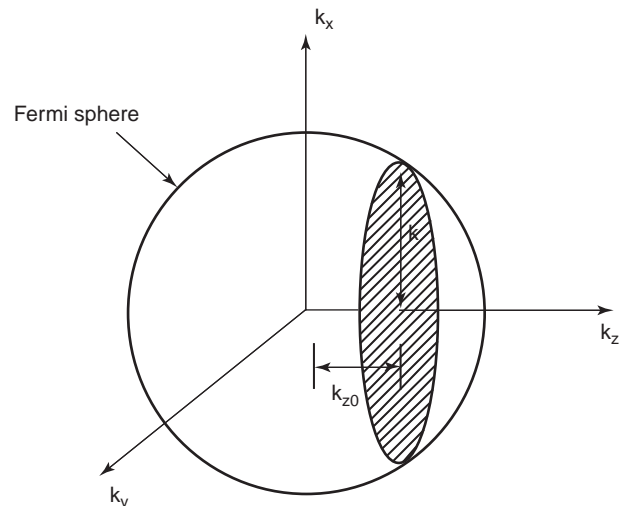


Figure 4. Fermi sphere for the degenerately doped emitter. The number of tunneling electrons is proportional to the area of the shaded disk.

with momentum k_{z0} is very small, or 0 at $T = 0$ K, when E_0 is larger than E_F . Their number then increases proportionally to the area of the shaded disk in Fig. 4 when $E_C < E_0 < E_F + E_C$. The electrons in the disk are in the resonant state. The area of the disk πk^2 is expressed as

$$\pi k^2 = \frac{2\pi m^*(E_F - (E_0 - E_C))}{\hbar^2} \quad (2)$$

In the simple approximation that ignores the band bending, E_C is linearly dependent on the applied voltage. This means that current increases linearly with increase in the applied voltage. Then, the number of electrons abruptly decreases when E_0 drops under E_C . Finally, nonresonant current increases with increasing applied voltage beyond this point. The nonresonant current arises from several mechanisms; examples are direct tunneling of thermally excited electrons, scattering, and imperfections of the structure. The result is the current–voltage characteristics shown in Fig. 3.

3. EFFECTS OF SCATTERING

Here, let us briefly consider the effects of scattering. Scattering destroys phase coherence and breaks the transition rule. Possible scattering centers include impurities, phonons, electrons, and interface roughness. Taking scattering into account in RTD theory is difficult and is still an evolving problem.

From a qualitative point of view, scattering in the well, which breaks the phase coherence of electrons, doesn't change the operating mechanism discussed above, if the scattering rate is not large enough to prevent energy-level formation. This is because the mechanism depends only on the fact that the electrons tunnel into the two-dimensional state in the well. It is called “sequential tunneling” when the scattering rate is large enough to destroy all coherence before electrons leave the well [5].

On the other hand, scattering plays an important role in determining peak and valley currents quantitatively [6]. In particular, it has been reported that scattering due to interface roughness has a significant effect on those currents [7]. The interface roughness breaks the translational symmetry in the xy plane, which results in broader resonance, and hence a larger valley current.

4. OPERATION SPEED

One of the most significant advantages of RTDs is their extremely high operation speed. In discussing the limit of the operation speed, it is important to differentiate two response times: the so-called “tunneling time” and the “ RC time.” The former is the time it takes electrons to tunnel through the RTD structure, and is related to quantum mechanics. The latter is the time required to charge the capacitance of the RTD, and is related to circuit theory.

Let us first consider the tunneling time [8]. Suppose that the electric field in the RTD structure changes from the nonresonant state to resonant state at a certain time t_0 . The amplitude of the wavefunction in the quantum well

changes to its steady-state value in response to this change. The tunneling time is the time required for this change. This time is of the order of the resonant state lifetime, τ_{life} , or the “escape” time, which is the time it takes an electron in the quantum well to escape from it. (In the most simple approximation, the tunneling time is the twice the escape time, because the tunneling time consists of two processes, tunneling into the well and from the well.) From simple theory, this time is determined by the energy level width Γ as

$$\tau_{\text{life}} = \frac{\hbar}{\Gamma} \quad (3)$$

The energy-level width Γ is determined as the half-width of the transmission probability function through the resonant state. Roughly speaking, Γ exponentially decreases with increasing barrier thickness and height. This means that a shorter tunneling time can be obtained with thinner and lower barriers, although there is a tradeoff against the peak-to-valley ratio. This time determines the fundamental speed limit for ideal RTDs, and it can be as short as 0.1 ps [9].

However, various nonidealities in the real RTDs affect the tunneling time. These nonidealities include barrier asymmetry, interface roughness, and inelastic scatterings. Several theoretical and experimental studies have been devoted to clarifying the tunneling time of RTDs. A time-resolved photoluminescent measurement using ultrashort pulses [10] has revealed that the escape time from a two-dimensional well agrees reasonably well with Eq. (3). On the other hand, the tunneling time was estimated from the high-frequency characteristics of quantum-well-base transistors [11]. These devices were heterojunction bipolar transistors with a base layer consisting of a resonant tunneling double barrier structure. The results again showed that the tunneling time is in reasonable agreement with Eq. (3). The resonant lifetime described in Eq. (3) is a useful guideline for designing high-speed RTDs, although further studies are necessary to clarify the tunneling time in real systems. In addition to the tunneling time, the transit time across the collector depletion layer affects RTD response when large spacer layers are used.

Next, we will discuss the operation speed limited by RC time. In most applications, the operation speed of RTDs is limited not by the intrinsic tunneling time but by the charging time of RTD capacitance. RTDs are accurately described by the equivalent circuit in Fig. 5. This circuit consists of a voltage-dependent current source $I_{\text{RTD}}(V)$, a voltage-dependent capacitor $C_{\text{RTD}}(V)$, and a series resistor R_s . Here, the parallel combination of $I_{\text{RTD}}(V)$ and $C_{\text{RTD}}(V)$ represents an intrinsic RTD, and the R_s is the sum of series resistances such as the contact resistances. An investigation of the capacitance $C_{\text{RTD}}(V)$ is extremely important in determining the maximum operation speed of RTD circuit. A schematic diagram of the capacitance–voltage curve is shown in Fig. 6 with the current–voltage curve as a reference. The capacitance of the RTD is extracted from the results of microwave S -parameter measurements [12]. In short, there are two main points: (1) the capacitance is roughly equal to that calculated from the undoped spacer layer and the depletion layer of the device, except for the

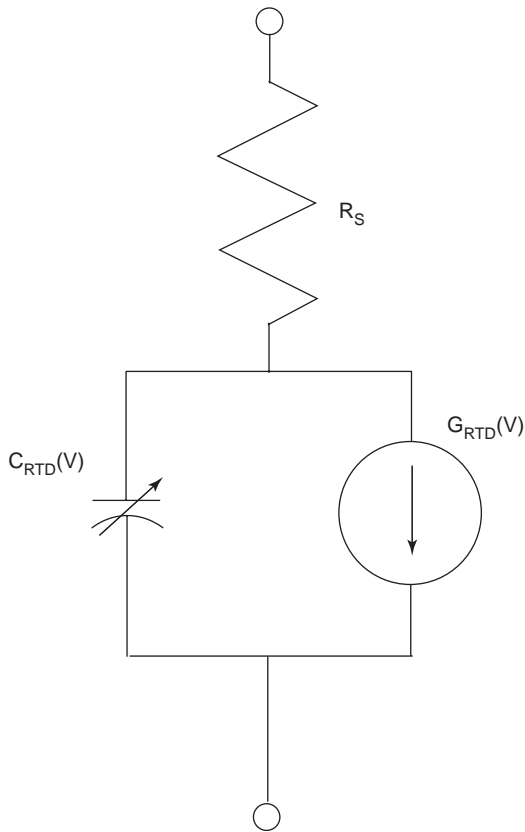


Figure 5. Equivalent circuit of the RTD. This circuit consists of a voltage-dependent current source, a voltage-dependent capacitor, and a series resistor.

voltage near the peak; and (2) there is an anomalous peak structure in the NDR region, as shown in Fig. 6. This peak is due to resonant electrons accumulated in the well. This must be taken into account to discuss operating speed precisely. Note that $I_{RTD}(V)$ and $C_{RTD}(V)$ do not depend on the frequency when the frequency is sufficiently smaller than the intrinsic limit determined by the lifetime discussed above. (Occasionally, quantum inductance was inserted to the equivalent circuit when the frequency approaches the intrinsic limit. This inductance, however, is difficult to discriminate from wiring inductance.)

Here, consider the operation speed limits for two typical applications. The first is an oscillator [13]. The NDR of RTDs can act as the basis for a very fast and simple oscillator. The maximum frequency of the oscillation f_{max} is expressed as

$$f_{max} = \frac{1}{2\pi C} \left[\frac{-G_{max}}{R_S} - G_{max}^2 \right]^{1/2} \quad (4)$$

where G_{max} is the maximum negative conductance in the NDR region and C is the capacitance at the voltage where G_{max} obtained. This is the frequency above which the dynamic current through the capacitance masks the NDR. Consequently, no oscillation occurs above this frequency. This frequency can be extremely high, for example, 1.24 THz [1].

The second example is the switching time for the resistance-load RTD circuit [14]. Figure 7 shows the load

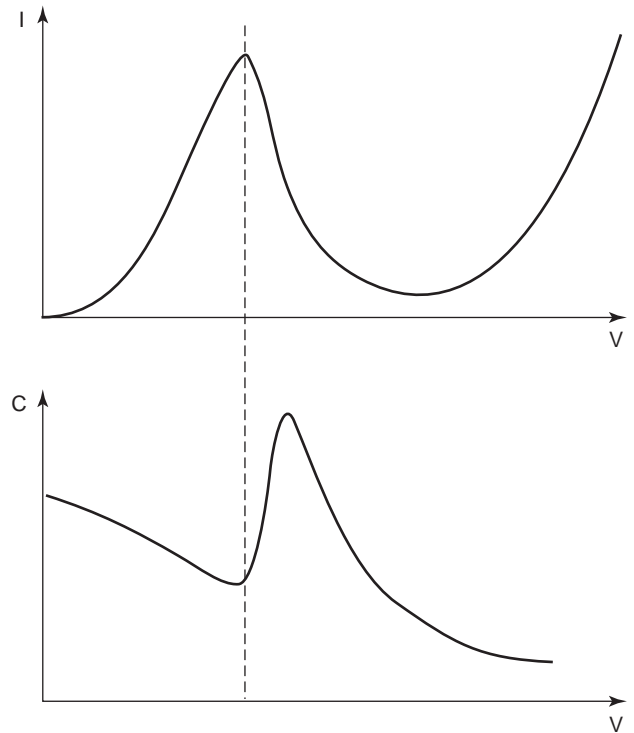


Figure 6. Schematic diagram of the capacitance–voltage curve with a current–voltage curve as a reference. An anomalous peak structure is shown in the NDR region.

diagram and the switching mechanism of the circuit. A small pulse applied to the bias terminal makes the circuit switch from OFF state to ON state. This switching time can be calculated from the equivalent-circuit model, and is approximated to be a few times RC , where C is the average capacitance in the NDR region and the R is the negative resistance. Extremely short switching times of 1.7 ps [15] and 1.5 ps [2] have been reported for InAs/AlSb and InAs/AlAs RTDs, respectively.

It is worth noting the advantages of RTDs compared to Esaki diodes, or tunnel diodes. The I – V curves of Esaki

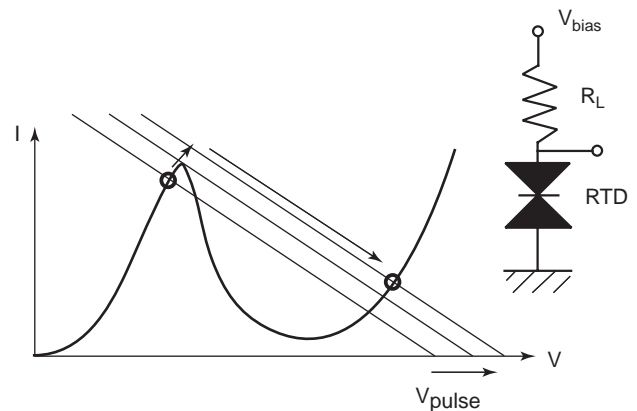


Figure 7. Load line diagram of the resistive load RTD switch circuit. The circuit switches its state in response to a small pulse (V_{pulse}) applied to the bias voltage. A small pulse applied to the bias terminal makes the circuit switch from OFF state to ON state.

diodes show NDR similar to RTDs, and several applications similar to RTDs have been studied. The one of most important advantages of the RTD is the ability to obtain a high peak current density with a relatively low capacitance. For example, an extremely high current density of 6.8 GA/m^2 is obtained with a capacitance of about 1.5 mF/m^2 [2]. These values indicate that the speed index, which is defined as the peak current density divided by the capacitance per unit area J_p/C , is as large as 4.55 V/ps . (The speed index corresponds to the speed of voltage variation, when the RTD capacitance is charged by its peak current.) This is much larger than those of Esaki diodes, which are smaller than 0.1 V/ps . This is possible because the current density of RTDs can be increased by changing the barrier and the well thicknesses, and this can be achieved without decreasing depletion layer thickness. On the other hand, one must increase impurity density to decrease tunnel barrier (= depletion-layer) thickness in order to increase current density in Esaki diodes. Consequently, the maximum operation speed of RTDs can be much higher than that of Esaki diodes. Furthermore, RTDs can avoid degradation observed in Esaki diodes due to impurity diffusion at the highly doped p-n junction.

5. RTD VARIATIONS

Several variations of RTDs have been studied. The one variation is an RTD with more than two barriers. The purpose of using multiple barriers is to obtain a multiple-peak I - V curve, which can be used for application for multiple-valued logic [16]. Also, the triple-barrier structures have been used to make a sharp peak. This is because the first quantum well plays the role of an energy filter [17].

Several materials other than GaAs/AlAs or In GaAs/InAlAs systems have also been studied. In particular, the AlSb/GaSb/InAs systems is attracting much attention because of its unique band lineups. Two different structures have been proposed for this material system [18,19]. One is the AlSb/InAs/AlSb double-barrier quantum-well structure, which has a band diagram similar to that of AlAs/GaAs. This heterostructure has a larger barrier height than AlAs/GaAs, so a larger peak-to-valley (P/V) current ratio can be obtained. The other is the resonant intervalley tunneling diode (RITD), which exploits the type II band alignment of the AlSb/GaSb/InAs system. (The conduction band minimum of InAs is lower than the valence band maximum of GaSb; see Fig. 8.) RITDs consist of a GaSb well sandwiched by AlSb barriers with InAs emitter/collector layers. In the GaSb well, quasibound states are formed in the valence band. This allows electrons in the emitter to tunnel through the valence band state of GaSb to the collector. In this structure, the bandgap of GaSb blocks the leakage current at the valley voltage. Consequently, an extremely high P/V ratio of more than 20 is possible at room temperature.

The implementation of RTDs with a Si-based material system has attracted increasing attention. Several types of devices were reported, which include an SiO_2/Si , SiGe/Si , CaF_2/Si , and $\gamma\text{-Al}_2\text{O}_3/\text{Si}$ systems [20]. Until now, only limited performance has been obtained for these systems

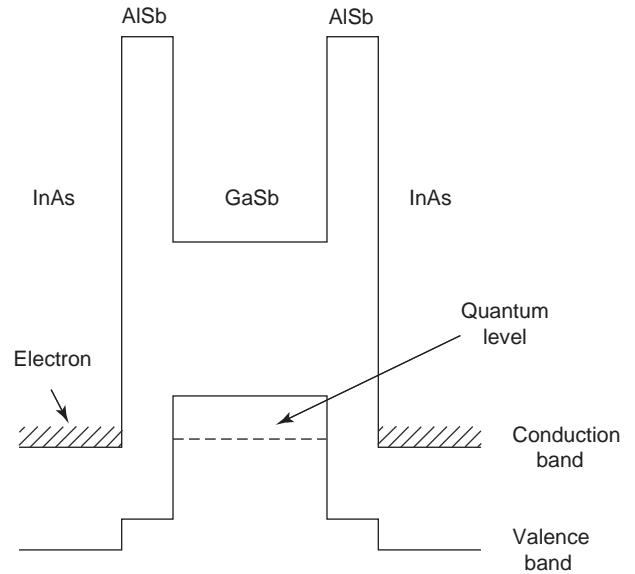


Figure 8. Conduction band diagram of the resonant intervalley tunneling diode.

(low P/V ratio, low peak current density). This is due to the higher electron mass in Si compared to that of the compound semiconductors. Further effort would be necessary to realize high-performance Si-based RTDs. However, the emergence of high-performance Si-based RTDs would have an extremely significant impact, because highly functional circuits using them could be implemented in Si VLSIs.

6. DEVICE MODELING

A device model of the RTDs suitable for circuit simulation is significant for designing circuits using RTDs. The equivalent-circuit model shown in Fig. 5 is generally used with a parasitic inductance L_s connected serially. For the I - V curve, the most simple model is the piecewise linear approximation. This is convenient to obtain general view of the circuit behavior. However, it's not sufficient for precise circuit design. Some model equations of RTD I - V curves have been proposed for circuit simulation. These equations are simple to use in circuit simulators, but can be closely fitted to experimental I - V curves. Among these, Schulman's model [21] is often used because it shows better fit for high-performance RTDs. Their equation is shown below, which is based on the physical current equation but some variables are treated as fitting parameters:

$$I(V) = I_{\text{RT}}(V) + I_{\text{NRT}}(V) \quad (5)$$

$$I_{\text{RT}}(V) = A \log \left[\frac{1 + \exp[(B - C + n_1 V)]}{1 + \exp[(B - C - n_1 V)]} \right] \times \left(\frac{\pi}{2} + \arctan \frac{C - n_1 V}{D} \right) \quad (6)$$

$$I_{\text{NRT}}(V) = A_0 \left(\exp \frac{V}{n_0} - 1 \right) \quad (7)$$

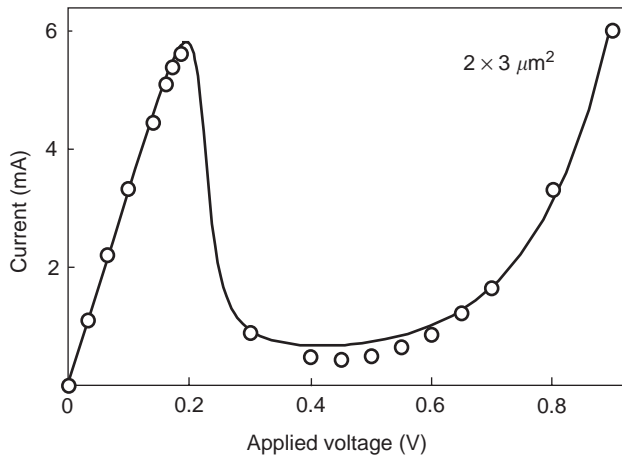


Figure 9. Model I - V curve fitted to the experimental data.

Here, $A_0, A, B, C, D, n_0, n_1$ are the fitting parameters. The model I - V curve is shown in Fig. 9 with the experimental one.

The C - V characteristics are more difficult to implement. This is because the precise measurement of capacitance for high-performance RTDs is very difficult because of its extremely small value and the difficulty in biasing the RTDs in NDR region. At present, capacitance calculated from the depletion layer thickness is often used for simulation. This is a reasonably good approximation in a moderate frequency range. However, for higher frequency ranges close to the cutoff frequency of the RTDs, it should be necessary to take the effect of electron accumulation in the well into account.

7. APPLICATIONS

Several possible RTD applications that exploit the NDR characteristics are now being developed. Although most of them are similar to those once proposed for Esaki diodes, progress in related device technology and the ultra-high-speed potential of RTDs open up new possibilities. The most attractive applications are microwave/millimeter-wave analog circuits [13]. They include an oscillator, a frequency multiplier, a mixer, and a trigger [22]. Some of these applications are discussed in detail here.

7.1. Oscillators

Oscillators based on NDR have been studied intensively. Oscillation frequencies up to 712 GHz with InAs/AlSb RTDs are the highest achieved to date and exceed those of any other solid-state devices [1]. The most significant problem that impedes use of RTD oscillators in real applications is the output power [23]. For example, output powers reported so far were 50 μ W at 205 GHz, 28 μ W at 290 GHz, and 0.3 μ W at 712 GHz. One of the most significant reasons for these small powers is the limited area of the RTD available in the circuit. This limitation is imposed to avoid oscillations in bias circuit. Small $V_v - V_p$ (V_v = valley voltage), and hence, large negative conductance makes this problem difficult to solve. Series integration of RTDs is one promising technique to overcome this

problem. However, biasing such series connected RTDs in the NDR region is unstable even when the total bias voltage V_{bias} satisfies the condition $nV_p < V_{\text{bias}} < nV_v$ (n = number of RTDs connected serially). In fact, the total voltage is distributed such that all RTDs are biased in the positive differential resistance regions. To solve this problem dynamic biasing techniques using a subfrequency excitation have been proposed [24]. Decreasing the parasitic resistance is also a significant problem for realizing high-frequency oscillators because this resistance restricts the available power as well as the maximum oscillation frequency. An interesting technique for decreasing collector contact resistance is to use the undoped Schottky contacts for the collector [25]. When the RTD is biased in the operating voltage, the forward-biased Schottky contact has no barrier that impedes electrons flowing from collector to the metal.

7.2. Mixers

The RTD has the ability to act as a mixer because of the rapid variation of the conductance with voltage. For a diode oscillating with a DC bias at the center of the NDR region, the time-varying small-signal dynamic conductance changes from a large negative value at the DC bias point to a small, perhaps positive, value at both extrema of the oscillation amplitude. Consequently, the RTDs can act as a mixer when the RF and LO signals are input.

7.3. Frequency Multipliers

As described above, the RTD shows a strong nonlinearity. The Fourier series of the conductance then has large coefficients at its first few harmonics, especially the even harmonics if the I - V curve is antisymmetric about the bias point. These harmonics can be used for frequency multipliers.

7.4. Clock Recovery Circuits and Frequency Dividers

Interesting applications relative to the resonant tunneling oscillators have been proposed. These are based on the injection-locking phenomenon, or more generally, the bifurcation phenomenon in the resonant tunneling oscillator circuits. First is an optoelectronic clock recovery circuit as shown in Fig. 10 [26]. The circuit consists of an oscillator, which is constructed with an RTD and a transmission line, and an extremely high-speed photodiode called UTC PD (uni-traveling-carrier photodiode). The essential synchronization principle is injection locking of the RTD oscillator using the photocurrent generated by UTC PD. It was reported that the integrated circuit fabricated on an InP substrate extracted an electrical 11.55-GHz clock signal from 11.55-Gbps RZ (return-to-zero) optical data streams in a wide locking range. Furthermore, the extraction of a subharmonic clock from 46.2 Gbps input datastreams was also reported. This indicates that this circuit also works as a frequency divider with an optical input.

The similar locking phenomenon was also adapted to a frequency divider shown in Fig. 11 [27]. This simple circuit can be regarded as a Van der Pol oscillator with an oscillating input. It is known in the field of nonlinear physics

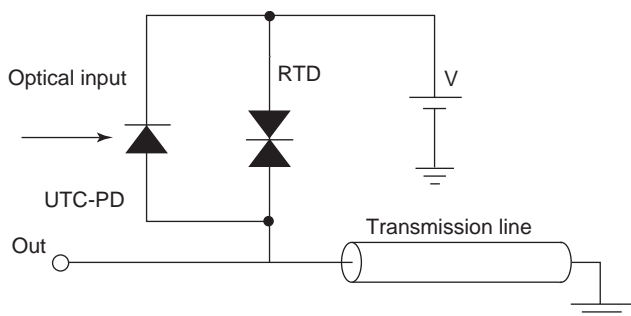


Figure 10. Circuit diagram of the clock recovery circuit.

that this type of circuit yields various signal patterns including long period signals, whose period T is integer-multiple of the input period T_0 ($T = nT_0$). This behavior is known as a *bifurcation phenomenon*, which is closely related to chaos. (In fact, this circuit also shows chaotic behavior under certain conditions, and several applications using controlled chaos could be realized, e.g., communication using chaos synchronization, and encryption.) Ultra-high-frequency operation at 88 GHz of the 1–2 frequency divider has been realized with this circuit.

Several circuits have also been proposed for digital applications [3]. The latching function due to the bistability of RTD circuits is the basis for most of these applications. A typical example of such a circuit is a (multiple-valued) memory, which uses RTDs connected in series or parallel with appropriate load.

8. RESONANT TUNNELING TRANSISTORS AND INTEGRATION WITH CONVENTIONAL TRANSISTORS

An RTD has only two terminals, which restricts the use of resonant tunneling phenomena. Adding a control terminal to RTDs extends their usability to a variety of applications. The most straightforward way to do this is to merge RTD with conventional transistors to make a composite device. This approach has been used to build resonant tunneling bipolar transistors (RTBTs) [3], resonant (tunneling) hot-electron transistors (RHET) [28], and gated RTDs. The RTBTs have a resonant tunneling structure at the emitter/base junction region or in the base. An RHET

is similar to RTBT and has a resonant tunneling structure at the emitter of the hot-electron transistor. Consequently, these devices have negative transconductance in emitter-grounded transistor characteristics. These nonlinear input–output characteristics can be applied to several circuits, such as an XOR (exclusive-OR) logic gate with only one transistor. On the other hand, gated RTDs have Schottky or junction gates around the emitter to control RTD area, and show an NDR with controlled peak current. These devices are used for a functional logic gate called a “MOBILE” (monostable–bistable transition logic element) [4], and are useful in investigating the physics of very small tunneling structures [29].

The other and more practical way to add control terminals is to connect RTDs with conventional transistors to make parallel or series circuits. Integration of RTDs with transistors is necessary in order to do this, but this has a significant advantage beyond merely adding a control terminal. One can use both RTD circuits and conventional transistor circuits according to their merits and demerits. Integration of RTDs with HEMTs or bipolar transistors have been proposed, and several circuits have been also reported using such devices [30–32].

In general, two configurations are used to connect an RTD and a transistor: parallel and serial configurations, as shown in Fig. 12. (Here, field-effect transistors are used for instance. The following discussion is valid for bipolar transistors.) The parallel circuit can be regarded as an NDR device capable of peak current modulation. On the other hand, the serial circuit, which has two options, connecting the RTD at source or drain, shows a negative transconductance. The former is used for the logic gate

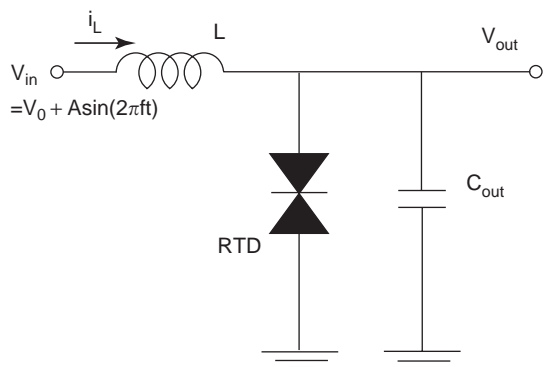


Figure 11. Circuit diagram of the chaos generator (frequency divider).

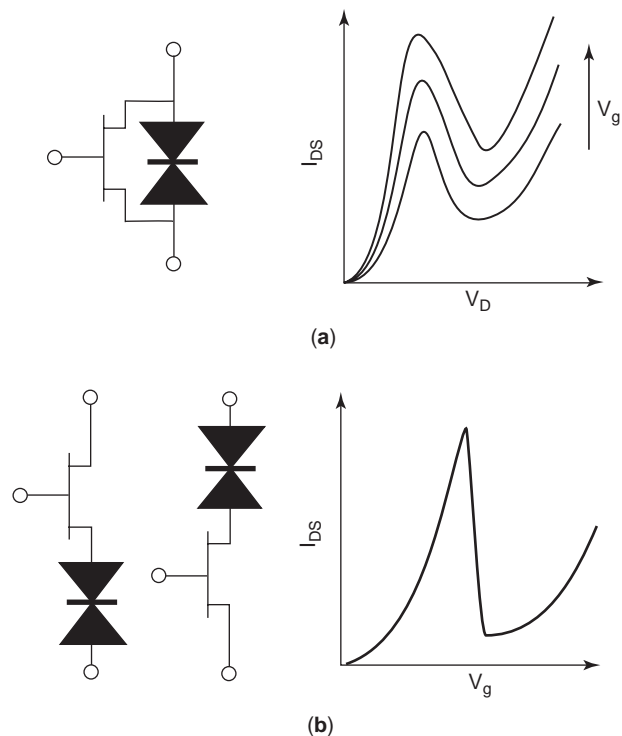


Figure 12. Basic configurations of the RTD/FET circuit together with its I - V characteristics.

MOBILE, and the latter is also used for various analog and digital applications. Here, some applications of these circuits will be discussed in detail.

8.1. MOBILE [Monostable-Bistable (Transition) Logic Element]

The MOBILE [33] is a functional logic gate exploiting the NDR of RTDs. It consists of two serially connected NDR devices with FET(s) connected parallel to the NDR device(s). The simplest form of the MOBILE, shown in Fig. 13, works as a clocked inverter, together with the load line diagram. The key point is that it employs the monostable-to-bistable transition of the circuit, and the circuit is driven by oscillating the bias voltage to produce the transition. A stable point S in the $V_{bias} < 2V_p$ region splits into two branches, S_1 and S_2 , when V_{bias} increases through $2V_p$. A small difference in the peak current between the two NDR devices determines the circuit's state after the transition. Therefore, the circuit forms a logic gate if the peak current of the NDR devices can be modulated according to input signals. The oscillatory varying bias voltage acts as a clock. The MOBILE switches its state only at the rising edge of the bias voltage (it works as a clock) and maintains its state while the bias voltage is high (edge-trigger and latch operation).

Several application circuits of the MOBILE have been reported, which include a 35-Gbps D-FF, and a 34-GHz T-FF. Moreover, replacing the input HEMT by a photodiode, a 80-Gbps optical D-FF has been demonstrated [34]. Owing to the function of the MOBILE, the numbers of devices used in the circuits have been reduced considerably in comparison to those of the conventional circuits.

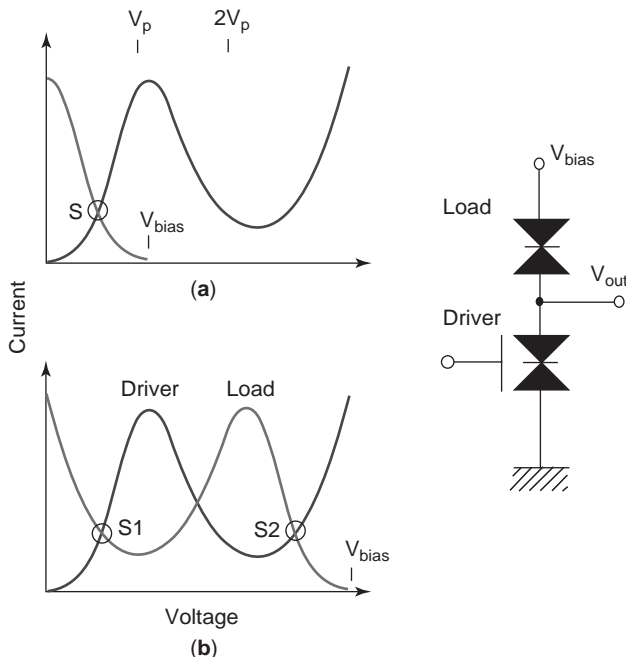


Figure 13. Operating principle of the MOBILE inverter: (a) basic configuration; (b) load diagrams for various V_{bias} .

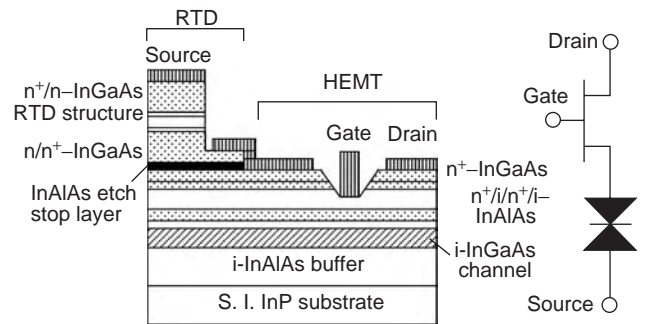


Figure 14. Schematic cross-sectional view of the RTHEMT with its equivalent circuit.

8.2. RTHEMT (Resonant Tunneling High-Electron-Mobility Transistor)

The RTHEMT [35,36] is one of the most promising devices, which incorporates an RTD at the source of a HEMT. It features a pronounced NDR and a negative transconductance. Figure 14 shows the schematic cross-section and the equivalent circuit of the RTHEMT. The RTD layers are grown on top of the HEMT layers. Its $I_{DS}-V_{GS}$ characteristics are shown in Fig. 15. As shown in the figure, strong nonlinear characteristics including negative transconductance, are observed for the RTHEMT. Note that this negative transconductance can be obtained in a wide range of the drain voltage due to the feedback of the nonlinear source resistance. This is in marked contrast with the configuration where the RTD is connected to the drain, which shows negative transconductance in relatively small range.

This folded $I_{DS}-V_{GS}$ curve is useful for fabricating frequency multipliers. A frequency doubler MMIC integrating RTHEMT and on chip impedance-matching circuit have been successfully fabricated. The discontinuous change in the drain current in $I_{DS}-V_{GS}$ characteristics is also valuable for various nonlinear circuits. This yields extremely high-order harmonics in its output. These high-order harmonics can be used for a pulse generator for the sampling phase detector and a signal source for injection-locking oscillator.

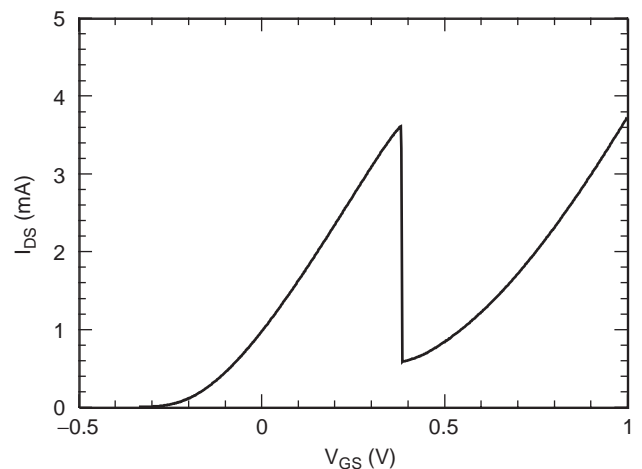


Figure 15. $I_{DS}-V_{GS}$ characteristics of the RTHEMT.

9. SUMMARY

Resonant tunneling diodes exploit the quantum tunneling effect emerging in nanometer-scale thin semiconductor heterostructures. The RTDs feature strong nonlinear current-voltage characteristics exhibiting negative differential resistance and also extremely high operation frequency. These features make the RTDs extremely useful for nonlinear microwave/millimeter-wave circuits as well as high-speed digital circuits. RTDs are excellent candidates for the high-frequency and low-power applications of the near future, and vigorous efforts to build and perfect them shall continue.

BIBLIOGRAPHY

1. E. R. Brown, J. R. Söderström, C. D. Parker, L. J. Mahoney, K. M. Molvar, and T. C. McGill, Oscillations up to 712 GHz in InAs. AlSb resonant-tunneling diodes, *Appl. Phys. Lett.* **58**:2291–2293 (1991).
2. N. Shimizu, T. Nagatsuma, T. Waho, M. Shinagawa, M. Yaita, and M. Yamamoto, In_{0.53}Ga_{0.47}As/AlAs resonant tunneling diodes with switching time of 1.5 ps, *Electron. Lett.* **31**:1695–1697 (1995).
3. F. Capasso, S. Sen, F. Beltram, and A. Y. Cho, Resonant tunneling and superlattice Devices: Physics and circuits, in F. Capasso, ed., *Physics of Quantum Electron Devices*, Springer-Verlag, Berlin, 1990.
4. K. Maezawa, T. Akeyoshi, and T. Mizutani, Functions and applications of monostable-bistable transition logic elements (MOBILEs) having multiple-input terminals, *IEEE Trans. Electron. Devices* **41**:148–154 (1994).
5. S. Luryi, Hot-electron injection and resonant-tunneling heterojunction devices, in F. Capasso and G. Margaritondo, eds., *Heterojunction Band Discontinuities*, North-Holland, Amsterdam, 1987.
6. S. Datta, *Electronic Transport in Mesoscopic Systems*, Cambridge Univ. Press, New York, 1995.
7. P. Roblin, R. C. Potter, and A. Fathimulla, Interface roughness scattering in AlAs/InGaAs resonant tunneling diodes with an InAs subwell, *J. Appl. Phys.* **79**:2502–2508 (1996).
8. D. K. Ferry, Theory of resonant tunnelling and surface superlattices, in F. Capasso, ed., *Physics of Quantum Electron Devices*, Springer-Verlag, Berlin, 1990.
9. T. C. L. G. Sollner, W. D. Goodhue, P. E. Tannenwald, C. D. Parker, and D. D. Peck, Resonant tunneling through quantum wells at frequencies up to 2.5 THz, *Appl. Phys. Lett.* **43**:588–590 (1983).
10. M. Tsuchiya, T. Matsusue, and H. Sakaki, Tunneling escape rate of electrons from quantum well in double-barrier heterostructures, *Phys. Rev.* **59**:2356–2359 (1987).
11. T. Waho, S. Koch, and T. Mizutani, Experimental analysis of resonant tunneling transit time using high-frequency characteristics of resonant tunneling transistors, *Superlatt. Microstruct.* **16**:205–209 (1994).
12. N. Shimizu, T. Waho, and T. Ishibashi, Capacitance anomaly in the negative differential resistance region of resonant tunneling diodes, *Jpn. J. Appl. Phys.* **36**:L330–L333 (1997).
13. T. C. L. G. Sollner, E. R. Brown, W. D. Goodhue, and H. Q. Le, Microwave and millimeter-wave resonant tunneling devices, in F. Capasso, ed., *Physics of Quantum Electron Devices*, Springer-Verlag, Berlin, 1990.
14. S. K. Diamond, E. Özbay, M. J. W. Rodwell, D. M. Bloom, Y. C. Pao, and J. S. Harris, Resonant tunneling diodes for switching applications, *Appl. Phys. Lett.* **54**:153–155 (1989).
15. E. Özbay, D. M. Bloom, D. H. Chow, and J. N. Schulman, 1.7ps, microwave, integrated-circuit-compatible InAs/AlSb resonant tunneling diodes, *IEEE Electron. Device Lett.* **14**:400–402 (1993).
16. T. Tanoue, H. Mizuta, and S. Takahashi, A triple-well resonant-tunneling diode for multiple-valued logic application, *IEEE Electron. Device Lett.* **9**:365–367 (1988).
17. T. Nakagawa, H. Imamoto, T. Kojima, and K. Ohta, Observation of resonant tunneling in AlGaAs/GaAs triple barrier diodes, *Appl. Phys. Lett.* **49**:73–75 (1986).
18. L. F. Luo, R. Beresford, and W. I. Wang, Resonant tunneling in AlSb/InAs/AlSb double-barrier heterostructures, *Appl. Phys. Lett.* **53**:2320–2322 (1988).
19. J. R. Söderström, D. H. Chow, and T. C. McGill, New negative differential resistance device based on resonant interband tunneling, *Appl. Phys. Lett.* **55**:1094–1096 (1989).
20. See, for example, *Ext. Abstr. 2001 Int. Conf. Solid State Devices and Materials*, Tokyo, 2001, pp. 582–589.
21. J. N. Schulman, H. J. De Los Santos, and D. H. Chow, Physics based RTD current-voltage equation, *IEEE Electron Device Lett.* **EDL-17**:220–222 (1996).
22. L. Yang, S. D. Draving, Dan E. Mars, and Mike R. T. Tan, A 50 GHz broad-band monolithic GaAs/AlAs resonant tunneling diode trigger circuit, *IEEE J. Solid-State Circuits* **29**:585–595 (1994).
23. H. Eisele and G. I. Haddad, Two-terminal millimeter-wave sources, *IEEE Trans. Microwave Theory Tech.* **46**:739–746 (1998).
24. R. Sun, O. B.-Lubecke, D.-S. Pan, and T. Itoh, Considerations and simulations of subfrequency excitation of series integrated resonant tunneling diodes oscillator, *IEEE Trans. Microwave Theory and Tech.* **43**:2478–2485 (1995).
25. M. Reddy, S. C. Martin, A. C. Molnar, R. E. Muller, R. P. Smith, P. H. Siegel, M. J. Mondry, M. J. W. Rodwell, H. Kroemer, and S. J. Allen, Jr., Monolithic Schottky-collector resonant tunnel diode oscillator arrays to 650 GHz, *IEEE Electron. Device Lett.* **18**:218–221 (1997).
26. K. Murata, K. Sano, T. Akeyoshi, N. Shimizu, E. Sano, M. Yamamoto, and T. Ishibashi, Optoelectronic clock recovery circuit using resonant tunnelling diode and uni-travelling-carrierphotodiode, *Electron. Lett.* **34**:1424–1425 (1998).
27. Y. Kawano, Y. Ohno, S. Kishimoto, K. Maezawa, T. Mizutani, and K. Sano, 88 GHz dynamic 2:1 frequency divider using resonant tunneling chaos circuit, *Electron. Lett.* **39**:1546–1547 (2003).
28. N. Yokoyama, S. Muto, H. Ohnishi, K. Imamura, T. Mori, and T. Inata, Resonant-tunneling hot electron transistors (RHET), in F. Capasso, ed., *Physics of Quantum Electron Devices*, Springer-Verlag, Berlin, 1990.
29. P. H. Beton, M. W. Dellow, P. C. Main, L. Eaves, and M. Henini, Magnetic-field dependence of the electrical characteristics of a gated resonant-tunneling diode, *Phys. Rev. B* **49**:2264–2264 (1994).
30. A. C. Seabaugh, E. A. Beame III, A. H. Taddiken, J. N. Randall, and Y.-C. Kao, Co-integration of resonant tunneling and double heterojunction bipolar transistor on InP, *IEEE Electron. Device Lett.* **14**:472–474 (1993).
31. J. Shen, S. Tehrani, H. Goronkin, G. Kramer, and R. Tsui, An exclusive-NOR based on resonant interband tunneling FET's, *IEEE Electron. Device Lett.* **17**:94–96 (1996).

32. K. J. Chen, K. Maezawa, T. Waho, and M. Yamamoto, Device technology for monolithic integration of InP-based resonant tunneling diodes and HEMTs, *IEICE Trans. Electron.* **E79-C**:1515–1524 (1996).
33. K. Maezawa and A. Foerster, Quantum transport devices based on resonant tunneling, in R. Waser, ed., *Nanoelectronics and Information Technology*, Wiley, Hoboken, NJ, 2003.
34. K. Sano, K. Murata, T. Otsuji, T. Akeyoshi, N. Shimizu, and E. Sano, An 80-Gb/s optoelectronic delayed flip-flop IC using resonant tunneling diodes and uni-traveling-carrier photodiode, *IEEE J. Solid State Circuits* **36**:281–289 (2001).
35. K. J. Chen, K. Maezawa, and M. Yamamoto, Novel current-voltage characteristics in a InP-based resonant tunneling high electron mobility transistor, *Appl. Phys. Lett.* **67**:3608–3610 (1995).
36. H. Fukuyama, K. Maezawa, M. Yamamoto, H. Okazaki, and M. Muraguchi, Large-signal microwave characteristics of resonant-tunneling high electron mobility transistors, *IEEE Trans. Electron. Devices* **46**:281–287 (1999).

RETRODIRECTIVE SYSTEMS

WAYNE A. SHIROMA
 RYAN Y. MIYAMOTO
 GRANT S. SHIROMA
 AARON T. OHTA
 MICHAEL A. TAMAMOTO
 BLAINE T. MURAKAMI
 University of Hawaii at Manoa
 Honolulu, Hawaii

Consider an electromagnetic wave in free space impinging on a flat metal sheet as shown in Fig. 1. If the direction of propagation is normal (i.e., perpendicular) to the metal surface, the wave reflects off the metal sheet in the same direction from which it originated. This is an example of *retrodirective* behavior, or simply, *retrodirectivity*. However, this does not imply that the metal sheet is a retrodirective system, because this behavior is observed only at normal incidence, when $\theta = 0^\circ$. If the incoming wave is incident at an arbitrary, nonnormal angle θ , the reflected wave does not bounce off the metal sheet at θ , as required for a retrodirective system, but instead at the specular angle $-\theta$ predicted by Snell's law. Moreover, if the direction of propagation is parallel to the metal surface ($\theta = 90^\circ$), the wave only grazes the sheet and there is no reflection at all. Retrodirectivity requires that the incoming wave bounce back in the same direction from which it originated, regardless of what that direction is.

Although one metal sheet cannot function as a retrodirective system, two or more metal sheets can. Figure 2 illustrates a retrodirective system formed by intersecting two mutually perpendicular, flat metal sheets. Since each quadrant forms a corner shape, the resulting structure is called a *corner reflector* [1], and provides retrodirectivity for any angle of incidence in the x - y plane. The system is easily extended to three dimensions by intersecting the two metal sheets in Fig. 2 with a third metal sheet that is

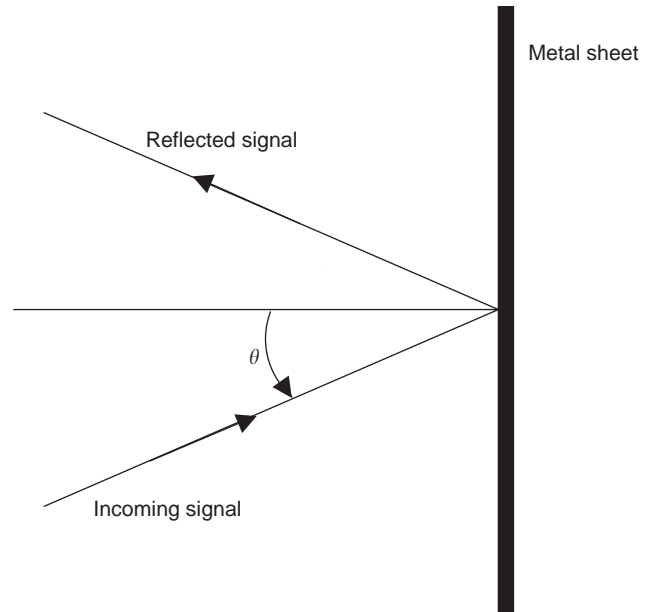


Figure 1. Reflection from a metal sheet. Retrodirective behavior occurs only at normal incidence ($\theta = 0^\circ$). At other angles of incidence, the reflected wave does not bounce back in the same direction from which it originated.

mutually perpendicular to both, creating a three-dimensional corner in all eight octants. Multiple reflections off of any one corner cause incoming waves from all possible angles in three-dimensional space to be reflected back in the same direction of the originating wave, giving rise to true retrodirectivity. We define a *retrodirective system*, then, as one that reacts to an incoming signal (often called an *interrogating* or *pilot signal*) from an unspecified direction by transmitting a response to that same direction, regardless of what that direction is. The response is completely automatic, and is performed without any prior knowledge of the location of the source.

Basic retrodirective systems such as the corner reflector were originally proposed as passive reflectors for use as radar targets, as they are capable of providing radar

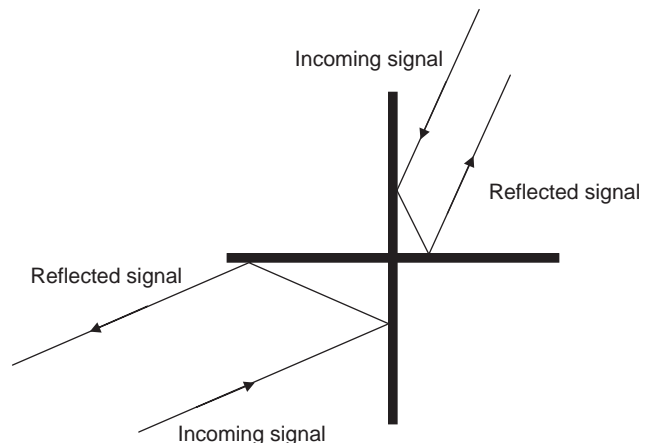


Figure 2. For a corner reflector, retrodirectivity is observed for waves incident from any angle in the x - y plane.

cross sections much larger than their physical size. But with advances in high-frequency electronics, more recently developed retrodirective systems have become more functional by providing modulation or gain, making them useful for wireless communication applications [2,3]. The autonomous beamsteering feature of retrodirective systems make them attractive for automatic pointing and tracking systems, microwave-tracking beacons, radio-frequency identification (RFID), solar power satellites, and crosslinks for small-satellite networks.

In each of these applications, the scenario is similar. An omnidirectional interrogating signal is transmitted in all directions. The retrodirective system, on receiving this signal, automatically transmits a response back to the interrogator. For microwave-tracking beacon applications, the interrogator uses this response to track the beacon's position. For RFID applications, the retrodirective tag's response includes inventory control information.

Retrodirective systems excel in applications where communication links are not fixed, as in base-to-mobile or mobile-to-mobile communications. The autonomous beamsteering is achieved at a purely hardware level, providing a means for creating secure, efficient, directive systems for satellite communications, wireless local-area networks, terrestrial peer-to-peer communications, or covert battlefield communications, without adding additional processing or system design strain.

One more recently proposed application of retrodirective systems is for the emerging area of small-satellite networks [4]. The smaller mass of nanosatellites (10 kg) and picosatellites (1 kg) make them more economical to develop and launch into orbit. Networks of small satellites promise increased mission flexibility and success by distributing the tasks and subsystems typical of a single large satellite. An autonomous small-satellite network also reduces the possibility of catastrophic single-point failure; if one satellite fails, others can take up the slack until a replacement is launched. However, the challenge in designing a distributed small-satellite network—especially a dynamically reconfigurable one—is in establishing and maintaining a reliable crosslink with other satellites in the network without a priori knowledge of their positions.

Omnidirectional antennas are the obvious choice for crosslinking satellites that are subject to constant repositioning, but this leaves the network susceptible to eavesdropping by unauthorized ground stations as well as by satellites outside the network but still within range of the constellation. Omnidirectional antennas are also inefficient, as power is radiated in all directions, not just in the direction of the receiver. Retrodirective crosslinks between satellites moving randomly in space provide the benefits of not only self-steering but also directivity. The high directivity associated with retrodirective systems improves not only network security but also the communication link efficiency by minimizing power consumption; this reduces the burden on transmitting and receiving amplifiers while still mainlining a reasonable link margin. The simplicity of the retrodirective approach is important for small satellites in which power is at a premium.

It is important to note that the automatic, self-steering function of retrodirective systems is performed autom-

atically, without the use of phase shifters, digital circuitry, or software. Compared to conventional phased-array antennas in which the phasing of the array is user controlled, a retrodirective system is self-phasing. Compared to smart antennas that rely on digital signal processing for beam control, retrodirective systems are much simpler and potentially faster because digital computations are not needed.

Much of the early work in retrodirective systems is reviewed in Ref. 5. This article focuses on more recent developments in antenna array systems that exhibit retrodirective behavior, and thus are called *retrodirective antenna arrays*. First, basic concepts in antenna arrays are reviewed, followed by a discussion of the two basic retrodirective array architectures. Next, methods for characterizing the arrays are reviewed. Finally, examples of more advanced retrodirective arrays and systems are presented.

1. BASIC RETRODIRECTIVE ARRAY ARCHITECTURES

Although the corner reflector is well suited for applications such as radar targets or markers, it is not particularly useful for wireless communications: (1) it is difficult to integrate electronics that are necessary for modulating the retrodirected signal; (2) corner reflectors must be large with respect to a wavelength to minimize the effects of edge diffraction, which distorts the retrodirected radiation pattern; and (3) the very nature of corner reflectors prohibits them from being planar and low-profile, which are desirable features for many applications.

For wireless applications, it is more common to use retrodirective *antenna arrays*, which lend themselves to integration with electronic circuits, are smaller and lighter than corner reflectors, and can be made planar and low-profile. An antenna array is composed of individual radiating elements. By combining individual antennas in an array, one can achieve higher directionality and the ability to steer the beam.

To illustrate, consider the four-element array shown in Fig. 3, consisting of four isotropic antennas spaced a

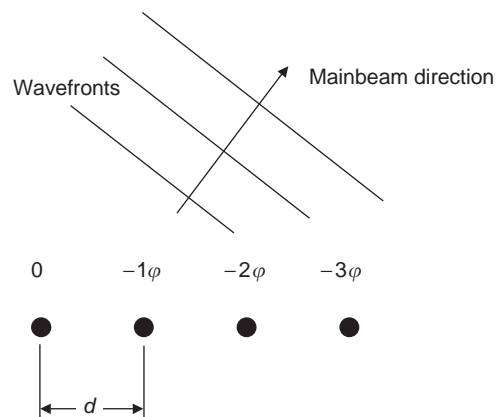


Figure 3. A four-element antenna array. If the elements are excited with a phase gradient that is increasingly negative from left to right, the mainbeam will appear to the right of broadside.

distance d apart. An isotropic antenna is one that radiates equally in all directions. The radiation from each element constructively interferes in certain directions (creating mainlobes and sidelobes) and destructively interferes in others (creating nulls), resulting in what is known as an *antenna radiation pattern*. An antenna's radiation pattern is the same whether it is transmitting or receiving.

The directions of constructive and destructive interference depend on the spacing between elements relative to the wavelength as well as the excitation of each element. For example, if each antenna element is excited at the same time (i.e., in phase), the radiation constructively interferes to create a mainbeam that forms in the broadside direction, defined as the two directions that are perpendicular to the array axis. If each antenna element is excited with a time delay between successive elements (i.e., with a progressive phase shift), the mainbeam forms in the direction corresponding to the amount of delay induced. The mainbeam direction is the one for which the path delay for each element compensates for the excitation delay for each element, resulting in a mainlobe that forms along the direction for which the radiation from each element adds in phase. It is therefore the phase gradient across the array that determines the direction of the mainbeam. If the element phase excitation is increasingly negative in moving from the left to the right, the mainbeam will appear to the right of the broadside direction, as shown in Fig. 3.

Conventional phased-array antennas are able to steer their beams by exciting elements with phase shifters. In contrast, retrodirective antenna arrays steer their beams automatically, without any phase shifters, in response to an interrogating signal.

1.1. Van Atta Arrays

Van Atta arrays [6] consist of pairs of antenna elements equally spaced from the center of the array with equal-length transmission lines (Fig. 4). The signal received by one antenna is reradiated by its pair, causing the order of reradiation to be flipped with respect to the center of the array. The phase gradient of the array is therefore re-

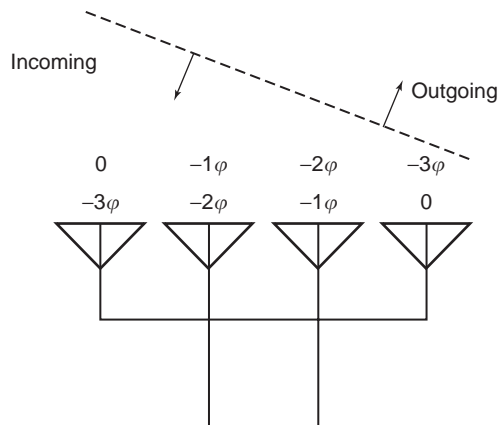


Figure 4. A Van Atta array, consisting of pairs of antennas connected with equal-length transmission lines.

versed (positive to negative, negative to positive) to achieve the proper phasing for retrodirectivity. Since the lengths of the connecting transmission lines are equal, the only frequency-dependent component in the Van Atta array is the antenna element. The use of broadband antennas and nondispersive transmission lines allows the array to perform over a wide bandwidth. However, this array configuration is restricted to planar wavefronts and planar topologies.

Figure 5 shows a microstrip patch antenna reflector array using the Van Atta architecture, developed at Texas A&M University [7]. The microstrip patch antennas are aperture-coupled with feedlines printed on the backside of the substrate, preventing undesired radiation from the feed networks and making the design compact. The array achieves wide angular coverage by taking advantage of both scattered and retrodirected fields. Radiation pattern measurements show a beamwidth larger than 120° , while a metal plate of the same size provides only a 10° beamwidth. Another type of Van Atta array, shown in Fig. 6, was developed at National Chiao Tung University [8]. The prototype array has six elements, each containing two slot antennas. Backradiation from the slot antennas is short-circuited with a metal reflector placed behind the array, which also serves to increase the radar cross section (RCS).

These two examples were proposed for intelligent vehicle highway system (IVHS) applications. The arrays successfully provide large radar cross sections in a wide angular range without any electronic circuitry, except for integrated switches in the transmission lines to provide modulation. The study shows promising results for other applications such as RFID.

1.2. Phase-Conjugating Arrays

A more popular technique for realizing retrodirective arrays is based on phase conjugation. This approach uses the same idea of the reversal of a phase gradient in the Van Atta array, but phase reversal is achieved at each antenna element instead of relying on antenna pairs.

In this scheme, shown in Fig. 7, heterodyne mixing [9] causes the incoming radiofrequency (RF) signal at each element to mix with a local oscillator (LO), creating the following mixing product:

$$\begin{aligned} V_{IF} &= V_{RF} \cos(\omega_{RF}t + \theta_n) \cdot V_{LO} \cos(\omega_{LO}t) \\ &= \frac{1}{2} V_{RF} V_{LO} [\cos((\omega_{LO} - \omega_{RF})t - \theta_n) \\ &\quad + \cos((\omega_{LO} + \omega_{RF})t + \theta_n)] \end{aligned} \quad (1)$$

If the LO frequency is twice the RF frequency, we obtain the following:

$$V_{IF} \propto \cos(\omega_{RF}t - \varphi) + \cos(3\omega_{RF}t + \varphi) \quad (2)$$

Note that the first term in (2), which is the lower sideband product (intermediate frequency, or IF signal) has the same frequency as the RF, but with a reversed, or

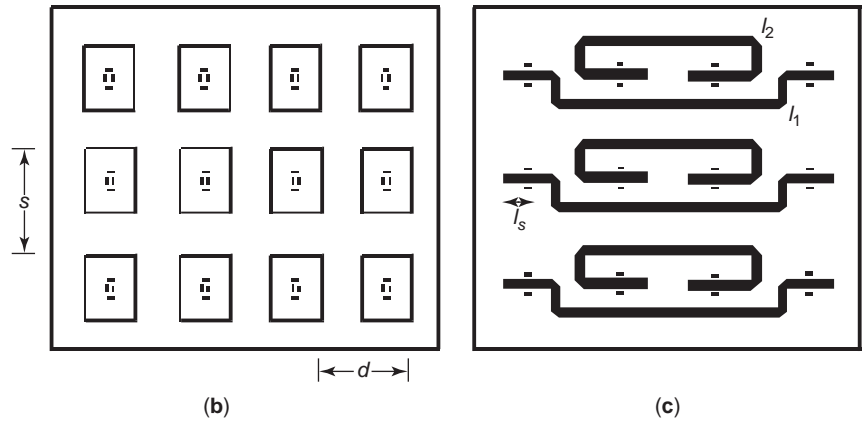
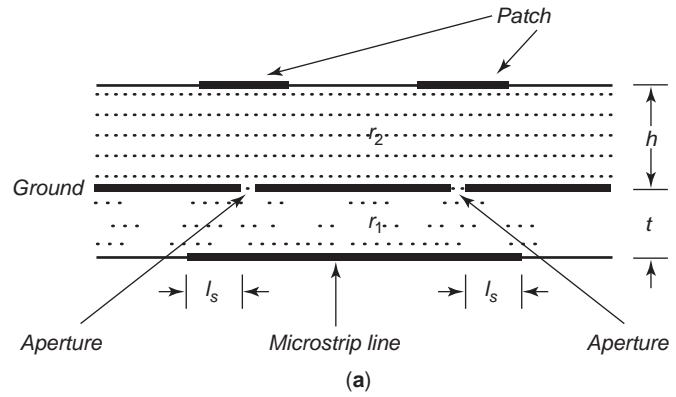


Figure 5. Planar Van Atta array using patch antennas: (a) side view; (b) antenna side; (c) feed side. (Courtesy of IEEE [7].)

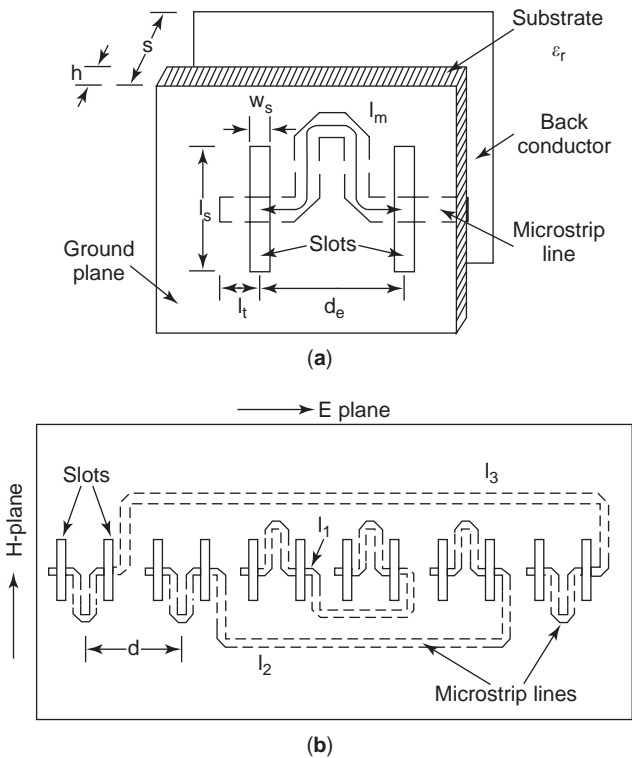


Figure 6. Planar Van Atta array using slot antennas: (a) unit cell; and (b) six-element array. (Courtesy of IEE [8].)

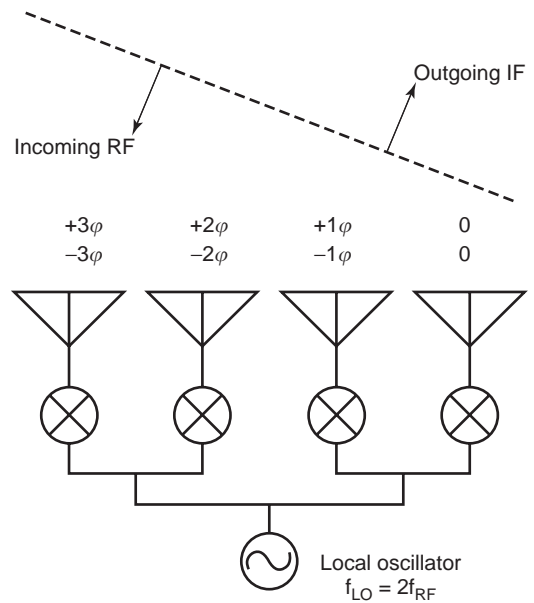


Figure 7. Phase-conjugating array using heterodyne mixers. The phase gradient associated with the incoming (RF) wave is conjugated, causing the outgoing (IF) wave to be retrodirected back toward the source.

conjugated phase. An array of such phase-conjugating elements causes the same kind of phase reversal as in the Van Atta array, resulting in a reradiated beam back toward the source direction.

In this method, it is important to eliminate undesired signals so that only the desired phase-conjugated signal radiates from the array. The upper sideband product in (2) and the LO leakage can easily be filtered and suppressed since their frequencies are far apart from the phase-conjugated signal frequency. Another signal that must be suppressed is the RF signal that leaks directly from the input to the output of the phase conjugator. This signal is exactly the same frequency as the desired IF signal, but is not phase-conjugated. The non-phase-conjugated RF leakage creates a specular beam that is the mirror image of the desired retrodirective beam. For example, if the retrodirected beam is formed at 20° , then the leakage signal will form at -20° .

Therefore, RF leakage suppression is one of the key challenges in the phase-conjugating heterodyne method. Since it is impossible to filter out the RF leakage, as its frequency is the same as that of the phase-conjugated signal, balanced mixer topologies are usually used to eliminate undesired signals.

1.2.1. Passive Phase-Conjugating Arrays. Figure 8 shows an example of the phase-conjugating architecture—an eight-element array using ratrace diode mixers that was developed at the University of California, Los Angeles (UCLA) [10]. Mounted between ports 2 and 4 of a dual-frequency ratrace coupler is a pair of series diodes, the center of which is short-circuited at the LO and RF/IF frequencies by two radial stubs. The 12-GHz LO and 6-GHz RF signals are applied through filters, which effectively isolate the LO from the RF/IF signals. RF-IF isolation is achieved by the balanced structure of the ratrace coupler. The measured conversion loss of the mixer is 5–7 dB over a RF frequency range from 5.5 to 6.5 GHz, while good RF-IF isolation is maintained over the range. The bidirectional characteristic of the circuit permits retrodirectivity for any polarization by using the two orthogonal modes of a patch antenna.

1.2.2. Active Phase-Conjugating Arrays. Passive, diode-based phase conjugators generally provide better RF-IF isolation than do active, transistor-based phase conjugators, especially when no bias is required. The major shortcoming of passive phase conjugators is the conversion loss, which limits the distance between the interrogator and the retrodirective array. The use of active devices such as metal semiconductor field-effect transistors (MESFETs) is attractive as they can provide conversion gain during the mixing process. Active phase conjugators make it possible for the retrodirective array to transpond an amplified signal back to the source location, without the need for additional amplifiers.

Figure 9 shows an example of this approach, developed at UCLA [11]. Like the design in Fig. 8, this circuit uses a dual-frequency ratrace coupler. The LO and RF signals are applied to FET mixers out of phase, resulting in cancellation of the RF and LO leakage while a phase-con-

jugated signal from each channel of the balanced mixer combines in phase at the output port. The measured conversion gain is about 6 dB, and the RF-IF isolation is better than 20 dB at the center frequency.

UCLA modified its phase conjugator design to eliminate the need for a dual-frequency combiner, thus simplifying the design and making it more compact [12]. As shown in Fig. 10, the interrogating RF signal is split into two channels that are 90° out of phase, while the LO is applied in phase. Phase-conjugated IF signals from the two channels are combined in phase, while the RF leakage is canceled before retransmission. The balanced structure suppresses the undesired RF leakage, achieving 20 dB of RF-IF isolation and a conversion gain of 3.2 dB. The array operates in the 6-GHz band, with a 12-GHz LO applied in phase to each phase conjugating element through a corporate feed network.

The strength of the phase-conjugating technique is the recreation of a wavefront. Unlike the Van Atta architecture, this technique allows an array to retrodirect a signal to the source through obstacles or in the near field [13], as shown in Fig. 11. It also accommodates nonplanar wavefronts and surfaces.

1.3. Characterization

Figure 12 illustrates the two standard measurements for characterizing the self-steering performance of a retrodirective antenna array: bistatic and monostatic radar cross sections (RCSs). In both cases, an interrogating signal provided by a horn antenna impinges on the array under test, whereupon the retrodirected signal is transmitted back (ideally in the same direction from which it originated) to a second receiving horn antenna. In the bistatic case, the interrogating antenna remains stationary while the receiving antenna is scanned. The resulting measurement shows a mainlobe in the direction of the source, with nulls or sidelobes in other directions. In the monostatic case, both the interrogating and receiving antennas are collocated and simultaneously scanned. Since the interrogating and retrodirected signals are both in the same direction, the peak of the array radiation will always be in the direction of the receiving antenna, and thus the monostatic pattern will exhibit a relatively flat pattern, without nulls.

Since the interrogating and retrodirected signals share the same frequency, there is always unavoidable coupling between the interrogating and receiving horns. In a phase-conjugating array or modified Van Atta array, this problem is overcome by slightly offsetting the frequencies so that the two signals can be resolved on a spectrum analyzer. For instance, the following frequencies could be used: an interrogating signal of 4.99 GHz, an LO signal of 10.00 GHz, and a retrodirected signal of 5.01 GHz. Phase conjugation is achieved even if the interrogating and retrodirected frequencies are not identical, but the deviation between these two frequencies leads to a pointing error in the return beam. The amount of the error depends on this frequency difference as well as the incoming beam angle, since the amount of progressive phase shift needed for array beamsteering is a function of antenna element spacing in terms of wavelength.

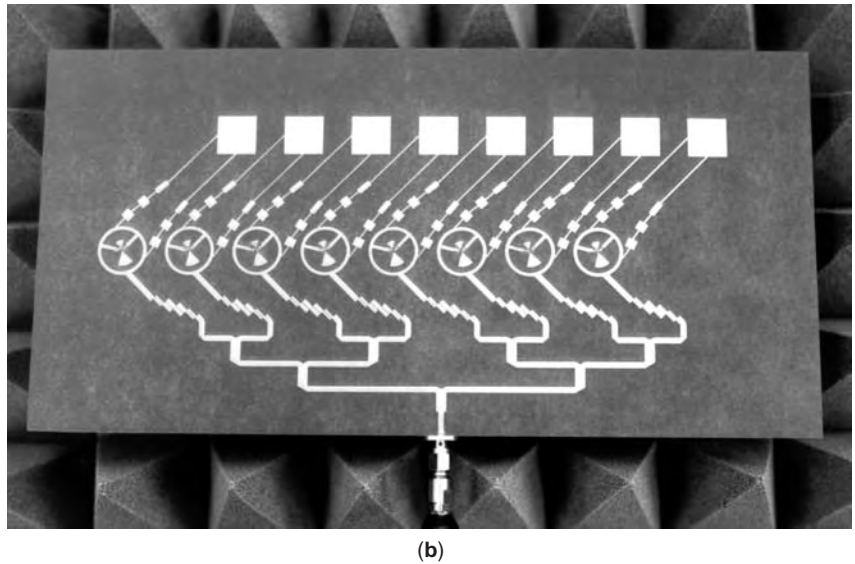
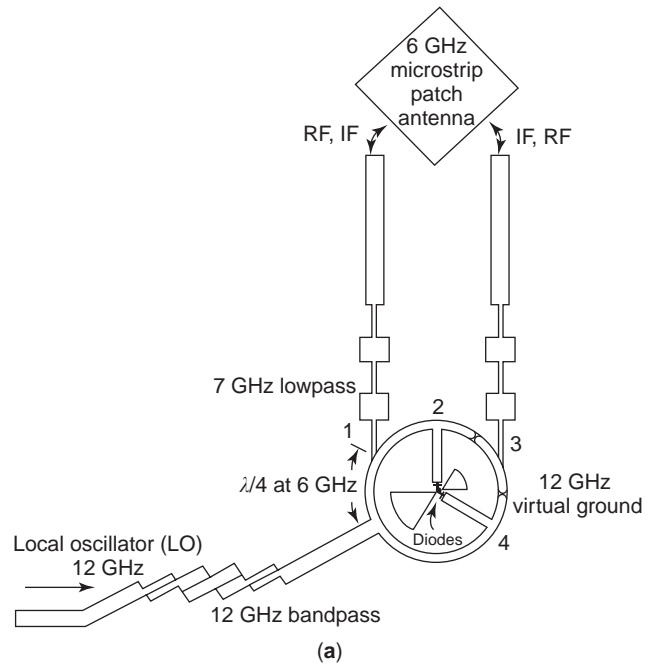


Figure 8. Passive phase-conjugating array using ratrace diode mixers: (a) phase-conjugating unit cell; (b) eight-element prototype. (Courtesy of IEEE [10].)

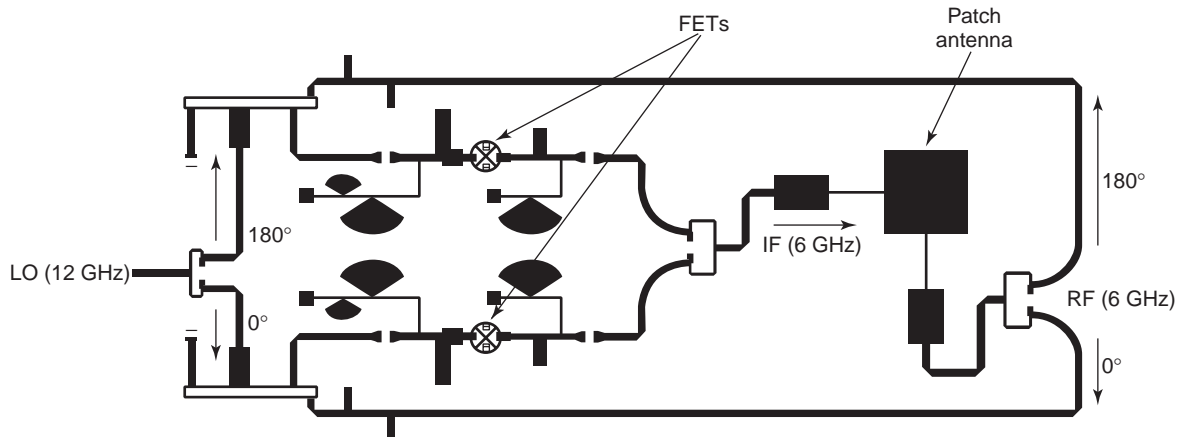


Figure 9. Balanced active phase conjugator integrated with antenna. (Courtesy of IEEE [11].)

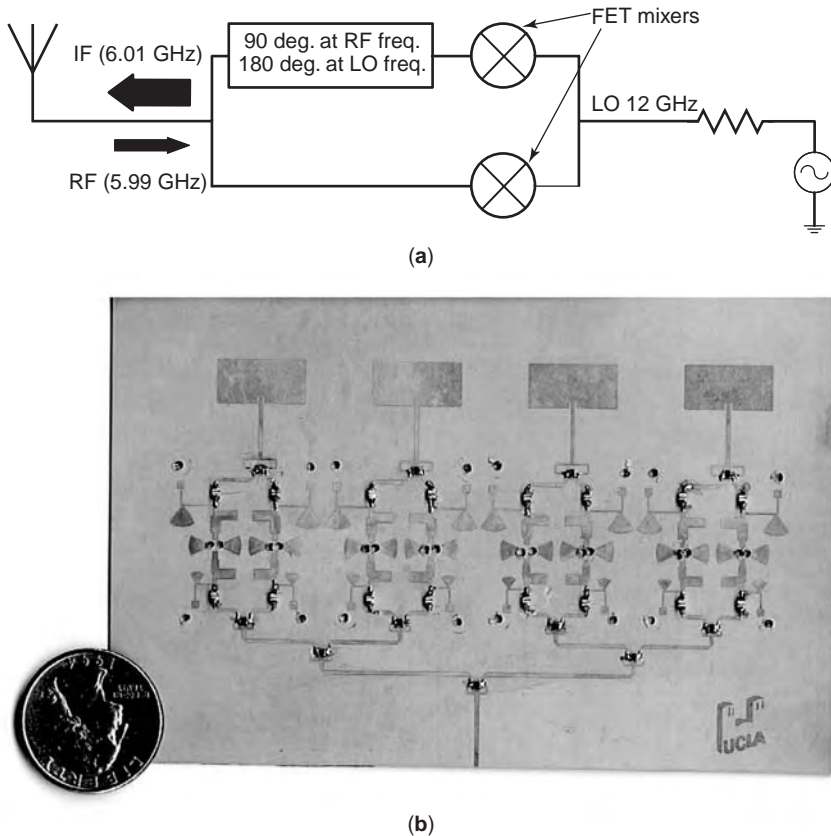


Figure 10. Active phase-conjugating array using MESFET mixers: (a) phase-conjugating unit cell; (b) four-element prototype (external LO not shown). (Courtesy of IEEE [12].)

Retrodirective arrays can be either one-dimensional, as in the examples presented previously, or two-dimensional, as presented in the next section. Bistatic and monostatic RCS measurements can therefore be taken over several planar cuts, as Fig. 13 shows. The theoretical bistatic RCS is given by

$$\begin{aligned} \sigma_{\text{bistatic}}(\theta, \theta_0, \phi, \phi_0) &= \frac{\lambda_0^2}{4\pi} G_c D_{\text{patch}}(\theta_0, \phi_0) D_{\text{patch}}(\theta, \phi) D_{\text{array}}(\theta, \theta_0, \phi, \phi_0) \end{aligned} \quad (3)$$

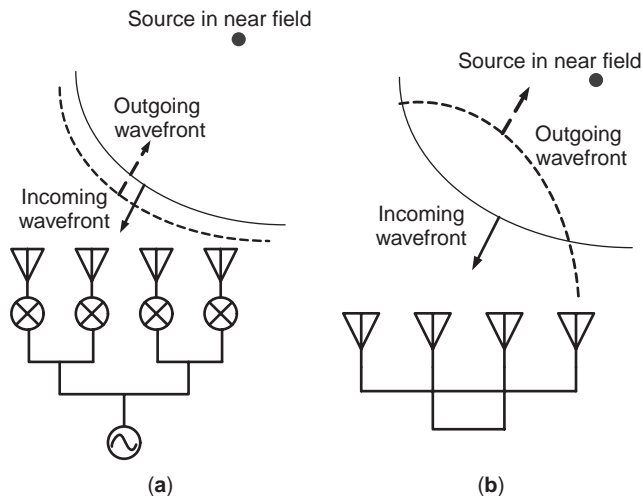


Figure 11. Reconstruction of the wavefront in a (a) phase-conjugating array and (b) a Van Atta array.

where θ_0, ϕ_0 are the RF source angles, G_c is the circuit gain, D_{patch} is the element directivity, and D_{array} is the directivity of the array, given by

$$\begin{aligned} D_{\text{array}}(\theta, \theta_0, \phi, \phi_0) &= \frac{|\text{AF}(\theta, \theta_0, \phi, \phi_0)|^2}{U_0(\theta_0, \phi_0)} \\ &= \frac{4\pi |\text{AF}(\theta, \theta_0, \phi, \phi_0)|^2}{\int_0^{2\pi} \int_0^\pi |\text{AF}(\theta', \theta_0, \phi', \phi_0)|^2 \sin \theta' d\theta' d\phi'} \end{aligned} \quad (4)$$

where AF is the array Factor.

In the bistatic RCS measurement, the radiation pattern of the array is fixed since the position of the RF interrogating source (i.e., θ_0, ϕ_0) is fixed, suggesting that the integration of the array factor U_0 is constant. Therefore, the directivity of the array simply depends on the angle θ

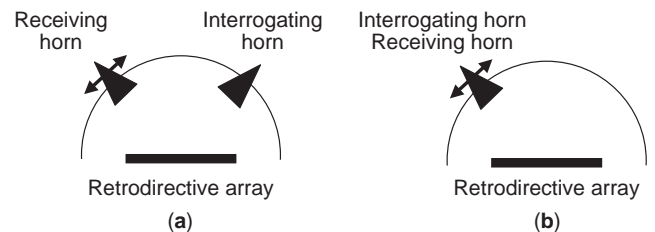


Figure 12. A retrodirective signal is characterized by (a) bistatic RCS and (b) monostatic RCS measurements.

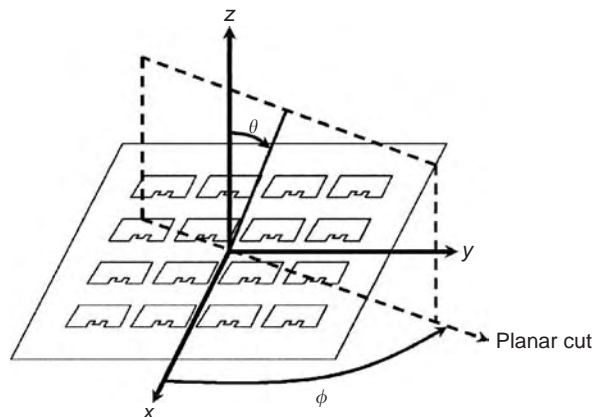


Figure 13. Coordinate system for the RCS measurement of a retrodirective array.

where the receiving horn is located. The normalized bistatic pattern is

$$\sigma'_{\text{bistatic}}(\theta, \phi)|_{\theta_0, \phi_0} = \frac{|\text{AF}(\theta, \phi)|_{\theta_0, \phi_0}|^2 D_{\text{patch}}(\theta, \phi)}{\max(|\text{AF}(\theta, \phi)|_{\theta_0, \phi_0}|^2 D_{\text{patch}}(\theta, \phi))} \quad (5)$$

where AF is the array factor. Since the array factor is maximum at the angle of the incoming RF signal, the mainlobe of the bistatic RCS pattern should point in the direction of the source. Typical bistatic RCS patterns are shown in Fig. 14.

In the monostatic RCS measurement, the interrogating and receiving antennas are collocated and moved together ($\theta = \theta_0, \phi = \phi_0$) to measure the radiation from the array, and thus the receiving antenna is always in the direction of the mainlobe. The monostatic RCS pattern is

given by

$$\sigma_{\text{monostatic}}(\theta, \phi) = \frac{\lambda_0}{4\pi} G_c D_{\text{patch}}^2(\theta, \phi) D_{\text{array}}(\theta, \phi) \quad (6)$$

In the monostatic RCS measurement, the radiation pattern varies as θ, ϕ changes. This implies that the array directivity at the peak is not constant, and depends on the scanning angle, that is, the position of the RF and IF horns, θ, ϕ [15,16]. The normalized monostatic pattern is given by

$$\sigma'_{\text{monostatic}}(\theta, \phi) = \frac{D_{\text{patch}}^2(\theta, \phi)/U_0(\theta, \phi)}{\max(D_{\text{patch}}^2(\theta, \phi)/U_0(\theta, \phi))} \quad (7)$$

A typical monostatic RCS pattern is shown in Fig. 15.

1.4. Array Design Considerations

In addition to the choice of architecture (Van Atta vs. phase conjugation, passive vs. active), the retrodirective system design must also include the appropriate choice of antenna element since this is often the limiting factor in the angular coverage of a retrodirective array. As shown in Fig. 16, the radiation pattern of the array is the product of the element and array factor directivities, but the maximum value of the product of these two directivities does not correspond to the peak of the array factor when a nonisotropic element is used. This results in a beam-pointing error, defined as the deviation of the mainbeam from that of the array factor pattern. Using an antenna element with low directivity, such as a microstrip patch, or increasing the number of elements reduces this error. Using a low-directivity element also decreases the dependence of the retrodirected power on the interrogation angle.

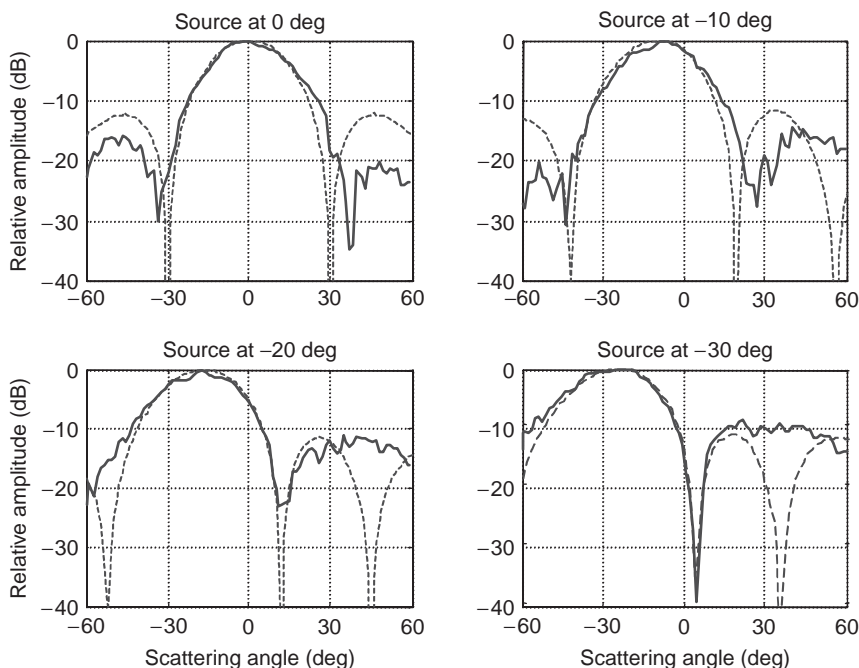


Figure 14. Examples of theoretical (dashed) and experimental (solid) bistatic RCS patterns when the interrogating signal is incident at $0^\circ, -10^\circ, -20^\circ,$ and -30° [14]. (This figure is available in full color at <http://www.mrw.interscience.wiley.com/erfme>.)

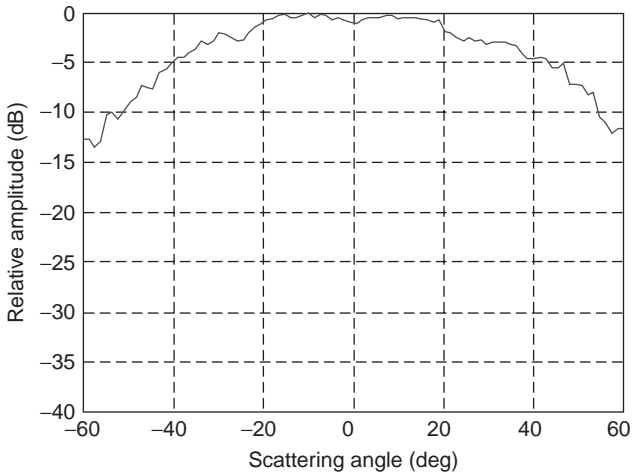


Figure 15. Example of a monostatic RCS pattern [14]. (This figure is available in full color at <http://www.mrw.interscience.wiley.com/erfme>.)

Additional insight into the beam pointing error, as well as methods for mitigating it, can be found in Ref. 17.

Another consideration is the spacing between elements in the array. As in other types of phased arrays, this

spacing limits the scanning range of a retrodirective array. To avoid grating lobes in the radiation pattern that result in scan angle limitations, the array spacing must satisfy the following condition for a given interrogation angle

$$d < \frac{\lambda_0}{(1 + |\sin \theta_{inc}|)} \tag{8}$$

where d is the array spacing, λ_0 is the free-space wavelength of the interrogating RF signal, and θ_{inc} is the incident angle of the incoming signal. For scanning from -90° to $+90^\circ$ without grating lobes, d must be less than a half-wavelength of the RF signal.

The monostatic RCS is useful in evaluating the wide-angle coverage of a retrodirective array. The bistatic RCS is useful for evaluating the antiintercept capability (low sidelobe power levels) beam-pointing errors, and scan angle limitations.

2. TWO-DIMENSIONAL RETRODIRECTIVE ARRAYS

While the one-dimensional (1D) retrodirective arrays discussed in the previous section may be suitable for terrestrial applications, two-dimensional (2D) retrodirectivity is

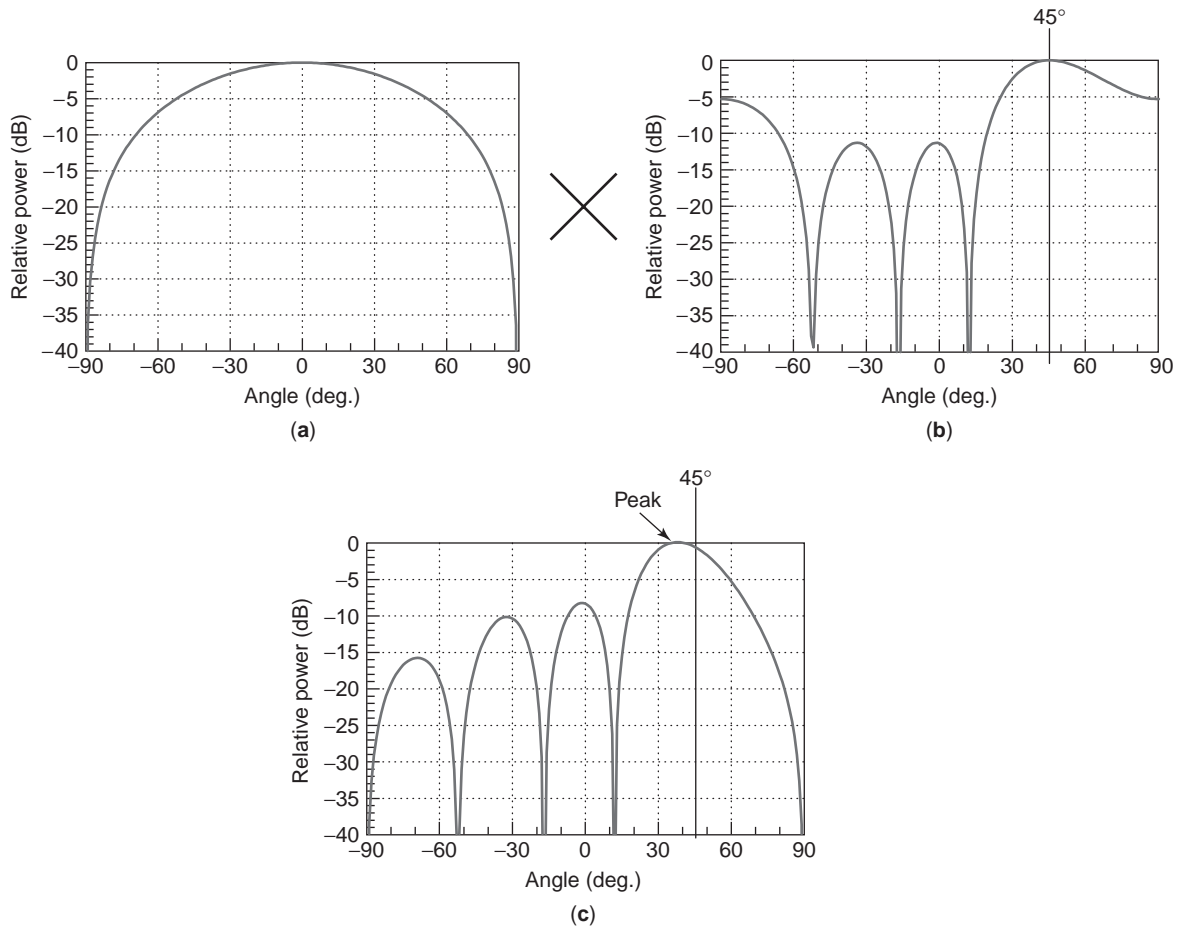


Figure 16. The beam-pointing error in a retrodirective array arises, in part, because of the directivity of the antenna element: (a) element pattern; (b) array factor pattern; (c) combined element-array pattern. (This figure is available in full color at <http://www.mrw.interscience.wiley.com/erfme>.)

necessary for terrestrial-to-space or space-to-space communications. However, implementing large 2D arrays based on traditional techniques is not as straightforward as simply adding more elements. For Van Atta arrays [18–20], the network of transmission lines connecting elements from one side of the array to the other becomes complicated as they must overlap each other. For phase-conjugating arrays, the maximum array size is limited by factors such as the complexity of a large corporate LO feed network and supplying enough LO power from a single source. In addition, the $\lambda/2 \times \lambda/2$ cell limitation for avoiding grating lobes have limited most 2D arrays to a maximum size of 4×4 elements. Several approaches have been proposed to overcome these issues.

2.1. Spatially Fed Local Oscillator

Researchers at the University of Hawaii (UH) developed a retrodirective diode grid array using a spatially fed LO [21]. Antiparallel diodes distributed over the grid enable third-order mixing. The LO is spatially applied to both front- and backsides of the grid, and mixed with the interrogating RF signal. The four-wave mixing scheme eliminates the need for an LO at twice the RF, allowing the system to use one frequency band for both RF and LO.

UH researchers developed a second phase-conjugating array in which the LO is spatially fed through slot-coupled patch antennas to eliminate LO feed networks [22]. Since there is no corporate feed network, each element of the

array is decoupled, allowing for 2D implementation without added complexity. A four-element 1D prototype was demonstrated at 5.35 GHz. The RF and LO signals received from patch antennas are combined through a diplexer and fed to the gate of a MESFET. The phase-conjugated IF from the drain is retransmitted through the IF patch antenna, which is cross-polarized to the RF antenna, reducing the coupling between the receiving and transmitting antennas. The measured results showed promising results for 2D implementation of this approach in the future.

2.2. Phase-Conjugating Arrays Using Self-Oscillating Mixers

A second type of phase-conjugating array developed at UH replaces the conventional mixers with self-oscillating mixers (SOMs) [23]. Phase-locking the SOM elements at the LO frequency while isolating them at the RF ensures proper operation. Since the LO signal is generated at each element, a corporate feed network is unnecessary, allowing for easier implementation of larger 2D arrays. This technique also makes it possible to provide enough LO power to each phase-conjugating element in a relatively large array.

UH's first experimental SOM array demonstrated retrodirectivity over 360° using a 96-element active antenna conformally wrapped around a dielectric cylinder [24]. More recently, a 16-element array using a different design was demonstrated in Ref. 25. As shown in Fig. 17, adjacent

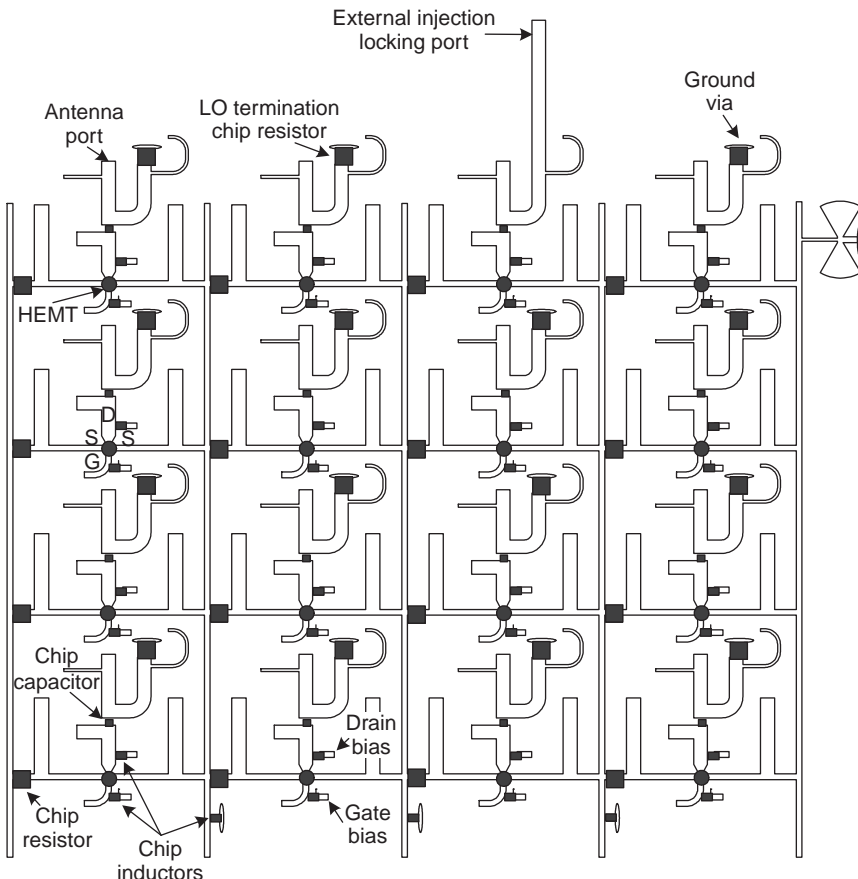


Figure 17. Layout of 2D retrodirective array using self-oscillating mixers. (Courtesy of IEEE [25].)

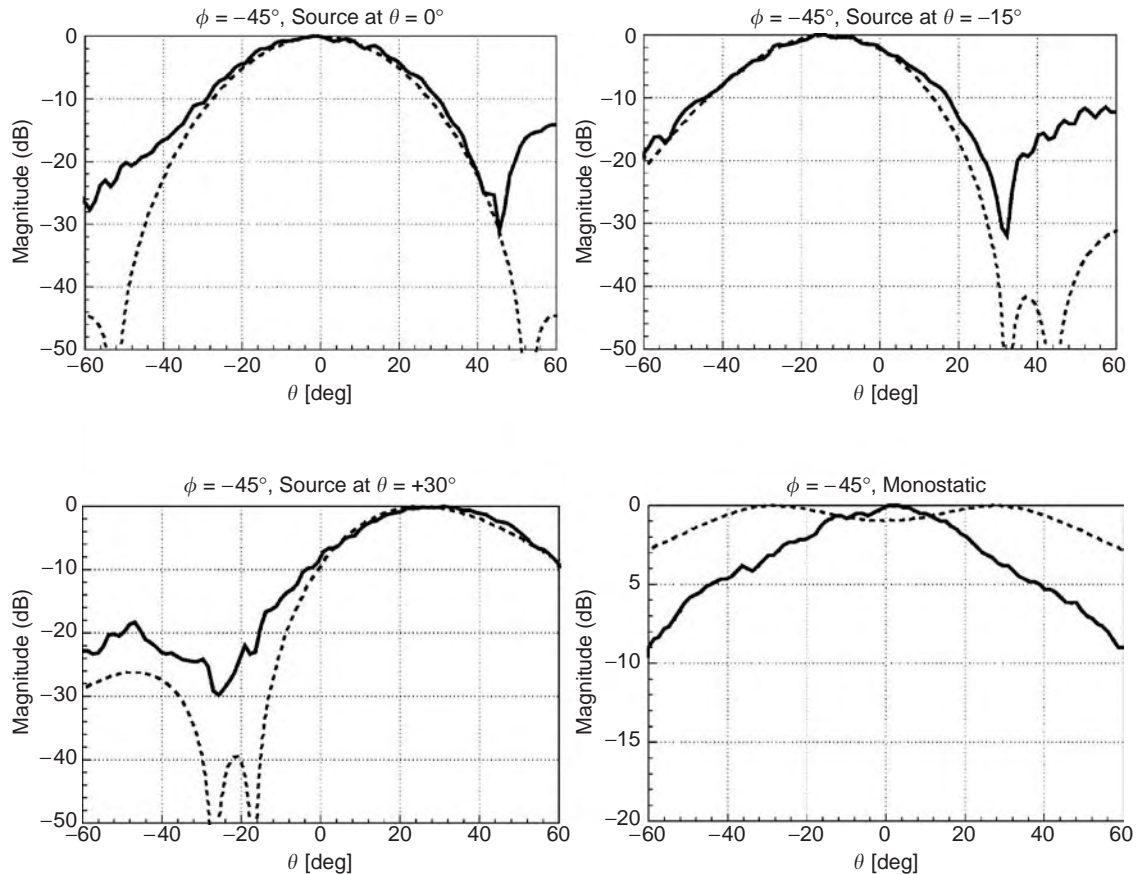


Figure 18. $\phi = -45^\circ$ bistatic RCS patterns for scattering angles of $\theta = 0^\circ$, $\theta = -15^\circ$, and $\theta = +30^\circ$ and monostatic radiation pattern. (Courtesy of IEEE [25].)

elements are coupled through the source of pseudomorphic high-electron-mobility transistors. Since the drain terminal is shared for RF, IF, and LO signals, a diplexer is inserted to ensure that the RF/IF sees the antenna only while the LO is terminated into a $50\text{-}\Omega$ load. By mounting the patch antennas in the back of the phase-conjugating circuitry, the unit cell size is reduced to $0.37\lambda \times 0.45\lambda$, satisfying (8). An external locking LO signal can be applied to an element at the edge to reduce phase noise or modulate the phase-conjugated signal. Measured monostatic and bistatic RCS patterns are shown in Fig. 18, illustrating retrodirectivity in both the azimuth and elevation planes.

3. RETRODIRECTIVE ARRAYS FOR MILLIMETER-WAVE SYSTEMS

Retrodirective arrays operating at millimeter-wave frequencies may have niche applications in 60-GHz satellite crosslink or 77-GHz automotive collision-avoidance applications. In addition, the millimeter-wave band offers the benefits of broader bandwidth and smaller size.

3.1. Millimeter-Wave Van Atta Arrays

Westinghouse Electric Corporation proposed a millimeter-wave retrodirective transponder for collision/obstacle avoidance and navigation/location [26]. The array is based

on the Van Atta architecture with modulators. The 8×1 array consists of five-element subarrays, allowing the system to both receive and transmit more power.

One of the first active retrodirective arrays to be demonstrated at millimeter-wave frequencies is a two-element Van Atta array [27]. Developed by researchers at the Queen's University of Belfast, this array receives a 65.5-GHz signal that is then downconverted to 62.5 GHz

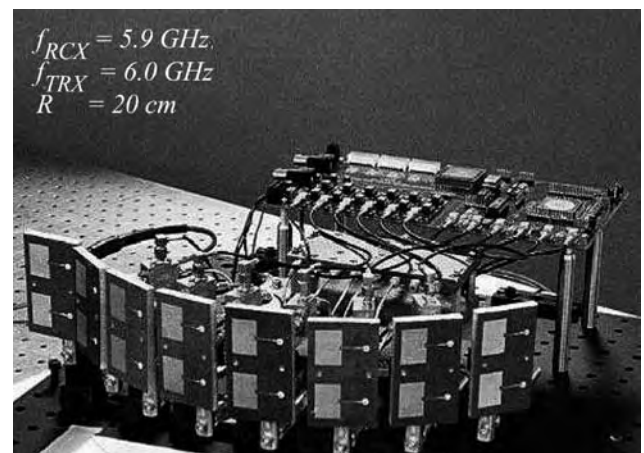


Figure 19. Full-duplex retrodirective array. (Courtesy of IEEE [30].)

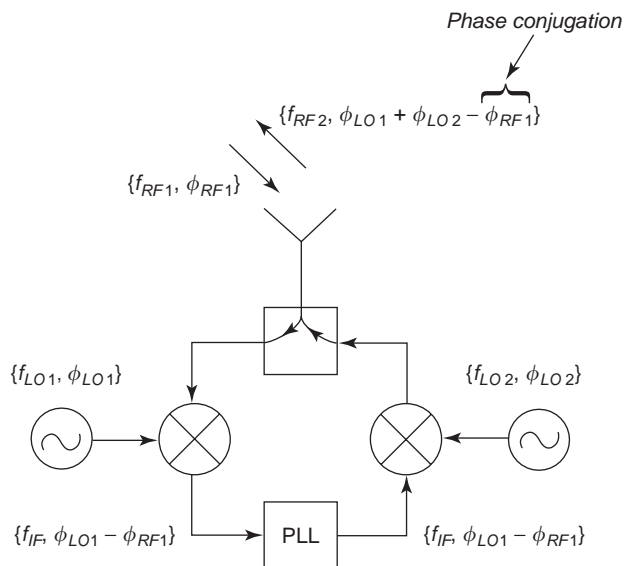


Figure 20. Phase conjugation using double mixing. (Courtesy of IEEE [30].)

and amplified with GaAs MMICs. By crossing the 62.5-GHz transmitting antennas, a Van Atta architecture is realized.

3.2. Millimeter-Wave Phase-Conjugating Arrays

Retrodirective arrays based on the phase-conjugating method are seldom feasible in the millimeter-wave band,

due to the requirement of having a LO at twice the RF frequency.

Recognizing this, Queen’s University of Belfast proposed using balanced subharmonic mixers for higher-frequency retrodirective arrays [28]. Subharmonic mixing halves the LO frequency requirement, while the balanced structure provides isolation between RF, IF, and LO frequencies, which typically may be less than a few percent apart. A prototype circuit based on two pairs of antiparallel diodes in a ratrace hybrid was built at RF, IF, and LO frequencies of 990, 970, and 980 MHz, respectively. This configuration exhibited good RF/IF and LO/IF isolation of 36 and 34 dB, respectively.

A second approach for higher-frequency applications is a dual-conversion phase-conjugating circuit [29]. Phase conjugation is achieved by mixing the incoming RF signal with an LO signal whose frequency is slightly higher than the RF. The resulting IF contains the phase conjugate of the RF and can be easily upconverted through a conventional mixer. This configuration reduces the cost of the system since the LO frequency is reduced to slightly higher than the RF frequency.

4. RETRODIRECTIVE SYSTEM EXAMPLES

The preceding sections have shown how retrodirective systems have evolved from high-reflectivity radar targets to components that can serve in wireless communication systems. This section presents four system-level examples in which retrodirective arrays show promise.

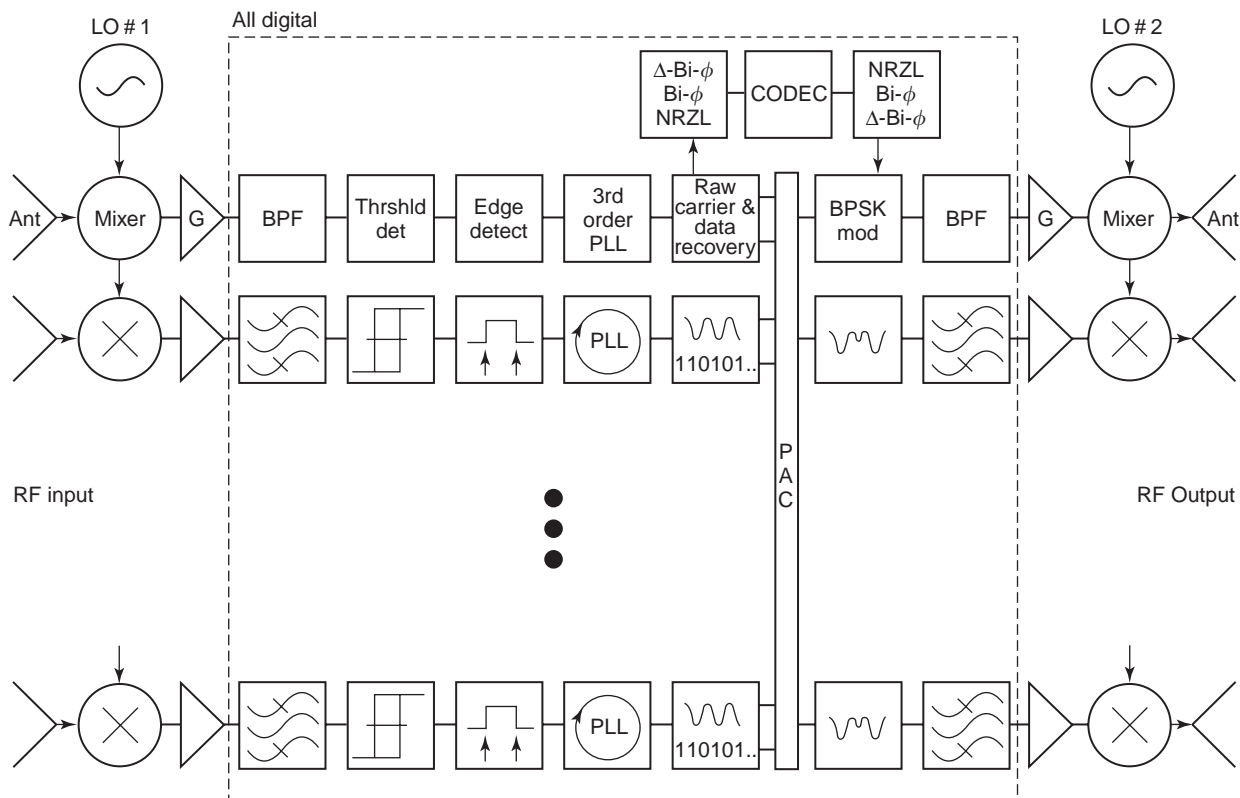


Figure 21. System architecture of the full-duplex array proposed in Ref. 30. (Courtesy of IEEE.)

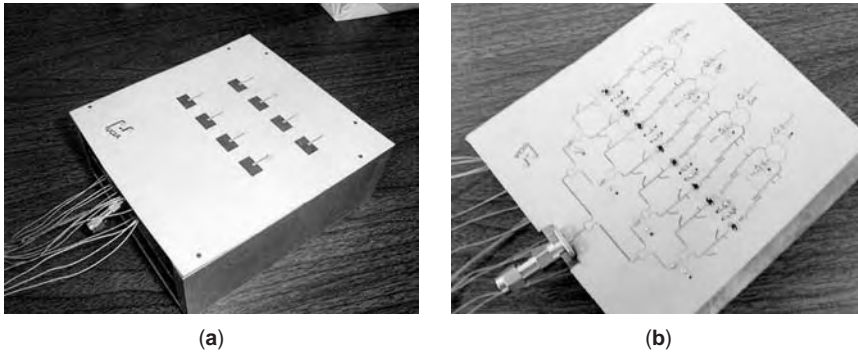


Figure 22. Photographs of the reconfigurable array in Ref. 31: (a) antenna side; (b) circuitry side. (Courtesy of IEEE.)

4.1. Full-Duplex Retrodirective Array

To enable duplex retrodirective communication, it is necessary for a retrodirective array to have a receiver function in addition to the transponder function. Figure 19 shows a full-duplex retrodirective array system developed at the University of Michigan [30]. Each phase conjugator employs two mixers. The frequency of the LO applied to the first mixer is slightly higher than that of the incoming RF signal. This mixing process generates a low-frequency phase-conjugated IF signal, which then proceeds to a carrier/data recovery circuit followed by a BPSK (binary phase shift keying) modulator as shown in Figs. 20 and 21. The output signal is upconverted by the second mixer and transmitted, and the recovered data are processed by an A/D converter. The carrier recovery system allows the retrodirective array to use the modulated RF signal as an interrogating RF signal, enabling full-duplex retrodirective array communications. Using a 78.125 kbps (kilobits per second) data rate, a full-duplex data transmission test resulted in a bit error rate of better than 10^{-6} for 10 dB signal-to-noise ratios without error correction.

4.2. Reconfigurable Retrodirective/Smart Antenna Array

Figure 22 shows a retrodirective/smart antenna array for wireless sensor systems, developed at UCLA [31]. The active integrated antenna array can be reconfigured as a direct-conversion receiver or a retrodirective transponder, simply by changing the LO frequency. If time-division duplexing is employed, the system can be used for half-duplex communications. Figure 23 shows the schematic of the reconfigurable circuit. The received signal is first amplified by a low-noise amplifier at the Σ port of a ratrace coupler and applied to the resistive FET mixers in phase.

An LO signal is divided into two paths, with one path experiencing a delay of 180° at 11.6 GHz and 45° at 2.9 GHz. When a 2.9-GHz LO is applied, the circuit serves as a sub-harmonic direct conversion receiver (receiving mode). I and Q channels are obtained through lowpass filters from the drain sides. When an 11.6-GHz LO is applied, the circuit functions as a phase conjugator (retrodirective transponder mode). The phase-conjugated signal is amplified by an amplifier at the Δ port of the ratrace coupler. It is also possible to modulate the phase-conjugated signal by applying data signals into the baseband ports of this circuit.

4.3. Fading Reduction in a Multipath Environment

When scatterers exist within the communication path, there are multiple paths of signal propagation that can lead to fading and interference. Researchers at Millilab in Finland and the University of Hawaii demonstrated how multipath propagation in the presence of a retrodirective

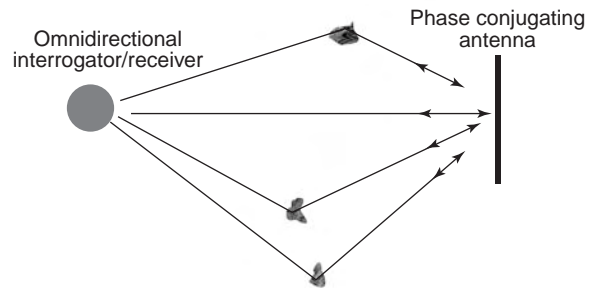


Figure 24. Ideal point-to-point communication with a phase-conjugating retrodirective antenna in a multipath environment with reflecting objects [32].

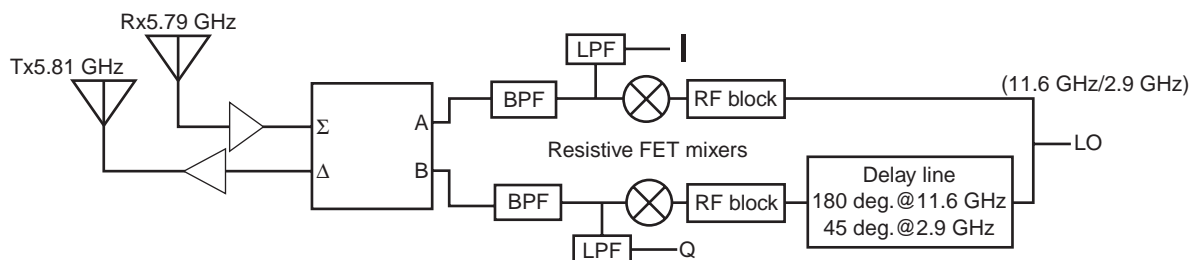


Figure 23. Schematic of the multifunctional circuit proposed in Ref. 31. (Courtesy of IEEE.)

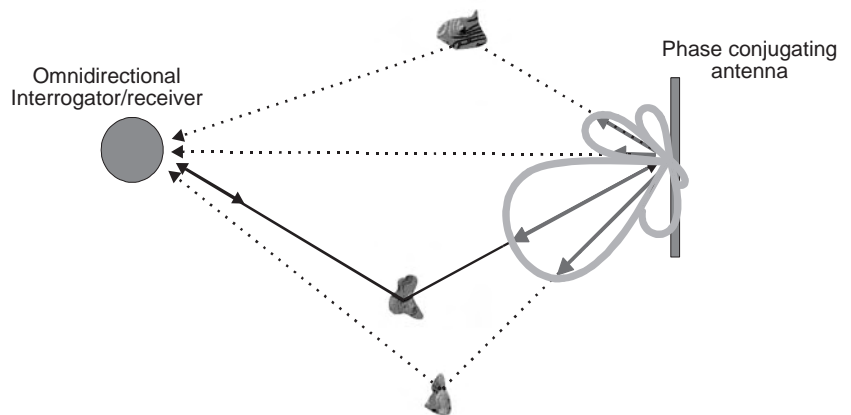


Figure 25. Retrodirected signal from a practical array in response to a single ray from the omnidirectional interrogator [32].

array could reduce fading [32]. The technique is based on the observation that retrodirected signals from a phase-conjugating retrodirective array coherently arrive at the interrogator. The received signal at each element of an array can be described as the sum of multiple signals from several directions. The phase conjugate of the received signal is therefore the sum of the phase conjugates of the multipath signals. Therefore, the radiation pattern of the retrodirective array has a beam toward each incoming direction, and the signals added in phase at the interrogating source point, as shown in the idealized case of Fig. 24. In the practical case of finite antenna size, beams reflect back from the retrodirective array through the mainbeam as well as the sidelobes (Fig. 25). The mainbeam rays add coherently while the sidelobe rays add incoherently, thus limiting the method in practical systems. Nevertheless, experimental results showed a 40 dB reduction in fading in a multipath environment.

4.4. Self-Steering Crosslinks for Picosatellite Networks

As mentioned at the beginning of this article, an interesting application of retrodirective arrays is its use in self-steering crosslinks in a picosatellite network. Designing for space applications presents new challenges. First, the zero-gravity, free-floating nature of picosatellites necessitates two-dimensional tracking, and therefore a two-dimensional retrodirective array. Moreover, since picosatellites are too small to have attitude control systems, it is impossible to determine the orientation of each satellite, thus requiring circular polarization to prevent polarization mismatch. Undergraduate students at the University of Hawaii developed 10-GHz circularly polarized, two-dimensional, phase-conjugating arrays based on quadruple subharmonic mixing, to relax the local oscillator frequency requirement [33]. These antennas will be used in a network of two picosatellites to be launched into low-Earth orbit. For a network containing multiple satellite nodes, each satellite would have both an onboard omnidirectional interrogator and retrodirective transponder. The link is initiated by one satellite's omnidirectional interrogating signal, which is coded for an intended receiver. That receiver then sends a retrodirective signal back to the interrogator, whereupon it switches to retrodirective mode and the link is established. The use of coded signals

prevents unauthorized third-party interrogation, and helps in setting up multiple links between nodes.

In addition to the four applications presented above, retrodirective systems are also applicable for non-communication-related applications as well, such as in solar power satellites. Although they cannot compete in many applications where smart antennas now dominate, retrodirective systems are expected to fill several niches where simplicity, small form factor, and minimal power requirements are needed.

BIBLIOGRAPHY

1. J. D. Kraus, *Antennas*, McGraw-Hill, New York, 1988.
2. R. Y. Miyamoto and T. Itoh, Retrodirective arrays for wireless communications, *IEEE Microwave Mag.* 71–79 (2002).
3. K. M. K. H. Leong, R. Y. Miyamoto, and T. Itoh, Moving forward in retrodirective arrays, *IEEE Potentials* 16–21 (2003).
4. B. T. Murakami, M. A. Tamamoto, A. T. Ohta, G. S. Shiroma, R. Y. Miyamoto, and W. A. Shiroma, Self-steering antenna arrays for distributed picosatellite networks, *Proc. 17th Annual AIAA/Utah State Univ. Conf. Small Satellites*, Logan, UT, 2003.
5. *IEEE Trans. Anten. Propag.* (special issue on active and adaptive antennas) **AP-12**:140–233 (1964).
6. L. C. Van Atta, *Electromagnetic Reflector*, U.S. Patent 2,908,002 (1959).
7. S.-J. Chung and K. Chang, A retrodirective microstrip antenna array, *IEEE Trans. Anten. Propag.* **46**:1802–1809 (1998).
8. W.-J. Tseng, C.-S. Hu, and S.-J. Chung, Planar retrodirective array reflector using dual-slot antennas, *Electron. Lett.* **34**: 1374–1376 (1998).
9. C. Y. Pon, Retrodirective array using the heterodyne technique, *IEEE Trans. Anten. Propag.* **AP-12**:176–180 (1964).
10. C. W. Pobanz and T. Itoh, A conformal retrodirective array for radar applications using a heterodyne phased scattering element, *IEEE MTT-S Int. Microwave Symp. Digest*, Orlando, FL, 1995, pp. 905–908.
11. R. Y. Miyamoto, Y. Qian, and T. Itoh, A retrodirective array using balanced quasi-optical FET mixers with conversion gain, *IEEE MTT-S Int. Microwave Symp. Digest*, Anaheim, CA, 1999, pp. 655–658.
12. R. Y. Miyamoto and T. Itoh, An active integrated retrodirective transponder for remote information retrieval-on-demand, *IEEE Trans. Microwave Theory Tech.* **49**:1658–1662 (2001).

13. Y. Chang, H. R. Fetterman, I. L. Newberg, and S. K. Panaretos, Microwave phase conjugation using antenna arrays, *IEEE Trans. Microwave Theory Tech.* **46**:1910–1919 (1998).
14. C. W. Pobanz, *Time-Varying Antennas*, Ph.D. dissertation, Dept. Electrical Engineering, Univ. California, Los Angeles, CA, 1998.
15. R. C. Hansen, *Phased Array Antennas*, Wiley, New York, 1997.
16. W. Stutzman and G. Thiele, *Antenna Theory and Design*, Wiley, New York, 1998.
17. S. L. Karode and V. F. Fusco, Self-tracking duplex communication link using planar retrodirective antennas, *IEEE Trans. Anten. Propag.* **47**:993–1000 (1999).
18. M. G. Christodoulou and D. P. Chrissoulidis, 2D Van Atta retrodirective array using dual polarized two-port square microstrip patches, *Proc. of 11th Int. Conf. on Anten. and Propag.*, 2001, pp. 814–816.
19. W.-J. Tseng and S.-J. Chung, Analysis and design of a planar two-dimensional retrodirective array reflector, *IEEE AP-S Int. Anten. and Propag. Symp. Digest*, Orlando, FL, 1999, pp. 1678–1680.
20. B. Nair and V. F. Fusco, Two-dimensional planar passive retrodirective array, *Electron. Lett.* **39**:768–769 (2003).
21. W. Ding, S.-T. Lei, and M. P. DeLisio, A retrodirective diode grid array using four-wave mixing, *IEEE MTT-S Int. Microwave Symp. Digest*, Phoenix, AZ, 2001, pp. 1851–1854.
22. W. E. Forsyth and W. A. Shiroma, A retrodirective antenna array using a spatially fed local oscillator, *IEEE Trans. Anten. Propag.* **50**:638–640 (2002).
23. G. S. Shiroma, C. Song, R. Y. Miyamoto, and W. A. Shiroma, An active self-steering array using self-oscillating mixers, *IEEE MTT-S Int. Microwave Symp. Digest*, Philadelphia, PA, 2003, pp. 1685–1688.
24. D. M. K. Ah Yo, W. E. Forsyth, and W. A. Shiroma, A 360° retrodirective self-oscillating mixer array, *IEEE MTT-S Int. Microwave Symp. Digest*, Boston, MA, 2000, pp. 813–816.
25. G. S. Shiroma, R. Y. Miyamoto, and W. A. Shiroma, A 16-element two dimensional active self-steering array using self-oscillating mixers, *IEEE Trans. Microwave Theory Tech.* **51**:2257–2264 (2003).
26. M. Cohn, A millimeter wave retrodirective transponder for collision/obstacle avoidance and navigation/location, *Proc. IEEE-IEE Vehicle Navigation and Information Systems Conf.*, 1993, pp. 534–538.
27. N. B. Buchanan, T. Brabetz, and V. F. Fusco, A 62/66 GHz frequency offset retrodirective array, *IEEE MTT-S Int. Microwave Symp. Digest*, Seattle, WA, 2002, pp. 315–318.
28. T. Brabetz, V. F. Fusco, and S. Karode, Balanced subharmonic mixers for retrodirective-array applications, *IEEE Trans. Microwave Theory Tech.* **49**:465–469 (2001).
29. M. I. Skolnik and D. D. King, Self-phasing array antennas, *IEEE Trans. Anten. Propag.* **AP-12**:142–149 (1964).
30. L. D. DiDomenico and G. M. Rebeiz, Digital communications using self-phased arrays, *IEEE Trans. Microwave Theory Tech.* **49**:677–684 (2001).
31. R. Y. Miyamoto, K. M. K. H. Leong, S.-S. Jeon, Y. Wang, Y. Qian, and T. Itoh, Digital wireless sensor server using an adaptive smart-antenna/retrodirective array, *IEEE Trans. Vehic. Tech.* **52**:1181–1188 (2003).
32. J. Tuovinen, G. S. Shiroma, W. E. Forsyth, and W. A. Shiroma, Multipath communications using a phase-conjugate array, *IEEE MTT-S Int. Microwave Symp. Digest*, Philadelphia, PA, 2003, pp. 1681–1684.
33. B. T. Murakami, J. D. Roque, S. S. Sung, G. S. Shiroma, R. Y. Miyamoto, and W. A. Shiroma, A quadruple subharmonic phase-conjugating array for secure picosatellite crosslinks, *IEEE MTT-S Int. Microwave Symp. Digest*, Fort Worth, TX, 2004, pp. 1687–1690.

RF CIRCUIT NOISE

W. MARSHALL LEACH Jr.
Georgia Institute of Technology
Atlanta, Georgia

1. NOTATION AND REFERENCES

The notation used here for voltages and currents correspond to the following conventions. Phasors are represented by uppercase letters and lowercase subscripts, for instance, V_s, I_s . Root-mean-square (RMS) values are represented by lowercase letters and lowercase subscripts, for example, v_s, i_s . Mean-square values are represented by the square of the RMS value, for instance, v_s^2, i_s^2 .

The low-noise literature contains a very large number of references. It is impossible to give a comprehensive list of these in an article of this scope. Only a selected list of references is given in the Bibliography.

2. THE V_N – I_N AMPLIFIER NOISE MODEL

A general noise model of an amplifier can be obtained by reflecting all internal noise sources to the input. In order for the reflected sources to be independent of the impedance of the signal source, two noise sources are required: a series voltage source and a shunt current source. In general, these sources are correlated. Figure 1 shows the amplifier noise model with a Thévenin input source, where V_s is the source voltage, $Z_s = R_s + jX_s$ is the source impedance, and V_{ts} is the thermal noise voltage generated by the source. The mean-square value of V_{ts} is given by the Nyquist formula

$$v_{ts}^2 = 4kTR_s\Delta f \quad (1)$$

where $k = 1.38 \times 10^{-23}$ J/K is the Boltzmann constant, T is the absolute temperature, and Δf is the bandwidth over which the noise is measured. The sources V_n and I_n are the noise sources representing the internal noise generated by the amplifier.

The amplifier output voltage V_o is given by

$$V_o = \frac{AZ_i}{Z_s + Z_i} \frac{Z_L}{Z_o + Z_L} [V_s + (V_{ts} + V_n + I_n Z_s)] \quad (2)$$

where A is the voltage gain, Z_i is the input impedance, Z_o is the output impedance, and Z_L is the load impedance. The equivalent noise input voltage V_{ni} is defined as the voltage in series with V_s that generates the same noise

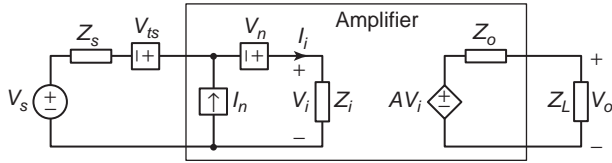


Figure 1. $V_n - I_n$ amplifier model with Thévenin source.

voltage at the output as all noise sources in the circuit. It consists of the terms in parenthesis in Eq. (2) and is given by

$$V_{ni} = V_{ts} + V_n + I_n Z_s \quad (3)$$

Note that this is the noise voltage across Z_i considering Z_i to be an open circuit; thus, it is the Thévenin input noise voltage.

The mean-square value of V_{ni} is given by

$$v_{ni}^2 = 4kTR_s \Delta f + v_n^2 + 2v_n i_n \text{Re}(\gamma Z_s^*) + i_n^2 |Z_s|^2 \quad (4)$$

where $\gamma = \gamma_r + j\gamma_i$ is the complex correlation coefficient between V_n and I_n and it is assumed that V_{ts} is independent of both V_n and I_n . The *signal-to-noise ratio* is given by

$$\text{SNR} = \frac{v_s^2}{v_{ni}^2} = \frac{v_s^2}{4kTR_s \Delta f + v_n^2 + 2v_n i_n \text{Re}(\gamma Z_s^*) + i_n^2 |Z_s|^2} \quad (5)$$

This is expressed in decibels by the relation $10 \log(v_s^2/v_{ni}^2)$.

Figure 2 shows the amplifier noise model with a Norton input source, where I_s is the source current, $Y_s = G_s + jB_s$ is the source admittance, and I_{ts} is the thermal noise current generated by the source. The mean-square value of I_{ts} is given by the Nyquist formula

$$i_{ts}^2 = 4kTG_s \Delta f \quad (6)$$

The amplifier output voltage V_o is given by

$$V_o = \frac{A}{Y_s + Y_i} \frac{Z_L}{Z_o + Z_L} [I_s + (I_{ts} + V_n Y_s + I_n)] \quad (7)$$

The *equivalent noise input current* I_{ni} is defined as the current in parallel with I_s that generates the same noise voltage at the output as all noise sources in the circuit. It consists of the terms in parenthesis in Eq. (7) and is given by

$$I_{ni} = I_{ts} + V_n Y_s + I_n \quad (8)$$

Note that this is the input noise current considering Y_i to be a short circuit, namely, the Norton input noise current.

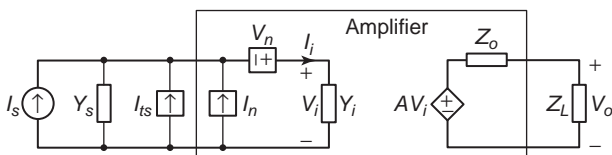


Figure 2. $V_n - I_n$ amplifier noise model with Norton source.

The mean-square value of I_{ni} is given by

$$i_{ni}^2 = 4kTG_s \Delta f + v_n^2 |Y_s|^2 + 2v_n i_n \text{Re}(\gamma Y_s) + i_n^2 \quad (9)$$

where it is assumed that I_{ts} is independent of V_n and I_n . The *signal-to-noise ratio* is given by

$$\text{SNR} = \frac{i_s^2}{i_{ni}^2} = \frac{i_s^2}{4kTG_s \Delta f + v_n^2 |Y_s|^2 + 2v_n i_n \text{Re}(\gamma Y_s) + i_n^2} \quad (10)$$

This is expressed in decibels by the relation $10 \log(i_s^2/i_{ni}^2)$.

3. NOISE FACTOR AND NOISE FIGURE

The *noise factor* F of an amplifier is defined as the ratio of its actual SNR to the SNR if the amplifier is noiseless, where the temperature is taken to be the *standard temperature* $T_0 = 290$ K. When it is expressed in decibels, it is called *noise figure* and is given by $\text{NF} = 10 \log(F)$. Often, it is convenient to express F in terms of the amplifier *noise resistance* R_n , its *noise conductance* G_n , its *correlation impedance* Z_γ , and its *correlation admittance* Y_γ . These are related to v_n^2 , i_n^2 , and γ by

$$R_n = \frac{v_n^2}{4kT_0 \Delta f} \quad (11)$$

$$G_n = \frac{i_n^2}{4kT_0 \Delta f} \quad (12)$$

$$Z_\gamma = R_\gamma + jX_\gamma = \gamma \frac{v_n}{i_n} = (\gamma_r + j\gamma_i) \frac{v_n}{i_n} \quad (13)$$

$$Y_\gamma = G_\gamma + jB_\gamma = \gamma^* \frac{i_n}{v_n} = (\gamma_r - j\gamma_i) \frac{i_n}{v_n} \quad (14)$$

Consider the amplifier driven by a Thévenin source in Fig. 1. If the amplifier is noiseless, its *signal-to-noise ratio* is given by $\text{SNR} = v_s^2/v_{ts}^2$, where v_s^2 is the mean-square source voltage and v_{ts}^2 is the mean-square thermal noise voltage generated by the source resistance R_s given by Eq. (1). The *noise factor* F is obtained by dividing the noiseless amplifier SNR by Eq. (5) to obtain

$$F = \frac{v_s^2/v_{ts}^2}{v_s^2/v_{ni}^2} = 1 + \frac{v_n^2 + 2v_n i_n \text{Re}(\gamma Z_s^*) + i_n^2 |Z_s|^2}{4kT_0 R_s \Delta f} \quad (15)$$

It follows that a noiseless amplifier has the *noise factor* $F = 1$. An alternate expression for F is obtained when the amplifier noise parameters are expressed in terms of R_n , G_n , and Z_γ . It is

$$F = 1 + \frac{R_n + 2G_n \text{Re}(Z_\gamma Z_s^*) + G_n |Z_s|^2}{R_s} \quad (16)$$

The value of Z_s that minimizes F is called the *optimum source impedance* and is denoted by $Z_{\text{opt}} = R_{\text{opt}} + jX_{\text{opt}}$. It is obtained by setting $\partial F/\partial R_s = 0$ and $\partial F/\partial X_s = 0$ and solving

for R_s and X_s . It is given by

$$Z_{\text{opt}} = [(1 - \gamma_i^2)^{1/2} - j\gamma_i] \frac{v_n}{i_n} = \left(\frac{R_n}{G_n} - X_\gamma^2 \right)^{1/2} - jX_\gamma \quad (17)$$

The corresponding minimum value of the noise factor is given by

$$F_{\text{min}} = 1 + \frac{v_n i_n}{2kT_0 \Delta f} [\gamma_r + (1 - \gamma_i^2)^{1/2}] = 1 + 2G_n(R_\gamma + R_{\text{opt}}) \quad (18)$$

It can be shown that F is related to F_{min} by

$$F = F_{\text{min}} + \frac{G_n}{R_s} |Z_s - Z_{\text{opt}}|^2 \quad (19)$$

If G_n , F_{min} , and Z_{opt} are given for an amplifier, it can be shown that

$$i_n^2 = 4kTG_n \Delta f \quad (20)$$

$$\gamma_i = \frac{-\text{sgn}(X_{\text{opt}})}{[1 + (R_{\text{opt}}/X_{\text{opt}})^2]^{1/2}} \quad (21)$$

$$v_n^2 = \left(\frac{X_{\text{opt}}}{\gamma_i} \right)^2 i_n^2 \quad (22)$$

$$\gamma_r = \frac{2kT_0 \Delta f}{v_n i_n} (F_{\text{min}} - 1) - (1 - \gamma_i^2)^{1/2} \quad (23)$$

where $\text{sgn}(X_{\text{opt}}) = X_{\text{opt}}/|X_{\text{opt}}|$.

If the amplifier driven by a Norton source in Fig. 2 is noiseless, the signal-to-noise ratio is given by $\text{SNR} = i_s^2/i_{\text{ts}}^2$, where i_s^2 is the mean-square source current and i_{ts}^2 is the mean-square thermal noise current generated by the source conductance G_s given by Eq. (6). The noise factor F is obtained by dividing the noiseless amplifier SNR by Eq. (10) to obtain

$$F = \frac{i_s^2/i_{\text{ts}}^2}{i_s^2/i_{\text{ni}}^2} = 1 + \frac{v_n^2 |Y_s|^2 + 2v_n i_n \text{Re}(\gamma Y_s) + i_n^2}{4kT_0 G_s \Delta f} \quad (24)$$

An alternate expression for F is obtained when the amplifier noise parameters are expressed in terms of R_n , G_n , and Y_γ :

$$F = 1 + \frac{R_n |Y_s|^2 + 2R_n \text{Re}(Y_\gamma Y_s) + G_n}{G_s} \quad (25)$$

The value of Y_s that minimizes F is called the *optimum source admittance* and is denoted by $Y_{\text{opt}} = G_{\text{opt}} + jB_{\text{opt}}$. It is obtained by setting $\partial F/\partial G_s = 0$ and $\partial F/\partial B_s = 0$ and solving for G_s and B_s . It is given by

$$Y_{\text{opt}} = [(1 - \gamma_i^2)^{1/2} + j\gamma_i] \frac{i_n}{v_n} = \left(\frac{G_n}{R_n} - B_\gamma^2 \right)^{1/2} + jB_\gamma \quad (26)$$

The corresponding minimum value of the noise factor is given by

$$F_{\text{min}} = 1 + \frac{v_n i_n}{2kT_0 \Delta f} [\gamma_r + (1 - \gamma_i^2)^{1/2}] = 1 + 2R_n(G_\gamma + G_{\text{opt}}) \quad (27)$$

It can be shown that F is related to F_{min} by

$$F = F_{\text{min}} + \frac{R_n}{G_s} |Y_s - Y_{\text{opt}}|^2 \quad (28)$$

If R_n , F_{min} , and $Y_{\text{opt}} = G_{\text{opt}} + jB_{\text{opt}}$ are given for an amplifier, it can be shown that

$$v_n^2 = 4kTR_n \Delta f \quad (29)$$

$$\gamma_i = \frac{\text{sgn}(B_{\text{opt}})}{[1 + (G_{\text{opt}}/B_{\text{opt}})^2]^{1/2}} \quad (30)$$

$$i_n^2 = \left(\frac{B_{\text{opt}}}{\gamma_i} \right)^2 v_n^2 \quad (31)$$

$$\gamma_r = \frac{2kT_0 \Delta f}{v_n i_n} (F_{\text{min}} - 1) - (1 - \gamma_i^2)^{1/2} \quad (32)$$

where $\text{sgn}(B_{\text{opt}}) = B_{\text{opt}}/|B_{\text{opt}}|$.

3.1. The Noise Factor Fallacy

The noise factor can be a misleading specification. If an attempt is made to minimize F by adding resistors either in series or in parallel with the source at the input of an amplifier, the SNR is always decreased. This is referred to as the *noise factor fallacy*. Potential confusion can be avoided if low-noise amplifiers are designed to maximize the SNR. This is accomplished by minimizing the equivalent noise input voltage or current. If a series resistor must be included at the amplifier input, its value should be much smaller than the source impedance. If a parallel resistor must be included at the amplifier input, its value should be much larger than the source impedance.

4. NOISE-MATCHING NETWORKS

Lossless noise-matching networks are used to transform the source impedance into the optimum impedance that minimizes the noise factor. These networks can be either lumped-element networks or microstrip networks. Two *noise matching networks* are described in the following examples.

Example 1. With a 50- Ω transmission line test fixture, the reflection coefficient seen looking out of the input terminals of an amplifier that minimizes its noise factor F at 900 MHz is determined to be $\Gamma_{\text{opt}} = 0.7 \angle 23.7^\circ$. Determine the lengths ℓ_1 and ℓ_2 of the transmission lines in the matching network of Fig. 3 that cause the source impedance seen by the amplifier to be the optimum source impedance Z_{opt} . The source resistance is $R_s = 50 \Omega$. The

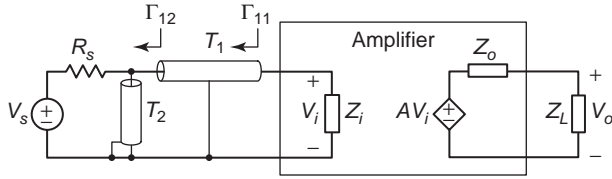


Figure 3. Transmission-line noise-matching network.

characteristic impedance of the two transmission lines in the network is $Z_{c1} = Z_{c2} = 75 \Omega$.

Solution: With $Z_c = 50 \Omega$, specifically, the line impedance of the text fixture used to measure Γ_{opt} , the optimum source impedance is calculated from

$$Z_{opt} = Z_c \frac{1 + \Gamma_{opt}}{1 - \Gamma_{opt}} \quad (33)$$

to obtain $Z_{opt} = 122.6 + j135.2 \Omega$. The reflection coefficient at the amplifier end of T_1 is calculated from

$$\Gamma_{11} = \frac{Z_{opt} - Z_{c1}}{Z_{opt} + Z_{c1}} \quad (34)$$

to obtain $\Gamma_{11} = 0.4230 + j0.3539$. This has the magnitude $|\Gamma_{11}| = 0.5988$. The reactance of T_2 is calculated from

$$X_2 = \pm Z_{c1} \left[\frac{1 - |\Gamma_{11}|^2}{|\Gamma_{11}|^2 (1 + Z_{c1}/R_s)^2 - (1 - Z_{c1}/R_s)^2} \right]^{1/2} \quad (35)$$

to obtain $X_2 = 42.58 \Omega$, where the positive solution has been used. The electrical length of T_2 is calculated from

$$\beta \ell_2 = \tan^{-1} \left(\frac{X_2}{Z_{c2}} \right) \quad (36)$$

to obtain $\beta \ell_2 = 29.58^\circ$. The reflection coefficient at the source end of T_1 is calculated from

$$\Gamma_{12} = \frac{R_s |jX_2 - Z_{c1}|}{R_s |jX_2 + Z_{c1}|} \quad (37)$$

to obtain $\Gamma_{12} = -0.4654 + j0.3767$. The electrical length of T_1 is calculated from

$$\beta \ell_1 = \frac{1}{2} \arg \left(\frac{\Gamma_{12}}{\Gamma_{11}} \right) \quad (38)$$

to obtain $\beta \ell_1 = 52.39^\circ$.

Example 2. For the amplifier of Example 1, determine X_1 and X_2 in the lumped-element noise-matching circuit shown in Fig. 4.

Solution: The source impedance is $R_s = 50 \Omega$ and the optimum impedance is $Z_{opt} = R_{opt} + jX_{opt} = 122.6 + j135.2 \Omega$. To transform R_s into Z_{opt} , X_1 is calculated from

$$X_1 = \pm \sqrt{R_s R_{opt} \left[1 + \left(\frac{X_{opt}}{R_{opt}} \right)^2 \right] - R_s^2} \quad (39)$$

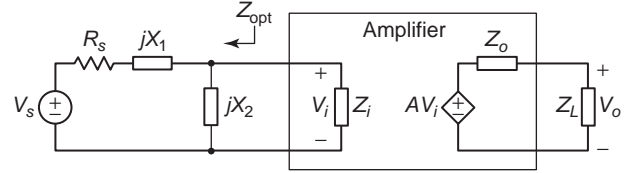


Figure 4. Lumped-element noise-matching network.

This yields $X_1 = \pm 105.3 \Omega$. X_2 is calculated from

$$X_2 = \frac{R_s^2 + X_1^2}{(R_s X_{opt}/R_{opt}) - X_1} \quad (40)$$

For $X_1 = +105.3 \Omega$, this gives $X_2 = -270.9 \Omega$. For $X_1 = -105.3 \Omega$, it gives $X_2 = +84.68 \Omega$.

5. NOISE TEMPERATURE

The internal noise generated by an amplifier can be expressed as an equivalent input-termination noise temperature. When the source is represented by a Thévenin equivalent circuit, the noise temperature T_n is the temperature of the source resistance that generates an open-circuit thermal noise voltage equal to the internal noise generated in the amplifier when referred to its input. The *noise temperature* is given by

$$T_n = \frac{v_n^2 + 2v_n i_n \operatorname{Re}(\gamma Z_s^*) + i_n^2 |Z_s|^2}{4kR_s \Delta f} \quad (41)$$

When the source is represented by a Norton equivalent circuit, the noise temperature is the temperature of the source conductance that generates a short-circuit thermal noise current equal to the internal noise generated in the amplifier when referred to its input. The noise temperature is given by

$$T_n = \frac{v_n^2 |Y_s|^2 + 2v_n i_n \operatorname{Re}(\gamma Y_s) + i_n^2}{4kG_s \Delta f} \quad (42)$$

The noise temperature is related to the noise factor by

$$T_n = (F - 1)T_0 \quad (43)$$

where the source temperature is taken to be the standard temperature T_0 . This holds for the amplifier with either the Thévenin or the Norton source.

6. MULTISTAGE AMPLIFIER

The noise factor of a *multistage amplifier* is given by

$$F = F_1 + \frac{F_2 - 1}{G_{a1}} + \cdots + \frac{F_N - 1}{G_{a1} G_{a2} \cdots G_{a(N-1)}} \quad (44)$$

where F_j is the noise factor of the j th stage, G_{aj} is its available power gain, and N is the number of stages. If G_{a1}

can be made large enough, this equation implies that $F \simeq F_1$. However, increasing G_{a1} may not make the second term arbitrarily small. For example, consider the case where $Z_{o1} = R_{o1} + j0$. In this case, it can be shown that $G_{a1} \propto R_{o1}$. Thus the second term in Eq. (44) can be written

$$\frac{F_2 - 1}{G_{a1}} \propto \frac{1}{4kT_0\Delta f} \left[\frac{v_{n2}^2}{R_{o1}^2} + \frac{2v_{n2}i_{n2}\text{Re}(\gamma_2)}{R_{o1}} + i_{n2}^2 \right] \quad (45)$$

where v_{n2}^2 and i_{n2}^2 , respectively, are the mean-square noise voltage and current of the second stage and γ_2 is the complex correlation coefficient between V_{n2} and I_{n2} . By increasing R_{o1} , G_{a1} can be made arbitrarily large. However, the second term in the expression for F cannot be made arbitrarily small by making R_{o1} arbitrarily large unless i_{n2}^2 is negligible.

Let T_n be the noise temperature of the overall amplifier and T_{nj} the noise temperature of the j th stage. It can be shown that T_n is given by

$$T_n = T_{n1} + \frac{T_{n2}}{G_{a1}} + \cdots + \frac{T_{nN}}{G_{a1}G_{a2}\cdots G_{a(N-1)}} \quad (46)$$

7. EFFECT OF A MATCHING NETWORK ON NOISE

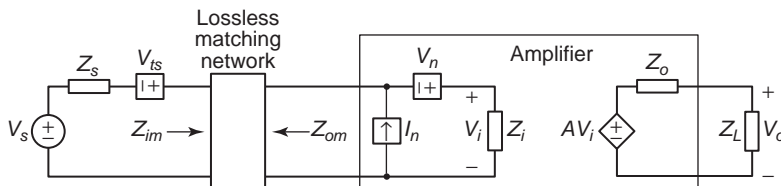
Lossless matching networks are commonly used between a source and the input to an amplifier to obtain either a maximum power gain or a minimum noise factor. For maximum power gain, the output impedance of the matching network must be equal to the conjugate of the amplifier input impedance. Such a network is called a *conjugate impedance-matching network*. For minimum noise factor, the output impedance of the matching network must be equal to the optimum source impedance. Such a network is called a *noise-matching network*.

Figure 5 shows a lossless matching network between the input to an amplifier having an input impedance $Z_i = R_i + jX_i$ and a Thévenin signal source having an output impedance $Z_s = R_s + jX_s$. Denote the input impedance of the matching network by $Z_{im} = R_{im} + jX_{im}$ and its output impedance by $Z_{om} = R_{om} + jX_{om}$. It can be shown that the mean-square equivalent noise input voltage in series with V_s is

$$v_{ni}^2 = 4kTR_s\Delta f + \frac{R_s}{R_{om}} [v_n^2 + 2v_n i_n \text{Re}(\gamma Z_{om}^*) + i_n^2 |Z_{om}|^2] \quad (47)$$

The noise factor is given by

$$F = \frac{v_{ni}^2}{4kTR_s\Delta f} = 1 + \frac{v_n^2 + 2v_n i_n \text{Re}(\gamma Z_{om}^*) + i_n^2 |Z_{om}|^2}{4kTR_{om}\Delta f} \quad (48)$$



This is the same as the noise factor calculated at the output of the matching network.

The noise factors at the source and at the output of the matching network are equal because a lossless matching network cannot add noise. Thus it follows that the signal-to-noise ratio is also the same at the input to the matching network as at the input to the amplifier. However, these conclusions do not hold for a lossy matching network.

Equation (48) can be used to predict the noise factor for any arbitrary matching network. For example, Z_{om} might be chosen to be the optimum source impedance to minimize F . Alternately, it can be chosen for a conjugate impedance match to maximize the power gain. For a conjugate match, Z_{om} is replaced with Z_i^* in Eqs. (47) and (48). Because v_{ni}^2 and F are then functions of Z_i , it is difficult to predict how changes in Z_i affect the noise. This is because V_n , I_n , and γ in the noise model are, in general, related to Z_i . For example, V_n , I_n , γ , and Z_i may all be functions of the bias current in the amplifier input stage. A change in the bias current to vary Z_i can cause a change in V_n , I_n , and γ . Thus the effects cannot be examined in detail unless the relations between the variables are known.

Example 3. An amplifier is driven from a source with a resistive output impedance $R_s = 50 \Omega$. At the operating frequency $f = 10$ MHz, the amplifier has a resistive input impedance $R_i = 25 \Omega$ and the noise parameters $v_n = 0.447$ nV/ $\sqrt{\text{Hz}}$, $i_n = 31$ pA/ $\sqrt{\text{Hz}}$, and $\gamma = 0.12 - j0.44$. Calculate the noise figure (a) with a conjugate impedance-matching network between the source and the amplifier and (b) assuming that the matching network is designed so that the amplifier sees its optimum source impedance.

Solution: (a) For a conjugate impedance match, the noise figure is

$$\text{NF} = 10 \log \left[1 + \frac{v_n^2 + 2v_n i_n \text{Re}(\gamma Z_i) + i_n^2 |Z_i^*|^2}{4kTR_i\Delta f} \right] = 5.062 \text{ dB}$$

(b) The optimum source impedance is given by Eq. (17):

$$Z_{opt} = [(1 - \gamma_i^2)^{1/2} - j\gamma_i] \frac{v_n}{i_n} = 13 + j6.35$$

Thus the minimum noise figure is

$$\begin{aligned} \text{NF}_{\min} &= 10 \log \left[1 + \frac{v_n^2 + 2v_n i_n \text{Re}(\gamma Z_{opt}^*) + i_n^2 |Z_{opt}|^2}{4kTR_{om}\Delta f} \right] \\ &= 4.414 \text{ dB} \end{aligned}$$

This is 0.648 dB lower than for part (a).

Figure 5. Amplifier with a Thévenin source and an input-matching network.

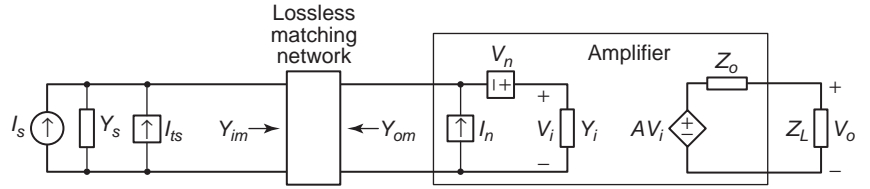


Figure 6. Amplifier with a Norton source and an input-matching network.

Figure 6 shows a lossless matching network between the input to an amplifier having an input admittance $Y_i = G_i + jB_i$ and a Norton source having an output admittance $Y_s = G_s + jB_s$. Denote the input admittance of the matching network by $Y_{im} = G_{im} + jB_{im}$ and its output admittance by $Y_{om} = G_{om} + jB_{om}$. It can be shown that the mean-square equivalent noise input current in parallel with I_s is

$$i_{ni}^2 = 4kTG_s\Delta f + \frac{G_s}{G_{om}}[v_n^2|Y_{om}|^2 + 2v_n i_n \text{Re}(\gamma Y_{om}) + i_n^2] \quad (49)$$

The noise factor is given by

$$F = \frac{i_{ni}^2}{4kTG_s\Delta f} = 1 + \frac{v_n^2|Y_{om}|^2 + 2v_n i_n \text{Re}(\gamma Y_{om}) + i_n^2}{4kTG_{om}\Delta f} \quad (50)$$

For a conjugate match, Y_{om} is replaced with Y_i^* in these equations.

8. NOISE CIRCLES

In RF design, the contours on the Smith chart for the reflection coefficient seen looking out of an amplifier input for constant F are important. These contours are circles. Thus they are called *noise circles*. These are described in this section for both the impedance and admittance Smith charts.

Figure 7 shows an amplifier with a Thévenin source and a lossless input matching network. Let the impedance seen looking into the output of the matching network be $Z_{om} = R_{om} + jX_{om}$. Let us write $Z_{om} = Z_{opt} + \Delta Z$, where $\Delta Z = \Delta R + j\Delta X$ represents the amount by which Z_{om} deviates from the source impedance Z_{opt} , which minimizes the noise factor. Define the variable z as

$$z = \frac{|1 - \Gamma_{opt}|^2}{4} \frac{|\Delta Z|^2}{Z_c R_{om}} \quad (51)$$

where Γ_{opt} is the reflection coefficient seen looking into the output of the matching network for the case $Z_{om} = Z_{opt}$ and

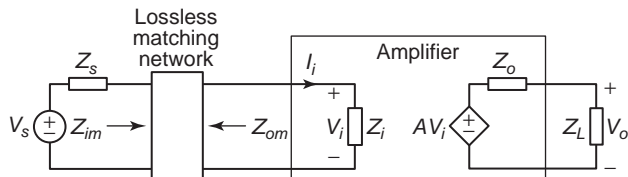


Figure 7. Amplifier with a Thévenin source and a lossless input-matching network.

Z_c is the characteristic impedance of the transmission line on which Γ_{opt} is calculated. It can be shown that the contours of constant F on an impedance Smith chart are circles of radius c centered at the point with rectangular coordinates (a, b) where

$$a = \frac{\text{Re}(\Gamma_{opt})}{1 + z} \quad (52)$$

$$b = \frac{\text{Im}(\Gamma_{opt})}{1 + z} \quad (53)$$

$$c = \left[\frac{z}{1 + z} \left(1 - \frac{|\Gamma_{opt}|^2}{1 + z} \right) \right]^{1/2} \quad (54)$$

On any noise circle, the noise factor is constant and is given by

$$F = F_{min} + G_n \frac{|\Delta Z|^2}{R_{om}} \quad (55)$$

Because b/a is independent of ΔZ , it follows that the centers of the noise circles lie on a straight line passing through the origin and the point Γ_{opt} on the Smith chart. Figure 8a shows an example impedance Smith chart with the point $\Gamma_{opt} = 0.5 \angle -135^\circ$ and three surrounding noise circles labeled Γ_1 , Γ_2 , and Γ_3 , corresponding to $z = 0.3$, $z = 0.5$, and $z = 0.7$, respectively.

Figure 9 shows an amplifier with a Norton source and a lossless input-matching network. Let the admittance seen looking into the output of the matching network be $Y_{om} = G_{om} + jB_{om}$. Let us write $Y_{om} = Y_{opt} + \Delta Y$, where $\Delta Y = \Delta G + j\Delta B$ represents the amount by which Y_{om} deviates from the source admittance Y_{opt} , which minimizes the noise factor. Define the variable y as

$$y = \frac{|1 + \Gamma_{opt}|^2}{4} \frac{|\Delta Y|^2}{Y_c G_{om}} \quad (56)$$

where Γ_{opt} is the reflection coefficient seen looking into the output of the matching network for the case $Y_{om} = Y_{opt}$ and Y_c is the characteristic admittance on the transmission line on which Γ_{opt} is calculated. It can be shown that the contours of constant F on an admittance Smith chart are circles of radius c centered at the point with rectangular coordinates (a, b) , where

$$a = \frac{\text{Re}(\Gamma_{opt})}{1 + y} \quad (57)$$

$$b = \frac{\text{Im}(\Gamma_{opt})}{1 + y} \quad (58)$$

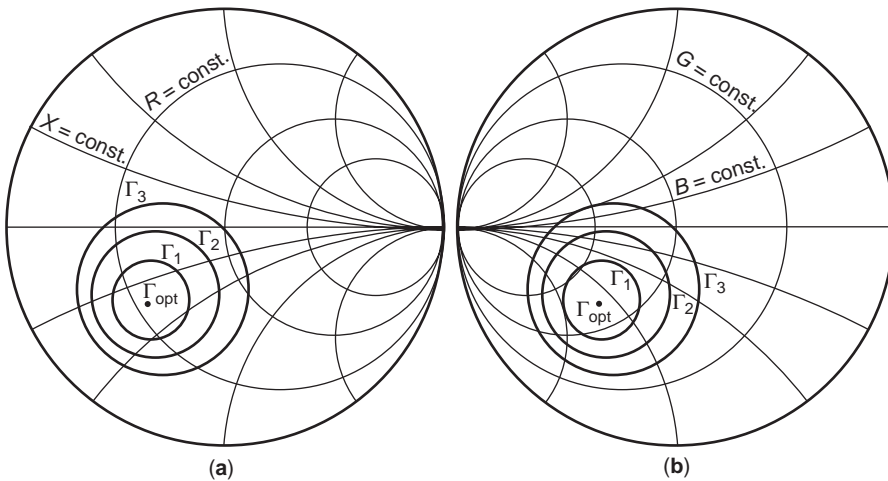


Figure 8. Smith charts showing the optimum reflection coefficient Γ_0 and three noise circles: (a) impedance chart; (b) admittance chart.

$$c = \left[\frac{y}{1+y} \left(1 - \frac{|\Gamma_{\text{opt}}|^2}{1+y} \right) \right]^{1/2} \quad (59)$$

On any circle, the noise factor is constant and is given by

$$F = F_{\text{min}} + R_n \frac{|\Delta Y|^2}{G_{\text{om}}} \quad (60)$$

Because b/a is independent of ΔY , it follows that the centers of the noise circles lie on a straight line passing through the origin and the point Γ_{opt} on the Smith chart.

Figure 8b shows an example admittance Smith chart with the point $\Gamma_{\text{opt}} = 0.5 \angle -135^\circ$ and three surrounding noise circles labeled Γ_1 , Γ_2 , and Γ_3 , corresponding to $y = 0.568$, $y = 0.983$, and $y = 1.33$, respectively. These values are chosen to give the same radii of the corresponding circles on the two charts. It follows from Eqs. (55) and (60), however, that the value of F on corresponding circles is not the same unless the following relation holds:

$$G_n \frac{|\Delta Z|^2}{R_{\text{om}}} = R_n \frac{|\Delta Y|^2}{G_{\text{om}}} \quad (61)$$

9. GAIN CIRCLES

Compromises are often made in RF amplifier design between lowest noise and highest gain. In this section, the contours of constant gain on the Smith chart are described. Like the noise factor contours, the constant gain contours are circles. Thus they are called *gain circles*. Given a Smith chart with both the noise circles and the gain circles plotted for a particular amplifier, the effect of the input-matching network on both noise and gain can be visualized.

Consider the amplifier model of Fig. 7, where the source is represented by a Thévenin equivalent. Let us write $Z_{\text{om}} = Z_i^* + \Delta Z$, where $\Delta Z = \Delta R + j\Delta X$ represents the amount by which Z_{om} deviates from Z_i^* . The relative efficiency of η of the input matching network can be

written

$$\eta = \frac{1}{1+h} \quad (62)$$

where h is given by

$$h = \frac{|\Delta Z|^2}{4R_i(R_i + \Delta R)} \quad (63)$$

It can be shown that the contours on an impedance Smith chart for which η is constant are circles of radius c centered at the point with rectangular coordinates (a, b) where

$$a = \frac{|Z_i/Z_c|^2 - 1}{|Z_i/Z_c|^2 + 2(R_i/Z_c)(1+2h) + 1} \quad (64)$$

$$b = \frac{-2(X_i/Z_c)}{|Z_i/Z_c|^2 + 2(R_i/Z_c)(1+2h) + 1} \quad (65)$$

$$c = \frac{4(R_i/Z_c)[h(1+h)]^{1/2}}{|Z_i/Z_c|^2 + 2(R_i/Z_c)(1+2h) + 1} \quad (66)$$

Because b/a is independent of h , it follows that the centers of the gain circles lie on a straight line passing through the origin of the Smith chart.

Consider the amplifier model of Fig. 9, where the source is represented by a Norton equivalent. Let the relative efficiency η of the input matching network be given by

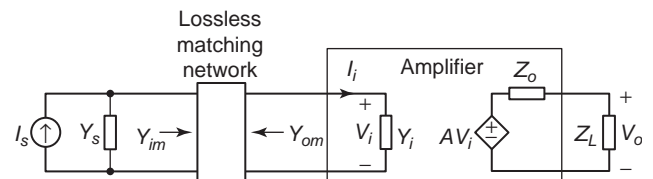


Figure 9. Amplifier with a Norton source and a lossless input-matching network.

Eq. (62), where h is given by

$$h = \frac{|\Delta Y|^2}{4G_i(G_i + \Delta G)} \quad (67)$$

It can be shown that the contours on an admittance Smith chart for which η is constant are circles of radius c centered at the point (a, b) , where

$$a = \frac{1 - |Y_i/Y_c|^2}{|Y_i/Y_c|^2 + 2(G_i/Y_c)(1 + 2h) + 1} \quad (68)$$

$$b = \frac{2(B_i/Y_c)}{|Y_i/Y_c|^2 + 2(G_i/Y_c)(1 + 2h) + 1} \quad (69)$$

$$c = \frac{4(G_i/Y_c)[h(1 + h)]^{1/2}}{|Y_i/Y_c|^2 + 2(G_i/Y_c)(1 + 2h) + 1} \quad (70)$$

Because b/a is independent of h , it follows that the centers of the gain circles lie on a straight line passing through the origin of the Smith chart.

Example 4. An amplifier designed to operate at the frequency $f = 1.9$ GHz from a source with an output impedance $Z_s = 50 \Omega$ has the specifications: optimum source reflection coefficient for minimum noise $\Gamma_{opt} = 0.52 \angle 68.8^\circ$, minimum noise figure $NF_{min} = 1.39$ dB, noise resistance $R_n = 20.4 \Omega$, input reflection coefficient $\Gamma_i = 0.68 \angle -86^\circ$. The reflection coefficients are measured with a test fixture having the characteristic impedance $Z_c = 50 \Omega$. (a) A noise-matching network is to be used between the source and the amplifier. On an admittance Smith chart, plot the point representing Γ_{opt} and the noise circle for which the noise is 0.25 dB higher than its minimum value. (b) A conjugate impedance matching network is to be used between the source and the amplifier. On the same chart, plot the point representing the reflection coefficient seen looking out of the amplifier input and the gain circle for which the gain is 1 dB lower than its maximum value.

Solution: (a) The point representing Γ_{opt} is shown on the admittance Smith chart in Fig. 10. At this point, the normalized source admittance is $Y_{opt}/Y_c = 0.443 - j0.589$ and the noise factor is

$$F_{min} = 10^{NF_{min}/10} = 1.377$$

For 0.25-dB higher noise, the noise figure is $NF_1 = NF_{min} + 0.25 = 1.64$. The corresponding noise factor is

$$F_1 = 10^{NF_1/10} = 1.459$$

Equations (56) and (60) can be combined to calculate y to obtain

$$y = \frac{|1 + \Gamma_{opt}|^2 F_1 - F_{min}}{4 R_n Y_c} = 0.082$$

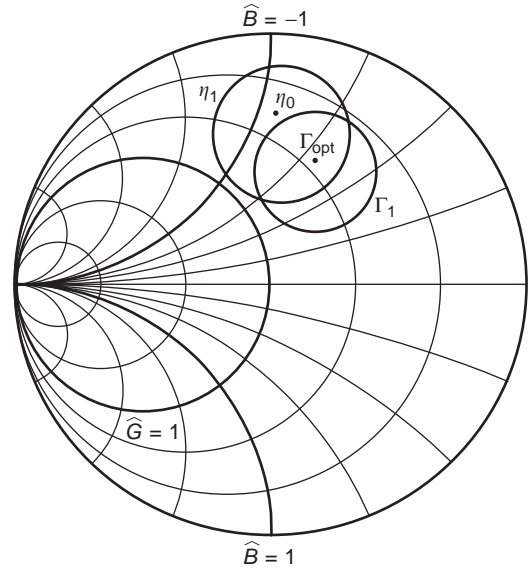


Figure 10. Admittance Smith chart for Example 3.

where $Y_c = 0.02$ S. The coordinates (a, b) of the center of the -0.25 -dB noise circle and its radius c are calculated from Eqs. (57)–(59) as follows:

$$a = \frac{\text{Re}(\Gamma_{opt})}{1 + y} = 0.174$$

$$b = \frac{\text{Im}(\Gamma_{opt})}{1 + y} = 0.448$$

$$c = \left[\frac{y}{1 + y} \left(1 - \frac{|\Gamma_{opt}|^2}{1 + y} \right) \right]^{1/2} = 0.239$$

The noise circle is shown labeled Γ_1 in Fig. 10.

(b) For a conjugate impedance-matching network, the reflection coefficient seen looking out of the amplifier input is $\Gamma_{om} = \Gamma_i^* = 0.68 \angle +86^\circ = 0.047 + j0.678$. This reflection coefficient maximizes the normalized gain of the matching network and is labeled η_0 in Fig. 10. On the gain circle for which the normalized gain of the matching network is -1 dB, the value of η in Eq. (62) is $\eta_1 = 10^{-1/10} = 0.794$. The corresponding value of h is $h_1 = 1/\eta_1 - 1 = 0.259$. The normalized amplifier input admittance is given by

$$\frac{Y_i}{Y_c} = \frac{G_i}{Y_c} + j \frac{B_i}{Y_c} = \frac{1 - \Gamma_i}{1 + \Gamma_i} = 0.345 + j0.871$$

The coordinates (a, b) of the center of the -1 -dB gain circle and its radius c are calculated from Eqs. (68)–(70) as follows:

$$a = \frac{1 - |Y_i/Y_c|^2}{|Y_i/Y_c|^2 + 2(G_i/Y_c)(1 + 2h) + 1} = 0.042$$

$$b = \frac{2B_i/Y_c}{|Y_i/Y_c|^2 + 2(G_i/Y_c)(1 + 2h) + 1} = 0.595$$

$$c = \frac{4(G_i/Y_c)[h(1+h)]^{1/2}}{|Y_i/Y_c|^2 + 2(G_i/Y_c)(1+2h) + 1} = 0.269$$

The gain circle is shown labeled η_1 in Fig. 10. If the source admittance lies in the intersection of the noise circle and the gain circle, the noise factor is within 0.25 dB of its minimum value and the relative power gain of the input matching network is within 1 dB of its maximum value.

10. MEASURING THE NOISE FACTOR

Consider the noise model of an amplifier given in Fig. 1. Consider the source to be a white-noise source having the spectral density $S_v(f) = v_s^2/\Delta f \text{ V}^2/\text{Hz}$ and a real output impedance $Z_s = R_s$. Let v_{o1} be the value of v_o with the input noise source set to zero: $S_v(f) = 0$. The temperature of R_s is specified to be the standard temperature $T_0 = 290 \text{ K}$. Let $S_v(f)$ be increased until the RMS output voltage increases by a factor r : $v_{o2} = rv_{o1}$. It can be shown that the noise factor is given by

$$F = \frac{S_v(f)}{(r^2 - 1) \times 4kT_0R_s} \quad (71)$$

In making measurements, a commonly used value for r is $r = \sqrt{2}$. In this case, the output noise voltage increases by 3 dB when the source is activated. Note that the expression for F is independent of the amplifier noise bandwidth, gain, and input impedance. However, the spectral density of the white noise input source must be known.

11. DETERMINATION OF NOISE PARAMETERS

Let the noise factor F be measured for N values of source admittance, where $N \geq 4$. Denote the noise factor values by F_i and the source admittance values by $Y_i = G_i + jB_i$. By Eq. (25), we can write

$$F_i = 1 + R_n \left(G_i + \frac{B_i^2}{G_i} \right) + 2R_n G_\gamma - 2R_n B_\gamma \frac{B_i}{G_i} + \frac{G_n}{G_i} \quad (72)$$

where $Y_\gamma = G_\gamma + jB_\gamma$ is the correlation admittance given by Eq. (14). The object is to use the measured values of F to determine the noise resistance R_n , the noise conductance G_n , and the correlation admittance Y_γ .

Define the mean-square error function

$$\begin{aligned} \varepsilon^2 = \sum \left[(F_i - 1) - R_n \left(G_i + \frac{B_i^2}{G_i} \right) \right. \\ \left. - 2R_n G_\gamma + 2R_n B_\gamma \frac{B_i}{G_i} - \frac{G_n}{G_i} \right]^2 \end{aligned} \quad (73)$$

where the summation extends over the range $1 \leq i \leq N$. The values of R_n , G_n , G_γ , and B_γ , which minimize ε^2 , represent a best estimate of the noise parameters. These values can be obtained by simultaneous solution of the set of equations $\partial \varepsilon^2 / \partial R_n = 0$, $\partial \varepsilon^2 / \partial G_n = 0$, $\partial \varepsilon^2 / \partial (R_n G_\gamma) = 0$, and

$\partial \varepsilon^2 / \partial (R_n B_\gamma) = 0$, where $R_n G_\gamma$ and $R_n B_\gamma$ are considered independent variables. This procedure leads to the following solution

$$\begin{bmatrix} R_n \\ 2R_n G_\gamma \\ -2R_n B_\gamma \\ G_n \end{bmatrix} = A^{-1} \begin{bmatrix} \sum \left(G_i + \frac{B_i^2}{G_i} \right) (F_i - 1) \\ \sum (F_i - 1) \\ \sum \frac{B_i}{G_i} (F_i - 1) \\ \sum \frac{1}{G_i} (F_i - 1) \end{bmatrix} \quad (74)$$

where the matrix A is given by

$$A = \begin{bmatrix} \sum \left(G_i + \frac{B_i^2}{G_i} \right)^2 & \sum G_i + \frac{B_i^2}{G_i} & \sum B_i + \frac{B_i^3}{G_i^2} & \sum 1 + \frac{B_i^2}{G_i^2} \\ \sum G_i + \frac{B_i^2}{G_i} & N & \sum \frac{B_i}{G_i} & \sum \frac{1}{G_i} \\ \sum B_i + \frac{B_i^3}{G_i^2} & \sum \frac{B_i}{G_i} & \sum \frac{B_i^2}{G_i^2} & \sum \frac{B_i}{G_i^2} \\ \sum 1 + \frac{B_i^2}{G_i^2} & \sum \frac{1}{G_i} & \sum \frac{B_i}{G_i^2} & \sum \frac{1}{G_i^2} \end{bmatrix} \quad (75)$$

The matrix A is singular if the ratios $a_{m1,n}/a_{m2,n}$ are equal for all elements in any two rows. With 4 rows, there are six combinations of two rows. It follows that the matrix is singular if the values of G_i and B_i lie on one of the contours defined by

$$G^2 + B^2 = k_1^2 \quad (76)$$

$$(G - k_2)^2 + B^2 = k_2^2 \quad (77)$$

$$G + (B - k_3)^2 = k_3^2 \quad (78)$$

$$B = k_4 G \quad (79)$$

$$G = k_5 \quad (80)$$

$$B = k_6 \quad (81)$$

where k_1 through k_6 are constants. Figure 11 shows example plots of these equations on the (G, B) plane. The k values are chosen so that the curves intersect at two common points. The curves labeled a – f correspond, in order, to Eqs. (76)–(81). Two curves labeled c , d , and f correspond to positive and negative values of k_3 , k_4 , and k_6 , respectively.

Given the solution for R_n , G_n , G_γ , and B_γ , the solutions for v_n^2 , i_n^2 , and γ are

$$v_n^2 = 4kT_0 R_n \Delta f \quad (82)$$

$$i_n^2 = 4kT_0 G_n \Delta f \quad (83)$$

$$\gamma = \frac{v_n}{i_n} (G_\gamma - jB_\gamma) \quad (84)$$

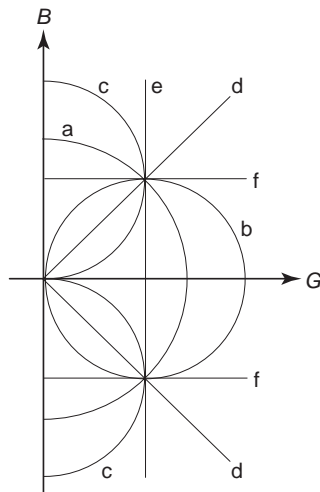


Figure 11. Example contours on which the matrix A is singular.

Because the quantity $(F - 1)$ is involved in the calculations, large percentage errors in $(F - 1)$ can be caused by small percentage errors in F when F has a value close to 1. Thus the solutions can be sensitive to experimental errors. Another problem lies in the choice of the values of G_i and B_i for which F is measured. If the values lie on or near one of the curves that makes the A matrix singular, the solutions can be unstable. To minimize this problem, the values of G_i and B_i should be chosen randomly.

BIBLIOGRAPHY

1. H. Rothe and W. Dahlke, Theory of noisy fourpoles, *Proc. IRE* **44**:811–818 (1956).
2. H. A. Haus (chairman), IRE standards on methods of measuring noise in linear twoports, 1959, *Proc. IRE* **48**: 60–68 (1960).
3. H. A. Haus (chairman), Representation of noise in linear two ports, IRE Subcommittee 7.9 on Noise, *Proc. IRE* **48**:69–74 (1960).
4. H. Fukui, Available power gain, noise figure and noise measure of two-ports and their graphical representations, *IEEE Trans. Circ. Theory* **13**:137–142 (1966).
5. C. R. Poole and D. K. Paul, Optimum noise measure terminations for microwave transistor amplifiers, *IEEE Trans. Microwave Theory Tech.* **MTT-33**:1254–1257 (1985).
6. M. Sannino, On the determination of device noise and gain parameters, *Proc. IEEE* **67**:1364–1366 (1979).
7. E. W. Strid, Measurement of losses in noise-matching networks, *IEEE Trans. Microwave Theory Tech.* **MTT-29**: 247–252 (1981).
8. G. Gonzalez, *Microwave Transistor Amplifiers Analysis and Design*, Prentice-Hall, Upper Saddle River, NJ, 1997.
9. D. M. Pozar, *Microwave Engineering*, Wiley, New York, 1998.
10. J. G. Webster, ed., *Wiley Encyclopedia of Electrical and Electronics Engineering*, Vol. 3, Wiley, New York, 1999.
11. J. G. Webster, ed., *The Measurement, Instrumentation, and Sensors Handbook*, CRC Press, Boca Raton, FL, 1999.

RF/WIRELESS PACKAGING

STEPHANE PINEL
 MANOS TENTZERIS
 DANIELA STAICNLESCU
 JOY LASKAR
 Georgia Institute of Technology
 Atlanta

The demand for increasingly higher rates of data, voice, and video and for the integration of various technologies (digital, analog, RF, optical) has driven in emerging high-performance applications such as personal communication networks, wireless local-area networks (WLAN), “last-mile” RF optical networks, and millimeter (mm)-wave sensors. These RF/wireless applications have defined a trend toward more flexible and reconfigurable systems, since they impose very stringent specifications never reached before in terms of low noise, high linearity, low power consumption, small size and weight, and low cost. The electronics packaging industry has proliferated to a point where its technology is at least as, if not more, important than, the semiconductor technology that it is designed to serve. The increase in silicon complexity and integration has imposed demanding requirements on packaging technology for higher I/O counts, finer lead pitch, enhanced heat dissipation, and high-speed, reliable interconnects. This places a further strain on packaging requirements. Microprocessor, RF and millimeter-wave packaging are undergoing major changes driven by technical, business, and economic factors. In its early evolution, the influence of the package on performance was limited; however, as the systems evolve to provide increasing performance and operation frequencies, the package must evolve to keep up, and packaging design must ensure that it can optimally enable the systems functionality. From the traditional role of a protective mechanical enclosure, the modern package has been transformed into a sophisticated thermal and electrical management platform. Furthermore, system architecture and design techniques have had a significant impact on the complexity and cost of packaging. The need to optimize the total solution (chip, package, board, and assembly) has never been more important to maximize performance and minimize cost.

More recent advances in high-frequency packaging indicate a migration from wirebond (where the chip or die is interconnected to the package only on the periphery of the die) to flip-chip (where the die is interconnected to the package using the entire die area); and from ceramic to organic packages, with cartridge and multichip technologies emerging as key form factors. With the “segmentation” of the high-frequency computing market (mobile, desktop, server, and associated subsegments), a significant proliferation of packaging types tailoring functionality and costs to the different applications specifications can be seen.

The RF front-end module is the core of these systems, and its integration poses a great challenge. Microelectronics technology, since the invention of the transistor, has

revolutionized many aspects of electronic products. The integration and cost path has led the microelectronics industry to believe that this kind of progress can continue forever, leading to the so-called system-on-chip (SoC) approach [1] for all applications. But it's becoming clear that it is still a dream to produce a complete on-chip solution for the novel wireless communication front-ends. Considering the characteristics of the RF front-end modules, such as high performance up to 100 GHz operating frequency, large number of high performance discrete passive components, design flexibility, reconfigurable architecture, low power consumption, compactness, customized product, short time to market, and low cost, the so-called system-on-package (SoP) approach [2,3] has emerged as the most effective means to provide a realistic integration solution. The strength of SoP is based on multilayer technology using low-cost and high-performance materials. Using this 3D topology, high-density hybrid interconnect schemes, as well as various compact passive structures, including inductors, capacitors, antennas, and filters can be directly integrated into the substrate. Thus, high-performance modules can be implemented while achieving simultaneously cost and size reduction.

In Section 1, we will give some background information on electronic packaging, including its evolution and the key driving forces. In Section 2 we will give further details on the current packaging technologies at the chip level and the board level. In Section 3 we will describe the so-called RF SoP concept and its application to the RF front-end module integration. Examples of practical implementation and futures trends will also be given. The modeling and the optimization techniques enabling fast and accurate designs will also be described.

1. BACKGROUND

Electronic packaging has been one of the greatest challenges of the semiconductor industry. The primary function of a package is to provide a means for electrical connectivity from the semiconductor device to a printed wiring board (PWB), also known as a printed-circuit board (PCB). It provides a path for power to be applied to the chip as well as a way for the data signals to be transmitted into and out of the chip. Its secondary function is to house and protect the fragile chip from harsh environmental conditions, such as moisture, light, and dust, that might hinder its performance. Finally, the package provides a pathway for dissipating the heat generated by the semiconductor device. This last function is becoming increasingly important and significantly more difficult to achieve at the beginning of this twenty-first century, as new applications require integrated circuit complexity, operating frequencies, and power consumption to reach new height [4]. Inherently, it is a synergy of various different factors (electrical, mechanical, thermal, material) that have to be considered during an accurate design and fabrication process, as shown in Fig. 1.

The major driving forces for the RF and wireless packaging technology are

- Material, Manufacturability and Cost
 - Materials: ceramic versus organic
 - Manufacturability depending on process control, cycle time, reparability, equipment downtime, design tolerances
 - Costs from fabrication, testing, rework, tuning (if required), yield loss

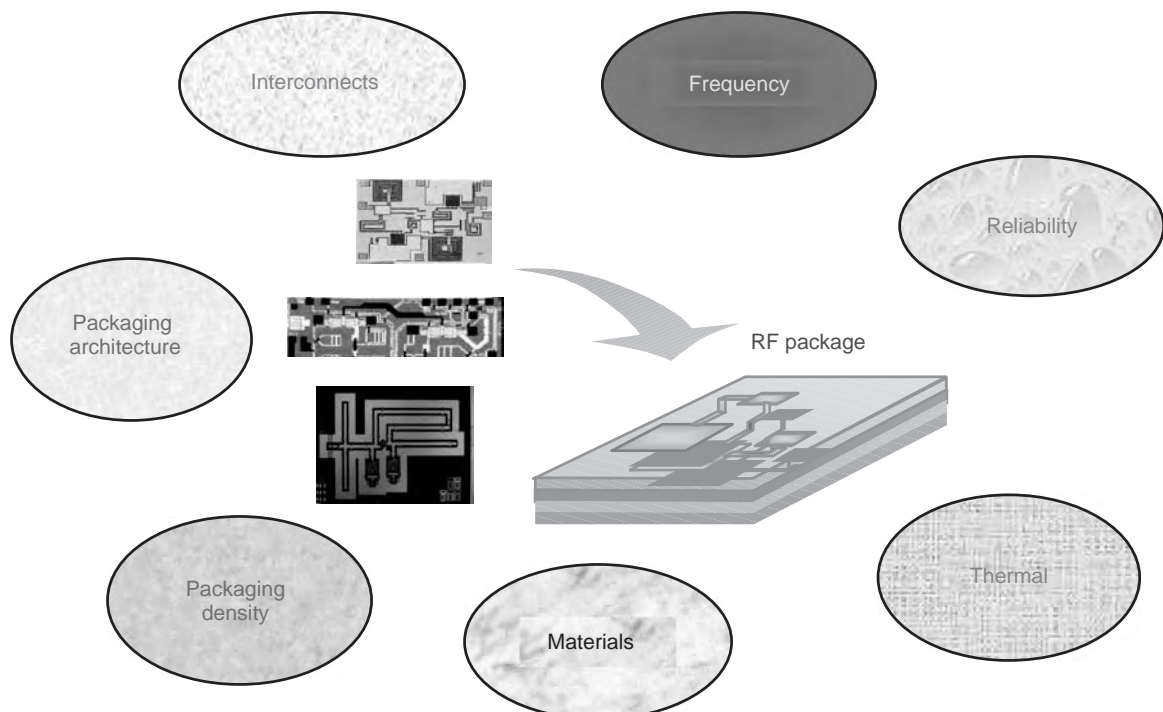


Figure 1. Critical factors along the design cycle of an RF package. (This figure is available in full color at <http://www.mrw.interscience.wiley.com/erfme>.)

- Electrical Design
 - Connectors, which play a dominant role in determining performance limits (each connection has parasitic capacitance, resistance, and inductance that limit speed, potentially distort signals, and add noise)
 - Interconnect density, 2D or 3D routing, crosstalk, transmission loss (resistive and radiation)
 - Matched impedances
 - Low ground resistance
- Thermal Design. The objective is to remove the heat from the junctions of the ICs by (1) preventing dopants from moving and (2) avoiding self-heating effects
 - How to remove heat (from the front or backside of the IC)
 - Thermal conductivity of the substrate
 - Forced air, liquid cooling, monophasic cooling, dual-phase cooling
- Reliability / Mechanical Design
 - Susceptibility to thermal stresses induced by CTE mismatch
 - Tensile modulus (“stiffness”)
 - Hermeticity
- Testability. There are two types and two phases:
 - On wafer: (1) in-process testing (nondestructive); (2) stress/reliability testing (destructive)
 - On MCMs: (1) substrate; (2) assembled module

1.1. 1970–1995

The original package devices were typically large. They were connected to the outside world by means of long leads, or pins that needed to be inserted through holes in the printed-circuit boards (PCBs). These devices came to be known as “through-hole” devices for that reason and were made of metal, ceramic, and plastic. The most predominant of these packages in the 1970s and 1980s was the dual-in-line package (DIP) [5], which is still in use today. The DIP’s main limitation was the lead count with an upper limit of 64 pins. After that point, the package simply became too large for any practical applications. A solution to this was the pin grid array (PGA) [6], which was using a two-dimensional array of pins protruding from the bottom of the package. The PGA package could have around 200 pins on average.

The main problem with through-hole devices was their size. Furthermore, despite recent improvements [7], their performance at high frequencies was quite limited. The trend in PCB manufacturing was to increase density while decreasing board area and increasing signal frequencies. Through-hole devices did not easily allow this to happen. In the 1980s, through-hole devices began to give way to a new packaging technology called *surface mount technology* (SMT) [8]. The leads from these packages were mounted directly to rectangular pads on the surface of the PCBs and did not require holes to be drilled into the PWBs. As a result, the width of the leads could be smaller and the

spacing between the leads (lead pitch) could be decreased. This allowed for a package with the same number of pins as a traditional through-hole device to be significantly smaller, despite the fact that both devices were made with the same materials. Common surface mount devices included the plastic leaded chip carrier (PLCC) and the small outline integrated circuit (SOIC). More recently, the quad flat pack (QFP) has become a predominant fine-pitch, high-lead-count package solution. Figure 2 illustrates most of the previous topologies, and Fig. 3 shows some popular packaging devices used through the 1980s and 1990s.

Both through-hole and surface mount devices mentioned above were connecting the silicon chip to the external package leads by means of a process known as *wire bonding* [9,10]. Very fine wires were attached directly to the silicon chip at one end and connected to the package leads at the other end. This process has been very well understood in the semiconductor industry and can be performed with very high yield for very low cost. It does, however pose problems, as I/O count, density, and operating frequencies increase and package lead pitch decreases. Another process for connecting to the outside world is tape-automated bonding (TAB) [9].

1.2. 1995–Today

Today, as semiconductor technology continues the mini-mization trend, the level of complexity on a single silicon chip is becoming greater and greater. This leads to more functionality in a smaller area, higher I/O counts, higher frequencies, and higher heat dissipation requirements. All the technologies listed up to this point have been inadequate and impractical to satisfy all of these requirements. This is not to say that they do not still have a place in modern integrated circuit design, but they will not meet the needs of leading-edge technologies and, in particular, in the case of very demanding high-frequency performance, such as that of RF and millimeter-wave integrated systems. So, new packaging technologies have emerged since the mid-1990s that are aimed at solving the I/O, frequency and heat challenges.

The first generation of these solutions continue to use the same wire bonding technology used in traditional packages, while accommodating advances in interconnect technology. Flip-chip technology [also called *direct chip attach* (DCA)] has emerged as a possible alternative to wire bonding [11]. Regardless of the interconnect technology, the most promising packaging technology being pursued at the present is the ball grid array (BGA) package, which is a descendant of the pin grid array (PGA) package discussed earlier. Instead of through-hole pins, the BGAs have small conductive balls that are soldered directly to the surface of printed-circuit boards. As the balls are located on the bottom of the package, an obvious disadvantage is the inability to visually inspect the connections between the package and the PWB. As a result, the assembly process for PWBs using BGA technology must be very precise with very low tolerance for error. Its advantages in I/O count, I/O density, and heat dissipation easily outweigh this somewhat minor disadvantage [12].

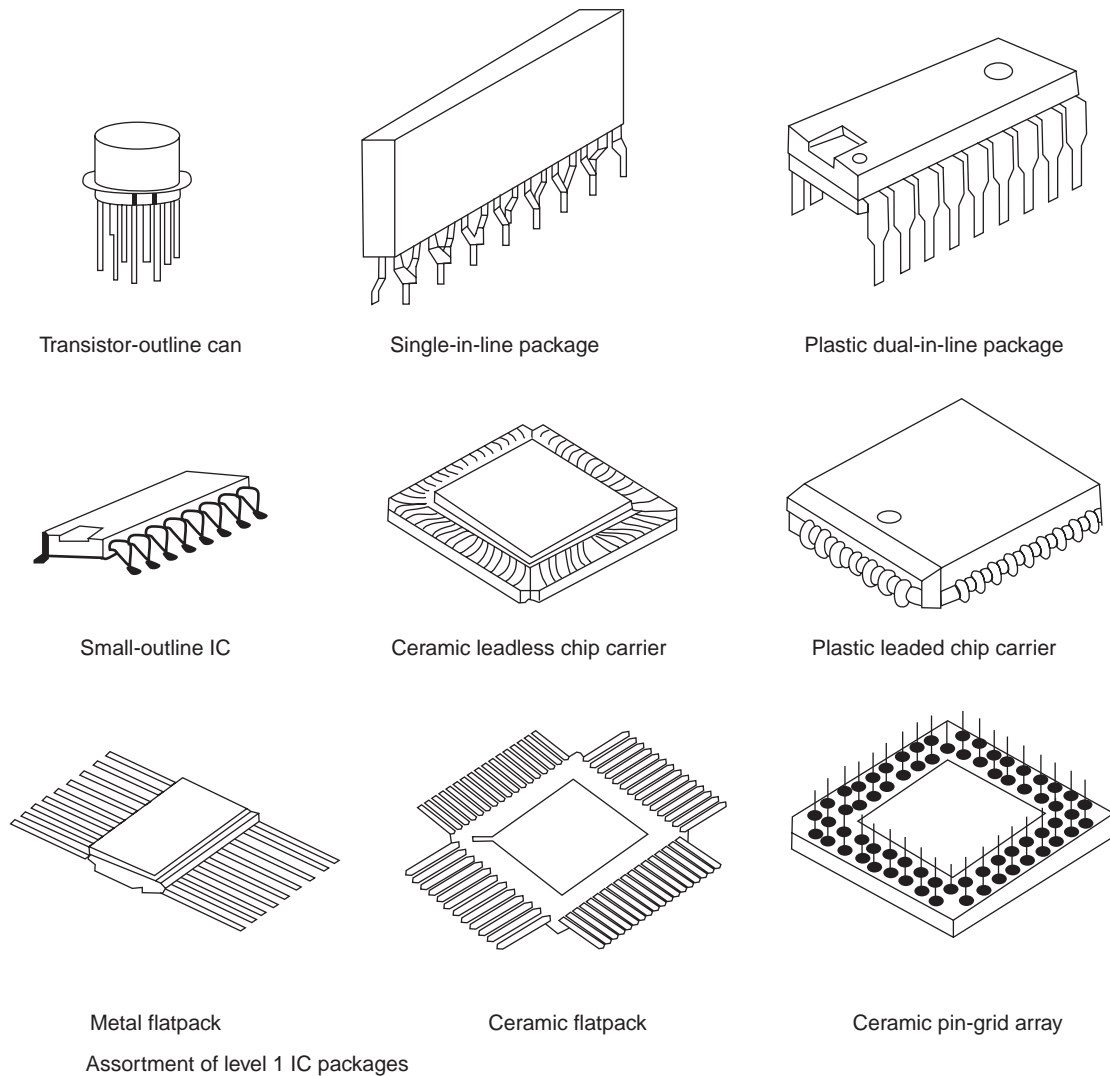


Figure 2. Various packaging topologies.

In 1999, the Semiconductor Industry Association (SIA) released *The National Technology Roadmap for Semiconductors* [13]. According to SIA, the increase in total I/O and I/O density, as packaging has evolved from PGA through QFP and now to BGA, has been quite dramatic, but represents only a first step along the required growth path. Growing at an average compound rate of 12.6%, high-performance package I/O has reached 2800 by the year 2004. Commodity products, while growing at a less aggressive 8.2% rate, require over 400 I/O. In the future, cost will be more than ever the driving factor. It is expected that packaging costs per pin will continue to decrease in the coming years, but the overall packaging pin count is expected to increase at a faster rate than the cost decrease. The increase in pin count is also expected to affect the substrate and the system-level costs. Packaging geometries are often classified in two independent areas of focus: single-chip and multichip packages. It is expected that devices such as QFPs will reach a maximum lead count of 300 and lead pitch will reach a minimum of 0.5 mm [9]. After this point, the package body size and

the surface mount assembly complexity become cost ineffective and multichip solutions have to be investigated.

Also, these recent years have highlighted the thermal management as a significant challenge. As a result, handheld or portable devices that do not use forced air and rely on the operator's hand to dissipate the heat from the unit need new heatsink technologies and materials with better thermal conductivity. On the other hand, the cost-performance market (desktop processors) requires forced-air cooling. Flip-chip could be a possible enhancement to the forced-air cooling as the backside of the silicon chip provides a "direct, efficient heat path from the chip to the heatsink." Existing heatsink solutions are predicted to be ineffective above 50 W in applications where forced air is not a viable solution because of market requirements. A reduction of internal thermal resistance and better air cooling techniques are critical for thermal solutions. The high-end market, with predicted power consumption between 110 and 120 W per chip, will pose an even greater challenge necessitating a closed-loop cooling system that meets market and customer requirements. In general,

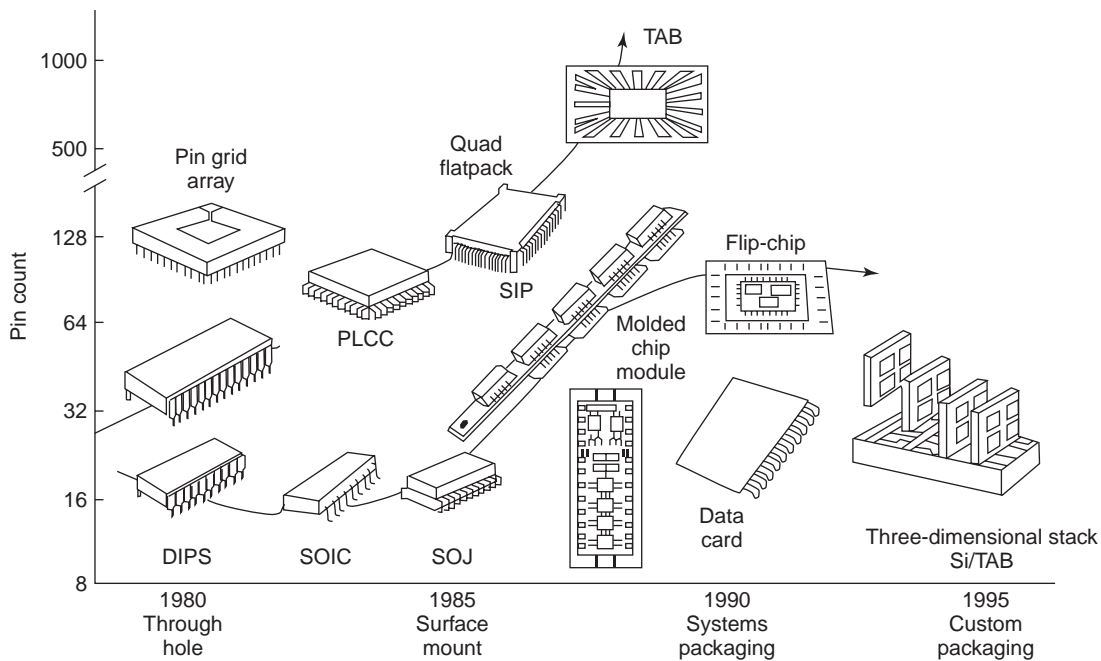


Figure 3. Popular packaging devices used through the 1980s and 1990s [9].

flip-chip is predicted to become the predominant technology for chip-to-next-level interconnect, since it enables the reduction of a level of interconnect. Commodity products will continue to use advanced forms of wire bonding until the cost of flip-chip becomes affordable for that market. Another important challenge is the matching of the coefficient of thermal expansion (CTE) between the silicon chip and the substrate. When using organic substrates, underfills will be required with high reliability, ease of manufacturability, stronger attachment at the interface, and higher resistance to moisture. Liquid-crystal polymers (LCPs) with engineered CTE could be a solution [14].

2. CURRENT PACKAGING TECHNOLOGIES

2.1. Chip Technology

2.1.1. Ball Grid Array (BGA). BGA packages allow for PWB space savings since an array of solder bumps (or

balls) is used in place of traditional package pins. The bumps have the advantage of shorter electrical patch to the motherboard, which improves the electrical performances at high frequencies. Also, they occupy a smaller area on the board for the same I/O count, while providing finer pitches and lower cost. Micro-BGA (μ BGA) is a chip-scale package that uses much smaller bumps than the traditional BGA. A typical BGA solder ball is 500–750 μ m in diameter and has a 1000–1250 μ m pitch, while a typical μ BGA NiAu ball is 50–100 μ m in diameter and has a 500–750 μ m pitch. An example of a BGA package developed for millimeter-wave application is presented in Fig. 4.

The BGA is made of an alumina substrate that acts as a carrier for the chip. Through-hole vias (signal, ground, and thermal) are realized by laser drilling and are filled with a CuW alloy. Thin-film metal (copper or gold) are deposited and patterned on both sides. Then the substrate is bumped with BGA or μ BGA balls. The chip is directly wired bonded on top of the substrate.

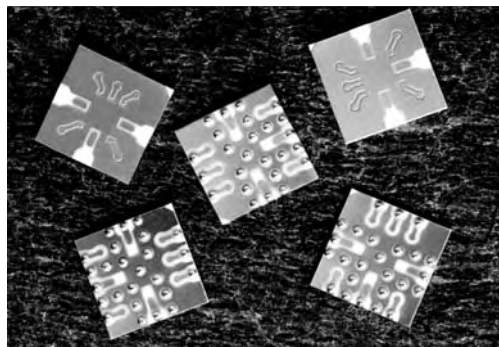
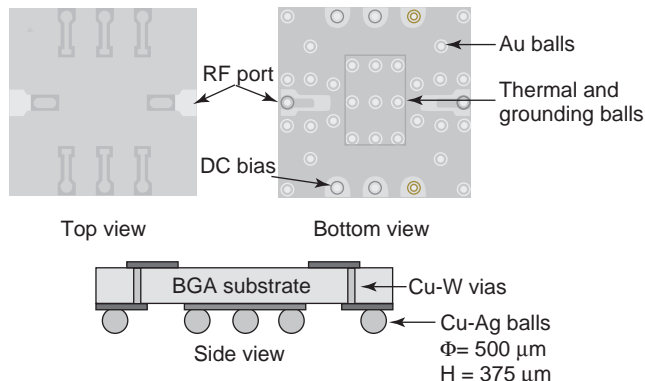


Figure 4. BGA package for millimeter-wave applications. (This figure is available in full color at <http://www.mrw.interscience.wiley.com/erfme>.)

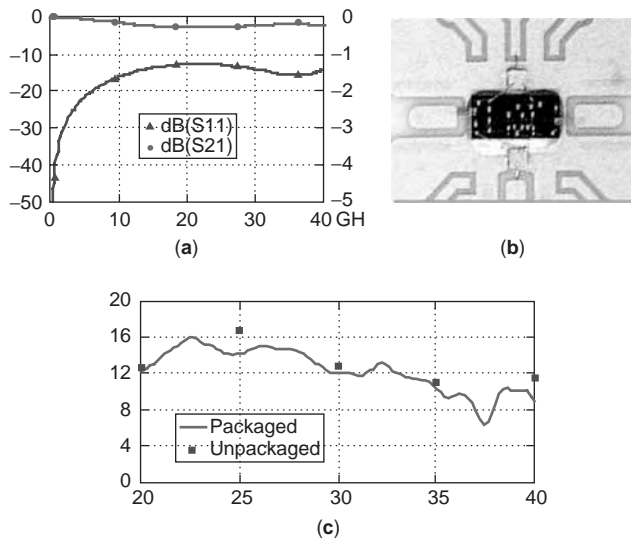


Figure 5. (a) Millimeter-wave performance of a single BGA transition; (b) 20–40 GHz wideband HP GaAs PHEMT MMIC amplifier on a BGA package; (c) millimeter-wave performance of the packaged amplifier. (This figure is available in full color at <http://www.mrw.interscience.wiley.com/erfme>.)

BGA and μ BGA packages have become more increasingly popular since the early 1990s for high-frequency applications up to 20 GHz. For the growing wireless communications systems operating at millimeter-wave frequencies such as local multipoint distribution services, BGA and μ BGA packages have also exhibited, with a proper transition design, excellent performance above 30 GHz. A single transition can exhibit an insertion loss of >0.3 dB at 36 GHz as shown in Fig. 5a. A 20–40-GHz wideband HP GaAs PHEMT MMIC amplifier mounted on a BGA package using conductive epoxy is shown in Fig. 5b. A comparison of performance (gain performance is depicted in Fig. 5c) of bare die and the package amplifier confirms that the BGA is a low-loss package and is applicable for millimeter-wave frequencies.

An example of a BGA applied to a 3D integrated module concept is presented in Fig. 6 [16]. In the proposed module concept, two stacked LTCC substrates are used and board-to-board vertical transition is insured by μ BGA balls [17,33]. Standard BGA balls ensure interconnection of this high-density module with a motherboard such as FR4 board. The top and the bottom substrates are dedicated respectively to the receiver and transmitter building

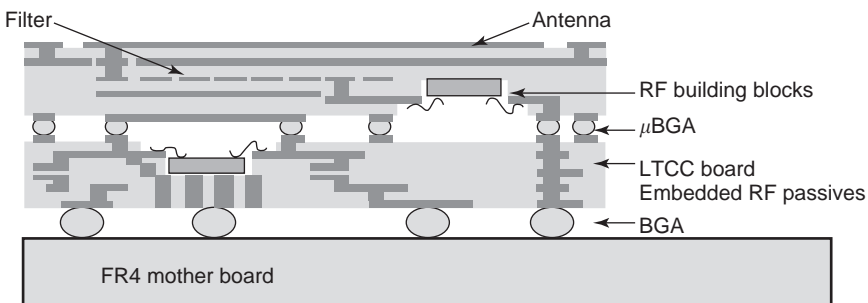


Figure 6. 3D integrated RF front-end module concept view using BGA and μ BGA. (This figure is available in full color at <http://www.mrw.interscience.wiley.com/erfme>.)

blocks of the RF front-end module. The two parts are separated by the μ BGA “layer” to improve the crosstalk performance of the module.

Ball grid arrays are expected to be the solutions for packages requiring over 200 pins and will be implemented using wirebonding in the lower I/O density parts and flip-chip in the higher-I/O-count and higher-power devices. Ultra-fine-pitch (UFP) wirebond technology will allow for a larger die to be placed on smaller substrates and effective pad pitches below $60 \mu\text{m}$. It is expected that increasing circuit density will enable the accommodation of more than 1000 I/Os and die shrinkage (size reduction) by 20–50%. Placing a larger die with more functionality on a smaller substrate results in significant cost savings, as the substrate is a driving factor in the cost of the device. Recent (as of 2004) trends indicate that I/O counts for leading-edge devices grow at a rate of approximately 10 times every 14 years.

Liquid encapsulant underfills will likely be needed to relieve the stress due to CTE differences between the chip and the BGA package substrates. Chip-scale packages using fine-pitch μ BGA with a size in the order of the chip size will be the next level of advancement for applications where low weight and small package size are required. As the technology matures and processes become cheaper, BGAs have the potential to become the workhorse of packaging technologies, as the DIP was for the 1970s and 1980s.

2.1.2. Flip-Chip Technology (FCT). Flip-chip is a technology dating back to the 1970s that matured in the late 1990s as a widely accepted and cost-effective method for the semiconductor industry, especially for high-frequency applications [18]. The term “flip-chip” refers to flipping a silicon die or chip and mounting it face down on a substrate. A typical flip-chip bump is $25\text{--}50 \mu\text{m}$ in diameter and has a $50\text{--}100 \mu\text{m}$ pitch. A schematic of a flip-chip transition from coplanar waveguide (CPW) to coplanar waveguide is presented in Fig. 7.

Of the 60 billion integrated circuits produced in 1998, approximately 1.5% of them were manufactured using flip-chip technology. From 1997 to 1998, the number of flip-chip dies grew by 40%. An average annual growth rate of 48% for flip-chip is expected in the near future. The flip-chip capabilities have been extended up to 75 GHz [19,20] and to optical applications using glass bumps that allow for waveguiding of optical waves [21].

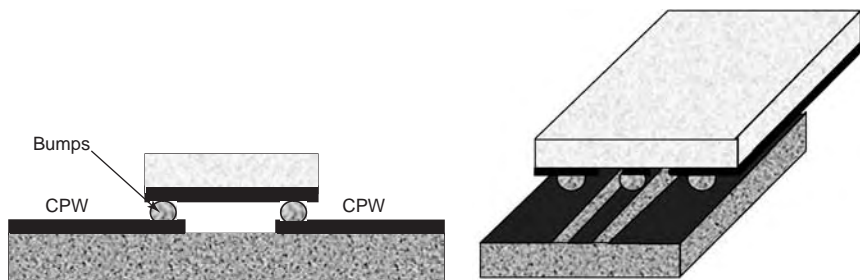


Figure 7. Schematic of a CPW-CPW flip-chip interconnection. (This figure is available in full color at <http://www.mrw.interscience.wiley.com/erfme>.)

An optimized transition for a CPW-CPW interconnect on alumina substrate is presented in Fig. 8a. The stud bumps on the die are soldered to the mounting substrate as shown in Fig. 8b. The optimization of the transition shows insertion loss of >2 dB and a return loss of >20 dB at 75 GHz.

Other issues related to flip-chip design include the presence of the resin underfill, for protecting the die from the environment, alleviating the CTE mismatch between the two substrates and increasing the fatigue life of joints. The resin changes the transition electrical performance and must be taken into account by the IC designer at the beginning of the design process. Also, a very important aspect is the development of scalable lumped-element models for the flip-chip transition. Typical models are presented in Fig. 9.

The capacitor C_1 represents the discontinuity capacitance at the chip, while the capacitor C_2 models the discontinuity capacitance at the motherboard. The inductor

L represents the inductance of the bump, and the resistors model the loss mechanism in the interconnection. For the T model, the capacitance C is due to the overlapping area of the feedline and the flipped chip and L_1 and L_2 model the inductance of the bump. The ultimate goal is to scale the values of the circuit elements with the physical attributes of the interconnection.

2.1.3. Flip-Chip versus Wirebond. Although new packaging and interconnection technologies have been introduced, wirebonding is still dominant in RF and wireless products, especially in applications up to 10 GHz, since it has strong benefits in cost and reliability. However, the stringent specifications of emerging communication systems and the use of higher frequency bands accentuate the drawbacks of the wirebonding, namely, parasitic effects and losses. When wirebonds are used as interconnects in microwave and millimeter-wave modules, they

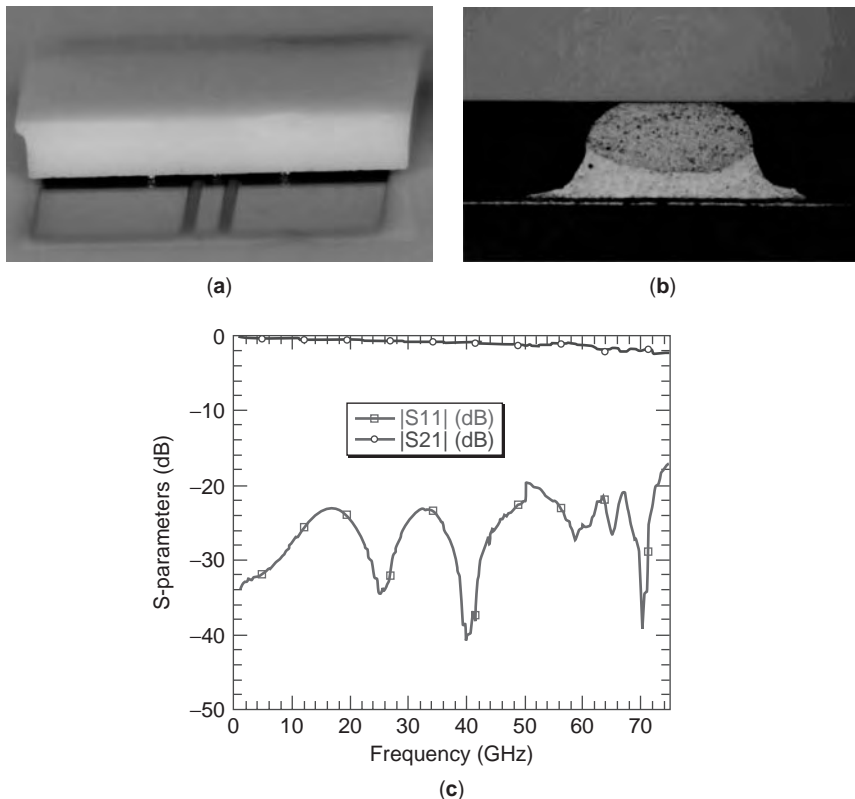


Figure 8. (a) Side view of flip-chip transition; (b) gold stud bump soldered to the substrate; (c) S-parameter results for optimized transition to 75 GHz. (This figure is available in full color at <http://www.mrw.interscience.wiley.com/erfme>.)

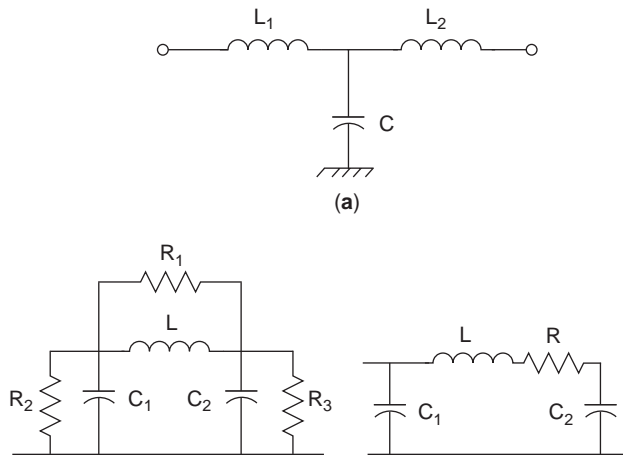


Figure 9. Various model topologies: (a) T model; (b,c) \square models.

exhibit a high characteristic impedance due to the high inductance of the thin wire and a small capacitance due to the small dielectric constant of the airgap between the wire and the ground plane. In addition, radiation loss resulting from wire discontinuity becomes significant, particularly in the millimeter-wave frequency range.

Vertical interconnection solutions have gained a significant interest because they provide features that can eliminate the problems associated with wirebonding: poor repeatability of the manufacturing process and a drastic increase of the losses associated with increased frequency. Along with showing better electrical performance, flip-chip technology allows several chips to be mounted together on the motherboard to increase density, improve system performance, and reduce cost. This packaging technique also allows combination of passive and active devices, Si and GaAs, analog, digital, and optical circuits on the same motherboard [22]. Furthermore, the compatibility with automatic manufacturing improves the reliability and reduces the assembly cost.

In addition to these benefits, since the flip-chip die is flipped upside down, all the chip area is available for interconnect, eliminating the wirebond restriction of having all the I/Os along the chip perimeter. This, along with the short electrical path, which eliminates coupling issues, allows true chip-scale packaging and therefore increased integration levels.

Another important issue in RF packaging structures is the transmission-line choice. The two most common choices for the transmission lines to be used in a flipped, monolithic microwave integrated circuit (MMIC) are microstrip and coplanar waveguides (CPW). Coplanar MMICs are more suited to flip-chip technology because of the immediate availability of all the grounds on one surface. In addition, coplanar circuitry requires no backside processing, eliminates the need for ground vias and allows the use of a thicker, more physically robust chip. Easier matching can be achieved because of the ground–signal–ground configuration. The more recently developed finite-ground coplanar waveguides (FG-CPWs) allow for a miniaturized implementation of these planar lines [23]. On the other hand, microstrip design tools are more mature, and MMIC manufacturers prefer to make full use of their capabilities.

However, thermal performance of flip-chip packages is poor compared to wirebond. Heatsinking is more efficient when the chip is firmly in place on the vertical stackup rather, with no contact with other components other than the interconnecting bumps. The coplanar design of the PCB eliminates the need for the vias, and shunt elements can be easily removed or added if tuning is necessary. From a mechanical reliability standpoint, flip-chip technology still needs to be improved. An underfill technology—to fill the gap between the chip die and board with a dielectric material—has been introduced to improve the heat dissipation and the mechanical stability and to compensate the CTE mismatch. However, it is difficult to apply underfill technology to RF modules, since the additional dielectric loss generated from the underfill material reduces the system efficiency. Moreover, the characteristic impedance of the transmission lines on a MMIC chip is significantly modified because of the higher dielectric constant of the underfill material. To avoid this problem, all MMIC circuits should be designed to compensate for the expected impedance change.

Figure 10 presents a review of the published electrical performance for wirebond, flip-chip and BGA [24]. The test structures used in these analyses are not identical and the individual characteristics are reflected in the S (scattering) parameters. However, it can be observed that flip-chip shows evidence of lower insertion loss over the entire frequency range than the wirebond. On the other hand, the BGA performance is poor compared with flip-chip, as a result of the larger dimensions and the use of more lossy substrates for the motherboard, especially for frequencies above 40 GHz. Similar results have been reported for return loss.

2.1.4. Chip-Scale Packaging (CSP). Chip-scale packaging (CSP) is generally considered the fundamental

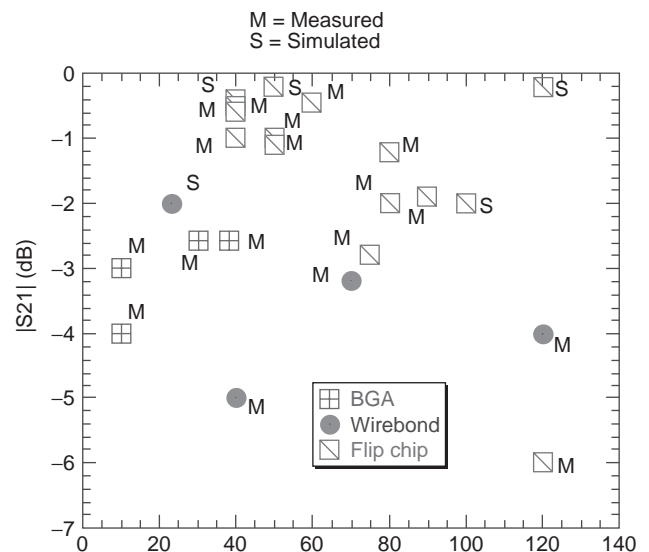


Figure 10. Electrical performance comparison between flip-chip, wirebond, and BGA. (This figure is available in full color at <http://www.mrw.interscience.wiley.com/erfme>.)

evolution required to meet most of the electronic packaging needs of the twenty-first century [25]. As defined by its proponents, CSP ranges in size from die equivalent area to, at its maximum, 120% of die area. Several configurations now in development include, among others, perimeter pad and leadframe packages, area array interposers, and μ BGAs, with target market segments ranging from low-cost consumer through high-end data processing, and I/O ranges up to 1000.

2.2. Board Packaging: MCM Definitions and Classifications

The term “multichip module” (MCM) refers to the packaging of multiple silicon dies into one device [26,27]. MCMs offer the ability to reduce package pin count by combining two or more high-pin-count devices, that would normally connect to each other at the board level, into one package, where the interconnect is performed at the chip level. The resulting packaged system needs only a reduced set of pins to connect power and signals from the outside world. It can also serve to reduce PWB real estate (an expensive commodity) and exhibits the following advantages:

- Improved performance, such as shorter interconnect lengths between dies (resulting in reduced delay time, lower RF parasitics and losses), lower power supply inductance, lower capacitance loading, less crosstalk, and lower off-chip driver power
- Miniaturization, since MCMs result in a smaller overall package size when compared to separate packaged components performing the same function, hence resulting in significant reduction of I/O to the system board
- Shorter time to market, making them attractive alternatives to ASICs (application-specific integrated circuits), especially for products with short lifecycles
- Low-cost silicon sweep, allowing integration of mixed semiconductor technology, such as SiGe or GaAs
- Hybrid configurations, including surface mount devices in the form of chip-scale or μ BGA packages and discrete chip capacitors and resistors
- Simplification of board complexity by integrating several devices onto one package, thereby reducing total opportunities for error at the board assembly level
- Capability of accommodating a variety of second-level interconnects (while BGAs are the most popular ones, leadframe solutions can be employed for plugability, enabling reconfigurability and modularity for upgrades)

The widespread use of MCMs has been hampered by a few factors. It is a relatively high-cost process. Since not all of the signals are connected to the outside world, package-level testing is difficult, so effort must be made to ensure that the die being put into the chip is good. Obtaining such “known good die” (KGD) is still a challenge. Also, the proliferation of flip-chip, BGA, and chip-scale packages for single-chip package solutions has reduced the need for chip-level system integration.

In the area of multichip packages, the SIA roadmap [13] identifies advancements in the following enabling technology solutions as requirements for the effective implementation of MCM:

- Design tools/simulators (integrated design environment)
- Flip-chip interconnect optimization
- Low-cost high-density substrate manufacturing
- Low-cost known good die (KGD).

These enabling technologies are interdependent and must be selected to be compatible to provide an integrated multichip solution. Bare chips must provide the same reliability, quality, and performance as packaged chips to be considered “known good.” Multichip packages containing two to three chips are in volume production today, and could evolve soon to include three to five chips. The evolution of these multichip packages into multichip modules with more than five chips will be driven by performance and cost requirements at the subsystem and system level, as well as improved chip reworkability and module testing techniques. The implementation and proliferation of multichip packages and modules will continue to be constrained by the availability of high-density substrates and “known good” die commensurate with the necessary cost and performance. Multichip modules will be driven by densification and cost reduction for low-end products and densification and performance for high-end products.

As mentioned above, a key factor in the development of MCM package is the availability of high-density substrates. There exist three commonly used substrate groups [9,26].:

1. *Laminate MCMs (MCM-Ls)*. These are manufactured through the lamination of sheet layers of organic dielectric, and are very similar to traditional PCB technology; in fact, the dielectric layers and the interconnects are developed in much the same way as for laminated printed-circuit boards. The line geometries and via diameters are typically half or less the size of those found in traditional circuit boards. These MCMs exhibit very low line losses up to relatively high frequencies because the lines are thick and wide; however, the vias are typically quite tall and also much wider than the lines, thus causing substantial impedance discontinuities and wavefront reflections for frequency components. A very special care has to be given for designs above 500 MHz.

2. *Ceramic MCMs (MCM-Cs)*. These MCMs are manufactured by stacking unfired layers of ceramic dielectric (i.e., in their flexible, unfired state), onto which liquid metal lines are “silk screened” using a metal ink process. The individual inked layers are then aligned, pressed together, and “cofired” at 800–900°C, or 1500–1600°C (depending on the composition of the ceramic material) into a solid planar structure, onto which integrated circuits can be installed. These MCMs can, if fabricated with excellent dimensional tolerance control, exhibit low line losses. They are for these reasons very popular for the integra-

Table 1. Comparison of MCM Technologies

Characteristic	MCM-L	MCM-C	MCM-D
Minimum linewidth (mm)	60–100	75–100	8–25
Line spacing (mm)	625–2250	125–450	25–75
Via diameter (mm)	300–500	100	8–25
Cost (\$/cm ²)	3–30	50–1000	800–8000

tion of high-frequency systems up to the millimeter-wave frequency range [28,29].

3. *Deposited (MCM-Ds)*. These components are manufactured through the deposition of organic or inorganic dielectrics onto a silicon or alumina support substrate. After each dielectric layer is deposited, one of several techniques is used to pattern metal lines as well as metal “vias” that penetrate the dielectric layers to connect adjacent metal layers. The chips are then installed on the upper surface, and attached electrically through wirebonds or other means such as tape-automated bond structures, or even by mounting the chips face down on the surface, with metal balls serving as the electrical connections between the chip and matching pads on the MCMs. The MCM-D line cross sections are typically smaller than for MCM-Cs or MCM-Ls, resulting in higher interconnect density but also higher resistive line losses; however, their via heights are typically quite small, and their via cross sections are equivalent to the linewidth, resulting in low levels of impedance discontinuity and wavefront reflections, in comparison to the MCM-Ls and MCM-Cs.

The different MCM line geometries and their respective cost are compared in Table 1.

In order to optimize cost and performance tradeoffs, the high performance of MCM-D at the low cost of MCM-L are desirable, leading to a hybrid technology called MCM-L/D, where substrate structures are formed as multiple layers of metal separated by dielectric material. Georgia Tech’s Packaging Research Center (PRC) “single-level-integrated module” (SLIM) implementation of the MCM-L/D para-

digim is shown in Fig. 11 [30,31]. This technical vision integrates all the packaging levels into one, containing layers for DC power distribution, high-density high-speed digital circuitry, embedded decoupling capacitors and termination resistors, embedded multilayer RF passives (i.e. inductors, filters, antennas), embedded optical waveguides, built-in MEMS devices, and built-in thermal management.

3. RF SoP MODULES

The dawn of the twenty-first century is witnessing a tremendous demand for wireless (untethered) communications services such as paging, analog, and digital cellular telephony, and emerging Personal Communications Services (PCS). Current commercial cellular and PCS systems are concentrated at frequency bands around 900 MHz and 1.8 GHz (S band); future allocations for PCS systems are expected around 2.4 and 5.8 GHz (through C band). Beyond the arena of mobile communications, there are numerous wireless applications, including RF identification (RFID), satellite communications, local multipoint distribution systems (LMDS), and wireless local-area networks (WLANs) operating at frequencies extending into the millimeter-wave regime (Ku to Q bands). The move to higher frequencies has been motivated by the need for more and more bandwidth for multimedia applications such as wireless real-time video transmission and internet access, and by the increased overcrowding of the lower frequency bands.

This rapid expansion of untethered communications services, along with the need for low-cost, high-efficiency system implementations, has led to an explosion in the development of integrated circuit approaches in the RF/microwave area. Highly integrated components such as frequency converters, low-noise and power amplifiers (LNAs and PAs), and frequency synthesizers are now commonplace, replacing hybrid circuits employing discrete semiconductor devices. These radiofrequency integrated circuits (RFICs) and monolithic microwave integrated

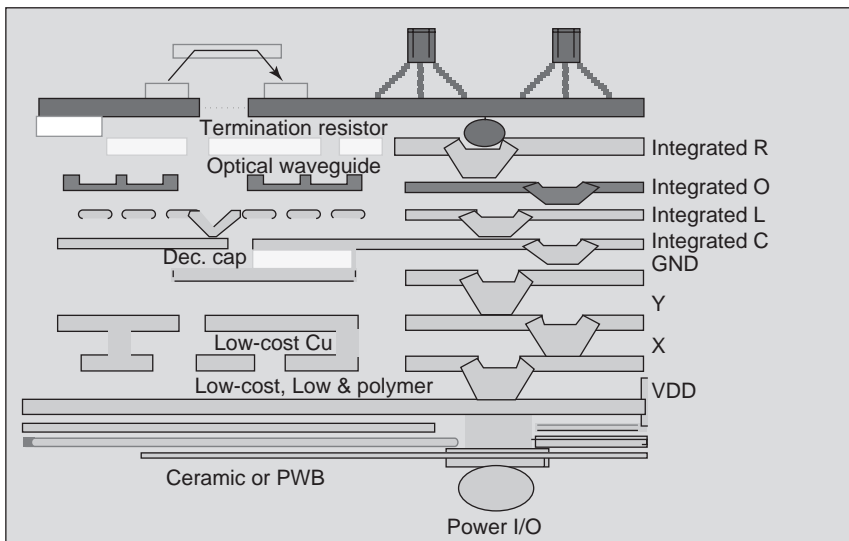


Figure 11. Georgia Tech’s Packaging Research Center (PRC) “single-level-integrated module” (SLIM) implementation of the MCM-L/D. (This figure is available in full color at <http://www.mrw.interscience.wiley.com/erfme>.)

circuits (MMICs) are generally packaged together with VLSI digital signal processing (DSP) and microprocessor (μ P) control chips on multilayer printed-circuit boards (PCBs). However, the system-on-chip movement has been ambushed by the cost of additional mask layers needed to marry digital logic with memory and analog function on one specific and optimum substrate. Therefore, many believe that the system-on-package (SoP) approach for the next-generation wireless solution is a more feasible option than system-on-chip (SoC), considering the obstacles faced today by SoC developers. The more recent development of materials and processes in packaging areas makes it possible to bring the concept of SoP into the RF world to meet the stringent needs in wireless communications. RF SoP is intended “to provide a complete packaging solution for RF module by integrating embedded passives components and MMIC at the package level.” SoP goes one step beyond MCM by enhancing overall performance and adding more functionalities. Wireless devices implementing complex functionality require a large amount of circuitry and consequently require a large conventional package or multichip-module (MCM) real estate. 3D integration techniques using multilayer high-density architectures in different technologies with vertical interconnect and embedded component integration are crucial for the design and development of a single package to a MCM. SoP is the art of bringing together at the system-level integrated circuits and embedded components following a codesign philosophy.

A strong alternative to complete single-chip integration is some advanced form of an MCM solution such as the one proposed in Fig. 12. It integrates antenna, filters, resonators, baluns, and other RF components. The multilayer 3D architectures have the major benefit of high integration

and compactness, while adding another degree of freedom in the module design. The materials suited for this technology include low-temperature cofired ceramic (LTCC) and high-temperature cofired ceramic (HTCC) [32], multilayer organic and LCPs (liquid crystal polymers) [33].

The basic philosophy here is to fabricate devices and circuits in the optimum available technology for their particular function (e.g., digital circuits in submicrometer CMOS, analog components in BiCMOS, RF components in GaAs or InP) and then integrate them into a system or subsystem using MCM technology. High-*Q* passive structures could potentially be embedded directly into the MCM structure. Multibeam antenna beamforming networks have been demonstrated in MCM technology. For the active analog/RF and digital/DSP functions, individual ICs can be interconnected using flip-chip bonding to eliminate bondwires (and their associated parasitic) and allow more compact MCM floor planning. An additional benefit of this approach is that complete system redesign is not necessarily needed to change one part of the subsystem/module; individual functional component dies could be upgraded as long as their interconnection scheme and footprint were kept the same to remain compatible with the MCM layout. This approach is referred to as “system on a package” (SoP), in contrast to “system on a chip.” The incorporation of MEMS, smart materials, smart antennas, and other components with mixed-signal integrated circuits in such an environment is now increasingly referred to as “mixed-technology” or “heterogeneous” integration.

To explain further the SOP concept, a general system configuration of a wireless transceiver is shown in Fig. 13. The module is composed of an MMIC chipset: power amplifier (PA), low-noise amplifier (LNA), up/down mixer (MIX), and voltage-controlled oscillator (VCO), and

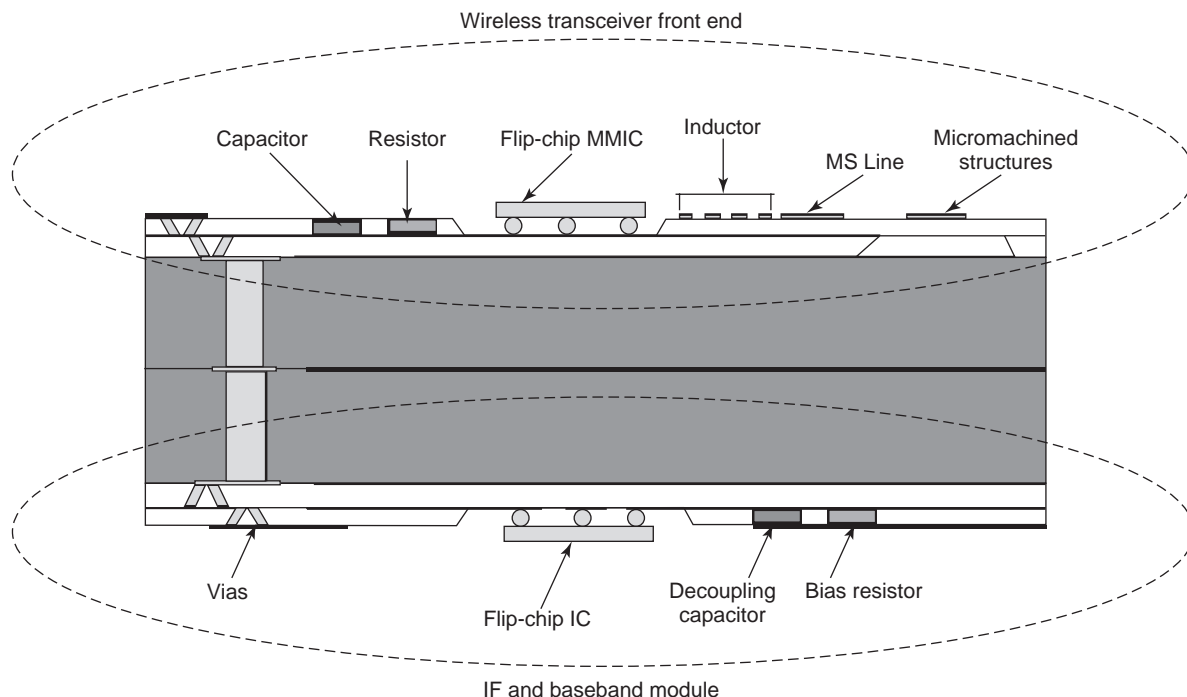


Figure 12. Advanced MCM solution for gigabit wireless module.

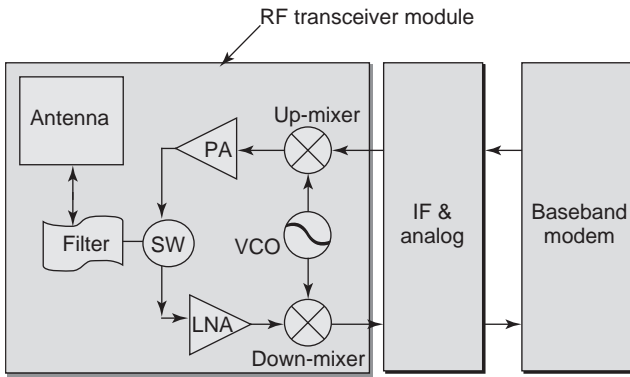


Figure 13. Block diagram of a typical RF front-end architecture.

passive components such as a filter, antenna, and external high- Q discrete passive elements for stringent blocks such as PA and VCO. The RF SoP approach includes replacing the discrete passives with embedded ones, adding more functional blocks, such as baluns and antennas, to the module and maximizing the performance of the MMIC chipset by replacing the on-chip passives with high- Q passives embedded in the package.

Figure 14 shows the technical mapping for ongoing and future RF SoP approach. It is important to note that the choice of the on-chip or off-chip (on-package) passives is dependent on the frequency band, modulation scheme, available device and packaging technology, such as the required linearity and efficiency of the PA. In VCO, the need for high- Q inductors on package is determined by the stringent phase noise specification that is coming from the modulation scheme.

Briefly, the advantages of RF SoP are

- Lower cost by using embedded passives instead of discrete components
- Flexibility for MMIC designers by embedding the high- Q passives in the package
- Minimum loss and parasitic effects by reducing the number of interconnections
- Size reduction by adopting multilayer packaging
- Easy-to-realize multifunctional RF modules in a single package

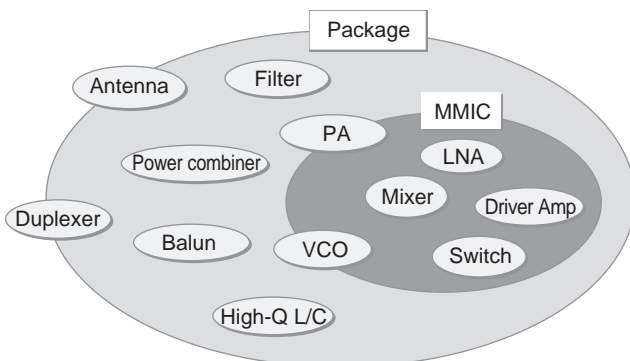


Figure 14. Technical mapping for the RF front-end SOP implementation.

- Better high-power-handling capability than MMIC chip

However, the SOP approach has various problems that are currently addressed by various research groups in the world:

- Interference between the blocks in the package
- Too many degrees of freedom in multilayer packaging to build design library
- Size constraint if antenna is included in the package

3.1. RF Front-End SoP Integration

3.1.1. SoP Integrated Passive. One of the key elements to be integrated in the RF front-end is the bandpass filter. An SoP integrated multilayer filter offers a more attractive implementation than do on-chip and discrete filters. An RF image-reject filter can be implemented with six layers of LTCC in a stripline configuration, whose three-dimensional view is illustrated in Fig. 15 [34]. Layers 6 and 0 are the top and bottom metallization which serve as the top and bottom ground planes. Two shunt inductors L_1 and L_2 were realized by the U-shaped strips fabricated on layers 4 and 3, which are located two and three layers underneath the top ground plane, respectively. The ends of the strips are connected to both grounds through vias. There is no metallization between layers 4 and 6; therefore, the top inductor strip on layer 4 is $180\ \mu\text{m}$ (two layers) away from the top ground plane while the bottom strip is 270 (three layers) away from the bottom ground plane. The required mutual inductive coupling is achieved by overlapping the L_1 and L_2 strips, which are one layer ($90\ \mu\text{m}$) apart. MIM capacitors with electrodes on layers 4 and 3 laid out beside the inductor strips were utilized to implement C_I and C_O . The V_{IC} topology was utilized to implement C_S , which is realized by two series capacitors of capacitance $2C_S$. Each of these capacitors is implemented in V_{IC} topology as a parallel combination of two capacitors with a value of C_S . Such implementation ensures the symmetry of the structure desirable for high frequency circuits. If C_S were implemented in MIM topology, the entire structure would not have been symmetric. The bottom plates of C_I and C_O are used as the top plates of the V_{IC} extended to layer 2 through via connections. The “dumb-bell”-shaped trace is inserted on layer 2 between layers 3 and 1 as the bottom plates of the V_{IC} . The extended top plates of the V_{IC} on layer 1 are used as the top MIM electrodes for the shunt capacitor C_R with the bottom ground on layer 0 as the bottom electrode. The filter prototype is given in the photograph in Fig. 16. Figure 16 also gives the measured insertion loss of 3 dB at 2.4 GHz with 40 dB rejection at 2 GHz.

3.1.2. RF SoP Integrated Module: 5.8-GHz OFDM. The integration of the antenna with the RF front-end in compact modules is one of the major challenges for the SoP implementation [35,36]. The size of the conventional patch antenna ($\lambda/2$) is often too large to be integrated with the rest of the module because it would unnecessarily increase the size of the entire system. Various approaches have

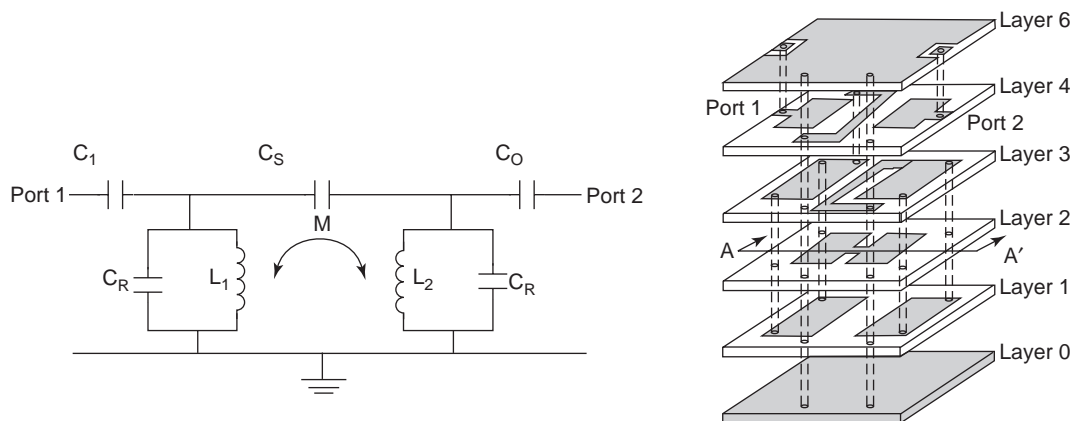


Figure 15. Configuration and 3D SOP filter.

been proposed for the miniaturization, the suppression of parasitic backside radiation (crosstalk) and the realization of multiband/multistandard antennas [37]. The concept view of the 3D integrated transceiver module with an antenna for 5.8 GHz is presented in Fig. 17. Three different multilayer subsystems—specifically, the transceiver, the filter, and the antenna—are vertically stacked and connected through vertical vias. The antenna and filter can be directly fabricated on the module using LTCC or LCP technology in order to reduce size and interconnection losses. The presented module has been designed for 20 LTCC layers. Before designing each of the embedded passives, the layers have been properly assigned. The antenna, filter, and transceiver utilize 8, 10, and 2 layers, respectively. The total size of the module is 14 × 19 × 2 mm, including all the RF functional blocks. The grounds are connected efficiently to suppress the unwanted parasitic modes. A photograph of the integrated module is shown in Fig. 17 [2].

To utilize the space of the module effectively, the geometries of the passive components are chosen very carefully. Also, innovative shielding solutions are currently investigated using metallized cavities [38] or electromagnetic bandgap (EBG) structures [39] as well as advanced simulation platforms to predict and minimize electromagnetic

interference and crosstalk within the different components of the module. In particular, electromagnetic bandgap (EBG) topologies are also used to confine the radiating field of antenna elements, therefore leading to more efficient isolation of the rest of the module, while achieving a reduction of size of the antenna, as was described in the above paragraph. Also, new design approaches based on optimization algorithms such as design of experiments (DoE) [40], feedforward neural networks [41], and genetic algorithms [42] are extensively studied and used to generate comprehensive models taking into account the fabrication and layout parameters and their impacts on electrical performances in multilayer configurations.

The RF functional blocks, including PA, LNA, mixers, and VCO, are attached on the top of the LTCC board. The specifications of the functional blocks are determined and verified through system simulations based on the IEEE 802.11a standard.

A two-section coupled stripline filter has been designed to be embedded inside the LTCC package with its input and output ports connected to the antenna and the duplexer switch through vias. A schematic view and measured performance are presented in Fig. 18. Coupled lines have been bent to fit into the module shape and via walls are used to connect ground planes and reduce

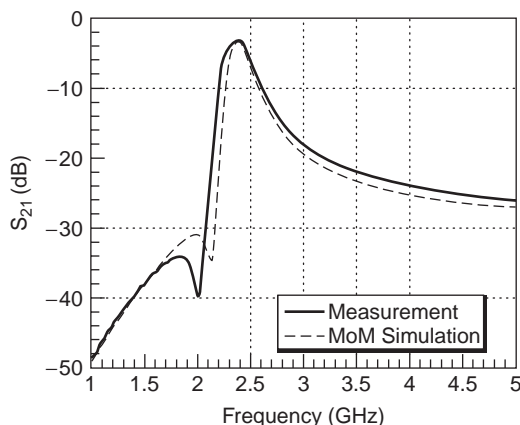
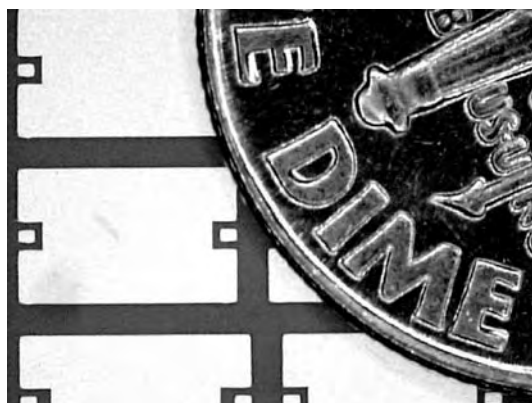


Figure 16. Photograph and measured and simulated insertion losses of the 3D SoP filter. (This figure is available in full color at <http://www.mrw.interscience.wiley.com/erfme>.)

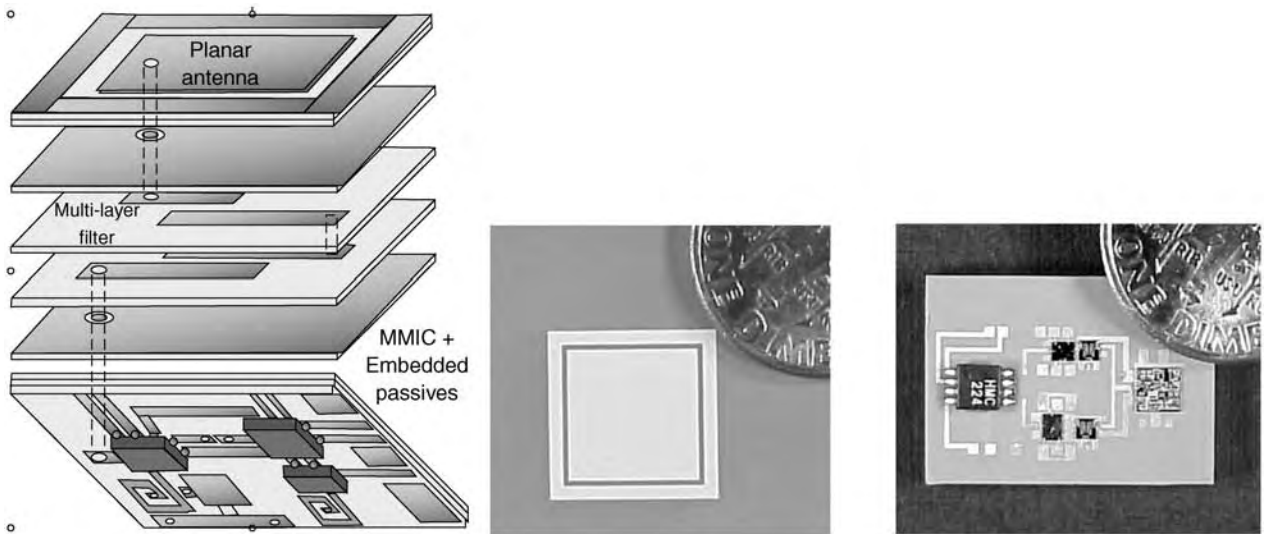


Figure 17. 3D integrated LTCC RF front-end module for 802.11a WLAN. (This figure is available in full color at <http://www.mrw.interscience.wiley.com/erfme>.)

parallel-plate modes. Filter performances have been measured separately and exhibit a -2.9 dB insertion loss, -20.8 dB return loss, and image rejection greater than -20 dB as shown in Fig. 19b.

A cavity-backed stacked-patch antenna (CBPA) has been designed for the module. Introduction of the “soft and hard surfaces” idea has allowed for further miniaturization of the antennas [43]. This antenna has been designed for IEEE 802.11a 5.8 GHz band as shown in Fig. 19. The heights of the lower and upper patches (400×400 mils) are 8 and 32 mils, respectively. The 10 dB return-loss bandwidth of the antenna is about 4%, fully covering the required band (5.725–5.825 GHz). Also this antenna has a desirable gain (near 6 dBi) and very low cross-polarization (less than -35 dBi).

Commercial GaAs MESFET processes have been used to implement Rx and Tx chipsets. The Rx chipset consists in LNA, downconverter mixer, and VCO as shown in Fig. 20. The Tx chipset includes a double-balanced diode ring mixer and RF amplifier as shown in Fig. 21.

The LNA gain is about 13 dB, and the LNA noise is about 2.2 dB. Figure 22a shows the output spectrum of the transmitter mixer demonstrating image signal rejection of 11 dBc, and LO-to-RF rejection of 40 dB, across the VCO tuning range between 4.5 and 5.5 GHz. It also shows less than 11 dB conversion loss between IF frequency from DC to 1 GHz. The RF amplifier demonstrates a measured gain of 7 dB as shown in Fig. 22b.

3.1.3. RF SoP Integrated Module: Ku-Band Transmitter.

The implementation of a compact transmitter module is the key issue for higher data rates and broadband transmission applications of satellite communication systems in the Ku/Ka-band range. One obstacle for a compact transceiver module is the large and heavy cavity filter that cannot be easily integrated into the module. A highly integrated LTCC-based transmitter module using GaAs MESFET MMICs for Ku-band satellite communication applications is shown in Fig. 23. [44] The upconverter MMIC integrated with a VCO exhibits a measured

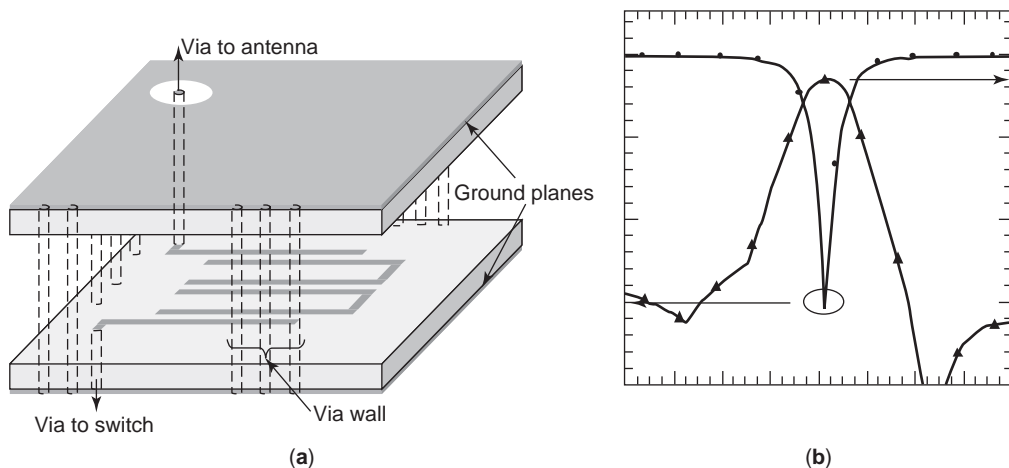


Figure 18. Embedded filter: (a) schematic; (b) performance chart. (This figure is available in full color at <http://www.mrw.interscience.wiley.com/erfme>.)

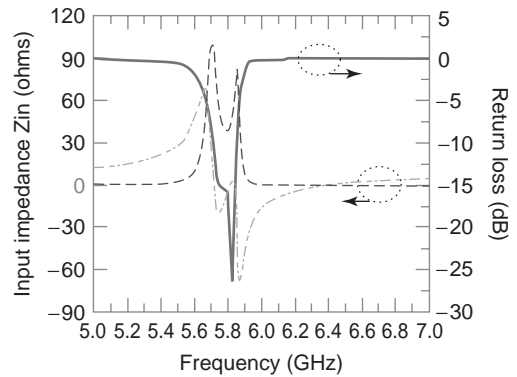
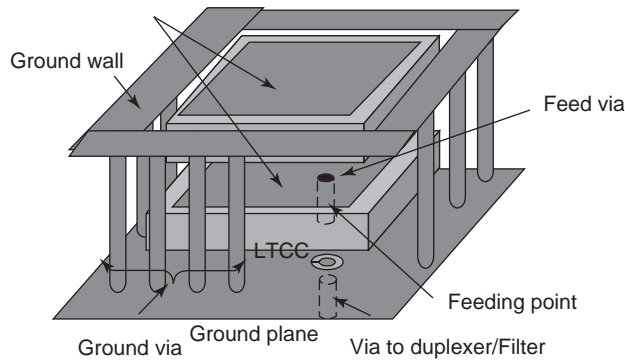


Figure 19. Cavity-backed patch antenna layout and performance. (This figure is available in full color at <http://www.mrw.interscience.wiley.com/erfme>.)

upconversion gain of 15 dB and an IIP3 (third-order input intercept point) of 15 dBm, while the power amplifier (PA) MMIC shows a measured gain of 31 dB and a 1 dB compression output power of 26 dBm at 14 GHz. Both MMICs were integrated on a compact LTCC module where an integrated front-end bandpass filter (BPF) with a measured insertion loss of 1.8 dB at 14.5 GHz was integrated. The bandpass filter for the transmitter module was implemented in a coupled-line filter topology on a multilayer LTCC substrate. The two stripline ground planes are physically connected by vias, and the actual input and output of the filter are connected to the RF amplifier and driver amplifier of the transmitter. Three segment folded edge coupled stripline filters, where the middle segment was deployed perpendicular to the first and third segments for compactness, have been designed to suppress the LO signal at 13 GHz as well as the harmonics and spurious signals. This is a balanced stripline topology where the coupled-line segments are sandwiched by two

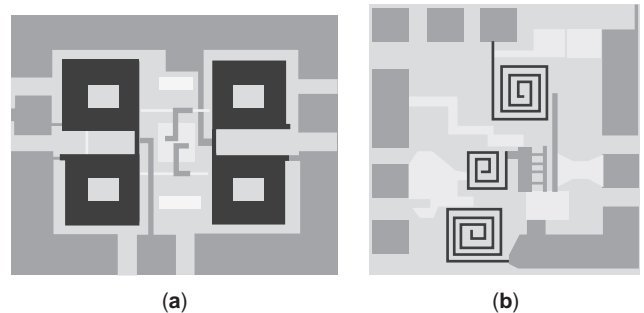


Figure 21. Photo of the Tx chipset used in the module: (a) mixer; (b) RF amplifier. (This figure is available in full color at <http://www.mrw.interscience.wiley.com/erfme>.)

ground planes at an equal distance of 17.5 mils (four LTCC tape layers).

The entire transmitter chain exhibits a total gain of 32 dB and output power of 26 dBm incorporating the

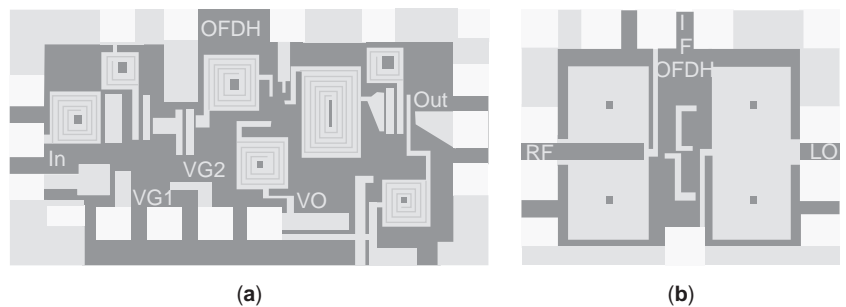
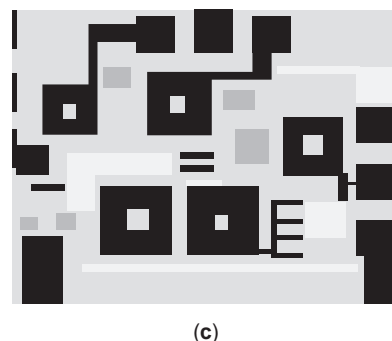


Figure 20. Photo of the Rx chipset used in the module: (a) LNA; (b) mixer; (c) VCO. (This figure is available in full color at <http://www.mrw.interscience.wiley.com/erfme>.)



(c)

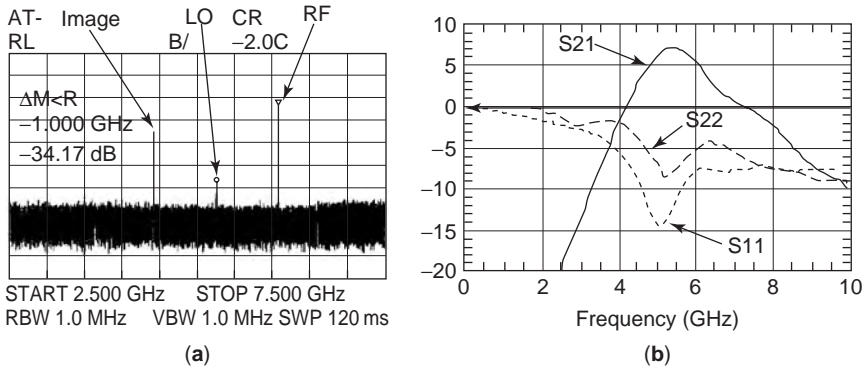


Figure 22. Tx module performances: (a) mixer output spectrum; (b) RF amplifier gain.

wirebond loss from 14 to 15 GHz and image rejection of more than 30 dBc at 12 GHz as shown in Fig. 24a. Figure 24b shows the overall system-level diagram of the entire transmitter chain based on the measurement of each transmitter blocks. The compact module was made possible by embedding the filter and thereby saving more than 40% of real estate compared to the module if it were implemented on a typical alumina substrate.

3.2. Package Modeling and Optimization

The current drawbacks of most commercially available microwave and millimeter-wave front-ends are their relatively large size, heavy weight caused primarily by discrete components such as the filters, and separately located modules. Multilayer ceramic (i.e., LTCC) and organic-based SoP implementation are capable of overcoming this limitation by integrating components as part of the module package that would have otherwise been acquired in discrete form. On-package components not only miniaturize the module but also eliminate or minimize the need for discrete components and thereby reduce the assembly time and cost as well. The optimization of

SoP structures requires the effective modeling of complex structures that involve mechanical motion and wave propagation. Because of computational constraints, many commercial simulators utilize various approximations in order to provide fast and relatively accurate results. Popular commercial EM simulation tools include HFSS (high-frequency structure simulator) [45], SONNET [46], MicroStripes [47], and IE3D [48]. Often the size or type of circuit that can be modeled is limited by these simulators. Either the approximations used limit the applicability to specific problems, or the simulation time and/or memory is excessive. To solve numerous innovative or 3D complex problems, custom simulators employing full-wave techniques can be used. Using a custom code, approximations can be made selectively and the effect on accuracy can be determined. Popular simulation techniques [49] include the method of moments (MoM), finite-element method (FEM) in the frequency domain and finite-difference time-domain (FDTD) method, transmission-line matrix (TLM), and multiresolution time-domain (MRTD) [50] in the time domain. Frequency-domain methods are often used to simulate complex structures and can naturally handle

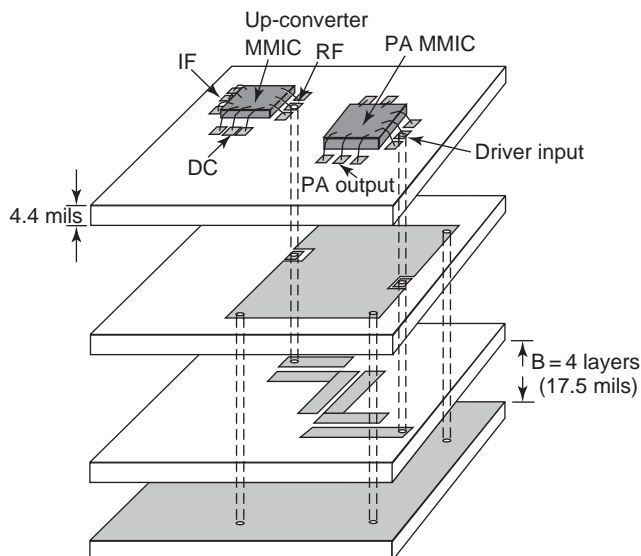


Figure 23. Configuration and picture of compact Ku-band transceiver module.

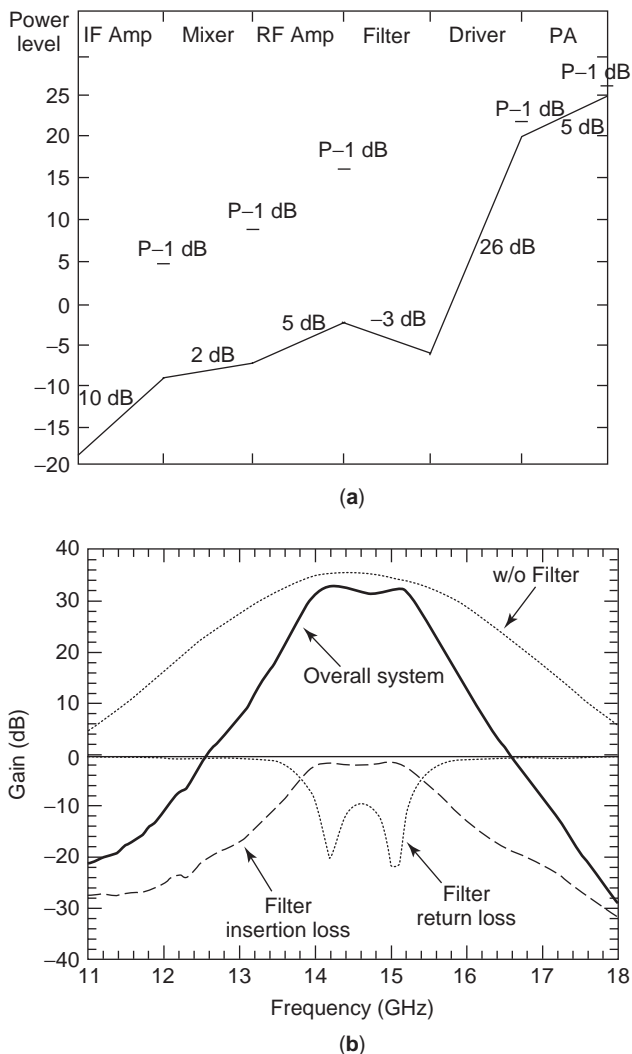


Figure 24. Measured gain of the module: (a) overall system gain; (b) gain variation at each level.

frequency-dependent parameters such as loss. Alternatively, time-domain simulation techniques allow the use of simple grids for complex structures, parallelize well on inexpensive hardware, and, through the use of a Fourier transform, can give the results for a wide frequency band using a single simulation. Both types of simulators can be used on most problems, although not with the same complexity.

Modern RF 3D modules and packages demand a high level of compactness and functionality. Full-wave EM numerical tools require computational complexity, which render this kind of design approach unpractical. Also, the low-frequency RF packaging design process often requires scalable equivalent circuits for the package itself. As the problems associated with the integration involve the consideration of an increasing number of factors, the design and optimization of such systems require more comprehensive and sophisticated tools. The current design and optimization methods, using the commercially available electromagnetic simulators, do not take into

account the specific effects of each of the factors involved in the design process, and the degree to which these factors interact with each other and their ranges of values. Only this type of thorough understanding of the entire system can enable the optimization and synthesis of any module or microsystem under different given conditions. An example of successful application of a combination of DoE (design of experiments) and RSM (response surface methods) is presented in Ref. 51. First, the factors that affect the performance of the system and the output figures of merit have to be identified. The next step involves the design of a factorial experiment with center-points based on a design space for these factors to determine the effect of each parameter, identify interaction between the parameters, and determine which ones are significant for each of the outputs. The experiment is run using electromagnetic simulations and/or microwave measurements, and the outputs are recorded and inputted into a statistical analysis software. After the statistical analysis of the data, significant factors are identified for all figures of merit, then RSM statistical methodology is applied for optimization. The result is an explicit set of equations that show how the outputs depend on the input variables, which are used to simultaneously optimize the figures of merit. Within the design space of the experiment, the optimized figures of merit and the required design parameters are identified.

The nonlinearity of the system, combined with the lack of analytical input-output description, suggest the use of soft computing algorithms also. Genetic algorithms (GAs) can be utilized as an optimization method of this kind. GAs search the parameter space stochastically, generating solutions that are close to the optimal. They also turn out to be very efficient for problems where small perturbations in the optimal solution lead to abrupt increase of the error.

An example of the EM/statistical hybrid method method was applied on a interdigitated coupled filter for 60-GHz applications [52]. The benchmarking structure is presented in Fig. 25. The filter is optimized for 60 GHz center frequency and maximum quality factor Q . The input variables are the linelength L and the three gaps between the lines G_1 , G_2 and G_3 .

The first-order statistical model validation showed curvature, so a second-order model has been developed and the equations describing the outputs as a function of

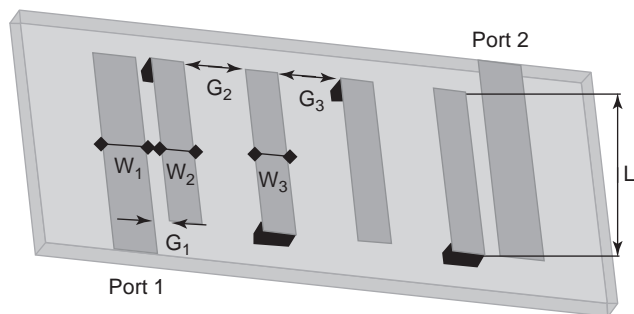


Figure 25. Benchmarking structure.

the inputs are

$$f_0 = 60.811 - 1.845 \left(\frac{L - 775}{25} \right) - 0.057 \left(\frac{G_1 - 60}{6} \right) + 0.164 \left(\frac{G_2 - 260}{25} \right) - 0.1 \left(\frac{G_3 - 260}{25} \right) + 0.07 \left(\frac{L - 775}{25} \right)^2 - 0.094 \left(\frac{G_2 - 260}{25} \right)^2$$

$$Q = 15.42 - 0.345 \left(\frac{L - 775}{25} \right) + 0.292 \left(\frac{G_1 - 60}{6} \right) + 1.104 \left(\frac{G_2 - 260}{25} \right) + 0.474 \left(\frac{G_3 - 260}{25} \right) - 0.104 \left(\frac{L - 775}{25} \right)^2 - 0.349 \left(\frac{G_2 - 260}{25} \right)^2$$

The filter was optimized on the basis of these equations, and the results were validated with a genetic algorithm optimization. The optimized filter insertion loss using the two methods is shown in Fig. 26.

These techniques are very flexible and can be applied to any type of design, especially in complex RF microsystems and packages where the number of factors increases and optimization is extremely difficult using only electromagnetic simulators. This gives a thorough understanding of the system behavior and integrates geometric, material, and functional parameters altogether. The approach is generic and independent of the choice of the electromagnetic simulator and statistical analysis software.

This approach has also been applied for RF and microwave flip-chip design rule development [53]. Previous work identified the factors to be considered in the design process and how they affect the assembly performance. The structure and the geometric factors are presented in Fig. 27. The design of the experimental method gave the possibility to bring all these factors together, quantify their significance, evaluate the interaction between them, and eliminate the insignificant ones from the analysis. The significant factors in this case have been found to

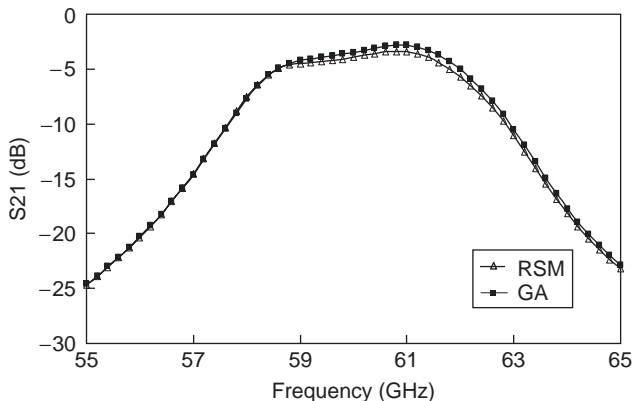


Figure 26. Comparison of the performance of the optimized filter using response surface methods and genetic algorithms.

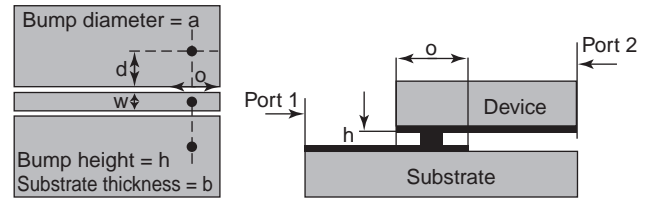


Figure 27. Geometric factors for flip-chip design rule development.

be the bump diameter and height, the CPW width, and the amount of transmission-line overlap around the transition. Also, the transition was optimized by considering not only the individual effects of the variables but also the interaction between them, which can be critical in determining the optimal factor combination. Finally, fully scalable lumped element models with all these factors were developed by applying regression models to the statistical data.

3.3. Testing

Such packages are tested and characterized using microwave measurements, and various deembedding techniques are used to extract the behavior of the device under test (DUT) (see Fig. 28). Microwave measurements require adapters or launches as interface between the measurement system (coaxial cable or on-wafer probes) and the DUT. The additional parasitics added to the measurements by these adapters and launches have to be deembedded to obtain the actual performance of the device [54–56].

There are a wide variety of deembedding techniques, some involving the calibration of the network analyzer such that the parasitic effects are eliminated from the measurement level, some involving separate measurements of the parasitics and using the deembedding capabilities of a circuit simulator such as Agilent's Advanced Design System (ADS) [57] or analytical approaches.

An example of the deembedding technique used for electrically long adapters is the “through-line-line” calibration [54]. This method obtains the effect of the launches by analytically computing its S parameters. It utilizes three deembedding components, one through and two lines (lines 1 and 2) (Fig. 29), without any reflecting components such as the TRL calibration technique. The measurement reference plane is $A'B'$, as shown in Fig. 28. After deembedding, the reference planes are moved back

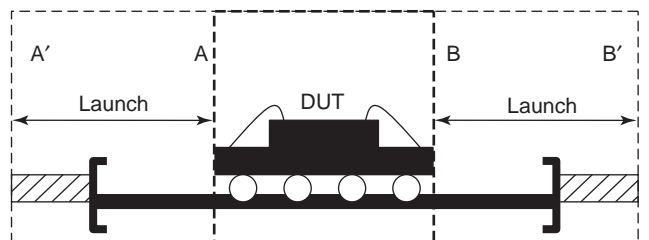


Figure 28. Illustration of typical deembedding application for a BGA structure.

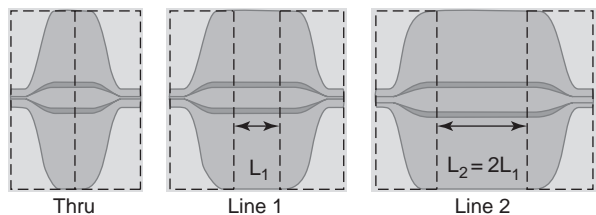


Figure 29. Lines “Thru,” “Line1,” and “Line2” designed for deembedding the coplanar waveguide launches.

to the device under test, at the *AB* plane. Figure 28 shows the application of this method to a BGA structure.

Figure 30a shows the *S* parameters of the BGA package test structure from both original measurement and deembedded data. In the deembedded data, the loss of the DUT is smaller than in the original measurement. In Figure 30b, the deembedding method is verified with the simulation of the BGA model and very good agreement is observed.

When the circuit complexity increases, a careful calibration design is sometimes not possible and more flexible methods need to be used. If the structure to be deembed-

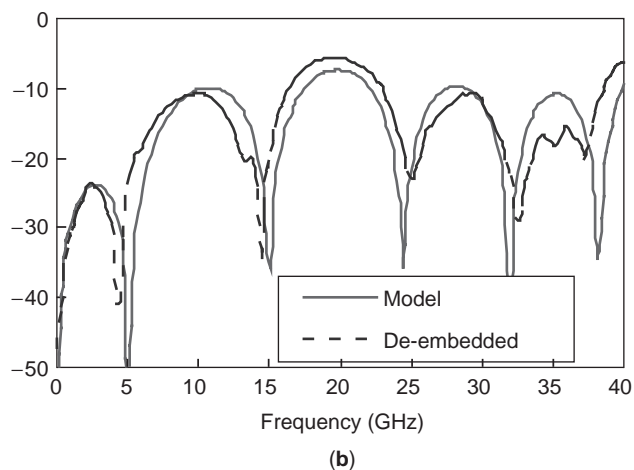
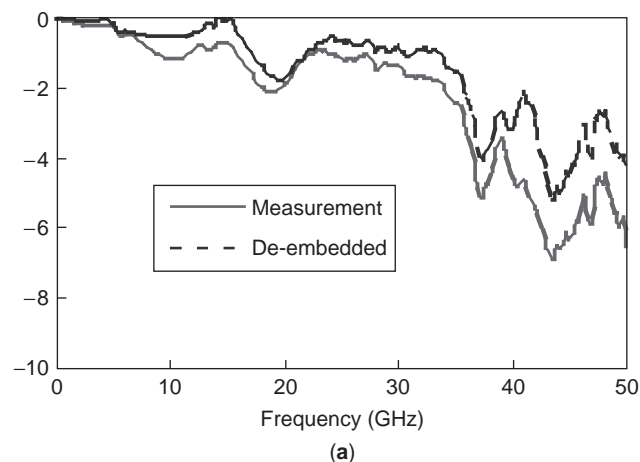


Figure 30. (a) Comparison of *S* parameters of the BGA test structure between the original measurement and deembedded data; (b) verification of the deembedded data with the BGA structure simulation. (This figure is available in full color at <http://www.mrw.interscience.wiley.com/erfme>.)

ded is measured or simulated (*AA'* and *BB'* in Fig. 28), its effect can be subtracted from the overall measurement (*A'B'*). First, two *S*-parameter measurements of the deembedding structure and of the entire system are recorded. Finally, the deembedding *S*-parameter block is cascaded in ADS on each side of the measured overall *S*-parameter block. All are simulated using the deembedding function of ADS, and then the deembedded DUT *S* parameters are obtained.

These deembedding techniques are also used for extracting the parasitic effects of the package itself for equivalent circuit model extraction [58]. These models are scalable and are very important to help the IC designer predict the entire system performance at the beginning of the design process.

3.4. Future Trends

More recent developments in advanced packaging technologies such as 3D multichip modules provide an opportunity for significant reduction in mass, volume, and power consumption. Simultaneously, emerging wireless communications applications in the RF/microwave/millimeter-wave regimes require miniaturization, portability, cost, and performance as key driving forces in the electronics packaging evolution. The system-on-package (SoP) approach [vs. the system-on-chip (SoC) technique] for module development has been proven to be the best approach for systems integration due to the real estate efficiency, cost-saving, size reduction, and performance improvement potentially involved in this integral functionality, and simultaneously satisfying the specifications of the next-generation wireless communication systems. However, current RF module integration is still based on low-density hybrid assembly technologies. Embedded ICs [59] and bumpless buildup layer (BBUL) [60] packaging technology are targeted for low-cost applications and provide great opportunities for the multigigahertz processor and ultracompact RF integrated system.

An example of this integration concept is illustrated in Fig. 31. A multilayer interconnect structure is built using modified MCM-D technology and advanced photosensitive epoxy. A low-loss interconnect is fabricated using buildup technology. Microvias with a minimum diameter of 40 μm are used to connect the different metal layers. Thus, high-density interconnect networks and integral passive components such as high-performance embedded inductors, filters, and antennas can be implemented within the multilayer wiring structure. Multigigahertz processor or RF

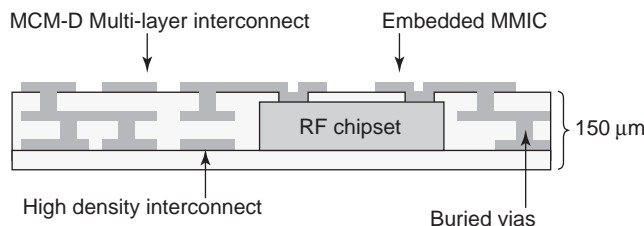


Figure 31. Embedded IC and bumpless build-up layer (BBUL) packaging technology concept view.

commercial chipset are placed into cavities created along the MCM-D process and covered by a final dielectric layer. Cavities provide self-alignment for the die with the interconnection structure. This approach avoids parasitics due to wirebonding, flip-chip, or BGA-type interconnection and parasitic interconnection length between the active circuitry and the passives components are greatly reduced.

New challenges such as RF MEMS integration and packaging are nowadays at the leading edge of the packaging research. Various approaches have been developed by universities or worldwide-leader packaging companies. Current techniques under investigations for the RF MEMS packaging are

- Wafer-to-wafer anodic bonding or polymer bonding/sealing at wafer scale [61]
- Thin-film encapsulation at wafer scale [62]
- Cavity in MCM-C, -L, or -D substrate combined with the use of a sealing cap [63].

Nevertheless, there is still a lack of standardization leading to excessive cost for the development of final products. Eventually, the ideal package technology will merge the standard functions (i.e., environmental protection, hermetic sealing, accelerated testing and vacuum encapsulation skills, signal isolation, mechanical stability) with design specific functions, such as the RF requirement for minimized package resonance, reduced parasitic effects, and so on.

4. CONCLUSION

Future RF and wireless communication and sensor systems will be increasingly complex, miniaturized, and reconfigurable enhancing the importance of packaging structures. High-integration technology is expected to reduce the chip size, number of components, and total system cost. Along with the migration of ICs to integrated system-on-chip (SoC), IC packaging is moving toward wafer-level packaging, and wafer-level test and burnin. The rapid progress of scaled CMOS technology and the introduction of SiGe technology since the late 1990s have improved the performance of silicon RF devices and circuits to meet the requirements. However, the difficulty in lowering the power consumption of RF and analog circuits and the size of passive components and analog transistors has diminished the appeal of the SoC approach. The SoP method will be the way to address these issues and lead to the successful transition from bulky board packaging to the multilayer micro-, nano-, and multifunctional boards for 2010 and beyond.

Acknowledgments

The authors would like to acknowledge the contribution of the Packaging Research Center at Georgia Tech, the Georgia Electronics Design Center, the National Science Foundation, NASA and DARPA.

BIBLIOGRAPHY

1. A. Matsuzawa, RF-SoC—expectations and required conditions, *IEEE Trans. Microwave Theory Tech.* **50**(1):245–253 (Jan. 2002).
2. K. Lim, S. Pinel, M. F. Davis, A. Sutono, C.-H. Lee, D. Heo, A. Obatoynbo, J. Laskar, M. Tentzeris, and R. Tummala, RF-SOP for wireless communications, *IEEE Microwave Mag.* **3**(1): 88–99 (March 2002).
3. R. R. Tummala and J. Laskar, Gigabit wireless: System-on-a-package technology, *Proc. IEEE* **92**(2):376–387 (Feb. 2004).
4. N. J. Koliass and R. C. Compton, Thermal management for high-power active amplifier arrays, *IEEE Trans. Microwave Theory Tech.* **44**(6):963–966 (June 1996).
5. M. DiOrio and S. Pinamaneni, Material effects on the performance and reliability of high-power molded dual-in-line packages, *Proc. 38th Electronics Components Conf.*, May 1988, pp. 406–410.
6. G. C. Phillips, Jr., Planar pin grid array (PGA) ceramic packaging, *Proc. 38th Electronics Components Conf.*, May 1988, pp. 350–354.
7. H. Liang, H. L. Barnes, J. Laskar, and D. Estreich, Application of digital PGA technology to K-band microcircuit and microwave subsystem packages, *IEEE Trans. Microwave Theory Tech.* **48**(12):2644–2651 (Dec. 2000).
8. R. Chronos, D. Mallik, and S. Prough, Packaging alternatives for high lead count, fine pitch, surface mount technology, *IEEE Trans. Compon. Hybrids Manuf. Technol.* **16**(Parts A–C)(4):396–401 (June 1993).
9. R. Tummala, E. Rymaszewski, and A. Klopfenstein, *Microelectronics Packaging Handbook—Part II*, 2nd ed., Kluwer Academic Publishers, 1997.
10. S. Ouimet and M.-C. Paquet, Overmold technology applied to cavity down ultrafine pitch PBGA package, *IEEE Trans. Adv. Pack.* **22**(2):123–128 (May 1999).
11. J. Darnauer, D. Chengson, B. Schmidt, E. Priest, D. A. Hanson, and W. G. Petefish, Electrical evaluation of flip-chip package alternatives for next generation microprocessors, *IEEE Trans. Adv. Pack.* **22**(Part B)(3):407–415 (Aug. 1999).
12. D. Dunn, BGAs given a couple of boosts, *Electronic Buyer's News*, CMP Media, Inc., Nov. 29, 1999.
13. *National Technology Roadmap for Semiconductors*, 1999 ed., Semiconductor Industry Association, 1999.
14. K. Brownlee, S. Bhattacharya, K.-I. Shinotani, C. P. Wong, and R. Tummala, Liquid crystal polymer for high performance SOP applications, *Proc. 8th Int. Symp. Advanced Packaging Materials*, March 2002, pp. 249–253.
15. H. Liang, J. Laskar, M. Hyslop, and R. Panicker, Development of a 36 GHz millimeter-wave BGA package, *2000 IEEE MTT-S Int. Microwave Symp. Digest*, June 11–16, 2000, Vol. 1, pp. 65–68.
16. S. Pinel, S. Chakraborty, S. Mandal, H. Liang, K. Lim, M. Roellig, R. Kunze, R. Tummala, M. Tentzeris, and J. Laskar, 3D integrated LTCC module using μ BGA technology for compact C-band RF front-end module, *Proc. IEEE Int. Microwave Symp.* June 2–7, 2002, pp. 1553–1556.
17. C. Mitchell, Assembly and reliability study for the micro-ball grid array, *Proc. 16th IEEE/CPMT IEMT Symp.*, Sept. 1994, pp. 344–346.
18. M. Christensen, Flip-chip: A technology reborn, in *Solid State Technology*, Pennwell Publishing, June 1999.
19. D. Staiculescu, J. Laskar, and M. Tentzeris, Design of experiments (DOE) technique for microwave/millimeter wave

- flip-chip optimization, *Int. J. Num. Model.* **16**(2):97–103 (March–April 2003).
20. D. Staiculescu, A. Sutono, and J. Laskar, Wideband scalable electrical model for microwave/millimeter wave flip chip interconnects, *IEEE Trans. Adv. Pack.* **24**(3):255–259 (Aug. 2001).
 21. J. Jahns, R. A. Morgan, H. N. Nguyen, J. A. Walker, S. J. Walker, and Y. M. Wong, Hybrid integration of surface-emitting microlaser chip and planar optics substrate for interconnection applications, *IEEE Photonics Tech. Lett.* **4**(12):1369–1372 (Dec. 1992).
 22. K. P. Jackson, High-density, array, optical interconnects for multi-chip modules, *Proc. Multi-Chip Module Conf.*, March 18–20, 1992, pp. 142–145.
 23. J. Papapolymerou, G. Ponchak, E. Dalton, A. Bacon, and M. M. Tentzeris, Crosstalk between finite ground coplanar waveguides over polyimide layers for 3D-MMIC's on Si substrates, *IEEE Trans. Microwave Theory Tech.* **52**(4):1292–1301 (April 2004).
 24. D. Staiculescu, K. Lim, A. Sutono, H. Liang, M. Tentzeris, and J. Laskar, Flip-chip vs. wirebond, *Printed Circ. Design Mag.* 12–16 (June 2002).
 25. B. C. Johnson, Overview of chip-level packaging, in *Electronic Materials Handbook*, Vol. 1, *Packaging*, ASM International, Materials Park, OH, 1989.
 26. B. K. Gilbert and G.-W. Pan, MCM packaging for present- and next-generation high clock-rate digital- and mixed-signal electronic systems: Areas for development, *IEEE Trans. Microwave Theory Tech.* **45**(10):1819–1835 (Oct. 1997).
 27. E. D. Perfecto, R. R. Shields, A. K. Malhotra, M. P. Jeanneret, D. C. McHerron, and G. A. Katopis, MCM-D/C packaging solution for IBM latest S/390 servers, *IEEE Trans. Adv. Pack.* **23**(3):515–520 (Aug. 2000).
 28. A. Sutono, D. Heo, Y.-J. Emery Chen, and J. Laskar, High-Q LTCC-based passive library for wireless system-on-package (SOP) module development, *IEEE Trans. Microwave Theory Tech.* **49**(10):1715–1724 (Oct. 2001).
 29. A. Sutono, A.-V. H. Pham, J. Laskar, and W. R. Smith, RF/microwave characterization of multilayer ceramic-based MCM technology, *IEEE Trans. Adv. Pack.* **22**(3):326–331 (Aug. 1999).
 30. R. R. Tummala, SLIM: Third generation of packaging beyond MCM, CSP, flipchip and micro-via board technologies, *Proc. 2nd Electronics Packaging Technology Conf.*, Dec. 8–10, 1998, pp. 1–8.
 31. R. R. Tummala, V. Sundaram, F. Liu, G. White, S. Hattacharya, R. M. Pulugurtha, M. Swaminathan, S. Dalmia, J. Laskar, N. M. Jokerst, and Y.-C. Sang, High density packaging in 2010 and beyond, *Proc. 4th Int. Symp. Electronic Materials and Packaging*, Dec. 4–6, 2002, pp. 30–36.
 32. O. Salmela and P. Ikalainen, Ceramic packaging technologies for microwave applications, *Proc. Wireless Communications Conf.*, Aug. 11–13, 1997, pp. 162–164.
 33. S. Pinel, M. Davis, V. Sundaram, K. Lim, J. Laskar, G. White, and R. Tummala, High Q passives on liquid crystal polymer substrates and μ BGA technology for 3D integrated RF front-end module, *IEICE Trans. Electron.* **E86-C**(8) (Aug. 2003).
 34. A. Sutono, J. Laskar, and W. R. Smith, Design of miniature multilayer on-package integrated image-reject filters, *IEEE Trans. Microwave Theory Tech.* **51**(1):156–162 (Jan. 2003).
 35. S. Chakraborty, K. Lim, A. Sutono, E. Chen, S. Yoo, A. Obatoyinbo, S.-W. Yoon, M. Maeng, M. F. Davis, S. Pinel, and J. Laskar, A 2.4-GHz radio front end in RF system-on-package technology, *IEEE Microwave Mag.* **3**(2):94–104 (June 2002).
 36. D. Heo, A. Sutono, E. Chen, Y. Suh, and J. Laskar, A 1.9-GHz DECT CMOS power amplifier with fully integrated multilayer LTCC passives, *IEEE Microwave Wireless Compon. Lett.* **11**(6):249–251 (June 2001).
 37. M. Tentzeris, R. Li, K. Lim, M. Maeng, E. Tsai, G. DeJean, and J. Laskar, Design of compact stacked-patch antennas on LTCC technology for wireless communication applications, *Proc. 2002 IEEE AP-S Symp.* June 2002, Vol. 2, pp. 500–503.
 38. H. Jiang, Y. Wang, J.-L. A. Yeh, and N. C. Tien, On-chip spiral inductors suspended over deep copper-lined cavities, *IEEE Trans. Microwave Theory Tech.* **48**:2415–2423 (Dec. 2000).
 39. Y. Rahmat-Samii and H. Mosallaei, Electromagnetic band-gap structures: Classification, characterization, and applications, *Proc. 11th Int. Conf. Antennas and Propagation*, April 2001, Vol. 2, pp. 560–564.
 40. D. C. Montgomery, *Design and Analysis of Experiments*, Wiley, New York, 1997.
 41. R. Hecht-Nielsen, *Neurocomputing*, Addison-Wesley, New York, 1990.
 42. N. Chaiyaratana and A. M. S. Zalzala, Recent developments in evolutionary and genetic algorithms: Theory and applications, *Proc. 2nd Int. Conf. Genetic Algorithms in Engineering Systems: Innovations and Applications*, Sept. 1997, pp. 270–277.
 43. R. L. Li, G. DeJean, J. Papapolymerou, J. Laskar, and M. M. Tentzeris, FDTD analysis of microstrip patch antennas and arrays on high dielectric-constant substrate surrounded by a soft-and-hard surface, *IEEE Trans. Magn.* **40**(2):1444–1447 (March 2004).
 44. C.-H. Lee, A. Sutono, S. Han, K. Lim, S. Pinel, E. M. Tentzeris, and J. Laskar, A compact LTCC-based Ku-band transmitter module, *IEEE Trans. Adv. Pack.* **25**(Part B)(3):374–384 (Aug. 2002).
 45. <http://www.ansoft.com/products/hf/hfss/>.
 46. <http://www.sonnetusa.com/>.
 47. <http://www.microstripes.com/>.
 48. <http://www.bay-technology.com/ie3d.htm>.
 49. T. Itoh, *Numerical Techniques for Microwave and Millimeter-Wave Passive Structures*, Wiley, New York, 1989.
 50. M. Krumpholz and L. P. B. Katehi, New time domain schemes based on multiresolution analysis, *IEEE Trans. Microwave Theory Tech.* **44**:555–561 (April 1996).
 51. N. Bushyager, L. Martin, S. Khushrushahi, S. Basat, and M. M. Tentzeris, Design of RF and wireless packages using fast hybrid electromagnetic/statistical methods, *Proc. IEEE-ECTC Symp.* May 2003, pp. 1546–1549.
 52. N. Bushyager, D. Staiculescu, L. Martin, J. H. Lee, N. Vasiloglou, and M. M. Tentzeris, Design and optimization of 3D RF modules, microsystems and packages using electromagnetic and statistical tools, *Proc. 2004 IEEE-ECTC Conf.*, June 2004, pp. 1412–1415.
 53. D. Staiculescu, J. Laskar, and M. M. Tentzeris, Design rule development for microwave flip-chip applications, *IEEE Trans. Microwave Theory Tech.* **48**(9):1476–148 (Sept. 2001).
 54. H. Liang, J. Laskar, and M. Hyslop, A broad band through-line-line de-embedding technique for BGA package measurements, *Proc. IEEE EPEP Conf.* Oct. 2001, pp. 125–128.
 55. L. Van Hauwermeiren, M. Botte, and D. De Zutter, A new de-embedding technique for on-board structures applied to the bandwidth measurement of packages, *IEEE Trans. Compon. Pack. Manuf. Technol.* **16**(3):300–303 (May 1993).

56. T. K. Sarkar, Z. A. Maricevic, and M. Kahrizi, An accurate de-embedding procedure for characterizing discontinuities, *Int. J. Microwavemillimeter-Wave Comput. Aided Eng.* 2(3):135–143 (1992).
57. <http://eesoftm.agilent.com/products/adsoview.html>.
58. T. S. Horng, S. M. Wu, and C. Shih, Electrical modeling of RFIC packages up to 12 GHz, *Proc. IEEE ECTC Conf.*, 1999, pp. 867–872.
59. S. Pinel, C.-H. Lee, S.-W. Yoon, S. Nuttinck, K. Lim, and J. Laskar, Embedded IC and high-Q passives technology for ultra-compact Ku-band VCO module, *IEEE Microwave Wireless Compon. Lett.* 14(2):80–82 (Feb. 2004).
60. S. Towle, H. Braunisch, C. Hu, R. D. Emery, and G. J. Vandentop, *Bumpless Build-Up Layer Packaging*, Intel Corp., (Components Research Intel Corp., 5000 W. Chandler Blvd., Chandler, AZ 85226; corresponding author: 480-552-0278, 480-552-4001 (fax), richard.d.emery@intel.com).
61. A. Margomenos, D. Peroulis, J. P. Becker, and L. P. B. Katehi, silicon micromachined interconnects for on-wafer packaging of MEMS devices, *2001 Topical Meeting on silicon Monolithic Integrated Circuits in RF Systems*, Sept. 2001, pp. 33–36.
62. Y. K. Park, Y. K. Kim, C. J. Kim, B. K. Ju, and J. O. Park, Innovative ultra thin packaging for RF-MEMS devices, *12th Int. Conf. Solid-State Sensors, Actuators and Microsystems*, 2003, pp. 903–906.
63. http://global.kyocera.com/prdct/semicon/ic_pkg/mems.html.

FURTHER READING

Some useful web links are as follows:

<http://www.chips.ibm.com/>.

<http://www.chips.ibm.com/micronews>.

<http://www.chips.ibm.com/products/interconnect/swg/interconnect.html>.

<http://sprocket.colorado.edu/centers/ycee-group/links/>.

<http://www.prc.gatech.edu/>.

<http://www.smta.org/>.

RING RESONATORS AND CIRCUITS

LUNG-HWA HSIEH
KAI CHANG
Texas A&M University
College Station, Texas

1. INTRODUCTION

The microstrip ring resonator was first introduced by P. Troughton in 1969 to measure the phase velocity and dispersive characteristics of a microstrip line [1]. Compared with the conventional half-wavelength resonator, the major advantage of using a ring resonator for these measurements is to avoid open-end effects. To understand the operation of a ring circuit, some complicated field

analyses based on electromagnetic field theory were developed [2]. In addition, simple transmission-line analyses were also proposed [3–5]. In the transmission-line approaches, the ring is modeled as equivalent circuits or equivalent lumped elements to overcome the field theory limitation described by dimensions and mode charts of the ring. Also, different types of rings such as microstrip, coplanar waveguide, dielectric, and slot-line rings were used to incorporate passive and active devices in MIC and MMIC [6–8]. A waveguide ring resonator is generally used for the applications need higher Q values and higher power handling [9]. With the advantages of compact size, low cost, easy fabrication, and low radiation loss, the planar ring resonator was widely used for the design of filters, oscillators, mixers, baluns, hybrids, magic T, couplers, frequency-selective surfaces, and antennas [10].

2. ANALYSIS AND MODELING OF RING RESONATORS

2.1. Field Analyses

The magnetic wall model introduced by Wolff and Knoppik was the most commonly used field theory to explain the

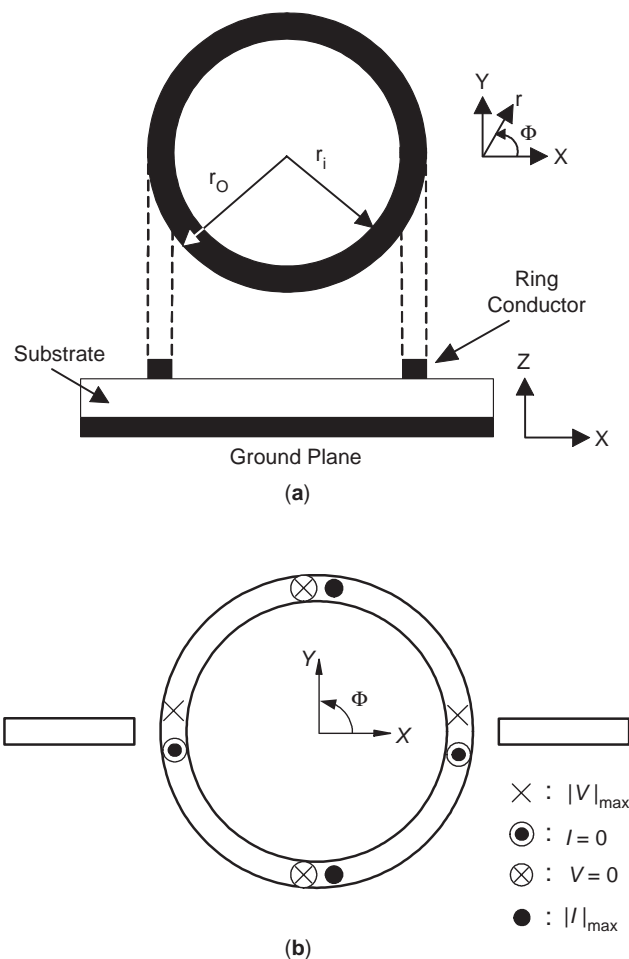


Figure 1. Ring resonator (a) configuration and (b) maximum and minimum field points.

56. T. K. Sarkar, Z. A. Maricevic, and M. Kahrizi, An accurate de-embedding procedure for characterizing discontinuities, *Int. J. Microwavemillimeter-Wave Comput. Aided Eng.* 2(3):135–143 (1992).

57. <http://eesof.tm.agilent.com/products/adsoview.html>.

58. T. S. Horng, S. M. Wu, and C. Shih, Electrical modeling of RFIC packages up to 12 GHz, *Proc. IEEE ECTC Conf.*, 1999, pp. 867–872.

59. S. Pinel, C.-H. Lee, S.-W. Yoon, S. Nuttinck, K. Lim, and J. Laskar, Embedded IC and high-Q passives technology for ultra-compact Ku-band VCO module, *IEEE Microwave Wireless Compon. Lett.* 14(2):80–82 (Feb. 2004).

60. S. Towle, H. Braunisch, C. Hu, R. D. Emery, and G. J. Vandentop, *Bumpless Build-Up Layer Packaging*, Intel Corp., (Components Research Intel Corp., 5000 W. Chandler Blvd., Chandler, AZ 85226; corresponding author: 480-552-0278, 480-552-4001 (fax), richard.d.emery@intel.com).

61. A. Margomenos, D. Peroulis, J. P. Becker, and L. P. B. Katehi, silicon micromachined interconnects for on-wafer packaging of MEMS devices, *2001 Topical Meeting on silicon Monolithic Integrated Circuits in RF Systems*, Sept. 2001, pp. 33–36.

62. Y. K. Park, Y. K. Kim, C. J. Kim, B. K. Ju, and J. O. Park, Innovative ultra thin packaging for RF-MEMS devices, *12th Int. Conf. Solid-State Sensors, Actuators and Microsystems*, 2003, pp. 903–906.

63. http://global.kyocera.com/prdct/semicon/ic_pkg/mems.html.

FURTHER READING

Some useful web links are as follows:

<http://www.chips.ibm.com/>.

<http://www.chips.ibm.com/micronews>.

<http://www.chips.ibm.com/products/interconnect/swg/interconnect.html>.

<http://sprocket.colorado.edu/centers/yclee-group/links/>.

<http://www.prc.gatech.edu/>.

<http://www.smta.org/>.

RING RESONATORS AND CIRCUITS

LUNG-HWA HSIEH
 KAI CHANG
 Texas A&M University
 College Station, Texas

1. INTRODUCTION

The microstrip ring resonator was first introduced by P. Troughton in 1969 to measure the phase velocity and dispersive characteristics of a microstrip line [1]. Compared with the conventional half-wavelength resonator, the major advantage of using a ring resonator for these measurements is to avoid open-end effects. To understand the operation of a ring circuit, some complicated field

analyses based on electromagnetic field theory were developed [2]. In addition, simple transmission-line analyses were also proposed [3–5]. In the transmission-line approaches, the ring is modeled as equivalent circuits or equivalent lumped elements to overcome the field theory limitation described by dimensions and mode charts of the ring. Also, different types of rings such as microstrip, coplanar waveguide, dielectric, and slot-line rings were used to incorporate passive and active devices in MIC and MMIC [6–8]. A waveguide ring resonator is generally used for the applications need higher *Q* values and higher power handling [9]. With the advantages of compact size, low cost, easy fabrication, and low radiation loss, the planar ring resonator was widely used for the design of filters, oscillators, mixers, baluns, hybrids, magic T, couplers, frequency-selective surfaces, and antennas [10].

2. ANALYSIS AND MODELING OF RING RESONATORS

2.1. Field Analyses

The magnetic wall model introduced by Wolff and Knoppik was the most commonly used field theory to explain the

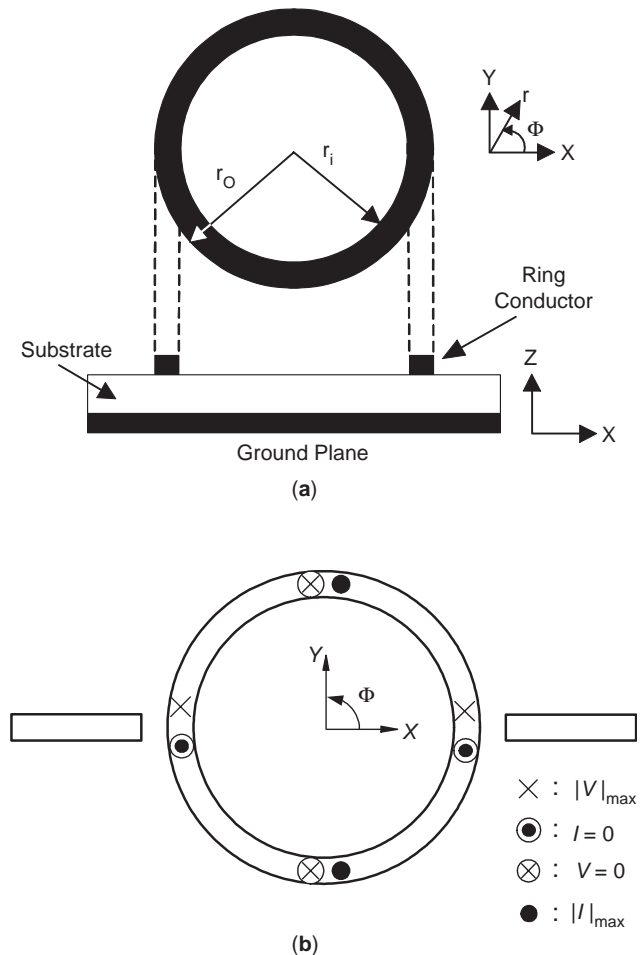


Figure 1. Ring resonator (a) configuration and (b) maximum and minimum field points.

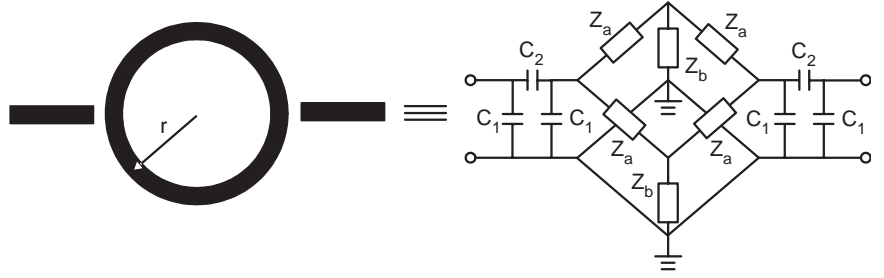


Figure 2. Ring resonator and its transmission-line model using a T network.

operation of the ring resonator [2]. This model including the curvature effects of the microstrip line can achieve an accurate expression for the physical size of the ring resonator corresponding to its electric characteristics. Also, using this analysis, Wolff and Knoppik obtained a good agreement for experiment and theoretical results in the resonant frequencies of the ring.

The ring resonator shown in Fig. 1a can be treated as a cavity resonator with electric walls on the top and bottom and magnetic walls on its sides. The electromagnetic fields are confined to the dielectric substrate between the ground plane and the ring resonator conductors. Assuming no z dependency ($\partial/\partial z = 0$), the fields are transverse magnetic (TM) in the z direction.

A solution of Maxwell's equations is

$$E_z = [AJ_n(kr) + BN_n(kr)] \cos(n\Phi) \quad (1a)$$

$$H_r = \frac{n}{j\omega\mu_0 r} [AJ_n(kr) + BN_n(kr)] \sin(n\Phi) \quad (1b)$$

$$H_\Phi = \frac{k}{j\omega\mu_0} [AJ'_n(kr) + BN'_n(kr)] \cos(n\Phi) \quad (1c)$$

where A and B are constants, k is the wavenumber, ω is the angular frequency, J_n and N_n are the Bessel function of the first and second kind of order n , and J'_n and N'_n are derivatives of the Bessel function with respect to the argument kr . With the boundary conditions $H_\Phi|_{r=r_o} = 0$ and $H_\Phi|_{r=r_i} = 0$, the eigenfunction derived from Eq. (1) is

$$J'_n(kr_o)N'_n(kr_i) - J'_n(kr_i)N'_n(kr_o) = 0 \quad (2)$$

where r_o and r_i are the outer and inner radii of the ring and $k = \omega\sqrt{\epsilon_o\epsilon_r\mu_0}$.

As r_i approaches to r_o , the eigenfunction in Eq. (2) reduces to [11]

$$[(kr_o)^2 - n^2][J_{n-1}(kr_o)N_n(kr_o) - J_n(kr_o)N_{n-1}(kr_o)] = 0 \quad (3)$$

The second term of Eq. (3) is nonzero, and thus

$$[(kr_o)^2 - n^2] = 0 \quad (4)$$

Substituting $k = 2\pi/\lambda_g$ into Eq. (4) yields the well-known equation

$$n\lambda_g = 2\pi r_o \quad (5)$$

Furthermore, a planar waveguide mode considering the fringe edge effects of the microstrip line was proposed to improve the magnetic wall model [12]. Beyond the magnetic wall model, some rigorous solutions for the ring resonator were also reported [13].

Figure 1b shows the maximum and minimum field points on the ring resonator that operates at its fundamental resonant frequency. These maximum and minimum field points indicate how the standing waves operate on the ring and can be simply derived by using a transmission-line model [14].

2.2. Transmission-Line Models

The magnetic wall model describes the physical dimensions of the ring resonator only with respect to its resonant frequencies. In addition, the rigorous solutions are limited because of their extensive computational time and difficulty for the use in applications. To extend the studies and applications, transmission-line models have been proposed [3–5]. In these models, the ring resonator is represented as an equivalent circuit; equivalent lumped elements in terms of G, L, C ; or distributed piecewise transmission lines.

Figure 2 shows a two-port ring and its equivalent circuit [3]. The ring resonator is divided into parallel transmission lines. Each line is modeled as a lossless T network as shown in Fig. 2. The equivalent impedances are given by

$$Z_a = jZ_0 \tan \frac{\beta l}{2}, \quad Z_b = -jZ_0 \csc(\beta l) \quad (6)$$

where Z_0 is the characteristic impedance of the ring resonator, β is the propagation constant, $l = \pi r$, and r is the mean radius of the ring resonator.

The input impedance of the ring circuit obtained with terminating any one of two ports is given as

$$Z_{in} = R_{in} + jX_{in} \quad (7)$$

Letting $X_{in} = 0$, we can find the resonant frequencies of the ring.

Table 1 shows the resonant frequencies compared with the magnetic wall model based on the RT/Duroid material and dimensions designed for the ring resonators as shown in Table 2. It can be seen that the transmission-line model accurately predicts the resonant frequencies within 1%. In addition, the coupling gaps between the feedlines and the ring resonator as shown in Fig. 2 affect the resonant

Table 1. Comparison between Transmission-Line and Magnetic Wall Models

Circuit	Transmission-Line Model Resonant Frequency Error (%)		Magnetic Wall Model Resonant Frequency Error (%)	
	$n = 1$	$n = 2$	$n = 1$	$n = 2$
1	0.79	0.6	0.78	0.89
2	0.56	0.28	0.63	0.38

frequency and insertion loss of the ring resonator [10]. The smaller (wider) is the gap size, the lower (higher) are the resonant frequency and insertion loss. Other coupling mechanisms can be found in the literature [15,16].

Figure 3 shows the ring resonator and its equivalent circuit in terms of G , L , and C , where α is the attenuation constant and ω_0 is the resonant angular frequency. The lumped elements G , L , and C are derived from $ABCD$, Y , and S parameters [5]. The unloaded Q of the ring can be directly calculated from G , L , and C . Table 3 shows a good agreement between the measured and calculated G , L , C , and unloaded Q of the ring resonator. The ring resonators were designed at the fundamental frequency of 2 GHz and fabricated on the dielectric constant (RT/Duroid 5870) of $\epsilon_r = 2.33$, the substrate thickness of $h = 10$ mil, the copper metallization thickness of $t = 0.7$ mil, and the width of $w = 0.74$ mm.

The distributed transmission-line model for the ring resonator is shown in Fig. 4 [4]. The whole ring resonator is divided into many small transmission-line elements. Therefore, the frequency response of the ring can be obtained by cascading many individual $ABCD$ matrices and Y and S parameters. Also, the effects of incorporated passive and active devices between any two small transmission-line elements can be easily calculated and predicted using this model. The model can also be used to study the effect of any perturbations incorporated into a portion of the ring.

3. MEASUREMENT USING RING RESONATORS

The ring resonator can be used to measure for dispersion, dielectric constant, and Q factor. By measuring the resonant frequencies of the ring resonator, the phase velocity and dispersive characteristics of a microstrip line can be obtained. The microstrip ring circuit shown in Fig. 2 consists of two feedlines, one closed-loop ring with two coupling gaps between the ring and the feedlines. The size of the coupling gaps should be large enough so that the coupling effects on the ring will not affect the resonant frequency. Equation (8) demonstrates that the ring supports waves with an integral multiple guided wavelengths equal

Table 2. Material and Dimensions of the Ring Resonator

Circuit	Substrate	Relative Permittivity	Thickness (mm)	Width (mm)	Mean Radius (mm)	Gap Size (mm)
1	6010	10.5	0.635	0.602	6.984	0.077
2	5880	2.2	0.254	0.838	4.9	0.069

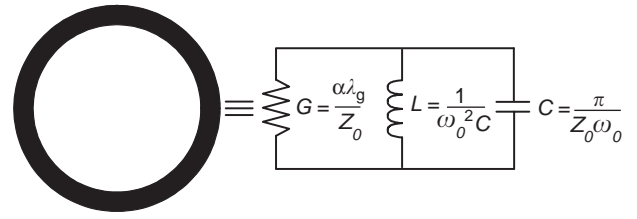
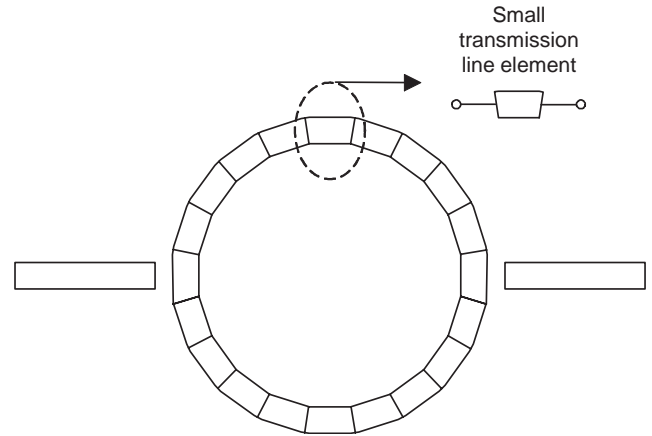

Figure 3. The ring resonator and its equivalent circuit in terms of G , L , and C .

Table 3. Measured and Calculated G , L , C , and Unloaded Q

Measurement	Calculation
$G = 0.495$ ms	$G = 0.508$ ms
$L = 1.55$ nH	$L = 1.52$ nH
$C = 4.25$ pF	$C = 4.17$ pF
Unload $Q = 105.78$	Unload $Q = 103.35$


Figure 4. Distributed transmission-line model.

to the mean circumference of the ring

$$n\lambda_g = 2\pi r, \quad n = 1, 2, 3, \dots \quad (8)$$

where n is the mode number and r is the mean radius. The dispersion in a microstrip line can be examined by the effective permittivity ϵ_{eff} . The *effective permittivity* is defined as the square of the ratio of the speed of light in free space c to the phase velocity v_p in a microstrip line:

$$\epsilon_{\text{eff}}(f) = \left(\frac{c}{f\lambda_g} \right)^2 = \left(\frac{\lambda_0}{\lambda_g} \right)^2 \quad (9)$$

Substituting Eq. (8) into Eq. (9) gives

$$\epsilon_{\text{eff}}(f_0) = \left(\frac{nc}{f_0 2\pi r} \right)^2 \quad (10)$$

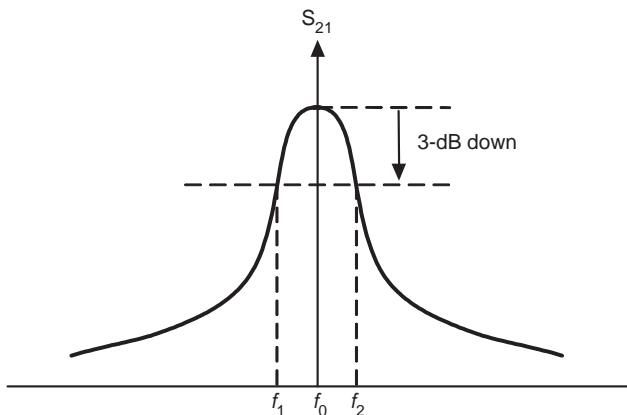


Figure 5. Frequency response of a resonator.

where f_0 is the resonant frequency. Thus, the dispersion of the microstrip line can be calculated from Eq. (10). The accuracy of the dispersion calculation depends on the accuracy of the measurement of the frequency and the total circumference of the ring.

A figure of merit for a ring resonator is its Q factor. The loaded Q factor of the ring can be measured by $Q_L = f_0 / (f_2 - f_1)$, where f_0 is the angular resonant frequency and $f_1 - f_2$ is the 3 dB (half-power) bandwidth. The corresponding frequency response is shown in Fig. 5. Moreover, the unloaded Q factor of the ring can be determined by measuring the loaded Q factor and the insertion loss of the ring at the resonance. The unloaded Q factor is calculated from

$$Q_u = \frac{Q_L}{(1 - 10^{-L/20})} \tag{11}$$

where L is the insertion loss in decibels at resonance of the ring.

4. RING FILTERS

The dual-mode bandpass filter was proposed by Wolff using asymmetric coupling feedlines as shown in Fig. 6 [17]. The asymmetries perturb the fields of the ring and generate two separated modes. These two modes couple each other and increase the passband of the ring resonator. The dual-mode effects are introduced by skewing one of feedlines with respect to the other, and/or by introduction of a discontinuity (notch, slit, patch, etc.) [10]. Later on, many new configurations using orthogonal feedlines with patch

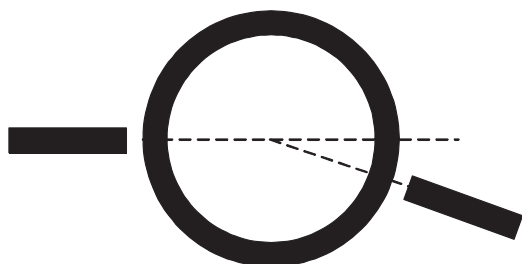


Figure 6. Asymmetrically coupling ring resonator.

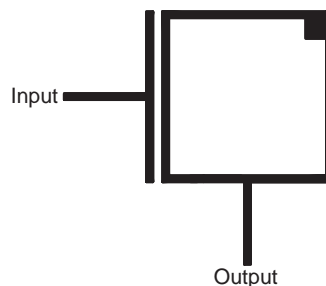


Figure 7. A dual-mode ring circuit with one single coupling gap [19]. (Permission from Electronics Letters.)

perturbation on a ring resonator were introduced [18–20]. The new configuration with orthogonal feedlines and a patch perturbation provides a quasielliptic function that has two transmission zeros close to the passband to reject adjacent channel interferences as shown in Fig. 7 [19]. Also, by cascading several resonators in series, various bandpass frequency responses can be designed [21].

4.1. Dual-Mode Bandpass Filters

Figure 8 shows a dual-mode bandpass filter. The square ring resonator is fed by a pair of orthogonal feedlines, and each feedline is connected to an L-shape coupling arm [15]. Figure 8b displays the scheme of the coupling arm, which consists of a coupling stub and a tuning stub. The tuning stub attached to the end of the coupling stub extends the coupling stub to increase the coupling periphery. In addition, the asymmetric structure perturbs the field of the ring resonator and excites two degenerate modes [17]. Without the tuning stubs, there is no perturbation on the ring resonator and only a single mode is excited [22]. Comparing the filter in Fig. 8 with conventional dual-mode filters [10], the conventional filters provide only a dual-mode characteristic without the benefits of enhanced coupling strength and performance optimization.

To improve the passband performance and stopband rejection, multiple-resonator filters are normally used. Figure 9 shows the filter layout using three cascaded resonators with the same dimensions as in Fig. 8. The filter was designed at the center frequency of 1.75 GHz and fabricated on a 50-mil-thickness RT/Duroid 6010.2 substrate

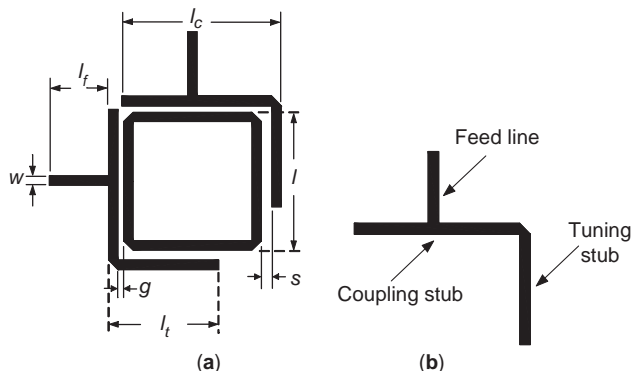


Figure 8. Dual-mode bandpass filter with enhanced coupling: (a) layout; (b) L-shape coupling arm [15]. (Permission from IEEE.)

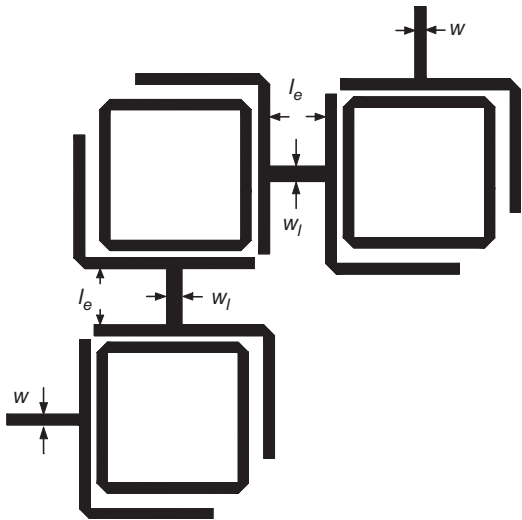


Figure 9. Layout of the filter using three resonators with L-shape coupling arms [15]. (Permission from IEEE.)

with a relative dielectric constant of 10.2. The dimensions of the filter were $w = 1.191$ mm, $l_f = 8$ mm, $g = 0.25$ mm, $s = 0.8$ mm, $l = 17.648$ mm, $l_t = 13.5$ mm, $l_c = 19.64$ mm, $l_e = 6.2$ mm, and $w_l = 1.691$ mm. Figure 10 shows the simulated and measured results. The simulation was completed using a IE3D electromagnetic simulator [23]. The filter had an insertion loss of 2.39 dB in the passband with a 3 dB bandwidth of 145 MHz. The stopband rejection was better than 30 dB within 1–1.62 GHz and 1.85–3 GHz, respectively.

4.2. Microstrip Ring Bandpass Filters with Two Transmission Zeros

By using asymmetrically feeding on the two open-loop ring resonators, the filter shown in Fig. 11 also provides two transmission zeros [24]. In comparison with the cross-coupled structure of Ref. 25, this configuration using only two resonators can also provide a sharp cutoff frequency

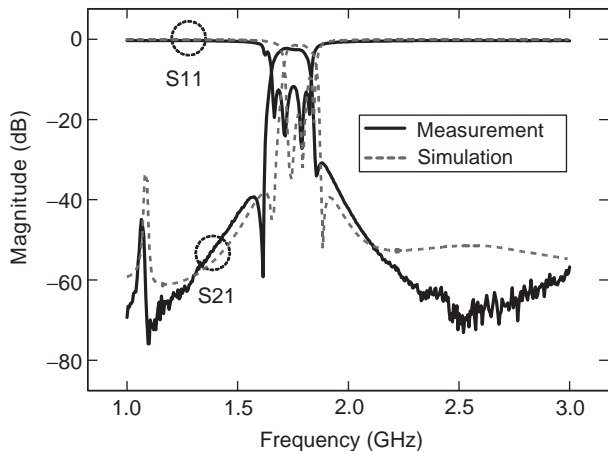


Figure 10. Simulated and measured results for the filter using three resonators with L-shape coupling arms [15]. (Permission from IEEE.) (This figure is available in full color at <http://www.mrw.interscience.wiley.com/erfme>.)

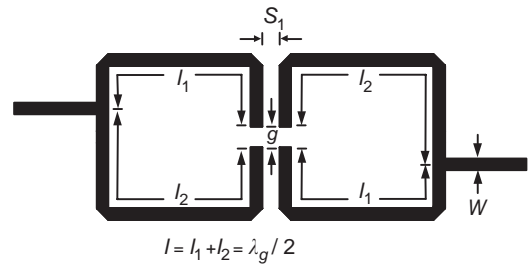


Figure 11. Layout of the filter using two open-loop ring resonators with asymmetric tapping feeders [24]. (Permission from IEEE.)

response but has lower insertion loss due to fewer conductor losses.

In Fig. 11, the total length of the resonator is $l = l_1 + l_2 = \lambda_g/2$, and the input and output feeders divide the resonators into two sections of l_1 and l_2 , where λ_g is the guided wavelength. By using *ABCD*, *Y*, and *S* parameter operations, the locations of the transmission zeros corresponding to the tapping position on the ring resonator are given by [24]

$$f_1 \cong \frac{nc}{4l_1\sqrt{\epsilon_{eff}}}, \quad f_2 \cong \frac{nc}{4l_2\sqrt{\epsilon_{eff}}}; \quad n = 1, 3, 5 \dots \quad (12)$$

To verify the calculation from Eq. (5), a filter was designed at the fundamental frequency of 2 GHz and fabricated on a RT/Duroid 6010.2 substrate with a thickness $h = 25$ mil and a relative dielectric constant $\epsilon_r = 10.2$. The dimensions of the filter are $g = 0.5$ mm, $s_1 = 0.35$ mm, $l_1 = 12.69$ mm, $w = 0.563$ mm, and $l_2 = 16.16$ mm. The measured results are shown in Fig. 12. The calculated and measured results shown in Table 4 agree well. The filter has an insertion loss of 0.95 dB at 2.02 GHz, return loss of greater than 20 dB from 1.98 to 2.06 GHz, and two transmission zeros at 1.69 GHz with -50.7 dB rejection and 2.5 GHz with -45.5 dB rejection, respectively. The 3 dB fractional bandwidth of the filter is 10.4%.

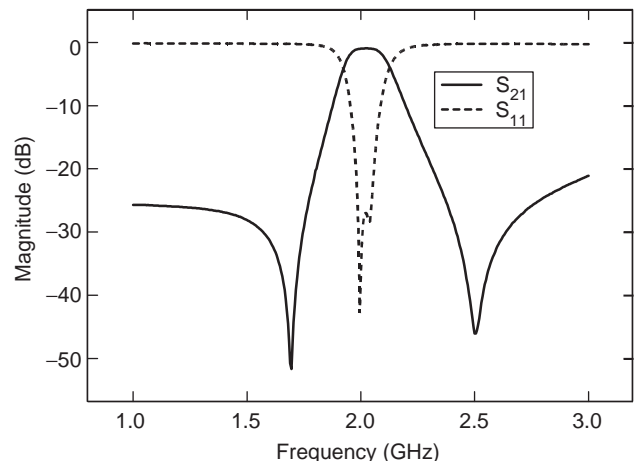


Figure 12. Measured results of the filter [24]. (Permission from IEEE.)

Table 4. Calculated and Measured Locations of Two Transmission Zeros

Calculation	Measurements
$f_1 = 1.79 \text{ GHz}, f_2 = 2.27 \text{ GHz}$	$f_1 = 1.83 \text{ GHz}, f_2 = 2.24 \text{ GHz}$

5. RING COUPLERS AND HYBRIDS

Hybrid ring couplers are widely used in various microwave integrated circuit (MIC) and monolithic microwave integrated circuit (MMIC) applications such as balanced amplifiers, balanced mixers, phase shifts, frequency discriminators, and feeding networks in antenna arrays [26–29]. The 180° hybrid ring couplers and 90° branchline couplers are commonly used in these applications. Rartrace hybrid rings and reverse-phase hybrid rings are well known for the 180° hybrid ring couplers [30,31]. Different types of hybrid couplers using slotline and coplanar waveguide structures have also been reported [6].

Figure 13 shows a microstrip hybrid ring coupler. When a unit amplitude wave is incident at port 4 of the coupler, the wave is divided into two components at the ring junction. These two components arrive in phase at ports 2 and 3, and 180° out of phase at port 1. Furthermore, if a unit amplitude is incident at port 1 of the coupler, the wave divides into two components that arrive at ports 2 and 3 with a net phase difference of 180° , and 180° out of phase at port 4.

According to the characteristics of the coupler, a balanced mixer can be built. The single balanced mixer shown in Fig. 14 consists of a hybrid ring coupler, two diodes, two RF chokes, two DC blocks, and one lowpass filter. The local oscillator (LO) is 180° out of phase at the RF port, providing the isolation between the LO and RF ports. The LO signal is split equally but is 180° out of phase at two diodes. The RF signal is split equally and in phase into two diodes. The phase noise of LO is thus canceled. Both RF and LO signals are mixed in the diodes to generate an IF signal at the output of the lowpass filter. The RF chokes provide a tuning mechanism and prevent the RF signal from leaking into ground. Figure 15 shows the measured results of a 94-GHz hybrid coupler mixer [29]. The mixer

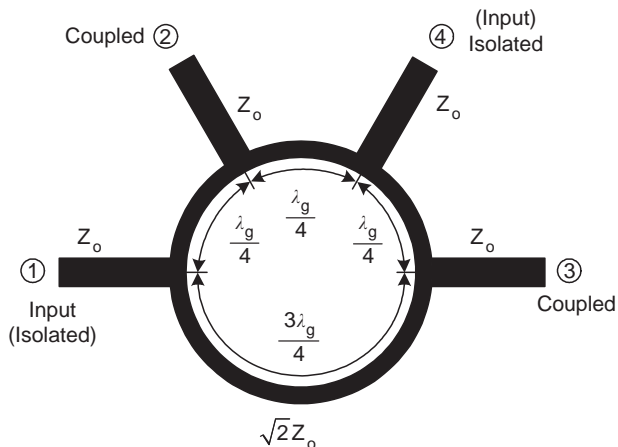


Figure 13. A microstrip hybrid ring coupler.

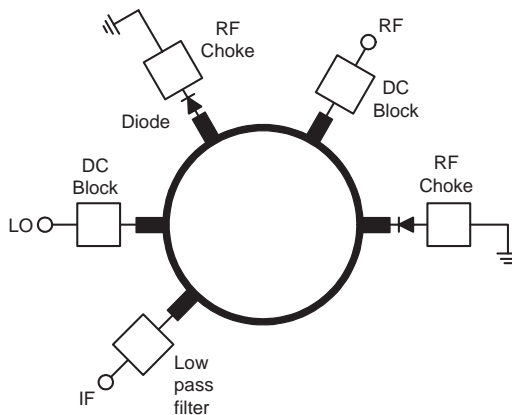


Figure 14. A hybrid coupler mixer.

has a conversion loss of less than 8 dB over a 3 GHz RF bandwidth using LO pump power of 8 dBm and less than 6.5 dB with LO pump power of 10 dBm.

6. RING ANTENNAS

In mid-1970s, microstrip antennas drew widespread attention because of their low cost and easy fabrication. Also, they could be easily used to design circularly polarized antennas, frequency-selective surface antennas, active antennas, phased arrays, reflect arrays, and so on [32–35]. New designs and applications of coplanar antennas are expected in modern wireless and personal communication systems.

6.1. Ring Antenna Circuit Models

The ring antenna shown in Fig. 16 consists of a close-loop ring conductor on one side of the substrate with a ground plane on the other side. The ring has an inside radius of r_i and an outside radius of r_o . The feedpoint radius is r_p . The total length of the ring antenna can be calculated from Eq. (8).

Since the thickness h is very small compared to the wavelength λ_0 , the variation of the electric field in the

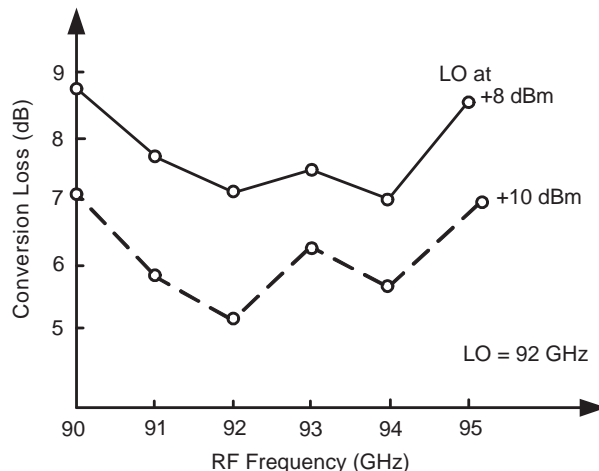


Figure 15. Performance of a 94-GHz hybrid coupler mixer [24].

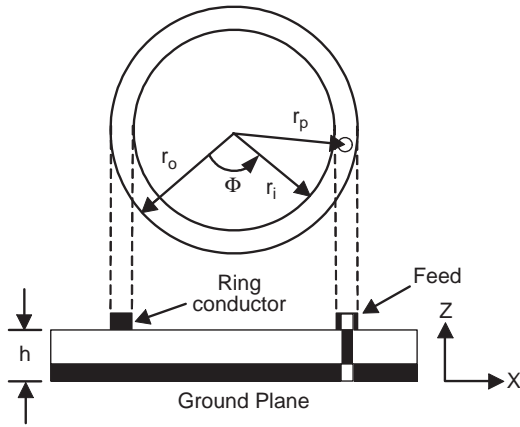


Figure 16. Configuration of a ring antenna.

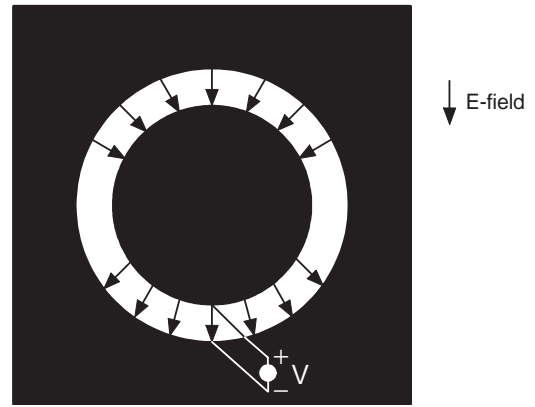


Figure 18. Slot ring feed method showing electric field.

z direction can be ignored. Without the Φ dependence, the TM modes of the electric and magnetic fields of the ring antenna are given by [36]

$$E_z(r) = A_n J_n(kr) + B_n N_n(kr) \tag{13}$$

$$H_\Phi(r) = -\frac{jk}{\omega\mu_0} [A_n J'_n(kr) + B_n N'_n(kr)] \tag{14}$$

These fields are used to define modal voltages and currents. The modal voltage is simply defined as $E_z(r)$. The modal current is rH_Φ or $-rH_\Phi$ for power propagation in the r direction, respectively. The admittance at any point r is expressed by

$$Y(r) = \frac{rH_\Phi(r)}{E_z(r)}, \quad r < r_p \tag{15}$$

$$Y(r) = -\frac{rH_\Phi(r)}{E_z(r)}, \quad r > r_p \tag{16}$$

6.2. Slot Ring Antennas

The slot antenna is a dual version of the microstrip ring antenna; a comparison is given in Fig. 17 [37]. It has a

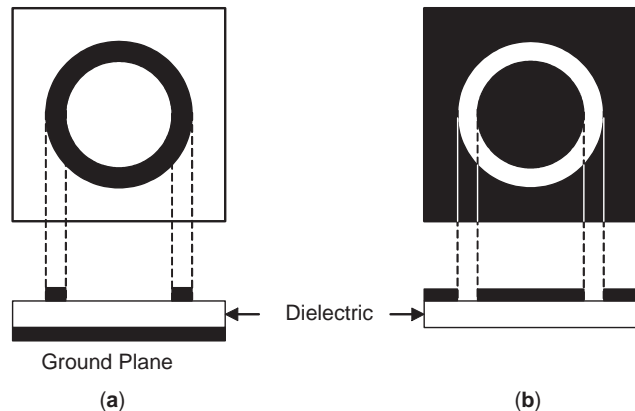


Figure 17. Comparison of (a) microstrip ring and (b) slot ring structures.

wider impedance bandwidth than does microstrip antenna. Therefore, the bandwidth of the slot antenna is greater than that of the microstrip antenna. By introducing some asymmetry to the slot antenna, a circular polarization (CP) radiation can be obtained. The slot ring antenna in the ground plane of a microstrip transmission line can be readily made into a corporate-fed array by implementing microstrip dividers.

To use the structure as an antenna, the first-order mode is excited as shown in Fig. 18 [37]. Also, the impedance seen by the voltage source is real at resonance. All the power delivered to the ring will be radiated [37]. The resonant frequency can be calculated using the transmission-line model [37].

Figure 19 shows a multifrequency annular slot antenna [38,39]. A 50-Ω microstrip feed is electromagnetically coupled to the slot ring at point A and is extended to point C. The circuit was etched on a Keene Corporation substrate with relative dielectric constant of 2.45 and height of 0.762 mm. The widths of the microstrip (w_m) and slot ring (w_s) were 2.16 and 2.9 mm, respectively. The mean circumference of the slot ring was 93.3 mm.

Ignoring the microstrip feed and treating the slot ring antenna as a transmission line, one expects the operating frequency to be the frequency at which the circumference

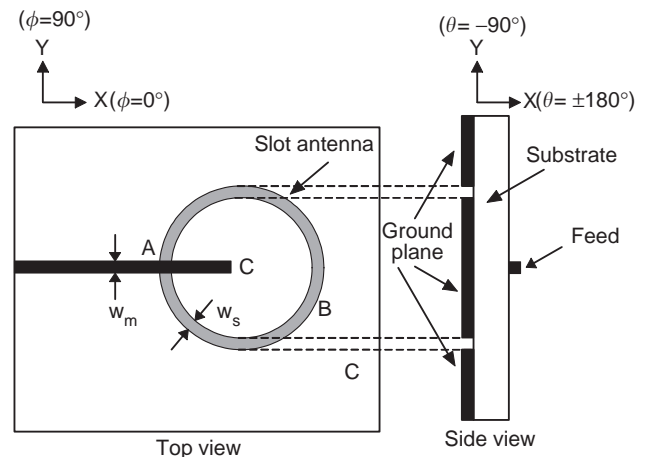


Figure 19. The configuration of the multifrequency annular antenna.

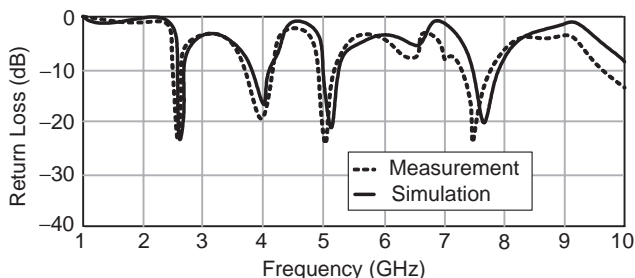


Figure 20. Measured and simulated return loss of the multifrequency antenna with AC=46.85 mm [38]. (Permission from IEEE.)

of the slot ring antenna becomes one guided wavelength of the slot (λ_{gs}). A slot guided wavelength for the frequency range of interest can be obtained from [40]

$$\lambda_{gs} = \lambda_0 \left\{ 1.045 - 0.365 \ln \epsilon_r + \frac{6.3(w_s/h)\epsilon_r^{0.945}}{(238.64 + 100w_s/h)} - \left[0.148 - \frac{8.81(\epsilon_r + 0.95)}{100\epsilon_r} \right] \ln \left(\frac{h}{\lambda_0} \right) \right\} \quad (17)$$

where λ_0 is the free-space wavelength and h is the thickness of the substrate. At 2.97 GHz, λ_{gs} is equal to the mean circumference of the antenna (93.3 mm). From this information, as a first-order approximation, first-operating frequency of the slot ring antenna is 2.97 GHz. The actual operating frequency of the microstrip-fed slot ring anten-

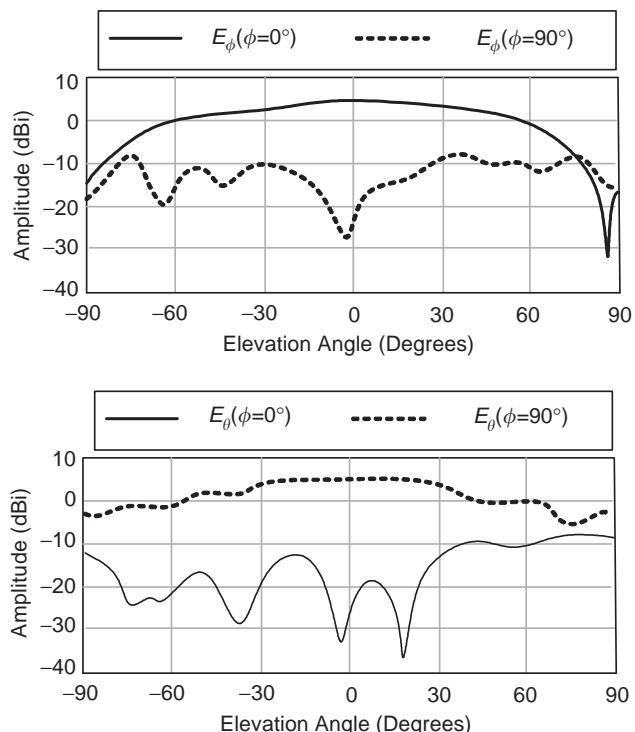
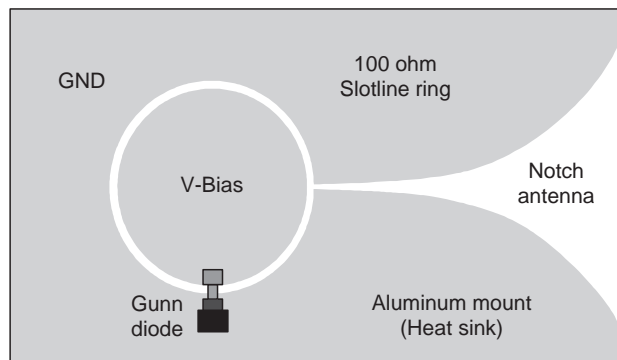
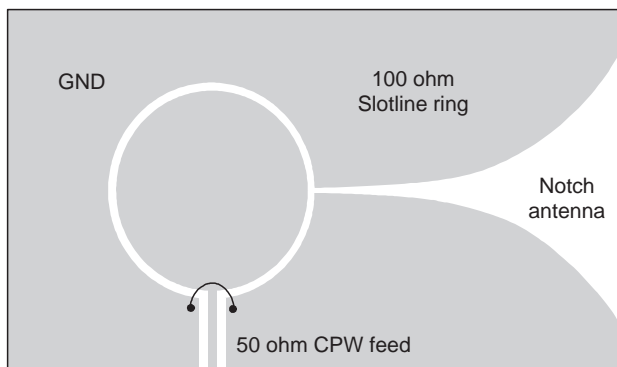


Figure 21. Radiation patterns of the multifrequency antenna with microstrip stub length AC=46.85 mm at 2.65 GHz [38]. (Permission from IEEE.)



(a)



(b)

Figure 22. Configuration of active antenna (a) Gunn diode active notch antenna using a slotline resonator (the wire for DC bias to the center of the ring is not shown) and (b) CPW-fed passive antenna (some dimensions in the figures are exaggerated to enhance detail) [34].

na can be either above or below this approximate frequency depending on the length of the microstrip stub.

The return loss of the multifrequency antenna and simulation results agree well and as shown in Fig. 20. The simulation was carried out by electromagnetic simulator [23]. Defining the operating frequency to be a frequency at which return loss is less than 10 dB, these experimental operating frequencies are centered at 2.58, 3.9, 5.03, and 7.52 GHz. The measured patterns of the antenna at resonant frequency of 2.65 GHz are shown in Fig. 21.

6.3. Active Ring Antennas

Active integrated antennas have the advantages of reducing the size, weight, and cost of many transmit and receive systems. Solid-state devices can be incorporated into an antenna to provide various functions. Two- and three-terminal solid-state devices have been integrated with various antennas to form switches, tuners, detectors, mixers, amplifiers, oscillators, Doppler sensors, and receivers. The choice between transistors and diodes is not clearcut. It depends on the type of microwave component required, operating frequency range, RF power output desired, available DC power input, and other considerations.

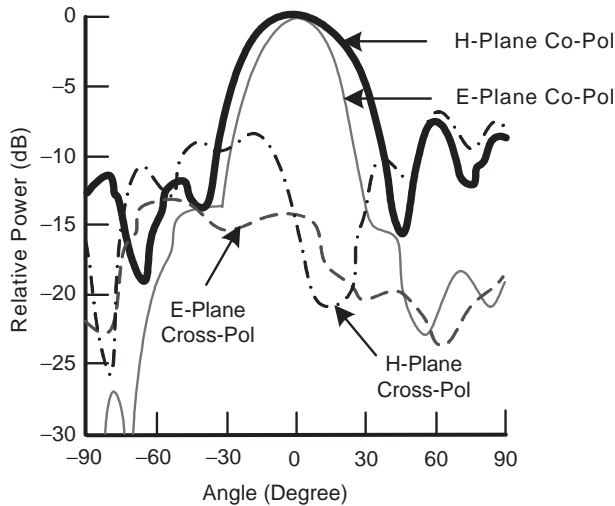


Figure 23. *E*-plane radiation pattern—half-power beamwidth (HPBW) = 33°, cross-polarization = 13.18 dB below copolarization; *H*-plane radiation pattern—HPBW = 47°, cross-polarization = 6.69 dB below copolarization [34]. (This figure is available in full color at <http://www.mrw.interscience.wiley.com/erfme>.)

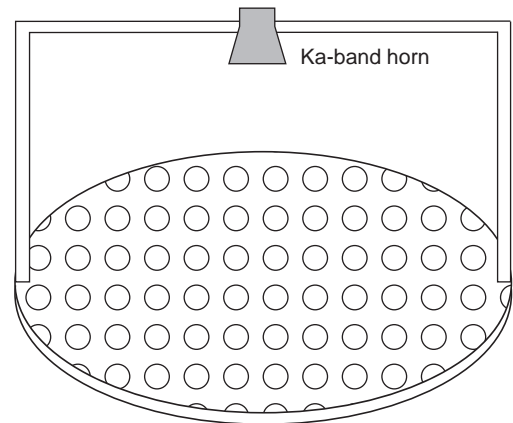
Unlike the design of a passive antenna, the design of an integrated active antenna needs to include the effects of device packages and bias lines. The effects often cause changes in operating frequencies, lower conversion efficiencies, and higher cross-polarization levels (CPLs).

As an example, the active antenna shown in Fig. 22 consists of a Gunn diode and a slotline notch antenna stabilized with a slotline ring resonator [34]. The Gunn diode is placed across the ring resonator at a low-impedance point to meet the conditions for oscillation. The slotline ring's resonant wavelength can be determined from

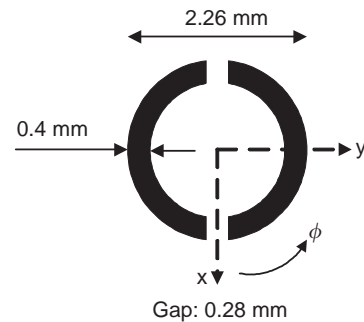
$$2\pi r = n\lambda_g, \quad n = 1, 2, 3, \dots \quad (18)$$

where r is the mean radius of the slotline ring, λ_g is the guided wavelength in the slotline ring, and n is the mode number.

Figure 22a shows the circuit configuration of the active antenna, while Fig. 22b shows the coplanar waveguide



(a)



(b)

Figure 24. Configuration of Ka-band reflectarray (a) setup and (b) ring antenna [35]. (Permission from *Electronics Letters*.)

(CPW)-fed passive antenna developed for radiation pattern comparison. The antennas were etched on Duroid 5870 board with a relative dielectric constant of 2.33, substrate thickness of 62 mils (1.575 mm), and 1-oz copper metallization. The antennas are truly uniplanar, requiring no backplane for excellent performance. The slotline ring has a mean radius of 3.81 mm and a slot width of 0.18 mm. The CPW feedline in the passive antenna has a

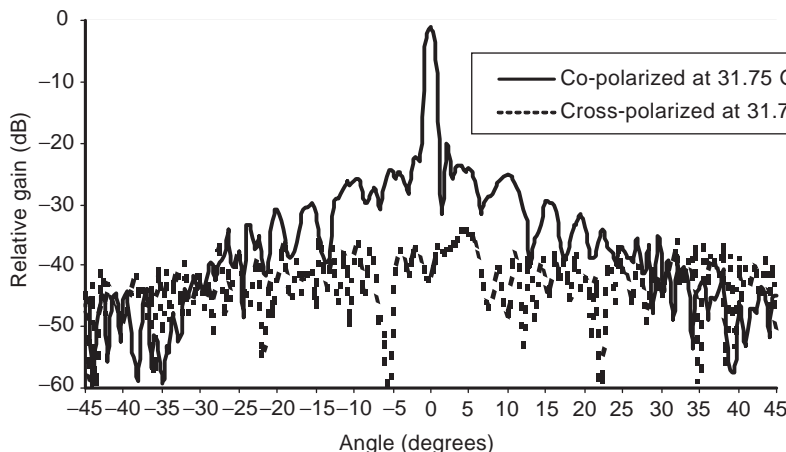


Figure 25. Measured radiation patterns [35]. (Permission from *Electronics Letters*.)

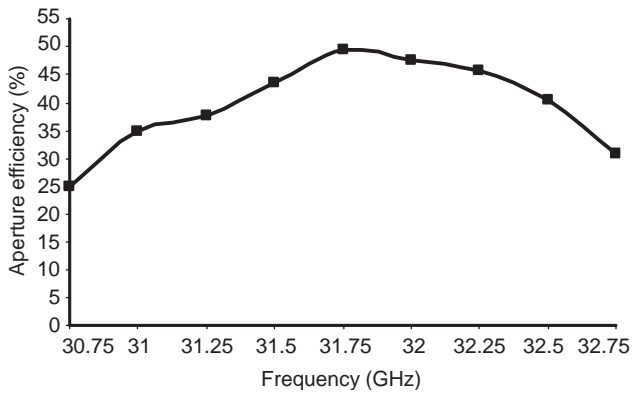


Figure 26. Measured aperture efficiency [35]. (Permission from *Electronics Letters*.)

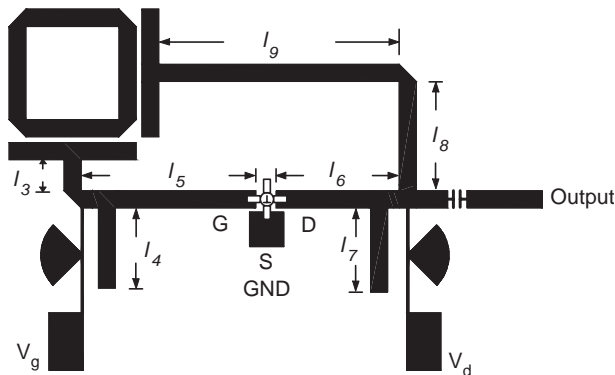


Figure 27. Feedback ring resonator oscillator [44]. (Permission from IEEE.)

center strip width of 1.2 mm and symmetric side gaps of 0.08 mm. A thin-wire airbridge is used to operate the CPW line in the even mode. The slotline notch antenna uses an exponential taper to match the impedance of the ring to free space. The antenna length is 6 cm, and the gap at the

feedpoint is 0.18 mm. The aluminum mount used in the active antenna also serves as the heatsink for the Gunn diode. The DC bias is provided directly to the center of the slotline ring. The active antenna radiates a clean spectrum at 9.26 GHz with a bias voltage of 10.0 V and draws 410 mA. The active antenna produces an effective power output of 27.1 mW and an effective isotropic radiated power (EIRP) of 720.0 mW. The spectrum has a phase noise of -95.33 dBc/Hz at 100 kHz from the carrier, while the second-harmonic radiation produced by the active antenna is 26.16 dB below the fundamental frequency. Figure 23 shows the radiation patterns of the active antenna.

The *E*-plane and *H*-plane patterns are smooth with cross-polarization levels of 13.18 and 6.69 dB below copolarization. The radiation *E* plane and *H* plane are 33° and 47°, respectively. The radiation pattern of the CPW-fed passive antenna is essentially similar with the exception that the cross-polarization levels are 18.74 and 16.51 or the *E* and *H* planes, respectively.

6.4. Reflect Array Using Ring Resonators

Microstrip reflectarrays have been shown to be good candidates for replacing the conventional parabolic reflector antennas. The technologies involve a flat printed array integrated with a space-feeding horn and have the advantages of low cost, low profile, easy fabrication, and flat surface [41].

Figure 24 shows the configuration of the reflectarray with a Ka-band feedhorn [35]. The reflectarray is constructed by ring resonators with two slits at the top and the bottom. Compared with the reflectarray using square patch antennas, this configuration using ring antennas can increase the operating bandwidth and reduce blockage when using in a dual-layer, dual-frequency application.

Because of the nature of reflection, an incident right-hand circularly polarized wave is reflected as a left-hand circularly polarized wave. However, by using these two slits on the ring, the reversal of polarization can be

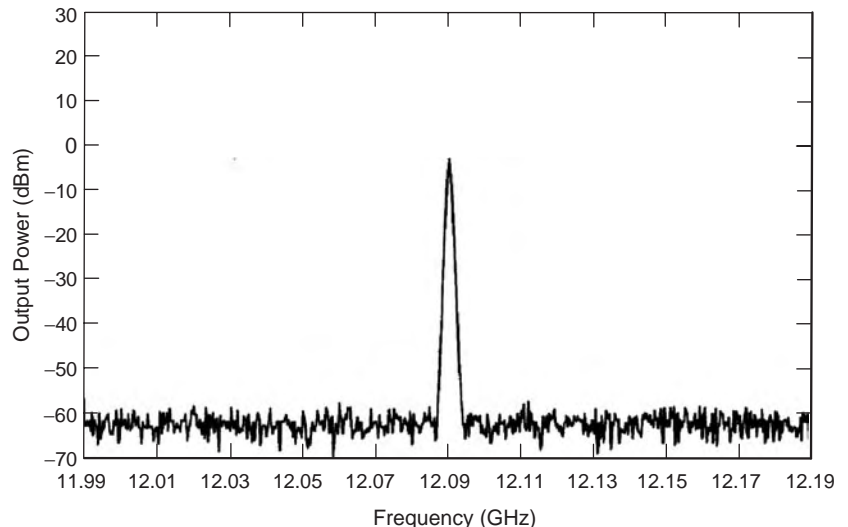


Figure 28. Output power for the feedback ring resonator oscillator operated at the second resonant mode of the ring resonator [44]. (Permission from IEEE.)

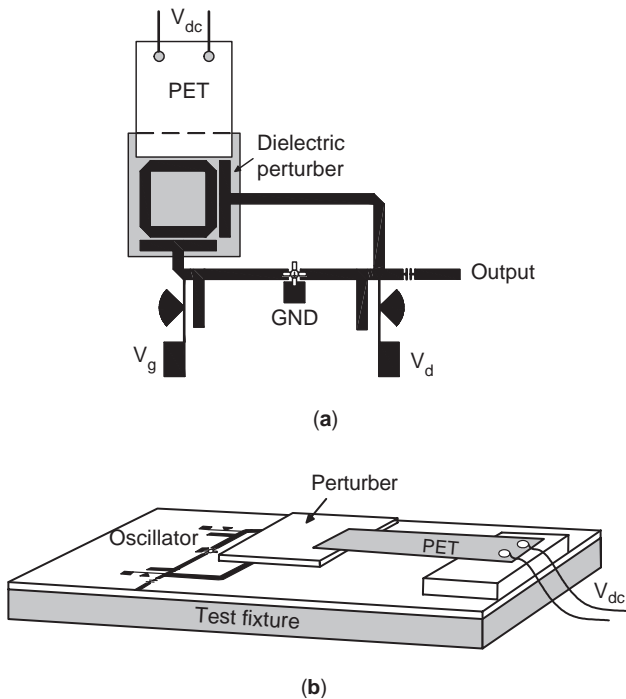


Figure 29. Configuration of the tunable oscillator using a PET: (a) top view; (b) 3D view [44]. (Permission from IEEE.)

anceled out. Also, a simple trigonometric relation is used to calculate the required additional pathlengths to create a parabolic phase front across an array's surface. Each ring antenna is rotated counterclockwise by ϕ radians at each position when 2ϕ radians are needed for compensating these additional pathlengths. For the whole reflectarray with a diameter of 0.5 m, the repetitious behaviors of array configurations are found to be more than 4 times that of a 2π radian.

A 0.5-m reflectarray has been designed for broadside radiation at a focal distance of 350 mm corresponding to

an f/D ratio of 0.7. The ring antennas are fabricated on RT/Duroid 5870 substrate with $\epsilon_r = 2.33$ and 0.508 mm thickness. The space between rings is 0.5 free-space wavelength, which is selected to avoid grating lobes. The measured results at 31.75 GHz are shown in Fig. 25. The mainbeam has a beamwidth of 1.3° . The cross-polarization level is 40.71 dB down at broadside, and the sidelobe suppression is greater than 19.47 dB, occurring at 2° . This cross-polarization level corresponds to an axial ratio of less than 0.5 dB. The relatively high peak sidelobe is due to feedhorn blockage effects. The measured efficiency of the reflectarray is shown in Fig. 26. The efficiency is better than 40% from 31.5 to 32.5 GHz. The highest efficiency is 50% at 31.75 GHz.

7. RING OSCILLATORS

With the advantages of high Q factor, low radiation loss, low cost, and easy fabrication, the ring resonator can be used to design an oscillator. Moreover, comparing to dielectric resonator oscillators, a varactor can be easily mounted in a ring oscillator to tune the oscillation frequency [42]. Several different types of oscillators using ring resonator have been introduced [43–45].

Figure 27 shows a feedback oscillator that consists of a feedback ring circuit and a two-port negative-resistance oscillator with input and output matching networks [44]. The closed-loop ring resonator using a pair of orthogonal feedlines suppresses odd resonant frequencies and operates at even resonant frequencies. This operation is characterized by high operating resonant frequencies, similar to those of push–push oscillators [45]. Also, the high- Q ring resonator is used to reduce the noise of the two-port negative-resistance oscillator.

The active device used is a NE32484A HEMT from NEC. The dimensions of the oscillator are $l_3 = 3$ mm, $l_4 = 6.95$ mm, $l_5 = 15.19$ mm, $l_6 = 10.69$ mm, $l_7 = 7.3$ mm, $l_8 = 9.47$ mm, and $l_9 = 21.19$ mm. The two-port negative-resistance oscillator uses the one open-end terminal as a

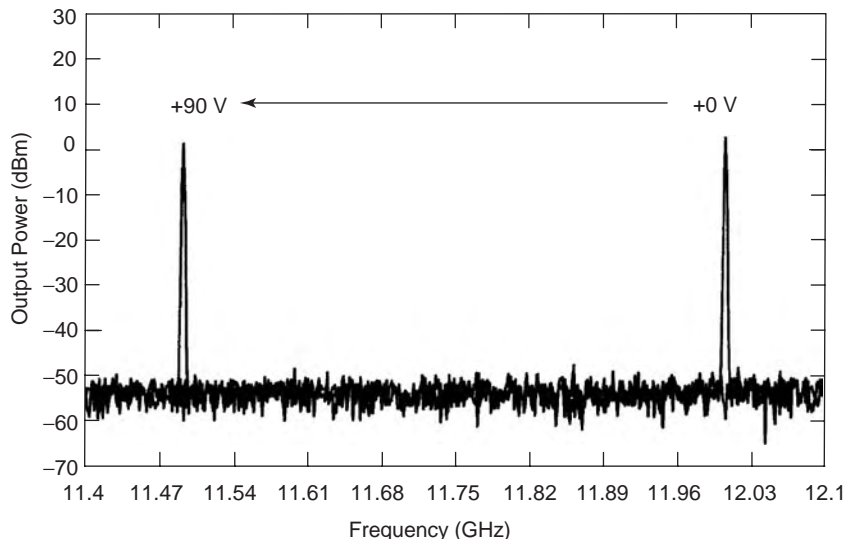


Figure 30. Measured tuning range of 510 MHz for the tunable oscillator using a PET [44]. (Permission from IEEE.)

series-feedback element to obtain a potential instability. Also, with input and output matching networks, the two-port oscillator with an applied bias of $V_{gs} = -0.65$ V and $V_{ds} = 1$ V has a negative resistance around 12 GHz.

Figure 28 shows a measured spectrum of the oscillator with applied voltages of $V_{gs} = -0.65$ V and $V_{ds} = 1$ V. Also, as shown in Fig. 28, the oscillator is operated at the second resonant mode of the ring resonator. The oscillator has the efficiency of 48.7% with output power of 3.41 mW at 12.09 GHz. The phase noise of the oscillator is -96.17 dBc/Hz at offset frequency of 100 kHz.

Figure 29 shows a configuration of the ring resonator oscillator integrated with a piezoelectric transducer (PET) with an attached dielectric perturber. When a DC voltage is applied to the PET, the PET moves the perturber up or down vertically to change the effective dielectric constant of the ring resonator, thus varying the resonant frequency of the ring resonator [44].

Figure 30 shows the measured results of the oscillator using the PET tuning. The perturber attached on the PET has a dielectric constant of $\epsilon_r = 10.8$ and thickness of $h = 50$ mil. The tuning range of the oscillator is from 11.49 GHz (at the applied voltage of +90 V to PET) with a power output of 3.17 dBm to 12 GHz (0 V) with a power output of 5.33 dBm.

8. CONCLUSIONS

A simple and useful ring resonator has been described. Because of its advantages of high Q , low radiation loss, low cost, and easy fabrication, it has been widely used in various applications such as dispersion measurement, filters, couplers, balanced mixers, balanced amplifiers, antennas, and oscillators. It is believed that many new applications could emerge in the future.

BIBLIOGRAPHY

- P. Troughton, Measurement techniques in microstrip, *Electron. Lett.* **5**(2):25–26 (Jan. 1969).
- I. Wolff and N. Knoppik, Microstrip ring resonator and dispersion measurements on microstrip lines, *Electron. Lett.* **7**(26):779–781 (Dec. 1971).
- K. Chang, T. S. Martin, F. Wang, and J. L. Klein, On the study of microstrip ring and varactor-tuned ring circuits, *IEEE Trans. Microwave Theory Tech.* **35**:1288–1295 (Dec. 1987).
- G. K. Gopalakrishnan and K. Chang, Bandpass characteristics of split-modes in asymmetric ring resonators, *Electron. Lett.* **26**(12):774–775 (June 1990).
- L.-H. Hsieh and K. Chang, Equivalent lumped elements G , L , C , and unloaded Q 's of closed- and open-loop ring resonators, *IEEE Trans. Microwave Theory Tech.* **50**(2):453–460 (Feb. 2002).
- C. Ho, L. Fan, and K. Chang, New uniplanar coplanar waveguide hybrid-ring couplers and magic-Ts, *IEEE Trans. Microwave Theory Tech.* **42**(12):2440–2448 (Dec. 1994).
- J. A. Navarro, and K. Chang, Varactor-tunable uniplanar ring resonators, *IEEE Trans. Microwave Theory Tech.* **41**(5):760–766 (May 1993).
- W. K. Hui and I. Wolff, Dielectric ring-gap resonator for application in MMIC's, *IEEE Trans. Microwave Theory Tech.* **39**(12):2061–2068 (Dec. 1991).
- C. Ho, L. Fan, and K. Chang, A new type of waveguide ring cavity for resonator and filter applications, *IEEE Trans. Microwave Theory Tech.* **42**(1):41–51 (Jan. 1994).
- K. Chang and L.-H. Hsieh, *Microwave Ring Circuits and Related Structures*, Wiley, New York, 2004.
- Y. S. Wu and F. J. Rosenbaum, Mode chart for microstrip ring resonators, *IEEE Trans. Microwave Theory Tech.* **21**:487–489 (July 1973).
- R. P. Owens, Curvature effect in microstrip ring resonators, *Electron. Lett.* **12**(14):356–357 (July 1976).
- S. G. Pintzos and R. Pregla, A simple method for computing the resonant frequencies of microstrip ring resonators, *IEEE Trans. Microwave Theory Tech.* **26**:809–813 (Oct. 1978).
- L.-H. Hsieh and K. Chang, Simple analysis of the frequency modes for microstrip ring resonators of any general shape and the correction of an error in literature, *Microwave Opt. Tech. Lett.* **38**:209–213 (Aug. 2003).
- L.-H. Hsieh and K. Chang, Dual-mode quasi-elliptic-function bandpass filters using ring resonators with enhanced-coupling tuning stubs, *IEEE Trans. Microwave Theory Tech.* **50**(5):1340–1345 (May 2002).
- G. K. Gopalakrishnan and K. Chang, Novel excitation schemes for the microstrip ring resonator with lower insertion loss, *Electron. Lett.* **30**(2):148–149 (Jan. 1994).
- I. Wolff, Microstrip bandpass filter using degenerate modes of a microstrip ring resonator, *Electron. Lett.* **8**(12):302–303 (June 1972).
- L. Zhu and K. Wu, A joint field/circuit model of line-to-ring coupling structures and its application to the design of microstrip dual-mode filters and ring resonator circuits, *IEEE Trans. Microwave Theory Tech.* **47**(10):1938–1948 (Oct. 1999).
- L.-H. Hsieh and K. Chang, Compact dual-mode elliptic-function bandpass filter using a single ring resonator with one coupling gap, *Electron. Lett.* **36**(19):1626–1627 (Sep. 2000).
- J. S. Hong and M. J. Lancaster, Bandpass characteristics of new dual-mode microstrip square loop resonators, *Electron. Lett.* **31**(11):891–892 (May 1995).
- L.-H. Hsieh and K. Chang, Compact, low insertion-loss, sharp-rejection, and wide-band microstrip bandpass filters, *IEEE Trans. Microwave Theory Tech.* **51**(4):1241–1246 (April 2003).
- J. S. Hong and M. J. Lancaster, Microstrip bandpass filter using degenerate mode of a novel meander loop resonator, *IEEE Microwave Guided Wave Lett.* **5**(11):371–372 (Nov. 1995).
- IE3D Version 8.0, Zeland Software Inc., Fremont, CA, January 2001.
- L.-H. Hsieh and K. Chang, Tunable microstrip bandpass filters with two transmission zeros, *IEEE Trans. Microwave Theory Tech.* **51**(2):520–525 (Feb. 2003).
- J. T. Kuo, M. J. Maa, and P. H. Lu, A microstrip elliptic function filter with compact miniaturized hairpin resonators, *IEEE Microwave Guided Wave Lett.* **10**(3):94–95 (March 2000).
- P. Akkaraekthalin, S. Jongjitaree, and V. Vivek, Coplanar waveguide balanced amplifier using bipolar junction transistors and backed ground-plane hybrids, *Electrical and Electronic Tech., TENCON, International Conference*, Vol. 2, pp. 732–735, 2001.

27. H. R. Ahn and I. Wolff, Asymmetric ring-hybrid phase shifters and attenuators, *IEEE Trans. Microwave Theory Tech.* **50**(4):1146–1155 (April 2002).
28. X. Xie, J. Khurgin, J. Kang, and F. S. Choa, Ring-assisted frequency discriminator with improved linearity, *IEEE Photon. Tech. Lett.* **14**(8):1136–1138 (Aug. 2002).
29. K. Chang, D. M. English, R. S. Tahim, A. J. Grote, T. Phan, C. Sun, G. M. Hayashibara, P. Yen, and W. Piotrowski, W-band (75–110 GHz) microstrip components, *IEEE Trans. Microwave Theory Tech.* **33**(12):1375–1382 (Dec. 1985).
30. C. Y. Pon, Hybrid-ring directional couplers for arbitrary power division, *IRE Trans. Microwave Theory Tech.* **9**:529–535 (Nov. 1961).
31. S. March, A wideband stripline hybrid ring, *IEEE Trans. Microwave Theory Tech.* **16**:361–369 (June 1968).
32. R. R. Ramirez, F. De Flaviis, and N. G. Alexopoulos, Single-feed circularly polarized microstrip ring antenna and arrays, *IEEE Trans. Anten. Propag.* **48**(7):1040–1047 (July 2000).
33. T. K. Wu and S. W. Lee, Multiband frequency selective surface with multiring patch elements, *IEEE Trans. Anten. Propag.* **42**(11):1484–1490 (Nov. 1994).
34. C. M. Montiel, L. Fan, and K. Chang, Active-notch antennas stabilized with a slotline-ring resonator for wireless applications, *IEEE Trans. Anten. Propag.* **46**(6):945–946 (June 1998).
35. C. Han and K. Chang, Ka-band reflectarray using ring elements, *Electron. Lett.* **39**(6):491–493 (March 2003).
36. A. K. Bhattacharyya and R. Garg, Self and mutual admittance between two concentric, coplanar, circular radiating current sources, *Proc. IEE* **130**(Part H)(6):217–219 (June 1984).
37. K. D. Stephan, N. Camilleri, and T. Itoh, A quasi-optical polarization-duplexed balanced mixer for millimeter-wave applications, *IEEE Trans. Microwave Theory Tech.* **31**(2):164–170 (Feb. 1983).
38. H. Tehrani and K. Chang, Multifrequency operation of microstrip-fed slot-ring antennas on thin low-dielectric permittivity substrates, *IEEE Trans. Anten. Propag.* **50**(9):1299–1308 (Sep. 2002).
39. H. Tehrani and K. Chang, A multi-frequency microstrip-fed annular slot antenna, *Proc. IEEE AP-S Int. Symp. Digest*, July 2000, pp. 632–636.
40. J. Huang and R. Pogorzelski, A Ka-band microstrip reflectarray with elements having variable rotation angles, *IEEE Trans. Anten. Propag.* **46**(5):650–656 (May 1998).
41. Y. D. Lee, M. H. Lee, K. H. Lee, W. P. Hong, and U. S. Hong, Voltage-controlled hair-pin resonator oscillator with new tuning mechanism, *Electron. Lett.* **36**(17):1470–1471 (Aug. 2000).
42. N. Popovic, Novel method of DRO frequency tuning with varactor diode, *Electron. Lett.* **26**(15):1162 (July 1990).
43. S. Qi, K. Wu, and Z. Ou, Hybrid integrated HEMT oscillator with a multiple-ring nonradiative dielectric (NRD) resonator feedback circuit, *IEEE Trans. Microwave Theory Tech.* **46**(10):1552–1558 (Oct. 1998).
44. L.-H. Hsieh and K. Chang, High-efficiency piezoelectric-transducer-tuned feedback microstrip ring-resonator oscillators operating at high resonant frequencies, *IEEE Trans. Microwave Theory Tech.* **51**(4):1141–1145 (April 2003).
45. F. X. Sinnesbichler, B. Hautz, and G. R. Olbrich, A Si/SiGe HBT dielectric resonator push-push oscillator at 58 GHz, *IEEE Microwave Guided Wave Lett.* **10**(4):145–147 (April 2000).

ROUGH-SURFACE SCATTERING: NUMERICAL SIMULATIONS AND APPLICATIONS IN MICROWAVE REMOTE SENSING

QIN LI

University of Washington
Seattle, Washington

MING YAO XIA
Peking University
Beijing, China

LEUNG TSANG
University of Washington
Seattle City

LIN ZHOU
Duke University
North Carolina

CHI HOU CHAN

ZHONG XIN LI

City University of Hong Kong

1. INTRODUCTION

There has been increasing interest in electromagnetic scattering from rough surfaces in with applications in active and passive remote sensing for soil, ocean, ice, and so on. Satellite microwave measurements of soil and ocean surface thermal emission and radar backscattering can provide the means to predict soil moisture and ocean properties. This interest has been fueled by satellites that were recently (as of 2004) launched or are being planned such as TRMM, EOS/AQUA, ADEOS II, Windsat, NPOESS, SMOS, and HYDROS. The small-perturbation method (SPM) and Kirchhoff approximation (KA) are classical theories of wave scattering of rough surfaces. They are limited in regimes of validity and do not give the correct frequency and polarimetric dependence of electromagnetic wave scattering. New analytic methods such as small-slope approximation (SSA) and the integral equation model (IEM) have also been developed to increase the regime of validity of classical theories. With the advent of modern computers, fast numerical simulations for rough-surface scattering have become attractive. The most common methods are the fast multipole method (FMM) and the sparse matrix canonical grid (SMCG) method. The computational complexity and memory requirement of the steepest-descent FMM (SDFMM) and SMCG are $O(N)$ and $O(N \log N)$, respectively, in these fast algorithms. Using these numerical methods, we have been developing the 3D numerical Maxwell model (NMM3D) for rough surface scattering applications. Through the simulations, the computed values of bistatic scattering and emissivities based on the numerical solutions of Maxwell equations will be tabulated and provided to the user's community. The goal is to have the tables for a variety of rough surface types and parameters. In a recent text [1], we have provided the details of numerical algorithms and applications in remote sensing. The SMCG method is limited by the RMS height. A Taylor expansion is made about the flat surface. The smallness parameter is the ratio of the height to the near-field distance. We have used six terms Taylor

expansion. If the height increases, then we need to use a larger near-field distance or use more terms in the Taylor expansion. Because of height limitations in the SMCG method, thus we are presently developing the multilevel UV method. In general the numerical simulations are limited by the fact that the surface area of the sample size must be much larger than both the correlation length (to ensure that the sample has many peaks and valleys and qualifies as a statistical sample) and the wavelength (so that the tapered wave can be used to approximate a plane wave). We expect that in the near future, with the advent of computers and numerical methods, NMM3D can replace all analytic theories when the RMS heights are within $1-2\lambda$ wavelengths and correlation lengths within 10λ .

This article deals with the forward problem, and discusses matching the theoretical simulations with measured data as an example of application of the theory. However, matching of forward computations with data is only a part of the picture. The real need or application is for an inversion or retrieval of soil moisture, for example, from backscatter or brightness temperature. Usually, a spaceborne instrument (radar or radiometer) may have one or two channels of measurements at L band as in the upcoming HYDROS Mission. Based on the comparisons with experimental data, we conclude that exponential spectrum is presently the best assumption. The knowledge of an accurate a priori roughness spectrum is not needed. In the NMM3D, only two parameters are needed: the RMS height and the correlation length. These two parameters do not add additional unknowns to the present inversion scheme [2–4] because the present inversion scheme of AMSR also uses two empirical parameters: H and Q . The advantages of a physically based NMM3D are that the parameters are physical and also can be used for both passive and active remote sensing. Furthermore the same physical parameters can be used for a wide frequency range rather than individual frequencies such as H and Q . The present NMM3D can be readily incorporated in the present inversion scheme by using the physical parameters of RMS height and correlation length to replace H and Q .

In this article, we address the applications of remote sensing of land and ocean. Land, applications include soil and roughness effects at the interface between the snow and the soil underneath. For such surfaces, the roughness generally exhibits large slopes with fine-scale irregular features. The RMS height is on the centimeter scale and is small to moderate at microwave frequencies. The surface scattering tends to be diffuse. Both coherent and incoherent waves are important. For ocean surface, the RMS slope is small; however, RMS height is large at microwave frequencies. Huge ocean waves can have heights exceeding 10 m. Thus the scattered wave is incoherent with strong scattering in the specular direction.

In the present article, we will cover only a few of the most recent research results pertain to the scope of the text here. In Section 2 we describe developments in numerical simulations methods and in Section 3, results that can be applied to microwave remote sensing. In Section 2, we describe the methods of computational

electromagnetics in rough-surface simulations. We start with the SMCG method, which has been extensively used in simulations of real-life problems. Then we describe the multilevel SMCG method and the multilevel UV method, both of which were developed recently and have the potential of drastically improving computational efficiency. In Section 2.1, we describe the SMCG method and the physics-based two-grid (PBTG) method for rough surface simulations. In Section 2.2, we describe the use of the Rao–Wilton–Glisson (RWG) basis functions and the combination of the SMCG method. In Section 2.3, we describe the method of using a single-integral equation (SIE) and the combination with the multilevel SMCG. In Section 2.4, we describe rough-surface scattering using the UV method with multilevel partitioning.

In Section 3, we describe the simulation results of some real-life problems using SMCG. In Section 3.1 we describe NMM3D applications in active remote sensing and in Section 3.2, in passive remote sensing.

2. METHODS OF NUMERICAL ALGORITHMS

This section introduces the readers to the state of the art of using numerical methods to simulate roughness response at microwave frequencies. Much work still needs to be done in extensive real life simulations. What we will show are simply the results at L and C bands at 1.4 GHz for soils and at 14 GHz for ocean.

2.1. The SMCG Method and the PBTG Method for Rough Surface Simulations

The scattering of electromagnetic waves by lossy dielectric surfaces with large permittivity [5,6] has broad applications in natural media. For wet soil, the relative permittivity can be as high as $17 + i2.0$ at 1.4 GHz; for ocean surfaces, the permittivity can be as high as $39.7 + i40.2$ at 14 GHz. A common implementation of the method of moments (MoM) is to use a grid of 8–10 points per wavelength to discretize the surface. We shall call such a gridding a *single coarse grid* (SCG). Two methods are used to treat lossy dielectric surfaces. The first method is to use impedance boundary conditions [7]. The impedance boundary condition ignores the propagation from one point to all other points through the dielectric medium. For wave scattering from metallic surfaces with very large permittivity, impedance boundary condition could be used because the wave in the medium cannot propagate to the other points. However, for lossy dielectric rough surfaces with high permittivity and fine-scale irregular features, there can be rapid spatial variations of the dielectric medium Green function and surface fields. Thus the impedance boundary method is not valid for such a case. The second method is to use a dense grid with a large number of points (say, 16–20 points) per wavelength. We shall call such a gridding a *single dense grid* (SDG). The disadvantage of this SDG is that there is a large increase in central processing unit (CPU) and required memory. We have developed the PBTG method [5,6], which is an improvement over the previous two alternatives in that it has the same accuracy as the SDG and yet has a CPU

comparable with that of the SCG. The PBTG method can calculate the emissivity accurately. In PBTG, two grids are used: a dense grid and a sparse grid. The sparse grid contains the usual 8–10 points per wavelength. The dense grid ranges from 16 or a higher number of points per wavelength depending on the relative permittivity of the lossy dielectric medium. The surface fields are calculated on the dense grid. In the formulation of the surface integral equations, two Green functions are used: the free space Green function and the Green function of the lossy dielectric medium. The PBTG is based on two observations: (1) the Green function of the lossy dielectric is attenuative (spatially limited) and (2) the Green function of free space is slowly varying on the dense grid (spatial frequency-limited). Because of the Kramer–Kronig relation, a large real part of dielectric constant is usually associated with a large imaginary part at high frequency. The first observation results in a sparse matrix for the Green function of the lossy dielectric. When this Green function acts on the surface fields on the dense grid, it will be just the product of a sparse matrix and a column vector. The second observation allows us, when using the free-space Green function to act on the surface fields of a dense grid, to first average the values of surface unknowns on the dense grid and then place them on the coarse grid. Thus, the PBTG speeds up the CPU and yet preserves the accuracy of the solution. It should be mentioned that the PBTG is different from the multigrid method. The multigrid method [8,9] tries to facilitate the convergence of iteration in iterative techniques. The present method is based on scattering physics. The purpose of PBTG is to speed up the matrix–vector product that corresponds to the convolution of two Green functions with the surface fields on the dense grid.

2.1.1. Formulation and Single-Grid Implementation. Consider an electromagnetic wave $\bar{E}_i(\vec{r})$ and $\bar{H}_i(\vec{r})$, with a time dependence of $e^{-i\omega t}$ impinging on a 2D dielectric rough surface with a random height profile $z=f(x, y)$. It is tapered so that the illuminated rough surface can be confined to the surface area $L_x \times L_y$ [10]. The direction of incident wave is $\hat{k}_i = \sin \theta_i \cos \phi_i \hat{x} + \sin \theta_i \sin \phi_i \hat{y} - \cos \theta_i \hat{z}$. The incident fields are given as

$$\bar{E}_i(\vec{r}) = \int_{-\infty}^{\infty} dk_x \int_{-\infty}^{\infty} dk_y e^{ik_x x + ik_y y - ik_z z} \cdot \mathbf{E}(k_x, k_y) \cdot \hat{\mathbf{e}}(-k_z) \quad (4)$$

$$\bar{H}_i(\vec{r}) = -\frac{1}{\eta_1} \int_{-\infty}^{\infty} dk_x \int_{-\infty}^{\infty} dk_y e^{ik_x x + ik_y y - ik_z z} \cdot \mathbf{E}(k_x, k_y) \cdot \hat{\mathbf{h}}(-k_z) \quad (5)$$

for TE wave incidence

$$\hat{\mathbf{e}}(-k_z) = \frac{1}{k_\rho} (\hat{x}k_y - \hat{y}k_x) \quad (6)$$

$$\hat{\mathbf{h}}(-k_z) = \frac{k_z}{kk_\rho} (\hat{x}k_y + \hat{y}k_x) + \frac{k_\rho}{k} \hat{z} \quad (4)$$

and for TM wave incidence

$$\hat{\mathbf{h}}(-k_z) = -\frac{1}{k_\rho} (\hat{x}k_y - \hat{y}k_x) \quad (5)$$

$$\hat{\mathbf{e}}(-k_z) = \frac{k_z}{kk_\rho} (\hat{x}k_x + \hat{y}k_y) + \frac{k_\rho}{k} \hat{z} \quad (6)$$

with $k_z = \sqrt{k_1^2 - k_\rho^2}$ and $k_\rho = \sqrt{k_x^2 + k_y^2}$, where k_1 and η_1 are the wavenumber and wave impedance of free space, respectively. The spectrum of the incident wave $E(k_x, k_y)$ is given as

$$E(k_x, k_y) = \frac{1}{4\pi^2} \int_{-\infty}^{\infty} dx \int_{-\infty}^{\infty} dy e^{-ik_x x - ik_y y} \cdot e^{i(k_{1x}x + k_{1y}y)(1+w)} \cdot e^{-t} \quad (7)$$

where $t = t_x + t_y = (x^2 + y^2)/g^2$ and

$$t_x = \frac{(\cos \theta_i \cos \phi_i x + \cos \theta_i \sin \phi_i y)^2}{g^2 \cos^2 \theta_i} \quad (8)$$

$$t_y = \frac{(-\sin \phi_i x + \cos \phi_i y)^2}{g^2} \quad (9)$$

$$w = \frac{1}{k_1^2} \left(\frac{2t_x - 1}{g^2 \cos^2 \theta_i} + \frac{2t_y - 1}{g^2} \right) \quad (10)$$

The parameter g controls the tapering of the incident wave. We use the Green functions G_1 and G_2 , which are the 3D Green functions of free space and the lower dielectric medium, respectively. They are given by

$$G_{1,2} = \frac{e^{ik_{1,2}R}}{4\pi R} \quad (11)$$

where $R = \{(x - x')^2 + (y - y')^2 + (f(x, y) - f(x', y'))^2\}^{1/2}$ and k_1 and k_2 are the wavenumbers of air and the lower dielectric medium, respectively. The Stratton–Chu formulation is used to derive the surface integral equation. Then

$$\begin{aligned} & \frac{\hat{\mathbf{n}} \times \bar{H}(\vec{r})}{2} - \hat{\mathbf{n}} \times \left\{ \int (-i\omega) \hat{\mathbf{n}}' \times \bar{E}(\vec{r}') \varepsilon_1 G_1 dS' \right. \\ & \left. + P \int [(\hat{\mathbf{n}}' \times \bar{H}(\vec{r})) \times \nabla' G_1 \right. \\ & \left. + \hat{\mathbf{n}}' \cdot \bar{H}(\vec{r}) \nabla' G_1] dS' \right\} = \hat{\mathbf{n}} \times \bar{H}^{\text{inc}}(\vec{r}) \end{aligned} \quad (12)$$

$$\begin{aligned} & \frac{\hat{n} \cdot \bar{\mathbf{E}}(\bar{\mathbf{r}})}{2} - \hat{n} \cdot \left\{ \int \hat{n}' \times \bar{\mathbf{H}}(\bar{\mathbf{r}}') i\omega\mu G_1 dS' \right. \\ & \left. + P \int [(\hat{n}' \times \bar{\mathbf{E}}(\bar{\mathbf{r}})) \times \nabla' G_1 \right. \end{aligned} \quad (13)$$

$$\begin{aligned} & \left. + \hat{n}' \cdot \bar{\mathbf{E}}(\bar{\mathbf{r}}) \nabla' G_1] dS' \right\} = \hat{n} \cdot \bar{\mathbf{E}}^{\text{inc}}(\bar{\mathbf{r}}) \\ & - \frac{\hat{n} \times \bar{\mathbf{E}}(\bar{\mathbf{r}})}{2} - \hat{n} \times \left\{ \int (i\omega) \hat{n}' \times \bar{\mathbf{H}}(\bar{\mathbf{r}}') \right. \end{aligned} \quad (14)$$

$$\begin{aligned} & \mu G_2 dS' + P \int [(\hat{n}' \times \bar{\mathbf{E}}(\bar{\mathbf{r}})) \nabla' G_2 \\ & \left. + \hat{n}' \cdot \bar{\mathbf{E}}(\bar{\mathbf{r}}) \frac{\epsilon_1}{\epsilon_2} \nabla' G_2 \right] dS' \left. \right\} = 0 \end{aligned} \quad (15)$$

$$\begin{aligned} & - \frac{\hat{n} \cdot \bar{\mathbf{H}}(\bar{\mathbf{r}})}{2} - \hat{n} \cdot \left\{ \int -\hat{n}' \times \bar{\mathbf{E}}(\bar{\mathbf{r}}') \right. \\ & \left. \times i\omega\epsilon_2 G_2 dS' + P \int [(\hat{n}' \times \bar{\mathbf{H}}(\bar{\mathbf{r}})) \times \nabla' G_2 \right. \\ & \left. + \hat{n}' \cdot \bar{\mathbf{H}}(\bar{\mathbf{r}}) \nabla' G_2] dS' \right\} = 0 \end{aligned}$$

The MoM is used to discretize the integral equation using the pulse basis functions and the method of point matching. The resulting matrix equations are

$$\begin{aligned} & \sum_{n=1}^N [Z_{mn}^{p1} I_n^{(1)} + Z_{mn}^{p2} I_n^{(2)} + Z_{mn}^{p3} I_n^{(3)} \\ & + Z_{mn}^{p4} I_n^{(4)} + Z_{mn}^{p5} I_n^{(5)} + Z_{mn}^{p6} I_n^{(6)}] = I_m^{(p)\text{inc}} \end{aligned} \quad (16)$$

for $p=1,2,3$, which correspond the surface integral equation when approaching the surface from free space and for $p=4,5,6$ when approaching the surface from the lower medium. The quantities of $I_m^{(p)\text{inc}}$ are zero for $p=4,5,6$, where

$$I_n^{(1)} = F_x(\bar{\mathbf{r}}) = S_{xy}(\bar{\mathbf{r}}_n) [\hat{n} \times \bar{\mathbf{H}}(\bar{\mathbf{r}}_n)] \hat{\mathbf{x}} \quad (17)$$

$$I_n^{(2)} = F_y(\bar{\mathbf{r}}) = S_{xy}(\bar{\mathbf{r}}_n) [\hat{n} \times \bar{\mathbf{H}}(\bar{\mathbf{r}}_n)] \hat{\mathbf{y}} \quad (18)$$

$$I_n^{(3)} = I_n(\bar{\mathbf{r}}) = S_{xy}(\bar{\mathbf{r}}_n) \hat{n} \cdot \bar{\mathbf{E}}(\bar{\mathbf{r}}_n) \quad (19)$$

$$I_n^{(4)} = I_x(\bar{\mathbf{r}}) = S_{xy}(\bar{\mathbf{r}}_n) [\hat{n} \times \bar{\mathbf{E}}(\bar{\mathbf{r}}_n)] \hat{\mathbf{x}} \quad (20)$$

$$I_n^{(5)} = I_y(\bar{\mathbf{r}}) = S_{xy}(\bar{\mathbf{r}}_n) [\hat{n} \times \bar{\mathbf{E}}(\bar{\mathbf{r}}_n)] \hat{\mathbf{y}} \quad (21)$$

$$I_n^{(6)} = F_n(\bar{\mathbf{r}}) = S_{xy}(\bar{\mathbf{r}}_n) \hat{n} \cdot \bar{\mathbf{H}}(\bar{\mathbf{r}}_n) \quad (22)$$

are surface unknowns and

$$S_{xy} = \left\{ 1 + \left[\frac{\partial f(x,y)}{\partial x} \right]^2 + \left[\frac{\partial f(x,y)}{\partial y} \right]^2 \right\}^{1/2}$$

The Z_{mn}^{pq} is the impedance elements and are determined by the free space Green function and the dielectric

medium Green function. The parameter N is the number of points we use to discretize the rough surface.

2.1.2. Physics-Based Two-Grid Method. We assume that the lower medium is lossy with large permittivity

$$\epsilon_2 = \epsilon_2' (1 + i \tan \delta) \quad (23)$$

where $\tan \delta$ stands for loss tangent. Let λ_1 and λ_2 represent the wavelength of the wave in the free space and the lower medium, respectively, and

$$n_2 = \text{integer}(\sqrt{\epsilon_2'}) \quad (24)$$

Then, the relationship between λ_1 and λ_2 can be expressed approximately by

$$\lambda_2 \approx \frac{\lambda_1}{n_2} \quad (25)$$

The number of sampling points needed in the lower medium should be n_2 times that of the free space.

In the physics-based two-grid method, we use two grids with samplings per wavelength of n_{scg} (coarse grid) and n_{sdg} (dense grid), respectively. Let N_{scg} and N_{sdg} be, respectively, the total number of points on the dense grid and the coarse grid

$$N_{\text{sdg}} = \left(n_{\text{sdg}} \frac{L_x}{\lambda_1} \right) \left(n_{\text{sdg}} \frac{L_y}{\lambda_1} \right) \quad (26)$$

$$N_{\text{scg}} = \left(n_{\text{scg}} \frac{L_x}{\lambda_1} \right) \left(n_{\text{scg}} \frac{L_y}{\lambda_1} \right) \quad (27)$$

For example, $n_{\text{scg}} = 8$ and $n_{\text{sdg}} = 8n_2$. We first write (16) using the dense grid with $N = N_{\text{sdg}}$

$$\begin{aligned} & \sum_{n=1}^{N_{\text{sdg}}} [Z_{mn}^{p1} I_n^{(1)} + Z_{mn}^{p2} I_n^{(2)} + Z_{mn}^{p3} I_n^{(3)} \\ & + Z_{mn}^{p4} I_n^{(4)} + Z_{mn}^{p5} I_n^{(5)} + Z_{mn}^{p6} I_n^{(6)}] = I_m^{(p)\text{inc}} \end{aligned} \quad (28)$$

where the integer subscripts m and n denote indexing with the dense grid. Note that in the PBTG method, the surface fields on the dense grid are calculated. To reduce the calculation, we make the following three observations:

1. The Green function in the lower region is heavily attenuative. A medium with a large real part of dielectric constant is normally associated with a large imaginary part at high frequency because of the Kramer-Kronig relation. Let k_2'' be the imaginary part of k_2 . If $k_2'' r > C$, where C is a constant, then the field interaction between the m th and the n th points is vanishingly small. We can define a distance limit as dictated by dissipative loss

$$r_l = \frac{C}{k_2''} \quad (29)$$

outside of which the lower medium Green function can be set equal to zero. Comparisons with the results from SMCG, indicate that C is fixed at 1.5 in this article. Based on this observation, we calculate the left-hand sides of (28) for $p = 4, 5, 6$ as follows by approximating

$$Z_{mn}^{pq} \approx \tilde{Z}_{mn}^{pq} = \begin{cases} Z_{mn}^{pq} r, & r_{mn} \leq r_l \\ 0, & r_{mn} \geq r_l \end{cases} \quad (30)$$

where r_{mn} is the distance between the m th point and the n th points on the dense grid. Thus, \tilde{Z}_{mn}^{pq} ($p = 4, 5, 6$) are sparse matrices and (28) for $p = 4, 5, 6$ becomes

$$\sum_{n=1}^{N_{\text{sdg}}} [\tilde{Z}_{mn}^{p1} I_n^{(1)} + \tilde{Z}_{mn}^{p2} I_n^{(2)} + \tilde{Z}_{mn}^{p3} I_n^{(3)} + \tilde{Z}_{mn}^{p4} I_n^{(4)} + \tilde{Z}_{mn}^{p5} I_n^{(5)} + \tilde{Z}_{mn}^{p6} I_n^{(6)}] = 0 \quad (31)$$

- For non-near-field interaction, the Green function for the upper medium is slowly varying on the dense grid. Thus, when performing matrix-column vector multiplication on the dense grid, as indicated in (28), the Green function of the upper medium is essentially constant over an area of $n_2 \times n_2$ points on the dense grid. Thus, we can write

$$\begin{aligned} \sum_{n=1}^{n_2^2} Z_{(m+l')(n+l)}^{pq} I_{n+l}^{(q)} &\approx Z_{n_{mp}n_{np}}^{pq(q)} \sum_{l=1}^{n_2^2} I_{n+l}^{(q)} \\ &= n_2^2 Z_{n_{mp}n_{np}}^{pq} \left(\frac{1}{n_2^2} \sum_{l=1}^{n_2^2} I_{n+l}^{(q)} \right) \end{aligned} \quad (32)$$

where $l' = 1, 2, \dots, n_2^2$ and the points with indexes m_{mp} and n_{mp} are the central point of the n_2^2 dense grid points of $m + 1, m + 2, \dots, m + n_2^2$, and $n + 1, n + 2, \dots, n + n_2^2$, respectively. What is performed in (32) is that the surface fields on the dense grid are first averaged before being multiplied by the upper medium Green function.

- The slowly varying nature of the Green function of the upper medium applies only to non-near-field interaction. For near-field interaction, Green functions G_1 and G_2 have similar variation rates. Thus we separate out a distance, say, 1λ , outside of which G_2 is much more rapidly varying than G_1 . On the basis of the observations above, we decompose the upper medium Green function into near-field and non-near-field interactions

$$\sum_{n=1}^{N_{\text{sdg}}} Z_{mn}^{pq(s)} I_n^{(q)} = \sum_{n=1}^{N_{\text{sdg}}} Z_{mn}^{pq(q)} I_n^{(q)} + \sum_{n=1}^{N_{\text{sdg}}} Z_{mn}^{pq(ns)} I_n^{(q)} \quad (33)$$

where $Z_{mn}^{pq(s)}$ and $Z_{mn}^{pq(ns)}$ are determined by

$$Z_{mn}^{pq(s)} = \begin{cases} Z_{mn}^{pq}, & r_{mn} \leq r_f \\ 0, & r_{mn} \geq r_f \end{cases} \quad (34)$$

$$Z_{mn}^{pq(ns)} = \begin{cases} 0, & r_{mn} \leq r_f \\ Z_{mn}^{pq}, & r_{mn} \geq r_f \end{cases} \quad (35)$$

Thus, r_f is the distance outside which the Green function of the lower medium is rapidly varying compared with that of free space Green function. Let \tilde{m} and \tilde{n} denote the coarse grid indices. The coarse grid has surface unknowns $\tilde{I}_{\tilde{n}}^{(q)}$, which are averages of the dense grid surface unknowns. Thus, if $\tilde{r}_{\tilde{n}}$ is centered in the group of the n_2^2 dense grid-points of $n + 1, n + 2, \dots, n + n_2^2$, we have

$$\tilde{I}_{\tilde{n}}^{(q)} = \frac{I_{n+1}^{(q)} + I_{n+2}^{(q)} + \dots + I_{n+n_2^2}^{(q)}}{n_2^2} \quad (36)$$

The Green function of the upper medium on the coarse grid is represented by $\tilde{Z}_{\tilde{m}\tilde{n}}^{pq}$. Then (28) for $p = 1, 2, 3$ becomes

$$\begin{aligned} \sum_{q=1}^6 \sum_{n=1}^{N_{\text{sdg}}} Z_{mn}^{pq(s)} I_n^{(q)} \\ + \sum_{q=1}^6 \left[\sum_{\tilde{n}=1}^{N_{\text{scg}}} \tilde{Z}_{\tilde{m}\tilde{n}}^{pq(ns)} \tilde{I}_{\tilde{n}}^{(q)} \right]_{\text{int}p} = I_m^{(p)\text{inc}} \end{aligned} \quad (37)$$

Note in (37) that $\sum_{n=1}^{N_{\text{sdg}}} Z_{mn}^{pq(s)} I_n^{(q)}$ includes N_{sdg} values of $m = 1, 2, \dots, N_{\text{sdg}}$ on the dense grid, while $\sum_{\tilde{n}=1}^{N_{\text{scg}}} \tilde{Z}_{\tilde{m}\tilde{n}}^{pq(ns)} \tilde{I}_{\tilde{n}}^{(q)}$ only has N_{scg} values of $n = 1, 2, \dots, N_{\text{scg}}$ on the coarse grid. Thus, we first compute $\sum_{\tilde{n}=1}^{N_{\text{scg}}} \tilde{Z}_{\tilde{m}\tilde{n}}^{pq(ns)} \tilde{I}_{\tilde{n}}^{(q)}$. Then we use linear interpolation of $\sum_{\tilde{n}=1}^{N_{\text{scg}}} \tilde{Z}_{\tilde{m}\tilde{n}}^{pq(ns)} \tilde{I}_{\tilde{n}}^{(q)}$ on the coarse grid to find N_{sdg} values on the dense grid. In (37), we use subscript $\text{int}p$ to represent that interpolation. Thus the computational steps for matrix-vector multiplication are associated with the number of surface unknowns on the coarse grid. The algorithm is depicted in Fig. 1. Note that surface field is obtained with the dense grid but the CPU time depends on the coarse grid. The PBTG is also used in conjunction with the SMCG used previously used in computing scattering

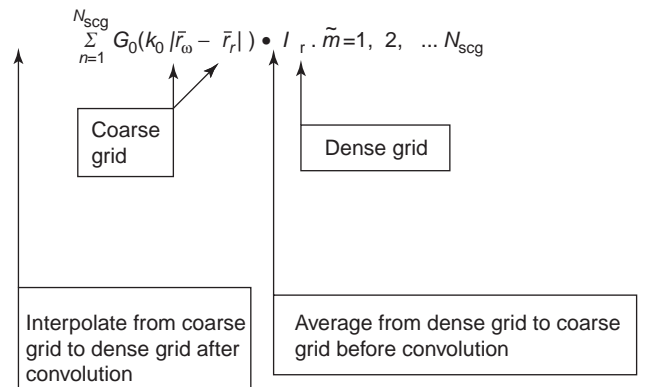


Figure 1. Illustration of physics-based two-grid method.

from 2D rough surfaces. The computational complexity of the combined algorithm of PBTG/SMCG is $O(N_{\text{scg}} \log(N_{\text{scg}}))$.

2.1.3. Bistatic Scattering Coefficient and Emissivity. The numerical simulation results are presented in terms of the bistatic scattering coefficients normalized by the incident power. For an incident wave with a polarization N_{sdg} , we have

$$\gamma_{\alpha\beta}(\theta_s, \phi_s; \theta_i, \phi_i) = \frac{|E_{\alpha}^s|^2}{2\eta_1 P_{\beta}^{\text{inc}}} \quad (38)$$

The incident power is

$$P_{\beta}^{\text{inc}} = \frac{2\pi^2}{\eta} \int_{k_{\rho} < k} dk_x dk_y |E(k_x, k_y)|^2 \frac{k_z}{k} \quad (39)$$

where $k_{\rho} = \sqrt{k_x^2 + k_y^2}$. The horizontal and vertical polarized scattered components are E_{α}^s , respectively

$$\begin{aligned} E_h^s &= \frac{ik}{4\pi} \int_{ds'} dx' dy' \exp(-ik\beta') \\ &\quad \{ I_x(x', y') \cos \theta_s \cos \phi_s \\ &\quad + I_y(x', y') \cos \theta_s \sin \phi_s \\ &\quad - I_x(x', y') \frac{\partial f(x', y')}{\partial x'} \sin \theta_s \\ &\quad - I_y(x', y') \frac{\partial f(x', y')}{\partial y'} \sin \theta_s \\ &\quad - \eta [F_x(x', y') \sin \phi_s \\ &\quad - F_y(x', y') \cos \phi_s] \} \end{aligned} \quad (40)$$

$$\begin{aligned} E_v^s &= \frac{ik}{4\pi} \int_{ds'} dx' dy' \exp(-ik\beta') \\ &\quad \{ I_x(x', y') \sin \phi_s - I_y(x', y') \cos \phi_s \\ &\quad + \eta [F_x(x', y') \cos \theta_s \cos \phi_s \\ &\quad + F_y(x', y') \cos \theta_s \sin \phi_s \\ &\quad - F_x(x', y') \frac{\partial f(x', y')}{\partial x'} \sin \theta_s \\ &\quad - F_y(x', y') \frac{\partial f(x', y')}{\partial y'} \sin \theta_s \} \end{aligned} \quad (41)$$

where $\beta = x' \sin \theta_s \cos \phi_s + y' \sin \theta_s \sin \phi_s + f(x', y') \cos \theta_s$. For scattering by a dielectric surface, the emissivity of the rough surface at incident angle (θ, ϕ_i) based on energy conservation and reciprocity is

$$\begin{aligned} e_{\beta}(\theta_i, \phi_i) &= 1 - \frac{1}{4\pi} \iint [\gamma_{h\beta}(\theta_s, \phi_s; \theta_i, \phi_i) \\ &\quad + \gamma_{v\beta}(\theta_s, \phi_s; \theta_i, \phi_i)] \sin \theta_s d\theta_s d\phi_s \end{aligned} \quad (42)$$

The brightness temperature is

$$T_B(\theta_i, \phi_i) = e_{\beta}(\theta_i, \phi_i) T \quad (43)$$

where T is the physical temperature of the medium in degrees kelvin. In Section 3.1, we will present numerical simulations using this approach for active and passive microwave remote sensing.

2.2. The use of RWG Basis Functions and Combination with the SMCG Method for Scattering from Rough-Surface Simulation

As described in Section 2.1, using the pulse basis functions and point matching, we have combined with SMCG method for rough-surface scattering. Researchers have applied the method to simulations of emissivities in passive microwave remote sensing. Johnson et al. [11] studied the case of ocean emissivity at nadir incidence using 8 points per wavelength and attained the accuracy of the impedance matrix elements by using a large order of integration quadrature. The PBTG method in Section 2.1 was developed such that dense sampling could be used and maintained comparable to the CPU and memory requirements. The SMCG/PBTG method was used to study a soil surface that was assumed to be a Gaussian random process with a Gaussian correlation function [1,11–13]. The results were compared with the second-order SPM method, which give the same results as does the SSA method for emissivity [14,15]. It was found that the second-order SPM method gives poor results for cases when the RMS slope is large. In the past, the numerical solutions were restricted mostly to Gaussian random surfaces with Gaussian correlation function [12]. But the use of Gaussian correlation function is not appropriate for soil surfaces because the backscattering coefficients based on such surfaces are many decibels below that of measurements. The exponential correlation function is a more realistic choice for soil surface and can be used to match active remote sensing experimental data. The exponential correlation function gives a rough surface with much more fine-scale features than a Gaussian correlation function of the same RMS height and correlation length. However, the use of pulse basis functions was not able to provide accurate results of emissivity for the exponential correlation functions although they provide adequate results for backscattering coefficients in decibel scale [16]. For the exponential correlation functions, we have tried using pulse basis functions with 16 points per wavelength and 32 points per wavelength with a very high order of integration quadrature to calculate the impedance matrix elements. However, there was no convergence in emissivity and the energy conservation was poor. Recent emphases on microwave remote sensing of soil moistures are moving toward combined active and passive remote sensing, particularly in the planned HYDROS satellite mission. Thus it is important to have the same characterization (i.e., exponential correlation functions) in both active and passive remote sensing. In this section, we show that by using RWG basis functions, the accuracy of emissivities calculations are improved significantly for the case of exponential correlation functions. We implemented the SMCG method with the RWG basis functions [17] by projecting the triangular elements into the canonical grid. To implement the RWG basis functions, we use

the PMCHW formulation [18] (after Poggio, Miller, Chang, Harrington, and Wu). Energy conservation checks are provided.

2.2.1. General Formulations. Consider a tapered plane wave [1] \bar{E}^{inc} and \bar{H}^{inc} , with a time dependence of $e^{-i\omega t}$, impinging on a 2D dielectric rough surface with a random height profile $z = f(x, y)$. Incident electric and magnetic fields E^{inc} and H^{inc} create equivalent electric and magnetic surface currents $J(r)$ and $M(r)$ on the rough surface. In the following, $\epsilon_{1,2}$ and $\mu_{1,2}$ represent the permittivity and the permeability, respectively, of the upper and lower half-spaces. Also, $k_{1,2} = \omega(\epsilon_{1,2}\mu_{1,2})^{1/2}$, and $\eta_{1,2} = (\mu_{1,2}/\epsilon_{1,2})^{1/2}$. To implement the RWG basis functions, it is convenient to use the PMCHW formulation, which is summarized below. To obtain J and M , the PMCHW formulation enforces the continuity of the tangential electric and magnetic field components across S

$$\bar{E}^{\text{inc}}(\bar{r})|_{\text{tan}} = (L_1 + L_2)\bar{J}(\bar{r})|_{\text{tan}} - (K_1 + K_2)\bar{M}(\bar{r})|_{\text{tan}} \quad (44)$$

$$\begin{aligned} \bar{H}^{\text{inc}}(\bar{r})|_{\text{tan}} &= (K_1 + K_2)\bar{J}(\bar{r})|_{\text{tan}} \\ &+ \left(\frac{1}{\eta_1}L_1 + \frac{1}{\eta_2}L_2\right)\bar{M}(\bar{r})|_{\text{tan}} \end{aligned} \quad (45)$$

where the operators $L_{1,2}$ and $K_{1,2}$ are defined by

$$\begin{aligned} L_{1,2}\bar{X}(\bar{r}) &= \int_S ds' [-i\omega\mu_{1,2}\bar{X}(\bar{r}')] \\ &+ \frac{-i}{\omega\epsilon_{1,2}} \nabla\nabla' \cdot \bar{X}(\bar{r}') g_{1,2}(\bar{r}, \bar{r}') \end{aligned} \quad (46)$$

$$K_{1,2}\bar{X}(\bar{r}) = \int_S ds' \bar{X}(\bar{r}') \times \nabla g_{1,2}(\bar{r}, \bar{r}') \quad (47)$$

and $\nabla g_{1,2}(\bar{r}, \bar{r}')$ is the scalar Green function in region 1 (air) and region 2 (lossy dielectric medium)

$$g_{1,2}(\bar{r}, \bar{r}') = \frac{\exp(ik_{1,2}|\bar{r} - \bar{r}'|)}{4\pi|\bar{r} - \bar{r}'|} \quad (48)$$

2.2.1.1. Emissivity and Brightness Temperature. The solution of the PMCHW yields the electric and magnetic surface current densities $J(r)$ and $M(r)$. These current densities can be used to evaluate the scattering field required in the computation of the bistatic scattering coefficient. The normalized bistatic scattering coefficient defined by

$$\gamma_{\beta\alpha}(\theta_s, \phi_s; \theta_i, \phi_i) = \frac{|S_{\beta}(\hat{k}_s)|^2}{2\eta_1 P_{\alpha}^{\text{inc}}} \quad (49)$$

where α and β indicate the polarization of the incident and scattered waves, respectively, P_{α}^{inc} is the incident power, and the vertical and horizontal polarized scattered

components are, respectively

$$\begin{aligned} S_v(\hat{k}_s) &= \frac{ik_1}{4\pi} \int_S ds [\hat{v}_s \cdot \eta_1 \bar{J} \\ &+ \hat{h}_s \cdot \bar{M}] \exp(-ik_1 k_s \cdot \bar{r}') \end{aligned} \quad (50)$$

$$\begin{aligned} S_h(\hat{k}_s) &= \frac{ik_1}{4\pi} \int_S ds [\hat{h}_s \cdot \eta_1 \bar{J} \\ &- \hat{v}_s \cdot \bar{M}] \exp(-ik_1 k_s \cdot \bar{r}') \end{aligned} \quad (51)$$

with $\hat{k}_s = \sin \theta_s \cos \phi_s \hat{x} + \sin \theta_s \sin \phi_s \hat{y} + \cos \theta_s \hat{z}$, $\hat{v}_s = \cos \theta_s \cos \phi_s \hat{x} + \cos \theta_s \sin \phi_s \hat{y} - \sin \theta_s \hat{z}$, and $\hat{h}_s = -\sin \phi_s \hat{x} + \cos \phi_s \hat{y}$, for scattering by a dielectric surface.

2.2.1.2. Energy Conservation Verification. An energy conservation check is essential because emissivity is based on energy conservation. If the energy conservation check is such that transmissivity plus scattering is not equal to unity, then there is an ambiguity whether emissivity should be equal to transmissivity or equal to one minus scattering. For a penetrable medium, absorptivity $\alpha(\theta_i)$ is equal to transmissivity. The absorptivity and reflectivity $r(\theta_i)$ can be calculated in terms of the surface fields

$$\alpha(\theta_i) = \frac{P_x}{P_{\text{inc}}} = \frac{\int_S ds \hat{n} \cdot \frac{1}{2} \text{Re}[\bar{E} \times \bar{H}]}{P_{\text{inc}}} \quad (52)$$

$$r(\theta_i) = \frac{P_s}{P_{\text{inc}}} = \frac{\int_S ds \hat{n} \cdot \frac{1}{2} \text{Re}[\bar{E}_s \times \bar{H}_s]}{P_{\text{inc}}} \quad (53)$$

where \bar{E} and \bar{H} are the total electrical and magnetic surface fields, respectively, while \bar{E}_s and \bar{H}_s are the surface scattered fields. They are calculated as

$$\bar{E}_s = \bar{E} - \hat{n} \times \bar{E}^{\text{inc}} = -\bar{M} - \hat{n} \times \bar{E}^{\text{inc}} \quad (54)$$

$$\bar{H}_s = \bar{H} - \hat{n} \times \bar{H}^{\text{inc}} = +\bar{J} - \hat{n} \times \bar{H}^{\text{inc}} \quad (55)$$

Numerical energy conservation is carried out by calculating absorptivity $\alpha(\theta_i)$ and reflectivity $r(\theta_i)$ using (52) and (53), to determine whether $\alpha(\theta_i) + r(\theta_i)$ is equal to unity.

2.2.2. Numerical SMCG/RWG Method. To solve the PMCHW equation, the Galerkin procedure is used to obtain the impedance matrix. Applying the RWG basis to (44) and (45) produces the matrix equation

$$[Z]I = V \quad (56)$$

In the SMCG method, the matrix equations (44) and (45) are solved in an iterative manner (e.g., conjugate-gradient method). The impedance matrix is decomposed into the sum of a sparse matrix $[Z^w]$, denoting the *strong near interactions*, and a dense matrix $[Z^f]$, denoting the *weak far interactions*. For the near-field interactions, we take the numerical integration over both the basis and testing functions, using numerical quadrature of 7-point rule. When the integral is evaluated for the self-term, an analytic approach is employed [19]. Since the Green

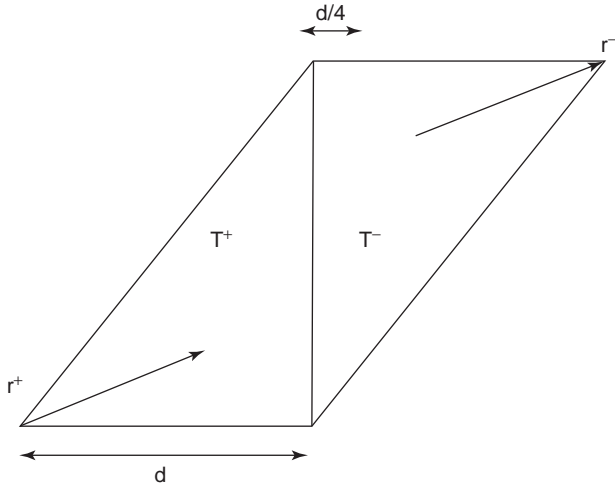


Figure 2. RWG basis function.

functions are smooth over the integration domains of the impedance matrix elements integrals in the far-field interactions, we use only the one-point approximation. We choose a point $(\frac{1}{4}, \frac{1}{4})$ in the triangle instead of the centroid $(\frac{1}{3}, \frac{1}{3})$, as depicted in Fig. 2.

The points at $(\frac{1}{4}, \frac{1}{4})$ of triangles fall in the canonical grid, as shown in Fig. 3 by cross-points. By using this judicious procedure, we only need to make Taylor expansion vertically and not horizontally to translate to the canonical grid in the SMCG implementation [17]. Efficient evaluation of the far-interaction contributions in matrix-vector multiplication is reduced to efficient convolution between the Green function and current vector.

We choose r_d as the neighborhood distance (e.g. $r_d = 2\lambda$). Let

$$\rho_R = \sqrt{(x - x')^2 + (y - y')^2} \tag{57}$$

be the horizontal separation between two points on the rough surface $x,y,f(x,y)$ and $x',y',f(x',y')$. Since the

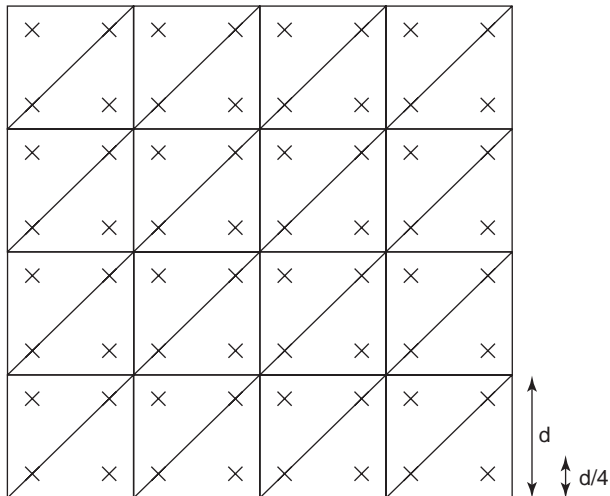


Figure 3. Projection of rough surface on the x - y plane and canonical grid depicted by cross-points.

weak-matrix elements satisfy the condition $\rho_R > r_d \gg |f(x,y) - f(x',y')|$, we can expand the Green function in a Taylor series about the flat surface. Thus, the Taylor-expanded Green function terms $g_{1,2}$ is

$$g_{1,2}(\bar{r} - \bar{r}') = \sum_{m=0}^M a_m^{(1,2)}(\rho_R) \left(\frac{z_d}{\rho_R} \right)^m \tag{58}$$

From $\nabla g = (\bar{r} - \bar{r}')G_{1,2}$, where $G_{1,2}(\bar{r} - \bar{r}') = [(ik_{1,2}|\bar{r} - \bar{r}'| - 1)] \exp(ik_{1,2}|\bar{r} - \bar{r}'|)/4\pi|\bar{r} - \bar{r}'|^3$, $G_{1,2}$ can be written as the form of Taylor expansion series

$$G_{1,2}(\bar{r} - \bar{r}') = \sum_{m=0}^M b_m^{(1,2)}(\rho_R) \left(\frac{z_d}{\rho_R} \right)^m \tag{59}$$

where $z_d = f(x,y) - f(x',y')$ and a_m and b_m are the coefficients of Taylor's series. Due to the translational invariable kernels in the Green functions, the weak-matrix vector multiplication can be efficiently performed via 2D fast Fourier transform (FFT). In this work, we use six terms of expansion series. Numerical results for passive and active microwave remote sensing will be described in Section 3.

2.3. An Efficient Algorithm for Electromagnetic Scattering from Rough Surfaces Using Single-Integral Equation and Multilevel SMCC Method

This is an algorithm presently being developed. The purpose of this algorithm is to reduce the number of surface unknowns by using the SIE. In this section, we present the efficient algorithm based on the SIE formulation in conjunction with a multilevel SMCG (MSMCG) method. The SIE method [20] needs only one unknown at each interior edge of the triangulated mesh, in contrast to using two or three unknowns by the coupling equations [21,22]. One advantage of using the SIE approach is the faster convergence for an iterative solution as revealed in Ref. 21. To extend the applicability of the original SMCG scheme [22,23] to rougher surfaces by using 3D FFT instead of 2D FFT, the MSMCG procedure [24,25] was proposed. By adjusting the expansion levels, the MSMCG scheme is applicable to surfaces with arbitrary roughness, while the number of terms of the Taylor series and the distance indicating whether the far interactions can be changed.

This section is organized as follows. In Section 2.3.1, formulations are provided for the method of moments using a single magnetic field integral equation along with the RWG basis functions. In Section 2.3.2, the solution procedure adopting the MSMCG method in solving the moment equations is outlined. In Section 2.3.3, a detailed description that the multiplication of the weak impedance matrices with a column vector can be calculated by means of FFT is illustrated. In Section 2.3.4, numerical examples are presented for bistatic scattering coefficients from surfaces with the Gaussian spectrum as well as wind-driven ocean spectrum. A short summary is given at the end.

2.3.1. Formulation by the Method of Moments. The time dependence adopted in this section is $e^{j\omega t}$. A dielectric random rough surface is depicted in Fig. 4. In the lower region, the fields may be expressed by a single *effective* surface current \mathbf{J}^{eff} beneath the interface as

$$\mathbf{E}_2 = L_2[\mathbf{J}^{\text{eff}}], \quad \mathbf{H}_2 = K_2[\mathbf{J}^{\text{eff}}] \quad (60)$$

where the operators are defined as

$$L_2[\mathbf{J}^{\text{eff}}] = -j\omega\mu_0 \int_S \left[G_2(R)\mathbf{J}^{\text{eff}}(\mathbf{r}') \right. \\ \left. + \frac{1}{k_2^2} \nabla G_2(R) \nabla' \cdot \mathbf{J}^{\text{eff}}(\mathbf{r}') \right] dS' \quad (61)$$

$$K_2[\mathbf{J}^{\text{eff}}] = \int_S [\nabla G_2(R) \times \mathbf{J}^{\text{eff}}(\mathbf{r}')] dS' \quad (62)$$

where $G_2 = e^{-jk_2 R} / 4\pi R$ is the Green function for the lower medium characterized by $(\epsilon_0 \epsilon_r, \mu_0)$. As an observer approaches the interface from the lower region, a pair of *equivalent* surface electric and magnetic currents can be defined as

$$\mathbf{J} = \hat{\mathbf{n}} \times \mathbf{H}_2 = \hat{\mathbf{n}} \times K_2[\mathbf{J}^{\text{eff}}] \\ = -\frac{1}{2} \mathbf{J}^{\text{eff}} + \hat{\mathbf{n}} \times (\text{PV})K_2[\mathbf{J}^{\text{eff}}] \quad (63)$$

$$-\mathbf{M} = \hat{\mathbf{n}} \times \mathbf{E}_2 = \hat{\mathbf{n}} \times L_2[\mathbf{J}^{\text{eff}}] \quad (64)$$

where $\hat{\mathbf{n}}$ is the normal upward and (PV) means the principal value integral with the singularity at $R=0$ removed. The scattering field in the air region may be found by

$$\mathbf{H}^{\text{s}} = \frac{1}{\eta_0} L_1[\mathbf{M}] + K_1[\mathbf{J}], \quad (65)$$

$$\eta_0 = \sqrt{\mu_0/\epsilon_0} \approx 377\Omega$$

where the operators L_1 and K_1 are the same as L_2 and K_2 but replacing the medium parameters $(\epsilon_0 \epsilon_r, \mu_0)$ with (ϵ_0, μ_0) and G_2 by G_1 (the air is seen as vacuum, and the permeability is assumed to be μ_0 for both regions). The total field in the air region is $\mathbf{H}_1 = \mathbf{H}^{\text{inc}} + \mathbf{H}^{\text{s}}$, where \mathbf{H}^{inc} is the

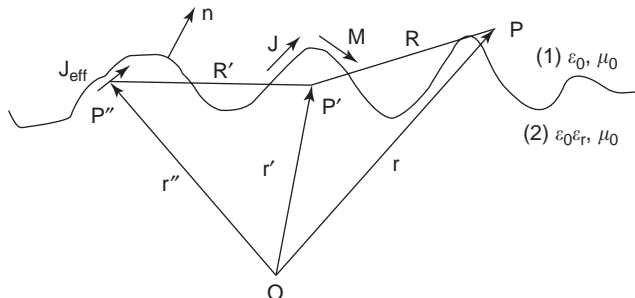


Figure 4. Configuration of a scattering problem from a random rough surface using a single-integral equation.

incident magnetic field. The boundary condition demands the continuity of the tangential magnetic field, that is, $\hat{\mathbf{n}} \times \mathbf{H}_2 = \hat{\mathbf{n}} \times \mathbf{H}_1$, which by (63) and (65) becomes

$$\mathbf{J} = \mathbf{J}^{\text{inc}} + \frac{1}{\eta_0} \hat{\mathbf{n}} \times L_1[\mathbf{M}] \\ + \frac{1}{2} \mathbf{J} + \hat{\mathbf{n}} \times (\text{PV})K_1[\mathbf{J}] \quad (66)$$

where $\mathbf{J}^{\text{inc}} = \hat{\mathbf{n}} \times \mathbf{H}^{\text{inc}}$ represents the equivalent incident electric current.

Using the method of moments with the RWG triangular basis functions [26], we can convert (63), (64), and (66) into linear equation sets

$$\left. \begin{aligned} [I^e] &= -\left(\frac{1}{2}[U] - [P_2]\right) \cdot [I^{\text{eff}}] \\ -[I^m] &= \eta_0 [Q_2] \cdot [I^{\text{eff}}] \end{aligned} \right\} \quad (67)$$

$$[I^e] = [I^{\text{inc}}] + \frac{1}{\eta_0} [Q_1] \cdot [I^m] + \left(\frac{1}{2}[U] + [P_1]\right) \cdot [I^e] \quad (68)$$

where $[U]$ is an identity matrix. Column vectors $[I^e]$, $[I^m]$, $[I^{\text{eff}}]$, $[I^{\text{inc}}]$ are the expansion coefficients of their corresponding vectors. For instance

$$\mathbf{J} = \sum_{n=1}^N I_n^e \mathbf{f}_n(\vec{r}), \quad (69a)$$

$$I_n^e \approx \frac{1}{l_n} \int_{l_n} (\hat{\mathbf{n}} \times \hat{l}_n) \cdot \mathbf{J} dl$$

$$\mathbf{M} = \sum_{n=1}^N I_n^m \mathbf{f}_n(\vec{r}), \quad (69b)$$

$$I_n^m \approx \frac{1}{l_n} \int_{l_n} (\hat{\mathbf{n}} \times \hat{l}_n) \cdot \mathbf{M} dl$$

where \mathbf{f}_n ($n=1, 2, \dots, N$) are the RWG basis functions associated with the N interior edges of the triangulated patches. The direction of the n th edge is labeled with \hat{l}_n , and $(\hat{\mathbf{n}} \times \hat{l}_n)$ defines the direction of the current flowing across the edge. The elements of $[P]$ and $[Q]$ are

$$P_i(m, n) = \frac{1}{l_m} \int_{l_m} \int_{l_n} [\hat{l}_m \cdot (\nabla G_i \times \mathbf{f}_n)] dS' dl \quad i=1, 2 \quad (70)$$

$$Q_i(m, n) = -jk_1 \frac{1}{l_m} \int_{l_m} \int_{l_n} \left[(\hat{l}_m \cdot \mathbf{f}_n) G_i \right. \\ \left. + \frac{1}{k_2^2} \frac{\partial G_i}{\partial l_m} (\nabla'_s \cdot \mathbf{f}_n) \right] dS' dl \quad i=1, 2 \quad (71)$$

Substituting (67) into (68), one obtains

$$[Z] \cdot [I^{\text{eff}}] = [I^{\text{inc}}] \quad (72)$$

$$[Z] = [Q_1] \cdot [Q_2] - \left(\frac{1}{2}[U] - [P_1]\right) \left(\frac{1}{2}[U] - [P_2]\right) \quad (73)$$

Solve (72) for $[I^{\text{eff}}]$, then restore $[I^e]$, $[I^m]$ via (67) and the equivalent currents by (69). Finally, instead of calculating the scattering fields by (65), we can compute the normalized bistatic scattering coefficients using the equivalent currents, which is defined by

$$\gamma_{ab}(\theta_s, \phi_s) = \lim_{r \rightarrow \infty} \frac{r^2 |E_a^s|^2}{2\eta_0 P_b^{\text{inc}}} = \frac{|S_a(\hat{\mathbf{k}}_s)|^2}{2\eta_0 P_b^{\text{inc}}} \quad (74)$$

where a and b indicate the polarization states of the scattering and incident waves, respectively, and P_b^{inc} is the power impinged on the surface. The scattering integral functions are

$$S_v(\hat{\mathbf{k}}_s) = -\frac{jk_1}{4\pi} \int_S (\hat{\mathbf{v}}_s \cdot \eta_0 \mathbf{J} + \hat{\mathbf{h}}_s \cdot \mathbf{M}) e^{jk_1 \hat{\mathbf{k}}_s \cdot \mathbf{r}'} dS' \quad (75)$$

$$S_h(\hat{\mathbf{k}}_s) = -\frac{jk_1}{4\pi} \int_S (\hat{\mathbf{h}}_s \cdot \eta_0 \mathbf{J} - \hat{\mathbf{v}}_s \cdot \mathbf{M}) e^{jk_1 \hat{\mathbf{k}}_s \cdot \mathbf{r}'} dS' \quad (76)$$

where $\hat{\mathbf{k}}_s = \sin \theta_s \cos \phi_s \hat{\mathbf{x}} + \sin \theta_s \sin \phi_s \hat{\mathbf{y}} + \cos \theta_s \hat{\mathbf{z}}$, $\hat{\mathbf{v}}_s = \hat{\mathbf{h}}_s \times \hat{\mathbf{k}}_s = \cos \theta_s \cos \phi_s \hat{\mathbf{x}} + \cos \theta_s \sin \phi_s \hat{\mathbf{y}} - \sin \theta_s \hat{\mathbf{z}}$, $\hat{\mathbf{h}}_s = \hat{\mathbf{z}} \times \hat{\mathbf{k}}_s / |\hat{\mathbf{z}} \times \hat{\mathbf{k}}_s| = -\sin \phi_s \hat{\mathbf{x}} + \cos \phi_s \hat{\mathbf{y}}$, where (θ_s, ϕ_s) is the scattering direction in spherical coordinate system.

2.3.2. Solution by the MSMCG Method. The SMCG method proved very successful in solving large-scale moment matrix equations encountered in analysis of rough-surface scattering. To use the method, we write each matrix as two parts, the strong part and the weak part:

$$[P_i] = [P_i^s] + [P_i^w], \quad [Q_i] = [Q_i^s] + [Q_i^w] \quad i = 1, 2 \quad (77)$$

Because the diagonal elements of $[P_i^s]$ are negligible with the singularity removed, it is possible to set $[P_i^s] = 0$ as long as the radius separating the far interactions is sufficiently small and the number of expansion levels is sufficiently large. Substituting (77) into (72), (73), one arrives at

$$[Z^s] \cdot [I^{\text{eff}}] = [I^{\text{inc}}] - [Z^w] \cdot [I^{\text{eff}}] \quad (78)$$

$$[Z^s] = [Q_1^s] \cdot [Q_2^s] - (\frac{1}{2}[U] - [P_1^s])(\frac{1}{2}[U] - [P_2^s]) \quad (79)$$

$$[Z^w] = [Z] - [Z^s] \quad (80)$$

Equation (78) will be solved by the conjugate-gradient method (CGM) on updating the right-hand side. Specifically, we assign $[I^{\text{eff}}] = [I_0^{\text{eff}}] = 0$ to the right-hand side of (78) and solve the equation using CGM for $[I^{\text{eff}}]$ to get $[I_1^{\text{eff}}]$. Then we assign $[I^{\text{eff}}] = [I_1^{\text{eff}}]$ to the right-hand side and solve for $[I^{\text{eff}}]$ to get $[I_2^{\text{eff}}]$. Convergence is admitted after k iterations if $\sqrt{\| [I_k^{\text{eff}}] - [I_{k-1}^{\text{eff}}] \| / \| [I^{\text{inc}}] \|} < 1\%$ is reached. For a small or mildly rough surface, the process converges rapidly. However, for very large or very rough surfaces, it may not converge through updating the right-hand side if the radius is not large enough. In this case, we move the last term back to the left-hand side. The resulting equation is again solved by CGM but using the

solution obtained in the last step of the updating approach as the initial solution.

In the SMCG method, the elements of the strong parts are calculated by exact numerical integration and stored in computer memory. However, the elements of the weak parts are not calculated and stored in common ways. Expand the Green function and its gradient as Taylor series about a three-dimensional cubic grid as shown in Fig. 5

$$G = \sum_{k=0}^K \frac{1}{k!} \frac{\partial^k G}{\partial \zeta^k} (\zeta - \zeta')^k = \sum_{k=0}^K C_k \sum_{l=0}^k \binom{k}{l} \zeta^l (-\zeta')^{k-l} \quad (81)$$

$$= \sum_{k=0}^K C_k \sum_{l=0}^k \kappa_{kl} \zeta^l (\zeta')^{k-l} \quad \nabla G = \sum_{k=0}^K \mathbf{D}_k \sum_{l=0}^k \kappa_{kl} \zeta^l (\zeta')^{k-l} \quad (82)$$

$$C_k = \frac{1}{k!} \left. \frac{\partial^k G}{\partial \zeta^k} \right|_{\zeta = \zeta' = 0},$$

$$\kappa_{kl} = (-1)^{k-l} \frac{k!}{l!(k-l)!},$$

$$\mathbf{D}_k = \hat{\mathbf{R}} \frac{1}{k!} \left. \frac{\partial^k}{\partial \zeta^k} \left(\frac{\partial G}{\partial \mathbf{R}} \right) \right|_{\zeta = \zeta' = 0}$$

where K truncates the number of terms of the Taylor series; C_k and \mathbf{D}_k are functions of the canonical grid coordinates. For instance, the expressions of the zeroth- and first-order terms are

$$C_0 = G(R_c), \quad C_1 = \frac{G'(R_c) z_c}{R_c}$$

$$\mathbf{D}_0 = G'(R_c) \hat{\mathbf{R}}_c, \quad \mathbf{D}_1 = \frac{z_c}{R_c}$$

$$\frac{G''(R_c) - G'(R_c)}{R_c} \hat{\mathbf{R}}_c + \frac{1}{R_c} G'(R_c) \hat{\mathbf{z}}$$

Inserting (81), (82) into (70), (71) and approximating the linear integration by the two-point rule (the endpoints of

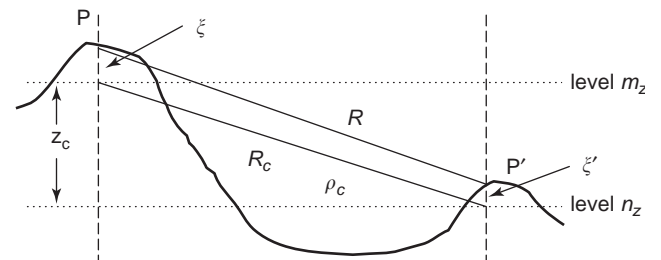


Figure 5. Schematic diagram for the Taylor expansion of the Green functions on a 3D grid system for the use of the MSMCG method.

an edge) and the surface integration over a triangle by three-point rule (the midpoints of the three edges), we can show that the weak elements, say, $[Q_2^w]$, have a form such as

$$Q_2^w(m, n) = \sum_{k=0}^K \sum_{l=0}^k f_{kl}(m) U_k(m-n) g_{kl}(n) \quad (83)$$

where $f_{kl}(m)$ is associated with a testing edge and $g_{kl}(n)$, with a source triangle. The matrix $[U_k]$ has the Toeplitz structure that may be stored as a column vector. In Section 2.3.3, $[f_{kl}]$, $[g_{kl}]$, and $[U_k]$ will be described in detail. For a three-dimensional canonical grid system, the grid indices in (83) should be understood as $m = (m_x, m_y, m_z)$ and $m-n = (m_x - n_x, m_y - n_y, m_z - n_z)$. Note that (m, n) in (83) refers to the grid indices, which in (71) refers to the numbering of the edges. There exists a corresponding relation between them through an index transform, say, a grid coordinate (m_x, m_y, m_z) corresponding to a deterministic midpoint of the m th edge.

The reduction of memory storage requirement is achieved as follows illustrated using $[Q_2]$. The storage of the matrix $[Q_2]$ is on the order of $O(N^2)$ in common sense. However, the storage of $[Q_2^s]$ is proportional to $O(N)$ because at each observation point only a few nearby source elements within a given distance are taken into account; the storage of $[U_k]$ is on the order of $O(2N)$, and so is $[f_{kl}]$ and $[g_{kl}]$ with N zeros padded to each of them to make use of the FFT. Thus, the total storage of $([Q_2^s] + [Q_2^w])$ is scaled down to $O(CN)$, where C is a constant, typically a few tens. Reduction of the memory storage requirement is remarkable when we think that N could be as big as several millions.

Using CGM to solve (72), the computing burden is dominated by matrix-vector multiplications. Multiplications of the strong parts with a column vector takes a little time, as the strong matrices are very sparse. Because of the approximation (83), the multiplication of the weak parts with a column vector $[x]$ can be accelerated greatly using the FFT technique such as

$$[Q_2^w] \cdot [x] = \sum_{k=0}^K \sum_{l=0}^k [f_{kl}] \cdot \text{FFT}^{-1} \{ \text{FFT} \{ [U_k] \} \cdot \text{FFT} \{ [g_{kl}] \cdot [x] \} \} \quad (84)$$

where the products between two column vectors are affected between their corresponding elements. The complexity directly computing the left-hand side of (84) is on the order of $O(N^2)$. Because the complexity of the three FFTs is $3 \times (2N \log 2N)$ and that of the three column vector products is $3 \times (2N)$, the total manipulation of the right-hand side is only $O(\beta N)$, where $\beta = \frac{1}{2}(K+1)(K+2)$ ($6 \log 2N + 6$), which may be seen as a constant as $\log 2N$ varies very slowly with N . Thus, the saving in CPU time for an iterative solution is substantial as β is typically several hundreds while N could be on the order of millions.

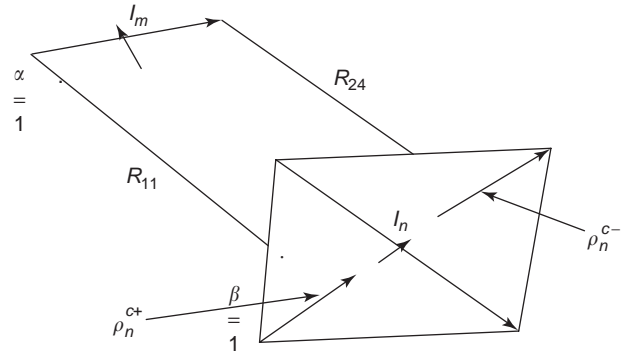


Figure 6. Pair of triangular patches connecting to the n th edge where the source is considered and the m th edge where the equation is tested.

2.3.3. Multiplication of Matrices with a Vector Using

FFT. In this subsection, we give a detailed description to the form of (84) that favors the multiplication of (84) by the FFT technique using FFTW software [27]. Refer to Fig. 6, in which a pair of RWG triangles is depicted along with an edge where the equation is tested. If the distance between the triangle pair and the testing edge is sufficiently large, we can approximate the linear integration along the m th edge by a two-point rule (the endpoints) and the surface integration over each triangle connecting to the n th edge by a three-point rule (the midpoint of each side). This allows us to write (71) as

$$Q_i^w(m, n) = -\frac{jk_1}{12} \hat{l}_m \cdot \sum_{\alpha=1}^2 \sum_{\beta=1}^5 G_{\alpha\beta} \vec{A}_\beta + \frac{4}{k_i^2 l_m} \sum_{\alpha=1}^2 \sum_{\beta=1}^5 (-1)^\alpha \text{sign}(3-\beta) G_{\alpha\beta} l_n \quad (85)$$

where the subscript $\alpha=1,2$ indicates the endpoints of the m th edge, while $\beta=1,2,3,4,5$ indicates the midpoint of a triangle pair connecting to the n th edge; $G_{\alpha\beta} = G(R_{\alpha\beta})$ with $R_{\alpha\beta}$ the distance between an endpoint of the testing edge and a midpoint of the source triangle as indicated in the figure; $\text{sign}(3-\beta)$ equals 1 if $\beta < 3$, 0 if $\beta = 3$, and -1 if $\beta > 3$; and \vec{A}_β equals ρ_n^{c+} if $\beta < 3$, $\rho_n^{c+} + \rho_n^{c-}$ if $\beta = 3$, and ρ_n^{c-} if $\beta > 3$. The vectors of ρ_n^{c+} and ρ_n^{c-} are also shown in the figure.

Actually, (85) can be rewritten in a more compact form

$$Q_i^w(m, n) = \sum_{\alpha, \beta} \sum_{q=1}^4 w_q^\alpha(m) G_{\alpha\beta} u_q^\beta(n) \quad (86)$$

where $q=1,2,3$ counts the first term of (86) because of three components involved, and $q=4$ counts the last term of (85); $w_q^\alpha(m)$ is associated with the testing edge while $u_q^\beta(n)$ is associated with the source triangle. Specifically, $w_q^\alpha(m) = (-jk_1/12)(\hat{q} \cdot \hat{l}_m)$ and $u_q^\beta(n) = (\hat{q} \cdot \vec{A}_\beta) l_n$, where $\hat{q} = \hat{x}, \hat{y}, \hat{z}$ for $q=1,2,3$, respectively; $w_4^\alpha(m) = (-jk_1/12)(1/k_i^2 l_m)(-1)^\alpha$ and $u_4^\beta(n) = \text{sign}(3-\beta) l_n$. Substitution of

the expansion (81) into (86) leads to

$$Q_i^w(m, n) = \sum_{k=0}^K \sum_{l=0}^k \sum_{\alpha, \beta} \sum_{q=1}^4 w_q^\alpha(m) (\kappa_{kl} \zeta_m^l) C_k(m_x - n_x + \Delta_x^{\alpha\beta}, m_y - n_y + \Delta_y^{\alpha\beta}, m_z - n_z) \zeta_n^{k-l} u_q^\beta(n) \quad (87)$$

where $\Delta_x^{\alpha\beta}$ and $\Delta_y^{\alpha\beta}$ are integer or half-integer numbers, representing the displacements due to the integration points over a triangle chosen to be the midpoint of each side, which may not be the gridpoints. If we set

$$\begin{aligned} \tilde{f}_{kl}(m) &= w_q^\alpha(m) (\kappa_{kl} \zeta_m^l), \\ \tilde{g}_{kl}(n) &= \zeta_n^{k-l} u_q^\beta(n) \\ \tilde{U}_k(m-n) &= C_k(m_x - n_x + \Delta_x^{\alpha\beta}, m_y - n_y + \Delta_y^{\alpha\beta}, m_z - n_z) \end{aligned} \quad (88)$$

then (87) would have the same form as (83) except for a triple summation over the indices α , β , and q . Figure 7 shows the projection of a rough surface on the x - y plane and the ordering of the edges. The currents crossing the edges can be sorted into three types according to their directions— x , y , and 45° directions, which will be distinguished by introducing an index $s = 1, 2, 3$. The ranges of m_x and n_x in (88) are chosen to range from 1 to N_x , and the ranges of m_y and n_y from 1 to N_y . It can also be shown that $-\frac{3}{2} \leq \Delta_x^{\alpha\beta}, \Delta_y^{\alpha\beta} \leq 1$. Thus, for a pair of (n_x, n_y) there are three corresponding edges distinguished by s denoting the edge type. Keeping this in mind, we use (88), recasting (87) as

$$Q_i^w(m, n) = \sum_{k=0}^K \sum_{l=0}^k \sum_{q=1}^4 \sum_{\alpha, \beta} \tilde{f}_{kl}(m) \tilde{U}_k(m-n) \tilde{g}_{kl}(n) \quad \text{for } s, s' = 1, 2, 3 \quad (89)$$

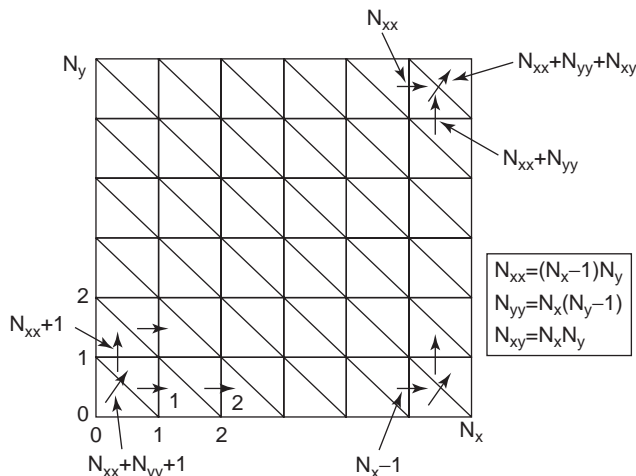


Figure 7. Projection of the rough surface on the x - y plane, and the ordering of the edges. The grid indices in the x and y directions are from 0 to N_x and from 0 to N_y .

where $s, s' = 1, 2, 3$ means that given a field edge type such as $s = 1$ and a source edge type such as $s' = 2$, the grid indices on the right-hand side correspond to a unique edge ordering index on the left-hand side. For instance, if $s = 1$ and $s' = 2$, and $m_x = m_y = n_x = n_y = 1$ for the right-hand side, then $m = 1$ and $n = N_{xx} + 1$ for the left-hand side. Because the matrix elements can be written as (89), which is in the form of (83), matrix-column vector multiplication can be performed using FFT for each set of α , β , and q . In order to improve the computing efficiency, the triple summations over α , β , and q may be lifted in some sense, accomplished as follows. If we allow m_x and n_x to vary from 1 to $N_x + 1$, and m_y and n_y from 1 to $N_y + 1$, we will get an extended version of $\tilde{U}_k(m-n)$ to be denoted by $U_k(m-n)$. This means that for any combination of (α, β) and (s, s') in (88), $\tilde{U}_k(m-n)$ is a subset of $U_k(m-n)$. Thus we need only store $U_k(m-n)$ and perform its own FFT, and do not need to compute the FFT of $\tilde{U}_k(m-n)$ for various (α, β) and (s, s') . The storage requirement and computing complexity of $U_k(m-n)$ is on the same order as those of $\tilde{U}_k(m-n)$. Because $U_k(m-n)$ is not relevant to the index β , it can be taken out of the summation over β , so that the summation over β for $u_q^\beta(n)$ can be performed before FFT. This means that we need not compute the FFT of $[\tilde{g}_{kl}] \cdot [x]$ for each β , where $[x]$ is a column vector to be multiplied with the matrix, but only the FFT of $\sum_{\beta, s'} [\tilde{g}_{kl}] \cdot [x]$. Taking these strategies into consideration, (89) eventually becomes equivalent to (83), which means that both the storage requirement and computing complexity for $[f_{kl}]$, $[U_k]$, and $[g_{kl}]$ in (83) are on the same orders as $[f_{kl}]$, $[\tilde{U}_k]$, and $[\tilde{g}_{kl}]$ in (89). We remind the reader that, because a column vector $[x]$ represents the surface currents, we may set $x(n_x, n_y, n_z) = 0$ except for $n_z = h(n_x, n_y)$, where $h(n_x, n_y)$ is the level closest to the surface. This implies that the elements of the product column vector $[g_{kl}] \cdot [x]$ are nonzero only for $n_z = h(n_x, n_y)$. Similar calculation can be performed for the multiplication of $[P_i^w]$ with a column vector. Multiplication of the transposed conjugate matrices of $[P_i^w]$ and $[Q_i^w]$ with a column vector can also be performed using the FFT technique.

2.3.4. Numerical Results and Discussion. To simulate the scattering from a truncated area of a boundless surface, an incident wave with limited beamwidth is necessary to minimize the errors caused by the surface boundaries. The Gaussian tapered incident wave adopted in this section is [28]

$$E_B^{\text{inc}} = \iint_{k_x^2 + k_y^2 \leq k_1^2} \mathbf{S}_E(k_x, k_y) \Phi_B(k_x - k_{ix}, k_y - k_{iy}) e^{-j(k_x x + k_y y - k_z z)} dk_x dk_y \quad (90)$$

where $k_z = \sqrt{k_1^2 - k_x^2 - k_y^2}$, and $\mathbf{S}_E(k_x, k_y) = \hat{p}_i \cdot (\hat{v}\hat{v} + \hat{h}\hat{h})$, where \hat{p}_i is \hat{v}_i for vertically polarized (TM waves) or \hat{h}_i for horizontally polarized (TE waves) incidences. The definitions of \hat{h} and \hat{v} are $\hat{h} = \hat{z} \times \hat{k} / |\hat{z} \times \hat{k}|$ and $\hat{v} = \hat{h} \times \hat{k}$, respectively, so that $(\hat{v}, \hat{h}, \hat{k})$ forms an orthonormal system. The incident magnetic field is obtained by replacing \mathbf{S}_E with $\mathbf{S}_H = \hat{k} \times \mathbf{S}_E / \eta_0 = \hat{p}_i \cdot (\hat{v}\hat{h} - \hat{h}\hat{v}) / \eta_0$. The function Φ_B is

a Gaussian tapered spectrum with center incident direction in (k_{ix}, k_{iy}, k_{iz}) , where $k_{iz} = \sqrt{k_1^2 - k_{ix}^2 - k_{iy}^2}$

$$\Phi_{\mathbf{B}}(k_x - k_{ix}, k_y - k_{iy}) = \frac{B_x B_y}{4\pi} \exp\left\{-\frac{1}{4}[(k_x - k_{ix})^2 B_x^2 + (k_y - k_{iy})^2 B_y^2]\right\} \quad (91)$$

where B_x and B_y control the tapering or the beamwidths and are typically chosen to be $B_x = L_x/5$ and $B_y = L_y/5$, where L_x and L_y are the sizes of a square area to be simulated. This procedure consists of three steps:

1. As a first check, we use a Gaussian randomly rough surface as an example to verify the correctness and accuracy of the present method, comparing the results with those obtained by the original SMCG method. The surface size is $64\lambda^2$, with RMS height $\sigma = 0.2\lambda$ ($k_1\sigma = 1.257$) and correlation length 1λ . The relative permittivity of the lower space is chosen to be $15 - 15j$. Figure 8 compares the bistatic scatter-

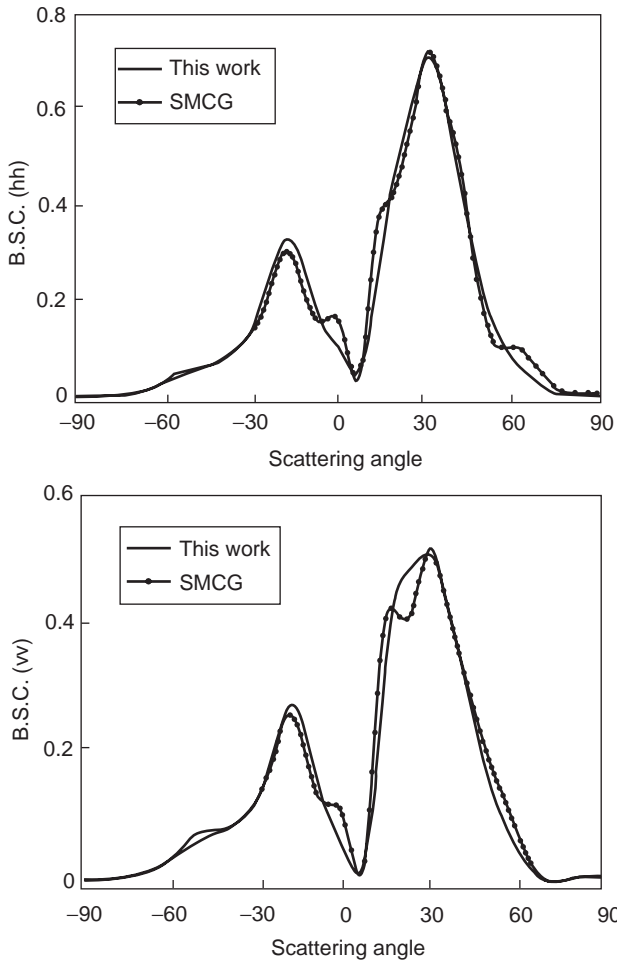


Figure 8. Comparison of the copolarized bistatic scattering coefficients (BSCs) from a $64\lambda^2$ surface area with RMS height 0.2λ using the original SMCG method and the present SMFIE-based MSMCG approach.

ing coefficients of copolarized components for a wave incident at -30° . Good agreement of the results demonstrates that both methods are reliable for predicting the bistatic scattering coefficients. The small discrepancy of the curves is understandable because of the difference between the two methods. The original SMCG method uses coupled equations with six unknowns per surface points, collocation method, and single-level expansion of the Green functions. The present method uses a single equation with one unknown per interior edge of the triangulated mesh representing the rough surface, RWG basis, and multilevel expansion. For this size and order of roughness surfaces, the overall iteration time using the present approach is around half that of the original SMCG method.

2. Next, to demonstrate the convergence of the proposed method for the large-RMS-height case, a very rough surface is analyzed. The simulated area is $256\lambda^2$ with RMS height $\sigma = 0.8\lambda$ ($k_1\sigma = 5.03$) and correlation lengths 1λ , and the relative permittivity of the lower region is set to be $8 - 4j$. The Green functions are expanded with 64 levels, and four Taylor series terms are retained. Figure 9 shows the simulation results of the bistatic scattering coefficients (BSCs) for a TE wave to z polarization incident at -30° . This example confirms that the present method converges to reasonable results as long as either the number of Taylor series terms or the number of expansion levels is sufficient. As a rule of thumb, the grid size in the z direction may be chosen to be $\Delta z \approx 1/|k_z|$. If the number of Taylor series terms is kept to be 4, the number of expansion levels is set to be around $(z_{\max} - z_{\min})/\Delta z$. If one more term of the Taylor series is added, the number of the expansion levels would be halved, and vice versa.
3. We perform some Monte Carlo simulations for bare soil surfaces over 50 realizations. A Gaussian spectrum is assumed, although an exponential spectrum may be more realistic. The permittivity of the wet soil is taken to be $25 - 3j$ at 1.5 GHz. The sizes of rough surfaces are 24×24 square wavelengths, with RMS height 0.25λ and correlation length 1λ . The results are shown in Fig. 10 for incidences at -30° .

In the following, we provide some results for wind-driven ocean surfaces. The ocean spectrum used is [29]

$$W(k, \phi) = \frac{1}{2\pi k} S(k) \Phi(k, \phi) \quad (92)$$

The spectral range used for simulations is $1 \leq k \leq 120 \text{ m}^{-1}$, and the surface sizes is chosen to be about 7.31 m by 7.31 m to sufficiently resolve the lower limit of the selected spectral range. At windspeed 10 m/s , the RMS height and slope are about 5 cm and 0.12 , respectively. At 1.5 GHz , the simulated area is about $36.6 \times 36.6\lambda^2$ with RMS roughness 0.25λ . The relative

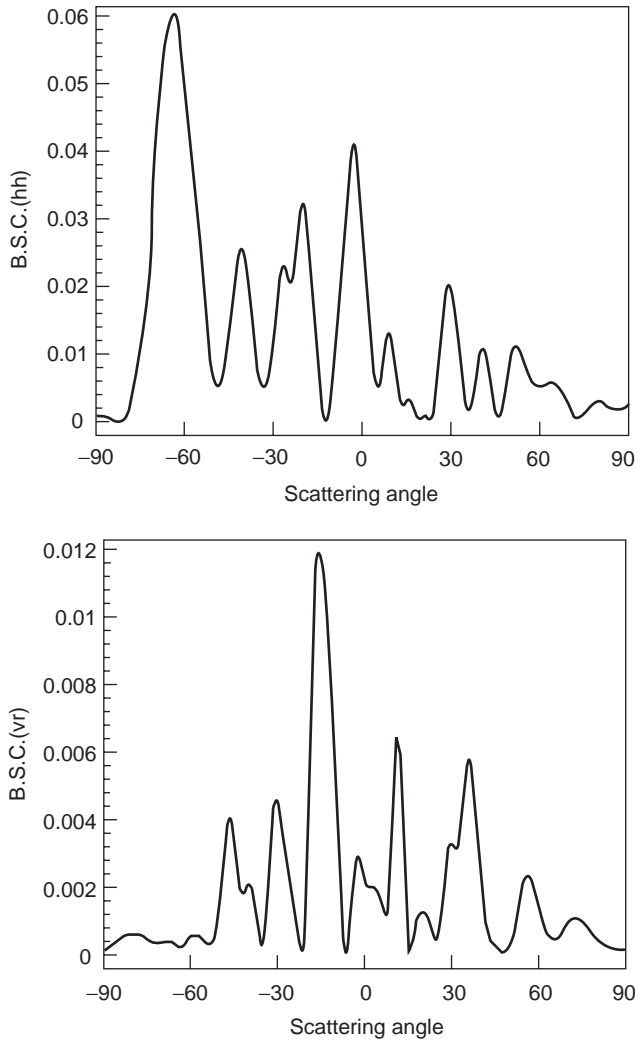


Figure 9. BSC from a $256\lambda^2$ rough surface area with RMS height 0.8λ for a TE wave incident at -30° .

permittivity of the seawater at the operating frequency is taken to be $74 - 61j$ at 15°C and 3.5% salinity.

First, it seems worth pointing out that (72) is a general and rigorous form, and some approximations may be made to speed up the computations within an acceptable loss of accuracy. If we set $[P_2]=[Q_2]=0$, then (67) would give $[I^m=0]$ and $[I^{\text{eff}}]=-2[I^e]$, and (72) would be reduced to the PEC (perfectly electric conducting) case. If only the diagonal elements are retained for $[Q_2]$ (the diagonal elements of $[P_2]$ are negligible with the singularity extracted), (72) would be commensurate with the impedance approximation method [30], and here we call it the *diagonal simplification method* (DSM). For a lossy half-space in which the Green function attenuates rapidly, it is always possible to discard the weak interactions in using the MSMCG scheme (i.e., letting $[P_2^w]=[Q_2^w]=0$), as long as the distance to distinguish the strong and weak interactions is appropriately large. This simplification, which would save nearly half of the CPU solution time, is referred to as the *neighborhood approximation method* (NAM). A comparison of the scattering coefficients for VV

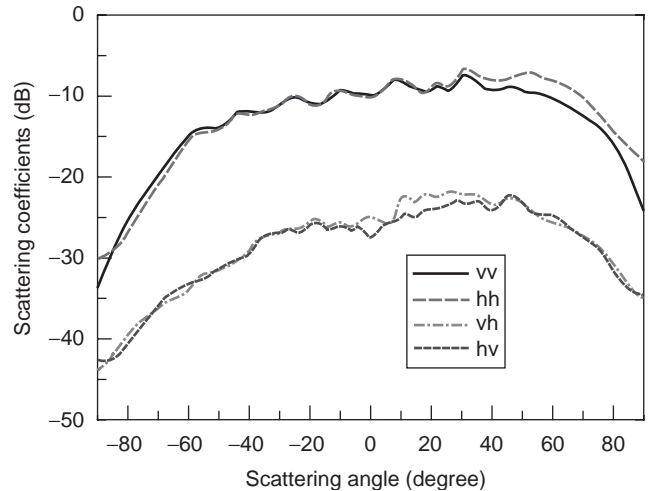


Figure 10. Scattering coefficients versus scattering angles for wet-soil surfaces. (This figure is available in full color at <http://www.mrw.interscience.wiley.com/erfme>.)

components is shown in Fig. 11, which illustrates that both DSM and NAM can well capture the features of the scattering coefficients, although DSM is less accurate than NAM and tends to overestimate the results in all of our numerical experiments.

Next, some Monte Carlo simulations are performed over 50 realizations for incidences at -20° , and the results are shown in Fig. 12 for three azimuth angles of incidences relative to the wind direction. The peak in the specular scattering direction for a wave incident in the crosswind direction is slightly stronger than that in the downwind and deadwind directions. The peak is 8.1 dB for crosswind incidence but only 6.7 dB for downwind and deadwind cases. This implies that the anisotropy of a wind-driven ocean surface is identifiable from the data of scattering measurements. Compared with Fig. 10, it can be seen that the scattering properties from Gaussian surfaces and oceanlike surfaces are basically distinguishable.

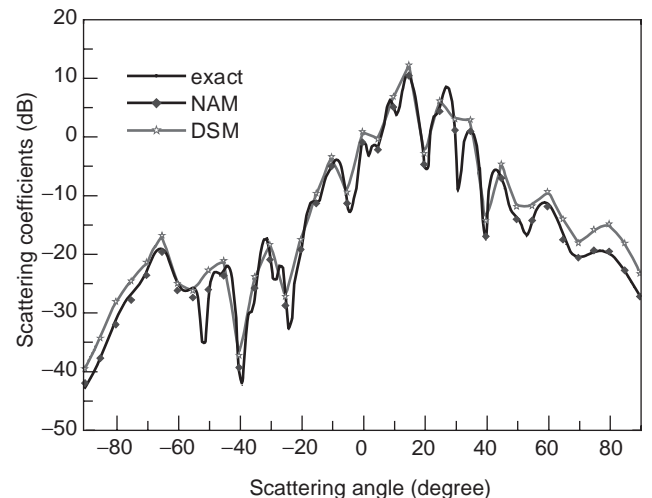


Figure 11. Comparison of approximate results using DSM and NAM with exact results. (This figure is available in full color at <http://www.mrw.interscience.wiley.com/erfme>.)

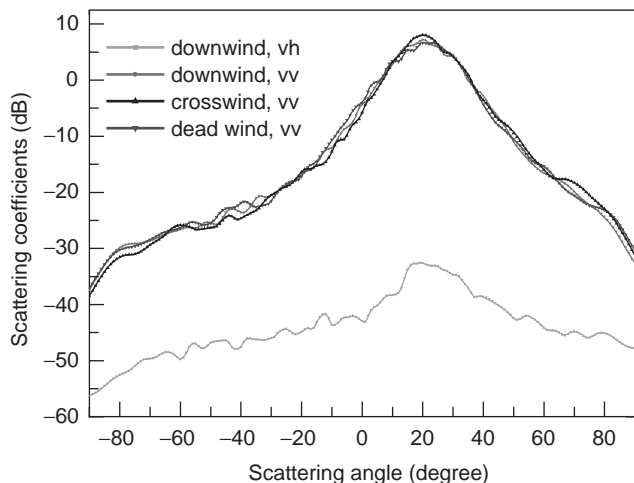


Figure 12. Scattering coefficients against scattering angles for wind-driven ocean surfaces. (This figure is available in full color at <http://www.mrw.interscience.wiley.com/erfme>.)

Finally, using the aforementioned NAM simplification, a very big oceanlike surface with sizes $128 \times 64\lambda^2$ is analyzed for which a permittivity of $45 - 30j$ has been used for the lower space [30]. The surface is modeled using 4,194,304 triangular patches, which results in a total of 6,288,384 unknowns for the *effective* surface electric currents using the single integral equation with the RWG basis functions. This number of unknowns would be doubled if two coupling integral equations were used. The results for incidence at -30° are shown in Fig. 13, which seems quite reasonable. The purpose of this example is to demonstrate the merits of our codes running on a newly constructed supercomputer that has 256 Alpha 800-MHz processors. The memory storage requirement for each processor is around 110 MB, and the total time is ~ 5 h for both polarizations combined. This efficiency is comparable with the Xia-Chan report [31] solving 10 million unknowns using 128 processors in 7 h.

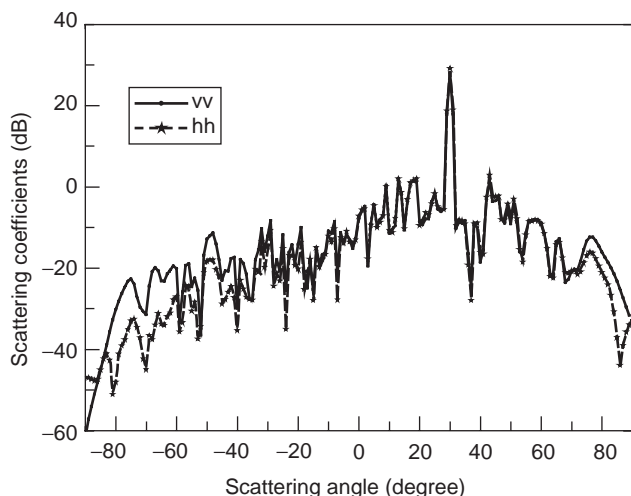


Figure 13. Scattering coefficients by a very large oceanlike surface.

2.4. Wave Scattering with UV Multilevel Partitioning Method: 3D Problem of Surface Scattering

We note that the SMCG method is limited by the RMS height. Also, when the RMS height is increased, the near-field neighborhood distance must be increased so that the number of terms in the Taylor series expansion can be limited. Furthermore, the PBTG requires an interpolation scheme. We have developed a multilevel UV method for rough-surface scattering. The basic of this method is described in this section.

Kapur and Long [32] proposed a QR decomposition method by using the property of the smoothness of the impedance matrix elements. The QR is applied to the matrix blocks with recursive partitioning and merging. The method has so far been demonstrated only for matrix block of moderate size in terms of wavelengths.

In this section, a UV method with multilevel partitioning (UV MLP) is developed to solve the wave scattering problem. The method consists of setting up a table of transmitting and receiving blocks of different sizes and separating them. For a specific scattering problem with given geometry, the scattering structure is partitioned into multilevel blocks. By looking up the rank in the static problem, the impedance matrix for a given transmitting and receiving block is expressed into a UV matrix product. In the method, we also apply the multilevel matrix partitioning (MLP) to partition the impedance matrix \bar{Z} . We demonstrate the technique for a 3D rough surface scattering problem. The surface area of the rough surface when projected onto the xy plane has a surface area up to 256 square wavelengths with the number of surface unknowns of 65,536. The RMS height is 0.5 wavelengths. In this case, the multilevel partitioning used is as done in the multilevel fast multipole method. Because the UV is applied independently to each level and each block, the procedure facilitates parallel implementation.

In Section 2.4.1, we describe the problem of independent rank determination. This is done for a flat surface and volume scattering. In Section 2.4.2, the formulation of the problem of wave impinging on a rough surface is given in terms of the surface integral equation, which is converted into a matrix equation using the method of moments (MoM). In Section 2.4.3, we describe the multilevel partitioning process, and in Section 2.4.4 we describe the UV method. In Section 2.4.5, the computational complexity of the proposed algorithm is derived.

2.4.1. Problem of Determination Independent Rank.

Consider a matrix \bar{Z} of dimension $N \times N$, which represents the interactions between two nonnear groups, each of which has N scatterers in the group, where the rank of \bar{Z} is r . We can use single-value decomposition (SVD) to determine rank. Let σ_1 be the largest singular value and the singular values be arranged in decreasing magnitude. Given a threshold ϵ , the rank r is such that $|\sigma_{r+1}/\sigma_1| \leq \epsilon$. The threshold used in the simulation is 1×10^{-5} in this article. Because of the smoothness of the matrix elements, the rank r is much less than the number of scatterers N . The rank r is determined mainly by the sizes of the

transmitting and receiving blocks and the separation distance between the two block centers.

Consider a transmitting block and a receiving block with N points in each block. The points are labeled \bar{r}_m , $m = 1, 2, \dots, N$ for the receiving block and \bar{r}_n , $n = 1, 2, \dots, N$, for the transmitting block. Then we have the matrix \bar{Z} of dimension $N \times N$ with elements

$$Z_{mn} = \frac{\exp(ik|\bar{r}_m - \bar{r}_n|)}{4\pi|\bar{r}_m - \bar{r}_n|} \quad (93)$$

For N , we assume 10 points per wavelength, which corresponds to 100 points per square wavelength and 1000 points per cubic wavelength.

The rank of the matrix can be determined. It is strongly dependent on the size of the transmitting and receiving blocks and the degree of separation between them.

2.4.1.1. Two Flat Sheets with Zero Vertical Separation.

Consider two flat sheets of sizes L_x and L_y placed on the same horizontal plane. The centers of the two planes are on the x axis, and R is the separation distance between the two centers. These requirements can be met for the problem of microstrip line and is usually assumed to be the current sheet. In the traditional method for determining the rank for such a problem, area sampling has to be used, which leads to a large number of sampling points and requires extensive CPU time and computer memory allocation. However, on the basis of Huygens principle, the equivalent sources are the boundary lines, which are the four sides of the sheet. Thus the radiation presumably originates from the enclosing boundary lines of the transmitting block to the boundary lines of the receiving block. We can actually use the boundary line sampling in the rank determination. Furthermore, due to the smoothness of Green function, we know that the rank is much less than the number of sampling points. Thus we can use coarse boundary sampling to further reduce the computational cost for the rank determination. In the Table 1, we list the ranks determined by these three methods, denoted as $L_z = 0$. For the area sampling, 100 points per square wavelength are used; for the boundary dense sampling, 10 points per wavelength are used. For the boundary coarse sampling, 4 points per wavelength are used. The ranks determined through them are comparable for the given physical sizes of the problem. Note that the ranks are substantially smaller than the block size N .

2.4.1.2. Volumetric Blocks and Enclosing Boundary Radiation. Next we consider volumetric blocks of sizes $L_x \times L_y \times L_z$. The centers of the blocks are placed on the x axis and separated by a distance R .

We also used three methods to determine the ranks for a given physical size of the problem: volume sampling, boundary dense sampling, and boundary coarse sampling. For the *boundary sampling*, the equivalent sources are now the boundary surfaces, which are the six sides of the block. Thus the radiation can be considered as radiation from the enclosing boundary surface of the transmitting block to the boundary surface of the receiving block. The

Table 1. Rank Table of Volume

$L_x = L_y$ (λ)	Points in Block	Distance (λ)	L_z (λ)	Rank
1.0	100	2.00	0	14 ^a , 13 ^b , 12 ^c
1.0	100	2.23	0	13, 13, 12
1.0	100	2.83	0	11, 9, 9
1.0	100	3.60	0	9, 9, 8
1.0	100	4.24	0	9, 8, 8
2.0	400	4.00	0	17, 15, 15
2.0	400	4.47	0	15, 14, 14
2.0	400	5.65	0	13, 12, 12
2.0	400	7.21	0	11, 11, 11
2.0	400	8.48	0	9, 10, 10
4.0	1,600	8.00	0	23, 20, 20
4.0	1,600	8.94	0	21, 18, 18
4.0	1,600	11.3	0	17, 16, 16
4.0	1,600	14.4	0	14, 13, 13
4.0	1,600	17.0	0	11, 12, 12
1.0	600	2.00	0.6	30 ^d , 34 ^e , 32 ^f
1.0	800	2.00	0.8	35, 37, 36
1.0	1,000	2.00	1.0	38, 43, 41
2.0	3,200	4.00	0.8	37, 41, 41
2.0	4,800	4.00	1.2	NA, g49, 50
2.0	8,000	4.00	2.0	NA, g65, 67
4.0	12,800	8.00	0.8	NA, g49, 49
4.0	38,400	8.00	2.4	NA, gNA, g81
4.0	64,000	8.00	4.0	NA, gNA, g116

^aArea sampling (100 points per square wavelength).

^bBoundary (line) dense sampling (10 points per wavelength).

^cBoundary (line) coarse sampling (4 points per wavelength).

^dVolume sampling (1000 points per cubic wavelength).

^eBoundary (surface) dense sampling (100 points per square wavelength).

^fBoundary (surface) coarse sampling (16 points per square wavelength).

^gNA = not available because of the limitation of computer resource.

ranks are also given in Table 1. For *volume sampling*, 1000 points per cubic wavelength are used. For *boundary dense sampling*, 100 points per square wavelength are used. For boundary coarse sampling, 16 points per square wavelength are used. Note that for the $4\lambda \times 4\lambda \times 4\lambda$, the number of points for volume sampling is 64,000, while for boundary coarse sampling the number of sampling points is only 1536. This will speed up the rank determination greatly for this case. We note that for the case of the $4\lambda \times 4\lambda \times 4\lambda$ with the $R = 8\lambda$ case, the number of points is $n = 40 \times 40 \times 40 = 64,000$. The rank from this case is only 116, meaning that significant matrix compression is possible. The table also shows that coarse sampling gives essentially the same rank as dense sampling. The rank can be determined quickly using coarse-coarse sampling.

2.4.1.3. Small Overestimation of Rank. In the SVD method, the rank determination is based on a threshold. Thus there is built in variation of rank due to variations in threshold. Furthermore, in applications as illustrated in this article, the exact rank is not required. Thus we usually are on the safe side using 10–20% above the “actual” rank.

We note that the block selection is dependent on the type of problem. However, once the static rank table is determined, the rank table can be applied to all cases within the same type of problem.

2.4.2. Wave Scattering Formulation. Consider a tapered scalar plane wave $\psi_{\text{inc}}(x, y, z)$ (Eq. 6.1.1 in Ref. 15) impinging on a 2D random rough surface with Dirichlet boundary condition and a random height profile $z=f(x, y)$. A Fredholm integral equation of the first kind can be formed. Let $\bar{r}' = \hat{x}x' + \hat{y}y' + \hat{z}f(x', y')$ denote a field point and $\bar{r} = \hat{x}x + \hat{y}y + \hat{z}f(x, y)$ denote a source point on the rough surface. Then the surface integral equation is [14]

$$0 = \psi_{\text{inc}}(\bar{r}) - \iint dx dy G_0(x, y, f(x, y); x', y', f(x', y')) U(x, y) \quad (94)$$

where $G_0 = [\exp(ik|\bar{r} - \bar{r}'|)] / (4\pi|\bar{r} - \bar{r}'|)$ is the free-space Green function and the unknown surface field is $U(x, y)$.

The method of moments (MoM) is used to discretize the integral equation. We use the pulse basis function and point matching method. The resulting matrix equation is

$$\bar{\bar{Z}} \cdot \bar{u} = \bar{b} \quad (95)$$

2.4.3. Multilevel Partitioning Process. Assuming that we have a square area as shown in Fig. 14a, we first split into four blocks as shown in Fig. 14b. Each of these four blocks is a subgroup at the P th level, which has the maximum group size. Then we split each subblock into another four small groups as shown in Fig. 14c. This splitting process is continued until we reach the smallest group size, which is at the first level. We decompose the full impedance matrix in Eq. (96) as the sum of P sparse matrixes as follows:

$$\bar{\bar{Z}} = \bar{\bar{Z}}^{(0)} + \bar{\bar{Z}}^{(1)} + \bar{\bar{Z}}^{(2)} + \dots + \bar{\bar{Z}}^{(P-1)} \quad (96)$$

Matrix $\bar{\bar{Z}}^{(0)}$ includes all the interactions among neighboring groups (including the self-group) at the first level. Matrix $\bar{\bar{Z}}^{(1)}$ includes all the interactions among neighboring groups at the second level. It consists of blocks at the

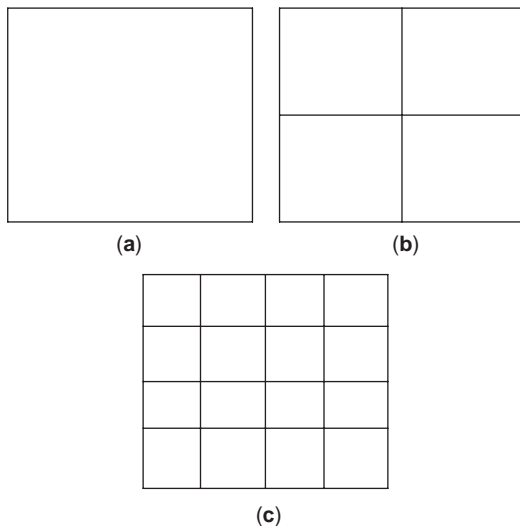


Figure 14. Illustration of multilevel partitioning process.

first level. Similarly, matrix $\bar{\bar{Z}}^{(i)}$ includes all the interactions among neighboring groups at the $(i+1)$ th level, but these consist of blocks at the i th level.

To facilitate understanding of the multilevel partitioning process, we give an example that has 64 subgroups at the first level. Assume that each group has M elements. For this example, the highest level is $P=3$. Thus $\bar{\bar{Z}} = \bar{\bar{Z}}^{(0)} + \bar{\bar{Z}}^{(1)} + \bar{\bar{Z}}^{(2)}$ and the impedance matrix of $\bar{\bar{Z}}$ is $64M \times 64M$ with $4096M \times M$ blocks.

In Fig. 15a, the 64 subgroups at the first level are denoted $1_1, 2_1, \dots, 64_1$. In Fig. 15b, the level 2 groups are denoted as $1_2, 2_2, \dots, 16_2$. Each of the level 2 groups has four level 1 groups. For example, group 3_2 has four groups of $5_1, 6_1, 13_1$, and 14_1 . In Fig. 15c, the level 3 groups are denoted as $1_3, 2_3, 3_3$, and 4_3 . Each of the level 3 groups has four level 2 groups. For example, group 2_3 has four groups of $3_2, 4_2, 7_2$, and 8_2 .

We use m_i to represent the group m of the level i . Then matrix $\bar{\bar{Z}}_{m_i, n_i}$ represents the interactions between the receiving group m and the transmitting group n of the i th level. Since the four level 1 groups form a level 2 group

57 ₁	58 ₁	59 ₁	60 ₁	61 ₁	62 ₁	63 ₁	64 ₁
49 ₁	50 ₁	51 ₁	52 ₁	53 ₁	54 ₁	55 ₁	56 ₁
41 ₁	42 ₁	43 ₁	44 ₁	45 ₁	46 ₁	47 ₁	48 ₁
33 ₁	34 ₁	35 ₁	36 ₁	37 ₁	38 ₁	39 ₁	40 ₁
25 ₁	26 ₁	27 ₁	28 ₁	29 ₁	30 ₁	31 ₁	32 ₁
17 ₁	18 ₁	19 ₁	20 ₁	21 ₁	22 ₁	23 ₁	24 ₁
9 ₁	10 ₁	11 ₁	12 ₁	13 ₁	14 ₁	15 ₁	16 ₁
1 ₁	2 ₁	3 ₁	4 ₁	5 ₁	6 ₁	7 ₁	8 ₁

(a)

13 ₂	14 ₂	15 ₂	16 ₂
9 ₂	10 ₂	11 ₂	12 ₂
5 ₂	6 ₂	7 ₂	8 ₂
1 ₂	2 ₂	3 ₂	4 ₂

(b)

3 ₃	4 ₃
1 ₃	2 ₃

(c)

Figure 15. Illustration of multilevel partitioning process with 64 subgroups at the first level.

and four level 2 groups form a level 3 group, we have

$$\bar{\bar{Z}}_{m_1 n_1} = \text{dimension of } M \times M$$

$$\bar{\bar{Z}}_{m_2 n_2} = \text{dimension of } 4M \times 4M$$

Examples are

$$\bar{\bar{Z}}_{3_2 5_2} = \begin{bmatrix} \bar{\bar{Z}}_{5_1 17_1} & \bar{\bar{Z}}_{5_1 18_1} & \bar{\bar{Z}}_{5_1 25_1} & \bar{\bar{Z}}_{5_1 26_1} \\ \bar{\bar{Z}}_{6_1 17_1} & \bar{\bar{Z}}_{6_1 18_1} & \bar{\bar{Z}}_{6_1 25_1} & \bar{\bar{Z}}_{6_1 26_1} \\ \bar{\bar{Z}}_{13_1 17_1} & \bar{\bar{Z}}_{13_1 18_1} & \bar{\bar{Z}}_{13_1 25_1} & \bar{\bar{Z}}_{13_1 26_1} \\ \bar{\bar{Z}}_{14_1 17_1} & \bar{\bar{Z}}_{14_1 18_1} & \bar{\bar{Z}}_{14_1 25_1} & \bar{\bar{Z}}_{14_1 26_1} \end{bmatrix} \quad (97)$$

$$\bar{\bar{Z}}_{6_2 5_2} = \begin{bmatrix} \bar{\bar{Z}}_{19_1 17_1} & \bar{\bar{Z}}_{19_1 18_1} & \bar{\bar{Z}}_{19_1 25_1} & \bar{\bar{Z}}_{19_1 26_1} \\ \bar{\bar{Z}}_{20_1 17_1} & \bar{\bar{Z}}_{20_1 18_1} & \bar{\bar{Z}}_{20_1 25_1} & \bar{\bar{Z}}_{20_1 26_1} \\ \bar{\bar{Z}}_{27_1 17_1} & \bar{\bar{Z}}_{27_1 18_1} & \bar{\bar{Z}}_{27_1 25_1} & \bar{\bar{Z}}_{27_1 26_1} \\ \bar{\bar{Z}}_{28_1 17_1} & \bar{\bar{Z}}_{28_1 18_1} & \bar{\bar{Z}}_{28_1 25_1} & \bar{\bar{Z}}_{28_1 26_1} \end{bmatrix} \quad (98)$$

$$\bar{\bar{Z}}_{1_3 2_3} = \begin{bmatrix} \bar{\bar{Z}}_{1_2 3_2} & \bar{\bar{Z}}_{1_2 4_2} & \bar{\bar{Z}}_{1_2 7_2} & \bar{\bar{Z}}_{1_2 8_2} \\ \bar{\bar{Z}}_{2_2 3_2} & \bar{\bar{Z}}_{2_2 4_2} & \bar{\bar{Z}}_{2_2 7_2} & \bar{\bar{Z}}_{2_2 8_2} \\ \bar{\bar{Z}}_{5_2 3_2} & \bar{\bar{Z}}_{5_2 4_2} & \bar{\bar{Z}}_{5_2 7_2} & \bar{\bar{Z}}_{5_2 8_2} \\ \bar{\bar{Z}}_{6_2 3_2} & \bar{\bar{Z}}_{6_2 4_2} & \bar{\bar{Z}}_{6_2 7_2} & \bar{\bar{Z}}_{6_2 8_2} \end{bmatrix} \quad (99)$$

There are three sets of blocks:

1. *The Blocks in $\bar{\bar{Z}}^{(0)}$.* In $\bar{\bar{Z}}^{(0)}$, we select interactions of the level 1 group with their nearest neighbors. For example, 20_1 have eight neighbors of 11_1 , 12_1 , 13_1 , 19_1 , 21_1 , 27_1 , 28_1 , and 29_1 . Thus $\bar{\bar{Z}}^{(0)}$ includes $\bar{\bar{Z}}_{11_1 20_1}$, $\bar{\bar{Z}}_{12_1 20_1}$, $\bar{\bar{Z}}_{13_1 20_1}$, $\bar{\bar{Z}}_{19_1 20_1}$, $\bar{\bar{Z}}_{20_1 20_1}$, $\bar{\bar{Z}}_{21_1 20_1}$, $\bar{\bar{Z}}_{27_1 20_1}$, $\bar{\bar{Z}}_{28_1 20_1}$, and $\bar{\bar{Z}}_{29_1 20_1}$, a total of nine matrices. Note that self-interaction is also included in here. We note that (a) block size of $\bar{\bar{Z}}_{m_1 n_1}$ is $M \times M$; (b) there are 36 interior level 1 groups of 9 blocks = $36 \times 9 = 324$ ($M \times M$) blocks; (c) 24 edge level 1 groups of 6 blocks = $24 \times 6 = 144$ ($M \times M$) blocks; (d) four corner level 1 groups of 4 blocks = $4 \times 4 = 16$ ($M \times M$) blocks. Thus $\bar{\bar{Z}}^{(0)}$ has a total of $324 + 144 + 16 = 484$ ($M \times M$) blocks.
2. *The Blocks in $\bar{\bar{Z}}^{(1)}$.* In $\bar{\bar{Z}}^{(1)}$, we select the interactions between level 2 groups and their nearest neighbors. For example, we need to include $\bar{\bar{Z}}_{6_2 5_2}$. However, we need to exclude those that have been included in $\bar{\bar{Z}}^{(0)}$. We define the impedance matrix primes

$$\bar{\bar{Z}}'_{6_2 5_2} = \begin{bmatrix} \bar{\bar{Z}}_{19_1 17_1} & \bar{0}_1 & \bar{\bar{Z}}_{19_1 25_1} & \bar{0}_1 \\ \bar{\bar{Z}}_{20_1 17_1} & \bar{\bar{Z}}_{20_1 18_1} & \bar{\bar{Z}}_{20_1 25_1} & \bar{\bar{Z}}_{20_1 26_1} \\ \bar{\bar{Z}}_{27_1 17_1} & \bar{0}_1 & \bar{\bar{Z}}_{27_1 25_1} & \bar{0}_1 \\ \bar{\bar{Z}}_{28_1 17_1} & \bar{\bar{Z}}_{28_1 18_1} & \bar{\bar{Z}}_{28_1 25_1} & \bar{\bar{Z}}_{28_1 26_1} \end{bmatrix} \quad (100)$$

where $\bar{0}_1$ is the zero matrix of dimension ($M \times M$).

Thus the $\bar{\bar{Z}}^{(1)}$, include all the $\bar{\bar{Z}}'_{m_2 n_2}$, where m_2 and n_2 are neighbors. As shown in Eq. (101), we note that the matrix $\bar{\bar{Z}}'_{m_2 n_2}$ (a) consists of blocks with size of $M \times M$, (b) each block consists of a transmitting region and a receiving region that are not neighbors of each other (e.g., in $\bar{\bar{Z}}'_{19_1 17_1}$, the receiving region is 19_1 and the transmitting region is 17_1 and the two are not neighbors of each other), and (c) the separation R between the transmitting and the receiving regions is at a minimum of $2S$ for $\bar{\bar{Z}}'_{19_1 17_1}$, where S is the block size. It is at a maximum of $R = 3\sqrt{2}S$ for $\bar{\bar{Z}}'_{44_1 17_1}$, which is in $\bar{\bar{Z}}'_{10_2 5_2}$. Thus $\bar{\bar{Z}}^{(1)}$ includes

3. Four interior level 2 groups that have eight neighbors, four of which have 12 blocks and four of which have 15 blocks. The total number of blocks is $4 \times (4 \times 12 + 4 \times 15) = 432$.
4. Eight edge level 2 groups that have five neighbors, three of which have 12 blocks and two of which have 15 blocks. The total number of blocks is $8 \times (3 \times 12 + 2 \times 15) = 528$.
5. Four corner level 2 groups, that have three neighbors, two of which have 12 blocks and one of which has 15 blocks. The total number of blocks is $4 \times (2 \times 12 + 1 \times 15) = 156$.
6. Thus matrix $\bar{\bar{Z}}^{(1)}$ includes $432 + 528 + 156 = 1116$ ($M \times M$) blocks.
7. *The Blocks in $\bar{\bar{Z}}^{(2)}$.* In $\bar{\bar{Z}}^{(2)}$, we select the interactions between level 3 groups and their nearest neighbors. For example, we need to include $\bar{\bar{Z}}'_{1_3 2_3}$. However, some of the interactions have already been included in $\bar{\bar{Z}}^{(0)}$ and $\bar{\bar{Z}}^{(1)}$ and need to be excluded. We define the prime impedance matrices

$$\bar{\bar{Z}}'_{1_3 2_3} = \begin{bmatrix} \bar{\bar{Z}}_{1_2 3_2} & \bar{\bar{Z}}_{1_2 4_2} & \bar{\bar{Z}}_{1_2 7_2} & \bar{\bar{Z}}_{1_2 8_2} \\ \bar{0}_2 & \bar{\bar{Z}}_{2_2 4_2} & \bar{0}_2 & \bar{\bar{Z}}_{2_2 8_2} \\ \bar{\bar{Z}}_{5_2 3_2} & \bar{\bar{Z}}_{5_2 4_2} & \bar{\bar{Z}}_{5_2 7_2} & \bar{\bar{Z}}_{5_2 8_2} \\ \bar{0}_2 & \bar{\bar{Z}}_{6_2 4_2} & \bar{0}_2 & \bar{\bar{Z}}_{6_2 8_2} \end{bmatrix} \quad (101)$$

Note that the building blocks of $\bar{\bar{Z}}'_{1_3 2_3}$ are level 2 blocks and are of size of $(4M \times 4M) = 16M \times M$. This is important that as the level increases, there will be a fourfold growth in block size as we go up each level. We have four level 3 groups, each of which has two neighbors with 12 level 2 blocks and one neighbor with 15 level 2 blocks. Thus, we have $4 \times (2 \times 12 + 1 \times 15) = 156$ level 2 blocks. Since each level 2 blocks has 16 level 1 blocks. Thus we have a total of $16 \times 156 = 2496$ level 1 block in $\bar{\bar{Z}}^{(2)}$.

Thus the total count is $484 + 1116 + 2496 = 4096$, and all the level 1 blocks are counted exactly once. To summarize, the block size in $\bar{\bar{Z}}^{(0)}$ is $M \times M$, in $\bar{\bar{Z}}^{(1)}$ is $M \times M$, and in $\bar{\bar{Z}}^{(2)}$ $4M \times 4M$. In applying UV decomposition, the UV

matrix is applied to each block for that level. Each block consists of a transmitting region and a receiving region that are not neighbors of each other. However, their separations are within a restricted range as indicated before.

2.4.4. UV Method Based on Interpolation Technique.

The matrix $\bar{\bar{Z}}_{m_i n_i}$, which represents the interactions between two nonneighbor groups' m_i and n_i , can be represented by UV decomposition. The matrix $\bar{\bar{Z}}_{m_i n_i}$ is of dimensions $4^{(i-1)}M \times 4^{(i-1)}M$. The rank of $\bar{\bar{Z}}_{m_i n_i}$, r , is much smaller than $4^{(i-1)}M$. For simpler notation, we denote $\bar{\bar{Z}}_{m_i n_i}$ by $\bar{\bar{A}}$, which has dimension of $N \times N$ and rank of r with $r \ll N$. Decomposition of $\bar{\bar{A}}$ by the SVD and Gram-Schmidt processes will consume CPU time because N is large. Note that in Section 3, we apply the SVD to find r . But because of coarse sampling, the selected matrices are roughly of dimension $r \times r$ only.

Let the column of $\bar{\bar{A}}$ be denoted by \bar{a}_l , where $l = 1, 2, \dots, N$; then $A_{mn} = (\bar{a}_n)_m$. The element A_{mn} is the m th element of the column vector \bar{a}_n . However, there are only r independent columns. In the transmitting region, we select r points from the N points. The r points must be uniformly distributed in the transmitting region.

We compute the r columns \bar{u}_l , $l = 1, 2, \dots, r$. Each column is of dimension of N and coincides with a column of $\bar{\bar{A}}$:

$$U_{ml} = (\bar{u}_l)_m = A_{mp(l)}, \quad m = 1, 2, \dots, N \quad (102)$$

where $p(l)$ is a column index of $\bar{\bar{A}}$ that depends on l . Note that to get U_{ml} , we need to go through all the N points in the receiving region. Thus the matrix \bar{U} has $N \times r$ elements.

Because of linear independence, any general column \bar{a}_m of $\bar{\bar{A}}$ is a linear combination of \bar{u}_l , that is

$$\bar{a}_m = \sum_{l=1}^r v_{lm} \bar{u}_l, \quad m = 1, 2, \dots, N \quad (103)$$

where v_{lm} are the coefficients to be determined.

We pick r rows of $\bar{\bar{A}}$ which has total of $N \times r$ elements. The r rows correspond to r points in the receiving group. The r points must be uniformly distributed in the receiving group. We first put these rows in a matrix of \bar{R} :

$$R_{m_a p} = A_{m(m_a)p}, \quad p = 1, 2, \dots, N \quad \text{and} \quad m_a = 1, 2, \dots, r \quad (104)$$

We pick the m_a rows in \bar{u}_l , $l = 1, 2, \dots, r$. That will give us a $r \times r$ matrix, which we will call \bar{U} , and we have $\bar{U}_{m_a n_a} = (\bar{u}_{n_a})_{m(m_a)}$. Then we set

$$R_{m_a l} = \sum_{n_a=1}^r \bar{U}_{m_a n_a} v_{n_a l}, \quad l = 1, 2, \dots, N \quad (105)$$

In matrix notation, $\bar{\bar{V}} = r \times N$, $\bar{\bar{R}} = r \times N$, $\bar{\bar{U}} = r \times r$, $\bar{\bar{R}} = \bar{\bar{U}} \bar{\bar{V}}$, and $\bar{\bar{V}} = (\bar{\bar{U}})^{-1} \bar{\bar{R}}$. This completes the UV decomposition:

$$\bar{\bar{A}} = \bar{\bar{U}} \bar{\bar{V}} \quad (106)$$

To summarize, we take r columns of $\bar{\bar{A}}$ and then r rows of N , which constitutes a total of $2r \times N$ elements. We need to

take the inverse of an $r \times r$ matrix $\bar{\bar{U}}$ and a matrix multiplication of the $r \times r$ matrix times a $r \times N$ matrix. The computational and memory efficiency is achieved when $r \ll N$.

2.4.5. Computational Complexity Analysis

2.4.5.1. Multilevel Group Sizes and Number of Groups. A rough surface is generated in a square area with \sqrt{N} points in x direction and \sqrt{N} points in y direction, so the total number of patches is N . We use various subgroup sizes at P level to partition the whole area as follows:

1. At P th level, we split the whole area as four groups. Each group has $N/4$ elements:

$$L_P = 4 = 2^{2(P-P+1)} \quad (107)$$

$$M_P = N/4 = \frac{N}{L_P} \quad (108)$$

2. where L_P is the number of groups and M_P is the number of elements of each group at P th level.
3. We split each group into four subgroups and continue this partitioning; at i th level, we have

$$L_i = 2^{2(P-i+1)} \quad (109)$$

$$M_i = \frac{N}{L_i} \quad (110)$$

4. At the first level, we have

$$L_1 = 2^{2P} \quad (111)$$

$$M_1 = \frac{N}{L_1} \quad (112)$$

2.4.5.2. Cost Function at i th Level. In $\bar{\bar{Z}}^{(i)}$, we select the interactions between level $(i+1)$ groups and their nearest neighbors. However, some of the interactions have already been included in the lower-level groups and must be excluded here. There are two kinds of neighboring groups: (1) that sharing only one common point and (2) that sharing one common edge.

1. *Sharing Only One Common Point.* For the neighboring groups of $m_{(i+1)}$ and $n_{(i+1)}$ shown in Fig. 16a, only one common point is shared between them. The impedance matrix that will be calculated is

$$\bar{\bar{Z}}_{m_{(i+1)} n_{(i+1)}} = \begin{bmatrix} \bar{\bar{Z}}_{m_i^{(1)} n_i^{(1)}} & \bar{\bar{Z}}_{m_i^{(1)} n_i^{(2)}} & \bar{\bar{Z}}_{m_i^{(1)} n_i^{(3)}} & \bar{\bar{Z}}_{m_i^{(1)} n_i^{(4)}} \\ \bar{\bar{Z}}_{m_i^{(2)} n_i^{(1)}} & \bar{0}_i & \bar{\bar{Z}}_{m_i^{(2)} n_i^{(3)}} & \bar{\bar{Z}}_{m_i^{(2)} n_i^{(4)}} \\ \bar{\bar{Z}}_{m_i^{(3)} n_i^{(1)}} & \bar{\bar{Z}}_{m_i^{(3)} n_i^{(2)}} & \bar{\bar{Z}}_{m_i^{(3)} n_i^{(3)}} & \bar{\bar{Z}}_{m_i^{(3)} n_i^{(4)}} \\ \bar{\bar{Z}}_{m_i^{(4)} n_i^{(1)}} & \bar{\bar{Z}}_{m_i^{(4)} n_i^{(2)}} & \bar{\bar{Z}}_{m_i^{(4)} n_i^{(3)}} & \bar{\bar{Z}}_{m_i^{(4)} n_i^{(4)}} \end{bmatrix} \quad (113)$$

The dimension of matrix $\bar{\bar{Z}}_{m_i n_i}$ is $M_i \times M_i$. The computational steps for $\bar{\bar{Z}}_{m_i n_i} \cdot \bar{b}_{M_i}$ through the UV is $2M_i r_i$, where r_i is the rank of $\bar{\bar{Z}}_{m_i n_i}$. In here we

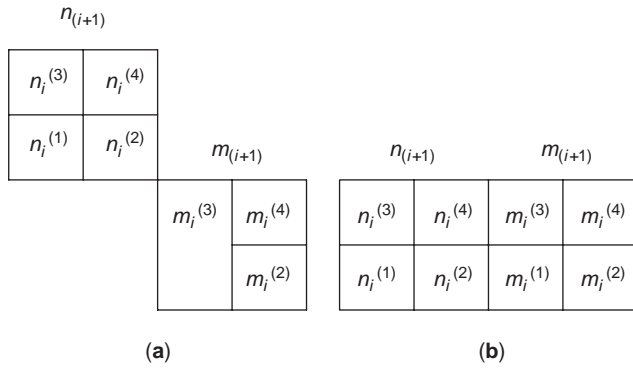


Figure 16. Illustration of block interactions at the i th level.

assume that the rank r_i of $\bar{\bar{Z}}_{m_i n_i}$ is same for all block interactions at the same level. There are 15 nonzero matrices of $\bar{\bar{Z}}_{m_i n_i}$ in the $\bar{\bar{Z}}'_{m_{i+1} n_{i+1}}$. The total computational steps for $\bar{\bar{Z}}'_{m_{i+1} n_{i+1}} \cdot \bar{b}'_{M_{i+1}}$ are $30M_i r_i$.

2. *Sharing One Common Edge.* For the neighboring groups of m_{i+1} and n_{i+1} shown in Fig. 16b, one common edge is shared between them. The impedance matrix that will be calculated is

$$\bar{\bar{Z}}'_{m_{i+1} n_{i+1}} = \begin{bmatrix} \bar{\bar{Z}}_{m_i^{(1)} n_i^{(1)}} & \bar{0}_i & \bar{\bar{Z}}_{m_i^{(1)} n_i^{(3)}} & \bar{0}_i \\ \bar{\bar{Z}}_{m_i^{(2)} n_i^{(1)}} & \bar{\bar{Z}}_{m_i^{(2)} n_i^{(2)}} & \bar{\bar{Z}}_{m_i^{(2)} n_i^{(3)}} & \bar{\bar{Z}}_{m_i^{(2)} n_i^{(4)}} \\ \bar{\bar{Z}}_{m_i^{(3)} n_i^{(1)}} & \bar{0}_i & \bar{\bar{Z}}_{m_i^{(3)} n_i^{(3)}} & \bar{0}_i \\ \bar{\bar{Z}}_{m_i^{(4)} n_i^{(1)}} & \bar{\bar{Z}}_{m_i^{(4)} n_i^{(2)}} & \bar{\bar{Z}}_{m_i^{(4)} n_i^{(3)}} & \bar{\bar{Z}}_{m_i^{(4)} n_i^{(4)}} \end{bmatrix} \quad (114)$$

There are 12 nonzero matrices of $\bar{\bar{Z}}_{m_i n_i}$ in the $\bar{\bar{Z}}'_{m_{i+1} n_{i+1}}$. The total computational steps for $\bar{\bar{Z}}'_{m_{i+1} n_{i+1}} \cdot \bar{b}'_{M_{i+1}}$ are $24M_i r_i$.

3. *Interior Groups.* The interior groups have eight neighbors, four of which share only one common point and four of which share one common edge. There are $(L_{i+1}^{1/2} - 2)^2$ interior groups at the $(i+1)$ th level. Thus the computational steps for the interior groups at the i th level are

$$\begin{aligned} & (L_{i+1}^{1/2} - 2)^2 (4 * 30M_i r_i + 4 * 24M_i r_i) \\ & = 216(L_{i+1}^{1/2} - 2)^2 M_i r_i \end{aligned} \quad (115)$$

4. *Edge Groups.* The edge groups have five neighbors, two of which share only one common point and three of which share one common edge. There are $4(L_{i+1}^{1/2} - 2)$ edge groups at the $(i+1)$ th level. Thus computational steps for the edge groups at the i th level are

$$\begin{aligned} & 4(L_{i+1}^{1/2} - 2)(2 * 30M_i r_i + 3 * 24M_i r_i) \\ & = 528(L_{i+1}^{1/2} - 2)M_i r_i \end{aligned} \quad (116)$$

5. *Corner Groups.* The corner groups have three neighbors. One of them shares only one common point, and two of them share one common edge. There are four corner groups at the $(i+1)$ th level. Thus computational steps for the corner groups at the i th level are

$$4(1 * 30M_i r_i + 2 * 24M_i r_i) = 312M_i r_i \quad (117)$$

6. *Total Computational Steps at i th Level:*

$$\begin{aligned} & 216(L_{i+1}^{1/2} - 2)^2 M_i r_i \\ & + 528(L_{i+1}^{1/2} - 2)M_i r_i + 312M_i r_i \\ & = 2M_i r_i (108L_{i+1} \\ & - 168L_{i+1}^{1/2} + 60) \end{aligned} \quad (118)$$

2.4.5.3. Cost Function for the Multilevel UV Method (nonnear). The total computational steps for nonneighbor block interactions through the multilevel UV decomposition are then

$$\sum_{i=1}^{P-1} 2r_i M_i [108L_{i+1} - 168L_{i+1}^{1/2} + 60] \quad (119)$$

Generally speaking, the rank of each block level will increase with increase in block size. For simplicity, we assume $r_i = \text{constant} = r$ here, and incorporating this r into Eq. (119), we have

$$27rN \log_2 \left(\frac{N}{M_1} \right) + 60rN - 120rM_1 \quad (120)$$

2.4.5.4. Cost Function for Near-Field Interactions in $\bar{\bar{Z}}^{(0)}$. All the near-field interactions are included in the matrix $\bar{\bar{Z}}^{(0)}$, which is computed directly as the original impedance matrix. The block size in $\bar{\bar{Z}}^{(0)}$ is of dimension of $M_1 \times M_1$. The computational steps for the block and block interaction are M_1^2 :

1. The interior group has nine blocks (including self-interaction). There are $(L_1^{1/2} - 2)^2$ interior groups at the first level. Thus computational steps for the interior groups at the first level are $9(L_1^{1/2} - 2)^2 M_1^2$.
2. The edge group has six blocks (including self-interaction). There are $4(L_1^{1/2} - 2)$ edge groups at the first level. Thus computational steps for the edge groups at the first level are $6(L_1^{1/2} - 2)M_1^2$.
3. The corner group has four blocks (including self-interaction). There are four corner groups at the first level. Thus the computational steps for the corner groups at level 1 are $4M_1^2$.

4. The total number of computational steps for near-field interaction is then

$$\begin{aligned} &9(L_1^{1/2} - 2)^2 M_1^2 + 6(L_1^{1/2} - 2)M_1^2 + 4M_1^2 \\ &= (9NM_1 - 12N^{1/2}M_1^{3/2} + 4M_1^2) \end{aligned} \quad (121)$$

2.4.6. Cost Function. The total computational steps for multilevel partitioning UV is the sum of the near and nonnear interactions and is given by

$$\begin{aligned} &27rN \log_2 \frac{N}{M_1} + 60rN \\ &- 120rM_1 + (9NM_1 \\ &- 12N^{1/2}M_1^{3/2} + 4M_1^2) \end{aligned} \quad (122)$$

2.4.7. Numerical Results and Discussion. The numerical simulation results are presented in terms of the bistatic scattering coefficients normalized by the incident power. Simulations are based on Gaussian random rough surfaces with Gaussian correlation functions. The computer used in the simulations is a Pentium single processor of 2.6 GHz with 2 GB memory. We have implemented both the SVD-based QR method and the UV method. First, we will illustrate the rank for the rough surface.

2.4.7.1. Rank Determination for Random Rough Surface.

For the rough-surface scattering problem, the difficulty is that the vertical sizes of the blocks are always changed because of the randomness of surface height. Thus we have to use the coarse-coarse area sampling to determine the rank. In the simulation, 16 (instead of 100) points per square wavelength are used for rank determination. In Table 2, we show the ranks as functions of the horizontal size, vertical size, and distance between two group centers. The vertical size is defined as the maximum height of the surface minus the minimum height of the surface in the same block. The results are obtained through one realization of rough-surface profiles with the given RMS height of 0.5λ and correlation length of 0.707λ .

2.4.7.2. CPU for the UV . In Table 3, we list the CPU time based on the UV method for different number of surface unknowns. The RMS height and correlation

Table 2. Rank Table of Rough Surface^a

$L_x = L_y$ (λ)	Points in Square	Distance (λ)	L_z (λ)	Rank
1.0	64	2.00	1.402	15
2.0	256	4.00	1.824	25(29)
4.0	1,024	8.00	3.219	35(44)

^aFrom one realization of rough surfaces with RMS height of 0.5λ and correlation length of 0.707λ . Surface area is 16×16 square wavelengths, 64 points per square wavelength are used in generating the rough surface. For rank determination, 16 points per square wavelength are taken uniformly from the rough surfaces.

Table 3. CPU for the UV Method

Number of Unknowns	Preprocessing(s)	Conjugate Gradient(s)	Total CPU(s)
4,096	$6^a + 5^b$	14	25
16,384	291 + 54	170	515
65,536	291 + 500	1220	2011

^aCPU for rank determination with coarse-coarse sampling.

^bCPU for building UV matrix.

length of the rough surface for all cases is 0.5λ and 0.707λ , respectively. The preprocessing time of the UV method is time used to find the rank on the basis of coarse-coarse sampling and the time to construct the UV matrix. The CPU time for CG means the CPU time spent for solving the matrix equation after the matrix filling and preprocessing is finished. For the case of 65,536 surface unknowns, it takes about 34 min for the total CPU.

2.4.7.3. Comparison of Bistatic Scattering Coefficients Simulated from Different Methods for Single Realization.

In Fig. 17, we plot the bistatic scattering coefficients as a function of the scattering angles. The RMS height and correlation length are 0.5λ and 0.707λ , respectively. The incidence angle is 20° . The surface lengths are 8×8 wavelengths, and we use 64 points per square wavelength to generate the rough surface. The results simulated from three methods are shown, which are the exact solution of the matrix equation, the solution based on the SVD-based QR method, and the solution of the UV method. All of them are in good agreement.

In Fig. 18a, we plot the same results except that the surface lengths are extended to 16×16 wavelengths. Because of the limitation of computer memory, we cannot

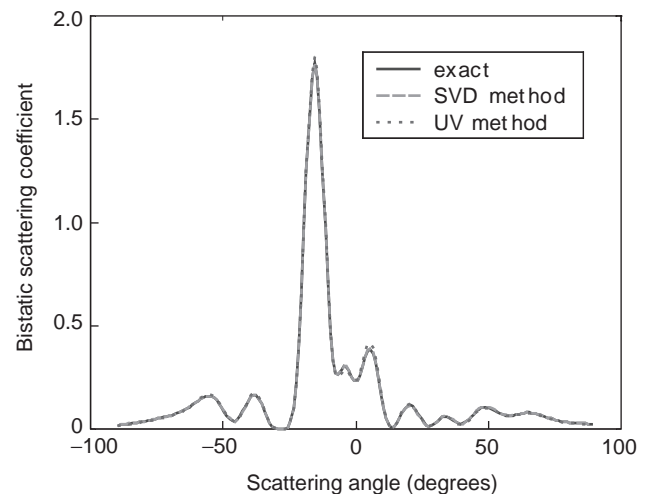


Figure 17. Comparisons of the bistatic scattering coefficients between numerical simulations from three approaches of exact solution, SVD-based QR method, and UV method. The RMS height and correlation length of the rough surface are 0.5λ and 0.707λ , respectively. The surface area is 8×8 squared wavelengths. The incident angle is 20° . (This figure is available in full color at <http://www.mrw.interscience.wiley.com/erfme>.)

solve the matrix equation with the exact solution. We only show the simulation results from the SVD-based QR and the *UV* method. The two results are in good agreement.

To demonstrate that the proposed algorithm can be used also for a large number of surface unknowns, we plot the simulation results for the case of RMS height of 0.5λ and correlation length of 0.707λ at an incidence angle of 20° in Fig. 18b. The surface lengths are 16×16 wavelengths, but we use 256 points per square wavelength to sample the rough surface. Again, very good agreement is observed at all scattering angles between the simulation results from the SVD-based QR method and the *UV*.

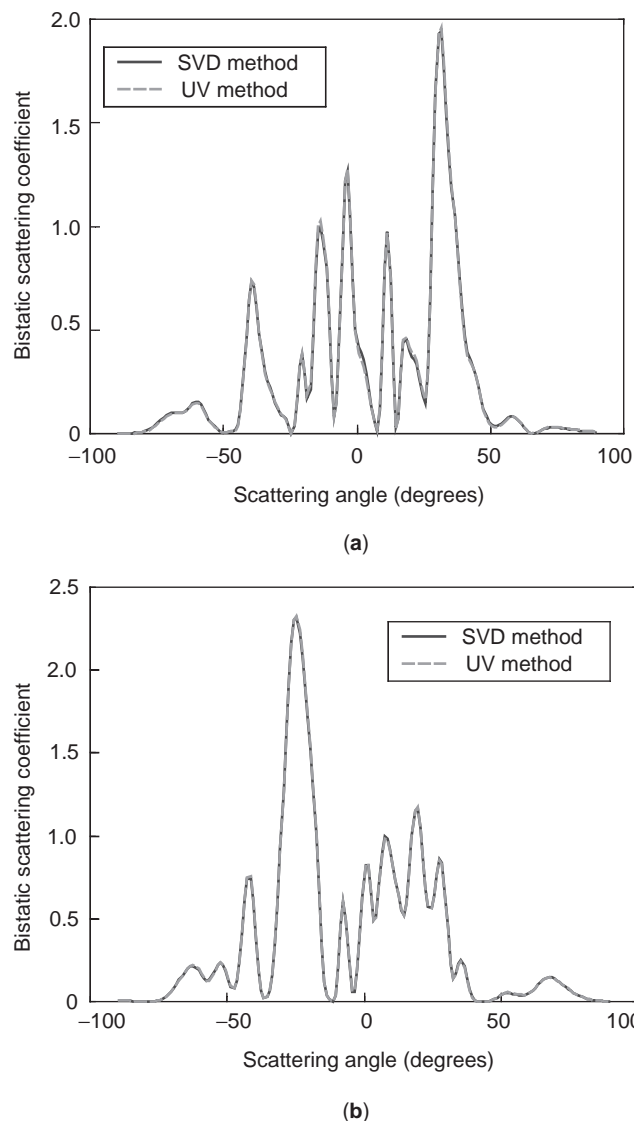


Figure 18. Comparisons of the bistatic scattering coefficients between the numerical simulations from two approaches of the SVD-based QR method and the *UV* method. The RMS height and correlation length of rough surface are 0.5λ and 0.707λ , respectively. Surface area is 16×16 squared wavelengths, with 64 points per square wavelength (a) and 256 points per square wavelength (b) used in the rough surface sampling. The incident angle is 20° . (This figure is available in full color at <http://www.mrw.interscience.wiley.com/erfme>.)

3. APPLICATIONS IN MICROWAVE REMOTE SENSING

Soil surface roughness is a major problem in land surface sensing. However, effects of vegetation cover are equally, if not more, important since very few land surfaces are not vegetation-covered. This article addresses roughness effects. We include both volume and surface scattering by considering a volume scattering layer above the rough surface; this is done using the NMM3D rough-surface results as a boundary condition for radiative transfer theory [33]. The model will be applied to vegetation effects over rough soil surface in a future paper.

Measurements of soil and ocean surface thermal emission at microwave frequency can provide the means to predict soil moisture and ocean wind velocity. In active microwave remote sensing, the radar backscattering response of soil surface at microwave frequencies is measured to evaluate the soil moisture and surface roughness parameters. The study of frequency, polarimetric, and angular dependence of the backscattering coefficients of rough surface is essential for retrieving soil moisture. In this section, we illustrate the numerical results from the NMM3D in active and passive remote sensing. In Section 3.1, NMM3D applications in active remote sensing will be described; in Section 3.2, we describe applications in passive remote sensing.

3.1. Application of NMM3D with Pulse Basis Function and Point-Matching Method in Active Remote Sensing

The backscattering coefficients of wet soil surfaces are studied with the three-dimensional Monte Carlo simulations using the Stratton–Chu formulation, pulse basis functions, and point matching. The method was described earlier in this article. The simulation results are compared with the experimental measurements for backscattering coefficients at L and C frequency bands and at multi-incidence angles. Fairly good agreements are obtained for the same physical surface roughness parameters at both frequency bands. The Monte Carlo simulation results of bistatic scattering from random rough surface in this section are averaged over 30 realizations.

The experimental data are taken from Oh et al. [34]. We choose these data because (1) they cover a wide range of surface roughness from smooth to very rough, (2) the RMS heights and correlation lengths of each field are given, (3) measurements are made for both dry and wet soils, and (4) the measurements are performed at three frequency bands of L, C, and X and incidence angles of 10 – 70° . There are four total surface fields used in the measurements. Fields 1 and 2 have similar surface roughness parameters and soil moisture levels, and they are very smooth. Field 3 is rough, and the field 4 is very rough. We will show the simulation results and their comparisons with the measurements for fields 1 and 3. For convenience, we list the measured rough surface parameters and relative permittivities of soil given by Oh et al. [34] and in Table 4. It was reported that these two rough-surface profiles are closer to an exponential correlation function

Table 4. Measured Surface Roughness Parameters and Relative Permittivities of Soil

Field	RMS Height (cm)	Correlation Length (cm)	Relative Permittivity			
			Wet Soil		Dry Soil	
			At 1.5 GHz	At 4.75 GHz	At 1.5 GHz	At 4.75 GHz
1	0.4	8.4	15.57 + i3.71	15.42 + i2.15	7.99 + i2.02	8.77 + i1.04
3	1.12	8.4	15.34 + i3.66	15.23 + i2.12	7.70 + i1.95	8.50 + i1.00

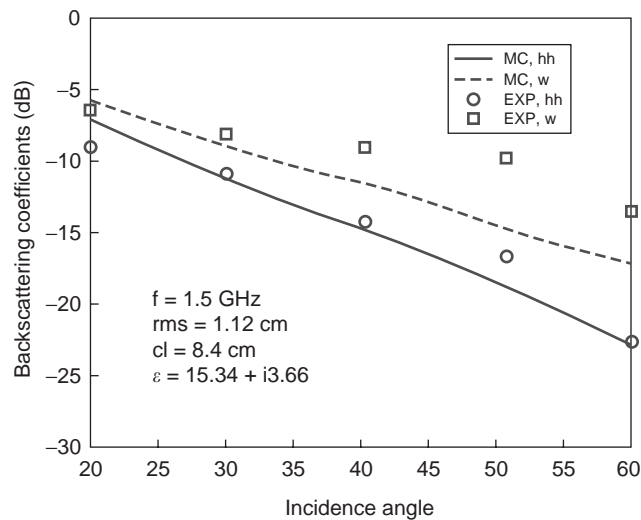
[34], so the numerical simulations of rough-surface scattering are conducted for the Gaussian rough surface with an exponential correlation function. The exponential correlation function is given by

$$C(x,y) = h^2 \exp - \frac{\sqrt{x^2 + y^2}}{l} \tag{123}$$

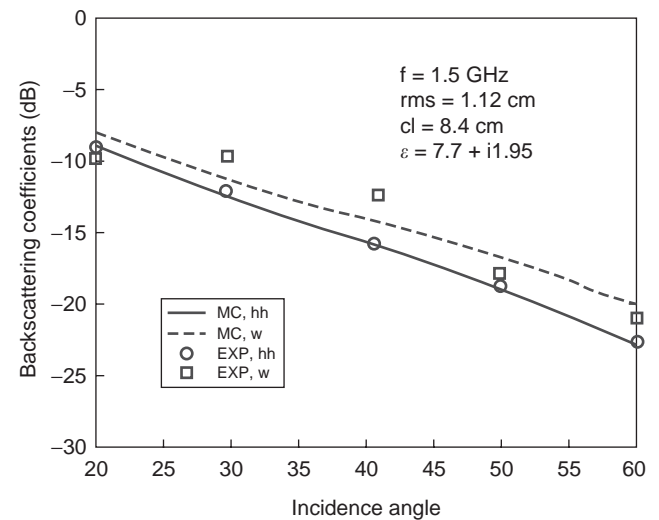
and its corresponding spectrum is

$$W(k) = \frac{h^2 l^2}{2\pi [1 + (kl)^2]^{3/2}} \tag{124}$$

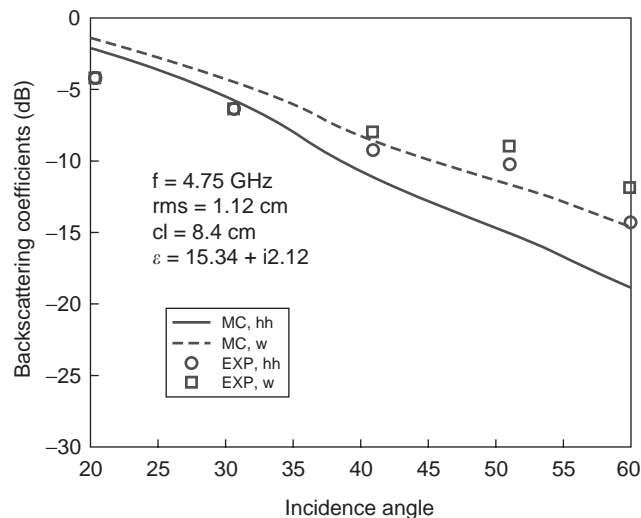
where parameter h is RMS height and l is correlation length.



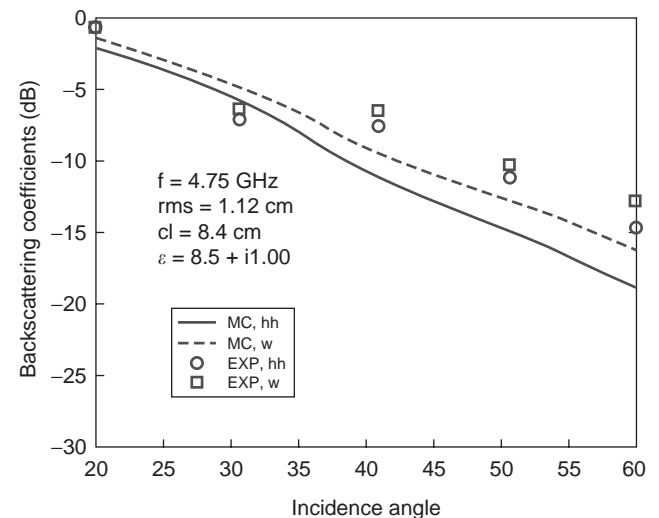
(a)



(a)



(b)



(b)

Figure 19. Comparisons of backscattering coefficients between numerical simulations and measurements for rough soil surface with wet-soil moisture conditions: (a) $f = 1.5$ GHz; (b) $f = 4.75$ GHz. (This figure is available in full color at <http://www.mrw.interscience.wiley.com/erfme>.)

Figure 20. Comparisons of backscattering coefficients between numerical simulations and measurements for rough soil surface with dry-soil moisture conditions: (a) $f = 1.5$ GHz; (b) $f = 4.75$ GHz. (This figure is available in full color at <http://www.mrw.interscience.wiley.com/erfme>.)

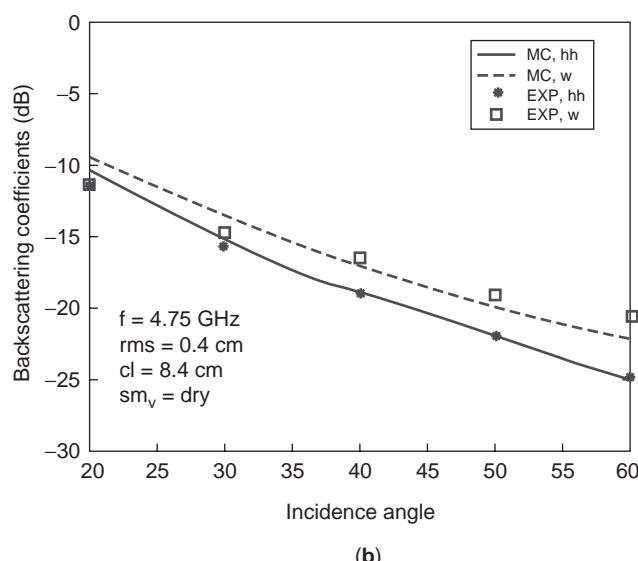
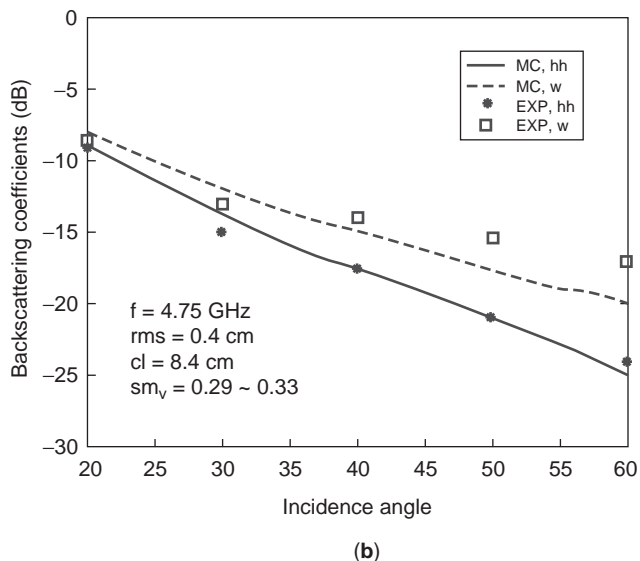
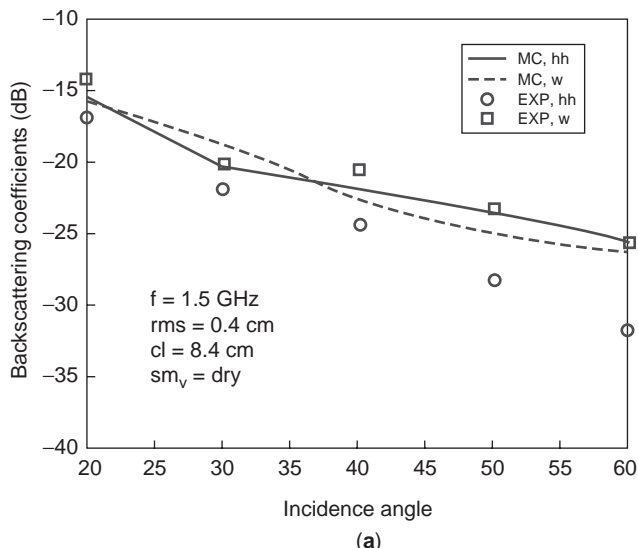
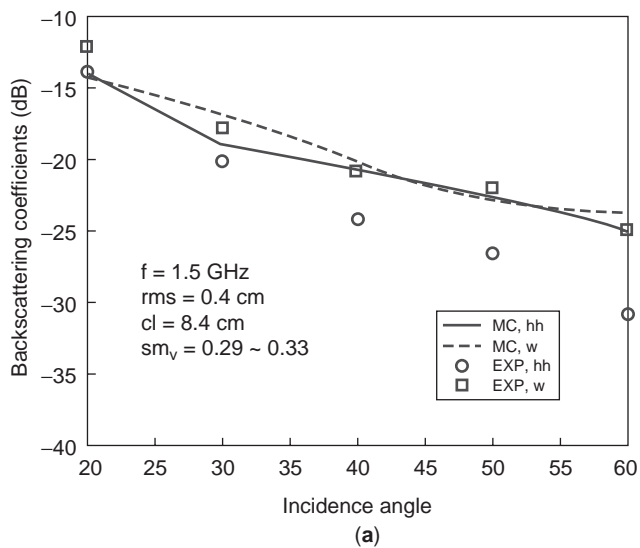


Figure 21. Comparisons of backscattering coefficients between numerical simulations and measurements for slightly rough soil surface with wet-soil moisture conditions: (a) $f = 1.5$ GHz; (b) $f = 4.75$ GHz. (This figure is available in full color at <http://www.mrw.interscience.wiley.com/erfme>.)

Figure 22. Comparisons of backscattering coefficients between numerical simulations and measurements for slightly rough soil surface with dry-soil moisture conditions: (a) $f = 1.5$ GHz; (b) $f = 4.75$ GHz. (This figure is available in full color at <http://www.mrw.interscience.wiley.com/erfme>.)

3.1.1. Comparison of Backscattering Coefficients for Wet and Dry Soils for Rough Surface of Field 3. In Figs. 19 and 20, we illustrate the results respectively for wet and dry soils. We show the backscattering coefficients obtained from the Monte Carlo simulations as a function of incidence angles and the comparisons with the experimental measurements for field 3. The surface roughness parameters and permittivities of soil are taken from the measurements given by Oh et al. [34]. The RMS height and correlation length of the measured soil surface are 1.12 cm and 8.4 cm, respectively. The relative permittivities of wet and dry soils are $15.34 + i3.66$ and $7.70 + i1.95$ at L band and $15.23 + i2.12$ and $8.50 + i1.0$ at C band. Figure 19 is simulated from wet-soil conditions and Fig. 20, from dry-soil conditions. Figures 19a and 20a

are for L band and Figs. 19b and 20b, for C band. Figure 20a gives the best match between the simulations and measurements; other figures (Figs. 19a,b, 20b) also show the fairly good agreement between the simulations and the measurements.

3.1.2. Comparison of Backscattering Coefficients for Wet and Dry Soils for Slightly Rough Surface of Field 1. In Figs. 21 and 22, we illustrate the results respectively for wet and dry soils of field 1. The field 1 is smoother than the field 3. The physical RMS height and correlation length are only 0.4 and 8.4 cm, respectively. There are also two sets of soil moisture conditions, wet and dry, similar to those for field 3. The relative permittivities of wet and dry soils are $15.57 + i3.71$ and $7.99 + i2.02$ at L band and 15.42

Table 5. Comparison between Wet and Dry Soils

Parameter	Polarization										
	HH (dB)					VV (dB)					
<i>a. Measurement Data with Frequency = 1.5 GHz, RMS = 1.2 cm, cl = 8.4 cm</i>											
Incidence angle	20	30	40	50	60	20	30	40	50	60	
Wet soil (15.34 + i3.66)	-9.6	-11.0	-13.8	-16	-22.6	-7.0	-8.5	-8.9	-9.3	-13.2	
Dry soil (7.7 + i1.95)	-8.8	-12.4	-16.2	-19.5	-23.5	-9.8	-10.2	-12.5	-18.9	-21.3	
Wet/dry-soil data difference	0.8	1.4	2.4	3.5	0.9	2.8	1.7	3.6	9.6	8.1	
Average difference	1.8						5.16				
<i>b. Numerical Simulations with Frequency = 1.5 GHz, RMS = 1.12 cm, cl = 8.4 cm</i>											
Incidence angle	20	30	40	50	60	20	30	40	50	60	
Wet soil (15.34 + i3.66)	-7.3	-11.5	-14.6	-18.9	-23.2	-6.1	-8.4	-11.6	-14.5	-17.5	
Dry soil (7.7 + i1.95)	-9.1	-12.9	-16.1	-19.8	-23.8	-8.0	-11.1	-14.0	-17.3	-20.1	
Wet/dry-soil data difference	1.8	1.4	1.9	0.9	0.3	1.9	2.7	2.4	2.8	2.6	
Average difference	1.26						2.48				
<i>c. Measurement Data with Frequency = 4.75 GHz, RMS = 1.12 cm, cl = 8.4 cm</i>											
Incidence angle	20	30	40	50	60	20	30	40	50	60	
Wet soil (15.23 + i2.12)	-4.1	-6.2	-8.8	-10.8	-14.2	-4.0	-6.3	-7.4	-9.3	-11.2	
Dry soil (8.5 + i1.00)	-0.4	-6.2	-7.8	-11	-14.5	-0.5	-5.3	-6.8	-10.1	-12.5	
Wet/dry-soil data difference	3.7	0	1	0.2	0.3	3.5	1.0	0.6	0.8	1.3	
Average difference	1.04						1.44				
<i>d. Numerical Simulations with Frequency = 4.75 GHz, RMS = 1.12 cm, cl = 8.4 cm</i>											
Incidence angle	20	30	40	50	60	20	30	40	50	60	
Wet soil (15.23 + i2.12)	-1.1	-4.2	-9.8	-13.8	-18.2	-0.4	-3.6	-8.0	-11.3	-14.8	
Dry soil (8.5 + i1.00)	-1.2	-5.3	-10.3	-13.5	-18.9	-1.8	-4.2	-9.0	-11.8	-15.5	
Wet/dry-soil data difference	0.1	1.1	0.5	0.3	0.7	1.4	0.6	1.0	0.5	0.7	
Average difference	0.54						0.84				
<i>e. Measurement Data with Frequency = 1.5 GHz, RMS = 0.4 cm, cl = 8.4 cm</i>											
Incidence angle	20	30	40	50	60	20	30	40	50	60	
Wet soil (15.57 + i3.71)	-13.8	-20.	-24.	-26.3	-30.7	-12.	-17.6	-20.3	-21.6	-25.0	
Dry soil (7.99 + i2.02)	-16.8	-21.6	-24.2	-28.3	-31.6	-14.3	-20.	-20.2	-22.8	-25.3	
Wet/dry-soil data difference	3.0	1.6	0.2	2.0	0.9	2.3	2.4	-0.1	1.2	0.3	
Average difference	1.54						1.22				
<i>f. Numerical Simulations with Frequency = 1.5 GHz, RMS = 0.4 cm, cl = 8.4 cm</i>											
Incidence angle	20	30	40	50	60	20	30	40	50	60	
Wet soil (15.57 + i3.71)	-13.8	-18.8	-20.3	-22.1	-25.3	-13.8	-16.8	-20.	-22.2	-23.3	
Dry soil (7.99 + i2.02)	-15.5	-20.1	-21.6	-23.2	-25.8	-15.6	-18.6	-22.3	-25.	-26.1	
Wet/dry-soil data difference	1.7	1.3	1.3	1.1	0.5	1.8	1.8	2.3	2.8	2.8	
Average difference	1.18						2.3				
<i>g. Measurement Data with Frequency = 4.75 GHz, RMS = 0.4 cm, cl = 8.4 cm</i>											
Incidence angle	20	30	40	50	60	20	30	40	50	60	
Wet soil (15.42 + i2.15)	-9.1	-15.	-17.9	-21.	-24.3	-8.7	-13	-13.6	-15.5	-16.4	
Dry soil (8.77 + i1.04)	-11.7	-15.6	-19.	-22.1.	-24.9	-11.6	-14.8	-16.3	-19.2	-20.8	
Wet/dry-soil data difference	2.6	0.6	1.1	1.1	0.6	2.9	1.8	2.7	3.7	4.4	
Average difference	1.2						3.1				
<i>h. Numerical Simulations with Frequency = 4.75 GHz, RMS = 0.4 cm, cl = 8.4 cm</i>											
Incidence angle	20	30	40	50	60	20	30	40	50	60	
Wet soil (15.42 + i2.15)	-9.0	-14.3	-17.8	-20.8	-24.7	-8	-12	-15.2	-17.7	20.0	
Dry soil (8.77 + i1.04)	-10.3	-15.3	-18.8	-21.8	-25	-9.3	-13.7	-16.8	-20	-20.2	
Wet/dry-soil data difference	1.3	1	1	1	0.3	1.3	1.7	1.6	2.3	0.2	
Average difference	0.92						1.42				

Table 6. Relative Permittivities of Soil Moisture in Weight at L Band

Moisture (%)	5	7.5	10.0	12.5	15.0	17.5	20.0	22.5	15.0
Permittivity	4.06 + i0.300	4.81 + i0.45	5.56 + i0.600	7.35 + i0.872	10.8 + i1.335	14.25 + i1.797	17.7 + i2.260	21.15 + i2.722	24.6 + i3.185

Table 7. Relative Permittivities of Soil Moisture in Volumetric Water Content (cm³/cm³) at L and C Bands

Moisture	0.05	0.10	0.15	0.20	0.25	0.30	0.35	0.40
Permittivity at L band	3.66 + i0.15	4.66 + i0.29	6.26 + i0.52	8.45 + i0.85	11.3 + i1.27	15.2 + i1.82	19.2 + i2.41	23.1 + i3.04
Permittivity at C band	3.62 + i0.19	4.52 + i0.44	5.94 + i0.85	7.90 + i1.42	10.4 + i2.17	13.9 + i3.22	17.4 + i4.30	20.8 + i5.30

Table 8. Calculated Emissivities^a

Moisture (%):	Correlation Length (in Wavelengths), Horizontal Polarization							
	0.33	0.4	0.5	0.6	0.7	0.8	0.9	1.0
5.00	0.8060	0.8011	0.7918	0.7841	0.7777	0.7720	0.7671	0.7636
7.50	0.7758	0.7693	0.7591	0.7514	0.7442	0.7377	0.7330	0.7286
10.0	0.7464	0.7393	0.7290	0.7205	0.7133	0.7072	0.7017	0.6973
12.5	0.7092	0.6964	0.6855	0.6743	0.6676	0.6614	0.6569	0.6520
15.0	0.6385	0.6236	0.6088	0.5990	0.5919	0.5862	0.5758	0.5766
17.5	0.5819	0.5668	0.5504	0.5393	0.5365	0.5248	0.5193	0.5149
20.0	0.5453	0.5309	0.5149	0.5042	0.4961	0.4896	0.4840	0.4792
22.5	0.5220	0.5077	0.4925	0.4827	0.4755	0.4695	0.4642	0.4596
25.0	0.4986	0.4826	0.4678	0.4577	0.4508	0.4454	0.4409	0.4366

^aParameters: RMS height = 0.1λ, observation angle = 50°.

Table 9. Calculated Emissivities^a

Moisture (%):	Correlation Length (in Wavelengths), Vertical Polarization							
	0.33	0.4	0.5	0.6	0.7	0.8	0.9	1.0
5.00	0.9565	0.9545	0.9541	0.9550	0.9563	0.9578	0.9592	0.9603
7.50	0.9437	0.9410	0.9400	0.9408	0.9423	0.9439	0.9454	0.9468
10.0	0.9308	0.9276	0.9261	0.9268	0.9284	0.9302	0.9318	0.9333
12.5	0.9081	0.9024	0.8995	0.8995	0.9006	0.9018	0.9031	0.9043
15.0	0.8568	0.8508	0.8469	0.8468	0.8480	0.8493	0.8510	0.8524
17.5	0.8202	0.8104	0.8036	0.8041	0.8054	0.8073	0.8091	0.8107
20.0	0.7841	0.7744	0.7684	0.7655	0.7696	0.7716	0.7734	0.7714
22.5	0.7535	0.7412	0.7361	0.7363	0.7382	0.7402	0.7423	0.7440
25.0	0.7272	0.7123	0.7048	0.7073	0.7092	0.7113	0.7134	0.7130

^aParameters: RMS height = 0.1λ, observation angle = 50°.

Table 10. Calculated Emissivities^a

Emissivity	Soil Moisture in Weight (%)								
	5.00	7.50	10.0	12.5	15.0	17.5	20.0	22.5	25.0
H (case 1)	0.8060	0.7758	0.7464	0.7092	0.6385	0.5819	0.5453	0.5220	0.4986
H (case 2)	0.8392	0.8053	0.7946	0.7519	0.6868	0.6376	0.6054	0.5804	0.5535
H (case 3)	0.8107	0.7820	0.7686	0.7252	0.6593	0.6110	0.5802	0.5653	0.5333
V (case 1)	0.9565	0.9437	0.9308	0.9081	0.8568	0.8202	0.7841	0.7535	0.7272
V (case 2)	0.9289	0.9123	0.8990	0.8667	0.8143	0.7698	0.7345	0.7064	0.6806
V (case 3)	0.9302	0.9154	0.9052	0.8758	0.8266	0.7840	0.7503	0.7227	0.6961

^aParameters

Case 1: RMS height = 0.1λ, correlation length = 0.333λ, observation angle = 50°.

Case 2: RMS height = 0.3λ, correlation length = 1.000λ, observation angle = 50°.

Case 3: RMS height = 0.3λ, correlation length = 1.000λ, observation angle = 55°.

Table 11. Calculated Emissivities^a

Emissivity	Volumetric Water Content (cm ³ /cm ³)							
	0.05	0.10	0.15	0.20	0.25	0.30	0.35	0.40
H (L band)	0.8434	0.8008	0.7490	0.6996	0.6446	0.5868	0.5553	0.5278
H (C band)	0.8626	0.8285	0.7900	0.7613	0.7160	0.6658	0.6313	0.6032
V (L band)	0.9615	0.9444	0.9181	0.8817	0.8424	0.7995	0.7593	0.7256
V (C band)	0.9393	0.9178	0.8867	0.8441	0.8045	0.7630	0.7284	0.6989

^aParameters: RMS height = 2.45 cm, correlation length = 8.0 cm, observation angle = 50°; L band— $F = 1.4$ GHz, C Band— $F = 5.0$ GHz.

+ $i2.15$, and $8.77 + i1.04$ at C band. Figure 21 shows numerical simulation results and their comparisons with the measurements for wet soil, Fig. 22 is for dry soil surface. Figures 21a and 22a are results at C band and Figs. 21b and 22b, at L band. For C-band results, both vertical and horizontal polarizations are in good agreement with the measurements at both wet and dry soil conditions. However, for L-band results, only those of vertical polarization are comparable with the experimental measurements at the full range of incident angles. For the horizontal polarization, the simulation results are consistent with the measurements at small incident angles, while at large incidence angle, some of the backscattering coefficients of horizontal polarization exceed those of vertical polarization. This is because a higher number of realizations is needed in the numerical simulations for the horizontal polarization to converge.

However, a major limitation of the simulations listed in Table 5 is that the surface has to be much larger than the wavelength so that the tapered wave can be used to approximate a plane wave. With limited computer resources, the present surface area is 8×8 wavelengths. With a finite surface area, the incident wave is not a plane wave in a single direction. It actually has an angular spectrum about the direction with the angular width roughly equal to the wavelength divided by the surface length. This means an incident angle of 40° actually has an angular spread of $\sim 40^\circ$. Thus the simulations will not be able to simulate the true results if there are large angular variations of backscattering. We have put the results of backscattering in tabulated form in Table 5. The table shows that the simulations do reveal dependence on soil moisture, although not as drastically as for the VV polarization in the experimental measurements.

3.2. Application in Passive Remote Sensing

In the NMM3D of rough-surface scattering, we solve Maxwell equations in three dimensions to calculate emis-

sivities for applications in passive microwave remote sensing of soil and ocean surfaces.

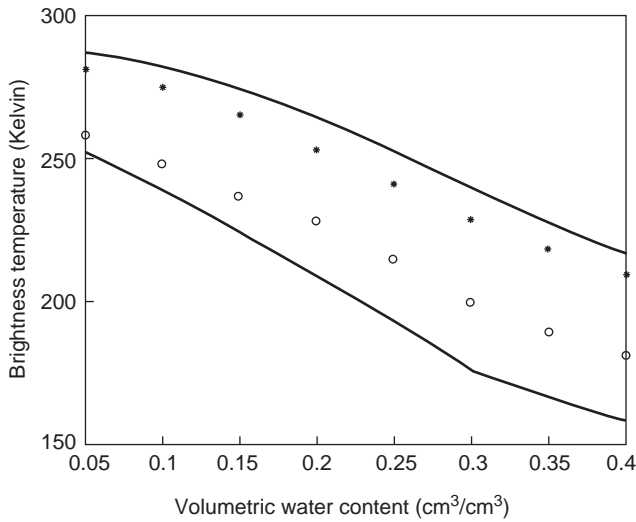
3.2.1. Application of NMM with Pulse Basis Function and Point Matching Method. In this section, we illustrate the numerical simulation results of emissivities of wet soils with a 2D rough surface (3D problem). Simulations are based on Gaussian random rough surfaces with Gaussian correlation functions. In the numerical results, the surface area used is 64 square wavelengths. We use 64 points per square wavelength as a coarse grid and 256 points per square wavelength as a dense grid, which leads to totally 98,304 surface unknowns. In our experiences of simulations for 1D lossy dielectric rough surfaces [6] within the range of relative permittivity, we found that 16 points per wavelength (256 points per square wavelength) can give accurate results for the emissivity for each single realization. For rough surfaces with an RMS height of 0.3λ , correlation length of 1.0λ , and relative permittivity of 17, the total CPUs for a single dense grid with SMCG are ~ 45 h for a TE wave and 49 h for a TM wave, respectively, on a DEC 3000/700 workstation. By using the PBTG with SMCG, the CPUs are about 8.5 h for TE and 9.0 h for TM, respectively, for the same case. We have shown that the SMCG is with the computational complexity of $O(N \log(N))$ in Refs. 35 and 36. The permittivities of wet soil by weight of the soil moisture at L band (1.4 GHz) [37] are listed in Table 6. The relative permittivity values of soil moisture in volumetric water content (cm³/cm³) [38,39] for L and C bands are given in Table 7. The C band is at 5 GHz. All cases were computed at an observation angle of 50°. In Tables 8–12, emissivities calculated are tabulated for interested readers. We also illustrate the brightness temperatures in Figs. 23 and 24. The physical temperature is taken as 300 K for all cases.

The brightness temperatures in passive microwave remote sensing are measured at L and C bands; thus it is useful to compare the brightness temperatures of soils at L and C bands using the same physical parameters of

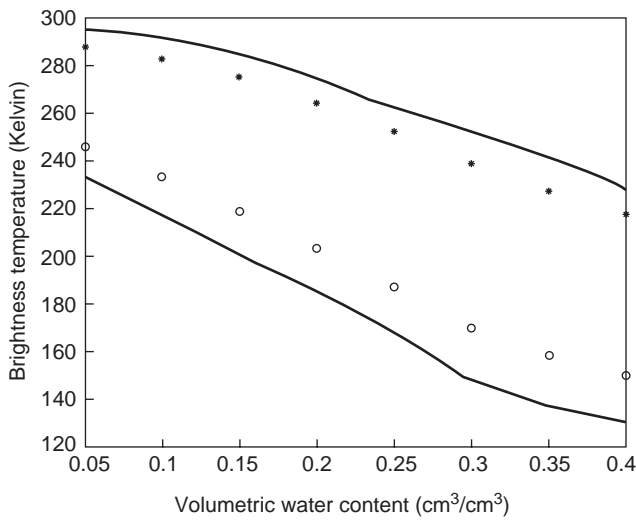
Table 12. Calculated Emissivities^a

Emissivity	Volumetric Water Content (cm ³ /cm ³)							
	0.05	0.10	0.15	0.20	0.25	0.30	0.35	0.40
H (L band)	0.7807	0.7258	0.6684	0.6198	0.5597	0.4915	0.4560	0.4354
H (C band)	0.8202	0.7793	0.7290	0.6778	0.6234	0.5656	0.5272	0.4990
V (L band)	0.9854	0.9747	0.9503	0.9132	0.8766	0.8426	0.8042	0.7633
V (C band)	0.9604	0.9430	0.9169	0.8820	0.8427	0.7968	0.7581	0.7254

^aParameters: RMS height = 0.73 cm, correlation length = 35.5 cm, observation angle = 50°; L band— $F = 1.4$ GHz, C Band— $F = 5.0$ GHz.



(a)



(b)

Figure 23. Variation of brightness temperatures with the soil moistures in volumetric water content at L and C bands using the permittivities in Table 7. The physical rough surface parameters are RMS height of 2.45 cm and correlation length of 8.0 cm (a) and RMS height of 0.73 cm and correlation length of 3.5 cm (b). The observation angle is 50°. The solid and dashed lines represent horizontal and vertical polarizations, respectively, at L band; circles and stars indicate horizontal and vertical polarizations, respectively, at C band.

roughness and soil moisture. In Fig. 23a, we plot the brightness temperatures as a function of soil moisture in volumetric water content at both L and C bands. The corresponding permittivities are taken from Table 7. The physical parameters are that the RMS height is 2.45 cm and correlation length is 8.0 cm. We can see that the brightness temperatures are higher at C band than at L band for horizontal polarization and lower at C band than at L band for vertical polarization. Since the permittivities between L and C bands are comparable, the results indicate that roughness has a greater effect on C band

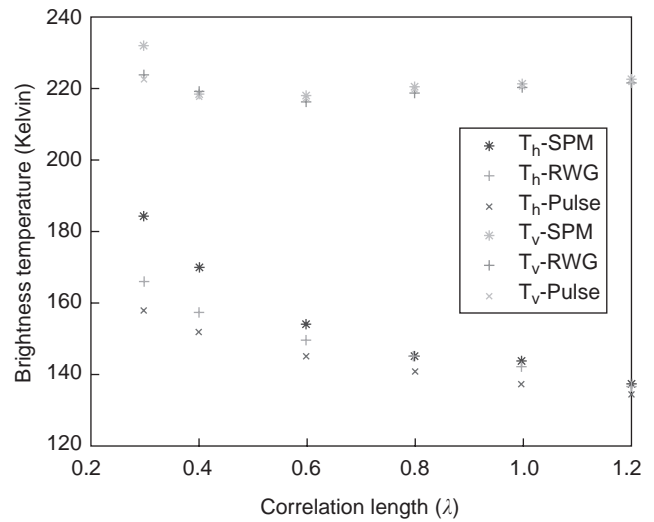


Figure 24. Brightness temperature of Monte Carlo simulations averaged over five realizations as a function of correlation length and comparisons with those from the second-order small-perturbation method, and from the PBTG/pulse. The case is for RMS height 0.1λ, relative permittivity 17 + 2i, and physical temperature of 283 K at observation angle 50°. (This figure is available in full color at <http://www.mrw.interscience.wiley.com/erfme>.)

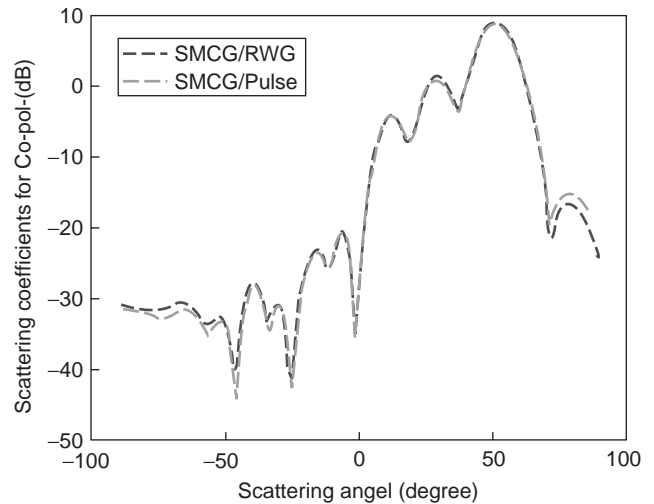


Figure 25. Comparison of the bistatic scattering coefficients between the SMCG/RWG and the SMCG/pulse for the TE wave incidence of copolarization. The case is for RMS height 0.1λ, correlation length of 1.0λ, and relative permittivity 17 + 2i at observation angle 50°. (This figure is available in full color at <http://www.mrw.interscience.wiley.com/erfme>.)

than at L band. In Fig. 23b, the results are shown with different rough-surface parameters. The RMS height is 0.73 cm, and the correlation length is 3.5 cm in this figure. Comparing the results of Figs. 23a and 23b indicates that as roughness decreases, the brightness temperatures of L and C bands are closer to each other.

3.2.2. With RWG Basis Function and Galerkin Method. In this section, we illustrate the numerical simulation

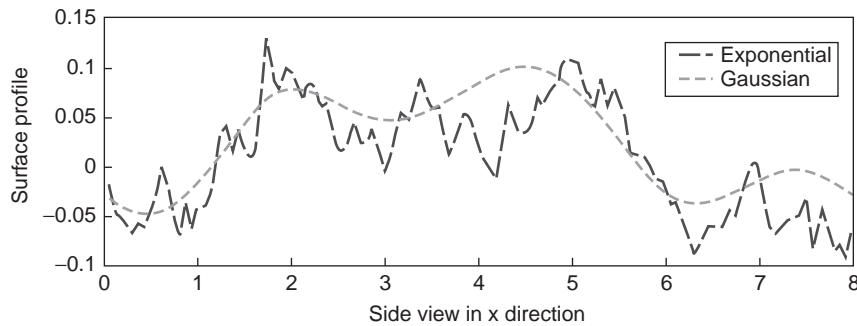


Figure 26. The profiles of surface side views by exponential and Gaussian correlation functions. (This figure is available in full color at <http://www.mrw.interscience.wiley.com/erfme>.)

results using the RWG basis functions and SMCG. Three types of random rough surfaces are studied: (1) Gaussian rough surfaces with Gaussian correlation function, (2) the exponential correlation function, and (3) the ocean spectrum. Surface area is 8×8 square wavelengths. As many as 96,266 current basis functions are used. Results are computed using parallel computations with the near interaction set at 2.1λ . We use $T = 283$ K as the physical temperature. Besides plotting the results, we also tabulate the results of emissivities so that the accuracies can be ascertained and to facilitate future comparisons for readers. Energy conservation checks are given by adding $a(\theta_i)$ and $r(\theta_i)$. We have gained extensive experience in our course of numerical simulations. On one hand, passive remote sensing requires great accuracy in energy conservation, which is not required in active remote sensing. On the other hand, passive remote sensing is easier than active remote sensing in other ways. For example, in active remote sensing, the results fluctuate from realization to realization because of speckle. However, in passive remote sensing, the emissivity requires an integration of bistatic scattering cross sections over solid angles over the hemisphere. The integration smooths out the fluctuations that exist in the bistatic coefficients. Our experience indicates that passive remote sensing requires for fewer realizations than does active remote sensing. Tests of convergence with realizations have also been done in the past. Five realizations were used for the results reported in this section. Checks have been used for selected cases using five or more realizations.

In the past, extensive studies have also been done with sample size varying from $8\lambda \times 8\lambda$ to $16\lambda \times 16\lambda$, and so on. The physical meaning is that the coherent interaction of waves is limited in extent. Thus if coherent interaction is limited to 8×8 square wavelengths, then incoherent

superposition can be exercised beyond 8×8 wavelengths. Numerical solutions of Maxwell equations need to be done for an area of 8×8 square wavelengths. Because of our previous experience in varying sample sizes, an $8\lambda \times 8\lambda$ area was used in this section. The surface length of 8λ is much larger than the correlation lengths.

The results of emissivities are tabulated. Energy conservation test for each case is given. Thus the accuracy of the emissivities values should be judged in relation to the test of energy conservation.

3.2.2.1. Emissivities and Bistatic Scattering Cross Sections of Gaussian Surfaces with Gaussian Correlation Function.

We compare the brightness temperature results of rough surfaces with Gaussian correlation function using three methods: SMCG with pulse basis functions (SMCG/pulse), SMCG with RWG basis functions (SMCG/RWG), and SPM. By *SPM*, we mean the common second-order SPM result of emissivity, which is computing the coherent field to second order and incoherent field to first order [40]. In Fig. 24, the brightness temperatures are shown as functions of correlation length from 0.3λ to 1.2λ with a fixed value of RMS height at 0.1λ , for both TE and TM waves. The observation angle is 50° , and the relative permittivity

Table 13. Measured Surface Roughness Parameters and Relative Permittivities of Wet Soil

	RMS Height (cm)	Correlation Length (cm)	Relative Permittivity	
			At 1.5 GHz	At 4.75 GHz
Field 1	0.4	8.4	$15.57 + i3.71$	$15.42 + i2.15$
Field 3	1.12	8.4	$15.34 + i3.66$	$15.23 + i2.12$

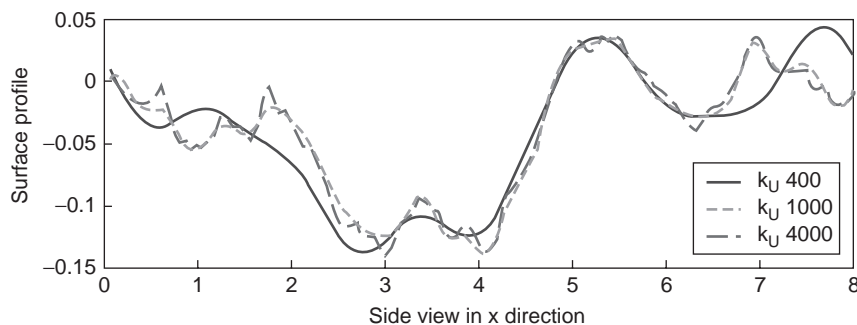
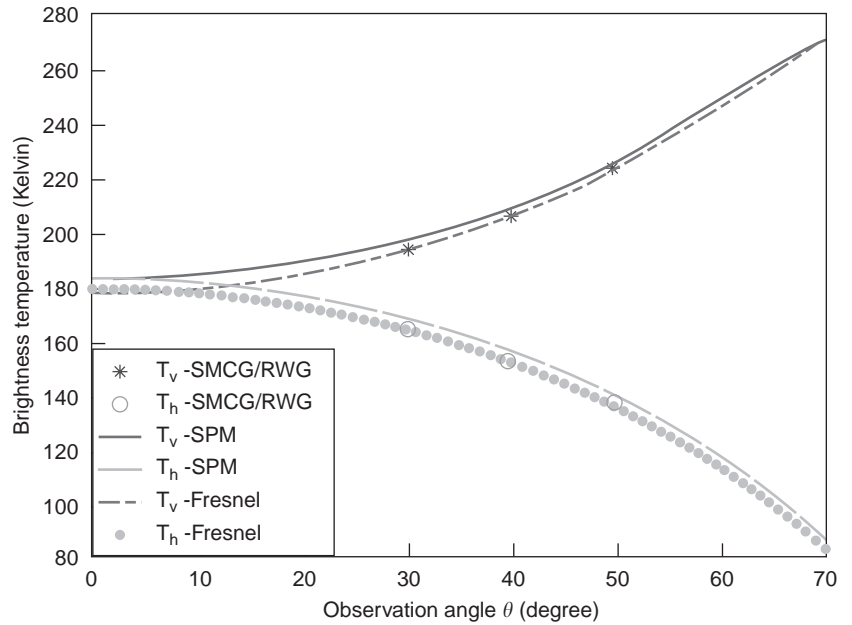
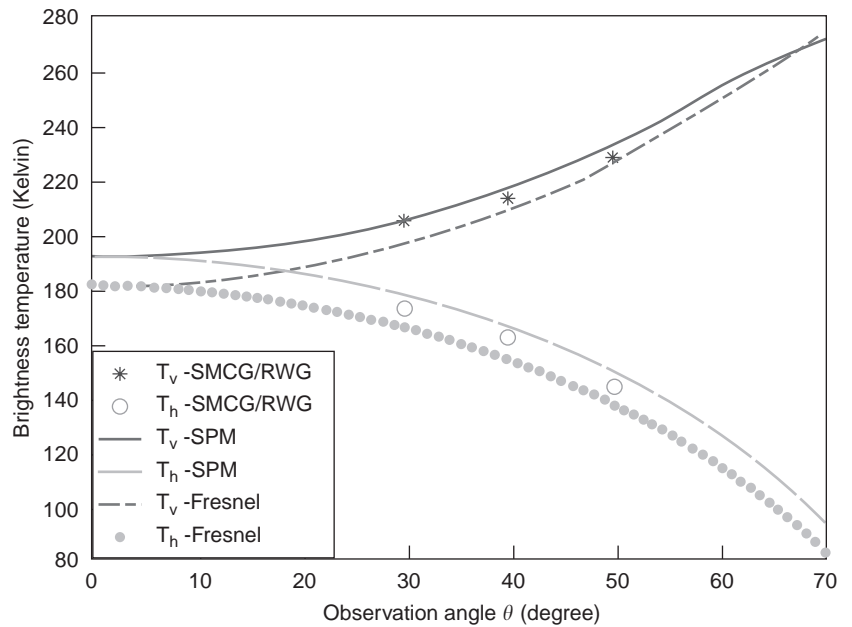


Figure 27. The profiles of surface side views by ocean spectrum with various values of upward limit k_U . (This figure is available in full color at <http://www.mrw.interscience.wiley.com/erfme>.)



(a)



(b)

Figure 28. The brightness temperature of Monte Carlo simulation averaged over five realizations as a function of observation angles and comparisons with those from the second-order small-perturbation method for field I with RMS height 0.40 cm, correlation length 8.4 cm, in L band (a) and in C band (b). (This figure is available in full color at <http://www.mrw.interscience.wiley.com/erfme>.)

Table 14. Emissivities of Soil Surfaces with RMS Height 0.40 cm, Correlation Length 8.4 cm, in L Band

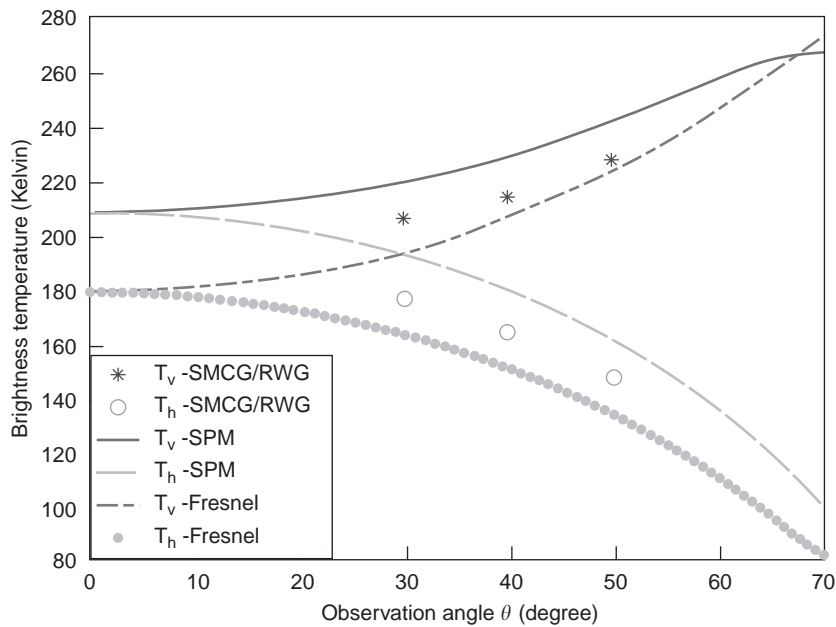
(1)	(2)	(3)	(4)	(5)	(6)
TE	30	0.5891	1.0065	0.5851	0.0040
TE	40	0.5465	0.9936	0.5413	0.0052
TE	50	0.4930	0.9926	0.4806	0.0124
TM	30	0.6951	1.0048	0.6893	0.0058
TM	40	0.7397	1.0040	0.7342	0.0055
TM	50	0.7997	1.0061	0.7969	0.0028

Columns: (1) polarization type (transverse electric or magnetic); (2) incident angle ($^{\circ}$); (3) emissivity (%); (4) energy conservation (%); (5) emissivity of flat surface (%); (6) rough/flat-surface emissivity difference (%).

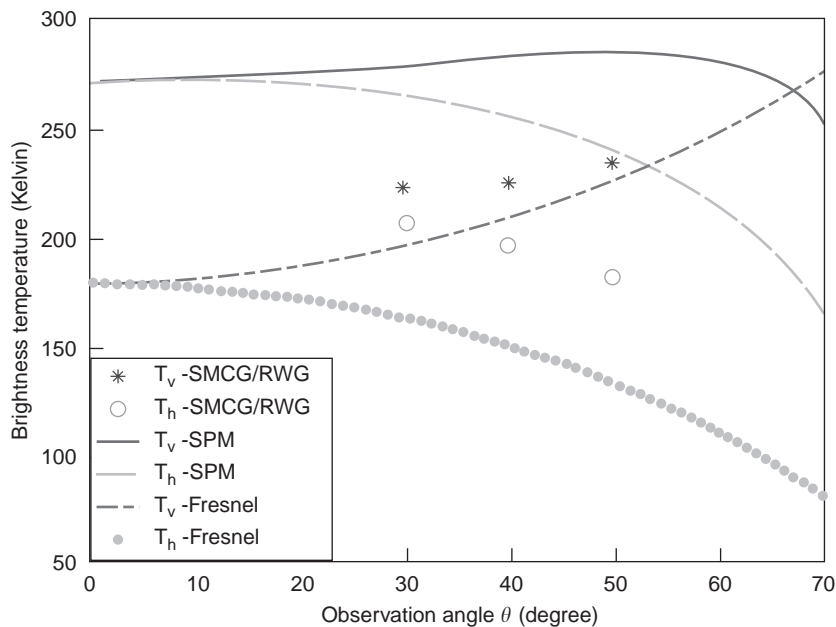
Table 15. Emissivities of Soil Surfaces with RMS Height 0.40 cm, Correlation Length 8.4 cm, in C Band

(1)	(2)	(3)	(4)	(5)	(6)
TE	30	0.6140	1.0078	0.5923	0.0217
TE	40	0.5752	0.9942	0.5485	0.0267
TE	50	0.5136	0.9936	0.4875	0.0261
TM	30	0.7219	0.9932	0.6964	0.0255
TM	40	0.7563	1.0034	0.7411	0.0152
TM	50	0.8086	1.0018	0.8035	0.0051

Columns: (1) polarization type (transverse electric or magnetic); (2) incident angle ($^{\circ}$); (3) emissivity (%); (4) energy conservation (%); (5) emissivity of flat surface (%); (6) rough/flat-surface emissivity difference (%).



(a)



(b)

Figure 29. The brightness temperature of Monte Carlo simulation averaged over five realizations as a function of observation angles and comparisons with those from the second-order small-perturbation method for field III with RMS height 1.12 cm, correlation length 8.4 cm in L band (a) and in C band (b). (This figure is available in full color at <http://www.mrw.interscience.wiley.com/erfme>.)

is $17 + i2.0$. It is shown that the results for the three approaches agree very well for the case of TM wave incidence. The exception for the TM case is the deviation from the numerical solutions by SPM at a correlation length of 0.3λ . In the case of TE wave incidence, SMCG/pulse gives lower results than does SMCG/RWG by about 5 K for a large RMS slope. SPM gives good comparison for small slopes but becomes inaccurate by as much as 20 K for large slopes.

In Fig. 25, the bistatic scattering coefficients of the same surfaces are compared between the SMCG/RWG and SMCG/pulse for the TE wave incidence at the incident angle of 50° . The RMS height and correlation length of

Table 16. Emissivities of Soil Surfaces with RMS Height 1.12 cm, Correlation Length 8.4 cm, in L Band

(1)	(2)	(3)	(4)	(5)	(6)
TE	30	0.6351	1.0031	0.5877	0.0474
TE	40	0.5944	0.9970	0.5439	0.0505
TE	50	0.5338	0.9968	0.4831	0.0507
TM	30	0.7380	1.0023	0.6919	0.0461
TM	40	0.7658	1.0045	0.7367	0.0291
TM	50	0.8140	1.0015	0.7992	0.0148

Columns: (1) polarization type (transverse electric or magnetic); (2) incident angle ($^\circ$); (3) emissivity (%); (4) energy conservation (%); (5) emissivity of flat surface (%); (6) rough/flat-surface emissivity difference (%).

Table 17. Emissivities of Soil Surfaces with RMS Height 1.12 cm, Correlation Length 8.4 cm, in C Band

(1)	(2)	(3)	(4)	(5)	(6)
TE	30	0.7388	1.0045	0.5947	0.1441
TE	40	0.7028	1.0062	0.5508	0.1520
TE	50	0.6535	1.0082	0.4898	0.1637
TM	30	0.7962	0.9912	0.6988	0.0974
TM	40	0.8058	0.9900	0.7434	0.0624
TM	50	0.8318	0.9869	0.8056	0.0262

Columns: (1) polarization type (transverse electric or magnetic); (2) incident angle ($^{\circ}$); (3) emissivity (%); (4) energy conservation (%); (5) emissivity of flat surface (%); (6) rough/flat-surface emissivity difference (%).

Gaussian surface are 0.1λ and 1.0λ , and the relative permittivity is $17 + 2i$. The results are for a single realization. The comparison in Fig. 25 shows good agreement between two approaches. This shows that pulse basis functions can give accurate results for bistatic scattering coefficients but less accurate results for passive remote sensing. We plot the surface profiles with the exponential correlation function, Gaussian correlation function, and ocean spectrum in Figs. 26 and 27. Figure 26 shows the fine irregular features that exist in exponential correlation function. This is the cause of the large emissivity differences between Gaussian correlation function and exponential correlation function. Figure 27 shows those new features of irregularity in the roughness profiles when the upper limit of ocean spectrum is increased. It is apparent that surfaces with exponential correlation function and ocean spectrum can have fine-scale features with large RMS slope. Although the Gaussian correlation function is inappropriate for soil surface, soil surface characterization remains an important problem. Exponential correlation function is just one better choice than the Gaussian correlation function. It is to be noted that the exponential correlation function does not have RMS slopes if the roughness spectrum upper limit is set at infinity. However, in actual implementation in this section, 16 points per wavelength is used to generate the roughness profile. This corresponds to setting an upper limit on the roughness spectrum.

Table 18. Comparison of Numerical Results (NMM) with Experimental Brightness Temperature Measurements (Surface RMS Height $\sigma = 2.6$ cm)

Dataset	Correlation Length (cm)	Relative Permittivity	Physical Temperature (K)	Flat Surface T_B (K)	NMM T_B (K)	Experiment
CM	37.0	$29.4 + i3.86$	296.0	160.45	217.0	216.8
CM	48.2	$20.05 + i2.57$	295.7	190.56	227.4	224.2
CM	87.6	$23.57 + i3.05$	303.7	177.68	223.6	221.1
CM	913.0	$15.98 + i2.03$	297.8	212.91	227.4	223.53

Table 19. Emissivities and Brightness Temperature with Various Values of k_U and $k_L = 100$ rad/m

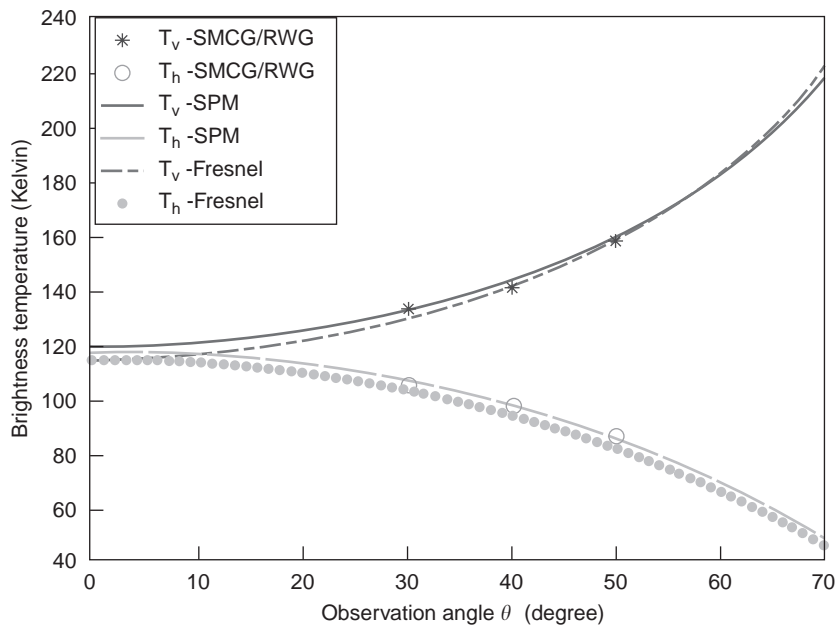
Polarization	k_U (rad/m)	Emissivity (%)	Energy Conservation (%)	Emissivity of Flat Surface (%)	T_B (K)	∇T_B (Rough-Flat)
TE	400	0.3118	0.9921	0.2872	88.2	6.96
TE	1000	0.3207	0.9920	0.2872	90.8	9.48
TE	4000	0.3233	0.9915	0.2872	91.5	10.22
TM	400	0.5477	0.9967	0.5594	155.0	-3.31
TM	1000	0.5550	0.9961	0.5594	157.1	-1.25
TM	4000	0.5604	0.9925	0.5594	158.6	0.30

3.2.2.2. Soil Surfaces. The experimental results are from Oh et al. [34]. The physical surface parameters, based on the exponential correlation function, are the same for both L and C bands. Field I is smooth, and field III is rough. The measured rough surface parameters and relative permittivities of wet soil are listed in Table 13. The upper limits of wavenumber in the spectrum are 3.55 and 11.24 cm^{-1} , respectively, in L and C bands. The numerical results are presented with various incident angles and compared with those from SPM.

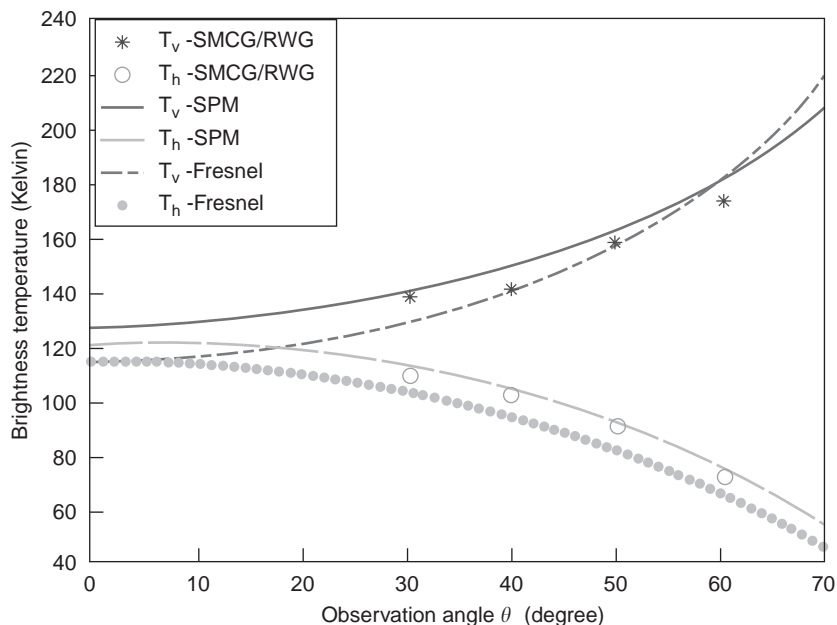
In Figs. 28a and 28b, we illustrate the brightness temperature results in L and C bands, respectively, for the smooth field I with RMS height 0.4 cm and correlation length 8.4 cm. The dashed-dotted curves are results of calculations from the Fresnel equations. It is shown that surface roughness increases the brightness temperature over flat surfaces for both horizontal and vertical polarizations. The difference of brightness temperature between rough surface and flat surface is larger in C band than in L band; this can be observed from both numerical results and SPM. In this case, the results from SPM are comparable to the numerical results. The numerical values of emissivities of field I are also tabulated in Tables 14 and 15, respectively, for L and C bands.

As the surface slope increases, the SPM cannot give the correct results of brightness temperature. We can see that from results for field III, which has RMS height of 1.12 cm and correlation length of 8.4 cm. In Figs. 29a and 29b, the brightness temperature results are illustrated for L and C bands, respectively. In this case, the SPM results are much higher than the numerical results. This means that the SPM is used beyond the limit of validity. We also see that the deviation of SPM results from numerical results is worse in C band than in L band. The numerical values of emissivities of field III are also tabulated in Tables 16 and 17, respectively, for L and C bands.

3.2.2.2.1. Comparison with Experimental Data. Numerical results are compared with measurements of soil surfaces [41]. The measurements were conducted at Texas



(a)



(b)

Figure 30. The brightness temperature of Monte Carlo simulation averaged over five realizations as a function of observation angles and comparisons with those from the second-order small-perturbation method for ocean surfaces with windspeeds of 10 m/s (a) and 20 m/s (b). (This figure is available in full color at <http://www.mrw.interscience.wiley.com/erfme>.)

Table 20. Emissivities of Ocean Surfaces at Windspeed 10 m/s with $k_L = 100 \text{ rad/m}$ and $k_U = 4000 \text{ rad/m}$

Polarization	Incident Angle ($^\circ$)	Emissivity (%)	Energy Conservation (%)	Emissivity of Flat Surface (%)	∇T_B (Rough-Flat)
TE	30	0.3723	1.0028	0.3662	1.72
TE	40	0.3427	0.9956	0.3319	3.06
TE	50	0.3056	0.9927	0.2872	5.21
TM	30	0.4744	0.9960	0.4555	5.35
TM	40	0.4991	1.0040	0.4971	0.57
TM	50	0.5534	0.9966	0.5594	-1.70

Table 21. Emissivities of Ocean Surfaces at Windspeed 20 m/s with $k_L = 100$ rad/m and $k_U = 4000$ rad/m

Polarization	Incident Angle ($^\circ$)	Emissivity (%)	Energy Conservation (%)	Emissivity of Flat Surface (%)	∇T_B (Rough–Flat)
TE	30	0.3863	1.0006	0.3662	5.69
TE	40	0.3584	0.9986	0.3319	7.5
TE	50	0.3233	0.9915	0.2872	10.2
TM	30	0.4898	0.9980	0.4555	9.7
TM	40	0.5015	0.9971	0.4971	1.25
TM	50	0.5604	0.9925	0.5594	0.30

A&M University [42,43] for 16 profiles of soil moisture and temperatures. The brightness temperatures were measured at nadir incidence of $\lambda = 21$ cm. Ground truth measurements of soil moisture and temperature were taken at several depths down to 15 cm. The standard deviation of height σ was also measured and was 2.6 cm. The permittivities are calculated by using the mixing formula at a wavelength of 21 cm [44], based on soil moisture measurements in each layer. Then, they are averaged from the soil depth of 0–2 cm. The weighted physical temperature, based on measurements, was used for each profile. Since there was no measurement of the horizontal correlation length, the correlation length within a reasonable range was chosen to match the data. In Table 18 we list the results for 4 of the 16 profiles; these 4 cases are with large permittivities.

In performing numerical simulations, the exponential correlation function with an upper wavenumber limit of 3.38/cm is employed to generate rough surfaces. The correlation length l is the same as that used in Ref. 41. As shown in Table 18, the numerical results are in agreement with the experiments data. The difference between them is no more than 3 K. Since the brightness temperature of rough surfaces with high permittivities can be more than 40 K higher than that of smooth surfaces, the discrepancy of 3 K between numerical results and measurements is acceptable.

3.2.3. Ocean Surfaces. To describe the wind-induced ocean surfaces, we use the semiempirical Durden–Vesecky spectrum [45], which was found to predict much of the observed dependence of the radar cross section on frequency, polarization, angle of incidence, and wind velocity [46–48]. In the model, a_0 is the absolute magnitude of the spectrum. Since a parametric analysis has been carried out showing that $a_0 = 0.008$ gives the best agreement with experiment data [46], a_0 of 0.008 is used for calculations in this section. The wavenumber cutoffs k_L and k_U are the key parameters in the spectrum, corresponding to the low and high frequency limits of the ocean spectrum, respectively. The quantities k_L and k_U can be selected to control the RMS height and fine-scale structures [46]. The physical temperature is 283 K. The permittivities of the seawater at 19 GHz are $28.9541 + i36.8340$.

For the sake of illustration, we show the results for hypothetical situations of windspeed 10 m/s and 20 m/s. It is to be noted that 20 m/s is closer to gale-force winds under hurricane conditions. With such high winds the ocean surface tends to have white capping and may not be simply represented by an ocean spectrum. In Fig. 27, the

ocean surfaces are generated at a windspeed 20 m/s with various k_U values, while k_L is equal to 100 rad/m. For larger values of k_U , there are more fine-scale structures. The corresponding results of emissivities and brightness temperature at incident angle of 50° are listed in Table 19, where k_U is chosen to be 400 rad/m, 1000 rad/m, and 4000 rad/m with fixed $k_L = 100$ rad/m. The roughness parameters k_σ for these three cases were 0.4263, 0.4415, and 0.4715, respectively. It is shown that the difference in brightness temperature between rough and flat surfaces increases with increase in k_U . This means that fine-scale structure plays an important role in calculating emissivities. Figure 30a illustrates the case for windspeed 10 m/s with corresponding $k_\sigma = 0.3156$, $k_L = 100$ rad/m, and $k_U = 4000$ rad/m. Brightness temperature values are also tabulated in Table 20. We can see that the numerical results agree well with the results from SPM for both horizontal and vertical polarizations. For windspeed of 20 m/s with $k_\sigma = 0.4715$, the brightness temperatures are plotted in Fig. 30b and listed in Table 21. The SPM results are in good agreement with numerical results for horizontal polarization, but are higher for vertical polarization.

Acknowledgments

The research in this article was supported by the City University of Hong Kong Research Grant 9380034 and Hong Kong RGC Competitive Earmarked Research Grant (CERG) 9040715 and RGC Central Allocation Grant 8730017.

BIBLIOGRAPHY

1. L. Tsang, J. A. Kong, K. H. Ding, and O. A. Chi, *Scattering of Electromagnetic Waves: Numerical Simulations*, Wiley Series in Remote Sensing, New York, 2001.
2. E. G. Njoku and D. Entekhabi, Passive microwave remote sensing of soil moisture, *J. Hydrol.* **184**(1):101–130 (1995).
3. E. G. Njoku and L. Li, Retrieval of land surface parameters using passive microwave measurements at 6–18 GHz, *IEEE Trans. Geosci. Remote Sens.* **37**(1):79–39 (1999).
4. E. G. Njoku, T. J. Jackson, V. Lakshmi, T. K. Chan, and S. V. Nghiem, Soil moisture retrieval from AMSR-E, *IEEE Trans. Geosci. Remote Sens.* **41**(2):215–229 (2003).
5. L. Tsang and Q. Li, Numerical solution of scattering of waves by lossy dielectric surfaces using a physics-based two-grid method, *Microwave Opt. Technol. Lett.* **16**(6):356–364 (Dec. 1997).
6. Q. Li, C. H. Chan, and L. Tsang, Monte-Carlo simulations of wave scattering from lossy dielectric random rough surfaces using the physics based two-grid method and canonical grid

- method, *IEEE Trans. Anten. Propag.* **47**(4):752–763 (April 1999).
7. J. T. Johnson, A numerical study of low-grazing angle backscatter from ocean-like impedance surfaces with the canonical grid method, *IEEE Trans. Anten. Propag.* **46**(1):114–120 (Jan. 1998).
 8. W. L. Briggs, A multigrid tutorial, *Proc. SIAM*, Philadelphia, PA, 1987.
 9. D. J. Donohue, H. C. Ku, and D. R. Thompson, Application of iterative moment-method solutions to ocean surface radar scattering, *IEEE Trans. Anten. Propag.* **46**(1):121–132 (Jan. 1998).
 10. K. Pak, L. Tsang, and J. Johnson, Numerical simulations and backscattering enhancement of electromagnetic waves from two-dimensional dielectric random rough surfaces with the sparse-matrix canonical grid method, *J. Opt. Soc. Am. A* **14**(7):1515–1529 (July 1997).
 11. J. T. Johnson, R. Shin, L. Tsang, K. Pak, and J. A. Kong, A numerical study of ocean polarimetric, polarimetric thermal emission, *IEEE Trans. Geosci. Remote Sens.* **37**(1):8–20 (1999).
 12. Q. Li, L. Tsang, K. S. Pak, and C. H. Chan, Bistatic scattering and emissivities of random rough dielectric lossy surfaces with the physics-based two-grid method in conjunction with the sparse-matrix canonical grid method, *IEEE Trans. Anten. Propag.* **48**(1):1–11 (Jan. 2000).
 13. Q. Li, L. Tsang, J. C. Shi, and C. H. Chan, Application of physics-based two-grid method and sparse matrix canonical grid method for numerical simulations of emissivities of soils with rough surfaces, *IEEE Trans. Geosci. Remote Sens.* **38**(4):1635–1643 (July 2000).
 14. V. G. Irisov, *Waves Random Media*, **7**:1–10 (1997).
 15. A. G. Voronovich, *Wave Scattering from Rough Surfaces*, Springer-Verlag, New York, 1994.
 16. Q. Li, L. Zhou, L. Tsang, and K. S. Chen, Numerical study of frequency and polarimetric dependence of the emissivities and backscattering coefficients of soil based on three dimensional Monte-Carlo simulations of Maxwell's equations, *Proc. International Geoscience and Remote Sensing Symposium*, Toronto, Canada, June 2002.
 17. S. M. Rao, D. R. Wilton, and A.W. Glisson, Electromagnetic scattering by surfaces of arbitrary shape, *IEEE Trans. Anten. Propag.* **30**(3):409–418 (May 1982).
 18. L. Medgyesi-Mitschang, J. Putnam, and M. Gedera, Generalized method of moments for three-dimensional penetrable scatterers, *J. Opt. Soc. Am. A* **12**(4):1383–1398 (1994).
 19. D. R. Wilton, S. M. Rao, A. W. Glisson, D. H. Schaubert, O. M. Al-Bundak, and C. M. Butler, Potential integrals for uniform and linear source distributions on polygonal and polyhedral domains, *IEEE Trans. Anten. Propag.* **32**(3):276–281 (March 1984).
 20. M. S. Yeung, Single integral equation for electromagnetic scattering by three-dimensional homogeneous dielectric objects, *IEEE Trans. Anten. Propag.* **47**(10):1615–1622 (Oct. 1999).
 21. V. Jandhyala, B. Shanker, E. Michielssen, and W. C. Chew, Fast algorithm for the analysis of scattering by dielectric rough surfaces, *J. Opt. Soc. Am. A* **15**(7):1877–1885 (1998).
 22. L. Tsang, C. H. Chan, and K. Pak, Backscattering enhancement of a two-dimensional random rough surface (three-dimensional scattering) based on Monte-Carlo simulation, *J. Opt. Soc. Am. A* **11**(2):711–715 (1994).
 23. K. Pak, L. Tsang, J. T. Johnson, Numerical simulations and backscattering enhancement of electromagnetic waves from two-dimensional dielectric random rough surface with the sparse-matrix canonical-grid method, *J. Opt. Soc. Am. A* **14**(7):1515–1529 (1997).
 24. S. Q. Li, C. H. Chan, M. Y. Xia, B. Zhang, and L. Tsang, Multilevel expansion of the sparse-matrix canonical-grid method for two-dimensional random rough surfaces, *IEEE Trans. Anten. Propag.* **49**(11):1579–1589 (2001).
 25. M. Y. Xia, C. H. Chan, S. Q. Li, B. Zhang, and L. Tsang, An efficient algorithm for electromagnetic scattering from rough surfaces using a single integral equation and multilevel sparse-matrix canonical-grid method, *IEEE Trans. Anten. Propag.* **51**(6):1142–1149 (June 2003).
 26. S. M. Rao, D. R. Wilton, and A. W. Glisson, Electromagnetic scattering by surfaces of arbitrary shape, *IEEE Trans. Anten. Propag.* **30**(3):409–418 (May 1982).
 27. M. Frigo and S. G. Johnson, FFTW: An adaptive software architecture for the FFT, *Proc. International Conference on Acoustic, Speech and Signal Processing*, 1998, Vol. 3, pp. 1381–1384 (see also <http://www.fftw.org>).
 28. H. Braunisch, Y. Zhang, C. O. Ao, S. E. Shih, Y. C. Eric Yang, K. H. Ding, J. A. Kong, and L. Tsang, Tapered wave with dominant polarization state for all angles of incidence, *IEEE Trans. Anten. Propag.* **48**(7):1086–1096 (July 2000).
 29. S. H. Yueh, Modeling of wind direction signals in polarimetric sea surface brightness temperature, *IEEE Trans. Geosci. Remote Sens.* **35**(6):1400–1418 (Nov. 1997).
 30. G. Soriano and M. Saillard, Scattering of electromagnetic waves from two-dimensional rough surfaces with an impedance approximation, *J. Opt. Soc. Am. A* **18**(1):124–133 (Jan. 2001).
 31. M. Y. Xia and C. H. Chan, Parallel analysis of electromagnetic scattering from rough surfaces, *Electron. Lett.* **39**(9):710–712 (May 2003).
 32. S. Kapur and D. E. Long, IES: A fast integral equation solver for efficient 3-dimensional extraction, *Proc. IEEE/ACM International Conference on Computer-Aided Design '97*.
 33. Y. Tan, Z. Li, L. Tsang, A. T. C. Chang, and Q. Li, Modeling the passive and active microwave remote sensing of snow using dense media radiative transfer theory with rough surface boundary conditions, *Proc. IGARSS*, 2004.
 34. Y. Oh, K. Sarabandi, and F. T. Ulaby, An empirical model and an inversion technique for radar scattering from bare soil surfaces, *IEEE Trans. Geosci. Remote Sens.* **30**(2):370–381 (March 1992).
 35. J. Johnson, L. Tsang, R. Shin, K. Pak, C. H. Chan, A. Ishimaru, and Y. Kuga, Backscattering enhancement of electromagnetic waves from two-dimensional perfectly conducting random rough surfaces: A comparison of Monte Carlo simulations with experimental data, *IEEE Trans. Anten. Propag.* **44**(5):748–756 (May 1996).
 36. K. Pak, L. Tsang, C. H. Chan, and J. Johnson, Backscattering enhancement of vector electromagnetic waves from two-dimensional perfectly conducting random rough surfaces based on Monte Carlo simulations, *J. Opt. Soc. Am. A* **12**(11):2491–2499 (Nov. 1995).
 37. L. Tsang and R. W. Newton, Microwave emissions from soils with rough surfaces, *J. Geophys. Res.* **87**(11):9017–9024 (Oct. 1982).
 38. J. R. Wang, T. J. Schmugge, An empirical model for the complex dielectric permittivity of soils as a function of water content, *IEEE Trans. Geosci. Remote Sens.* **GE-18**:288–295 (Oct. 1980).
 39. J. R. Wang, P. E. O'Neill, T. J. Jackson, and E. T. Engman, Multi-frequency measurements of the effects of soil moisture,

- soil texture and surface roughness, *IEEE Trans. Geosci. Remote Sen.* **GE-21**:44–51 (Jan. 1983).
40. L. Tsang and J. A. Kong, *Scattering of Electromagnetic Waves: Advanced Topics*, Wiley-Interscience, New York, 2001.
 41. L. Tsang, and R. W. Newton, Microwave emissions from soils with rough surfaces, *J. Geophys. Res.* **87**(11):9017–9024 (Oct. 1982).
 42. R. W. Newton, *Microwave Remote Sensing and Its Application to Soil Moisture Detection*, Technical Report RSC-81, Remote Sensing Center, Texas A&M Univ., College Station, TX, 1977.
 43. R. W. Newton, and J. W. Rouse, Microwave radiometer measurements of soil moisture content, *IEEE Trans. Anten. Propag.* **AP-28**:680–686 (1980).
 44. T. J. Schmugge, T. Wilheit, W. Webster, Jr., and P. Gloersen, *Remote Sensing of Soil Moisture with Microwave Radiometers*, II, NASA TND-8321, Goddard Space Flight Center, Greenbelt, MD, 1976.
 45. S. P. Durden and J. F. Vesecky, A physical radar cross section model for a wind driven sea with swell, *IEEE J. Oceanic Eng.* **OE-10**:445–451 (1985).
 46. S. H. Yueh, R. Kwok, F. K. Li, S. V. Nghiem, W. J. Wilson, and J. A. Kong, Polarimetric passive remote sensing of ocean wind vectors, *Radio Sci.* **29**(4):799–814 (July–Aug. 1994).
 47. J. T. Johnson, J. A. Kong, R. T. Shin, S. H. Yueh, S. V. Nghiem, and R. Kwok, Polarimetric thermal emission from rough ocean surfaces, *J. Electromagn. Waves Appl.* **8**(1):43–59 (1994).
 48. L. Zhou, L. Tsang, and D. Chen, Polarimetric passive microwave remote sensing of wind vectors with foam covered rough ocean surfaces, *Radio Sci.* **38**(4) (Aug. 2003).

SATELLITE ANTENNAS

R. B. DYBDAL
The Aerospace Corporation

Antennas for satellite systems have developed and increased in performance since the 1950s and greatly contribute to satellite capabilities. The preponderance of this antenna development has been for communication systems, and other development has been for remote sensing applications. Early satellite systems provided not only proof of concept but also a useful initial operating capability. The payload constraints of early satellites together with primitive attitude control systems limited antennas to simple narrow-bandwidth, broad-coverage designs, a far cry from today's sophisticated antenna systems with substantial throughput capabilities. Similarly, early users needed large ground terminal antennas to achieve the required link performance, and terrestrial links were provided to other system users. Today, systems are being developed to communicate to individual users with handheld terminals [1].

Both spaceborne and user antenna systems have requirements and development issues that are unique to satellite systems. In addition, satellite system antennas have testing requirements and objectives that differ from other antenna applications. Antenna technology, requirements and development issues, and test methods and objectives are described.

1. SPACE SEGMENT ANTENNAS

Spaceborne antennas have unique requirements and development issues. Like all satellite subsystems, much design attention is paid to three important parameters: weight, power, and volume. Likewise, reliability is a key requirement because an anticipated lifetime exceeding 10 years is expected without the possibility of repair or servicing. Spaceborne antenna designs must be sufficiently rugged to survive the rigors of launch environments. In addition to these physical requirements, the RF requirements differ from common antenna specifications. Spaceborne antennas provide performance over prescribed coverage areas containing the user segment; the pattern of the antenna projected on Earth's surface is referred to as its *footprint*. Antenna systems are specified by their minimum performance within the specified coverage area rather than their peak performance levels. This discussion uses different coverage area requirements to describe space segment antennas.

1.1. Earth Coverage Antennas

The simplest spaceborne antenna design is one that matches its coverage area with the available field of view from the satellite. These antennas are generally re-

ferred to as Earth coverage designs, and their beamwidth subtends the field of view plus the angular uncertainties of the satellite's attitude stability. Early satellite attitude control systems had both limited attitude control and uncertain reliability, so simple antenna designs with broad coverage were used. However, today's attitude control systems provide stabilities on the order of one-tenth of a degree, so that Earth coverage antennas can be essentially matched to the field of view. Thus, for geosynchronous satellites, an antenna with an 18° beamwidth is required; lower altitude LEO and MEO satellites require a correspondingly larger beamwidth for their larger field of view.

A typical Earth coverage design for geosynchronous altitudes is a corrugated horn antenna [2], which can be easily constructed and has a rotationally symmetric, low-sidelobe pattern for an efficient fit to the design coverage area. These horns are typically wide-flare designs chosen to maintain the same beamwidth and coverage over a wide bandwidth. Thus, a single horn together with a diplexer to isolate the receiver and transmitter can be used for both uplink and downlink frequencies. A design alternative at higher EHF frequencies is separate uplink and downlink horn antennas because these horns are very small and lightweight. Since the uplink and downlink frequencies are widely separated at EHF, the transmit diplexing filter is inherent because the transmit waveguide is cutoff at the receive frequencies and a modest physical separation may provide adequate isolation to meet the receive diplexing filter requirement of avoiding receiver saturation at the transmit frequency. Thus, the weight of a second horn antenna is offset because a diplexer is not required and performance is not degraded by the insertion loss of the diplexer.

At lower LEO and MEO altitudes, the broader field of view requirements can be met with an open-ended waveguide surrounded by corrugations to produce low sidelobes and beam symmetry. At these lower altitudes, the range differences between the subsatellite point and the edge of the earth become more significant and thus users at the edge of the coverage experience less sensitivity from the satellite antenna. In these cases, a shaped beam that provides more gain at the edge of Earth than the subsatellite point may be desired. Such shaped-beam antennas can be realized by an array of horns with properly selected excitation to meet the beamshaping requirement. However, such shaped-beam designs have more design complexity than a simple horn, and weight and volume are important satellite parameters. A well-known example of shaped beam designs is the array antenna used by the GPS satellites to broadcast navigational information. The GPS satellites are in a 12-h orbit, and the antenna array [3] is designed to deliver a uniform flux density to users within the earth's field of view.

1.2. Tracking, Telemetry, and Command Antennas

Every satellite requires a TT&C (tracking, telemetry, and command) subsystem to assist in determining the

satellite's orbital position, reporting the satellite's health and status to the ground-based satellite control segment, and providing a means to command and validate changes to the satellite's operation. The TT&C antennas have two distinct coverage requirements. One requirement is to provide complete spatial coverage during launch operations so that corrective commands or, in the worst case, a command for destruction can be delivered irrespective of the satellite's orientation. The second requirement is to provide coverage over Earth's field of view once on-orbit so that different terminals within the ground-control network can access the satellite. TT&C antennas must be both simple in design and highly reliable since the control of satellite operation is critical.

The broad coverage requirements of the TT&C antennas provide several design challenges. Aside from the impossibility of an ideal isotropic antenna with uniform sensitivity in all directions, the presence of the spacecraft blocks the antenna coverage. As a result, two antennas that strive for hemispheric coverage are used with one hemisphere being Earth facing and the other hemisphere facing away from Earth. During launch operations, the antenna having the higher signal strength is used and once the satellite is stable in its orbital position, the Earth facing antenna is used. In principle, somewhat better on-orbit performance could be achieved with an Earth coverage antenna, but the additional antenna and required switching increase weight and volume and add switch reliability risks. Since TT&C data rate requirements are low, ample link performance is readily achieved by ground-based control terminals.

Achieving and quantifying the performance of hemispheric coverage antenna elements remain challenges. Satellites have irregular shapes and appendages such as solar arrays whose positions vary to *sun-track* and maximize their power output. The hemispheric coverage required by TT&C antennas is degraded by blockage and diffraction effects from the satellite structure. Controlling wide-angle sidelobes and backlobes of a simple, electrically and physically small antenna is difficult to do but is needed to minimize antenna interactions with satellite structure. Extending the antenna from the spacecraft to reduce interactions results in deployment risk. Analytic projections of the antenna coverage in the presence of the spacecraft are challenged by the design complexity and the wide variety of satellite designs. Measurements of the antenna performance have all the problems of testing broad coverage antenna designs. Certainly, measurements using flight hardware not only have practical limitations such as the inability to deploy solar arrays but also moving and positioning flight hardware for the measurements have unacceptable risks. Generally, these problems are addressed by a combination of selecting a satellite antenna location with a clear field of view, analytic estimates of the effects of nearby satellite structure, scale model measurements, and ample margin in the ground segment.

Typically, TT&C systems operate at the lower microwave frequencies. Generally, a single uplink/downlink antenna is used to minimize weight and volume and avoid mutual blockage. The difference between uplink and

downlink frequencies often spans a significant percentage bandwidth. These considerations typically result in selecting a frequency independent antenna design such as a spiral to achieve the broad coverage requirements.

1.3. Spot Coverage Antennas

Spot coverage antennas service only a portion of the available field of view. These antenna designs provide higher gain levels than Earth coverage antennas because of their narrower beamwidths. This higher gain performance may be traded for higher data rate transfer, reduced user antenna dimensions, or increased link margin. In addition, spot beam antenna designs can provide coverage that is confined to geographic areas [4] and avoid worldwide licensing requirements. Thus, these designs are widely used to serve national or regional requirements. Several different design implementations have been developed to satisfy these needs.

The easiest design solution is to select a sufficiently large antenna so that its beamwidth matches the required coverage area and any variations caused by attitude uncertainty. Such a design might consist of a reflector whose size is selected to meet the desired beamwidth and a single feed horn, a simple design approach. In such a design, any variations in coverage requirements during the satellite lifetime can be accomplished by mechanically repositioning the antenna to serve a different coverage area. Such a capability is commonly used in military satellites so that coverage to different geographic areas within the field of view can be provided to service changing political needs.

A wide variety of designs has been developed to service more irregular coverage areas. These coverage areas may be bounded by geopolitical borders, different time zones, and other delineations. A standard means of providing such coverage is to synthesize the coverage area by combining different beams generated by a cluster of feed elements in the focal region of a reflector antenna. Each feed has its own pointing direction, and the collection of beams subtends the desired coverage area. The individual beams being combined are required to have a common phase center so that grating lobes do not degrade coverage characteristics. Thus, the collection of beams is generated by a common aperture. The arrangement of individual beams and their corresponding feed elements mimic the desired coverage area. The reflector antenna size is much larger than that needed to provide coverage over the composite area. When active devices are used in the feed elements prior to combining, design attention must be paid to their amplitude and phase tracking. The precision of fitting to the design coverage area can be increased by using a larger number of beams at the expense of design complexity and a larger overall aperture size.

In addition to the complexity of the additional number of feeds and the larger reflector required by this approach, the design complexity also increases because the individual feeds are no longer located at the focal point of the reflector but instead are distributed within the focal region. The off-axis feeds are not ideally focused, and suffer gain loss and pattern degradation. These problems are shared with multiple beam designs and, as will be

discussed, result in dual reflector designs to limit beam degradation when a large number of beam are combined.

Another design approach has developed to provide coverage over irregular areas. This design uses a single feed, and the irregular coverage area is generated by deforming the reflector surface [5]. Synthesis procedures have been developed [6] to specify the required deformation of the reflector surface. This design approach has the advantage of a simple feed design rather than a cluster of feed elements and combining, but requires developing and maintaining controlled reflector surface distortion. If the coverage requirements change, a new surface deformation is required. This approach also precludes changing the coverage areas on-orbit by using beam switching techniques.

A final design alternative for spot coverage is an adaptive uplink antenna. The pattern within the coverage area is adaptively controlled to service desired users within the design coverage area to the extent practical while reducing received interference by forming pattern nulls in the direction of interference sources. This capability is principally required for military systems whose users desire protection from intentional interference. When interference is not present, a quiescent pattern provides coverage over the design region. When interference is initiated, the antenna responds under adaptive control to form pattern nulls.

Adaptive antennas require a means to distinguish desired signals from interference, to detect the initiation of interference, and to determine a set of complex weighting values that combine antenna elements to satisfy an optimization criteria. Several different discriminates have been employed to distinguish desired signals from interference: spectral characteristics, power levels, and signal arrival directions. When systems also use spread spectrum modulation for additional interference protection, the properties of the spread-spectrum codes provide a basis to distinguish interference from desired signals. Interference initiation can be detected by increased received power levels that do not have spread spectrum modulation components; correlation processes are normally used to indicate interference power. An optimization criterion such as maximum SINR (signal-to-interference-plus noise ratio) is used to establish complex weighting coefficients to combine antenna elements. Generally, a recursion relation based on measured correlation values and the optimization criteria is derived to form a control algorithm. The combination of the complex weighted antenna elements produces a pattern containing null in the direction of interference, and equivalently, the received interference power is minimized.

Two types of antenna designs have been investigated for these adaptive systems [7,8]. One approach uses a thinned array where the elements are combined to generate pattern nulls when interference is present and a set of weighting coefficients for interference-free cases. The potential advantage of this approach is that the resolution between desired users and interference is enhanced by increasing the array element spacing. However, the separation between array elements produces additional nulls within the coverage area referred to as grating nulls that

degrade coverage characteristics. The separation of the array elements results in the inherent frequency scanning properties of an array creating dispersion that limits cancellation performance over the required bandwidth. In addition, the coverage of the array elements generally extends beyond the desired coverage area, resulting in susceptibility to interference beyond the coverage area. Finally, the thinned array design generally results in reduced G/T performance within the coverage area.

The second design approach uses an offset reflector with a cluster of feeds in the focal region. In interference-free conditions, a set of quiescent weighting values for the individual feeds maintains performance over the design coverage area. The initiation of interference produces correlation products associated with the interference that are used to derive complex weighting values. The advantage of this design approach is that all beams generated by the feed cluster have the same phase center location so that the dispersion inherent in array designs is not present and broad bandwidth cancellation performance is achieved. The resolution between interference and desired signals is limited by the beamwidth of the individual beams. This resolution depends on the amount of G/T margin that the user can sacrifice and the interference source's location on the earth, as illustrated in Fig. 1. A comparison between the performance of a thinned array design and a multiple feed design is presented in Fig. 2. The grating nulls are apparent in the thinned array contours, which reduces the coverage available to users.

Several performance measures are used with adaptive antenna designs. The threshold SNIR establishes a bound for acceptable communication performance that can be measured using BER (bit error rate) values by injecting both desired signals and residual interference into the receiver. The null depth performance and its variation over the required bandwidth as measured between the quiescent pattern and the pattern after adaption are sometimes used to judge nulling performance. The amount of time the adaptive process takes to convert the quiescent pattern to the nulled pattern is referred to as the convergence time and measures the transient performance of the system. Finally, for this uplink application, the amount of the design coverage area that exceeds the threshold SNIR value is another measure for space segment antennas. These performance measures depend on the number of interference sources and their locations, and their power levels and spectral characteristics; this description of the interference is referred to as a scenario. Adaptive systems are commonly developed using a simulation that varies the scenario parameters on a Monte Carlo basis to provide statistical measures of the performance parameters. The simulation is then validated by using hardware measurements on a limited number of scenario cases in order to avoid the impractical amount of time required to test on a Monte Carlo basis.

1.4. Multiple-Beam Antennas

Multiple-beam antenna systems (MBA) [9] greatly increase the on-orbit satellite capabilities. These antennas simultaneously produce more than one antenna beam

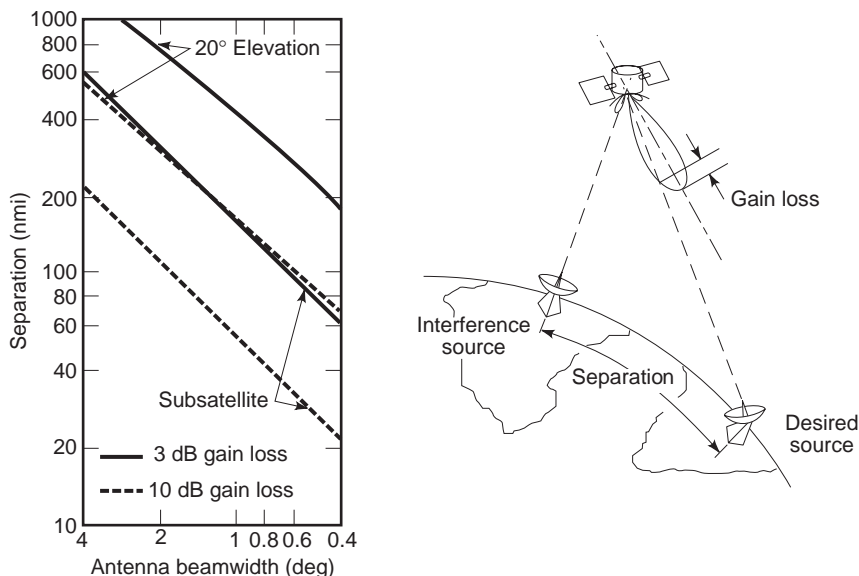


Figure 1. Adaptive antenna resolution (after Ref. 8).

from a single aperture. For space applications, a single aperture is a significant savings in space required on the satellite and the overall weight compared with multiple aperture alternatives. When the coverage area is subdivided by different beams, the gain available to users increases, permitting higher data rates or reduced user terminal performance. A further advantage of multiple beam antennas is that beams directed to different geographic locations are isolated by their spatial separation. Thus, the same frequency bands can be used simultaneously at both beam locations increasing the information that can be transferred by a single satellite. These advantages are the reasons for the wide application of multiple-beam antennas.

The antenna design has several different requirements. Independent beams must be efficiently generated with high pattern fidelity and minimal gain degradation over the required field of view. Isolation between different beams must be maintained so that signals using the same frequency subband are not degraded by cochannel interference. Beamforming networks that combine signals from the antenna beam outputs to and from the satellite transponder must be developed. The transponder must provide a means to map the uplink information in each beam position to the downlink beam positions.

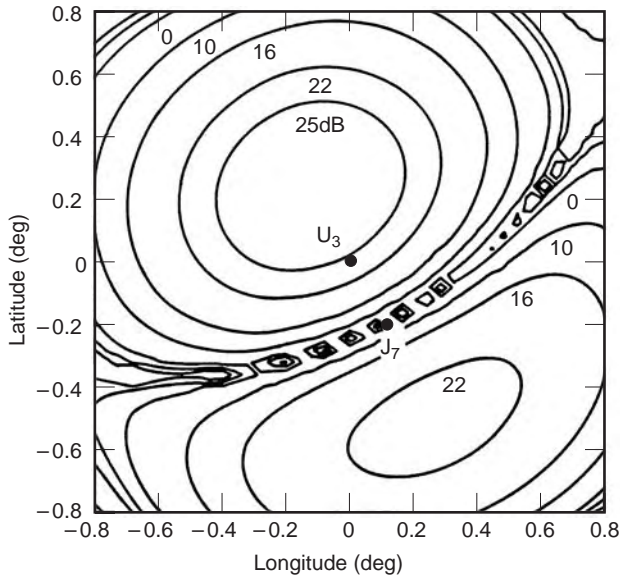
One design issue is to efficiently generate independent beams with high pattern fidelity over the required field of view. When optical designs (i.e., reflector and lens antennas) are used, each feed produces an independent beam in a different direction, but not all of the feeds are ideally focused. As a consequence, some of the feeds experience phase distortions that degrade the pattern characteristics and reduce the gain compared to the feeds that are well focused [10]. Several different techniques in the design of the optics are used to minimize the degradation. One technique is to select a long f/D ratio to reduce off-axis phase distortions. The popularity of dual-reflector designs in these applications results in part from their increase of

the effective f/D , and careful attention to the optics can produce excellent results [11,12]. The dual-reflector designs in an offset configuration also provide the ability to achieve very good polarization purity. Other techniques have been applied to selecting lens surface contours [13].

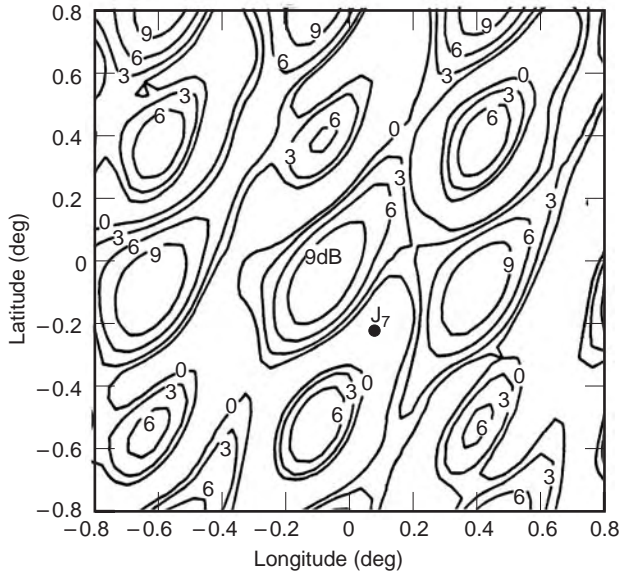
In addition to achieving good pattern and gain performance over the required field of view for an individual feed, another set of design challenges exists with the cluster of feeds. The problem is a conflict among beam isolation, the crossover level between adjacent beams, the sidelobe levels of the beams, and the antenna efficiency. On the one hand, low sidelobe patterns are desired to enhance the beam isolation, which requires the feed to produce an amplitude taper over the aperture, resulting in a relatively large feed. The physical interference between large adjacent feeds results in a relatively low tangential crossover level (the pattern level relative to the beam boresight at an equal distance between beam centers) between beams. The consequence of the low crossover level is that the minimum gain within the field of view is reduced. On the other hand, high beam crossover levels result a higher minimum gain level within the field of view, but beam patterns with high sidelobes having reduced beam isolation. High beam crossover levels also result in beam coupling loss [14], which degrades antenna efficiency.

These conflicts have resulted in several different design approaches. One technique is to couple signal samples from adjacent feed elements [15] to achieve high crossover levels, low sidelobe patterns, and reasonable antenna efficiency. Another technique [16] uses a underilluminated aperture with the feeds displaced from the focal region. This approach requires a somewhat larger reflector than in the focused case, but at EHF frequencies where compact antennas result from the small wavelength, the size increase may be unimportant.

The required isolation between beams depends on the susceptibility of the signal modulation to cochannel interference and the dynamic range of the system users. Thus,



(a) Multiple beam contours



(b) Thinned array contours

Figure 2. Comparison of multiple-beam antennas and thinned array performance (after Ref. 8).

the required isolation level must be derived for each application. Isolation between adjacent beams can be achieved in two ways. One way, referred to as frequency reuse, divides the allotted bandwidth into subbands. A frequency plan is devised to adequately separate the beams using the same subband to meet the isolation requirement. Since the same frequency subband is simultaneously used in different beam positions, the plan is referred to as a frequency reuse plan.

A second way of increasing isolation referred to as polarization reuse uses orthogonal polarizations together with frequency subbands in applications requiring high isolation. Orthogonal polarization is also used in applications demanding as much capacity as possible because the same beam position can transfer twice the information.

These techniques require antennas with high polarization purity; a typical requirement is to suppress cross polarization levels at least 27 dB lower than the principal polarization. Generally, satellite systems use circular polarization so that the user does not have to align to a linear polarization. However, inclement weather can cause coupling between polarizations, reducing the isolation. This effect is less severe for linear polarization, so that orthogonal linear polarization is sometimes used. This combination of polarization and frequency reuse is commonly used by commercial systems to obtain as much capacity as possible from a single satellite.

Multiple-beam antennas are generally considered as designs covering the available field of view. As the beamwidth of the individual beams decreases, the required number of beams greatly increases as shown in Fig. 3, larger aperture sizes are required and the complexity of beam routing increases. In some applications, multiple beams are used in a limited geographical region [4,17]. The Ka-band multiple-beam system described in Ref. 17 has such small beamwidths that active tracking of a ground beacon is required to compensate for satellite attitude variations.

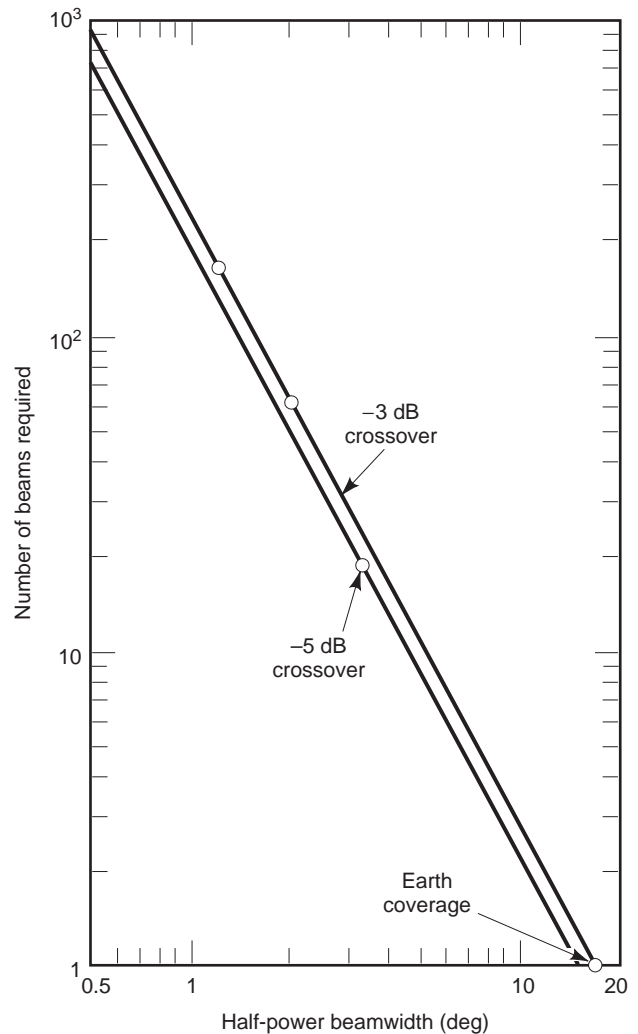


Figure 3. Number of beams to cover FV (after Ref. 9).

The ability to process and direct the information on the collection of multiple beams requires beamforming networks that separate information on the uplink beams and combine information on the downlink beams. A wide variety of beamforming networks have been developed. The simplest design is a fixed beamformer network that simply combines beams in a fixed pattern. This beamformer, together with transponder channelization, maps the uplink beam patterns into the downlink patterns. Other beamformer designs use cascaded networks on switches or variable power dividers so that the beam patterns can be changed on-orbit. Still other beamformers use adaptive processing on the uplink beamformer to negate interference. Yet other systems route the uplink information to a terminal on the ground, referred to as a *gateway*, where the uplink beams are mapped into the downlink collection.

The beamformers have different requirements for the uplink beams and downlink beams. The system noise temperature on the uplink can be established by preamplifiers that are followed by the beamformers. In this way the system sensitivity is not degraded by the insertion loss of the beamformers, and lightweight networks and diode switching can be used in the beamformer implementation. The downlink beamformer network must be placed between the transmitters and the beam ports, so that power handling and insertion loss are important design parameters. In addition, switching for redundant transmitters is also required. These requirements depend on the application.

The development of multiple-beam antenna systems has been pursued principally for geosynchronous satellites, and future design challenges exist to develop multiple-beam designs for LEO and MEO (low- and medium-Earth orbit) satellites. While offset reflector antennas are commonly used in geosynchronous satellites, these antennas are examples of limited scan antennas [14], which are not appropriate for the wider field of view at the lower altitudes. These lower altitudes also need wider beamwidths than geosynchronous designs to maintain reasonable footprint dimensions, and thus the overall antenna size is electrically smaller. Array antennas are commonly used to meet performance requirements for these orbits. With their smaller electrical size compared with geosynchronous designs, a reasonable number of array elements is required.

The trend toward using digital technology in the transponder also naturally leads to considering digital beamforming techniques in the array design. On the uplink, the received signal at each element is preamplified, downconverted to baseband, and transformed into the digital domain by an analog-to-digital converter (ADC). Digital samples from each array element are combined using a complex matrix multiplier containing the complex coefficients that perform the beamsteering. Parallel complex multipliers are required to form multiple beams. The same constraints on beam isolation exist for multiple beam operation. The downlink antenna follows the same procedure in reverse. The input digital datastream is complex-matrix-multiplied to obtain the properly weighted samples for each array element for the beamsteering, and a digital-to-analog converter (DAC) provides

conversion to the analog domain. This analog baseband is upconverted to the transmit frequency and suitably amplified to the required element power level. Experience with digital array designs is described in Ref. 18; an adaptive array using digital technology to increase beam isolation is described in Ref. 19.

The downlink array designs for multiple-beam operation also present challenges in transmit power control. The element transmit power is shared with each of the beams transmitted by the array. The relative amplitude and phase between the array elements must be maintained to achieve the desired downlink pattern. In addition, the total power in the array elements must be maintained near saturation to achieve the design ERP performance and maximum power efficiency. However, the total power must not extend into the transmitter's non-linear region, which would degrade performance by producing intermodulation products and signal suppression. The challenge is to maintain the required amplitude and phase excitation for each beam while allotting each beam an equitable share of the downlink transmit power.

1.5. Remote Sensing Antennas

Satellite antennas also include designs for remote sensing applications. Two types of sensors are used: active, or radar, and passive, or radiometric, sensors. These systems are used in low-orbiting satellites to provide both global coverage and high resolution of terrain features.

Radar sensitivity is commonly measured by the power aperture product of the design, and thus, in addition to high peak power levels, a physically large aperture size is required [20]. Antenna designs for active applications generally require deployment to achieve the required aperture size. A conflict exists in these designs. Large apertures can be obtained from low-frequency arrays where a reasonable number of elements are required and the mechanical tolerance is not overly stringent, but the resolution of these systems is lower than higher-frequency designs. The better resolution of the higher-frequency designs is accompanied by the requirements of additional array elements and more stringent mechanical tolerance. The size, weight, and prime power requirements for these sensors make their development an ambitious effort, but future systems designs, particularly those using synthetic aperture processing, can be anticipated.

Passive sensors are commonly used for both meteorological and terrain remote sensing [21]. Two types of antenna designs are used in these applications. One type of antenna, generally an offset reflector, is mechanically rotated at a constant angle from the satellite's nadir to generate a conical trace on the ground at a constant elevation angle. As the satellite proceeds in its orbit, a swath on the ground is swept out. The requirements for these antennas include design attention to minimize insertion loss to achieve high sensitivity, good polarization purity to discern the radiometric contrast for oblique incidence angles used by these sensors, low sidelobes so that the emission received by the mainbeam is not degraded by sidelobe returns, and a narrow beamwidth to obtain good resolution

of terrain features. Commonly, these antennas are specified by their solid beam efficiency performance. This parameter is defined by the power received for the specified polarization over a required angular region to the total power received from all space assuming the antenna is uniformly illuminated from all directions. This parameter is defined to provide a means to quantify the degree to which the power received by the sensor is isolated to its specified coverage area. This system design commonly operates at several different frequency bands using the same aperture.

A second type of antenna has a much simpler design and is used in sensors referred to as *sounders*. In this design, the antenna boresight is aligned with the satellite nadir. These designs operate at frequencies selected from peak of molecular absorption resonances, which occur at EHF frequencies. Several different IF bandwidths are used in these designs. As the bandwidth straddles more of the molecular resonance, the absorption toward the bandwidth edges reduces from the peak value at the resonant frequency. This reduced absorption at the bandwidth edges permits the sensor to view emission closer to Earth's surface. Thus, by examining the emission received at different IF bandwidths, a profile for different altitudes may be observed. The antennas used in these sounder designs are generally corrugated horn designs selected for their low insertion loss and rotationally symmetric, low sidelobe patterns.

2. USER SEGMENT ANTENNAS

User segment antennas also have requirements specific to satellite applications. In addition to meeting G/T and ERP requirements for link closure, the user antennas generally need to align their mainbeams with the appropriate satellite. Other design issues include the control of interference to and the reduction of interference from other systems. With the increased number of satellite users, terminal costs including the antenna, transportability to alternative locations, and in future personal communication systems, techniques to reduce interactions with the surrounding environment form the principal development issues.

2.1. Radiofrequency Issues

The most common user antenna is a reflector design capable of reasonable RF performance with a modest cost. Other antenna technologies, such as phased arrays, have more complexity which results in higher manufacturing costs, and therefore are used when compelling reasons exist for their design. For example, aerodynamic constraints for high-performance aircraft may dictate the development of conformal array designs.

The trend toward increased numbers of users results in the terminal costs having a significant fraction of the total system costs. This trend in turn requires sufficient performance from the satellite to minimize terminal performance requirements. An excellent example is provided by direct-broadcast satellite TV services where both the user terminal size and costs have dramatically shrunk.

More generally, the present development of systems for VSATs (very-small-aperture terminals) illustrates this trend. A very important part of system planning is to insure that adequate satellite performance is available to minimize user performance requirements, and thereby control the total system cost as well as provide a minimum amount of equipment, particularly for those users with mobility requirements.

The increased number of satellites in orbit has also resulted in additional requirements for the antennas. Concern regarding interference to and from satellites that are closely spaced in orbit has resulted in sidelobe envelope requirements to reduce interference levels. These requirements are mandated on antenna manufacturers. A typical example of these requirements has been levied by the CCIR [International Radio Consultative Committee, technical branch of International Telecommunication Union (ITU)] [22], which results in a sidelobe envelope constraint that depends on the electrical size of the antenna.

Sidelobe control is one antenna technique that reduces interference for both reception and transmission. Another technique for reducing received interference is to construct an adaptive cancellation system. A typical design for ground terminal applications called a *sidelobe canceler* [23] assumes the desired signal is received by the main-beam and that the interference arrives through the antenna sidelobes. The antenna hardware consists of a main reflector antenna and a set of auxiliary antenna elements that are combined with complex weighting values with the main reflector antenna to cancel interference. The principal issue for this design approach is the dispersion inherent in the main reflector's sidelobe response. The sidelobe response of reflector antenna includes radiation from edge diffraction, direct feed radiation and spillover, scattering and blockage contributions, and leakage from the panels composing the reflector surface. The complex sum of these individual radiation mechanisms varies over the operating bandwidth so that effective cancellation requires frequency-dependent weighting values. Such frequency-independent weighting values can be achieved by adaptive equalization circuitry using a transversal filter with adaptive weighting coefficients at each time-delay tap. An example of this interference reduction approach may be found in Ref. 24, which describes the design and the measured results of a demonstration of cancellation capabilities.

The trend toward increased microwave users and systems extends beyond satellite applications. This trend also increases the possibility of interference to user terminals from nearby terrestrial systems. A particular concern is the possibility of out-of-band receiver compression from high-level pulse systems such as radars that suppresses desired signal levels and creates intermodulation products degrading receiver performance. Design attention must be paid to the receiver's dynamic range and RF filtering to protect the receiver from high-level interference. However, RF filtering, while necessary has insertion loss, which degrades sensitivity by reducing the received signal and increasing the system temperature.

Inexpensive, low noise receiver front ends and relatively low sky temperature values [25] provide the potential of

low system temperatures that increase system performance and reduce the required antenna size. Controlling antenna spillover and wide-angle sidelobe levels by both efficient rotationally symmetric feed designs and reflector geometry choice produces low antenna temperature values [26]. Low antenna temperature values also require minimizing feed and transmission line losses. Filter loss even in a high- Q medium becomes the dominant insertion loss, but such receiver protection is necessary. These steps permit development of terminals that meet the required G/T with a minimum size antenna. These factors result in the popularity of offset reflector antennas for user applications. The efficiency of offset reflectors is enhanced by the absence of feed blockage; their high-level spillover lobes are directed toward the lower sky temperature instead of the ambient Earth temperature, and their low sidelobe levels minimize the antenna temperature while also complying with sidelobe envelope requirements.

User antennas for future personnel communication systems face additional challenges. These antennas must provide broad coverage so that antenna pointing is not required, particularly since the LEO and MEO orbits used in these systems produce ever-changing angular positions between the user and the satellite. One problem inherent in broad-coverage antennas, as previously discussed for TT&C antennas, is the sensitivity of the antenna performance to the environment surrounding the antenna. For the personal communication application, there exists a wide variety of environments with varying degrees of multipath (i.e., scattering from human-made and terrain features). In addition, link performance can be degraded by foliage attenuation and blockage from terrain features. These development issues are being actively pursued for both satellite systems and terrestrial cellular networks that operate at somewhat lower frequencies. Development of techniques to mitigate these degradations is also being actively pursued; techniques such as RAKE receivers, which provide adaptive diversity combining and equalization are being evaluated.

2.2. Antenna Pointing Techniques

User antennas must also be aligned with the desired satellites for signal reception. The satellite's orbital position is specified by its ephemeris which describes the satellite's altitude, eccentricity of orbit, inclination, longitude of ascension, and time of epoch. The satellite ephemeris and the user location are required to determine the antenna pointing angles. Typically, this information is transferred to the antenna control unit where the required pointing angles are computed and the necessary commands to the antenna positioner are issued. The requirements for antenna pointing depend on the antenna beamwidth, the uncertainty in the satellite's location, and the orbital dynamics. For communication applications, a pointing accuracy of one-tenth of a beamwidth is typically specified to minimize signal loss caused by pointing errors.

In some cases, antenna pointing is trivial. For example, the antennas for personal communication systems are purposely designed with broad coverage antennas, so that the user has no pointing requirements. Another com-

mon example is a small user antenna for direct-broadcast satellite reception from geosynchronous satellites. These antennas are roughly aligned using the user's geographic location, verified by signal peaking techniques, and rigidly secured. The combination of the relatively wide beamwidth from the small antenna and the stationary position of the geosynchronous satellite and its station keeping results in a fixed pointing requirement.

In other applications where satellites have inclined orbits or orbits that are not geosynchronous, the satellite undergoes dynamic motion with respect to the user, and a means must be provided to follow the satellite in orbit. For users with relatively broad beamwidths compared to the orbital uncertainty, the knowledge of the satellite ephemeris and the user location may be adequate to simply command the user's antenna position. This open-loop procedure is commonly referred to as *program tracking*.

If some uncertainty exists in the antenna pointing, such as ephemeris data that are not current, another open-loop technique referred to as *step track* is commonly used to verify correct alignment with the satellite's position. The user's antenna is pointed at the nominal position of the satellite as might be obtained from program track. The antenna is then commanded to move in equal and opposite angular positions from this nominal pointing direction. If the antenna is correctly aligned with the satellite, the received signal level should be reduced by the same amount at both angular offsets. If the signal levels at both positions are not identical, the difference in the power level provides the angular correction to the nominal position. This process is repeated in the orthogonal plane to properly position the antenna in two angular coordinates.

These two open-loop antenna pointing techniques are commonly used together. The step track procedure is periodically exercised to validate the correctness of the program track pointing. A significant advantage of these techniques is that minimal equipment is required. The antenna positioner is required and simple software commanding is needed to execute the angular offsets. The power measurements at the different angular offsets may be obtained from a simple measurement of the receiver's automatic gain control (AGC) voltage with the appropriate calibration and linearity verification.

When user antennas have beamwidths that approach 10 times the uncertainty in satellite position or a significant amount of orbital dynamics exist, closed-loop tracking techniques are required. These techniques are commonly used in radar systems to locate targets and are referred to as *monopulse* designs. This term is derived from radar applications because the tracking information is obtained from each radar pulse. In radar applications, the received signal level varies as the target changes aspect angle and typically has a significant dynamic range. Thus, tracking information is derived from each radar pulse so that the dynamics of the target return do not degrade antenna pointing performance. Monopulse systems for communication applications have requirements easier than those for radar systems. The received signal level has a relatively constant amplitude, so that the monopulse signals can be sequentially sampled, reducing hardware

requirements. The antenna pointing accuracy depends on aligning the antenna with sufficient accuracy to minimize signal loss as compared to locating a radar target with the maximum precision practical.

Monopulse systems operate by forming two types of antenna beamshapes: a sum beam, which receives the desired signal; and a difference beam, which has a null on the antenna boresight axis. The signal power in the sum beam is maximized by positioning the antenna to the null of the difference pattern. The ratio of the signal levels in the sum and difference beams is independent of the power density of the received signal, and provides a measure of the angular displacement from the antenna's axis. This ratio can be used in a closed loop system so that the antenna will align to the received signal and will follow any variations in the signal location.

Two different types of feed designs are commonly used to generate the sum and difference beams. One feed design [27] uses a conventional feed for the sum beam and an additional four small feed elements to produce the difference beam. The second design [28] uses a higher-order waveguide mode to produce the difference beam, which is sampled by couplers. In both cases, the difference beam outputs are coupled into the sum channel and switched sequentially. The resulting AM modulation on the sum signal is processed to derive the antenna pointing measurements.

3. SATELLITE ANTENNA TESTING

While antenna testing is widely developed for many applications, satellite antenna systems pose some unique testing challenges. Rigorous testing is required for spaceborne antenna systems because of their reliability requirements and the inability to service on-orbit antennas. This discussion illustrates the trends toward increased integration of antennas with payload electronics, and testing where the antenna performance depends on both the antenna hardware and system electronics further increases testing complexity. The user segment also follows the trend of increased integration with terminal requirements. Finally, the demands for capacity also result in more stringent than normal testing requirements, such as validating the polarization purity requirements for systems using polarization reuse.

Spaceborne antenna testing generally has three distinct phases:

Development testing that demonstrates design compliance with system specifications

Qualification testing that ensures flight hardware not only meets the RF performance demonstrated in development testing but also is capable of surviving the launch and on-orbit environments and meets weight and power requirements

On-orbit testing that validates system compliance with system specifications and provides diagnostic evaluation of system shortfalls during the orbital lifetime

These three test phases have a scope that greatly exceeds the normal testing to define the component level performance of antennas. This situation is particularly true with the trend toward incorporating payload electronics into the antenna system, which results in antenna system performance that depends on not only the antenna components but also the electronics performance.

The development testing has the objective to demonstrate the designs fully comply with the system specifications. The testing in this phase of the program is most closely related to conventional antenna testing and quantifies gain values, pattern characteristics, polarization purity, impedance properties, bandwidth variations, and so on, as is typically performed. These RF characteristics can generally be performed using conventional RF test facilities and general-purpose instrumentation. The antenna components are designed on a prototype or engineering model basis, so that weight projections and compliance with thermal and mechanical requirements for launch can also be evaluated.

The qualification testing has the objective of determining whether the flight hardware is capable of the performance established for the design whose compliance has been demonstrated in the development testing. An important part of the program test planning is a requirements' flowdown that identifies the testing necessary to demonstrate overall system compliance and assurance of flight-worthiness. The principal concern in this phase of the testing is how to perform the testing without risk to flight hardware. Moving flight hardware to conventional antenna test facilities poses an unacceptable risk in many cases. Testing very lightweight antenna designs may be precluded because they can be destroyed by wind or become contaminated and the effects of gravity can degrade the ability to project on-orbit performance. The development of portable near-field test facilities is viewed as a need to permit detailed antenna testing in payload assembly areas. Another important part of the test planning in the early part of the program is the identification of test ports for system evaluation and the required development and calibration of any specialized test fixture. Qualification testing must also evaluate performance variations in the thermal variations and vacuum conditions, and the ability to survive the shock and vibration levels experienced during launch. Other issues such as the reliability of deployment mechanisms, if used, must be demonstrated.

On-orbit testing is conducted using specialized test terminals, which are often a part of the satellite control networks. The testing at this phase is generally conducted shortly after the satellite arrives at its orbital location. This testing generally concentrates on system-level performance parameters, such as uplink G/T, downlink ERP, and payload antenna pointing alignment, to establish overall performance compliance. After this initial performance evaluation, these test facilities are used to periodically assess on-orbit performance, and together with the telemetry information provide a means for on-orbit diagnostics. An important part of the test planning is an examination of the adequacy of the telemetry and test terminal information for identifying failed components

and their potential substitution with redundant components.

Satellite systems also have some specialized testing requirements peculiar to their environment. One problem with satellite systems is the static charging of components on-orbit. Typically, this charging occurs on dielectric materials used for thermal protection not only for the antenna but also for other satellite subsystems. The charge builds up on these components until discharge occurs. This phenomenon is referred to as ESD (electrostatic discharge), and the spectral components of the discharge may have sufficient intensity to interfere with payload receivers. The ESD spectral content is typically measured by embedding a sample of the material in an electron beam and using a pickup probe antenna and a spectrum analyzer or very wide bandwidth oscilloscope.

Another problem that results from high power operation in vacuum conditions is multipaction. In this case, the RF energy may be sufficient to strip electrons from the surfaces of materials exposed to the high power, which will damage the component. The potential for multipaction is typically evaluated by testing the components associated with high power in an evacuated bell jar and using a spectrum analyzer to observe any RF noise associated with multipaction. Such testing can also evaluate any power-handling and microarcing limitations of the components by examining the components after the test for damage. Temperature increases from high-power operation can also be measured.

A third problem is also associated with high-power operation and is referred to as PIM (passive intermodulation). This problem results from exposing junctions with high power. Dissimilar metals or contamination forms weak diode junctions whose nonlinearity generates intermodulation products. Such junctions can occur in transmission-line components, filters and diplexers, and joints within the antenna structure. Those components exposed to high power are tested by injecting two tones at high-power levels (higher-power transmitters than the operational ones are sometimes used to insure the observed intermodulation does not result from products generated by a saturated transmitter) and observing any intermodulation products generated by the components under test with a spectrum analyzer.

User antenna testing also has some unique issues for satellite systems [29]. One problem results from testing on ground terminal antennas, where the physical size of the antenna precludes testing in conventional antenna test facilities. A test technique using the emission from astronomical sources is used to measure the G/T [30]. The flux density of these emissions has been well established, and a variety of sources exist. The emission from the sun has a high level, but the angular width of the solar disk limits this technique to relatively wide beamwidths. Other sources such as the moon and radio stars such as Cassiopeia A are used for narrower beamwidths. The positions of these sources are also well known, and thus, the opportunity to validate the accuracy of the antenna positioning systems is also available. The antenna gain in the transmit bandwidth can also be established by connecting a

low-noise preamplifier in place of the transmitter, measuring the G/T, separately measuring the system temperature, and multiplying to obtain the transmit antenna gain. While this technique was developed for large ground terminal antennas [31] with the available low-noise preamplifiers, useful measurements can be made on much smaller antennas. This technique is particularly useful for those antennas that follow the trend of integrating the antenna feed and receiver front end without connectors for test purposes.

Other electromagnetic measurements are required in the development of both user and spaceborne systems to validate EMI/EMC (electromagnetic interference/electromagnetic compatibility) issues. Part of the system planning for satellite systems involves frequency planning to avoid such problems; measurements at the assembly level are performed to ensure that on-orbit performance will not be degraded by interference between subsystems. User terminal designs are also evaluated to insure the design is not susceptible to outside interference as well as not creating interference to other systems that may be located nearby.

4. SUMMARY

Satellite antenna development is a significant part of present-day antenna technology. Much progress in antenna systems for both the space and user segments has been made. However, future requirements such as the development of satellite systems for personal use provide a rich opportunity for further development and challenges to meet the increased performance levels demanded in future systems and applications.

BIBLIOGRAPHY

1. F. Ananasso and F. D. Prisco, The role of satellites in personal communication services, *IEEE Select. Areas Commun. SAC-13*:180-195 (1995).
2. A. W. Love, *Electromagnetic Horn Antennas*, IEEE Press, New York, 1976.
3. C. T. Brumbaugh et al., Shaped beam antenna for the global positioning satellite system, *1976 IEEE AP-S Symp. Digest*, Amherst, MA, Oct. 11-15, 1976, pp. 117-120.
4. K. Ueno et al., Design and characteristics of a multiband communication satellite antenna system, *IEEE Trans. Aerospace Electron. Syst.* **AES-31**:600-607 (1995).
5. T. Katagi and Y. Takeichi, Shaped beam horn reflector antenna, *IEEE Trans. Anten. Propag.* **AP-23**:757-763 (1982).
6. O. M. Bucci et al., Antenna pattern synthesis: A new general approach, *Proc. IEEE* **82**:358-371 (1994).
7. J. T. Mayhan, Area coverage adaptive nulling from geosynchronous satellites: Phased arrays versus multiple beam antenna, *IEEE Trans. Anten. Propag.* **AP-27**:410-419 (1986).
8. K. M. SooHoo and R. B. Dybdal, Resolution performance of an adaptive multiple beam antenna, *IEEE MILCOM '89 Symp. Digest Session 7*, Boston, MA, 1989.

SCHOTTKY BARRIER DIODES AND THEIR APPLICATIONS

W. ALAN DAVIS

The University of Texas at
Arlington

1. INTRODUCTION

The original point contact diodes were made by pressing a tungsten wire onto a semiconductor such as Ge or Si. These early forms of the Schottky barrier diode were used as detectors and mixers in radar systems. Although times have changed, the Schottky barrier diode remains an important component in many systems because of its unique features. They act in some ways like the pn junction, but they also have some important differences. In particular, the Schottky barrier diode is a majority carrier device, so they lack the diffusion capacitance associated with the minority carrier storage effects, which makes them ideal for fast switching and high-frequency mixer applications. The discussion will first focus on the origin of the energy bands and their relationship to the Fermi level. The simple theory is later modified by the barrier-lowering effect and the presence of surface states. The reverse bias depletion capacitance and, subsequently, the forward current characteristics are determined. Equivalent circuit models are discussed that are useful for circuit design. Finally, some comments are made about recent progress in wide bandgap Schottky barrier diodes. The applications sections emphasize mixer design, as this seems to be the predominant use of Schottky devices.

2. ENERGY LEVELS IN A METAL AND SEMICONDUCTOR

Conceptually, two materials, one a metal and the other a semiconductor, can be initially far removed from one another and then brought together into intimate contact. The electrons in both materials obey the Pauli exclusion principle, and hence their energy levels can be described in terms of the Fermi-Dirac distribution function. For both the metal and the semiconductor, these distributions functions are:

$$f_{Dm}(\mathcal{E}) = \frac{1}{1 + \exp[(\mathcal{E} - \mathcal{E}_{Fm})/kT]} \quad (1)$$

$$f_{Ds}(\mathcal{E}) = \frac{1}{1 + \exp[(\mathcal{E} - \mathcal{E}_{Fs})/kT]} \quad (2)$$

Thus the probability that an electron is located either above or below the Fermi level, \mathcal{E}_F , is $1/2$ when $\mathcal{E} = \mathcal{E}_F$.

The total allowed energy states is $g(\mathcal{E})$, the total number of filled states is $n(\mathcal{E})$, and the total number of empty states is $v(\mathcal{E})$. For both the metal and the semiconductor, the number of filled states is the product of the total number of available states and the probability that it is full, whereas the total number of vacant states is what is left

9. R. B. Dybdal, Multiple beam communication satellite antenna systems, *IEEE ICC Conf. Digest*, 27D-1-5, Minneapolis, MN, June 17-19, 1974.
10. A. W. Love, *Reflector Antennas*, IEEE Press, New York, 1978.
11. C. M. Rappaport, An offset bifocal reflector antenna design for wide angle beam scanning, *IEEE Trans. Anten. Propag.* **AP-32**:1196-1204 (1984).
12. R. Jorgensen, P. Balling, and W. J. English, Dual offset reflector multibeam antenna for international communications satellite applications, *IEEE Trans. Anten. Propag.* **AP-33**:1304-1312 (1985).
13. C. M. Rappaport and A. I. Zagloul, Optimized three dimensional lenses for wide angle scanning, *IEEE Trans. Anten. Propag.* **AP-33**:1227-1236 (1985).
14. R. J. Mailloux, *Phased Array Antenna Handbook*, Artech House, Norwood, MA, 1994.
15. K. S. Rao et al., Development of a 45-GHz multiple beam antenna for military satellite communications, *IEEE Trans. Anten. Propag.* **AP-43**:1036-1047 (1995).
16. P. Ingerson and C. A. Chen, The use of non-focusing aperture for multibeam antennas, *1983 IEEE AP-S Symp. Digest*, 1983, pp. 330-333.
17. F. Carducci and M. Francesi, The ITALSAT satellite system, *Int. J. Satellite Commun.* **13**:49-81 (1995).
18. R. Miura et al., Beamforming experiment with a DBF multibeam antenna in a mobile satellite environment, *IEEE Trans. Anten. Propag.* **AP-45**:707-713 (1997).
19. T. Gebauer and H. G. Gockler, Channel individual adaptive beamforming for mobile satellite communications, *IEEE J. Select. Areas Commun.* **SAC-11**:439-448 (1995).
20. Special issue on SIR-C/X-SAR, *IEEE Trans. Geosci. Remote Sens.* **33** (1995).
21. K. Tomiyasu, Remote sensing of the earth by microwaves, *Proc. IEEE* **62**:86-92 (1974).
22. CCIR Recommendation 465-3.
23. P. W. Howells, *Intermediate Frequency Sidelobe Canceller*, U.S. Patent 3,202,990 (Aug. 24, 1965).
24. K. M. SooHoo and W. Masenten, Adaptive sidelobe canceller designs for large earth terminals, *1984 IEEE MILCOM Symp. Digest*, paper 40.5 (classified).
25. E. K. Smith, Centimeter and millimeter wave attenuation and brightness temperature due to atmospheric oxygen and water vapor, *Radio Sci.* **17**:1455-1464 (1982).
26. R. C. Rudduck and K. Lambert, Calculation and verification of antenna temperature for earth-based reflector antennas, *Radio Sci.* **27**:23-30 (1992).
27. J. DiTullio, A high performance feed for earth station satellite communications, *19th Annu. USAF Antenna R&D Symp. Digest*, Robert Allerton Park, IL, Oct. 15-17, 1968.
28. Y. H. Chong, K. R. Goudey, and L. O. Bryans, Theory and design of a Ku-band TE₂₁ mode coupler, *IEEE Trans. Microwave Theory Tech.* **MTT-30**:1862-1866 (1982).
29. R. B. Dybdal, Measurement of satellite ground terminals, *1991 AMTA Symp. Digest*, Boulder, CO, Oct. 7-11, 1991, pp. 6-9, 13.
30. J. W. M. Baars, Measurement of large antennas with cosmic radio sources, *IEEE Trans. Anten. Propag.* **AP-21**:461-473 (1973).
31. D. F. Wait, Precision measurement of antenna system noise using radio stars, *IEEE Trans. Instrum. Meas.* **IM-32**:110-116 (1983).

over.

$$n(\mathcal{E}) = g(\mathcal{E}) \cdot f_D(\mathcal{E}) \tag{3}$$

$$v(\mathcal{E}) = g(\mathcal{E}) \cdot [1 - f_D(\mathcal{E})] \tag{4}$$

Thus, at $\mathcal{E} = \mathcal{E}_F$, the energy state has equal probability of being full or empty. In a metal, the Fermi level lies within the conduction band, whereas for a typical semiconductor, the Fermi level lies inside the forbidden energy gap. Figure 1 shows the energy levels for a metal and a semiconductor when the two are separated far enough apart so that their energy levels do not interact with one another. Shown are diagrams for both n- and p-type semiconductors. Another energy level located above the conduction band may be identified as the vacuum or free electron energy level, \mathcal{E}_0 , which is the minimum energy required to remove an electron from the surface of the metal or semiconductor. The difference between this and the Fermi level is called the *work function*, ϕ .

$$q\phi = \mathcal{E}_0 - \mathcal{E}_F \tag{5}$$

In a semiconductor, this is a function of the doping density, because \mathcal{E}_F varies with doping density. For an n-type semiconductor, \mathcal{E}_F is closer to the conduction band, and for a p-type semiconductor, \mathcal{E}_F is closer to the valence band. However, the *electron affinity*, χ , is the difference between the vacuum energy, \mathcal{E}_0 and the conduction band energy, \mathcal{E}_C , which does not vary with doping concentration.

$$q\chi = \mathcal{E}_0 - \mathcal{E}_C \tag{6}$$

These parameters are useful in giving an explanation of the behavior of a metal semiconductor junction described in Section 3.

3. FUNDAMENTALS OF THE IDEAL METAL-SEMICONDUCTOR JUNCTION

Assume that the metal and semiconductor materials are brought into contact so that electrons can flow between them [1]. The flow of charge from the metal to the semiconductor is proportional to the number of filled states in the metal, $n_m(\mathcal{E})$, and is also proportional to the number of empty states in the semiconductor, $v_s(\mathcal{E})$. On the other hand, the amount of charge flowing from the semiconductor to the metal is proportional to the number of filled

states in the semiconductor, $n_s(\mathcal{E})$, and the number of empty states in the metal ready to receive the charge, $v_m(\mathcal{E})$. At equilibrium, the charge flow between the semiconductor and metal is equal in both directions.

$$n_m(\mathcal{E})v_s(\mathcal{E}) = n_s(\mathcal{E})v_m(\mathcal{E}) \tag{7}$$

When this equation is written in terms of the Fermi–Dirac distribution functions, it is found that the Fermi energies of both materials are equal to one another. Substituting Eqs. (3) and (4) into Eq. (7) demonstrates this statement.

$$g_m f_{Dm} \cdot g_s (1 - f_{Ds}) = g_s f_{Ds} \cdot g_m (1 - f_{Dm}) \tag{8}$$

$$g_m f_{Dm} g_s = g_s g_m f_{Ds} \tag{9}$$

which is true if

$$\mathcal{E}_{Fm} = \mathcal{E}_{Fs} \tag{10}$$

The Fermi levels of the two materials line up at their junction.

Three principles can be used to draw the energy level diagram for the metal semiconductor junction: (1) the equality of the Fermi levels on both sides of the junction, (2) the constancy of the electron affinity in all regions of the materials, and (3) the continuity of the free electron energy levels. In regard to the last principle, a discontinuity of \mathcal{E}_0 would be a violation of energy conservation. Figure 2 shows how the energy bands bend in the transition from metal to semiconductor. In the choice of materials illustrated in Fig. 2, the work function in the metal is larger than that for the semiconductor.

$$q\phi_m > q\phi_s \tag{11}$$

$$\mathcal{E}_{Fs} > \mathcal{E}_{Fm} \tag{12}$$

The abrupt shift of the energy bands in the semiconductor near the junction is the barrier potential. For an n-type semiconductor, this is given by

$$q\phi_{Bn} = q(\phi_m - \chi) \tag{13}$$

When $\phi_m > \phi_s$, as assumed in Fig. 2(a), the average energy of the electrons is greater in the semiconductor than in the metal. Electrons will flow from the semiconductor into the metal. The higher values of \mathcal{E}_C and \mathcal{E}_V near the junction

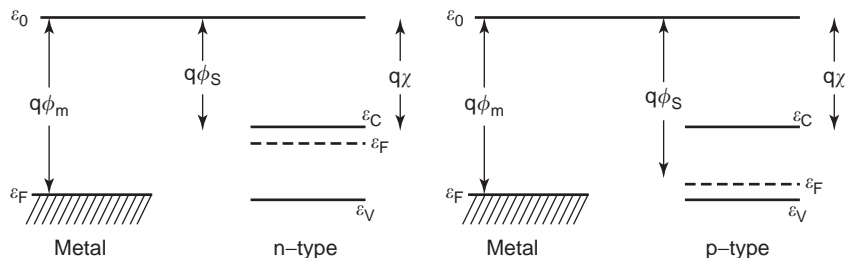


Figure 1. The energy bands of a metal and semiconductor when separated: (a) n-type semiconductor, and (b) p-type semiconductor.

(a)

(b)

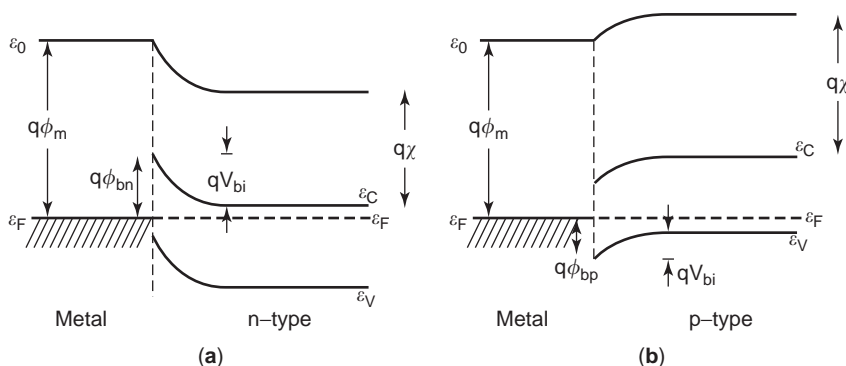


Figure 2. The energy bands of a metal and semiconductor when brought into contact with one another: (a) n-type semiconductor, and (b) p-type semiconductor.

are a result of the charge transfer to the metal. An electric field is formed that increases the net energy of the electrons in this vicinity. The electrons left behind in the semiconductor have a higher average energy, and thus the distance between the conduction band and the Fermi level increases (Fig. 2(a)). The barrier height between a metal and p-type semiconductor is illustrated in Fig 2(b). If the energy gap between the conduction band and valence band is \mathcal{E}_G , then the barrier height is

$$q\phi_{Bp} = \mathcal{E}_G - q(\phi_m - \chi) \quad (14)$$

The electric field, the potential, and finally the capacitance resulting from this charge motion can now be described. The approximation is made that all mobile charges are removed from the region of the semiconductor near the junction up to a distance, x_d , the depletion, or space charge region. What is left is the bound charge associated with the ionized atoms. The maximum electric field at the metal-semiconductor interface is found from $\nabla \cdot \mathbf{D} = \rho$.

$$E_m = \frac{-qN_D x_d}{\epsilon_s} \quad (15)$$

In this equation, ϵ_s is the semiconductor permittivity, q is the electron charge, and N_D is the donor concentration for the n-type semiconductor. The built-in potential, V_{bi} , is the voltage across the depletion region. It is the amount the conduction band goes up inside the n-type semiconductor from the semiconductor bulk to the junction. In the p-type semiconductor, it is the amount the conduction band shifts downward between the semiconductor bulk and the junction. The built-in potential is the integral of the electric field between the junction and the edge of the depletion region, x_d , in the semiconductor bulk.

$$V_{bi} = - \int_0^{x_d} E dx = \frac{1}{2} \frac{qN_D x_d^2}{\epsilon_s} \quad (16)$$

The immobile space charge in this region with cross-sectional area, A , is

$$\begin{aligned} Q_s &= AN_D q x_d \\ &= A \sqrt{2q\epsilon_s N_D V_{bi}} \end{aligned} \quad (17)$$

or when an applied external voltage, V_a , is applied,

$$Q_s = A \sqrt{2q\epsilon_s N_D (V_{bi} - V_a)} \quad (18)$$

The stored charge results in a depletion junction capacitance.

$$C = - \frac{\partial Q_s}{\partial V_a} \quad (19)$$

$$= A \sqrt{\frac{q\epsilon_s N_D}{2(V_{bi} - V_a)}} \quad (20)$$

$$= \frac{C_0}{(1 - V_a/V_{bi})^{3/2}} \quad (21)$$

This equation is similar in form to that of an abrupt junction pn diode where $\gamma = 1/2$. Sign confusion is reduced if Eq. (21) is written the way it is shown above with a negative sign. If the diode is reverse biased at, for example, $V_a = -5$ V, then the denominator of Eq. (21) is $(1 + 5/V_{bi})^{3/2}$.

4. BARRIER LOWERING

The analysis in Section 3 assumed that the barrier potential, ϕ_B , is independent of an applied voltage. However, there is some reduction in ϕ_B that is proportional to fourth root of the applied voltage, which is known as the Schottky effect. When a negative charge is placed a certain distance, x , from a conducting plane, it will induce a positive charge on that plane and be attracted to it. The forces on the charge would be unchanged if the conducting plane were replaced with a positive charge of the same magnitude but a distance x on the opposite side of the plane. The force on the actual charge in the semiconductor with a dielectric constant, ϵ_s , can easily be found from Coulomb's law.

$$F(x) = \frac{-q^2}{4\pi\epsilon_s (2x)^2} \quad (22)$$

The energy required to bring the charge to a distance x away from the metal is found by integrating

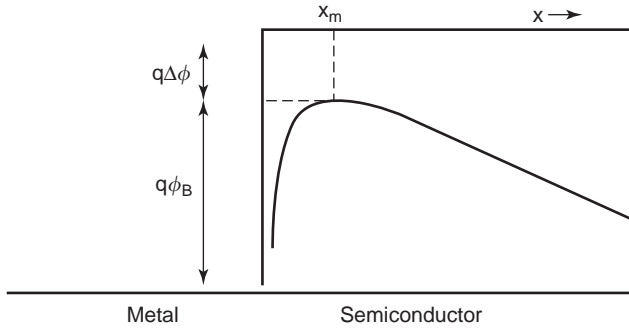


Figure 3. The barrier lowering effect caused by the image force on electrons in the semiconductor but close to the metal.

from $x = \infty$ to x .

$$\mathcal{E} = \int_{\infty}^x F(x) dx = \frac{q^2}{16\pi\epsilon_s x} \quad (23)$$

which represents the energy of the charge associated with its image force. In the presence of an electric field, E , the total potential energy is measured downward relative to the x -axis in Fig. 3 where the reference energy is $q\phi_B(V_a = 0)$ above the Fermi level.

$$PE(x) = \frac{q}{16\pi\epsilon_s x} + qEx \quad (24)$$

The position, x_m , where the maximum potential occurs, results from setting the derivative of Eq. (24) to zero.

$$x_m = \sqrt{\frac{q}{16\pi\epsilon_s E}} \quad (25)$$

The potential energy at this position is the amount the potential barrier is reduced as a result of an applied electric field.

$$PE(x_m) = q\Delta\phi = q\sqrt{\frac{qE}{4\pi\epsilon_s}} \quad (26)$$

when for example, in a metal-silicon interface, where $\epsilon_s = 11.7 \cdot \epsilon_0$, $E = 10^5$ V/cm, the values for $x_m = 17.54$ Å and $\Delta\phi = 3.51 \cdot 10^{-2}$ V.

The variation of the current from the metal into the semiconductor changes with the field-dependent value of $\Delta\phi$. The current, at room temperature, will obey the Maxwell-Boltzmann distribution.

$$J = J_0 \exp\left(\frac{\sqrt{q^3 E / 4\pi\epsilon_s}}{kT}\right) \quad (27)$$

If x_d is eliminated between Eq. (15) and Eq. (16) and the built-in voltage, V_{bi} , is modified by the applied voltage, $V_{bi} - V_a$, then the field is seen to be proportional to the

square root of the applied voltage.

$$E = \sqrt{\frac{2qN_D(V_{bi} - V_a)}{\epsilon_s}} \quad (28)$$

Consequently, the current under reverse bias depends only on the fourth root of the applied voltage.

5. SURFACE STATES

The barrier height, as seen from Eq. (13), is determined by the metal work function. In addition, surface states that develop from imperfections and discontinuities at the junction can play an important role. The interfacial states cause a surface charge layer that is so thin that it does not impede the flow of electrons, but they can modify the voltage drop across the junction. The analysis of the effect of the surface states was carried out by Crowley and Sze [3]. The energy level at the surface of the semiconductor is designated as $q\phi_0$. Before joining the semiconductor with the metal, it would be

$$q\phi_0 = \mathcal{E}_F - \mathcal{E}_V \quad (29)$$

which specifies that all states below $q\phi_0$ must be filled. As a result of the presence of surface states when the metal and semiconductor are joined (Fig. 2), $q\phi_0$ reaches from \mathcal{E}_V to somewhere below the Fermi level. If the density of surface states is D_s states/cm²/eV, then the barrier potential can be found for two extreme states [3]. When $D_s \rightarrow \infty$, the barrier height for an n-type semiconductor is

$$q\phi_{Bn} = (\mathcal{E}_G - q\phi_0) - q\Delta\phi \quad (30)$$

and when $D_s \rightarrow 0$

$$q\phi_{Bn} = q(\phi_m - \chi) - q\Delta\phi \quad (31)$$

When there is a large number of surface states, the barrier potential is independent of the metal work function. A least squares fit for a variety of semiconductor-metal systems has been developed. A summary of these relations is given in Table 1. The large scatter in data for CdS makes the expression for this material less certain.

Table 1. Empirical Expressions for the Barrier Height [3]

Semiconductor	ϕ_{Bn} (eV)	Slope Error	Intercept Error (eV)
Si	$0.27\phi_m - 0.55$	± 0.05	± 0.22
GaP	$0.27\phi_m - 0.01$	± 0.05	± 0.13
GaAs	$0.074\phi_m + 0.49$	± 0.05	± 0.24
CdS	$0.38\phi_m - 1.20$	± 0.16	± 0.77

6. FORWARD BIAS CURRENT-VOLTAGE CHARACTERISTICS

Two basic mechanisms exist for the flow of current when the Schottky barrier is forward biased: thermionic emission and diffusion [2]. In both cases, the result is in the form of the Shockley diode equation where the externally applied voltage is V_a .

$$J = J_s(e^{qV_a/kT} - 1) \quad (32)$$

Of the two theories, thermionic emission is seen to prevail at room temperatures for Ge, Si, and GaAs with electric fields in the 10^4 to 10^5 V/cm range. The thermionic emission theory shows that J_s is especially dependent on the temperature, and the diffusion theory shows that J_s is more strongly dependent on the applied voltage.

6.1. Thermionic Emission

The thermionic emission theory, which was first developed by Bethe [4] and reviewed by Sze [2], was based on the assumptions that (1) $q\phi_{Bn} \gg kT$, (2) thermal equilibrium exists at the junction, and (3) superposition of forward and reverse currents is accurate.

First, the current from the semiconductor to the metal, $J_{s \rightarrow m}$, is found, which is the current that develops from the electrons that have sufficient energy to overcome the barrier potential.

$$J_{s \rightarrow m} = \int_{\mathcal{E}_F + q\phi_{Bn}}^{\infty} qv_x dn \quad (33)$$

The carrier velocity in the semiconductor is v_x , and the number density of electrons is n . The incremental number of electrons is the number of available states for the electrons and the probability of them being filled [5].

$$dn = N(\mathcal{E})f_D(\mathcal{E})d\mathcal{E} \quad (34)$$

$$= \frac{8\pi p^2 dp}{h^3} f_D(\mathcal{E}) \quad (35)$$

$$= 4\pi \left(\frac{2m_n^*}{h^2} \right)^{3/2} (\mathcal{E} - \mathcal{E}_C)^{1/2} f_D(\mathcal{E}) d\mathcal{E} \quad (36)$$

The incremental momentum from p to $p + dp$ is found by determining the change in the spherical volume in momentum space and recognition that the crystal momentum is $p_x = h/\lambda$. An extra factor of 2 is included to account for electron spin. The kinetic energy expressed in terms of momentum, p , is expressed in terms of energy in Eq. (36). When $\mathcal{E} > 3kT$ above or below the Fermi level, the Fermi-Dirac distribution can be approximated by the Maxwell-Boltzmann distribution. Under this condition, the incremental change in the electron density is

$$dn = 4\pi \left(\frac{2m_n^*}{h^2} \right)^{3/2} (\mathcal{E} - \mathcal{E}_C)^{1/2} \exp[-(\mathcal{E} - \mathcal{E}_F)/kT] d\mathcal{E} \quad (37)$$

If all the electron energy above the conduction band is kinetic energy, so that

$$\mathcal{E} - \mathcal{E}_C = \frac{m_n^* v^2}{2} \quad (38)$$

$$d\mathcal{E} = m_n^* v dv \quad (39)$$

then

$$dn = 2 \left(\frac{m_n^*}{h} \right)^3 e^{(\mathcal{E} - \mathcal{E}_F)/kT} \cdot e^{m_n^* v^2 / 2kT} \quad (40)$$

The velocity is decomposed into its three Cartesian coordinates.

$$v^2 = v_x^2 + v_y^2 + v_z^2 \quad (41)$$

$$dv_x dv_y dv_z = v^2 \sin \theta dv d\theta d\phi = 4\pi v^2 dv \quad (42)$$

which is used to integrate Eq. (33). It should be noted that the integrals in the v_y and v_z directions are of the form $\int_{-\infty}^{\infty} r e^{-ar^2} dr = \sqrt{\pi/a}$. The lower limit on the integral in the x -directed velocity is v_{ox} , which is the minimum electron velocity needed to overcome the barrier. As a result, the current going from the semiconductor to the metal is given below.

$$J_{s \rightarrow m} = 2q \left(\frac{m_n^*}{h} \right)^3 e^{(\mathcal{E}_C - \mathcal{E}_F)/kT} \cdot \frac{1}{2} \left(\frac{2kT}{m_n^*} \right) e^{-m_n^* v_{ox}^2 / 2kT} \sqrt{\frac{\pi 2kT}{m_n^*}} \cdot \sqrt{\frac{\pi 2kT}{m_n^*}} \quad (43)$$

The minimum energy

$$\frac{m_n^* v_{ox}^2}{2} = qV_{bi} - V_a \quad (44)$$

and the barrier height

$$q\phi_{Bn} = qV_{bi} + (\mathcal{E}_C - \mathcal{E}_F) \quad (45)$$

are substituted into Eq. (43). The thermionic current density is thus given in terms of the Richardson constant, A^* ,

$$J_{s \rightarrow m} = A^* T^2 e^{q\phi_{Bn}/kT} \cdot e^{-qV_a/\eta kT} \quad (46)$$

where

$$A^* = \frac{4\pi q m_n^* k^2}{h^3} \quad (47)$$

The only parameter in A^* that will vary from one material to another is the effective electron mass, m_n^* . Values for these can be found in [6]. The ideality factor, η , in a pn junction is 1 when diffusion current dominates and is 2 when recombination current dominates. For many Schottky barrier devices, $\eta \approx 1.08$ for either Si or GaAs.

When the applied voltage $V_a = 0$, thermal equilibrium occurs and

$$J_{m \rightarrow s} = J_{s \rightarrow m} = -A^* T^2 e^{-q\phi_{Bn}/kT} \quad (48)$$

As this does not change with applied voltage, the total current with an applied voltage is the total electron current.

$$\begin{aligned} J_n &= J_{s \rightarrow m} + J_{m \rightarrow s} \\ &= \left(A^* T^2 e^{-q\phi_{Bn}/kT} \right) \cdot \left(e^{qV_a/\eta kT} - 1 \right) \end{aligned} \quad (49)$$

6.2. Diffusion Theory

The diffusion theory is based on balancing the diffusion current with the conduction current in the diode [1].

$$\begin{aligned} J_n &= \frac{q^2 D_n N_c}{kT} \left[\frac{2q(V_{bi} - V_a) N_D}{\epsilon_s} \right]^{1/2} \\ &\quad \times e^{-q\phi_{Bn}/kT} \cdot \left(e^{qV_a/\eta kT} - 1 \right) \end{aligned} \quad (50)$$

The diffusion theory predicts that the saturation current varies with the $\sqrt{V_a}$ and is inversely proportional to temperature, which is in contrast with the thermionic theory where the saturation current is proportional to T^2 . Both theories have been incorporated into one to highlight the predominance of the thermionic mechanism at room temperature [2]. The effective thermal velocity and the diffusion velocity are respectively

$$\begin{aligned} v_R &= \frac{A^* T^2}{q N_C} \\ \frac{1}{v_D} &= \int_{x_m}^W \frac{q}{\mu kT} \exp \left[-\frac{q\psi(x)}{kT} \right] dx \end{aligned} \quad (51)$$

where ψ is the electron potential energy difference between the top of the barrier and the bottom of the conduction band in the semiconductor as a function of position, x , x_m is the point where the electron potential energy is maximum, and μ is the mobility. Neglecting optical phonon scattering and quantum-mechanical reflection of electrons, the revised ‘‘Richardson constant’’ is designated as A^{**} .

$$A^{**} = \frac{A^*}{1 + v_R/v_D} \quad (52)$$

7. SCHOTTKY BARRIER DEVICE CIRCUIT MODEL

The simplest model for a Schottky barrier diode is a voltage variable resistance. In addition, the depletion capacitance exists when the diode is in reverse or slightly

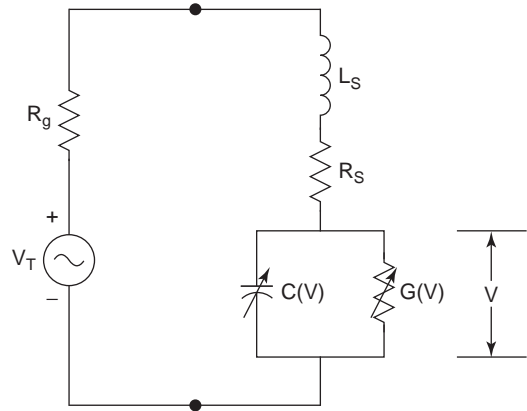


Figure 4. The Schottky diode circuit model with additional inductance necessary to fit data [7].

forward bias. The analysis in [7] shows the importance of the parasitic inductance in predicting the waveshape for the junction voltage, v (Fig. 4). One practical consequence is the discovery that burnout is associated with an over voltage rather than too much power, and this is only obvious after including the parasitic inductance in the calculations. As a reference point, the device parameters used in [7] at 9 GHz are $R_s = 8.5 \Omega$, $C_o = 0.08 \text{ nF}$, $L_s = 1.7 \text{ nH}$, $n = 1.1$, $I_s = 10^{-13} A^{**}$, $V_{bi} = 0.9 \text{ V}$, and $R_g = 50 \Omega$.

Applications for Schottky barrier diodes at millimeter and sub-millimeter frequencies have required that the diode model take into consideration skin effect, carrier inertia, and displacement current [8]. If the device radius is b and the contact radius is a , then clearly $a < b$. When $a \ll b$, the total diode impedance is the sum of the spreading and skin effects.

$$Z = Z_{sp} + Z_{skin} \quad (53)$$

$$Z_{sp} = \frac{1}{4\sigma a} \left[\frac{1}{1 + j(\omega/\omega_s)} + j(\omega/\omega_d) \right]^{-1} \quad (54)$$

$$\begin{aligned} Z_{skin} &= \left[\frac{\ln(b/a)}{2\pi} \right] \sqrt{\frac{j\omega\mu_0}{\sigma}} \\ &\quad \times \left[\frac{1}{1 + j(\omega/\omega_s)} + j(\omega/\omega_d) \right]^{-1/2} \end{aligned} \quad (55)$$

The definition of the dielectric relaxation frequency and scattering frequency are defined as

$$\omega_d = \frac{\sigma}{\epsilon} \quad (56)$$

$$\omega_s = \frac{q}{m^* \mu} \quad (57)$$

In these expressions, σ is the semiconductor conductivity, q is the charge of an electron, m^* is the effective mass of the carrier in the semiconductor, and μ is the carrier mobility. The equivalent circuit for the impedance, Eq. (53), is shown in Fig. 5 where the inertial inductance is

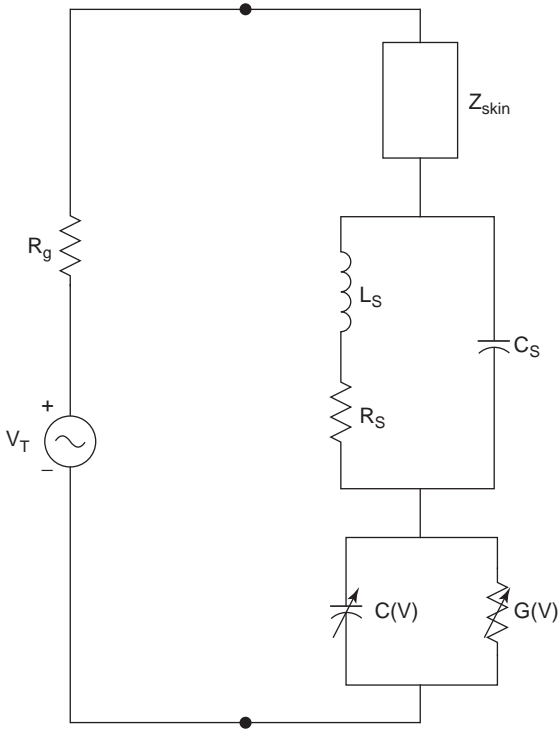


Figure 5. The Schottky diode circuit model incorporating spreading resistance, displacement capacitance, and inertial inductance [8].

$L_s = R_s / \omega_s$, the DC spreading resistance is R_s , and the displacement capacitance is $C_s = 1/R_s \omega_d$. The classic definition for the cutoff frequency is

$$\omega_c = \frac{1}{R_s C(v)} \Big|_{v=0} \quad (58)$$

but should now be found from the expression.

$$0 = \Re\{Z_{skin}\} + \Re\{Z_{sp}(\omega_c)\} - \frac{1}{\omega_c C(v=0)} \quad (59)$$

The cutoff frequency for an n-type GaAs Schottky barrier diode is as much as six times lower than what is predicted by Eq. (58), whereas for n-type Si, the results from Eq. (58) and Eq. (59) are quite close [8]. In any case, the theory shows that the smaller the contact radius, a , the higher the cutoff frequency.

The topology assumed by both [8,9] is a circular contact. An attempt was made in [10] to determine if alternative contact geometries might produce higher cutoff frequency devices. The finite element analysis of various geometries showed that for a given constant contact area, the skin effect resistance, R_{skin} , is minimized for a rectangular shape.

The analytical understanding of mixer and multiplier design will require simplification of the model described above. If the Schottky diode can be expressed as a nonlinear conductance based on Eq. (32), where J_s is

independent of voltage, then the conductance is

$$G(V_a) = \frac{dJA}{dV_a} = \frac{J_s}{V_T} A e^{V_a/V_T} \approx \frac{J(V_a)A}{V_T} \quad (60)$$

For a sinusoidal excitation given by

$$V_a = V_{dc} + V_1 \cos \omega t \quad (61)$$

the conductance can be expressed in terms of the modified Bessel functions.

$$G(t) = \frac{J_s A}{V_T} e^{V_{dc}/V_T} \left[I_0(V_1/V_T) + \sum_{n=1}^{\infty} I_n(V_1/V_T) \cos n\omega t \right] \quad (62)$$

In this expression, $V_T = kT/q$. The assumed sinusoidal excitation is a simplification of the analysis given in [7].

8. RECENT SiC SCHOTTKY BARRIER DESIGNS

The crystal structure of silicon carbide can take on a wide variety of stacking sequences with the same chemical composition. The stack can be viewed as alternating hexagonal planes of carbon and silicon atoms. Every silicon atom is bonded to four nearest neighbor carbon atoms, and each carbon atom is bonded to four nearest neighbor silicon atoms. The number of layers of SiC couples in the repeating sequence is designated by an integer. The most important values for a periodic stacking sequence in SiC are 3, 4, or 6. In addition, the crystal shapes of the material is designated as C for cubic, H for hexagonal, and R for rhombohedral. The published values for the number of polytypes have ranged from 170 to 250. Technologically, the most important polytypes of silicon carbide are designated as 3C-SiC, 4H-SiC, or 6H-SiC. Approximate values for some important properties of these materials are compared with those of Si in Table 2.

The wide bandgap of SiC (≈ 3 eV) compared with that of Si (≈ 1.1 eV) and GaAs (≈ 1.43 eV) makes this material ideal for high-power, high-temperature, and radiation-resistant applications. Silicon carbide also has high thermal conductivity and high saturated electron velocities. The most obvious difference between Si and SiC is the value for the intrinsic carrier concentration. The lower value for n_i in SiC makes the thermally generated leakage currents orders of magnitude smaller than that found for Si, thereby allowing much higher operating temperatures [12].

The choice of the metal used in the diode determines the tradeoff between low forward voltage drop and low reverse saturation current. A low barrier Schottky diode gives small forward voltage but a large reverse current. A high barrier Schottky gives a large forward voltage drop but a low reverse current. For mixer applications, a low forward voltage drop improves conversion loss.

Table 2. Physical Properties of SiC [1,11]

Parameter	Symbol	Units	Silicon	3C-SiC	4H-SiC	6H-SiC
Bandgap Energy	\mathcal{E}_G	eV	1.12	2.37	3.25	3.0
Intrinsic carrier concn.(300 K)	n_i	cm^{-3}	$1.45 \cdot 10^{10}$	–	$2 \cdot 10^{-8}$	$2 \cdot 10^{-6}$
Breakdown Field	E_C	V/cm	$3 \cdot 10^5$	$1.8 \cdot 10^6$	$1.5 - 4 \cdot 10^6$	$1.5 - 4 \cdot 10^6$
Electron mobility	μ_n	cm^2/Vs	1350	900	–	–
to c-axis			–	–	1050	100
⊥ to c-axis			–	–	800	375
Saturation velocity	v_s	cm/s	$1 \cdot 10^7$	$2 \cdot 10^7$	$2.2 \cdot 10^7$	$1.9 \cdot 10^7$
Thermal conductivity	κ	W/(cm K)	1.412	3.3	3.3	3.3

Nitrogen has been used for n-type doping in both the 4H- and 6H- materials with concentrations as high as $5 \cdot 10^{18} \text{ cm}^{-3}$. Both aluminum and boron have been used as p-type dopants for SiC, but Al gives the lowest resistivity and can have carrier concentrations as high as 10^{21} cm^{-3} . The design of a Schottky device not only involves determining the barrier potential at the Schottky junction, but also the design of the Ohmic contact on the other side of the semiconductor. The Ohmic contact for 6C-SiC is more difficult to form than for 3C-SiC. Both the barrier height and the Ohmic contact are heavily influenced by the polytype [11, p. 212].

A small-signal and large-signal model for a SiC microwave Schottky barrier diode was given in [13] using the basic topology given in Fig. 4, where L_s was not used. The saturation current was found from Eq. (49) where the Richardson constant was found to be $A^* = 151 \text{ A} \cdot \text{cm}^{-2} \text{ K}^{-2}$. Careful accounting of mobility, junction reverse capacitance, forward current density, reverse biased tunneling current, and barrier-lowering effect caused by the image force, resulted in a diode model that predicted both forward and reverse current with reasonable accuracy. The cutoff frequency available from SiC, however, still falls short of what can be achieved with GaAs Schottky barrier diodes [13].

Examination of the properties of SiC can be illustrated by the requirements for a mixer design. The desired mixer properties include achieving good linearity, high dynamic range, low conversion loss, low noise (especially $1/f$ noise), and low local oscillator power requirements. A measure of the linearity is the third-order intercept point, IP_3 , which is defined as the point on the IF output power vs. RF input power curves where the desired IF power and the third-order product intersect. Basically, the larger the IP_3 , the better. Schottky barrier diodes made with SiC offer some unique characteristics in regard to these parameters. Both the linearity and the conversion loss of the mixer may be enhanced by increasing the LO power. By sacrificing the low local oscillator power, conversion loss can vary from 26 dB to 5.2 dB as the local oscillator power changes from 0 dBm to 30 dBm [13]. At the same time, the IP_3 varied from 13 dBm to 31 dBm as the local oscillator power varied from 10 to 30 dBm. Similar results were obtained independently for local oscillator power levels up to 19 dBm

[14]. The improved conversion loss of the mixer is qualitatively the same as found by Torrey and Whitmer [9, p. 157]. The increase in linearity and the decrease in conversion loss comes at the cost of larger local oscillator power requirements. In absolute terms, wide bandgap Schottky barrier single ended mixer can achieve similar values for intermodulation distortion than a more complex resistance loaded, multiple device per branch double balanced Si mixer [14].

Low frequency $1/f$ noise properties of the Schottky barrier device become important in receiver designs. A variety of mechanisms have been suggested for the existence of this noise in Schottky barrier devices: Fluctuations in the number of charge carriers associated generation-recombination noise in the depletion region and trapping of carriers in a multistep tunneling process. However, for a Si Schottky barrier the spectral short circuit current is

$$S_I \propto \frac{I_F^\beta}{A^\gamma f^\delta} \quad (63)$$

where I_F is the forward current, A is the diode area, and f is the frequency. Typically, β and δ are near unity. However, the fluctuation in the number of charge carriers model would give $\beta \approx 2$. For this to correlate with Eq. (63), the low-frequency noise mechanism would have to be caused by fluctuations in the mobilities of the free carriers [15]. It was verified that the thermionic emission model for Richardson's equation was valid as given in Eqs. (46), (47). However, these equations do not contain mobility, so that $1/f$ noise is not present in ideal diodes. However, the modified Richardson's constant, A^{**} , is dependent on mobility, which does lead to the conclusion that mobility fluctuations results in current fluctuations [15]. A similar explanation for $1/f$ noise was found experimentally for 6H-SiC Ti Schottky diodes. For a wide bandgap material, the generation-recombination of carriers is much lower than in a Si device [16].

Other wide bandgap materials that have received considerable interest are AlN, InN, GaN, and AlGaIn, with the most attention for high-frequency devices centered on the latter two. The GaN material has an energy bandgap of 3.4 eV and a saturation velocity of $2 \cdot 10^7 \text{ cm/s}$, which is

similar to that found in SiC. All three materials, SiC, GaN, and AlGaIn, will probably play a much greater role in high-speed electronic devices in the near future.

9. MIXERS

Schottky diodes are the predominant diode type for microwave and millimeter wave mixers. Silicon diode ring and star connections of four diodes are readily available for use in double balanced mixers. GaAs offers improved conversion loss and noise performance over what is possible for silicon [17]. The saturation current is much higher in silicon than GaAs, and this leads to increased shot noise in silicon. The nonlinear conductance given in Eq. (60) is primarily responsible for the mixing properties of the Schottky barrier diode.

The conversion loss of a mixer along with its noise figure are the primary figures-of-merit for a mixer. The mixer is usually placed in the first or second stage of a receiver where it receives a low power signal. The theory on mixers was first developed based on the assumption of a sinusoidal voltage local oscillator waveform across the diode junction. As shown in [18], the waveform can be more accurately taken as a rectangular pulse. Nevertheless, the theory based on the sinusoidal waveform gives clearer analytical insight into mixer design and will be used here even though it may be less accurate.

9.1. Volt–Ampere Relationship for Mixing Frequencies

If the total voltage and current can be expressed as the sum of local oscillator values (v_p and i_p) and all the rest of the small signal components, then

$$v_t = v_p + v'_s \quad (64)$$

$$i_t = i_p + i'_s \quad (65)$$

The v'_s and i'_s are the sum of the RF input signal and all the rest of the sideband components. It is assumed from the outset that the RF input signal voltage is much less than the local oscillator pump voltage, so that the only frequencies generated are $m\omega_p \pm \omega_s$. The pumped conductance can be expressed in terms of a Fourier series.

$$G(v_p) = \sum_{m=-\infty}^{\infty} G_m e^{jm\omega_p t} \quad (66)$$

This equation multiplied by the small-signal sideband voltages,

$$v'_s = \sum_{m=-\infty}^{\infty} V_{np+s} e^{j(n\omega_p + \omega_s)t} + \sum_{n=-\infty}^{\infty} V_{np-s} e^{j(n\omega_p - \omega_s)t} \quad (67)$$

will give the current sidebands.

$$\begin{aligned} i'_s &= \sum_{m=-\infty}^{\infty} \sum_{n=-\infty}^{\infty} V_{np+s} e^{j(n\omega_p + \omega_s)t} G_m e^{jm\omega_p t} \\ &+ \sum_{m=-\infty}^{\infty} \sum_{n=-\infty}^{\infty} V_{np-s} e^{j(n\omega_p - \omega_s)t} G_m e^{jm\omega_p t} \end{aligned} \quad (68)$$

As each of the summations extend to $\pm\infty$, no change in the sum occurs if a finite shift in m exists. Hence, with m replaced by $m - n$, the sideband currents can be found.

$$\begin{aligned} i'_s &= \sum_{m=-\infty}^{\infty} \sum_{n=-\infty}^{\infty} V_{np+s} G_{m-n} e^{j(m\omega_p + \omega_s)t} \\ &+ \sum_{m=-\infty}^{\infty} \sum_{n=-\infty}^{\infty} V_{np-s} G_{m-n} e^{j(m\omega_p - \omega_s)t} \end{aligned} \quad (69)$$

The sideband current components can be expressed individually for a given m .

$$I_{mp+s} = \sum_{n=-\infty}^{\infty} V_{np+s} G_{m-n} \quad (70)$$

$$I_{mp-s} = \sum_{n=-\infty}^{\infty} V_{np-s} G_{m-n} \quad (71)$$

The goal now is to find an appropriate finite matrix that will describe the current–voltage characteristics of the device based on Eqs. (70) and (71). For example, if $m = 0$, the current at the signal frequency is seen to be the result of voltages at a variety of sideband frequencies.

$$\begin{aligned} I_s &= \cdots + V_{-3p+s} G_3 + V_{-2p+s} G_2 + V_{-p+s} G_1 + V_s G_0 \\ &+ V_{p+s} G_{-1} + V_{2p+s} G_{-2} + V_{3p+s} G_{-3} + \cdots \end{aligned} \quad (72)$$

$$\begin{aligned} I_{-s} &= \cdots + V_{-3p-s} G_3 + V_{-2p-s} G_2 + V_{-p-s} G_1 + V_{-s} G_0 \\ &+ V_{p-s} G_{-1} + V_{2p-s} G_{-2} + V_{3p-s} G_{-3} + \cdots \end{aligned} \quad (73)$$

If the voltages and current in Eqs. (70) and (71) are expressed in trigonometric form, then clearly the coefficients of the sine and cosine terms would be real, which implies that the coefficients of the exponential series on either side of zero are complex conjugates.

$$\begin{aligned} V_{-x} &= V_x^* \\ I_{-x} &= I_x^* \end{aligned} \quad (74)$$

Furthermore, the G_{m-n} coefficients are real. As a result, Eqs. (70) and (71) produce twice as many equations as necessary because one can be written as the complex conjugate of the other. Equations (70) and (71) can be expanded like Eqs. (72) and (73) for other values of m to give

a truncated matrix representation of the mixer.

$$\begin{bmatrix} I_s \\ I_{p-s}^* \\ I_{p+s} \\ I_{2p-s}^* \\ \vdots \end{bmatrix} = \begin{bmatrix} G_0 & G_1 & G_{-1} & G_2 & \dots \\ G_{-1} & G_0 & G_{-2} & G_1 & \dots \\ G_1 & G_2 & G_0 & G_3 & \dots \\ G_{-2} & G_{-1} & G_{-3} & G_0 & \dots \\ \vdots & \vdots & \vdots & \vdots & \ddots \end{bmatrix} \begin{bmatrix} V_s \\ V_{p-s}^* \\ V_{p+s} \\ V_{2p-s}^* \\ \vdots \end{bmatrix} \quad (75)$$

This matrix relates currents to voltages at different frequencies and thus differs from the usual conductance matrix.

A similar matrix can be found for the current-voltage relation resulting from the pumped capacitance.

$$\begin{bmatrix} I_s \\ I_{p-s}^* \\ I_{p+s} \\ I_{2p-s}^* \\ \vdots \end{bmatrix} = \begin{bmatrix} j\omega_s C_0 & j\omega_{p-s} C_1 & j\omega_{p+s} C_1 & j\omega_{2p-s} C_2 & \dots \\ j\omega_s C_{-1} & j\omega_{p-s} C_0 & j\omega_{p+s} C_{-2} & j\omega_{2p-s} C_1 & \dots \\ j\omega_s C_1 & j\omega_{p-s} C_2 & j\omega_{p+s} C_0 & j\omega_{2p-s} C_3 & \dots \\ j\omega_s C_{-2} & j\omega_{p-s} C_{-1} & j\omega_{p+s} C_{-3} & j\omega_{2p-s} C_0 & \dots \\ \vdots & \vdots & \vdots & \vdots & \ddots \end{bmatrix} \times \begin{bmatrix} V_s \\ V_{p-s}^* \\ V_{p+s} \\ V_{2p-s}^* \\ \vdots \end{bmatrix} \quad (76)$$

The classic theory for the mixer is based on Eq. (75) and, for parametric amplifiers and upconverters, on Eq. (76). When both the nonlinear conductance and nonlinear capacitance are significant, the two effects can be added together. Physically, the generated frequencies are

$n\omega_p \pm \omega_s$, but only those frequencies shown in Fig. 6 are used to arrive at Eq. (75).

9.2. Mixer Conversion Loss

The typical mixer (Fig. 7) will have an RF small signal coming from the receive antenna, a large amplitude local oscillator of frequency ω_p , and the difference frequency called the intermediate or IF frequency. The customary notation for these frequencies, and other higher order terms, is given by the relationship

$$\omega_n = \omega_0 + n\omega_p \quad (77)$$

Figure 6 shows these frequencies where the RF signal, $\omega_1 > \omega_p$. The IF frequency is then ω_0 . For synthesis purposes, Eq. (75) is truncated to include only ω_0, ω_1 , and the image frequency ω_{-1} . Based on these three frequencies, the conversion loss and the optimum input conductance can be determined [9]. The conversion loss has been defined by [9] as the ratio of the input and output available powers. The theory based on this definition has been well developed.

The available power from the signal generator and from the IF output of the mixer is given below.

$$P_G = \frac{I_G^2}{8G_G} \quad (78)$$

$$P_0 = \frac{I_0^2}{8G_{out}} \quad (79)$$

In order to make the conversion loss a positive number when expressed in dB, it is defined as the reciprocal of the available gain.

$$L_a = \frac{P_G}{P_0} \quad (80)$$

The different frequency terms can be expressed in the way used in Eq. (70) and Eq. (71), or they can be expressed in the more usual mixer notation of Eq. (77). Some simplifying assumptions can now be made to the conductance matrix representing the mixer diode. First, only the RF, IF, and image voltages are nonzero. These correspond to the currents (applying the notational shift) $I_{p+s} = I_1, I_s = I_0$, and $I_{p-s}^* = I_{-1}^*$, respectively. In the former notation, I_s was considered the low-frequency input, but in typical mixer application, the lowest frequency is the IF. In short, the "s" does not really stand for the RF signal frequency anymore.

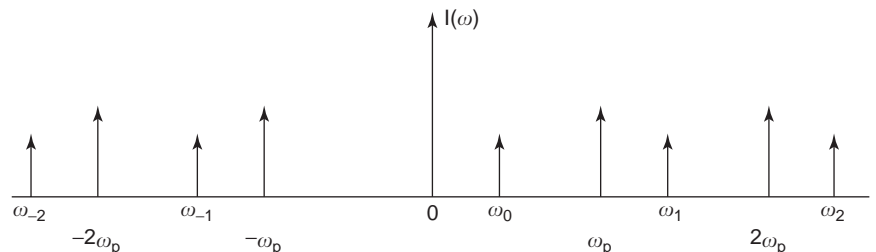


Figure 6. The spectrum of frequencies necessary to analyze the nonlinear conductance of a Schottky diode mixer.

The effect of the local oscillator voltage is to pump the diode, so this does not need to be further considered in the small signal analysis of the mixer other than through $G(v_p)$.

Equation (75) can be truncated still further to retain only the RF signal, IF output, and the image frequencies. Using the above revised notation, Eq. (75) is written as

$$\begin{bmatrix} I_1 \\ I_0 \\ I_{-1}^* \end{bmatrix} = \begin{bmatrix} G_0 & G_1 & G_2 \\ G_{-1} & G_0 & G_1 \\ G_{-2} & G_1 & G_0 \end{bmatrix} \begin{bmatrix} V_1 \\ V_0 \\ V_{-1}^* \end{bmatrix} \quad (81)$$

$$= \begin{bmatrix} y_{11} & y_{12} & y_{13} \\ y_{21} & y_{22} & y_{23} \\ y_{31} & y_{32} & y_{33} \end{bmatrix} \begin{bmatrix} V_1 \\ V_0 \\ V_{-1}^* \end{bmatrix} \quad (82)$$

Second, certain approximations can often be made in Eq. (81) or Eq. (82) that makes the analysis simpler. As the image and RF frequencies are typically close together, and the mixer is typically a broad-band circuit, it can be assumed that the external loads, $G_{image} = G_G$, and that conversion from the RF port to another port will be the same as the conversion from the image port to that same port (Fig. 7). Consequently,

$$y_{32} = y_{12}^* = G_{-1} = G_1 \quad (83)$$

$$y_{23} = y_{21}^* = G_1 = G_{-1} \quad (84)$$

$$y_{31} = y_{13}^* = G_{-2} = G_2 \quad (85)$$

$$g_{33} = y_{11}^* = G_0 = G_0 \quad (86)$$

so that for real matrix elements

$$\begin{bmatrix} I_1 \\ I_0 \\ I_{-1}^* \end{bmatrix} = \begin{bmatrix} g_{11} & g_{12} & g_{13} \\ g_{21} & g_{22} & g_{21} \\ g_{13} & g_{12} & g_{11} \end{bmatrix} \begin{bmatrix} V_1 \\ V_0 \\ V_{-1}^* \end{bmatrix} \quad (87)$$

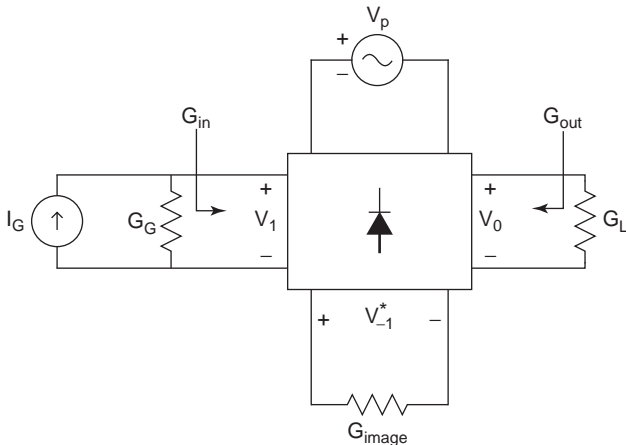


Figure 7. Mixer circuit that includes terminations at the RF input signal, the IF output signal, and the image frequency.

If I_1 is replaced by $-G_G V_1$, I_0 is replaced by $+G_{out} V_0$ and I_{-1}^* is replaced by $-G_G V_{-1}^*$, then Eq. (88) becomes singular and only can be solved when the determinate is 0, which results in an equation that can be solved for G_{out} , the IF output admittance.

$$\begin{aligned} G_{out} &= g_{22} + \frac{2g_{12}g_{21}[g_{13} - (g_{11} + G_G)]}{(g_{11} + G_G)^2 - g_{13}^2} \\ &= g_{22} - \frac{2g_{12}g_{21}}{g_{13} + g_{11} + G_G} \end{aligned} \quad (88)$$

If in the IF port, $G_L = \infty$, then the IF voltage $V_0 = 0$. The current entering the RF port is $I_G - G_G V_1$, and the current entering the image port (where $G_{image} = G_G$) is $-G_G V_{-1}^*$. Solution of Eq. (87) for this condition leads to an expression for I_G and I_0 in terms of the RF voltage V_1 .

$$I_G = (g_{11} + G_G)V_1 - \frac{g_{13}g_{31}}{g_{11} + G_G}V_1 \quad (89)$$

$$I_0 = \left(g_{21} - \frac{g_{21}g_{13}}{g_{11} + G_G} \right) V_1 \quad (90)$$

By eliminating V_1 between these two expressions, I_0 can be related to I_G .

$$I_0 = \frac{g_{21}I_G}{g_{11} + G_G + g_{13}} \quad (91)$$

The conversion loss can be found now from Eqs. (78)–(80).

$$\begin{aligned} L_a &= \frac{P_G}{P_0} \\ &= \frac{G_{out}(g_{11} + G_G + g_{13})^2}{G_G g_{21}^2} \end{aligned} \quad (92)$$

The value for G_{out} in Eq. (88) is substituted into Eq. (92) to give the conversion loss in terms of the mixer diode properties and G_G only.

$$L_a = \frac{g_{12}}{g_{21}} \frac{(g_{11} + g_{13} + G_G)[g_{22}(g_{11} + g_{13} + G_G) - 2g_{12}g_{21}]}{G_G g_{21} g_{12}} \quad (93)$$

At this point, Torrey and Whitmer [9] normalized conductances in Eq. (93) with respect to g_{11} . If

$$\begin{aligned} x &= \frac{G_G}{g_{11}} \\ a &= 1 + \frac{g_{13}}{g_{11}} \\ b &= \frac{2g_{12}g_{21}}{g_{11}g_{22}} \end{aligned}$$

then

$$L_a = \frac{2g_{21}g_{11}}{g_{12}} \cdot f(x) \quad (94)$$

where $f(x)$ is defined as

$$f(x) = \frac{(a+x)(a+x-b)}{bx} \quad (95)$$

The value of $x = x_o$ that minimizes $f(x)$ is found by taking a derivative.

$$x_o = \sqrt{a(a-b)} \quad (96)$$

Substituting this result back into Eq. (95) gives the value for $f(x)$ that minimizes the conversion loss.

$$L_{a-min} = \frac{2g_{21}}{g_{12}} \frac{1 + \sqrt{1 - b/a}}{1 - \sqrt{1 - b/a}} \quad (97)$$

where

$$\frac{b}{a} = \frac{2g_{12}g_{21}}{g_{22}(g_{11} + g_{13})} \quad (98)$$

The optimum conductance for the RF port is found from $x_o g_{11}$.

$$\begin{aligned} G_{G-opt} &= g_{11} a \sqrt{1 - b/a} \\ &= (g_{11} + g_{13}) \sqrt{1 - b/a} \end{aligned} \quad (99)$$

and the optimum conductance for the IF port is found from Eq. (88).

$$G_{out-opt} = g_{22} \sqrt{1 - b/a} \quad (100)$$

Equations (97)–(100) can now be written in terms of the pumped conductance parameters Eqs. (83)–(86).

$$\frac{b}{a} = \frac{2G_1^2}{G_0(G_0 + G_2)} \quad (101)$$

$$L_{a-min} = 2 \frac{1 + \sqrt{1 - b/a}}{1 - \sqrt{1 - b/a}} \quad (102)$$

$$G_{G-opt} = (G_0 + G_2) \sqrt{1 - b/a} \quad (103)$$

$$G_{out-opt} = G_0 \sqrt{1 - b/a} \quad (104)$$

Values for G_0 , G_1 , G_2 , etc., are best obtained experimentally.

For a known mixer diode, Eqs. (103)–(105) and Eq. (102) give the design procedure and a predicted value for the minimum conversion loss. These are, as mentioned earlier, based on the assumption of a sinusoidal pump voltage at the diode terminals.

An alternative definition for conversion loss is the reciprocal of the transducer power gain, which is defined as the power available from the source to the IF power delivered to the load [17]. The 3×3 matrix Eq. (81) is converted to a 2×2 matrix, and the resulting matrix elements are used in the standard transducer power gain equation [18, p. 131].

Barber [19] determined the mixer conversion loss, noise figure, optimum G_G , and G_{out} as a function of the pulse duty ratio for three conditions: $G_{image} = G_G$, $G_{image} = \infty$, and $G_{image} = 0$. The pulse duty ratio is the ratio, t/T , where t is the time the local oscillator pulse is on and T is the total period of the local oscillator pulse generator, which is seen to be more accurate than an assumed sinusoidal voltage on the diode junction. It was found that the conversion loss was smallest when $t/T \rightarrow 0$. The minimum theoretical conversion loss (and noise figure) was shown to be 3 dB when $G_{image} = G_G$ and 0 dB when $G_{image} = \infty$ or 0.

9.3. Mixer Noise

The source of noise in a Schottky barrier diode can be considered to be from $1/f$ flicker noise at low frequencies, from shot noise at intermediate frequencies (which is essentially white noise), and noise associated with electron transit time effects at high frequencies. The transit time noise component was the subject emphasized in [20] for Si devices.

Achieving the lowest possible noise figure in a mixer requires cooling the devices to cryogenic temperatures. A double sideband (DSB) receiver noise temperature of 62 K was achieved at 100 GHz when the mixer was cooled to 20 K [21]. Their data also show an average DSB noise temperature of 75 K over the frequency range of 80 to 115 GHz. Single sideband noise temperature would be 124 K because the input signal is twice as large in the DSB measurement.

The shot noise component was addressed in [19] by associating the nonlinear conductance terms of the diode with the current components that gives rise to the shot noise, which implies that the mixer gain and noise are functions of the single variable, the AC input signal amplitude. Formulas given in [19] show noise figure for the three cases when the image conductance is infinite, is zero, and is equal to the source conductance.

The noise characteristics of Schottky barrier diodes become very important for mixer design for radio astronomy applications or millimeter-wave sensors. High-frequency devices require small areas to reduce capacitance, but small areas have been known to exhibit noise temperatures much greater than what would be predicted at cryogenic temperatures. The larger than expected noise has been seen to be the result of interfacial stress between the GaAs device and the SiO_2 , where the latter material is used to define the location and size of the metal contact on the GaAs [22]. The large difference in the expansion coefficients of the materials seems to produce stress, which in turn was responsible for higher than expected noise.

10. FREQUENCY MULTIPLIERS

The nonlinearity available in the Schottky barrier diode can also be used in frequency multipliers. In the Schottky barrier diode, both the forward conduction current, which provides nonlinear conductance, and the reverse biased charge storage in the depletion capacitance can contribute to the frequency multiplication process, which is in

contrast to the pn junction varactor that uses only the nonlinear capacitance (but might include diffusion capacitance). The varactor multipliers are more efficient and less noisy than Schottky diode resistive multipliers, but they are more sensitive to circuit tuning. Schottky barrier diodes used in broad-band frequency multipliers are more easily tuned and have fewer unwanted frequencies than their varactor counterpart. A discussion of combining $G(v)$ and $C(v)$ is found in [23], with regard to a mixer application.

The Manley–Rowe equations [24,25], which are basically a statement of energy conservation, show that the lossless varactor multiplier output power is proportional to the output to input frequency ratio, n , which is good news when the output frequency is higher than the input frequency, and bad news when the output frequency is lower. In contrast, for the resistive multiplier, the power at $n\omega_1$ is

$$P_n \leq \frac{P_1}{n^2} \quad (105)$$

and the remaining power is converted to DC.

$$P_{DC} \geq (n^2 - 1)P_1 \quad (106)$$

BIBLIOGRAPHY

- R. S. Muller, and T. I. Kamins, *Device Electronics for Integrated Circuits*, 3rd Ed., Wiley, New York, 2003.
- S. M. Sze, *Physics of Semiconductor Devices*, 2nd Ed., Wiley, New York, 1981.
- A. M. Cowley and S. M. Sze, Surface states and barrier height of metal-semiconductor systems, *J. Appl. Phys.*, **36**:3212–3220 (1965).
- H. A. Bethe, Theory of the boundary layer of crystal rectifiers, *MIT Radiation Lab. Report*, 43-12, 1942.
- R. F. Pierret, *Advanced Semiconductor Fundamentals*, Vol. 4, 2nd Ed., Prentice Hall, Upper Saddle River, NJ, 2003, pp. 88–96.
- C. R. Cromwell, The Richardson constant for thermionic emission in Schottky barrier diodes, *Solid State Electron.*, **8**:395–399 (1965).
- D. A. Fleri, and L. D. Cohen, Nonlinear analysis of the Schottky-barrier mixer diode, *IEEE Trans. Microwave Theory Tech.*, **MTT-21**:39–43 (1973).
- K. S. Champlin and G. Eisenstein, Cutoff frequency of submillimeter Schottky-barrier diodes, *IEEE Trans. Microwave Theory Tech.*, **MTT-26**:31–34 (1978).
- H. C. Torrey and C. A. Whitmer, *Crystal Rectifiers* (Massachusetts Institute of Technology Radiation Laboratory Series, Vol. 15), McGraw-Hill, New York, 1948.
- J. S. Campbell and G. T. Wrixon, Finite element analysis of skin effect resistance in submillimeter wave Schottky barrier diodes, *IEEE Trans. Microwave Theory Tech.*, **MTT-30**: 744–749 (1982).
- M. W. Cole and P. C. Joshi, Ohmic contacts to SiC for high power and high temperature device applications, in Z. C. Feng and J. H. Zhao, eds., *Silicon Carbide Materials, Processing, and Devices*, Taylor & Francis, New York, 2004.
- J. A. Cooper, Silicon Carbide MOSFET's, in F. Ren and J. C. Zolper, eds., *Wide Energy Bandgap Electronic Devices*, World Scientific: New Jersey, 2003, p. 344.
- J. Eriksson, N. Rorsman, and H. Zirath, 4H-Silicon carbide Schottky barrier diodes for microwave applications, *IEEE Trans. Microwave Theory Tech.*, **51**:796–804 (2003).
- R. N. Simons and P. G. Neudeck, Intermodulation-distortion performance of silicon-carbide Schottky-barrier RF mixer diode, *IEEE Trans. Microwave Theory Tech.*, **51**:669–672 (2003).
- T. G. M. Kleinpenning, Low-frequency noise in Schottky barrier diodes, *Solid State Electron.*, **22**:121–128 (1979).
- L. Anghel, T. Ouisse, T. Billon, P. Laasanga, and C. Jaussaud, Experimental investigation of noise sources in silicon carbide Schottky barriers, *Int. Semiconduct. Conf.*, **2**, October 9–12, pp. 539–542.
- S. A. Maas, *Nonlinear Microwave Circuits*, 2nd Ed., Artech House, Norwood, MA, 1988.
- W. K. Chen, *Active Network and Feedback Amplifier Theory*, McGraw-Hill, New York, 1980.
- M. R. Barber, Noise figure and conversion loss of the Schottky barrier mixer diode, *IEEE Trans. Microwave Theory Tech.*, **MTT-15**:629–635 (1967).
- M. Trippe, G. Bosman, and A. van der Ziel, Transit-time effects in the noise of Schottky-barrier diodes, *IEEE Trans. Microwave Theory Tech.*, **34**:1183–1192 (1986).
- C. R. Predmore, A. V. Räisänen, N. R. Erickson, P. F. Goldsmith, and J. L. R. Marrero, A broad-band, ultra-low-noise Schottky diode mixer receiver from 80 to 115 GHz, *IEEE Trans. Microwave Theory Tech.*, 498–507 (1984).
- G. K. Sherrill, R. J. Mattauch, and T. W. Crowe, Interfacial stress and excess noise in Schottky-barrier mixer diodes, *IEEE Trans. Microwave Theory Tech.*, **MTT-34**:342–345 (1986).
- M. Akaike and K. Ohnishi, A nonlinear analysis of Schottky-barrier diode upconverters, *IEEE Trans. Microwave Theory Tech.*, **MTT-25**:1059–1064 (1977).
- J. M. Manley and H. E. Rowe, Some general properties of nonlinear elements—Part I. General energy relations, *Proc. IRE*, **44**:904–913 (1956).
- H. E. Rowe, Some general properties of nonlinear elements: Part II—Small signal theory, *Proc. IRE*, **46**:850–860 (1958).

SCHOTTKY BARRIERS

S. ASHOK
The Pennsylvania State
University
University Park, Pennsylvania

The Schottky barrier, one of the earliest and simplest semiconductor interfaces studied, consists of a metal in contact with a semiconductor. It is named after Walter Schottky, who in the 1930s developed a comprehensive theory of such contacts, and traced their properties to the electrical barrier that forms at the metal-semiconductor (MS) interface. If the barrier height is relatively large, the current–voltage (I – V) characteristics exhibit an asymmetric rectifying behavior, while a symmetric linear I – V response results from a low barrier. The rectifying MS

contact is called the *Schottky diode*, whereas the nonrectifying device is simply referred to as an *ohmic contact*.

The first observation of asymmetric conduction in solids was made by Ferdinand Braun in 1874, when he studied the properties of metal contacts to metallic sulfides (later identified as semiconductors). The subsequent advent and rapid growth of radiocommunication led to widespread use of these contacts as “point contact” diode detectors. These naturally occurring semiconducting minerals suffered from high levels and variable distribution of impurities, which made the devices rather unreliable. Reproducible, high-quality MS interfaces had to await the post-World War II development of synthesized semiconductors of extremely high purity (such as Ge and Si) and the use of vacuum deposition techniques. Exhaustive studies of an enormous assortment of metal–semiconductor contacts have led to a better—although still incomplete—understanding of the mechanism of barrier formation. Other phenomena (such as carrier transport) are well understood, and Schottky contact technologies may be considered mature for most semiconductors.

Because of its inherent high speed, the Schottky diode is widely used in micro- and millimeter-wave detection and mixing, while the Schottky interface itself is a key element in important amplifying devices such as the *metal semiconductor field-effect transistors* (MESFETs) and the more recent heterostructure FET (HFET), as well as in a variety of radiation detectors. Commonly used metals generally form high barriers on n-type semiconductors, and this is also the usually desired situation in devices because of the higher mobility of electrons. The ohmic contact with negligible voltage drop across itself is essential for all external and internal connections to the elements of semiconductor devices; the theory of the Schottky barrier is also of relevance to the choice of metals for ohmic contacts.

1. THEORY OF SCHOTTKY BARRIER FORMATION

It is important to distinguish between two different types of MS interfaces: (1) those prepared on semiconductor surfaces freshly formed (by cleaving, or sputtering and annealing, or in situ epitaxy) in ultrahigh vacuum (UHV, with pressures $< 10^{-10}$ torr) and, hence, unexposed to the ambient; and (2) those prepared on chemically etched surfaces with the metallization done under simple high vacuum (pressure $\approx 10^{-6}$ torr). The former are of great importance in basic studies of Schottky barrier formation. These involve mono- and submonolayer coverage of the metal on freshly cleaved semiconductor surfaces and in situ evaluation of the barrier height as well as microscopic interactions between the metal and the semiconductor through sophisticated surface analytical tools. All practical Schottky barriers are formed on chemically etched surfaces and result in extremely reproducible electrical characteristics. Regardless of the specific MS interface, it turns out that the same physical models generally apply. This is true even for the special case of reacted metal–semiconductor contacts such as between metallic silicides and silicon. The silicide Schottky barriers are of interest from both fundamental and practical viewpoints, as the

MS interface here is buried inside the semiconductor bulk, thus obviating the deleterious influence of surface oxides and other contamination.

We will consider here two basic models, the earlier one due to Schottky and the later one inspired by Bardeen’s postulation of the surface states. Exhaustive reviews of the physical models and experimental data on the Schottky barrier may be found in Refs. 1–3.

2. THE INTIMATE SCHOTTKY CONTACT MODEL

This model, originally proposed by Schottky as well as Mott, assumes an intimate interface between the metal and the semiconductor with no interfacial layer between the two. Consider a metal with workfunction ϕ_m greater than the electron affinity χ_s of an n-type semiconductor. Figure 1a shows the electron energy lineup in the metal and the semiconductor before contact. When the contact is made (Fig. 1b), the workfunction (or, equivalently, electronegativity) difference forces a momentary net flow of electrons from the semiconductor to the metal until the MS system as a whole reaches thermal equilibrium with a single constant Fermi energy E_F . The consequences of this process are twofold: (1) an energy barrier ϕ_b separating the electrons in the metal from the empty conduction band states of the semiconductor at the interface and (2) a space

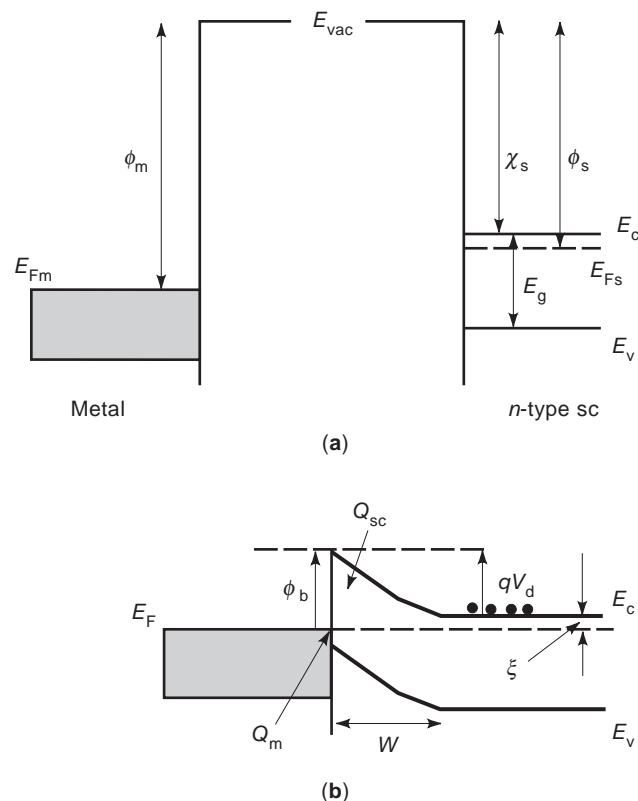


Figure 1. Electron energy band diagram of a metal and an n-type semiconductor under thermal equilibrium before (a) and after (b) contact. The workfunction of the metal ϕ_m is assumed to be greater than the semiconductor electron affinity χ_s .

charge or depletion region of width W on the semiconductor side of the interface. The electrical properties of the Schottky barrier arise principally from this space charge layer. The positive charge in the latter (Q_{sc}), consisting of ionized donors, compensates the negative electron charge in the metal (Q_m). Correspondingly, the space charge region develops a band bending qV_d in a manner similar to that in a p-n junction. From Fig. 1, the Schottky barrier height ϕ_b^n and (zero-bias) band bending qV_d or diffusion potential V_d are readily shown to be

$$\phi_b^n = \phi_m - \chi_s \quad (1)$$

$$qV_d = \phi_m - \phi_s \quad (2)$$

The space region width W is given by

$$W = \left[\frac{2\epsilon_s V_d}{qN_D} \right]^{1/2} \quad (3)$$

where ϵ_s is the dielectric permittivity of the semiconductor, q the electron charge, V_d the diffusion potential, and N_D the bulk donor concentration.

It is possible to form Schottky barriers on p-type semiconductors also, in which case we need $\phi_m < \phi_s$, and the Schottky barrier height ϕ_b^p (for holes, measured from E_{Fm} to E_v at the interface) becomes

$$\phi_b^p = E_g + \chi_s - \phi_m \quad (4)$$

Equations (1) and (4) predict a linear dependence of barrier height on metal workfunction, with a slope parameter $S_\phi = |d\phi_b/d\phi_m|$ equal to unity. However, experimental values of S_ϕ are significantly less than unity for most semiconductors, thus requiring a more elaborate model postulating the presence of an interfacial layer *and* interfacial charge. The first proposal for the interfacial charge was made by Bardeen, who recognized that the discontinuity of the crystal lattice at the surface would give rise to surface states or traps located physically at the semiconductor surface and energetically within the bandgap.

Addition of Eqs. (1) and (4) yields the relation

$$\phi_b^n + \phi_b^p = E_g \quad (5)$$

for any metal–semiconductor combination. While Eqs. (1) and (4) invariably fail to describe experimental results on Schottky barriers, the Schottky barrier heights of similarly prepared contacts on n-type and p-type semiconductors often add up to the bandgap as given by Eq. (5) for a variety of semiconductors and metals.

2.1. The MIS Schottky Contact Model

The MIS Schottky model incorporates the following changes to the intimate Schottky contact model: (1) an (ultrathin, tunnelable) interfacial layer (I) of thickness δ between the metal and the semiconductor and (2) interface traps of density D_{it} ($\text{cm}^{-2} \text{eV}^{-1}$) located at the IS interface and with occupancy controlled by the metal Fermi energy E_{Fm} . By Gauss' law, a surface charge density Q_{it} in

the interface traps would give rise to a potential (Δ/q) across the I layer as shown in Fig. 2. The resulting realignment of the semiconductor band bending then alters the barrier height, making it less dependent on the metal workfunction. In view of the electrical transparency of the I layer, note that the Schottky barrier height is still given by the difference between the semiconductor conduction band edge at the surface and the Fermi energy in the metal. With the additional source of charge, the charge neutrality condition becomes

$$Q_m + Q_{it} + Q_{sc} = 0 \quad (6)$$

It is convenient to define a “neutral level” ϕ_0 for the interface traps, such that the net interface trap charge Q_{it} is zero when E_{Fm} lies at ϕ_0 . From the band diagram of Fig. 2, using Gauss' law and a few simplifying assumptions, it can be shown (see Ref. 2, p. 20) that

$$\phi_b^n = \gamma(\phi_m - \chi_s) + (1 - \gamma)(E_g - \phi_0) \quad (7)$$

where $\gamma = \epsilon_i / (\epsilon_i + q\delta D_{it})$. Now the slope parameter $S_\phi = \gamma < 1$, and decreases monotonically with increase in the interface trap density D_{it} and interface layer thickness δ . In the extreme case when $(\delta D_{it}) \rightarrow \infty$, $\phi_b^n = (E_g - \phi_0) = \text{constant}$, independent of the metal workfunction ϕ_m —the so-called Bardeen limit. This situation is also referred to as (surface) Fermi level pinning, because E_{Fn} is now pinned

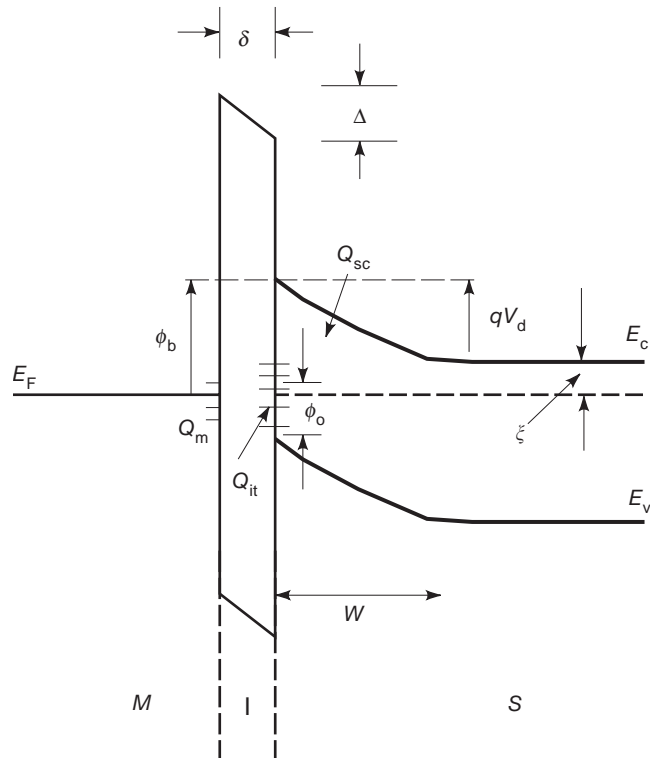


Figure 2. Electron energy band diagram for the MIS Schottky model under thermal equilibrium, with an ultrathin, tunnelable interfacial layer I .

to the neutral level ϕ_0 of the interface traps. If, on the other hand, $(\delta D_{it}) \rightarrow 0$, then Eq. (4) reduces to Eq. (1), which applies to the (intimate) Schottky limit.

If we use an upper limit of $\delta = 20 \text{ \AA}$ for a good Schottky diode and assume an $\varepsilon = 4\varepsilon_0$, the Bardeen limit is approached for $D_{it} \gtrsim 10^{13} \text{ cm}^{-2} \text{ eV}^{-1}$. Using a surface atomic density of 10^{15} cm^{-2} for a solid, this corresponds to about one interface trap for every 100 surface atoms. Such a high level of interface trap density contrasts with $D_{it} < 10^{10} \text{ cm}^{-2} \text{ eV}^{-1}$ obtained for the high-quality thermal SiO_2/Si interface used in Si MOS technology.

Experimental verification of Eq. (7) requires deposition of metals of widely differing workfunction on identically prepared samples, rather than compiling data reported by different authors in the literature. Such studies on Si have yielded a γ in the range 0.15–0.22 depending, evidently, on surface preparation [4]. However, phenomena such as metal–semiconductor reaction, interfacial strain, and aging effects could profoundly influence the MS interface, so strict adherence of relations such as Eq. (7) should not be expected for all metal–semiconductor combinations. The principal success of the model is in explaining semiquantitatively those trends observed in measurements.

An expression similar to that in Eq. (7) can be derived for the MIS Schottky barrier on a p-type semiconductor, and again ϕ_b^n and ϕ_b^p add up to the bandgap E_g of the semiconductor as with the intimate Schottky model [see Eq. (5)]. Experimental data on a number of semiconductors confirm this trend (Ref. 2, Sec. 2). Thus a high barrier height on an n-type semiconductor implies a low barrier on the p-type. A practical conclusion from the MIS Schottky model, as with the intimate Schottky model, is that high barrier heights require metals of large workfunction for n-type materials and small workfunction metals for p-type materials. Measured barrier heights are typically in the range 0.6–0.8 eV for n-type Si, and 0.75–0.95 eV for n-type GaAs. Clearly, the higher the bandgap E_g , the higher will be the expected Schottky barrier height.

The stipulation of the I layer in this model is a logical one for Schottky barriers formed on chemically etched semiconductor surfaces. Most semiconductors form a native insulating oxide, 10–20 Å thick, on inevitable exposure to room ambient before the samples are introduced into the vacuum chamber for metallization. The MIS model, however, could also be applied to UHV-prepared intimate contacts because an atomic level separation between Q_m and Q_{it} is all that is needed to simulate the I layer; here the two sheet charges essentially constitute an atomic dipole.

The origin of the interface traps has been a subject of some controversy over the years, with at least two distinct schools of thought: (1) the unified defect model, where the surface Fermi level is pinned at discrete acceptor- and donorlike defect states induced by the metal deposition and (2) the continuum metal-induced gap states (MIGSs) that arise from the decay of the metal electron wavefunctions into the semiconductor, as originally proposed by Heine in 1965. More recent studies of both UHV and chemically etched samples appear to favor the MIGS theory although some anomalies persist, requiring an additional secondary

mechanism of metal deposition-induced defect states. These issues have been reviewed at length by Mönch [3,5].

The MIS Schottky model is most effective in giving a qualitative explanation for the observed weak dependence of barrier height on the metal workfunction. Quantitative, predictive interpretations using Eq. (7) are beset not merely by second-order phenomena, such as metal–semiconductor interdiffusion, but the more basic problem of choosing the right value for the workfunction ϕ_m . The workfunction of a solid contains surface as well as volume contributions, and both the intimate and MIS Schottky models tacitly assume that ϕ_m and χ_s do not change (at least differentially) when the metal and the semiconductor are brought into contact. This may not be true in practice, so other parameters of the metal such as electronegativity have been proposed over the years for correlating to barrier height. Other empirical correlations studied include the heat of formation of silicides, effective workfunction, and the interfacial crystal structure. Detailed discussions of these aspects can be found in an article by Werner and Rao [4] on silicon, and in the review by Brillson [6] on other types of semiconductors.

3. CARRIER TRANSPORT

The current flow across the Schottky barrier may be visualized as an extension of electron emission from a metal to vacuum. As seen in Fig. 1a, the energy barrier for this process is the metal workfunction ϕ_m , which constitutes the activation energy for over-the-barrier thermionic emission current [proportional to $\exp -(\phi_m/kT)$]. With the metal in contact with the semiconductor (Fig. 1b or 2), the effective barrier for electron emission changes to the Schottky barrier height ϕ_b , as empty states are available in the conduction band of the semiconductors to receive the emitted electrons. Further, unlike vacuum, the semiconductor is also a source of electrons for emission back into the metal. Most importantly, we can control this latter flow by applying a voltage V of proper polarity—the so-called forward bias where the n-type semiconductor is negatively biased—that raises the conduction (and valence) band edge upward by an amount qV relative to thermal equilibrium. As shown in Fig. 3, the energy barrier for electrons in the semiconductor reduces from qV_d to $q(V_d - V)$, which results in an exponential increase of current with the applied voltage. The path for this over-the-barrier-thermionic emission is shown as (a) in Fig. 3.

The current–voltage (I – V) characteristics of a Schottky barrier are then dominated by the thermionic emission process, with the following expression for current:

$$I = I_0 \left(\frac{\exp qV}{nkT} - 1 \right) \quad (8)$$

I_0 is the so-called saturation current given by

$$I_0 = A \cdot A^{**} \cdot T^2 \exp -\frac{\phi_b}{kT} \quad (9)$$

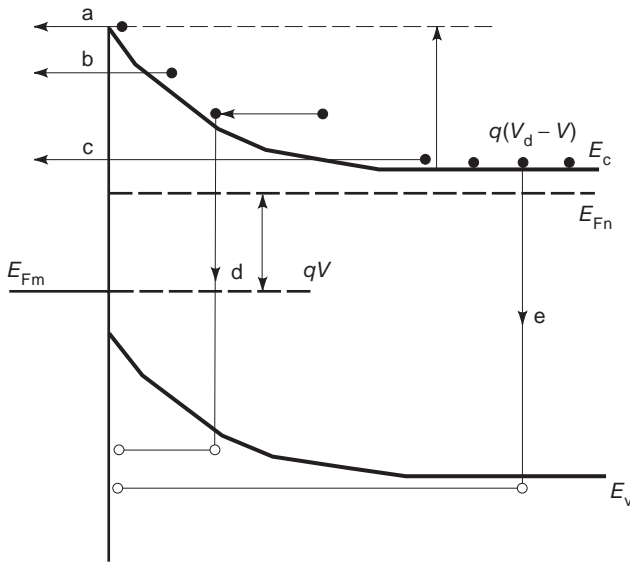


Figure 3. The band diagram of a metal/n-type semiconductor interface under an applied forward bias voltage V , displaying the various carrier transport mechanisms.

where A is the area of the Schottky contact; A^{**} is the modified Richardson constant, which is dependent on the semiconductor band structure; k is Boltzmann's constant; and T is the temperature in kelvins. Equation (8) also contains the so-called ideality factor n , which has a value slightly greater than unity. This n factor is a consequence of second-order effects such as the image force reduction of the Schottky barrier height, and the presence of any interfacial layer that drops part of the applied voltage and thus reduces the voltage across the semiconductor. High-quality, intimate Schottky barriers made on moderately doped semiconductors can have $n \leq 1.01$, while increased doping and presence of I layers can raise the value to as high as 1.1.

According to Eq. (8), the log I - V plot should be linear for $V \geq 3 kT$, with the zero-voltage extrapolation giving the saturation current I_0 . Using Eq. (9) and assuming the value of A^{**} ($112 \text{ A cm}^{-2} \text{ K}^{-2}$ for n -Si and $4.4 \text{ A cm}^{-2} \text{ K}^{-2}$ for n -GaAs), one can then extract the value of the Schottky barrier height ϕ_b . In the reverse direction, that is, for $V < 0$, the current will remain constant at the saturation value I_0 (typical range 10^{-10} – 10^{-6} A/cm^2) until the junction breaks down under large reverse bias. It is evident that Eq. (8) represents highly asymmetric I - V characteristics, leading to the use of the Schottky barrier as a rectifier in the Schottky diode.

Thermionic emission is the dominant transport mechanism at room temperature and above for Schottky barriers formed on moderately doped, single-crystal semiconductors, but a number of other mechanisms are also simultaneously present. Most of these are parallel processes and are illustrated in Fig. 3, where process b represents the thermionic field emission or thermally assisted tunneling process, where the electron climbs part way up the barrier thermally and tunnels through the rest; process c is field emission or direct tunneling across

the entire barrier; process d is recombination in the depletion region; and process e is recombination in the semiconductor bulk of injected minority holes.

Thermionic field emission and field emission become important as the dopant concentration is increased [with corresponding reduction in depletion width W , Eq. (3)] or temperature is reduced, and they have I - V relations similar in form to Eq. (8), but with an n factor increasing substantially above unity. In the extreme case of field emission, the (nT) product becomes a constant, giving a temperature-independent slope for the log I - V plots. In highly defective or disordered materials such as amorphous and polycrystalline semiconductors, one sometimes observes nonthermionic characteristics even at room temperature and at doping levels where direct field or thermionic field emission is impossible. These are attributed to "multistep" tunneling through impurity and defect levels in the depletion region.

Recombination in the depletion region (process d) and hole injection (process e) are identical to the phenomena that occur in a p-n junction. The former gives an additional current component similar to Eq. (8), but with an ideality factor n that is usually close to 2. If the corresponding I_0 is larger than that for thermionic emission, this component will show up as a shoulder in the log I - V plots under low forward bias. The (minority) hole injection component has a form similar to that in Eq. (8), but with $n = 1$. As the corresponding I_0 is invariably orders of magnitude lower than that for the majority electron thermionic emission, minority carrier injection into the semiconductor is only rarely observed in Schottky barriers, corresponding to unusually large barrier heights and high forward bias. Note that the electrons injected from the n-type semiconductor into the metal are still majority carriers in the metal, unlike those injected from the n- to the p-side of a p-n junction. Thus there is no minority-carrier storage in the Schottky diode, making it an extremely fast switching device.

All the current flow mechanisms identified in the preceding text are parallel processes. However, the thermionic emission process itself is in series with diffusion of majority electrons from the bulk towards the interface. Nevertheless, except in some very low mobility semiconductors, the rate-limiting step is thermionic emission, not diffusion. Thermionic emission and diffusion limits in a Schottky barrier are analogous to water flow in a pipe limited by the orifice and internal bulk friction, respectively. Further details of current flow in a semiconductor may be found in Ref. 2.

4. BARRIER HEIGHT MEASUREMENTS

The most commonly used technique for measuring the Schottky barrier height is the I - V measurement. As noted earlier, extrapolation of the forward log I - V plot yields I_0 , which is related to ϕ_b through Eq. (9). A simple room-temperature I - V measurement will suffice here if the value of A^{**} is assumed. However, the barrier height measured includes the effect of image force, a reduction on the order of 0.01–0.04 eV depending on the material and

doping. The error due to uncertainties in the value of A^{**} (due to the interfacial layer, etc.) is small (<0.02 eV for a factor of 2 change in A^{**}) due to its logarithmic influence on ϕ_b . For any meaningful interpretation of the log I - V data using the thermionic emission theory, it is important to verify that the linear region extends over at least two decades of current and that the n factor is less than 1.1.

An added degree of freedom in Schottky barrier measurement can be gained if the I - V measurements are made at different temperatures, typically at room temperature and above where thermionic emission is likely to dominate. Then an activation energy plot of $\log(I/T^2)$ versus $1/T$ should yield a straight line, whose slope gives the barrier height and the y -axis intercept yields the value of A^{**} . This approach hence does not require any knowledge of the Richardson's constant, and is particularly effective for the assessment of Schottky barriers containing intentionally introduced I layers for barrier height control.

Another frequently used electrical measurement is based on the depletion capacitance $C = \epsilon_s (A/W)$, which is a function of applied voltage V through Eq. (3) [modified by replacing V_d with $(V_d - V)$ under bias]. To avert the influence of strong conduction under forward bias, the capacitance-voltage (C - V) measurement is usually done under reverse bias (i.e., $V < 0$). Assuming that the dopant concentration is constant, a plot of $[1/C^2]$ versus V will then give a straight line with an x -axis intercept at V_d . Figures 1 and 2 show the relation between V_d and ϕ_b ; however, by including the effect of carriers at the depletion region edge through a correction term kT , one obtains the relation

$$\phi_b = qV_d + \zeta + kT \quad (10)$$

For intimate Schottky contacts on uniformly doped substrates, the agreement between I - V - and C - V -determined barrier height is quite close. However, the C - V technique fails to yield the correct barrier height with I layers of substantial thickness and interface traps that may respond to the AC measurement signal. Incidentally, the slope of the $1/C^2$ plot gives the doping concentration N_D , which turns out to be valid even for nonuniform doping. A convenient way of obtaining the doping profile of a semiconductor wafer is to use a mercury contact as a temporary Schottky barrier.

One of the most direct measurements of Schottky barrier height involves photoexciting the electrons in the metal over the barrier. This *internal* photoemission process requires photons of energy $h\nu$ lying between ϕ_b and E_g to avert fundamental absorption in the semiconductor. The photoyield Y (photoelectron per absorbed photon) is given approximately by

$$Y \simeq B[h\nu - \phi_b]^2$$

where B is a constant. A plot of $Y^{1/2}$ versus $h\nu$ gives a straight line with an x -axis intercept at ϕ_b . As with I - V measurements, this barrier height includes the image force reduction effect. The variable wavelength illumination needed for this measurement may be obtained using a

high-intensity white-light source and a monochromator. If the illumination is on the metal side, the thickness of the metal should be small ($\approx 100 \text{ \AA}$) because otherwise the photoexcited, *hot* electron with its limited mean free path cannot reach the interface.

5. MATERIAL SYSTEMS

Schottky barriers may be formed on literally any semiconductor, and in most cases it is easier to obtain a high barrier on n-type than on p-type material. There are exceptions such as InP, where the barrier height on n-type material is very low, seriously limiting the application potential of this important optoelectronic semiconductor in MESFETs. Most practical applications of Schottky contacts require a high barrier to minimize the leakage current I_0 , and this, coupled with the higher electron mobility, makes n-type semiconductors the preferred choice for Schottky-based devices.

The choice of the metal is also based on metallurgical considerations involving interfacial stability. Metal-semiconductor interdiffusion may occur at high operating temperatures and current densities, so practical contacts may involve multilayers, and refractory and other metals and their alloys. Metallic silicides (e.g., PtSi, Co_2Si) are particularly attractive Schottky contact materials for Si as well as compound semiconductors and are widely used.

The technique of metal deposition is also crucial in determining the barrier height. Thermal evaporation in high vacuum ($<10^{-6}$ torr) is the most innocuous method for Schottky barrier formation, while sputtering and related ion-beam/plasma techniques introduce defects close to the MS interface and significantly modify the Schottky barrier height [7].

6. SCHOTTKY BARRIER MODIFICATION

Modification and control of the Schottky interface have been the subject of intense interest since the 1970s, from both fundamental and practical viewpoints. The interest in basic studies stems from the possibility of "passivating" the interface traps with suitable chemical treatment so that one may achieve the Schottky limit. Studies have also focused on introducing insulating as well as semiconducting nanoscale interlayers (e.g., Al/Si/GaInP, Metal/ Si_3N_4 /Si) to form deliberate MIS structures for barrier modification [8]. Interface doping can also be used to alter ϕ_b . An elegant practical technique is that proposed by Shannon [9]. By using a very shallow ($\approx 100 \text{ \AA}$) implanted layer between the metal and the semiconductor, the shape of the barrier is altered, thereby changing the effective barrier height. If the implanted species are of the same conductivity type as the substrate, the increased electric field and thinning of the barrier near the top causes carrier tunneling. This effectively reduces barrier height. With an implant of the opposite conductivity type, the dopant compensation causes electric field reversal near the top, thereby increasing barrier height.

More recent contributions to the understanding of Schottky barriers have come about from the study of

epitaxial silicide/Si interfaces where the crystallographic effects are very much in evidence. A very interesting result is the difference in barrier height of 0.13 eV between NiSi₂ and Si(111) depending on whether both have the same orientation or are rotated 180° about the $\langle 111 \rangle$ direction.

A closer inspection of the electrical and structural properties has also forced one to consider the inherent inhomogeneities at Schottky interfaces. The spatial potential fluctuations effectively yield a distributed system of parallel Schottky barriers of varying barrier heights. Hence, the net carrier transport can be profoundly influenced through the exponential dependence of current on ϕ_b [see Eqs. (8), (9)]. These issues are discussed at length in Ref. 4.

BIBLIOGRAPHY

1. H. K. Henisch, *Semiconductor Contacts: An Approach to Ideas and Models*, Clarendon, Oxford, 1984.
2. E. H. Rhoderick and R. H. Williams, *Metal-Semiconductor Contacts*, 2nd ed., Clarendon, Oxford, 1987.
3. W. Mönch, *Semiconductor Surfaces and Interfaces*, 2nd ed., Springer-Verlag, Berlin, 1995.
4. J. H. Werner and U. Rao, Schottky contacts on silicon, in J.-F. Luy and P. Russer, eds., *Silicon-Based Millimeter-Wave Devices*, Springer-Verlag, Berlin, 1994.
5. W. Mönch, On the physics and metal-semiconductor interfaces, *Rep. Prog. Phys.* **53**:221 (1990).
6. L. J. Brillson, The structure and properties of metal-semiconductor interfaces, *Surface Sci. Rep.* **2**:123 (1982).
7. S. Ashok, Low-energy ion bombardment modification of silicon surface barriers, in D. Stievenard and J. C. Bourgoin, eds., *Ion Implantation*, Trans Tech Publications, Switzerland, 1988, p. 187.
8. W. Mönch, Electronic properties of ideal and interface-modified metal-semiconductor contacts, in S. Ashok et al., eds. *Defect and Impurity Engineered Semiconductors and Devices*, Materials Research Society, Pittsburgh, 1995, pp. 378, 811.
9. J. M. Shannon, Control of Schottky barrier height by using heavily doped surface layers, *Solid State Electron.* **19**:537 (1996).

SiC DEVICE TECHNOLOGIES

M. Östling
S.-M. KOO
M. DOMEIJ
E. DANIELSSON
C.-M. ZETTERLING
Royal Institute of Technology
Kista-Stockholm, Sweden

1. INTRODUCTION

The characteristic properties of semiconductor materials play a key role for the performance of the fabricated electronic devices. In this respect, silicon carbide (SiC) devices offer great advantages to overcome the physical device limitations in silicon (Si) devices set by the materials

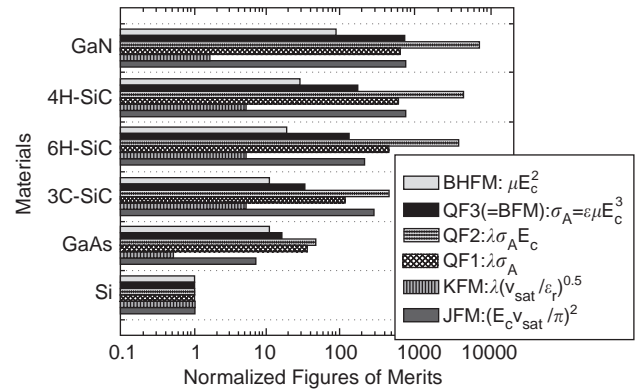


Figure 1. Figures of merit for various semiconductors. All values are normalized with respect to Si, including Johnson's figure of merit (FoM) (JFM in diagram) for basic limits on the device performance (high power and frequency) and Keyes' FoM (KFM in diagram) for the switching speed of transistor. Quality factors QF1–3 take thermal properties into consideration (QF1) for the heatsink material and the active-device area in power devices. QF2 assumes a perfect heatsink. QF3 is based on no heatsink nor geometric factors. Baliga's FoM (BFM in diagram) can be used for evaluation of high-frequency application.

properties in Si. The theoretical performances of SiC can be compared to Si and other common semiconductors using appropriate figures of merit [1] (see Fig. 1).

Si devices are generally used below a maximum junction temperature of $\sim 200^\circ\text{C}$ and confined to blocking voltages of a few kilovolts. Because of its large bandgap, SiC possesses a very high breakdown field and low intrinsic carrier concentration, which consequently makes high voltage and high temperature operation possible. SiC is also suitable for high-frequency device applications, because of the high saturation drift velocity and low permittivity. The material quality and the diameter of silicon carbide wafers have steadily been improved and the micropipe densities have been reduced to $\sim 10\text{ cm}^{-2}$ at production level ($\sim 0.9\text{ cm}^{-2}$ for a 50-mm 4H SiC wafer in research stage) [2,3]. This is promising for future fabrication of larger than millimeter-sized devices. Presently, 6H and 4H SiC wafers of n and p types with a diameter of 75 mm are commercially available, while wafers of 100 mm diameter are shown as viable demonstrators expected to be in production within a few years. Most of the key SiC process technologies including doping, dry etching, oxide growth, and Schottky and Ohmic contacts, and are relatively mature and compatible to those in Si processing. However, some key processing issues that are critical must still be overcome for device commercialization. In this article, the progress and the current status of SiC device technologies are discussed.

2. PROCESS TECHNOLOGY

A good feature with SiC is the excellent behavior to be thermally oxidized to form SiO₂, which is crucial in both fabricating devices with MOS structures as well as passivation of surfaces. SiC is normally oxidized at higher

temperatures ($> \sim 1150^\circ\text{C}$) and at slower rate, due to the stronger Si–C bonds compared to Si–Si bonds [4]. The interface properties of SiO_2/SiC have recently been improved by H_2 treatment prior to the oxidation or by postoxidation annealing in NO or N_2O [5]. A serious problem with oxidation of SiC is the low MOS channel mobility. The highest values reported for the n-channel inversion mobility in $6H$ SiC is $70\text{--}100\text{ cm}^2/\text{V}\cdot\text{s}$, whereas values of $1\text{--}20\text{ cm}^2/\text{V}\cdot\text{s}$ are commonly found for the inversion channel mobility in $4H$ SiC [6].

High-voltage termination technique is crucial to high power devices. Most passivation techniques in Si devices are also applicable to SiC, which includes guard rings, field plate termination, and junction termination extensions (JTEs). Other passivation techniques suggested are the high-dose implantation of inert ions (either Ar or B) forming a high-resistivity region or to create a beveled surface region by etching. Power switching devices appear to perform well with these passivation treatments even though the inadequate passivation affects the subthreshold or the microwave characteristics of JFETs [7] and MESFETs [8].

Whereas the large Si–C bonding energy makes silicon carbide attractive for applications in harsh environments, it becomes problematic in etching SiC. Because of the high bond energies between silicon and carbon, the conventional wet chemical etching is not possible at practical process temperatures. Hence plasma-based dry etching plays a crucial role in SiC for the device pattern transfer process. Plasma etching is used for junction termination in mesa structures, devices with various structures such as U-MOSFETs, buried-gate JFETs, BJTs, or via-hole etching in SiC. Plasma etching of SiC in F-based chemistry has been proved to work well [9]. Etch rates as high as $1.35\text{ }\mu\text{m}/\text{min}$ in helicon reactor and $970\text{ nm}/\text{min}$ by inductively coupled plasma reactive ion etching in a SF_6/O_2 plasma have been reported. Electrical properties of Schottky and Ohmic contacts on etch damaged surfaces are of interest, and more recent studies show that the damage from a low-energy etched $4H$ SiC can be recovered by a sacrificial oxidation annealing [10].

All devices need good low-Ohmic contacts. They are particularly important for applications using high current densities that result in large voltage drops across even small resistances. The specific contact resistance to n- and p-type SiC is normally in the range of $10^{-4}\text{--}10^{-6}\text{ }\Omega\text{ cm}^2$ and $10^{-3}\text{--}10^{-5}\text{ }\Omega\cdot\text{cm}^2$, respectively, and are highly dependent on the surface doping concentration, choice of the metal, sample preparation, and the postmetallization heat treatment. The surface of SiC can be terminated by either Si or C and will greatly affect the contact properties. Normally contacts are made to Si-surface-oriented device structures, which has proved to yield reliable properties. Ohmic contacts to n-type SiC seem to be acceptable for device applications. However, because of the higher barrier height, it is yet more difficult to obtain lower specific contact resistance (ρ_c) for p-type SiC. Generally, Ni-based and aluminum-based contacts have been widely used for n-type and p-type SiC, respectively. The lowest contact resistivities yet reported for p-type SiC is in the $5 \times 10^{-6}\text{ }\Omega\cdot\text{cm}^2$ range using CoSi_2 by sequential evaporation

of Co and Si on $6H$ SiC [11]. Various interesting approaches can be found in the literature. Epitaxially grown TiC on $4H$ SiC has shown good Ohmic contact properties (5×10^{-6} and $3 \times 10^{-5}\text{ }\Omega\cdot\text{cm}^2$ for n- and p-type $4H$ SiC epilayers) by using coevaporation with an e-beam for Ti and a Knudsen cell for C60 in a UHV system, which required an annealing temperature of only $\sim 500^\circ\text{C}$ [12].

3. DEVICE APPLICATIONS

3.1. High-Voltage Devices

SiC offers a high voltage capability that can be realized on much thinner drift layers than in Si or GaAs. High breakdown voltage with lower on-state resistance can be achieved because of the high critical electric field of SiC. Schottky diodes are approaching the unipolar limit of $4H$ SiC and are today commercially produced by Infineon and Cree Inc. with voltage ratings up to 600 V. The SiC Schottky diodes are free from reverse recovery, and this reduces switching power losses, thus allowing higher switching frequencies in converter circuits. In the development and research laboratories, several Schottky prototypes approaching 2000 V have been demonstrated. SiC junction barrier Schottky (JBS) diodes are interesting candidates to Schottky diodes in the 600–3300 V blocking voltage regime. JBS diodes [11] combine the excellent switching behavior of Schottky diodes with a low leakage current approaching that of PN diodes. The process technology of JBS diodes is, on the other hand, more complex than for Schottky diodes. Figure 2 shows a performance comparison between Schottky and JBS diodes [13].

PN diodes become advantageous for voltages above $\sim 3\text{--}4\text{ kV}$ because of their lower on resistance obtained through conductivity modulation. Cree Inc. have reported the highest breakdown voltage for a PN diode [14] to date with $\sim 19.2\text{ kV}$ and a low forward voltage drop of 4.9 V at $100\text{ A}/\text{cm}^{-2}$ that clearly indicates conductivity modulation. This type of very-high-voltage diode has potential

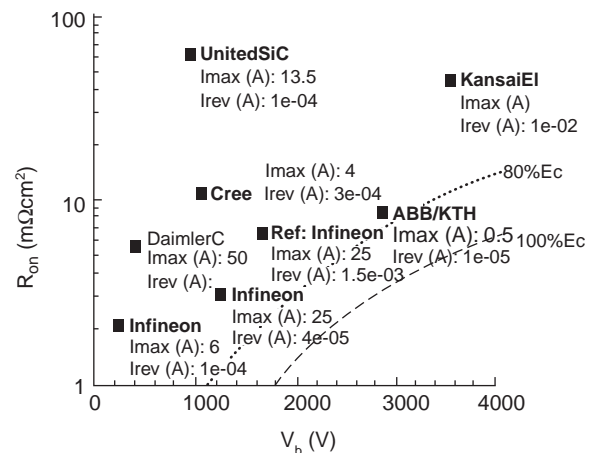


Figure 2. Performance comparison between Schottky and JBS diodes.

application with substantial system benefits, for instance, in high-voltage DC power transmission. Very-high-voltage diodes are, however, interesting mainly for applications with high currents of 100 A and more. This requires chip sizes in the range of 1 cm^2 , and a commercially viable production of such diodes therefore requires significant improvements regarding crystal imperfections such as micropipes, screw and edge dislocations, and low-angle grain boundaries. Another problem that needs to be solved is the long-term degradation of bipolar SiC devices caused by recombination assisted defect generation and motion discovered in 2002 [15].

Among switching power devices, MOSFETs, JFETs, bipolar junction transistors, and thyristors have been experimentally demonstrated. In $4H$ SiC MOSFETs, the measured ON-state resistance is relatively poor due to a low effective channel mobility. More recently, however, MOSFETs fabricated on $6H$ and $15R$ SiC as well as on the $(11\bar{2}0)$ or $(03\bar{3}8)$ surface of $4H$ SiC showed impressive performances. Double-implanted MOSFETs in $6H$ SiC showed properties exceeding 30 times the Si theoretical limit with V_B of 1.8 kV and R_{ON} of $46 \text{ m}\Omega \cdot \text{cm}^2$ [16]. Static channel expansion MOSFETs with 5.0 kV and R_{ON} of $88 \text{ m}\Omega \cdot \text{cm}^2$ have been demonstrated in $4H$ SiC, using an accumulated MOS gate and a pn-junction gate [17,18]. Additionally, the highest blocking voltage for a SiC switching device (6.5 kV) was obtained with an accumulation-mode MOS gated device [19]. Technological challenges for SiC MOSFETs are improvements regarding channel mobility and oxide reliability.

JFETs, which are unipolar devices without any Schottky or MOS interface, have advantages due to the built in potential and inherent stability of the pn-junction gate and do not suffer from the low channel mobility of the MOSFETs. Thus they are suitable for applications in which the normally ON characteristic is not a severe disadvantage. The best performance published to date in a SiC majority-carrier active switch was in a vertical JFET with R_{ON} of $26 \text{ m}\Omega \cdot \text{cm}^2$ for devices with 3.5 kV breakdown voltage [20]. Those types of JFETs are connected with Si MOSFETs in a cascode configuration to obtain a module with normally OFF characteristics. SiC JFETs combine low ON-state resistance with fast switching and excellent short-circuit withstand times in the range of milliseconds.

Progress has been made in development of SiC bipolar junction transistors (BJTs) with an ON-state resistance of only $10.8 \text{ m}\Omega \cdot \text{cm}^2$ for a device blocking 1.8 kV [21]. The BJTs combine a very low ON-state resistance with fast switching, thanks to the thin drift layer needed for SiC devices. Most of the reported SiC BJTs have epitaxially grown emitter regions and common-emitter current gains in the range of 10–50. Increased complexity in drive circuitry and the low current gains are drawbacks of BJTs compared to FETs, whereas normally OFF characteristics are an advantage compared to the JFET.

Promising results have been reported also for thyristors with a gate turnoff GTO thyristor capable of blocking 2.6 kV and turning off 12 A [28]. Thyristors are, however, like PN diodes, mainly interesting in large chip sizes and therefore depend on improvements in material quality for a potential commercialization.

Table 1. Summary of High-Voltage SiC Devices

Device (Polytype)	V_{BD} (kV)	R_{ON} ($\text{m}\Omega \cdot \text{cm}^2$)	V_{BD}^2/R_{ON} (MW/cm^2)	Ref
PIN diode ($4H$)	19.5	65	5850	14
PIN diode ($4H$)	4.5	42	482	20
JBS diode ($4H$)	2.8	8	980	11
Schottky diode ($4H$)	4.9	43	558	22
DMOSFET ($4H$)	2.4	42	137	23
SIAFET ($4H$)	6.1	732	51	19
SEMOSFET ($4H$)	5	88	284	17
ACCUFET ($4H$)	1.4	15.7	125	24
DMOSFET ($6H$)	1.8	46	70	16
JFET ($4H$)	5.5	218	139	25
VJFET ($4H$)	2	70	57	26
VJFET ($4H$)	3.5	25	490	20
VJFET ($4H$)	1.7	3.6	802	47
BJT ($4H$)	1.8	10.8	300	21
BJT ($4H$)	1	17	59	27
BJT ($4H$)	1.3	8	211	29

The breakdown voltage squared over the ON-state resistance (V_{BD}^2/R_{ON}) is compared in general, as shown in Table 1. In Fig. 3, the results are plotted with the ideal ON-state resistance of Si, $6H$ SiC, and $4H$ SiC devices. As can be seen, diodes have been more successful so far, and are very close to the ideal R_{ON} . To calculate the forward voltage drop, the R_{ON} should be multiplied by the current density. For the bipolar devices there is an additional voltage drop because of the built-in voltage of the pn junction, around 0.7 V for Si and 2.5 V for SiC. For the MOSFETs in Table 1 and Fig. 3, the ON-state resistance is, to a large extent, the channel resistance, since the mobility of the inversion channel is still a problem.

3.2. RF Power Devices

SiC devices have shown considerable improvement and superior RF power performance compared to those

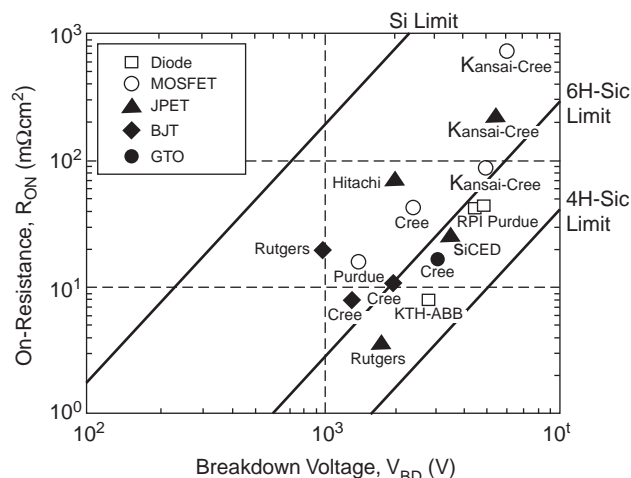


Figure 3. ON-state resistance versus blocking voltage performances for reported SiC devices.

Table 2. Summary of High-Frequency SiC Devices

Device (Polytype)	Frequency (GHz)	Power Density (W/mm)	Ref.
IMPATT diode (4H)	9.9	300 mW (pulsed)	30
IMPATT diode (4H)	7.2	9 kA/cm ² (pulsed)	31
MESFET (4H)	3.5	5.2 (pulsed, total 62 W)	32,33
MESFET (4H)	10	4.5 (pulsed, total 54 W)	32
MESFET (4H)	2	4 (CW, total 8 W)	34
MESFET (4H)	3	1.9 (CW, total 27 W)	35
MESFET (4H)	3.5	3.8 (CW)	36
SIT (4H)	1.3	1.67 (pulsed, total 400 W)	37
SIT (4H)	2.9	1.51 (pulsed, total 78 W)	38
SIT (4H)	1.3	1.55 (pulsed, total 35 W)	39
GaN HEMT	3.5	12.1 (pulsed, total 145 W)	33
AlGaN HEMT	10	4.2 (pulsed, total 50.1 W)	33
AlGaN HEMT	20	6.6 (CW, total 1.32 W)	40
MOSFET (Si)	1.9	0.32 (CW, total 2.4 W)	41
LDMOSFET (Si)	3.2	1 (pulsed)	42
MODFET (GaAs)	2.16	2.22 (pulsed, total 200 W)	43

available from Si or GaAs devices. Better high frequency figures of merits are attributed to improved materials properties such as bandgap, critical electric field, and thermal conductivity as well as the saturation electron velocity, and also to a reduced capacitance from decreased device area. The most recent results demonstrated on SiC RF power devices are listed in Table 2. The RF power available from an impact ionization avalanche transit time (IMPATT) diode in SiC is ~ 100 times higher than in Si or GaAs. Promising devices have been demonstrated for IMPATT diodes with X-band operation and microwave power of 300 mW [30].

SiC MESFETs are developed as power transistors for operating frequencies in the 1–10 GHz range (from UHF through X band). Cree Inc. is marketing MESFETs with a best performance of 5.2 W/mm at 3.5 GHz and 63% power-added efficiency (PAE) for a $0.7\text{ }\mu\text{m} \times 48\text{-mm}$ device and monolithic microwave IC (MMIC) amplifiers based on these devices are also demonstrated with a power 36.3 W, associated gain of 0.5 dB, and PAE of 20.6% [33].

Static induction transistors (SITs) are also unipolar devices with a pn junction or a Schottky controlled gate. Normally, a SIT has a vertical channel structure for higher power density but is restricted to lower frequencies (UHF to C band) compared to MESFET with a lateral channel.

High-electron-mobility transistors (HEMTs) based on the AlGaN/GaN heterostructure show very promising device operation at frequencies of 10 GHz and higher. In this structure, a 5-times-higher two-dimensional electron gas (2DEG) than in the AlGaAs/GaAs structures allows a higher current capability. However, conventional GaN devices on sapphire substrates are not well suited because of a poor lattice match between GaN and sapphire ($\sim 13\%$) and thus high defect density ($\sim 10^8/\text{cm}^2$). By using a SiC substrate, the lattice mismatch can be decreased and the efficient heatsink is considerably better because of higher thermal conductivity in SiC.

There are several figures for comparing high-frequency devices, such as maximum operating frequency (f_T) or maximum frequency of oscillation (f_{max}). It is common to scale the output power with the gate width when compar-

ing devices with different dimensions at the operating frequency. Any device used in a circuit to measure the output power needs an f_T and f_{max} about 5–10 times higher than the operating frequency as a rule of thumb (see Fig. 4).

There are other aspects to consider when designing high-frequency devices. One is impedance matching, which influences linearity and bandwidth of an amplifier. The RF power devices in silicon today have output impedances in the order of $2\text{ }\Omega$, requiring complicated frequency-dependent matching circuits. The wide-bandgap materials have an advantage here in terms of breakdown voltage. Due to high critical fields, the devices in the GHz range can have breakdown voltages in the order of 200 V, which is necessary for high power delivery directly to a $50\text{-}\Omega$ load. For example, 30 W of power delivered to such a load requires a voltage swing of 55 V, and a device with a breakdown voltage safely above twice this value. However, in order to utilize this advantage the parasitic

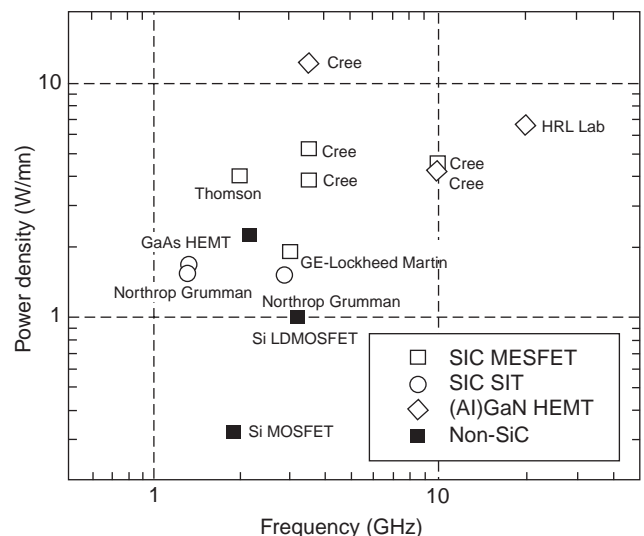


Figure 4. Output power density versus operating frequency for some more recent high-frequency devices.

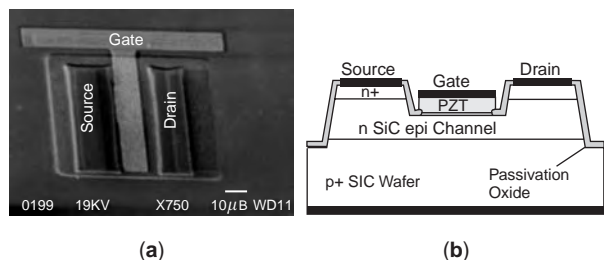


Figure 5. (a) A SEM image and (b) a schematic cross section of the 4H SiC ferroelectric FET in SiC.

elements have to be controlled, since higher output impedances are more sensitive to parasitics. Output impedances for 1-mm²-sized 4H SiC MESFETs are between 20 and 40 Ω.

3.3. Other Application Areas

A SiC application very close to commercial use is catalytic gas sensors. The basic principle is to use a catalytic metal (Pt, Pa, Ir, etc.) as gate on a metal–oxide–semiconductor (MOS) structure. Some gases will crack or decompose on the catalytic metal, and hydrogen ions can be sensed on the gate by the shift in flatband voltage that the extra charge incurs. Several devices based on this principle have been demonstrated in several different sensor applications for combustion processes [44].

More recently, the structural and electrical properties of ferroelectric PZT/Al₂O₃/4H SiC diode structures are proved to be promising for device applications [45], and the experimental results in the ferroelectric FETs (FeFET) in SiC showed nonvolatile operations (see Fig. 5). As shown in Fig. 6, it can be clearly seen that I_D – V_G characteristics exhibited memory effect; depending on the sweep direction, two different values of I_D can be measured for the same gate voltage [46]. The results are promising for other smart sensing applications utilizing high-temperature and high-frequency properties of ferroelectrics.

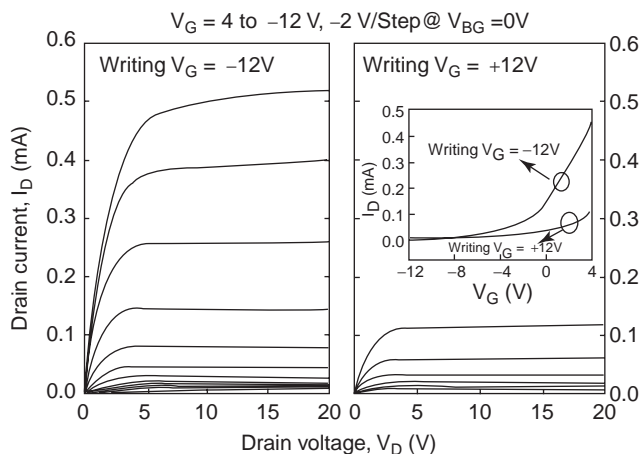


Figure 6. Static drain current versus drain voltage characteristics of a typical SiC ferroelectric FET after different V_G of +12 and –12 V has been applied.

4. SUMMARY

A discussion of the advantageous physical material properties of SiC that allows for high power, high frequency, and high temperature applications was presented. An updated review of the state-of-the-art performance was given for high-voltage as well as RF power devices. Although serious defect problems still remain to be overcome before large-area devices can be economically viable, the development of fabrication processes for SiC is at a relatively advanced stage and superior to most other wide-bandgap semiconductors. New emerging device applications such as the FeFET were presented.

BIBLIOGRAPHY

1. T. P. Chow, N. Ramungul, and M. Ghezzi, Recent advances in high-voltage SiC power devices, *Proc. High-Temperature Electronic Materials, Devices and Sensors Conf.* (Cat. IEEE), New York, 1998, p. 55.
2. Cree Inc., Durham, NC, USA, <http://www.cree.com>.
3. S. G. Mueller, M. Brady, B. Brixius, G. Fechko, R. Glass, D. Henshall, D. Hobgood, J. Jenny, R. Leonard, D. Malta, A. Powell, V. F. Tsvetkov, and J. C. H. Carter, High quality SiC substrates for semiconductor devices: From research to industrial production, *Proc. Int. Conf. Silicon Carbide and Related Materials*, Tsukuba, Japan, 2001.
4. C.-M. Zetterling, *Process Technology for Silicon Carbide Devices*, in EMIS Processing Series, IEE, London; 2002.
5. G. Y. Chung, C. C. Tin, J. R. Williams, K. McDonald, R. K. Chanana, R. A. Weller, S. T. Pantelides, L. C. Feldman, O. W. Holland, M. K. Das, and J. W. Palmour, Improved inversion channel mobility for 4H-SiC MOSFETs following high temperature anneals in nitric oxide, *IEEE Electron. Device Lett.* **22**:176–178 (2001).
6. M. K. Das, B. S. Um, and J. A. Cooper, Jr., Anomalous high density of interface states near the conduction band in SiO₂/sub 2//4H-SiC MOS devices, *Mater. Sci. Forum* **338**:1069–1072 (2000).
7. A. O. Konstantinov, P. A. Ivanov, N. Nordell, S. Karlsson, and C. I. Harris, High-voltage operation of field-effect transistors in silicon carbide, *IEEE Electron. Device Lett.* **18**:521–522 (1997).
8. K. P. Hilton, M. J. Uren, D. G. Hayes, P. J. Wilding, H. K. Johnson, J. J. Guest, and B. H. Smith, Surface induced instabilities in 4H-SiC microwave MESFETs, *Mater. Sci. Forum* **338**:1251–1254 (2000).
9. H. Cho, P. Leerungnawarat, D. C. Hays, S. J. Pearton, S. N. Chu, R. M. Strong, C. M. Zetterling, M. Östling, and F. Ren, Ultradeep, low-damage dry etching of SiC, *Appl. Phys. Lett.* **76**:739–741 (2000).
10. E. Danielsson, S. K. Lee, C. M. Zetterling, and M. Östling, Inductively coupled plasma etch damage in 4H-SiC investigated by Schottky diode characterization, *J. Electron. Mater.* **30**:247–252 (2001).
11. F. Dahlquist, J. O. Svedberg, C. M. Zetterling, M. Östling, B. Breitholtz, and H. Lendenmann, A 2.8 kV forward drop JBS diode with low leakage, *Mater. Sci. Forum* **338**:1179–1182 (2000).
12. S. K. Lee, C. M. Zetterling, E. Danielsson, M. Östling, J. P. Palmquist, H. Högborg, and U. Jansson, Electrical character-

- ization of TiC ohmic contacts to aluminum is implanted 4H-Silicon carbide, *Appl. Phys. Lett.* **77**:1478–1480 (2000).
13. F. Dahlquist, *Junction Barrier Schottky Rectifiers in Silicon Carbide—Aspects on Digest and Fabrication*, licentiate thesis, Royal Institute of Technology, Stockholm, Sweden, 2001; F. Dahlquist, private communication.
 14. Y. Sugawara, D. Takayama, K. Asano, R. Singh, J. Palmour, and T. Hayashi, 12–19 kV 4H-SiC pin diodes with low power loss, *Proc. 13th Int. Symp. Power Semiconductor Devices & ICs (ISPSD '01)*, 2002, pp. 27–30.
 15. H. Lendenmann, F. Dahlquist, J. P. Bergman, H. Bleichner, and C. Hallin, High-power SiC diodes: Characteristics, reliability and relation to material defects, *Mater. Sci. Forum* **389–393**: 1259–1264 (2002).
 16. D. Peters, R. Schorner, P. Friedrichs, J. Volkl, H. Mitlehner, and D. Stephani, An 1800 V triple implanted vertical 6H-SiC MOSFET, *IEEE Trans. Electron. Devices* **46**:542–545 (1999).
 17. Y. Sugawara, K. Asano, D. Takayama, S. Ryu, R. Singh, J. Palmour, and T. Hayashi, 5.0 kV 4H-SiC SEMOSFET with low RonS of 88mWcm, *Mater. Sci. Forum* **389–393**:1199–1202 (2002).
 18. Y. Sugawara, K. Asano, D. Takayama, S. Ryu, R. Singh, J. Palmour, and T. Hayashi, 5.0 kV 4H-SiC SEMOSFET with low RonS of 88mWcm, *Proc. Int. Conf. Silicon Carbide and Related Materials*, Tsukuba, Japan, 2001.
 19. D. Takayama, Y. Sugawara, T. Hayashi, R. Singh, J. Palmour, S. Ryu, and K. Asano, Static and dynamic characteristics of 4–6 kV 4H-SiC SIAFETs, *Proc. IEEE Int. Symp. Power Semiconductor Devices and ICs (ISPSD)*, 2001, pp. 41–44.
 20. P. Friedrichs, H. Mitlehner, R. Schörner, K.-O. Dohnke, R. Elpelt, and D. Stephani, Application oriented unipolar SiC switching devices, *Mater. Sci. Forum* **389–393**:1185–1190 (2002).
 21. S. Ryu, A. K. Agarwal, R. Singh, and J. W. Palmour, 1800 V NPN bipolar junction transistors in 4H-SiC, *IEEE Electron. Device Lett.* **22**:124–126 (2001).
 22. H. M. McGlothlin, D. T. Morissette, J. A. Cooper, Jr., and M. R. Melloch, 4 kV silicon carbide Schottky diodes for high-frequency switching applications, *57th Annual Device Research Conf. Digest*, 1999, pp. 42–43.
 23. S. H. Ryu, A. Agarwal, M. Das, L. Lipkin, J. Palmour, and N. Saks, Large area (3.3 mm × 3.3 mm) power MOSFETs in 4H-SiC, *Mater. Sci. Forum* **389–393**:1195–1198 (2002).
 24. J. Tan, J. A. Cooper, Jr., and M. R. Melloch, High-voltage accumulation-layer UMOSFETs in 4H-SiC, *IEEE Electron. Device Lett.* **19**:487–489 (1998).
 25. K. Asano, Y. Sugawara, S. Ryu, R. Singh, J. Palmour, T. Hayashi, and D. Takayama, 5.5 kV normally-off low RonS 4H-SiC SEJFET, *Proc. IEEE Int. Symp. Power Semiconductor Devices and ICs (ISPSD)*, 2001, pp. 23–26.
 26. H. Onose, A. Watanabe, T. Someya, and Y. Kobayashi, 2 kV 4H-SiC Junction FETs, *Mater. Sci. Forum* **389–393**:1227–1230 (2002).
 27. Y. Luo, J. Zhang, P. Alexandrov, L. Fursin, J. H. Zhao, and T. Burke, High-voltage (>1 kV) and high current gain(32) 4H-SiC power BJTs using Al-free Ohmic contact to the base, *IEEE Electron. Device Lett.* **24**:695–697 (2003).
 28. A. Agarwal, S.-H. Ryu, R. Singh, O. Kordina, and J. W. Palmour, 2600 V, 12 A, 4H-SiC, assymetrical gate turn off (GTO) thyristor development, *Mater. Sci. Forum* **338–342**:1387–1390 (2000).
 29. A. Agarwal, S.-H. Ryu, C. Capell, J. Richmond, J. W. Palmour, B. Phan, J. Stambaugh, H. Bartlow, and K. Brewer, SiC BJT's for high power switching and RF applications, *Proc. Int. Conf. Silicon Carbide and Related Materials*, 2003.
 30. K. V. Vassilevski, A. V. Zorenko, K. Zekentes, K. Tsagaraki, E. Bano, C. Banc, and A. A. Lebedev, 4H-SiC IMPATT diode fabrication and testing, *Mater. Sci. Forum* **389–393**:1353–1358 (2002).
 31. L. Yuan, J. A. Cooper, K. J. Webb, and M. R. Melloch, Demonstration of IMPATT diode oscillators in 4H-SiC, *Proc. Int. Conf. Silicon Carbide and Related Materials*, Tsukuba, Japan, 2001.
 32. R. A. Sadler, S. T. Allen, W. L. Pribble, T. S. Alcorn, J. J. Sumakeris, and J. W. Palmour, SiC MESFET hybrid amplifier with 30-W output power at 10 GHz, *Proc. IEEE/Cornell Conf. High Performance Devices*, Piscataway, NJ, 2000, pp. 173–177.
 33. J. W. Palmour, S. T. Sheppard, R. P. Smith, S. T. Allen, W. L. Pribble, T. J. Smith, Z. Ring, J. J. Sumakeris, A. W. Saxler, and J. W. Milligan, Wide bandgap semiconductor devices and MMICs for RF power applications, *Int. Electron Devices Meeting (IEDM) Technical Digest*, 2001, pp. 17.4.1–17.4.4.
 34. O. Noblanc, C. Arnodo, C. Dua, E. Chartier, and C. Brylinski, Power density comparison between microwave power MESFET's processed on conductive and semi-insulating wafer, *Mater. Sci. Forum* **338**:1247–1250 (2000).
 35. A. P. Zhang, L. B. Rowland, E. B. Kaminsky, J. W. Kretchmer, R. A. Beaupre, J. L. Garrett, J. B. Tucker, B. J. Edward, J. Foppes, and A. F. Allen, Microwave power SiC MESFETs and GaN HEMTs, *Solid-State Electron.* **47**:821–826 (2003).
 36. S. Sriram, A. Ward, C. Janke, T. Alcorn, H. Hagleitner, J. Henning, K. Wieber, J. Jenny, J. Sumakeris, and S. Allen, RF performance and reliability of SiC's on high purity semi-insulating substrates, *Proc. Int. Conf. Silicon Carbide and Related Materials*, 2003.
 37. R. C. Clarke, A. W. Morse, P. Esker, and W. R. Curtice, A 16 W, 40% efficient, continuous wave, 4H SiC, L-band SIT, *Proc. IEEE/Cornell Conf. on High Performance Devices*, Piscataway, NJ, 2000, Vol. 274, pp. 141–143.
 38. R. C. Clarke, C. D. Brandt, S. Sriram, R. R. Siergiej, A. W. Morse, A. K. Agarwal, L. S. Chen, V. Balakrishna, and A. A. Burk, Recent advances in high temperature, high frequency SiC devices, *Proc High-Temperature Electronic Materials, Devices and Sensors Conf. (Cat. IEEE)*, New York, 1998, pp. 96–97.
 39. A. K. Agarwal, L. S. Chen, G. W. Eldridge, R. R. Siergiej, and R. C. Clarke, Ion-implanted static induction transistors in 4H-SiC, *IEEE Device Research Conf. Digest*, Charlottesville, VA, 1998, pp. 94–95.
 40. J. S. Moon, M. Micovic, P. Janke, P. Hashimoto, W.-S. Wong, R. D. Widman, L. McCray, A. Kuidoghlian, and C. Nguyen, GaN/AlGaIn HEMTs operating at 20 GHz with continuous-wave power density >6 W/mm, *Electron. Lett.* **37**:528–530 (2001).
 41. I. Yoshida, M. Katsueda, Y. Maruyama, and I. Kohjiro, A highly efficient 1.9-GHz Si high-power MOS amplifier, *IEEE Trans. Electron. Devices* **45**:953–956 (1998).
 42. J. Olsson, N. Rorsman, L. Vestling, C. Fager, J. Ankarcrona, H. Zirath, and K. H. Eklund, 1 W/mm RF power density at 3.2 GHz for a dual-layer RESURF LDMOS transistor, *IEEE Electron. Device Lett.* **23**:206–208 (2002).
 43. H. Ishida, T. Yokoyama, H. Furukawa, T. Tanaka, M. Maeda, S. Morimoto, Y. Ota, D. Ueda, and C. Hamaguchi, 200 W GaAs-based MODFET power amplifier for W-CDMA base stations, *Int. Electron Devices Meeting (IEDM) Technical Digest*, 1999, pp. 393–396.

44. A. L. Spetz, P. Tobias, L. Uneus, H. Svenningstorp, L. G. Ekedahl, and I. Lundstrom, High temperature catalytic metal field effect transistors for industrial applications, *Sensors Actuators B* 1–3 (2000).
45. S.-M. Koo, S. I. Khartsev, C.-M. Zetterling, A. M. Grishin, and M. Östling, Ferroelectric Pb(Zr,Ti)O₃/Al₂O₃/4H-SiC diode structures, *Appl. Phys. Lett.* **81**:895–897 (2002).
46. S.-M. Koo, S. I. Khartsev, C.-M. Zetterling, A. M. Grishin, and M. Östling, Towards ferroelectric field effect transistors in 4H-silicon carbide, *Mater. Res. Soc. Symp. Proc.*, **711** (2002).
47. J. H. Zhao, K. Tone, X. Li, P. Alexandrov, L. Fursin, and M. Weiner, 3.6 mΩcm², 1726 V 4H-SiC normally-off trench-and-implanted vertical JFETs, *Proc. 15th IEEE Int. Symp. Power Semiconductor Devices and ICs*, April 14–17, 2003 (IS-PSD'03), pp. 50–53.

SIGNAL FADING IN RADIOCOMMUNICATIONS

RAMAKRISHNA JANASWAMY
University of Massachusetts
Amherst, Massachusetts

1. INTRODUCTION

THE term *fading* generally refers to the fluctuation of a radiofrequency (RF) signal with respect to time due to wave interference associated with time-varying propagation multipath. Multipath may be caused by reflections, refractions, diffractions, or scattering of the radio signals by obstacles dispersed around the transmitter and receiver. Time variation is caused by the motion of the transmitter, or the receiver, or the multipath environment, or combinations thereof. Depending on the time scales of variation, fading is characterized either as short-term (also referred to as *fast fading*) or long-term (also referred to as *slow fading*). Long-term variations are usually associated with obstacles causing shadowing and blockage of signals, and these influence the attenuation of the mean signal level. Examples are large buildings, trees, and solar or meteorological influences, all extending over at least a few tens of wavelengths of the RF signal. In terrestrial mobile communications, the long-term timescales can vary from few tenths of a second to a few seconds depending on the mobile speed and the angle of arrival of the multipath waves. In HF communications, timescales can range from a few minutes to a even a few hours depending on solar activity and meteorological influences; in many cases the long-term variation includes components that are diurnal, seasonal, or annual, or even involve the 11-year sunspot cycle. The availability of a channel in a wireless communication system is determined by long-term fading, whereas short-term fading variations affect the details of received waveform structure and system performance parameters such as the error rate. Because of the complexity and variety of the multipath environment, one often resorts to a statistical description of long-term and short-term fading. In most wireless systems, long-term fading and short-term fading coexist, and these variations

are superimposed on the gross variation of signal strength resulting from wave spreading in space. However, it is reasonable to assume that the long-term variability is sufficiently slow such that the short-term fading statistics are locally stationary; thus the channel statistics of the latter can be regarded fixed over an interval of interest. This assumption facilitates independent handling of the two statistics and greatly simplifies system analysis. Section 5 of this article describes short-term fading and the parameters of interest in a system design. Section 5 describes long-term fading and its effect on the determination of a cell size in a cellular type of system. Section 5 discusses current work and research topics in the area.

2. SHORT-TERM FADING

Short-term fading is a direct consequence of multipath and motion. When the radio environment consists of many scatterers, multiple copies of the transmitted signal waveform appear at the receiver, and this phenomenon is termed *multipath*. In addition, if there is motion at the transmitter or receiver, or in the environment, the received signal time and frequency characteristics are altered as a result of constructive and destructive interference of the multipath wave components. In the general case, the propagation channel can be conveniently treated as a time-varying linear system. However, it is instructive to discuss the narrowband case and the wideband case separately to gain a better understanding of the fading phenomena.

When a pure tone of frequency f_c and amplitude A_c is transmitted through a time-varying discrete multipath channel, the latter imposes amplitude and phase fluctuations on the carrier. One consequence of this is that the frequency of the carrier experiences a *Doppler shift*, whose maximum value, f_{dM} , depends on the transmitted wavelength λ and the maximum speed of motion v_0 :

$$f_{dM} = \frac{v_0}{\lambda} = 1.4815 f_{\text{GHz}} v_{0\text{mph}} \quad (1)$$

where the frequency f_{GHz} in the latter is expressed in GHz (gigahertz) and the speed of motion $v_{0\text{mph}}$ is expressed in miles per hour. For example, if the frequency of operation is 1 GHz and the receiver moves at a speed of 100 mph, the maximum Doppler shift is 148.15 Hz. The reciprocal of the maximum Doppler shift defines a timescale of variation of short time fading. In the example above, we say that radio channel has a variability over timescales of the order of 6.75 ms. More precise parameters such as the Doppler spread B_D , the level crossing rate N_A , and the average fade duration τ_A will be defined later. When a pure tone experiences fading, signal fluctuations of 40 dB or more about the mean level are not uncommon, with successive minima occurring every half-wavelength or so at the carrier frequency. In the design of digital systems, the data rate must be chosen so that there is no loss of coherence over the symbol as received. A rule of thumb is to choose the symbol rate to be at least two orders of magnitude greater than the maximum Doppler frequency.

When an electromagnetic wave of certain polarization enters a medium consisting of arbitrarily oriented scatterers, its polarization gets altered as a result of multiple scattering. One may expect to receive power from all polarizations even though it may be dominant in one polarization. For the sake of simplicity, we ignore polarization aspects and treat only scalar wave propagation here. Assuming a discrete multipath model, the complex envelope¹ of the total received signal could be written as

$$z(t) = A_c \sum_{n=1}^N a_n e^{j(2\pi\nu_n t + \phi_n)} \quad (2)$$

The time-varying equivalent lowpass transfer function $H(t)$ of the channel is thus

$$H(t) = \sum_{n=1}^N a_n e^{j(2\pi\nu_n t + \phi_n)} \triangleq a(t) e^{j\varphi(t)} \triangleq X(t) + jY(t) \quad (3)$$

The Doppler frequency ν_n depends not only on ν_0 and λ , but also on the angles of arrival (θ_n, ϕ_n) of the n th multipath wave relative to the direction of motion. Also, the amplitude a_n , the phase ϕ_n , and the number of independently varying multipath components N can all be treated as random numbers changing from location to location. It is seen from (2) that the time variation of the channel is a consequence of the Doppler shift experienced by the carrier. If the number of multipath components is large enough (typically $N \geq 5$), then, by the central-limit theorem, $H(t)$ will converge to a complex Gaussian random process, namely, the in-phase component $X(t)$ and the quadrature phase component $Y(t)$ of the complex envelope $H(t)$ will be independently distributed Gaussian random processes, or equivalently, the actual envelope $a(t) = \sqrt{X^2(t) + Y^2(t)}$ will be Rayleigh distributed and the phase $\varphi(t) = \text{atan}(Y(t)/X(t))$ will be uniformly distributed. Denoting the instantaneous signal power received with $A_c = 1$ as $S = \frac{1}{2}|H(t)|^2$ and its mean as $\sigma_S^2 = \langle S \rangle$, where angle brackets denote statistical expectation, the probability density functions (pdf's) for the phase envelope, and power are given by

$$p(\varphi) = \frac{1}{2\pi}, \quad 0 \leq \varphi \leq 2\pi \quad (\text{uniform distribution}) \quad (4)$$

$$p(a) = \frac{a}{\sigma_S^2} e^{-a^2/2\sigma_S^2}, \quad 0 \leq a < \infty \quad (5)$$

(Rayleigh distribution)

$$p(S) = \frac{1}{\sigma_S^2} e^{-S/2\sigma_S^2}, \quad 0 \leq S < \infty \quad (6)$$

(exponential distribution)

¹The complex envelope $u(t)$ of a real signal $s(t)$ relative to a nominal frequency f_c is defined as $s(t) = \Re[u(t)e^{j2\pi f_c t}]$, where \Re denotes *real part*. For a linear filter the impulse response $g(t)$ is related to the equivalent lowpass complex impulse response $h(t)$ as $g(t) = 2\Re[h(t)e^{j2\pi f_c t}]$.

For the Rayleigh distribution, the mean envelope level is $\bar{a} = \sqrt{\pi/2}\sigma_S$. Other distributions have been proposed in the literature, which purportedly match better with measured results around the mean or median signal level. For example, the Nakagami- m distribution for the envelope a given by

$$p_m(a) = \frac{2}{\Gamma(m)} \left(\frac{m}{2\sigma_S^2} \right)^m a^{2m-1} e^{-ma^2/2\sigma_S^2}, \quad a > 0, \quad (7)$$

$$m \geq \frac{1}{2} \quad (\text{Nakagami-}m \text{ distribution})$$

$$p_m(a) = \frac{2}{\Gamma(m)} \left(\frac{m}{2\sigma_S^2} \right)^m a^{2m-1} e^{-ma^2/2\sigma_S^2}, \quad a < 0,$$

$$m \geq \frac{1}{2} \quad (\text{Nakagami-}m \text{ distribution})$$

where $\Gamma(\cdot)$ is the gamma function, has been suggested by some researchers as a better model for describing the fluctuating signal. Note that $m = 1$ recovers the Rayleigh distribution. The corresponding distribution for power $S = a^2/2$ transforms to a gamma distribution:

$$p_m(S) = \frac{m^m S^{m-1} e^{-(mS/\sigma_S^2)}}{\Gamma(m)\sigma_S^{2m}} \quad (\text{gamma distribution}). \quad (8)$$

Once again $m = 1$ recovers the exponential power distribution (6) corresponding to the Rayleigh envelope (5).

Note that the characterizations in (2) and (3) assume that all the multipath components are random and that there is no steady component. If a steady component with mean power S_0 exists along with the random components, the distribution of the phase and envelope will be modified to

$$p(\varphi) = \frac{e^{-K} \left[1 + \sqrt{\pi K} \cos \varphi e^{K \cos^2 \varphi} \right] \left[1 + \text{erf} \left(\sqrt{K} \cos \varphi \right) \right]}{2\pi},$$

$$0 \leq \varphi \leq 2\pi \quad (9)$$

$$p(a) = \frac{a}{\sigma_S^2} e^{-a^2/2\sigma_S^2} e^{-K} I_0 \left(a\sqrt{2K}/\sigma_S \right),$$

$$0 \leq a < \infty \quad (\text{Ricean distribution}) \quad (10)$$

where $I_0(\cdot)$ is the modified Bessel function of the first kind of order zero and $K = S_0/\sigma_S^2$, known as the *Ricean K factor*, is the ratio of the power contained in the steady component to that contained in the random part. It is seen that the phase of the signal will no longer be uniformly distributed, but will peak around the phase of the steady component. Furthermore, the amount of fluctuations experienced under Rayleigh fading will be more severe than that under Ricean fading; consequently most system designers are concerned with evaluating system performance under Rayleigh fading.

Second-order statistical functions such as the autocorrelation and the autocovariance functions define the rate of variation of the fading signal. Assuming that the short-term fading is wide-sense stationary, the autocorrelation and the autocovariance functions of the envelope are defined as $\mu_a(\tau) = \langle a(t+\tau)a(t) \rangle$ and $v_a(\tau) = \mu_a(\tau) - \langle a(t) \rangle \langle a(t+\tau) \rangle$, respectively. The normalized envelope correlation coefficient is defined as

$$\rho_a(\tau) = \frac{v_a(\tau)}{[(\langle a^2(t) \rangle) - |\langle a(t) \rangle|^2]} \approx |e^{-j[\omega_{\text{dM}}\tau \cos(\gamma_0 - \phi) \sin \theta]}|^2 \quad (11)$$

where $\omega_{\text{dM}} = 2\pi f_{\text{dM}}$, (θ, ϕ) are the angles of arrival (random) of the incoming waves, and γ_0 is the azimuth angle of motion of the receiver. It is seen that the correlation properties of the signal will depend on the angular spectrum of arriving waves and are proportional to the Fourier transform of the angular spectrum. The signals received at two different time instants will be more correlated in the case when waves arrive through a narrower angular extent than when they arrive through wider angles. Using $x = v_0\tau$, Eq. (11) can also be used to describe the spatial correlation of the received envelope as a function of distance x . From the distribution of angles of arrival, related parameters such as the mean angle (first moment of the angular pdf) and rms angular spread (variance of the angular pdf) can be defined both for the azimuth angle and the elevation angle. A simple model, known as *Clarke's 2D model*, is where the waves are assumed to propagate in a two-dimensional plane (azimuth plane) and arrive with equal likelihood from all angles. For the Clarke's 2D model, the envelope correlation can be found as

$$\rho_a(\tau) = J_0^2(\omega_{\text{dM}}\tau) = J_0^2(k_0x) \triangleq \rho_e(x) \quad (12)$$

where $k_0 = 2\pi/\lambda$ is the wavenumber and $J_0(\cdot)$ is the zeroth-order Bessel function of the first kind. In general, the envelope correlation will decrease as τ or x are increased. As a rule of thumb, the signals at 2 times separated by time lag $f_{\text{dM}}\tau$ (or spatial points separated by k_0x) are considered to be correlated if $\rho_e(\tau) \leq 0.7$. For the Clarke's 2D model, the demarcation between correlated and uncorrelated signal occurs at $f_{\text{dM}}\tau = k_0x = 0.825$. Thus signals at two points separated by more than 0.13λ will be uncorrelated. Conversely, the correlation between two points separated more than 0.13λ will be less than 0.7. For example, the spatial correlation coefficient between two points separated by $\lambda/2$ is equal to $J_0^2(\pi) \approx 0.1$. If waves arrive uniformly from all angles in three dimensions (Clarke's 3D model), then the envelope correlation can be found using the second of (11) as

$$\rho_a(\tau) = \left[\frac{\sin(\omega_{\text{dM}}\tau)}{\omega_{\text{dM}}\tau} \right]^2 \quad (13)$$

To indicate the rate and severity of the fading signal, system parameters such as the level crossing rate and the average fade duration can also be extracted from the second-order statistics of the received signal. The *level cross-*

ing rate N_A (in Hertz) is the expected rate at which the envelope of the received signal crosses a specified level A in the positive-going (or negative-going) direction. The *average fade duration* τ_A (in seconds) below a specified level $a = A$ is the average of all durations for which the envelope is below that level. For Clarke's 2D model, the level crossing rate and the average fade duration can be shown to be

$$N_A = \frac{\sqrt{\pi}f_{\text{dM}}A}{\sigma_S} e^{-A^2/2\sigma_S^2} \quad (14)$$

$$\tau_A = \frac{1}{N_A} [1 - e^{-A^2/2\sigma_S^2}] \quad (15)$$

The level crossing rate is small at small and large values of A . Its maximum value occurs at $A = \sigma_S$ and is equal to $\sqrt{\pi}/e f_{\text{dM}} \approx 1.075f_{\text{dM}}$. The average fade duration increases with increasing values of A . Since the time taken to travel one wavelength is $\lambda/v_0 = 1/f_{\text{dM}}$, dividing N_A by f_{dM} and multiplying τ_A by f_{dM} gives, respectively, the number of crossings per wavelength and the average fade duration in wavelengths. As an example, using $f = 1$ GHz, $v_0 = 60$ mph, $A = \sigma_S$ yields $N_A = 96.75$ per second or 1.075 positive-going crossings per wavelength, and $\tau_A \approx 4.1$ ms or 0.37 wavelength. In order to capture fades at the level $A = \sigma_S$, the envelope must be sampled every 4.1 ms or every 0.37 wavelength. In actual wireless systems, the correlation properties of the received signal will also be influenced by electromagnetic mutual coupling, and this needs to be considered as well in system design.

For a general time-varying linear system representing the radio channel, the impulse response $g(\tau; t)$ is related to the equivalent lowpass impulse response $h(\tau; t)$ as

$$g(\tau; t) = 2\Re\{h(\tau; t) e^{j2\pi f_c \tau}\} \quad (16)$$

where the variable t represents the time variation of the channel due to Doppler frequency and the variable τ represents the propagation delay variable. The impulse response $h(\tau; t)$ represents the complex response of the channel at time t for an impulse applied τ seconds in the past. For a channel comprised of discrete multipath waves, the complex impulse response can be written as

$$h(\tau; t) = \sum_{n=1}^N a_n \delta(\tau - t_n) e^{j2\pi[v_n t - f_c t_n] + j\psi_n} \quad (17)$$

where the random quantities (a_n, v_n, ψ_n, t_n) respectively are the amplitude, Doppler shift, phase, and delay associated with the n th multipath wave. The phase $2\pi f_c t_n$ could be combined with ψ_n to define a new phase $\varphi_n = \psi_n - 2\pi f_c t_n$. A Fourier transformation of (17) with respect to the delay variable \mathcal{F}_τ results in the frequency-selective channel transfer function $H(f; t)$

$$H(f; t) = \int_{-\infty}^{\infty} h(\tau; t) e^{-j2\pi f \tau} d\tau \triangleq \mathcal{F}_\tau[h(\tau; t)] \quad (18)$$

where the frequency f represents translation relative to the nominal frequency f_c . At each frequency denoted by f ,

$H(f; t)$ represents the *time-varying* envelope and phase received with a single tone transmitted at that frequency. As described previously, as a result of the central-limit theorem, this is characterized by a zero-mean complex Gaussian random process. If the transmitted signal has a complex envelope $u(t)$ and a corresponding frequency spectrum $U(f)$, the received signal will have a complex envelope

$$z(t) = \int_{-\infty}^{\infty} h(t - \tau; t) u(\tau) d\tau = \int_{-\infty}^{\infty} H(f; t) U(f) e^{j2\pi f t} df \quad (19)$$

where it has been assumed that multipath returns at all delays will be observed. For the discrete multipath model of (17), the received complex envelope could be written as

$$z(t) = \sum_{n=1}^N a_n u(t - t_n) e^{j[2\pi\nu_n t + \phi_n]} \quad (20)$$

For a bandlimited transmitted signal $u(t)$, the multipath components cannot be resolved with infinite precision as can be done with impulse type of signals. All those delays arriving within a time duration much less than the reciprocal of the bandwidth W of $u(t)$ will appear together. The set of t_n s can be partitioned into L disjoint sets A_ℓ , $\ell = 1, 2, \dots, L$ and a representative delay τ_ℓ is associated with each set A_ℓ such that $t_n \in A_\ell$ if $u(t - t_n) \approx u(t - \tau_\ell)$. This will be true if the differences $\tau_\ell - t_n$ are much smaller than the reciprocal bandwidth of $u(t)$. Assuming single-bounce scattering, multipath components with a fixed delay τ_ℓ will appear to arrive from points distributed on an ellipsoid drawn in space such that the total pathlength traveled from the transmitter to the receiver via the ellipsoid is equal to $c\tau_\ell$, where c is the speed of light. The thickness of the sheath around the ellipsoid is of the order of the reciprocal bandwidth of $u(t)$ and will contribute to the set A_ℓ . With this approximation

$$z(t) = \sum_{\ell=1}^L u(t - \tau_\ell) \sum_{n_\ell} a_n e^{j[2\pi\nu_n t + \phi_n]} \quad (21)$$

where n_ℓ is the set of integers such that $t_n \in A_\ell$. Writing $\sum_{n_\ell} a_n \exp(j[2\pi\nu_n t + \phi_n]) = \alpha_\ell(t)$ and taking the Fourier transform on both sides of (21) with respect to the delay variable while treating $\alpha_n(t)$ terms as constants, the frequency-selective multipath description of fading channels

$$Z(f; t) = U(f) \sum_{\ell=1}^L \alpha_\ell(t) e^{j2\pi f \tau_\ell} \quad (22)$$

with the transfer function

$$H(f; t) = \sum_{\ell=1}^L \alpha_\ell(t) e^{j2\pi f \tau_\ell} \quad (23)$$

is obtained. The coefficient $\alpha_\ell(t)$ is a complex random quantity, and if n_ℓ is a sufficiently large, the sum defining it will contain different random terms. Moreover, note that we

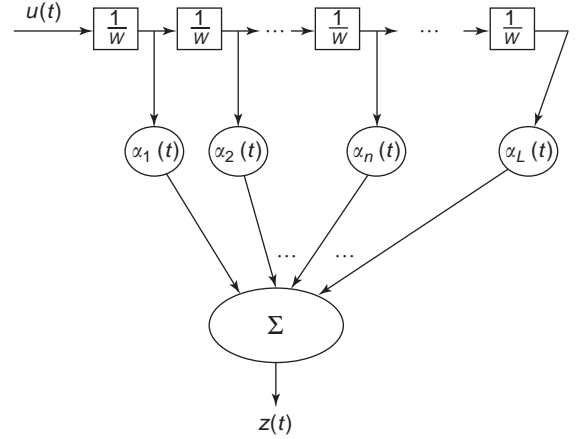


Figure 1. Tapped delay-line model for a frequency-selective channel. Note that $\tau_{\ell+1} - \tau_\ell \approx 1/W$.

have treated them as being constants while taking the Consequently, from the central-limit theorem, the $\alpha_\ell(t)$ terms, $\ell = 1, \dots, L$ can be regarded as i.i.d. (independent, identically distributed) complex, zero-mean, Gaussian random variables. The phase of $\alpha_\ell(t)$ will be uniformly distributed in $[0, 2\pi]$, and the envelope $|\alpha_\ell(t)|$ will be Rayleigh distributed. A tapped delay-line model derived from (22) is frequently employed for a frequency-selective channel and is shown in Fig. 1. When only a single tone is transmitted, then $u(t) = A_c$ and (20) reduces to (2). In situations where the duration of the symbol transmitted is very small in comparison to the inverse of f_{DM} , there will be negligible change in the structure of the transfer function over one symbol duration, and one may regard the spectrum of the received signal to be $Z(f; t) = U(f)H(f; t)$. Thus the channel imposes multiplicative fading on the transmitted spectrum at each frequency.

To characterize the behavior of the transfer function at different frequencies and at different times, we define the following correlation functions

$$R_h(\tau_1, \tau_2; t_1, t_2) = \langle h(\tau_1; t_1) h^*(\tau_2; t_2) \rangle \quad (24)$$

$$R_H(f_1, f_2; t_1, t_2) = \langle H(f_1; t_1) H^*(f_2; t_2) \rangle \quad (25)$$

$$R_T(f_1, f_2; \nu_1, \nu_2) = \langle T(f_1; \nu_1) T^*(f_2; \nu_2) \rangle \quad (26)$$

$$R_S(\tau_1, \tau_2; \nu_1, \nu_2) = \langle S(\tau_1; \nu_1) S^*(\tau_2; \nu_2) \rangle \quad (27)$$

where $T(f; \nu)$ and $S(\tau; \nu)$ are the Fourier transform of $H(f; t)$ and $h(\tau; t)$, respectively, with respect to t . The relationships between the various system functions are shown in Fig. 2 and between the various correlation functions, in Fig. 3.

For a wide-sense stationary (WSS) random process, the correlation functions depend only on the timelag $\Delta t = t_2 - t_1$. This also implies that the returns at different Doppler frequencies will be uncorrelated. Likewise, if the channel is wide-sense stationary in the frequency variable, the correlation functions will depend only on the frequency difference $\Delta f = f_2 - f_1$. This assumption is also known as *uncorrelated scattering* (US) for it implies that the returns arriving from different delays will be uncorrelated. The

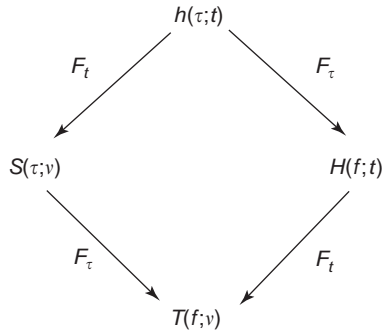


Figure 2. Relationships between the various system functions. \mathcal{F}_x denotes Fourier transformation with respect to the variable x .

US assumption has been derived for tropospheric scattering where multiple scattering phenomena are negligible. For terrestrial wireless multipath channels, the wave can be multiply scattered before arriving at the receiver. However, the US assumption has continued to be adopted by the wireless community owing to its simplicity. For a WSSUS channel, then, the various correlation functions simplify to

$$R_h(\tau_1, \tau_2; t_1, t_2) = \delta(\tau_2 - \tau_1) P_h(\tau_1; \Delta t) \quad (28)$$

$$R_H(f_1, f_2; t_1, t_2) = R_H(\Delta f; \Delta t) \quad (29)$$

$$R_T(f_1, f_2; \nu_1, \nu_2) = \delta(\nu_2 - \nu_1) P_T(\Delta f; \nu_1) \quad (30)$$

$$R_S(\tau_1, \tau_2; \nu_1, \nu_2) = \delta(\tau_2 - \tau_1) \delta(\nu_2 - \nu_1) P_S(\tau_1; \nu_1) \quad (31)$$

where $\delta(\cdot)$ is the delta function. The US assumption in the model is evident from the presence of $\delta(\tau_2 - \tau_1)$ in Eqs. (28) and (31). The quantity $P_S(\tau_1; \nu_1)$ is known as the *delay-Doppler channel scattering function* and describes the power spectral density of scattered waves arriving from delay τ_1 and Doppler shift ν_1 . The frequency selectivity of fading is characterized by $R_H(\Delta f; 0)$. In general, a wireless channel is frequency-selective. However, over a transmission bandwidth B for which $R_H(\Delta f; 0) \approx R_H(0; 0)$, all signal components fade together and $H(f; t)$ in effect acts like an allpass filter with a transfer function approximately equal

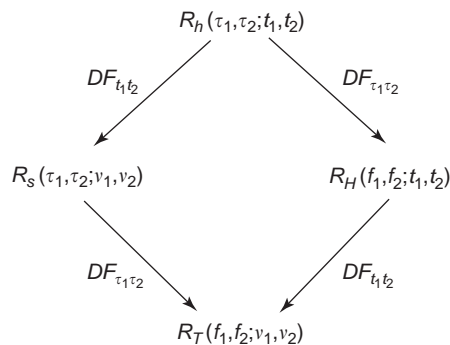


Figure 3. Relationships between the various correlation functions. $\mathcal{D}\mathcal{F}_{xy}$ denotes double Fourier transformation with respect to the variables x and y .

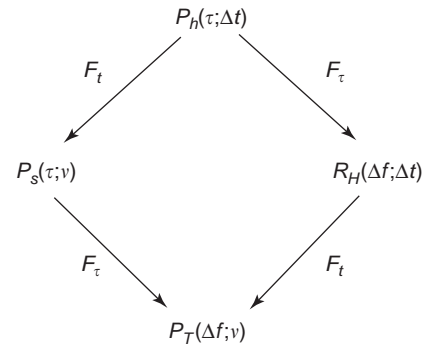


Figure 4. Relationships between the various correlation functions in a WSSUS channel.

to $H(0; t)$. Such a case is termed *frequency-nonselective fading or flat fading*. From Eq. (19), it is seen that the received complex envelope in such a case reduces to $z(t) = u(t)H(0; t)$, in a form similar to fading of a pure tone with a multiplicative channel gain. The relationships between the various correlation functions in a WSSUS channel are shown in Fig. 4.

It is useful to characterize the timescales over which fading can be treated as being essentially nonvarying. To determine this, we express the autocorrelation function of the received signal in terms of the transmitted signal $u(t)$ and $P_S(\tau, \nu)$:

$$R_z(t_1, t_2) = \langle z(t_1) z^*(t_2) \rangle = \int_{-\infty}^{\infty} \int_{-\infty}^{\infty} u(t_1 - \tau) u^* \times (t_2 - \tau) P_S(\tau; \nu) e^{-j2\pi\nu(t_2 - t_1)} d\tau d\nu \quad (32)$$

If a pure tone with unit amplitude is transmitted, then $u(t) = 1$, and writing $\Delta t = t_2 - t_1$, we get

$$R_z(\Delta t) = \int_{-\infty}^{\infty} \left[\int_{-\infty}^{\infty} P_S(\tau; \nu) d\tau \right] e^{-j2\pi\nu\Delta t} d\nu \triangleq \int_{-\infty}^{\infty} P_0(\nu) e^{-j2\pi\nu\Delta t} d\nu \quad (33)$$

where $P_0(\nu)$, known as the *Doppler spectrum*, is the observed power spectrum, equal to the sum of spectra contributed by all delays. The nominal width of this power spectrum is termed the *Doppler spread* B_D and is defined as

$$B_D = \left[\frac{\int_{-\infty}^{\infty} \nu^2 P_0(\nu) d\nu}{\int_{-\infty}^{\infty} P_0(\nu) d\nu} \right]^{1/2} \quad (34)$$

The fade rate at the median envelope level can be shown to be equal to $1.475 B_D$. For Clarke's 2D model, whose Doppler spectrum is the Fourier transform of $J_0(\omega_{dM}\tau)$, it can be shown that $B_D = f_{dM}/\sqrt{2}$. Thus, as mentioned earlier, the maximum Doppler shift f_{dM} is a measure of the fading rate of the channel. For a pure tone transmitted, we can also show that $R_z(\Delta t) = R_H(0; \Delta t)$. Hence, for a pure tone transmitted, coherent integration in reception is

possible only over timespans Δt for which the autocorrelation function $R_H(0;\Delta t)$ remains constant. The width Δt of $R_H(0;\Delta t)$ is known as the *channel coherence time* and is approximately equal to the reciprocal of the Doppler spread B_D . The channel Doppler spread is an important parameter and plays a key role in system design. In coherent systems the channel must be estimated at least one order of magnitude faster than the symbol rate, and we assert that the symbol duration $T \ll 1/B_D$. In adaptive systems (filters or antennas), the adaptive weights must be updated at least two orders of magnitude faster than the Doppler spread.

The value $P_h(\tau;0) = P_h(\tau)$ is the mean intensity of the channel in the delay variable and describes the dispersive behavior of the channel. This is known as the *power delay profile*. In terms of the function $P_h(\tau)$, the correlation function of the received complex envelope for zero timelag can be expressed as

$$R_z(t,t) = \int_{-\infty}^{\infty} |u(t-\tau)|^2 P_h(\tau) d\tau \approx P_h(t) \quad (35)$$

where the latter approximation is valid when the time duration of the transmitted symbol is much smaller than the spread of $P_h(t)$ and when its energy has been normalized to unity. The parameters of practical interest are the *mean delay* $\bar{\tau}$ and the root-mean-square (RMS) *delay spread* τ_{RMS} :

$$\bar{\tau} = \frac{\int \tau P_h(\tau) d\tau}{\int P_h(\tau) d\tau} \quad (36)$$

$$\tau_{\text{RMS}}^2 = \frac{\int (\tau - \bar{\tau})^2 P_h(\tau) d\tau}{\int P_h(\tau) d\tau} \quad (37)$$

For frequency-nonselctive fading we require the delay spread to be a small fraction of the symbol duration: $\tau_{\text{RMS}} \ll T$. This is also the requirement to avoid intersymbol interference. The requirement for coherent detection of symbols using matched filters is that $\tau_{\text{RMS}} \ll T \ll 1/B_D \Rightarrow \tau_{\text{RMS}} B_D \ll TB_D \ll 1$. A reasonable symbol time that satisfies both limits is to pick it to be the geometric mean of the two limits: $T \simeq \sqrt{\tau_{\text{RMS}}/B_D}$ or a symbol rate of $\sqrt{B_D/\tau_{\text{RMS}}}$. The quantity $\tau_{\text{RMS}} B_D$ is known as the *spread factor* of the wireless channel, and it is desirable to keep it less than unity for coherent detection. The spread factor depends on the RF frequency, speed of motion, angular spectrum of arriving waves, and buildup of the multipath environment.

Typical values of RMS delay spread vary from a few hundred nanoseconds for rural environments to few tens of microseconds for hilly terrain in terrestrial mobile communications. In HF skywave communication, delay spread arises due to multiple hops, electron density variation with height, from magnetoionic effects causing polarization-dependent paths (ordinary and extraordinary waves) and from inhomogeneities of the ionosphere. Typical values of τ_{RMS} due to multiple hops are 20–40 μs , and those due to electron density variation and magnetoionic effects vary from 100–200 μs . Typical values of Doppler

spread are less than 1–2 Hz, resulting in a spread factor of about 0.1 or less. In troposcatter links, the delay spread remains below 100–200 ns and the Doppler spread is in the range 0.1–10 Hz. In Earth–satellite links, fading (also referred to as *scintillation*) depends on the orbital radius as well as whether the terrestrial link is fixed or mobile on an airplane. Typical delay spreads are less than 10 ns, while the fade rates are in the range of fractional hertz to a few hertz. In underwater acoustic communication links with ranges within 10–100 mi, delay spreads range from a few seconds, while the Doppler spread often exceeds 1 Hz. Thus the channel is generally overspread, requiring non-coherent waveform processing.

For a WSSUS radio channel, the autocorrelation function $R_H(\Delta f;\Delta t)$ and $P_h(\tau;\Delta t)$ are related through the Fourier transform relationship as indicated in Fig. 4. As in the case of power delay profile, it is customary to consider zero timelag $\Delta t = 0$ and drop the second argument from the autocorrelation function. The resulting function, $R_H(\Delta f)$, is known as the *frequency correlation function* and is related to the power density profile through

$$R_H(\Delta f) = \int_{-\infty}^{\infty} P_h(\tau) e^{-j2\pi\Delta f\tau} d\tau \quad (38)$$

The *coherence bandwidth* B_{coh} is the nominal width of this function about $\Delta f = 0$. A common definition is to take B_{coh} as the smallest value for which the correlation falls to a prescribed value, say, –5 dB below the peak. The coherence bandwidth will be inversely proportional to the RMS delay spread and it is usual to assume $B_{\text{coh}} \approx 0.5/\tau_{\text{RMS}}$.

Having described the statistics of short term fading, we can easily ascertain its effects on the performance of a communication system. As an example, the bit error rate of BPSK in the presence of additive white Gaussian noise is equal to

$$P_e(\gamma) = \frac{1}{2} \text{erfc}(\sqrt{\gamma}) \quad (39)$$

where $\text{erfc}(\cdot)$ is the complementary error function and γ is the SNR per bit. In the presence of Rayleigh fading, γ will vary randomly, and the probability of error $P_b(\Gamma)$ will be obtained by considering (39) as a conditional probability, conditioned on the instantaneous SNR γ and writing

$$P_b(\Gamma) = \int_0^{\infty} P_e(\gamma) p(\gamma) d\gamma = \frac{1}{2} \left(1 - \sqrt{\frac{\Gamma}{1+\Gamma}} \right) \quad (40)$$

where $p(\gamma)$ is the pdf of γ and equal to [following from Eq. (6)]

$$p(\gamma) = \frac{1}{\Gamma} e^{-\gamma/\Gamma} \quad (41)$$

and Γ is the mean SNR per bit. The effect of fading is to drastically increase the bit error rates relative to those achieved in free space.

3. LONG-TERM FADING

Long-term fading generally occurs over spatial scales of the order of tens of wavelengths at the RF frequency and is attributed to blocking or shadowing by large obstacles. It is also known as *shadow fading*. It is obtained from the received signal by removing short-term fading after performing an average over spatial scales of the order of a few wavelengths or so. In terrestrial mobile communications, shadow fading is typically found to exhibit *lognormal distribution*; specifically, the sector averaged received signal power expressed on a decibel (dB) scale follows a Gaussian distribution. A lognormal distribution in built-up areas can be conceived from the central-limit theorem if the signal *sequentially* passes features of the environment that impart independent random fluctuations to its amplitude. Such features include random variation in building heights, gaps between buildings, variation in building design and construction material, and the presence of trees. In mobile communications, the standard deviation $\sigma_d = 20 \log(\bar{\sigma})$ of lognormal distribution has been found to lie in the range $6 \leq \sigma_d \leq 12$ dB. If $\bar{a}_d = 20 \log(\bar{a})$ is the mean envelope level in dB, where \bar{a} is the mean envelope level as a fraction, and $\bar{\mu}_d = 20 \log(\bar{\mu})$ is the area mean in dB, then the lognormal distribution can be expressed as

$$\begin{aligned} p(\bar{a}_d) &= \frac{1}{\sqrt{2\pi}\sigma_d} \exp\left[-\frac{(\bar{a}_d - \bar{\mu}_d)^2}{2\sigma_d^2}\right] \\ &= \frac{1}{\sqrt{2\pi}\sigma_d} \exp\left[-\frac{1}{2}\left(\frac{\ln[\bar{a}/\bar{\mu}]}{\ln(\bar{\sigma})}\right)^2\right] \text{ (lognormal distribution)} \end{aligned} \quad (42)$$

The instantaneous power received at a distance r from the transmitter for a signal undergoing lognormal fading with standard deviation σ_d (dB) can be expressed as

$$P_r(r) = \bar{P}_r(r) + \tilde{X} \quad (\text{dBW}) \quad (43)$$

where $\bar{P}_r(r)$ is the mean power received at r and \tilde{X} is a zero mean, Gaussian random variable with standard deviation σ_d . The mean signal power $\bar{P}_r(r)$ generally obeys the relation

$$\bar{P}_r(r) = \bar{P}_r(r_0) - 10\gamma \log \frac{r}{r_0} \quad (44)$$

where $\bar{P}_r(r_0)$ is the mean power received at some reference distance r_0 from the transmitter and γ is known as the *path loss exponent*. In terrestrial mobile communications, its value can range from 1.5 to 6. Given that the instantaneous power received can vary about the mean power, it is apt to ask the question ‘‘What is the probability $P_{X_0}(r)$ that the signal received at r falls below some threshold power X_0 [dBW]?’’ Using the pdf for a Gaussian random

variable, it is easy to see that

$$\begin{aligned} P_{X_0}(r) &= \int_{-\infty}^{X_0} \frac{1}{\sqrt{2\pi}\sigma_d} e^{-[x - \bar{P}_r(r)]^2 / 2\sigma_d^2} dx \\ &= \frac{1}{2} \operatorname{erfc}\left(\frac{\bar{P}_r(r_0) - 10\gamma \log(r/r_0) - X_0}{\sqrt{2}\sigma_d}\right) \end{aligned} \quad (45)$$

Given the parameters γ , σ_d , X_0 , $\bar{P}_r(r_0)$, and r_0 , Eq. (45) can be used to determine the radius of a cell $r = R$ about the transmitter such that the signal level on its boundary falls below the threshold for only a fraction β of the time. Hence

$$\log \frac{R}{r_0} = \frac{\bar{P}_r(r_0) - X_0 - \sqrt{2}\sigma_d \operatorname{erfc}^{-1}(2\beta)}{10\gamma} \quad (46)$$

As an example, if $\beta = 0.25$, $X_0 = -100$ dBm, $\sigma_d = 9$ dB, $\gamma = 4.8$, $r_0 = 1$ mi, $\bar{P}_r(r_0) = -77$ dBm (at 850 MHz), then $R = 3.6$ km.

4. COMBINED SHORT- AND LONG-TERM FADINGS

It is possible to combine the short-term distributions with long-term distributions and come up with a single model for the composite variation of the signal. For example, the statistics of a non-line-of-sight (NLoS) signal can be treated as a mixture of Rayleigh distribution whose mean power varies lognormally, resulting in what is known as *Suzuki distribution* for the envelope:

$$\begin{aligned} P_s(a; \sigma_d, \mu_d) &= \int_0^\infty \frac{a}{\sigma^2} e^{-a^2/2\sigma^2} \Big|_{\sigma = \bar{a}\sqrt{2/\pi}} \cdot \frac{1}{\sqrt{2\pi}\sigma_d} \\ &\quad \times \exp\left[-\frac{1}{2}\left(\frac{\ln[\bar{a}/\bar{\mu}]}{\ln(\bar{\sigma})}\right)^2\right] d\bar{a} \end{aligned} \quad (47)$$

Although Suzuki distribution is sound on physical grounds, it has limited practical utility as no closed-form expression is available for the integral given above. A similar mixture can also be defined for LoS situations where Ricean distribution is used instead of the Rayleigh distribution for short-term fading.

5. CURRENT WORK AND RESEARCH TOPICS

With the advent of antenna arrays for interference reduction (smart antennas), mitigation of fading (spatial or polarization diversity antennas), exploitation of multipath fading itself to increase system capacity [multiple-input/multiple-output (MIMO) systems], and position location (direction finding systems), it becomes necessary to develop more advanced models than the ones based on uniform angles of arrival in 2D or 3D space as were assumed in the previous sections. It has already been demonstrated in (11) that even though the statistics of fluctuation (i.e., pdf of fluctuations) may remain the same, the temporal or spatial correlation of the signal in a dynamic multipath

environment depends on the angular spectrum of the arriving waves at the receiver. Furthermore, when electromagnetic waves strike arbitrarily oriented, finite obstacles, there will be transfer of power from copolar components to the cross-polar components. Geometric scattering models, introduced during the era of troposcatter communications, are now being used to simulate various wireless environments. In these models, waves are singly scattered from point scatterers and arrive at the receiver. Various models exist that all differ in the distribution of scatter density to simulate either multipath around base stations, multipath around mobile stations, or combinations of both. Using these models it is possible to get the PDF in the angles and times of arrival as well as the power spectra in angles and delay. Other quantities such as the envelope correlation can be obtained from these statistics. Janaswamy compares the various geometric models with each other as well as with measurements. As an example, the Gaussian scatter density model gives the following expression for the spatial correlation, ρ , between two points separated by a distance d

$$\rho \approx \exp(jk_0 d \cos \bar{\phi}) \exp \left[-\frac{1}{2} \left(\frac{k_0 d \sigma_s \sin \bar{\phi}}{D} \right)^2 \right], \quad (48)$$

$$\sigma_s \ll D,$$

where D is the distance between the mobile station (MS) and the base station (BS), $\bar{\phi}$ is the angle between the line joining the two spatial points and the line joining BS and MS, and σ_s is a measure of the effective radius of scatterers about the MS. The envelope correlation is equal to $|\rho|^2$. All the existing geometric scattering models are scalar in nature. An empirical polarimetric model for fixed wireless applications is described by Oestges et al. With the introduction of MIMO systems, there is certainly a need to develop full polarimetric models that also take into account multiple scattering of waves. Jensen and Wallace give a good summary of the antenna and propagation issues for MIMO systems.

6. CONCLUSION

In this article we have described the mathematical models of short-term and long-term fading. Statistical distributions for signal fading such as Rayleigh distribution, Ricean distribution, lognormal distribution, and models for wide-band channel characterization have been introduced. Various propagation parameters, including Doppler spread, delay spread, angular spread, spatial correlation, have been discussed. The effect of short-term fading on system performance and the effect of long-term fading on the design of a wireless cell size has been demonstrated. Finally, topics of current research in fading have been discussed.

BIBLIOGRAPHY

1. R. B. Ertel, P. Cardieri, K. W. Sowerby, T. S. Rappaport, and J. H. Reed, Overview of spatial channel models for antenna array communication systems, *IEEE Pers. Commun.* **5**:10–22 (Feb. 1998).
2. C. Oestges, V. Eerceg, D. V. Janvier, and A. Paulraj, Propagation modeling of multi-polarized fixed wireless channels, *IEEE Trans. Veh. Technol.* **53**(3):644–654 (May 2004).
3. W. C. Jakes, ed., *Microwave Mobile Communications*, IEEE Press, New York, 1995.
4. R. Janaswamy, *Radiowave Propagation and Smart Antennas for Wireless Communications*, Kluwer Academic Publishers, Boston, 2000.
5. R. Janaswamy, Angle and time of arrival statistics for the Gaussian scatter density model, *IEEE Trans. Wireless Commun.* **1**(3):488–497 (July 2002).
6. M. A. Jensen and J. W. Wallace, A review of antennas and propagation for MIMO wireless communication systems, *IEEE Trans. Anten. Propag.* (in press).
7. R. S. Kennedy, *Fading Dispersive Communication Channels*, J Wiley, New York, 1969.
8. A. Papoulis and S. Unnikrishna Pillai, *Probability, Random Variables, and Stochastic Processes*, 4th ed., McGraw-Hill, New York, 2002.
9. J. D. Parsons, *The Mobile Radio Propagation Channel*, Pentech Press, London, 1992.
10. J. G. Proakis, *Digital Communications*, 4th ed., McGraw-Hill, New York, 2000.
11. T. S. Rappaport, *Wireless Communications*, Prentice-Hall, Upper Saddle River, NJ, 2000.
12. M. Schwartz, W. R. Bennett, and S. Stein, *Communication Systems and Techniques*, Part III, McGraw-Hill, New York, 1966.
13. S. Stein, Fading channel issues in systems engineering, *IEEE J. Select. Areas Commun.* **SAC-5**(2):68–89 (Feb. 1987).

SILICON-GERMANIUM

HERMANN SCHUMACHER
University of Ulm
Ulm, Germany

1. INTRODUCTION

By a wide margin, Silicon is the most used semiconductor material in electronics today. Its main advantages are its abundant supply (it is fabricated from SiO₂, which is as abundant as sand on a beach), its mechanical robustness (which allows very large wafers to be fabricated, currently up to 300 mm in diameter), its high thermal conductivity (which not only allows power semiconductor devices to be fabricated, but also is a prerequisite for the integration of millions of transistors on one chip), and most importantly, its highly stable native oxide, SiO₂. The most common transistor device technology in use today, the metal-oxide-semiconductor field-effect transistor, or MOSFET, uses this native oxide extensively both in the fabrication process and in the completed device.

Compared with other semiconductor materials—Silicon (Si), Germanium (Ge), or Gallium-Arsenide (GaAs)—the semiconducting alloy Silicon-Germanium (SiGe) has been a late arrival on the stage of high-speed electronics. SiGe layers are never used alone, but always in combination

with Si layers, and they allow significant enhancement of electronic device performance in a variety of ways.

- Si/SiGe heterostructure bipolar transistors (HBTs) have been commercially available since 1998. SiGe is being used in the base layer in two different ways.
 - A graded $\text{Si}_{1-x}\text{Ge}_x$ layer with a low Ge content x near the emitter and a higher Ge content near the collector of a bipolar transistor creates a strong electric field in the base and significantly increases the speed of electrons traversing the base, increasing the current-gain cutoff frequency f_T .
 - In another concept, the Ge content is already substantial at the emitter-base junction, creating an energy barrier for the unwanted injection of holes from the base into the emitter, which allows significant increase of the base doping concentration, leading to a much reduced base resistance, and increases primarily the microwave power gain of these transistors.
- Si/SiGe heterostructures can also be advantageously used to confine charge carriers in the channel of a field-effect transistor (FET). The primary goal of this confinement (forming a two-dimensional electron or hole gas) is an improvement in the charge carriers' mobility, which in turn increases the device speed. At the time of this writing (2004), no Si/SiGe heterostructure FET processes are commercially available, but the area is experiencing intense research.
- The fact that the introduction of Ge into the Silicon crystal lattice also increases the lattice constant can be used to fabricate Silicon films with a built-in tensile strain, which can equally increase the charge carrier mobility. Such "strained-Si" channels are one of the options for next-generation metal-oxide-semiconductor field-effect transistors (MOSFETs), holding great promise for an increase in the speed of operation of highly integrated digital and analog integrated circuits.

The large interest in Si/SiGe heterostructure devices is caused by the fact that they fully exploit the vast body of technological advances in Silicon semiconductor processing in general. The concept of "bandgap engineering," the modification of the semiconductor energy band structure, introduces new degrees of freedom in the design of advanced devices, yet requires only minor modifications to existing processes.

By combining bandgap engineering for the vertical layer sequence of a semiconductor device with the deep sub- μm lateral scaling made possible by advances in Silicon processing, SiGe HBTs (the most mature Si/SiGe device concept) have shown dramatic improvements in their cutoff frequencies: a record transit frequency $f_T = 350$ GHz characterizes the state-of-the-art today in laboratory experiments [1], whereas more readily available devices show both f_T and the maximum frequency of oscillation f_{max} in the 100–200 GHz range. The demonstrated Si/SiGe HBT performance enables monolithic microwave integrated circuits (MMICs) with good performance well into the

upper microwave and lower millimeter-wave range. The mature Silicon fabrication processes into which the SiGe devices are being embedded allow for high-complexity designs. Device cutoff frequencies have progressed to a point where raw device speed is no longer the bottleneck in the design of Si-based MMICs, but rather passive circuit element performance and layout issues. Additionally, breakdown voltages of Si/SiGe HBTs optimized for high cutoff frequencies are too low for some higher power applications.

Although circuits using Si/SiGe heterostructure devices are making inroads into areas traditionally held by GaAs technologies, such as short-range radar sensors, it is evident that they will not replace these technologies entirely. Demanding applications in terms of either low receiver noise figure or significant radio frequency (RF) output power at elevated frequencies will continue to use GaAs-based heterostructure technologies.

Si/SiGe ICs are best when

- large market volumes can be expected
- the specific application benefits from multifunctional, high-complexity monolithic ICs
- optimum RF performance is not required, but rather low cost.

2. A CLOSER LOOK

Commonly, electronic devices are fabricated in a crystal lattice that consists of one semiconductor only—Silicon, which has a chemical composition made up from only one atom. Other mono-element semiconductors are Ge, or C in its crystalline form—diamond.

2.1. Compound Semiconductors and Bandgap Engineering

Other semiconductor materials, such as GaAs, are composed of two or more chemical elements—they are compound semiconductors. Semiconducting alloys may have several advantages over mono-element semiconductors, like strong electro-luminescence (conversion of an electric current into light), or high electron mobility.

Most important, however, is the added degree of freedom in device design obtained by the ability to change the chemical composition of the lattice within a single crystal. Such a structure with varied stoichiometry within a single semiconducting crystal is called a semiconductor heterostructure.

In solid-state physics terms, the most striking feature of any semiconductor is the band structure, characterized by a valence band energy E_V (which is the highest energy of bound electrons at absolute temperature $T = 0$ K), a conduction band energy E_C (which is the lowest energy of a free electron—free to move about in the lattice), and the forbidden energy range in between, which does not contain any allowed energy states an electron can occupy. This forbidden energy region is called the bandgap.

The exact band structure depends strongly on the chemical composition of the semiconductor material: By modifying the chemical structure, we can tailor the band

structure according to our needs—we perform bandgap engineering. In 1982, Herbert Kroemer formulated the central design principle of semiconductor heterostructures, saying; “Heterostructures modify the distribution and flow of charge carriers in semiconductors” [2].

Most compound semiconductor materials are formed by combining elements of the third and fourth column of the periodic table of elements, like Gallium (3rd column) and Arsenic (5th column). These compounds are called “three-five semiconductors.”

2.1.1. The Silicon-Germanium Compound Heterostructure. Silicon and Germanium are both elements from the fourth column of the periodic table of elements. Their alloy, $\text{Si}_{1-x}\text{Ge}_x$, is also a semiconductor whose properties can be modified by changing the Germanium mole fraction x .

An important observation is that when we modify the chemical composition of a semiconducting crystal, we not only modify the energy band structure, but also the geometry of the lattice, characterized by the lattice constant. Both effects are typically represented in a graph similar to Fig. 1. Note that for the ternary compound semiconductor formed by the alloy of GaAs and AlAs— $\text{Al}_x\text{Ga}_{1-x}\text{As}$ —the bandgap can be varied in a wide range by an appropriate Al mole fraction x , whereas the lattice constant remains essentially unchanged. In $\text{Si}_{1-x}\text{Ge}_x$, not only the bandgap but also the lattice constant is being significantly modified by the Ge mole fraction. The corresponding change in the geometry of the lattice will lead to strong mechanical strain in the crystal, which will eventually cause crystallographic defects, which restricts the modification of chemical composition to very thin layers where the mechanical energy can be stored by elastic deformation of the lattice; the strained layer has to be thinner than a critical layer thickness, which is a function of the material composition of the layers forming the heterostructure.

Current semiconductor devices employing $\text{Si}/\text{Si}_{1-x}\text{Ge}_x$ heterostructures exploit the ability to modify the bandgap. The change in lattice constant is a complicating side effect. SiGe heterostructures are being used in two different ways.

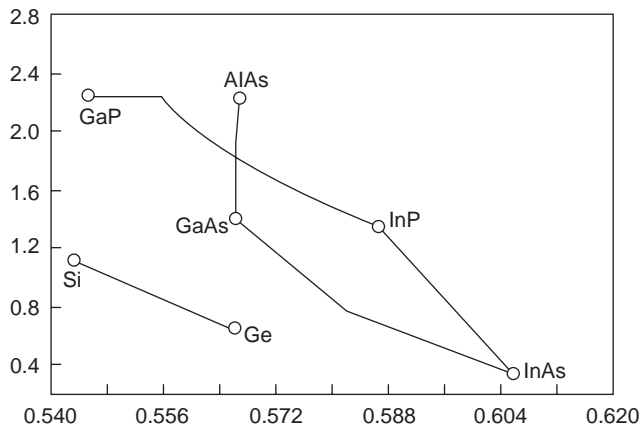


Figure 1. Lattice constant (horizontal axis) and bandgap (vertical axis) of important compound semiconductor structures.

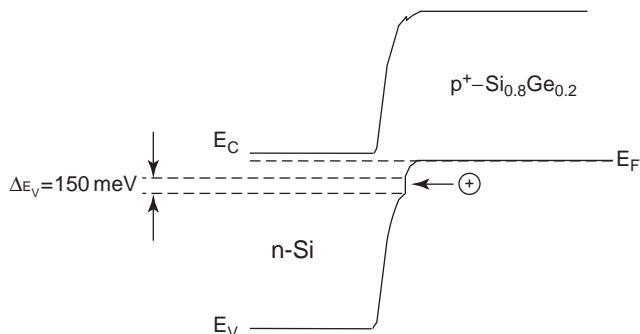


Figure 2. Abrupt n-Si/p-SiGe heterostructure: hole-blocking barrier in the valence band.

1. Abrupt Si/SiGe junctions can be used to construct energy barriers, e.g., for holes in the valence band, see Fig. 2. The situation shown is found in the “wide-gap emitter” concept of heterostructure bipolar transistors (HBTs) and will be described in more detail below. Another application of abrupt Si/SiGe heterostructures is the formation of confining energy barriers for the channel region of field-effect transistors. Figure 3 shows the concept for the case of a hole channel.
2. Graded Si/SiGe heterostructures can be used to create a built-in electric field through a variation of the bandedge, for one carrier species only, see Fig. 4. This concept is being used in Si/SiGe drift transistors, where electrons in the base of an npn bipolar transistors experience a significant reduction in base transit time by the additional drift field.

In all of these applications, the effect of mechanical strain has to be carefully observed. Crystallographic defects have to be avoided by choosing the thickness of the strained layer to be lower than a critical thickness d_{crit} . Figure 5 shows the most common case, a thin strained $\text{Si}_{1-x}\text{Ge}_x$ layer on relaxed Si [3]. Note that two different definitions of the critical thickness exist: The lower curve is the

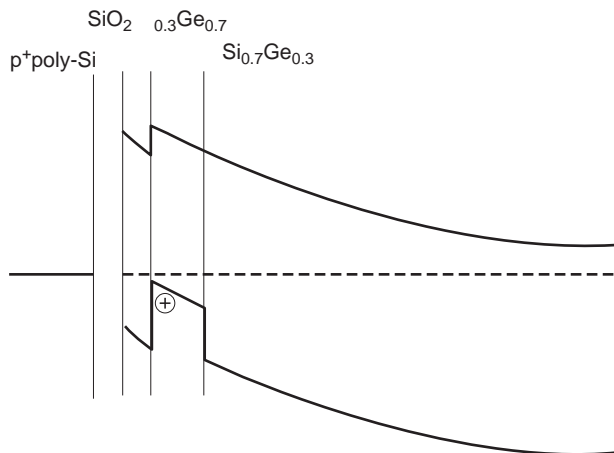


Figure 3. Two abrupt Si/SiGe heterostructures provide confinement for holes in a p-channel field-effect transistor.

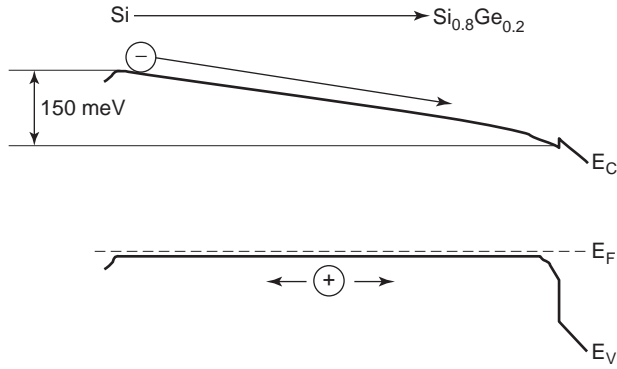


Figure 4. Creation of a built-in drift field acting on electrons only, through a gradual variation of the Ge concentration x in a p-doped $\text{Si}_{1-x}\text{Ge}_x$ layer.

equilibrium limit. Layers with combinations of Ge content and layer thickness below this line can be considered stable even at elevated processing temperatures. The upper line is an empirical fit to published data on strained SiGe layers. Layers with Ge content and layer thickness combinations above this line will most likely result in plastic deformation of the lattice and crystallographic defect formation. The medium range is called the metastable regime. Layers in the metastable regime can be defect-free, provided that the thermal budget of process steps after the SiGe film deposition is being carefully monitored.

In an elastically strained SiGe film, the strain will affect the band structure. Here, we need to take a closer look at the three fundamentally different ways in which the conduction and valence bands in a semiconductor heterostructure can line up.

- In a “type I” heterostructure, the valence band of the material with the wider gap is below, and the

conduction band is above, the respective band in the material with the smaller bandgap, or in other words, the forbidden gap of the material with the smaller bandgap is completely within the forbidden gap of the material with the larger bandgap.

- In a “type II” heterostructure, both the valence band and the conduction band of one material are below the respective bands in the other material, leading to a staircase-like impression.
- In a “type III” heterostructure, the conduction band of one material is energetically below the valence band of the other material.

Elastically deformed Si/SiGe heterostructures can have a type I or a type II band lineup, depending on the strain built into the lattice. Figure 6 shows a chart, published by Schäffler [4], which allows determination of the conduction band (ΔE_C) and valence band (ΔE_V) discontinuities of abrupt SiGe/Si heterostructures.

2.2. The Si/SiGe/Si Heterostructure Bipolar Transistor

To understand the central design dilemma of the bipolar transistor, addressed by the introduction of heterostructures, consider the way in which the collector current is controlled by the base-emitter voltage. We will restrict our discussion to npn-type transistors, where the emitter is n-doped, the base p-doped, and the collector again n-doped. Equal arguments can be found for the pnp-type transistor by considering holes instead of electrons.

The base of a bipolar transistor is hence bordered by two pn-junctions: one, the emitter-base diode, is forward biased in active operation, whereas the other, the base-collector diode, is reverse biased. Through the forward bias $V_{BE} > 0$ across the emitter-base diode, the minority carrier density (here, the electron density in the p-doped base, n_p) in the base layer at $y = 0$ (the base-side edge of the emitter-base space charge region) is increased.

$$n_p(y=0) = n_{p0} \exp\left(\frac{V_{BE}}{V_T}\right) = \frac{n_{i,B}^2}{N_{AB}} \exp\left(\frac{V_{BE}}{V_T}\right) \quad (1)$$

where $n_{i,B}$ is the intrinsic carrier concentration in the base layer, N_{AB} is the acceptor doping concentration, and $V_T = kT/q$ is the thermal voltage (approximately 26 meV at room temperature). We are assuming that all acceptors have been ionized.

The reverse bias $V_{CB} > 0$ across the collector-base junction lowers the minority carrier concentration at $y = W_B$, the base-side edge of the collector-base space charge region

$$n_p(y=W_B) = n_{p0} \exp\left(\frac{-V_{BC}}{V_T}\right) = \frac{n_{i,B}^2}{N_{AB}} \exp\left(\frac{-V_{BC}}{V_T}\right) \approx 0 \quad (2)$$

in the active forward regime, as $n_p(W_B)$ can be neglected vs. $n_p(0)$.

The base layer is so thin that recombination can be neglected across the base (short-base diode). In this case, the minority carrier concentration is a linear function of the

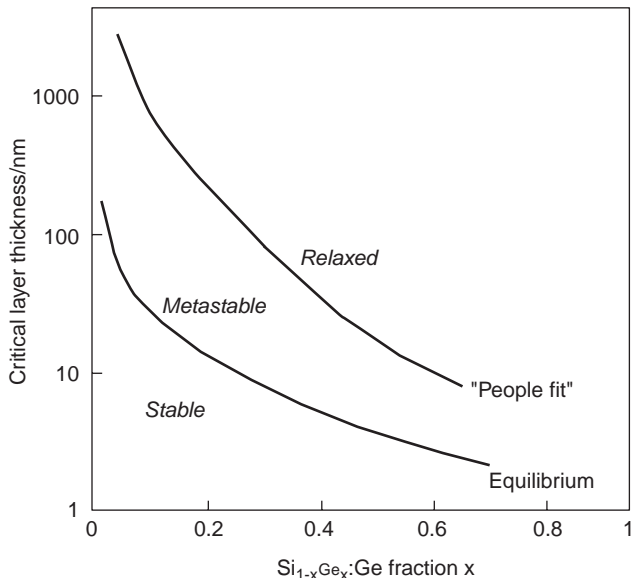


Figure 5. Critical thickness of strained $\text{Si}_{1-x}\text{Ge}_x$ layers on Si, vs. Ge mole fraction x , after [3].

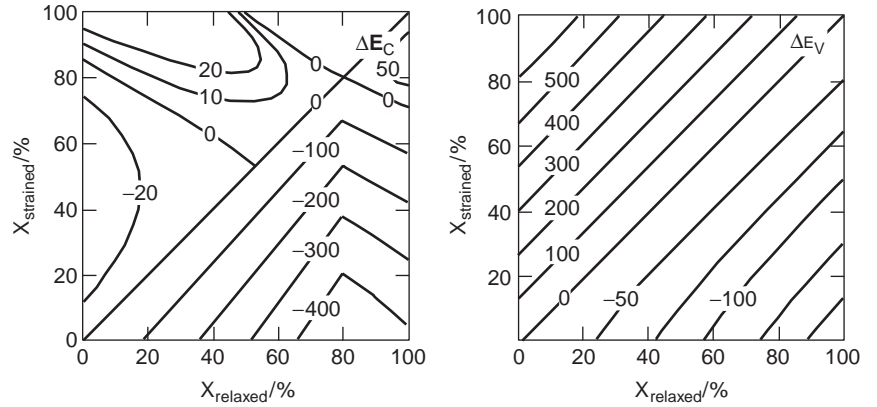


Figure 6. Conduction band and valence band discontinuities of Si/SiGe heterostructures as a function of the composition of the relaxed layer and the strained layer, after [4].

coordinate y

$$n_p(y) = n_p(0) - \frac{n_p(0) - n_p(W_B)}{W_B} y \approx n_p(0) \times \left(1 - \frac{y}{W_B}\right) \text{ for } 0 < y < W_B \quad (3)$$

Neglecting any potential difference across the neutral base layer (the voltages drop across the space charge regions), the electrons move across the base driven by diffusion only and the collector current density J_C is proportional to the minority carrier gradient

$$J_C = qD_{n,B} \frac{dn_p(y)}{dy} \approx -qn_{p0} \frac{D_{n,B}}{W_B} = -q \frac{D_{n,B}n_{i,B}^2}{W_B N_{AB}} \exp\left(\frac{V_{BE}}{V_T}\right) \text{ for } 0 < y < W_B \quad (4)$$

Here, q is the electron charge and $D_{n,B}$ is the diffusion constant of electrons in the base.

Likewise, we consider the emitter region as a short-base diode bordered by the base emitter at $y = -d_{BE}$ and an ideal recombination contact at $y = -W_E$, which forces $p_n(-W_E) = 0$. We further assume that the thickness of the base-emitter space charge region d_{BE} is much smaller than the emitter width W_E . The forward-biased emitter-base junction injects holes from the base to the emitter, leading to a base current density J_B

$$J_B = -qD_{p,E} \frac{dp_n}{dy} = -q \frac{D_{p,E}n_{i,E}^2}{W_E N_{DE}} \exp\left(\frac{V_{BE}}{V_T}\right) \text{ for } -W_E < y < -d_{BE} \quad (5)$$

where $n_{i,E}$ is the intrinsic carrier concentration in the emitter layer and N_{DE} the donor doping concentration there. Equations (4) and (5) allow us to find the common

emitter current gain of the bipolar transistor

$$B = \frac{J_C}{J_B} = \frac{D_{n,B}}{D_{p,E}} \frac{W_E}{W_B} \frac{N_{DE}}{N_{AB}} \frac{n_{i,B}^2}{n_{i,E}^2} \quad (6)$$

In a conventional homojunction bipolar transistor, where emitter and base layers are composed of the same material, the intrinsic carrier concentrations in the emitter $n_{i,E}$ and the base $n_{i,B}$ will be identical (neglecting small differences because of doping-dependent bandgap narrowing effects), so the last term in Eq. (6) is close to one. The ratio of diffusion constants in the base and the emitter (the first term) reflects the ratio of electron and hole mobilities, which in Silicon is a little less than three. The emitter and base width (the layer thicknesses, in the third term) will be comparable, as the emitter width cannot be increased without a significant increase in emitter resistance. Hence, a current gain $B \gg 1$ will require $N_{DE} \gg N_{AB}$.

This requirement now constitutes the central design dilemma of the bipolar transistor. The base resistance R_B is an important element in the high-frequency performance of the bipolar transistor—an increased R_B :

- lowers the maximum frequency of oscillation according to the approximation

$$f_{\max} = \left(\frac{f_T}{8\pi R_B C_{BC}}\right)^{\frac{1}{2}} \quad (7)$$

where f_T is the transit frequency and C_{BC} the base-collector capacitance

- increases the noise figure F and the equivalent noise resistance R_n , see, e.g., [5]
- leads to an inhomogeneous current density distribution over the emitter-base junction area (displacement of the current toward the emitter edge, see, e.g., [6])

The base resistance scales with base width and base doping concentration as

$$R_B \sim (W_B N_{AB})^{-1} \quad (8)$$

On the other hand, the base transit time, a crucial factor determining f_T , scales with the square of the base width. In a homogeneously doped base, the electrons will move across the neutral base by diffusion only

$$\tau_B = \frac{W_B^2}{D_{n,B}} \quad (9)$$

Optimizing a bipolar transistor for f_T by lowering W_B will hence come at the price of an increased R_B , deteriorating f_{\max} and noise performance, while trying to avoid the R_B increase by increasing N_{AB} will lower the current gain B.

Possible solutions can be found by examining Eqs. (6) and (9) again.

In Eq. (6), the last term, the ratio of intrinsic carrier concentrations in the base and the emitter, $n_{i,E}$ could be made much smaller than $n_{i,B}$ if a material with a higher bandgap energy E_G was chosen, because

$$n_i = (N_C N_V)^{1/2} \exp\left(\frac{-E_G}{2kT}\right) \quad (10)$$

where N_C and N_V are the conduction and valence band densities of states, k is Boltzmann's constant, and T is the absolute temperature.

Equation (6) can now be rewritten as

$$B = \frac{J_C}{J_B} = \frac{D_{n,B}}{D_{p,E}} \frac{W_E}{W_B} \frac{N_{DE}}{N_{AB}} \frac{N_{C,B}}{N_{C,E}} \frac{N_{V,B}}{N_{V,E}} \exp\left(\frac{E_{G,E}}{E_{G,B}}\right) \quad (11)$$

The important term here is the exponential one. The possible vast improvement in current gain B will be used to drastically increase N_{AB} (and lower N_{DE}), opening the way to reduced R_B despite thinner base layers W_B .

This approach, the "wide-gap emitter structure" has already been described shortly after the invention of the bipolar transistor [7], yet technological problems prevented the creation of the necessary semiconductor heterostructures at the time.

A different optimization strategy can be found by examining the assumptions leading to Eq. (9). We assumed that the minority carriers in the neutral base move by virtue of diffusion only, without the assistance of an electrical field. If we now allow a built-in drift field E_{bi} in the neutral base, the base transit time expression becomes [8]

$$\tau_B = \frac{W_B^2}{2 \left(1 + \left(q \frac{E_{bi} W_B}{kT} \right)^{3/2} \right) D_{n,B}} \quad (12)$$

The built-in field can be realized through a doping variation in the base (higher N_A at the base-emitter junctions than at the base-collector junction), but it is much more efficiently implemented using a bandgap variation across

the base (larger bandgap at the base-emitter junction than at the base-collector junction), and without the otherwise inevitable reduction in the average base doping concentration.

Both strategies can be pursued using a Silicon-Germanium alloy in the base layer.

2.2.1. The Si/SiGe/Si Wide-Gap Emitter Structure. The concept of the Si/SiGe/Si wide-gap emitter HBT is identical to that of HBTs fabricated from compound semiconductors of the third and fifth column of the periodic table of elements and has been pursued primarily by DaimlerChrysler [9] and, more recently, Atmel [10].

The base is fabricated from a $\text{Si}_{1-x}\text{Ge}_x$ alloy with a fixed Ge mole fraction x , with typically $x = 0.2$. The SiGe layer is elastically strained between unstrained Si layers (emitter and collector), so turning to Fig. 6, we find that for $x = 0.2$, the conduction band discontinuity is negligible at slightly less than -20 meV, whereas the valence band discontinuity is substantial at 150 meV. The large valence band and negligible conduction band discontinuity is ideal for npn-type transistors, as it avoids the conduction band parasitic barrier found, for example, in abrupt AlGaAs/GaAs heterojunctions. Figure 7 shows a qualitative representation of the band structure at thermodynamic equilibrium. Note that a valence band discontinuity exists both at the emitter-base and base-collector junction; the first is desired. The latter is because of the fact that the SiGe layer has to be thin because of the lattice mismatch, and hence the collector has to be fabricated from Si, leading necessarily to a double heterostructure. It will have a detrimental effect on high-current operation, as will be explained later.

The exponential factor in Eq. (11) is 1.18×10^4 at room temperature and allows the emitter and base doping concentration ratio to be reversed, i.e., the higher doping concentration is now in the base, whereas the emitter doping concentration immediately adjacent to the emitter-base junction is lowered to prevent tunneling. To control the emitter series resistance, the low-doped emitter region is narrow and the doping is increased in the top part of the emitter, see Fig. 8.

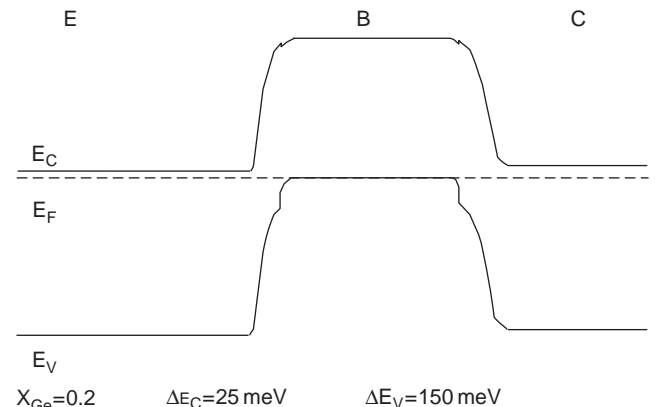


Figure 7. Qualitative band diagram of a Si/SiGe/Si wide-gap emitter bipolar transistor.

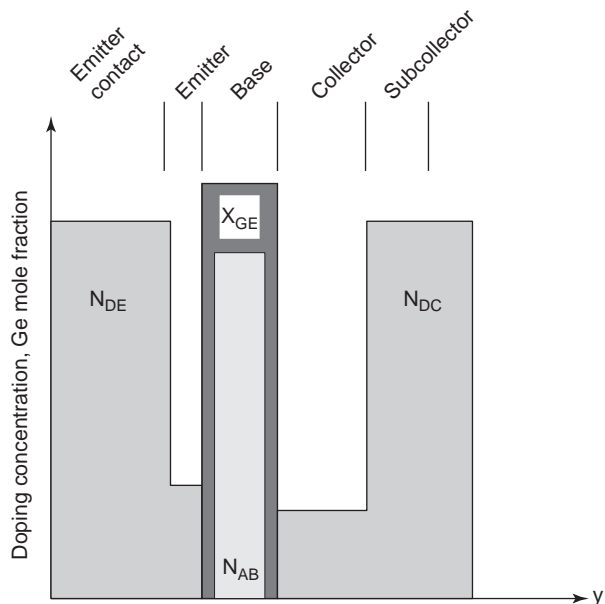


Figure 8. Schematic representation of Ge mole fraction and doping concentrations in a Si/SiGe/Si wide-gap emitter HBT.

The combination of $x_{Ge}=0.2$ and typical base thicknesses of 30–50 nm places these structures into the metastable regime of Fig. 5. The built-in strain of the base is substantial, precluding high-temperature processing steps after deposition of the SiGe layer. Still, both dedicated bipolar and BiCMOS processes have been realized using this concept and are commercially available. Its prime advantage is the very low base sheet resistance possible using this concept, which allows high cutoff frequencies without aggressive lateral scaling of the emitter, e.g., 80 GHz f_T and f_{max} with 0.5 μm minimum feature size [11]. There are no known reliability concerns in normal mode of operation stemming from the high built-in strain in the base.

2.2.2. The Si/SiGe/Si Graded Base Structure. Full compatibility with CMOS processing temperatures, even after the deposition of the SiGe layer, requires a substantially lower Ge concentration in the base; the combination of Ge mole fraction and layer thickness needs to be below the equilibrium limit in Fig. 5. As this simultaneously decreases the valence band discontinuity, see again Fig. 6, the wide-gap emitter concept becomes less powerful.

Instead, the optimization strategy suggested by Eq. (12) is being pursued; the Ge mole fraction at the emitter-base junction is zero or very low and gradually increases toward the base-collector junction, where it is reduced to zero again for the collector layer. As Fig. 9 shows, the conduction band in the neutral base is tilted toward the collector now and creates a very strong built-in field for electrons only, whereas the conduction band is essentially unchanged (except for the effect of the changing density of states in the valence band with the Ge mole fraction, neglected here for simplicity).

This concept has been introduced by IBM [12]. Typical maximum Ge mole fractions (at the base-collector inter-

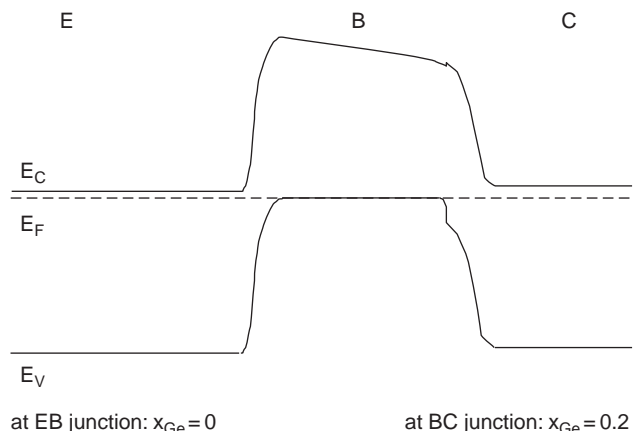


Figure 9. Qualitative band diagram of a Si/SiGe/Si graded-base bipolar transistor.

face) are $x = 0.15\text{--}0.20$, leading to an average mole fraction of 7.5–10%, resulting in a substantially lower built-in strain in the base.

Note that here, too, a valence band discontinuity exists at the base-collector junction.

Figure 10 shows the doping and Ge mole fraction profile for the graded-base structure. The lack of an emitter-base bandgap difference requires a emitter-base doping ratio that is similar to a conventional bipolar transistor. The base sheet resistance is thus higher than in the wide-gap emitter concept; the required low-base resistance has to be realized here by a more aggressive lateral scaling of the emitter width, e.g., a production technology with $f_T = 72$ GHz and $f_{max} = 75$ GHz has a feature size of 0.35 μm [13].

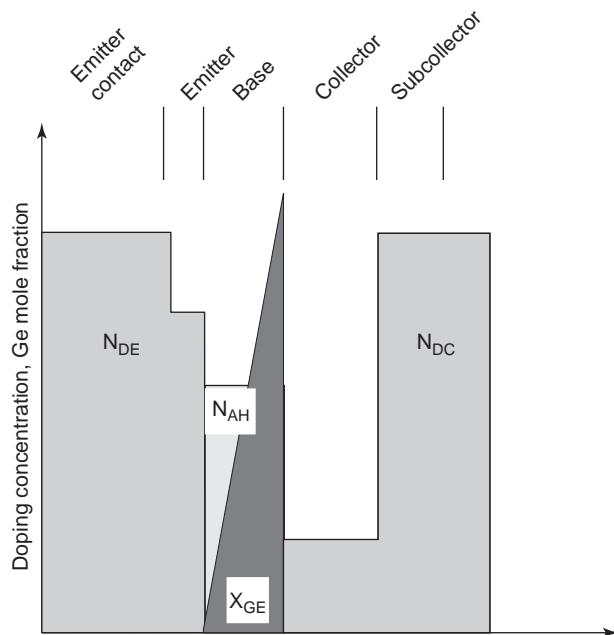


Figure 10. Schematic representation of Ge mole fraction and doping concentrations in a Si/SiGe/Si graded-base HBT.

2.2.3. The Base-Collector Heterostructure Effect. As pointed out, the severe lattice mismatch between practical SiGe layers and the embedding Si forces SiGe heterostructure bipolar transistors to have a second heterostructure at or near the base-collector junction.

Generally, this heterostructure is undesirable as it might introduce a conduction band energy barrier (“spike”) that negatively affects the collection of base minority carriers (electrons in npn transistors) by the collector. In the special case of S/SiGe/Si HBTs, no noticeable conduction band spike will occur as the conduction band discontinuity for strained SiGe layers versus unstrained Si is negligible (see again Fig. 6).

The situation changes when higher collector current densities are present, but shows an onset prior to that of the Kirk effect. In the classic Kirk effect, the injected minority carriers from the base have a sufficient density to effectively neutralize the fixed charge in the collector space-charge region. The space charge will disappear at the base-collector junction, the neutral base will extend into the base (“base push-out”). As a consequence, the effective base width will increase, the current gain decrease [see Eq. (6)], and the base transit time will increase drastically, see Eq. (9).

In the case of the double heterostructure, as pointed out by Tiwari in 1988 [14], partial compensation of the collector space charge will lead to the appearance of an electron barrier in the conduction band, which can be intuitively understood when considering that in a conventional bipolar transistor, the weakening of the space charge will lead to a decreased potential barrier not only for electrons, but also for holes. If the base-collector junction is replaced by a heterojunction with a significant valence band discontinuity, the increasing injection of holes from the base into the collector is blocked. Holes will instead accumulate against the barrier, their increased density pushes the valence and conduction bands upward, leading to the observed decrease in current gain B and transit frequency f_T , which is much more pronounced than what is observed in homojunction bipolar transistors. It is significant because in high-speed operation, bipolar transistors need to be operated at or close to the collector current density for maximum f_T . Large-signal CAD models for SiGe HBTs will hence have to predict the high-current rolloff very accurately, which will occur immediately beyond the optimum f_T bias point.

In SiGe HBTs, the effect of this base-collector heterostructure effect can be lessened by introducing a retrograde SiGe profile extending into the collector layer, by slightly displacing the SiGe/Si heterojunction into the collector, or by increasing the collector doping concentration immediately adjacent to the base [15]. In the first two cases, the increased strain because of the lattice mismatch has to be observed, whereas the latter solution will compromise the maximum frequency of oscillation (through an increase in the base-collector capacitance) and the collector-base breakdown voltage.

2.2.4. Carbon Codoping in the SiGe Base Layer. As pointed out, the main attractions of introducing an SiGe heterostructure into Si bipolar transistors is the possible

decrease in the base resistance by increasing the base doping concentration. Simultaneously, the vertical base thickness is decreased to reduce the base transit time. This technological development leads invariably to very steep doping profiles in the base layer.

Very steep doping gradients, in turn, increase the risk of dopant outdiffusion from the base layer into the emitter and collector regions, with very detrimental effects.

- Especially in wide-gap emitter structures, outdiffusion into the emitter places the emitter-base pn junction into the emitter and the heterojunction into the base. The hole-blocking valence band discontinuity is no longer effective, whereas the heterostructure inside the p-doped region will lead to a conduction band barrier decreasing electron injection from the emitter into the base. As a result, the current gain B will be dramatically decreased.
- The base-collector heterostructure will be placed into the base layer as the p-dopant diffuses into the collector, displacing the pn junction. Again, this will cause a conduction band barrier for electrons and particularly worsen the high-current base-collector heterostructure effect discussed in Section 2.2.3.

Traditionally, base dopant outdiffusion has been anticipated through the introduction of undoped setback layers in the base, which absorbed the outdiffusing base dopant and placed the pn junctions in the proper place [16]. However, as the vertical base width is decreased, these setback layers have to be scaled down or eliminated. Also, the necessity to accurately predict the amount of outdiffusion makes the processing windows for the epitaxial growth much smaller.

As the lateral transistor sizes are scaled down, the fact that the dopant not only diffuses vertically, but also laterally, becomes visible. The problem is that in many processes, the extrinsic base is doped highly by ion implantation (usually with BF_2). The resulting crystallographic damage creates a significant density of interstitial defects that enhances the outdiffusion of the predominant base dopant, Boron. Similar defect-induced enhanced diffusion effects can occur because of high-level emitter implant doses.

Rather than anticipating dopant outdiffusion through setback layers and relaxed lateral scaling rules, it is better to reduce the diffusivity of the dopant. A very efficient way of doing this is the use of Carbon codoping [17]. Codoping denotes the incorporation of low ($< 10^{20} \text{ cm}^{-3}$) concentrations of Carbon, as opposed to ternary SiGeC compounds, which are under investigation to reduce the lattice mismatch toward Si. The codoped Carbon atoms are electrically inactive, but dramatically reduce the transient enhanced diffusion (TED) of Boron [18], enabling steep Boron gradients without doping setbacks, and simultaneously enabling the aggressive lateral scaling that has made transit frequencies in excess of 300 GHz possible in SiGe HBTs.

2.2.5. State of the Art. The performance of Si/SiGe HBTs rivals that of its competitors from III-V compound

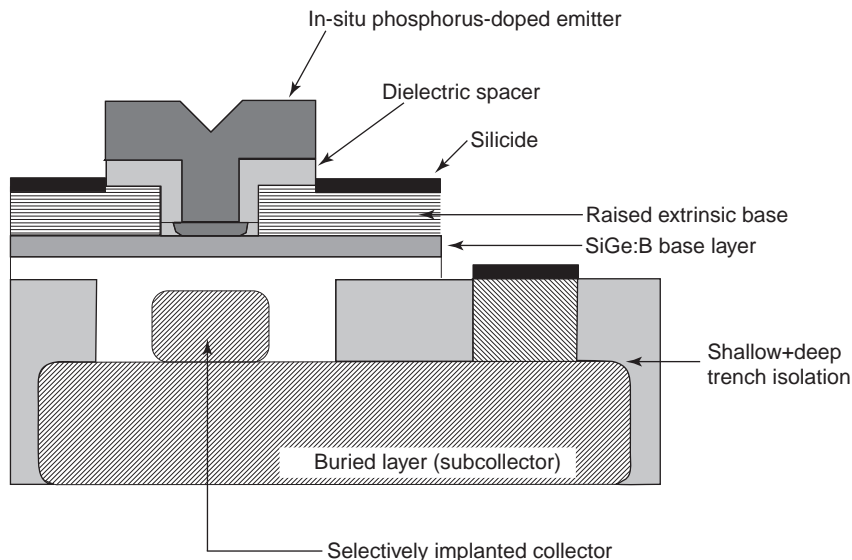


Figure 11. Cross-section of a state-of-the-art box-shaped SiGe HBT, after [19].

semiconductors. The combination of bandgap engineering in the base and drastic reductions in base and collector layer thicknesses with aggressive lateral scaling made possible by advances in modern CMOS processing resulted in record transit frequencies of $f_T = 350$ GHz in 2002 [19], or a total emitter-to-collector transit time $\tau_{EC} = 0.45$ ps. The base has a Ge mole fraction of 25%, with a Boron sheet concentration of $5 \times 10^{13} \text{ cm}^{-3}$. The lateral emitter width has been scaled down to 120 nm. Although the intrinsic base resistance benefits from the high Boron dose, the extrinsic base resistance has been lowered using raised base contact layers, which have been grown in a self-aligned fashion.

The box-like transistor cross section, shown in Fig. 11, reduces particularly the base-collector capacitance. For the f_T -optimized design, the authors reported a maximum frequency of oscillation, determined from Mason's unilateral gain, of 170 GHz. In this design, the radical reduction of base and collector layer thicknesses increases R_B and C_{BC} , respectively, leading to the rather low f_{max} compared with f_T .

Optimizing the device in a more practical way, for similar f_T and f_{max} , the authors obtained $f_T = 270$ GHz and $f_{max} = 260$ GHz. The peak f_T in these transistors occurs at a high collector current density of $17 \text{ mA}/\mu\text{m}^2$.

The negative aspect of the lateral scaling, especially of the collector layer, is the reduction in breakdown voltage. For the record device, the open-base collector-emitter breakdown voltage BV_{CEO} is only 1.4 V, in part because of the very high current gain of 2300. The more practical device design with 260 GHz f_T has $BV_{CEO} = 1.6$ V. As the authors point out, the product of breakdown voltage and f_T is 490 V GHz and 416 V GHz, respectively, and much beyond the commonly assumed Johnson limit of 200 V GHz, and the breakdown voltages for short-circuited base terminal (BV_{CBO}) are 5 V and 5.5 V, respectively, but still the low breakdown voltages present significant challenges in practical micro- and millimeter-wave applications of ad-

vanced SiGe HBTs. The general trend in breakdown voltages in HBTs using Si/SiGe can be found in Fig. 12.

The inferiority of Si/SiGe HBTs versus its III-V competitors in terms of breakdown voltage for a given f_T is because of

- the higher electric field at the onset of avalanche breakdown in GaAs and InP
- the lower average carrier velocity in Si at moderate electric fields

In essence, devices with an Si collector will pay a higher price in breakdown voltage reduction when the collector is being scaled for a given collector transit time τ_C .

It can be argued that for practical micro- and millimeter-wave applications requiring at least moderate power levels (1 V_{p-p} amplitude corresponds to only 4 dBm into a 50 Ω load), the low breakdown voltage is now the most

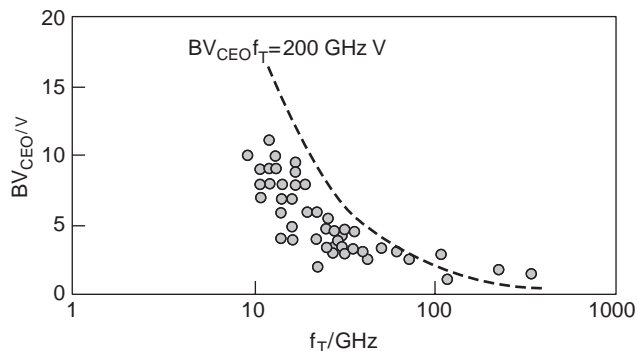


Figure 12. Comparison of breakdown voltage trends in Si-, GaAs-, and InP-based HBTs, vs. transit frequency f_T . The dashed curve is the often-quoted "Johnson limit" of 200 GHz V for the product of f_T and the open-base breakdown voltage BV_{CEO} (data partly from the SiGe Microsystems website).

significant challenge in the development of SiGe HBTs, not the cutoff frequencies.

2.3. The Si/SiGe/Si Heterostructure Field-Effect Transistor

2.3.1. Quantum-Well Channels for Electrons and Holes.

The use of Si/SiGe heterostructures in field-effect transistors has not yet (in 2004) reached the commercialization stage, but is, after slow beginnings, gaining momentum in research, as it holds promise for advances in high-speed CMOS beyond those offered by geometry scaling. The reasons for the slower market introduction of SiGe heterostructure field-effect transistors, compared with SiGe HBTs, is not only the significant performance improvement that has been experienced in scaled Si CMOS, but also the fact that, as we will see, high-performance SiGe HFETs need strain-relaxed SiGe buffer layers (“quasisubstrates” with a larger lattice constant than Si), making process integration not as straightforward as in SiGe HBTs.

When comparing Silicon with III-V compound semiconductors, it cannot be overlooked that III-V semiconductors, like GaAs and especially InGaAs, have significant advantages in terms of the low-field electron mobility μ_n . The hole low-field mobility μ_p in Si is larger than in GaAs or InGaAs, but still significantly lower than μ_n . The following challenges therefore develop, for which SiGe heterostructures promise potential solutions:

- Increase the electron mobility μ_n —in III-V semiconductors, an often used solution is the reduction of electrostatic interaction (Coulomb scattering) between free charge carriers (here, electrons) and fixed charge stemming from ionized doping atoms (here, positively charged donors), which is the concept of the high electron mobility transistor, or HEMT, and requires the physical separation of dopants and free charge. The physical separation can be created by confining the free charge to a quantum well apart from the fully depleted supply layer and requires a heterostructure.
- Increase the hole mobility μ_p ; here, reduction of Coulomb scattering will help as well, but the observation of a significantly higher hole mobility in Ge as compared with Si points into a different direction: Increase the Ge mole fraction in a SiGe hole channel.

The formation of a quantum-well channel with separation of free holes and fixed ionized acceptors, useful for p-channel FETs, is quite straightforward and can use the heterostructure system discussed for Si/SiGe HBTs. Figure 13 (a) shows a suitable layer structure. The supply layers are 20 nm thick Si, doped with Boron to $p = 10^{19} \text{ cm}^{-3}$. The quantum well is formed in a $\text{Si}_{0.85}\text{Ge}_{0.15}$ layer of 40 nm thickness. Two 2 nm wide undoped Si spacer layers create the physical separation of free holes and fixed ionized acceptor charge. Two two-dimension hole gas channels form at the Si/SiGe heterointerfaces in this structure [20]. Figure 13 (b) demonstrates the difference in low-field hole mobility between the cases of doped and undoped SiGe well; a factor of 2 at room temperature, increasing to

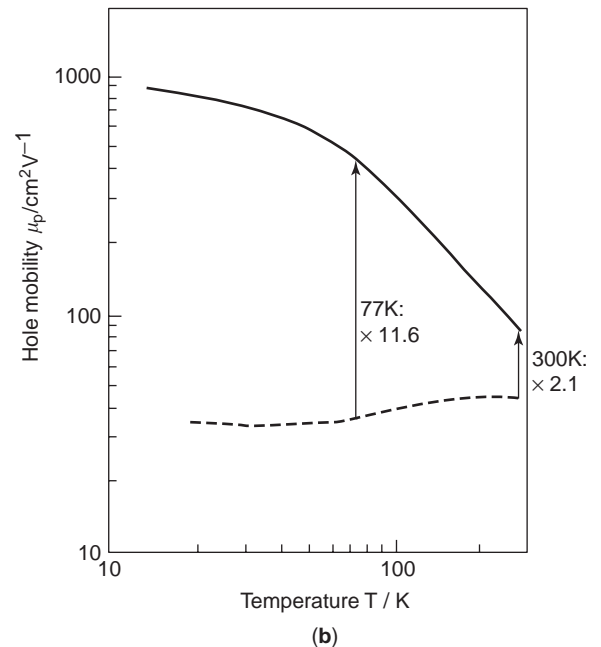
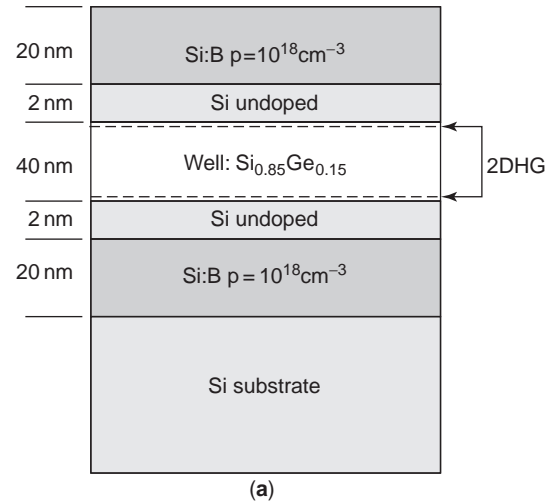


Figure 13. (a) Si/SiGe/Si heterostructure with formation of a two-dimensional hole gas (2DHG). (b) Low-field hole mobility μ_p for doped and undoped wells (after [20]).

a factor of almost 12 at 77 K, where the limitation because of phonon scattering is less pronounced.

Even higher gains in hole mobility are possible if the Ge concentration in the well is increased. Figure 14 provides a survey of literature values [21]; the index x demotes the Ge mole fraction in the $\text{Si}_{1-x}\text{Ge}_x$ channel, whereas y is the Ge mole fraction in the underlying $\text{Si}_{1-y}\text{Ge}_y$ quasisubstrate, which will be explained below. Almost a factor of 10 can be gained when moving from $\text{Si}_{0.85}\text{Ge}_{0.15}$ to a pure Ge channel ($x = 1$).

Also note that the hole mobility can even be improved when straining a pure Si channel ($x = 0$) by an underlying SiGe film (here, $y = 0.25$), which has a larger lattice constant and hence provides a tensile strain to the Si layer, which is the concept pursued in “strained-Si” CMOS, which will not be treated here any further.

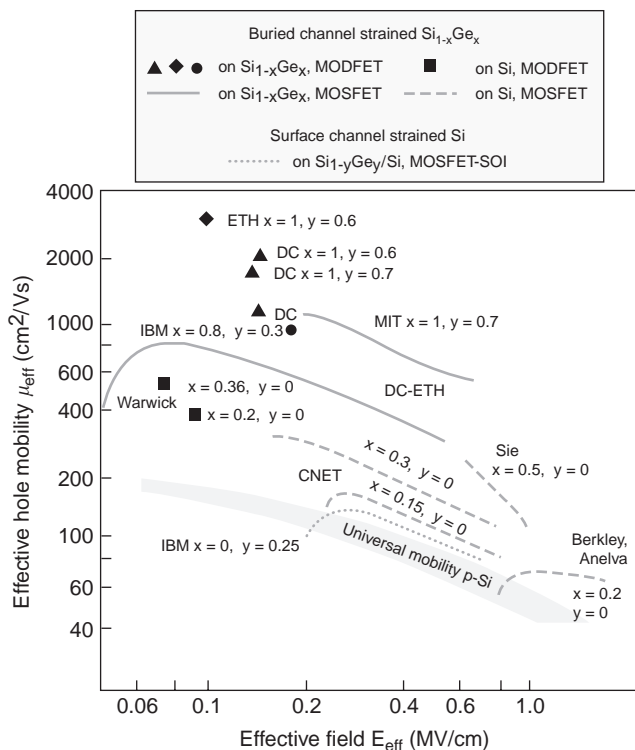


Figure 14. Effective hole mobilities in SiGe heterostructures, vs. electric field, after [21]. DC = DaimlerChrysler, ETH = ETH Zurich, Si = Siemens, Warwick = University of Warwick, Berkeley = University of California, Berkeley.

Referring back to Fig. 5, we readily notice that high Ge mole fractions will lead to extremely small critical thickness values. The resulting very thin quantum wells will no longer provide an effective confinement to the holes and lead to an increase of Coulomb scattering. Practical high-Ge channels therefore need a SiGe substrate with significant Ge content.

Such SiGe quasisubstrates are realized on Si substrates by growing layers that are deliberately unstrained (relaxed). The challenge is to provide strain-relaxed buffer layers that are ideally free of defects at the top (where the device structure will be grown) and as thin as possible.

First experiments to produce strain-relaxed virtual substrate layers involved the growth of thick (2–5 μm) graded Si_{1-x}Ge_x layers, starting with x=0–0.05 at the the Si substrate and ending in typically x=0.3–0.4 at the top of the layer.

A reduced thickness will improve the integrability of the technology, but even more importantly, it will reduce the overall thermal resistance. It has been reported [22] that Si_{0.6}Ge_{0.4} has an 18-fold lower thermal resistance than Si. A reduction of the relaxed buffer thickness from 5 μm to 0.5 μm led to a reduction of the overall thermal resistance seen by the FET structure by a factor of 3.

The growth of thin strain-relaxed quasisubstrates with low defect density generally requires the restriction of dislocations to certain parts of the layer, using various growth methods, e.g., low-energy plasma-enhanced chemical vapor deposition (LEPECVD, [23]), very low temper-

ature epitaxy (VLTE, [24]), or by postdeposition relaxation through He implantation and annealing (HELAX, [25]).

An example for a SiGe-channel p-MOSFET is shown in Fig. 15. A strain-relaxed Si_{0.7}Ge_{0.3} buffer is grown onto Si and forms the quasisubstrate. The channel region itself has a Ge concentration of 0.7 and is therefore experiencing tensile strain. Figure 6 predicts a negligible conduction band discontinuity of 5 meV and a significant valence band discontinuity of 300 meV, the desired situation. Figure 15 also provides the qualitative band diagram of the structure, indicating the location of the buried hole channel. The Silicon cap layer between the Si_{0.3}Ge_{0.7} well and the oxide serves two purposes.

1. It improves the quality of the gate oxide; a direct oxidation of the SiGe compound should be avoided.
2. It removes the free carriers from the oxide interface, which further improves the mobility.

Note the second valence band maximum at the oxide-Si interface. A parasitic surface channel with lower mobility

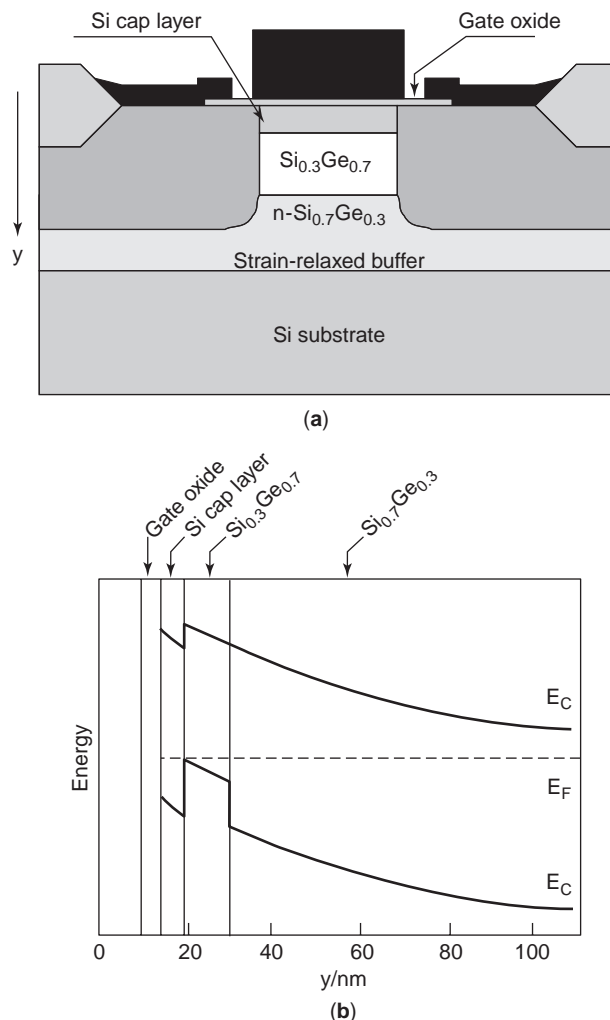


Figure 15. (a) Cross section of a SiGe-channel p-MOSFET (after [26]) (b) corresponding band diagram under the gate.

may form here if the device is strongly forward biased, which has to be avoided by proper device design.

Aside from MOSFET structures with charge control through an MOS diode, MODFET structures with channel control through a Schottky gate (as in III-V HEMTs) have also been realized, see, e.g., [27].

The use of SiGe heterostructures for n-channel FETs is less obvious; the heterostructures considered so far all had significant valence band offsets, yet negligible conduction band discontinuities and were therefore unable to provide confinement in a conduction band well. However, consider the case of a strained Si film on unstrained $\text{Si}_{1-x}\text{Ge}_x$ (e.g., for $x=0.3$). Figure 6 gives a valence band offset of -55 meV and a conduction band offset of -160 meV . The negative sign denotes that the conduction band in the strained Si is below the conduction band in the unstrained SiGe; this is a type II heterostructure. An efficient electron confinement is now possible in the strained Si layer.

Figure 16 provides a synopsis of low-field mobility data. The significant improvement over the universal electron mobility curve is clearly visible, especially for buried channel structures, where an up to eight-fold improvement is observed.

Figure 17 shows the layer structure of an n-channel SiGe MODFET [28]. The electron channel forms in the 9 nm thick Si layer, which is sandwiched between two $\text{Si}_{0.6}\text{Ge}_{0.4}$ spacer layers (undoped, 3 resp. 4 nm thick). A double-doped MODFET structure is adopted here, with 5 nm thick Sb-doped supply layers above ($2 \times 10^{19}\text{ cm}^{-3}$) and below ($2 \times 10^{18}\text{ cm}^{-3}$) the channel. The Schottky gate sits on top of a 3.5 nm thick Si cap layer; the authors report that an increased gate leakage current was noticed, which is likely because of the bandgap lowering in the strained Si. The quasisubstrate is provided by a 240 nm thick strain-relaxed buffer ($\text{Si}_{0.6}\text{Ge}_{0.4}$) grown by VLTE. With a T-gate and a gate length of $L_G = 0.1\ \mu\text{m}$, the devices showed peak $f_T = 43\text{ GHz}$ and $f_{\text{max}} = 95\text{ GHz}$.

It is interesting to note that p-channel devices (channel in SiGe) and n-channel devices (channel in Si) can use the

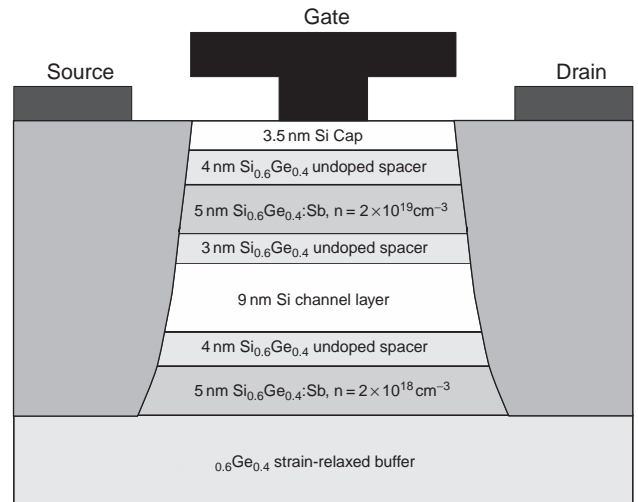


Figure 17. Cross section of an n-channel Si/SiGe heterostructure MODFET, after [28].

same SiGe quasisubstrate, opening the way to complementary Si/SiGe MOSFET technologies [29].

As SiGe heterostructure MOSFETs and MODFETs all provide significantly increased low-field mobilities through the combination of strain, high Ge content in the channel (for p-channel devices), reduction of Coulomb scattering (in MODFET structures), and suppression of oxide interface scattering (in MOSFET structures, through the buried channel), they will be particularly suitable in providing low-noise amplification at microwave frequencies [30].

2.3.2. SiGe HFETs: State of the Art. Using gate lengths down to 90 nm, transit frequencies up to 90 GHz have been demonstrated in n-channel Si/SiGe MODFETs [31]. The f_T still scaled well with the inverse gate length. A technological problem that remains to be solved is the high source access resistance, which lowers the extrinsic transconductance and hence the f_T . With this problem solved, and with gate lengths comparable with experimental Si NMOS technologies (down to 40 nm), f_T values significantly in excess of 200 GHz can be predicted.

Owing to the metal gates and also a low output conductance, Si/SiGe HFETs already show impressive maximum frequencies of oscillation, reported up to 188 GHz [32]. Figure 18 shows a comparison of values reported in the literature. It is obvious that Si/SiGe HFET structures have most pronounced advantages for p-channel devices, where they now have comparable properties with current Si NMOS, holding great promise for high-speed fully complementary circuits.

Also obvious, however, is that SiGe HBTs offer 100 GHz f_{max} values at much relaxed lateral scaling requirements.

2.3.3. Microwave and Millimeter-Wave Circuits Using SiGe HBTs and HFETs. The motivation to use Si/SiGe heterostructure devices lies not in their properties as discrete devices, but in their ability to be easily integrated

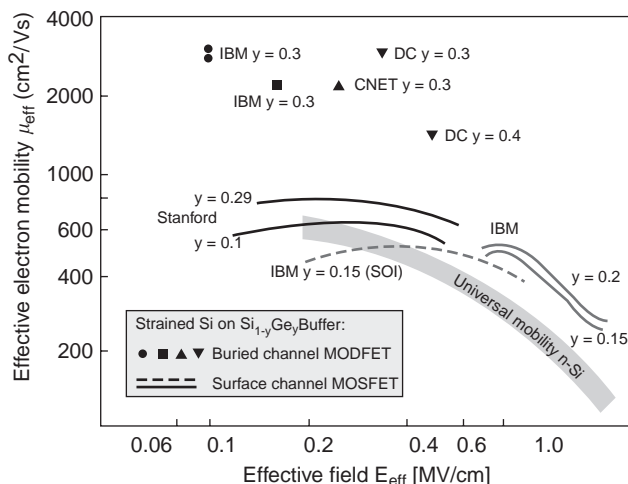


Figure 16. Effective electron mobilities in SiGe heterostructures, vs. electric field, after [21].

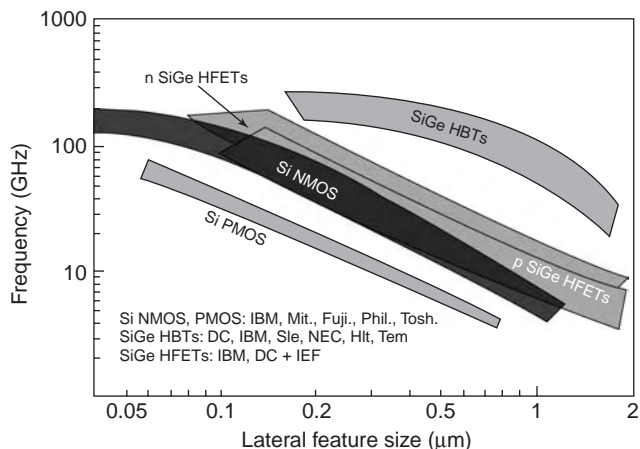


Figure 18. Comparison of literature values for the maximum frequency of oscillation for various classes of Si-based high-speed devices, after [21].

into mature Silicon IC processes. A brief look at microwave and millimeter-wave ICs (MMICs) realized using Si/SiGe heterostructures shall therefore conclude this chapter.

Significant differences exist between Si-based MMICs and their counterparts realized from III-V compound semiconductors, in terms of circuit complexity, the density of active elements on chip, and in the total chip size.

Traditionally, MMICs have been borrowing heavily from hybrid microwave circuit design, using transmission line segments to realize reactances and for impedance transformations. GaAs substrates in MMIC fabrication are semiinsulating, with resistivities $> 10^7 \Omega\text{cm}$, and hence suitable for circuit design techniques originally conceived for non-semiconducting substrates such as alumina, sapphire, or PTFE. Si-based MMICs may use high-resistivity substrates (e.g., $1000 \Omega\text{cm}$), but are more often realized on medium-to-low resistivity substrates (e.g., $20 \Omega\text{cm}$).

Distributed passive structures are hence in danger of suffering from prohibitive substrate losses and have to be avoided in Si MMIC design. Instead, quas lumped passive circuit elements are being used even at millimeter-wave frequencies, such as spiral inductors and metal-insulator-metal (MIM) capacitors. The necessary compact layout techniques have the added benefit of resulting in very compact chips, adding to the cost benefit of Si/SiGe ICs.

The lossy nature of the Silicon substrates will have to be accounted for in various ways. Transmission line segments can be described as lossy-backplane thin film microstrip lines or coplanar waveguides backed by a lossy backplane [33], depending on the geometry. Such lines show pronounced dispersion in the form of slow-wave effects at low frequencies, which disappear at higher frequencies (typically above 2–3 GHz), see Fig. 19. Thin film microstrip lines can also be placed in higher metalization layers, using the first metalization layer as a backplane, providing shielding from the substrate. Such lines no longer suffer from substrate effects, but the thin dielectric

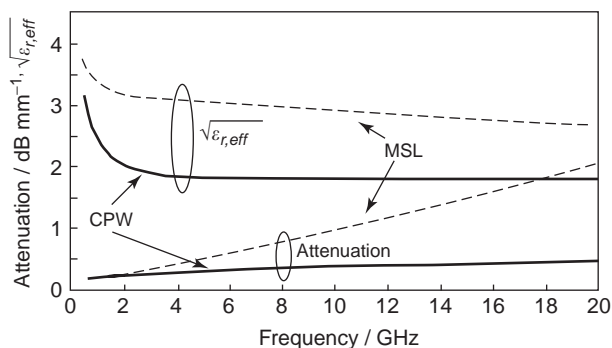


Figure 19. Measured attenuation and slowing factor for $4.2 \mu\text{m}$ wide microstrip (MSL—dashed curves) and coplanar transmission lines (CPW—solid curves) on $20 \Omega\text{cm}$ Silicon substrate, after [33].

layer makes signal lines very narrow, leading to nonnegligible Ohmic metalization losses.

Spiral inductor models on conducting substrates need to take Eddy currents in the substrate into account, at least at lower frequencies where necessary self-inductance and hence geometric size are large [34]. Eddy currents will lower the inductance of the planar coil and reduce the quality factor. At millimeter-wave frequencies, with typical inductances of less than 1 nH, the modeling of spiral inductors simplifies as the skin-effect metalization losses dominate over substrate effects. Ground shields (either in the lowest metalization layer or using a buried highly doped semiconductor layer) are sometimes used to reduce substrate losses, but under inductors they have to be slotted to avoid excessive Eddy current effects. Ground-coupled noise can be a significant problem in applications such as low-noise amplifiers and can be addressed equally by ground shields.

Integration density and the high yield of mature Silicon processes make MMICs with a high number of integrated functions possible. As an example, refer to Fig. 20, which shows a fully integrated downconverter IC for the 24 GHz ISM band [35]. The IC contains all necessary circuit blocks: a three-stage preamplifier (lower left), a voltage-controlled oscillator using an active inductance concept, a

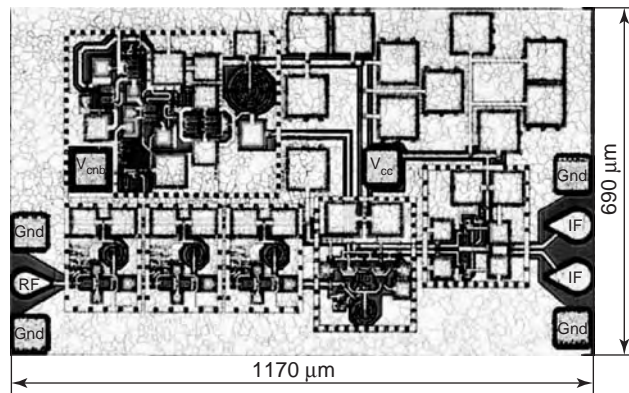


Figure 20. Chip photograph of a fully integrated 24 GHz receiver IC using Si/SiGe HBT technology, after [35].

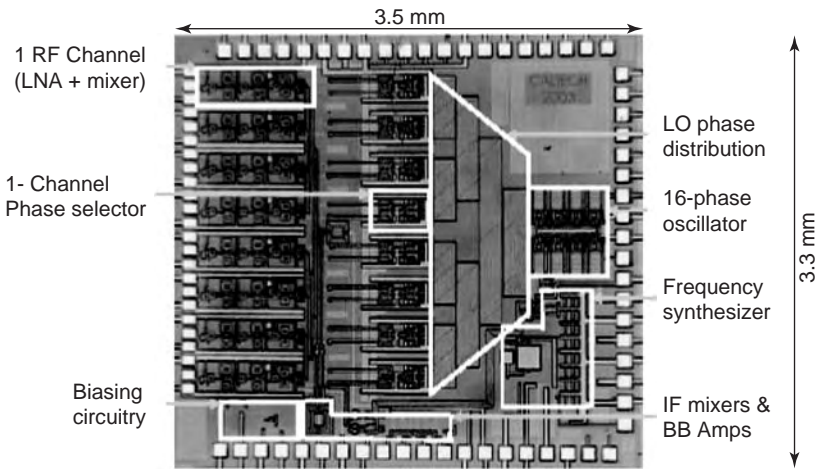


Figure 21. Chip photo of an 8 channel phased-array receiver for 24 GHz in a SiGe BiCMOS technology, after [36].

Gilbert cell mixer, and IF output buffers (lower right). The circuit has been realized in the Atmel SiGe1 technology, which, as a first-generation SiGe HBT technology, has f_T and f_{max} of 50 GHz and is at its limits at 24 GHz. Still, the receiver is fully functional and provides a conversion gain of 16 dB. Circuits for the 24 GHz ISM band have also been realized in Si/SiGe BiCMOS processes, where they can take advantage of the excellent microwave properties of the npn Si/SiGe HBTs and realize lower frequency high-complexity circuit blocks in CMOS. Hashemi et al. [36] realized the highly complex 8 channel receiver chip for 24 GHz phased-array systems shown in Fig. 21. An interesting research topic will be the efficient testing of such RF systems-on-a-chip in production lines, however.

Using state-of-the-art SiGe HBT technologies, ICs can be realized with frequencies of operation in excess of 100 GHz. Figure cc shows the concept and the sensitivity of a dynamic frequency divider realized using an SiGe HBT technology with $f_T = 200$ GHz [37]. In a dynamic divider, whose concept is shown in Fig. 22 (a), any spectral component at one-half f_1 at port 1 of the mixer is sufficient to produce $f_1 \pm$ one-half f_1 at port 3. The active mixer has a low-pass characteristic that suppresses the higher frequency component and passes the one-half f_1 spectral component, which is amplified and fed back to the mixer in a regenerative fashion. The useful input sensitivity in this circuit extended beyond 110 GHz, the highest measurement frequency, see Fig. 22 (b). The circuit consumed 310 mW from a 5 V power supply.

Micro- and millimeter-wave circuit applications of Si/SiGe HFETs are still quite rare as of this writing (2004), reflecting the fact that most of the research is still in fundamental issues such as optimized thin quasisubstrate layers. A first ultra-wideband MMIC amplifier structure has been realized using an n-channel MODFET technology described in [38].

The transistors are characterized by a transconductance $g_m = 175$ mS/mm, a transit frequency f_T of 52 GHz, and a maximum frequency of oscillation $f_{max} = 148$ GHz extracted from Mason’s unilateral gain U. The transistors used in the circuit design had a gate length of 0.1 μ m and a

total gate width of 100 μ m. Models for the coplanar transmission lines on the virtual SiGe substrate were developed using test structures on similar wafers and fitting the parameter set for coplanar transmission lines in Agilent ADS, which was also used for the complete circuit design.

The distributed amplifier realized in this technology has six identical stages [39]. The gate transmission line has segments of 450 μ m length with a center conductor width of 20 μ m and signal-to-ground gaps of 60 μ m, whereas the drain transmission line has segments of 530 μ m length, with a center conductor width of 20 μ m and gaps of 40 μ m. Figure 23 shows a chip photograph.

The distributed amplifier realized in this technology has six identical stages. The gate transmission line has segments of 450 μ m length with a center conductor width

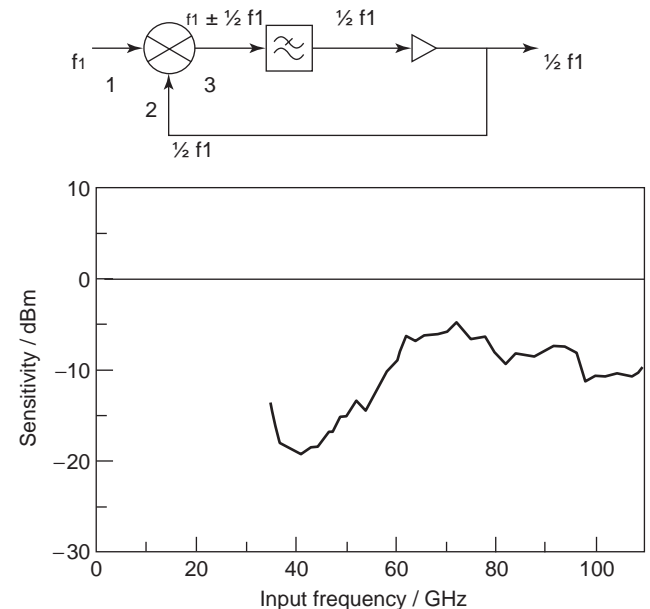


Figure 22. (a) Block diagram of a dynamic frequency divider (b) input sensitivity vs. frequency of a dynamic frequency divider realized using an $f_T = 200$ GHz SiGe HBT technology, after [37].

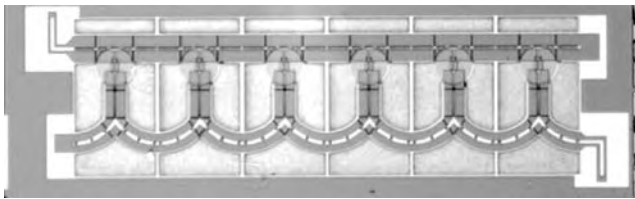


Figure 23. Chip photograph of a distributed amplifier using Si/SiGe n-channel MODFETs, after [39].

of 20 μm and signal-to-ground gaps of 60 μm , whereas the drain transmission line has segments of 530 μm length, with a center conductor width of 20 μm and gaps of 40 μm . The circuit draws 45.7 mA from a 2.3 V supply, the gate bias is held at $V_{\text{GS}} = -0.16$ V. At this bias point, the amplifier exhibits a power gain of 5.5 dB \pm 0.8 dB up to 32 GHz.

3. CONCLUSIONS

Si/SiGe heterostructure devices introduce the advantages of bandgap engineering to Si-based microelectronics and open up options for the optimization of RF performance that go beyond lateral and vertical geometric scaling. The significant lattice mismatch between Si and Ge introduces a high mechanical strain into Si/SiGe heterostructures that needs to be carefully observed. As a consequence, SiGe alloy layers need to be very thin, or strain-relaxed buffer layers (quasisubstrates with a larger lattice constant than Si) need to be used.

SiGe heterojunction bipolar transistors are firmly established in commercial production and have provided impressive circuit results, both in terms of circuit complexity and in terms of frequency of operation, which surpasses 100 GHz in special cases.

SiGe heterostructure field-effect transistors are still at a research stage, but demonstrate an equally impressive performance potential.

The most significant challenge in the design of Si-based micro- and millimeter-wave circuits is no longer the raw speed of the active devices, but rather the control of substrate losses, and the very low breakdown voltages of high- f_T SiGe HBTs.

BIBLIOGRAPHY

- J.-S. Rieh, B. Jagannathan, H. Chen, K. T. Schoenberg, D. Angell, A. Chinthakindi, J. Florkey, F. Golan, D. Greenberg, S.-J. Jeng, M. Khater, F. Pagette, C. Schnabel, P. Smith, A. Stricker, K. Vaed, R. Volant, D. Ahlgren, G. Freeman, K. Stein, and S. Subbanna, SiGe HBTs with Cut-Off Frequency of 350 GHz, International Electron Device Meeting, San Francisco, CA, December 8–11, 2002, pp. 771–774.
- H. Kroemer, Heterostructure bipolar Transistors and integrated circuits, *Proc. IEEE*, **70**:13–25 (1982).
- A. Gruhle, SiGe Heterojunction Bipolar Transistors, in J. F. Luy and P. Russer, eds., *Silicon-Based Millimeter-Wave Devices*, Springer-Verlag, New York, 1994, pp. 149–189.
- F. Schäffler, in E. Kasper, ed., *Properties of Strained and Relaxed Silicon Germanium*, EMIS Datareviews Series No. 12, IEE, INSPEC, London, 1995.
- R. J. Hawkins, Limitations of Nielsen's and related noise equations applied to microwave bipolar transistors, and a new expression for the frequency and current-dependent noise figure, *Solid-State Electron.*, **20**:191–196 (1977).
- H. Groendijk, Modeling base crowding in a bipolar transistor, *IEEE Trans. Elec. Dev.*, **ED-20**:329–330 (1973).
- H. Kroemer, Theory of a wide-gap emitter for transistors, *Proc. IRE*, **45**:1535–1537 (1957).
- Bart van Zeghbrouk, University of Colorado (online) available at http://ece-www.colorado.edu/~bart/book/book/chapter5/ch5_5.htm.
- A. Schüppen, U. Erben, A. Gruhle, H. Kibbel, H. Schumacher, and U. König, Enhanced SiGe heterojunction bipolar transistors with 160 GHz f_{max} , *IEEE Int. Elec. Dev. Meeting*, Technical Digest, pp. 30.4.1–30.4.4 (1995).
- M. Bopp and A. Schüppen, SiGe Transistor Technology for RF Applications, *Microwave J.* **42**:22–39 (1999).
- V. Dudek, J. Berntgen, P. Maier, M. Tortschanoff, and W. Kraus, DC and RF performance of a cost-effective SiGe technology, 1st International SiGe Technology and Device Meeting, Nagoya, Japan, January 15–17, 2003.
- G. L. Patton, D. L. Harame, J. M. C. Stork, B. S. Meyerson, G. J. Scilla, and E. Ganin, Graded SiGe base/poly emitter heterojunction bipolar transistors, *IEEE Elec. Dev. Lett.* **10**:537–539 (1989).
- W. Klein and B. H. Klepser, 75 GHz bipolar production technology for the 21st century, *Proc. ESSDERC*, 88–94 (1999).
- S. Tiwari, A new effect at high current densities in heterostructure bipolar transistors, *IEEE Elec. Dev. Lett.*, **9**:142–144 (1988).
- A. J. Joseph, J. D. Cressler, D. M. Richey, and G. Niu, Optimization of SiGe HBTs for operation at high current densities, *IEEE Trans. Elec. Dev.* **46**:1347–1354 (1999).
- E. J. Prinz, P. M. Garone, P. V. Schwartz, X. Xiao, and J. C. Sturm, The effects of base dopant outdiffusion and undoped $\text{Si}_{1-x}\text{Ge}_x$ junction spacer layers in $\text{Si}/\text{Si}_{1-x}\text{Ge}_x/\text{Si}$ heterojunction bipolar transistors, *IEEE Elec. Dev. Lett.* **12**:42–44 (1991).
- H. J. Osten, D. Knoll, B. Heinemann, and P. Schley, Increasing process margin in SiGe heterojunction bipolar technology by adding carbon, *IEEE Trans. Elec. Dev.*, **46**:1910–1912 (1999).
- L. D. Lanzarotti, J. C. Sturm, E. Stach, R. Hull, T. Buyuklimanli, and C. Magee, Suppression of boron outdiffusion in SiGe HBTs by carbon incorporation, *IEDM Tech. Dig.*, 249–252 (1996).
- J.-S. Rieh, B. Jagannathan, H. Chen, K. T. Schoenberg, D. Angell, A. Chinthakindi, J. Florkey, F. Golan, D. Greenberg, S.-J. Jeng, M. Khater, F. Pagette, C. Schnabel, P. Smith, A. Stricker, K. Vaed, R. Volant, D. Ahlgren, G. Freeman, K. Stein, and S. Subbanna, SiGe HBTs with cut-off frequency of 350 GHz, *Int. Elec. Dev. Meeting*, San Francisco, CA, December 8–11, 2002, pp. 771–774.
- B. S. Meyerson, UHV/CVD growth of Si and Si:Ge alloys: chemistry, physics, and device applications, *Proc. IEEE*, 1592–1608 (1992).
- Th. Hackbarth, M. Zeuner, and U. König, The future of SiGe beyond HBT applications, Uniaxis “Chip” magazine, July 2002. (online) available at <http://semiconductors.uniaxis.com/en/download/The%20Future%20of%20SiGe.pdf>.

22. T. Hackbarth, H-J. Herzog, K-H. Hieber, U. König, M. Bollani, D. Chrastina, and H. von Känel, Reduced self-heating in Si/SiGe field-effect transistors on thin virtual substrates prepared by low-energy plasma-enhanced chemical vapor deposition, *Appl. Phys. Lett.*, **83**:5464–5466 (2003).
23. C. Rosenblad, M. Kummer, H. D. Deller, T. Graf, A. Dommann, T. Hackbarth, G. Höck, E. Müller, and H. von Känel, Low energy plasma enhanced chemical vapor deposition—plasma enhanced deposition of epitaxial Si and Ge, *Mat. Res. Soc. Symp. Proc.*, **696**:N4.7.1–N4.7.12 (2002).
24. K. Lyutovich, M. Bauer, E. Kasper, H. J. Herzog, T. Perova, R. Maurice, C. Hofer, and C. Teichert, Thin SiGe buffers with high Ge content for n-MODFETs, *Mat. Sci. Engin. B*, **89**:1–3 (2002).
25. S. Mantl, S. M. Hogg, B. Holländer, S. Lenk, M. Luysberg, M. Grimm, H. Trinkaus, H-J. Herzog, T. Hackbarth, R. Loo, and M. Bauer, Strain relaxed ultrathin SiGe buffer layers on blanket and patterned Si and SOI wafers for strained Si produced by He ion implantation and annealing, *Proc. IEDM*, (2002).
26. U. König, M. Zeuner, G. Höck, T. Hackbarth, M. Glück, T. Ostermann, and M. Saxarra, n- and p-type SiGe HFETs and circuits, *Solid-State Electron.*, **43**:1383–1388 (1999).
27. M. Arafa, K. Ismail, J. O. Chu, B. S. Meyerson, and I. Adesida, A 70 GHz f_T low operating bias self-aligned p-type SiGe MODFET, *IEEE Electron Dev. Lett.*, **17**:586–588 (1996).
28. M. Encisco-Aguilar, N. Zerounian, F. Aniel, T. Hackbarth, H-J. Herzog, K. Lyutovich, and E. Kasper, High frequency performance of strained Si n-MODFET on very thin SiGe buffers, *Proc. 11th GaAs Symp.*, Munich, 2003, pp. 183–186.
29. A. Sadek, K. Ismail, M. A. Armstrong, D. A. Antoniadis, and F. Stern, Design of Si/SiGe heterojunction complementary metal-oxide-semiconductor transistors, *IEEE Trans. Electron Dev.*, **43**:1224–1232 (1996).
30. A. G. O'Neill and D. A. Antoniadis, Investigation of Si/SiGe-based FET geometries for high frequency performance by computer simulation, *IEEE Trans. Electron Dev.*, **44**:80–88 (1997).
31. M. Zeuner, A. Fox, T. Hackbarth, D. Behammer, and U. König, 90 GHz f_T SiGe HFET with fully optical self-aligned sub-100 nm gate, *DRC 2002, Tech. Digest*, IIB.
32. M. Enciso-Aguilar, F. Aniel, P. Crozat, R. Adde, H. J. Herzog, T. Hackbarth, U. König, and H. von Känel, DC and high frequency performance of 0.1 μm n-type Si/Si_{0.6}Ge_{0.4} MODFET with $f_{\text{max}} = 188$ GHz at 300 K and $f_{\text{max}} = 230$ GHz at 50 K, *Electron. Lett.*, **39**:149–151 (2003).
33. W. Dürr, U. Erben, A. Schüppen, H. Dietrich, and H. Schumacher, Investigation of microstrip and coplanar transmission lines on lossy silicon substrates without backside metalization, *IEEE Trans. Microwave Theory Techn.*, **46**:712–715 (1998).
34. A. C. Wilson, D. Melendy, P. Francis, K. Hwang, and A. Weisshaar, Comprehensive compact-modeling methodology for spiral inductors in silicon-based RFICs, *IEEE Trans. Microwave Theory Techn.*, **52**:849–857 (2004).
35. E. Sönmez, A. Trasser, K-B. Schad, P. Abele, and H. Schumacher, A single-chip 24 GHz receiver front-end using a commercially available SiGe HBT foundry process, *RFIC Conference*, Seattle, WA, June 2–4, 2002, pp. 159–162.
36. H. Hashemi, X. Guan, and A. Hajimiri, A fully integrated 24-GHz 8-path phased-array receiver in silicon, *ISSCC 2004*, San Francisco, CA, February 15–18, 2004.
37. H. Knapp, M. Wurzer, T. F. Meister, K. Aufinger, J. Böck, S. Boguth, and H. Schäfer, 86 GHz static and 110 GHz dynamic frequency dividers in SiGe HBT technology, *Int. Microwave Sympos.*, Philadelphia, PA, June 8–13, 2003, Paper WE6C-5.
38. T. Mack, T. Hackbarth, H-J. Herzog, H. Von Känel, M. Kummer, J. Ramm, and R. Sauer, Si/SiGe FETs grown by MBE on LEPECVD grown virtual substrate, *Mat. Sci. Eng.*, **B39**:368–372 (2002).
39. P. Abele, M. Zeuner, I. Kallfass, J. Müller, H. L. Hiwilepo, D. Chrastina, H. Von Känel, U. König, and H. Schumacher, A 32 GHz MMIC distributed amplifier based n-channel SiGe MODFETs, *Electron. Lett.*, **39**:1448–1449 (2003).

SIX-PORT NETWORKS

XINYU XU
 KE WU
 RENATO G. BOSISIO
 Ecole Polytechnique de Montreal
 Montreal, QC, Canada

1. INTRODUCTION

A *software-defined radio* (SDR) is a radio in which the operating parameters, including the frequency range, modulation type, and maximum radiated or conducted output power can be altered by making a change in software without making any hardware changes.

The essence of an SDR is the ability, without introducing new hardware, to change operating characteristics by changing software programs executing in processing resources. In SDR, operating parameters are determined for the most part by software. This enables a single wireless device to be reprogrammed to allow different modulation schemes, coding, and access protocols. SDR allows more efficient use of spectrum by facilitating spectrum sharing and allowing equipment to be reprogrammed for various modulation schemes. The ability of SDR to be programmed also enhances interoperability between different radio services. Figure 1 shows a block diagram of an ideal SDR. Broadband RF signals are converted to baseband and fed to high-speed A/D converter (ADC) and programmable digital filter or channel decoder to select the desired channel signal such that demodulation means of RF signals with various bandwidths, transmission rates and modulation schemes are readily programmed. The hardware for this procedure requires downconversion to baseband of the entire bandwidth for various mobile standards and different frequency bands. This baseband signal is digitized, and all the subsequent processing is implemented in software [1–4].

SDR has been identified as a potential method to enhance flexible wireless communication systems. The operation speed of an analog/digital converter (ADC) and processing ability of digital signal processors (DSPs) and chips are key factors in the development of SDR for useful commercial applications. More recent advances in semiconductor processing technology and the development of reconfigurable devices such as digital signal processors (DSP) and field-programmable gate arrays (FPGA) reduce the development time of commercial products. SDR in conjunction with six-port receivers has promising

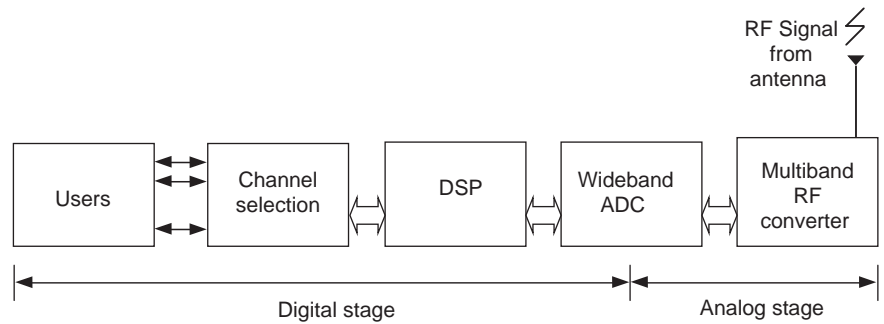


Figure 1. Block diagram of an Ideal Software Defined Radio Receiver.

applications for use in wireless LANs, audio and television broadcasting, and interoperability between different radio services, as seen by new studies on the use of six-port technology [5] in various design aspects of a new SDR receiver. The objective is to realize an application of SDR to provide a multichannel, multimode wireless direct digital receiver. The combination of SDR and six-port technology provides great flexibility in system configuration, significant reduction in hardware cost, particularly at millimeter-wave frequencies, and potential for software reuse. Different types of six-port circuits have been designed, with center frequencies at 2.4, 5.8, 24, and 28 GHz [6–9], operating over large frequency bands. Some six-port circuits are based on microstrip structures, fabricated with hybrid microwave integrated circuit (MHMIC) or monolithic microwave integrated circuit (MMIC) technology at both microwave and millimeter-wave frequencies. Other circuits use a novel substrate-integrated waveguide (SIW) structure [10], which allows integration of planar integrated circuit structure with waveguide structure. The performances of these six-port circuits in digital receivers are reported in relation to signal modulation schemes, noise performance analysis calibration, and coding. Bit error rate simulation and measurement results obtained with demodulation algorithms are given for QPSK and QAM-16 signals under a variety of operating conditions [11]. It is shown that this type of receiver can provide bit error rates as low as 1×10^{-6} for E_b/N_0 of 11 dB (for QPSK) and 15 dB (for QAM-16). Initial results show promising applications of six-port technology for direct digital conversion demodulation reception, needed in future low-cost SDR communication systems [11]. Measurement and

simulated demodulation results obtained with coding algorithms are also given in Section 7.

The six-port receiver approach offers wideband accommodation to ever-changing communication specifications required in a SDR as much of its functionality is defined in software and it can offer widebands from 2 to 2200 MHz [12].

SDR can be considered to be an information transfer system (ITS) combining technology from historically separate fields of computers and radios. Emerging from military applications, SDR has received much attention by researchers investigating wireless communications, and several Websites are providing detailed information [13–15]. An SDR is a radio in which the operating parameters, including the frequency range, modulation type, and maximum radiated or conducted output power can be altered by changes in software without need to make hardware changes [1]. Taking advantage of state-of-the-art digital signal processing technology, the performances of SDR systems depend more on DSPs with low-cost RF hardware. Of course, this goal can be achieved by less stringent requirements for expensive RF circuit fabrication and more flexibility for diverse communication systems.

The ideal SDR receivers must be wideband with high-speed ADCs and effective operating algorithms. Data signals from antenna are converted from analog to digital, and remaining tasks are processed in the DSP. Limited by the ability of current ADC and reprogramming device, present SDR receiver systems convert signals from analog to digital after downconversion to baseband. A block diagram of a typical superheterodyne receiver with double-stage downconversion is shown in Fig. 2; a typical direct

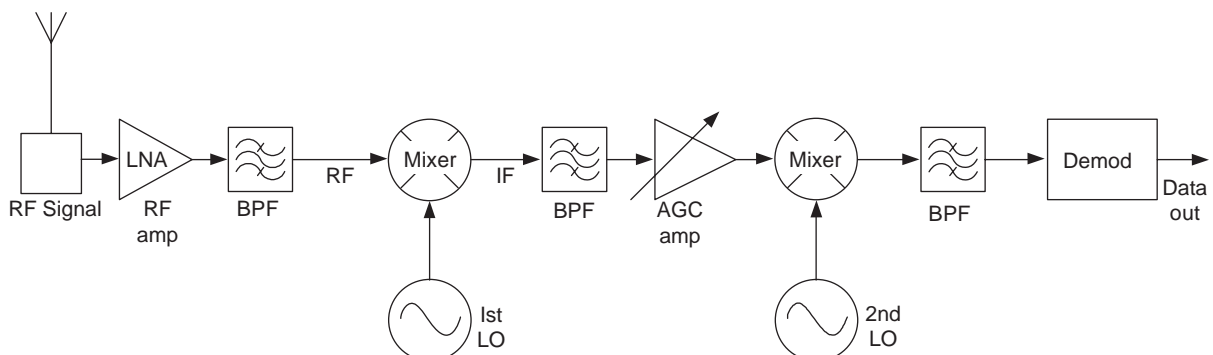


Figure 2. Block diagram of a typical double-stage downconversion superheterodyne digital receiver.

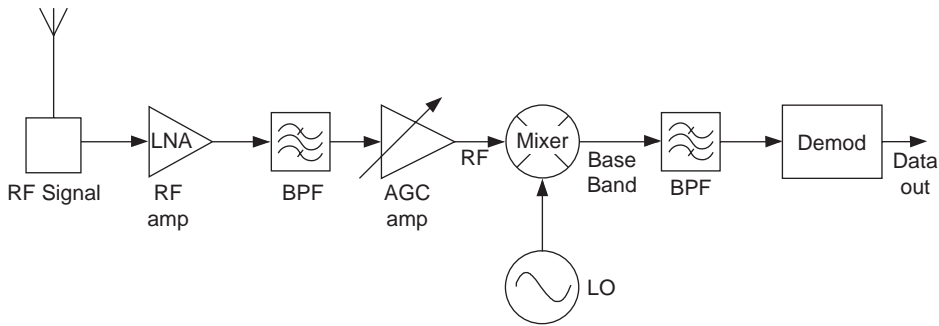


Figure 3. Block diagram of a typical direct digital receiver.

digital receiver is shown in Fig. 3, and a typical six-port receiver is shown in Fig. 4.

In all three receiver types the phases and amplitudes are measured to determine I,Q data by signal processing means. However, the conversion of data from RF signal to baseband signal is quite different and more simple by using six-port circuit approach (Fig. 4) in conjunction with integrated circuits, SIW, and wideband operational six-port circuits.

In general, digital receivers used in RF communication systems can be divided into two categories: superheterodyne receivers and direct-conversion receivers. Figure 2, as mentioned, illustrates a simplified block diagram of a typical superheterodyne digital receiver. The received RF signal is amplified first and then converted into a lower frequency (intermediate frequency). The desired signal is filtered to eliminate noise and interference and a succeeding high-gain AGC amplifier stabilizes the output signal level as the input RF signal level may vary because of a fading transmission channel. The superheterodyne receiver offers advantages such as high sensitivity and high frequency selectivity, and it has been the de facto standard configuration in most communication systems. However, this receiver uses many components, including several bandpass filters and IF amplifiers, and it is less suited for high-level circuit integration fabrication means needed to satisfy SDR mass production markets.

On the other hand, Fig. 3 shows the block diagram of a typical direct digital receiver. The received RF signal is converted with a mixer directly from RF to baseband. The direct-conversion receiver offers several advantages; it is simpler and less costly than superheterodyne receiver, since there is no IF amplifier, IF bandpass filter, or IF local oscillator required for final downconversion. Therefore,

the overall configuration of the direct receiver is expected to be much simpler than superheterodyne receiver, leading to a potentially cost-effective solution. Another important advantage of direct conversion is that there is no image frequency. Since the mixer difference frequency is effectively zero, and the sum frequency, equal to twice the local-oscillator (LO) frequency, is easily filtered. However, one important disadvantage of direct receivers is that the LO must be very stable, and it is hence costly, especially for millimeter-wave frequencies. In addition, wideband downconverters are not readily available at millimeter-wave frequencies. An alternative method is the use of six-port based direct digital receiver architecture (Fig. 4). More recent results [16,17] with carrier recovery from QPSK signals offer an interesting approach used in six-port-type receivers to reduce LO costs without imposing serious limits on wideband operation.

The six-port-based SDR receiver shown in Fig. 4 also uses a direct conversion scheme, and the baseband signal is digitized at four output terminals of the six-port circuit. The six-port-based digital receiver in SDR targets multi-modulation and multiband wireless communication systems at low cost for mass-market millimeter-wave applications.

The concept of the six-port-based receiver is derived from six-port technology, developed as an amplitude and phase measurement methodology for high-frequency signals [18]. In 1994, a paper proposed application of six-ports for direct receivers [5]. Several six-port receivers have been developed since then for microwave and millimeter-wave communications. The carrier recovery method for six-port receiver has advanced, and LO frequency can be retrieved from the RF input by carrier recovery means [7,19]. Six-port receivers have been proposed for being

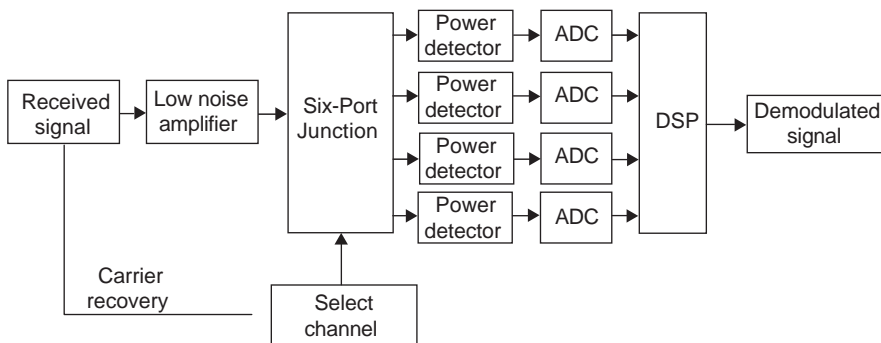


Figure 4. Block diagram of typical direct software six-port receiver.

robust and offering low manufacturing cost and low power consumption. More investigations are needed, however, and present studies indicate that a six-port receiver has a strong potential to solve a number of current communication and marketing problems, including multiuser modulation, seamless radio reception, low cost, and wideband operation.

2. DSP IN SOFTWARE-DEFINED RADIO

Figure 5 is a photograph of a typical DSP board with two A/Ds and D/As (12 bit sampling rate of 65 MHz), an FPGA chip (EP20K1500EBC652-1X) and two digital input/output ports, configuration ports, and an external clock connector. Several DSP boards may be operated in parallel by cabling digital I/O ports.

Today the evolution toward practical software radios is accelerating through a combination of techniques. These include smart antennas, multiband antennas, and wideband RF devices. Nowadays wideband analog-to-digital converters (ADCs) and digital-to-analog converters (DACs) can access gigahertz range of spectra instantaneously. Intermediate frequency (IF), baseband, and bit-stream processing is implemented in increasingly general-purpose programmable processors with application-specific integrated circuits (ASICs), Field-programmable gate arrays (FPGAs), digital signal processors (DSPs), and general-purpose (GP) processor technologies are being introduced in SDR designs. SDR is becoming practical as costs per millions of instructions per second (mips) of DSPs, and general-purpose central processor units (CPUs) have dropped below \$10 per mips. The economics of software radios become increasingly compelling as demands for flexibility increase while numerical processing costs continue to drop by a factor of 2 every few years, but RF parts and subassembly costs tend to remain high, particularly at millimeter-wave frequencies. At the same time, absolute processing capacities continue to climb into the

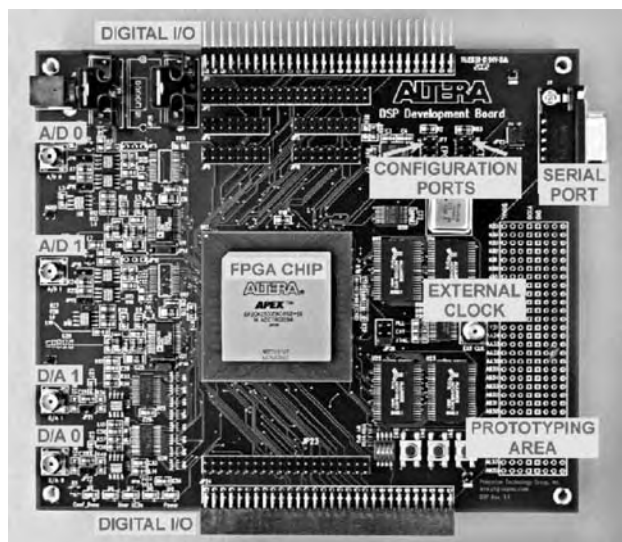


Figure 5. Photograph of a typical DSP board.

hundreds of millions of floating-point operations per second (mflops) to billions of flops (gflops) per chip. At present time, software radio technology can be cost-effectively implemented for commercial first-generation (1G) analog and second-generation (2G) digital mobile cellular radio air interfaces. Over time, wideband third-generation (3G) air interfaces will also yield to software techniques on wideband RF platforms possibly at millimeter-wave frequencies. The resulting software-defined radio extends the evolution of programmable hardware, increasing flexibility via increased programmability. The ideal software radio represents the point of maximum flexible programmability in this evolution. In addition, ADCs and DACs are available as low-cost chips and single-board open-architecture configurations offer bandwidths of tens of megahertz with the dynamic range required for software radio applications. Multimedia requirements for desktop and wireless personal digital assistants (PDAs) continue to exert downward pressure on parts count and on power consumption of such chipsets. This trend will push the ideal software radio technology from the base station to the mobile terminal. Although the tradeoffs among analog devices, low-power ASICs, DSP cores, and embedded microprocessors in handsets remain fluid, cutting-edge base stations are beginning to employ software radio architectures. New designs for high-end mobile radio nodes such as military vehicular radios are now largely based on some type of software radio approach. Finally, the multiband, multimode, and multiuser flexibility of software radios appears central to the goal of seamless integration of personal communications systems (PCS) and land mobile and satellite mobile services (including truly nomadic computing).

Compared to the traditional hardware radio, the main advantage of software radio is the fact that it can support various modulation schemes with a unique hardware. On the other hand, its main disadvantage is still the present high cost of digital programmable devices. This situation can change with the rapid development in semiconductor processing technology and the development of reconfigurable devices in combination with six-port receiver technology.

2.1. Combination of SDR and Six-Port Technology

One key point of SDR is to possess a digital processing kernel with almost infinite processing ability. Although DSP and semiconductor technology have developed rapidly since the early 1990s, it is still difficult for the operating speed level of current DSP chip to completely support a high-speed multichannel multimodulation SDR at IF level. In the interim, SDR implementations will require a mix of hardware-intensive techniques such as ASICs. Certain software radio systems adopt multichip architecture and parallel algorithms, thereby increasing the design complexity and potential cost.

Instead of digitizing signals at IF, microwave/millimeter-wave signals can be digitized at baseband with six-port technology, and hence reduce the processing requirement for DSP chips. This new solution to SDR design is based on direct demodulation with "six-port technology,"

downconverting RF signal to baseband directly with a six-port module. This work presents more recent results obtained on the six-port receiver suitable for SDR use in multimode microwave/millimeter-wave wireless mass-market communications.

2.2. Broader Implications of the Software Radio

The prospect of a new technology for multiband, multi-mode software radio handsets and infrastructure has social and political implications, particularly for type certification authorities charged with administering the equitable use of the radio spectrum. Among other factors, these authorities certify that radio equipment meets legally imposed constraints. The software radio introduces new levels of complexity in the communication hardware certification process.

In addition, software radios may operate on any RF band that is within the capabilities of the underlying radio platform, and with any mode for which a software load image is available. This raises the possibility of truly novel approaches to spectrum management. One of the more interesting is the possibility that software radios could use a spectrum rental protocol to autonomously share the spectrum. Another is that by incorporating advanced technology such as neural networks [20–22], SDR can develop its own protocols to achieve a radio system called “cognitive radio.” Cognitive radio is an advanced research topic based on the software radio concept.

3. ARCHITECTURE AND OPERATING PRINCIPLE OF SIX-PORT RECEIVER

Six-port technology has been under development since the early 1970s starting with microwave and millimeter-wave measurement applications; in 1994 a six-port receiver was first proposed as a direct digital receivers [5]. In principle, the six-port consists of linear circuits with dividers and combiners interconnected in such a way that four or ‘ N ’ different vectorial additions of reference signal and signal to be measured (receiver signal) are obtained. The use of different phase shifts and attenuation between the components such that the two RF input signals generate different phases at four output ports by vector addition of the input phasors. The signal levels of the four baseband output signals are detected using Schottky diode detectors or another RF quadratic detector including a power detector. By applying suitable baseband signal processing algorithms, the magnitude and phase of the unknown received signal can be determined for given modulation and coding scheme [5,23].

3.1. Six-Port Circuit Reflectometer and Six-Port Receiver

The block diagram of a conventional six-port reflectometer is shown in Fig. 6. RF signal a_1 is normally connected to port 1 as reference signal and RF signal a_2 to port 2 as unknown signal. The other four output ports are connected to RF quadratic detectors or power detectors. The unknown signal of the six-port circuits can be obtained from

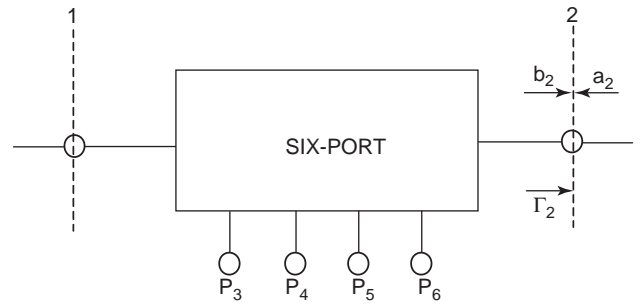


Figure 6. Block diagram of six-port reflectometer.

four output power level readings [24–26]:

$$p_3 = |b_3|^2 = |Aa_2 + Bb_2|^2 \quad (1)$$

$$p_4 = |b_4|^2 = |Ca_2 + Db_2|^2 \quad (2)$$

$$p_5 = |b_5|^2 = |Ea_2 + Fb_2|^2 \quad (3)$$

$$p_6 = |b_6|^2 = |Ga_2 + Hb_2|^2 \quad (4)$$

where $A \dots H$ are eight complex constants, to be known by physical calibration procedures, described below

$$|b_2|^2 = \sum_{i=3}^6 \beta_i P_i$$

and β_i are real coefficients, functions of $A \dots H$ complex coefficients.

The measurement of $|b_2|$ in the reflectometer shown in Fig. 6 determines one measurement of interest. The six-port reflectometer is usually designed in such a way that the response of one of the power detectors is proportional to $|b_2|^2$. The fourth port is chosen for normalization. Referring to Eq. (2), the first design objective is for $C = 0$. Hence

$$p_4 = |D|^2 |b_2|^2 \quad (5)$$

In order to explicitly display the measurements of interest, (1), (3), and (4) may be written as follows:

$$p_3 = |A|^2 |b_2|^2 |\Gamma_2 - q_3|^2 \quad (6)$$

$$p_5 = |E|^2 |b_2|^2 |\Gamma_2 - q_5|^2 \quad (7)$$

$$p_6 = |G|^2 |b_2|^2 |\Gamma_2 - q_6|^2 \quad (8)$$

When A , E , and G are known by calibration procedures, then $|b_2|$ and Γ_2 can be determined from Eqs. (6)–(8).

Consider the case of a six-port receiver at a reference plane 2-2'. The “incident wave” a_2 and the “reflected wave” b_2 have frequencies f_{RF} , f_{LO} and have arbitrary relative relationships φ_1 , φ_2 , so that

$$a_2 = |a| e^{j(2\pi f_{RF} t + \varphi_1)} \quad (9)$$

$$b_2 = |b| e^{j(2\pi f_{LO} t + \varphi_2)} \quad (10)$$

If their frequency difference is small, the S parameters of the six-port to be calibrated can be regarded as being constant at each frequency and the equivalent reflection coefficient becomes

$$\Gamma_2 = \frac{b_2}{a_2} = \left| \frac{b}{a} \right| e^{j(2\pi\Delta f t + \Delta\phi)} \quad (11)$$

where $\Delta f = f_{LO} - f_{RF}$ and $\Delta\phi = \phi_2 - \phi_1$

The frequency difference Δf can be readily obtained from the derivative of $\theta(t)$

$$\Delta f = \frac{\theta(t_2) - \theta(t_1)}{t_2 - t_1} \quad (12)$$

where the time interval between two samples $\Delta t = t_2 - t_1$ is properly chosen for best accuracy. It is to be noted that the sign of Δf is direct indication of relative position of f_{RF} and f_{LO} . In this way, we can determine the ratio of amplitude, frequency and phase between LO signal (port 1) and RF signal (port 2) from the power levels at the four output ports. Thus

$$\Gamma_2 = \frac{\sum_{i=3}^6 X_i P_i}{\sum_{i=3}^6 Y_i P_i} \quad (13)$$

where X_i, Y_i are complex constants that can be obtained by calibration procedures. However I,Q data for a given channel can be determined directly from output signals on six-port circuit by use of digital or analog decoder circuit [27].

3.2. Architecture of Six-Port SDR Receiver

The structure of a software six-port receiver was shown in Fig. 3. The six-port junction works as a direct RF downconverter in the proposed receiver. Port 2 connects to RF signal and port 1 connects to LO signal; the other four ports are connected to power detectors. RF signals from port 1 and port 2 are directly downconverted from radiofrequency to baseband frequency from the output levels of the power detectors. The baseband signal levels from power detectors are digitized and sent to DSP. The DSP stage is in charge with suitable algorithms of baseband signal processing such as demodulation and decoding. Six-port receivers were designed at CRP to operate at a center frequency of 24 GHz for SIW, 28, 24, 5.8, and 2.4 GHz for MMIC or MHMIC technology six-port circuits.

3.3. Analysis of Six-Port Circuit

One of the design criteria for an ideal six-port junction as suggested by Engen [26] is as follows. For the ideal situation, a six-port circuit can obtain highest accuracy for all ranges of operation if the six-port circuit q points (complex numbers) correspond to the condition $|q_3| = |q_5| = |q_6|$ and their arguments differ by 120° .

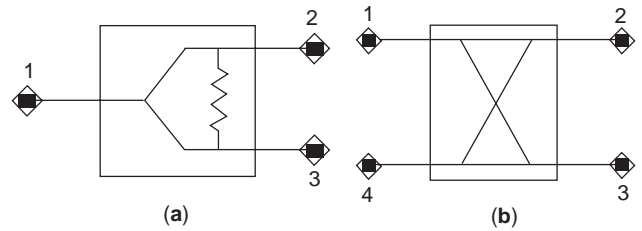


Figure 7. (a) Wilkinson power divider; (b) 90° hybrid coupler.

Suppose that ports 1 and 2 are completely isolated, and then the equivalent q_i point can be expressed as

$$q_i = \frac{S_{i1}}{S_{i2}} \quad (14)$$

In practical circumstances, it is difficult to find such a circuit, especially if extremely broadband operation is required. In general, the more the magnitudes of q_i are equal and the greater the differences between arguments of q_i , the better is the performance of the circuit. According to Stumper [31], the six-port can yield good results even when the ratios of the magnitudes of q_i exceed 4 and the angles between q_i are smaller than 25° . For QPSK hard receivers, the angle separation of q_i points is 90° and their amplitudes are equal.

A typical six-port junction presented below consists of a Wilkinson power divider and a number of 90° hybrid couplers. Figure 7 shows the symbols of these two components.

The scattering parameters of the Wilkinson power divider and 90° coupler are

Wilkinson power divider [S]

$$= \begin{bmatrix} 0 & -\frac{j}{\sqrt{2}} & -\frac{j}{\sqrt{2}} \\ -\frac{j}{\sqrt{2}} & 0 & -\frac{j}{\sqrt{2}} \\ -\frac{j}{\sqrt{2}} & 0 & -\frac{j}{\sqrt{2}} \end{bmatrix} \quad (15)$$

90° hybrid coupler [S]

$$= \begin{bmatrix} 0 & \frac{j}{\sqrt{2}} & \frac{1}{\sqrt{2}} & 0 \\ \frac{j}{\sqrt{2}} & 0 & 0 & \frac{1}{\sqrt{2}} \\ \frac{1}{\sqrt{2}} & 0 & 0 & \frac{j}{\sqrt{2}} \\ 0 & \frac{1}{\sqrt{2}} & \frac{j}{\sqrt{2}} & 0 \end{bmatrix} \quad (16)$$

A block diagram of six-port circuit architecture is shown in Fig. 8. The circuit consists of one power divider and three 90° hybrid couplers.

From (15) and (16), the reflected wave at ports 3–6 can be expressed as follows:

$$\begin{aligned} b_3 &= -\frac{a_1}{2} + \frac{a_2}{2}j \\ b_4 &= -\frac{a_1}{2}j + \frac{a_2}{2}j \\ b_5 &= \frac{a_1}{2}j + \frac{a_2}{2} \\ b_6 &= -\frac{a_1}{2} - \frac{a_2}{2} \end{aligned} \quad (17)$$

Assuming that all six ports are perfectly matched, then $b_1 = b_2 = b_3 = b_4 = b_5 = b_6 = 0$; and

$$[b] = [S] \cdot [a] \quad (18)$$

The scattering parameters for an ideal six-port junction are as follows:

$$\begin{bmatrix} b_1 \\ b_2 \\ b_3 \\ b_4 \\ b_5 \\ b_6 \end{bmatrix} = \begin{bmatrix} 0 & 0 & \frac{1}{2}e^{j180^\circ} & \frac{1}{2}e^{-j90^\circ} & \frac{1}{2}e^{-j90^\circ} & \frac{1}{2}e^{j180^\circ} \\ 0 & 0 & \frac{1}{2}e^{j90^\circ} & \frac{1}{2}e^{j90^\circ} & \frac{1}{2}e^{j0^\circ} & \frac{1}{2}e^{j180^\circ} \\ \frac{1}{2}e^{j180^\circ} & \frac{1}{2}e^{j90^\circ} & 0 & 0 & 0 & 0 \\ \frac{1}{2}e^{-j90^\circ} & \frac{1}{2}e^{j90^\circ} & 0 & 0 & 0 & 0 \\ \frac{1}{2}e^{-j90^\circ} & \frac{1}{2}e^{j0^\circ} & 0 & 0 & 0 & 0 \\ \frac{1}{2}e^{j180^\circ} & \frac{1}{2}e^{j180^\circ} & 0 & 0 & 0 & 0 \end{bmatrix} \cdot \begin{bmatrix} a_1 \\ a_2 \\ a_3 \\ a_4 \\ a_5 \\ a_6 \end{bmatrix} \quad (19)$$

where a_1 and a_2 represent the incoming signal and the reference LO signal, respectively.

4. SIX-PORT DESIGNS

Based on the analysis of an ideal six-port junction, we now provide various six-port circuit designs. One objective is to design a six-port circuit that is to be used in an SDR receiver operated at a center frequency of 24 GHz with good receiver stability and high sensitivity. This leads to the following design objectives:

- Minimum of insertion loss between the RF input port and power detector ports such as to increase power levels at output ports
- Maximum isolation between RF input port and LO port to reduce leakage to antenna

The q_i points of the six-port circuit should be equal in magnitude and 120° apart in phase. When RF input port and LO ports are completely isolated, the equivalent q_i points of the six-port circuit can be expressed as

$$q_3 = \frac{S_{31}}{S_{32}}, q_4 = \frac{S_{41}}{S_{42}}, q_5 = \frac{S_{51}}{S_{52}}, q_6 = \frac{S_{61}}{S_{62}}$$

Different six-port circuits were designed and fabricated at 24 and 28 GHz. Circuit designs are based on microstrip structure (MHMIC) and substrate-integrated waveguide (SIW) structure [10]. Circuit simulations of these two six-port circuits were made using ADS and HFSS software of Agilent Technologies. In addition, an MMIC six-port circuit was designed at 28 GHz and fabricated using a pseudomorphic high-electron-mobility transistor (PHEMT) process on a GaAs compound semiconductor [17]. Other six-port circuits for six-port receivers were designed at much lower frequencies [7,28].

4.1. Microstrip Six-Port Circuit

Microstrip six-port circuits were designed at 24 and 28 GHz. The 24-GHz circuit was fabricated in MHMIC technology (on a 250- μm ceramic substrate with a relative permittivity $\epsilon_r = 9.9$) with the layout shown in Fig. 9 and photographed in Fig. 10. The circuit at 28 GHz was fabricated in MMIC technology using PHMET process on GaAs and (See Fig. 11). The MHMIC chip measures 9.5×8.4 mm and the MMIC chip, 2×3 mm. Simulated and measured S parameters of the MHMIC six-port circuit are summarized in Table 1, with center frequency at 24 GHz. The reflection coefficients S_{11}, S_{22} are lower than -19.8 dB and the isolation between the RF port and LO port S_{12} is lower than -23.8 dB at center frequency. The transmission coefficients are close to the theoretical predicted value (-6 dB). Similar agreement between measurement and simulated S parameters was found for the MMIC six-port operating from 24 to 30 GHz.

The simulated and measured operating bandwidth results for the microstrip structure six-port MHMIC are shown in Fig. 12. The simulated and measured results agree well over the operating bandwidth. The isolation

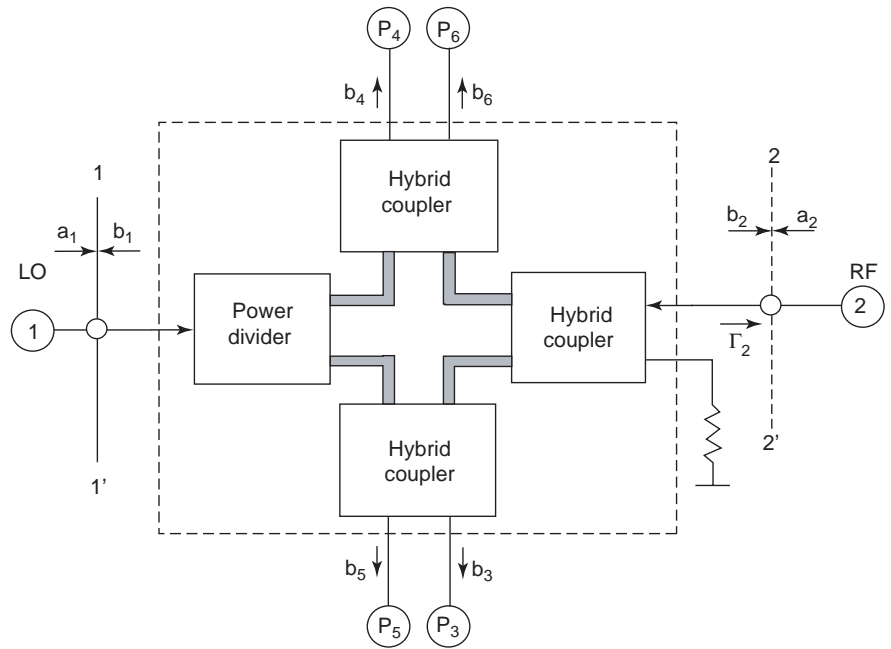


Figure 8. Six-port circuit block diagram.

between RF and LO ports is found to be at least 15 dB, and the transmission coefficients are within ± 0.5 dB of the theoretical predicted value (-6 dB).

4.2. Substrate-Integrated Waveguide (SIW) Structure Six-Port Circuit

Rectangular waveguide components have been widely used in millimeter-wave systems, but their high cost and difficult integration to planar circuits prevent these components from being used in low-cost high-volume applications. The recently proposed substrate-integrated waveguide (SIW) scheme (Fig. 13) provides an interesting alternative. In this case, the rectangular waveguide components are synthesized using arrays of metallic vias and

convenient transitions to planar structures (microstrip, CPW) are designed and integrated on a single substrate. Hence, high-Q rectangular waveguide components and planar circuits can be integrated together on the same planar platform at low cost using standard PCB or compound semiconductor substrates.

SIW is fabricated with a periodic via structure to realize bilateral waveguide edge walls. This periodic structure is much more complex for analysis than the conventional rectangular waveguide. A simulation of the integrated waveguide using a finite-element method that

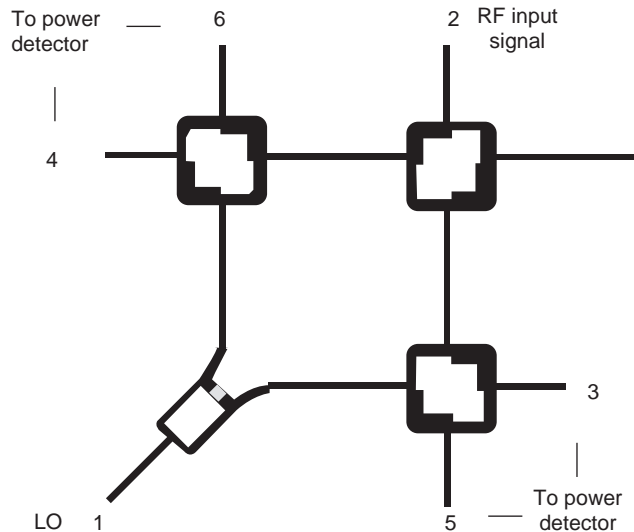


Figure 9. Design layout of the MHMIC six-port circuit.

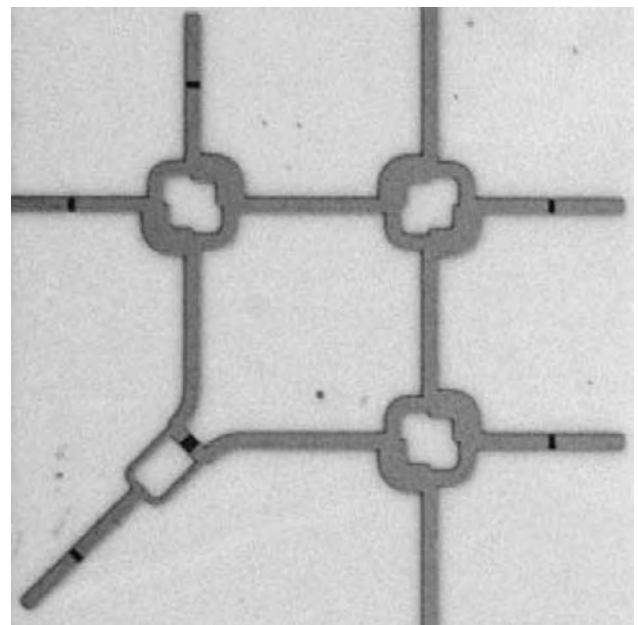


Figure 10. Photograph of MHMIC six-port circuit.

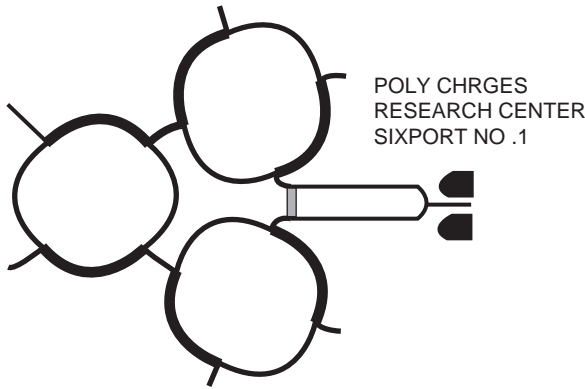


Figure 11. Photograph of MHMIC six-port circuit.

requires abundant resources and its design is not straightforward. To improve the design efficiency, the SIW is transformed to an equivalent rectangular waveguide. It is shown [10] that a TE_{10} -like mode in the SIW has dispersion characteristics almost identical to those of the TE_{10} mode of a dielectric-filled rectangular waveguide of an equivalent width.

For a six-port circuit, it is necessary to match the SIW to a microstrip or CPW transmission line. It is well known that a three-port matched network must be lossy. For a microstrip based six-port circuit, a Wilkinson power divider containing a $100\text{-}\Omega$ resistance is used. For the SIW structure, it is difficult to realize impedance inside a waveguide. Therefore, a Wilkinson power divider structure cannot be used in SIW. In the proposed SIW six-port circuit, the power divider is replaced with a coupler to ensure that its output 14 ports are well matched.

The SIW six-port circuit layout is shown in Fig. 6. The circuit was designed on a 0.508-mm substrate with relative permittivity $\epsilon_r = 2.2$, the via diameter is $d = 0.75\text{ mm}$, and the distance between the bilateral via sidewalls is $a = 6.682\text{ mm}$. The equivalent width a_{eqv} of the waveguide for HFSS simulation is 6.20 mm to operate in desired frequency band. Simulated S parameters of the SIW six-port circuit are summarized in Table 2 at a center frequency of 24 GHz . The reflection coefficients S_{11} and S_{22} are less than -27 dB and the isolation between RF port and LO port S_{12} is less than -37 dB . The transmission coefficients are close to the theoretical predicted value (-6 dB).

The simulated operating bandwidth results for the SIW structure six-port circuit are shown in Fig. 15. The return loss at output ports is less than -20 dB and the isolation between RF and LO ports is -33 dB at center frequency of 24 GHz . Over the operating bandwidth, the isolation

between RF and LO ports is at least -20 dB and the transmission coefficients are very close ($\pm 0.05\text{ dB}$) to the theoretical predicted value (-6 dB).

4.3. Comparison between Microstrip Structures and SIW Circuit Structure for Six-Port Circuit

Compared to microstrip structure, SIW structure can achieve higher Q value, which means smaller energy loss of the whole circuit. Simulation results show that the SIW structure can achieve smaller insertion loss between the RF input port and the power detector ports and more isolation between the RF input port and the LO port. In addition, the SIW structure can work at frequencies above 30 GHz , whereas the high loss of planar microstrip circuit makes this structure unacceptable above 30 GHz . However, the MMIC structure has definite dimensional advantages in the frequency ranges below 10 GHz and between 15 and 35 GHz .

An SIW structure can be effectively converted to an equivalent conventional rectangular waveguide. The SIW can then be modeled by conventional waveguide techniques, and all the existing design methods for the rectangular waveguide can be applied. With an appropriate choice of diameter, the radiation loss can be decreased to a negligible level. These characteristics make the SIW six-port structure a good choice for an SDR working at millimeter-wave frequencies above 40 GHz .

However, the SIW six-port circuit is much larger than the MMIC microstrip six-port circuit operated at 30 GHz . The SIW structure is not suited to low-frequency communications, and at typical microwave frequencies below 10 GHz , microstrip MHMIC or MMIC structure six-port is a better choice.

5. CALIBRATION

It is possible to calculate the ratio of amplitude, frequency, and phase between LO signal (port 1) and RF signal (port 2) from the four output power levels determining the complex constants X_i, Y_i by calibration procedures. We now examine the six-port calibration method and the six-port receiver demodulation results obtained with calibration. Among the many algorithms that have been proposed for the physical calibration of six-port reflectometers (SPRs) [18], Engen's six-port-to-four-port reduction [26,30] seems to be the most attractive. This procedure determines the dependencies between the different power meter readings, yielding five real-valued reduction parameters that permit transformation of the SPR into a virtual four-port. No

Table 1. Measured and Simulated S Parameters of Microstrip Structure MHMIC Six-Port ($f = 24\text{ GHz}$)

S Parameters	Simulations (dB)	Measurements (dB)	S Parameters	Simulations (dB)	Measurements (dB)
S_{11}	-25.8	-20.5	S_{16}	-6.5	-6.3
S_{22}	-22.7	-19.8	S_{23}	-6.5	-6.5
S_{12}	-26.4	-23.8	S_{24}	-6.3	-6.4
S_{13}	-6.3	-6.4	S_{25}	-6.5	-6.6
S_{14}	-6.3	-6.4	S_{26}	-6.0	-6.3
S_{15}	-6.4	-6.5	—	—	—

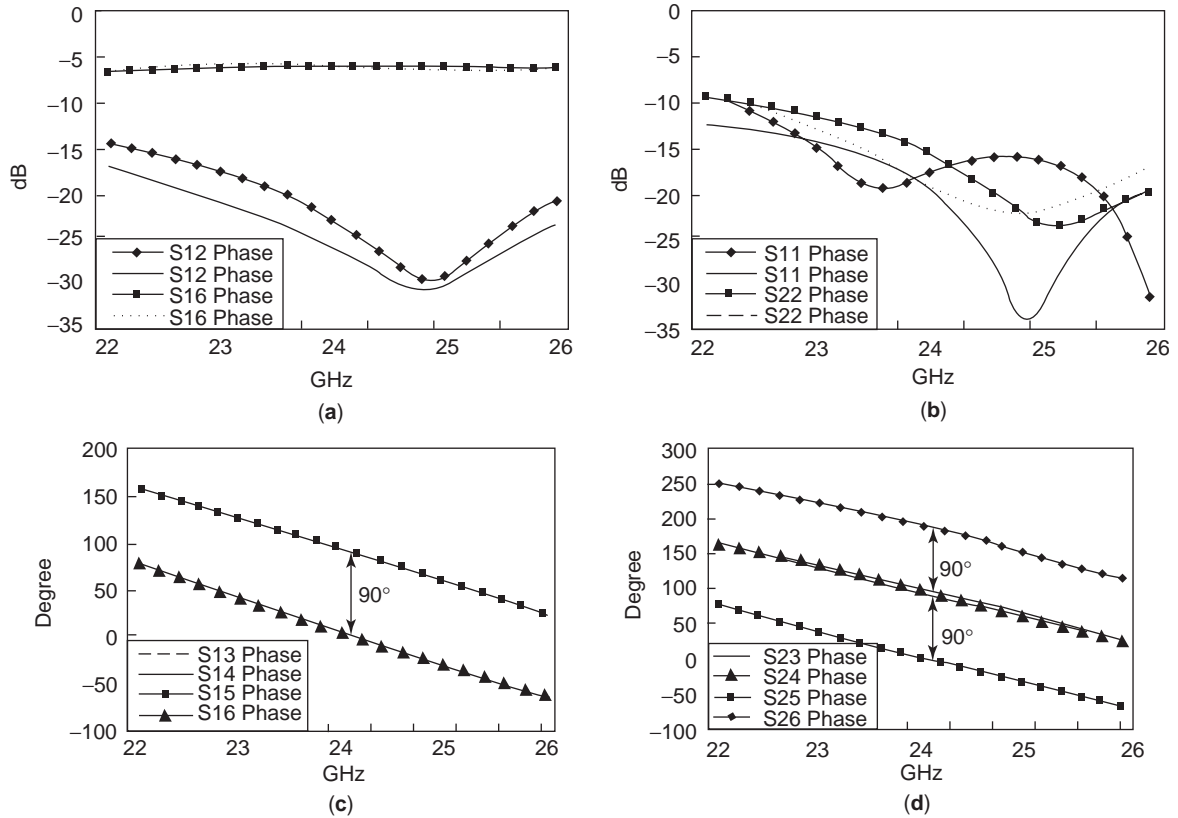


Figure 12. Simulated and measured scattering parameters of the MHMIC six-port circuit.

known standards are required for this reduction. The value measured by the virtual four-port is related to the reflection coefficient of the device under test by an “error box” transformation. The three complex parameters of this transformation may be found by using one of the many existing methods for the calibration of traditional network analyzers.

More recently, some real-time six-port calibration algorithms have been proposed. These calibration algorithms are designed for six-port direct receivers, a brief description of these calibration methods are given here.

5.1. Physical Six-Port Calibration Method

5.1.1. W-Plane Calibration of Six-Port Circuit. Using the same annotation as Stumper [31], the six-port to four-port reduction is given by the equations

$$p_1 = |w|^2 \tag{20}$$

$$Zp_2 = |w - w_1|^2 \tag{21}$$

$$Rp_3 = |w - w_2|^2 \tag{22}$$

where w is the complex reflection coefficient at the input of the imaginary ideal four-port reflectometer and the p_i denote the power levels from p_1 to p_3 , measured with the SPR significantly. However, good initial estimates of the

five parameters are needed for measured at the ports labeled 1–3, normalized with respect to the power value measured at the reference port 4 of the SPR. The five reduction parameters to be determined by the calibration are the values of the real positive variables Z , R , and w_1 , and the real and imaginary parts of the complex variable w_2 .

The variable may be eliminated from (9) to (11), yielding the nonlinear constraint equation

$$\begin{aligned} Ap_1^2 + BZ^2P_2^2 + CR^2P_3^2 + (C - A - B)ZP_1P_2 \\ + (B - C - A)RP_1P_3 + A(A - B - C)ZRP_2P_3 \\ + A(A - B - C)P_1 + B(B - C - A)ZP_2 \\ + C(C - A - B)RP_3 + ABC = 0 \end{aligned} \tag{23}$$

where

$$A = |w_1 - w_2|^2 \tag{24}$$

$$B = |w_2|^2 \tag{25}$$

Equation (9) can be solved by measuring at least 9 (usually 13 in practice) arbitrary different terminations. The solution of (9) $[A, B, C, Z, R]$ allows transformation of six-port to a perfect four-port reflectometer in a notional W

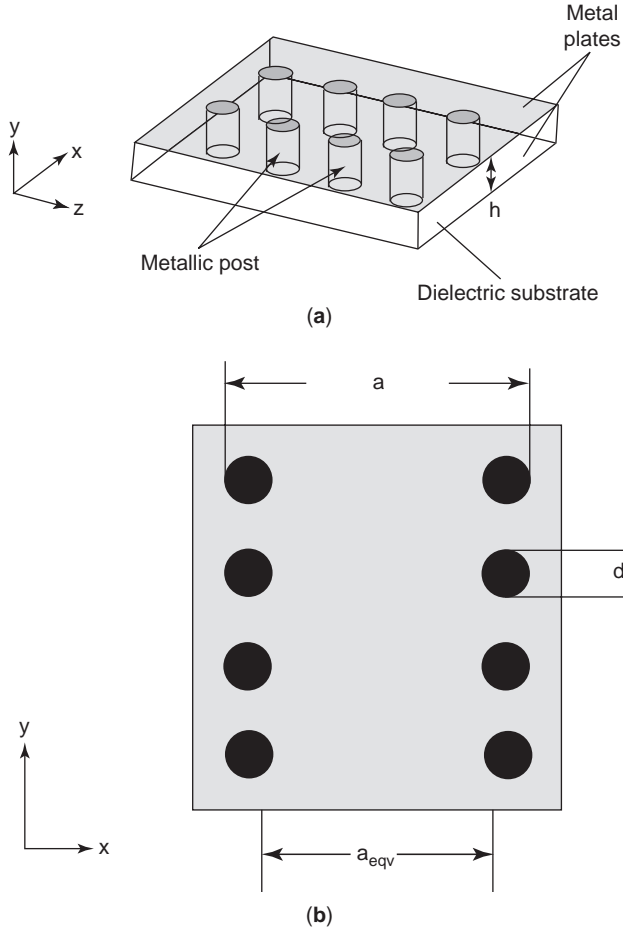


Figure 13. Topology of a substrate-integrated waveguide (SIW).

complex plane. The W -plane reflection coefficient is

$$W = \frac{p_1 - Z^2 p_2 + C}{2\sqrt{C}} + j \frac{[C(A+B-C) + (A-B+C)p_1 - (A-B-C)Z^2 p_2 - 2CR^2 p_3]}{\pm 2\sqrt{C(2AB + 2BC + 2AC - A^2 - B^2 - C^2)}} \quad (26)$$

5.1.2. Error-Box Calibration. A two-port error box is inserted between the notional four-port and the DUT (device under test) such that the virtual reflection reading from the notional perfect reflectometer obtained by W -plane calibration are transferred to the real reflection coefficients Γ . This is done through a bilinear transformation

$$\Gamma = \frac{e - W}{cW - d} \quad (27)$$

where c , d , and e are complex constants related to the S parameters of the error box

$$c = -S_{22}$$

$$d = S_{12}S_{21} - S_{11}S_{22}$$

$$e = S_{11}$$

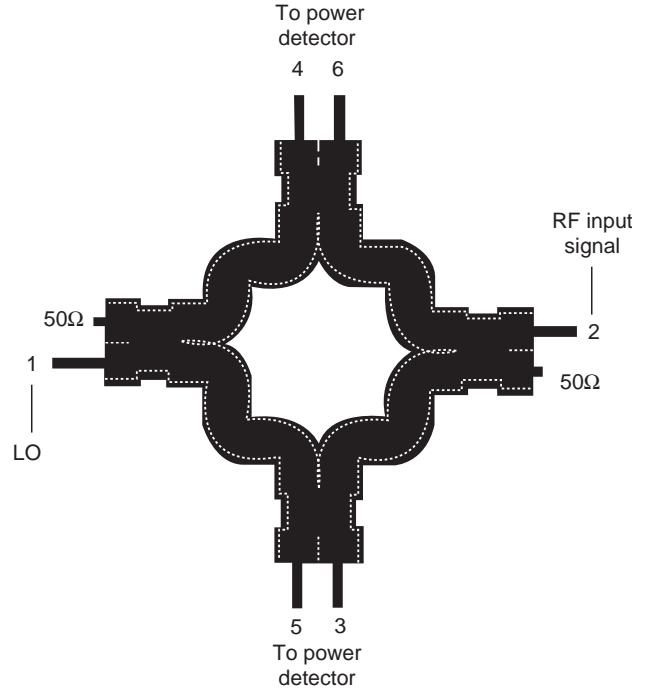


Figure 14. Design layout of the SIW six-port circuit [29].

W -planet- Γ -plane bilinear transformation is shown in Fig. 16.

After six-port-to-four-port reduction and error box calibration, $|b_2|$ and Γ can be determined. Therefore the phase difference and amplitude ratio of a_1 and a_2 can be obtained.

5.2. Real-Time Calibration Method for Six-Port Receiver [32]

The physical six-port calibration method uses external physical standard terminals to its input port. However, for a six-port receiver, it would be entirely impractical. It is therefore necessary to develop a calibration method free from any external connection. To accomplish this goal, a new six-port calibration methods is achieved by feeding a RF signal other than the reference source into DUT port of the six-port. This signal can be either a unmodulated signal carrier with a frequency adjacent to the six-port local source frequency, or a digital modulated signal with a frequency equal to or close to the local source frequency. The resulting output waveforms of the diode detectors of the six-port are actually beat signals of the two RF signals.

Table 2. Simulated S Parameters of SIW Structure Six-Port ($f = 24$ GHz)

S Parameters	Simulations (dB)	S Parameters	Simulations (dB)
S_{11}	-27.5	S_{16}	-6.05
S_{22}	-30.2	S_{23}	-6.04
S_{12}	-36.9	S_{24}	-6.04
S_{13}	-6.01	S_{25}	-6.02
S_{14}	-6.05	S_{26}	-6.05
S_{15}	-6.03	—	—

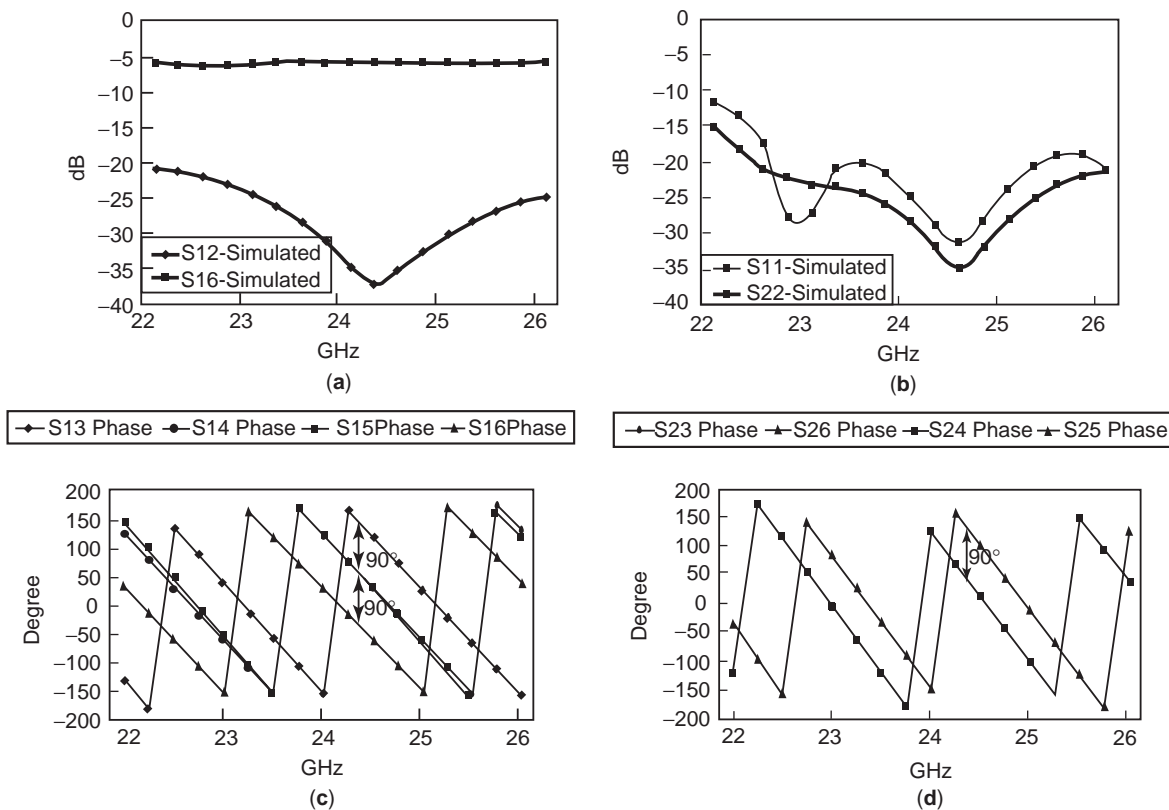


Figure 15. Simulated results of SIW structure six-port circuit.

The voltage readings corresponding to a group of widely distributed terminations are acquired by properly sampling these waveforms.

As we know, the leakage of the received signal to the local-oscillator reference port is small, and may be neglected. In this case, the relationship between the output data of SPR and the three power ratios of the detectors of the six-port become linear, and can be expressed as follows

$$\Gamma_r = A_{r1}p_1 + A_{r2}p_2 + A_{r3}p_3 + C_r \tag{28}$$

$$\Gamma_i = A_{i1}p_1 + A_{i2}p_2 + A_{i3}p_3 + C_i \tag{29}$$

where Γ_r , Γ_i are the calculated output data, whereas A_{rj} , A_{ij} ($j = 1,2,3$) and C_r , C_i are calibration parameters to be determined. Power ratios at the output detectors of the six-port are p_1, p_2, p_3 .

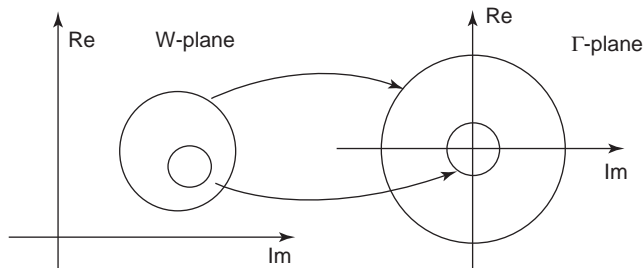


Figure 16. W-plane- Γ -plane bilinear transformation.

It is clear that from the equations above that a total of eight parameters should be determined from the calibration procedure. Therefore, four known sets of I,Q values or signal spread-spectrum (SS) standards should be used to obtain eight linear equations for solution of the preceding eight parameters of calibration A_{rj} , A_{ij} and C_r , C_i . These four known sets of I,Q values are ideally selected as being the four different states in QPSK. However, simulation shows that the calculation diverges when the four known sets of I,Q values have the same amplitude. Hence, at least the amplitude of one signal standard should be different from the remaining three. Therefore, we choose three sets of I,Q values from the four states of a QPSK signal and a zero signal at the input of the receiver as the fourth known I,Q set. The zero signal input can be achieved by applying a large bias to drive the low-noise amplifier (LNA) in the receiver front end far beyond cutoff. An alternative method is to insert an attenuation for example, 3 or 6 dB in the fourth set of QPSK signals.

From the four sets of I,Q values above or signal standards, we have four sets of detector output power ratios of the six-port, namely, Q with $k = 1,2,3,4$ and $j = 1,2,3$. Substituting $Q_{k,j}$ into Eq. (12) and equating the left-hand k, j side of these equations to the standard I,Q values, (1,1), (-1,1), (-1,-1), and (0,0) we have two systems of four linear equations. One of them corresponds to Eq. (13), and the other to Eq. (14). Solving these systems of linear equations, we obtain the parameters $A_{rj}, A_{ij}, j = (1,2,3)$ and C_r, C_i from which the calculations of the receiver output I,Q data

Table 3. Demodulation Data Results for QPSK Signal

Input	Output	Input	Output
$1 \angle 45^\circ$	$1.0205 \angle 46.66^\circ$	$1 \angle 225^\circ$	$1.0000 \angle 224.68^\circ$
$1 \angle 135^\circ$	$0.9595 \angle 139.42^\circ$	$1 \angle 315^\circ$	$1.0365 \angle 315.45^\circ$

are made using the ratios of the output readings of the power detectors in Eq. (12).

6. DEMODULATION ALGORITHM RESULTS

The complex constants related to six-port circuit X_i, Y_i that are obtained from calibration to arrive at required receiver demodulation. Table 3 and 4 show the simulated demodulation results for virtual six-port circuit for QPSK and QAM16 modulations 17 when using suitable algorithms.

The simulated demodulation results show that the receiver has an accuracy of $\pm 5^\circ$ in phase and ± 0.4 dB in amplitude. It is found that actual six-port circuits do indeed comply with above resolution in phase and amplitude.

Within the operating frequency band of the SIW six-port circuit based receiver (22–26 GHz), two modulation schemes (QPSK and QAM-16) are selected to test the performance of algorithms in SDR.

6.1. QPSK demodulation

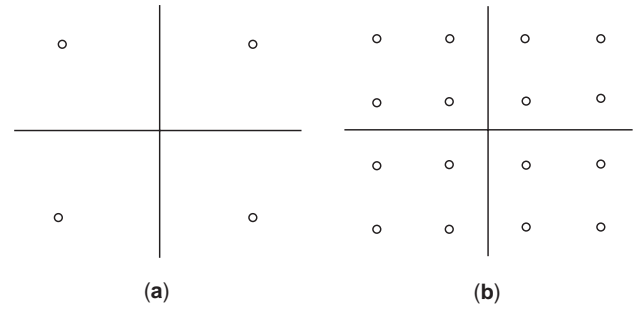
The input and output waveform and phase of QPSK are shown in Fig. 18. The INPUT is a pseudorandom bit sequence QPSK signal. The OUTPUT signal is obtained at the output port of the receiver. It is seen that the output signals (demodulation signals) are the same as input signals, and this confirms the operating principle of the receiver algorithm. Figure 19 shows the simulated output QPSK signal constellations for various signal-to-noise ratios (SNRs). A white noise is added to the input signal and the output constellations are presented in Figs. 19a–19c for QPSK signal with SNR equal 30, 10, and 4 dB, respectively. Demodulation results are presented in Fig. 19d.

Figure 20 shows the simulated output signal constellations for QPSK with different RF and LO power levels; the power level of RF and LO is changed from -10 to -30 dBm. By defining the demodulation error as follows

$$\text{Error} = \frac{|\text{output_signal} - \text{input_signal}|}{|\text{input_signal}|} \quad (30)$$

Table 4. Demodulation Data Results for QAM-16 Signal

Input	Output	Input	Output
$4.2426 \angle 45^\circ$	$4.1636 \angle 47.46^\circ$	$1.4142 \angle 225^\circ$	$1.5123 \angle 227.20^\circ$
$3.1623 \angle 18.43^\circ$	$3.1548 \angle 18.90^\circ$	$3.1623 \angle 251.56^\circ$	$3.1305 \angle 249.71^\circ$
$1.4142 \angle 45^\circ$	$1.2892 \angle 43.18^\circ$	$4.2426 \angle 225^\circ$	$4.2693 \angle 224.02^\circ$
$3.1623 \angle 71.56^\circ$	$2.9562 \angle 43.15^\circ$	$3.1623 \angle 198.43^\circ$	$3.1952 \angle 201.29^\circ$
$3.1623 \angle 341.57^\circ$	$3.2395 \angle 341.25^\circ$	$3.1623 \angle 108.44^\circ$	$2.9198 \angle 111.52^\circ$
$4.2426 \angle 315^\circ$	$4.3099 \angle 341.82^\circ$	$1.4142 \angle 145^\circ$	$1.2758 \angle 143.24^\circ$
$3.1623 \angle 288.44^\circ$	$3.1222 \angle 287.17^\circ$	$3.1426 \angle 161.57^\circ$	$3.0527 \angle 166.60^\circ$
$1.4142 \angle 315^\circ$	$1.4511 \angle 311.64^\circ$	$4.2426 \angle 145^\circ$	$3.9331 \angle 141.67^\circ$

**Figure 17.** Input signal constellations for QPSK (a) and QAM-16 (b) modulation.

it is seen that when the LO power level exceeds the RF power level, the highest error is under 5%, and when the LO power level is the same as the RF power level, the highest error is about 15%. To reduce the error of QPSK demodulation, the LO power level should exceed the RF input power level.

Simulated and theoretical BER versus E_b/N_0 for QPSK modulation is presented in Fig. 21 where E_b is the average energy of a modulated bit and N_0 is the noise power spectral density. For carrier power P_{RF} is (-21 dBm) and local-oscillator power P_{LO} is (-16 dBm) and the bit rate of QPSK signals is 1 Mbps (megabits per second), it is seen that the simulated BER curve matches the theoretical BER curve very well, as the BER is found to be less than 1×10^{-3} for E_b/N_0 higher than 7 dB over the frequency range within the operating band.

6.2. QAM-16 Demodulation Algorithm

Results on input and output waveforms and phase of QAM-16 are shown in Fig. 22. The INPUT is a pseudorandom bit sequence QAM-16 signal. The OUTPUT is the signal obtained at the output port of the receiver. It can be seen the output signals (demodulation signals) are the same as input signals.

Figure 23 shows the simulated output QAM-16 signal constellations for various signal-to-noise ratios (SNRs). A white noise is added to the input signal, and the output constellations are presented in Figs. 23a–23c for a QAM-16 signal with SNR equal 30-, 15-, and 8 dB, respectively. Targeted demodulation results are presented in Fig. 23d.

Figure 24 shows the algorithm simulated output signal constellations for QAM-16 with different RF and LO power levels; the power level of RF and LO is changed from -10

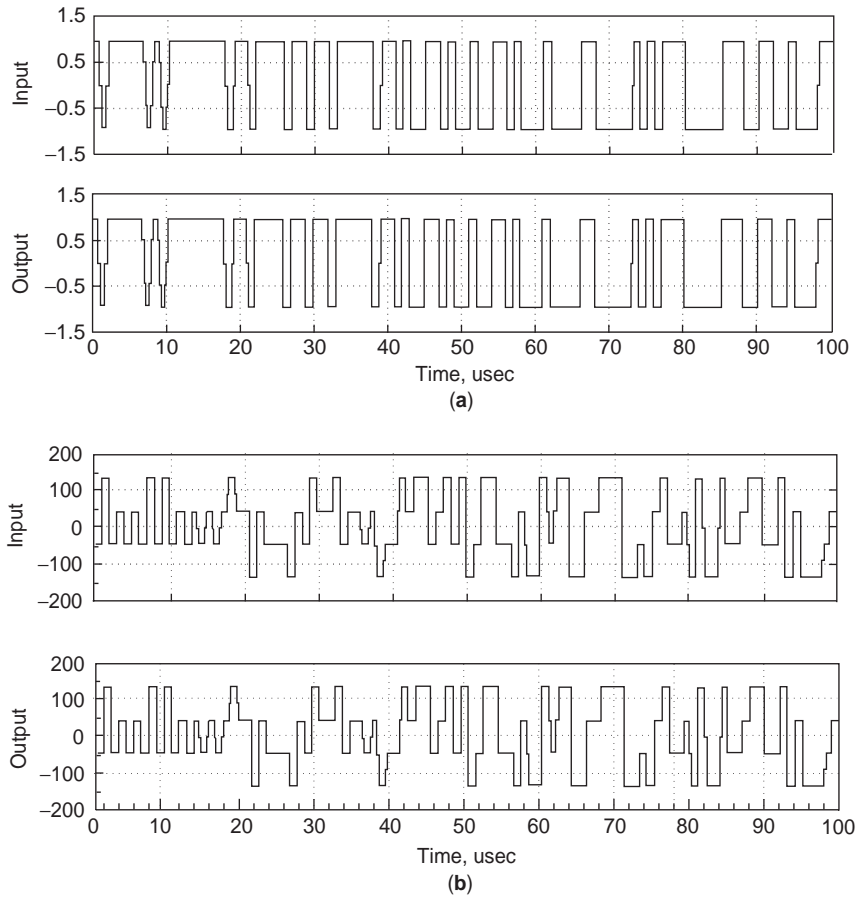


Figure 18. Receiver simulation results of QPSK: input/output waveform (a) and phase (b) as functions of time.

to -30 dBm. We can see that when the LO power level is bigger than RF power level, the highest error is under 5%, and when the LO power level is same as RF power level, the highest error is about 17%. It is seen that the to reduce

the error of QAM-16 demodulation, power level of LO should exceed the power level of RF input.

Simulated and theoretical BER versus E_b/N_0 for QAM-16 algorithm demodulation is presented in Fig. 25. The

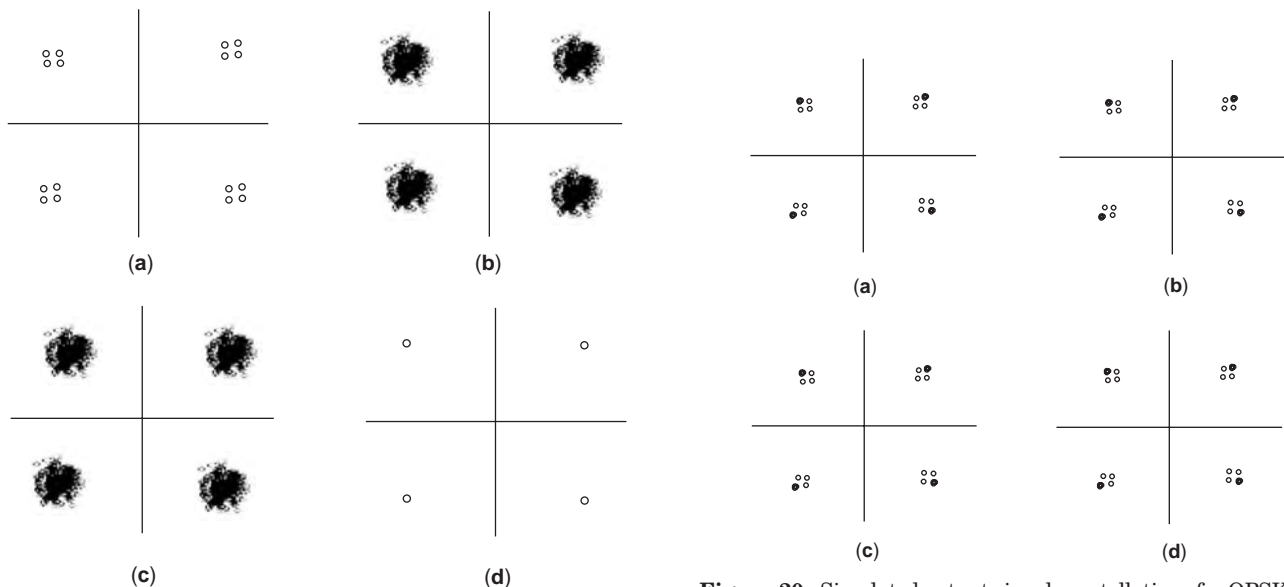


Figure 19. Simulated output signal constellations for QPSK with different SNR values: (a) SNR = 30 dB; (b) SNR = 10 dB; (c) SNR = 4 dB; (d) demodulation result.

Figure 20. Simulated output signal constellations for QPSK with different RF and LO power levels: (a) RF = -20 dBm, LO = -10 dBm; (b) RF = -20 dBm, LO = -20 dBm; (c) RF = -30 dBm; LO = -10 dBm; (d) RF = -30 dBm; LO = -20 dBm.

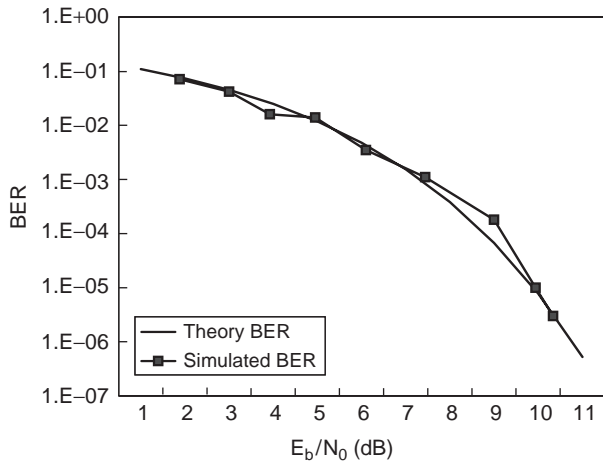


Figure 21. Simulated and predicted BER for QPSK modulation.

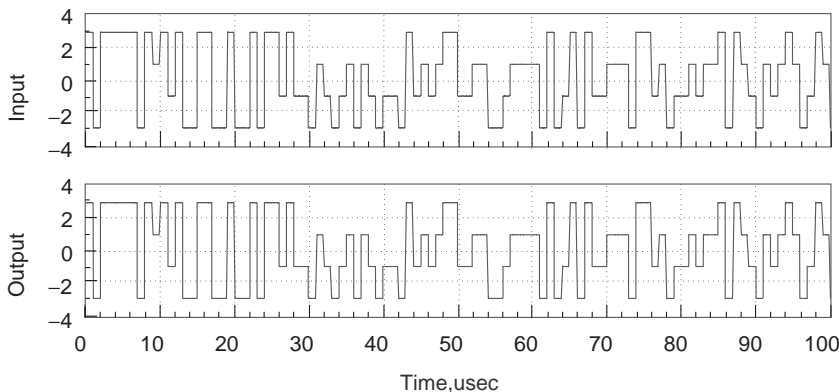
carrier power P_{RF} is -21 dBm and local oscillator power P_{LO} is -16 dBm. The signal bit rate is 1 Mbps. It is seen that the simulated BER curve matches the theoretical BER curve very well; the BER is less than 1×10^{-3} for E_b/N_0 higher than 11 dB (QAM-16) over the frequency range within the operating band.

7. CODING AND CDMA TECHNOLOGY

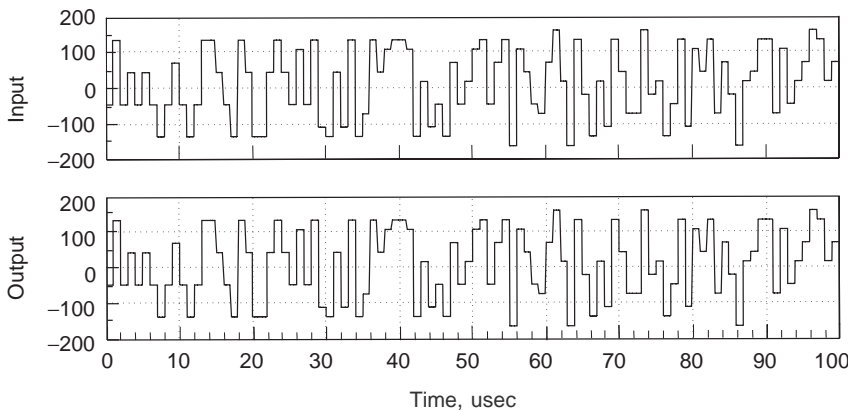
7.1. Channel Coding

Channel coding [33–35] refers to the class of signal transformations designed to improve communications performance by enabling the transmitted signals to better withstand the effects of various channel impairments, such as noise, interference, and fading. These signal processing techniques can be thought of as a means for accomplishing desirable system tradeoffs (e.g., error performance vs. bandwidth, power vs. bandwidth). The use of very large-scale integrated circuits (VLSI) and high-speed signal processing (DSP) techniques have made it possible to provide as much as 10 dB performance improvement through these methods, at much less cost than by the use of other methods such as high-power transmitters or larger antennas.

According to information theory and the Shannon limit, coding theory has developed rapidly. Many kinds of error control codes such as block code, cyclic code, convolutional code, and turbo code are available. Many early codes were developed for deep-space and satellite communication systems. With the emergence of digital cellular telephony, HDTV, high-density storage, coding technology promises to predominate not only in scientific



(a)



(b)

Figure 22. Receiver simulation results obtained with algorithm QAM-16: input/output waveform (a) and phase (b) as functions of time.

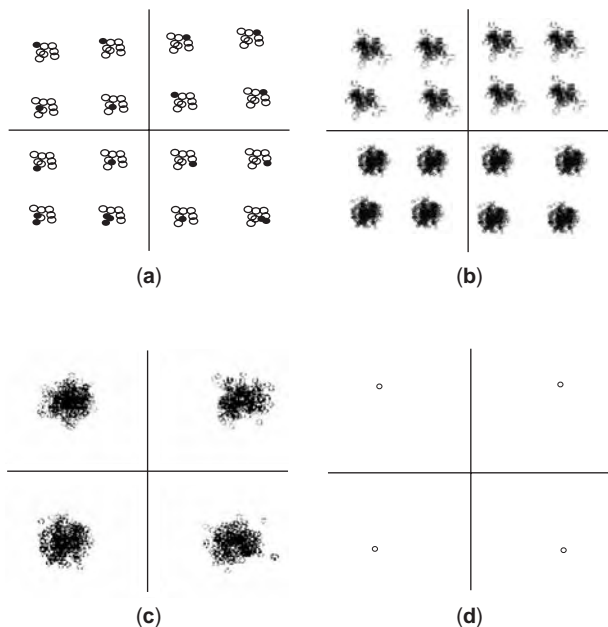


Figure 23. Simulated output signal constellations for QAM-16 with different SNR values: (a) SNR = 30 dB; (b) SNR = 15 dB; (c) SNR = 4 dB; (d) targeted demodulation result.

and military applications but also in numerous commercial applications [36–38].

7.2. Convolutional Encoder [33,34]

A convolutional code is described by three integers, n , k , and K , where the ratio k/n is the coding rate, and the integer K is a parameter known as *constraint length*, representing the number of k -tuple stages in the encoding

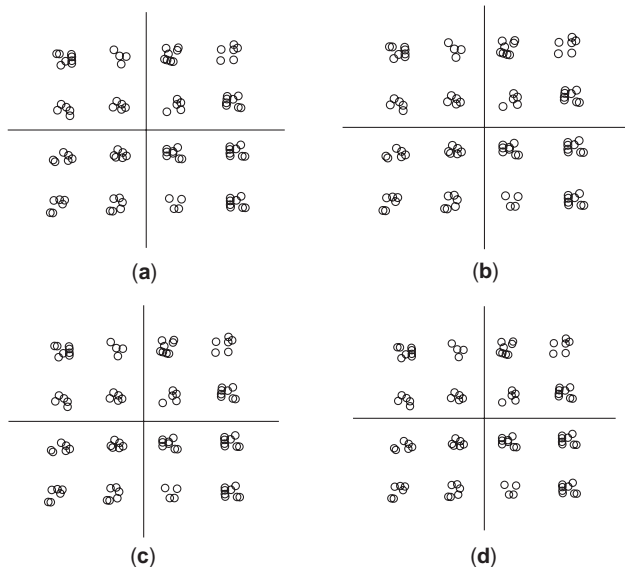


Figure 24. Algorithm-simulated output signal constellations for QAM-16 with different RF and LO power levels: (a) RF = -20 dBm, LO = -10 dBm; (b) RF = -20 dBm, LO = -20 dBm; (c) RF = -30 dBm, LO = -10 dBm; (d) RF = -30 dBm, LO = -20 dBm.

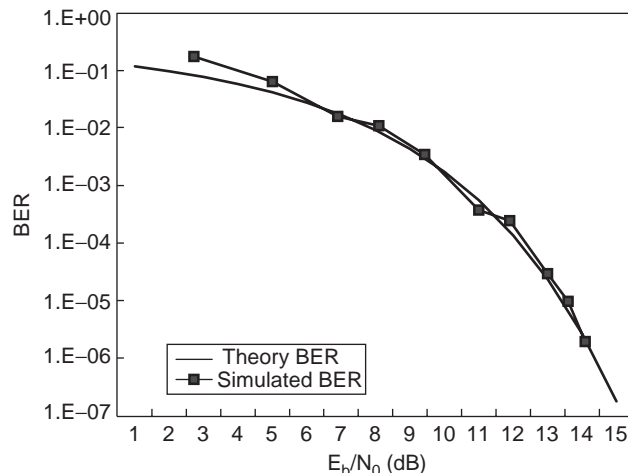


Figure 25. Simulated and predicted BER for QAM-16 modulation.

shift register. An important characteristic of convolutional codes, different from block codes, is that the encoder has memory—the n -tuple emitted by the convolutional encoding procedure is a function not only of an input k -tuple but is also of the previous $K - 1$ input k tuples. In practice, n and k are small integers and K is varied to control the capability and complexity of the code.

Convolutional code can be used in the six-port receiver as in any other receivers because this coding is done in baseband immediately available in proposed receiver as shown in Fig. 26, where convolutional code is used as the channel code. Figure 27 is a convolutional code encoder diagram. The code rate is set to $R = \frac{1}{2}$, and the constraint length $K = 7$, $g[0,0] = 1 + z + z^2 + z^3 + z^6$ with octal number 171, $g[0,1] = 1 + z^2 + z^3 + z^5 + z^6$ with octal number 133.

7.3. Turbo Code Encoder [39]

The component encoders are recursive systematic convolutional (RSC) encoders, specifically, systematic convolutional encoders with feedback. Figure 28 is a schematic diagram of a constituent encoder. The constraint memory length is 2. The generator polynomials are $1 + z + z^2$ and $1 + z^2$.

For systematic codes, the information sequence is part of the codeword, which corresponds to the direct connection from the input to one of outputs. For each input bits, the encoder generates two codeword bits.

The turbo encoder uses two parallel-concatenated RSC (recursive systematic convolutional) encoders with an interleaver before the second RSC encoder shown in Fig. 29. The two recursive convolutional codes are termed the *constituent codes of the turbo code*. The outputs of the constituent encoders are punctured and repeated to achieve



Figure 26. System encoder diagram with six-port receiver.

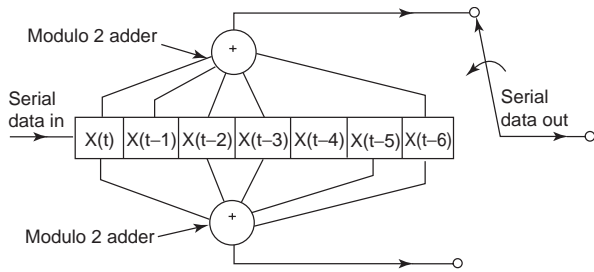


Figure 27. Convolutional code schematic.

the $(N_{turbo} + 6)/R$ output symbols. A common constituent code (RSC code) is used for turbo codes of rates $\frac{1}{2}$, $\frac{1}{3}$, and $\frac{1}{4}$. Initially, the states of the constituent encoder registers are set to 0. In our system, the overall rate of the encoder is $\frac{1}{2}$.

7.4. CDMA Application In Six-Port Receiver [38]

The initial application of spread-spectrum (SS) techniques was in the development of military guidance and communication systems. The techniques are called *spread spectrum* because the transmission bandwidth employed is much greater than the minimum bandwidth required transmitting the information. With the wide-bandwidth characteristics of six-port receiver, the CDMA technology can be readily applied. A system is defined as a SS system if it fulfills the following requirements:

1. The signal occupies a bandwidth much in excess of the minimum bandwidth necessary to send the information.
2. Spreading is accomplished by means of a spreading signal, often called a *code signal*, which is independent of the data.
3. At the receiver, despreading (recovering the original data) is accomplished by the correlation of the receiver spread signal with a synchronized replica of the spreading signal used to spread the information.

Spread-spectrum multiple-access techniques allow multiple signals occupying the same RF bandwidth to be transmitted simultaneously without interfering with one another. For the CDMA there are two schemes of spread spectrum: (1) frequency-hopped code-division multiple access (FH/CDMA), and (2) direct sequence code-division multiple access (DS/CDMA).

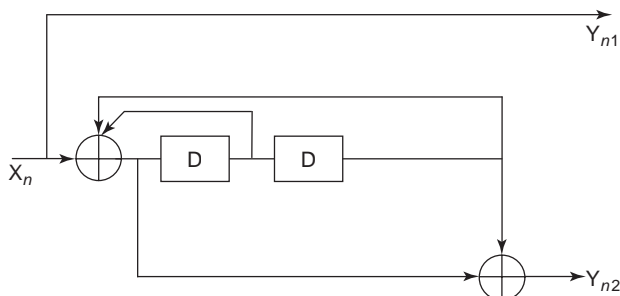


Figure 28. RSC constituent encoder.

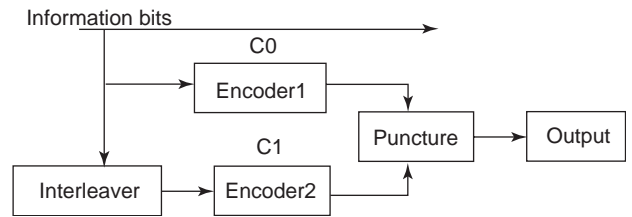


Figure 29. Block diagram of general turbo encoder.

7.5. Six-Port Circuits for Multiuser CDMA Technology [38]

The six-port circuits are able to receive any signals, not only QPSK, BPSK, and QAM but also the random complex signals. In the wireless communication system, there are many users talking or sending information at the same time. This means that the received signal at the receiver is a combination of signals from different users with noise and multipath signal characteristics. In order to demodulate the signal from a specific user, the six-port technology in combination with the CDMA approach has the ability to demodulate any random complex signals.

From the power readers of $P_3, P_4, P_5,$ and P_6 , we can use the output value to calculate the complex envelope signal:

$$a_5 = A_{LO} * \exp(j\omega_0 t)$$

$$a_6 = A_{RF} * \text{env}(t) * \exp(j\omega_0 t) \tag{31}$$

$$\text{env}(t) = I(t) + jQ(t)$$

The following is the relationship between the input and output signals of the six-port circuits. The outputs at baseband are digitized for DSP operations:

$$b_1 = -j \frac{a_5}{2} + j \frac{a_6}{2}$$

$$b_2 = \frac{a_5}{2} + j \frac{a_6}{2}$$

$$b_3 = \frac{a_5}{2} + \frac{a_6}{2}$$

$$b_4 = j \frac{a_5}{2} - j \frac{a_6}{2} \tag{32}$$

7.6. Multiuser Six-Port Receiver with CDMA Technology

After the envelope of the RF signal has been obtained, pseudonoise (PN) code is used to decode different user information.

In Fig. 30, at the transmitter end the user, data are first modulated to IF signal and then through the upconverter to RF signal and then multiplied by its own PN code. At the receiving end the RF signal is first multiplied by its own PN code, and then the resultant signal is output to the six-port for demodulation. The PN code can be changed to receive different user’s data information.

In addition, the six-port receiver can be used with another type of transmitter/receiver structure as shown in

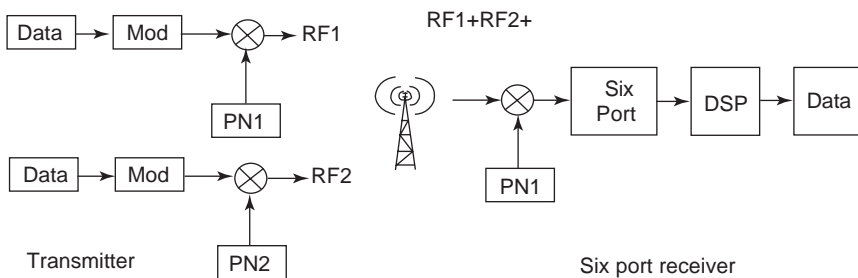


Figure 30. Six-port receiver with CDMA communication technology.

Fig. 31. A PN code is first used on the data, and then the resultant signal is modulated to IF signal frequency and upconverted to the desired RF frequency. At the receiver end, the six-port receiver directly demodulates the RF signal to obtain the baseband data. This desired user data are obtained with the proper PN code.

7.7. Channel Coding Results

At the transmitting end, a convolutional code is used as the channel code. The coding rate is $\frac{1}{2}$, the modulation type is QPSK, and the RF central frequency is 26.5 GHz. At the receiving end, a six-port receiver is used to downconvert the RF signal directly to baseband signal; a judgment circuit is connected to the output of the six-port receiver. After obtaining the channel bits (hard decision), the decoding module is used to obtain the user data. BER measurement equipment is used to calculate the bit error rate versus the bit energy over the noise density. In this system, the channel is assumed to be an AWGN (additive white Gaussian noise) channel [40]. For the turbo convolutional code (TCC), code rate R is $\frac{1}{2}$. The BER curve versus E_b/N_0 is shown in the Fig. 32.

Based on the direct six-port receiver, both convolutional code and turbo code are investigated as the channel codes for the six-port receiver. The improved performance of the six-port receiver is shown in Fig. 32. This new receiver presents a viable alternative for mobile terminals; at a BER of 1×10^{-7} , using the convolutional code, a 3 dB coding gain can be obtained. Using the turbo code the bit error rates are close to the Shannon limit with a coding gain of at least 8 dB.

Based on the direct six-port receiver, both convolutional code and turbo code are investigated as the channel codes for the six-port receiver. The improved performance of the six-port receiver is shown in Fig. 32. This new receiver presents a viable alternative for mobile terminals;

at a BER of 1×10^{-7} , using the convolutional code, a 3 dB coding gain can be obtained. Using the turbo code the bit error rates are close to the Shannon limit with a coding gain of at least 8 dB.

7.8. CDMA Six-Port Receiver Results

At first, the receiver characteristics are examined with respect to bandwidth and validity of six-port receiver simulations. The simulation validity is seen by comparing performance of the actual six-port receiver and ideal six-port receiver. Figure 33 shows an excellent agreement in BER (bit error rate) results between the two types of receivers. The bandwidth of an actual six-port receiver is seen to be at least 3 GHz (Fig. 35).

For the code-division multiple-access (CDMA) application, the six-port receiver can receive any kind of complex envelope signals. In order to obtain the data information of a specific user, the CDMA technology is used in conjunction with six-port receiver and the results are presented. A six-port receiver simulation was performed for one and two users as shown in Fig. 37 with different non-synchronous Walsh codes (0.5 chip delay) in CDMA technology. The results for two users with synchronous Walsh codes show exactly the same performance as for results obtained with one user only.

The curve in Fig. 33 is the BER curve of one user or more users in synchronism with QPSK modulation. This type of receiver can demodulate random complex envelope signals such as BPSK, QPSK, QAM, and 16-QAM.

Using the S parameters of an actual six-port, at 24 GHz, the bit error rate curve is compared with ideal six-port results shown in Fig. 34. From the results it can be seen that the ideal six-port receiver and practical six-port receiver are in very good agreement.

Figure 35 shows BER curves of a SIW six-port receiver at 23 and 26 GHz. The return loss of each ports of the

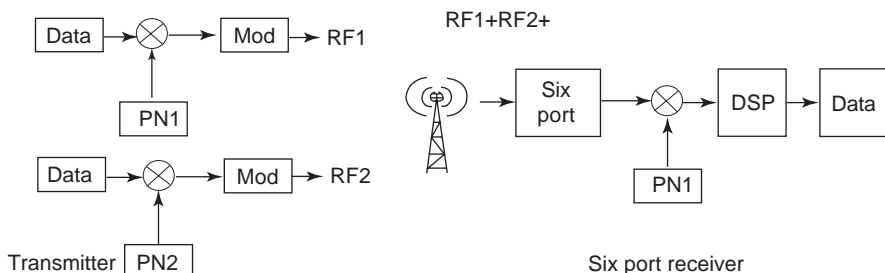


Figure 31. Six-port receiver with CDMA communication technology.

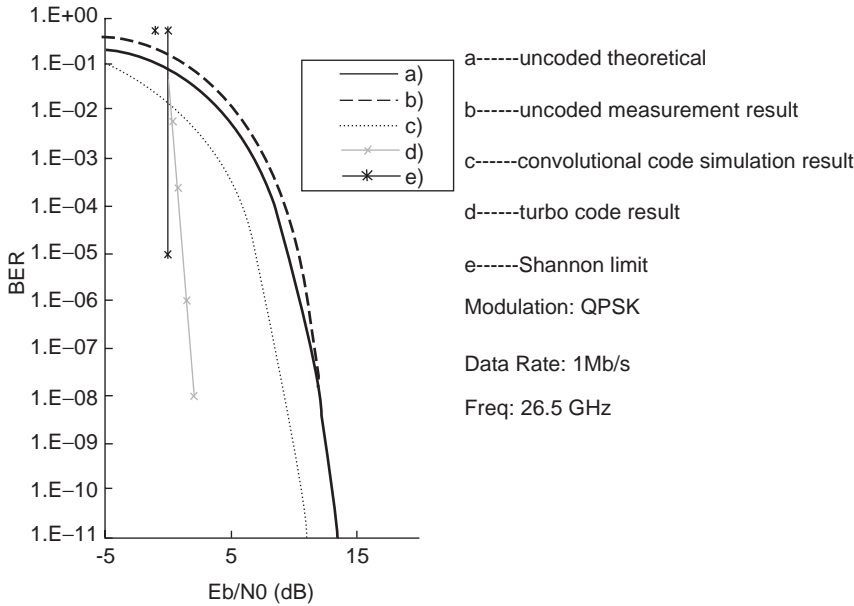


Figure 32. Simulation and measurement BER versus E_b/N_0 for various codes [40].

six-port is less than -20 dB during this frequency band. From this figure, we can see that six-port receiver is performing well and has a wide operation band if all ports are match-tested with a chip rate of 1 Mbps in a CDMA system.

For an actual circuit at 24 GHz tested under two users' conditions, the input and output waveforms of user 1 are identical as shown in Fig. 36 (the transmitted power of each user is the same). The curve shown presents waveforms of I and Q channels, when each user possesses individual orthogonal Walsh codes.

Figure 37 shows the bit error rate of one user in the presence of a second user for a nonsynchronous case (0.5 chip delay).

8. CONCLUSIONS

The development of SDR technology based on the six-port receiver scheme has been investigated, and some simulations and experimental results obtained particularly at

millimeter-wave frequencies are presented. The six-port based receiver can support multimodulation and multi-band communication and should achieve better performance than existing superheterodyne or direct-conversion receivers when coding, carrier recovery, and a higher level of circuit integration technology are implemented. The six-port receiver scheme is strongly motivated by the fact that the speed and present state-of-the-art reconfigurable devices such as digital signal processors (DSPs) and field-programmable gate arrays (FPGAs) are already satisfactory, and increased performance with price reduction are foreseen. On the other hand, the cost of the microwave components for the six-port receiver can be reduced mainly because of increased circuit integration means and the six-port receiver approach. Therefore, a receiver configuration that shifts the complexity to digital signal processing and alleviates problems associated with RF

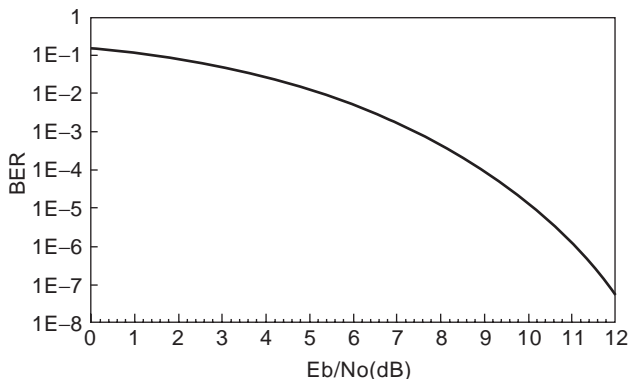


Figure 33. Simulation results of BER curve of one user or more in synchronism for CDMA.

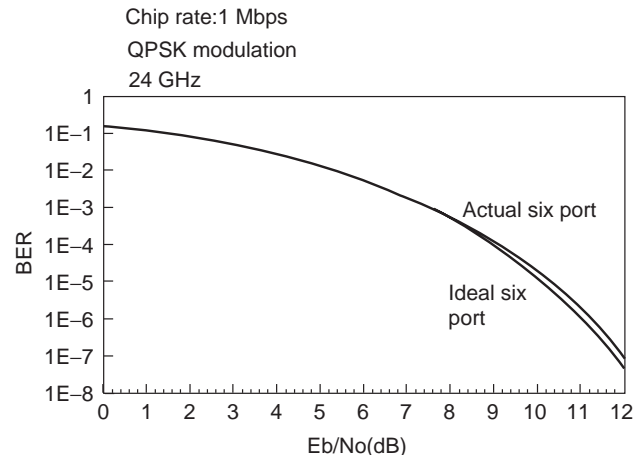


Figure 34. Simulation BER comparison between ideal six-port and actual six-port.

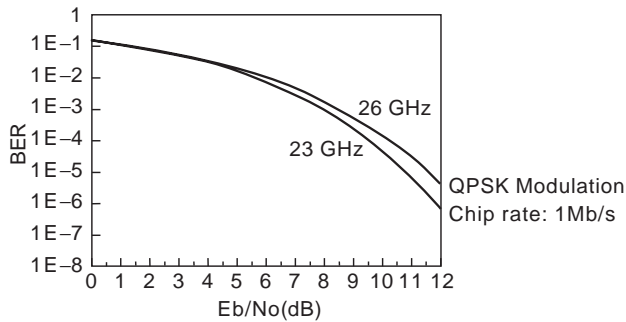


Figure 35. Simulation BER curve at 23 and 26 GHz of actual six-port circuit.

components can be viable in terms of cost, functionality, and market penetration.

The proposed six-port SDR receiver scheme is part of the direct-conversion receiver. In addition, it meets important technical and marketing criteria as mentioned in previous paragraphs. A six-port SDR receiver testbench and testbed is under construction at Centre de Recherches Poly-Grames to further evaluate six-port technology in SDR. The following factors favor further development of SDR:

- Amplification of RF signals were expensive in the past and had to be carried out at a low frequency (i.e., IF). Today, low-cost, wideband, high-gain microwave transistors have considerably decreased in cost.
- Wideband microwave amplifier design techniques have matured to maintain uniform gain and noise figure over a wide frequency band. The nonuniform sensitivity of the early direct receiver has been avoided, and such amplifiers, suitable for mass-production means, are now available and can be integrated with six-port circuits.
- “Online” SPR calibration reduces error related to imperfect circuit fabrication, allowing the six-port receiver to be flexible and yet accurate.
- Coding technology can be used to reduce the bit error rate and to allow multiuser modulation schemes (e.g., CDMA).

Figure 36. Input/output simulation waveform of user 1 in presence of second user.

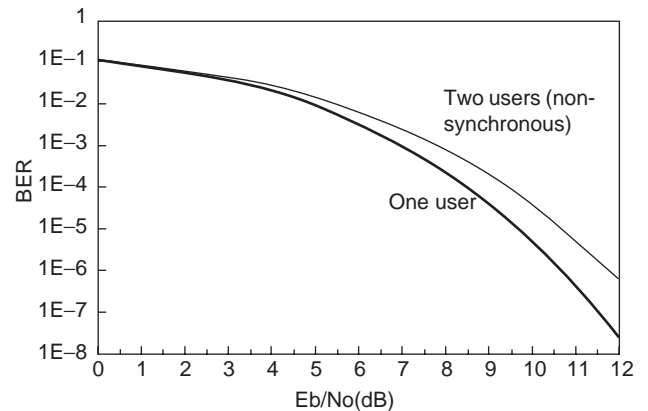
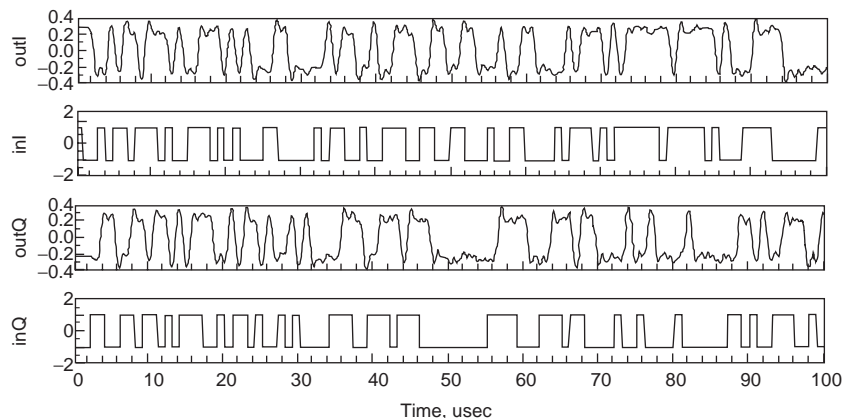


Figure 37. Six-port receiver bit error rate CDMA simulation results for one and two users with nonsynchronous signals (0.5 chip delay).

- The present state in the development of VLSI and ASIC technology makes high-speed digital signal processing practical and cost-effective in six-port receiver technology.

Research work described in this article narrows the gap between six-port technology and emerging SDR. It is shown through a number of computer simulations and measurements that combined SDR and SPR offer a great flexibility in system configuration, reduction in system development cost, and a high potential for software reuse. The characteristics of six-port receiver are simulated and measured using hybrid and monolithic integrated six-port circuits. A new SIW six-port circuit with improved transmission characteristics has been introduced. The results of BER versus E_b/N_0 of the SDR receiver obtained with algorithm for two different modulation schemes have been presented. Simulation and measurement results show that the proposed receiver is flexible and stable, and it has a strong potential for future SDR terminals in various wireless communication systems.

Acknowledgments

The financial support of the National Science Engineering Research Council (NSERC) of Canada is gratefully accepted.

The authors would like to acknowledge Serioja Ovidiu Tatu, Emilia Moldovan, Zhiyan Song, Eric Marsan, Traian Antonescu Yansheng Xu, and all technical personnel of Centre de Recherche Poly-Grames (CRP) of École Polytechnique for their valuable contributions to this research.

BIBLIOGRAPHY

1. J. Mitola, The software radio architecture, *IEEE Commun. Mag.* (May 1995).
2. Software radio technology challenges and opportunities, paper presented at the 1st European Workshop on Software Radios, May 1997.
3. W. Tuttlebee, The impact of software radio, paper presented at the Software Radio Workshop, Brussels, Belgium, May 1997.
4. V. Bose, M. Ismert, M. Welborn, and J. Guttag, Virtual radios, *IEEE/JSAC, Special Issue on Software Radios*, 591–602, (April 1999).
5. J. Li, R. G. Bosisio, and K. Wu, Computer and measurement simulation of a new digital receiver operating directly at millimeter-wave frequencies, *IEEE Trans. Microwave Theory Tech.* **43**(12):2766–2772 (Dec. 1995).
6. J. F. Gagné, J. Gauthier, and R. G. Bosisio, High speed low cost architecture of direct conversion digital receiver, *Proc. IEEE Int. Microwave Symp.*, Phoenix, AZ, May 20–25, 2001, Vol. 2, pp. 1093–1096.
7. E. Marsan, J.-C. Schiel, G. Brehm, K. Wu, and R. G. Bosisio, High speed carrier recovery suitable for direct digital QPSK transceivers, *Proc. RAWCON IEEE Radio and Wireless Conf.*, Boston, Aug. 11–14, 2002, pp. 103–106.
8. X. Xu, S. O. Tatu, E. Moldovan, R. G. Bosisio, and K. Wu, Analysis of FDSS ultra-wideband six-port receiver, *Proc. RAWCON IEEE Radio and Wireless Conf.*, Boston, Aug. 11–14, 2002, pp. 87–90.
9. S. O. Tatu, E. Moldovan, K. Wu, and R. G. Bosisio, A new direct millimeter wave six-port receiver, *IEEE Trans. Microwave Theory Tech.* (special issue) **49**(12): 2517–2522 (Dec. 2001).
10. D. Deslandes and K. Wu, Integrated microstrip and rectangular waveguide in planar form, *IEEE Microwave Guided Wave Lett.* **11**(2):68–70 (Feb. 2001).
11. X. Y. Xu, K. Wu, and R. G. Bosisio, Software defined radio receiver based on six-port technology, *Proc. IEEE-IMS Symp.*, Philadelphia, June 8–13, 2003, pp. 1059–1062.
12. J. Hesselbarth, F. Wiedmann, and B. Huyart, Two new six-port reflectometers covering very large bandwidths, *IEEE Trans. Instrum. Meas.* **46**(4):966–970 (Aug. 1997).
13. <http://www.jtrs.saalt.army.mil>.
14. <http://www.sdrforum.org>.
15. <http://www.crc.ca/scari>.
16. S. O. Tatu, E. Moldovan, K. Wu, and R. G. Bosisio, A new carrier recovery method for a six-port millimeter wave receiver, *Proc. Int. Sympo. Microwaves and Optical Technologies (ISMOT)*, Montreal, Quebec, Canada, June 19–23, 2001, pp. 211–214.
17. S. O. Tatu, E. Moldovan, G. Brehm, K. Wu, and R. G. Bosisio, Ka band direct digital receiver, *IEEE Trans. Microwave Theory Tech.* **50**(11):2436–2442 (Nov. 2002).
18. G. F. Engen, The six-port reflectometer: An alternative network analyzer, *IEEE Trans. Microwave Theory Tech.* **MTT-25**(12) (Dec. 1977).
19. S. O. Tatu, E. Moldovan, K. Wu, and R. G. Bosisio, A rapid carrier recovery loop for direct conversion receivers, *Proc. RAWCON IEEE Radio and Wireless Conf.*, Boston, Aug. 10–13, 2003.
20. O. Mireux, J. J. Brault, and R. G. Bosisio, Unsupervised learning network decoders for six port receivers (SPR). *Proc. Int. Symp. Microwaves and Optical Technologies (ISMOT)*, Montreal, Quebec, June 20–22, 2001, pp. 215–218.
21. O. Mireux, J. J. Brault, and R. G. Bosisio, Results on a direct digital receiver operated with fast learning networks, *Proc. IEEE-MTT Symp.*, Seattle, June 2–4, 2002, Vol. 1, pp. 497–500.
22. J. Brault, K. Wu, and R. G. Bosisio, Neural networks in microwave/millimeter wave six port, *Proc. NIMIA 2001 Symp.*, Sep. 2001.
23. T. Visan, J. Beauvais, and R. G. Bosisio, New phase and gain imbalance correction algorithm for six-port based direct digital millimetric receivers, *Microwave Opt. Technol. Lett.* **27**(6):432–438 (Dec. 2000).
24. F. M. Ghannouchi and R. G. Bosisio, An alternative explicit six-port matrix calibration formalism using five standards, *IEEE Trans. Microwave Theory Tech.* **36**(3) (1988).
25. T. Visan, J. Beauvais, and R. G. Bosisio, New phase and gain imbalance correction algorithm for six port based direct digital millimetric receivers, *Microwave Opt. Technol. Lett.* **27**(6) (2000).
26. G. F. Engen, Calibrating the six-port reflectometer by means of sliding terminations, *IEEE Trans. Instrum. Meas.* **MTT-26** (Dec. 1978).
27. S. O. Tatu, E. Moldovan, K. Wu, and R. G. Bosisio, Analog signal treatment in six-port technology, *Proc. Canadian Conf. Electrical and Computer Engineering (CCECE)*, Montreal, May 4–7, 2003.
28. M. Abe, N. Sasho, V. Brankovic, and D. Krupezevic, Direct conversion receiver MMIC based on six-port technology, *Proc. European Conf. Wireless Technology (ECWT 2000)*, Oct. 2000, pp. 139–142.
29. X. Xu, *Software Defined Radio Receiver Based on Six-Port Technology*, Ph.D. thesis, École Polytechnique de Montreal, April 10, 2003.
30. G. F. Engen and C. A. Hoer, Thru-reflect-line: An improved technique for calibrating the dual six-port automatic network analyzer, *IEEE Trans. Microwave Theory Tech.*, **MTT-27**: 987–993 (Dec. 1979).
31. U. Stumper, Finding initial estimates needed for the Engen method of calibrating single six-port reflectometers, *IEEE Trans. Instrum. Meas.* **38** (July 1990).
32. Y. Xu and R. G. Bosisio, On the real-time calibration of six-port receivers (SPRs), *Microwave Opt. Technol. Lett.* **20**(5) (March 5, 1999).
33. J. G. Proakis, *Digital Communication*, McGraw-Hill, New York, 1995.
34. B. Sklar, *Digital Communications Fundamentals and Applications*, 2nd Edition, Prentice Hall PTR, Indianapolis, 2001.
35. Y. Gao, *Design and Implementation of Non-binary Convolutional Turbo Code*, thesis, Dept. Electrical Engineering, Concordia Univ., Montreal, Dec, 2001.
36. T. S. Rapport, *Wireless Communications: Principles and Practices*, Prentice-Hall, Inc. Upper Saddle River, NJ, 1996.
37. K. Hiramatsu, M. Hayashi, and O. Kato, Overview of IMT-2000 CDMA TDD, *Matsushita Tech. J.* **47**:15 (2001).

38. L.-L. Yang and L. Hanzo, Performance of generalized multi-carrier DS-CDMA over Nakagami-m fading channels, *IEEE Trans. Commun.* **50**:956 (2002).
39. C. Berrou, A. Glavieux, and P. Thitimajshima, Near Shannon limit error correcting coding and decoding: Turbo-codes, *Proc. 1993 IEEE Int. Conf. on Communications*, Geneva, Switzerland, 1993, pp. 1064–1070.
40. Z. Song, S. Tatu, M. R. Soleymani, K. Wu, and R. G. Bosisio, Initial coding results with millimeter wave six-port QPSK receiver, *Microwave Opt. Technol. Lett.* **36**(6):465–467 (March 20, 2003).
- R. J. Collier and N. A. El-Deeb, On the use of a microstrip three-line system as a six-port reflectometer, *IEEE Trans. Microwave Theory Tech.* **MTT-27**:847–853 (Oct. 1979).
- D. Woods, Analysis and calibration theory of the general six-port reflectometer employing four amplitude detector, *Proc. IEEE* **126**:221–228 (Feb. 1979).
- G. F. Engen, A least square solution for use in the six-port measurement technique, *IEEE Trans. Microwave Theory Tech.* **MTT-28**(12):1473–1477 (Dec. 1980).
- A. L. Cullen, S. K. Judah, and F. Nikraves, Impedance measurement using a six-port directional coupler, *IEEE Proc.* **127**(Part H)(2):92–98 (April 1980).
- A. Iketa, K. Araka, Y. Naito, and M. Iwakuni, A design of six-port compensating circuits for circulators, *Trans. Inst. Electron. Commun. Eng. Jpn.* (Sec. E) **E63**(1):68–69 (Jan. 1980).
- M. D. Rafal and W. T. Joines, Optimizing the design of the six-port junction, *IEEE MTT-S Int. Microwave Symp. Digest*, 1980, pp. 437–439.
- G. P. Riblet, Transmission phase measurement with a single six-port, *IEEE MTT-S Int. Microwave Symp. Digest*, 1980, pp. 431–433.
- S. H. Li and R. G. Bosisio, The automatic measurement of N-port microwave junctions by means of the six-port technique, *IEEE Trans. Instrum. Meas.* **31**(1):40–43 (1982).
- T. E. Hodget and E. J. Griffin, *A Unified Treatment of the Theory of Six-Port Reflectometer Calibration Using the Minimum of Standards*, Report 83003 RSRE Malvern, Aug. 1983.
- A. N. El-Deeb, The calibration and performance of microstrip six-port reflectometer, *IEEE Trans. Microwave Theory Tech.* **MTT-31**(7) (July 1983).
- E. R. B. Hansson and G. P. Riblet, An ideal six-port network consisting of a matched reciprocal lossless five-port and a perfect directional coupler, *IEEE Trans. Microwave Theory Tech.* **MTT-31**:284–289 (March 1983).
- S. Li and R. G. Bosisio, Analysis and optimized circuit design of the six-port reflectometer, *Acta Electronica Sinica* (China) **11** (1983).
- D. Woods, Simplified calibration technique for general six-port reflectometer requiring only two coaxial airline standards, *IEEE Proc. A* 250–253 (1983).
- P. I. Somlo, The case for using a marched load standard for six-port calibration, *Electron. Lett.* **19**(23) (1983).
- L. Kaliouby and R. G. Bosisio, A new method for six-port swept frequency automatic network analysis, *IEEE Trans. Microwave Theory Tech.* **MTT-32**(12):1678–1682 (Dec. 1984).
- J. R. Juroshek and C. A. Hoer, A dual six-port network analyzer using diode detectors, *IEEE Trans. Microwave Theory Tech.* **MTT-32**:51–57 (Jan. 1984).
- R. G. Bosisio, C. Q. Li, and S. H. Li, CAD/CAM microwave modeling with six-port automatic network analyzers, *Microwave J.* **27**(5):193–203 (1984).
- C. T. Qian, An improved method for six-port reflectometer calibration, *IEEE Trans. Instrum. Meas.* **IM-34**:611–615 (Dec. 1985).
- D. A. Zein, Solution of a set of non linear algebraic equations for general purpose CAD programs, *IEEE Circuit Syst. Mag.* **1**(5) (Sept. 1985).
- J. R. Juroshek and C. A. Hoer, A technique for extending the dynamic range of the dual six-port network analyzer, *IEEE Trans. Microwave Theory Tech.* **MTT-33**(6):453–459 (June 1985).
- J. D. Hunter and P. I. Somlo, Simple derivation of six-port reflectometer equations, *Electron. Lett.* **21**:370–371 (April 1985).

FURTHER READING

- C. A. Hoer, The six-port coupler: A new approach to measuring voltage, current, power, impedance and phase, *IEEE Trans. Instrum. Meas.* **IM-21**:466–470 (Dec. 1972).
- G. F. Engen and C. A. Hoer, Application of an arbitrary 6-port junction to power measurement problems, *IEEE Trans. Instrum. Meas.* **IM-21**(4):470–474 (Nov. 1972).
- C. A. Hoer, The six-port coupler: A new approach to measuring voltage, Current, power, impedance and phase, *IEEE Trans. Instrum. Meas.* **IM-21**(4):466–470 (Nov. 1972).
- C. A. Hoer, A network analyzer incorporation two six-port reflectometer, *IEEE Trans. Microwave Theory Tech.* **MTT-25**(12):1070–1074 (Dec. 1973).
- G. F. Engen, Calibration of arbitrary six-port junction for measurement of active and passive circuit parameters, *IEEE Trans. Instrum. Meas.* **IM-22**(4):295–299 (Dec. 1973).
- G. F. Engen and C. A. Hoer, Analyzer of a six-port for measuring v, i, a, b, z, and phase, *Proc. IMEKO Symp. Acquisition and Processing of Measurement Data for Automation*, June 17–13, 1973.
- C. A. Hoer, Using an arbitrary six-port junction to measure complex voltage ratios, *IEEE Trans. Microwave Theory Tech.* **MTT-23**(12):978–984 (1975).
- G. F. Engen, The six-port reflectometer: an alternative network analyzer, *IEEE Trans. Microwave Theory Tech.* **MTT-25**:1075–1079 (Dec. 1977).
- C. A. Hoer, A network analyzer incorporating two six port reflectometer, *IEEE Trans. Microwave Theory Tech.* **MTT-25**:1070–1074 (Dec. 1977).
- H. M. Cronson and L. Susman, A six-port automatic network analyzer, *IEEE Trans. Microwave Theory Tech.* **MTT-25**(12):1086–1091 (Dec. 1977).
- G. F. Engen, An improved circuit for implementing the six-port technique of microwave measurement, *IEEE Trans. Microwave Theory Tech.* **MTT-25**(12):1080–1083 (Dec. 1977).
- G. F. Engen, Calibrating the six-port reflectometer by means of sliding terminations, *IEEE Trans. Microwave Theory Tech.* **MTT-26**:951–957 (Dec. 1978).
- G. F. Engen, The six-port measurement technique—a status report, *Microwave J.* **21**:18–89 (1978).
- G. F. Engen, C. A. Hoer, and R. A. Speciale, The application of “thru-short-delay” to the calibration of the dual six-port, *IEEE MTT-S Symp. Digest*, 1978, pp. 179–180.
- G. F. Engen and C. A. Hoer, Thru reflect line: An improved technique for calibrating the dual six-port automatic network analyzer, *IEEE Trans. Microwave Theory Tech.* **MTT-27**:987–993 (Dec. 1979).
- C. A. Hoer, Performance of a dual six-port automatic network analyzer, *IEEE Trans. Microwave Theory Tech.* **MTT-27**(12):993–998 (Dec. 1979).

- J. D. Hunter and P. I. Somlo, An explicit six port calibration using five standards, *IEEE Trans. Microwave Theory Tech.* **MTT-33**:69–72 (Jan. 1985).
- O. Tokuo and K. Welter, Stokes vector representation of the six-port network analyzer: Calibration and measurement, *IEEE MTT-S Digest*, 1985, pp. 503–506.
- T. Oishi and W. K. Kahn, Stoke vector representation of six port network analyzer. Calibration and measure, *IEEE MTT-S Int. Symp. Digest*, 1985, pp. 503–506.
- M. Riazat and M. G. Zdasiuk, Waveguide star junction used in Ka band dual six-port measurement, *IEEE MTT-S Digest*, 1985, pp. 593–594.
- F. M. Ghannouchi and R. G. Bosisio, *Calibration and Measurement of Six-Port Reflectometer Using a Matrix Approach Part I: Description and Performance*, technical report EPM/RT-86/46, École Polytechnique de Montréal, Canada, Oct. 1986.
- F. M. Ghannouchi and R. G. Bosisio, *Calibration and Measurement of Six-Port Reflectometer Using a Matrix Approach Part II: Description and Performance*, technical report EPM/RT 86/47, École Polytechnique de Montréal, Canada, Oct. 1986.
- F. M. Ghannouchi and R. G. Bosisio, *L'analyseur de Réseau Hyperfréquentiel à Six-accès et sa Calibration par une Méthode Matricielle*, 54e congrès de l'ACFAS, Univ. Montréal, May 1986, p. 189.
- F. M. Ghannouchi and R. G. Bosisio, *Calibration and Measurement of Six-Port Reflectometer Using a Matrix Approach Part II: Description and Performance*, technical report EPM/RT-86/47, École Polytechnique de Montreal, 1986.
- Z. H. Feng, Broadband dielectric waveguide coupler and six-port network, *IEEE MTT-S Digest*, 1986, pp. 237–240.
- M. Malkomes and R. Walsdorf, Integrated fin-line six-ports for MM-wave network analyzers, *IEEE MTT-S Digest*, 1986, pp. 669–671.
- F. M. Ghannouchi and R. G. Bosisio, A new six port calibration method using four standards and avoiding singularities, *IEEE Trans. Instrum. Meas.* 204–211 (Dec. 1987).
- M. Berman, P. I. Somlo, and M. J. Buckley, A comparative statistical study of some proposed six-port junction designs, *IEEE Trans. Microwave Theory Tech.* **MTT-35**:971–977 (Nov. 1987).
- F. M. Ghannouchi and R. G. Bosisio, An alternative explicit six-port matrix calibration formalism using five standards, *IEEE Trans. Microwave Theory Tech.* (Oct. 1987).
- F. M. Ghannouchi and R. G. Bosisio, Modelling and simulation of six-port reflectometer, *IMACS and IEEE Int. Symp.*, Québec, Aug. 1987, pp. 301–308.
- F. M. Ghannouchi, Mesures Micro-ondes Assistées par Ordinateur Utilisant un Nouveau Corrélateur Six Port, thesis, École Polytechnique, June 1987.
- F. M. Ghannouchi and R. G. Bosisio, A new explicit six-port calibration method using for standards, *IEEE Conf. Proc.* Boston, April 1987, pp. 149–153.
- F. M. Ghannouchi and R. G. Bosisio, *L'Utilisation d'Une Charge Adaptée Mobile dans la Calibration du Reflectomètre Hyperfréquentiel à Six-accès*, 55e Congrès de l'ACFAS, Univ. Ottawa, 1987, p. 154.
- F. M. Ghannouchi and R. G. Bosisio, The six-port reflectometer and its complete calibration by four standard terminations, *IEEE Proc.* **135**(4):285–288 (Aug. 1988).
- I. Ohta, A new six-port microwave network: Six-port magic junction, *IEEE Trans. Microwave Theory Tech.* **MTT-36**:859–864 (May 1988).
- A. Mahmoodshahi, *Polarization Measurement Using Six-Port Network Analyzer: A Theoretical and Experimental Approach*, dissertation, George Washington Univ., Washington, DC, March 1988.
- F. M. Ghannouchi and R. G. Bosisio, An alternative explicit six-port matrix calibration formalism using five standards, *IEEE Trans. Microwave Theory Tech.* **MTT-36**:434–439 (March 1988).
- S. K. Judah and A. S. Wright, A second generation dual six port network analyzer, *IEEE Trans. MTT-S Digest*, 1988, pp. 295–296.
- F. M. Ghannouchi and R. G. Bosisio, An improved sliding load formulation for use in six-port calibration methods, *Alta Frequenza* **LVII**(8):497–499 (1988).
- F. M. Ghannouchi and R. G. Bosisio, A comparative worst-case error analysis of some proposed six-port designs, *IEEE Trans. Instrum. Meas.* **37**(4):552–556 (1988).
- G. Colef, M. Ettenberg, and P. R. Karmel, Performance of an integrating six-port reflectometer operated with pulse signals, *Proc. 1989 IEEE Instrumentation and Measurement Technology Conf.*, April 1989, pp. 522–525.
- F. M. Ghannouchi and R. G. Bosisio, Simultaneous microwave impedance and power flow measurements using six-port techniques, *Proc. 2nd Int. Symp. Recent Advances in Microwave Technology* (ISRAMT '89), 1989, pp. 135–140.
- S. Li and R. G. Bosisio, A new tri-six-port automatic network analyzer, *Proc. 2nd Int. Symp. Recent Advances in Microwave Technology* (ISRAMT '89), 1989, pp. 123–126.
- V. A. Yankin, Effect of quantization, amplifier noise and the parameters of the calibration elements on the accuracy of measurement using a six-port microwave ampli-phase-meter, *Radioelectron. Commun. Syst.* **32**(8):110–112 (1989).
- F. M. Ghannouchi, R. G. Bosisio, and R. Hajji, Polarization measurement of microwave/millimeter wave antennas using six-port techniques, *Proc. Int. Conf. Electromagnetics in Aerospace Applications*, 1989.
- F. M. Ghannouchi and R. G. Bosisio, Measurement of microwave permittivity using a six-port reflectometer with an open-ended coaxial line, *IEEE Trans. Instrum. Meas.* **38**(2):505–508 (1989).
- E. Bergeault, B. Huyart, G. Geneves, and L. Jallet, Measurement error for six port analyzer, *IEE Proc. H (Microwaves Anten. Propag.)* **137**(6):415–416 (Dec. 1990).
- J. Sun, The new method of measuring the RCS of a target by means of the six-port reflectometer, *Microwave Opt. Technol. Lett.* **3**(11):398–399 (Nov. 1990).
- M. Christ, Parallel digital signal processor 320C40, *Elektronik Industrie* **21**(11):20, 22, 24, 26 (Nov. 1990).
- C. M. Fortgang, S. P. Jachim, C. Geisik, W. D. Gutscher, E. F. Natter, and J.B. Niesen, Heavy beam loading measurements of an RF accelerating cavity under amplitude and phase control, *Rev. Sci. Instrum.* **61**(11):3405–3411 (Nov. 1990).
- T. Kobashi, T. Yakabe, and H. Yabe, Calibration of a six-port network analyzing system, *Bull. Univ. Electro-Communications* **3**(1):23–29 (June 1990).
- W. K. Kahn, Theory of polarization derived from real power received by general four-element antenna array, *Proc. Polarimetric Technology Workshop*, May 1990, Vol. 1, pp. 361–369.
- S. Wang, *A CAD/CAM Wide Band Microwave Six-Port Junction*, mémoire de maîtrise, École Polytechnique de Montréal, Feb. 1990.
- J. D. Hunter and J. E. Peters, An efficient six-port procedure for power meter calibration, *Conf. Precision Electromagnetic Measurements (CPEM '90) Digest* (Cat. 90CH2822-5), 1990, pp. 57–58.

- E. Bergeault, G. Geneves, B. Huyart, and L. Jallet, The design of a six-port reflectometer with frequency-independent calibration procedure, *Conf. Precision Electromagnetic Measurements (CPEM '90) Digest* (Cat. 90CH2822-5), 1990, pp. 398–399.
- E. Bergeault, et al., Accuracy analysis for six-port automated network analyzers, *IEEE Trans. Instrum. Meas.* **39**(3):492–496 (1990).
- K.-P. Tsao, N. Zhu, and T. Pham, A high performance memory compiler for multi-port RAMs, *Proc. 3rd Annual IEEE ASIC Seminar and Exhibit* (Cat. 90TH0303-8), 1990, pp. 3–6.
- H. Ohnuki, N. Hosaka, J. Yamada, and T. Kobayashi, Computer aided design of low-loss SAW filters employing IIDT for high performance mobile radio duplexer, *Proc. IEEE 1990 Ultrasonics Symp.* (Cat. 90CH2938-9), 1990, Vol. 1, pp. 123–127.
- F. M. Ghannouchi and R. G. Bosisio, A millimeter wave (18–40 GHz) coaxial and homodyne vector network analyzer, *Conf. Precision Electromagnetic Measurements (CPEM '90) Digest* (Cat. 90CH2822-5), 1990, pp. 55–56.
- T. E. Hodgetts, A new approach to “TRL” calibration for dual six-ports and network analyzers, *Conf. Precision Electromagnetic Measurements (CPEM '90) Digest* (Cat. 90CH2822-5), 1990, pp. 53–54.
- U. Stumper, Simple millimeter-wave six-port reflectometers, *Conf. Precision Electromagnetic Measurements (CPEM '90) Digest* (Cat. 90CH2822-5), 1990, pp. 51–52.
- T. Guldbrandsen, Analysis of diodes used as precision power detectors above the square law region, *Conf. Precision Electromagnetic Measurements (CPEM '90) Digest* (Cat. 90CH2822-5), 1990, p. 48.
- J. Sun, The new analysis of the target's radar cross section by means of the six-port technique, *Proc. Conf. Communication Systems: Towards Global Integration. Singapore ICCS '90*, 1990, Vol. 2, pp. 24-9/1–2.
- N. M. Ridler, The development of a broadband VHF six-port for high precision impedance measurements, *IEE Colloquium on What's New in Microwave Measurements* (Digest 174), 1990, pp. 6/1–7.
- A. S. Wright, A. J. Wilkinson, and S. K. Judah, Reducing the effects of random errors in six-port network analyzers, *1990 IEEE MTT-S Int. Microwave Symp. Digest* (Cat. 90CH2848-0), 1990, Vol. 3, pp. 1041–1044.
- J. V. Bellantoni and R. C. Compton, A vector network analyzer integrated into coplanar-waveguide probes, *1990 IEEE MTT-S Int. Microwave Symp. Digest* (Cat. 90CH2848-0), 1990, Vol. 3, pp. 1025–1028.
- V. Bilik, V. Raffaj, and J. Bezek, A new extremely wideband lumped six-port reflectometer, *Proc. 20th European Microwave Conf.*, 1990, Vol. 2, pp. 1473–1478.
- J. M. Rebollar, J. Esteban, and C. Blanco, Computer aided design of non-symmetric six-port branch-waveguide directional couplers, *Proc. 20th European Microwave Conf.*, 1990, Vol. 2, pp. 1041–1046.
- L. Brunetti, Geometrical estimator use in six-port reflectometer study, *Conf. Precision Electromagnetic Measurements (CPEM '90) Digest* (Cat. 90CH2822-5), 1990, pp. 402–403.
- V. K. Tripathi and A. Biswas, Coplanar and broadside coupled finline six port hybrids, *Proc. 20th European Microwave Conf.*, Budapest, 1990, Vol. 2, pp. 1033–1038.
- Z. Feng, J. She, J. Wang, K. Gong, and B. Xu, W-band six port reflectometer using a symmetric 5-port junction and a coupler, *Int. Conf. Millimeter Wave and Far-Infrared Technology (ICMWFIT '90) Supplementary Digest* (Cat. 90TH0317-8), 1990, pp. 131–134.
- H. Shinohara, N. Matsumoto, K. Fujimori, S. Kato, A flexible multi-port RAM compiler for data path, *Proc. IEEE 1990 Custom Integrated Circuits Conf.* (Cat. 90CH2860-5), 1990, pp. 16.5/1–4.
- Y. Demers, R. G. Bosisio, and F. M. Ghannouchi, Repetitive and single shot pulse microwave six-port reflectometer, *IEEE Trans. Instrum. Meas.* **39**(1):195–200 (1990).
- F. M. Ghannouchi, R. Larose, and R. G. Bosisio, Y. Demers, A six-port network analyzer load-pull system for active load tuning, *IEEE Trans. Instrum. Meas.* **39**(4):628–631 (1990).
- E. Bergeault, B. Huyart, G. Geneves, and L. Jallet, Characterization of diode detectors used in six-port reflectometers, *IEEE Trans. Instrum. Meas.* **40**(6):1041–1043 (Dec. 1991).
- F. M. Ghannouchi and R. G. Bosisio, A wideband millimeter wave six-port reflectometer using four diode detectors calibrated without a power ratio, *IEEE Trans. Instrum. Meas.* **40**(6):1043–1046 (Dec. 1991).
- M. Kamarei, Vector voltmeter applications in microwave imaging, *Microwave J.* **34**(11):102, 104, 108–110, 112, 114 (Nov. 1991).
- J. Esteban and J. M. Rebollar, Generalized scattering matrix of generalized two-port discontinuities: Application to four-port and non-symmetric six-port couplers, *IEEE Trans. Microwave Theory Tech.* **39**(10):1725–1734 (Oct. 1991).
- Y. Zhang, G. Colef, Y. Li, and G. Eichmann, Six-port optical reflectometer, *IEEE Trans. Instrum. Meas.* **40**(5):869–871 (Oct. 1991).
- L. Brunetti, Six-port reflectometer: some geometric gamma-estimators, *IEEE Trans. Instrum. Meas.* **40**(5):866–869 (Oct. 1991).
- J. M. Thiebaut and G. Roussy, Extension of the six-port circuit theory for using a practical directional coupler in measuring RF impedances and RF power, *Meas. Sci. Technol.* **2**(9):856–859 (Sept. 1991).
- S. P. Yeo and C. L. Lau, First-order model of symmetrical six-port microstrip ring coupler, *IEEE Trans. Microwave Theory Tech.* **39**(9):1666–1669 (Sept. 1991).
- F. M. Ghannouchi, R. G. Bosisio, L'analyseur de réseaux à six-ports pour l'asservissement de dispositifs micro-ondes non linéaires transportés à bord des satellites, *Proc. SPS 91 Space Power, 2nd Int. Symp.*, Paris/Gif-sur-Yvette, France, Aug. 27–30, 1991, pp. 561–563.
- J. Cao, J. Sun, and Z. Qishao, A six-port technique application of measuring complex permittivity and permeability, *Microwave Opt. Technol. Lett.* **4**:376–378 (Aug. 1991).
- B. Huyart, E. Bergeault, G. Geneves, and L. Jallet, Design and measurement results of a six-port network analyzer in the 1–18 GHz frequency band, *Annal. Telecommun.* **46**(7–8):443–451 (July–Aug. 1991).
- N. Fourikis, K. W. Eccleston, N. Lioutas, and M. J. Sorell, Scalar network analyzers operating at Ka- and W-bands, *Int. J. Infrared Millimeter Waves* **12**(7):819–843 (July 1991).
- K. Gong, Z. Feng, J. She, and J. Wang, Estimation of the uncertainty of MMW six-port reflectometer, *Int. J. Infrared Millimeter Waves* **12**(7):799–802 (July 1991).
- R. Larose, *Caractérisation de Transistors Micro-onde en Régime Non Linéaire Utilisant la Technologie des Six-Ports*, mémoire de maîtrise, École Polytechnique de Montréal, July 1991.
- F. M. Ghannouchi, R. Larose, and R. G. Bosisio, A new multi-harmonic loading method for large-signal microwave and millimeter-wave transistor characterization, *IEEE Trans. Microwave Theory Tech.* **39**(6):986–992 (June 1991).

- G. Riddels and V. F. Fusco, A quasi-lumped six-port reflectometer for cellular radio use, *Microwave Opt. Technol. Lett.* **4**(5):191–194 (April 1991).
- H. Shinohara, N. Matsumoto, K. Fujimori, Y. Tsujihashi, H. Nakao, S. Kato, Y. Horiba, and A. Tada, A flexible multiport RAM compiler for data path, *IEEE J. Solid-State Circ.* **26**(3):343–349 (March 1991).
- Y. V. Rysanyi, O. B. Zhuravleva, and V. P. Pologrudov, Optimizing the structure of six-port transducers, *Meas. Tech.* **34**(3):286–288 (March 1991).
- H. Shinohara, N. Matsumoto, K. Fujimori, and S. Kato, A flexible multi-port RAM compiler for data path, *Proc. IEEE 1990 Custom Integrated Circuits Conf.* (Cat. 90CH2860-5), March 1991, pp. 16.5/1–4.
- N. A. El-Deeb, Calibration and performance of an automatic microstrip six-port reflectometer, *IEEE Trans. Instrum. Meas.* **40**(1):51–54 (Feb. 1991).
- J. Sun, J. Cao, and Q. Zhang, A study on X-band swept-frequency dual six-port ANA, *Acta Electron. Sinica.* **19**(1):126–129 (Jan. 1991).
- R. M. Ghannouchi and R. G. Bosisio, Six-port junctions for the control of phased array antennas on microwave power satellites, *Proc. 2nd Int. Symp. SPS91, Power from Space*, 1991, pp. 561–562.
- S. P. Yeo and W. L. Wong, Using the symmetrical six-port waveguide junction as a six-port reflectometer, *IEEE Instrumentation and Measurement Technology Conf. Record* (Cat. 91CH2940-5), 1991, pp. 236–240.
- V. Bilik, An improved method of determining the reference port characteristics of six-port reflectometers, *Proc. 21st European Microwave Conf.*, 1991, pp. 521–526.
- F. M. Ghannouchi and R. G. Bosisio, A six-port reflectometer with a variable test port impedance suitable for nonlinear microwave device characterization, *IEEE Instrumentation and Measurement Technology Conf. Record* (Cat. 91CH2940-5), 1991, pp. 180–182.
- J. Esteban and J. M. Rebolgar, Rigorous field theory analysis of four-port and six-port branch guide couplers, *Proc. 2nd Int. Conf. Electromagnetics in Aerospace Applications*, 1991, pp. 465–468.
- L. Accatino, B. Piovano, and S. Contu, Advanced design of Ku-band BFNs for satellite applications, *Proc. 2nd Int. Conf. Electromagnetics in Aerospace Applications*, 1991, pp. 457–459.
- H. P. Groll, Trends in measurement in the mm-wave range, *Proc. 21st European Microwave Conf. (Microwave '91)*, 1991, pp. 99–107.
- R. Garreis, 90 degrees optical hybrid for coherent receivers, *Proc. Int. Soc. Opt. Eng.* **1522**:210–219 (1991).
- N. Fourikis, K. W. Eccleston, N. Lioutas, and M. J. Sorell, Scalar network analyzers operating at Ka- and W-bands, *Int. J. Infrared Millimeter Waves* **12**(7):819–843 (July 1991).
- J. Sherman, A PIN diode switch that operates at 100 watts CW at C-band, *1991 IEEE MTT-S Int. Microwave Symp. Digest* (91CH2870-4), 1991, Vol. 3, pp. 1307–1310.
- S. Sebechlebsky, V. Raffaj, and V. Bilik, Synthesis of reflectors for wide-band lumped six-port reflectometers, *Elektrotechnicky Casopis* **42**(9–10):449–470 (1991).
- S. Aouchahine, B. Huyart, E. Bergeault, and L. Jallet, Design and evaluation of a millimeter wave six-port reflectometer in the W frequency band (75–110 GHz), *Annal. Télécommun.* **47**(11–12):536–538 (Nov.–Dec. 1992).
- Z. Feng, J. She, K. Gong, J. Wang, and B. Xu, W-band six-port reflectometer: Its design, calibration and accuracy, *J. Infrared Millimeter Waves* **11**(6):459–466 (Dec. 1992).
- V. Bilik, Calibrating the six-port reflectometer using a matched load and four unity-reflection standards. 2. Sliding termination, *Radio-engineering* **1**(2):2–8 (Dec. 1992).
- F. M. Ghannouchi and R. G. Bosisio, An automated millimeter-wave active load-pull measurement system based on six-port techniques, *IEEE Trans. Instrum. Meas.* **41**(6):957–962 (Dec. 1992).
- A. Duenas-Jimenez, A. Serrano-Santoyo, and F. J. Mendieta, On the synthesis of some ring junctions for six-port measurement applications, *Microwave Opt. Technol. Lett.* **5**(11):559–563 (Oct. 1992).
- V. Bilik, Calibrating the six-port reflectometer using a matched load and four unity-reflection standards. Perfectly matched load, *Radio-engineering* **1**(1):10–13 (Oct. 1992).
- N. M. Ridler, J. C. Medley, A. J. Baden Fuller, et al., Computer generated equivalent circuit models for coaxial-line offset open circuits, *IEE Proc. A Sci. Meas. Technol.* **139**(5):229–231 (Sept. 1992).
- M. N. Solomon, P. S. Weitzman, and C. P. McClay, A monolithic six-port module, *IEEE Microwave Guided Wave Lett.* **2**(8):334 (Aug. 1992).
- G. Colef, Bandwidth extension for six-port reflectometers via a simple numerical method, *Microwave Opt. Technol. Lett.* **5**(8):374–377 (July 1992).
- J. J. Laurin, R. G. Bosisio, and F. M. Ghannouchi, Calibration of a monitoring system for arrays based on six-port junctions, *Proc. IEEE Antennas and Propagation Society Int. Symp.*, July 1992, Vol. 1, pp. 458–461.
- Y. Cassivi, F. M. Ghannouchi, and R. G. Bosisio, Six-port junctions in a phased array antenna for accurate beam-steering, *Proc. IEEE Antennas and Propagation Society Int. Symp.* (Cat. 92CH3178-1), July 1992.
- N. M. Ridler and C. J. Medley, *Uncertainty Budget for VHF and UHF Reflectometers*, Nat. Phys. Lab., Teddington, UK, May 1992.
- R. J. Collier and M. F. D'Souza, Phase shifters for dielectric guides, *IEE Proc. H (Microwaves Anten. Propag.)* **139**(2):202–204 (April 1992).
- F. M. Ghannouchi and R. G. Bosisio, Source-pull/load-pull oscillator measurements at microwave/MM wave frequencies, *IEEE Trans. Instrum. Meas.* **41**(1):32–35 (Feb. 1992).
- D. J. Bannister, J. P. Ide, and M. Perkins, Improved six-port reflectometer based on symmetrical five-port junction, *Electron. Lett.* **28**(4):406–408 (Feb. 13, 1992).
- S. D'Agostino, G. D'Inzeo, and L. Tudini, Analytical modeling and design criteria for traveling-wave FET amplifiers, *Travel. Wave FET Amp.* **40**(2):202–208 (Feb. 1992).
- A. Mahmoodshahi and W. K. Kahn, Polarization state measurements derived from a general six-port analyzer: A theoretical and experimental approach, *Direct and Inverse Methods in Radar Polarimetry, Proc. NATO Advanced Research Workshop*, 1992.
- R. Honigbaum and U. Stumper, High-frequency efficiency standard measuring apparatus to 40 GHz, *Mikrowellen HF Mag. Telecommun.* **18**(3):157–161 (1992).
- E. Bergeault, B. Huyart, Y. Delisle, and R. G. Bosisio, A MMIC six-port reflectometer, *Proc. 35th Midwest Symp. Circuits and Systems* (Cat. 92CH3099-9), 1992, Vol. 2, pp. 1485–1488.

- F. M. Ghannouchi, Y. Cassivi, and R. G. Bosisio, Six-port junctions for the control of phased array antennas on microwave power satellites, *Space Power* **11**(2):133–140 (1992).
- U. Stumper, Six-port reflectometers in PTB-calibration study, *Mikrowellen HF Mag. Telecommun.* **18**(3):162–169 (1992).
- S. P. Yeo, Analysis of symmetrical six-port junction when configured as a six-port reflectometer, *IEEE Trans. Instrum. Meas.* **41**(2):193–197 (1992).
- G. O. Bolme, P. M. Denney, W. D. Gutscher, S. P. Jachim, K. F. Johnson, C. K. Little, R. D. Patton, A. H. Regan, and O. R. Sander, Analysis of high-power conditioning for accelerator cavities using a six-port reflectometer, *Proc. 1992 Linear Accelerator Conf.* (AECL-10728), 1992, Vol. 1, pp. 136–138.
- D. F. Hornbachner, M. A. Schreiblehner, W. R. Leeb, and A. L. Scholtz, Experimental determination of power penalty contributions in an optical Costas-type phase-locked loop receiver, *Proc. SPIE* (Int. Society for Optical Engineering) **1635**:10–18 (1992).
- M. Cicolani, et al., Phase and amplitude automatic measurements on pulsed RF signals, *Proc. Microwave Exhibitions and Publishers Conf. 1992*, 1992, Vol. 2, pp. 931–936.
- F. M. Ghannouchi and R. G. Bosisio, A millimeter wave active load-pull measurement system, *Proc. IMTC '92, IEEE Instrumentation and Measurement Technology Conf.* (Cat. 92CH3151-8), 1992, pp. 395–398.
- B. Galwas and S. Palczewski, Idea of six-port vector-voltmeter with homodyne phase-sensitive detectors, *Proc. IMTC '92, IEEE Instrumentation and Measurement Technology Conf.* (Cat. 92CH3151-8), 1992, pp. 380–384.
- C. S. Hartmann, D. P. Chen, and J. Heighway, Experimental determination of COM model parameters for SAW transversely coupled resonator filter, *Proc. IEEE 1992 Ultrasonics Symp.* (Cat. 92CH3118-7), 1992, Vol. 1, pp. 211–214.
- W. K. Kahn, Automated polarization measurement, *Proc. NTC-92, National Telesystems Conf.* (Cat. 92CH3120-3), 1992, pp. 2/13–15.
- B. Galwas and S. Palczewski, Ratio of complex amplitudes measurement by means of six-port with homodyne phase-sensitive, *Proc. 22nd European Microwave Conf.*, 1992.
- F. M. Ghannouchi, D. Maurin, M. Cuhaci, and R. G. Bosisio, A miniaturized frequency-compensated six-port junction using MHMIC technology, *Microwave Opt. Technol. Lett.* **6**(10):573–575 (Aug. 1993).
- F. M. Ghannouchi, A calibration and measurement method of a tri-six-port network analyzer suitable for on-wafer characterization of three-port devices, *IEEE Trans. Instrum. Meas.* **42**(4):864–866 (Aug. 1993).
- J. Mlakar, Circuit model for a symmetrical condensed TLM node, *Int. J. Num. Model.: Electron. Networks, Devices Fields*, **6**(3):183–193 (Aug. 1993).
- T. Sieverding and F. Arndt, Rigorous analysis of the rectangular waveguide six-port junction, *IEEE Microwave Guided Wave Lett.* **3**(7):224–226 (July 1993).
- G. Potter and C. M. Hjipteris, Ultra-broadband reflectometer using the six-port technique, *MOP 93 Conf. Digest*, Sindelfingen, Germany, May 25–27, 1993.
- M. E. Bialkowski and A. P. Dimitrios, A step-frequency six-port network analyzer with real-time display, *Archiv Elektron. Uebertragungstechnik* **47**(3):193–197 (May 1993).
- C. Akyel and F. M. Ghannouchi, High power six-port reflectometer using hybrid stripline/waveguide technology, *Conf. Record IMTC/93*, May 1993, pp. 653–656.
- F. M. Ghannouchi and R. G. Bosisio, Device line characterization of Gunn diodes using six-port techniques, *Conf. Record IMTC/93*, May 1993, pp. 323–326.
- M. N. Solomon, C. P. McClay, H. M. Cronson, A. Chu, and P. S. Weitzman, A monolithic six-port module for built-in-test applications, *Conf. Record IMTC/93*, May 1993.
- J. M. Wilson, T. V. Parry, and A. Marshall, *Operational Wear in the Impeller of a Vertical Shaft Impact Breaker*. Univ. Science Lab, Durham, England, April 13, 1993, *Wear*, Vol. 162–64, Part B, pp. 1022–1024.
- J. Munoz, M. Rojo, and J. Margineda, A method for measuring the permittivity without ambiguity using six-port reflectometer, *IEEE Trans. Instrum. Meas.* **42**(2):222–226 (April 1993).
- S. A. Chahine, B. Huyart, E. Bergeault, and L. Jallet, A six-port reflectometer calibration using Schottky diodes operating in AC detection mode, *IEEE Trans. Instrum. Meas.* **42**(2):505–510 (April 1993).
- E. Bergeault, J. Achkar, M. Valon, and B. Huyart, A national intercomparison between automatic network analyzers, *IEEE Trans. Instrum. Meas.* **42**(2):511–515 (April 1993).
- S. Abouchahine, B. Huyart, E. Bergrault, and L. Jallet, Millimetric network analyzer using a single six-port reflectometer, *Electron. Lett.* **29**(3):256–258 (Feb. 4, 1993).
- P. Landsberg, C. Tretz, and C. Zukowski, An efficient macro-model for static CMOS multi-port memories, *Proc. IEEE 1993 Custom Integrated Circuits Conf.* (Cat. 93CH3214-4), 1993, pp. 8.2.1–8.2.4.
- M. N. Solomon, et al., A monolithic six-port module, *IEEE Microwave Guided Wave Lett.* **2**:334–336 (1992).
- G. Potter and C. M. Hjipteris, Robust six-to four-port reduction algorithm, *1993 IEEE MTT-S Int. Microwave Symp. Digest* (Cat. 93CH3277-1), 1993, Vol. 3, pp. 12263–12266.
- F. M. Ghannouchi, F. Beauregard, and A. B. Kouki, Measurement of microwave absolute power with the aid of a six-port junction with four diodes, *Proc. 1993 Canadian Conf. Electrical and Computer Engineering* (Cat. 93TH0590-0), 1993, Vol. 2, pp. 925–926.
- A. J. Belfort de Oliveira and S. P. Xavier Neto, The six-port technique: A brief review, *Proc. 1993 SBMO Int. Microwave Conf./Brazil* (IEEE Cat. 93TH0555-3), 1993, Vol. 2, pp. 717–722.
- F. Arndt, Advances in the mode-matching simulation and CAD of waveguide components, *Proc. 23rd European Microwave Conf.*, 1993, Vol. 2, p. 45.
- G. Potter and C. M. Hjipteris, A novel 250 MHz–26.5 GHz reflection analyzer, *Proc. 23rd European Microwave Conf.*, 1993, Vol. 1, pp. 302–304.
- S. Abou Chahine, B. Huyart, E. Bergeault, and L. Jallet, A millimeter dual six-port network analyzer in the W frequency band (75–110 GHz), *Proc. 23rd European Microwave Conf.*, 1993, Vol. 1, pp. 299–301.
- Marconi Instruments, Design of a six-port microwave instrument, *Marconi Instruments Tech. J.* **93**(2):6–7 (1993).
- S. Luo, A. Biswas, and V. K. Tripathi, Fin-line multi-port couplers, *IEEE Trans. Microwave Theory Tech.* **42**(12)(Part 1):2208–2215 (Dec. 1994).
- S. P. Yeo and M. Cheng, New technique for measuring the scattering coefficients of two-port devices, *Electron. Lett.* **30**(23):1951–1953 (Nov. 10, 1994).
- T. Yakabe, M. Kinoshita, and H. Yabe, Complete calibration of a six-port reflectometer with one sliding load and one short, *IEEE Trans. Microwave Theory Tech.* **42**(11):2035–2039 (Nov. 1994).

- F. Deshours, E. Bergeault, L. Jallet, and B. Huyart, An active load-pull measurement system using two six-port reflectometers, *Microwave Opt. Technol. Lett.* **7**(14):679–684 (Oct. 5, 1994).
- F. M. Ghannouchi, F. Beaugard, and A. B. Kouki, Power added efficiency and gain improvement in MESFET amplifiers using an active harmonic loading technique, *Microwave Opt. Technol. Lett.* **7**(13):625–627 (Sept. 1994).
- D.-L. Le and F.M. Ghannouchi, Source-pull measurements using reverse six-port, *IEEE Trans. Microwave Theory Tech.* **42**(9)(Part 1):1589–1595 (Sept. 1994).
- F. M. Ghannouchi, Y. Xu, and R. G. Bosisio, One-step connection method for the measurement of N-port microwave networks using six-port techniques, *IEE Proc. Microwaves Anten. Propag.* **141**(4):285–289 (Aug. 1994).
- J.-M. Moreau, A. E. Idrissi, and C. Tibaudo, Permittivity measurements of materials during heating by microwaves, *Meas. Sci. Technol.* **5**(8):996–1001 (Aug. 1994).
- H. How, T.-M. Fang, C. Vittoria, and R. Schmidt, Design of six-port strip-line ferrite junction circulators, *IEEE Trans. Microwave Theory Tech.* **42**(7)(Part 1):1272–1275 (July 1994).
- M. Kinoshita, H. Suzuki, T. Yakabe, and H. Yabe, Variance distribution of reflection coefficients in six-port reflectometer, *IEICE Trans. Electron.* **E77-C**(6):930–934 (June 1994).
- F. M. Ghannouchi, F. Beaugard, and A. B. Kouki, Large-signal stability and spectrum characterization of a medium power HBT using active load-pull techniques, *IEEE Microwave Guided Wave Lett.* **4**(6):191–193 (June 1994).
- P. Berini, M. Desgagne, F. M. Ghannouchi, and R. G. Bosisio, An experimental study of the effects of harmonic loading on microwave MESFET oscillators and amplifiers, *IEEE Trans. Microwave Theory Tech.* **42**(6):943–950 (June 1994).
- F. M. Ghannouchi, Z. Guoxiang, and F. Beaugard, Simultaneous load-pull of intermodulation and output power under two-tone excitation for accurate SSPA's design, *IEEE Trans. Microwave Theory Tech.* **42**(6):929–934 (June 1994).
- T. Yakabe and H. Yabe, A simple adapter de-embedding method in the six-port calibration process using a scalar analyzer, *IEICE Trans. Electron.* **E77-C**(6):925–929 (June 1994).
- T.-J. Chen and T.-H. Chu, A micro-strip five-port network analyzer for reflection and transmission coefficient measurement. *Proc. National Science Council, Republic of China, Part A (Phys. Sci. Eng.)* **18**(3):274–279 (May 1994).
- C. Akyel, F. M. Ghannouchi, and M. Caron, A new design for high-power six-port reflectometers using hybrid strip-line/waveguide technology, *IEEE Trans. Instrum. Meas.* **43**(2):316–321 (April 1994).
- F. M. Ghannouchi, A. B. Kouki, and F. Beaugard, A new implementation of the device line measurement technique for accurate microwave oscillator design, *IEEE Trans. Instrum. Meas.* **43**(2):311–315 (April 1994).
- K.-H. Kim and S. E. Lindberg, High-precision measurements of mercury vapor in air: Design of a six-port-manifold mass flow errors controller system and evaluation of mass flow at atmospheric pressure, *J. Geophys. Res.* **99** Iss. (D3):5379–5384 (March 20, 1994).
- F. M. Ghannouchi, Compact circuit performs swept vector measurements, *Microwaves RF* **33**(2):67–68 (Feb. 1994).
- N. M. Ridler, New VHF impedance measuring instrument for UK national standard, *IEE Proc. Sci. Meas. Technol.* **141**(1):71–74 (Jan. 1994).
- M. J. Cryan, P. R. Shepherd, and S. R. Pennock, A comparison of three wide FETs configured as controllable couplers, *IEE Colloquium on Modeling, Design and Application of MMIC's* (Digest 1994/092), 1994, 6/1–6.
- M. Wojcicki and A. Lisowiec, A method for determination of basic electrical parameters of piezoelectric resonators in a wide frequency range, *J. Piezoelectric Resonators Wide Freq. Range* **27**(3–4):143–154 (1994).
- V. Bilik and J. Bezek, Vector reflectometer system for industrial applications, *Proc. 24th European Microwave Conf.* 1994, Vol. 2, pp. 1010–1015.
- J. M. Rebollar, J. Esteban, and J. E. Page, Design of a compact Ka-band three-way power divider, *IEEE Antennas and Propagation Society Int. Symp. 1994 Digest* (Cat. 94CH3466-0), 1994, Vol. 2, pp. 1074–1077.
- D. Maurin, Y. Xu, B. Huyart, K. Wu, M. Cuhaci, and R. G. Bosisio, CPW millimeter-wave six-port reflectometers using MHMIC and MMIC technologies, *Proc. 24th European Microwave Conf.* 1994, Vol. 1, pp. 911–915.
- B. Huyart, M.-L. Comet, M. Cuhaci, D. Maurin, J.-J. Laurin, and R. G. Bosisio, Adaptive antenna system (AAS) using a sixport module, *Proc. Symp. Antenna Technology and Applied Electromagnetics 1994*, 1st ed., 1994, pp. 63–66.
- J. Li, R. G. Bosisio, and K. Wu, Performing PSK demodulation using six-ports, *Proc. Symp. Antenna Technology and Applied Electromagnetics 1994*, 1st ed., 1994, pp. 15–18.
- V. Bilik and J. Bezek, High-power 2.45 GHz waveguide vector reflectometer for industrial applications, *Proc. Microwaves 94, The Applications of RF Microwave and Millimeter Wave Technologies*, 1994, pp. 21–25.
- M. Begin, F. M. Ghannouchi, F. Beaugard, L. Selmi, B. Ricco, and V. Borelli, Characterization of transient effects in the S-parameters of GaAs MESFETs by means of pulsed measurements, *Proc. ESSDERC '94, 24th European Solid State Device Research Conf.*, 1994, pp. 639–642.
- J. M. Rebollar, J. Esteban, and J. E. Page, Design of a compact Ka-band three-way power divider, *IEEE Antennas and Propagation Society Int. Symp. 1994 Digest* (Cat. 94CH3466-0), 1994, Vol. 2, pp. 1074–1077.
- E. Eid, F. M. Ghannouchi, and F. Beaugard, Self-calibration of six-port reflectometers using active loads, *1994 Conf. Precision Electromagnetic Measurements Digest* (Cat. 94CH3449-6), 1994, pp. 121–122.
- C. Jiang, A swept six-port reflectometer with real-time response at Ka band, *Proc. 10th Anniversary IEEE IMTC/94 Advanced Technologies in Instrumentation and Measurement Conf.* (Cat. 94CH3424-9), 1994, Vol. 2, pp. 1001–1003.
- D.-L. Le and F. M. Ghannouchi, Network analysis of nonlinear devices under multi-frequency excitation, *Proc. 10th Anniversary IEEE IMTC/94 Advanced Technologies in Instrumentation and Measurement Conf.* (Cat. 94CH3424-9), 1994, Vol. 2, pp. 998–1000.
- L. Qiao and S. P. Yeo, Efficient four-standard calibration procedure for six-port reflectometers, *Proc. 10th Anniversary IEEE IMTC/94 Advanced Technologies in IEEE Instrumentation and Measurement Conf.* (Cat. 94CH3424-9), 1994, Vol. 2, pp. 994–997.
- H.-G. Krekels and B. Schiek, A full model calibration algorithm for a dual six-port network analyzer, *Proc. 10th Anniversary IEEE IMTC/94 Advanced Technologies in Instrumentation and Measurement Conf.* (Cat. 94CH3424-9), 1994, Vol. 2, pp. 990–993.
- M. Begin, F. M. Ghannouchi, L. Selmi, and B. Ricco, Instantaneous S parameters measurements of MESFETs under burst bias conditions, *Proc. 10th Anniversary IEEE IMTC/94 Advanced Technologies in Instrumentation and Measurement Conf.* (Cat. 94CH3424-9), 1994, Vol. 2, pp. 858–861.

- M. Caron, C. Akyel, and F. M. Ghannouchi, High power microwave impedance measurements system suitable for in-situ thermo-dielectric material characterization, *1994 IEEE MTT-S Int. Microwave Symp. Digest* (Cat. 94CH3389-4), 1994, Vol. 1, pp. 443–446.
- J. Li, R. G. Bosisio, and K. Wu, A six-port direct digital millimeter wave receiver, *1994 IEEE MTT-S Int. Microwave Symp. Digest* (Cat. 94CH3389-4), 1994, Vol. 3, pp. 1659–1662.
- J. Li, R. G. Bosisio, and K. Wu, A collision avoidance radar using six-port phase/frequency discriminator (SPFD), *1994 IEEE MTT-S Int. Microwave Symp. Digest* (Cat. 94CH3389-4), 1994, Vol. 3, pp. 1553–1556.
- S. Abou Chahine, B. Huyart, E. Bergeault, and L. Jallet, Measurement performance of a millimetric dual six-port network analyzer in the W frequency band (75–110 GHz), *1994 Conf. Precision Electromagnetic Measurements Digest* (Cat. 94CH3449-6), 1994, pp. 9–10.
- F. Deshours, E. Bergeault, L. Jallet, and B. Huyart, Large signal load-pull measurements using six-port reflectometers, *1994 Conf. Precision Electromagnetic Measurements Digest* (Cat. 94CH3449-6), 1994, pp. 294–295.
- J. Li, R. G. Bosisio, and K. Wu, A six-port direct digital millimeter wave receiver, *Proc. 1994 IEEE National Telesystems Conf.* (Cat. 94CH3419-9), 1994, pp. 79–82.
- J. Li, R. G. Bosisio, and K. Wu, A collision avoidance radar using six-port phase/frequency discriminator (SPFD), *Proc. 1994 IEEE National Telesystems Conf.* (Cat. 94CH3419-9), 1994, pp. 55–58.
- B. Huyart, F. Wiedmann, L. Jallet, E. Bergeault, R. Benelbar, and R. G. Bosisio, Microwave measurement using Wheatstone's bridges, *Proc. 24th European Microwave Conf.*, 1994, Vol. 1, pp. 928–933.
- S. Abou Chahine, B. Huyart, B. Vujik, E. Bergeault, and L. A. Jallet, Millimeter network analyzer incorporating a single six-port junction, *Proc. 24th European Microwave Conf.*, 1994, Vol. 1, pp. 916–921.
- M. J. Cryan, P. R. Shepherd, and S. R. Pennock, A monolithic voltage controlled directional coupler, *Proc. 24th European Microwave Conf.*, 1994, Vol. 1, pp. 752–757.
- B. Kuyart, J. J. Laurin, R. G. Bosisio, and D. Roscoe, A direction-finding antenna system using an integrated six-port circuit, *IEEE Trans. Anten. Propag.* **43**(12):1508–1512 (Dec. 1995).
- J. Li, R. G. Bosisio, and K. Wu, Computer and measurement simulation of a new digital receiver operating directly at millimeter-wave frequencies, *IEEE Trans. Microwave Theory Tech.* (Dec. 1995).
- J. Li, R. G. Bosisio, and K. Wu, Modeling of the six-port discriminator used in a microwave direct digital receiver, *Proc. Canadian Conf. Electrical and Computer Engineering*, Sept. 1995, pp. 1164–1165.
- D.-L. Le and F. M. Ghannouchi, Noise measurements of microwave transistors using an uncalibrated mechanical stub tuner and a built-in reverse six-port reflectometer, *IEEE Trans. Instrum. Meas.* **44**(4):847–852 (Aug. 1995).
- M. E. Bialkowski, J. Bornemann, V. P. Waris, and P. W. Davis, Simplified mode-matching techniques for the analysis of coaxial-cavity-coupled radial E-plane power dividers, *IEEE Trans. Microwave Theory Tech.* **43**(8):1875–1880 (Aug. 1995).
- A. J. B. De Oliveira and S. P. X. Neto, A single six-port reflectometer measures the scattering parameters of two-port microwave devices, *Proc. 1995 SBMO/MTT-S Int. Microwave and Optoelectronics Conf.* (Cat. 95TH8080), July 24–27, 1995, Vol. 2, pp. 671–674.
- A. M. Affandi and A. M. Rushdi, An accurate six-port micro-strip reflectometer, *Proc. 1995 SBMO/IEEE MTT-S Int. Microwave and Optoelectronics Conf.* (Cat. 95TH8080), July 24–27, 1995, Vol. 2, pp. 563–568.
- F. M. Ghannouchi, G. Zhao, and F. Beaugard, Simultaneous AM-AM/AM-PM distortion measurements of microwave transistors using active load-pull and six-port techniques, *IEEE Trans. Microwave Theory Tech.* **43**(7)(Part 1):1584–1588 (July 1995).
- L. Qiao and S. P. Yeo, Improved implementation of four-standard procedure for calibrating six-port reflectometers, *IEEE Trans. Instrum. Meas.* **44**(3):632–636 (July 1995).
- J. Achkar, A 90 MHz–40 GHz “six-port” vector network analyzer, *Revue Générale l'Électricité* (5):36–44 (May 1995).
- S. Abou Chahine, B. Huyart, E. Bergeault, and L. Jallet, Design realization and evaluation of a millimeter-wave network analyzer using a single six-port reflectometer, *Microwave Opt. Technol. Lett.* **8**(2):84–87 (Feb. 5, 1995).
- C. Tzong-Jyh and C. Tah-Hsiung, A wide-band six-port polarimetric measurement system, *IEEE Antennas and Propagation Society Int. Symp. 1995 Digest* (Cat. 95CH35814), 1995, Vol. 4, pp. 1694–1697.
- D. Berude, F. M. Ghannouchi, P. Savard, and I. Jolicoeur, Correction of discontinuities in measurements of complex permittivity with the aid of a coaxial probe, *Proc. 1995 Canadian Conf. Electrical and Computer Engineering* (Cat. 95TH8103), 1995, Vol. 1, pp. 497–500.
- S. Abou Chahine, B. Huyart, B. Vujik, E. Bergeault, and L. Jallet, A millimeter network analyzer incorporating a single six-port junction, *Proc. 24th European Microwave 1995*, Vol. 1, pp. 916–921.
- J. Li, R. G. Bosisio, and K. Wu, Modeling of the six-port discriminator used in a microwave direct digital receiver, *Proc. 1995 Canadian Conf. Electrical and Computer Engineering* (Cat. 95TH8103), 1995, Vol. 2, pp. 1164–1165.
- D.-L. Le and F. M. Ghannouchi, Multi-frequency measurement system for optimizing the performance of nonlinear microwave devices, *Proc. 1995 Canadian Conf. Electrical and Computer Engineering* (Cat. 95TH8103), 1995, Vol. 2, pp. 1011–1014.
- M. Caron, C. Akyel, and F. M. Ghannouchi, A versatile easy to do six-port based high-power reflectometer, *J. Microwave Power Electromagn. Energy* **30**(4):231–239 (1995).
- A. Afandi and G. Al-Rawi, A novel eight port 5-dB hybrid ring, *Proc. ICECS '95 Int. Conf. Electronics, Circuits and Systems*. 1995, pp. 486–488.
- A. Coffey, Employment issues [Transmanche Link Region], *IEE Colloquium on Eurotunnel: Social and Economic Implications (Digest 1995/173)*, 1995, pp. 4/1–8.
- I. T. Sylla, R. Hajji, and F. M. Ghannouchi, CAD of an integrated six-port reflectometer in MMIC technology, *Proc. 1995 Canadian Conf. Electrical and Computer Engineering* (Cat. 95TH8103), 1995, Vol. 2, pp. 1170–1172.
- A. J. B. De Oliveira and P. R. Lima, The six-port reflectometer: Choosing a calibration method, *Proc. SBMO/IEEE MTT-S International Microwave and Optoelectronics Conference*. Rio de Janeiro: SBMO, 1995. Vol. 2. pp. 675–680.
- S. Hrabar, S. Margetic, and R. Kovacevic, Some experiences with implementation of the Neumeyer six-port calibration method, *Proc. 37th ELMAR Int. Symp.* 1995, pp. 175–178.
- A. Rahal and R. G. Bosisio, A stable Ka band planar Gunn diode dielectric resonator oscillator (DRO), *Proc. 1995 Canadian Conf. Electrical and Computer Engineering* (Cat. 95TH8103), 1995, Vol. 2, pp. 734–737.

- W. K. Kahn and I. L. Gheorghisor, Calibration of a self-aligning polarization analyzer, *Proc. 1995 Int. Geoscience and Remote Sensing Symp. (IGARSS '95), Quantitative Remote Sensing for Science and Applications* (Cat. 95CH35770), 1995, Vol. 1, pp. 77–79.
- A. Rahal and R. G. Bosisio, A stable Ka band planar Gunn diode dielectric resonator, *Proc. 1995 Canadian Conf. Electrical and Computer Engineering* (Cat. 95TH8103), pp. 1995, Vol. 2, pp. 734–737.
- J. H. Yun, H. J. Lee, and J. K. Kim, Design and analysis of six port-TEM cell for generating standard electromagnetic fields, *Electron. Lett.* **32**(23):2127–2128 (Nov. 1996).
- J. C. Coetzee and M. M. Nieuwoudt, The design of single-section and wideband symmetrical three-line micro-strip couplers, *Microwave Opt. Technol. Lett.* **13**(3):165–169 (Oct. 20, 1996).
- H. How, T. M. Fang, C. Vittoria, and R. Schmidt, Magnetic losses in strip-line/micro-strip circulators, *J. Appl. Phys.* **79**(8)(Part 2B):5739–5741 (April 15, 1996).
- A. Zucchetti, W. Vogel, and D.-G. Welsch, Quantum-state homodyne measurement with vacuum ports, *Phys. Rev. A (Atomic Molec. Opt. Phys.)* **54**(1):856–862 (July 1996).
- S. P. Yeo and M. Cheng, Novel nine-port network analyzer for measuring scattering coefficients of two-port devices, *IEE Proc. Microwaves Anten. Propag.* **143**(2):137–140 (April 1996).
- L. Yi, Calibrating an industrial microwave six-port instrument using the artificial neural network technique, *IEEE Trans. Instrum. Meas.* **45**:651–656 (April 1996).
- K. Fanmin, C. Gangwu, et al., A calibration method of open-ended coaxial line and six-port for dielectric measurement, *Acta Electron. Sinica.* **24**(3):74–76 (March 1996).
- D. Tarach and G. Trenkler, Calibration of inductive voltage dividers at extremely low frequencies, *Metrologia* **32**(5):367–370 (March 1996).
- S. Abou Chahine, B. Huyart, E. Bergeault, and L. Jallet, Design, realization and performance of a millimetric six-port network analyzer, *Annal. Télécommun.* **51**(1–2):11–18 (Jan.–Feb. 1996).
- M. Begin, F. M. Ghannouchi, F. Bearegard, L. Selmi, and B. Ricco, Characterization of the transient behavior of a GaAs MESFET using dynamic I–V and S-parameter measurements, *IEEE Trans. Instrum. Meas.* **45**(1):231–237 (Feb. 1996).
- J. Li, R. G. Bosisio, and K. Wu, Dual-tone calibration of six-port junction and its application to the six-port direct digital millimetric receiver, *IEEE Trans. Microwave Theory Tech.* **44**(1):93–99 (Jan. 1996).
- B. A. Galwas, S. Palczewski, and Z. Pienkowski, A dual six-port with homodyne phase-sensitive detectors as new option of microwave network analyzer, *1996 IEEE Conf. Precision Electromagnetic Measurements Digest* (Cat. 96CH35956), 1996, pp. 602–603.
- O. O. Drobakhin, V. F. Borulko, and V. A. Karlov, Millimeter apparatus for transmission line and dielectric material measurements by multi-frequency methods, *1996 Conf. Precision Electromagnetic Measurement Digest* (Cat. 96CH35956), 1996, pp. 598–599.
- F. Wiedmann, B. Huyart, E. Bergeault, and L. Jallet, New structure for a six-port reflectometer in MMIC technology, *1996 Conf. Precision Electromagnetic Measurements Digest* (Cat. 96CH35956), 1996, pp. 534–535.
- P. Poiré and F. M. Ghannouchi, Immunity of six-port measurement techniques to the AM-PM noise of the microwave signal generator, *Proc. Quality Measurements: The Indispensable Bridge between Theory and Reality (No Measurement? No Science!) Joint Conf. 1996, IEEE Instrumentation and Measurement*, 1996, Vol. 2, pp. 1259–1262, 1515.
- C. M. Krowne, 3D dyadic Green's function for radially inhomogeneous circular ferrite circulator, *1996 IEEE MTT-S Int. Microwave Symp. Digest* (Cat. 96CH35915), 1996, Vol. 1, pp. 121–124.

SKIN EFFECT

FRANK OLYSLAGER
DANIËL DE ZUTTER
Ghent University
Ghent, Belgium

1. INTRODUCTION

The term *skin effect* is used to indicate that electromagnetic waves penetrate only a small distance into a conductor. Equivalently, the skin effect is the phenomenon that time-varying current densities are concentrated in a thin layer near the surface or skin of a conductor. The current densities are concentrated at the side of the conductor exposed to the source of these currents. These currents are often referred to by the term *eddy currents*.

For time-harmonic fields the amplitude of these fields decays exponentially with the distance from the surface. The distance over which the amplitude of the fields, and hence of the current density, decreases by a factor e is called the skin depth δ given by

$$\delta = \sqrt{\frac{2}{\omega\mu\sigma}} \quad (1)$$

Thus, the layer in which the fields are concentrated becomes thinner when the frequency $f = \omega/(2\pi)$ increases, the permeability μ increases, or the conductivity σ increases. In the limit of perfect conductors, fields and current density are concentrated in a vanishingly thin layer at the surface of the conductor.

If a current flows in a conductor with finite conductivity, this will cause a voltage drop along the flow of the current. The ratio of the voltage drop to the current is the internal impedance of the conductor. If the current density is concentrated in a thin layer at the surface of the conductor, this internal impedance, expressed per unit square, that is, for a unit length and a unit width of the conductor, is called the surface impedance Z_s . For a cylindrical wire with radius r this amounts to an internal impedance $Z_s/(2\pi r)$ per unit length. The surface impedance Z_s is given by

$$Z_s = \frac{1+j}{\sigma\delta} = \frac{1+j}{\sqrt{2}} \sqrt{\frac{\omega\mu}{\sigma}} \quad (2)$$

If Z_s is decomposed in its real and imaginary parts as $Z_s = R_s + j\omega L_1$, then R_s is the surface resistance and L_1 is the internal inductance per unit square. The surface impedance also expresses the ratio between the tangential electric field and tangential magnetic field at the surface of a conductor.

For a conductor several skin depths thick, the electromagnetic fields will not penetrate through the conductor. For a hollow conductor, such as a coaxial cable, this means that the internal electromagnetic field is decoupled from the external field. This is the electromagnetic shielding property of conductors. Since for copper at 60 Hz the skin depth $\delta = 8.5$ mm, the skin effect not only is important at radiofrequencies but also plays an important role for the design of power transmission lines, electrical machines, and electrification of railways. Because of the concentration of the current density at the surface of the wires, the Ohmic losses per unit length and voltage drops per unit length are substantially higher than what would be expected from a uniform distribution of the current density over the cross section of the wire. This concentration also imposes a limitation on the useful diameter of wires for power transmission.

The dissipated power per unit length P_d by a current I in the skin layer is given by

$$P_d = \frac{1}{2} R_s |I|^2 = \frac{1}{2} \sqrt{\frac{\omega\mu}{2\sigma}} |I|^2 \quad (3)$$

It is thus seen that for a given current this dissipation increases with frequency and permeability and decreases with conductivity.

Strictly speaking, the previous expressions for δ , Z_s , and P_d are valid only in good conductors with planar surfaces. However, if the radii of curvature of the conductor surface are large compared to the skin depth δ , these formulas are still good approximations. Table 1 shows the skin depth δ and surface resistance R_s for a number of conductors. Except for iron, the relative permeability μ/μ_0 , with μ_0 the free-space permeability, is equal to one for all metals.

When the surface of the conductor is rough, the losses inside the conductor will increase because the surface resistance increases. Porosity of the surface also will increase the surface resistance considerably.

To take the skin effect into account in numerical electromagnetic simulations, two approaches are possible. First, one can replace the boundary condition of a vanishing tangential electric field for a perfect conductor by an impedance boundary condition relating the tangential

Table 1. Conductivities, Skin Depths, and Surface Resistances for a Number of Conductors (f in Hz).

	σ	δ	R_s
Gold	41 MS/m	79 mm/ \sqrt{f}	310 n $\Omega\sqrt{f}$
Silver	61.7 MS/m	64.1 mm/ \sqrt{f}	253 n $\Omega\sqrt{f}$
Copper	58 MS/m	66.1 mm/ \sqrt{f}	261 n $\Omega\sqrt{f}$
Aluminium	37.2 MS/m	82.5 mm/ \sqrt{f}	326 n $\Omega\sqrt{f}$
Brass	15.7 MS/m	127 mm/ \sqrt{f}	501 n $\Omega\sqrt{f}$
Iron ($\mu_r = 120$)	10 MS/m	15 mm/ \sqrt{f}	6.88 n $\Omega\sqrt{f}$
Tin	8.69 MS/m	171 mm/ \sqrt{f}	674 n $\Omega\sqrt{f}$
Mercury	1.04 MS/m	494 mm/ \sqrt{f}	1.95 n $\Omega\sqrt{f}$
Zinc	17.4 MS/m	121 mm/ \sqrt{f}	476 n $\Omega\sqrt{f}$
Lead	4.8 MS/m	230 mm/ \sqrt{f}	910 n $\Omega\sqrt{f}$
Platinum	9.66 MS/m	162 mm/ \sqrt{f}	639 n $\Omega\sqrt{f}$
Human tissue (~ 1 GHz)	1.2 S/m	460 m/ \sqrt{f}	1.81 m $\Omega\sqrt{f}$

electric field to the tangential magnetic field through the surface impedance. In most cases this is an approximation, but it can be a very good one. A second approach is to also perform a simulation of the fields inside the conductor. For numerical techniques such as finite-element techniques, finite-difference techniques, or volume integral equation techniques, which discretize the volume of the conductors, a fine discretization is needed in order to accurately model the exponential decay of the fields inside the conductors. For boundary integral equation techniques the second approach, except for an increase in computational complexity, does not entail extra complications.

2. THEORY

2.1. Plane Interfaces

To study the skin effect quantitatively consider the structure of Fig. 1, consisting of a conductor with planar interface that occupies the semiinfinite region $z > 0$ and that is characterised by the material parameters ϵ , μ and σ . The region $z < 0$ is assumed to be free space with parameters ϵ_0 and μ_0 . Outside the conductor and in the absence of sources, the electromagnetic fields in time-harmonic regime $e^{j\omega t}$ satisfy the Maxwell curl equations

$$\nabla \times \mathbf{E} = -j\omega\mu_0\mathbf{H} \quad (4)$$

$$\nabla \times \mathbf{H} = j\omega\epsilon_0\mathbf{E} \quad (5)$$

Inside the conductor the fields satisfy

$$\nabla \times \mathbf{E} = -j\omega\mu\mathbf{H} \quad (6)$$

$$\nabla \times \mathbf{H} = (j\omega\epsilon + \sigma)\mathbf{E} \approx \sigma\mathbf{E} \quad (7)$$

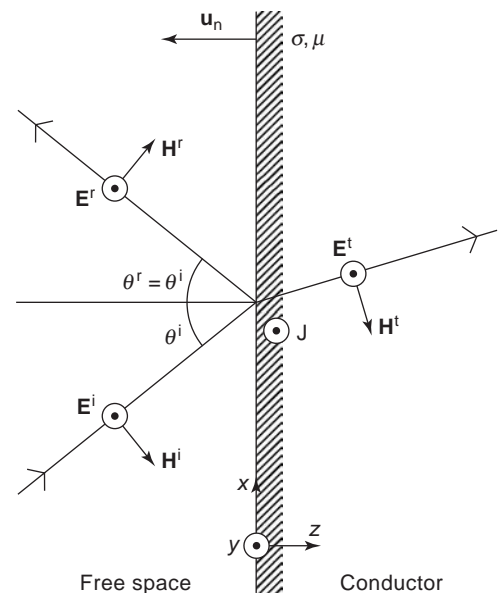


Figure 1. Incident plane electromagnetic TE wave on a plane conductor with conductivity σ and permeability μ . The angle of incidence is θ^i .

In the last equation the displacement current term was neglected compared to the conduction current term, which is allowed for all practical conductors at practical frequencies. For example, in platinum $\omega\varepsilon$ becomes comparable to σ only at 1.5 pHz. Taking the curl of Eqs. (4) and (6), substituting Eqs. (5) and (7), and using the Maxwell divergence equations $\nabla \cdot \mathbf{E} = \nabla \cdot \mathbf{H} = 0$ in both free space and the conductor shows that the electric field in free space satisfies the Helmholtz equation

$$\nabla^2 \mathbf{E} + k_0^2 \mathbf{E} = 0 \quad (8)$$

where $k_0^2 = \omega^2 \varepsilon_0 \mu_0$ and in the conductor the Helmholtz equation

$$\nabla^2 \mathbf{E} - j\omega\mu\sigma \mathbf{E} = 0 \quad (9)$$

Now illuminate the conductor by a plane electromagnetic wave (see Fig. 1). Assume that this plane wave has TE (transverse electric) polarization and that, according to the coordinate system of Fig. 1, the electric field has a component only in the y direction. The incident electric field is given by

$$\mathbf{E}^i = E_0 \mathbf{u}_y e^{-jk_x x} e^{-jk_z z} \quad (10)$$

where \mathbf{u}_y is the unit vector in the y direction. Substituting in Eq. (8) and taking into account an angle of incident θ^i yields $k_x = k_0 \sin \theta^i$ and $k_y = k_0 \cos \theta^i$. From Eq. (4) the incident magnetic field is then found to be

$$\mathbf{H}^i = \frac{k_x \mathbf{u}_z - k_z \mathbf{u}_x}{\omega\mu_0} E_0 e^{-jk_x x} e^{-jk_z z} \quad (11)$$

where \mathbf{u}_x and \mathbf{u}_z are unit vectors in x and z directions, respectively. The incident plane wave will give rise to a reflected plane wave in free space and a transmitted plane wave in the conductor. All these plane waves will have the same phase variation $e^{-jk_x x}$ in the x direction along the interface, and they will all be TE-polarized. This means that the reflected plane wave takes the form

$$\mathbf{E}^r = RE_0 \mathbf{u}_y e^{-jk_x x} e^{jk_z z} \quad (12)$$

$$\mathbf{H}^r = \frac{k_x \mathbf{u}_z + k_z \mathbf{u}_x}{\omega\mu_0} RE_0 e^{-jk_x x} e^{jk_z z} \quad (13)$$

where R is the reflection coefficient, which is still to be determined. The transmitted electric field in the conductor takes the form

$$\mathbf{E}^t = E_0 \mathbf{u}_y e^{-jk_x x} f(z) \quad (14)$$

Substituting in Eq. (9) shows that $f(z)$ satisfies

$$\frac{d^2 f(z)}{dz^2} - (j\omega\mu\sigma + k_x^2) f(z) = 0 \quad (15)$$

Because $k_x = k_0 \sin \theta^i$ is of the same order of magnitude as k_0 , we neglect the term k_x^2 in the previous equation on the

same grounds for neglecting $\omega\varepsilon$ in Eq. (7). Taking into account that $f(z)$ should remain bounded for $z \rightarrow +\infty$ yields that $f(z) = T e^{-(1+j)z/\delta}$ with δ the skin depth as defined in Eq. (1). From Eqs. (14) and (6) the fields in the conductor are thus found to be

$$\mathbf{E}^t = TE_0 \mathbf{u}_y e^{-jk_x x} e^{-(1+j)z/\delta} \quad (16)$$

$$\mathbf{H}^t = \frac{k_x \mathbf{u}_z - (1-j)/\delta \mathbf{u}_x}{\omega\mu} TE_0 e^{-jk_x x} e^{-(1+j)z/\delta} \quad (17)$$

where T is the transmission coefficient. It is seen that the amplitudes of the fields decrease by a factor of e when they propagate over a distance perpendicular to the interface equal to the skin depth δ . The reflection and transmission coefficients follow from imposing the continuity of the tangential fields, that is, of E_y

$$1 + R = T \quad (18)$$

and H_x

$$-\frac{k_z}{\omega\mu_0} + R \frac{k_z}{\omega\mu_0} = -\frac{(1-j)T}{\omega\mu\delta} \quad (19)$$

at the interface $z = 0$. The solution to this set of equations is

$$R = \frac{k_z \mu_r \delta + 1 - j}{k_z \mu_r \delta - 1 + j} \quad (20)$$

and

$$T = \frac{2k_z \mu_r \delta}{k_z \mu_r \delta - 1 + j} \quad (21)$$

At the interface $z = 0$ the relation between the tangential electric field \mathbf{E}_t and the tangential magnetic field \mathbf{H}_t can be expressed as

$$\mathbf{E}_t = Z_s \mathbf{u}_n \times \mathbf{H}_t \quad (22)$$

where Z_s is the surface impedance as defined in Eq. (2) and $\mathbf{u}_n = -\mathbf{u}_z$ for the configuration of Fig. 1. Indeed, from Eq. (16) it follows that $\mathbf{E}_t = TE_0 \mathbf{u}_y e^{-jk_x x}$ and from Eq. (17) that $\mathbf{H}_t = -(1-j)/(\omega\mu\delta) TE_0 \mathbf{u}_x e^{-jk_x x}$ and hence that Z_s is as given by Eq. (2).

The current density \mathbf{J} in the conductor is $\sigma \mathbf{E}$, and from Eq. (16)

$$\mathbf{J} = \sigma TE_0 \mathbf{u}_y e^{-jk_x x} e^{-(1+j)z/\delta} \quad (23)$$

The total current per unit length I flowing in the conductor from the integration of Eq. (23) over all $z > 0$ is given by $I = \mathbf{J}_s \cdot \mathbf{u}_y$ with

$$\mathbf{J}_s = \int_0^{+\infty} \sigma TE_0 \mathbf{u}_y e^{-jk_x x} e^{-(1+j)z/\delta} dz = \frac{\sigma\delta}{1+j} TE_0 \mathbf{u}_y e^{-jk_x x} \quad (24)$$

where the notation \mathbf{J}_s indicates that this can be viewed as an equivalent surface current density. When this current flows across the conductor in the y direction over a unit distance it causes a voltage drop V equal to $\mathbf{E}^t(z=0) \times \mathbf{u}_y = TE_0e^{-jk_x x}$. The ratio V/I can be seen as the internal impedance per unit square of the conductor and is given by the surface impedance Z_s . The real part of the surface impedance is the surface resistance R_s and the imaginary part is the internal reactance ωL_i , which are both equal to $1/(\sigma\delta)$. This means that the surface resistance can be seen as the resistance per unit square when all the current is homogeneously distributed over and concentrated in a layer with thickness δ at the surface of the conductor, that is, as the DC resistance of a planar conductor with thickness δ .

The dissipated power P_d in the skin layer, per unit distance in the x direction due to Ohmic losses is given by

$$P_d = \frac{1}{2} \Re \int_0^{+\infty} \mathbf{J}^* \cdot \mathbf{E}^t dz = \frac{\sigma}{2} \int_0^{+\infty} |\mathbf{E}^t|^2 dz = \frac{\sigma\delta}{4} |E_0|^2 |T|^2 \tag{25}$$

From Eq. (24) it follows that

$$|I| = \frac{\sigma\delta}{\sqrt{2}} |T||E_0| \tag{26}$$

which allows one to recast Eq. (25) as

$$P_d = \frac{|I|^2}{2\sigma\delta} = \frac{1}{2} R_s |I|^2 \tag{27}$$

This shows that P_d can be seen as the power dissipated per unit length in the surface impedance by the surface current I .

The skin depth δ and the surface impedance Z_s are independent of $k_x = k_0 \sin \theta^i$, that is, independent of the angle of incidence of the plane wave. The previous derivations can also be repeated for a TM (transverse magnetic) polarized plane wave leading to the same conclusions. Only the expressions Eqs. (20) and (21) for R and T will change. This means that the previous analysis remains valid for arbitrary plane waves incident on the conductor surface. The amplitudes of the fields inside the conductor will always decrease by a factor e after having traveled a distance δ given by Eq. (1), and the surface impedance Z_s is always given by Eq. (2) independent of the angle of incidence. Since an arbitrary incident field can always be expressed as a superposition of plane waves, these conclusions remain valid for arbitrary illuminations of the conductor. For more on the plane-wave interaction with conductors, we refer the reader to Stratton [1].

2.2. Curved Interfaces

To investigate the effect of curvature on the penetration of electromagnetic fields in a conductor, consider the structure of Fig. 2 consisting of a round wire, with radius r_0 ,

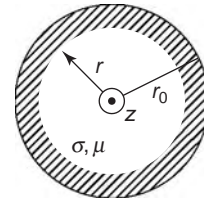


Figure 2. Round wire with radius r_0 , conductivity σ , and permeability μ stretched along the z axis.

conductivity σ , and permeability μ stretched along the z axis (see also Ref. 2). It is assumed that some time-harmonic z -directed current flows inside the wire that depends only on the radial coordinate r . Since $\mathbf{J} = \sigma\mathbf{E}$, it follows from Eq. (9) that the longitudinal current density J_z satisfies the equation

$$\frac{d^2 J_z}{dr^2} + \frac{1}{r} \frac{dJ_z}{dr} - j\omega\mu\sigma J_z = 0 \tag{28}$$

A general solution of this equation is $J_z = AJ_0[(1-j)r/\delta] + BY_0[(1-j)r/\delta]$ where $J_0(x)$ is the Bessel function and $Y_0(x)$ is the Neumann function of order zero and argument x . Since the current density needs to remain finite at the center of the wire, B should be zero. If J_z , at $r=r_0$, is denoted by $J_{z,0}$ then J_z can be expressed as

$$J_z = J_{z,0} \frac{J_0[(1-j)r/\delta]}{J_0[(1-j)r_0/\delta]} \tag{29}$$

In Fig. 3 $|J_z/J_{z,0}|$ is shown for different values of $a = \delta/r_0$ and compared with

$$\left| \frac{J_z}{J_{z,0}} \right| = |e^{-(1+j)(r_0-r)/\delta}| = e^{-(r_0-r)/\delta} \tag{30}$$

for a planar conductor with $r_0 - r$ the distance from the surface [see Eq. (23) with a change of coordinates]. One

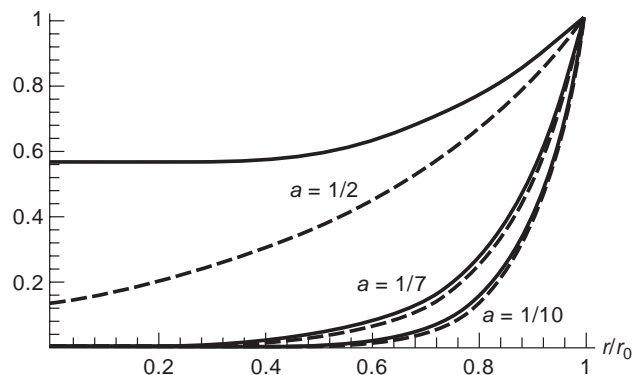


Figure 3. Current density distribution in a conducting wire (continuous lines) compared with the current distribution in a plane conductor (dashed lines) for different values of $a = r_0/\delta$ where r_0 is the radius of the wire and δ the skin depth.

notes that for $r_0 > 7\delta$ there is a good agreement between both results. This means that for $r_0 > 7\delta$ the conductor can be regarded to be planar (i.e., the curvature can be neglected) with respect to the skin effect.

The total current I flowing inside the wire is given by

$$\begin{aligned} I &= \oint_S \mathbf{J}_z dS = 2\pi \int_0^{r_0} J_{z,0} \frac{J_0[(1-j)r/\delta]}{J_0[(1-j)r_0/\delta]} dr \\ &= -\sqrt{2}\pi r_0 J_{z,0} (1+j)\delta \frac{J_0'[(1-j)r_0/\delta]}{J_0[(1-j)r_0/\delta]} \end{aligned} \quad (31)$$

The voltage drop V per unit length is given by $E_z = J_z/\sigma$ at $r = r_0$ or

$$V = \frac{J_{z,0}}{\sigma} \quad (32)$$

From Eqs. (31) and (32) it follows that the internal impedance per unit length of the wire is given by

$$\begin{aligned} Z_i &= \frac{V}{I} = -\frac{1-j}{2\sqrt{2}\pi r_0 \sigma \delta} \frac{J_0[(1-j)r_0/\delta]}{J_0'[(1-j)r_0/\delta]} \\ &= \frac{Z_s}{2\pi r_0} \frac{j}{\sqrt{2}} \frac{J_0[(1-j)r_0/\delta]}{J_0'[(1-j)r_0/\delta]} \end{aligned} \quad (33)$$

Comparing Z_i with $Z_s/(2\pi r_0)$ gives an indication of the radius of curvature above which it is possible to use the surface impedance Z_s for a planar conductor to calculate the internal impedance of a curved conductor. For a 10% error on R_s it is easily determined that r_0/δ should be larger than 5.5 and for the same error on ωL_i , r_0/δ should be larger than 2.2. In [3] the results shown in Fig. 3 are compared to spherically curved surfaces.

2.3. Thin Conducting Layer

Instead of a semiinfinite conducting space as shown in Fig. 1, consider a thin conducting layer with thickness d , conductivity σ , and permeability μ . This thin layer between $z=0$ and $z=d$ is embedded in free space. Assume fields inside this layer that only depend on the z coordinate. Taking an x and y dependence into account will not change the conclusions of this section. Assume also, without loss of generality, that the electric field is oriented along the y axis and the magnetic field along the x axis. If the displacement current in the layer is neglected, the total current I flowing in the conductor per unit length in the x direction is given by $I = \mathbf{J}_s \cdot \mathbf{u}_y$ with

$$\begin{aligned} \mathbf{J}_s &= \mathbf{u}_z \times [\mathbf{H}(z=d) - \mathbf{H}(z=0)] \\ &= [H_x(z=d) - H_x(z=0)] \mathbf{u}_y \end{aligned} \quad (34)$$

Maxwell's equations Eqs. (6) and (7) relate the electric and magnetic fields at $z=d$ and $z=0$:

$$\begin{aligned} H_x(z=d) &= -\frac{j}{Z_s \sin[(1-j)d/\delta]} \\ &\times \left\{ \cos\left[\frac{(1-j)d}{\delta}\right] E_y(z=d) - E_y(z=0) \right\} \end{aligned} \quad (35)$$

$$\begin{aligned} H_x(z=d) &= -\frac{j}{Z_s \sin[(1-j)d/\delta]} \\ &\times \left\{ E_y(z=d) - \cos\left[\frac{(1-j)d}{\delta}\right] E_y(z=0) \right\} \end{aligned} \quad (36)$$

From Eq. (34) it now follows that

$$I = -\frac{j[\cos[(1-j)d/\delta] - 1]}{Z_s \sin[(1-j)d/\delta]} [E_y(z=d) + E_y(z=0)] \quad (37)$$

The voltage drop over a unit distance caused by the current I is with good approximation given by $V \approx E_y(z=d/2) \approx \frac{1}{2}[E_y(z=d) + E_y(z=0)]$. This approximation is valid as long as the conductor is thin compared to the wavelength in free space. Hence, the internal impedance per unit square of the thin layer is given by

$$Z_i = \frac{V}{I} = \frac{Z_s \sin[(1-j)d/\delta]}{2j\{1 - \cos[(1-j)d/\delta]\}} = \frac{Z_s}{2j} \tan \frac{(1-j)d}{(2\delta)} \quad (38)$$

This means that under the aforementioned restrictions a thin conducting layer can be replaced with an infinitely thin conducting sheet with impedance Z_i .

In the low-frequency limit, that is, in the limit where the thickness d of the layer is small compared to the skin depth δ , one verifies that

$$Z_i = \frac{1}{\sigma d} \quad (39)$$

In this case the current density is homogeneously distributed over the conductor and the internal impedance becomes equal to the DC resistance of a planar conductor with thickness d .

At high frequencies, that is, when the thickness d of the layer exceeds several skin depths δ , one verifies that

$$Z_i = \frac{Z_s}{2} \quad (40)$$

In this case all the current is concentrated in thin sheets at the top and the bottom of the layer. Each of these current sheets yields an internal impedance Z_s . Since both impedances are in parallel, the total internal impedance is $Z_s/2$.

2.4. Surface Roughness

Because of the increased surface area, the surface resistance increases when the conductor has a rough surface. For limited surface roughness the relative increase of the surface resistance $\Delta R_s/R_s$ is proportional to the RMS

roughness ρ according to the empirical law

$$\frac{\Delta R_s}{R_s} = 0.29 \frac{\rho}{\delta} \quad (41)$$

This law is valid up to $\rho/\delta \approx 1.5$, independent of the type of material or frequency. At $\rho/\delta \approx 3$ the relative increase saturates at $\Delta R_s/R_s \approx 0.6$ [4]. Not only surface roughness but also porosity of the surface will substantially increase the surface resistance. The increase in resistivity will result in an increase of the dissipation according to the first part of Eq. (3).

2.5. Numerical Simulations

In numerical electromagnetic simulation techniques the finite conductivity is most easily taken into account by imposing the impedance boundary condition Eq. (22) instead of $\mathbf{E}_t = 0$ for perfect conductors. The relation Eq. (22) can also be expressed as

$$\mathbf{E}_t = Z_s \mathbf{J}_s \quad (42)$$

where \mathbf{J}_s is the current density concentrated at the surface.

Consider the electric field integral equation for perfect conductors of the form

$$0 = \lim_{r \rightarrow S} \left[\mathbf{E}_t^i(\mathbf{r}) + \int_S \overline{\overline{G}}_{tt}(\mathbf{r}|\mathbf{r}') \cdot \mathbf{J}_s(\mathbf{r}') dS' \right] \quad (43)$$

where $\mathbf{E}^i(\mathbf{r})$ is an incident electric field and $\overline{\overline{G}}_{tt}$ is the electric–electric Green dyadic. This integral equation is a Fredholm equation of the first kind. For a conductor with finite conductivity this integral equation is replaced by

$$Z_s \mathbf{J}_s = \lim_{r \rightarrow S} \left[\mathbf{E}_t^i(\mathbf{r}) + \int_S \overline{\overline{G}}_{tt}(\mathbf{r}|\mathbf{r}') \cdot \mathbf{J}_s(\mathbf{r}') dS' \right] \quad (44)$$

which is a Fredholm integral equation of the second kind.

Inclusion of the surface impedance in the finite-element method goes along the same lines as for integral equation techniques. Consider the functional for a volume V with surface S and internal sources \mathbf{J}

$$F(\mathbf{E}) = \frac{1}{2} \int_V [(\nabla \times \mathbf{E}) \cdot (\nabla \times \mathbf{E}) - k^2 \mathbf{E} \cdot \mathbf{E} + 2j\omega\mu \mathbf{E} \cdot \mathbf{J}] dV + j\omega\mu \int_S \mathbf{E} \cdot (\mathbf{u}_n \times \mathbf{H}) dS \quad (45)$$

where \mathbf{u}_n is the unit normal pointing into V and $k^2 = \omega^2 \epsilon \mu$. The surface impedance is now taken into account by replacing $\mathbf{u}_n \times \mathbf{H}$ in the surface integral term by $Z_s \mathbf{E}$.

The finite-difference time-domain technique is more complicated because of the frequency dependence of Z_s . Equation (22) has to be expressed in the time domain,

which involves a convolution integral

$$\mathbf{e}_t(t) = \mathbf{u}_n \times \int_0^t z_s(t-\tau) \mathbf{h}_t(\tau) d\tau \quad (46)$$

where $z_s(t)$ is the inverse Fourier transform of Z_s . After discretization with respect to time this convolution implies that in principle the magnetic fields of all previous time-steps need to be remembered. However, several techniques [5] have been developed to limit the number of field values that have to be stored. In these techniques the surface impedance is approximated by a series of first-order rational functions in ω .

When analyzing the eigenmodes of resonators, an important quantity is the quality factor of the resonances. If the walls of the resonator consist of good conducting material, the quality factor Q can be estimated very well from a calculation of the eigenmodes in a resonator with perfectly conducting walls followed by a perturbation analysis taking into account the wall losses due to the skin effect. If \mathbf{H}_m are the magnetic fields corresponding to a mode in the resonator, then Q is given by

$$Q = \frac{2}{\delta} \frac{\int_V |\mathbf{H}_m|^2 dV}{\int_S |\mathbf{u}_n \times \mathbf{H}_m|^2 dS} \quad (47)$$

where V is the volume of the resonator and S its surface [6].

For an eigenmode in a waveguide with conducting walls, the skin effect will give rise to an attenuation of the eigenmodes. Just as the quality factor for a resonator, the attenuation constant α_m of an eigenmode can be estimated from the fields \mathbf{E}_m and \mathbf{H}_m of the eigenmode propagating in a waveguide with perfectly conducting walls. If the waveguide is oriented along the z axis, then α_m is given by

$$\alpha_m = \frac{R_s}{2} \frac{\oint_c |\mathbf{u}_n \times \mathbf{H}_m|^2 dc}{\int_S (\mathbf{E}_m \times \mathbf{H}_m^*) \cdot \mathbf{u}_z dS} \quad (48)$$

where S is the crosssection of the waveguide and c is the contour cut out of the crosssection by the perfectly conducting walls. The attenuation of the eigenmode in dB/m is then given by $8.69 \alpha_m$.

In numerical simulations a thin conducting layer can be replaced by an infinitely thin sheet with a sheet condition given by

$$\mathbf{E}_t = Z_i \mathbf{u}_n \times \Delta \mathbf{H}_t \quad (49)$$

where Z_i is as given by Eq. (38) and $\Delta \mathbf{H}_t$ is the jump in the tangential magnetic field over the sheet. The tangential electric field \mathbf{E}_t remains continuous over the sheet.

BIBLIOGRAPHY

1. J. A. Stratton, *Electromagnetic Theory*, McGraw-Hill, New York, 1951, pp. 500, 605.

2. S. Ramo and J. R. Whinnery, *Fields and Waves in Modern Radio*, Wiley, New York, 1945, p. 196.
3. C. M. Butler and J. Van Bladel, Electromagnetic fields in a spherical cavity embedded in a dissipative medium, *IEEE Trans. Anten. Propag.* **AP-12**:110–118 (1964).
4. T. S. Saad, *The Microwave Engineers' Handbook*, Vol. 2, Artech House, Dedham, MA, 1971, p. 186.
5. K. S. Oh and J. E. Schutt-Aine, An efficient implementation of surface impedance boundary conditions for the finite-difference time-domain method, *IEEE Trans. Anten. Propag.* **AP-43**:660–666 (1995).
6. J. Van Bladel, *Electromagnetic Fields*, Hemisphere Publishing, Washington, DC, 1985, p. 305.

SKY WAVE PROPAGATION AT LOW FREQUENCIES

J. RALPH JOHLER
Johler Associates

Radiowaves generated by manufactured transmitters near the surface of the earth or radiowaves generated by such natural causes as cloud-to-ground lightning strokes propagate to great distances in a lateral direction between the surface of the earth and the ionized region between approximately 60 km and 100 km above the earth. This region is known as the lower ionosphere or the D and E regions of the ionosphere [1–8]. These radiowaves are called low-frequency (LF) *sky waves* in reference to this propagation phenomenon.

It is common practice to specify 30 kHz to 300 kHz as the LF part of the radio spectrum. This is somewhat arbitrary, and theoretical considerations described herein have been found to be useful far above and below this range of frequencies. In fact, the LF sky wave propagation theory can be used at the lower end of the very low-frequency (VLF) radio spectrum, and at the higher end of the medium-frequency (MF) radio spectrum. Traditionally, the mode theory is used at VLF [9], but the theoretical presentations herein can provide an interesting alternative.

Although LF sky waves have been used since the earliest days of radio science, vigorous study of these waves occurred mainly between 1950 and 1970 (see FURTHER READING). This research was in large measure a consequence of the development of precision pulsed ground-wave radio navigation and positioning systems. Although the ground wave is very stable with time of day, season, and so on, the ionospheric waves vary with time, and if such waves were not somehow sidestepped, the accuracy and precision of the navigation or positioning system would deteriorate. Thus, from an engineering point of view, LF sky waves were a problem in developing navigation systems such as Loran-C or Loran-D. One direct consequence of this research was the development of the *wave hop theory* of LF sky wave propagation, which will be introduced here. A discussion of Loran-C 100 kHz sky waves is given in Ref. 10.

1. EXPERIMENTS TO DETECT LOW-FREQUENCY SKY WAVES

An experimental pulse was radiated from a transmitter located in New York State during the 1953 preliminary tests of the Loran-C radio navigation system [2]. Figure 1(a,b,c) shows oscillograms of the observed pulse at distances west of the transmitter of 0, 1065, and 1381 km (or 0, 662, 858 statute miles), respectively. The electromagnetic (EM) field near the transmitter is vertically polarized and consists of a pulse that rises to a crest in 4 cycles, or 40 μ s. The observation at 1065 km was recorded at 12:55 A.M. EST and therefore includes reflections from the nighttime ionosphere at altitudes as great as 90 km. At 1381 km, the second pulse was recorded at 4:00 A.M. EST, and the shape reflects the changes that occur between day and night. Finally, the daytime pulse is shown at the distance 1381 km. Here, at 9:55 A.M., a daytime sky wave from the D region of the ionosphere dominates the pulse.

It is not difficult to realize that the severe distortion of the pulse is a consequence of multiple reflections from the ionosphere. Thus, many discrete pulses may arrive at the receiver at different delayed points in local times t' . Both the different propagation times and phase distortions resulting from reflection process cause constructive and destructive phase-type interference between the cycles of each pulse.

2. ELEMENTARY THEORETICAL CONSIDERATIONS

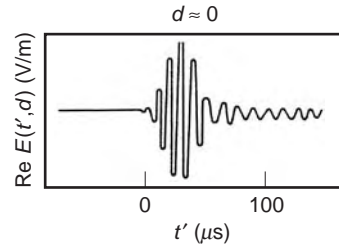
A theory to explain these observed phenomena has been constructed by applying Maxwell's equations to a model of the ionosphere and the earth. Before describing this theory, let us use some simple intuition and a simple model for the propagation environment. Consider the relationship between time and frequency:

$$\mathbf{E}(t', d) = \frac{1}{2\pi} \int_{-\infty}^{\infty} \exp(i\omega t) \mathbf{E}(\omega, d) f_s(\omega) d\omega \quad (1)$$

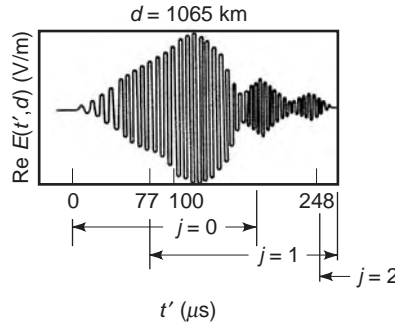
where $\mathbf{E}(t', d)$ is the propagated field at time t' at a distance d .

Here the transformed field $\mathbf{E}(\omega, d)$ depends on the frequency ω , and $t' = t - d/c$, where $c = 0.299792458$ m/ns, a constant, $\mathbf{E}(\omega, d)$, and $f_s(\omega)$ are transforms of the field and the source, respectively. The observed pulse is $\mathbf{E}(t, d)$, and Re in Fig. 1 denotes the real part [2].

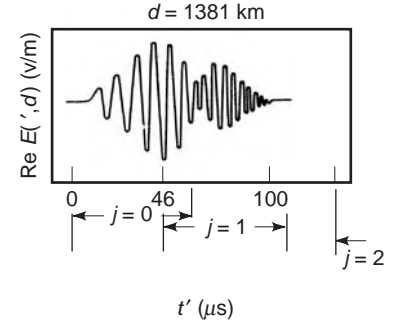
The earliest pulse to arrive at the receiver travels the shortest distance from the transmitter over the geodesic, d . This is the ground-wave pulse with the indexed order $j=0$. Pulses are also reflected from the ionosphere, but these pulses always arrive later in the local time (t')-domain. The earliest sky wave to arrive at the receiver at the greater distances occurs during daylight hours. The arrival of the first hop sky-wave is between 30 μ s and 40 μ s later than the arrival of the earliest precursor of the ground-wave pulse. Thus, the natural world allows only 30 μ s to 40 μ s of pure ground-wave pulse, in daylight hours, for operation of Loran-C. This difficulty was overcome by time-domain data sampling on the leading edge of



(a)



(b)



(c)

Figure 1. (a) Experimental LF pulse radiation close to the transmitter distance, $d \approx 0$, with a characteristic frequency of 100 kHz. (By permission of IEEE, Ref. 2). (b) Pulse observed at distance $d = 1065$ km at 12:55 A.M. EST, illustrating nighttime LF sky wave pulses, with characteristic frequency at 100 kHz. (By permission of IEEE, Ref. 2). (c) Pulse observed at a distance of 1381 km at 4:00 A.M. EST, illustrating early morning LF sky wave pulses. (By permission of IEEE, Ref. 2).

the pulse at a point (say less than $30 \mu\text{s}$ to $40 \mu\text{s}$) where pure ground-wave pulse energy can be found.

Figure 2 is a diagrammatic representation of the LF sky waves, valid in both the time and frequency domains of Eq. (1) [2,12]. The concept of a somewhat localized system of reflection coefficients, R and T , at the ground and at the ionosphere respectively is introduced there. For a spherical model of the earth with a concentric ionosphere as depicted in Fig. 2(a,b), a coordinate system is used such that the distance from the center of the earth to the surface of the ground is $r = a$ and at the ionosphere is $r = a + h$, where r is the radial distance from the center of the earth. The *geodesic distance* is $d = a\theta$, where θ is the angle at the earth's center. The lines connecting the source or transmitter (S) with the observer or receiver (O), via the various local reflecting regions both at the ground and at the ionosphere, are called *geometric-optical rays* [13] or *wave hops* [14], where the latter include diffraction around the curve of the earth. The ionosphere lower boundary is located at $r = a + h = g$. For $r\theta$ coordinates, the earth's surface is $r = a$. The earliest part of each sky wave pulse arrives at a time D_j/c , where

$$D_j = 2j[(a + h) \cos \phi_{i,j} - a \cos \tau_j]$$

in which

$\phi_{i,j}$ = angle of incidence on the ionosphere
 τ_j = angle of incidence on the earth

If the ionosphere were perfectly conducting (i.e., sharply bounded and of very high conductivity), the reflection coefficient would be $T = -1$. The composite reflection process with reflections at the ground, R , for any index j

would be

$$C_j = (-1)^j p_0^j R_e^{j-1} \quad (2)$$

where

R_e^{j-1} = $(j - 1)$ th earth reflection coefficient
 p_0^j = ionosphere-ground curvature focusing-defocusing factor.

If the ionosphere is simply imperfectly reflecting with a finite conductivity, an ionospheric reflection coefficient T can be introduced:

$$C_j = (T_{ee})^j p_0^j R_e^{j-1} \quad (3)$$

The subscript *ee* denotes vertical electric (TM, or transverse magnetic) polarization at both the source and the receiver (vertical means in the r direction).

As extensively discussed in the literature (Refs. 15–17, for example), the reflection process at the ionosphere is complicated by the effects of the earth's magnetic field on the reflection process. Thus, notwithstanding the fact that the excitation waves generated at the transmitter are pure vertical polarization (TM) waves, such waves arriving at the receiver, after reflecting from the ionosphere magnetoplasma, contain horizontally polarized (TE) wave components. These components of the reflected waves are shown in Fig. 2(a,b) as dashed lines. These dashed geometric-optical lines always originate at the ionosphere magnetoplasma. The ground, for most practical purposes, is considered to be isotropic.

The wave $j = 1$ is independent of the TE waves if the receiving antenna is a vertical structure (i.e., receives only TM waves). However, the wave $j = 2$ depends on the TE

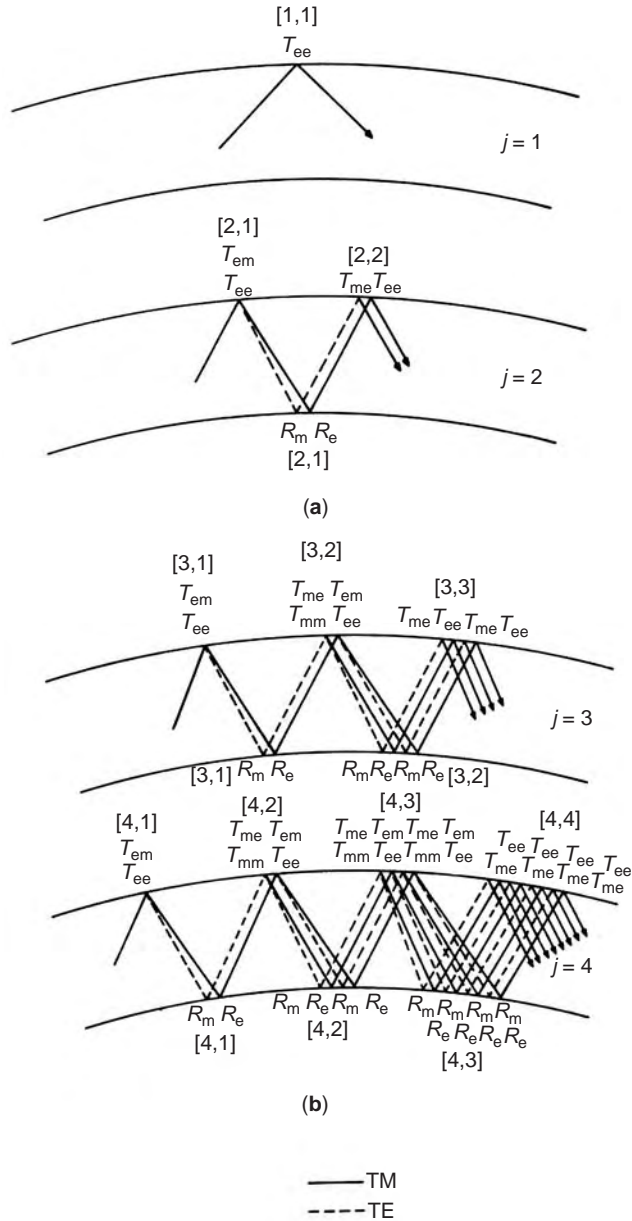


Figure 2. (a) Diagrammatic representation of LF sky waves, depicting an indexing method for identification of a series of time-domain pulses traveling laterally between the ground and the ionosphere, $j = 1, 2, 3, \dots$. Reflecting regions at the ionosphere are indicated as (j, k) , $j = 1, 2, 3, \dots$, $k = 1, 2, 3, \dots$. (From Ref. 11) (b) Diagrammatic representation of LF sky waves, depicting an indexing method for identification of a series of time-domain pulses traveling laterally between the ground and the ionosphere, $j = 2, 4, \dots$. Reflecting regions at the ionosphere are indicated as (j, k) , $j = 1, 2, 3, \dots$, $k = 1, 2, 3, \dots$. (From Ref. 11).

component, because this component is converted into TM waves at the second reflection point. Thus, in principle, one cannot escape the TE waves that originate in the ionosphere by using vertically polarized transmitting and receiving antennas.

The following reflection coefficients for TM and TE waves are defined as:

T_{ee} is the coefficient for the TM incident, TM reflected wave.

T_{mm} is the coefficient for the TE incident, TE reflected wave.

T_{em} is the TM-incident-TE-reflected conversion coefficient.

T_{me} is the TE-incident-TM-reflected conversion coefficient.

The coupling coefficients for transmission between vertically polarized transmission and reception can now be written as

$$C_1 = T_{ee}$$

$$C_2 = R_e T_{ee}^2 + R_m T_{em} T_{me}$$

$$C_3 = 2R_e R_m T_{ee} T_{em} T_{me} + R_e^2 T_{ee}^3 + R_m^2 T_{mm} T_{em} T_{me} \quad (4)$$

⋮

These equations can be generalized using matrix notation, for vertically polarized transmitters and receivers

$$G_e = \begin{bmatrix} R_e & 0 \\ 0 & -1 \end{bmatrix} \quad (5)$$

$$T = \begin{bmatrix} T_{ee} & T_{em} \\ T_{me} & T_{mm} \end{bmatrix} \quad (6)$$

$$G_m = p_0 \begin{bmatrix} 1 & 0 \\ 0 & -R_m \end{bmatrix}, \quad 1 = \begin{bmatrix} 1 & 0 \\ 0 & 1 \end{bmatrix} \quad (7)$$

$$(G_m T G_e)^{j-1} G_m T = p_0^j \begin{bmatrix} C_j & x_j \\ y_j & z_j \end{bmatrix} \quad (8)$$

3. THEORY OF PROPAGATION OF LOW-FREQUENCY SKY WAVES

As Eq. (1) is independent of Maxwell's equations, it is necessary only to construct a model for the propagation of the E field in the frequency-domain [2,12]. The propagation model usually employed to describe the LF sky waves in their natural environment is a finitely conducting spherical earth with radius $r = a$. This spherical earth is surrounded by a *magnetoplasma* comprising electrons, ions, and neutral particles with a superposed terrestrial magnetic field and a finite frequency of collision between particles. These particles go from random into orbital motion when excited by the LF electro-magnetic waves. Each particle has a finite collision frequency, which tends to dampen the activity. As the earth's magnetic field changes the particle motion from linear to orbital, and the direction of propagation of the EM wave may vary with respect to the terrestrial magnetic field, the ionospheric reflection process becomes anisotropic.

The detailed structure of the lower ionosphere between approximately 60 km and 100 km above the surface of the earth is well documented in the literature [3,18]. In the daytime, a layer of such plasma placed at 60 km and concentric with the earth usually serves as a simple model. This can be improved by introducing a large number of such concentric shells of plasma as a function of altitude, to take account of the variation of electron and ion density with altitude. Application of Maxwell's equations to this model results in a rigorous full-wave solution, if the ionosphere is assumed to be isotropic [1]. As is indicated in the discussion leading to Eq. (8) and in Refs. 4,15-17, the curved, concentric, isotropic ionosphere reflection coefficient is normally replaced by a suitable planar anisotropic reflection coefficient. This replacement involves the magneto-ionic theory with a full-wave (plane-wave) reflection coefficient. The spherical-wave focusing effect of the curve ionosphere can be retained in this process.

The LF radiowave field for a transmitter and receiver on the surface of the earth separated by a distance d can be represented rigorously by a system of waves traveling in the radial (r) direction

$$E_r = A \sum_{n=0}^{\infty} G(\theta, n) F(r, n) \tag{9}$$

Here

$$A = \frac{I_0 L \mu_0 c}{4\pi k_{-1}^2 a^4}$$

where $I_0 L$ is the current moment of the source, $\mu_0 = 4\pi \times 10^{-7}$ F/m, $c = 0.299792458$ m/ns, and the wave-number for the earth-ionosphere space is $k_{-1} = \omega/c$. We also define

$$k_{-2} = \frac{\omega}{c} \sqrt{\epsilon_{-2} - i \frac{\sigma_{-2}}{\epsilon_0 \omega}}$$

where σ_{-2} is the ground conductivity (s/m), $\omega = 2\pi f$, $\epsilon_0 = 1/c^2 \mu_0$, ϵ_{-2} is the relative dielectric constant of the ground, and f is the frequency (Hz). Furthermore,

$$G(\theta, n) = n(n+1)(2n+1)P_n(\cos \theta)$$

where $P_0(z) = 1, P_1(z) = z$, and

$$P_{n+1}(z) = \frac{2n+1}{n+1} z P_n(z) - \frac{1}{n+1} P_{n-1}(z), \quad n = 1, 2, \dots$$

Finally,

$$F(r, n) = \frac{\zeta_{-1a}^{(1)} \zeta_{-1a}^{(2)}}{\zeta_{-1a}^{(1)} \zeta_{-1a}^{(2)}} \frac{(1+R)(1+p_0 T_{ee})}{1-p_0 R T_{ee}} \tag{10}$$

where

$$p_0 = \frac{-\zeta_{-1a}^{(1)} - \zeta_{-1g}^{(2)}}{\zeta_{-1a}^{(2)} \zeta_{-1g}^{(1)}} \tag{11}$$

$$\zeta_{n+1}^{(1,2)}(z) = \frac{2n+1}{z} \zeta_n^{(1,2)}(z) - \zeta_{n-1}^{(1,2)}(z)$$

$$\zeta_0^{(1,2)}(z) = \pm \exp(\mp iz) \tag{12}$$

$$\zeta_{-1}^{(1,2)}(z) = \exp(\mp iz)$$

The abbreviation $\zeta_{-1a}^{(1,2)}$ means $\zeta_{-1}^{(1,2)}(k_{-1}a)$. The earth's reflection coefficient for the spherical waves is

$$R_e = \frac{\ln' \psi_{-1a} - \frac{k_{-1}}{k_{-2}} \ln' \psi_{-2a}}{-\ln' \zeta_{-1a}^{(2)} + \frac{k_{-1}}{k_{-2}} \ln' \psi_{-2a}}$$

$$\psi_n(z) = \frac{1}{2} [\zeta_n^{(1)}(z) + \zeta_n^{(2)}(z)]$$

where \ln' is the logarithmic derivative defined by

$$\ln' \psi_{-1a} = \left[\frac{\psi_n'(z)}{\psi_n(z)} \right]_{z=k_{-1}a}, \quad \psi_n'(z) = \frac{d}{dz} \psi_n(z)$$

These spherical wave functions are given in Ref. 19.

Equation (10) is derived from this isotropic model by identification of T_{ee} as the reflection coefficient of the lower boundary of this model. If T_{ee} is calculated by the recursion process described in Ref. 1, a rigorous solution of the problem for an arbitrary variation of the electron and ion densities with altitude can be found.

4. GEOMETRIC SERIES REPRESENTATION

Equation (10) can be expanded into a geometric series

$$F(r, n) = (1+R)(1+p_0 T_{ee}) \times \left(1 + \sum_{j=1}^{\infty} (p_0 R T_{ee})^j \right) \zeta_{-1a}^{(1)} \zeta_{-1a}^{(2)} \tag{13}$$

for

$$|p_0 R T_{ee}| < 1 \tag{14}$$

which converges absolutely. The propagated field of Eq. (9) can now be written

$$E_r = E_{r,0} + \sum_{j=1}^{\infty} E_{r,j} \tag{15}$$

where at the surface of the ground the zero-order term is the ground wave

$$E_{r,0} = B \sum_{n=0}^{\infty} G(\theta, n) \zeta_{-1a}^{(1)} \zeta_{-1a}^{(2)} (1+R_e) \tag{16}$$

Here

$$B = \frac{\mu_0 c}{8\pi} \frac{I_0 L}{k_{-1}^2 a^4}$$

and R_e is the ground reflection coefficient

$$1 + R_e = \frac{2i}{\zeta_{-1a}^{(1)} \zeta_{-1a}^{(2)} [-\ln' \zeta_{-1a}^{(2)} + (k_{-1}/k_{-2}) \ln' \zeta_{-1a}^{(2)}]}$$

where the logarithmic derivative is

$$\ln' \zeta_{-1a}^{(1,2)} = \left[\frac{\zeta_{-1a}^{(1,2)'}(z)}{\zeta_{-1a}^{(1,2)}(z)} \right]_{z=k_{-1}}$$

with

$$\zeta_n^{(1,2)'}(z) = \frac{d}{dz} \zeta_n^{(1,2)}$$

The quantity B contains $I_0 L$, the source dipole current moment, and $I_0 L = 1 \text{ A} \cdot \text{m}$ determines the \mathbf{E} -field amplitude.

A particular sky wave can now be written

$$E_{r,j} = B \sum_{n=0}^{\infty} G(\theta, n) \zeta_{-1a}^{(1)} \zeta_{-1a}^{(2)} (1 + R_e)^2 p_0 R_e^{j-1} T_{ee}^j \quad (17)$$

The anisotropic sky waves can now be written using Eqs. (5)–(8)

$$F(r, n) = (1 + R_e) \frac{|1 + G_m T|}{|1 - G_m G_e T|} \zeta_{-1a}^{(1)} \zeta_{-1a}^{(2)} \quad (18)$$

whereon expansion of the determinate ratio in a geometric series yields

$$F(r, n) = \zeta_{-1a}^{(1)} \zeta_{-1a}^{(2)} (1 + R_e) \times \left| \mathbf{I} + (\mathbf{I} + G_e) \sum_{j=1}^{\infty} (G_m G_e T)^{j-1} G_m T \right| \quad (19)$$

with

$$\mathbf{I} = \begin{bmatrix} 1 & 0 \\ 0 & 1 \end{bmatrix}$$

and so

$$E_{r,j} = \sum_{n=0}^{\infty} G(\theta, n) \zeta_{-1a}^{(1)} \zeta_{-1a}^{(2)} (1 + R_e)^2 p_0^j C_j \quad (20)$$

As the ground wave [17] has been removed as a separate entity, the summation of all the j -terms generalized by Eq. (19) is a full-wave solution for the LF sky waves in the presence of an anisotropic ionosphere. The method for inserting anisotropy is discussed in detail in

Refs. 1,14,10,21. Reference 11 describes a computer program to calculate this equation directly.

The ratio of the two determinants in Eq. (18) can be written

$$\frac{|\mathbf{I} + G_m T|}{|\mathbf{I} - G_m G_e T|} = \left| \left(\mathbf{I} + \sum_{j=1}^{\infty} G_m G_e T \right)^j (\mathbf{I} + G_m T) \right| \quad (21)$$

which is equivalent to the determinant in Eq. (19). This is analogous to the determinant given by Eq. (7) in Ref. 10.

Equation (21) was central to the development of a widely distributed computer program [22,23] based on the use of the asymptotic computation methods for spherical wave functions of complex, noninteger order n . This approach is based on Ref. 14.

The j -series expansion discussed above is called by its author the *wave hop series*. In this approach, Eq. (9) is rewritten in the complex v plane where a suitable contour c is used [24]:

$$E_r = \int_c f(v) (1 + R_e) \frac{|\mathbf{I} + G_m T|}{|\mathbf{I} - G_m G_e T|} dv \quad (22)$$

Here

$$f(v) = -iA \frac{v^3}{\cos v\pi} P_{v-1/2}(-\cos \theta) \zeta_{-1a}^{(1)} \zeta_{-1a}^{(2)} \quad (23)$$

where $P_{v-1/2}(-\cos \theta)$ is the Legendre function of complex order. The function [23] is the complex-order analog to

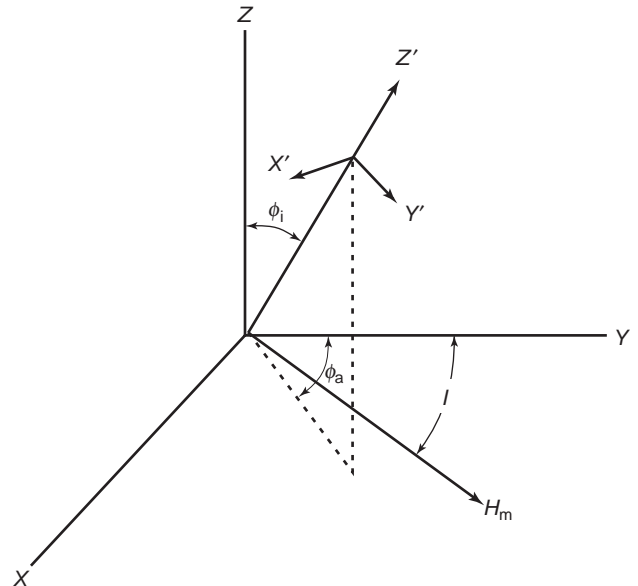


Figure 3. Coordinate system for each reflecting region of the ionosphere.

that given in Eq. (9), and we have [13].

$$\zeta_{-1a}^{(1,2)} = \zeta_{v-1/2}^{(1,2)}(k_{-1}a), \quad \zeta_{v-1/2}^{(1,2)}(z) = \sqrt{\frac{\pi z}{2}} H_v^{(1,2)}(z)$$

where $H_v^{(1,2)}(z)$ is the well-known Hankel function [24].

The spherical reflection coefficients introduced in Fig. 2 and used in Eqs. (16) and (17) can now be written

$$R_e = \frac{\zeta_{-1a}^{(1)'} - \frac{k_{-1}}{k_{-2}} D_{-2a} \zeta_{-1a}^{(1)}}{-\zeta_{-1a}^{(2)} + \frac{k_{-1}}{k_{-2}} D_{-2a} \zeta_{-1a}^{(2)}} \quad (24)$$

where

$$D_{-2a} = \frac{\zeta_{-2a}^{(m)'}}{\zeta_{-2a}^{(m)}} \approx (-1)^m \sqrt{\left(\frac{v}{k_{-2}a}\right)^2 - 1}$$

provided $n = v - \frac{1}{2}$. This is called the Debye approximation; it is used extensively in the literature, for example, Refs. 9,12,14,20,24, and 25. The isotropic reflection from the ionosphere lower boundary located at altitude h above the

earth, or $r = g = a + h$, is

$$T = T_{ee}^s = \frac{-\zeta_{1g}^{(2)}}{\zeta_{1g}^{(2)}} T_{ee} \quad (25)$$

$$T_{ee}^s = \frac{\zeta_{1g}^{(2)} - \frac{k_{-1}}{k_3} D_{3g} \zeta_{1g}^{(2)}}{-\zeta_{1g}^{(1)} + \frac{k_{-1}}{k_3} D_{3g} \zeta_{1g}^{(1)}} \quad (26)$$

where K_3 is an isotropic wavenumber representing a simple model ionosphere reflector. The angle of incidence on the ionosphere and the earth shown in Fig. 2(a-d) can now be identified

$$\phi_{ij} = \sin^{-1} \frac{v}{k_{-1}g}, \quad \tau_j = \sin^{-1} \frac{v}{k_{-1}a} \quad (27)$$

Using the expansion given in Eq. (21) for an anisotropic ionosphere and integrating each term of the series along a suitable contour in the complex v plane again gives the ground-wave analog of Eq. (16) and a series of terms, each of which is a particular sky wave analog of Eq. (17).

The reduction of Eq. (22) is detailed in Refs. 14 and 20.

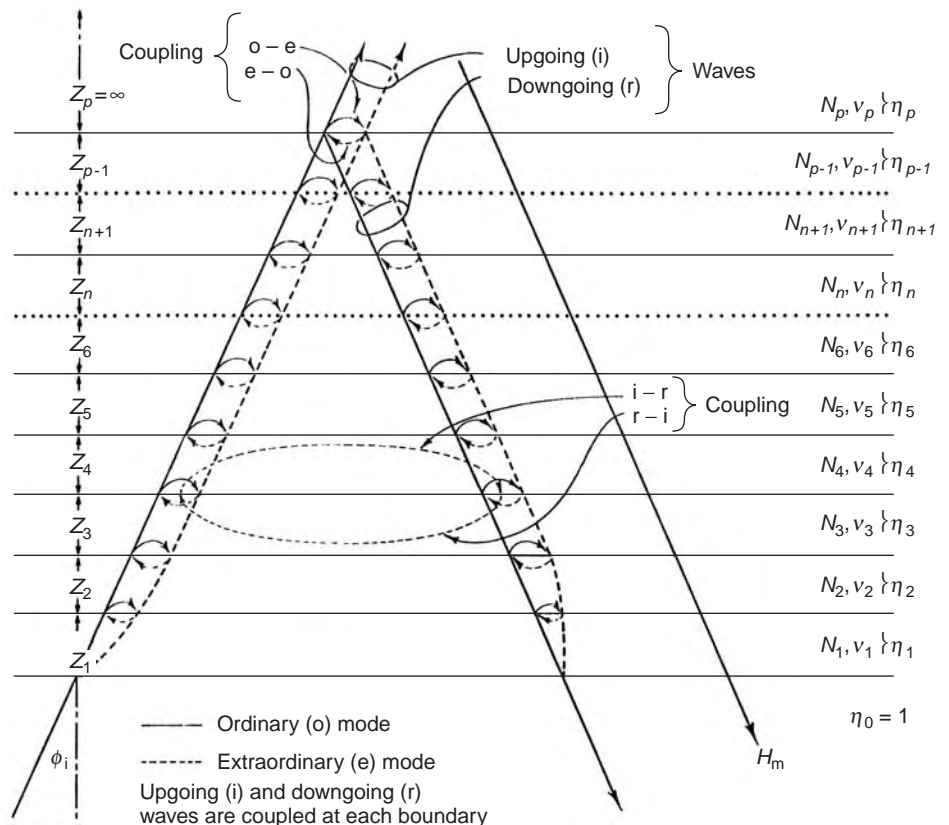


Figure 4. Magnetoplasma model showing detailed structure of the system of waves. The model is flexible, and the number of layers can be increased and the thickness decreased until convergence is obtained on electron-ion density profiles of the lower ionosphere. (After Ref. 2, by permission of IEEE).

The wave hop series now becomes

$$E_r = \int_c f(v)(1 + R_e) dv + \sum_{j=1}^{\infty} \int_c f(v)(1 + R_e)^2 p_0^j (a_j T_{ee} + c_j T_{me}) dv \quad (28)$$

$$\begin{bmatrix} a_j & b_j \\ c_j & d_j \end{bmatrix} = G_m^1 G_e T \begin{bmatrix} a_{j-1} & b_{j-1} \\ c_{j-1} & d_{j-1} \end{bmatrix} \quad (29)$$

where

$$G_m^1 = \frac{G_m}{p_0}$$

$$a_1 = 1 \quad c_1 = 0$$

$$a_j = R_e(T_{ee} a_{j-1} + T_{me} c_{j-1}) \quad \text{for } j \geq 2$$

$$c_j = R_m(T_{em} a_{j-1} + T_{mm} c_{j-1}) \quad \text{for } j \geq 2$$

Notwithstanding the fact that only TM waves have been excited and only TM waves are received at the receiver, a TE-type ground reflection coefficient is required at the ground as a result of the effects of the earth's magnetic

Table 1. Coefficients of Quartic Equation for an Electron Plasma

$$\begin{aligned} a_L &= \sin \phi_i \cos \phi_a, \quad a_T = \sin \phi_i \sin \phi_a \\ a_0 &= S_2^2 \left(1 - \frac{s}{s^2 - h^2} \right) + S_2 \left(\frac{1}{s} + \frac{s-2}{s^2 - h^2} + \frac{a_1^2 h_T^2}{s(s^2 - h^2)} \right) + \frac{s-1}{s(s^2 - h^2)} \\ a_1 &= 2 \frac{h_L h_T a_L}{s(s^2 - h^2)} S_2 \\ a_2 &= \left[2 \left(1 - \frac{s}{s^2 - h^2} \right) + \frac{h_L^2}{s(s^2 - h^2)} \right] S_2 + \frac{h_T^2 a_T^2}{s(s^2 - h^2)} + \frac{s-2}{s(s^2 - h^2)} \\ a_3 &= 2 \frac{h_L h_T a_L}{s(s^2 - h^2)} - a_L \sec^2 \phi_i \\ a_4 &= 1 - \frac{s^2 - h_L^2}{s(s^2 - h^2)} \\ s &= \frac{\omega^2}{\omega_N^2} \left(1 - i \frac{v}{\omega} \right), \quad S_2 = \sin^2 \phi_i - 1 \\ h &= \frac{\omega_H \omega}{\omega_N^2}, \quad h_L = h \sin I, \quad h_T = h \cos I \\ \omega_N^2 &= \frac{N e^2}{\epsilon_0 m} \\ \omega_H &= \frac{\mu_0 e H_m}{m} = \text{gyrofrequency} \end{aligned}$$

N and m are the electron number density and mass. H_m is the earth's magnetic intensity; I is the magnetic declination.

field on the ionosphere. Thus because of anisotropy, the TE ground reflection coefficient is required, as found explicitly in Refs. 20 and 23

$$R_m = \frac{\zeta_{-1a}^{(1)'} - \frac{k-2}{k-1} D_{-2a} \zeta_{-1a}^{(1)}}{\zeta_{-1a}^{(2)'} + \frac{k-2}{k-1} D_{-2a} \zeta_{-1a}^{(2)}} \frac{\zeta_{-1a}^{(2)}}{\zeta_{-1a}^{(1)}} \quad (30)$$

5. THEORY OF REFLECTION FROM THE IONOSPHERE

There remains to be explained a reflection process that leads to the four ionosphere reflection coefficients

$$T_{ee}, T_{mm}, T_{em}, T_{me}$$

The details leading to the mathematical theory of this reflection process are given in Refs. 4,15–17. Consider one of the reflecting regions at the ionosphere depicted in Fig. 2(a,b). The reflection process at one such region will now be given in detail.

The particle statistics of the electron-ion-neutral gas with superposed electrodynamic and magnetostatic fields was first treated in radio science between 1927 and 1931 [5–8] (see also Ref. 26, pp. 59–99).

The use of the full magneto-ionic theory to model LF sky wave propagation is given in Ref. 14. A local coordinate system is set up at a particular reflecting region depicted in Fig. 2. This Cartesian xyz coordinate system is shown in Fig. 3. The terrestrial magnetic field vector is contained in the yz plane. The EM wave propagates in the z' direction, and the wavefronts are contained in the $x'y'$ plane. The directions relative to the magnetic field vector are as follows:

ϕ_i is the angle of incidence.

ϕ_a is the magnetic azimuth.

I is the magnetic dip angle.

$\phi_{i,j}$ is now abbreviated to ϕ_i .

Figure 4 depicts a flexible model for the lower ionosphere. The plasma electron density is divided into layers. The thickness of each layer is decreased and the number of layers is increased until a stable reflection coefficient set is obtained for a particular electron number density, collision frequency, and so on. Figure 4 depicts ordinary and extraordinary propagation components coupled at each boundary. Each plasma slab, $n = 1, 2, 3, \dots, p$, becomes smaller as the number of slabs, p , is increased. The complex index of refraction for each layer in the model is obtained from a simultaneous solution of Maxwell's equations and the equation of motion in the velocity \mathbf{V} :

$$\begin{aligned} \nabla \times \mathbf{E} + \mu_0 \frac{\partial \mathbf{H}}{\partial t} &= 0 \\ \nabla \times \mathbf{H} - \mathbf{J} - \epsilon_0 \frac{\partial \mathbf{E}}{\partial t} &= 0 \end{aligned} \quad (31)$$

$$m \frac{d\mathbf{V}}{dt} + m v \mathbf{V} + \mu_0 e \mathbf{V} \times \mathbf{H} + e \mathbf{E} = 0 \quad (32)$$

Table 2. Reflection and Transmission Coefficient Matrices

$$\begin{bmatrix}
 a_{11}a_{12}a_{13}a_{14}a_{15}a_{16} \\
 b_{11}b_{12}b_{13}b_{14}b_{15}b_{16} \\
 c_{11}c_{12}c_{13}c_{14}c_{15}c_{16} \\
 d_{11}d_{12}d_{13}d_{14}d_{15}d_{16} \\
 \\
 a_{23}a_{24}a_{25}a_{26}a_{27}a_{28}a_{29}a_{2(10)} \\
 b_{23}b_{24}b_{25}b_{26}b_{27}b_{28}b_{29}b_{2(10)} \\
 c_{23}c_{24}c_{25}c_{26}c_{27}c_{28}c_{29}c_{2(10)} \\
 d_{23}d_{24}d_{25}d_{26}d_{27}d_{28}d_{29}d_{2(10)} \\
 \\
 a_{37}a_{38}a_{39}a_{3(10)}a_{3(11)}a_{3(12)}a_{3(13)}a_{3(14)} \\
 b_{37}b_{38}b_{39}b_{3(10)}b_{3(11)}b_{3(12)}b_{3(13)}b_{3(14)} \\
 c_{37}c_{38}c_{39}c_{3(10)}c_{3(11)}c_{3(12)}c_{3(13)}c_{3(14)} \\
 d_{37}d_{38}d_{39}d_{3(10)}d_{3(11)}d_{3(12)}d_{3(13)}d_{3(14)} \\
 \\
 \dots \\
 \dots \\
 \dots \\
 \dots \\
 \\
 a_{p(p+4)} \dots a_{p(p+9)} \\
 b_{p(p+4)} \dots b_{p(p+9)} \\
 c_{p(p+4)} \dots c_{p(p+9)} \\
 d_{p(p+4)} \dots d_{p(p+9)}
 \end{bmatrix}
 +
 \begin{bmatrix}
 T_{em} & T_{mm} \\
 T_{ee} & T_{me} \\
 U_{eio}^{(1)} & U_{mio}^{(1)} \\
 U_{eic}^{(1)} & U_{mie}^{(1)} \\
 U_{ero}^{(1)} & U_{mro}^{(1)} \\
 U_{ere}^{(1)} & U_{mre}^{(1)} \\
 U_{eio}^{(2)} & U_{mio}^{(2)} \\
 U_{eie}^{(2)} & U_{mie}^{(2)} \\
 U_{ero}^{(2)} & U_{mro}^{(2)} \\
 U_{ere}^{(2)} & U_{mre}^{(2)} \\
 \dots & \dots \\
 \dots & \dots \\
 \dots & \dots \\
 U_{eio}^{(p-1)} & U_{mio}^{(p-1)} \\
 U_{eie}^{(p-1)} & U_{mie}^{(p-1)} \\
 U_{ero}^{(p-1)} & U_{mro}^{(p-1)} \\
 U_{ere}^{(p-1)} & U_{mre}^{(p-1)} \\
 U_{eio}^{(p)} & U_{mio}^{(p)} \\
 U_{eic}^{(p)} & U_{mie}^{(p)}
 \end{bmatrix}
 +
 \begin{bmatrix}
 a_{oe} & a_{om} \\
 b_{oe} & b_{om} \\
 c_{oe} & c_{om} \\
 d_{oe} & d_{om}
 \end{bmatrix}
 = 0$$

where $\mu_0 = 4\pi \times 10^{-7}$ H/m, ν is the collision frequency, m is the electronic mass, and e is the electronic charge. Reference 4 extends these equations to include ions, and Ref. 17 provides an extension for collision rate proportional to energy [27–29]. The lower boundary of the model electron plasma (Fig. 3), below which ($z < 0$) the ionization is nil ($N = 0$), is taken as the xy plane. The region above the xy plane ($z > 0$) is characterized by an electron number density N , which, along with the collision frequency, varies with altitude z . A plane-wave incident on the ionosphere is assumed to be

$$\mathbf{E}_i = |\mathbf{E}_i| \exp \left[i \left(\omega t - \frac{\omega}{c} \eta D \right) \right] \tag{33}$$

Below the ionosphere, $\eta = \eta_0 = 1$. Here

$$D = x \sin \phi_i \sin \phi_a + y \sin \phi_i \cos \phi_a + z \cos \phi_i$$

A wave transmitted into the ionosphere is assumed to have the form

$$\mathbf{E}_t = |\mathbf{E}_t| \exp \left[i \left(\omega t - \frac{\omega}{c} \eta D \right) \right] \tag{34}$$

Elimination of the vectors \mathbf{V} and \mathbf{H} results in a quartic equation

$$\eta D = x \sin \phi_i \sin \phi_a + y \sin \phi_i \cos \phi_a + z \xi \tag{35}$$

$$a_4 \xi^4 + a_3 \xi^3 + a_2 \xi^2 + a_1 \xi + a_0 = 0$$

The detailed explicit expressions for the coefficients of this quartic are given in Table 1 for an electron

Table 3. Elements of Matrix Equation

$a_{11} = \cos \phi_i$	$b_{11} = -\sin \phi_i$
$a_{12} = -\cos \phi_i \sin \phi_a$	$b_{12} = -\cos \phi_i \cos \phi_a$
$a_{13} = -Q_{1o}^{(1)}$	$b_{13} = -1$
$a_{14} = -Q_{1e}^{(1)}$	$b_{14} = -1$
$a_{15} = -Q_{1ro}^{(1)}$	$b_{15} = -1$
$a_{16} = -Q_{1re}^{(1)}$	$b_{16} = -1$
$a_{23} = -a_{13} \exp\left(-i \frac{ga}{c} z_1 \zeta_{1o}^{(1)}\right)$	$b_{23} = \exp\left(-i \frac{ga}{c} z_1 \zeta_{1o}^{(1)}\right)$
$a_{24} = -a_{14} \exp\left(-i \frac{ga}{c} z_1 \zeta_{1e}^{(1)}\right)$	$b_{24} = \exp\left(-i \frac{ga}{c} z_1 \zeta_{1e}^{(1)}\right)$
$a_{25} = -a_{15} \exp\left(-i \frac{ga}{c} z_1 \zeta_{1ro}^{(1)}\right)$	$b_{25} = \exp\left(-i \frac{ga}{c} z_1 \zeta_{1ro}^{(1)}\right)$
$a_{26} = -a_{16} \exp\left(-i \frac{ga}{c} z_1 \zeta_{1re}^{(1)}\right)$	$b_{26} = \exp\left(-i \frac{ga}{c} z_1 \zeta_{1re}^{(1)}\right)$
$a_{27} = -Q_{2o}^{(2)}$	$b_{27} = -1$
$a_{28} = -Q_{2e}^{(2)}$	$b_{28} = -1$
$a_{29} = -Q_{2ro}^{(2)}$	$b_{29} = -1$
$a_{37} = -a_{27} \exp\left(-i \frac{ga}{c} z_2 \zeta_{2o}^{(2)}\right)$	$b_{37} = \exp\left(-i \frac{ga}{c} z_2 \zeta_{2o}^{(2)}\right)$
\vdots	\vdots
$a_{p(p+9)} = -Q_{1e}$	$b_{p(p+9)} = -1$

magnetoplasma. The coefficients for an electron-ion magnetoplasma are given in Ref. 4. The quartic equation is readily solved numerically with various computer programs that exist in the literature, such as Refs. 11 and 22. The complex index of refraction of a particular layer in the model now can be found

$$\eta^2 = \zeta^2 + \sin^2 \phi_i \quad (36)$$

The significance of the four roots of the quartic equation is depicted in Fig. 4. There are two upgoing waves, called the ordinary and the extraordinary upgoing wave. There are two downgoing waves, the ordinary and the extraordinary downgoing wave. These four waves are coupled at each boundary in the model and hence are modified by the change in electron density on each side of the boundary.

The boundary of each stratum, or plasma slab, is introduced through the continuity of the tangential \mathbf{E} and \mathbf{H} field components in Maxwell's equations. This is accomplished by equating the fields immediately above and

Table 4. Elements of Matrix Equation

$c_{11} = -\cos \phi_i \sin \phi_a$	$d_{11} = -\cos \phi_i \cos \phi_a$
$c_{12} = -\cos \phi_a$	$d_{12} = \sin \phi_a$
$c_{13} = -(a_L P_{1o}^{(1)} - \zeta_{1o}^{(1)})$	$d_{13} = -(\zeta_{1o}^{(1)} Q_{1o}^{(1)} - a_T P_{1o}^{(1)})$
$c_{14} = -(a_L P_{1e}^{(1)} - \zeta_{1e}^{(1)})$	$d_{14} = -(\zeta_{1e}^{(1)} Q_{1e}^{(1)} - a_T P_{1e}^{(1)})$
$c_{15} = -(a_L P_{1ro}^{(1)} - \zeta_{1ro}^{(1)})$	$d_{15} = -(\zeta_{1ro}^{(1)} Q_{1ro}^{(1)} - a_T P_{1ro}^{(1)})$
$c_{16} = -(a_L P_{1re}^{(1)} - \zeta_{1re}^{(1)})$	$d_{16} = -(\zeta_{1re}^{(1)} Q_{1re}^{(1)} - a_T P_{1re}^{(1)})$
$c_{23} = -c_{13} \exp\left(-i \frac{ga}{c} z_1 \zeta_{1o}^{(1)}\right)$	$d_{23} = -d_{13} \exp\left(-i \frac{ga}{c} z_1 \zeta_{1o}^{(1)}\right)$
$c_{24} = -c_{14} \exp\left(-i \frac{ga}{c} z_1 \zeta_{1e}^{(1)}\right)$	$d_{24} = -d_{14} \exp\left(-i \frac{ga}{c} z_1 \zeta_{1e}^{(1)}\right)$
$c_{25} = -c_{15} \exp\left(-i \frac{ga}{c} z_1 \zeta_{1ro}^{(1)}\right)$	$d_{25} = -d_{15} \exp\left(-i \frac{ga}{c} z_1 \zeta_{1ro}^{(1)}\right)$
$c_{26} = -c_{16} \exp\left(-i \frac{ga}{c} z_1 \zeta_{1re}^{(1)}\right)$	$d_{26} = -d_{16} \exp\left(-i \frac{ga}{c} z_1 \zeta_{1re}^{(1)}\right)$
$c_{27} = -(a_L P_{2o}^{(2)} - \zeta_{2o}^{(2)})$	$d_{27} = -(\zeta_{2o}^{(2)} Q_{2o}^{(2)} - a_T P_{2o}^{(2)})$
$c_{28} = -(a_L P_{2e}^{(2)} - \zeta_{2e}^{(2)})$	$d_{28} = -(\zeta_{2e}^{(2)} Q_{2e}^{(2)} - a_T P_{2e}^{(2)})$
$c_{29} = -(a_L P_{2ro}^{(2)} - \zeta_{2ro}^{(2)})$	$d_{29} = -(\zeta_{2ro}^{(2)} Q_{2ro}^{(2)} - a_T P_{2ro}^{(2)})$
$c_{210} = -(a_L P_{2re}^{(2)} - \zeta_{2re}^{(2)})$	$d_{210} = -(\zeta_{2re}^{(2)} Q_{2re}^{(2)} - a_T P_{2re}^{(2)})$
$c_{37} = -c_{27} \exp\left(-i \frac{ga}{c} z_2 \zeta_{2o}^{(2)}\right)$	$d_{37} = -d_{27} \exp\left(-i \frac{ga}{c} z_2 \zeta_{2o}^{(2)}\right)$
\vdots	\vdots
$c_{p(p+9)} = -(a_L P_{1e}^{(p)} - \zeta_{1e}^{(p)})$	$d_{p(p+9)} = -(\zeta_{1e}^{(p)} Q_{1e}^{(p)} - a_T P_{1e}^{(p)})$

immediately below each boundary, which results in the matrix equation in Table 2.

Using Fig. 3, the following transmission and reflection coefficients can be recovered by a numerical solution of the matrix equation in Table 2:

$$T_{ee} = \frac{E_{y'r}}{E_{y'i}}, \quad T_{em} = \frac{E_{x'r}}{E_{y'i}}$$

$$T_{me} = \frac{E_{y'r}}{E_{x'i}}, \quad T_{mm} = \frac{E_{x'r}}{E_{x'i}}$$

$$U(n)_{eio} = \frac{E_{yio}^{(n)}}{E_{y'i}}, \quad U(n)_{mio} = \frac{E_{yio}^{(n)}}{E_{x'i}}$$

$$U(n)_{eie} = \frac{E_{yie}^{(n)}}{E_{y'i}}, \quad U(n)_{mie} = \frac{E_{yie}^{(n)}}{E_{x'r}}$$

Table 5. Elements of Matrix Equation

$$\begin{aligned}
 a_{oe} &= \cos \phi_i \sin \phi_a & a_{om} &= \cos \phi_a \\
 b_{oe} &= \cos \phi_i \sin \phi_a & b_{om} &= -\sin \phi_a \\
 c_{oe} &= -\cos \phi_a & c_{om} &= \cos \phi_i \sin \phi_a \\
 d_{oe} &= \sin \phi_a & d_{om} &= \cos \phi_i \cos \phi_a \\
 A_1 &= -\left(a_L \zeta + \frac{h_T h_L}{s(s^2 - h^2)}\right) \left(1 - a_L^2 - \zeta^2 - \frac{s}{s^2 - h^2}\right) \\
 B_1 &= \left(a_L a_T - i \frac{h_L}{s^2 - h^2}\right) \left(a_T \zeta - i \frac{h_T}{s^2 - h^2}\right) \\
 C_1 &= -\left(1 - a_s^2 - \frac{s^2 - h_L^2}{s(s^2 - h^2)}\right) \left(a_L a_T - i \frac{h_L}{s^2 - h^2}\right) \\
 D_1 &= \left(a_T \zeta + i \frac{h_T}{s^2 - h^2}\right) \left(a_L \zeta + \frac{h_L h_T}{s(s^2 - h^2)}\right) \\
 E_1 &= \left(1 - a_s^2 - \frac{s^2 - h_L^2}{s(s^2 - h^2)}\right) \left(1 - a_L^2 - \zeta^2 - \frac{s}{s^2 - h^2}\right) \\
 F_1 &= -\left(a_T \zeta + i \frac{h_T}{s^2 - h^2}\right) \left(a_T \zeta - i \frac{h_T}{s^2 - h^2}\right) \\
 P &= \frac{A_1 + B_1}{E_1 + F_1} & Q &= \frac{C_1 + D_1}{E_1 + F_1}
 \end{aligned}$$

Here $\zeta = \zeta^{(n)}$, $P = P^{(n)}$, $Q = Q^{(n)}$ for a particular slab (Fig. 4), and $a_s = \sin \phi_i$; io, ie, ro, re refer to the four roots of Eq. (35).

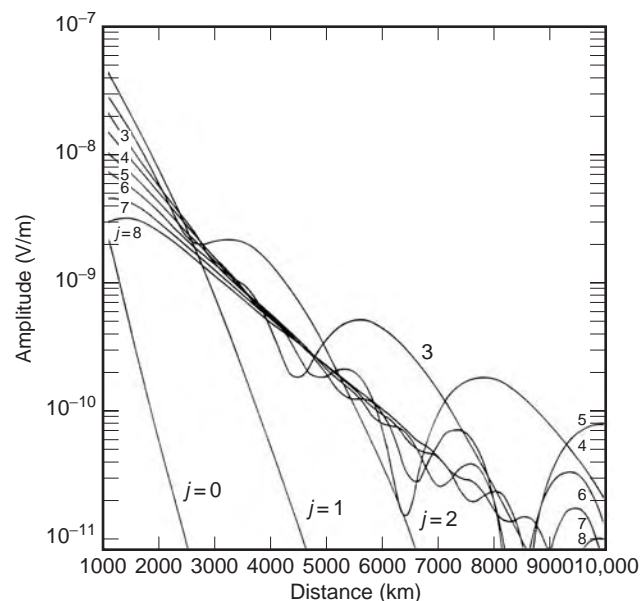


Figure 5. Amplitude of the total E field as a function of distance along the surface of the earth, together with the individual wave hops, $j=0$ (the ground wave), 1, 2, 3, ..., illustrating propagation in the presence of an ionosphere with infinite conductivity. (From Ref. 11 by permission IEEE [2].)

using the ratios $Q = E_x/E_y$, and $P = E_z/E_y$, where (Fig. 2) $n = 1, 2, 3, \dots, p-1$. The elements of the matrix equation in Table 2 are defined in Tables 3, 4, and 5 for an electron magnetoplasma.

6. SKY WAVE DIFFRACTION

The angle of incidence of the sky wave on the earth [Eq. (26)] is in general complex:

$$\tau_j = \frac{v}{k_{-1} a}$$

This is implied in the full-wave solutions given by Eqs. (16), (17), and (26). LF sky wave diffraction theory has been treated in Refs. 25, 30, and 31. However, it can now be demonstrated that the full-wave solution discussed herein implies sky wave diffraction into the earth's shadow region. The hypothetical ionosphere reflection was set equal to that of a perfect reflector [Eq. (2)], and Eqs. (16)

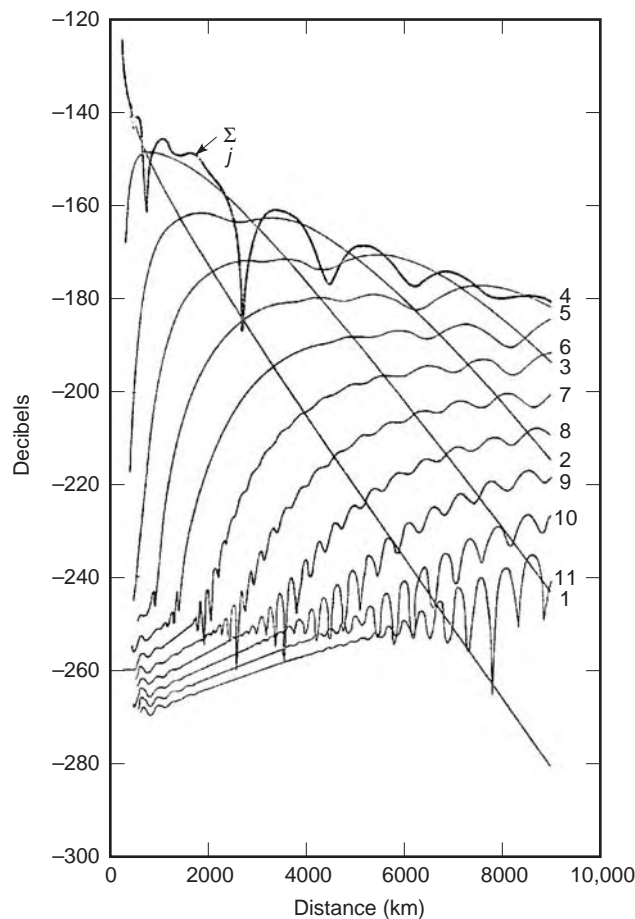


Figure 6. Amplitude of the total E field as a function of distance along the surface of the earth, together with the individual wave hops, $j=0$ (the ground wave), 1, 2, 3, ..., illustrating propagation in the presence of a sharply bounded semiinfinite plasma slab placed at the height $h=65$ km for a signal at 26.1 kHz and an assumed ratio of electron number density to collision frequency equal to 9.375 [1]. (From Ref. 1, by permission of AGU.)

and (17) were used to generate the wave hop series shown in Fig. 5. Each wave hop in Fig. 5— $j=0$ (the ground wave) and $j=1, 2, 3, \dots$ —will ultimately go beyond the geometric-optical horizon, and the attenuation finally takes on a slope as a function of distance like the ground wave. The conductivity of the ground is assumed to be 0.005 S/m with a dielectric constant of 15 relative to space. The frequency is 26 kHz, and the ionosphere height $h=65$ km.

A more sophisticated model of the ionosphere is shown in Fig. 6. Here a single sharply bounded electron plasma slab is placed at 65 km and extends uniformly out to infinity with a constant ratio of electron density to collision frequency of 9.375 [1]. The frequency is again 26 kHz. The influence of a finitely conducting ionosphere is here introduced into the model. Again, each sky wave at great distance attenuates with a slope parallel to that of the ground wave on this linear distance–decibel (logarithmic) amplitude scale. A rather interesting set of standing waves as a function of distance appears at shorter distances on the higher order wave hops. The total field, which sums the wave hops together with the ground wave, does not give any evidence of the existence of these waves.

It is concluded from Fig. 6 that the inclusion of a finitely conducting ionosphere is an important improvement in the modeling technique. At this juncture, one could still go further with the full-wave solution and use concentric spherical shells that follow known electron-density–collision-frequency profiles such as given in Ref. 1. However, this would not take into account the effects of the earth's magnetic field on the propagation. By following the procedures dictated by Eq. (20) or by using the asymptotic methods used with Eq. (28), the effects of a more realistic model can be generated as shown in Fig. 7.

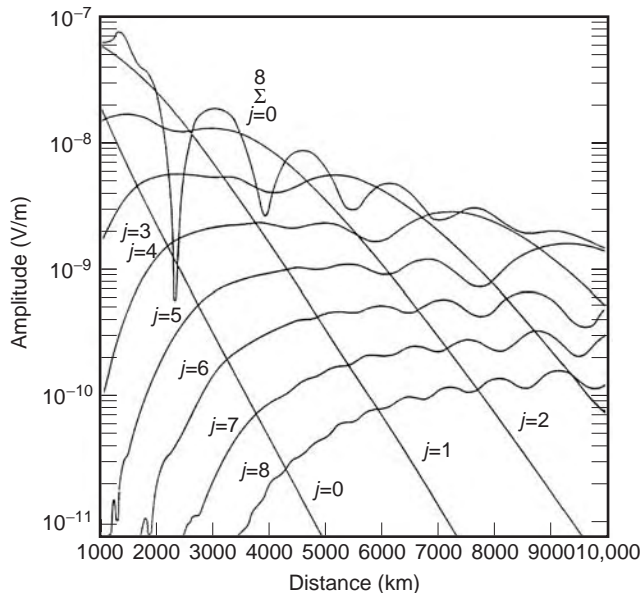


Figure 7. Sample wave hop calculation using the full magneto-ionic theory for the model given in Table 2, for a propagation path over sea water with magnetic parameters and ionosphere electron density profiles given in Ref. 11.

The electron density profile for the ionosphere is given in Ref. 11.

It is interesting to note that the standing waves on the individual wave hops are more highly damped as a function of distance. This is quite reasonable, because the ionosphere lower boundary is more diffuse (gradual) in this model. It therefore seems quite justified to use this more sophisticated model.

BIBLIOGRAPHY

1. J. R. Johler, Spherical wave theory for MF, LF, and VLF propagation, *Radio Sci.*, **5**:1429–1443 (1970).
2. J. R. Johler, Propagation of the low-frequency radio signal, *Proc. IRE*, **50**(4):404–427 (1962).
3. J. S. Belrose, L. A. Bound, and L. W. Hewitt, Ground based radio wave propagation studies of the lower ionosphere, *Proc. Conf.*, April 11–15, 1966, Defence Research Telecommunications Establishment, Radio Physics Lab., Defense Research Board, Dept. of National Defence, Shirley Bay, Ottawa, Canada, 1967.
4. J. R. Johler and L. A. Berry, On the effect of heavy ions on LF propagation, with special reference to a nuclear environment, *Natl. Bur. Stand. Tech. Note 313*, Washington, D.C.: U.S. Govt. Printing Office, 1965.
5. D. R. Hartree, *Proc. Cambridge Philos. Soc.*, **25**:27 (1927).
6. D. R. Hartree, The propagation of electro-magnetic waves in a refracting medium in a magnetic field, *Proc. Cambridge Philos. Soc.*, **27**:143 (1931).
7. E. V. Appleton, *J. Inst. Elec. Eng.*, **71**:642 (1932).
8. J. A. Ratcliffe, *The Magneto-ionic Theory and Its Applications to the Ionosphere*, Cambridge, UK: Cambridge Univ. Press, 1959.
9. J. R. Wait, *Electromagnetic Waves in Stratified Media*, New York: Pergamon, 1962.
10. G. Hefley, *The Development of Loran-C Navigation and Timing*, NBS Monograph 129, Washington, D.C.: U.S. Govt. Printing Office, 1972.
11. J. R. Johler and C. Mellecker, Theoretical LF, VLF field calculations with spherical wave functions of integer order, ESSA Tech. Rep. ERL 165ITS 106, Boulder, CO: U.S. Dept. of Commerce, Inst. for Telecommunication Sciences (ITS), 1970.
12. J. R. Johler, Propagation of an electromagnetic pulse from a nuclear burst, *IEEE Trans. Antennas Propag.*, **AP-15**: 256–263 (1967).
13. H. Bremmer, *Terrestrial Radio Waves*, New York: Elsevier, 1949.
14. L. A. Berry, Wave hop theory of long distance propagation of LF radio waves, *J. Res. Natl. Bur. Stand.*, **68D**:1275–1282 (1964).
15. J. R. Johler and J. D. Harper, Jr., Reflection and transmission of radio waves at a continuously stratified plasma with arbitrary magnetic induction, *J. Res. Natl. Bur. Stand.*, **66D**: 81–91 (1962).
16. J. R. Johler and J. D. Harper, Jr., On the effect of a solar disturbance on the LF ionosphere reflection process, *6th AGARD (NATO) Ionospheric Research Meeting*, May 15–18, 1961, Italy, New York: Pergamon, 1963.
17. J. R. Johler, On radio wave reflections at a continuously stratified plasma with collisions proportional to energy and arbitrary magnetic induction, *Proc. Int. Conf. Ionosphere*,

Imperial College, London, July, 1962, London: Inst. Phys., Phys. Soc., Chapman & Hall, 1963.

18. R. M. Davis and L. A. Berry, A revised model of the electron density in the lower ionosphere, Alexandria, VA: Defense Documentation Center, Cameron Station, 1977.
19. M. Abramowitz and I. A. Stegun, *Handbook of Mathematical Functions*, NBS, AMS 55, Washington, D.C.: U.S. Govt. Printing Office, 1964.
20. L. A. Berry, G. Gonzalez, and J. L. Lloyd, Wave hop series for an anisotropic ionosphere, *Radio Sci.*, 4:1021–1027 (1969).
21. J. R. Johler, Zonal harmonics in low frequency terrestrial radio wave propagation, Natl. Bur. Stand. Tech. Note 335, Washington, DC.: Supt. of Documents, U.S. Govt. Printing Office, 1966.
22. L. A. Berry and J. E. Herman, A wave hop propagation program for an anisotropic ionosphere, OT/ITS Res. Rep. 11, Boulder, CO: U.S. Dept. of Commerce, Inst. for Telecommunication Sciences (ITS), 1971.
23. J. K. Oliver, Jr., G. Gonzalez, and J. L. Lloyd, LF–VLF propagation analysis computer program documentation, RADC-TR-68-453, Rome, NY: Rome Air Development Center, 1968.
24. J. R. Johler and L. A. Berry, *A Complete Mode Sum for LF, VLF, ELF Terrestrial, Radio Wave Fields*, NBS Monograph 78, Washington, D.C.: U.S. Govt. Printing Office, 1964.
25. J. R. Wait, A diffraction theory for LF sky-wave propagation, *J. Geophys. Res.*, 66:1713–1724 (1961).
26. K. Davies, *Ionospheric Radio Propagation*, NBS Monograph 80, Washington, D.C.: U.S. Govt. Printing Office, 1965.
27. A. V. Phelps, Propagation constants for electromagnetic waves in weakly ionized, dry air, *J. Appl. Phys.*, 21: 1723–1729 (1960).
28. P. Molmud, Langevin equation and the ac conductivity of non-maxwellian plasmas, *J. Phys. Res.*, 114:29–32 (1959).
29. R. B. Dingle, D. Arndt, and S. K. Roy, The integrals $E_p(x)$ and $D_p(x)$ and their tabulation, *Appl. Sci. Res.*, 6B:155–164 (1956).
30. L. A. Berry and M. C. Chrisman, Numerical values for the path integrals for low and very low frequencies, NBS Tech. Note 319, Washington, D.C.: U.S. Govt. Printing Office, 1965.
31. O. E. H. Rydbeck, On the propagation of radio waves, *Trans. Chalmers Univ.*, 34, 1944.

FURTHER READING

- L. A. Berry and R. M. Jones, A time-varying electron density model for LF/VLF propagation calculations, OT/ITSTM 3, Boulder, CO: U.S. Dept. of Commerce, Inst. for Telecommunication Sciences (ITS), 1970.
- J. R. Johler, On the analysis of LF ionospheric radio propagation phenomena, *J. Res. Natl. Bur. Stand Radio Propag.*, 65D:5 (1961).
- J. R. Johler, Theory of propagation of low frequency terrestrial radio waves—mathematical techniques for the interpretation of D-region propagation studies, 1966 *Ottawa Conf. Proc.*, 2:399–422 (1967). See also Ref. 3.
- J. R. Wait, Terrestrial propagation of very low frequency radio waves, *J. Res. Natl. Bur. Stand. D Radio Propag.*, 64D:183–204 (1960).

SKY WAVE PROPAGATION AT MEDIUM AND HIGH FREQUENCIES

KENNETH DAVIES
National Oceanic and
Atmospheric Administration

1. SPECTRUM CONSIDERATIONS

Medium frequencies and high frequencies are usually defined as the frequency bands from 300 kHz to 3000 kHz and from 3 MHz to 30 MHz, respectively. However, as far as ionospheric propagation is concerned, there are no sharp divisions. The medium-frequency band is dominated by the amplitude modulated (AM) broadcasting band between about 500 kHz and 1700 kHz, which is designed primarily for ground-wave usage. On the other hand, high-frequency systems are designed for long-distance sky wave propagation and for some 50 years (from about 1925 to about 1975) provided the primary vehicle for global communications. High frequencies are still used extensively for communications because of the following advantages: (1) low cost of terminal equipment, (2) low power requirements, and (3) adequate bandwidths. By contrast, medium frequencies suffer heavy ionospheric absorption during daytime and, therefore, there is relatively little cochannel interference; whereas by night, when the absorption is small, interference between closely spaced channels is common. High-frequency sky waves suffer from several disadvantages brought about by (1) the temporal and geographical variability of the ionosphere, (2) the large number of possible propagation paths and the consequent time dispersion of the resulting signal, (3) large and rapid amplitude and phase fluctuations, (4) high interference because of spectrum congestion, and (5) frequency distortion of wideband signals. An important disadvantage is the occurrence of several types of ionospheric disruptions caused by solar disturbances. These disruptions can be hemispheric, such as those on the dayside caused by bursts of solar X rays (sudden ionospheric disturbances) or confined mostly to high latitudes (e.g., polar cap disturbances and ionospheric storms that originate in the auroral zones and spread to populated middle latitudes). Ionospheric storms are major concerns for high-frequency (HF) users. They occur mostly at high sunspot numbers when the higher critical frequencies help to mitigate their adverse effects.

In this article, we shall discuss the following topics:

1. Basic physical properties of sky wave propagation (namely, refraction, reflection, penetration, and absorption)
2. relationships between vertical propagation and oblique propagation
3. ionospheric models
4. characteristics of medium frequencies
5. characteristics of high frequencies

- Imperial College, London, July, 1962, London: Inst. Phys., Phys. Soc., Chapman & Hall, 1963.
18. R. M. Davis and L. A. Berry, A revised model of the electron density in the lower ionosphere, Alexandria, VA: Defense Documentation Center, Cameron Station, 1977.
 19. M. Abramowitz and I. A. Stegun, *Handbook of Mathematical Functions*, NBS, AMS 55, Washington, D.C.: U.S. Govt. Printing Office, 1964.
 20. L. A. Berry, G. Gonzalez, and J. L. Lloyd, Wave hop series for an anisotropic ionosphere, *Radio Sci.*, 4:1021–1027 (1969).
 21. J. R. Johler, Zonal harmonics in low frequency terrestrial radio wave propagation, Natl. Bur. Stand. Tech. Note 335, Washington, DC.: Supt. of Documents, U.S. Govt. Printing Office, 1966.
 22. L. A. Berry and J. E. Herman, A wave hop propagation program for an anisotropic ionosphere, OT/ITS Res. Rep. 11, Boulder, CO: U.S. Dept. of Commerce, Inst. for Telecommunication Sciences (ITS), 1971.
 23. J. K. Oliver, Jr., G. Gonzalez, and J. L. Lloyd, LF–VLF propagation analysis computer program documentation, RADC-TR-68-453, Rome, NY: Rome Air Development Center, 1968.
 24. J. R. Johler and L. A. Berry, *A Complete Mode Sum for LF, VLF, ELF Terrestrial, Radio Wave Fields*, NBS Monograph 78, Washington, D.C.: U.S. Govt. Printing Office, 1964.
 25. J. R. Wait, A diffraction theory for LF sky-wave propagation, *J. Geophys. Res.*, 66:1713–1724 (1961).
 26. K. Davies, *Ionospheric Radio Propagation*, NBS Monograph 80, Washington, D.C.: U.S. Govt. Printing Office, 1965.
 27. A. V. Phelps, Propagation constants for electromagnetic waves in weakly ionized, dry air, *J. Appl. Phys.*, 21: 1723–1729 (1960).
 28. P. Molmud, Langevin equation and the ac conductivity of non-maxwellian plasmas, *J. Phys. Res.*, 114:29–32 (1959).
 29. R. B. Dingle, D. Arndt, and S. K. Roy, The integrals $E_p(x)$ and $D_p(x)$ and their tabulation, *Appl. Sci. Res.*, 6B:155–164 (1956).
 30. L. A. Berry and M. C. Chrisman, Numerical values for the path integrals for low and very low frequencies, NBS Tech. Note 319, Washington, D.C.: U.S. Govt. Printing Office, 1965.
 31. O. E. H. Rydbeck, On the propagation of radio waves, *Trans. Chalmers Univ.*, 34, 1944.

FURTHER READING

- L. A. Berry and R. M. Jones, A time-varying electron density model for LF/VLF propagation calculations, OT/ITSTM 3, Boulder, CO: U.S. Dept. of Commerce, Inst. for Telecommunication Sciences (ITS), 1970.
- J. R. Johler, On the analysis of LF ionospheric radio propagation phenomena, *J. Res. Natl. Bur. Stand Radio Propag.*, 65D:5 (1961).
- J. R. Johler, Theory of propagation of low frequency terrestrial radio waves—mathematical techniques for the interpretation of D-region propagation studies, 1966 *Ottawa Conf. Proc.*, 2:399–422 (1967). See also Ref. 3.
- J. R. Wait, Terrestrial propagation of very low frequency radio waves, *J. Res. Natl. Bur. Stand. D Radio Propag.*, 64D:183–204 (1960).

SKY WAVE PROPAGATION AT MEDIUM AND HIGH FREQUENCIES

KENNETH DAVIES
National Oceanic and
Atmospheric Administration

1. SPECTRUM CONSIDERATIONS

Medium frequencies and high frequencies are usually defined as the frequency bands from 300 kHz to 3000 kHz and from 3 MHz to 30 MHz, respectively. However, as far as ionospheric propagation is concerned, there are no sharp divisions. The medium-frequency band is dominated by the amplitude modulated (AM) broadcasting band between about 500 kHz and 1700 kHz, which is designed primarily for ground-wave usage. On the other hand, high-frequency systems are designed for long-distance sky wave propagation and for some 50 years (from about 1925 to about 1975) provided the primary vehicle for global communications. High frequencies are still used extensively for communications because of the following advantages: (1) low cost of terminal equipment, (2) low power requirements, and (3) adequate bandwidths. By contrast, medium frequencies suffer heavy ionospheric absorption during daytime and, therefore, there is relatively little cochannel interference; whereas by night, when the absorption is small, interference between closely spaced channels is common. High-frequency sky waves suffer from several disadvantages brought about by (1) the temporal and geographical variability of the ionosphere, (2) the large number of possible propagation paths and the consequent time dispersion of the resulting signal, (3) large and rapid amplitude and phase fluctuations, (4) high interference because of spectrum congestion, and (5) frequency distortion of wideband signals. An important disadvantage is the occurrence of several types of ionospheric disruptions caused by solar disturbances. These disruptions can be hemispheric, such as those on the dayside caused by bursts of solar X rays (sudden ionospheric disturbances) or confined mostly to high latitudes (e.g., polar cap disturbances and ionospheric storms that originate in the auroral zones and spread to populated middle latitudes). Ionospheric storms are major concerns for high-frequency (HF) users. They occur mostly at high sunspot numbers when the higher critical frequencies help to mitigate their adverse effects.

In this article, we shall discuss the following topics:

1. Basic physical properties of sky wave propagation (namely, refraction, reflection, penetration, and absorption)
2. relationships between vertical propagation and oblique propagation
3. ionospheric models
4. characteristics of medium frequencies
5. characteristics of high frequencies

- 6. prediction programs for ionospheric sky wave performance
- 7. real-time channel evaluation

There is extensive literature in the field of ionospheric radio propagation, and the interested reader is referred to books by Davies [1], Goodman [2], Hunsucker [3], and McNamara [4] and the bibliographies therein. Groundwaves are particularly important on medium frequencies (see RADIOWAVE PROPAGATION CONCEPTS).

2. PROPAGATION CHARACTERISTICS

2.1. The Ionosphere

Sky waves result from radio refraction and reflection from the ionosphere. The ionosphere is usually defined as that part of the upper atmosphere where sufficient ionization exists to affect the propagation of radiowaves. The ionosphere lies between about 50 km and about 2000 km. The peak electron density usually occurs in the F region (above 140 km) (Fig. 1). The F region often contains two layers: the lower F1 layer and the upper F2 layer. Below the F region is the E region (90 km to 140 km), which contains the normal E layer and sporadic E. The D region (50 km to 90 km) contains the D layer and the C, or cosmic ray, layer. Above the F peak is the topside, and above about 2000 km is the protonosphere. The boundaries between these regions are not well defined. The alphabetic nomenclature was introduced by Appleton (see Ref. 1, Sec. 1.1), who used the letter E for electric and F for field. These letters left room for the discovery of other layers. Ionospheric electron densities vary by orders of magnitude depending on altitude, time of day, season, sunspot number, solar distur-

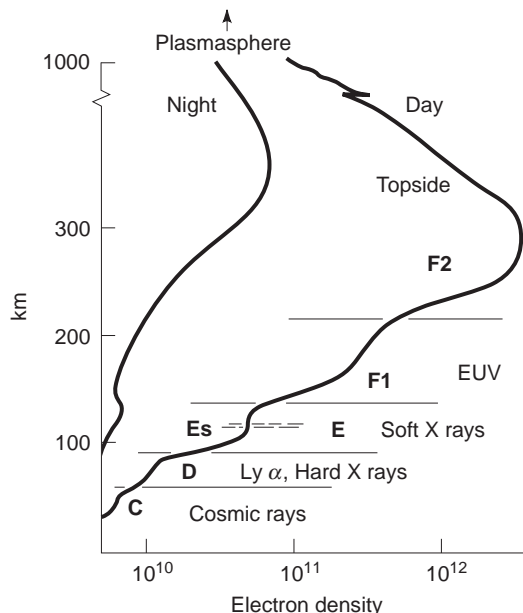


Figure 1. Ionospheric structure on a summer day and night in middle latitudes, and the main bands of solar and cosmic-ray ionizing radiations.

bances, and geographical location. It is this variability that renders sky waves so difficult to manage.

2.2. Refraction, Reflection, and Penetration

In an ionized plasma, with electron density $N \text{ el} \cdot \text{m}^{-2}$, in the absence of collisions and an external magnetic field, the radio refractive index μ of a wave of frequency f Hz, is given by

$$\mu^2 = 1 - (f_N/f)^2 = 1 - 80.5N/f^2 \tag{1}$$

where f_N is the plasma frequency in Hz. Ionospheric electron densities are such that typical E layer and F layer plasma frequencies lie in the range from 0.5 MHz to 30 MHz. Thus, for medium and high frequencies, the refractive index of the ionosphere is less than unity and application of Snell's law shows that, on entry into the ionosphere, a wave is refracted away from the vertical. When the electron density is sufficient, the direction of propagation becomes horizontal and reflection occurs. The main sky wave propagation mechanisms are illustrated in Fig. 2: absorption, reflection, scatter, and penetration. When the maximum electron density is insufficient, the wave penetrates; this is essential for ground-to-satellite communication. As ionospheric scatter propagation is considered elsewhere, it will not be discussed in detail in this article.

2.3. Absorption

The neutral atmosphere affects the propagation of radiowaves because of electron-neutral collisions that convert

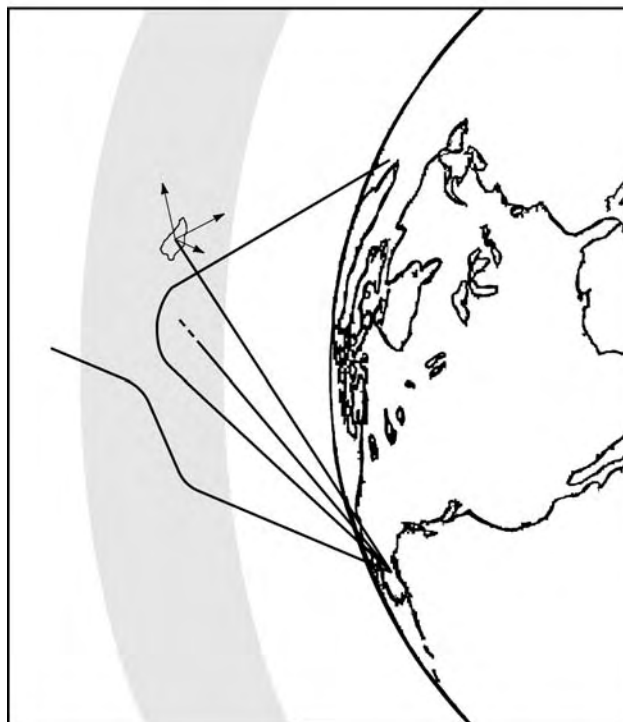


Figure 2. The four main mechanisms in MF and HF sky wave propagation: absorption, reflection, scatter, and penetration.

the ordered momentum of the wave into heat and electromagnetic noise. To a first approximation, the loss L , in decibels per kilometer, is

$$L = 0.00117N\nu/\mu f^2 \quad (2)$$

where ν is the number of collisions made by one electron per second. From Eq. (2), we see that with $\mu \approx 1$, the non-deviative absorption is inversely proportional to the frequency squared so that, in general, signals are stronger on high frequencies than on medium frequencies. The product $N\nu$ maximizes in the D region. The loss L can be large where $\mu \approx 0$; this deviative absorption occurs near reflection, or where there is pronounced refraction of the wave.

2.4. Effects of the Earth's Magnetic Field

The earth's magnetic field affects sky waves by splitting the incident wave into ordinary and extraordinary waves that are oppositely polarized and by affecting the global structure of the ionosphere (see ELECTROMAGNETIC WAVES IN THE IONOSPHERE). The ordinary (o) wave is polarized such that, with the thumb pointing in the direction of the earth's magnetic field, the electric field rotates in a left-handed sense, whereas the extraordinary (x) wave rotates in a right-handed sense. For example, an incident, vertically polarized wave on exit from the ionosphere will be elliptically polarized, which depends on the relative amplitudes and polarizations of the emerging o and x waves. The relative amplitudes of the o and x waves are determined by the extent to which the incident power is divided between the two component waves and the relative absorptions of the two waves thereafter. The relative absorptions are

$$L(o, x) = A/(f \pm f_H)^2 \quad (3)$$

where the $+$ sign refers to the ordinary wave and the $-$ sign to the extraordinary wave, and A is essentially the same for both waves. The electron gyrofrequency f_H is the natural frequency of rotation of an electron (right-handed) about the magnetic field. In the ionosphere, f_H varies from about 0.8 MHz at the magnetic equator to about 1.6 MHz near the magnetic poles. Current models of the geomagnetic field are available on the Internet (e.g., see Ref. 5). Equation (3) shows that the absorption of the ordinary wave is less than that of the extraordinary wave, so that an antenna should be designed to excite as much of the ordinary wave as possible (see Ref. 1, Sec. 7.6).

The global effects of the geomagnetic field are two-fold. Near the magnetic equator there is an F2-layer anomaly in which the peak electron densities maximize in the late afternoon at magnetic latitudes near $\pm 15^\circ$. Magnetic latitude Φ is defined in terms of the dip angle I by which the earth's magnetic field dips below the horizontal.

$$\tan \Phi = 0.5 \tan I \quad (4)$$

Another way in which the earth's field affects the ionosphere is via the precipitation of magnetospheric charged particles into the polar caps and the auroral zones (65° to

70° magnetic latitude), where energy is deposited that produces ionospheric storms. In the auroral zones, D-region electron densities are enhanced producing auroral absorption. Energetic solar protons enter the atmosphere over the polar caps (latitudes $> 70^\circ$) and produce intense polar cap absorption (PCA) that can black out HF signals for several days.

3. VERTICAL AND OBLIQUE PROPAGATION

3.1. Equivalence of Vertical and Oblique Reflection

Equation (1) shows that, with a radiowave incident at an angle ϕ with the vertical on a plane ionosphere, reflection occurs when

$$f_N = f \cos \phi \quad (5)$$

With vertical propagation, $\phi = 0^\circ$, so $f = f_N$ and, therefore, for a given maximum electron density (i.e., maximum f_N) a maximum, or critical, frequency is reflected. With oblique propagation, the maximum frequency depends jointly on the critical frequency and on the incident angle, which is determined by the ground range and the layer height. The subject of vertical-to-oblique conversion has been discussed extensively by numerous authors (e.g., Ref. 1, Chapter 6; Ref. 2, Chapter 4; Ref. 4, Chapter 4). With a flat earth and flat ionosphere, the relationship between a frequency f_o incident obliquely at an angle ϕ and a frequency f_v reflected vertically from the same true height is

$$f_o = f_v \sec \phi = f_v [1 + (D/2h')^2]^{1/2} \quad (6)$$

where D is the ground range and h' is the virtual height of reflection. The variation of virtual height with frequency is called an ionogram, and the relationship between $\sec \phi$ and h' , when presented graphically, is called a transmission curve. The intersection of a transmission curve with the ionogram trace gives the virtual heights of reflection of the obliquely traveling signal. When the transmission curve is tangent to the ionogram, we have the maximum reflected frequency. On frequencies below the maximum frequency, there are two intersections of the transmission curve and the ionogram trace (for a single layer) showing that, for a given ground range, there is a low-angle ray and a high-angle ray. Modifications to the plane ionosphere geometry are required for ground ranges over about 200 km and for the extraordinary ray that determines the maximum frequency, but the principles are essentially the same (the reader is referred to the aforementioned texts and references therein).

3.2. Parabolic Layer Theory

Transmission curves were used extensively for the determination of maximum usable frequencies (MUF) for a number of years (approximately 1940 to 1980). With the advent of inexpensive and fast computers, an alternative method has come to the fore. Essentially, the method consists of using ionogram data to approximate the electron-density profile by an analytic function such as a parabola,

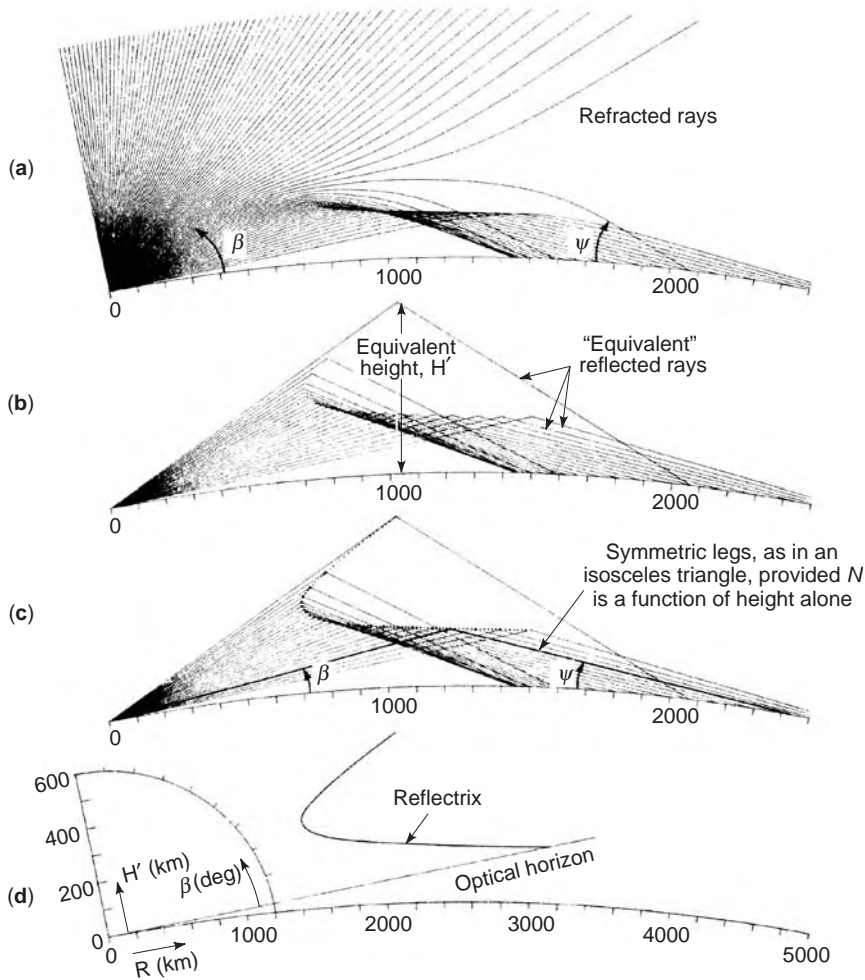


Figure 3. (a) Real rays in a concentric earth and Chapman ionosphere, $f = 8$ MHz, $f_c = 4$ MHz, $h_{\max} = 300$ km, semi-thickness = 200 km. (b) Equivalent or virtual paths reflected at the apexes of the fictitious triangular paths. (c) The reflectrix as the locus of the virtual reflection heights. (d) The reflectrix as a function of virtual height, range, and elevation angle. (Adapted from Croft [9] by permission of the American Geophysical Union.)

or a quasiparabola, and calculating the maximum frequency. A parabolic profile is defined by its critical frequency f_c , the semithickness y_m , and the height of the peak h_m . More complicated ionospheres can be approximated by two (or more) parabolas or by two parabolas joined by linear segments. The International Reference Ionosphere [6] also uses a segmented profile. The ground range in each segment is calculated analytically.

3.3. Ray Tracing

With realistic profiles obtained by ionogram inversion, which have horizontal and vertical structures and cannot be represented by simple analytical formulas, there is recourse to ray tracing. This involves starting with a ray from a specified transmitting site and with specified angles of elevation and azimuth, and plotting the flow of energy step by step until it returns to earth or escapes into space. This is a complicated procedure and is feasible only with adequate computers. A comprehensive three-dimensional ray tracing program has been constructed by Jones and Stephenson [7] and is available on the Internet [8]. In Fig. 3a, we see what happens to the ray paths (on a given frequency) as the angle of elevation slowly increases. For

low angles, the ground range is long. As the elevation increases, the ground range decreases until the skip is reached, after which the range increases rapidly. Eventually penetration occurs. Figure 3b shows the equivalent triangular paths for different angles of elevation. The apexes of the equivalent triangles lie on a smooth curve, called a reflectrix, as shown in Fig. 3c. The ray with its apex at the “nose” of the reflectrix is the skip ray and its frequency is the MUF. Rays reflected at lower virtual heights are low-angle rays, and rays reflected on the upper side of the reflectrix are high-angle rays. For a given reflectrix, the relationship between virtual height and angle of elevation (β) is given by Fig. 3d [9].

3.4. Maximum Frequencies

When the ground range, D , is plotted against the angle ϕ we find that, for $f > f_c$, there is a minimum range, D_s , called the skip distance, within which no power is received via the normal reflection process. However, signal power in the skip zone may result from ground waves, ground scatter, and scatter from ionospheric irregularities. At the edge of the skip zone, the signal frequency corresponds to the maximum usable frequency for the skip distance,

MUF(D_s). The MUF for a distance D is related to the critical frequency by

$$\text{MUF}(D) = f_c M(D) \quad (7)$$

where $M(D)$ is called the MUF factor corresponding to the distance D . The $M(3000)F_2$ is used extensively both as a reference and as a measure of the height of the F2 layer.

4. IONOSPHERIC MODELS

Ionospheric models are of two types: (1) empirical models based on data and (2) physical models based on production, loss, and movement of plasma by winds and/or electric fields. For long-term sky wave predictions, it is customary to use monthly median models of the main ionospheric characteristics, such as critical frequencies (f_oE_{hmE} , fE_{sh_mF2} , f_oF1 , f_oF2) and layer heights (h_mE , h_mF2) or equivalent M factors. The diurnal, seasonal, and sunspot number dependencies of the regular E and F1 layers are well behaved and are represented by analytical expressions (e.g., see Ref. 1, Chapter 5). However, the most important (F2) layer varies irregularly, and its characteristics are expressed in the form of numerical maps of median values. The day-to-day variability is expressed in terms of upper-decile and lower-decile values. D-region absorption, although highly variable in space and time, is represented by an analytical expression (see Ref. 1, Eq. 12.12). Electron-density profiles can be represented numerically or, for ray tracing, more conveniently by integrable segments. Several such approximations are discussed in Davies (Ref. 1, Sec. 5.3.2, 5.3.4, and 5.3.5). Of particular interest is the International Reference Ionosphere (IRI), which produces electron-density profiles, ion- and electron-temperature profiles, layer heights, and so on and is available from World Data Centers on the Internet [5,8]. Some models, such as PRISM [10], can be updated using current ionospheric data, such as total electron contents (see Ref. 1, Chapter 8) and/or critical frequencies.

5. PROPAGATION ON MEDIUM FREQUENCIES

5.1. Importance of Medium Frequencies

The medium-frequency (MF) band is dominated by the AM broadcast band (≈ 500 kHz to 1700 kHz), which during daytime depends on ground-wave propagation. This frequency band has a major economic, social, and political impact on everyday life and is intensively used. Knowledge of sky wave properties in the MF band is restricted because of (1) the congested spectrum, (2) high ionospheric absorption, (3) the role of the earth's magnetic field, (4) difficulty in separating deviative ($\mu \approx 0$) from nondeviative ($\mu \approx 1$) effects, (5) effects of collisions, and (6) the medium not always slowly varying on the lower frequency end, so that ray theory may be inapplicable. For efficient use of the MF band it is essential for several users to operate on the same, or adjacent, channels with minimum interference. Thus determination of the signal strength in distant

regions is important in channel sharing [11]. Atmospheric radio noise on the MF band has been modeled by Herman and DeAngelis [12]. It is difficult to collect sky wave data during the daytime because the signals are weak and/or over short distances the ground wave may mask the sky wave. For estimating sky wave field strengths, the Radio Communications Sector of the International Telecommunications Union (ITU) has recommended the Wang [11] method for North America and the CCIR (Consultative Committee on International Radio) [13] Recommendation 435-8 elsewhere. These two methods are in reasonable agreement throughout Europe.

5.2. Temporal Variations

5.2.1. Diurnal Variations. As the MF band is dominated by the broadcast band, relatively little is known about the sky wave signal structure. Yet this band has the heaviest usage. During daylight, high D-region absorption suppresses sky wave signals to an extent sufficient for interference-free broadcasting in most areas. However, in areas remote from an MF transmitter, weak sky waves may suffice to produce unwanted interference. Shortly after sunset, when the electron content of the D region essentially disappears, sky wave strengths increase and AM stations can be received at distances of several thousand kilometers. During daytime, MF waves are reflected from the E layer, but during nighttime, sky waves may be received from both E and F layers, especially on the upper end of the MF band.

5.2.2. Seasonal Variations. Measurements in Europe (see Ref. 14, Report 431-4) show equinoctial maxima of signal strength and minima in summer and winter, the summer minimum being the more pronounced. The overall seasonal variation may be as much as 15 dB at the lower end of the MF band, decreasing to about 3 dB at the upper end of the band. Over the western hemisphere there is little seasonal variation, and over the United States there is a slight minimum in summer. The sensitivity to length of day and to magnetic disturbance of broadcast signals received in Canada is illustrated in Fig. 4. This figure shows the frequency-integrated power in the AM broadcast band (550 kHz to 1600 kHz) received in Arviat, Northwest Territories during a six-month interval, September 1994 through April 1995. Local time is on the vertical axis, with local midnight (0600 UT) near midscale. The figure shows the normal diurnal pattern of MF sky wave reception in that signals are strong at night (middle of the figure) and weak during the day (top and bottom of the figure). The span of reception extends from near sunset (≈ 00 UT) to near sunrise (≈ 12 UT), corresponding to the seasonal variations of the terminator. The reception is longest near midwinter. In summer, reception is short lived. There is an asymmetry between the dawn and dusk terminators: The dawn terminator produces a sharper transition between nighttime conditions and daytime conditions than is the case near dusk. This phenomenon results from the prompt production of the D layer at sunrise versus the relatively slow decay of the D layer after sunset.

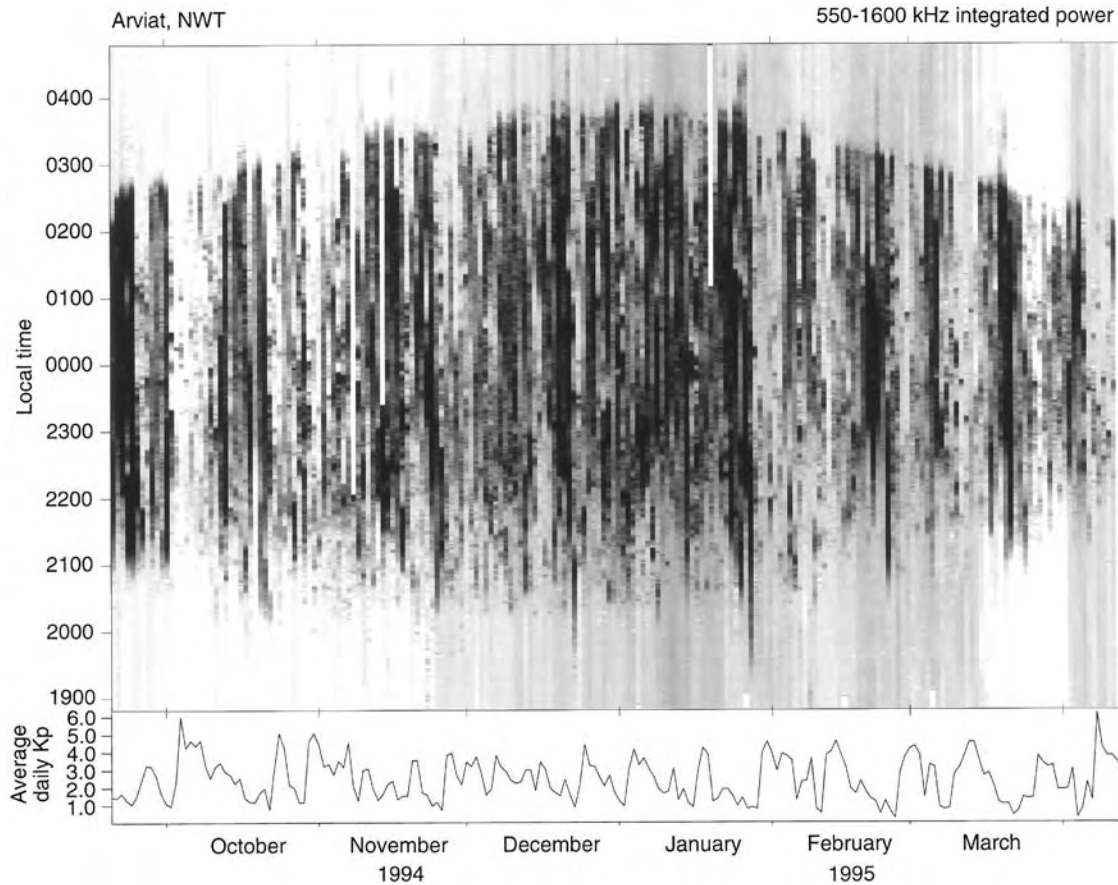


Figure 4. Integrated power in the frequency range 550 kHz to 1600 kHz received in Arviat, Northwest Territories, Canada from September 1994 through April 1995. Local meridian (270°E) time is on the vertical axis. The reception is best near the winter solstice. (Courtesy of J. La-Belle.)

The lower panel in Fig. 4 shows the daily magnetic index from September 1994 to April 1995 and illustrates the dependence on geomagnetic activity of the high-latitude reception of distant AM broadcast band transmissions. Several-day intervals with high magnetic disturbance correlate one-to-one with intervals when the integrated power in the AM broadcast band at night is nearly the same as it is during the day. The latter intervals appear as light vertical bands in the top panel of Fig. 4. On shorter timescales, prompt absorption of distant AM transmissions is a sensitive indicator of auroral disturbance [15]. Another indication of the seasonal variation is the average daily number of hours of MF reception at Fairbanks, Alaska of signals from five stations in the United States and Canada: Hunsucker and DeLana [16] found these hours to be 13.3 h in winter and spring, 4.0 in summer, and 11.0 in autumn. Daytime field strengths, though weak, are higher in winter than in summer. The winter-to-summer ratio is typically 10 dB to 20 dB. For planning purposes, “annual median” field strengths are used (Ref. 11, Sec. 4.1). Measurements indicate that the annual median value at noon is some 42.5 dB lower than at 6 hours after sunset, which is the reference time used by Europeans.

5.2.3. Sunspot Dependence. In Europe, Ebert [17] found that the 11-month smoothed midnight signal,

$F(11)$, and the corresponding smoothed sunspot number, $R(11)$, are related by

$$F(11) \approx 60 - 0.02R(11) \text{ dB} \quad (8)$$

The sensitivity to sunspot number depends on the hour of observation. In Europe, the reference hour is normally 6 h after sunset, whereas in North America it is customary to use sunset + 2 h, at which the difference between field strengths at sunspot maximum and sunspot minimum during 1944 through 1947 was 14 dB compared with only 8 dB at sunset + 6 h.

5.3. Dependence on Wave Frequency

Some measurements indicate that the signal strength increases with wave frequency, whereas others suggest a decrease of signal strength with increase of frequency. Both these conclusions have some basis because, at night, an appreciable fraction of the ionospheric absorption may occur near the reflection level (i.e., deviative absorption, which may increase with increasing frequency; see Ref. 1, Sec. 11.5.3, which gives several formulas for the frequency dependence of MF field strengths). For many practical purposes, it is sufficient to take the field strength on 1000 kHz as representative of the entire band.

5.4. Dependence on the Geomagnetic Field

The CCIR [13] basic loss factor is

$$K = 3.2 + 0.19f^{0.4} \tan^2(\Phi + 3) \quad (9)$$

where the frequency, f , is in kHz and Φ is the magnetic latitude at the center of the path for $\Phi \leq 60^\circ$ and $\Phi = 60^\circ$ for magnetic latitudes greater than 60° . Thus reception is poor near the auroral zones. This is illustrated in Fig. 4, which shows gaps in the reception of signals on days with high magnetic indexes. This is the result of increased auroral absorption on the path because of increased D-region electron content and equatorial motion of the auroral zone. MF signals are sensitive to auroral absorption and, above a certain threshold of disturbance, are blacked out.

For east–west and west–east propagation in low magnetic latitudes (e.g., in Africa), polarization coupling loss is important. This develops because the electric field, from a vertical antenna, is perpendicular to the (horizontal) magnetic field and excites only an extraordinary wave, which suffers high D-region absorption [see Eq. (3), with $f \approx f_H$].

5.5. Predicting Field Strengths

Methods for predicting MF sky wave field strengths are given in CCIR [see Ref. 13, pp. 311–390; PoKempner [18], and Davies [1], Sec. 11.7]. The CCIR method takes into account antenna gain, propagation loss, polarization coupling, and, where appropriate, sea gain.

5.6. Fading on MF

Nearly all sky waves fluctuate, or fade, with time as a result of interference between component echoes, absorption changes, polarization changes, and so on. To determine a station's sky wave service area and its interference potential, it is important to know the percentage of time that a given field strength is exceeded. For example, fields exceeded for 1% and 10% of the time are about 13 dB and 8 dB, respectively, higher than the median. In high geomagnetic latitudes, the corresponding differences are 15 dB and 10 dB [19].

6. PROPAGATION ON HIGH FREQUENCIES

6.1. The Available Spectrum

The HF sky wave spectrum is bounded on the upper end by the MUF, which is essentially determined by the maximum electron density in the reflecting layer, and on the lower end by the lowest usable frequency (LUF), which is determined by D-region absorption and/or by E-layer cut-off. As a result of day-to-day fluctuations ($\approx 15\%$ about the monthly median) of the F2 critical frequencies, operation on the MUF would provide reception for 50% of the time at a particular hour. To ensure communications 90% of the time, it is customary to operate at, or below, the optimum working frequency (or FOT from the French initials), which is defined empirically as 0.85 of the monthly median MUF. As the MUF can be defined in several ways, the CCIR (Ref. 14, Recommendation 373-5) has adopted the

following: (1) Basic MUF is the highest frequency by which a radiowave can propagate between given terminals, on a specified occasion, by ionospheric refraction alone; and (2) operational MUF, or simply MUF, is the highest frequency that would permit acceptable operation of a radio service between given radio terminals at a given time under specified working conditions (such as antennas, transmitter power, class of emission, information rate, and required signal-to-noise ratio).

The operational MUF refers to propagation in the actual ionosphere and includes effects of scattering, partial reflection, and so on, whereas the basic MUF essentially depends only on ionospheric refraction. Hence, in general, the operational MUF is equal to or greater than the basic MUF.

6.2. Path Structure

The layered structure of the ionosphere can produce complicated oblique echoes. A composite echo may consist of the following: high- and low-angle rays from the E (including E_s), F1, and F2 layers (See CHARACTERISTICS OF THE IONOSPHERE for a discussion of ionospheric structure and variability); one-hop, two-hop, and so on echoes; and scatter from the ground and from ionospheric irregularities. Figure 5 shows a sample oblique ionogram taken, during magnetically quiet conditions, over a geographically east–west path. The traces are sharp and the maximum, or junction (J), frequency of the one-hop F₂ trace is well defined. The high-angle, or Pedersen, trace can be seen for the one-hop trace. Splitting of the high (H)-angle, two-hop trace into ordinary and extraordinary traces can be seen. The time spread sets a limit to the rate of transmission of information because overlapping echoes can result in errors. Roughly speaking, the maximum rate of transmission (in binary units per second) is equal to the reciprocal of the time spread, which is a function of signal frequency, path length, geographical location, season, sunspot number, and so on. Ionospheric structures, both vertical and horizontal, produce echoes with various angles of elevation and azimuth. The interested reader should consult Ref. 4, Chapters 12–15, for a detailed discussion of direction finding.

6.3. Fading on HF

When the ionosphere changes with time and/or space with moving terminal(s), the relative phases of the component echoes change and the resultant signal fluctuates or fades. Fading may result from interference between (1) echoes reflected from different parts of the ionosphere; (2) ordinary and extraordinary waves, called polarization fading; (3) reflection or penetration, called MUF fading or skip fading; (4) absorption fading; and (5) focusing. The fading rate depends largely on the type of fading and may range from 100/s (flutter fading) to once per day (MUF fading). The speed of interference fading is related to the width of the fading power spectrum. The autocorrelation falls to 0.37 after a time, t , called the fading time, given by

$$t = \lambda/4\pi v \quad (10)$$

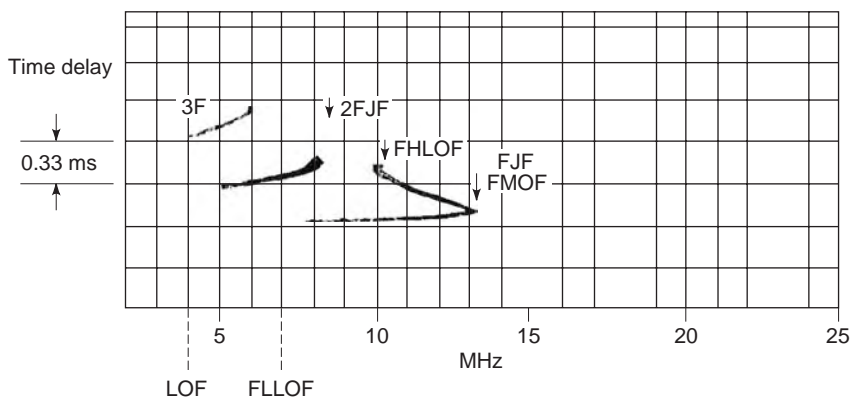


Figure 5. Oblique ionogram for the 2370 km, geographic approximately west–east path from Boulder, Colorado, to Sterling, Virginia, September 1, 1954, 2112 (90° West Meridian Time). Here the junction frequency (FJF) or basic MUF is the same as the maximum observed frequency (FMOF). LOF is the lowest observed frequency.

where λ is the signal wavelength and v is a measure of the velocity of the reflecting sources.

For practical purposes, it is customary to make fading allowances to ensure that the field strength is exceeded a certain percentage (e.g., 90%) of the time. Circuit planning requires comparison of the strengths of the wanted signal relative to (1) natural and synthetic noise, and (2) cochannel and adjacent channel interference (called electromagnetic compatibility). Hence, in addition to monthly medians, fading allowances are necessary that depend on short-term (<1 h) and long-term (day-to-day) fading of the wanted signal and the background interference. Some proposed fading allowances are discussed in ITU [20], Recommendations 339 and 411.

In high magnetic latitudes, rapid ionospheric motions ($\approx 1 \text{ km} \cdot \text{s}^{-1}$) result in Doppler frequency shifts and, hence, frequency spreading on great-circle paths of 0.1 Hz to 0.5 Hz. On nongreat-circle paths, spreading of 5 Hz to 10 Hz is typical. Some typical time-delay spreads are 100 ms to 200 ms. Sky wave fading models are available (e.g., see [21]). Further, in high latitudes, vertical antennas, which generate vertical electric fields, are preferred to horizontal antennas because they excite ordinary waves, which suffer less absorption than extraordinary waves.

6.4. HF Propagation Programs

As the ionosphere varies in space and time (local time, season, sunspot numbers, etc.), so does the usable frequency spectrum and, also, the characteristics of the received signals (e.g., signal strength, fading). Hence, knowledge of the variability of the ionosphere has been invaluable in the design and operation of point-to-point and broadcasting HF systems. For continuous operation of a given point-to-point circuit, a set of frequencies is required to avoid MUF failure (e.g., at night) and excessive ionospheric absorption by day. For long-term planning, the f_oF2 is the most important single parameter in controlling the MUF, and it is highly variable. In spite of the increase in the number of solar disturbances, HF sky wave propagation is better near sunspot maximum than near sunspot minimum because of the broader available frequency band.

When the f_oF2 and the layer height [or $M(3000)F2$] are known, from vertical soundings, the basic MUF can be calculated by graphical methods or by parabolic theory. The behaviors of the E and F1 layers are regular and are expressed by analytic formulas (see Ref. 1, Sec. 5.2) and are such that the smaller $F1M$ factor essentially compensates for the higher f_oF1 so that the products, the MUFs, for both layers are nearly equal. During daytime, the E layer is usually the controlling layer for distances up to about 2000 km and the F1 layer for distances between 2000 km and 3000 km. Over distances of 4000 km and longer, the F2 is normally the controlling layer. Single-hop propagation is limited to paths shorter than about 4000 km. Empirically, it has been found that as the distance increases beyond the “limit,” sky wave propagation is maintained by such mechanisms as ionospheric and ground scatter, high-angle rays that have longer one-hop limits, and ionospheric tilts that produce “super-modes” such as those that occur on transequatorial circuits. Propagation fails only when the ionosphere fails to support propagation at one of two “control points” on the great-circle path at 2000 km from each end (see Ref. 1, Sec. 12.2). The path MUF is the lower of the two MUFs for 4000 km with the ionospheric parameters at the control points. In the cases of the E, Es, and F1 layers for paths longer 2000 km, control points 1000 km from each end are used and the MUFs for a range of 2000 km are calculated (the lower of the two MUFs is taken as the circuit MUF). Global numerical maps of f_oF2 are available at reference high- and low-sunspot numbers (or equivalent indexes), and the values for other sunspot numbers are obtained by interpolation or extrapolation. There is a saturation of f_oF2 at sunspot numbers ≥ 150 so that for sunspot numbers greater than 150, the value is set at 150. The monthly median f_oF2 correlates better with the 12-month smoothed sunspot number than with the individual monthly number. For prediction purposes, the zero distance MUF ($=f_oF2 + 0.5f_H$) together with the MUF at a reference distance (e.g., 3000 km or 4000 km) and, for paths with other lengths, the MUFs are found by interpolation. The $M(3000)$ is related to the virtual height, in km, by

$$M(3000) = (67.6542 - 0.014938h') / \sqrt{h'} \quad (11)$$

The optimum working frequency (FOT) is 0.85 (monthly median MUF), and it ensures sky wave propagation 90% of the days of the month at a particular hour (usually local or universal time). Operating on the monthly median MUF results in sky wave reliability of 50%. The highest probable frequency, or HPF, is exceeded 10% of the time. The higher the signal frequency the greater is the signal strength, but this has to be balanced against the spectrum congestion caused by many operators using similar circuits. An advantage of using a frequency close to the MUF is that the time dispersion is a minimum.

In planning a circuit, it is necessary to determine (1) the maximum MUF for the various layers and, hence, the FOT; (2) the radiation angle for the appropriate layer; (3) the power delivered to a receiver (using spatial spreading, ionospheric absorption, fading and polarization losses, antenna gains); and (4) the noise and interference (see RADIO NOISE).

Before about 1970, individual circuit evaluations were necessary using laborious methods, and graphical techniques were customary for the determination of sky wave propagation parameters such as those discussed previously. Today, these laborious methods are replaced by convenient user-friendly computer programs, many written for personal computers, that only require basic circuit information, such as time of day, month, sunspot number (or equivalent), and path terminals (or area coverage for broadcasting). The computer programs normally include

numerical maps, or formulas, for calculating the necessary ionospheric characteristics and noise and interference; the more comprehensive models include reference antennas for calculation of received signal-to-noise ratios. The sophistication of these PC programs ranges from basic frequency outputs to broad coverage. A list of some commercially available programs is given in Goodman (Ref. 2, Table 5.16; see also Ref. 22, Resolution ITU-R25). An example of a prediction program is the Ionospheric Communications Enhanced Profile Analysis and Circuit (ICEPAC), which includes, in addition to a global ionospheric model, models of the subauroral trough, auroral zones, and polar caps. This software is available (free) on the Internet [23]. A sample output from ICEPAC is shown in Fig. 6, which includes contours of signal strength around a broadcasting transmitter that has an isotropic antenna.

Besides the basic sky wave characteristics, such as MUF, FOT, and LUF, the more comprehensive of these computer programs give signal-to-noise ratio for a given circuit performance (see RADIO NOISE) and the following characteristics that depend on the ionosphere (see Ref. 2, Sec. 5.11, and references therein). Mode availability, Q ($0 < Q < 1$), is the fraction of time that a path is available (see Ref. 1, Sec. 12.6.2). To a first approximation, the standard deviation of f_oF_2 about the monthly average is about 15%. On the median MUF, $Q = 0.5$; on the FOT, $Q = 0.9$; and on the HPF, $Q = 0.1$.

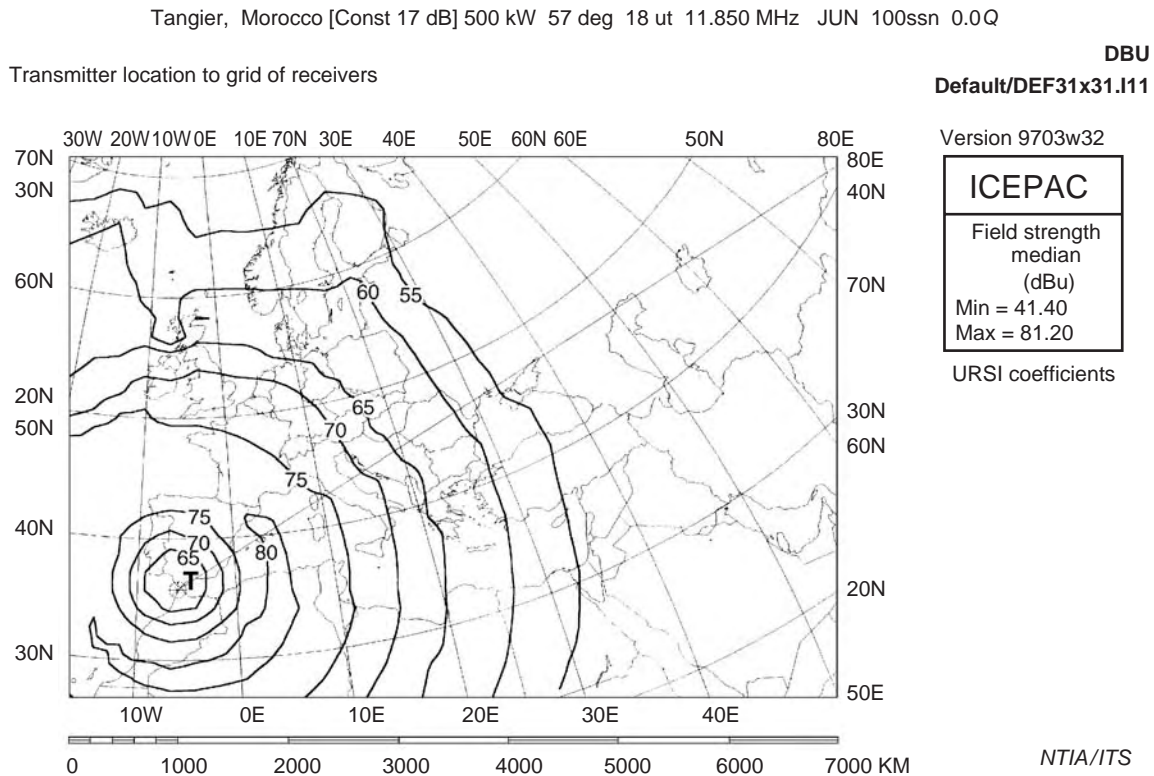


Figure 6. Contours of signal strength on the ground around a transmitter at Tangier at 1800 UT in June with sunspot number of 100. Transmitter power is 100 kW; signal strength is decibels above $1 \mu\text{V}$ per meter with an isotropic antenna obtained from the ICEPAC program. (Courtesy of G. Hand.)

Circuit reliability, ρ , ($0 < \rho < 1$) is the fraction of days that successful communication may be expected at a given hour of a month on a specified operating frequency

$$\rho = QP \quad (12)$$

where P is the probability that the mean received signal-to-noise ratio exceeds a specified level. The reliability, ρ , depends on P increasing with increasing frequency, whereas Q decreases with increasing frequency.

Grade of service defines the quality of communication desired (for example, the percentage of error-free messages in teletype transmitted or the percentage of satisfied customers of a given service). Service probability is the fraction of time that a specified grade of service (e.g., signal to noise) or better is achieved.

Above-the-MUF loss, L_m , accounts for the fact that signals may be received on frequencies above the basic MUF (e.g., resulting from ionosphere scatter, E_s , etc.). The CCIR [14], Report 252-2, recommends

$$L_m = 130\{(f/MUF) - 1\}^2 \quad (13)$$

To account for a wide variety of ionospheric effects, such as E_s , spread F, off-great-circle propagation, focusing, day-to-day variability, and aurora, ITU [20] Report 252 contains information on additional system loss resulting from these extra effects.

Compatibility is defined as the percentage of time during which a specified criterion of service quality is achieved at a receiver in the presence of interference, relative to the value that would be obtained if only noise were present.

6.5. Digital System Considerations

Digital systems are particularly affected by ionospheric dispersion, which produces fading (e.g., by multipath, polarization, etc.). The performance of a digital system is characterized by its bit error rate, which is the probability that a transmitted binary digit is wrongly detected by the receiver. On HF, intervals with high error densities alternate with intervals of low error densities. Error bursts occur when the signal-to-noise ratio temporarily falls below a critical level (e.g., selective fading). Curves are available in the ITU [20] Report 197, that gives the duration and probability of fades as a function of the signal level for specific circuits. In the absence of fading, the signal-to-noise ratio (SNR) is the controlling factor for digital transmission speed. The theoretical error-free channel capacity, C , is

$$C = B \log_2(1 + \text{SNR}) \text{bits} \cdot \text{s}^{-1} \quad (14)$$

where B is the channel bandwidth (Hz). As a result of all the effects described above, these ionospheric channels usually operate far below the theoretical capacity (Eq. (14)).

6.6. Real-time Channel Evaluation

Although the prediction systems discussed previously are valuable for circuit planning and frequency allocation, they have limited value for operational purposes, primarily because of the high hour-to-hour and day-to-day variability of the F2 layer. To meet operational requirements, several real-time circuit evaluation (RTCE) systems have been developed (see Ref. 14, Report 889-1). The first such system involved oblique sweep-frequency sounding over the operational circuit and, from the oblique ionogram, selection of a suitable frequency with low time dispersion, adequate signal, and minimum noise and interference. The channel selection is normally limited by the channel allocation. A critical feature of this technique is the interval between soundings. When the interval is long, changing ionospheric conditions can catch the operator unaware. On the other hand, too frequent soundings generate excessive interference to other services. An alternative, and less bothersome, approach is channel sounding on the allocated channels only. This technique has the following advantages: simpler equipment, lower installation costs, and less interference. When the optimum channel is identified, a message is dispatched to the sender, who can commence transmission. This method assumes reciprocity (that is, the sender-to-receiver conditions are the same as the receiver-to-sender conditions). This is usually a good assumption. Adaptive systems are essential for RTCE in order to respond to rapidly changing sky wave conditions. An adaptive system needs (1) a fast frequency response, (2) antenna agility, and (3) the ability to adjust rates of information.

Use of RTCE allows adaptive frequency management by which usage of the HF spectrum can be maximized. Such an approach is preferable to increasing the transmitter power and/or transmitting simultaneously on all allocated frequencies, both of which may be self-defeating. The term *channel estimation* is used to describe the process of monitoring channel characteristics with the aim of describing the states of a set of channels. Real-time adaptive systems are of particular value when one of the terminals is mobile (e.g., ship, airplane, vehicle) and the other is fixed, so that the fixed terminal can avail itself of high power and directive antennas. One advantage of RTCE over prediction is to maximize above-the-median MUF propagation, in which interference is usually lower than on the FOT.

7. CONCLUSIONS

The medium-frequency and high-frequency bands have great commercial, social, and scientific value and are used extensively for broadcasting and for point-to-point communications. The pronounced (orders of magnitude) variability of the ionosphere makes sky wave communications problematic, both as a means of communicating and as a source of interference. Using HF systems, frequency agility is essential for continuous operation and, therefore, a set of suitable assigned frequency channels. Even with such a frequency allocation, by the appropriate national authority, sky wave propagation is liable to disruption by

several solar disturbances and synthetic disturbances (e.g., nuclear explosions and ionospheric modification). For many purposes, satellite communications, on giga-Hertz frequencies, have replaced HF for global communications. However, sky waves will continue to be used well into the foreseeable future.

BIBLIOGRAPHY

1. K. Davies, *Ionospheric Radio*, London: P. Peregrinus on behalf of the Inst. Elec. Eng., 1990.
2. J. M. Goodman, *HF Communication, Science and Technology*, New York: Van Nostrand Reinhold, 1991.
3. R. D. Hunsucker, *Radio Techniques for Probing the Terrestrial Ionosphere*, Berlin: Springer-Verlag, 1991.
4. L. F. McNamara, *The Ionosphere: Communications, Surveillance, and Direction Finding*, Malibar, FL: Krieger, 1991.
5. National Space Science Data Center, (online) 1998, available at <http://nssdc.gsfc.nasa.gov/space/model/models/iri.html>.
6. D. Bilitza, ed., *International Reference Ionosphere 1990*, Greenbelt, MD: National Space Science Center, NSSDC 90-20, 1990.
7. R. M. Jones and J. J. Stephenson, A versatile three-dimensional ray tracing program for radio waves in the ionosphere, *OT Report 75-76*, Washington, DC: Government Printing Office, 1975.
8. Ionospheric Physics Group, (online) 1998, available at <http://www.ngdc.noaa.gov/stp/IONO/ionohome.html>.
9. T. A. Croft, HF radio focussing caused by the electron distribution between ionospheric layers, *J. Geophys. Res.*, **72**:2343–2355 (1967).
10. D. N. Anderson, The development of global, semi-empirical ionospheric specification models, in J. M. Goodman, ed., *Proc. Ionospheric Effects Symp.*, Alexandria, VA: TCI/BR Communications, 22314, pp. 353–363, 1993.
11. J. C. H. Wang, LF/MF skywave propagation at daytime, *IEEE Trans. Broadcast.*, **41**:23–27 (1995).
12. J. R. Herman and X. A. DeAngelis, Bandwidth expansion effects on the voltage deviation parameter (V_d) of MF and HF atmospheric radio noise, *Radio Sci.*, **22**:26–36 (1987).
13. CCIR, Sky-wave field-strength prediction method for the broadcasting service in the frequency range of 150 to 1600 kHz, Recommendation 435-7, 19–43, in *1992 CCIR Recommendations*, Geneva, Switzerland: Int. Telecommun. Union, 1992.
14. CCIR, Recommendations and Reports of the *CCIR 1986*, VI, Propagation in Ionized Media, Geneva, Switzerland: Int. Telecommun. Union, Report 431-4, 374–390, 1986.
15. J. LaBelle, et al., The spectrum of LF/MF/HF radio noise at ground level during substorms, *Geophys. Res. Lett.*, **21**:2749–2752 (1994).
16. R. D. Hunsucker and B. S. DeLana, High-latitude field-strength measurements of standard broadcast skywave transmission monitored at Fairbanks, Alaska, Geophysical Inst., Fairbanks, AK: Univ. Alaska, 1986.
17. W. Ebert, Ionospheric propagation on long and medium waves, *Tech Doc. 3081*, Brussels, Belgium: European Broadcasting Union, 1962.
18. M. PoKempner, Comparison of available methods for predicting medium frequency sky-wave field strengths, *NTIA Report 80-42*, Boulder, CO: Nat. Telecommun. Inf. Admin., 1980.
19. R. D. Hunsucker, B. S. DeLana, and J. C. H. Wang, Medium frequency sky-wave propagation at high latitudes: Results of an FCC sponsored study, *Proc. 42nd Broadcast Eng. Meeting*, Nat. Assoc. Broadcasters, 1988.
20. ITU, Fading allowances in HF broadcasting, Vol. X—Part 1, Broadcasting service (sound), XVII Plenary Assembly, Geneva, Switzerland: Int. Telecommun. Union, 1990.
21. C. C. Watterson, J. R. Juroshek, and W. D. Bensema, Experimental confirmation of an HF channel model, *IEEE Trans. Com. Tech.*, **COM-18**(6):792–803 (1970).
22. ITU, Computer programs for the prediction of ionospheric characteristics, sky-wave transmission loss, and noise, III, Propagation, XVIII Plenary Assembly, Geneva, Switzerland: Int. Telecommun. Union, 1994.
23. (Online) available at <http://elbert.its.blrdoc.gov/hf.html>.

SLOT ANTENNAS

HISAMATSU NAKANO
Hosei University
Koganei, Tokyo, Japan

1. INTRODUCTION

The advantages of a slot antenna (a slot cut in a conducting sheet) are that it is simple and robust. The slot can radiate either a linearly polarized wave or a circularly polarized wave. Numerous slot antennas have been proposed for radiocommunication systems [1–3]. This article focuses on representative slot antennas, including straight, bow-tie, loop, curl, and spiral slot antennas, and reveals their radiation characteristics.

First, a thin straight slot [4] is discussed in Section 2, assuming a sinusoidal electric field over the slot. The radiation pattern and the radiation conductance are formulated under the condition that a conducting sheet, in which the thin slot is cut, is of infinite extent. Subsequently, a relationship between the impedances of a slot

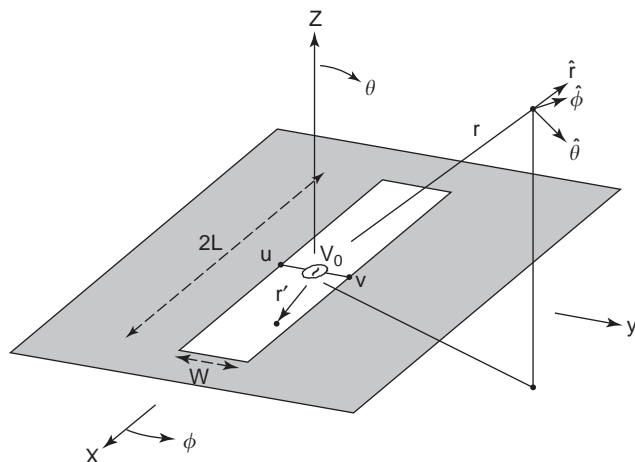


Figure 1. Thin straight slot cut in a conducting sheet of infinite extent.

antenna and a corresponding plate antenna, both having the same shape, is discussed in Section 3. This relationship, called “Babinet’s principle [4,5],” is then applied to the aforementioned thin slot antenna and its radiation conductance is again discussed.

The conducting sheet used for the derivation of Babinet’s principle is of *infinite* extent. However, in practice, the conducting sheet is of *finite* extent and Babinet’s principle cannot be applied to a slot cut in a finite sheet. To overcome the limitation regarding the size of the conducting sheet, an analysis method called the *finite-difference time-domain method* (FDTD) [6–8] is presented in Section 4. Evaluation of antenna characteristics (including the input impedance, radiation pattern, and gain) based on the FDTD is briefly described. Note that the FDTD can be used for both a slot in a finite sheet and in an infinite sheet.

Sections 5–10 present the analysis results for the representative slot antennas (including the straight, bowtie, loop, curl, and spiral slot antennas), obtained by using the FDTD.

The antenna characteristics of a straight half-wavelength slot as a function of the source location are analyzed in Section 5 (note that the slots in Sections 2 and 3 are fed from their centerpoints). It is found that the straight

half-wavelength slot shows a purely resistive input impedance, when it is fed from an off-center feedpoint. The gain as a function of the source location is also revealed.

Effects of the finiteness of a conducting sheet on the radiation characteristics of a half-wavelength slot are revealed in Section 6, where an x -directed slot is cut in a sheet with an x -directed side length of S_{GPx} and a y -directed side length of S_{GPy} [9,10]. Variations in the input impedance, radiation pattern, and gain are evaluated as a function of S_{GPx} , holding S_{GPy} constant. Similarly, variations in the input impedance, radiation pattern, and gain are evaluated as a function of S_{GPy} , holding S_{GPx} constant.

A variation on the shape of the straight slot (width w) is the bowtie slot, whose width increases along the slot axis. The increase in the width is specified by the bowtie angle ϕ_{bow} . The size of this angle affects the antenna characteristics [11,12]. Fixing the length of the bowtie to be a half-wavelength, the effects of the bowtie angle on the antenna characteristics are revealed in Section 7 [13]. The frequency responses of the half-power beamwidth and the gain are also presented and discussed.

A loop slot presented in Section 8 has a closed-arm structure, as opposed to the straight and bowtie slots. The antenna characteristics of the loop slot as a function of the loop circumference are evaluated under the condition that the conducting sheet, in which the loop slot is cut, is of infinite extent [14]. In addition, a comparison between loop slots with finite and infinite conducting sheets is made to clarify the differences in the radiation patterns and the gains.

The straight slot in Sections 5 and 6, the bowtie slot in Section 7, and the loop slot in Section 8 radiate a *linearly* polarized wave. The antennas discussed in Sections 9 and 10 radiate a *circularly* polarized wave.

A curl slot antenna, discussed in Section 9, has a triplate transmission-line structure [15–17], where the curl slot is cut in the upper plate of the triplate transmission line. The middle plate of the triplate transmission line forms the feed probe for the slot. The radiation from the curl is unidirectional by virtue of the lower plate, which acts as a reflector. After investigating the curl slot, dual-curl slots are arrayed to realize a high gain of more than 30 dBi [18].

A spiral slot with two arms [19] is discussed in Section 10. Finite arm lengths are considered for practicality. The frequency responses of the radiation pattern, gain, and input impedance for this finite arm-length case are evaluated and the wideband characteristics within a frequency range of 3–7 GHz are discussed [20].

Finally, some comments on slot antennas are added, referring to recent research work [21–25].

2. THIN STRAIGHT SLOT

A straight slot antenna is a simple radiation element, similar to the straight wire antenna. This section discusses how to calculate the radiation field and the radiation conductance of the straight slot antenna. For the calculation, the slot is assumed to have a very small width relative to the wavelength; that is, the slot is assumed to be thin.

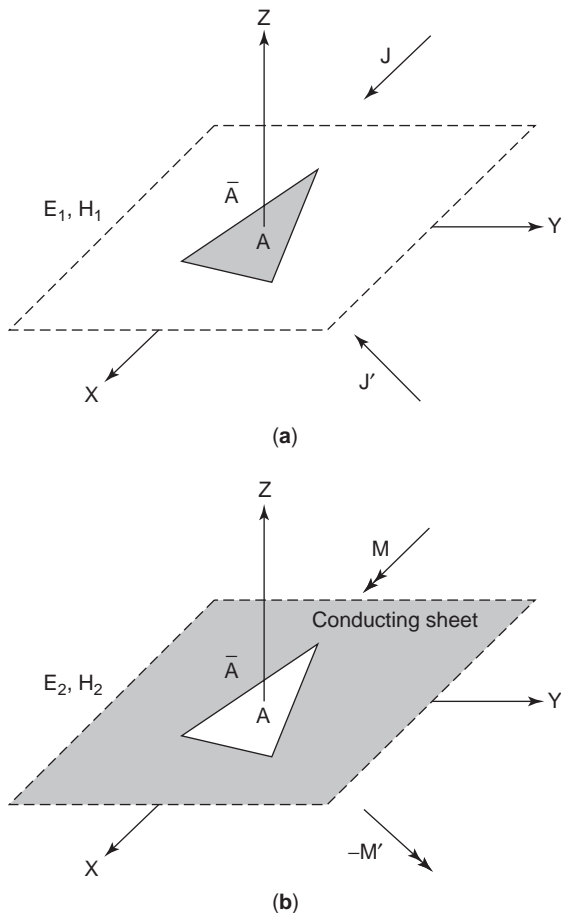


Figure 2. Complementary structures: (a) conducting plate of area A ; (b) slot of area A in a conducting sheet of infinite extent.

2.1. Radiation Field

Figure 1 shows a thin straight slot cut in a conducting sheet of infinite extent, where the length and width of the slot are denoted as $2L$ and w , respectively. The slot is excited with a voltage source at its center. We assume that the electric field over the slot is

$$E_y = E_m \sin[k_0(L - |x'|)],$$

$$-L \leq x' \leq L \text{ and } -\frac{w}{2} \leq y' \leq \frac{w}{2} \quad (1)$$

where k_0 is the wavenumber ($= 2\pi/\lambda$, where λ is the wavelength in free space).

The radiation field $\mathbf{E}(r, \theta, \phi) = E_\theta(r, \theta, \phi)\hat{\theta} + E_\phi(r, \theta, \phi)\hat{\phi}$ in the $+z$ side of the sheet is calculated using the equivalence principle [26] as

$$E_\theta(r, \theta, \phi) = -\frac{jk_0}{4\pi} \frac{e^{-jk_0r}}{r} \int_{-(w/2)}^{w/2} \int_{-L}^L M_\phi e^{jk_0\hat{r}\cdot\mathbf{r}'} dx' dy' \quad (2)$$

$$E_\phi(r, \theta, \phi) = \frac{jk_0}{4\pi} \frac{e^{-jk_0r}}{r} \int_{-(w/2)}^{w/2} \int_{-L}^L M_\theta e^{jk_0\hat{r}\cdot\mathbf{r}'} dx' dy' \quad (3)$$

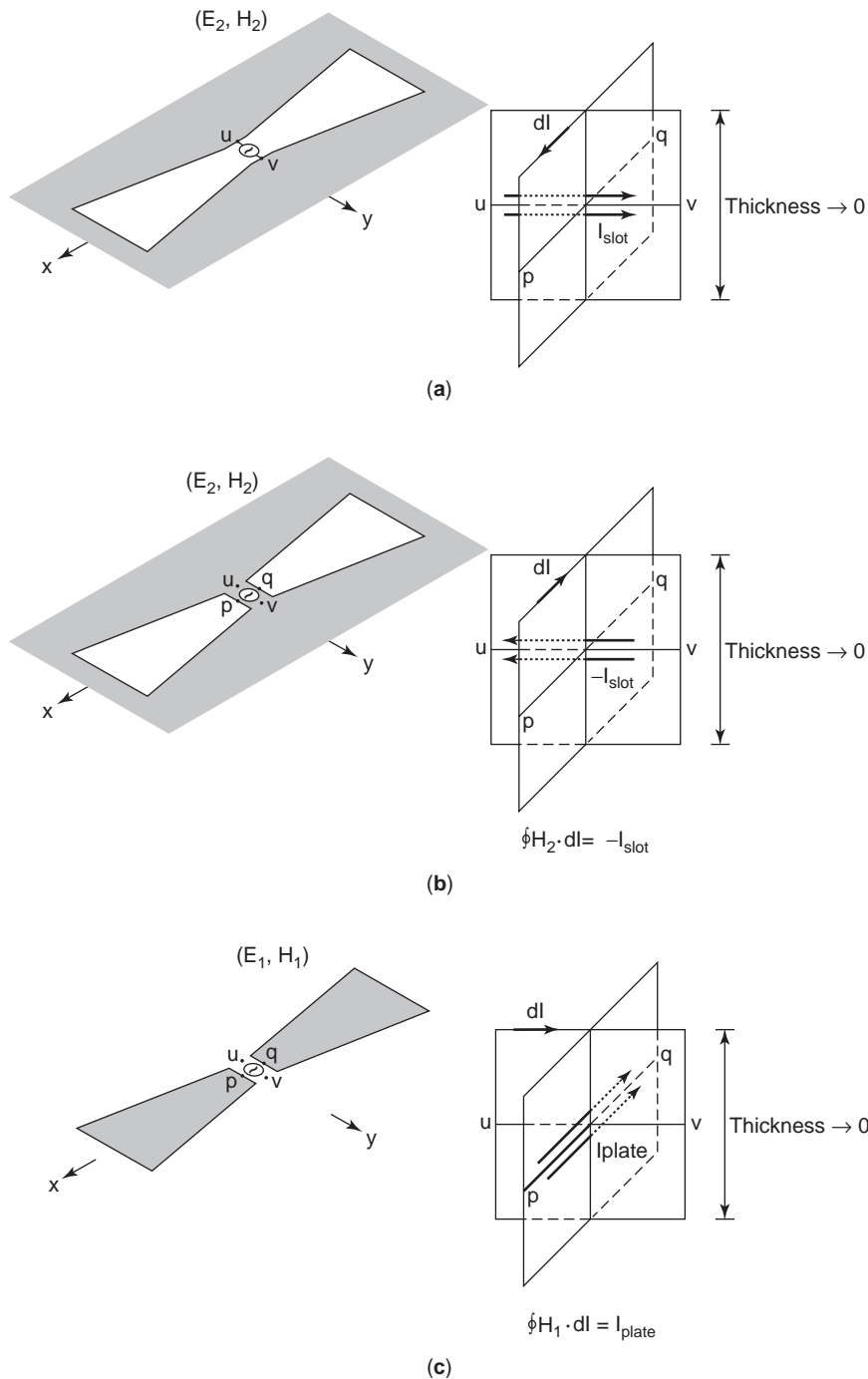


Figure 3. Babinet's principle: (a) slot excited by a voltage source (original problem); (b) slot excited by magnetic current source (equivalent to Fig. 3a); (c) conducting plate excited by a voltage source (complementary to Fig. 3b).

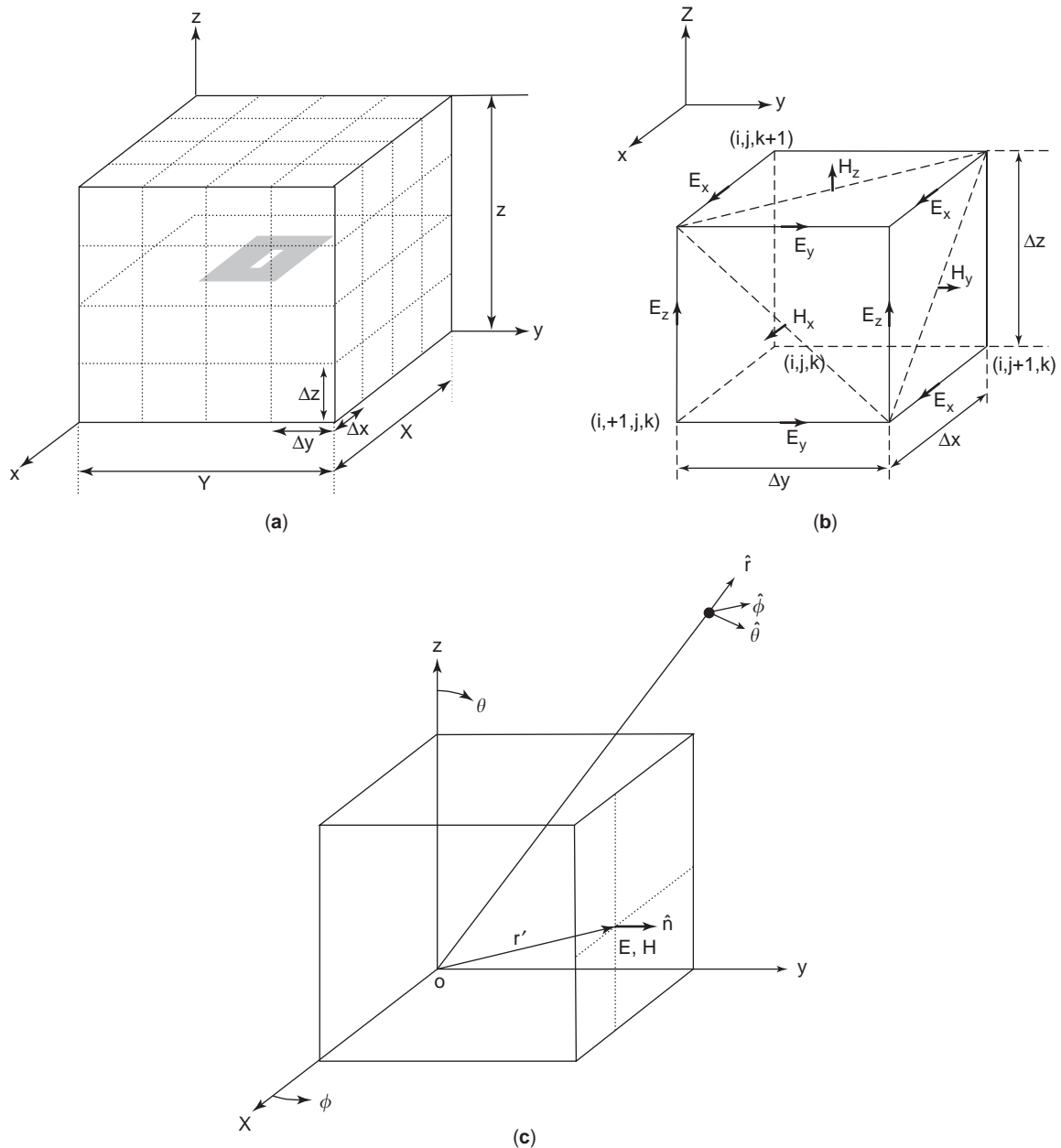


Figure 4. Finite-difference time-domain method: (a) analysis space, which is subdivided into numerous cells; (b) assignment of electric field \mathbf{E} and magnetic field \mathbf{H} on a cell; (c) radiation field calculation using equivalence theorem.

where r , θ , and ϕ are spherical coordinates and \hat{r} , $\hat{\theta}$, and $\hat{\phi}$ are the corresponding unit vectors; M_θ and M_ϕ are the components of the magnetic current density \mathbf{M} (equivalent source density) over the slot

$$M_\phi = -2E_y \sin \phi \quad (4)$$

$$M_\theta = 2E_y \cos \theta \cos \phi \quad (5)$$

Note that $\mathbf{r}' [= \mathbf{r}'(x', y')]$ in Eqs. (2) and (3) is the position vector from the coordinate origin to a point within the slot, and hence

$$\hat{r} \cdot \mathbf{r}' = x' \sin \theta \cos \phi + y' \sin \theta \sin \phi \quad (6)$$

When the slot length $2L$ is a half-wavelength and $k_0 y' \rightarrow 0$, Eqs. (2) and (3) become

$$E_\theta = \frac{j}{\pi} \frac{e^{-jk_0 r}}{r} V_0 \sin \phi \frac{\cos \left[\frac{\pi}{2} \sin \theta \cos \phi \right]}{1 - \sin^2 \theta \cos^2 \phi} \quad (7)$$

$$E_\phi = \frac{j}{\pi} \frac{e^{-jk_0 r}}{r} V_0 \cos \theta \cos \phi \frac{\cos \left[\frac{\pi}{2} \sin \theta \cos \phi \right]}{1 - \sin^2 \theta \cos^2 \phi} \quad (8)$$

where $V_0 = \omega E_m$, which is the voltage across the center terminals u and v . Note that Eqs. (7) and (8) in the x - z

plane ($\phi = 0$) are

$$E_\theta = 0 \quad (9)$$

$$E_\phi = \frac{j}{\pi} \frac{e^{-jk_0 r}}{r} V_0 \frac{\cos\left[\frac{\pi}{2} \sin \theta\right]}{\cos \theta} \quad (10)$$

and Eqs. (7) and (8) in the y - z plane ($\phi = \pi/2$) are

$$E_\theta = \frac{j}{\pi} \frac{e^{-jk_0 r}}{r} V_0 \quad (11)$$

$$E_\phi = 0 \quad (12)$$

As will be shown later, the radiation fields in the two principal planes, as given above, are in good agreement with those obtained using the finite-difference time-domain method.

2.2. Radiation Conductance

Using Eqs. (7) and (8), we calculate the total power P radiated in the $+z$ space from a thin half-wavelength slot (shown in Fig. 1). Integrating the Poynting power over the surface of a hemisphere of radius r leads to

$$\begin{aligned} P &= \int_{\theta=0}^{\pi/2} \int_{\phi=0}^{2\pi} \frac{1}{2Z_0} (|E_\theta|^2 + |E_\phi|^2) r^2 \sin \theta d\theta d\phi \\ &= \frac{1}{2Z_0} \frac{1}{\pi^2} \frac{1}{r^2} V_0^2 \int_{\theta=0}^{\pi/2} \int_{\phi=0}^{2\pi} (\sin^2 \phi + \cos^2 \theta \cos^2 \phi) \\ &\quad \times \frac{\cos^2\left(\frac{\pi}{2} \sin \theta \cos \phi\right)}{(1 - \sin^2 \theta \cos^2 \phi)^2} r^2 \sin \theta d\theta d\phi \end{aligned} \quad (13)$$

where Z_0 is the intrinsic impedance of free space: $Z_0 = 120\pi \Omega$.

Equation (13) becomes (see Appendix)

$$\begin{aligned} P &= \frac{V_0^2}{4\pi Z_0} [\ln 2\pi\gamma - \text{Ci}(2\pi)] \\ &= 73 \frac{V_0^2}{Z_0^2} \end{aligned} \quad (14)$$

where $\ln \gamma = 0.5772$ (Euler's constant) and $\text{Ci}(x)$ is the cosine integral:

$$\text{Ci}(x) = - \int_x^\infty \frac{\cos x}{x} dx \quad (15a)$$

$$\int_0^x \frac{1 - \cos x}{x} dx = \ln x\gamma - \text{Ci}(x) \quad (15b)$$

The total power P can alternatively be written, using the radiation conductance G_r , as

$$P = \frac{1}{2} G_r V_0^2 \quad (16)$$

From Eqs. (14) and (16), G_r is given as

$$\begin{aligned} G_r &= \frac{2(73)}{Z_0^2} \\ &= 1.03 \times 10^{-3} \text{ mhos} \end{aligned} \quad (17)$$

Note that the radiation conductance in Eq. (17) applies for a slot radiating only in the $+z$ space. The radiation conductance will be discussed again in Section 3.2.

3. IMPEDANCE RELATIONSHIP BETWEEN COMPLEMENTARY STRUCTURES

The conductance determined in the previous section can be evaluated directly from Babinet's principle [4,5,29]. Before applying Babinet's principle to a slot antenna, let us understand what Babinet's principle is.

3.1. Babinet's Principle

For derivation of Babinet's principle, we consider an arbitrarily shaped conducting plate of area A in the x - y plane, shown in Fig. 2a. Let the shape of the conducting plate be exactly the same as the aperture (slot) cut in a conducting sheet of infinite extent, as shown in Fig. 2b, where the conducting sheet of area \bar{A} is located in the x - y plane. The two structures, where $A + \bar{A}$ covers the entire x - y sheet, are said to be "complementary" to each other.

\mathbf{J} and \mathbf{J}' in Fig. 2a are electric currents, which are located symmetrically with respect to the x - y plane. The electric and magnetic fields for this case are specified by \mathbf{E}_1 and \mathbf{H}_1 , respectively. Similarly, the electric and magnetic fields for the case shown in Fig. 2b are specified by \mathbf{E}_2 and \mathbf{H}_2 , where antisymmetric magnetic currents \mathbf{M} and $-\mathbf{M}'$ exist [5,29].

Maxwell's curl equations for Figs. 2a and 2b are written as

$$\nabla \times \mathbf{E}_1 + j\omega\mu\mathbf{H}_1 = 0 \quad (18)$$

$$\nabla \times \mathbf{H}_1 - (j\omega\epsilon + \sigma)\mathbf{E}_1 = \mathbf{J} \quad (z > 0) \quad (19a)$$

$$\nabla \times \mathbf{H}_1 - (j\omega\epsilon + \sigma)\mathbf{E}_1 = \mathbf{J}' \quad (z < 0) \quad (19b)$$

$$\nabla \times \mathbf{E}_2 + j\omega\mu\mathbf{H}_2 = -\mathbf{M} \quad (z > 0) \quad (20a)$$

$$\nabla \times \mathbf{E}_2 + j\omega\mu\mathbf{H}_2 = \mathbf{M}' \quad (z < 0) \quad (20b)$$

$$\nabla \times \mathbf{H}_2 - (j\omega\epsilon + \sigma)\mathbf{E}_2 = 0 \quad (21)$$

If the magnetic currents are chosen to be $(\mathbf{M}, \mathbf{M}') = (Z_\sigma \mathbf{J}, Z_\sigma \mathbf{J}')$, then Eqs. (20a), (20b), and (21) are transformed,

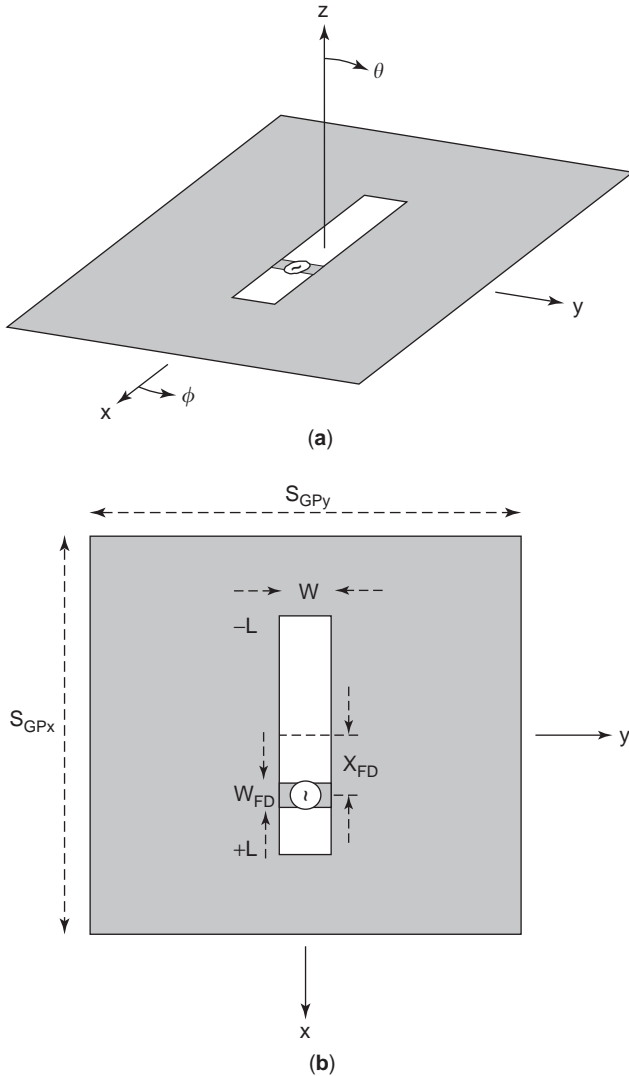


Figure 5. Half-wavelength straight slot excited by an off-center voltage source: (a) perspective view; (b) top view.

respectively, to

$$\nabla \times \left(-\frac{1}{Z_\sigma} \mathbf{E}_2 \right) - (j\omega\epsilon + \sigma)(Z_\sigma \mathbf{H}_2) = \mathbf{J} \quad (z > 0) \quad (22a)$$

$$\nabla \times \left(\frac{1}{Z_\sigma} \mathbf{E}_2 \right) - (j\omega\epsilon + \sigma)(-Z_\sigma \mathbf{H}_2) = \mathbf{J}' \quad (z < 0) \quad (22b)$$

$$\nabla \times (Z_\sigma \mathbf{H}_2) + j\omega\mu \left(-\frac{\mathbf{E}_2}{Z_\sigma} \right) = 0 \quad (23)$$

where Z_σ is

$$Z_\sigma = \left(\frac{j\omega\mu}{j\omega\epsilon + \sigma} \right)^{1/2} \quad (24)$$

These electric and magnetic fields $(\mathbf{E}_1, \mathbf{H}_1)$ and $(\mathbf{E}_2, \mathbf{H}_2)$ must satisfy the boundary conditions on the areas A

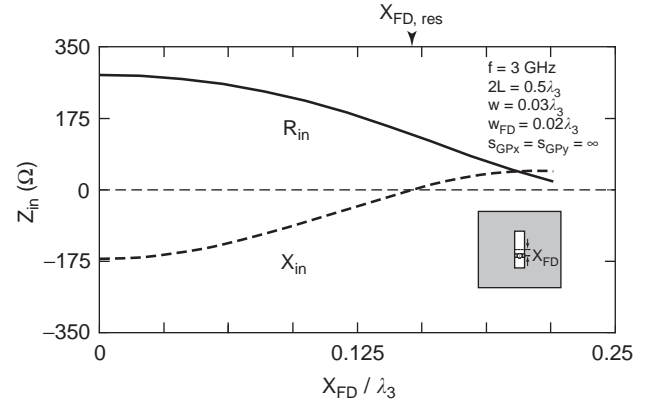


Figure 6. Input impedance Z_{in} of a half-wavelength straight slot as a function of the source location x_{FD} .

and \bar{A} [5,29]

$$\mathbf{E}_1 \times \hat{n} = \mathbf{H}_1 \cdot \hat{n} = 0 \quad \text{on } A \quad (25a)$$

$$\mathbf{E}_1 \cdot \hat{n} = \mathbf{H}_1 \times \hat{n} = 0 \quad \text{on } \bar{A} \quad (25b)$$

$$\mathbf{E}_2 \times \hat{n} = \mathbf{H}_2 \cdot \hat{n} = 0 \quad \text{on } \bar{A} \quad (26a)$$

$$\mathbf{E}_2 \cdot \hat{n} = \mathbf{H}_2 \times \hat{n} = 0 \quad \text{on } A \quad (26b)$$

where \hat{n} is the unit vector normal to the x - y plane. Equations (25b) and (26b) are derived from the symmetric electric currents and antisymmetric magnetic currents, respectively.

Comparing Eqs. (18), (19a), and (19b) to Eqs. (23), (22a), and (22b), respectively, and taking into account the boundary conditions Eqs. (25) and (26), we have

$$\mathbf{H}_1 = \mp \frac{1}{Z_\sigma} \mathbf{E}_2 \quad (z \geq 0) \quad (27a)$$

$$\mathbf{E}_1 = \pm Z_\sigma \mathbf{H}_2 \quad (z \geq 0) \quad (27b)$$

This means that, once the electric and magnetic fields are obtained for either case of Fig. 2a or Fig. 2b, the fields for the remaining case can be calculated using Eq. (27). Such a principle is referred to as *Babinet's principle*.

Similarly, if we choose the magnetic currents as $(\mathbf{M}, \mathbf{M}') = (\mathbf{J}, \mathbf{J}')$, as Kotani did [5,29], the field equations for Babinet's principle can be written as

$$\mathbf{H}_1 = \mp \mathbf{E}_2 \quad (z \geq 0) \quad (28a)$$

$$\mathbf{E}_1 = \pm Z_\sigma^2 \mathbf{H}_2 \quad (z \geq 0) \quad (28b)$$

3.2. Application of Babinet's Principle to a Slot Antenna

The purpose of this section is to obtain the radiation conductance of the slot antenna shown in Fig. 3a, using Babinet's principle. For this, the voltage and the current across terminals u and v are denoted as V_{slot} and I_{slot} ,

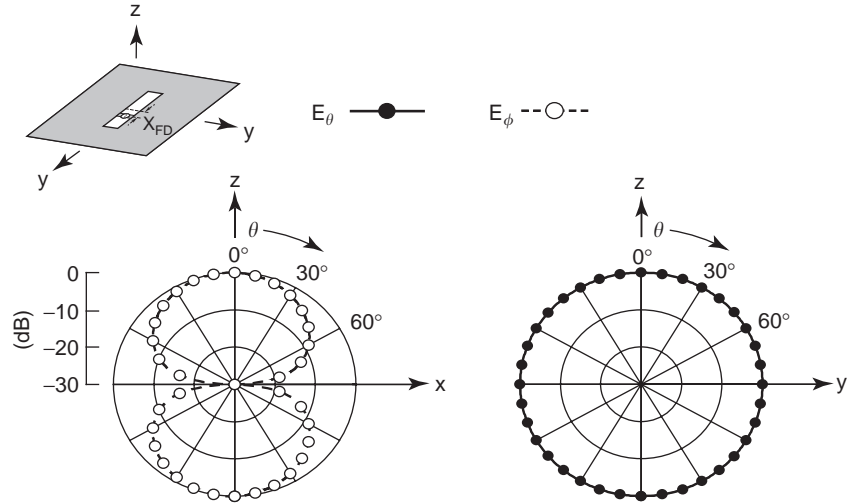


Figure 7. Radiation pattern of a half-wavelength straight slot excited by an off-center source.

$$f = 3 \text{ GHz}, 2L = 0.5\lambda_3, w = 0.03\lambda_3, w_{FD} = 0.02\lambda_3, x_{FD} = 0.15\lambda_3, S_{GPx} = S_{GPy} = \infty$$

respectively. In addition, the electric and magnetic fields for this case are specified by \mathbf{E}_2 and \mathbf{H}_2 , respectively.

We replace the voltage source in Fig. 3a with a magnetic current source, as shown in Fig. 3b. The magnetic current source surrounds a conducting plate section connecting points p and q . In other words, the directions of the magnetic current in the front and back of this section are opposite to each other [5]. It follows that Fig. 3b corresponds to Fig. 2b. Note that the electric and magnetic fields in Fig. 3b are specified by the initial \mathbf{E}_2 and \mathbf{H}_2 , respectively, so that Fig. 3b is equivalent to Fig. 3a.

Figure 3c shows the complementary structure of Fig. 3b. The voltage and the current across terminals p and q are denoted by V_{plate} and I_{plate} , respectively. The electric and magnetic fields for this case are specified by \mathbf{E}_1 and \mathbf{H}_1 , respectively. Note that Fig. 3c corresponds to Fig. 2a.

To solve the original problem shown in Fig. 3a, we apply Babinet's principle to Figs. 3b and 3c with Eq. (27)

$$\begin{aligned} V_{\text{slot}} &= - \int_u^v \mathbf{E}_2 \cdot d\mathbf{l} = \int_u^v (Z_\sigma \mathbf{H}_1) \cdot d\mathbf{l} \\ &= \frac{1}{2} \oint (Z_\sigma \mathbf{H}_1) \cdot d\mathbf{l} = \frac{Z_\sigma}{2} I_{\text{plate}} \end{aligned} \quad (29)$$

$$\begin{aligned} V_{\text{plate}} &= - \int_p^q \mathbf{E}_1 \cdot d\mathbf{l} = - \int_p^q (Z_\sigma \mathbf{H}_2) \cdot d\mathbf{l} \\ &= - \frac{1}{2} \oint (Z_\sigma \mathbf{H}_2) \cdot d\mathbf{l} = \frac{Z_\sigma}{2} I_{\text{slot}} \end{aligned} \quad (30)$$

where $d\mathbf{l}$ is a line element vector. The input impedance of the slot antenna Z_{slot} and that of the plate antenna Z_{plate} are given as

$$Z_{\text{slot}} = \frac{V_{\text{slot}}}{I_{\text{slot}}} \quad (31)$$

$$Z_{\text{plate}} = \frac{V_{\text{plate}}}{I_{\text{plate}}} \quad (32)$$

Therefore, from Eqs. (29) and (30), we have

$$Z_{\text{slot}} \cdot Z_{\text{plate}} = \frac{Z_\sigma^2}{4} \quad (33)$$

Note that this relationship can also be derived using Eq. (28) [5,29].

When $Z_{\text{plate}} = 73 \Omega$ and $Z_\sigma = 120\pi \Omega \equiv Z_0$ (for $\sigma = 0$), Eq. (33) becomes

$$Z_{\text{slot}} = \frac{Z_0^2}{4(73)} \quad (34)$$

Hence, the radiation conductance G_{slot} is written as

$$G_{\text{slot}} = \frac{4(73)}{Z_0^2} \quad (35)$$

It is emphasized that Eq. (35) is derived under the condition that the slot radiates in both the $+z$ and $-z$ spaces. When the slot radiates only in the $+z$ space, as discussed

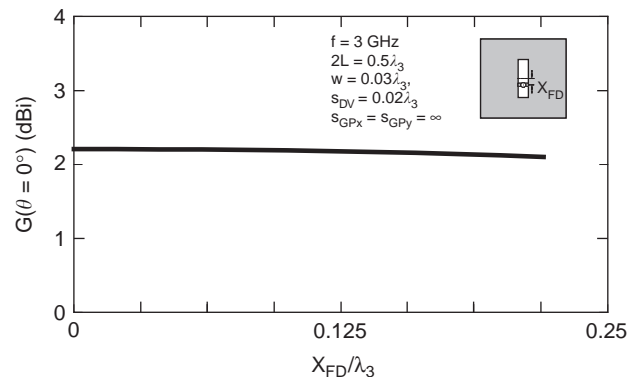


Figure 8. Gain of a half-wavelength straight slot as a function of the source location x_{FD} .

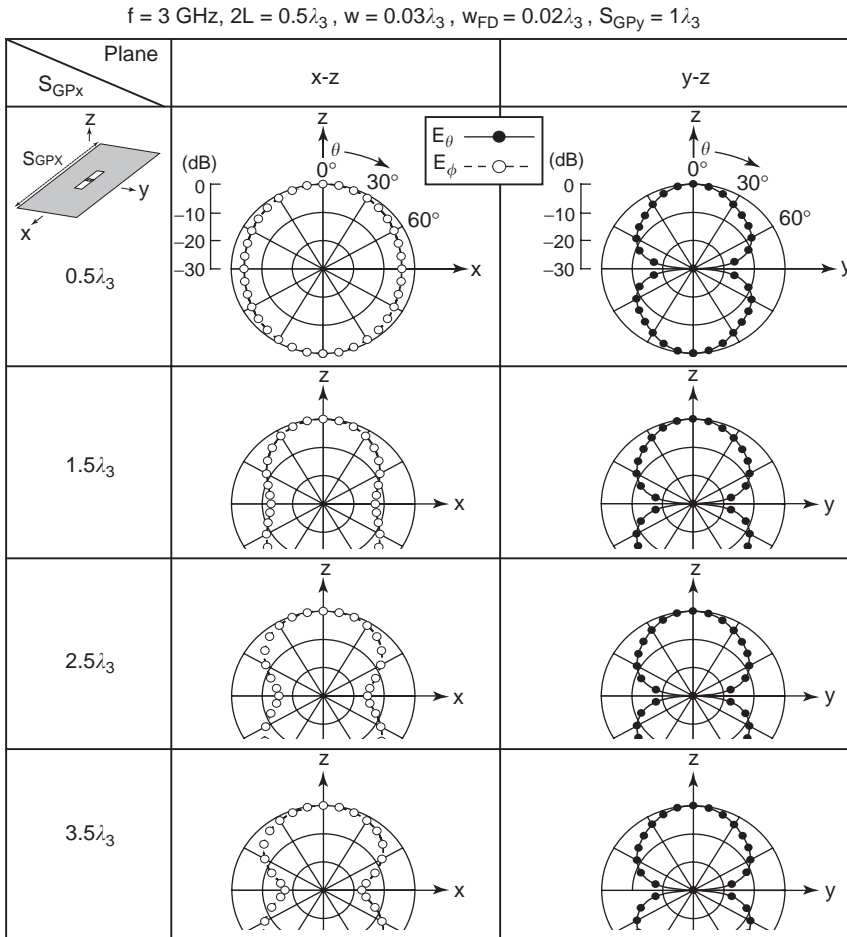


Figure 9. Radiation pattern of a center-fed half-wavelength straight slot as a function of the side length in the x direction, S_{GPX} .

in Section 2, the radiation conductance is given as one-half of G_{slot} :

$$\frac{1}{2}G_{slot} = \frac{2(73)}{Z_0^2} \quad (36)$$

This equals Eq. (17).

4. NUMERICAL TECHNIQUES

The discussion in Section 2 starts with the assumption that the electric field distribution over a straight slot can be represented by Eq. (1). The value of the slot width w for Eq. (1) is not explicitly mentioned. The width is described only as “thin.” The radiation conductance given by Eq. (17) is the value for the limited case where the slot width w approaches zero.

As will be described later, the radiation pattern depends on the size of the conducting sheet in which the slot is cut. Equations (7) and (8) are derived under the condition that the conducting sheet is of infinite extent. However, in practice, the conducting sheet is of finite extent.

One powerful tool for analyzing the slot antenna, taking into account the slot width w and finite sheet size, is the finite-difference time-domain method (FDTD) [6–8].

The FDTD is a numerical solver for the electric field \mathbf{E} and the magnetic field \mathbf{H} . On the basis of the fields obtained using the FDTD, we can evaluate the antenna characteristics.

4.1. FDTD

As shown in Fig. 4a, we form an analysis space of $X \times Y \times Z$ such that it encloses the antenna to be considered. This

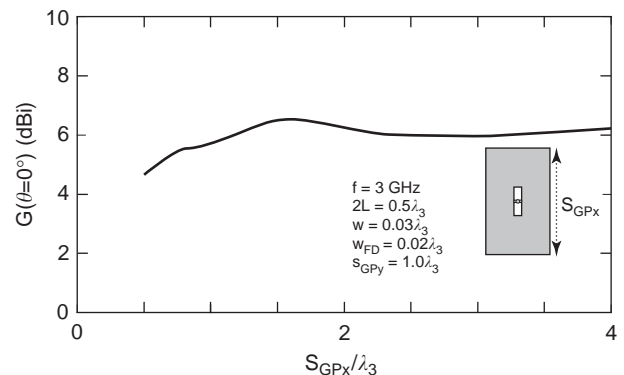


Figure 10. Gain of a center-fed half-wavelength straight slot as a function of the side length in the x direction, S_{GPX} .

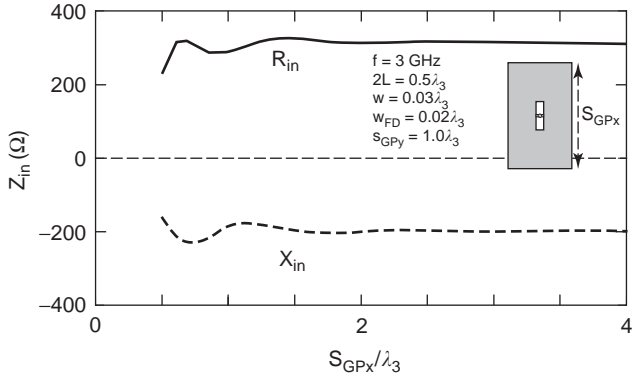


Figure 11. Input impedance of a center-fed half-wavelength straight slot as a function of the side length in the x direction, S_{GPx} .

analysis space consists of numerous cells, each having a volume of $\Delta x \times \Delta y \times \Delta z$. To apply Maxwell's equations to the analysis space, the field components on a cell are assigned, as shown in Fig. 4b, where the Cartesian coordinates are expressed as $(x, y, z) = (i\Delta x, j\Delta y, k\Delta z)$ with i, j , and k being integers.

To terminate the outer surface of the analysis space, we express the tangential electric field components E_y and E_z

at the boundary $x = \xi_x$ as $E_y(t + \Delta t, \xi_x)$ and $E_z(t + \Delta t, \xi_x)$, respectively, and denote them as $E(t + \Delta t, \xi)$ for simplicity, where t and Δt denote the time coordinate and timestep, respectively. Similarly, the tangential electric field components at $y = \xi_y$ and $z = \xi_z$ are expressed as $E(t + \Delta t, \xi)$. Liao shows that this $E(t + \Delta t, \xi)$ is updated using $E(t, \xi)$, $E(t, \xi - \Delta \xi)$, $E(t, \xi - 2\Delta \xi)$, $E(t - \Delta t, \xi)$, $E(t - \Delta t, \xi - \Delta \xi)$, $E(t - \Delta t, \xi - 2\Delta \xi)$, $E(t - \Delta t, \xi - 3\Delta \xi)$, and $E(t - \Delta t, \xi - 4\Delta \xi)$ [8]. In this article, we use Liao's result as the absorbing boundary condition.

The time coordinate t is expressed as $n\Delta t$, where n is an integer. For simplicity, a function $g(x, y, z, t) = g(i\Delta x, j\Delta y, k\Delta z, n\Delta t)$ is denoted as $g^n(i, j, k)$ in the FTDDM. Then, derivatives with respect to x and t are approximated with central finite differences as follows:

$$\frac{\partial g^n(i, j, k)}{\partial x} \approx \frac{g^n\left(i + \frac{1}{2}, j, k\right) - g^n\left(i - \frac{1}{2}, j, k\right)}{\Delta x} \quad (37)$$

$$\frac{\partial \mathbf{E}}{\partial t} \Big|_{t=[n-(1/2)]\Delta t} \approx \frac{\mathbf{E}^n - \mathbf{E}^{n-1}}{\Delta t} \quad (38)$$

$$\frac{\partial \mathbf{H}}{\partial t} \Big|_{t=n\Delta t} \approx \frac{\mathbf{H}^{n+(1/2)} - \mathbf{H}^{n-(1/2)}}{\Delta t} \quad (39)$$

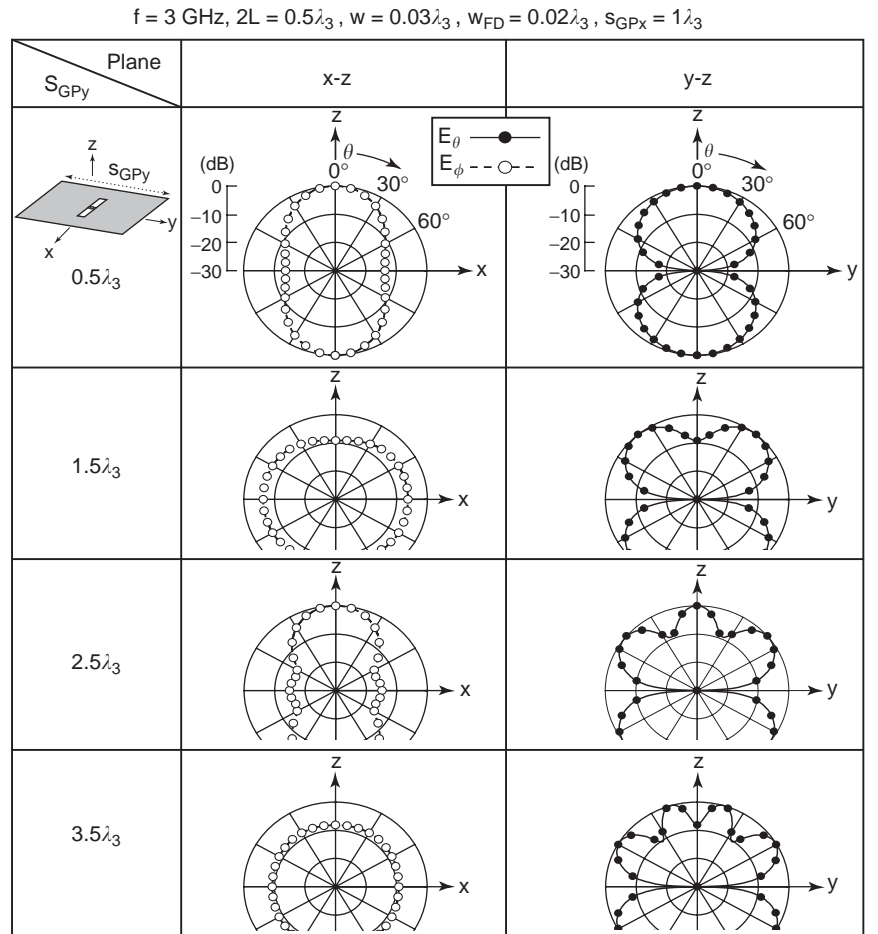


Figure 12. Radiation pattern of a center-fed half-wavelength straight slot as a function of the side length in the y direction, S_{GPy} .

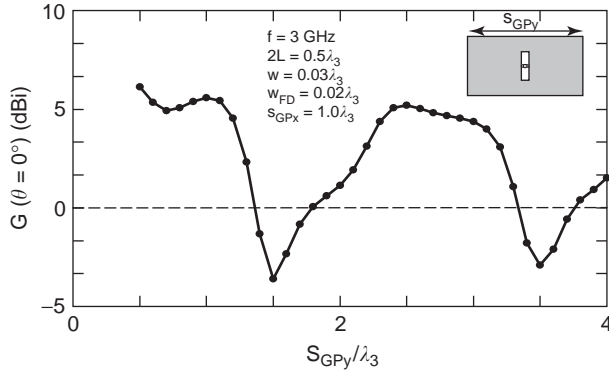


Figure 13. Gain of a center-fed half-wavelength straight slot as a function of the side length in the y direction, S_{GPy} .

Using Eqs. (38) and (39), Maxwell's curl equations

$$\nabla \times \mathbf{E} = -\mu \frac{\partial \mathbf{H}}{\partial t} \quad (40)$$

$$\nabla \times \mathbf{H} = \sigma \mathbf{E} + \varepsilon \frac{\partial \mathbf{E}}{\partial t} \quad (41)$$

are transformed to

$$\mathbf{E}^n = \frac{2\varepsilon - \sigma\Delta t}{2\varepsilon + \sigma\Delta t} \mathbf{E}^{n-1} + \frac{2\Delta t}{2\varepsilon + \sigma\Delta t} \nabla \times \mathbf{H}^{n-(1/2)} \quad (42)$$

$$\mathbf{H}^{n+(1/2)} = \mathbf{H}^{n-(1/2)} - \frac{\Delta t}{\mu} \nabla \times \mathbf{E}^n \quad (43)$$

where ε , μ , and σ are the permittivity, permeability, and conductivity, respectively. Note that the time at which $\sigma \mathbf{E}$ in Eq. (41) is evaluated is $t = [n - (1/2)]\Delta t$, corresponding to the time at which $\partial \mathbf{E}/\partial t$ is evaluated. This $\sigma \mathbf{E}$ is expressed as $\sigma \mathbf{E}^{n-(1/2)}$ and approximated by the average of $\sigma \mathbf{E}^n$ and $\sigma \mathbf{E}^{n-1}$ to obtain Eq. (42).

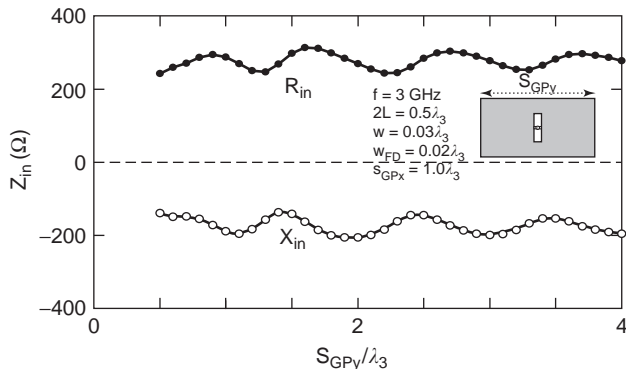


Figure 14. Input impedance of a center-fed half-wavelength straight slot as a function of the side length in the y direction, S_{GPy} .

Using Eq. (37), the finite-difference form for the x component of Eq. (42) is written as

$$\begin{aligned} E_x^n \left(i + \frac{1}{2}, j, k \right) &= e_{x/0} \left(i + \frac{1}{2}, j, k \right) E_x^{n-1} \left(i + \frac{1}{2}, j, k \right) \\ &+ e_{x/y} \left(i + \frac{1}{2}, j, k \right) \left[H_z^{n-(1/2)} \left(i + \frac{1}{2}, j + \frac{1}{2}, k \right) \right. \\ &\quad \left. - H_z^{n-(1/2)} \left(i + \frac{1}{2}, j - \frac{1}{2}, k \right) \right] \\ &- e_{x/z} \left(i + \frac{1}{2}, j, k \right) \left[H_y^{n-(1/2)} \left(i + \frac{1}{2}, j, k + \frac{1}{2} \right) \right. \\ &\quad \left. - H_y^{n-(1/2)} \left(i + \frac{1}{2}, j, k - \frac{1}{2} \right) \right] \end{aligned} \quad (44)$$

where

$$\begin{aligned} e_{x/0} \left(i + \frac{1}{2}, j, k \right) &= \frac{2\varepsilon \left(i + \frac{1}{2}, j, k \right) - \sigma \left(i + \frac{1}{2}, j, k \right) \Delta t}{2\varepsilon \left(i + \frac{1}{2}, j, k \right) + \sigma \left(i + \frac{1}{2}, j, k \right) \Delta t} \end{aligned} \quad (45)$$

$$\begin{aligned} e_{x/y} \left(i + \frac{1}{2}, j, k \right) &= \frac{2\Delta t}{2\varepsilon \left(i + \frac{1}{2}, j, k \right) + \sigma \left(i + \frac{1}{2}, j, k \right) \Delta t} \frac{1}{\Delta y} \end{aligned} \quad (46)$$

$$\begin{aligned} e_{x/z} \left(i + \frac{1}{2}, j, k \right) &= \frac{2\Delta t}{2\varepsilon \left(i + \frac{1}{2}, j, k \right) + \sigma \left(i + \frac{1}{2}, j, k \right) \Delta t} \frac{1}{\Delta z} \end{aligned} \quad (47)$$

The two other components of the electric field \mathbf{E}^n and three components of the magnetic field $\mathbf{H}^{n+(1/2)}$ are similarly formulated.

After determining \mathbf{E} and \mathbf{H} , the current along the antenna conductor I is obtained by integrating the magnetic field \mathbf{H} around the antenna conductor (Ampere's law). The input impedance $Z_{in} = R_{in} + jX_{in}$ is given as $V_{in}(\omega)/I_{in}(\omega)$, where $V_{in}(\omega)$ and $I_{in}(\omega)$ are the input voltage and current in the frequency domain, respectively. These $V_{in}(\omega)$ and $I_{in}(\omega)$ are obtained by Fourier-transforming the time-domain voltage and current, $V_{in}(t)$ and $I_{in}(t)$, respectively.

The radiation field \mathbf{E}_{rad} is calculated using the equivalence theorem [26]. The θ and ϕ components of the

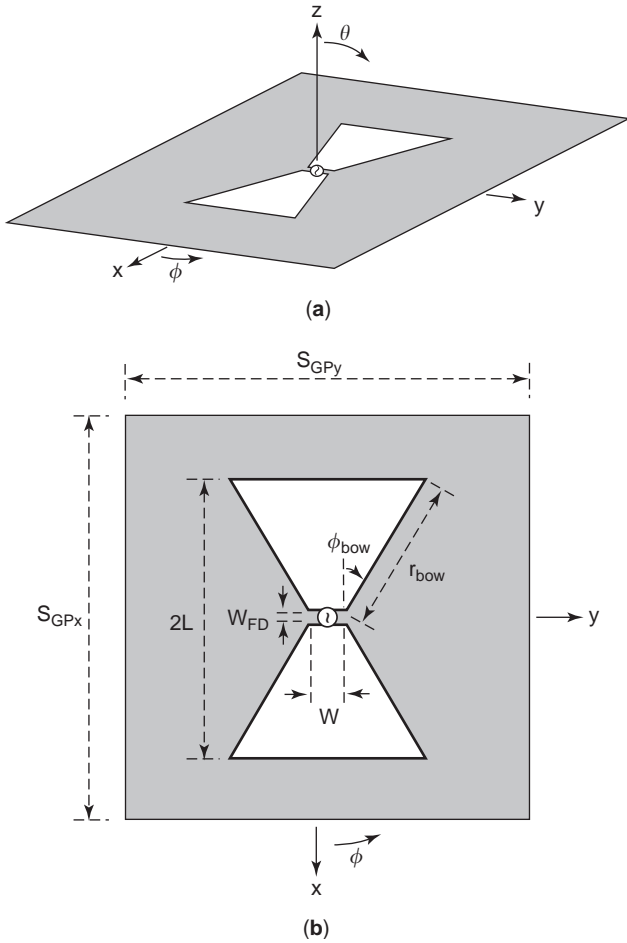


Figure 15. Bowtie slot antenna: (a) perspective view; (b) top view.

radiation field (in the frequency domain) are given as

$$E_{\theta}(\omega) = -\frac{jk_0}{4\pi} \frac{e^{-jk_0 r}}{r} [Z_0 \mathbf{N}(\omega) \cdot \hat{\theta} + \mathbf{L}(\omega) \cdot \hat{\phi}] \quad (48)$$

$$E_{\phi}(\omega) = -\frac{jk_0}{4\pi} \frac{e^{-jk_0 r}}{r} [Z_0 \mathbf{N}(\omega) \cdot \hat{\phi} - \mathbf{L}(\omega) \cdot \hat{\theta}] \quad (49)$$

where

$$\mathbf{N}(\omega) = \int_{\text{closed surface}} \mathbf{J}_s(\omega, \mathbf{r}') e^{jk_0 \hat{\mathbf{r}} \cdot \mathbf{r}'} dS' \quad (50)$$

$$\mathbf{L}(\omega) = \int_{\text{closed surface}} \mathbf{M}_s(\omega, \mathbf{r}') e^{jk_0 \hat{\mathbf{r}} \cdot \mathbf{r}'} dS' \quad (51)$$

Z_0 is the intrinsic impedance ($120\pi \Omega$) and k_0 is the wave-number. Note that the $\mathbf{J}_s(\omega, \mathbf{r}')$, and $\mathbf{M}_s(\omega, \mathbf{r}')$ are, respectively, the Fourier transforms of the time-domain currents $\mathbf{J}_s(t, \mathbf{r}') = \hat{\mathbf{n}} \times \mathbf{H}(t, \mathbf{r}')$ and $\mathbf{M}_s(t, \mathbf{r}') = \mathbf{E}(t, \mathbf{r}') \times \hat{\mathbf{n}}$, where \mathbf{r}' is the position vector from the coordinate origin to the point at which $\mathbf{E}(t, \mathbf{r}')$ and $\mathbf{H}(t, \mathbf{r}')$ are evaluated on the closed surface and $\hat{\mathbf{n}}$ is the outward unit vector normal to the closed surface (see Fig. 4c).

For the axial ratio (AR) calculation, the radiation field ($\mathbf{E}_{\text{rad}} = E_{\theta} \hat{\theta} + E_{\phi} \hat{\phi}$) is decomposed into two circularly polarized (CP) wave components

$$\begin{aligned} \mathbf{E}_{\text{rad}}(r, \theta, \phi) = & E_R(r, \theta, \phi)(\hat{\theta} - j\hat{\phi}) \\ & + E_L(r, \theta, \phi)(\hat{\theta} + j\hat{\phi}) \end{aligned} \quad (52)$$

where the first term represents a right-hand CP wave component and the second represents a left-hand CP wave component. Using these two components, the axial ratio is given as $\text{AR} = (|E_R| + |E_L|) / |E_R - E_L|$.

The antenna gain at a far-field point (r, θ, ϕ) is defined as $G = (|E_{\theta}|^2 + |E_{\phi}|^2) r^2 / 30P_{\text{in}}$, where P_{in} is the power input to the antenna. Since a relationship of $|E_{\theta}|^2 + |E_{\phi}|^2 = 2(|E_R|^2 + |E_L|^2)$ is obtained from Eq. (52), the gain is written as $G = (|E_R|^2 + |E_L|^2) r^2 / 30P_{\text{in}}$. Therefore, the gains for a right-hand circularly polarized wave and left-hand circularly polarized wave are calculated as $G_R = |E_R(r, \theta, \phi)|^2 r^2 / 30P_{\text{in}}$ and $G_L = |E_L(r, \theta, \phi)|^2 r^2 / 30P_{\text{in}}$, respectively.

For $|E_R| > |E_L|$, G_R increases and G_L decreases as the axial ratio AR decreases, in accordance with $G_R = G / [1 + \{(AR - 1)/(AR + 1)\}^2]$ and $G_L = G / [1 + \{(AR + 1)/(AR - 1)\}^2]$. Note that $G_R = G$ and $G_L = 0$ when $\text{AR} = 1$ (i.e., the polarization is perfectly circular with a right-hand sense).

5. ANTENNA CHARACTERISTICS OF A HALF-WAVELENGTH STRAIGHT SLOT AS A FUNCTION OF SOURCE LOCATION x_{FD}

We continue our analysis of a half-wavelength straight slot cut in a conducting sheet of infinite extent using the FDTD. As shown in Fig. 5, the slot is excited with a voltage source at $x = x_{\text{FD}}$. No assumption about the electric field over the slot is made for the analysis, unlike the analysis in Section 2. In addition, the analysis is performed with an explicit slot width w [9].

Figure 6 shows the input impedance Z_{in} as a function of the source location x_{FD} , where the slot width is chosen to be $w = 0.03\lambda_3$ (λ_3 : the wavelength in free space at 3 GHz). It is found that the input impedance has a purely resistive value at $x_{\text{FD, res}}$ off the centerpoint ($x_{\text{FD}} = 0$).

The source location x_{FD} does not affect the radiation pattern. Figure 7 shows a representative radiation pattern at $x_{\text{FD}} = x_{\text{FD, res}}$. The radiation is *linearly polarized*. The half-power beamwidth (HPBW) is approximately 76° in the x - z plane [which is nearly equal to the HPBW for an infinitesimally thin slot (78° for $w \rightarrow 0$)]. Note that the radiation pattern is symmetric with respect to the x - y plane.

Figure 8 shows the gain in the z direction as a function of x_{FD} . The fact that the HPBW remains almost unchanged with x_{FD} leads to nearly constant gain. The gain is approximately 2.2 dBi at $x_{\text{FD}} = 0$. This value is very close to the gain of a center-fed cylindrical dipole antenna (2.16 dBi) [27].

6. EFFECTS OF FINITENESS OF CONDUCTING SHEET ON RADIATION CHARACTERISTICS OF A CENTER-FED HALF-WAVELENGTH STRAIGHT SLOT

The discussion above is based on the condition that the half-wavelength straight slot is cut in a conducting sheet

$$f = 3 \text{ GHz}, 2L = 0.5\lambda_3, w = 0.03\lambda_3, w_{FD} = 0.02\lambda_3, s_{GPx} = s_{GPx} = 1\lambda_3$$

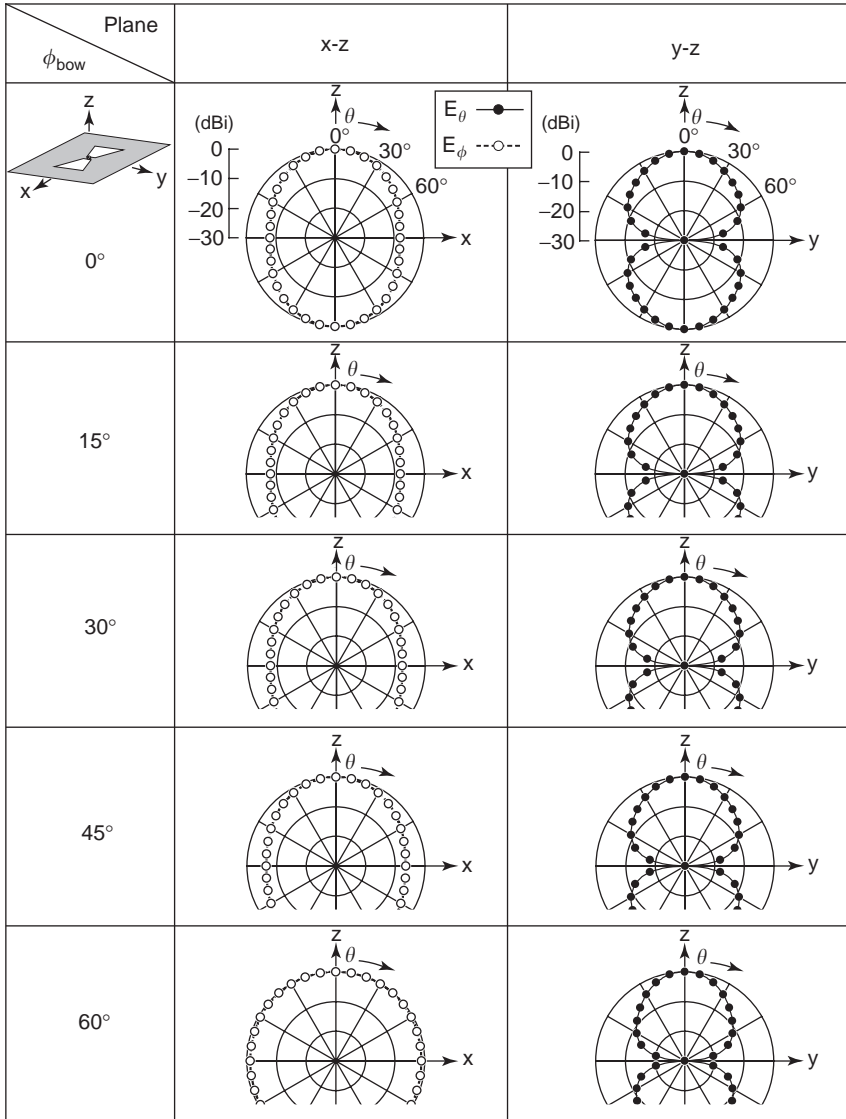


Figure 16. Radiation pattern of a bowtie slot as a function of the bowtie angle ϕ_{bow} .

of infinite extent ($s_{GPx} = \infty$ and $s_{GPy} = \infty$). In this section, the conducting sheet is chosen to be of finite extent [9,10]. Note that the slot width is fixed to be $w = 0.03\lambda_3$ (the same value used in Section 5) and the voltage source is located at $x = 0$ throughout this section.

6.1. Effects of Side Length in x Direction, s_{GPx}

Figure 9 shows the radiation pattern as a function of the side length in the x direction s_{GPx} , where the side length in the y direction s_{GPy} is fixed to be $1\lambda_3$ (λ_3 : the wavelength in free space at 3 GHz). The radiation pattern is symmetric with respect to the x - y plane, and hence the radiation pattern in the $-z$ region is not fully shown except for $s_{GPx} = 0.5\lambda_3$. It is clear that the radiation pattern in the x - z plane is affected by the finiteness of the conducting sheet. This leads to a gain higher than that for an infinite conducting sheet (2.2 dBi), as shown in Fig. 10.

Figure 11 shows the input impedance as a function of the side length s_{GPx} . The variation in the input impedance is relatively small for s_{GPx} greater than two wavelengths. As seen later, this behavior contrasts with that of the impedance as a function of the side length in the y direction, s_{GPy} .

6.2. Effects of Side Length in y Direction, s_{GPy}

Noticeable effects of the finiteness of the conducting sheet on the antenna characteristics are found when the side length in the y direction, s_{GPy} , is varied. Figure 12 shows the radiation pattern as a function of the length s_{GPy} , where the side length in the x direction is fixed to be $s_{GPx} = 1\lambda_3$. Note that the radiation patterns are symmetric with respect to the x - y plane.

As the side length s_{GPy} increases, the radiation pattern in the y - z plane undulates. This undulation results from

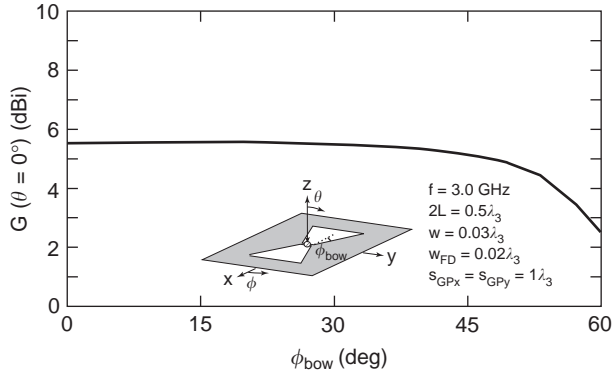


Figure 17. Gain of a bowtie slot as a function of the bowtie angle ϕ_{bow} .

radiation fields from the following three sources [10]: (1) the y -directed electric field source over the slot, (2) the y -directed electric field source distributed along the x -directed edge at $y = \frac{1}{2}s_{\text{GP}y}$, and (3) the y -directed electric field source distributed along the x -directed edge at $y = -\frac{1}{2}s_{\text{GP}y}$. The maximum and minimum values of the undulation occur at

$$\theta = \sin^{-1} \frac{n\lambda}{s_{\text{GP}y}} \quad (53)$$

where n is an integer. If $\cos \delta$ (where δ is the phase difference of the edge sources 2 and 3 with respect to source 1) is positive, then maxima are obtained with even values of n and minima with odd values of n .

The effects of the variation in the radiation pattern clearly appear in the gain. Figure 13 shows the z -direction gain as a function of the side length $s_{\text{GP}y}$. The gain drops at $s_{\text{GP}y} = 1.5\lambda_3$ and $3.5\lambda_3$ are due to the decrease in the radiation field intensity in the z direction (see the radiation patterns at $s_{\text{GP}y} = 1.5\lambda_3$ and $3.5\lambda_3$ in Fig. 12).

The input impedance is also clearly varied with the side length in the y direction, $s_{\text{GP}y}$. Figure 14 shows the input impedance as a function of $s_{\text{GP}y}$. It is observed that the input impedance varies periodically with $s_{\text{GP}y}$.

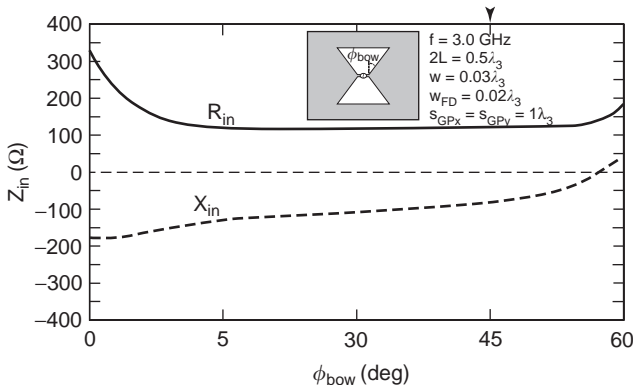


Figure 18. Input impedance of a bowtie slot as a function of the bowtie angle ϕ_{bow} .

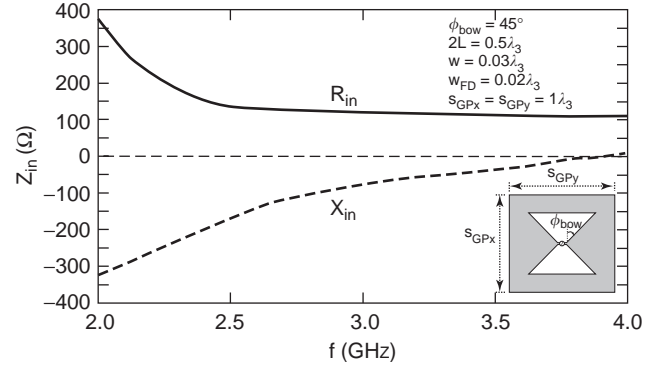


Figure 19. Input impedance of a bowtie slot as a function of frequency.

7. BOWTIE SLOT ANTENNA

A bowtie slot antenna is created by linearly increasing the width of a straight slot antenna, shown in Fig. 1, from its center to both ends (see Fig. 15). The following parameters specify the bowtie: the inner width w , radial length r_{bow} , and bowtie angle ϕ_{bow} .

A bowtie cut in a conducting sheet of finite extent ($s_{\text{GP}x} \times s_{\text{GP}y} = 1\lambda_3 \times 1\lambda_3$, where λ_3 is the wavelength in free space at 3 GHz) is investigated in this section, where the bowtie length and the inner width are fixed to be $2L = 0.5\lambda_3$ and $w = 0.03\lambda_3$, respectively [13]. The excitation of this half-wavelength bowtie is performed with a voltage source located at $x = 0$.

Here we describe the effects of the bowtie angle ϕ_{bow} on the antenna characteristics. Figures 16 and 17 show, respectively, the radiation pattern and gain as a function of ϕ_{bow} . The effects of the bowtie angle on the radiation pattern are more noticeable in the x - z plane than in the y - z plane. As the bowtie angle increases, the half-power beamwidth in the x - z plane gradually increases, leading to the gradual decrease in the gain. The gain is approximately 5.2 dBi at $\phi_{\text{bow}} = 45^\circ$ and 2.6 dBi at $\phi_{\text{bow}} = 60^\circ$.

Note that the gain at $\phi_{\text{bow}} = 0^\circ$ in Fig. 17, which is the gain of a half-wavelength straight slot in a $1\lambda_3 \times 1\lambda_3$ conducting sheet, is approximately 5.5 dBi. This value is

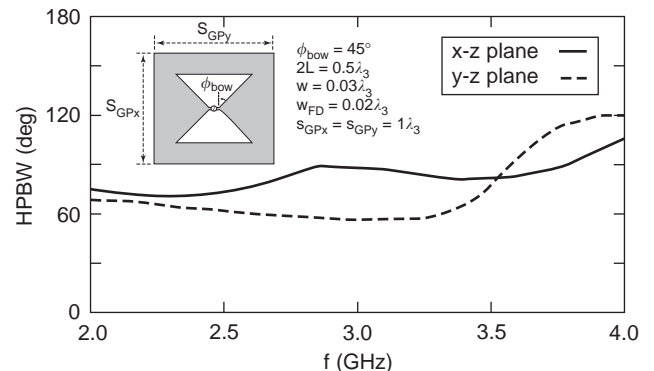


Figure 20. Half-power beamwidths of a bowtie slot as a function of frequency.

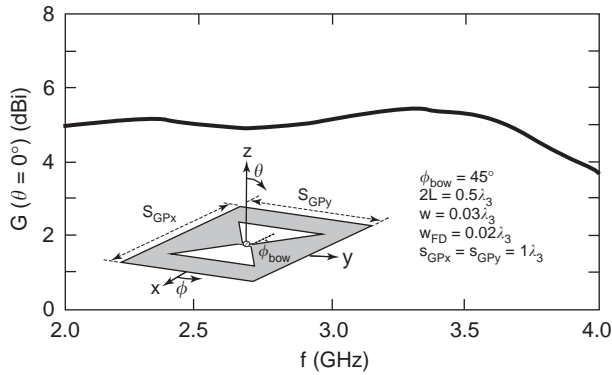


Figure 21. Gain of a bowtie slot as a function of frequency.

3.3 dBi higher than the gain of a half-wavelength straight slot cut in an *infinite* conducting sheet (approximately 2.2 dBi, as described in Section 5).

Figure 18 shows the input impedance as a function of the bowtie angle ϕ_{bow} . The impedance seamlessly changes

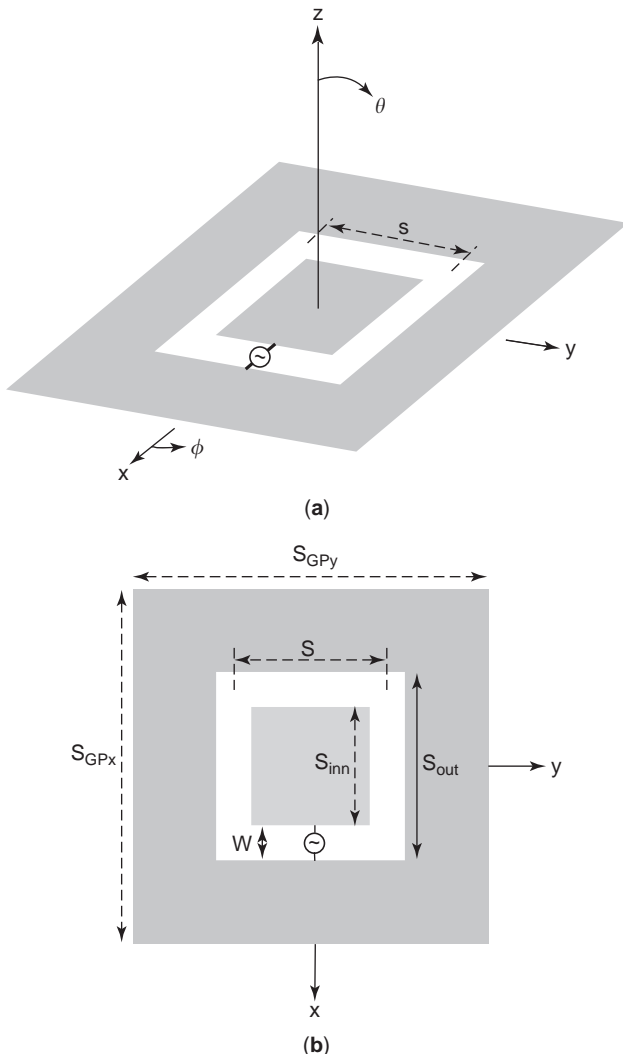


Figure 22. Loop slot antenna: (a) perspective view; (b) top view.

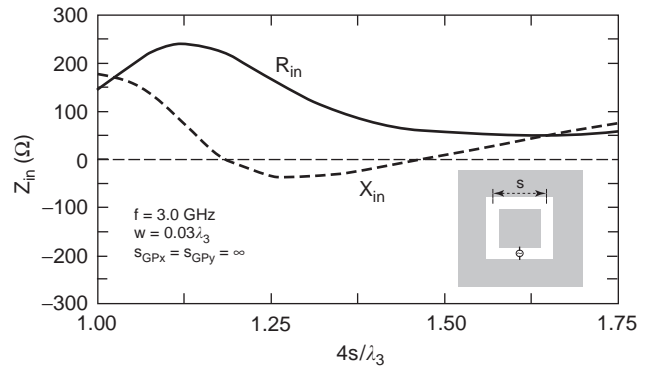


Figure 23. Input impedance of a loop slot as a function of the circumference.

with the bowtie angle. From this fact it is expected that the input impedance will vary smoothly when the frequency is changed. Figure 19 confirms this expectation, where the bowtie angle is chosen to be $\phi_{\text{bow}} = 45^\circ$.

We further investigate the frequency response of the bowtie with $\phi_{\text{bow}} = 45^\circ$. Figures 20 and 21 show, respectively, the half-power beamwidth and gain as a function of frequency. It is found that an average value of the half-power beamwidths in the two principal planes (x - z and y - z planes) is relatively constant below 3.5 GHz, corresponding to a relatively constant gain at frequencies below 3.5 GHz. The lower gain at 4 GHz corresponds to the wider half-power beamwidths.

8. LOOP SLOT ANTENNA

The slots analyzed in the previous sections have distinct ends, while the slot in this section forms a loop (see Fig. 22). The loop is specified by the outer side length s_{out} and inner side length s_{inn} . The slot width is given as $w = \frac{1}{2}(s_{\text{out}} - s_{\text{inn}})$ and an average value of the outer and inner lengths of the loop (simply called “loop circumference”) is given as $4s$, where $s = \frac{1}{2}(s_{\text{out}} + s_{\text{inn}})$. The loop slot is excited with a voltage source on the x axis.

First, we analyze the loop slot under the condition that the loop is cut in a conducting sheet of infinite size ($S_{\text{GPx}} = \infty$ and $S_{\text{GPy}} = \infty$) [14]. Figures 23 and 24 show, respectively, the input impedance and the radiation pattern as a function of the loop circumference $4s$, where the frequency and the slot width are fixed to be $f = 3 \text{ GHz}$ and $w = 3 \text{ mm} = 0.03\lambda_3$, respectively. It is found that the input impedance becomes purely resistive at two loop circumferences below $1\frac{3}{4}$ wavelengths. It is also found that, as the loop circumference $4s$ is increased, the radiation pattern in the x - z plane becomes increasingly asymmetric with respect to the z axis. Note that the radiation pattern in the y - z plane is always symmetric with respect to the z axis.

The cross-polarization component in the y - z plane (E_θ) is due to the radiation from the two x -directed slots, which are part of the loop slot (one is located on the $+y$ side of the x - y plane, and the other is located on the $-y$ side of the x - y plane). The electric field distributed along the

$$f = 3 \text{ GHz}, w = 0.03\lambda_3, s_{GPx} = s_{GPy} = \infty$$

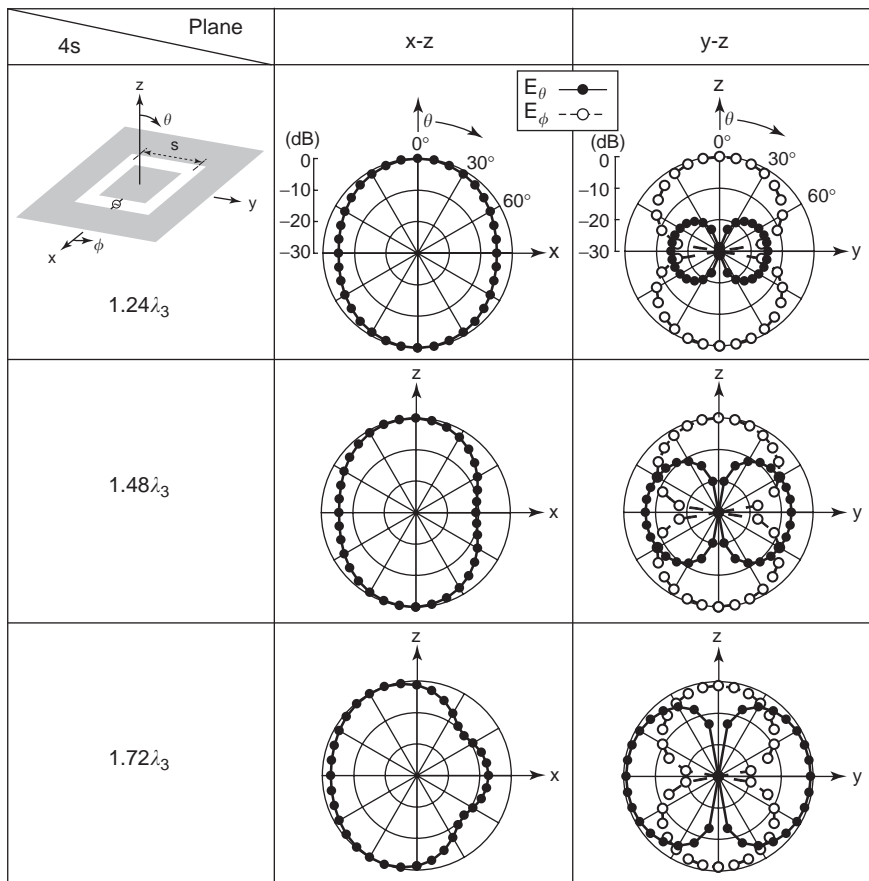


Figure 24. Radiation pattern of a loop slot as a function of the circumference.

x -directed slot on the $+y$ side has the same amplitude as that along the x -directed slot on the $-y$ side. However, the phase difference between these electric fields is 180° . Therefore, the resulting radiation field E_θ in the z direction is always zero. The radiation pattern of the E_θ depends on the distance between these two slots.

The asymmetric pattern in the x - z plane and the increase in the intensity of the E_θ component in the y - z plane affect the gain in the z direction, $G(\theta = 0^\circ)$. Figure 25 shows the gain as a function of the loop circumference $4s$. A gain of approximately 4 dB_i, observed at $4s = 1\frac{1}{2}\lambda_3$, is decreased to 1.1 dB_i at $4s = 1\frac{3}{4}\lambda_3$.

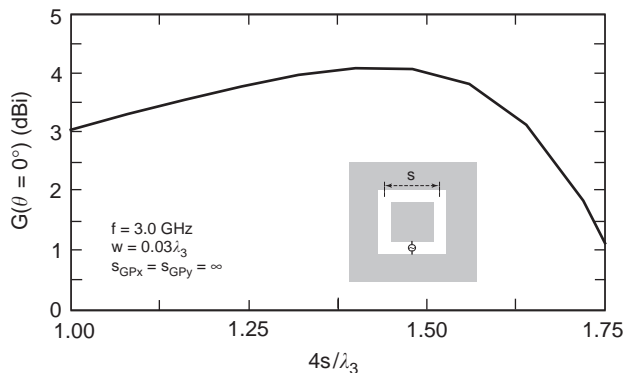


Figure 25. Gain of a loop slot as a function of the circumference.

The discussion above is based on the condition that the conducting sheet, in which the loop slot is cut, is of infinite extent. It is worth comparing the radiation characteristics of a loop slot in an infinite sheet with those of a loop slot in a finite sheet [14]. For comparison, we choose the loop circumference to be $4s = 1\lambda_3$.

Figures 26a and 26b show the radiation patterns of the loop slot in an infinite sheet and a finite sheet, respectively, where the finite sheet is square with side lengths $s_{GPx} = s_{GPy} = 1\lambda_3$. It is found that, in the x - z plane, an almost omnidirectional radiation pattern is obtained for the infinite sheet, while a figure-eight-shaped radiation pattern is obtained for the finite sheet. The difference in the radiation patterns appears as a difference in the gains; the gain for the infinite sheet is 3.0 dB_i and the gain for the finite sheet is 5.4 dB_i. Note that the input impedance for the finite sheet ($s_{GPx} = s_{GPy} = 1\lambda_3$) is found to be almost equal to that for the infinite sheet.

9. CURL SLOT ANTENNA

The radiation from the straight, bowtie, and loop slot antennas in the previous sections is linearly polarized. The radiation from the curl slot antenna to be discussed in this section is circularly polarized. Note that the curl is a simplified spiral structure with an extremely small number of turns.

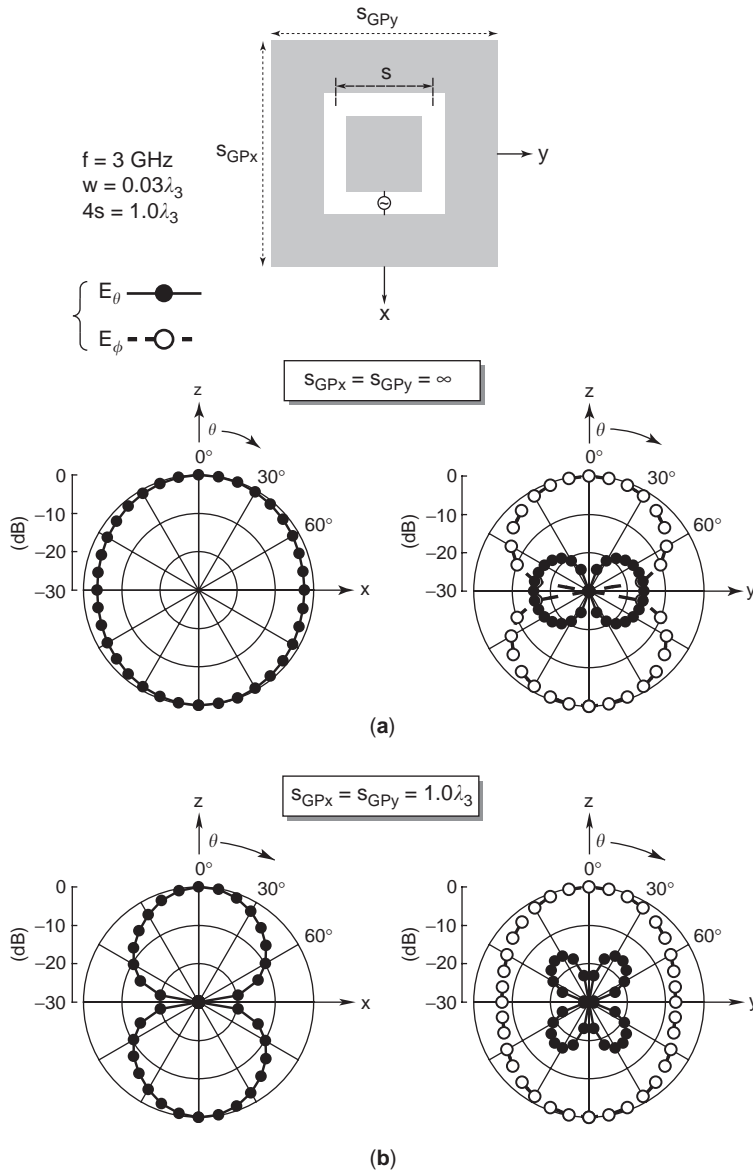


Figure 26. Radiation patterns: (a) loop slot cut in an infinite conducting sheet; (b) loop slot cut in a finite conducting sheet.

9.1. A Circularly Polarized Wave from a Curl Slot Antenna

Figure 27 shows a curl slot cut in the upper conducting plate of a triplate transmission line. The curl slot is defined by an Archimedean spiral function of $r = a_{sp}\phi_s$, where r is the radial distance from the center of the curl to the centerline of the slot arm, a_{sp} is the spiral constant, and ϕ_s is the winding angle (starting at ϕ_{st} and ending at ϕ_{end}). The width of the curl slot is denoted by w .

A feed stripline of width w_{strip} , which is made from the middle plate of the triplate, is sandwiched by dielectric sheets of low relative permittivity ϵ_r . The feed stripline is not in contact with the curl slot. The electromagnetic energy flowing along the stripline is coupled to the curl slot at point P_c . This kind of coupling is called *proximity coupling*. Note that the length of the stripline from point P_c to the open end P_e is chosen to be one-quarter wavelength at the design frequency.

The curl slot is designed to radiate a circularly polarized wave at 11.85 GHz. For this, we optimize the end angle of the curl ϕ_{end} by observing the axial ratio [17]. Figure 28 shows the axial ratio AR as a function of ϕ_{end} . It is found that the radiation is circularly polarized near $\phi_{end} = 8.16\pi \text{ rad} \equiv \phi_{end, opt}$. In the following discussion, we fix the end angle to be $\phi_{end, opt}$.

The radiation from the curl slot is unidirectional by virtue of the lower conducting plate of the triplate transmission line (which acts as a reflector). Figure 29 shows unidirectional radiation patterns, where the radiation field is decomposed into two components: a right-hand circularly polarized wave component E_R and a left-hand circularly polarized wave component E_L . The E_R component results from a dominant magnetic current flowing from the inner slot end toward the outer slot end. Note that the E_L component results from a minor reverse magnetic current flowing from the outer slot end toward the

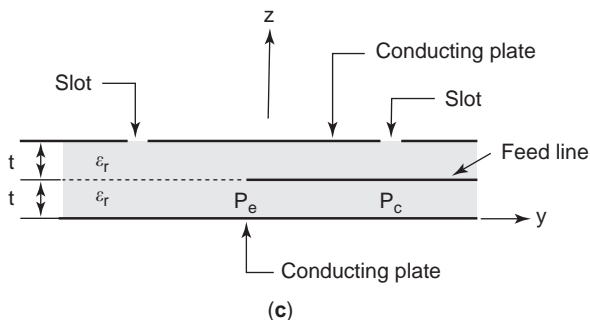
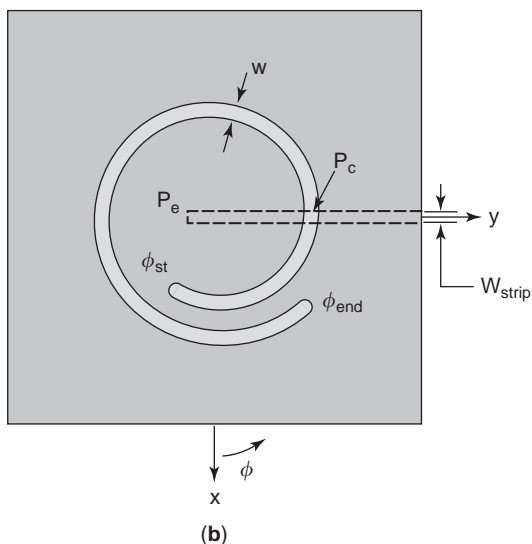
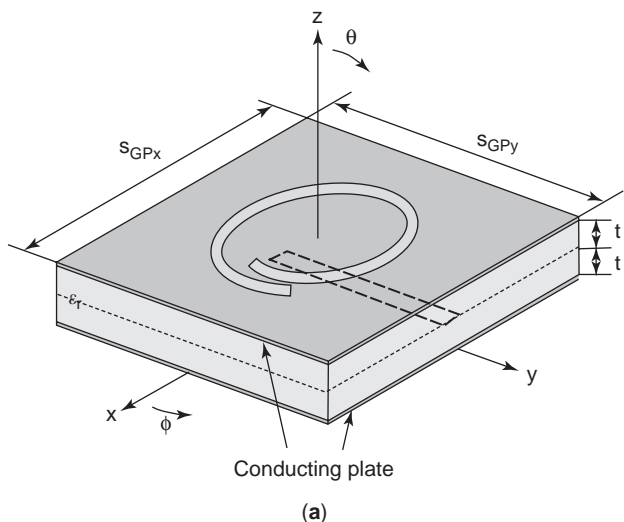


Figure 27. Curl slot antenna: (a) perspective view; (b) top view; (c) side view.

inner slot end. The E_L component is undesirable because it deteriorates the axial ratio.

Figure 30 shows the axial ratio as a function of frequency. The frequency bandwidth for a 3-dB axial ratio criterion is calculated to be 6.2%. Within this axial ratio bandwidth the directivity in the z direction is relatively constant with a maximum value of approximately 6.4 dB.

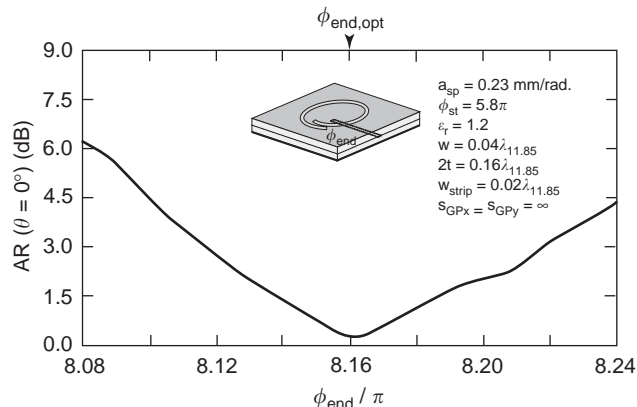


Figure 28. Axial ratio of a curl slot as a function of the end angle.

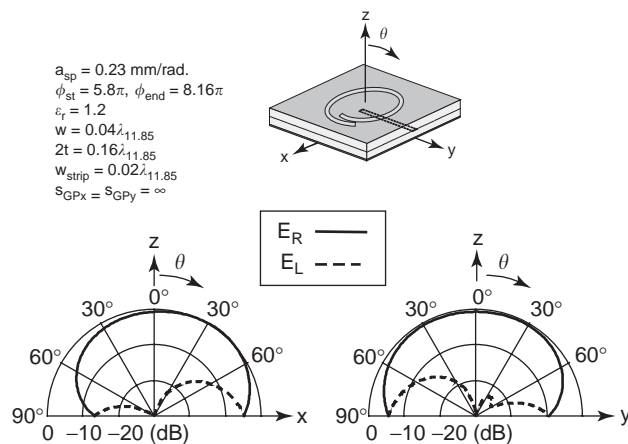


Figure 29. Radiation pattern of a curl slot.

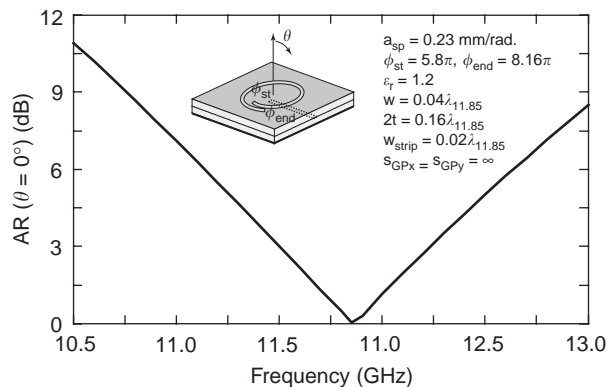


Figure 30. Axial ratio of a curl slot as a function of frequency.

Note that impedance matching between the triplate transmission line and the curl can be performed by inserting a matching network (e.g., quarter-wavelength transformer) into the feed stripline.

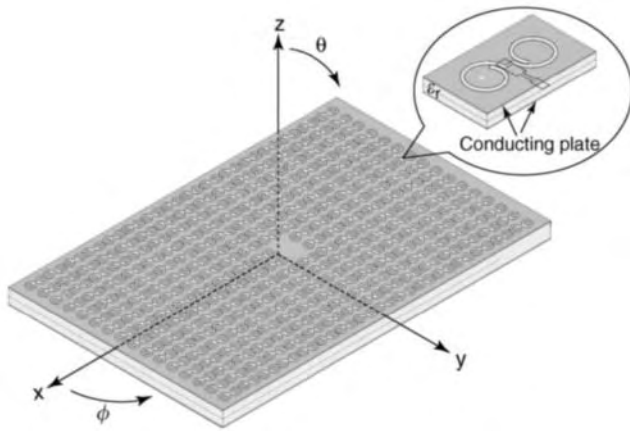


Figure 31. Dual-curl slot array.

9.2. Dual-Curl Slot Array

We are able to realize a high-gain antenna radiating a circularly polarized wave by arraying radiation elements. Figure 31 shows an example of such arrays, where the array element (array unit) is a pair of curl slots, whose outer slot arm ends are connected to the ends of a short straight slot. This array element is called a *dual-curl slot* (DCS) or *dual-spiral slot*. The DCS has the advantage that it is simultaneously coupled to a single feedline.

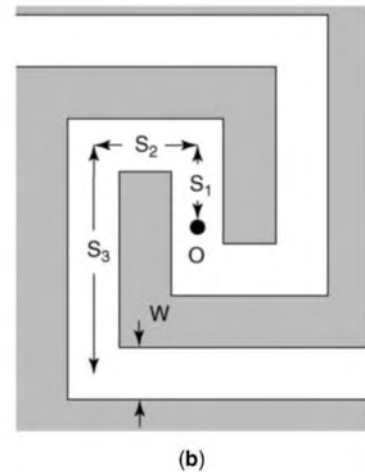
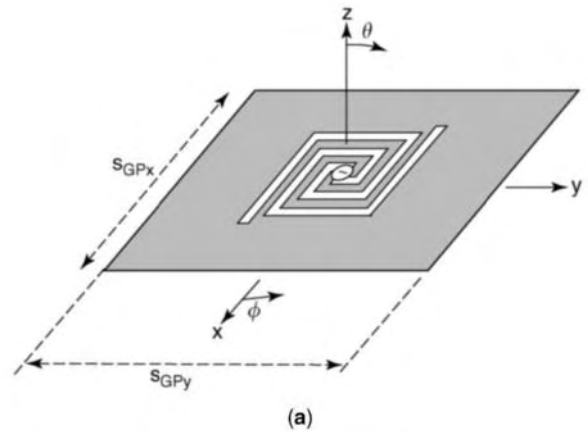


Figure 33. Spiral slot antenna: (a) perspective view; (b) top view.

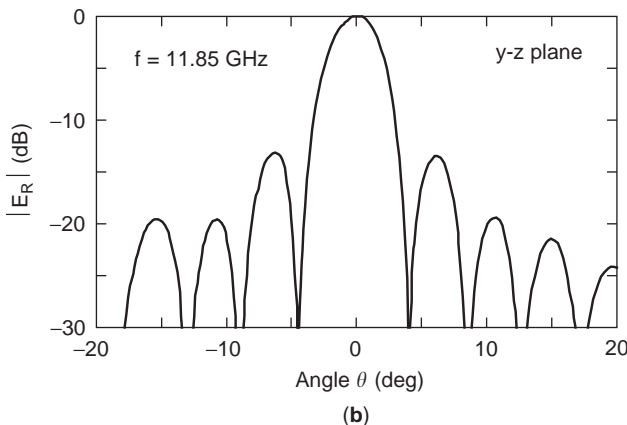
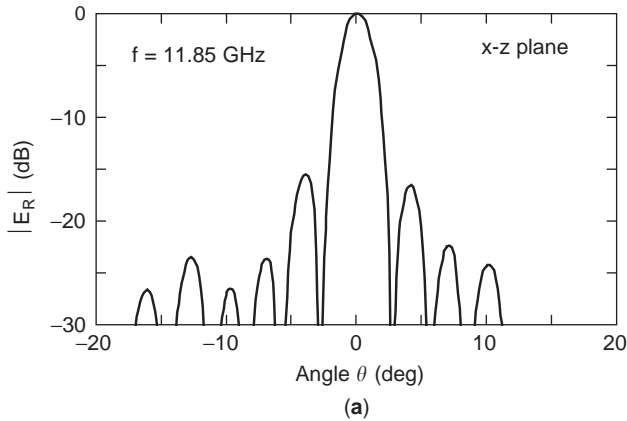


Figure 32. Radiation pattern of a dual-curl slot array: (a) radiation pattern in the x - z plane; (b) radiation pattern in the y - z plane.

The design procedure for the DCS array and the optimized configuration parameters of the DCS are presented in Ref. 18. Figure 32 shows an example of the measured radiation patterns of a DCS array antenna, where 254 DCS elements are used. These elements are excited with the same amplitude and phase. This array antenna shows a gain of more than 31 dB within a frequency range of 11.7–12 GHz (direct-broadcasting satellite frequency band).

10. SPIRAL SLOT ANTENNA

It is known that a spiral *wire* antenna of *infinitely* long arms has wideband characteristics with respect to the radiation pattern, input impedance, and gain [28]. In this section, we use a slot arm, instead of the wire, as shown in Fig. 33. Note that the arm length is finite, as opposed to that of the wire spiral, and the conducting sheet is assumed to be of infinite extent ($s_{GPx} = \infty$ and $s_{GPy} = \infty$) [20].

The antenna is composed of two arms, each having N straight slots of width w . The first slot length along its center line is s_1 , and the n th slot length is $s_n = 2(n - 1)s_1$, $n = 2, 3, \dots, N$. The spiral slot is excited at point o (the coordinate origin) with a voltage source.

$$w = 2.0 \text{ mm}, s_1 = 2.0 \text{ mm}, N = 10, S_{GPx} = S_{GPy} = \infty$$

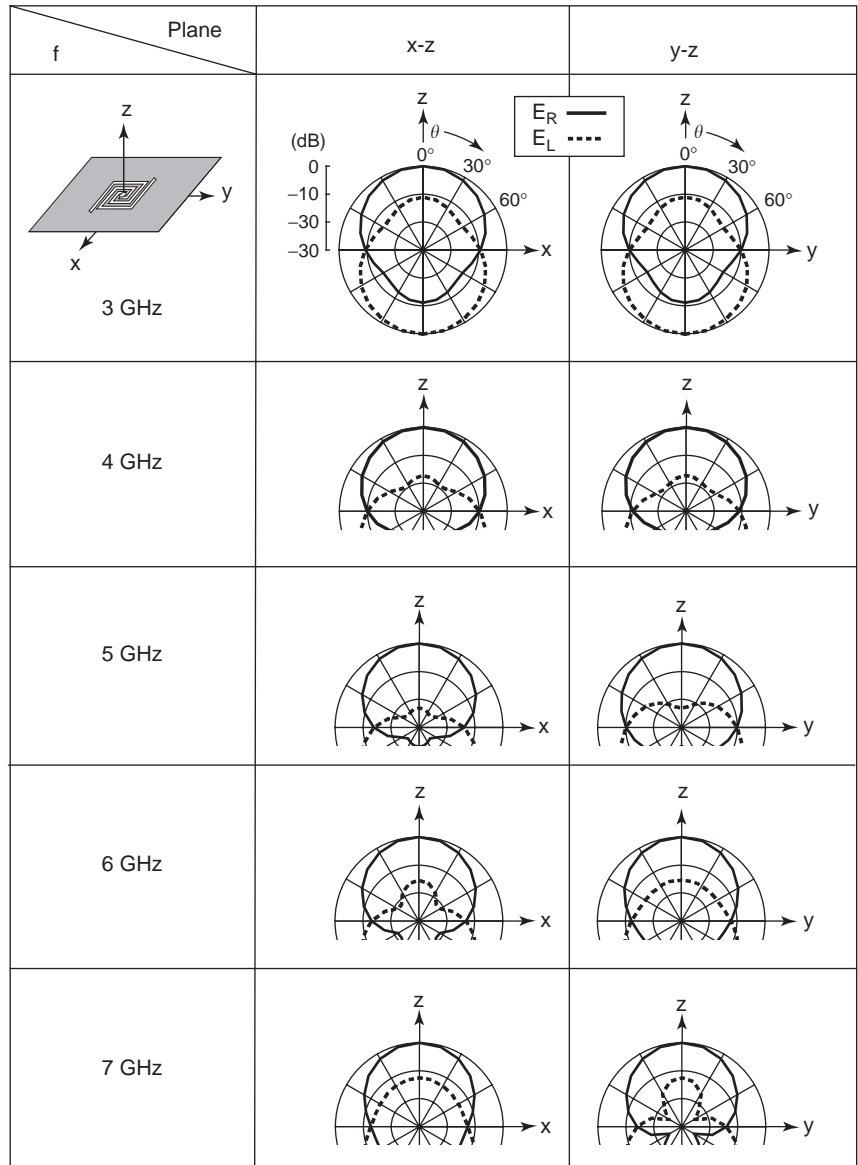


Figure 34. Radiation pattern of a spiral slot antenna as a function of frequency.

The periphery of the spiral, defined as $C_{\text{spiral}} = 4s_N$, must be more than one wavelength to support first-mode radiation [28], which yields a circularly polarized wave. The spiral to be considered here has a periphery of $C_{\text{spiral}} = 1.4\lambda_3$ at 3 GHz, satisfying the requirement for first-mode radiation.

Figure 34 shows the radiation pattern as a function of frequency. The radiation pattern is symmetric with respect to the x - y plane and only half of the radiation pattern is illustrated except at 3 GHz. It is found that the bidirectional radiation is circularly polarized around the z axis.

As seen from Fig. 34, as the frequency increases, the half-power beamwidth gradually decreases. This gradual decrease in the half-power beamwidth leads to a mild variation in the gain, as shown in Fig. 35. The gain

variation within the 3–7 GHz frequency band is only approximately 1.6 dBi.

In addition to the gain, the input impedance also has a wideband characteristic. Figure 36 shows the input impedance as a function of frequency. It is revealed that the input impedance in this analysis range is almost purely resistive with a relatively constant value.

11. ADDITIONAL INFORMATION

Applications of straight slots for array antennas are found in the literature [2,3,21,22]. The straight slots in Ref. 2 and in Chap. 12 of Ref. 3 are cut in a rectangular waveguide, and those in Refs. 21 and 22 are cut in the upper plate of a radial waveguide. Note that the radiation from

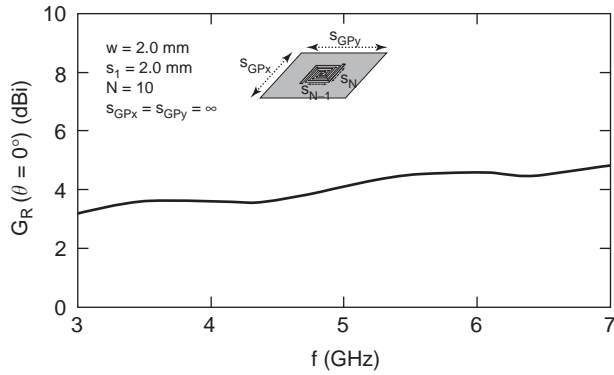


Figure 35. Gain of a spiral slot antenna as a function of frequency.

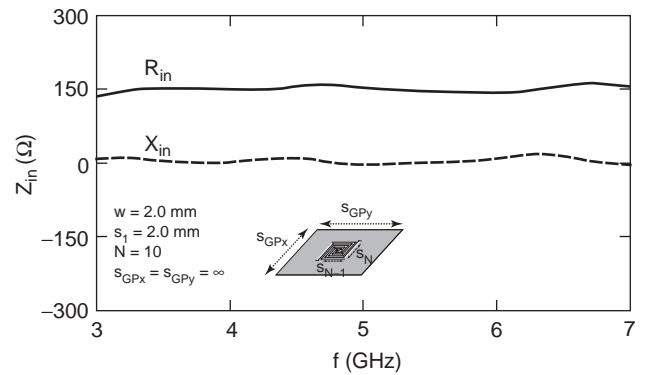


Figure 36. Input impedance of a spiral slot antenna as a function of frequency.

the arrays in Refs. 2 and 3 is linearly polarized and that from the arrays in Refs. 21 and 22 are circularly polarized.

The bowtie in Section 7 is composed of two identical triangular slots. A recent study reveals that a bowtie antenna composed of two different-size triangular slots has a dual-frequency operation mode. The design process for realizing resonances at 2.45 and 5.2 GHz is presented in Ref. 23.

The loop slot in Section 8 radiates a linearly polarized wave. It is possible to obtain a circularly polarized wave by making use of a loop slot structure. Figure 37 shows such a loop slot structure, where the loop slot, cut in the upper conducting plate of a triplate transmission line, has two perturbation sections of length d_p and width w_p [24]. These perturbation sections are designed to generate a traveling-wave magnetic current along the slot [25]. Figure 38 demonstrates that the radiation from the slot is circularly polarized with the help of the perturbation sections. Note that, since the lower plate of the triplate acts as a reflector, the radiation becomes unidirectional, as was the case for the curl slot antenna discussed in Section 9.

Finally, a numerical experiment based on a relationship between a thin-slot element and a thin-wire element is worth mentioning. A slot of width w and length s , cut in

a conducting sheet of *infinite* extent, is equivalent to a wire of radius $w/4$ and length s , isolated in free space. The radiation characteristics of the equivalent wire can be analyzed using the method of moments (MoM) [30]. Note that the radiation fields E_ϕ and E_θ obtained using MoM correspond to E_θ and E_ϕ , respectively, for the FDTD. In this article, some slots, each cut in an infinite conducting sheet, are analyzed using both the FDTD and MoM. The FDTD results (see Figs. 6–8, 23–26a, 34–36) are in good agreement with the MoM results (not presented). This agreement confirms the validity of the FDTD results.

Acknowledgments

I appreciate the kind assistance of V. Shkawrytko in the preparation of this manuscript. Also, I would like to thank the following people for their assistance in verifying the results of the analyses: K. Motoyama for Sections 5 and 6 (straight slot antennas), N. Ohki for Section 7 (bowtie slot antennas), M. Seto for Section 8 (loop slot antennas), S. Shimada for Section 9 (curl slot antennas), T. Goto for Section 10 (spiral slot antennas), and T. Nakajima for Section 11 (circularly polarized loop slots).

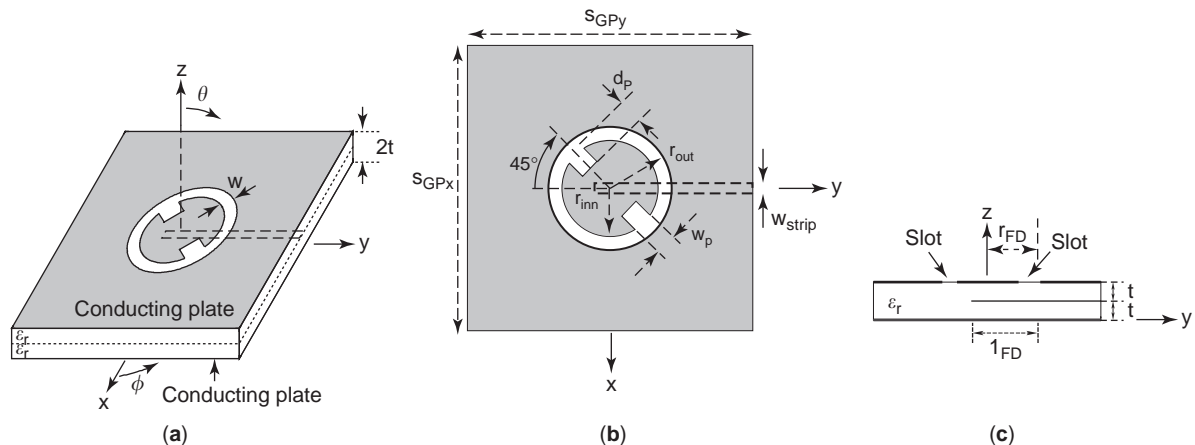


Figure 37. Loop slot antenna radiating a circularly polarized waver: (a) perspective view; (b) top view; (c) side view.

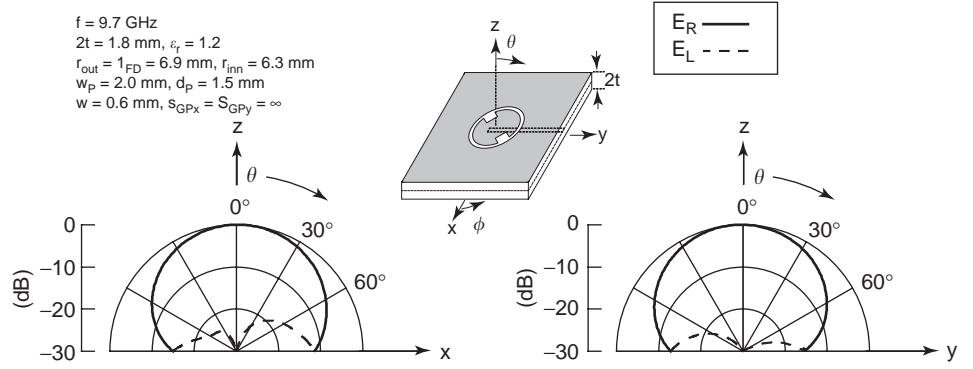


Figure 38. Radiation pattern of a loop slot antenna radiating a circularly polarized wave.

12. APPENDIX

Equation (13) is written as

$$P = \frac{1}{2Z_0} \frac{1}{\pi^2} \frac{1}{r^2} V_0^2 \int_{\phi=0}^{2\pi} \int_{\theta=0}^{\pi/2} \frac{\cos^2\left(\frac{\pi}{2} \sin \theta \cos \phi\right)}{(1 - \sin^2 \theta \cos^2 \phi)} \times r^2 \sin \theta d\theta d\phi \quad (A.1)$$

Using angles ξ and ζ , which are defined in Fig. 39, Eq. (A.1) is transformed into

$$P = \frac{1}{2Z_0} \frac{1}{\pi^2} \frac{1}{r^2} V_0^2 \int_{\zeta=-(\pi/2)}^{\pi/2} \int_{\xi=0}^{\pi} \frac{\cos^2\left(\frac{\pi}{2} \cos \xi\right)}{1 - \cos^2 \zeta} \times r^2 \sin \xi d\xi d\zeta \quad (A.2)$$

Note that the small surface area ($r^2 \sin \theta d\theta d\phi$) in Eq. (A.1) is replaced with ($r^2 \sin \xi d\xi d\zeta$) in Eq. (A.2). We define I_{integral} as

$$I_{\text{integral}} \equiv \int_0^{\pi} \frac{\cos^2\left(\frac{\pi}{2} \cos \xi\right)}{\sin \xi} d\xi \quad (A.3)$$

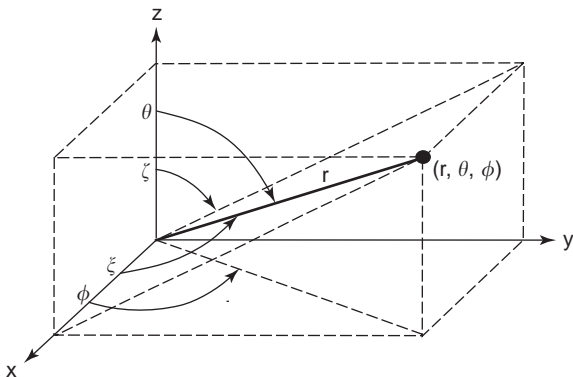


Figure 39. Definition of angles ξ and ζ .

Then, Eq. (A.2) is written as

$$P = \frac{1}{2Z_0} \frac{1}{\pi} V_0^2 I_{\text{integral}} \quad (A.4)$$

Replacing $\cos \xi$ in Eq. (A.3) with $1 - v$, we transform Eq. (A.3) into

$$I_{\text{integral}} = \frac{1}{2} \int_0^2 \frac{1 - \cos \pi v}{v} dv \quad (A.5)$$

This can be written as

$$I_{\text{integral}} = \frac{1}{2} \int_0^{2\pi} \frac{1 - \cos x}{x} dx \quad (A.6)$$

where πv in Eq. (A.5) is replaced with x .

Using the cosine integral Ci [see Eqs. (15a) and (15b)], we obtain

$$I_{\text{integral}} = \frac{1}{2} [\ln 2\pi\gamma - \text{Ci}(2\pi)] \quad (A.7)$$

Substituting Eq. (A.7) into Eq. (A.2), P is expressed as

$$P = \frac{V_0^2}{Z_0} \frac{1}{4\pi} [\ln 2\pi\gamma - \text{Ci}(2\pi)] = 73 \frac{V_0^2}{Z_0^2} \quad (A.8)$$

BIBLIOGRAPHY

1. W. Rudge, K. Milne, A. D. Olver, and P. Knight, *The Handbook of Antenna Design*, Peter Peregrinus, London, UK, 1986, pp. 521–526.
2. R. C. Johnson and H. Jasik, *Antenna Engineering Handbook*, 2nd ed., McGraw-Hill, New York, 1984, Chaps. 8 and 9.
3. Y. T. Lo and S. W. Lee, *Antenna Handbook*, Van Nostrand-Reinhold, New York, 1988. pp. 3.31, 9.68–9.72; Chap. 12, pp. 20.85–20.86, 20.90, 30.13.
4. R. Collin and F. Zucker, *Antenna Theory*. McGraw-Hill, New York, 1969, Chap. 14.

5. Y. Mushiake, *Antennas and Radio Propagation*, 21st ed., Corona, Tokyo, 1980, pp. 88–91.
6. K. S. Yee, Numerical solution of initial boundary value problems involving Maxwell's equations in isotropic media, *IEEE Trans. Anten. Propag.* **14**(3):302–307 (May 1966).
7. A. Taflove, *Computational Electrodynamics: The Finite-Difference Time Domain Method*, Artech House, Norwood, MA, 1995.
8. Z. P. Liao, H. L. Wong, B. P. Yang, and Y. F. Yuan, A transmitting boundary for transient wave analyses, *Sci. Sinica A* **27**(10):1063–1076 (1984).
9. K. Motoyama, private report, June 2003.
10. J. Kraus, *Antennas*, 2nd ed., McGraw-Hill, New York, 1988, Chap. 13.
11. G. Sakamoto, J. Yamauchi, and H. Nakano, Slot bow-tie antenna, *Proc. 2002 IEICE* (Institute of Electronics, Information and Communication Engineers) *Society Conf.*, Miyazaki, Japan, Sept. 2002, p. B-1-32.
12. G. Sakamoto, J. Yamauchi, and H. Nakano, A strip-fed slot bow-tie antenna, *Proc. 2003 IEICE General Conf.* Sendai, Japan, March 2003, p. B-1-134.
13. N. Ohki, private report, June 2003.
14. M. Seto, private report, June 2003.
15. H. Nakano, K. Nakayama, H. Mimaki, and J. Yamauchi, Single arm spiral slot antenna fed by a triplate transmission line, *Electron. Lett.* **22**(22):2088–2090 (Oct. 1992).
16. K. Hirose, K. Nakayama, and H. Nakano, Monofilar Archimedean spiral slot antennas, *Electromagnetics* **14**(3–4):415–426 (July–Dec. 1994).
17. S. Shimada, private report, June 2003.
18. K. Hirose and H. Nakano, Dual-spiral slot antennas, *IEE Proc. H* **138**(1):32–36 (Feb. 1991).
19. H. Nakano, S. Okuzawa, and H. Mimaki, Two-arm slot spiral antenna, *Electromagnetics* **14**(3–4): 397–413 (July–Dec. 1994).
20. T. Goto, private report, June 2003.
21. H. Sasazawa, Y. Oshima, K. Sakurai, M. Ando, and N. Goto, Slot coupling in a radial line slot antenna for 12 GHz band satellite TV reception, *IEEE Trans. Anten. Propag.* **AP36**(9):1221–1226 (1998).
22. M. Bailkowski and P. Davis, Analysis of a circular patch antenna radiating in a parallel-plate guide, *IEEE Trans. Anten. Propag.* **50**(2):180–187 (2002).
23. N. Ohki, J. Yamauchi, and H. Nakano, A dual-frequency slot bow-tie antenna, *Proc. 2003 IEICE Society Conf.* Niigata, Japan, Sept. 2003, p. B-1-32.
24. T. Nakajima, private report, June 2003.
25. K. Hirose, H. Horiuchi, and H. Nakano, Dual-loop slot array antenna radiating circularly polarized wave, *Electron. Lett.* **22**(3):179–180 (Feb. 1990).
26. R. F. Harrington, *Time-Harmonic Electromagnetic Fields*, McGraw-Hill, New York, 1961, pp. 106–110.
27. D. K. Cheng, *Fields and Wave Electromagnetics*, 2nd ed., Addison-Wesley, Reading, MA, 1989, pp. 617–621.
28. J. A. Kaiser, The Archimedean two-wire spiral antenna, *IRE Trans. Anten. Propag.* **AP-8**:312–323 (May 1960).
29. H. Uchida and Y. Mushiake, *VHF Antenna*, 6th ed., Corona, Tokyo, 1970, Chap. 13.
30. R. F. Harrington, *Field Computation by Moment Methods*, Macmillan, New York, 1968.

SLOTLINE COMPONENTS

LU FAN
KAI CHANG
Texas A&M University
College Station, Texas

Slotline components, just as the term implies, are the microwave circuit components consisting of slotlines and combinations of slotlines and other transmission lines such as microstrip and coplanar waveguides (CPWs).

Slotline is a nontransverse electromagnetic (non-TEM) uniplanar transmission structure using a single slot etched on a dielectric-supported layer of metal without a backside ground plane [1]. The slotline configuration is useful in circuits requiring high-impedance lines, series stubs, short-circuited ends, and easy series and shunt connections of passive and active solid-state devices without via holes. With its advantages of small size, light weight, and low cost, the slotline has emerged as an alternative transmission line for applications in microwave integrated circuits (MICs) and monolithic microwave integrated circuits (MMICs). These circuits include filters, couplers, ferrite devices, and other components as well as complete circuits.

The slotline can also be combined with the microstrip and CPW for many circuit applications. These types of hybrid combinations allow flexibility in the design of MIC and MMIC components. For example, a wide range of line impedance, compact circuit structure, easier device mounting, and better integration are achievable in printed form. These features have led to many novel circuits such as hybrid couplers, magic Ts, oscillators, mixers, receivers, and antennas. In spite of these numerous advantages and uses, the description of the slotline components is generally hidden in many papers and books. Because of limited space, this article is intended to present merely the typical slotline components. By outlining their basic operation principle, an overview of the general function of the important circuit components is given. The basic characteristics of slotlines, such as wavelength, characteristic impedance, quality factor, and its discontinuities, can be found in *SLOTLINES*.

This article first discusses the fundamental slotline elements such as various T junctions, resonators, and transitions. After these general topics, several kinds of passive slotline integrated circuits are presented through a discussion of filters, hybrid couplers, and nonreciprocal devices. Finally, the applications of slotline to solid-state integrated circuits, that is, mixers, oscillators, modulators, and frequency doublers, are described. These applications are supported by real circuit demonstrations and actual circuit performances. The implementation of solid-state devices for the tuning and switching of resonances is also discussed.

1. BASIC SLOTLINE CONFIGURATIONS

1.1. Slotline T Junctions

Slotline T junctions appear very frequently in slotline-microstrip circuits (double-sided MICs) and slotline-CPW circuits (uniplanar MICs). Figure 1 shows the physical

5. Y. Mushiake, *Antennas and Radio Propagation*, 21st ed., Corona, Tokyo, 1980, pp. 88–91.
6. K. S. Yee, Numerical solution of initial boundary value problems involving Maxwell's equations in isotropic media, *IEEE Trans. Anten. Propag.* **14**(3):302–307 (May 1966).
7. A. Taflove, *Computational Electrodynamics: The Finite-Difference Time Domain Method*, Artech House, Norwood, MA, 1995.
8. Z. P. Liao, H. L. Wong, B. P. Yang, and Y. F. Yuan, A transmitting boundary for transient wave analyses, *Sci. Sinica A* **27**(10):1063–1076 (1984).
9. K. Motoyama, private report, June 2003.
10. J. Kraus, *Antennas*, 2nd ed., McGraw-Hill, New York, 1988, Chap. 13.
11. G. Sakamoto, J. Yamauchi, and H. Nakano, Slot bow-tie antenna, *Proc. 2002 IEICE* (Institute of Electronics, Information and Communication Engineers) *Society Conf.*, Miyazaki, Japan, Sept. 2002, p. B-1-32.
12. G. Sakamoto, J. Yamauchi, and H. Nakano, A strip-fed slot bow-tie antenna, *Proc. 2003 IEICE General Conf.* Sendai, Japan, March 2003, p. B-1-134.
13. N. Ohki, private report, June 2003.
14. M. Seto, private report, June 2003.
15. H. Nakano, K. Nakayama, H. Mimaki, and J. Yamauchi, Single arm spiral slot antenna fed by a triplate transmission line, *Electron. Lett.* **22**(22):2088–2090 (Oct. 1992).
16. K. Hirose, K. Nakayama, and H. Nakano, Monofilar Archimedean spiral slot antennas, *Electromagnetics* **14**(3–4):415–426 (July–Dec. 1994).
17. S. Shimada, private report, June 2003.
18. K. Hirose and H. Nakano, Dual-spiral slot antennas, *IEE Proc. H* **138**(1):32–36 (Feb. 1991).
19. H. Nakano, S. Okuzawa, and H. Mimaki, Two-arm slot spiral antenna, *Electromagnetics* **14**(3–4): 397–413 (July–Dec. 1994).
20. T. Goto, private report, June 2003.
21. H. Sasazawa, Y. Oshima, K. Sakurai, M. Ando, and N. Goto, Slot coupling in a radial line slot antenna for 12 GHz band satellite TV reception, *IEEE Trans. Anten. Propag.* **AP36**(9):1221–1226 (1998).
22. M. Bailkowski and P. Davis, Analysis of a circular patch antenna radiating in a parallel-plate guide, *IEEE Trans. Anten. Propag.* **50**(2):180–187 (2002).
23. N. Ohki, J. Yamauchi, and H. Nakano, A dual-frequency slot bow-tie antenna, *Proc. 2003 IEICE Society Conf.* Niigata, Japan, Sept. 2003, p. B-1-32.
24. T. Nakajima, private report, June 2003.
25. K. Hirose, H. Horiuchi, and H. Nakano, Dual-loop slot array antenna radiating circularly polarized wave, *Electron. Lett.* **22**(3):179–180 (Feb. 1990).
26. R. F. Harrington, *Time-Harmonic Electromagnetic Fields*, McGraw-Hill, New York, 1961, pp. 106–110.
27. D. K. Cheng, *Fields and Wave Electromagnetics*, 2nd ed., Addison-Wesley, Reading, MA, 1989, pp. 617–621.
28. J. A. Kaiser, The Archimedean two-wire spiral antenna, *IRE Trans. Anten. Propag.* **AP-8**:312–323 (May 1960).
29. H. Uchida and Y. Mushiake, *VHF Antenna*, 6th ed., Corona, Tokyo, 1970, Chap. 13.
30. R. F. Harrington, *Field Computation by Moment Methods*, Macmillan, New York, 1968.

SLOTLINE COMPONENTS

LU FAN
KAI CHANG
Texas A&M University
College Station, Texas

Slotline components, just as the term implies, are the microwave circuit components consisting of slotlines and combinations of slotlines and other transmission lines such as microstrip and coplanar waveguides (CPWs).

Slotline is a nontransverse electromagnetic (non-TEM) uniplanar transmission structure using a single slot etched on a dielectric-supported layer of metal without a backside ground plane [1]. The slotline configuration is useful in circuits requiring high-impedance lines, series stubs, short-circuited ends, and easy series and shunt connections of passive and active solid-state devices without via holes. With its advantages of small size, light weight, and low cost, the slotline has emerged as an alternative transmission line for applications in microwave integrated circuits (MICs) and monolithic microwave integrated circuits (MMICs). These circuits include filters, couplers, ferrite devices, and other components as well as complete circuits.

The slotline can also be combined with the microstrip and CPW for many circuit applications. These types of hybrid combinations allow flexibility in the design of MIC and MMIC components. For example, a wide range of line impedance, compact circuit structure, easier device mounting, and better integration are achievable in printed form. These features have led to many novel circuits such as hybrid couplers, magic Ts, oscillators, mixers, receivers, and antennas. In spite of these numerous advantages and uses, the description of the slotline components is generally hidden in many papers and books. Because of limited space, this article is intended to present merely the typical slotline components. By outlining their basic operation principle, an overview of the general function of the important circuit components is given. The basic characteristics of slotlines, such as wavelength, characteristic impedance, quality factor, and its discontinuities, can be found in *SLOTLINES*.

This article first discusses the fundamental slotline elements such as various T junctions, resonators, and transitions. After these general topics, several kinds of passive slotline integrated circuits are presented through a discussion of filters, hybrid couplers, and nonreciprocal devices. Finally, the applications of slotline to solid-state integrated circuits, that is, mixers, oscillators, modulators, and frequency doublers, are described. These applications are supported by real circuit demonstrations and actual circuit performances. The implementation of solid-state devices for the tuning and switching of resonances is also discussed.

1. BASIC SLOTLINE CONFIGURATIONS

1.1. Slotline T Junctions

Slotline T junctions appear very frequently in slotline-microstrip circuits (double-sided MICs) and slotline-CPW circuits (uniplanar MICs). Figure 1 shows the physical

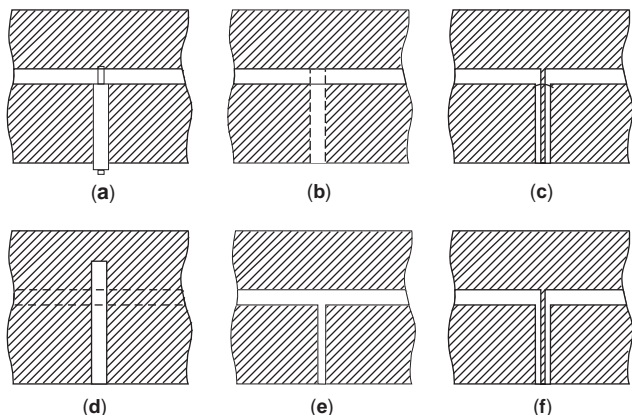


Figure 1. Various slotline T junctions: (a) coax-slot T; (b) microstrip-slotline T; (c) CPW-slotline T; (d) slotline-microstrip series T; (e) slotline T; and (f) CPW (even mode)-slotline series T. Solid lines show slotlines and CPW lines on the substrate. Dotted lines show microstrip lines on the back side of the substrate.

configurations of various slotline T junctions. In accordance with the input and output transmission lines, the T junctions can be classified into parallel and series types. The parallel T junctions (Figs. 1a–1c) require the unbalanced line (coaxial line, microstrip, or CPW) as an input transmission line, while the series T junctions (Figs. 1d–1f) require the balanced line (slotline). It is necessary to note that the CPW (without bonding wire) in Fig. 1f is the coupled slotline that operates in coupled-slotline mode (also called the CPW even mode). Figure 2 shows equivalent transmission-line circuits and schematic expression of the circuit behavior for the parallel and series T junctions of Fig. 1. The arrows in the figure indicate the electric field distribution in the circuits. For the parallel tee as shown in Fig. 2a when an incident wave fed to port 1 propagates through the input line, at the T junction it will divide into two components that both arrive in phase at ports 2 and 3. For series tee as shown in Fig. 2b when an incident wave fed to port 1 propagates through the input line, at the T junction it will divide into two components that arrive at ports 2 and 3 with a 180° phase difference.

Both series and parallel T junctions can be combined to realize hybrid circuits and balanced circuits. In addition, it is worth mentioning that the T junctions in Figs. 1c, 1e, and 1f can be fabricated using only one side of the substrate. This is a great advantage in developing uniplanar MICs as discussed in later sections.

1.2. Slotline Transitions

To test slotline circuits, a transition between slotline and the measuring transmission lines is necessary. A coaxial (coax) slotline transition is first used for this purpose. To increase the application of slotlines, transitions from slotline to other transmission lines are also useful. Such transitions are slotline to microstrip and slotline to CPW. These three types of transitions discussed in this section are based on the slotline T junctions of Fig. 1. Interested readers may refer to Refs. 1–5.

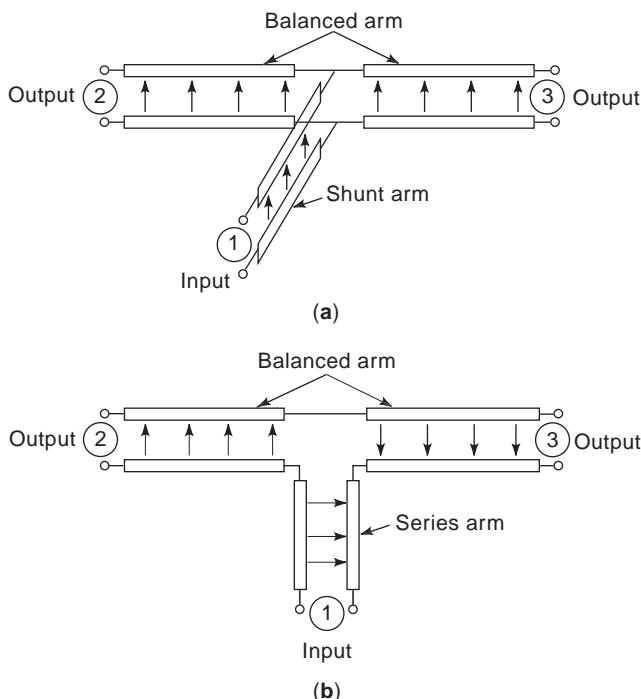


Figure 2. Equivalent transmission-line models of the slotline T junctions of Fig. 1: (a) shunt model of the slotline T junctions for Figs. 1a–1c; (b) series model of the slotline T junctions for Figs. 1d–1f.

1.2.1. Coax-Slotline Transitions. Figure 3 shows a commonly used coax slotline transition reported by S. B. Cohn [2] in 1969. It consists of a miniature semirigid coaxial line placed at the end of an open slotline. Both the inner and outer conductors of the coaxial line are electrically connected (with solder or epoxy) to the conductive plating on the two sides of the slot. As mentioned above, this transition is based on the coax slotline T junction of Fig. 1a. This T junction works like a power divider with an open termination at one of its output ports. The transition was constructed with a slot width of 0.79 mm on a 1.57-mm-thick Trans-Tech D-16 substrate ($\epsilon_r = 16.3$). The slotline impedance corresponding to these dimensions is about 75Ω. The voltage standing-wave ratio (VSWR) looking into the 50-Ω coaxial line was less than 1.2 over a 500 MHz bandwidth at 3 GHz.

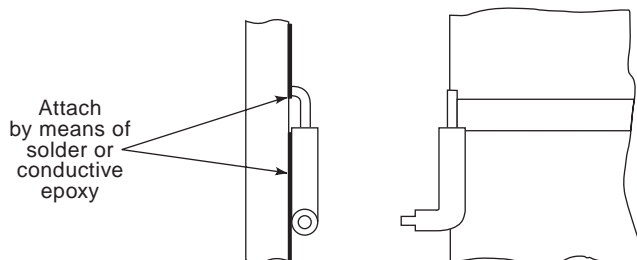


Figure 3. A coax slotline transition that is a wideband transition between slotline and miniature cross section coaxial line. (From Ref. 2 with permission, ©1969 IEEE.)

1.2.2. Microstrip–Slotline Transitions. Microstrip–slotline transitions are transformers between unbalanced and balanced lines. The majority of transitions are based on the well-known concept of the Marchand balun. Since 1969 when the first microstrip–slotline transition was reported, various microstrip–slotline transitions have been developed for double-sided MICs that use a combination of microstrip and slotlines on both sides of the substrate. Various microstrip–slotline transitions are shown in Fig. 4. In Figs. 4a–4e, the transitions consist of uniform and nonuniform impedance stubs as well as soldered and virtually shorted (short-circuited) microstrip stubs. They are based on the microstrip–slotline T junctions of Figs. 1b and 1d with a different termination at one of the T junction output ports. Modeling and experimental investigation on these transitions was carried out by Schuppert [3]. The back-to-back connection of two transitions shown in Fig. 4e has a bandwidth of approximately one decade. The bandwidth of a single transition will obviously be larger than that of two transitions. It was also found that the transition with a microstrip short (circuit) shown in Fig. 4b has a larger bandwidth than the transition with a microstrip open stub. However, its implementation needs a via hole grounding that may sometimes be difficult. The transition shown in Fig. 4f is not based on the type of Marchand baluns, but on a six-port junction. Although this transition has good performance over a broadband from 2 to 9 GHz, it occupies more substrate space.

1.2.3. CPW–Slotline Transitions. Coplanar waveguide and slotline are the fundamental transmission lines and are useful in uniplanar MICs and MMICs. CPW–slotline transitions are realized on one substrate side without metallization on the backside. This feature can significantly reduce the substrate processing complexity and consequently the cost. To fully utilize the advantages of uniplanar structures, the transition between CPW and slotline is necessary. Extensive study and modeling

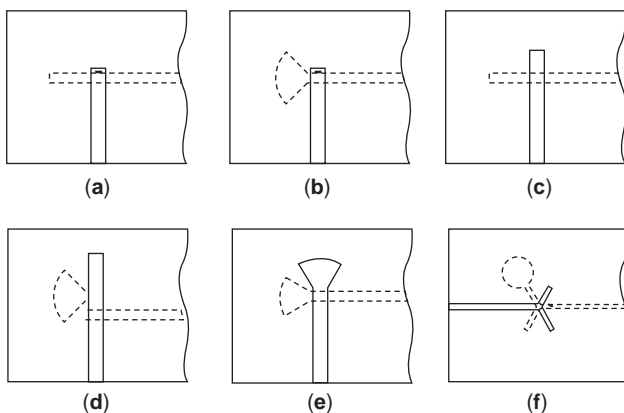


Figure 4. Circuit configurations of microstrip–slotline transitions with different terminations: (a, c) transitions with uniform impedance stubs; (b–e) transitions with nonuniform impedance stubs; (f) double Y-junction microstrip–slotline transition. Solid lines show microstrip lines on the substrate. Dotted lines show slotlines on the backside of the substrate.

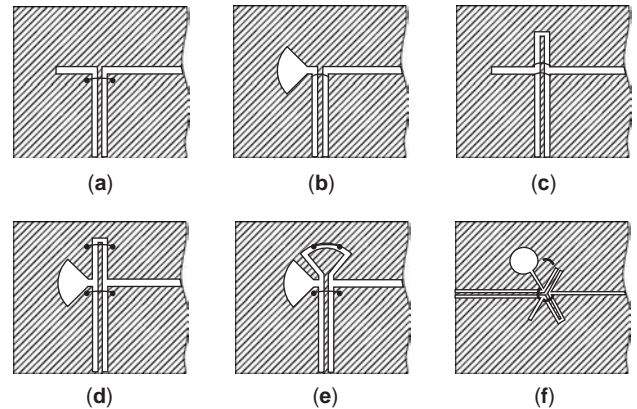


Figure 5. Circuit configurations of CPW–slotline transitions with different terminations: (a) a CPW short with a uniform slotline short stub; (b) a CPW short with a nonuniform slotline short stub; (c) a uniform CPW open stub with a uniform slotline short stub; (d) a uniform CPW open stub with a nonuniform slotline short stub; (e) a nonuniform CPW open stub with a nonuniform slotline short stub; (f) a uniplanar double Y-junction CPW–slotline transition.

have been carried out to investigate various transition configurations. CPW–slotline transitions that are equivalent to the microstrip–slotline transitions of Fig. 4 are shown in Fig. 5. They have been evaluated both experimentally [4] and theoretically [5]. The transition in Fig. 5a is based on the CPW–slotline T junction of Fig. 1c. One of the output ports of the T junction is terminated in a quarter-wavelength slotline short stub that provides tuning capability. To improve the bandwidth, the short stub has been replaced by a radial slotline stub in Fig. 5b. Figures 5c–5e show the transition where a quarter-wavelength CPW open stub or a CPW radial stub is used instead of CPW shorts of the transitions in Figs. 5a and 5b. Overall, the transition with nonuniform radial stubs has larger bandwidth than that with uniform stubs. Experimental investigations of these transitions show that the transition in Fig. 5b gives the best performance with a 5.2–1 bandwidth and insertion loss of less than 1 dB. Other transitions of Figs. 5a and 5c–5e have a bandwidth ranging from 1.6:1 to 4.1:1. Similar to the microstrip–slotline transition in Fig. 4f, the transition shown in Fig. 5f uses a double-Y junction between CPW and slotline. This transition has better performance than do other uniplanar transitions except for its need for more substrate room. The measured results of this transition show less than a 1.6 VSWR and 0.7 dB insertion loss for a bandwidth ratio of 6:1.

1.3. Slotline Resonators

Slotline resonators are basic elements served as wavelength measurements, filters, and other MIC components. The slotline resonator is a uniplanar structure etched on one substrate side without back metallization. As shown in Fig. 6a, a half-wavelength rectangular slot is a typical resonator used exclusively for the various filters. If necessary, the rectangular resonator slot can be made by

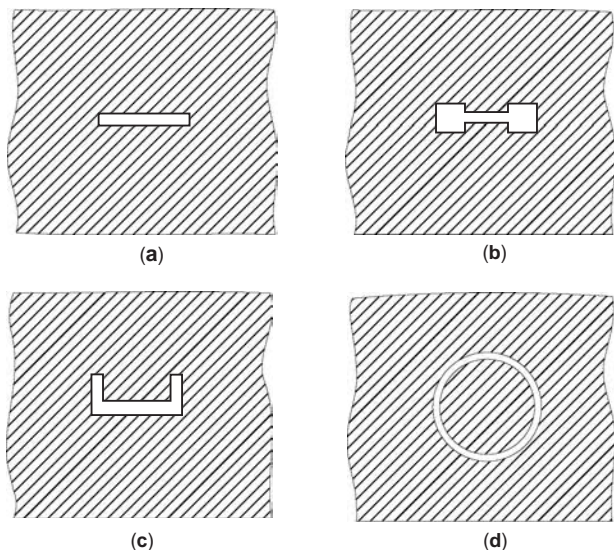


Figure 6. Slotline resonators: (a) rectangle; (b) rectangle with capacitive loading; (c) bent rectangle; (d) ring.

capacitive loading over a portion of its length to reduce its resonator frequency as in Fig. 6b or by bending it as in Fig. 6c to conserve length with relatively little effect on the resonant frequency.

The slotline ring resonator as shown in Fig. 6d is widely used in many circuit applications [6]. Coupling between the feedlines and slotline ring can be the following three types: microstrip coupling, CPW coupling, and slotline coupling. Figure 7 shows these three possible coupling schemes. The microstrip coupling is a capacitive coupling. The length of input and output microstrip coupling stubs can be adjusted to optimize the loaded Q

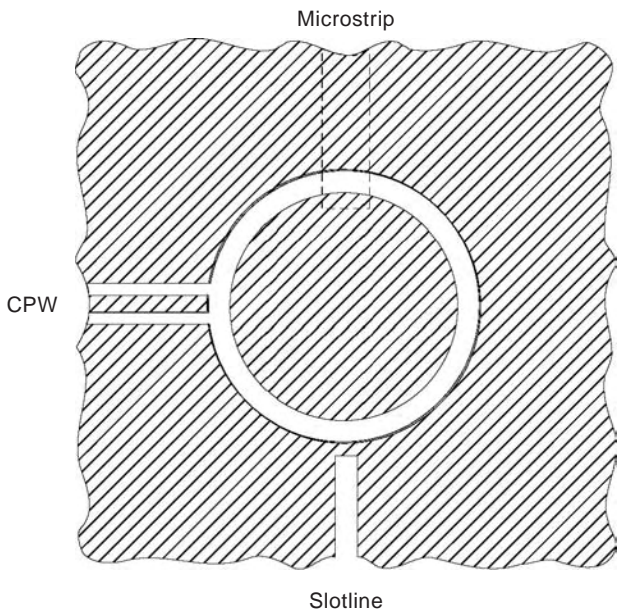


Figure 7. Circuit configuration of slotline ring resonator with different coupling schemes: microstrip-fed, CPW-fed, and slotline-fed slotline rings. (From Ref. 9 with permission, © 1993 IEEE.)

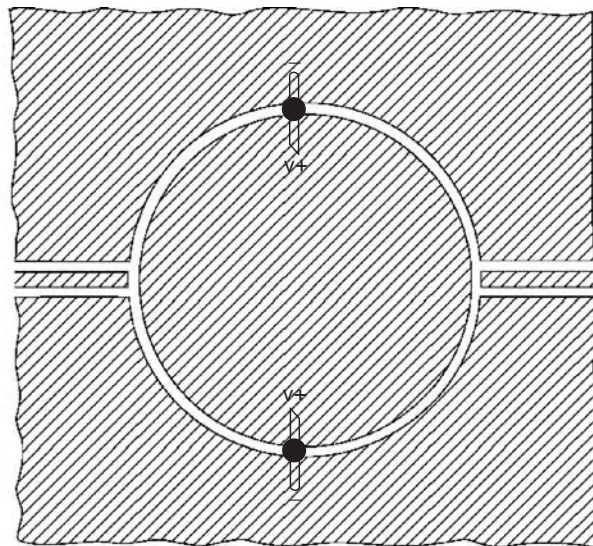


Figure 8. Varactor-tunable slotline ring resonator with CPW feeds. Two 50- Ω CPW lines feed an 85- Ω slotline ring through a 0.05 mm series gap. The ring has a mean radius of 11.26 mm and uses a 0.5-mm slotline on a 0.63-mm-thick RT-Duroid 6010 substrate ($\epsilon_r = 10.5$). (From Ref. 7 with permission, © 1993 IEEE.)

values. However, less coupling may effect the coupling efficiency and cause higher insertion loss. The tradeoff between the loaded Q and coupling loss depends on the application. CPW coupling is also a capacitive coupling and is formed by a small coupling gap between the CPW feed lines and the slotline ring. The loaded Q value and insertion loss are dependent on the gap size. The smaller gap size will cause a lower loaded Q and smaller insertion loss. Unlike microstrip and CPW couplings, the slotline ring coupled to slotline feed is an inductively coupled ring resonator. The metal gap between the slotline ring and slotline feed is for the coupling of magnetic field energy. Therefore, the maximum electric field points of this resonator are opposite those of the capacitively coupled slotline ring resonators.

The last two types of slotline ring resonators are truly coplanar and also allow easy series and shunt device mounting. Varactor diodes can be incorporated into the ring resonators to make the resonant frequencies electronically tunable. For example, Fig. 8 shows varactor-tunable slotline ring resonator [7]. The varactors located at 90° and 270° along the ring tune the even modes of the resonator and allow a second mode electronic tuning bandwidth of more than 22% from 3.13 to 4.07 GHz. The frequency responses of the circuit agree very well with those calculated using a distributed transmission line model.

2. PASSIVE SLOTLINE COMPONENTS

Based on the discussion of the fundamental slotline elements in the previous section, this section describes passive slotline components such as filters, magic Ts, and various hybrid couplers in detail.

2.1. Slotline Filters

The slotline on high dielectric substrate provides a microwave medium for fabricating bandpass and bandstop filters that have been used in MICs. In 1970, Mariani and Agrios [8] reported two types of bandpass filters using the end-coupled and quarter-wave-coupled resonant slots as shown in Fig. 9. For example, a three-resonator end-coupled bandpass filter was designed and constructed on a D-16 substrate ($\epsilon_r = 16.3, h = 1.6$ mm). Important dimensions are shown in Fig. 9b. The distance X was adjusted experimentally for matching external loading of the end resonators. The measured response as shown in Fig. 9c was in reasonable agreement with the design goals. The filter had a 3 dB bandwidth of 145 MHz centered at 2998 MHz. The insertion loss, including the losses of the coax slotline transition, was 4.5 dB, which corresponds to Q_u of about 150.

Slotline bandstop filters are easily implemented by using the combination of slotline and microstrip as shown in Fig. 10a. The slot resonators are etched on the ground

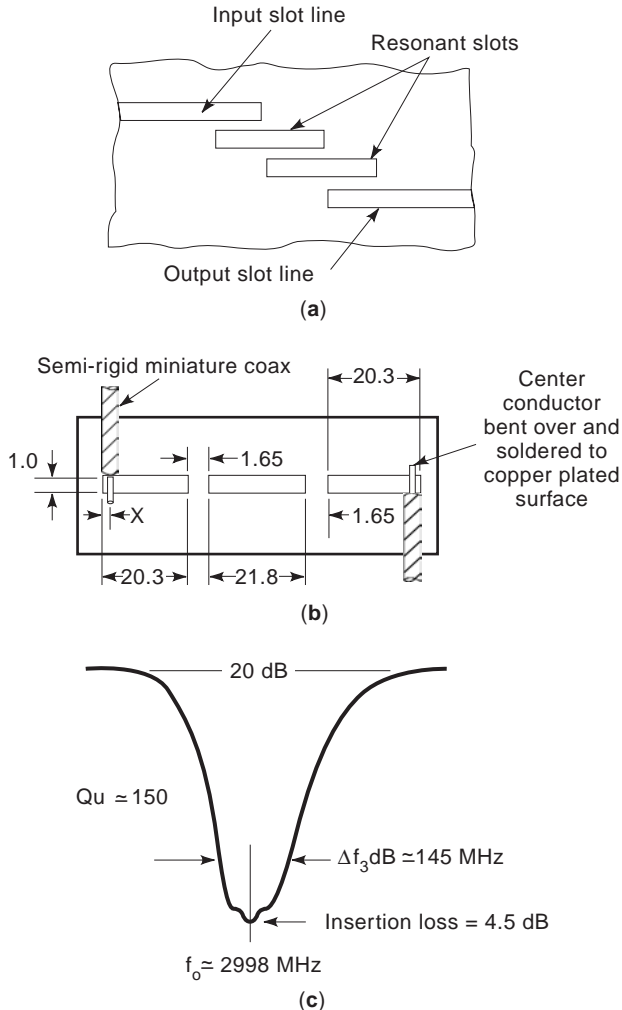


Figure 9. Slotline bandpass filters: (a) configuration of quarter-wavelength-coupled slot resonator filter; (b) circuit configuration of end-coupled slot resonator filter; (c) bandpass response of (b). (From Ref. 8 with permission, © 1970 IEEE.)

plane of the microstrip line, which acts as the terminating line. Such a two-resonator bandstop filter was built on a 1.6-mm-thick D-16 substrate using the same configuration as that in Fig. 10a. The slots had an impedance of 85Ω , were approximately $\lambda_g/2$ long, and had a separation of $3\lambda_m/4$ (λ_m is the wavelength of the microstrip line). Figure 10b shows a rejection response of about 15% at the 20 dB level for the filter.

Another application of slotline–microstrip combination in filters is the microstrip-fed slotline dual-mode bandpass filter [9]. By using microstrip tuning stubs on the backside of the slotline ring at 45° and 135° , the dual resonant mode can be excited. Figure 11a shows the physical configuration of the slotline dual-mode bandpass filter. The microstrip feedlines located at 0° and 270° are used to extract both sine and cosine resonant modes that are orthogonal to each other in the ring structure. Figure 11b shows the measured insertion and return loss as for the slotline dual-mode bandpass filter with mode number $n = 3$. The dual-mode filter has a 12% bandwidth at the center frequency of 3.5 GHz, a stopband attenuation of more than 30 dB, and a sharp gain slope transition. Compared with the microstrip dual-mode filter, the slotline dual-mode filter has a better

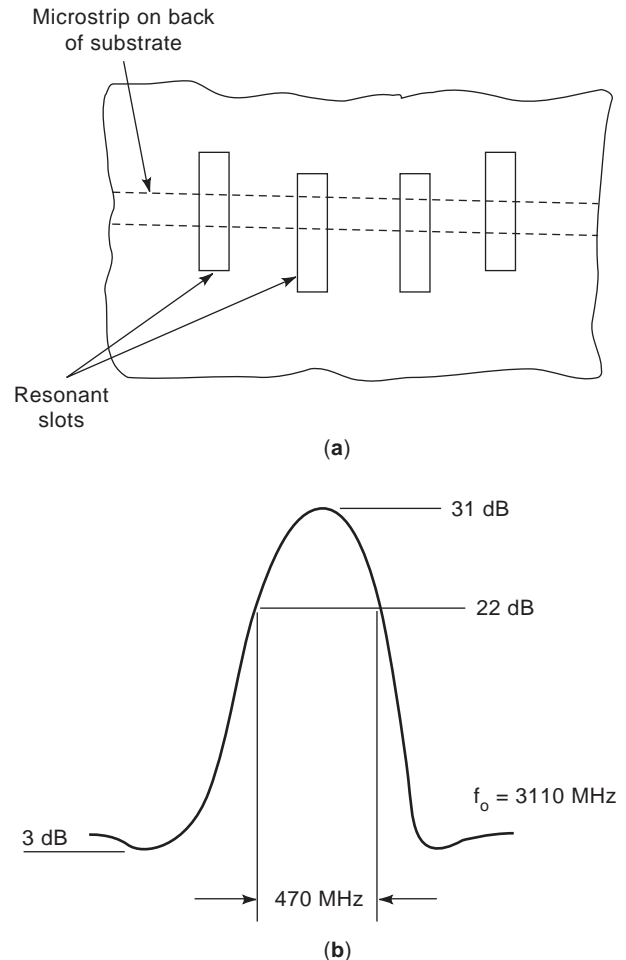


Figure 10. (a) Configuration and (b) characteristic response for slotline bandstop filter. (From Ref. 8 with permission, © 1970 IEEE.)

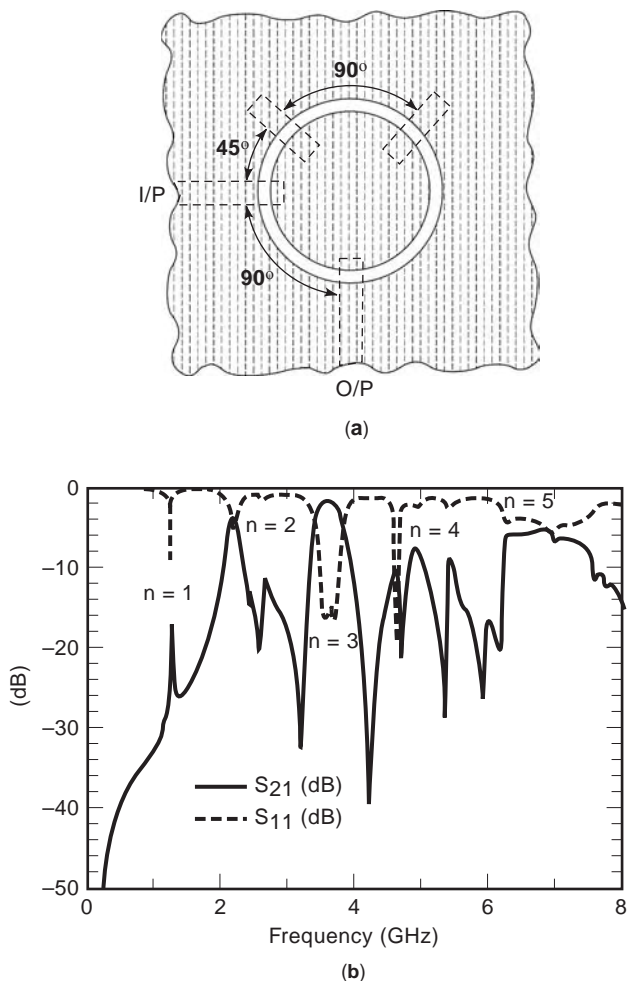


Figure 11. Slotline ring dual-mode bandpass filter: (a) physical circuit etched on a RT-Duroid 6010 substrate ($\epsilon_r = 10.5$, $h = 0.63$ mm); (b) measured frequency responses of insertion loss and return loss. (From Ref. 9 with permission, © 1993 IEEE.)

in-band and out-of-band performance. Also, the slotline ring dual-mode filter has the advantages of flexible tuning and ease of adding series and shunt devices.

2.2. Ferrite Devices

Slotline application to ferrite devices was reported in 1969 when the slotline was first introduced as an alternative transmission line for microwave integrated circuits [10]. Based on the existence of an elliptically polarized magnetic field, slotline was used for the design of planar ferrite phase shifters, circulators, and isolators. The design procedure for the slotline ferrite devices is the same as that for the microstrip line. However, the experimental results reported so far indicate that the performance of the slotline ferrite devices is not superior to those using a microstrip line.

2.3. Slotline Branchline Couplers, Hybrid Couplers, and Magic Ts

Hybrids and couplers form an indispensable component group in modern MIC and MMIC technology. With the inventions of new planar transmission lines like CPW,

slotline, coplanar stripline (CPS), coupled microstrip–slotlines, and their derivatives, many types of hybrids and couplers have been developed over the past several decades. This growth is due to the rapidly expanding applications in wireless communications, radar, sensors, electronic warfare, and space technology.

This section describes different types of slotline branchline couplers, hybrid couplers, and magic Ts and their applications.

2.3.1. Parallel-Coupled Slotline Directional Coupler. The first attempt in fabricating a parallel-coupled slotline coupler was successful by Mariani and Agrios in 1970 [8]. The coupler used a D-16 dielectric substrate ($\epsilon_r = 16.3$, $h = 1.6$ mm) with aluminum tape metallization. The actual circuit dimensions are shown in Fig. 12 along with the measured results. Unlike the backward coupling (electric coupling) in the case of parallel microstrip-coupled line couplers, the coupling of the coupled slotline coupler is magnetic coupling in the forward direction as in the case of the waveguide narrow-wall coupler. As shown in Fig. 12b, the coupler had a 4 dB coupling (3 dB is ideal coupling) over a wideband of about 600 MHz. The insertion loss was nearly 1 dB, which includes the coax-slotline transitions. The isolation bandwidth of 18 dB was 400 MHz centered at 2.8 GHz (about 14% bandwidth). According to their experiments, the reporters indicated that

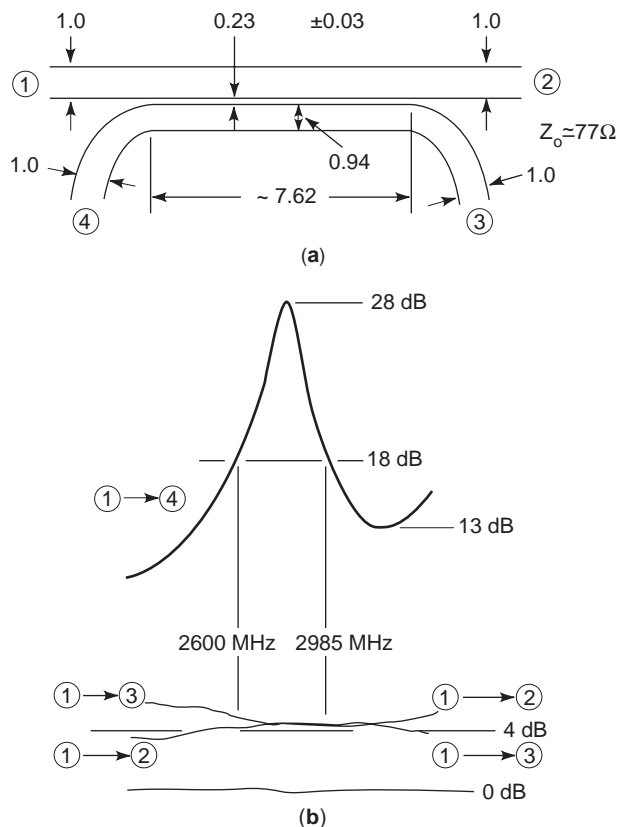


Figure 12. Parallel-coupled slotline coupler: (a) physical configuration (all dimensions in millimeters); (b) measured frequency responses of insertion loss and return loss. (From Ref. 8 with permission, © 1970 IEEE.)

(1) the performance of the slotline coupler could be improved by optimizing the various important physical dimensions such as the separation, coupling length, and slot width; and (2) a 3 dB coupling implementation in using parallel-coupled slotline is quite practical and a wider bandwidth of 40% is possible.

2.3.2. Uniplanar Branchline Couplers. It is well known that microstrip branchline couplers are basic components in applications such as power dividers, balanced mixers, frequency discriminators, and phase shifters. The concept and analysis of the branchline couplers can be found in many microwave textbooks. This section presents two uniplanar branchline couplers using slotline and CPW structures [4]. The design technique for the slotline branchline coupler uses series branchlines. The design technique for the slotline–CPW hybrid branchline coupler uses shunt branchlines.

Figure 13a shows the physical configuration of the slotline two-branchline coupler [11]. For the case of 3 dB coupling, when a signal is applied to port 1 the outputs appear at ports 2 and 3 and are equal in amplitude and differ in phase by 90°. Port 4 is the isolation port. Figure 13b shows the equivalent transmission-line model of the slotline branchline coupler. The through arms and branch arms are connected in series. The corresponding line characteristic impedances of the slotline through and branch arms, in terms of the termination impedance Z_0 , can be expressed as

pressed as

$$Z_{S1} = \sqrt{2}Z_0; \quad Z_{S2} = Z_0 \quad (1)$$

where Z_{S1} is the characteristic impedance of the slotline through arms and Z_{S2} is the characteristic impedance of the slotline branch arms.

The measured performance is summarized below. The amplitude imbalance of 1 dB is within a bandwidth of less than 20% at the 3 GHz center frequency. The measured isolation between ports 1 and 4 is greater than 30 dB at the center frequency of 3 GHz. A computer program based on the equivalent transmission-line model of Fig. 13b was developed and was used to analyze the circuit. The calculated results agree very well with the measured results.

Another type of uniplanar branch coupler is a slotline–CPW hybrid branchline coupler consisting of a rectangular slotline ring coupled with two parallel slotline feeds. The uniplanar hybrid branchline coupler is dual to the slotline branchline coupler in Fig. 13a. Figure 14a shows the physical configuration of the branchline coupler [13]. The two CPW through arms are fed by input and output slotlines and connected by two slotline shunt branch arms. The equivalent transmission-line model of the coupler is shown in Fig. 14b. Adding bonding wires at the circuit's discontinuities is important to prevent the coupled slotline mode from propagating on the CPW arms. The corresponding line characteristic impedances of slotline and CPW branch arms for 3 dB coupling, in terms of the termination impedance Z_0 , can be expressed as

$$Z_{CPW} = \frac{Z_0}{\sqrt{2}}; \quad Z_S = Z_0 \quad (2)$$

where Z_{CPW} is the impedance of the CPW arms and Z_S is the impedance of the slotline shunt branch arms. According to the Eq. (2), a truly uniplanar hybrid branchline coupler was built on a 1.27-mm-thick RT/Duroid ($\epsilon_r = 10.8$) substrate. To test the hybrid branchline coupler, the wideband slotline–CPW transitions shown in Fig. 4b was connected at ports 1–4. The measurements were performed on an HP-8510 network analyzer using standard subminiature (SMA) connectors. The performance includes two coax CPW transitions and two CPW–slotline transitions. Figure 14c shows the measured frequency responses of the hybrid branchline coupler. Over a 40% bandwidth centered at 3 GHz, the power dividing balance and phase difference between ports 2 and 3 are ± 1 dB and $83^\circ \pm 3^\circ$, respectively. The isolation between ports 1 and 4 is greater than 20 dB, and the return loss is more than 19 dB over the same bandwidth. This slotline–CPW hybrid branchline coupler exhibits superior broadband performance over conventional microstrip branchline couplers.

2.3.3. De Ronde's Couplers. In 1970 de Ronde proposed a new coupler that has been named after him. The de Ronde coupler is particularly suitable for tight coupling such as in 3-dB hybrids in MIC technology. The coupler configuration consists of a microstrip–slotline coupling

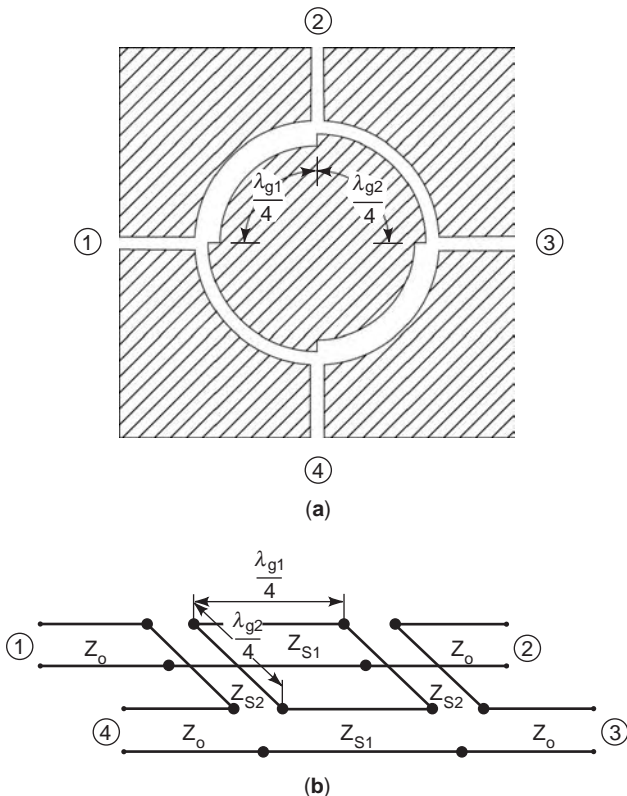


Figure 13. Slotline branchline coupler: (a) physical configuration; (b) equivalent transmission-line model. Two branch arms are connected to the through arms in series. (From Ref. 12.)

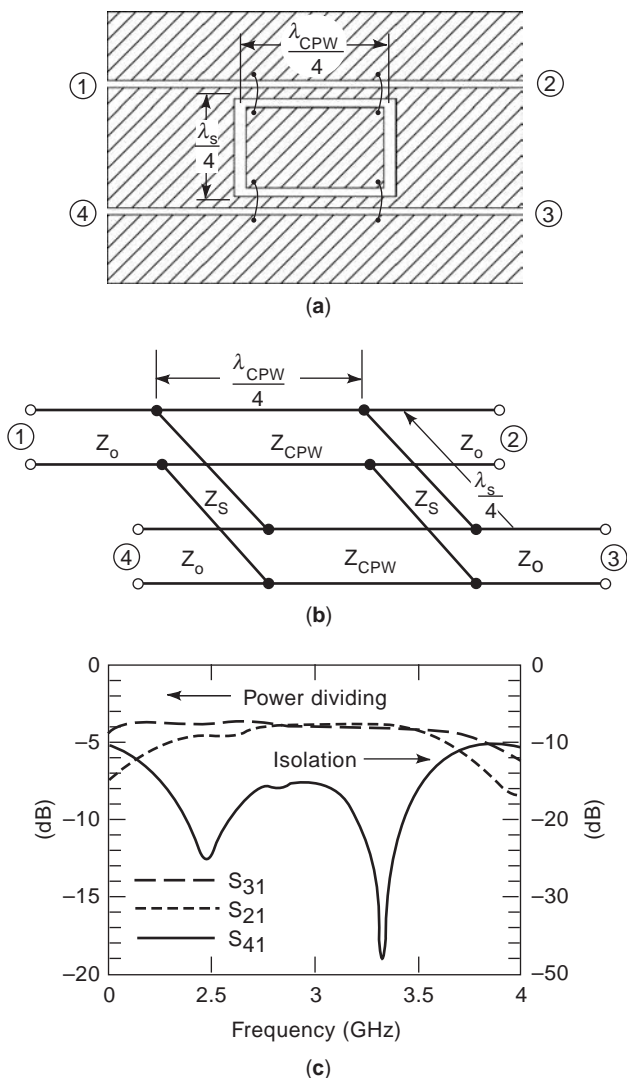


Figure 14. Uniplanar slotline-CPW hybrid branchline coupler: (a) physical configuration; (b) equivalent transmission-line model; (c) measured frequency responses of power dividing and isolation. (From Ref. 4 with permission, © 1993 IEEE.)

section (with a strip on top of the substrate and a slot in the ground plane) connected by four microstrip output lines as shown in Fig. 15a. An analysis of the coupler has been made by Schiek [12] with the aid of the equivalent transmission-line model of the hybrid branchline coupler. From this design theory, an empirical de Ronde's 3-dB coupler was built at X band with a measured performance as shown in Fig. 15b, which is close to the expected behavior. A complete analysis of de Ronde's coupler has been carried out by Hoffman and Siegl [13] using the method of the even-odd mode of four-port network with double symmetry. The scattering parameters of the couplers were derived and the compensated couplers were also demonstrated. In 1995, Ho et al. [14] presented a uniplanar de Ronde CPW-slotline directional coupler. The new coupler uses parallel and series CPW-slotline connections. Both the CPW and slotline are on the same side of substrate. A truly uniplanar de Ronde's CPW-slotline direc-

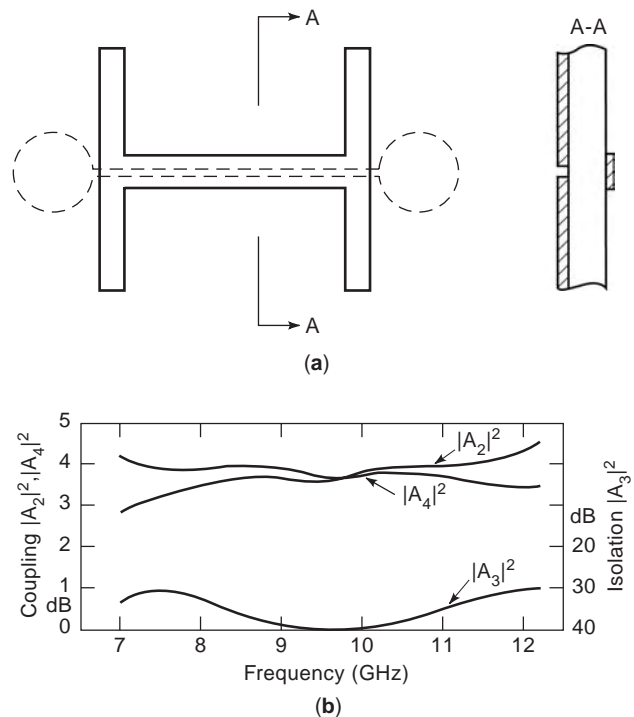


Figure 15. Microstrip-slotline de Ronde coupler: (a) physical configurations (left—top view; right—side view); (b) measured performance for the coupler's couplings and isolation. (From Ref. 14 with permission, © 1974 IEEE.)

tional coupler with 5 dB coupling was demonstrated for use from 2.4 to 3.4 GHz.

Figure 16a shows the physical configuration of the uniplanar de Ronde CPW-slotline directional couplers [16]. The couplers consist of sections of CPW and slotline that are in close proximity and are continuously coupled. The slotline coupling section with a compensation length L_S is terminated with a slotline radial stub on both ends, as shown in Fig. 16a. The purpose of adding an extended slotline section L_S is to compensate for the difference of phase velocity between the even- and odd-mode coupling. The output four ports are formed by two CPW-slotline T junctions. Figure 16b shows the equivalent transmission-line model of the coupler.

To test the coupler, a wideband CPW-slotline transition was used to connect to ports 1-4. The measurements were made using standard SMA connectors and an HP-8510 network analyzer. Experimental results showed that the uniplanar de Ronde coupler achieved a greater than 30% bandwidth from 2.4 to 3.4 GHz, a power coupling of 5.5 dB (including insertion loss), a >14 dB return loss, greater than 17 dB isolation, and $90^\circ \pm 4^\circ$ phase difference between ports 2 and 3. The poor return loss is due to the mechanical tolerances, misalignments, and connectors.

2.3.4. 180° Reverse-Phase Hybrid Ring Couplers. The microstrip ratrace hybrid ring has been widely used in microwave power dividers and combiners. Figure 17a shows the physical configuration of the hybrid ring coupler consisting of three $\lambda_m/4$ sections, $3\lambda_m/4$ delay section, and four

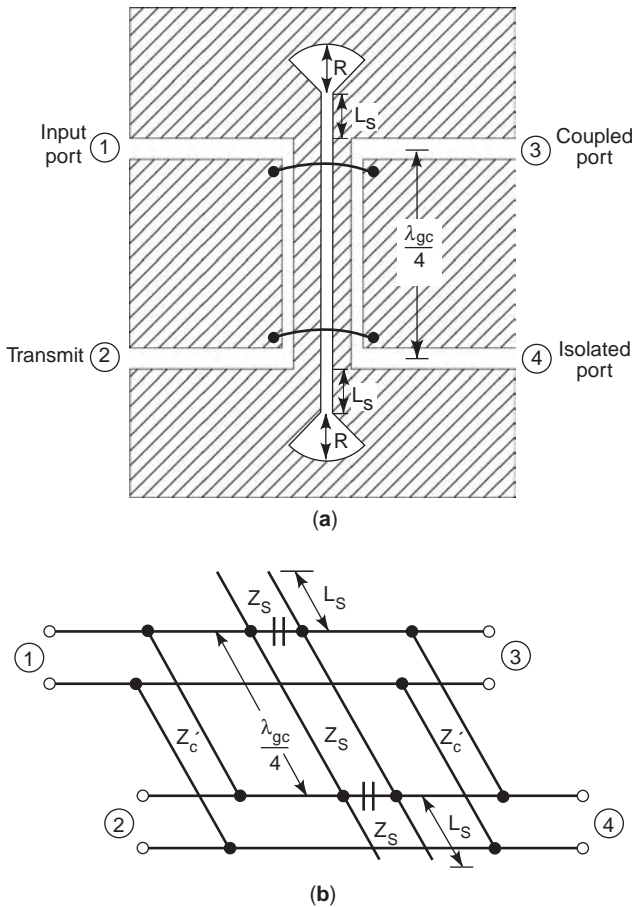


Figure 16. Uniplanar de Ronde CPW-slotline directional coupler: (a) physical configuration; (b) equivalent transmission-line model. (From Ref. 16 with permission, © 1995 IEEE.)

microstrip T junctions. Typically this coupler has a bandwidth of 20–25%. To extend the bandwidth, a modified version of this coupler was proposed by Chua in 1971 [15]. This modified reverse-phase hybrid ring coupler used a $\lambda_s/4$ section of a pair of microstrip-slotline transitions to replace the $3\lambda_m/4$ section of the conventional $3\lambda_m/2$ microstrip ratrace hybrid ring coupler as shown in Fig. 17b. The microstrip-slotline transitions provide a remaining 180° phase delay. Since the phase change of the microstrip-slotline transition is frequency-independent, the resulting reverse-phase hybrid ring coupler has a bandwidth of greater than an octave. Although the modified version gives good performance with a wide bandwidth, the double-sided implementation of a curved $3\lambda_m/4$ microstrip line with an inserted $\lambda_s/4$ slotline is not easy for the photolithography process. Also, ground pins are needed for the microstrip shorts.

More recently, uniplanar transmission lines have emerged as alternatives to microstrip in planar microwave integrated circuits. A narrowband uniplanar hybrid coupler was proposed by Hirota et al. in 1987 [16]. The circuit is based on a slotline ring with three in-phase CPW feeds via an airbridge. More recently, a broadband uniplanar hybrid ring coupler [5] operating over an octave bandwidth was developed using a one-wavelength cross-

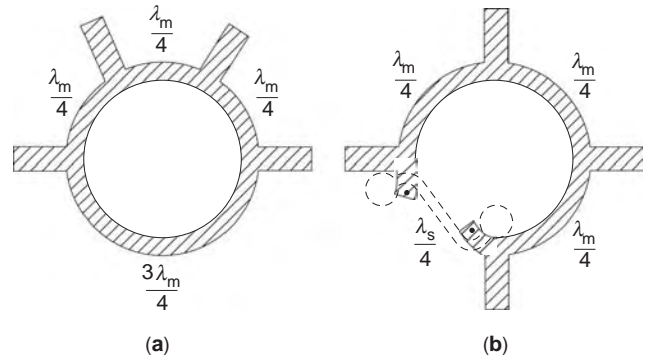


Figure 17. Circuit configurations of microstrip hybrid ring couplers: (a) ratrace hybrid ring coupler using microstrip lines only; (b) reverse-phase hybrid ring coupler using a $\lambda_s/4$ slotline section instead of the $3\lambda_m/4$ microstrip line in (a).

over slotline ring and a one-wavelength crossover CPW ring structure. However, these devices consist of $\lambda/4$ sections that occupy large areas in MIC applications and the bandwidth is limited by the electrical linelength. To overcome these problems for monolithic integration, a uniplanar reverse-phase hybrid ring coupler [17] was proposed using a slotline-CPW ring with a 180° reverse-phase slotline-CPW back-to-back balun and four CPW feeds as shown in Fig. 18a. The circuit consists of four CPW-slotline T junctions and one 180° reverse-phase slotline-CPW back-to-back balun that is formed using a pair of slotline-CPW transitions. Figure 18b shows the equivalent transmission-line model. The twisted transmission line represents the 180° reverse-phase CPW-slotline balun. The characteristic impedance of slotline Z_S and CPW Z_C in terms of CPW feedline impedance Z_{co} and θ are given by

$$Z_S = Z_C = Z_{co} \sqrt{2(1 - \cot^2 \theta)} \quad (3)$$

In this design, $\theta = 72^\circ$ (i.e., $\lambda_{gs}/5$) was chosen, resulting in the characteristic impedances Z_S and $Z_C = 66.9\Omega$. The hybrid ring coupler was fabricated on a 1.524-mm-thick RT/Duroid 6010 ($\epsilon_r = 10.5$) substrate. Experimental measurements presented in Fig. 18c show that the hybrid ring coupler has a 1.3-octave bandwidth centered at 4 GHz, a maximum power dividing imbalance of 0.4 dB, and a 2.5° maximum phase imbalance. Compared to microstrip reverse-phase hybrid ring coupler, the reduced-size slotline-CPW hybrid ring coupler has the advantages of uniplanar structure, small size, and broadband operation.

2.3.5. Magic Ts. Magic Ts (also known as “magic tees”) are widely used as 0° and 180° power dividers or combiners in microwave circuits such as balanced mixers, balanced amplifiers, and frequency discriminators. The matched waveguide double-T is a well-known and commonly used waveguide magic T. In 1964, Kraker [18] first proposed a planar magic T that uses an asymmetric coupled transmission-line directional coupler and Schiffman’s phase shift network [19]. In 1980, Aikawa and Ogawa [20] proposed a double-sided magic T that is constructed with

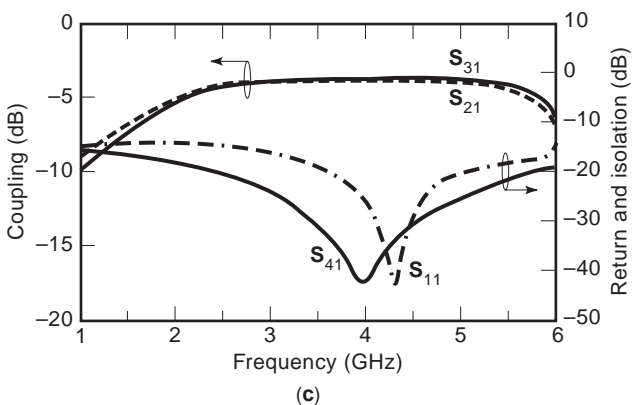
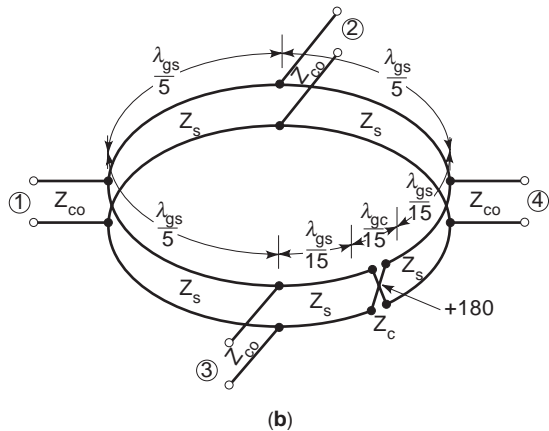
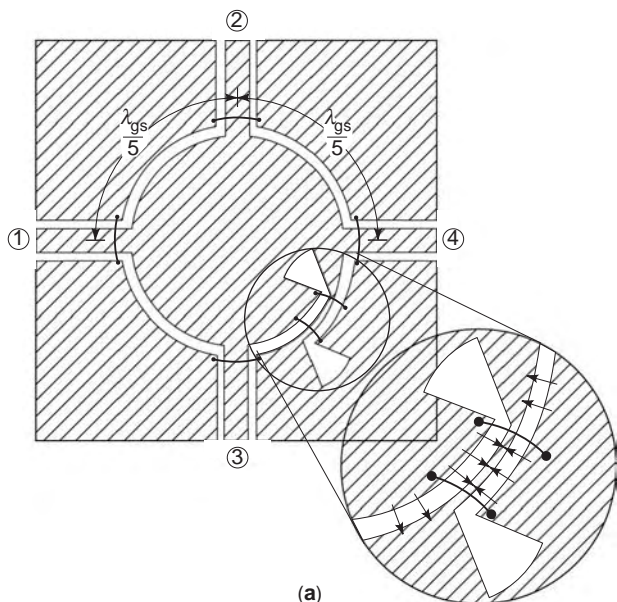


Figure 18. Uniplanar reduced-size reverse-phase hybrid ring coupler: (a) circuit configuration; (b) equivalent transmission-line model; (c) measured frequency responses of coupling, return loss, and isolation. (From Ref. 17 with permission, © 1995 IEEE.)

microstrip–slotline T junctions and coupled slotlines. The two balanced arms of the double-sided magic T are on the same side and do not need a crossover connection. The double-sided magic T has a bandwidth from 2 to 10 GHz.

More recently, uniplanar magic Ts have been preferred for planar microwave integrated circuits because they allow easy series and shunt connections of passive and active solid-state devices without via holes. In 1987, Hirota et al. [16] proposed a uniplanar magic T that uses three CPW–slotline T junctions and a slotline T junction. The in-phase CPW excitation is via an airbridge, and the slotline T junction is used as a phase inverter. The uniplanar magic T has a narrow bandwidth. We next present a double-sided slotline magic T [21], then a uniplanar slotline magic T will be discussed [22]. These two magic Ts are based on a 180° phase reversal of the slotline T junction as shown in Fig. 1e. Finally, a reduced-size uniplanar magic T will be discussed [17] with its equivalent circuit. Since the out-of-phase CPW–slotline T junction is basically frequency-in-

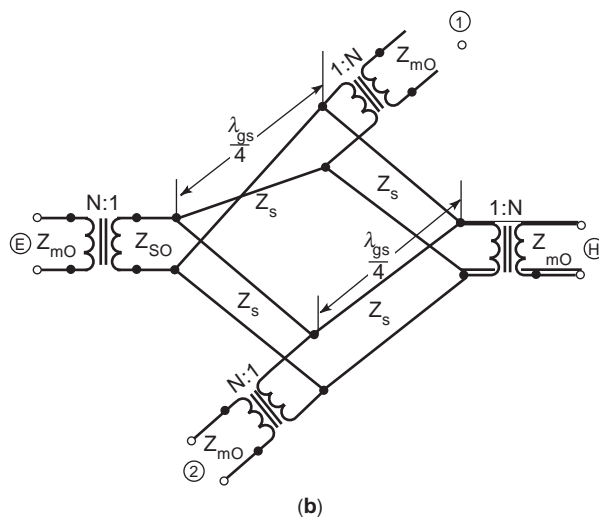
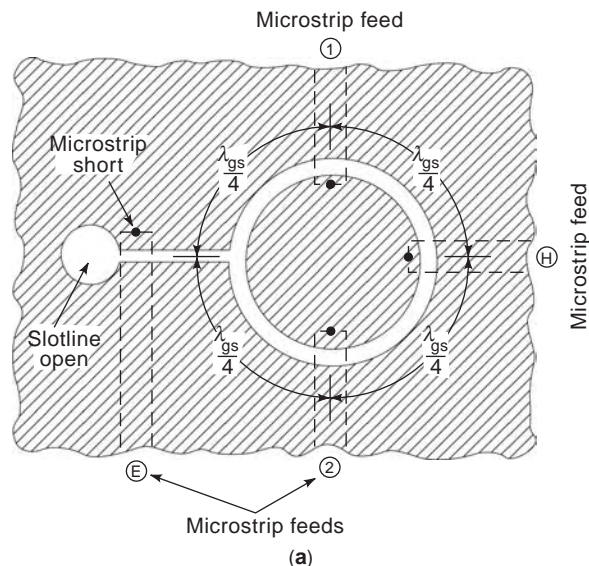


Figure 19. Double-sided slotline magic T with microstrip feeds: (a) physical configuration; (b) equivalent circuit. (From K. Chang, *Microwave Ring Circuits and Antennas*, 180 degree double-sided slotline ring magic-Ts, New York: Wiley & Sons, p 203, © 1996. Reprinted by permission of John Wiley & Sons, Inc.)

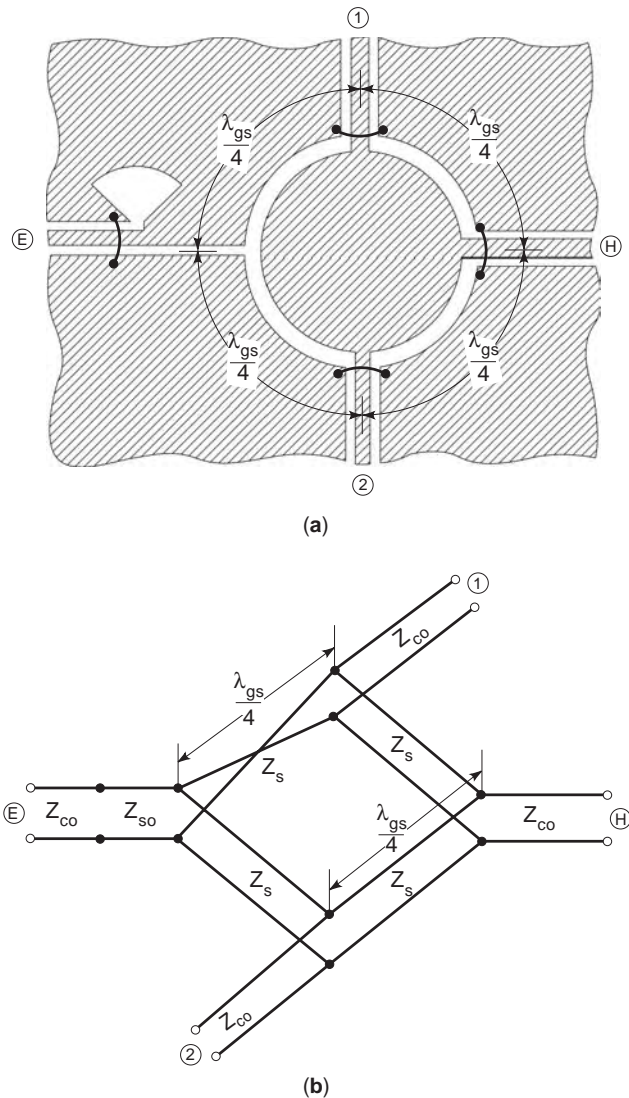


Figure 20. Uniplanar slotline magic T using a 180° reversed-phase slotline T junction: (a) physical configuration; (b) equivalent transmission-line model. (From K. Chang, *Microwave Ring Circuits and Antennas*, 180 degree double-sided slotline ring magic-Ts, New York: Wiley & Sons, pp. 207–208, © 1996. Reprinted by permission of John Wiley & Sons, Inc.)

dependent, the resulting magic T has a broad bandwidth with good performance.

2.3.5.1. 180° Double-Sided Slotline Magic T. Figure 19a shows the circuit configuration of the double-sided slotline magic T [21]. The circuit simply consists of a slotline T junction connected to a slotline–microstrip transition and a slotline ring with three microstrip feeds. The slotline T junction is a well-known 180° reverse-phase T junction and is used as a phase inverter in the slotline magic T. In Fig. 19a, ports *E* and *H* correspond to the *E* and *H* arms of the conventional waveguide magic T, respectively. Ports 1 and 2 are the power-dividing balanced arms. The equivalent transmission-line model of the slotline magic T is shown in Fig. 19b. The twisted transmission line represents the phase reversal of the slotline T junction. The

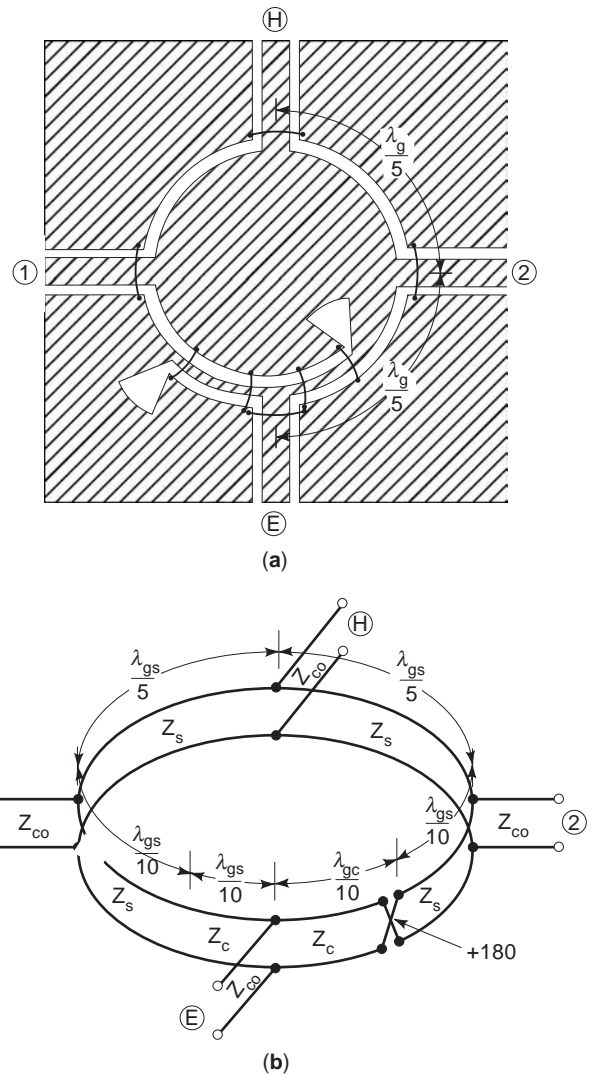


Figure 21. Reduced-size uniplanar hybrid magic T using a $4\lambda_g/5$ circumference CPW-slotline ring that is 20% smaller than comparable designs: (a) circuit configuration; (b) equivalent transmission-line model. The magic T has a bandwidth of 1.6 octaves centered at 4 GHz with a 0.4 dB power dividing imbalance and a 2.5° phase imbalance. (From Ref. 17 with permission, © 1995 IEEE.)

characteristic impedance of the slotline Z_S in terms of the input–output characteristic impedance Z_{S0} is given by $Z_S = \sqrt{2}Z_{S0}$. The radius of the slotline ring is determined by $2\pi r = \lambda_{gs}$, where λ_{gs} is the guide wavelength of the slotline ring. The test circuit was built on a RT/Duroid 6010.8 substrate ($\epsilon_r = 10.8$, $h = 1.27$ mm). Measured results show that the slotline magic T has an excellent isolation of greater than 35 dB and a good power-dividing balance of 0.2 dB over an 80% bandwidth. The calculated results from the equivalent model agreed very well with the measured data.

2.3.5.2. 180° Uniplanar Slotline Magic T. Figure 20 shows the physical configuration of the uniplanar slotline magic T and its equivalent circuit [16]. Similar to the double-sided slotline magic T, the *E* arm of the uniplanar

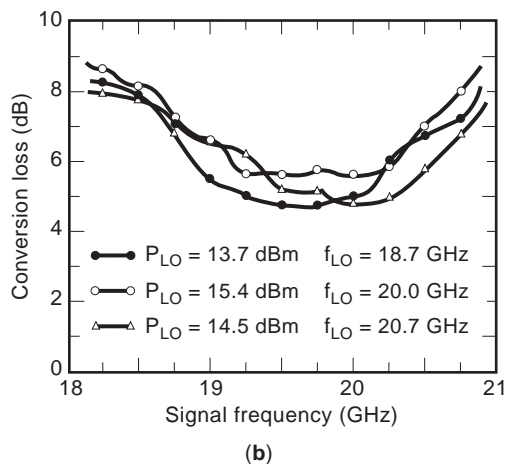
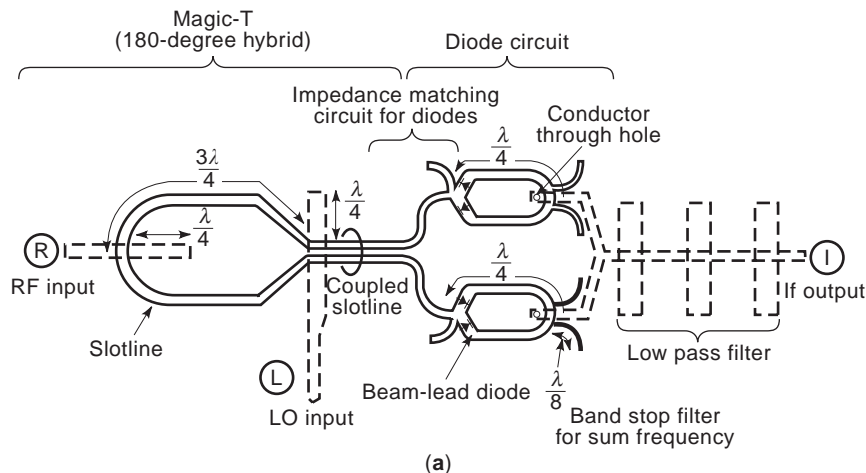


Figure 22. (a) Physical configuration of double-balanced mixer. Solid lines show slotlines and coupled slotlines on the substrate. Dotted lines show microstrip lines on the backside of the substrate. (b) Conversion loss of the mixer. (From Ref. 23 with permission, © 1980 IEEE.)

magic T is fed through a slotline connected to a broadband slotline-CPW transition. The slotline T junction is used as a phase inverter to achieve the 180° phase reversal. The H arm and output balanced arms are all fed by CPW lines. This uniplanar slotline magic T also has good performance over a bandwidth of one octave from 2 to 4 GHz with ±0.25 dB power-dividing balance and ±1° phase balance.

2.3.5.3. Reduced-Size Uniplanar Magic T. Figure 21a shows the circuit configuration of the magic T consisting of one out-of-phase and three in-phase CPW-slotline T junctions [17]. The out-of-phase T junction serves as a phase inverter. In Fig. 21a, ports E and H correspond to the E and H arms of the conventional waveguide magic T, respectively. Ports 1 and 2 are the balanced arms. Figure 21b shows the equivalent transmission-line model of the magic T. The twisted transmission line represents the phase reversal of the CPW-slotline T junction.

3. SOLID-STATE INTEGRATED CIRCUITS (ACTIVE COMPONENTS) USING SLOTLINES

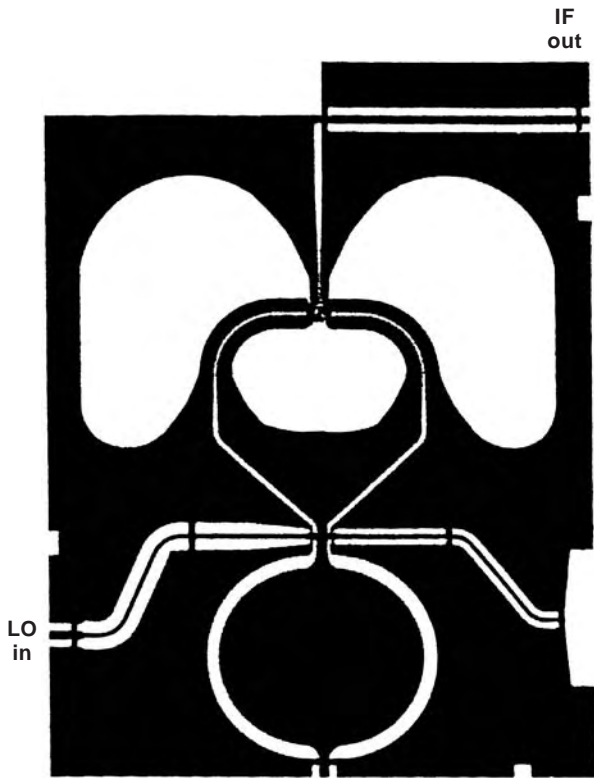
This section presents various microwave integrated circuits such as mixers, oscillators, modulators, and frequency doublers constructed by using slotlines or the combination

of the slotlines and other transmission lines with solid-state devices. A few quasioptical circuits integrated with slotline antennas are also briefly described.

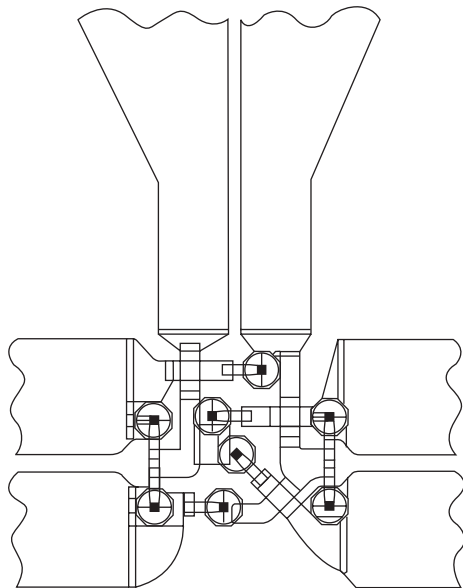
3.1. Mixers

There are three basic types of mixer circuits: single-ended, single-balanced, and double-balanced, which are commonly used in microwave applications. Some examples of planar mixer circuits with slotline follow.

3.1.1. Double-Balanced Mixer. In 1980, Ogawa et al. [23] described a MIC double-balanced mixer. The mixer consists of a magic T for combining the radiofrequency (RF) and local-oscillation (LO) signals, and a balun transition circuit for separating the RF(LO) and intermediate-frequency (IF) signals as shown in Fig. 22a. These circuits are constructed by using combinations of microstrip lines, slotlines, and coupled slotlines, together with four beam-lead Schottky barrier diodes. In Fig. 22a through the magic T, the RF and LO signals are supplied to two pairs of diodes in phase and 180° out of phase, respectively. The IF signal is derived from port I composed of a microstrip low-pass filter, which is used to suppress undesired signals. The diode circuit in Fig. 22a consists of two impedance-matching slotline sections, four λ/4 slotlines, two pairs of



(a)



(b)

Figure 23. Double-double-balanced mixer: (a) photograph of the circuit, chip size $4.57 \times 6.1 \times 0.4 \text{ mm}^3$; (b) detail of dual diode ring connection to the circuit. (From Ref. 24 with permission, © 1991 IEEE.)

beam-lead diodes, six $\lambda/8$ slotline shorted stubs, and two cylindrical conductors used for connecting slotlines and microstrip lines through holes in the substrate. These $\lambda/4$ slotlines are used to utilize effectively the RF and LO pow-

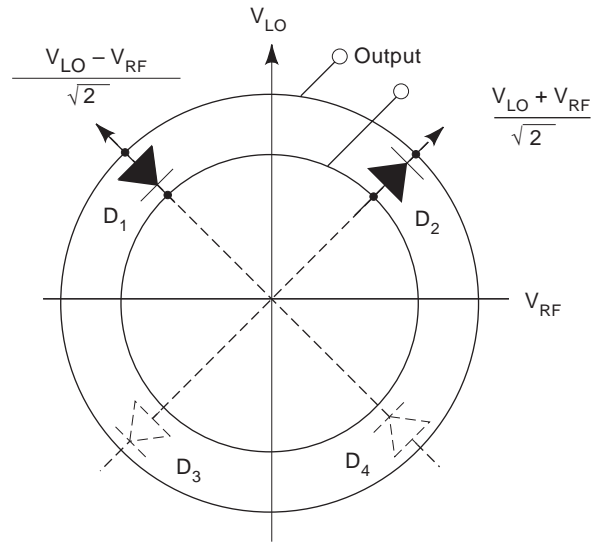


Figure 24. Quasi-optical slotline ring mixer. Four diodes are separated by 90° along the ring, and the basic operation of the mixer is in a balanced polarization-duplexed mode. (From Ref. 25 with permission, © 1983 IEEE.)

ers fed to the diodes. The six $\lambda/8$ slotline shorted stubs serving as bandstop filters are connected to the slotlines in order to suppress the sum frequency.

The double-balanced mixer was fabricated on a 0.3-mm-thick alumina substrate with a dielectric constant of 9.6. Figure 22b shows the measured conversion loss for several LO frequencies. The minimum conversion loss of the mixer is 4.7 dB at a signal frequency of 9.6 GHz, and isolation between the three ports is greater than 20 dB from 18 to 21 GHz. This type of double-balanced mixer can be easily fabricated using ordinary MIC techniques and can be applied to other balanced devices like balanced modulators and upconverters.

3.1.2. Uniplanar Double-Double-Balanced MMIC Mixer.

An arrangement for a double-double-balanced mixer (DDBM) using slotlines, coplanar waveguides (CPW), and coplanar strips (CPSs) is shown in Fig. 23 [24]. The DDBM is composed of a 180° hybrid, an IF balun, and eight GaAs Schottky diodes. The circuit uses a balanced LO input and an unbalanced RF input. The LO signal is applied to the difference port, and the RF signal is fed to the sum port. The 180° hybrid couples the RF signal in phase and LO signal opposite phase to the diodes. Matching between the hybrid and diodes is accomplished by a slotline section and a CPS section in cascade. The IF output is through the IF balun consisting of a CPW-slotline transition followed by a slotline-CPS transition.

The MMIC mixer was fabricated on a 0.4-mm-thick GaAs substrate without the use of via holes. The resulting DDBM operated over a RF bandwidth of 6 GHz, a LO bandwidth of 8–18 GHz, and IF bandwidth of 2–7 GHz with conversion loss ranging from 6.2 to 9.8 dB. Isolations

between the three ports were all greater than 20 dB. The mixer was analyzed using the harmonic-balance method, and the measured and simulated results were in reasonable agreement.

3.1.3. Quasioptical Slotline Ring Mixer. The slotline ring discussed in the previous section was also used as an antenna to build a quasioptical mixer [25]. Figure 24 shows the circuit arrangement. The RF signal arrives as a horizontally polarized plane wave incident perpendicular to the antenna. The LO signal is vertically polarized, and can arrive from either side of the structure. V_{LO} and V_{RF} are the electric field vectors on the antenna plane. By resolving each vector into two perpendicular components, it is easy to see that the mixer diode D_1 receives $(V_{LO} - V_{RF})/\sqrt{2}$, while D_2 receives $(V_{LO} + V_{RF})/\sqrt{2}$. In effect, each diode has its own independent mixer circuit with the intermediate-frequency (IF) outputs added in parallel. The IF signal appears as a voltage between the central metal disk and the surrounding ground plane and is removed through an RF choke. A double-balanced mixer

with improved isolation can be made by adding two additional diodes D_3 and D_4 , as indicated.

The antenna mixer has good LO-to-RF isolation because of the symmetry provided by the balanced configuration. A conversion loss of 6.5 dB was measured for this quasioptical mixer operating at X band.

3.2. Oscillators

Oscillators are one-port circuits generating sinusoidal signals, and are widely applied in microwave transmission and measurement systems. Early oscillator circuits were made using waveguide or coaxial-line technology. Modern designs are often made in planar technology such as microstrip, CPW, slotline, and their combination technologies as well as MIC and MMIC technologies. Examples of oscillator circuits using slotlines follow.

3.2.1. MMIC Varactor-Tuned Oscillator Using a Slotline Resonator. Varactor-tuned oscillators provide more constant output power, wider tuning range, and faster

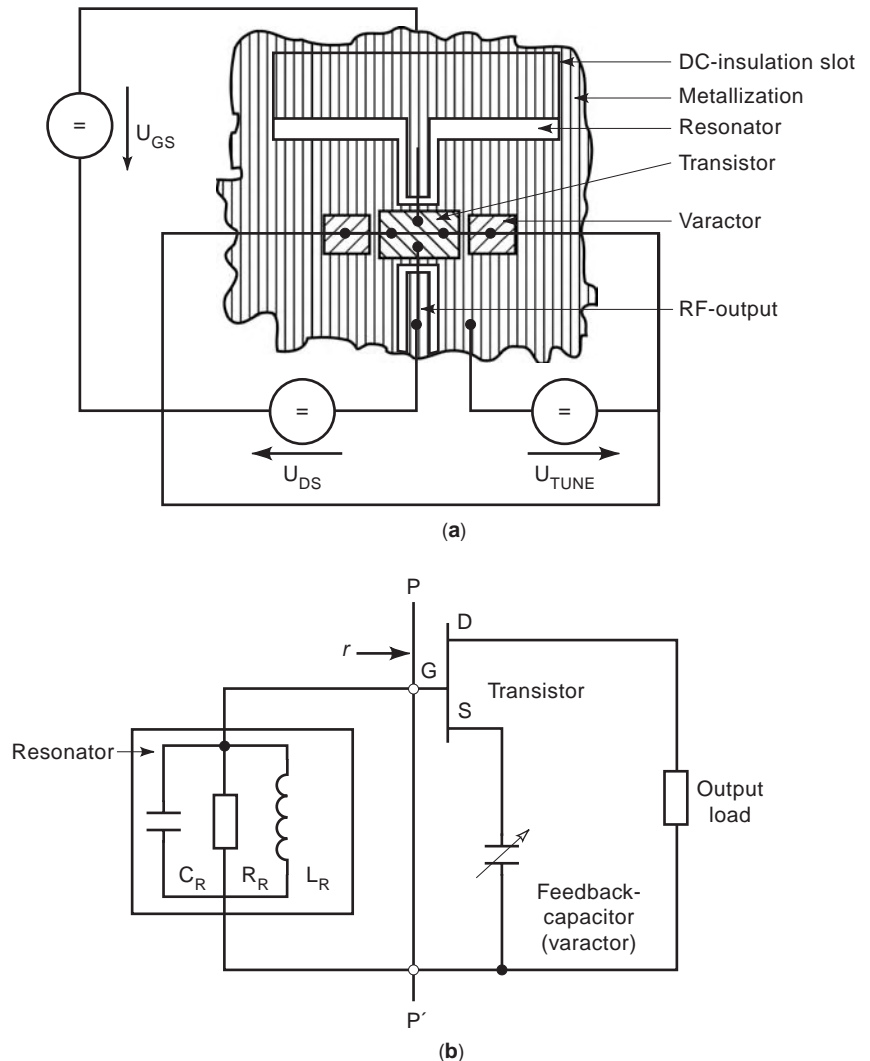


Figure 25. MMIC varactor-tuned oscillator using slotline resonator: (a) physical configuration; (b) equivalent circuit for calculation of RF behavior. (From Ref. 26, reprinted with permission from *Microwave Journal*, Sept. 1990, p. 223.)

response than those of bias tuning oscillators. Figure 25a shows an MMIC varactor-tuned oscillator using a slotline resonator proposed by Roth et al. [26] in 1990. The oscillator was driven by a GaAs field-effect transistor (FET) connected in common source with a capacitive serial feedback. Coupling was realized by a GaAs varactor integrated on the same substrate with the FET. A slotline resonator was built as a linear resonator with coplanar waveguide (CPW) coupling to the FET gate. Bonding wires were used to connect the circuit elements while the output CPW connection was made with a microwave probe. The equivalent circuit of the oscillator as shown in Fig. 25b was used for circuit simulation and predicting circuit performance. The capacitive serial feedback of the FET provides a reflection coefficient r greater than unity in the plane $p-p'$. The resonant frequency was determined by the resonant circuit and the feedback varactor. A test circuit was fabricated and measured. A tuning range of nearly one octave was achieved with 10 mW output power. The experimental results had good agreement with the calculated electrical properties.

Another varactor-tuned oscillator driven by a Gunn diode was built on CPW and slotline [27] as shown in Fig. 26a. The circuit consists of a Gunn diode, a varactor diode, a CPW resonator, a slotline lowpass filter for RF choke and diode biases, and a slotline-microstrip transition for coupling power to output. This VCO provides 16.3 ± 0.35 dB output power throughout a 350 MHz tuning range centered at 10.37 GHz. Figure 26b shows the power output as a function of frequency and varactor bias. The output power is fairly constant over the tuning range.

3.2.2. Active Slot Antennas Driven by Oscillators. Slot resonators have been used as radiators for antenna applications. A ring-stabilized Gunn oscillator coupled with a

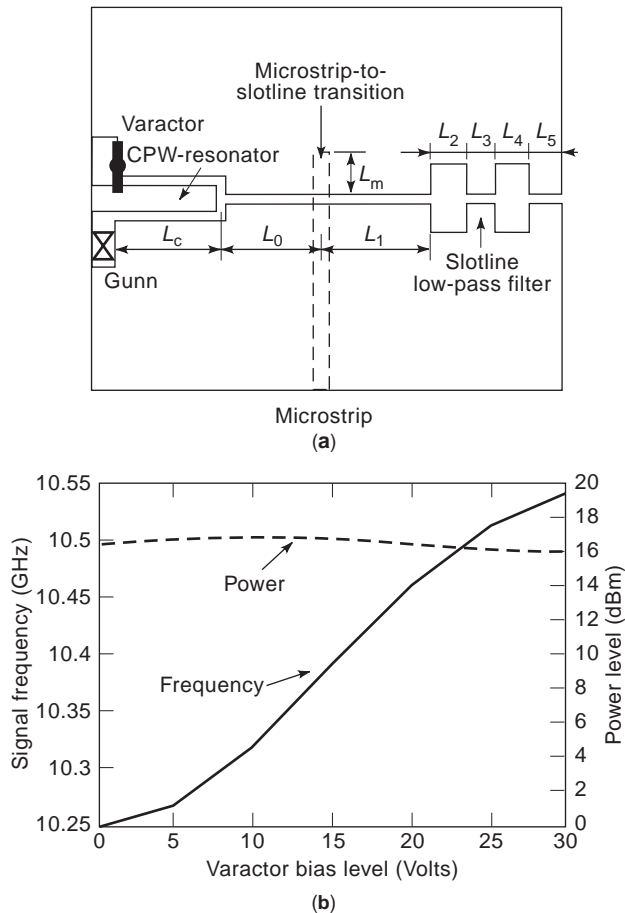


Figure 26. Varactor-tuned CPW/slotline Gunn oscillator: (a) physical configuration; (b) varactor bias voltage versus frequency and power output. Packaged Gunn (MA49106) and varactor (MA46602F) diodes from M/A COM were used for the circuit integration. The circuit was fabricated on a 0.635-mm-thick RT/Duroid 6010 substrate ($\epsilon_r = 10.5$). (From Ref. 27 with permission, © 1991 IEEE.)

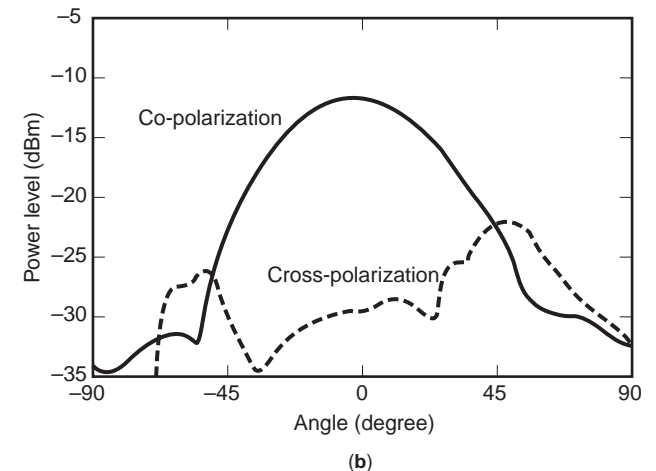
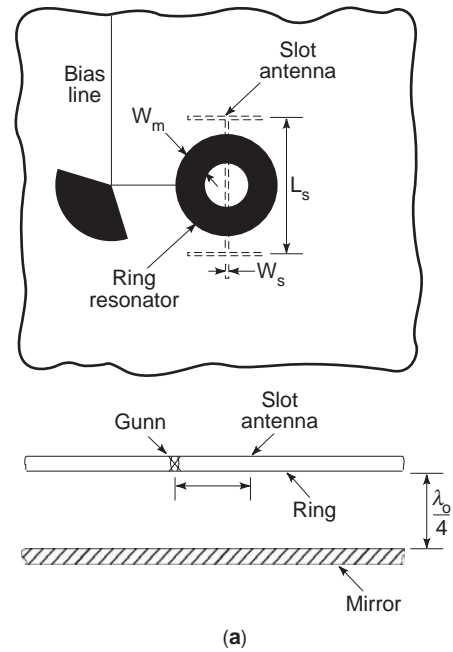


Figure 27. Gunn oscillator driving slot antenna: (a) circuit configuration; (b) H -plane pattern of the antenna. The antenna circuit was fabricated on RT/Duroid 5880 dielectric substrate of $\epsilon_r = 2.20$ and thickness $h = 1.57$ mm with Gunn diodes of model number MA49135 from M/A COM. (From Ref. 28 with permission, © 1995 IEEE.)

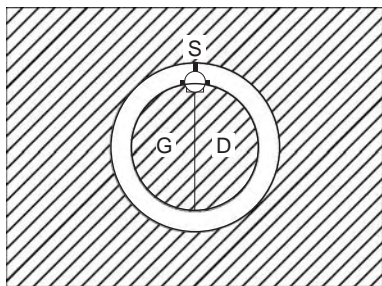


Figure 28. Circuit configuration of an FET active slotline ring antenna. The circuit was etched on RT/Duroid 5870 board with the following dimensions: relative dielectric constant $\epsilon_r = 2.20$; substrate thickness $h = 1.57$ mm; inner radius of the slotline ring $d_1 = 9.54$ mm; outer radius of the slotline ring $d_0 = 11.54$ mm. The active device used in the circuit is an Avantek ATF-26836 FET. (From Ref. 29 with permission from *Electronics Letters*.)

slot radiator to form an active antenna was reported in 1995 [28]. The circuit configuration is shown in Fig. 27a. A circular microstrip ring is used as the resonant element of the oscillator. A slot on the ground plane of the substrate coupled with the microstrip ring served as the radiating element. A Gunn diode is mounted between the ring and the ground plane of the substrate at either side of the ring. A metal mirror block is introduced a quarter-wavelength behind the ring to avoid any backscattering. The operating frequency of the active antenna was designed to be close to the first resonant frequency of the circular microstrip ring. A radiated power of 16 dBm at 5.5 GHz was obtained with the bias level of 12.6 V. The H -plane radiation patterns are shown in Fig. 27b.

An FET oscillator integrated with a slotline ring antenna was also developed [29]. Figure 28 shows the physical configuration. A simple transmission-line method was used to predict the resonant frequency. The FET oscillator-driven slotline antenna radiated 21.6 mW at 7.7 GHz with 18% DC-to-RF efficiency.

3.3. Modulators

A number of digital modulators have been developed for digital communication systems. Digital modulators are classified into three types: the amplitude shift keying (ASK) modulator, the phase shift keying (PSK) modula-

tor, and the frequency shift keying (FSK) modulator. The basic information about modulation can be found elsewhere in this encyclopedia (see the article MODULATION ANALYSIS FORMULA). Here we introduce some examples of modulator circuits using slotlines.

3.3.1. ASK Modulator Using Double-Sided MIC. There are three types of ASK modulators: reflection, transmission, and balanced. Reflection-type modulators need circulators to separate input and output power or hybrid couplers to maintain perfect matching, while transmission-type modulators use isolators instead of circulators. Balanced-type modulators require balanced/unbalanced hybrid transitions for transformation from unbalanced modes to balanced modes, or vice versa. Generally, non-reciprocal components or the matching resistance are necessary to implement ASK modulators.

In 1989, an ASK modulator that does not require circulators and matching resistances was proposed [30]. The circuit using double-sided (slotlines and microstrips) MIC is shown in Fig. 29. It consists of two $\lambda/4$ slotlines, a slotline-microstrip transition, and two beam-lead p-i-n diodes. The measurements for the ASK modulator were performed in the frequency range from 25.0 to 29.5 GHz. A 2.8 dB insertion loss, a 12 dB return loss, and an ON/OFF ratio of greater than 40 dB were obtained. This balanced ASK modulator had a size more compact than that of other types of ASK modulators because no circulators and hybrid couplers were needed, and it had a fairly high ON/OFF ratio because of the balanced circuit configuration.

3.3.2. Integrated Balanced Biphase Shift Keying (BPSK) and Quadriphase Shift Keying (QPSK) Modulators. PSK modulators have two types of reflection and transmission (balanced). The basic principle of the reflection-type PSK modulators is similar to that of the ASK modulators. Transmission-type PSK modulators use the difference in pathlengths for carriers. By selecting a quarter-wavelength for the carrier pathline, a 0° - 180° (BPSK) modulator can be produced. If a one-eighth wavelength of the carrier line is selected, a 0° - 90° (QPSK) modulator can be obtained.

3.3.2.1. Balanced BPSK Modulators. Balanced BPSK modulators are commonly used as digital modulators.

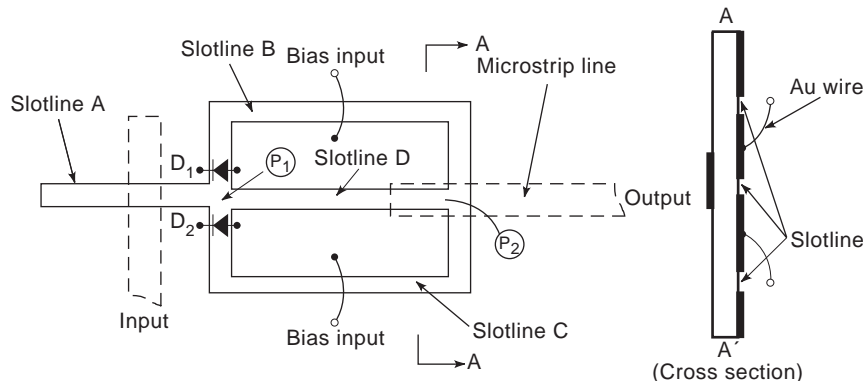


Figure 29. Circuit configuration of the balanced ASK modulator. Solid lines represent slotlines on the substrate. Dotted lines show microstrips on the backside of the substrate. (From Ref. 30 with permission, © 1987 IEEE.)

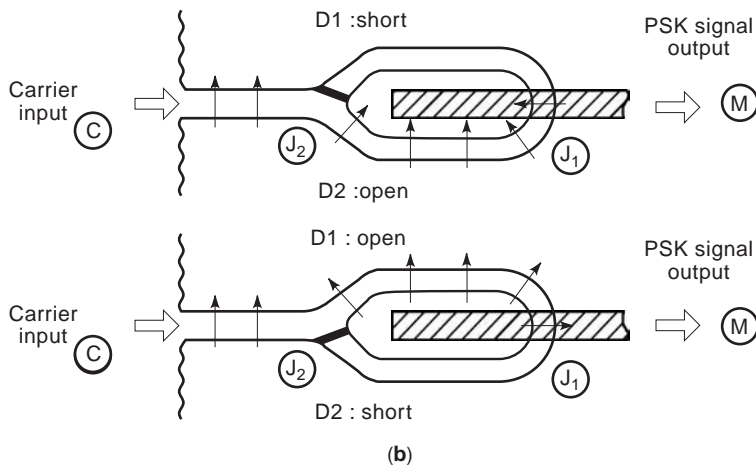
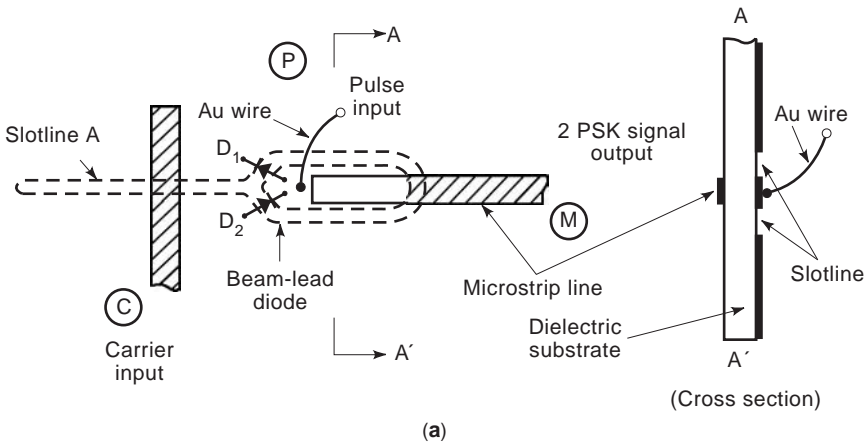


Figure 30. (a) Circuit configuration; (b) operating principle of balanced biphase shift keying (BPSK) modulator. (From Ref. 31 with permission, © 1982 IEEE.)

Figure 30a shows the circuit configuration of a single-balanced BPSK modulator proposed [31] for use in Ka band. The circuit consists of two $\lambda/4$ slotlines, two switching diodes, two slotline–microstrip transitions, and a gold wire used to supply modulating pulses to the diodes. The BPSK modulator operates as shown in Fig. 30b. The arrows represent the electric field of the carrier propagating along the slotlines. When the carrier is supplied to port C, the bias states of the diodes determine which path the carrier takes as the data alternately switch the diodes ON and OFF. The carrier takes path 1 or path 2, producing a biphase output signal because the direction of the electric field at the junction J_1 is 180° out of phase, as shown in Fig. 30b. The modulated carrier is then fed to the microstrip port M through the slotline–microstrip transition. The performance of the BPSK modulator has 2.2 dB insertion loss at a carrier frequency of 27 GHz and a greater than 25 dB isolation over a 1 GHz bandwidth. The phase error and amplitude deviation were less than 1° and 0.5 dB, respectively.

3.3.2.2. Balanced QPSK Modulators. A balanced QPSK modulator is important for digital wireless or satellite communication systems because it allows effective use of frequencies and has also been applied to microwave and millimeter-wave transceivers. A QPSK modulator using

double-sided MIC techniques was reported in 1984 [32] for directly modulating a 60 GHz carrier frequency. Figure 31 shows a block diagram and circuit layout of the QPSK modulator. The circuit consists of a Wilkinson power divider with 90° phase shift in one arm, two biphase switches (BPSK modulators) using coupled slotline–microstrip structure, and a microstrip–waveguide transition at the output.

The circuit operates as follows. The unmodulated RF carrier enters the circuit on microstrip and goes to the in-phase power divider. The carrier is divided into two signals with equal amplitude and in phase. One arm of the power divider drives biphase switch 1 directly. A 90° phase shifter is introduced at the input of biphase switch 2 by increasing the microstrip pathlength between the power divider and biphase switch 2. The biphase switches introduce an additional 0° or 180° phase shift to each signal as the data inputs switch the Schottky diodes. The two biphase-modulated signals are then summed in an in-phase power combiner producing a quadriphase-modulated signal. The QPSK modulator has the following design features and advantages:

1. High isolation between the carrier input port and the modulated carrier output port is obtained because of the balanced configuration.

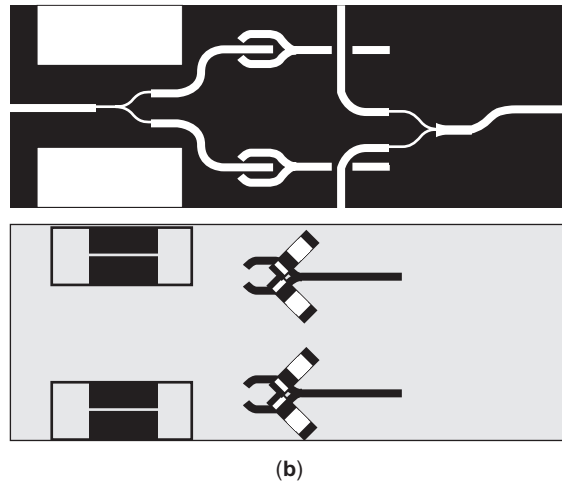
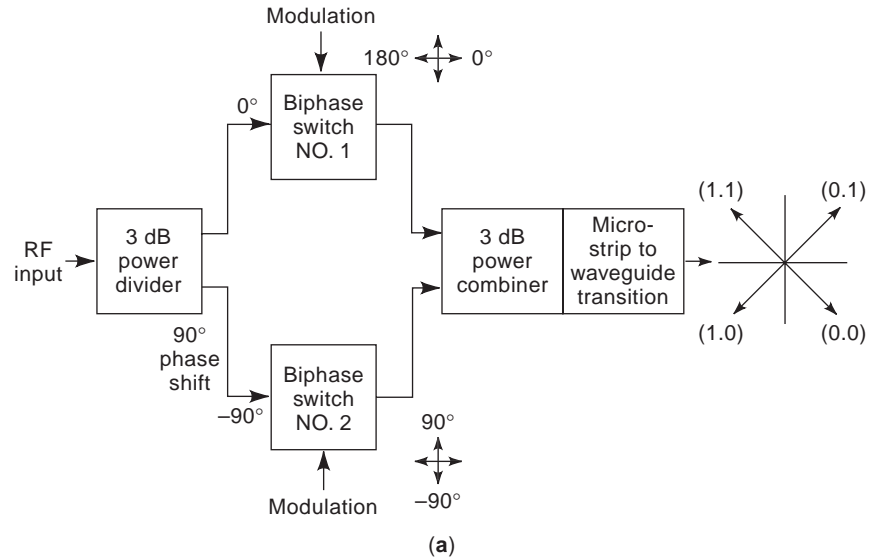


Figure 31. (a) Block diagram; (b) circuit layout of a quadriphase shift keying (QPSK) modulator chip (shown are both sides of the chip). (From Ref. 32 with permission, © 1984 IEEE.)

2. A DC return path is not required because a slotline is used.
3. The 90° phase shift is introduced by an additional pathlength instead of using a 90° hybrid (this simplifies the design since a low-loss, well-balanced 90° hybrid is difficult to realize at 60 GHz).
4. The 180° phase shift is introduced by the built-in field distribution of the slotting.
5. A simple configuration using only a wire bonding is sufficient for a baseband input circuit.
6. Small size is achieved by using a sapphire substrate.

The QPSK modulator chip was integrated with a Gunn voltage-controlled oscillator (VCO), a subharmonic mixer, and a microstrip–waveguide transition to form the RF exciter/modulator module. The modulator demonstrated excellent performance at 60 GHz with an output phase error of less than 3° and maximum amplitude error of 0.5 dB.

3.4. Frequency Multiplier

Microwave and millimeter-wave signals can be generated by frequency multiplication of lower-frequency signals produced by a quartz-controlled generator. Frequency multipliers are usually used to realize this conversion. Figure 32 shows a block diagram of frequency multiplier. A signal of angular frequency ω_0 is fed to a nonlinear device (varactor diodes or transistors), which generates harmonics at angular frequencies $n\omega_0$. The output signal at the desired frequency is then selected by a bandpass filter.

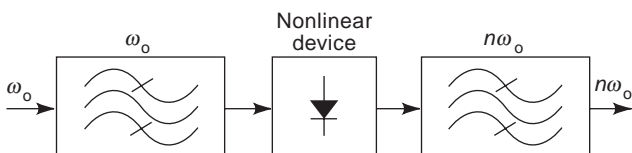


Figure 32. Block diagram of frequency multiplier.

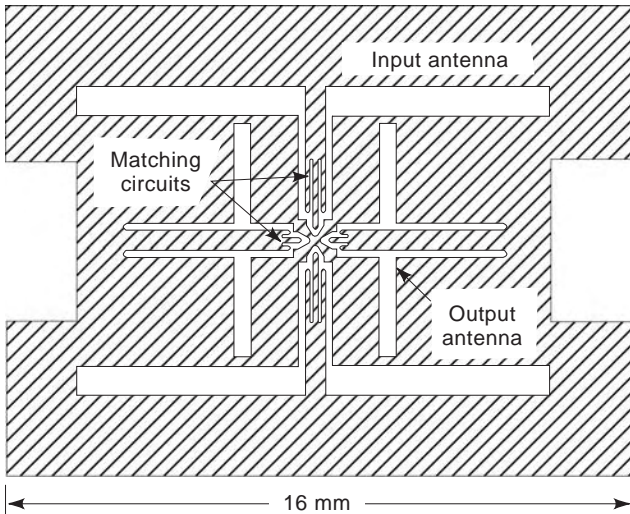


Figure 33. Configuration of an X/K-band quasioptical frequency multiplier. The circuit is built on a thin quartz substrate and mounted on a stycast-filled ($\epsilon_r = 3.9$) parabola. (From Ref. 33 with permission, © 1997 IEEE.)

Two examples of quasioptical frequency multipliers using slot antennas follow.

3.4.1. Quasioptical Frequency Multipliers Using Slot Antennas. Using a uniplanar structure of slotline and CPW, a parabola-feed frequency multiplier for millimeter- and submillimeter-wave signal renovation has been recently reported [33]. The multiplier uses a quadbridge diode configuration to provide effective isolation between input and output signals. Two pairs of double-slot antennas with orthogonal polarizations directly couple input and output signals to the diodes without the need for hybrid couplers in conventional balanced circuits. Figure 33 shows the circuit configuration of the frequency multiplier implemented on a parabola feed with two pairs of slot antennas. The two input antennas receive a vertically polarized signal in phase while sending the signal to the diodes with opposite phase. The output signal generated by the diodes will be transmitted in phase through the two

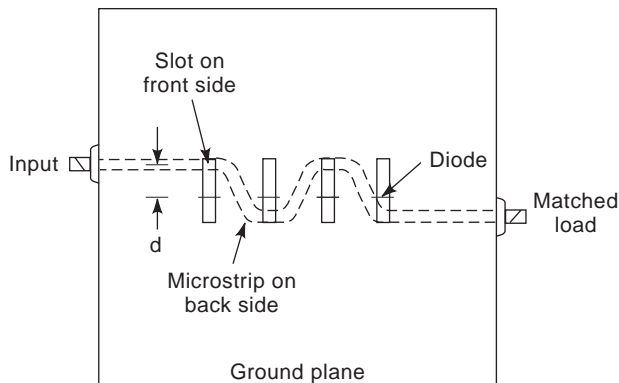


Figure 34. Configuration of frequency multiplier using microstrip-fed slot array. (From Ref. 34 with permission, © 1987 IEEE.)

horizontally polarized antennas. The input and output signals are then coupled to free space by placing the multiplier circuit on an electrically thick substrate lens (a dielectric-filled parabola in this case). This configuration maintains the same conversion efficiency as single-diode multipliers but quadruples the power-handing capability. Measurement results of an X/K-band multiplier show frequency conversion loss of 6.8 dB at the 20.3 GHz output frequency.

Another quasioptical frequency multiplier using double-sided MIC (coupled slot microstrip) techniques was proposed [34] in 1987. The configuration shown in Fig. 34 uses a meander microstrip line to feed an array of diode-loaded slot antennas that are positioned in correct phase to maximize the radiation performance of the multiplier. A 26 dBm, 5.4 GHz input multiplied to 10.8 GHz, was achieved for the circuit. With a planar structure, controllable power coupling, and flexibility in array geometry, the quasioptical frequency multiplier is suited for MIC and MMIC applications.

BIBLIOGRAPHY

1. K. C. Gupta et al., *Microstrip Lines and Slotlines*, 2nd ed., Artech House, Norwood, MA, 1996.
2. S. B. Cohn, Slot line on a dielectric substrate, *IEEE Trans. Microwave Theory Tech.* **MTT-17**(10):768–778 (1969).
3. B. Schuppert, Microstrip/slotline transition: Modeling and experimental investigation, *IEEE Trans. Microwave Theory Tech.* **MTT-36**(8):1272–1282 (1988).
4. C. H. Ho, L. Fan, and K. Chang, Broad-band uniplanar hybrid-ring and branch-line couplers, *IEEE Trans. Microwave Theory Tech.* **MTT-41**(12):2116–2125 (1993).
5. C. H. Ho, L. Fan, and K. Chang, New uniplanar coplanar waveguide hybrid-ring couplers and magic-T's, *IEEE Trans. Microwave Theory Tech.* **MTT-42**(12):2440–2448 (1994).
6. K. Chang, *Microwave Ring Circuits and Antennas*, Wiley, New York, 1996.
7. J. A. Navarro and K. Chang, Varactor-tunable uniplanar ring resonators, *IEEE Trans. Microwave Theory Tech.* **MTT-41**(5):760–766 (1993).
8. E. A. Mariani and J. P. Agrios, Slot-line filters and couplers, *IEEE Trans. Microwave Theory Tech.* **MTT-18**(12):1089–1095 (1970).
9. C. H. Ho, L. Fan, and K. Chang, Slotline annular ring elements and their applications to resonator, filter and coupler design, *IEEE Trans. Microwave Theory Tech.* **MTT-41**(9):1648–1650 (1993).
10. G. H. Robinson and J. L. Allen, Slot-line application to miniature ferrite devices, *IEEE Trans. Microwave Theory Tech.* **MTT-17**(12):1097–1101 (1969).
11. C. H. Ho, *Slotline, CPW Ring Circuits and Waveguide Ring Cavities for Coupler and Filter Application*, Ph.D. dissertation, Texas A&M Univ., College Station, TX, 1994.
12. B. Schiek, Hybrid branchline coupler—a useful new class of directional couplers, *IEEE Trans. Microwave Theory Tech.* **MTT-22**(10):864–869 (1974).
13. R. Hoffmann and J. Siegl, Microstrip-slot coupler design—Part I and Part II, *IEEE Trans. Microwave Theory Tech.* **MTT-30**(8):1205–1216 (1982).

14. C. Ho, L. Fan, and K. Chang, Uniplanar de Ronde's CPW-slot directional couplers *IEEE MTT-S Int. Microwave Symp. Digest*, 1995, Vol. 3, pp. 1399–1402.
15. L. W. Chua, New broad-band matched hybrids for microwave integrated circuits, *Proc. 2nd European Microwave Conf.*, 1971, pp. C4/5:1–C4/5:4.
16. T. Hirota, Y. Tarusawa, and H. Ogawa, Uniplanar MMIC hybrids—a proposed new MMIC structure, *IEEE Trans. Microwave Theory Tech.* **MTT-35**(6):576–581 (1987).
17. L. Fan et al., Wide-band reduced-size uniplanar magic-T, hybrid-ring, and de Ronde's CPW-slot couplers, *IEEE Trans. Microwave Theory Tech.* **MTT-43**(12):2749–2758 (1995).
18. D. I. Kraker, A symmetric coupled-transmission-line magic-T, *IEEE Trans. Microwave Theory Tech.* **MTT-12**(11):595–599 (1964).
19. B. M. Schiffman, A new class of broad-band microwave 90-degree phase shifters, *IRE Trans. Microwave Theory Tech.* **MTT-6**(4):232–237 (1958).
20. M. Aikawa and H. Ogawa, A new MIC magic-T using coupled slot-line, *IEEE Trans. Microwave Theory Tech.* **MTT-28**(6):523–528 (1980).
21. K. Chang, *Microwave Ring Circuits and Antennas*, Wiley, New York, 1996, pp. 202–206.
22. K. Chang, *Microwave Ring Circuits and Antennas*, Wiley, New York, 1996, pp. 207–213.
23. H. Ogawa, M. Aikawa, and K. Morita, K-band integrated double-balanced mixer, *IEEE Trans. Microwave Theory Tech.* **MTT-28**(3):180–185 (1980).
24. J. Eisenberg, J. Panelli, and W. Ou, A new planar double-double balanced MMIC mixer structure, *IEEE MTT-S Int. Microwave Symp. Digest*, 1991, Vol. 1, pp. 81–84.
25. K. D. Stephan, N. Camilleri, and T. Itoh, A quasi-optical polarization-duplexed balanced mixer for millimeter-wave applications, *IEEE Trans. Microwave Theory Tech.* **MTT-31**(2):164–170 (1983).
26. B. Roth, M. Joseph, and A. Beyer, A varactor-tuned oscillator using MMIC technology, *Microwave J.* **33**(9):223–225 (1990).
27. J. A. Navarro, Y. Shu, and K. Chang, A novel varactor tunable coplanar waveguide-slotline Gunn VCO, *IEEE MTT-S Int. Microwave Symp. Digest*, 1991, Vol. 3, pp. 1187–1190.
28. Z. Ding, L. Fan, and K. Chang, A new type of active antenna for coupled Gunn oscillator driven spatial power combining arrays, *IEEE Microwave Guided Wave Lett.* **5**(8):264–266 (1995).
29. C. H. Ho, L. Fan, and K. Chang, New FET active slotline ring antenna, *Electron. Lett.* **29**(6):521–522 (1993).
30. Y. Tarusawa, H. Ogawa, and T. Hirota, A new constant-resistance ASK modulator using double-sided MIC, *IEEE Trans. Microwave Theory Tech.* **MTT-35**(9):819–822 (1987).
31. H. Ogawa, M. Aikawa, and M. Akaike, Integrated balanced BPSK and QPSK modulators for the Ka-band, *IEEE Trans. Microwave Theory Tech.* **MTT-30**(3):227–234 (1982).
32. A. Grote and K. Chang, 60-GHz Integrated-circuit high data rate quadriphase shift keying exciter and modulator, *IEEE Trans. Microwave Theory Tech.* **MTT-32**(12):1663–1667 (1984).
33. M. Kim et al., A planar parabola-feed frequency multiplier, *IEEE Microwave Guided Wave Lett.* **7**(3):60–62 (1997).
34. S. Nam, T. Uwano, and T. Itoh, Microstrip-fed planar frequency multiplying space combiner, *IEEE Trans. Microwave Theory Tech.* **MTT-35**(12):1271–1276 (1987).

SLOTLINES

CHUNG-YI LEE
Qualcomm, Inc.
TATSUO ITOH
UCLA

The propagation and radiation of high-frequency signals are getting more important as the technology progresses. For example, the clock rate for digital circuitry is over hundreds of megahertz. The booming wireless applications have pushed the low-cost and high-volume products to the gigahertz range. Engineers need to understand the behavior of high-frequency signals to have a proper and efficient layout when they design a new circuit. This article introduces one type of high-frequency transmission line called the slotline. The configuration, terminology, analysis, and applications are discussed in subsequent sections.

A slotline is an uniplanar wave-guiding structure proposed by Cohn in 1968 [1]. Figure 1(a) shows the basic configuration of a slotline. It consists of a narrow slit between two metal planes that are on one side of the substrate. It is different from a microstrip line that has a strip and a ground plane on the opposite sides of a substrate. The substrate property (μ, ϵ) and thickness h , the slot width w , and the metal thickness t are parameters determining slotline characteristics. The electromagnetic fields of a slotline concentrate around the slot region and propagate along the longitudinal direction as depicted in Fig. 1(b). The main electric field lines are on the transverse plane, and there are more lines in the substrate region because it has a higher dielectric constant. The propagation mode is nontransverse electromagnetic (non-TEM). Unlike the non-TEM metal waveguide, the slotline has no cutoff frequency because it has two separated metals. We will use the spectral domain approach to analyze the slotline. The propagation constant and the characteristic impedance are obtained from this rigorous analysis.

Microwave circuits are frequently packaged in a metal shield. That is, the bottom of the substrate in Fig. 1(a) is attached to a metal plane. Figure 2 shows a conductor-backed slotline (CBSL). The additional bottom ground plane provides better mechanical strength and heat-sinking ability. However, the presence of the conductor backing can cause a serious problem, which is power leakage in the transverse direction. This power loss results in undesirable package and crosstalk effects. The leakage phenomenon is easy to understand. Besides the slotline mode, the conductor-backed slotline also supports a parallel-plate mode in a region away from the open slit. A slotline mode is a non-TEM wave and has its fields spread in both the substrate and air regions. A parallel-plate mode is a TEM wave and has all its energy confined in the substrate between two metal planes. Therefore, the effective dielectric constant of a parallel-plate mode is always higher than that of a slotline mode. Under these circumstances, the parallel-plate mode behaves as the dominant mode,

14. C. Ho, L. Fan, and K. Chang, Uniplanar de Ronde's CPW-slot directional couplers *IEEE MTT-S Int. Microwave Symp. Digest*, 1995, Vol. 3, pp. 1399–1402.
15. L. W. Chua, New broad-band matched hybrids for microwave integrated circuits, *Proc. 2nd European Microwave Conf.*, 1971, pp. C4/5:1–C4/5:4.
16. T. Hirota, Y. Tarusawa, and H. Ogawa, Uniplanar MMIC hybrids—a proposed new MMIC structure, *IEEE Trans. Microwave Theory Tech.* **MTT-35**(6):576–581 (1987).
17. L. Fan et al., Wide-band reduced-size uniplanar magic-T, hybrid-ring, and de Ronde's CPW-slot couplers, *IEEE Trans. Microwave Theory Tech.* **MTT-43**(12):2749–2758 (1995).
18. D. I. Kraker, A symmetric coupled-transmission-line magic-T, *IEEE Trans. Microwave Theory Tech.* **MTT-12**(11):595–599 (1964).
19. B. M. Schiffman, A new class of broad-band microwave 90-degree phase shifters, *IRE Trans. Microwave Theory Tech.* **MTT-6**(4):232–237 (1958).
20. M. Aikawa and H. Ogawa, A new MIC magic-T using coupled slot-line, *IEEE Trans. Microwave Theory Tech.* **MTT-28**(6):523–528 (1980).
21. K. Chang, *Microwave Ring Circuits and Antennas*, Wiley, New York, 1996, pp. 202–206.
22. K. Chang, *Microwave Ring Circuits and Antennas*, Wiley, New York, 1996, pp. 207–213.
23. H. Ogawa, M. Aikawa, and K. Morita, K-band integrated double-balanced mixer, *IEEE Trans. Microwave Theory Tech.* **MTT-28**(3):180–185 (1980).
24. J. Eisenberg, J. Panelli, and W. Ou, A new planar double-double balanced MMIC mixer structure, *IEEE MTT-S Int. Microwave Symp. Digest*, 1991, Vol. 1, pp. 81–84.
25. K. D. Stephan, N. Camilleri, and T. Itoh, A quasi-optical polarization-duplexed balanced mixer for millimeter-wave applications, *IEEE Trans. Microwave Theory Tech.* **MTT-31**(2):164–170 (1983).
26. B. Roth, M. Joseph, and A. Beyer, A varactor-tuned oscillator using MMIC technology, *Microwave J.* **33**(9):223–225 (1990).
27. J. A. Navarro, Y. Shu, and K. Chang, A novel varactor tunable coplanar waveguide-slotline Gunn VCO, *IEEE MTT-S Int. Microwave Symp. Digest*, 1991, Vol. 3, pp. 1187–1190.
28. Z. Ding, L. Fan, and K. Chang, A new type of active antenna for coupled Gunn oscillator driven spatial power combining arrays, *IEEE Microwave Guided Wave Lett.* **5**(8):264–266 (1995).
29. C. H. Ho, L. Fan, and K. Chang, New FET active slotline ring antenna, *Electron. Lett.* **29**(6):521–522 (1993).
30. Y. Tarusawa, H. Ogawa, and T. Hirota, A new constant-resistance ASK modulator using double-sided MIC, *IEEE Trans. Microwave Theory Tech.* **MTT-35**(9):819–822 (1987).
31. H. Ogawa, M. Aikawa, and M. Akaike, Integrated balanced BPSK and QPSK modulators for the Ka-band, *IEEE Trans. Microwave Theory Tech.* **MTT-30**(3):227–234 (1982).
32. A. Grote and K. Chang, 60-GHz Integrated-circuit high data rate quadriphase shift keying exciter and modulator, *IEEE Trans. Microwave Theory Tech.* **MTT-32**(12):1663–1667 (1984).
33. M. Kim et al., A planar parabola-feed frequency multiplier, *IEEE Microwave Guided Wave Lett.* **7**(3):60–62 (1997).
34. S. Nam, T. Uwano, and T. Itoh, Microstrip-fed planar frequency multiplying space combiner, *IEEE Trans. Microwave Theory Tech.* **MTT-35**(12):1271–1276 (1987).

SLOTLINES

CHUNG-YI LEE
Qualcomm, Inc.
TATSUO ITOH
UCLA

The propagation and radiation of high-frequency signals are getting more important as the technology progresses. For example, the clock rate for digital circuitry is over hundreds of megahertz. The booming wireless applications have pushed the low-cost and high-volume products to the gigahertz range. Engineers need to understand the behavior of high-frequency signals to have a proper and efficient layout when they design a new circuit. This article introduces one type of high-frequency transmission line called the slotline. The configuration, terminology, analysis, and applications are discussed in subsequent sections.

A slotline is an uniplanar wave-guiding structure proposed by Cohn in 1968 [1]. Figure 1(a) shows the basic configuration of a slotline. It consists of a narrow slit between two metal planes that are on one side of the substrate. It is different from a microstrip line that has a strip and a ground plane on the opposite sides of a substrate. The substrate property (μ, ϵ) and thickness h , the slot width w , and the metal thickness t are parameters determining slotline characteristics. The electromagnetic fields of a slotline concentrate around the slot region and propagate along the longitudinal direction as depicted in Fig. 1(b). The main electric field lines are on the transverse plane, and there are more lines in the substrate region because it has a higher dielectric constant. The propagation mode is nontransverse electromagnetic (non-TEM). Unlike the non-TEM metal waveguide, the slotline has no cutoff frequency because it has two separated metals. We will use the spectral domain approach to analyze the slotline. The propagation constant and the characteristic impedance are obtained from this rigorous analysis.

Microwave circuits are frequently packaged in a metal shield. That is, the bottom of the substrate in Fig. 1(a) is attached to a metal plane. Figure 2 shows a conductor-backed slotline (CBSL). The additional bottom ground plane provides better mechanical strength and heat-sinking ability. However, the presence of the conductor backing can cause a serious problem, which is power leakage in the transverse direction. This power loss results in undesirable package and crosstalk effects. The leakage phenomenon is easy to understand. Besides the slotline mode, the conductor-backed slotline also supports a parallel-plate mode in a region away from the open slit. A slotline mode is a non-TEM wave and has its fields spread in both the substrate and air regions. A parallel-plate mode is a TEM wave and has all its energy confined in the substrate between two metal planes. Therefore, the effective dielectric constant of a parallel-plate mode is always higher than that of a slotline mode. Under these circumstances, the parallel-plate mode behaves as the dominant mode,

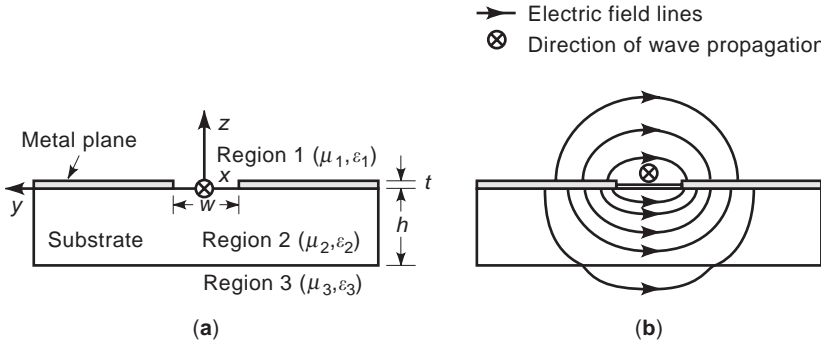


Figure 1. Slotline configuration: (a) cross-sectional view, (b) electric field distribution and wave direction.

and the slotline mode is the first higher order mode on the dispersion curves. Therefore, the energy in the slotline mode tends to leak to the parallel-plate mode. This leaky energy propagates at an angle with the longitudinal direction and is frequency-dependent. A rigorous analysis to predict the leaky performance and some methods to reduce the energy loss are discussed in Section 1.

Slotlines can be built using the same fabrication process for the microstrip line and the coplanar waveguide (CPW). All these transmission lines have planar geometries and are very useful in integrated circuit designs. The easy integration of these structures on a substrate provides an additional design choice. It becomes important to understand completely the transition between different transmission lines. Slotline discontinuities, coaxial-to-slotline, microstrip-to-slotline, and CPW-to-slotline transitions are investigated in this article. Compared with a microstrip line and a CPW, the slotline has high dispersive characteristics and a divergent field distribution. Therefore, the slotline is not commonly used as a long transmission line but rather as a short high-impedance line or a radiating geometry. As another application, the slotline has an elliptically polarized magnetic field that makes it suitable for use with a ferromagnetic material to build a nonreciprocal device [2].

1. THEORETICAL ANALYSIS

Several methods can be used to analyze a uniform slotline. They range from a closed form expression, a quasistatic approach, to full-wave frequency- and time-domain approaches [3–9]. The closed form and quasistatic approach are time efficient but have limited accuracy. The rigorous full-wave methods, on the other hand, provide accurate data with a lengthy formulation and programming

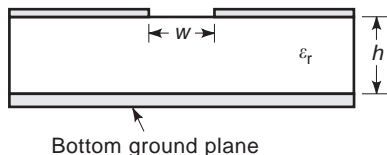


Figure 2. Conductor-backed slotline that has a good mechanical strength and heat-sinking capability.

process. As a result of the progress in computer technology, a well-written simulation code can give complete characteristics of a transmission line within few minutes on a personal computer. We will concentrate on one of the most versatile numerical methods called spectral domain analysis, and also known as the spectral domain approach (SDA) [10]. This technique is very efficient in analyzing multilayered planar structures. Moreover, the same formulation can be extended to analyze circuit discontinuities. Readers who are interested in closed form expressions can refer to Ref. 11.

1.1. Spectral Domain Analysis

1.1.1. Formulation of the Dyadic Green's Function.

Figure 1(a) shows a single-layered slotline with its coordinate system. The metal and substrate extend into infinity in the transverse, $\pm y$, direction. The wave propagates along the $+x$ direction. The conductor thickness t and loss from metal and dielectric are neglected in the following derivation. We can easily extend the procedures to a multilayered and lossy slotline. The formulation is based on the concept of Hertz potentials [10,12]. If we define TE-to- z and TM-to- z Hertz potentials as ϕ_i^e and ϕ_i^h , the field components can be expressed as

$$E_{xi}(x, y, z) = \frac{\partial^2 \phi_i^e(x, y, z)}{\partial x \partial z} - j\omega\mu_i \frac{\partial \phi_i^h(x, y, z)}{\partial y} \quad (1a)$$

$$E_{yi}(x, y, z) = \frac{\partial^2 \phi_i^e(x, y, z)}{\partial y \partial z} + j\omega\mu_i \frac{\partial \phi_i^h(x, y, z)}{\partial x} \quad (1b)$$

$$E_{zi}(x, y, z) = \left(\frac{\partial^2}{\partial Z^2} + k_i^2 \right) \phi_i^e(x, y, z) \quad (1c)$$

$$H_{xi}(x, y, z) = j\omega\epsilon_i \frac{\partial \phi_i^e(x, y, z)}{\partial y} + \frac{\partial^2 \phi_i^h(x, y, z)}{\partial x \partial z} \quad (1d)$$

$$H_{yi}(x, y, z) = -j\omega\epsilon_i \frac{\partial \phi_i^e(x, y, z)}{\partial x} + \frac{\partial^2 \phi_i^h(x, y, z)}{\partial y \partial z} \quad (1e)$$

$$H_{zi}(x, y, z) = \left(\frac{\partial^2}{\partial Z^2} + k_i^2 \right) \phi_i^h(x, y, z) \quad (1f)$$

$$k_i = \omega\sqrt{\mu_i\epsilon_i} \quad (1g)$$

where a harmonic time dependence of $e^{j\omega t}$, $\omega = 2\pi f$, is assumed and $i = 1, 2$, and 3 refer to regions 1, 2, and 3, respectively. ε_i and μ_i are the electric permittivity and magnetic permeability of each region. Hertz potentials satisfy the Helmholtz wave equation

$$(\nabla^2 + k_i^2)\phi_i^{e,h} = 0 \tag{2}$$

Equations (1a)–(1f) and (2) are second-order partial differential equations. However, they can be simplified into ordinary differential equations by (1) assuming the x -dependence as $e^{-j\alpha x}$ and (2) defining the spatial Fourier transform in the y direction as

$$\tilde{\phi}_i^{e,h}(\beta, z) = \sum_{-\infty}^{\infty} \phi_i^{e,h}(y, z) e^{j\beta y} dy \tag{3}$$

With these definitions, the transformed fields of Eqs. (1a)–(1f) and (2) are

$$\tilde{\mathbf{E}}_{xi}(\beta, z) = -j\alpha \frac{d\tilde{\phi}_i^e}{dz} - \omega\mu_i\beta\tilde{\phi}_i^h \tag{4a}$$

$$\tilde{\mathbf{E}}_{yi}(\beta, z) = -j\beta \frac{d\tilde{\phi}_i^e}{dz} + \omega\mu_i\alpha\tilde{\phi}_i^h \tag{4b}$$

$$\tilde{\mathbf{E}}_{zi}(\beta, z) = \left(\frac{d^2}{dz^2} + k_i^2\right)\tilde{\phi}_i^e \tag{4c}$$

$$\tilde{\mathbf{H}}_{xi}(\beta, z) = \omega\varepsilon_i\beta\tilde{\phi}_i^e - j\alpha \frac{d\tilde{\phi}_i^h}{dz} \tag{4d}$$

$$\tilde{\mathbf{H}}_{yi}(\beta, z) = -\omega\varepsilon_i\alpha\tilde{\phi}_i^e - j\beta \frac{d\tilde{\phi}_i^h}{dz} \tag{4e}$$

$$\tilde{\mathbf{H}}_{zi}(\beta, z) = \left(\frac{d^2}{dz^2} + k_i^2\right)\tilde{\phi}_i^h \tag{4f}$$

$$\left(\frac{d^2}{dz^2} - \gamma_i^2\right)\tilde{\phi}_i^{e,h}(\beta, z) = 0 \tag{4g}$$

where $\gamma_i^2 = \alpha^2 + \beta^2 - k_i^2$. Equation (4g) is an ordinary second-order wave equation. The general solutions of this wave equation at each region in Fig. 1(a) are

$$\tilde{\phi}_1^e = A_1 e^{-\gamma_1 z} \tag{5a}$$

$$\tilde{\phi}_1^h = A_2 e^{-\gamma_1 z} \tag{5b}$$

$$\tilde{\phi}_2^e = B_1 \sinh[\gamma_2(h+z)] + B_2 \cosh[\gamma_2(h+z)] \tag{5c}$$

$$\tilde{\phi}_2^h = B_3 \sinh[\gamma_2(h+z)] + B_4 \cosh[\gamma_2(h+z)] \tag{5d}$$

$$\tilde{\phi}_3^e = C_1 e^{-\gamma_3(h+z)} \tag{5e}$$

$$\tilde{\phi}_3^h = C_2 e^{-\gamma_3(h+z)} \tag{5f}$$

where $A_1, A_2, B_1, B_2, B_3, B_4, C_1$, and C_2 are unknown coefficients. All solutions are functions of the spatial variable z only. We use the hyperbolic functions to represent the standing wave nature of fields at the stratified region 2. The decaying feature of energy in air regions above and

below the substrate is in the form of an exponential function. Substituting Eqs. (5a)–(5f) in Eqs. (4a)–(4f), we have the general field solutions. There are a total eight unknowns in Eqs. (5a)–(5f). We need eight independent equations to get the dyadic Green's function. The next step is to match the transformed boundary conditions: At $z = -h$,

$$\tilde{\mathbf{E}}_{x2} = \tilde{\mathbf{E}}_{x3} \tag{6a}$$

$$\tilde{\mathbf{E}}_{y2} = \tilde{\mathbf{E}}_{y3} \tag{6b}$$

$$\tilde{\mathbf{H}}_{x2} = \tilde{\mathbf{H}}_{x3} \tag{6c}$$

$$\tilde{\mathbf{H}}_{y2} = \tilde{\mathbf{H}}_{y3} \tag{6d}$$

At $z = 0$,

$$\tilde{\mathbf{E}}_{x1} = \tilde{\mathbf{E}}_{x2} = \tilde{\mathbf{e}}_x \tag{7a}$$

$$\tilde{\mathbf{E}}_{y1} = \tilde{\mathbf{E}}_{y2} = \tilde{\mathbf{e}}_y \tag{7b}$$

$$\tilde{\mathbf{J}}_x = \tilde{\mathbf{H}}_{y2} - \tilde{\mathbf{H}}_{y1} \tag{7c}$$

$$\tilde{\mathbf{J}}_y = \tilde{\mathbf{H}}_{x1} - \tilde{\mathbf{H}}_{x2} \tag{7d}$$

By eliminating eight unknown coefficients using boundary conditions in Eqs. (6a)–(6d) and (7a)–(7d), we have a set of dyadic Green's function

$$\begin{bmatrix} \tilde{\mathbf{J}}_x \\ \tilde{\mathbf{J}}_y \end{bmatrix} = \begin{bmatrix} \tilde{\mathbf{G}}_{xx} & \tilde{\mathbf{G}}_{xy} \\ \tilde{\mathbf{G}}_{yx} & \tilde{\mathbf{G}}_{yy} \end{bmatrix} \begin{bmatrix} \tilde{\mathbf{e}}_x \\ \tilde{\mathbf{e}}_y \end{bmatrix} \tag{8}$$

where $(\tilde{\mathbf{e}}_x, \tilde{\mathbf{e}}_y)$ and $(\tilde{\mathbf{J}}_x, \tilde{\mathbf{J}}_y)$ are electric fields and currents at the slot and the conductor of the $z = 0$ plane, respectively. In the formulation, all unknown coefficients in Eqs. (5a)–(5f) are only functions of two variables $(\tilde{\mathbf{e}}_x, \tilde{\mathbf{e}}_y)$. The field characteristic of a slotline is solved if we can find proper functions to describe the slot fields accurately. This task is done using the method of moment (MoM). One such technique, called the Galerkin's method, is discussed in Section 1.1.2.

1.1.2. Galerkin's Method. To solve the propagation constant α and field distributions, we can use Galerkin's method. The Galerkin method uses the same weighting function as the basis function. Suppose that the aperture electric field is expressed as

$$\tilde{\mathbf{e}}_x(\beta) = \sum_{m=1}^M a_m \tilde{\mathbf{f}}_{xm}(\beta) \tag{9a}$$

$$\tilde{\mathbf{e}}_y(\beta) = \sum_{n=1}^M b_n \tilde{\mathbf{f}}_{yn}(\beta) \tag{9b}$$

where $\tilde{\mathbf{f}}_{xm}$ and $\tilde{\mathbf{f}}_{yn}$ are complete basis functions with unknown coefficients a_m and b_n . As the electric fields and currents are nonzero in complementary regions at the interface $z = 0$, we can multiply both sides of Eq. (8) by the complex conjugate of aperture electric fields. Then, integrating the product at $z = 0$, we obtain a set of eigenvalue

equations

$$\begin{bmatrix} \tilde{Z}_{xx} & \tilde{Z}_{xy} \\ \tilde{Z}_{yx} & \tilde{Z}_{yy} \end{bmatrix} = 0 \quad (10)$$

By setting the determinant of Eq. (10) equal to zero, all modes supported by the slotline are solved from the root-searching results of α . The unknown coefficients in Eqs. (9a) and (9b) are also obtained during this process. Substituting the solved Eqs. (9a) and (9b) into Eqs. (4a)–(4g) and (5a)–(5f), the electric and magnetic fields can be calculated.

1.1.3. Characteristic Impedance. There is no unique definition of characteristic impedance for a non-TEM transmission line. Power-and-current, power-and-voltage, and voltage-and-current are three commonly used definitions in calculating the characteristic impedance. The characteristic impedance of a slotline is usually defined in terms of the power-and-voltage relation

$$Z_0 = \frac{V^2}{2P_{avg}} \quad (11)$$

where V is the voltage across the slot. This potential difference is calculated by integrating the electric field

$$V = \int_{slot} E_y(y) dy \quad (12)$$

The time-averaged power P_{avg} propagated along the slotline is

$$P_{avg} = \frac{1}{4\pi} \text{Re} \iint [\tilde{E}_y(\beta, z)\tilde{H}_z^*(\beta, z) - \tilde{E}_z(\beta, z)\tilde{H}_y^*(\beta, z)] dz d\beta \quad (13)$$

where * means the complex conjugate.

1.1.4. Dispersion Behaviors of a Slotline. A computer code based on Eqs. (10) and (11) is written for analyzing a slotline. Figure 3 shows the propagation constant and impedance of a slotline as a function of substrate thickness. As the substrate thickness increases, the effective dielectric constant of a slotline increases because there is more energy in the substrate. Also, the slotline is a slow wave structure because the normalized propagation constant is always greater than one. Besides the characteristics of the dominant mode, a full-wave analysis also provides the information of higher order, evanescent, and leaky modes [8,11].

As the fields of a slotline are concentrated around the narrow slot, any parameter changes at this area affect the slotline characteristic. Kitazawa analyzed the effect of finite metal thickness on the slotline performance with the modified SDA [13]. He added a narrow, thin air region of the height of the metal thickness into the formulation as shown in Fig. 4. Then two sets of basis functions were set at the top and bottom edges of the narrow slot region.

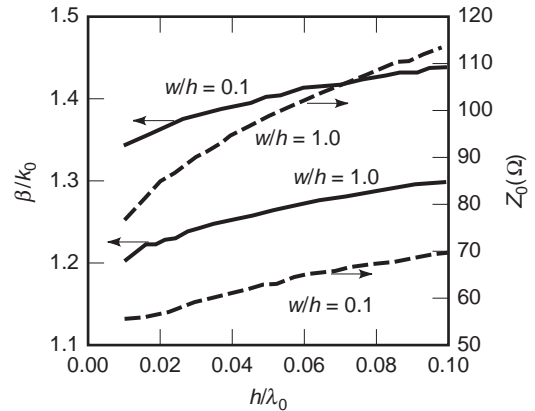


Figure 3. Normalized propagation constant and characteristic impedance of slotline ($\epsilon_r = 4.5$). The slotline characteristics are determined by its constituent parameters.

Figure 5 depicts the normalized propagation constant and impedance of a slotline with different metal thicknesses. As the slot is modeled as an air-filled region, there is increasing energy in the air when the metal thickness increases. Therefore, the propagation constant decreases with increasing metal thickness. Obviously the metal thickness influences the slotline. It is important to incorporate the metal thickness into consideration in designing slot-type transmission lines (e.g., the slotline and the coplanar waveguide).

1.1.5. Choice of Basis Functions [10,12]. The accuracy and efficiency of the final solution depend on the accuracy with which the basis functions represent the true electric field. The entire domain basis functions (e.g., the sinusoidal functions or Chebyshev polynomials) are preferred in the analysis of a uniform transmission line. Only two or three terms can yield a very accurate result. On the other hand, the subdomain basis functions (e.g., rectangular and triangular functions) are commonly used in the analysis of circuit discontinuities. Table 1 compares the results of using the entire and subdomain basis functions in analyzing a uniform slotline.

1.1.6. Leaky Phenomenon and Control on Conductor-Backed Slotline. Recently, some work has been done to investigate and reduce the leaky phenomena in various planar structures [14–19]. This power leakage in terms of

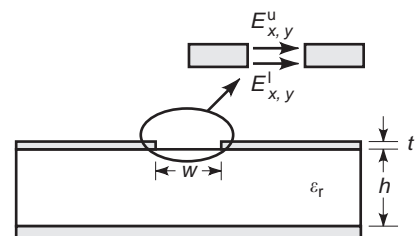


Figure 4. Basis functions used to simulate a slotline with a finite conductor thickness t in SDA.

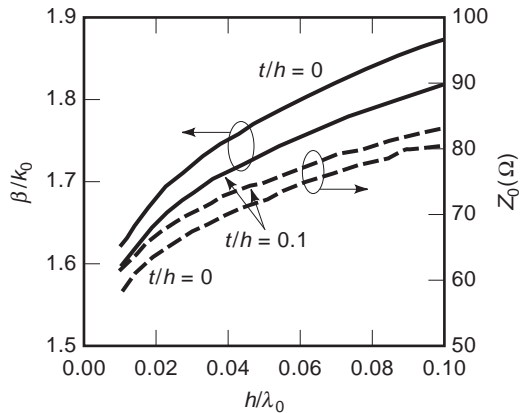


Figure 5. Normalized propagation constant and characteristic impedance of slotline with different conductor thickness ($\epsilon_r = 10.5, w/h = 0.5$). The conductor thickness has an obvious influence on slotline performance.

other guided waves is an interesting behavior and can be analyzed easily with a little modification on the conventional SDA. The integration path of a conventional SDA is along the real axis of the spectral variable β . In order to include the contribution of leaky waves, special attention should be paid to the integration path [20]. For a leaky transmission line, the model field is no longer bounded, and the propagation constant becomes complex instead of real. Therefore, a deformed integration path or residue calculation is commonly used to handle the leaky waves as depicted in Fig. 6. The deformed integration path is numerically easily implemented. However, it suffers from the numerical divergence when the integration path is close to leaky-wave poles. In this case, the residue calculation is preferred for an accurate and general formulation.

1.1.7. Leaky Phenomenon. The conductor-backed slotline shown in Fig. 2 has the inherent problem of power leakage in the transverse direction. This is so because the slotline mode of a CBSL has a lower effective dielectric constant than that of a parallel-plate mode. Figure 7 depicts the dispersion curves for both modes. Clearly, the phase constant of the slotline mode is always less than that of a parallel-plate mode. With the complex root-searching method, the attenuation constant (the imaginary part of α) exists over all frequencies. It says that the

Table 1. Analysis of a Uniform Slotline^a

Number of Basis Function	Entire Domain Function	Subdomain Function
1	1.9083	1.8977
2	1.8715	1.8795
3	1.8695	1.8751
4	1.8693	1.8734
5	1.8692	1.8725
10	1.8692	1.8708

^aThe entire domain function is more suitable in analyzing a uniform slotline.

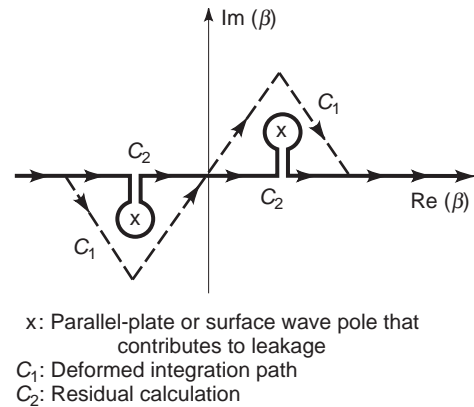


Figure 6. Integration paths in the spectral domain analysis to calculate the leaky wave-guiding structures.

guided slotline mode loses energy when it propagates. The leakage phenomenon is also frequency-dependent. Shigesawa et al. conducted a comprehensive analysis and measurement of this issue [14].

1.1.8. Leakage Control. The leakage problem shadows the CBSL. It is important to eliminate or reduce the power leakage that causes unwanted coupling and energy loss. Figure 8 depicts some proposed configurations to control the power leakage [15–17]. The basic idea is to make the effective dielectric constant of the slotline mode higher than that of a parallel-plate mode with the additional dielectric compensation [Fig. 8(a,b)]. Or, we can physically confine the fields within the slot region using metal vias in the substrate [Fig. 8(c)]. Figure 8(a) can be easily analyzed using the SDA. Figure 9 demonstrates the leakage control of a CBSL with a proper material combination. It must be pointed out that the leaky phenomenon is caused by the so-called LSM mode in Fig. 8(a) because there are two substrates between metal plates. The attenuation becomes zero when the propagation constant of a slotline

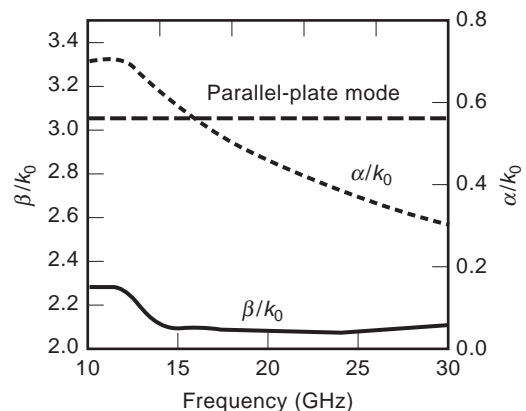


Figure 7. Normalized propagation constant of CBSL and parallel-plate mode. $\epsilon_r = 9.5, h = 1 \text{ mm}, w = 0.25 \text{ mm}$. There is a nonzero attenuation constant because the phase constant of a slotline is always less than that of a parallel-plate mode.

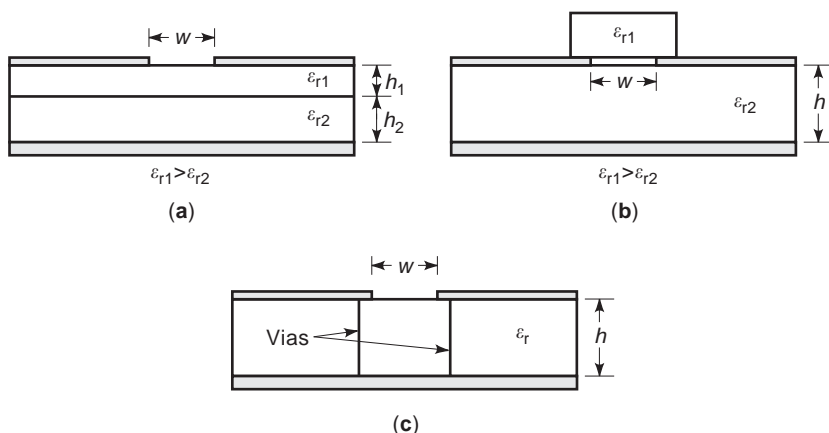


Figure 8. Configurations to reduce or eliminate the leakage on a CBSL: (a) with an additional substrate layer, (b) with a superstrate for dielectric compensation, (c) with periodic vias in the substrate.

is higher than the LSM mode. There is a transition region between then leaky and nonleaky regions. Some researchers have studied this microscopic picture of mode transitions [21,22].

1.2. Slotline Discontinuities

The short end and the open end are two single-ended slotline discontinuities. These two discontinuities are frequently used as parts of slotline components. Their characteristics are, therefore, important for understanding the component behavior.

1.2.1. Short End. The short end is realized by connecting one end of the slotline shown in Fig. 1 with metalization. This discontinuity has been analyzed both theoretically and experimentally [23–25]. Figure 10 plots the comparison for the normalized end reactance. The short-end slotline exhibits inductive loading because the reactance is positive. It means that the stored energy is mainly in the form of magnetic energy. Besides the reactive energy, there is a radiation and surface wave loss

caused by this discontinuity. The loss makes the reflection coefficient less than one, which can be modeled as a resistor in the equivalent circuit. Figure 11 shows the normalized resistance of a shorted slotline using a full-wave analysis technique [25]. Figures 10 and 11 say that the inductive loading and the radiation loss gets stronger as the frequency increases.

1.2.2. Open End. Unlike the microstrip line, an open-ended slotline is difficult to realize and is sometimes impractical in circuit applications. Figure 12 depicts some variations of an open-ended slotline. There is a very strong radiation loss for the configurations in Fig. 12(a,b). Although it is not a good candidate in circuit applications, Fig. 12(b) is commonly used in the end-fired antenna design. Figures 12(c,d) have confined energy and are experimentally studied by Chramiec [26]. If the operating frequency is higher than the resonant frequency of the disk resonator, Fig. 12(c,d) behaves like an open circuit.

1.3. Transitions

Transitions between the slotline and other wave-guiding structures extend the design and test capabilities of a

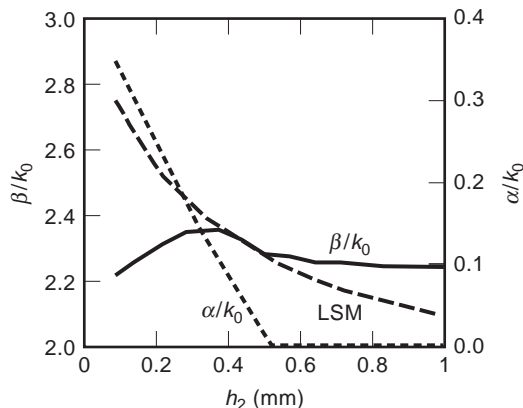


Figure 9. Normalized propagation constant of a nonleaky CBSL with an additional substrate layer. $\epsilon_{r1} = 9.5$, $\epsilon_{r2} = 2.33$, $h_1 = 1$ mm, $w = 0.25$ mm, frequency = 20 GHz. The attenuation constant becomes zero when the phase constant of a slotline is higher than that of a LSM.

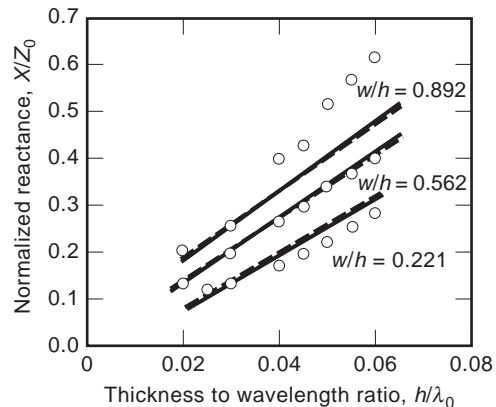


Figure 10. Normalized end reactance of a shorted slotline, $\epsilon_r = 12$. The shorted slotline is inductively loaded. Dots are measured data; solid and dashed lines are calculated results. (Reprinted with permission from Ref. 25, © 1988 IEEE.)

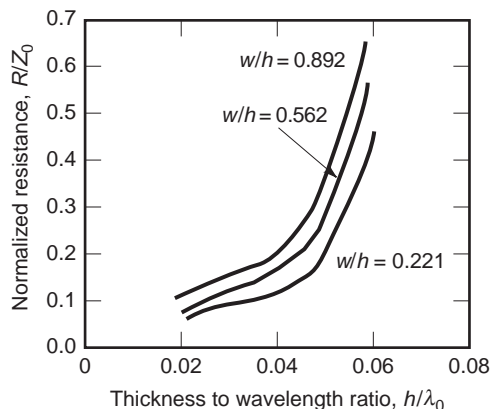


Figure 11. Normalized end resistance of a shorted slotline, $\epsilon_r = 12$. This resistance represents the energy loss of a shorted slotline. (Reprinted with permission from Ref. 25, © 1988 IEEE.)

slotline. For example, a coaxial-to-slotline transition is needed to test the slotline in a standard microwave measurement system. There are several different ways to combine two transmission lines. The one with a natural field match at the junction region gives maximum energy transfer. That is, for a good transition, the orientations of electric and magnetic fields should match each other. In the following sections, we will discuss several practical transitions.

1.3.1. Coaxial-to-Slotline Transition. Most microwave measurement systems use the coaxial cable as the input/output transmission line. It needs a good coaxial-to-slotline transition to test the slotline performance. Figure 13 depicts the coaxial-to-slotline transition. These two structures cross each other with a right angle to have the proper field match. The center conductor of the coaxial

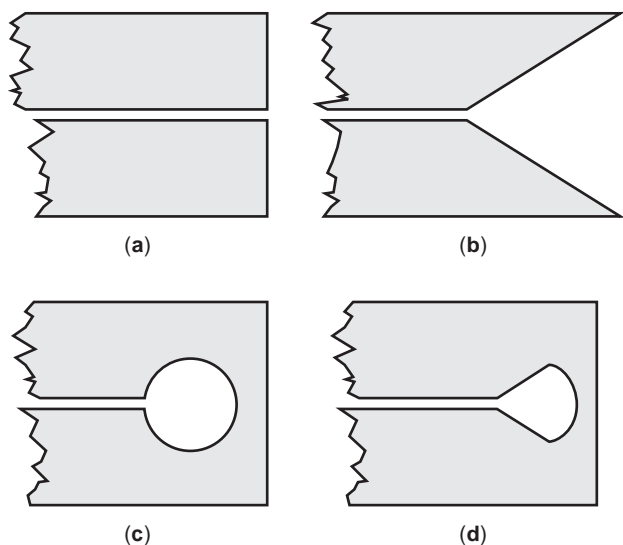


Figure 12. Various structures for slotline open end: (a) an abrupt discontinuity; (b) with a flared angle; (c) with a circular disk; and (d) with a flared slot and half-disk (Reprinted with permission from *Microstrip Lines and Slotlines* by K. C. Gupta et al., Artech House, Inc., Norwood, MA, USA. <http://www.artech-house.com>.)

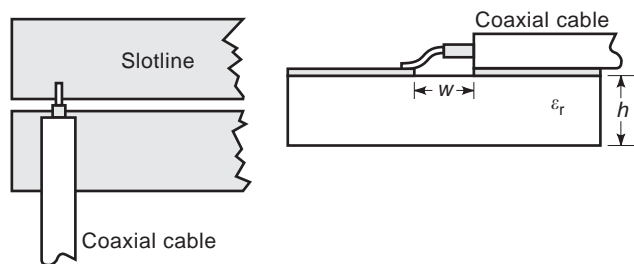


Figure 13. Coaxial-to-slotline transition. (Reprinted with permission from Ref. 27, © 1974 IEEE.)

line is connected to one of the slotline metal planes, and the outer conductor is connected to the other one. With the open end at one side of the slotline, the energy propagates along the uniform section. This configuration is also useful in exciting a slotline antenna, which is a double short-ended slotline. Knorr analyzed and measured this transition with a 50 Ω microstrip line and a 75 Ω slotline [27]. It has a good voltage standing-wave ratio (VSWR) for frequencies less than 4 GHz. The performance of the transition gets worse at higher frequencies

The open end of the slotline shown in Fig. 13 may cause unwanted radiation loss. Although it has low return loss, it does not mean that there is a maximum energy transfer in the form of a guided wave. To reduce this radiation loss, a movable short-end configuration is proposed [11]. As a result of the resonant wavelength, this type of transition has an optimal VSWR over a narrow frequency range.

1.3.2. Microstrip-to-Slotline Transition. Microstrip circuits are most widely used in microwave integrated circuits. The microstrip-to-slotline transition expands applications for both the microstrip line and the slotline. Also, the fabrication is very easy and accurate by etching the metallization on both sides of the substrate. It makes the double-sided circuit design feasible. A branch-line coupler based on this transition has been demonstrated [28]. Figure 14 shows the transition with both lines crossing at a right angle and extending about a quarter wavelength beyond each other. Chambers et al. used an approximate transmission line method to analyze this transition [29]. More rigorous full-wave methods were also reported [25,30,31]. All simulations agree well with the experiment done by Knorr at the lower frequency, but there is a large discrepancy at the high-frequency end. The deviation may be caused by fabrication tolerance. Besides, the substrate used in the experiment [27] is Custom Hik 707-20

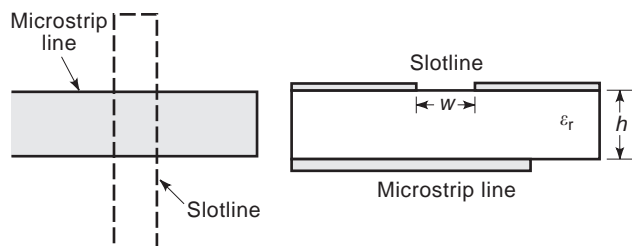


Figure 14. Microstrip-to-slotline transition.

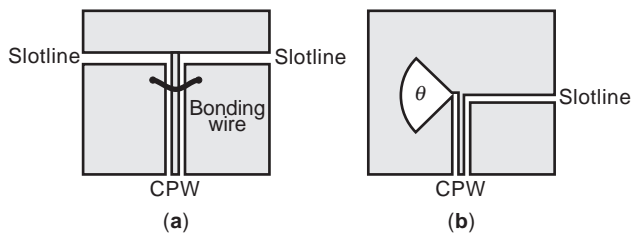


Figure 15. CPW-to-slotline transitions: (a) two slotline outputs, (b) single slotline output. (Reprinted with permission from Refs. 36 and 39, © 1987 and 1993 IEEE.)

($\epsilon_r = 20$), which is usually very lossy at higher frequencies. This loss parameter was not included in the previously mentioned simulations.

Figure 14 is a narrow-band transition. The bandwidth limitation is a result of the frequency dependence of the quarter wavelength sections. Several papers have tried to improve the bandwidth with different approaches [32–35]. It is found that the bandwidth is related to the stub reactance and impedance. The lowest VSWR occurs when the reactances cancel each other for the quarter wavelength sections. Moreover, there is a maximum bandwidth when the characteristic impedance of the microstrip stub is 2.618 times the characteristic impedance of the slotline stub [35].

1.3.3. Coplanar Waveguide-to-Slotline Transition. Unlike the microstrip-to-slotline transition, the coplanar waveguide (CPW)-to-slotline transition can be built on the same side of metallization. This configuration is preferred in the monolithic microwave integrated circuits (MMICs), where all metals are on one side of the substrate only. Much effort has been made to study this transition [36–39]. Figure 15 shows some of the representative configurations. Figure 15(a) is a CPW-to-slotline T-junction that behaves like a power divider. Two output ports on the slotline are available in Fig. 15(a). If a single output is necessary, the other port can be shorted at a quarter wavelength from the junction. The bonding wire is used to suppress the unwanted mode on the CPW. To increase the bandwidth, a radial stub is used as shown in Fig. 15(b), even though it requires a large circuit space. It is found that Fig. 15(b) has the best performance in terms of bandwidth and return loss [39]. The 1 dB insertion loss bandwidth for this transition is more than 5.2:1. Unlike coaxial and microstrip-to-slotline transitions discussed previously, one design advantage of this transition is that the I/O lines can have an angle from 0° to 90° . The optimal transition can be obtained with a modification of circuit dimensions.

BIBLIOGRAPHY

1. S. B. Cohn, Slotline on a dielectric substrate, *IEEE Trans. Microw. Theory Tech.*, **MTT-17**:768–778 (1969).
2. L. Courtois and M. de Vecchis, A new class of non-reciprocal components using slotline, *IEEE Trans. Microw. Theory Tech.*, **MTT-23**:511–516 (1975).

3. R. Garg and K. C. Gupta, Expressions for wavelength and impedance of slotline, *IEEE Trans. Microw. Theory Tech.*, **MTT-24**:532 (1976).
4. R. Janaswamy and D. H. Schaubert, Characteristic impedance of a wide slotline on low permittivity substrate, *IEEE Trans. Microw. Theory Tech.*, **MTT-34**:900–902 (1986).
5. J. B. Knorr and K. D. Kuchler, Analysis of coupled slots and coplanar strips on dielectric substrates, *IEEE Trans. Microw. Theory Tech.*, **MTT-23**:541–548 (1975).
6. T. Itoh and R. Mittra, Dispersion characteristics of slotlines, *Electron. Lett.*, **7**:364–365 (1971).
7. R. Janaswamy and D. H. Schaubert, Dispersion characteristics for wide slotlines on low permittivity substrate, *IEEE Trans. Microw. Theory Tech.*, **MTT-33**:723–726 (1985).
8. J. Citerne, S. Toutain, and L. Racz, Fundamental and higher order modes in microslot lines, *Proc. 5th Eur. Microw. Conf.*, pp. 273–277, 1975.
9. G. C. Liang, Y-W. Liu, and K. K. Mei, Full-wave analysis of coplanar waveguide and slotline using the time-domain finite-difference method, *IEEE Trans. Microw. Theory Tech.*, **MTT-37**:1949–1957 (1989).
10. T. Itoh, *Numerical Techniques for Microwave and Millimeter-Wave Passive Structures*, New York: Wiley, 1989.
11. K. C. Gupta, et al., *Microstrip Lines and Slotlines*, 2nd ed., Norwood, MA: Artech House, 1996.
12. B. Bhat and S. K. Koul, *Analysis, Design and Applications of Fin Lines*, Norwood, MA: Artech House, 1987.
13. T. Kitazawa, Y. Hayashi, and M. Suzuki, Analysis of the dispersion characteristics of slot line with thick metal coating, *IEEE Trans. Microw. Theory Tech.*, **MTT-28**:387–392 (1980).
14. H. Shigesawa, M. Tsuji, and A. A. Oliner, Conductor-backed slotline and coplanar waveguide: Dangers and full-wave analysis, *IEEE MTT-S Int. Microw. Symp. Dig.*, **1**:199–202 (1988).
15. Y. Liu and T. Itoh, Control of leakage in multilayered conductor-backed coplanar structures, *IEEE MTT-S Int. Microw. Symp. Dig.*, **1**:141–144 (1994).
16. J-W. Huang and C-K. C. Tzuang, Mode-coupling-avoidance of shielded conductor-backed coplanar waveguide (CBCPW) using dielectric lines compensation, *IEEE MTT-S Int. Microw. Symp. Dig.*, **1**:149–152 (1994).
17. N. K. Das, Two conductor-backed configurations of slotline or coplanar waveguide for elimination or suppression of the power-leakage problem, *IEEE MTT-S Int. Microw. Symp. Dig.*, **1**:153–156 (1994).
18. D. Nghiem, et al., Leakage of the dominant mode on stripline with a small air gap, *IEEE Trans. Microw. Theory Tech.*, **MTT-43**:2549–2556 (1995).
19. N. K. Das, Spectral-domain analysis of complex characteristic impedance of a leaky conductor-backed slotline, *IEEE MTT-S Int. Microw. Symp. Dig.*, **1**:1791–1794 (1996).
20. C-Y. Lee, et al., Analysis and application of non-leaky uniplanar structures with conductor backing, *J. Microw. Millimeter-Wave Comput. Aided Eng.*, **6**:319–327 (1996).
21. Y-D. Lin, J-W. Sheen, and C-Y. Chang, Surface-wave leakage properties of coplanar strips, *IEEE MTT-S Int. Microw. Symp. Dig.*, **1**:229–232 (1995).
22. H. Shigesawa, M. Tsuji, and A. A. Oliner, Simultaneous propagation of bound and leaky dominant modes on printed-circuit lines: A new general effect, *IEEE Trans. Microw. Theory Tech.*, **MTT-43**:3007–3019 (1995).
23. J. B. Knorr and J. Saenz, End effect in a shorted slot, *IEEE Trans. Microw. Theory Tech.*, **MTT-21**:579–580 (1973).

24. R. Jansen, Hybrid mode analysis of end effects of planar microwave and millimeter wave transmission lines, *Proc. Inst. Elec. Eng.*, **128**:77–86 (1981).
25. H. Yang and N. G. Alexopoulos, A dynamic model for microstrip-slotline transition and related structures, *IEEE Trans. Microw. Theory Tech.*, **MTT-36**:286–293 (1988).
26. J. Chramiec, Reactances of slotline short and open circuits on alumina substrate, *IEEE Trans. Microw. Theory Tech.*, **MTT-37**:1638–1641 (1989).
27. J. B. Knorr, Slotline transitions, *IEEE Trans. Microw. Theory Tech.*, **MTT-22**:548–554 (1974).
28. C-Y. Lee and T. Itoh, Full-wave analysis and design of a new double-sided branch-lines coupler and its complementary structure, *IEEE Trans. Microw. Theory Tech.*, **MTT-43**:1895–1901 (1995).
29. D. Chambers, et al., Microwave active network synthesis, *Semiannual Report, Stanford Res. Inst.*, June 1970.
30. Y. M. M. Antar, A. K. Bhattacharyya, and A. Ittipiboon, Microstrip-slotline transition analysis using the spectra domain technique, *IEEE Trans. Microw. Theory Tech.*, **MTT-40**:515–523 (1992).
31. N. K. Das, Generalized multiport reciprocity analysis of surface-to-surface transitions between multiple printed transmission lines, *IEEE Trans. Microw. Theory Tech.*, **MTT-41**:1164–1177 (1993).
32. G. H. Robinson and J. L. Allen, Slotline application to miniature ferrite devices, *IEEE Trans. Microw. Theory Tech.*, **MTT-17**:1097–1101 (1969).
33. F. C. de Ronde, A new class of microstrip directional couplers, *IEEE MTT-S Int. Microw. Symp. Dig.*, **1**:184–189 (1970).
34. A. Podcameni and M. L. Coimbra, Slotline-microstrip transition on iso/anisotropic substrate: A more accurate design, *Electron. Lett.*, **16**:780–781 (1980).
35. B. Schuppert, Microstrip/slotline transitions: Modeling and experimental investigations, *IEEE Trans. Microw. Theory Tech.*, **MTT-36**:1272–1282 (1988).
36. H. Ogawa and A. Minagawa, Uniplanar MIC balanced multiplier—A proposed new structure for MICs, *IEEE Trans. Microw. Theory Tech.*, **MTT-35**:1363–1368 (1987).
37. W. Grammer and K. S. Yngvesson, Coplanar waveguide transitions to slotline: Design and microprobe characterization, *IEEE Trans. Microw. Theory Tech.*, **MTT-41**:1653–1658 (1993).
38. T. Q. Ho and S. M. Hart, A broad-band coplanar waveguide to slotline transition, *IEEE Microw. Guided Wave Lett.*, **2**:415–416 (1992).
39. C. H. Ho, L. Fan, and K. Chang, Broad-band uniplanar hybrid-ring and branch-line couplers, *IEEE Trans. Microw. Theory Tech.*, **MTT-41**:2116–2125 (1993).

SLOW WAVE STRUCTURES

KE WU
École Polytechnique de Montréal

1. GUIDED WAVES AND WAVEGUIDES

Electromagnetic wave propagation, which is fundamentally governed by Maxwell's field equations, is usually

characterized by its propagation constant. The propagation constant is used to derive its phase and group velocity and attenuation relative to frequency or wavelength. The phase velocity of a freely propagating wave is reduced or increased compared with the speed of light if such a propagation takes place in material other than air or vacuum. Guided-wave phenomena [1–4] are electrically or magnetically bounded waves propagating in air- or material-filled tubes or strips, or called wave-guides or sometimes transmission lines, and are the physical foundation for designing and manufacturing radiofrequency (RF), microwave, and optical components and systems. A waveguide can also be defined as a structure that causes a wave to propagate in a chosen direction because of some measure of confinement in the plane transverse to the direction of propagation. The topological view of a waveguide is graphically sketched in Fig. 1(a), which may involve materials of different properties and multiple conductors with or without a specifically shaped dielectric or conducting enclosure. Dielectric guides, hollow-pipe waveguides, and planar guides are the most important building blocks in practical use to date.

Generally, the guided-wave properties of a waveguide depend on physical aspects, such as boundary conditions, materials, and frequency. Conventional uniform waveguides (rectangular metallic waveguides without physical variations in the longitudinal direction, for example) exhibit phase velocities of wave propagation greater than the velocity of light, or in other words, guided wavelengths are longer than the free-space wavelength: these structures are usually called fast-wave structures. Fast-wave structures, in most cases have cutoff frequencies below which wave propagation is halted.

The slow wave is a particular type of wave propagation, usually of the guided-wave type, and it is described mostly in the frequency-domain. Slow-wave structures [5–7] are wave-guides or transmission lines in which the wave travels with a phase velocity equal to or less than a certain predesignated velocity of wave propagation. In other words, the slow wave should be interpreted relative to its fast-wave counterpart compared with a velocity of reference, such as the speed of light in a hollow metallic waveguide. However, it may be disputable how to choose the velocity of reference that is directly connected with the slow-wave structure. Of course, one may always choose the speed of light as the reference velocity (classic consideration) to distinguish slow-wave propagation from other guided waves. This was the common practice in very early studies of slow-wave structures probably because the early slow-wave development was closely related to the rectangular and circular waveguiding structures. Since the emergence of planar integrated dielectric-layered geometry, such a classic definition of slow-wave structure was somewhat altered by the relative dielectric and magnetic properties of the materials of the structure. It is now widely accepted that a slow-wave structure can support wave propagation that has a phase velocity less than the attainable value because of the inherent properties of the waveguiding material, such as permittivity and permeability.

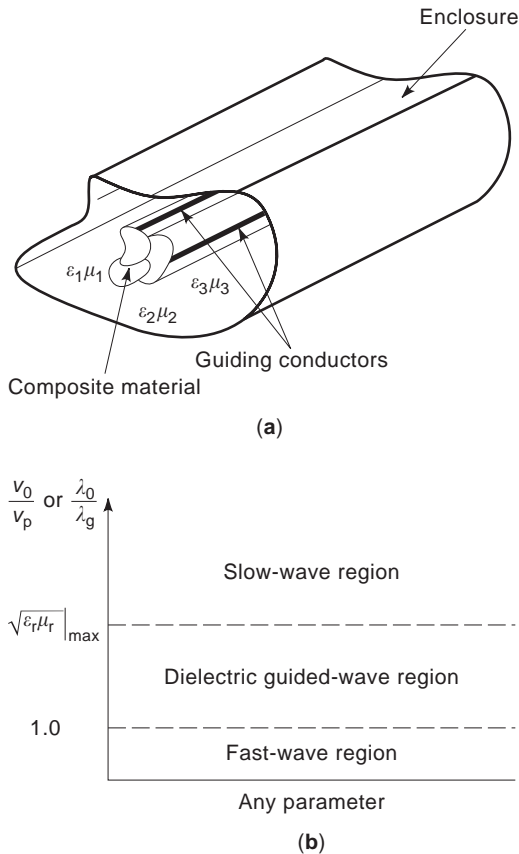


Figure 1. Graphic illustration of a generalized waveguide problem and its guided waves, (a) Physical view of an arbitrary waveguiding structure and (b) concise description of any potential guided-wave propagation along its axial direction, which are classified in terms of three types of waves: slow wave, dielectric guided wave, and fast wave. The waveguide consists of a composite medium with three blocks of different relative permittivities, ϵ_r , and permeabilities, μ_r , with the subscript r denoting 1, 2, and 3. The outer enclosure may be in the form of a dielectric or metallic boundary. The classification of guided waves is made by measuring the free-space counterpart v_0 relative to its guided-wave phase velocity v_p , or equivalently the freespace wavelength λ_0 versus the guided-wave wavelength λ_g . The abscissa in (b) refers to any susceptible physical and electrical parameter connected with wave propagation.

Figure 1(b) depicts schematically a concise classification of guided-wave structures by comparing the normalized guided wavelength with its free-space counterpart. We consider the basic waveguiding geometry of Fig. 1(a) as the reference in which the maximum permittivity and permeability of a relevant subregion sets up the border between material-related guided-wave and slow-wave propagation. In most cases, only linear isotropic dielectric materials are used in waveguides. In this description, the slow- and fast-wave-guiding properties are simply characterized by a popular technical term called the effective permittivity, which may involve the effect of permeability if the relative permeability is not equal to one, even though the concept of a separate effective permeability is valid.

2. FUNDAMENTALS OF SLOW-WAVE STRUCTURES

Generally, a slow wave cannot be obtained without artificial guided-wave structures. Special mechanisms in a guided-wave structure need to be designed to generate slow-wave propagation. The basic and absolute condition of a guided-wave structure that supports slow-wave propagation is that this structure should provide separate storage of electric and magnetic energy in space either in the axial or transverse directions. Obviously, any susceptible slow-wave generation depends on the geometry and/or the core materials of a guided-wave structure subject to some particular criteria of construction, that lead to a critical separation of energy in space. The effective spatial separation of electric (capacitive effect) and magnetic (inductive effect) energy constitutes the fundamental principle for designing a slow-wave structure.

There are two fundamental classes of slow-wave structures, several typical examples of which are shown in Figs. 2 and 3. One is the periodic structure (Fig. 2) in the axial or longitudinal direction, and the other consists of uniform structures that have special geometry designed in the transverse direction (Fig. 3). Periodic structures can be formed with two configurations: (1) structures with continuous but periodically varying material properties and (2) structures with periodically loaded sections or periodic boundary conditions. The most common type is the latter. Uniform slow-wave structures usually consist of multilayered or composite materials that have a specially arranged thickness ratio and dielectric/magnetic property. The best known example today in this category is probably the metal-insulator-semiconductor (MIS) transmission line described by the examples of Fig. 3. In this case, planar transmission lines are deposited onto a very thin insulator that is formed, depleted, or grown by using a semiconductor

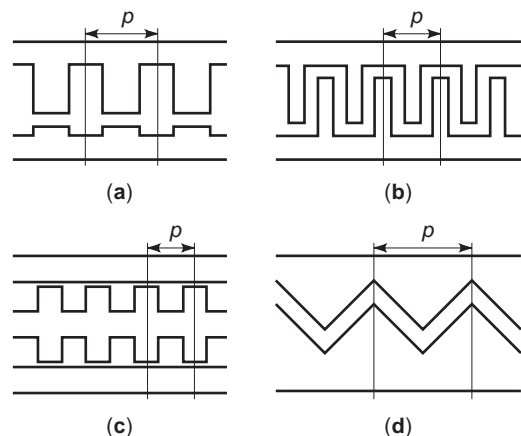


Figure 2. Bidimensional view of generalized periodic slow-wave structures that may depict conventional metallic waveguides and planar transmission lines with a class of typical periodically nonuniform physical layout or patterns (slots or strips) along the propagative axis. p refers to the length of a periodic cell or block. (a) A corrugated waveguide or comb-like line. (b) Either an interdigital line (strip case) or a meander line (slot case). (c) Either a stub-loaded planar line or waveguide. (d) A zigzag nonuniform coupled transmission line.

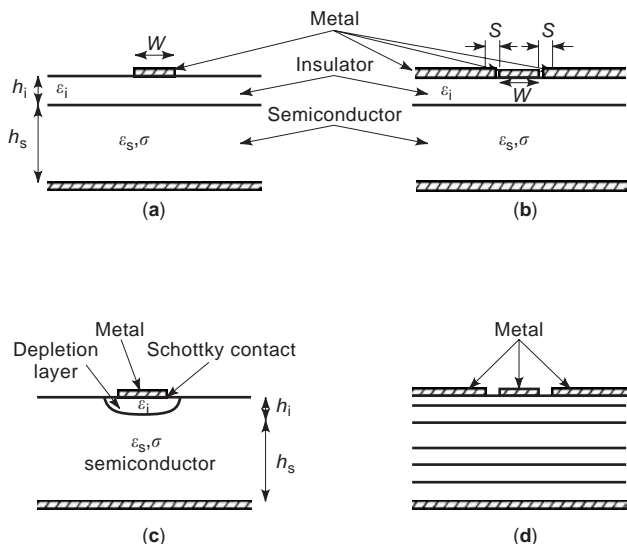


Figure 3. Cross-sectional view of various metal-insulator-semiconductor (MIS) planar slow-wave transmission lines with low-loss or ideally lossless insulator and doped lossy semiconductor. (a) An MIS microstrip structure. (b) An MIS coplanar waveguide (CPW). (c) A Schottky-contact slow-wave microstrip line with a depletion layer that can be regarded as a special case of the MIS structures. (d) A general multilayered planar structure that may involve quantum-well layers. This structure is subject to slow-wave propagation. Mathematical symbols used in the figure are as follows: w and s stand for the widths of the center conductor and slot, respectively. Subscripts i and s refer to the insulating and semiconductor layers, respectively. ϵ is the dielectric permittivity, σ is the conductivity of the doped semiconductor, and h is the thickness of layer.

microfabrication process on an appropriately doped semiconductor substrate. Interestingly, slow-wave generation in periodic structures is achieved by separating electric and magnetic energy in the longitudinal space, whereas the uniform structures, such as MIS lines, use storage of electric and magnetic energy separated in the transverse direction.

Based on the building block, periodic structures usually require a three-dimensional (3-D) description, whereas uniform slow-wave structures are simply two-dimensional (2-D) problems. The slow-wave characteristics of the two classes of structures differ in some aspects, but they also share some common features. Slow-wave propagation is related to particular electromagnetic modes of the structure, and its fundamental characteristic parameters are the slow-wave factor and propagation loss even though they may be represented differently in some cases. As for other conventional waveguides or transmission lines, characteristic impedance is useful for design purposes, but it may be difficult to define for some structures. To accurately describe the guided-wave properties of slow-wave structures, Maxwell's field equations are required to calculate the electrical parameters and to plot the distribution of the field quantities over the structures. The calculation is usually done numerically except for some classic periodic waveguides. These are typical boundary value problems. Normally, the guided-wave properties of a

slow-wave structure are dispersive or frequency-dependent, and they can also be greatly modified by changing structure parameters, which are of paramount importance for design purposes.

Now, let us consider some physical aspects of slow-wave structures via two classic examples of periodic structure (see Fig. 4), helix and cavity-chain waveguide, and two popular examples of MIS structures (see Fig. 3), the coplanar waveguide (CPW) and the Schottky-contact microstrip line. Of course, slow-wave generation along MIS structures differs, but its physical principle remains similar to that of periodic structures.

A practical helical slow-wave structure typically consists of a metal wire or tape wound in the form of a helix, supported by a longitudinal dielectric rod/bar. The entire structure may also be enclosed in a dielectric/metallic envelope, depending on its intended use. Figure 4(a) shows a typical geometry for a single-tape or single-wire helix that was studied by J. R. Pierce [8] and S. Sensiper [9]. The field is guided at the velocity of light along the helical path if no dielectric rod is involved, so that the velocity along the axial or z -direction is considerably less than the velocity of light. Obviously, the tighter the helix is wound, the smaller the pitch p , and the more slowly the wave appears to travel in the axial direction. If an electron beam introduced into the above structures travels along the axis with the same axial velocity as the wave, cumulative field interactions take place, and we have a form of traveling-wave tube. Interestingly, the induced inductance over one helical period prevails over the capacitance, leading to the separation of electric and magnetic energy in the axial direction.

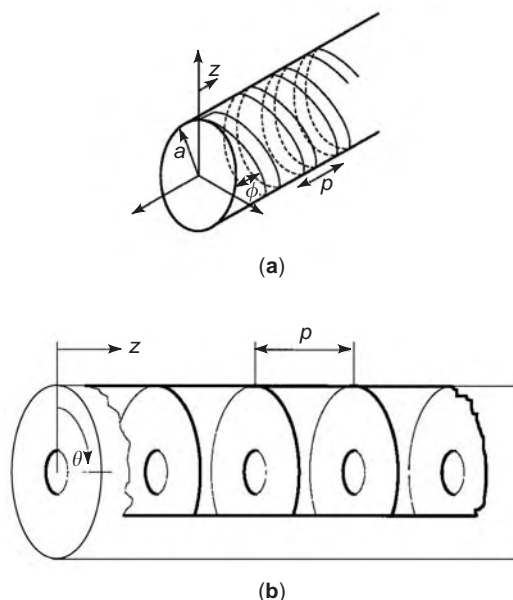


Figure 4. Two examples of classic periodic waveguides. (a) A simple helix slow-wave structure made of tape or wire. p is the pitch, θ the pitch angle, and a the radius. (b) A periodically disk-loaded (cavity-chain) circular waveguide. p is the periodic spacing of the disks. In both cases, z is the propagation direction of the slow waves.

Figure 4(b) presents an example of metallic waveguides loaded periodically by a series of obstacles, fins in this instance, which slow the wave, as they would slow a stream of water running through the pipe. The smaller the center holes, the greater the reduction in field velocity through the pipe. This structure belongs to the class of cavity-chain, slow-wave structures, each of which consists of a chain of coupled resonant cavities. These cavities are very frequency-selective. Electrons, of course, can be introduced to flow along the axis with a velocity that allows them either to absorb power from or to deliver power to the circuit wave. This mechanism can be used to realize forward-wave traveling-wave amplifiers or backward-wave oscillators, “Carcinatron.” Similarly, it can be observed from guided-mode concepts that the spatial separation of electric and magnetic fields satisfy the critical condition of slow-wave guidance.

The basic slow-wave MIS structures consist of planar transmission lines usually in the form of a few or a hundred micrometer-size microstrip, CPW, or other planar patterns, which are fabricated on a doped thin or thick semiconductor substrate, such as N^+ silicon (Si) or GaAs. In an MIS CPW, as shown in Fig. 3(b), the metals are separated from the doped semiconductor by a low-loss or ideally lossless insulating layer, such as silicon dioxide (SiO_2) or silicon nitride (Si_3N_4), that is usually extremely thin and ranges from the submicrometer range to two micrometers. The presence of back metallization usually has a negligible influence on slow-wave propagation, whereas in the Schottky-contact microstrip described in Fig. 3(c), a low-loss depletion region is formed by applying a negative bias voltage over the microstrip with respect to the ground plane. Such a depletion region is equivalent to the insulator of an MIS structure but inhomogeneous in profile over the cross section. Therefore, the Schottky-contact line can be regarded as a special MIS structure. The existence of slow-wave propagation along these MIS structures can be explained in the following manner. The low-impedance doped semiconductor, which is a nonmagnetic material, is virtually invisible to the magnetic field. Therefore, the magnetic field freely penetrates into the semiconductor layer, and it is nearly identical to that of an undoped CPW structure. However, the electric field is highly confined in the insulating layer between the semiconductor and the center strip of the CPW. This field distribution corresponds to separate storage of electric and magnetic energy in space, which is the well-known condition for a slow-wave mode to propagate. Obviously, transmission loss is inevitable and is often the main design problem because MIS structures always contain a doped semiconductor layer. Heuristically, applying different bias voltages on these MIS structures should modify the physical profile of the insulating layer or depletion region, thereby changing the slow-wave propagation. This feature is exploited in designing electronically tunable MIS devices.

3. A BRIEF HISTORY OF SLOW-WAVE DEVELOPMENT

Based on their classification, the development of the electro-magnetic slow-wave structures passed two historical

landmarks: the periodic structure and the metal-insulator-semiconductor (MIS) structure. Of course, the MIS structure is not unique for generating slow-wave propagation on the basis of a uniform line made of special material. Slow-wave effects are also observed in waveguides that involve ferromagnetic, plasma, or other complex media, such as chiral materials, if the mechanism and conditions of generating slow-wave propagation in those structures exist. In other words, the spatial separation of electric and magnetic energy takes place.

The very early development of slow-wave structures can be traced back to World War II, when there was an explosion of activity in the microwave electronics field. In 1939, a high-frequency tube, known as the klystron, was developed by W. W. Hansen and the Varian brothers, following the invention of the high-power magnetron by A. W. Hull in 1921. At that time, slow-wave structures were built by cascading resonant cavities, which usually provided tremendous power gains over relatively short waveguiding length, but the frequency bandwidth was very limited. These cavity-connected and ladder-type slow-wave structures are still widely used today for highly frequency-selective devices, such as narrowband filters, multiplexers, and field polarization control devices.

In the early 1940s, R. Kompfner [10], reflecting on the relative inefficiency and narrow bandwidth offered by the klystron, reasoned that if an electron beam were to interact continuously with a wave on a helix, it would interact more efficiently. This is the velocity-matching principle for the electron beam and electromagnetic wave, which are supposed to travel at equal speeds in the ideal case, such that maximum field interaction or energy exchange occurs between the two waves. Furthermore, the helix would not be strongly resonant at any frequency, and therefore it would have a broad bandwidth. Kompfner's first traveling-wave tube (TWT) was successfully developed in 1943, which marked the beginning of slow-wave structures. In fact, a similar concept was proposed but not explicitly described in the patent filed by Percival in 1935 [11] for distributed circuits. Subsequently, the TWT was refined by Bell laboratory workers during and after World War II. Among them, J. R. Pierce is perhaps most prominent. He worked on the TWT theory and built high-performance tubes [8]. Since then, a large class of broad-band and high-performance traveling-wave electronic devices has been proposed and developed on the basis of various slow-wave structures [9,12]. These include distributed TWT amplifiers, oscillators, and linear particle accelerators [13–16]. In addition, the slow-wave phenomena were also observed and studied for other classes of structures including plasma- and ferrite-filled waveguides [17]. In those early times, periodic structures were sometimes called delay structures instead of slow-wave structures.

Since the mid 1950s, there has been tremendous research and development into planar transmission lines and high-frequency integrated circuits printed on low-loss dielectric substrates or semiconductor wafers. These transmission lines may be in the form of microstrip lines, coplanar waveguides (CPW), slot lines, and other derivatives. The concept of hybrid microwave integrated circuits (HMICs) and monolithic MICs (MMICs) was eventually

proposed in the early 1960s. Such microwave integrated circuits (MICs) may be designed on lossy semiconductor substrates. Slow-wave propagation along these layered structures was predicted in 1967 [18], and immediately an extensive and detailed study on MIS (Si-SiO₂) slow-wave microstrip lines was published in [19]. Subsequently, a Schottky contact microstrip line [20,21] was used as a variable slow-wave structure with an external voltage control.

Periodic structures using planar fabrication techniques had basically received no attention until the emerging design requirement of the broad-band or high-directivity microstrip line coupler in the early 1970s. A coupled parallel-line system had been used to design couplers whose electrical performance is usually limited by the mismatch in the phase velocity of the even and odd modes. An effective solution to this problem was introduced by Podell [22] by wiggling the edges of coupled lines. It is used to deliberately control the ratio of capacitance and inductance, leading to the equalization of even and odd mode velocities. This marked the beginning of planar periodic structures that effectively generate slow-wave propagation [23].

Since the early 1970s, research on both MIS and planar periodic slow-wave structures have continued, and a selected set of publications issued before 1987 was presented for MIS-related topics [7]. Other published works related to MIS-based and planar periodic slow-wave structures can easily be found in the *IEEE MTT Transactions*, letters and conference publications (*Microwave Theory and Techniques*), *IEE Proceedings* (Part-H), and *Electronics Letters*. Recent advances include (1) the use of hybrid MIS and periodic structures (cross-tie overlay) for low-loss, slow-wave enhancement; (2) the observation of slow-wave effects because of lossy conductor strips at low frequency; (3) the proposal of inhomogeneous doping techniques for improving MIS transmission loss; and (4) the development of slow-wave structures using new materials, such as chiral media, photonic bandgap structures, and quantum-barrier traveling-wave devices. Some of these new developments are discussed in a subsequent section. Readers are encouraged to consult those periodicals and publications for more detailed information on this subject.

4. BASIC THEORY OF SLOW-WAVE STRUCTURE

It is known that periodic and MIS structures yield slow-wave propagation, depending on whether the fundamental condition of spatial separation of electric and magnetic energy is sustained. This is to say that slow-wave propagation does not necessarily occur along these structures under certain circumstances. This critical requirement for slow-wave propagation depends, in turn, on the physical layout of the structure and the working range of frequency. The question is, how shall we describe them electromagnetically at a given frequency and also on which theoretical platform should we rely to predict slow-wave propagation? Furthermore, characteristic parameters must be identified to formulate such guided-wave proper-

ties clearly because they are very important for understanding and designing slow-wave structures and circuits.

To begin with, let us consider Figs. 2–4, which show a class of planar and nonplanar periodic and MIS structures. We realize, first of all, that the electric \vec{E} and magnetic \vec{H} fields along these structures should always satisfy Maxwell's equations, which are usually formulated in the frequency-domain (angular frequency $\omega = 2\pi f$ and f frequency) for slow-wave guiding structures. Maxwell's field equations are easily found elsewhere [1–4,6]. To study guided-wave properties, slow-wave structures are usually assumed to be infinitely long. This stipulation is not just a practical one imposed to simplify matters, as indeed it does, but it turns out that fields and guided-wave characteristics are rather useful and accurate for practical design of a finitely but sufficiently long structure. In addition, results obtained for an infinitely long structure may approach results for its finitely long counterpart quite accurately if both ends are terminated or matched, so as to satisfy the boundary conditions. In this case, the slow-wave structures can be characterized simply by the classic transmission-line theory in a unified lumped-circuit way, that is, the complex propagation constant $\gamma = \alpha + j\beta$ and characteristic impedance Z_0 derived from a generic ladder network are described by its constituent circuit elements *RGLC* that stand for distributed resistance, conductance, inductance, and capacitance per unit of length for a uniform line or per period for periodic structures. Guided-wave properties, such as γ and Z_0 , can be rigorously modeled by applying Maxwell's equations with appropriate boundary conditions. This may call for numerical approaches if simple analytical or closed-form techniques fail to extract the characteristic parameters. This is true in particular for planar periodic and MIS slow-wave structures.

A unified transmission line model is introduced for both periodic and MIS structures because they can be considered special classes of transmission lines. In addition, it can be shown that transmission line theory (circuit aspect) is consistent with Maxwell's equations (field aspect) for such guided-wave structures. This model mathematically confirms the origin and existence of slow-wave propagation once an effective spatial separation of electric and magnetic energy takes place. In addition, it should reveal some guided-wave properties of the slow-wave structure. Based on the difference in geometry compared with the uniform MIS slow-wave line, the periodic structure may be subject to some unique mathematical theorems and treatments, which are described following, together with other pertinent definitions frequently used with slow-wave structures.

4.1. Periodicity or Floquet's Theorem

The periodicity theorem helps us to formulate the guided-wave properties of a linear, periodic, slow-wave system, that is, to determine modes of electric and magnetic fields subject to periodic boundary conditions. This theorem is sometimes called Floquet's theorem, a generalized mathematical theorem for differential equations with periodic coefficients. A *mode* denotes a particular solution to

Maxwell's equations or to the wave equations at a certain frequency. A slow-wave could be composed of a number of modes in a hybrid form called hybrid mode, depending on the nature of the structure. The electric and magnetic fields over the cross section should be identical for the infinitely long helix and periodic waveguide, but with a phase shift given by the factor $e^{-j\beta p}$ from any point z to the point $z + p$, where β and p are the fundamental propagation constant and the periodic length, respectively. Without loss of generality, let us consider only electric fields in a Cartesian coordinate system for the periodic cavity-chain waveguide. Floquet's theorem in Cartesian coordinates states that

$$\begin{aligned}\vec{E}(x, y, z + p) &= \vec{E}(x, y, z) \cdot e^{-j\beta p} \\ &= \vec{E}(x, y, z) \cdot e^{-j\beta_n p} \\ \beta_n &= \beta + \frac{2n\pi}{p}\end{aligned}\quad (1)$$

in which $n = 0, \pm 1, \pm 2, \pm 3, \dots$ and so forth, which stand for the index terms of space harmonics. This equation suggests that the electromagnetic solution to a periodic cell with space-harmonic expansion constitutes the completeness of a field solution for the entire periodic structure. Equation (1) implies that "local" waves contained to some extent in the periodic cells that interact with "guided" waves eventually yield a space separation of electric and magnetic energy. The exponent says that the n th mode has a propagation constant β_n on the basis of a Fourier (space harmonic) expansion and that the periodic phase shift of the structure is always dictated by the term or βp or φ .

The determination of β at a given frequency ω is the central problem in a periodic slow-wave structure. The solution is sometimes called the ω - β diagram, or dispersion curve. Note that the concept of a space harmonic differs from that of a mode in that a space harmonic is the inseparable component of a wave containing the explicit exponent factor and it may be a component of a mode. A single space harmonic rarely satisfies all of the boundary conditions, and it may or may not satisfy Maxwell's equations. Nevertheless, under some circumstances, the space harmonic expansion may correspond directly to the modes. Sometimes in the literature, this expansion of fields over a periodic cell is called spatial harmonics, or sometimes Hartree harmonics, to represent the guided-wave properties of the complete structure.

Of the infinite number of spatial harmonics, half are forward waves, whereas the other half are backward waves. This interesting and useful feature of periodic slow-wave structures is discussed following.

5. ($\omega - \beta$) DISPERSION DIAGRAM AND SLOW-WAVE PARAMETERS

Our general understanding of the behavior of slow-wave structures depends greatly on ω - β dispersion curves, sometimes called the Brillouin diagram. This is a plot of

ω against β . In some cases, the phase shift φ ($\varphi = \beta p$) may also be used (ω - φ curves) for periodic structures. This classic graphic representation is popular for periodic structures but not for uniform MIS structures, which use other alternatives, such as a slow-wave factor. Figure 5 depicts a typical ω - β dispersion curve for a slow-wave periodic structure. The phase and group velocities are calculated from

$$\begin{aligned}v_p &= \frac{\omega}{\beta} \\ v_g &= \frac{\partial \omega}{\partial \beta}\end{aligned}\quad (2)$$

The phase velocity v_p of a mode is the velocity with which an observer must travel to keep in step with this mode, and it stands for the phase transmission characteristic of each frequency relative to the frequency of reference. Usually, v_p differs from mode to mode on the basis of Floquet's theorem. The group velocity v_g yields the energy transmission (or power flow) velocity at a finite frequency. The concept of dispersion is used to measure the degree of field variation over the cross section or periodic cell of a structure as the frequency changes. If v_g remains constant over a range of frequency, signal information carried by these frequencies travel with the same velocity in the structure. In other words, a structure may be dispersionless if its ω - β curves are simply straight lines or the two characteristic parameters are linearly related to each other. Interestingly, in a periodic structure, the group velocity is the same for all the modes because $\partial \omega / \partial \beta_n = \partial \omega / \partial \beta$ is always satisfied according to Eq. (1). Thus the group velocity is a parameter for an entire wave. If β is positive in Fig. 5, v_g is positive at point A, meaning that the signal power flows in the $+z$ -direction (forward wave), whereas v_g negative at point B means that the signal power flows in the $-z$ -direction (backward wave). At point C, the wave is cutoff or

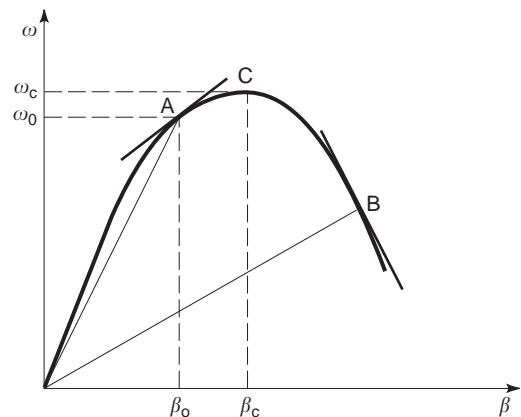


Figure 5. Characteristic dispersion curve, or ω - β diagram, for a slow-wave structure (typically for periodic structures). ω is angular frequency, β propagation constant (usually β is for the fundamental mode of a periodic slow-wave structure). Points A and B represent forward and backward propagating waves in the case of a positive β , respectively, and point C is the cutoff frequency at which energy flow is halted.

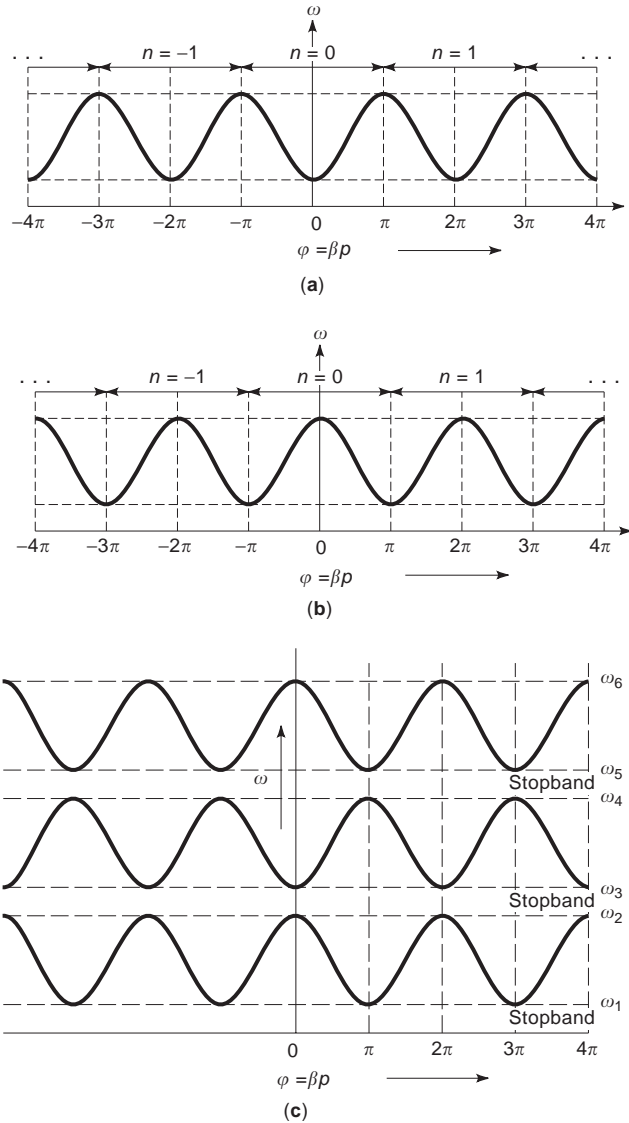


Figure 6. A general form of ω - φ dispersion curve, or Brillouin diagram, for a typical periodic waveguide structure. (a) Forward wave ω - φ relationship and curve slopes for space harmonics with the energy flowing in the $+z$ -direction ($\beta_n = \beta + 2n\pi/p$) for the solid lines; and with the energy flowing in the $-z$ -direction ($\beta_n = -\beta + 2n\pi/p$) for the dotted line. (b) Backward wave ω - φ relationship and curve slopes for space harmonics with energy flowing in the $+z$ -direction ($\beta_n = -\beta + 2n\pi/p$) for the solid lines, and with energy flowing in the $-z$ -direction ($\beta_n = \beta + 2n\pi/p$) for the dotted line. (c) Composite ω - φ diagram showing alternated passbands and stopbands. The first three characteristic passbands feature forward and backward spatial harmonics. The bandwidths of the three stopbands are not necessarily the same.

in a state of local resonance where v_g becomes zero. The forward and backward waves are the fundamental physical attributes of periodic waveguides. Obviously, the forward and backward waves are not related only to positive β .

Figure 6 gives a set of ω - φ dispersion curves for a typical periodic waveguide structure. The fundamental forward and backward slow waves are described in Fig. 6(a)

and Fig. 6(b), respectively, via the sign of β and slope of ω - φ dispersion curves relative to the space harmonics. There are two possible scenarios for realizing forward waves as shown in Fig. 6(a): (1) the dispersion curves have positive slopes ($v_g > 0$, and the energy propagates in the $+z$ -direction) because $\beta_n = \beta + 2n\pi/p$; or (2) the dispersion curves have negative slopes ($v_g < 0$, and the energy propagates in the $-z$ -direction) because $\beta_n = -\beta + 2n\pi/p$. Obviously, forward wave propagations take place if and only if $\partial\omega/\partial\beta_n = \partial\omega/\partial\beta$ and ω/β have the same sign at a given frequency. Similarly, there are also two corresponding scenarios for achieving backward waves, as shown in Fig. 6(b): (1) the dispersion curves have positive slopes ($v_g > 0$, and the energy propagates in the $+z$ -direction) because $\beta_n = -\beta + 2n\pi/p$; or (2) the dispersion curves have negative slopes ($v_g < 0$, and the energy propagates in the $-z$ -direction) because $\beta_n = \beta + 2n\pi/p$. In this case, the backward wave propagations take place if and only if $\partial\omega/\partial\beta_n = \partial\omega/\partial\beta$ and ω/β have opposite signs at a given frequency. It is helpful to remember that the propagative direction of the fundamental mode guidance differs from that of the energy flow. Based on the difference of dispersion curve behavior between the two classes of waves ($\beta = 0$, for example), the slow-wave structure design for forward wave propagations may differ from those of backward waves. The forward wave structures have been used to design amplifiers, such as TWT, usually on the basis of the fundamental mode ($n = 0$). The space harmonics ($n \neq 0$) are often involved in spurious field interactions. The backward wave structures have been popular in designing voltage-controlled oscillators. Space harmonics ($n \neq 0$) could sometimes be used to obtain lower control voltages.

Figure 6(c) shows a composite diagram or general form of $(\omega - \varphi)$ dispersion curve, which involves the frequency response of spatial harmonics for three characteristic curves. A transverse electric and magnetic (TEM) mode periodic line may be considered when $\omega_1 = 0$. Otherwise, this is for a non-TEM mode structure. The frequency ranges between the extremes of an $\omega - \varphi$ curve are called passbands, that is $\omega_1 - \omega_2, \omega_3 - \omega_4$, and $\omega_5 - \omega_6$ because β_0 is real and the fields carry real power through the structure. A frequency range between two passbands is a stopband, that is $0 - \omega_1, \omega_2 - \omega_3$, and $\omega_4 - \omega_5$ within which no real power can flow because the fields decay exponentially away from the reference source. This important feature is of considerable significance in designing filters and other components based on periodic structures.

Passband and stopband characteristics are unique for periodic structures. In the MIS structures, the wave propagation depends, first of all, on the fundamental characteristics of a planar line. A microstrip line is different from a slotline [7,24], for example. The slow-wave characteristics of an MIS structure are characterized by a complex propagation constant and a complex characteristic impedance. In turn, the complex propagation constant can be expressed by the slow-wave factor η and loss α in dB/mm. The slow-wave factor is simply defined as

$$\eta = \frac{v_0}{v_p} = \frac{\lambda_0}{\lambda_g} = \frac{\beta}{\beta_0} = \sqrt{\epsilon_{\text{eff}}} \quad (3)$$

where λ_0 and λ_g denote the free-space and guided wavelengths, respectively. β_0 and ϵ_{eff} are the free-space propagation constant (or wavenumber) and the effective dielectric constant, respectively. Obviously, the slow-wave factor, which is identical to the effective index commonly used in optics, can also be applied to the characterization of periodic structures. The central problem in MIS research work is to obtain the highest slow-wave factor possible at higher frequencies, and the lowest line loss is desired. Potential dielectric, ohmic, and radiative losses contribute to the whole loss. Generally speaking, each loss effect is strongly frequency-dependent. In addition, the physical layout may be designed with some expected impedance value. Sometimes, the MIS slow-wave propagation is measured by a quality factor or figure-of-merit as Q as follows:

$$Q = \frac{\eta}{\alpha} \tag{4}$$

There is no consistency in the literature for the definition of Q , which is also defined elsewhere as $(\alpha \cdot \lambda_g)^{-1}$ [25] or $\beta/2(\alpha)$ [26].

5.1. Unified Transmission Line Model

For the periodic and MIS structures shown in Figs. 2–4, the slow-wave propagation of a mode can be represented simply by an equivalent transmission line model with the characteristic lumped elements whether per unit length or per periodic cell, denoted by *RGLC*. Conventionally, R and G (resistance and conductance per unit length) are caused by the longitudinal current flow on the lossy conductor and transverse current dissipation in the dielectric

region, respectively. L and C (inductance and capacitance per unit length) are produced by the longitudinal current flow and transverse electric field effect, respectively. As multiple modes possibly exist in a waveguide, for instance, the periodic waveguides, multiple lossy network topologies are required to characterize different guided-wave properties of these modes, such as lowpass, highpass, and bandpass prototypes. Nevertheless, any network topology can be theoretically transformed from the fundamental lowpass prototype, shown in Fig. 7. Therefore, a unified transmission line model can be set up to interrelate line voltages and currents at an interval of a unit or a period, which is very informative in analyzing slow-wave properties.

In the frequency-domain, the transmission line equations (or telegraph equations) can be expressed by

$$\frac{dV(z)}{dz} = -(R + j\omega L)I(z) \tag{5a}$$

and

$$\frac{dI(z)}{dz} = -(G + j\omega C)V(z) \tag{5b}$$

Uncoupling these two equations leads to wave equations for the voltage and current on the line

$$\frac{d^2V(z)}{dz^2} = \gamma^2 V(z) \tag{6a}$$

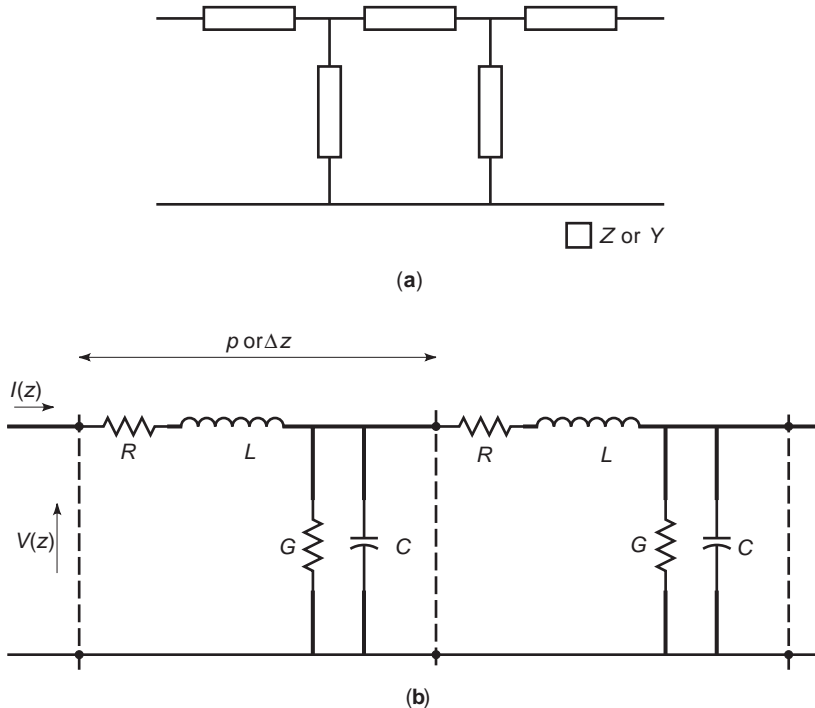


Figure 7. Unified network prototypes or equivalent transmission line model of the slow-wave structures, characterizing frequency responses or guided-wave properties through a set of lumped elements. (a) Arbitrary T or π network representation for any type of slow-wave transmission line. Z and Y stand for complex impedance and admittance, respectively. (b) A general cascaded *RGLC* lumped-element transmission line model for the periodic and MIS slow-wave structures with the concept of distributed voltages and currents.

and

$$\frac{d^2 I(z)}{dz^2} = \gamma^2 I(z) \quad (6b)$$

where $\gamma = \alpha + j\beta = \sqrt{(R + j\omega L)(G + j\omega C)}$ is the complex propagation constant and the complex characteristic impedance of the line can be calculated from $Z_0 = Z_{0r} + Z_{0i} = \sqrt{(R + j\omega L)/(G + j\omega C)}$.

The propagation constant may be expanded in a Taylor series to show the asymptotic behavior of the loss and the phase velocity. For high frequency and low loss, such that $R \ll \omega L$ and $G \ll \omega C$, the first-order approximation is easily made to obtain the following formulas:

$$\alpha \approx \frac{1}{2} \left(R \sqrt{\frac{C}{L}} + G \sqrt{\frac{L}{C}} \right) \quad (7a)$$

and

$$\beta \approx \omega \sqrt{LC} \quad (7b)$$

Similarly, the complex characteristic impedance can be approximated for low-loss lines such that the real and imaginary parts are given by

$$Z_{0r} \approx \sqrt{\frac{L}{C}} \quad (8a)$$

and

$$Z_{0i} \approx -\frac{1}{2\omega} \sqrt{\frac{L}{C}} \left(\frac{R}{L} - \frac{G}{C} \right) \quad (8b)$$

Of course, the phase velocity of a slow-wave structure can be directly derived from Eq. (7b) via

$$v_p \approx \frac{1}{\sqrt{LC}} \quad (9)$$

This simple equation reveals the fundamental requirements for a guided-wave structure to allow slow-wave propagation: either a large inductance or a large capacitance per unit of length or per period, or both, along the signal path by spatially separating electric and magnetic energy. In a periodic structure, a large reactance (inductance and/or capacitance) is induced by the periodic cell, whereas the MIS structure produces only an excess capacitance and its inductance remains basically unchanged with reference to its normal line counterpart. Based on other equations, the loss may be critical in using an MIS structure as opposed to a periodic structure because the lossy semiconductor layer is always required in constructing an MIS structure, and both conductance and resistance could be significant at high frequencies. The transmission attenuation of a periodic structure is essentially caused by the conductive (ohmic) loss and potential radiation loss (discontinuity effect). The change in v_p should affect the other line parameters. Consider a helix

slow-wave structure that generates a large inductance. Its characteristic impedance may be high, whereas the MIS structure yields a low impedance because of its large capacitance. In fact, the lumped elements can be obtained by approximate and quasistatic models for the slow-wave structures.

6. APPROXIMATE AND QUASISTATIC MODELS

As some slow-wave structures like helical and planar periodic lines are complex, it is rather difficult or even impossible to solve these problems analytically. In the earlier days, high-speed computing resources and modeling capacity were quite limited, and it was not practical to generate tedious field solutions for design purposes. Approximate and quasistatic models that are common in engineering practice were widely used to obtain, within an acceptable margin of error, guided-wave properties and design databases for a large class of slow-wave structures including helical and lumped-element models of planar transmission lines. The approximate models are usually developed on the basis of a much simplified geometry that neglects some physical effects and parameters, whereas the quasistatic models are generated simply by considering the limiting case of $f = 0$. The approximate models can be applied to any slow-wave structures, but the quasistatic models are applicable only to those supporting TEM modes or static field solutions. Generally, all of these models are amenable to simple analytical procedures or sometimes closed-form solutions. Advantages of the quasistatic models are that they allow one to gain insight easily into the slow-wave properties of a structure through its extracted lumped elements.

As the models and analysis techniques of waveguide slow-wave structures are easily found in the literature and technical books [1,2,6,8,13–15,17], our attention in this article is focused on slow-wave models and characteristics of planar structures, which are also recent subjects of interest in research and development. Selected quasistatic and lumped-element models are briefly presented to showcase earlier development of modeling and design tools.

6.1. Sheath-Helix Model

Probably the best known approximate model of periodic structures is the sheath-helix model introduced by P. R. Pierce and then refined by Sensiper. Subsequently, it was extensively used for a large class of helices. This model is not presented in this article because it is well documented [6,8,9,14]. Other recently published textbooks contain detailed information [2,3]. The sheath-helix has dispersion, or $(\omega - \beta)$ curves, that approximate the reality of a helical structure remarkably well. In this model, the actual helix of a finite thickness, whether made of wire or tape, is replaced by a fictitious cylindrical tube model, which has such features as (1) an infinitesimal thickness; (2) a radius equal to the mean radius of the actual helix of finite thickness; and (3) anisotropic conductivity, such that the sheath conductivities are infinite and zero in directions parallel and perpendicular to the helical winding direction,

respectively. The sheath-helix model would be closer to the actual situation if the helix is more tightly wound.

6.2. Model for Planar Periodic Structure

As a typical and simplified example of planar periodic structures, Fig. 8 shows a linear and isotropic microstrip line consisting of its double-layered geometrical layout with an infinitely thin periodic strip conductor. Its lumped-element equivalence is built on the basis of quasistatic or quasi TEM mode propagation or low-frequency operation such that the length p of a periodic cell is much smaller than the wavelength. The structure is considered lossless for most quasistatic models even though the ohmic dissipation in a conductor may be significant at higher frequency. Obviously, the wide line section W_1 generates a capacitive effect, whereas the narrow line section is responsible for an inductive effect. In this way, the separation of electric and magnetic energy is achieved in longitudinal space, potentially leading to slow-wave propagation. The lumped capacitance C and inductance L per cell section can be effectively calculated, and the voltage and current are considered stationary over the periodic section. The phase velocity and characteristic impedance

can be readily obtained if L and C are calculated. Therefore, the slow-wave problem is simply reduced to calculations of L and C per periodic cell. The approach, as described in Ref. 23, can be applied to other quasistatic periodic structures.

6.2.1. Capacitance Calculation. Electrostatic field problems are usually handled via the 3-D Poisson equation, which operates on scalar potential functions. With reference to the symmetrical structure of Fig. 8, which is divided into two cross-sectional regions I and II, the periodic cell section is bounded by magnetic walls over which there are no normal electric fields. This is a consequence of the quasistatic condition. The 2-D electric charge density distributed over the periodic conductor surface is denoted by $\rho_e(x, z)$. The electrostatic potentials are expanded in a Fourier series considering boundary conditions. Such expansions are usually in the form of infinite series summations of trigonometric functions, which satisfy the bidimensional boundary conditions over the periodic cells [23]. The infinite summation is subject to a convergence-allowable truncation in numerical calculations. This procedure involves some unknown coefficients. The total energy W_e stored in a periodic section is simply given by $0.5 \int_0^p \int_0^a \epsilon |\vec{E}|^2 dv$, in which the electric fields are derived from the scalar potential functions. To eliminate the unknown coefficients, a set of boundary conditions at $y = h_2$ are used. In this case, the coefficients are formulated by $\rho_e(x, z)$. Therefore, the energy is explicitly expressed by

$$W_e = \frac{2}{ap} \sum_{m=1}^{\infty} \sum_{n=0}^{\infty} G_e(m, n) \cdot \left[\int_0^p \int_0^a \rho_e(x, z) \sin \frac{m\pi x}{a} \cos \frac{n\pi z}{p} dx dz \right]^2 \quad (10a)$$

$$G_e(m, n) = \frac{1}{\delta(n)k_{mn}} (\epsilon_1 \coth k_{mn} h_1 + \epsilon_2 \coth k_{mn} h_2)^{-1} \quad (10b)$$

$$\delta(n) = \begin{cases} 1 & (n \neq 0) \\ 2 & (n = 0) \end{cases} \quad (10c)$$

In Eq. (10b), the term G_e denotes Green's function for this electrostatic field problem. Now, capacitance per periodic section is given by $C = Q/V = Q^2/(2W_e)$, where $Q = \int_0^p \int_0^a \rho_e(x, z) dx dz$. Q is the total electric charge on the conductor, and it is calculated from the charge density function $\rho_e(x, z)$.

6.2.2. Inductance Calculation. As a result of the structural symmetry, the inductance L can be calculated by applying a procedure similar to that for calculating the capacitance. Otherwise, the L calculations are not so simple, and it may require vectorial magnetic potentials that are related to the current density distributed over the conductor. Nevertheless, the magnetic fields in this case have only normal components at the interface $y = h_2$ outside the conductor strip. This is a complementary problem

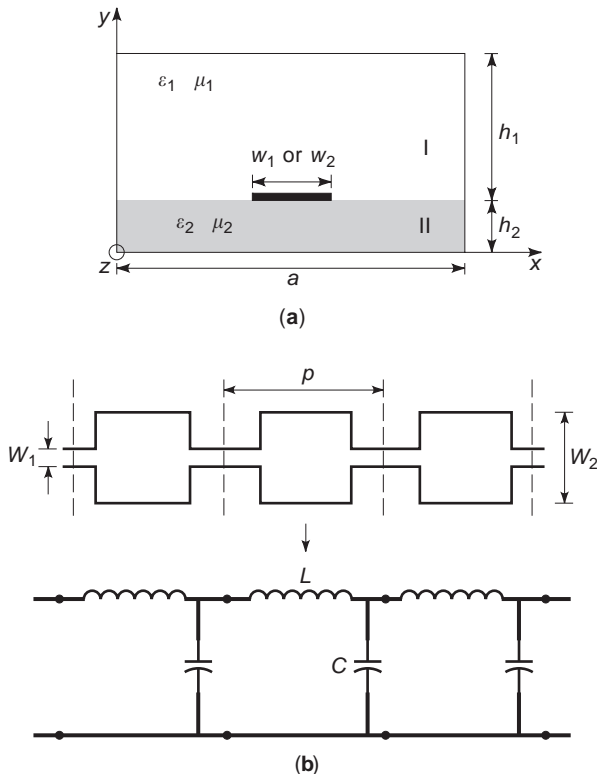


Figure 8. (a) Cross-sectional view (b) longitudinal view and network equivalence of a generalized periodic microstrip slow-wave line sandwiched by two different linear and isotropic dielectric substrates. This periodic line is simply represented by a lumped-element LC model in the absence of both losses and conductor thickness. Geometrical dimensions and substrate parameters sketched in the figure are similar to the previous illustrations. The lumped elements are extracted by an approximate quasistatic model.

of duality. The scalar magnetostatic potentials proportional to the magnetic fields ($H = -\psi_m$) are used to satisfy the Poisson equation, and they can be expanded with a set of unknown coefficients. At the boundary between the two layers, the normal component of the magnetic flux density is continuous.

In contrast with the electrostatic case, the magnetic flux density is a hypothetical term, and of course, its normal component cannot exist on the conductor surface ($\rho_m = 0$ on the conductor). Similarly, the unknown expanded coefficients can be effectively eliminated, and the total magnetostatic energy is easily obtained by equations in magnetic identity similar to Eq. (10), except that ϵ is replaced by μ^{-1} . The inductance L is given by $L = \Phi/I = \Phi^2/(2W_m)$ with $\Phi = \int_0^p \int_0^a \rho_m(x,z) dx dz$. Φ is the total magnetic flux interlinking the strip conductor. As the magnetic flux across one side of the conductor is equal in magnitude and opposite in sign to that over the other side, it can be calculated from the one-side flux density function $\rho_m(x, z)$.

6.2.3. Charge Density Calculation. To complete our calculations of capacitance and inductance, we need to know the electric and magnetic charge density functions. Usually, various techniques connected to the method of moments, such as the Rayleigh–Ritz variational procedure, may be applied to solve this problem. To do so, the unknown charge density functions are expanded in terms of well-behaved basis functions with unknown coefficients, even though the actual charge densities may be very complex. In the C calculation, for example, the electric charge density function may be expressed in terms of known basis functions f_k of finite series, such that $\rho_e(x,z) = \sum_{k=1}^K \alpha_k f_k(x,z)$, in which α_k are unknown coefficients. The purpose of applying a method of moments is to calculate the unknown coefficients, and then an approximate solution to the problem can be obtained. The L calculation can be made similarly. With the calculated L and C , the slow-wave velocity and characteristic impedance can be derived by applying Eqs. (7–9). The theory and applications of the method of moments can be found in the literature [27]. Details on applying the variational principle are described in Ref. 23, which also presents a number of typical theoretical and experimental results of single and coupled microstrip periodic structures.

6.3. Model for Planar MIS Structure

Various approximate models were proposed for modeling an MIS microstrip line and CPW, whose cross sections are shown in Fig. 3 with a unified equivalent circuit model, as described in Fig. 9. Details of these classic techniques are well formulated in technical papers and books, and they include the parallel-plate waveguide model for the microstrip line [21] and the conformal mapping technique for both the microstrip line and the CPW [26]. Valid use of these techniques is always subject to careful approximations or assumptions about geometrical dimensions and physical parameters. The Schottky-contact microstrip line, which is regarded as a special case of the MIS microstrip line, can be treated similarly to the MIS structure.

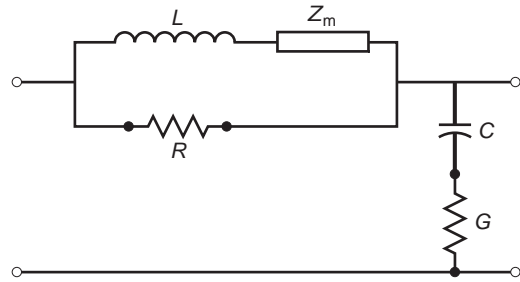


Figure 9. Unified equivalent circuit model for an MIS slow-wave structure including microstrip and CPW lines (see Fig. 3). In addition to the previously defined lumped-elements $RGLC$, Z_m is used to account for the conductor loss, which can be obtained by the calculating surface impedance Z_s , for example.

Of course, the MIS structure consists of an unavoidable lossy semiconductor layer and an extremely thin insulator usually with very narrow guiding strips. Therefore, the loss is a critical factor in analyzing and designing an MIS structure. There are three potential difficulties encountered in modeling planar MIS structures: (1) accurate characterization of conductor loss; (2) accurate calculation of fringing fields (usually in the case of the parallel-waveguide model); and (3) the quasistatic multilayer model.

Three different modes of propagation exist along an MIS structure as frequency varies [19,21,26], called “slow-wave mode,” “dielectric quasiTEM mode,” and “skin-effect mode,” respectively. Generally, these modes are roughly distinguished by three characteristic frequencies, namely, the dielectric relaxation frequency f_d , the characteristic skin-effect frequency f_s , and the relaxation frequency of interfacial polarization $f_p = f_d(\epsilon_s h_1)/(\epsilon_i h_2)$ in which the physical parameters are specified in Fig. 3. The lumped-element $RGLC$ depicted in Fig. 9 is easily derived from the quasistatic (TEM mode) models [19,21,26]. Table 1 summarizes quasistatic approximations of the lumped elements for the MIS microstrip (including Schottky-contact line) and CPW. In Table 1, ϵ_0 and μ_0 are the permittivity and permeability of free space, respectively, and F is a geometrical factor stemming from the conformal mapping model, which is approximated by

$$F = \begin{cases} \frac{\ln \left[\frac{2(1 + \sqrt{k})}{(1 - \sqrt{k})} \right]}{\pi} & \text{for } 0.707 \leq k \leq 1 \\ \frac{\pi}{\ln \left[\frac{2(1 + \sqrt{k'})}{(1 - \sqrt{k'})} \right]} & \text{for } 0 \leq k \leq 0.707 \end{cases} \quad (11)$$

in which $k = W/(W + 2S)$ and $k' = \sqrt{1 - k^2}$. The parameter K in Table 1, which can be numerically calculated by an exact static model, accounts for the effect of fringing fields, and its value is slightly greater than 1.0. The effect of conductor loss is reflected in its complex impedance Z_m . It can be derived by several techniques, such as the incremental inductance rule [7], phenomenological loss equivalence [28], and surface impedance approach [7]. Other parameters are described in Fig. 3.

Table 1. Basic Characteristic Frequencies and Lumped-Element Equations of the Approximate Quasistatic Model for MIS and Schottky-Contact Microstrip Lines and MIS Coplanar Waveguides (CPW)

Line Type	Lumped Elements						
	f^a	f^s	R	G	L	C	Z^m
MIS and Schottky-Contact Microstrip	$\frac{\sigma}{2\pi\epsilon_0\epsilon_s}$	$\frac{1}{\pi\sigma\mu_0 h_2^2}$	$\frac{3}{\sigma h_2 w}$	$\frac{w}{\sigma h_2}$	$\mu_0 \frac{(h_1 + h_2)}{w}$	$\epsilon_0 \epsilon_i \frac{w}{h_1}$	$\frac{Z_s}{w}$
MIS CPW	$\frac{\sigma}{2\pi\epsilon_0\epsilon_s}$	$\frac{1}{\pi\sigma\mu_0 (w/2 + s)^2}$	$\frac{1}{\sigma \delta w}$	$2\sigma F$	$\frac{\mu_0}{4F}$	$\frac{\epsilon_0 \epsilon_i w}{h_1} K$	$\frac{Z_s}{w}$

^aThe model validity may be subject to certain limiting conditions. Physical and electrical parameters refer to Fig. 3. The geometrical factor F is calculated by Eq. (11). The complex impedance of conductor Z_m can be derived from the surface impedance Z_s that can be modeled by several well-documented techniques (see relevant references and literature for more details). The K value, usually slightly greater than 1, is used to assess the effect of fringing fields, and it can be numerically calculated by an exact static model.

7. ACCURATE AND HYBRID-MODE FIELD MODELS

Accurate field models are usually required when approximate models are no longer valid or the operating frequency is too high to use a quasistatic approximation. In other cases, the use of hybrid-mode field techniques are mandatory because the slow-wave structures cannot support a quasiTEM mode propagation, such as the corrugated periodic waveguide and the fin line, to name two typical examples. Some physical approximations simplify or make a field model useful before its analytical development. Therefore, the choice of an appropriate field model is critically important for its expected accuracy and efficiency when applied to the structure of interest. There are many techniques available today, whose solutions are usually in numerical form. They include the method of moments and finite-difference and finite-element techniques. Readers are referred to other articles and literature for details on the numerical techniques. There is no “lumped-element” consideration in the field models to account for the spatial separation of electric and magnetic energy in contrast with the quasistatic models.

In the past, a number of efficient techniques were applied to various periodic waveguides (3-D problems) and MIS multilayered planar transmission lines (2-D problems). Earlier models for the waveguide problems were usually related to modal expansion or mode-matching techniques. Planar periodic structures were studied with a spectral-domain approach [24,29,30], which can also be applied to MIS slow-wave structures. In this case, the conductor thickness is usually assumed to vanish even though its effect may be included in the model. In fact, the conductor loss with a finite thickness in the field-based models can be evaluated by various techniques, such as the surface impedance scheme [7] and the self-consistent technique [31]. The semiconductor layer of an MIS structure may be inhomogeneous under certain circumstances, such as a depletion region of the Schottky-contact structures and partially doped MIS lines. Therefore, a generalized technique may be required to handle such complex topologies. In Sections 7.1 and 7.2, two typical techniques are presented narratively to showcase modeling using field theory.

7.1. Model for Planar Periodic Waveguide

Electromagnetic fields in a planar multilayered periodic structure are described by scalar electric and magnetic potential functions that also satisfy Helmholtz equations and boundary conditions [30]. Such potentials can be expanded as functions of trigonometric functions in their infinite summations by considering Floquet’s spatial harmonic representation in the periodic cell. Similarly to the static model, the infinite summation must be truncated. As detailed in Ref. 30, the Floquet harmonics can be regarded as “modal spectra” in the Fourier sense or as a “natural Fourier transform” in the half-periodic cell ($p/2$). As such, a double Fourier expansion is developed over the planar periodic fin line or slotline cell along the x - z plane, as shown in Fig. 10. The resulting formulation suggests that a procedure called “higher order resonant harmonic decoupling” can be readily applied, meaning that even and odd harmonics in the z -direction ($p/2$) can be separated regardless of the fundamental mode. This argument translates the Floquet’s theorem into a linear superposition of the spatial harmonics in a periodic cell with fictitious electric and magnetic walls defined at the periodic boundaries with the interval ($p/2$), as indicated in Fig. 10.

This decoupling procedure provides us with a powerful bidimensional Fourier transform tool in the x - z plane. In addition, this consideration allows predicting the existence of two modes: TM (even harmonics) and TE (odd harmonics). In this way, the Helmholtz equations can be transformed into y -dependent, ordinary differential equations that are solved analytically along the layered transverse direction. This corresponds to a set of transmission line equations in the spectral-domain. The use of the transmission line equations and additional boundary conditions leads to algebraic, spectral-domain-coupled, Green’s function $\tilde{\mathbf{Y}}$ in the form of a matrix at the periodic discontinuity:

$$\begin{bmatrix} \tilde{\mathbf{Y}}_{xx}(\alpha_m, \xi_n, \beta) & \tilde{\mathbf{Y}}_{xz}(\alpha_m, \xi_n, \beta) \\ \tilde{\mathbf{Y}}_{zx}(\alpha_m, \xi_n, \beta) & \tilde{\mathbf{Y}}_{zz}(\alpha_m, \xi_n, \beta) \end{bmatrix} \cdot \begin{bmatrix} \tilde{\mathbf{E}}_x(\alpha_m, \xi_n) \\ \tilde{\mathbf{E}}_z(\alpha_m, \xi_n) \end{bmatrix} = \begin{bmatrix} \tilde{\mathbf{J}}_x(\alpha_m, \xi_n) \\ \tilde{\mathbf{J}}_z(\alpha_m, \xi_n) \end{bmatrix} \quad (12)$$

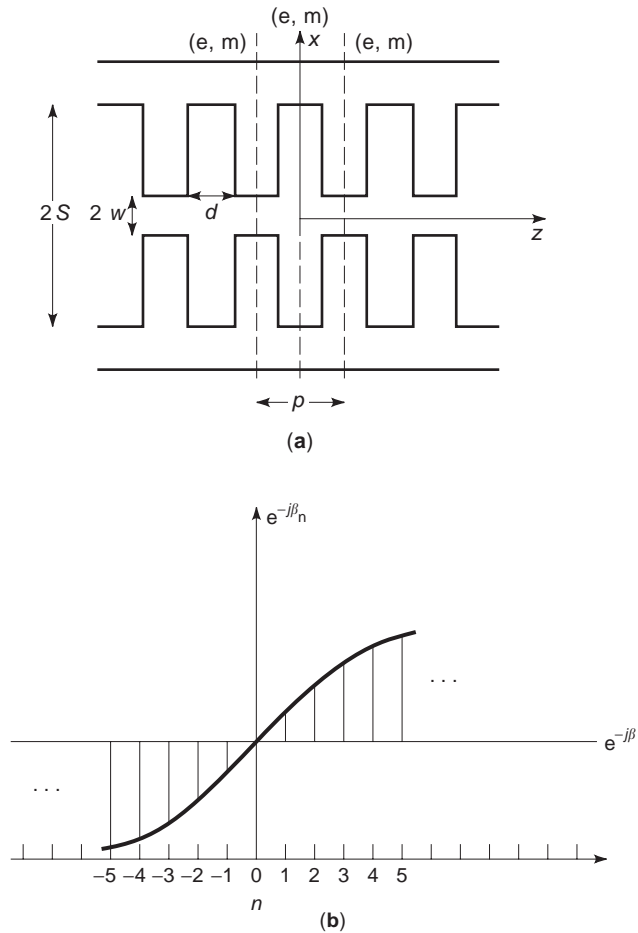


Figure 10. Two-dimensional physical layout description (a) and spatial-harmonics representation (b) of a periodically loaded planar slotline or fin line whose periodic cell is defined by d (the spacing between two adjacent stubs along the axial direction), $2w$ (the gap between the inline stubs), and $2s$ (the distance between the two bottom lines). The cross section of this structure may be in the form of multilayer dielectrics, whereas the spatial harmonics are transformed into a linear superposition of even (magnetic) and odd (electric) harmonics in a single periodic cell for a hybrid-mode model.

Obviously, the elements in Green’s function are related to α_m (the x -oriented spectral variable), $\xi_n = 2\pi n/p$ (the z -oriented spectral variable), and the unknown β . Then, the unknown aperture fields E and currents J can be expanded in terms of bidimensional basis functions with unknown coefficients, and Galerkin’s technique is applied to derive a coefficient matrix equation in the spectral-domain.

A nontrivial solution for the propagative constant is obtained by setting the determinant of the coefficient matrix $M(\beta)$ equal to zero. Several algorithms may be applied to search for solutions of this resulting nonlinear equation (eigenvalue problems). As explained in Ref. 30, the basis functions can be defined as functions of two types, namely, “guided” and “stored” basis functions. The field quantities and other parameters can be calculated once the fundamental propagation constant is

obtained, leading to the visualization of the field profile over the structure.

7.2. Model for Planar MIS Structure

As the MIS structures are a class of typical planar lossy transmission lines with a multilayered dielectric, a broad range of field-based techniques can be applied. However, the spectral-domain approach, the method of lines, and the mode-matching technique are the widely accepted schemes for modeling these structures because the MIS structures have such special features that the ratio of thickness among the multiple layers is relatively large and also the line width may be critically small compared with other structures. In addition, an inhomogeneous doping profile is possible for improving line performance [32]. Therefore, those fine details must be efficiently taken into account if a successful model is to be obtained. These arguments recommend that a model free of space discretization from layer to layer is favored, which includes the previous schemes. The following presentation is limited to an overview of the method of lines [25], which is a popular alternative to the spectral-domain approach when applied to the same problem. In particular, this method has some unique features, and it allows handling complex cross-sectional geometries, as in an inhomogeneously doped layer.

To begin with, an ideal lossless guiding conductor of vanishing thickness is considered for simplifying the model description. The same field equations as in the modeling of planar periodic structures are used herewith with the two potential functions. The whole MIS structure depicted in Fig. 3 is sampled by a set of alternating electric and magnetic lines perpendicular to the conducting strip plane. The potentials of each of the sampling lines must satisfy the Sturm–Liouville and Helmholtz equations. The Sturm–Liouville equations allow one to account for an inhomogeneous profile [25]. Using finite-difference techniques, these partial differential equations are cast into spatially coupled ordinary differential equations for each layer of the MIS guiding structure. Then they can be decoupled by matrix diagonalization via matrix eigenvalue techniques to yield simple transverse transmission line equations.

In our model, the lower boundary is a perfect electric wall under the ground plane, whereas the upper boundary may be infinity, corresponding to a matched transverse transmission line. Starting from both boundaries with the aid of transverse transmission concepts, we enforce field continuity at each interface. Finally, by equating the upper and lower tangential field components at the entire interface of the conducting strip, a characteristic matrix relationship may be derived from the matrix transformation back in the original space-domain. Extracting the sampling lines that intersect the conductor over which the tangential electric fields are null, we obtain a smaller matrix. The complex propagation constant is obtained from its nontrivial solution.

In contrast with the spectral-domain approach, the method of lines is always formulated in the semidiscrete

space-domain. The underlying advantages are its rigorous approach, simple convergent behavior, and fast algorithm with small memory requirements.

8. SLOW-WAVE SUMMARY AND APPLICATIONS

The two classes of slow-wave structures discussed previously, periodic structures and MIS transmission lines, have their own distinct characteristics because the mechanism of generating slow-wave propagation differs in separating electric and magnetic energy in space. The difference between them can be largely seen from their parameters, such as the slow-wave factor, transmission loss, characteristic impedance, bandwidth, frequency response, dispersion, and power handling capability. Modeling strategies for both types also differ. In fact, different groups of periodic structures and MIS lines also exist, based on the fundamental building block's geometry. The hybrid periodic MIS structures (sometimes called cross-tie overlay MIS structures) are also interesting in their own right, because they share some of the common characteristics of both periodic and MIS structures.

Slow-wave structures are characterized theoretically and experimentally for design purposes. There are several experimental techniques available, such as classic measurement methods for both periodic and MIS structures [7,30]. Other alternative methods, such as the ring-resonator technique, electrooptical sampling, time-domain measurements, and on-wafer probing techniques are also useful. Figure 11 shows an example of the measurement test setups for periodic structures, which allow one to extract the slow-wave factor and transmission loss.

Slow-wave structures are very useful in practice and play roles of paramount importance in the electrical and electronic fields. They are used and will continue to be used in diversified applications, including a broad range of passive and active circuits and devices in radio-frequency, microwave and millimeter-wave, and lightwave technologies. Now, slow-wave structures are categorized in terms of guided-wave properties, and various applications are also presented to highlight the importance of slow-wave structures in high-frequency electromagnetic engineering.

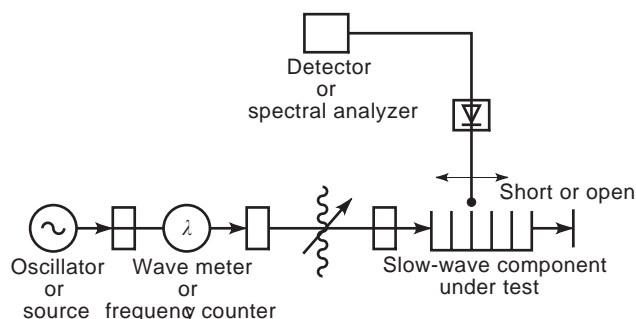


Figure 11. An example of the illustrative measurement setup of a conventional experimental procedure for a periodic structure in the frequency-domain.

8.1. Slow-Wave Structures and Properties

8.1.1. Periodic Structures. There are two classes of periodic structures: nonplanar and planar. The nonplanar structures include metallic waveguides, coaxial lines, and dielectric waveguides, whereas the planar structures are related to the integrated planar dielectric layers on which periodic metallic patterns are formed or printed. The periodic structures have quasiperiodic frequency response in the form of bandpass and bandstop (see Fig. 6 and Ref. 29 for an illustration), and they are quite dispersive. Low-loss, slow-wave transmission usually occurs in the bandpass region, and the structures may exhibit relatively high dispersion. A broad range of characteristic impedance and bandwidths are achievable on the basis of flexible and simultaneous separation of electric and magnetic energy in space. The nonplanar periodic structure may provide high-power handling capability and high Q (low loss) over its planar counterpart.

Three categories among the periodic structures in the form of nonplanar structures that have a relatively long history are the helix, the periodically obstructed waveguide, and the serpentine line. Planar structures may have similar periodic patterns, but they are formed on the 2-D plane, whereas the non-planar structures have 3-D features, and they are more flexible in structural design.

The helix (wire or tape) has continued to enjoy widespread use since its inception in a TWT. Three typical structures of the helix are the simple helix; the bifilar helix, also called the folded helix, made of two contrawound helices of equal but reversed pitches; and a ring-and-bar structure [14]. The last two helix-derived structures may have improved performance over the simple helical structure, such as higher allowable voltage, better thermal conditions, higher interactive impedance, and higher gain, when used in a TWT. However, the simple helix has the largest bandwidth. Similar helical patterns could also be realized by planar means, but very few examples are known to date because they are not useful for high-power applications.

Periodic waveguides supporting nonTEM modes usually behave as high-pass or bandpass filters, depending on the geometry of periodic obstacles or patterns. The topological form of such periodic obstacles characterizes the slow-wave properties. Typical examples include cavity-to-cavity chain structures. The intercavity couplings are made through capacitive or inductive schemes with various shapes, such as slot, cloverleaf, annular ring, and disk. Using the planar technique, the cavity can be easily made in the form of a patch or other geometry, and it can be coupled via gaps and other means.

Some typical examples of the serpentine line structure are the folded waveguide, including the meander-type line and the interdigital structure. Obviously, these structures can be realized easily by planar techniques. A number of these lines exhibit TEM-mode slow-wave propagation and usually the dispersion is low over a wide frequency range. Typical stationary field profiles and mode description over the periodic cell are shown in Fig. 12 for a fin-line structure at its fundamental resonance [30].

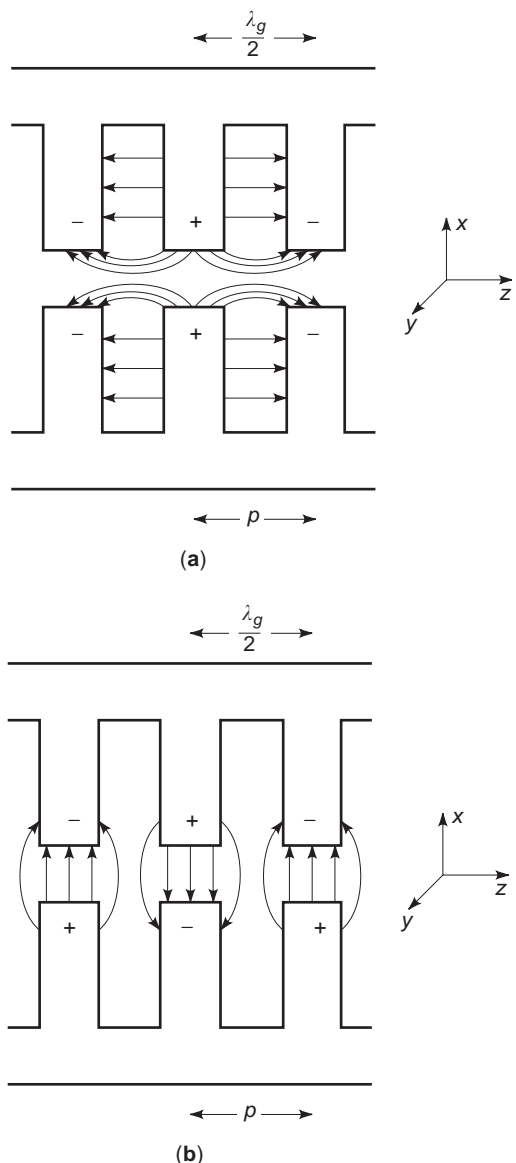


Figure 12. Typical electric field patterns or fundamental mode profiles in the $(x-z)$ section of a resonant periodic slow-wave structure (the periodic length p is equal to half of the guided-wave length $\lambda_g/2$ in this circumstance), which are generated by a hybrid-mode modeling technique. (a) TM_{11} mode; and (b) TE_{10} mode, in the case of a slotline or fin-line structure, as indicated in Fig. 10.

8.1.2. MIS Transmission Lines. The MIS structures consist of thin (several micrometers) and thick-film (several hundred micrometers) types on the basis of the thickness of the semiconductor (Si, GaAs, or InP) layer. The insulating layer (SiO_2 or Si_3N_4) is always kept very thin at around the order of less than $2 \mu m$. The fundamental characteristics of an MIS structure depend, first of all, on its line pattern. The thin-type MIS line was developed much earlier than its thick-type counterpart. Generally speaking, the thin-type semiconductor layer is less doped than the thick film for a much higher slow-wave factor, but its dispersion is also relatively high. The thick type is usually

heavily doped and has low dispersion over a wide frequency range. The low-loss propagation of a thick-film type may easily exceed 10 GHz with moderate slow-wave factors and easy-to-match impedance, whereas the thin-film type is limited to several GHz. There is also a difference between the normal MIS structures and Schottky-contact lines. Usually, the Schottky-contact line may require a voltage bias for practical use, and it is usually made of a microstrip line even though other lines are still feasible. The normal MIS structures may have any form of line patterns, such as microstrip, CPW, coplanar strip, fin line and slotline, and so on.

As mentioned in its lumped-element model, the MIS structure presents three basic characteristic frequencies with which it is convenient to design a “characteristic frequency map” in connection with the doping conductivity and frequency, as shown in Fig. 13. This map indicates the three possible modes of propagation identified in an MIS structure:

1. *Dielectric QuasiTEM Mode.* This is for the region where $f_d < f < f_s$. In this range, $\omega\epsilon_s > \sigma$, such that the doped semiconductor layer acts like a normal dielectric and confines most of the guided-wave energy in it. The propagation is usually lossy.
2. *Skin-Effect Mode.* When $f_s < f < f_d$, the doped semiconductor layer behaves as a lossy conductor wall to the wave because $\omega\epsilon_s \ll \sigma$. Hence, the depth of penetration or the skin depth $\delta = \sqrt{2/(\omega\mu_0\sigma)}$ becomes smaller than h_2 . The propagation is significantly dispersive.
3. *Slow-Wave Mode.* This is for the region where $f \ll f_d$ and $f \ll f_s$ as indicated in the map. In this case, f is perceived as not so “high” with the moderate value of σ .

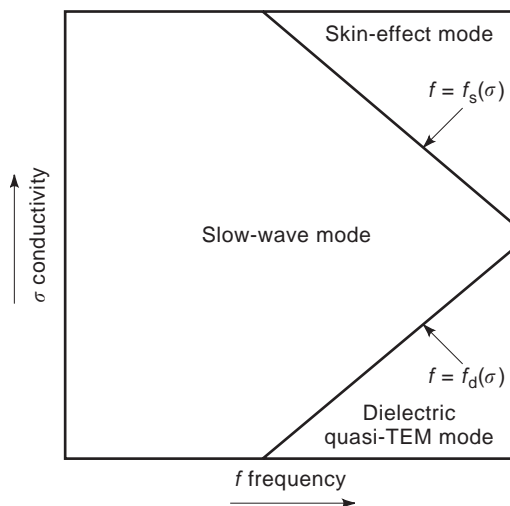


Figure 13. $\sigma - f$ characteristic frequency map of a typical MIS slow-wave structure (TEM-mode type lines) that characterizes three modes: slow-wave mode, dielectric quasiTEM mode, and skin-effect mode. This symbolic map is useful in designing an MIS structure with preliminary consideration of parametric effects on its slow-wave factor and transmission loss.

The electric field is confined within the insulator, whereas the magnetic field penetrates freely over the cross section, resulting in energy separation in space.

The conductor loss is an important aspect in designing an MIS structure. The loss may be accurately calculated by a self-consistent approach [25,31]. In this case, the conductor of a finite thickness is modeled merely as a normal lossy dielectric layer with intrinsic conductivity. For an MIS line operating in the slow-wave mode, the conductor contributes largely to the total loss at low frequency, over which the semiconductor loss is relatively small.

8.2. Slow-Wave Applications

It is known that slow-waves are not limited to periodic and MIS structures. Other structures that generate slow-wave propagation may be competitive in finding applications. Conductors, including superconductors [31,33], for example, exhibit slow-wave effects at low frequency. In this case, the field may penetrate into the conductor, leading to a significant increase in line inductance. Complex media, such as chiral waveguides, may support slow-wave propagation with specially arranged and coupled electric and magnetic properties to separate electric and magnetic energy. A photonic bandgap structure presents merely periodic lattice geometry, which is also subject to slow-wave propagation. Nevertheless, most slow-wave applications known so far rely essentially on the periodic and MIS structures.

The basic applications for slow-wave structures are usually related to the following uses as passive circuits and active devices: circuit miniaturization, frequency-selective devices and filters, traveling-wave devices, antennas, time-delay lines, phase shift and equalization, impedance match, mode polarization, energy conversion, amplification, oscillation, pulse shaping, and signal synchronization. Table 2 presents a general comparison and summary of performance among the periodic waveguides

and MIS lines for slow-wave propagation based on the previous discussion. The table provides a critical choice of these structures for various applications, such as high-power traveling-wave devices, integrated microwave circuits, high-speed signal interconnects, optoelectronics, and superconducting devices. Selected devices and circuits are discussed following to highlight some uniquely useful features of slow-wave structures.

Phase Shifter and Delay Line. Both periodic and MIS structures can be used to design these devices as hybrids or monoliths. Usually, the periodic slow-wave structures present fixed-phase shifting and long time-delay lines. In this case, superconducting technology may be used to significantly reduce the intrinsic conductive loss, for example, a physically very long line required to achieve more than several nanoseconds of group delay. Delay-line concepts were developed much earlier with periodic waveguide structures, whereas the phase shifter has been a popular research topic using the MIS slow-wave structures, especially in designing tunable phase shifters [34].

Linear and Nonlinear Traveling-Wave Devices. Some classic slow-wave examples are high-power traveling-wave tubes, backward-wave oscillators, amplifiers, and linear accelerators using periodic waveguides. The planar technologies allow designing similar distributed devices based on transistors and nonlinear transmission lines (NLTL) for broad-band devices including broad-band impedance matching networks, field grating devices, and of course, broad-band amplifiers [35]. On the other hand, the velocity-match mechanism of electrical and optical signals can be realized by using periodic electrodes and also the control of MIS slow-wave guidance on traveling-wave electrooptical modulators and photodetectors for wideband applications [36].

Filtering and Pulse-Control Devices. A class of filters and multiplexer can be designed with periodic

Table 2. Critical View and Comparison of High-Frequency Electrical and Mechanical Characteristics of Periodic and MIS Slow-Wave Structures Judging from their Passive Circuit Applications

		Basic Characteristics				
		Maximum Limiting Frequency	Transmission loss	Slow-Wave Factor	Structural Size	Frequency Dispersion
Slow-Wave Structures	Metallic and dielectric periodic waveguides	Extremely high	Very low	Low to moderate	Large to very large	High
	Planar periodic waveguides	High or relatively high	Moderate to low	Low to moderate	Small to medium	Medium to high
	Thin-film MIS lines	Low (several GHz)	Medium to relatively high	Very high	Extremely small (hundred μm)	Relatively high
	Thick-film MIS lines	Medium (possibly up to 30 GHz)	Relatively low	Moderate	Miniaturized to several μm	Low

^aAs compared with the MIS lines, the periodic waveguides present usually bandpass and bandstop characteristics, thereby leading to high dispersion of frequency. On the other hand, the unavoidable lossy semiconductor layer in the MIS structures exhibits adversely higher loss of transmission. The performances of the MIS structures refer basically to the Si-SiO₂ building block. The thin and thick films are distinguished by the thickness of the doped semiconductor, which is in the range of several microns and several hundred microns in thickness of the doped semiconductor, respectively.

structures, using their bandpass and bandstop characteristics. Extremely low-loss and linear-phase narrowband filters are realized from superconducting slow-wave lines that have various periodic patterns [37]. Frequency-selective devices and some traveling-wave antennas can also benefit from the advantageous features of periodic slow-wave structures. Pulse-control lines, including pulse-shaping devices, are often seen in high-speed digital circuits and interconnects. In this case, the MIS structures may play an important role in designing low-dispersion and signal-synchronized-pulse routine lines [38].

BIBLIOGRAPHY

- J. C. Slater, *Microwave Electronics*, Princeton, NJ: Van Nostrand, 1950.
- S. Ramo, J. R. Whinnery, and T. Van Duzer, *Fields and Waves in Communication Electronics*, New York: Wiley, 1984.
- R. E. Collin, *Field Theory of Guided Waves*, 2nd ed., New York: IEEE Press, 1991.
- R. F. Harrington, *Time-Harmonic Electromagnetic Fields*, New York: McGraw-Hill, 1961.
- L. Brillouin, *Wave Propagation in Periodic Structures*, 2nd ed., New York: Dover, 1953.
- R. M. Bevensee, *Electromagnetic Slow Wave Systems*, New York: Wiley, 1964.
- T. Itoh, ed., *Planar Transmission Line Structures*, New York: IEEE Press, 1987 (see Part X).
- J. R. Pierce and L. M. Field, Traveling-wave tubes, *Proc. IRE*, **35**:108–111 (1947), see also J. R. Pierce, *Traveling Wave Tubes*, 1st ed., Princeton, NJ: D. Van Nostrand, 1950.
- S. Sensiper, Electromagnetic wave propagation on helical structures, *Proc. IRE*, **43**:149–161 (1955).
- R. Kompfner, The traveling wave valve, *Wireless World*, **52**:369–372 (1946), see also The traveling-wave tube as amplifier at microwaves, *Proc. IRE*, **35**:124–127 (1947).
- W. S. Percival, *Improvements in and Relating to Thermionic Valve Circuits*, British Patent Specification 460, 562 (1936).
- A. A. Oliner and W. Rotman, Periodic structures in through waveguide, *IRE Trans. Microwave Theory Tech.*, **MTT-7**:134 (1959).
- A. H. W. Beck, *Space-Charge Waves*, New York: Pergamon, 1958. (Vol. 8 of *International Series of Monographs on Electronics and Instrumentation*, D. W. Fry and W. A. Higinbotham, eds.
- B. N. Basu, *Electromagnetic Theory and Applications in Beam-Wave Electronics*, Singapore: World Scientific, 1996.
- S. Y. Liao, *Microwave Electron-Tube Devices*, Englewood Cliffs, NJ: Prentice-Hall, 1988.
- A. S. Gilmour, Jr., *Microwave Tubes*, Dedham, MA: Artech House, 1986.
- A. W. Trivelpiece, *Slow-Wave Propagation in Plasma Waveguides*, San Francisco: San Francisco Press, 1967.
- H. Guckel, P. A. Brennan, and I. Palocz, A parallel-plate waveguide approach to microminiaturized, planar transmission lines for integrated circuits, *IEEE Trans. Microwave Theory Tech.*, **MTT-15**:468–476 (1967).
- H. Hasegawa, M. Furukawa, and H. Yanai, Properties of microstrip line on Si-SiO₂ system, *IEEE Trans. Microw. Theory Tech.*, **MTT-19**:869–881 (1971).
- J. Jaffe, A high-frequency variable delay line, *IEEE Trans. Electron Devices*, **ED-19**:1292–1294 (1972).
- D. Jäger, Slow-wave propagation along variable Schottky-contact microstrip line, *IEEE Trans. Microw. Theory Tech.*, **MTT-24**:566–573 (1976).
- A. Podell, A high directivity microstrip coupler technique, *1970 G-MTT Symp. Digest*, pp. 33–36, 1970.
- T. Sugiura, Analysis of distributed-lumped strip transmission lines, *IEEE Trans. Microw. Theory Tech.*, **MTT-25**:656–661 (1977).
- T. Kitazawa and R. Mittra, An investigation of striplines and fin-lines with periodic stubs, *IEEE Trans. Microw. Theory Tech.*, **MTT-32**:684–688 (1984).
- K. Wu and R. Vahldieck, Hybrid-mode analysis of homogeneously and inhomogeneously doped low-loss slow-wave coplanar transmission lines, *IEEE Trans. Microw. Theory Tech.*, **MTT-39**:1348–1360 (1991).
- Y. R. Kwon, V. M. Hietala, and K. S. Champlin, Quasi-TEM analysis of “slow-wave” mode propagation on coplanar microstructure MIS transmission lines, *IEEE Trans. Microw. Theory Tech.*, **MTT-35**:545–551 (1987).
- R. F. Harrington, *Field Computation by Moment Methods*, Malabar, FL: Krieger, 1982.
- H. Y. Lee and T. Itoh, Phenomenological loss equivalence method for planar quasi-TEM transmission lines with a thin normal conductor or superconductor, *IEEE Trans. Microw. Theory Tech.*, **MTT-37**:1904–1909 (1989).
- F. J. Glandorf and I. Wolff, A spectra-domain analysis of periodically nonuniform microstrip lines, *IEEE Trans. Microw. Theory Tech.*, **MTT-35**:336–343 (1987).
- K. Wu, V. Dzuganov, and P. Saguet, Complete theoretical and experimental analysis on properties of planar periodic waveguides, *IEE Proc.*, **135**:27–33 (1988).
- K. Wu, et al., The influence of finite conductor thickness and conductivity on fundamental and higher order modes in Miniature Hybrid MIC's (MHMIC's) and MMIC's, *IEEE Trans. Microw. Theory Tech.*, **MTT-41**:421–430 (1993).
- K. Wu, New prospective coplanar metal-insulator-semiconductor (MIS) monolithic structure, *Electron. Lett.*, **24**(5):262–264 (1988).
- C. Y. E. Tong and K. Wu, Propagation characteristics of thin film superconducting microstrip line for terahertz applications, *Electron. Lett.*, **27**:2299–2300 (1991).
- C. M. Krowne and E. J. Cukauskas, GaAs slow-wave phase shifter characteristics at cryogenic temperature, *IEEE Trans. Electron. Dev.*, **ED-34**:124–129 (1987).
- W. Heinrich and H. L. Hartnagel, Wave propagation on MESFET electrodes and its influence on transistor gain, *IEEE Trans. Microw. Theory Tech.*, **MTT-35**:1–8 (1987).
- K. S. Giboney, M. J. W. Rodwell, and J. E. Bowers, Traveling-wave photodetector theory, *IEEE Trans. Microw. Theory Tech.*, **MTT-45**:1310–1319 (1997).
- M. J. Lancaster, et al., Miniature superconducting filters, *IEEE Trans. Microw. Theory Tech.*, **MTT-44**:1339–1346 (1996).
- H. Hasegawa and S. Seki, Analysis of interconnection delay on very high-speed LSI/VLSI chips using an MIS microstrip line model, *IEEE Trans. Microw. Theory Tech.*, **MTT-32**:1721–1727 (1984).

SMALL ANTENNAS

KYOHEI FUJIMOTO
University of Tsukuba
Tsukuba, Japan

1. GENERAL

What is a small antenna? This question then leads to another question. How small is small in small antennas? When one looks at a millimeter-wave horn antenna of a palm size (Fig. 1), the antenna is said to be small, simply because the physical size is small. On the other hand, when one takes a look at a photo of Marconi's antenna used for the first transoceanic communication in 1901 (Fig. 2), the antenna is surely said to be "a quite big antenna." The Marconi's antenna had a vertical fan-like structure supported by a horizontal wire stretched between two masts about 48 meters high and 60 meters apart [1]. It is natural that smallness might be judged by its physical dimensions. However, smallness of an antenna is not only viewed by the physical size, but also the electrical size defined in comparison with the operating wavelength. When the aperture size of a millimeter-wave horn antenna is much larger than the operating wavelengths, it is not called small, but large in terms of the electrical size, although the physical size is small. In turn, the Marconi's antenna can be said to be small in terms of the wavelength, because it is measured to be about one-tenth of the operating wavelength. Use of the electrical size often is more meaningful than the physical size, because the antenna characteristics and performances are more reasonably dealt with in terms of the operating wavelength.

The smallness of an antenna can be viewed in other ways. For example, low-profile antennas such as the Inverted-L antenna [Fig. 3(a)], planar antennas such as the patch antenna, microstrip antenna (MSA) [Fig. 3 (b)], and so forth, may be classified into small antennas, as the height or thickness, one part of these antennas, is constrained to an electrically small size. In this case, the term "physically constrained small" is considered appropriate.

Another way to classify an antenna as being small is an attribute of its functions. When an antenna has attained either additional functions or enhanced performances without significant change in its dimensions, the antenna is said to be equivalently small, as the corresponding functions would not otherwise be obtained without enlarging the dimension. An example is a case where beam steering function (Fig. 4) is endowed to an antenna without any change in the dimensions; that is to say, the antenna of smaller dimensions is altered to give a beam

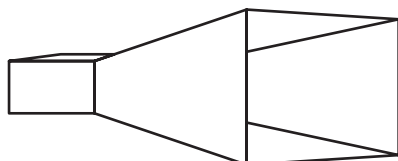


Figure 1. Microwave horn antenna.

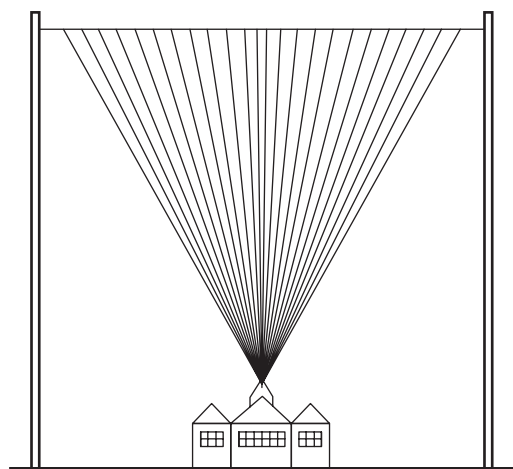


Figure 2. Marconi's first transoceanic communication antenna.

steering function, which cannot be realized by smaller antennas. This type of antenna is classified into "functionally small antenna."

Then small antennas are categorized into four types [2]: Electrically Small Antenna (ESA), Physically Small Antenna (PSA), Physically Constrained Small Antenna (PCSA), and Functionally Small Antenna (FSA). Although one uses four categories, the classification is not necessarily distinct, so that one class of antenna can be classified into more than one class; for instance, when a patch antenna has the edge (radiating aperture) of one-fifth wavelength in its peripheral, the antenna is referred to as both ESA and PCSA.

Two major subjects exist in small antennas: (1) investigation of characteristics and performance of small antennas, and (2) exploitation of methods to attain small antenna, particularly ESA. The former is mainly concerned with fundamentals of electrically small antennas. The essentials of small antennas have long been studied by many investigators; however, many problems must still be solved. Among them, limitations of small antennas is the most significant and interesting subject remaining of the important problems. It is directly concerned with how to realize small antennas with reasonably high gain or broad bandwidth. The physical limitation was first discussed by Wheeler [3] and then Chu [4], in 1947 and 1948, respectively. Since then, small antenna problems have been discussed among many investigators, particularly regarding

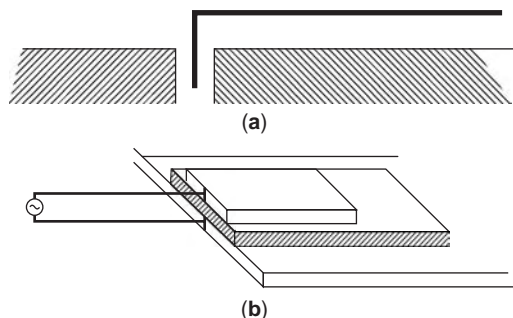


Figure 3. Low-profile antennas. (a) Inverted-L antenna. (b) Patch antenna.

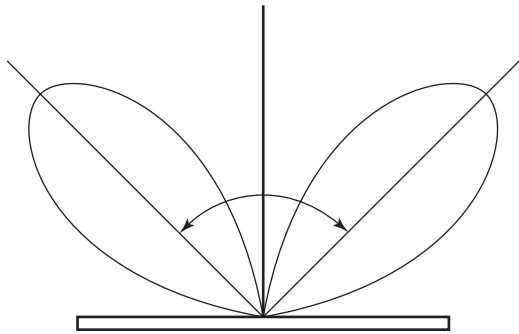


Figure 4. Beamsteering antenna.

antenna quality factor Q , gain, bandwidth, and efficiency [5–10] in conjunction with the limitation.

Meanwhile, various efforts to accomplish practically useful small antennas have continuously been made, and at the same time, attempts were made to realize antennas having performance as close as possible to the limitations. Among them, realization of ESA has been a continuously interesting one in the field of antennas and communications, because small antennas have been required for a variety of wireless systems and downsizing of systems subsequently demand downsizing of antennas rather urgently at the same time. Recent progress in miniaturization of electronic components, devices, and thus circuitries is notable, whereas antenna sizes have not necessarily followed it. The concept of downsizing in antennas is essentially different from that of other electronic components or devices, because antenna problems are inherently concerned with the physical nature of electromagnetic waves in open space, whereas circuitry is concerned with problems within closed space.

Nevertheless, there have been increasing demands for small antennas in a variety of situations. The most urgent requirements in recent years are for the fields of mobile communications, where the number of small terminals such as mobile phones has explosively increased and the antennas for such mobile terminals are required to be not only small, but also to be built into the unit, and yet to have higher or at least similar performance without appreciable degradation. In practice, gain and bandwidth should be maintained the same as that before the size reduction. Furthermore, with the advancement of systems, there have often been encountered the need for antennas that have capability for multiple-band or wideband operation for some systems. Other growing demands also have developed in various wireless systems, which are applied to transmission of not only information, but also data, video signals, and control signals. A typical example is the wireless LAN (Local Area Network) system, including indoor as well as outdoor networks. Another important requirement is for reception of the Digital Television (DTV) broadcasting. Small, wideband and yet reasonably high-gain antennas are demanded. The demands are not only outdoor and indoor antennas, but also vehicle-mount antennas, which should be as small and light as possible. Diversity or adaptive control function is inevitable for vehicle antennas.

Various types of small antennas have so far been developed. Planar and low-profile antennas are typical. Practical examples are Planar Inverted-F antenna (PIFA) [Fig. 5(a)], patch antennas, and microstrip antennas (MSA) [Fig. 5(b)], whereas examples of linear antennas are Normal Mode Helical Antennas (NMHA) [Fig. 5(c)], Meander Line Antennas (MLA) [Fig. 5(d)], Inverted-L antennas (ILA), and so forth. Materials such as ferrites and dielectrics are used to reduce the antenna size. Ceramic Chip Antennas (CCA) [Fig. 5(e)] and ferrite coil antennas [Fig. 5(f)] are practical examples. Among them, a very small Ceramic Chip Antenna exists made up with dimensions of several-millimeter square for applications to small mobile terminals in 1–5 GHz frequency regions, which is considered the physically smallest antenna to be used for small mobile terminals that can be produced by the present state of the art.

2. DEFINITION

“Small antennas” are categorized into four types according to the dimensions or the functions: Electrically Small Antenna (ESA), Physically Constrained Small Antenna

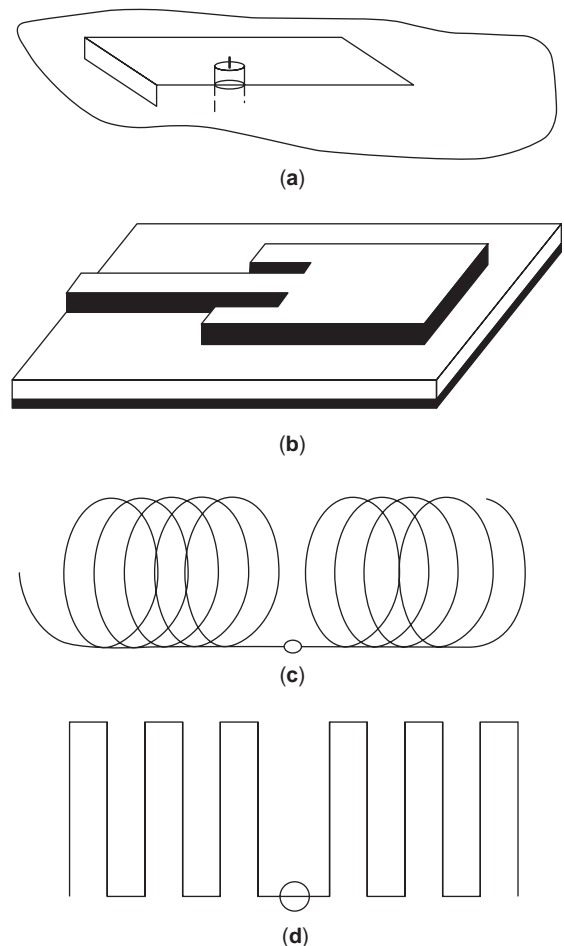


Figure 5. Various examples of small antenna. (a) Planar inverted-F antenna. (b) Microstrip antenna. (c) Normal mode helical antenna (NMHA).

(PCSA), Functionally Small Antenna (FSA), and Physically Small Antenna (PSA) [2].

- ESA is an antenna that has much smaller dimensions as compared with the wavelength. Conventionally, an antenna that has a much smaller volume than a virtual sphere, called “radian sphere” having radius r of $\lambda/2\pi$ (λ : wavelength) (Fig. 6), is referred to as ESA [11]. The radius of $\lambda/2\pi$ is significant in small antenna, because near space around a small antenna is occupied mainly by the stored energy of its electric field or a magnetic field, and the surface of the radian sphere is the transition region from where the energy flow produced by the small antenna changes mainly to the radiation energy.

However, two other terms were previously proposed to define ESA: (1) when an antenna has its greatest dimension less than one-tenth of wavelength [12] and (2) when it has less than one-eighth λ [13]. Although a radian sphere is referred to in the definition of ESA, an antenna may no longer be said to be ESA when it has a length equal to the diameter of the radian sphere; that is, $2 \times \lambda/2\pi$ (0.32λ). Thus, it is reasonable to say that an antenna having the size less than one-tenth λ should be classified to be ESA.

- PCSA is an antenna that is not necessarily categorized as an ESA, but has a shape that has considerably reduced size in one part of the antenna. A low-profile antenna with the height of say one-fiftieth λ or so, like a small MSA, can be classified into PCSA.
- FSA is an antenna that has additional functions or higher performance than an antenna with the same or smaller dimensions. FSA may not necessarily satisfy the above two categories, ESA and PCSA. For instance, an antenna accomplishing a beam steering function that would ordinarily be realized by an antenna of greater dimensions can be classified into FSA.
- PSA is an antenna that is not categorized in any of the above, but still regarded as small in a relative sense; that is, an antenna is judged to be small by its appearance. When the volume is bounded by 30 cm or

less in one length, the antenna can be called PSA. No strict physical meaning exists in the definition of PSA. An example is a microwave horn antenna, which can be placed on a palm. An MSA can be PCSA and also PSA.

These definitions cannot be analytically formulated in practice, because an antenna may be differently classified depending on the practical situation. For instance, when a short monopole categorized as ESA is placed on a rectangular conducting plate of one-quarter λ , as shown in Fig. 7, radiation performance of the monopole may be enhanced, as the effective length is extended by the addition of the conducting plate. Then one may consider that the addition of the conducting plate to the monopole antenna forms a new size-extended antenna system, which no longer belongs to ESA. In other words, performance of an ESA can be enhanced with assistance of a conducting material besides the antenna element. A small chip antenna placed on the ground plane in a small mobile terminal is a typical example.

3. REQUIREMENTS FOR SMALL ANTENNAS

General requirements for small antennas are listed below.

- (1) General
 - dimensions (small)
 - light weight
 - compactness
 - low profile
 - built-in
 - low cost
 - easy construction
- (2) Electrical performances
 - gain (high) *1
 - efficiency (high)*1
 - bandwidth (wide)*1
 - low interaction (desired)*1
 - radiation pattern (desired)*2
 - polarization *2

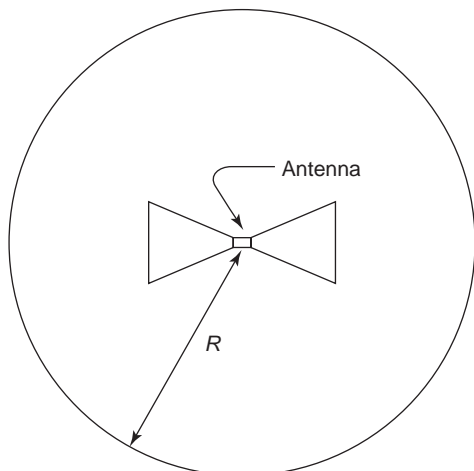


Figure 6. Radiansphere.

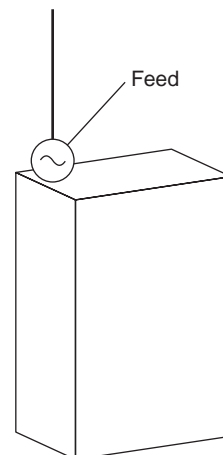


Figure 7. A monopole mounted on a rectangular conducting box.

*1 as high/wide/low value as obtainable

*2 realization as is expected

4. MAJOR SUBJECTS RELATED WITH SMALL ANTENNAS

One of the practical and indispensable problems that concern small antennas is the study of the limitation of antennas and another is how to realize small antennas, especially ESA. Study of the limitation is particularly important because knowledge of the limitation is necessary as a guiding principle when development of a new antenna is attempted or small antennas are designed.

The physical limitation of small antenna was first discussed by Wheeler [3], and then by Chu [4], followed by Harrington [8], Hansen [9], McLean [10,11], and Grimes [12]. Recently, Geyi has shown an extended theory of limitation [13] from Chu's theory to include cases for arbitrary geometry and excitation of antennas and discussed the minimum Q and the largest G/Q in antennas.

The essential problem regarding Q is the relationships between antenna size and the lowest bound of antenna Q , which is the inverse of the bandwidth. Antenna designers often encounter practical problems asking how wider bandwidth or how higher efficiency could be obtained with a given size of small antenna. Thiele treated problems of Q based on the superdirective theory, as a small antenna is essentially a superdirective antenna. He obtained a lowest bound of Q in practical point of view and verified why practical antennas do show much higher Q than the theoretically lowest Q by showing some examples of typical antennas [14].

Recent needs for small antenna are urgent, as the downsizing in wireless systems has advanced rapidly and antennas to be applied to these systems should also meet the requirement that is downsizing. It is well known that the smaller the antenna size, the lower the radiation efficiency and narrower the bandwidth. The practical problem is how to keep the antenna performance unchanged or equivalent, even though the size is made smaller. Antenna designers must design antennas that satisfy the requirements, even when the size becomes smaller. With knowledge of the limitation, antenna design turns out to be an effort on how to approach a limitation as closely as possible, for instance, how to obtain wider bandwidth with a given small-sized antenna.

The fundamental concepts of making an antenna small in practice are (1) filling space (two or three dimensionally) effectively that encloses the antenna, (2) realizing uniform current distributions on the antenna element, (3) increasing radiation modes, (4) making self-resonance within an antenna system, and (5) adding functions.

The concept of filling space is based on Chu's theory, in which he derived minimum Q of a small antenna enclosed in a radian sphere. In practical antennas, the minimum Q can hardly be realized without fully using the volume of the sphere. As small dipoles or loops do not use the spherical volume effectively, their lower bound of Q is relatively high and, hence, the theoretically obtainable wideband characteristics can never be realized. In order to overcome the inherent narrow bandwidth problem in small anten-



Figure 8. A uniform current distribution on a small dipole antenna.

nas, filling space effectively enclosing an antenna as much as possible is significant and useful. Space is not necessarily three dimensional, but also two or one dimensional depending on an antenna structure. For example, fractal antennas may have fairly wide bandwidth, as they can occupy the space two dimensionally surrounding the antenna.

Chu also had shown that the ideal current distribution to attain the maximum gain is uniform (Fig. 8) [4]. However, uniform distribution on a dipole cannot ordinarily be realized by a small antenna structure, because current distribution goes to zero toward the end of an antenna element. The current distribution on a small dipole is assumed to be a triangular shape with zero at the end of the element (Fig. 9). One way to obtain uniform current distribution is to load an impedance component. The most popular example is top loading. The longer the linear antenna size is, the nearer the current distribution approaches to uniform, as the distribution is gradually changed more smoothly than a shorter antenna, which is usually assumed to be triangular. By using a traveling wave structure, an equivalently long antenna structure can be attained.

Integration technique, by which an antenna system is constituted with combination of devices or circuitry and an antenna, is another method to obtain uniform distribution, although it may not be perfect, but nearly uniform.

Increasing radiation mode is another important method. Hansen discussed in [9] that antenna Q will be reduced by half with excitation of TE and TM modes at the same time.

Achieving self-resonance in an antenna structure is an important concept of making an antenna small. If self-resonance is attained in a small antenna, one may increase radiation efficiency or avoid the degradation because of loss in the matching circuitry. Without using a reactive matching component with loss, connection between an antenna and the RF front end can be made simple and cost effective.

Self-resonance can be accomplished by (1) loading techniques, (2) using traveling wave structures, and (3) applying IAS (Integrated Antenna Systems) techniques.

Loading of an impedance component, including an antenna element, is essentially to change the current distributions on the antenna element so that the resonance condition is attained. Loading of a conjugate impedance is



Figure 9. A triangular current distribution on a dipole antenna.

to attain resonance for a wide frequency range, that is, wide bandwidth. Complementary structures do not only aim at achieving self-resonance condition, but also obtaining frequency-independent characteristics.

By adding function into an antenna, either enhancement of antenna performance or improvement of antenna characteristics can be expected. It depends on the functions to be integrated into an antenna system. If integration of amplification function could result in the increase of the antenna gain, it would conversely mean the reduction of an antenna size with the gain kept unchanged.

The integration technique may bring evolutionary antenna systems that cannot be realized by the conventional method. Either passive or active integration, or a combination, are possible, and either improvement of antenna characteristics or enhancement of antenna performance could be expected as a result of integration. Typical examples are enlargement of bandwidth, improvement of radiation efficiency, control of radiation patterns, and so forth. Enhancement of antenna performance or improvement of antenna characteristics may bring novel antennas with small size that cannot practically be realized by conventional antennas, although sometimes it would not be as easy as expected.

Application of nonmetallic materials to reduce an antenna dimensions and/or enhance antenna performance is also another important method, by which not only realizing very small antennas, but also having high-efficiency small antennas would be possible.

Realizing small antennas is, in other words, achieving either wider bandwidth or higher efficiency while maintaining the antenna size unchanged.

The practical systems sometimes require a very small antenna to fit to the unit having very small size. Antenna designers thus should attempt to realize an antenna having the practically obtainable performances for the required size, although some difficulty may still exist.

5. PROPERTIES OF SMALL ANTENNAS

5.1. General

Small antennas have some characteristics that distinguish them from ordinary antennas. A very small antenna can be considered essentially as an electric dipole or a magnetic dipole, and the reactive impedance is highly capacitive or inductive, whereas the resistive impedance is very small. With this impedance characteristic, particular care must be taken for small antennas. If the length of a dipole is shorter than one-tenth λ , a perfect match to the load of $50\ \Omega$ is very difficult. However, it is interesting to note that the effective aperture of it is about $0.119\ \lambda^2$ [Fig. 10(a)], when the antenna is perfectly matched, which is only an 8.5% smaller value than that of the one-half λ dipole, the effective aperture of which is $0.13\ \lambda^2$ [Fig. 10(b)] [15], which can be understood by inspecting the flow of the Poynting vector into a small antenna, as shown in Fig. 11 [16]. The figures illustrate cases for when (a) a short dipole is not matched, so the energy passes through the antenna, resulting in no energy absorption, (b) a very

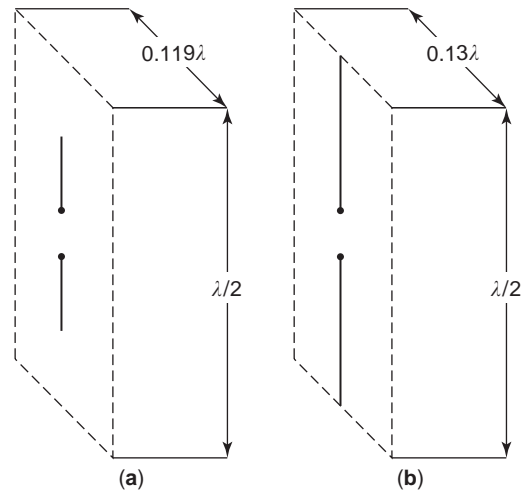


Figure 10. Effective aperture. (a) A small dipole. (b) A half-wave dipole.

short dipole is perfectly matched and the incoming energy is efficiently absorbed, and (c) a matched one-half λ -dipole is used.

In practice, however, matching of a small antenna to the load of $50\ \Omega$ is not so easy, because the input impedance has inherently very low radiation resistance and very high reactive impedance. Matching to the load of $50\ \Omega$ thus needs a high conjugate reactance component to compensate the high antenna reactive impedance and a transformer to transform the low antenna resistance to $50\ \Omega$. When a small antenna is a type of electric dipole, high radiation efficiency may not be expected even if perfect matching could be attained.

The radiation efficiency η is given by

$$\eta = R_{\text{rad}} / (R_{\text{rad}} + R_{\text{loss}}) \quad (1)$$

where R_{rad} denotes the radiation resistance and R_{loss} is the loss resistance, which is composed of $R_{\text{L}a}$ and $R_{\text{L}c}$ existing in the antenna and the matching circuit, respectively. In a small electric dipole antenna, the reactive component of the input impedance is capacitive, so an inductive impedance is required for matching. When the dipole is a short stub of $0.16\ \lambda$ with thickness of $3.3 \times 10^{-4}\ \lambda$, R_{rad} is $0.1\ \Omega$ and X_{rad} (input reactance impedance) is $-2071\ \Omega$. In order to achieve matching, an inductive component of $2071\ \Omega$ is used. When Q_{L} of this component is 100, $R_{\text{L}c}$ is $20.7\ \Omega$. The radiation efficiency η in this case is about 0.005, or 0.5%. With Q_{L} of 400, η increases to 0.019, or 1.9%, which is still very low. A loss resistance because of the inductive component, which is used for the matching circuit, may far exceed the radiation resistance and, consequently, causes low radiation efficiency. It will become a serious problem in designing a small dipole antenna, as very small size is required.

Meanwhile, when a small magnetic dipole of the circumference $0.1\ \lambda$ with the same thickness as the above dipole is used, η is 9.28% with $Q_{\text{L}c}$ of 1000. If $Q_{\text{L}c}$ is 4000, η becomes 21.1%. As a capacitive component can give higher Q than that of an inductive component (a coil), a small

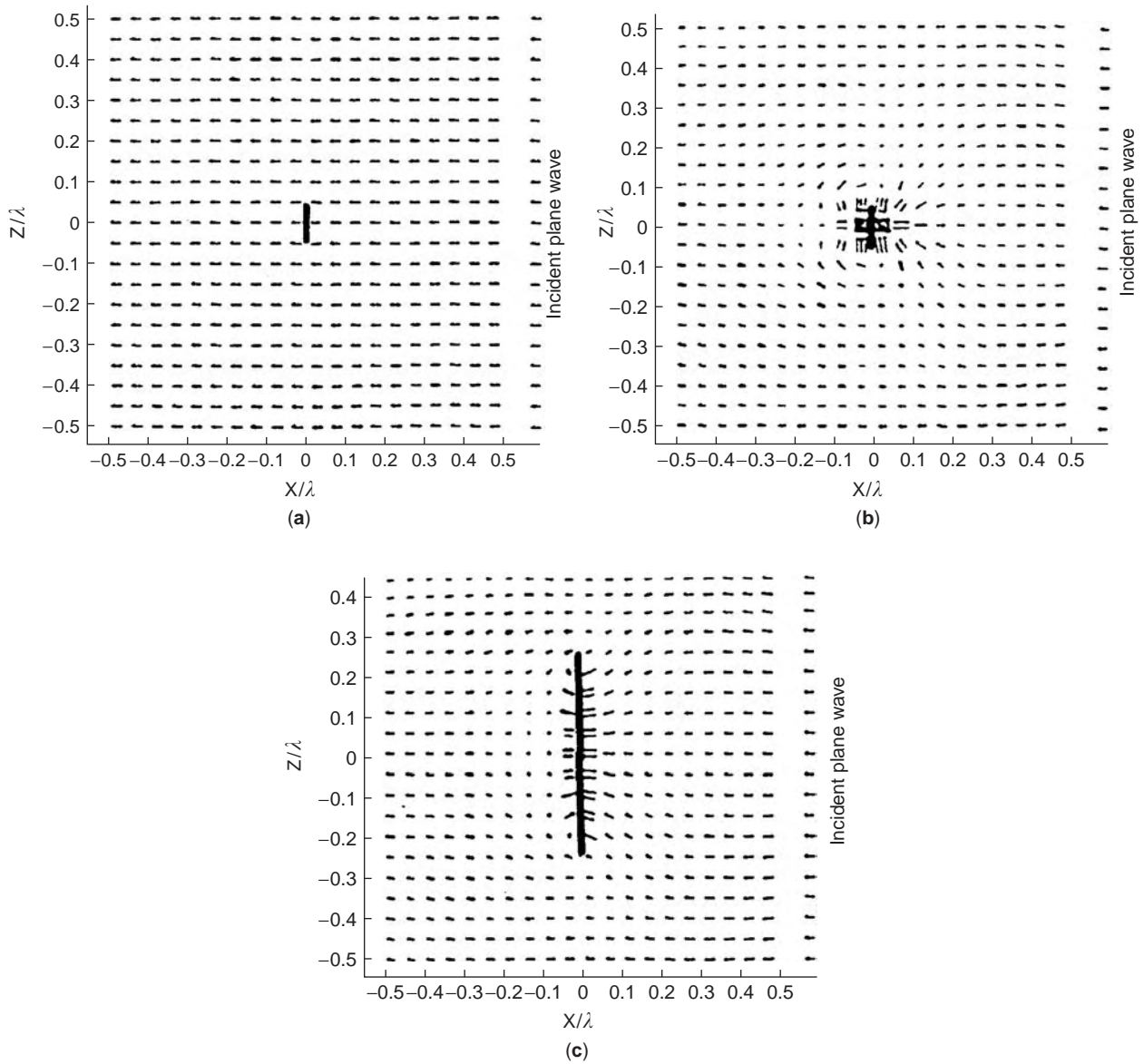


Figure 11. Poynting vector flow in the vicinity of a dipole antenna. (a) A small antenna is not matched. (b) A small antenna is perfectly matched. (c) A half-wave dipole is matched. (From Ref. 16 with permission from Wiley and IEICE.)

magnetic dipole is preferred in order to obtain higher radiation efficiency when about the same size of small antenna is required.

Gain G of an antenna is defined by

$$G = \eta D M \mathbf{p} \tag{2}$$

where D is the directivity, M is the impedance matching factor, and \mathbf{p} is the polarization matching factor. M is given by using the reflection factor Γ at the input terminals as

$$M = 1 - |\Gamma|^2 \leq 1 \tag{3}$$

$$= 4S / (1 + S)^2 \tag{4}$$

where S is VSWR and related with Γ by

$$S = (\Gamma + 1) / (\Gamma - 1) \tag{5}$$

The polarization factor \mathbf{p} is given by

$$\mathbf{p} = |\rho_H, \rho_E|^2 = |\cos \phi_p|^2 \leq 1 \tag{6}$$

where ρ_H and ρ_E are unit vectors of the wave with horizontal and vertical polarization, respectively, and ϕ_p is the angle between the two vectors. Here, the electric fields E_H and E_E of incoming waves, respectively, are described as

$$\mathbf{E}_H = \rho_H E_H \tag{7}$$

$$\mathbf{E}_E = \rho_E E_E \tag{8}$$

Gain of a very small antenna is determined almost by η and M , because D is 1.5 [4] without regarding the size, and p is usually taken as unity, because polarization matching is made in almost all cases. The radiation efficiency η of a dipole shown above was for cases where $M = 1$. If $M \neq 1$, the gain G is lowered as M decreases.

Another important factor in small antennas is Q . Q , in general, is defined as

$$Q = 2\omega X / \text{Prad} \tag{9}$$

where X denotes the reactive energy stored in an antenna, $\omega = 2\pi f$ (f : frequency), and Prad expresses the radiated power from an antenna. When Q is smaller than 10, the reverse of Q can be taken to be the bandwidth B . Either Q or bandwidth B is an essential factor in small antenna design, because in small antenna, Q rapidly increases, and as a consequence, bandwidth B decreases rapidly, as the size of antenna reduces. The lowest Q or highest obtainable B , and the highest possible G/Q have been studied by many investigators. Chu calculated G and Q of a linearly polarized omnidirectional antenna by using spherical mode expansions, by which the fields around the hypothetical antenna enclosed by a sphere of radius (a) are expressed [4]. He discussed about the possibility of wide bandwidth with an antenna of the maximum dimensions of $2r$ when the gain is equal to or less than $4r/\lambda$, which is the gain obtained by a current distribution of uniform amplitude and phase along a line of the length $2r$. He also mentioned that efficient use of the volume of the hypothetical sphere is essential for realizing the minimum Q , thus the wide bandwidth. Chu showed the directivity of a small antenna was 1.5, independent of the size. Later, Hansen discussed the limitation of antennas [9] and mentioned that the minimum obtainable Q shown by Chu could only be approached and never be equaled. He illustrated minimum obtainable Q with respect to the size (kr) of an antenna, as Fig. 12 shows. In the figure, Q 's for dipoles of both thin and thick radius and Goubau's antenna are shown for comparison with the Chu's results. Limitation problems will be described in Section 5.3.

Specialty in small antennas is observed in not only its properties but also the evaluation of the properties, particularly when the size becomes very small. The instrument itself for the measurements may disturb the antenna characteristics or the performance when the size is similar or larger compared with the antenna size. Errors in the measurement may often be observed especially when a small antenna has complicated structure, as proper connection of instrument to the antenna may hardly be made. These problems will be discussed in Section 5.3.

5.2. Characteristics of Small Antennas

5.2.1. Impedance. Theoretical input impedance Z_{dip} of a thin linear short dipole antenna having the length $2h$ and the thickness $2a$ is given as function of kh by [17]

$$Z_{\text{dip}} = R_{\text{dip}} + jX_{\text{dip}} \tag{10}$$

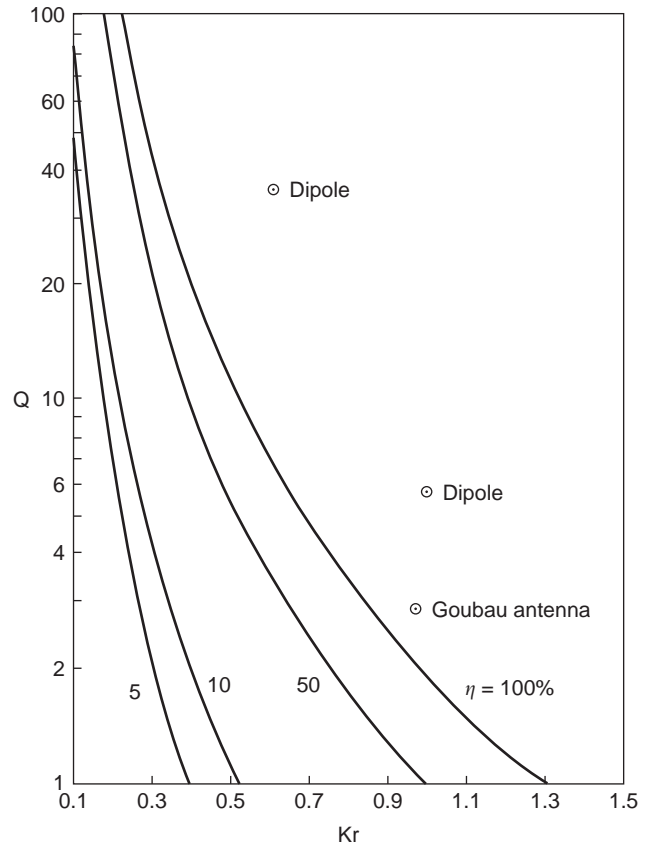


Figure 12. Minimum obtainable Q with respect to antenna dimensions kr . (From Ref. 9 with permission from Wiley and IEEE.)

where

$$R_{\text{dip}} = 20(kh)^2 \tag{11}$$

and

$$X_{\text{dip}} = -j120\{\ln(h/a) - 1\}/kh \tag{12}$$

R_{dip} and X_{dip} with respect to kh are drawn in Fig. 13 [18], where a parameter $\Omega = 2\ln(\frac{2h}{a})$ is used. The resistive component R_{dip} decreases rapidly as kh decreases, whereas the reactive component X_{dip} increases rapidly. When kh is 0.314, i.e., $2h = 0.1\lambda$, R_{dip} is 1.97Ω and X_{dip} is $-3.8 \times 10^3\Omega$.

Theoretical input impedance Z_{loop} of a thin small circular loop antenna having radius (a), and the thickness $2d$ is given by [19]

$$Z_{\text{loop}} = R_{\text{loop}} + jX_{\text{loop}} \tag{13}$$

where

$$R_{\text{loop}} = 20\pi^2(\beta a)^4 \tag{14}$$

$$X_{\text{loop}} = \omega L \tag{15}$$

and

$$L = \mu_0 a [\ln(8a/d) - 2] \tag{16}$$

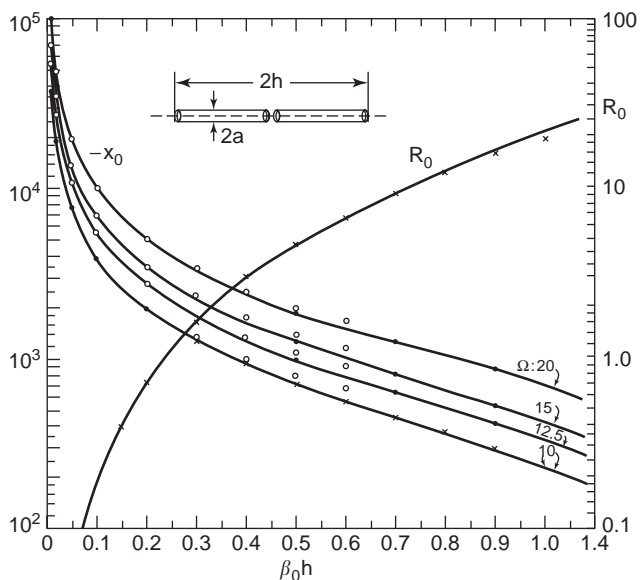


Figure 13. Input impedance of a small dipole. (After Ref. 18.)

Resistive component R_{loop} and inductive component L are shown in Fig. 14 (a) and (b), respectively. When (a) is 0.05λ and the thickness is 0.005λ , R_{loop} is 15.8Ω , and X_{loop} is 202Ω .

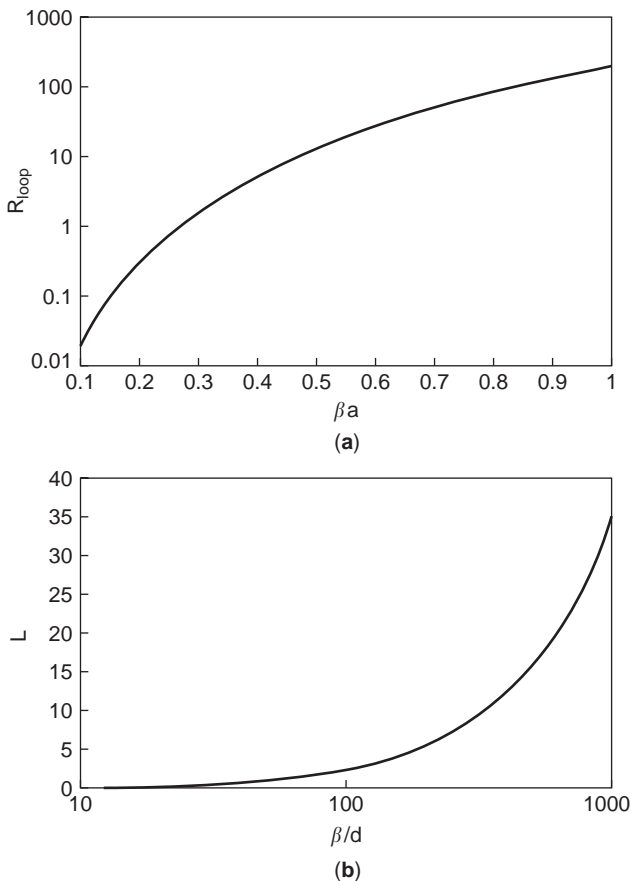


Figure 14. Input impedance of a small loop.

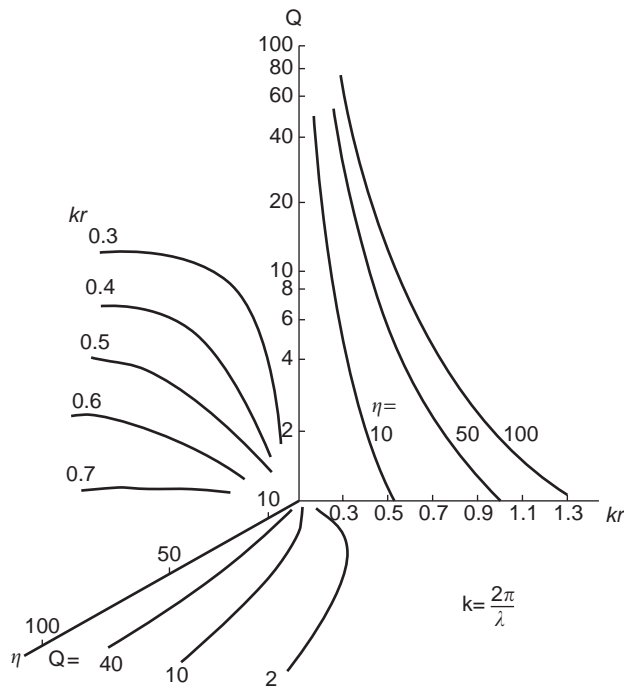


Figure 15. Relationships between Q , η , and kr modified from the graph in Fig. 12.

5.2.2. Bandwidth. The bandwidth Δf is the range of frequencies on either side of a center frequency, at which the antenna characteristics, such as impedance, gain, radiation efficiency, and so forth, are within an acceptable range of those at the center frequency. For narrowband antennas like small antennas, a ratio of $\Delta f/f_0 = B$ is defined as

$$B = \Delta f / f_0 = (f_1 - f_2) / f_0 \tag{17}$$

where f_1 and f_2 , respectively, are the higher and the lower frequencies at which the power declines 3 dB from the

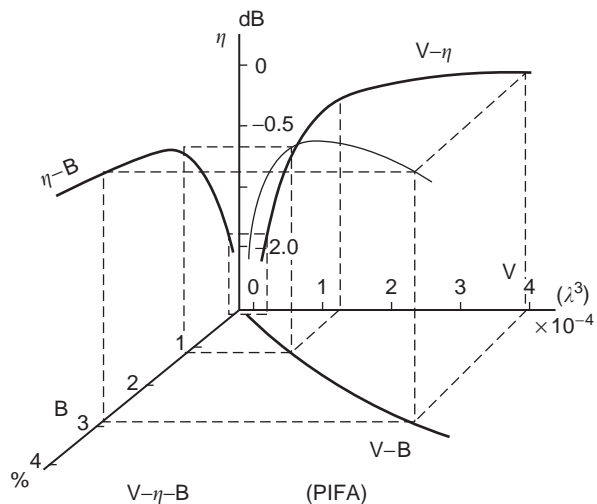


Figure 16. Antenna volume V , relative bandwidth B , and efficiency η of a practical PIFA.

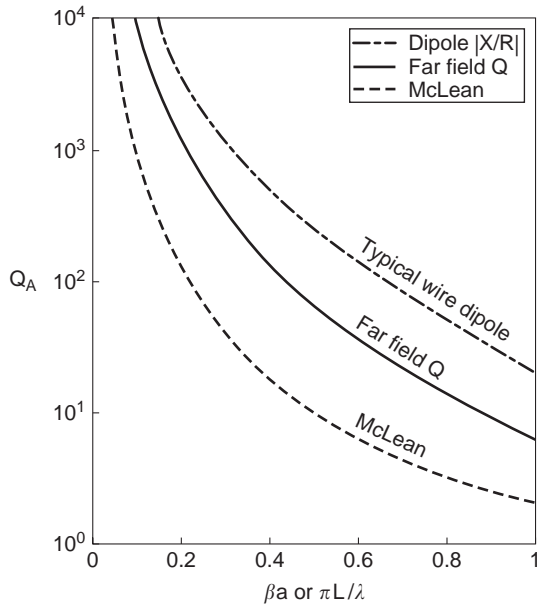


Figure 17. Radiation Q with respect to antenna dimensions (βa and L/λ): McLean's curve is the lower bound for an ideal dipole, which has a uniform current distribution. Far-field Q is the lower bound for a dipole with sinusoidal current distribution. Top curve is a typical radiation Q for a thin wire dipole. (From Ref. 14 with permission from IEEE.)

maximum and f_0 is the center frequency of the bandwidth Δf . This B is referred to as the relative bandwidth and is practically used instead of the bandwidth Δf . The center frequency f_0 is given by

$$f_0 = (f_1 + f_2)/2 \tag{18}$$

Quality factor Q can be used instead of the relative bandwidth B when the bandwidth Δf is narrow ($B \ll 10\%$),

$$B = 1/Q \tag{19}$$

Q of an antenna is generally defined as [20]

$$Q_A = 2\omega W_e / Pr, \quad W_e > W_m \tag{20a}$$

or

$$Q_A = 2\omega W_m / Pr, \quad W_m > W_e \tag{20b}$$

where ω is the radian frequency $2\pi f$, Pr is the radiated power, and W_e and W_m , respectively, are the time average

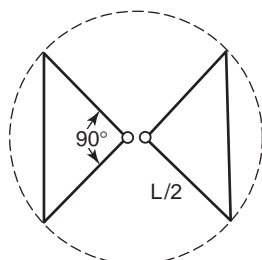


Figure 18. A wire type bow-tie antenna. (From Ref. 14 with permission from IEEE.)

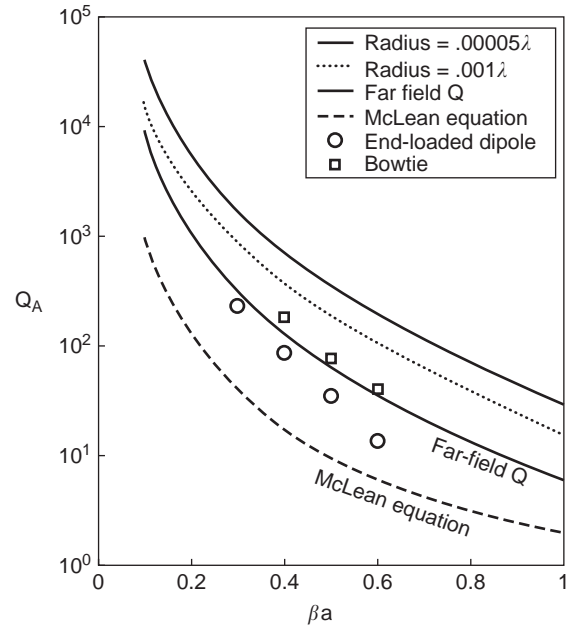


Figure 19. Radiation Q with respect to antenna dimensions (βa): McLean's curve is the lower bound for a ideal dipole, which has a uniform current distribution. Far-field Q is the lower bound for an dipole with sinusoidal current distribution. Top curve is Q for a thin wire dipole obtained by using X/R . Q 's for bow-tie and end-loaded dipole are shown for comparison. (From Ref. 14 with permission from IEEE.)

nonpropagating stored electric energy and the time average nonpropagating stored magnetic energy.

As the size of antenna decreases, Q increases greatly and the bandwidth Δf becomes smaller. Q of a small dipole is expressed by [10]

$$Q = (kr)^{-3} + (kr)^{-1}, \quad kr < 1 \tag{21}$$

where r is the radius of a virtual sphere, which encloses the antenna.

The relationships between the antenna size kr , the relative bandwidth B , and the efficiency η are illustrated by Fig. 15, which is modified from Fig. 12 in [9]. In practical small antennas, variation of Q with respect to the size is

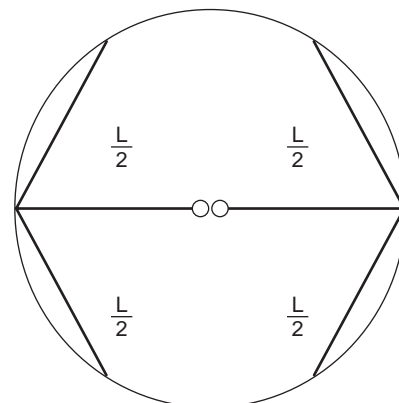


Figure 20. An end-loaded dipole with wire.

not necessarily the same as that of Q shown in Figs. 12 and 15. Figure 16 illustrates an example, showing variation of B and η with respect to the size (volume V) of a practical PIFA (Planar Inverted-F Antenna). In practice, $B(Q)$ increases (decreases) as the volume V of antenna increases (decreases), which seems somehow in conflict with the tendency shown in Fig. 12. The reason for it is that efficiency varies with change of the antenna size as well as the bandwidth, in contrast with the curves shown in Fig. 12, where curves are drawn with constant efficiency.

5.2.3. Radiation Patterns. As the size of antenna becomes small, directivity D_{\max} approaches 1.5, which implies the radiation pattern fills two-thirds of the entire solid angle of a space, and the pattern is simply a donut-shaped $\sin \theta$ pattern.

5.3. Limitation of Small Antennas

The reduction of antenna size imposes a fundamental limitation on the antenna performance. Antennas such as ESA having dimensions much less than the wavelength are subject to the limitations. Fundamental properties of small antennas were first treated by Wheeler [3], as was mentioned previously. Wheeler used the radiation power factor Pr , which was defined as a measure of radiation of a small antenna by taking a ratio of the radiation power to the reactive energy. In his treatment, a small antenna was assumed to have dimensions much smaller than the wavelength and, at most, less than one radiansphere ($= \lambda/2\pi$) in space. In small antennas, because the reactive energy exceeds the radiation power, an antenna is equivalently expressed by either a capacitance C or inductance L , both of which occupy a volume V . He discussed that Pr is proportional to volume and also concerned with antenna shape factor. Radiation efficiency η , which is defined as $Pr/(Pr + P_{\text{loss}})$, where P_{loss} is loss power factor, decreases with antenna size, because Pr is small whereas P_{loss} relatively increases with the size reduction.

Chu showed a fundamental limitation in small antennas by using spherical function expansions, expressing fields with a sum of spherical modes [4]. The antenna was assumed to be enclosed by a virtual sphere (Fig. 6), and the electromagnetic (EM) fields produced by the antenna located in the sphere were expressed with modes in a spherical harmonic series. By using the spherical functions, fields in open space can be treated with radial modes as well as the fields in a closed space like a circular waveguide. In his treatment, no azimuthal variations exist, i.e., the radiation is omnidirectional in the azimuth plane. An equivalent circuit was derived based on the field expressions obtained from mode expansions, from which mode impedance can be derived as a ratio of the mode voltages to the mode currents in the equivalent circuit. The antenna quality factor Q is then obtained for each mode with respect to the antenna dimensions, and the lowest limitation of Q was discussed.

As in small antennas bandwidth is the inverse of Q , the largest bandwidth can be found for antenna dimensions. Chu also showed maximum obtainable gain G and then a ratio of G to Q .

Chu's treatment of small antennas was followed by many investigators, and problems regarding limitations of antenna were subsequently discussed.

Fante worked on the antenna Q based on the spherical wave function expansion for the fields outside the circumscribing sphere of the antenna [21], along with Collin and Rothschild's idea, by which the stored energy was treated as the difference of total field energy and the asymptotic limit of the energy density at infinity [22]. Hansen also discussed limitations of small antennas essentially based on Chu's theory and illustrated relationships between antenna Q and antenna size taking radiation efficiency as the parameter [9]. He had shown that when both TE and TM fields are considered at the same time, Q will become one-half of that of the single mode. McLean improved Chu's theory by deriving an exact result for the antenna Q using the field for TM_{01} mode directly. His results were similar to Chu's; however, he found a slightly higher lower bound on Q for antennas, the length of which is approaching to a length of one-third λ .

Chu and McLean's results provide the lowest Q , however, as this lower bound Q can hardly be realized by a practical antenna, because uniform current distributions on the antenna system should be presumed and also the sphere enclosing an antenna should be used fully by the antenna. Foltz and McLean attempted to overcome this problem by expanding the fields around an antenna using prolate spheroidal functions, instead of spherical functions, and obtained a little higher Q , which was a more practical value than Chu's results. This result can be understood in that a dipole can be better represented by a prolate spheroidal volume than a spherical volume, as it occupies higher fraction of the volume inside the prolate spheroid than a sphere.

Thiele took a different approach to find a lower bound on the radiation Q_A for ESA [14]. His approach is based on the concept of superdirectivity R_{SD} [23], which is defined as the ratio of an integration of the far-field pattern function over all space (i.e., visible + invisible) to an integration over visible space as follows:

$$R_{SD} = \frac{\int_{-\infty}^{\infty} |f(u)|^2 du}{\int_{-\frac{\pi L}{\lambda}}^{\frac{\pi L}{\lambda}} |f(u)|^2 du} \quad (22)$$

where $f(u)$ is the normalized far-field pattern function in u space, $u = (\beta L/2) \cos \theta$, and L is the length of the linear source. Here it is assumed that the source is along the z axis with constant phase and the main beam direction is broadside. R_{SD} is equal to $(Q_A + 1)$ [14] if

$$Q_A = \frac{\int_{-\infty}^{-\frac{\pi L}{\lambda}} |f(u)|^2 du + \int_{\frac{\pi L}{\lambda}}^{\infty} |f(u)|^2 du}{\int_{-\frac{\pi L}{\lambda}}^{\frac{\pi L}{\lambda}} |f(u)|^2 du} \quad (23)$$

However, he discussed validity of using $f(u)$ only in Eq. (22) and then added the element pattern function

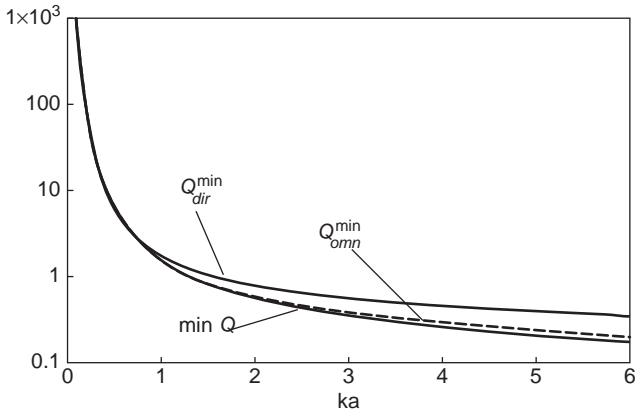


Figure 21. Minimum possible Q and minimized Q. (From Ref. 13 with permission from IEEE.)

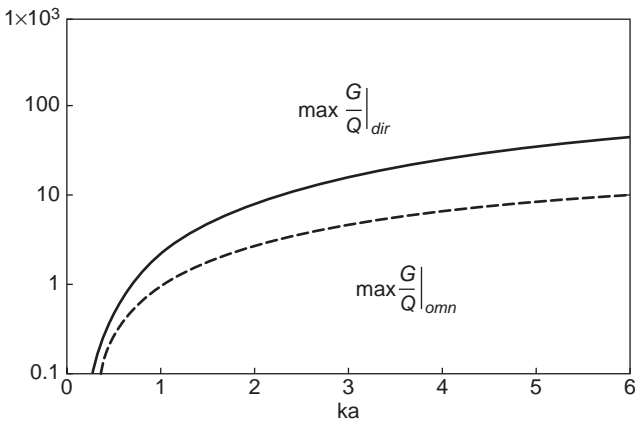


Figure 22. G/Q for antenna with and without directivity. (From Ref. 13 with permission from IEEE.)

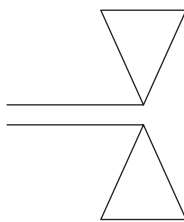


Figure 23. A planar bow-tie antenna.

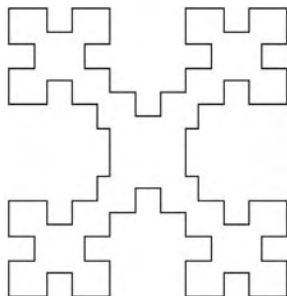


Figure 24. An example of fractal structure.

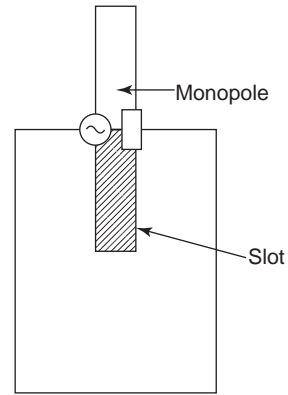


Figure 25. An example of self-complementary structure.

$g(u)$ to $f(u)$ in Eq. (23), whereby consistency with Q_A defined by Eq. (21) is kept. Q_A is then expressed by

$$Q_A = \frac{\int_{-\infty}^{-\pi/L} |E_n(u)|^2 du + \int_{\pi/L}^{\infty} |E_n|^2 du}{\int_{-\pi/L}^{\pi/L} |E_n|^2 du} \quad (24)$$

where $E_u = f(u)g(u)$ normalized field pattern. For a dipole of arbitrary length L along the z axis with a sinusoidal current distribution,

$$E_n(u) = \frac{\cos u - \cos\left(\frac{\beta L}{2}\right)}{\left[1 - \cos\left(\frac{\beta L}{2}\right)\right] \sqrt{1 - \left(\frac{2u}{\beta L}\right)^2}} \quad (25)$$

Examples of radiation Q_A 's obtained by Eqs. (24) and (25) are shown in Fig. 17. A curve on top in the figure is typical radiation Q_A of a thin linear dipole obtained as a ratio of antenna input reactance to antenna input resistance, by using the method of moment. A curve at bottom shows the lower bound Q_A for an ideal or Hertzian dipole, which has uniform current distribution. McLean derived this Q_A by using the lowest order TM mode and that mode only. TM_{01} mode generates fields equivalent to the fields produced by a dipole of uniform current distribution, which corresponds to an ideal dipole. When the current distributions are sinusoidal, the lower bound of radiation Q_A is higher than that of antennas with uniform current

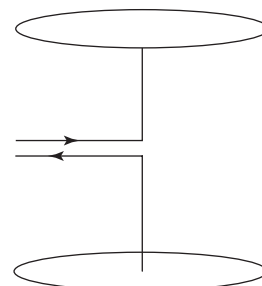


Figure 26. A capacitor plate-loaded dipole.

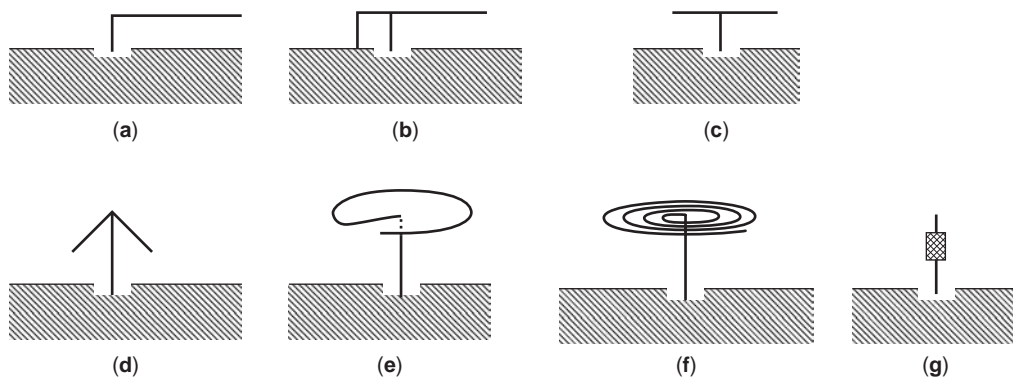


Figure 27. Various examples of loaded monopole on the ground plane. (a) Inverted-L, (b) Inverted-F, (c) T-shaped, (d) Umbrella type, (e) Loop-loaded, (f) Spiral-loaded, and (g) Device integrated.

distributions, which is considered to be a more practical case. The middle curve, denoted “far-field Q_A ,” is obtained by using Eq. (25) for a dipole of a sinusoidal current distribution. The curve is in between the top and the bottom ones. Q_A of a bow-tie dipole, which fits into the spherical volume of radius $L/2$ as shown in Fig. 18, has slightly higher values than the far-field Q_A , as Fig. 19 shows by a curve plotted with \square -symbols. An end-loaded dipole, shown in Fig. 20, has nearly uniform current distribution on the radiating element, so its radiation Q_A lies between McLean’s curve and the typical radiation Q_A , as shown by a curve plotted with \circ -symbols in Fig. 19. With increasing size, current distribution gradually varies to sinusoidal from uniform, and then the Q_A approaches to McLean’s curve. The top two curves show effects of antenna thickness, that is, increasing Q_A with decreasing the

thickness of a dipole antenna. Thiele also discussed Q_A with variation of radiation efficiency.

When an antenna is excited by both of the lowest modes TM_{01} and TE_{01} , the lowest Q , which is one-half that for either mode alone, is obtained [9]. In this case, the field is circularly polarized. The practical example is a case where both a small electric dipole and a small loop are used for the circular polarization. Q of this two-antenna system is one-half that of either the dipole or the loop alone. However, when circular polarization is generated by a cross dipole system with a $\pi/2$ phase difference, the Q will differ from the dipole-loop system and also differ from the Q of either element alone.

Grimes and Grimes have shown that Q of a crossed-Hertzian electric dipole approaches one-third that of a single dipole as the dipole becomes electrically small [12].

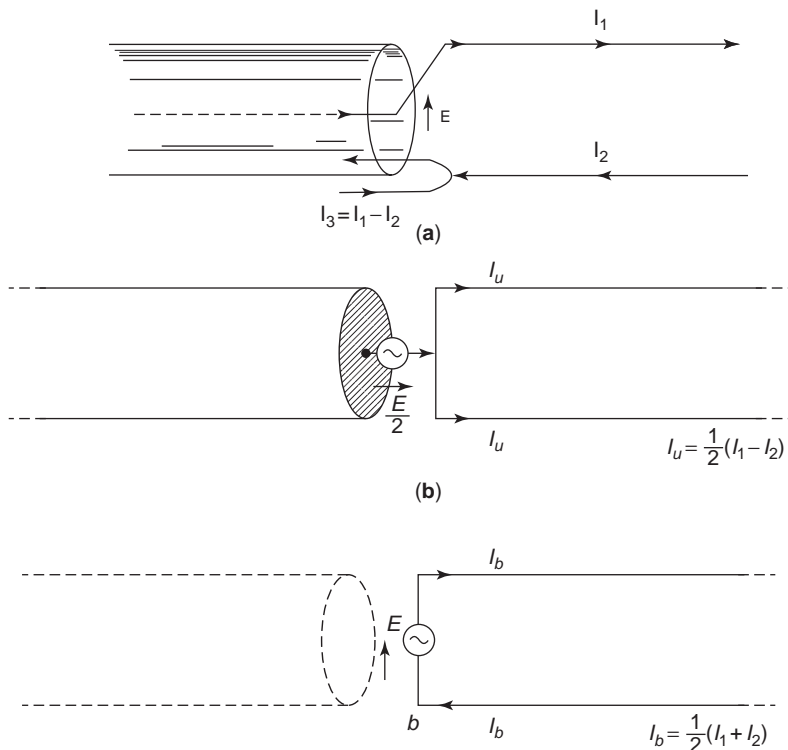


Figure 28. Connection of unbalanced line to balanced line. (a) Direct connection of a coaxial cable to a two-wire transmission line.(b) Equivalent expression of unbalanced mode. (c) Equivalent expression of balanced mode.

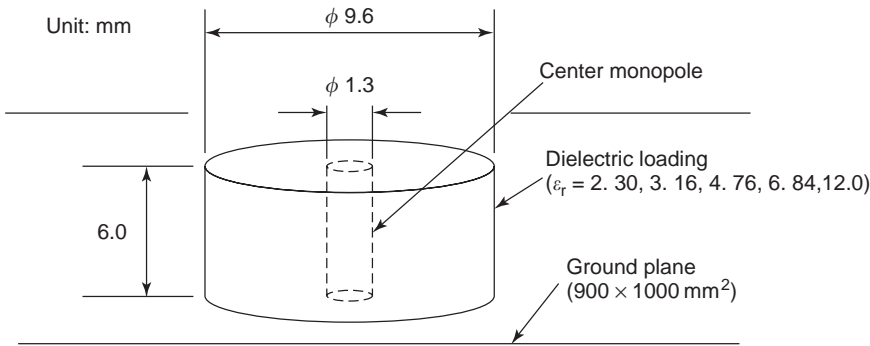


Figure 29. A dielectric material-loaded small monopole antenna used for evaluation of very small radiation resistance. (After Ref. 25.)

They used a time-dependent Poynting theorem. This factor one-third cannot be obtained by using frequency-domain approaches, because the near fields of the two dipoles are coupled and a phase difference exists between them.

Geyi further extended Chu’s theory to include antennas of arbitrary geometry and excitation. He has first derived the minimum possible antenna Q and then the maximum possible ratio of gain G over Q, based on the spherical mode theory. Fante had shown Q for directional antennas previously; however, Geyi examined Fante’s approach and pointed out that was incorrect. He discussed fundamental limitation of antenna by showing minimum possible Q and

maximum possible G/Q for both omnidirectional and directional antennas. They are expressed by [13] for directive antennas,

$$\max \frac{G}{Q}_{dir}^{small} \approx \frac{6(ka)^3}{2(ka)^2 + 1} \quad (26)$$

$$Q_{dir}^{small}|_{small} \approx \frac{1}{ka} + \frac{1}{2(ka)^3}, G_{dir}^{small}|_{small} \approx 3 \quad (27)$$

for omnidirectional antennas,

$$\max \frac{G}{Q}_{omn}^{small} \approx \frac{3(ka)^3}{2(ka)^2 + 1} \quad (28)$$

$$Q_{omn}^{min} \approx \frac{1}{ka} + \frac{1}{2(ka)^3}, G_{omn}^{max}|_{small} \approx 1.5 \quad (29)$$

For small antennas, which are considered here as antennas with the length less than one-eighth λ, the max G/Q and min Q can be achieved simultaneously. Gmax, given by Eq. (27), corresponds to the directivity of an infinitesimally small dipole. Therefore, an omnidirectional antenna, which can achieve maximum bandwidth, has the same directivity as that of an infinitesimally small dipole.

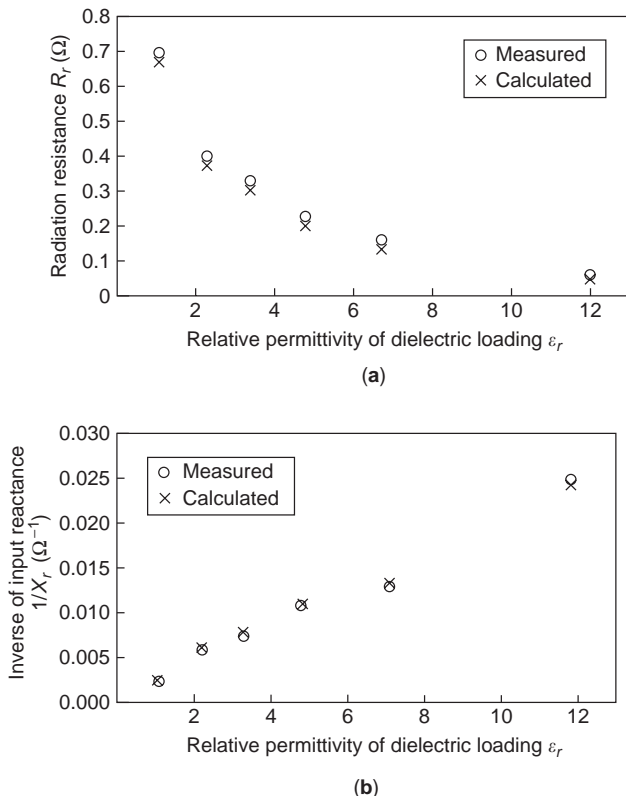


Figure 30. Measured results. (a) Radiation resistance vs. relative permittivity of loaded material. (b) Inverse of input reactance vs. relative permittivity of loaded material. (After Ref. 25.)

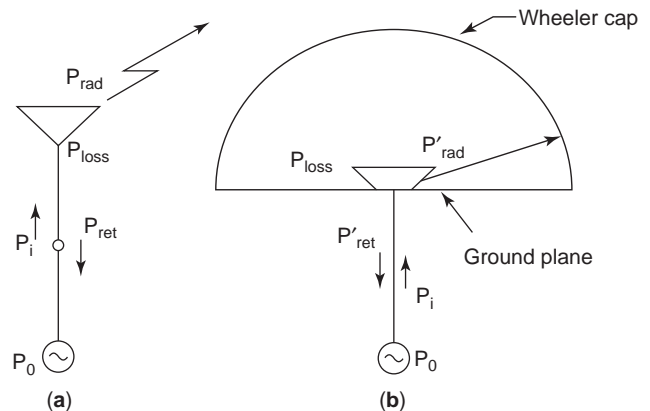


Figure 31. Wheeler-cap method for the radiation efficiency measurement. (From Ref. 24 with permission from Artech House.)

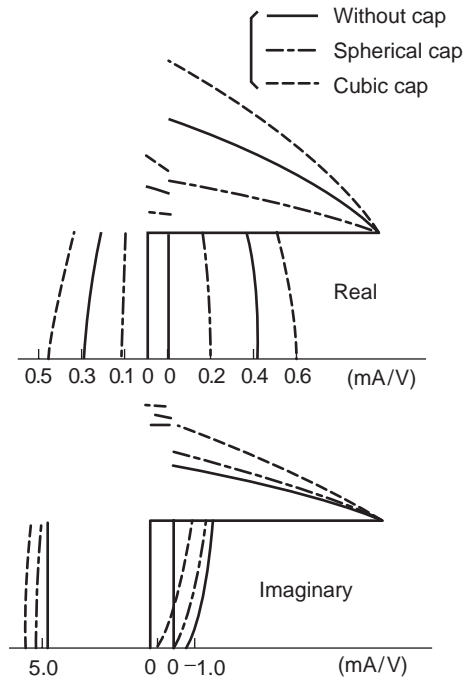


Figure 32. Variation of current distribution on an inverted-L element under the effect of Wheeler-cap. (From Refs. 24,27 with permission from Artech House.)

$Q_{\min}|_{\text{dir}}$, $Q_{\min}|_{\text{omn}}$, and minimum Q are shown in Fig. 21, where it is observed that $Q_{\min}|_{\text{dir}} > Q_{\min}|_{\text{omn}} > \text{minimum } Q$, excepting for $Ka < 1$. $G/Q|_{\text{dir}}$ and $G/Q|_{\text{omn}}$ are depicted in Fig. 22, where $G/Q|_{\text{dir}}$ is seen always larger than $G/Q|_{\text{omn}}$, which can be easily understood that a directional antenna may have higher gain even when Q is kept near the same value.

6. REALIZATION OF SMALL ANTENNAS

Various practical ways exist of making an antenna small.

First, applying the space-filling concept to an antenna structure is the most significant. Chu discussed this concept, stating that gain increase with minimum Q can be accomplished by effectively filling space within which an antenna is enclosed. He also showed that uniform current distribution on a dipole antenna leads to achieving maximum gain. The concept is not only associated with three-

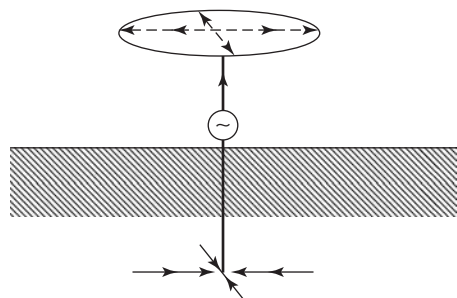


Figure 33. A planar-cap loaded small monopole on the ground plane.

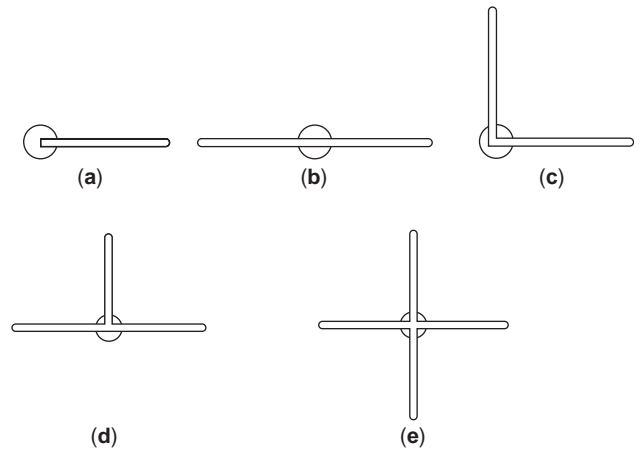


Figure 34. Various models of top-loaded monopoles.(a) A bar loaded at one side. (b) A bar loaded at both side. (c) T-bar loaded. (d) L-bar loaded. (e) Cross-bar loaded.

dimensional structures, but also one- or two-dimensional structures. A planar structure is a simple case in which the problem is how to constitute an antenna that can occupy the space to the greatest extent possible. A bow-tie antenna is an example (Fig. 23). More effective space filling is seen in fractal structures (Fig. 24), by which space to be filled will be increased by increasing the number of modes. Recently, much attention has been paid to the fractal structure by many investigators in great expectations of developing small antennas having wide bandwidth.

Second, accomplishing self-resonance in an antenna structure is significant. In a small dipole, for example, the shorter the antenna size becomes, the harder achieving the resonance within the antenna structure becomes, as the radiation resistance decreases to very small values, whereas the capacitive reactance increases greatly. Then a very high inductive reactance is required for matching. This high inductive reactance, which introduces a higher loss resistance than the radiation resistance, will degrade the radiation efficiency. On the contrary, if self-resonance condition can be satisfied in the antenna structure, such a loss can be avoided and achievement of appreciable radiation efficiency can be expected.

Self-resonance can be attained by integrating conjugate components into an antenna structure, as the reactive impedance is compensated. A composite antenna structure, for instance, a combination of a small dipole and a small loop, produces the self-resonance condition in the antenna system by compensating their reactance components against each other. If an antenna adopts complementary structure, self-resonance for a wide frequency range may be attained. The complementary structure (Fig. 25) has inherently frequency-independent property when it is constituted on an infinite platform.

Third, realizing uniform current distribution is another important concept for obtaining small antenna. However, in a practical antenna system like a dipole, uniform current distributions can hardly be realized, as the current diminishes at the end of the dipole element. One way to realize nearly uniform current distribution on an element is to load an impedance component or an antenna element

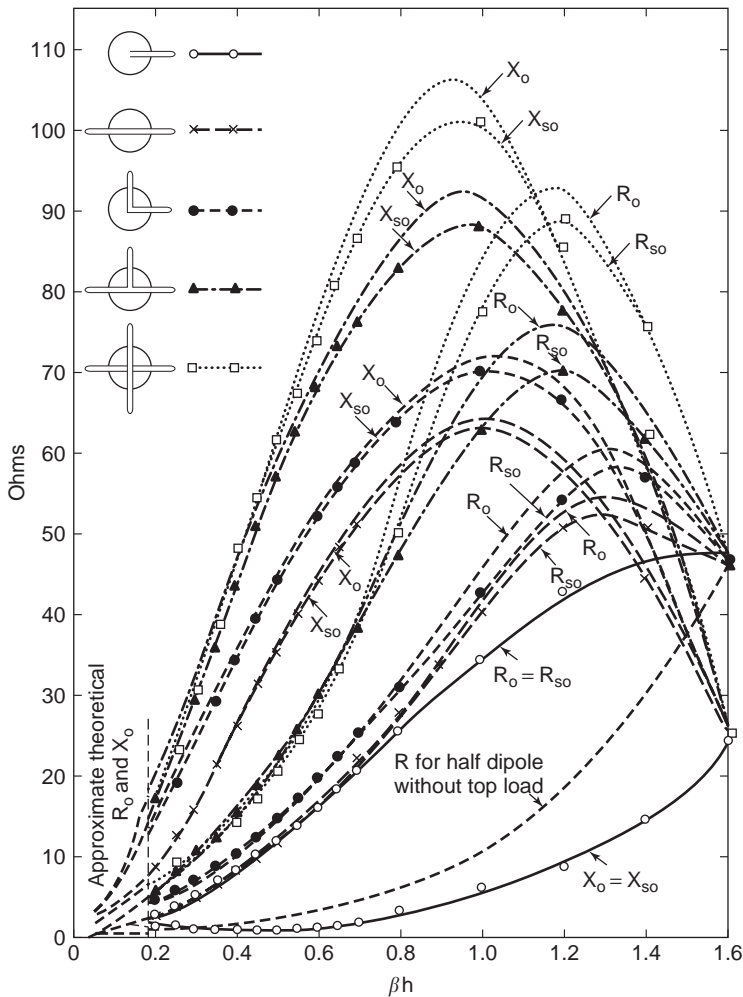


Figure 35. Input impedance characteristics of top-loaded monopoles shown in Fig. 34. (After Ref. 51.)

within the antenna. Top loading is an example. A capacitor plate is attached on top of a monopole standing on the ground so that the current on the monopole can be adjusted to have nearly uniform amplitude, as shown in Fig. 26. Loading of wire elements on top of a monopole, as Fig. 27 shows, is another method. The figure shows various types of top-loaded antennas; (a) inverted-L, (b) inverted-F, (c) T-shape, (d) umbrella-shape, (f) loop-loaded, and (e) spiral-loaded. By integrating some devices or circuitry into the antenna structure, current distributions may be modified to realize distribution of as near to uniform as possible [Fig. 27(g)].

Fourth, a more significant concept is to increase the modes. Gain increase or bandwidth enhancement can be expected with increase of modes. Two radiation modes can be produced by exciting an antenna with both TE and TM modes. A practical example is combination of a dipole and a slot. If they have complementary structure and are constructed on an infinite platform, it has frequency-independent characteristics. In practice, however, because an antenna structure can hardly be constituted on an infinite platform, perfect frequency-independent characteristics

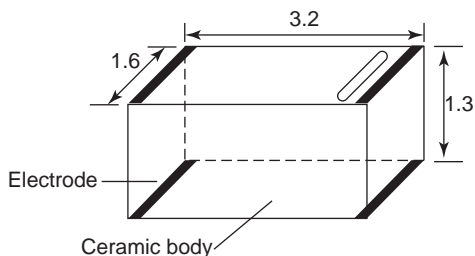


Figure 36. A small ceramic chip antenna. (Courtesy of Murata Mfg. Co.)

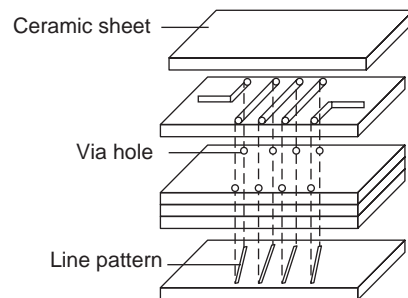


Figure 37. Exploded view of a multilayered chip antenna. (Courtesy of Murata Mfg. Co.)

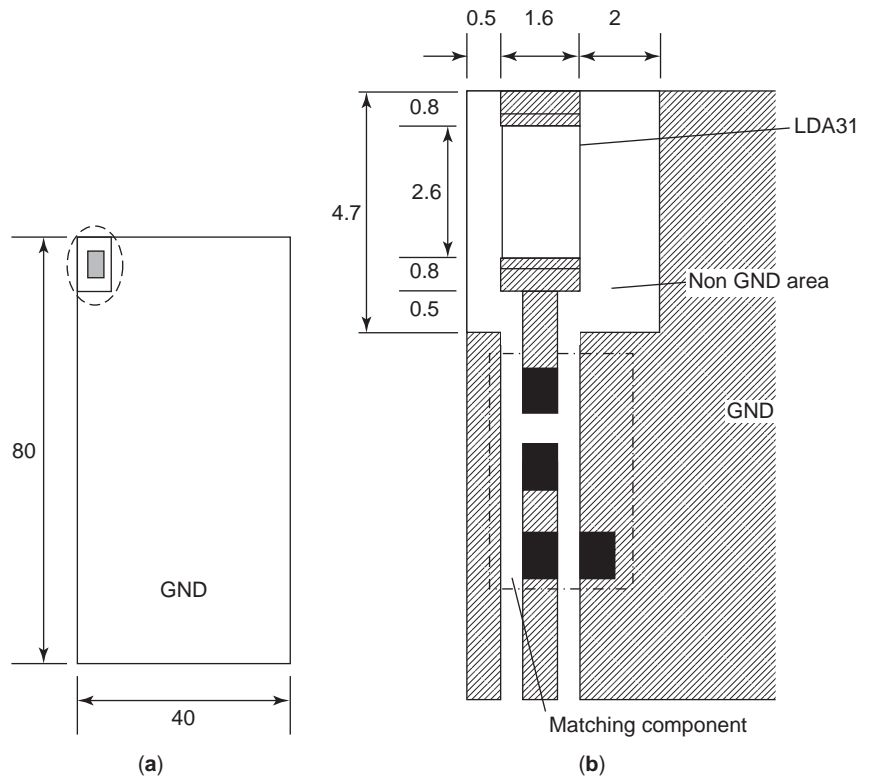


Figure 38. A chip antenna mounted on a ground plane. (a) A chip antenna placed at a corner of ground plane. (b) Detail of chip antenna mounting. (Courtesy of Murata Mfg. Co.)

cannot be accomplished. Nevertheless, an antenna with fairly wideband characteristics, and yet small size, can be realized, even with imperfect complementary structure.

Fifth, integration of devices or circuitry into an antenna structure is a useful technique to obtain either improvement of the antenna characteristics or enhancement of the antenna performance. By means of this technique,

possibility of gain increase, bandwidth enhancement, or improvement of radiation efficiency in a small antenna may exist. It does not mean, however, that these improvements and/or enhancements cannot always be accomplished, but it is dependent on antenna structure, integrating devices, method of integration, operating frequency, and so forth.

Application	Module	Cellular phone	PDA	Laptop PC
Mock-up board (non GND area 8 × 12) [unit: mm]				
f ₀ (MHz)	2450	2450	2450	2450
B.W (MHz)	450	160	210	140
Peak gain (dBi)	+2.0 (ZX plane)	+3.7 (YZ plane)	+2.7 (YZ plane)	+3.3 (XY plane)
Typical directivities — vertical — horizontal				

Figure 39. Various applications of chip antenna. (a) Module, (b) Cellular phone, (c) PDA, (d) Laptop personal computer. (Courtesy of Murata Mfg. Co.)

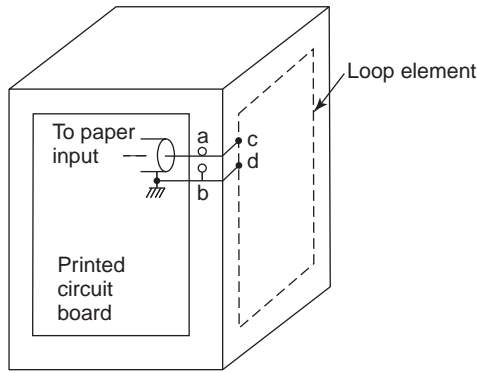


Figure 40. A rectangular loop antenna used for a pager. (From Ref. 29 with permission from Research Studies Press.)

7. MEASUREMENTS [24]

7.1. Considerations Necessary Prior to the Measurement of Small Antennas

It seems no essential difference exists in small antenna measurement from the ordinary antenna measurement. However, the difference of small-antenna performance from that of ordinary antennas gives rise to the difference in their measurement. The reduction of antenna size presents various problems to the antenna designers because of the performance penalties in antenna characteristics, such as impedance, efficiency, bandwidth, and so forth. As far as the small antenna is concerned, the problems are not only associated with antenna design, but also with its measurements. The smaller the antenna size, the

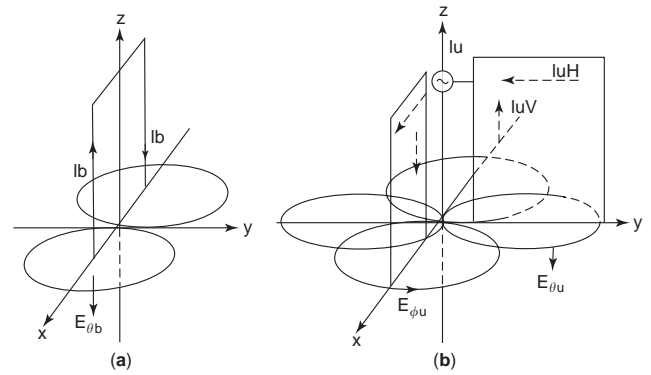


Figure 42. Equivalent expression of pager antenna system. (a) Balanced mode (loop mode). (b) Unbalanced mode (dipole mode). (From Ref. 29 with permission from Research Studies Press.)

harder is the determination of its performance. The difficulty in small antenna measurements is attributed to the performance penalties as well as the antenna structure, which may have an asymmetric configuration. Problems will become complicated when a small antenna is mounted on or built into a platform in a unit of wireless systems. The antenna system then assumes a composite structure of an antenna and the unit body as an antenna system, and thus the measurement must perform to evaluate the performance of such composite antenna system. Special care is necessary to obtain a reliable determination of small antenna performance. Some typical cases to which particular attention should be paid are as follows:

- a. When the size of the antenna is very small compared with the wavelength or the size of nearby conducting materials.
- b. When the antenna structure is asymmetric.
- c. When some proximity effects exist on the antenna.

Although particular considerations are given to the measurement of small antennas, some cases may exist where no effective method is found for the accurate determination of antenna characteristics. For example, when the size of the antenna is extremely small, the resistance becomes too small to be determined. Another case is where the antenna structure is so complicated that precise measurement becomes very difficult to perform. When the antenna size is very small, difficulty in the measurement develops from not only the specific antenna performance, but also subjects related to antenna structure, proximity effect, and so forth.

Antenna measurements are often made by using an image plane as the ground plane (GPL). With an image (ground) plane, measurements can be made simpler and more accurate as compared with measurements without an image (ground) plane. When an antenna under test has simple and symmetric structure, half the antenna structure can be replaced by an image plane, and convenient measurements may then be made on one-half of the antenna. By using a GPL, a coaxial cable can be used for feeding of a test antenna. As almost all of the instruments have unbalanced mode output terminals, a coaxial cable is

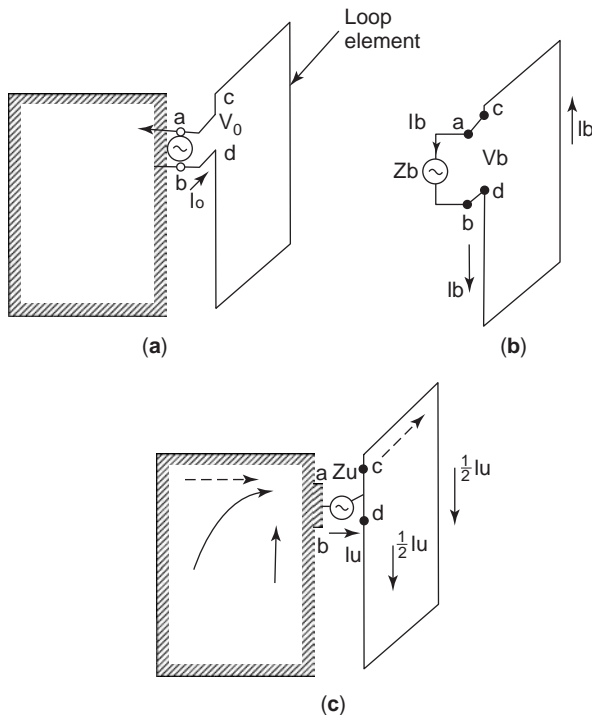


Figure 41. Schematic of pager input terminals. (From Ref. 29 with permission from Research Studies Press.)

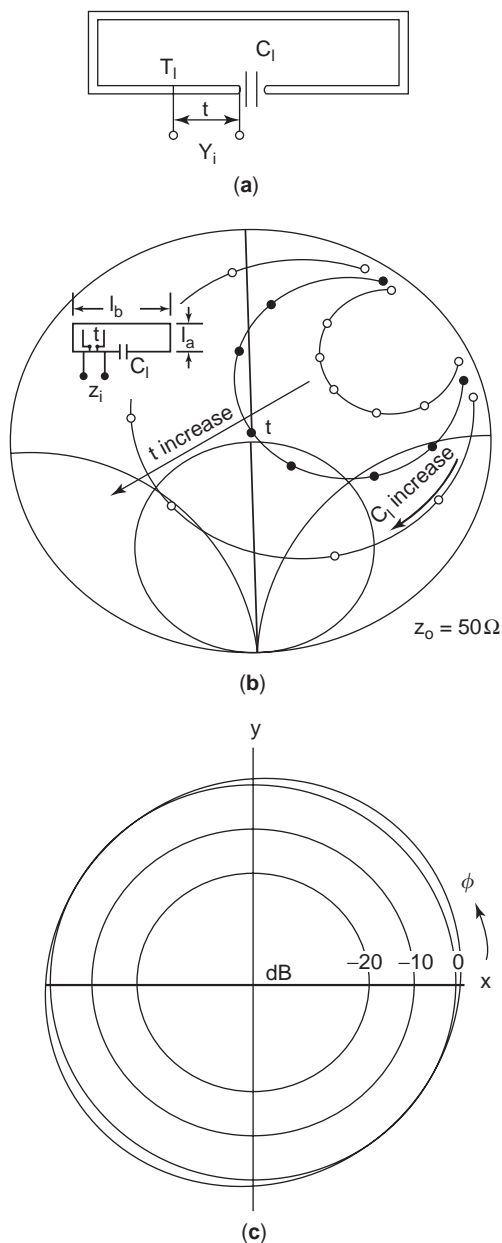


Figure 43. Receiving patterns. (a) Pattern produced by a balanced mode. (b) Patterns produced by unbalanced mode. (c) Combined pattern resulted in omnidirectional pattern. (From Ref. 29 with permission from Research Studies Press.)

used in ordinary measurements. Use of a coaxial cable is convenient and simple, and no Balun (balanced-unbalanced transformation) is necessary. In addition, a stable measurement can be performed, as noise and interference can be isolated from the antenna feed. The feature of using a coaxial cable feed behind the GPL is not concerned about the unbalanced current that disturbs the measurement.

When an antenna has balanced feed terminals and is connected by an unbalanced cable to feed, an unbalanced current may be easily produced on the feed cable. Similar situations are encountered when a small antenna is composed of asymmetrical, irregular, or complicated struc-

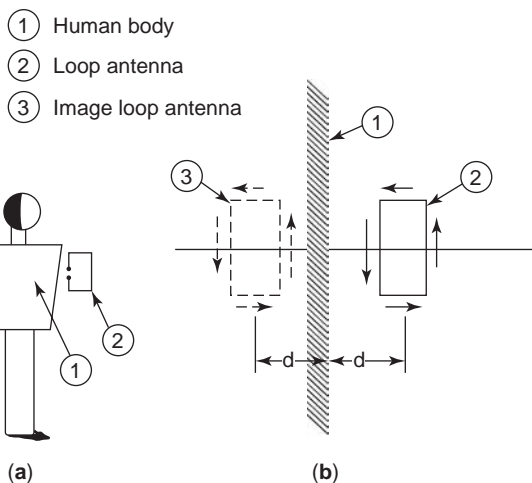


Figure 44. Self-resonance of a small loop antenna. (a) Variable parameters; feeding gap t and series capacitor C . (b) Variation of input impedance with variation of t and C .

tures. Use of a Balun is a must, and every means must be taken to avoid coupling, proximity effects, and so forth.

As a practical GPL cannot be made with infinite size, an undesired unbalanced current may be induced on the plane and further flow behind the plane. Thus, the determination of the antenna impedance becomes uncertain and radiation patterns are distorted. Hence, a usual compromise is to use a conducting plane of several wavelengths or more to obtain antenna performance nearly that of free space. For this purpose, use of a high-impedance ground plane (HIG), designed based on the electronic bandgap (EBG) concept, is recommended. However, one should be careful about the frequency dependence of the HIG.

7.2. Antenna Structure

When the size of antenna under test is comparable with or smaller than that of the instrument connected to the test antenna, electromagnetic coupling is likely to exist between the antenna element and nearby objects, including cables, instruments, and so forth. Such coupling effects may disturb the measurement. For example, if a coaxial cable is connected to an antenna element, the cable couples electromagnetically with the antenna element, and the impedance of the antenna may be measured with an error.

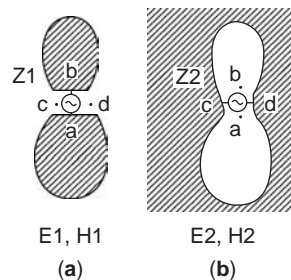


Figure 45. Complementary structure. (a) A planar element. (b) A complementary slot.

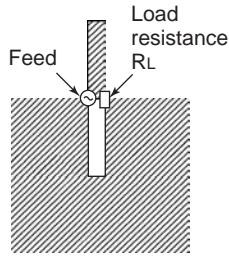


Figure 46. A typical complementary antenna; a monopole and a slot.

Environmental condition may likely affect antenna performance, and thus some errors will be produced in the measurement. When an antenna has a complicated structure, such environmental conditions may likely affect the antenna performance. A typical example is a case where an antenna is used for small mobile terminals, where the

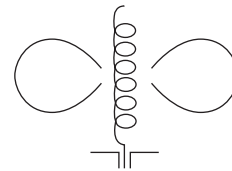
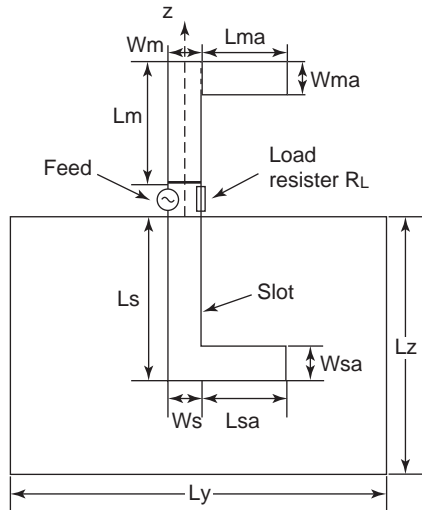


Figure 48. Normal mode helical antenna (NMHA).

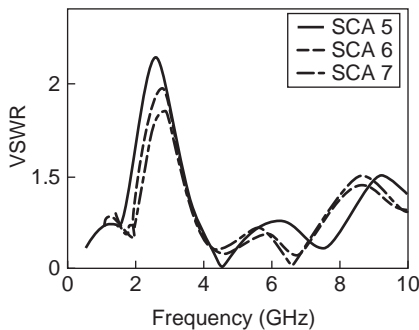
mobile unit effectively acts as a part of radiator, as the antenna element excites the conducting materials in the unit. In this case, a combination of the antenna element and the unit constitutes an equivalent antenna system, and the measurement will be on the equivalent antenna system.

When undesired mode current exists in the antenna systems, uncertainty of the measurements is increased and exact antenna performance cannot be determined.

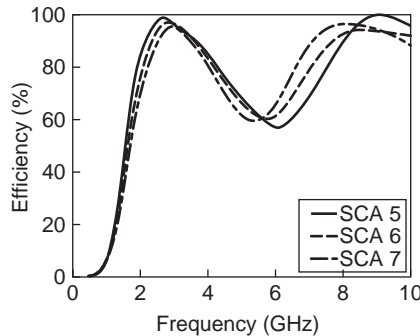


Model	Lsa-Lma (mm)	Ls-Lm (mm)	Others (mm)	RL=188 ohms
SCA5	6	21	Lm+Lma-27, Ly=46, Lz=60	
SCA6	12	15	Ws=Wm=4, Wsa=Wma=3	
SCA7	15	12	Thickness=0.5	

(a)



(b)



(c)

Figure 47. L-shaped small self-complementary antenna. (a) Antenna configuration. (b) Impedance characteristics. (c) Efficiency characteristics. (From Ref. 31 with permission from IEEE.)



Figure 49. Equivalent expression of NMHA.

7.3. Balanced and Unbalanced Transformation

When a coaxial cable, which has an unbalanced mode, is connected directly to a two-wire line, which has a balanced mode [Fig. 28(a)], the system is equivalently expressed by two parts: an unbalanced mode [Fig. 28 (b)] and a balanced mode [Fig. 28(c)]. The unbalanced mode current I_u contributes to produce radiation, whereas the balanced mode current I_b does not. If the unbalanced mode current exists on the outside of the outer conductor of the coaxial cable, it may produce undesired radiation and may cause an error in the measurement of impedance and radiation patterns.

7.4. The Effect of Nearby Conducting Materials

The effect of nearby conducting materials on an antenna system, which is called the proximity effect, is an undesired phenomenon for small-antenna measurements. The usual attempt is to remove the proximity effect or to keep it as small as possible in the measurement system. If any proximity effect exists near a feed point, antenna current may be varied so that antenna characteristics such as impedance and efficiency are varied as well.

When some materials are located very near to an antenna element, removal of the proximity effect is not feasible. If an appreciable amount of radiation current flows

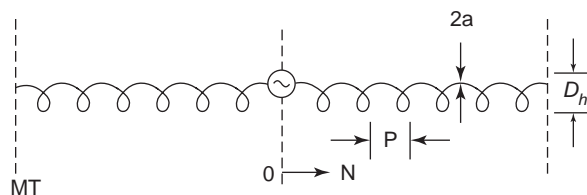


Figure 50. A model of normal mode helical antenna. (From Ref. 33 with permission from Research Studies Press.)

on the materials, the materials are considered a part of the “radiator,” and the antenna element and the materials together are considered as a combined radiator. In this case, the measurement is performed for the combined radiator. A typical example is a mobile phone unit, in which the mobile phone body and antenna element act as an antenna system.

7.5. The Accuracy, Precision, and Stability of the Instrument

If the antenna under test has such small size that its resistance is, for example, several ohms, the instrument to be used should have high enough accuracy and precision to measure such a low resistance value. A typical case is where the efficiency of an ESA that has dimensions on the order of one-tenth λ or less is determined. When an antenna impedance in the VHF-UHF ranges or higher is less than 0.5Ω , for example, no way to determine the true impedance may exist because an instrument with high enough accuracy to determine such a small value may not be available.

A successful measurement for such small impedance with reasonable accuracy was reported in [25], in which very low impedances of dielectric material-loaded dipoles (Fig. 29) are introduced. The results are shown in Fig. 30, where small values of radiation resistance and inverse of input reactance with respect to the relative permittivity of loaded dielectric material are shown. Efficiency-bandwidth ratio, which corresponds to Wheeler’s radiation power factor, is used to evaluate small values of radiation

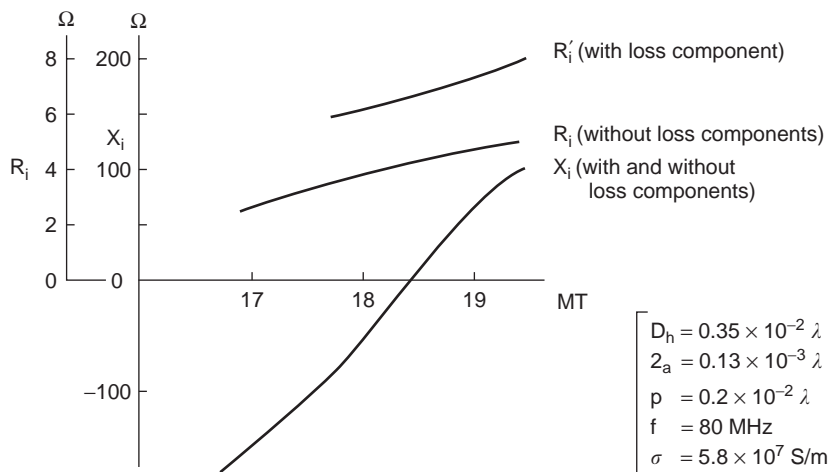


Figure 51. Input impedance of a NMHA. (From Ref. 33 with permission from Research Studies Press.)

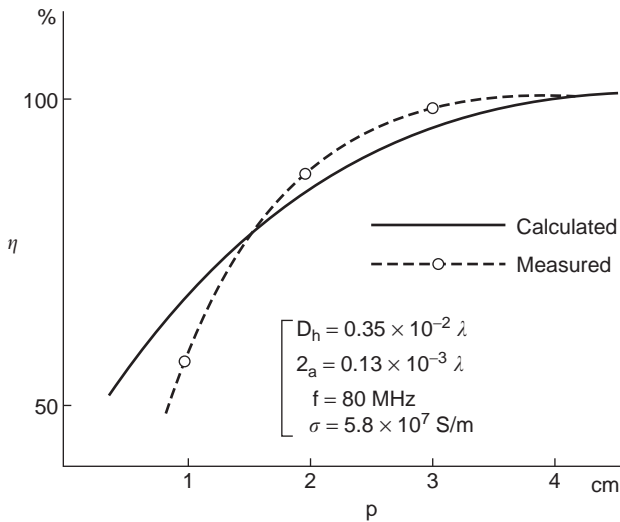


Figure 52. Radiation efficiency η versus pitch P . (From Ref. 33 with permission from Research Studies Press.)

resistance along with Wheeler-cap method for efficiency measurement.

Stability of the instrument is also important because, if the instrument is not stable enough, errors because of fluctuation in the measurement system become involved in the measured results. For instance, when a small impedance of an ESA, e.g., about $1\ \Omega$ is measured, stability of the instrument must be high enough to determine one-tenth of $1\ \Omega$ or so. The results obtained by the measurement with an unstable instrument are meaningless.

7.6. Measurement of Radiation Efficiency

There are three typical methods to determine the antenna efficiency: pattern integration method, Q-factor method, and Wheeler method [26].

The pattern integral method determines Prad from the integration of the radiation pattern intensity, which is obtained from the far-field measurement. Although pattern integration method is considered the most accurate available, especially when the absolute efficiency of an antenna is desired, it usually takes a rather long time, because it needs to measure radiation patterns and to perform integration of the radiation patterns over a spherical surface completely enclosing the antenna.

On the contrary, Q-factor and Wheeler methods have the advantage of being quick and easy to employ, as compared with the pattern integration method. These two methods relate with antenna efficiency to the input impedance rather than the far-field pattern integration. The two methods have the advantage that the measurement does not require any particular system, but can employ ordinary methods and also be performed in ordinary laboratory rooms. However, there is a tradeoff between the accuracy and ease of the measurement because the accuracy of the antenna efficiency obtained by these two methods is relatively lower than by the pattern integration method.

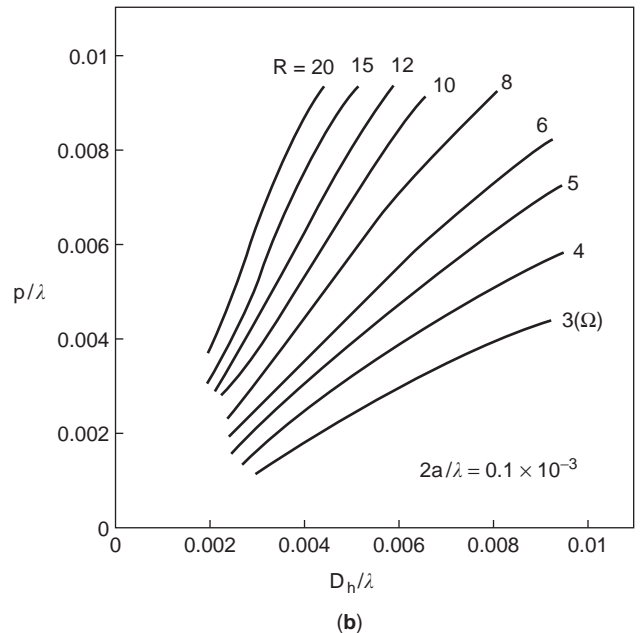
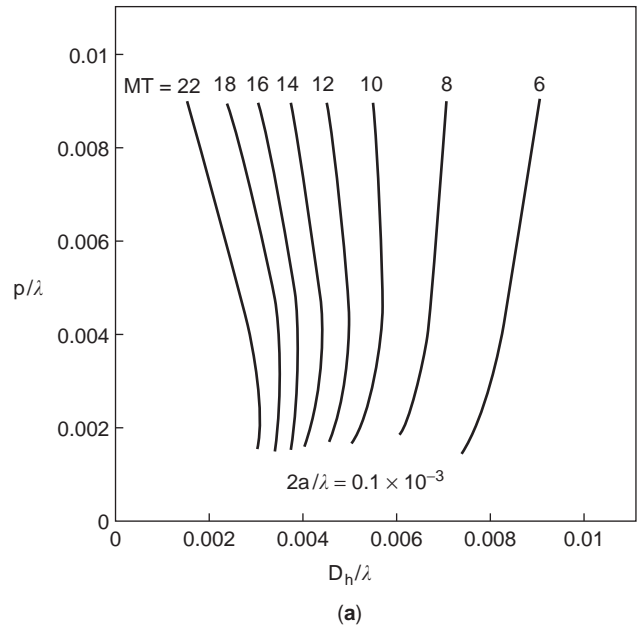


Figure 53. Design chart of NMHA. (a) Dh vs. P with respect to number of turns MT . (b) Dh vs. P with respect to resonance resistance R . (From Ref. 33 with permission from Research Studies Press.)

The Q-factor method is based on a measurement of two antenna Q values; one is the Q_{RL} of the test antenna and another is the Q_R of an ideal antenna. Q_{RL} can be determined by measuring the impedance of the test antenna. Q_r can be determined from calculations based on Chu's theory. If the Q of an antenna is high, it can be interpreted as the reciprocal of the relative bandwidth B. The B can be known from the impedance-frequency characteristics. B is defined as the bandwidth for the half-power frequencies that occur for a power reflection coefficient of 0.5 (VSWR = 5.83). As a result of the inherent difficulty in determining

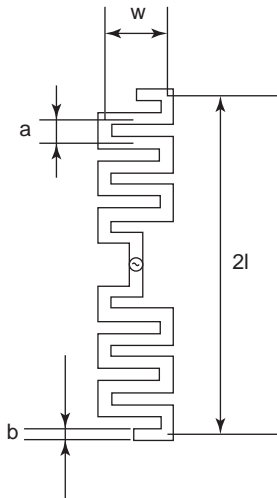


Figure 54. Model of meander-line antenna. (From Ref. 34 with permission from IEICE.)

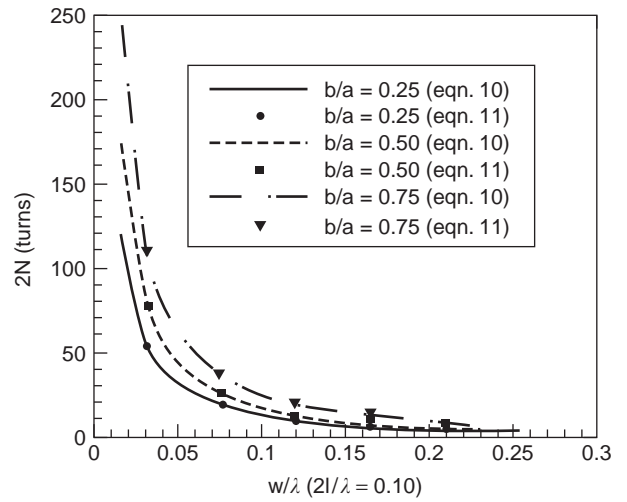


Figure 57. Number of turns N vs. meander-line width w/λ . (From Ref. 34 with permission from IEICE.)

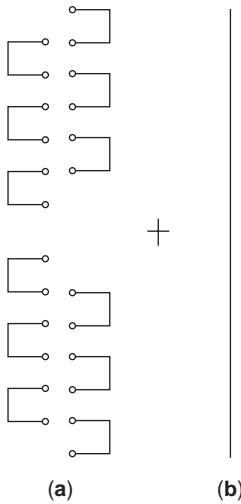


Figure 55. Equivalent expression of meander-line antenna. (From Ref. 34 with permission from IEICE.)

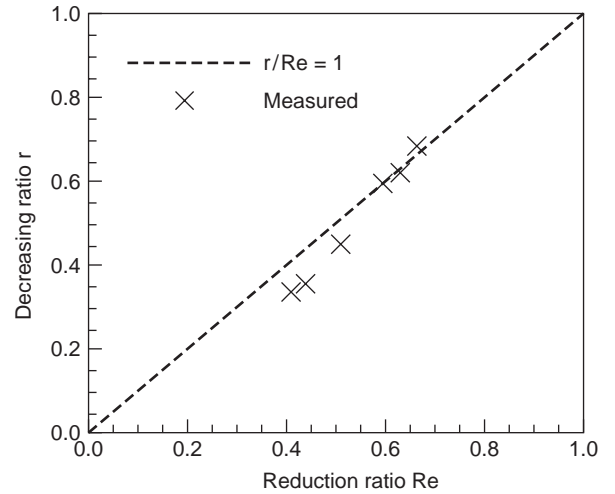


Figure 58. Size decreasing ratio with respect to reduction ratio. (From Ref. 34 with permission from IEICE.)

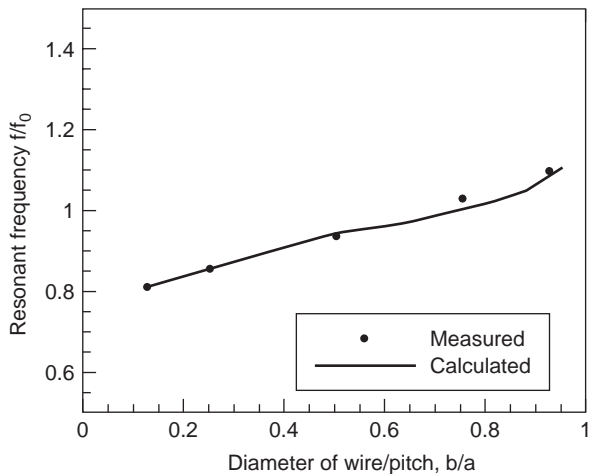


Figure 56. Resonant frequency vs. diameter of wire/pitch. (From Ref. 34 with permission from IEICE.)

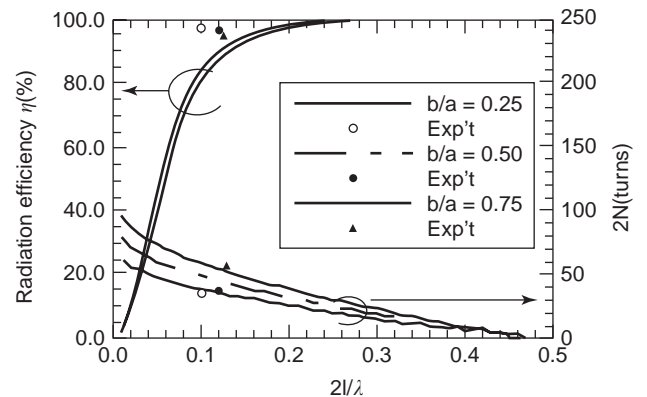


Figure 59. Radiation efficiency η with respect to length l/λ . (From Ref. 34 with permission from IEICE.)

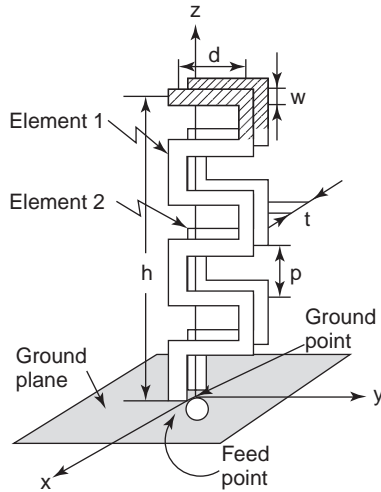


Figure 60. Meander-line antenna composed of two strips in parallel. (From Ref. 35 with permission from IEICE.)

Q_R , the Wheeler method is recommended because it is simpler in practice.

In the Wheeler method (Fig. 31), the antenna resistance is measured in two ways: R_{in} of an antenna reradiating into free space and R_{loss} of an antenna placed within a Wheeler cap, which eliminates radiation from the antenna. By using these two resistances, R_{loss} and R_{in} , R_{rad} can be found, because $R_{in} = R_{rad} + R_{loss}$. Then the efficiency η is calculated from

$$\eta = R_{rad} / (R_{rad} + R_{loss}) \tag{30}$$

The dimension of a cap is recommended to be about $\lambda/2\pi$ or less, although no exact theories to prove this idea exist. From the experimental results, no severe limitation in the cap size seems to exist unless it does not greatly exceed $\lambda/2\pi$. For the shape of a cap, either a hemisphere or cubic shape can be used. The shape somehow depends on the size and type of test antennas. For a thin, short monopole, both hemispheric and cubic shapes can be used. A cubic shape seems to be better for antennas, such as an inverted-F antenna, because it has elements parallel to the sides of the cap, and the distance between the antenna element and the cap can be made nearly equal; thereby, variation

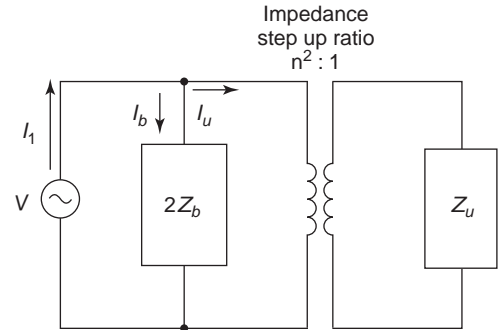


Figure 62. Equivalent circuit of two-strip meander-line antenna. (From Ref. 35 with permission from IEICE.)

in the antenna current is made small after the cap covers the antenna.

In any case, care must be observed for the resonance or antiresonance of the antenna, cap, or both. Note that the principle of the Wheeler method is based on the measurement of the series resistance or the parallel conductance at or near resonance or antiresonance frequencies; resistance or conductance becomes very low or approaches an infinitely large value, and no consistency in the measured values can be expected.

The inner surface of a cap should be plated to reduce the ohmic loss. Usually, the interaction of the cap surface current with the antenna current is ignored because it can be assumed to be very small. However, it may become an appreciable value when the antenna element approaches the inner surface of the cap because the cap surface current may interact with antenna current. Then the cap surface loss becomes included in the antenna loss. Plating the cap surface with gold is best.

Another problem in the Wheeler method lies in an assumption that the antenna current is not changed in the Wheeler cap, which is not really true. Figure 32 shows that the antenna current of an inverted-F antenna varies because of a Wheeler cap [27]. Variation of the current depends on the shape and the size of the Wheeler cap as well as the type and the size of the antenna. Errors in the measurement are greatly increased, especially at the frequency of resonance or antiresonance, which depend on the type and size of the antenna as well as the shape and size of the Wheeler cap.

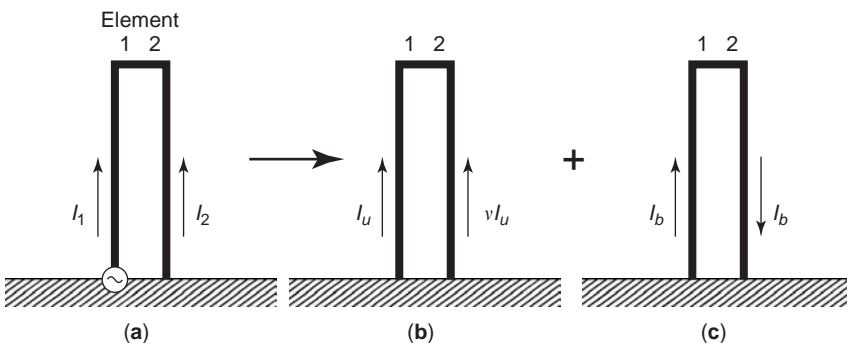


Figure 61. Equivalent expressions of two-strip meander-line antenna. (From Ref. 35 with permission from IEICE.)

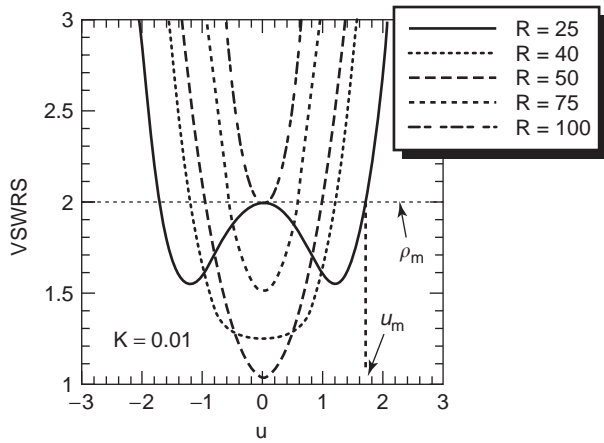


Figure 63. VSWR vs. $u = (Q2\Delta f/f_0)$. (From Ref. 35 with permission from IEICE.)

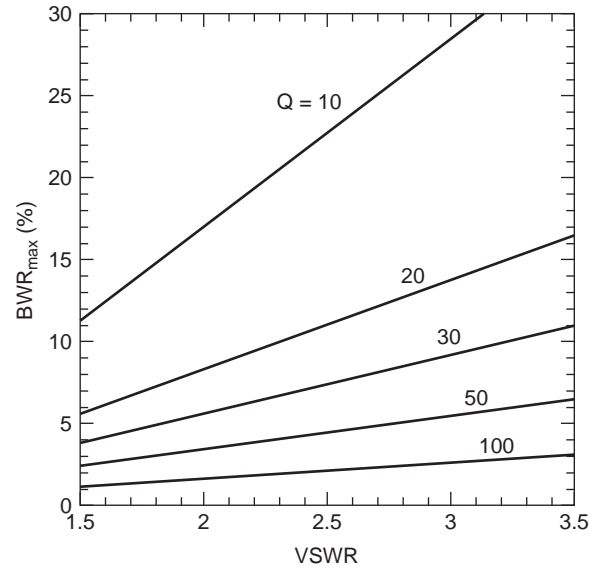


Figure 65. Bandwidth ratio vs. VSWR. (From Ref. 35 with permission from IEICE.)

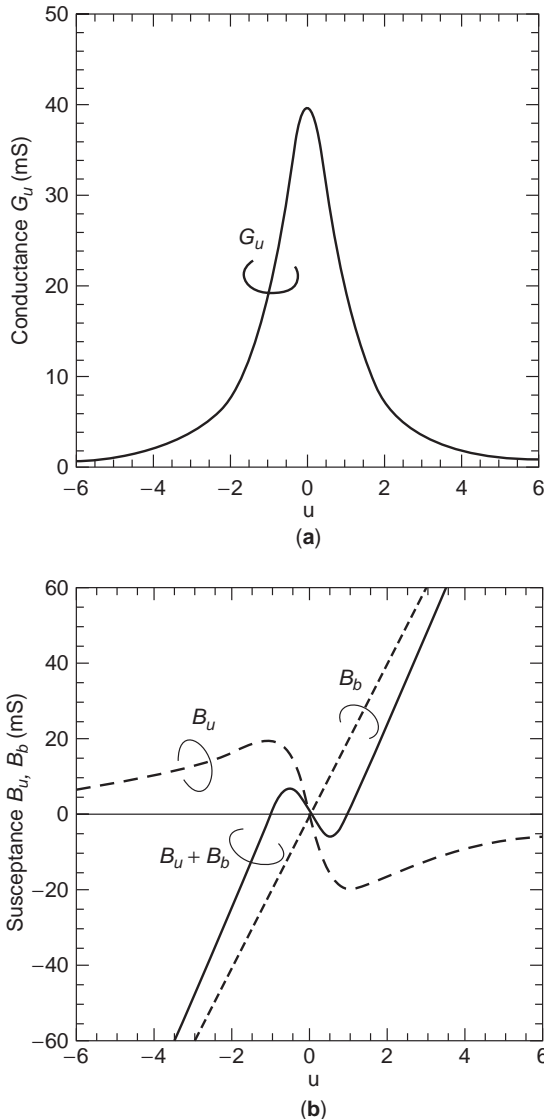


Figure 64. Input admittance of a meander-line antenna. (a) Conductance G_u vs. u . (b) Susceptances B_u and B_b vs. u . (From Ref. 35 with permission from IEICE.)

8. PRACTICAL SMALL ANTENNAS

8.1. ESA

8.1.1. Self-Resonance Structure

8.1.1.1. Short Monopole with Capacitor Cap Top-Loading. A capacitor cap is placed on top of a monopole standing on the ground plane (GPL) (Fig. 33) in order to increase the radiation resistance of a short monopole. With assistance of an image presumed below the GPL, the antenna system is considered as a dipole with end-loading. The input resistance R_r is one-half that of the dipole, which is given by [17]

$$R_r = 1000(h/\lambda)^2 \quad (31)$$

8.1.1.2. Short Monopole with Wire Top-Loading. Figure 34 depicts a top view of various top-loaded antennas: (a) a bar one-side loaded, (b) a bar both-side loaded, (c) L-bar loaded, (d) T-bar loaded, and (e) cross-bar loaded.

The impedance characteristics of these antennas are shown in Fig. 35 [51].

8.1.2. Material Loading

8.1.2.1. Ceramic Chip Antenna. This example may be the world's smallest antenna at present; the size of the ceramic substrate measures 1.6 mm wide, 3.2 mm long, and 1.3 mm high, as depicted in Fig. 36. Figure 37 illustrates an exploded view of the antenna structure. The thin ceramic substrate is composed of multilayered thin ceramic sheets. The type of antenna is a normal mode helix, which is formed in the substrate by connecting printed patterns on the top layer and bottom layer via wires. This antenna has been practically used for small mobile terminals, in which the antenna is placed on a corner of the ground plane (GPL), as shown in Fig. 38. It is usual that a small part of the ground plane beneath the antenna

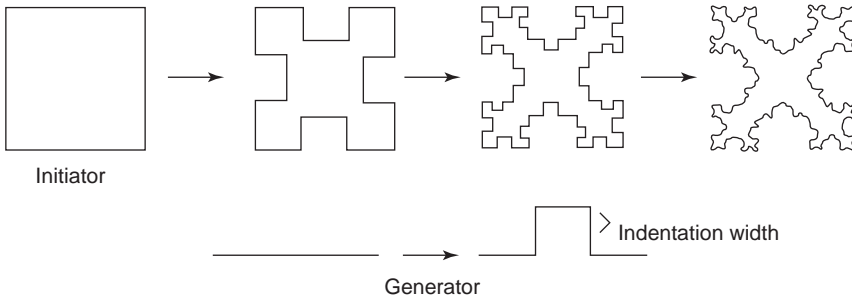


Figure 66. The iterative-generation procedure for a Minkowski island fractal. (From Ref. 36 with permission from IEEE.)

element is taken out in order to avoid excessive loss because of the GPL. However, the antenna needs the help of the GPL. In other words, this antenna actually excites the GPL so that the small antenna and the GPL work as a combined antenna system. Thus, the antenna performance depends on the size of the GPL and how and where the antenna element is placed on the GPL. Some examples of antenna applications are shown in Fig. 39, in which antenna mounting; operating frequency; and antenna performance, such as gain, bandwidth, and radiation patterns are presented.

This type of antenna has features in having a resonant frequency controlled by an easily adjustable structure, has reasonably high gain and wide bandwidth, in addition to being very small in size and very lightweight. Typically, it has the gain of -5 to $+10$ dBi and the bandwidth of about 100 MHz in 5 GHz regions.

8.1.3. Composite Structure

8.1.3.1. Small Rectangular Loop Antenna. This is an example of an ESA with composite structure, consisting of a small loop and an equivalent dipole structure [28]. The size of this antenna is 0.007λ . The design of this antenna was based on the important concepts of realizing small antennas, which are (1) increasing modes, (2) accomplishing self-resonance, and (3) use of magnetic current source and its image. The antenna was practically applied to a small pager unit, as shown in Fig. 40. A rectangular small loop antenna is directly connected to the receiver input as Fig. 41(a) shows. Without using a Balun for the connection between the loop and the receiver input, both balanced and unbalanced currents are produced at the feeding

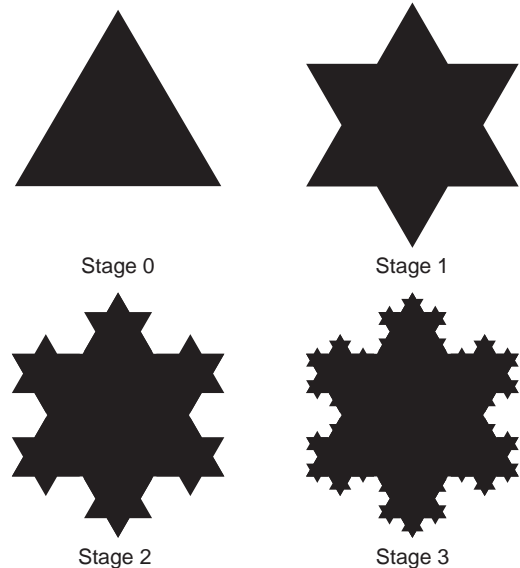


Figure 68. The first three stages of Koch snowflake. (From Ref. 38 with permission from IEEE.)

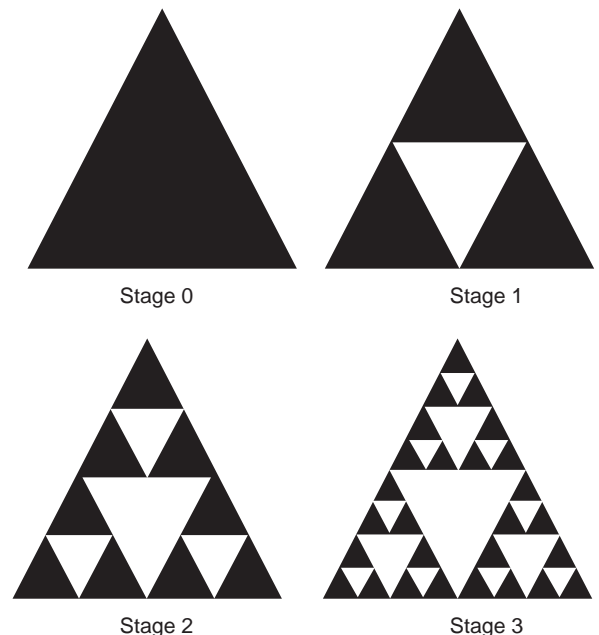


Figure 69. The first three stages of a Sierpinski gasket fractal. (From Ref. 38 with permission from IEEE.)

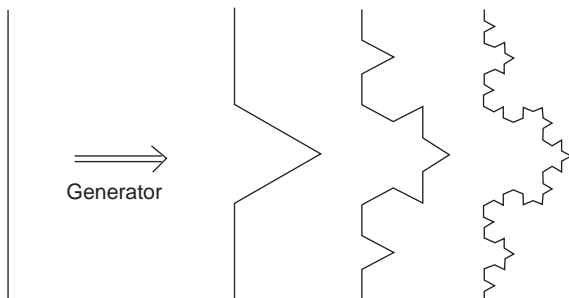


Figure 67. Three successive iteration of a Koch fractal. (From Ref. 39 with permission from IEEE.)

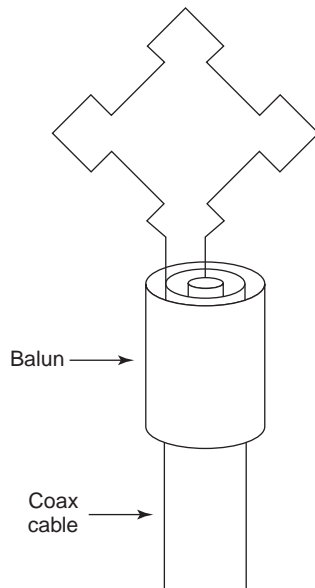


Figure 70. Experimental model of a first iteration of a Minkowski fractal. (From Ref. 36 with permission from IEEE.)

terminals, as shown in Fig. 41(b) and (c), respectively, resulting in creating two modes, a loop mode and a dipole mode, in the antenna system. The balanced part is the original loop antenna, whereas the unbalanced part forms

an equivalent dipole, being composed of the ground plane as one part and the loop structure as another part. Then the combined antenna system performs combined performances of both loop and dipole. The receiving patterns, for example, are nearly omnidirectional, as shown in Fig. 42, where (a) shows the loop pattern, (b) shows both the loop and the dipole patterns, and (c) shows the combined pattern of these. It is interesting to know that the pattern on the plane normal to the receiver unit is omnidirectional. With a single loop antenna, the pattern is only a figure 8-shaped pattern. The omnidirectional pattern is favorable, because a pager should have sensitivity without regarding direction of the signal incidence while moving.

Self-resonance was attained by integrating a capacitor C in series near the loop input and adjusting the gap t of input terminals [Fig. 43(a)], so that matching to the load of $50\ \Omega$ can be attained. Figure 43(b) shows how self-resonance, and thus matching conditions, can be attained by adjusting C and t .

Another point is that the loop element is placed normal to the wide side of the unit so that the loop faces normal to the human body when the unit is placed in a chest pocket [Fig. 44(a)]. By this means, image of the loop presumed inside the human body produces the additive magnetic field on the surface of the human body [Fig. 44(b)], so that the receiver sensitivity can be made about 3 dB higher as compared with that of a receiver in free space.

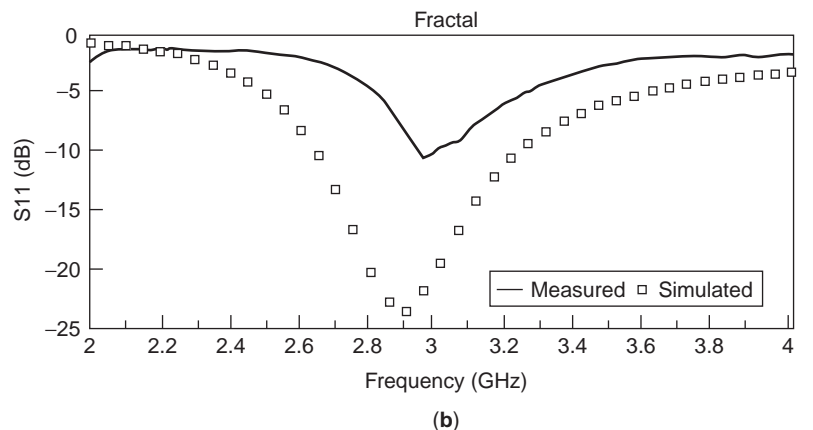
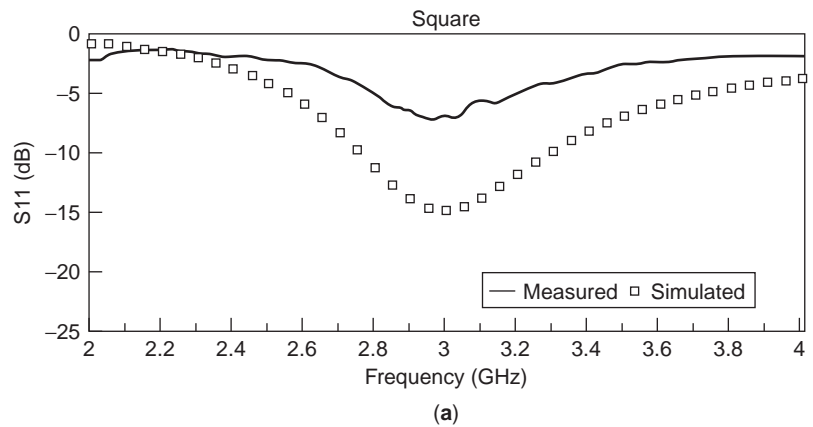


Figure 71. The input match characteristics. (a) A corner-fed square loop \square . (b) The first iteration Minkowski fractal loop \square . (From Ref. 36 with permission from IEEE.)

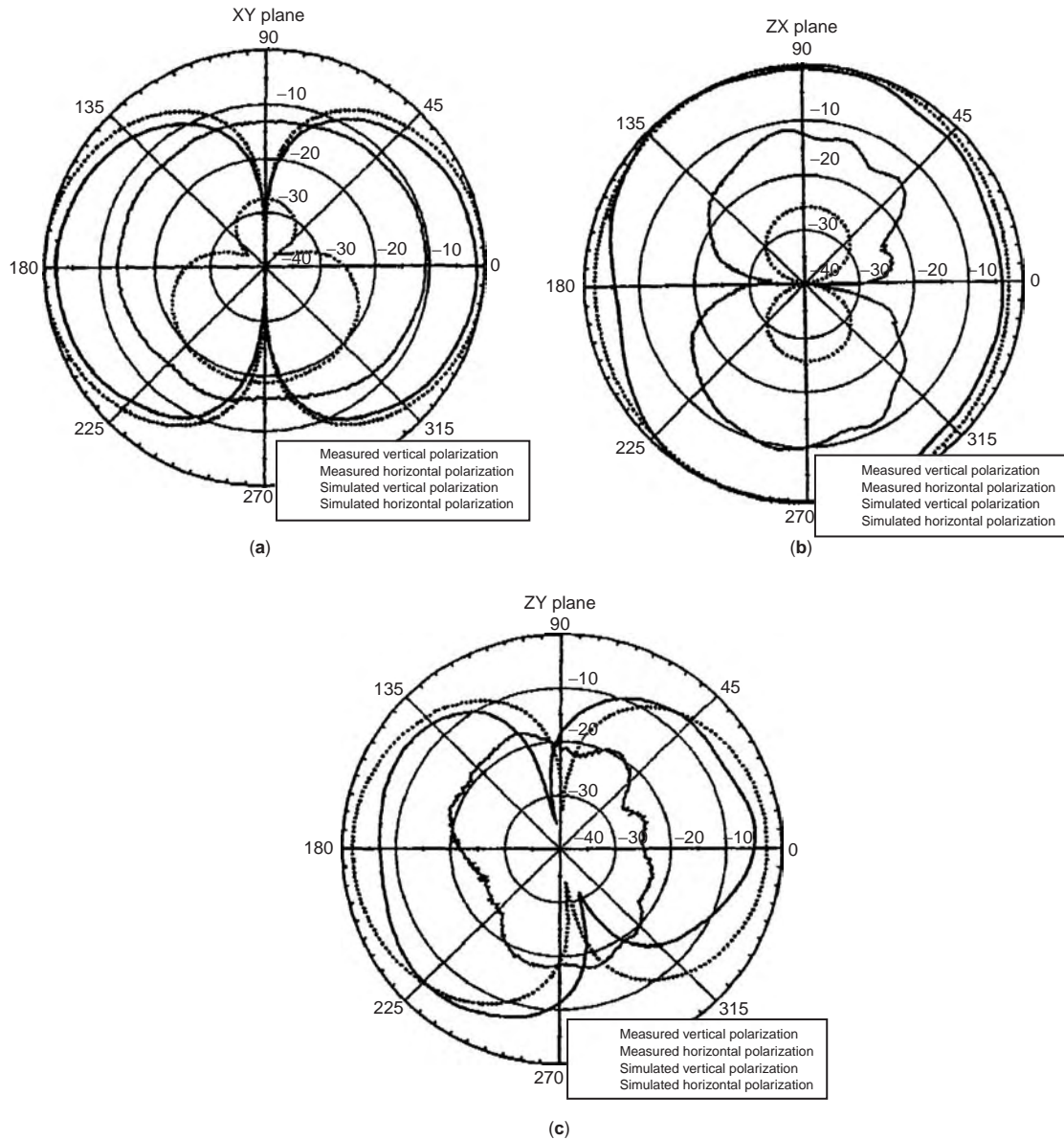


Figure 72. The far-field patterns of the first-order Minkowski fractal loop antenna: measured and computed results. (a) XY plane. (b) ZX plane. (c) ZY plane. (From Ref. 36 with permission from IEEE.)

The design concepts of this type of composite antenna, such as realization of self-resonance, utilization of unbalanced component, and use of magnetic current source as an additional radiator, can be applied to any other type of small antennas.

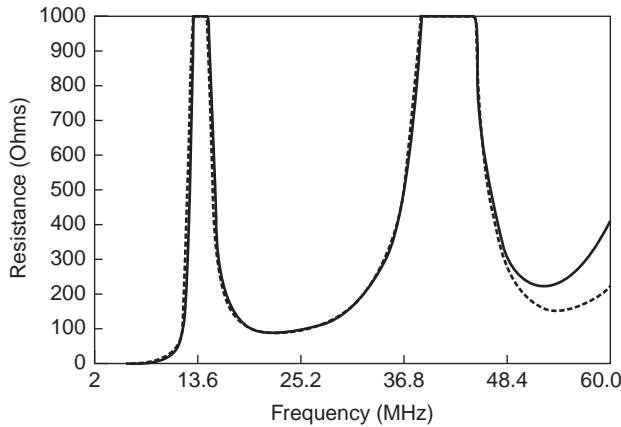
8.1.3.2. Complementary Antenna

8.1.3.2.1. general. The principle of the self-complementary antenna (SCA) was first introduced by Mushiake in 1948 [29,30], where SCA had shown to be an antenna system having constant input impedance, independently of the source frequency and shape of the antenna. The concept of SCA has been applied to create various types of wideband antennas, and subsequently practical applications have been made so far.

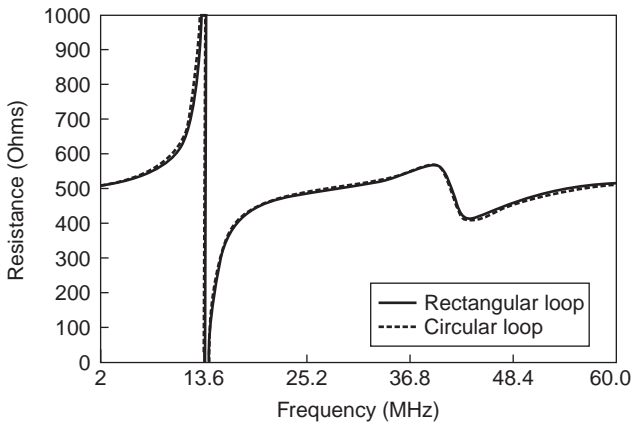
8.1.3.2.2. theory. Here, we assume a pair of mutually complementary antennas, as shown in Fig. 45, where (a) depicts an arbitrarily shaped planar antenna and (b) its complementary slot antenna. The electromagnetic fields E_1, H_1 for Fig. 45(a) and E_2, H_2 for Fig. 45(b) satisfy the duality relationship as follows:

$$E_2 = \mu H_1 \text{ and } H_2 = \pm \gamma E_1 \tag{32}$$

where $\gamma = (j\omega\epsilon + \sigma)/(j\omega\mu)$, ϵ , μ , and σ are permittivity, permeability, and conductivity of the medium, respectively. The input impedance Z_1 and Z_2 of the planar antenna and slot antenna, in Fig. 45(a) and (b), can be expressed by the ratio of the input voltages and input currents at the



(a)



(b)

Figure 73. Impedance of the Euclidean loop antennas. (a) Resistance. (b) Reactance. (From Ref. 39 with permission from IEEE.)

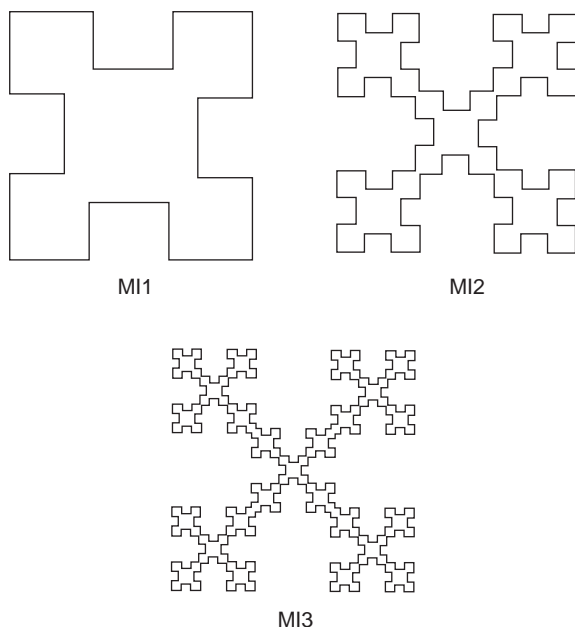


Figure 74. The Minkowski fractal loop antennas. (From Ref. 39 with permission from IEEE.)

respective feeding terminals a–b and c–d as follows:

$$Z_1 = \int_b^a E_1 \cdot dl / 2 \int_c^d H_1 \cdot dl \tag{33}$$

$$Z_2 = \int_d^c E_2 \cdot dl / 2 \int_b^a H_2 \cdot dl \tag{34}$$

where dl denotes the line element, and the integral is performed in the vicinity of the feed terminals. From Eqs. (32)–(34), the following relationships can be derived:

$$Z_1 Z_2 = (Z_0 / 2)^2 \tag{35}$$

where Z_0 is the intrinsic impedance of the medium, which is approximately equal to 120π ohms in free space. If an antenna is identical to its complementary structure, the antenna is referred to as the self-complementary antenna (SCA). The input impedance Z_1 of the original structure is equal to that of its complementary structure Z_2 , and is assumed to be Z , then

$$Z_1 = Z_2 = Z = Z_0 / 2 = 60 \pi \tag{36}$$

which is referred to as Mushiake’s relationship [27], which means that input impedance is a constant, independent of the source frequency and of the shape of the structure.

In other words, SCA has infinite bandwidth in terms of the input impedance. However, in practical antenna systems, infinite structure can never be realized so that constant impedance would only be approximate in practice. Thus, truncation effect because of the finite structure will always bring more or less deterioration of the bandwidth. However, study has shown even with finite dimensions, antenna systems having self-complementary structure have fairly wide bandwidth that can be used practically for various wideband wireless systems [31].

A typical example of SCA with small size is depicted in Fig. 46, where a monopole and its complementary slot are used to compose an SCA. Three antenna models shown in Fig. 47(a) are introduced here. In Fig. 47(a), the antenna dimensions and other parameters are also given. The antenna performances such as VSWR, radiation efficiency, and radiation patterns are illustrated in Fig. 47(b). As can be seen in the figures, the antenna has fairly wide bandwidth that cannot be obtained by other antennas of similar size.

8.1.3.3. Traveling Wave Structure

8.1.3.3.1. normal mode helical antenna (NMHA). Normal mode helical antenna is a helical antenna that radiates in the direction normal to the helical axis and the radiation patterns are essentially the same as that of a short dipole (Fig. 48). The dimensions of the helix are usually taken much smaller than the operating wavelength, the length of an individual turn being a small fraction of a wavelength λ and the axial length being also much less than a one-quarter λ . With this structure, an NMHA is equivalently expressed by an array of small loops and short monopoles (Fig. 49) [32]. Inductive imped-

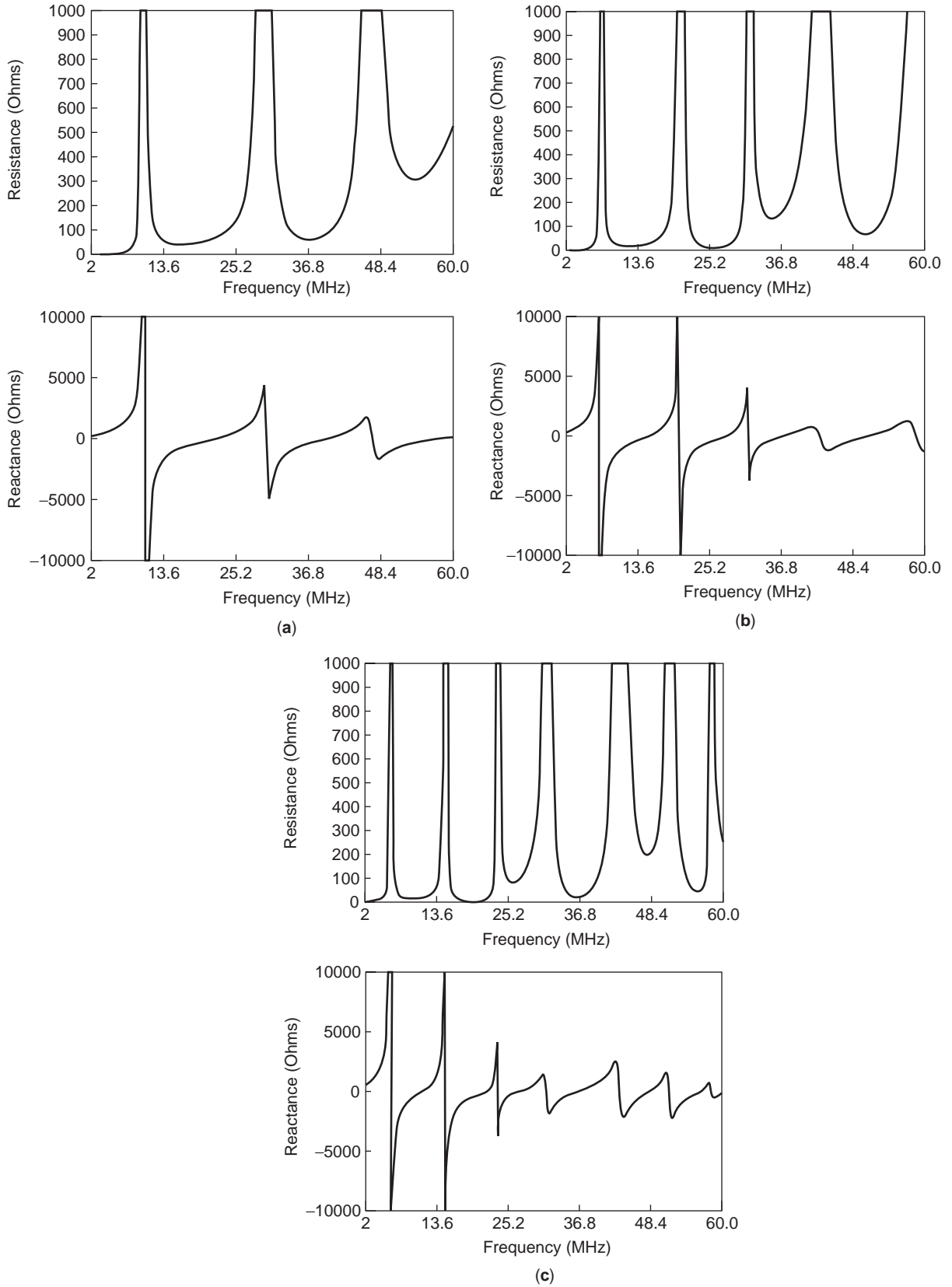


Figure 75. The impedances of the Minkowski island fractal antennas. (a) M11 fractal loop antenna. (b) M12 fractal loop antenna. (c) M13 fractal loop antenna. (From Ref. 39 with permission from IEEE.)

Table 1. The Performance Properties of the Euclidean Loop Antennas (From Ref. 39 with permission from IEEE.)

	Rectangular Loop		Circular Loop	
Resonant frequency (MHz)	29.22	56.33	29.22	57.72
Feed-point resistance (Ω)	134.2	268.6	139.6	183.8
SWR wrt 50 ohms	2.68	5.37	2.79	3.68
2:1 SWR bandwidth wrt resonant resistance (%)	8	8.9	8.3	6.2
Radiation efficiency (%)	99.3	99.6	99.4	99.4
Peak gain (dBi)	3.23	2.9	3.6	3.0
Overall dimensions (λ) (length by width or dia.)	0.273×0.259	0.526×0.50	0.332	0.656
Total enclosed area (λ^2)	0.071	0.263	0.087	0.338
Total wire length (λ)	1.065	2.054	1.044	2.061

Table 2. A Comparison of the Performances of the M10, M11, M12, and M13 Fractal Loop Antenna at their Resonant Frequencies (From Ref. 39 with permission from IEEE.)

	M10		M11		M12		M13	
Resonant frequency (MHz)	29.22	56.33	21.33	39.48	15.19	27.89	11.48	21.83
Feed-point resistance (Ω)	134.2	268.6	57.8	77.75	28.1	19.1	17.6	9.6
2:1 SWR bandwidth wrt resonant resistance (%)	8	8.9	3.14	2.1	1.18	0.39	0.61	0.13
Radiation efficiency (%)	99.3	99.6	98.1	98.1	94.1	89.5	81.8	66.7
Peak gain (dBi)	3.23	2.9	2.38	4.5	1.83	3.5	1.0	2.1
Overall dimensions (λ)	0.273×0.259	0.526×0.50	0.199×0.185	0.368×0.350	0.142×0.135	0.261×0.247	0.106×0.099	0.201×0.189
Total wire length (λ)	1.065	2.054	1.161	2.152	1.397	2.564	1.749	3.326

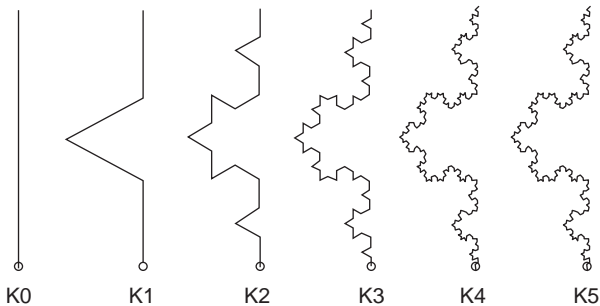


Figure 76. The geometrical configurations of the Koch fractal monopole antennas. (From Ref. 39 with permission from IEEE.)

Table 3. The Resonant Performance Characteristics of the Koch Fractal Monopole (From Ref. 39 with permission from IEEE.)

Koch Fractal Iteration	Resonant Frequency (MHz)	Resonant Resistance (ohms)	2:1 SWR Bandwidth (%)
K0	1201	36.8	8.5
K1	981.5	24.3	5.6
K2	835.2	18.5	4.3
K3	745.3	15.4	3.5
K4	691	13.8	3.1
K5	673.7	14.5	3.2

ance is increased by the array of loops and compensates the capacitive impedance of short monopoles. As a consequence, the helical structure can be arranged to have self-resonance property, although the antenna length (in the axial direction) is considerably shorter than that of a conventional resonant monopole or dipole antenna. Then the antenna efficiency can be improved, and extension of the antenna length may lead to increased bandwidth. The NMHA has been used in modern mobile phones worldwide.

An antenna model shown in Fig. 50 is considered. The impedance characteristics of an antenna having dimensions of the helical diameter $Dh = 0.018\lambda$, the pitch

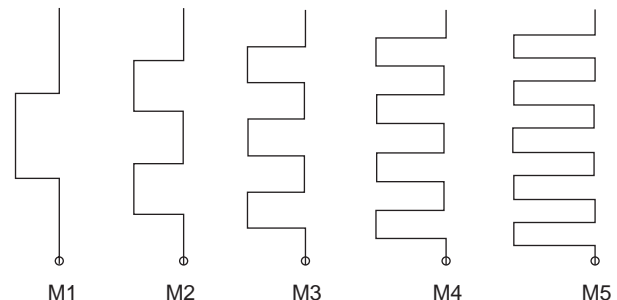


Figure 77. Meander-line antennas. (From Ref. 39 with permission from IEEE.)

Table 4. The Resonant Performance of the Meander-Line and NMHA Fractal Antennas (From Ref. 39 with permission from IEEE.)

Antenna Iteration	Resonant Frequency (MHz)	Resonant Resistance (ohms)	2:1 SWR Bandwidth (%)
K0	1201	36.8	8.5
M1	989.8	25.0	5.8
M2	809.5	17.7	4.0
M3	662.5	12.8	2.9
M4	544	9.8	2.1
M5	446.5	7.8	1.6
H1	975.7	24.6	5.7
H2	786.5	17.3	3.9
H3	634.6	12.4	2.7
H4	513.3	9.2	1.8
H5	413.6	7.3	1.4

$P = 0.006 \lambda$, and the wire diameter $2a = 0.0002 \lambda$ are shown in Fig. 51, where number of turns MT is taken as the variable parameter. Figure 52 shows the radiation efficiency with respect to the pitch. The design chart, by which design parameters can be found, are provided in Fig. 53 [33], where relationships between Dh and P are given. In Fig. 52, the parameter used in (b) is the number of turns MT, whereas that in (c) is the radiation resistance R at resonance.

8.1.3.3.2. meander line antenna. A meander line antenna is an antenna that has a periodical array structure of alternative square patterns as shown in Fig. 54. With this pattern, the extended wire length can be made much longer than the initial antenna (dipole) length so that the self-resonance can be attained. The resonance frequency is then lower and radiation resistance is higher than that of a dipole with the same length, which in turn implies that the antenna is effectively made small.

Here, a meander line dipole antenna shown in Fig. 54, where dimensional parameters are given, is considered [34]. Figure 55 shows the equivalent expression of the antenna, which is composed of a series connection of shorted two-wire transmission lines (a) and a monopole (b). By using this model, design parameters can be found. At first, a relationship between the resonance frequency f_0 and the wire radius B /pitch p is obtained, as Fig. 56 shows. Here, the planar line of width B is replaced equivalently by a

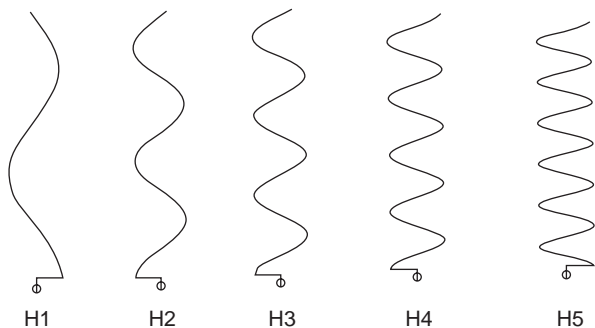


Figure 78. Normal mode helical antennas. (From Ref. 39 with permission from IEEE.)

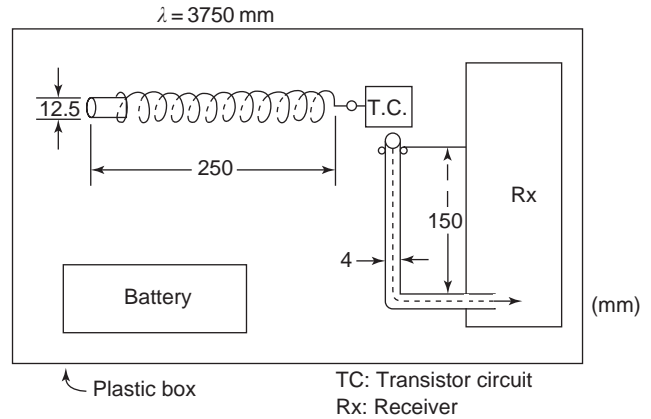


Figure 79. Inverted-L IAS. (From Ref. 40 with permission from Research Studies Press.)

wire of diameter d . When the resonance frequency f_0 is given, the number of turns N can be determined with prior knowledge of the wire radius B and the antenna width w by using Fig. 57. As the antenna length becomes shorter, the radiation resistance R_{rad} decreases. The ratio of the R_{rad} to that of a half-wave dipole is shown in Fig. 58 as a function of the antenna length-reduction ratio R_e . Figure 59 shows radiation efficiency η and number of turns N with respect to the length l (el) of the antenna.

In order to enhance the bandwidth, a meander line antenna is constituted with two strips in parallel, as shown in Fig. 60, where dimensional parameters are also given [35]. The antenna, which stands on a ground plane, can be equivalently modeled by a shorted two-wire transmission line with one line shorted at the ground plane [Fig. 61(a)] and further divided into two parts: balanced and unbalanced modes, respectively, as Fig. 61(a) and (b) show. Thus, a meander line antenna composed of two strips can be treated by an equivalent circuit shown in Fig. 62, where Z_u denotes impedance related with the unbalanced mode and Z_b with the balanced mode (the subscript u denotes the unbalance mode and B the balanced mode). With this model, antenna characteristics can be found and parameters necessary for the design are determined. Fig. 63 illustrates VSWR S with respect to frequency f along with various values of radiation resistance R_{rad} . Here, parameter $u = Q(2\Delta f)/f_0$, where Q is the quality factor of the antenna and $\Delta f = (f - f_0)$. An example of the antenna admittance $Y (= Gu + j(Bu + Bb))$ is shown in Fig. 64, where Gu and Bu , respectively, are conductance and susceptance of the balanced mode and Bb is susceptance of the balance mode. Relative bandwidth $Bm (= 2\Delta f_m/f_0)$ vs. VSWR S_m is shown in Fig. 65, where Δf_m is the maximum Δf and S_m is the maximum VSWR required.

8.1.3.3.3. fractal structure. Fractal structure is applied to miniaturization of antenna by using its space-filling property. The fractal geometry is known as a structure having infinitely iterative intricate fine contour. Starting from a Euclidean square (the initiator), for example, and replacing each segment of the geometry with the generator, Minkowsky fractal island is generated, as shown in Fig. 66 [36]. Significance of application of a fractal

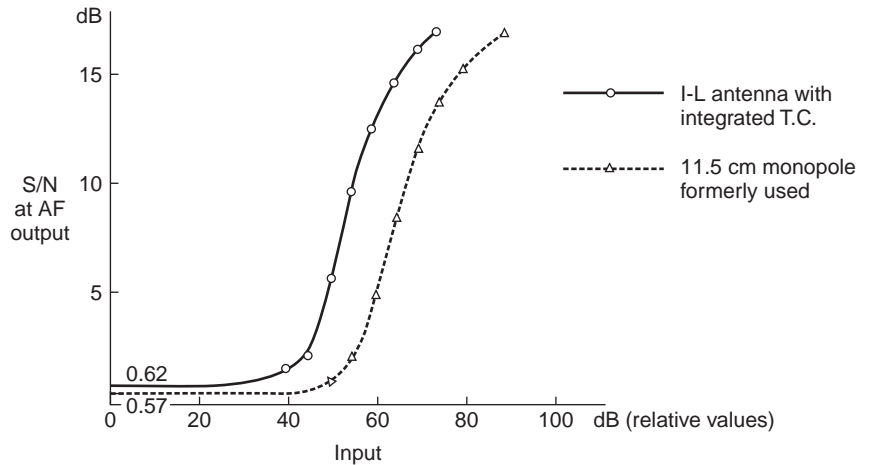


Figure 80. S/N gain performance of inverted-L IAS. (From Ref. 40 with permission from Research Studies Press.)

structure to antennas is two-fold; one is to endow the antenna with increased space-filling ability, attributed to the intricate shape to fit into a smaller physical area and bring an increase in the electrical length, by which resonance frequency can be lowered. Another is to increase the radiation resistance as a consequence of increase in the electrical length. These are effective ways to realize small antennas that have higher gain or lower Q as compared with the same size of conventional antennas.

The first example of how a fractal structure could be used for miniaturizing an antenna was the Koch fractal monopole (Fig. 67) [33], in which an antenna with better performance in terms of Q than the Euclidean monopole was demonstrated. Later, more intricate dipole structures have been analyzed [37]. These results have shown that the bandwidth of an antenna was improved when the antenna used more effectively the available volume of the virtual sphere that surrounds the antenna.

The geometrical configuration of the Koch fractal monopole antenna starts out as an equilateral triangle in a plane and forms snowflake shapes that are constructed by adding smaller and smaller triangles to the original structure in an iterative fashion, as Fig. 68 shows. Another popular fractal structure is Sierpinski gasket fractal, which is depicted in Fig. 69 [38]. This fractal is

constructed by removing smaller and smaller triangles, opposite to the Koch fractal, from the original structure.

Miniaturization of a loop antenna, as an example, is shown in Fig. 70, where the generation procedure starting from a square loop and the initiator are depicted [36]. The fractal is formed by displacing the middle third of each straight segment by some fraction of one-third, which is called the indentation width w that takes value from 0 to 1. The resulting structure has five segments for every one of the previous iteration, but not all of the same scale.

Antenna performance of a corner-fed small square loop and a first iteration Minkowsky fractal loop shown in Fig. 70 is compared in terms of input match, as shown in Fig. 71. It is observed that with the fractal structure the resonance frequency is lowered and better matching can be made, although the Minkowsky fractal has 15% smaller height than the small square loop. Radiation patterns are illustrated in Fig. 72, in which it is shown that the fractal structure produced an appreciable amount of horizontal

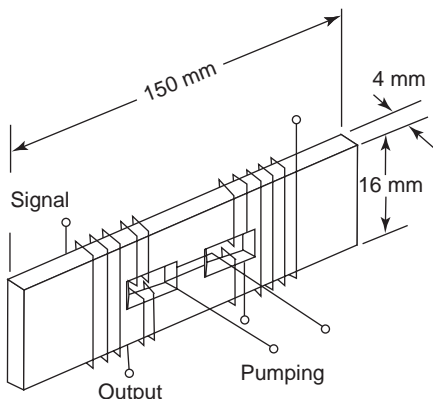


Figure 81. Ferrite IAS. (From Ref. 41 with permission from IEEE.)

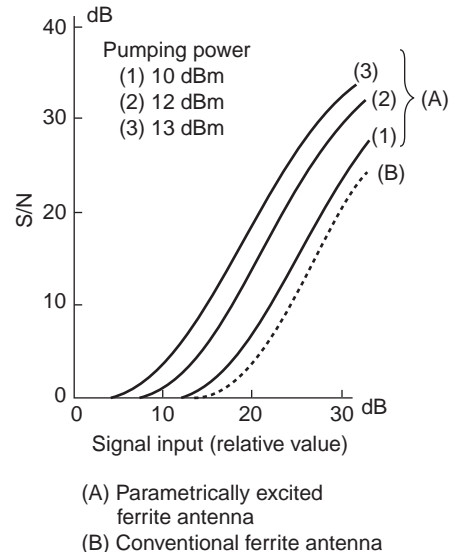


Figure 82. S/N gain performance of Ferrite IAS. (From Ref. 41 with permission from IEEE.)

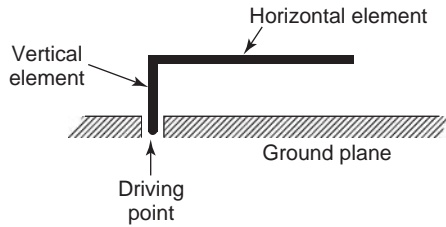


Figure 83. Inverted-L antenna.

patterns, as it has some horizontal components in its shape.

Various antenna performances have been studied for various types of fractal antennas [39]. For comparison, a square loop having a size of 2.66 m × 2.8 m and a circular loop having a radius of 1.704 m have been used. The impedances of these two antennas are shown in Fig. 73, whereas the impedance characteristics of fractal loops are shown in Fig. 74. Minkowsky fractals are shown in Fig. 75. The performances such as resonant frequency, feed point resistance, VSWR, radiation efficiency, dimensions, and so forth, are provided in Tables 1 and 2, where parameters are presented at the two lowest series-resonance frequencies. The progressive decrease in resonance frequency is observed; however, as the fractal iteration increases, the decrease in resonant frequency begins to converge to a lower limit, which implies that the benefit of lowering resonant frequency diminishes with a progressive increase in the fractal iteration.

Koch fractal monopoles shown in Fig. 76 have impedance properties presented in Table 3 and the resonant performance characteristics of other types of fractal structure, such as meander line (Fig. 77) and normal mode helix structure (Fig. 78), are shown by Table 4.

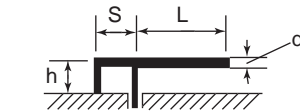
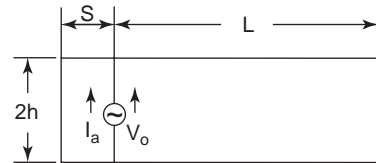
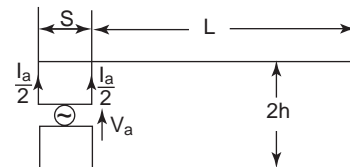


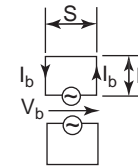
Figure 85. Inverted-F antenna.



(a)



(b)



(c)

Figure 86. Equivalent expression of inverted-F antenna. (a) Equivalent model of an inverted-F antenna with its image. (b) Part related with radiation. (c) Part related not with radiation.

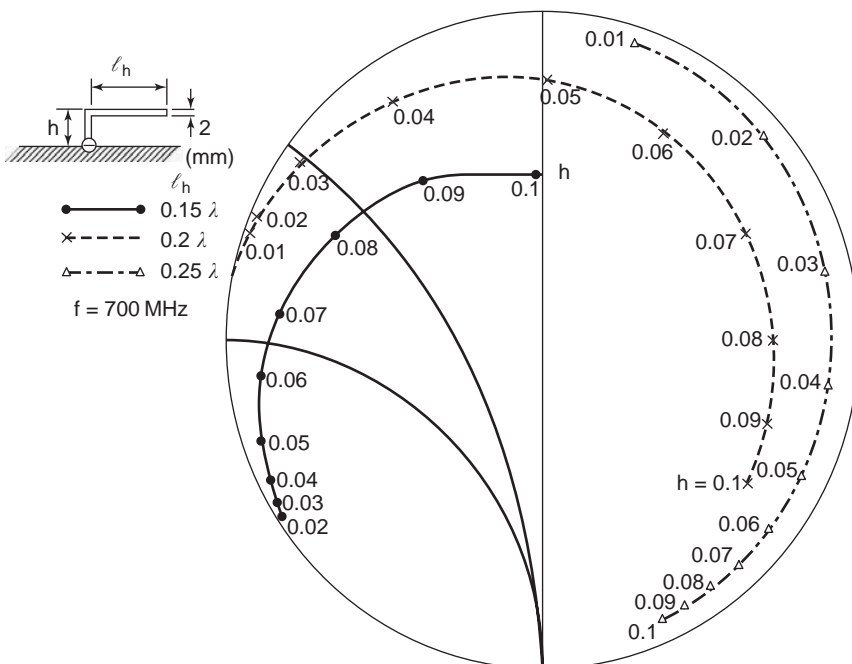


Figure 84. Input impedance of an inverted-L antenna. (From Refs. 43,45 with permission from Research Studies Press.)

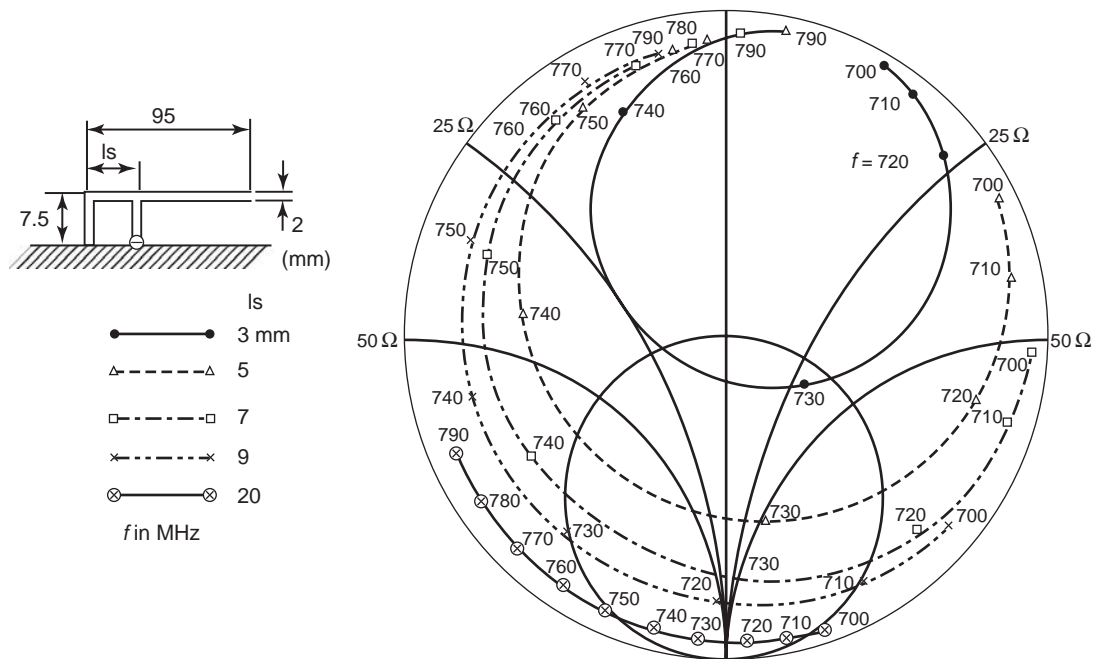


Figure 87. Input impedance of an inverted-F antenna. (From Ref. 43 with permission from Research Studies Press.)

8.1.4. Integrated Antennas Systems (IAS)

8.1.4.1. Inverted-L Integrated Antenna System. A transistor circuit was integrated into the middle of an inverted-L element, by which a long monopole antenna previously used was replaced [40]. With the Inverted-L

IAS, about 10 dB higher S/N gain over the conventionally used monopole antenna of about a one-third wavelength was attained. Figure 79 shows the antenna installed inside an 80 MHz small portable receiver. Figure 80 shows receiver S/N gain improvement over that when the monopole was used. This IAS can be referred to functionally small antenna, because downsizing of the antenna was attributed to integration of amplification function.

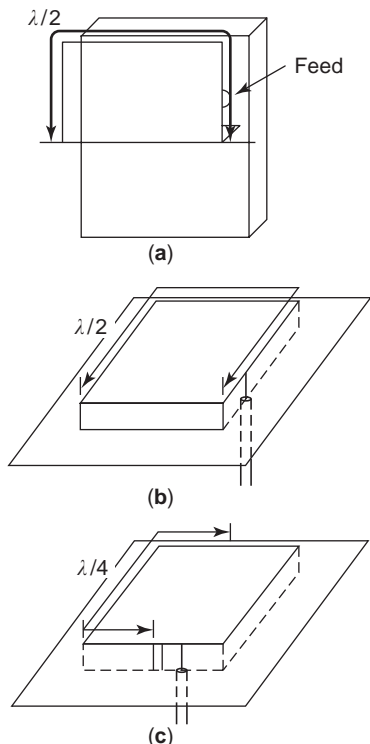


Figure 88. A slot mounted on the side of a rectangular conducting box.(a) Initial model. (b)A half-wavelength slot mounted on a rectangular conducting body.(c) Planar inverted-F antenna.

8.1.4.2. Ferrite AIAS (Active Integrated Antenna System). Gain of a small ferrite antenna was drastically increased by integrating parametric excitation into a ferrite antenna [41]. Figure 81 illustrates the antenna structure along with signal, pump, and output circuits. By the parametric excitation to a rectangular ferrite bar with pumping of 3 MHz, signal input of 1 MHz is transformed into output of 2 MHz with higher S/N gain than that of the same size ferrite antenna. S/N gain performance obtained is shown in Fig. 82, in which about 10 dB higher S/N gain can be seen.

This ferrite AIAS is a real “active” antenna, whereas in general active antennas, the radiator is not really “active,”

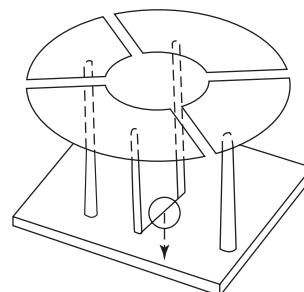


Figure 89. Goubau antenna. (From Ref. 45 with permission from IEEE.)

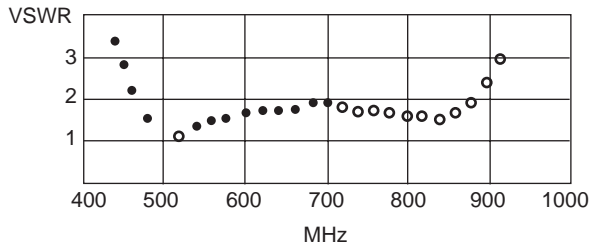


Figure 90. Bandwidth characteristics of Goubau antenna. (From Ref. 45 with permission from IEEE.)

but inherently passive, although it is called “active antenna.” In this ferrite AIAS, the part that is concerned with radiation (receiving) performs like a real “active” radiator as a consequence of the parametric excitation.

This antenna can be also classified into an FSA, as the smallness of antenna was achieved by integration of amplification function.

8.2. PCSA

8.2.1. Inverted-L Antenna. Inverted-L antenna (ILA) is an antenna that is composed of a short vertical element and a little longer horizontal element attached to the vertical element, as shown in Fig. 83. The ILA is a class of low-profile antenna and is classified in a physically constrained small antenna, because the height of the antenna is, in almost all cases, constrained to a fraction of the operating wavelength. The horizontal element is not necessarily short, but the length is usually shorter than a quarter wavelength (Fig. 84).

This type of antenna was used in ships in the early days of wireless communications and later at home for reception of broadcasting, as the antenna is very simple and easily built by using thin wires. As ILA has a feature of low profile and simple structure, it has been applied to various communication systems, particularly mobile communications. ILA does not have, however, really favorable characteristics, because the radiation resistance is very low and reactive impedance is very high, as shown in Fig. 85 [42]. Then, in practical applications, various modified antennas have been developed and used. The typical one is the inverted-F antenna (IFA), from which the planar inverted-F antenna (PIFA) has evolved. PIFA and its variations have been widely applied to mobile phones.

8.2.2. Inverted-F Antenna (IFA). IFA shown in Fig. 85 can be treated by an antenna shown in Fig. 86 (a) with

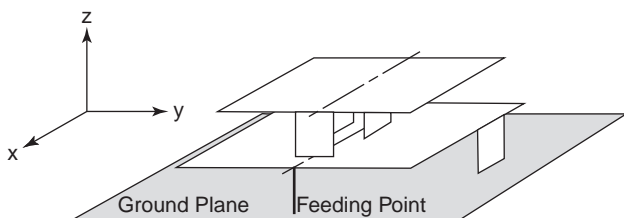


Figure 91. Multilayered antenna. (From Ref. 46 with permission from IEICE.)

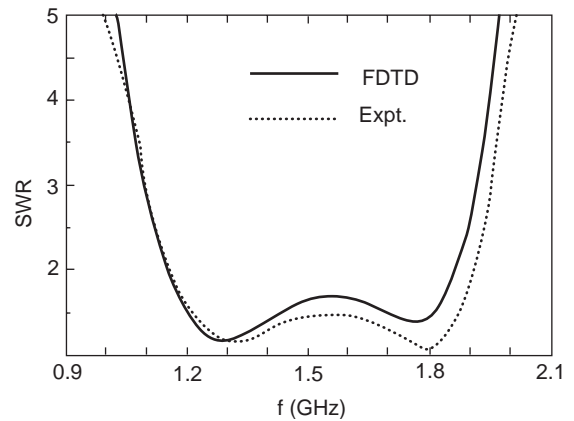


Figure 92. Bandwidth of the Multilayered antenna. (From Ref. 46 with permission from IEICE.)

its image. This IFA shown in Fig. 86(b) is equivalently decomposed into two parts: an ILA with its image and two two-wire shorted transmission lines, as Fig. 86(c) expresses. The two-wire transmission lines compensate capacitive

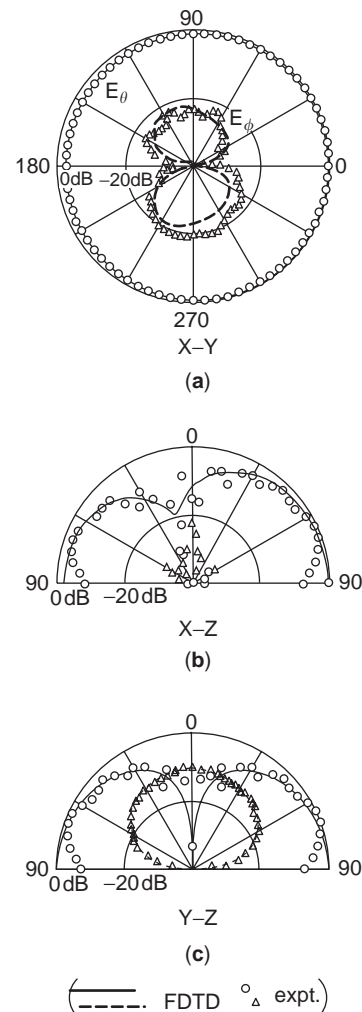


Figure 93. Radiation patterns of Multilayered antenna. (a) XY plane. (b) XZ plane. (c) YZ plane. (From Ref. 46 with permission from IEICE.)

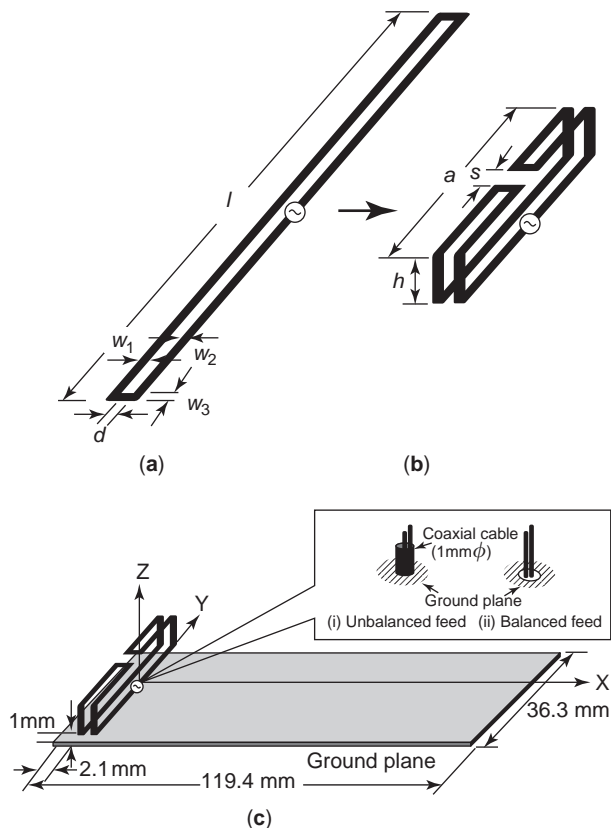


Figure 94. Folded-loop antenna. (a) Initial loop antenna. (b) Folded loop. (c) Antenna mounted on a ground plane. (From Ref. 47 with permission from IEICE.)

impedance of the ILA and, at the same time, stepup the input impedance so that matching to the 50 ohm load is made feasible. The input impedance of IFA is expressed by

$$Z_{in} = 4Za \cap 2Zb \tag{37}$$

where Za denotes the input impedance of the antenna shown in Fig. 86(b), Zh is the impedance of the shorted two-wire transmission line having the length h and

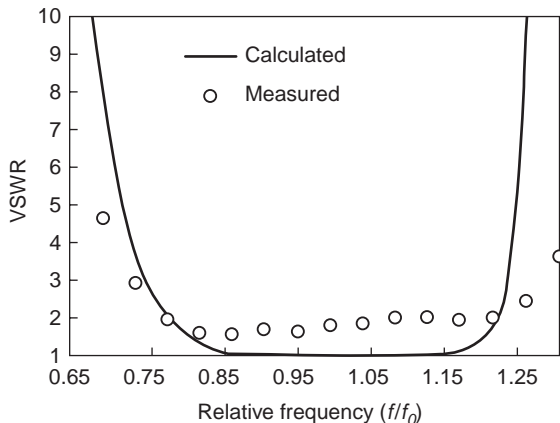


Figure 95. VSWR characteristics of folded-loop antenna. (From Ref. 47 with permission from IEICE.)

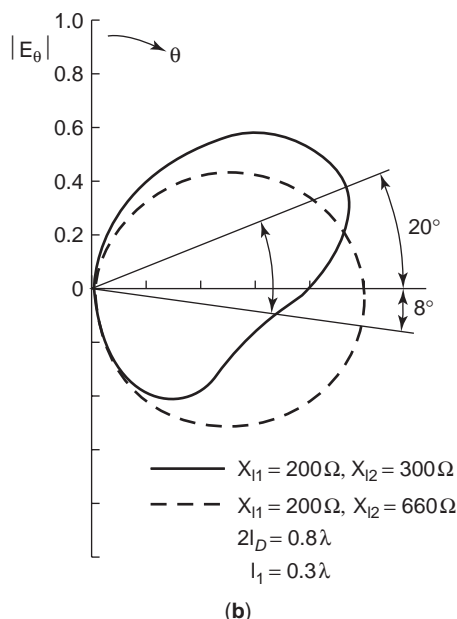
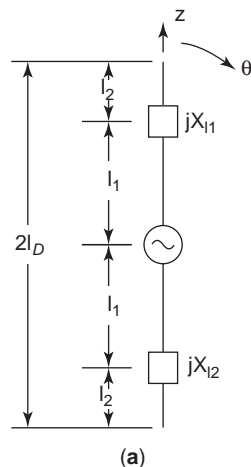


Figure 96. Two-reactance component integrated dipole antenna. (a) Antenna model. (b) Beam shifting performance of two-reactance component integrated antenna. (From Ref. 48 with permission from Research Studies Press.)

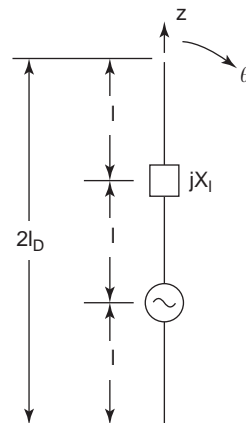


Figure 97. One-reactance component integrated dipole antenna. (From Ref. 48 with permission from Research Studies Press.)

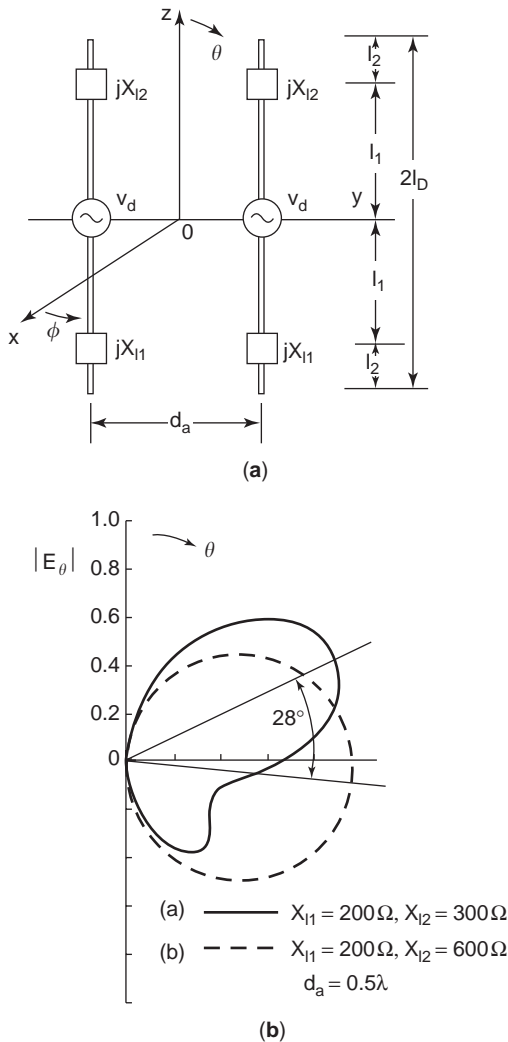


Figure 98. Array of two-reactance component integrated dipole antennas. (From Ref. 49 with permission from Research Studies Press.)

the width S , and \square expresses parallel combination of impedances.

The input impedance of an IFA can be adjusted by selecting S and h appropriately. An example is shown in Fig. 87 [43].

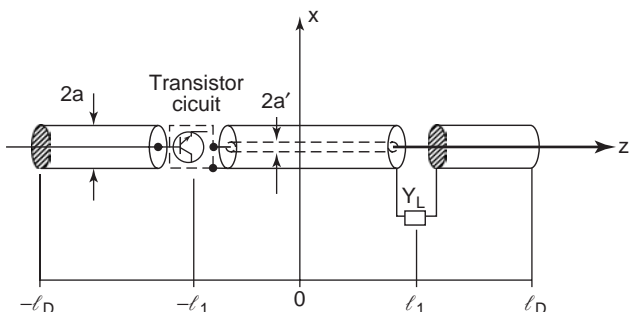


Figure 99. Transistor-circuit integrated inverted-L antenna. (From Ref. 50 with permission from Research Studies Press.)

8.2.3. Planar Inverted-F Antenna (PIFA). PIFA is a modified antenna from IFA being composed of a short vertical element and a planar horizontal element. However, it should be noted that PIFA is not an IFA, from which the horizontal element is simply replaced by a planar element. The principle of the PIFA performance differs from that of the IFA, because the source of radiation of PIFA is nearly a half wavelength aperture formed along the peripheral of the horizontal element, whereas that of IFA is a short vertical element and a quarter wavelength horizontal element. PIFA has initially started with a slot antenna placed on the side of a rectangular conducting body, as shown in Fig. 88(a). The slot has the length nearly a half wavelength and is fed at a point near a shorted end. The idea was born in the process of development of handset antennas. The basic concept is based on the handset antenna having a small and low-profile structure, and magnetic current as a source of radiation is recommended. This slot antenna satisfies these requirements. Meanwhile, the microstrip antenna (MSA) had been known as a useful planar antenna, having a small and low-profile structure. Then an attempt was made to place that slot antenna on a ground plane to form a planar structure like an MSA [Fig. 88(b)], and the performance was confirmed to be satisfactory for handset use. Finally, the antenna configuration was arranged to have a structure, as illustrated in Fig. 88(c), in which the shorted part is shown with reduced size for making the antenna size small. In a PIFA, its peripheral aperture of a half wavelength contributes to radiation, whereas in MSA, a patch end of a quarter wavelength does to radiation.

An initial attempt was made for increasing the bandwidth of a linear IFA by replacing the linear horizontal element with a planar element; however, it was not successful, as the bandwidth increase obtained was only 1–2%, unless otherwise increasing the height.

8.2.4. Disk-Loaded Antennas. Goubau developed a multielement sectored-disk antenna [44], which had a VSWR bandwidth of about 2 to 1. Figure 89 illustrates the antenna configuration. Two of the posts are connected to the ground plane, whereas two other posts are used for feed connections. The wideband performance is shown in Fig. 90.

Friedman later demonstrated a simple disk-loaded antenna, which had shown wideband performance of 2 to 1 or 3 to 1 in terms of VSWR [45]. He developed a wideband matching method to achieve a low VSWR over a desired bandwidth for small antennas and applied it to a small disk-loaded antenna, obtaining comparative wide bandwidth with the Goubau antenna. The disk antenna is integrated with impedance matching circuits, consisting of two parallel side posts and a conductive biconical center post located in the space under the disk. The concept of the matching circuit is basically a wideband double-tuning to impedance match to a line resistance.

8.2.5. Multilayered Antenna. A multilayered antenna demonstrated by Tokumaru has a small, low-profile, and

lightweight structure, and yet features very wideband performance [46]. The wide bandwidth was accomplished by the two-layered plate structure, with which multi-resonance performance was attained. The antenna structure and its dimensions are shown in Fig. 91. The SWR performance is illustrated in Fig. 92, by which wideband performance can be observed to be about 48%. The radiation patterns at 1.5 GHz are shown in Fig. 93. Similar radiation patterns were obtained at 1.8 GHz but not shown here. The measure of size reduction is evaluated by using a size reduction ratio $S = V/\lambda^3$, where V is the physical volume of the antenna. S of various antennas are compared. S of this antenna is 0.0057 when the dimensions are $60 \times 60 \times 20$ (mm) (1.5 GHz), whereas 0.0004 for a Planar Inverted-F antenna when the dimensions are $45 \times 30 \times 10$ (mm) (0.92 GHz), and 0.0052 for a stacked-MSA when the dimensions are $3.8 \times 3.8 \times 1.8$ (mm) (20 GHz).

8.2.6. Folded-Loop Antenna. A wideband folded-loop antenna, depicted in Fig. 94(c), has been demonstrated in [47]. The antenna is originally a one-wavelength rectangular loop, as shown in Fig. 94(a), and is folded to constitute a small, low-profile antenna, as shown in Fig. 94(b). Three resonance modes exist in the antenna structure that contributes to make this antenna wideband. The wideband performance in the 1 GHz band is illustrated in Fig. 95, in which about 40% or wider bandwidth can be observed.

This antenna is not really an ESA; however, because this sort of wideband characteristics may not ordinarily be accomplished by the same-sized antennas, this antenna may be said to be a functionally small antenna.

This antenna is designed to be used as a builtin antenna in a handset unit. In Fig. 94(c), two feeding methods, with either balanced line or unbalanced line, are shown. Use of the balanced linefeed is meaningful for antennas used in a handset, because it is effective to avoid an operator's hand effect on the antenna system, as the undesired current flow on the feeding cable can be reduced. This antenna has, however, the self-balance property, and hence either balanced or unbalanced feed can be used.

8.3. FSA

8.3.1. Integrated Antenna System

8.3.1.1. Reactance Component-Integrated Dipole Antenna (RCDA). Beam shifting or steering realized by a single dipole was demonstrated by using a 0.8-wavelength antenna, into which one or two reactance components were integrated [48], which is a typical example of FSA, because beam shifting, which usually needs at least two antennas, was accomplished by a single dipole, although the length was a little longer than a half wavelength. Beam shifting is attributed to asymmetrical current distributions on the dipole that was accomplished by asymmetrical integration of reactance components, as shown in Fig. 95, where two different reactance components were used. An example of beam shifting pattern is shown in Fig. 96, where parameters used are also shown.

When one reactance component, instead of two, is integrated into a dipole element, the reactance component is placed symmetrically with respect to the feed point so that asymmetrical current distribution on the dipole element is achieved, thereby beam shifting is attained. Figure 97 illustrates an example.

When beam steering or scanning is required, it can be achieved by varying the integrated-reactance values through electronic means.

8.3.1.2. Array of RCDA. Two elements of reactance component-integrated dipoles are arrayed, as shown in Fig. 98(a), and beam shifting achieved is shown in Fig. 98(b) [49]. As two-dimensional pattern control is feasible by using a RCDA, three-dimensional pattern control may be possible by array of two RCDA's, which implies possibility of array thinning by using RCDA.

8.3.1.3. Transistor Circuit-Integrated Dipole Antenna. Electronic beam control can be realized by integrating a transistor circuit into a dipole antenna. Figure 99 depicts an example [50], where a transistor circuit is placed asymmetrically with respect to the feed point, so that asymmetrical current distribution is realized. By varying the bias voltage to the transistor circuit, the circuit parameters are varied, resulting in pattern control.

BIBLIOGRAPHY

1. J. Rumsay, Highlight of antenna history, IEEE AP-S News Letter, Dec. 1981.
2. K. Fujimoto, A. Henderson, K. Hirasawa, and J. R. James, *Small Antennas*, Research Studies Press, Letchworth, Hertfordshire UK, 1987.
3. H. A. Wheeler, Fundamental limitations of small antennas, *Proc. IEEE*, **35**:1479-1484 (1947).
4. L. J. Chu, Physical limitations of omnidirectional antennas, *J. Appl. Phys.*, **19**:1163-1175 (1948).
5. H. A. Wheeler, The radiansphere around a small antenna, *Proc. IRE*, **47**:1325-1321 (1959).
6. R. W. P. King, *The Theory of Linear Antennas*, Harvard University Press, Cambridge, MA, 1956.
7. S. A. Shelkunoff and H. T. Friis, *Antenna Theory and Practice*, Wiley, New York, 1952.
8. R. F. Harrington, Effect of antenna size on gain, bandwidth and efficiency, *J. Res. Nat. Bur. Stand.*, **64**-D:1-12 (1960).
9. R. C. Hansen, Fundamental limitations in antennas, *Proc. IEEE*, **69**:170-182 (1981).
10. J. S. McLean, A re-examination of the fundamental limits on the radiation Q of electrically small antennas, *IEEE Trans. Ant. Propagat.*, **44**:672-675 (1991).
11. H. D. Foltz and J. S. McLean, Limits on the radiation Q of electrical small antenna restricted to oblong boundary regions, *IEEE AP-S Int. Symp.*, **4**:2702-2705 (1999).
12. D. M. Grimes and C. A. Grimes, Radiation Q of dipole-generated fields, *Radio Sci.*, **34**(2):281-296 (1999).
13. W. Geyi, Physical limitations of antennas, *IEEE Trans. Ant. Propagat.*, **51**(8):2116-2123 (2003).
14. G. A. Thiele, P. L. Detweiler, and R. P. Penno, On the lower bound of the radiation Q for electrically small antennas, *IEEE Trans. Ant. Propagat.*, **51**(6):1263-1269 (2003).

15. J. D. Kraus, *Antennas for All Applications*, 3rd ed., McGraw-Hill, New York, 2002, p.35.
16. K. Ishizone, Poynting vector flow in the vicinity of a dipole antenna, *IEICE Tech Report*, **AP-88**:38 (1981).
17. C. T. Tai, Cylindrical dipoles, 4-5, 4-6, in *Antenna Engineering Handbook*, 2nd ed., H. Jasik, ed., McGraw-Hill, New York (1984).
18. R. W. P. King, *The Theory of Linear Antennas*, Harvard University Press, Cambridge, MA, 1956.
19. W. L. Weeks, *Antenna Engineering*, McGraw-Hill, New York, 1968, pp. 41–46.
20. R. F. Harrington, *Time-harmonic Electromagnetic Transmissions*, McGraw-Hill, New York, 1961, p. 305.
21. R. L. Fante, Quality factor of general ideal Q, *IEEE Trans. Ant. Propagat.*, **AP-17**:151–155 (1969).
22. R. E. Collin and S. Rothschild, Evaluation of antenna Q, *IEEE Trans. Ant. Propagat.*, **AP-12**:23–27 (1964).
23. C. H. Walter, *Traveling Wave Antennas*, CAL Peninsula, CA, Los Altos, 1990.
24. K. Hirasawa and M. Haneishi, eds., *Analysis, Design, and Measurement of Small and Low-Profile Antennas*, Chapt. 9, Artech House, London, 1992.
25. I. Ida, T. Sekizawa, H. Yoshimura, and K. Ito, Dependence of the efficiency-bandwidth product of small dielectric loaded antennas on the permittivity, *Proc. ISAP*. 1:61–64 (2000).
26. E. D. Newman, P. Bohley, and C. H. Walter, Two methods for measurement of antenna efficiency, *IEEE Trans. Ant. Propagat.*, **AP-23**(3):457–461 (1975).
27. R. Y. Chao, K. Hirasawa, and K. Fujimoto, Wire antenna current distributions within a Wheeler cap, *Trans. IEICE*, **J71-B**(11):1370–1372 (1988).
28. pp. 86–106 in [2].
29. Y. Muashiake, The input impedance of a slot antenna, Joint Convention Record of Tohoku Section of IEE and IEIC of Japan, 1948, pp. 25–26.
30. Y. Mushiake, *Self-Complementary Antenna*, Springer-Verlag, New York, 1996.
31. P. Xu and K. Fujimoto, L-shaped self-complementary antenna, *IEEE APS Int. Symp.*, **3**:95–98 (2003).
32. J. D. Kraus, *Antennas for All Applications*, 3rd ed., McGraw-Hill, New York, 2002, pp. 293–294.
33. pp. 60–66 in [2].
34. T. Endo, Y. Sunahara, S. Satoh, and T. Katagi, Resonant frequency and radiation efficiency of meander line antenna, *Trans. IEICE*, **J80 B-II**(12):1044–1049 (1997). (in Japanese)
35. K. Noguchi, M. Mizusawa, T. Yamaguchi, Y. Okumura, and S. Betsudan, Increasing the bandwidth of a small meander line antenna consisting of two strips, *Trans. IEICE*, **J82-B**(3): 402–409 (1999). (in Japanese)
36. J. P. Gianvittorio and Y. R. Samii, Fractal antenna: a novel antenna miniaturization technique and applications, *IEEE AP Mag.*, **44**(1):20–36 (2002).
37. P. Baharda, C. Romeu, A. Cardama, The Koch monopole: a small fractal antenna, *IEEE Trans. Ant. Propagat.*, **AP-48**(11): 1773–1781 (2000).
38. D. H. Werner, An overview of fractal antenna engineering research, *IEEE AP Mag.*, **45**(1):38–56 (2003).
39. S. R. Best, Discussion on the significance of geometry in determining the resonant behavior of fractal and other non-Euclidean wire antennas, *IEEE AP Mag.*, **45**(3):9–28 (2003).
40. pp. 130–135 in [2].
41. K. Tamura and K. Fujimoto, A parametric-excitation-integrated ferrite antenna, *IEEE Trans. MAG-8*, **3**:384 (1972).
42. K. Fujimoto, A. Henderson, K. Hirasawa, and J. R. James, *Small Antennas*, Research Studies Press, UK, 1987, pp. 116–130.
43. pp. 120–121 in [2].
44. G. Goubau, Multi-element monopole antenna, *Proc. ECOM-ARO Workshop on Electronically Small Antennas*, Fort Monmouth, NJ, 1976, pp. 63–67.
45. C. H. Friedman, Wide-band matching of a small disk-loaded monopole, *IEEE Trans. Ant. Propagat.*, **AP-33**(10):1142–1148 (1985).
46. J. W. Yang, T. Iijima, and S. Tokumaru, Multiplates: low profile antenna, *Trans. IEICE*, **J80-BII**(12):1050–1057 (1997). (in Japanese)
47. S. Hayashida, H. Morishita, and K. Fujimoto, A wideband folded loop antenna for handsets, *Trans. IEICE*, **J86-B**(9):1739–1805 (2003).
48. pp. 152–159 in [2].
49. pp. 160–164 in [2].
50. K. Fujimoto, A. Henderson, K. Hirasawa, and J. R. James, *Small Antennas*, Research Studies Press, UK, 1987, pp. 164–181.
51. R. W. P. King and C. H. Harrison, *Antennas and Waves*, The MIT Press, 1969, p. 473.

SMART MATERIALS

OSAMA O. AWADELKARIM
 SAMIA A. SULIMAN
 The Pennsylvania State
 University
 University Park, Pennsylvania

1. INTRODUCTION

Since the industrial revolution in the second half of the eighteenth century engineering has made enormous advances in the design and manufacture of machinery and systems. All these advancements were based on traditional materials, which do not have particularly special physical or chemical properties. The traditional materials included metals, such as steel and gold, and insulators, such as glass. The machinery and systems developed included the wooden wheel, steam engine, and gaseous electronics.

Contemporary research on new machines and systems, however, focuses on the development of new materials and engineered material structures that possess unique properties that may be utilized in new engineering applications. This research involves the tailoring of some special material systems and structures in order to realize a particular physical or chemical property needed for a certain application. Alternatively, the research involves the discovery of new properties in some special groups of materials; these properties may open up the door for several new and exciting engineering applications.

15. J. D. Kraus, *Antennas for All Applications*, 3rd ed., McGraw-Hill, New York, 2002, p.35.
16. K. Ishizone, Poynting vector flow in the vicinity of a dipole antenna, *IEICE Tech Report*, **AP-88**:38 (1981).
17. C. T. Tai, Cylindrical dipoles, 4-5, 4-6, in *Antenna Engineering Handbook*, 2nd ed., H. Jasik, ed., McGraw-Hill, New York (1984).
18. R. W. P. King, *The Theory of Linear Antennas*, Harvard University Press, Cambridge, MA, 1956.
19. W. L. Weeks, *Antenna Engineering*, McGraw-Hill, New York, 1968, pp. 41–46.
20. R. F. Harrington, *Time-harmonic Electromagnetic Transmissions*, McGraw-Hill, New York, 1961, p. 305.
21. R. L. Fante, Quality factor of general ideal Q, *IEEE Trans. Ant. Propagat.*, **AP-17**:151–155 (1969).
22. R. E. Collin and S. Rothschild, Evaluation of antenna Q, *IEEE Trans. Ant. Propagat.*, **AP-12**:23–27 (1964).
23. C. H. Walter, *Traveling Wave Antennas*, CAL Peninsula, CA, Los Altos, 1990.
24. K. Hirasawa and M. Haneishi, eds., *Analysis, Design, and Measurement of Small and Low-Profile Antennas*, Chapt. 9, Artech House, London, 1992.
25. I. Ida, T. Sekizawa, H. Yoshimura, and K. Ito, Dependence of the efficiency- bandwidth product of small dielectric loaded antennas on the permittivity, *Proc. ISAP*. 1:61–64 (2000).
26. E. D. Newman, P. Bohley, and C. H. Walter, Two methods for measurement of antenna efficiency, *IEEE Trans. Ant. Propagat.*, **AP-23**(3):457–461 (1975).
27. R. Y. Chao, K. Hirasawa, and K. Fujimoto, Wire antenna current distributions within a Wheeler cap, *Trans. IEICE*, **J71-B**(11):1370–1372 (1988).
28. pp. 86–106 in [2].
29. Y. Muashiake, The input impedance of a slot antenna, Joint Convention Record of Tohoku Section of IEE and IEIC of Japan, 1948, pp. 25–26.
30. Y. Mushiake, *Self-Complementary Antenna*, Springer-Verlag, New York, 1996.
31. P. Xu and K. Fujimoto, L-shaped self-complementary antenna, *IEEE APS Int. Symp.*, **3**:95–98 (2003).
32. J. D. Kraus, *Antennas for All Applications*, 3rd ed., McGraw-Hill, New York, 2002, pp. 293–294.
33. pp. 60–66 in [2].
34. T. Endo, Y. Sunahara, S. Satoh, and T. Katagi, Resonant frequency and radiation efficiency of meander line antenna, *Trans. IEICE*, **J80 B-II**(12):1044–1049 (1997). (in Japanese)
35. K. Noguchi, M. Mizusawa, T. Yamaguchi, Y. Okumura, and S. Betsudan, Increasing the bandwidth of a small meander line antenna consisting of two strips, *Trans. IEICE*, **J82-B**(3): 402–409 (1999). (in Japanese)
36. J. P. Gianvittorio and Y. R. Samii, Fractal antenna: a novel antenna miniaturization technique and applications, *IEEE AP Mag.*, **44**(1):20–36 (2002).
37. P. Baharda, C. Romeu, A. Cardama, The Koch monopole: a small fractal antenna, *IEEE Trans. Ant. Propagat.*, **AP-48**(11): 1773–1781 (2000).
38. D. H. Werner, An overview of fractal antenna engineering research, *IEEE AP Mag.*, **45**(1):38–56 (2003).
39. S. R. Best, Discussion on the significance of geometry in determining the resonant behavior of fractal and other non-Euclidean wire antennas, *IEEE AP Mag.*, **45**(3):9–28 (2003).
40. pp. 130–135 in [2].
41. K. Tamura and K. Fujimoto, A parametric-excitation-integrated ferrite antenna, *IEEE Trans. MAG-8*, **3**:384 (1972).
42. K. Fujimoto, A. Henderson, K. Hirasawa, and J. R. James, *Small Antennas*, Research Studies Press, UK, 1987, pp. 116–130.
43. pp. 120–121 in [2].
44. G. Goubau, Multi-element monopole antenna, *Proc. ECOM-ARO Workshop on Electronically Small Antennas*, Fort Monmouth, NJ, 1976, pp. 63–67.
45. C. H. Friedman, Wide-band matching of a small disk-loaded monopole, *IEEE Trans. Ant. Propagat.*, **AP-33**(10):1142–1148 (1985).
46. J. W. Yang, T. Iijima, and S. Tokumaru, Multiplates: low profile antenna, *Trans. IEICE*, **J80-BII**(12):1050–1057 (1997). (in Japanese)
47. S. Hayashida, H. Morishita, and K. Fujimoto, A wideband folded loop antenna for handsets, *Trans. IEICE*, **J86-B**(9):1739–1805 (2003).
48. pp. 152–159 in [2].
49. pp. 160–164 in [2].
50. K. Fujimoto, A. Henderson, K. Hirasawa, and J. R. James, *Small Antennas*, Research Studies Press, UK, 1987, pp. 164–181.
51. R. W. P. King and C. H. Harrison, *Antennas and Waves*, The MIT Press, 1969, p. 473.

SMART MATERIALS

OSAMA O. AWADELKARIM
 SAMIA A. SULIMAN
 The Pennsylvania State
 University
 University Park, Pennsylvania

1. INTRODUCTION

Since the industrial revolution in the second half of the eighteenth century engineering has made enormous advances in the design and manufacture of machinery and systems. All these advancements were based on traditional materials, which do not have particularly special physical or chemical properties. The traditional materials included metals, such as steel and gold, and insulators, such as glass. The machinery and systems developed included the wooden wheel, steam engine, and gaseous electronics.

Contemporary research on new machines and systems, however, focuses on the development of new materials and engineered material structures that possess unique properties that may be utilized in new engineering applications. This research involves the tailoring of some special material systems and structures in order to realize a particular physical or chemical property needed for a certain application. Alternatively, the research involves the discovery of new properties in some special groups of materials; these properties may open up the door for several new and exciting engineering applications.

Traditional materials, on one hand, have very well established and limited physical properties that cannot be significantly altered. For example, metals have high electrical conductivities that change very slightly with temperature, and glass remains insulating over a wide temperature range. “Smart materials,” on the other hand, have properties that can be dramatically altered. For example, “semiconductors” are a special group of materials in which electrical conductivity can change by orders of magnitude as their temperatures and/or compositions are very slightly changed. Moreover, the optical properties of semiconductors can be significantly modulated by engineering a multitude of semiconductor structures incorporating different semiconductor films. Needless to say, these properties of semiconductors paved the way for a revolution in information technology, communication, and nanotechnologies. This revolution is fueled by advancements in nanoscale electronics, optics, and mechanics.

The group of smart materials reviewed in this article includes (1) semiconductors, (2) superconductors, (3) piezoelectric materials, and (4) shape memory materials. Our choice of these materials for review in this article does not limit the list of smart materials to this group of materials. Indeed, it is very well known by now that several other materials, such as liquid crystals and rheostatic materials, possess very interesting properties that are widely employed in many exciting engineering applications. However, the group of smart materials discussed here is particularly important to the advancement of the rapidly expanding fields of nanoelectronics and integrated circuits (ICs), nano/micromechanical systems (N/MEMS), optoelectronics, and communication.

2. SEMICONDUCTORS

To fabricate ICs or N/MEMS, many different kinds of bulk materials and thin films are used. We will refer to these bulk materials and thin films used in IC and N/MEMS fabrication as *electronic materials* [1]. The bulk materials are predominantly semiconductor materials. The most important semiconductors in IC fabrication are silicon and gallium arsenide. The thin films used in IC fabrication can be classified into four groups: thermal silicon dioxide, dielectric layers, polycrystalline silicon (poly-Si), and metal films. The dielectric layers include deposited silicon dioxide (sometimes referred to as *the oxide*), and silicon nitride. These dielectrics are used for insulation between conducting layers, for diffusion and ion implantation masks, for structural components in N/MEMS, and for passivation to protect devices from impurities, moisture,

and scratches. Poly-Si is used as a gate electrode in metal-oxide-semiconductor (MOS) devices, as a conductive material for multilevel metallization, as a contact material for devices with shallow junctions, and as a structural material in N/MEMS. Metal films are used to form low-resistance interconnections and rectifying metal-semiconductor barriers. The thermal oxide is usually a better quality oxide (compared to deposited oxide) and is used for the gate oxide layers in field effect transistors. It is, hence, apparent that semiconductors are the backbone for ICs and N/MEMS since they are used in both their crystalline and polycrystalline forms as well as they are used in the chemical growth of dielectric films needed for device operation and protection. The sections below focus on the properties of semiconductors and demonstrate the multitude of smart characteristics associated with these materials.

2.1. Electrical and Chemical Properties of Semiconductors

Semiconductors are inorganic materials made from elements in the fourth column (group IV) of the periodic table. Semiconductor materials from group IV elements in the periodic table include silicon, germanium, and carbon (diamond); semiconductors from group IV elements are called *elemental semiconductors*. Semiconductor materials can also be made from a combination of elements from either group III and group V or group II and group VI; these are called *compound semiconductors*. Examples of these are gallium arsenide and zinc telluride materials. The term *semiconductor* is given to these materials because above certain temperature regimes they are able to exhibit good electrical conduction properties, and below these temperature regimes they behave as insulators.

Among the elemental semiconductors, Si is by far the most commonly used semiconductor. Si is the most important material for nano/microelectronics and IC technology. Also, Si-based compounds and technologies are becoming the major cornerstones for the rapidly developing fields of N/MEMS and nanofabrication. For this reason we will be emphasizing Si and use it in demonstrating several semiconductor properties. Table 1 lists a few of the mechanical, electrical, and thermal properties of single-crystalline silicon. GaAs, on the other hand, is the most common of the compound semiconductors, and it is widely used in fabricating optical and high-speed devices.

The crystal structure of many semiconductors, including Si and GaAs, is the *diamond lattice* (Fig. 1a). Diamond structure is that of two interleaved face-centered cubic arrays with one array displaced a fraction of the interatomic distance from the other. In the GaAs type of

Table 1. Electrical, Mechanical, and Thermal Properties of Crystalline Silicon

Electrical		Mechanical		Thermal	
Resistivity (P-doped)	1–50 $\Omega \cdot \text{cm}$	Yield strength	$7 \times 10^9 \text{ N/m}^2$	Thermal conductivity	1.6 W/cm \cdot $^\circ\text{C}$
Resistivity (Sb-doped)	0.005–10 $\Omega \cdot \text{cm}$	Young's modulus	$1.9 \times 10^{11} \text{ Pa}$	Thermal expansion	$2.3 \times 10^{-6} \text{ }^\circ\text{C}^{-1}$
Resistivity (B-doped)	0.005–50 $\Omega \cdot \text{cm}$	Density	2.3 g/cm ³		
Minority-carrier lifetime	30–300 μs	Dislocations	<500/cm ²		

Source: Ref. 1.

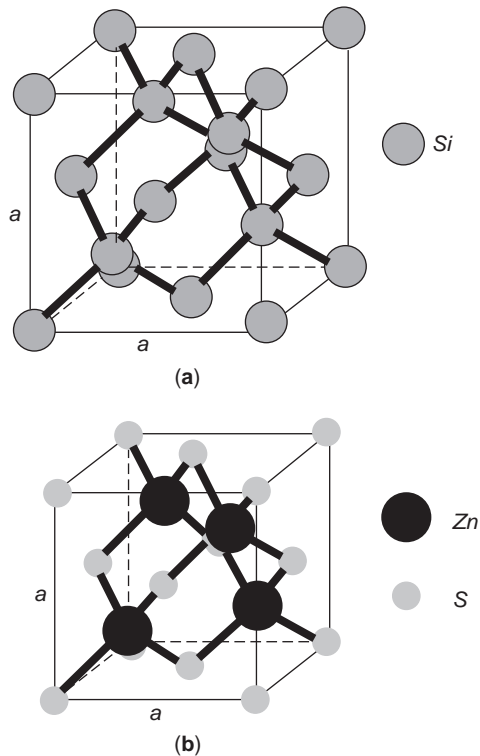


Figure 1. Semiconductor crystal structures: (a) diamond; (b) zincblende.

compound, one of the two arrays is composed entirely of Ga atoms, while the other array is composed of As atoms. This particular class of the diamond structure, called the *zincblende*, is shown in Fig. 1b for the II–VI compound semiconductor zinc sulfide. In the diamond lattice each atom has four nearest neighbors. In both elemental and compound semiconductors, there is an average of four valence electrons per atom. Each atom is thus held in the crystal by four covalent bonds with two electrons participating in each bond. In a perfect semiconductor crystal and at absolute zero temperature the number of electrons available would exactly fill the inner atomic shells and the covalent bonds. At temperatures above absolute zero some of these electrons gain enough thermal energy to break loose from these covalent bonds and become *free electrons*. This thermal energy relates to a quantum-mechanical property of the semiconductor crystal called the *energy gap*, often written as E_g and expressed in electronvolts (eV). The smaller the energy gap, the lower the temperature at which the semiconductor becomes conducting. Free electrons are responsible for electrical conduction across the semiconductor crystal. Some of the physical properties of selected elemental and compound semiconductor crystals are given in Table 2.

2.2. Growth and Deposition: Single-Crystalline and Polycrystalline Silicon

To demonstrate the methods of growing semiconductors we will consider growth of single-crystal silicon in details. We choose silicon since it is the most utilized semiconduc-

Table 2. Structure and Lattice Properties for Some Known Semiconductors^a

Material	Lattice Structure	Lattice Constant (Å)	Energy Gap (eV)
Ge	Diamond	5.66	0.66
Si	Diamond	5.43	1.12
InSb	Zincblende	6.46	0.18
InAs	Zincblende	6.04	0.33
InP	Zincblende	5.86	1.25
GaAs	Zincblende	5.64	1.44
GaSb	Zincblende	6.12	0.78
PbSe	Zincblende	6.14	0.27
PbTe	Zincblende	6.34	0.30

^aThe lattice constant a (see Fig. 2) and bandgap are given at $T = 300$ K. Source: Ref. 1.

tor in nano/microelectronics and N/MEMS. Basically, the technique used for silicon crystal growth from the melt is the *Czochralski technique* [2]. The technique starts from a pure form of sand (SiO_2) called *quartzite* placed in a furnace with different carbon-releasing materials such as coal and coke. Several reactions take place inside the furnace and high purity metallurgy-grade silicon (MGS) is produced. The Czochralski technique uses the apparatus shown in Fig. 2, called the *puller*. The puller comprises

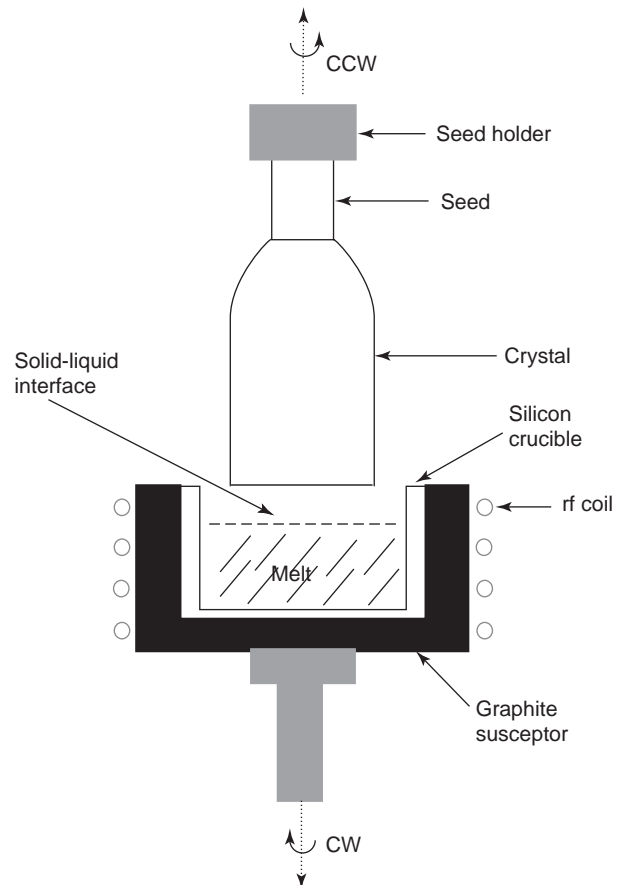


Figure 2. A schematic view of the puller: the apparatus used in the Czochralski growth of Si [1].

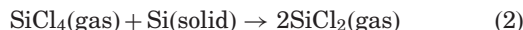
three main parts: (1) a furnace that consists of a fused-silica (SiO_2) crucible, a graphite susceptor, a rotation mechanism, a heating element, and a power supply; (2) a crystal pulling mechanism, which is composed of a seed holder, and a rotation mechanism; and (3) an ambient control, which includes a gas source (usually an inert gas), a flow control, and an exhaust system. In the crystal growth process, MGS is placed in the crucible and the furnace is heated above the melting temperature of Si. An appropriately oriented seed crystal (e.g., [100]) is suspended over the crucible in a seed holder. The seed is lowered into the melt. Part of it melts but the tip of the remaining seed crystal still touches the liquid surface. The seed is then gently withdrawn. Progressive freezing at the solid-liquid interface yields a large single crystal ingot. Finally the ingot is sliced by diamond saw into wafers.

The method for growing single-crystal silicon layer on a substrate wafer is *epitaxial* process where the substrate wafer acts as a seed crystal. Epitaxial processes are different from crystal growth from the melt in that the epitaxial layer can be grown at a temperature very much below the melting point. Among various epitaxial processes, vapor-phase epitaxy (VPE) is the very common process for single-crystal silicon layer growth.

A schematic of the VPE apparatus is shown in Fig. 3. The figure shows a horizontal susceptor made from graphite blocks. The susceptor mechanically supports the wafer, and in induction-heated reactor it also serves as the source of thermal energy for the reaction. Several silicon sources are usually used: silicon tetrachloride (SiCl_4), dichlorosilane (SiH_2Cl_2), trichlorosilane (SiHCl_3), and silane (SiH_4). The typical reaction temperature for silicon tetrachloride is $\sim 1200^\circ\text{C}$. The overall reaction in the case of silicon tetrachloride is reduction by hydrogen [2]:



A competing reaction, which would occur simultaneously, is



In reaction (1) silicon is deposited on the wafer, whereas in reaction (2) silicon is removed (*etched*). Therefore if the

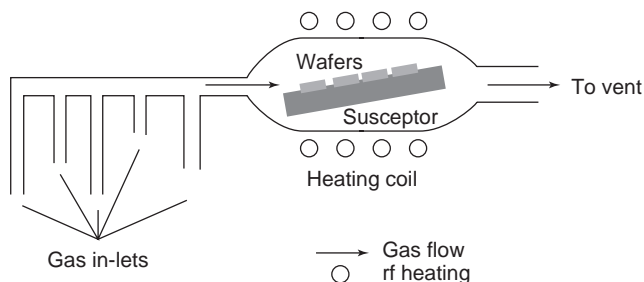
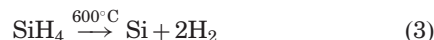


Figure 3. A schematic view of a typical VPE apparatus [1].

concentration of SiCl_4 is too high, etching rather than growth of silicon will take place.

An alternative epitaxial process for single-crystal silicon layer growth is molecular-beam epitaxy (MBE), which is an epitaxial process involving the reaction of a thermal beam of silicon atoms with a silicon wafer surface under ultrahigh vacuum conditions ($\sim 10^{-10}$ Torr). MBE can achieve precise control in both chemical composition and impurity (if introduced intentionally) profiles. Single-crystal multilayer structures with dimensions of the order of atomic layers can be made using MBE.

Polycrystalline silicon is often used as a structural material in N/MEMS. Poly-Si is also used in ICs and N/MEMS for electrode formation and as a conductor or high-value resistor depending on its doping level. A low-pressure reactor, such as the one shown in Fig. 3, operated between 600 and 650°C is used to deposit poly-Si by pyrolyzing silane according to the following reaction [2]:



The most common low-pressure processes used for poly-Si deposition are the ones that operate at pressures between 0.2 and 1.0 torr using 100% silane. Another process for poly-Si deposition involves a diluted mixture of 20–30% silane in nitrogen.

2.3. Doping

A pure semiconductor with insignificantly low concentrations of “impurities” is referred to as an *intrinsic semiconductor*. However, when impurities are intentionally added to a semiconductor the semiconductor is said to be “doped” with impurities. Figure 4a shows a hypothetical two-dimensional Si crystal in which one Si atom is replaced (or substituted) by an atom from group V elements in the periodic table, namely, phosphorus. Phosphorus has five valence electrons as opposed to Si, which has only four. The phosphorus atom will share four of its electrons with four neighboring Si atoms in covalent bonds. The remaining fifth valence electron in phosphorus is loosely bound to the phosphorus nucleus. Using the hydrogen atom model, one can estimate the ionization energy of E_d , an impurity atom in a semiconductor crystal as

$$E_d = \left(\frac{\epsilon_0}{\epsilon_s}\right)^2 \left(\frac{m_n^*}{m}\right) E_n \quad (4)$$

where ϵ_0 is the permittivity of free space, ϵ_s is that of the semiconductor, m is the electron’s mass, and m_n^* is its effective mass in the semiconductor crystal. When the phosphorus atom in Si is ionized, the released electron becomes a free electron, which is available for conduction. The phosphorus atom is, hence, called a *donor* atom since it donates a free electron to the crystal. All atoms with five valence electrons can potentially do the same thing done by phosphorus to the Si crystal, that is, donate a free electron to the semiconductor crystal; however, the amount of energy needed E_d for this process to occur may differ from one type of donor atom to another. Atoms

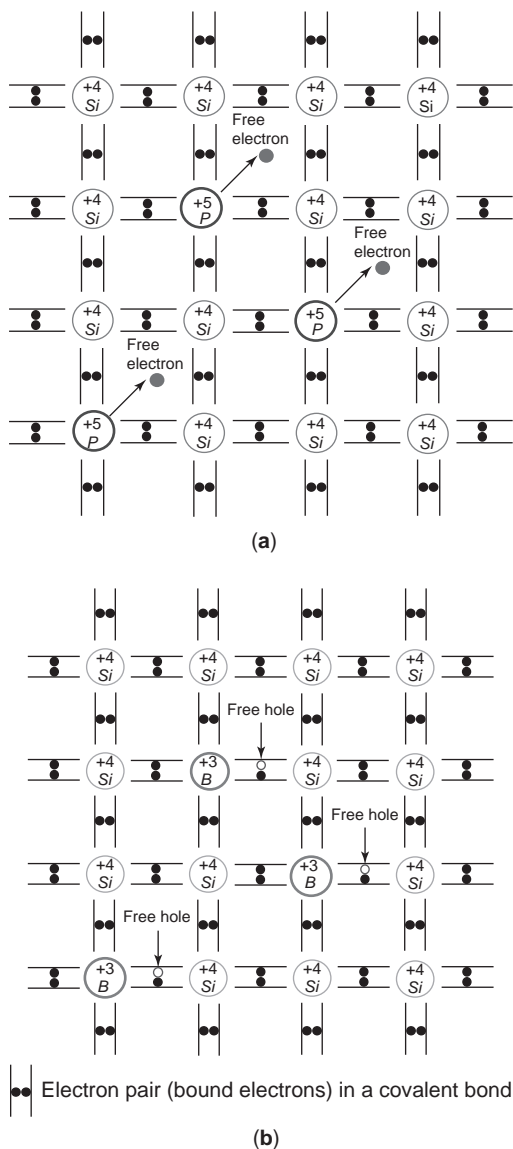


Figure 4. The effects of doping on a hypothetical two-dimensional Si crystal: (a) ntype; (b) ptype.

with five valence electrons are those in group V of the periodic table. These atoms will donate electrons if they substitute for host atoms in crystals of group IV elemental semiconductors. The atoms in group V of the periodic table, such as phosphorus or arsenic, are called *donor atoms* or simply *donors*, and the doped semiconductor is now called *extrinsic semiconductor*.

If one is able to introduce a large concentration of phosphorus atoms in an otherwise pure Si crystal, such as a phosphorus atom concentration of $\sim 10^{15} \text{ cm}^{-3}$, then with a minimal energy supply, these phosphorus atoms will donate each an electron to the crystal amounting to a concentration of electrons in the conduction band of the order of 10^{15} cm^{-3} at room temperature. This concentration of electrons is to be contrasted with the concentration of conduction electrons in an intrinsic Si at room temperature, which is of the order of 10^{10} cm^{-3} . With this doping level a five-order-of-magnitude increase in the free-electron

concentration is achieved. Note that in a solid there are $\sim 10^{22}\text{--}10^{23} \text{ atoms/cm}^3$ and a doping level of $\sim 10^{15} \text{ cm}^{-3}$ is equivalent to merely replacing one Si atom in every $10^7\text{--}10^8 \text{ atoms/cm}^3$ by a phosphorus atom. Clearly this level of doping introduces a very insignificant change in the overall crystal structure, but its effect on the free-electron concentration is apparently very significant. Therefore, conduction in phosphorus-doped Si is dominated by electrons. This type of extrinsic semiconductor, or more specifically Si, is called *n-type semiconductor* or *n-type Si*. The term *n type* indicates that the charge carriers are the negatively charged electrons. The example discussed above was specific to Si doped with phosphorus; however, the conclusions arrived at will generally apply to all elemental semiconductors doped with atoms of a group V element; thus, any elemental semiconductor doped with atoms from group V elements becomes an n-type semiconductor. The ionization energies E_d for several group V donors in Si are given in Table 3.

We now consider the situation where our elemental semiconductor is doped with atoms from an element in group III of the periodic table, specifically, atoms that have only three valence electrons. To be more specific, we will take as an example Si doped with boron as is shown in the hypothetical two-dimensional Si lattice in Fig. 4b. As can be seen from Fig. 4b, the net effect of having a boron atom substituting for Si is the creation of a free “hole” (an electron deficiency in a covalent bond). This hole, which is essentially a positively charged particle with the same charge magnitude as that in an electron, is generated as follows. Since boron has three valence electrons, three neighboring Si atoms will be bonded covalently with boron; however, the fourth nearest-neighbor Si atom has one of its four valence electrons sitting in a dangling bond—thus the whole system of the boron atom and the four neighboring Si atoms is missing one electron. An electron from a neighboring Si-Si covalent bond may replace the missing electron, thereby creating an electron deficiency (a hole) at the neighboring bond. The net effect is hence the generation of a *free hole* in the Si crystal. Therefore this type of extrinsic semiconductor, Si in this particular example, is called *p-type semiconductor* or *p-type Si*. It is p-type because electrical conduction is carried out by positively charged free holes. Common acceptor atoms to silicon are listed in Table 3.

Diffusion and *ion implantation* are the two key processes used to introduce controlled amounts of dopants

Table 3. Common Donor and Acceptor Atoms in Si Together with Their Ionization Energies

Atom	Atomic Number	Type	Ionization Energy in Si (eV)
Boron	5	Acceptor	0.045
Aluminum	13	Acceptor	0.057
Phosphorus	15	Donor	0.044
Gallium	31	Acceptor	0.065
Arsenic	33	Donor	0.049
Indium	49	Acceptor	0.160
Antimony	51	Donor	0.039

Source: Ref. 2.

into semiconductors. These two processes are used to selectively dope the semiconductor substrate to produce either n-type or a p-type region. In the diffusion method the dopant atoms are placed on the surface of the semiconductor by deposition from the gas phase of the dopant or by using doped-oxide sources. Diffusion of dopants is typically done by placing the semiconductor wafers in a furnace and passing an inert gas that contains the desired dopant through it. Temperatures for doping range between 800 and 1200°C for silicon. The diffusion process is described in terms of Fick's diffusion equation [3]

$$\frac{\partial C}{\partial t} = D \frac{\partial^2 C}{\partial x^2} \quad (5)$$

where C is the dopant concentration, D is the diffusion coefficient, t is time, and x is measured from the wafer surface in a direction perpendicular to the surface. Typical values for D at $\sim 900^\circ\text{C}$ are of the order of $10^{-14} \text{ cm}^2/\text{s}$ [4].

Ion implantation is the process whereby high-energy ions are thrown at a semiconductor substrate. Typical ion energies used in ion implantations are in the range 20–200 keV, and ion densities could vary between 10^{11} and 10^{16} ions/cm² incident on the wafer surface. Commonly implanted elements are boron, phosphorus, and arsenic for doping elemental n- or p-type semiconductors. After implantations wafers are rapidly thermally annealed to electrically activate the dopants. Oxygen is also implanted in silicon wafers to form buried oxide layers.

2.4. Piezoresistivity in Semiconductors

Piezoresistivity is defined as the change in the resistivity of a material when subjected to a mechanical stress. The prefix *piezo* is Greek for “to press.” All materials probably have a piezoresistance effect to some extent, but it is particularly important in some semiconductors. Silicon exhibits piezoresistivity in either one of its p-type or n-type forms and because of this silicon is very commonly used in the fabrication of strain gauges and force/pressure sensors. The fact that Si crystal is anisotropic has made the relation between the change in resistivity and the applied stress more complex. For a three-dimensional Si crystal of resistivity ρ , the change in resistivity tensor $\Delta\rho$ and the stress tensor (σ values for the normal stress components and τ values for shear stress components) are related via a 6×6 piezoresistive coefficient matrix [π] as [5,6]

$$\frac{1}{\rho} \begin{bmatrix} \Delta\rho_{xx} \\ \Delta\rho_{yy} \\ \Delta\rho_{zz} \\ \Delta\rho_{xy} \\ \Delta\rho_{yz} \\ \Delta\rho_{zx} \end{bmatrix} = \begin{bmatrix} \pi_{11} & \pi_{12} & \pi_{12} & 0 & 0 & 0 \\ \pi_{12} & \pi_{11} & \pi_{12} & 0 & 0 & 0 \\ \pi_{12} & \pi_{12} & \pi_{11} & 0 & 0 & 0 \\ 0 & 0 & 0 & \pi_{44} & 0 & 0 \\ 0 & 0 & 0 & 0 & \pi_{44} & 0 \\ 0 & 0 & 0 & 0 & 0 & \pi_{44} \end{bmatrix} \begin{bmatrix} \sigma_{xx} \\ \sigma_{yy} \\ \sigma_{zz} \\ \tau_{xy} \\ \tau_{yz} \\ \tau_{zx} \end{bmatrix} \quad (6)$$

where we notice that only three piezoresistive coefficients— π_{11} , π_{12} , and π_{44} —are nonzero for Si. π_{11} and π_{12} are associated with the normal stress components σ_{xx} , σ_{yy} ,

Table 4. Piezoresistance Coefficients for Si at Room Temperature

	ρ	π_{11} in $10^{-11}(\text{Pa})$	π_{12} in $10^{-11}(\text{Pa})$	π_{44} in $10^{-11}(\text{Pa})$
p-type Si	7.8	+6.6	−1.1	+138.1
n-type Si	11.7	−102.2	+53.4	−13.6

Source: Ref. 7.

and σ_{zz} , whereas the coefficient π_{44} is associated with the shear stress components. The values of these coefficients in Si at room temperature are given in Table 4. If we denote the piezoresistive coefficients of a piezoresistor along the longitudinal and transverse directions by π_L and π_T , respectively, then the relative change in resistance $\Delta R/R$ of the piezoresistor may be written as

$$\frac{\Delta R}{R} = \pi_L \sigma_L + \pi_T \sigma_T \quad (7)$$

where σ_L and σ_T are the longitudinal and tangential stresses, respectively. The piezoresistive coefficients for p-type Si piezoresistor in the longitudinal (x -axis) and tangential (y -axis) directions are given in Table 5.

2.5. Temperature Effects on Semiconductors

Thermoresistors are those materials for which the resistivity is a strong function of temperature. There are two types of thermoresistors: metal thermoresistors and semiconducting thermoresistors. The term *thermistor* is generally given to a semiconductor thermoresistor. The use of intrinsic semiconductors as thermistors is attractive because the resistivity's dependence on temperature is practically controlled by the carrier generation mechanism, namely, free-carrier concentrations n for electrons and p for holes as functions of temperature, rather than the “mobilities” of electrons and holes in the semiconductor. This is because the temperature-dependence of mobility in intrinsic semiconductors is much weaker than that of n and p . In an intrinsic semiconductor the dependence of resistivity ρ on temperature can be expressed as

$$\rho = A \exp \left[\frac{E_g(0)}{2k_B T} \right] \quad (8)$$

where T is temperature in kelvins, $E_g(0)$ is the energy bandgap at the absolute zero temperature, k_B is Boltz-

Table 5. Longitudinal and Tangential Piezoresistive Coefficients for Si

Crystal Plane	Orientation $\langle x \rangle$	Orientation $\langle y \rangle$	π_L	π_T
(100)	$\langle 100 \rangle$	$\langle 100 \rangle$	+0.02 π_{44}	0.02 π_{44}
(100)	$\langle 110 \rangle$	$\langle 100 \rangle$	+0.5 π_{44}	0
(100)	$\langle 110 \rangle$	$\langle 110 \rangle$	+0.5 π_{44}	−0.5 π_{44}
(100)	$\langle 111 \rangle$	$\langle 211 \rangle$	+0.66 π_{44}	−0.33 π_{44}

Source: Ref. 8.

mann's constant, and A is a preexponential factor that varies very slowly with temperature. If one defines the *temperature coefficient of resistivity* (TCR) α as

$$\alpha = \frac{1}{\rho_0} \frac{d\rho}{dT} \quad (9)$$

where ρ_0 denotes the resistivity at some reference temperature T_0 , often taken to be 0°C . From (8) we find out that for intrinsic semiconductors TCR is given by

$$\alpha \approx -\frac{E_g(0)}{2k_B T^2} \quad (10)$$

Unfortunately, silicon does not exhibit an intrinsic behavior that can be reliably utilized for temperature sensing. This is because the lowest concentration of electrically active impurities, and therefore dopant atoms obtainable in silicon is $\sim 10^{12} \text{cm}^{-3}$, which is two orders of magnitude higher than the intrinsic carrier concentration n_i in silicon at room temperature, which is $\sim 10^{10} \text{cm}^{-3}$. However, another elemental semiconductor, germanium, is successfully utilized in measuring cryogenic temperatures in the range 1–35 K [9].

2.6. Optical Absorption and Photoconductivity in Semiconductors

Radiation is absorbed by a semiconductor, and the degree of absorption varies with the material optical properties and the radiation energy. In this context the term *optical* does not necessarily imply that the photons absorbed are in the visible part of the electromagnetic spectrum. In fact, many semiconductors absorb photons in the infrared region, which is included in the term *optical absorption*. In semiconductors the major process that leads to the absorption of radiation is that of creating an *electron-hole pair*. Photons with energies greater than the bandgap of the semiconductor (i.e., $h\nu > E_g$) are absorbed by the semiconductor, whereas photons of energies lower than the bandgap (i.e., $h\nu < E_g$) are not absorbed and, instead, transmitted through the semiconductor. The electron and hole created are called *excess carriers*. The optical absorption is determined by the properties of the semiconductor via a parameter called *absorption coefficient*. The absorption coefficient α is a measure of the fractional decrease in incident radiation intensity I_0 with distance into the material x measured from the surface exposed to the radiation

$$I(x) = I_0 e^{-\alpha x}, \quad \alpha = -\frac{1}{I} \frac{dI}{dx} \quad (11)$$

where $I(x)$ is the intensity of radiation at x . Figure 5 shows a typical α/λ plot where we note that at long wavelengths ($hc/\lambda \ll E_g$) there is no significant absorption of radiation and considerable absorption of photons with larger energies ($hc/\lambda \geq E_g$).

Photoconductive cells are semiconductor resistor structures that are used as optical sensors that utilize the photoconductivity effect, in which light striking the resis-

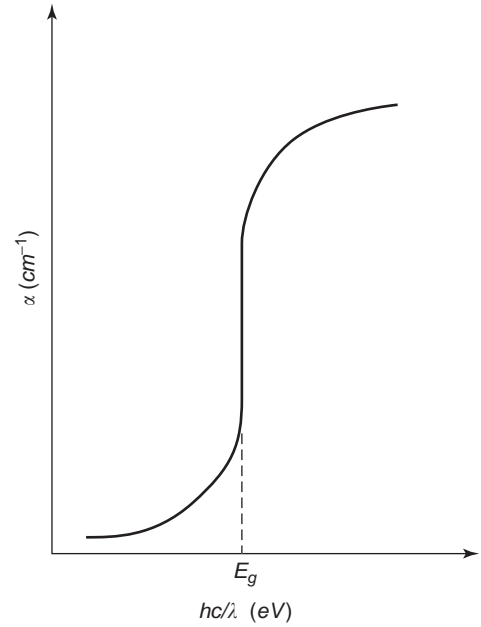


Figure 5. A typical α/λ plot in a semiconductor.

tor reduces its resistance. The optical sensitivity of a semiconductor is assessed in terms of its optical generation rate G_{op} , the concentration of excess carriers generated per unit time. If the lifetimes, defined as the mean time each carrier spends before it is annihilated, is $\bar{\tau}_n$ or $\bar{\tau}_p$ for electrons and holes, respectively, one may write

$$\Delta n = G_{op} \bar{\tau}_n, \quad \Delta p = G_{op} \bar{\tau}_p \quad (12)$$

Accordingly, the photoconductivity change $\Delta\sigma$ in the semiconductor is

$$\Delta\sigma = eG_{op}(\mu_n \bar{\tau}_n + \mu_p \bar{\tau}_p) \quad (13)$$

This change in conductivity translates into a change in overall resistance ΔR of the semiconductor cell given by

$$\Delta R = \frac{1}{\Delta\sigma t} \left(\frac{l}{w} \right) \quad (14)$$

where t is the thickness and (l/w) is the aspect ratio of the cell.

2.7. Magnetoresistance in Semiconductors

Let us consider a slab of a semiconductor such as the one shown in Fig. 6 with the magnetic and electric fields orientations indicated in the figure. As they drift in the semiconductor, free carriers, namely, electrons and holes, will experience *Lorentz force*, which tends to deflect carriers to one of the semiconductor surfaces (top or bottom). This will continue until an electric field, called the *Hall field*, develops along the y axis. This field produces a force on the carrier that is exactly equal to the Lorentz force. Hence, in the steady state the total current in the y direction must be zero, and the Hall field will increase

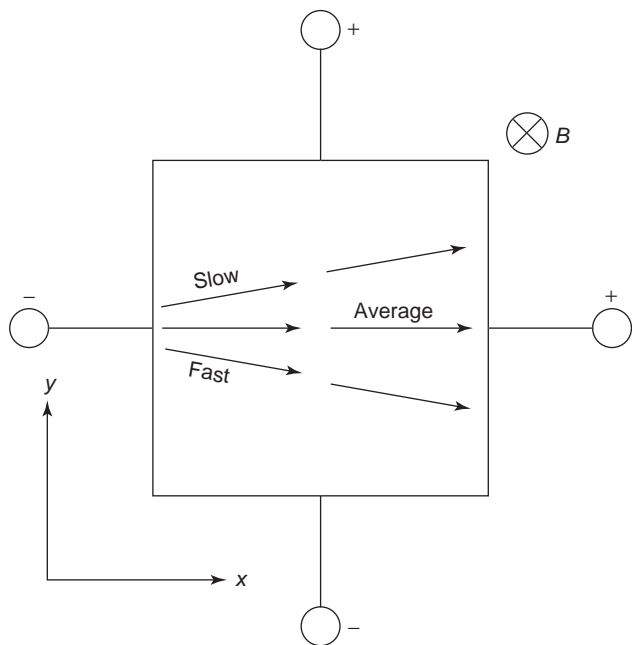


Figure 6. A slab of a biased semiconductor placed in a magnetic field.

until this is the case. However, we also note that the Lorentz force is directly proportional to the velocity of the carrier, and that not all carriers have the same velocity. In the steady state, for some charge carriers the Lorentz force is larger than the force due to the Hall field and for other carriers the opposite is true. This will cause some carriers to deflect upward and some to deflect downward, as shown in Fig. 6. The path of these charge carriers as they cross the slab is somewhat longer, and this leads to an increase of the resistance in the semiconductor. This effect is called *physical magnetoresistance*. Physical magnetoresistance is not severe in semiconductors as compared to metals. This is because the carrier mobilities in semiconductors are too small to induce any change in resistance for such a small change in the carrier's path. However, when coupled with the right geometry, magnetoresistance could be made significant in semiconductors. The dependence of the resistance of the semiconductor slab on the magnetic field is of the form [10]

$$R = R_0(1 + k_{ar}\mu^2B) \quad (15)$$

where k_{ar} is an aspect ratio parameter, R_0 is the resistance at zero magnetic field, and μ is the carrier mobility.

2.8. Chemical Interactions and Semiconductors as Chemoresistors

Back in 1953 it was discovered that the adsorption of some gases into the surfaces of some semiconductors could produce large changes in the resistivity. These semiconductors are primarily compound metal oxides such as ZnO, TiO₂, In₂O₃, or SnO₂. The latter is the most commonly used semiconductor in gas sensors, especially combustible gases, such as methane (CH₄). In an oxygen-rich

environment SnO₂ acts as a n-type semiconductor. However, oxygen can occupy a lattice vacant site in SnO₂ and acts as a single electron or double *electron trap*, in which the oxygen atom, once it occupies the lattice site, is able to bind one (to become O⁻) or two free electrons (to become O²⁻) to its core and therefore restricts the free motion of the electron or the two electrons. These trapped electrons are no longer free electrons, and the net effect is a reduction in the free-electron concentration n . This way the incorporation of oxygen in the crystal lattice of SnO₂ increases its resistivity. The electron-trapping process is reversed, however, by the exposure of the oxygen containing SnO₂ resistor to a gas such as CH₄. CH₄ reacts with the single negatively (O⁻) or double negatively (O²⁻) charged oxygen to produce CO₂. As this reaction is completed O⁻ or O²⁻ give back to the crystal of SnO₂ one or two free electrons, respectively. This reaction enhances the free-electron concentration and decreases the resistance.

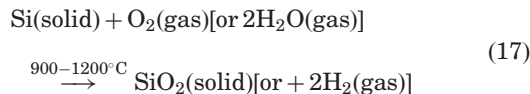
A simple theory predicts an increase in the conductivity $\Delta\sigma$ of the semiconductor, which can be related to the increase in carrier concentration Δn and, from the reaction kinetics, to a fractional power m of the gas concentration [11]

$$\Delta\sigma = e\mu_n\Delta n \propto [X]^m \quad \text{where } 0.5 < m < 1 \quad (16)$$

where [X] represents the gas concentration.

2.9. Insulator-on-Semiconductor Structures: Oxidation/Nitridation of Silicon and Oxide/Nitride Deposition

2.9.1. Thermal Oxidation. Thermal oxidation is the method by which a thin film of SiO₂ is grown on top of a silicon wafer. It is the key method of producing thin SiO₂ layers in modern IC and N/MEMS technologies. Thermal oxidation of silicon in oxygen or water vapor can be described by the following chemical reactions [1,2]:



The silicon-silicon dioxide interface moves into the silicon during the oxidation process. Using the densities and molecular weights of silicon and silicon dioxide, one can show that growing an oxide thickness x consumes a layer of silicon that is $0.44x$ thick. Oxidation in high-pressure steam or oxygen can produce substantial acceleration in the growth rate and is often used in growing thick oxides. One advantage to high-pressure oxide growth is that oxides can be grown at significantly lower temperatures and at reasonable growth rates.

The basic structural unit of thermal SiO₂ is a silicon atom surrounded tetrahedrally by four oxygen atoms as shown in Fig. 7. The silicon-oxygen and oxygen-oxygen internuclear distances are 1.6 and 2.27 Å, respectively. SiO₂ or silica has several crystalline structures (e.g., quartz) and an amorphous structure. Typically amorphous SiO₂ has a density of $\sim 2.2 \text{ g/cm}^3$, whereas quartz

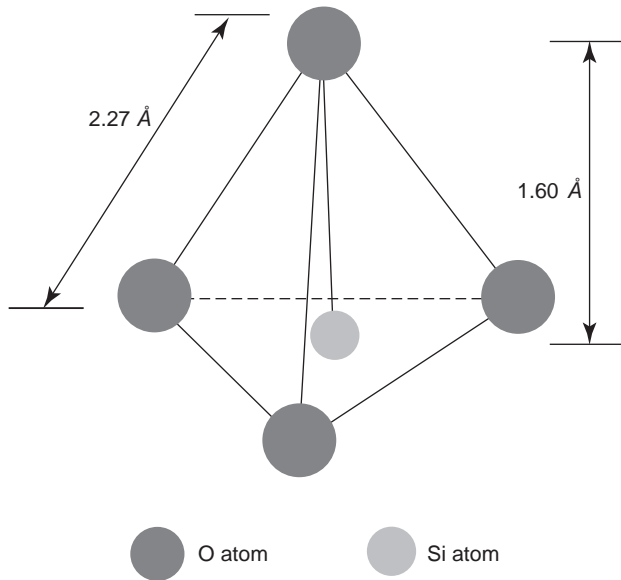


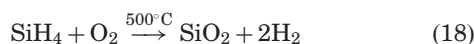
Figure 7. The basic structural unit of SiO_2 .

has a density of $\sim 2.7 \text{ g/cm}^3$. Thermally grown oxides are usually amorphous.

2.9.2. Silicon Oxide and Silicon Nitride Deposition.

Three deposition methods, all based on *chemical vapor deposition* (CVD), are commonly used in forming a thin dielectric film on a substrate: atmospheric-pressure chemical vapor deposition (APCVD), low-pressure chemical vapor deposition (LPCVD), and plasma-enhanced chemical vapor deposition (PECVD). The latter method is an energy-enhanced CVD method. The appropriate method from among these three deposition methods is based on the substrate temperature, the deposition rate and film uniformity, the morphology, the electrical and mechanical properties, and the chemical composition of the dielectric films.

CVD is used extensively in depositing SiO_2 and silicon nitride (Si_3N_4). CVD deposited SiO_2 does not replace thermally grown SiO_2 , which has electrical and mechanical properties superior to those of CVD oxide. However, CVD oxides are used instead to complement thermal oxides and in many cases to form oxide layers that are much thicker than thermal oxides in relatively very short timeframes. SiO_2 can be CVD-deposited by several methods. It can be deposited from reacting silane and oxygen in a LPCVD reactor at $\sim 300\text{--}500^\circ\text{C}$ [1,2]:



It can also be LPCVD-deposited by decomposing tetraethylorthosilicate, $\text{Si}(\text{OC}_2\text{H}_5)_4$. The compound, abbreviated TEOS, is vaporized from a liquid source. TEOS decomposes as follows:

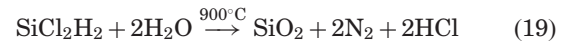


Table 6 compares different SiO_2 films deposited by different methods and contrasts them with thermally grown oxides. Likewise, Si_3N_4 can be LPCVD-deposited by an intermediate-temperature process or a low-temperature PECVD process. In the LPCVD process, which is the more common process, dichlorosilane and ammonia react according to



3. SUPERCONDUCTORS

Superconductors are materials that exhibit no resistance to current flow. This definition implies that electrical resistance in these materials is zero, which suggests that once current is initiated in these materials, it continues to flow indefinitely without the need for maintaining the applied voltage that was necessary to produce the current. *Superconductivity* occurs in materials below a certain temperature that is specific for a given material. This temperature is referred to as the *transition* or *critical temperature* T_C .

3.1. Types of Superconductors

Superconductivity was discovered in 1911 by Kammerlingh Onnes in Leiden University in the Netherlands [12]. Kammerlingh Onnes cooled mercury down to liquid helium temperature (4.2 K) and found out that mercury loses its DC resistance below that temperature, which then becomes the critical temperature for mercury. Subsequent to Kammerlingh Onnes' discovery, several materials exhibited superconductivity at T_C , which is much higher than 4.2 K. Superconductors that have low T_C are often categorized as *low-temperature superconductors* (LTSs). The LTS category of superconductors consists mainly of metals and metalloids that show *some* conductivity at room temperature. They require extremely low temperature (in the neighborhood of 4.2 K) to slow down core vibrations sufficiently and inhibit electron scattering by phonon, which impedes electron flow.

Table 6. Properties of Deposited and Thermally Grown Oxide Films

Property	Composition	Step Coverage	Density (gm/cm^3)	Refractive Index	Dielectric Strength (V/cm)
Thermally grown at 1000°C	SiO_2	—	2.2	1.46	$> 10^{-5}$
Deposited from $\text{SiH}_4 + \text{O}_2$ at 450°C	$\text{SiO}_2(\text{H})$	Nonconformal	2.1	1.44	8×10^{-6}
Deposited from TEOS at 700°C	SiO_2	Conformal	2.2	1.46	10^{-5}
Deposited from $\text{SiCl}_2\text{H}_2 + \text{N}_2\text{O}$ at 900°C	$\text{SiO}_2(\text{Cl})$	Conformal	2.2	1.46	10^{-5}

Source: Ref. 1.

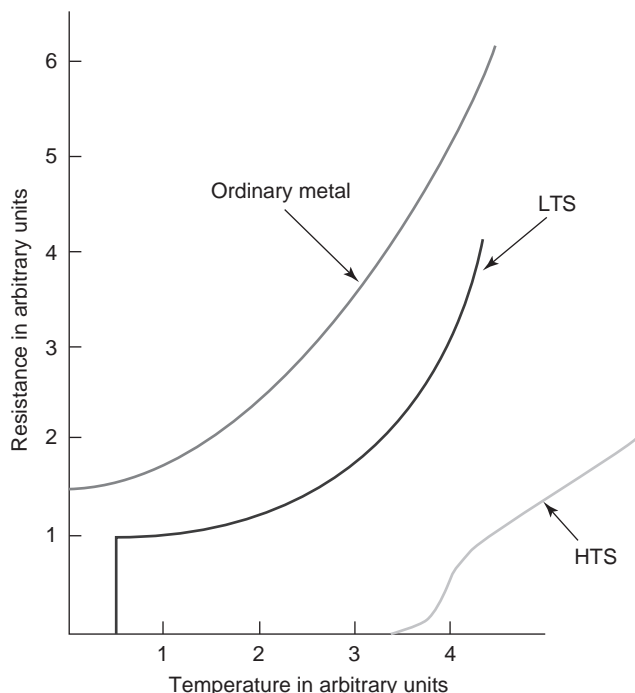


Figure 8. The resistance dependence on temperature for an ordinary metal and low- and high-temperature superconductors (LTS, HTS).

In 1986 superconductivity was discovered in a new group of materials that have a significantly higher transition temperature ($T_C \sim 40$ K or above) [13]. T_C in this group of materials is at least 10 K higher than the highest T_C in LTS. Therefore, this group of superconductors are referred to as *high temperature superconductors* (HTSs). Except for a very few elements, HTS comprises metallic compounds and alloys. One prominent class of these compounds is the *perovskites*. Reported T_C values in HTS have reached ~ 140 K and are projected to reach 200 K or higher. The temperature dependence of the resistance in an ordinary metal is shown in Fig. 8 and contrasted with those in low-temperature and high-temperature superconductors. Also, Table 7 gives T_C for a selected group of superconductors.

3.2. The Meissner Effect

We now consider a hypothetical perfectly pure metal at $T = 0$ K in which the resistance is zero because of the absence of phonon scattering. This perfect conductor with a vanishing resistance is a perfect *diamagnet*; thus if placed in a magnetic field, the perfect conductor would expel the magnetic field and the magnetic field intensity within the perfect conductor would be zero. Conversely, if the hypothetical perfectly pure metal is placed in a magnetic field at $T > 0$ K (phonon scattering is present and the metal resistance is nonzero), a nonzero magnetic field develops within the metal. However, if the metal temperature is lowered to 0 K, at which point the metal becomes a perfect conductor, the magnetic field within the now perfect conductor remains trapped within. Both of these effects are derived from *Lenz' law*, which imply that current loops would be generated to exactly cancel the imposed field. Therefore, a solely zero resistance model for the superconductor in a magnetic field would behave similar to a perfect conductor.

However, the situation in a superconductor is found to be unexpectedly different from that in a perfect conductor. A superconductor in a magnetic field would have a nonzero magnetic field at $T > T_C$ as shown in Fig. 9a. In contrast to the perfect conductor, however, and when temperature is lowered to $T \leq T_C$ the magnetic field within the superconductor vanishes and the magnetic flux is expelled as shown in Fig. 9b; thus, the superconductor has a zero effective *permeability*. It was concluded that in a weak magnetic field and at $T \leq T_C$ a superconductor is a perfect diamagnet except for a thin surface layer of the body, which is ~ 100 nm deep. This effect is called the *Meissner effect* in superconductors [16].

The preceding discussion assumes a weak magnetic field. However, a superconductor loses its superconducting state at magnetic fields higher than a *critical field* value B_C . The critical field at any temperature is given as

$$B_C = B_C^0 \left[1 - \left(\frac{T}{T_C} \right)^2 \right] \tag{21}$$

Table 7. Properties of Some Selected Superconductors

Element/Compound	T_C (K)	2Δ (meV)	$B_C(T)$ (tesla)	Atomic Density ($\times 10^{28} \text{ m}^{-3}$)
Nb	9.25	3.05	0.206 (0 K)	5.56
Pb	7.196	2.73	0.0803 (0 K)	3.30
La	6.00	1.9	0.1096 (0 K)	2.70
Hg	4.154	1.65	0.0411 (0 K)	4.26
In	3.408	1.05	0.0281 (0 K)	3.83
Al	1.175	0.34	0.0105 (0 K)	6.02
TlBa ₂ Ca ₂ Cu ₃ O _y	115	—	10 (77 K)	—
(Bi,Pb) ₂ Sr ₂ Ca ₂ Cu ₃ O _x	107	—	3 (30 K), 1 (77 K)	—
YBa ₂ Cu ₃ O _{7-x}	92	—	10 (77 K)	—
Nb ₃ Ge	23.2	—	36 (4.2 K)	—
Nb ₃ Sn	18.4	—	22 (4.2 K)	—

Source: Refs. 14 and 15.

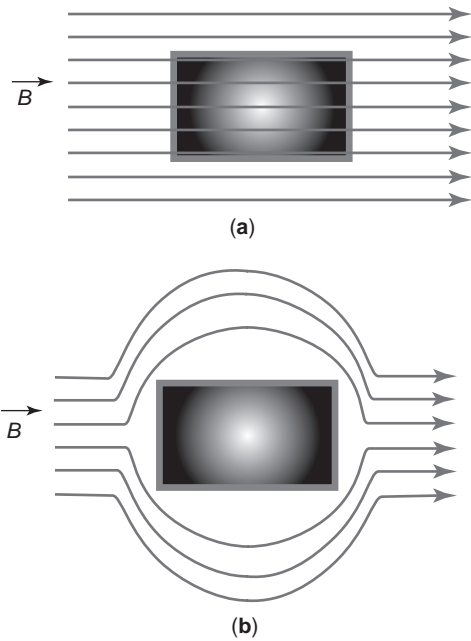


Figure 9. A superconductor in a magnetic field (a) at $T > T_C$ and (b) at $T < T_C$.

where B_C^0 is a constant [17]. Table 7 gives the critical field for a number of superconductors.

3.3. Microscopic Theories of Superconductivity

The microscopic theory of superconductivity was developed by the trio Bardeen, Cooper, and Schrieffer (BCS) in 1957, and this theory is widely referred to as the BCS theory [18]. This theory describes the metal LTSs very successfully, and it leads to results that quantitatively agree with experimental results. Later in 1972 Bardeen, Cooper and Schrieffer were awarded the Nobel prize in physics for their BCS theory.

The basic hypothesis of the BCS theory of the superconducting state is that the electrons occupy the momentum states in pairs, which are attracted to one another. In a pair of electrons, referred to as *Cooper pair*, the two electrons occupy the momentum states \mathbf{k} and $-\mathbf{k}$ with opposite spins. In the superconducting ground state ($T=0$ K) the energy necessary to separate electrons in the pairs is called the *energy gap* Δ . The BCS theory relates Δ to T_C as

$$2\Delta = 3.52k_B T_C \quad (22)$$

where k_B is Boltzmann's constant. Also in the superconducting ground state ($T=0$ K) the probability of pair occupation of momentum states is reminiscent of the normal *Fermi-Dirac* occupation probability at $T=0$ K. At $T > 0$ K some of the pairs are separated and the generated single electrons obey Fermi-Dirac statistics. The energy gaps for selected superconductors are given in Table 7.

In spite of the remarkable success of the BCS theory in describing superconductivity in metal LTSs, there is, as yet, no acceptable microscopic theory for HTSs. The main

reason for this is that HTSs are highly anisotropic and their superconducting response depends very strongly in their crystallographic structure. Note that the BCS theory is based on the isotropic electron gas in a metal.

3.4. Superconductor Applications

The most obvious application of superconductors would be in power transmission lines. More than 10% of the generated electricity is dissipated as heat in the transmission lines, and the prospect of zero-loss superconducting transmission lines is appealing. However, the hurdle for such an application is the cooling below T_C requirement. Niobium-titanium with $T_C \sim 10$ K and $B_C \sim 15$ tesla is used in superconducting magnets applications. Superconducting magnets are essential to magnetic resonance imaging (MRI) of the human body. MRI requires very strong and uniform magnetic fields that can be generated only by superconducting coils.

Another prominent application of superconductors is in the *superconducting quantum interference device* (SQUID), which consists of two superconductors separated by insulating layers, thereby forming two parallel Josephson junctions. SQUID is able to detect minute magnetic fields such as the ones occurring in living organisms and animal brains.

4. PIEZOELECTRIC MATERIALS

4.1. The Piezoelectric Effect

Piezoelectricity is the development of electric polarization in a crystal produced by an applied mechanical stress (direct) and the converse process of development of mechanical elastic strain in a crystal by the application of an electric field (indirect). Piezoelectricity is therefore an electromechanical phenomenon that occurs in piezoelectric materials. In simple terms piezoelectric materials can produce a voltage if subjected to a mechanical stress. The reverse process, that is, the application of a voltage to a piezoelectric material, can change its shape.

For a crystal to be piezoelectric its structure must have no center of symmetry. Hence a stress applied to such a crystal will modify the separation between positive and negative charge sites and consequently results in a net polarization at the crystal surface. This polarization gives rise to the potential difference generated in the crystal. In piezoelectric materials, coupling between the electrical and mechanical parameters gives [1]

$$\sigma_{ij} = c_{ijkl}^E S_{kl} - e_{kij} E_k, \quad D_i = e_{ikl} S_{kl} + \epsilon_{ik}^s E_k \quad (23)$$

where σ and S are second order stress and strain tensors, respectively, and i and j assume values of 1, 2, or 3 (x , y , or z). The former tensor is expressed in pascals (Pa), and the latter is unitless. c^E , given in pascals, is the *elastic stiffness constant* at a given electric field E , measured in V/m , with the k th component E_k . e is the *piezoelectric constant* in units of C/m^2 and ϵ , given in F/m , is the permittivity of the piezoelectric material. D_i is the i th component of the electric displacement measured in C/m^2 .

The two equations in (23) are referred to as the *piezoelectric constitutive equations*. In matrix notation they take the form

$$[\sigma] = [c][S] - [e^T]E, \quad D = [e][S] + [\varepsilon]E \quad (24)$$

where $[e]$ is a 3×6 matrix with its elements depending on the symmetry of the piezoelectric crystal and $[e^T]$ is the transpose of the matrix $[e]$. With $e = 0$, Eqs. (23) and (24) reduce to the familiar *Hooke's law* and the familiar relation between electric field and displacement vectors $D = \varepsilon E$. Hence, D can be nonzero in the absence of any electric field ($E = 0$) provided that the crystal undergoes a strain, whereas the application of an electric field can result in strain in the absence of mechanical stress ($\sigma = 0$).

4.2. Piezoelectric Materials and Their Preparation

Piezoelectric materials are predominantly ceramic solids and a number of polymers. Piezoelectricity is exhibited by a number of natural crystals such as quartz, sodium potassium tartrate, and tourmaline. Among the synthesized piezoelectric crystals are the Rochelle salt, barium titanate ($BaTiO_3$), lead zirconate titanate (PZT), zinc oxide, aluminum nitride, and the polymer polyvinylidene fluoride (PVDF).

Piezoelectric films are commonly used in semiconductor sensor and N/MEMS applications. The most popular piezoelectric films for these applications are ZnO, AlN, and PZT. Advantages of these films over others include (1) high electromechanical coupling, (2) good adhesion to substrates, (3) stable and not significantly affected by environment, (4) compatible with CMOS processing, and (5) relatively low cost. Major applications of these films are in pressure and gas microsensors, acoustic resonators, accelerometers, filters, and microactuators. Several methods for the preparation of piezoelectric films are employed depending on which material and substrate are used.

The major preparation methods for piezoelectric films are vacuum deposition and solgel [19]. The latter method is used exclusively for piezoceramic films, such as PZT and PLZT, deposition. The solgel method involves the spinning of a chemical solution, which allows for a better control of composition and film homogeneity. Also solgel deposition is very low cost compared to vacuum deposition methods and is very suitable for large-area film preparation. However, solgel deposition may not be appropriate for the deposition of thick piezoelectric ($\geq 1\text{-}\mu\text{m}$) films because of localized microscopic cracks that could develop in thicker films, especially if subsequent thermal annealing of the film is part of the final device processing. Piezoelectric films with cracks have very low piezoelectric coupling and results in very poor device performance.

Vacuum deposition methods comprise sputtering and direct, indirect, or reactive evaporations [20–22]. Reactive evaporation is particularly important in depositing ZnO and AlN films. ZnO and AlN are also deposited using variations of sputtering: “triode sputtering,” “RF sputtering,” and “magnetron sputtering” [23]. ZnO sputtering employs a pure zinc target that is reactively sputtered in an oxygen/inert-gas mixture. Improved ZnO film deposi-

tions are obtained with triode sputtering at submicron pressures. Also higher sputtering rates and excellent film qualities have resulted from DC and RF magnetron sputtering. RF magnetron sputtering was also applied to AlN growth at low temperatures. Early preparations of AlN films have used metallorganic chemical vapor deposition (MOCVD) methods [24].

4.3. Piezoelectric Material Applications

Piezoelectric materials form essential components for transducer devices that convert mechanical signals to electrical ones. Likewise, piezoelectric materials form essential components for actuator devices, which convert electrical signals to mechanical ones.

To understand the electrical-to-mechanical energy conversion process and, hence, illustrate the actuation application of piezoelectric materials, we consider the hypothetical two-dimensional piezoelectric crystal in Fig. 10. Figure 10a shows the piezoelectric crystal in the absence of any applied stress or electric field with the vertical separation l between positive and negative charge centers. When an electric field E is applied in the direction shown in Fig. 10b, the positive and negative ion centers are displaced; positive ions are displaced upward, whereas negative ions are displaced downward. This increases the separation l between ions and results in crystal expansion—a net positive strain occurs in the crystal in this case. Similarly, by changing the applied electric field polarity, negative strain develops in the crystal as shown in Fig. 10c. This is a case of unidirectional loading, which is very common in many piezoelectric transducer applications. Instead of using the complex relations given in Eqs.

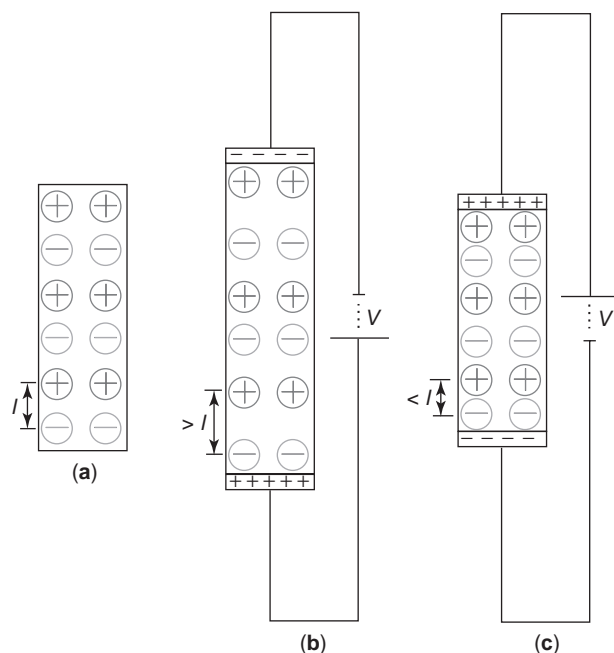


Figure 10. A piezoelectric crystal (a) in the absence of electric field, (b) with applied electric field, and (c) with applied electric field in a direction opposite that in (b).

(23) and (24) engineers often use the simple relation [25]

$$S = dE \tag{25}$$

where, as in Section 4.1, S and E are the strain and the magnitude of the electric field, respectively, and d is a *piezoelectric coefficient*, which is dependent on the piezoelectric material and is given in units of meters per volt. d relates to e in Eqs. (23) and (24) through c and ϵ .

Conversely, in sensor applications of piezoelectric materials and for unidirectional loading of the electric field, resulting from the application of a mechanical stress to the piezoelectric crystal, is simplified by the relation [25]

$$E = f\sigma \tag{26}$$

where f is another material dependent piezoelectric coefficient and satisfies the relation

$$\frac{1}{fd} = c \tag{27}$$

The effectiveness of the conversion of mechanical energy to electrical energy and vice versa is gauged via an electromechanical conversion factor K defined as follows [25]:

$$K^2 = \frac{\text{mechanical energy output}}{\text{electrical energy input}} \quad \text{or} \tag{28}$$

$$K^2 = \frac{\text{electrical energy output}}{\text{mechanical energy input}}$$

The piezoelectric coefficient d as well as the conversion factor K for common piezoelectric crystals are given in Table 8.

5. SHAPE MEMORY MATERIALS

5.1. Shape Memory Alloys

5.1.1. The Shape Memory Effect in Alloys. The *shape memory effect* (SME) is a property of a group of alloys that exhibit *martensitic transformation* [27]. The shape memory alloy (SMA) undergoes a deformation in the low-temperature phase and recovers its original shape on heating to a critical temperature called the *reverse transformation (RT) temperature*. Martensitic transformation (MT) is a diffusionless process in which atoms move collectively by a shearlike mechanism. Usually the *parent*

Table 8. Piezoelectric Coefficients d and conversion factors K for Selected Piezoelectric Materials

Piezoelectric Crystal	$d \times 10^{-12}$ m/V	K
Quartz (SiO ₂)	2.3	0.1
Barium titanate (BaTiO ₃)	100–190	0.49
Lead zirconate titanate, PZT, (PbTi _{1-x} Zr _x O ₃)	480	0.72
Polyvinylidene fluoride (PVDF)	18	—

Source: Refs. 25 and 26.

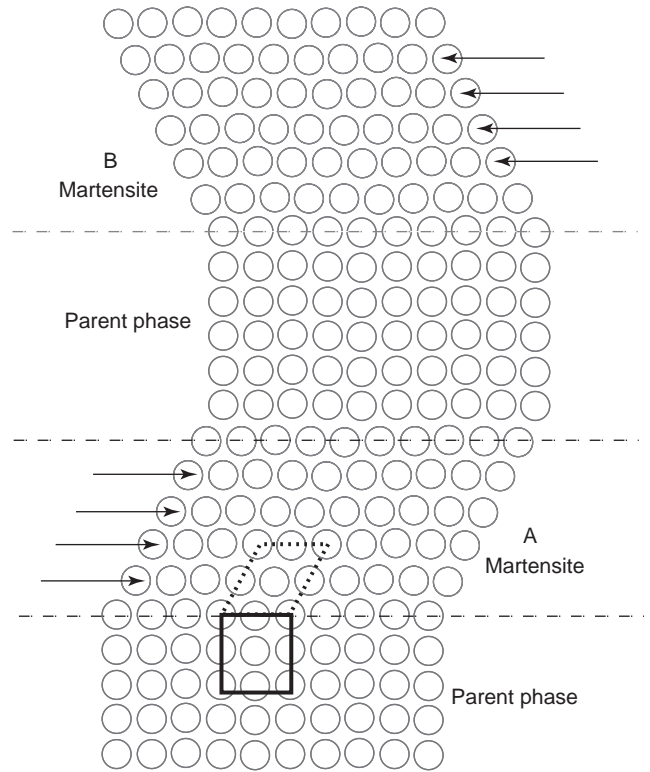


Figure 11. A martensitic transformation in a SMA showing the martensite and parent phases. (This figure is available in full color at <http://www.mrw.interscience.wiley.com/erfme>.)

phase, which occurs at a high temperature, is cubic; and the martensite phase, which occurs at a low temperature, has a lower symmetry. MT is schematically shown in Fig. 11, where as, the temperature is lowered, the parent phase yields the two martensites A and B, which have the same crystal structure but two different orientations. The two martensites A and B are called the *correspondence variants* (CVs). Since the martensite phase is of a lower symmetry than the parent phase, many variants could be formed from the parent phase. For example a MT in which the parent phase is face-centered cubic (fcc) and the martensite phase is body-centered tetragonal (bct) comes with three CVs. MT is normally accompanied by either slip or twinning, depending on the kind of alloys; this is why twins or dislocations are normally observed in martensites under electron microscopy. MT may occur as a result of temperature change; however, a uniaxial stress would always assist MT giving rise to a *stress-induced martensitic* (SIM) *transformation*. Now, if the temperature of the alloy is raised high enough to render the martensite phase unstable, a reverse transformation (RT) occurs, if it is crystallographically reversible, and the martensite reverts back to the parent phase, hence giving rise to SME.

Figure 12 illustrates the SME by showing the parent phase of a single-crystal SMA (Fig. 12a) transforming into a self-accommodated martensite phase (Fig. 12b) on cooling to a temperature T between T_M^s and T_M^f , where the former temperature is the martensite start temperature and the latter is the martensite finish temperature. As the

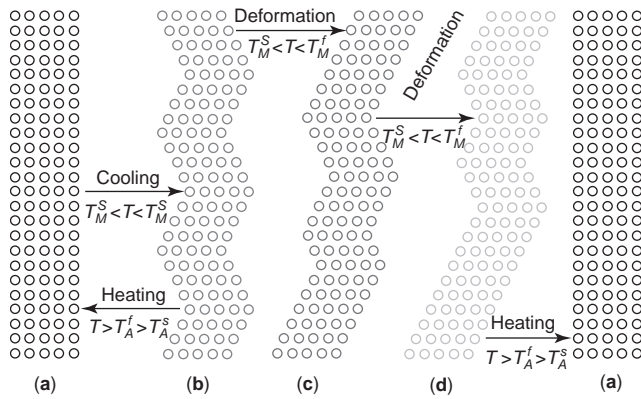


Figure 12. The SME effect and transformation paths over different temperature and deformation cycles in a SMA. (This figure is available in full color at <http://www.mrw.interscience.wiley.com/erfme>.)

temperature of the crystal is increased to $T > T_A^f > T_A^s$, where T_A^s and T_A^f are the start and finish temperatures of RT, respectively, the crystal regains its original shape. Also, a deformation in martensite (Figs. 12c and 12d), resulting from any kind of stress such as tensile, compressive, or bending, may proceed by the growth of one variant at the expense of the others (e.g., twinning or detwinning). As long as the strain is below some critical value, the deformed crystal reverts back to its original shape in Fig. 12a as the temperature is increased beyond T_A^f .

Figure 13 provides a tensile stress–strain behavior in a typical SMA. At $T_M^s < T < T_M^f$ the stress–strain curve is as shown in Fig. 13a: SIM occurs and is stable; hence a substantial strain remains on load removal and absence of stress. This strain is eliminated and the material returns to its original shape as indicated by the dotted line in Fig. 13a upon increasing the temperature to $T > T_A^f$. On the contrary, when the SMA is tensile-stressed at $T > T_A^f$, strains recover simply by unloading (Fig. 13b). One notes that often SMAs have another unique property called *superelasticity* at $T > T_A^f$. Superelastic materials are those materials exhibiting large ($\sim 20\%$) nonlinear recoverable strain on loading and unloading.

5.1.2. Shape Memory Alloys and Their Processing. Some selected SMAs are given in Table 9 together with their composition and structural change. TiNi-based alloys are the most prominent SMAs with good strength properties, ductility and resistance to corrosion, as well as excellent SME characteristics. However, TiNi-based alloys are expensive, which make them unsuitable for many applications. Cu-based SMAs, however, are rather inexpensive

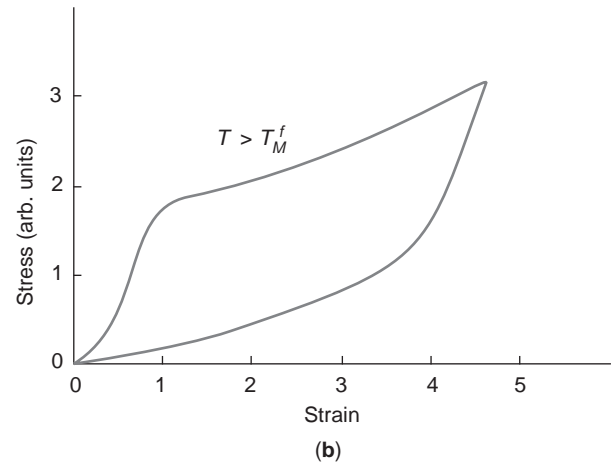
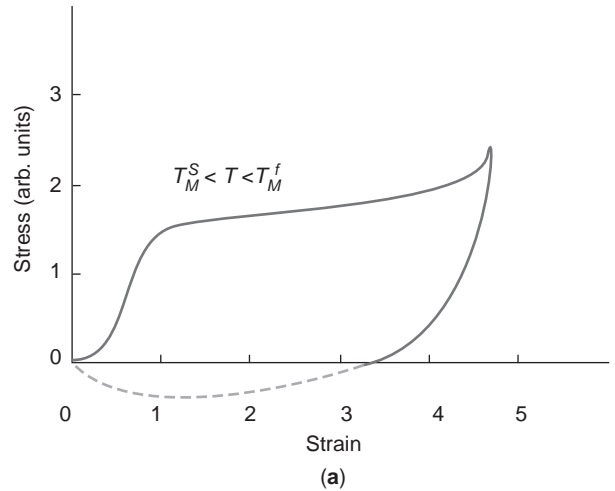


Figure 13. A tensile stress–strain behavior in a SMA.

and have been extensively studied for several applications. They are superior to TiNi-based SMAs in electrical and thermal conductivities and in deformability. Among the Cu-based SMAs that are widely investigated are CuZn and CuAl.

The fabrication of commercial SMAs involves three major steps [28]: (1) melting and casting, (2) hot- and coldworking, and (3) shape memory treatment. The control of the alloy composition is very important to the SMA characteristics. In particular, room temperature is very sensitive to composition. For example, a 1% shift in Ni content results in 100 K changes in T_M^s and T_A^f of TiNi SMA. Melting is usually performed at high temperatures (~ 1500 K and higher) in high vacuum or an inert-gas atmosphere since the molten metals would often be very

Table 9. Properties of Some Selected SMAs

SMA	Composition	T_M^s (K)	T_M^f (K)	T_A^s (K)	T_A^f (K)
Polycrystalline CuAlNi	—	191	203	213	225
Crystalline FePt	25% Pt	131	—	—	148
Crystalline FePd	30% Pd	179	—	—	183
Crystalline FeMnSi	30%Mn–1% Si	300	—	410	—

Source: Ref. 28.

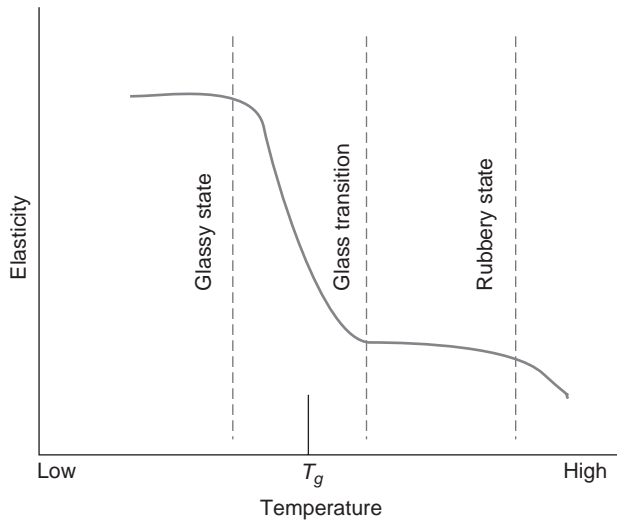


Figure 14. Elasticity–temperature behavior in a polymer.

reactive to oxygen. A high-frequency induction melting method is commonly used. Advantages of induction melting include the homogeneity and controllability of chemical composition throughout the ingot. Other melting methods utilize electron beams. Electron-beam melting comes with the lowest impurity content in the SMA; however, controllability of the composition is much less precise. Hot- or coldworking is used to forge and roll the ingot into a bar, a wire, or a slab with appropriate size.

5.2. Shape Memory Polymers

Certain polymers show SME; however, the mechanism involved is completely different from that in SMA. Rubberlike polymers show elastic behavior at room temperature; they exhibit large strains in response to applied stresses and completely recover their original shapes when the stresses are removed [28]. However, when the temperature of the strained rubberlike polymer is decreased to very low levels, the strained polymer may lose its elasticity and may not revert back to its original shape on the removal of stress. The low temperature at which this happens for a particular polymer is called the *glass temperature* T_g of the polymer (Fig. 14). When the temperature of the unloaded polymer is increased above T_g , the polymer returns back to its prestress shape, thus exhibiting a SME. Polymers that show the SME are referred to as the *shape memory polymers* (SMPs). The properties of SMAs and SMPs are compared in Table 10. Among SMPs are polynorbornene, polyisoprene, polyurethane, and polyethylene.

5.3. Applications of Shape Memory Materials

The most important applications of SM materials are in thermal actuation, which results in the generation of force and/or motion. The *thermal actuator* is a device that converts thermal energy to mechanical energy via the thermomechanical properties of a shape memory material. The most commonly used shape memory material element in an SM actuator is a coil spring since this form makes

Table 10. Comparison between SMA and SMP Properties

Physical Property	SMPs	SMAs
Density (g/cm^3)	0.9–1.1	6–8
Deformation (%)	250–800	6–7
Recovery temperature ($^{\circ}\text{C}$)	25–90	10–100
Stress required for deformation (MPa)	1–3	50–200
Recover stress (MPa)	1–3	150–300

Source: Ref. 28.

possible the generation of high degrees of large force and motion. The major application of SM actuators is in thermally actuated valves. Other applications for SM actuators are the ones where the actuator is used as both a sensor and an actuator. These applications include thermal protection devices for domestic water filtration units, steam traps for passenger train steam heating units, and thermally actuated electric switches for diesel engine radiator fans.

SMAs and SMPs are also used in N/MEMS. These include robotic micromanipulators [29] and microgrippers [30]. Moreover, SME have more recently been used successfully in dental and medical fields. Examples of SME applications in dental fields are the use of TiNi alloys in dental arc wires [31], dental implants [32], and partial dentures [33]. In medical applications, however, bone plates made of TiNi alloys are attached with screws for fixing broken bones.

BIBLIOGRAPHY

1. J. W. Gardner, V. K. Varadan, and O. O. Awadelkarim, *Microsensors, MEMS, and Smart Devices*, Wiley, New York, 2001.
2. S. M. Sze, *Semiconductor Devices, Physics, and Technology*, Wiley, New York, 1985.
3. J. Crank, *Mathematics of Diffusion*, Oxford Univ. Press, Oxford, UK, 1975.
4. H. C. Casey and G. L. Pearson, Diffusion in semiconductors, in J. H. Crawford and L. M. Slifkin, eds., *Point Defects in Solids*, Vol. 2, Plenum Press, New York, 1975.
5. C. S. Smith, *Phys. Rev.* **94**:42 (1954).
6. L. E. Hollander, G. L. Vick, and T. J. Diesel, *Rev. Sci. Instrum.* **31**:323 (1960).
7. P. J. French and A. G. R. Evans, Piezoresistance in single crystal and polycrystalline Si, *Proc. INSPEC*, 1988, pp. 94–103.
8. J. Bryzek, K. Petersen, J. R. Mallon, Jr., L. Christel, and F. Pourahmadi, *Silicon Sensors and Microstructures*, NovaSensors, Fremont, CA, 1991.
9. G. Urban, A. Jachimowicz, F. Kohl, H. Kuttner, F. Olcaytug, and H. Kamper, *Sensors Actuators A*:21–23, 650 (1990).
10. S. Middelhoek and S. A. Audet, *Silicon Sensors*, Academic Press, London, 1989.
11. J. W. Gardner, *Microsensors Principles and Applications*, Wiley, 1994.
12. H. Kammerlingh Onnes, *Akad. van Wetenschappen* (Amsterdam) **14**:113 (1911).
13. J. G. Bednorz and K. A. Muller, *Z. Phys. B* **64**:189–193 (1986).

14. C. Kittel, *Introduction to Solid State Physics*, 7th ed., Wiley, New York, 1996.
15. B. W. Roberts, *J. Phys. Chem. Ref. Data* **5**(3):581–821 (1976).
16. W. Meissner and R. Ochsenfeld, *Naturwissenschaften* **21**:787–788 (1933).
17. T. van Duzer and C. W. Turner, *Superconductive Devices and Circuits*, 2nd ed., Prentice-Hall PTR, 1999.
18. J. Bardeen, L. N. Cooper, and J. R. Schrieffer, *Phys. Rev.* **108**:1175–1204 (1957).
19. M. E. Motamedi and R. M. White, Acoustic sensors, in S. M. Sze, ed., *Semiconductor Sensors*, Wiley, 1994, pp. 97–151.
20. N. F. Foster, *Proc. Joint IEEE-IEE Conf. Application of Thin Film in Electronics Engineering*, London, 1996.
21. J. de Klerk and E. F. Kelly, *Rev. Sci. Instrum.* **36**:506 (1965).
22. R. M. Malbon, D. J. Walsh, and D. K. Winslow, *Appl. Phys. Lett.* **10** (1967).
23. N. F. Foster, *IEEE Trans. Sonic Ultrason.* **SV-15**:28 (1968).
24. K. Tsubouchi, K. Sugai, and N. Mikoshiba, *Proc. IEEE 1981 Ultrasonics Symp.*, 1981, pp. 375–380.
25. D. Askeland, *The Science and Engineering of Materials*, 3rd ed., PWS Publishing, Boston, 1994.
26. S. O. Kasap, *Principles of Electrical Engineering Materials and Devices*, Irwin, Chicago, 1997.
27. E. C. Bains, *Trans. AIME* **70**:25 (1924).
28. K. Otsuka and C. M. Wayman, *Shape Memory Materials*, Cambridge Univ. Press, 1998.
29. Y. Miwa, *Seimitsu Kougakkaishi* (Jpn.), **53**(2):15 (1987).
30. K. Ikuta, *Proc. IEEE Int. Conf. Robotics and Automation*, 1990, p. 2156.
31. C. J. Burstone, B. Qin, and J. Morton, *Am. J. Orthod.* **187**:445 (1985).
32. S. Fukuyo, Y. Suzuki, and E. Sairenji, in T. W. Duerig et al., eds., *Engineering Aspects of Shape Memory Alloys*, Butterworth-Heinemann., 1990, p. 452.
33. S. Miyazaki, S. Fukutsuji, and M. Taira, *Proc. ICOMAT-92*, Monterey, CA, 1993, p. 1235.
- D. Schoenberg, *Superconductivity*, Cambridge Univ. Press, Cambridge, UK, 1965.
- M. Tinkham, *Introduction to Superconductivity*, 2nd ed., McGraw-Hill, New York, 1996.

Piezoelectrics

- T. Ikeda, *Fundamentals of Piezoelectricity*, Oxford Univ. Press, Oxford, New York, 1996.
- C. Z. Rose, B. V. Hiremath, and R. Newnham, *Key Papers in Physics: Piezoelectricity*, American Institute of Physics, New York, 1992.
- W. G. Cady, *Piezoelectricity: An Introduction to the Theory and Applications of Electromechanical Phenomena in Crystals*, Dover, New York, 1964.

Shape Memory Materials

- K. Battacharya, *Oxford Series on Materials Modelling 2: Microstructure of Martensite; Why It Forms and How It Gives Rise to the Shape Memory Effect*, Oxford Univ. Press, Oxford, 2003.
- A. V. Srinivasan and D. M. McFarland, *Smart Structures: Analysis and Design*, Cambridge Univ. Press, Cambridge, UK, 2001.
- I. P. Lipscomb and L. D. M. Nokes, *The Application of Shape Memory Alloys in Medicine*, MEP, Bury St. Edmonds, UK, 1996.
- M. Fremond and S. Miyazaki, *Shape Memory Alloys*, Springer, Vienna, New York, 1996.
- S. Eucken, ed., *Progress in Shape Memory Alloys*, DGM Informationsgesellschaft, Oberursel, Germany, 1992.

SMITH CHART

LEONARD M. SCHWAB
Germaine Development Corp.

FURTHER READING

Semiconductors

- R. A. Smith, *Semiconductors*, 2nd ed., Cambridge Univ. Press, New York, 1978.
- C. M. Wolfe, N. Holonyak, Jr., and G. E. Stillman, *Physical Properties of Semiconductors*, Prentice-Hall, Englewood Cliffs, NJ, 1989.
- D. H. Navon, *Semiconductor Microdevices and Materials*, Holt, Rinehart & Winston, New York, 1986.
- S. Wolf and R. N. Tauber, *Silicon Processing for the VLSI Era*, Vol. 1, *Process Technology*, Lattice Press, Sunset Beach, CA, 1986.
- S. M. Sze, *VLSI Technology*, McGraw-Hill, New York, 1988.
- D. A. Neamen, *Semiconductor Physics and Devices, Basic Principles*, McGraw-Hill, New York, 2003.

Superconductors

- M. Tinkham, *Superconductivity*, Gordon & Breach, New York, 1965.
- F. London, *Superfluids, Microscopic Theory of Superconductivity*, Vol. 1, Dover, New York, 1960.
- B. S. Deaver, C. M. Falco, J. H. Harris, and S. A. Wolf, eds., *Future Trends in Superconductive Electronics*, American Institute of Physics, New York, 1978.

The origin of the Smith chart as a fast and accurate graphical design tool is rooted in the predigital computer era of the 1930s. The original paper chart format was routinely used to solve difficult transmission-line matching problems in a variety of broadcasting, microwave, circuit design, and telecommunication applications. While it has since evolved almost exclusively into a software format, the original paper forms remain a convenient detailed medium for print output of finished work from software implementations of Smith's graphical method.

Phillip H. Smith, inventor and developer of the Smith chart, was affiliated with Bell Telephone Laboratories for his entire engineering career after graduating from Tufts College in 1928. At Bell Labs, Smith repeatedly demonstrated his incisive, pragmatic, problem-solving abilities on a variety of technical problems. In his first decade on the job he developed the chart to its common present form through an iterative trial process of several more rudimentary forms Smith's original intended application was to simplify the tedious work of installing and matching open wire transmission lines for antennas. During this period he almost single-handedly developed and proved

the concept of using a graphical chart as a viable solution method. One can certainly appreciate his desire to minimize tedious slide-rule calculations required to solve transmission line equations involving hyperbolic functions. Smith [1] cited his routine need to obtain impedance solutions using Fleming's [2] telephone equation as a driving force to consider a graphical solution alternative. (Readers interested in greater detail on the life of Phillip Smith are referred to the Foreword section of Ref. 3 for a written transcript of the memorial session in Phillip Smith's honor presented at the 1990 IEEE MTT/S Symposium. An on-line IEEE source [4] also provides good detail on Smith's back-ground.)

The Smith chart was first published in a usable developmental form in 1939 by Smith [5]. A subsequent publication [6] in 1944 described the refined form known and used today. A standard preprinted paper chart in this format is shown in Fig. 1a, and Fig. 1b shows only the enlarged central portion around the normalized point $z = (1 + j0)$. In each of Smith's publications the fundamental equations and methods are provided along with demonstrations of the utility of the chart method. Certainly the ability to represent and mathematically manipulate a complete impedance data vector on a single compact graphical paper chart was a significant step forward at the time for the telecommunication and emerging electronics industries at the onset of World War II.

1. THE ATTRACTION OF A GRAPHICAL SOLUTION METHOD

The essential objective in using the Smith chart is stated simply. An impedance (or equivalent admittance) locus over a frequency range is systematically repositioned on the chart in well-defined ways by the progressive effects of series or shunt elements, thereby placing the passband portion of the impedance vector in the central area of the chart and the stopband portion at the outer periphery of the chart. The circuit elements commonly used include distributed elements such as transmission lines and quarter-wave stubs, discrete elements such as inductors and capacitors, and any combination of these and related elements. Resistance elements are seldom intentionally used.

There is no need for a graphical method as an aide to solve a straightforward equation such as Ohm's law. However, the more difficult general equation for the input impedance ("sending impedance" in early-twentieth-century parlance) of a transmission line with an arbitrary value of load impedance ("receiving impedance") is another matter. The presence of multiple hyperbolic functions in Fleming's equation is shown in Table 1, line 1. Figure 2a illustrates the concentric circular arc movement on the interior of the chart for a value of load impedance Z_L connected to a length l/λ of transmission line to produce an input impedance of Z_i . The input impedance

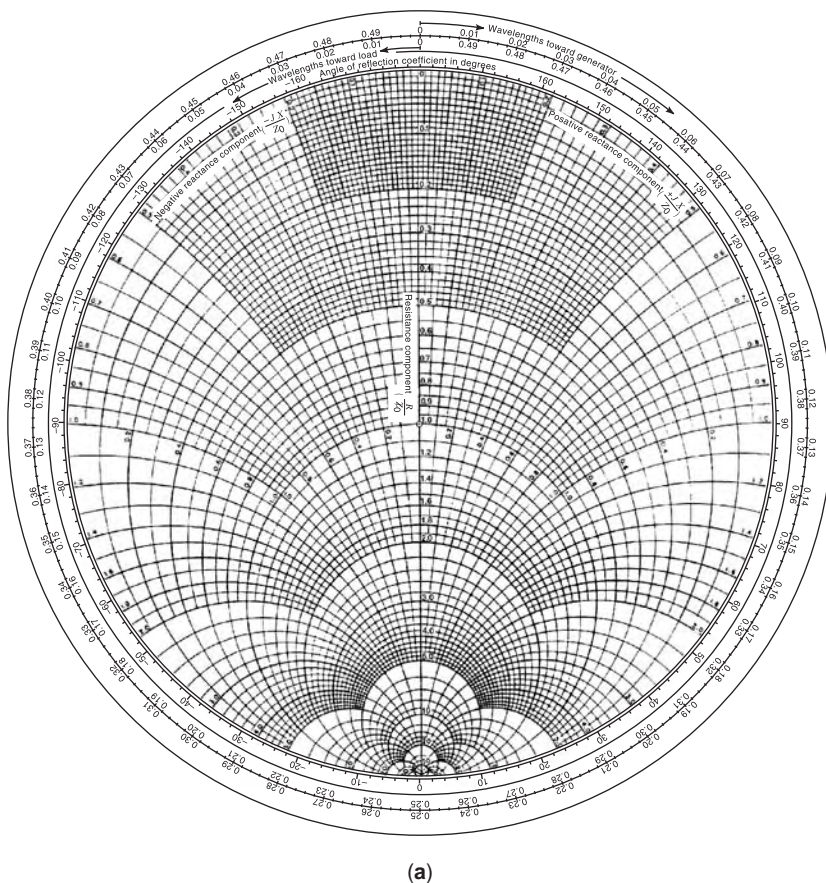


Figure 1. Full-size Smith chart grid; (b) enlarged center portion of the chart.

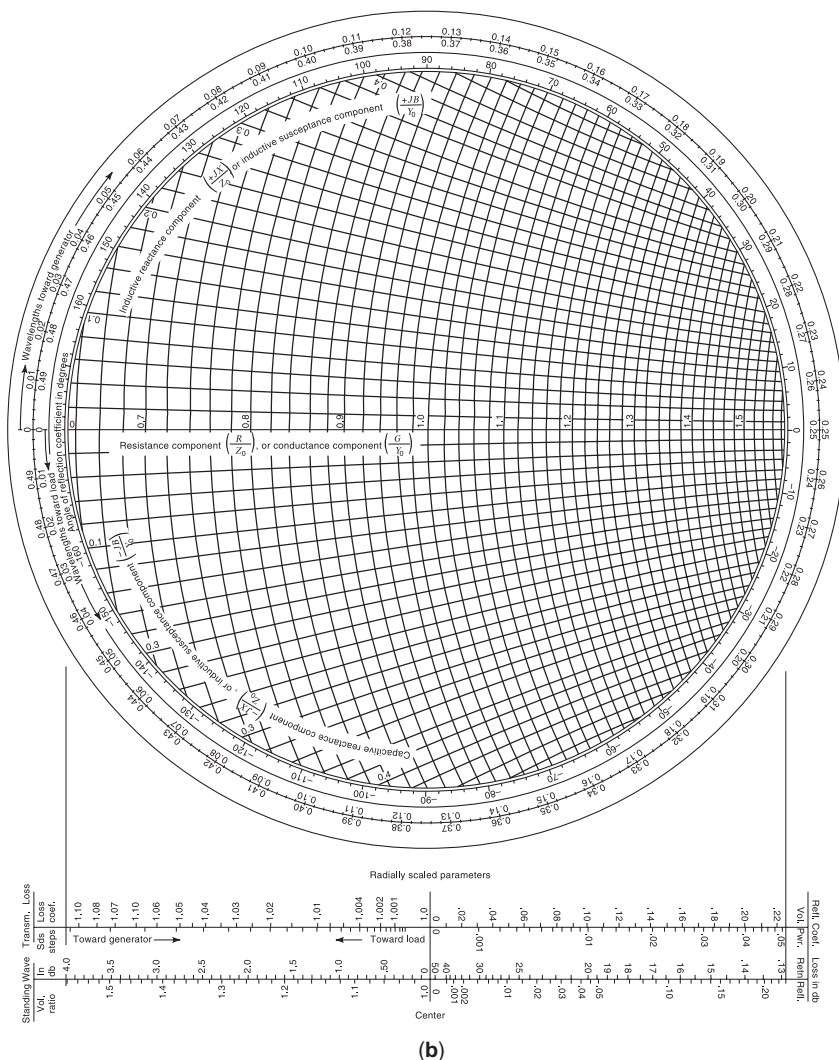


Figure 1. (Continued).

equations for transmission-line stubs (i.e., lengths of line typically less than a half-wavelength, with short-circuit and open-circuit load impedance values) are given by the equations of Table 1, lines 2 and 3, respectively. Figure 2b illustrates the concentric circular arc movement along the periphery of the chart for a value of load impedance ($Z_L = 0$ for the short-circuit stub and $Z_L = \infty$ for the open-circuit stub), connected to a stub with length l/λ , to produce an input impedance of Z_i .

The equation of Table 1, line 2 shows the effective parallel LC circuit tuning effect for a short-circuit stub, and line 3 illustrates the effective series LC circuit tuning effect for the case of an open-circuit stub. At relatively higher frequencies for which the length of the stub is greater than a half-wavelength, these tuning effects repeat unlike the effect of discrete (lumped element) parallel or series LC circuits.

The repetitive nature of these three equations when line length exceeds a half-wavelength is evident when one

Table 1. Distributed and Lumped-Element Components Commonly Used in Smith Chart Analysis and the Direction of Progression with Frequency on the Chart

Element Type	Defining Equation	Motion on the Smith Chart
Transmission line	$Z_{in} = Z_0 (Z_L + Z_0 \tanh \gamma l) / (Z_0 + Z_L \tanh \gamma l)$	CW along a circle centered at $Z_0 = 1 + j0$ (see Fig. 2a)
Short-circuit stub	$Z_{in} = jZ_0 \tan \gamma l$	CW along chart perimeter with region near ∞ especially useful ($l = \lambda/4$) (see Fig. 2b)
Open-circuit stub	$Z_{in} = -jZ_0 \cot \gamma l$	CW along chart perimeter with region near 0 especially useful ($l = \lambda/4$) (see Fig. 2b)
Inductance	$E = IX_L; X_L = j\omega L$	CW along constant- R circles (see Fig. 2c)
Capacitance	$E = IX_C; X_C = 1/j\omega C$	CCW along constant- R circles (see Fig. 2c)
Resistance	$E = IR$	To right along constant- X arcs toward $R = \infty$

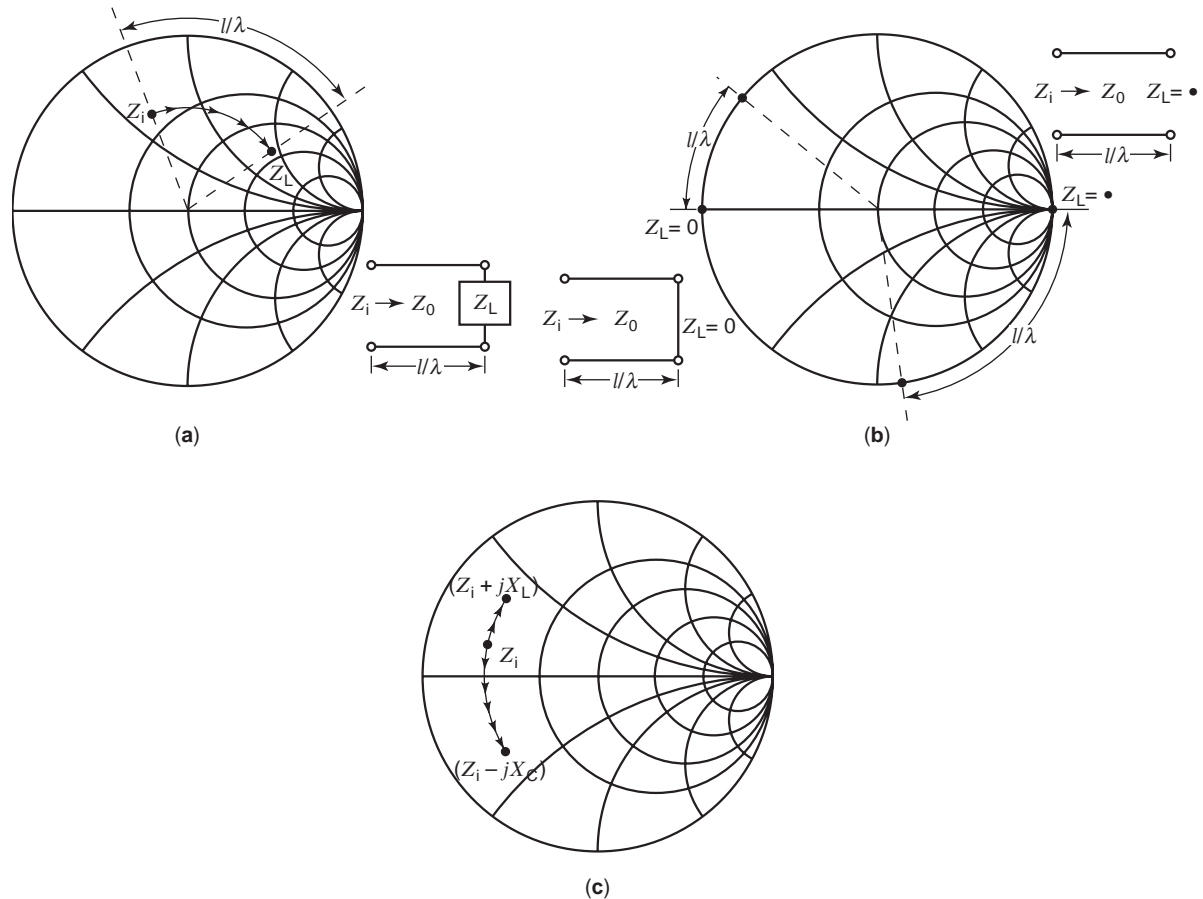


Figure 2. (a) Concentric circular movement along the chart interior to a value of input impedance Z_i resulting from addition of a transmission line to a load impedance Z_L ; (b) concentric circular chart movement along the chart periphery for the input impedance of a short-circuit ($Z_L = 0$) and an open-circuit ($Z_L = \infty$) stub; (c) movement along circular arcs of constant resistance for addition of a capacitance (downward) and inductance (upward) to a load impedance Z_L .

looks at them plotted on the chart. Likewise, the tuning effects of discrete elements is also calculable and treated on the chart. The inductor and capacitor are used especially in typical equalizer, filter, and matching circuits. The resistor element, while it can also be treated on the chart, is seldom used except in cases such as ultrabroadband (i.e., multioctave to decade bandwidth) tuning of electrically short antennas to meet a VSWR specification. The equations for the discrete elements and the relative motion of their locus on the chart is given in Table 1, lines 4, 5, and 6. Figure 2c illustrates the movement on the chart along arcs of constant resistance for some load impedance Z_L when a capacitance or inductance is placed in series.

The Smith chart's power as a graphical solution method comes from its versatility to design cascade and parallel circuits made up of any combination of distributed and lumped circuit elements defined by the equations given in Table 1. In addition, algorithmic methods such as the design of transmission-line impedance transformers can also be implemented directly on the chart. Design aids such as a voltage standing-wave ratio (VSWR) goal plotted as a circle concentric to the center of the chart and other geometric constructs such as forbidden areas and boundary circles make the design process straightforward. These

design aids as well as the line entries in Table 1 are discussed in greater detail in subsequent sections.

2. MATHEMATICAL STRUCTURE OF THE CHART

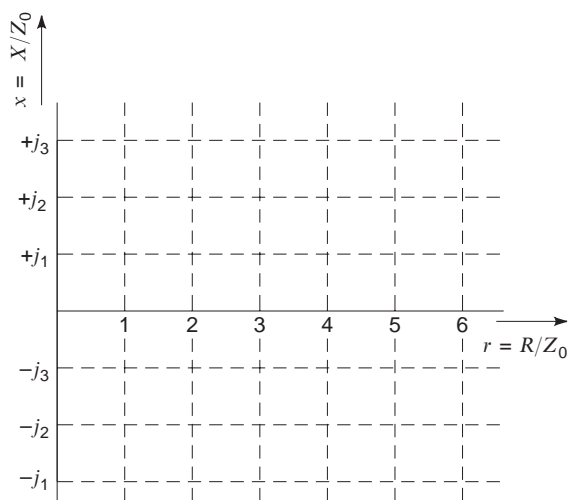
The mathematical basis of the Smith chart is a conformal bilinear transformation for which all data values approaching infinitely large values on the $\{(R, X)$ or $\{(G, B)\}$ complex plane map to a single uniquely defined finite point. In implementing the transformation, the simple, familiar, straight-lined, rectangular, impedance grid with resistance (or conductance) on the positive abscissa and reactance (or susceptance) on both positive and negative axes of the ordinate map into two families of circles that intersect orthogonally to one another. This holds true for charts scaled for impedance or admittance.

The equations that uniquely define the bilateral transformation between complex normalized impedance and complex reflection coefficient are given as

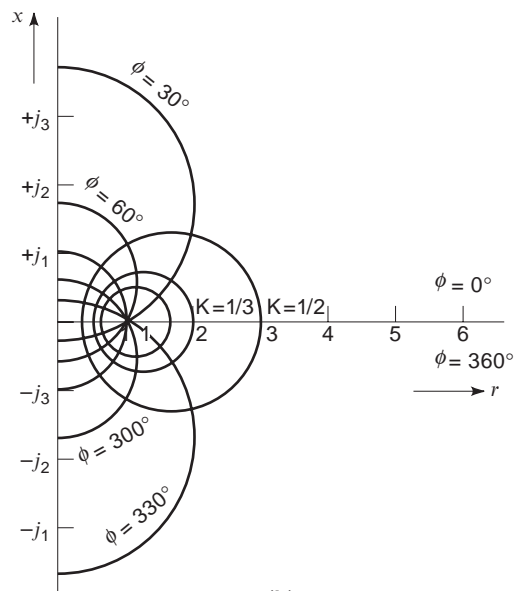
$$z = \frac{1+k}{1-k} \quad \text{and} \quad k = \frac{z-1}{z+1} \quad (1)$$

where z represents normalized impedance (Z/Z_0), k is the complex reflection coefficient at the point where z is measured, and Z_0 is the reference or normalizing value of impedance.

The generality of the underlying bilinear transformation is seen by plotting normalized impedance values (or analogously admittance values) on the right half of a Cartesian coordinate plane and evaluating the paired Eq. (1) for reflection coefficient loci that have constant values of magnitude with varying modulus as well as constant modulus (angle) values with varying magnitudes. Figure 3a illustrates normalized impedance plotted in a Cartesian frame, with the dashed lines indicating constant-resistance and constant-reactance values (hereafter referred to as constant- R and constant- X , respectively). Figure 3b



(a)

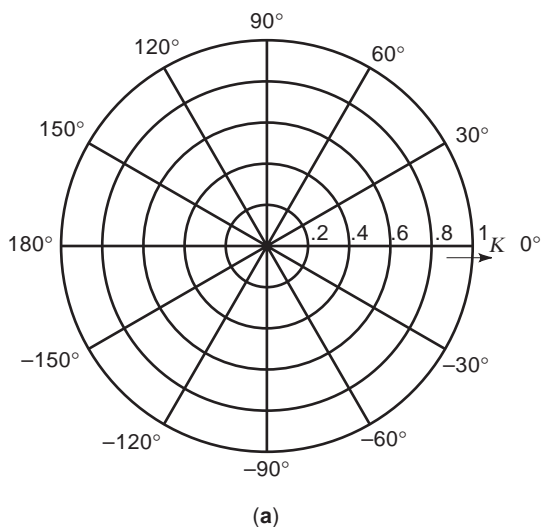


(b)

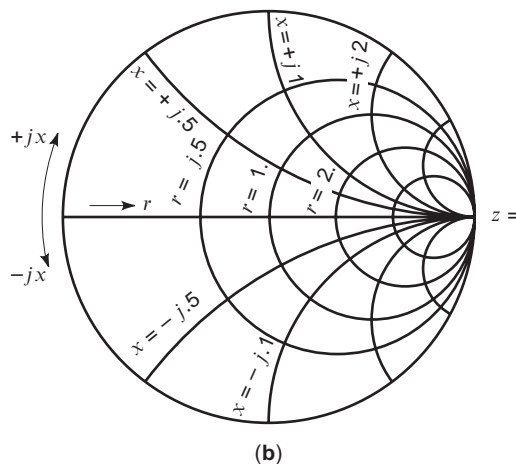
Figure 3. (a) Plots of normalized constant R and constant X on a Cartesian frame; (b) loci of constant- k (full circles) and constant- ϕ angle (circular arcs).

uses the same frame to depict loci of constant- k values as solid-lined full circles, and it uses loci of constant phase angle values for variable- k magnitudes as solid-lined partial circles. The constant angle value loci all intersect at the single point $z = (1 + j0)$ for which $k = (0 + j0)$.

Alternately, one can plot the complex reflection coefficient [$k = K \exp(j\phi)$] in two-dimensional cylindrical (i.e., polar) coordinates as shown in Fig. 4a, with $k = (0 + j0)$ located at the center and cylindrical angle representing the reflection coefficient angle ϕ . Then the transformation to complex normalized impedance using Eq. (1) results in loci for constant- R and constant- X values that are again full circles and partial circles, respectively, as illustrated in Fig. 4b. These circles and circular arcs have progressively offset centers located along the orthogonal axes defined by the horizontal line at $x = 0$ and the vertical line tangent to the outer circle at the right side point. Figure 4 illustrates the orthogonality features in both domains of (a) reflection coefficient and (b) normalized impedance.



(a)



(b)

Figure 4. (a) Two-dimensional cylindrical coordinate plot of loci of constant reflection coefficient magnitude and constant reflection coefficient angle; (b) loci of constant- R circles and constant- X circular arcs scaled to fit on the reflection coefficient loci plot of part (a).

The latter grid of circle and circular arcs represent exactly the chart solution method first proposed by Smith to the radio engineering community.

The radii and centers of the constant- R circles and constant- X circular arcs of Fig. 4b are derived relative to the center of the cylindrical coordinate plot of complex reflection coefficient. The radii are given by Eq. (2), where the value of either r or x is held constant. The geometric locations of the centers of the constant- R circles are given by Eq. (3), and the positions of the centers of the constant- X circular arcs are given by Eq. (4)

$$r_k = \frac{[(r^2 - 1 + x^2)^2 + 4x^2]^{1/2}}{(r+1)^2 + x^2} \quad (2)$$

$$(k_R^x, k_R^y) = \left(\frac{r}{r+1}, 0 \right) \quad (3)$$

$$(k_X^x, k_X^y) = \left(1, \frac{1}{x} \right) \quad (4)$$

where the subscripts R and X denote constant- R circles and constant- X arcs, respectively, and the superscripts x and y denote the directional components.

3. NORMALIZATION OF THE CHART

For commonality and other reasons, it is useful to deal with normalized rather than unnormalized charts. Both full-size and enlarged central area charts are normalized by dividing values of resistance (R) and reactance ($\pm X$) by the real reference value (Z_0). This scaling results in all real axis values to the left of the centerpoint having values between 0 and 1, and all real axis values to the right of the centerpoint represent values between 1 and infinity. Charts that plot admittance values are analogously normalized using the reference value $Y_0 = 1/Z_0$. The usage of normalized impedance values on the Smith chart grid facilitates the computation of reflection coefficient, VSWR, and return loss from the chart. Design examples given in subsequent sections for transmission-line problems illustrate the advantage of using normalized values for chart-based computation.

4. GRID-BASED FEATURES OF THE SMITH CHART

A number of useful design features result from the final form of the chart grid as derived by Smith. In addition to the interrelation of VSWR, return loss, and reflection coefficient, one is also able to read length ($1/\lambda$) along a transmission-line segment from the rim of the chart and use boundary circles as a design aid. These features are reviewed below, but the reader is referred to Smith's seminal text [7] for added detail on these and other features. This reference also contains an exhaustive bibliography on publications related to the Smith chart through 1969.

4.1. VSWR Circles

The relationship between VSWR and reflection coefficient is given by Eq. (5), where K is the magnitude of the complex reflection coefficient written as $k = K \exp(j\phi)$:

$$\text{VSWR} = \frac{1+K}{1-K} \quad (5)$$

On the Smith chart, loci of constant VSWR are concentric circles with all centers located at $K=0$, and radii are nonuniformly distributed between unity and infinity for values of K ranging from 0 to 1.

4.2. Chart Perimeter as Transmission-Line Length

The classical transmission-line equation (see Table 1, line 1) clearly illustrates that impedance, and hence VSWR, varies in a repetitive fashion every half-wavelength in distance along a lossless line. On the Smith chart this is equivalent to repeated values for reflection coefficients with every complete rotation around the chart relative to the center of the chart. The entire perimeter of the Smith chart calibrates uniformly as a \pm quarter-wavelength distance relative to a reference location. Clockwise rotation around the chart's periphery is equivalent to moving along the line in a direction toward the source (generator), and counterclockwise rotation around the chart is equivalent to moving toward the load.

4.3. Impedance and Admittance Locus Movement for Discrete Circuit Elements

Electronic circuit impedance matching is easily performed utilizing the Smith chart. Typically one desires to use only lossless components to accomplish a match. The addition of a discrete circuit element such as a capacitance or an inductance in a matching circuit has a well-defined effect on moving the locus of a load impedance vector on the chart grid. The four key discrete circuit elements commonly used in circuit matching are given as follows along with their effects on motion of an impedance locus (for series elements) or an admittance locus (for shunt elements):

- Series inductance rotates an impedance locus CW on a constant- R circle
- Series capacitance rotates an impedance locus CCW on a constant- R circle
- Shunt inductance rotates an admittance locus CCW on a constant- G circle
- Shunt capacitance rotates an admittance locus CW on a constant- G circle

Here CW and CCW denote clockwise and counterclockwise motion, respectively, on the specified circles.

4.4. Boundary Circles

The chart-centered circle for a finite value of VSWR leads directly to the useful design construct known as *boundary circles*, which serve as a visual aid to determine the correct value of a circuit element that will provide the proper

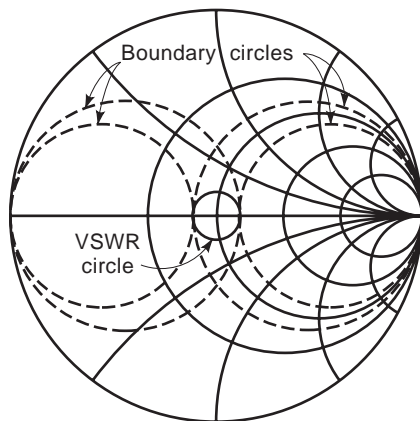


Figure 5. VSWR circle and its associated boundary circle pairs for a value $VSWR = 1.25$.

amount of rotation of an impedance or admittance locus for acceptable matching (i.e., that meets the VSWR requirement).

For a specified VSWR there are two related pairs of boundary circles. Each pair consists of two circles that are centered on the $x = 0$ line and are doubly tangent to both the VSWR circle and the periphery of the chart, where the magnitude of the reflection coefficient is unity. Figure 5 shows the combination of a $VSWR = 1.25$ circle along with its associated pair of boundary circles. Knowing the directions of rotation for an impedance or admittance locus caused by the addition of series or shunt elements, respectively, one immediately determines that impedance values over a very large portion of the chart—namely, the interior portions of both small boundary circles, as well as the upper and lower exclusion areas outside both of the larger boundary circles—cannot be matched to within a specified value of VSWR with a single matching element.

5. OTHER IMPORTANT OPERATIONS EXECUTABLE ON THE SMITH CHART

5.1. Two-Element Matching over the Entire Chart

In contrast to the case just shown where impedance values over much of the chart area cannot be matched with a single element, it can be shown that all single-frequency impedance values anywhere on the chart exclusive of the outer rim circle ($r = 0$) can always be perfectly matched to a value of $r = (1 + j0)$ by use of a two-element circuit. Smith [8] and a current software chart implementation [9] provide overlay diagrams of the eight possible ell-type circuits (four L - C , two L - L , and two C - C), each with its associated allowed area and supplementary forbidden area on the Smith chart. (The same diagrams are also illustrated in Ref. 10, p. 40.) Any point within an allowed area can always be perfectly matched using the associated ell circuit.

5.2. Transmission-Line Transformers

Frequently the design of an impedance-matching circuit must be implemented using distributed parameter ele-

ments such as transmission lines. Somlo [11] has shown how a single-frequency design for a transmission-line transformer is graphically implemented using a Smith chart. Narrow-bandwidth-matching designs are also achievable using the same method. The Somlo technique is implemented as a utility tool in the software implementations of Refs. 9 and 12.

The ability to graphically analyze the matching effects of a variety of transmission-line circuit elements (e.g., open- or short-circuit stubs as well as transmission-line sections and impedance transformers in both series and shunt configurations) gives the Smith chart more versatility than do software synthesis tools, which are typically unable to treat a full array of transmission-line elements.

6. EXAMPLE

A circuit-matching design exercise is described here to illustrate the methods used in obtaining a solution on the Smith chart. To keep the charts visually succinct, each of the intermediate plotting steps including $Z \rightarrow Y$ and $Y \rightarrow Z$ inversions as well as the effects of individual branch-by-branch circuit constructions are presented on a set of individual charts. The traces plotted on the charts use the convention of Z_N or Y_N for the driving point impedance or admittance when looking toward the load from branch N . Readers who wish to study a variety of antenna-matching problems executed in step-by-step detail can consult Ref. 13.

In this problem a device, such as an antenna, has a highly capacitive input impedance vector as given in Table 2 for the range of 850–925 MHz. The objective is to produce a matching circuit that meets a VSWR requirement of 2.5:1 over the reduced frequency range of 855–920 MHz with the restriction that no lumped circuit inductors be used in the matching circuit.

The bandwidth requirement of about 8.5%, the highly capacitive values, and the implementation restriction of no lumped inductors all imply that additional elements beyond a simple two-element L configuration will be required to implement a satisfactory matching circuit. The two solutions derived by use of a software chart method are described in Table 3, giving all the circuit element parameter values. The first solution uses transmission lines and short-circuit stub elements exclusively and is illustrated in the set of successive charts in Fig. 6. The second solution requires fewer elements but includes a capacitance and a short-circuit stub having a low value of Z_0 that is virtually impossible to implement. It is presented in the second part of Table 3 for purposes of contrast only.

Table 2. Load Impedance Values for Example Matching Problem

Frequency (MHz)	Load impedance (Ω)
850	$15.0 - j250$
875	$19.0 - j227$
900	$21.5 - j192$
925	$25.0 - j180$

Table 3. Component Types and Values for the Solutions of Example Problem

Element No.	Element Type	Parameter Values ($v/c =$ Group Velocity)
<i>Primary Solution^a</i>		
1	Transmission line	$Z_0 = 234 \Omega$, 2.60 cm, $v/c = 0.69$
2	Shunt short-circuit stub	$Z_0 = 10.1 \Omega$, 4.84 cm, $v/c = 0.69$
3	Transmission line	$Z_0 = 76.22 \Omega$, 0.70 cm, $v/c = 0.69$
4	Shunt short-circuit stub	$Z_0 = 6.53 \Omega$, 6.25 cm, $v/c = 0.69$
<i>Contrasting Solution</i>		
1	Transmission line	$Z_0 = 100 \Omega$, 4.91 cm, $v/c = 0.69$
2	Shunt capacitance	9.4 pF
3	Transmission line	$Z_0 = 42.8 \Omega$, 5.84 cm, $v/c = 0.69$
4	Shunt short-circuit stub	$Z_0 = 3.12 \Omega$, 5.91 cm, $v/c = 0.69$

^aSee Fig. 6 for associated chart traces.

The first element in the matching circuit must be either of the two inductive types: a short-circuit stub or a transmission line of sufficient length to rotate the load impedance trace toward the inductive reactance portion (i.e., upper half) of the chart. There is, however, a distinct observable difference in how the two candidate initial elements cause the load impedance trace to rotate on the chart. A series-wired short-circuit stub will move the load trace CW and upward along constant- R gridlines, causing

the rotated impedance vector to lie closer to the center of the chart, but extending it over the chart to a greater degree than would be caused by a series transmission line. Conversely, the series transmission line keeps the rotated load trace further out toward the chart periphery. A compromise for the initial element is to use a short length of transmission line with high Z_0 . This has an impedance-transforming effect in bringing the load trace toward the center of the chart, but the short length keeps the trace

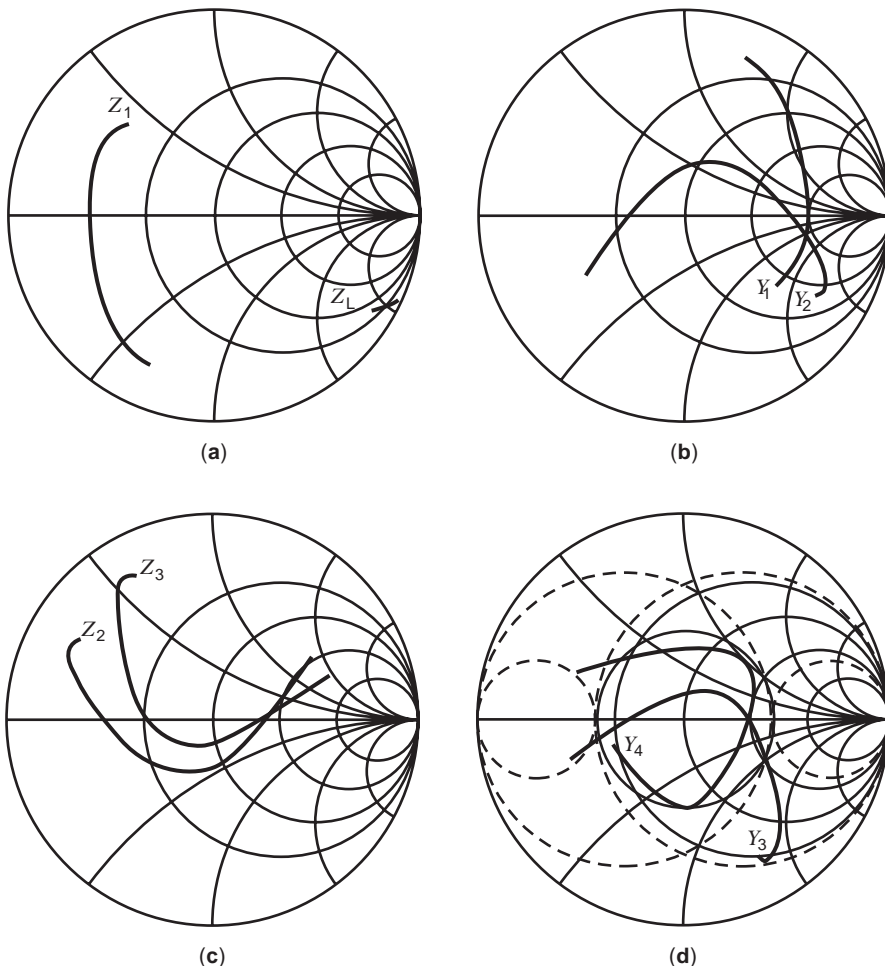


Figure 6. Solution to the example impedance-matching problem requiring no lumped-element inductors: (a) Z_L trace and Z_1 trace after adding series transmission-line section; (b) Y_1 trace and Y_2 trace after adding shunt short-circuit stub; (c) Z_2 trace and Z_3 trace after adding series transmission line section; (d) Y_3 trace and Y_4 trace after adding shunt short-circuit stub.

located mostly on the capacitive side of the chart. In this case the characteristic impedance and length of the transmission-line element are selected to rotate the impedance locus such that it approximately straddles the lower-left crescent of the boundary circles associated with the specified VSWR.

The second element, a shunt position short-circuit stub, rotates the Y_1 trace CCW and downward to position the ends of the Y_2 trace on the inductive susceptance side of the chart with the trace approximately surrounding the center of the chart. This begins the process of pulling the ends of the trace inward toward accomplishing the ultimate goal of collapsing the final trace into a loop configuration and positioning it inside the 2.5:1 VSWR circle.

The third element, a length of transmission line, rotates the Z_2 trace CW to an approximately vertical orientation with about half of the trace in each of the top and bottom halves of the chart. With the central portion of the Z_3 locus inside the VSWR circle, the sole purpose of the fourth and final element will be to complete the process of collapsing the trace into the needed loop and place it inside the VSWR circle.

The fourth element, a shunt-wired short-circuit stub, adds sufficient compensating susceptance (inductive susceptance at the low frequencies and capacitive susceptance at the high frequencies) to further close the loop. To provide the necessary magnitude of compensating susceptance given by $B_{\text{stub}} = -(\cot \gamma l/Z_0)$, the characteristic impedance required for the shunt short-circuit stub element is a small value. This also keeps the Y_4 trace tightly looped. In practice, this low value of Z_0 is typically accomplished with four equal-length stubs wired in parallel and each having a Z_0 of about 25Ω , which is a practical physical lower limit. Frequency interpolation is used to confirm that the VSWR specification is met for the frequency range of 855–920 MHz.

The contrasting solution listed in Table 3 follows much the same sequence used in the first solution. The primary difference in the two methods is that use of a capacitance for the second element places its associated Y_2 trace in a more vertical orientation with the extremes of the trace spread further out from the VSWR circle. That causes the value of characteristic impedance for the short-circuit stub used for the fourth element to be much lower than that for the first solution method, where more of the admittance locus for the third element is already within the VSWR circle. This second solution is clearly not a physically realizable situation. Hence, the associated chart traces are not shown.

7. REVITALIZATION OF THE SMITH CHART IN SOFTWARE

The original printed paper versions of the Smith chart were primarily used in industrial research and World War II development efforts through the 1940s. For the following three decades, these paper charts became a mainstay tool in every transmission-line course in academia as well as a broad-based industry design tool. Beginning about 1980 with the onset of a variety of numerical design tools such as the real-frequency method pioneered by Yarman

and Carlin [14] and implemented in commercial software [15], the paper version of the Smith chart fell into relative disuse. However, beginning about 1990, a number of software tools [9,10,12,16,17] became available that implemented the core operations of the Smith chart on a computer screen.

These software implementations of the Smith chart alleviated most or all of the key difficulties encountered with manual use of the paper charts. These advantages include (1) elimination of math errors since the software internally performs all the background calculations of branch impedance or admittance values including normalization, (2) elimination of errors due to using an incorrect rotation direction on the chart, (3) elimination of interpolation errors when plotting data onto or reading value off of the chart, (4) requiring the user to select a proper value of group velocity for a transmission line ($v/c < 1$), (5) having the software internally perform spline calculations to plot smoothly contouring line vectors on the chart, (6) the dramatic speed improvement factor over hand-drawn Smith charts, and (7) toggled screen presentation of VSWR and boundary circles as convenient design aids. In addition, an attractive feature of the software versions is their ability to plot the finished work in excellent detail on a preprinted paper Smith chart form for delivery or publication purposes.

With the availability of software-based Smith chart programs, the professional circuit designer, student, and researcher can take full advantage of the clarity and simplicity of graphical methods with a minimum investment of labor and time to obtain the needed solution. More important, one gains the value of personal insight into the process of design of a matching circuit when using this graphical method.

The value of the Smith chart as a potent graphical design tool was well stated by Carlin [18] at a 1983 IEEE MTT/S professional workshop on broadband matching: "So far the 'best' transfer functions analytic theory has to offer are based on Chebyshev polynomials and almost invariably these yield matching structures which can be surpassed in performance by significantly simpler equalizers. In effect the old-fashioned procedure of 'playing around' on the Smith chart may produce better results than sophisticated theory."

As software-based Smith chart tools evolve to include additional capabilities such as built-in circuit optimization functions and IEEE 488 interfaces to port measured impedance data from network analyzers, it is expected that they will enjoy continued future usage by a variety of technical practitioners and students.

BIBLIOGRAPHY

1. P. H. Smith, Introduction section, *Electronic Applications of the Smith Chart*, McGraw-Hill, New York, 1969; subsequent reprints Krieger Publishing, Malabar, FL, 1983; Noble Publishing, Tucker, GA, 1996.
2. J. A. Fleming, *The Propagation of Electric Currents in Telephone and Telegraph Conductors*, Van Nostrand, New York, 1911.

3. L. M. Schwab, *Advanced Automated Smith Chart, Version 2*, Artech House, Boston, 1995.
4. Available online at http://www.ieee.org/history_center/oral_histories/abstracts/smith3_abstract.html.
5. P. H. Smith, Transmission line calculator, *Electronics* (Jan. 29, 1939).
6. P. H. Smith, An improved transmission line calculator, *Electronics* (Jan. 30, 1944).
7. P. H. Smith, *Electronic Applications of the Smith Chart*, McGraw-Hill, New York, 1969; subsequent reprints Krieger Publishing, Malabar, FL, 1983; Noble Publishing, Tucker, GA, 1996.
8. Ref. 7, pp. 116–117.
9. L. M. Schwab, *Automated Smith Chart, Version 3* (MS Windows 95/NT), Artech House, Boston, 1998.
10. L. M. Schwab, *Automated Smith Chart* (DOS), Artech House, Boston, 1991.
11. P. I. Somlo, A logarithmic transmission line chart, *IRE Trans. Microwave Theory Tech.* **8**:463 (1960).
12. L. M. Schwab, *Advanced Automated Smith Chart, Version 2* (MS Windows 3.1), Artech House, Boston, 1995.
13. W. N. Caron, *Antenna Impedance Matching*, American Radio Relay League, Newington, CT, 1989.
14. B. S. Yarman and H. J. Carlin, A simplified “real frequency” technique applied to broadband multistage microwave amplifiers, *IEEE Trans. Microwave Theory Tech.* **30**(12):2216–2222 (1982).
15. *Complex Match II*, synthesis software by Compact Software, Inc. Paterson, NJ, 1988.
16. W. Hayward, *MicroSmith* (DOS), American Radio Relay League, Newington, CT, 1992.
17. Eagleware, *winSMITH* (MS Windows), Noble Publishing, Tucker, GA, 1995.
18. H. J. Carlin, Keynote speech: That perennial problem of broadband matching, *1983 IEEE MTT/S Symp. Workshop on Broadband Matching and Design of Microwave Amplifiers*.

SPACEBORNE RADAR

RONALD KWOK
SIMON H. YUEH
LEE-LUENG FU
California Institute of
Technology

Spaceborne remote sensing instruments allow the acquisition of global and synoptic information for Earth science investigations. In particular, active microwave observations have the added advantage of providing diurnal measurements and are relatively uncontaminated by the intervening atmosphere. Here, we review three different applications of active microwave remote sensing that have contributed geophysical measurements on a scale and accuracy that surpass what could be accomplished with airborne or in situ observations. These are synthetic aperture radar interferometry, scatterometry, and altimetry. For each of these areas, we describe the measurement princi-

ple, the current technology, the applications, and give a brief look into the future.

1. SPACEBORNE IMAGING RADAR INTERFEROMETRY

1.1. Background

Radar interferometry is a technique for combining coherent radar images recorded by antennas at different locations or at different times to form interferograms that permit the detection of small differences in range, to better than the wavelength (λ) of the signal, between the two points of observation. The measurements are extremely useful for construction of high-resolution topographic maps and surface change maps. The observational geometry of across-track interferometry is depicted in Fig. 1. For a given set of repeat-pass observations, from the i th and j th epochs, with baseline B_{ij} and look angle θ , the interferometric phase difference at each sample is

$$\begin{aligned} \Delta\phi_{ij} &= (4\pi/\lambda)B_{ij} \sin(\theta - \alpha_{ij}) + (4\pi/\lambda)\Delta\rho_{ij} \\ &= \phi_{\text{topography}} + \phi_{\text{displacement}} \end{aligned} \quad (1)$$

where α is the tilt of the baseline with respect to the horizontal. The difference in the slant range pathlength $|\mathbf{r}_i - \mathbf{r}_j|$ is approximated by $\mathbf{B} \cdot \mathbf{r}$. The first term $\phi_{\text{topography}}$ contains phase contributions from the topography of the Earth surface relative to the interferometric baseline. The sensitivity of the measurements to surface relief is directly proportional to the length of the baseline. If the scatterers are displaced by $\Delta\rho_{ij}$ in the range direction between the two observations, then the observed phase will include a second contribution of $(4\pi/\lambda)\Delta\rho_{ij}$ due to this displacement. This additional term $\phi_{\text{displacement}}$ is independent of the spatial baseline. When the i th and j th observations are acquired at the same time (single-pass interferometry), only the first term is relevant. If the i th and j th observations are separated by a time interval, it is generally referred to as repeat-pass interferometry. In the case where more than one observation is available, it is known as multiple-pass interferometry. The reader is referred to the following articles for a more detailed description of the principles of imaging radar interferometry [1–4].

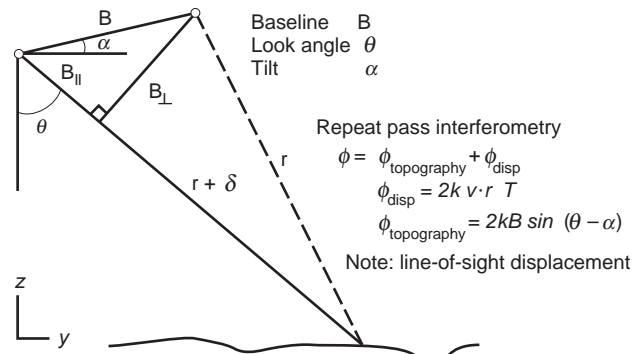


Figure 1. Radar interferometry—imaging geometry.

Here, we consider the more important practical limitations to the solution of Eq. (1) that affect the accuracies of the derived topography or motion field: phase unwrapping; baseline length/orientation; and phase noise. A digital interferogram is the product of two coregistered complex images I_i and I_j^* (* is the complex conjugate). The measured phases are modulo- 2π of the absolute phase $\Delta\phi_{ij}$ in Eq. (1). In order to create relative measurements, this phase field needs to be unwrapped to remove the 2π ambiguity. This is a difficult task, especially if the phase noise (introduced by the radar system) is high or if the phase field has high spatial frequency [2]. The unwrapped phase differs from the absolute interferometric phase $\Delta\phi_{ij}$ by an integer number of cycles for the entire phase field. Assuming $\phi_{\text{displacement}} = 0$ in the following discussion, a simple method to determine this constant would be to find one target in the interferogram with known position relative to the interferometer. Other methods for estimating absolute phase have been proposed and are used in different types of processing. Another significant error source results from errors in knowledge of the baseline length and orientation. It is impossible to separate an error in the baseline angle knowledge from a slope in the surface topography. Hence, the sensitivity of interferometer to surface relief is a function of baseline length and orientation. Extremely precise knowledge of the baseline geometry and length is required if absolute height estimates are needed. Phase noise results from various factors including thermal noise, sampling and processing artifacts, and the correlation of individual radar echoes before they are combined to form the interferogram. Uncertainties in baseline orientation cause slowly varying error whereas phase noise (expected to be random) describes the statistical variability of elevation estimates at each sample.

If an interferogram contains a mixture of topography and motion components in the observed phase, additional information is required to separate the two measurements. Much of it depends on the nature and magnitude of the motion field. For example, if a digital elevation model (DEM) of the region of interest is available, then the topographic phase could be removed. On the other hand, multiple interferograms could be used to estimate the two parameters. Some examples in the following sections illustrate several interesting uses of spaceborne interferometric datasets.

1.2. Evolution of the Technology

Imaging radar interferometry involves a mix of radar technology and data/signal processing techniques. Similar to most application technologies, the rate of development was limited by available datasets for experimentation and verification. Graham [5] of Goodyear Aerospace Corporation first demonstrated the feasibility of operating an airborne imaging radar system in the interferometric mode to generate elevation maps using optically processed data. Their interferometer consists of two antennas mounted one above the other on a side-looking moving gimbal. Subsequently, Zebker and Goldstein [1] at the Jet Propulsion Laboratory (JPL) refined these techniques using digitally processed complex data from a side-

looking synthetic aperture radar mounted on the NASA CV990 aircraft. Gray and Ferris-Manning [6] of the Canada Center for Remote Sensing (CCRS) also reported the results of a repeat-track implementation. The single-pass airborne systems of JPL and CCRS have generated extensive datasets for a number of years. Since then, there have been a growing number of interferometric systems developed for high-resolution topographic mapping and for studies in geology, glaciology, hydrology, and forestry. The current JPL TOPSAR system has two interferometers, both flush-mounted to the fuselage of the DC-8 aircraft and operating at L and C bands. The CCRS system uses the C-band channel of radar on the Convair CV-580 aircraft. Other airborne interferometers were developed by the following organizations: Environmental Research Institute of Michigan [7]; Norden Systems; and United Technologies. The Technical University of Denmark and Dornier of Germany both have operational airborne interferometers.

Researchers at JPL first demonstrated that interferometric procedures could be applied to satellite SAR data acquired on separate SEASAT passes [2,3]. Differential interferometry (using multiple interferograms) was used by Gabriel et al. [8] for detection of subcentimeter surface displacements over a large area. The SEASAT satellite, launched in 1978, provided a key source of satellite data for interferometric studies until the launch of the European Remote Sensing Satellite (ERS-1) in July 1991. The SEASAT SAR was operated at L band (25 cm wavelength) and the ERS-1 SAR was operated at C band. Both provided temporal baselines close to 3 days, but the longer wavelength of SEASAT makes that data less prone to temporal decorrelation. At shorter wavelengths, the data are more prone to temporal decorrelation, due to their sensitivity to small-scale changes in the scattering characteristics of the natural medium. The Japanese J-ERS1 radar, launched in 1992, has an L-band SAR, which also provided repeat-pass interferometric datasets. The repeat period of 44 days, however, was rather long for certain applications. Numerous Earth science studies have been carried out using these datasets.

The Spaceborne Imaging Radar (SIR-C/X-SAR) missions (both approximately 10 days) were flown in April and October 1994 and tested the technology of repeat-pass radar interferometry for topographic mapping of Earth and for detection of surface change. The multifrequency radars mounted in the shuttle bay were operated at L, C, and X bands. The L- and C-band radars had vertical and horizontal transmit and receive capabilities for collecting multipolarization observations. These radar datasets allowed an assessment of the relative merits of repeat-pass interferometers for mapping the Earth surface.

During late 1995 and early 1996, the ERS-1 and ERS-2 (launched in 1995) SARs were flown in tandem to collect a near-global dataset suitable for repeat-pass interferometric analysis. The orbits were maintained such that the repeat tracks of the two radars were separated by one day, thus providing 1-day intervals between data acquired for interferometry. Subsequently, ERS-1 was decommissioned as an operational sensor. Late in 1995, the Canadian RADARSAT (another C-band SAR with 24-day repeat) was

launched but the orbits were not routinely adjusted to the baseline tolerances required for interferometry. However, it still provided subsets of data suitable for interferometric studies.

These satellite systems have collected significant volumes of repeat-pass datasets. The use of these data for Earth science investigations has grown considerably.

1.3. Applications in Earth Science

We provide examples of three Earth science areas where the use of radar interferometry has blossomed: topographic mapping; measurement of glacial ice motion; and monitoring of earthquakes. The most direct application of radar interferometry is topographic mapping. Accurate DEMs are required by a number of Earth science disciplines, including hydrology, ecology, glaciology, geomorphology, and atmospheric circulation [9]. For example, the JPL/NASA TOPSAR system exhibits errors of about 1 m rms in flatter regions and 3 m in mountainous areas. By comparison, the standard United States Geological Survey (USGS) product generally available has a 30 m posting and a level of accuracy of approximately 7 m. The achievable accuracy is better than standard U.S. maps. For parts of the world that are relatively poorly mapped, topographic mapping using radar interferometry is an alternative to traditional photogrammetric surveys. This is especially attractive in regions where the cloud cover precludes the use of visible sensors.

Goldstein et al. [10] produced the first map of ice motion over the Rutford Ice Stream in Antarctica. In their demonstration, they used an image pair with very small baseline (~ 4 m) to avoid contamination due to surface relief. The sensitivity to line-of-sight motion is better than 1 m/year, and comparison of derived measurement with ground-based observations showed good agreement. Subsequently, Joughin et al. [11] and Rignot et al. [12] both demonstrated the observability of ice motion on the Greenland Ice Sheet after the removal of the topographic component of the signal. Kwok and Fahnestock [13] used a sequence of interferograms to separate the motion and topographic components of the measured interferometric phase with the assumption that the motion is constant over the observation period. Other studies have progressed further in the use of interferometric observations to produce maps of grounding lines and multiple

observations to derive three-dimensional velocities. As an illustration, Fig. 2 shows a map of the motion field of the Ross Ice Shelf in Antarctica just east of Roosevelt Island; the topographic component of the phase was removed. Flow patterns east of Roosevelt Island are explained by the flow of ice through the channel bounded by the Shirase Coast (400–500 m/year). The situation is more complicated west of Roosevelt Island, where large rifts extend away from the Bay of Whales and slice through the ice shelf. Eventually, these large blocks of ice will separate (an event known as calving) from the shelf ice and flow off as icebergs. Observations such as this have given glaciological investigators an unprecedented view of the velocity fields of the various regimes of glacial ice flow. By analyzing only a few synthetic aperture radar (SAR) images, these interferometric procedures can provide dense fields of observation that otherwise would require many years of extremely expensive fieldwork to compile.

The mapping of coseismic displacement of earthquakes was demonstrated by Massonnet et al. [14,15] and Zebker et al. [16]. Massonnet et al. [14] used two images (before and after an earthquake) and removed the topographic component using a simulated topographic phase field generated using an available DEM. Zebker et al. [16] used three complex SAR images: one before and two after the main Landers earthquake in June 1992. The topographic phase is removed by differencing two interferograms—one with surface motion and one without. Again, these techniques have been used routinely to monitor the effects of earthquakes in the past several years. Figure 3 shows a map of ground motion in the aftermath of an earthquake. This figure of the area around Kobe, Japan was created by combining two JERS-1 synthetic aperture radar images acquired 2.5 years apart to form an interferogram, which contains a record of the topography of the surface and the change in topography between the imaging times. Because the JERS-1 satellite imaged the area from nearly the same path on orbit (baseline = 0 m at the top of the scene and about 100 m at the bottom of the scene), there is very little sensitivity in the interferogram to the topography; the steep mountains north of the city of Kobe cannot be seen in the signature of the interferogram. However, the surface changed dramatically over the 2.5 years because the magnitude 7 Kobe earthquake occurred between imaging times. Most of the gray level variations on Awaji island and in the city of Kobe are the signature of strong

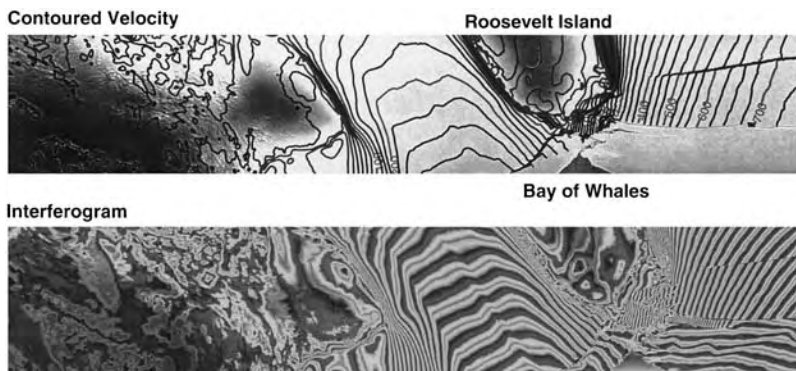


Figure 2. Ice motion of the Ross Ice Shelf, Antarctica near Roosevelt Island. This ERS tandem phase data was recorded at the U.S. McMurdo Reception Facility in Antarctica in January 1996.

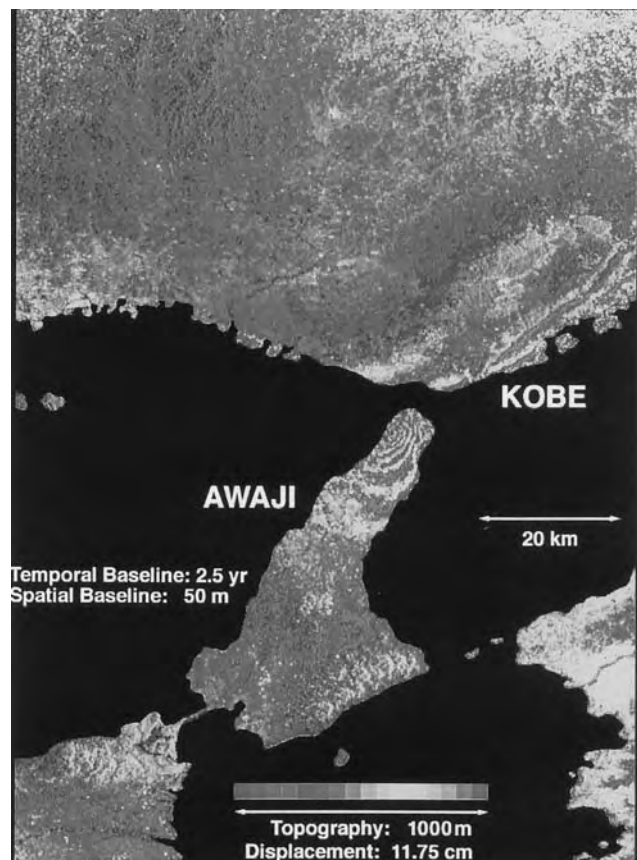


Figure 3. Image showing surface displacement due to the magnitude 7 earthquake in Kobe, Japan derived from JERS-1 data. (Courtesy of Dr. P. Rosen, Jet Propulsion Laboratory, California Institute of Technology.)

displacement of the surface due to the earthquake. The distance that the ground moved is depicted as gray level contours, with 11.75 cm of distance shown as one cycle of color variation. It can be seen that the ground moved by greater than 1 m from before to after the earthquake. Very noisy signals along the port areas east of Kobe indicate massive surface disruption from liquefaction of the surface and collapse of structures.

1.4. Future Perspectives

Radar interferometry is rapidly maturing into a routine tool for providing important measurements for supporting Earth science investigations and other applications. There are a number of spaceborne radar systems on the horizon designed to provide interferometric observations as one of their primary missions.

In 1999, the Shuttle Radar Topography Mission (SRTM) was launched with the purpose of producing the most accurate and complete topographic map of the Earth surface. The SRTM mission is a joint project of the Department of Defence's National Imagery and Mapping Agency (NIMA), NASA, and the German and Italian Space Agencies. SRTM planned to build on the technology of the earlier SIR-C/X-SAR missions that were flown in

1994. The objective of the 1999 mission was to collect elevation measurements of nearly 80% of Earth's land surface. These observations were to be assembled into DEMs. These DEMs had a planimetric resolution of 30 m and a relative height accuracy of 10 m. Maps of this accuracy can be used for a large number of scientific, civilian, and military applications. The SRTM interferometer will operate at two frequencies (C and X bands). The interferometer had a baseline of approximately 60 m. A set of antennas were mounted in the bay of the shuttle, and another set were mounted at the end of a boom deployed from the shuttle bay after orbit insertion. The interferograms were obtained from complex SAR data collected from the two sets of antennas. In this case, we will have a C-band and X-band interferograms were provided for most of the Earth surface. The entire dataset was acquired in an 11-day mission. The bulk of the data processing to convert the radar signal data to DEMs took more than a year.

The European Space Agency (ESA) launched ENVISAT in late 1998 as a follow-up to the ERS satellites, and the Canadian Space Agency (CSA) launched RADARSAT II in 1999. The proposed NASA LightSAR was an imaging satellite that would use advanced technologies to reduce the cost and enhance the quality of images taken with SAR technology. All these spaceborne missions had an interferometry component. The data from these missions have provided quantitative measurements at an unprecedented spatial and temporal scale into the present century.

2. SPACEBORNE SCATTEROMETRY: OCEAN WINDS

2.1. Background

Wind scatterometers are radars specifically designed to measure wind velocities over the oceans. During the early 1960s, an aircraft radar measurement program conducted by the Naval Research Laboratory indicated that ocean radar clutter was dependent on windspeed and sea state [17,18]. Thereafter, NASA sponsored the development of airborne radars with extensive field programs to help interpret scatterometer measurements in terms of oceanic parameters. In 1966, Moore and Pierson [19] proposed a spaceborne scatterometer on a polar-orbiting satellite to obtain ocean surface wind measurements. During the 1970s, NASA sponsored improved aircraft (AAFE RADSCAT) and Skylab-193 scatterometer programs [20,21] that paved the way for a full-blown demonstration of a spaceborne sensor: the SASS experiment.

On June 28, 1978, SASS was launched on SEASAT to provide global measurements of ocean surface wind vectors [22,23]. Although SEASAT operated only for three months, SASS demonstrated the feasibility of ocean wind measurements from space. The scientific results can be found in the special issue of *Journal of Geophysical Research* [88(C3) (Feb. 28, 1983)].

Following the SASS experiment, the ERS series of satellites with onboard C-band microwave scatterometers [24] have provided surface wind measurements since 1991. The NASA Scatterometer (NSCAT) aboard the Japanese Advanced Earth Observation Satellite (ADEOS) was launched on August 17, 1996. Although ADEOS-1

ceased operation after June 1997, due to the solar paddle failure, NSCAT has been found to have had a significant impact on numerical weather forecasting, storm monitoring, and many other scientific applications. This prompted NASA to decide to launch a copy of the Sea Winds Scatterometer in early 1999 to fill in the data gap between the NSCAT and ADEOS-2/SeaWinds missions. Subsequent NASA and ESA satellite scatterometers were planned to extend the time series of satellite wind products to the twenty-first century.

2.2. Measurement Principle

Scatterometers measure ocean surface winds based on the dependence of radar backscatter (σ_0) on ocean surface roughness, which is a function of surface wind velocity. Here, σ_0 is defined as the normalized radar cross section of the sea surface. Wind-roughened surfaces in the form of gravity and capillary waves, breaking waves and foam, are due to the balance of wind input and dissipative processes. Changes in wind velocity cause changes in the roughness of these surface waves. Directional response of the ocean surface to wind forcing makes the profiles of gravity and capillary waves rougher in the along-wind direction than those across. Additionally, the nonlinear interaction of long and short ocean waves makes the short ocean waves rougher on the leeward faces of the long waves than on the windward faces [26,27]. These surface waves interact with radar waves, and the strength of the returned echoes is modulated by the windspeed and direction.

The typical dependence of microwave ocean backscatter on surface wind velocities is illustrated in Fig. 4. As shown, σ_0 is a monotonically increasing function of wind-speed at incidence angles above 20° , and has a few decibels (dB) of variation over azimuth angles. σ_0 is larger in the upwind direction than in the crosswind direction (upwind-crosswind asymmetry), and there is a small difference between upwind and downwind observations (upwind-downwind asymmetry). These asymmetries are caused by the preferential directional features of surface waves described in the foregoing. At small incidence angles ($<10^\circ$), the backscatter signal is dominated by the specular reflection by the surface, usually referred to as geometric optics scattering. Because the short ocean waves reduce the specular reflectivity of the surface, σ_0 has a negative wind speed sensitivity at near normal incidence angles. However, geometric optics scattering is insensitive to wave direction at less than 15° incidence angles. Hence, microwave scatterometers typically operate at above 20° incidence for near-surface wind velocity measurements.

To facilitate the retrieval of surface wind velocities from radar measurements, a geophysical model function (GMF) relating the microwave ocean backscatter to the surface wind velocity is required. In principle, if there is an accurate mathematical representation of ocean surface waves and an accurate scattering theory accounting for the interaction of electromagnetic waves with ocean surfaces, the relationship of σ_0 and ocean surface parameters can be established for any observation angles and fre-

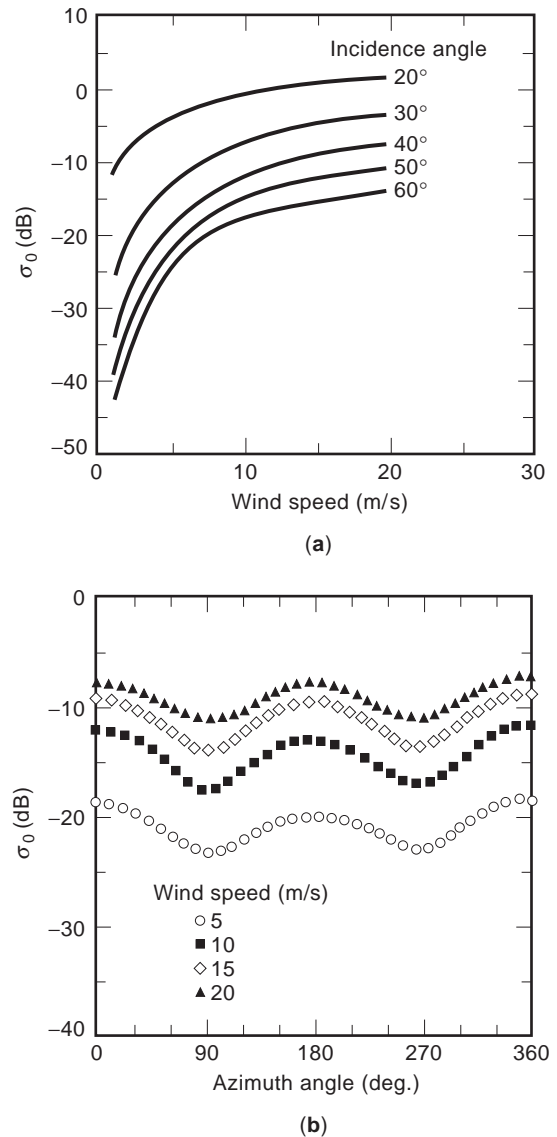


Figure 4. The dependence of microwave ocean backscatter on surface wind velocities at Ku band derived from NSCAT-1 geophysical model function. 0° , 90° , and 180° azimuth angles correspond to upwind, crosswind, and downwind. Incidence angle is the angle between the direction of surface normal and the radar observation direction.

quencies. However, present hydrodynamic and electromagnetic theories are not yet mature enough to produce an accurate geophysical model function for operational considerations. An alternative approach for deriving the scatterometer GMF is to empirically correlate the radar measurements with in situ data. A variety of input winds, including numerical weather model winds and buoys, have been considered for the development of such an empirical function [28–30]. For example, the C-band geophysical model function [30] developed for the European Space Agency (ESA) is based on the colocated European Centre for Medium-Range Weather Forecasts (ECMWF) analysis field and ERS-1 scatterometer measurements. A similar approach using the National Center for Environmental

Prediction (NCEP) and ECMWF winds together with the Special Sensor Microwave/Imager windspeed products was employed to derive the first version of NSCAT model function (see Fig. 4).

Since σ_0 depends on both windspeed and direction, a single σ_0 measurement is inadequate for the retrieval of both variables (see Fig. 4). To retrieve the wind vector, multiple σ_0 measurements are made at several different azimuthal angles. Figure 5 depicts the measurement geometries of SASS, ERS, NSCAT, and SeaWinds scatterometers. SASS collected σ_0 measurements at two azimuth angles separated by 90° , and there are up to four possible wind directions for the SASS measurement geometry. To reduce the number of wind direction solutions (ambiguities), ERS scatterometers and NSCAT added one antenna beam to the SASS antenna geometry. Without measurement noise, ERS scatterometers and NSCAT measurements allow unique determination of the correct wind direction. However, the upwind and downwind asymmetry of ocean σ_0 are not significant, and, the correct wind direction (closest to the true) and the one in the opposite direction are often confused by noise. Hence, the ambiguity selection skill, which is defined as the probability that the correct wind direction solution is selected, is a very important parameter for scatterometer performance.

The scatterometer wind accuracy is limited by the accuracies of radar measurements and geophysical model functions. The sources of radar measurement errors result from uncertainties in instrument calibration, background and instrument thermal noise, radar integration time-bandwidth product, and propagation loss through the atmosphere. Instrument calibration errors typically appear

as biases and may drift as a function of time. Thermal noise and limited time-bandwidth product uncertainties are expected to be random and are important at low winds because of low signal-to-noise ratio. Atmospheric loss is expected to be smaller for ERS scatterometers operating at C band (5.3 GHz) than NSCAT operating at Ku band (13.995 GHz), but will introduce biases in the retrieved windspeed if left uncorrected. In particular, the error caused by atmospheric loss can be significant at high winds typically associated with thick cloud cover and rain. The other major error source for wind retrieval is the uncertainty of the geophysical model function, which may be influenced by many other geophysical parameters besides the winds, such as wave height and sea and air temperatures.

2.3. Current Technology

The NSCAT is a follow-on instrument to SASS. It operates at Ku band and employs antenna fan beams and Doppler filtering to determine the cell resolution. However, based on the study of SASS data, significant improvements have been made to address NASA science requirements. These include the addition of a third antenna beam for each side of the swath and an onboard digital Doppler processor to replace the analog filtering employed by SASS. The detailed design and implementation of each of these subsystems are described in Ref. 31.

The NSCAT antenna subsystem consists of two sets of three antenna fan beams. All NSCAT antenna beams are dual-polarized. The midbeam can transmit and receive vertical and horizontal polarizations, but NSCAT was


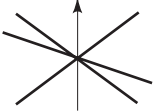
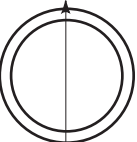

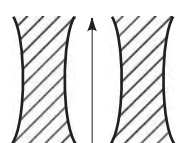
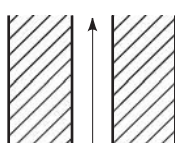
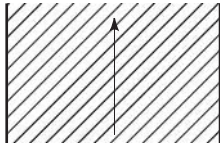
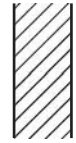
	SASS	NSCAT	SeaWinds	ERS-1/2
Frequency	14.6 GHz	13.995 GHz	13.402 GHz	5.3 GHz
Scan pattern				
Polarization	V-H, V-H	V, V-H, V	V, H	V only
Beam resolution	Fixed Doppler	Variable Doppler	Spot	Range gate
Resolution	50/100 km	25/50 km	20/25 km	25/50 km
Swath				
Daily / 2-day coverage	Variable	77/97%	93/100%	41%
Dates	6/78 - 10/78	8/96 - 6/97	11/98 - 11/00 +, 8/00 - 8/03	91 +

Figure 5. Measurement geometries of SASS, ERS scatterometers, NSCAT, and SeaWinds.

designed to excite only the vertical polarization ports of fore and aft antenna beams. The baseline operation scans sequentially through these eight antenna ports in 3.746 s, leading to a sampling resolution of 25 km along the track. The scanning sequence is determined by a beam sequence table containing 8 beam numbers stored in the on-board computer. The addition of a third antenna beam to the SASS design is to improve the ambiguity selection skill of NSCAT. The results of postlaunch NSCAT calibration and validation studies have suggested that NSCAT multiple antenna measurements without additional meteorological information allow the selection of the closest solution more than 90% of the time, representing a significant improvement over SASS.

Another improvement of NSCAT over SASS is the use of onboard digital Doppler filtering. Due to the relative motion of spacecraft and Earth surfaces, the Doppler shift of the return echos varies across the swath. The onboard DSS divides the swath into 25 cells based on the Doppler shift. The Doppler center and bandwidth of each of these cells are adjusted as a function of spacecraft orbit location to maintain the swath location and across-track cell resolution. A table containing the constants necessary for the calculation of Doppler frequencies on orbit is called the "binning table" and is used by the NSCAT on-board computer for real-time calculations. Because the binning and beam sequence tables can be updated and uploadable to the satellite, the along- and across-track resolutions of each NSCAT cell are adjustable. For example, NSCAT has been configured to operate at 6.25 and 12.5 km measurement resolutions for about 2 days during the first three months of operation. The resulting high-resolution data have enabled the observations of the significant effects of land surface topography on coastal ocean winds.

SeaWinds is the follow-on to NSCAT. SeaWinds also operates at Ku band. The SeaWinds system represents a major design change of NASA scatterometers. Instead of using the fan beam design, SeaWinds uses a conically scanning reflector. This is due to the limited space available on ADEOS-2, which does not provide a clear field of view for NSCAT-like fan beam antennas with broad elevation antenna beam patterns. As mentioned earlier, the first copy of SeaWinds Scatterometer went on a U.S. satellite in early 1999. The second copy of SeaWinds will be aboard ADEOS-2 as planned for a year 2000 launch.

The SeaWinds reflector is illuminated by two offset antenna feedhorns, resulting in two spot beams illuminating the Earth surface at 46° and 54° incidence angles. The outer beam operates at vertical polarization, and the inner beam operates at horizontal polarization. Because the horizontally polarized ocean backscatter has a larger upwind-downwind asymmetry than in the vertically polarized response, the mixed polarization combination was determined to have a better ambiguity selection skill than the other combinations. The antenna reflector is mounted on a spinning assembly with a nominal rotation rate of 18 rpm. The antenna footprints produced by these two antenna beams will trace out two circles on the surface, enabling two to four azimuth radar observations for a given spot on the surface. The relative azimuth angles of these observations vary across the swath, unlike the fan beam

designs where the relative azimuth angles are essentially constant from near to far swath. The varying azimuth geometry degrades the measurement performance at outer swath and near nadir track where the fore and aft looks reduce to one or have 180° separation.

Because of the change of antenna design, the signal detection principle and hence the electronics design of SeaWinds is also different from those of NSCAT. The resolution of the SeaWinds radar footprints is basically defined by the size of the antenna reflector and is about 35 km in range and 26 km in azimuth. To improve the range resolution, the SeaWinds radiofrequency electronics were designed to chirp the transmit signal over 375 kHz in one pulse length (1.5 m). Onboard digital processing then applied range compression to divide the radar echo into range bins, resulting in about 5 km resolution in range. This makes the size of the SeaWinds measurement cell comparable to the nominal resolution of NSCAT.

Another important feature of the SeaWinds scanning geometry is that the measurement swath is contiguous without a gap near the subsatellite nadir track, which is present in fan-beam scatterometer designs. Although the accuracy of retrieved wind velocity near the spacecraft nadir track is not as good as that in the midswath, a contiguous swath does allow SeaWinds to image 90% of global ice-free oceans in 1 day compared with 2 days required for NSCAT.

The ESA has launched two ERS scatterometers since July 1991. ERS scatterometers are part of the Active Microwave Instrument (AMI) on ERS satellites. AMI operating at a frequency of 5.3 GHz (C band) consists of three operational modes: the image mode, the wave mode, and the wind mode. In the image and wave modes, AMI is configured as a synthetic aperture radar, while in the wind mode, it is configured as a scatterometer. These modes time-share the operation in orbit [24].

The ERS scatterometers employ a fan-beam antenna design with three vertically polarized antennas looking to the right-hand side of the satellite. The midbeam is perpendicular to the ERS-1 ground track and the fore and aft antenna beams are offset by 45° in azimuth with respect to the midbeam. The antenna beamwidths are 26° in elevation and 0.9° in azimuth for fore and aft beams and 24° in elevation and 1.4° in azimuth for aft beam. These antenna beams provide three radar images of the ocean surface with a swath width of 500 km. However, unlike SASS and NSCAT designs based on Doppler filtering, ERS scatterometers employ short transmit pulses and range gate the return echos to sharpen the resolution along the broad-beam direction. This design eliminates the complexity of Doppler filtering, but an on-orbit yaw steering of ERS satellites was required to compensate for the Doppler shift.

The other distinct feature of ERS scatterometers is the use of high transmit power. Because the traveling-wave-tube amplifier (TWTA) used for ERS AMI provides an output peak power of 4 kW, the transmit power of ERS scatterometers is much larger than the nominal 100 W output power used by SASS, NSCAT, and SeaWinds. Although 100 W transmit power has been shown to be adequate for fan-beam scatterometers as demonstrated by NSCAT performance, a significantly higher transmit power raises the

signal-to noise ratio (SNR) and reduces the signal detection uncertainties of low wind σ_0 at high incidence angles.

The difference in transmit frequencies between ERS and NASA scatterometers leads to several performance differences in geophysical retrieval. The lower operating frequency makes ERS scatterometers less sensitive to atmospheric water vapor and clouds than Ku-band scatterometers; hence C-band scatterometers are expected to outperform Ku-band scatterometers under severe weather conditions. However, C-band backscatter is less sensitive to wind direction, particularly at low winds, and has smaller upwind and downwind backscatter differences. Consequently, Ku-band scatterometers have better wind direction accuracy than C-band scatterometers. It was observed that ERS scatterometers are very inadequate in discriminating the upwind and downwind ambiguities.

2.4. Applications in Earth Science

As the largest source of momentum to the upper ocean, winds drive oceanic motions on scales ranging from surface waves to basinwide current systems. Winds over the ocean modulate air-sea fluxes of heat, moisture, gases, and particulates, regulating the crucial coupling between atmosphere and ocean that establishes and maintains global and regional climates. Figure 6 is an example of global ocean surface winds provided by satellite scatterometers, illustrating the wind velocities over the Pacific Ocean on September 21, 1996, acquired by NSCAT. Gray levels in the image represent windspeed in meters per second. Dark shading shows low speeds, and light shading shows high speeds. In the tropical areas just north of the

equator, called the Intertropical Convergence Zone, winds from the Northern and Southern Hemispheres collide and force an upwelling of air. In the subtropical areas, air sinks back, creating a zone of divergence and low winds that was long ago called the Horse Latitudes. To the south (north) of the Horse Latitudes in the northern (southern) hemisphere, there are strong, steady winds known as Trade Winds. At latitudes greater than the Horse Latitudes, the Coriolis force is strong. High vorticity in this area creates the cyclones characterizing Earth's weather system. The light spiral features in the upper left near Japan are typhoons Violet and Tom.

Measurement of surface wind velocities can be assimilated into regional and global numerical weather models, thus improving our ability to predict future weather. Satellite wind data, such as those from ERS scatterometers and NSCAT, have generated more accurate forecasts and extended the useful range of weather forecasts by more than 24 h in the Southern Hemisphere. The mapping of wind fields in the equatorial areas of the Pacific Ocean is particularly useful for the prediction of El Niño events, leading to changes of rain patterns and weather worldwide. The ability of satellite scatterometers in the prediction of El Niño and other seasonal and annual climate changes will benefit the management of global agriculture, fisheries, and water reserves.

Scatterometer wind data are also valuable for various commercial applications, including storm warning, ship routing, oil production, and marine food harvesting. In a collaborative effort with NASA/JPL, National Oceanic and Atmospheric Administration (NOAA) was able to measure surface winds from NSCAT data within 3 hours after data acquisition for operational use. The scatterometer data can pinpoint the location, structure, and strength of storms [32], as indicated in Fig. 6. Severe marine storms, including hurricanes near America and typhoons in the western Pacific, are among the most destructive of all natural hazards. The use of satellite scatterometer wind data facilitates the monitoring and forecasting of tropical and midlatitude storms. Captains of ocean ships can rely on regular scatterometer data with large-scale coverage to choose routes that avoid heavy seas, high head winds, and severe weather systems. As oil production is ongoing at many offshore platforms around the world, long time series of scatterometer wind data will be indispensable for the design of drilling platforms and warnings of impending storms. Because winds drive the ocean currents that transport heat and nutrients, scatterometer data together with other types of spaceborne sensors can be used to study the biogeochemical balance of the ocean-atmosphere system. Detailed wind data from satellite scatterometers can aid in the harvesting of natural seafood crops.

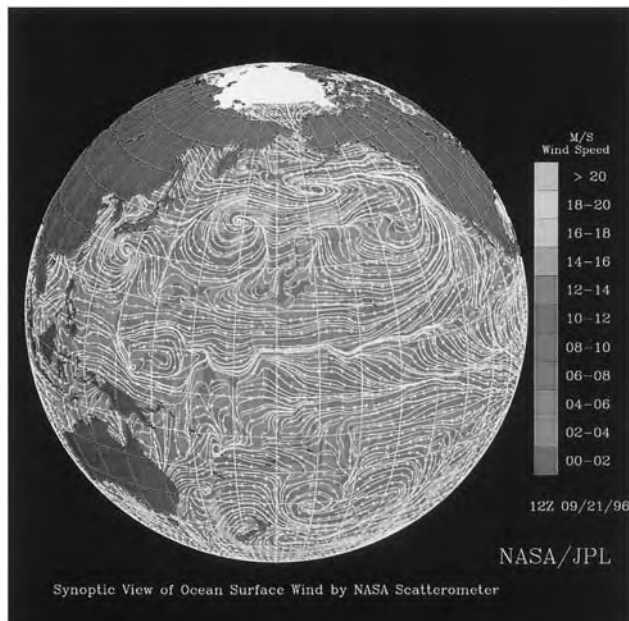


Figure 6. Ocean surface winds provided by NSCAT of the Pacific Ocean on September 21, 1996. The image represents windspeed in meters per second. Dark shading represents low speeds and light shading high speeds. (Courtesy of Drs. W. T. Liu and W. Tang, Jet Propulsion Laboratory, California Institute of Technology.)

2.5. Future Perspectives

As the use of scatterometers becomes more widespread in meteorology, oceanography, and operational weather forecasting, there are several challenges for the development and applications of spaceborne scatterometer technology in the twenty-first century.

Although satellite scatterometers have already demonstrated a significant impact on climate research and weather forecasting, the volume, mass, and cost of a spaceborne scatterometer mission remains high, creating a significant barrier for these instruments to be flown on operational weather satellites. For instance, the cost of NSCAT and SeaWinds science missions are in the range of 100–200 million dollars for a mission life of 3 years, and both instruments weigh about 300 kg. It is necessary to incorporate new technologies to reduce the size, weight, and power of scatterometers. For example, reducing the noise figure of low-noise amplifiers will enable the reduction of transmit power, hence leading to a smaller demand on spacecraft power. Advanced electronics technology will allow the use of fewer and smaller components, but with more capabilities, resulting in a decrease of size and weight. This in turn will allow the use of a smaller launch vehicle and make it easier to accommodate the instruments on the spacecraft. Furthermore, if the mission lifetime can be extended beyond 3–5 years through the use of more reliable components and technologies, spaceborne scatterometry will be more cost-effective.

The temporal coverage and spatial resolution of spaceborne scatterometers need to be improved to enable the study of many natural phenomena with high variability and resolution. The radar footprint size and sampling resolution of ERS scatterometers, NSCAT and SeaWinds are in the range of 25–50 km, which is inadequate for imaging high-resolution features in the weather fronts, wind fields with high vorticity near the eyewall of tropical cyclones, tropical convective cells, and coastal winds. In addition, NSCAT and SeaWinds require a few days to complete coverage of the tropical oceans, where there are significant diurnal-period variations. A more frequent coverage is needed to resolve these variations for investigating tropical air–sea interaction dynamics. These issues will demand a high-resolution scatterometer with an improved swath coverage or a constellation of low-cost instruments.

The main objective of spaceborne scatterometers is to provide surface wind measurements over the global oceans. However, scatterometers also acquire radar measurements over land surfaces and polar sea ice, together occupying more than 30% of the Earth surface. Recent investigations of ERS scatterometers and NSCAT data have indicated that scatterometers have a strong potential for studies of the dynamics and changes of land surface and polar regions, for example, tropical deforestation monitoring, glacier ice sheets, sea ice extent, and sea ice motion. The challenge is to come up with an accurate geophysical interpretation of scatterometer data collected over these targets and to develop algorithms for a consistent, quantitative retrieval of geophysical parameters.

3. ALTIMETRY: LARGE-SCALE OCEAN DYNAMICS

3.1. Background

Radar altimetry is used to measure the precise height of sea surface relative to the geocenter, a very useful variable for geophysical studies. Many physical processes affect the height of the sea surface. The dominant factor is the spa-

tially varying gravity field of Earth, making the sea surface follow Earth's gravitational equipotential surface, or the geoid. This effect creates a sea surface relief of hundreds of meters. For instance, the height of the Tropical Indian Ocean is lower than that of the western Tropical Pacific Ocean by more than 100 m. The reader is referred to McAdoo and Marks [33] for an example of the applications of altimetry to the study of Earth's gravity field. Apart from the geoid are sea surface variations of magnitude from centimeters to meters caused by various oceanographic phenomena, such as tides, waves, currents, and storm surges. Among these, the effect of currents is most interesting in the study of large-scale ocean dynamics that is key to understanding the Earth's climate. The application of altimetry to the measurement of sea surface height for the study of ocean dynamics is the focus of this section.

The fundamental relation between sea surface height and ocean current is the geostrophic balance [34], a balance between the pressure gradient at the sea surface and the Coriolis force resulting from the movement of water on a rotating Earth. The pressure gradient is derived from the ocean topography, defined as the elevation of the sea surface relative to the geoid. The ocean topography is directly related to the ocean surface current velocity as follows

$$u = -\frac{g}{f} \frac{\partial h}{\partial y}$$

$$v = \frac{g}{f} \frac{\partial h}{\partial x}$$

where u is the eastward velocity, v is the northward velocity, x is the east coordinate, y is the north coordinate, h is the elevation of the ocean topography, $f = 2\Omega \sin(\text{latitude})$; $\Omega = 7.29 \times 10^{-5} \text{ s}^{-1}$ (rotation rate of Earth), and g is the local gravitational acceleration at the sea surface. The velocity determined in this way is not the total surface velocity, but the important component that penetrates the deep ocean. There is a surface boundary layer of directly wind-driven current (called the Ekman layer; see Ref. 34) that has no signatures in ocean topography and hence is invisible to altimeters. This aspect makes altimetry particularly useful for the study of the circulation of the entire water column.

The relief of the global ocean topography is on the order of 1 m, a small signal to retrieve from space. This signal has to be measured with an accuracy of a few centimeters in order to calculate the precise change in the ocean circulation. For instance, a 1 cm tilt of the ocean topography implies the transport of up to several million metric tons of water per second, which is a significant fraction of the transport carried by the major ocean current systems. The challenge of altimetry is to achieve this centimeter accuracy for oceanographic studies.

For a general introduction to altimetry the reader is referred to Stewart [35], Wunsch and Gaposchkin [36], and Chelton et al. [37]. The basic concept is straightforward. The radar altimeter bounces microwave pulses from the sea surface and measures the round-trip travel time to

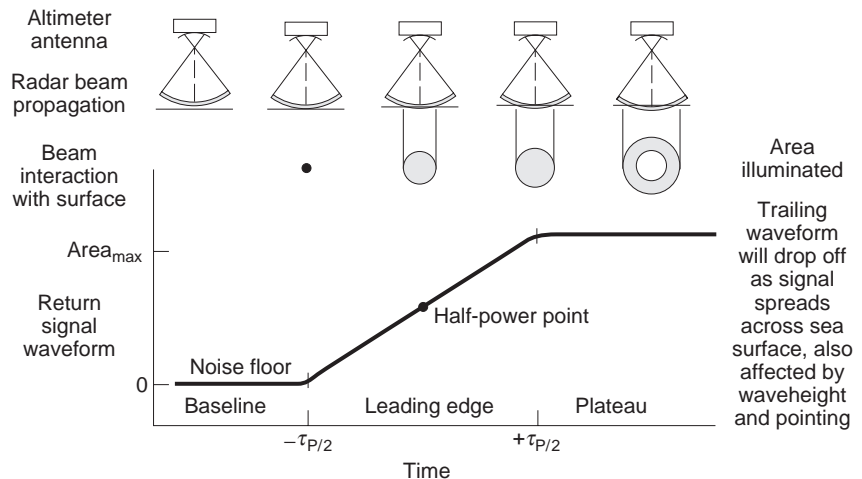


Figure 7. Altimeter pulse interaction with the sea surface and the characteristic return waveform generated by the altimeter electronics (From Zieger et al. [39]).

determine the altitude of the spacecraft above the sea surface. By subtracting this altitude from the distance between the spacecraft and the geocenter, a distance determined by the technique of precision orbit determination [38], one can thus obtain the height of the sea surface relative to the geocenter.

Shown in Fig. 7 (adapted from Ref. 39) is a schematic representation of the technique of pulse ranging by a radar altimeter. It shows the variation with time of area illuminated by a short, widebeam pulse. The power of the return pulse is proportional to the area of illumination and thus has a similar dependence on time. The time of the arrival of the leading edge of the return pulse is used to determine the range from the sea surface to the radar antenna. In the presence of ocean waves, the wave crests reflect the pulse back to the altimeter sooner than do the wave troughs, creating a further stretch of the leading edge. The extent of the leading edge of the return pulse can thus be used to determine the height of the waves. The frequency used by most radar altimeters is in the range of the Ku band (~ 14 GHz, which corresponds to a wavelength of about 2 cm). At vertical incidence in the case of a radar altimeter, the return signal strength decreases with the amplitude of these centimetric waves, which are extremely sensitive to windspeed. When the wind is weak, the sea surface is smooth and hence reflects more radar signals than does a rough sea resulting from a strong wind. A strong return pulse is thus related to low windspeed, and a weak return pulse is related to high windspeed. Therefore, an altimeter can also measure ocean windspeed.

To obtain the centimeter measurement accuracy, a host of technical challenges arises despite the apparent simplicity of the basic measurement principle of radar altimetry. For example, the radar pulse needs to be compressed to resolve travel time in nanoseconds; thousands of pulses need to be transmitted and received every second to average out the noise in the return signals; the delay of electromagnetic waves due to the dry and wet air mass in the troposphere as well as the free electrons in the ionosphere needs to be accounted for; the distance between the center

of mass of the spacecraft and the geocenter needs to be determined within a few centimeters (a precision of one in ten millions).

3.2. Evolution of the Technology

The early satellite altimeters were primarily flown for proving the concept of this potentially powerful remote sensing tool [40]. The noise levels of the altimeters on board Skylab (1974), GEOS-3 (1975–1978), and Seasat (1978) were 60, 25, and 10 cm, respectively. The Seasat altimeter [41] was the first to have reached a precision level useful for oceanographic studies. Unfortunately, Seasat lasted only slightly over 100 days. The next satellite altimeter was flown by the U.S. Navy's Geosat (1985–1989). This instrument has several improvements over the Seasat altimeter (42), notably the longer radar pulse ($102.4\ \mu\text{s}$ instead of $3.2\ \mu\text{s}$). This long pulse, plus some other hardware improvements, has reduced the peak power requirement from 2 kW (for Seasat and GEOS-3) to 20 W, making the instrument more robust. The Geosat altimeter has lasted for four years and generated a rich data set for oceanographic and geophysical studies [the Geosat special issues of the *Journal of Geophysical Research* **95**(C3,10): 1990 [43].

Despite the success of Geosat, it has several limitations. The altimeter has only one frequency channel (13.5 GHz) and hence is not able to retrieve the pulse delay caused by the ionospheric free electrons. This delay can create an error of 2–20 cm. An altimeter operating at two properly separated frequencies would be able to determine this delay from the difference in pulse travel time between the two signals. The pulse delay by the water vapor in the troposphere creates another source of error of up to 40 cm. This delay requires knowledge of the water vapor content of the atmosphere whose determination would require a microwave radiometer. Such a radiometer was missing in Geosat. Moreover, the uncertainty in the radial position of the Geosat orbit was determined only with an accuracy of 1 m, making the applications to large-scale ocean dynamics difficult.

Launched in August 1992, the United States/France joint TOPEX/POSEIDON Mission [44] has provided a state-of-the-art altimeter system that is specifically designed to meet the challenge posed by the requirement of measuring the largescale, small signals in sea surface height caused by ocean currents. There are two radar altimeters on board the satellite. The primary one (provided by the United States) operates at two frequencies (13.6 and 5.3 GHz) for retrieving the ionospheric pulse delay. The secondary one (provided by France) is a solid-state, single-frequency (13.65 GHz) system to demonstrate low-power, low-cost technology for future altimeter missions. The primary NASA altimeter has several improvements over the Geosat altimeter [39]. The 13.6 GHz channel has a pulse rate of 4000/s compared to Geosat's 1020/s, resulting in reduction of noise level to an RMS magnitude of 1.7 cm. The instrument software in waveform sampling and analysis is also improved. The French altimeter, using a different design, performs at a noise level of 2 cm. TOPEX/POSEIDON also carries a three-frequency radiometer for measuring the total columnar water vapor content along the altimeter line of sight. This measurement is used to determine the pulse delay caused by the water vapor. The total error in the altimeter range measurement is estimated to be 3.2 cm (RMS) at the rate of one measurement per second, covering an along-track distance of 6.2 km.

The precise location of the satellite in orbit is determined by three independent tracking systems [38].

Conventional laser tracking was performed by an onboard laser retroreflector array with a worldwide ground network of laser stations. A dual-frequency microwave Doppler system called DORIS (Doppler Orbitography and Radio-positioning Integrated by Satellite) was provided by the French, involving an onboard receiver and a worldwide, densely populated network of ground beacons. An experimental Global Positioning System (GPS) receiver was carried as the third system, which involves the constellation of the GPS satellites and a network of ground stations. The accuracy of the satellite radial orbital position calculated from these measurements with the use of a state-of-the-art model of Earth's gravity field [45] has reached a level of less than 3 cm. The total uncertainty in the measurement of sea surface height has therefore reached a level of 4 cm, making the signals created by the variability of basinwide ocean circulation detectable from space for the first time.

Radar altimeters are also part of the payload of the ERS satellite series [46]. Single-frequency altimeters were flown on both the ERS-1 (1991–1996) and ERS-2 (1995 to the present) satellites. The level of performance of these two altimeters was somewhere between Geosat and TOPEX/POSEIDON. The accuracy of the orbit determination for ERS-2 has been significantly improved by the Precise Range and Range-Rate Equipment (PRARE) system, which failed to work on board ERS-1. However, it has been demonstrated that by adjusting the ERS-1 data to simultaneous TOPEX/POSEIDON data it was possible to

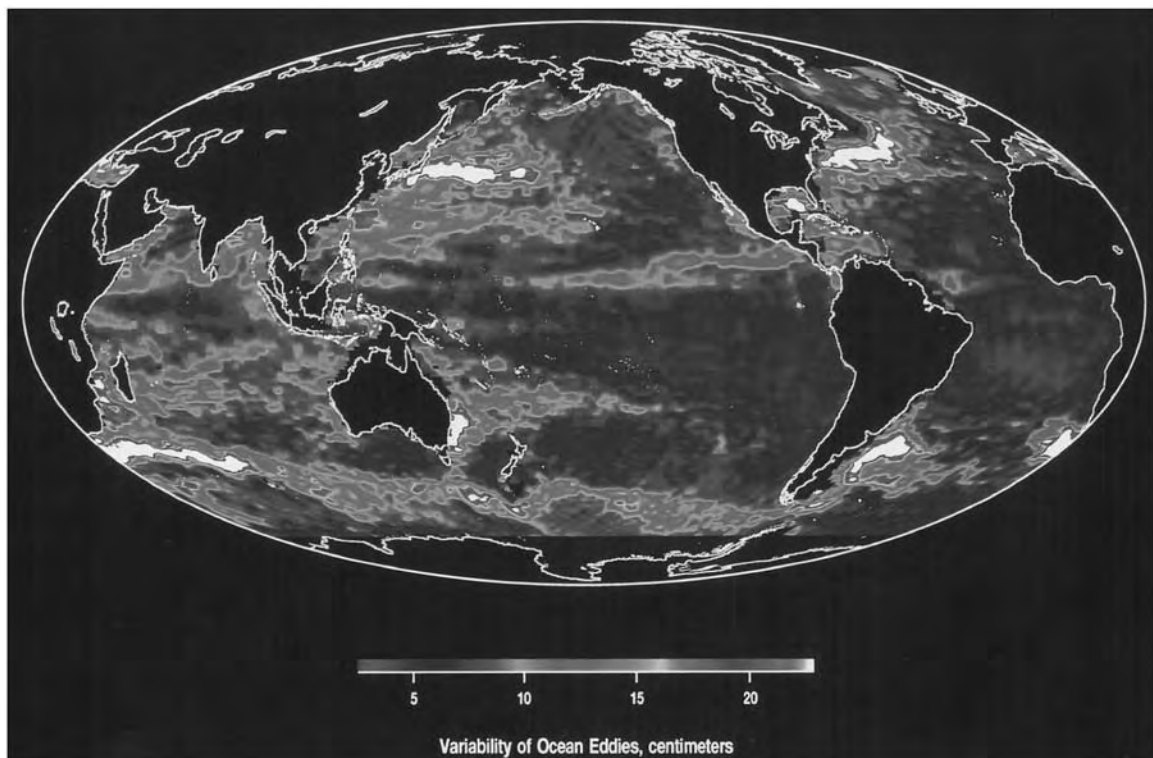


Figure 8. Standard deviation (in centimeters) of the sea surface height variability over the global oceans based on the first year of the TOPEX/POSEIDON data. The white areas represent variabilities larger than 25 cm with peak values larger than 50 cm.



Figure 9. TOPEX/POSEIDON observation (lower) and computer simulation (upper) of the sea level in the Pacific Ocean during December 1994, when the 1994–95 El Niño event reached its peak. The excessive heat associated with the anomalously high sea level in the central equatorial Pacific altered the path of the atmospheric jet stream and caused unusual weather worldwide. (From Fu and Smith [52]).

minimize the orbit errors in the ERS-1 data [47]. A major disadvantage of the ERS system is the lack of a second channel for determining the ionospheric pulse delay.

3.3. Applications to Large-Scale Ocean Dynamics

TOPEX/POSEIDON has opened a new door to the study of large-scale ocean circulation and its governing dynamics. A wealth of results can be found in two special issues of the *Journal of Geophysical Research* [99(C12): 1994; 100(C12): 1995], as well as Wunsch and Stammer [48]. For the first time scientists can obtain snapshots of the global ocean topography every 10 days and monitor its changes over weeks to years. The ocean is turbulent on a wide range of scales from millimeters to thousands of kilometers, from seconds to years and decades. However, most of the kinetic energy of ocean currents is concentrated at the so-called mesoscales: 100 km in space and 100 days in time. This is the scale of ocean storms, or eddies [49]. Figure 8 shows a map of the global distribution of the sea surface variability associated with the ocean eddies. The map was constructed from data taken over one year. It

reveals the regions of energetic ocean currents such as the Gulf Stream, the Japan Current (the Kuroshio), the Brazil/Malvinas Current, and the Antarctic Circumpolar Current among others. This type of map is very useful for testing the performance of computer models of ocean circulation [50–52], which, when properly calibrated and validated, are powerful tools for studying Earth's climate system.

Altimetry data are often analyzed in the form of sea surface anomalies, which are deviations of ocean topography from its time average and represent the variations of ocean currents that are affecting climate variability. Shown in Fig. 9 is a comparison of the sea surface anomalies in the Pacific Ocean derived from the TOPEX/POSEIDON data and the simulation by a state-of-the-art ocean circulation model [52]. The degree of similarity is striking, although the amplitude of the anomalies is generally weaker in the model simulation. In December 1994, the 1994/95 El Niño (see Ref. 53 on the subject) reached its peak. Note the manifestation of the El Niño as high (dark area) in the central equatorial Pacific in both the data and the model, indicating the capability of the model in

simulating major ocean anomalies. However, the quantitative accuracy of the model still needs to be improved. One effective approach is to apply data assimilation techniques (54) to combining the data with the model such that the information of the sea surface height observation can be used to improve the model simulation of the circulation, as well as temperature and salinity at depths [55,56].

3.4. Future Perspectives

The accuracy and precision of the TOPEX/POSEIDON observation has set the standard for future altimetric missions. Since the ocean circulation and its effect on climate has timescales from years to decades and longer, we need to establish a long record of high-quality altimeter data to gain significant understanding of the ocean's role in climate and to improve its prediction. A series of follow-on missions to TOPEX/POSEIDON, called Jason, was developed by France and the United States to extend the TOPEX/POSEIDON-class data record into the twenty-first century. The first of these series, Jason-1, was launched in 2000. This was intended as a solid-state, dual-frequency altimeter based on the heritage of the French altimeter on TOPEX/POSEIDON. The satellite was also equipped with a three-frequency water vapor radiometer as well as DORIS, GPS, and laser tracking devices. The objectives were to achieve a performance at the TOPEX/POSEIDON level with a goal of approaching 1 cm accuracy in sea surface height. Some new challenges are to develop new algorithms that would allow (1) recovery of signals over extremely calm seas or rain cells that produce an impulselike return waveform, and (2) better determination of the electromagnetic bias (a sea surface height bias toward the ocean wave troughs) that needs to be removed from the data. Another important task is calibration and validation of the system for consistency with TOPEX/POSEIDON to ensure continuity of the data for detecting long-term sea level trends and global change.

Two other altimetry missions were scheduled for the next five years. The U.S. Navy's Geosat Follow-On (GFO), launched in 1998, was equipped with a single-frequency altimeter and a two-frequency water vapor radiometer. Its challenge was to make ionospheric correction using models and data from other sources such as GPS. The ESA's Environment Satellite (ENVISAT), launched in 1999, carried a dual-frequency altimeter and a water vapor radiometer among several other instruments. The measurement performance was probably be close to that of TOPEX/POSEIDON. However, the satellite flew in an orbit that was not optimized for large-scale ocean dynamics due to multiple mission objectives.

Given the missions noted above, the prospects of future altimetric observations are excellent. The bilateral commitment of France and the United States to the continuation of TOPEX/POSEIDON-quality measurement via the Jason series has laid the foundation for a global observing system for monitoring the ocean in the present century. The quality promised by the Jason measurements will underlie their utility in serving as a framework to integrate other satellite observations into a powerful datastream for assimilation by sophisticated numerical

models. Such a system of data and models will make routine scientific diagnosis and reliable prediction of the ocean and climate changes a reality.

Acknowledgment

This work was carried out by the Jet Propulsion Laboratory, California Institute of Technology, under a contract with the National Aeronautics and Space Administration.

BIBLIOGRAPHY

1. H. A. Zebker and R. Goldstein, Topographic mapping from interferometric SAR observations, *J. Geophys. Res.* **91**(B5):4993–4999 (1986).
2. R. M. Goldstein, H. A. Zebker, and C. Werner, Satellite radar interferometry: Two-dimensional phase unwrapping, *Radio Sci.* **23**(4):713–720 (1988).
3. F. Li and R. M. Goldstein, Studies of multi-baseline interferometric synthetic aperture radars, *IEEE Trans. Geosci. Remote Sens.* **28**:88–97 (1990).
4. E. Rodriguez and J. Martin, Theory and design of interferometric SARs, *Proc. IEEE* **139**(2):147–159 (1990).
5. L. C. Graham, Synthetic interferometer radar for topographic mapping, *Proc. IEEE* **62**:763–768 (1974).
6. A. L. Gray and P. J. Ferris-Manning, Repeat-pass interferometry with airborne synthetic aperture radar, *IEEE Trans. Geosci. Remote Sens.* **31**(1):180–191 (1993).
7. H. W. Klimach and G. T. Sos, High performance interferometric SAR description and capabilities, *Proc. 1st Int. Airborne Remote Sensing Conf. and Exhibition*, Strasbourg, France, Sept. 11–15, 1994.
8. A. K. Gabriel, R. M. Goldstein, and H.A. Zebker, Mapping small elevation changes over large areas: differential radar interferometry, *J. Geophys. Res.* **94**(B7):9183–9191 (1989).
9. D. L. Evans, T. G. Farr, H. A. Zebker, J. J. van Zyl, and P. M. Mouganis-Mark, Radar interferometry studies of the Earth's topography, *EOS Trans. AGU* **73**(52).
10. R. M. Goldstein, H. Engelhardt, B. Kamb, and R. M. Frolich, Satellite radar interferometry for monitoring ice sheet motion: Application to an Antarctic Ice Stream, *Science* **262**:1525–1530 (1993).
11. I. R. Joughin, D. P. Winebrenner, and M. A. Fahnestock, Observations of ice sheet motion in Greenland using satellite radar interferometry, *Geophys. Res. Lett.* **22**(5):571–574 (1995).
12. E. Rignot, K. Jezek, and H. Sohn, Ice flow dynamics of Greenland ice sheet from SAR interferometry, *Geophys. Res. Lett.* **22**(5):575–578 (1995).
13. R. Kwok and M. A. Fahnestock, Ice sheet motion and topography from radar interferometry, *IEEE Trans. Geosci. Remote Sens.* **34**:189–200 (1996).
14. D. Massonnet, M. Rossi, C. Carmona, F. Adragna, G. Peltzer, K. Feigi, and T. Rabaute, The displacement field of the Landers earthquake mapped by radar interferometry, *Nature* **364**:138–142 (1993).
15. D. Massonnet, K. Feigi, M. Rossi, and F. Adragna, Radar interferometric mapping of deformation in the year after the Landers earthquake, *Nature* **369**:227–230 (1994).
16. H. A. Zebker, P. A. Rosen, R. M. Goldstein, C. Werner, and A. Gabriel, On the derivation of coseismic displacement fields using differential radar interferometry, *J. Geophys. Res.*

17. W. Guinard, J. T. Ransome, Jr., and J. C. Daley, Variation of the NRCS of the sea with increasing roughness, *J. Geophys. Res.* **76**:1525 (Nov. 1971).
18. C. Daley, Wind dependence of radar sea return, *J. Geophys. Res.* **78**:7823–7833 (Nov. 1973).
19. K. Moore and W. J. Pierson, Worldwide oceanic wind and wave predictions using a satellite radar-radiometer, *J. Hydro-naut.* **5**:52–60 (1971).
20. L. Jones, L. C. Schroeder, and J. L. Mitchell, Aircraft measurements of the microwave scattering signature of the ocean, *IEEE J. Oceanic Eng.* **OE-2**:52–61 (1977).
21. K. Moore and J. D. Young, Active microwave measurements from space of sea surface wind, *IEEE J. Oceanic Eng.* **OE-2**:309–317 (1977).
22. L. Grantham, E. M. Bracalente, W. Linwood Jones, and J. W. Johnson, The SeaSat—A satellite scatterometer, *IEEE J. Oceanic Eng.* **OE-2**:200–206 (1977).
23. L. Jones, L. C. Schroeder, D. Boggs, E. M. Bracalente, R. A. Brown, G. J. Dome, W. J. Pierson, and F. J. Wentz, The SEA-SAT—A satellite scatterometer: The geophysical evaluation of remotely sensed wind vectors over the ocean, *J. Geophys. Res.* **87**(C5):3297–3317 (1982).
24. E. P. W. Attema, The active microwave instrument on-board the ERS-1 Satellite, *Proc. IEEE* **79**:791–799 (1991).
25. L. Tsang, J. A. Kong, and R. T. Shin, *Theory of Microwave Remote Sensing*, Wiley-Interscience, New York, 1985.
26. A. M. Reece, Modulation of short waves by long waves, *Boundary Layer Meteorol.* **13**:203–214 (1978).
27. A. Donelan and W. J. Pierson, Radar scattering and equilibrium ranges in wind-generated waves with applications to scatterometry, *J. Geophys. Res.* **92**(C5):4971–5029 (1987).
28. H. Freilich and R. S. Dunbar, Derivation of satellite wind model functions using operational surface wind analysis: An altimeter example, *J. Geophys. Res.* **98**(C8):14,633–14,649 (Aug. 15, 1993).
29. C. Rufenach, A new relationship between radar cross section and ocean surface wind speed during ERS-1 scatterometer and buoy measurements, *Int. J. Remote Sens.* **16**(18):3629–3647 (1995).
30. A. Stoffelen and D. Anderson, Scatterometer data interpretation—estimation and validation of the transfer function CMOD4, *J. Geophys. Res.* **102**(C3):5767–5780 (1997).
31. M. Naderi, M. H. Freilich, and D. G. Long, Spaceborne radar measurement of wind velocity over the ocean—an overview of the NSCAT scatterometer system, *Proc. IEEE* **79**:850–866 (1991).
32. W. T. Liu, W. Tang, and R. S. Dunbar, Scatterometer observes extratropical transition of Pacific typhoons, *EOS Trans. AGU* **78**(23):237 (June 10, 1997).
33. D. C. McAdoo and K. M. Marks, Gravity fields of the Southern Ocean from Geosat data, *J. Geophys. Res.* **97**:3247–3260 (1992).
34. J. Pedlosky, *Geophysical Fluid Dynamics*, Springer-Verlag, New York, 1979.
35. R. H. Stewart, *Methods of Satellite Oceanography*, Univ. California Press, Berkeley, CA, 1985.
36. C. Wunsch and E. M. Gaposchkin, On using satellite altimetry to determine the general circulation of the oceans with application to geoid improvement. *Rev. Geophys. Space Phys.* **18**(4):725–745 (1980).
37. D. B. Chelton, E. J. Walsh, and J. L. MacArthur, Pulse compression and sea level tracking in satellite altimetry, *J. Atmos. Oceanic Technol.* **6**:407–438 (1989).
38. B. D. Tapley, J. C. Ries, G. W. Davis, R. J. Eanes, B. E. Schutz, C. K. Shum, M. M. Watkins, J. A. Marshall, and R. S. Nerem, B. H. Putney, S. M. Klosko, S. B. Luthcke, D. Pavlis, R. G. Williamson, and N. P. Zelensky, Precision orbit determination for TOPEX/POSEIDON, *J. Geophys. Res.* **99**:24383–24404 (1994).
39. A. R. Zieger, D. W. Hancock, G. S. Hayne, and C. L. Purdy, NASA radar altimeter for the TOPEX/POSEIDON Project, *Proc. IEEE* **79**:810–826 (1991).
40. L. L. Fu, Recent progress in the application of satellite altimetry to observing the mesoscale variability and general circulation of the oceans, *Rev. Geophys. Space Phys.* **21**:1657–1666 (1983).
41. W. F. Townsend, An initial assessment of the performance achieved by the Seasat-1 radar altimeter, *IEEE J. Oceanic Eng.* **OE-5**:80–92 (1980).
42. J. L. MacArthur, P. C. Marth, and J. G. Wall, The GEOSAT radar altimeter, *Johns Hopkins APL Tech. Digest* **8**:176–181 (1987).
43. L. L. Fu and R. E. Cheney, Applications of satellite altimetry to ocean circulation studies: 1987–1994, *Rev. Geophys.* **32**(Suppl.):213–223 (1995).
44. L. L. Fu, E. J. Christensen, C. Yamarone, M. Lefebvre, Y. Menard, M. Dorrer, and P. Escudier, 1994: TOPEX/POSEIDON Mission Overview, *J. Geophys. Res.* **99**:24369–24381 (1994).
45. B. D. Tapley, M. M. Watkins, J. C. Ries, G. W. Davis, R. J. Eanes, S. R. Poole, H. J. Rim, B. E. Schutz, and C. K. Shum, R. S. Nerem, F. J. Lerch, J. A. Marshall, S. M. Klosko, N. K. Pavlis, and R. G. Williamson, The Joint Gravity Model 3, *J. Geophys. Res.* **101**:28029–28049 (1996).
46. European Space Agency, *ERS-1 Special Issue*, ESA Bulletin 65, European Space Agency, Paris, 1991.
47. P. Y. Le Traon, P. Gaspar, F. Bouyssel, and H. Makhmaraa, Use of Topex/Poseidon data to enhance ERS-1 data. *J. Atmos. Oceanic Technol.* **12**:161–170 (1995).
48. C. Wunsch and D. Stammer, Satellite altimetry, the marine geoid and the oceanic general circulation, *Ann. Rev. Earth Plan. Sci.* (in press).
49. A. R. Robinson, ed., *Eddies in Marine Science*, Springer-Verlag, New York, 1983.
50. A. J. Semtner, Modeling ocean circulation, *Science* **269**:1379–1385 (1995).
51. D. Stammer, R. Tokmakian, A. Semtner, and C. Wunsch, How well does a 1/4° global circulation model simulate large-scale oceanic observations? *J. Geophys. Res.* **101**:25779–25811 (1996).
52. L. L. Fu and R. D. Smith, Global ocean circulation from satellite altimetry and high-resolution computer simulation, *Bull. Am. Meteorol. Soc.* **77**:2625–2636 (1996).
53. S. G. Philander, *El Nino, La Nina, and Southern Oscillation*, Academic Press, Boston, 1990.
54. M. Ghil and P. Malanotte-Rizzoli, Data assimilation in meteorology and oceanography, *Adv. Geophys.* **33**:141–266 (1991).
55. I. Fukumori, Assimilation of TOPEX sea level measurements with a reduced-gravity, shallow water model of the tropical Pacific Ocean, *J. Geophys. Res.* **100**:25027–25039 (1995).
56. D. Stammer and C. Wunsch, The determination of the large-scale circulation of the Pacific Ocean from satellite altimetry using model Green's functions, *J. Geophys. Res.* **101**:18409–18423 (1996).

SPATIAL AND QUASI-OPTICAL POWER COMBINING

Dr. JULIO A. NAVARRO
Boeing-Phantom Works
Seattle, WA

1. HISTORICAL BACKGROUND

During the first few decades of the twentieth century, operating frequencies of several hundred megahertz were mostly ignored and “microwaves” were not yet deemed necessary. It was not until the advent of World War II, where the detection of enemy ships and aircraft became the key to national defense and the method of radio detection and ranging (radar) was born. The British used longwave radar to detect German bombers approaching the English shore and then scramble fighters to intercept the aircraft. However, longwave radar was limited by poor resolution and large ground interference. As a radar’s resolution (i.e., the minimum object size that it can detect) is inversely proportional to the frequency of operation, shorter operating wavelengths are better suited to detect smaller objects. Although resolution improves with shorter wavelengths, higher operating frequencies require improved circuits, antennas, and sources. With respect to radiofrequency (RF) power sources, it was not until Randall and Boot developed the internal cavity magnetron [1] that shorter wavelengths could be used effectively in radar applications. A magnetron source demonstrated 10 kW of pulsed power at S-band (2–4 GHz). The technology was carried over to the United States and developed through the efforts of the Radiation Laboratory of the Massachusetts Institute of Technology. The development of the magnetron and similar tube-type devices in the early 1940s gave the allies a definitive edge in detecting enemy attacks and shortened the duration of the war considerably.

The MIT Radiation Lab also developed a wide range of waveguide circuits and antenna components that continue, nearly unchanged, to this day. These microwave circuits have since become an integral part of modern society used in many space, scientific, and commercial applications. The term *microwave* refers to that part of the frequency spectrum from 300 MHz to 300 GHz. Another more recent term, *millimeter waves* refer to the subset of the microwave range where the operating wavelength is one millimeter long (i.e., ≥ 30 GHz).

A radar’s performance is determined by its operating frequency, bandwidth, power output, antenna gain, and receiver sensitivity. Higher operating frequencies and higher output power combined with larger antennas, improved receiving, and processing circuits allow longer detection ranges, higher resolution, and improved perimeter protection. The success of microwave radar has enabled the development of a wide range of devices and components. The availability of these components has facilitated the introduction of many other applications such as point-to-point data communication links, telemetry, medical imaging, wireless local area networks, motion and presence sensing systems, remote sensing and imaging, selec-

tive heating of tumors, and spectroscopy for material identification. For example, police radar started at X-band (10.525 GHz) and later, with the improvement of components, moved to K-band (24.1 GHz), then to Ka-band (35.5 GHz), and Laser frequencies. At the same time, a new consumer market emerged to detect the presence of police radar with radar detectors. In a similar fashion, automatic door openers, perimeter surveillance, and detection systems have been successfully deployed at S-band, X-band, and now at K-band.

As more applications are introduced, overcrowding and interference tend to push new applications toward higher operating frequencies. Crowded spectrum has pushed many satellite communication systems from C- to X- to Ka-band. Higher operating frequencies provide larger instantaneous bandwidth, which can translate to faster data rate and larger information throughput. Higher operating frequencies also provide greater antenna directive gain for a given aperture size. At higher frequencies, however, devices perform poorly with respect to power and efficiency, distribution circuits have higher losses and require significantly improved and often complicated fabrication methods. Low-loss materials and complex fabrication methods also increase the cost of materials and components. Another problem is that high-frequency circuit models are often over-simplified and inaccurate, which leads to more design iterations, loss in delivery schedules, and higher system costs.

Over the last decade, many improvements in personal computing power, commercial software tools, and emerging consumer markets has propelled significant improvements in materials, processes, devices, components, and systems. Regardless of the specific application, complete low-cost system solutions require the successful combination of materials, mechanical parts, and electronic components as well as reasonable manufacturing, assembly, and test processes. Substrate material properties continue to improve in terms of dielectric constant, loss tangent, mechanical stability, and lot-to-lot repeatability. Mechanical parts are being fabricated in larger volumes with tighter dimensional tolerances at relatively low costs (i.e., casting, molding, plating, etc.). Electronic devices continue to improve in efficiency and frequency performance while the device packages are more robust, less expensive, and easier to handle with automatic pick-and-place machines. Similarly, printed wiring board fabrication methods are improving with respect to multiple-layer registration, laminations, via-plating, drilling, and routing. These improvements have resulted in reduced per unit component costs and improved performance, which has, in turn, opened up new markets and applications. The synergy between the various areas has contributed to an explosion of new products.

This article discusses various aspects of power combining techniques, including devices, integrated antennas, and methods for power combining. Section 2 briefly describes vacuum tube devices used in RF power generation and reasons for replacing them with solid-state devices. This description is followed by power combining classifications and descriptions of quasioptical and spatial power combiners.

2. RF POWER GENERATION

Types of devices used to generate RF power at millimeter wavelengths include magnetrons, klystrons, traveling-wave tubes (TWT), cross-field amplifiers (CFA), and solid-state devices. Tubes are very efficient at high power levels and continue to be used in many critical applications. However, tubes tend to be costly, bulky, and not as reliable as solid-state devices. Tubes require heaters for cathodes, finite warm-up time, high-voltage power supplies, oil-filling or encapsulation, and a large space for implementation.

Semiconductors, on the other hand, do not require heaters, are not limited by warm-up delays, can use low-voltage supplies, and can be implemented in relatively compact spaces. Tubes tend to operate in bandwidths less than 20%, whereas solid-state devices can operate over broader bandwidths (~50%). Solid-state devices are fabricated using photolithographic techniques and can be integrated monolithically within circuits of varying functions that exhibit consistent, repeatable performance and greater mean time between failures (MTBF).

However, solid-state devices, in general, provide relatively little power as compared with tube-type devices or similar high-power microwave sources [2,3]. Single solid-state electronic devices have thermal and impedance limitations that limit the RF output power and power-added efficiencies. These deficiencies get progressively worse with increasing frequency and limits their use in many high-power military and commercial applications.

Solid-state devices, however, continue to hold the promise of higher operating frequencies with lower costs, higher reliability, increased repeatability, and greater MTBF. To address and overcome the RF power and efficiency issues of combining many distributed sources [4], several techniques at microwave [5] and millimeter [6] wavelengths have been proposed and demonstrated in both industry and academia.

3. POWER COMBINING TECHNIQUES

Power combining techniques have been implemented at various levels such as chip, circuit, and spatial levels. In the area of spatial combiners, two references detail components and configurations implemented up to 1995 [7,8]. The references describe individual active antenna ele-

ments and grid configurations used in a wide range of applications, including spatial power combining.

In some applications, a component may employ several levels of combining to achieve the desired output power. Power combining classifications are listed below and shown in Fig. 1 [9].

1. Chip level [10,11]: Clustering or grouping of multiple devices in sub-wavelength lattices. Single wafer implementation is preferred, but chip devices can be diced and grouped together after wafer fabrication.
2. Circuit level (waveguides and planar media)
 - a. Resonant cavities [12–14]
 - b. Nonresonant [15–17]
 - i. N-way combiners [18–22]
 - ii. Corporate combiners [23]
3. Spatial Power Combining
 - a. Open resonator cavities [24–27]
 - b. Array of resonant radiators
 - c. Arrays of nonresonant radiators [28] and Grids [29]

Chip-level combining of solid-state devices can be accomplished monolithically on the wafer if yields and consistency throughout the process can be tightly controlled. If yields are not high, then good devices on the wafer can be diced and die-attached to a carrier plate for DC biasing, RF matching, and power combining. Chip-level combining has much tighter sub-wavelength lattice spacing over similar circuit-level combiners. Circuit-level combining has been used extensively in a broad range of media and combining configurations. As listed above, circuit-level combining can take many forms, including resonant cavities and nonresonant circuits. Resonant cavities may include rectangular and cylindrical waveguides or similar planar resonant structures. Nonresonant circuits include N-way and corporate combiners. N-way combiners include radial line, conical waveguide, and Wilkinson combiners, whereas corporate combiners include hybrid-coupled and chain-coupled circuits.

Circuit-level power combiners are limited by ohmic and dielectric losses, which increases proportionally with the number of devices combined. Overmoding is an issue with resonant combiners, and device-to-device isolation often limits the graceful degradation that distributed sources exhibit. Free-space combining provides an alternative

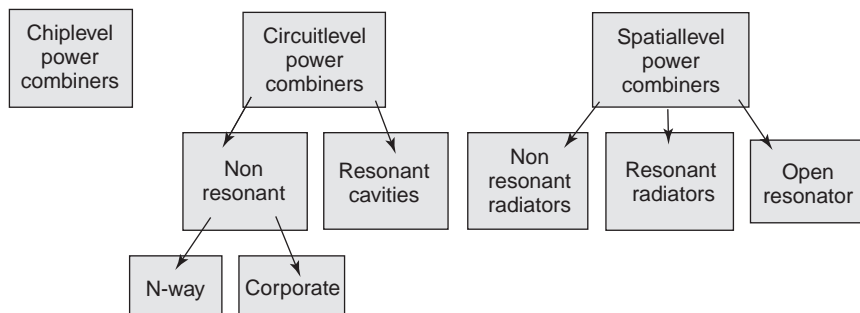


Figure 1. Power combining classifications.

method of power combining that addresses some of these deficiencies.

Spatial power combiners overcome circuit losses by combining in free space. Spatial combiners include open resonator arrays of resonant and nonresonant antennas (i.e., grids). Similar to chip-level combiners, grids tend to be tightly spaced, nonresonant individual devices clustered in a two-dimensional lattice. Several grids can be layered to develop many other components, such as filters [30,31], multipliers [32], oscillators [33,34], mixers [35], amplifiers [36], variable impedance surfaces [37], nonferrite isolators [38,39], polarization converters, and voltage-controlled frequency-selective surfaces [40].

4. OPEN RESONATOR SPATIAL POWER COMBINER

The open resonator was first proposed by J. Mink. It uses a spatial combining array within a quasioptical cavity. The distributed, self-running sources are injection locked to a quasioptical resonant mode of an open cavity as shown in Fig. 2 [41].

Open resonators are referred to as quasioptical because of the similarities with laser cavities at optical frequencies (i.e., Fabry–Perot). Open-cavity power combiners relax fabrication tolerances of typical circuit resonant cavities and avoid dielectric and ohmic losses of circuit-level combiners. Open resonators replace transmission line circuits with free space and use the open-cavity modes to synchronize all of the free-running sources. These open-cavity modes have high quality factors, which enhance stability and phase-spectra of the output signal. The large open-cavity dimensions allow the combination of many devices while avoiding multimode issues of circuit-level resonant cavities. A partially transparent reflector is used to maintain the open resonator mode while still coupling power out for system use. Open resonator combiners have been demonstrated using both two- and three-terminal devices that are clustered at the beam waist of the dominant mode. Partial reflector, which provides feedback for sustaining the open resonator mode, also allows transmission for energy radiation. DC biasing of the array of sources, thermal management, mode stability, and modulation are

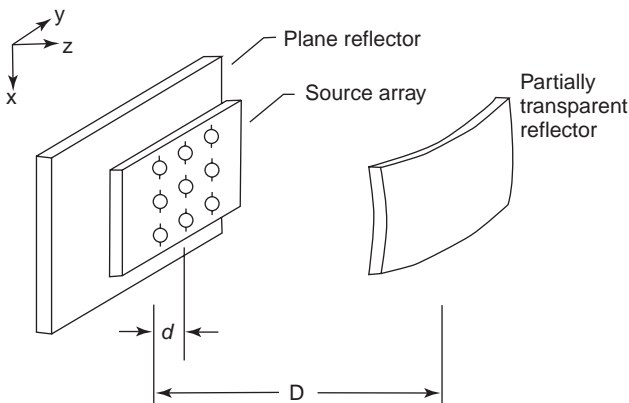


Figure 2. Open resonator spatial power combiner from Mink.

issues that require some careful attention for this quasi-optical combiner.

5. ANTENNA ARRAYS IN SPATIAL POWER COMBINERS

Spatial power combiners using an array of free-running sources also relax fabrication tolerances of circuit cavity combiners and avoid dielectric and ohmic losses of circuit-level combiners. Spatial power combiners radiate freely as large planar arrays of distributed sources synchronized to produce a single higher output power signal. Unlike the open resonator, spatial combiners require alternative methods for synchronization, such as mutual coupling, external circuitry, partial reflection for external feedback, or an external source as shown in Fig. 3. Spectral purity and stability of the spatial combiner will depend on the injection locking method and the qualities of the injection locking source used.

Spatial power combiners are not limited to the open resonator beam waist dimensions, so many more sources can be injection-locked and combined in a larger area without open resonator moding concerns. The single, coherent transmitter spatial power combiner output has predictable EIRP, beamwidth, and bandwidth. Spatial power combiners can be designed and modeled using standard oscillator and planar array theory. The antenna element normally serves as a resonator, radiator, and the conduit to supply DC power to the active devices. As always, DC biasing and control must be carefully implemented to avoid degrading the co- and cross-polarization components of the active antennas. Thermal gradients across the aperture degrade the overall combining efficiency and performance of the spatial combiner by detuning individual sources.

Spatial power combiners require the design and fabrication of a large number of similar sources. However, many electrical and mechanical difficulties exist that

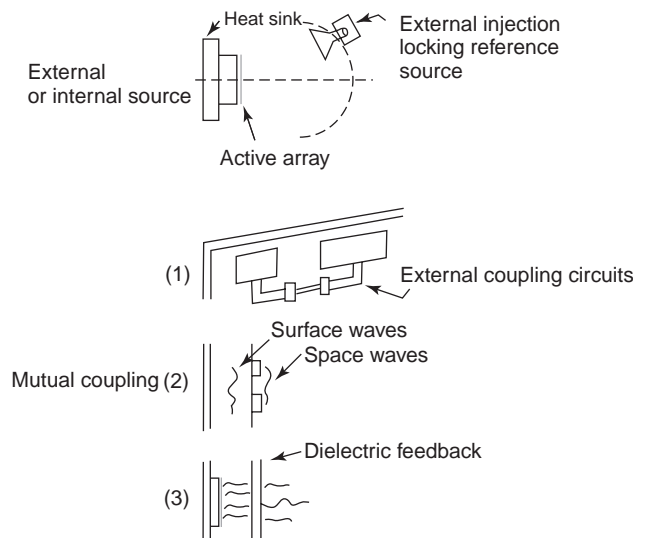


Figure 3. Methods for active antenna synchronization in a spatial power combiner.

work against the fabrication of nearly identical sources. The individual device parameters and package parasitics vary throughout the process. Similarly, assembly tolerances and die placement vary along with wire bonding and alignment. These variations create differences between the theoretical expectations and measured parameters. These differences are further compounded by mutual coupling in the array environment, which will vary as a function of frequency and element position within the array. The phase of an individual of active antenna synchronized within a spatial combining array depends on the difference between its self-oscillating frequency and the array injection-locked operating frequency. Mutual coupling tends to pull the oscillating frequency of individual active antennas and incur a phase offset on each of the sources. As mutual coupling varies with respect to array location, many identical sources could exhibit varying phase offsets across the aperture. These offsets, if not accounted for, can reduce power combining efficiency and overall array performance. On the other hand, these phase offsets have been controlled to develop a spatial power combiner with array beam steering capabilities [42–45].

The resulting spatial power combiner can be classified by its frequency stability, noise content, and spectral purity. The spatial combiner may also have issues like frequency jumping, pulling, or pushing and spurious signals. If the array of distributed sources remains locked, the spatial combiner should exhibit graceful degradation and have much higher reliability and MBTF than a comparable tube device.

6. ACTIVE ANTENNA OSCILLATORS

As active antennas are radiating oscillators, the same qualities used to describe circuit oscillators apply to active antennas used for spatial power combiners. There are several types of sinusoidal oscillators, including sub-harmonic, fundamental, and harmonic oscillators. Oscillators provide power at each of its harmonics. If the embedding circuit is designed to operate at the first harmonic and suppress others, it is called a fundamental oscillator. Similarly, sub-harmonic oscillators operate at fractional multiples below the fundamental, and harmonic oscillators operate at integer multiples above the fundamental. The performance of an oscillator can be gauged by several qualities listed below:

1. **Stability:** Ability of an oscillator to return to the original operating point after experiencing a slight electrical or mechanical disturbance.
2. **Noise**
 - Amplitude modulation (AM) noise: amplitude variations of the output signal.
 - FM noise: unwanted frequency variations.
 - Phase noise: unwanted phase variations.
3. **Quality (Q) factor**
 - Unloaded: accounts for resonator losses R_{loss} only.

- External: accounts for the load resistor R_{load} only and assumes $R_{loss} = 0$.
 - Loaded: accounts for both resonator losses and external loading.
4. **Frequency**
 - Jumping: Discontinuous change in oscillator frequency because of nonlinearities in the device impedance.
 - Pulling: Change in oscillator frequency vs. a specified load mismatch over 360° of phase variation.
 - Pushing: Change in oscillator frequency vs. DC bias point variation.
 5. **Spurious signals:** Output signals at frequencies other than the desired oscillation carrier.
 6. **Post-Tuning drift:** Frequency and power drift of a steady-state oscillator because of heating of the solid-state device.
 7. **Thermal stability:** Change in output power and frequency vs. temperature.

Each of these traits are applicable to active antennas and because the antenna serves as the resonant circuit as well as the radiator for the source, it will affect the overall performance of the spatial power combiner. A DC bias line delivers the proper voltage and current for the active device to generate electromagnetic energy. The resonator circuit provides the necessary reactive storage that compensates for the active device reactance. Oscillations occur at the frequency where the overall circuit reactance cancels out.

Figure 4 shows the Gunn diode equivalent circuit along with the imbedding circuit. The imbedding circuit could be a typical circuit resonator, an isolated antenna, or an antenna in an array environment. The imbedding circuit is depicted by $(Z_c = R_c + jX_c)$ and the Gunn diode by $(Z_d = R_d + jX_d)$. Similar schematics are applicable for three-terminal devices. Derivations and analysis for

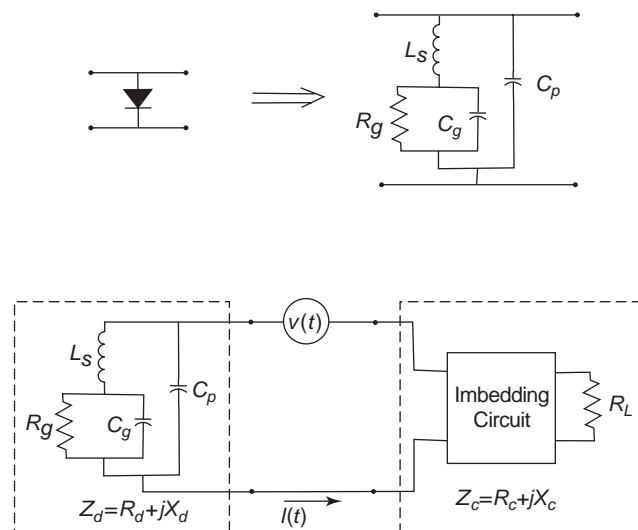


Figure 4. Gunn diode and active antenna equivalent circuit.

stability [46], noise in synchronized oscillators [47–49], external quality factors, and injection locking characteristics [50] have been derived and described in literature.

Oscillation start-up occurs because of noise or DC bias transients. The power level builds up until the active device is saturated. The device achieves steady-state equilibrium by continually restoring the power delivered to and dissipated within the circuit. As the device impedance is a function of the RF current, the oscillation frequency may change as the device reaches its steady state. At equilibrium, the oscillation frequency and amplitude remain unchanged.

For a free-running, steady-state oscillator, the sum of the circuit (Z_c) and device (Z_d) impedances must be zero at the device's operating point as shown by

$$Z_d(V_{dc}, I_{dc}, \omega_n, I_{rf}, T, \dots) + Z_c(\omega_n) = 0 \quad (1)$$

where the circuit impedance varies only with frequency and the device impedance is a function of its DC operating point (V_{dc} , I_{dc}), operating frequency components (ω_n), RF current amplitude (I_{rf}), and temperature (T). The subscript n refers to the harmonic or sub-harmonic frequency. The conditions for oscillation are then summarized as

$$\begin{aligned} R_c &\leq |R_d| \\ X_d &= -X_c \end{aligned} \quad (2)$$

where R_d is the device negative resistance and R_c is the resistance presented to the device terminals by the circuit. Similarly, X_d is the device reactance and X_c is the reactance presented to the device terminals by the circuit.

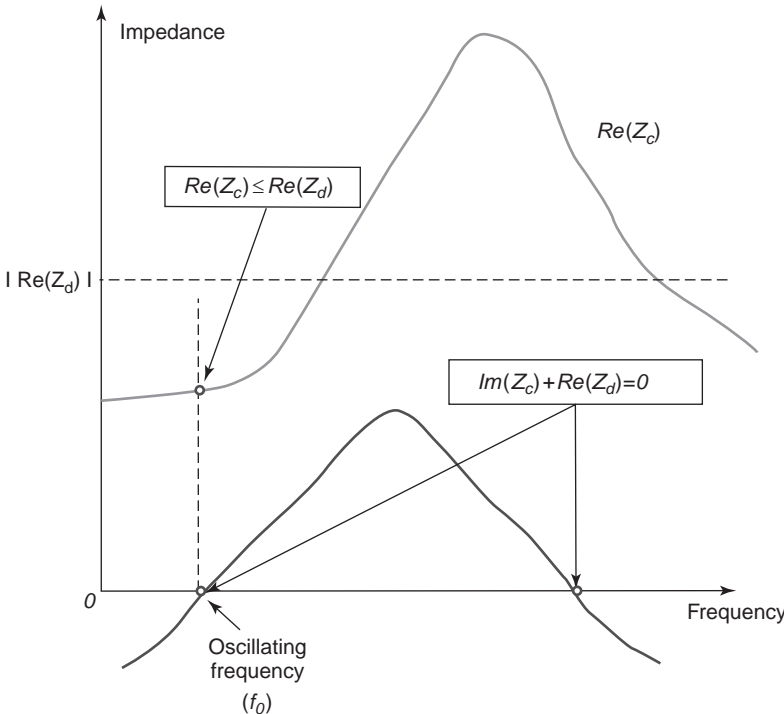


Figure 5 shows a typical circuit response presented to the device terminals at resonance. As shown, the real part of the imbedding circuit's impedance presented to the diode ($\text{Re}[Z_c]$) must be less than the real part of the diode's impedance ($\text{Re}[Z_d]$) to satisfy the oscillation condition in Equation (2). The figure also shows the zero cross-over points of ($\text{im}[Z_c] + \text{im}[Z_d]$). One of the two zero-crossings satisfies both conditions and serves as the oscillation frequency (f_0).

Figure 6 shows the Gunn diode I-V characteristics, including the threshold voltage (V_{th}), threshold current (I_{th}), DC operating current (I_{op}), and DC operating voltage (V_{op}). Impressed on the graph is an RF variation at the operating frequency ($f_0 = \frac{c}{\lambda}$) that simulates oscillation conditions.

7. SPATIAL POWER COMBINER FIGURES-OF-MERIT

Active antennas and spatial power combiners are measured in antenna ranges or anechoic chambers. Active antennas exhibit low Q-factor values and are easily affected by the environment. Care must be taken to ensure proper biasing and minimal load pulling as the antenna is rotated. Using standard gain horns, the Effective Isotropic Radiated Power (EIRP) of the active antenna or spatial power combiner can be determined through the use of the Friis transmission equation:

$$EIRP = \frac{P_{rec}}{G_{std}} \left(\frac{4\pi R}{\lambda} \right)^2 \quad (3)$$

where the receive horn gain is (G_{std}), power received at the horn is (P_{rec}), the range length is R , and the operating wavelength is (λ).

Figure 5. Imbedding circuit characteristics at resonance.

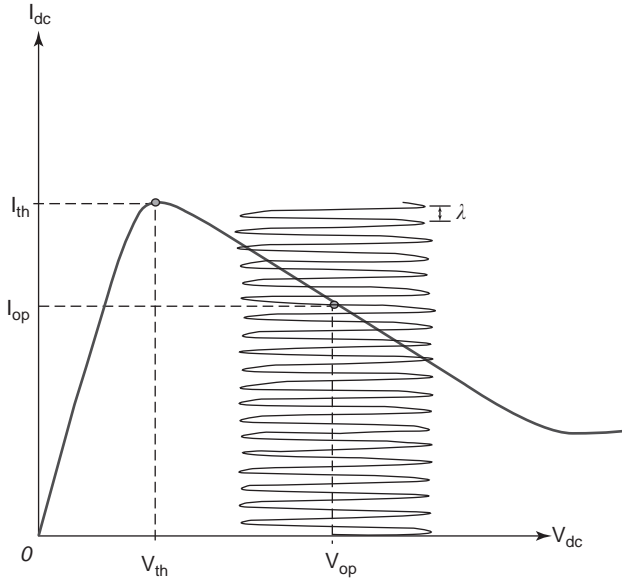


Figure 6. Gunn diode I-V characteristics.

The EIRP measurement and the estimated gain of the integrated antenna (G_a) is then used to determine the output power (P_o) of the integrated active device or array of devices:

$$P_o = \frac{EIRP}{G_a} \quad (4)$$

In the case of a spatial power combiner, the aperture gain (G_a) can be approximated by the total projected area of the array, which are typically rectangular or, as in the case of most open resonators, circular.

$$G_a = 4\pi \frac{\text{Array Area}}{\lambda^2} \quad (5)$$

Given the large number of distributed sources with varying power and phase levels, the spatial power combiner can be analyzed using array theory to determine directivity drop and sidelobe level increase from random amplitude and phase errors. Other key parameters of an active antenna include its locking gain (G_L) and its locking bandwidth (Δf), which determine the amount of injected power (P_{inj}) required to keep the active antenna synchronized to an external source.

Within the measurement chamber, an antenna of known gain (G_{std}) placed at a specified distance (R) is used to inject a signal on the active antenna at wavelength (λ). The Friis transmission equation is used again to determine how much power is injected (P_{inj}) at the active device terminals from a known source of power (P_{source}):

$$P_{inj} = G_a G_{std} P_{source} \left(\frac{\lambda}{4\pi R} \right)^2 \quad (6)$$

where the source power level (P_{source}) is varied to obtain different levels of injected power (P_{inj}) on the active device over a range of operating frequencies.

This data is used to determine the locking gain ($G_L = \frac{P_o}{P_{inj}}$) and locking bandwidth (Δf) of the radiating oscillator or spatial power combiner. With the values above, the external Quality-factor of the active antenna can also be calculated

$$Q_{ext} = 2 \frac{f_0}{\Delta f_{max}} \sqrt{\frac{P_{inj}}{P_0}} \frac{1}{\sin(\psi)} \quad (7)$$

where ψ is the angle at the intersection of the device line and the imbedded antenna impedance presented to the device terminals. Although there are no hard rules for comparison, the external Q-factor (Q_{ext}) and power-added efficiency ($PAE = \frac{P_{RFout} - P_{DCin}}{P_{RFIn}}$) are useful figures-of-merit that are used to compare the performance of active antennas spatial power combiners. In [51], Gouker presents a good review and suggestions on the development of figures-of-merit for more equitable comparisons between various spatial power combining oscillators and amplifiers.

As previously stated, a large number of relatively low-power active antennas are clustered and synchronized to develop a large high-power source with the benefits of semiconductor technologies and the graceful degradation afforded by distributed sources. To date, only certain aspects of true spatial power combining sources have been implemented commercially, and tube devices are likely to stay in use in many critical high-power applications for the next few decades.

Significant improvements in power densities, power-added efficiencies, and thermal management are required to reach power levels comparable with current high-power tube devices. Recent improvements in basic materials and device technologies continue to advance the attainable power levels from spatial power combining techniques. New technologies such as Gallium Nitride, ferroelectrics, reliable Micro-Electro-Mechanical Systems (MEMS), micromachining [52], and nanotechnologies continue to provide additional features that will improve the current state-of-the-art. Improvements in processing and assembly tolerances are also allowing the fabrication of a larger number of nearly identical sources that are more easily grouped and synchronized. As the power output levels increase, thermal dissipation and thermal gradients across the face of the combiner degrade performance and are also being addressed [53].

Grids and similar nonresonant arrays have shown great promise in monolithic integration and in the development of more compact, stable oscillators, higher power amplifiers [54], and many other quasioptical components previously referenced. Along with the advancement of sources, significant developments in spatial power combining amplifiers [55], phased arrays [56], retro-directive arrays [57,58], smart antennas, and active integrated transceivers [59] continue to increase in both functionality and quality. In time, these developments will increase both function and performance at reasonable costs for new products in emerging global markets.

BIBLIOGRAPHY

1. H. A. H. Boot and J. T. Randall, The cavity magnetron, *J. Inst. Elect. Eng.*, **93**(pt. IIIA):928–938 (1946).
2. D. Yaogen, The State-of-the-art and trend of the high power klystron, *Vacuum Electron.*, **2**:1–17 (1995).
3. R. J. Barker and E. Schamiloglu, eds., *High Power Microwave Sources and Technologies*, New York: IEEE Press/ Wiley, 2001.
4. D. Staiman, M. E. Breese, and W. T. Patton, New technique for combining solid-state sources, *IEEE J. Solid-State Circuits*, **SC-3**:238–243, (1968).
5. K. J. Russel, Microwave power combining techniques, *IEEE Trans. Microwave Theory Techn.*, **MTT-27**(5): 472–478 (1979).
6. K. Chang and C. Sun, Millimeter-wave power-combining techniques, *IEEE Trans. Microwave Theory Techn.*, **MTT-31**(2): 91–107 (1983).
7. J. A. Navarro and K. Chang, eds., *Active Antennas and Spatial Power Combining*, New York: Wiley, 1996.
8. R. A. York and Z. B. Popovic, eds., *Active and Quasi-Optical Arrays for Solid-State Power Combining*, New York: Wiley, 1997.
9. K. Chang, *Microwave Solid-State Circuits and Applications*, New York: Wiley, 1994, pp. 287–290.
10. J. G. Josenhans, Diamond as an insulating heat sink for a series combination of IMPATT diodes, *Proc. IEEE*, **56**:762–763 (1968).
11. C. T. Rucker, et al., Multi-chip IMPATT power combining, a summary with new analytical and experimental results, *IEEE Trans. Microwave Theory Techn.*, **MTT-27**:951–957 (1979).
12. K. Kurokawa, The single-cavity multiple device oscillator, *IEEE Trans. Microwave Theory Techn.*, **19**(10):793–801 (1971).
13. R. S. Harp and H. L. Stover, Power combining of X-band IMPATT circuit modules, *1973 IEEE-ISSCC Digest Technical Papers*, **XVI**:118–119 (1973).
14. J. Bae, T. Unou, T. Fujii, and K. Mizuno, Spatial power combining of Gunn diodes using an overmoded-waveguide resonator at millimeter wavelengths, *IEEE Trans. Microwave Theory Techn.*, **46**(12):2289–2294 (1998).
15. C. E. Saavedra, W. Wright, and R. C. Compton, A circuit, waveguide, and spatial power combiner for millimeter-wave amplification, *IEEE Trans. Microwave Theory Techn.*, **47**(5):605–613 (1999).
16. N. S. Cheng, A. Alexanian, M. G. Case, D. B. Rensch, and R. A. York, 40-W CW broad-band spatial power combiner using dense finline arrays, *IEEE Trans. Microwave Theory Techn.*, **47**(7):217–227 (1999).
17. N. S. Cheng, P. Jia, D. B. Rensch, and R. A. York, A 120W X-band spatially combined solid-state amplifier, *IEEE Trans. Microwave Theory Techn.*, **47**(12):2557–2561 (1999).
18. E. J. Wilkinson, An N-way hybrid power divider, *IRE Trans. Microwave Theory Techn.*, **MTT-8**:116–118 (1960).
19. N. Nagai, E. Maekawa, and K. Ono, New N-Way hybrid power dividers, *IEEE Trans. Microwave Theory Techn.*, **MTT-25**(12):1008–1012 (1977).
20. J. M. Schellenberg and M. Cohn, A wideband radial power combiner for FET amplifiers, *IEEE ISSCC Dig.*, 164–165 (1978).
21. M. A. Gouker, R. G. Beaudette, and J. T. Delisle, A hybrid-circuit tile approach architecture for high-power spatial power combined transmitters, IEEE National Telesystems Conference 1994, pp. 47–50.
22. M. A. Gouker, J. T. Delisle, and S. M. Duffy, A 16-element subarray for hybrid-circuit tile approach spatial power combining, *IEEE Trans. Microwave Theory Techn.*, **44**(11):2093–2098 (1996).
23. S. Mizushina, 2nd oscillators combined with 3-dB directional couplers for output power summing, *Proc. IEEE*, **55**:2166 (1967).
24. L. Wandinger and V. Nalbandian, Quasi-optical millimeter-wave power combiner, Proc. 6th Int. Conf Infrared and Millimeter Waves.
25. H. Kondo, M. Hieda, M. Nakayama, T. Tanaka, K. Osakabe, and K. Mizuno, Millimeter and sub-millimeter wave quasi-optical oscillator with multi-elements, *IEEE Trans. Microwave Theory Techn.*, **40**(5):857–863 (1992).
26. J. E. Ge, S. F. Li, and Y. Y. Chen, Millimetre wave quasi-optical power combiner, *Electron. Lett.*, **27**(10):880–882 (1991).
27. J. Bae, Y. Aburakawa, H. Kondo, T. Tanaka, and K. Mizuno, Millimeter and sub-millimeter wave quasi-optical oscillator with Gunn diodes, *IEEE Trans. Microwave Theory Techn.*, **41**(10):1851–1855 (1993).
28. M. Rahman, T. Ivanov, and A. Mortazawi, A 26-MESFET spatial power combining oscillator, *IEEE Microwave Guided Wave Lett.*, **7**(4):100–102 (1997).
29. F. Nusseibeh, T. W. Nuteson, J. Patwardhan, M. A. Summers, C. E. Christoffersen, J. Kreskovsky, and M. B. Steer, Computer aided engineering environment for spatial power combining systems, *IEEE Int. Microwave Sympos. Dig. 1997*, 1073–1076 (1997).
30. A. A. M. Saleh, An adjustable quasi-optical bandpass filter-Part I: Theory and design formulas, *IEEE Trans. Microwave Theory Techn.*, **22**(7):728–734 (1974).
31. A. A. M. Saleh, An adjustable quasi-optical bandpass filter-Part II: practical considerations, *IEEE Trans. Microwave Theory Techn.*, **22**(7):734–739 (1974).
32. R. J. Hwu, L. P. Sadwick, N. C. Luhmann, Jr., and D. B. Rutledge, DC and millimeter-wave performance of watt-level barrier-intrinsic-N+ diode grid frequency multiplier fabricated on III-V compound semiconductors, *IEEE IEDM*, 191–194 (1988).
33. Z. B. Popovic, R. M. Weikle II, M. Kim, and D. B. Rutledge, A 100-element planar grid oscillator, *IEEE Trans. Microwave Theory Techn.*, **39**(2):193–199 (1991).
34. S. C. Bundy and Z. B. Popovic, A generalized analysis for grid oscillator design, *IEEE Trans. Microwave Theory Techn.*, **42**(12): 2486–2491 (1994).
35. J. B. Hacker, R. M. Weikle II, M. Kim, M. P. Delisio, and D. B. Rutledge, A 100-element planar Schottky diode grid mixer, *IEEE Trans. Microwave Theory Techn.*, **40**(3):557–562 (1992).
36. R. M. Weikle II, M. Kim, J. B. Hacker, M. P. Delisio, Z. B. Popovic, and D. B. Rutledge, Transistor oscillator and amplifier grids, *Proc. IEEE*, **80**(11):1800–1809 (1992).
37. L. B. Sjogren, H. X. Liu, X. Qin, C. W. Domier, and N. C. Luhmann, Jr., Phased array operation of a diode grid impedance surface, *IEEE Trans. Microwave Theory Techn.*, **42**(4):565–572 (1994).
38. S. Hollung, W. Shiroma, M. Markovic, and Z. B. Popovic, A quasi-optical isolator, *IEEE Microwave Guided Wave Lett.*, **6**(5):205–206 (1996).
39. J. J. Taub, Comments on a quasi-optical isolator, *IEEE Microwave Guided Wave Lett.*, **6**(11):423 (1996).
40. W. A. Shiroma, S. C. Bundy, S. Hollung, B. D. Bauernfeind, and Z. B. Popovic, Cascaded active and passive quasi-optical

- grids, *IEEE Trans. Microwave Theory Techn.*, **MTT-43**(12):2904–2909 (1995).
41. J. W. Mink, Quasi-optical power combining of solid-state millimeter-wave sources, *IEEE Trans. Microwave Theory Techn.*, **MTT-34**(2):273–279 (1986).
 42. K. D. Stephan, Inter injection-locked oscillators for power combining and phased arrays, *IEEE Trans. Microwave Theory Techn.*, **MTT-34**(10):1017–1025 (1986).
 43. J. A. Navarro and K. Chang, Electronic beam-steering of active antenna arrays, *Electron. Lett.*, **3**:302–304 (1993).
 44. R. A. York, Nonlinear analysis of phase relationships in quasi-optical oscillator arrays, *IEEE Trans. Microwave Theory Techn.*, **MTT-41**(10):1799–1809 (1993).
 45. H. C. Chang, X. Cao, U. K. Mishra, and R. A. York, Phase noise in coupled oscillators: theory and experiment, *IEEE Trans. Microwave Theory Techn.*, **MTT-45**(5):604–615 (1997).
 46. B. D. Bates and P. J. Khan, Stability of multifrequency negative resistance oscillators, *IEEE Trans. Microwave Theory Techn.*, **MTT-32**(10):1310–1318 (1968).
 47. K. Kurokawa, Noise in synchronized oscillators, *IEEE Trans. Microwave Theory Techn.*, **MTT-16**(4):234–240 (1968).
 48. J. C. Nallatamby, M. Prigent, J. C. Sarkissian, R. Quere, and J. Obregon, A new approach to nonlinear analysis of noise behavior of synchronized oscillators and analog-frequency dividers, *IEEE Trans. Microwave Theory Techn.*, **MTT-46**(8):1168–1171 (1998).
 49. K. F. Schunemann and K. Behm, Nonlinear noise theory for synchronized oscillators, *IEEE Trans. Microwave Theory Techn.*, **MTT-27**(5):452–458 (1979).
 50. E. Shumakher and G. Eisenstein, On the noise properties of injection-locked oscillators, *IEEE Trans. Microwave Theory Techn.*, **MTT-52**(5):1523–1537 (2004).
 51. M. Gouker, Toward standard figures-of-merit for spatial and quasi-optical power-combined arrays, *IEEE Trans. Microwave Theory Techn.*, **43**(7):1614–1617 (1995).
 52. Y. Lee, J. R. East, and L. P. B. Katehi, Micromachined millimeter-wave module for power combining, *IEEE Int. Microwave Sympos. Dig.*, 2004, 349–352 (2004).
 53. W. Batty, C. E. Christoffersen, A. B. Yakovlev, J. F. Whitaker, A. Mortazawi, A. Al-Zayed, M. Ozkar, S. Ortiz, R. M. Reano, K. Yang, K. Yang, L. P. B. Katehi, C. M. Snowden, and M. B. Steer, Global coupled EM-electrical-thermal simulation and experimental validation for a spatial power combining MMIC array, *IEEE Trans. Microwave Theory Techn.*, **50**(12):2820–2833 (2002).
 54. M. P. Delisio, et al., A Ka-band grid amplifier module with over 10 watts output power, *IEEE Int. Microwave Sympos. Dig.* 2004, 83–86 (2004).
 55. F. C. E. Tsai and M. E. Bialkowski, An X-band spatial power combiner using a planar array of stacked patches for bandwidth enhancement, *IEEE Int. Microwave Sympos. Dig.* 2004, 95–98 (2004).
 56. Phased arrays for the new millenium, *2001 IEEE Antennas Propagation/URSI Sympos.*, July 8–13, 2001, Boston, Massachusetts.
 57. C. T. Rodenbeck, M. Y. Li, and K. Chang, A phased-array architecture for retrodirective microwave power transmission from the space solar power satellite, *IEEE Int. Microwave Sympos. Dig.* 2004, 1679–1682 (2004).
 58. B. T. Murakami, J. D. Roque, S. S. Sung, G. S. Shiroma, R. Y. Miyamoto, and W. A. Shiroma, A quadruple subharmonic phase-conjugating array for secure picosatellite crosslinks, *IEEE Int. Microwave Sympos. Dig.* 2004, 1687–1690 (2004).
 59. R. Flynt, L. Fan, J. A. Navarro, and K. Chang, Low cost and compact active integrated antenna transceiver for system applications, *IEEE Trans. Microwave Theory Techn.*, 1642–1649 (1996).

SPICE

WILLIAM H. MORONG
Consultant

1. INTRODUCTION TO SPICE

Since the advent of electronic computers, programs have been developed to simulate physical phenomena. Electronic circuits are among the phenomena having thus been simulated. An enduring and popular electronic simulation program developed at the University of California, Berkeley, is SPICE, an acronym meaning “Simulator Program with Integrated Circuit Emphasis.” It is beneficial not to be misled by its name to believe that SPICE is limited to circuits destined for monolithic integration. SPICE simulates as easily as integrated circuits, discrete circuits, and even purely electrical circuits containing only such components as voltage and current sources, resistors, capacitors, and inductors.

SPICE is most useful when a need exists to simulate circuits at the component level. Many other simulation programs offer higher degrees of abstraction to free the user from handling a plethora of individual components. Cases where component-level simulation is helpful include, but are not limited to, analog circuits, the structures within digital circuits in which such analog behavior as transitions must be studied, RF circuitry, and the instruction of students in circuit theory.

SPICE includes such ideal components as independent and dependent voltage and current sources, resistors, capacitors, inductors, and transmission lines, and provides a means for assigning a numerical quantities to each instance of such components. It further provides for inclusion in circuits of externally supplied components as models or as subcircuits.

A SPICE circuit comprises a “netlist” that expresses the chosen components and their interconnections. The “netlist,” an example of which is shown in Fig. 1, is essentially an alpha-numeric text expression of a circuit diagram. Each component or external connection and each terminal thereof is assigned a name. Each group of uniquely interconnected component terminals is called a “node” and assigned a name. The SPICE simulation program, through extensive iteration in accordance with the netlist and components thereof, calculates the behavior of the circuit. This behavior approximately satisfies, often with great precision, the requirements of such fundamental circuit equations as Ohm’s law and Kirchhoff’s law. Adherence to such laws is implicit in SPICE simulation.

Until recently, the most common means of passing input to the SPICE application has been alpha-numeric text in a command line, or even Hollerith cards. The total input

NODE	REFERENCE	PIN #	PIN NAME	PIN TYPE	PART VALUE
[00001]	N001				
	V1	1	+	Passive	3.6
	L1	1	A	Passive	300n
	C1	1	A	Passive	39p
	R3	1	A	Passive	1k00
	R6	2	B	Passive	10
	R7	2	B	Passive	10
	D2	2	-	Passive	MMBD101
	D3	1	+	Passive	D
[00002]	0				
	V1	2	-	Passive	3.6
	V2	2	-	Passive	1.225
	R1	2	B	Passive	240
	R5	1	A	Passive	5k11
	R8	2	B	Passive	240
	R9	2	B	Passive	240
	V4	2	-	Passive	5
[00003]	N002				
	L1	2	B	Passive	300n
	C1	2	B	Passive	39p
	X1	1	C	Passive	Bfp405f
	D1	2	-	Passive	MMBD101

Figure 1. Sample portion of a SPICE netlist. (This figure is available in full color at <http://www.mrw.interscience.wiley.com/erfme>.)

for a given circuit to SPICE is still often called a “deck.” Such entry has been language readable by computers, necessitated by the former inability of computers to economically process more humanly intuitive communications. However, in electronic engineering, far older and more comfortable language exists, in which most engineers are fluent. That language is the circuit (schematic) diagram. Undoubtedly, engineers who do not share a spoken tongue, or even an alphabet, can read each others’ diagrams. Recent advances in Graphic User Interfaces (GUIs) now render circuit diagrams computers readable. Modern SPICE applications offer “schematic entry” as the default input method. Figure 2 shows a typical SPICE schematic entry environment.

However tedious alpha-numeric text input may be, interpretation of nongraphical numeric output data seems even more difficult for humans. Therefore, SPICE has long included provisions for graphing the voltage at any node of a circuit or the current in a terminal of a component. Modern SPICE applications make this facility even more comfortable. The means of obtaining graphical output is now often a cursor resembling an oscilloscope probe, and the output often looks like an oscilloscope or spectrum analyzer output. Figure 3 shows typical SPICE output for the circuit of Fig. 2. The GUIs of some SPICE applications are now so good that it is possible for an engineer with decades of bench experience to forget that he or she is working in a virtual environment of which the soldering iron is no part. Figure 4 shows the SPICE GUI environment offered by a typical SPICE application.

In addition to schematic input and graphical output, many SPICE applications import and export netlists as .cir files, allowing a circuit generated in one SPICE application to be simulated in another. Some SPICE applications also filter and export their netlists in a number of proprietary formats readable by a number of popular Printed Circuit Board (PCB) layout applications. Moreover, some SPICE applications also provide easy graphical capture of on-screen diagrams and plots that can be easily picked up in popular graphics editing applications. Most of the files thus generated are of surprisingly modest size. All these facilities make it very easy for engineers to share designs and their outputs over networks, including the Internet.

SPICE is now available to operate under a variety of operating systems. Proprietary SPICE versions are often distinguished by their user interfaces and by the libraries they supply. The cost of a fully functional SPICE application varies from several thousand dollars to free. Some versions use standard Berkeley SPICE syntax, whereas others use similar syntax that is largely humanly understandable but not necessarily compatible. In addition, SPICE has been tailored for particular engineering disciplines. For instance, several software suppliers offer special versions directed toward RF design or power-conversion circuitry.

SPICE software may be accessed in a variety of ways. One may purchase a proprietary SPICE application. Complete SPICE applications are also offered as “freeware” [1] for download over the Internet. Such applications are usually less than 20 megabytes in size and will run reasonably quickly even on obsolete computers with

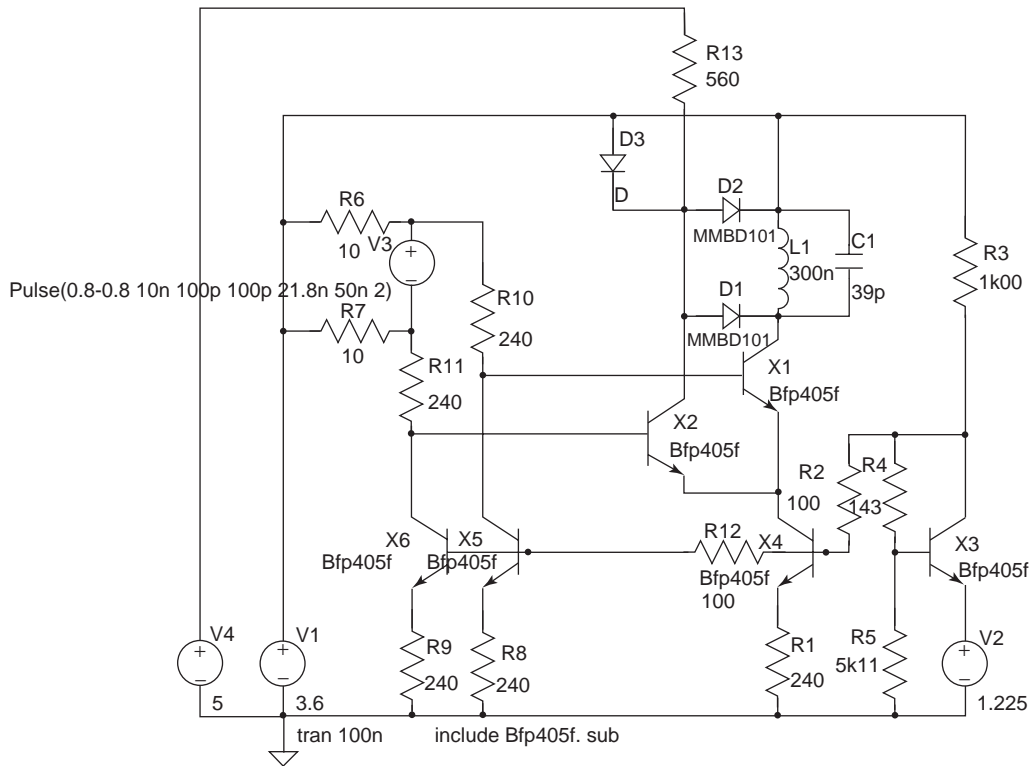


Figure 2. Schematic diagram image from SPICE GUI.

processor speeds below 200 Mhz. Free applications [2] sometimes include extensive libraries of the parts offered by the manufacturer supplying that application. Such libraries often do not encumber one's use of the program,

can be very convenient, and can easily be supplemented by models from other vendors. Some component vendors enter into arrangements with vendors of proprietary SPICE applications to provide applications largely dedicated to

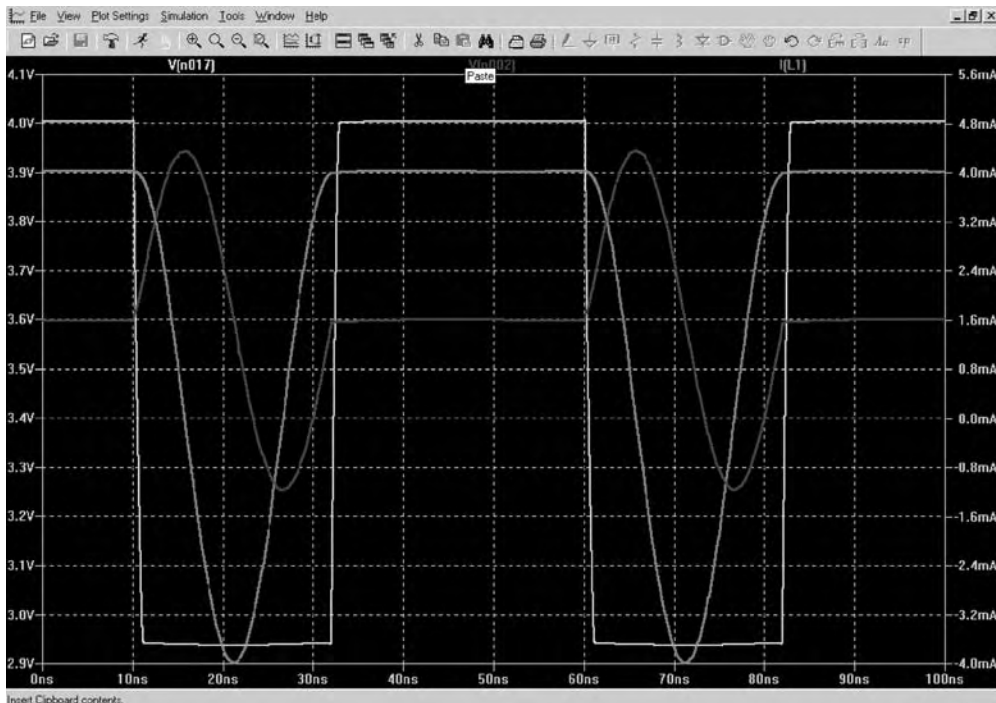


Figure 3. Voltage and current waveforms from SPICE GUI. (This figure is available in full color at <http://www.mrw.interscience.wiley.com/erfme>.)

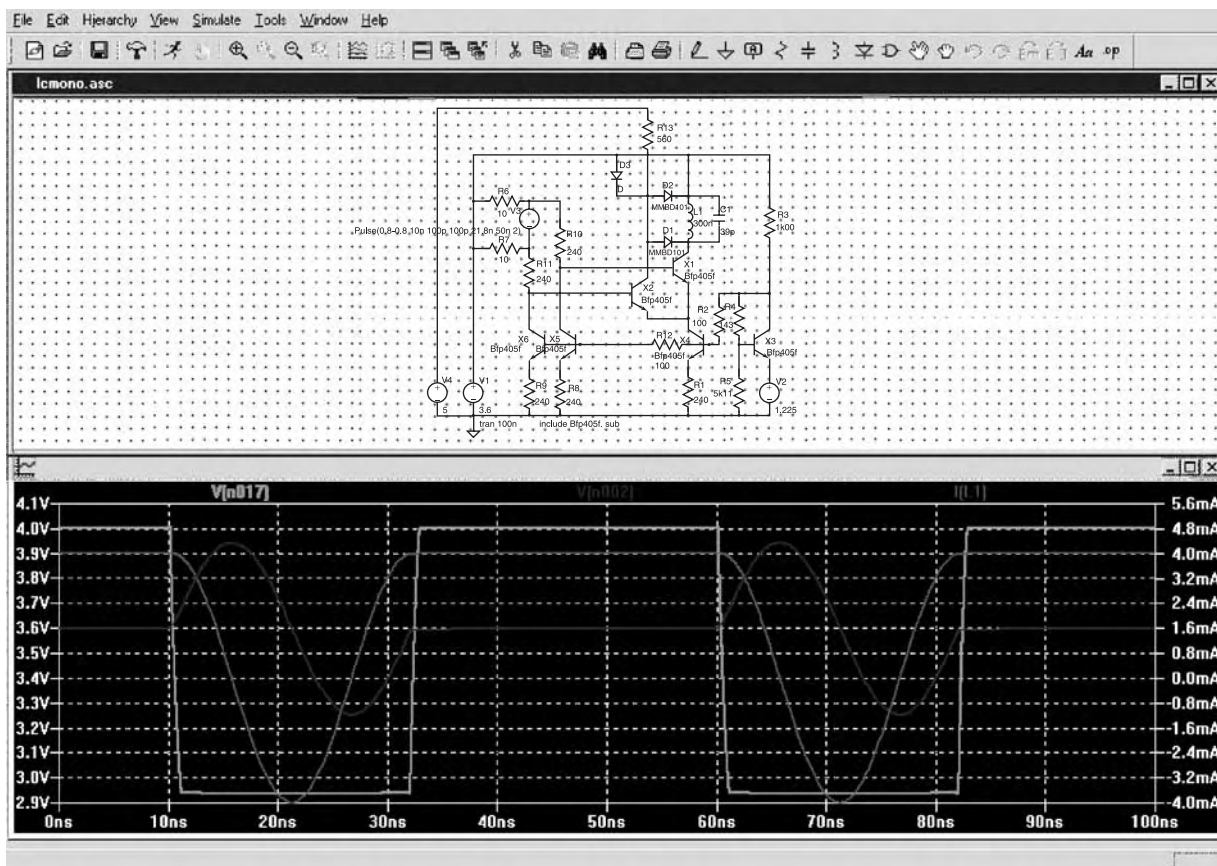


Figure 4. Typical SPICE GUI showing schematic and waveforms.

the components they offer or to limited applications such as power-conversion circuitry. Some of these dedicated applications are available for download [3], whereas others reside at the component vendor’s Website and are usable over the Internet [4]. It is wise to thoroughly explore these options without regard for the names of the applications. One offering named to indicate dedication to switching power supplies is actually a totally free, full-featured, and largely generic version of SPICE with a generous and convenient GUI, and operates under both Windows and Linux operating systems.

Although such primitive elements as resistors and capacitors are an integral part of SPICE, even the ubiquitous 2N3904 transistor is not. However, primitive frameworks of transistors are integral parts of SPICE. SPICE recognizes, as models, groups of parameters that together define the behavior of transistors. For each transistor type, SPICE requires a model that comprises parameters equated with corresponding numerical values. The transistors that SPICE is endowed to recognize are Bipolar Junction Transistors (BJTs), both NPN and PNP; Junction Field Effect Transistors (JFETs), both N and P channel; and Metal-Oxide Semiconductor Field Effect Transistors (MOSFETS), both N and P channel. SPICE also sets forth parameters for, and recognizes, models of semiconductor diodes.

A model is a brief text file that retains the alpha-numeric character of earlier SPICE inputs. Models begin

with the syntax “.model” followed by the name of the model, for example 2N3904. A primitive SPICE description follows, such as NPN for the 2N3904.

Its complement the 2N3906 would be “PNP.” SPICE recognizes .model and NPN and will associate these with the name 2N3904. Terminal numbers are assumed; in the case of a NPN BJT, these are usually 1, 2, and 3, the collector, base, and emitter, respectively.

Letters grouped with numbers follow, either in parentheses or on lines starting with “+” a list of parameters, each group containing “=”, for instance, “BF = 100.” Each group is a named quantity that SPICE has been endowed to recognize as a particular characteristic of device that it recognizes. Thus SPICE recognizes that the NPN called 2N3904 has a Beta Forward (BF) of 100. There are many SPICE-recognizable parameters for each device type. The mythical model below illustrates the typical syntax of a model.

```
.model XBT9999 NPN
+ Is = 7.931f   Xti = 3           Eg = 1.11           Vaf = 58.74
+ Bf = 76      Ne = 1.342       Ise = 5.911f       Ikf = 13.93m
+ Xtb = 1.5    Br = 1.297       Nc = 2             Isc = 0
+ Ikr = 0      Rc = 1.61        Cjc = 4.017p       Mjc = .3174
+ Vjc = .75    Fc = .5              Cje = 4.973p       Mje = .4146
+ Vje = .75    Tr = 4.687n          Tf = 820.4p        Itf = .35
+ Vtf = 4      Xtf = 7           Rb = 10
```

Complete lists of SPICE-recognizable parameters for diodes and transistors of all recognizable types are set forth in detail in literature published by UC Berkeley [5] and summarized [6,7] and published by other entities. Both the complete parameter descriptions and their summaries are freely available for download over the Internet. For MOSFETS, SPICE recognizes both electrical models, including electrical parameters and geometric models, the latter often including lengths and widths of MOSFET features expressed in microns.

Devices that are not single devices primitively recognizable to SPICE may also be similarly called. These are described as subcircuits. A subcircuit is brief text file including a plethora of SPICE-recognizable devices interconnected by a net list and having terminals like, and called like a single component. A subcircuit may contain many BJTs, resistors, capacitors, or other components. A subcircuit may encompass even a complex subsystem. The syntax is similar to that for models, beginning with ".subckt," followed by the name of the subcircuit, which is followed by several alpha-numeric expressions separated by spaces, representing the external nodes of the subcircuit. This opening is followed by a netlist of the subcircuit and any models included therein, finally ending with ".ends." Comments lines beginning with an asterisk may be included anywhere in the text. It is safest to completely include all models used in a subcircuit in its text to avoid corrupting a subcircuit when transporting it to a SPICE application with a different library. The filename of a subcircuit is usually the name of that subcircuit with the suffix ".sub." The syntax of a subcircuit is illustrated by the mythical subcircuit named DIFFECL.sub follows below.

```
*ECL DIFFERENTIAL RECEIVER
.Subckt DIFFECL Vcc Vee Vin + Vin - Vout + Vout -
I2 Q22_E Vee 2.95m
Q21 Vcc R11_N Vout + 0 HFGADJ
Q22 R12_N Vin + Q22_E 0 HFGADJ
Q12 Vcc R12_N Vout - 0 HFGADJ
Q11 R11_N Vin - Q22_E 0 HFGADJ
R12 Vcc R12_N 270
R11 Vcc R11_N 270

.MODEL HFGADJ NPN
+ IS = 3.84e-16    BF = 124.9      NF = 1.05      VAF = 11.9
+ VJS = 0.75      IKF = 0.027     MJS = 0        ISE = 1.0e-14
+ FC = 0.5        NE = 2.17       TF = 8.7e-12   BR = 1
+ XTF = 18        NR = 1.05       VTF = 19.1     ITF = 0.082
+ PTF = 0 ISC = 0 TR = 0.635e-9  NC = 2         EG = 1.11
+ RE = 0.6        XTB = 0           RB = 17.9     XTI = 3
+ RBM = 1.02      KF = 0            IRB = 4.01e-4 AF = 1
+ RC = 10.5       CJE = 0.358e-12  VJE = 0.71    MJE = 0.5
+ CJC = 0.162e-12 VJC = 0.79       MJC = 0.64    XCJC = 0
+ CJS = 0
.ends
```

Subcircuits have many uses. Subcircuits provide a way for SPICE to simulate both usual and unusual components. For example, it is unlikely that the authors of SPICE had vacuum tubes (valves) in mind when they wrote a program nominally having "integrated circuit emphasis." However, certain audio enthusiasts find that

subcircuits representing triode and pentode vacuum tubes are convenient for simulating their circuits. The monolithic IC designer may use subcircuits to abstract repetitive structures. The discrete analog designer will doubtless encounter manufacturers' macromodels of such devices as operational amplifiers, which are, in fact, subcircuits that mimic the behavior of such components. The HF RF designer may use models, but the very high frequency (VHF) and ultra-high frequency (UHF) designer must usually use models embedded in subcircuits representing the package parasitics of their devices.

Modern SPICE applications often include model and subcircuit libraries that SPICE searches by default for their contents. Additionally, many SPICE applications are endowed by their software authors with such libraries already supplied with common components. Models of devices are often supplied by manufacturers, and may usually be downloaded over the Internet. This is often the source of the most accurate models, although some manufacturers supply models with errors. Some users learn no more about models than how to download them and to install them in their SPICE libraries.

The RF designer and the high-speed analog and digital designer may need models of other circuit elements that neither SPICE nor device manufacturers can supply. At high frequencies and speeds, the parasitic, or stray, resistance, capacitance, and inductance of the interconnects between devices is often far from negligible and may even dominate circuit performance. Therefore, if SPICE is to simulate such circuits accurately, these parasitic elements must be included in the simulation. Obtaining models of parasitic elements can be challenging.

Other computer simulation programs may be used to provide models of parasitic elements. Some electromagnetic (EM) field solvers [8] provide for drafting entry of such geometric features as may occur on a PCB, in hybrid circuitry, or in a monolithic IC. Such programs also often provide import capability for graphics files. Some EM field solvers output both S-parameter and SPICE models that may be useful to the high-frequency SPICE user. Lacking an EM field solver, it is sometimes useful to treat interconnects as transmission line sections that are easily included in the SPICE simulation.

Another need for subcircuits and models develops with mixed-signal design. To simulate circuits containing both analog and digital devices, at least the input and output characteristics of the digital parts must be modeled in SPICE-recognizable format. One common format for digital interfaces is IBIS. IBIS-to-SPICE conversion applications [9] facilitate SPICE simulation including digital components. In the case of such digitally simple parts as buffers and inverters, the IBIS-to-SPICE conversion may be all the treatment that the digital components require.

2. USING SPICE

The first entry on a SPICE schematic diagram should be the ground (earth) symbol; SPICE will not correctly simulate any circuit lacking a ground.

SPICE will also balk at a circuit containing nodes for which it cannot compute a DC operating point relative to ground. A capacitor left with one open terminal is unacceptable. Analogous to the open capacitor is the shorted inductor, the current of which is unknown. Some SPICE applications will accept a resistor with one open terminal, whereas others will not. Despite the fact that coaxial cable, microstrip, or other transmission lines obviously exhibit longitudinal conduction, SPICE does not recognize what one may ordinarily take for granted. For simulation, circuits connected by transmission line may require resistors to ground at the far end of the line. Such resistors may be arbitrarily large, i.e., 1 gig-ohm. Other circuits inadvertently containing galvanically isolated nodes may require similar treatment. Examples of such are certain M-derived filters, isolation amplifiers, isolated DC-DC power supplies, and transformer-coupled RF circuitry. It is usually advisable to connect normally isolated circuit portions to the grounded parts of the schematic diagram using a resistor. Once the simulation is performed, one can examine this resistor for common-mode currents. If the circuit has been thoroughly modeled, it will contain the stray coupling elements between the isolated section and ground. In transformer-coupled circuitry, the common-mode potential imposed on a secondary winding may often have a peak voltage as high as the power supply on the primary side. The current in the connecting resistor should be commensurate with that which is to be expected. The discipline of examining this current is helpful in appreciating and controlling common-mode currents in RF circuits and DC-DC converters.

Although most SPICE applications have libraries of models and subcircuits, the manipulation of such files varies from application to application, and even within applications. For example, one application groups all semiconductors, models, and subcircuits alike into a single file. Another has a separate folder in which each subcircuit is a separate file. In the latter application, other components, passive and active, are grouped in files within another folder, a file for resistors, another for capacitor, yet another for inductors, a file for BJTs, etc. However, the latter application also includes other components not kept in such files, such as switches. In the latter application, switches are defined by a SPICE directive, a snippet of text edited in a dialog box and deposited on the schematic diagram.

A few words are needed about the use of the ideal components available in SPICE. Unless other inputs are given, SPICE components and sources are ideal! Resistors have no capacitance or inductance. Capacitors have no resistance or inductance. Inductors have no resistance or capacitance. Voltage sources can supply megaamps, and current sources have compliances of megavolts, whether dependent or independent sources. *If your simulation needs less than ideal components to be correct, you must explicitly add the necessary nonidealities to your schematic diagram, or in some SPICE applications, to the component descriptions!* At first, those unaccustomed to ideal components may experience some disorientation. For example, although a real current

source usually must be connected to a voltage more extreme than greatest compliance desired therefrom, an ideal current source needs no such connection. It may be connected to ground or to any appropriate return. Even more disconcerting is the fact that an ideal current source, unlike most real current sources, can swing to voltages beyond the power supply voltages provided in the schematic diagram. If one were to apply an ideal current source to the capacitor of a ramp generator, and then not reset that generator soon enough, one might see several kilovolts across that capacitor.

Additionally, diode and transistor models may not include breakdown voltages. In a real circuit, a positive current source applied to the emitter of an NPN BJT will merely cause zener conduction, but because the zener breakdown base-emitter junctions is commonly not included in SPICE models, the emitter voltage in simulation may increase to astounding levels.

The effects of ideal voltage sources are more misleading for SPICE users because they are seldom so dramatic. Build a DC-DC converter fed by an ideal voltage source and no ripple will be conducted to another connected circuit. Power the real version of the same circuits with a battery and the circuits sharing the battery may be inundated with noise. To obtain the truth, one must endow that ideal voltage source with battery-like nonidealities. If one remembers to observe the current in the ideal voltage source, the need for proper bypassing and decoupling becomes obvious.

Independent sources in SPICE may be made to provide a steady voltage or current, AC voltage or current for AC analysis, or waveforms with or without DC components. Available waveforms are pulse, sine-wave, exponential, piece-wise linear (PWL), and single-frequency FM. Although these sources largely correspond to what the engineer expects in bench instruments, a few accommodations are to be made. One accustomed to a function generator with sine-, square-, and triangle-wave outputs may at first miss the last. However, two triangle-wave sources are implicit in SPICE. The pulse source has programmable rise and fall time. A pulse consisting entirely of rise and fall is a triangle wave. One accustomed to the usual engineering practice of measuring pulses at their 50% points may at first not obtain the expected pulse waveforms from SPICE, in which the waveform is specified as having an implied off-time, a rise, an on-time, a fall, and a period. The second triangle-wave generator is the PWL source. Using this source, the times and levels at the tips of the wave may be defined.

In addition to independent sources, dependent sources are available in SPICE. These are four-terminal devices having either a voltage or a current input and a voltage or a current output. One must at least enter a value of gain or transconductance for these devices.

Another SPICE source is the nonlinear dependent (in some applications called behavioral) source. These are a two-terminal voltage or current sources, the output of which is a mathematical expression. The output of such a source might, for example, be a voltage twice the sine of the square of the voltage on some other node on the schematic diagram.

When any component or source is entered in SPICE, no error is entered with it. Some SPICE applications include Monte Carlo analysis, but, in the absence of that feature, one can be misled by inadvertent and unrealistic matching of components. If any question about such errors exists, it is wise to deliberately introduce appropriate errors and recheck simulation results.

Having entered a schematic diagram and incorporated in one's library, the models, and subcircuits it contains, one must direct SPICE to do the desired analysis. The time-domain oriented engineer will often choose transient analysis. The output of transient analysis is essentially the same as using an oscilloscope to probe a real circuit. In transient analysis, SPICE must be given at least a stop time at which to discontinue the simulation. During simulation, a dialog box may drop asking what node voltages or component currents are to be plotted. In many applications, one may, after simulation, examine these voltages and currents by clicking a probe-shaped cursor on a corresponding part of the schematic diagram. In transient analysis, a time to start collecting data to be plotted, a maximum step time (time resolution), and sometimes a minimum step time, may be entered.

Another engineer may choose AC analysis. In this case, the result after simulation of clicking the probe on a given node of the schematic is the generation of a Bode plot, as shown in Fig. 5. For this analysis, one enters a start frequency, a stop frequency, whether the output interval is to be in octaves or decades, and the number of points per interval. It does not matter at all to SPICE whether the circuit is operating from 1 to 10 MHz or 1 to 10 GHz, the computation is equally quick. For a given cir-

cuit, AC analysis is usually much quicker than transient analysis.

SPICE offers intuitive bridges between the frequency-domain and the time-domain. It is a trivial task to perform both transient and AC analysis of the same circuit. Making a habit of doing so can greatly sharpen one's intuitive grasp of the relationship between these domains. For example, one can observe the transient response of a feedback amplifier and then consider its Bode plot. Examination of the ripples in the transient response are easily related to discontinuities shown on the Bode plot. With a little practice of this discipline, it becomes difficult not to know how to compensate an amplifier. Were that not enough, many applications include FFT capability that is easily applied to the output data. Such capability, shown in Fig. 6, can be very useful for observing harmonics and intermodulation products.

Noise analysis is invoked similarly to AC analysis. The obvious difference is that for noise analysis the circuit itself provides the signal.

DC analysis is usually performed by default before more complex analyses are done, but may be separately invoked. Pole-zero analysis and sensitivity analysis are part of SPICE and are not explicitly accessible in many applications. Transfer function analysis is also part of SPICE, fully explicitly available in some applications and explicitly available only for DC in others.

Circuits capable of energy storage can require inordinate simulation times in SPICE. To overcome this problem, SPICE contains the ability to set initial conditions. For example, an L-C oscillator with a high-Q tank may take hundreds or thousands of cycles to attain the

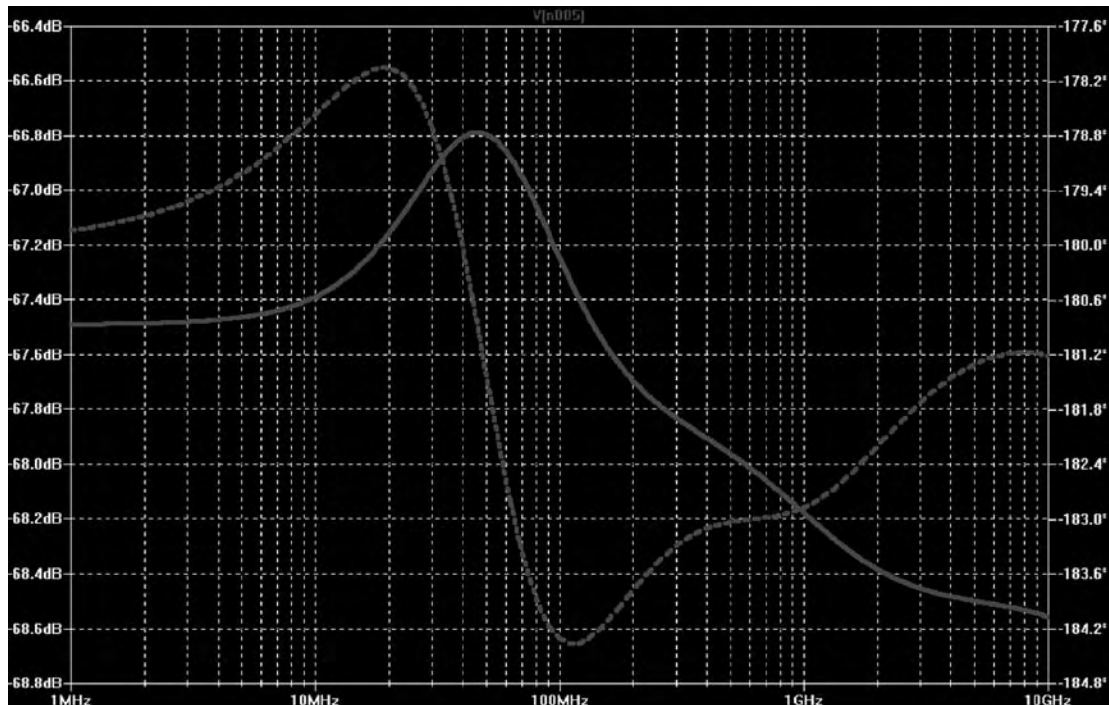


Figure 5. Bode plot image from SPICE GUI. (This figure is available in full color at <http://www.mrw.interscience.wiley.com/erfme>.)

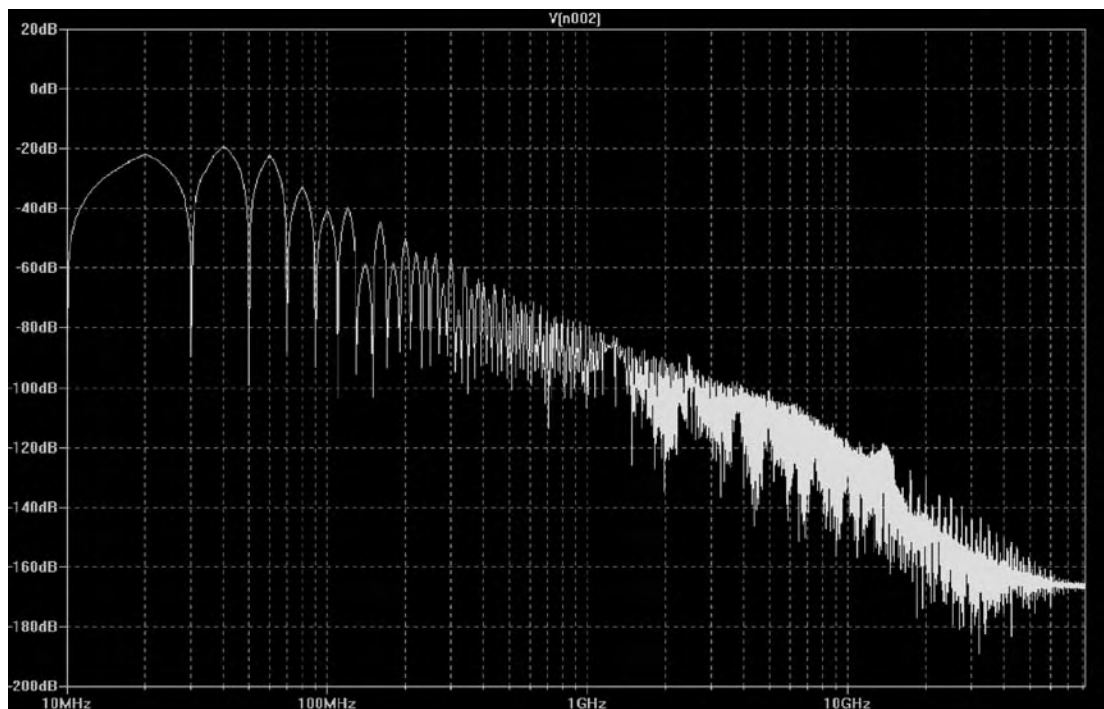


Figure 6. FFT image from SPICE GUI. (This figure is available in full color at <http://www.mrw.interscience.wiley.com/erfme>.)

steady state. If one is not interested in its turnon behavior, one may invoke an initial condition to start the circuit fully charged with energy. For example, one might use the syntax “.ic I(L1)=18m” (meaning the initial condition of L1 is to have a flow of 18 mA) to preload the inductor with 18 mA. If this current is correctly chosen in accordance with the equations governing the inductor’s peak current in the steady state, the oscillator may start immediately. In inductive circuits, it is not unusual to obtain plots indicating several KV, with power supplies of a few volts. This problem is often solved by setting an inductor initial condition to zero, or to some reasonable value. Likewise, if one has no interest in the turnon of an A-M envelope detector, one may precharge its filter capacitor with such syntax as “.ic V(n017) = 1.347 V,” where the terminal of the capacitor attached to node 17 needs to be charged to that voltage. The initial condition is almost indispensable for examining the ripple of DC-DC converters. When initial conditions are not specified and should be, not only does transient simulation often become lengthy, but also the SPICE iterations needed initially to establish DC conditions may become so slow as to strain one’s patience waiting for actual simulation to commence.

RF and power-conversion circuits often involve transformer coupling. Transformers in SPICE are simply coupled inductors. The windings to be coupled are entered having polarity dots if needed and their respective self-inductances. Remember that inductance varies as the square of turns; turns-ratio in SPICE is a dependent variable derived from the square root of the inductance ratio. One enters the windings on the schematic as if they were perfectly coupled. To implement less than complete

coupling, the syntax is usually something like “K1 L1 L2 0.5,” meaning that the windings L1 and L2 are 50% coupled. Many windings can usually be included in that syntax.

One might wonder how, without the expense of an EM field solver, to model parasitic elements. Free resources, some available online give, either as charts in text [10] or as calculators [11,12], the impedance of microstrip and other common structures given dielectric constant, or material, and dimensions. If one merely treats one’s interconnects as such structures, one can ascertain their impedances as transmission lines. The same facilities usually relate their timelengths to physical lengths. To convert timelength at a given impedance to lumped elements, use $C = T/Z_0$ and $L = T \cdot Z_0$, where T is the timelength, Z_0 is the characteristic impedance, C is the capacitance of the section, and L is the inductance of the section. Thus, one can approximate, for example, the stray capacitance and stray inductance of a run on PCB. The reason for simulating using lumped elements rather than transmission line sections for connections is that SPICE does not comprehend transmission lines as DC connections.

As SPICE may compute the characteristics of sections of transmission lines with far greater smoothness than is practically realizable, simulations involving transmission lines are often slow. More reasonable simulations are often obtained using lumped-element lines when the “lumpiness” is chosen to have little effect on circuit operation. Using many small sections can approximate the smoothness of a continuous line.

Although a few SPICE applications add some thermal capability, many do not. In the world of SPICE, simulated

components can be far more tolerant of excessive dissipation than in actual circuits. One must, therefore, account for the dissipation of one's components before assuming that a design that performs flawlessly in simulation is complete. Having manually determined that a temperature increase will occur, no difficulty exists in causing SPICE to simulate at the higher temperature. Some applications include a menu entry for temperature, whereas others require syntax such as "temp 100." Although some manufacturers supply models with temperatures in Kelvin degrees, many SPICE applications require Celsius degrees and produce anomalous results when given Kelvin degrees. Likewise, many active device models do not include voltage breakdown. A 60 V transistor with 200 V on its collector may simulate flawlessly. High SWR that may destroy real transistors may not be noticed in SPICE unless voltages and currents are examined.

Habituation to real-world circuits usually does not encourage observation of currents. However, in SPICE, observation of voltages and currents is equally practical. It is helpful to cultivate the habit of observing currents in RF circuits. For example, in RF circuits it is not uncommon for ground planes to resonate with bypass capacitors. The tell-tale sign in real circuits is that a capacitor with good ESR exhibits far more voltage drop than its capacitive reactance and the available power-supply voltage would seem to permit. Q of the resonant tank formed by plane and bypass is the culprit. With strays correctly modeled, the resonance will also occur in SPICE, but the current in the bypass will be directly observable.

As well as simulating common components, SPICE also facilitates simulation of functions incorporating LaPlace transforms. Some applications offer explicit LaPlace blocks, ideal components with infinite input impedances and infinitesimal output impedances, into which can be inserted numerical expressions of the form "6347/(s+355)." In other applications, the LaPlace functions are less obvious. In some, dependent voltage and current sources may be endowed with values including the LaPlacian, using such syntax as "LaPlace = 5473/(s + 23495)." In addition to their use as ideal components, LaPlacian sources, when embedded in circuitry yielding the appropriate nonidealities, often provide effective replacement models when component models are not available.

3. ACCOMMODATING SPICE AND MODEL ANOMALIES

Like any tool, SPICE is not perfect. One annoying problem is that sometimes a circuit portion that has been totally disabled will generate simulation artifacts. If one sees in simulation what appears to be low-level interference or crosstalk from a source that has been reduced to zero volts, it is good not to be surprised. This problem looks just like RF leakage, but it is not. Saving a version of the circuit and eliminating the offending source therein usually causes the problem to disappear, thus proving the problem to be an artifact.

Another perplexing problem can develop because of the default resolutions of SPICE applications. For instance, the leakage currents of some MOSFETS are in the femtoamps. If one's application defaults to 1 nanoamp resolution, it is understandable that measurements on the picoamp and femtoamp regions will appear to wander aimlessly as SPICE dithers between minimal levels at maximum resolution. If one needs to work in extreme areas, it is wise to examine the defaults of the SPICE application.

Most problems encountered using SPICE do not originate in the SPICE application; models and subcircuits are the most abundant source of errors. At this time, most engineers obtain their models over the Internet. For SPICE models, macromodels, and subcircuits, as for other information, the Internet offers an abundant wellspring of undifferentiated truth and error. The Internet abounds with SPICE models, some totally erroneous. The best are usually offered by device manufacturers, but even some of these are rife with errors.

Although some engineers feel that SPICE models are sacred and should be preserved inviolate, such a stance denies one the ability to correct obvious errors. It is not uncommon, even with manufacturer-supplied models, to encounter errors. As many component characteristics are also supplied in datasheets, it is wise to compare datasheet values with SPICE models. If something seems wrong with a transistor's parameters, examination of the datasheet may resolve the problem. For example, a BJT model that exhibited an unusually high Vbe (base-emitter voltage) had given for its parameter "N = 2.4." The Vbe was noticeably higher than indicated by the datasheet. Similar transistors of the same family by the same manufacturer had "N = 1.4." The 2.4 was a typographical error. Some manufacturers' datasheets have decimal point errors that misrepresent parameters by two orders of magnitude. Usually, such a gross error is made manifest by the data explicitly or implicitly provided on the datasheet.

For this reason and others, it is wise not to "fly blind" with SPICE. The definitions of SPICE itself and the parameters of its models are freely available on the Internet. The descriptions given are succinct. The SPICE user will be amply rewarded by the insight gained from the minimal investment required to understand SPICE and its parameters.

Another kind of understanding is helpful for getting the most from SPICE. One should try to understand the physics of the situation. For example, a manufacturer's subcircuit for a 45 GHz SiGe transistor seems to behave in a manner that violates Kirchoff's law when a reversal of emitter current exists. When the emitter current of the transistor is plotted, it is reported in the forward direction, but not in the reverse direction. Current in a resistor uniquely in series with the emitter is plotted as bidirectional. The subcircuit comprises a transistor and some diode models embedded in parasitics representing the device package. In numbering the nodes to which the subcircuit elements are connected, an error was made. Diode model terminals, obviously part of the chip, were mistakenly numbered by the device manufacturer

to be connected to external package connections. It is obvious that a few bits of metal embedded in epoxy cannot function as a diode. Examination of the subcircuit file reveals this obvious error, and simple renumbering of the diode terminals moves it electrically to the inside of the package strays and onto the chip, where it belongs.

The correction of model and subcircuit errors requires editing of same. There are other uses for editing. For example, one may copy and edit a BJT model into several related BJTs, one set perhaps representing the minimum and maximum betas of the parent device. One may similarly scale model resistances and currents to obtain sets of related devices with different current densities. Such scaling is very applicable to the mismatches encountered in differential pairs of transistors of a given type.

Models of transistors with transition frequencies approaching 1 GHz and above are often given with the model of the transistor itself in a convenient, ready-to-use form, and the package parasitics given in a separate not so easy-to-use table, tempting one to use only what is convenient. It is wise to resist that temptation. If a schematic is drawn including the BJT model alone, biased with a current, having its base and collectors connected together, the simulation usually yields a well-behaved diode drop of voltage at the collector and base. If, however, the subcircuit representing the packaged transistor is similarly treated, a violent oscillation, perhaps of 10 to 20 GHz, will likely result. A 100 Ohm resistor in series with the base will likely restore peace. Such transistors and their packages are often designed to operate properly with certain impedances on their terminals. Omission of the package from the simulation can produce erroneous expectations. If you must enter into your library numerous instances of similar transistors made by the same manufacturer and packaged in the same package, it may prove efficient to copy and rename the subcircuit of the first and replace the semiconductor models therein with the easy-to-use models pertaining to the latter subcircuit. Some datasheets are so inconvenient as to require one to construct a subcircuit from the data given. If this is needed, one may simply draw a small schematic diagram of the package with the semiconductor contained therein. The parts and nodes must then be named and numbered. The syntax for the subcircuit may be copied from a known, working, similar device, edited to substitute the names and numbers of the small schematic and the models contained therein.

BIBLIOGRAPHY

1. *Simetrix/SIMPLIS*, Catena Software Ltd. (online), available at <http://www.catena.uk.com/>.
2. *LTSpice/SwitcherCADIII*, Linear Technology, June 23, 2004 (online).
3. *Intusoft Spice Simulator*, On Semiconductor (online, CDROM), available at <http://www.onsemi.com/site/support/models>.
4. *Webench Amplifiers Simulation*, National Semiconductor (online), available at http://www.national.com/appinfo/webench/scripts/my_webench.cgi/.
5. T. Quarles, A. R. Newton, D. O. Pederson, and A. Sangiovanni-Vincentelli, *SPICE3 Version3f3 User's Manual*, University of California, May 1993 (online), available at http://soc.ajou.ac.kr/data/ppt/document%20data/Spice3/man_spice3.pdf.
6. *Agilent 85190A IC-CAP 2002 Nonlinear Device Models*, Agilent Technologies, 2002 (online), available at http://eesoftm.agilent.com/docs/iccip2002/ic_mdl/icim014.html.
7. Agilent Technologies (online), available at http://eesoftm.agilent.com/docs/iccip2002/ic_mdl/icim024.html.
8. *Sonnet Lite 9.53*, Sonnet Software Inc., June 24, 2004 (online, CDROM), available at <http://www.sonnetsoftware.com/products/lite/download.asp>.
9. *IBIS2SPICE*, Intusoft, October 23, 2003 (online), available at <http://www.intusoft.com/cgi/regnow.exe?from=utilities.htm&for=software/IBIS2SPICE.zip>.
10. *MECL System Design Handbook HB205/D*, On Semiconductor, April 3, 2003 (online), available at <http://www.onsemi.com/pub/Collateral/HB205-D.PDF>.
11. *PCB Trace Impedance Calculator*, University of Missouri-Rolla (online), available at <http://www.emclab.umr.edu/pcbtlc/index.html#structure>.
12. *PCB Impedance calculator*, SunMan Engineering Inc., 2004 (online), available at http://www.sunmantechology.com/resources/cal_cat00.shtml.

SPIRAL ANTENNAS

THOMAS P. CENCICH
DEJAN S. FILIPOVIC
University of Colorado at
Boulder
Boulder, Colorado

1. INTRODUCTION

Found in many natural phenomena (galaxies, DNA, tornado, spiderweb, ramhorns, seashells, the face of a sunflower, human fingerprints, etc.), the spiral form has intrigued mathematicians and physicists from ancient times to the modern era. Radar developments after World War II, particularly the need for broadband (from L to Ku bands) circularly polarized antennas for electronic warfare, influenced antenna engineers to look into radiating structures of the spiral shape. Although the obvious needs existed at the time, the first spiral antenna was realized by a curiosity of Edwin Turner [1]. In 1954 he wound a long wire dipole into a spiral form and connected its terminals to a two-wire feedline. The largest antenna bandwidths at that time were on the order of one octave, but the results obtained with the first spiral experiment were so encouraging that an immediate research effort was launched. Half a century down the road with hundreds of papers and patents published and awarded, and thousands of antennas already in the use, the spiral shape is still being heavily investigated by many researchers throughout the world.

Spiral antennas are inherently circularly polarized radiators with relatively constant input impedance and

radiation patterns maintained over wide frequency ranges. Bandwidth is determined by the fine precision of the feeding region (high frequencies) and overall spiral aperture size (low frequencies). Often the balun feed limits antenna performance, although very wideband feeds have been devised. Spirals can be designed in various planar or conical shapes, and the most common configurations include the equiangular [2–4] and Archimedian spirals [5]. The finite features of equiangular aperture prohibit its frequency-independent [6] operation for wavelengths greater than the antenna aperture circumference and lower than the diameter of its feeding region. Spirals operate in a so-called three-way (3W): as a fast wave, leaky wave, and traveling-wave antenna. Basically, the *traveling-wave* form of the excited currents on the spiral arms allows for its broadband performance. This wave is *fast* because of the mutual coupling between neighboring arms, and *leaks* energy while propagating on the line to produce radiation.

Spirals can be designed with different numbers of arms, but typically two or four arms are used. The number of arms and their excitation phase/amplitude difference determines both near- and the far-field antenna performance, which is frequently described using spiral modes. Until relatively recently it was considered that the number of broadband spiral modes that can be excited using an N -arm spiral is $N-1$ [7, pp. 108–109]. However, a broadband dual-mode operation of a two-arm slot spiral was demonstrated for the first time by the authors [8]. Two-arm spirals are most frequently used to operate in the first (mode 1, sum or Σ) mode, which is obtained when the arms are excited 180° out of phase. Leaking (radiation) occurs throughout the propagation path of the current traveling wave, with the most efficient radiation from the ring one wavelength in circumference. When operating in this mode the spiral directs its radiation toward broadside.

Spiral antennas can be classified (with respect to the type of transmission line supporting the excited traveling wave) in two major groups: (1) printed or wire spirals and (2) slot spirals. Although the first published records of spiral research were on slot spirals [1,3,4], the majority of publications and patenting have occurred for printed geometries [5,7,9]. The main reason is that the multiarm designs are much easier with printed spirals. Additionally, once the multioctave broadband matching techniques were developed, vertical feeds were realized and many aperture designs became feasible. Other spiral designs have also been introduced, including the spiral-mode microstrip (SMM) antennas, realized from microstrip lines wound into a spiral shape [10].

In this article, various aspects of spiral antenna engineering are discussed. Basic theory of spiral operation, characteristic geometries and shapes, and multiarm and multimode configurations, as well as theoretical and practical aspects needed for successful design and understanding of spiral antennas, are reviewed. Special attention is given to understanding the modal performance of multiarm spiral antennas and its importance to overall antenna characteristics, analysis theory, mode-forming networks, and related topics. Dual-polarized spiral designs, including inside/out-fed spirals and modulated armwidth (MAW) spirals, are also described.

2. HISTORICAL HIGHLIGHTS

The following is a brief timeline of developments in spiral antenna technology:

Year	Development	Researcher [Ref.]
1954	Two-arm spiral antenna	Turner [1]
1955	Two-arm complementary equiangular spiral	Rumsey [2]
1959	Two-arm slot spiral	Dyson [3,4]
1959	Infinite balun	Dyson [3,4]
1959	Two-arm conical spiral	Dyson [3,4]
1959	Impedances of complementary structures	Deschamps [17]
1960	Mode 2 spiral	Donnellan [13]
1960	Four-arm dual-mode spiral	Shelton [34]
1961	Explanation of spiral radiation regions	Wheeler [35]
1967	Sum-difference feed network (patent)	Shelton and Chadwick [36]
1966	Spiral mode impedances	Bruce [37]
1971	Multiple-polarization spiral (patent)	Kuo and Liu [38]
1977	Helix-loaded spiral (patent)	Grieser [39]
1979	Broadband center-fed antenna (patent)	Lamberty and Andrews [40]
1986	Modulated armwidth spiral (patent)	Ingerson [14]
1983	Spiral mode-matching transformer (patent)	Ohara et al. [41]
1986	Direction-finding antenna interface (patent)	Corzine and Mosko [7]

3. BASIC THEORY OF OPERATION

The radiating ring theory, also known as a *band theory* [5], is used to describe the theoretical principles behind operation of spiral antennas. The band theory will be demonstrated on the simplest and most commonly used spiral antenna: a two-arm, planar, wire spiral operating in the first mode (mode 1, sum or Σ). As depicted in Fig. 1, the spiral is fed from its center at ports A and A' , with ideally equal amplitudes and a 180° phase difference. When fed with an ideal balanced line, and assuming discontinuity-free aperture, the spiral will support propagation of the forward traveling wave. Mode 1 radiation will predominantly occur from a ring with approximately one guided wavelength (λ) circumference. When excited to operate in this mode, spiral currents at points B and B' , which belong to neighboring arms, will be directed the same way; specifically, they will have the same phase value. The same is the case with diametrically opposite points C and C' (see Fig. 1). The nonradiated traveling-wave currents will flow past this region, and if size of the spiral permits, radiate in the next properly phased section. This will occur at the three-guided-wavelength circumference (mode 3 for a two-arm spiral), or they will reach the end of the spiral arms, where they are either absorbed or reflected back toward

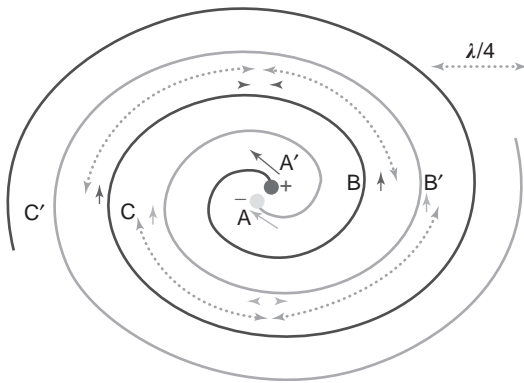


Figure 1. Mode 1 radiating region for a two-arm spiral. (This figure is available in full color at <http://www.mrw.interscience.wiley.com/erfme>.)

the spiral center. Note that if the spiral is large enough in size, the in-phase current conditions will show up at odd guided-wavelength circumferences of the spiral and higher-order modes will radiate. This condition is often referred to as *overmoding*. If attenuation of the forward-traveling wave through radiation and dissipation in the lossy termination are insufficient, the currents will reflect back from the end of the spiral and the backward-traveling waves will be generated. Since the wrap direction currents now have the opposite sense, the corresponding radiation of this current wave will be cross-polarized. The majority of backward current wave power will also leak in the odd wavelength circumference regions. Any remaining power will arrive at the spiral input ports (if perfectly matched) and show up as increased input VSWR.

This similar radiation process occurs with other modes and different numbers of arms. For example, a four-arm spiral fed in mode 1 (total phase progression of 360° at the input ports, i.e., where the feed phase vector is $\{0^\circ, 90^\circ, 180^\circ, 270^\circ\}$) will radiate higher modes of orders 5, 9, $4m + 1$, $m = 1, 2, \dots$, and so on if the spiral large enough to support those modes. When fed with 720° phase progression between input ports (where the feed phase vector is

$\{0^\circ, 180^\circ, 0^\circ, 180^\circ\}$), the spiral will operate in the second mode (mode 2, difference or Δ), and overmoding will show up at radiating rings at 6, 10, $\dots 4m + 2$, $m = 1, 2, \dots$ guided wavelength circumferences. Mode 1 and 2 regions of a four-arm spiral are shown in Fig. 2. Undesired modes sometimes occurs as a result of imperfections in the feed circuitry, loose or improperly attached cables, material impurities, and other conditions capable of alternating the natural progression of the current traveling wave.

4. SPIRAL ANTENNA TYPES, CHARACTERISTICS, AND TECHNOLOGY

4.1. Archimedean and Equiangular Spirals

The most frequently used spiral shapes are that of Archimedean and equiangular spirals in planar or conical form. These shapes in planar form are depicted in Fig. 3. The Archimedean spiral has constant armwidth and constant separation between arms through the entire aperture. The defining equation for this antenna is $r = r_0 + a\Phi$, where r_0 is the starting radius, a is the growth rate, and Φ is the progressive growth angle. The equiangular spiral has progressively increased armwidth and separation between the arms as they open toward the outside. This shape can be entirely described by angles and is the basis for the frequency-independent principles [6]. The defining equation for an equiangular spiral is $r = r_0 e^{a\Phi}$, where r_0 is starting radius, a is the growth rate and Φ is the progressive growth angle. Another term frequently used to describe tightness of the equiangular spirals is the so-called expansion factor (EXP), defined as $EXP = e^{2\pi a}$. For an expansion factor of 2, the spiral radius as well as the armwidth and separation between the arms will double for each turn.

4.2. Spiral Modes

Spiral modes were first theoretically studied in early 1960s [11,12], when radiation conditions for orthogonal radiation modes of infinite arm spirals were derived. The

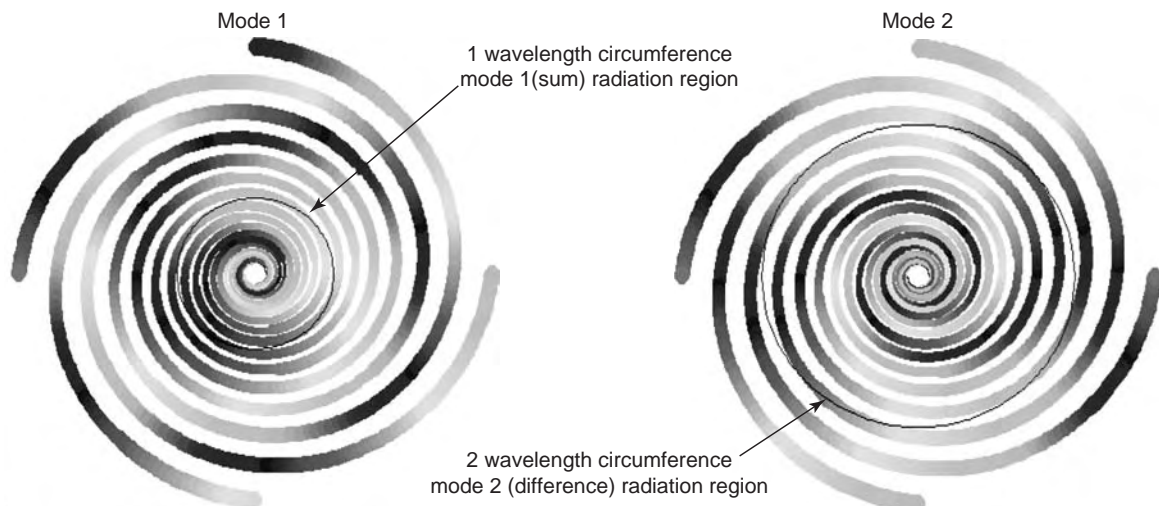


Figure 2. Four-arm spiral currents depicting mode 1 and mode 2 radiation. (This figure is available in full color at <http://www.mrw.interscience.wiley.com/erfme>.)

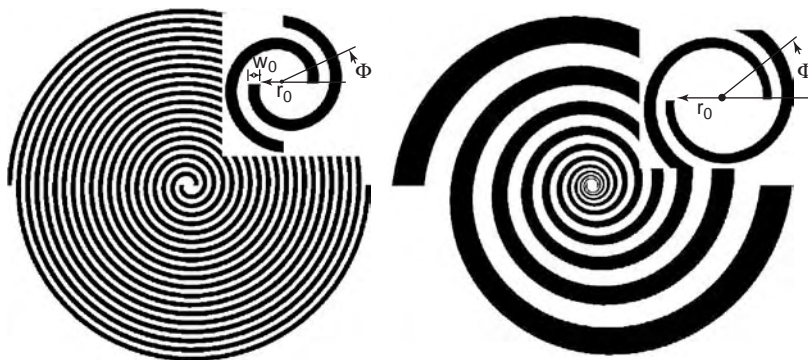


Figure 3. Two-arm Archimedean (left) and equiangular (right) spirals.

notion of spiral modes is associated with either the dominant (desired) or the higher-order (undesired) radiation conditions from a spiral aperture. Dominant modes are those for which the proper phase progressions at the feed are devised; for mode m an overall phase progression of $m \times 360^\circ$ is needed. They radiate a circularly polarized wave from the $m\lambda$ circumference rings and have a far-field phase (on a cone) progression with m cycles of 360° . Only mode 1, with both right circular polarization (RCP) and left circular polarization (LCP), has any boresight component. Other modes have an on-axis null. Higher-order modes are typically unwanted and they are formed due to existence of the nonradiated currents on the spiral aperture outside the nominal radiating ring. They can be suppressed by reducing the size of the spiral, so that its circumference is smaller than $m\lambda$, where m is the unwanted mode. Improving the efficiency of the radiation through the dominant radiating ring can reduce the negative effects of these modes, and this is recommended for spiral antenna designers. Radiated power of the higher-order modes is to blame for scalloping spiral patterns and significantly increased amplitude wobble on conical spiral pattern cuts (the parameter often termed as WoW [7,9]).

A NEC-generated numerical model of a 16-arm equiangular spiral is used to compute the radiation patterns for dominant modes supported by this antenna, and the radiation patterns are shown in Fig. 4. Each higher-order spiral mode peaks successively further from boresight.

Approximate beam peak angles and directivities for the first nine spiral modes are shown in Table 1. These values are typical, but there will be minor variations based on spiral design and frequency. To demonstrate the overmoding on a two-arm spiral antenna, a first higher-order mode, mode 3, was computed for several equiangular spirals with various growth rates. As seen in Fig. 5, tighter growth rates can be utilized to design antennas with high-cross-mode difference gains and thus improved patterns. The maximum value shown for mode 3 radiation is -18 dB below the mode 1 gain at 18 GHz, resulting in only a 2 dB azimuth ripple (WoW).

4.3. Number of Spiral Arms

The first spiral antennas were realized with two arms and operated in a single mode. Initially, they were fed by a balanced two-wire transmission line, and they were the best broadband antennas at that time (2–1 bandwidths were considered extremely wide). The interest in spirals with more than two arms was ignited by Paul Shelton in 1960. He proposed three- and four-arm spiral designs for multimode operation (see App. A in Ref. 7 for a copy of the original letter). Shelton recognized that for proper phase progression at the input ports an extra arm (reference) was needed; thus, to achieve two broadband modes, at least three arms were required. His finding heavily impacted funded research conducted in several labs that had

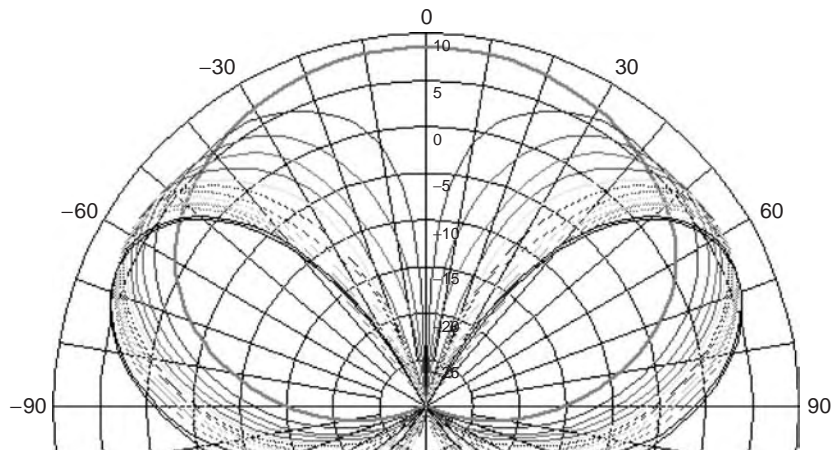


Figure 4. Radiation patterns of ideal modes from a 16-arm spiral. (This figure is available in full color at <http://www.mrw.interscience.wiley.com/erfme>.)

Table 1. Directivity and Beam Peak Position for Spiral Modes in Free Space

	Mode								
	1	2	3	4	5	6	7	8	9
Beam peak (deg)	0	40	45	49	52	54	56	58	60
Directivity (dBic)	8.5	6.3	6.3	6.3	6.3	6.3	6.3	6.3	6.3

been trying to obtain two broadband modes from two-arm spiral antennas [13]. Since then, it has been generally accepted that an N -arm spiral can radiate $N-1$ broadband modes. Therefore, the minimum number of arms for a multimode spiral is 3. A unique feature of the three-arm spiral is that the first and second modes have the same impedance. However, four arms are generally used because of the more complex feed network, often called *beamformer* or *modeformer*, for a three-arm spiral (feed phase vectors are mode 1 {0, 120, 240°} and mode 2 {0, 240, 480°}). For dual-polarized spirals, such as the modulated armwidth (MAW) spiral [14], a minimum of five arms are required for multimode operation. Because of the beamformer simplicity, six or eight arms are generally used. Finally, single-arm spirals have also been investigated [15], and some narrowband applications were found where these antennas provide satisfactory performance. However, they do not have conventional spiral behavior and will not be discussed here.

4.4. Pattern Modal Decomposition

To investigate the composition of the modes in a radiation pattern of a spiral antenna, a technique referred to as a *pattern modal decomposition* is often used [16]. The radiating modes of an N -arm spiral can be obtained by producing a phase progression between adjacent arms at the feedpoints equal to $2\pi m/N$, where $m = 1, 2, \dots$ is the desired mode of operation. To compute the modal content of the

radiated field, the phase progression is applied to the arms of the spiral through complex voltage coefficients defined by

$$V_{k,m} = V_{0m} \cdot e^{[-j2\pi m(k-1)]/N} \tag{1}$$

where $k = 1, \dots, N$ denotes the arm, V_{0m} is a constant amplitude, and j equals $\sqrt{-1}$. Equation (1) has the restriction

$$\sum_{k=1}^N V_{k,m} = 0 \tag{2}$$

for each mode. A determination of the modal fields in terms of the measured pattern

$$E_m(\theta) \cong \frac{1}{N(\phi)} \cdot \sum_{k=1}^{N\phi} V_{k,m}^* \cdot E(\theta, \phi_k) \tag{3}$$

The modal decomposition, $E_m(\theta)$, are the coefficients to the discrete Fourier series representation of $E(\theta, \phi_k)$. $N\phi$ is the number of points per conic cut (at a constant θ value), in the far-field pattern data, and the highest number of ambiguity free modes that can be resolved is equal to $(N\phi/2 - 1) \cdot E(\theta, \phi_k)$ can be measured pattern data or calculated from electromagnetic models. To demonstrate the capabilities of this technique, the beamformed patterns of an eight-arm spiral are decomposed into modes as shown in Fig. 6. Both, left- and right-handed modes supported by this structure are measured and as seen, the power in cross-polarized modes (negative ones) is much smaller than that of the copolarized fields. Also clear from this figure is that the higher-order modes “turn on” at progressively higher frequencies. A single-arm measurement without beamformer can also be decomposed into basic spiral modes, thus providing significant amount of data (i.e., all possible spiral modes) from a single-port measurement.

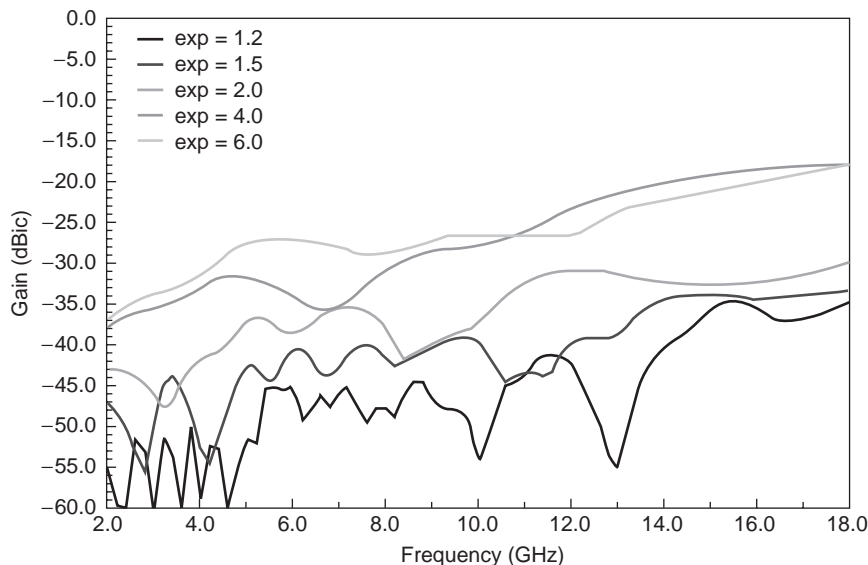


Figure 5. Mode 3 content (relative to mode 1), of a 2.4-in.-diameter two-arm equiangular spiral with various growth rates. (This figure is available in full color at <http://www.mrw.interscience.wiley.com/erfme>.)

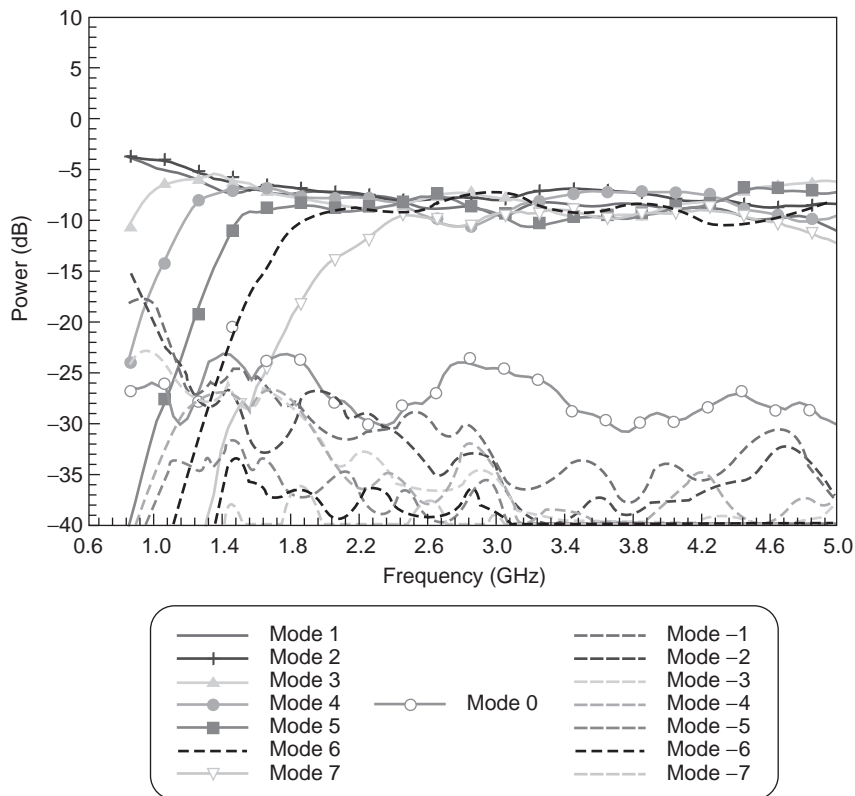


Figure 6. Power in each mode for a single arm of a 25-cm-diameter eight-arm spiral. (This figure is available in full color at <http://www.mrw.interscience.wiley.com/erfme>.)

4.5. Spiral Impedance

The input impedance to the ground for a self-complementary N -arm structure in free space is derived by Deschamps [17] and is given as

$$Z_m^{fs,comp} = \frac{\eta_0/4}{\sin\left(\frac{m \cdot \pi}{N}\right)} \tag{4}$$

where $\eta_0 = 120\pi \Omega$ is the impedance of the free space. The integer m denotes the eigenvalue or characteristic mode ($m = 1, 2, \dots, N-1$) where N is the number of arms on the structure. Modal impedances for self-complementary two-through eight-arm spirals are computed using (4), and results are shown in Table 2. As seen, only a three-arm spiral has the same modal impedances for modes 1 and 2. As discussed in the previous section, the complexity of the beamforming network for this antenna reduce its practical

application. In practice, these theoretical impedances are lowered because of the finite thickness of the metallic parts on an antenna as well as inevitable dielectric loading (used for mechanical support).

To impedance-match the spiral to a particular mode, the arm-to-gapwidth ratio (A/G) at the spiral feedpoints can be adjusted to match to the feed cable impedance (usually 50Ω). Since spirals radiate most efficiently as self-complementary structures, the noncomplementary feed region should be slowly transformed back to complementary before the first desired radiation region. As with most impedance transformers, this transition should be at least a quarter of a guided wavelength long at the lowest frequency of operation. A drawing of a tapered A/G feed region for an eight-arm spiral is shown in Fig. 7. For this antenna, to simultaneously match both modes 2 and 3 to $50\text{-}\Omega$ coax (coaxial cable), the predicted optimum A/G ratio is about 14 (see Fig. 8).

Table 2. Input Impedance (in Ω) of Free-Space Self-Complementary Spirals

Number of Arms	Spiral Mode						
	1	2	3	4	5	6	7
2	94.2	—	—	—	—	—	—
3	108.8	108.8	—	—	—	—	—
4	133.3	94.2	133.3	—	—	—	—
5	160.3	99.1	99.1	160.3	—	—	—
6	188.5	108.8	94.2	108.8	188.5	—	—
7	217.2	120.5	96.7	96.7	120.5	217.2	—
8	246.3	133.3	102.0	94.2	102.0	133.3	246.3

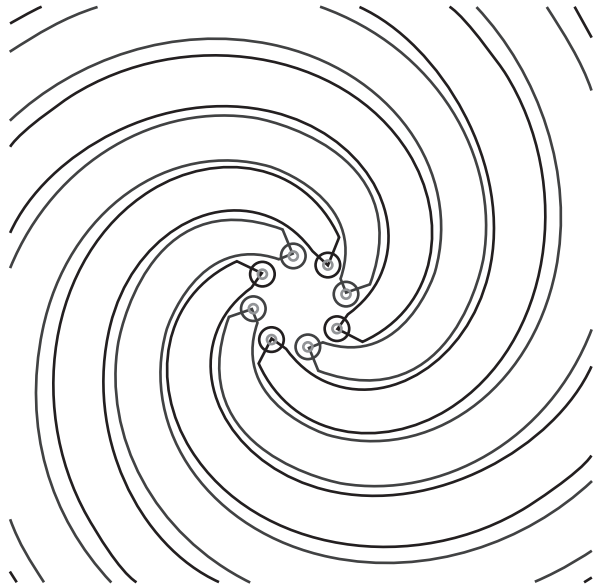


Figure 7. Impedance transformer for an eight-arm spiral. (This figure is available in full color at <http://www.mrw.interscience.wiley.com/erfme>.)

Simultaneous matching of spiral mode impedances is a challenging problem, and several methods have been devised. These methods utilize a feedline structure that is highly decoupled at the beamformer input (all input ports are 50Ω, regardless of mode), and strongly coupled at the spiral interface (impedance is dependant on input excitation). In the feedline section, near the spiral, coupling is obtained similar to that between the arms in a spiral antenna. A six-arm spiral with a coaxial type coupled feedline [18] had maximum return loss of -13, -17, and -16 dB for the first three modes. Average return loss over the 4:1 bandwidth was -18, -22, and -24 dB for these same modes.

4.6. Spiral Feeding Methods

A number of different feeding techniques have been developed for spiral antennas. Some include not only balanced-to-unbalanced (balun) transitions but also impedance

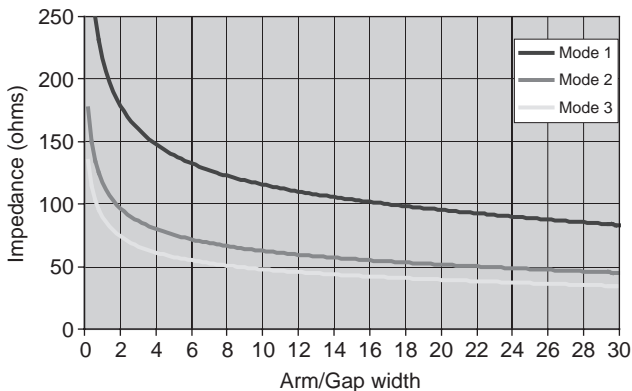


Figure 8. Theoretical input impedance versus arm-to-gapwidth ratio for modes 1, 2, and 3 of an eight-arm spiral antenna on a 0.010-in.-thick 2.1 dielectric substrate. (This figure is available in full color at <http://www.mrw.interscience.wiley.com/erfme>.)

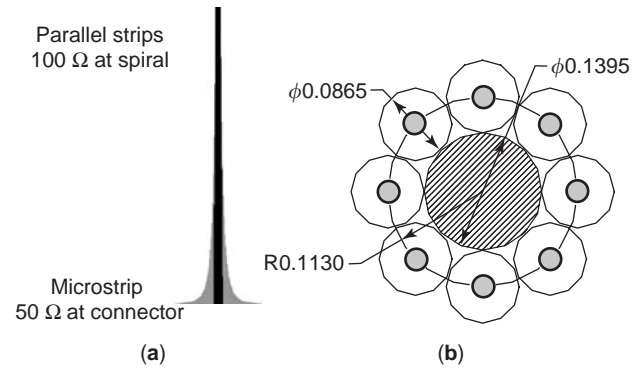


Figure 9. Microstrip tapered balun (a) and coaxial cluster feed (b). (This figure is available in full color at <http://www.mrw.interscience.wiley.com/erfme>.)

transformation. The tapered microstrip balun [19], Marchand balun [20], and 180° hybrids with coaxial feeds are commonly used for two-arm printed spirals. The tapered microstrip balun, shown in Fig. 9a, has the advantage that the spiral impedance can be matched by tapering the width of the strips. It can be designed for bandwidths several octaves wide. For more than two arms, coaxial feedlines are used; one realization is shown in Fig. 9b. The outer conductors of these coaxial cables are soldered together to form a compact coaxial cluster. To further reduce unwanted feed line radiation, absorber paint is sometimes used to coat the outer conductor of the coaxial feedline cables between the beamformer and spiral. The so-called infinite balun developed by Dyson [3] is the most commonly used feeding method for slot spirals. The outer conductor of the coaxial cables is soldered to the metallic portion of the spiral (in between the slot arms), and a transition to the slotline is provided in the center. A recently proposed dual Dyson balun for a four-arm slot spiral [21] is shown in Fig. 10. In this configuration the dummy cable (used with two-arm configurations to provide symmetry) is replaced by another feed cable, and proper mode 2 phasing is obtained using a simple power divider.

4.7. Spiral Start and End Radius Guidelines

In this section, recommendations for start and end radii of spiral apertures are provided. If the spiral start radius is too large, excessive energy will leak through the mode

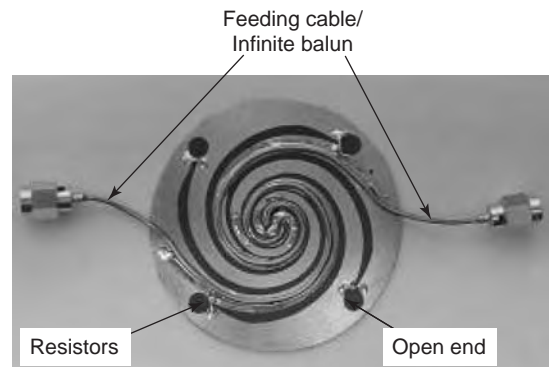


Figure 10. Directivity–gain for various modes of a four-arm equiangular spiral.

1 radiation region. Spiral size permitting, this energy will radiate in higher order modes, thus significantly contaminating its far field. The guideline given in Eq. (5) is for the spirals with relatively small growth rates ($EXP < 2$):

$$R_{start} = \frac{\lambda_{high} m_{lowest}}{6\pi} \tag{5}$$

where λ_{high} is the guided wavelength of the highest frequency of operation and m_{lowest} is the mode order of the lowest desired mode of operation. Additionally, the feed region of the spiral can interact with the feeding cables and create currents that propagate on the outside of the cables. This can severely deteriorate the radiation patterns and also provide unwanted interference. Since multiarm spirals are commonly fed with some form of coaxial clusters, special care must be exercised when the minimum spiral radius is determined. The approximate upper frequency limits for quality mode 1 radiated patterns for various coaxial cable sizes are summarized in Table 3. The outer shields of these coax clusters are usually soldered together to reduce unwanted cluster radiation.

As discussed earlier, a spiral needs to be $m\lambda$ in circumference to support the radiation of mode m . Since the radiation region is actually a finite width ring, it will be severely truncated if the circumference is only $m\lambda$. A good rule to avoid unnecessary truncation of the radiating ring of tightly wound spiral ($EXP < 2$) is expressed in (6)

$$D \geq \frac{(m_{highest} + 0.5)\lambda_{lowest}}{2\pi} \tag{6}$$

where λ_{lowest} is the guided wavelength of the lowest frequency of operation and $m_{highest}$ is the mode order of the highest desired mode of operation. For higher spiral efficiency, the numerator of Eq. (6) should be increased to $(m_{highest} + 1)\lambda_{lowest}$. Loss (directivity minus gain) versus spiral circumference for a four-arm printed equiangular spiral over an absorptive cavity is shown in Fig. 11. At least 3 dB of this loss can be attributed to absorbing the back hemisphere pattern of the spiral.

4.8. Slot Spirals

The slot spiral antenna [1,3] can be considered as a complement to the more frequently used wire or printed spirals, thus their performance is quite similar. The basic transmission line used to support the forward traveling wave is slotline-wrapped in the spiral form. To maintain input impedance of a two-arm design close to $50\ \Omega$ and allow for “clean” slot mode excitation, a metal to slot ratio is typically larger than 1. The proper mode excitation of

Table 3. Maximum Mode 1 Frequency (GHz) for Coaxial Cable Feeding Arrangements

Number of Coaxial Lines	Coaxial Cable Diameter (in.)			
	0.141	0.085	0.047	0.034
2	7	12	>18	>18
4	6	10	18	>18
6	5	8	14	>18
8	4	6	12	16

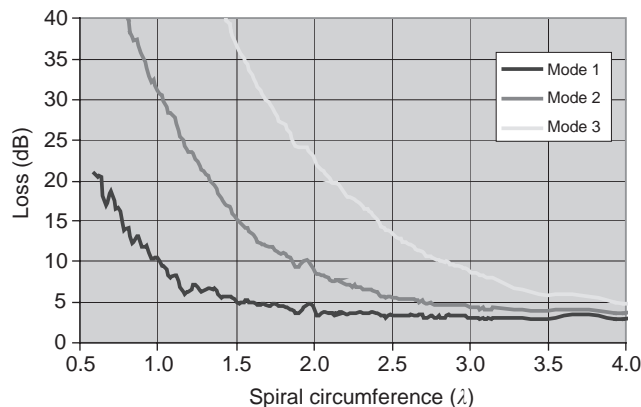


Figure 11. Four-arm slot spiral with dual Dyson balun feed. (This figure is available in full color at <http://www.mrw.interscience.wiley.com/erfme>.)

the slot spiral has been best obtained by utilizing a Dyson infinite balun [3], shown in Fig. 10. This feed provides almost perfect balance, and its bandwidth is restricted only by the spiral aperture and excitation of the higher-order coaxial cable and connector modes. The disadvantages of Dyson baluns include difficult fabrication, restriction on the spiral growth rate (thus somewhat lesser coupling in the active region), high-frequency losses, and increased scattering from the cables if the balun is placed outside the cavity. Other techniques for feeding slot spirals including the microstrip feed [22] and vertical balanced excitation, have been proposed, but significant improvements are still necessary (microstrip radiation and coupling into the slot outside the transition region, both negatively affecting the crosspol).

The design of the termination region is crucial for slot spirals. Because of the smaller attenuation through the active region (to be discussed later), the residual traveling wave on the slotline not only radiates in the higher-order modes but also undergoes strong reflections from the spiral arm ends and severely deteriorates the pattern and impedance performance at low- and midband frequencies. Excellent treatment of the slotline termination is provided in Ref. 23. A photo of the 15-cm slot spiral fed with Dyson balun and terminated with a 30 resistors per arm Klopfenstein taper [24] is shown in Fig. 12.

4.9. Beamforming

Beamformers, also known as *modeformers*, are used to provide proper phasing of the spiral arms to achieve the desired mode excitations. Phase excitations for the first two modes of four-arm RCP and LCP spirals are shown in Fig. 13. For a counterclockwise (CCW)-wound RCP spiral, phase excitation of successive spiral arms is given by $P = [-360m(n - 1)]/N$ (in degrees), where $m = 1, 2$ is the mode number, $n = 1, 2, 3, 4$ is the arm number, and $N = 4$ is the number of arms. Note that the theoretical phase distributions are identical for modes 2 RCP and LCP and that spiral’s wrap direction determines the polarization sense. The beamforming networks are typically stripline circuits built as a combination of 90° and 180° hybrids and phase



Figure 12. Two-arm slot spiral with coaxial Dyson balun feed.

shifters. An excellent treatment of spiral beamformers can be found in Ref. 7.

The modal decomposition of the mode 1 input of a 4×4 Butler matrix beamformer (shown as inset) is depicted in Fig. 14. Complex S_{N1} data are measured from the mode 1 input to each of the four outputs of the beamformer ($N = 1, 2, 3, 4$). These data are then decomposed into the four spiral modes. Both amplitude and phase imbalances contribute to the modal contamination. The top curve denotes the insertion loss for mode 1; while the remaining curves (modal isolation > 25 dB) represent the contamination level of each of undesired modes 2, 3, and 4. An ideal spiral integrated with this beamformer will have these modal pattern errors, assuming the spiral is large enough to support all the modes. Modal purity of other ports (modes 2–4) is determined in the same manner. Mode 4 will not radiate well from a four-arm spiral, but the beamformer modal contamination should be low so it will not excite direct radiation from the spiral feed structure.

4.10. Cavity Types

A planar spiral antenna radiates bidirectionally, with opposite polarization senses in the two hemispheres. For many applications unidirectional radiation is required.

The most commonly utilized approaches for eliminating the backward radiation of a planar spiral are use of either a reflective or absorber filled cavity. Absorptive cavities dissipate backward radiation using carbon filled materials in some form of honeycomb, syntactic foam or polyurethane foam, to mention just a few. A graded absorber is used to taper match the air to the heavily loaded carbon material. If the absorber is placed too close to the spiral element, additional attenuation of the forward traveling wave will occur (more than the 3 dB of expected cavity loss). To decrease the loss due to the absorptive cavity, a contact dielectric lens can be placed on the top of spiral [25]. The lens enhances direct coupling to free space and typical gain increases of 1–2 dB have been observed.

A reflective cavity or ground plane can also be used over limited bandwidths. Fields reflected off the metallic bottom undergo polarization reversal and constructively add in the far field if the bottom is a quarter-wavelength from the spiral. Overmoding will occur if the spiral size permits creation of higher-order mode active regions. Thus, an effective way for suppressing overmoding effects is to increase the number of spiral arms such that the active region of the lowest-order parasitic mode falls outside of the spiral aperture. For example, if we want to design a mode 1 spiral to operate in 2–20 GHz range with 5 cm aperture diameter and absorber free metallic backing, how many arms should we consider? Assuming ideal conditions on the spiral (zero width of the active region, no miniaturization and ideal arms termination), and knowing that the circumference of the active region for the first parasitic mode is $(N + 1)\lambda_{\text{high}}$, we can compute that the number of arms as $N \geq D\pi/\lambda_{\text{high}} - 1$; thus, at least $N = 10$ arms are needed. A more appropriate inequality for computing the number of arms for this type of spiral antenna is

$$N = \left\lfloor \frac{f_{\text{high}}}{f_{\text{low}}} (m + \Delta) \right\rfloor - m + 1 \quad (7)$$

where f_{high} and f_{low} are highest and lowest frequencies of operation, m is the desired mode of operation ($m = 1$ in the given example), $\lfloor x \rfloor$ is the integer part of x , and Δ is the safety factor depending on the width of the active region, depth of metallic backing, and established criteria for tolerable cross-modal difference (typical values for Δ are ~ 0.5 – 1). Note that multiarm designs have higher complexity and price associated primarily with the beamformer. Often the increase in antenna efficiency

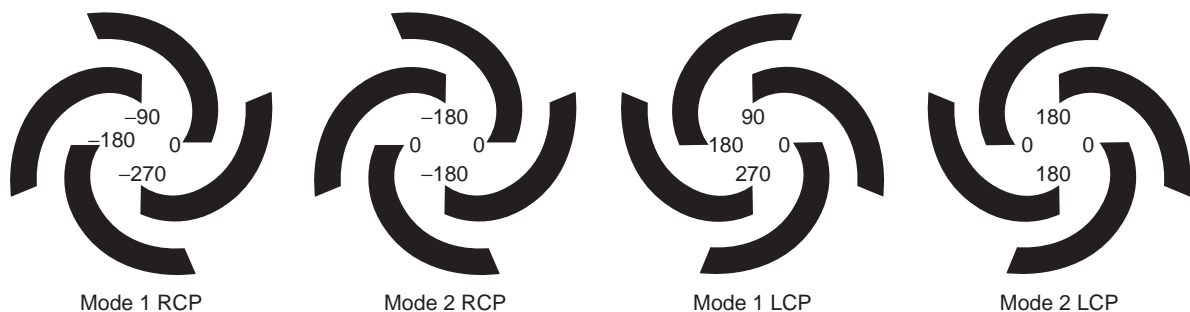


Figure 13. Four-arm phase excitations.

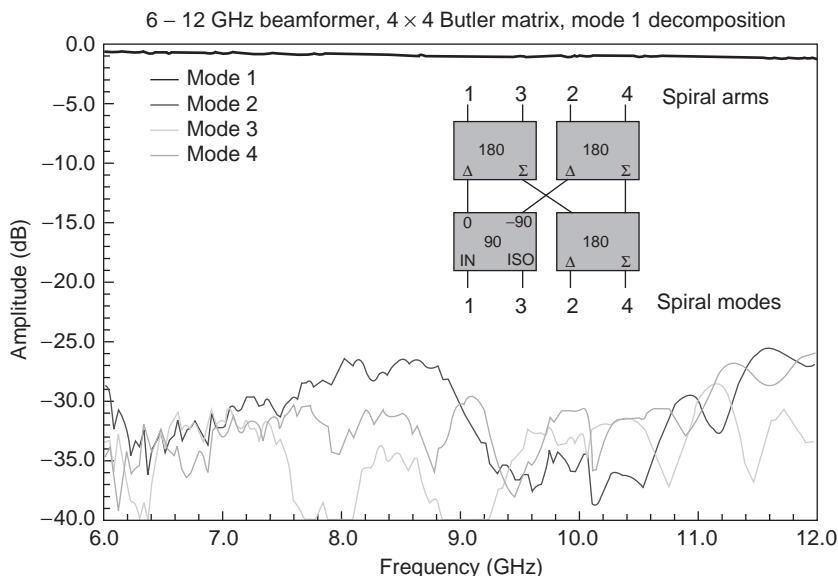


Figure 14. Modal decomposition of mode 1 for a 4 × 4 Butler matrix beamformer. (This figure is available in full color at <http://www.mrw.interscience.wiley.com/erfme>.)

does not compensate for the excessive cost (remember that the beamformer must have the same bandwidth as the antenna; thus for a 12-arm spiral, maintaining 30° phase progression between neighboring ports over a decade bandwidth is very respectable task).

Effects of the metal backing are clearly depicted in Fig. 15, where modal content of metal backed and freestanding two-arm spirals are compared. As seen, the power radiated by the higher-order modes of the freestanding spiral is significantly lower. Note that the cross-modal difference of 10 dB typically causes WoW on the order of 6 dB on wide-angle conical cuts.

A metallic backing spaced further than $\lambda/4$ will begin to degrade the boresight gain. At a height of $\lambda/2$, the mode 1

pattern will have a null on boresight and still maintain mode 1 phase characteristics. Several designs utilizing tapered absorber filled and absorber free conical cavities can be found in Ref. 23.

4.11. Spiral Cross-Polarization

Cross-polarization is determined primarily by the effectiveness of radiation through the spiral region and the quality of the spiral termination. Feedline radiation can also generate cross-polarization, particularly with slot spirals when a microstrip feed is used. A drawing of the microstrip feed of a four-arm slot spiral is shown in Fig. 16. The microstrip line not only enhances cross-polarization

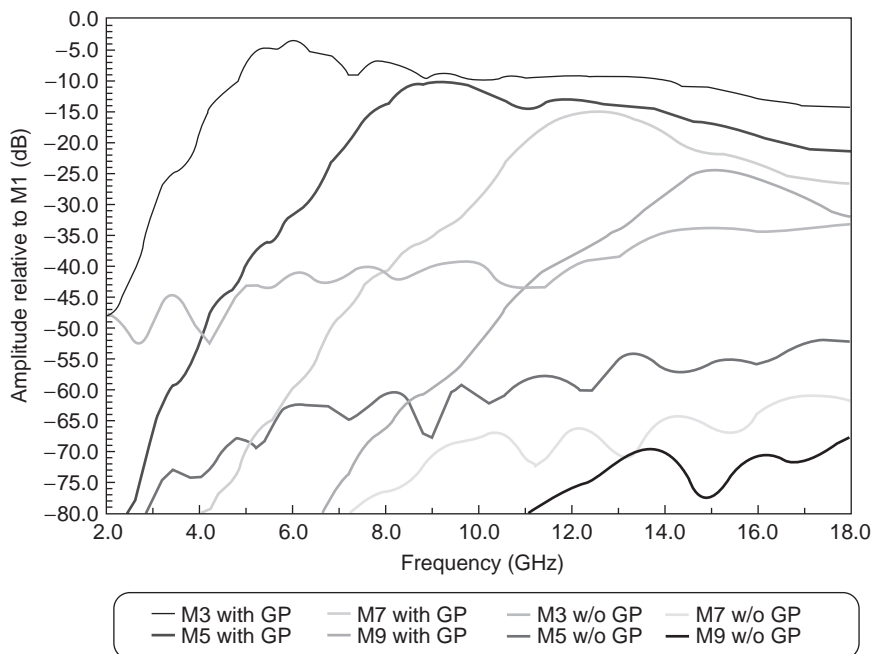


Figure 15. Modal contamination of cavity-backed and freestanding two-arm spiral. (This figure is available in full color at <http://www.mrw.interscience.wiley.com/erfme>.)

directly (by radiation), but the microstrip also couples into the slot spiral and creates an inward slotline wave (cross-polarization due to the direction of travel). In the case of coaxial clusters, a monopole type radiation with dominant vertically polarized field component (due to excited currents on the outside conductors on the cluster) creates the cross-polarization. A reflective cavity also contributes to the increased cross-polarization levels.

4.12. Attenuation through the Active Region

As discussed earlier, spirals are traveling/fast/leaky-wave antennas realized by wrapping a transmission line into a spiral shape. If a spiral is considered as a lossy transmission line, it should be designed to ensure large radiation loss for the traveling wave passing through the active region. Attenuation through the active region is usually directly correlated with the ability of a spiral antenna to efficiently radiate. The faster the wave on the spiral (i.e., the more the arms that couple), the greater is the attenuation through the active region. The radiation efficiency (and attenuation through the active region) increases when the spiral is on a thin, low-loss dielectric constant substrate. This efficiency also improves as the spiral is more tightly wound. In practice, one should allow at least one turn before the active region. Excellent discussion on this subject is given in Ref. 9.

4.13. Arm Termination Methods

When attenuation through the active region(s) is insufficient, the residual traveling wave will reach arm ends, encounter a discontinuity (open end for printed and short end for slot spirals), and reflect back. Simultaneous existence of two oppositely directed traveling waves on the spiral create conditions for standing wave, thus reducing bandwidth and increased cross-polarization. To mitigate these effects, a special care must be taken in the design of arm terminations. Various techniques for terminating the

spiral arms are devised in the past, including

- Distributed resistive loading in a form of matched taper such as exponential or Klopfenstein tapers (preferred method for slot spirals)
- Resistive termination to the spiral cavity
- $50\ \Omega$ termination in the form of a microstrip or strip-line transition (for outside ports)
- Absorber ring around spiral perimeter, either on the top (contact) or inside the cavity
- Helix loaded spiral (absorber loads the helix at low frequencies; see Fig. 17a)
- A thin (thus lossy) multiple turns wire at the spiral perimeter, sometimes painted with lossy material
- Absorber paint on the last turn (or a few turns)

The rule of thumb is that the termination section should be at least quarter of a guided wavelength long at the lowest frequency of the spiral.

4.14. Reduced-Size Spirals

A spiral is fast leaky wave antenna that performs at its best when the traveling-wave phase velocity is as high as possible. Thus slowing the wave on the spiral arms, though possible, must be exercised with extreme care. Among techniques for slowing the wave on the spiral arms are loading the spiral with higher contrast/thickness dielectric material, increasing the length of the spiral arms using modulations or a modified spiral shape, capacitive and inductive loading of the line, and so on. Although some techniques result in acceptable patterns and improved matching conditions, the antenna efficiency typically is reduced (for dielectric loading) and some pattern contamination occurs (for all methods). A good example of extended low-frequency performance is the helix-loaded spiral [7]. A 25-cm spiral demonstrated good patterns down to 250 MHz. A similar commercially available realization is shown in Fig. 17a. In Ref. 26 a 15-cm-diameter two-arm meanderline slot spiral, shown in Fig. 17b, had good performance down to 250 MHz. A very interesting property of an Archimedian spiral has been derived [27]. More specifically, if spiral miniaturization/loading technique can be characterized through an effective dielectric constant ϵ^{ef} , then the input impedance scales as $(\epsilon^{ef})^{-1/2}$, while the radiating region scales as $(\epsilon^{ef})^{-1/4}$. This result showed why the gain curves translate to the lower frequencies with much smaller miniaturization factor as in the case of resonant dipoles.

5. OTHER SPIRAL ANTENNA GEOMETRIES

Spiral antennas have been fabricated in a wide range of geometries not only for improved performance but also for the reasons of packaging, arraying, conformal and flush-mounting and so forth. For example, square spirals (see Fig. 18) allow closer packaging in an array environment and, due to longer circumference than round spirals, provide some inherent miniaturization factor ($MF=4/\pi$) for improved low frequency operation. Wiggly spirals

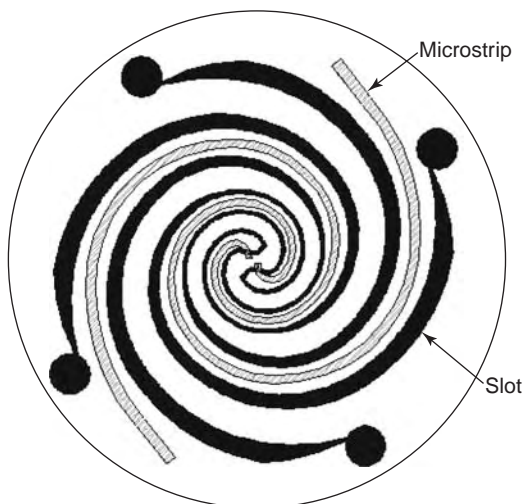
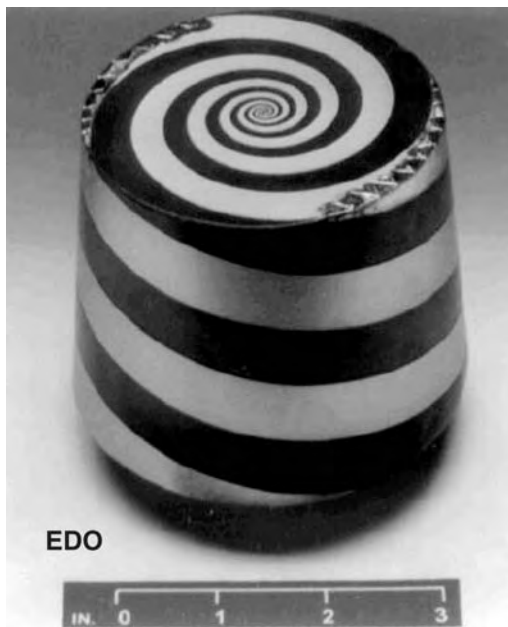


Figure 16. Sketch of a microstrip feed for a four-arm slot spiral antenna.



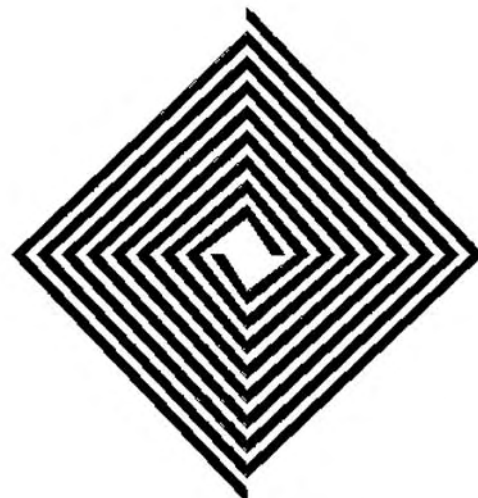
(a)



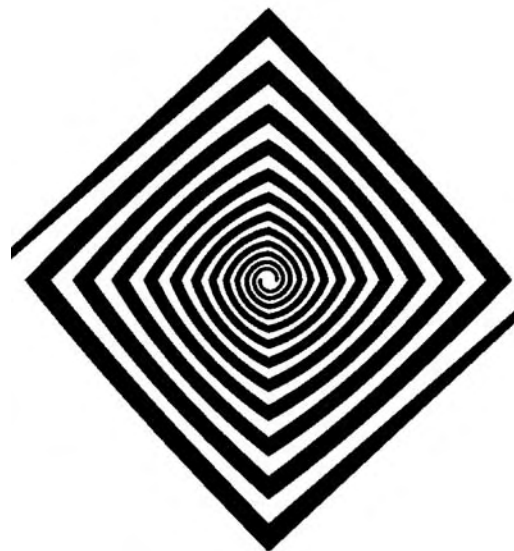
(b)

Figure 17. Helix-loaded spiral (courtesy of EDO) and meanderline slot spiral (b).

have modulations in the form of zigzag, sinusoid, or meanderline added to the spiral arms to make armlengths longer and also enhance low-frequency performance. These methods can improve low-frequency performance, but overmoding is still present at higher frequencies. The ambidextrous spiral, shown in Fig. 19, has phase centers spaced closer together, which reduces ambiguities for high-frequency interferometer applications. This antenna can be also designed in a four-aperture configuration for quadrant coverage applications. Spirals can be conformal and embedded into the leading edge of aircraft wings. Spirals have also been made on parabolic reflector surfaces.



(a)



(b)

Figure 18. Square (a) and hybrid (b) four-arm spiral designs.

5.1. Conical Spirals

To reduce the bidirectional radiation of a spiral, Dyson wrapped the spiral onto a cone [4]. This increases radiation toward the cone apex and reduces backward-traveling hemisphere radiation. Various photographs of the first conical spiral antennas can be found in Ref. 28. Printed and slot designs, including spirals with outer coaxial conductors playing the role of arms, have been realized, and they were fed with some form of Dyson balun. Dyson used his experimental brilliancy to determine that when the spiral currents reduce by 3 dB on the high-frequency end (at the top of the cone) and 15 dB (at the bottom of the cone), the radiation characteristics seldom change significantly. This finding was important for truncation of the spiral, thus simplifying fabrication while reducing the feed coaxial length, and the height of the cone. A computed front-to-back (F/B) ratios for various cone



Figure 19. Ambidextrous spiral (courtesy of BAE).

apex angles of a four-arm conical spiral are shown in Fig. 20. As the cone angle is decreased (the spiral gets taller), the backlobe is reduced and the directivity increases. Directivity also increases when the spiral is wrapped tighter since more turns cross the active region and coupling between them is enhanced.

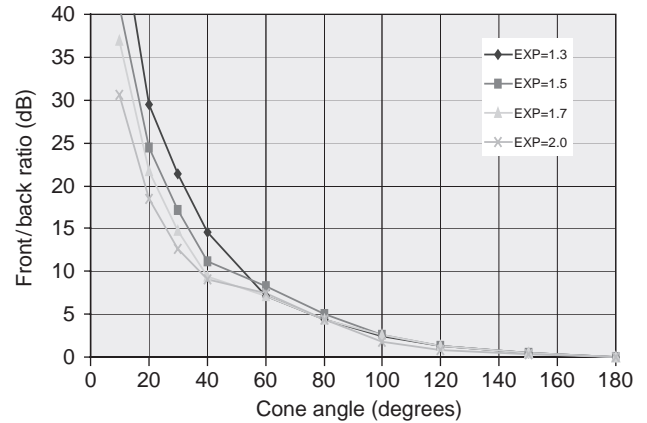
Conical spirals designed to operate in the mode 2 have been utilized for surveillance applications [29]. It was shown that the cone apex angle and other parameters of the spiral can be adjusted to peak the beam at desired angles.

5.2. Simultaneous Inside/Outside-Fed Spiral

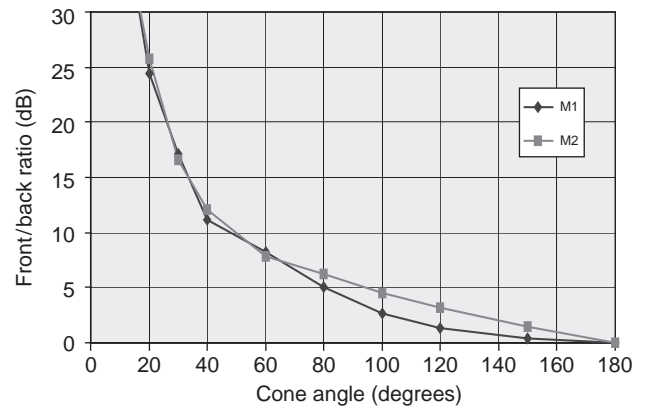
A spiral can be fed from either the inner ports or outer ports, or both simultaneously. Spiral polarization can be determined using the right-hand rule, so that a CCW wound spirals fed from the inside radiates RCP. The same spiral when fed from the outer ports radiates LCP. Simultaneous excitation can result in the broadband dual-polarized operation. Feeding from the outside has the additional advantage of ample room to provide impedance-matching networks. Stripline or microstrip transitions can be designed to match to $50\ \Omega$ and broadband match for multiple modes can be readily achieved. A major disadvantage of outside feeding is that the highest-order mode of excitation will radiate first, thus limiting the effective bandwidth of this type of antenna. To increase the bandwidth, more arms must be added, thus increasing cost (a more complicated and expensive beamforming network). A higher-order (for this structure sometimes also called “parasitic”) mode free dual-polarized bandwidth of inside/outside-fed spirals can be found using the expression

$$B \leq \frac{N + 2}{2(M_h + \pi\Delta)} \quad (8)$$

where B is the bandwidth ($f_{\text{high}}/f_{\text{low}}$), N is the minimum number of arms, M_h is the highest order mode used, and Δ is the width of the radiation band (typically $\Delta = 0.18$).



(a)



(b)

Figure 20. Conical spiral front-to-back ratio versus cone angle for various growth rates (a) and modes (b). (This figure is available in full color at <http://www.mrw.interscience.wiley.com/erfme>.)

Computed bandwidths for multiple arms and multi-mode operation of inside/outside-fed spiral are shown in Table 4. As seen, with this spiral for octave bandwidth dual-mode and dual-polarization performance, at least eight arms are required (1.95:1 bandwidth). For a four-arm spiral, the dual-mode dual-polarization bandwidth is only about 17%. By relaxing the requirements for the gain and WoW, the bandwidth will increase.

When spiral is fed from outside, a continuous conductive ring is required to keep coaxial feed outside conductors at the same potential. This can be accomplished by using a mounting flange just outside the spiral cavity. Microstrip or stripline is used to transform the impedance from $50\ \Omega$ (at the outside port connectors) to match to the spiral arm ending width. This works well for small growth rates towards the spiral perimeter. A drawing of an outer microstrip transition is shown in Fig. 21.

5.3. Modulated Armwidth (MAW) Spiral

The MAW spiral was introduced by Ingerson [14]. It was the first center-fed spiral antenna with multioctave dual-polarized operation. The MAW spiral incorporates arm impedance modulations for creation of bandstop regions. A bandstop (often called *band-reflect*) region utilizes a series of quarter wavelength high/low-impedance sections, which

Table 4. Bandwidth of a Mode-free Dual Spiral (Inside/Outside-Fed)

N	Mode		
	1	2	3
3	1.6	—	—
4	1.9	1.2	—
6	2.5	1.5	1.1
8	3.1	1.9	1.4

provide a broadband method for reflecting the spiral’s traveling wave, thus in turn generating the backward oppositely polarized wave. These reflected currents generate modes similar to the outside-fed spiral described above, but without the overmoding limitations. The MAW spiral bandwidth has the same limits as for the regular spiral; thus the highest frequency is determined by the fineness of the central region, and the lowest limit is determined by the diameter of the spiral. Because of its ability to support both forward and backward waves in dominant active regions, multimode operation can be achieved by increasing the number of arms. For a MAW spiral to operate with m useful modes, the minimum number of arms is $N = 2m + 1$. Thus for a single-mode dual-polarized operation the MAW must have at least three arms.

The 4, 6, and 8-arm MAW spirals are shown in Fig. 22. The band-reflect region is set at the circumference of $N/2$ guided wavelengths, where N is the number of arms. A four-arm spiral will reflect the currents at the 2λ circumference, thus limiting this antenna to single-mode operation, but preserving the dual circularly polarized capability. So, how does the port phasing work for the MAW spiral? Assume a clockwise-wound four-arm printed MAW spiral. This antenna (center-fed) will produce LCP mode 1 radiation for feed phasing vector $\{0^\circ, 90^\circ, 180^\circ, 270^\circ\}$. Now, if we excite the feed ports with the vector $\{0^\circ, -90^\circ, -180^\circ, -270^\circ\}$, this corresponds to the mode -1 for the LCP spiral. This phase progression is identical to the phase vector $\{0^\circ, 270^\circ, 540^\circ, 810^\circ\}$, which creates $3 \times 360^\circ$ conical far-field progression and represents the mode 3 phase vector. Thus, the forward traveling wave will pass the mode 1 radiation region without radiation, arrive at its bandstop region, undergo reflection, and become a backward-traveling wave spiraling back toward spiral center. At the 1λ circumference, phasing is correct to radiate mode -1 and a RCP mode pattern is generated.

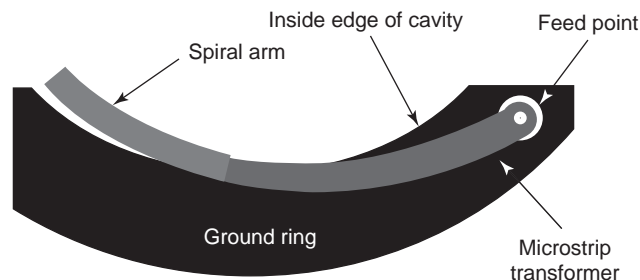


Figure 21. Outside feed of the spiral using microstrip transition.

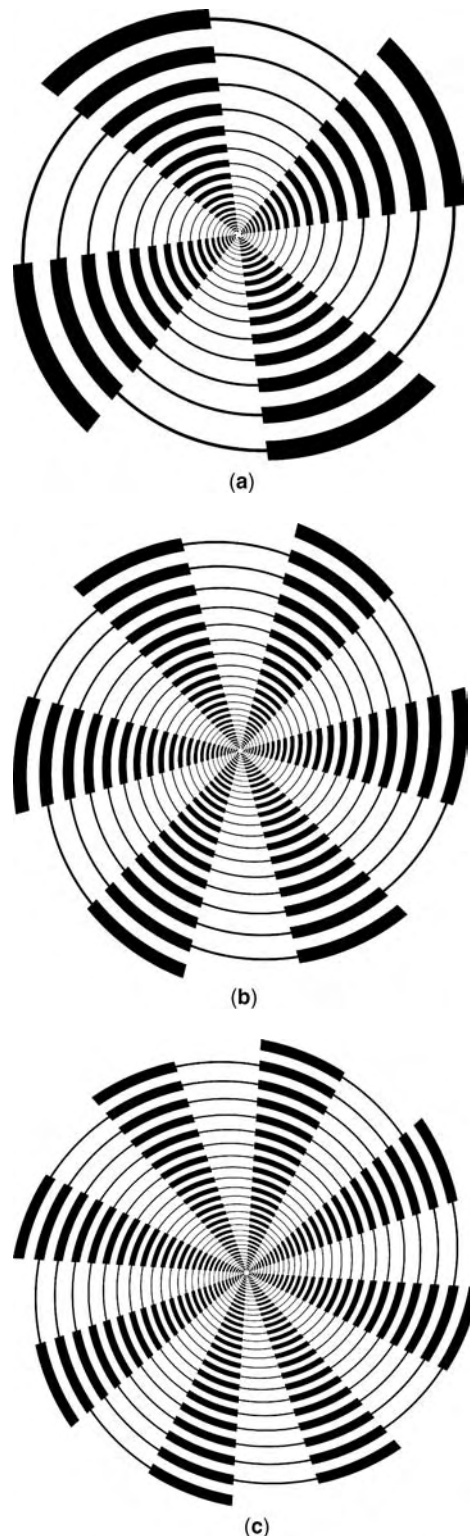


Figure 22. MAW spirals with four (a), six (b), and eight (c) arms.

The band-reflect section is not required in the low frequency region. For example, an eight-arm 25-cm-diameter spiral will have good mode 2 radiation at 800 MHz; however, the mode 4 band-reject ring need not exist since the spiral will not radiate mode -2 (m_6). Since a reflection

from the end of the arm is desired, end loading should not be used for most MAW spirals. Also, the inner band-reject region does not need to exist until it is required for rejecting the highest frequency of the lowest mode. Making this inner portion a traditional spiral, with no modulations, leaves room for impedance matching. Modulation ratios (wide section/thin section) should be in the 4:1 to 15:1 range for a good band-reflect region.

MAW spirals with multidecade bandwidths have been demonstrated. The six-arm MAW can support dual polarization for two modes, and the eight-arm MAW can support three modes. Spiral pathlengths, and therefore losses, will be higher for the reflected modes. Measured data shows only minor gain degradations for a properly designed MAW spiral. Conical MAW spirals have also been realized, but they exhibited different patterns for the reflected modes. This is because the phasing between turns is different for the reflected modes. This also applies to the conical spiral when fed from the outside.

5.4. Spiral with Narrowband Dual Polarization

A spiral antenna can radiate dual polarization over narrow bandwidths without the aid of inside/outside feeding or modulations. The reverse polarization mode can be obtained by feeding the spiral with a negative mode (for a RCP spiral). If the spiral is not large enough to radiate the energy, currents will reflect off the spiral open ends and reradiate at the one wavelength circumference ring in the opposite polarization (LCP) since they are now traveling inward (clockwise) [30]. This can be accomplished by feeding from either the inner or outer ports. For single mode and dual polarization, bandwidths (f_{hi}/f_{low}) are approximately 1.3 for four arms, 2.7 for six arms, and 4.0 for eight-arm spirals. Using this method, 8 to 10 arms will be required for a dual-polarized and dual-mode spiral over an octave bandwidth, for typical gain and WoW requirements.

5.5. Reflector Feed Spirals

Since spirals have approximately constant beamwidths, they make ideal reflector feeds if broadband circular polarization is required. For planar absorptive cavity spirals, a reflector F/D of approximately 0.35 is optimal for mode 1. The spiral phase center is relatively stable across wide frequency ranges and is slightly in front of the spiral element, outside of the cavity, for this configuration. Figure 23 shows amplitude taper loss (ATL) and spillover loss (SPL) versus F/D , for both modes 1 and 2, using measured patterns of a four-arm spiral feeding a center-fed reflector. Maximum mode 1 aperture efficiency is at a 0.42 F/D . Mode 2 is most efficient at a 0.37 F/D . Simultaneous illumination is best at $F/D = 0.40$. Note the ATL + SPL curves are relatively flat and optimal F/D may be chosen on the basis of other factors such as maximum mode 1 gain or lower sidelobes. With a reflective cavity, the spiral directivity increases and the optimum F/D ratios increase to 0.45 for mode 1, 0.38 for mode 2, and 0.45 for simultaneous illumination of both modes.

Conical spirals have also been used as reflector feeds. The major advantage of conical spirals is improved efficiency (due to backlobe reduction). A disadvantage is that

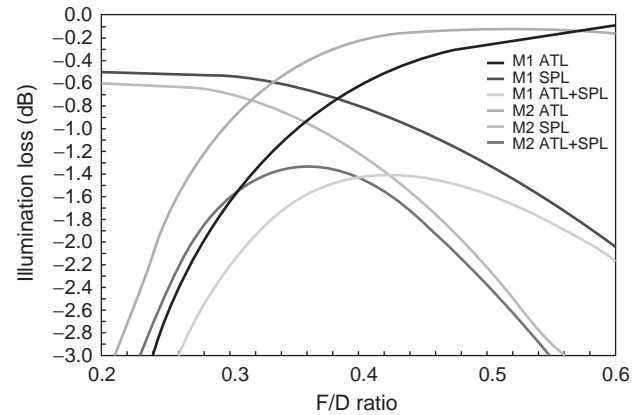


Figure 23. Aperture losses for a center-fed reflector with a four-arm spiral feed. (This figure is available in full color at <http://www.mrw.interscience.wiley.com/erfme>.)

the phase center moves with frequency resulting in a quadratic phase loss with frequency for a symmetric reflector. For this reason, the conical spiral can have optimal performance at only one frequency. Also, phase centers are not collocated for multiple modes at the same frequency. When used in an offset reflector, a conical feed will have beam squint versus frequency due to phase center movement. Even with these limitations, conical spirals can be efficient feeds over broad bandwidths. Illumination losses of less than 1.5 dB for 10–1 bandwidths using cone angles ($2\theta_0$) of 20 to 40° are demonstrated in Ref. 31.

6. NUMERICAL MODELING

The complexity of the spiral geometry and absence of appropriate computational tools (including methods for numerical electromagnetics) in the 1950s limited the study of spiral antennas to primarily experimental efforts. The first theoretical analysis of a spiral antenna was published in 1960 [32], where the spiral geometry was approximated by semicircles, and the vector potentials were computed by employing the appropriate Green function. Although this was a simplified model, the physical understanding of the spiral's operation, including the low- and high-frequency limits, were obtained from this analysis. The availability of faster computers and the introduction of rigorous analysis methods for solving integral equations (numerical methods) were critical for comprehensive theoretical investigation of spiral antennas. Nevertheless, while integral equation methods have traditionally been used for freestanding printed and wire spirals, and non-cavity-backed slot spirals partial-differential equation and volume modeling methods are more appropriate for the cavity-backed spirals and spirals on a finite substrate. The finite element-boundary integral method (FE-BI), developed especially for the cavity-backed Archimedian slot spirals [33], was introduced more recently. This method combines triangular and quadrilateral prismatic finite elements to obtain the best representation of the electric fields inside an extremely narrow slotline. This field modeling secures the convergence of the method for geometries that contain a number of small details, along with the

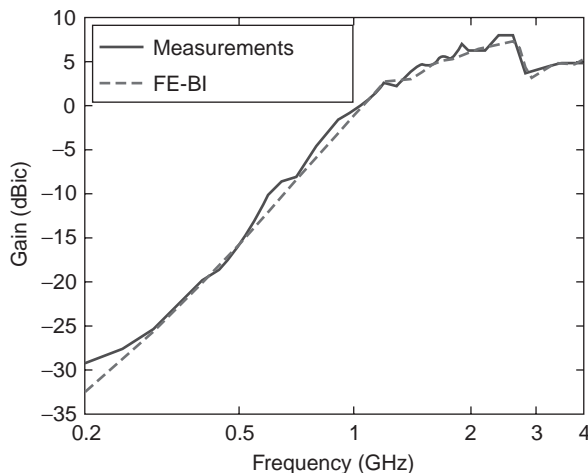


Figure 24. Measured versus computed (FE-BI) broadside gain of a two-arm slot spiral. (This figure is available in full color at <http://www.mrw.interscience.wiley.com/erfme>.)

inherent capability of a FEM for modeling of inhomogeneous materials inside the cavity [27]. An example depicting the capability of this technique is given in Fig. 24, where the computed gain of a cavity-backed slot spiral is compared with measurement. Excellent agreement between measurements and simulations over a wide dynamic range of >40 dB, predictions of the TM_{110} cavity resonance and antenna response after the resonance, fully validate this simulation tool. The slot spiral parameters were $d = 14.9$ cm, $D = 1.27$ cm, $w = 0.0762$ cm, $t = 0.0508$ cm, $\epsilon_r = 3.38$, and 60 resistors per arm Klopfenstein taper [23]. For more detailed discussion and reference list regarding spiral analysis, see Ref. 27.

Analysis of spiral antennas have also been performed using commercially available numerical tools, including MoM (method-of-moments) codes such as NEC, FEKO, Ansoft Designer, and IE3D, etc., as well as finite-element software tools such as HFSS and extended finite-difference time-domain XFDTD.

BIBLIOGRAPHY

1. E. M. Turner, *Spiral Slot Antenna*, U.S. Patent 2,863,145 (1958).
2. V. H. Rumsey, Frequency independent antennas, *IRE Natl. Convent. Rec.* **1**:114–118 (1957).
3. J. D. Dyson, The equiangular spiral antenna, *IRE Trans. Anten. Propag.* **AP-7**:181–187 (1959).
4. J. D. Dyson, The unidirectional equiangular spiral antenna, *IRE Trans. Anten. Propag.* **AP-7**:329–334 (1959).
5. J. Kaiser, The Archimedean two-wire spiral antenna, *IRE Trans. Anten. Propag.* **AP-8**:312–323 (1960).
6. V. H. Rumsey, *Frequency-Independent Antennas*, Academic Press, New York, 1966.
7. R. Corzine and J. Mosko, *Four-Arm Spiral Antennas*, Artech House, Norwood, MA, 1990.
8. D. S. Filipovic, M. Lukic, Q. Mathews, and T. P. Cencich, Broadband dual-mode performance of a two arm spiral, *Proc. Annual Symp. IEEE AP/URSI*, 2004.
9. R. H. DuHammel and J. P. Scherer, Frequency-independent antennas, in *Antenna Engineering Handbook*, McGraw-Hill, New York, 1993, Chap. 14.
10. J. Wang and V. Tripp, Design of multi-octave spiral-mode microstrip antennas, *IEEE Trans. Anten. Propag.* **39**:332–335 (1991).
11. B. Cheo, V. Rumsey, and W. Welch, A solution to the frequency-independent antenna problem, *IRE Trans. Anten. Propag.* **AP-9**:527–534 (1961).
12. R. Sivan-Sussman, Various modes of the equiangular spiral antenna, *IEEE Trans. Anten. Propag.* **AP-11**:533–539 (1963).
13. J. Donnellan, Second-mode operation of the spiral antenna, *IRE Trans. Anten. Propag.* **AP-8**: 637 (1960).
14. P. G. Ingerson, Modulated arm width (MAW) log-spiral antennas, *Proc. 20th Annual Symp.*, USAF Antenna Research and Development Program, 1970.
15. H. Nakano, Y. Shinma, and J. Yamauchi, A monofilar spiral antenna and its array above a ground plane-formation of a circularly polarized fan beam, *IEEE Trans. Anten. Propag.* **45**:1506–1511 (1997).
16. T. Milligan, Parameters of multiple-arm spiral antenna from single-arm measurements, *IEEE Anten. Propag. Mag.* **40**: 65–69 (1998).
17. G. Deschamps, Impedance properties of complementary multiterminal planar structures, *IRE Trans. Anten. Propag.* **AP-7**:371–378 (1959).
18. T. P. Cencich, and D. Walcher, *Simultaneous Mode Matching Feedline*, U.S. Patent 6,549,175 (2003).
19. D. F. Bowman, Impedance matching and broadbanding, in *Antenna Engineering Handbook*, McGraw-Hill, New York, 1984, Chap. 43.
20. N. Marchand, Transmission lines conversion transformer, *Electronics* **17**:142–145 (1944).
21. N. Stutzke and D. S. Filipovic, Four-arm 2nd mode equiangular slot spiral antenna with infinite balun feed, *Proc. IA-EST Antenna Radiation Propagation*, 2004.
22. M. W. Nurnberger and J. L. Volakis, A new planar feed for slot spiral antennas, *IEEE Trans. Anten. Propag.* **44**:130–131 (1996).
23. M. W. Nurnberger, *The Broadband, Shallow, Reflecting Cavity-Backed Slot Spiral Antenna*, Ph.D. thesis, Univ. Michigan, Ann Arbor, 2002.
24. R. Klopfenstein, A transmission line taper of improved design, *Proc. IRE* **44**:31–35 (1956).
25. J. Craven, Dielectric lens for second-mode spiral, *IRE Trans. Anten. Propag.* **AP-9**:499 (1961).
26. D. S. Filipovic and J. L. Volakis, A broadband meanderline slot spiral antenna, *IEE Proc. Microwave Anten. Propag.* **149**:98–105 (2002).
27. D. S. Filipovic, *Multi-functional Slot Spiral Based Antennas for Airborne and Automotive Applications*, Ph.D. thesis, Univ. Michigan, Ann Arbor, 2002.
28. Antennas on the Web, picture archive: Illinois Historic Archive, Univ. Illinois, <http://www.ece.uiuc.edu/pubs/antenna/> (July 8, 2004).
29. J. D. Dyson and P. E. Mayes, New circularly-polarized frequency-independent antennas with conical beam or omnidirectional patterns, *IRE Trans. Anten. Propag.* **AP-8**:334–342 (1960).
30. O. K. Kim and J. D. Dyson, A log spiral with selectable polarization, *IEEE Trans. Anten. Propag.* **AP-19**:675–677 (1971).

31. T. A. Milligan, *Modern Antenna Design*, 2nd ed., Wiley, New York, 2004.
32. W. Curtis, Spiral antennas, *IRE Trans. Anten. Propag.* **AP-8**:298–306 (1960).
33. T. Ozdemir, J. L. Volakis, and M. W. Nurnberber, Analysis of thin multioctave cavity-backed slot spiral antennas, *IEEE Proc. Microwave Anten. Propag.* **146**:447–454 (1999).
34. J. P. Shelton, Four Arm Spiral Direction Finding System, 1960, in Appendix A of *Four-Arm Spiral Antennas* I. R. Corzine, J. Mosko 1st Edition, Artech House, 1990.
35. M. S. Wheeler, On the radiation from several regions in spiral antennas, *IRE Trans. Antennas Propag.*, **AP-9**:100–102 (1961).
36. Chadwick and Shelton, *Sum-Difference Feed Network*, U.S. Patent 3,346,861 Oct 1967.
37. J. D. Bruce, The Impedances of Arbitrarily Fed Planar Self-Complimentary Structures, U.S. Naval Ordnance Test Station, China Lake, Calif., July 1966 (NAVWEPS Report 8975).
38. Kuo and Liu, *Multiple Polarization Spiral Antenna*, U.S. Patent 3,562,756 (Feb. 1971).
39. Greiser, *Helix-loaded Spiral Antenna*, U.S. Patent 4,012,744 (March 1977).
40. Lamberty and Andrews, *Broadband Center Fed Spiral Antenna*, U.S. Patent 4,243,993 (Jan, 1981).
41. O'Hara, et al., *Matching Section for Multi-arm Spiral Antennas*, U.S. Patent 4,396,921 (Aug. 1983).

SQUIDS

ROBERT L. FAGALY
Tristan Technologies

Since the development of the Superconducting QUantum Interference Device (SQUID) in the late 1960s and its commercial introduction in 1970, SQUID-based instruments have proven to be the most sensitive measurement devices not only for magnetization measurements but also for several other electrical measurements. Their device noise (well below 1 mK), frequency response to dc, and low drift permit electromagnetic measurements at levels far below those of conventional techniques.

SQUID instruments consist of a SQUID amplifier or sensor and a detection circuit that transforms the signal of interest into a magnetic flux that is detected by the SQUID sensor. Associated control electronics transform this signal into a room temperature voltage that is available for additional signal processing if needed. The SQUID amplifier and the detection coils are superconducting devices. Thus some type of refrigerant (e.g., liquid helium or nitrogen) or refrigeration device is needed to maintain the SQUID (and detection coil) in the superconducting state. Additional signal-conditioning electronics may be needed to improve the signal-to-noise ratio.

1. THE JOSEPHSON EFFECT

SQUIDS combine two phenomena—flux quantization where the flux $\phi = \mathbf{B} \cdot \mathbf{A}$ penetrating a superconducting loop is quantized in steps of $1 \phi_0 = h/2e = 2.068 \times 10^{-15}$

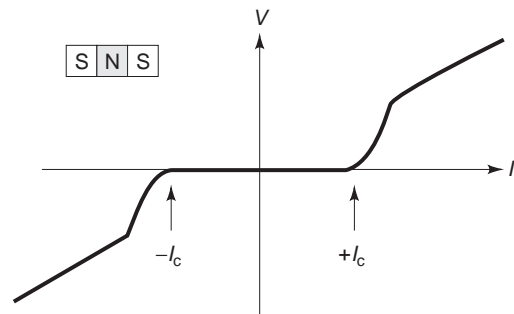


Figure 1. *IV* curve of a Josephson tunnel junction.

I_C , and the Josephson effect [1] (electrons tunneling from one superconducting region to another separated by a resistive barrier). Currents smaller than a critical current I_C , can penetrate the barrier (usually called a weak link) with no voltage drop (Fig. 1).

A typical weak link might have a critical current of $10 \mu\text{A}$. If the loop has a diameter of 2 mm, this is equivalent to several flux quanta. In a superconductor loop interrupted by a weak link Josephson junction, magnetic flux threading through a superconducting loop sets up a current in the loop. As long as the current is below the critical current, the complete loop behaves as if it was superconducting. Any changes in the magnetic flux threading through the loop induce a shielding current that generates a small magnetic field to oppose the change in magnetic flux. The weak link can be a region in which the current flowing is greater than the current needed to drive the superconductor normal I_C . Details on the Josephson effect and the theory of SQUIDS can be found in Refs. 2, 3, and 4.

2. SQUID OPERATION

SQUIDS are operated as either RF (radiofrequency) or dc SQUIDS. The prefix RF or dc refers to whether the Josephson junction(s) is biased with an alternating current (RF) or a dc current.

2.1. The RF SQUID

For the RF SQUID [5], flux is normally (inductively) coupled into a SQUID loop containing a single Josephson junction via an input coil (which connects the SQUID to the experiment) and an RF coil that is part of a high- Q resonant circuit to read out current changes due to induced flux in the SQUID loop (Fig. 2).

This tuned circuit is driven by a constant current RF oscillator that is weakly coupled to the SQUID loop. The detected RF output is found to be the periodic function (Fig. 3).

One way to measure the change in input coil current is to simply count the number of periods it produces in the detected RF output. A more common mode of operation is a feedback scheme (Fig. 2), which locks in on either a peak or a valley in the triangle pattern output from the RF peak detector. A feedback flux is applied to the SQUID through the RF coil that just cancels the change in flux from the input coil.

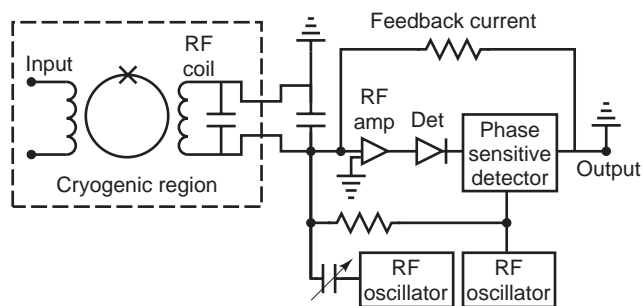


Figure 2. Block diagram of SQUID input and electronics for locked-loop operation.

2.2. The dc SQUID

The dc SQUID (Fig. 4) differs from the RF SQUID in the manner of biasing the Josephson junction (dc rather than ac) and the number of junctions (two rather than one).

The dc SQUID is biased with a dc current approximately equal to twice I_C and develops a dc voltage across the junctions. A change in the flux penetrating the SQUID loop enhances the current through one Josephson junction and reduces the current through the other, driving one junction normally and the other superconducting. This asymmetry, which is periodic in ϕ_0 , provides a feedback current that nulls the flux penetrating the SQUID loop. Although total flux within the SQUID loop is in multiples of ϕ_0 , by measuring the voltage drop across the feedback resistor, resolutions of external flux changes at the 10^{-6} level can be achieved. The linearity of flux-locked loop SQUID systems are typically better than 1 ppm. Like the RF SQUID, this feedback current (presented as a voltage at the output) is a direct measure of changes in flux applied to the SQUID.

2.2.1. Control Electronics. The system output voltage is the voltage drop across the feedback resistor in a negative feedback loop controlled by the SQUID electronics. The feedback signal is generated in response to changes in the output signal of the SQUID sensor. The output of the SQUID sensor is periodic in the field coupled into the SQUID loop. Negative feedback (similar to a phase-locked loop technique) maintains the system operating point at a particular (and arbitrary) flux quantum. When operated in this mode, the system is in a flux-locked loop.

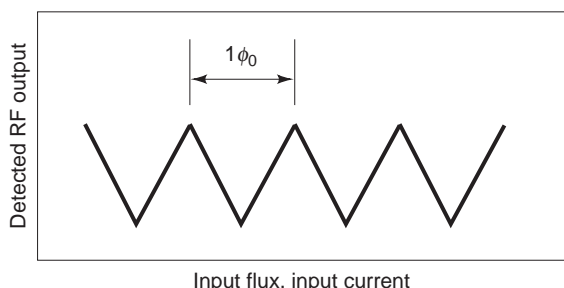


Figure 3. Triangle pattern showing detected output voltage as a function of flux in the SQUID.

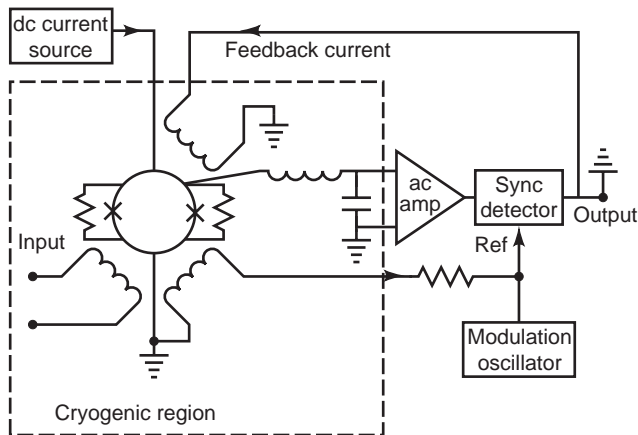


Figure 4. Block diagram of a typical dc SQUID.

One important factor of SQUID design is such that the feedback electronics be able to follow changes in the shielding currents. If the shielding current changes so fast that the flux in the SQUID loop changes by more than $\phi_0/2$, it is possible that the feedback electronics will lag behind the rapidly changing flux. When the electronics finally “catch up,” they can lock on an operating point (Fig. 3) different from the original. In this case, the SQUID has “lost lock” because the SQUID has exceeded the maximum slew rate of the electronics. This places an upper limit on the bandwidth of the system. The typical bandwidth of commercially available SQUID systems is dc to 50 + kHz. Custom electronics have been built extending bandwidths above 5 MHz. Typical slew rates for SQUIDs are in the range of 10^5 – $10^6 \phi_0/s$.

Even though one may not need or want to observe rapidly changing signals, situations may arise when ambient noise (e.g., 60 Hz) may determine the slew rate requirements of the system. To recover a signal from such interference, the system must be able to track all signals present at the input, including the noise. When system response is sped up to handle very fast signals, sensitivity to RF interference and spurious transients is also increased. Because the ability to remain locked while subjected to strong electrical transients is greatest when the maximum slew rate is limited (slow), whereas ability to track rapidly varying signals is greatest when the maximum slew rate is greatest (fast), it is desirable to be able to match the maximum slew-rate capability to the measuring situation. As a matter of convenience, many commercial SQUID systems offer user-selectable slew rates along with high-pass and low-pass filters for noise reduction.

2.3. Sensitivity

Because of the varying input impedances of SQUID sensors, the sensitivity of SQUID devices is best discussed in terms of the energy sensitivity:

$$E_N = L_i I_N^2 = \frac{\phi_N^2}{L_i} \tag{1}$$

where L_i is the input inductance of the device, I_N is the current noise, and ϕ_N is the flux sensitivity. E_N is often expressed in terms of Planck's constant $h = 6.6 \times 10^{-34}$ J/Hz.

The major limiting factor in the noise of an RF SQUID is the bias frequency f_0 used to excite the tank circuit and that RF SQUID noise is proportional to $1/\sqrt{f_0}$ [6]. As f_0 increases, the complexity of the electronics also tends to increase.

The minimum noise energy for a dc SQUID is given by [7]

$$E_N = k_B T \sqrt{L_{\text{loop}} C} \quad (2)$$

where k_B is Boltzmann's constant, L_1 is the inductance of the SQUID loop, and C is the capacitance of the junction. Substituting appropriate numbers indicates that the minimum noise energy E_N for a dc SQUID is on the order of $h/2$. Devices with sensitivities of $\sim h$ have been constructed. These extremely low noise levels are achieved by limiting dynamic range and avoiding feedback. The need for practical (useful) devices requires that feedback be used and that the SQUID have a reasonable dynamic range. Commercially available RF SQUIDS have noise levels of 10^{-29} J/Hz; commercial dc SQUIDS are typically $\sim 10^{-31}$ J/Hz.

In addition to the frequency independent (white) component of system noise, a low-frequency contribution exists that increases as the frequency decreases. The onset of this $1/f$ noise can be dependent on the ambient magnetic field when the SQUID sensor is cooled. When cooled in the earth's magnetic field, the point at which the $1/f$ noise equals the white (frequency independent) noise is typically ~ 1 Hz. Cooling the SQUID sensor in low ambient magnetic fields (less than $1 \mu\text{T}$) may improve the $1/f$ performance by as much as an order of magnitude. A large contribution to this noise in some dc SQUIDS can arise from the presence of the dc current bias. By chopping the dc bias in combination with the conventional flux modulation techniques, it is possible to reduce this added $1/f$ noise. This ac bias reversal approach [8] separates the original signal waveform from the noise associated with the dc bias and can reduce $1/f$ noise at very low frequencies.

The major difference between RF and dc SQUIDS is that the dc SQUID offers lower noise. From a historical viewpoint, although the dc SQUID was the first type of SQUID magnetometer made, the early development was with RF SQUIDS because of the difficulty in fabricating two nearly identical Josephson junctions in a single device. With modern thin film fabrication techniques and improvements in control electronics design, the dc SQUID offers clear advantages over the RF SQUID for many applications.

2.4. Limitations on SQUID Technology

It is important to bear in mind several fundamental limitations in designing SQUID-based measurement systems and data reduction algorithms.

1. A fundamental limitation of SQUIDS is that they are sensitive to *relative* (field or current) changes only. This is a consequence of the fact that the output voltage of a SQUID is a periodic function (Fig. 3) of the flux penetrating the SQUID loop. The SQUID is "flux locked" on an arbitrary maximum (or minimum) on the $V - \Phi$ curve, and the SQUID output is sensitive to flux changes relative to this lock point.
2. A second limitation exists on the system bandwidth. Although the SQUID has an intrinsic bandwidth of several gigahertz, when operated with standard flux-locked loop electronics using ac flux modulation, the maximum bandwidth is typically 50 kHz to 100 kHz. Another limitation is the presence of $1/f$ noise. High Temperature Superconducting (HTS) SQUIDS [and early commercial Low Temperature Superconducting (LTS) dc SQUIDS] exhibit excess $1/f$ noise due to critical current fluctuations of the Josephson junctions. This noise can be reduced by reversing the dc bias voltage (ac bias). This limits the maximum bandwidths less than half the bias reversal frequency. If the bias reversal frequency is too high, noise can be induced due to voltage spikes in the transformer coupled preamplifier input circuit. Because of this, the maximum bandwidth of present day HTS SQUIDS is ~ 30 kHz. If megahertz bandwidths are required, the ac bias is not used; however, there will be excess noise below 1 kHz.
3. Finally, SQUID magnetometers are vector magnetometers. For a pure magnetometer operating in the earth's magnetic field, a 180° rotation will sweep out a total field change of $\sim 100 \mu\text{T}$. If the magnetometer has a sensitivity of $10 \text{ fT}/\sqrt{\text{Hz}}$, tracking the total field change requires a dynamic range of $100 \mu\text{T}/10 \text{ fT} = 200 \text{ dB}$, well beyond the capabilities of current electronics. In addition, the rotational speed must not cause the current flowing through the SQUID sensor to exceed its slew rate limitations. An ideal gradiometer is insensitive to a uniform field and would not suffer this dynamic range limitation.

3. INPUT CIRCUITS

Whether an RF or dc SQUID, a SQUID system can be considered as a black box that acts like a current- (or flux-) to-voltage amplifier with extremely high gain. In addition, it offers extremely low noise, high dynamic range ($> 140 \text{ dB}$), excellent linearity ($> 1 : 10^7$), and a wide bandwidth that can extend down to dc.

Today, SQUIDS are fabricated as planar devices. In this configuration, the superconducting loop, Josephson junctions, and coils (input, feedback, and modulation) are patterned on the same device. Multilayer deposition techniques are used (primarily in LTS devices), and coils are normally in the form of a square washer. The planar configuration leads to quite small devices, occupying only a few cubic millimeters compared with $5 + \text{cm}^3$ ($1.2 \text{ cm diam.} \times 5 \text{ cm}$) for older toroidal RF SQUIDS [9]. Another advantage of the planar device is that it is

possible to have the detection coils as part of the SQUID sensor, eliminating the need for separate (three-dimensional) detection coils. Such an integrated sensor has the potential to reduce the complexity of multichannel systems significantly.

Although it is possible to couple magnetic flux directly into the SQUID loop, environmental noise considerations (see Fig. 9) make this difficult, if not impossible, in an unshielded environment. In addition, the area of a typical SQUID loop is small ($< 0.1 \text{ mm}^2$), and its resulting sensitivity to external flux changes ($\Delta\Phi = A \cdot \Delta B$) is also small. Although a larger loop diameter would increase the SQUID's sensitivity to external flux, it would also make it much more susceptible to environmental noise. For this reason, external flux is normally inductively coupled to the SQUID loop by a flux transformer.

Conceptually, the easiest input circuit to consider for detecting changes in magnetic fields is that of a SQUID sensor connected to a simple superconducting coil (Fig. 5).

Because the total flux in a superconducting loop is conserved, any change in external field through the signal coil will induce a current in the flux transformer that must satisfy

$$\Delta\Phi = NA\Delta B = (L_{\text{coil}} + L_i)\Delta I \quad (3)$$

where ΔB is the change in applied field; N , A , and L_{coil} are the number of turns, area, and inductance of the detection coil; L_i is the inductance of the SQUID input coil; and ΔI is the change in current in the superconducting circuit. If the lead inductance is not negligible, it must be added to L_{coil} and L_i .

To calculate the sensitivity and noise level of a simple detection coil system, the inductance of the detection coil must be known. The inductance of a flat, tightly wound, circular multiturn loop of superconducting wire is given by [10].

$$4 \times 10^{-3} N^2 \pi r \left[\ln \left(\frac{8r}{\rho} \right) - 2 \right] \frac{\mu\text{H}}{\text{cm turn}^2} \quad (4)$$

where r is the radius of the detection coil and ρ is the radius of the (superconducting) wire. Knowing the coil inductance L_{coil} , we can rewrite Eq. (3) as

$$\Delta B = (L_{\text{coil}} + L_i)\Delta I/NA \quad (5)$$

Because the SQUID system has an output proportional to the input current, maximum sensitivity is obtained by using the input circuit that provides the maximum current

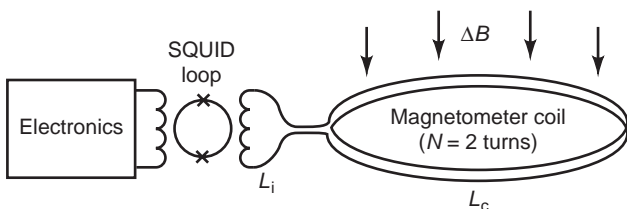


Figure 5. Schematic diagram of typical SQUID input circuit.

into the SQUID and satisfies all other constraints of the experimental apparatus. For a pure magnetometer, the maximum sensitivity will occur when the impedance of the detection coil matches that of the SQUID sensor ($L_{\text{coil}} = L_i$).

3.1. Detection Coils

Several factors affect the design of the detection coils [11]. These include the desired sensitivity of the system, the size and location of the magnetic field source, and the need to match the inductance of the detection coil to that of the SQUID. The ability to separate field patterns caused by sources at different locations and strengths requires a good signal-to-noise ratio. At the same time, one has to find the coil configuration that gives the best spatial resolution. Unfortunately, these two tasks are not independent. For example, increasing the signal coil diameter improves field sensitivity but sacrifices spatial resolution. In practice, system design is restricted by several constraints: the impedance and noise of the SQUID sensors, the size of the dewar, and the number of channels, along with the distribution and strength of noise sources.

It is extremely important for dc response that the detection coil(s) be superconducting. Resistance in the detection circuit has two effects: (1) attenuating the signal and (2) adding Nyquist noise. Resistive attenuation is important only below a frequency f_0 , such that the resistive impedance is equal to the sum of the inductive impedances in the circuit (e.g., $f_0 \approx R/L_t$, where L_t is the total inductive impedance of the circuit). Resistive noise is important only if it becomes comparable with other noise sources or the signal ($< 10^{-30} \text{ J/Hz}$ for biomagnetism, $< 10^{-26} \text{ J/Hz}$ for geophysics). For a SQUID with $E_N \approx 10^{-30} \text{ J/Hz}$, the total resistance of the circuit, including any joints, must be less than $1.4 \times 10^{-13} \Omega$ [12]. Thus it is very important that all solder joints, press-fits, or connections have as low a joint resistance as possible.

Figure 6 displays a variety of detection coils. The magnetometer [Fig. 6(a)] responds to the changes in the field penetrating the coil. More complicated coil configurations provide the advantage of discriminating against unwanted background fields from distant sources while retaining sensitivity to nearby sources.

Because of the present inability to make flexible wire or make true superconducting joints in HTS materials, three-dimensional HTS coil structures [e.g., Figs. 6(b,d-f)] are not possible. Present day HTS magnetometers are fabricated as planar devices and are available only as pure magnetometers [Fig. 6(a)] and planar gradiometers [Fig. 6(c)]. As a result, commercially available HTS devices are currently in the form of magnetic-sensing rather than current-sensing devices.

3.2. Gradiometers

Magnetometers are extremely sensitive to the outside environment. This may be acceptable if one is measuring ambient fields. If what is to be measured is close to the detection coil and weak, outside interference may prevent measurements at SQUID sensitivities. If the measurement is of a magnetic source close to the detection coil, a

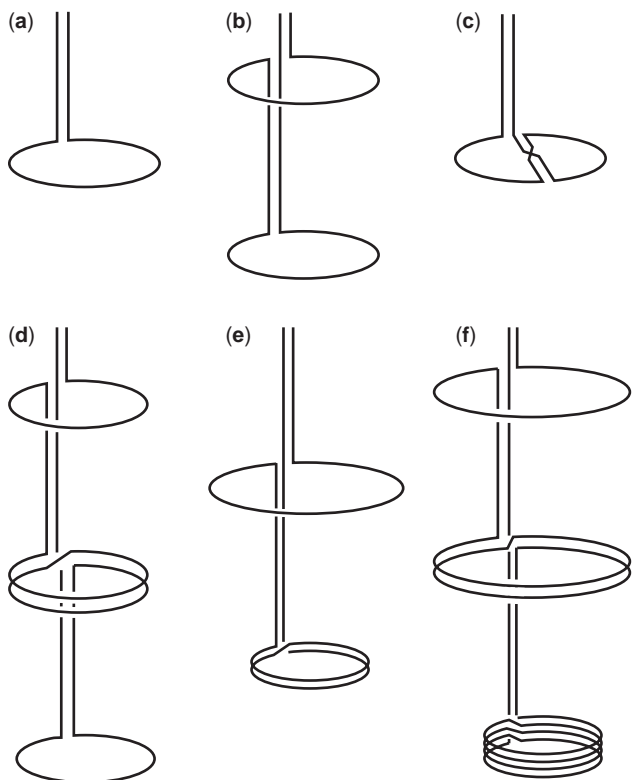


Figure 6. (a) Magnetometer, (b) first derivative gradiometer, (c) planar gradiometer, (d) second derivative gradiometer, (e) first derivative asymmetric gradiometer, and (f) second derivative asymmetric gradiometer. Courtesy of S. J. Williamson.

gradiometer coil may be preferred. The field of a magnetic dipole is inversely proportional to the cube of the distance between the dipole and the sensor. It follows that the field from a distant source is relatively uniform in direction and magnitude at the sensor. If we connect in series two identical and exactly parallel loops wound in opposite senses, separated by a distance b (the base-line), we obtain a coil [Fig. 6(b)] that will reject uniform fields.

Because the response of a single coil to a magnetic dipole goes as $1/r^3$, an object that is much closer to one coil than the other will couple better to the closer coil than the more distant. Sources that are relatively distant will couple equally into both coils. For objects that are closer than $0.3 b$, the gradiometer acts as a pure magnetometer, while rejecting more than 99% of the influence of objects more than $300 b$ distant (Fig. 7). In essence, the gradiometer acts as a compensated magnetometer. It is possible to use two gradiometers connected in series opposition [Fig. 6(d)] to further minimize the response of the system to distant sources. This can be extended to higher orders by connecting in series opposition two second-order gradiometers, and so on. Doing so, however, reduces the sensitivity of the instrument to the signal of interest and may not significantly improve the signal-to-noise ratio.

Rejection of distant noise sources depends on having a precise match (or balance as it is sometimes referred to) between the number of area-turns in the coils. A symmetric gradiometer [Fig. 6(b) requires that $N_s A_s = N_c A_c$,

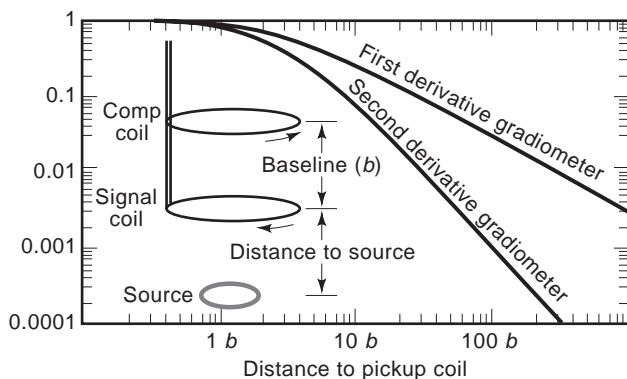


Figure 7. Response of gradient coils relative to magnetometer response ($1/r^3$ suppressed).

where N is the number of turns and A is the area of the signal and compensation coils, respectively. An asymmetric design [Fig. 6(e,f)] has the advantage that the inductance (L_s) of the signal coil(s) is much greater than the compensation coils (L_c); greater sensitivity is achieved than with a symmetric design. Another advantage is that the signal coil diameter is reduced, leading to potentially higher spatial resolution. The optimum conditions for the number of turns in an asymmetric signal coil is given by [13]:

$$(L_s + L_c + L_i + L_l) - N_s \frac{\partial}{\partial N_s} (L_s + L_c + L_i + L_l) = 0 \quad (6)$$

If the gradiometer is perfectly made (balanced), it will reject uniform fields. However, if one coil has a larger effective diameter than the other, the response will not be that of a perfect gradiometer, but that of a gradiometer in series with a magnetometer. Mathematically, the balance, β can be defined as $V_t \propto \mathbf{G} + \beta \cdot \mathbf{H}$, where V_t is the system response, \mathbf{G} is the coil's response to a gradient field, and \mathbf{H} is the applied uniform fields. Typically, coil forms that wind gradiometers can be machined (grooved) to achieve balances β that range from 0.01 to 0.001. Planar devices, through photolithography, can achieve lower levels—a factor of 10 or better. Superconducting trim tabs placed within the detection coils can improve β to the parts per million level. High degrees of balance can allow a SQUID gradiometer to operate in relatively large (millitesla) ambient fields while maintaining sensitivities in the tens of femtotesla.

For multichannel systems (such as are used in biomagnetism), it is not possible to use externally adjustable trim tabs—each tab tends to interfere with the others. Electronic balancing [14] can provide balance ratios at the parts per million level. In this situation, portions of (additional) magnetometer reference channel response are summed electronically with the gradiometers' input to balance out its effective magnetometer response. Eight-element tensor arrays as reference channels can further improve external noise rejection. The major advantage of electronic balancing is significant improvement in immunity to low-frequency environment noise.

4. REFRIGERATION

The superconducting nature of SQUIDs require them to operate well below their superconducting transition temperature (9.3 K for Nb and 93 K for $\text{YBa}_2\text{Cu}_3\text{O}_{7-\delta}$). The thermal environment for the SQUID sensor and detection coil has typically been liquid helium or liquid nitrogen contained in a vacuum-insulated vessel known as a dewar (Fig. 8). The cryogen hold time depends on the boil-off rate (heat load) and the inner vessel volume.

The major heat load on dewars is the result of thermal conduction down the neck tube and a magnetometer probe along with black body radiation. The space between the inner and outer walls is evacuated to prevent thermal conduction between room temperature and the cryogen chamber. Within the vacuum space, a thermal shield (anchored to the neck tube) acts to reduce heat transfer by thermal (black body) radiation. The thermal shield either can be vapor cooled—using the enthalpy of the evaporating helium or nitrogen gas—or have the shield thermally connected to a liquid nitrogen reservoir. Dewars with removable sections use liquid-nitrogen-cooled shields.

If the experiment involves measurements interior to the dewar, then a metallic dewar is preferable. Metallic dewars offer significant shielding from environmental noise at frequencies above 10 Hz to 100 Hz. If the system is to measure magnetic fields exterior to the dewar, the dewar must be magnetically transparent, and metallic construction is not appropriate. Dewars for external field measurements are normally constructed of nonmetallic, low-susceptibility materials to minimize their magnetic interactions with the SQUID sensors and detection coils.

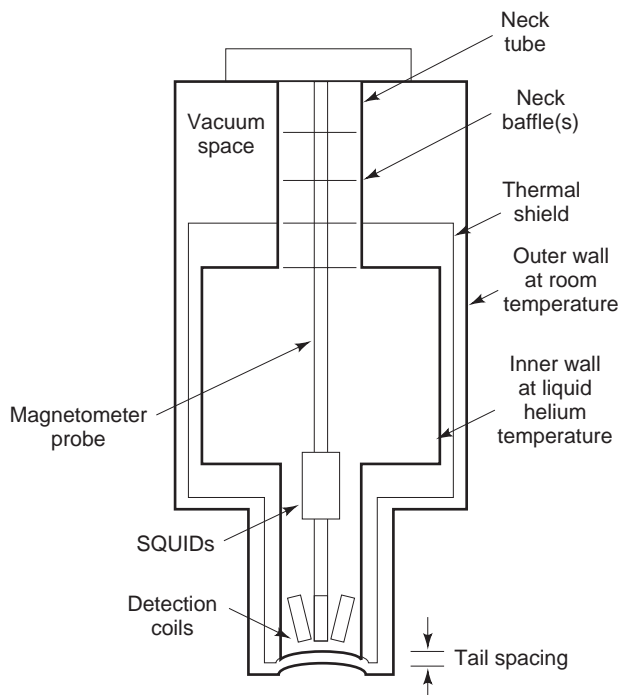


Figure 8. Typical design of a fiberglass dewar used for biomagnetic measurements.

Materials used are typically glass-fiber epoxy composites such as G-10. In an effort to get the detection coil(s) as close as possible to the object being measured, a “tailed” design is often used. This decreases the forces on the bottom of the dewar and allows the use of thinner end pieces (closer tail spacing). Dewars for biomagnetic measurements often have curved tails to get closer to the head.

The major advantage of high-temperature superconductivity is the simplified cryogenics and reduced spacing between cryogenic regions and room temperature. The thermal load (due to conduction and black body radiation) is less, and the heat capacity of what needs to be cooled is larger (implying smaller temperature variations for a given heat load). Because the latent heat/unit volume of liquid nitrogen is 60 times larger than liquid helium, hold times become months rather than days for an equivalently sized dewar.

4.1. Closed Cycle Refrigeration

As an alternative to liquid cryogens, closed cycle refrigeration would be desirable for several reasons. These include reduction of operating costs, use in remote locations, operation in nonvertical orientations, avoiding interruptions in cryogen deliveries, safety, and the convenience of not having to transfer every few days. Although one mechanically cooled SQUID system has been built [15], the inherent vibration and magnetic signature of present day closed cycle refrigerators prevent them from widespread use. The development of pulse tube refrigerators [16] offers promise for magnetometer operation without cryogens.

4.2. Environmental Noise

The greatest obstacle to SQUID measurements is external noise sources. If the object being measured is within the cryostat (such as is typical in most laboratory experiments), metallic shielding can minimize external noise (e.g., act as a low-pass eddy current shield). Superconducting shields essentially eliminate all external field variations. This assumes that any electrical inputs to the experimental region have been appropriately filtered. Powerline or microprocessor clock frequencies can severely degrade performance.

When measuring external fields, the SQUID magnetometer must operate in an environment—the magnetic field of the earth—that can be ten orders of magnitude greater than its sensitivity (Fig. 9). The magnetic field at the surface of the earth is generated by several sources. A background field of $\sim 50 \mu\text{T}$ exists with a daily variation of $\pm 0.1 \mu\text{T}$. In addition, there is a contribution (below 1 Hz) from the interaction of the solar wind with the magnetosphere. The remaining contributions to external magnetic fields are primarily man-made. These can be caused by structural steel and other localized magnetic materials such as furniture and instruments that distort the earth’s field and result in field gradients; moving vehicles that generate transient fields; electric motors; elevators; radio, television, and microwave transmitters; and the ever-present powerline electromagnetic field and its harmonics.

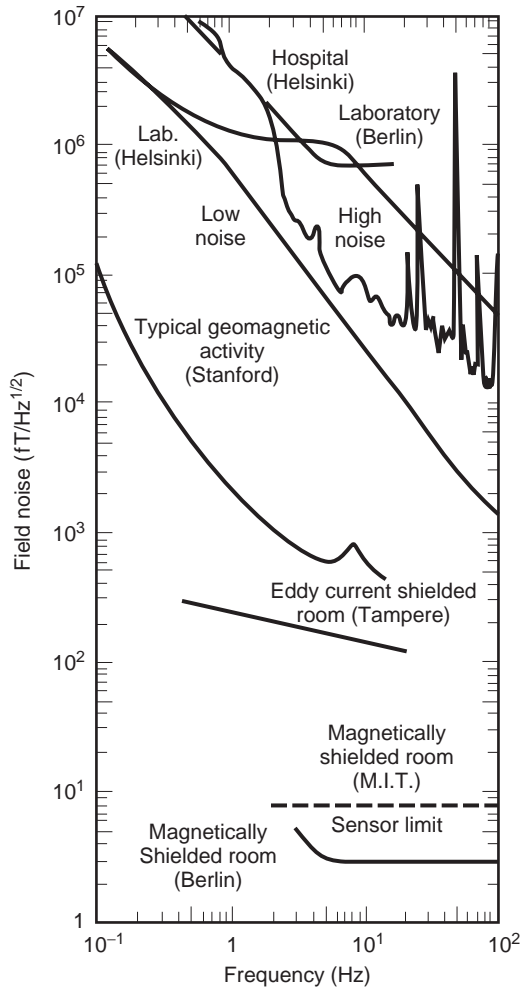


Figure 9. Rms field noise spectra in various environments as a function of frequency. Courtesy of S. J. Williamson.

4.3. Noise Reduction

One method to attenuate external noise sources is with an eddy current shield that generates fields that act to cancel the externally applied fields within the conducting material. The shielding effect is determined by skin depth λ . For a sinusoidal varying wave

$$\lambda = \sqrt{\rho / \pi \mu_0 f} \quad (7)$$

where f is the frequency of the applied field, ρ is the electrical resistivity, and μ_0 is the magnetic permeability of free space. In situations where the wall thickness $t \ll \lambda$, external fields are attenuated by

$$\frac{H_i}{H_e} = \frac{1}{1 + (2\pi f L / R)^2} \quad (8)$$

where L is the inductance of the enclosure and R is the resistance along the path of current flow. Unfortunately, induced currents in the shield generate noise. For a

cylindrical shape,

$$B_{\text{rms}} = \sqrt{\frac{64\pi k_B T t}{h d \rho}} \quad (9)$$

where h is the length and d is the diameter of the can. The cutoff frequency is given by $f_{-3\text{dB}} \approx \rho / 4\pi d t$. Because of noise considerations, eddy current shields that are to be placed near the detection coils should be made from relatively poor conductors such as BeCu.

4.4. Shielded Rooms

Another approach is to use eddy current shielding to shield the entire measurement system. An eddy current room constructed with 2 cm high purity aluminum walls can achieve shielding > 40 dB at 60 Hz with improved performance at higher frequencies. The equivalent field noise is less than $200 \text{ fT} / \sqrt{\text{Hz}}$ at frequencies above 1 Hz.

The need for shielding at lower frequencies has led to the use of magnetically shielded rooms (MSR). In the situation where $t \gg \lambda$, the attenuation goes as $(r/\lambda)e^{t/\lambda}$. Using pure eddy current shielding would require wall thicknesses that could exceed 1 m or more (below 1 Hz). For a ferromagnetic material, the permeability of the material $[\mu = \mu_0(1 + \chi)]$ replaces μ_0 in Eq. (8). The shielding is due to the fact that flux prefers the path with the highest permeability. Because magnetically “soft” materials (e.g., mu-metal[®]) can have permeabilities that exceed 10^4 , the external magnetic flux is routed around the walls, avoiding the interior. Multiple shields can act to further shield the interior of an MSR. For the six-layer Berlin MSR (Fig. 9), shielding factors exceeded 10^4 at frequencies above 0.01 Hz with noise levels below $3 \text{ fT} / \sqrt{\text{Hz}}$.

5. APPLICATIONS

Many applications (Fig. 10) configure the SQUID as a magnetometer. SQUIDS can also be configured to measure a wide variety of electromagnetic properties (Fig. 11).

The state of the art in materials processing limits the variety of superconducting input circuits that can be used with HTS SQUIDS. As already mentioned, there is no existing method for making superconducting connections to SQUIDS with HTS wire. As a result, commercially available HTS devices are currently in the form of magnetic sensing [Fig. 6(b)] rather than current sensing devices [Fig. 6(a,c-f)].

5.1. Laboratory Applications [4,8,17]

Table 1 shows typical capabilities of commercially available SQUID-based instruments. The number in the parenthesis refers to the corresponding Fig. 11.

5.1.1. Current. One common use of a SQUID is as an ammeter [Fig. 11(a)]. The input can be connected to an experiment at liquid helium temperatures or to room temperature. If the signal is to be inductively coupled to a detection coil that is connected to the SQUID input,

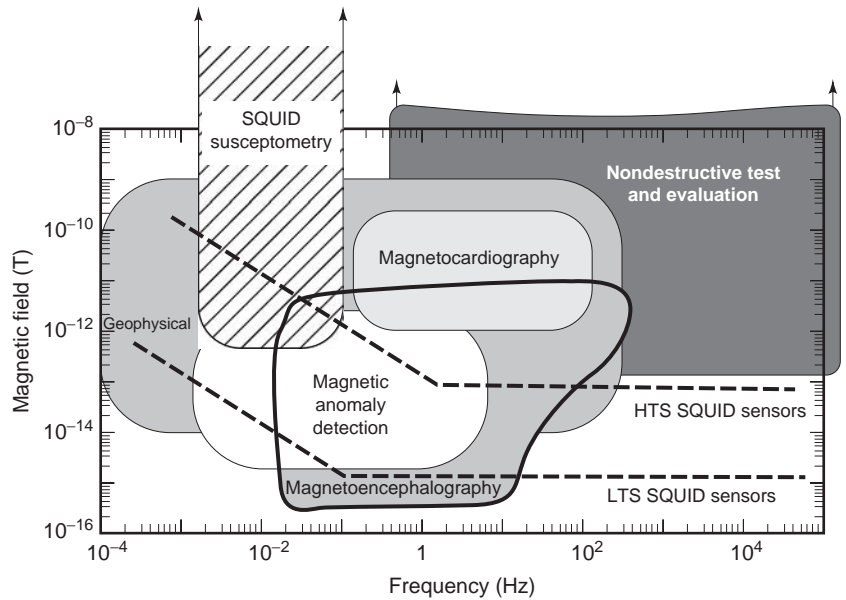


Figure 10. Field sensitivities and bandwidths typical of various applications. The lines indicate the sensitivity of commercially available SQUIDS.

then the circuit must be superconducting if dc response is desired.

If the measurement is of a current that passes through the detection coil, a toroidal geometry for the detection coil has the advantage of extremely good coupling to the source while rejecting contributions due to external sources. Because the measurement is inductive, there is no loading of the current-generating elements.

5.1.2. Voltage. Typically most applications use superconducting circuits. There are, however, several applications where resistive circuits are used. One example is

the detection of extremely small voltages or resistances (Fig. 12).

When a voltage V_I is applied across the input terminals, a current is generated in the SQUID input coil. In this situation, the feedback current (I_F) that would normally be applied to the SQUID loop is fed back via RF through r_s until the voltage drop across r_s is equal to V_I and there is no net current through the SQUID. V_O measures the voltage drop across RF and r_s with $V_I = V_O r_s / (R_F + r_s)$. The voltage gain of the system is determined by the ratio of R_F / r_s . Typical values for R_F and r_s are 3 and $30 \mu\Omega$, respectively, giving a voltage gain of

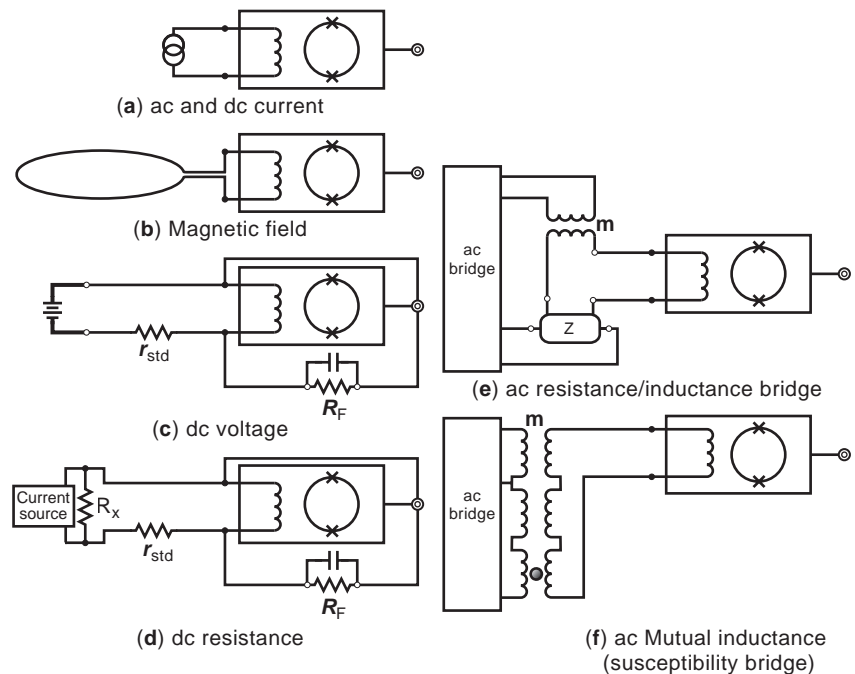


Figure 11. (a) ac and dc current, (b) magnetic field, (c) dc voltage, (d) dc resistance, (e) ac resistance/inductance bridge, and (f) ac mutual inductance (susceptibility bridge).

Table 1. Typical Capabilities of SQUID-based Instruments

Measurement	Sensitivity
Current [Fig. 11(a)]	10^{-12} A/ $\sqrt{\text{Hz}}$
Magnetic fields [Fig. 11(b)]	10^{-15} T/ $\sqrt{\text{Hz}}$
dc voltage [Fig. 11(c)]	10^{-14} V
dc resistance [Fig. 11(d)]	10^{-12} Ω
Mutual/self inductance [Fig. 11(e)]	10^{-10} H
Magnetic moment [Fig. 11(f)]	10^{-10} emu

10^8 . The standard resistor r_s is typically at 4.2 K. The voltage source, however, may be at a completely different temperature.

The input noise of a SQUID picovoltmeter ($\sim 10^{-14}$ V) is a function of the source resistance and temperature ($R \propto T_s$), the inherent voltage noise (due to r_s), and the inherent current noise of the SQUID. Measurement of the Johnson noise in a resistor ($\langle V^2 \rangle = 4k_B TR \Delta f$ where Δf is the bandwidth of the measurement) can determine absolute temperature. Commercially available LTS SQUIDS have equivalent device temperatures

With the addition of an appropriate current source [Fig. 11(d)], it is possible to measure resistance. Resolutions of $10^{-11} \Omega$ can be achieved for $R_x < 10^{-2} \Omega$. Other applications of picovoltmeters include measurements of thermopower, thermal electromotive forces (emfs) (thermocouples), and infrared bolometers.

5.1.3. Ac Susceptibility [4]. The SQUID can also be the null detector in an ac bridge circuit (Fig. 13) to measure both resistive and reactive components of a complex impedance. The unknown impedance Z is excited by a current generated by an oscillator voltage, which is attenuated by a precision ratio transformer λ . The difference between the voltage developed across the unknown impedance Z and that developed in the secondary of a nulling mutual inductor m is applied to the input of the SQUID circuit. The primary current in m is proportional to the oscillator voltage and defined by the setting of the ratio transformer α . An additional reactive current is supplied by a second ratio transformer β , which causes the

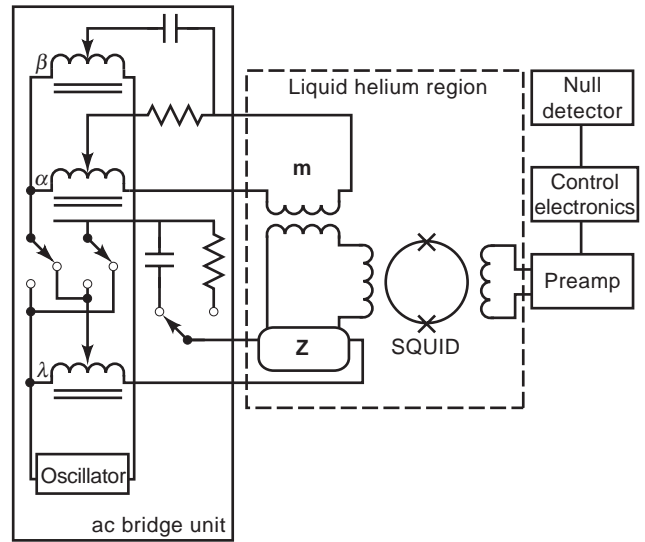


Figure 13. Block diagram of ac bridge.

primary current to be passed through a capacitor rather than a resistor, thus generating a 90° phase shift in the voltage applied to m . The amplified off-balance signal, which appears at the output of the SQUID control electronics, can be displayed by means of a lock-in amplifier tuned to the oscillator frequency.

As mentioned earlier, the sensitivity is limited inherently by Johnson noise in the resistive components of the unknown (including the potential connections) and by the device noise of the SQUID sensor. Assuming $I_N \approx 1$ pA/ $\sqrt{\text{Hz}}$, such a system is capable of measuring R between 10^{-10} to 0.5Ω and L (self and mutual) between 10^{-12} and 10^{-3} H. Using a current comparator as the bridge excitation V , a 0.1 ppm resistance bridge can be constructed.

5.1.4. SQUID Magnetometer/Susceptometers [16]. Instead of using a secondary ac excitation coil [Fig. 11(f)], a dc field can magnetize samples. Typically the field is fixed, and the sample is moved into the detection coil's region of sensitivity. The change in detected magnetization is directly proportional to the magnetic moment of the sample. Because of the superconducting nature of SQUID input circuits, true dc response is possible.

Commonly referred to as SQUID magnetometers, these systems are properly SQUID susceptometers. They have a homogeneous superconducting magnet to create a very uniform field over the entire sample measuring region and the superconducting pick-up loops. The magnet induces a moment allowing a measurement of magnetic susceptibility. The superconducting detection loop array is rigidly mounted in the center of the magnet [17]. This array is configured as a gradient coil to reject external noise sources. The detection coil geometry determines what mathematical algorithm calculates the net magnetization. Oppositely paired Helmholtz, first and second derivatives, have all been successfully used. Coupling two axial channels of differing gradient order can significantly improve noise rejection.

Sensitivities of 10^{-8} emu have been achieved, even at applied fields of 9 T. Placement of secondary excitation

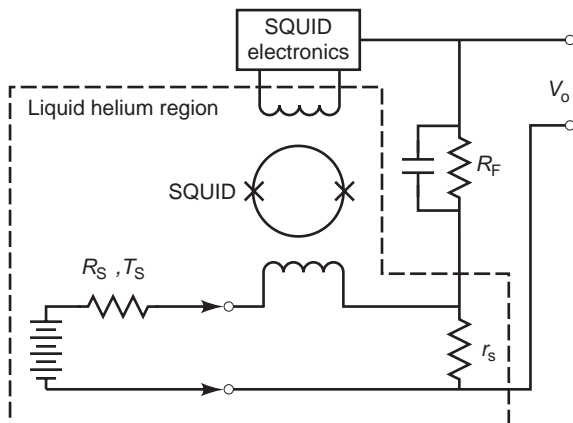


Figure 12. Block diagram of SQUID picovolt measuring system. Negative feedback is applied to the cryogenic input circuit through the voltage divider formed by R_F and r_s .

coils can allow ac susceptibility measurements to be made in the presence of a significant dc bias field. Variable temperature capability (1.7 K to 800 K) is achieved by placing a reentrant cryostat within the detection coils.

5.1.5. Other Laboratory Applications. NMR signals [18] can be measured by placing a sample (e.g., protons or ^{19}F) in the center of SQUID detection coils and either sweeping the external field or applying an RF excitation to the sample. The same experimental concept can measure electron paramagnetic resonance (EPR) signals. SQUIDs have been used for more esoteric applications including temperature measurements with resolution near 10 K to 12 K. SQUIDs have also measured position for gravity wave detectors with sub-Ångstrom resolution and tests of Einstein's General Theory of Relativity. Because SQUID magnetometers are vector devices, they can detect rotations better than 10^{-3} arc-seconds in the earth's magnetic field. SQUIDs have been used in searches for dark matter such as Weak Interacting Massive Particles (WIMPs) along with attempts at detecting magnetic monopoles and free quarks.

5.2. Geophysical Applications [19,20]

SQUID magnetometers measure the earth's magnetic field (Fig. 9) at frequencies ranging between 1 kHz and 10^{-4} Hz. A technique known as magnetotellurics [21] can determine the electrical conductivity distribution of the earth's crust by measuring the earth's electric and magnetic field. Because the earth is a good electrical conductor compared with the air, the electrical field generated in the ionosphere (as a result of solar wind) is reflected at the earth's surface, with components of both the electric and magnetic field decaying as they penetrate into the earth. The decay length or skin depth $\delta = 500\sqrt{\rho\tau}$, where ρ is the electrical resistivity of the earth and τ is the period of the electromagnetic wave.

In magnetotellurics, the electric field (as a function of frequency) is related to the magnetic field via an impedance tensor where $\mathbf{E}(\omega) = \mathbb{Z}\mathbf{H}(\omega)$. The impedance tensor \mathbb{Z} contains four complex elements Z_{xx} , Z_{xy} , Z_{yx} , and Z_{yy} and is related to the resistivity by $\rho_{ij} = 0.2|Z_{ij}(\omega)|^2\tau$ where \mathbb{Z} has units of mV/km-nT.

Magnetic anomaly detection uses the five unique spatial components of $\nabla\mathbf{B}$ to locate a magnetic dipole uniquely. This has potential uses in mineralogical surveys and detection of unexploded ordnance.

5.3. Nondestructive Test and Evaluation [22,23]

Magnetic-sensing techniques such as eddy current testing have been used for many years to detect flaws in structures. A major limitation on their sensitivity is the skin depth [Eq. (7)] of metallic materials. Because SQUID sensors have true dc response and superior sensitivity, they can see "deeper" into metallic structures. dc response also means that they can detect remnant magnetization—without the need for externally applied magnetic fields. Their flat frequency response and zero phase distortion allows for a wide range of applications. One potential application of SQUIDs is in detection of stress or corrosion in reinforcing rods used in bridges, aircraft runways, or

Table 2. NDE Measurement Techniques

Imaging
Intrinsic currents
Remnant magnetization
Flaw-induced perturbations in applied currents
Johnson noise in metals
Eddy currents in an applied ac field (flaws)
Embedded magnetic sensors
Hysteretic magnetization due to:
Cyclic stress (strain)
Simultaneous dc and ac magnetic fields
Magnetization of paramagnetic, diamagnetic and ferromagnetic materials in dc magnetic fields

buildings. Table 2 shows some of the measurement techniques that can be used with SQUID sensors.

SQUID magnetometers have made noncontact measurements of timing circuits [24]—one instrument has better than $10\ \mu\text{m}$ resolution [25]. Such instruments with megahertz bandwidths could be used for circuit board and integrated circuit (IC) mapping.

5.4. Medical Applications of SQUIDs [23,26–29]

Bioelectric signals as a diagnostic tool is well known in medicine [e.g., the electrocardiogram (ECG) for the heart and the electroencephalogram (EEG) for the brain]. The electrical activity that produces the surface electrical activity that is measured by EEG and ECG also produces magnetic fields. The analogous magnetic measurements are known as the magnetocardiogram (MCG) and the magnetoencephalogram (MEG). Other physiological processes also generate electrical activity with analogous magnetic fields (Fig. 14).

Magnetic fields from active electrical sources in the body can be measured passively and external to the body by placing the magnetometer in close proximity to the body's surface. It has been shown that a population of neurons in the brain can be modeled as a current dipole that generates

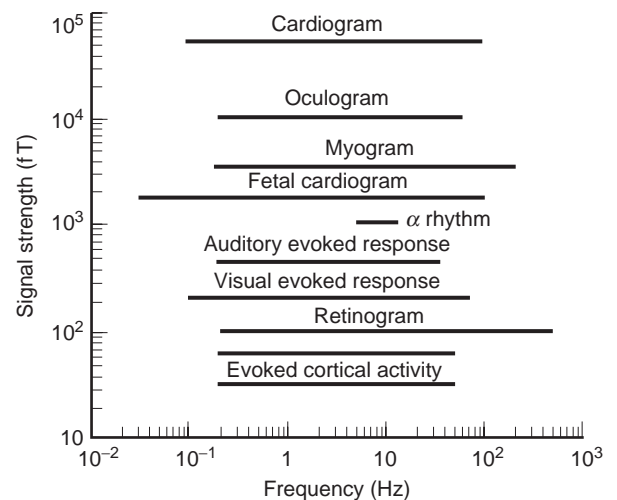


Figure 14. Typical amplitudes and frequency ranges for various biomagnetic signals.

Table 3. Medical Applications of SQUIDS

Studies of the brain—neuromagnetism
Epilepsy
Presurgical cortical function mapping
Drug development and testing
Stroke
Alzheimer's
Neuromuscular disorders
Prenatal brain disorders
Performance evaluation
Studies of the heart—magnetocardiography
Arrhythmia
Heart muscle damage
Fetal cardiography
Other medical applications
Studies of the stomach—gastroenterology
Intestinal ischemia
Noninvasive in vivo magnetic liver biopsies
Lung function and clearance studies
Nerve damage assessment

a well-defined magnetic field profile. Mapping of these field profiles can infer the location of the equivalent active dipole site region to within millimeters. Using evoked response techniques, the location of signal pathways and information processing centers in the brain can be mapped at different delay times (latencies) after the stimulus.

There are also magnetic measurements for which there are no electrical analogs. These are measurements of static magnetic fields produced by ferromagnetic materials ingested into the body and measurements of the magnetic susceptibility of materials in the body. In particular, information on the quantity and depth of diamagnetic or paramagnetic materials (such as iron stored in the liver) can be obtained by using magnetizing and detection coils of differing sizes in the same instrument and measuring the induced field as a function of distance. This technique is already being used to monitor patients suffering from iron overload diseases such as thalassemia and hemochromatosis.

The development of the SQUID has allowed the development of noninvasive clinical measurements of biomagnetic fields. Gradiometers can allow measurements to be made in unshielded environments at sensitivities below $20 \text{ fT}/\sqrt{\text{Hz}}$. Typically, however, neuromagnetic measurements are made in room-sized MSRs that will allow measurements of the magnetic field of the brain over the entire surface of the head (>150 positions simultaneously). Table 3 gives some of the areas in which SQUID magnetometers are currently being used in medical research.

BIBLIOGRAPHY

1. B. D. Josephson, Possible new effect in superconductive tunneling, *Phys. Lett.*, **1**:251–253 (1962).
2. J. Clarke, SQUID fundamentals, in H. Weinstock, ed., *SQUID Sensors: Fundamentals, Fabrications and Applications*, Dordrecht: Kluwer, 1997.
3. T. Van Duzer and C. W. Turner, *Principles of Superconductive Devices and Circuits*, New York: Elsevier, 1981.
4. T. P. Orlando and K. A. Delin, *Foundations of Applied Superconductivity*, Reading, MA: Addison-Wesley, 1991.
5. R. P. Giffard, R. A. Webb, and J. C. Wheatley, Principles and methods of low-frequency electric and magnetic measurements using an rf-biased point-contact superconducting device, *J. Low Temp. Phys.*, **6**:533–610 (1972).
6. R. J. Prance et al., Fully engineered high performance UHF SQUID magnetometer, *Cryogenics*, **21**:501–506 (1981).
7. C. D. Tesche and J. Clarke, DC SQUID: noise and optimization, *J. Low Temp. Phys.*, **29**:301–331 (1982).
8. M. B. Simmonds and R. P. Giffard, *Apparatus for reducing low frequency noise in dc biased SQUIDS*, U.S. Patent 4,389,612 (1983).
9. R. L. Fagaly, Superconducting magnetometers and instrumentation, *Sci. Prog., Oxford*, **71**:181–201 (1987).
10. F. W. Grover, *Inductance Calculations, Working Formulas and Tables*, New York: Dover, 1962.
11. J. P. Wikswo, Jr., Optimization of SQUID differential magnetometers, *AIP Conference Proc.*, **44**:145–149 (1978).
12. R. B. Stephens and R. L. Fagaly, High temperature superconductors for SQUID detection coils, *Cryogenics*, **31**:988–992 (1991).
13. R. Illmonemi et al., Multi-SQUID devices and their applications, in D. F. Brewer, ed., *Progress in Low Temperature Physics*, vol. XII, Amsterdam: Elsevier, 1989.
14. J. Vrba, SQUID gradiometers in real environments, in H. Weinstock, ed., *SQUID Sensors: Fundamentals, Fabrications and Applications*, Dordrecht: Kluwer, 1997.
15. D. S. Buchanan, D. N. Paulson, and S. J. Williamson, Instrumentation for clinical applications of neuromagnetism, in R. W. Fast, ed., *Advances in Cryogenic Engineering*, vol. 33, New York: Plenum, 1988, pp. 97–106.
16. C. Heiden, Pulse tube refrigerators: A cooling option, in H. Weinstock, ed., *SQUID Sensors: Fundamentals, Fabrications and Applications*, Dordrecht: Kluwer, 1997.
17. R. E. Sarwinski, Superconducting instrumentation, *Cryogenics*, **17**:671–679 (1977).
18. R. A. Webb, New technique of improved low-temperature SQUID NMR measurements, *Rev. Sci. Instrum.*, **48**:1585 (1977).
19. J. Clarke, Geophysical applications of SQUIDS, *IEEE Trans. Mag.*, **MAG-19**:288–294 (1983).
20. H. Weinstock and W. C. Overton, Jr., eds., *SQUID Applications to Geophysics*, Tulsa: Society of Exploration Geophysicists, 1981.
21. K. Vozoff, The magnetotelluric method in the exploration of sedimentary basins, *Geophysics*, **37**:98–114 (1972).
22. G. B. Donaldson, SQUIDS for everything else, in H. Weinstock and M. Nisenoff, eds., *Superconducting Electronics*, New York: Springer-Verlag, 1989.
23. J. P. Wikswo, Jr., SQUID magnetometers for biomagnetism and non-destructive testing: Important questions and initial answers, *IEEE Trans. Appl. Supercond.*, **5**:74–120 (1995).
24. R. L. Fagaly, SQUID detection of electronic circuits, *IEEE Trans. Magn.*, **MAG-25**:1216–1218 (1989).
25. J. Kirtley, Imaging magnetic fields, *IEEE Spectrum*, **33**(12):40–48 (1996).
26. S. J. Williamson and L. Kaufman, Biomagnetism, *J. Magn. Mag. Mat.*, **22**:129–202 (1981).
27. G.-L. Romani, S. J. Williamson, and L. Kaufman, Biomagnetic instrumentation, *Rev. Sci. Instrum.*, **53**:1815–1845 (1982).
28. R. L. Fagaly, Neuromagnetic instrumentation, in S. Sato, ed., *Advances in Neurology, Vol. 54: Magnetoencephalography*, New York: Raven Press, 1990.
29. C. Aine et al., *Advances in Biomagnetism Research: Biomag96*, New York: Springer-Verlag, 1997.

STABILITY OF NONLINEAR SYSTEMS

GUANRONG CHEN
City University of Hong Kong
Kowloon, Hong Kong, China

1. INTRODUCTION

A *nonlinear system* refers to a set of nonlinear equations (algebraic, difference, differential, integral, functional, or abstract operator equations, or a combination of some of these) used to describe a physical device or process that otherwise cannot be clearly defined by a set of linear equations of any kind. *Dynamical system* is used as a synonym for mathematical or physical system when the describing equations represent evolution of a solution with time and, sometimes, with control inputs and/or other varying parameters as well.

The theory of nonlinear dynamical systems, or *nonlinear control systems* if control inputs are involved, has been greatly advanced since the nineteenth century. Today, nonlinear control systems are used to describe a great variety of scientific and engineering phenomena ranging from social, life, and physical sciences to engineering and technology. This theory has been applied to a broad spectrum of problems in physics, chemistry, mathematics, biology, medicine, economics, and various engineering disciplines.

Stability theory plays a central role in system engineering, especially in the field of control systems and automation, with regard to both dynamics and control. Stability of a dynamical system, with or without control and disturbance inputs, is a fundamental requirement for its practical value, particularly in most real-world applications. Roughly speaking, stability means that the system outputs and its internal signals are bounded within admissible limits (the so-called bounded-input/bounded-output stability) or, sometimes more strictly, the system outputs tend to an equilibrium state of interest (the so-called asymptotic stability). Conceptually, there are different kinds of stabilities, among which three basic notions are the main concerns in nonlinear dynamics and control systems: the stability of a system with respect to its equilibria, the orbital stability of a system output trajectory, and the structural stability of a system itself.

The basic concept of stability emerged from the study of an equilibrium state of a mechanical system, dated back to as early as 1644, when E. Torricelli studied the equilibrium of a rigid body under the natural force of gravity. The classical stability theorem of G. Lagrange, formulated in 1788, is perhaps the best known result about stability of conservative mechanical systems, which states that if the potential energy of a conservative system, currently at the position of an isolated equilibrium and perhaps subject to some simple constraints, has a minimum, then this equi-

librium position of the system is stable [23]. The evolution of the fundamental concepts of system and trajectory stabilities then went through a long history, with many fruitful advances and developments, until the celebrated Ph.D. thesis of A. M. Lyapunov, *The General Problem of Motion Stability*, finished in 1892 [21]. This monograph is so fundamental that its ideas and techniques are virtually leading all kinds of basic research and applications regarding stabilities of dynamical systems today. In fact, not only dynamical behavior analysis in modern physics but also controllers design in engineering systems depend on the principles of Lyapunov's stability theory. This article is devoted to a brief description of the basic stability theory, criteria, and methodologies of Lyapunov, as well as a few related important stability concepts, for nonlinear dynamical systems.

2. NONLINEAR SYSTEM PRELIMINARIES

2.1. Nonlinear Control Systems

A continuous-time nonlinear control system is generally described by a differential equation of the form

$$\dot{\mathbf{x}} = \mathbf{f}(\mathbf{x}, t; \mathbf{u}), \quad t \in [t_0, \infty) \quad (1)$$

where $\mathbf{x} = \mathbf{x}(t)$ is the *state* of the system belonging to a (usually bounded) region $\Omega_{\mathbf{x}} \subset \mathbf{R}^n$, \mathbf{u} is the *control* input vector belonging to another (usually bounded) region $\Omega_{\mathbf{u}} \subset \mathbf{R}^m$ (often, $m \leq n$), and \mathbf{f} is a Lipschitz or continuously differentiable nonlinear function, so that the system has a unique solution for each admissible control input and suitable initial condition $\mathbf{x}(t_0) = \mathbf{x}_0 \in \Omega_{\mathbf{x}}$. To indicate the time evolution and the dependence on the initial state \mathbf{x}_0 , the *trajectory* (or *orbit*) of a system state $\mathbf{x}(t)$ is sometimes denoted as $\varphi_t(\mathbf{x}_0)$.

In control system (1), the initial time used is $t_0 \geq 0$, unless otherwise indicated. The entire space \mathbf{R}^n , to which the system states belong, is called the *state space*. Associated with the control system (1), there usually is an *observation* or *measurement* equation

$$\mathbf{y} = \mathbf{g}(\mathbf{x}, t; \mathbf{u}) \quad (2)$$

where $\mathbf{y} = \mathbf{y}(t) \in \mathbf{R}^\ell$ is the *output* of the system, $1 \leq \ell \leq n$, and \mathbf{g} is a continuous or smooth nonlinear function. When both $n, \ell > 1$, the system is called a *multiinput/multioutput* (MIMO) system; while if $n = \ell = 1$, it is called a *single-input/single-output* (SISO) system. MISO and SIMO systems are similarly defined.

In the discrete-time setting, a nonlinear control system is described by a difference equation of the form

$$\begin{cases} \mathbf{x}_{k+1} = \mathbf{f}(\mathbf{x}_k, k; \mathbf{u}_k) \\ \mathbf{y}_k = \mathbf{g}(\mathbf{x}_k, k; \mathbf{u}_k), \end{cases} \quad k = 0, 1, \dots \quad (3)$$

where all notations are similarly defined. This article usually discusses only the control system (1), or the first equation of (3). In this case, the system state \mathbf{x} is also considered as the system output for simplicity.

A special case of system (1), with or without control, is said to be *autonomous* if the time variable t does not appear separately (independently) from the state vector in the system function \mathbf{f} . For example, with a state feedback control $\mathbf{u}(t) = \mathbf{h}(\mathbf{x}(t))$, this often is the situation. In this case, the system is usually written as

$$\dot{\mathbf{x}} = \mathbf{f}(\mathbf{x}), \quad \mathbf{x}(t_0) = \mathbf{x}_0 \in \mathbf{R}^n \tag{4}$$

Otherwise, as (1) stands, the system is said to be *nonautonomous*. The same terminology may be applied in the same way to discrete-time systems, although they may have different characteristics.

An *equilibrium*, or *fixed point*, of system (4), if it exists, is a solution, \mathbf{x}^* , of the algebraic equation

$$\mathbf{f}(\mathbf{x}^*) = 0 \tag{5}$$

It then follows from (4) and (5) that $\dot{\mathbf{x}}^* = 0$, which means that an equilibrium of a system must be a constant state. For the discrete-time case, an equilibrium of system

$$\mathbf{x}_{k+1} = \mathbf{f}(\mathbf{x}_k), \quad k = 0, 1, \dots \tag{6}$$

is a solution, if it exists, of equation

$$\mathbf{x}^* = \mathbf{f}(\mathbf{x}^*) \tag{7}$$

An equilibrium is *stable* if some nearby trajectories of the system states, starting from various initial states, approach it; it is *unstable* if some nearby trajectories move away from it. The concept of system stability with respect to an equilibrium will be precisely introduced in Section 3.

A control system is *deterministic* if there is a unique consequence to every change of the system parameters or initial states. It is *random* or *stochastic*, if there is more than one possible consequence for a change in its parameters or initial states according to some probability distribution [6]. This article deals only with deterministic systems.

2.2. Hyperbolic Equilibria and Their Manifolds

Consider the autonomous system (4). The Jacobian of this system is defined by

$$J(\mathbf{x}) = \frac{\partial \mathbf{f}}{\partial \mathbf{x}} \tag{8}$$

Clearly, this is a matrix-valued function of time. If the Jacobian is evaluated at a constant state, say, \mathbf{x}^* or \mathbf{x}_0 , then it becomes a constant matrix determined by \mathbf{f} and \mathbf{x}^* or \mathbf{x}_0 .

An equilibrium \mathbf{x}^* of system (4) is said to be *hyperbolic* if all eigenvalues of the system Jacobian, evaluated at this equilibrium, have nonzero real parts.

For a p -periodic solution of system (4), $\tilde{\mathbf{x}}(t)$, with a fundamental period $p > 0$, let $J(\tilde{\mathbf{x}}(t))$ be its Jacobian evaluated

at $\tilde{\mathbf{x}}(t)$. Then this Jacobian is also p -periodic:

$$J(\tilde{\mathbf{x}}(t+p)) = J(\tilde{\mathbf{x}}(t)) \quad \text{for all } t \in [t_0, \infty)$$

In this case, there always exist a p -periodic nonsingular matrix $M(t)$ and a constant matrix Q such that the fundamental solution matrix associated with the Jacobian $J(\tilde{\mathbf{x}}(t))$ is given by [4]

$$\Phi(t) = M(t)e^{tQ}$$

Here, the fundamental matrix $\Phi(t)$ consists of, as its columns, n linearly independent solution vectors of the linear equation $\dot{\mathbf{x}} = J(\tilde{\mathbf{x}}(t))\mathbf{x}$, with $\mathbf{x}(t_0) = \mathbf{x}_0$.

In the preceding, the eigenvalues of the constant matrix e^{pQ} are called the *Floquet multipliers* of the Jacobian. The p -periodic solution $\tilde{\mathbf{x}}(t)$ is called a *hyperbolic periodic orbit* of the system if all its corresponding Floquet multipliers have nonzero real parts.

Next, let \mathcal{D} be a neighborhood of an equilibrium, \mathbf{x}^* , of the autonomous system (4). A *local stable* and *local unstable manifold* of \mathbf{x}^* is defined by

$$W_{\text{loc}}^s(\mathbf{x}^*) = \{\mathbf{x} \in \mathcal{D} \mid \varphi_t(\mathbf{x}) \in \mathcal{D} \ \forall t \geq t_0 \text{ and } \varphi_t(\mathbf{x}) \rightarrow \mathbf{x}^* \text{ as } t \rightarrow \infty\} \tag{9}$$

and

$$W_{\text{loc}}^u(\mathbf{x}^*) = \{\mathbf{x} \in \mathcal{D} \mid \varphi_t(\mathbf{x}) \in \mathcal{D} \ \forall t \leq t_0 \text{ and } \varphi_t(\mathbf{x}) \rightarrow \mathbf{x}^* \text{ as } t \rightarrow -\infty\} \tag{10}$$

respectively. Furthermore, a *stable* and *unstable manifold* of \mathbf{x}^* is defined by

$$W^s(\mathbf{x}^*) = \{\mathbf{x} \in \mathcal{D} \mid \varphi_t(\mathbf{x}) \cap W_{\text{loc}}^s(\mathbf{x}^*) \neq \phi\} \tag{11}$$

and

$$W^u(\mathbf{x}^*) = \{\mathbf{x} \in \mathcal{D} \mid \varphi_t(\mathbf{x}) \cap W_{\text{loc}}^u(\mathbf{x}^*) \neq \phi\} \tag{12}$$

respectively, where ϕ denotes the empty set. For example, the autonomous system

$$\begin{cases} \dot{x} = y \\ \dot{y} = x(1 - x^2) \end{cases}$$

has a hyperbolic equilibrium $(x^*, y^*) = (0, 0)$. The local stable and unstable manifolds of this equilibrium are illustrated by Fig. 1a, and the corresponding stable and unstable manifolds are visualized by Fig. 1b.

A hyperbolic equilibrium only has stable and/or unstable manifolds since its associated Jacobian has only stable and/or unstable eigenvalues. The dynamics of an autonomous system in a neighborhood of a hyperbolic equilibrium is quite simple—it has either stable (convergent) or unstable (divergent) properties. Therefore, complex dynamical behaviors such as chaos are seldom associated with isolated hyperbolic equilibria or isolated hyperbolic

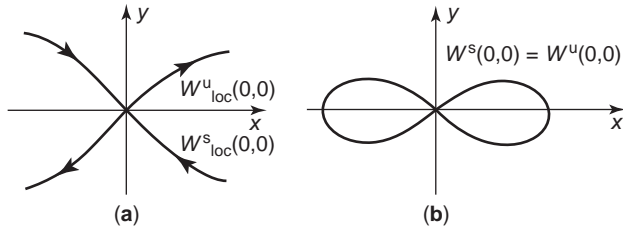


Figure 1. Stable and unstable manifolds.

periodic orbits [7,11,15] (see Theorem 16, below); they generally are confined within the *center manifold*, $W^c(x^*)$, where $\dim(W^s) + \dim(W^c) + \dim(W^u) = n$.

2.3. Open-Loop and Closed-Loop Systems

Let S be an MIMO system, which can be linear or nonlinear, continuous-time or discrete-time, deterministic or stochastic, or any well-defined input–output map. Let U and Y be the sets (sometimes, spaces) of the admissible input and corresponding output signals, respectively, both defined on the time domain $\mathcal{D} = [a, b]$, $-\infty \leq a < b \leq \infty$ (for control systems, usually $a = t_0 = 0$ and $b = \infty$). This simple relation is described by an open-loop map

$$S : \mathbf{u} \rightarrow \mathbf{y} \text{ or } \mathbf{y}(t) = S(\mathbf{u}(t)) \tag{13}$$

and its block diagram is shown in Fig. 2. Actually, every control system described by a differential or difference equation can be viewed as a map in this form. But, in such a situation, the map S can be implicitly defined only via the equation and initial conditions.

In the control system (1) or (3), if the control inputs are functions of the state vectors, $\mathbf{u} = \mathbf{h}(\mathbf{x}; t)$, then the control system can be implemented via a closed-loop configuration. A typical closed-loop system is shown in Fig. 3, where usually S_1 is the plant (described by \mathbf{f}) and S_2 is the controller (described by \mathbf{h}); yet they can be reversed.

2.4. Norms of Functions and Operators

This article deals only with finite-dimensional systems. For an n -dimensional vector-valued functions, $\mathbf{x}(t) = [x_1(t) \dots x_n(t)]^T$ where superscript “T” denotes transpose, let $\|\cdot\|$ and $\|\cdot\|_p$ denote its *Euclidean norm* and *L_p norm*, defined respectively by the “length”

$$\|\mathbf{x}(t)\| = \sqrt{x_1^2(t) + \dots + x_n^2(t)}$$

and

$$\|\mathbf{x}\|_p = \left(\int_a^b \|\mathbf{x}(t)\|^p dt \right)^{1/p}, \quad 1 \leq p < \infty$$

$$\|\mathbf{x}\|_\infty = \text{ess sup}_{\substack{a \leq t \leq b \\ 1 \leq i \leq n}} |x_i(t)|$$

Here, a few remarks are in order:

1. The term “ess sup” means “essential supremum” (i.e., the supremum except perhaps over a set of

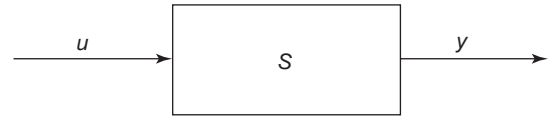


Figure 2. The block diagram of an open-loop system.

measure zero). For a piecewise continuous function $f(t)$, actually

$$\text{ess sup}_{a \leq t \leq b} |f(t)| = \sup_{a \leq t \leq b} |f(t)|$$

2. The main difference between the “sup” and the “max” is that $\max |f(t)|$ is attainable but $\sup |f(t)|$ may not. For example, $\max_{0 \leq t < \infty} |\sin(t)| = 1$ but $\sup_{0 \leq t < \infty} |1 - e^{-t}| = 1$.
3. The difference between the Euclidean norm and the L_p norms is that the former is a function of time but the latter are all constants.
4. For a finite-dimensional vector $\mathbf{x}(t)$, with $n < \infty$, all the L_p norms are equivalent in the sense that for any $p, q \in [1, \infty]$, there exist two positive constants α and β such that

$$\alpha \|\mathbf{x}\|_p \leq \|\mathbf{x}\|_q \leq \beta \|\mathbf{x}\|_p$$

For the input–output map in Eq. (13), the so-called operator norm of the map S is defined to be the maximum gain from all possible inputs over the domain of the map to their corresponding outputs. More precisely, the *operator norm* of the map S in (13) is defined by

$$\|S\| = \sup_{\substack{\mathbf{u}_1, \mathbf{u}_2 \in U \\ \mathbf{u}_1 \neq \mathbf{u}_2}} \frac{\|\mathbf{y}_1 - \mathbf{y}_2\|_Y}{\|\mathbf{u}_1 - \mathbf{u}_2\|_U} \tag{14}$$

where $\mathbf{y}_i = S(\mathbf{u}_i) \in Y$, $i = 1, 2$, and $\|\cdot\|_U$ and $\|\cdot\|_Y$ are the norms of the functions defined on the input–output sets (or spaces) U and Y , respectively.

3. LYAPUNOV, ORBITAL, AND STRUCTURAL STABILITIES

Three different types of stabilities, namely, the Lyapunov stability of a system with respect to its equilibria, the orbital stability of a system output trajectory, and the structural stability of a system itself, are of fundamental importance in the studies of nonlinear dynamics and control systems.

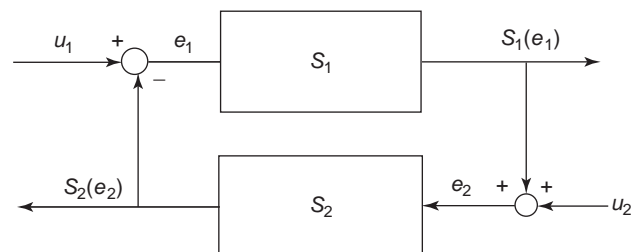


Figure 3. A typical closed-loop control system.

Roughly speaking, the Lyapunov stability of a system with respect to its equilibrium of interest is about the behavior of the system outputs toward the equilibrium state—wandering nearby and around the equilibrium (stability in the sense of Lyapunov) or gradually approaches it (asymptotic stability); the orbital stability of a system output is the resistance of the trajectory to small perturbations; the structural stability of a system is the resistance of the system structure against small perturbations [3,13,16,17,19,20,23,25,26,29,35]. These three basic types of stabilities are introduced in this section, for dynamical systems without explicitly involving control inputs.

Consider the general nonautonomous system

$$\dot{\mathbf{x}} = \mathbf{f}(\mathbf{x}, t), \quad \mathbf{x}(t_0) = \mathbf{x}_0 \in \mathbf{R}^n \tag{15}$$

where the control input $\mathbf{u}(t) = \mathbf{h}(\mathbf{x}(t), t)$, if it exists [see system (1)], has been combined into the system function \mathbf{f} for simplicity of discussion. Without loss of generality, assume that the origin $\mathbf{x} = 0$ is the system equilibrium of interest. Lyapunov stability theory concerns various stabilities of the system orbits with respect to this equilibrium. When another equilibrium is discussed, the new equilibrium is first shifted to zero by a change of variables, and then the transformed system is studied in the same way.

3.1. Stability in the Sense of Lyapunov

System (15) is said to be *stable in the sense of Lyapunov* with respect to the equilibrium $\mathbf{x}^* = 0$, if for any $\varepsilon > 0$ and any initial time $t_0 \geq 0$, there exists a constant, $\delta = \delta(\varepsilon, t_0) > 0$, such that

$$\|\mathbf{x}(t_0)\| < \delta \Rightarrow \|\mathbf{x}(t)\| < \varepsilon \quad \text{for all } t \geq t_0 \tag{16}$$

This stability is illustrated by Fig. 4.

It should be emphasized that the constant δ generally depends on both ε and t_0 . It is particularly important to point out that, unlike autonomous systems, one cannot simply fix the initial time $t_0 = 0$ for a nonautonomous system in a general discussion of its stability. For example, consider the following linear time-varying system with a discontinuous coefficient:

$$\dot{x}(t) = \frac{1}{1-t}x(t), \quad x(t_0) = x_0$$

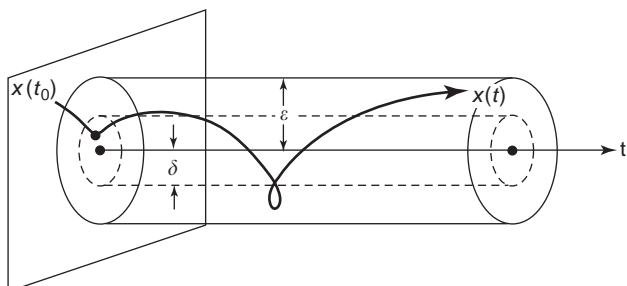


Figure 4. Geometric meaning of stability in the sense of Lyapunov.

It has an explicit solution

$$x(t) = x_0 \frac{1-t_0}{1-t}, \quad 0 \leq t_0 \leq t < \infty$$

which is stable in the sense of Lyapunov about the equilibrium $x^* = 0$ over the entire time domain $[0, \infty)$ if and only if $t_0 = 1$. This shows that the initial time, t_0 , does play an important role in the stability of a nonautonomous system.

The above-defined stability, in the sense of Lyapunov, is said to be *uniform* with respect to the initial time, if the existing constant $\delta = \delta(\varepsilon)$ is indeed independent of t_0 over the entire time interval $[0, \infty)$. According to the discussion above, uniform stability is defined only for nonautonomous systems since it is not needed for autonomous systems (for which it is always uniform with respect to the initial time).

3.2. Asymptotic and Exponential Stabilities

System (15) is said to be *asymptotically stable* about its equilibrium $\mathbf{x}^* = 0$, if it is stable in the sense of Lyapunov and, furthermore, there exists a constant, $\delta = \delta(t_0) > 0$, such that

$$\|\mathbf{x}(t_0)\| < \delta \Rightarrow \|\mathbf{x}(t)\| \rightarrow 0 \quad \text{as } t \rightarrow \infty \tag{17}$$

This stability is visualized by Fig. 5.

The asymptotic stability is said to be *uniform* if the existing constant δ is independent of t_0 over $[0, \infty)$, and is said to be *global* if the convergence, $\|\mathbf{x}\| \rightarrow 0$, is independent of the initial state $\mathbf{x}(t_0)$ over the entire spatial domain on which the system is defined (e.g., when $\delta = \infty$). If, furthermore

$$\|\mathbf{x}(t_0)\| < \delta \Rightarrow \|\mathbf{x}(t)\| \leq ce^{-\sigma t} \tag{18}$$

for two positive constants c and σ , then the equilibrium is said to be *exponentially stable*. The exponential stability is visualized by Fig. 6.

Clearly, exponential stability implies asymptotic stability, and asymptotic stability implies the stability in the sense of Lyapunov, but the reverse need not be true. For illustration, if a system has output trajectory $x_1(t) = x_0 \sin(t)$, then it is stable in the sense of Lyapunov about 0, but is not asymptotically stable; a system with output

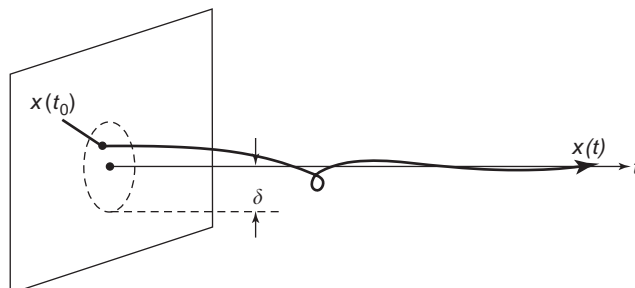


Figure 5. Geometric meaning of the asymptotic stability.

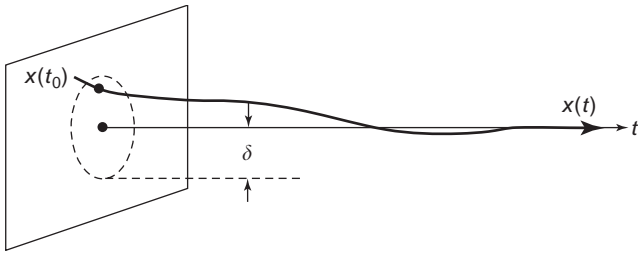


Figure 6. Geometric meaning of the exponential stability.

trajectory $x_2(t) = x_0(1+t-t_0)^{-1}$ is asymptotically stable (so also is stable in the sense of Lyapunov) if $t_0 < 1$ but is not exponentially stable about 0; however, a system with $x_3(t) = x_0e^{-t}$ is exponentially stable (hence, is both asymptotically stable and stable in the sense of Lyapunov).

3.3. Orbital Stability

The orbital stability differs from the Lyapunov stabilities in that it concerns with the stability of a system output (or state) trajectory under small external perturbations.

Let $\varphi_t(\mathbf{x}_0)$ be a p -periodic solution, $p > 0$, of the autonomous system

$$\dot{\mathbf{x}}(t) = \mathbf{f}(\mathbf{x}), \quad \mathbf{x}(t_0) = \mathbf{x}_0 \in \mathbf{R}^n \quad (19)$$

and let Γ represent the closed orbit of $\varphi_t(\mathbf{x}_0)$ in the state space, namely,

$$\Gamma = \{\mathbf{y} \mid \mathbf{y} = \varphi_t(\mathbf{x}_0), \quad 0 \leq t < p\}$$

If, for any $\varepsilon > 0$, there exists a constant $\delta = \delta(\varepsilon) > 0$ such that for any \mathbf{x}_0 satisfying

$$d(\mathbf{x}_0, \Gamma) := \inf_{\mathbf{y} \in \Gamma} \|\mathbf{x}_0 - \mathbf{y}\| < \delta$$

the solution of the system, $\varphi_t(\mathbf{x}_0)$, satisfies

$$d(\varphi_t(\mathbf{x}_0), \Gamma) < \varepsilon, \quad \text{for all } t \geq t_0$$

then this p -periodic solution trajectory, $\varphi_t(\mathbf{x}_0)$, is said to be *orbitally stable*.

Orbital stability is visualized by Fig. 7. For a simple example, a stable periodic solution, particularly a stable equilibrium of a system is orbitally stable. This is because all nearby trajectories approach it and, as such, it becomes a nearby orbit after a small perturbation and so will move back to its original position (or stay nearby). On the contrary, unstable and semistable (saddle-type of) periodic orbits are orbitally unstable.

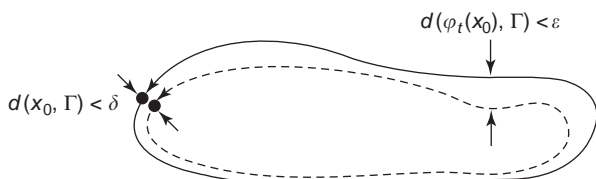


Figure 7. Geometric meaning of the orbital stability.

A more precise concept of orbital stability is given in the sense of Zhukovskij [37].

A solution $\varphi_t(\mathbf{x}_0)$ of system (19) is said to be stable in the sense of Zhukovskij, if for any $\varepsilon > 0$, there exists a $\delta = \delta(\varepsilon) > 0$ such that for any $\mathbf{y}_0 \in B_\delta(\mathbf{x}_0)$, a ball of radius δ centered at \mathbf{x}_0 , there exist two functions, $\tau_1 = \tau_1(t)$ and $\tau_2 = \tau_2(t)$, satisfying

$$\|\mathbf{x}_{\tau_1}(\mathbf{x}_0) - \mathbf{x}_{\tau_2}(\mathbf{x}_0)\| < \varepsilon$$

for all $t \geq t_0$, where τ_1 and τ_2 are homeomorphisms (i.e., a continuous map whose inverse exists and is also continuous) from $[0, \infty)$ to $[0, \infty)$ with $\tau_1(0) = \tau_2(0) = 0$.

Furthermore, a Zhukovskij stable solution $\varphi_t(\mathbf{x}_0)$ of system (19) is said to be asymptotically stable in the sense of Zhukovskij, if for any $\varepsilon > 0$, there exists a $\delta = \delta(\varepsilon) > 0$ such that for any $\mathbf{y}_0 \in B_\delta(\mathbf{x}_0)$, a ball of radius δ centered at \mathbf{x}_0 , there exist two functions, $\tau_1 = \tau_1(t)$ and $\tau_2 = \tau_2(t)$, satisfying

$$\|\mathbf{x}_{\tau_1}(\mathbf{x}_0) - \mathbf{x}_{\tau_2}(\mathbf{x}_0)\| \rightarrow 0$$

as $t \rightarrow \infty$, where τ_1 and τ_2 are homeomorphisms from $[0, \infty)$ to $[0, \infty)$ with $\tau_1(0) = \tau_2(0) = 0$.

It can be verified that (asymptotic) Zhukovskij stability implies (asymptotic) Lyapunov stability about an equilibrium. However, the converse may not be true. Moreover, these two types of stabilities are equivalent if the orbit $\varphi_t(\mathbf{x}_0)$ is an equilibrium of the system.

3.4. Structural Stability

Two systems are said to be *topologically orbitally equivalent*, if there exists a homeomorphism that transforms the family of trajectories of the first system to that of the second while preserving their motion directions. Roughly, this means that the geometrical pictures of the orbit families of the two systems are similar (no one has extra knots, sharp corners, bifurcating branches, etc.). For instance, systems $\dot{x} = x$ and $\dot{x} = 2x$ are topologically orbitally equivalent, but are not so between $\dot{x} = x$ and $\dot{x} = \sqrt{x}$. These three system trajectories are shown in Fig. 8.

Return to the autonomous system (19). If the dynamics of the system in the state space changes radically, for example by the appearance of a new equilibrium or a new periodic orbit, due to small external perturbations, then the system is considered to be structurally unstable.

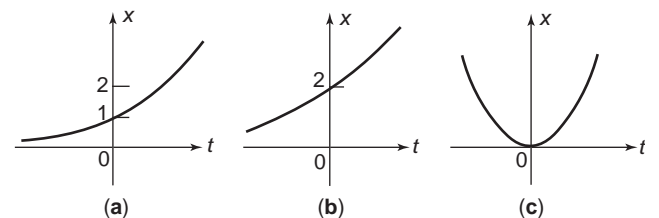


Figure 8. Trajectories of three systems for comparison: (a) $\dot{x} = x$; (b) $\dot{x} = 2x$; (c) $\dot{x} = \sqrt{x}$.

To be more precise, consider the following set of functions:

$$\mathcal{S} = \left\{ \mathbf{g}(\mathbf{x}) \mid \|\mathbf{g}(\mathbf{x})\| < \infty, \left\| \frac{\partial \mathbf{g}(\mathbf{x})}{\partial \mathbf{x}} \right\| < \infty \text{ for all } \mathbf{x} \in \mathbf{R}^n \right\}$$

If, for any $g \in \mathcal{S}$, there exists an $\varepsilon > 0$ such that the orbits of the two systems

$$\dot{\mathbf{x}} = \mathbf{f}(\mathbf{x}) \text{ and } \dot{\mathbf{x}} = \mathbf{f}(\mathbf{x}) + \varepsilon \mathbf{g}(\mathbf{x})$$

are topologically orbitally equivalent, then the autonomous system (19), namely, the first (unperturbed) system above, is said to be *structurally stable*.

For example, $\dot{x} = x$ is structurally stable but $\dot{x} = x^2$ is not, in a neighborhood of the origin. This is because when the second system is slightly perturbed, to become, say, $\dot{x} = x^2 + \varepsilon$, where $\varepsilon > 0$, then the resulting system has two equilibria, $x_1^* = \sqrt{\varepsilon}$ and $x_2^* = -\sqrt{\varepsilon}$, which has more numbers of equilibria than the original system that possesses only one, $x^* = 0$.

4. VARIOUS STABILITY THEOREMS

Consider the general nonautonomous system

$$\dot{\mathbf{x}} = \mathbf{f}(\mathbf{x}, t), \quad \mathbf{x}(t_0) = \mathbf{x}_0 \in \mathbf{R}^n \tag{20}$$

where $\mathbf{f}: \mathcal{D} \times [0, \infty) \rightarrow \mathbf{R}^n$ is continuously differentiable in a neighborhood of the origin, $\mathcal{D} \subseteq \mathbf{R}^n$, with a given initial state $\mathbf{x}_0 \in \mathcal{D}$. Again, without loss of generality, assume that $\mathbf{x}^* = 0$ is a system equilibrium of interest.

4.1. Lyapunov Stability Theorems

First, for the autonomous system (19), an important special case of (20), with a continuously differentiable $\mathbf{f}: \mathcal{D} \rightarrow \mathbf{R}^n$, the following criterion of stability, called the *first (or indirect) method of Lyapunov*, is very convenient to use.

Theorem 1 (First Method of Lyapunov: For Continuous-Time Autonomous Systems). Let $J = [\partial \mathbf{f} / \partial \mathbf{x}]_{\mathbf{x} = \mathbf{x}^* = 0}$ be the system Jacobian evaluated at the zero equilibrium of system (19). If all the eigenvalues of J have a negative real part, then the system is asymptotically stable about $\mathbf{x}^* = 0$.

First, note that this and the following Lyapunov theorems apply to linear systems as well, for linear systems are merely a special case of nonlinear systems. When $\mathbf{f}(\mathbf{x}) = A\mathbf{x}$, the linear time-invariant system $\dot{\mathbf{x}} = A\mathbf{x}$ has the only equilibrium $\mathbf{x}^* = 0$. If A has all eigenvalues with negative real parts, Theorem 1 implies that the system is asymptotically stable about its equilibrium since the system Jacobian is simply $J = A$. This is consistent with the familiar linear stability results.

Note also that the region of asymptotic stability given by Theorem 1 is local, which can be quite large for some nonlinear systems but may be very small for some others. However, there is no general criterion for determining the

boundaries of such local stability regions when this and the following Lyapunov methods are applied.

Moreover, it is important to note that this theorem cannot be applied to a *general* nonautonomous system, since for general nonautonomous systems this theorem is neither necessary nor sufficient [36]. A simple counterexample is the following linear time-varying system [17,34]:

$$\dot{\mathbf{x}}(t) = \begin{bmatrix} -1 + 1.5 \cos^2(t) & 1 - 1.5 \sin(t) \cos(t) \\ -1 - 1.5 \sin(t) \cos(t) & -1 + 1.5 \sin^2(t) \end{bmatrix} \mathbf{x}(t)$$

This system has eigenvalues $\lambda_{1,2} = -0.25 \pm j0.25\sqrt{7}$, both having negative real parts and being independent of the time variable t . If this theorem is used to judge the system, the conclusion would be that the system is asymptotically stable about its equilibrium 0. However, the solution of this system is

$$\mathbf{x}(t) = \begin{bmatrix} e^{0.5t} \cos(t) & e^{-t} \sin(t) \\ -e^{0.5t} \sin(t) & e^{-t} \cos(t) \end{bmatrix} \begin{bmatrix} x_1(t_0) \\ x_2(t_0) \end{bmatrix}$$

which is unstable, for any initial conditions with a bounded and nonzero value of $x_1(t_0)$, no matter how small this initial value is. This example shows that by using the Lyapunov first method *alone* to determine the stability of a general time-varying system, the conclusion can be wrong.

This type of counterexamples can be easily found [35]. On the one hand, this demonstrates the necessity of other general criteria for asymptotic stability of nonautonomous systems. On the other hand, however, a word of caution is that this types of counterexamples do not completely rule out the possibility of applying the first method of Lyapunov to *some* special nonautonomous systems in case studies. The reason is that there is no theorem saying that “the Lyapunov first method cannot be applied to *all* nonautonomous systems.” Because of the complexity of nonlinear dynamical systems, they often have to be studied class by class, or even case by case. It has been widely experienced that the first method of Lyapunov does work for some, perhaps not too many, *specific* nonautonomous systems in case studies (e.g., in the study of some chaotic systems [7]; see also Theorem 18, below). The point is that one has to be very careful when this method is applied to a particular nonautonomous system; the stability conclusion must be verified by some other means at the same time.

Here, it is emphasized that a rigorous approach for asymptotic stability analysis of general nonautonomous systems is provided by the second method of Lyapunov, for which the following set of class \mathcal{K} functions are useful:

$$\mathcal{K} = \{g(t) : g(t_0) = 0, g(t) > 0 \text{ if } t > t_0,$$

$$g(t) \text{ is continuous and nondecreasing on } [t_0, \infty)\}$$

Theorem 2 (Second Method of Lyapunov: For Continuous-Time Nonautonomous Systems). The system (20) is globally (over the entire domain \mathcal{D}), uniformly (with respect to the initial time over the entire time interval $[t_0, \infty)$), and asymptotically stable about its zero equilibrium, if there

exist a scalar-valued function, $V(\mathbf{x}, t)$, defined on $\mathcal{D} \times [t_0, \infty)$, and three functions $\alpha(\cdot), \beta(\cdot), \gamma(\cdot) \in \mathcal{K}$, such that

- (a) $V(0, t_0) = 0$.
- (b) $V(\mathbf{x}, t) > 0$ for all $\mathbf{x} \neq 0$ in \mathcal{D} and all $t \geq t_0$.
- (c) $\alpha(\|\mathbf{x}\|) \leq V(\mathbf{x}, t) \leq \beta(\|\mathbf{x}\|)$ for all $t \geq t_0$.
- (d) $\dot{V}(\mathbf{x}, t) \leq -\gamma(\|\mathbf{x}\|) < 0$ for all $t \geq t_0$.

In Theorem 2, the function V is called a *Lyapunov function*. The method of constructing a Lyapunov function for stability determination is called the *second* (or *direct*) *method of Lyapunov*.

The geometric meaning of a Lyapunov function used for determining the system stability about the zero equilibrium may be illustrated by Fig. 9. In this figure, assuming that a Lyapunov function, $V(\mathbf{x})$, has been found, which has a bowl shape as shown based on conditions (a) and (b). Then, condition (d) is

$$\dot{V}(\mathbf{x}) = \left[\frac{\partial V}{\partial \mathbf{x}} \right] \dot{\mathbf{x}} < 0 \tag{21}$$

where $[\partial V / \partial \mathbf{x}]$ is the gradient of V along the trajectory \mathbf{x} . It is known, from calculus, that if the inner product of this gradient and the tangent vector $\dot{\mathbf{x}}$ is constantly negative, as guaranteed by condition (21), then the angle between these two vectors is larger than 90° , so that the surface of $V(\mathbf{x})$ is monotonically decreasing to zero (this is visualized in Fig. 9). Consequently, the system trajectory \mathbf{x} , the projection on the domain as shown in the figure, converges to zero as time evolves.

As an example, consider the following nonautonomous system

$$\dot{\mathbf{x}} = A\mathbf{x} + \mathbf{g}(\mathbf{x}, t)$$

where A is a stable constant matrix and \mathbf{g} is a nonlinear function satisfying $\mathbf{g}(0, t) = 0$ and $\|\mathbf{g}(\mathbf{x}, t)\| \leq c\|\mathbf{x}\|$ for a constant $c > 0$ for all $t \in [t_0, \infty)$. Since A is stable, the following *Lyapunov equation*

$$PA + A^T P + I = 0$$

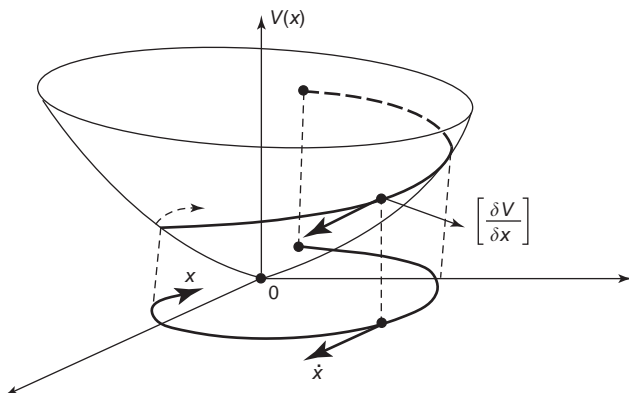


Figure 9. Geometric meaning of the Lyapunov function.

has a unique positive definite and symmetric matrix solution, P . Using the Lyapunov function $V(\mathbf{x}, t) = \mathbf{x}^T P \mathbf{x}$, it can be easily verified that

$$\begin{aligned} \dot{V}(\mathbf{x}, t) &= \mathbf{x}^T [PA + A^T P] \mathbf{x} + 2\mathbf{x}^T P \mathbf{g}(\mathbf{x}, t) \\ &\leq -\mathbf{x}^T \mathbf{x} + 2\lambda_{\max}(P)c\|\mathbf{x}\|^2 \end{aligned}$$

where $\lambda_{\max}(P)$ is the largest eigenvalue of P . Therefore, if the constant $c < 1/(2\lambda_{\max}(P))$ and if the class \mathcal{K} functions

$$\begin{aligned} \alpha(\zeta) &= \lambda_{\min}(P)\zeta^2, & \beta(\zeta) &= \lambda_{\max}(P)\zeta^2, \\ \gamma(\zeta) &= [1 - 2c\lambda_{\max}(P)]\zeta^2 \end{aligned}$$

are used, then conditions (c) and (d) of Theorem 2 are satisfied. As a result, the above system is globally, uniformly, and asymptotically stable about its zero equilibrium. This example shows that the linear part of a weakly nonlinear nonautonomous system can indeed dominate the stability.

Note that in Theorem 2, the uniform stability is guaranteed by the class \mathcal{K} functions α, β, γ stated in conditions (c) and (d), which is necessary since the solution of a nonautonomous system may sensitively depend on the initial time, as seen from the numerical example discussed in Section 3.1. For autonomous systems, these class \mathcal{K} functions [hence, condition (c)] are not needed. In this case, Theorem 2 reduces to the following simple form.

Theorem 3 (Second Method of Lyapunov: For Continuous-Time Autonomous Systems). The autonomous system (19) is globally (over the entire domain \mathcal{D}) and asymptotically stable about its zero equilibrium, if there exists a scalar-valued function $V(\mathbf{x})$, defined on \mathcal{D} , such that

- (a) $V(0) = 0$.
- (b) $V(\mathbf{x}) > 0$ for all $\mathbf{x} \neq 0$ in \mathcal{D} .
- (c) $\dot{V}(\mathbf{x}) < 0$ for all $\mathbf{x} \neq 0$ in \mathcal{D} .

Note that if condition (c) in Theorem 3 is replaced by (d) $\dot{V}(\mathbf{x}) \leq 0$ for all $\mathbf{x} \in \mathcal{D}$, then the resulting stability is only in the sense of Lyapunov but may not be asymptotic. For example, consider a simple model of an undamped pendulum of length ℓ described by

$$\begin{cases} \dot{x} = -\frac{g}{\ell} \sin(y) \\ \dot{y} = x \end{cases}$$

where $x = \dot{\theta}$ is the angular variable defined on $-\pi < \theta < \pi$, with the vertical axis as its reference, and g is the gravity constant. Since the system Jacobian at the zero equilibrium has one pair of purely imaginary eigenvalues, $\lambda_{1,2} = \pm \sqrt{-g/\ell}$, Theorem 1 is not applicable. However, if one uses the Lyapunov function

$$V = \frac{g}{\ell} (1 - \cos(y)) + \frac{1}{2} x^2$$

then it can be easily verified that $\dot{V} = 0$ over the entire domain. Thus, the conclusion is that the undamped

pendulum is stable in the sense of Lyapunov but may not be asymptotically, consistent with the physics of the undamped pendulum.

Theorem 4 (Krasovkii Theorem: For Continuous-Time Autonomous Systems). For the autonomous system (19), let $J(\mathbf{x}) = [\partial \mathbf{f} / \partial \mathbf{x}]$ be its Jacobian evaluated at $\mathbf{x}(t)$. A sufficient condition for the system to be asymptotically stable about its zero equilibrium is that there exist two real positive definite and symmetric constant matrices, P and Q , such that the matrix

$$J^T(\mathbf{x})P + PJ(\mathbf{x}) + Q$$

is seminegative definite for all $\mathbf{x} \neq 0$ in a neighborhood \mathcal{D} of the origin. For this case, a Lyapunov function is given by

$$V(\mathbf{x}) = \mathbf{f}^T(\mathbf{x})P\mathbf{f}(\mathbf{x})$$

Furthermore, if $\mathcal{D} = \mathbf{R}^n$ and $V(\mathbf{x}) \rightarrow \infty$ as $\|\mathbf{x}\| \rightarrow \infty$, then this asymptotic stability is also global.

Similar stability criteria can be established for discrete-time systems [10]. Two main results are summarized as follows.

Theorem 5 (First Method of Lyapunov: For Discrete-Time “Autonomous” Systems). Let $\mathbf{x}^* = 0$ be an equilibrium of the discrete-time “autonomous” system

$$\mathbf{x}_{k+1} = \mathbf{f}(\mathbf{x}_k) \tag{22}$$

where $\mathbf{f}: \mathcal{D} \rightarrow \mathbf{R}^n$ is continuously differentiable in a neighborhood of the origin, $\mathcal{D} \subseteq \mathbf{R}^n$, and let $J = [\partial \mathbf{f} / \partial \mathbf{x}_k]_{\mathbf{x}_k = \mathbf{x}^* = 0}$ be the Jacobian of the system evaluated at this equilibrium. If all the eigenvalues of J are strictly less than one in absolute value, then the system is asymptotically stable about its zero equilibrium.

Theorem 6 (Second Method of Lyapunov: For Discrete-Time “Nonautonomous” Systems). Let $\mathbf{x}^* = 0$ be an equilibrium of the “nonautonomous” system

$$\mathbf{x}_{k+1} = \mathbf{f}_k(\mathbf{x}_k) \tag{23}$$

where $\mathbf{f}_k: \mathcal{D} \rightarrow \mathbf{R}^n$ is continuously differentiable in a neighborhood of the origin, $\mathcal{D} \subseteq \mathbf{R}^n$. Then, system (22) is globally (over the entire domain \mathcal{D}) and asymptotically stable about its zero equilibrium, if there exists a scalar-valued function, $V(\mathbf{x}_k, k)$, defined on \mathcal{D} and continuous in \mathbf{x}_k , such that

- (a) $V(0, k) = 0$ for all $k \geq k_0$.
- (b) $V(\mathbf{x}_k, k) > 0$ for all $\mathbf{x}_k \neq 0$ in \mathcal{D} and for all $k \geq k_0$.
- (c) $\Delta V(\mathbf{x}_k, k) := V(\mathbf{x}_k, k) - V(\mathbf{x}_{k-1}, k-1) < 0$ for all $\mathbf{x}_k \neq 0$ in \mathcal{D} and all $k \geq k_0 + 1$.
- (d) $0 < W(\|\mathbf{x}_k\|) < V(\mathbf{x}_k, k)$ for all $k \geq k_0 + 1$, where $W(\tau)$ is a positive continuous function defined on \mathcal{D} , satisfying $W(\|\mathbf{x}_{k_0}\|) = 0$ and $\lim_{\tau \rightarrow \infty} W(\tau) = \infty$ monotonically.

As a special case, for discrete-time “autonomous” systems, Theorem 6 reduces to the following simple form.

Theorem 7 (Second Method of Lyapunov: For Discrete-Time “Autonomous” Systems). Let $\mathbf{x}^* = 0$ be an equilibrium for the “autonomous” system (22). Then the system is globally (over the entire domain \mathcal{D}) and asymptotically stable about this zero equilibrium if there exists a scalar-valued function, $V(\mathbf{x}_k)$, defined on \mathcal{D} and continuous in \mathbf{x}_k , such that

- (a) $V(0) = 0$.
- (b) $V(\mathbf{x}_k) > 0$ for all $\mathbf{x}_k \neq 0$ in \mathcal{D} .
- (c) $\Delta V(\mathbf{x}_k) := V(\mathbf{x}_k) - V(\mathbf{x}_{k-1}) < 0$ for all $\mathbf{x}_k \neq 0$ in \mathcal{D} .
- (d) $V(\mathbf{x}) \rightarrow \infty$ as $\|\mathbf{x}\| \rightarrow \infty$.

To this end, it is important to emphasize that all the Lyapunov theorems stated above only offer *sufficient* conditions for asymptotic stability. On the other hand, usually more than one Lyapunov function may be constructed for the same system. For a given system, one choice of a Lyapunov function may yield a less conservative result (e.g., with a larger stability region) than other choices. However, no conclusion regarding stability may be drawn if, for technical reasons, a satisfactory Lyapunov function cannot be found. Nevertheless, there is a necessary condition in theory about the existence of a Lyapunov function [15], as follows.

Theorem 8 (Massera Inverse Theorem). Suppose that the autonomous system (19) is asymptotically stable about its equilibrium \mathbf{x}^* and \mathbf{f} is continuously differentiable with respect to \mathbf{x} for all $t \in [t_0, \infty)$. Then a Lyapunov function exists for this system.

4.2. Some Instability Theorems

Once again, consider a general autonomous system

$$\dot{\mathbf{x}} = \mathbf{f}(\mathbf{x}), \quad \mathbf{x}(t_0) = \mathbf{x}_0 \in \mathbf{R}^n \tag{24}$$

with an equilibrium $\mathbf{x}^* = 0$. To disprove the stability, the following instability theorems may be used.

Theorem 9 (A Linear Instability Theorem). In system (24), let $J = [\partial \mathbf{f} / \partial \mathbf{x}]_{\mathbf{x} = \mathbf{x}^* = 0}$ be the system Jacobian evaluated at $\mathbf{x}^* = 0$. If at least one of the eigenvalues of J has a positive real part, then $\mathbf{x}^* = 0$ is unstable.

For discrete-time systems, there is a similar result. A *discrete-time “autonomous” system*

$$\mathbf{x}_{k+1} = \mathbf{f}(\mathbf{x}_k), \quad k = 0, 1, 2, \dots,$$

is unstable about its equilibrium $\mathbf{x}^* = 0$ if at least one of the eigenvalues of the system Jacobian is larger than 1 in absolute value.

The following two negative theorems can be easily extended to nonautonomous systems in an obvious way.

Theorem 10 (A General Instability Theorem). For system (24), let $V(\mathbf{x})$ be a positive and continuously differentiable function defined on a neighborhood \mathcal{D} of the origin, satisfying $V(0)=0$. Assume that in any subset, containing the origin, of \mathcal{D} , there is an $\hat{\mathbf{x}}$ such that $V(\hat{\mathbf{x}})>0$. If, moreover

$$\frac{d}{dt} V(\mathbf{x}) > 0 \quad \text{for all } \mathbf{x} \neq 0 \text{ in } \mathcal{D}$$

then the system is unstable about the equilibrium $\mathbf{x}^* = 0$.

One example is the system

$$\begin{cases} \dot{x} = y + x(x^2 + y^4) \\ \dot{y} = -x + y(x^2 + y^4) \end{cases}$$

which has equilibrium $(x^*, y^*) = (0, 0)$. The system Jacobian at the equilibrium has a pair of imaginary eigenvalues, $\lambda_{1,2} = \pm \sqrt{-1}$, so Theorem 1 is not applicable. On the contrary, the Lyapunov function

$$V = \frac{1}{2} (x^2 + y^2)$$

leads to $\dot{V} = (x^2 + y^2)(x^2 + y^4) > 0$ for all $(x, y) \neq (0, 0)$. Therefore, the conclusion is that this system is unstable about its zero equilibrium.

Theorem 11 (Chetaev Instability Theorem). For system (24), let $V(\mathbf{x})$ be a positive and continuously differentiable function defined on \mathcal{D} , and let Ω be a subset, containing the origin, of \mathcal{D} , (i.e., $0 \in \mathcal{D} \cap \Omega$). If (a) $V(\mathbf{x}) > 0$ and $\dot{V}(\mathbf{x}) > 0$ for all $\mathbf{x} \neq 0$ in \mathcal{D} and (b) $V(\mathbf{x}) = 0$ for all \mathbf{x} on the boundary of Ω , then the system is unstable about the equilibrium $\mathbf{x}^* = 0$.

This instability theorem is illustrated by Fig. 10, which graphically shows that if the theorem conditions are satisfied, then there is a gap within any neighborhood of the origin, so that a system trajectory can escape from the neighborhood of the origin along a path in this gap [23].

As an example, consider the system

$$\begin{cases} \dot{x} = x^2 + 2y^5 \\ \dot{y} = xy^2 \end{cases}$$

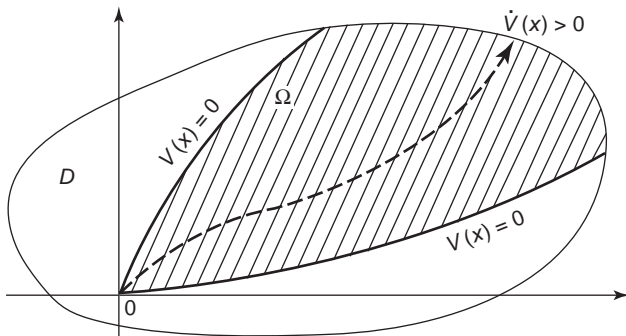


Figure 10. Illustration of the Chetaev theorem.

with the Lyapunov function

$$V = x^2 - y^4$$

which is positive inside the region defined by

$$x = y^2 \quad \text{and} \quad x = -y^2$$

Let \mathcal{D} be the right half-plane and Ω be the shaded area shown in Fig. 11. Clearly, $V=0$ on the boundary of Ω , and $V>0$ and $\dot{V}=2x^3 > 0$ for all $(x, y) \in \mathcal{D}$. According to the Chetaev theorem, this system is unstable about its zero equilibrium.

4.3. LaSalle Invariance Principle

Consider again the autonomous system (24) with an equilibrium $\mathbf{x}^* = 0$. Let $V(\mathbf{x})$ be a Lyapunov function defined on a neighborhood \mathcal{D} of the origin. Let also $\varphi_t(\mathbf{x}_0)$ be a bounded solution orbit of the system, with the initial state \mathbf{x}_0 and all its limit states being confined in \mathcal{D} . Moreover, let

$$E = \{\mathbf{x} \in \mathcal{D} \mid \dot{V}(\mathbf{x}) = 0\} \tag{25}$$

and $M \subset E$ be the largest invariant subset of E in the sense that if the initial state $\mathbf{x}_0 \in M$, then the entire orbit $\varphi_t(\mathbf{x}_0) \subset M$ for all $t \geq t_0$.

Theorem 12 (LaSalle Invariance Principle). Under the assumptions above, for any initial state $\mathbf{x}_0 \in \mathcal{D}$, the solution orbit satisfies $\varphi_t(\mathbf{x}_0) \rightarrow M$ as $t \rightarrow \infty$.

This invariance principle is consistent with the Lyapunov theorems when they are applicable to a problem [11,19]. Sometimes, when $\dot{V}=0$ over a subset of the domain of V , a Lyapunov theorem is not easy to directly apply, but the above LaSalle invariance principle may be convenient to use. For instance, consider the system

$$\begin{cases} \dot{x} = -x + \frac{1}{3}x^3 + y \\ \dot{y} = -x \end{cases}$$

The Lyapunov function $V = x^2 + y^2$ yields

$$\dot{V} = \frac{1}{2} x^2 \left(\frac{1}{3} x^2 - 1 \right)$$

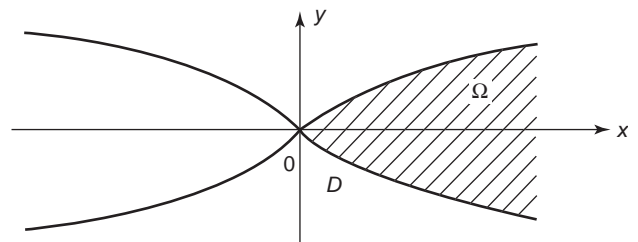


Figure 11. The defining region of a Lyapunov function.

which is negative for $x^2 < 3$ but is zero for $x = 0$ and $x^2 = 3$, regardless of variable y . Thus, Lyapunov theorems do not seem to be applicable, at least not directly. However, observe that the set E defined above has only three straight lines: $x = -\sqrt{3}$, $x = 0$, and $x = \sqrt{3}$, and that all trajectories that intersect the line $x = 0$ will remain on the line only if $y = 0$. This means that the largest invariant subset M containing the points with $x = 0$ is the only point $(0, 0)$. It then follows from the LaSalle invariance principle that starting from any initial state located in a neighborhood of the origin bounded within the two stripes $x = \pm \sqrt{3}$, say, located inside the disk

$$\mathcal{D} = \{(x, y) \mid x^2 + y^2 < 3\}$$

the solution orbit will always be attracted to the point $(0, 0)$. This means that the system is (locally) asymptotically stable about its zero equilibrium.

4.4. Comparison Principle and Vector Lyapunov Functions

For large-scale and interconnected nonlinear (control) systems, or systems described by differential inequalities rather than differential equations, the stability criteria above may not be directly applicable. In such cases, the comparison principle and vector Lyapunov function methods turn out to be advantageous [18,24,32].

To introduce the comparison principle, consider the general nonautonomous system

$$\dot{\mathbf{x}} = \mathbf{f}(\mathbf{x}, t), \quad \mathbf{x}(t_0) = \mathbf{x}_0 \tag{26}$$

where $\mathbf{f}(\mathbf{0}, t) = 0$ is continuous on a neighborhood \mathcal{D} of the origin, $t_0 \leq t < \infty$.

In this case, since \mathbf{f} is only continuous (but not necessarily satisfying the Lipschitz condition), this differential equation may have more than one solution [12]. Let $\mathbf{x}_{\max}(t)$ and $\mathbf{x}_{\min}(t)$ be its maximum and minimum solutions, respectively, in the sense that

$$\mathbf{x}_{\min}(t) \leq \mathbf{x}(t) \leq \mathbf{x}_{\max}(t) \quad \text{componentwise, for all } t \in [t_0, \infty)$$

where $\mathbf{x}(t)$ is any solution of the equation, and $\mathbf{x}_{\min}(t_0) = \mathbf{x}(t_0) = \mathbf{x}_{\max}(t_0) = \mathbf{x}_0$.

Theorem 13 (The Comparison Principle). Let $\mathbf{y}(t)$ be a solution of the following differential inequality:

$$\dot{\mathbf{y}}(t) \leq \mathbf{f}(\mathbf{y}, t) \quad \text{with } \mathbf{y}(t_0) \leq \mathbf{x}_0 \quad \text{componentwise}$$

If $\mathbf{x}_{\max}(t)$ is the maximum solution of system (26), then

$$\mathbf{y}(t) \leq \mathbf{x}_{\max}(t) \quad \text{componentwise for all } t \in [t_0, \infty)$$

The next theorem is established based on this comparison principle. First, recall that a vector-valued function, $\mathbf{g}(\mathbf{x}, t) = [g_1(\mathbf{x}, t) \cdots g_n(\mathbf{x}, t)]^T$ is said to be *quasimonotonic*, if

$$\begin{aligned} x_i = \tilde{x}_i \quad \text{and} \quad x_j \geq \tilde{x}_j \quad (j \neq i) \\ \Rightarrow g_i(\mathbf{x}, t) \geq g_i(\tilde{\mathbf{x}}, t), \quad i = 1, \dots, n \end{aligned}$$

Theorem 14 (Vector Lyapunov Function Theorem). Let $\mathbf{v}(\mathbf{x}, t)$ be a vector Lyapunov function associated with the

nonautonomous system (26), $\mathbf{v}(\mathbf{x}, t) = [V_1(\mathbf{x}, t) \cdots V_n(\mathbf{x}, t)]^T$ in which each V_i is a continuous Lyapunov function for the system, $i = 1, \dots, n$, satisfying $\|\mathbf{v}(\mathbf{x}, t)\| > 0$ for $\mathbf{x} \neq 0$. Assume that

$$\dot{\mathbf{v}}(\mathbf{x}, t) \leq \mathbf{g}(\mathbf{v}(\mathbf{x}, t), t) \quad \text{componentwise}$$

for a continuous and quasimonotonic function \mathbf{g} defined on \mathcal{D} . Then

- (a) If the system

$$\dot{\mathbf{y}}(t) = \mathbf{g}(\mathbf{y}, t)$$

is stable in the sense of Lyapunov (or asymptotically stable) about its zero equilibrium $\mathbf{y}^* = 0$, then so is the nonautonomous system (26).

- (b) If, moreover, $\|\mathbf{v}(\mathbf{x}, t)\|$ is monotonically decreasing with respect to t and the preceding stability (or asymptotic stability) is uniform, then so is the nonautonomous system (26).
- (c) If, furthermore, $\|\mathbf{v}(\mathbf{x}, t)\| \geq c \|\mathbf{x}\|^\sigma$ for two positive constants c and σ , and the preceding stability (or asymptotic stability) is exponential, then so is the nonautonomous system (26).

A simple and frequently used comparison function is

$$\mathbf{g}(\mathbf{y}, t) = A\mathbf{y} + \mathbf{h}(\mathbf{y}, t), \quad \lim_{\|\mathbf{y}\| \rightarrow 0} \frac{\|\mathbf{h}(\mathbf{y}, t)\|}{\|\mathbf{y}\|} = 0$$

where A is a stable M matrix (Metzler matrix). Here, $A = [a_{ij}]$ is an M matrix if

$$a_{ii} < 0 \quad \text{and} \quad a_{ij} \geq 0 \quad (i \neq j), \quad i, j = 1, \dots, n$$

4.5. Orbital and Structural Stability Theorems

Theorem 15 (Orbital Stability Theorem). Let $\tilde{\mathbf{x}}(t)$ be a p -periodic solution of an autonomous system. Suppose that the system has Floquet multipliers λ_i , with $\lambda_1 = 0$ and $|\lambda_i| < 1$ for $i = 2, \dots, n$. Then this periodic solution $\tilde{\mathbf{x}}(t)$ is orbitally stable.

Theorem 16 (Peixoto Structural Stability Theorem). Consider a two-dimensional autonomous system. Suppose that \mathbf{f} is twice differentiable on a compact and connected subset \mathcal{D} bounded by a simple closed curve Γ , with an outward normal vector $\tilde{\mathbf{n}}$. Assume that $\mathbf{f} \cdot \tilde{\mathbf{n}} \neq 0$ on Γ . Then the system is structurally stable on \mathcal{D} if and only if

- (a) All equilibria are hyperbolic.
- (b) All periodic orbits are hyperbolic.
- (c) If x and y are hyperbolic saddles (probably $x = y$), then $W^s(x)$ and $W^u(y)$ are transversal.

5. LINEAR STABILITY OF NONLINEAR SYSTEMS

The first method of Lyapunov provides a linear stability analysis for nonlinear autonomous systems. In this section, the following general nonautonomous system is

considered:

$$\dot{\mathbf{x}} = \mathbf{f}(\mathbf{x}, t), \quad \mathbf{x}(t_0) = \mathbf{x}_0 \in \mathbf{R}^n \tag{27}$$

which is assumed to have an equilibrium $\mathbf{x}^* = 0$.

5.1. Linear Stability of Nonautonomous Systems

In system (27), Taylor-expanding the function \mathbf{f} about $\mathbf{x}^* = 0$ gives

$$\dot{\mathbf{x}} = \mathbf{f}(\mathbf{x}, t) = J(t)\mathbf{x} + \mathbf{g}(\mathbf{x}, t) \tag{28}$$

where $J(t) = [\partial \mathbf{f} / \partial \mathbf{x}]_{\mathbf{x}=0}$ is the Jacobian and $\mathbf{g}(\mathbf{x}, t)$ is the residual of the expansion, which is assumed to satisfy

$$\|\mathbf{g}(\mathbf{x}, t)\| \leq a \|\mathbf{x}\|^2 \quad \text{for all } t \in [t_0, \infty)$$

where $a > 0$ is a constant. It is known from the theory of elementary ordinary differential equations [12] that the solution of equation (28) is given by

$$\mathbf{x}(t) = \Phi(t, t_0)\mathbf{x}_0 + \int_{t_0}^t \Phi(t, \tau)\mathbf{g}(\mathbf{x}(\tau), \tau)d\tau \tag{29}$$

where $\Phi(t, \tau)$ is the fundamental matrix associated with matrix $J(t)$.

Theorem 17 (A General Linear Stability Theorem). For the nonlinear nonautonomous system (28), if there are two positive constants c and σ such that

$$\|\Phi(t, \tau)\| \leq ce^{-\sigma(t-\tau)} \quad \text{for all } t_0 \leq \tau \leq t < \infty$$

and if

$$\lim_{\|\mathbf{x}\| \rightarrow 0} \frac{\|\mathbf{g}(\mathbf{x}, t)\|}{\|\mathbf{x}\|} = 0$$

uniformly with respect to $t \in [t_0, \infty)$, then there are two positive constants, γ and δ , such that

$$\|\mathbf{x}(t)\| \leq c\|\mathbf{x}_0\|e^{-\gamma(t-t_0)}$$

for all $\|\mathbf{x}_0\| \leq \delta$ and all $t \in [t_0, \infty)$.

This result implies that under the theorem conditions, the system is locally, uniformly, and exponentially stable about its equilibrium $\mathbf{x}^* = 0$.

In particular, if the system matrix $J(t) = J$ is a stable constant matrix, then the following simple criterion is convenient to use.

Theorem 18 (A Special Linear Stability Theorem). Suppose that in system (28), the matrix $J(t) = J$ is a stable constant matrix (all its eigenvalues have a negative real part), and $\mathbf{g}(0, t) = 0$. Let P be a positive definite and symmetric matrix solution of the Lyapunov equation

$$PJ + J^T P + Q = 0$$

where Q is a positive definite and symmetric constant matrix. If

$$\|\mathbf{g}(\mathbf{x}, t)\| \leq a\|\mathbf{x}\|$$

for a constant $a < \frac{1}{2}\lambda_{\max}(P)$ uniformly on $[t_0, \infty)$, where $\lambda_{\max}(P)$ is the maximum eigenvalue of P , then system (28) is globally, uniformly, and asymptotically stable about its equilibrium $\mathbf{x}^* = 0$.

This actually is the example for illustration of Theorem 2 discussed in Section 4.1.

Again consider system (27) with equilibrium $\mathbf{x}^* = 0$.

Theorem 19 (The Lyapunov Converse Theorem). Suppose that \mathbf{f} is continuously differentiable in a neighborhood of the origin, and its Jacobian $\mathbf{J}(t)$ is bounded and Lipschitz in the neighborhood, uniformly in t . Then, the system is exponentially stable about its equilibrium if and only if its linearized system $\dot{\mathbf{x}} = \mathbf{J}(t)\mathbf{x}$ is exponentially stable about the origin.

5.2. Linear Stability of Nonlinear Systems with Periodic Linearity

Consider a nonlinear nonautonomous system of the form

$$\dot{\mathbf{x}} = \mathbf{f}(\mathbf{x}, t) = J(t)\mathbf{x} + \mathbf{g}(\mathbf{x}, t), \quad \mathbf{x}(t_0) = \mathbf{x}_0 \in \mathbf{R}^n \tag{30}$$

where $\mathbf{g}(0, t) = 0$ and $J(t)$ is a p -periodic matrix ($p > 0$):

$$J(t + p) = J(t) \quad \text{for all } t \in [t_0, \infty)$$

Theorem 20 (Floquet Theorem). In system (30), assume that $\mathbf{g}(\mathbf{x}, t)$ and $\partial \mathbf{g}(\mathbf{x}, t) / \partial \mathbf{x}$ are both continuous in a bounded region \mathcal{D} containing the origin. Assume, moreover, that

$$\lim_{\|\mathbf{x}\| \rightarrow 0} \frac{\|\mathbf{g}(\mathbf{x}, t)\|}{\|\mathbf{x}\|} = 0$$

uniformly on $[t_0, \infty)$. If the system Floquet multipliers satisfy

$$|\lambda_i| < 1, \quad i = 1, \dots, n, \quad \text{for all } t \in [t_0, \infty) \tag{31}$$

then system (30) is globally, uniformly, and asymptotically stable about its equilibrium $\mathbf{x}^* = 0$.

Note that if $\mathbf{g}(\mathbf{x}, t) = 0$ in system (28) or (30), all the linear stability results presented above still hold and are consistent with the familiar results from the linear systems theory.

6. TOTAL STABILITY: STABILITY UNDER PERSISTENT PERTURBANCES

Consider a nonautonomous system of the form

$$\dot{\mathbf{x}} = \mathbf{f}(\mathbf{x}, t) + \mathbf{h}(\mathbf{x}, t), \quad \mathbf{x}(t_0) = \mathbf{x}_0 \in \mathbf{R}^n \tag{32}$$

where \mathbf{f} is continuously differentiable, with $\mathbf{f}(0, t) = 0$, and \mathbf{h} is a *persistent perturbation* in the sense that for any $\varepsilon > 0$, there are two positive constants, δ_1 and δ_2 , such that if $\|\mathbf{h}(\tilde{\mathbf{x}}, t)\| < \delta_1$ for all $t \in [t_0, \infty)$ and if $\|\tilde{\mathbf{x}}(t_0)\| < \delta_2$, then $\|\tilde{\mathbf{x}}(t)\| < \varepsilon$.

The equilibrium $\mathbf{x}^* = 0$ of the unperturbed system [system (32) with $\mathbf{h} = 0$ therein] is said to be *totally stable*, if the persistently perturbed system (32) remains to be stable in the sense of Lyapunov.

As the next theorem states, all uniformly and asymptotically stable systems with persistent perturbations are totally stable, namely, a stable orbit starting from a neighborhood of another orbit will stay nearby [13,15].

Theorem 21 (Malkin Theorem). If the unperturbed system (32), that is, with $\mathbf{h} = 0$ therein, is uniformly and asymptotically stable about its equilibrium $\mathbf{x}^* = 0$, then it is totally stable, namely, the persistently perturbed system (32) remains to be stable in the sense of Lyapunov.

Next, consider an autonomous system with persistent perturbations:

$$\dot{\mathbf{x}} = \mathbf{f}(\mathbf{x}) + \mathbf{h}(\mathbf{x}, t), \quad \mathbf{x} \in \mathbf{R}^n \tag{33}$$

Theorem 22 (Perturbed Orbital Stability Theorem). If $\varphi_t(\mathbf{x}_0)$ is an orbitally stable solution of the unperturbed autonomous system (33) (with $\mathbf{h} = 0$ therein), then it is totally stable, that is, the perturbed system remains to be orbitally stable under persistent perturbations.

7. ABSOLUTE STABILITY AND FREQUENCY-DOMAIN CRITERIA

Consider a feedback system in the Lur’e form

$$\begin{cases} \dot{\mathbf{x}} = \mathbf{A}\mathbf{x} + \mathbf{B}\mathbf{h}(\mathbf{y}) \\ \mathbf{y} = \mathbf{C}\mathbf{x} \end{cases} \tag{34}$$

where A, B, C are constant matrices, in which A is non-singular but B and C are not necessarily square (yet, probably, $B = C = I$), and \mathbf{h} is a vector-valued nonlinear function. By taking the Laplace transform with zero initial conditions, and denoting the transform by $\hat{\mathbf{x}} = \mathcal{L}\{\mathbf{x}\}$, the state vector is obtained as

$$\hat{\mathbf{x}} = [sI - A]^{-1}B\mathcal{L}\{\mathbf{h}(\mathbf{y})\} \tag{35}$$

so that the output is given by

$$\hat{\mathbf{y}} = CG(s)\mathcal{L}\{\mathbf{h}(\mathbf{y})\} \tag{36}$$

with the system transfer matrix

$$G(s) = [sI - A]^{-1}B \tag{37}$$

This can be implemented via the block diagram shown in Fig. 12, where, for notational convenience, both time- and frequency-domain symbols are mixed.

The Lur’e system shown in Fig. 12 is a closed-loop configuration, where the feedback loop is usually considered as a “controller.” Thus, this system is sometimes written in the following equivalent form:

$$\begin{cases} \dot{\mathbf{x}} + \mathbf{A}\mathbf{x} + \mathbf{B}\mathbf{u} \\ \mathbf{y} = \mathbf{C}\mathbf{x} \\ \mathbf{u} = \mathbf{h}(\mathbf{y}) \end{cases} \tag{38}$$

7.1. SISO Lur’e Systems

First, single-input/single-output Lur’e systems are discussed, where $u = h(y)$ and $y = \mathbf{c}^T\mathbf{x}$ are both scalar-valued functions:

$$\begin{cases} \dot{\mathbf{x}} = \mathbf{A}\mathbf{x} + \mathbf{b}u \\ y = \mathbf{c}^T\mathbf{x} \\ u = h(y) \end{cases} \tag{39}$$

Assume that $h(0) = 0$, so that $\mathbf{x}^* = 0$ is an equilibrium of the system.

7.1.1. The Sector Condition. The Lur’e system (39) is said to satisfy the *local (global) sector condition* on the nonlinear function $h(\cdot)$, if there exist two constants, $\alpha < \beta$, such that

- 1. Local sector condition:

$$\begin{aligned} \alpha y^2(t) \leq y(t)h(y(t)) \leq \beta y^2(t) \quad \text{for all} \\ a \leq y(t) \leq b \quad \text{and } t \in [t_0, \infty) \end{aligned} \tag{40}$$

- 2. Global sector condition:

$$\begin{aligned} \alpha y^2(t) \leq y(t)h(y(t)) \leq \beta y^2(t) \quad \text{for all} \\ -\infty < y(t) < \infty \quad \text{and } t \in [t_0, \infty) \end{aligned} \tag{41}$$

Here, $[\alpha, \beta]$ is called the *sector* for the nonlinear function $h(\cdot)$. Moreover, the system (39) is said to be (globally) *absolutely stable within the sector* $[\alpha, \beta]$ if the system is (globally) asymptotically stable about its equilibrium $\mathbf{x}^* = 0$ for any nonlinear function $h(\cdot)$ satisfying the

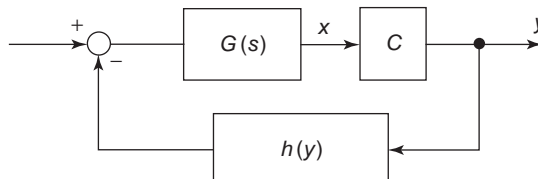


Figure 12. Configuration of the Lur’e system.

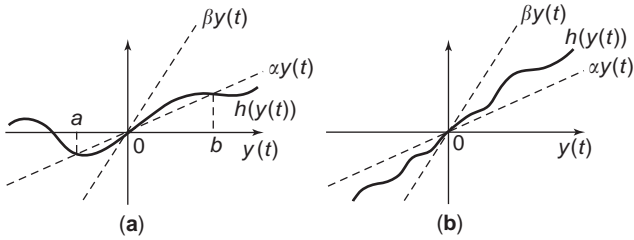


Figure 13. Local and global sector conditions.

(global) sector condition. These local and global sector conditions are visualized by Figs. 13a and 13b, respectively.

7.1.2. The Popov Criterion.

Theorem 23 (Popov Criterion). Suppose that the SISO Lur’e system (39) satisfied the following conditions:

- (a) A is stable and $\{A, \mathbf{b}\}$ is controllable.
- (b) The system satisfies the global sector condition with $\alpha = 0$ therein.
- (c) For any $\varepsilon > 0$, there is a constant $\gamma > 0$ such that

$$\text{Re}\{(1 + j\gamma\omega)G(j\omega)\} + \frac{1}{\beta} \geq \varepsilon \quad \text{for all } \omega \geq 0 \quad (42)$$

where $G(s)$ is the transfer function defined by (37), and $\text{Re}\{\cdot\}$ denotes the real part of a complex number (or function). Then, the system is globally asymptotically stable about its equilibrium $\mathbf{x}^* = 0$ within the sector.

The Popov criterion has the following geometric meaning. Separate the complex function $G(s)$ into its real and imaginary parts, namely

$$G(j\omega) = G_r(\omega) + jG_i(\omega)$$

and rewrite condition (C) as

$$\frac{1}{\beta} > -G_r(\omega) + \gamma\omega G_i(\omega) \quad \text{for all } \omega \geq 0$$

Then the graphical situation of the Popov criterion shown in Fig. 14 implies the global asymptotic stability of the system about its zero equilibrium.

7.1.3. The Circle Criterion. The Popov criterion has a natural connection to the linear Nyquist criterion

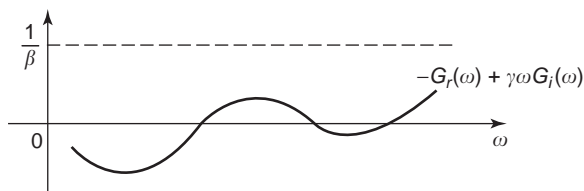


Figure 14. Geometric meaning of the Popov criterion.

[17,26,27,29]. A more direct generalization of the Nyquist criterion to nonlinear systems is the following.

Theorem 24 (Circle Criterion). Suppose that the SISO Lur’e system (39) satisfies the following conditions:

- (a) A has no purely imaginary eigenvalues, and has κ eigenvalues with positive real parts.
- (b) The system satisfies the global sector condition.
- (c) One of the following situation holds:
 - (1) $0 < \alpha < \beta$ —the Nyquist plot of $G(j\omega)$ encircles the disk $D[-(1/\alpha), -(1/\beta)]$ counterclockwise κ times but does not enter it.
 - (2) $0 = \alpha < \beta$ —the Nyquist plot of $G(j\omega)$ stays within the open half-plane $\text{Re}\{s\} > -(1/\beta)$.
 - (3) $\alpha < 0 < \beta$ —the Nyquist plot of $G(j\omega)$ stays within the open disk $D[-(1/\beta), -(1/\alpha)]$.
 - (4) $\alpha < \beta < 0$ —the Nyquist plot of $-G(j\omega)$ encircles the disk $D[(1/\alpha), (1/\beta)]$ counterclockwise κ times but does not enter it.

Then, the system is globally asymptotically stable about its equilibrium $\mathbf{x}^* = 0$.

Here, the disk $D[-(1/\alpha), -(1/\beta)]$, for the case of $0 < \alpha < \beta$, is shown in Fig. 15.

7.2. MIMO Lur’e systems

Consider a multiinput/multioutput Lur’e system, as shown in Fig. 12, described by

$$\begin{cases} \mathbf{x}(s) = G(s)\mathbf{u}(s) \\ \mathbf{u}(t) = -\mathbf{h}(\mathbf{y}(t)) \end{cases} \quad (43)$$

with $G(s)$ as defined in (37). If this system satisfies the following Popov inequality

$$\int_{t_0}^{t_1} \mathbf{y}^T(\tau)\mathbf{x}(\tau)d\tau \geq -\gamma \quad \text{for all } t_1 \geq t_0 \quad (44)$$

for a constant $\gamma \geq 0$ independent of t , then it is said to be hyperstable.

The linear part of this MIMO system is described by the transfer matrix $G(s)$, which is said to be positive real if

1. There are no poles of $G(s)$ located inside the open half-plane $\text{Re}\{s\} > 0$.
2. Poles of $G(s)$ on the imaginary axis are simple, and the residues form a semipositive definite matrix.

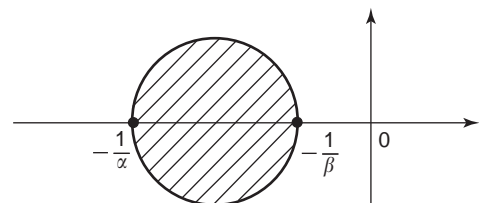


Figure 15. The disk $D[-(1/\alpha), -(1/\beta)]$.

3. The matrix $[G(j\omega) + G^T(j\omega)]$ is a semipositive definite matrix for all real values of ω that are not poles of $G(s)$.

Theorem 25 (Hyperstability Theorem). The MIMO Lur’e system (43) is hyperstable if and only if its transfer matrix $G(s)$ is positive real.

7.3. Describing Function Method

Return to the SISO Lur’e system (39) and consider its periodic output $y(t)$. Assume that the nonlinear function $h(\cdot)$ therein is a time-invariant odd function, and satisfies the property that for $y(t) = \alpha \sin(\omega t)$, with real constants ω and $\alpha \neq 0$, only the first-order harmonic of $-h(y)$ in its Fourier series expansion is significant. Under this setup, the specially defined function

$$\Psi(\alpha) = -\frac{2\omega}{\alpha\pi} \int_0^{\pi/\omega} h(\alpha \sin(\omega t)) \sin(\omega t) dt \quad (45)$$

is called the *describing function* of the nonlinearity $-h(\cdot)$, or of the system [1,26,27].

Theorem 26 (First-Order Harmonic Balance Approximation). Under the conditions stated above, if the first-order harmonic balance equations

$$G_r(j\omega)\Psi(\alpha) = 1 \quad \text{and} \quad G_i(j\omega) = 0$$

have solutions ω and $\alpha \neq 0$, then

$$y^{(1)}(t) = \frac{j\alpha}{2} e^{-j\omega t} - \frac{j\alpha}{2} e^{j\omega t}$$

is the first-order approximation of a possible periodic orbit of the output of system (39); but if the preceding harmonic balance equations have no solution, then the system is unlikely to have any periodic output.

When solving the equation $G_r(j\omega)\Psi(\alpha) = 1$ graphically, one can sketch two curves in the complex plane: $G_r(j\omega)$ and $-1/\Psi(\alpha)$ by increasing gradually ω and α , respectively, to find their crossing points:

1. If the two curves are (almost) tangent, as illustrated by Fig. 16a, then a conclusion drawn from the describing function method will not be satisfactory in general.
2. If the two curves are (almost) transversal, as illustrated by Fig. 16b, then a conclusion drawn from the describing function analysis will generally be reliable.

Theorem 27 (Graphical Stability Criterion for a Periodic Orbit). Each intersection point of the two curves above, $G_r(j\omega)$ and $-1/\Psi(\alpha)$, corresponds to a periodic orbit, $y^{(1)}(t)$, of the output of system (39). If the points, near the intersection and on one side of the curve $-1/\Psi(\alpha)$ where $-\alpha$ is increasing, are not encircled by the curve $G_r(j\omega)$, then the corresponding periodic output is stable; otherwise, it is unstable.

8. BIBO STABILITY

A relatively simple, and also relatively weak, notion of stability is discussed in this section. This is the *bounded-input/bounded-output (BIBO) stability*, which refers to the property of a system that any bounded input to the system produces a bounded output throughout the system [8,9,17].

It can be verified that the linear system $\dot{\mathbf{x}} = \mathbf{A}\mathbf{x} + \mathbf{B}\mathbf{u}$ is BIBO stable if the matrix \mathbf{A} is asymptotically stable.

Here, the focus is on the input-output map (13), with its configuration shown in Fig. 2.

The system S is said to be *BIBO stable* from the input set U to the output set Y , if for each admissible input $\mathbf{u} \in U$ and the corresponding output $\mathbf{y} \in Y$, there exist two non-negative constants, b_i and b_o , such that

$$\|\mathbf{u}\|_U \leq b_i \Rightarrow \|\mathbf{y}\|_Y \leq b_o \quad (46)$$

Since all norms are equivalent for a finite-dimensional vector, it is generally insignificant to distinguish under what kind of norms for the input and output signals the BIBO stability is defined and achieved. Moreover, it is important to note that in the definition above, even if b_i is small and b_o is large, the system is still considered to be BIBO-stable. Therefore, this stability may not be very practical for some systems in certain applications.

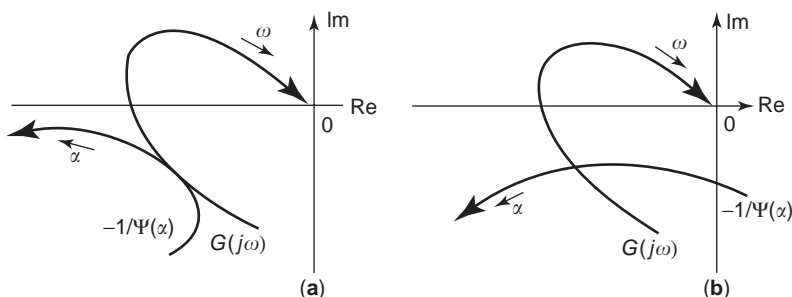


Figure 16. Graphical depiction of describing function analysis.

8.1. Small-Gain Theorem

A convenient criterion for verifying the BIBO stability of a closed-loop control system is the small-gain theorem [8,9,17], which applies to almost all kinds of systems (linear and nonlinear, continuous-time and discrete-time, time-delayed, of any dimensions), as long as the mathematical setup is appropriately formulated to meet the theorem conditions. The main disadvantage of this criterion is its overconservativity.

Return to the typical closed-loop system shown in Fig. 3, where the inputs, outputs, and internal signals are related via the following equations:

$$\begin{cases} S_1(e_1) = e_2 - u_2 \\ S_2(e_2) = u_1 - e_1 \end{cases} \quad (47)$$

It is important to note that the individual BIBO stability of S_1 and S_2 is not sufficient for the BIBO stability of the connected closed-loop system. For instance, in the discrete-time setting of Fig. 3, suppose that $S_1 \equiv 1$ and $S_2 \equiv -1$, with $u_1(k) \equiv 1$ for all $k = 0, 1, \dots$. Then S_1 and S_2 are BIBO-stable individually, but it can be easily verified that $y_1(k) = k \rightarrow \infty$ as the discrete-time variable k evolves. Therefore, a stronger condition describing the interaction of S_1 and S_2 is necessary.

Theorem 28 (Small-Gain Theorem). If there exist four constants, L_1, L_2, M_1, M_2 , with $L_1L_2 < 1$, such that

$$\begin{cases} \|S_1(e_1)\| \leq M_1 + L_1\|e_1\| \\ \|S_2(e_2)\| \leq M_2 + L_2\|e_2\| \end{cases} \quad (48)$$

then

$$\begin{cases} \|e_1\| \leq (1 - L_1L_2)^{-1}(\|u_1\| + L_2\|u_2\| + M_2 + L_2M_1) \\ \|e_2\| \leq (1 - L_1L_2)^{-1}(\|u_2\| + L_1\|u_1\| + M_1 + L_1M_2) \end{cases} \quad (49)$$

where the norms $\|\cdot\|$ are defined over the spaces that the signals belong. Consequently, (48) and (49) together imply that if the system inputs (u_1 and u_2) are bounded then the corresponding outputs [$S_1(e_1)$ and $S_2(e_2)$] are bounded.

Note that the four constants, L_1, L_2, M_1, M_2 , can be somewhat arbitrary (e.g., either L_1 or L_2 can be large) provided that $L_1L_2 < 1$, which is the key condition for the theorem to hold [and is used to obtain $(1 - L_1L_2)^{-1}$ in the bounds (49)].

In the special case where the input-output spaces U and Y are both the L_2 space, a similar criterion based on the system passivity property can be obtained [9,17]. In this case, an inner product between any two vectors in the space is defined by

$$\langle \xi, \eta \rangle = \int_{t_0}^{\infty} \xi^T(\tau)\eta(\tau) d\tau$$

Theorem 29 (Passivity Stability Theorem). If there exist four constants, L_1, L_2, M_1, M_2 , with $L_1 + L_2 > 0$, such that

$$\begin{cases} \langle e_1, S_1(e_1) \rangle \geq L_1\|e_1\|_2^2 + M_1 \\ \langle e_2, S_2(e_2) \rangle \geq L_2\|e_2\|_2^2 + M_2 \end{cases} \quad (50)$$

then the closed-loop system (47) is BIBO-stable.

As mentioned, the main disadvantage of this criterion is its overconservativity in providing the sufficient conditions for the BIBO stability. One resolution is to transform the system into the Lur'e structure, and then apply the circle or Popov criterion under the sector condition (if it can be satisfied), which can usually lead to less conservative stability conditions.

8.2. Contraction Mapping Theorem

The small-gain theorem discussed above, by nature, is a kind of contraction mapping theorem. The contraction mapping theorem can be used to determine the BIBO stability property of a system described by a map in various forms, provided that the system (or the map) is appropriately formulated. The following is a typical (global) contraction mapping theorem.

Theorem 30 (Contraction Mapping Theorem). If the operator norm of the input-output map S , defined on \mathbf{R}^n , satisfies $\|S\| < 1$, then the system mapping

$$\mathbf{y}(t) = S(\mathbf{y}(t)) + \mathbf{c}$$

has a unique solution for any constant vector $\mathbf{c} \in \mathbf{R}^n$. This solution satisfies

$$\|\mathbf{y}\| \leq (1 - \|S\|)^{-1}\|\mathbf{c}\|$$

In particular, the solution of the equation

$$\mathbf{y}_{k+1} = S(\mathbf{y}_k), \mathbf{y}_0 \in \mathbf{R}^n, k = 0, 1, \dots$$

satisfies

$$\|\mathbf{y}_k\| \rightarrow 0 \text{ as } k \rightarrow \infty$$

9. CONCLUDING REMARKS

This article has offered a brief introduction to the basic theory and methodology of Lyapunov stability, orbital stability, structural stability, and input-output stability for nonlinear dynamical systems. More subtle details for stability analysis of general dynamical systems can be found in the literature [3,5,9,11-13,16,17,19,20,23,26,27,29,30]. In cases where control was explicitly involved, stability and stabilization issues have also been studied [8,17,25,28,33].

Several important classes of nonlinear (control) systems have been omitted in the discussion of various stability issues: some general functional systems such as

systems with time delays [14], measure ordinary differential equations such as systems with impulses [2,31], and some weakly nonlinear systems such as piecewise linear and switching (non)linear systems. Discussion of more advanced nonlinear systems, such as singular nonlinear systems (perhaps with time delays), infinite-dimensional (non)linear systems, spatiotemporal systems described by nonlinear partial differential equations, and nonlinear stochastic (control) systems, are beyond the scope of this elementary expository article.

Finally, for more recent studies of system stability theories, the reader is referred to the reviews edited by Martynuk [22].

BIBLIOGRAPHY

1. D. P. Atherton, *Nonlinear Control Engineering* (student ed.), Van Nostrand Reinhold, New York, 1982.
2. D. D. Bainov and P. S. Simeonov, *Systems with Impulse Effect: Stability, Theory and Applications*, Ellis Horwood, Chichester (UK), 1989.
3. N. P. Bhatia and G. P. Szegö, *Stability Theory of Dynamical Systems*, Springer-Verlag, Berlin, 1970.
4. F. Brauer and J. A. Nohel, *The Qualitative Theory of Ordinary Differential Equations: An Introduction*, 1969; Dover, New York, 1989.
5. L. Cesari, *Asymptotic Behavior and Stability Problems in Ordinary Differential Equations*, Springer-Verlag, New York, 1971.
6. G. Chen, G. Chen, and S. H. Hsu, *Linear Stochastic Control Systems*, CRC Press, Boca Raton, FL, 1995.
7. G. Chen and X. Dong, *From Chaos to Order: Methodologies, Perspectives and Applications*, World Scientific, Singapore, 1998.
8. R. J. P. de Figueiredo and G. Chen, *Nonlinear Feedback Control Systems: An Operator Theory Approach*, Academic Press, San Diego, 1993.
9. C. A. Desoer and M. Vidyasagar, *Feedback Systems: Input-Output Properties*, Academic Press, New York, 1975.
10. H. Freeman, *Discrete-Time Systems: An Introduction to the Theory*, Wiley, New York, 1965.
11. P. Glendinning, *Stability, Instability and Chaos*, Cambridge Univ. Press, New York, 1994.
12. R. Grimshaw, *Nonlinear Ordinary Differential Equations*, CRC Press, Boca Raton, FL, 1993.
13. W. Hahn, *Stability of Motion*, Springer-Verlag, Berlin, 1967.
14. J. Hale, *Theory of Functional Differential Equations*, Springer-Verlag, New York, 1973.
15. F. C. Hoppensteadt, *Analysis and Simulation of Chaotic Systems*, Springer-Verlag, New York, 1977.
16. D. W. Jordan and P. Smith, *Nonlinear Ordinary Differential Equations*, 2nd ed., Oxford Univ. Press, New York, 1987.
17. H. K. Khalil, *Nonlinear Systems*, 2nd ed., Prentice-Hall, Upper Saddle River, NJ, 1996.
18. V. Lakshmikantham, V. M. Matrosov, and S. Sivasundaram, *Vector Lyapunov Functions and Stability Analysis of Nonlinear Systems*, Kluwer Academic, Boston, 1991.
19. J. P. LaSalle, *The Stability of Dynamical Systems*, SIAM, Philadelphia, 1976.
20. S. Lefschetz, *Differential Equations: Geometric Theory*, 2nd ed., 1963; Dover, New York, 1977.
21. A. M. Lyapunov, *The General Problem of Stability of Motion* (100th Anniversary), Taylor & Francis, London, 1992.
22. A. A. Martynuk, ed., *Advances in Stability Theory at the End of the 20th Century*, Taylor & Francis, London, 2003.
23. D. R. Merkin, *Introduction to the Theory of Stability*, Springer-Verlag, New York, 1997.
24. A. N. Michel and R. K. Miller, *Qualitative Analysis of Large Scale Dynamical Systems*, Academic Press, New York, 1977.
25. N. Minorsky, *Theory of Nonlinear Control Systems*, New York: McGraw-Hill, 1969.
26. R. R. Mohler, *Nonlinear Systems*, Vol. 1, *Dynamics and Control*, Prentice-Hall, Englewood Cliffs, NJ, 1991.
27. K. S. Narendra and J. H. Taylor, *Frequency Domain Criteria for Absolute Stability*, Academic Press, New York, 1973.
28. H. Nijmeijer and A. J. van der Schaft, *Nonlinear Dynamical Control Systems*, Springer-Verlag, New York, 1990.
29. P. C. Parks and V. Hahn, *Stability Theory*, Prentice-Hall, New York, 1981.
30. S. Yu. Pilyugin, *Introduction to Structurally Stable Systems of Differential Equations*, Birkhäuser, Boston, 1992.
31. A. M. Samoilenko and N. A. Perestyuk, *Impulsive Differential Equations*, World Scientific, Singapore, 1995.
32. D. D. Siljjack, *Large Scale Dynamic Systems: Stability and Structure*, North-Holland, Amsterdam, 1978.
33. E. D. Sontag, *Mathematical Control Theory: Deterministic Finite Dimensional Systems*, 2nd ed., Springer-Verlag, New York, 1998.
34. F. Verhulst, *Nonlinear Differential Equations and Dynamical Systems*, Springer-Verlag, Berlin, 1990.
35. M. Vidyasagar, *Nonlinear Systems Analysis*, 2nd ed., Prentice-Hall, Englewood Cliffs, NJ, 1993.
36. M. Y. Wu, A note on stability of linear time-varying systems, *IEEE Trans. Automat. Control* (April 1974), p. 162.
37. N. E. Zhukovskij, On solidity of motion, in *Collection of Works*, Leningrad Press, Moscow, 1948, Vol. 1, p. 67.

STANDING WAVE METERS AND NETWORK ANALYZERS

BURKHARD SCHIEK
ANDREAS GRONEFELD
Ruhr-Universität Bochum

1. MEASUREMENT OF NETWORKS AT MICROWAVE FREQUENCIES

Determining the characteristics of electrical networks (network analysis) is an important measurement tool both for developers of electrical circuits and systems and in production testing. The measurement of network characteristics at microwave frequencies employs different concepts than are used at lower frequencies, where measuring port voltages and currents readily allows determination of impedance (Z) or admittance (Y) parameters. At higher frequencies, neither high-impedance voltage probes nor low-impedance current measurements are feasible, because parasitic capacitance and inductance of

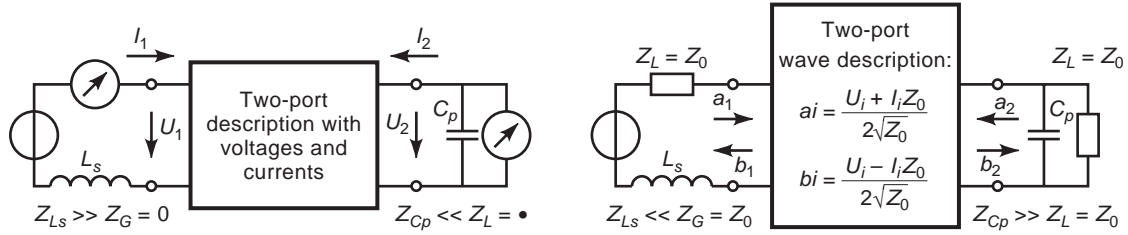


Figure 1. Drawbacks of voltage and current measurement versus the wave concept.

probes (L_s and C_p in Fig. 1) cannot be made small enough. Also, the physical dimensions of microwave circuits typically are no longer small with respect to the wavelength. A cable, connecting the port of a device under test with the measurement equipment, may easily transform the intended open circuit into a short, if its length happens to be an odd multiple of $\lambda/4$. Furthermore, short- or open-circuiting network ports, invariably linked to voltage and current measurements, may alter the behavior of microwave circuits (e.g., an amplifier, operated at those impedance extremes, may oscillate). And in waveguides, voltage and current are not even defined.

The above difficulties are circumvented if the network is embedded between defined generator and load impedances Z_0 (typically real and $50\ \Omega$) and described in terms of its power transfer characteristics. The “scattering” of the incident power wave a_1 into the transmitted wave b_2 and the reflected wave b_1 fully characterizes the two-port network of Fig. 1 in the forward direction.

Conceptually, waves represent the propagation of energy along a transmission line. The incident (forward) wave $a = U_f/\sqrt{Z_0}$ travels along the line, with a portion of it ($b = U_r/\sqrt{Z_0}$) being reflected at the line’s end. Adding both complex quantities in every location along the transmission line yields a sine-shaped pattern, the standing wave (Fig. 2). The ratio of its maximum to its minimum voltage is called the voltage standing wave ratio (VSWR) and is directly linked to the magnitude of the impedance Z_L , terminating the line.

$$\text{VSWR} = \frac{|U_f| + |U_r|}{|U_f| - |U_r|} = \frac{U_{\max}}{U_{\min}} = \begin{cases} \left| \frac{Z_L}{Z_0} \right|, & |Z_L| > Z_0 \\ \left| \frac{Z_0}{Z_L} \right|, & |Z_L| < Z_0 \end{cases} \quad (1)$$

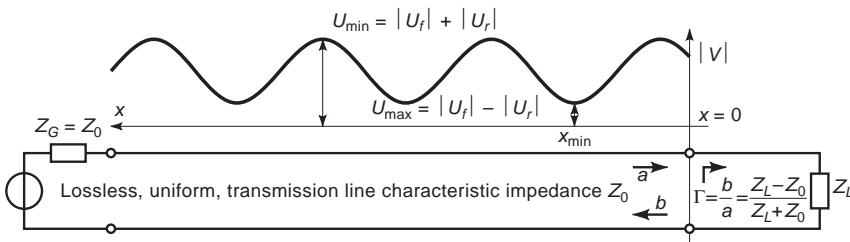


Figure 2. Standing waves along a transmission line, terminated in Z_L .

The incident and reflected waves a_i and b_i at a network port (Fig. 1) are defined as linear combinations of the port currents and voltages:

$$a_i = \frac{U_i + I_i Z_0}{2\sqrt{Z_0}}, \quad b_i = \frac{U_i - I_i Z_0}{2\sqrt{Z_0}}$$

making it easy to compute the impedance Z_i at that port:

$$Z_i = \frac{U_i}{I_i} = Z_0 \frac{1 + \frac{b_i}{a_i}}{1 - \frac{b_i}{a_i}} = Z_0 \frac{1 + \Gamma_i}{1 - \Gamma_i}, \quad \Gamma_i = \frac{b_i}{a_i} \quad (2)$$

Γ is called the reflection coefficient. Similarly, the portion of the incident power transmitted from port i to port j is obtained by the transmission factor $t_{ji} = b_j a_i$.

In general, a two-port network is fully characterized by its 2×2 scattering matrix,

$$\begin{pmatrix} b_1 \\ b_2 \end{pmatrix} = \begin{bmatrix} S_{11} & S_{12} \\ S_{21} & S_{22} \end{bmatrix} \begin{pmatrix} a_1 \\ a_2 \end{pmatrix}$$

which is composed of

$$\text{Reflection coefficients: } S_{11} = \left. \frac{b_1}{a_1} \right|_{a_2=0}, \quad S_{22} = \left. \frac{b_2}{a_2} \right|_{a_1=0}$$

$$\text{Transmission coefficients: } S_{21} = \left. \frac{b_2}{a_1} \right|_{a_2=0}, \quad S_{12} = \left. \frac{b_1}{a_2} \right|_{a_1=0}$$

The exact determination of scattering parameters, however, still requires the locus, where they are valid, to be fixed. If the measurement port at $x = 0$ in Fig. 2 is shifted to the left, the phase of incident and reflected waves changes and so does the reflection coefficient, which therefore depends on the locus. Especially at small wavelengths, measurement of S parameters stipulates the exact definition of

where the waves are recorded, leading to the concept of *measurement or reference planes*. These planes are thought to perpendicularly intersect the transmission lines leading to the ports of the network, such that the phase of the waves in each plane is constant. For scattering parameter S_{ij} , the incident wave in plane j is thus the reference for the emanating wave in plane i . S_{ij} therefore describes the transmission of energy between those planes.

As scattering parameters are ratios of emanating and incident waves, their computation does not require absolute measurement of the wave quantities. This important advantage allows the measurement of scattering parameters (with network analyzers) to inherently exhibit much higher precision than can be expected from a spectrum analyzer that relies on absolute measurement of its input power.

The remainder of this article will present a number of measurement systems for the determination of reflection coefficients (one-port network analyzer or reflectometer) and for full characterization of two-port networks. Although the concept of S -parameters is easily extended to N -ports, measurement of networks with more than two ports will not be covered, because most commercially available hardware is built for two-port measurements and can be used to characterize N -ports by simply terminating the unused $N-2$ ports in Z_0 .

2. REFLECTION MEASUREMENT TECHNIQUES

2.1. The Slotted Line for VSWR and Impedance Measurements

A very old technique for measuring the VSWR on a transmission line, to determine the impedance connected at its end, makes use of a slotted transmission line of characteristic impedance Z_0 (see, for example, Ref. 1, Chap. 2, for a very detailed outline; or see Ref. 2, Chap. 4).

The slot allows a small enough probe, as not to disturb the line's field, to be moved along the x axis of the transmission line and sample its electric field. The high-frequency voltage is converted to direct current (dc) by a diode detector and brought to an instrument for readout. Since the signal level of the probe must be kept low in order to avoid loading of the line, the detector operates in its square-law region and its output is proportional to the detected *power*, or the square of the voltage. Noting the maximum and minimum values of the detector output, while varying the position of the probe, allows computation of the VSWR, provided that the slot is long enough to reach both maximum and minimum.

As indicated by Eq. (1), measurement of the scalar VSWR is not sufficient to uniquely determine the complex impedance Z_L , terminating the line. In fact, since

$$\begin{aligned} \text{VSWR} &= \frac{|U_f| + |U_r|}{|U_f| - |U_r|} = \frac{1 + \left| \frac{U_r}{U_f} \right|}{1 - \left| \frac{U_r}{U_f} \right|} = \frac{1 + \left| \frac{b}{a} \right|}{1 - \left| \frac{b}{a} \right|} \\ &= \frac{1 + |\Gamma|}{1 - |\Gamma|} \rightarrow |\Gamma| = \frac{\text{VSWR} - 1}{\text{VSWR} + 1} \end{aligned}$$

only the *magnitude* of the reflection coefficient Γ is available. The *phase* of Γ is obtained by noting the *position* x_{\min} of the first minimum, appearing when the probe is moved away from Z_L . With the propagation constant

$$\beta = \frac{2\pi}{\lambda_{sl}}$$

of the slotted transmission line, the phase of Γ becomes

$$\varphi = 2\beta x - \pi$$

such that

$$\Gamma = |\Gamma|e^{j\varphi} = \frac{\text{VSWR} - 1}{\text{VSWR} + 1} e^{j(2\beta x - \pi)}$$

and the complex impedance Z_L may be computed from Γ using Eq. (2).

Although conceptionally simple, the slotted line technique suffers from several drawbacks and limitations:

1. The slotted transmission line is a costly precision device, exhibiting precise line impedance Z_0 , low losses, negligible loading due to the probe, and mechanical stability of the probe depth over the entire moving range.
2. Linearity errors and the limited dynamic range of the detectors reduce the accuracy, when measuring large VSWRs. By modulating the radiofrequency (RF) source and selective reception of the modulation frequency, noise can be reduced, increasing sensitivity and thus measurement dynamic (the so-called "modulated frequency technique").
3. The measurement procedure requires manual interaction and, in its simple form of Fig. 3, does not allow for swept frequency impedance measurements. If, however, only the magnitude of the reflection coefficient is of interest, Sorger [3] describes a setup that uses two slotted lines for swept frequency VSWR measurement.

Because slotted line reflection measurements are a very old technique, much research has been undertaken to alleviate the above limitations. Many ideas and extensions can be found in Ref. 2, covering the topic in more detail.

2.2. Using the Slotline with Multiple Probes

The biggest drawback of slotline measurements, the need for manual interaction, can be overcome if more than one

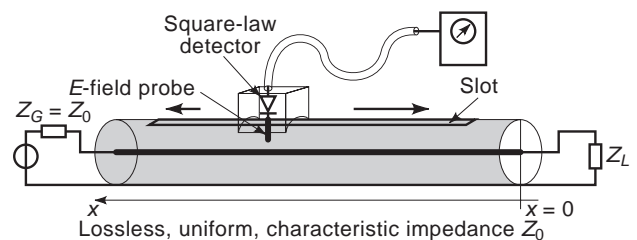


Figure 3. The slotted line measurement setup.

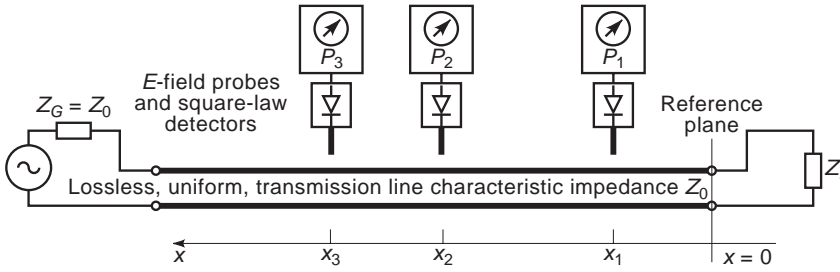


Figure 4. The multiprobe reflectometer.

probe taps to the field of the line in known and fixed positions. Figure 4 shows a system proposed by Caldecott [4] that uses three probes in arbitrary but known positions x_1 , x_2 , and x_3 . Caldecott proved that

$$\Gamma_L \approx \frac{P_1(e^{-j2\beta x_2} - e^{-j2\beta x_3}) + P_2(e^{-j2\beta x_3} - e^{-j2\beta x_1}) + P_3(e^{-j2\beta x_1} - e^{-j2\beta x_2})}{\sin[2\beta(x_2 - x_3)]\sin[2\beta(x_3 - x_1)] + \sin[2\beta(x_1 - x_2)]}$$

even providing complex measurability of the reflection coefficient, although only scalar power measurements ($P_1 \dots P_3$) are used.

Another interesting multiprobe reflectometer for swept frequency/swept power applications reported in Ref. 5 even provided an automatic Smith-chart display of the measured impedance.

2.3. The Six-Port Reflectometer

The idea of the foregoing section can be generalized to the so-called six-port reflectometer, developed by Hoer [6] and Engen [7] in the early 1970s. Figure 5 shows a general six-port junction, driven by a signal generator at port 5, ports 1 through 4 connected to power sensors (diode detectors, bolometers, thermocouple, etc.), and port 6 interfacing to the unknown impedance with reflection coefficient Γ_L .

As the mathematical derivation of the six-port theory is rather lengthy, the interested reader should refer to Refs. 2, 6, or 7 for details. In essence the 6×6 S-matrix of the six-port network is reduced to the form

$$b_i = Q_i a_6 + R_i b_6, \quad i = 1, \dots, 4 \quad (3)$$

by using $\Gamma_i = a_i/b_i$ to eliminate $a_1 \dots a_5$ (b_5 is also eliminated by omitting the fifth equation). The powers P_i are related to b_i by

$$P_i = |b_i|^2(1 - |\Gamma_i|^2)$$

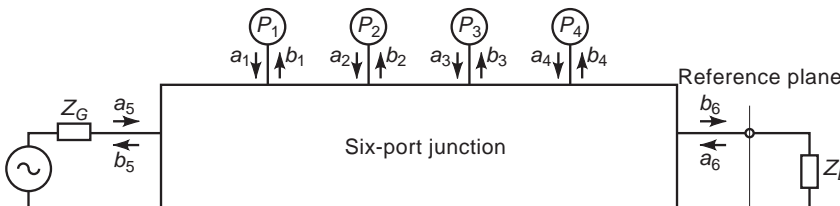


Figure 5. The six-port reflectometer.

and, using Eq. (3), can be expressed as

$$P_i = (1 - |\Gamma_i|^2)\{|R_i|^2|b_6|^2 + 2\text{Re}(Q_i^* R_i) \text{Re}(a_6 b_6^*) + 2 \text{Im}(Q_i^* R_i) \text{Im}(a_6 b_6^*) + |Q_i|^2|a_6|^2\}$$

which may be written in matrix form as

$$(P_1 P_2 P_3 P_4)^T = [D](|b_6|^2 \text{Re}(a_6 b_6^*) \text{Im}(a_6 b_6^*) |a_6|^2)^T \quad (4)$$

with $[D]$ being a real-valued 4×4 matrix. Inverting Eq. (4) gives access to its right-hand-side vector, provided that $[D]$ is known and invertible with $[C]$ being its inverse,

$$(|b_6|^2 \text{Re}(a_6 b_6^*) \text{Im}(a_6 b_6^*) |a_6|^2)^T = [C](P_1 P_2 P_3 P_4)^T$$

such that Γ_L can be computed as

$$\Gamma_L = \frac{a_6}{b_6} = \frac{a_6 b_6^*}{b_6 b_6^*} = \frac{\text{Re}(a_6 b_6^*) + j \text{Im}(a_6 b_6^*)}{|b_6|^2} = \frac{\sum_{n=1}^4 C_{2n} P_n + j \sum_{n=1}^4 C_{3n} P_n}{\sum_{n=1}^4 C_{1n} P_n} \quad (5)$$

With just 12 of the 16 real-valued elements of $[C]$ appearing in Eq. (5), only 11 need to be computed, as Eq. (5) may be normalized to one of the 12 terms. They are determined by measuring *six known* reflection coefficients and using the complex equation [Eq. (5)] to establish a set of 12 linear, real-valued equations in the 12 unknowns.

Although such a calibration procedure to determine the elements of $[C]$ *must* be carried out before the six-port can be used for reflection measurements, it has the added advantage of providing error-corrected results. No a priori knowledge about the six-port is necessary, because the

calibration sufficiently characterizes $[C]$, which reflects the properties of the six-port junction.

Further advantages of this kind of instrument are that neither the signal generator nor the power sensors need to be perfectly matched. The mismatch of the power sensors must however be constant. Because only ratios of measured powers enter the calculation of Γ_L , the power sensors do not need to be absolutely calibrated for power measurements.

However, the power sensors must be linear; and because of their broadband nature, care must be taken to suppress spurious emissions from the signal generator.

Evaluation of Eq. (5) and the determination of $[C]$ require some amount of numerical processing. Six-port reflectometers are therefore almost always combined with microcontrollers to automate the process of calibration and measurement.

Internally, the six-port must be built such that the reduced matrix $[D]$ is invertible at all measurement frequencies. Details of the design process are outlined in Ref. 8 with a practical realization, using 0° and 90° couplers described in Ref. 9.

2.4. Reflection Measurement with the Directional Coupler

All of the impedance measurement methods described thus far evaluate the *sum* of incident and reflected waves, requiring at least two independent measurements for calculation of the reflection coefficient.

Alternatively, forward and reflected waves may be separated using a directional coupler. Such devices are common building blocks in microwave engineering and exist in a wide variety of designs, many of which are treated in Ref. 10, Chap. 8. The interested reader may also refer to Ref. 11 for some less common coupler structures and unusual applications. Figure 6 depicts the associated symbol of a directional coupler and its scattering matrix.

The important property of the directional coupler, used to separate incident and reflected wave, is in its decoupled port. Figure 7 illustrates that feeding a wave a_1 into port 1 results in wave $b_2 = \tau a_1$ and $b_3 = \kappa a_1$ being emitted at ports 2 and 3 with no energy being fed to port 4, the decoupled port. Similarly, port 2 is decoupled from port 3. Driving the coupler at port 1, terminating port 3 in Z_0 , and connecting a matched power detector to port 4 allows measurement of unknown reflection coefficients connected to port 2.

Directional couplers, also called “VSWR-bridges” or “reflection coefficient bridges,” appear in various forms, with the microstrip coupler, the resistive coupler, and the Wilkinson divider (Fig. 8) being the variants most often found.

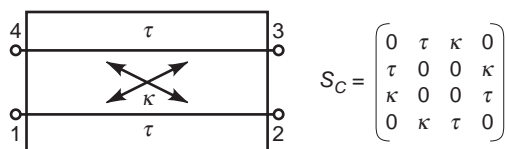


Figure 6. The directional coupler.

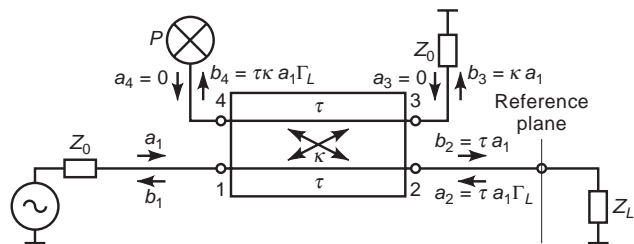


Figure 7. Reflection measurement using a directional coupler.

All practical realizations of directional couplers exhibit finite *directivity*, meaning that a small amount of the power fed to port 1 will leak to port 4, even if port 2 and 3 are perfectly terminated in Z_0 . The directivity of a coupler is defined as

$$d = \frac{S_{14}}{\kappa\tau}$$

Mismatch at port 2 and even at the driving port 1 will further add to erroneous reflections being indicated by the wave b_4 , which ideally should be a measure of the reflection of Z_L only. All these errors must be kept low if the coupler is to be used for precision reflection measurement. Narrow-band precision couplers, exhibiting more than 50 dB directivity, have been built in waveguide and broad-band couplers, typically of the resistive bridge type, and exhibit more than 36 dB directivity over a bandwidth of more than three decades. As a rule of thumb, the directivity should be at least 10 dB better than the expected reflection coefficient of the measured device under test (DUT).

3. ARCHITECTURES OF NETWORK ANALYZERS

In order to measure the entire scattering matrix of a two-port, some means of measuring the transmitted waves as well as the reflected waves must be provided. Because reflection measurements, nowadays, are almost always carried out with directional couplers, we will use its symbol for denoting measurement of reflected waves. As in Fig. 7, the “mixer” symbol will denote a measurement point, at which the wave to be measured may be further processed in one of the following ways:

1. With power detectors, leading to scalar measurement of the wave

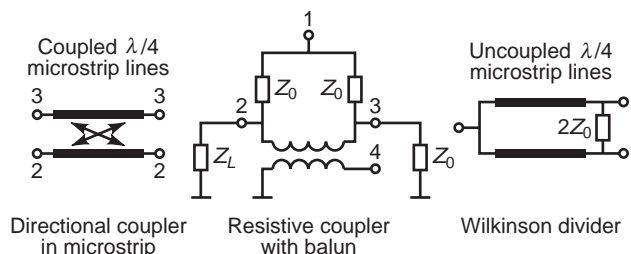


Figure 8. Some commonly used directional couplers.

2. With a homodyne receiver, potentially capable of providing amplitude and phase information
3. With a heterodyne receiver (hence the mixer symbol), providing amplitude and phase information

Depending on the type of detector used, network analyzers (NAs) are classified into one of the following types of analyzer:

3.1. Scalar Network Analyzer

The simplest and most economic approach to the measurement of scattering-parameters employs power (diode) detectors. Because these provide no phase information, only the magnitude of the S -parameters can be measured, hence the term *scalar network analyzer* (SNA). For many applications, however, the magnitude may be all that is needed. Calibration techniques, as described in Section 4, however, require the phase information and consequently cannot be applied to SNAs. Instead, normalization is all that can be employed with such an instrument.

Other drawbacks of SNAs are the limited dynamic range and the broad-band nature of the power detectors. As they record the entire power of a wave, regardless of its spectral origin, these instruments are susceptible to spurs or harmonics of the generator. If, for example, the harmonics of the radiofrequency (RF) source are suppressed by 30 dB, and the DUT has a high-pass or bandstop characteristic (return loss of a filter or an antenna), the SNA will show no less than -30 dB attenuation or return loss, regardless of the DUT's real properties.

It should be emphasized that the mere use of power detectors does not necessarily yield a scalar network analyzer. The six-port reflectometer, as described in Section 2.3, employs four scalar detectors to determine the complex reflection coefficient; a complete vector NA can be built by using two such reflectometers (see Refs. 8, 9, and 12), retaining all vector error-correction capabilities of those instruments [13,14], as discussed in Section 4.

3.2. Heterodyne (Vector) Network Analyzer

If the wave quantities are processed by heterodyne receivers, the phase information can be preserved by phase-locking the heterodyne oscillator to the RF source driving the DUT (Fig. 9), and complex measurement of the scattering parameters is possible. Besides providing a much higher dynamic range (over 120 dB for recent industry products versus 70 dB for SNAs), the ability to measure the complex S -parameters has the added benefit of allowing calibration techniques to enhance measurement accuracy. On the other hand, the inherent higher complexity of heterodyne vector network analyzers (VNAs) results in more expensive hardware. For broad-band systems, the heterodyne oscillator and its Phase Locked Loop (PLL) add considerably to the cost, because they must cover the system's entire bandwidth.

A cost reducing alternative exists by employing "harmonic mixing" (e.g., Ref. 35). In this case the local oscillator (LO) in Fig. 9 has to cover only one octave with all higher frequencies that are needed being supplied by the LO's harmonics. Harmonic mixing, however, leads to

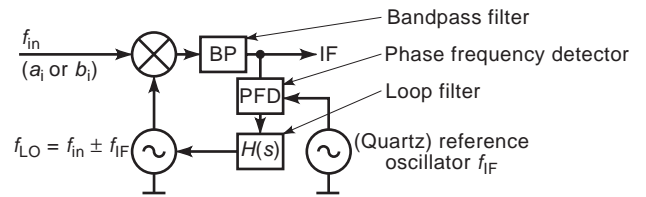


Figure 9. Heterodyne receiver (LO): Local Oscillator, IF: Intermediate Frequency, BP: Bandpass filter, PFD: Phase-Frequency Detector, $H(s)$: Loopfilter.

higher mixer conversion loss and thus also reduces the instrument's dynamic range.

3.3. Homodyne Network Analyzers

In order to circumvent the need for a second microwave source and phase-locking circuitry, homodyne systems use the same generator for down-conversion that drives the DUT. Because the homodyne mixing process provides only the real part of the wave quantity, homodyne NAs need additional hardware (phase-shifters) to extract the complex information from two or more measurements (e.g., Ref. 15). Although relatively simple hardware concepts have been developed [16], homodyne NAs also suffer from their sensitivity to generator harmonics, limiting dynamic range. It is for that reason that homodyne systems are rarely used in the laboratory, although some realizations exist for industrial measurements.

Regardless of the kind of detector used, all practical realizations of the NA architectures introduced in the next sections should be built to provide:

- Good port match, properly terminating the DUT in the system impedance Z_0
- High directivity of the directional coupler for precise reflection measurement
- Low variation of transmission losses over the bandwidth of the system

3.4. Reflection and Transmission Measurement with the Unidirectional Network Analyzer

Unidirectional network analyzers (Fig. 10) extend the capability of a simple reflectometer to measure S_{11} and S_{21} of a two-port DUT.

With the measured quantity m_1 being proportional to a_1 , m_2 presenting a measure for the reflection b_1 , and m_3 presenting a measure for the transmission b_2 , S_{11} , and S_{21} can be expressed as

$$S_{11} = c_{11} \frac{m_2}{m_1}, \quad S_{21} = c_{21} \frac{m_3}{m_1} \quad (6)$$

The proportionality constants are usually obtained through normalization measurements of known reflection/transmission coefficients. Connecting a "Short" with $S_{11} = -1$ to port 1 yields

$$c_{11} = -1 \frac{m_1^S}{m_2^S}; \quad \text{and} \quad c_{21} = 1 \frac{m_1^T}{m_3^T}$$

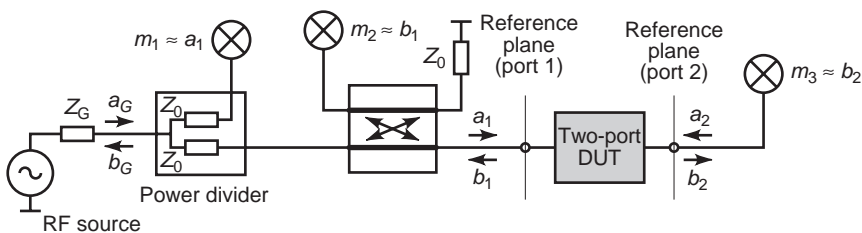


Figure 10. Unidirectional network analyzer.

is obtained by connecting both ports (“Through”), such that $S_{21} = 1$.

For measurement of S_{22} and S_{12} (reverse direction), the DUT must be connected to the unidirectional NA with its ports reversed.

3.5. The Three-Receiver Network Analyzer Architecture for Full Two-Port Measurements

The need for manually reversing the DUT can be eliminated if a switch and another directional coupler is introduced into the system of Fig. 11. With the switch in position I, the RF source is connected to port 1 of the DUT, m_1 is proportional to a_1 , m_2 is a measure for b_1 , and m_3 is a measure for b_2 . The second contact of the switch terminates the coupler at port 2 in Z_0 , ensuring proper port match. With the switch in position II, port 2 of the DUT is excited, the coupler connected to port 1 of the DUT is terminated in Z_0 , and m_1 is now a measure for a_2 . As the three receivers m_1 , m_2 , and m_3 now provide different readings, depending on the position of the switch, their measurement values will from now on be referred to as m_i^I and m_i^{II} , the superscript denoting the position of the switch. The S -parameters of the DUT are therefore determined as

$$S_{11} = c_{11} \frac{m_2^I}{m_1^I}, \quad S_{21} = c_{21} \frac{m_3^I}{m_1^I}$$

$$S_{22} = c_{22} \frac{m_3^{II}}{m_1^{II}}, \quad \text{and} \quad S_{12} = c_{12} \frac{m_2^{II}}{m_1^{II}}$$

with the proportionality constants resulting from normalization measurements. Using a “Short” at port 1 and

port 2 and a “Through” connecting both ports yields

$$c_{11} = -1 \frac{m_1^I}{m_2^I}, \quad c_{21} = 1 \frac{m_1^I}{m_3^I}$$

$$c_{22} = -1 \frac{m_1^{II}}{m_3^{II}}, \quad \text{and} \quad c_{12} = 1 \frac{m_1^{II}}{m_2^{II}}$$

The switch should be well matched to keep measurement errors low, must be reproducible, and must provide sufficient isolation in order not to limit the dynamic range of the instrument.

3.6. The Four-Receiver Vector Network Analyzer

There seems to be little gained in extending the above-described three-receiver NA with a fourth receiver, as outlined in Fig. 12, because the complete S -matrix of a two-port can already be measured with three receivers. For *vector* network analyzers (VNA), however, the additional receiver provides simultaneous measurement capability of all waves and makes the architecture completely symmetrical around the DUT, resulting in interesting calibration capabilities, detailed in Sections 4.5, 4.6, and 5. The subtle change of moving the switch from *between* two receivers to *in front* of the receiver pairs radically alters the error model, even reducing the requirements of the switch (see Section 4.5). For measurements *without* error correction, however, the switch must, again, be as ideal as possible with respect to match, repeatability, and isolation.

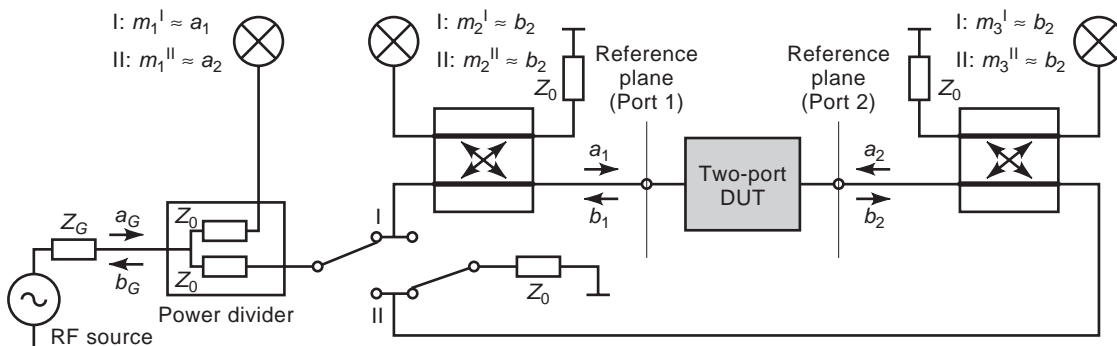


Figure 11. Bidirectional network analyzer with three receivers.

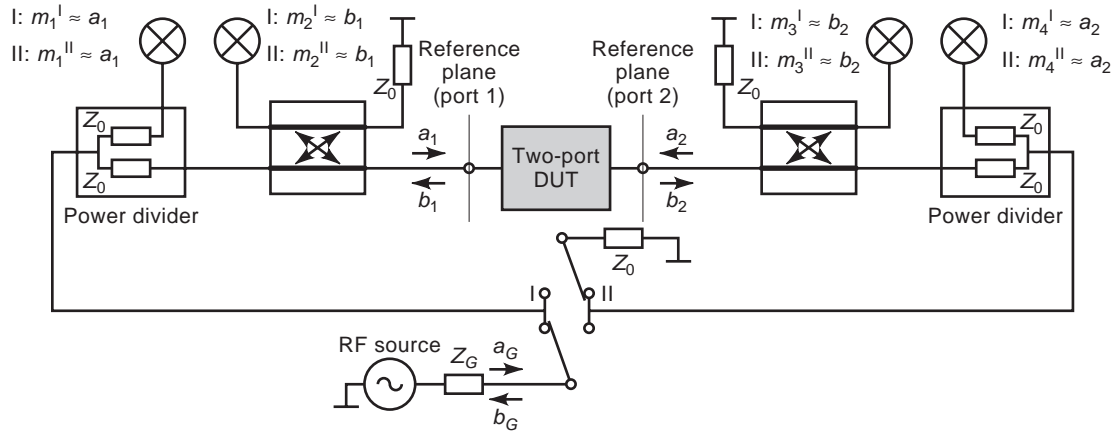


Figure 12. Bidirectional vector network analyzer with four receivers.

A four-receiver VNA measures the S -matrix of a two-port DUT as

$$S_{11} = c_{11} \frac{m_2^I}{m_1^I}, \quad S_{21} = c_{21} \frac{m_3^I}{m_1^I}$$

$$S_{22} = c_{22} \frac{m_3^II}{m_4^II}, \quad \text{and} \quad S_{12} = c_{12} \frac{m_2^II}{m_4^II}$$

with the proportionality factors determined through normalization measurements as described before.

4. ERROR MODELS, CALIBRATION, AND ERROR CORRECTION

For a long time, precision NAs required carefully designed and expensive hardware, ensuring a good port match for embedding the DUT between proper terminations and high coupler directivity for precise reflection measurement. Losses in the hardware had to be accounted for by reference measurements of devices with a known characteristic. With the advent of microprocessors, however, the focus has shifted toward calibration techniques that allow the imperfections of the hardware to be taken into account and corrected mathematically. An error model is needed for this purpose, and its parameters are determined through measurement of well-known one- or two-ports (calibration). This mathematical description of the non-ideal hardware is then used to correct the measurement of the DUT.

The error models, covered in subsequent sections, are used to model and correct all the linear errors of the VNA: transmission losses between the generator, the receivers, and the DUT; port match; and coupler directivity. Theoretically, the hardware of a VNA that provides these error-correction capabilities need no longer be built to high standards. Yet, commercially available systems still strive for good hardware performance for two reasons: first, in an effort to assist the calibration through good hardware performance and achieve even better accuracy; and, second, to provide an instrument that does not depend on time-consuming calibration procedures, allowing unco-

rected measurements for all those applications that can tolerate the reduced accuracy. However, commercially available instruments use the calibration capabilities for a considerable extension of their usable bandwidth. When the directivity of the directional couplers decreases to unsatisfactory values below a certain frequency, a built-in error correction mathematically enhances the directivity to usable values, extending the frequency range to as low as 9 kHz.

As all error models presented herein are linear and deterministic, a stringent requirement remains that the VNA hardware be linear (errors due to compression of receivers cannot be corrected) and stable.

With modern equipment achieving a short-term stability in the millidecibel range, the most prominent source of error in many cases remains in the cabling between the VNA and the DUT and the associated interface contacts. These contacting errors are statistical in nature and must be minimized by proper cable and connector selection and maintenance. As the transmission phase of coaxial cables varies over temperature and may change if the cable is bent, VNAs are usually equipped with special test-port cables, optimized for phasestability and mechanically protected against overbending.

The mathematical descriptions of the error models presented in the following sections make heavy use of matrix representations, leading to very compact expressions and similar structures for the different models. Alternatively, flowgraph techniques could be applied as in Refs. 17 and 18, leading to comparable results.

4.1. The Three-Term Error Model for Reflection Measurements

A reflectometer like the one of Fig. 13 can always be represented by a linear four-port, driven at the left port by the RF source, two ports connected to the receivers for measurement of the incident and reflected waves, and the DUT placed at the port to the right. In this general form, the underlying hardware of the reflectometer becomes unimportant, much like the fact that internal structure of the six-port reflectometer was of no concern in Section 2.3.

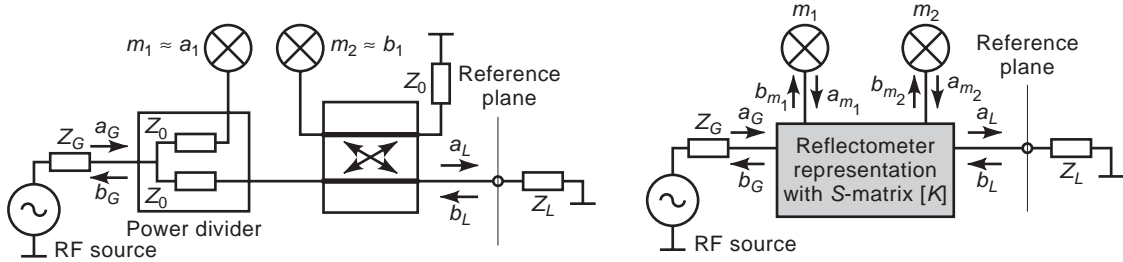


Figure 13. Four-port description of a reflectometer.

The waves incident to and reflected from this four-port relate to its S -matrix by

$$\begin{pmatrix} b_{m_1} \\ b_{m_2} \\ a_L \\ b_G \end{pmatrix} = [K] \begin{pmatrix} a_{m_1} \\ a_{m_2} \\ b_L \\ a_G \end{pmatrix} \quad (7)$$

The measured quantities m_1 and m_2 are proportional to the incident waves of the receivers ($m_1 = \eta_1 b_{m_1}$, $m_2 = \eta_2 b_{m_2}$), with the receiver constant η_i representing the entire transfer characteristics of the i th receiver, comprising mixer conversion, intermediate frequency (IF) amplification, and so on. Architectural details of the receiver are of no concern at this point. The only requirement is that η_i must be constant, implying stability of the receiver's phase and amplitude response. Let r_i be the reflection coefficients of the receiver inputs such that the conditions

$$\begin{aligned} m_1 &= \eta_1 b_{m_1}, & m_2 &= \eta_2 b_{m_2}, \\ a_{m_1} &= r_1 b_{m_1}, & a_{m_2} &= r_2 b_{m_2} \end{aligned} \quad (8)$$

result. Their use allows the elimination of the generator waves a_G and b_G in Eq. (7), according to the following scheme: The third equation of Eq. (7) is solved for a_G , and the result is inserted into the first two equations. In these, b_{m_i} is expressed through a_{m_i} and a_{m_i} in turn expressed by m_i , using Eq. (8). The resulting two equations relate the measured quantities m_1 and m_2 to the waves at the DUT and are arranged in matrix form as

$$\begin{pmatrix} b_L \\ a_L \end{pmatrix} = \begin{bmatrix} G_{11} & G_{12} \\ G_{21} & G_{22} \end{bmatrix} \begin{pmatrix} m_2 \\ m_1 \end{pmatrix} = [G] \begin{pmatrix} m_2 \\ m_1 \end{pmatrix} \quad (9)$$

Every element of $[G]$ evolves as a function of K_i , r_i , and η_i , which need not be explicitly known. It suffices to determine $[G]$ through a process called calibration, in order to calculate the correct waves at the DUT from the raw measurements m_i :

$$\Gamma_L = \frac{b_L}{a_L} = \frac{G_{11}m_2 + G_{12}m_1}{G_{21}m_2 + G_{22}m_1} \quad (10)$$

Interestingly, this four-port/two-port reduction with its elimination of the generator waves has freed the error model [Eq. (9)] from any influence of the RF source. Power or impedance variations do not introduce measurement errors, provided that m_1 and m_2 are measured simultaneously.

Equation (10) can be further simplified by dividing numerator and denominator by m_1 and defining

$$m_{11} = \frac{m_2}{m_1} = \frac{\eta_2 b_{m_2}}{\eta_1 b_{m_1}} \quad (11)$$

as the uncorrected (raw) reflection measurement [compare with Eq. (6)] such that the error-corrected reflection coefficient becomes

$$\Gamma_L = \frac{b_L}{a_L} = \frac{G_{11}m_{11} + G_{12}}{G_{21}m_{11} + G_{22}} \quad (12)$$

The importance of Eq. (11) is twofold:

1. The ratio of two measurements enters the computation of the error-corrected result. Relative, rather than absolute, measurements are therefore still sufficient if an error model and error correction is used. And with the reflected wave measurement m_2 being referenced to the incident wave measurement m_1 , the theoretically derived insensitivity of the error model to power variations of the RF source becomes obvious.
2. The ratio of η_1/η_2 appearing in Eq. (11) indicates that amplitude and phase drifts of the receivers cancel if both receivers are built *equal*.

Both properties are essential for the high accuracy achievable with VNAs. The use of the latter property is especially important for accurate phase measurements at high frequencies.

4.1.1. Calibration of the Three-Term Error Model. Before error-corrected measurements using Eq. (12) can be carried out, the error matrix $[G]$ must be determined. For this calibration procedure, several one-ports (calibration standards) with known reflection coefficients are needed. As numerator and denominator of Eq. (12) may be multiplied by any complex number without altering the result, one of the error terms may arbitrarily be set to 1, with the other

three remaining to be computed. Without loss of generality, let $G_{11} = 1$ and Eq. (12) can be rearranged to yield a linear equation in the three remaining error terms:

$$-G_{12} + \Gamma^i m_{11}^i G_{21} + \Gamma^i G_{22} = m_{11}^i \quad (13)$$

The superscript i denotes the i th calibration measurement with known reflection coefficient Γ^i and the corresponding measured value m_{11}^i . Performing calibration measurements with three distinct and known reflection standards yields three linear inhomogeneous and independent forms of Eq. (13), sufficient to solve for the needed error terms.

In order to maximize the independence of the three equations, the three-term calibration is typically performed with those three impedances, which are furthest apart in the reflection plane:

$$\text{Open: } \Gamma^O = 1, \quad \text{Short: } \Gamma^S = -1,$$

$$\text{Match: } \Gamma^M = 0$$

Three-term reflectometer calibration is therefore also referred to as OSM calibration.

4.2. The Five-Term Error Model for Unidirectional Vector Network Analyzers

Extending a single reflectometer with a third receiver for transmission measurements yields the unidirectional NA of Fig. 10. Its error model comprises two parts: The reflectometer hardware to the left of the DUT, which is again represented by an error two-port $[G]$; and the hardware to the right of the DUT, which constitutes a physical two-port with a corresponding 2×2 S -matrix (Fig. 14).

As in Section 4.1, the reflection coefficient r_3 and the transfer characteristics η_3 of the receiver m_3 establish the conditions

$$a_{m_3} = r_3 b_{m_3} \quad \text{and} \quad m_3 = \eta_3 b_{m_3}$$

which are used to reduce $[T]$ to an error two-port that relates the waves a_2 and b_2 of the DUT to the measured value m_3 :

$$\begin{pmatrix} b_2 \\ a_2 \end{pmatrix} = \begin{bmatrix} H_{11} & H_{12} \\ H_{21} & H_{22} \end{bmatrix} \begin{pmatrix} m_3 \\ 0 \end{pmatrix} = [H] \begin{pmatrix} m_3 \\ 0 \end{pmatrix}$$

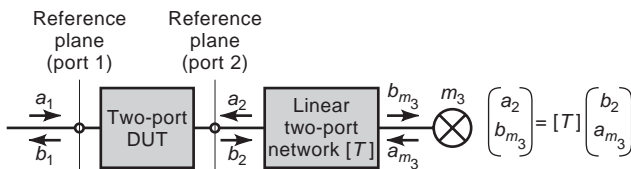


Figure 14. Hardware description of the transmission receiver m_3 .

Together with the error two-port of the reflectometer

$$\begin{pmatrix} b_1 \\ a_1 \end{pmatrix} = \begin{bmatrix} G_{11} & G_{12} \\ G_{21} & G_{22} \end{bmatrix} \begin{pmatrix} m_2 \\ m_1 \end{pmatrix} = [G] \begin{pmatrix} m_2 \\ m_1 \end{pmatrix}$$

and the definition of the DUT's S -matrix

$$\begin{pmatrix} b_1 \\ b_2 \end{pmatrix} = \begin{bmatrix} S_{11} & S_{12} \\ S_{21} & S_{22} \end{bmatrix} \begin{pmatrix} a_1 \\ a_2 \end{pmatrix} \quad (14)$$

the error model (Fig. 15) can be expressed as

$$\begin{aligned} \begin{pmatrix} b_1 \\ b_2 \end{pmatrix} &= \begin{pmatrix} G_{11}m_2 + G_{12}m_1 \\ H_{11}m_3 \end{pmatrix} \\ &= [S] \begin{pmatrix} G_{21}m_2 + G_{22}m_1 \\ H_{21}m_3 \end{pmatrix} = [S] \begin{pmatrix} a_1 \\ a_2 \end{pmatrix} \end{aligned} \quad (15)$$

It is obvious that the two equations of Eq. (15) are not sufficient to solve for the entire S -matrix of the DUT. On the other hand, the “forward” S -parameters S_{11} and S_{21} cannot be error-corrected by themselves without the knowledge of S_{12} and S_{22} .

Error correction is therefore only possible if a second measurement with the DUT reversed is made. Denoting the measured values with superscripts f and r for forward and reverse measurement of the DUT, both vector equations of Eq. (15) can be combined into a matrix equation

$$\begin{aligned} &\begin{bmatrix} G_{11}m_2^f + G_{12}m_1^f & H_{11}m_3^r \\ H_{11}m_3^f & G_{11}m_2^r + G_{12}m_1^r \end{bmatrix} \\ &= [S] \begin{bmatrix} G_{21}m_2^f + G_{22}m_1^f & H_{21}m_3^r \\ H_{21}m_3^f & G_{21}m_2^r + G_{22}m_1^r \end{bmatrix} \end{aligned} \quad (16)$$

Again, Eq. (16) may be normalized to the incident waves m_1^f and m_1^r such that only the unconnected measurement ratios

$$\begin{aligned} m_{11} &= \frac{m_2^f}{m_1^f} = \frac{\eta_2 b_{m_2}^f}{\eta_1 b_{m_1}^f}, & m_{21} &= \frac{m_3^r}{m_1^f} = \frac{\eta_3 b_{m_3}^r}{\eta_1 b_{m_1}^f} \\ m_{12} &= \frac{m_3^r}{m_1^r} = \frac{\eta_3 b_{m_3}^r}{\eta_1 b_{m_1}^r}, & m_{22} &= \frac{m_2^f}{m_1^r} = \frac{\eta_2 b_{m_2}^f}{\eta_1 b_{m_1}^r} \end{aligned}$$

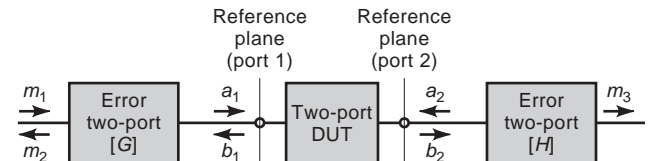


Figure 15. Error model of the unidirectional vector network analyzer.

remain [compare with Eq. (6)]. Solving the normalized version of Eq. (16) for $[S]$ yields the error-correction formula

$$[S] = \begin{bmatrix} G_{11}m_{11} + G_{12} & H_{11}m_{12} \\ H_{11}m_{21} & G_{11}m_{22} + G_{12} \end{bmatrix} \times \begin{bmatrix} G_{21}m_{11} + G_{22} & H_{21}m_{12} \\ H_{21}m_{21} & H_{21}m_{22} + G_{22} \end{bmatrix}^{-1} \quad (17)$$

4.2.1. Calibration of the Five-Term Error Model. Not all of the eight error terms contained in $[G]$ and $[H]$ are needed for error correction with Eq. (17), where H_{12} and H_{22} do not appear. Furthermore, the structure of Eq. (17) reveals its invariance to multiplication of *all* error terms with a constant. The remaining error terms may therefore be computed by rearranging Eq. (17) into a linear, homogeneous system of equations in the error terms,

$$\begin{bmatrix} -m_{11}^i & -1 & S_{11}^i m_{11}^i & S_{11}^i & 0 & S_{12}^i m_{21}^i \\ 0 & 0 & S_{21}^i m_{11}^i & S_{21}^i & -m_{21}^i & S_{22}^i m_{21}^i \\ 0 & 0 & S_{12}^i m_{22}^i & S_{12}^i & -m_{12}^i & S_{11}^i m_{12}^i \\ -m_{22}^i & -1 & S_{22}^i m_{22}^i & S_{22}^i & 0 & S_{21}^i m_{12}^i \end{bmatrix} \times \begin{pmatrix} G_{11} \\ G_{12} \\ G_{21} \\ G_{22} \\ H_{11} \\ H_{21} \end{pmatrix} = 0 \quad (18)$$

setting one error term to unity and solving the resulting inhomogeneous system of equations. $[S^i]$ denotes the S -matrix of the i th calibration standard. Five independent equations are needed to solve for the remaining five independent error terms, hence the name five-term error model.

The problem of *how many* two-port standards are needed and how they must be built to ensure five independent equations can be tackled in the following way: A suitable combination of standards must always comprise at least one standard with transmission ($S_{21} \neq 0$ and $S_{12} \neq 0$); otherwise, H_{11} and H_{21} cannot be determined [$S_{21} = S_{12} = 0$ implies $m_{21} = m_{12} = 0$, such that the fifth and sixth column

of Eq. (18) vanish]. Numerical investigations reveal that a two-port standard exhibiting transmission contributes at least two equations and may contribute four if it is not symmetric (i.e., $S_{11} \neq S_{22}$).

Because the use of reflection standards ($S_{21} = S_{12} = 0$) implies $m_{21} = m_{12} = 0$, the second and third equation of Eq. (18) degenerate, leaving only the first and fourth equation for determination of $[G]$; and with $S_{11} = \Gamma_s$, the first equation corresponds directly to Eq. (13) (three-term calibration) with $G_{11} = 1$. Transmissionless standards therefore contribute one equation per reflection coefficient connected to port 1.

Even though the general nature of Eq. (18) allows for calibration with any set of standards that yields five independent equations, traditionally the five-term model is calibrated using the three reflection standards Open, Short, and Match (contributing three equations), together with a direct connection of both reference planes, the Through standard (furnishing the remaining two equations). Figure 16 depicts this commonly used set of standards. Another name for this commonly used procedure is SOLT, which stands for Short, Open, Load, and Through.

Of course, care must be taken as to build the calibration standards such that their S -matrix or reflection coefficients match the postulated values used in the calibration process. All deviations of the standards' *real* values from the postulated *ideal* of Fig. 16 lead to inconsistencies in the equations of Eq. (18). Keeping these inconsistency errors small requires a smart choice and precisely built or modeled standards.

Because the Through standard requires a direct connection of both measurement ports, it is typically a very easy standard to realize in coaxial media. The same holds for the Short, which is easily manufactured to high precision ($< 1^\circ$ deviation at 20 GHz) in coaxial media. However, care must be taken as to ensure that the Short is connected directly to the reference plane, which is a potential problem if sexed connectors (N, SMA, K) are used. Bridging same-sexed connectors with adapters introduces a phase shift $2\beta l$ into the reflection coefficient, which must be known in order to substitute the shorts reflection coefficient by $-1e^{-2\beta l}$. The same holds if offset shorts with electrical length $2\beta l$ are used. For a frequency band where $2\beta l$ is between 40° and 320° , the latter can replace the open standard, which typically suffers from fringing capacities and radiation losses. Therefore, the open standards contained in commercially available calibration kits come with detailed information on those imperfections, modeling the frequency dependence of the open's capacitance by a polynomial to enhance accuracy. For the absolute impedance reference, the Match standard, precision crafting is needed for precision measurements.

4.3. The 10-Term Error Model for Vector Network Analyzers with Three Receivers

For all practical purposes, the applicability of the five-term error model is somewhat impaired by the need for manually reversing the DUT in order to obtain

Figure 16. Calibration standards for the TMSO five-term procedure. Through: $[S^T] = \begin{bmatrix} 0 & 1 \\ 1 & 0 \end{bmatrix}$, Open: $S_{11}^O = 1$, Short: $S_{11}^S = -1$, Match: $S_{11}^M = 0$

error-corrected results. If a switch is incorporated into the VNA, as depicted in Fig. 11, this manual interaction can be automated, easing error-corrected measurements considerably.

In essence, the error model of the resulting bidirectional VNA with three receivers (see Section 3.5) consists of *two* five-term error models (Fig. 17). Because of the switch being located *between* m_1 and m_2 and m_1 and m_3 , different error two-ports are needed for either position of the switch.

With the switch in position I, the reflectometer comprising m_1 and m_2 can be represented by an error two-port $[G^I]$ and the reflectometer terminated in Z_0 and comprising m_3 by an error two-port $[H^I]$. In the second state of the switch, the four-port comprising m_1 and m_3 can be reduced to the error two-port $[G^{II}]$ and the reflectometer terminated in Z_0 and comprising m_2 by an error two-port $[H^{II}]$ with

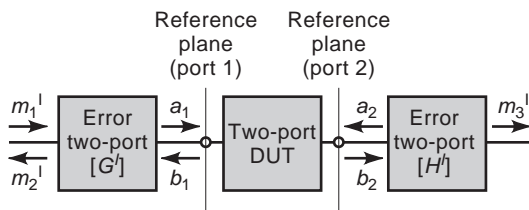
$$\begin{aligned} \begin{pmatrix} b_1 \\ a_1 \end{pmatrix} &= [G^I] \begin{pmatrix} m_2^I \\ m_1^I \end{pmatrix}, & \begin{pmatrix} b_2 \\ a_2 \end{pmatrix} &= [H^I] \begin{pmatrix} m_3^I \\ 0 \end{pmatrix} \\ \begin{pmatrix} b_1 \\ a_1 \end{pmatrix} &= [H^{II}] \begin{pmatrix} m_2^{II} \\ 0 \end{pmatrix}, & \begin{pmatrix} b_2 \\ a_2 \end{pmatrix} &= [G^{II}] \begin{pmatrix} m_3^{II} \\ m_1^{II} \end{pmatrix} \end{aligned}$$

Using these relations together with Eq. (14) yields a vector equation for either state of the switch that can be combined into a matrix equation, very similar to Eq. (16):

$$\begin{aligned} &\begin{bmatrix} G_{11}^I m_2^I + G_{12}^I m_1^I & H_{11}^{II} m_2^{II} \\ H_{11}^I m_3^I & G_{11}^{II} m_3^{II} + G_{12}^{II} m_1^{II} \end{bmatrix} \\ &= [S] \begin{bmatrix} G_{21}^I m_2^I + G_{22}^I m_1^I & H_{21}^{II} m_2^{II} \\ H_{21}^I m_3^I & G_{21}^{II} m_3^{II} + G_{22}^{II} m_1^{II} \end{bmatrix} \end{aligned}$$

Normalization to the incident waves m_1^I and m_1^{II} now yields

$$\begin{aligned} &\begin{bmatrix} G_{11}^I m_{11} + G_{12}^I & H_{11}^{II} m_{12} \\ H_{11}^I m_{21} & G_{11}^{II} m_{22} + G_{12}^{II} \end{bmatrix} \\ &= [S] \begin{bmatrix} G_{21}^I m_{11} + G_{22}^I & H_{21}^{II} m_{12} \\ H_{21}^I m_{21} & G_{21}^{II} m_{22} + G_{22}^{II} \end{bmatrix} \end{aligned} \quad (19)$$



Error model for switch in position I

with

$$\begin{aligned} m_{11} &= \frac{m_2^I}{m_1^I} = \frac{\eta_2 b_{m_2}}{\eta_1 b_{m_1}}, & m_{21} &= \frac{m_3^I}{m_1^I} = \frac{\eta_3 b_{m_3}}{\eta_1 b_{m_1}} \\ m_{12} &= \frac{m_2^{II}}{m_1^{II}} = \frac{\eta_2 b_{m_2}}{\eta_1 b_{m_1}}, & m_{22} &= \frac{m_3^{II}}{m_1^{II}} = \frac{\eta_3 b_{m_3}}{\eta_1 b_{m_1}} \end{aligned}$$

where comparison with the five-term error model shows that m_2^{II} and m_3^{II} have switched their position as have the error terms for the second state of the switch, a consequence of the switch now reversing the DUT and the error two-ports.

With error correction according to the 10-term error model applied, the requirements of the switch as detailed in Section 3.5 become somewhat relaxed, because its mismatch errors and transmission losses are now accounted for. However, repeatability and leakage errors (finite isolation) are not contained in the error model.

4.3.1. Calibration of the 10-Term Error Model. As was the case with the five-term model, not all 16 error terms appear in Eq. (19). H_{12}^I , H_{22}^I , H_{22}^{II} , and H_{22}^{II} are not needed for error correction and cannot be determined by the calibration procedure.

Rearranging Eq. (19) as a linear homogeneous system of equations in the remaining error terms, as demonstrated in Section 4.2.1 finds the four equations to be decoupled: Two equations depend solely on error terms of $[G^I]$ and $[H^I]$, and the other two equations depend only on $[G^{II}]$ and $[H^{II}]$:

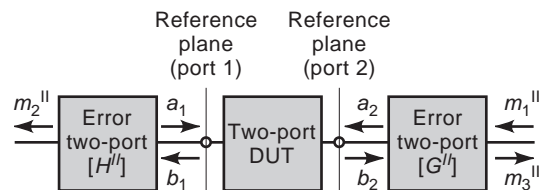
$$\begin{bmatrix} -m_{11}^i & -1 & S_{11}^i m_{11}^i & S_{11}^i & 0 & S_{12}^i m_{21}^i \\ 0 & 0 & S_{21}^i m_{11}^i & S_{21}^i & -m_{21}^i & S_{22}^i m_{21}^i \end{bmatrix} \mathbf{e}^I = 0,$$

$$\mathbf{e}^I = (G_{11}^I, G_{12}^I, G_{21}^I, G_{22}^I, H_{11}^I, H_{21}^I)^T$$

$$\begin{bmatrix} 0 & 0 & S_{12}^i m_{22}^i & S_{12}^i & -m_{12}^i & S_{11}^i m_{12}^i \\ -m_{22}^i & -1 & S_{22}^i m_{22}^i & S_{22}^i & 0 & S_{21}^i m_{12}^i \end{bmatrix} \mathbf{e}^{II} = 0,$$

$$\mathbf{e}^{II} = (G_{11}^{II}, G_{12}^{II}, G_{21}^{II}, G_{22}^{II}, H_{11}^{II}, H_{21}^{II})^T$$

With one of the error terms of both \mathbf{e}^I and \mathbf{e}^{II} set to 1 (e.g., $G_{11}^I = G_{11}^{II} = 1$), two sets of five independent equations must be supplied by the calibration measurements in order to solve the resulting inhomogeneous system for the remaining 10 error terms.



Error model for switch in position II

Figure 17. Error model of the bidirectional vector network analyzer with three receivers.

A similar reasoning (compared with Section 4.2.1) as to how many and what kind of standards are needed is applicable here. At least one standard with transmission ($S_{21} \neq 0$ and $S_{12} \neq 0$) is needed in order to determine $[H^I]$ and $[H^{II}]$. Because of the different error terms, such a standard will supply a total of four equations for both positions of the switch. Reflection two-ports ($S_{21} = S_{12} = 0$), on the other hand, still contribute one equation for each of their two reflection coefficients S_{11} and S_{22} .

The same standards as with the five term error model (referred to as TMSO, Through-Match-Short-Open, or SOLT, Short-Open-Load-Through) are commonly used to calibrate the 10-term model, with the reflection standards now being reflection two-ports.

Because of the decoupled nature of Eq. (19), the reflection two-ports may be realized as one-ports by first connecting the calibration impedance to port 1 and noting the measurement values with the switch in position I. Then the appropriate calibration impedance is connected to port 2 and the measurements are taken with the switch in the second position [because these standards do not exhibit transmission, the corresponding transmission receiver (m_3^I, m_2^{II}) need not be considered]. With respect to the commonly used TMSO standards, this sequential procedure eliminates the need for two identical reflection standards but allows usage of one physical match—short and open—as reflection one-ports.

4.4. The Crosstalk Including 12-Term Error Model for Three-Receiver VNAs

Several commercially available VNAs provide a 12-term calibration capability [17], expanding the above-described 10-term error model by two error terms that characterize forward and reverse isolation. Their inclusion aims at extending the dynamic range for measurements where finite isolation of the switch or coupling over the DUT adversely affects measurement accuracy at high insertion loss levels of the DUT.

For that purpose, an additional isolation standard (no transmission) with, for now, arbitrary reflection coefficients r_1 and r_2

$$[S^X] = \begin{bmatrix} r_1 & 0 \\ 0 & r_2 \end{bmatrix} \rightarrow [M^X] = \begin{bmatrix} m_{11}^X & m_{12}^X \\ m_{21}^X & m_{22}^X \end{bmatrix}$$

must be measured (alternatively the transmission measurement of one of the reflection standards may be exploited). The transmission terms m_{12}^X and m_{21}^X of its measurement matrix are a measure of the crosstalk level and can be used for correcting the measured transmission values of the DUT:

$$[S] = \begin{bmatrix} G_{11}^I m_{11} + G_{12}^I & H_{11}^{II} (m_{12} - m_{12}^X) \\ H_{11}^I (m_{21} - m_{21}^X) & G_{11}^{II} m_{22} + G_{12}^{II} \end{bmatrix} \\ \times \begin{bmatrix} G_{21}^I m_{11} + G_{22}^I & H_{21}^{II} (m_{12} - m_{12}^X) \\ H_{21}^I (m_{21} - m_{21}^X) & G_{21}^{II} m_{22} + G_{22}^{II} \end{bmatrix}^{-1}$$

However, this simple correction scheme can only improve results if the reflection coefficients of the isolation standard match the reflection coefficients of the DUT. For well-matched DUTs, the isolation terms can be taken from the measurement of the Match standard $[S^M]$. High transmission dynamic DUTs (e.g., filters), however, typically exhibit strongly varying reflection coefficients over frequency. If two identical DUTs are available, an isolation standard that satisfies the above condition can be generated by connecting the first DUT with port 1 to port 1 of the VNA and the second DUT with port 2 to the VNAs second port. The unused ports of the DUTs are terminated in Z_0 . Consequently, the isolation measurement must be repeated with a suitable isolation standard whenever DUTs with differing reflection coefficients are to be measured.

Considering the above limitations, the cross-talk reduction with the 12-term model should be regarded as a cross-talk *normalization* rather than as a *calibration*.

In Section 4.6, it will be shown that for an error model to correctly include cross-talk, eight error terms are needed for its characterization.

4.5. The Seven-Term Error Model for Vector Network Analyzers with Four Receivers

The addition of a fourth receiver to independently measure all four waves at the DUT, as depicted in Fig. 12, leads to very interesting instrument properties and calibration possibilities. The DUT is now embedded in a symmetrical test set, consisting of two reflectometers, each of which can be represented by an error two-port (see Section 4.1, which discusses four-port/two-port reduction).

The subtle but far-reaching advantages of this architecture and the accompanying error-model are as follows

1. The error model (Figs. 18 and 19) is valid for *either* position of the switch, reducing the number of error terms to eight and the number of two-port calibration standards required to three.
2. The four-receiver architecture provides redundant information in the calibration measurements that can be exploited to allow calibration with *partially unknown* standards. Section 5 details these important and powerful techniques.
3. The switch is no longer part of the error two-ports. Instead it has been moved into the generator port of the reflectometers, whose waves were eliminated during the four-port/two-port reduction. Therefore, the imperfections of the switch no longer influence the quality of an error-corrected measurement. The

$$\text{Through: } [S^T] = \begin{bmatrix} 0 & 1 \\ 1 & 0 \end{bmatrix}, \quad \text{Open: } [S_{11}^O] = \begin{bmatrix} 1 & 0 \\ 0 & 1 \end{bmatrix} \\ \text{Short: } [S^S] = \begin{bmatrix} -1 & 0 \\ 0 & -1 \end{bmatrix}, \quad \text{Match: } [S^M] = \begin{bmatrix} 0 & 0 \\ 0 & 0 \end{bmatrix}$$

Figure 18. Calibration standards for the TMSO (SOLT) 10-term procedure.

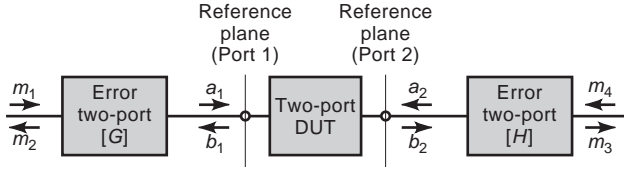


Figure 19. Seven-term error model of the bidirectional vector network analyzer with four receivers.

switch may be mismatched, may exhibit transmission losses and finite isolation, and does not even need to be repeatable.

The mathematical derivation of the seven-term error model unfolds in the usual way. With

$$\begin{pmatrix} b_1 \\ a_1 \end{pmatrix} = [G] \begin{pmatrix} m_2 \\ m_1 \end{pmatrix}, \quad \begin{pmatrix} b_2 \\ a_2 \end{pmatrix} = [H] \begin{pmatrix} m_3 \\ m_4 \end{pmatrix}, \quad (20)$$

and

$$\begin{pmatrix} b_1 \\ b_2 \end{pmatrix} = [S] \begin{pmatrix} a_1 \\ a_2 \end{pmatrix}$$

vector equations for both positions of the switch (I and II) are obtained and combined into a matrix equation:

$$\begin{bmatrix} G_{11}m_2^I + G_{12}m_1^I & G_{11}m_2^{II} + G_{12}m_1^{II} \\ H_{11}m_3^I + H_{12}m_4^I & H_{11}m_3^{II} + H_{12}m_4^{II} \end{bmatrix} = [S] \begin{bmatrix} G_{21}m_2^I + G_{22}m_1^I & G_{21}m_2^{II} + G_{22}m_1^{II} \\ H_{21}m_3^I + H_{22}m_4^I & H_{21}m_3^{II} + H_{22}m_4^{II} \end{bmatrix} \quad (21)$$

The eight measurement values contained in Eq. (21) can be condensed to four by expanding Eq. (21) as

$$\begin{aligned} & \begin{bmatrix} G_{12} & 0 \\ 0 & H_{12} \end{bmatrix} \begin{bmatrix} m_1^I & m_1^{II} \\ m_4^I & m_4^{II} \end{bmatrix} \\ & + \begin{bmatrix} G_{11} & 0 \\ 0 & H_{11} \end{bmatrix} \begin{bmatrix} m_2^I & m_2^{II} \\ m_3^I & m_3^{II} \end{bmatrix} \\ & = [S] \left\{ \begin{bmatrix} G_{22} & 0 \\ 0 & H_{22} \end{bmatrix} \begin{bmatrix} m_1^I & m_1^{II} \\ m_4^I & m_4^{II} \end{bmatrix} \right. \\ & \quad \left. + \begin{bmatrix} G_{21} & 0 \\ 0 & H_{21} \end{bmatrix} \begin{bmatrix} m_2^I & m_2^{II} \\ m_3^I & m_3^{II} \end{bmatrix} \right\} \end{aligned}$$

and right-multiplying both sides with the inverse measurement matrix of the first and fourth receiver. The

result is much simplified error-model representation

$$\begin{aligned} & \begin{bmatrix} G_{12} & 0 \\ 0 & H_{12} \end{bmatrix} + \begin{bmatrix} G_{11} & 0 \\ 0 & H_{11} \end{bmatrix} [M] \\ & = [S] \left\{ \begin{bmatrix} G_{22} & 0 \\ 0 & H_{22} \end{bmatrix} + \begin{bmatrix} G_{21} & 0 \\ 0 & H_{21} \end{bmatrix} [M] \right\} \end{aligned} \quad (22)$$

with a 2×2 measurement matrix

$$[M] = \begin{bmatrix} m_2^I & m_2^{II} \\ m_3^I & m_3^{II} \end{bmatrix} \begin{bmatrix} m_1^I & m_1^{II} \\ m_4^I & m_4^{II} \end{bmatrix}^{-1} = \begin{bmatrix} m_{11} & m_{12} \\ m_{21} & m_{22} \end{bmatrix}$$

With the measurement values pertaining to the incident waves m_1^I and m_4^I residing on the main diagonal of the right submatrix and the off-diagonal elements being small, the matrix is guaranteed to be invertible. For $m_4^I = m_1^{II} = 0$ (three receiver analogy), the entries of $[M]$ are normalized with respect to the incident waves m_1^I and m_4^I . The measurement matrix $[M]$ is therefore attributed S -parameter character. Furthermore, the computation of $[M]$ provides a first level of error correction, because finite isolation of the switch is eliminated. This is achieved by the fourth receiver, which precisely measures the level of the switch's leakage signals through m_1^{II} and m_4^I .

Equation (22) is easily returned to the structure of Eq. (21), with the four measurement values now being direct counterparts of the corresponding error-corrected S -parameters of the DUT:

$$\begin{aligned} & \begin{bmatrix} G_{11}m_{11} + G_{12} & G_{11}m_{12} \\ H_{11}m_{21} & H_{11}m_{22} + H_{12} \end{bmatrix} \\ & = [S] \begin{bmatrix} G_{21}m_{11} + G_{22} & G_{21}m_{12} \\ H_{21}m_{21} & H_{21}m_{22} + H_{22} \end{bmatrix} \end{aligned} \quad (23)$$

It may be interesting to note that $[G]$ and $[H]$ are of the cascading *transfer matrix* type. This type of matrix also appears in all other error models introduced in this section. The fact that transfer matrices exhibit a singularity if the underlying network has zero transmission can safely be ignored as far as error two-ports of practical reflectometer or network analyzer realizations are concerned. Those networks *must* exhibit transmission in order to perform the desired function. The device under test, however, may be perfectly isolating and should therefore always be represented by its S -matrix (Section 5.1.1 introduces *pseudo-transfer matrices* to work around that singularity).

4.5.1. Calibration of the Seven-Term Error Model. With Eq. (23) being of the same structure as the five-term model [Eq. (16)] and the 10-term model [Eq. (19)], the determination of the error terms proceeds in the same way. Equation (23) is rearranged into a linear homogeneous system

of equations

$$\begin{bmatrix} -m_{11}^i & -1 & S_{11}^i m_{11}^i & S_{11}^i & 0 & 0 & S_{12}^i m_{21}^i & 0 \\ 0 & 0 & S_{21}^i m_{11}^i & S_{21}^i & -m_{21}^i & 0 & S_{22}^i m_{21}^i & 0 \\ -m_{12}^i & 0 & S_{11}^i m_{12}^i & 0 & 0 & 0 & S_{12}^i m_{22}^i & S_{12}^i \\ 0 & 0 & S_{21}^i m_{12}^i & 0 & -m_{22}^i & -1 & S_{22}^i m_{22}^i & S_{22}^i \end{bmatrix} \mathbf{e} = 0,$$

$$\mathbf{e} = (G_{11}, \dots, G_{22}, H_{11}, \dots, H_{22})^T$$

with every calibration measurement i contributing four equations. One error term is set to 1, and seven independent equations are required to solve for the remaining seven error terms. It turns out that the eight equations stemming from the measurement of two calibration two-ports are not sufficient to provide the necessary rank of 7. Measurement of a third calibration two-port is needed such that a total of 12 equations exist.

The resulting surplus in information can be used in one of the following ways:

1. The linear system with all 12 equations is solved in the least-squares sense (e.g., see Ref. 19), using the extra equations to minimize residual errors (contacting or repeatability errors).
2. Even though contacting errors cannot be accounted for due to their statistical nature, in Ref. 20, the extra information is used to assess these errors by deriving error bounds. As these techniques are not yet widely used, they will not be further treated here.
3. The calibration standards can be permitted to have unknown parameters [13,21], which are determined using the extra information contained in the additional equations. Because the construction of standards, which do not have to be fully known, can result in considerable savings, this “self-calibration” technique is of much practical importance. Section 5 has the details.

Performing a seven-term calibration with completely known standards is most easily done using the TMS procedure, where the three calibration two-ports

$$\text{Through: } [S^T] = \begin{bmatrix} 0 & 1 \\ 1 & 0 \end{bmatrix}, \quad \text{Match: } [S^M] = \begin{bmatrix} 0 & 0 \\ 0 & 0 \end{bmatrix}$$

$$\text{Short: } [S^S] = \begin{bmatrix} -1 & 0 \\ 0 & -1 \end{bmatrix}$$

are used. Comparison with the 10-term and the 5-term model shows that the third reflection standard is no longer needed. Using a short, instead of an open, as the third standard is in many cases the more convenient choice, because shorts can be manufactured to higher precision in coaxial media or waveguides (see Section 4.2.1). At low frequencies, however, using an open may be the more

advantageous choice, as the test port serves as a comparatively good open up to about 100 MHz.

The computed error terms are used for error correction by simply solving Eq. (23) for $[S]$:

$$[S] = \begin{bmatrix} G_{11}m_{11} + G_{12} & G_{11}m_{12} \\ H_{11}m_{21} & H_{11}m_{22} + H_{12} \end{bmatrix} \times \begin{bmatrix} G_{21}m_{11} + G_{22} & G_{21}m_{12} \\ H_{21}m_{21} & H_{21}m_{22} + H_{22} \end{bmatrix}^{-1}$$

4.5.2. Calibration of the Seven-term Error Model using an Unknown Through. For applications where a Through standard of known properties is not available, the seven-term error model may be calibrated by performing simple reflectometer calibrations for the error two-ports $[G]$ and $[H]$, according to Section 4.1.1, and using a transmission standard whose only known property is its reciprocity (e.g., $S_{21} = S_{12}$).

Such a calibration method may, for instance, be desirable for on-wafer measurements where nonaligned measurement ports render a known Through difficult to build [22]. Calibration without an unknown Through was first introduced in Ref. 23 and is very simple to derive if the cascade structure of the error model (Fig. 19) is written using transfer matrices. With the error two-ports $[G]$ and $[H]$ already in that notation [Eq. (20)], the difference to Eq. (22) is in the description of the DUT

$$\begin{pmatrix} b_1 \\ a_1 \end{pmatrix} = [\Sigma] \begin{pmatrix} a_2 \\ b_2 \end{pmatrix} = \frac{1}{S_{21}} \begin{bmatrix} -\Delta S & S_{11} \\ -S_{22} & 1 \end{bmatrix} \begin{pmatrix} a_2 \\ b_2 \end{pmatrix} \quad (24)$$

and in the evolving measurement matrix

$$\begin{bmatrix} m_1^I & m_1^H \\ m_2^I & m_2^H \end{bmatrix} \begin{bmatrix} m_3^I & m_3^H \\ m_4^I & m_4^H \end{bmatrix}^{-1} = [P] = [G]^{-1}[\Sigma][H]$$

with the latter now also being a transfer matrix.

Performing reflectometer calibrations, as described in Section 4.1.1, for both error two-ports establishes three of the four error terms in $[G]$ and $[H]$, leading to the preliminary error matrices $[\tilde{G}]$ and $[\tilde{H}]$, with one error term normalized to 1. Without loss of generality, let us assume $\tilde{G}_{11} = \tilde{H}_{11} = 1$. This knowledge of $[G]$ and $[H]$, except for a common factor, can be expressed as

$$[P] = [G]^{-1}[\Sigma][H] = \frac{1}{K_G} [\tilde{G}]^{-1}[\Sigma]K_H[\tilde{H}]$$

$$= \alpha [\tilde{G}]^{-1}[\Sigma][\tilde{H}]$$

$$\alpha = \frac{K_H}{K_G}$$

The still unknown term α can be regarded as the seventh error term, still needed for a full two-port calibration. As the determinant of the transfer matrix of a reciprocal

two-port is unity, using such a device for calibration produces the equation

$$\begin{aligned} \det[P^{\text{reci}}] &= \alpha^2 \det[\tilde{G}]^{-1} \det[\Sigma^{\text{reci}}] \det[\tilde{H}] \\ &= \alpha^2 \frac{\det[\tilde{H}]}{\det[\tilde{G}]} \end{aligned}$$

which is solved for α :

$$\alpha = \pm \sqrt{\frac{\det[\tilde{G}]}{\det[\tilde{H}]} \det[P^{\text{reci}}]} \quad (25)$$

According to Ref. 23, the correct root in Eq. (25) is most easily found using

$$S_{21}^{\text{reci}} = \frac{\alpha}{P_{22}^{\text{reci}}}$$

if the phase of the reciprocal transmission-factor is known to $\pm 90^\circ$.

4.6. The Crosstalk Correcting 15-Term Error Model for Four-Receiver VNAs

Whenever energy emanating from the measurement planes finds a path to leak around the DUT or a coupling path between the reflectometers of the VNA exists (Fig. 20), the error models of Sections 4.2–4.5 cannot adequately handle the associated cross-talk error. On-wafer measurements typically suffer from this kind of leakage error, due to the small separation of the measurement planes and the radiation of the probe tips.

An error model, capable of accounting for those leakage errors, was first detailed in Ref. 24 and is also termed *full-model* [14]. It can be derived by describing the four-receiver VNA's hardware as a general eight-port. The coupling between the reflectometers may be arbitrary and nonreciprocal but must be linear and not affected by the parameters of the DUT. Comparable with the four-port/two-port reduction, introduced in Section 4.2.1, the reflection coefficients and conversion constants of the four

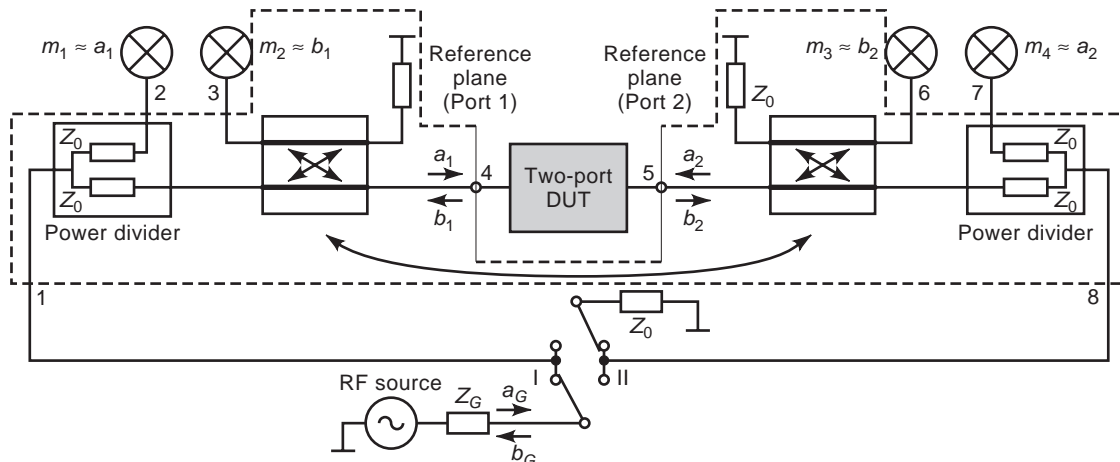


Figure 20. Eight-port hardware representation of the vector network analyzer, including coupling of the reflectometers.

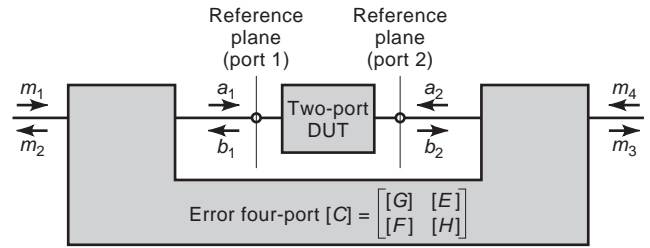


Figure 21. Fifteen-term error-model of the four-receiver vector network analyzer.

receivers are used to eliminate the reflected waves at the receivers and the generator waves a_G and b_G .

The resulting error four-port $[C]$ (Fig. 21) relates the measured values m_i ($i = 1, 2, 3, 4$) to the waves a_1, a_2, b_1, b_2 at the DUT such that its S -matrix can be computed from the measurement data and $[C]$. Because the switch is not part of the error network and the waves of the RF source are eliminated in Eq. (26), the properties of the switch have no influence on the quality of error correction, and the same error network may be used for either state of the switch.

The mathematical formulation of the error model is derived by partitioning the 4×4 matrix $[C]$ into four 2×2 matrices. With

$$\begin{pmatrix} b_1 \\ b_2 \\ a_1 \\ a_2 \end{pmatrix} = [C] \begin{pmatrix} m_1 \\ m_4 \\ m_2 \\ m_3 \end{pmatrix} = \begin{bmatrix} [G] & [E] \\ [F] & [H] \end{bmatrix} \begin{pmatrix} m_1 \\ m_4 \\ m_2 \\ m_3 \end{pmatrix} \quad (26)$$

the two vector equations

$$\begin{pmatrix} b_1 \\ b_2 \end{pmatrix} = [G] \begin{pmatrix} m_1 \\ m_4 \end{pmatrix} + [E] \begin{pmatrix} m_2 \\ m_3 \end{pmatrix}$$

$$\begin{pmatrix} a_1 \\ a_2 \end{pmatrix} = [F] \begin{pmatrix} m_1 \\ m_4 \end{pmatrix} + [H] \begin{pmatrix} m_2 \\ m_3 \end{pmatrix}$$

can be derived to express the waves at the DUT as

$$[G] \begin{pmatrix} m_1 \\ m_4 \end{pmatrix} + [E] \begin{pmatrix} m_2 \\ m_3 \end{pmatrix} = [S] \left\{ [F] \begin{pmatrix} m_1 \\ m_4 \end{pmatrix} + [H] \begin{pmatrix} m_2 \\ m_3 \end{pmatrix} \right\}$$

An equation of this type is obtained for measurement in either position of the switch, and combining both vector equations into a matrix equation yields

$$[G] \begin{bmatrix} m_1^I & m_1^{II} \\ m_4^I & m_4^{II} \end{bmatrix} + [E] \begin{bmatrix} m_2^I & m_2^{II} \\ m_3^I & m_3^{II} \end{bmatrix} \\ = [S] \left\{ [F] \begin{bmatrix} m_1^I & m_1^{II} \\ m_4^I & m_4^{II} \end{bmatrix} + [H] \begin{bmatrix} m_2^I & m_2^{II} \\ m_3^I & m_3^{II} \end{bmatrix} \right\}$$

which simplifies to

$$[G] + [E][M] = [S]([F] + [H][M]) \quad (27)$$

by introduction of the measurement matrix

$$[M] = \begin{bmatrix} m_2^I & m_2^{II} \\ m_3^I & m_3^{II} \end{bmatrix} \begin{bmatrix} m_1^I & m_1^{II} \\ m_4^I & m_4^{II} \end{bmatrix}^{-1} = \begin{bmatrix} m_{11} & m_{12} \\ m_{21} & m_{22} \end{bmatrix}$$

Comparison with the formulation of the seven-term model [Eq. (22)] reveals the very close relationship, because their structure and even the measurement matrix are identical. In fact, the seven-term error model evolves as a special case of the more general 15-term model. Consequently, the eight off-diagonal error terms that default to zero in Eq. (21), where no leakage is assumed, are needed in the 15-term model to correctly describe the crosstalk.

4.6.1. Calibration of the 15-Term Error Model. Determination of the 16 error terms in the error quadrants $[G]$, $[E]$, $[F]$, and $[H]$ is achieved by expanding Eq. (27) into a system of four linear equations in the error terms per calibration measurement [25]. One error term may be arbitrarily set to one, and the resulting inhomogeneous system may be solved for the remaining 15 error terms. Care must be taken to choose one of the error terms *on* the diagonal of the error-quadrants for this normalization, because the *off*-diagonal elements vanish in the case of a leakage-free error four-port.

It turns out that at least five completely known and distinct calibration two-ports must be measured to determine the 15 error terms [25,26]. With five calibration measurements, 20 equations in the 15 unknowns exist, but only 15 are needed. Analogous to Section 4.5, either five suitable equations may be neglected or the system of 20 equations in 15 unknowns is solved in the least-squares sense. Use of partially unknown standards and their

determination through self-calibration is the third option and is outlined in Section 5.3.

An especially well-suited combination of standards for the 15-term model, first mentioned in Ref. 25, consists of a Through two-port and the three reflection one-ports match, short, and open, combined to yield four reflection two-ports such that calibration is performed with the five two-ports of Fig. 22.

Contrary to the 7-term, 5-term, or 10-term error-models, the 15-term model does not allow reflection two-ports to be measured sequentially, by separating the reflection measurements at both ports. Due to the presence of crosstalk that must be precisely measured, both ports need to be terminated in the prescribed impedance while performing the calibration measurement. Cyclically interchanging the three reflection one-ports to create the calibration standard lets this Tms0 procedure get by with one match-, short-, and open standard. Lowercase letters are used to indicate that match, short, and open are one-ports and need to be combined to form the necessary calibration two-ports.

Once all error terms are known, the measured values of an arbitrary DUT are to be error-corrected. Contrary to the calibration process, error correction is performed with every measurement. Numerical efficiency is therefore in demand.

Equation (27) is easily solved for the S -matrix $[S]$ of the DUT

$$[S] = \{[G][M] + [E]\} \{[H][M] + [F]\}^{-1}$$

and devises a very simple algorithm for the error-correction process. Only 2×2 matrices need to be manipulated.

Figure 23 (taken from Ref. 27) demonstrates the capabilities of the 15-term procedure in the presence of an artificial leakage error between the measurement planes. Figure 24 depicts the setup. The DUT is a 20 dB attenuator, and the crosstalk is modeled by a second 20 dB attenuator in parallel to the DUT.

Although the presence of the leakage error corrupts the result in a way that the uncorrected data bears no resemblance with the transfer characteristics of the DUT, correcting the data according to the 15-term procedure recovers the attenuation value with good precision, even though the amount of crosstalk is of the same magnitude as the DUT's transmission.

5. MODERN SELF-CALIBRATION TECHNIQUES FOR FOUR-RECEIVER VNAs

Calibration of four-receiver VNAs according to the 7-term or the 15-term error model yields five redundant equations that are not needed for the computation of the error terms. Using this extra information for the determination of unknown parameters of the calibration standards is a

Figure 22. Calibration standards for the 15-term Tms0 procedure. $S^T = \begin{bmatrix} 0 & 1 \\ 1 & 0 \end{bmatrix}$, $S^{MS} = \begin{bmatrix} 0 & 0 \\ 0 & -1 \end{bmatrix}$, $S^{OM} = \begin{bmatrix} 1 & 0 \\ 0 & 0 \end{bmatrix}$, $S^{SO} = \begin{bmatrix} -1 & 0 \\ 0 & 1 \end{bmatrix}$, $S^{OS} = \begin{bmatrix} 1 & 0 \\ 0 & -1 \end{bmatrix}$

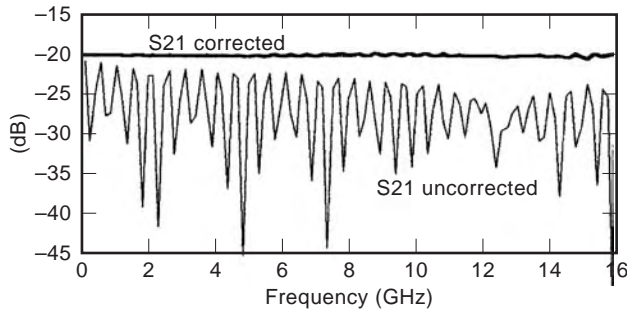


Figure 23. Transmission measurement of a 20 dB attenuator (corrected/uncorrected). (From Ref. 27, with permission.)

very powerful technique that allows the calibration to be performed with *partially known* standards. Besides reducing the cost of standards, self-calibration techniques also enhance the accuracy of the calibration as inconsistency errors are reduced.

One of the most popular self-calibration representative, introduced in 1979 by Engen and Hoer [13] for the double six-port reflectometer (seven-term error model), is the TLR procedure. It allows calibration with the following standards:

- (T)hrough (direct connection of both measurement planes)
- (L)ine (a line of unknown electrical length, between 20° and 160° , perfectly matched)
- (R)eflect (unknown, but symmetrical reflection standard)

The L standard and the R standard are only partially known, with no requirements imposed on the reflect, except that the same reflect has to be used on both measurement planes. Its value and the exact electrical length of the line are determined through the self-calibration process. Different methods can be employed for the determination of the unknown parameters of the standards, three of which are as follows:

1. The *linear* system of equations in the error terms [Eqs. (23) and (27)] is treated as a *nonlinear* system in the error terms *and* the unknowns of the standards. This nonlinear system is solved iteratively

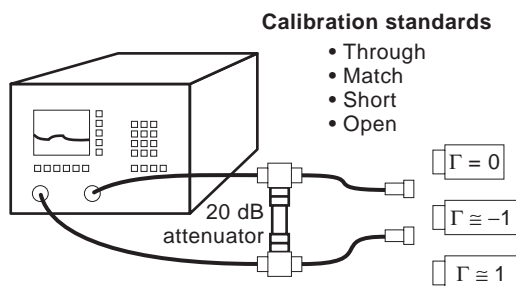


Figure 24. Measurement setup of a network analyzer with artificial cross-talk.

[28] or, where possible, analytically, providing a simultaneous solution of error terms and unknowns of the standards [17,18,29].

2. For a unique solution of the error terms to exist, 5 of the 12 (respectively, 20) equations must be linearly dependent. If the 12×8 (20×16) coefficient matrix of the homogeneous linear system of equations [Eqs. (23) and (27)] can be *analytically* brought to tridiagonal form, the last five lines are required to vanish, resulting in five equations in which only measurement values and parameters of the standards appear. It may be argued that the analytical reduction of a 20×16 or even a 12×8 matrix to tridiagonal form is impracticable. However, Eqs. (23) and (27) are sparse enough to render the derivation of self-calibration equations according to this scheme feasible, even for the 15-term error model (30). Once the unknown parameters of the standards are determined, the standards are completely known and so are all nonzero entries of the tridiagonal matrix, which is then used to compute the error terms by a backsubstitution process [19, p. 37].
3. The formulation of the error model is rearranged to yield relations between the standards' *S*-parameters and the measured values, eliminating the error terms. These relations are exploited to solve for the unknown parameters of the calibration standards which are then completely known and can be used to solve the linear system of equations [Eqs. (23) and (27)] for the error terms. In the following sections, this method, which is based on similarity transformations [21,27], will be presented for the 7-term and the 15-term error model.

5.1. Self-Calibration for the Seven-Term Error Model

Elimination of the error parameters to arrive at a relation between the standards' parameters and the measurement values was first described by Eul and Schiek [21] and is most easily achieved by using transfer parameters to describe the cascade structure of the error model (Fig. 19). See Eq. (24) in Section 4.5.2.

As transfer parameters exhibit a singularity for transmissionless two-ports ($S_{21} = 0$), this representation of the error model is less suited for the computation of the error terms, which is why the *S*-parameter representation [Eq. (22)] was chosen in Section 4.5. The seven-term error model, however, may as well be written using Eq. (24) with the three calibration measurements yielding three such equations.

Solving the *i*th calibration measurement for [*H*]

$$[H] = [\Sigma_i]^{-1}[G][P_i]^{-1} \quad (28)$$

and substituting Eq. (28) into the remaining calibration measurements *j* and *k* yields

$$\begin{aligned} [P_j][P_i]^{-1} &= [G]^{-1}[\Sigma_j][\Sigma_i]^{-1}[G] \quad \text{and} \\ [P_k][P_i]^{-1} &= [G]^{-1}[\Sigma_k][\Sigma_i]^{-1}[G] \end{aligned} \quad (29)$$

Recognizing Eq. (29) as similarity transformations, the equality of the eigenvalues of the similar matrices is equivalent to the equality of their determinants and traces; hence

$$\begin{aligned} [A] &= [X][B][X]^{-1} \Rightarrow \det[A] = \det[B] \\ \text{trace}[A] &= a_{11} + a_{22} = \text{trace}[B] = b_{11} + b_{22} \end{aligned}$$

which yields the four equations

$$\begin{aligned} \det\{[P_j][P_i]^{-1}\} &= \beta_1 = \det\{[\Sigma_j][\Sigma_i]^{-1}\}, \\ \text{trace}\{[P_j][P_i]^{-1}\} &= \beta_2 = \text{trace}\{[\Sigma_j][\Sigma_i]^{-1}\} \\ \det\{[P_k][P_i]^{-1}\} &= \beta_3 = \det\{[\Sigma_k][\Sigma_i]^{-1}\}, \\ \text{trace}\{[P_k][P_i]^{-1}\} &= \beta_4 = \text{trace}\{[\Sigma_k][\Sigma_i]^{-1}\} \end{aligned} \quad (30)$$

The combination of both equations in Eq. (29) leads to a fifth condition for the standards' parameters:

$$\begin{aligned} \text{trace}\{[P_j][P_i]^{-1}[P_k][P_i]^{-1}\} \\ = \beta_5 = \text{trace}\{[\Sigma_j][\Sigma_i]^{-1}[\Sigma_k][\Sigma_i]^{-1}\} \end{aligned} \quad (31)$$

These five equations in Eqs. (30) and (31), in which only the transfer parameters of the standards and measurement values appear, can be used to compute a maximum of five unknown parameters of the standards.

5.1.1. The General TAN Procedure. One possibility to distribute the five unknowns among the three calibration standards is the general TAN procedure, where a Through standard (of known transmission factor t), a well-matched Attenuator (with unknown forward and reverse attenuation k_f and k_r), and a symmetrical, but not necessarily reciprocal, Network standard (with unknown reflection r and unknown transmission coefficients u_f and u_r) are used for calibration:

$$\begin{aligned} [\Sigma_T] &= \begin{bmatrix} t & 0 \\ 0 & 1/t \end{bmatrix}, \quad [\Sigma_A] = \begin{bmatrix} k_r & 0 \\ 0 & 1/k_f \end{bmatrix} \\ [\Sigma_N] &= \frac{1}{u_f} \begin{bmatrix} u_f u_r - r^2 & r \\ -r & 1 \end{bmatrix} \end{aligned}$$

The inclusion of the known parameter t is for convenience if connector sex dictates the use of a nonzero length Through.

As the A -standard may also turn into a well-matched Line standard (L) with $k_f = k_r = e^{-\gamma l}$, or into a double Match standard (M) with $k_f = k_r = 0$, and as the N standard may degenerate to a Reflection standard (R) with $u_f = u_r = 0$, the general TAN procedure also covers the most popular TLR and TMR self-calibration procedures.

However, the singularity of the transfer matrices $[\Sigma_A]$ and $[\Sigma_N]$ and the accompanying measurement matrices $[P_A]$ and $[P_N]$ for the case of vanishing transmission (M, R standard) must be taken care of. For that purpose, pseu-

dotransfer matrices are introduced [31] by separating the matrix of the measured quantities $[P]$ from its determinant Δm , which may be zero. The residual part of the matrix is denoted $[\tilde{P}]$

$$\begin{aligned} [P] &= \begin{bmatrix} m_1^I & m_1^{II} \\ m_2^I & m_2^{II} \end{bmatrix} \frac{1}{m_3^I m_4^{II} - m_3^{II} m_4^I} \begin{bmatrix} m_4^{II} & -m_3^{II} \\ -m_4^I & m_3^I \end{bmatrix} \\ &= \frac{1}{\Delta m} [\tilde{P}] \end{aligned} \quad (32)$$

with

$$\begin{aligned} \Delta m &= m_3^I m_4^{II} - m_3^{II} m_4^I \text{ and} \\ [\tilde{P}] &= \begin{bmatrix} m_1^I & m_1^{II} \\ m_2^I & m_2^{II} \end{bmatrix} \begin{bmatrix} m_4^{II} & -m_3^{II} \\ -m_4^I & m_3^I \end{bmatrix} \end{aligned}$$

Combination of the determinant of the measurement matrix with the transfer matrix of the standard belonging to it yields the pseudotransfer matrices

$$\begin{aligned} \Delta m_A[\Sigma_A] &= \frac{\Delta m_A}{k_f} \begin{bmatrix} k_r k_f & 0 \\ 0 & 1 \end{bmatrix} = \begin{bmatrix} \kappa_r & 0 \\ 0 & 1/\kappa_f \end{bmatrix} = [\Sigma_A^p] \\ \Delta m_N[\Sigma_N] &= \frac{\Delta m_N}{u_f} \begin{bmatrix} u_f u_r - r^2 & r \\ -r & 1 \end{bmatrix} = \frac{1}{\mu_f} \begin{bmatrix} \mu_f \mu_r - \rho^2 & \rho \\ -\rho & 1 \end{bmatrix} \\ &= [\Sigma_N^p] \end{aligned}$$

with

$$\begin{aligned} \kappa_f &= \frac{k_f}{\Delta m_A}, \quad \kappa_r = k_r \Delta m_A, \\ \mu_f &= \frac{u_f}{\Delta m_N}, \quad \mu_r = r_r \Delta m_N, \quad \rho = r \end{aligned} \quad (33)$$

and modifies Eqs. (30) and (31) as

$$\begin{aligned} \det\{[\tilde{P}_A][P_T]^{-1}\} &= \beta_1 = \det\{\Delta m_A[\Sigma_A][\Sigma_T]^{-1}\} \\ &= \det\{[\Sigma_A^p][\Sigma_T]^{-1}\} \\ \text{trace}\{[\tilde{P}_A][P_T]^{-1}\} &= \beta_2 = \text{trace}\{\Delta m_A[\Sigma_A][\Sigma_T]^{-1}\} \\ &= \text{trace}\{[\Sigma_A^p][\Sigma_T]^{-1}\} \\ \det\{[\tilde{P}_N][P_T]^{-1}\} &= \beta_3 = \det\{\Delta m_N[\Sigma_N][\Sigma_T]^{-1}\} \\ &= \det\{[\Sigma_N^p][\Sigma_T]^{-1}\} \\ \text{trace}\{[\tilde{P}_N][P_T]^{-1}\} &= \beta_4 = \text{trace}\{\Delta m_N[\Sigma_N][\Sigma_T]^{-1}\} \\ &= \text{trace}\{[\Sigma_N^p][\Sigma_T]^{-1}\} \end{aligned}$$

$$\begin{aligned} \text{trace}\{[\tilde{P}_A][P_T]^{-1}[\tilde{P}_N][P_T]^{-1}\} &= \beta_5 \\ &= \text{trace}\{[\Sigma_A^p][\Sigma_T]^{-1}[\Sigma_N^p][\Sigma_T]^{-1}\} \end{aligned} \quad (34)$$

Because at least one standard must exhibit transmission, this property is, without loss of generality, attributed to the T standard, which therefore may be represented by a regular transfer matrix.

With β_i being nonsingular complex values, computed from the measurement values of the four receivers, according to Eq. (32), the first two equations of Eq. (34) can be used to determine the transmission coefficients of the A standard,

$$\frac{\kappa_r}{\kappa_f} = \beta_1, \quad \frac{\kappa_r}{t} + \frac{t}{\kappa_f} = \beta_2$$

which compute as

$$\kappa_r = t \left(\frac{\beta_2}{2} \pm \sqrt{\frac{\beta_2^2}{4} - \beta_1} \right) \quad \text{and} \quad \kappa_f = \frac{\kappa_r}{\beta_1} = \frac{t^2}{t\beta_2 - \kappa_r} \quad (35)$$

Similarly, the other parameters may be derived from the remaining equations in Eqs. (34) as

$$\mu_f = \frac{t^2 - \kappa_f \kappa_r}{t\kappa_f(\beta_5 - \kappa_r\beta_4)}, \quad \mu_r = \mu_f \beta_3 \quad (36)$$

$$\rho = \pm \sqrt{\mu_f \mu_r - \frac{\beta_4 \mu_f}{t} + \frac{1}{t^2}} \quad (37)$$

Using Eq. (33), the parameters of the transfer matrices of the standards $[\Sigma_A]$ and $[\Sigma_N]$ are computed from the above-derived pseudotransfer parameters.

The root ambiguity in Eq. (35) is solved with a priori knowledge of the A standard's transmission factor. If the standard exhibits attenuation ($|k_r| < 1$), the root whose magnitude is below 1 will be chosen, because the standard is passive. If a line standard with $|k_f| = |k_r| \approx 1$ is used, the phase of the line's transmission factor must be known to $\pm 90^\circ$ in order to select the correct root.

The root choice in Eq. (37) requires the same kind of information about the phase of the N standard's reflection coefficient, which must be known to $\pm 90^\circ$.

Equations (35)–(37) allow the computation of the calibration standards for the general TAN calibration procedure, also accounting for the special cases of the TMN, TMR, TAR, TLN, and TLR procedures, where the second and/or third standard are double one-ports without transmission.

Calibrating with TMN standards ($k_f = k_r = 0$), for instance, reduces Eqs. (35)–(37) to

$$\mu_f = \frac{\beta_2}{\beta_5}, \quad \mu_r = \frac{\beta_2 \beta_3}{\beta_5}, \quad \rho = \pm \sqrt{\mu_f \mu_r - \frac{\beta_4 \mu_f}{t} + \frac{1}{t^2}}$$

TAR (TLR), on the other hand, has arbitrary k_f and k_r with $\mu_f = \mu_r = 0$, reducing the set of unknowns to

$$\kappa_r = t \left(\frac{\beta_2}{2} \pm \sqrt{\frac{\beta_2^2}{4} - \beta_1} \right), \quad \kappa_f = \frac{\kappa_r}{\beta_1}$$

$$\rho = \pm \frac{1}{t} \sqrt{1 - \frac{\beta_4(t^2 - \kappa_f \kappa_r)}{\kappa_f(\beta_5 - \kappa_r \beta_4)}}$$

For the TMR procedure [32], $k_f = k_r = 0$ and $\mu_f = \mu_r = 0$. Only the unknown reflection r needs to be determined, yielding

$$\rho = \pm \frac{1}{t} \sqrt{1 - t \frac{\beta_2 \beta_4}{\beta_5}}$$

As before, the reflection coefficient must be known a priori to $\pm 90^\circ$ in order to resolve the root ambiguity. Technically this is done by choosing the solution that is closest to the estimated reflection coefficient of the R standard. Its choice as a short or an open is common practice (although not required) and provides the necessary information. Furthermore, the *true* value of r is determined by the self-calibration process and can be used to check the quality of the calibration, in those cases in which the R standard is completely known.

It should be noted that the perfect match of the A , L , or M standard in the above-described procedures is the only absolute impedance standard and must always be a known quantity, determining the reference impedance of the calibration. The R standard is not required to be known exactly, and the only demand is that the same reflection is presented to both ports. By connecting the same reflection standard first to port 1 and then to port 2, this requirement is easily met. Possible inconsistencies between the phase-reference planes of the different standards, which may creep in without the use of self-calibration, can therefore not occur. The postulated symmetry of the R standard uniquely sets the phase reference at equal offsets to the test ports. These offsets are zero if the transmission factor t of the through corresponds to its true electrical length.

Besides allowing the calibration of the seven-term error model with partially known standards, self-calibration also provides an interesting means of verifying the quality of the calibration if the calibration standards are fully known. In this case, all deviations of the computed parameters of the standards from their *known* values indicate imperfections of the calibration process.

5.2. Employing Self-Calibration for s_r -Measurements

The scheme introduced above for determining the transmission factor of the A standard can be used in a straightforward manner to obtain error-corrected measurements of the electrical length of an unknown line: Measurements of a through and the unknown line yield the measurement matrices $[P_T]$ and $[\tilde{P}_A]$ which using Eq. (34) make β_1 and β_2

available. With the transmission factor of a line being

$$e^{-\gamma l} = k_f = k_r = \frac{k_r}{\Delta m_A}$$

Eq. (35) can be used to solve for γl . Furthermore, if the mechanical length l of the line is known, the complex propagation constant γ containing ϵ_r is available with very high precision, even though up to this point no calibration has been performed.

5.3. Self-Calibration for the 15-Term Error Model

Contrary to the above-presented self-calibration scheme for the seven-term error model, self-calibration formulas for the 15-term model can be derived without the need for transfer parameters and their associated singularity problems.

As was shown in Section 4.6, the 15-term model is calibrated using five calibration measurements

$$[G] + [E][M_n] = [S_n]([F] + [H][M_n]) \quad (n = 1, \dots, 5) \quad (38)$$

Using four of those equations, named i, j, k , and l , most of the error parameters can be eliminated, arriving at

$$\begin{aligned} & \Delta M_{j,k}^{-1} \Delta M_{i,j} \Delta M_{i,l}^{-1} \Delta M_{l,k} \\ &= ([H] + [F][M_k])^{-1} \Delta S_{j,k}^{-1} \Delta S_{i,j} \\ & \quad \times \Delta S_{i,l}^{-1} \Delta S_{l,k} ([H] + [F][M_k]) \end{aligned} \quad (39)$$

with

$$\Delta S_{m,n} = [S_m] - [S_n], \quad \Delta M_{m,n} = [M_m] - [M_n] \quad (m, n = 1, \dots, 5)$$

see Ref. 27 for a comprehensive outline of the derivation).

Equation (39) again constitutes a similarity transform, resulting in the two nonlinear relations

$$\begin{aligned} & \text{Trace}\{\Delta M_{j,k}^{-1} \Delta M_{i,j} \Delta M_{i,l}^{-1} \Delta M_{l,k}\} \\ &= b_1 = \text{Trace}\{\Delta S_{j,k}^{-1} \Delta S_{i,j} \Delta S_{i,l}^{-1} \Delta S_{l,k}\} \\ & \text{Det}\{\Delta M_{j,k}^{-1} \Delta M_{i,j} \Delta M_{i,l}^{-1} \Delta M_{l,k}\} \\ &= b_2 = \text{Det}\{\Delta S_{j,k}^{-1} \Delta S_{i,j} \Delta S_{i,l}^{-1} \Delta S_{l,k}\} \end{aligned} \quad (40)$$

between the measured values $[M_n]$ and the standards' S -parameters (invariance of the eigenvalues of similar matrices).

Because only four calibration measurements are used by Eq. (39), the fifth standard $[S_m]$, $[M_m]$ may be substituted into Eq. (39) to yield two more similarity transformations:

$$\begin{aligned} & \Delta M_{j,k}^{-1} \Delta M_{m,j} \Delta M_{m,l}^{-1} \Delta M_{l,k} \\ &= ([H] + [F][M_k])^{-1} \Delta S_{j,k}^{-1} \Delta S_{m,j} \\ & \quad \times \Delta S_{m,l}^{-1} \Delta S_{l,k} ([H] + [F][M_k]) \end{aligned} \quad (41)$$

(i th standard replaced by m th standard) and

$$\begin{aligned} & \Delta M_{m,k}^{-1} \Delta M_{i,m} \Delta M_{i,l}^{-1} \Delta M_{l,k} \\ &= ([H] + [F][M_k])^{-1} \Delta S_{m,k}^{-1} \Delta S_{i,m} \\ & \quad \times \Delta S_{i,l}^{-1} \Delta S_{l,k} ([H] + [F][M_k]) \end{aligned} \quad (42)$$

(j th standard replaced by m th standard).

Together with Eq. (40), the resulting trace and determinant equalities provide six nonlinear self-calibration equations, sufficient for computation of the maximally five unknowns that the 15-term error model allows for.

It is interesting to note that the derivation of Eq. (39) holds as long as the structure of the error model [Eq. (38)] is unchanged. The calibration standards and/or the measurement matrix $[M]$ may therefore also be expressed in T -(transfer) parameters or even in chain parameters, using voltages and currents instead of waves. Even the extension to the error model of an N -port VNA, as described in Ref. 24, is straightforward. In this case, all quadrants of the error matrix, the standards' S - (T -) matrix, and the measurement matrices are $N \times N$ matrices. The invariance of the eigenvalues of the two similar matrices in Eq. (39) yields N relations between the measured values and the standards.

5.3.1. The Tmrg Procedure. The self-calibration equations [Eqs. (39), (41), and (42)] permit construction of a multitude of self-calibration procedures, allowing calibration with the set of standards, best suited for a specific application. A particularly interesting variant, the Tmrg procedure, refining the Tmso procedure of Section 4.6 shall now be introduced.

Whereas Tmso requires a *perfect* match, short and open, the above-derived formalism allows the reflection coefficients of the short and open to be computed through self-calibration. Furthermore, a nonzero but known reflection coefficient may be used as the m standard, reducing its requirement from *perfect* to *known*.

Comparable with Fig. 22, Fig. 25 shows the five standards to be constructed from a Through (with known transmission factor t) and three reflection one-ports with reflection coefficients m, r , and g . The first four standards suffice for the determination of the unknown reflection coefficients r and g .

Substituting the standards i, j, k , and l into Eq. (39) and evaluating the product of S -matrix differences yield

$$\begin{aligned} & \Delta S_{j,k}^{-1} \Delta S_{i,j} \Delta S_{i,l}^{-1} \Delta S_{l,k} = [B] \\ &= \frac{1}{t_2 - rm} \begin{bmatrix} t^2 C_1 - m^2 C_2 & t(m C_2 - g C_1) \\ t(r C_1 - m C_2) & t^2 C_2 - rg C_1 \end{bmatrix} \end{aligned}$$

with

$$C_1 = \frac{r - m}{r - g}, \quad C_2 = \frac{g - r}{g - m}$$

$$[S_{(t)}^T] = \begin{bmatrix} 0 & t \\ t & 0 \end{bmatrix}, \quad [S_{(m)}^m] = \begin{bmatrix} r & 0 \\ 0 & m \end{bmatrix}, \quad [S_{(g)}^{mg}] = \begin{bmatrix} m & 0 \\ 0 & g \end{bmatrix}, \quad [S_{(t)}^g] = \begin{bmatrix} g & 0 \\ 0 & r \end{bmatrix}, \quad [S_{(m)}^{tg}] = \begin{bmatrix} r & 0 \\ 0 & g \end{bmatrix}$$

Figure 25. Calibration standards for the 15-term Tmrg self-calibration procedure.

resulting in

$$\begin{aligned} & \text{trace}\{\Delta M_{j,k}^{-1} \Delta M_{i,j} \Delta M_{i,l}^{-1} \Delta M_{l,k}\} \\ & = \text{trace}[B] = b_1 = \frac{m^2(g-m+gr(m-r))+t^2(r-g)}{(rm-t^2)(m-g)} \end{aligned} \quad (43)$$

$$\begin{aligned} & \det\{\Delta M_{j,k}^{-1} \Delta M_{i,j} \Delta M_{i,l}^{-1} \Delta M_{l,k}\} \\ & = \det[B] = b_2 = \frac{(t^2-mg)(r-m)}{(t^2-rm)(m-g)} \end{aligned} \quad (44)$$

Equation (44) can be solved to yield a linear relation for r

$$r = \frac{b_2 t^2 (g-m) + m(gm-t^2)}{b_2 m (g-m) + (gm-t^2)} \quad (45)$$

and can be combined with Eq. (43) to form a quadratic equation for g

$$g^2 - g \frac{2mt^2 a_1 a_2}{m^2 a_3 - t^2 b_2^2} + \frac{t^4 a_3 - t^2 m^2 b_2^2}{m^2 a_3 - t^2 b_2^2} = 0 \quad (46)$$

with

$$\begin{aligned} a_1 &= b_1 - 1 - 2b_2, \quad a_2 = b_2 + 1 \\ a_3 &= (b_1 - 1)(b_2 + 1) - b_2(2 + b_2) \end{aligned}$$

Choosing the proper root for g requires knowledge about the sign of that reflection standard. Using a short for g and an open for r provides the necessary sign information and makes the standards sufficiently distinct for subsequent use as fully known calibration standards.

The only parameters that must be known are the transmission coefficient t of the T standard and the reflection m . The quantity m should be small for numerical reasons and must be known, but the standard is not required to be an *ideal* match.

As only one set of reflection one-ports is physically required, the postulated equality of the reflection coefficients that enter the different standards is guaranteed, an important advantage over calibration procedures, which require the *same* reflection coefficient to be connected to both ports simultaneously.

6. OUTLOOK AND RELATED TOPICS

The continuously growing need for fast (production) and precision (laboratory) network measurements has led to the development of sophisticated instrumentation equipment [33–35] and many optimized calibration procedures. This process is expected to continue, with the focus shifting toward even higher frequencies (>110 GHz), on-wafer crosstalk correction, and N -port measurements [36,37]. A lot of interest is spawned by the communication

industry—for instance, in the characterization of IC packages (N -port measurements) and in high production throughput. Semiautomatic calibration procedures, avoiding the necessity of reconnecting the calibration standards for every calibration, address this need but are not covered here. The interested reader is referred to Ref. 38 for an overview. References 39 and 40 describe commercially available solutions.

Finally, Refs. 20 and 41 present statistical methods to assess errors not originally contained in the error model, like repeatability or contacting errors. Because these errors meanwhile constitute the accuracy limit of error-corrected network analyzer measurements, their inclusion is expected to further boost measurement accuracy.

BIBLIOGRAPHY

1. M. Sucher and J. Fox, *Handbook of Microwave Measurements*, Vol. 1, Brooklyn, NY: Polytechnic Press of the Polytechnic Institute of Brooklyn, 1963.
2. P. I. Somlo and J. D. Hunter, *Microwave Impedance Measurements*, *IEE Electrical Measurement Series*, Vol. 2, Stevenage, U.K.: Peregrinus, 1985.
3. G. U. Sorger, Coaxial swept-frequency VSWR measurements using slotted lines, *IEEE Trans. Instrum. Meas.*, **IM-17**: 403–412 (1968).
4. R. Caldecott, The generalized multiprobe reflectometer and its application to automated transmission line measurements, *IEEE Trans. Antennas Propag.* **AP-21**:550–554 (1973).
5. C. L. J. Hu, A novel approach to the design of multiple-probe high-power microwave automatic impedance measuring schemes, *IEEE Trans. Microw. Theory Tech.*, **MTT-28**: 1422–1428 (1980).
6. C. A. Hoer, The six-port coupler: A new approach to measuring voltage, current, power, impedance and phase, *IEEE Trans. Instrum. Meas.*, **IM-21**:466–470 (1972).
7. G. F. Engen, The six-port reflectometer: An alternative network analyzer, *IEEE Trans. Instrum. Meas.*, **IM-21**: 1075–1080 (1972).
8. P. I. Somlo and J. D. Hunter, A six-port reflectometer and its complete characterization by convenient calibration procedures, *IEEE Trans. Microw. Theory Tech.*, **MTT-30**:186–192 (1982).
9. G. F. Engen, An improved circuit for implementing the six-port technique of microwave measurements, *IEEE Trans. Microw. Theory Tech.*, **MTT-25**:110–112 (1977).
10. D. M. Pozar, *Microwave Engineering*, Reading, MA: Addison-Wesley, 1990.
11. S. Uysal, *Nonuniform Line Microstrip Directional Couplers and Filters*, Norwood, MA: Artech House, 1993.
12. H. M. Churchill and L. Susman, A six-port automatic network analyser, *IEEE Trans. Microw. Theory Tech.*, **MTT-25**: 1086–1091 (1977).
13. G. F. Engen and C. A. Hoer, Thru-reflect-line: An improved technique for calibrating the dual six port automatic network analyzer, *IEEE Trans. Microw. Theory Tech.*, **MTT-27**: 987–993 (1979).

14. H.-G. Krekels and B. Schiek, A full model calibration algorithm for a dual six-port network analyzer, *Proc. IEEE Instrum. Meas. Conf. (IMTC)*, Hamamatsu, Japan, 1994, pp. 990–993.
15. R. J. King, *Microwave Homodyne Systems*, Stevenage, U.K.: Peregrinus, 1978.
16. U. Gärtner and B. Schiek, A broad-band homodyne network-analyzer with binary phase-modulation, *IEEE Trans. Microw. Theory Tech.*, **MTT-34**:902–906 (1986).
17. D. Rytting, An analysis of vector measurement accuracy enhancement techniques, Hewlett Packard, April 1981.
18. D. Rytting, Appendix to an analysis of vector measurement accuracy enhancement techniques, Hewlett Packard, April 1981.
19. W. H. Press, et al., *Numerical Recipes in C*, Cambridge, U.K.: Cambridge Univ. Press, 1988.
20. H. Van Hamme and M. Vanden Bosche, Flexible vector network analyzer calibration with accuracy bounds using an 8-term or a 16-term error correction model, *IEEE Trans. Microw. Theory Tech.*, **MTT-42**:976–987 (1994).
21. H.-J. Eul and B. Schiek, A generalized theory and new calibration procedures for network analyzer self-calibration, *IEEE Trans. Microw. Theory Tech.*, **MTT-39**:724–731 (1991).
22. A. Ferrero, Two-port network analyzer calibration using an unknown “Thru”, *IEEE Microwave Guided Wave Lett.*, **2**: 505–507 (1992).
23. B. Saswata and L. Hayden, An SOLR calibration for accurate measurement of orthogonal on-wafer DUTs, *Proc. IEEE MTT-S Int. Microw. Symp.*, Denver, CO, 1997, pp. 1335–1338.
24. R. A. Speciale, A generalization of the TSD network-analyzer calibration procedure, covering n -port scattering-parameter measurements, affected by leakage errors. *IEEE Trans. Microw. Theory Tech.*, **MTT-25**:1100–1115 (1977).
25. K. J. Silvonen, Calibration of 16-term error-model, *Electron. Lett.*, **29**:1544–1545 (1993).
26. H. Heuermann and B. Schiek, Results of network analyzer measurements with leakage errors corrected with the TMS-15-term procedure, *Proc. IEEE MTT-S Int. Microw. Symp.*, San Diego, CA, 1994, pp. 1361–1364.
27. A. Gronefeld and B. Schiek, Network-analyzer self-calibration with four or five standards for the 15-term error-model, *Proc. IEEE MTT-S Int. Microw. Symp.*, Denver, CO, 1997, pp. 1655–1658.
28. G. L. Madonna, A. Ferrero, and U. Piani, Multiport network-analyzer self-calibration: A new approach and some interesting results, *49th ARFTG Conf. Dig.*, Denver, CO, 1997, p. 142.
29. K. J. Silvonen, LMR 16—a self-calibration procedure for a leaky network analyzer, *IEEE Trans. Microw. Theory Tech.*, **MTT-45**:1041–1049 (1997).
30. A. Gronefeld and B. Schiek, Eine neue Methode zur Generierung von Selbstkalibrierverfahren für Netzwerkanalysatoren, anwendbar auf alle bekannten Fehlermodelle, *Kleinheubacher Berichte 1998*, Band 41, pp. 117–126.
31. H. Heuermann and B. Schiek, Robust algorithms for Txx network analyzer self-calibration procedures, *IEEE Trans. Instrum. Meas.*, **IM-43**:18–23 (1994).
32. H.-J. Eul and B. Schiek, Thru-match-reflect: One result of a rigorous theory for de-embedding and network analyzer calibration, *Proc. 18th Eur. Microw. Conf.*, Stockholm, Sweden, 1988, pp. 909–914.
33. O. Ostwald and C. Evers, Vector network analyzer family ZVR, to the heart of the chart, *News from Rohde & Schwarz*, **150**:6–9 1996.
34. A. Wiltron, 360/37XXXA/B Series Vector Network Analyzers, Application Note AN360B/37XXXA/B-1, May 1996.
35. Hewlett Packard, “HP8510”, Product information.
36. A. Ferrero, F. Sanpietro, and U. Pisani, Multiport vector network analyzer calibration: A general formulation, *IEEE Trans. Microw. Theory Tech.*, **MTT-42**:2455–2461 (1994).
37. J. C. Tippet and R. A. Speciale, A rigorous technique for measuring the scattering matrix of a multiport device with a 2-Port network-analyzer, *IEEE Trans. Microw. Theory Tech.*, **MTT-30**:661–666 (1982).
38. H.-G. Krekels and B. Schiek, A novel procedure for an automatic network-analyzer calibration, *IEEE Trans. Instrum. Meas.*, **IM-44**:291–294 (1995).
39. H. G. Krekels, AutoKal: Automatic calibration of vector network analyzer ZVR, *Rohde & Schwarz Application Note 1EZ30 IE*, 1996.
40. Hewlett Packard, *Ecal*, Product information.
41. R. B. Marks, A multiline method of network analyzer calibration, *IEEE Trans. Microw. Theory Tech.*, **MTT-39**: 1205–1215 (1991).

STRIP TRANSMISSION LINES

PROTAP PRAMANICK
K & L Microwave, Inc.
Salisbury, Maryland
PRAKASH BHARTIA
Natel Engineering Co., Inc.
Chatsworth, California

1. BASIC CONFIGURATION

The stripline, shown in Fig. 1 is the oldest planar transmission line that has been in use in microwave integrated circuits since its creation by R.M. Barrett in 1950 [1]. In its simplest form, it consists of a conducting strip, of width W and thickness t , separated from a pair of common conducting ground planes of theoretically infinite extent compared to the width W of the strip conductor, $W \ll a$; where a is the width of the ground plane. The ground planes are separated by a thickness b , and the entire space is homogeneously filled with a dielectric material of complex dielectric constant $\epsilon_r(1 - j \tan \delta)$. The ground planes are kept at the same potential. In a balanced stripline, the strip conductor is equidistant from the ground planes. In an unbalanced stripline, there is an offset and the strip is not

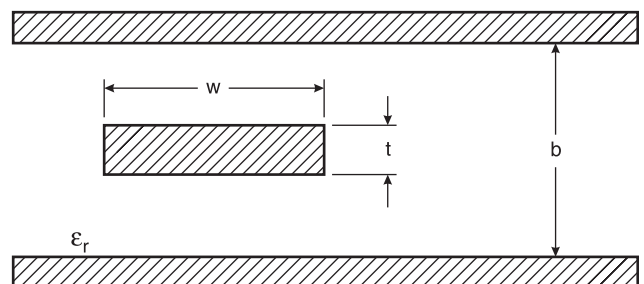


Figure 1. Balanced stripline configuration.

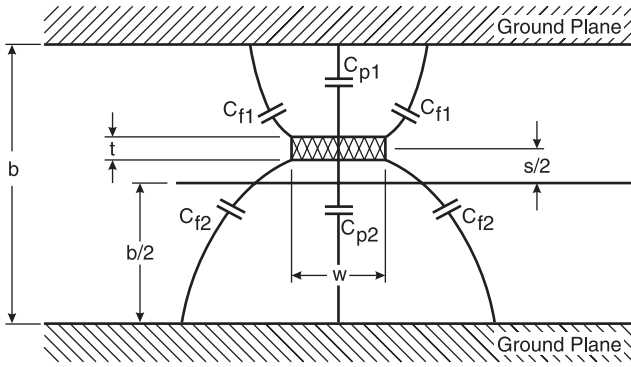


Figure 2. Unbalanced stripline configuration.

equidistant from the two ground planes as shown in Fig. 2. The first significant theoretical investigation on stripline was carried out by S. Cohn in the mid 1950s [2]. While Sanders Associates used the tradename *triplate* [3], the term *stripline* was first introduced by Airborne Instruments Laboratories (AIL).

2. MODES IN A STRIPLINE AND THE MAXIMUM USABLE FREQUENCY

Although striplines can support waveguide-type modes (TE or TM), the fundamental mode of propagation is the transverse electromagnetic (TEM) mode having no cutoff frequency. The field configuration for the fundamental mode is shown in Fig. 3. The usable single-mode bandwidth of a stripline is determined by the cutoff frequency of the lowest-order waveguide mode. For that mode, the two ground planes have the same potential, the electric field is normal to the strip, and the ground planes and the longitudinal electric field are zero with cutoff frequency [4]

$$f_c = \frac{c}{\sqrt{\epsilon_r} \left(2 \frac{W}{b} + 4 \frac{d}{b} \right) b} \quad (1)$$

where c is the velocity of light in free space (3×10^8 m/s) and $4b/d$ is a function of the cross section of the stripline. For a balanced stripline when $t/b = 0$ and $W/b > 0.35$, then $4d/b$ is a function of b/f_c alone and is given in Table 1 in [4].

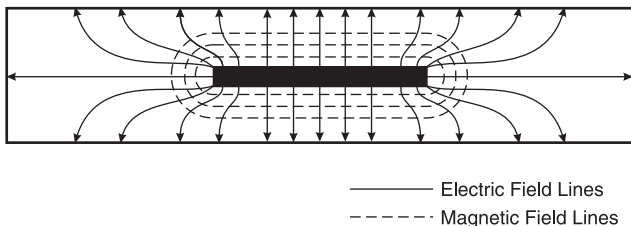


Figure 3. Field configuration of the fundamental mode of stripline.

3. CHARACTERISTIC IMPEDANCE OF A BALANCED STRIPLINE

The characteristic impedance of a balanced strip transmission line can be accurately calculated from [5]

$$Z_0 = \frac{60}{\sqrt{\epsilon_r}} \ln \left[\frac{4b}{\pi d} \right] \quad (2)$$

For $W/b < 0.35$, where

$$d = \frac{W}{2} \left[1 + \frac{t}{\pi W} \left(1 + \ln \frac{4\pi W}{t} + 0.51\pi \left(\frac{t}{W} \right)^2 \right) \right] \quad (3)$$

and

$$Z_0 = \frac{94.15}{\sqrt{\epsilon_r}} \frac{1}{\frac{C_f}{\epsilon} + \frac{W}{b \left(1 - \frac{t}{b} \right)}} \Omega \quad (4)$$

for $W/b \geq 0.35$, where

$$\frac{C_f}{\epsilon} = \frac{1}{\pi} \left\{ \frac{2}{1 - \frac{t}{b}} \ln \left(\frac{1}{1 - \frac{t}{b}} + 1 \right) \right\} - \frac{1}{\pi} \left\{ \left(\frac{1}{1 - \frac{t}{b}} - 1 \right) \ln \left(\frac{1}{\left(1 - \frac{t}{b} \right)^2} - 1 \right) \right\} \quad (5)$$

where $2C_f/\epsilon$ is the per unit length fringing field capacitance between the strip and each ground plane and $\epsilon = \epsilon_0 \epsilon_r$; $\epsilon_0 = 8.854e^{-12}$ F/m (permittivity of free space).

4. CHARACTERISTIC IMPEDANCE OF AN UNBALANCED STRIP TRANSMISSION LINE

The characteristic impedance of an unbalanced stripline (shown in Fig. 2) is given by [5]

$$Z_0 = \frac{120\pi}{\sqrt{\epsilon_r} \frac{C}{\epsilon}} \quad (6)$$

where C/ϵ is the per unit length static capacitance between the strip and the two ground planes, normalized by the permittivity ϵ of the medium:

$$\frac{C}{\epsilon} = \frac{C_{p1}}{\epsilon} + \frac{C_{p2}}{\epsilon} + \frac{2C_{f1}}{\epsilon} + \frac{2C_{f2}}{\epsilon} \quad (7)$$

$$\frac{C_{p1}}{\epsilon} = \frac{2 \frac{W}{b-s}}{1 - \frac{t}{b-s}} \quad (8)$$

$$\frac{C_{p2}}{\epsilon} = \frac{2 \frac{W}{b+s}}{1 - \frac{t}{b+s}} \quad (9)$$

The per unit length fringe field capacitances C_{f1} and C_{f2} are obtained from Eq. (5) by replacing b with $(b - S)$ and

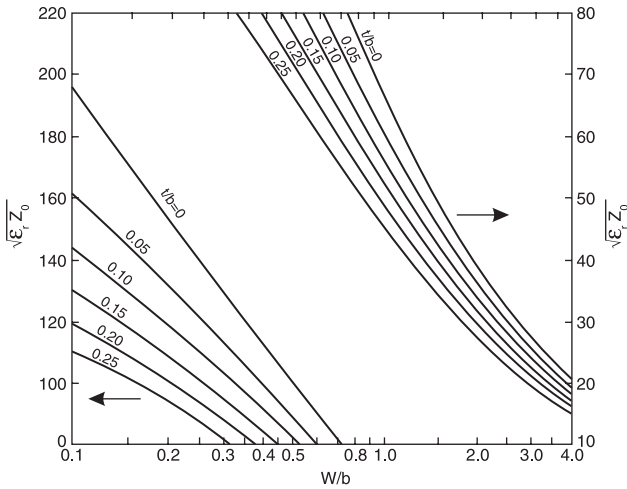


Figure 4. Variation of characteristic impedance Z_0 with W/b and t/b .

$(b + S)$ respectively. The above formulae are applicable to single strips only. Figure 4 shows the variations of Z_0 with W/b for various values of t/b , for a balanced stripline.

5. THE PROPAGATION CONSTANT IN A STRIPLINE

The propagation constant β of a stripline is given by

$$\beta = \frac{2\pi}{\lambda_g} = \frac{2\pi\sqrt{\epsilon_r}}{\lambda_0} \text{ radians per unit length} \quad (10)$$

where λ_g and λ_0 are the wavelengths in the stripline and free space, respectively.

6. SYNTHESIS OF STRIPLINES

In order to obtain the structural dimensions for a stripline to be designed, when the characteristic impedance Z_0 and the substrate dielectric constant ϵ_r are given, the following formulas are used [6]:

$$W = W_0 - \Delta W_0 \quad (11)$$

$$W_0 = \frac{8(b - t)\sqrt{B + 0.568}}{\pi(b - 1)} \quad (12)$$

$$\Delta W_0 = \frac{t}{\pi} \left\{ 1 - 0.5 \ln \left[\left(\frac{t}{2b - t} \right)^2 + \left(\frac{0.0796t}{W_0 - 0.26t} \right)^m \right] \right\} \quad (13)$$

$$B = e^{(Z_0\sqrt{\epsilon_r})/30} \quad (14)$$

$$m = 6 \left[\frac{b - t}{3b - t} \right] \quad (15)$$

There is no closed-form design equation for the unbalanced stripline shown in Fig. 2. An iterative procedure based on analysis and optimization is used to synthesize an unbalanced stripline for a given characteristic impedance Z_0 and substrate dielectric constant ϵ_r .

7. ATTENUATION CONSTANT IN STRIPLINES

The attenuation constant of a stripline, balanced or unbalanced, is given by [4]

$$\alpha = \alpha_c + \alpha_d \text{ nepers per unit length} \quad (16)$$

The attenuation constant α_c due to conductor loss in the line at a frequency f in gigahertz is obtained from [7]

$$\alpha_c = \frac{\pi\sqrt{\epsilon_r}f}{0.2998} \left[1 - \frac{Z_0'}{Z_0} \right] \text{ Np/m} \quad (17)$$

where Z_0 is the characteristic impedance of the line and Z_0' is the characteristic impedance of the line when W , t , and b are replaced by $W = W + \delta_s$, $t + \delta_s$, and $b - \delta_s$, respectively in Eqs. (2)–(5) and

$$\delta_s = 0.0822\sqrt{\frac{\delta_s}{f}} \text{ mils} \quad (18)$$

is the skin depth at the frequency f in GHz and δ is the conductivity relative to copper.

The attenuation constant α_d due to dielectric loss is given by

$$\alpha_d = \frac{\beta \tan \delta}{2} \text{ Np/m} \quad (19)$$

The Q factor of a stripline is given by

$$Q = \frac{8.686\pi\sqrt{\epsilon_r}}{\lambda_0\alpha} \quad (20)$$

8. THE POWER-HANDLING CAPABILITY OF STRIPLINES

The average power P (in kilowatts) that can be carried by a matched balanced stripline with rounded edges is shown in Fig. 5 [4]. The ground plane–ground plane thickness is measured in inches. Although the strip edges are assumed to be round, an approximate value of Z_0 can be obtained from either Fig. 4 or from the analysis equations presented above.

9. STRIPLINE DISCONTINUITIES

Stripline discontinuities are as essential an element of microwave circuits as their uniform line counterparts. Any arbitrary discontinuity in a stripline can be decomposed into a few basic forms of discontinuity: an abrupt change in width or step discontinuity, a gap, a circular hole in the strip, an open-end, a cross junction, a T junction, and an angled bend. The appearance of discontinuities causes alterations in the electromagnetic field configurations of an otherwise uniform stripline. Therefore the modified field configuration can be taken into account by appropriate incorporation of a shunt or a series capacitance or inductance. For example, an open-end can be represented by a shunt capacitance. Figure 6 shows the

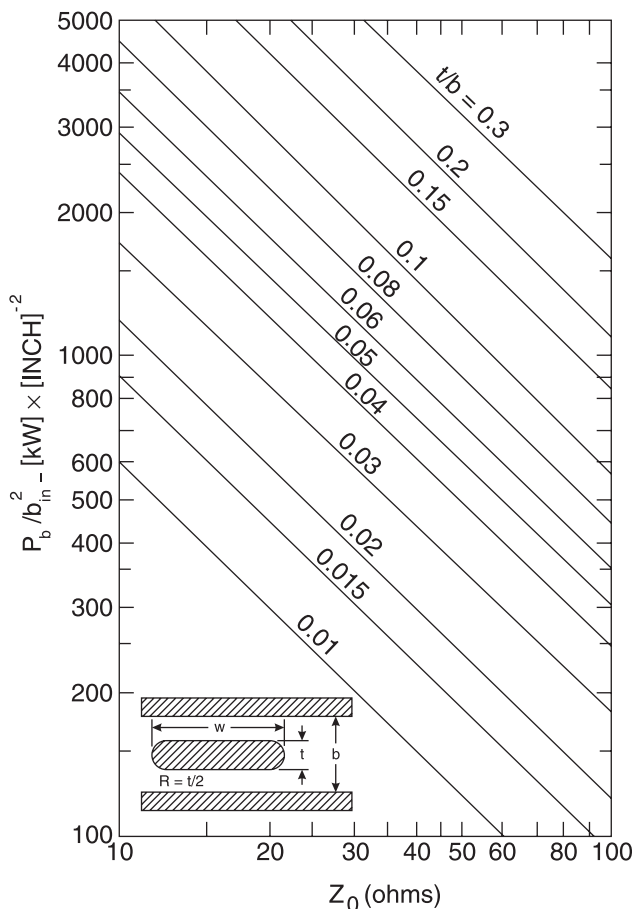


Figure 5. Average power-handling capability of a stripline with rounded trip edges.

configurations and the corresponding equivalent circuits of the discontinuities [8–10]. The equivalent width D , shown by the dashed lines, is obtained by conformal mapping techniques

$$D = b \frac{K(k)}{K(k')} + \frac{t}{\pi} \left(1 - \ln \frac{2t}{b} \right) \quad (21)$$

for $W/b \leq 0.5$, where $K(k)$ is the complete elliptic integral of the first kind:

$$k = \tanh \left(\frac{\pi W}{2b} \right) \quad (22)$$

$$K(k) = \int_0^1 \frac{dx}{\sqrt{(1-x^2)(1-k^2x^2)}} \quad (23)$$

The associated complementary elliptic integral is defined as

$$K(k') = K(\sqrt{1-k^2}) \quad (24)$$

and

$$D = W + \frac{2b}{\pi} \ln 2 + \frac{t}{\pi} \left(1 - \ln \frac{2t}{b} \right) \quad (25)$$

for $W/b > 0.5$.

9.1. Step Discontinuity

A change in strip width or step discontinuity is essential for the design of stripline matching transformers and low-pass filters. The equivalent-circuit parameters, shown in Fig. 6a, are given by

$$X = Z_1 \frac{2D_1}{\lambda_g} \ln \csc \frac{\pi D_2}{D_1} \quad (26)$$

$$l_1 = -l_2 = \frac{b \ln 2}{\pi} \quad (27)$$

The normalized scattering matrix of the discontinuity can be written as

$$[S] = \frac{1}{\Delta S} \begin{bmatrix} S_{11} & S_{12} \\ S_{21} & S_{22} \end{bmatrix}$$

$$S_{11} = (Z_2 - Z_1 + jX) e^{-j2\beta l_1}$$

$$S_{12} = S_{21} = 2\sqrt{Z_1 Z_2} \quad (28)$$

$$S_{22} = (Z_1 - Z_2 + jX) e^{-j2\beta l_2}$$

$$\Delta S = S_{11}S_{22} - S_{12}S_{21}$$

The equivalent network for equal normalizations at the input and the output ports includes a transformer as shown in Fig. 6a.

9.2. Gap Discontinuity

A series capacitance in a stripline is realized by a gap discontinuity as shown in Fig 6b. The equivalent circuit is, however, a π -network of one series and two shunt capacitances. The series component is due to the fringing capacitance from one strip to the other strip, and the shunt components are due to the field disturbance at the edge of each strip. As the gap increases, the series capacitance decreases and the two shunt capacitances tend toward that of an open-ended stripline. The normalized susceptance parameters of the equivalent π -network are given by

$$\overline{B}_A = \frac{1 + \overline{B}_a \cot(\beta s/2)}{\cot(\beta s) - \overline{B}_a} = \frac{\omega C_1}{Y_0} \quad (29)$$

$$2\overline{B}_B = \frac{1 + (2\overline{B}_b + \overline{B}_a) \cot(\beta s/2)}{\cot(\beta s/2) - (2\overline{B}_b + \overline{B}_a)} - \overline{B}_A = \frac{2\omega C_{12}}{Y_0} \quad (30)$$

$$\lambda \overline{B}_a = 2b \ln \left\{ \operatorname{sech} \left(\frac{2b}{\pi s} \right) \right\} \quad (31)$$

$$\lambda \overline{B}_b = b \ln \left\{ \coth \left(\frac{\pi s}{2b} \right) \right\} \quad (32)$$

9.3. Circular Hole Discontinuity

A hole discontinuity in a stripline is introduced to realize reactive tuning in filters and resonators. Such discontinuities are predominantly inductive in nature. The most common hole discontinuity is a circular hole discontinuity

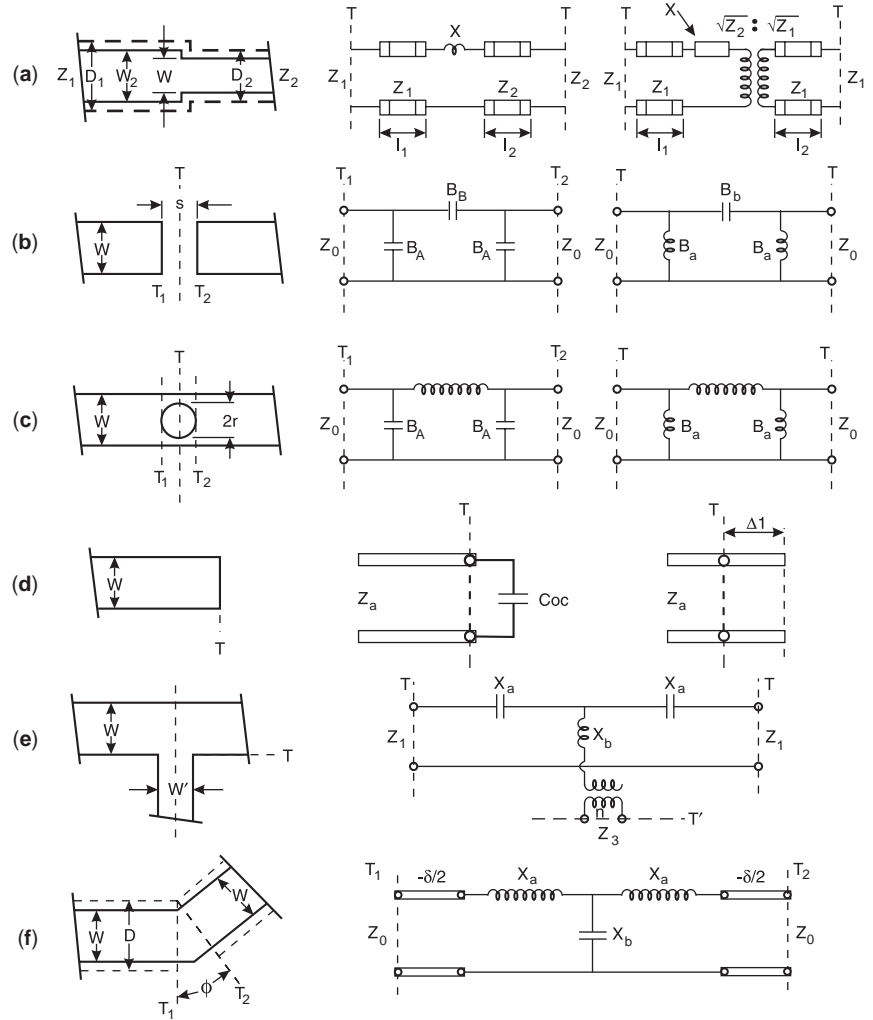


Figure 6. Stripline discontinuities and the equivalent networks: (a) step; (b) gap; (c) circular hole; (d) open-end; (e) T junction; (f) bend.

as shown in Fig. 6c. The susceptance parameters of the equivalent π -network are given by

$$\overline{B}_A = \frac{1 + \overline{B}_a \cot(\beta r)}{\cot(\beta r) - \overline{B}_b} \quad (33)$$

$$2\overline{B}_B = \frac{1 + 2\overline{B}_a \cot(\beta r)}{\cot(\beta r) - \overline{B}_b} - \overline{B}_A \quad (34)$$

where

$$\overline{B}_b = -\left(\frac{3bD}{16\beta r^3}\right), \quad \overline{B}_a = \frac{1}{3B - b} \quad (35)$$

It is to be noted that the equivalent networks for gap and circular hole discontinuities depend on where the reference plane is considered to be situated.

9.4. Open-End Discontinuity

An open-end discontinuity occurs whenever an open-circuited stripline stub is used in matching networks, filters, and so on. Figure 6d shows a stripline open-end and two equivalent networks. The network can be a shunt capacitance C_{oc} or an extended length Δl . The second

representation assumes that a perfect magnetic wall exists at a distance Δl from the physical open circuit. The open-circuit capacitance is given by

$$C_{oc} = \frac{1}{\omega Z_0} \tan^{-1} \left[\frac{\xi + 2W}{4\xi + 2W} \tan(\beta\xi) \right] \quad (36)$$

where

$$\lambda = \frac{\lambda_0}{\sqrt{\epsilon_r}}, \quad \beta = \frac{2\pi}{\lambda}, \quad \xi = 0.2206b \quad (37)$$

The length extension Δl can be obtained from the open-end capacitance

$$\Delta l = \frac{1}{\beta} \tan^{-1}(Z_0 \omega C_{oc}) \quad (38)$$

The reflection coefficient from the open-end discontinuity can be calculated as

$$S_{11} = \frac{1 - jZ_0 \omega C_{oc}}{1 + jZ_0 \omega C_{oc}} \quad (39)$$

In the equations above, Z_0 is the characteristic equation of the stripline.

9.5. T-Junction Discontinuity

A T-junction discontinuity occurs in stripline stub matching, stub-loaded lowpass and bandpass filters, branchline couplers, hybrid rings, and many other components. Figure 6e shows the stripline T junction and the equivalent network. The network parameters are obtained from

$$\frac{X_a}{Z_1} = - (0.785n)^2 \frac{D_3^2}{D_1\lambda} \quad (40)$$

$$\begin{aligned} \frac{X_b}{Z_1} = & -\frac{X_a}{2Z_1} + \frac{1}{n^2} \left\{ \frac{B_1}{2Y_1} + \frac{2D_1}{\lambda} \left[0.6931 + \frac{\pi D_3}{6D_1} + 1.5 \left(\frac{D_1}{\lambda} \right)^2 \right] \right\} \end{aligned} \quad (41)$$

for $D_3/D_1 < 0.5$, and

$$\frac{X_b}{Z_1} = -\frac{X_a}{2Z_1} + \frac{2D_1}{\lambda n^2} \left\{ \ln \frac{1.43D_1}{D_3} + 2 \left(\frac{D_1}{\lambda} \right)^2 \right\} \quad (42)$$

for $D_3/D_1 > 0.5$. The transformer turns ratio n is given by

$$n = \frac{\sin \left(\frac{\pi D_3}{\lambda} \right)}{\frac{\pi D_3}{\lambda}} \quad (43)$$

and

$$\frac{B_1}{2Y_1} = \frac{2D_1}{\lambda} \left[\ln \csc \frac{\pi D_1}{2D_1} + 0.5 \left(\frac{d_1}{\lambda} \right)^2 \cos^4 \frac{\pi D_3}{2D_1} \right] \quad (44)$$

In these equations D_1 and D_3 are the widths of the equivalent parallel-plate waveguides for strips of widths W and W' , respectively; Z_1 and Z_3 are the corresponding characteristic impedances; and Y_1 and Y_3 are the respective characteristic admittances. The normalized scattering matrix of the T junction is obtained from

$$S_{11} = S_{22} = \frac{j2(Z_3/n^2)X_a - (Z_1^2 + 2X_a X_b + X_a^2)}{(Z_1 + jX_a)\Delta} \quad (45)$$

$$S_{12} = S_{21} = \frac{2Z_1(Z_3/n^2 + jX_a)}{(Z_1 + jX_b)\Delta} \quad (46)$$

$$S_{13} = S_{23} = S_{31} = S_{32} = \frac{2\sqrt{Z_1 Z_2}/n^2}{\Delta} \quad (47)$$

$$S_{33} = \frac{Z_1 - 2(Z_3/n^2) + j(X_a + 2X_b)}{\Delta} \quad (48)$$

and

$$\Delta = Z_1 + \frac{2Z_3}{n^2} + j(X_a + 2X_b) \quad (49)$$

9.6. Bend Discontinuity

A bend discontinuity occurs mainly in stripline transitions and hybrids. Figure 6f shows a stripline bend discontinuity and the equivalent network. The parameters of the network are obtained from the following equations, derived from Babinet's principle and the equivalent parallel-plate waveguide model:

$$\lambda \bar{X}_a = 2D \left\{ \psi(x) + 1.9635 + \frac{1}{x} \right\} \quad (50)$$

$$\bar{X}_b = -\frac{\lambda}{2\pi D} \cot \frac{\theta}{2} \quad (51)$$

With θ , in degrees, x is given by

$$x = 0.5 \left\{ 1 + \frac{\theta}{180} \right\} \quad (52)$$

and

$$\psi(x) = 0.5223 \ln(x) + 0.394 \quad (53)$$

Equation (53) is an approximation of the T function [11]. Accurate values of the T function for various x values are available in Ref. 11.

The reference planes T_1 and T_2 meet at an angle θ . This modifies the scattering parameters of the bend by multiplying S_{11} and S_{22} by $e^{j2\beta\zeta}$ and S_{12} and S_{21} by $e^{j\beta\zeta}$, where

$$\zeta = (D - W) \tan \frac{\theta}{2} \quad (54)$$

10. STRIPLINE COMPONENTS

Virtually every microwave circuit component can be realized using stripline technology. Its planar form makes the components inexpensive and easily mass-producible using the printed circuit board technique. Presence of top and ground shields makes the components almost completely radiation-free. In addition to that, the homogeneous dielectric filling offers the minimum frequency dispersion of component characteristics. The only limitations are relatively high insertion loss due to lossy plastic-type dielectric filling and low power-handling capability compared to waveguides and onset of waveguide modings at high frequencies.

The passive components that can be realized using stripline technology are the direct-coupled hybrids, power dividers, directional couplers, filters, and matching transformers. Such components in conventional forms

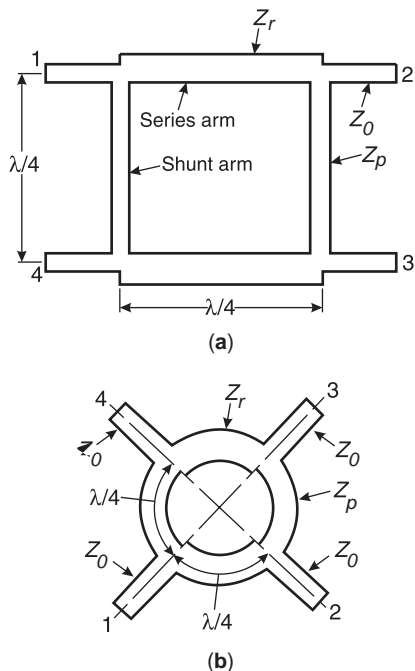


Figure 7. (a) Single section branchline coupler; (b) circular form of branchline coupler.

are completely uniplanar and do not need any via holes or groundings through the substrate. Figure 7 shows the simplest form of a direct-coupled hybrid, which is a 90° branchline hybrid. Figure 7a shows the layout of the metallization between the circuit boards, and Fig. 7b shows the circular form of a branchline hybrid. It consists of two mainlines coupled by two λ/4 line sections spaced λ/4 apart, where λ is the wavelength at the center frequency of the operating band. The coupling factor is determined by the ratio of the impedances of the shunt and the series arms and is optimized to satisfy the impedance match over a desired bandwidth. For a 90° phase difference between the two output ports the following conditions hold good:

$$\frac{P_2}{P_3} = \left(\frac{Z_0}{Z_p}\right)^2 \tag{55}$$

$$\left(\frac{Z_0}{Z_R}\right)^2 = \left(\frac{Z_0}{Z_P}\right)^2 + 1 \tag{56}$$

A two-branch, or a single-section, hybrid is a very common structure. However, it has a very narrow bandwidth. This drawback is overcome by using a multisection branchline hybrid as shown in Fig. 8. However, such multisection branchline hybrids often pose another problem. They require too wide a range of impedances, which in turn

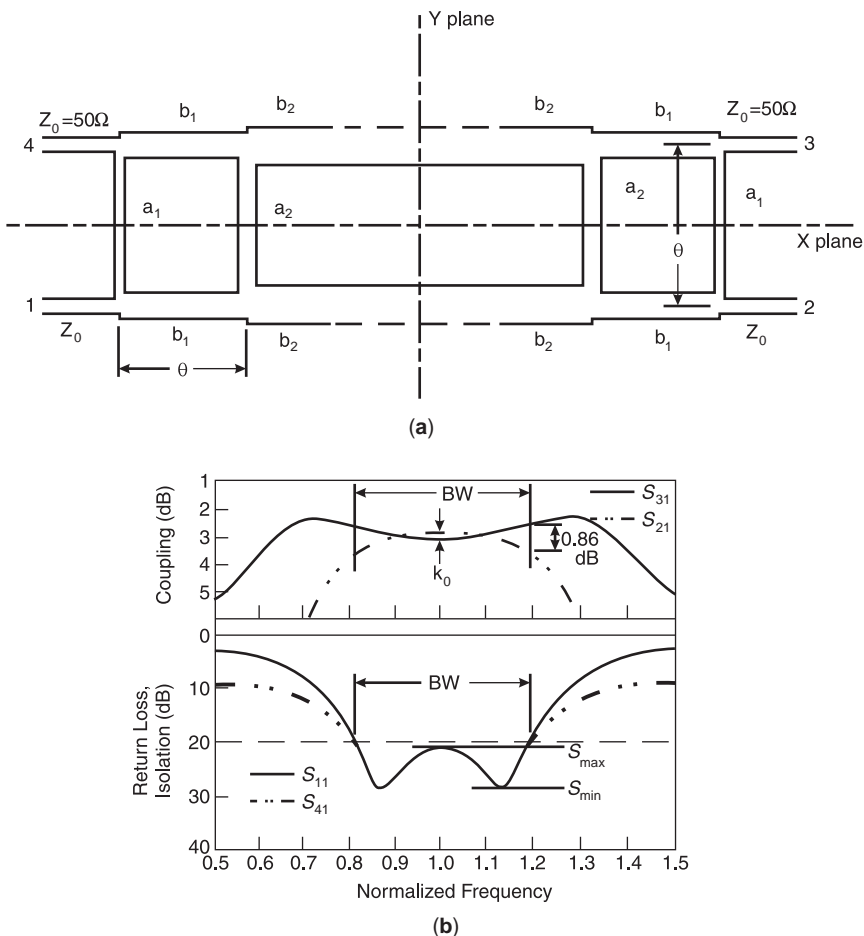


Figure 8. A multisection branchline hybrid for wide bandwidth.

requires very narrow or very wide and physically realizable striplines. Analytical design methods for branchline hybrids are available in Refs. 12 and 13.

A matched hybrid ring magic T is a special type of ring form of the branchline hybrid in which the circumference is an odd multiple of $3\lambda/2$. As a result, the phase difference between split powers that meet at different ports is either 0° or 180° .

The conductor pattern of the simplest version of stripline hybrid is shown in Fig. 9a. If a signal is input to port B, it splits into equal halves and these equal halves meet at ports A and C with 0° phase difference and with 180° phase difference at port D. Typical frequency response of a stripline hybrid T is shown in Figs. 9b and 9c [13]. Usually around 20% bandwidth is obtained in a stripline hybrid T. In addition, the 180° phase difference is more frequency-dependent than the 0° response as shown in Fig. 9c. Stripline hybrid T is used in single-sideband generators and mixers.

Figure 10a shows the conductor pattern of a stripline inline power divider. It is a broadband equal phase power

splitter. An inline power divider was invented by Wilkinson [14] in 1960. Hence they are also known as “Wilkinson power dividers.” The one shown in Fig. 10a is known as the uncompensated power divider. Figure 10b shows the compensated version. The compensated divider offers a slightly better performance. A single section Wilkinson power divider offers one octave bandwidth. For larger bandwidth multisection power divider, shown in Fig. 11, is used. For excellent accounts of Wilkinson power dividers, one should consult Refs. 14 and 15.

The schematic of a parallel-coupled line coupler is shown in Fig. 12a. There can be two types of parallel coupling in stripline. Figure 12b shows edge coupling, and Fig. 12c shows broadside coupling. Both are very popular in many applications where weak coupling (< 10 dB) is required. However, broadside couplers can achieve tighter couplings up to -3 dB. The coupling coefficient is given by

$$C = -20 \log |S_{12}| = -20 \log \left| \frac{Z_{oe} - Z_{oo}}{Z_{oe} + Z_{oo}} \right| \text{dB} \quad (57)$$

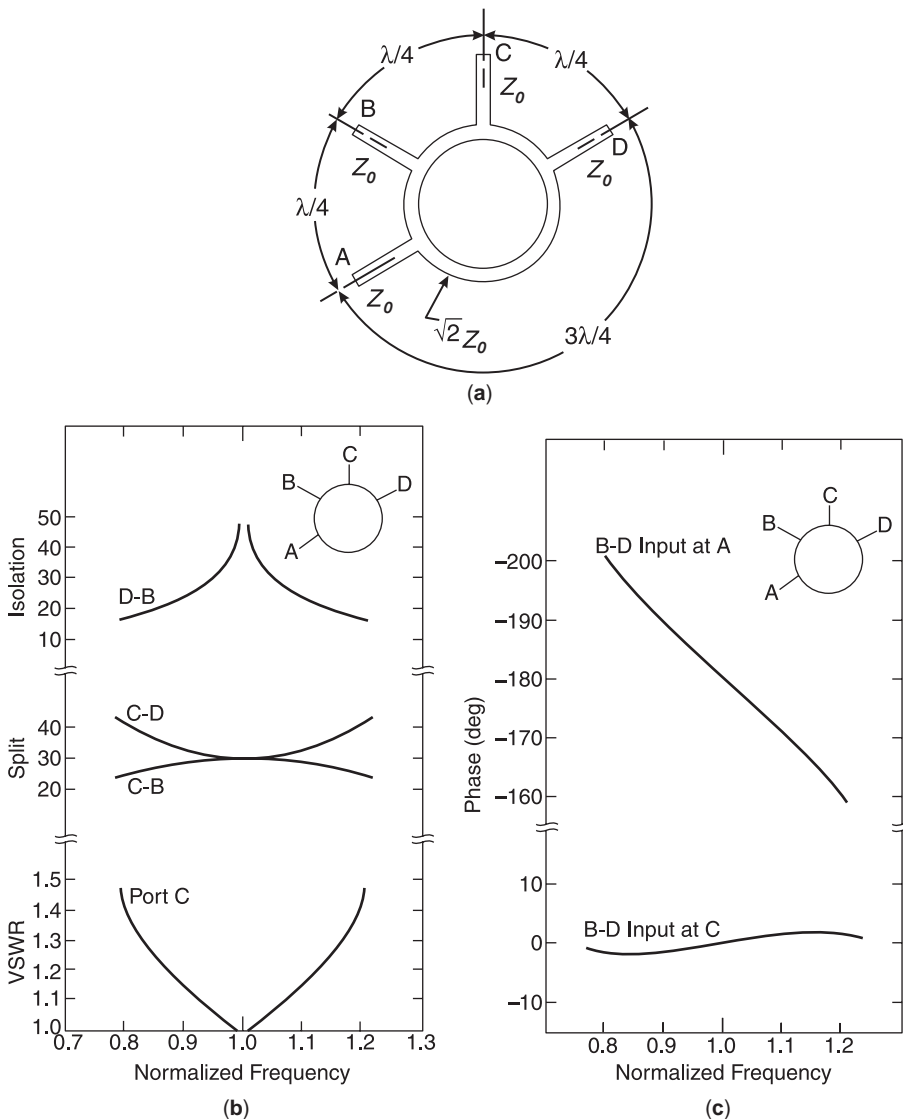


Figure 9. (a) Conductor pattern of stripline hybrid ring; (b) response curve for $(\frac{3}{2}\lambda)$ hybrid ring magic T, with power split and isolation expressed in dB; (c) phase response curve.

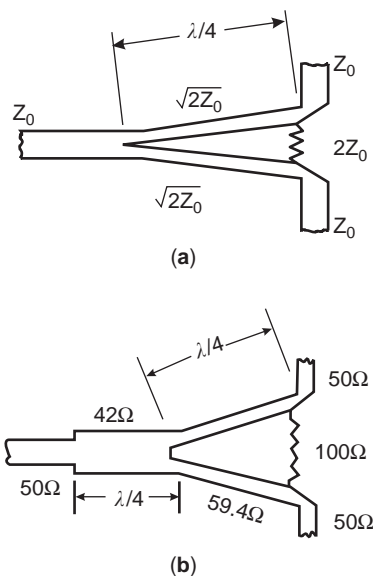


Figure 10. (a) Uncompensated single-section Wilkinson power divider; (b) compensated single-section Wilkinson power divider.

Moreover, for a system impedance of Z_0 , the perfect matching condition gives

$$Z_0^2 = Z_{oe}Z_{oo} \tag{58}$$

Equations (57) and (58) are valid only at the center frequency of the operating band where the electrical length of the coupled section is exactly 90° , or in other words, the coupled section is quarter wavelength long.

For a specified coupling coefficient, the design equations become

$$Z_{oe} = Z_0 \sqrt{\frac{1 + 10^{-C/20}}{1 - 10^{-C/20}}} \tag{59}$$

$$Z_{oo} = Z_0 \sqrt{\frac{1 - 10^{-C/20}}{1 + 10^{-C/20}}} \tag{60}$$

Once Z_{oe} and Z_{oo} are known, the physical dimension of the coupled-line structure can be obtained from coupled stripline equations [16, 17]. The frequency response of a par-

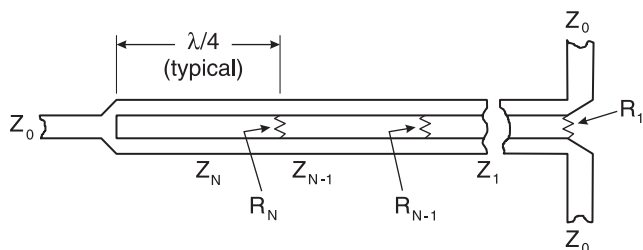


Figure 11. Multisection Wilkinson power divider.

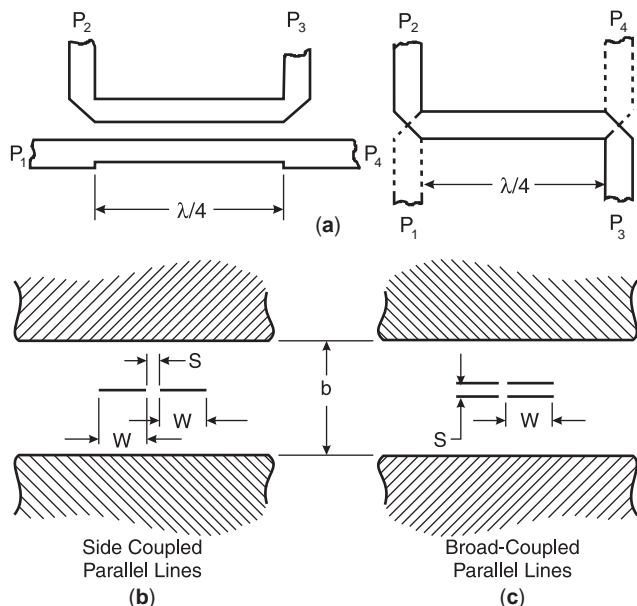


Figure 12. (a) Schematic of parallel coupled line coupler; (b) edge-coupled stripline; (c) broadside coupled stripline; (d) frequency response of a stripline coupler.

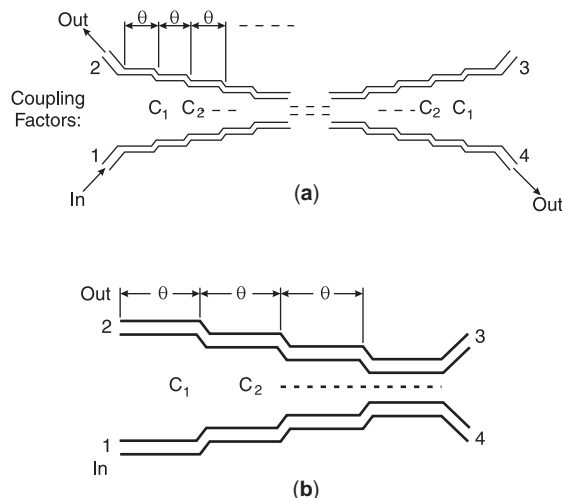


Figure 13. Multisection stripline: (a) symmetric and (b) asymmetric couplers.

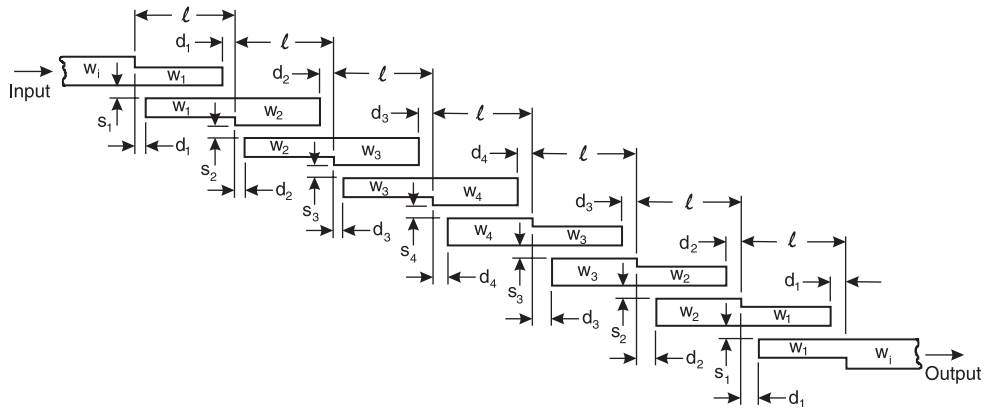


Figure 14. Parallel coupled half-wavelength bandpass filters.

allel-coupled stripline coupler is given by

$$C(\theta) = \frac{jC \sin \theta}{\sqrt{1 - C^2 \cos \theta + j \sin \theta}} \quad (61)$$

where C is the midband coupling and θ is the electrical length of the coupled section. As stripline is a transmission line with homogeneous dielectric filling, it has infinite directivity at the center frequency. Figure 12d shows the typical frequency response of a stripline parallel-coupled line coupler.

For many applications, the single-section coupler offers inadequate bandwidth. Therefore, the designer should

have recourse to a multisection design. A multisection coupler is a cascaded combination of more than one single-section couplers as shown in Fig. 13 [5,18].

The coupling coefficient for an n -section symmetric coupler can be written as

$$C(\theta) = \left| \frac{V_2}{V_1} \right| = C_1 \sin(n\theta) + (C_2 - C_1) \sin[(n - 2)\theta] + \dots + (C_i - C_{i-1}) \sin[(n - 2i + 2)\theta] + \dots + (C_{[(n+1)/2]} - C_{[(n-1)/2]}) \sin \theta \quad (62)$$

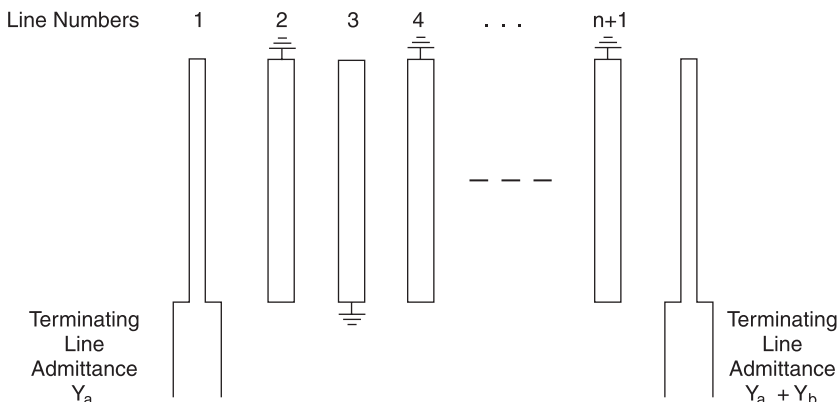
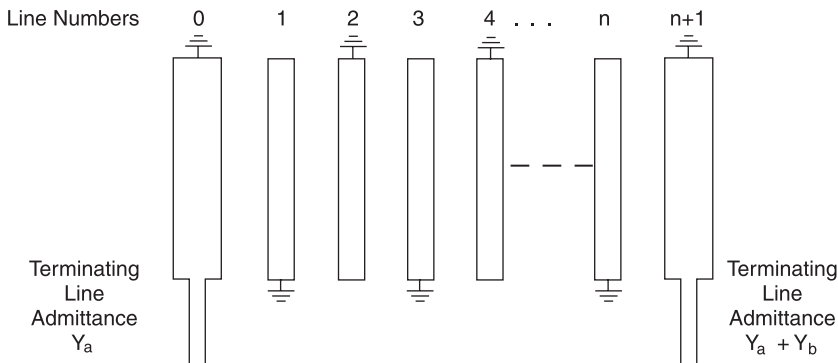
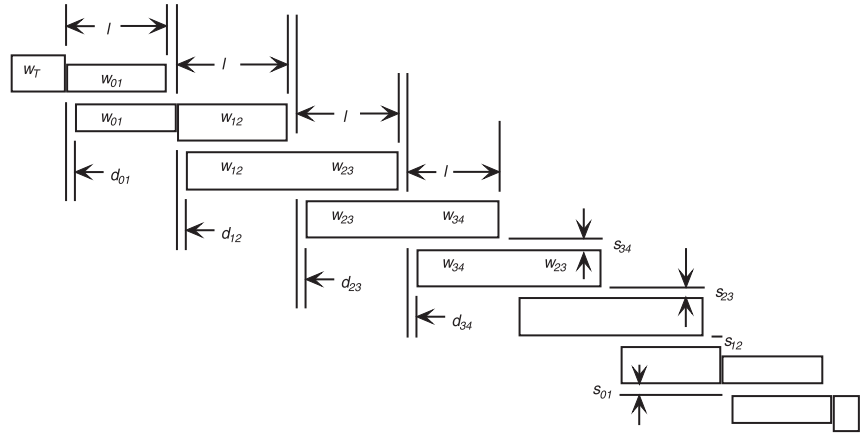


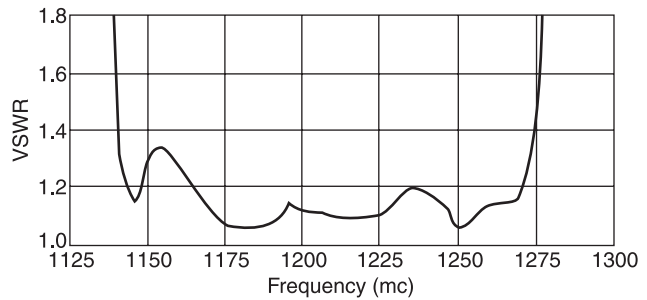
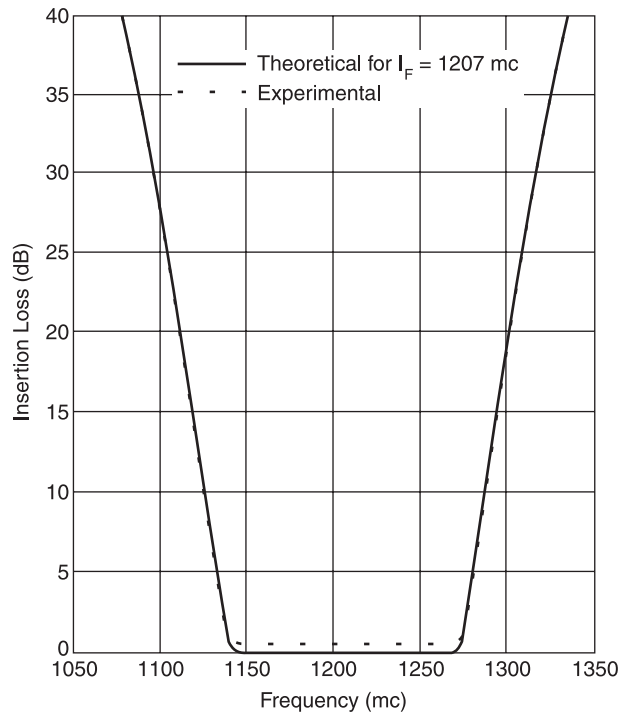
Figure 15. Interdigital quarter-wavelength bandpass filters.

$j, j+1$	W (mils)	S (mils)	D (mils)
01	236	21	73
12	346	110	84
23	360	158	85
34	361	361	85



Ground plane spacing = 500 mils, Resonator length $l = 1532$ mils, Substrate dielectric constant = 2.55

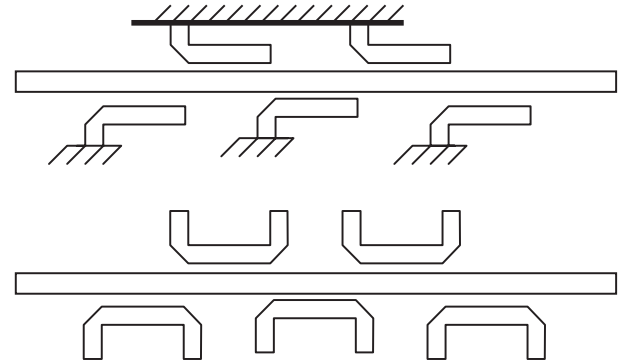
(a)



(b)

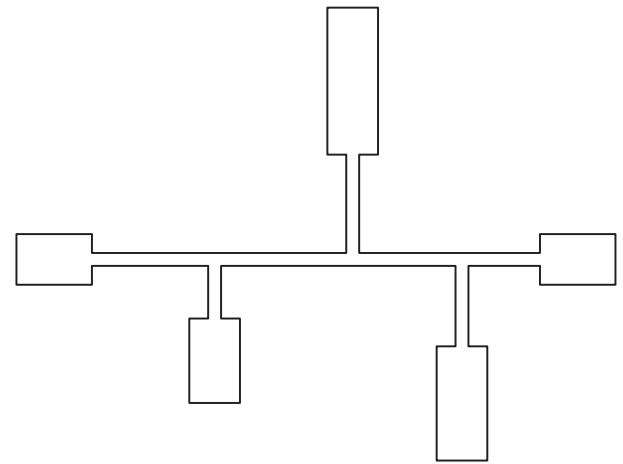
Figure 16. (a) Conductor pattern; (b) insertion loss response of a stripline edge coupled bandpass filter. (After L. Young [26], 1972, Artech House, reprinted with permission.)

filter. Therefore, the designer of a stripline coupler has to synthesize only a two-port in place of a four-port with the reflection coefficient response the same as the desired coupling coefficient response of directional coupler. For a

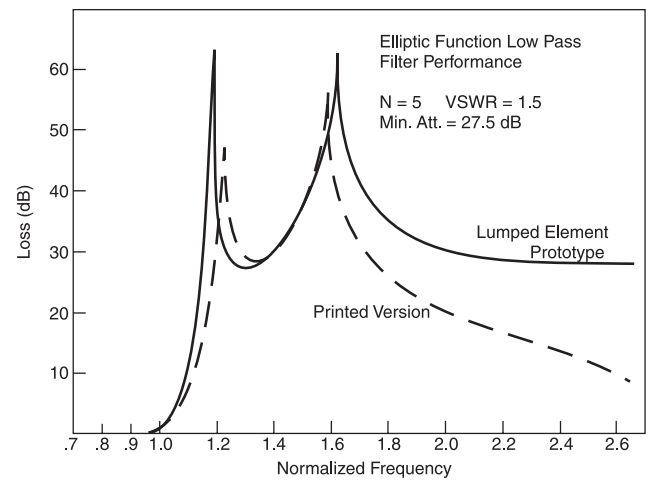


Coupled Resonator Band Stop Filters with Shorted or Open Resonators

(a)



(b)

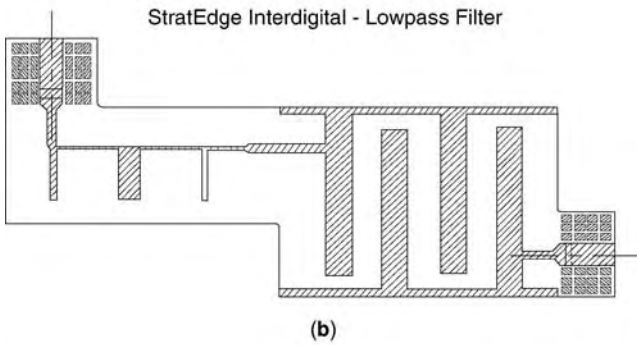


(c)

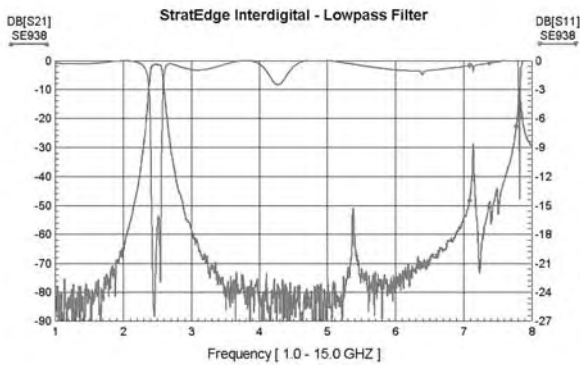
Figure 18. Conductor patterns of stripline (a) bandstop, (b) low-pass, and (c) highpass filters.



(a)



(b)



(c)

Figure 17. (a) Photograph of hard substrate stripline bandpass filter package; (b) layout of the filter in (a); (c) measured frequency response of the filter. (Courtesy of StratEdge Corp., San Diego.) (This figure is available in full color at <http://www.mrw.interscience.wiley.com/erfme>.)

If the desired coupling response is maximally flat, then C_i satisfies a set of $\frac{1}{2}(n - 1)$ linear equations obtained from

$$\left[\frac{d^r C(\theta)}{d\theta^r} \right]_{\theta = \pi/2} = 0 \tag{63}$$

$$r = 2.4.6, \dots, n - 1$$

The design concept is based on the fact that the backward coupled wave of TEM (transverse electromagnetic mode) coupler corresponds to the reflected wave of a quarter-wave

detailed account of the parallel-coupled stripline coupler, the reader is referred to the article by Fubini et al. [18].

Virtually all types of filters can be realized using stripline technology. Stripline filter technology is as old as stripline technology itself. Fubini et al. [19] reported the oldest work on high- Q stripline components. It was followed by Bradley's work [20]. However, it was Seymore Cohn's paper on parallel-coupled transmission-line resonator filters that presented the first methodical approach and realization of stripline bandpass filters [24]. Figure 14 shows the conductor pattern of several capacitively coupled stripline resonator filters. The reader is referred to the article by Cohn [23] for design information. Since each resonator is a half-wavelength long at the center frequency of the passband, the lowest-frequency spurious passband occurs at twice the center frequency.

Figure 15 shows the conductor pattern of stripline interdigital filter as reported by Matthaei [21] and Cristal [22].

Unlike the half wavelength resonators in filters reported by Cohn [23], interdigital filters use quarter-wavelength resonators that need grounding of one of two ends of a resonator. However, the interdigital configuration has two advantages: (1) it is compact, and (2) since each resonator is a quarter-wavelength long at the center frequency of the passband, the lowest-frequency spurious passband occurs at thrice the center frequency of the passband. The reader is referred to Ref. 22 for design information. Ozaki and Ishi [24] and Young's reprint volume [26] present thorough discussions of the theories of parallel-coupled stripline bandpass filters. Most stripline bandpass filters use Teflon or plastic-type substrate having moderate or high dielectric loss. Hence dielectric loss plays the dominant role in filter's insertion loss. Figure 16 shows the insertion loss response of a typical stripline edge-coupled bandpass filter.

Considerable interest has developed in the recent (as of 2004) past in hard substrate stripline technology. In this technology the top and the bottom halves of a ceramic substrate stripline are glued together using a glass-based material. Filters using this technology offer very good insertion loss performance. Figure 17 shows the photograph of an X-band alumina substrate bandpass filter. Such filters are extremely rugged and have excellent reliability, especially for space born applications.

Besides bandpass filters, other types of filters are also successfully realized using stripline technology. Figure 18 shows the conductor patterns of stripline lowpass, bandstop, and highpass filters. Design information on these structures is available in Refs. 25 and 26. Figure 19 compares the frequency response of a stripline elliptic function lowpass filter with that of its lumped-element version. The conductor pattern of the filter has been shown in the inset.

Besides the passive components described above, there are a large number of microwave active components and subsystems that use stripline passive components.

BIBLIOGRAPHY

1. R. M. Barrett, Microwave printed circuits—the early years, *IEEE Trans. Microwave Theory Tech.* **MTT-32**:883–900 (Sept. 1984).
2. S. B. Cohn, Characteristic impedance of shielded strip transmission lines, *IRE Trans. Microwave Theory Tech.* **MTT-2**:52–55 (July, 1954).
3. R. W. Peters et al., *Handbook of Triplate Microwave Components*, Sanders Associates, Nashua, NH, 1956.
4. G. Matthaei, L. Young, and E. M. T. Jones, *Microwave Filters, Impedance Matching Networks and Coupling Structures*, Artech House, Dedham, MA, 1974.
5. H. Howe, Jr., *Stripline Circuit Design*, Artech House, Dedham, MA, 1974.
6. H. A. Wheeler, Transmission line properties of a stripline between parallel planes, *IEEE Trans. Microwave Theory Tech.* **MTT-26**(11):866–876 (Nov. 1978).
7. S. M. Perlow, Analysis of edge coupled shielded strip and slabline structures, *IEEE Trans. Microwave Theory Tech.* **MTT-35**:522–529 (May, 1987).
8. A. A. Oliner, Equivalent circuits for discontinuities in balanced strip transmission line, *IRE Trans. Microwave Theory Tech.* **MTT-3**:134–143 (March, 1955).
9. H. M. Altschuler, and A. A. Oliner, Discontinuities in the center conductor of a strip transmission line, *IRE Trans. Microwave Theory Tech.* **MTT-8**:328–339 (May, 1960).
10. K. C. Gupta, R. Garg, and R. Chadha, *Computer Aided Design of Microwave Circuits*, Artech House, Norwood, MA, 1981.
11. E. Jhanke and F. Emde, *Table of Functions*, Dover, New York, 1945, p. 16.
12. O. Muraguchi, M. Y. Takeshi, Y. Naito, Optimum design of 3-dB branchline couplers using microstriplines, *IEEE Trans. Microwave Theory Tech.* **MTT-31**:674–678 (Aug. 1983).
13. H. Howe, Jr., *Stripline Circuit Design*, Artech House, Norwood, MA, 1974, pp. 77–94.
14. E. Wilkinson, An N-way hybrid power divider, *IEEE Trans. Microwave Theory Tech.* **MTT-8**:116–118 (Jan. 1960).
15. H. Howe, Jr., *Stripline Circuit Design*, Artech House, Norwood, MA, 1974, pp. 94–110.
16. S. Cohn, Shielded coupled strip transmission lines, *IEEE Trans. Microwave Theory Tech.* **MTT-3**:29–37 (Oct. 1955).
17. S. Cohn, Characteristic impedances of broadside coupled strip transmission lines, *IEEE Trans. Microwave Theory Tech.* **MTT-8**:633–637 (Nov. 1960).
18. P. Pramanick and P. Bhartia, in I. J. Bahl and P. Bhartia, eds., *Hybrids and Couplers in Microwave Solid State Circuit Design*, Wiley-Interscience, Hoboken, NJ, 2003.
19. E. G. Fubini, W. E. Fromm, and H. S. Keen, Microwave applications of high- Q strip components, *IRE Convent. Rec.* (Part 8):98–103 (April, 1956).
20. E. A. Bradley, Design and development of stripline filters, *IRE Trans.* 4:86–93 (April, 1956).
21. G. L. Matthaei, Interdigital bandpass filters, *IRE Trans.* **MTT-10**:479–491 (Nov. 1962).
22. E. G. Cristal, New design equations for a class of microwave filters, *IEEE Trans. Microwave Theory Tech.* **MTT-19**:486–490 (May, 1971).
23. S. Cohn, Parallel coupled transmission line resonator filters, *IRE Trans. Microwave Theory Tech.* **MTT-6**(2):224–231 (April, 1958).
24. H. Ozaki and J. Ishii, Synthesis of a class of strip-line filters, *IRE Trans. Circuit Theory* **CT-5**(2):104–109 (June, 1958).
25. L. Young, *Microwave Filters Using Parallel Coupled Lines*, Artech House, Norwood, MA, 1972.
26. H. Howe, Jr., *Stripline Circuit Design*, Artech House, Norwood, MA, 1974, pp. 181–189, 207–210, 257–258.

STRIPLINE COMPONENTS

R. M. BARRIO-GARRIDO

Universidad Carlos III de Madrid

M. SALAZAR-PALMA

Universidad Politécnica de Madrid

T. K. SARKAR

Syracuse University

R. S. ADVE

Research Associates for Defense Conversion Inc.

A stripline is a signal-carrying conductor sandwiched between two layers of dielectric that are shielded by ground planes. The simplest and classic cross section of a stripline is shown in Fig. 1. In this standard stripline, the dielectric is homogeneous and both the ground plates are held at the same potential. The resultant structure implies that the balanced homogeneous stripline supports ideally perfect transverse electromagnetic (TEM) waves, which is in contrast to the microstrip line, shown in Fig. 2, where not only the signal-carrying conductor is exposed and may radiate, but also this structure operates in a highly inhomogeneous environment and, hence, it supports a fundamental mode that is strictly a hybrid mode but can be approximated within certain limits by a quasi-TEM mode. Analysis of striplines is usually easier than the analysis of a microstrip circuit.

In practice, however, actually the interest is focused on stripline-like circuits based on multilayered and inhomogeneous configurations. First, the practical stripline is not an ideal one, but a three-layer configuration with the center conductor to be offset and surrounded by a thin airgap, because small airgaps are often inadvertently introduced during the fabrication process [1]. The model used by researchers for the analysis of such practical structure is shown in Fig. 3. On the other side, in practical antenna feed and new environments such as monolithic microwave integrated circuits (MMIC) and printed circuit boards (PCB), multilayer stripline structures like that of the Fig. 4 are employed. These structures are usually composed of a metal strip conductor sandwiched by two layers of different dielectric constant and upper/lower planes that may not be symmetrically located. Finally, the suspended stripline configuration (SSL) is actually in spread use for coupler and filter applications, caused primarily by its high unloaded Q-factor. Suspended stripline has the center conductor pattern etched on a very thin layer of low dielectric constant; both the conductor and thin dielectric layer are suspended in the air between the two ground planes, as shown in Fig. 5. In some cases, strip conductors are placed on both sides of the dielectric layer, to construct directional couplers of high coupling parameter.

As a result of the inhomogeneous configurations used by engineers in practice, it is impossible for a pure TEM wave to propagate along such a transmission line. These

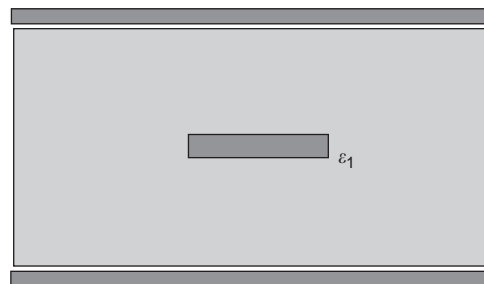


Figure 1. Cross section of a stripline.



Figure 2. Cross section of a microstrip line.

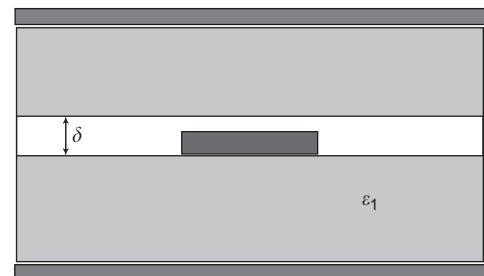


Figure 3. Air-gap layer in striplines circuits caused by fabrication process.

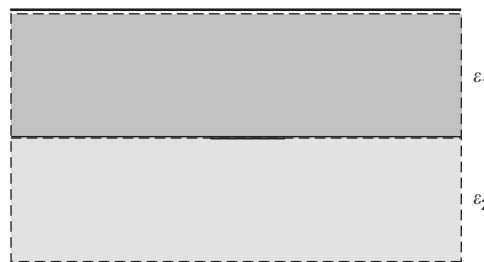


Figure 4. Cross section of a multilayer stripline.

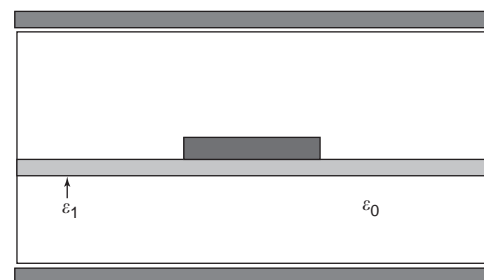


Figure 5. Suspended stripline configuration.

structures are referred in the literature as striplines (usually, multilayer or inhomogeneous stripline). In the case of SSL, some authors refer to it as inverted or suspended microstrip. However, because of the almost negligible thickness of the dielectric layer that sustains the metal strip, and the presence of two ground planes, most of the authors consider that this structure is a particular case of stripline.

1. SOME ADVANTAGES AND DRAWBACKS. MAIN CHARACTERISTICS AND APPLICATIONS

Both stripline and microstrip circuits are planar structures in that their properties can be controlled by changing one dimension of the circuit. This is requirement key for a transmission structure to be suitable as a circuit element in microwave integrated circuits. For example, the characteristic impedance of a stripline can be controlled by changing the width of the line [2].

In antenna applications, we find the greatest use of the stripline in the feed structure. A popular modern antenna element is a microstrip patch radiating element being fed by a stripline. We can use the stripline, however, in various sections of the feed structures. Some common applications include power dividers, directional couplers, coupled parallel lines, mixers, and switches. We also extensively use stripline components such as bandpass and bandstop filters and direct coupled hybrids.

In such applications, striplines can provide some significant advantages [3]. The stripline is compact and can hence replace bulky waveguides. Producing stripline components on a large scale requires the manufacturing and testing of only one component. An unlimited number of identical components can be manufactured with the same template. Therefore, in commercial applications, striplines can be significantly less expensive than waveguides. In addition, all components required to make up the complete circuit can be placed on a single substrate, which allows for compact circuit designs and circuits that can be flush-mounted on any desired surface. This property is particularly useful to engineers in the design of airborne antenna arrays and wireless communication antennas. Furthermore, the placement of all components on a single substrate eliminates the need for interconnections, usually the source of unreliable manufacturing.

At lower frequencies, a good choice of the substrate material can lead to significant savings in circuit size, which reduces the weight and cost of many transmit and receive systems. Although traditional waveguides can usually handle higher power levels than striplines can, in most applications, the stripline feed structures have adequate power-handling capabilities. In fact, the power-handling capability of the stripline is greater than that of microstrip circuits. Also, the structured design of a stripline circuit allows for the easy interchange of components to replace defective ones. Moreover, the stripline provides an important advantage in some millimeter-wave antenna applications over the microstrip feed: Although microstrip is a radiating element in nature, especially at higher

frequencies, the stripline has probed its effectiveness in suppressing backradiation from the antenna.

Along with these advantages, several drawbacks should be taken into account in the design of stripline components. For example, the manufacturing of a stripline circuit is a complex task because of its sensitivity to small manufacturing errors. At microwave frequencies, all dimensions of the circuit are important, and small errors can lead to serious degradations in the operation of stripline circuits. In addition, and in contrast to microstrip lines, small adjustments or tuning cannot be easily incorporated after the circuit has been fabricated because it is an enclosed medium. A stripline circuit also suffers from some practical difficulties because the line must be excited by either a coaxial line or a waveguide. In either case, the connection is a sharp discontinuity requiring matching circuits to reduce reflections.

The multilayer structure of the practical stripline leads to dielectric-dielectric and dielectric-metal interfaces. Therefore, the electromagnetic fields must satisfy different boundary conditions at these interfaces. A complete analysis of stripline circuits is hence a complex electromagnetic problem requiring extensive computer resources. Usually, a quasi-TEM (quasi-static) analysis suffices to characterize the transmission line by means of the characteristic impedance and the transmission constant. However, even a quasi-static analysis of multiple striplines in proximity to each other is a complicated task, and actually a lack of useful design models and closed-form equations suitable for the analysis of multilayer three-dimensional (3-D) packaging structures exists. Moreover, the unbalanced inhomogeneous multilevel and multiconductor geometries employed by engineers in antenna feed and MMIC boards give rise to leaky modes and residual wave currents that result in increased attenuation, crosstalk, and other undesirable spurious effects. To minimize these effects and enhance the performance of the stripline configurations, in many cases, it is not only desirable, but necessary, to perform a full-wave analysis that takes into account the high-order evanescent and spurious modes. A continuous effort has been made in the last years in this field, and some numerical techniques employed in the classic and recent literature are presented in Section 3.

2. SOME INITIAL DESIGN CONSIDERATIONS

The design of a stripline circuit begins with the choice of dielectric material to form the substrate over which the circuit is to be printed. No one material is ideal for all stripline applications. The desired properties of the dielectric material are usually in conflict with each other, which results in a tradeoff for each requirement. Some aspects of the material that require attention are the dielectric constant and its variation with temperature or frequency, the energy dissipation in the material, and the homogeneity of the material. Other characteristics that play a part in circuit design are the dimensional stability of the material as the operating temperature or humidity changes, the resistance of the material to water, and the chemicals involved in the printing. The tensile and structural strength

of the material, its machinability, and thermal conductivity are also important material properties [1].

The choice of dielectric material helps determine the losses, the characteristic impedance, and the power-handling capability of the line. The choice depends on whether we are interested in peak power or continuous-wave (CW) power. For example, in pulsed radar systems, the peak power is significantly higher than the average power, which may lead to arcing in the dielectric substrate. Sharp edges that lead to concentration of fields are a principal cause of arcing. Smoother bends, such as a mitered bend, can help reduce the effect of a sharp corner. The average power capability is mainly a function of the permissible temperature rise of the center conductor and the surrounding material. The thermal conductivity and dielectric losses play a key role in determining the maximum permissible CW power [1,4]. In a recent study, both transmission line theory and thermal modeling based on finite element analysis were combined to estimate the temperature rise within a stripline [5]. This study defines a method for assessing the effect of stripline design on its thermal performance, and it shows that higher dielectric materials used by engineers for size reduction of the circuit, despite their higher power loss, can produce smaller striplines with similar internal temperature rise than that of standard materials. This capability is because of the higher thermal conductivity of the materials with higher dielectric constant.

The combination of guided wave circuits with radiating elements leads to a new set of tradeoffs. The properties of materials and structures that enhance printed circuit performance tend to reduce radiation performance. Furthermore, direct-current (dc) biased circuits and the packaging for the stripline feed structure disturb antenna characteristics [6].

Stripline feed circuits usually work at power levels lower than those of waveguides. Hence, a coaxial cable to stripline transition usually launches a signal onto the feedline. The coaxial cable supports a pure TEM mode, whereas the multilayer and practical stripline supports a quasi-TEM mode, which makes the transition relatively simple, and matching circuits can be designed to ensure a good match. A transition section is needed if the ground spacing of the stripline is not the same as the dimensions of the cable. If the transition from cable to stripline is ignored, the high capacitance at the transition can lead to effective shorts circuits, which causes most of the transmitted energy to be reflected. Broadwall transitions from the side of cable are also possible.

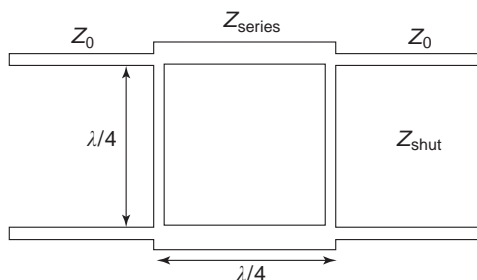


Figure 6. Narrowband directional coupler.

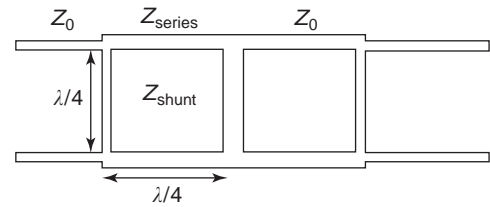


Figure 7. Multisection directional coupler.

3. APPLICATIONS AND ANALYSIS

The simplest and least expensive directional couplers or power dividers are by a direct coupled line or a branch line, which allows for single-plane construction as shown in Fig. 6. The ratio of the series and shunt impedances determines the coupling coefficients. This structure is narrowband in nature, and a more broad-band coupler can be made by extending the circuit to include multiple sections as shown in Fig. 7. A three-section stripline coupler is about the maximum that can be designed without the lines getting too thin to be reliably manufactured [1]. Broadband couplers can also be designed by having a main line parallel to a secondary line as shown in Fig. 8. This configuration, or coupled parallel lines, is one of the most useful and widely applied stripline structures for broad-band applications in the design of planar hybrids, bandpass filters, and directional couplers. Moreover, the conventional wideband stripline flat coupler formed by two coupled parallel lines presents some advantages with respect to the microstrip coupler. Not only does it present ultra-wideband operation, but it also presents flat coupling over the band, smaller size and volume, and perfect shielding [1].

Suspended stripline couplers have also been widely used by engineers. In this case, the coupled line consists of two strip conductors on both sides of a thin dielectric substrate, inside an air environment and enclosed by two ground planes. To improve directivity, a novel suspended stripline coupler has been recently reported [7]. In this configuration, parallel capacitance is added to each port of the coupled line to reduce the difference of the phase velocities between the even and the odd mode, which improves the performance of the device in its return losses and isolation. A direct application of this structure is a low-loss serial power combiner suitable for amplifier applications.

Another common application of striplines is the stripline circulator. In the traditional stripline circulator, or ferrite junction circulator, the striplines conforms the

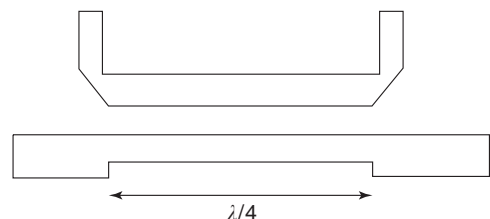


Figure 8. Broad-band directional coupler.

ports of the device and merges a metal disk sandwiched by two ferrite disks on top and bottom. Magnetic dc bias field is applied perpendicular to the plane of the ferrite disks [8]. Recently, novel designs have been proposed in the literature, and a growing interest in the ferrite coupled line (FCL) circulators has taken place [9]. Such a device is a possible alternative to conventional ferrite junction circulators, mainly because it is simpler and cheaper to fabricate, it needs only a weak biasing field, and its bandwidth is potentially very wide. It can be realized by cascading an FCL section, which resembles two parallel coupled lines embedded in a ferrite substrate, with a T-junction or hybrid coupler. In these devices, the FCL sections are typically much larger than the T-junctions or hybrid couplers. Therefore, the losses in the circulators are mainly caused by the FCL sections. The potential disadvantages of such a long narrow shape and its associated problems related to losses and ferrite fabrication can be alleviated by appropriate folding techniques, such as those reported in Ref. 10.

Stripline filter design is well documented in classic literature [1]. The most common bandpass filter in general use by engineers for stripline applications is the side-coupled filter, which makes use of open-circuit sections of stripline that act as half-wave resonators. To package the filter in an overall stripline circuit, it may be desirable to fold side-coupled filters to avoid the large size of the half-wave resonators. An alternative half-wave resonator filter is the end-coupled filter, in which the resonators are coupled by small capacitive gaps. This configuration can be meandered in a serpentine fashion to minimize its overall length. For wideband applications, the most effective type of filter is the direct-coupled stub filter, formed by a series of short-circuited quarter-wavelength stubs separated by quarter-wavelength sections of line. We may use equivalent circuit elements in place of the quarter-wavelength stub to achieve the actual impedance levels necessary for the short-circuited sections.

Recently, however, interest has been focused on the multilayered striplines filters, to obtain high-quality factors or tunable filters, like those based on suspended stripline configurations, and to employ them in LTCC environments. Low-temperature cofire ceramic or LTCC is one of the key technologies for integration of millimeter-wave systems and RF module applications because of its good metal conductivity, excellent high-frequency characteristics, and three-dimensional integration capability. For high-performance LTCC applications, stripline structures represent the most ideal transmission line, because dispersion and radiation are negligible and ground planes provide effective shielding. In this way, multiconductor stripline structures, with four or more layers and via holes or excitation vias connecting the different conductor layers, have been reported on the design of LTCC stripline filters for millimeter waves [11,12].

The suspended stripline is a versatile transmission medium for millimeter-wave frequencies, because of its low loss and the option of fabricating double-sided circuits. Its low unloaded Q-factor makes the suspended stripline an attractive approach for implementation of filters at high frequencies [13]. One major drawbacks of these filters is

the filter length. A miniature suspended stripline filter has been reported in Ref. 14. This filter is based on an interdigital structure in which its key element is a short-circuit, branched, and folded quarter-wave resonator that allows a reduction of its length by about 75% in the overall structure. Suspended stripline has been also used by engineers in the design of tunable interdigital filters. The varactor-tuned RF filter [15] is similar to the capacitively loaded combline filter, but it is adapted for interdigital topology and conforms to a symmetric filter of coupled resonators. The tuning element is a reversed-biased varactor diode. The resonators are shortened fingers of suspended strips with varactor diodes at the ends. The filter has a 60% tuning range at about 1 GHz with insertion loss better than 3 dB. Another way to improve the Q-factors of stripline resonators, instead of using suspended stripline configuration, is the implementation of small air cavities over the strip conductor and the bottom ground plane [16] in LTCC substrate.

In antenna applications, a stripline is the feedline to the antenna. The stripline must be shielded from the radiating element. In most applications, the stripline feeds the radiating element through a slot in a ground plane. An example of a stripline feed exciting a microstrip antenna element is shown in Fig. 9.

For good radiation characteristics, the patch antenna in Fig. 6 must be built on low relative permittivity materials ($\epsilon_r \approx 1$) to reduce the concentration of fields in the substrate. Furthermore, the substrate should be thick so that the fields caused by the patch and its image do not cancel each other. Thick substrates are also useful to engineers in building antennas with large bandwidths. A material that satisfies these properties is foam [2]. The microstrip antenna is etched on one side of a thick foam layer with the ground plane on the other side of the foam. The nonresonant slot is cut into the ground plane with a stripline under the ground plane exciting the slot. This stripline-slot-foam-inverse-patch (SSFIP) structure was introduced in Ref. 3.

The stripline could be etched on a foam without the ground plane backing the antenna element. However, the antenna must be mounted on some surface. If the ground plane is removed, the feed structure is affected by the

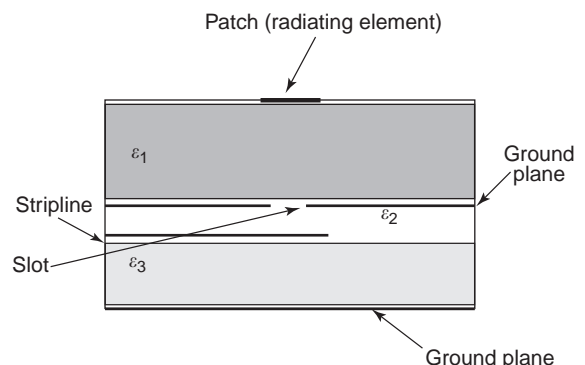


Figure 9. Microstrip patch antenna fed by a stripline through a slot.

mounting. The metal ground plane protects the stripline from the surface. The mounting surface must be distant from the feed, whereas for maximum coupling, the feed must be as close as possible to the slot. Hence, the feed is an unbalanced stripline. Furthermore, the SSFIP element is designed with metal walls to eliminate the propagation of parallel plate modes.

The stripline feed is compact and efficient and it presents some advantages over a microstrip feed, because the cross-polarization level is lower and the interactions between the radiating elements and the feeding network, such as the shift in the resonant frequency and the backradiation from the feeding network, are suppressed. But stripline feed leads to some complications. To have sufficient coupling across the slot, the widths of the stripline must be greater than that of the microstrip. Furthermore, completely enclosed striplines can lead to resonant frequencies or parallel plate modes, presented in the multilayer feeding structures. Mode suppression pins or electrical posts or vias that short the two ground planes in some strategic points can prevent resonant modes. The resulting structure can be complicated, and design of the feed structure requires considerable effort. Beyond the fabrication complexity involved, these posts create imperfect waveguides that might considerably affect the predictability of the circuit performance. It has been demonstrated, by means of full-wave analysis based on method of moments (MoM), that vias considerably modify the impedance and resonant characteristics of the patch antenna [17]. This effect becomes substantial and must be included in the design tool. In this work, the radiation efficiency of patch antennas with and without vias is studied, and proper location of the posts is shown to drastically reduce power in the parallel-plate mode. At higher frequencies, smaller via-spacing must be used by engineers around the slot to ensure that resonances do not occur. One way we could avoid the posts would be to use striplines with two different dielectric layers, but this is only acceptable as long as coupling to both sides of the stripline is not necessary. A new solution proposed involves such inhomogeneous stripline only in the vicinity of the microstrip-to-stripline coupling slot [18]. The TEM parallel plate mode is excited in such structure at a much lower level. Recently, the frequency-dependent behavior of the spurious mode power ratio to the input power of the antenna has been discussed, and it has been found that this ratio is very small when the antenna is operated at the resonant frequency of the patch [19]. This efficient method can avoid excessively geometrical complex solutions for the suppression of the parallel plate mode in the stripline feed.

Striplines can feed other particular antenna structures, such as meander slot antennas, Vivaldi notch antenna arrays, bowtie antennas, and cylindrical rectangular microstrip antennas.

However, a complete analysis of stripline feeds is a complicated task. In general, no closed-form solutions exist for the currents on the striplines and the fields in the surrounding media. Engineers have used a numerical solution, using such techniques as the MoM [20–23], to solve for the fields and currents on the stripline. The initial solution techniques accounted for only the quasi-TEM dominant mode; that is, they applied a quasi-static analysis.

In Ref. 24, the authors analyzed the crosstalk and coupling between multiconductor transmission lines such as striplines, suspended striplines, and microstrip lines based on modal analysis in the frequency domain. This approach is extended in the commercially available software packages LINPAR [25] and MATPAR [26]. A time-domain analysis of the multiconductor transmission problem [27] allows for the tracking of digital waveforms as the propagate along the stripline.

In Ref. 28, a dual-polarized slot-coupled printed antenna with a stripline feed is analyzed. They assumed a quasi-TEM mode on the stripline associated with the standing wave because of the serial impedance caused by the slot. Stripline feeds for infinite arrays can be analyzed with Floquet modes [29]. In Ref. 29, the stripline feeds an open slot array. Electric and magnetic currents are used by engineers in conjunction with the equivalence principle to separate the feed region from the radiation region. The currents on the feed structure are obtained by solving the coupled integral equations for the two regions [30].

Nowadays, as the frequency of operation and power levels have increased, the quasi-TEM approximation is less applicable. Full-wave techniques account for all modes, propagating and evanescent [31]. Furthermore, for high-performance circuits, where spurious and high-order modes effects must be taken into account in complex multilayered geometries, full-wave analysis is needed. In fact, the existence of leaky modes that leak power into the parallel plate surrounding medium on printed-circuit transmission lines has recently been the subject of considerable interest. These modes are usually undesirable because they result in increased attenuation, crosstalk, and interference with bound modes. The part of the continuous spectrum not represented by leaky modes has been studied, and it was termed *residual wave*. Some authors have studied the excitation of leaky modes and residual waves [32,33] in multilayered stripline structures. In these studies, a quasi-analytical method and closed-form representation are derived, which can help the proper understanding of these spurious effects. The practical reduction in the crosstalk and parallel plate mode coupling between adjacent striplines in LTCC packages is commonly accomplished by the insertion of plated via holes, in a fashion similar to the stripline antenna feeding structures. Full-wave three-dimensional simulators have been used by engineers to analyze the impact of the via holes in the stripline structure. It has been demonstrated that the radiation loss and the coupling increases if the fences are placed too close to the stripline [34,35]. In Ref. 34, it is shown that placement of a via hole fence closer than three times the substrate height to the strips increases radiation and coupling. It must be apparent that shorting posts must be performed carefully in the stripline and antenna feeding designs. Moreover, from the point of view of planar process, shorting posts increase significantly the fabrication complexity. An alternative leakage suppression structure with a two-dimensional photonic bandgap lattice etched in the ground planes has been reported [36].

Because of the application of via holes in striplines structures to suppress the leakage parallel-plate modes, the necessity of 3-D full-wave analysis becomes more

apparent. With the increase of operating frequencies and higher circuit densities, issues like crosstalk, signal delay, and distortion are becoming more predominant in the design procedure. At high frequencies, we must take great care with physical layout and interconnects to minimize parasitics, and technological effort in high-density packaging is leading to the design of true three-dimensional circuits, in which accurate signal timing depends on three-dimensional analysis of interconnect, for which we cannot use conventional two-dimensional analysis.

The most popular approach to analyze striplines and microstrip lines is the integral equation (IE) formulation in either the space [37] or spectral domain [38,39]. In Ref. 39, a cylindrical cavity-backed SSL antenna is analyzed. The SSL feed is particularly attractive in the higher microwave and millimeter frequency regions. In Ref. 40, the analysis of a similar structure, the cavity backed circular aperture antenna with suspended stripline feed, using the finite element method (FEM) is reported. A more rigorous analysis of metal-dielectric bodies such as stripline feeds is possible with subsectional analysis [41]. The finite difference time-domain (FDTD) method is also used by engineers in the analysis of multilayered striplines. In Ref. 42, the current and electric field distribution of a PCB stripline structure is reported applying the FDTD method. In Ref. 43, FDTD analyzes an endfire tapered slot phased array with stripline feed. In this study, the effect of the plated vias is included in the analysis, and this allows us to place the vias in the proper points to eliminate impedance anomalies in the antenna. The FDTD method presents the advantage that it provides the transient response as well as the frequency domain data, but it is a time-consuming technique. MoM and FEM techniques, as we have seen before, are also extensively used by engineers in the stripline analysis. MoM offers the advantage, in this particular case of multilayered striplines, of only requiring the discretization of the conducting interconnects, and hence, it can simulate bigger and more complicated structures. The integral equation technique starts with the development of the Green functions for the problem. MoM is then applied to the integral equation to obtain an approximate solution for the currents in the interconnects. A significant part of the computational effort in MoM is associated with the calculation of the elements in the reaction or impedance matrix. These elements can be represented as Sommerfeld-type integrals, which are highly oscillatory and slowly convergent. A full-wave layered-interconnect simulator (UA-FWLIS) that claims to overcome this problem has been recently reported [44]. In this method, the reaction elements of the MoM have been analytically evaluated. The method is directly involved in the analysis of coupling in a multilayered stripline circuit.

BIBLIOGRAPHY

- H. Howe, Jr., *Stripline Circuit Design*, Artech House, Norwood, MA, 1982.
- K. C. Gupta, R. Garg, and I. J. Bahl, *Microstrip Lines and Slotlines*, 2nd ed., Artech House, Norwood, MA, 1996.
- J.-F. Zurcher and F. E. Gardiol, *Broadband Patch Antennas*, Artech House, Norwood, MA, 1992.
- P. Shiffres, How much CW power can stripline handle? *Microwaves*. June: (1966) 25–34.
- R. Wilcoxon, The effects of geometry and dielectric material on stripline and microstrip internal temperatures, *2004 IEEE 20th Annual Semiconductor Thermal Measurement and Management*, March 9–11, 2004, pp. 308–313.
- J. Navarro and K. Chang, Inverted stripline antennas integrated with passive and active solid-state devices, *IEEE Trans. Microw. Theory Tech.* **43**:2059–2065 (1995).
- Y. Tahara, et al., A low-loss serial power combiner using novel suspended stripline couplers, *2001 IEEE MTT-S Int. Microw. Symp. Dig.* 1:20–25 (2001).
- B. S. Yildirim and E.-B. El-Sharawy, Finite-difference time-domain analysis of a striplinedisc-junction circulator, *1998 IEEE MTT-S Int. Microw. Symp. Dig.* **2**:629–632 (1998).
- C. K. Queck and L. E. Davis, Broad-band three-port and four-port stripline ferrite coupled line circulators, *IEEE Trans. Microw. Theory Tech.* **52**(2):625–632 (2004).
- C. K. Queck and L. E. Davis, Novel folding technique for planar ferrite-coupled-line circulators, *IEEE Trans. Microw. Theory Tech.* **52**(5):1369–1374 (2004).
- V. Kondratyev, M. Lahti, and T. Jaakola, On the design of LTCC filter for millimeter-waves, *2003 IEEE MTT-S Int. Microw. Symp. Dig.* **3**:1771–1773 (2003).
- T. Ohwada, et al., A Ku-band low-loss stripline low-pass filter for LTCC modules with low-impedance lines to obtain plural transmission zeros, *2002 IEEE MTT-S Int. Microw. Symp. Dig.* **3**:1617–1620 (2002).
- A. Basu and S. K. Koul, Design and implementation of a wide-band band pass filter in suspended stripline, *2000 Asia-Pacific Microw. Conf.*, December 2000, pp. 512–515.
- W. Menzel, A novel miniature suspended stripline filter, *2003 33rd European Microwave Conference*, 2003, pp. 1047–1050.
- A. R. Brown and G. M. Rebeiz, A varactor-tuned RF filter, *IEEE Trans. Microw. Theory Tech.* **48**(7):1157–1160 (2000).
- Y. C. Lee and C. S. Park, A novel high-Q LTCC stripline resonator for millimeter-wave applications, *IEEE Microw. Wireless Components Lett.* **13**(12):499–501 (2003).
- A. Bhattachayya and O. Fordham, Analysis of stripline-fed slot-coupled patch antennas with vias for parallel-plate mode suppression, *IEEE Trans. Antennas Propag.* **46**(4):538–545 (1998).
- N. I. Herscovici, N. K. Das, and J. Klugman, A microstrip array fed by a non-homogeneous stripline feeding network, *4th International Kharkov Symposium on Physics and Engineering of Millimeter and Sub-millimeter Waves*, Vol. 1, 2001, pp. 123–125.
- M. Yamamoto and K. Itoh, Behaviour of the parallel plate mode in a stripline slot-coupled patch antenna, *IEE Proc. Microw. Antennas Propag.* **147**:385–389 (2000).
- R. F. Harrington, *Field Computation by Moment Methods*, Krieger, Melbourne, FL, 1982.
- T. K. Sarkar, et al., Analysis of arbitrarily shaped microstrip patch antennas utilizing the Sommerfeld formulation, *Int. J. Microw. Millimeter Wave Comput. Aided Eng.* **3**(2):168–178 (1992).
- T. K. Sarkar, S. M. Rao, and A. R. Djordjevic, Electromagnetic scattering and radiation from finite microstrip structures, *IEEE Trans. Microw. Theory Tech.* **38**:1568–1575 (1990).
- S. M. Rao, et al., Electromagnetic scattering and radiation from finite conducting and dielectric structures: Surface/surface formulation, *IEEE Trans. Antennas Propag.* **39**:1034–1038 (1991).

24. C. Wei, et al., Multiconductor transmission lines in multilayered dielectric media, *IEEE Trans. Microw. Theory and Tech.* **32**:439–450 (1984).
25. A. Djordjevic, et al., *Scattering Parameters of Microwave Networks with Multiconductor Transmission Lines: Software and User's Manual*, Artech House, Norwood, MA, 1990.
26. A. Djordjevic, et al., *Matrix Parameters for Multiconductor Transmission Lines: Software and User's Manual*, Artech House, Norwood, MA, 1989.
27. A. Djordjevic, et al., *Time-Domain Response of Multiconductor Transmission Lines: Software and User's Manual*, Artech House, Norwood, MA, 1989.
28. P. Brachat and J. M. Baracco, Dual-polarization slot-coupled printed antennas fed by stripline, *IEEE Trans. Antennas Propag.* **43**:738–742 (1995).
29. D. Schaubert, et al., Moment method analysis of infinite stripline-fed tapered slot antenna arrays with a ground plane, *IEEE Trans. Antennas Propag.* **42**:1161–1166 (1994).
30. M. Kahrizi, T. K. Sarkar, and Z. Maricevic, Analysis of wide radiating slot in the ground plane of a microstrip line, *IEEE Trans. Microw. Theory Tech.* **41**:29–37 (1993).
31. T. Itoh, *Numerical Techniques for Microwave and Millimeter-Wave Passive Structures*, Wiley, New York, 1989.
32. C. Di Nallo, F. Mesa, and D. R. Jackson, Excitation of leaky modes on multilayer stripline structures, *IEEE Trans. Microw. Theory Tech.* **46**(8):1062–1071 (1998).
33. P. Baccarelli, et al., An accurate analytical representation of the continuous spectrum excited on multilayer stripline structures in spectral-gap regions, *2003 IEEE MTT-S Int. Microw. Symp. Dig.* **2**:809–812 (2003).
34. G. E. Ponchak, D. Chun, and J.-G. Yook, The use of metal filled via holes for improving isolation in LTCC RF and wireless multichip packages, *IEEE Trans. Adv. Packaging* **23**(1):88–99 (2000).
35. J. Gipprich and D. Stevens, A new via fence structure for crosstalk reduction in high density stripline packages, *2001 IEEE MTT-S Int. Microw. Symp. Dig.* **3**:1719–1722 (2001).
36. K.-P. Ma, et al., Leakage suppression in stripline circuits using a 2-D photonic bandgap lattice, *1999 IEEE MTT-S Int. Microw. Symp. Dig.* **1**:73–76 (1999).
37. J. R. Mosig and T. K. Sarkar, Comparison of quasi-static and exact electromagnetic fields from a horizontal electric dipole above a lossy dielectric backed by an imperfect ground plane, *IEEE Trans. Microw. Theory Tech.* **34**:379–387 (1986).
38. R. H. Jansen, The spectral-domain approach for microwave integrated circuits, *IEEE Trans. Microw. Theory Tech.* **33**:1043–1056 (1985).
39. J. C. Goswami and M. Sachidananda, Cylindrical cavity-backed suspended stripline antenna—theory and experiment, *IEEE Trans. Antennas Propag.* **41**:1155–1160 (1993).
40. D. Chun, R. N. Simons, and L. P. B. Katehi, Modeling and characterization of cavity backed circular antenna with suspended stripline probe feed, *2000 IEEE Antennas and Propagation Society International Symposium*, Vol. 2, July 2000, pp. 774–777.
41. B. M. Kolundzija, et al., *Analysis of Composite Metallic and Dielectric Structures: Software and User's Manual*, Artech House, Norwood, MA, 1997.
42. Y.-K. Kim, FDTD analysis on the current and electric field distribution in a PCB stripline structure, *2000 IEEE International Symposium on Electromagnetic Compatibility*, Vol. 2, August 2000, pp. 691–694.
43. H. Holter, T.-H. Chio, and D. H. Schaubert, Elimination of impedance anomalies in single- and dual-polarized endfire tapered slot phased arrays, *IEEE Trans. Antennas Propag.* **48**(1):122–124 (2000).
44. S. Kabir, S. L. Dvorak, and J. L. Prince, Reaction analysis in stripline circuits, *IEEE Trans. Adv. Packaging* **24**(3):347–356 (2001).

SUBMARINE ANTENNAS

DAVID F. RIVERA
 Naval Undersea Warfare Center
 Newport, Rhode Island
 RAJEEV BANSAL
 University of Connecticut
 Storrs, Connecticut

1. HISTORICAL PERSPECTIVE

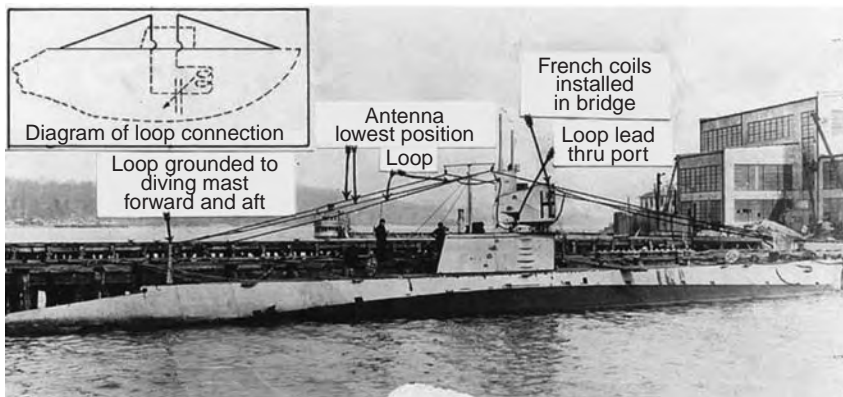
The introduction of radio (or “wireless”) telegraphy into the U.S. fleet in 1910 marked the beginning of the submarine’s role as a capable ally with the surface ship in times of conflict. In those early years, submarine antennas were of either the hull-terminated loop type (introduced in 1919) or the flat-top (T) variety; the latter were modeled after those found on small aircraft and surface ships of the period. Figures 1a and 1b are views of these post- and pre-World War I (WWI) antennas, respectively. Operationally, the antennas were used for reception under water at very low frequencies (to a depth of ≤ 20 feet at 16 kHz), but had to be exposed by raising the vessel to the ocean surface for the purpose of transmission.

Throughout the late 1920s and early 1930s antenna designs grew in sophistication as the introduction of radar and other intelligence gathering functions became part of the submarine’s sensor suite. Figure 2 is a photograph of a typical antenna system aboard a WWII-era diesel-powered submarine. With the arrival of nuclear propulsion in the mid-1950s, antenna technology was pushed still further, as the new submarine was able to remain submerged for months while still maintaining communications with the outside world using the *buoyant cable antenna* (BCA, discussed in Section 3).

Submarine antenna technology thus owes its evolution to developments in naval operational requirements as well as advances in the applied sciences. In this article, some important elements of submarine antenna design are discussed and some representative examples are shown.

2. THE SEA AS A WAVE PROPAGATION MEDIUM

The electrical properties of the ocean play an important role in determining how a submarine antenna is to be used effectively. Whether the antenna is on, near, or below the surface, these properties influence not only the appropriate type of antenna to use but also the rate of data



(a)



(b)

Figure 1. Antennas on early submarines (ca. 1920): (a) hull-terminated loop antenna on submarine *USS H-2* (SS-29); (b) view of T-antenna feedthrough insulator from the bridge of submarine *USS H-3* (SS-30).

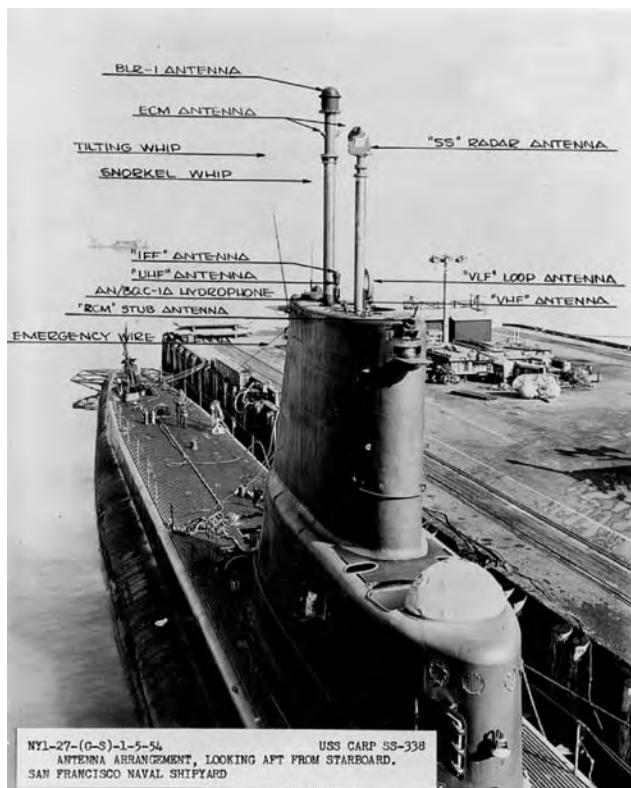


Figure 2. Antenna systems used on diesel submarine *USS Carp* (SS-338).

transfer, which in most cases is of paramount importance when timely decisions must be made and actions carried through. Thus, an understanding of these properties is a part of a submarine antenna designer's repertoire and is briefly discussed here.

Aside from its important thermodynamic properties, water is an electrically polar material with a nonzero net molecular dipole moment that causes the molecule to rotate in the presence of an applied alternating electric field. Over a wide spectrum of frequencies, the rotation of an ensemble of water molecules has been shown to possess a loss peak in the vicinity of 17 GHz at 20°C, commonly called the *relaxation* frequency. The reciprocal of the corresponding angular frequency is the time constant required for the molecules to reach spatial equilibrium once the field is removed (about 9.3 ps). Above and below the relaxation frequency, the loss decreases. The real part of the permittivity decreases above the relaxation frequency but is a constant below it over a wide frequency range with a value of 80, a commonly quoted figure.

The difference between seawater and freshwater is the presence of ionic conductivity, due to the inclusion of natural salts. On a perkilogram basis, the world-average salt content in seawater at 3.5°C is about 35 g (written as 35 parts per thousand, or 35‰), which corresponds to a conductivity σ of 3.2 siemens per meter (S/m). The widely used conductivity value of 4 S/m is equivalent to a salinity of 29‰ at 20°C.

As a propagation medium of electromagnetic waves, seawater permits, with minimal attenuation, the

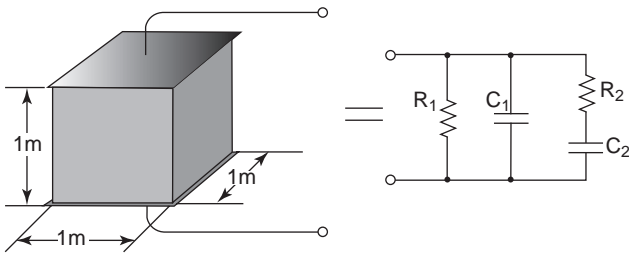


Figure 3. Suboptical wavelength model of seawater at room temperature. In the circuit, $R_1 = 250 \Omega$, $R_2 = 21 \text{ m}\Omega$, $C_1 = 43 \text{ pF}$, and $C_2 = 583 \text{ pF}$. The circuit model is valid for frequencies from near DC to 40 GHz.

penetration of extremely long (greater than 300 Mm) or optical (blue-green spectrum, near 500 nm) wavelengths. Between these extremes the dielectric properties of seawater limit the wave’s depth of penetration and thus determine how antennas are to be advantageously used.

The dielectric properties of seawater below optical frequencies may be visualized with the diagram in Fig. 3. In the figure, a hypothetical cube (1 m on the side) of seawater is placed between two conducting plates to form a capacitor. Since the relative complex permittivity ϵ_r of seawater has been shown to vary with frequency [1], the corresponding complex admittance Y (S/m) across the capacitor terminals may be modeled by a lumped RC network which permits a simple interpretation [2]. In the circuit, R_1 is the reciprocal of the ionic conductivity σ . Resistor R_2 and capacitor C_2 represent the rotational behavior the water molecules constituting the cube in the presence of an applied alternating field. The product $\tau = R_2 C_2$ is the time constant or *relaxation time* required for the molecules to reach spatial equilibrium (12.3 ps). Finally, capacitor C_1 represents the dielectric constant of water at near-infrared frequencies, the limit of the model. In terms of the circuit admittance Y , the relative complex permittivity ϵ_r and attenuation α (Np/m) of seawater are computed by

$$\epsilon_r = \frac{\eta_0 Y}{jk} \tag{1}$$

$$\alpha = \text{Re}(\sqrt{jk\eta_0 Y})$$

where k is the free-space propagation constant ($2\pi/\lambda$) and η_0 is the intrinsic wave impedance of free space (approximately $120\pi \Omega$). Figure 4 is a plot of the plane-wave attenuation of water with ionic conductivity σ (S/m) as a parameter.

3. ANTENNA TYPES AND SERVICES

Because of the need for living and working space of personnel, weapon storage and deployment machinery, and numerous other devices, the submarine antenna is designed to occupy as little space as possible. Since modern submarine communications are carried out over a multi-decade frequency range from 30 Hz to 50 GHz, antennas exhibiting broadband behavior (with respect to either terminal impedance or pattern) to accommodate multiple

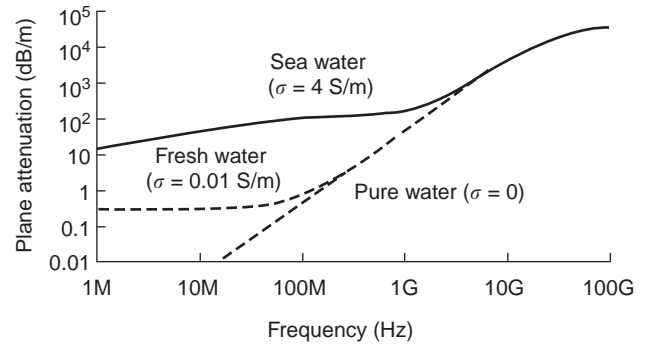


Figure 4. Plane-wave attenuation of water (20°C) with ionic conductivity (σ) as the parameter.

functions are highly desirable. Moreover, careful attention is paid in the early design stages to cositing issues, in order to pinpoint and mitigate electromagnetic interference between various groups of antennas.

Submarine antennas generally fall into one of two broad categories: mast and buoyant. A *mast antenna* is a structure that is extended electromechanically from the topmost portion of the ship known as the *sail*, which breaks through the ocean surface to enable communications. In this posture, the antenna is said to be deployed at *periscope depth* (P/D). A buoyant antenna, in contrast, is deployed from the submerged vessel and allowed to float upward to the ocean surface or to a predetermined depth, depending on the frequency. Once deployed, the antenna is either trailed behind the vessel or fixed in a stationary position. Buoyant towed systems, which are generally low in profile, are thus said to be operated at *speed and depth* (S/D). Figure 5 illustrates the various antenna categories used by a submarine, as determined by its operational posture at sea.

Submarine antennas are typically surrounded by insulation to protect against the effects of corrosion and hydrostatic pressure. For masts, the dielectric is usually a structural composite such as fiberglass or other nonmetallic material with a high strength-to-weight ratio. Buoyant systems may use rigid syntactic foams, hollow fiberglass housings and/or flexible foam polymers to withstand pressure or accommodate storage on a reel within

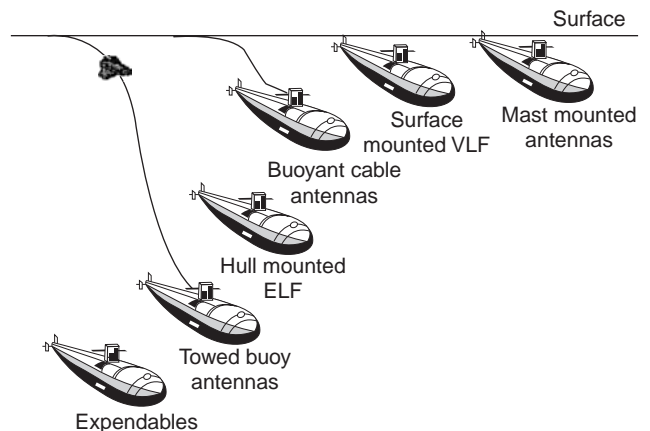


Figure 5. Antenna deployment with submarine depth.

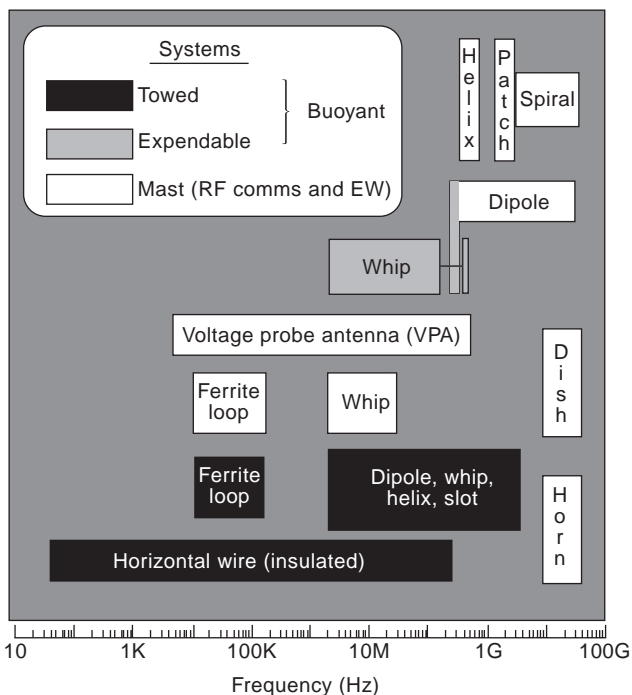


Figure 6. Antenna types by category of use and frequency.

the vessel. Figure 6 plots antennas by generic type (whip, loop, etc.) as a function of frequency.

3.1. Mast Antennas

Mast antennas are structurally attached to the submarine and are exposed above the ocean surface at periscope depth (or with the vessel on the surface) to permit communication or detect signals. They are divided into two categories, by function:

1. *Radiofrequency Communications (RF Comms)*. These are antennas used for services ranging from VLF navigation through UHF satellite (with low to moderate gain); above 10 GHz, large aperture (high gain) antennas are employed.
2. *Electronic Warfare (EW)*. This category describes a suite of antenna sensors used (singly or in groups) to

identify the presence and/or direction of electromagnetic emission(s) generated by friendly or hostile forces over multidecade wavelengths from VLF through millimeter waves. Depending upon the nature of the emission(s), electronic warfare antennas may be used in a variety of ways within three functional groups.

- *Electronic Attack (EA)*. This subcategory comprises antennas used either (1) for jamming or deception (nondestructive) or (2) as a weapon for degrading or neutralizing an electromagnetic energy source emitted by a hostile force (destructive).
- *Electronic Protection (EP)*. These are passive or active sensors designed to protect or mask personnel, facilities, and equipment from the effects of directed energy emission from hostile or friendly sources.
- *Electronic Warfare Support (ES)*. Formally known as *electronic surveillance measures (ESM)*, the antennas and subsystems in this group are used for locating [i.e., direction finding (DF)] and identifying electromagnetic sources for targeting, threat recognition, and other tactical actions.

The physical disposition of the various mast antenna types found on a typical submarine sail is shown in Fig. 7a. Radiofrequency communication masts are, in general, standalone (i.e., dedicated) systems. Electronic warfare mast systems differ in packaging; they are either standalone or mechanically integrated with other functions. An example of the latter includes antennas placed together with the submarine’s periscope optics system, to acquire visual information while simultaneously collecting electromagnetic emission data.

Depending on the frequency and specific use, the antennas generally assume a multitude of forms such as monopoles, loops, or quadrifilar helices. Figure 8a is a photograph of typical mast antennas used in the UHF (225–400 MHz) range; Fig. 8b is an EW antenna stack consisting of spiral, dipole and horn antennas for 200 MHz–40 GHz. More recently, emerging requirements for real-time data exchange with other battle groups have shifted emphasis toward the design of antennas with larger apertures (and hence higher gain). These requirements are generally met at frequencies above 10 GHz, where efficient

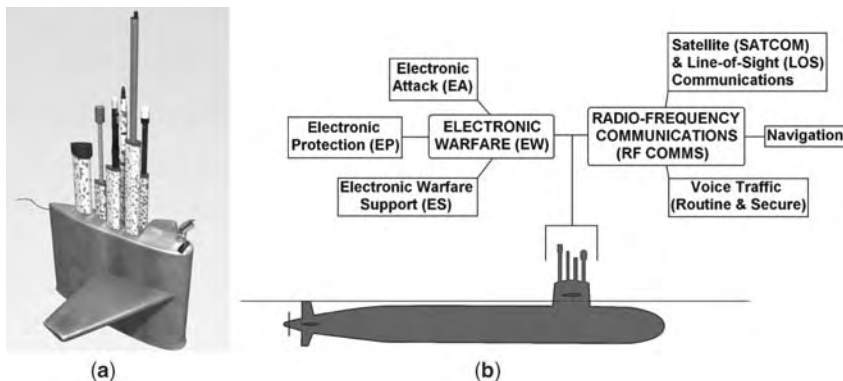


Figure 7. Mast antenna systems: (a) systems erected from the submarine sail; (b) tree diagram of typical functions.

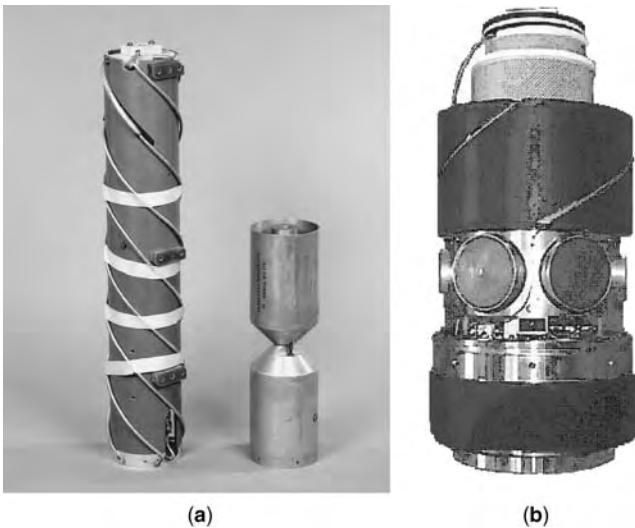


Figure 8. Mast antennas: (a) UHF antennas (RF communications); (b) multiband DF/ES system (periscope).

antennas are not unduly large. One key relationship for selecting the approximate size of an antenna for a given maximum directivity D_{\max} is given by [3]

$$D_{\max} = (ka_e)^2 + 2ka_e \quad (2)$$

where a_e is the equivalent radius of a sphere that has the same overall volume as the antenna and k is the propagation constant (defined earlier). Figure 9 is a plot of (2) for some selected antennas at a given frequency (250 MHz).

Larger directivities with the added advantage of beam-steering are achievable with phased arrays; a comprehensive review of these larger aperture systems applied to submarines is given by Craig [4].

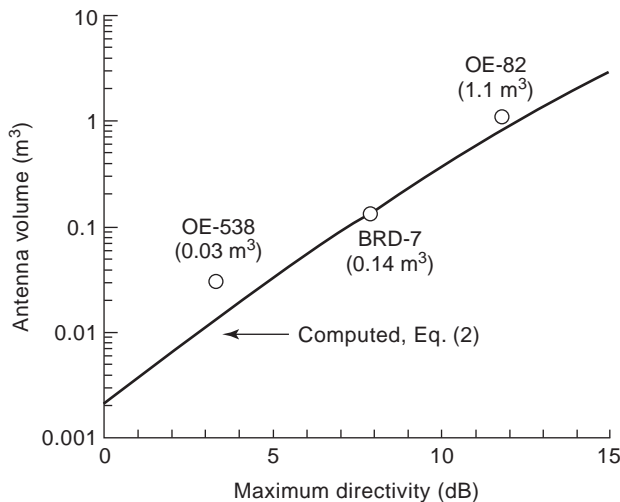


Figure 9. Variation of maximum directivity with antenna volume at 250 MHz.

3.2. Buoyant Antennas

In contrast with mast systems, buoyant antennas are deployed when the vessel is submerged. There are two sub-categories of buoyant systems typically used by a submarine:

1. *Towed.* A towed antenna is one that is deployed from the submerged submarine, typically from a location near the trailing edge of the sail. The antenna floats upward toward a predetermined equilibrium position near or on the ocean surface, whereupon it is dragged behind the vessel at a certain velocity. The velocity and depth with which the antenna is towed behind the submarine is dictated by the operating frequency, together with hydrodynamic and other considerations. There are several types of towed antennas, each with different purposes as described below:

- *Buoyant Cable Antenna (BCA).* The BCA is a thin (nominal overall diameter of 0.65 in.) insulated wire antenna terminated at the far end to seawater with a suitable grounding electrode. The mainstay of low-silhouette communications since 1960, the frequency range of the BCA extends from about 30 Hz to 180 MHz and is used for navigation, voice, and related tasks,
- *Towed Buoy.* A towed buoy is a device that is used to keep a trailed insulated wire (or other) antenna at a steady depth beneath (or above) the ocean surface, or as a platform for carrying an antenna on the sea surface.

2. *Expendable.* An expendable antenna is used for emergency signaling applications. After reaching the sea surface when jettisoned from a submerged vessel, the antenna performs its intended function and afterward “scuttles” or self-destructs after a preset time limit.

As noted above, buoyant antennas take numerous forms depending on their intended application. The challenge in their design lies in simultaneously satisfying numerous constraints which are generally competitive in nature.

3.2.1. Buoyant Cable Antenna (BCA).

Since the early 1960s the mainstay of low-silhouette submarine communications has been the buoyant cable antenna (BCA). The BCA is essentially a transmission line antenna, as shown in Fig. 10, consisting of an insulated flexible wire. It derives its buoyancy from a foamed watertight polyethylene jacket that envelops the antenna element and transmission line and derives its tensile strength with Kevlar strength members imbedded between the jacket and insulated wire. The antenna structure as a whole is also resilient in that long-term exposure to large hydrostatic pressures—as experienced during deep submergence—does not seriously degrade its buoyancy over its operational life. Its evolution from transmission line to antenna is shown succinctly in Fig. 11; Fig. 12 is a collection of BCA electrodes.

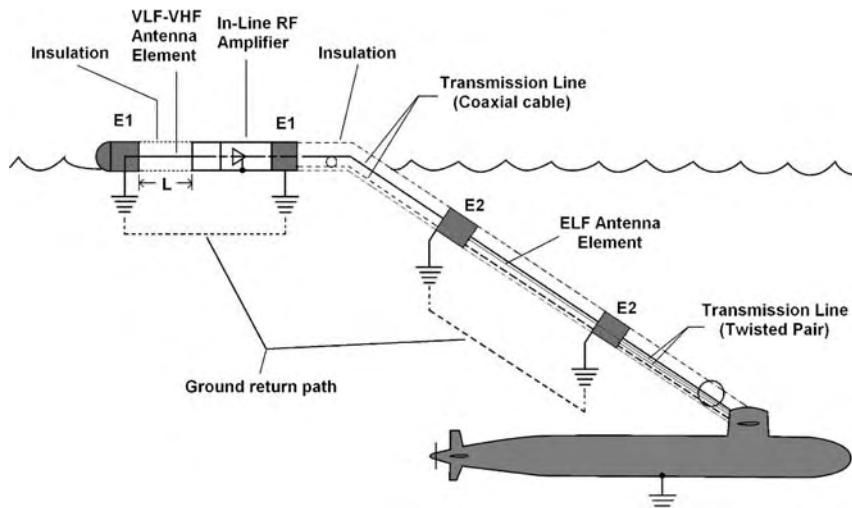


Figure 10. Buoyant cable antenna (BCA). Electrodes E_1 and E_2 in the diagram are grounding electrodes. Antenna size relative to submarine is exaggerated to show detail.

The reception of extremely low frequency (ELF; 30–300 Hz) broadcasts uses two helical grounding electrodes similar to E_2 (see Fig. 10), which are molded into the transmission-line portion of the BCA; the distance between them is about 1000 f. With only one end of each electrode connected to a lead from a twisted-pair transmission line, the insulated conductor spanning the distance between them serves as the antenna element. This aspect is discussed in further detail later.

3.2.1.1. BCA Input Impedance. Two important properties of the buoyant cable antenna are discussed in this section: (1) the circuit characteristics, which permit the determination of the feedpoint impedance and (2) the radiation pattern, which is due to the current distributed along its length. Given the physical dimensions of the antenna, both properties may be used to determine, for example, its range of transmission (or reception) or the operating bandwidth in the presence of seawater.

As shown in Fig. 11, the conversion from a conventional coaxial transmission line into an antenna amounts to splitting a symmetric structure, followed by an exchange of the outer shell from metal—with very high conductivity—to a finitely conducting medium.

The impedance presented at the feedpoint of a conventional transmission line, it will be recalled, is represented by

$$Z_{in} = Z_0 \frac{[Z_L + Z_0 \tanh(\gamma L)]}{[Z_0 + Z_L \tanh(\gamma L)]} \tag{3}$$

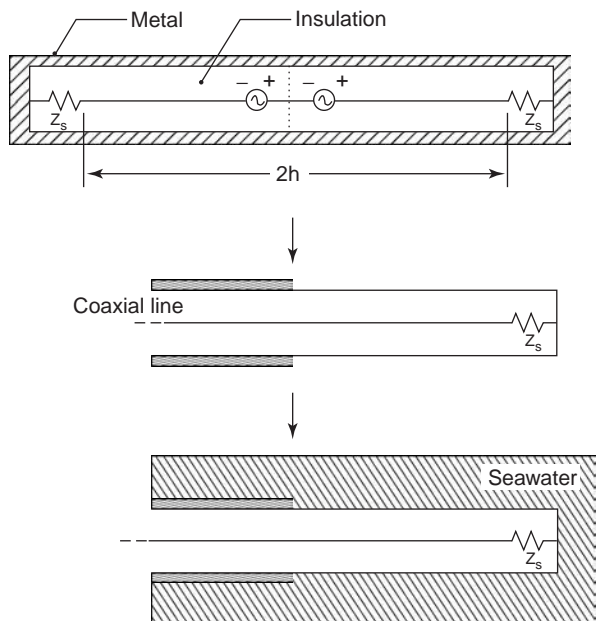


Figure 11. Evolution of a buoyant cable antenna. Starting from the top: a coaxial line with metal outer conductor; stripping away of the outer conductor, exposing the insulation; replacement of the outer conductor with seawater. The transmission line’s center conductor is terminated to the outer conductor (metal or seawater) through an impedance Z_s . Practical BCAs generally use a short circuit ($Z_s \rightarrow 0$) termination. (© 2004 IEEE.)

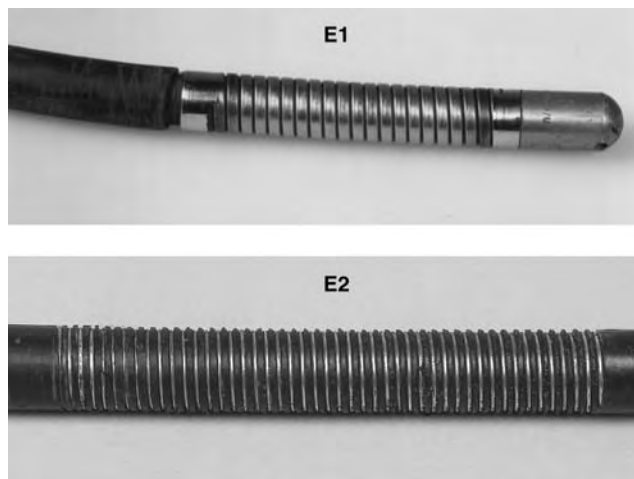


Figure 12. BCA grounding electrodes (see Fig. 10).

where Z_0 is the characteristic impedance of the line, Z_L is the termination (or load) impedance, γ and L are the complex propagation constant and length of the line, respectively.

Because the antenna cross section is small compared with its length (for flexibility), the equivalent circuit of the antenna retains a transmission-line-like character (subject to certain conditions) and is described through *distributed* circuit elements as in the former case. The constants Z_0 and γ are thus modified to account for the presence of seawater [5].

3.2.1.2. BCA Radiation Pattern and Gain. With reference to the coordinate system shown in Fig. 13, Figs. 14a–14c are plots of the computed magnitude of the pattern factors for a 100-ft-long antenna element VLF-VHF BCA element (length L in Figs. 10 and 13) with a short-circuit termination, attached to a coaxial transmission line [6].

Figure 15 depicts a calculation of the total system gain. In the plot, the length of the transmission line connecting

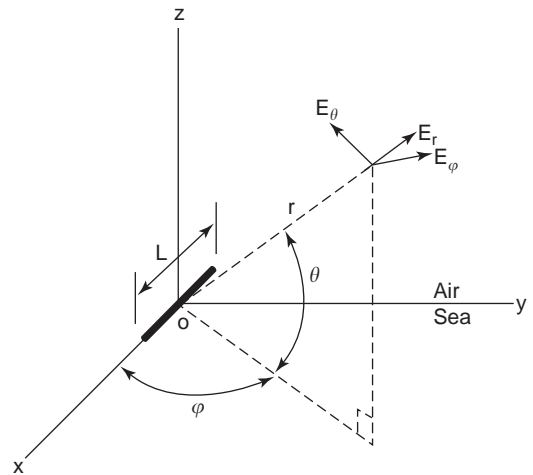


Figure 13. VLF-VHF buoyant cable antenna element of length L : orientation in space.

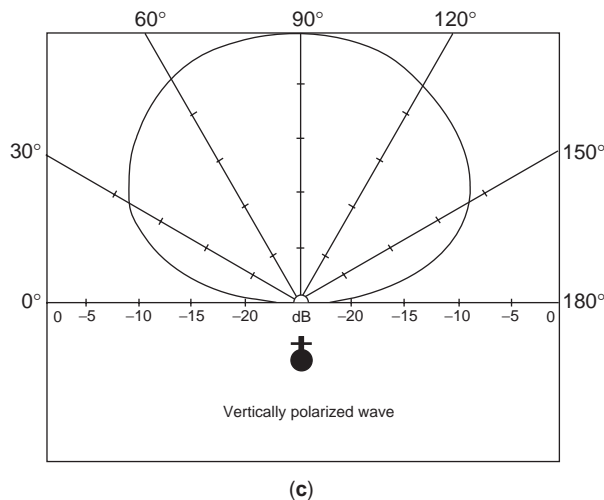
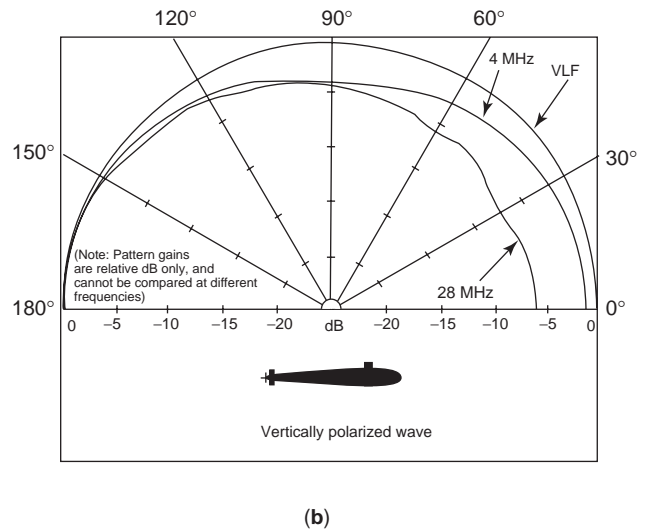
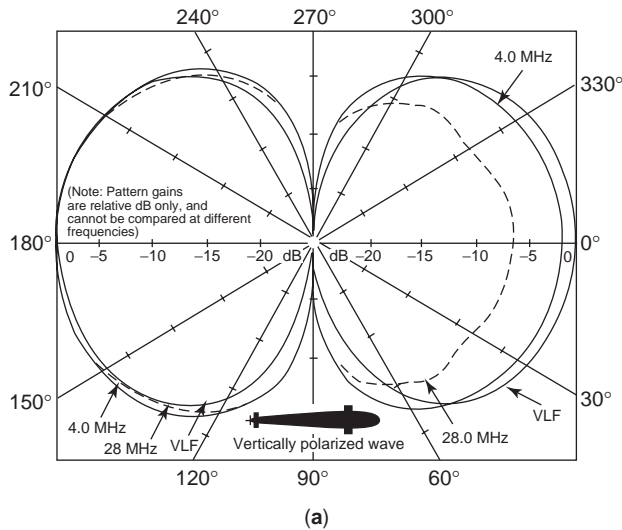


Figure 14. Patterns in the x - y plane (a), x - z plane (b), and y - z plane (c) (where $|E|$ is a function of θ at $\phi = 90^\circ$). (© 2004 IEEE.)

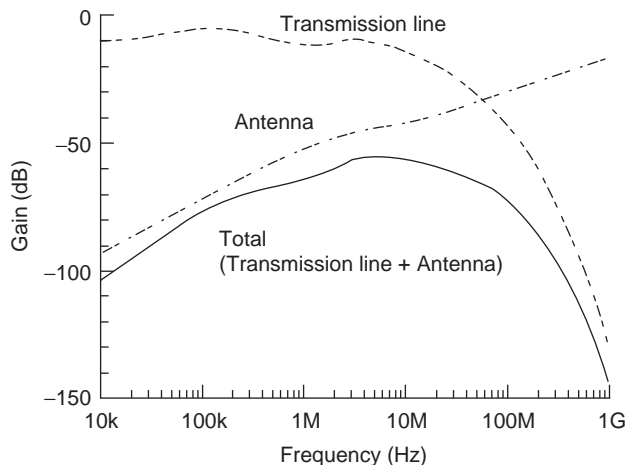


Figure 15. Gain ($\theta = 0^\circ$ and $\varphi = 0^\circ$) of the VLF-VHF portion of the buoyant cable antenna system with a short-circuited termination shown in Figs. 10–14. (© 2004 IEEE.)

the antenna to the ship is assumed to be 1500 ft; the antenna is a 0.65-in.-diameter cable, 100 ft long, with a short-circuited termination. As the plot indicates, the system gain in this case has a maximum value of -55 dB at 5 MHz. Thus a 500-W transmitter attached to the input terminals of the BCA results in an output power of 1.5 mW, sufficient in some cases for long-haul HF ionospheric communications.

3.2.1.3. Frequency Range of the VLF-VHF BCA. As indicated by Fig. 15, the frequency range of the higher-frequency portion of the BCA is bounded by the gains of the transmission line and the antenna element. It should be noted that the gain is negative for both the (lossy) transmission line and the antenna. The overall peak gain in the range of 2–30 MHz enables the BCA to be used for transmitting in a limited fashion; for reception, it is generally useful from 10 kHz to 180 MHz; the upper limit is that frequency where the coaxial transmission-line attenuation and amplifier gain are equal in magnitude. Several models of the solid-state inline amplifier are shown in Fig. 16.

3.2.1.4. ELF Reception with the BCA. As mentioned earlier, the reception of ELF is made with the antenna element between grounded electrodes E_2 . Although the antenna is physically long (1000 ft), its length is a very small fraction of a wavelength in that part of the spectrum and the antenna is operating within the near (or quasi-static) zone. In this instance its field pattern is, in general, a function of the radial distance away from the antenna. For a given electric field E penetrating the ocean, an open-circuit voltage V will exist at the input terminal of the antenna that varies directly with electrode spacing d . This can be written as

$$V = |E|d \quad (4)$$



Figure 16. Solid-state inline amplifiers for a buoyant cable antenna: *left*—rigid chassis design (ca. 1970); *right*—flexible bellows model (1980–present).

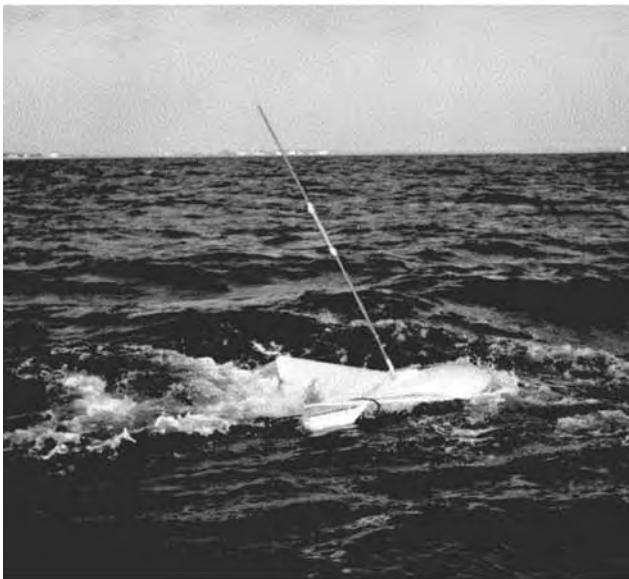
where $|E|$ is the magnitude of the electric field. The ELF antenna is located away from the submarine to minimize the pickup of hull-generated noise.

3.2.2. Towed Buoy. Towed buoys are buoyant bodies that are used whenever a submerged submarine is too deep to deploy a buoyant cable antenna. The body may be used stabilize the position of an antenna, affixed to it, at some shallow distance beneath the ocean surface, or as a means for carrying antennas on the surface. Since the early 1960s, the U.S. Navy has developed various antenna/tow body configurations for operation at various sea conditions and frequencies. The tow bodies were designed by various organizations within the Navy, and Fig. 17 is a composite of some early designs. The design shown in part (a) was known as the AN/BRA-10, the first static (non-towed) buoy. The antenna, mounted topside, is a VHF/UHF whip. The configuration in (b) was known as the AN/BRA-27, which was perhaps the first *dynamic* radio buoy. It played an important role during the 1962 Cuban missile crisis [6].

Advances in tow body research through the years have resulted in hydrodynamic shapes with improved tow speed, reliability, wake, and depth control characteristics. Figure 18 shows several of these newer designs. Pressure transducers placed inside the tow bodies become part of an electromechanical feedback system that provides depth control when coupled to a winch; other designs use buoyancy tanks within the buoy to regulate the depth.



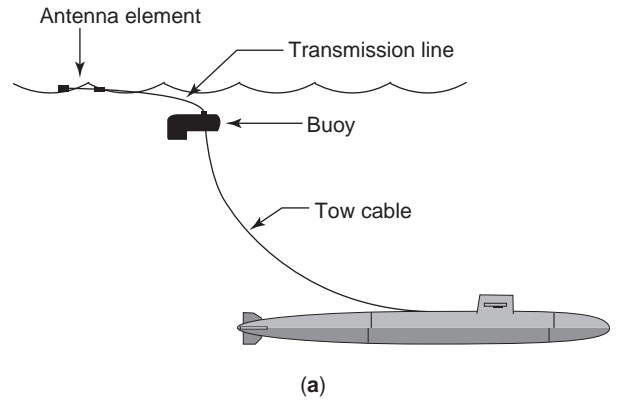
(a)



(b)

Figure 17. Early antenna/tow body configurations: (a) AN/BRA-10, the first *static* buoy (ca. 1960); (b) AN/BRA-27, the first *dynamic* buoy (ca. 1962).

With the exception of experimental work with HF and UHF antennas, the tow bodies in Fig. 18a have been used for towing ferrite core loop antennas to permit continuous VLF reception. More recently, improvements in antenna



(a)

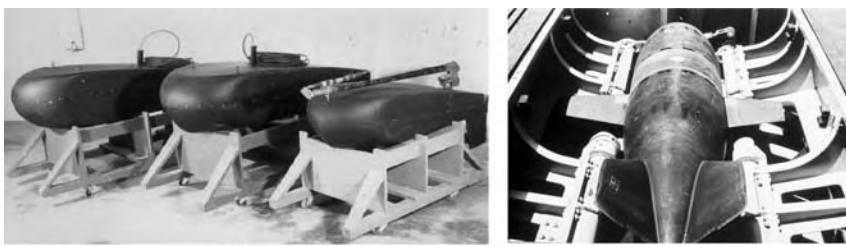


(b)

Figure 19. High-lift auxiliary wire: (a) antenna being towed; (b) ferrite core loop assembly.

design to address the need for hemispherical coverage have resulted in the development of the HF (2–30-MHz) high-lift auxiliary wire. In this system, an insulated buoyant wire and loop antenna are placed collinearly, and, with their output signals properly combined, generate the desired hemispherical coverage pattern. Figure 19 shows the towed system and loop antenna.

The most recent work on the *low-profile antenna* (LPA), a UHF (240–320-MHz) transmit/receive system, has focused on both antenna and tow body designs. Figure 20 shows the tow body under test. Generically of the *planing craft* variety, the slender tow body (or module, with a length-to-diameter ratio of 16) is able to generate lift during tow to minimize signal outages due to seawater washover during tow [7]. This important design feature ensures more consistent performance when towed against



(a)

(b)

Figure 18. Towed buoys: (a) designs with pressure transducers or buoyancy tanks (*back*—OE-305; *middle*—AN/BRR-6; *foreground*—AN/BSQ-5 with collapsible HF and UHF antennas topside); (b) lift-producing buoy (AN/BRA-8, now obsolete) in its berthing cage.

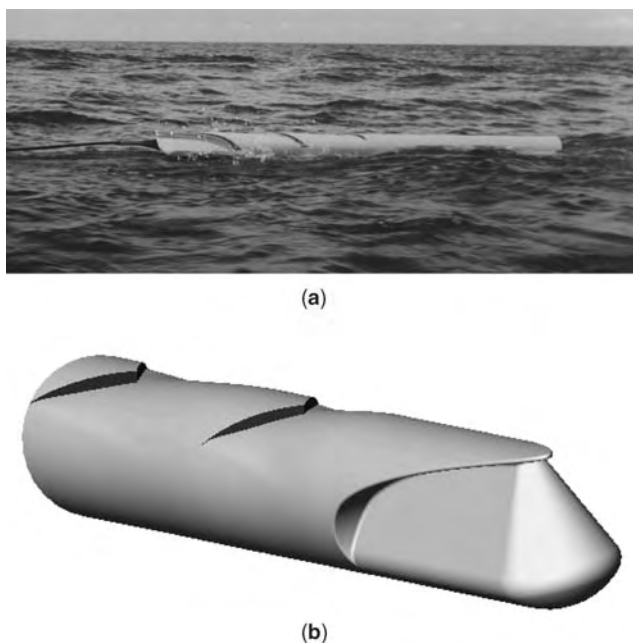


Figure 20. UHF LPA tow body: (a) antenna module under tow; (b) closeup of spray diverter.

or along ocean wave crests and troughs (known as cross or following sea, respectively). It is also fitted with spray diverters over the top (skyward) side as a secondary means for washover reduction.

In Fig. 21, several antennas enclosed within the module are shown. Figure 21a is a small tunable UHF slotted-cylinder antenna (dielectrically loaded), while Fig. 21b is a GPS/iridium phone antenna. When mounted on a two-axis gimbal, the low center of gravity resulting from its conical shape forces this phone antenna to always face upward, regardless of the pitch and yaw movement of the tow body.

3.2.3. Expendables. An expendable antenna is used in emergency situations. Its purpose is to call for assistance in case a submarine is disabled. Over the years, various types of expendables have been devised, but their main operational characteristic involves the one-way transmission of a message. The general sequence of operation is as follows:

1. *Deployment*—the antenna unit is ejected from the submerged vessel,
2. *Formation*—the antenna unit surfaces and assumes its operational position. In some cases the buoy arrives at the ocean surface in a compressed shape, whereupon the use of an explosive charge or gas pressure exerts forces that cause the antenna to unfurl for operation.
3. *Transmission*—the sending of a prerecorded message,
4. *Destruction*—self-disposal of the unit.

The expendable system includes a miniature battery-powered transmitter, together with the necessary circuitry for data storage and retrieval. Built-in test equipment (BITE) for pinpointing problems that would impede operation on deployment, are integrated within some of these devices. The expendables shown in Fig. 22 are of the free-floating (FF) type, meaning that they are untethered.

4. DESIGN CONSIDERATIONS

4.1. Mast Antennas

The design of mast antennas is similar in principle to the design of antennas used in commercial systems, except for the following special precautions:

- *Size*—antenna weight is part of the total submarine payload and must be accounted for.
- *Bandwidth*—the antenna bandwidth is determined by its physical size relative to the wavelength; a tradeoff must be performed with weight considerations to arrive at a satisfactory compromise.
- *Heat dissipation*—there must be provisions for heat-sink design when antennas dissipate considerable heat (typically generated by impedance matching circuits for electrically short monopoles enclosed in a radome).
- *Shock load*—the antenna structure must be able to withstand high impulsive forces, such as those experienced during explosions.
- *Vortex shedding on masts*—a vertical structure of arbitrary cross section towed against a fluid (in this case a mast against seawater) sets up a series of alternating low pressure zones in the fluid, which are

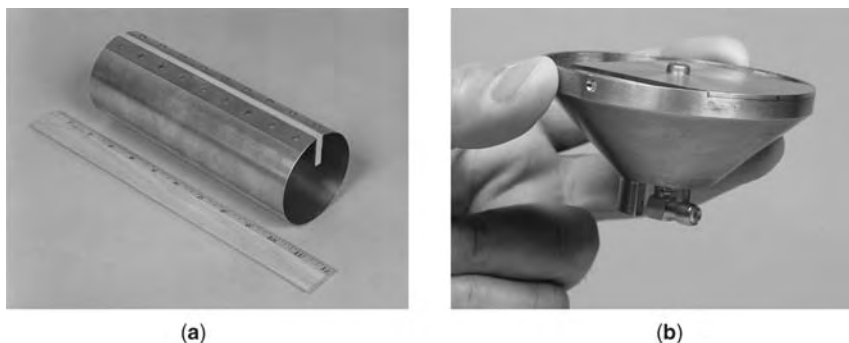


Figure 21. LPA antennas: (a) dielectrically loaded UHF (240–320 MHz, tunable slot antenna; (b) GPS/iridium phone antenna (1.2–1.8 GHz).

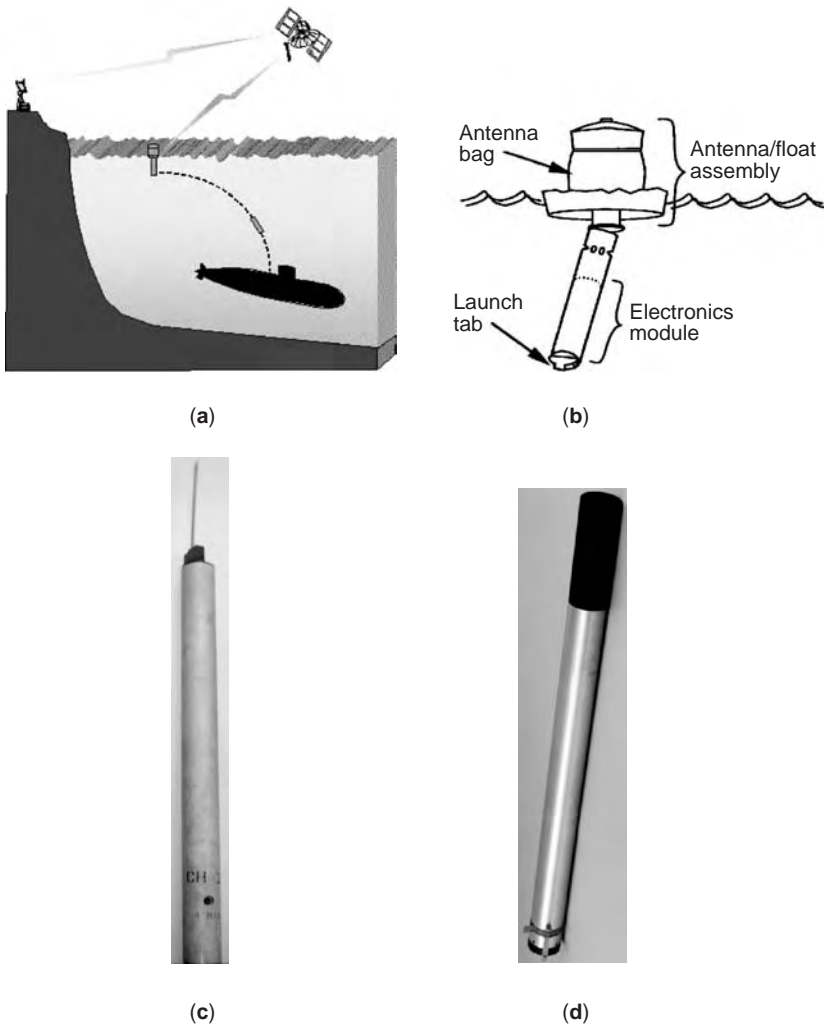


Figure 22. Expendable antennas: (a) ejection from submerged vessel; (b) formation of UHF folded dipole antenna (AN/BRT-6) on sea surface; (c) VHF (160–175 MHz) submarine launched one way transmitting (SLOT) buoy (AN/BRT-1); (d) UHF (406 MHz) submarine emergency position indicating radio beacon (SEPIRB, T-1630/SRT). In (c) the whip antenna is exposed, while in (d) the antenna is under the protective black cap, respectively.

located at the wake or trailing edge of the mast. The resulting movement of the mast toward and away from these zones can cause a structural resonance in the mast at a certain critical tow velocity, often with destructive effects. The satisfactory design of a mast shape thus begins with an understanding of the operating envelope the structure it is likely to work within (subject to numerous other factors) followed by experiments on scale models, combined with numerical fluiddynamic computations.

- *Wave slap*—a term used to describe the pressure load a fluid places against an immovable object. A pressure of 9 lb/in.² above atmospheric is used as the most stringent figure for an acceptable design.
- *Vibration*—the ship vibration spectrum must be considered in order to properly locate the antenna for optimum operation.
- *Pressure tolerance*—the completed system (antennas and radome) must withstand large hydrostatic pressures; a minimum of 450 lb/in.² is typical.
- *Ease of repair/maintainability*—the antenna must be simple to repair or replace on site (pier-side) or at a

maintenance depot with a minimum of effort. This forces the design to be robust with a minimum of tuning screws, adjustment bars, and other devices.

- *Placement*—spacing between antennas within and between masts must be chosen properly to prevent interference by mutual coupling.

4.2. Towed Buoy and Buoyant Cable Antennas

Antennas for tow bodies must withstand very large hydrostatic pressure yet must be light enough to float on the ocean surface. The following precautions, when added to the criteria outlined above, represent a comprehensive (although not exhaustive) set of guidelines:

- *Stability*—the tow body must be hydrodynamically stable with minimal mechanical hysteresis.
- *Tow body drag*—this must be kept to a minimum so that leader cable “strumming” and other stress effects are minimized.
- *Hydrophobicity*—the tow body’s surface must be able to quickly shed water spay, usually accomplished with paints or other special coatings.

- *Corrosion resistance*—careful selection of metals is needed to minimize or prevent the generation of galvanic currents (and its resultant destructive effects).

The buoyant cable antenna is a relatively simple structure, which can be maintained with a minimum of equipment, or disposed of if it is considered to be beyond repair.

5. MATERIALS

The materials chosen for the structural and electrical performance of submarine antennas are dictated by requirement. In certain applications where the design may be a “one-time use” device, inexpensive materials are chosen; at the other end of the spectrum, where high strength is required, resilient materials are needed.

5.1. Metals

For prototyping work, various grades of brass, copper, or aluminum are used; the choice is determined primarily by cost or application. Silver, gold or bronze are used whenever RF connectors, grounding electrodes, or circuit board mating pins are required to have high conductivity, corrosion resistance, or hardness, respectively. In special cases, stainless steel or titanium is used whenever resistance to corrosion or strength combined with light weight is desired.

5.2. Insulators and Dielectrics

Most ceramics and glasses used in submarine antenna applications require moderate dielectric constants ($\epsilon_r' 3\text{--}7$) and moderately low-loss tangents ($\tan \delta < 10^{-2}$). In instances where heat dissipation is necessary, ceramics such as beryllium oxide (BeO) or aluminum nitride (AlN) are usually employed. For applications requiring high dielectric strength and very low loss ($\tan \delta < 10^{-4}$), Teflon (TFE) or Noryl (PPO) are typically used. Noryl has been used as a radome material for microwave antennas. More recently, the introduction of printed antennas in submarine mast applications has utilized low-loss TFE laminates. Certain buoyant antennas have made use of syntactic foam, a strong and lightweight material that is made by mixing glass microspheres with a binding agent, such as epoxy. In critical applications requiring low dielectric loss, care must be exercised when choosing each component. For certain radome applications, electrical-grade fiberglass (G-10) and (more recently) quartz epoxy composites have been used.

6. TESTING

The electrical and mechanical testing facilities for submarine antennas are unique. In this section, brief overviews of the facilities used by the U.S. Navy are presented.

6.1. Electrical

The measurement of the low-angle radiation pattern and input impedance of BCA and mast antennas is carried out at the Navy’s Fisher’s Island facility in Long Island

Sound, NY, a location far from human-produced noise (Fig. 23). The facility has a naturally formed saltwater tidal pond (a) that serves as the BCA testbed. With the antenna floating on the pond, measurement “cuts” in the azimuth plane are made at a distance of approximately one mile from the pond (b) at a very shallow (about $\frac{1}{23}$ rd of a degree) elevation angle.

The circular area located near the tidal pond, to the right in Fig. 23c, is the mast antenna testing facility (c). It comprises a concrete pool lined with radials to simulate a ground plane. When testing is required, the pool is filled with seawater from the neighboring Sound. A control room immediately below the pool (not shown) serves as an instrument room where measurements are taken. Mast and BCA antenna measurements are made over the frequency range of 10 kHz–400 MHz.

The test site denoted by Fig. 23d is the *submarine sensor test platform* (SSTP), used for measuring the radar cross section (RCS) of mast antennas over seawater and under realistic time-varying conditions. Shown closer in Fig. 24, the sledlike steel structure comprises ballast tanks in the forward section for controlling the degree of buoyancy; the crane/mounting platform assembly is located in the rear. In operation, the platform is operated by a winch and is guided by a rail system to a location 900 ft offshore. At this location, important parameters such as antenna impedance, azimuthal plane patterns, and RCS measurements are determined. An RCS measurement range that complements the SSTP is shown in Fig. 25. In that setup, the RCS target is calibrated in free space, away from multipath and clutter effects to obtain meaningful results from the SSTP.

In addition to the measurements performed at the Fisher’s Island facility, antenna and RCS measurements are made at one of the two radiofrequency anechoic chambers that simulate freespace, located at the laboratory grounds. This is done in order to compare the performance of the antennas with and without the presence of seawater. The larger tapered chamber shown in Fig. 26a is used

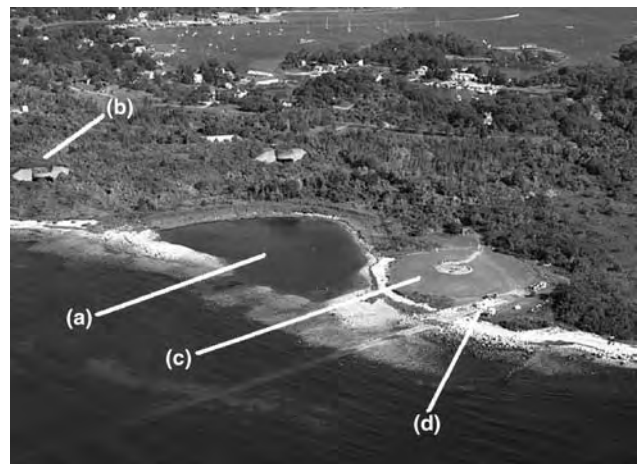


Figure 23. Aerial view of Fisher’s Island, NY testing facility: (a) BCA tidal pond testbed; (b) mile-site, (c) mast antenna radial ground plane test range; (d) submarine sensor test platform (SSTP; see text).



Figure 24. SSTP (with a mast system mounted topside) transiting on guiderails toward test position in Long Island Sound, NY. The frequency range of testing is 100 MHz–18 GHz.

for measuring pattern and RCS data in the frequency range of 100 MHz–50 GHz; the smaller (compact) range is used from 2 to 50 GHz.

Another unique facility for testing antennas under controlled conditions is the overwater arch, shown in Figs. 26b and 26c. The arch is a 70 × 90-ft concrete bed filled with seawater to enable radiation pattern testing in the 100 MHz–18 GHz range. With the antenna under test (AUT) placed in the center of the pool, a source antenna above “illuminates” the AUT throughout a predetermined range of elevation angles. The platform on which the AUT is mounted can be rotated to obtain pattern data in the azimuthal plane.

6.2. Mechanical

The ultimate success and adoption of an antenna design for submarine application is not dependent solely on

the satisfactory meeting of desired electrical characteristics. Its ability to survive repeated exposure in the ocean environment, together or separately with other effects such as explosions, which deliver the extremes of hydrostatic pressure, temperature, vibration, and shock on it, thus requires significant effort in its mechanical design. In order to verify a submarine antenna’s mechanical design integrity, the laboratory has numerous devices and methods suited for this purpose. In this section, a brief overview of the more common mechanical test devices is presented.

6.2.1. Ship Motion, Vibration, and Shock. The forces imparted on a mast due to the typical movements of a ship at sea (roll, heave, pitch, and yaw) are satisfactorily simulated with the device shown in Fig. 27a. This device, known as the *submarine mast-mounted motion table* (SMMT), is computer-controlled and permits 6 degrees of freedom in movement at selected velocities. In this manner, the resultant bending, twisting, or other related movements of the mast and antenna (viewed as a load) may be assessed. A related device, shown in Fig. 27b, is used for generating vibrational forces. As in the case of the motion table, the vibrating table is computer controlled to create a time-dependent vibration profile with respect to frequency, intensity, duration, or cycling.

Shock testing is typically performed in a large open area, such as a pond or a lake to permit the propagation of shock waves due to an intense underwater explosion (UNDEX). The amount and type of explosive charge used depends on the device tested. A high-brissance (large shock/shear-wave-generating) explosive, such as HBX-1, is typically used. Figure 27c is a view of the UNDEX facility at Briar Point pond, operated by the Naval Surface Warfare Center (Carderock, MD Division) and under the auspices of the Army’s Aberdeen Proving Grounds.

6.2.2. Hydrostatic Pressure and Environmental Testing. The hydrostatic tank in Fig. 28a is used for testing the



(a)



(b)

Figure 25. Elevated RCS calibration range (2–18 GHz). The target (b) is 70 ft above ground and the source (a) is 1400 ft away. It is located in an area clear of multipath and clutter effects and is used with the SSTP.

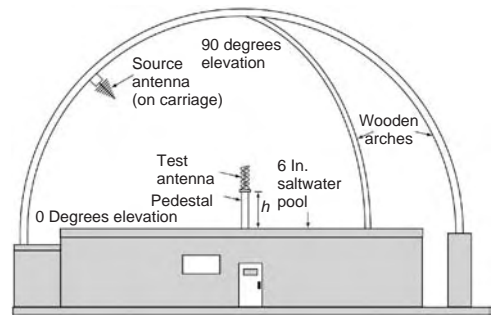
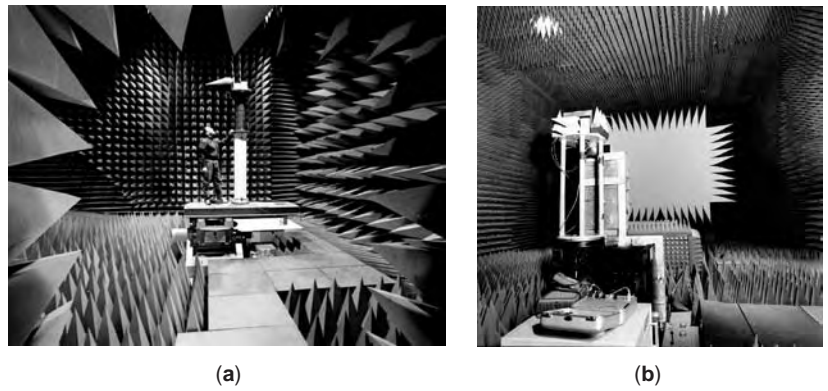


Figure 26. Submarine antenna testing facilities: (a) tapered anechoic chamber; (b) compact range; (c) overwater arch (*left*—front view; *right*—illustration of rear view).



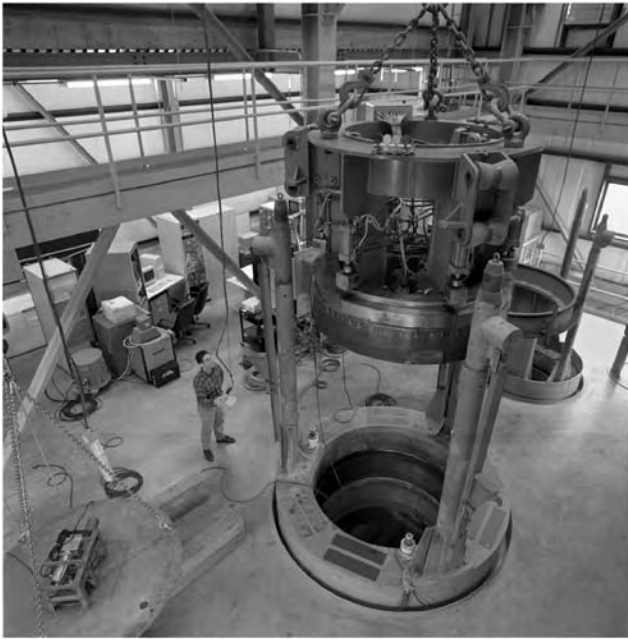
(a)

(b)



(c)

Figure 27. (a) Six-axis motion table with mast and antenna load; (b) vibration table; (c) UNDEX facility (Aberdeen Proving Grounds, MD).



(a)



(b)

Figure 28. (a) Hydrostatic pressure tank; (b) temperature/humidity chamber.

pressure tolerance of mast or buoyant antennas and their associated components. The device under test (DUT) is placed inside the tank, which is filled with water. On closure and sealing of the thick-domed cover, the pressure in the tank may be raised from the ambient atmospheric level to values in excess of 5000 lb/in.². After removal from the tank, the DUT may be visually checked for leaks, cracks, or other destructive effects. Properties such as an antenna's input impedance may be made to determine the effects of pressure on it.

The effects of temperature and humidity on an antenna are determined with the chamber shown in Fig. 28b. The chamber is capable of producing wide extremes in either quantity to examine effects such as variations in brittleness or pliability of candidate insulating materials for

antennas, copper plating delamination of printed antennas, and for first-article tests to determine the degree of compliance of a given DUT with prescribed military standards.

Acknowledgements

The authors would like to thank the following individuals for their encouragement and guidance in the preparation of this article (in no particular order): Tony Susi (BCA program manager, retired) John Merrill (former department head, Submarine Electromagnetic Systems Department, New London CT Laboratory, retired), Earle Pearson (retired), Jim Clark, Frank Zannini, Kurt Hafner, Jr. (retired), Raffi Khokasian, Paul Medeiros, Phil Amidon, Chris Cooney, George Nichols, Dr. John Casey, Rich Allen, Dan Craw (Archivist, NUWC Data Center), and Steve Finnigan (Curator, U.S. Navy Submarine Force Museum, Groton Connecticut).

BIBLIOGRAPHY

1. J. A. Saxton, and J. A. Lane, Electrical properties of sea water, *Wireless Eng.* **29**:269–275 (1952).
2. G. H. Brown, C. N. Hoyle, and R. A. Bierwirth, *Theory and Application of Radio-Frequency Heating*, Van Nostrand, New York; 1947, pp. 226–233.
3. R. F. Harrington, Effect of antenna size on gain, bandwidth, and efficiency, *Radio Sci.* **64D**(1):1–12 (1960).
4. W. P. Craig, Electronically steered array antennas for submarine connectivity, *NUWC Technical Digest*, Sept. 2002, pp. 26–36.
5. R. W. P. King, and G. S. Smith, *Antennas in Matter*, MIT Press, Cambridge, MA, 1981, Chap. 1.
6. D. F. Rivera, and R. Bansal, Towed antennas for U.S. submarine communications: A historical perspective, *IEEE Anten. Propag. Mag.* **46**(1):23–36 (2004).
7. J. H. Clark, Hydrodynamic mitigation of washover effects associated with surface towed antennas bodies, *Conf. Proc. 2001 ISOPE*, 2001, Vol. II, pp. 333–338.

SUPERCONDUCTING CAVITY RESONATORS

HASAN PADAMSEE
Cornell University

A key component of the modern particle accelerator [1] is the device that imparts energy to the charged particles. This is an electromagnetic radio frequency (RF) cavity resonating at microwave frequencies typically between 50 MHz and 3000 MHz. Traditionally, accelerating devices are normal conducting cavities typically made from copper [1]. One of the main incentives for using superconducting cavities is that the dissipation in the walls of the copper structure can be substantially reduced. This is especially beneficial for accelerators that operate in a continuous wave (CW) mode or at a high duty factor

(e.g., $>1\%$). Superconducting cavities economically provide high CW operating fields. Another benefit is that superconducting cavities can be designed to have a large beam aperture that reduces the beam cavity interactions, allowing higher beam quality and higher beam current.

There are two distinct types of superconducting cavities, depending on the velocity of the particles. The first category is for accelerating charged particles that move at nearly the speed of light, such as electrons in a high-energy linear accelerator [e.g., at TJNAF [2] at Jefferson Lab in Newport News, VA] or a storage ring [e.g., LEP [3] at CERN in Switzerland]. The second type is for particles that move at a small fraction (e.g., 0.01 to 0.3) of the speed of light, such as the heavy ions emerging from a dc high-voltage Van de Graaff accelerator. ATLAS [4] at Argonne National Lab, Argonne, IL is the longest-running heavy ion accelerator facility. Figure 1(a) is a sketch of the typical superconducting accelerating structure of the first type, and Fig. 2(a) is a corresponding photograph [5].

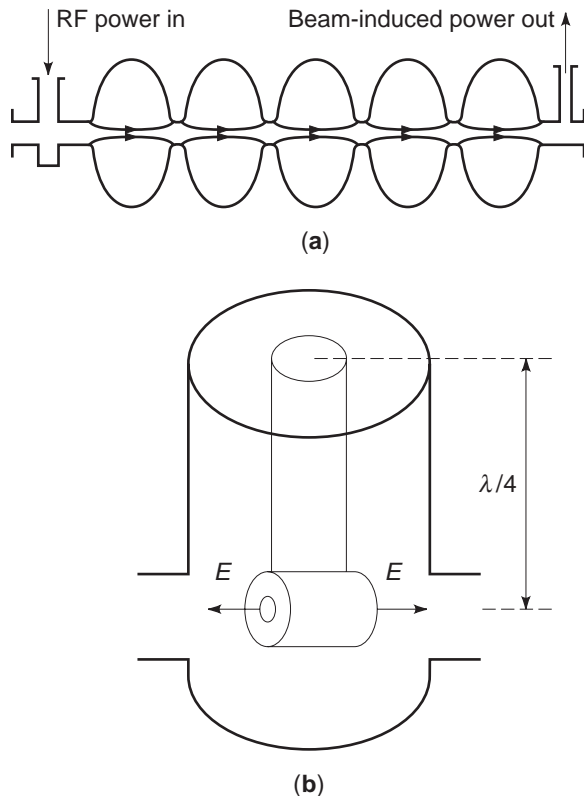


Figure 1. (a). An accelerating structure for velocity of light particles. The resonant frequency for superconducting structures is typically between 350 MHz and 3000 MHz. The cell length is half a wavelength ($\lambda/2$) long. The phase of the electric field on the axis of each cell is shown for the accelerating mode. Ports outside the cell region are for input power couplers and higher order mode power output couplers. In many applications, the power induced by the beam in higher order modes has to be removed by output couplers. (b) An accelerating structure for low-velocity particles, such as heavy ions. The resonant frequency is typically between 50 MHz and 150 MHz. The accelerating gaps are $\beta_1\gamma_2$ in length, where $\beta = v/c$ and v is the velocity of the heavy ions.

There are five accelerating cells that resonate in the transverse magnetic $(TM)_{010}$ mode of the cylindrical cavity. As the particle traverses each half-wavelength ($\lambda/2$) accelerating gap in half a radio-frequency (RF) period, it sees a longitudinal electric field pointing in the same direction for continuous acceleration. Figure 1(b) is a sketch for a structure for low velocity particles, and Fig. 2(b) is a corresponding photograph [6]. A coaxial transmission line a quarter wavelength long resonates in the transverse electromagnetic (TEM) mode. A drift tube is suspended from the end of the hollow center conductor. The structure has two accelerating cells between the ends of the drift tube and the beam hole openings located in the outer conductor of the coax. The accelerating gap is $\beta\lambda/2$, where $\beta = v/c$. As β is small, λ must be chosen to be large, to achieve a useful

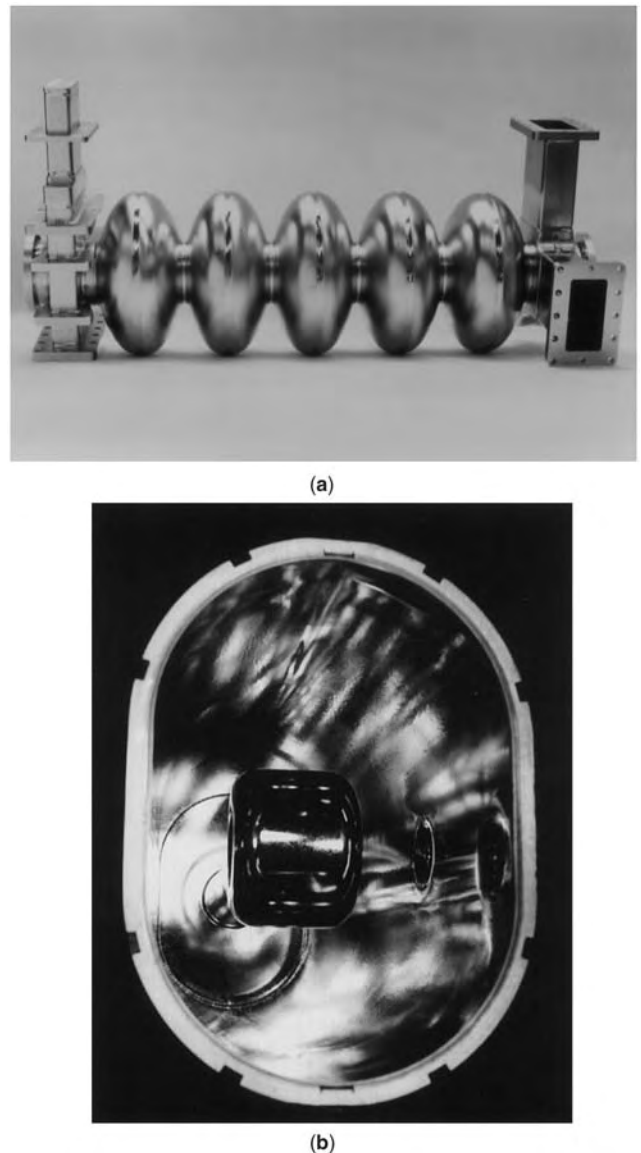


Figure 2. (a) Five-cell 1.5 GHz niobium cavity developed at Cornell University (Ithaca, NY), now used at TJNAF. (b) A quarter-wave resonator from niobium developed for the JAERI (Tokai, Japan) heavy ion linac.

acceleration. Therefore, a low resonant frequency is chosen, typically 100 MHz. The wavelength also sets the height of the quarter-wave resonator. The example of Fig. 2 has a manageable height of less than 1 m.

Large-scale application of superconducting cavities to electron and ion accelerators is now established at many laboratories around the world [7]. These accelerators provide high-energy electron and positron beams for elementary particle research, medium-energy electron beams for nuclear physics research, low-energy, heavy ion beams for nuclear research, and high-quality electron beams for free electron lasers. Altogether more than 500 m of superconducting cavities have been installed worldwide and successfully operated at accelerating fields up to 6 MV/m to provide a total of more than 2.5 GV for a variety of accelerators.

The two most salient characteristics of an accelerating cavity are its average accelerating field, E_{acc} , and the quality factor Q_0 . The typical accelerating field at which $\beta \approx 1$ superconducting cavities are now operated routinely is $E_{acc} = 5$ MV/m, and the typical Q_0 value is 2×10^9 . The corresponding numbers for low-velocity structures are 3 MV/m and 10^9 . Accelerating fields as high as 40 MV/m and Q_0 values as high as 10^{11} have been reached in high-performance $\beta \approx 1$ superconducting test cavities.

The strongest incentive to use superconducting cavities is in accelerators that operate in a CW mode, or at a high duty factor ($> 1\%$). For CW operation, the power dissipation in the walls of a structure built from normal conducting material (such as copper) is substantial. Therefore, the typical CW operating field for a copper cavity is usually kept below 1 MV/m. The microwave surface resistance of a superconductor is typically five orders of magnitude lower than that of copper, and therefore, the Q_0 is five orders of magnitude higher. For applications demanding high CW voltage, such as increasing the energy of electron storage rings, the advantage of superconducting cavities becomes clear. As the dissipated power increases with the square of the operating field, only superconducting cavities can economically provide the needed voltage. For example, LEP requires 2.5 GV to double its energy from 50 GeV to 100 GeV per beam. If copper cavities were to be used, both the capital cost of the klystrons and the ac power operating cost would become prohibitive at the higher accelerating field. Several megawatts/meter of ac power would be required to operate a copper cavity at 5 MV/m. There are also practical limits to dissipating high power in the walls of a copper cavity. When more than 100 kW is dissipated in a copper cell, the surface temperatures exceeds 100°C , causing vacuum degradation, stresses, and metal fatigue due to thermal expansion. High accelerating fields (≈ 100 MV/m) can be produced in copper cavities, but only for microseconds, and the peak RF power needed [1] becomes enormous (many hundreds of megawatts).

Apart from the general advantages of reduced RF capital and reduced RF associated operating costs, superconductivity offers certain special advantages that stem from the low-cavity wall losses. Because of the low-power dissipation at high accelerating field, one can afford to make the beam hole of the superconducting cavity much larger

than for a normal conducting cavity. The large beam hole substantially reduces the beam-cavity interaction [or wake fields [1]], allowing better beam quality and higher current for improving the precision and reaction rates of physics experiments. For the intense proton linacs, where scraping of the proton beam tails is a major worry because of radio-activation of the accelerator, the wide beam hole greatly reduces the risk of beam-loss-induced radioactivity.

1. RF SUPERCONDUCTIVITY BASICS

The remarkable properties of superconductivity are attributed to the condensation of charge carriers into Cooper pairs, which move frictionlessly. At $T = 0$ K, all charge carriers are condensed. At higher temperatures, some carriers are unpaired; the fraction of unpaired carriers increases exponentially with temperature, as $e^{-\Delta/kT}$, until none of the carriers are paired above T_c . Here 2Δ is the energy gap of the superconductor, the energy needed to break up the pairs. In this simplified picture, known as the *London two-fluid model*, when a dc field is turned on, the pairs carry all the current, shielding the applied field from the normal electrons. Electrical resistance vanishes.

In the case of RF currents, however, dissipation does occur for all $T > 0$ K, albeit very small compared with the normal conducting state. Although the Cooper pairs move frictionlessly, they do have inertial mass. For high-frequency currents to flow, forces must be applied to bring about alternating directions of flow. Hence an ac electric field will be present in the skin layer, and it will continually accelerate and decelerate the normal carriers, leading to dissipation proportional to the square of the RF frequency. The two-fluid model provides a simple explanation for the quadratic frequency and the exponential temperature dependence of the RF surface resistance. The power dissipated is proportional to the internal electric field (proportional to the RF frequency) and to the normal component of the current. The “normal” component of the current, being proportional to the interior electric field, gives another factor proportional to the RF frequency. The normal component of the current also depends on the number of carriers thermally excited across the gap 2Δ and is given by the Boltzmann factor $e^{-\Delta/kT}$.

Besides the phenomenally low RF surface resistance, other important fundamental aspects are the maximum surface fields that can be tolerated without increasing the microwave surface resistance substantially or without causing a breakdown of superconductivity. The accelerating field, E_{acc} , is proportional to the peak surface RF electric field (E_{pk}), as well as the peak surface RF magnetic surface field (H_{pk}).

The ultimate limit to the accelerating field is the RF critical magnetic field. Theoretically, this is equal to the superheating critical magnetic field. In the Ginzburg-Landau phenomenological theory of superconductivity [8], surface energy considerations lead to estimates for superheating critical field in terms of the thermodynamic critical field, H_c , and the Ginzburg-Landau parameter, κ ,

as follows:

$$\begin{aligned} H_{\text{sh}} &\approx \frac{0.89}{\sqrt{\kappa}} H_c & \text{for } \kappa \ll 1 \\ H_{\text{sh}} &\approx 1.2 H_c & \text{for } \kappa \approx 1 \\ H_{\text{sh}} &\approx 0.75 H_c & \text{for } \kappa \gg 1 \end{aligned} \quad (1)$$

For the most commonly used superconductor, niobium, H_{sh} , is about 230 mT, which translates to a maximum accelerating field of 55 MV/m for a typical $\beta = 1$ niobium structure and roughly 30 MV/m for a $\beta < 1$ niobium structure.

Typically, cavity performance is, however, significantly below the theoretically expected surface field. One important phenomenon that limits the achievable RF magnetic field is “thermal breakdown” of superconductivity, originating at submillimeter-size regions of high RF loss, called “defects.” When the temperature outside the defect exceeds the superconducting transition temperature, T_c , the losses increase, because large regions become normal conducting. Several measures have been developed to overcome thermal breakdown, such as (a) improving the thermal conductivity of niobium by purification or (b) using thin films of niobium (or lead) on a copper substrate cavity.

In the early stages of the development of superconducting cavities, a major performance limitation was the phenomenon of “multipacting.” This is a resonant process in which a large number of electrons builds up within a small region of the cavity surface because the secondary electron emission coefficient of the surface is greater than unity. The avalanche absorbs RF power, making it impossible to raise the fields by increasing the incident RF power. The electrons impact the cavity walls, leading to a large temperature rise and eventually to thermal breakdown. With the invention of the spherical cavity shape [9] (and later the elliptical cavity shape [10]), multipacting is no longer a significant problem for velocity-of-light structures. Multipacting is still an impediment for structures for low-velocity particles but can be reduced by long periods of exposure to high RF power, called *conditioning*, during which the secondary electron emission is reduced by long-term electron bombardment.

In contrast to the magnetic field limit H_{sh} , there is no known theoretical limit to the tolerable surface electric field. Continuous wave electric fields up to 145 MV/m [11] and pulsed electric fields up to 220 MV/m [12] have been imposed on a superconducting niobium cavity surface without any catastrophic effects. However, at high electric fields, an important limitation to the performance of superconducting cavities arises from the emission of electrons from high electric field regions of the cavity. Power is absorbed by the electrons and deposited as heat when electrons impact the cavity walls. If the emission grows intense, it can even initiate thermal breakdown. There have been extensive studies about the nature of field emission sites as well as development of techniques to avoid emission sites and to destroy them [13].

For low-velocity accelerators, there is an important additional performance consideration. Ambient acoustic

noise (microphonics) excites mechanical vibrational modes of the cavity, causing the resonant frequency to vary. The resonant cavities are extended, loaded structures (e.g., drift tubes supported by pipes) and generally have reduced mechanical stability. The cavity RF phase must be synchronized with an RF clock. This requires rapidly tuning the cavity to cancel the effects of acoustically induced mechanical distortions [14].

2. FIGURES OF MERIT FOR A SUPERCONDUCTING CAVITY

We show how to calculate the important physical quantities, such as resonant frequency, accelerating field, peak electric and magnetic fields, power dissipation, quality factor Q_0 , and shunt impedance for a simple cavity, the cylindrically symmetric pillbox. The treatment is basic to both normal conducting and superconducting cavities (see CAVITY RESONATORS). We also work out illustrative values. Similar analytic calculations can be carried out for a coaxial (TEM) quarter-wave resonator, as illustrative of an accelerating structure for low-velocity particles. Only simple structures can be calculated analytically. For real structures with beam holes, it is necessary to use field computation codes, such as (a) URMEL [15] for cylindrically symmetric structures and (b) MAFIA [16] for three-dimensional geometries.

For a cylinder of length d and radius R , the electric (E) and magnetic (H) fields for the standing wave TM_{010} mode are

$$\begin{aligned} E_z &= E_0 J_0 \left(\frac{2.405 \rho}{R} \right) e^{i\omega t}, \\ H_\phi &= -i \sqrt{\frac{\epsilon_0}{\mu_0}} E_0 J_1 \left(\frac{2.405 \rho}{R} \right) e^{i\omega t} \end{aligned} \quad (2)$$

where all other field components are 0. J_0 and J_1 are Bessel functions of the radial coordinate. The angular resonant frequency $\omega = 2\pi f$ is given by

$$\omega_{010} = \frac{2.405 c}{R} \quad (3)$$

Note that the resonant frequency, f , is independent of the cavity length.

Assume an electron traveling nearly at the speed of light (c). It enters the cavity at time $t = 0$ and leaves at a time $t = d/c$. To receive the maximum kick from the cavity, the time it takes the particle to traverse the cavity is to equal one half of an RF period, that is,

$$t = \frac{d}{c} = \frac{1}{2} T_{\text{RF}} = \frac{\pi}{\omega} \quad (4)$$

Under this condition, the electron always sees a field pointing in the same direction. The accelerating voltage (V_{acc}) for a cavity is

$$V_{\text{acc}} = \left| \int_{z=0}^{z=d} E_{\text{el}} dz \right| \quad (5)$$

For an electron accelerator with energy > 10 MeV, it is sufficiently accurate to use $v = c$, so that $t(z) = z/c$. Thus

$$V_{\text{acc}} = \left| \int_{z=0}^{z=d} E_z(\rho = 0, z) e^{i\omega z/c} dz \right| \quad (6)$$

$$V_{\text{acc}} = E_0 \left| \int_{z=0}^{z=d} e^{i\omega z/c} dz \right| = dE_0 \frac{\sin\left(\frac{\omega d}{2c}\right)}{\frac{\omega d}{2c}} = dE_0 T \quad (7)$$

Here T is referred to as the “transit time factor.” At 1.5 GHz, we have $d = c\pi/\omega = 10$ cm, and Eq. (7) simplifies to

$$V_{\text{acc}} = 0.064 \text{ m} \cdot E_0$$

The average accelerating electric field (E_{acc}) is given by

$$E_{\text{acc}} = \frac{V_{\text{acc}}}{d} = \frac{2E_0}{\pi} \quad (8)$$

Here E has the dimensions of V/m.

3. PEAK SURFACE FIELDS

To achieve a high accelerating field in a cavity, it is important to minimize the design ratios of the peak fields to the accelerating field. For the TM_{010} mode in a pillbox cavity, we have

$$E_{\text{pk}} = E_0, \quad H_{\text{pk}} = \sqrt{\frac{\epsilon_0}{\mu_0}} J_1(1.841) E_0 = \frac{E_0}{647\Omega} \quad (9)$$

Thus we obtain the following ratios:

$$\begin{aligned} \frac{E_{\text{pk}}}{E_{\text{acc}}} &= \frac{\pi}{2} = 1.6, \\ \frac{H_{\text{pk}}}{E_{\text{acc}}} &= 2430 \frac{\text{A/m}}{\text{MV/m}} = 3.05 \frac{\text{mT}}{\text{MV/m}} \end{aligned} \quad (10)$$

The units for magnetic field used are teslas.

4. POWER DISSIPATION AND Q_0

In order to support the electromagnetic fields, currents flow within a thin surface layer of the cavity walls. If the surface resistance is R_s , the power dissipated/unit area (P_a) due to Joule heating is

$$P_a = \frac{1}{2} R_s H^2 \quad (11)$$

The quality, Q_0 , is related to the power dissipation by the definition of Q_0 :

$$Q_0 = \omega \frac{\text{Energy stored}}{\text{Power dissipated}} = \frac{\omega U}{P_c} \quad (12)$$

where U is the stored energy and P_c is the dissipated power.

The total energy in the cavity and the power dissipated are

$$U = \frac{1}{2} \mu_0 \int_v |H|^2 dv, \quad P_c = \frac{1}{2} R_s \oint_s |H|^2 ds \quad (13)$$

where the integral is taken over the volume of the cavity. Thus

$$Q_0 = \frac{\omega \mu_0 \int_v |H|^2 dv}{R_s \oint_s |H|^2 ds}, \quad Q_0 = \frac{G}{R_s}, \quad (14)$$

$$G = \frac{\omega \mu_0 \int_v |H|^2 dV}{\oint_s |H|^2 ds}$$

Here G is called the *geometry factor*. It only depends on the cavity shape and not on its size. For the TM_{010} mode in a pillbox cavity, we obtain

$$U = \frac{\pi \epsilon_0 E_0^2}{2} J_1^2(2.405) d R^2 \quad (15)$$

$$P_c = \frac{\pi R_s E_0^2 \epsilon_0}{\mu_0} J_1^2(2.405) R[R+d] \quad (16)$$

$$G = \frac{453 R d}{(R^2 + R d)} \Omega \quad (17)$$

Combining Eqs. (3) and (4), we find that in order to obtain the maximum accelerating voltage from the cavity, we require

$$\frac{R}{d} = \frac{2.405}{\pi} \quad (18)$$

so that $G = 257 \Omega$. A typical observed surface resistance for a well-prepared superconducting Nb cavity is $R_s = 20$ n Ω . Thus we have a Q_0 value of

$$Q_0 = \frac{G}{R_s} = 1.3 \times 10^{10} \quad (19)$$

For a typical cavity length of $d = 10$ cm (at 1.5 GHz), we obtain $R = 7.65$ cm. For an accelerating voltage of 1 MV, we obtain the following results:

$$E_{\text{acc}} = \frac{V_{\text{acc}}}{d} = 10 \text{ MV/m}$$

$$E_{\text{pk}} = E_0 = \frac{\pi}{2} E_{\text{acc}} = 15.7 \text{ MV/m}$$

$$H_{\text{pk}} = 2430 \frac{\text{A/m}}{\text{MV/m}} E_{\text{acc}} = 24.3 \text{ kA/m} = 30.5 \text{ mT} \quad (20)$$

$$U = \frac{\pi \epsilon_0 E_0^2}{2} J_1^2(2.405) d R^2 = 0.54 \text{ J}$$

$$P_c = \frac{\omega U}{Q_0} = 0.4 \text{ W}$$

The performance of a superconducting cavity is evaluated by measuring the Q_0 as a function of the cavity field level.

This gives information on the average behavior of the RF surface.

5. THERMOMETRY BASED DIAGNOSTICS

To resolve the local distribution of RF losses from the various mechanisms described above, temperature mapping is used as a diagnostic technique. A chain of rotating carbon thermometers, or an array of fixed thermometers, samples the temperature of the outer wall of the cavity. Temperature mapping with carbon thermometers has played a key role in improving the understanding of mechanisms that lead to residual resistance, multipacting, thermal breakdown, and field emission. Carbon makes a sensitive thermometer at liquid helium temperatures because, as a semiconductor, its resistance increases exponentially with decreasing temperature. Above the superfluid temperature (2.17 K), temperature increments of the cavity wall of a few mK can be easily detected. A single rotating arm bearing 10 to 20 thermometers per cell is appropriate for locating stable field emitters or thermal defects in sizable structures, such as a multicell cavity. For temperature mapping in superfluid helium, thermometers need to be isolated from the superfluid bath so that movable elements do not provide good sensitivity. A large array of fixed thermometers is preferred. These are brought in intimate contact with the cavity wall by the use of spring-loaded contacts. Grease applied between the cavity wall and the thermometer element improves heat transfer and keeps the superfluid away. Due to the large number of thermometers and leads, the fixed method is suitable for investigations with single-cell cavities. An example of a fixed thermometry system is shown in Fig. 3, and a typical temperature map is shown in Fig. 4 [17].

Figure 3. (a) A single-cell niobium cavity surrounded by an array of ≈ 700 carbon thermometers that make close contact with the outer wall of the cavity. (b) There are 19 thermometers placed on each board that is contoured to closely follow the cavity profile. (c) A single thermometer consists of a 100 Ω carbon resistor embedded in an epoxy housing. It is held by a spring-loaded pin inserted into holes in the board. The surface of the thermometer is ground so that the carbon element is exposed and subsequently covered with a thin layer of varnish to provide electrical insulation. The leads are made of a low-thermal-conductivity alloy, such as manganin.

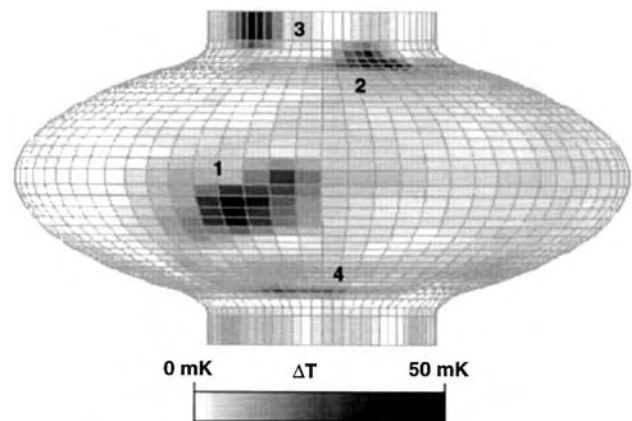
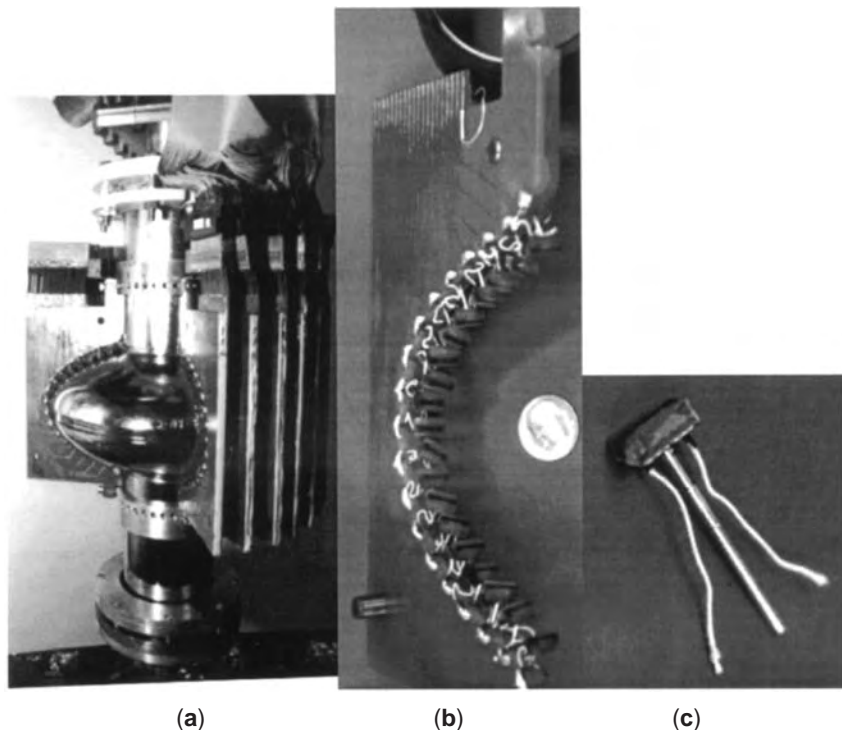


Figure 4. Temperature map at 40 mT of a single-cell 1.5 GHz cavity showing heating at a defect site near the cavity equator (labeled 1) and field emission sites (labeled 2, 3, and 4) near the cavity iris.

6. REFRIGERATOR REQUIREMENTS

Although the power dissipated in the superconducting cavity is very small, the losses will be dissipated in the liquid He bath. Together with the static heat leak to the cryostat, these losses comprise the cryogenic loss. Typically the ac power needed to operate the refrigerator is larger than the dissipated power in 2 K liquid He by a factor of 750. One part of this factor comes from the technical efficiency (η) of the refrigerator, typically $\eta = 0.2$ for a large system, and the other part comes from the Carnot efficiency η_c , which at 2 K is

$$\frac{1}{\eta_c} = \frac{300 - 2}{2} \quad (21)$$

At 10 MV/m, the required refrigerator ac power due to the RF loss would be 300 W for the case of a single-cell 1.5 GHz cavity. For a copper cavity of the same geometry, with a typical $R_s = 3 \text{ m}\Omega$, the RF power dissipation in the cavity would be 60 kW for an accelerating field $E_{\text{acc}} = 10 \text{ MV/m}$. Furthermore, the ac wall power will be a factor of 2 higher because of the typical klystron efficiency. Thus, the ac power cost of running a copper cavity in CW mode would be several hundred times higher than the cost for an Nb cavity.

7. SHUNT IMPEDANCE

An important quantity used to characterize the losses in a cavity at a given accelerating voltage is the shunt impedance (R_a) as typified by a parallel RLC circuit:

$$R_a = \frac{V_{\text{acc}}^2}{P_c} \quad (22)$$

in which case P_c = power dissipated and V_{acc} is the acceleration voltage. Hence the shunt impedance is in ohms.

Ideally the shunt impedance should be large for the accelerating mode so that the dissipated power is small. This is particularly important for copper cavities, where the wall power dissipation is a major issue and we wish to have as large an accelerating field as possible. For the TM_{010} mode pillbox cavity and R_s of 20 n Ω , we have

$$R_a = \frac{4\mu_0 d^2}{\pi^3 R_s \epsilon_0 J_1^2(2.405) R[R+d]} = 2.5 \times 10^{12} \Omega \quad (23)$$

Note that the ratio of R_a/Q is given by

$$\frac{R_a}{Q_0} = \frac{V_{\text{acc}}^2}{\omega U} \quad (24)$$

which is independent of the surface resistance. For the pillbox TM_{010} mode, we have

$$\frac{R_a}{Q_0} = 150 \Omega \frac{d}{R} = 196 \Omega \quad (25)$$

By applying computer codes to determine electromagnetic fields, the computed figures of merit for the Cornell/TJNAF five-cell cavity are given in Table 1. Note that due to the presence of the beam holes, the shunt impedance is reduced and the peak surface fields are enhanced, relative to the pillbox case. For a realistic cavity shape, R/Q_0 is lowered due to the presence of the beam holes, typically by a factor of 2.

Table 1. Figures of Merit for the Cornell/CEBAF Five-Cell Cavity

G	290 Ω
R/Q (per 5-cell cavity)	480 Ω
$E_{\text{pk}}/E_{\text{acc}}$	2.6
$H_{\text{pk}}/E_{\text{acc}}$	4.7 mT/(MV/m)

^aData taken from Ref. 4.

8. RF SURFACE RESISTANCE

Based on the very successful BCS theory [18], expressions for the superconducting surface impedance have been worked out by Mattis and Bardeen [19]. These expressions involve material parameters, such as the London penetration depth λ_L , the coherence distance ξ_0 , the Fermi velocity V_F , and the electron mean free path l . They are in a rather difficult form to obtain general formulas to work with. Computer programs have been written—for example, by Turneaure [20] and Halbritter [21]. Figure 5 gives the results from Halbritter's programs for niobium and lead and Nb_3Sn . Table 2 gives the material parameters used for the calculations. Calculations from the theory agree well with experimentally measured R_s for $T/T_c > 0.3$. At lower temperatures, the residual resistance term dominates.

A simplified form of the temperature dependence of Nb for $T_c/T > 2$ and for frequencies much smaller than $2\Delta/h \approx 10^{12} \text{ Hz}$ is

$$R_s = A(1/TJ)f^2 \exp(-\Delta(T)/k_B T) + R_0 \quad (26)$$

Here k_B is Boltzmann's constant. The second term, R_0 , is called the *residual resistance*. Typical R_0 values for Nb cavities fall in the range from 10^{-7} to $10^{-8} \Omega$. The record for the lowest surface resistance is $1-2 \times 10^{-9} \Omega$ [22]. For comparison, the surface resistance of copper at 1.5 GHz is 3 m Ω .

The operating temperature of a superconducting cavity is usually chosen so that the first term in Eq. (26) is reduced to an economically tolerable value. R_0 , referred to as the *residual resistance*, is influenced by several factors. Some of the sources are extraneous to the superconducting surface—for example, lossy joints between components of the structure. Other factors originate at the superconducting surface. A well-understood and controllable source of residual loss is trapped dc magnetic flux from insufficient shielding of the earth's magnetic field, or other dc magnetic fields in the vicinity of the cavity. To get the highest Q_0 , a superconducting cavity must be well shielded from the earth's field. Typically, at 1 GHz, R_0 is $10 \mu\Omega/\text{mT}$ [23]. Another important residual loss

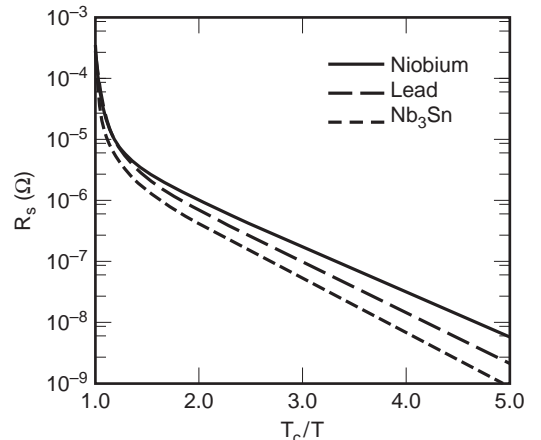


Figure 5. Theoretical surface resistance at 1.5 GHz of lead, niobium, and Nb_3Sn as calculated from Halbritter's program [20]. The values used for the material parameters are given in Table 2.

Table 2. Material Parameters Used for the Calculations of Fig. 5

Material-Parameter	Pb	Nb	Nb ₃ Sn
T_c [K]	7.19	9.20	18.00
Energy gap, Δ/kT_c	2.10	1.86	2.25
Penetration depth λ [Å]	280.00	360.00	600.00
Coherence length ξ [Å]	1110.00	640.00	60.00
Mean free path ℓ [Å]	10,000.00	500.00	10.00

mechanism arises when the hydrogen dissolved in bulk niobium precipitates as a lossy hydride at the RF surface [24]. This residual loss is a subtle effect that depends on the rate of cooldown and the amount of other interstitial impurities present in niobium. The effect can be severe enough to lower the Q_0 to 10^8 depending on the amount of hydrogen dissolved and the cooldown rate of the cavity. More than 2 ppm wt of hydrogen can be dangerous.

9. CAVITY FABRICATION AND SURFACE PREPARATION

Niobium cavities can be constructed from sheet niobium using the techniques of forming (e.g., deep drawing or spinning) followed by electron beam welding [25]. Another method is to deposit a thin niobium film onto a preformed copper cavity substrate [26]. The copper cavity is made in essentially the same way as the sheet niobium cavity, except for surface preparation before film deposition. If the cavity has more than one cell, the cells need to be tuned relative to each other, by adjusting the dimensions, so that the accelerating field is the same for each cell. Dimensional variations between cells are sufficient to alter the field profile substantially. Typical fabrication tolerances are in the range of a few tenths of a millimeter.

The purity of niobium used is important, both in terms of bulk impurity content and in terms of inclusions from manufacturing steps, such as rolling. Inclusions on the RF surface play the role of normal conducting sites for thermal breakdown. Dissolved impurities serve as scattering sites for the electrons not condensed into Cooper pairs. These impurities lower the thermal conductivity, impede the heat transfer to the helium, and limit the maximum tolerable surface magnetic field before the onset of thermal breakdown. The accompanying decrease in electrical conductivity, or the RRR value, serves as a convenient measure of the purity of the metal. The formal definition of RRR is

$$RRR = \left(\frac{\text{resistivity at 300 K}}{\text{residual resistivity at low temperature (normal state)}} \right) \quad (27)$$

Here low temperature means the temperature at which the dc resistivity in the normal state becomes residual. A convenient relationship between thermal conductivity and RRR for niobium is

$$k \approx 0.25 RRR \left(\frac{\text{W}}{\text{mK}} \right) \quad (28)$$

This relationship can be derived from the Wiedemann-Franz law [27] and from the ratio of the superconducting to

normal conducting state thermal conductivities [28]. To achieve the optimum RF performance, the surface of the cavity must be prepared to approach as close as possible the ideal. Microscopic contaminants can limit the performance, either by thermal breakdown or by field emission [29]. A clean RF surface is achieved by chemically etching away a surface layer, rinsing thoroughly with ultraclean water, and then taking precautions so that no contaminants come in contact with the clean RF surface. The resistivity of the water should be close to theoretically pure (18 MΩ-cm), and the water should be filtered to eliminate particles larger than 1 μm. After etching, water is recirculated for several hours through the cavity in series with the water purification system so as to continuously and thoroughly remove any chemical and particulate residue from the niobium surface. For a review of cavity fabrication and preparation procedures, see Ref. 28.

Many laboratories have found that the RF surface can be made even cleaner if chemistry is followed by high-pressure rinsing (HPR) of the cavity with ultrapure water [30]. At TJNAF, for example, water at a pressure of 70 bar to 80 bar is sprayed through stainless steel nozzles each having a 0.3 mm diameter orifice [31]. The potent jets of water are scanned across all parts of the RF surface to dislodge and sweep away microscopic contaminants that have adhered to the surface.

After rinsing, the cavity is transported into a dust-free clean room where the water is drained. The cavity surface thus only comes in contact with filtered air. The level of cleanliness required is comparable with that in the semiconductor industry where a clean room environment of Class 10–100 is routine. Class 10 refers to the number of particles of size 0.5 μm or larger in 1 ft³ of air. The surface of the cavity must be dried before the cavity is evacuated, placed inside a cryostat, and cooled down for RF tests. During final assembly, the laboratory workers in the vicinity need to wear special particulate-free clothing and follow strict protocols to reduce particulate generation.

During these various stages of cavity production and preparation, there are many opportunities for defects to enter the cavity. Therefore great care must be exercised during the manufacture of sheet metal, deep drawing of cups, electron beam welding, chemical etching, rinsing, drying, and insertion of coupling devices, as well as in the final attachment of the cavity to the vacuum system of the test stand or the accelerator. Two examples of defects that caused thermal breakdown are shown in Fig. 6 [32]. On a statistical basis, we expect that the number of defects increases with cavity surface area.

10. OVERCOMING FIELD EMISSION

The temperature mapping diagnostic technique for superconducting cavities shows that emission arises from particular spots, called “emitters,” located in high electric field regions. The electrons that emerge from the emitters travel in the RF fields of the cavity and impact the surface (Fig. 7). Some electrons may be captured in the axial fields and accelerated along with the beam. These produce unwanted “dark current,” which may spoil the beam quality

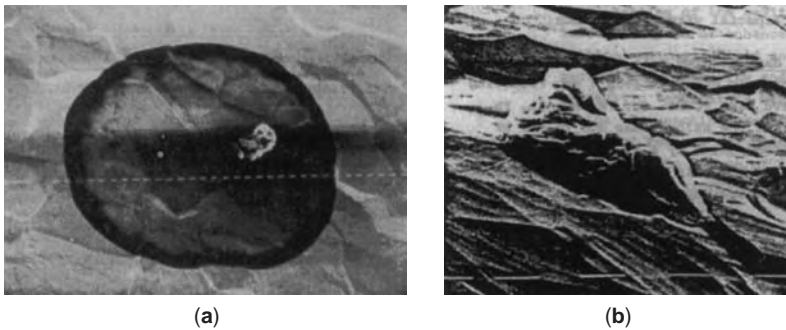


Figure 6. Scanning electron microscope (SEM) micrographs of defects that caused thermal breakdown. (a) A chemical or drying stain 440 μm in diameter. The small crystal on the right side contains K, Cl, and P. This defect quenched at $E_{\text{acc}} = 3.4 \text{ MV/m}$. (b) A 50 μm crystal containing S, Ca, Cl, and K. This defect quenched at $E_{\text{acc}} = 10.7 \text{ MV/m}$. These defects were located by temperature maps. (Courtesy of CERN.)

or impact the walls of adjacent cavities. The pattern of temperature rise as a function of position along a given meridian contains implicit information about the location and characteristics of the source. The power deposited by the impacting electrons depends on the trajectory as well as on the intrinsic properties of the emitter.

In their basic theory of field emission [33], Fowler and Nordheim (FN) showed that in the presence of an electric field, electrons tunnel out of the metal into the vacuum because of their quantum wave-like nature. However, a comparison with the observed currents reveals that, at a given field, emission is substantially higher than the FN predictions. Traditionally, the excess has been attributed to a “field enhancement factor,” which is believed to be related to the physical properties of the emitter discussed below. Both RF and dc studies reveal that emitters are micron- to submicron-size contaminant particles [14]. Figure 8 shows an example of a region of emitting particles found in a niobium cavity [34]. The properties of the emitter that lead to enhanced emission are (a) the microgeometry of the particle [35], (b) the nature of condensed gases or adsorbates on the surface of the particle [36], and (c) the interface between the particle and the underlying metal RF surface [37]. Accordingly, a high level of cleanliness is necessary for cavity surface preparation. Field emission-free performance has been achieved with HPR [31]. Recently, many nine-cell 1.3 GHz structures were prepared at DESY by using HPR [38]. A sample of their results is shown in Fig. 11.

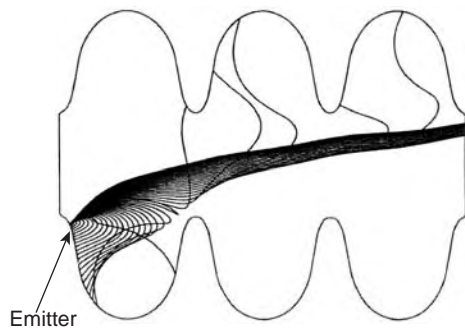
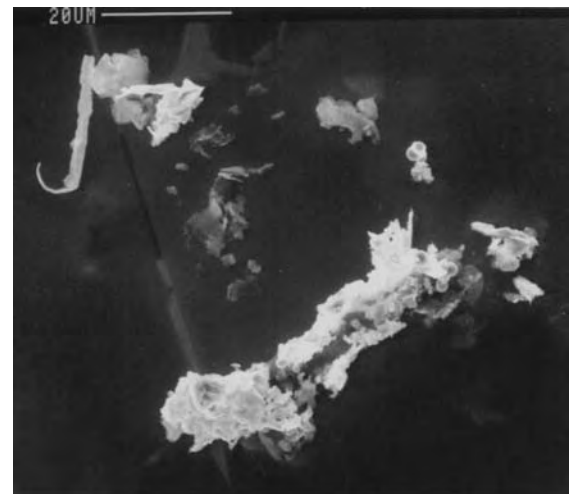
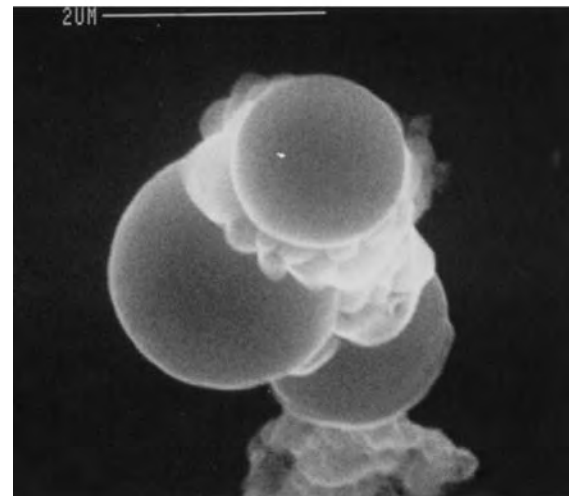


Figure 7. Calculated electron trajectories in a three-cell 1.5 GHz cavity operating at $E_{\text{pk}} = 50 \text{ MV/m}$. The emitter is located in the end cell, where the surface electric field is 44 MV/m. Note that a significant number of field-emitted electrons bend back and strike the wall near the emitter. Others are accelerated through the cavity structure and could produce unwanted “dark current” that may be accelerated in adjacent cavities.

When raising the RF electric field in a superconducting cavity for the first time, the field emission often decreases abruptly; the cavity is said to “process” or “condition.” There has been much progress in characterizing processed



(a)



(b)

Figure 8. (a) SEM micrograph of field emitting particles. Note the cluster of small spherical balls that indicate that a part of the site melted. EDX analysis shows that the particles are stainless steel. Note also the jagged microgeometry of the particles believed responsible for field enhancement. (b) The melted cluster is expanded.

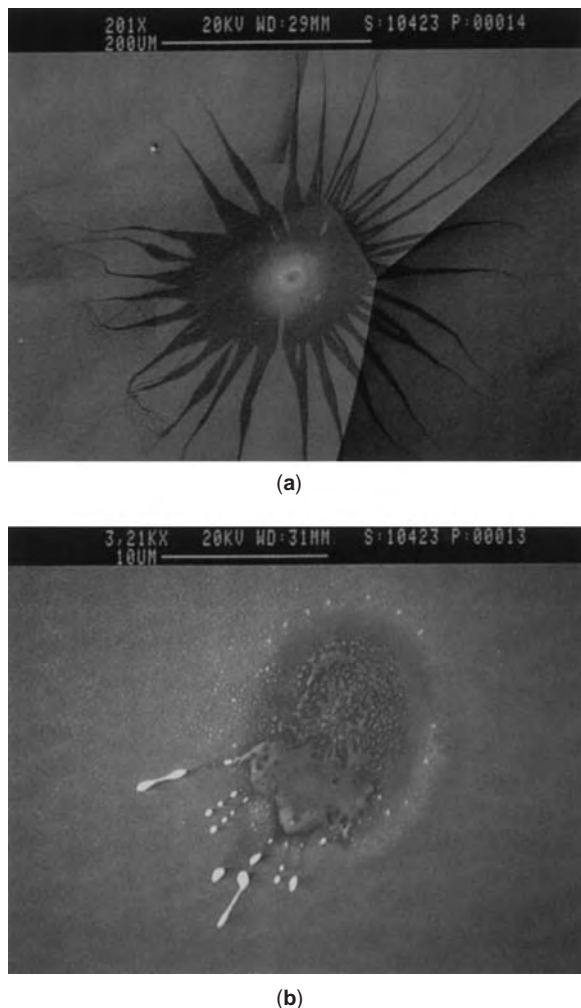


Figure 9. SEM pictures of the processed site found at the location predicted via temperature maps. (a) Low magnification; (b) high magnification of crater region within the starburst of (a). The molten splashes in the crater region were found to contain indium, presumably from the indium wire seals used to make vacuum joints.

emitters at a microscopic level using techniques such as SEM, EDX, Auger, and AFM. These studies reveal that emitter processing is an explosive event that accompanies what we usually refer to as a “spark” or a “discharge,” or

the “electrical breakdown” of the insulating vacuum [39]. Figure 9 shows a typical SEM micrograph of an exploded emitting site [40].

To reach the highest accelerating fields, the highest thermal conductivity is essential to avoid thermal breakdown, and a high level of cleanliness is essential to avoid field emission. High-pressure water rinsing is a very successful cleaning technique to avoid field emission. In multicell structures with large surface area, there is always a significant probability that a few emitters will eventually find their way on to the cavity surface. There is also the danger of dust falling into cavities during installation of power coupling devices as well as during installing of the structure into the accelerator.

A technique that eliminates field emitters in situ is high-pulsed power RF processing (HPP) [41]. The essential idea is to raise the surface electric field at the emitter as high as possible, even if for a very short time (\ll milliseconds). As the field rises, the emission current rises exponentially to the level at which melting, evaporation, gas evolution, plasma formation, and ultimately a microdischarge (RF spark) take place. The ensuing explosive event destroys the emitter. An important benefit of HPP is that the technique can be applied to recover cavities after their final installation. It can also be used to recover the performance of cavities, which may be accidentally contaminated, as, for example, in a vacuum mishap. To achieve emission-free performance at a desired E_{acc} , processing must be carried out at $\approx 2 \times E_{acc}$. Figure 10 shows the improvement in performance achieved by HPP [42]. [Recently, many nine-cell 1.3 GHz structures were prepared at DESY by using HPR techniques [38]. A sample of their results is shown in Fig. 11. Occasionally it is possible to achieve field emission-free performance, as shown by the best curve of Fig. 11.]

11. OVERCOMING THERMAL BREAKDOWN

The most effective cure for thermal breakdown caused by millimeter- to submillimeter-size defects is to (a) use better quality material that is free of such defects or (b) to raise the thermal conductivity of the niobium so that remaining defects will be able to tolerate more power before driving the neighboring superconductor into the normal state [43]. A simple analysis of the thermal breakdown shows that the maximum magnetic surface field is

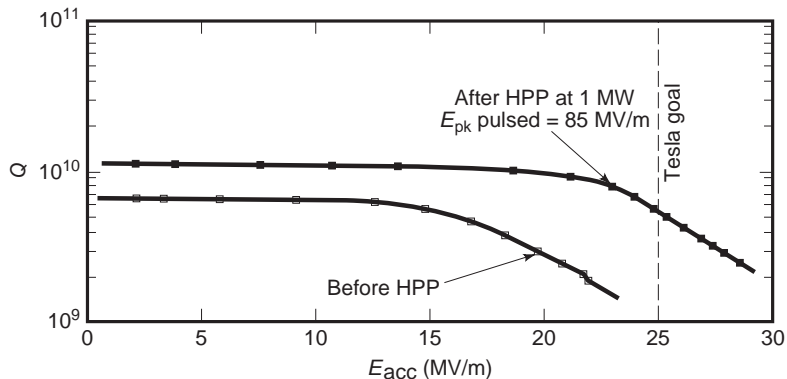


Figure 10. Performance of a five-cell 1.3 GHz niobium cavity improved by HPP. Before HPP, the maximum field was limited by heavy field emission to $E_{acc} = 22$ MV/m. After applying 1 MW of power and reaching $E_{pk} = 90$ MV/m in the pulsed mode, the field emission was processed away and $E_{acc} = 28$ MV/m was possible in the CW mode.

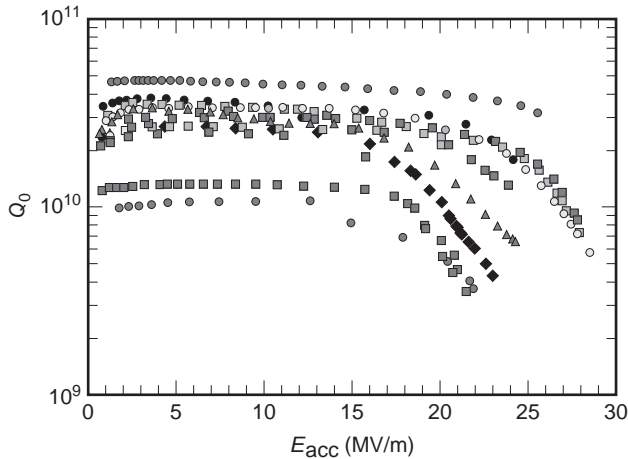


Figure 11. High performance of several nine-cell 1.3 GHz cavities achieved by high-pressure rinsing.

given by

$$H_{\max} = \sqrt{\frac{4k(T_c - T_b)}{aR_n}}, \quad \text{i.e., } H_{\max} \propto \sqrt{k} \propto \sqrt{RRR} \quad (29)$$

Here k is the thermal conductivity, T_c is the superconducting transition temperature, T_b is the bath temperature, a is the radius of the defect, and R_n is the surface resistance of the defect. This dependence on RRR is supported by detailed numerical simulations of thermal breakdown, as well as by experiments on cavities made from Nb of different RRR (Fig. 12).

Figure 13 shows the thermal conductivity of three samples of niobium that have different histories of heat treatment [44]. The common feature of all three curves is the

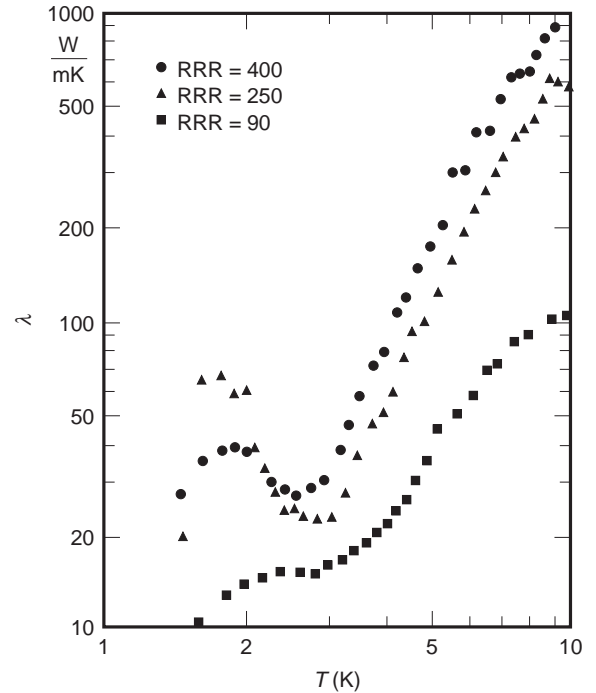


Figure 13. Thermal conductivity (λ) of niobium with $RRR = 90$ (as received), $RRR = 400$ after postpurification with yttrium, and $RRR = 250$ after annealing the postpurified sample for 6 hours at 1400°C. (Courtesy of Wuppertal.)

sharp drop below $T_c = 9.2$ K, as more and more electrons condense into Cooper pairs. At the higher temperatures ($4\text{K} < T < T_c$), a significant, although small, fraction of electrons is not frozen into Cooper pairs and can carry heat effectively, provided that the electron-impurity scattering is low. As the temperature in the neighborhood of the

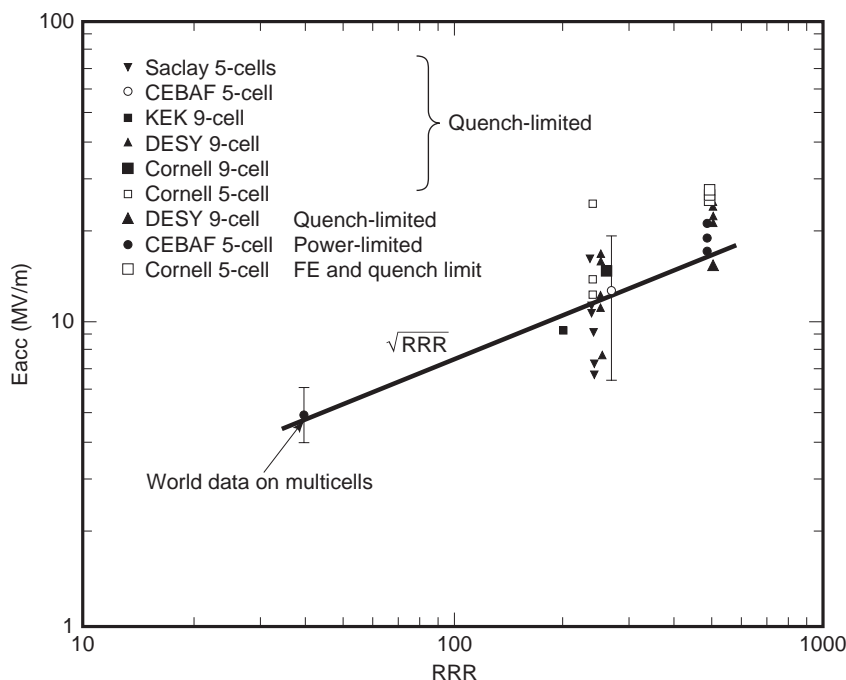


Figure 12. A summary of the results of multi-cell cavities [40]–[44] showing the importance of high RRR coupled with emission reduction techniques such as HPP and HPR. The line shows a \sqrt{RRR} dependence expected from the simple theory of thermal breakdown.

Table 3. Expected RRR for 1 ppm wt of Major Impurities^a

Element	RRR
H	2640
N	4230
C	4380
O	5580
Ta (1000 ppm wt)	1140

^aNote that the effect of Ta is given in terms of 1000 ppm wt.

defect is between the bath temperature and T_c , the high-temperature thermal conductivity is the most important and has the strongest effect on thermal breakdown. The higher the RRR , the higher the thermal conductivity in this temperature range.

Below 4 K, as electrons condense into Cooper pair, electron-phonon scattering also decreases. As a result, the thermal conductivity from phonons begins to increase, leading to the phonon peak near 2 K. With decreasing temperature, the number of phonons decreases $\propto T^c$. The value of the phonon conductivity maximum is limited by phonon scattering from lattice imperfections, of which the grain boundary density is the most important. If the crystal grains of niobium are very large (e.g., because of annealing at high temperature), one observes a large phonon peak, as shown in the thermal conductivity behavior of the sample with $RRR = 250$, which was annealed at 1400°C. As the phonon peak is at about 2 K, it does not help to thermally stabilize defects that heat up in the RF field.

The light, interstitially dissolved impurities have the strongest effect on the RRR . Among these, oxygen is dominant. The other interstitials are carbon, nitrogen, and hydrogen. Among the metallic impurities, tantalum is found in the highest concentration (typically 500 ppm by weight) because all naturally occurring ores contain some tantalum. This impurity level is not a problem because tantalum is a substitutional impurity and does not substantially affect the electronic properties. However, Ta can become a problem if clustering occurs. The Nb used to fabricate a cavity has been checked, for example, by an eddy current scanning technique [45] to look for large defects such as Ta clusters. Next in abundance are the higher temperature, refractory elements, such as tungsten, zirconium, hafnium, and titanium, usually found at the level of 10–50 ppm wt. The electron-scattering effectiveness of the various impurities are shown in Table 3 in terms of their effect on the RRR [46].

To obtain the net RRR , one must add the resistance contributions for each impurity element in parallel. The contributions of the phonons is always present, so that the highest theoretical RRR for niobium is 35,000 [47]. Experimentally, the highest RRR ever achieved in a niobium sample was 28,000 [48].

The most convenient method to obtain high-purity niobium for superconducting cavities is to remove the interstitials during the electron-beam melting stages of the ingot. Multiple melts and progressive improvements in the furnace chamber vacuum have led to a steady increase in the RRR of commercial niobium over the last decade from 30, typical of commonly available “reactor grade”

niobium, to 300 [49]. The RRR of commercially available Nb continues to improve. Recently, niobium sheet of $RRR = 500$ –700 became available from a Russian source [50].

If RF surface magnetic fields higher than 50 mT are desired on a consistently reproducible basis, the thermal conductivity of the niobium must be improved to $RRR > 300$. In one method called *postpurification*, the purity of the niobium is increased by solid-state gettering of oxygen using yttrium [51] or titanium [52] at high temperature. The foreign metal is vapor-deposited on the niobium surface. In the same step, the high temperature decreases the diffusion time of the oxygen in niobium. Over a few hours, oxygen is trapped in the deposited getter layer. If yttrium is used, the best temperature is 1200–1250°C because both the vapor pressure of yttrium and the diffusion rate of oxygen in niobium are sufficiently high. If titanium is used, temperatures of 1350–1400°C are required because of the lower vapor pressure of titanium. Typically during postpurification, the RRR improves by a factor of two in a few hours. An important disadvantage of the postpurification is that the yield strength of niobium falls substantially due to the high-temperature treatment. Also, titanium diffusion into the bulk along grain boundaries demands additional etching.

12. Nb/Cu CAVITIES

As we mentioned, thin Nb films on higher thermal conductivity copper is another way to avoid thermal breakdown. The technique of sputter coating niobium has been developed by CERN for 350 MHz structures and applied successfully to hundreds of structures [26]. In the most successful coating method to date, thin film deposition is carried out by cylindrical magnetron sputtering. Before the coating stage, the copper cavity is degreased, chemically polished ($\approx 20 \mu\text{m}$), rinsed with high-purity, dust-free water and alcohol, and dried under clean laminar airflow. After bakeout of the copper cavity to reach a good vacuum, a typical coating time is 4 hours. The coating thickness is a few microns at a substrate temperature of 180–200°C. The RRR of the deposited niobium serves as one of the monitors of film quality. The sputtering rate and substrate temperature are optimized to reach an RRR greater than 20. Note that the low RRR relative to bulk niobium is not a problem because the film is very thin. The rod-like grains of the niobium film are up to 1 μm long and 10–150 nm in diameter. When studied with transmission electron microscopy, the individual grains show a high density of defects, consisting of dislocations and point defect agglomerates [53]. The distance between two defects varies from 2 to 20 nm. The onset T_c of as-deposited films is 9.6 K, but the transition width is larger than for bulk niobium (typically a few tenths of a kelvin). The large transition width (5 K in some cases) is indicative of poor film quality.

Although Q_0 values $\approx 10^{10}$ are obtained at low fields, the RF losses of Nb/Cu cavities increase steadily with field. This effect is attributed to intergrain losses in the niobium films, which become more severe at higher frequency. Recently [54], there is evidence to show that

impurities buried in the films can also account for increased losses at high fields.

13. FUTURE DIRECTIONS, NEW MATERIALS

Based on the fundamental aspects, for a material to be useful in accelerators, the primary requirements are a high transition temperature and a high superheating critical magnetic field. Among the elemental superconductors, niobium has the highest T_c . Although lead, coated on to a copper cavity, has been very useful in early studies and heavy-ion accelerator applications, the higher T_c and H_c has made niobium the more attractive choice. Technical considerations, such as ease of fabrication and the ability to achieve uniformly good material properties over a large surface area, have also proven favorable for niobium. The realm of superconducting compounds has been much less explored because of technical complexities that govern compound formation. In looking at candidates, such as Nb_3Sn , NbN , and the new high-temperature superconductors (HTS), such as $YBa_2Cu_3O_7$, it is important to select a material for which the desired compound phase is stable over a broad composition range. With this criterion, formation of the compound may prove more tolerant to variations in experimental conditions, which in turn would make it possible to achieve the desired single phase over a large surface area. With a T_c of 18 K, Nb_3Sn is the most successful compound explored to date [55]. At low fields, residual resistance values comparable with niobium have been achieved. However, the maximum fields reached to date are far lower than those for sheet niobium cavities. The new HTS are even further from the performance level desired for application to accelerators. Figure 14 compares the measured RF surface resistance at low fields of several superconductors: HTS, Nb_3Sn , and Nb [56]. The surface resistance of Nb at 1.3 K, Nb_3Sn at 4.2 K, and copper at 77 K are included for comparison.

Early enthusiasm over the remarkable strides made in the transition temperature of HTS are now tempered with difficulties in achieving useful properties, such as a high critical current density. The coherence lengths of the cuprates are very short (17 Å within the copper-oxygen planes and 3 Å perpendicular to the planes, respectively). There is also a large anisotropy of the magnetic and electrical properties between the c axis and the ab planes, with superior behavior when the current flow is in the ab plane. To produce good quality HTS films, it is therefore necessary to orient the grains so that the c axis is normal to the RF surface everywhere. This restriction will be a significant challenge for realizing HTS in existing accelerating cavity shapes. It is also essential to have the right stoichiometry and oxygen content. Because of the short coherence length, transport properties are extremely sensitive to minute defects, such as grain boundaries and their associated imperfections. Decoupling of superconducting grains is believed to occur because the coherence lengths approach the scale of the grain boundary thickness, forming only weak links between individual grains. As a result, the intergrain critical current is two to three orders of magnitude lower than intragrain critical current. Even at

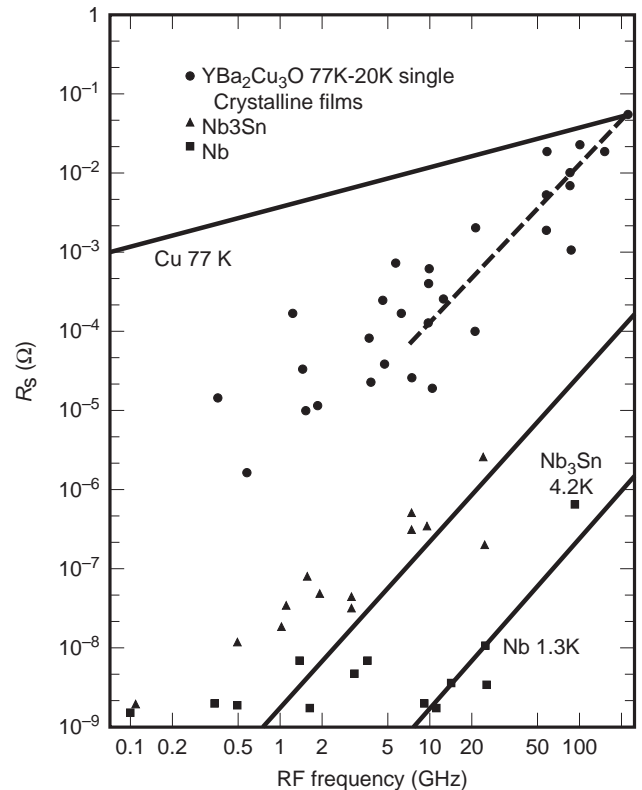


Figure 14. Measured surface resistance of HTS compared with the same for Nb (1.3 K) and Nb_3Sn (4.2 K). In the case of HTS, the resistance is quoted at 77 K if it is already residual; if the resistance is still decreasing with temperature, the residual is obtained at 20 K. The solid lines show the calculated surface resistance of copper at 77 K, Nb_3Sn at 4.2 K, and Nb at 1.3 K.

a clean grain boundary, the scale of the disorder that exists from breaking up of a unit cell can exceed the coherence length, especially in the direction of the c axis [57].

14. CONCLUSION

Even at the modest fraction of the ultimate potential, many attractive applications are now in place, and new ones are forthcoming. As our understanding of field limiting mechanisms continues to improve, new techniques emerge to further advance gradients, such as high-purity niobium to raise the thermal conductivity, high-pressure rinsing to provide cleaner, field emission-free surfaces, and high pulsed power processing to destroy residual emitters. The new techniques for bulk niobium cavities have demonstrated that gradients can be improved to between 20 and 30 MV/m in multicell structures. If such gradients can be reliably achieved, exciting new applications are on the horizon, such as the TeV electron-positron linear collider [58] or a multi-TeV muon collider [59].

BIBLIOGRAPHY

1. P. Wilson, in R. A. Carrigan, F. R. Huson, and M. Month, eds., *Physics of High Energy Particle Accelerators* (Fermilab

- Summer School, 1981), AIP Conf. Proc., no. 87, American Institute of Physics, 1982.
2. J. Preble, in B. Bonin, ed., *Proc. 7th Workshop RF Supercond.*, Gif-sur-Yvette, France, CEA/Saclay 96 080/1, 1995, p. 173.
 3. G. Geschonke, in B. Bonin, ed., *Proc. 7th Workshop RF Supercond.*, Gif-sur-Yvette, France, CEA/Saclay 96 080/1, 1995, p. 143.
 4. L. M. Bollinger, *Annu. Rev. Nucl. Particle Sci.*, **36**:475 (1987).
 5. R. Sundelin, *IEEE Trans. Nucl. Sci.*, **NS-32**:3570 (1985).
 6. S. Takeuchi, in K. W. Shepard, ed., *Proc. 3rd Workshop RF Supercond.*, Argonne National Laboratory, Argonne, IL, ANL-PHY-88-1, 1988, p. 429.
 7. H. Padamsee, K. Shepard, and R. Sundelin, *Annu. Rev. Nucl. Particle Sci.*, **43**:635 (1993).
 8. V. L. Ginsburg and L. D. Landau, *Zh. Eksperim. i. Theor. Fizike*, **20**:1064 (1950).
 9. U. Klein and D. Proch, in J. S. McCarthy and R. R. Whitney, eds., *Proc. Conf. Future Possibilities Electron Accelerators*, Charlottesville, VA:University of Virginia, 1979, P.N1-N17.
 10. P. Kneisel, R. Vincon, and J. Halbritter, *Nucl. Instrum. Meth.*, **188**:669 (1981).
 11. D. Moffat, in Y. Kojima, ed., *Proc. 4th Workshop RF Supercond.*, KEK, Tsukuba, Japan, Rep. 89-21, 1990, p. 445.
 12. J. Delayen and K. W. Shepard, *Appl. Phys. Lett.*, **57**(5):514 (1990).
 13. H. Padamsee, in Latham, ed., *High Voltage Vacuum Insulation*, New York: Academic Press, 1995, p. 431.
 14. J. Delayen, in Y. Kojima, ed., *Proceedings of the 4th Workshop on RF Superconductors*, Tsukuba, Japan: KEK, Rep. 89-21, 1990, p. 249.
 15. U. Laustroer, U. van Rienen, and T. Wieland, DESY M-87-03, 1988.
 16. R. Klatt, DESY M-86-07, 1987.
 17. J. Knobloch and H. Muller, *Rev. Sci. Instrum.*, **65**(11):3521 (1994).
 18. J. Bardeen, L. N. Cooper, and J. R. Schrieffer, *Phys. Rev.*, **108**:1175 (1957).
 19. D. C. Mattis and J. Bardeen, *Phys. Rev.*, **111**:412 (1958).
 20. J. P. Turneaure, Ph.D. thesis, Stanford University, 1967; see also J. M. Pierce, in L. Marton, ed., *Methods of Experimental Physics*, Vol. 11, 1974, p. 541.
 21. J. Halbritter, *Z. Physik*, **238**:466 (1970).
 22. See J. P. Turneaure, *Proc. Appl. Supercond. Conf.*, Annapolis, MD, 1972, p. 621.
 23. C. Vallet et al., in E. H. Henke et al., eds., *Proc. 1992 European Particle Accelerator Conf.*, Editions Frontieres, 1992, p. 1295.
 24. B. Bonin and R. Roeth, in D. Proch, ed., *Proc. 5th Workshop RF Supercond.*, Hamburg, Germany:DESY, DESY-M-92-01, 1991, p. 210.
 25. J. Kirchgessner, in K. W. Shepard, ed., *Proc. 3rd Workshop RF Supercond.*, Argonne, IL: Argonne National Laboratory, ANL-PHY-88-1, 1988, p. 533.
 26. C. Benvenuti, in D. Proch, ed., *Proc. 5th Workshop RF Supercond.*, Hamburg; Germany: DESY, DESY-M-92-01, 1991, p. 189.
 27. Aschroft and Mermin, *Solid State Physics*, W. B. Saunders, 1976, p. 20.
 28. L. P. Kadanoff and P. C. Martin, *Phys. Rev.* **124**:670 (1961).
 29. H. Padamsee, J. Knobloch, and T. Hays, *RF Superconductivity for Accelerators*, New York: Wiley, 1998.
 30. P. Bernard et al., in H. Henke et al., eds., *Proc. 3rd Eur. Particle Accelerator Conf.*, Editions Frontieres, 1992, p. 1269.
 31. P. Kneisel, B. Lewis, and L. Turlington, in R. M. Sundelin, ed., *Proc. 6th Workshop RF Superconductivity*, Newport News, VA: CEBAF, 1994, p. 628.
 32. H. Padamsee, J. Tuckmantel, and W. Weingarten, *IEEE Trans. Magn.*, **Mag-19**: 1308 (1983).
 33. R. H. Fowler and L. Nordheim, *Proc. R. Soc. London*, **A119**:173 (1928).
 34. J. Knobloch et al., in *Proc. 1995 Particle Accelerator Conf.*, Dallas, TX: 1995, p. 1623.
 35. M. Jiminez et al., *J. Phys. D:Appl. Phys.* **27**:1038 (1994).
 36. Q. S. Shu et al., in *IEEE Trans. Magn.*, **25**:1868 (1989).
 37. N. S. Xu, in R. V. Latham, ed., *High Voltage Vacuum Insulation*, New York: Academic Press, 1995, p.116.
 38. W. D. Moeller and M. Pekeler, in S. Myers et al., ed., *Proc. 5th European Particle Accelerator Conf.*, Barcelona, Spain, Bristol, UK: IOPP Publishing, 1996, p.2013.
 39. D. Moffat et al., *Particle Accel.*, **40**:85 (1992).
 40. J. Graber et al., *Nucl. Instrum. Meth. Phys. Res.*, **A 350**:582 (1994).
 41. J. Graber et al., *Nucl. Instrum. Meth. Phys. Res.*, **A 350**:572 (1994).
 42. C. Crawford et al., *Particle Accel.*, **49**:1 (1995).
 43. H. Padamsee, *Proc. 1st Workshop RF Supercond.*, Karlsruhe, Germany: KFK, KFK-3019, 1980, p. 145.
 44. G. Mueller, in K. W. Shepard, ed., *Proc. 3rd Workshop RF Supercond.*, Argonne, IL: Argonne National Laboratories, ANL-PHY-88-1, 1988, p. 331.
 45. W. Singer, in E. Palmieri, ed., *Proc. 8th Workshop on RF Supercond.*, Abano Terme, Italy, 1997, in press.
 46. K. K. Schulze, *J. Metals*, **33**:33 (1981).
 47. K. Schulze, Niobium, in H. Stuart, ed., *Proc. Int. Symp.*, San Francisco. The Metallurgical Society of AIME, 1981, p. 163.
 48. A. Gladun et al., *J. Low Temp. Phys.*, **27**:873 (1977).
 49. H. Padamsee, in R. M. Sundelin, ed., *Proc. 6th Workshop RF Supercond.*, Newport News, VA: CEBAF, 1994, p. 515.
 50. A. V. Elyutin, et al., in D. Proch, ed., *Proc. 5th Workshop RF Supercond.*, Hamburg, Germany: DESY, DESY-M-92-01, 1991, pp. 354, 426.
 51. H. Padamsee, in H. Lengeler, ed., *Proc. 2nd Workshop RF Supercond.*, Geneva, Switzerland: CERN, 1984, p. 339.
 52. P. Kneisel, *J. Less Common Metals*, **139**:179 (1988).
 53. C. Durand and W. Weingarten, *IEEE Trans Appl. Supercond.*, **5**:1107 (1995).
 54. S. Calatroni, in E. Palmieri, ed., *Proc. 8th Workshop RF Supercond.*, Abano Terme, Italy, 1997, in press.
 55. M. Peiniger, in K. W. Shepard, ed., *Proc. 3rd Workshop RF Supercond.*, Argonne, IL: Argonne National Laboratory, ANL-PHY- 88-1, 1988, p. 503.
 56. D. Busch et al., in R. M. Sundelin, ed., *Proc. 6th Workshop RF Supercond.*, Newport News, VA: CEBAF, 1994, p. 173.
 57. G. Mueller, in Y. Kojima, ed., *Proc. 4th Workshop RF Supercond.*, Tsukuba, Japan: KEK, Rep. 89-21,1990, p. 267.
 58. R. Brinkmann, in *Proceedings of the 1995 Particle Accelerator Conference*, Cat. No. 95CH35843, 1995, p. 674.
 59. $\mu^+ \mu^-$ Collider, *A Feasibility Study*, BNL-52503, 1996.

SUPERCONDUCTING ELECTROMAGNETS

JOHN E.C. WILLIAMS
Massachusetts Institute of
Technology
Cambridge, Massachusetts

The design and construction of superconducting magnets has been made possible by the development of technical superconductors. There are three principal materials: the alloy niobium–titanium (NbTi), the intermetallic compound niobium–tin (Nb₃Sn), and the collective high-temperature superconductors (HTSs) based on copper oxide layers in a perovskite structure. Nb₃Sn and NbTi were developed in the early 1960s. A small solenoid made of Nb₃Sn achieved a field of 10 T in 1963, and the alloy NbTi was also first examined as a wire for a superconducting magnet in that year. In the time that has elapsed since those first steps, superconducting magnets weighing up to many hundreds of tonnes have been built and operated.

Technical superconductors are a class having special properties that allow superconductor operation in high magnetic fields and with useful current densities. Superconductors are of two types; both can support the flow of electrical current without resistance only below a combination of maximum temperature, field, and current density, with critical parameters T_c , B_c , and J_c [1]. For type I superconductors, typical values of T_c and B_c are 9 K and 0.1 T, respectively. Flux is excluded from the bulk of a type I superconductor, and current flows only in a surface layer, about 10^{-4} mm thick. The current is carried by electron pairs of equal and opposite momentum. (This momentum includes terms arising from both velocity and linked flux.) Since flux is excluded from the interior of a type I superconductor, and current flows only on the surface, a useful overall current density can be obtained only in wires of a diameter unacceptably small for magnet construction. Consequently, a type I superconductor cannot be used to construct a useful magnet, even if the critical field were to be higher than 0.1 T. Examples of type I superconductors are lead, indium, mercury, and pure annealed niobium.

By contrast, type II superconductors allow flux to penetrate into the bulk of the lattice in the form of an array of flux quanta. A circulating supercurrent surrounds each flux quantum (2.07×10^{-15} V · s) [2]. If a net transport current flows along a type II superconducting wire, a density gradient of flux quanta exists across the wire. The flux density gradient is given by

$$\frac{dB}{dx} = -\mu_0 J_c \quad (1)$$

where J_c is a bulk critical current density and μ_0 is the permeability of free space.

However, a type II superconductor is not necessarily a technical superconductor. The interaction of the net transport current flow with the flux quanta creates a Lorentz force that causes a migration of the flux across the superconductor. Such a migration appears as a voltage gradient along the superconductor, which causes a dissipation; that is, the superconductor appears to be resistive. For these

reasons pure annealed type II superconductors are resistive with a transport current in the presence of a field. Because of the penetration of flux, the maximum temperatures and fields below which superconductivity arises in them are up to 18 K and 25 T, respectively. The latter is the upper critical field B_{c2} , at which the lattice is fully packed with flux quanta. The penetration of flux into the lattice begins at a lower critical field B_{c1} .

The technical superconductor is a type II superconductor in which this migration of flux quanta is inhibited. This is achieved by the introduction of lattice defects, in the form of crystal boundaries, impurities, vacancies, or dislocations [3]. At these defects flux quanta tend to become pinned against further movement, at least until the Lorentz force increases.

To the extent that mechanical models assist in the understanding of quantum effects, a typical pinning center may be imagined as a long hole through the lattice of the superconductor. If a flux quantum, or an integral number of flux quanta, were located in this hole, the associated circulating current would lie in the material around the hole. If the flux quantum were to move away from the hole, the current would have to become elongated so as to continue to flow in solid material. That would increase the interactive force between flux and current, so tending to force the flux back into the hole. The movement of flux quanta through an array of pinning centers is also influenced by thermal vibration. Since the temperature at which electron pairs can form is low, thermally induced lattice vibration is comparable in energy density with that of the pinning strength of the centers. Thus a flux quantum trapped at a pinning center may be dislodged by a large enough random thermal movement. That flux quantum would then migrate down the Lorentz force gradient to another pinning center. On the macroscopic scale this effect will reduce the flux density gradient and hence the Lorentz force. So, under conditions of constant transport current and external field, the random movement of flux quanta will die away until the current, field, or temperature changes. This process is known as *flux creep*. It is central to the manner in which technical superconductors can be used in magnets [4].

The continuous movement of flux across an annealed type II superconductor appears as a voltage gradient along it. Similarly, the process of flux creep through a field of pinning centers creates a voltage gradient, and through the interaction with the transport current, it gives rise to dissipation. The faster the flux creep, the greater is the local dissipation. Thus with flux creep is associated a local temperature rise. Since the specific heat of materials is small at low temperatures, the dissipation associated with flux creep can cause significant temperature rise. (At room temperature the energy of dissipation through flux creep would generate little temperature rise.) Thus the dissipative effect of flux creep can lead to a runaway flux movement. As the temperature rises, the critical current density decreases. According to Eq. (1), that in turn leads to an increased flux movement and thence to more dissipation. In the extreme case the temperature rises above the critical value, and superconductivity ceases. This process is known as a *flux jump* [5]. In a magnet

wound with superconducting wire, the sudden reversion to the normal state of a small length of the wire will result in the dissipation of the stored magnetic energy at high density in a volume that expands through thermal diffusion. If the stored energy is large enough and the thermal diffusion slow enough, the temperature rise at the point of initiation may exceed the melting point of the wire. The essence of the design of superconducting magnets is the suppression or control of this fundamental thermal instability.

1. TECHNICAL SUPERCONDUCTORS

The major properties of the three technical superconductors are typically as shown in Table 1. T_c is the highest temperature below which superconductivity can exist (electron pairs can form) in zero field and with zero current. B_{c2} is the upper critical field at 0 K at which the lattice is fully packed with flux quanta. $J_{c \text{ typ}}$ is a typical operating current density at useful values of field and temperature. (Below the lower critical field B_{c1} , the technical superconductor behaves as a type I superconductor; that field is typically 0.01 T.) The two leading HTS materials are based on yttrium or on bismuth. The critical parameters refer to typical bismuth-based HTS.

Figure 1 illustrates the typical variation of critical current density with field and temperature for the two low-temperature technical superconductors. Depending on the local values of any two of the parameters, the third has a local critical value. In a magnet conductor, B and J are usually fixed, so T is the critical parameter. The distance between the operating values B , J , and T and the critical surface is the margin. In fact, since current and field are locally fixed, only the temperature can vary. Thus the temperature margin determines the susceptibility of the conductor to disturbance. The higher the margin, the more stable it will be. Since NbTi must operate at the lowest temperatures, it is the least stable. The HTS, by contrast, can operate with such high-temperature margins that they are very stable. However, that also leads to a problem of protection that must be addressed carefully in the future design of large HTS magnets.

Despite its low-temperature margin NbTi is the most widely used technical superconductor. It is a ductile alloy, compatible in metallurgical processing with copper and cupronickel. However, Nb₃Sn must be used in magnets or sections of magnets generating fields above about 12 T. HTS materials are now also beginning to be used in small magnets. Almost all magnets are wound with wire or a large cross-sectional conductor. (In principle, a magnet might be formed from a block of superconductor into

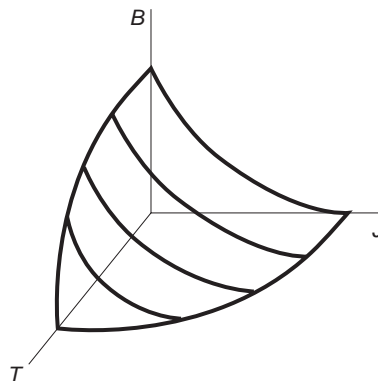


Figure 1. Variation of critical current density of a technical superconductor as a function of field and temperature.

which a field is frozen, e.g., by applying a field and then lowering the temperature. Instability makes that infeasible in low-temperature superconductors, but HTS may make such monolithic magnets possible.)

1.1. Composite Superconductors

The suppression of instability and the protection of the conductor in the event of an instability are the predominant problems in the design of superconducting magnets. If a magnet is to operate reliably, the tendency for a runaway magnetothermal effect to trigger a full transition from the superconductive to the normal conducting state must be suppressed. Two methods have been developed to achieve that: the elimination of flux jumping and the limiting of its consequences through cryogenic stabilization [5].

The essence of the stabilization of a technical superconductor is its subdivision into fine filaments. In the composite conductor, this is achieved by embedding a large number of fine filaments in a matrix. The matrix is usually high-conductivity copper, although aluminum has also been used. The copper serves several functions. It rapidly conducts heat away from the surface of the fine filaments; since its resistivity is much lower than that of the superconductor in its normal state, it allows current to flow with relatively low dissipation when the adjacent superconductor has become normal through an instability.

1.2. Niobium–Titanium

Figure 2 shows a typical cross section through a NbTi composite superconductor. It is manufactured by a co-drawing process [6]. Typical wire diameters lie in the range of 0.1–3 mm with critical currents at 4.2 K and 8 T of between 5 and 500 A. The insulation is typically Formvar (polyvinylformal). The diameter of the superconducting filament is determined largely by stability but also by hysteresis loss. The latter is the integrated effect of dissipation by flux creep during the rise of current and field in a magnet. Hysteresis loss is minimized by decreasing the diameter of the filaments. Typically the number of filaments in a wire may lie between 10 and 100,000.

Table 1. The Critical Properties of the Principal Technical Superconductors

	NbTi	Nb ₃ Sn	HTS
T_c (K)	10	18	90
B_{c2} (T)	13	27	> 100
$J_{c \text{ typ}}$ (A/mm ²)	1000	5000	1000

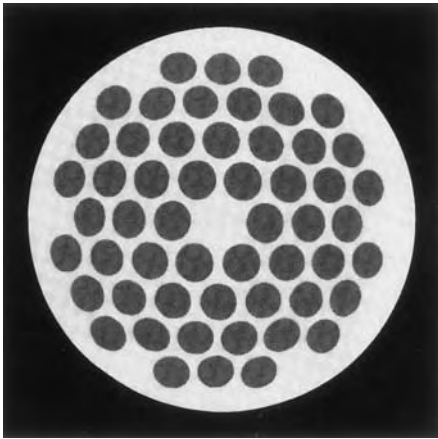


Figure 2. Cross section of a typical niobium–titanium composite superconductor. (Courtesy of Vacuumschmelze GMBH).

1.3. Niobium–Tin

Nb_3Sn is a brittle compound, and its use in a magnet winding is considerably more complex than NbTi. The predominant method of forming the compound is the diffusion of tin into niobium at a high temperature [6]. The tin is contained either internally within filamentary niobium tubes or in a tin-rich bronze surrounding solid niobium filaments. The niobium has typically up to 5% of tantalum for improved critical current density. The stock wire is unreacted for winding and is insulated with a glass braid, such as silica glass. After winding, the coil is reacted at about 700°C for up to 200 h. During this reaction the tin diffuses into the niobium and forms the compound Nb_3Sn . For adequate diffusion the diameter of the niobium filament must be no greater than 0.005 mm. After reaction the wire is brittle and cannot tolerate bending. Therefore the winding must be consolidated by vacuum impregnation with epoxy resin. Figure 3 shows a typical cross section through a bronze route superconducting wire before reaction.

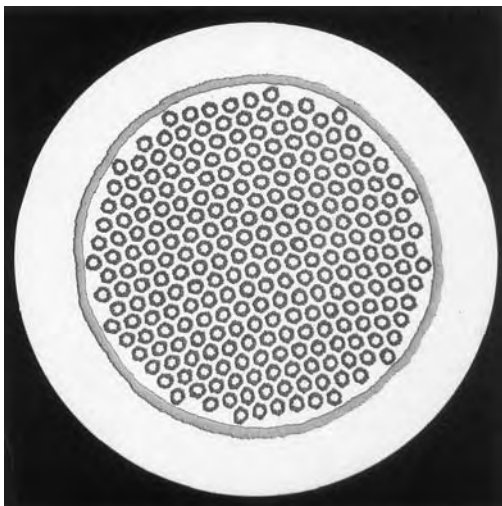


Figure 3. Cross section of a typical niobium–tin superconductor. (Courtesy of Vacuumschmelze GMBH).

As in the NbTi composite, copper is required as a stabilizer and for protection. In order to preserve the low resistivity of the copper, tin must not be allowed to diffuse into it during the reaction. (That would, in any case, dilute the tin available for diffusion into the niobium.) A barrier is inserted between the bronze and the copper matrix to prevent such unwanted diffusion. This barrier is in the form of a thin wrap of tantalum or niobium.

1.4. High-Current Conductors

To form high-current conductors in either NbTi or Nb_3Sn , cables of small wires are usually embedded in a copper or aluminum matrix. In this way NbTi composite conductors with critical currents of up to 100,000 A can be constructed. Similarly high-current Nb_3Sn composites can be constructed by carefully cabling prereacted wires and soldering the cable into a copper matrix. Handling such pre-reacted Nb_3Sn conductors requires exacting quality control procedures [7].

An important form of high-current conductor is the so-called *cable-in-conduit* (CiC). A cable of composite strands is inserted into a closed sheath, usually of stainless steel. Liquid helium (sometimes in the superfluid state at a temperature below 2.17 K) is circulated through the gaps between the strands of the cable [8]. This arrangement combines good support of the strands against the Lorentz forces with a low shielding loss and high current (see Section 6).

Another development in Nb_3Sn conductors is a pre-reacted cable of very fine wires. The strands are so thin that bending radii appropriate to normal winding techniques can be tolerated [9].

2. HIGH-TEMPERATURE SUPERCONDUCTORS

At present only a very few superconducting magnets use these materials. These superconductors all contain copper oxide layers in a perovskite crystal structure [10]. Two major types are being actively developed for application to magnets: yttrium-based and bismuth-based.

2.1. Yttrium HTS

This material has the chemical composition $\text{YBa}_2\text{Cu}_3\text{O}_7$, abbreviated YBCO. It has a critical temperature of 80 K. Its critical field at 4.2 K has not been directly measured but is believed to be about 100 T. Wire is manufactured in the form of a tape, samples of which have achieved a critical current density of 7000 A/mm^2 at 5 T and 77 K. Lengths of wire suitable for the construction of magnets have not yet been produced. Their manufacture suffers from the disadvantage of a highly anisotropic critical current density; that is, the critical current depends strongly on the orientation of the local field relative to the crystal orientation. Nevertheless, magnets operating at liquid nitrogen temperatures will probably use this material in the near future.

2.2. Bismuth HTS

This material is manufactured in two forms, with chemical compositions of $\text{Bi}_2\text{Sr}_2\text{CaCu}_2\text{O}_7$, abbreviated 2212, or $(\text{BiPb})_2\text{Sr}_2\text{Ca}_2\text{Cu}_3\text{O}_7$, abbreviated 2223. Both of these are being manufactured in lengths of up to 1000 m, and small magnets have been wound from them. The 2212 requires lower temperatures for high-field operation than the 2223. However, it is more easily fabricated and coils of the 2212 have been tested in external fields to show that useful currents can be carried at 30 T and 4.2 K. Either of these BSCCO materials may soon be the choice for inserts in very high field solenoids.

3. STABILITY

3.1. Adiabatic Stability

Regrettably, the flux jump is not the only source of heating sufficient to raise the temperature above the local critical value. Movement of a wire under the influence of the Lorentz forces in the body of a winding can generate local frictional heat sufficient to raise the temperature of a wire above the local critical value, especially where the temperature margin is small. A further precaution that must therefore be exercised in a magnet designed to avoid flux jumping is the consolidation of the winding so that no sudden frictional movement can occur to generate heat. This is achieved by impregnating the winding with epoxy resin, or another agent, in order to prevent sudden movement between wires, or between wires and stationary structure such as coil forms. This is the form of winding of the *adiabatic magnet*, which is so termed because no thermal sink exists within the winding.

Despite the use of fine filaments and winding techniques to avoid mechanical disturbances, the adiabatic winding is susceptible to sudden local transition from the superconductive to the normal state, if only through failure of the cryogenic environment. The resulting spreading normal zone is a process known as *quenching*. It may be precipitated by the relief of local stresses, which may merely be the repositioning of a wire, or cracking in a resin impregnant, and it may result in quenching at a current and field below design values. On recooling and recharging, the next premature occurrence of quenching can be at a higher current. This sequential improvement in the operating current is known as *training*. It is a common characteristic of large adiabatic magnets, especially of magnets with complex topology, such as particle-beam-handling magnets.

Despite the disadvantages associated with instability, quenching, and training, adiabatic magnets are the most common embodiment because they achieve the highest overall current densities in the windings. They enable the most compact magnets and the highest fields.

3.2. Cryostability

A second method of stabilization exploits the powerful cooling effect of liquid helium to maintain the temperature of a conductor below the local critical value even in the presence of flux jumping or other severe perturbations.

This is achieved by paralleling the superconductor with sufficient copper or aluminum cooled by liquid helium [11]. Now, even though all the transport current were to flow in the copper, the temperature would be kept below the critical value of the superconductor if sufficient surface were presented to the helium. This is the principle of cryostability. The governing expression for this mode of operation of a superconductor is

$$\frac{I^2 \rho}{A} = hP \quad (2)$$

where ρ is the resistivity of the copper, A is the copper cross section, h is the heat transfer rate, and P is the wetted perimeter of the copper. If the value for h is chosen to be about 1000 W/m^2 , this becomes a conservative stability criterion but leads to a low overall current density in a winding because the cross section of the stabilizing copper is large.

The earliest large magnets (mainly for bubble chambers built in the late 1960s) were designed in accordance with this principle. However, the boiling heat transfer curve for liquid helium has two branches, as shown in Fig. 4: nucleate boiling, line (a), with high heat transfer coefficient and film boiling; line (c) with lower coefficient (1000 W/m^2 is typically the lowest value of heat transfer rate in the film boiling regime). Intermediate between these is a region of unstable boiling, line (b). During an instability some or all of the current may transfer locally from the superconductor to the copper. The local generation of heat in such an extended region is line (f), rising from zero where no current flows in the copper to the full heating where all the current flows in the copper. The areas (d) and (e) then represent respectively regions where more heat is removed than generated and where more heat is generated than removed.

The sharing of current between the superconductor and copper results in the following expression for the local temperature

$$\frac{I(I - I_s)\rho}{A} = q(\theta - \theta_b)P \quad (3)$$

where I is the total current, I_s is the current still in the superconductor, ρ is the resistivity of the copper, and q is the heat transfer coefficient at the temperature difference $\theta - \theta_b$ between the copper and the helium bath. A good approximation for the current in the superconductor at a temperature θ is

$$I_s = \frac{I_c(\theta_c - \theta)}{(\theta_c - \theta_b)} \quad (4)$$

where I_c is the critical current at θ_b , the bath temperature. Equations (2)–(4) are represented together with the boiling heat transfer in Fig. 4. If the cooling exceeds the heating, area (d) greater than area (e), then recovery of superconductivity will occur. The normal region will collapse from the cold ends. This type of stability, called *cold end recovery*, allows higher values of h to be assumed in Eq. (2); 3000 W/m^2 is commonly accepted. This in turn allows a smaller cross section of copper and a more compact winding [12].

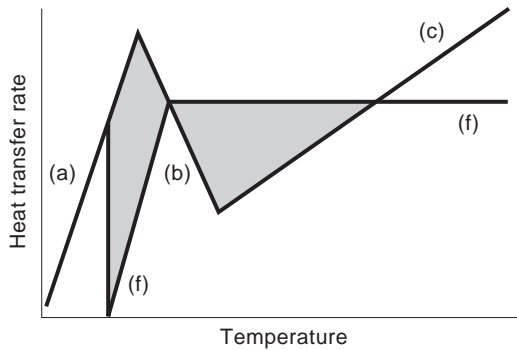


Figure 4. Boiling heat transfer curve for liquid helium and the heat generation curve for a composite superconductor.

4. PROTECTION

The other crucial issue in the design of superconducting magnets is protection. In both the adiabatic and cryostable types, the consequences of quenching must be anticipated. The methods by which this is achieved are quite different in the two types.

4.1. Adiabatic Protection

In this winding the conductors are in a compact array without an internal heatsink but with close thermal coupling between conductors. Therefore, when a conductor becomes normal through a perturbation, not only does the normal zone travel along the wire but the local heating rapidly causes adjacent conductors to heat up and become normal. Quenching then expands as a three-dimensional zone of increasing volume and surface area. The volume of normal conductor at any instant is approximated by

$$V_n \propto v_1 v_2 v_3 t^3 \quad (5)$$

where $v_{1,2,3}$ are effective velocities of quench propagation along the wire and transverse to it and t is the elapsed time. Thus the magnetic energy stored in the field is dissipated in a rapidly expanding volume of conductor. The velocities of propagation depend, among other things, on the local temperature margin; the greater the margin, the slower are the velocities. Although not as high as the velocity along the wire, the dominant velocities are those between turns and between layers. Rapid propagation of quenching between turns is desired in order to spread the temperature rise over a large volume. For that reason HTS winding may be more difficult to protect than those with the smaller temperature margins of Nb_3Sn or NbTi .

Two criteria are applied to this process to gauge the vulnerability of the magnet winding to quenching: (1) the final temperature of the wire at the point of initiation of quenching and (2) the voltage appearing between layers or turns of the winding. The latter criterion involves complex computation of the spatial distribution of normal and superconducting regions during the quench. However, the peak temperature generally dominates the criteria. This must clearly neither exceed the allowable temperature for the insulation or impregnant nor produce unacceptable

local stresses due to differential thermal expansion. A rule of thumb for acceptable peak temperature is 100 K. To achieve such limit (and simultaneously limit the voltage), sufficient copper must parallel the superconducting filaments so that the integrated heating in the copper does not exceed the acceptable peak value. Because of the rather complex time dependency of the current in a quenching adiabatic magnet, this criterion is best illustrated by reference to the protection of a cryostable magnet.

4.2. Cryostable Protection

In this type of magnet no propagation of a quench zone occurs between adjacent conductors. Furthermore the one-dimensional propagation of quench along a conductor is slow. If, for example, the level of liquid helium is low so that a length of conductor is exposed to helium vapor and has quenched, no propagation will occur, and the normal zone will be stationary. In such a case protection of the conductor against excessive temperature rise must be by external discharge of the stored magnetic energy. Interturn voltage is hardly ever a dominant effect in the protection of a cryostable magnet. The limiting criterion is therefore the temperature rise of the conductor at the point of quench initiation. Just as for the adiabatic magnet, a generally accepted criterion is a rise of no more than 100 K. The prediction of the temperature rise is now rather simple. If the magnet is discharged exponentially, the governing equation is

$$J_{\text{Cu}}^2 \rho(\theta) dt = c(\theta) d\theta \quad (6)$$

The left-hand side of Eq. (6) represents the heat being generated in the resistance of the copper, and the right-hand side represents the same heat being absorbed by its enthalpy. The quantities $\rho(\theta)$ and $c(\theta)$ are the temperature-dependent resistivity and volumetric specific heat of the copper.

Equation (6) may be rewritten as

$$\int_0^\infty J_{\text{Cu}}^2 dt = \int_{4.2}^{\theta_{\text{max}}} \left\{ \frac{c(\theta)}{\rho(\theta)} \right\} d\theta \quad (7)$$

In this expression the right-hand side is a function of the copper, or some other conducting material, between a low temperature, generally assumed to be that of liquid helium boiling at atmospheric pressure, 4.2 K, and the allowable upper temperature, generally 100 K [13]. (It is sometimes called the “ G function” but not in the original reference.) If the discharge of the magnet is exponential, Eq. (7) becomes

$$\frac{1}{2} J_{0\text{Cu}}^2 \tau = G(\theta_{\text{max}} - 4.2) \quad (8)$$

where $J_{0\text{Cu}}$ is the initial maximum current density in the copper. For copper at 100 K, the value of the G function is typically $6 \cdot 10^{16} \text{ A}^2 \text{ m}^{-4} \text{ s}^{-1}$. In order to achieve the required time constant of discharge, the voltage across the magnet must be as large as the inductance demands. As an example, a large magnet might have a stored energy of

100 MJ, an operating current of 10,000 A, and a copper cross section of 500 mm². The inductance would be 2 henries and $J_{0\text{Cu}}$ would be 2×10^7 A/m². The time constant of discharge would have to be 17.32 s, and the maximum initial discharge voltage 1.154 kV.

4.3. Winding Topology

The design of a winding array is dictated by the desired field properties. The basic expression governing the field produced by a winding is the Biot–Savart law, expressed as

$$dB = \frac{I \cdot dl \sin(\theta)}{r^2} \quad (9)$$

where $I \cdot dl$ is a current element, and θ is the angle between that element and the radius vector r to the field point. The direction of the field vector is perpendicular to both the current element and the radius vector. This expression is integrated in closed form for the fields of solenoids and of long linear windings. The forward computation of field produced by a given current array is straightforward. It can be performed for any configuration of currents, although the closed-form calculation is easy only for circular or straight arrays. The reverse computation, of a current array to produce a given field topology, is possible only for a few simple configurations, specifically for the axially symmetric field of a current ring and the circular field of an infinite straight current. The off-axis fields of a circular current array involve elliptic integrals. Numerical methods for the solution of the off-axis field of a current arc are routinely available as commercial codes. Most field geometries are produced by combinations of straight currents and current arcs. Generally the design problem proceeds by the iterative recomputation of the fields generated by incrementally modified straight or arc current arrays.

5. OPERATION IN TIME-VARYING FIELDS

Although most superconducting magnets constructed to date have been designed for steady-state operation, a few have been constructed for use either under AC conditions or with a rapidly changing field [14]. The design of a conductor for such operation involves the reduction of dissipative mechanisms in the superconductor. One source of dissipation under conditions of changing field has been described, that is, flux creep. That loss is generally called *hysteresis loss* and is approximated per unit volume by the expression

$$Q \approx \frac{1}{4} \Delta B d_w J_c \quad (10)$$

where ΔB is the field change, d_w is the wire diameter, and J_c is the critical current density. It is seen that the dissipation is smallest for thin wires.

Other sources of dissipation are found in composite superconductors. The most important of those is what is called *shielding loss*. It arises as follows. To reduce hysteresis loss and to improve the stability of a supercon-

ductor against flux jumping, the superconductor is finely divided into filaments in a (typically) copper matrix. However, it may be seen that the collection of filaments will still tend to exclude flux unless the filaments are transposed. Full transposition of any but a single layer of filaments is impossible within the matrix. However, a compromise is the twisting of the conductor. A short twist pitch or high resistivity of the matrix will allow flux to penetrate through the layers of filaments [15]. The time constant of penetration is given roughly by

$$\tau = \left(\frac{\mu_0}{2\rho} \right) \left(\frac{L}{2\pi} \right)^2 \quad (11)$$

where ρ is the resistivity of the matrix and L is the twist pitch. External field change will generate dissipation roughly given by

$$Q = \left(\frac{B^2}{2\mu_0} \right) \left(\frac{\tau}{\tau + t} \right) \quad (12)$$

where t is the time constant of the field change B . If the change is very rapid compared with the time constant of penetration of the conductor, the dissipation approaches the energy density of the magnetic field. Some magnets have been made with superconductors that have a matrix of cupronickel. The resistivity of cupronickel is high, which leads to a short time constant for flux penetration. However, the conductor is not well stabilized, and in the event of a quench it is not well protected against local hot spot. The CiC conductor, described above, also minimizes the shielding losses.

6. FORCES AND STRESSES

The force on a conductor in a field is given by the expression

$$F = BI \quad (13)$$

where I is the current in amperes, B is the component of the field in tesla perpendicular to the current vector, and F is the force per unit length in newtons which is directed perpendicular to the current and field vectors. The calculation of stresses in the conductors of a winding can be performed in closed form for only a few simple cases. For an isolated circular loop, the hoop stress averaged over a section of wire (whose cross section may include superconducting filaments, copper, depleted bronze, etc.) is given by

$$\sigma = BJr \quad (14)$$

where B is the average field at the wire perpendicular to the plane of the loop, J is the current density averaged over the wire section, and r is the mean radius of the loop. If J is in A/m², and r is in meters, then σ is in pascals. In a multilayered solenoidal winding the stresses in the wire are influenced by the transmission of radial forces between layers and by axial forces generated by radial components of field at the ends of the solenoid. The analysis of these stresses usually is performed by standard programs.

However, Eqs. (13) and (14) provide a useful rough guide to the stresses that will be encountered in a solenoidal winding.

The forces in long straight windings, such as extended dipoles, may be similarly estimated by the summation of the forces found from Eq. (13). The stresses in solenoidal windings are often supported by the conductor alone. Since the stresses are predominantly tangential, they produce tension in the components of the wires. In NbTi composites the stresses tend to be divided roughly equally between the NbTi superconductor and the copper unless the latter is annealed. In Nb₃Sn conductors most of the tensile load appears in the Nb₃Sn superconductor itself because the Young’s modulus is high, 172 GPa. The other components of a Nb₃Sn composite tend to be annealed by the heat treatment.

6.1. Examples of Superconducting Magnets

Common applications of superconducting magnets include the following: magnetic resonance imaging (MRI), laboratory magnets (for NMR analysis, susceptibility measurement), particle-beam handling, subatomic particle analysis, power conditioning, energy storage, open gradient magnetic separation, and magnetohydrodynamic (MHD) power generation. All superconducting magnets are wound. The most common winding topologies are solenoids and extended linear windings. The latter are in general of the form of armature windings, having straight sections with end turns of complex shape. Solenoids are used in magnets for MRI, most laboratory magnets, particle analysis, and energy storage. Extended linear windings are used in particle-beam-handling magnets, in rotating machines (rotor windings), for particle focusing (quadrupoles, hexapoles), and in MHD power generation. Occasionally a superconducting winding has an associated ferromagnetic flux path. (In such so-called superferric magnets, the iron is usually included in the magnet’s cryogenic environment, to avoid the transmission of high forces between low temperature and room temperature.)

Although most superconducting magnets are solenoids or extended dipoles and multipoles, a few magnets of more complex shape have been manufactured. These include

Table 2. Major Characteristics of a 750-MHz NMR Solenoid

Type	Solenoid
Materials	NbTi and Nb ₃ Sn
Energy	15 MJ
Center field	17.6 T
Bore at 4.2 K	74 mm
Typical weight	250 kg

very large “ying–yang” coils for the mirror fusion test facility (MFTF) [16], saddle coils for experiments on magnetohydrodynamic (MHD) power generation [17] and toroidally shaped coils for several Tokamak fusion experiments [18]. (Toroidal field magnets for fusion devices are D-shaped coils that are arrayed around a circular plasma path; in the absence of orthogonal—poloidal—fields, the conductors of these coils experience pure tension as in a solenoid.)

All are large magnets, storing energy in the range of 100 MJ. The stored magnetic energy is a rough classification of the size and cost of a magnet, and not necessarily of the difficulty of design and construction. Very high-field, compact magnets present more difficulty because of small operating margins, high stresses, and high-energy densities during quenching.

One of the largest superconducting magnets under construction is the model central solenoid for the International Thermonuclear Experimental Reactor (ITER). It stores 650 MJ and weighs 100 tonnes [19]. The most precisely engineered have been the high-field NMR magnets. They now have reached fields of 18.8 T with homogeneity of 10^{−9} in a 10 mm spherical volume.

NMR and MRI magnets operate in persistent mode. After energizing, a superconducting switch is closed across the winding so that the current continues to flow in an essentially resistanceless circuit. These are the most commonly produced commercial magnets [20].

Superconducting particle-beam-handling magnets have made possible the very high-energy accelerators in operation at BNL, CERN, DESY, and the Fermi Laboratory. Superconducting dipole magnets are typically 10 m

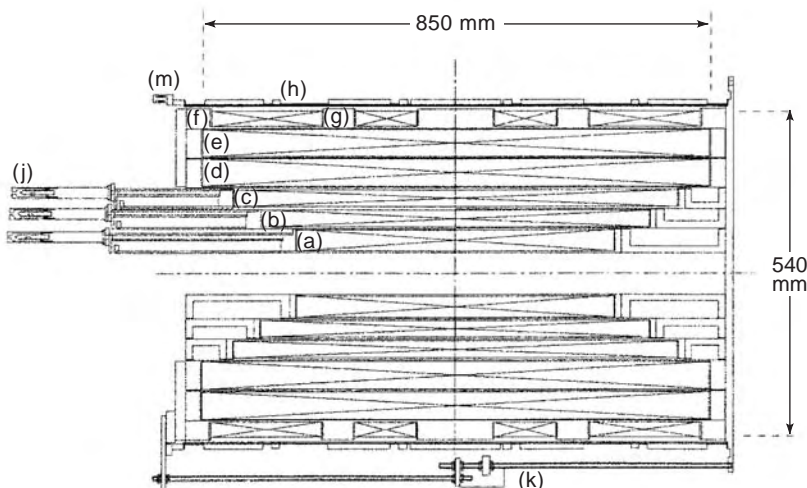


Figure 5. The winding profile of a typical commercial NMR magnet. (Courtesy of Magnex Scientific PLC.)

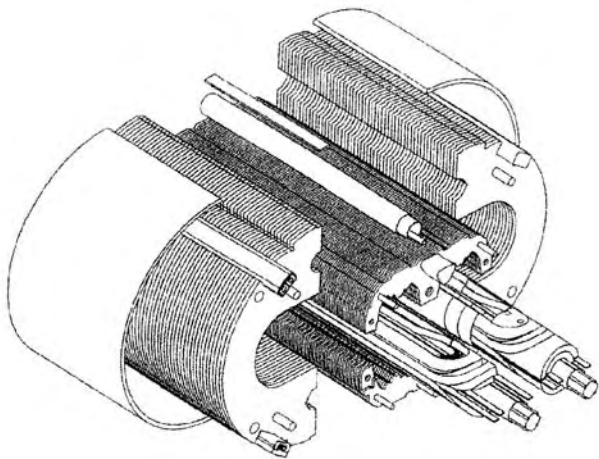


Figure 6. An illustrative view of the LHC dipole construction, showing the windings and the structural yokes. (Courtesy of CERN.)

long or greater, generating transverse fields of up to 8 T to provide the deflection required to bend the particle beam to a circular orbit. The requirement for uniformity of field is about 10^{-4} over 25 mm width. Superconducting quadrupole magnets are used for focusing of the particle beam and typically provide field gradients of up to 25 T/m.

6.2. Specific Examples

6.2.1. NMR Magnet for 750 MHz Proton Frequency [21]. Superconducting magnets for NMR and MRI are described separately within this encyclopedia. However, as they typify solenoidal magnets, the 750 MHz magnet is described here in outline. Figure 5 gives the profile of the windings of

a commercial magnet along with some of the structural details. The global characteristics are listed in Table 2.

In the figure the windings are labeled (a) through (g). Windings (a), (b), and (c) are of Nb_3Sn . The wire size is largest in section (a), where the field is highest and the critical current density lowest. In fact, section (a) consists of three grades of wire in order to maximize the local winding current density. Sections (d) and (e) are the main NbTi winding, again graded to maximize overall current density. Sections (f) and (g) compensate the axial gradients introduced by the full-length sections. All magnets used for NMR are operated in persistent mode. The windings are connected in series through superconducting joints. After energizing, the windings are closed through a superconducting switch (k). The joints (j) between the Nb_3Sn sections provide the best performance (highest critical current) in low field. Therefore they are mounted away from the windings on posts that rigidly support the brittle conductor. Surrounding the windings is an array of shim coils (h) that provides for fine adjustments. Each shim set has its own switch (m).

6.2.2. Particle Accelerators. The Fermilab energy doubler/saver is typical of the use of superconducting beam-bending magnets used in particle accelerators [22,23]. The field generated by the magnet is oriented vertically and extends over a length of 6 m. High-energy protons are slightly deflected by the field-length product of the magnet. The transverse force on the particle beam is as predicted by the Lorentz equation [13]. A large number of these dipoles (774), quadrupoles (216), and sextupoles are arranged to produce a total deflection of 360° . In the Fermilab energy doubler each dipole magnet produces a mere 0.47° deflection at maximum beam energy.

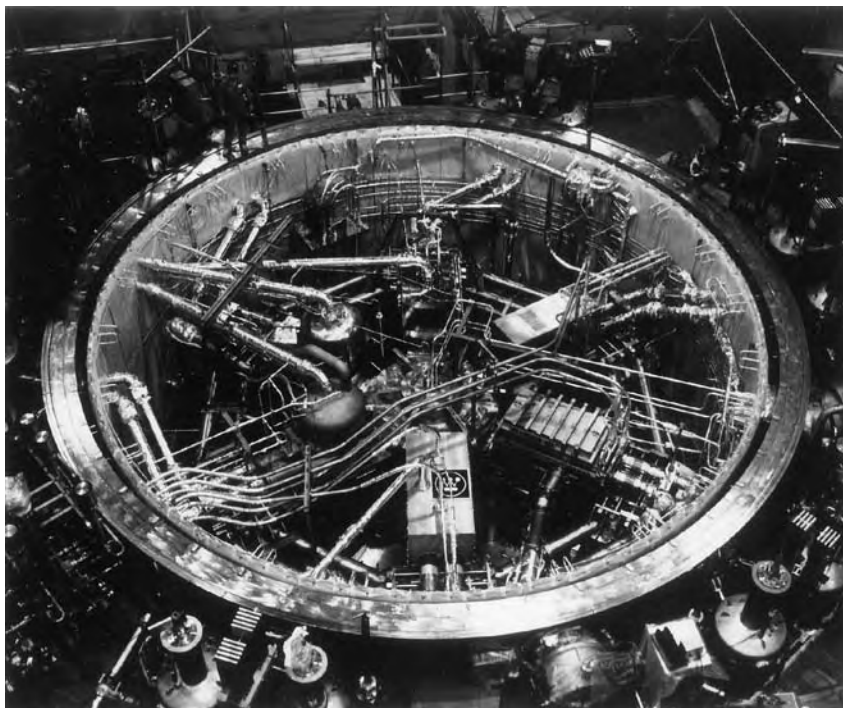


Figure 7. The six dee coils of the Large Coil Task installed in the test cryostat. (Courtesy of the Oak Ridge National Laboratory.)

Table 3. Major Characteristics of the Coils in the Large Coil Task

		<i>Global</i>			
		Design field	8 T		
		Total stored energy	600 MJ		
		Operating temperature	4.5 K		
		Inside height (each coil)	3.5 m		
		Inside span (each coil)	2.5 m		
		Inside radius	1.25 m		
		<i>Individual</i>			
Origin	Conductor Type	Inductance (H)	Peak Field (T)	Current (kA)	Energy (MJ)
EU	NbTi FF	1.57	9.01	11.40	200
WH	Nb ₃ Sn FF	0.75	8.23	17.76	202
GE/ORNL	NbTi PB	1.81	8.89	10.50	193
GD	NbTi PB	1.81	7.72	10.20	136
JAERI	NbTi PB	2.00	8.81	10.22	198
CH	NbTi FF	1.00	7.86	13.00	123

A more recent project involving superconducting beam-handling magnets is the Large Hadron Collider (LHC) at CERN. This also uses a sequence of long dipoles, quadrupoles, and sextupoles in two adjacent rings in which protons, or other heavy particles, will circulate in opposite directions to collide at energies up to 14 TeV. The cross section of the winding and associated structure is shown in Fig. 6. The conductors are located so as to approximate a cosine distribution of current density. That arrangement generates a field uniform throughout the center region of each beam. The outward forces on the conductors are constrained by a stainless-steel collar. This cold assembly is supported within an iron yoke that provides a return path for the flux. The yoke is assembled from transformer iron laminations, welded in a set of long steel girders.

6.2.3. Large Coil Task [24]. Six coils were built, one each by the following groups: EURATOM (EU), The Swiss Institute for Nuclear Science (CH), The Japanese Atomic Energy Research Institute (JAERI), Westinghouse Electric (WH), General Dynamics (GD), and General Electric/Oak Ridge National Laboratory (GE/ORNL). Each coil was a constant tension dee coil [18], but each used a different form of conductor. The Westinghouse coil alone used Nb₃Sn, in a CiC configuration; all the others used NbTi in a cryostable (helium-cooled) configuration. The cooling method was either forced-flow (FF) or pool-boiling (PB). The purpose of the program was to demonstrate stability of the coils under conditions of combined toroidal and pulsed poloidal fields. This international program has resulted in the construction of a model toroidal coil array as shown in Fig. 7. The main specifications were as listed in Table 3.

BIBLIOGRAPHY

1. A. C. Rose-Innes, *Introduction to Superconductivity*, 2nd ed., Elsevier Science, Amsterdam, The Netherlands, 1994.
2. H. Trauble and U. Essmann, Flux-line arrangement in superconductors as revealed by direct observation, *J. Appl. Phys.* **39**:4052–4057 (1968).
3. E. J. Kramer, Scaling laws for flux pinning in hard superconductors, *J. Appl. Phys.* **44**:1360–1370 (1973).
4. P. A. Anderson and Y. B. Kim, Hard superconductivity: Theory of the motion of Abrikosov flux lines, *Rev. Mod. Phys.* **36**:39–45 (1964).
5. M. N. Wilson, Superconducting magnets, *Monographs on Cryogenics*, Clarendon Press, Oxford, 1983, p. 131.
6. E. Gregory, Conventional wire and cable technology, *Proc. IEEE* **77**:1110–1123 (1989).
7. M. J. Leupold, A 42 cm bore superconducting coil using pre-reacted Nb₃Sn, *IEEE Trans. Magn.* **24**:1413–1416 (1988).
8. M. O. Hoenig, Internally cooled cabled superconductors, *Cryogenics* **22**(Part 1):373–389; (Part 2):427–434 (1980).
9. S. Pourrahimi and K. Demoranville, Development of flexible Nb₃Sn CiCC suitable for the react-then-wind approach, *IEEE Trans. Appl. Supercond.* **7**:816–819 (1997).
10. D. C. Larbalestier, The road to conductors of high temperature superconductors: 10 years does make a difference, *IEEE Trans. Appl. Supercond.* **7**:90–97 (1997).
11. A. R. Kantrowitz and Z. J. J. Stekly, A new principle for the construction of stabilized superconducting coils, *Appl. Phys. Lett.* **6**:65–67 (1965).
12. B. J. Maddock, G. B. James, and W. T. Norris, Superconducting composite: Heat transfer and steady state stabilisation, *Cryogenics* **9**:261 (1969).
13. B. J. Maddock and G. B. James, Protection and stabilisation of large superconducting coils, *Proc. Inst. Electric. Eng.* **115**:543 (1968).
14. O. Miura et al., Development of high-field ac superconducting magnet using ultrafine multifilamentary Nb-Ti superconducting wire with designed artificial pins, *Cryogenics* **35**:181–188 (1995).
15. M. N. Wilson, *Superconducting magnets, Monographs on Cryogenics*, Clarendon Press, Oxford, 1983, p. 159.
16. T. Kozman et al., Construction and testing of the mirror fusion test facility magnets, *IEEE Trans. Magn.* **23**:1448–1463 (1986).
17. S.-T. Wong et al., Design and construction of a large superconducting MHD magnet for the coal-fired flow facility at the University of Tennessee Space Institute, *Proc. Int. Cryogenic Engineering Conf.*, June 1980, IPC Science Technology Press, Guildford, pp. 785–789.
18. J. File, R. G. Mills, and G. V. Sheffield, Large superconducting magnet designs for fusion reactors, *IEEE Trans. Nucl. Sci.* **4**:277–282 (1971).
19. R. Jayakumar et al., Fabrication of ITER central solenoid model coil inner module, *IEEE Trans. Appl. Supercond.* **7**(Part 1):981–984 (1997).

20. D. G. Hawksworth, Superconducting magnets systems for MRI, *Int. Symp. New Developments Appl. Supercond.*, Singapore: World Scientific, 1989, pp. 731–744.
21. A. Zhukovsky et al., 750 MHz NMR magnet development, *IEEE Trans. Magn.* **28**:644–647 (1992).
22. P. V. Livdahl et al., Status of the Fermilab energy doubler/saver project, *IEEE Trans. Nucl. Sci.* **24**:1218–1221 (1977).
23. J. Ahlback et al., Electromagnetic and mechanical design of a 56 mm aperture model dipole for the LHC, *IEEE Trans. Magn.* **30**:1746–1749 (1994).
24. S. S. Shen et al., First results of the full array LCT coil tests, *IEEE Trans. Magn.* **23**:1678–1682 (1987).

FURTHER READING

More information may be found in the following books and articles:

- A. C. Rose-Innes, *Introduction to Superconductivity*, 2nd ed., Elsevier Science, Amsterdam, The Netherlands: 1994. (This book describes the fundamental physics of superconductivity and its application to conductors for superconducting magnets.)
- Proc. IEEE*, special supplement on superconductivity, **77**: 1110–1287 (1989). (This IEEE review contains comprehensive contributions on magnets, conductors, power devices, and electronics. Despite the date of publication, the contents are still appropriate.)
- H. Desportes, Three decades of superconducting magnet development, *Cryogenics* (ICEC suppl.) **34**:46–56 (1994). (This is one of the more recent reviews of superconducting magnet development but contains less detail than the *Proc. IEEE* issue above.)
- Reference 10 above is a concise review of the status of HTS conductors and their applicability to superconducting magnetic construction.
- P. Schmuser, in M. Month and M. Diennes, eds., *The Physics of Particle Accelerators: Superconducting Magnets for Particle Accelerators*, AIP Conf. Proc., 1992, Vol. 249, pp. 1099–1103.

SUPERCONDUCTING FILTERS AND PASSIVE COMPONENTS

JUAN M. O'CALLAGHAN
CARLOS COLLADO
Technical University of
Catalonia (UPC)

SALVADOR H. TALISA
Johns Hopkins University

JORDI MATEU
Telecommunications
Technological Center of
Catalonia (TTC)

The advent of high-temperature superconducting (HTS) materials has enabled a number of applications in passive microwave electronics. Superconductors exhibit very low losses at microwave frequencies and, although finite, at the practical operating temperature of 77 K (boiling point of nitrogen), these losses are more than two orders of

magnitude lower than normal conductors at frequencies of 10 GHz and below. This has allowed the possibility for high-performance planar microwave components because high-quality epitaxial films can be deposited on both sides of low microwave loss, single-crystal substrates allowing the fabrication of components in planar configurations such as microstrip, stripline, and coplanar waveguide. These configurations are widely used throughout the microwave community in a variety of technologies ranging from GaAs microwave monolithic integrated circuits (MMIC) to integrated circuits using ceramic and laminated substrates. Figure 1 shows a schematic cross section of all three most common planar microwave structures. The use of HTS in these circuit configurations results in passive devices such as resonators, filters, and delay lines with performance far superior to conventional planar technology and with the attractive feature that many well-established design techniques can be used for HTS circuits as well.

The discussion in this article will focus mostly on HTS microwave planar filters, because they are the majority of microwave HTS devices built nowadays. They are also representative of other devices like duplexers and multiplexers, which may contain several filters to separate signals at different frequencies.

Microwave filters are made of several coupled resonators. This article will describe the details of resonators currently used in HTS microwave filters. There are other applications that also use HTS resonators to take advantage of the unique features of HTS materials, for example, in the frequency stabilization of microwave oscillators. These applications will not be described in detail. The interested reader is referred to the reading list for further details.

Planar microwave circuits with HTS materials are also used for some applications that do not involve the use of resonators. Of particular significance are the devices that include planar delay lines. A short overview of these devices is given in this article. Further details can be found in the reading list and in the references therein.

The HTS microwave technology is discussed in this article with the understanding that conventional low-temperature superconductors (LTS), for example, Nb or NbN, can also be used in the same fashion. Practical LTS materials operate typically at 4.2 K, the boiling temperature of liquid He. Furthermore, it should be kept in mind that a larger variety of substrates can be used in LTS technology because it does not require single-crystal epitaxial films. For example, Nb microwave and digital circuits have been demonstrated on Si and single-crystal sapphire substrates [1].

1. HIGH-TEMPERATURE SUPERCONDUCTING FILM PROCESSING TECHNOLOGY

The basic elements of HTS thin film technology from the point of view of microwave applications will be discussed here briefly. Only epitaxial thin films will be addressed because, to date, significantly better properties can be obtained from epitaxial material than from polycrystalline,

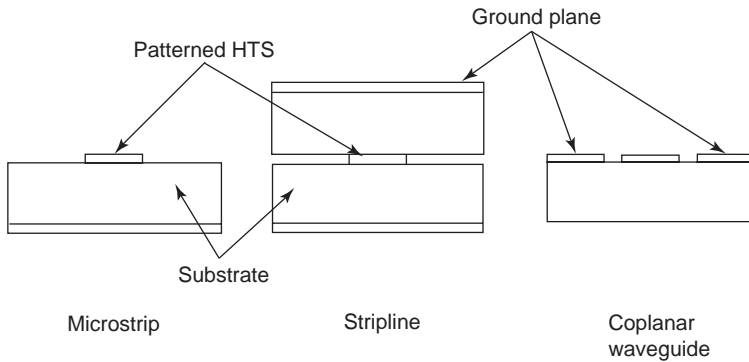


Figure 1. HTS technology lends itself to the fabrication of microwave planar devices such as those schematically depicted here in cross section. One advantage of coplanar waveguide (and its variant slotline, not shown) is that only one patterned HTS film is needed. One disadvantage of stripline is that it is difficult to package. HTS devices have been demonstrated in all three structures.

nonepitaxial techniques. Most, if not all, of the developments covered in this article, however, are valid for the case of polycrystalline materials. The main advantage of these materials is cost and coating of nonplanar surfaces like the inside of a cylinder to form a high-Q cavity resonator [2].

Among the various high-temperature superconductors, there are two that have achieved a level of maturity and acceptance in the industry: (1) $\text{YBa}_2\text{Cu}_3\text{O}_7$, usually referred to as YBCO, and (2) $\text{Tl}_2\text{Ba}_2\text{CaCu}_2\text{O}_8$ or TBCCO. High-quality epitaxial thin films of these materials can be deposited on both sides of a variety of low microwave loss, single-crystal substrates by several deposition techniques. Evaporation is the dominant technique for production of large-area YBCO films [3,4], whereas sputtering [5], laser ablation [6], and metal-organic chemical vapor deposition (MOCVD) [7] are used in some YBCO processes and, as detailed below, as a part of most TBCCO processes.

YBCO is typically grown in situ as an epitaxial single-crystal film with thickness ranging from 300 nm to 700 nm. This means that the desired crystalline phase of the material is formed as the film grows because the growth conditions can be adjusted to obtain such results. In contrast, TBCCO films have to be grown in two steps because of the high volatility of thallium. In a first step, a thallium-free epitaxial film containing barium, calcium, copper, and oxygen is formed following the deposition techniques mentioned above. Then, the film is annealed in a thallium atmosphere to form the TBCCO film with the adequate composition and crystalline structure [8].

Despite the complications in the fabrication of TBCCO films, they have the advantage of a higher critical temperature (Table 1) and are typically grown with thickness close to 1 μm . These are advantages because practical devices must be made with thicknesses two or three times greater than the London penetration depth (200 nm to 300 nm) at 77 K (see Section 2.1.). TBCCO films thus offer a greater operating margin than YBCO films.

1.1. Substrates

To date, the two most common substrates used to grow HTS films on are LaAlO_3 (LAO) and MgO. Circuits on sapphire have been demonstrated, but they are much more difficult to make with a YBCO thickness of at least 500 nm. YBCO films thicker than 300 nm tend to crack because of the difference in the coefficients of thermal ex-

pansion of the YBCO and the sapphire substrate. Both LAO and MgO substrates are available commercially from a variety of suppliers around the world and can be readily obtained in circular wafers up to 7.6 cm in diameter and 250 μm to 700 μm in thickness. At 77 K and for frequencies between 1 GHz and 10 GHz, the loss factor ($\tan \delta$) of LAO and MgO is, at most, on the order of 10^{-5} , which is 10 to 100 times smaller than most practical microwave substrates and is compatible with the low conductor loss of HTS.

These two preferred substrates for HTS planar devices have significant differences among them. LAO has a cubic crystal structure above about 450°C. Below that temperature it transitions to a rhombohedral structure, which is only a slight distortion from the cubic structure consisting of a very small stretching of the cubic unit cell along its diagonal. In order to release stress, the crystal will form twin structures, symmetrically related regions oriented in different directions. Noncubic crystals are anisotropic and, as a result of this twinning, the LAO substrate is made up of slightly anisotropic regions randomly distributed throughout the substrate [9]. The net result is an average dielectric constant with a uniformity of approximately 1%

Table 1. Basic Characteristics of the Most Used Thin Films and Dielectric Substrates for Microwave Applications

HTS Films	YBCO	TBCCO
Critical Temperature (T_c)	90 K	110 K
Surface resistance (R_s) at 77 K and 10 GHz (f^2 dependence)	0.2–0.5 m Ω	0.2–0.5 m Ω
Film thickness	300–700 nm	800–1000 nm
Critical dc current density (J_c) at 77 K	2 MA/cm ²	1 MA/cm ²
Penetration depth (nm)	200 nm	200 nm
Substrates	(LaAlO ₃) LAO	MgO
Relative dielectric constant (ϵ_r) at 77 K	23.6	9.7
Dissipation factor ($\tan \delta$) at 77 K	10^{-5}	$<10^{-6}$
Typical dimensions	5, 7.5, 10 cm diameter 250 and 500 μm thick	5 and 7.5 cm diameter 250 and 500 μm thick

Note: Both types of HTS films can be grown in either substrate.

that, among other effects, may provoke unacceptably large tolerances in the resonant frequencies of the resonators that make up a planar filter. In contrast, MgO, which is cubic, has a dielectric constant uniformity of 0.1% [10].

The relative dielectric constant of LAO is $\epsilon_r = 23.4$ at 77 K. This is a higher value than most common microwave substrates whose dielectric constants usually do not exceed 10 ($\epsilon_r = 9.7$ for MgO). This high permittivity makes invalid some of the models that are used in standard planar microwave circuit design, like, for example, the models of quarter-wave-coupled microstrip sections, which are not valid for $\epsilon_r > 18$.

The most important characteristics of these two HTS materials and their substrates are given in Table 1. The properties listed are those a microwave designer would want to know if engaged in an HTS device design project.

1.2. Device Processing

Fabrication of microwave devices using either YBCO and TBCCO follows relatively straightforward photolithographic techniques. Patterning of the superconducting layer is typically accomplished by Ar-ion milling. The processing may include the deposition and patterning of low-resistivity contacts for interfacing with other devices or instrumentation. These are typically made by depositing a thin (200 nm to 300 nm) layer of gold or silver through a shadow mask on the contact areas [11]. Another possibility is to deposit a layer of gold or silver over the whole HTS film and then selectively remove the metal in the photolithographic process. The latter option allows for an in situ deposition of the metal in the same chamber where the HTS film is grown, without breaking vacuum, favoring a low-resistance contact between the HTS and the metal. Interfacing with other devices via coaxial connectors or directly to other substrates, superconducting or otherwise, can be accomplished using gold wire or ribbon attached to the low-resistivity contacts by ultrasonic thermal compression bonding or gap-welding (ribbons). Fabrication details of filters and delay lines made at Northrop Grumman can be found in Ref. 12. Other institutions follow similar procedures.

1.3. Microwave Packaging of High-Temperature Superconducting Devices

Proper packaging of cryogenic microwave devices is critical to the success of the technology. In general, planar microwave devices are made up of a dielectric or semi-insulating substrate, typically mounted on a metallic package or carrier by means of conducting epoxy or soldering. The mounted device then interfaces with other devices or measurement instrumentation most commonly via coaxial connections. In this case, the metallic carrier forms part of the ground terminal by connecting to both the outer jacket of the coaxial interconnection and the ground plane defined on the substrate. This means that microwave currents flow into the planar device through the center conductor of the coaxial interface and back out through the ground plane on the substrate, the metallic carrier, and its connection to the coaxial connector outer jacket. This current flow into the packaging assembly must occur without appreciable impedance mismatch or discontinuity. Figure 2 illustrates these points schematically with an example for a microstrip device.

The criticality of these connections among substrate, carrier, and connectors is exacerbated when cryogenic cooling of the microwave package is required because a large thermal mismatch between the various components may cause cracking of the substrate or degradation of the interface between substrate and carrier or connector. Furthermore, the quality of the interface between the cryoelectronic substrate and the outside world must be preserved through many temperature cycles between ambient and cryogenic temperature to allow for repeated testing of the device and an operational environment, which may require that the device warm up to room temperature while not in use. Suitable microwave package designs must therefore include one or more of the following elements: (1) the use of thermally matched materials, (2) adhesives that remain sufficiently pliable at cryogenic temperatures, and (3) configurations that allow the various parts of the package to contract and expand freely while maintaining good electrical contact.

When considering materials that are thermally matched to HTS substrates, the important parameter is the total contraction between room temperature and the

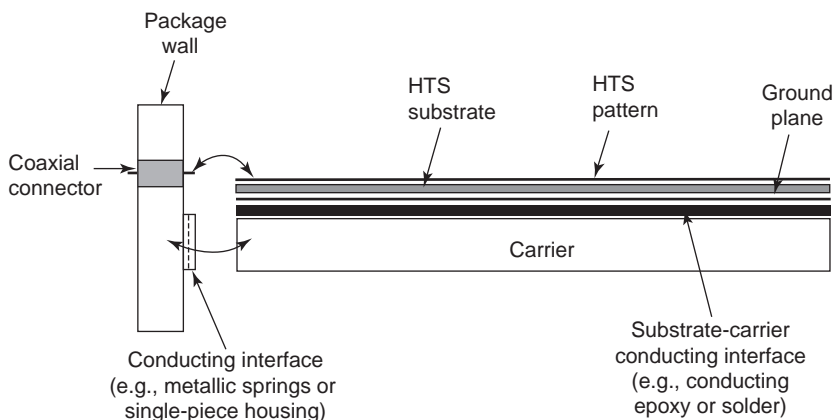


Figure 2. Microwave packaging of HTS devices is challenging because mechanical and electrical integrity must be maintained when the device is cycled from ambient to cryogenic temperatures. Special attention must be paid to the ground-current return path so as not to introduce parasitic reactances that could severely affect the performance.

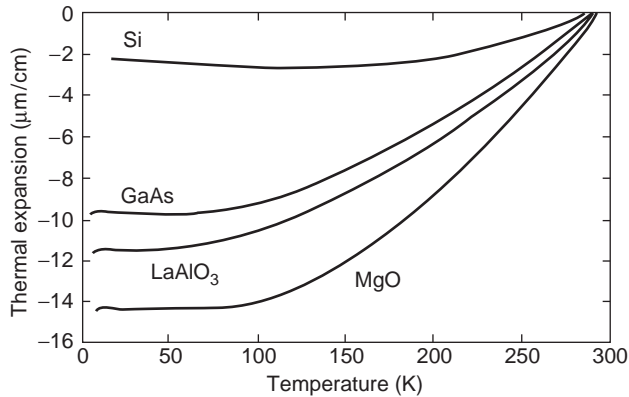


Figure 3. Measured relative thermal contraction of several materials of interest in HTS technology, including Si and GaAs. These or similar data should be used in the selection of carrier materials and the packaging of hybrid HTS-semiconductor components. If a good thermal match between parts that must remain in intimate mechanical and electrical contact cannot be obtained, sufficiently pliable conductive adhesives may be adequate for some applications, particularly if the mismatched parts are small.

operating temperature, for example, 77 K, and not the thermal coefficient of expansion. Figure 3 shows the relative thermal contraction for several materials, including LAO and MgO, in $\mu\text{m}/\text{cm}$ (i.e., at a given temperature, a 1 cm-long piece of material shrinks so many microns from its length at 300 K). As can be seen, the slope of this curve, that is, the thermal coefficient of expansion, varies greatly with temperature over the range of interest, making it a practically useless parameter for the selection of appropriate materials. Although there are some differences in the rate of contraction as the materials shrink from room temperature, the key parameter is the total contraction at 77 K. For example, Nb and LAO are fairly well matched at 77 K, even though their rate of contraction as a function of temperature is slightly different. This is borne out by extensive experimentation [12]. Other substrate/carrier material pairs have been successfully used as well.

2. MICROWAVE PROPERTIES OF SUPERCONDUCTORS—DYNAMIC RANGE BENEFITS

The key reason for developing a microwave HTS technology is the exploitation of the low loss afforded by HTS compared with conventional metals like gold and copper. High-performance, low-loss devices using conventional materials can generally be made at the expense of high volume, usually in the form of hollow or partially dielectric-filled waveguide components. The potential of HTS is to enable components with the same or better performance in a much reduced volume that must include the cryocooler. Figure 4 shows a comparison between calculated losses in several common types of transmission line, including HTS microstrip on LAO, for the parameters listed in Table 1. For calibration, included in this comparison is Au microstrip at 77 K, also on LAO. For the microstrip cases, only the conductor and dielectric losses were calculated; radiation losses or coupling to spurious surface modes were ignored. Also included are the losses in X-

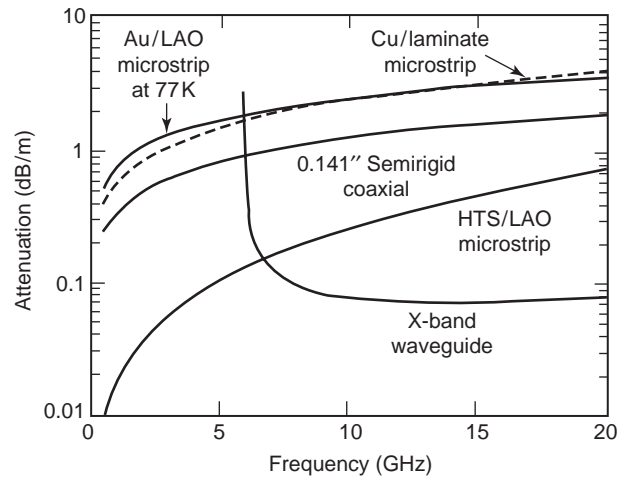


Figure 4. Calculated attenuation comparison for various transmission-line types including HTS and gold microstrip on 500 mm-thick LAO substrates. The line impedance for each line was $50\ \Omega$. All microstrip substrates were assumed to be $500\ \mu\text{m}$ thick. Notice that X-band waveguide has lower loss than HTS microstrip (for the parameters chosen). However, HTS microstrip has broader bandwidth and the potential for smaller volume because it facilitates the integration of several microwave components.

Band waveguide, which are lower than HTS for the parameters chosen, although HTS microstrip offers the advantage of much wider bandwidth and ready integration of several components into a small volume. Notice that the useful frequency range for X-band waveguide is typically only 8 GHz to 12 GHz. Integration capability combined with low loss are key elements of HTS technology because most systems insertion opportunities will develop for applications offering significant size advantages with respect to conventional approaches.

A different and useful way of getting insight into the advantages of HTS planar circuits is from the point of view of resonant structures, which form the basic building block of passband filters. This can best be discussed in terms of quality factor, Q , which is the ratio between stored and dissipated energy, represented as

$$Q = \frac{\text{Stored energy}}{\text{Dissipated energy}} \quad (1)$$

For empty electromagnetic cavity-type resonators, this is, in essence, a figure-of-merit measuring the degree of compromise between volume (stored energy) and surface area (microwave losses on the conducting surfaces). In general, both stored and dissipated energy depend on the dielectric constant and the geometric configuration used, the dissipated energy also depends on the surface resistance of the (super) conducting surfaces and the losses in the dielectric. In practice, there could be other types of losses such as radiation, which, for simplicity, will be neglected in this discussion. In principle, the performance of any passive device can be projected from the Q of the type of structure used to make up the device. For example, a resonator made up of a section of microstrip line can be calculated from well-known expressions [13]. The insertion loss of a

filter can, in turn, be estimated from the Q of the resonators that make up the filter [14].

Figure 5 is a plot comparing the Q and volume, as a function of frequency, of resonators made up of a microstrip line section and an empty metallic cube, respectively. As the dimensions of the resonator are specified at each frequency, the volume calculated is that of the smallest cube capable of resonating at a given frequency. The microstrip HTS resonator volume was calculated assuming it is in an enclosure with cross section as shown in the

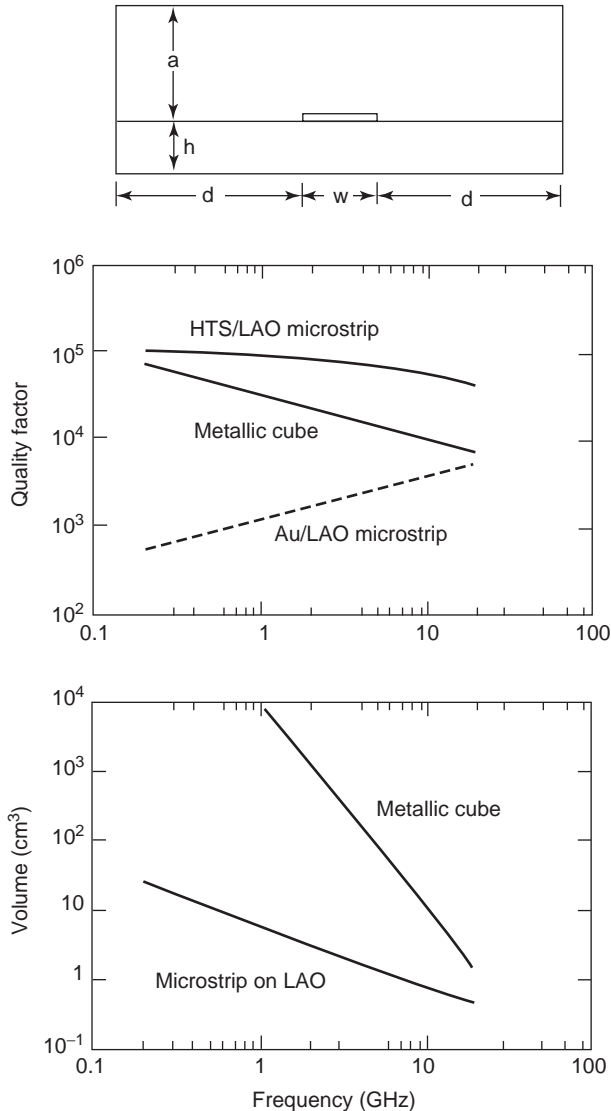


Figure 5. Calculated comparison of quality factor (Q) and volume for two types of resonators: 50 Ω HTS microstrip on 500 μm -thick LAO and a metallic cube. The Q of a gold-on-LAO microstrip at 77 K was also calculated as a reference. The metallic cube is representative of a simple cavity resonator and was chosen because its Q is easy to calculate [15]. The volume for the microstrip was chosen as a device with the cross section shown in the figure with $a/h = 10$, $d/h = 20$, and a length of $(l/2 + 4h)$. This assumed cross section is independent of wavelength and loses its meaning at the higher frequencies plotted, where the substrate would, in practice, be thinner, making the microstrip always smaller than the waveguide.

figure, where the walls and the lid are sufficiently far away from the superconducting strip that their contribution to the loss is negligible. The Q of HTS microstrip, although higher, is within the same order of magnitude as the Q of the cube resonator. However, the estimated volume can be two or more orders of magnitude smaller, especially at the lower microwave frequencies.

Although to first order the main feature distinguishing HTS from conventional planar microwave passive devices is low loss, other important differences exist and are discussed in the following sections.

2.1. Surface Impedance and Penetration Depth

The surface impedance of a conductor is the characteristic impedance seen by a plane-wave incident perpendicularly on a planar (super)conducting surface. For both normal (e.g., copper, gold) conductors and superconductors, the surface impedance is given by [9,15]

$$Z_S = R_S + jX_S = \sqrt{\frac{j\omega\mu}{\sigma}} \quad (2)$$

where ω is the angular frequency, μ is the permeability, and σ is the conductivity, which is real for normal conductors but is complex for superconductors. In both cases, the RF fields decay exponentially inside the material, defining a field penetration depth. In the case of superconductors, however, this parameter—called the London penetration depth—is independent of frequency and is orders of magnitude smaller than the normal conductor penetration depth (usually referred to as the skin depth). The reasons are derived from the perfect diamagnetism of superconductors, the so-called Meissner effect, and are explained by the Gorter–Casimir and London two-fluid model of superconductivity [9,16].

Table 2 summarizes the differences between normal and superconductors from the point of view of their microwave surface impedance. Notice that the surface resistance of superconductors, R_s , has a frequency-squared (f^2) dependence. In contrast, normal conductors depend on the square root of frequency (\sqrt{f}). Figure 6 shows the difference between copper at 300 K and 77 K, and HTS at 77 K. This must be taken into consideration, especially when designing wideband components. The figure also highlights the large difference between copper and HTS at frequencies below 1 GHz.

As with planar microwave devices using normal conductors, best performance control is obtained when the geometric inductance of the circuit dominates the internal inductance of the superconductor. That is, from a practical point of view, the thickness of the superconductor must be at least two to three times larger than the penetration depth at the temperature of operation. The London penetration depth is a strong function of temperature, and for HTS, it is given approximately by [9,16]

$$\lambda_L = \frac{\lambda_L(0)}{\sqrt{1 - \left(\frac{T}{T_c}\right)^4}} \quad (3)$$

Table 2. Microwave Surface Impedance Comparison Between Normal Conductors and Superconductors

Normal Conductors	Superconductors
$\sigma = \text{Real}$	$\sigma = \text{Complex}$
Penetration (skin) depth: $\delta = \sqrt{\frac{1}{\pi f \mu \sigma}}$	Penetration depth: $\lambda_L(T) = \frac{\lambda_L(0)}{\sqrt{1 - \left(\frac{T}{T_C}\right)^2}}$
$R_S = X_S = \frac{1}{\sigma \delta} \propto \sqrt{f}$	$\lambda_L(0) \cong 150 \text{ nm}$ for YBCO $R_S \propto f^2$ $X_S \cong 2\pi f \mu \lambda_L$
Copper at 300 K: $\delta = \frac{2.1}{\sqrt{f}} \mu\text{m}$ $R_S = 8.24 \sqrt{f} \text{ m}\Omega$	YBCO at 77 K: $\lambda_L(77) \cong 0.2 \mu\text{m}$ $R_S = 5f^2 \mu\Omega$
Copper at 77 K: $\delta = \frac{0.9}{\sqrt{f}} \mu\text{m}$ $R_S = 3.4 \sqrt{f} \text{ m}\Omega$	

Note: The frequency f is in GHz in the numerical equations for δ and R_S above.

where $\lambda_L(0)$, the penetration depth at 0 K, is a fundamental parameter of the material, T is the temperature, and T_C is the critical temperature. For YBCO, $\lambda_L(0) \cong 150 \text{ nm}$, which results in $\lambda_L(77 \text{ K}) \cong 214 \text{ nm}$. The HTS film must be at least 500 nm to 600 nm thick for operation at 77 K, in order for the kinetic inductance effects to be negligible with respect to the total inductance of the circuit.

For practical microwave design purposes, this allows treating the superconductor as a normal conductor with a surface resistance that can be obtained from measured values and a frequency-squared scale factor. It has become customary for workers in the field to normalize the surface resistance to 10 GHz and 77 K, although measured data may have been taken at a different frequency. Devices where the kinetic inductance is allowed to dominate have been demonstrated [17]. However, they are lossy, difficult to fabricate, and quite dependent on temperature because

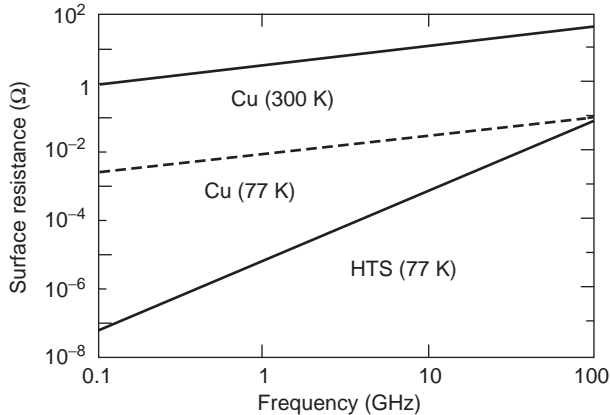


Figure 6. Surface resistance of HTS at 77 K and copper at 77 K and 300 K as a function of frequency. The surface resistance of copper scales with frequency as $f^{1/2}$; for HTS, it scales as f^2 .

of the strong temperature dependence of the penetration depth.

2.2. Nonlinear Effects

A fundamental characterization of the nonlinear behavior and power handling in HTS materials is through the surface impedance and its dependence on the RF magnetic field H_{RF} [18–23].

$$Z_S(H_{RF}) = R_S(H_{RF}) + jX_S(H_{RF}) \quad (4)$$

The essence of the nonlinear dependence of the surface impedance on signal power level or, equivalently, H_{RF} is intuitively grasped by observing the response of a microstrip resonator, shown in Figure 7. As the input power is increased, the resonator Q degrades (R_S dependence on H_{RF}) and the resonance shifts to lower frequencies (X_S dependence on H_{RF}). Several regimes have been identified in the study of nonlinear phenomena in HTS [20]. A linear region at sufficiently low power levels, a weakly nonlinear region where nonlinear behavior is dominated by grain-boundary weak links (Josephson-junction-like defects in the crystalline make-up of the HTS film) and a strongly nonlinear region dominated by hysteretic vortex penetration. Above this regime, breakdown of the superconducting state occurs, with the surface resistance increasing abruptly because of heating and the formation of normal-state domains [20].

If the magnetic field exceeds its critical value, the material becomes a normal conductor and dissipates heat that must be removed by the cryocooler in the system and can even damage the device. The device ceases to operate as a superconducting device and, if no damage has occurred, must recover after the high-power source has been removed. The related topic of intentionally provoking a superconducting-to-normal transition as a switching mechanism has been studied extensively [24–26].

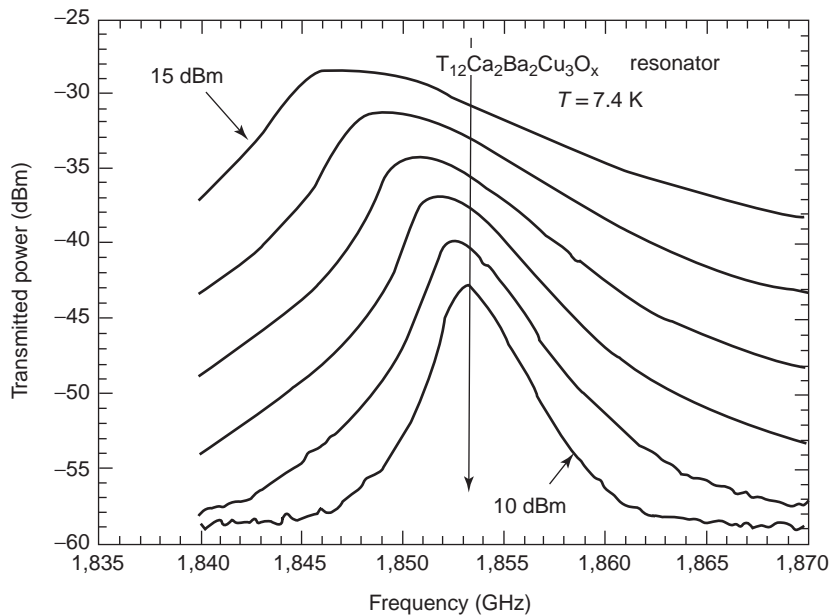
2.3. Dynamic Range Considerations: Noise Figure

An important consideration for any electronic device is its dynamic range, or range of signal power levels over which the device will operate properly. In the case of passive HTS devices, they are expected to be linear over a certain dynamic range, limited below by noise and above by the onset of nonlinear behavior.

Starting at the lower end, the noise generated in a passive device will generally be of a thermal nature. A measure of how much noise any device generates is given by the noise figure [27], which is, by definition, related to the excess noise generated in the device when a matched resistor at 290 K (ambient temperature) is placed at the input. Thus the noise figure would be equal to 1 (or, equivalently, 0 dB) if the device were perfectly noiseless or if it were an ideally lossless passive device. The accepted noise figure definition as a function of device temperature is [27]

$$F_{dB} = 10 \cdot \log \left[1 + (L - 1) \cdot \frac{T}{290} \right] \quad (5)$$

Figure 7. Effects of increasing the input power level on a superconducting microstrip resonator. This measurement (courtesy of Dr. M. Golosovsky, Hebrew University of Jerusalem) captures the essence of the nonlinear RF power dependence of the surface impedance $Z_s = R_s + jX_s$. As power level increases, so does R_s , and the resonance Q decreases. On the other hand, the effect of increased power level on X_s manifests itself on a shift of the resonance toward lower frequencies [20].



Here, L is the insertion loss of the device as a number greater than or equal to 1 (i.e., $10 \log(L) \geq 0$ dB), and T is the temperature in degrees Kelvin. For a passive, lossy device at 290 K, the noise figure turns out to be equal to its insertion loss, a rule that system designers commonly use when dealing with passive components such as filters or lengths of transmission line. HTS devices, however, because they operate at cryogenic temperatures (77 K, typically), will have a lower noise figure, according to the accepted definition [27]. Figure 8 shows this expression graphically as a function of the insertion loss of the device for 77 K and 290 K (ambient temperature). Thus, in considering the dynamic range of HTS devices, the lower end of the range will tend to be lower than for conventional devices, not only because of their inherent low loss, but also because they operate at cryogenic temperatures. Measurements reported in the literature [28] confirm, to first order at least, that the noise in HTS passive devices is indeed thermal in nature.

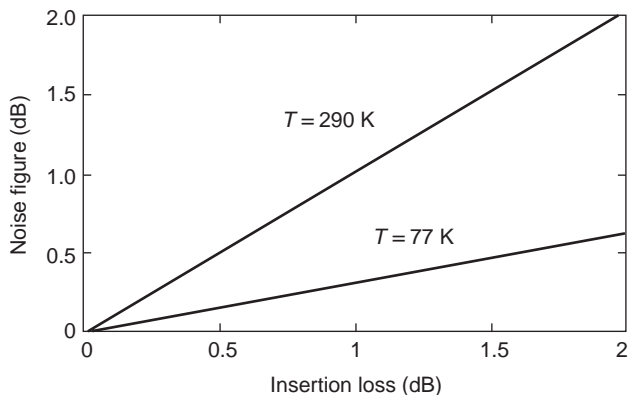


Figure 8. Noise figure of a cryogenically cooled passive device as a function of insertion loss. Notice that the noise figure equals the loss at 290 K (by definition), but it is lower for devices operating at a lower temperature.

2.4. Dynamic Range Consideration: Nonlinearity and Power Handling

The upper limit of the dynamic range of HTS passive devices is limited by nonlinearities in the superconductor. This is in contrast to conventional technology, for which this upper limit could be orders of magnitude higher, generally limited by such phenomena as the voltage breakdown of air or the dielectric used, or melting of the metallic pattern because of high currents. HTS, on the other hand, is fundamentally limited by the dependence of its surface impedance on the magnetic field shown in Eq. (4). In a linear media, there is no dependence between surface impedance and magnetic field, so Eq. (4) implies that the fields at the surface of the HTS film will have distortions with respect to the ones in a linear material.

Of particular importance is the intermodulation distortion (IMD), whose most distinctive feature is the generation of third-order mixing products at frequencies $2f_1 - f_2$ and $2f_2 - f_1$ when a device is driven by two harmonic signals at f_1 and f_2 . The upper end of the dynamic range is then reached when the power level of the applied signals is such that the third-order products rise above the noise floor and can be mistaken and processed by the system as real signals.

Nonlinear effects are exacerbated in HTS devices where the microwave fields are nonuniformly distributed. For example, an HTS microstrip line has much higher current density (and magnetic field) near the edges of the line than along the center. Thus, as the signal power level is increased, the current density at the line edges will generate nonlinearities and increased losses, degrading the performance of the device. As a result, the linearity condition, which may be a relatively minor issue with conventional filter technology, is, in contrast, very key in HTS filter technology.

A system dynamic range can, in turn, be determined from that of its components. An important example is that

of a microwave receiver front-end, usually consisting of a low-noise amplifier (LNA) placed after the antenna, which is then followed by one or more downconversion stages. The dynamic range of the receiver is greatly determined by the noise figure, gain, and IMD of the LNA, with the components that follow having much less influence. Many applications demand a preselector filter between the antenna and the LNA to reject strong interfering signals that could generate unwanted mixing products because of the nonlinearity of the LNA [28]. The preselector filter must not significantly degrade the receiver dynamic range, and so it must have low insertion loss (i.e., low noise figure) and an IMD sufficiently lower than the LNA's with respect to both in-band signals and the rejected out-of-band interfering signals. This is an important example because HTS filter technology is a strong candidate for this type of preselector in some applications like wireless communications base-station receivers [29].

Nonlinear properties of HTS bandpass filters are strongly dependent on frequency. This is because of the frequency dependence of current and field amplitudes on the resonators that form the filter, which, on some of the resonators, have sharp peaks at the frequencies close to the edge of the passband [30]. As a result, the nonlinear properties of HTS filters are normally set by these resonators, and the frequencies close to the edge of the passband are typically the ones where IMD and other nonlinear effects are more prominent (see Figure 9). This is an important consideration in HTS preselector filters, which may be subject to strong out-of-band interfering signals.

Although IMD is normally tested with two tones to check for the generation of mixing products, the signals applied to HTS filters are often not sinusoidal, and it may be difficult to predict the nonlinear effects from the

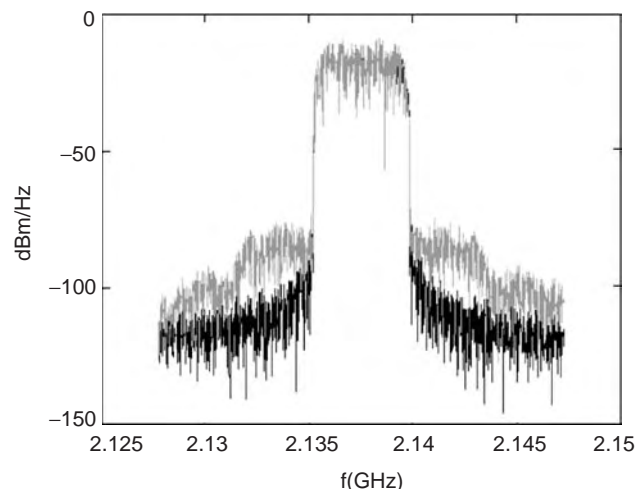


Figure 10. Simulated WCDMA spectrum before (black) and after (grey) an HTS filter showing the effect of the nonlinearities in the regrowth of the spectrum outside the passband.

two-tone characterization. This happens, for example, when HTS filters are driven with spread-spectrum signals, like those used in CDMA- or WCDMA-based communication systems. The IMD in this case causes a broadening of the band-limited spectrum, which may mask the signals in adjacent channels (see Figure 10). Prediction of this type of effects requires using nonlinear numerical techniques [31].

3. HIGH-TEMPERATURE SUPERCONDUCTING FILTERS

One of the most important applications of HTS microwave technology are high-performance passband filters because they can be made in planar configurations. Filters are often the dominant contributor to system volume, in particular when banks of low-loss filters are required. As discussed earlier, high-Q structures can be obtained at the expense of high volume. HTS planar configurations like microstrip or coplanar waveguide have Q comparable with cavities at a much smaller volume (see Figure 5), and so HTS is an attractive approach to reducing the volume of high-performance filters.

3.1. Insertion Loss and Q

A straightforward way of thinking of bandpass filters is as coupled resonators. The performance of a resonator is characterized by its quality factor Q , defined in Eq. (1). When the resonator forms part of an electrical circuit, the circuit delivers and takes back energy from the resonator, affecting its characteristics. The unloaded Q of a resonator, Q_u , is its intrinsic quality factor, without the effects of an external circuit. A first-order filter consists of a single resonator. Its bandwidth can be adjusted by the degree of coupling into the resonator by the external circuit. In a lightly coupled resonator, little disturbance is introduced by the input and output circuits, and its resonant conditions and bandwidth are close to those of an ideal, unloaded resonator. When coupling into the resonator is strong, the disturbance is large and the Q is now dominated by

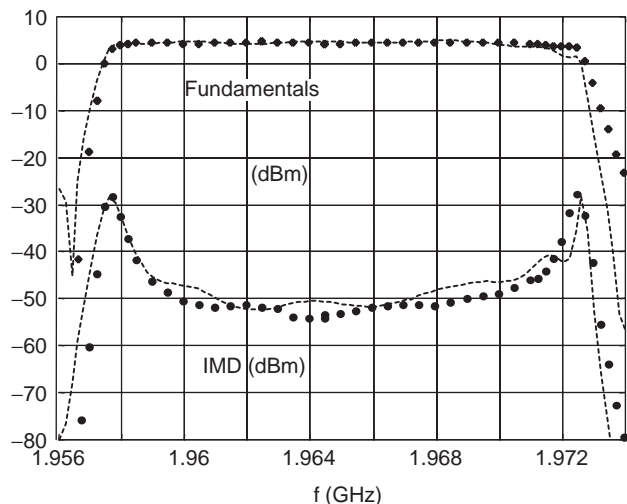


Figure 9. Frequency response and intermodulation distortion in a 8-pole quasielliptic planar HTS filter subject to two tones spaced by 100 KHz. The power of the fundamental signals (upper trace) follows the transfer response of the filter, whereas the intermodulation products (lower trace) peak at the edges of the passband. The figure also compares measurements (dots) with simulations (lines) made with nonlinear numerical techniques [31].

both the resonator and the external circuit, making the total or loaded Q lower than the ideal, unloaded Q, and therefore the filter bandwidth is now wider. For a higher order filter made up of various resonators coupled together, the idea is the same. Narrow-band filters require that the resonators be loosely coupled to each other, and the minimum bandwidth is limited by the unloaded Q of the resonators. Wider bandwidth filters will have tighter coupling among resonators. Clearly, then, narrow-band filters are a desirable application for HTS because its inherent high Q enables narrow bandpass filters with low loss and small volume. This was illustrated in Fig. 5, which helps to convey the significance of the loss-volume tradeoff from the point of view of using HTS and metallic cavity resonators to make filters. There is also a tradeoff between bandwidth, filter order (number of resonators), and insertion loss. The following is an approximate expression for the mid-band insertion loss of a filter [14], in dB, which reflects this tradeoff in Chebychev filters as

$$L_{dB,n} \cong \frac{4.34}{B} \cdot \sum_{k=1}^n \frac{g_k}{Q_{uk}} \quad (6)$$

Here, n is the filter order, g_k is the normalized series inductance and shunt capacitance values of the low-pass prototype filter [14], B is the filter bandwidth as a fraction of the center frequency, and Q_{uk} is the unloaded Q of the k th resonator. For the purposes of estimation, it is reasonable to assume that all the resonators in the filter will have the same Q_u . Figure 11 illustrates the tradeoff between insertion loss, bandwidth, and filter order as a function of resonator Q. It shows how Eq. (6) can be used to estimate the potential of a certain filter technology, in this

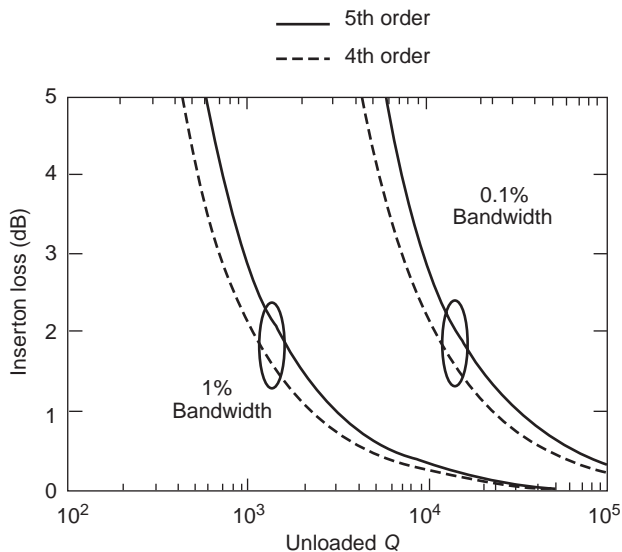


Figure 11. Estimated insertion loss of fourth- and fifth-order Chebychev passband filters of 1% and 0.1% fractional bandwidths as a function of the unloaded Q of the resonators that make up the filter. It was assumed that all the resonators have the same Q. The chart shows the increase in insertion loss caused by increasing the filter order by one and reducing the fractional bandwidth by a factor of ten.

case HTS, and understand its limitations. The insertion loss was estimated for Chebychev-type filters [14] of the fourth and fifth orders, respectively, and for 1% and 0.1% fractional bandwidths. The purpose of this chart is to point out the difference in loss caused by increasing the filter order by one and by increasing the fractional bandwidth by a factor of ten. Figure 11 complements Fig. 5 by helping to make a connection between the insertion loss of a filter of a given order and bandwidth and a specific structure and its volume. The information provided by these two figures can readily be extended to cover other structures and technologies.

3.2. Selectivity and Q—Types of HTS Filter Designs

Besides having an effect on the insertion loss, the quality factor of the resonators that form a filter also affect the steepness of the frequency response at edges of the passband. Steep filter skirts demand high Q_u in the resonators and make possible a sharp transition between the stopband (where an insertion loss L_s is guaranteed) and the passband (where a return loss L_r is guaranteed). The width of this transmission band δf is limited by the Q_u of the resonators in the filter. For the particular case where $L_s = L_r = -23\text{ dB}$ and a maximum of 20% of the incident power is allowed to be dissipated in the filter (i.e., maximum insertion loss caused by dissipation is about 1 dB), the minimum width of the transition band δf is given by [30]

$$\delta f \leq 8\pi\beta_0 \frac{f_0}{Q_u} \quad (7)$$

where f_0 is the center frequency of the filter and $\beta_0 \approx 0.75$ for Chebychev filters and 0.25 for elliptic filters [30].

From Equation (7), it is clear that the width of the transition band also depends on the type of filter design through the coefficient β_0 , with Chebychev filters providing wider transition bands than elliptic filters.

Most modern HTS filters use couplings between non-adjacent resonators to produce elliptic or quasielliptic responses having transmission zeros close to the edge of the passband. This type of coupling is not used in Chebychev filters, which do not have transmission zeros in their frequency response. Elliptic filters, on the other hand, need the highest number of nonadjacent interresonator couplings, but require fewer resonators than Chebychev filters for a given ratio between the bandwidth and the width of the transmission region. For example [30], a filter with a center frequency of 2 GHz, 20 MHz bandwidth, 400 KHz transition width, requiring a 20 dB return loss in the passband, and 85 dB of insertion loss in the stopband, would need 48 resonators in a Chebychev design and 15 in an elliptic design. The elliptic design would have 14 transmission zeros in the stopband.

Chebychev and elliptic designs represent extreme cases of filter design, where either full advantage is taken from nonadjacent interresonator couplings (elliptic filters), or this type of coupling is not used at all (Chebychev). There is a wide range of intermediate designs (quasielliptic filters) depending on how many interresonator couplings are used and how many transmission zeros are synthesized.

Many HTS filters use at least a single pair of transmission zeros at the edge of the passband.

3.3. Planar Resonator Designs

There are four main features that HTS filter designers seek in a planar resonator:

1. Miniaturization
2. Low interresonator coupling vs. distance
3. High power handling
4. High Q

Obviously, a single resonator design will not optimize all these four features. Rather, a certain resonator shape represents a compromise between several of them. For example, miniaturized resonators tend to have large current densities, and this tends to degrade their quality factor and power handling. In the paragraphs below, we will discuss each of these features and give some examples of representative HTS resonator designs.

Miniaturization of the size of the planar resonators has been a trend in HTS filter design since shortly after its beginning. The high Q of HTS resonators allows the design of filters with many resonators without significant degradation of the insertion loss. This, together with substrate cost and the limitations in the substrate size, has motivated filter designers to try to fit as many resonators as possible on a given substrate area. Early HTS filters were made with straight microstrip transmission line resonators, and the need for miniaturization has motivated the use of other types of resonators that use less real state. One possibility is the use of quasilumped elements as in Figure 12. Other possibilities include several ways of folding the transmission line in forms of loops, hairpins, spirals, or even fractal shapes. Some of these geometries will be discussed below.

Miniaturization of the space that the resonators take is not the only requisite to have small HTS planar filters. One also needs to have resonators that can be placed close to each other while keeping a low degree of coupling among them. Low coupling is necessary to make narrow-band filters, and traditional layouts need high interresonator spacings to achieve this. To avoid the use of large

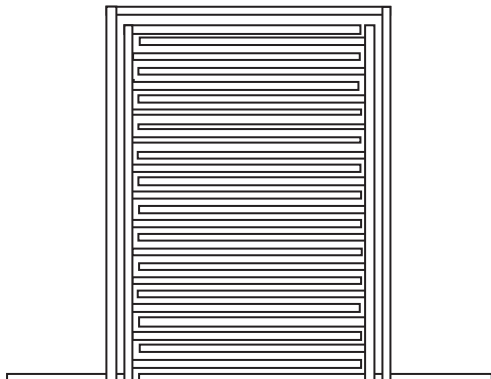


Figure 12. Example of a quasilumped resonator having an inductor and an interdigital capacitor (US patent 6,438,394). Courtesy of Superconductor Technologies Inc.

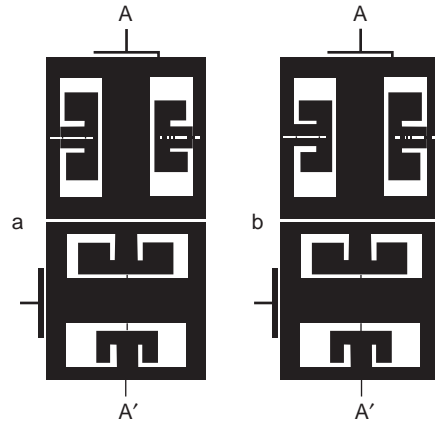


Figure 13. Example of resonators with low interresonator coupling. In this design, perfectly symmetrical resonators would be uncoupled. The degree of coupling is set by small disturbances in the resonators that break the symmetry [37] © 1999 IEEE.

areas of substrate, some resonators are designed to have low interresonator coupling, and make it little sensitive with interresonator spacing. An example of such type of resonators is shown in Figure 13.

Resonators with high Q and high power handling have a common requirement: low current densities in the HTS. As explained earlier, current crowding along the edges of typical planar transmission lines (e.g., microstrip, stripline, and coplanar waveguide) ultimately limits the maximum power level that can be handled. Improved filter designs are based on planar structures that avoid the effects of significant current crowding at the edges, as is the case of low-impedance microstrip lines [32].

Another approach involves the use of resonators with parallel segments of microstrip transmission lines having symmetrical currents, so the fields between transmission line segments tend to cancel (see inset in Figure 14). This reduces the current-crowding effects at the adjacent edges of the transmission line segments. The resonator layout is then based on folding a line in several segments, and having the segment with the strongest current density surrounded by adjacent segments with symmetrical currents. This is achieved at the even resonances of the spiral-in spiral-out resonators of Figure 14 [33].

Another significant type of HTS resonators with high power handling are the structures based on the circular TM_{010} mode [34–36]. The most salient features of this approach are shown in Figures 15(a) and (b), which show the electromagnetic fields and current profile in a microstrip and a disk resonator, respectively. In the latter, the RF magnetic fields do not close above the substrate but within it, under the disk. Thus the current density does not peak at the edges of the resonator and its distribution is more uniform. The only possible drawback of this approach is that the fields are more confined to the disk resonator, and intercoupling between resonators to form a filter may be more difficult, perhaps requiring three-dimensional structures for proper control of the coupling. This would eliminate some of the planar integration advantages. Fully planar filters using this concept, however, have been successfully demonstrated [34].

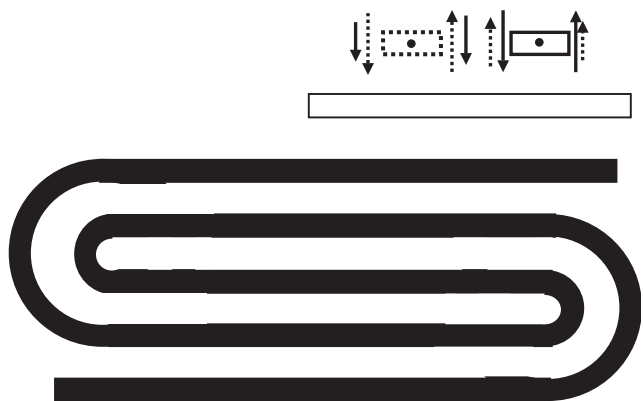


Figure 14. Layout of a spiral-in spiral-out resonator. Symmetrical currents in the various segments of the transmission line (and particularly on those with strongest currents at resonance) reduce current crowding effects, enhancing the quality factor and the power handling of the resonator [33]. Inset: detail on how symmetric currents reduce the fields between the strips. Similarly, antisymmetric currents would enhance the fields in the region between strips and increase the current densities at the adjacent edges of the strips. Courtesy of Superconductor Technologies Inc.

Obtaining high Q planar HTS resonators involves using HTS materials with low surface resistance and keeping current densities low. Both of these aspects have been discussed previously. A third requirement to obtain high Q in these resonators is to avoid package losses. These losses are usually because of the currents on the metallic walls of the package induced by the currents in the resonator. To prevent them, it is important to avoid resonator shapes that, at resonance, would launch propagating modes that would propagate in the direction perpendicular to the substrate, and generate high currents on the metal lid [37].

3.4. Examples: Filters for Base Stations of Wireless Communication Systems

There are many examples of planar filters that can be found in the literature and on the world wide web [38,39]. As an example of the performance achievable with this technology, Figure 16 shows the response of a 17-pole filter made by Cryoelectra GmbH, and Figure 17 shows a front end including several filters and low-noise amplifiers for base stations of third-generation wireless communication systems.

Example 1. Four-Channel Passband Multiplexer. Figure 18 shows a diagram of a multiplexer architecture [12,40]. It can accommodate as many channels as the bandwidth of the 90° hybrid coupler covers. Input microwave energy is equally split at the first coupler. If the frequency is within the passband of the two identical filters connected to the coupler, it passes through the filters and adds in-phase at the output port of the output hybrid coupler for Channel 1. If the frequency is not within the passband of the Channel 1 filters, the signal is reflected back to the input coupler where it recombines such that it is out-of-phase at the input port and in-phase at the input of the second channel hybrid coupler. The process then repeats itself until the signal exits the device through the appropriate channel port. Figure 19 presents details of one implementation of this device [12,41] showing one input, four outputs, and a through port terminated in an external (coaxial) load. Additional channels could be connected to this port provided they are still within the bandwidth (about 10%) of the hybrid coupler used in this demonstration. Figure 19 also shows a detail of the assembly, which includes the internal HTS interconnections between filters and the integrated thin film resistive terminations at the out-of-phase port of the output hybrid in each channel.

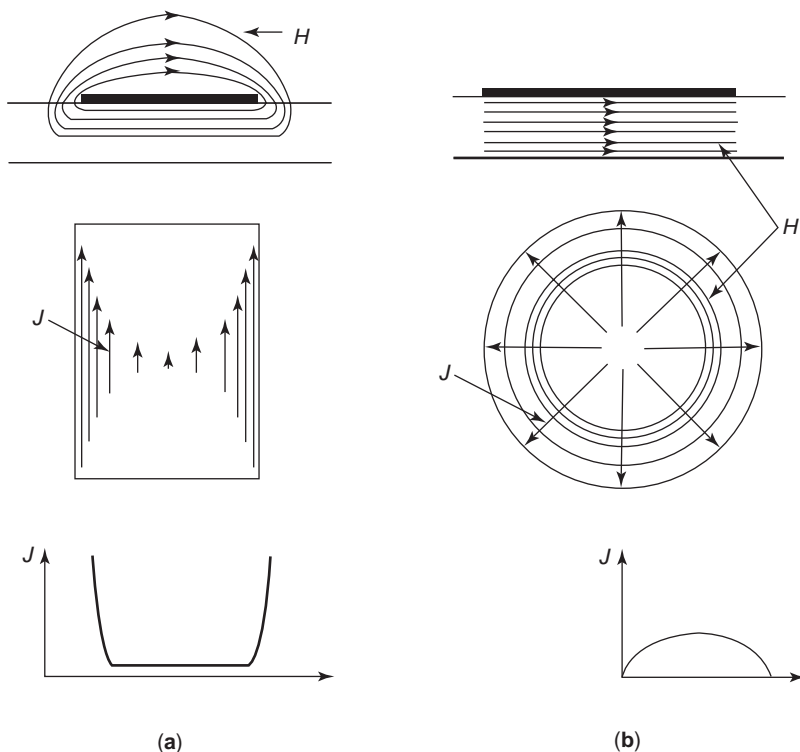


Figure 15. Diagram (courtesy of Dr. Z-Y Shen, E.I. du Pont de Nemours and Co.) [34], showing the magnetic field and current distribution in a $\lambda/2$ microstrip resonator (a) and a TM_{010} printed disk resonator (b). In the disk, the magnetic field lines are circular and remain on the plane of the disk, so the current is not highly nonuniform, as is the case of the rectangular microstrip resonator. The advantage of the disk is that it can handle much higher power levels [34–36].

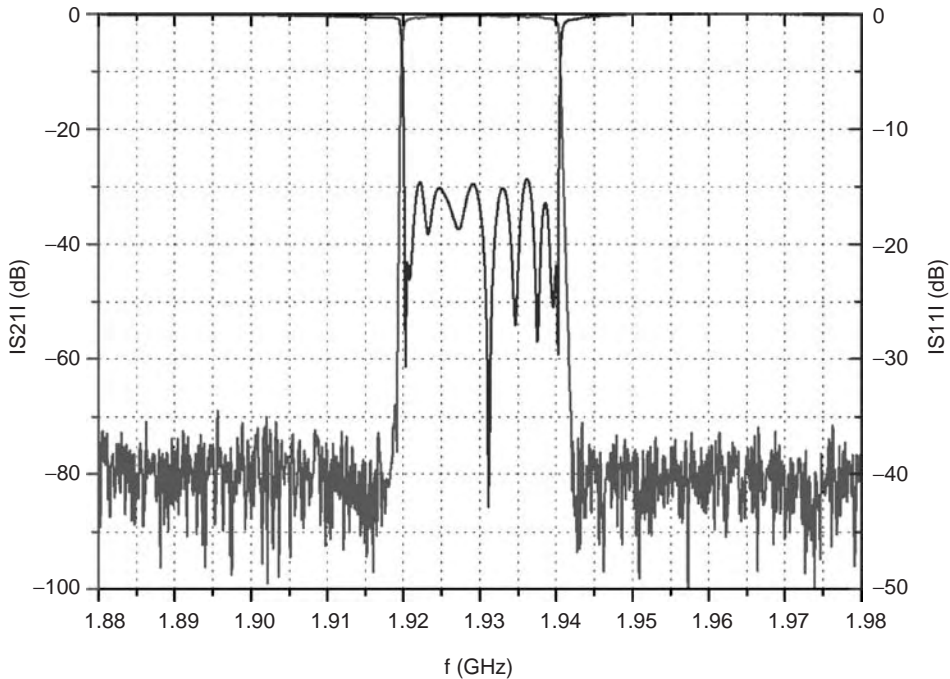


Figure 16. Frequency response of a 17-pole elliptic filter for UMTS applications [50].

The HTS material used for this work was YBCO thin film deposited on 500 μm -thick LAO substrates. The package included an Aluminum frame holding the external coaxial connectors and niobium carriers onto which the LAO substrate pieces were mounted. Niobium has a good thermal expansion match to LAO, so the electrical and mechanical integrity of the device was preserved when cycling from ambient temperature to near 77 K. The substrate-carrier assemblies were mounted on the Aluminum frame using a beryllium-copper spring arrangement. Figure 20 shows the measured performance. The

low-frequency skirts of Channels 2, 3, and 4 show some level of interaction between channels that can be eliminated using a wider guardband between channels. Refs. 12 and 41 include a full discussion of the design, fabrication, and measurements on this device.

This unit was one of a series of demonstration devices delivered to the U.S. Navy's High-Temperature Superconductivity Experiment II program by several contractors for inclusion into the space package [42].

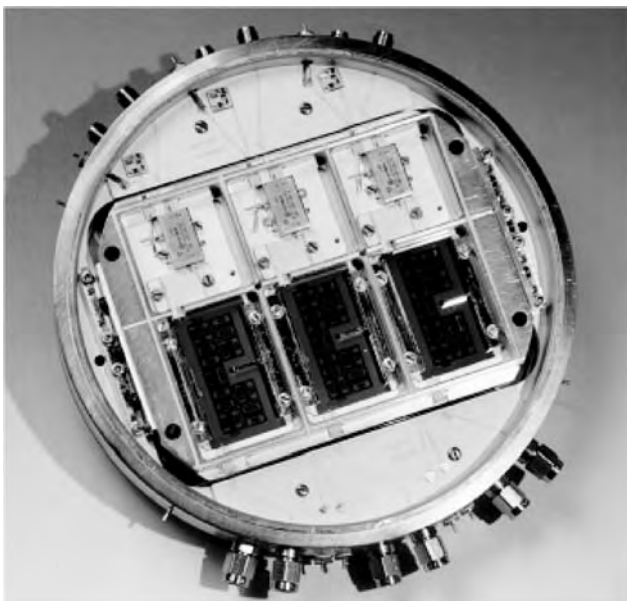


Figure 17. Picture of a front end with six highly selective HTS filters and LNAs (three on each side of the ring) developed within the ACTS project SUCOMS.

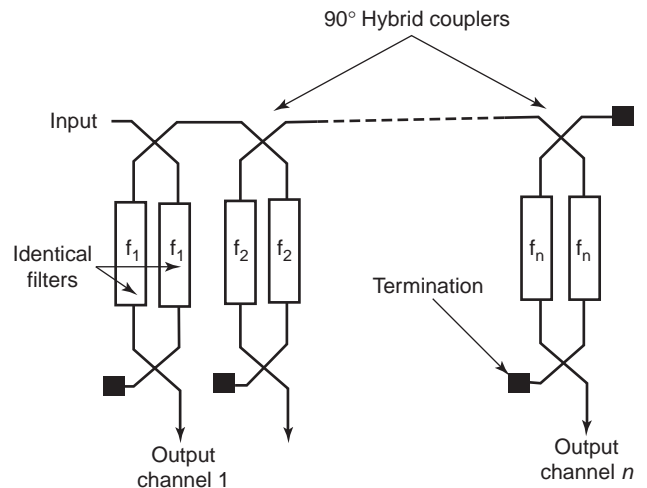


Figure 18. Multiplexer architecture used to demonstrate a four-channel HTS microstrip device. This configuration has the advantage of allowing as many channels as the bandwidth covered by the 90° hybrid. Each filter is terminated in $50\ \Omega$ and is essentially isolated from the others. Other schemes require that the impedance terminations in each filter be adjusted to account for the presence of all the filters in the multiplexer, practically limiting the maximum number of filters to ten or twelve.

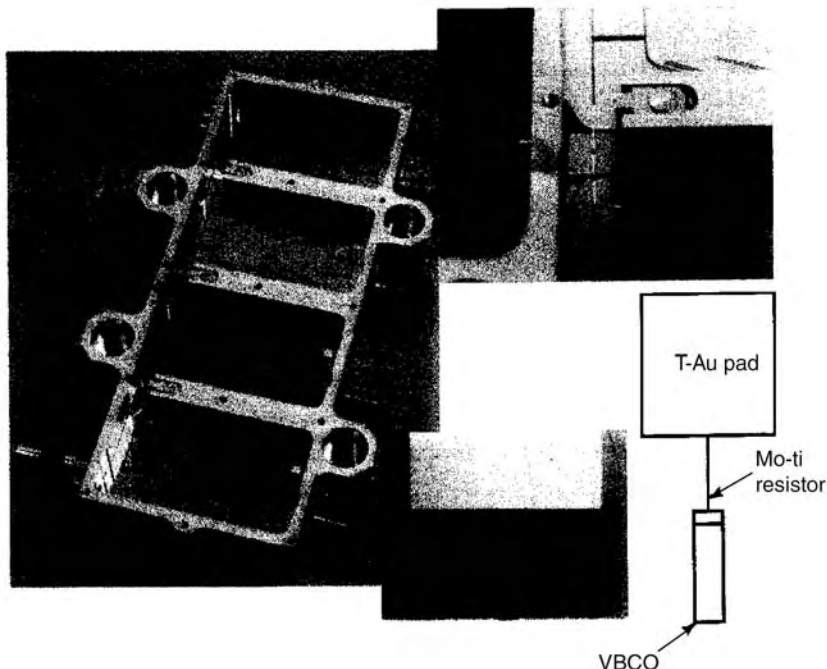


Figure 19. Photo montage of a four-channel YBCO-on-LAO microstrip multiplexer demonstrated under the U.S. Navy's High Temperature Superconductivity Space Experiment II (HTSSE-II). Details of the design, fabrication, and assembly of this device can be found in Refs. 12 and 41.

4. HIGH-TEMPERATURE SUPERCONDUCTING DELAY LINES

Work on superconducting delay lines started at Lincoln Laboratory well before the advent of high-temperature superconductivity, and concentrated mostly on linearly dispersive delay lines for analog signal processing. Linearly dispersive delay lines have delay characteristics that vary linearly with frequency over a certain operating bandwidth and can be used to perform pulse compression, a technique to process and detect small signals that may be below the receiver noise floor [1]. The pioneering work at Lincoln Laboratory in this area using LTS and, more recently, HTS thin film technologies has been extensively documented in the literature [1,43].

Nondispersive delay lines have a constant delay-versus-frequency characteristic and are typically used as

analog memory elements that can store a signal for, say, up to a few hundred nanoseconds while the system is engaged in other processing steps. Work on HTS nondispersive delay lines has also been significant [44–47], including two instantaneous frequency measurement subsystems based on banks of delay lines [44–47]. Clearly, the advantages of superconductivity are that a long length of line can be fabricated in a small volume by defining a long, planar transmission line on a wafer. Reference [46] compares conventional nondispersive delay lines, which require amplifiers between sections of transmission line (e.g., coaxial), with HTS delay lines using projections based on measurements made on relatively short (22 ns) delay lines. Key delay-line parameters are delay, bandwidth, insertion loss, and third-order intercept point. Conventional delay lines that must resort to amplification to boost the signal are limited in dynamic range by the amplifiers.

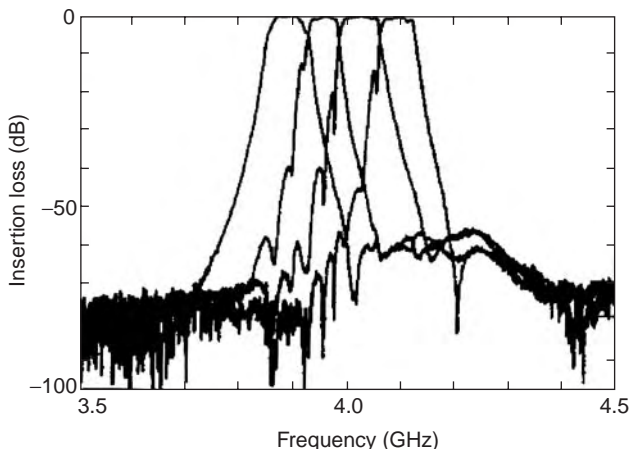


Figure 20. Measured response of the four-channel HTS multiplexer. Further details can be found in Refs. 12 and 41.

5. CRYOCOOLERS AND CRYOGENIC PACKAGING

Key to the insertion of superconducting microwave circuits into electronic systems is the integration of the HTS components with a cryogenic refrigerator and its associated control electronics. Clearly, for HTS technology to be ultimately successful, the user must be rendered able to ignore the fact that cryogenics are used at all, by providing long-lifetime cryocoolers and optimally small cryogenic packages with standard envelop characteristics and interfaces (e.g., 19 inch rack mounts and backplane blind-mate connectors).

Many important considerations enter into the design of a cryogenic package suitable for a microwave HTS subsystem. Figure 21 is a schematic representation of this package, showing its main elements and the various heat inputs that must be considered for an appropriate thermal

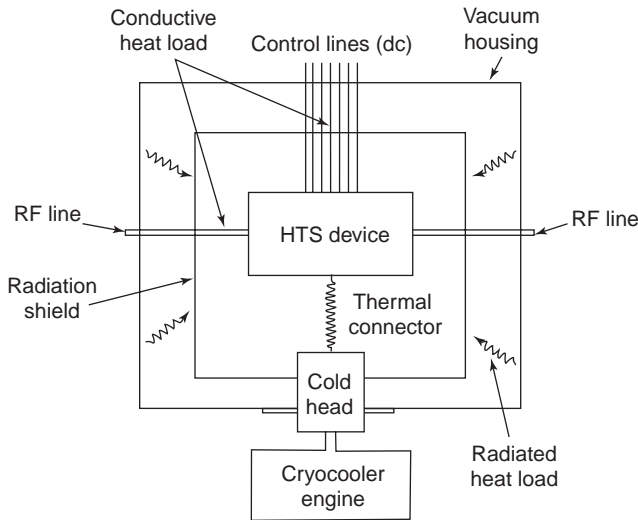


Figure 21. Schematic diagram of the cryogenic package for a hypothetical HTS device showing conducted heat inputs through input/output RF and control lines and the mechanical support of the cold head, as well as the radiated heat input from the (warm) wall of the vacuum housing. The purpose of this diagram is to show the main elements that affect the design of the cryogenic package.

design. References 48,49 provide specific details on the cryogenic aspects of a communications filter subsystem, including packaging.

Cryogenic receiver front ends, including HTS filters, have pushed the development of cryocoolers. The use of

Table 3. Sample Requirements That Will Affect the Choice of Cooler and Cryogenic Packaging Approach

Requirement	Comments
Size and weight	Stringent in almost all applications
Cool-down time	Some applications may require very fast turn-on time (e.g., a few minutes). They would be a driver toward higher cooler power and lower HTS device thermal mass
Vibration	For example, a minute amount of mechanical distortion on a circuit caused by vibration from the cooler may generate a phase modulation that degrades the circuit performance
Power consumption and power supply type	E.g., 120 Vac
Mode of operation	E.g., continuous, intermittent, short missions and then mostly idle, etc.
Temperature stability and control	While any fine temperature feedback control loop ($< \pm 0.01$ K) tends to be done using heater and a temperature sensor, some applications may require a certain degree of cooling engine control ($< \pm 0.5$ K)
Unattended lifetime	Some applications (e.g., space) may require a lifetime on the order of 10 years or more
Vacuum lifetime	All-welded construction; use of getters in a clean, well-conditioned (baked) system

these front ends in communications ground stations at remote locations operating unattended for a long time requires cryocoolers with high reliability and low power consumption. Nowadays, most cryocoolers deployed in base stations of wireless communication systems use the Stirling-cycle [48]. However, when HTS was discovered, the applications of this type of cryocooler were mostly limited to airborne military applications requiring the use of a small cooler, and communications ground stations required a larger, more reliable refrigerator using the Gifford–McMahon cycle.

The choice of a cryocooler will depend on the system and the cooling requirements imposed by the component or subsystem to be cooled, which determines the amount of cooling power required at the operating temperature. Typical sample system and cooling requirements and some comments as to their significance are given in Tables 3 and 4, respectively.

Table 4. Cooling Requirements That Will Influence the Cooling Power (Heat Lift) Required for a Given Application

Requirement	Comments
Power dissipated in the device	A filter with a 0.5 dB insertion loss that must pass a 20 W signal will dissipate 2 W of heat that must be removed by the cryocooler. Also, semiconductor devices such as low-noise amplifiers, which improve in noise and gain performance when cooled, always dissipate a certain amount of heat which must be taken into consideration
Number of microwave and dc control leads	These are the electrical interface between the cryocooled device and the outside world. For example, a filter might require two microwave leads (input and output) and two pairs of dc control lines for the heat sensor and a small heater to keep the temperature constant. These conductors represent a heat loss that the cooler must overcome because they connect the outside ambient temperature with the cold device. While the dc control lines are typically made of thin low-thermal-conductivity, high-resistivity wire (e.g., gauge 32 manganin), the microwave leads must achieve a compromise between insertion and thermal loss
Surface area	Radiation loss is another form of heat loss that the cooler must overcome and therefore must be minimized. The total surface area and their infrared radiation emissivity are important design parameters. Low emissivity radiation shields are typically used between the warm vacuum vessel wall and the cold device
Thermal mass	For those applications that have a cool-down time requirement, the thermal mass of the device to be cooled is important and will be affected by the microwave packaging material and its shape

Table 5. Some Cryogenic Refrigerator Types Suitable for HTS Technology

Cooler Type	Heat-Lift Range Available at 80 K	Comments
Split Stirling	0.5–3 W	Available from many manufacturers, used primarily in the tactical military infrared industry. Has a cold head Separated from a compressor by a metallic transfer line up to 15 cm long
Integral Stirling	0.5–5 W	Also used in infrared detectors. Several versions are being used in HTS front-ends for wireless communications base stations. The compressor and cold finger are integrated in a single unit.
Gifford–McMahon	2–>200 W	Widely used in the support of vacuum systems for semiconductor industry; highly reliable and versatile. The compressor and cold head are separate units connected by fluid lines that can be several meters long
Throttle-cycle	~ 4 W	Reliable and low cost. The compressor and cold heat are separate units connected by fluid lines that can be several meters long
Jule–Thomson	0.5–2 W	Generally used as an open-cycle cooling system for short tactical missile IR detector applications
Pulse tube	0.5–2 W	Emerging technology. It avoids moving parts on the cold part of the cooler, avoiding vibrations and increasing reliability. It has been used in a number of prototypes of HTS front-ends for wireless communications base stations

Cryocoolers suitable for microwave HTS technology will typically have from 3 W to 10 W of cooling capacity [49]. A primary concern systems designers have is the reliability of cryogenic refrigerators, which varies greatly depending on their type and size. Leveraging developments in other fields, such as infrared detectors, the reliability of small, military tactical cryocoolers has steadily increased in recent years, with some manufacturers claiming up to 40,000 h of mean-time to failure (MTTF). On the other hand, larger laboratory or industrial units and specialized coolers for aerospace applications operate for 5 years to 10 years and require minimal servicing. Table 5 lists some of the cryocooler types of interest. The intent here is not to be all-inclusive but to provide a basic reference to the type of coolers most likely to be employed in HTS microwave technology. Reference [49] is a good source of the latest developments in cryocooler technology. Figure 22 is a photograph of a commercial HTS filter

subsystem, showing the cryocooler and associated electronics in their open package.

6. CONCLUSION

High-temperature superconductor microwave technology offers unique advantages derived from the low microwave loss of HTS materials and the inherent low thermal noise in cryogenically cooled components. The main applications to date are related to increased microwave receiver sensitivity, and this is most likely to have an impact on wireless military and commercial communications systems. The reason is that receiver sensitivity and dynamic range must be preserved in the presence of a large number of spurious signals that, if unfiltered, degrade receiver performance. Generation of clean transmitted signals requires filtering in the transmitter, which, coupled with

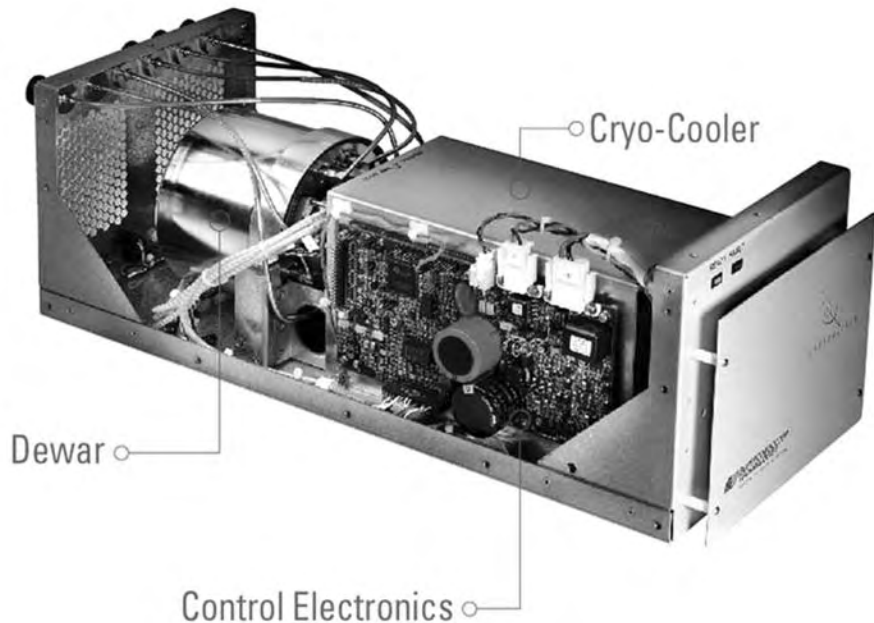


Figure 22. Photograph of an HTS filter assembly for commercial wireless applications (courtesy of Superconductor Technologies, Inc.).

the need to reject unwanted high-power signals at the receiver, has spurred work on high power handling in HTS filters. Interest in the United States and abroad exists in the wireless commercial communications market, and several companies are testing and deploying base station receiver front ends consisting of cryogenically cooled filter-LNA subassemblies.

HTS microwave filters are therefore a promising technology, especially at frequencies below 3 GHz where the loss in conventional microwave materials force high-performance filters to be very large in order to achieve the required low insertion losses and selectivity. Leveraging developments in infrared imaging detector technology and perhaps new developments of cooled semiconductor components for fast computer workstations, cryocooler technology is progressing to the point where long lifetimes and small-size, low-weight coolers are now widely available.

BIBLIOGRAPHY

- R. S. Withers and R. W. Ralston, Superconductive analog signal processing devices, *Proc. IEEE*, **77**:1247–1263 (1989). This paper contains many references to earlier work by the authors.
- P. A. Smith, et al., YBCO thick films for high Q resonators, *IEEE Trans. Appl. Supercond.*, **7**:1763–1765 (1997).
- W. Prusseit, B. Utz, P. Berberich, and H. Kinder, High-quality $\text{YBa}_2\text{Cu}_3\text{O}_7$ films on 4-in. wafers of sapphire, gallium arsenide, and silicon. *J. Supercond.*, **7**(1):231–233 (1994).
- P. Berberich, B. Utz, W. Prusseit, and H. Kinder, Homogeneous high-quality $\text{YBa}_2\text{Cu}_3\text{O}_7$ films on 3" and 4" substrates, *Physica-C*, **219**(3–4):497–504 (1994).
- D. W. Face, et al., Large area $\text{YBa}_2\text{Cu}_3\text{O}_7$ films for high power microwave applications, *IEEE Trans. Appl. Supercond.*, **5**:1581–1586 (1995).
- A. Pique, et al., Microwave compatible $\text{YBa}_2\text{Cu}_3\text{O}_{7-x}$ films on ferrimagnetic garnet substrates, *Appl. Phys. Lett.*, **67**:1778–1780 (1995).
- E. J. Smith, J. Musolf, and E. Soares, Composition controlled MOCVD as a route to high Q HTS thin film devices, *Proc. 3rd Jt. ISTE/C/MRS Int. Workshop Supercond.: Suitable Mater. Proces. HTS Appl. Towards Next Decade*, 1997, p. 145.
- T. C. Pluym, et al., Superconducting TBCCO thin films prepared by post-annealing in flow-through multiple-zone furnace, *IEEE Trans. Appl. Supercond.*, **5**(2):1339–1342 (1995).
- Z.-Y. Shen, *High-Temperature Superconducting Microwave Circuits*, Norwood, MA: Artech House, 1994.
- Unpublished data obtained jointly by Northrop Grumman, NASA Lewis Research Center, and Superconductor Technology, Inc, 1989.
- J. W. Ekin, A. J. Panson, and B. A. Blankenship, Method for making low-resistivity contacts to high Tc superconductors, *Appl. Phys. Lett.*, **52**:331–333 (1988).
- S. H. Talisa, et al., High-temperature superconducting space-qualified multiplexers and delay lines, *IEEE Trans. Microw. Theory Tech.*, **44**:1229–1239 (1996).
- R. K. Hoffmann, *Handbook of Microwave Integrated Circuits*, Norwood, MA: Artech House, 1987.
- G. L. Matthaei, L. Young, and E. M. T. Jones, *Microwave Filters, Impedance-Matching Networks, and Coupling Structures*, Dedham, MA: Artech House, 1980.
- S. Ramo, J. R. Whinnery, and T. Van Duzer, *Fields and Waves in Communication Electronics*, New York: Wiley, 1965.
- I. Vendik and O. Vendik, in E. Kollberg, ed., *High Temperature Superconductor Devices for Microwave Signal Processing*, St. Petersburg, Russia: Skladen, 1997, 3 parts.
- K. R. Carroll, J. M. Pond and E. J. Cukauskas, Superconducting kinetic-inductance microwave filters, *IEEE Trans. Appl. Supercond.*, **3**:8–16 (1993).
- D. E. Oates, et al., Nonlinear surface resistance in $\text{YBa}_2\text{Cu}_3\text{O}_{7-x}$ thin films, *IEEE Trans. Appl. Supercond.*, **3**:1114–1119 (1993).
- C. Wilker, et al., Nonlinear effects in high-temperature superconductors: 3rd order intercept from harmonic generation, *IEEE Trans. Appl. Supercond.*, **5**:1665–1670 (1995).
- M. Golosovsky, Physical mechanisms causing nonlinear microwave losses in high-Tc superconductors, *8th Workshop RF Supercond.*, Abano Terme, Italy, 1997, Invited Paper.
- S. Sridhar, Non-linear microwave response of superconductors and ac response of the critical state, *Appl. Phys. Lett.*, **65**:1054–1056 (1994).
- J. H. Oates, et al., A nonlinear transmission line model for superconducting stripline resonators, *IEEE Trans. Appl. Supercond.*, **7**:17–22 (1993).
- D. E. Oates, et al., Microwave power dependence of $\text{YBa}_2\text{Cu}_3\text{O}_7$ thin-film Josephson edge junctions, *Appl. Phys. Lett.*, **68**:705–707 (1996).
- I. Vendik and O. Vendik, *High Temperature Superconducting Devices for Microwave Signal Processing*, St. Petersburg, Russia: Skladen, 1997, Part 2, Chap. 7.
- B. S. Karasik, et al., Subnanosecond switching of YBaCuO films between superconducting and normal states induced by current pulse, *J. Appl. Phys.*, **77**:4064–4070 (1995).
- I. Vendik, et al., The superconducting microwave devices based on S-N transition in HTS films, *27th Eur. Microw. Conf. Proc.*, 1997, pp. 909–914.
- W. W. Mumford and E. H. Scheibe, *Noise Performance Factors in Communication Systems*, Dedham, MA: Horizon House-Microwave, 1968, UMI Out-of-Print Books on Demand.
- S. H. Talisa, et al., Dynamic range considerations for high-temperature superconducting filter applications to receiver front-ends, *IEEE MTT-S Int. Microw. Symp. Dig.*, **2**:997–1000 (1994).
- G. Koepf, Superconductors improve coverage in wireless networks, *Microw. RF*, **37**(4):63–74 (1998).
- H. Chaloupka, in H. Weinstock, ed., *Applications of Superconductivity*, Dodrecht, The Netherlands: Kluwer, 2000, Chapter 6.
- C. Collado, et al., Prediction of nonlinear distortion in HTS filters for CDMA communication systems, *IEEE Trans. Appl. Supercond.*, **13**(2):328–331 (2003).
- G.-C. Liang, et al., High-temperature superconducting microstrip filters with high power handling capability, *IEEE MTT-S Int. Microw. Symp. Dig.*, **1**:191–194 (1995).
- B. A. Willemsen, A. H. Cardona, N. O. Fenzi, and R. J. Forse, *High temperature superconducting structures and methods for high Q, reduced intermodulation resonators and filters*, U.S. Patent 6,026,311 (2000).
- Z.-Y. Shen, et al., Power handling capability improvement of high-temperature superconducting microwave circuits, *IEEE Trans. Appl. Supercond.*, **7**:2446–2453 (1997).
- H. Chaloupka, et al., Superconducting planar disk resonators and filters with high power handling capability, *Electron. Lett.*, **32**:1735–1736 (1996).

36. S. Kolesov, et al., Planar HTS structures for high-power applications in communication systems, *J. Supercond.*, **10**:179–187 (1997).
37. M. Reppel and H. Chaloupka, Novel approach for narrowband superconducting filters, *IEEE MTT-S Int. Microw. Symp. Dig.*, **4**:1563–1566 (1999).
38. <http://www.conectus.org/>
39. <http://www.suptech.com/index.html>
40. R. R. Mansour, et al., Design considerations of superconductive input multiplexers for satellite applications, *IEEE Trans. Microw. Theory Tech.*, **44**:1213–1228 (1996).
41. S. H. Talisa, et al., High-temperature superconducting four-channel filterbanks, *IEEE Trans. Appl. Supercond.*, **5**:2079–2082 (1995).
42. T. G. Kawecki, et al., The high temperature superconductivity space experiment (HTSSE-II) design, *IEEE Trans. Microw. Theory Tech.*, **44**:1198–1212 (1996).
43. W. G. Lyons, et al., High temperature superconductive wide-band compressive receivers, *IEEE Trans. Microw. Theory Tech.*, **44**:1258–1278 (1996).
44. G. C. Liang, et al., Space-qualified superconductive digital instantaneous frequency-measurement subsystem, *IEEE Trans. Microw. Theory Tech.*, **44**:1289–1299 (1996).
45. N. Fenzi, et al., Development of high temperature superconducting 100 nanosecond delay line, *SPIE Proc.*, **2156**:143–151 (1994).
46. S. H. Talisa, et al., High-temperature superconducting wide band delay lines, *IEEE Trans. Appl. Supercond.*, **5**:2291–2294 (1995).
47. M. Biehl, et al., A 4-bit instantaneous frequency meter at 10 GHz with coplanar YBCO delay lines, *IEEE Trans. Appl. Supercond.*, **5**:2279–2282 (1995).
48. H. Weinstock and M. Nisenoff, eds., *Microwave Superconductivity*, Chapt. 15, Dordrecht, the Netherlands: Kluwer, 2001.
49. H. Weinstock and M. Nisenoff, eds., *Microwave Superconductivity*, Chapt. 11, Dordrecht, the Netherlands: Kluwer, 2001.
50. Z. Kolesov, et al. Cryogenic BTS receiver front end demonstrator, *30th European Microwave Conference*, 2000, pt. 3, p. 230–232 vol.3.

FURTHER READING

- H. Weinstock and M. Nisenoff, eds., *Microwave Superconductivity*, Dordrecht, the Netherlands: Kluwer, 2001.
- M. J. Lancaster, *Passive Microwave Device Applications of High-Temperature Superconductors*, Cambridge, UK: Cambridge University Press, 1997.
- Z-Y. Shen, *High-Temperature Superconducting Microwave Circuits*, Norwood, MA: Artech House, 1994.
- R. R. Mansour, Microwave Superconductivity, *IEEE Trans. Microw. Theor. Tech.*, **50**(3):750–759 (2002).
- B. A. Willemsen, HTS filter subsystems for wireless telecommunications, *IEEE Trans. Applied. Supercond.*, **11**(1):60–67 (2001).
- N. Klein, High-frequency applications of high-temperature superconductor thin films, *Rep. Prog. Phys.*, **65**:1387–1425 (2002).
- A. V. Narlikar, ed., *High Temperature Superconductivity 2: Engineering Applications*, Berlin, Germany: Springer, 2004, Chapter 14.
- R. W. Simon, R. B. Hammond, S. J. Berkowitz, and B. A. Willemsen, Superconducting microwave filter systems for cellular telephone base stations, *Proc. IEEE*, **92**(10):1585–1596 (2004).

SUPERCONDUCTING MICROWAVE TECHNOLOGY

DURGA P. CHOUDHURY
S. SRIDHAR
Northeastern University

Superconductivity is a remarkable state of matter in which electric current can flow inside materials without any detectable resistance. This phenomenon was discovered by the Dutch physicist H. K. Onnes in 1911. While studying the temperature dependence of the electric resistance of mercury in his newly invented helium liquefier, Onnes found that below a temperature of about 4 K, the resistance abruptly fell to below measurable limits.

In a superconductor, perfect electric conductivity or zero resistivity occurs only below a “critical temperature” T_C . This happens because the electric current, instead of being carried by single electrons, is carried by pairs of electrons called Cooper pairs, which have the ability to conserve energy because of quantum mechanical reasons. A direct current induced in a superconducting ring has been shown to persist for over 2 years without any measurable decay. From this type of experiment, the upper limit on resistivity ρ is $\sim 10^{-25} \Omega \cdot \text{m}$. As ρ for copper is $\sim 10^{-8} \Omega \cdot \text{m}$, a factor of 10^{17} larger, it is believed that the electric resistance of a superconductor is truly zero.

Another important characteristic of superconductors was the discovery by W. Meissner and R. Ochsenfeld in 1933 that a superconductor expels all magnetic flux from its interior; that is, a superconductor is also a perfect diamagnet. This phenomenon is known as the Meissner effect.

A key area of technological applications of superconductors is in high-frequency devices, particularly at frequencies in the radiowave, microwave, and millimeter-wave spectral ranges. Broadly speaking, two principal areas of high-frequency applications can be identified:

- *Passive devices*, typically using resonant and transmission line structures, exploiting the low-loss properties of superconductors.
- *Active elements*, such as oscillators, mixers, logic elements, and other similar devices, which exploit a macroscopic quantum coherence property of the charge carriers, called the Josephson effect.

The price to pay to achieve the superior performance is the need to cool the superconducting device to temperatures well below room temperature. This means the use of cryogenic fluids like liquid nitrogen or liquid helium, or a mechanical cryocooler. Despite the need for a cryogenic environment, there are many applications where the superior performance of superconductors prevails over conventional devices.

1. SUPERCONDUCTING MATERIALS

Superconductivity has been observed in diverse types of materials including pure metals, alloys, semimetals,

organic materials, semiconductors, polymers, and even elemental insulators. Presently, at least 26 of the naturally occurring elements are known to be superconducting at sufficiently low temperatures at ambient pressure, and the number of alloys and intermetallic compounds are well above 1000.

A significant advancement in understanding superconductivity was the theory of Bardeen, Cooper, and Schrieffer in 1957. This theory successfully described the microscopic mechanism of superconductivity and explained the properties of most superconductors for nearly 30 years.

Then came the era of high-temperature superconductivity, with the groundbreaking discovery by Bednorz and Müller in 1986 of superconductivity in a Ba—La—Cu—O compound with T_C around 30 K, which subsequently earned them a Nobel Prize. This discovery rekindled the interest in superconductivity and spurred the hopes of finding new technological applications. The efforts led to the discovery of other copperoxide-based superconductors that have critical temperatures well in excess of the boiling point of nitrogen (77 K), an easily available and cheap cryogenic fluid usable for commercial applications. Presently the highest critical temperature is about 150 K at high pressures in $\text{HgBa}_2\text{Ca}_2\text{Cu}_3\text{O}_8$.

Superconductors fall in two broad categories, namely, “high critical temperature” (or “high- T_C ”) and “low critical temperature” (or “low- T_C ”) materials. (There are many other ways of classifying them, such as Type I and Type II superconductors, heavy fermion, and conventional superconductors.) Some examples of low- T_C superconductors, particularly relevant to commercial applications, are niobium and its alloys, such as NbN and Nb_3Ge . These have critical temperatures in the region of 10 K to 20 K. The high- T_C superconductors that are most commonly used include $\text{YBa}_2\text{Cu}_3\text{O}_7$ (commonly referred to as YBCO or Y-123, $T_C \sim 93$ K), $\text{Bi}_2\text{Sr}_2\text{CaCu}_2\text{O}_8$ (commonly referred to as BSCCO or Bi-2212, $T_C \sim 90$ K), and $\text{Tl}_2\text{Ba}_2\text{Ca}_2\text{Cu}_3\text{O}_{10}$ (TBCCO or Tl-2223, $T_C \sim 125$ K).

Besides the critical temperature, some other relevant physical parameters that characterize a superconductor are as follows:

- *The London penetration depth* (λ_L): The depth to which an applied direct current (dc) magnetic field is confined because of the Meissner effect.

- *The coherence length* (ξ): The length scale over which the two electrons forming the Cooper pairs are separated.
- *The (thermodynamic) critical field* (H_C): The magnetic field whose associated free energy is equal to the free energy change in the superconducting transition. A “Type I” superconductor will completely expel the applied field below H_C and will become normal abruptly as the applied field exceeds this magnitude, assuming no demagnetization effects. For “Type II” superconductors (which includes practically all of the superconductors of technological interest), the field starts to penetrate in the form of vortices at a “lower critical field” H_{C1} ($< H_C$), but superconductivity is not quenched until the applied field exceeds the “upper critical field” H_{C2} ($> H_C$).

Some superconductors of relevance to microwave applications are described in Table 1 along with their relevant properties (λ_L , ξ , H_{C1} , and H_{C2} quoted are extrapolated to $T = 0$ K).

1.1. Substrates for Thin-Film Superconductors

For most electronic applications, including microwave devices, superconductors are necessarily used in the form of thin films. This requires the use of a foreign material for a substrate. Some of the popular substrates include sapphire ($\alpha\text{-Al}_2\text{O}_3$), lanthanum aluminate (LaAlO_3), and magnesium oxide (MgO). Ferroelectric substrates like strontium titanate (SrTiO_3) and $\text{KTa}_{1-x}\text{Nb}_x\text{O}_3$ are also used to achieve tunability at the expense of additional dielectric loss.

The electrical parameters that characterize the properties of a substrate material are its dielectric constant ϵ and its loss tangent $\tan \delta$. (The loss tangent of a substrate is defined as $\tan \delta = \sigma/\omega\epsilon$, where σ is the conductivity.) Other factors such as environmental stability, mechanical strength, chemical inertness, and absence of magnetic moment are also important. Close lattice match between the deposited film and the substrate is essential to achieve good epitaxial growth. These parameters have been measured and investigated by various researchers using different techniques for most substrate materials.

In general, the dielectric constant would be more or less frequency independent unless the frequency is close to a

Table 1. Some Commercially Used Superconducting Materials and Their Physical Properties

Material	T_C (K)	λ_L (nm)	ξ (nm)	H_{C1} (Oe)	H_{C2} (Oe)	Crystal Structure
Pb	7.2	37	83.00	803	803	Face-centered cubic
Nb	9.2	32	39.00	~ 1600	~ 3200	Body-centered cubic
NbN	16.0	50	4.00	300		BI
Nb_3Ge	23.2				3.6×10^{5a}	A15
YBCO ^b	93.0	140	~ 2.00	200	$\sim 10^6$	Orthorhombic
TBCCO ^b	127.0	220 ^c	2.60 ^c			Tetragonal
BSCCO ^b	~ 90.0	500	0.16			Tetragonal

^aAt 4.2 K.

^bYBCO, TBCCO, BSCCO, and most other high- T_C superconductors are highly anisotropic. The values given are for microwave current flowing in the ab -plane, which is often the plane of epitaxial growth and the desired geometry in most technological applications.

^cAverage of ab -plane and c -axis value.

Table 2. Some Commonly Used Substrate Materials for Superconducting Thin-Film Devices

Material	Dielectric Constant	Loss Tangent	Crystal Structure	Growth Surface	Remarks
LaAlO ₃	25.00	5×10^{-6}	Rhombohedral	(110)	Usually twinned
YAlO ₃	16.00	10^{-5}	Orthorhombic	(110)	
MgO	9.65	6.2×10^{-6}	Cubic	(100)	Good lattice match
Sapphire	8.60	3.8×10^{-8}	Hexagonal	(11 02)	Very low loss
NdGaO ₃	23.00	3.2×10^{-4}	Orthorhombic	(110)	Good for multilayer circuits
SrTiO ₃	300.00	3×10^{-4}	Cubic	(100)	Good for tunable device applications
YSZ	27.00	7.4×10^{-4}	Cubic	(100)	

resonance frequency of the material. The dielectric constant is also expected to have a weak temperature dependence for nonferroelectric substances. The loss tangent is expected to increase with temperature. Table 2 provides the most commonly accepted values of these material parameters for some of the substrates, measured at 10 GHz and 77 K unless otherwise stated.

Most of these materials have high ϵ ; this imposes certain restrictions, especially for high-frequency applications. A high ϵ reduces the dimension of the device and thus imposes stringent dimensional tolerance, especially in the millimeter-wave region. But consideration of dielectric constant has to be sacrificed for some even more important parameters, namely, a lattice match between the substrate and the film, and not widely different thermal expansivity from the superconductor. A lattice mismatch would create atomic level strain and leads to poor superconducting properties. Another criterion is that losses in the substrate must be negligible compared with the losses in the superconductor. Heavy twinning in materials like LaAlO₃ creates problems in multilayer films. When the substrate is reheated for the deposition of a new layer, the thermally induced movement of the twin boundaries strain the previously deposited layers.

There are numerous methods of depositing superconducting films on substrates, the most common being pulsed laser deposition (PLD), coevaporation, and off-axis sputtering or physical vapor deposition (PVD). Each of these methods has its pros and cons. For example, PLD produces high-quality films at a fast rate (a few angstroms per second) but only over relatively small areas, typically less than 2 in. diameter. The PVD method is useful for producing larger area films, but the deposition rate is only a fraction of an angstrom per second. Another method of film deposition, namely, metal-organic chemical vapor deposition (MOCVD), popular in the semiconductor industry, has also been tried for high- T_C superconductors, although somewhat less successfully owing to the chemical and structural complexity of the high- T_C materials. We refer the reader interested in deposition technique to some useful resources (see, for example, Ref. 1).

The “quality” of a deposited superconducting film is characterized by several parameters, such as the critical temperature T_C , the transition width ΔT_C , and the critical current density J_C , which is the maximum lossless current per unit cross-sectional area that the film can carry. The higher the T_C and J_C and the lower the ΔT_C , the better the film.

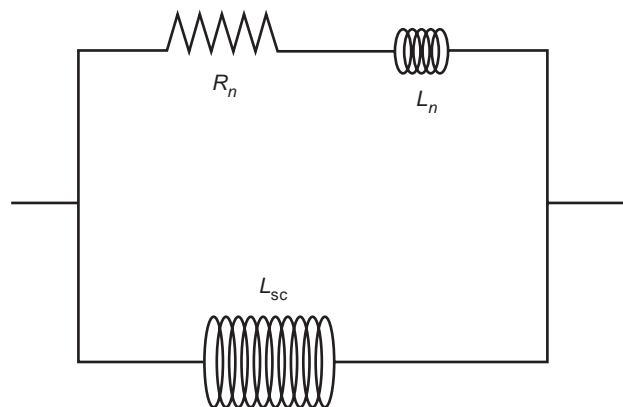
2. THE SUPERCONDUCTOR–MICROWAVE INTERACTION

A superconductor has zero electrical resistance only at zero frequency (dc). At any finite frequency, it exhibits losses that increase with frequency. A superconductor can be regarded as being composed of two types of charge carriers, one consisting of the lossless Cooper pairs and the other being lossy “quasiparticles.” Such a description is known as the “two-fluid model” and is applied to all known superconductors.

The finite frequency [alternating current (ac)] response of a superconductor is characterized in terms of a generalization of Ohm’s law: $\mathbf{J} = \sigma_s \mathbf{E}$, where \mathbf{E} is the applied electric field and $\sigma_s = \sigma_1 - i\sigma_2$ is the complex conductivity. The normal part σ_1 comes from the motion of the quasiparticles, and the imaginary part σ_2 comes from that of the Cooper pairs. For most superconductors well below the transition temperature, $\sigma_2 \gg \sigma_1$. The frequency ω , wave vector \mathbf{k} , temperature T , and current density \mathbf{J} dependence of σ_s contains all the information about the electrical properties of the superconductor. For a normal metal, $\sigma_s = \sigma_n$ is purely real.

Figure 1 shows a lumped circuit equivalent of a superconductor. The large inductive element L_{sc} represents the lossless carriers, and the parallel branch with a series combination of a resistor R_n and an inductance L_n represents the quasiparticles. At dc, the large inductor shorts out the resistive branch, leading to zero resistance, whereas at finite frequencies, there is always dissipation.

As the excitation frequency increases, the impressed electromagnetic field is confined closer to the surface. In a normal metal, this is known as the skin effect and the

**Figure 1.** Two-fluid model equivalent circuit of a superconductor.

characteristic length of confinement (the “skin depth”) is given by $\delta_n = (2/\mu\omega\sigma_n)^{1/2}$, where σ_n is the (normal) conductivity. δ_n for Copper at 10 GHz and 77 K is 0.55 μm . In a superconductor at temperature $T \ll T_c$, the skin depth is replaced by the “London penetration depth” $\lambda_L = 1/(\mu\omega\sigma_2)^{1/2}$. The penetration depth is typically independent of frequency from dc to microwave frequencies and is comparable with the London penetration depth in Table 1.

The interaction of a time-varying electromagnetic field and a metal (normal or superconducting) at microwave frequencies is best described in terms of the surface impedance defined as $Z_s = R_s + iX_s = (i\mu\omega/2\sigma)^{1/2}$. R_s and X_s are the surface resistance and reactance, respectively. As can be seen, R_s and $X_s \propto \omega^{1/2}$ in a normal metal, where $\sigma = \sigma_n$. On the other hand, $R_s \propto \omega^2$ and $X_s \propto \omega$ in an “ideal” superconductor. This can be easily verified by assuming σ_1 and λ_L to be frequency independent and $\sigma_2 \gg \sigma_1$.

The property that makes superconductors attractive for passive microwave circuits is that their surface resistance is orders of magnitude lower than that of normal metals. For example, thin-film YBCO has a surface resistance of <0.1 m Ω at 77 K and 10 GHz compared to 8.7 m Ω of copper under identical conditions, and this difference is even higher at lower temperatures. Figure 2 shows the measured frequency and temperature dependence of R_s of some of the most common superconducting and nonsuperconducting materials [3].

2.1. Nonlinearity in High- T_c Superconductors

For most superconductors, particularly the high- T_c superconductors, the surface impedance increases with applied microwave power, even for moderate power levels (<0.1 W). In other words (unlike normal metals), they act as nonlinear circuit elements. This nonlinear response often poses serious constraints on the utility of superconductors in practical devices. Some specific examples of such limitations are as follows:

- Degradation of insertion loss with increasing power.
- Generation of harmonic frequencies: For an applied signal at frequency f , most of the harmonic power is generated at a frequency of $3f$. Given today’s tight use of the electromagnetic spectrum, practically all frequency ranges have been preassigned by the appropriate authorities (e.g., the Federal Communication Commission in the United States) with just the required amount of bandwidths. Thus, radiation by a device at frequencies far outside the designated frequency of operation is unacceptable.
- Frequency mixing, leading to intermodulation products (intermods): For two nearby frequencies f_1 and f_2 , the strongest intermods are produced at $2f_1 - f_2$ and $2f_2 - f_1$. The result is that spurious frequencies are produced in devices.

Figure 3 shows the effect of nonlinearity on a suspended line resonator with a resonance frequency of 3.73 GHz [4]. At low power levels, the response in the frequency domain is close to a Lorentzian. As the input power is

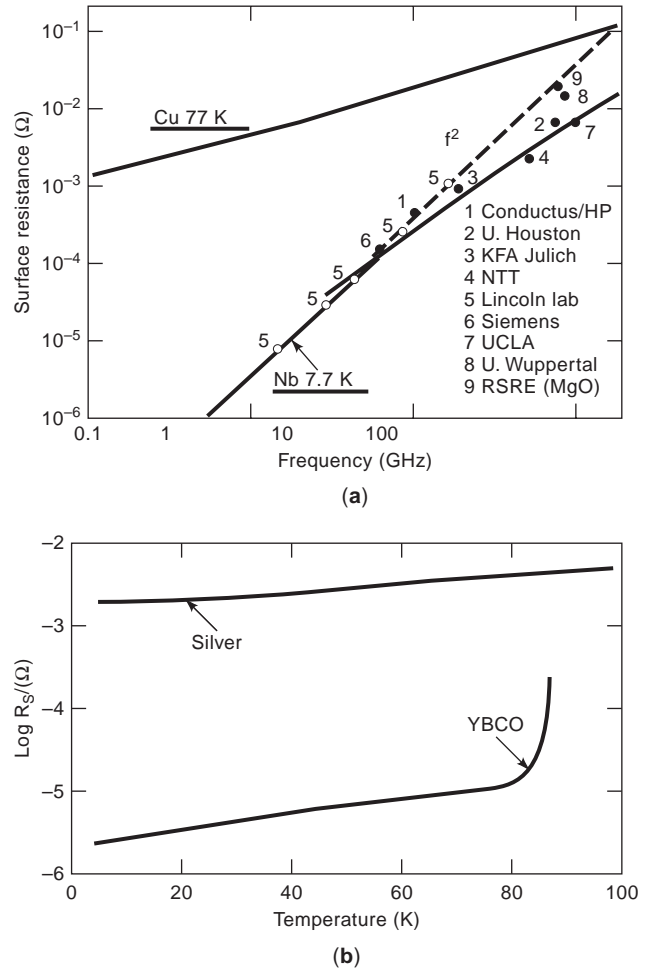


Figure 2. (a) Comparison of the surface resistance of YBCO at 77 K with other superconducting materials. The horizontal bands represent YBCO. (From Ref. 3, with permission.) (b) Temperature dependence of the surface resistance of YBCO grown by several techniques compared with niobium and niobium-tin superconductors at the same reduced temperature. The scale on the upper axis refers to the reduced temperature for the Nb₃Sn and Nb, whereas the lower scale refers to the actual temperature of the YBCO films. The T_c of the three materials coincides. $f = 8$ GHz.

increased, the shape begins to distort, and the Q and the resonance frequency go down. This also highlights the point that at high power levels, the Q of a superconducting resonator cannot be defined in terms of a “3 dB bandwidth.” A quantitative measure of the nonlinearity of a device is specified in terms of its third-order intercept (TOI), defined as the input power at which power output at the fundamental and the third harmonic equal each other. Single-tone TOI for most commercially used HTSC materials is at least 70 dBm (10 kW).

These effects together limit the maximum power that a passive superconducting circuit can handle, and raising the power handling capacity has been one of the prime concerns of material scientists and engineers alike. Much of the nonlinearity of the high- T_c materials is ascribed to material properties (e.g., granularity and “flux pinning”) and is expected to improve with synthesis and deposition

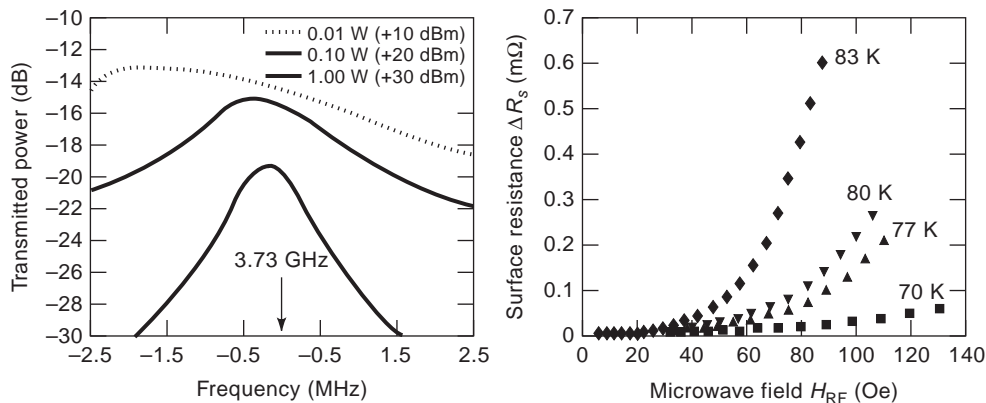


Figure 3. (Left) Frequency-domain response of a suspended resonator. Notice the deviation from a Gaussian shape as the input power increases. (Right) The R_s of a similar resonator against applied power at different temperatures. (From Ref. 4, with permission.)

techniques. From a design point of view, nonlinearities can be suppressed by increasing the surface area of the device, leading to lower current densities and avoiding current crowding at the edges. Thus, a planar filter can handle significantly higher power than a stripline, and a cavity resonator has Q value orders of magnitude higher than one built out of a transmission line, even factoring out the losses in the substrate. However, higher dimensional circuits are not always practical for many applications because they take up more space and often have the problem of mode degeneracy (i.e., more than one mode of oscillation at the same frequency). The latter problem can often be solved by making the circuit slightly asymmetrical, but then modeling them with a computer becomes more cumbersome.

3. PASSIVE MICROWAVE CIRCUITS

Passive microwave circuits are some of the most promising applications of superconductors to date. In the following we shall focus on the advantages of high-temperature superconductors (HTS) materials and the special considerations that applies to them. General ideas about passive microwave devices are available in the literature. For a good review of the current state of the art, see Ref. 5. For a more elementary introduction, see Ref. 6.

Superconductors are an attractive alternative to “conventional” materials for three principal reasons:

1. *Very low surface resistance* compared with normal metals: For example, insertion loss of a superconducting filter (~ 0.1 dB) is usually at least 3 dB lower than one made out of high-quality metal (e.g., oxygen-free high-purity copper) under equivalent conditions. Thus in applications where the signal strength is low, superconductors are the material of choice.
2. *A frequency-independent penetration depth.* In normal metals, the skin depth is proportional to the inverse square root of the frequency of the signal, giving rise to strong dispersion of a wideband signal,

unacceptable in many applications. In superconductors, the penetration of electromagnetic field is dominated by the “London penetration depth,” which is independent of frequency, giving rise to phase dispersion-free propagation in the transverse electromagnetic (TEM) mode.

3. *The ability to be fabricated in extremely compact geometries,* arising from the low loss mentioned above. Thus, a several-meter-long coaxial delay line made out of a normal conductor can be replaced with a superconducting one that is only a few square centimeters in area, and bulky dielectric resonator filters can be replaced by compact planar superconducting filters.

3.1. Transmission Line

A microwave transmission line can be constructed in several geometries, each having its pros and cons. The most common geometries are microstrip, stripline, and coplanar. Many other novel geometries such as the suspended line and coplanar strips are also used for special-purpose applications. The basic concepts behind transmission line and distributed circuits is the same whether or not they are made out of superconductors, and the interested reader can find them elsewhere (see, for example, Ref. 7). Here we will briefly discuss only those issues that are specific to superconducting transmission lines.

The two major distinctions between superconducting and nonsuperconducting transmission lines stem from the temperature and frequency dependence of the characteristic impedance of the line, defined as $Z_0 = (L/C)^{1/2}$ where L and C are the equivalent lumped inductance and capacitance, respectively. In addition to the usual geometric inductance, superconductors have temperature-dependent kinetic inductance because of the presence of the Cooper pairs. Also, for sufficiently low temperatures ($T \ll T_C$, or more pertinently, $\lambda_L \ll \delta$), the penetration depth is independent of the frequency, giving rise to a phase dispersion-free propagation for the TEM mode. Nonlinear effects are another major complication in dealing with superconducting transmission lines, as has been discussed. The

nonlinear effects are particularly worse in the edges of the line where the current density is maximum. Therefore, a good design for a passive superconducting circuit tends to avoid sharp edges as much as possible. Owing to these, full-wave analysis of superconducting transmission lines is quite a daunting task that cannot be done satisfactorily using most commercially available CAD programs and often must be carried out for individual needs.

One of the most promising applications of superconducting transmission lines is in the form of hybrid interconnects between components, both semiconducting and superconducting and both analog and digital.

3.2. Resonators

The “quality factor” (Q) of a resonator is defined to be $Q = U/f_0/P$, where U is the total energy stored in the oscillator, f_0 is the resonance frequency, and P is the power dissipated per cycle. As $P = \int R_s H^2 dA$, where the integral is over the surface of the material comprising the resonator walls, the Q can then be written as $Q = \Gamma/R_s$, where Γ is a geometric factor, for a resonator entirely comprising a single material.

The advantage of a superconducting resonator over a normal metal one is the very high Q owing to the much smaller surface resistance of the former. At 10 GHz, Q as high as 10^{11} can be achieved (using niobium cavities in TE₀₁₁ mode), compared with a maximum Q of around 10^4 using copper. Superconducting cavities are typically operated in the TE₀₁₁ mode because this has no electric fields on the cavity walls. Cavities have been made out of both low-temperature and high-temperature superconductors [8], although the latter is a lot harder to make owing to the ceramic nature of the material. Superconducting cavities such as these play an important role as a research tool for precision measurements of surface impedance of superconductors and other materials. Figure 4 shows a picture

of a niobium cavity that was fabricated at Northeastern University and is used to measure the surface impedance of other crystalline superconductors using the cavity perturbation technique [9].

A major application of superconducting cavities is in providing large high-frequency electric fields for accelerating subatomic and atomic particles. The fields in a cavity resonator are given by $E_{\max} = \gamma(QP_{\text{abs}})^{1/2}$ so that significantly larger fields can be achieved with high Q cavities for much lower absorbed powers P_{abs} . A notable example is the continuous electron beam accelerator facility (CEBAF) for heavy ions, which uses superconducting niobium cavities operating at megahertz frequencies.

Superconducting microwave cavity resonators are among the most stable frequency standards available today owing to their very high Q values. One of the applications of such high-stability frequency standards is in satellite and deep-space communications, where it is important to maintain precise clocks on board the satellite to improve synchronization between the ground-based clock and the satellite or space vehicle’s on-board clock.

Another potential application is in the master oscillator of a Doppler radar. A Doppler radar identifies the target velocity by measuring the frequency shift of the reflected beam. Clearly, for the measurement to be reliable, the frequency of the source has to be highly stable. This is especially important for detecting targets flying close to the ground (e.g., a cruise missile), because reflections from the ground (the “ground noise”) can completely mask the signal.

3.3. Filters

A filter is realized by a set of coupled resonators with closely spaced resonance frequencies. The response of each resonator is represented as a pole in the frequency domain. Thus a filter with n resonating elements is called

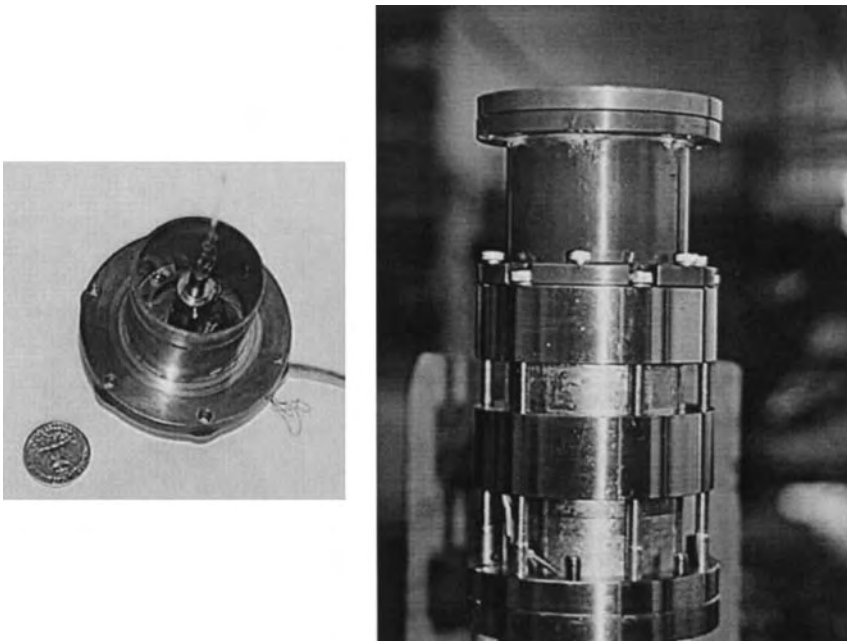


Figure 4. A superconducting niobium cavity used for surface resistance measurement. The specimen under test is thermally insulated from the cavity using a sapphire rod, allowing it to be probed up to nearly room temperature while the cavity is still superconducting. (Right) The disassembled cavity showing the sapphire sample mount. (Left) The packaged structure. Q values of $\sim 10^7$ to 10^8 at 4.2 K are routinely obtained in this setup. (Courtesy of Z. Zhai and H. Srikanth.)

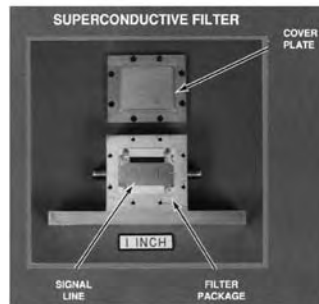


Figure 5. A four-pole superconducting filter and its measured performance. (Courtesy of Dr. Daniel Oates, MIT Lincoln Laboratory.)

an n -pole filter. The resonators can be lumped (e.g., tank LC oscillators) or distributed (e.g., half-wave transmission lines.) Clearly, the greater the number of poles in a filter, the greater the bandwidth that can be achieved for a pre-set filter skirt and band ripple, or the steeper the filter skirt and smaller the band ripple for a given bandwidth. Both are desirable. However, increasing the number of elements increases the insertion loss proportionally. Thus, many applications that require *both* a small insertion loss and steep filter skirt with low band ripple cannot be realized using conventional materials such as high-purity copper.

Alternative technologies such as surface acoustic wave (SAW) devices do produce better results, but are still too lossy (typically 2 dB to 4 dB). Dielectric resonator based filters have low loss, but are too bulky for many lucrative applications. This is precisely why superconductors are the material of choice for making high-performance filters. The extremely low surface resistance allows a designer to use a lot more elements for a given amount of insertion loss.

Figure 5 shows a four-pole microstrip Chebyshev filter fabricated at the MIT Lincoln Laboratory with a 4.8 GHz center frequency and 100 MHz bandwidth patterned on an LaAlO_3 substrate with YBCO film. The filter uses a “hair pin try”; that is, the resonators are bent with a U-turn to save wafer space. The right-hand side of Fig. 4 shows the measured insertion loss (S_{21}) of the filter at 77 K temperature. Also shown for reference is the performance of equivalent elements made out of silver (Ag) at 77 K and gold (Au) at room temperature (300 K). The advantages of high- T_C superconducting filters are quite obvious.

One of the problems in working with HTS material is the lack of availability of large wafers of acceptable quality. The maximum size of high-quality HTS films are presently limited to about 5 cm, compared with 30 cm wafers of semiconductors. This poses a problem in two cases: (1) where the center frequency is low, requiring the length of the transmission lines of a distributed filter to be long, and (2) where the bandwidth is tight (a fraction of 1%), requiring very weak coupling, and hence large separation between elements. The first problem calls for miniaturization of the device, and there are several means of accomplishing this, including the use of lumped resonators [10] and high-dielectric-constant substrates. The second problem is usually solved by a technique called staggering.

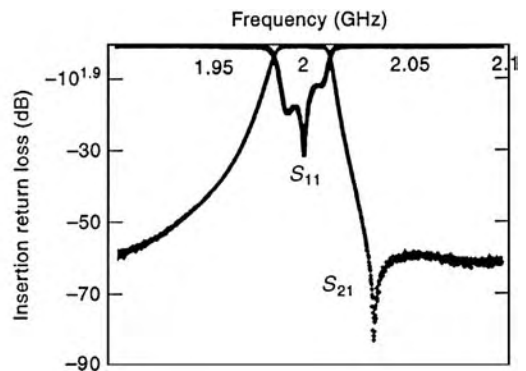


Figure 6 shows a photograph of a high-performance lumped-element nine-pole Chebyshev filter.

3.3.1. Frequency Agile Devices. A filter is much more useful if it can be tuned. Several innovative approaches to tune a passive filter have been tried. One method consists of changing the resonance frequency of the individual resonators (due to change in the kinetic inductance) with temperature. The desired variation in temperature is achieved by a control line in the form of a heating element placed close to the resonators. A better method is to build the filter on a ferroelectric substrate with a low Curie temperature such as $\text{KTa}_{1-x}\text{Nb}_x\text{O}_3$ and $\text{Sr}_{1-x}\text{Pb}_x\text{TiO}_3$ [11]. The permittivity of the substrate can be changed by applying a bias voltage, thus providing the necessary tuning. The optimal temperature of operation is slightly above the Curie temperature of the substrate to avoid hysteresis and to produce maximum tunability for a given bias voltage. Impedance matching of the input and output is done with a set of ferroelectric transformers. As these techniques essentially manipulate the electrical length of the filter elements, the same methods can also be used to tune the parameters of other passive structures.

Another important type of filter is a “chirp” filter. A “chirp” is essentially a frequency-modulated signal whose frequency increases (“upchirped”) or decreases (“downchirped”) with time. One of the applications of chirp signals is in Doppler radars to optimize power output and bandwidth, both of which are desirable. Using a simple sinusoidal signal, however, both cannot be achieved

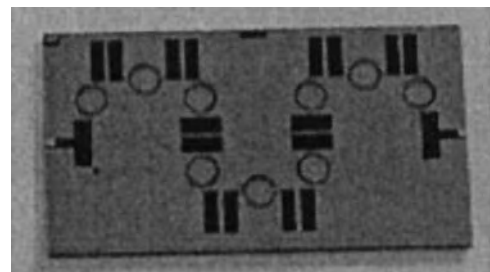


Figure 6. A nine-pole lumped Chebyshev filter from Superconductor Technologies Inc. (Courtesy of Dr. Balam Willemsen, Superconductor Technologies, Inc.)

simultaneously. A higher bandwidth means a shorter pulsewidth, which limits the maximum power transmitted per pulse and vice versa. A chirped waveform gets around this limitation. Another application is to compensate the distortion of a wave packet after passing through a dispersive transmission line. The principal advantage of constructing a chirp filter out of superconducting material is low dispersiveness.

A superconducting chirp filter in microstrip geometry consists of a series of quarter-wave forward-coupled transmission lines that are deliberately decoupled for a specified length between the couplings. The transmission line is wound in the form of a spiral to optimally use the film surface. As a pulse is applied to the input, the individual frequency components couple to the output line that corresponds to their resonance frequencies. Depending on whether the resonators are increasing or decreasing in length down the line, a downchirped or upchirped signal is obtained at the output.

3.4. Antenna

Using superconducting antennas can improve efficiency enormously because of their lower loss (for a general discussion of antennas, see Ref. 12). In particular, there are three situations when a superconducting antenna can outperform one made out of a normal metal sufficiently to merit its use:

1. *Electrically Short Antennas.* A dipole antenna has maximum radiation efficiency when its characteristic length is an integral multiple of the wavelength being radiated. For low-frequency applications (such as underwater communication, which involves frequencies of the order of 15 kHz), this length can be unrealistically large, and hence a shorter antenna has to be deployed. The radiated power P is proportional to $(l/\lambda)^2$ for a linear (electric dipole) antenna and $P \propto (D/\lambda)^4$ for a circular loop (magnetic dipole) antenna, where l is the length of the linear antenna, D is the diameter of the loop antenna, and λ is the radiated wavelength. For $l, D \ll \lambda$, the impedance of the antenna is mostly reactive and most of the power

is dissipated as ohmic losses in the antenna and the feed network. Therefore, introduction of superconducting radiating elements and feed networks can dramatically improve the radiation efficiency at low-frequency regions.

2. *Superdirective Antennas.* A superdirective antenna [13] has directional gain much larger than a conventional one. This can be of advantage in radio beacons and radar transmitters. A superdirective antenna is realized in practice by an array of closely spaced (separation \ll wavelength) dipole elements that are excited approximately 180° out of phase with respect to their neighbor. Such a structure has a low efficiency when built out of normal metal because ohmic losses in each individual element add up. In addition, these antennas have inherently low radiation efficiency because of cancellation of the radiation field, and use of HTS material can enhance efficiency.
3. *Millimeter-Wave Antennas and Feed Networks.* Superconducting antennas also improve the performance of antenna arrays and other distributed feed systems, where the power gain because of the distributed structure has to compete with the loss in an increasing number of elements. In a copper microstrip antenna, the overall gain begins to decrease beyond about 40 elements, whereas the same antenna employing superconducting elements shows an increase in gain up to about 400 elements. This increase in gain can be crucial in mission critical applications such as military target tracking systems.

Figure 7 is a photograph of a 16-element phased-array antenna that was developed at the U.S. Air Force Rome Laboratory.

3.5. Delay Lines

Requirements for a good delay line are low loss, low dispersion, and large delay for unit size/weight of the material. Superconducting delay lines are far superior to normal metal ones in satisfying these requirements, so

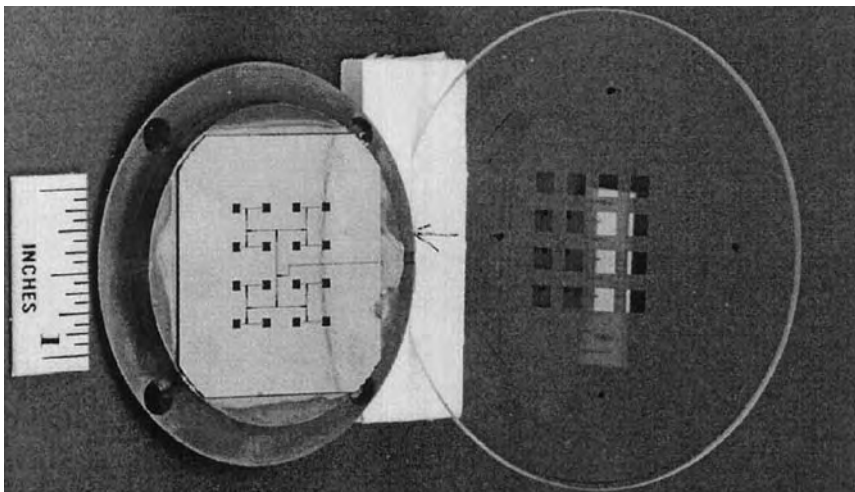


Figure 7. A 16-element superconducting phase array antenna and the feed network. An LaAlO_3 substrate is holding the HTS film. To the right of it is a 1 mm quartz plate holding the corresponding copper patches that provides an electromagnetic coupling to room temperature environment. A 0.5 mm vacuum between the two and low thermal conductivity spacers provide the required thermal isolation. The quartz plate has the necessary mechanical strength to withstand the atmospheric pressure and also serves as a radome. The antenna operates at 20 GHz. (Courtesy of Dr. Jeffrey Herd, U.S. Air Force Research Laboratory.)

much so that superconducting delay lines were in application even before the advent of high- T_C superconductivity [14]. Delays of the order of 20 ns can be routinely achieved with HTS materials on a substrate with an area of a few square inches, with good possibilities of achieving more than 100 ns in the near future. A copper coaxial line has to be several meters long for producing the same amount of time delay and would have a high insertion loss.

A novel application of a delay line is the measurement of instantaneous frequency of a nonperiodic signal [15]. This is achieved by splitting the input signal power equally between a series of n phase discriminating units, where n is the number of bit of frequency resolution desired. Each phase discriminating unit consists of a mixer, one port of which is fed by the signal directly and the other one by the same signal delayed.

4. ACTIVE MICROWAVE CIRCUITS

In 1962 B. D. Josephson predicted that when two superconductors are separated by a thin layer of metal or an insulator, a lossless current can flow up to a certain critical value I_C before a voltage appears across the junction. This is the manifestation of the phenomena that the Cooper pairs that carry lossless electric current can tunnel through the potential barrier represented by the junction material. Josephson’s remarkable prediction was verified experimentally the following year and is known as the Josephson effect. The Josephson effect opened the way for several new applications of superconductors, which

exploit the fact that superconductivity is actually an amazing manifestation of quantum mechanics on a macroscopic scale. The most noteworthy of these is the superconducting quantum interference device (SQUID) magnetometer. With sensitivities approaching 10^{-15} T/Hz^{1/2} values, SQUIDS can measure magnetic field with precision that is unimaginable with any conventional techniques. The interested reader is referred to some useful reference for further details (see, for example, Ref. 16). In the following, we shall describe some of the microwave applications of the Josephson effect that have the potential to radically alter the future of microelectronics.

The Josephson current I is related to the phase difference θ between the Cooper pair on the two sides of the junction as $I = I_C \sin \theta$. When current across the junction exceeds the critical value, a voltage V appears across it that is related to time rate of change of θ as $\partial\theta/\partial t = 4\pi eV/h$ (i.e., the phases of Cooper pairs on the two sides of the junction begin to “slip” relative to each other.) Figure 8(a) shows a lumped circuit equivalent of a Josephson junction (JJ), called a resistively shunted junction (RSJ model). The conductance and the capacitance represent the resistive and displacement current flow across the junction. The static characteristics of the circuit is given in terms of Stewart–McCumber parameter [17,18] $\beta = 4\pi eI_C C/hg^2$.

Elementary mathematical analysis of Fig. 8(b) shows that the time-domain response of the circuit can be written as $I/I_C = \beta d^2\theta/d\phi^2 + d\theta/d\phi + \sin \theta$, where $\phi = 4\pi eI_C t/hg$, t being time. This is equivalent to the equation describing the motion of a simple pendulum in a gravitational field. Thus the Josephson current behaves like a

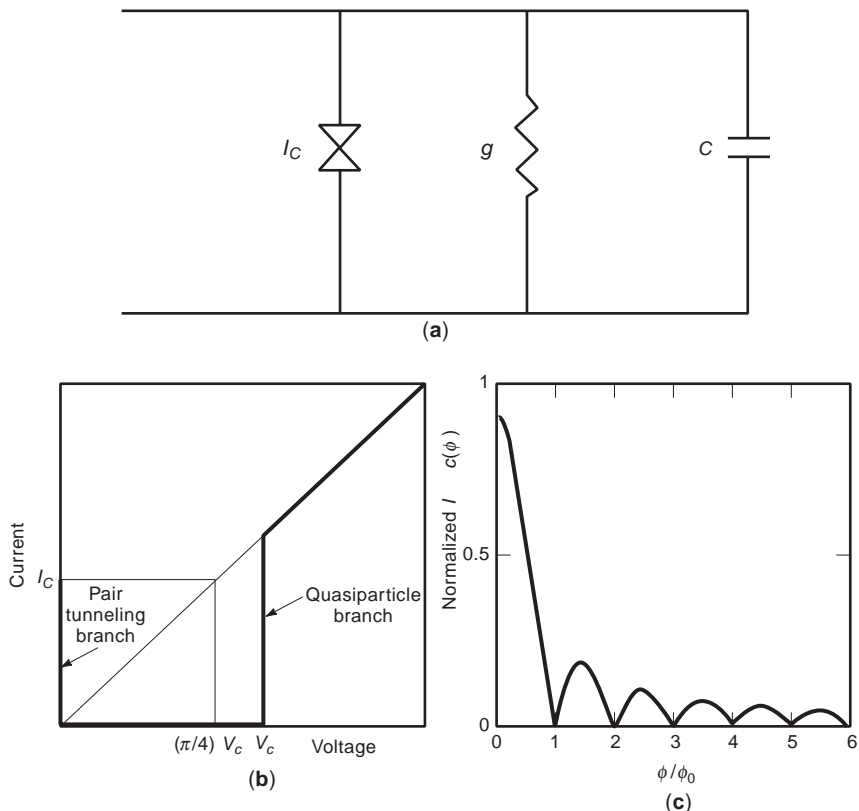


Figure 8. (a) Lumped equivalent of a superconductor-insulator-superconductor (SIS) Josephson junction. (b) I - V characteristics of an SIS Josephson junction. (c) Dependence of junction critical current on the threaded flux.

damped harmonic oscillator for small currents, which is underdamped for $\beta < 1/4$ and overdamped for $\beta > 1/4$. This also implies a hysteretic $I-V$ behavior in the a region $I_{\min} < I < I_C$, and the value of I_{\min} must be obtained by solving the above equation. The value of I_{\min} decreases monotonically with increasing β . Another useful property of a JJ is the flux dependence of the critical current. If the JJ has a flux Φ threaded to it, then the critical current is given by $I_{C\Phi} = I_C \sin(\pi\Phi/\Phi_0)/(\pi\Phi/\Phi_0)$, where $\Phi_0 = h/2e = 2 \times 10^{-15}$ Wb is the “flux quantum.” (The flux threaded through any superconducting ring must be an integral multiple of Φ_0 .) This is shown in Fig. 8(c).

To date, the most promising applications of superconducting active devices have been demonstrated only in low-temperature superconductors, most notably lead, niobium, and niobium nitride with aluminum oxide (AlO_x), magnesium oxide (MgO), and lead oxide (PbO) as the insulating barriers. For a Cooper pair to tunnel coherently across a junction, its thickness must be comparable with the coherence length of the material, which is extremely small for high- T_C superconductors (see Table 1). The critical current in these materials is also rather high (of the order of milliamperes), which is required for the Josephson coupling energy $\hbar I_C/4\pi e$ to overcome the thermal energy $k_B T$, but it produces excessive Joule heating in the resistive shunts and high voltages across inductances. There are additional factors arising out of complex crystal structure and presence of “weak links” (i.e., small angle grain boundaries) that make fabrication of JJs difficult in these materials. There are several possible analog and digital applications of the Josephson effect in microwave frequency regime, some of which are outlined in the following.

4.1. Superconducting Digital Logic Circuits

From the early days of its discovery, the JJ has been eyed as a potential replacement of semiconducting logic gates (a detailed review is provided by Ref. 19). Josephson junctions are inherently bistable (with zero and finite resistivity). However, the real driving force behind a “superconducting supercomputer” comes from three different sources:

- Josephson junctions can be switched *much* faster than a CMOS logic gate, where the parasitic and junction capacitance limits the minimum switching time. For a JJ, however, the theoretical limit on switching time is $\hbar/2\pi\Delta$, where \hbar is Planck’s constant and Δ is the superconducting energy gap. For niobium, this corresponds to 0.22 ps, and practical circuits with switching times of 1.5 ps have been fabricated. The large difference between the theoretical upper limit in switching speed and those practically achieved stems from parasitic capacitance in the junction. However, there are no space-charge effects in a JJ, and hence these capacitances are much smaller compared with semiconductor circuits.
- Average power dissipation per gate in a JJ is at least two orders of magnitude lower than equivalent semiconductor gates. This means that the gates can be

packed closer together, thereby reducing the propagation delay of the signal, another constraint in high-speed digital circuits. As an example, a four-bit microcontroller fabricated out of JJ and clocked at 770 MHz dissipated 5 mW, in contrast to a replica made out of gallium arsenide (GaAs) and clocked at 72 MHz that dissipated 2.2 W.

- Digital circuits operating over ~ 100 GHz must use superconducting interconnects, because the inherent dispersion and loss in metal interconnects will degrade the signal sufficiently to make the circuit inoperable.

Owing to the hysteretic $I-V$ characteristics of the JJ, switching between zero resistance and finite resistance states (logic 0 and logic 1 in our convention) cannot be achieved as fast as it would be in a nonhysteretic device. If the current is reduced slightly below the value at which a logic 0 to logic 1 switching takes place, the circuit will remain in logic 1 state. Owing to this property, such circuits are called “latching circuits.” The maximum clocking speed of these circuits cannot exceed a few gigahertz. To solve this problem, JJs are shunted with resistors that make them nonhysteretic. These circuits, called rapid single flux quantum (RSFQ) devices, are the basic building block of superconducting logic circuits. They differ from “conventional” logic in a fundamental way: The logic state is not decided by the voltage level of the gate but by the presence or absence of voltage pulse generated by the motion of single fluxons. Practical superconducting digital circuits with significantly higher performance have been demonstrated. Using niobium technology, a 4 bit microprocessor has been fabricated by Fujitsu and a 1 kbit random access memory (RAM) chip has been made by NEC (for a good review of recent progress in Josephson IC fabrication, see Ref. 20). Many other leading manufacturers are also pursuing this technology [21].

There are a few rather unusual problems in the practical realization of a superconducting computing device. It is impractical to realize a high-speed computer in a Von Neumann-type architecture that involves massive data transfer between a central processor and the memory, which are physically separated over a relatively long distance. An order-of-magnitude estimate of the maximum allowable data path (assuming microstrip interconnects on a substrate with dielectric constant ~ 20) of a computer operating at 300 GHz is ~ 0.3 mm. Clearly, this is very difficult to realize on a circuit board. However, applications such as dedicated digital signal processor with on-board cache memory and multichip modules can have phenomenal speed and performance increase if built using RSFQ logic.

4.2. Detectors and Mixers

The nonlinearity of a Josephson junction can be exploited to make a mixing device. In addition to the low noise and high efficiency that these devices offer, they can easily be integrated to an all-superconductor radiofrequency (RF) receiver front end.

The general principles of mixing due to photon-assisted tunneling was derived and applied to superconductor-insulator-superconductor (SIS) junctions by Tucker [22,23]. There can be two types of mixers using Josephson junctions: those using Cooper pair tunneling operating near zero bias voltage and those using quasiparticle tunneling operating near gap voltage. Quasiparticle mixers are usually preferable over Cooper pair mixers for several reasons. For one, the junction capacitance has to be small so that most of the current comes from Cooper pair tunneling and not displacement electric field. This means the use of point contact junctions that are difficult to fabricate reproducibly. Second, they are noisy because of harmonic mixing of all frequencies up to the gap frequency. According to the quantum theory of mixing, strong nonlinearity in I - V characteristics (more precisely, when $I_{dc}(V_{dc} + hv/e) - I(V_{dc}) \gg I_{dc}(V_{dc}) - I_{dc}(V_{dc} - hv/e)$) can result in conversion gain exceeding unity and conversion efficiency approaching the quantum limit even in a purely resistive mixer. Third, the shot noise in a quasiparticle mixer is lower than that in Cooper pair tunneling mixers. SIS quasiparticle mixers have been used in radio astronomy for quite a while.

4.3. Analog-to-Digital Converters

Analog-to-digital converters (ADCs) are another type of circuit where phenomenal performance improvement has been demonstrated using superconducting circuitry. While superconducting ADCs can be and have been fabricated in most architectures and have the usual advantage of a large bandwidth because of their fast switching capability, there is the additional advantage that when exploiting the multithreshold characteristics of a JJ [see Fig. 8(c)], an n -bit flash ADC requires only n comparators as opposed to $2^n - 1$ that would be normally required [24]. This allows high-bandwidth and high-resolution ADCs to be fabricated reliably and compactly.

4.4. Precision Voltage and Frequency Sources

The Josephson relation $\partial\theta/\partial t = 4\pi eV/h$ can be used both as a source of high-frequency radiation and as a dc voltage standard. The power radiated by the oscillating Josephson current in response to a small dc bias (483.5 GHz/mV) is usually too very small (a few nanowatts) to be of much practical use, but coherent Josephson arrays have been fabricated that can output as much as a few microwatts, and power levels of up to 1W have been predicted. On the other hand, when irradiated with microwaves, a JJ develops a dc voltage across it. As frequency of such radiation can be accurately controlled and measured, such devices are one of the accepted precision voltage standards today.

4.4.1. The Future of Superconducting Microwave Electronics. How are these myriad of possible superconducting circuits realized in practice? Just like any other microelectronic circuit, they are lithographically patterned on a substrate through a similar sequence of steps in a semiconductor [25]. Thus, the vast assortment of techniques developed during the last several decades for and by the

semiconductor industry can be ported into commercialization of superconducting electronics. For a complete self-contained system, many of the subsystems have to be built out of semiconductor devices [e.g., the (IF) amplifiers for an RF transceiver]. An efficient way of manufacturing these systems is to mix HTS and high electron mobility transistor (HEMT) semiconductor circuits on the same substrate as a multichip module (MCM) [26]. Typically the HTS film is grown on a GaAs substrate with a thin buffer layer for better lattice match. Semiconductor devices perform better at lower temperatures because of enhanced carrier mobility, so the overall performance increases. Decrease of thermal noise is another desirable byproduct. Also, with the increase in the packing density of the semiconductor circuitry, a decrease in operating temperature, and the advent of high-temperature superconductors, the disparity between the operating voltage levels associated with the two types of circuits is going down, minimizing the possibility of ground loops between these two types of elements. Any large-scale commercial application of HTS microwave circuit will rely on the ability to integrate them, either as a hybrid component or as a monolithic component, with active semiconductor components.

There are many hurdles in the road to success of superconducting devices. The absence of a room-temperature superconductor, essential for consumer market, is one of them. Even if there was a room-temperature superconductor, the vast amount of techniques developed by the semiconductor industry for precise and predictable control of material properties are unavailable in the superconductor industry. The reason for this is obvious: The whole phenomenon of high-temperature superconductivity is only understood phenomenologically at best. There is no equivalent of "bandgap engineering" for superconductors. If we knew the material to dope to change the superconducting bandgap, we could then produce a room-temperature superconductor!

However, consumer electronics, although a large share of the market, still is not all of the market. There are niche markets, mostly in the defense sector and commercial/military wireless communication, who would pay the extra dollar to have the advantages of superconducting electronics (see, for example, Ref. 27). For example, the low insertion loss and steep skirt of a superconducting filter makes it cost effective in a cellular base station where the receiving/transmitting antenna must operate within tight bandwidth tolerance and divide up the available bandwidths among as many customers as possible. Such filters are available from many vendors, and several are being field-tested by cellular service providers. One example of a large-scale attempt to use HTSC microwave circuits in communication application is the U.S. Naval Research Laboratory's "High Temperature Superconductivity Space Experiments" (HTSSE) [28]. The U.S. Air Force is another major player in this field and expects to use low-loss superconducting antennas in the next-generation radar systems. System integration is a crucial aspect toward commercialization, and significant progress has been made to this end. Integration of individual superconducting microwave components to produce a complete

self-contained RF receiver/transmitter front end has been successfully demonstrated by many researchers. Integration of superconducting and semiconducting electronics on the same device has also been carried out.

At the present rate of progress, we can safely say that the growth of superconducting electronics will steadily increase with time. Whether it would radically alter the present state of the art, similar to the effect the advent of solid-state circuits had over the vacuum tube technology, will be seen in the years to come.

Acknowledgments

This work was supported by NSF-ECS-9711910. I am grateful to the following people for providing me with figures and associated data: Dr. Daniel Oates of MIT Lincoln Laboratory for Fig. 5, Dr. Balam Willemsen of Superconductor Technologies Inc. for Fig. 6, and Dr. Jeffrey Herd of the U.S. Air Force Research Laboratory for Fig. 7.

BIBLIOGRAPHY

1. McConnell, Wolf, and Noufi, eds., *Science and Technology of Thin Film Superconductors*, Vols. 1–2, New York: Plenum, 1988, 1990.
2. J. D. Jackson, *Classical Electrodynamics*, 3rd ed., New York: Wiley, 1999.
3. M. J. Lancaster, *Passive Microwave Applications of High-Temperature Superconductors*, Cambridge, UK: Cambridge University Press, 1997.
4. B. A. Willemsen, J. S. Derov, and S. Sridhar, Non-linear response of suspended high temperature superconducting microwave resonators, *IEEE Trans. Appl. Supercond.*, **5**: 1753–1755 (1995).
5. *IEEE Trans. Microw. Theory Tech.*, **44**(7): (1996).
6. R. Chatterjee, *Elements of Microwave Engineering*, Ellis Horwood Series on Electrical and Electronic Engineering, Chichester, UK: Ellis Horwood, 1986.
7. R. A. Chipman, *Transmission Lines*, Schaum Outline Series, New York: McGraw-Hill, 1968.
8. C. Zahopoulos, W. L. Kennedy, and S. Sridhar, Performance of a fully superconducting microwave cavity made of the high T_c superconductor $Y_1Ba_2Cu_3O_y$, *Appl. Phys. Lett.*, **52**:2168 (1988).
9. S. Sridhar and W. L. Kennedy, Novel technique to measure the microwave response of high T_c superconductors between 4.2 and 200 K, *Rev. Sci. Instrum.*, **59**:531 (1988).
10. G. L. Hey-Shipton et al., *High temperature superconductor lumped element band-reject filters*, U.S. Patent 5,616,539 (1997).
11. S. Das, U.S. Patent 5,496,795 (1996).
12. R. J. Dinger, D. R. Bowling, and A. M. Martin, A survey of possible passive antenna applications of high-temperature superconductors, *IEEE Trans. Microw. Theory Tech.*, **39**:1498–1507 (1991).
13. R. W. Conrad, U.S. Patent No. H000653, 1989.
14. J. T. Lynch et al., U.S. Patent No. 4,499,441, 1985.
15. G.-C. Liang et al., Superconductive digital instantaneous frequency measurement subsystem, *IEEE Trans. Microw. Theory Tech.*, **41**:2368 (1993).
16. J. C. Gallop, *SQUIDS, the Josephson Effects and Superconducting Electronics*, Adam Hilger Series on Measurement Science and Technology, Philadelphia, PA: Adam Hilger, 1991.
17. W. C. Stewart, Current–voltage characteristics of Josephson junctions, *Appl. Phys. Lett.*, **12**:227–280 (1968).
18. D. E. McCumber, Effect of ac impedance on dc voltage–current characteristics of superconductor weak link junctions, *J. Appl. Phys.*, **39**:3113–3118 (1968).
19. K. K. Likharev and V. K. Semenov, RSFQ logic/memory family: A new Josephson–junction technology for sub-terahertz-clock-frequency digital systems, *IEEE Trans. Appl. Supercond.*, **1**:3 (1991).
20. K. Hara, ed., *Superconductivity Electronics*, Ohmsha, Japan: Prentice-Hall, 1988.
21. Oleg A. Mukhanov, *Three-part Josephson memory cell for superconducting digital computer*, U.S. Patent 5,365,476 (1994).
22. J. R. Tucker, Quantum limited detection in tunnel junction mixers, *IEEE J. Quantum Electron.*, **QE-15**:1234–1258 (1979).
23. Predicted conversion gain in superconductor–insulator–superconductor quasiparticle mixer, *Appl. Phys. Lett.*, **36**: 477–479 (1980).
24. P. D. Bradley, *Flash analog-to-digital converter employing Josephson junctions*, U.S. Patent 5,400,026 (1995).
25. Q. Ma and W. N. Hardy, *Superconductor logic and switching circuits*, U.S. Patent 5,345,114 (1994).
26. A. D. Smith and A. H. Silver, *Integrated superconductive heterodyne receiver*, U.S. Patent 5,493,719 (1996).
27. F. W. Patten and S. A. Wolf, The ARPA high temperature superconductor program, *IEEE Trans. Appl. Supercond.*, **5**:3203 (1995).
28. M. Nisenoff et al., The high-temperature superconductivity space experiments: HTSSE I components and HTSSE II subsystems and devices, *IEEE Trans. Appl. Supercond.*, **3**:2885–2890 (1993).

FURTHER READING

The literature of microwave applications of superconductivity is quite extensive, and citations relevant to a particular subtopic have already been given wherever appropriate. A nonexhaustive list of periodicals and monographs of general interest in this area is provided below:

- *IEEE Transactions on Microwave Theory and Techniques* (Periodical).
- *IEEE Transactions on Applied Superconductivity* (Periodical).
- M. J. Lancaster, *Passive Microwave Device Applications of High-Temperature Superconductors*, Cambridge, UK: Cambridge University Press, 1997.
- Z.-Y. Shen, *High-Temperature Superconducting Microwave Circuits*, Norwood, MA: Artech House, 1994.
- S. T. Ruggiero D. A. Rudman, eds., *Superconducting Devices*, New York: Academic Press, 1990.
- R. D. Parks, ed., *Superconductivity* (in two volumes), New York: Marcel Dekker, 1969.
- T. Van Duzer and C. W. Turner, *Principles of Superconductive Devices and Circuits*, Amsterdam: Elsevier, 1981.
- H. Weinstock and M. Nisenoff, eds., *Superconducting Electronics*, NATO Advanced Study Institute Series, New York: Springer-Verlag, 1989.

SURFACE ACOUSTIC WAVE APPLICATIONS

DONALD C. MALOCHA
University of Central Florida

Since the introduction of the surface acoustic wave (SAW) interdigital transducer in the late 1960s, SAW devices have tremendously affected a broad range of systems. The key to this technology is the ability to sense or tap a traveling electroacoustic wave on a piezoelectric substrate whose velocity is 10^5 times slower than an electromagnetic wave. The velocity and photolithographic line resolution determine the practical SAW operating frequency range from approximately 30 MHz to 3 GHz. Typical devices are manufactured in volumes from a few cubic millimeters at high frequencies to a few cubic inches at lower frequencies. Typically, the high-frequency devices have a small volume and low cost. Using various SAW components depending on the required specifications, it is possible to provide precise frequency filtering, frequency resonance, time-pulse shaping, and signal processing. The passive, solid-state SAW devices provide very high performance relative to their volume, weight, and cost, which is the reason for their widespread use. The highest cost precision devices are typically used for military and satellite systems, which have the most demanding specifications; the intermediate cost devices are used in modest volume military man packs, military base stations, and commercial base stations; and the lowest cost devices are used in a broad range of commercial and consumer applications.

During the 1970s and early 1980s, military applications guided the development of the technology providing the ability to implement new and, up to that time, unachievable systems. A broad range of applications included dispersive devices and filter banks for radars, filters, and resonators for conventional communication systems, delay lines for systems and weapons, and coded devices, encoded modulator devices, and convolvers for spread-spectrum systems requiring secure communications. These systems encouraged the development of most of the components still in use by SAW devices today. The advent of enormous commercial opportunities in mobile and wireless systems in the 1990s ushered in a renaissance in SAW technology and has spawned technological innovation in devices and systems.

In addition to device technological innovation, research and development on other propagating Rayleigh-like modes, called pseudo-SAW, and new substrate materials, such as lithium tetraborate and langasite, have provided lower loss, higher frequency, and wider bandwidth devices. These material and device enhancements allow SAW devices to compete for insertion in the RF, IF, and processing sections of modern communication systems. Commercial and consumer applications include cellular and mobile phones, car and garage door openers, VCRs, CATV, fiber optic repeaters, spread-spectrum systems, sensors, identification tags, satellite communication systems, and many more [1-4].

1. SAW TVIF FILTER

The SAW TVIF filter stands alone as the first significant commercial application of SAW devices for the television intermediate-frequency (TVIF) filter and deserves a highlighted discussion. Development began in the 1970s when SAW technology was just emerging. Design, analysis, fabrication, and packaging were all extremely challenging for SAW devices at that time. However, it was recognized that a significant technological advance would be achieved if a single, solid-state component could replace the bulky, multiple LC tank circuits in the IE, which were both expensive to build and insert into the chassis. In addition, the LC sections drifted with temperature and aged with time producing a profoundly negative effect on video reception. The SAW TVIF filters were first introduced to the market in the late 1970s and demonstrated that high-volume manufacturing of the devices was feasible. Today, every TV manufactured has a SAW TVIF filter.

Figure 1 compares the SAW versus LC implementation of filtering in a TVIF section [5]. The SAW TVIF filter is interesting because it demonstrates that the SAW transversal filter can meet a demanding design and cost specification. The TV system requirements have been in place since TV's inception and vary by country around the world. The U.S. system requirement is typical and is used as the example. The video and audio transmission format have remained the same for compatibility over the years and were determined from the original transmission specifications. These specifications required a nonsymmetrical template for the magnitude of the TVIF filter response and a precise dispersive group-delay response. The nonsymmetrical magnitude response sets the relative video and audio carrier levels and shapes the chroma response. The group delay must vary precisely with frequency to reproduce a sharp image and accurate colors. Early SAW TVIF filter insertion losses were greater than 20 dB, which reduced the internal SAW device triple transit echo (TTE) to approximately 46 dB. A TTE greater than -40 dB produces a noticeable ghost picture that would be unacceptable to the consumer. Lower loss devices using new transducer and

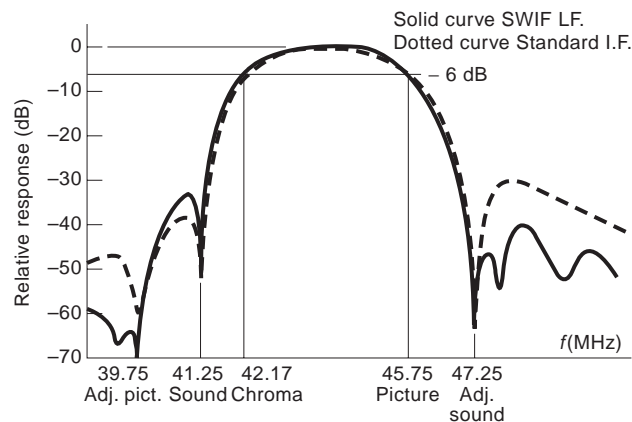


Figure 1. Early comparison of the SAW TVIF filter and the LC equivalent circuits used in U.S. television sets. (Reproduced with permission of the IEEE, *Proceedings of the IEEE*, 64(5):672 (1976).)

device embodiments reduce the loss below 20 dB while maintaining the specifications and costs required in the TV.

SAW devices are manufactured by using many of the previously developed integrated circuit techniques. Multiple devices on a single crystal substrate using aluminum electrodes fabricated by conventional photolithographic techniques is very attractive. Similar to silicon technology, high-volume manufacturing provided the vehicle for advancing the technology so that costs were reduced. Costs for SAW TVIF filters dropped from several dollars per device in the 1980s to under \$0.50 for current devices and are currently manufactured in volumes of millions per month. The SAW technology and device embodiments have been changed and refined to provide better performance at a lower cost [4]. As the first high-volume commercial SAW application, the TVIF filter can be credited for the confidence that companies had when developing the current wide range of high-performance, low-cost commercial SAW products.

2. TYPICAL WIRELESS COMMUNICATION SYSTEM

There are tremendous numbers of different wireless communication systems for audio, video, and data transmis-

sion. Rather than attempting to focus on any one system that has its own specific characteristics, a more generic approach is taken. Figure 2 shows a schematic for a typical transmitter and receiver system. The radiofrequency (RF) section eliminates spurious responses and establishes the noise figure for the system, and the intermediate frequency (IF) sections provide the channel selectivity and limit the noise bandwidth. To reduce cost, the second IF section is eliminated when possible. The oscillator/synthesizer is used for channel selection and may be used as the system clock. The postprocessing of the signal may also contain SAW devices in many coded and secure communication systems. The gray blocks represent elements in which SAW devices may be inserted, depending on specifications.

2.1. RF SAW Devices

The receivers of interest operate in the frequency range between approximately 30 MHz and 3 GHz where typical SAW devices find application. The RF section center frequency and bandwidth are consistent with the channel requirements, and fractional bandwidths can be from fractions of a percent to tenths of a percent. The RF section consists of one or two RF filters and a low-noise amplifier

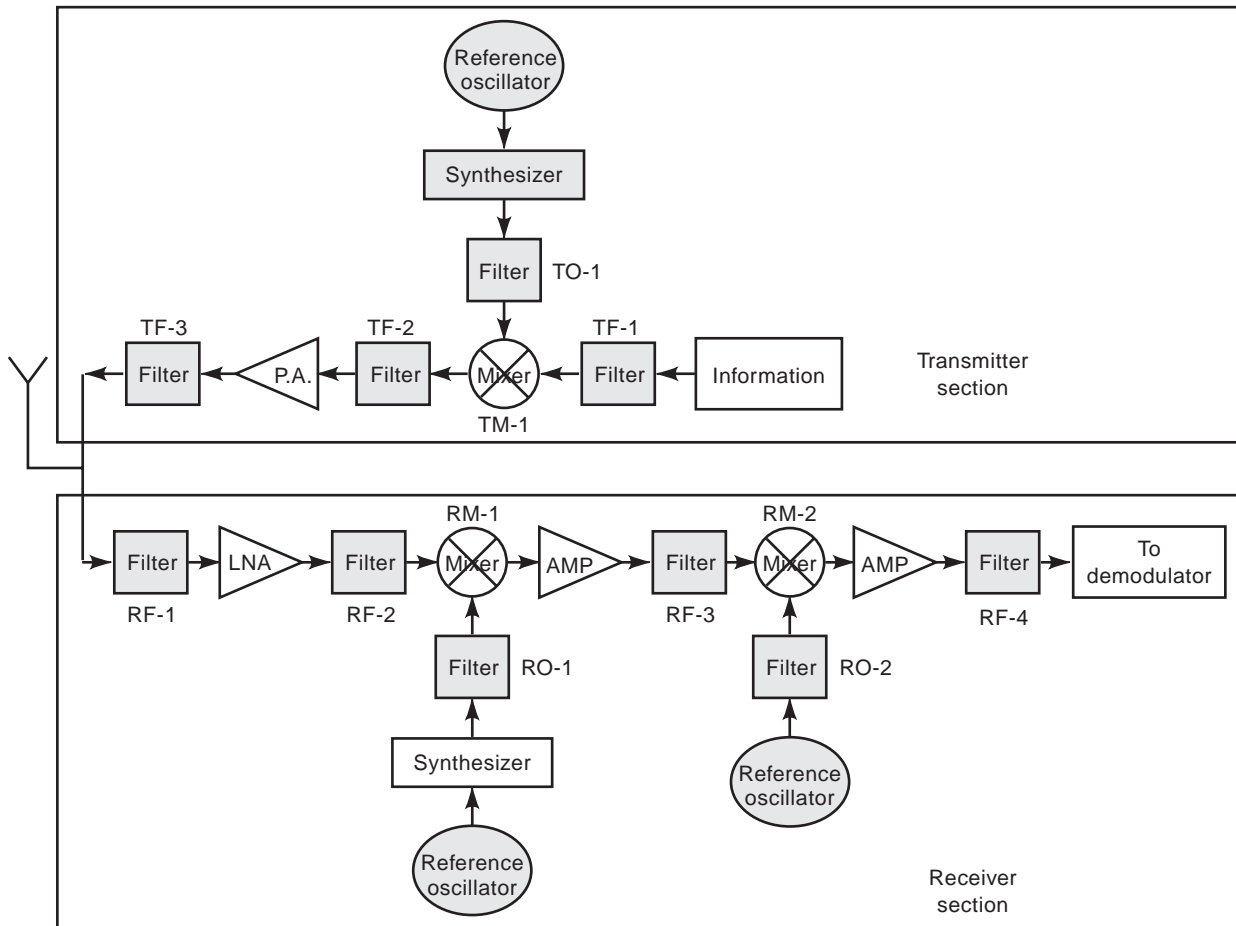


Figure 2. Schematic diagram of a generic transmitter/receiver (transceiver) system. The transceiver has a common antenna. The system can be separated into a transmitter and receiver by eliminating the common antenna. The gray blocks represent possible SAW elements within the RF and IF transceiver sections.

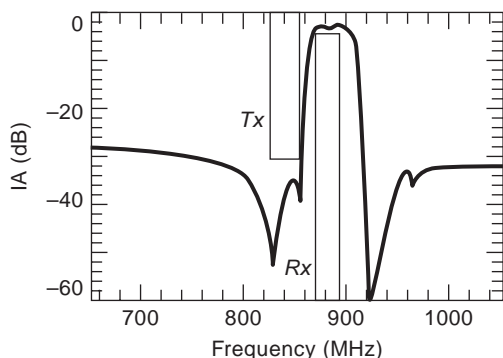


Figure 3. An 870 MHz SAW filter with a 3% fractional bandwidth and 2.0 dB insertion loss. This filter uses a multiresonator approach in a ladder-type network. This filter is used as the front-end RF filter in the Advanced Mobile Phone System (AMPS). (Reproduced with permission of the IEEE, J. Machui et al., 1995 *IEEE Ultrasonics Symposium Proceedings*, pp. 121–130.)

(LNA). As an example, a typical mobile telephone system's center frequencies vary from approximately 450 MHz to more than 2 GHz with fractional bandwidths of 1% to 5%. One RF filter that has very low loss and good selectivity is desired. However, two filters may be necessary, the first with very low loss and marginal selectivity and a second filter with a higher loss and better selectivity. Any loss before the LNA is a direct reduction in signal-to-noise ratio. Therefore, RF filters require extremely low loss, typically between 1 dB and 3 dB. Figure 3 shows a typical SAW front-end RF filter for a mobile phone application at 870 MHz with an insertion loss of approximately 2.0 dB and a 25 MHz bandwidth [6]. Typically nulls are designed at the adjacent transmit/receive frequencies for a transceiver, and sidelobe rejection depends on the design approach. The second RF filter can have a relaxed insertion loss specification but typically has greater out-of-band spurious suppression. Figure 4 shows a SAW interstage filter at 950 MHz with approximately 3 dB insertion loss implemented by using a transversely coupled resonator approach [6]. SAW filter design techniques for RF filters

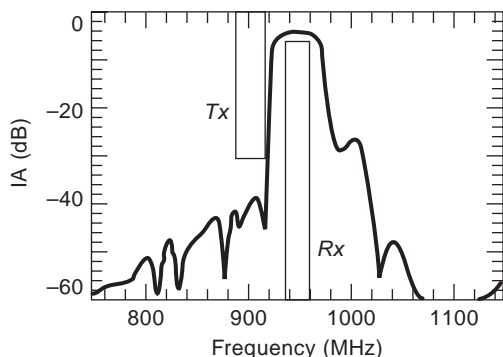


Figure 4. A 950 MHz SAW filter with an approximate 3% fractional bandwidth and 3 dB insertion loss. This filter uses a transversely coupled resonator filter, which provides a two-pole response and good ultimate sidelobe rejection. This filter is used in the Global System for Mobile communication (GSM). (Reproduced with permission of the IEEE, J. Machui et al., 1995 *IEEE Ultrasonics Symposium Proceedings*, pp. 121–130.)

include two-transducer low-loss designs, interdigitated interdigital transducers, single and multitrack resonant structures, and ladder/lattice impedance filters. For cellular applications, the antenna is common to both the transmitter and receiver, and it may be necessary for the RF receiver filter to accept large input power at the transmission frequencies. SAW ladder/lattice filters are currently of great interest because they handle high power and provide low loss and acceptable selectivity. Other important considerations are the temperature coefficient of frequency and the material coupling coefficient. The bandwidth must be increased to accommodate operation over the required temperature range, and the coupling coefficient determines the maximum achievable bandwidth for a given insertion loss.

2.2. IF SAW Devices

The IF filter typically has greater selectivity and higher insertion loss than the RF filter. The IF center frequency is chosen for good image rejection and adjacent channel selectivity and is lower than the transceiver operating frequency, typically from tens to hundreds of megahertz. The IF filter must have a narrow transition band and low sidelobe levels to limit the noise within the system and may also have specific traps to reduce adjacent channels, intermodulation, or other spurious carrier responses. The insertion loss is usually not as stringent a requirement as in the RF filter because the signal-to-noise ratio is set before this stage and amplification is typically low cost and available. IF stage insertion loss can range from several decibels to as much as 50 dB depending on the fractional bandwidth and system requirements. Figure 5 shows a typical SAW IF bandpass filter at 70 MHz, insertion loss of 22 dB, 8 MHz bandwidth, and group-delay variation of approximately 40 ns. The filter is a conventional two-transducer, SAW transversal implementation that demonstrates the excellent passband shaping, extremely sharp skirts, and near-constant group-delay response.

2.3. SAW Resonator Oscillator Applications

The oscillator/synthesizer often uses a SAW resonator for the frequency-control element having a center frequency

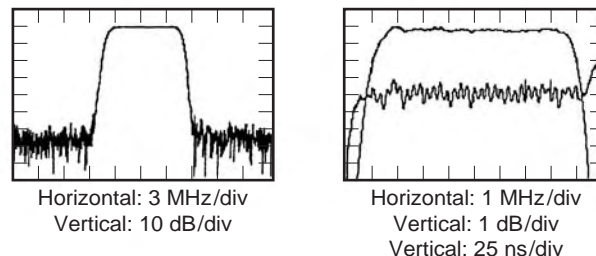


Figure 5. A typical 70 MHz IF filter having a typical insertion loss of 22 dB, 3 dB bandwidth of 8 MHz, and sidelobe rejection of greater than 55 dB. The passband has less than 0.25 dB ripple and group-delay variation of approximately 40 ns. The passband ripple and group-delay variation are primarily caused by TTE. The 70 MHz IF frequency is popular for military applications. (Reproduced with permission from Sawtek, Inc.)

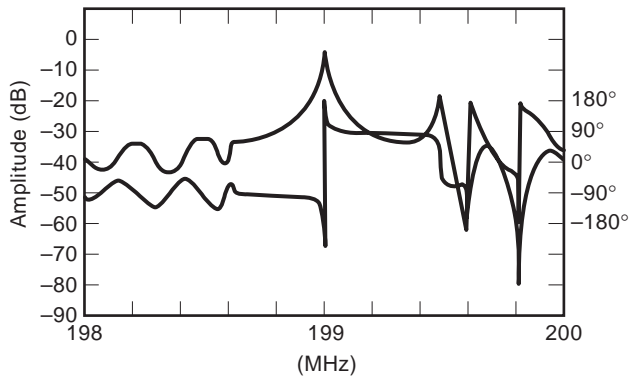


Figure 6. Magnitude and phase response of a 199 MHz, two-port, SAW resonator on quartz. (Reproduced with permission from Sawtek, Inc.)

such that, when mixed with the incoming carrier, it results in a signal at the IF center frequency. The oscillator frequency is chosen on the basis of a wealth of system considerations including the reception frequency, single versus double conversion, inter- and cross-modulation products, and other specifications. It is desired that the resonator be high *Q*, low loss, and have excellent temperature stability versus frequency. As an example, Fig. 6 shows a 199 MHz, quartz, two-port SAW resonator response. The peak to spurious level typically needs to be greater than 10 dB to ensure that any excessive loop gain in the oscillator does not result in oscillator instability. SAW resonator *Q*'s are typically several thousand and can be designed to tens of thousands. SAW oscillators often compete with bulk acoustic wave (BAW) devices that typically operate at much lower frequencies and use multipliers to obtain the frequencies of interest. Both SAW and BAW-based oscillators are often called crystal oscillators (XO). Oscillators have frequency drift primarily caused by the crystal temperature coefficient of frequency (TCF) and often have sophisticated electronics and temperature control to achieve long-term and short-term stabilities. Various configurations include the voltage-controlled (VCXO), temperature-controlled (TCXO), oven-controlled (OCXO), and microprocessor-controlled (MCXO) crystal oscillators.

Using a narrowband SAW resonator, it is also possible to produce a notch filter [7]. Notch filters are used to eliminate a narrow carrier that is produced within a radio, such as in the oscillator, or they are used to eliminate an external signal, such as an adjacent channel carrier frequency. Various circuit configurations are used with resonators to produce a notch. The notch filter should have good temperature stability and a notch bandwidth adequate to track over the required operating temperature range. Multiple coupled resonators are used to obtain a larger notch bandwidth than are the conventional single-pole resonators.

3. SIGNAL PROCESSING APPLICATIONS

3.1. Coded and Quadrature Modulators

3.1.1. PSK SAW Filter. Because each tap in a SAW device is independently controlled, it is very easy to implement simple-phase, shift-keying (PSK) biphasic coding into a device. A schematic of a typical PSK-coded SAW used for coding the data in a spread-spectrum system is shown in Fig. 7. A digital datastream is converted into a series of impulses whose polarity corresponds to the sign of each data bit. The input transducer launches the wave whose phase depends on the sign of the input pulse and which is then convolved with the coded transducer. The SAW-coded transducer is composed of a series of time chips. The sign of each chip is implemented by properly connecting of each electrode to the appropriate busbar. The overall SAW impulse-response length is equal to the data bit length. The output from the SAW-coded transducer can be further modulated for transmission. A similar SAW filter can be used as the matched filter at the receiver where a compressed pulse is achieved whose phase is a function of the original data stream. The frequency bandwidth is determined by the chip impulse-response length, and the processing gain is a function of the number of chips per bit. Figure 8 shows the measured time response of a 128 chip PSK correlator, which exhibits a peak-to-sidelobe ratio of approximately 21 dB, as expected.

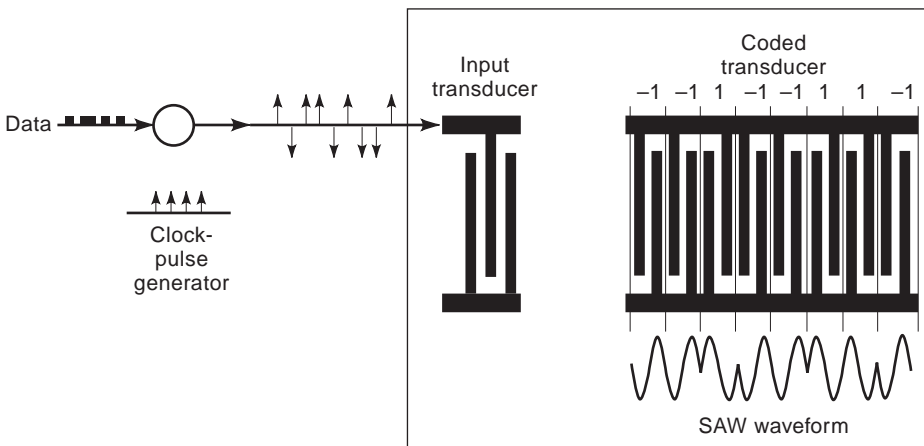


Figure 7. Schematic diagram of a typical SAW PSK-type coded filter. The input data are converted into a series of phase-modulated impulses that then produce the SAW output-coded waveform.

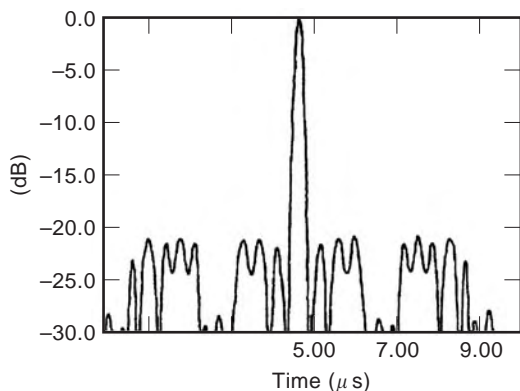
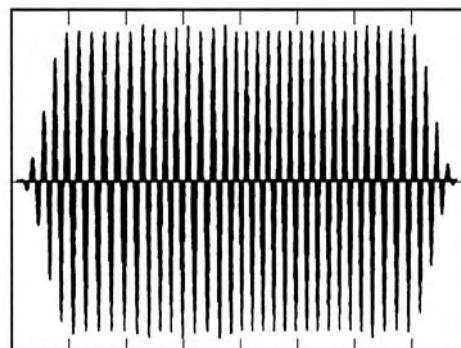


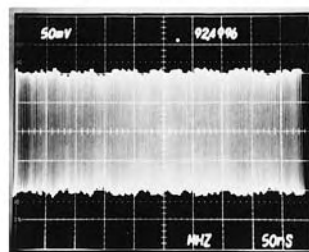
Figure 8. Measured time-domain response of a 128 chip PSK SAW correlator. (Reproduced with permission from Sawtek, Inc.)

3.2. Continuous-Phase Frequency-Modulation Devices

SAW devices are designed in both the time and frequency domains. The ability to pulse shape allows developing and implementing precise modulation schemes that are very difficult to implement with other technologies. Quadrature modulation techniques are very popular for transmission, they include quadrature-phase shift keying (QPSK), minimum shift keying (MSK), and others. The MSK waveform, along with many others, forms a class of continuous-phase frequency modulation (CPFM), encodes the information in the phase and frequency of each chip or bit, and has a uniform amplitude envelope. The phase continuity and uniform amplitude provide minimum distortion when transmitting through power amplifiers, which are often nonlinear. These advantages are obtained at the expense of a wider chip null bandwidth, which reduces data rates. A schematic of a simple way to implement a CPFM system is shown in Fig. 9 where the SAW device provides pulse shaping when excited by an impulse. For MSK, the pulse envelope shape is a simple one-half cycle cosine whose length is equal to the required bit length. The data bit length is one half the MSK impulse-response length, and therefore, the device impulse response from a given data bit impulse overlaps adjacent data bits to form a nearly continuous, flat-envelope code stream. The predicted and measured SAW MSK waveforms are shown in Fig. 10.



Predicted MSK waveform including effects of input transducer



Measured MSK waveform including effects of input transducer and the equalized cosine transducer

Figure 10. Predicted and measured time-domain response of a SAW MSK system at 300 MHz and a 92.5 MHz data rate. The predicted response has approximately 4% amplitude modulation compared with the 7% measured. The main cause for amplitude modulation is hardware system implementation.

3.3. Synchronous Optical Network

The synchronous optical network (SONET) has critical and demanding timing for data transmission. When transmitting over long distances, such as transoceanic, it is necessary to recover the clock from the actual nonreturn-to-zero (NRZ) datastream to retime the data at intermediate points along the network. One popular method is to use a SAW filter within the clock-recovery circuit, as shown in Fig. 11. Figure 12 shows a high *Q*, 622 MHz, quartz, SAW filter used in a SONET clock-recovery system. The device has a typical insertion loss of 16 dB, and a quartz substrate is used to minimize temperature drift

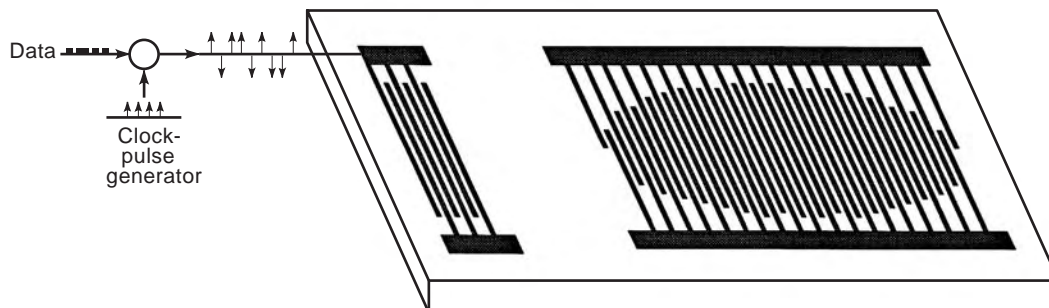


Figure 9. Schematic diagram of a typical SAW MSK-type coded filter. The input data are converted into a series of phase-modulated impulses, which then produce the SAW output-coded waveform.

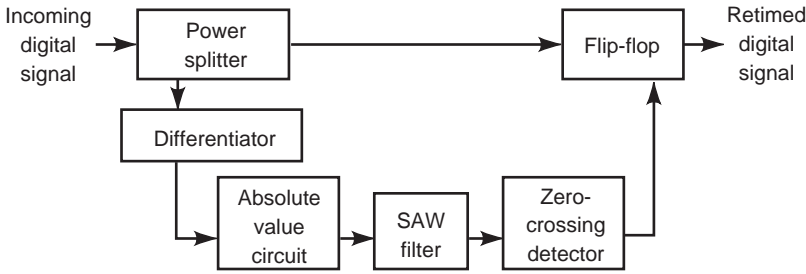


Figure 11. A simple schematic diagram of a SONET clock-recovery circuit using a SAW filter.

effects. In addition to the clock recovery, SAW devices may be used in SONET as delay elements for timing or for data pulse shaping to minimize intersymbol interference and reduce the probability of error in data recovery.

3.4. Channelizers

In wideband communication systems that have multiple channels, it is often required to break the receiving bandwidth into adjacent channels. Sometimes these channels are processed independently, or there are times when multiple channels may be combined into a wider band channel. This requires a sophisticated system that has well-matched individual channels and an electronic system that provides the required switching network. SAW channelized receivers have met this demanding requirement for both military and commercial applications. A complete integrated SAW channelizer system allows dynamic, active switching in or out of one or more channels. The superimposed frequency response from a seven-channel, 330 MHz SAW filter bank is shown in Fig. 13. The uniformity of amplitude and out-of-band rejection (approximately 50 dB) between channels require precise filter design and system integration.

3.5. Dispersive Devices

3.5.1. Radar. One of the earliest and technologically important applications of SAW devices was in radar systems. The simplest radar in concept is the pulse radar. To obtain the greatest accuracy in determining an object's distance from a source, it is desirable to transmit a very narrow pulse from the source, which is subsequently reflected from an object and received. The delay corresponds to the round-trip distance difference. The maximum

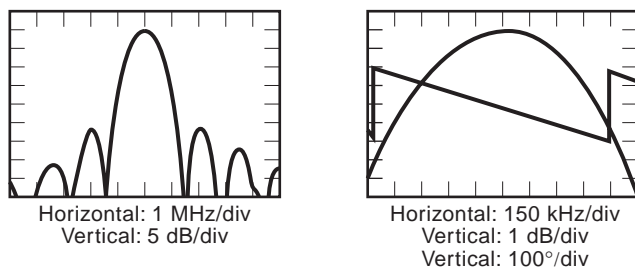


Figure 12. Frequency response of a 622.08 MHz SAW filter used in a SONET clock-recovery circuit. The device has a typical insertion loss of 16 dB, a 3 dB bandwidth of 0.93 MHz, a delay of 700 ns, and is fabricated on quartz. (Reproduced with permission from Sawtek, Inc.)

viewing distance is limited by the path loss and the minimum detectable signal-to-noise ratio. Therefore, it is desirable to transmit very narrow, high-amplitude pulses or to extend the pulsewidth. The former approach requires a very low duty factor and high-power transmitters, whereas the latter lengthens the pulse, which limits distance accuracy. The solution to these two conflicting requirements is to use a dispersive transmit pulse that changes the instantaneous carrier frequency with time. A chirp radar uses a SAW dispersive (or chirp) filter to transmit a long dispersive pulse that has significantly more energy than a simple, single-carrier frequency pulse [8]. Then the return signal is sent to a matched SAW chirp filter that compresses the pulse. The SAW input/output devices are a matched set whose transmit filter is an upchirp and receive filter is a downchirp. Figure 14 shows a schematic representation of an upchirp and downchirp SAW filter. For a linear chirp, the frequency changes at a given chirp rate (Hz/s) from some minimum to some maximum value across the device. The processing gain, which is approximately given by ratio of the output compressed pulsewidth to the transducer impulse response length, is a direct function of the device's time-bandwidth product. Devices can be produced using simple dispersive transducers or by using long reflector structures called reflective array correlators (RAC) [8]. Time-bandwidth products from several hundred to tens of thousands have been achieved. The time-domain responses of the transmitted or received chirps may be weighted to produce a more optimum

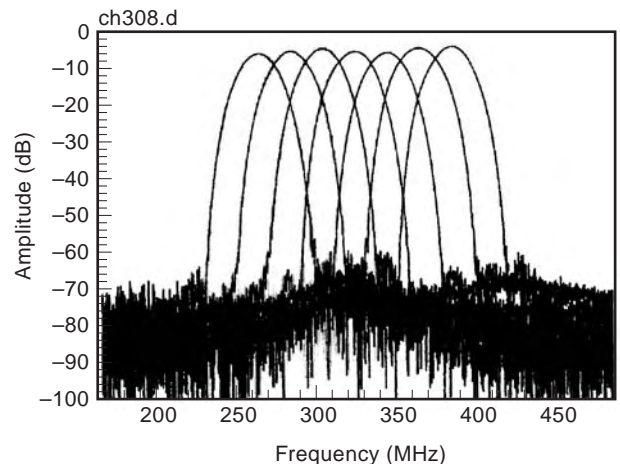


Figure 13. The superimposed frequency response of all channels of a seven-channel SAW filter bank at a center frequency of 330 MHz. (Reproduced with permission from Sawtek, Inc.)

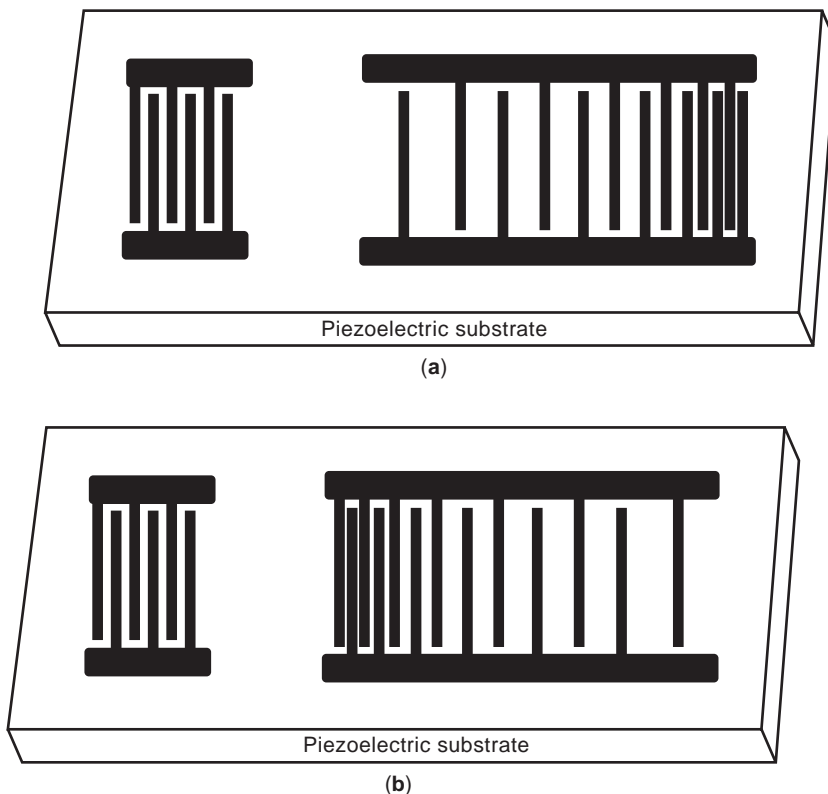


Figure 14. (a) Schematic of an upchirp SAW filter. (b) Schematic of a downchirp SAW filter.

time-domain pulse-compression response at the receiver. Figure 15 shows the frequency responses of an expander/compressor matched pair at a center frequency of 1 GHz having a bandwidth of 450 MHz, a dispersive delay of 0.45 μs, and a time-delay slope of 1000 MHz/μs. The compressed-time matched-correlator response has a compressed pulsewidth inversely proportional to the bandwidth (2.22 ns as compared with 2.9 ns measured) and a typical peak-to-sidelobe ratio of approximately 10 × log (time-bandwidth product), which is 23 dB.

3.5.2. SAW Chirp Fourier Transformer. Another application of SAW dispersive devices is in a chirp Fourier trans-

form system that performs a real-time Fourier transform of a given input signal, which is confined to the system bandwidth. Given a function $f(t)$ that has a Fourier transform, $F(\omega)$, the frequency domain function is written as

$$F(2\pi\mu t) = \int_{-\infty}^{\infty} f(\tau)e^{-j2\pi\mu t\tau} d\tau$$

where $\omega = 2\pi\mu t$.

Using the identity $2t\tau = t^2 + \tau^2 - (t - \tau)^2$, the equation is rewritten as

$$F(2\pi\mu t) = e^{-j\pi\mu t^2} \int_{-\infty}^{\infty} f(\tau)e^{-j\pi\mu\tau^2} e^{j\pi\mu(t-\tau)^2} d\tau$$

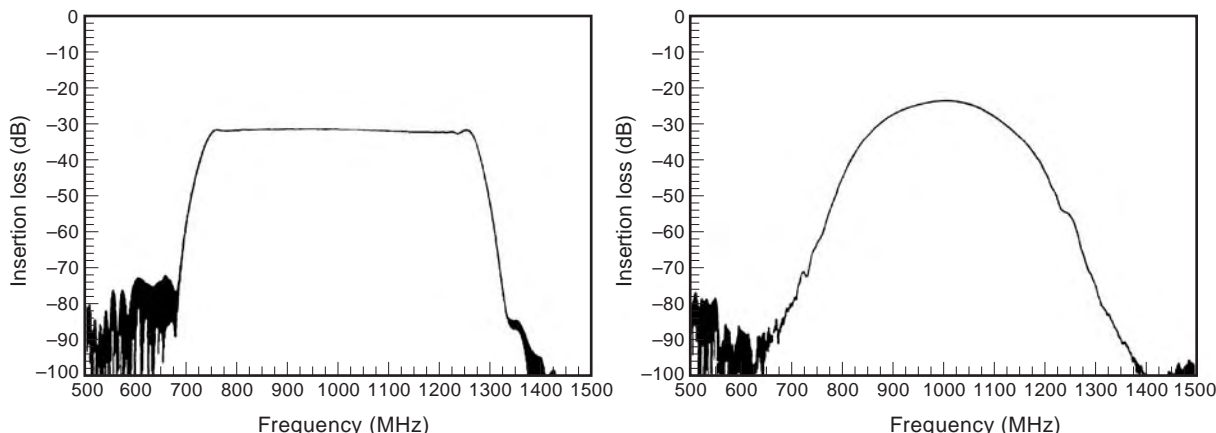


Figure 15. A dispersive SAW expander and compressor matched filter pair. The center frequency is 1.0 GHz, a 450 MHz bandwidth, 0.45 μs delay, and 1000 MHz/μs dispersion. (a) Expander and (b) weighted compressor. (Reproduced with permission from Sawtek, Inc.)

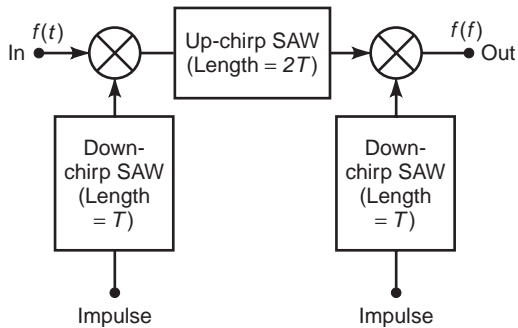


Figure 16. Schematic diagram of a SAW chirp Fourier transform system.

This is the equation form of the chirp Fourier transform that is a time function multiplied by a complex chirp, convolved with a second chirp, and then multiplied by a third chirp. A typical SAW implementation of a multiply-convolve-multiply (MCM) chirp transform system is shown in schematic form in Fig. 16. The convolve chirp is usually twice the length of the multiply chirps. The first multiply chirp conditions the input signal by adding the dispersive delay, and then the second chirp sorts the input signal frequencies in the time domain through the convolution process, providing the amplitude-frequency response curve. The final chirp multiply is necessary only if the phase information is desired and does not affect the amplitude response. Figure 17 shows a schematic representation of the system output for an input signal composed of three different frequencies. The convolve chirp is an up-chirp that sorts the frequencies from low with the smallest delay to high with the longest delay. The output signals have a finite time length due to the limited bandwidth of the SAW chirp system. The SAW implementation of the chirp transform system is not an exact implementation of the chirp Fourier transform because it is limited in both time length and frequency bandwidth. However, it works

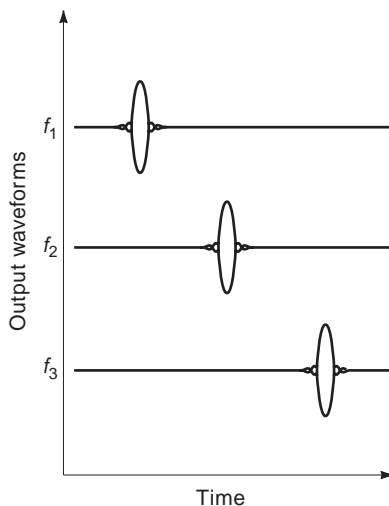


Figure 17. Schematic representation of the output waveform of a SAW chirp system given the sum of three tones having equal amplitude as the input waveform.

well for bandlimited and multitone input waveforms used in radar and other military systems.

3.5.3. SAW Elastic Convolver. Spread-spectrum systems need some type of matched filter, correlator, or convolver to extract the transmitted signal from noise and interfering sources. SAW elastic convolvers were studied in the 1970s for use in militarily secure, spread-spectrum communication systems [8,9]. The SAW convolver is a three-port device that uses the nonlinear portion of the crystal constants to perform a real-time convolution on any two arbitrary input signals within the operating bandwidth and time length of the device. The device is shown schematically in Fig. 18. The device consists of two input interdigital transducers (IDT), two beam compressors, and a long output plate between the two beam compressors. The input IDT provides the input signal from the receiver, and the reference IDT provides the known reference code signal. To enhance the nonlinear effect within the crystal, the power density is increased by compressing the SAW beam to only a few wavelengths. The beam compressors are usually either multistrip couplers, a horn-type waveguide, or self-focusing IDTs with typical compression ratios of 5 to 20. The two counterpropagating waves are compressed and then trapped under the electrode waveguide, which is only a few wavelengths wide, where they eventually slide by each other. The nonlinear crystal parameters provide point-source multiplication, and the long solid electrode provides the summing bus that is proportional to the integration time. The output signal is the convolution of the two SAW input waveforms at twice the carrier frequency of the inputs. The processing gain of the system is given by the device's time-bandwidth product. Typical devices have time lengths of several microseconds and bandwidths of tens to hundreds of megahertz. A convolver with a 10 microsecond integration length and a 100 MHz bandwidth has a processing gain of 30 dB. Typical convolver efficiency is between -50 dBm to -75 dBm, which depends on the substrate material, bandwidth, integration time, and device design. Figure 19 shows the predicted and measured results of a $22 \mu\text{s}$ long, real-time SAW convolution of a coded MSK signal. The agreement between measurements and the theory of the compressed pulse are excellent.

4. SAW REMOTE SIGNALING AND SENSORS

4.1. Identification Tags

SAW devices are used in the passive mode as identification tags or in remote sensing. A schematic of a pulse-excited, time-reflective type of a coded SAW tag is shown in Fig. 20. The tag is composed of an antenna, a transducer, and a series of partial reflectors. A remote transmitter sends an interrogation pulse that is received by the antenna and excites the SAW transducer, which launches a wave. The SAW is partially reflected at each reflector and is sent back to the SAW transducer where it is retransmitted back to the interrogator. The center position of the reflector provides a series of delayed pulses that provide the unique code for identification. The device is totally passive, and the antenna and SAW chip are integrated into a single,

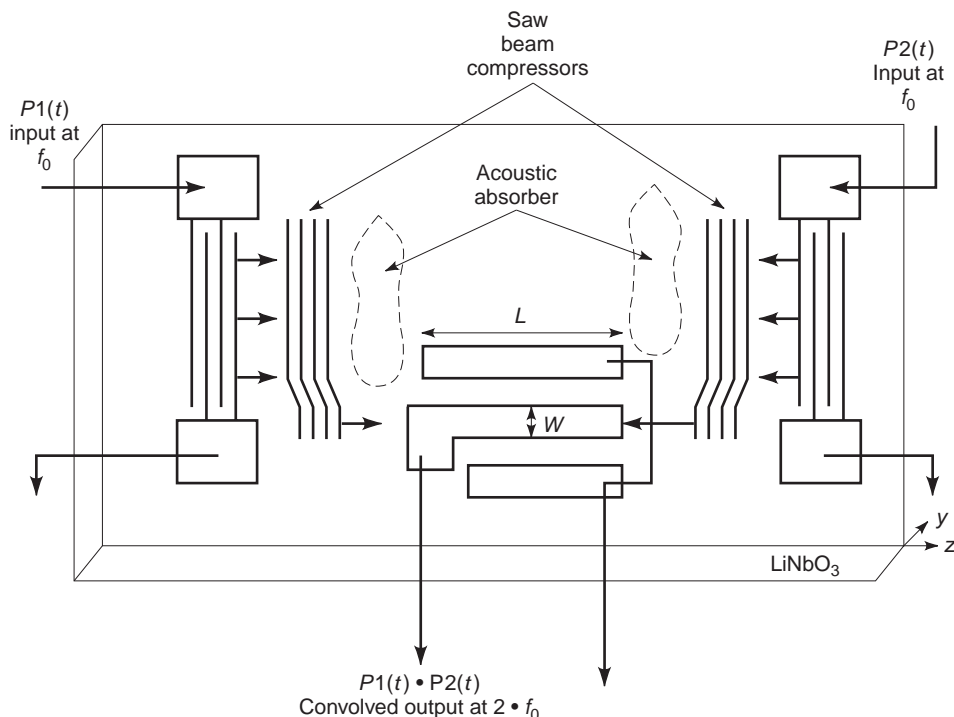


Figure 18. Schematic view of a SAW beamwidth compression elastic convolver.

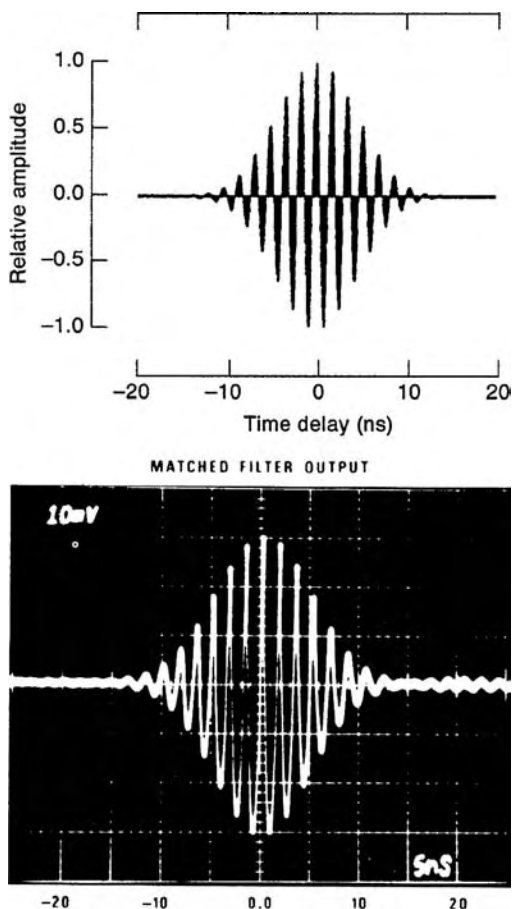


Figure 19. Correlation of a compressed-pulse time-response of a SAW elastic convolver.

low-cost package. Figure 21 shows the measured time-domain results for a reflective, coded, passive SAW tag. The time pulses are relatively uniform and discrete, which makes demodulation of the tag information easy and accurate.

4.2. Remote Signaling

Remote signaling has become very desirable and accepted by consumers and industry. Examples include remote car door openers, car accessory operation, garage door openers, remote lights, power utility meters, and others. It makes some very simple operations even simpler and faster, increases industrial productivity, and is used in inaccessible places and environments for control and sensing. The acceptance of such systems is based on the relatively small size and cost. As an example, a transmitter for a keyless automobile entry is embedded on the actual key with minimal increase in size. A simple system used for a keyless entry system is shown in Fig. 22 [9]. The system consists of two SAW filters, an amplifier, an integrated circuit for the code generator, and a battery. The two SAW filters and amplifier are placed in a single package, and a custom ASIC is designed and programmed for the specific code generator. The integrated circuit provides the code data, and the data format is simple on-off shift keying (OOSK). One SAW is used in the oscillator as the frequency-control element, and the second SAW filter is used to remove unwanted harmonics and spurious responses from the oscillator.

4.3. Sensors

Sensing the external environment using SAW technology is a relatively new and growing market. The different

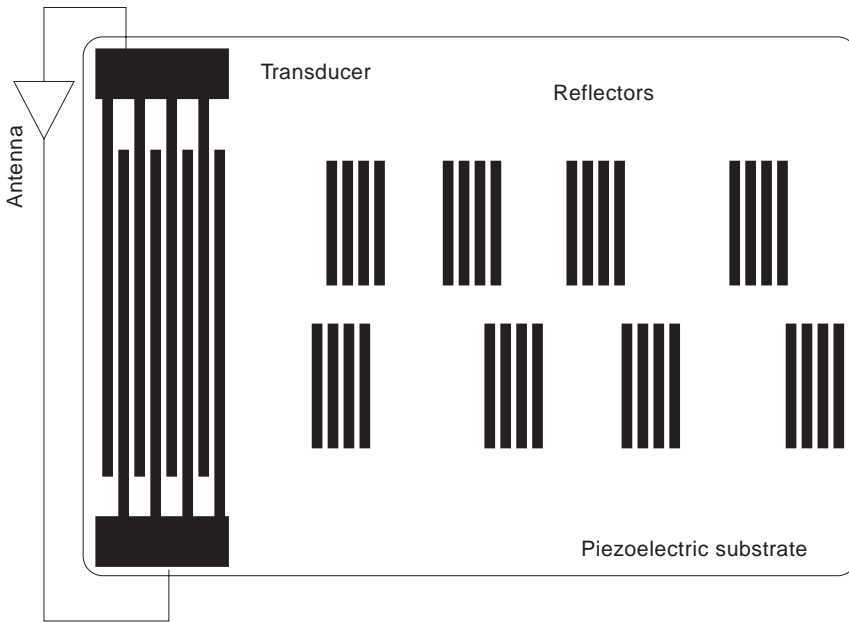


Figure 20. A schematic of pulse-excited, time-reflective type of a coded SAW tag. The device consists of a transmit/receive antenna, a dual-purpose input/output transducer, and a series of reflectors that have centers of reflection corresponding to a pulse position code.

number and types of SAW sensor devices and systems cannot be adequately presented here [10]. SAW sensors are under investigation to sense gases, temperature, acceleration, pressure, and other parameters. The two critical issues are to find a sensitive sensing mechanism for the parameter of interest while eliminating or compensating for all other environmental elements, thereby isolating the measurement to only a single environmental element (gas, temperature, etc.). One popular method for measuring gases is to use a SAW delay line having a gas sensitive film in an oscillator circuit on the substrate surface. As the gas absorbs and desorbs, there is a change in the film's

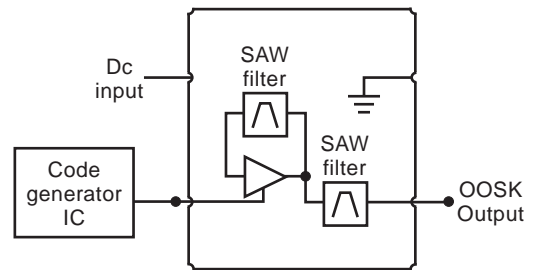


Figure 22. Schematic of a simple, low-cost SAW-based remote keyless entry system using on-off shift keying. (From RF Monolithics data sheet, HX1000.)

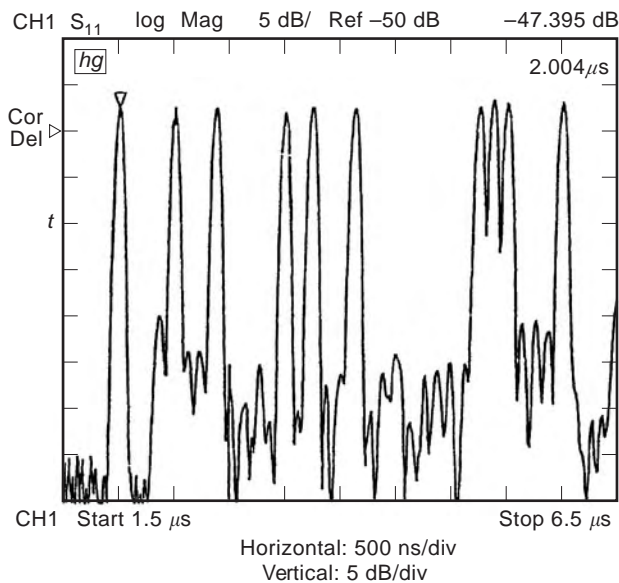


Figure 21. The measured time-domain results for a reflective coded passive SAW tag. The time pulses are relatively uniform and discrete, which makes easy and accurate demodulation of the tag information. (Reproduced with permission from Sawtek, Inc.)

elastic properties that creates a change in acoustic velocity, delay, and insertion loss. This is translated into a frequency shift in the oscillator. The change in frequency versus gas absorption is often determined in parts per

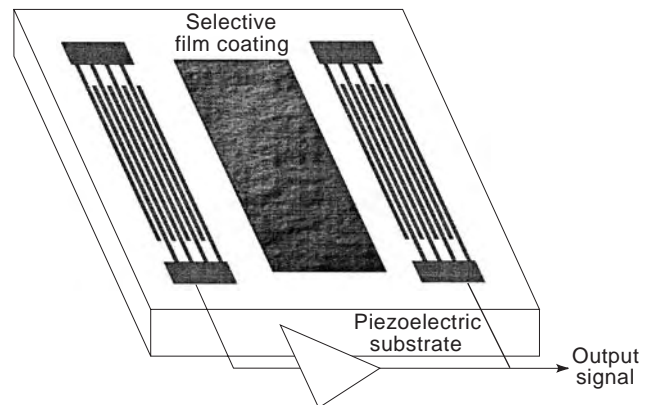


Figure 23. A schematic of a simple SAW sensor composed of a two-transducer-delay line with a selective absorbing film, which changes the amplitude, phase, and/or insertion loss of the delay line.

million for a well-calibrated system. A schematic of a simple SAW sensor is shown in Fig. 23. Sensing is developing into a very large market. Combining sensing with wireless transmission results in remote sensing applicable to a huge number of applications in transportation, medical, environmental, manufacturing, and many other fields.

BIBLIOGRAPHY

1. Special issue on surface acoustic wave devices and applications, *IEEE Proc.*, **64**(5) (1976).
2. Special Issue on Applications, *IEEE Trans. Ultrason. Ferroelectr. Freq. Control*, **40**(5) (1993).
3. C. Campbell, *Surface Wave Devices and Their Signal Processing Applications*, San Diego, CA: Academic Press, 1989.
4. C. C. W. Ruppel et al., SAW devices for consumer applications, *IEEE Trans. Ultrason. Ferroelectr. Freq. Control*, **40**:438–452 (1993).
5. A. J. DeVries and R. Adler, Case history of a surface wave TV IF filter for color television receivers, *IEEE Proc.*, **64**:671–676 (1976).
6. J. Machui et al., SAW devices in cellular and cordless phones, *1995 Ultrasonics Symp. Proc.*, pp. 121–130.
7. C. S. Hartmann, J. C. Andle, and M. B. King, SAW notch filters, *1987 IEEE Ultrasonics Symp.*, pp. 131–138.
8. D. P. Morgan, *Surface Wave Devices for Signal Processing Applications*, New York: Elsevier, 1991, Chaps. 9 and 10.
9. K. Tsubouchi et al., Full duplex transmission operation of a 2.45 GHz asynchronous spread spectrum using a SAW convolver, *IEEE Trans. Ultrason. Ferroelectr. Frequency Control*, **40**:478–482 (1993).
10. RF Monolithics Application Note, Hx 1000, 1994.
11. D. S. Ballantine et al., *Acoustic Wave Sensors, Theory, Design, Physico-Chemical Applications*, San Diego, CA: Academic Press, 1997.

SURFACE ACOUSTIC WAVE DELAY LINES

LEONHARD M. REINDL
Albert Ludwigs Universitat
Freiburg, Germany
CLEMENS C.W. RUPPEL
EPCOS AG
Munich, Germany

1. INTRODUCTION TO SAW TECHNOLOGY

1.1. SAW Devices

Surface acoustic waves (SAWs) are mechanical waves whose associated particle displacements are bounded to the surface [1]. The typical penetration into the volume is in the order of one acoustical wavelength λ . Figure 1 shows a finite-element analysis of the particle displacement caused by a special surface acoustic wave, the so-called Rayleigh wave. The particle displacement in Fig. 1, however, is enlarged to make the displacement (or strain) visible. The actual displacements are in the order of some angstroms.

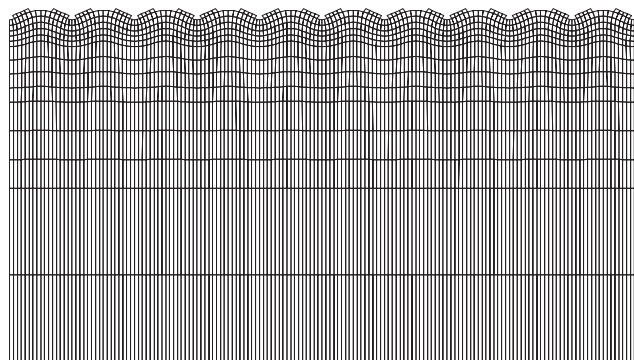


Figure 1. Finite-element analysis of the particle displacement caused by a surface acoustic wave.

On piezoelectric substrates SAWs can easily be generated by using so-called interdigital transducers (IDTs) shown in the left part of Fig. 2 [2]. A SAW device consists of metallic structures on top of a highly polished piezoelectric substrate, such as one or several of these IDTs and reflection or coupling gratings. Typically aluminum is used for the metallization. For an IDT, the widths and spacings of the electrodes and strips determine together with the phase velocity v the operating frequency f . The sum of the electrode width and spacing gives the geometric period p (pitch) of the IDT. In the plainest transducer, the pitch p is constant over the entire IDT. The resonance condition is given by a SAW wavelength λ of

$$\lambda = 2p \quad (1)$$

The operating frequency f of the IDT is thereby given by

$$f = \frac{v}{\lambda} = \frac{v}{2p} \quad (2)$$

The number of pitches N of the transducer gives its length in the time domain, which determines the bandwidth B of operation by

$$B = \frac{v}{2Np} \quad (3)$$

The input and output IDTs are electrically connected, for example, via bond wires to the pins of a hermetically sealed package (see Fig. 3). Triggered by the piezoelectric effect, an electrical microwave input signal at the transmitting IDT stimulates a microacoustic wave that propagates along the surface of the elastic solid body. In

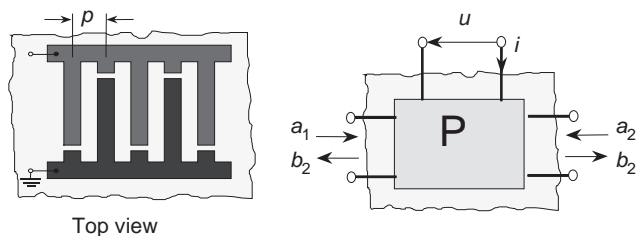


Figure 2. Schematic of an interdigital transducer with pitch p and associated P -matrix model, where u and i are respectively the electrical voltage and current and a and b denote the incident and outgoing acoustic waves respectively.

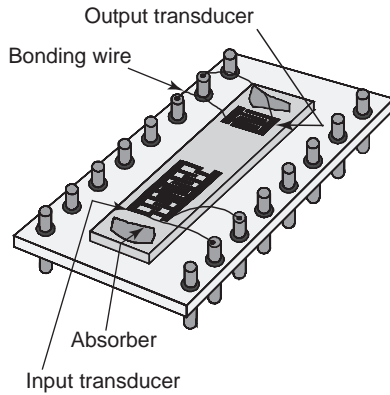


Figure 3. Schematic drawing of a SAW filter.

contrast, a SAW propagating through an IDT generates an electric charge distribution at the receiving IDT, causing a microwave electrical output signal [3–10]. To suppress unwanted reflections from the edges absorbers become fixed to the ends of the chips.

The main advantages of the SAW technology are the low velocity of the acoustic waves, which allows the implementation of a large number of wavelengths or significant delay times within a small chip, and the high quality factor of the materials, which results in low attenuation factors. Both factors together allow for filters with relative bandwidths from 0.1% up to almost 100% with flat pass-band response, steep skirts, high selectivity, and precise phase characteristics.

Since the early 1990s, driven by the booming wireless technology business, great and important progress in SAW device performance has been made and a variety of innovative applications developed. Most telecommunication systems, in particular mobile radio and satellite systems, depend on extremely high-performance SAW filters. Large and, to an increasing extent, smaller radar systems have utilized pulse compression SAW filters. High-frequency SAW-based oscillators replace the low-frequency quartz crystal sources and the required frequency multiplier chains in many electronic systems. All modern television and televisionlike receivers contain SAW filters for Nyquist IF filtering.

Many digital spread-spectrum systems use SAW band-pass filters in the IF and RF stage up to 2.5 GHz [11]. Up to now wideband spread-spectrum systems were used mainly in military applications. Digital technology, however, allows the realization of spread-spectrum systems only with low bandwidths and long integration times. Therefore, most commercial systems are based on this technology. For digital CDMA systems, however, analog IF antialiasing filters are required; therefore SAW filters offering steep passband skirts, flat amplitude response, and linear phase are used. For indoor applications with strong interference a bandwidth higher than the coherence bandwidth is needed [12]. In spread-spectrum systems with high bandwidths SAW devices are the only choice for real-time signal processing such as correlation and spectrum shaping. Fixed-code matched filters have opened up a wide range of signal processing capabilities. SAW-based chirp spread-spectrum wireless system applications with extremely high data

rates have been demonstrated very successfully and are now in the pioneering stage on the market. Today digital signal processors (DSPs) can handle some 10 MHz bandwidth, while SAW devices can deal easily with some hundreds of megahertz of bandwidth. This advantage of SAW devices over DSPs will become smaller one day with progress in the development of digital circuits.

SAW sensors for many physical (electrical, mechanical, thermal, etc.), chemical, and biological quantities as measurands are now becoming mature and commercially feasible. Radio SAW sensing is under investigation at many laboratories, and a few new products are on the market. Wireless identification tagging and reading based on passive SAW interrogator labels (SAW tags) have recently been introduced to the market.

SAW technology has evolved since the mid-1970s and now allows the routine design of filters in the range from 20 MHz to 3 GHz [13]. This frequency band is used in many new wireless communication systems and for sensor applications, especially within the ISM frequency at 2.5 GHz, which is also used for the intermediate frequency for broadband systems operating at higher frequencies [14]. Currently, the submicrometer manufacturing and material techniques are improving greatly and are encompassing even higher frequencies of ≤ 10 GHz. Delay-time lengths are limited by the size of standard wafer dimensions to 16 μ s. Precise simulation tools for SAW devices are available. Thus it is possible to optimize the SAW devices on a computer before fabrication of the first samples. Very accurate SAW devices performing complex signal processing in communication systems may be designed.

1.2. Materials and IDTs

The invention of the IDT in 1965 [2] as a most efficient technique for the generation and detection of SAWs on a piezoelectric substrate immediately paved the way to two major microwave engineering product design directions, with quite different thrusts. At one end of the scale, in the high-volume, low-cost-component market, the challenge was related to whether mass-produced SAW filters and resonators could be competitive in price and performance with established technologies. At the opposite end, the focus was on low-volume, high-cost components for radar signal processing and maximum emphasis was given to the efficient implementation of SAW pulse compression filters with very large compression gains. Between these two extremes, a wide range of other SAW device configurations and applications began to receive intensive research scrutiny.

SAW devices are based on excitation, propagating, reflection, and detection of microacoustic waves. On the basis of a variety of physical principles, methods and techniques have been developed for the microwave–microacoustic transduction, for reflecting, guiding, focusing, and amplifying the waves, and for introducing controlled dispersion. The use of transduction and reflection, which are the basic mechanisms in most SAW devices, is discussed by way of a two-port resonator illustrated in Fig. 4. Both the IDTs and the reflectors are distributed elements, consisting of an array of metallic electrodes or strips. The

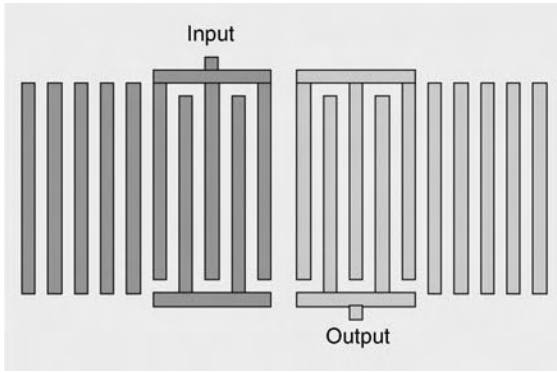


Figure 4. Schematic layout of a two-port SAW resonator. Two IDTs (input and output) are backed by several reflector strips forming a cavity.

(active) IDTs exploit piezoelectricity to launch and detect the SAW waves. The (passive) reflector gratings, usually a set of metal strips that can be short- or open-circuited, act within their stopband as a mirror reflecting the incident waves, thus forming a cavity. Elements combining transduction and reflection with a predefined phase relation (Fig. 5) are in use for advanced SAW IF filters. They enable single-phase unidirectional transducers (SPUDTs) and contribute to the size reduction of IF filters by using resonances within the transducers.

For an arrangement of strips with a width of $\lambda/4$ and a pitch of $\lambda/2$, reflections add up constructively. Therefore a sequence of alternatively polarized type 1 structures will result in both strong transduction and reflection. On the other hand, using an arrangement of strips with a width of $\lambda/8$ and a pitch of $\lambda/4$ (split finger), (e.g., type 2, 3, or 4), reflections add up destructively. Cell types 2 and 4 will launch a transduction with opposite sign, while a type 3 cell will introduce no transduction and reflection.

The first basic design parameter is the phase velocity v , because according to Eqs. (2) and (3) it determines the spacing and number of pitches of a transducer for a given operating frequency f and bandwidth B . The second basic design parameter is the electromechanical coupling coefficient k^2 , which is a measure of the efficiency in converting an applied microwave signal into mechanical energy associated with the microacoustic wave. It also determines the minimum insertion attenuation of a SAW device for a given relative bandwidth. Because of the piezoelectric effect, the SAW velocity differs little between free or metallized

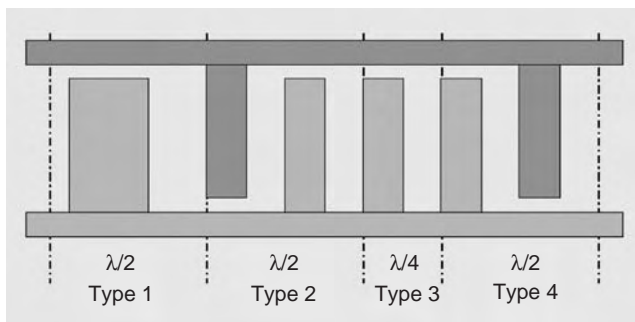


Figure 5. Basic cells for building a generalized SPUDT.

Table 1. Properties of Frequently Used SAW Substrate materials

Material	Orientation ^a		v (m/s)	k^2 (%)	TCD (ppm/K)
	Cut	Prop			
Quartz	ST	X	3158	0.1	0
	37°rotY	90°rotX	5094	0.1	0
LiNbO ₃	Y	Z	3488	4.1	94
	41°rotY	X	4750	15.8	69
	128°rotY	X	3980	5.5	75
LiTaO ₃	36°rotY	X	4220	6.6	30

^a“Orientation cut” denotes the crystalline orientation of the substrate surface normal; “orientation prop” gives the orientation of the wave propagation direction.

surface, or within an IDT. Again, k^2 gives the relative difference between the velocities with electrically open/short-circuited surface. Both v and k^2 depend on the material tensor elements of elasticity, piezoelectricity and dielectric permittivity, and on the mass density (among others).

A wide variety of single-crystalline substrates such as quartz (SiO₂), lithium tantalate (LiTaO₃), and lithium niobate (LiNbO₃) are commonly used for SAW devices. The wave types propagating on these substrate materials show velocities v between 3000 and 5000 m/s, which is slower by a factor of 10^5 compared to that of guided electromagnetic waves, such as waves guided by microstrip transmission lines. Thus, devices operating in the VHF/UHF frequency region can be fabricated with linewidths in the order of micrometers or below, which can be produced very accurately and reproducibly using optical projection printing techniques.

Table 1 gives an overview on the fundamental SAW properties of some of the most frequently used cuts. Quartz crystal cuts show excellent temperature stability, which is given by the temperature coefficient of delay, (TCD). The coupling coefficient k^2 , however, is low, which limits the relative bandwidth that can be electrically matched without losses to some percent. Therefore, quartz crystal cuts are used mainly for narrowband devices down to 0.1% relative bandwidth, or when steep skirts in the transfer function are specified. SAW devices on quartz are used in the IF stages of mobile phones, for resonators or delay lines used in local oscillators, and for dispersive delay lines used in radar applications. The coupling coefficient k^2 of LiNbO₃ is much larger than that of quartz, allowing medium-loss devices for wideband applications with relative bandwidths up to $\sim 10\%$. SAW devices on LiNbO₃ are used for IF filtering in TV or satellite receiver sets, for example. Some special cuts, like the 41°rotY cut of LiNbO₃ or the 36°rotY cut of LiTaO₃ show extreme high coupling coefficients, which makes these cuts highly suited for low-loss and wideband applications needed in the RF stages of mobile phones.

1.3. SAW Design

The design of SAW devices is based mainly on signal theory. Signal theory algorithms such as impulse response modeling [15] allows for a first-order design because the impulse response $h(t)$ of the IDT is—with the help of the

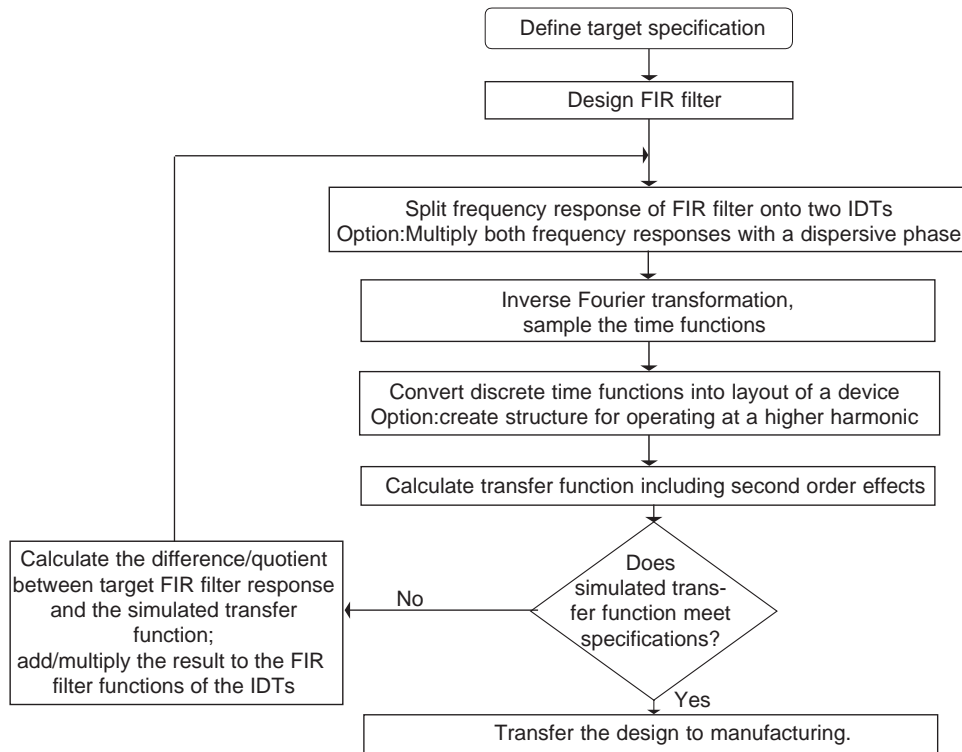


Figure 6. Flowchart for the design algorithm of a SAW delay line.

SAW velocity v —directly related to the overlap and spacing of the electrodes if reflections are not dominant. The frequency response $H(f)$, which is the Fourier transform of $h(t)$, therefore can be computed quite straightforwardly from the electrode pattern. This procedure can also be reversed and used for filter synthesis. To achieve a given transfer function for a transducer, for example, the overlaps can be weighted (apodized) according to the corresponding impulse response. Figure 6 is a flowchart for a typical design algorithm of a SAW delay line.

SAW tapped, reflective, or transducer-coded delay lines are specified mainly in the time domain. SAW linear, pulseshaping, and nonlinear phase delay lines, on the other hand, are specified mainly in the frequency domain. To start the design, these specifications must be transferred into a finite impulse response [15–19].

In the next step, the target frequency response has to be split up onto two IDTs, which can be achieved by using one apodized and one uniform transducer, with one or both transducers being dispersive, or by using two dispersive and amplitude weighted transducers. If an uniform IDT is chosen, the frequency response of the weighted transducer is given by the overall frequency response $H(f)$ divided by the frequency response of the uniform IDT. When using two weighted IDTs, the frequency response can be split using the square-root method [19]. If dispersive transducers are chosen, their appropriate phase or chirp functions have to be multiplied additionally by the frequency response of each individual transducer. The chirp functions can be adapted to improve the matching conditions for the IDTs. After transforming the frequency response of each individual transducer into the time

domain, a linear or a nonlinear sampling method is applied to both time functions, which allows a synthesis of an initial guesses for the two IDTs of the delay line [19]. To transfer this sampled IDT into a geometric layout, the SAW velocity within the transducer v_{IDT} has to be determined quite accurately. The group delay time specification of the device can be achieved by a proper shift of these building blocks by using the SAW velocity on free space v .

Filters operating at the third harmonic can be designed at their nominal frequencies and, instead of taking every tap, only every third active tap is realized. For IDTs operating at even higher harmonics, every fifth, seventh, and higher active tap may be selected.

Signal theory guidelines, however, are not adequate for accounting for microwave and microacoustic effects. These so-called second-order effects include the acoustic reflections at strips and electrodes, effects due to the charge distribution on electrodes; mechanical loading effects such as mass loading, stress loading, and topographical loading at strip edges; the microacoustic attenuation and dispersion; the diffraction and refraction of the waves, beamsteering due to anisotropy of the substrate; the generation of spurious bulk acoustic waves (BAWs) in the IDTs and/or the conversion of SAWs into BAWs, ohmic losses of the strips; and electromagnetic feedthrough between IDTs. This second-order effects can be treated only by using network theory or field theory algorithms.

The quantitative characterization of the second-order effects is solved by field theory approaches [20], by test chip measurements, and by a combination of both [21]. In order to store the results in databases, they are fitted to simple, mostly analytic expressions depending on

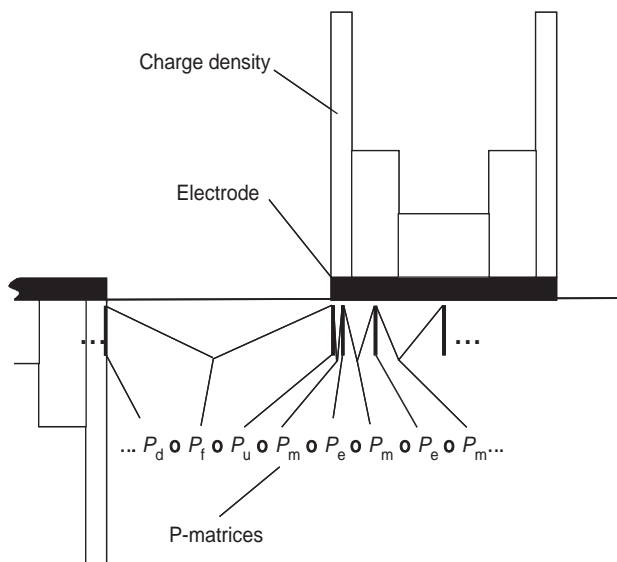


Figure 7. Basic cells for the *P*-matrix model. The transversal finger structure is divided into several substructures, which can be simulated in a straightforward manner. P_d , for instance, gives the *P* matrix of a “down” step, P_f of a free surface, P_u of a “up step,” P_m of metallized surface, P_e of an electrical charge, and so on; *o* is the symbol for the *P*-matrix cascading algorithm.

frequency, geometric parameters (e.g., metallization height, metallization ratios), and material parameters (e.g., coupling coefficient or mass density). Bond wires, chip layout effects, and package parasitics are accounted for using adequate lumped-element models.

For a SAW analysis, the SAW structures are subdivided into substructures that are further subdivided into basic two-port (with two acoustic ports) or three-port cells (with two acoustic and one electric port), as depicted in Fig. 7. A typical basic cell, for example, may be a single electrode as well as a detail of an electrode. This may be necessary when the charge distribution on the electrodes (depicted in Fig. 8) or edge effects are modeled. The electrical and acoustical descriptions of the substructures are then

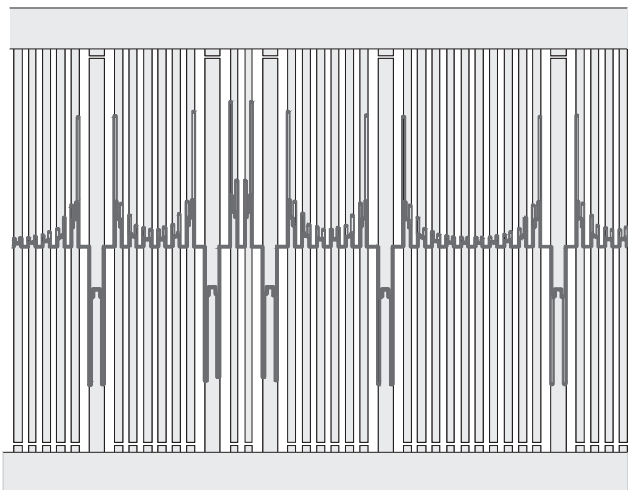


Figure 8. Electrical charge distribution on the electrodes in a section of an IDT.

cascaded using network theory algorithms. Popular techniques include various lumped-element methods such as equivalent-circuit modeling techniques, matrix manipulation techniques such as *P*-matrix formalisms (Figs. 2 and 7), or coupling-of-modes (CoM) techniques [22]. By cascading all the subcells, and by including the microwave parasitics and electrical matching structures, the electrical terminal behavior of the microacoustic device, which gives the simulated transfer function, can be analyzed. To simulate diffraction effects, an extended angular spectrum of the straight-crested waves model can be used [23,24].

The deviations of the simulated transfer function from the target frequency response can be used in an optimization process to modify the two frequency responses defining both IDTs. This gives two new IDT functions, which build the starting point of the next synthesis, the next simulation, and, if necessary, the next optimization. The number of necessary iterations of this optimization process depends on the specifications of the delay line, but typically 5–10 iterations are sufficient. If the simulated transfer function of the final optimization run comes close enough to the specified target frequency response, the geometry of this design is transferred to the technology for manufacturing.

1.4. Manufacturing

SAW manufacturing is based on the technology of integrated circuits [13]. The basic prerequisite for the reproducible manufacturing of SAW components is that the wafer material be as perfect as possible. Only a defect-free monocrystal and a good standard of surface polish will ensure constant propagation velocity and low damping of the waves. In contrast to the semiconductor process, only one single metallization layer has to be manufactured, but with a much higher demand with respect to geometric precision of the linewidth and thickness uniformity. For instance, projection printing using a wafer stepper is a reliable fabrication technique that provides the required high resolution and positional accuracy as well as a low defect density. In conjunction with a single-level liftoff or etching process (see Fig. 9), this provides the best dimensional stability and reproducibility of the aluminum structure, together with the smooth finger edges that are particularly important for the propagation properties of the acoustic waves. Small variations of the electrical performance are introduced by misalignments of the orientation of the wafers, variations of the metallization height, and deviations from the desired mark:pitch ratio.

The pattern of small SAW devices is repeated several times on the mask so that a large number of devices can be exposed simultaneously. For larger SAW devices, such as long delay lines, tapped delay lines, chirp filters, and convolvers, the devices have to be composed on the wave using a programmable wafer stepper. Wafers with diameters of ≤ 5 in. are used in today’s high volume fabrication. For special applications crystal substrates with lengths of ≤ 25 cm are available, which, in principle, enables SAW devices having delays times up to $40 \mu\text{s}$.

The maximum operation frequency is given by the minimum linewidth. Very fine lines can be obtained by X-ray

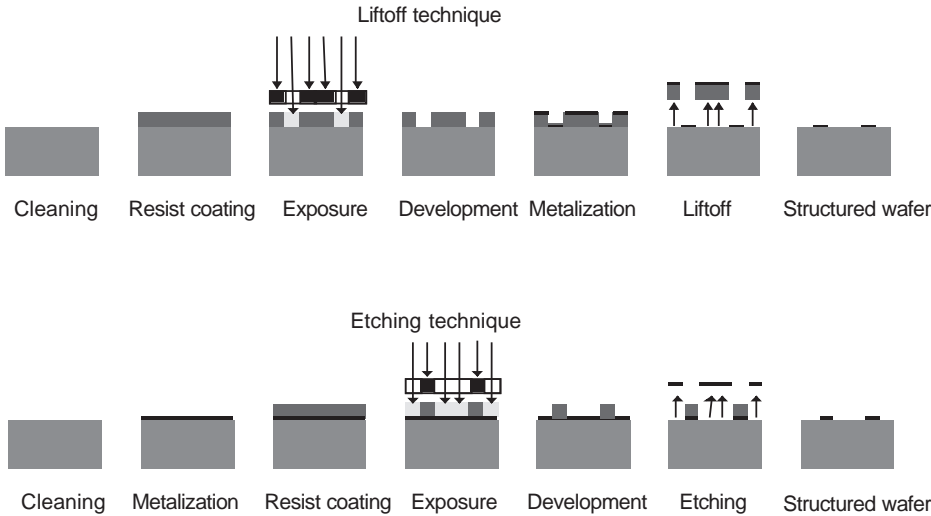


Figure 9. Process flow of SAW device fabrication (*top*—liftoff technology; *bottom*—etching technology).

[25] or electron-beam exposure [26], deep UV, or ion projection [27], which allow linewidths down to $0.1\ \mu\text{m}$ and fundamental frequency responses up to 10 GHz. However, those techniques are still, in the experimental stage. SAW companies often use optical lithography, which allows a patterning down to $0.3\ \mu\text{m}$ with a high precision of linewidth [28]. As is seen from Fig. 10, high resolution and good edge quality are achieved. Using this process, the fabrication of SAW devices operating up to 2.45 GHz in the fundamental mode has been demonstrated.

From the packaging point of view the most commercial challenge today is the miniaturisation of SAW filters and their integration into front-end modules [29]. Epcos, for instance, has developed a highly miniaturised chip-size package technology (see Fig. 11). The SAW chip is flip-chip mounted onto a chip carrier serving as the bottom part of the package. The electrical connections to the chip are bonded with solder bumps. An underfiller attaches the SAW chip solidly to the chip carrier. Thus, the backside of the chip can also serve as part of the package. To protect the surface of the acoustically active area of the SAW chip, a cavity is built on the wafer with photolithographic process in two steps. First, a closed polymeric wall is placed

around the active filter structure. Using the same process, this wall is then covered with a roof. Using this technology, Epcos could introduce SAW filters for 2 GHz applications, such as personal communication networks and systems and UMTS (Universal Mobile Telephone System) devices available in a $2 \times 2 \times 0.8\text{-mm}^3$ -chip package technology. The technology, moreover, allows for a further miniaturisation of SAW filters beyond a $1\ \text{mm}^2$ footprint area.

2. TWO-PORT DEVICES

The two-port devices of the SAW delay lines can be subdivided into linear phase, dispersive, and tapped delay lines. This devices are mainly used for expanding, compressing, or pulshaping in the IF part of radar or spread-spectrum communication systems. Additional applications for linear phase delay lines are in the feedback loop of an oscillator or for the signal delay necessary in military surveillance systems or in calibration routines for radar systems.

2.1. Linear Phase Delay Lines

Linear phase delay lines with long delay times are needed mainly for military surveillance systems [16] and for the

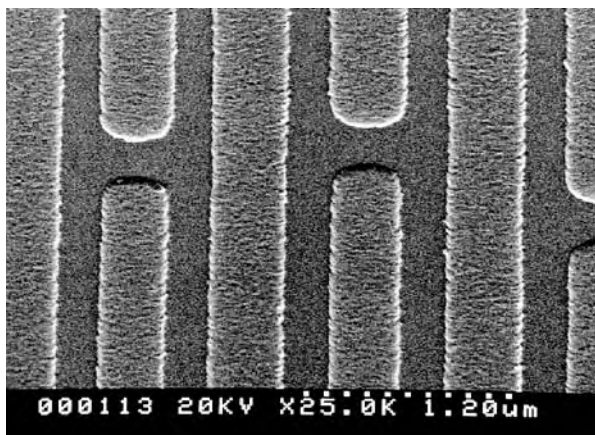


Figure 10. SEM photograph of part of an IDT with $0.6\ \mu\text{m}$ periodicity and $0.4\ \mu\text{m}$ linewidth.

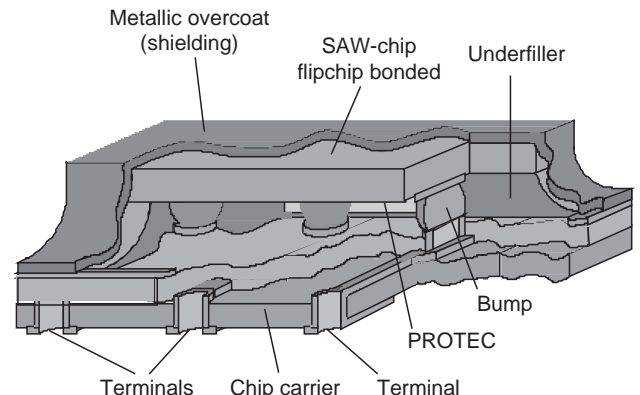


Figure 11. Chip-size package technology (© Epcos, Munich, Germany).

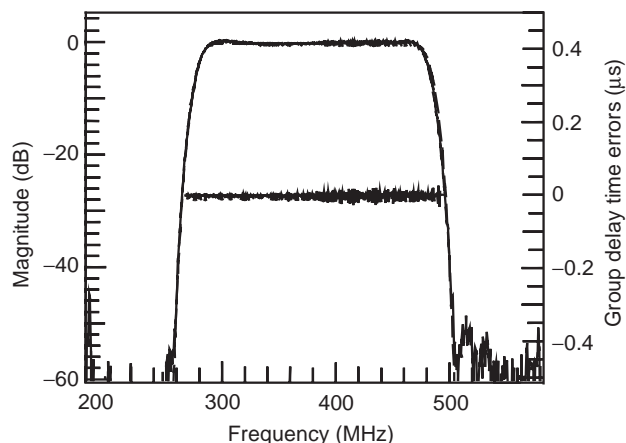


Figure 12. Normalized measured transfer function of a delay line operating at a center frequency of 384 MHz with a relative bandwidth of more than 50%.

linearization of radar systems [28,30]. For both systems large absolute bandwidths are requested. A special application of linear phase delay lines are spectrum-shaping filters like PSK to MSK conversion filters.

Figure 12 shows an example for a typical transfer function (normalized) of a linear phase delay line [31] achievable in SAW technique operating at a centre frequency of 380 MHz and covering a relative bandwidth of 52%. The insertion attenuation is approximately 25 dB. The delay time is $0.75 \mu\text{s}$. The amplitude deviations within the pass-band are less than $\pm 0.5 \text{ dB}$. The ripple on the group delay response is caused by acoustic reflections. If these reflections are gated in the time domain, group delay errors are within $\pm 1 \text{ ns}$.

For SAW devices with large absolute bandwidths, a high center frequency, which lowers the required relative bandwidth, is of advantage. Furthermore, a great variety of amplifiers and other circuitries are available for the ISM band from 2.4 to 2.5 GHz. Therefore, nowadays many commercial radar systems use this frequency band for IF operation. Figure 13 presents the layout of a linear phase SAW delay line incorporating a shielding pad between

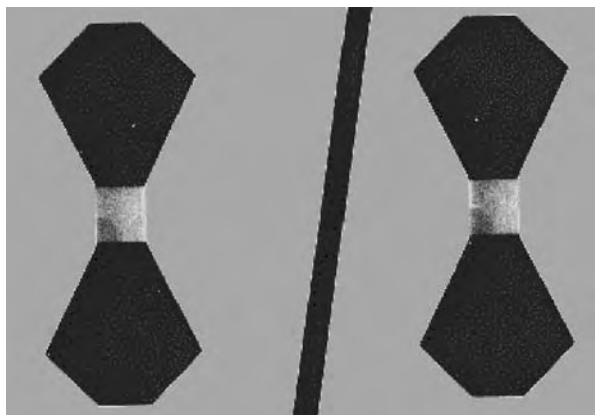


Figure 13. Typical layout of a linear phase delay line for a center frequency of 2.45 GHz.

both IDTs (dark gray area) to lower electromagnetic feedthrough. The bulky black hexagonal areas are the bonding pads. The center frequency of this delay line is 2.45 GHz, and group delay times of 1.0, 1.5, and $2.0 \mu\text{s}$ have been realized. The area of an IDT directly scales with the acoustic wavelength and thus shrinks when increasing the center frequency. For the bonding pads, on the other hand, a minimum area is needed for a safe bonding process. Thus, for high frequencies the bonding pads become larger than the acoustically active area of the IDT. The filter has been designed for operation bandwidths of 400, 600, and 800 MHz, respectively. The devices exhibit excellent passband characteristics and low group delay distortions similar to those shown in Fig. 12. The insertion attenuation is approximately 25 dB. Stopband attenuation is better than 30 dB close-in.

2.2. Pulseshaping Linear Phase Delay Lines

The amplitude and phase of the transfer function of a SAW delay line filter can be designed independent of each other, as pointed out in Section 1. Thus signals, which are limited in both the time and frequency domains, can be shaped by SAW delay-line filters. For example, it is possible to design SAW delay lines having a rectangular impulse response with constant phase, which results in a sinc transfer characteristic and linear phase in the frequency domain.

Phase-shift-keyed (PSK) signals are quite easily generated digitally. A PSK signal consists of a sequence of contiguous chips of duration T_c and uses two signal phases: -0° and 180° . If the state of two consecutive chips remains the same, then the phase of the signal does not change. If the chip state changes (from 0 to 1, or 1 to 0), the phase of the signal changes by 180° . A MSK signal also consists of a sequence of contiguous chips of duration T_c , but there are no phase shifts at the transitions between adjacent chips. Instead, the instantaneous frequency of the carrier takes on a value f_1 in some of the chips and a value of f_2 in others, again in a pseudorandom sequence. The phase of a MSK signal is everywhere continuous, and so is its first time derivative since the transitions between f_1 and f_2 occur at the peaks of the waveform. Because of this “smoother” nature of the waveform, the amplitude of the spectral sidelobes falls more rapidly with the distance from the center frequency confining 99.5% spectral energy within its mainlobe, compared to 92% of a PSK signal. Also, MSK signals show a 33% higher spectrum efficiency when compared to PSK signals and thus allow higher bit rates or lower bit error rates (BER) for the same given bandwidth.

In contrast to PSK signals, minimum-shift-keyed (MSK) signals are more difficult to generate. In order to convert a PSK signal into a MSK signal, the convolution with a rectangular time function has to be performed [6,32]. The length of the rectangular time function must be one chip length of the PSK signal. This can be done easily with a SAW delay line. This spectrum-shaping feature can also be implemented in the SAW IF filter of a superheterodyne receiver, and it can be included in a SAW tapped delay line, as shown in Section 2.4.

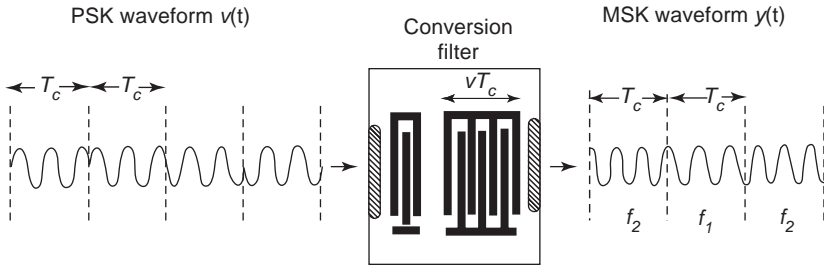


Figure 14. SAW-based PSK-to-MSK conversion filter [6, p. 191].

Figure 14 [6, p. 291] shows a sketch of this PSK-to-MSK signal conversion with the help of a SAW conversion filter. A PSK waveform at an angular frequency f_1 and a chip length T_c is fed to the SAW conversion filter with an impulse response of a time length of T_c at an angular frequency f_2 . The output signal then is a MSK waveform whereby the code is represented by the two angular frequencies f_1 and f_2 . An almost rectangular impulse response is generated using one very short IDT and one with a length vT_c . The two angular frequencies f_1 and f_2 are chosen to satisfy the condition

$$(f_2 - f_1) T_c = \frac{1}{2} \tag{4}$$

This means that a f_2 chip contains an extra one-half cycle of carrier as compared to a f_1 chip.

In Fig. 15 the measured frequency and impulse responses of a PSK-to-MSK conversion filter for a system using a chip rate of 60 ns are shown. Deviations in the upper frequency band are caused by electrical feed-through. Spurious signals in the time domain are below 30 dB.

2.3. Nonlinear Phase Delay Lines

First applications of nonlinear phase (sometimes called *dispersive*) SAW filters were in radar systems for pulse expansion and pulse compression [33–35]. Typical characteristics of these filters were bandwidths of a few percent and integration times up to 20 μ s. The nonlinear phase function in the frequency domain of an expander and the appropriate compressor filter have to cancel each other to

result in an overall linear phase function of the system. In subsequent systems the expanded signals were generated digitally and SAW filters were used only for compression of the expanded signals.

SAW dispersive delay lines were also used as spreading and despreading filters in spread-spectrum transmission systems, and for very fast broadband channel sounding [36,37]. The spreading/despreading function can be implemented as a special feature in the SAW IF filters of the transmitter and receiver. Thereby, no further components or wiring is needed to upgrade a conventional transceiver to a spread-spectrum system. For this application, SAW dispersive filters and SAW tapped delay lines (see Section 2.4) are used. Dispersive filters generate compressed impulses with a much lower sidelobe level. However, in contrast to tapped delay lines, only two (almost) orthogonal codes can be implemented using SAW dispersive delay lines, an “up” chirp and a “down” chirp.

Two different filter techniques were used for the building of a dispersive delay line; in the first, the input and output transducers are arranged in parallel acoustic tracks and the signal is shaped by chevron-type reflectors, which connect the input and output transducers acoustically. These devices are called *reflective array compressors* (RACs) [38–40]. As the length of the crystal chip is used twice, the integration time can be extended up to 40 μ s for standard 3-in SAW wafers. The second configuration consists of two inline transducers, and the weighting function is implemented in both transducers [17,19,41].

As an example, a pulse compression filter covering a long chirp time of 12 μ s over a bandwidth of approximately 6 MHz is shown in Fig. 16. The main second-order effect of

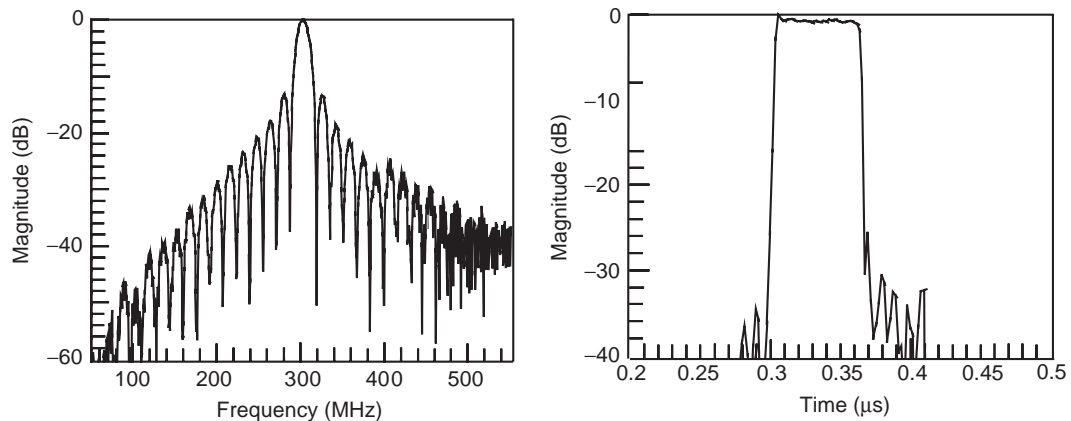


Figure 15. Normalized measured frequency and impulse responses of a PSK-to-MSK conversion filter for a system using a 60 ns chip rate.

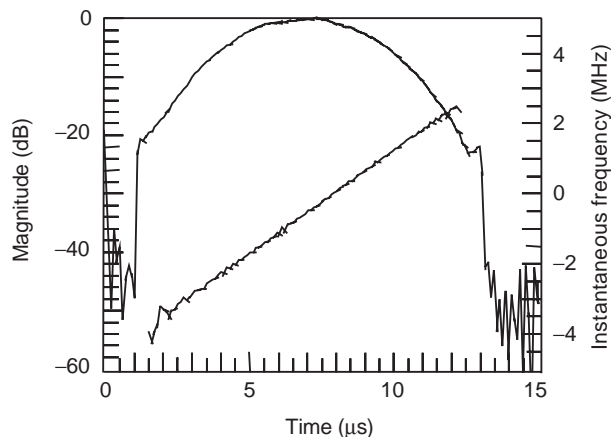


Figure 16. Impulse response of a dispersive delay line with a chirp time of $12\ \mu\text{s}$ and a bandwidth of 6 MHz. The filter is used as compressor in a pulse compression system. Therefore, the amplitude of the filter is weighted according to a Hamming function.

a SAW device of such specification is due to diffraction effects caused by the long delay time. By compensating these diffraction effects, the suppression of close-in spurious signals of the compressed impulse can be improved significantly, as demonstrated in Fig. 17.

The software for the design of chirped SAW devices for pulse expansion and compression has been improved continuously. In the 1980s it was necessary to utilize the principle of stationary phase to compensate second-order effects. Starting from the 1990s, it became possible to design pulse compression filters even with a low time-bandwidth product using optimization techniques [19]. As an example, two dispersive filters (expander and compressor) are shown in Fig. 18. These filters were designed using optimization techniques.

2.4. Tapped Delay Lines

One of the key technologies of modern RF consumer communications is the spread spectrum technique [12]

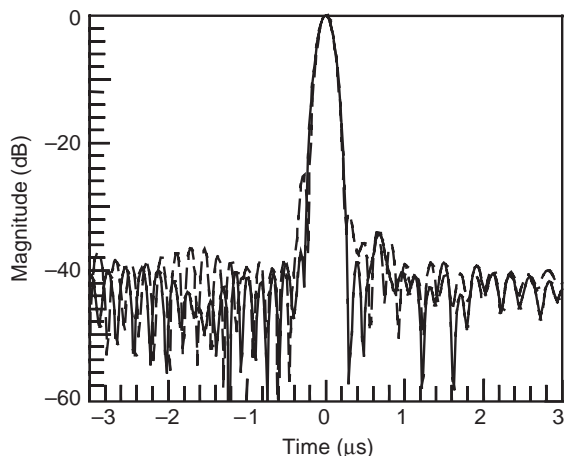


Figure 17. Compressed pulse using the compressor of Fig. 16 (solid line—final design including compensation of diffraction; broken line—first design).

which originated in the military arena with a flurry of developments during and following World War II. Spread-spectrum communication became the standard for military signaling since it reduces the friendly communicator's detectability and combats the enemy-introduced interference.

Because of its inherent wideband transmission and the occurring processing gain, spread-spectrum communication also shows excellent performance in preventing multipath phenomena and allows to transmission of signals over noisy channels with a high degree of signal security.

Driven by the immense progress of communication systems, in the mid-1980s research groups began to develop wireless spread-spectrum demonstrators, shifting spread-spectrum from military to commercial applications. The radio channel of modern portable cordless telephone systems, for example, in indoor cells such as business and public administration buildings, shows a large coherence bandwidth and small delay spread (typically 30 MHz and 100 ns). These channel properties are optimally exploited by a spread-spectrum system using a higher bandwidth than the coherence bandwidth. Therefore, throughout the world, civil spread-spectrum systems are now in practical use, such as in wireless LAN products. The ongoing trend toward spread-spectrum communication is due to its excellent robustness in indoor radio channels, the demand for user privacy, with low-power, unlicensed communication devices, and also low cost of systems.

Modern commercial spread-spectrum systems use a frequency hopping (FH) or the direct-sequence code-division multiple access (DS CDMA) system, both combined with time-division multiple access (TDMA). Most modern DS CDMA systems use pseudonoise (PN) codes for channel separation. The RF energy, thereby, is spread across a wide frequency band by replacing each data bit by a number of chips, namely, multiple subbits, which occupy the same time interval. The more the signal is spread, the lower is the interference threat to or from other systems using the same frequency band. For that reason, in most countries regulatory bodies insist on a minimum processing gain of 10 dB. The upper limit of processing gain is determined mainly by the available RF bandwidth. Some new concepts, however, use a chirp function instead of the pseudonoise codes, resulting in a chirp spread-spectrum system (see Section 2.2). In a CDMA or chirp system the correlation of the received signal with a given time function (code or chirp function) has to be performed in the receiver.

Among the encoding and decoding techniques necessary in all spread-spectrum systems [12], analogue SAW matched delay lines can be used for code generation and as matched filtering to despread the received information signal [31,42]. Using SAW matched delay lines [43,44], the correlation can be carried out asynchronously, and the front-end hardware can be implemented simply and compactly. SAW matched delay lines easily exhibit moderate correlation gain values in the order of 20–30 dB, which cannot be met by digital matched filter implementations. For many systems a fixed-code SAW tapped delay line (TDL) is feasible as a matched filter.

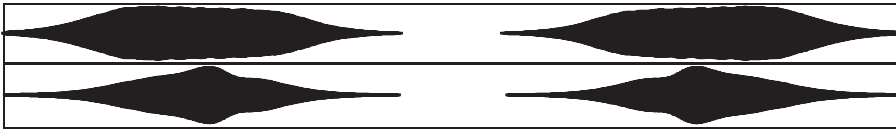


Figure 18. Geometry of the expander (top) and compressor (bottom) filter. The meander line through the active taps is depicted.

In SAW dispersive matched delay lines, different phase (and eventually amplitude) spread-spectrum modulation schemes can be implemented. Two, three, or more phase states for the code chips extend the variety of signals with good correlation properties and high resistance against interference in buildings. Exclusively binary signals do not offer this variety, and their detection after hardlimiter sampling is very sensitive to sinusoidal interference [36,37].

The desired correlation function can be realized in the SAW delay line and defines the impulse response of the delay line. In addition, an optional frequency limitation may be built in. A schematic layout of a PSK tapped delay line is depicted in Fig. 19. Additional weighting functions necessary to convert the PSK signal to an MSK signal can be implemented easily.

A SAW tapped delay line basically is a transversal SAW filter incorporating an input interdigital transducer (IDT) and an output IDT, one of which is phase-coded like the one shown in Fig. 19 for binary phase shift keying (BPSK) modulation. The chip-defining reversal of the waveform cycles is simply achieved by an appropriate polarity reversal of the IDT fingers.

Instead of BPSK modulation, which gives a theoretical sidelobe suppression of 13 dB, a MSK modulation scheme can also be applied. This can be achieved, for instance, by using an input IDT according to Fig. 19, having a time length of one chip. Thereby, this IDT will perform an additional convolution with a rectangular time function of one chip length to PSK transfer function. The impulse response of a MSK tapped delay line is depicted in Fig. 20. The instantaneous frequency is directly related to the code, here a PN code sequence with a length of 128 chips. The time sequence of the two different frequencies of the MSK modulation scheme can easily be seen.

Figure 21 gives the power spectrum of the MSK-modulated tapped delay line. In comparison to BPSK, a MSK modulation results in a 10 dB additional sidelobe suppression and a falloff increased by 6 dB. The insertion attenuation of this delay line is approximately 18 dB. The binary pattern of the tapped delay line cannot be seen in the frequency domain, but the bandlimitation of the

output IDT is obvious. Additional weighting of the spectrum for generating a Gaussian MSK is possible.

The performance of a tapped delay line is characterised by the correlation response. The correlation gain obtainable depends on the choice and length of the binary code. In our example the length of the code is 128 chips, the correlation gain is 21 dB, and the peak:sidelobe ratio is approximately 15 dB, as shown in Fig. 22.

3. ONE-PORT DEVICES

The one-port devices of SAW delay lines are mainly wired to antennas and used for passive marks in identification or sensor systems.

3.1. Operating Principle of a SAW-Based Wireless Passive ID or Sensor System

SAW devices can be used as identification and sensor elements not requiring a power supply for measuring wirelessly physical, chemical, and biological quantities such as temperature, pressure, torque, acceleration, and humidity [14,45,46]. These applications are based mainly on the invention and implementation of SAW identification (ID) tags and their combination with traditional SAW sensor techniques.

The operating principle of such a system is schematically depicted in Fig. 23. A radiofrequency electromagnetic (RF) readout signal is transmitted by the reader unit, which contains a radar transceiver. A small portion of this signal is picked up by the antenna of the passive SAW transponder, where an IDT, connected to the antenna, converts the received signal into a SAW.

The microacoustic wave is stored for a certain time in the SAW device and coded according to the code number or the sensor variable of interest. This storing of the acoustic

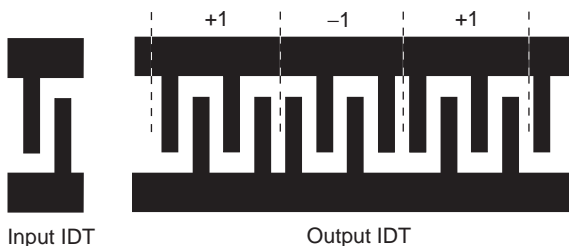


Figure 19. Schematic layout of a PSK tapped delay line.

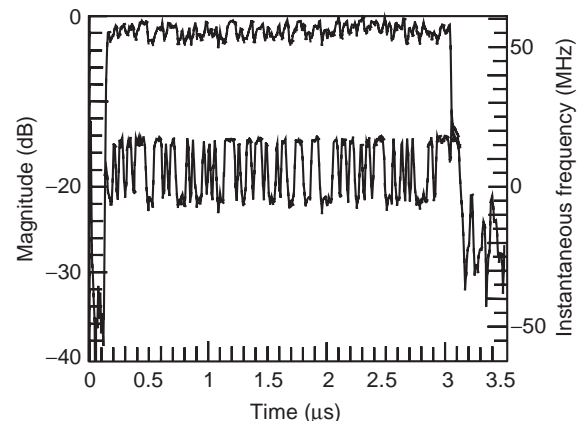


Figure 20. Impulse response and instantaneous frequency of a tapped delay line applying a MSK modulation scheme.

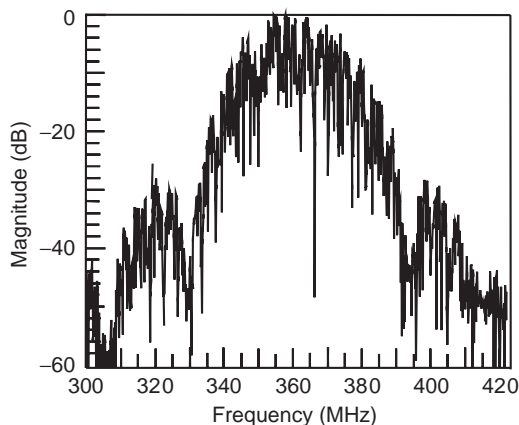


Figure 21. Normalized frequency response of the MSK-modulated tapped delay line.

energy can be done using either a delay-line configuration or a resonator. If the storing is done using a delay-line configuration, the information is encoded in the number, the time positions, and the phases of the response pulses. This coding can be achieved by using either a coded transducer, as depicted in Fig. 25, or reflector array, as shown in both Figs. 23 and 26. If resonant structures are used for storing, the information is encoded by the center frequencies and the respective phases. The temporarily stored and coded microacoustic signal is reconverted into electrical signals by the IDT and retransmitted to the radar transceiver unit via the transponder antenna.

Because of the low velocity of SAWs, long delay times in the range of some microseconds can be achieved using rather small SAW chips. Therefore, at VHF/UHF frequencies, environmental echoes caused by electromagnetic multipath propagation phenomena are already safely faded out when the sensor response arrives at the radar transceiver (see Fig. 24). Hence, the response signal of the SAW ID tag or sensor can easily be separated from environmental echoes in the time domain.

The response signal of the SAW ID tag or sensor contains all information about the number and geometries of the coding structures as well as the propagation and

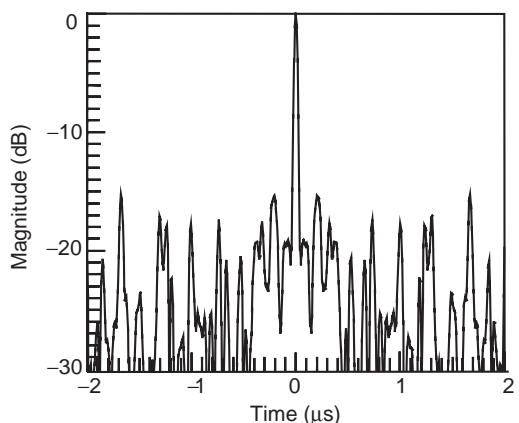


Figure 22. Autocorrelation function of the tapped delay line shown in Figs. 20 and 21.

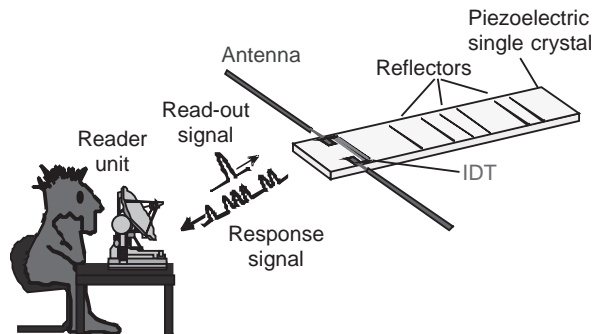


Figure 23. Schematic of a SAW-based radiolink system that uses a reflective delay line.

reflection properties of the SAW. Its evaluation in the radar unit may allow for the extraction of the desired information, which may include the sensor effect to a certain measurand or a specific ID number. As the distance between the radar transceiver and the SAW transponder is unknown or may even vary, differential evaluation of the signals are usually employed and differences in amplitudes, phases, frequencies, and propagation time delays are evaluated.

SAW transponders are passive components without any active logic on chip. Therefore, they cannot be addressed individually. To access more than one transponder, a frequency-division multiple access (FDMA), time-division multiple access (TDMA), code-division multiple access (CDMA), space-division multiple access (SDMA), or any combination of these must be realized. For FDMA orthogonal frequency bands or subbands must be used for each individual transponder. This technique is feasible for several resonant transponders [47,48]. When implementing a TDMA scheme, different time positions for each reflected signal must be chosen for minimising intersymbol interference. Typical 10 TDMA reflective SAW delay lines, each with three or four reflectors, can be realized. Using CDMA and the corresponding signal processing, again approximately 10 transponders having orthogonal codes can be addressed [49,50]. For SDMA techniques a space separation of the transponders has to be ensured. Because of the field attenuation of Rx (receiver) power with r^4 , the near-far problem limits the multiple access of passive radio transponders.

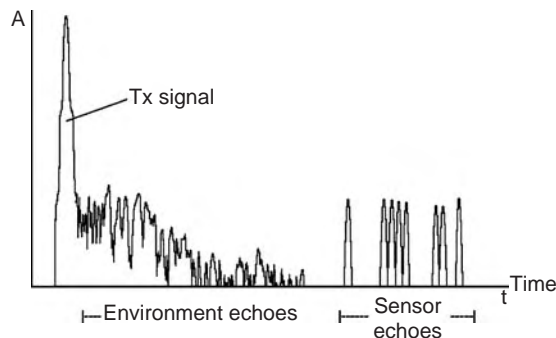


Figure 24. Response signal of a SAW ID tag or wireless sensor.

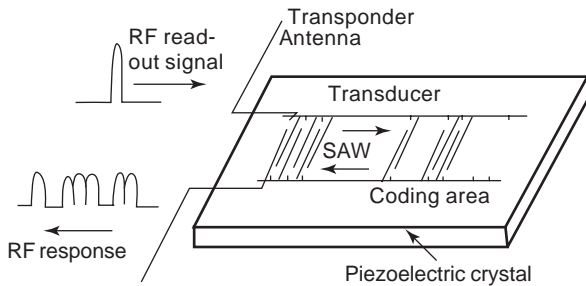


Figure 25. Schematic layout of a SAW ID tag with several coding transducers electrically connected to a common busbar.

Dipole, patch, slot, or loop antennas are used for passive SAW transponders. In the VHF/UHF frequency range, the insertion attenuation of SAW transponders is in the order of 20–60 dB [14,45,46], depending on the operating frequency, the substrate material, and the number of reflectors. The achievable access rate is up to 10^5 per second. The latter fact allows for communication with fast-moving objects or vehicles.

The reader units for SAW ID tags or wireless sensor system applications [14,46] resemble those used in traditional radar systems. For fast-moving or fast-changing measuring conditions, pulse radar or pulse compression radar systems have been used; in cost-sensitive applications, FMCW (frequency-modulated carrier wave) or stepped-frequency systems are used.

In Europe, only two frequency bands suitable for SAW ID tags and/or wireless sensor applications are allocated for unlicensed low-power devices (LPDs) such as industrial, scientific, or medical (ISM) apparatus: 433.07–434.77 MHz and 2.4–2.4835 GHz. The allowed equivalent isotropically radiated power (EIRP) in these bands is $P_0 = 25$ mW. Applying this power level, the typical readout distance for a SAW ID tag or wireless sensor is in the order of several meters. Table 2 summarizes typical resolution values that can be achieved using passive SAW sensors read out wirelessly by a radar transceiver [14].

3.2. Identification Tags

For ID tags, a great amount of individual coding is required. A SAW ID tag usually incorporates a coupling IDT and a coding area [51–54]. There are two ways of designing the coding area—either reflectors are used (see

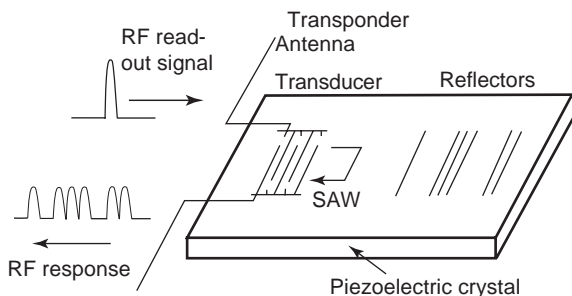


Figure 26. Schematic layout of a reflective delay line.

Fig. 26) or, alternatively, several coding transducers are wired together by a common busbar (see Fig. 25). The layout of a delay line with several coding transducers is similar to that of a tapped delay line, whereby the tapped transducers are connected by a long busbar to the coupling transducer to build up a one-port device. On high-coupling materials with a high dielectric constant, there might already arise some electrical phase shifts on this busbar, deteriorating the overall performance. In principle, the coded transducers could also be electrically connected to the coupling transducer and the antenna via a circulator, a phase combining network, or bonding wires.

Most SAW ID tags and passive sensors are designed using a reflective delay line, like the one sketched in Fig. 26. The surface acoustic wave in a reflective delay line propagates toward reflectors distributed in a characteristic barodelike pattern and is partially reflected at each reflector. Using reflectors reduces the chip length by a factor 2 compared to the nonreflective arrangement shown in Fig. 25. Furthermore, the electrical impedance of the transducers remains unaffected by the actual code.

The coding of a SAW ID tag depends on the applied modulation technique. In the simplest case, this coding is done by a binary amplitude shift keying ASK (ON/OFF); each predetermined possible symbol position is occupied either by a transducer or reflector (ON bit) or not (OFF bit). Figure 27 shows a measurement of an ID tag using a reflective delay line structure and an ASK modulation scheme. Using 32 symbol positions, 2^{32} different tags can be coded. ID tags with ASK modulation are already in use, such as in German subway systems operating at 2.45 GHz [45].

The ASK ON/OFF keying is outperformed by other modulation techniques such as phase shift keying (PSK). A binary PSK (BPSK) modulation obtains the same bit error rate at a 6 dB lower signal-to-noise ratio compared to an ASK modulation, thus enhancing the maximum readout distance by a factor of approximately 40%. Higher-order PSK-like quadrature PSK (QPSK) use fewer symbols (reflectors) and therefore need less chip size and result in a lower insertion attenuation, but a higher signal-to-noise ratio is needed for the detection.

The requirements for a SAW transponder used in a phase modulation system, however, become more stringent, because all influences that change the delay time of a signal, such as SAW velocity variations or the accuracy of the fabrication process, must be controlled within a small fraction of one SAW wavelength.

A good choice for the modulation technique used in SAW ID tags might be a pulse position modulation (PPM) (see Fig. 28), which achieves the code density of a higher phase modulation scheme but avoids their stringent sensitivity on small inaccuracies during the fabrication process [54]. In a pulse position modulation scheme the symbol occupies one of several possible timeslots. In most radar systems, the accuracy in the time resolution for one target is much higher than the time separation needed to resolve two targets. Therefore, using a PPM modulation the timeslots can be arranged much more densely, compared to the symbol separation in a ASK modulation.

Table 2. Typical Resolution of Wireless SAW Sensor Systems

Measured Quantity	Measurement Result	Resolution
Identification number	Change of signal pattern	32 bits
Temperature	Variation of SAW velocity	0.1 K
Mechanical quantities such as pressure, force, torque, acceleration, friction	Variation of elastic constants	1% of full scale
Impedance sensors	Variation of amplitude and phase of reflected signal	5% of full scale
Distance	Change of signal delay	20 cm
Relative position	Change of Doppler phase	2 cm
Angular position	Change Doppler phase	3°

3.3. Delay-Line Sensors

For a wireless SAW sensor, fewer symbols or reflectors are required compared than for an ID tag [14,46,56]. In most cases four to five symbols and/or reflectors are sufficient for one transponder. Figure 29 is a photo of a SAW reflective delay line for temperature sensing mounted in a surface mount device (SMD) package. The tag works in the 2.45-GHz ISM band. On the left side the IDT can be seen, and to the right there are four reflectors placed on the chip.

For sensing purposes, the delay time between the symbols and the respective phase differences have to be examined very accurately. Figure 30 shows the impulse response of the signal received from a SAW sensor incorporating five reflectors. The corresponding baseband signal is depicted in a polar diagram to show the phase relations between the symbols. Symbols R1, R2, R3, R4, and R5 denote the signals reflected from reflectors 1, 2, 3, 4, and 5, respectively. φ_{2-1} gives the phase difference between signals 1 and 2. Because the delay time between signals 4 and 5 is short, there is a slight intersymbol interference (ISI) between these two signals.

The evaluation of the carrier phase differences results in a huge enhancement in resolution, when compared to the evaluation of the delay-time differences. The enhancement is in the order of f_0/B , whereby f_0 gives the center frequency and B the bandwidth of the system. The resolution is comparable to a GPS (global positioning system), in which the evaluation of the carrier phase results in a

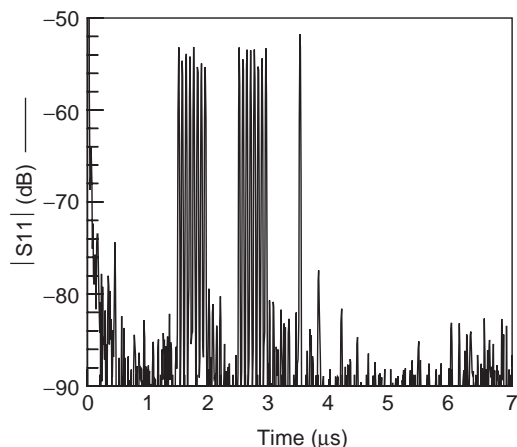


Figure 27. Measurement of the SAW ID tag with 8 ON/8 OFF/8 ON/8 OFF symbols, and 1 ON symbol.

resolution of parts of a millimeter, whereby the evaluation of the delay times gives an accuracy of some meters only.

The evaluation of the phase differences, however, induces an ambiguity when the phase shift exceeds 360° . This ambiguity of the phase evaluation can be overcome by using a precise evaluation of the delay times. Figure 31 gives the continuous phase difference φ_{3-1} of a wireless SAW reflective delay line as a function of temperature.

Lithium niobate, LiNbO_3 , is an ideal material for temperature sensors, because of its large temperature coefficient of delay TCD between approximately -70 and -85 ppm/ $^\circ\text{C}$, depending on the cut angle, and its high electroacoustic coupling factor [14,57,58]; for instance, SAW radio-requestable temperature sensors have been used to monitor the temperature of high-voltage surge arresters [59]. Also, the feasibility has been shown to monitor the temperature of a brake disk of a railcar during train braking [60] or the rotor temperature of an asynchronous motor during rotation [59]. The typical temperature resolution is in the order of 0.2°C . Up to about 200°C , standard assembly, interconnect, and packaging techniques can be used. Using special materials, such as lanthanite, and titanium for electrode material, operation up to temperatures as high as 1000°C have been demonstrated [58].

Using reflective delay lines for measuring mechanical parameters, such as pressure [61], force, strain, or acceleration, an adapted mounting and packaging technique is required. Wireless SAW pressure sensors are formed using a quartz diaphragm that bends under hydrostatic pressure. Figure 32 shows a schematic layout [62]. An “all-quartz package,” consisting of the SAW delay-line chip

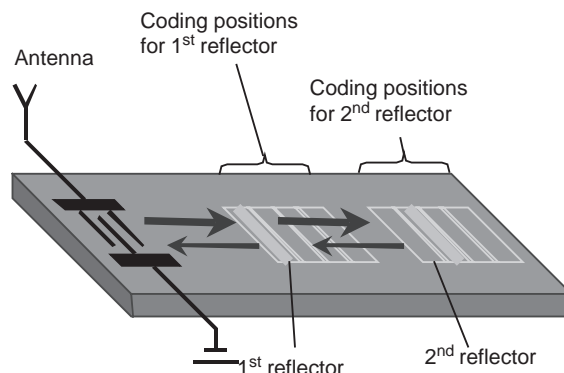


Figure 28. Schematic of a SAW ID tag applying a pulse position coding scheme [55].

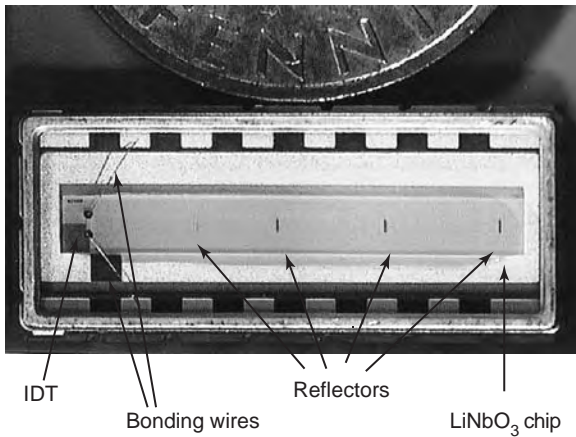


Figure 29. Photo of an assembled SAW reflective delay-line sensor for temperature sensing.

together with a cover and a lid formed of the same material, results in minimal thermal stresses and therefore minimizes cross-sensitivity to temperature. Using this all-quartz package, one obtains a pressure resolution of about 1% of the full range.

Adding an inertial mass in an appropriate way, a radio-readable SAW accelerometer can be built up [63]. With the help of a SAW reflective delay line, monitoring of the friction coefficient between a car tire and the road surface, a key parameter when stabilizing a vehicle in critical situations, has been demonstrated [64]. The friction coefficient can be determined by evaluating the mechanical strain in the tire-road contact area by utilising the deformation of a tread element.

As is demonstrated with a torque sensor, a high sensitivity can be attained even if the temperature effects superpose the sensor signal [45]. The SAW reflective delay lines measure, comparable to resistive strain gauges, the torque indirectly by detecting the strain or stress distribution generated by a torque acting on the shaft. The fact

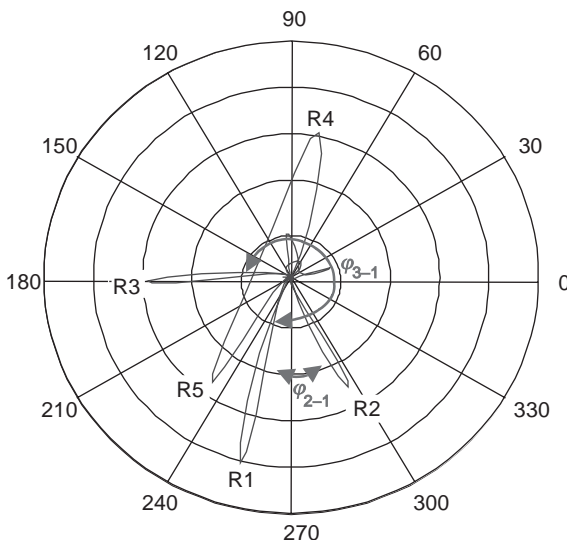


Figure 30. Polar map of the SAW impulse response of a reflective delay line in the base band.

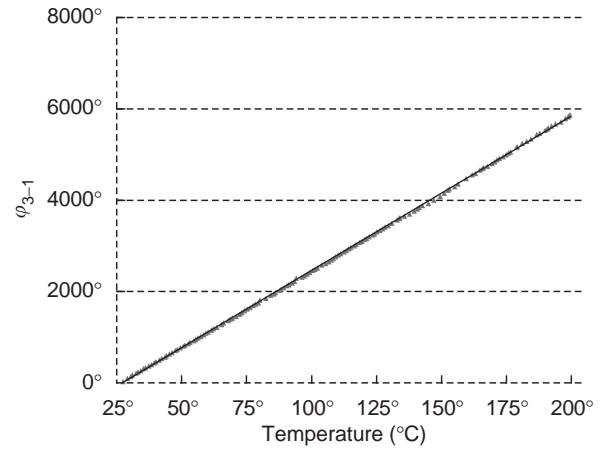


Figure 31. Variation of the continuous phase difference ϕ_{3-1} between the first and third responses of a reflective delay line as a function of temperature.

that the strain has an opposite sign in $\pm 45^\circ$ orientation relative to the shaft axis can be used for temperature compensation. The potential use of quartz and LiNbO₃ as substrate materials has been investigated [65,66].

3.4. Chirped Delay-Line Sensors

The sensitivity with respect to the delay time of a SAW delay-line transponder can be enhanced by using chirped reflectors and/or transducers [45,67,68]. In a dispersive device, the delay time τ of a transmitted signal depends on the frequency f . For a linear dispersion with bandwidth B , dispersion time T , and center frequency f , we can calculate for all frequencies within the passband, with

$$\tau(f) = \tau_0 \pm \frac{T}{B} f \tag{5}$$

where the plus/minus (\pm) sign represents an up/down-chirp law. A variation Δv of the SAW velocity v now affects both the time τ_0 and the synchronous frequency f , and both result in a change of the delay time τ . Therefore, we get in first order a shift and in addition a small tilt of the chirp function $f(t)$. This feature is similar to the impact of a Doppler shift to a FMCW radar system.

Neglecting the small tilt, we obtain the following equation in first order:

$$\frac{\Delta\tau}{\tau_0} = \left[1 \mp \frac{T}{B} \frac{f_0}{\tau_0} \right] \frac{\Delta v}{v} \tag{6}$$

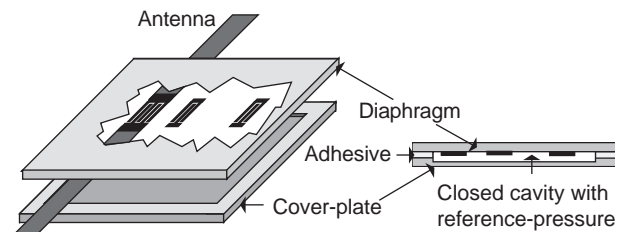


Figure 32. Schematic drawing of a pressure sensor based on a SAW reflective delay line assembled in an all-quartz package.

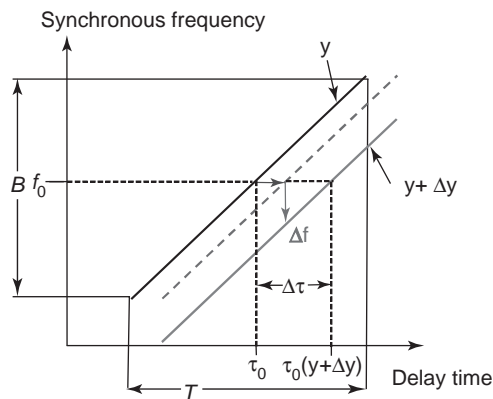


Figure 33. Illustration of the amplification effect for the sensitivity of the delay time using dispersive delay lines.

The expression in the brackets of this equation can be interpreted as an amplification factor for the sensitivity of the group delay, due to the usage of chirped devices. Figure 33 illustrates this amplification effect for the sensitivity of the delay time. The horizontal arrow gives the shift of the delay time of the area of the synchronous frequency and the vertical arrow, the shift in the synchronous frequency by a variation of the SAW velocity. The delay time to the new area with the correct synchronous frequency results from both effects and the chirp rate.

An increase by a factor of 10–100 is possible; even a change in the sign is possible. Figure 34 shows measurements of dispersive SAW sensors, and the amplification effect can be seen. This amplification, however, is effective only in the group delay time. In the phase variation, we get the same dependence as we would obtain by using a nonchirped device.

3.5. Combination with External Sensors

It is possible to wirelessly read out signals of arbitrary sensors, that is, of non-SAW sensors, as long as these sensors operate as impedance sensors [53,69,70]. In that case, a second IDT deposited on the SAW transponder can be

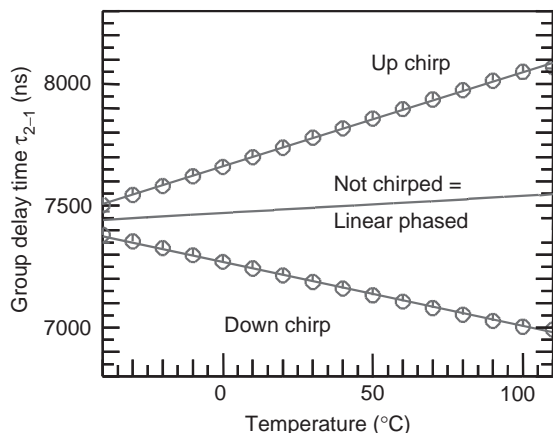


Figure 34. Measurement of the amplification effect for the sensitivity of the delay time by using dispersive delay lines.

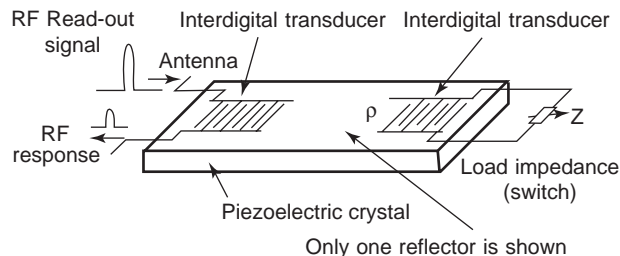


Figure 35. Schematic layout of a passive SAW reflective delay-line device combined with an external sensor.

electrically loaded by the external sensor, which changes the IDT’s microacoustic reflectivity (see Fig. 35).

The reflectivity of an interdigital transducer as a function of a complex termination impedance Z_{load} at its electrical port is given in the well-known P -matrix formalism with P_{11} :

$$P_{11}(Z_{load}) = P_{11}^{sc} + \frac{P_{13}^2}{P_{33} + \frac{1}{Z_{load}}} \quad (7)$$

The measuring signal changes the value of the load impedance, thus changing the reflection characteristics of the IDT and thereby the time function of the retransmitted signal of the transponder. To enhance the sensor effect, a substrate with a high coupling coefficient, resulting in a high P_{13} and a low P_{33} , should be used. Figures 36 and 37 show the acoustic reflectivity of a split-finger ($\lambda/8$) IDT on $LiNbO_3$ as a function of its electrical load.

Using this technique, for instance, the remote measurement of high electrical currents or of the water content of soil has been demonstrated [45,71,72]. In 2001, a SAW-based tire pressure measuring system designed for commercial vehicular applications has been introduced [73]. This novel system shows an accuracy of ± 15 kPa within a pressure range of 100–400 kPa, an excess pressure stability of 600 kPa, and a high heat stability up to 130°C.

3.6. Resonant Delay-Line Sensors

The required delay time required to overcome environmental echoes can also be obtained by using one-port SAW resonator configurations [47,48]. An RF burst impulse

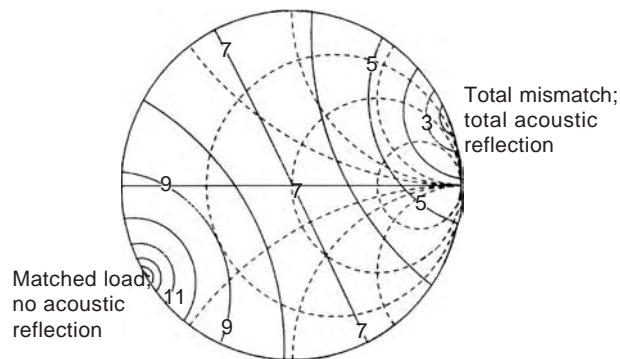


Figure 36. Acoustic reflection factor P_{11} of a split-finger IDT on $LiNbO_3$ as function of the complex reflection coefficient of its load impedance Z_L (Smith chart representation). The diagram shows lines of constant acoustic reflection. For line n , $|P_{11}|$ is $n(-5$ dB).

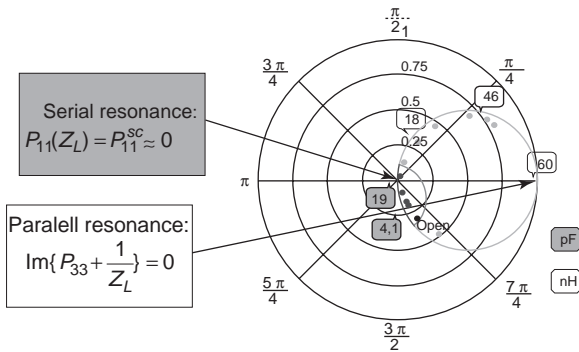


Figure 37. Measured amplitude and phase of the acoustic reflection factor P_{11} (polar chart representation) of a split-finger IDT with capacitive and inductive load impedance Z_L .

excites a high- Q resonator. The retransmitted RF burst of this resonator can still be seen even when all multipath echoes have faded. The sensitivity of these resonator-type transponders is comparable to that of a reflective delay-line transponder, however, with a significant reduction in SAW chip size. The combination of resonant SAW transponders with an external sensor as a variable load can also be used for pulling the resonator frequency. This is similar to the combination of a reflective delay line and external sensors.

4. CONCLUSION

Surface acoustic wave linear and nonlinear phased delay lines play a key role in the radiofrequency (RF) and intermediate-frequency (IF) stages of wideband radar systems. Pulse shaping filters allow a simple generation of complex signals used in modern digital telecommunication systems. Chirped and tapped delay lines enable wideband spread-spectrum systems, much broader than what can be obtained by using modern digital circuitry. Reflective delay lines and transducer-connected delay lines allow the construction of identification and sensor systems using passive transponders that can be wirelessly addressed using a radiolink.

Acknowledgment

Many of the results reported in this contribution were obtained by a common effort of all of our former colleagues and students in the department ZT MS 1 of Siemens AG. The authors want to especially acknowledge the contributions of W. E. Bulst, K. Wagner, G. Scholl, F. Schmidt, T. Ostertag, and Dr. W. Ruile. We also gratefully acknowledge the contributions of Prof. Franz Seifert and A. Pohl from the University of Technology in Vienna and Prof. R. Weigel from the University of Erlangen, Prof. E. Schrüfer from the Technical University of Munich, and their students.

BIBLIOGRAPHY

1. B. A. Auld, *Acoustic Fields and Waves in Solids*, Vols. I and II. Wiley, New York, 1973.

2. R. M. White and F. W. Voltmer, Direct piezoelectric coupling to surface elastic waves, *Appl. Phys. Lett.* **7**:314–316 (1965).

3. H. Matthews, ed., *Surface Wave Filters*, Wiley, New York, 1977.

4. A. Oliner, ed., *Acoustic Surface Waves*, Springer, Berlin, 1978.

5. E. A. Ash and E. G. S. Paige, *Rayleigh Wave Theory and Application*, Springer, Berlin, 1985.

6. D. P. Morgan, *Surface-Wave Devices for Signal Processing*, Elsevier, Amsterdam, 1985.

7. S. Datta, *Surface Acoustic Wave Devices*, Prentice-Hall, Englewood Cliffs, NJ, 1985.

8. C. Campbell, *Surface Acoustic Wave Devices and Their Signal Processing Application*, Academic Press, San Diego, 1989.

9. M. Feldmann and J. Henaff, *Surface Acoustic Waves for Signal Processing*, Artech House, Boston, 1989.

10. S. V. Biryukov, Y. V. Gulaev, V. V. Krylov, and V. P. Plessky, *Surface Acoustic Waves in Inhomogeneous Media*, Springer, Berlin, 1995.

11. C. C. W. Ruppel, R. Dill, A. Fischerauer, G. Fischerauer, W. Gawlik, J. Machui, F. Müller, L. Reindl, W. Ruile, G. Scholl, I. Schropp, and K. Ch. Wagner, SAW devices for consumer communication applications, *IEEE Trans. Ultrason. Ferroelectric. Freq. Control* **UFFC-40**:438–452 (1993).

12. R. C. Dixon, *Spread spectrum Systems with Commercial Applications*, Wiley, New York, 1994.

13. U. Knauer, J. Machui, and C. C. W. Ruppel, Design, fabrication, and application of GHz SAW devices, *Proc. IEEE Int. Microwave Symp.*, Denver, 1997, pp. 1821–1824.

14. L. Reindl, A. Pohl, G. Scholl, and R. Weigel, SAW-based radio sensor systems, *IEEE Sensors J.* **SJ-1**:69–78 (2001).

15. C. S. Hartmann, D. T. Bell, and R. C. Rosenfeld, Impulse model design of acoustic surface-wave filters, *IEEE Trans. Microwave Theory Tech.* **MTT-21**:162–175 (1973).

16. H. R. Stocker, W. E. Bulst, G. Eberharter, and R. Veith, Octave bandwidth high performance SAW delay line, *Proc. IEEE Ultrasonics Symp.*, 1980, pp. 386–390.

17. M. Solal, High performance SAW dispersive delay lines for low time bandwidth using periodically sampled transducers, *Proc. IEEE Ultrasonics Symp.*, 1988, pp. 175–178.

18. C. C. W. Ruppel, A. A. Sachs, and F. J. Seifert, A review of optimization algorithms for the design of SAW transducers, *Proc. IEEE Ultrasonics Symp.*, 1991, pp. 73–83.

19. C. C. W. Ruppel, L. Reindl, and K. Ch. Wagner, Optimum design of low time bandwidth product SAW filters, *Proc. IEEE Ultrasonics Symp.* 1994, pp. 61–65.

20. R. Weigel, Efficient modelling of microacoustic structures in terms of electromagnetic field concepts, *Proc. Int. Symp. Antennas and Propagation (ISAP)*, Chiba, Japan, 1996, pp. 897–900.

21. R. Thomas, T. W. Johannes, W. Ruile, and R. Weigel, Determination of phase velocity and attenuation of surface acoustic waves with improved accuracy, *Proc. IEEE Int. Ultrasonics Symp.*, Sendai, Japan, 1998, pp. 277–300.

22. F. Seifert and R. Weigel, SAW-based wireless sensor and communication techniques, *Proc. European Microwave Conf.*, Jerusalem, Israel, 1997, pp. 1323–1346.

23. G. Visintini, A.-R. Baghai-Wadji, and O. Männer, Modular two-dimensional analysis of SAW filters—Part I: Theory, *IEEE Trans. Ultrason. Ferroelectric. Freq. Control* **UFFC-39**:61–72 (1992).

24. G. Visintini, C. Kappacher, and C. C. W. Ruppel, Modular two-dimensional analysis of SAW filters—Part II: Analysis and

- compensation results, *IEEE Trans. Ultrason. Ferroelectric. Freq. Control* **UFFC-39**:73–81 (1992).
25. N. Yoshioka, A. Sakai, H. Morimoto, K. Hosono, Y. Watakabe, and S. Wadaka, Fabrication of surface acoustic wave devices by using X-ray lithography, *J. Vac. Sci. Technol.* **B-7**:1688–1691 (1989).
 26. H. Odagawa and K. Yamanouchi, 10 GHz range extremely low-loss surface acoustic wave filter, *Electron. Lett.* **34**:865–866 (1998).
 27. W. H. Brunger, L.-M. Buchmann, M. Kreutzer, M. Torkler, G. Zwicker, and B. Fleischmann, Fabrication of 3,5 GHz surface acoustic wave filters by ion projection lithography, *Microelectron. Eng.* **17**:245–248 (1992).
 28. L. Reindl, C. C. W. Ruppel, S. Berek, U. Knauer, M. Vossiek, P. Heide, and L. Oreans, Design, fabrication, and application of precise SAWdelay lines used in a FMCWradar system, *IEEE Trans. Microwave Theory Tech.* **MTT-49**:787–794 (2001).
 29. H. Meier, T. Baier, and G. Riha, Miniaturization and advanced functionalities of SAWdevices, *IEEE Trans. Microwave Theory Tech.* **MTT-49**:743–748 (2001).
 30. M. Vossiek, P. Heide, M. Nalezinski, and V. Magori, Novel FMCWradar system concept with adaptive compensation of phase errors, *Proc. 26th European Microwave Conf. (EuMC)*, 1996, pp. 135–139.
 31. C. C. W. Ruppel and L. Reindl, SAWdevices for spread spectrum applications, *Proc. IEEE Int. Symp. Spread Spectrum Techniques and Applications*, Mainz, Germany, 1996, pp. 713–719.
 32. W. R. Smith, SAWfilters for CPSMspread spectrum communication, *Proc. IEEE Ultrasonics Symp.*, 1977, pp. 524–528.
 33. J. R. Klauder et al. The theory and design of chirp radars, *Bell Syst. Tech. J.* **39**:745–808 (1960).
 34. R. H. Tancrell, M. B. Schulz, H. H. Barrett, L. Davies, and M. G. Holland, Dispersive delay lines using ultrasonic surface waves, *Proc. IEEE* **57**:1211–1213 (1969).
 35. P. Hartemann and E. Dieulesaint, Intrinsic compensation of sidelobes in a dispersive acoustic delay line, *Electron. Lett.* **5**:219–220 (1969).
 36. A. Springer, M. Huemer, L. Reindl, C. C. W. Ruppel, A. Pohl, F. Seifert, W. Gugler, and R. Weigel, A robust ultra-broadband wireless communication system using SAWchirped delay lines, *IEEE Trans. Microwave Theory Tech.* **MTT-46**:2213–2219 (1998).
 37. A. Springer, W. Gugler, M. Huemer, R. Koller, and R. Weigel, A wireless spread-spectrum communication system using SAWchirped delay lines, *IEEE Trans. Microwave Theory Tech.* **MTT-49**:754–760 (2001).
 38. R. C. Williamson and H. I. Smith, Large time-bandwidth product surface-wave pulse compressor employing reflective gratings, *Electron. Lett.* **8**:401–402 (1972); see also, R. C. Williamson and H. I. Smith, The use of surface elastic wave reflection gratings in large time-bandwidth pulse compression filters, *IEEE Trans. Microwave Theory Tech.* **MTT-21**:195–205 (1973).
 39. G. Riha, H. R. Stocker, R. Veith, and W. E. Bulst, RACfilters with position weighted metallic strip arrays, *Proc. IEEE Int. Ultrasonics Symp.*, 1982, pp. 83–87.
 40. W. Ruile, F. Muller, and G. Riha, Metal-RACs with track interference weighting, *Proc. IEEE Int. Ultrasonics Symp.*, 1986, pp. 147–151.
 41. G. W. Judd, Technique for realizing low time sidelobe levels in small compression ratio chirp waveforms, *Proc. IEEE Int. Ultrasonics Symp.*, 1973, pp. 478–481.
 42. S. T. Costanza, P. J. Hagon, and L. A. MacNevin, Analog matched filter using tapped acoustic surface wave delay line, *IEEE Trans. Microwave Theory Tech.* **MTT-17**:1042–1043 (1969).
 43. P. W. Baier, K. Dostert, and M. Pandit, A novel spread-spectrum receiver synchronization scheme using a SAWtapped delay line, *IEEE Trans. Commun.* **COM-30**(5):1037–1047 (May 1982).
 44. R. Weigel, F. Kalabic, G. Ostermayer, A. Pohl, F. Seifert, and L. Reindl, Design of a SAWexpander and compressor on LiT-aO₃ for a TCDMAspread spectrum system, *IEEE Trans. Microwave Theory Tech.*, **MTT-45**:2468–2492 (1997).
 45. L. Reindl, G. Scholl, T. Ostertag, H. Scherr, U. Wolff, and F. Schmidt, Theory and application of passive SAWradio transponder as sensors, *IEEE Trans. Ultrason. Ferroelectric. Freq. Control* **UFFC-45**:1281–1292 (1998).
 46. A. Pohl, A review of wireless SAWsensors, *IEEE Trans. Ultrason. Ferroelectric. Freq. Control* **UFFC-47**:317–332 (2000).
 47. W. Buff, SAWsensors, *Sens. Actuators* **A-42**:117–121 (1992).
 48. A. Pohl, G. Ostermayer, and F. Seifert, Wireless sensing using oscillator circuits locked to remote high-Q SAWresonators, *IEEE Trans. Ultrason. Ferroelectric. Freq. Control* **UFFC-45**:1161–1168 (1998).
 49. G. Ostermayer, A. Pohl, L. Reindl, and F. Seifert, Multiple access to SAWsensors using matched filter properties, *Proc. IEEE Ultrason. Symp.*, Toronto, 1997, pp. 339–342.
 50. G. Ostermayer, A. Pohl, R. Steindl, and F. Seifert, SAWsensors and correlative signal processing—a method providing multiple access capability, *Proc. ISSSTA 98*, South Africa, 1998, pp. 902–906.
 51. P. A. Nysen, H. Skeie, and D. Armstrong, *System for Interrogating a Passive Transponder Carrying Phase-Encoded Information*, U.S. Patents 4,725,841, 4,625,207 and 4,625,208 (1983).
 52. K. Yamanouchi, G. Shimizu, and K. Morishita, 2.5-GHz SAWpropagation and reflection characteristics and application to passive electronic tag and matched filter, *Proc. 1993 IEEE Ultrasonics Symp.*, 1993, pp. 1267–1270.
 53. L. Reindl and W. Ruile, Programmable reflectors for SAW-ID-tags, *Proc. 1993 IEEE Ultrasonics Symp.*, 1993, pp. 125–130.
 54. V. P. Plessky, S. N. Kondratiev, R. Stierlin, and F. Nyffeler, SAWtags: New ideas, *Proc. 1995 IEEE Ultrasonics Symp.*, 1995, pp. 117–120.
 55. Baumer AG (online), <http://www.baumerident.com>
 56. F. Seifert, W. E. Bulst, and C. C. W. Ruppel, Mechanical sensors based on surface acoustic waves, *Sens. Actuators* **A-44**:231–239 (1994).
 57. X. Q. Bao, W. Burkhard, V. V. Varadan, and V. K. Varadan, SAWtemperature sensor and remote reading system, *Proc. 1987 IEEE Ultrasonics Symp.*, 1987, pp. 583–585.
 58. L. Reindl, R. Steindl, A. Pohl, J. Hornsteiner, E. Riha, and F. Seifert, Passive SAWsensors for temperature and other measurands, *Proc. Tempmeko 99*, The Netherlands, 1999, pp. 424–429.
 59. G. Scholl, F. Schmidt, T. Ostertag, L. Reindl, H. Scherr, and U. Wolff, Wireless passive SAWsensor systems for industrial and domestic applications, *Proc. 1998 IEEE Frequency Control Symp.*, 1998, pp. 595–601.
 60. A. Pohl and F. Seifert, Wireless interrogable SAW-sensors for vehicular applications, *Proc. IEEE Instrumentation and Measurement Conf. 1996*, 1996, pp. 1465–1468.

61. A. Pohl, G. Ostermayer, L. Reindl, and F. Seifert, Monitoring the tire pressure at cars using passive SAWsensors, *Proc. IEEE Ultrasonics Symp.*, Toronto, 1997, pp. 471–474.
62. H. Scherr, G. Scholl, F. Seifert, and R. Weigel, Quartz pressure sensor based on SAWreflective delay line, *Proc. 1996 IEEE Ultrasonics Symp.*, 1996, pp. 347–350.
63. A. Pohl, R. Steindl, and L. Reindl, Measurements of vibration and acceleration utilizing SAWsensors, *Proc. SENSOR'99*, Germany, 1999, Vol. 2, pp. 53–58.
64. A. Pohl, R. Steindl, and L. Reindl, The “intelligent tire” utilizing passive SAWsensors—measurement of tire friction, *IEEE Trans. Instrum. Meas.* **48**(6):1041–1046 (Dec. 1999).
65. T. Sachs, R. Grossmann, J. Michel, and E. Schrüfer, Remote sensing using quartz sensors, *Proc. SPIE 1996 Symp. Smart Structures and Materials*, 1996, SPIE Vol. 2718, pp. 47–58.
66. U. Wolff, F. Schmidt, G. Scholl, and V. Magori, Radio accessible SAWsensors for simultaneous noncontact measurement of torque and temperature, *Proc. 1996 IEEE Ultrasonics Symp.*, 1996, pp. 359–362.
67. L. Reindl, U. Rösler, C. Ruppel, R. Obertreis, and R. Weigel, Chirped SAWdevices for wireless passive sensors, *Proc. IEEE Ultrasonics Symp.*, 1997, pp. 343–348.
68. T. Pankratz, H. Scherr, L. Reindl, C. Ruppel, and R. Weigel, Low TB radio SAWsensors incorporating chirped transducers and reflectors for wireless pressure sensing applications, *Proc. 1998 IEEE MTT-S Int. Microwave Symp.*, 1998, pp. 845–848.
69. R. Steindl, A. Pohl, L. Reindl, and F. Seifert, SAWdelay lines for wirelessly requestable conventional sensors, *Proc. 1998 IEEE Ultrasonics Symp.*, 1998, pp. 351–354.
70. R. Steindl, A. Pohl, and F. Seifert, Impedance loaded SAWsensors offer a wide range of measurement opportunities, *Proc. IEEE MTT-S 1999*, Anaheim, CA, 1999, pp. 1453–1456.
71. R. Steindl, C. Hausleitner, A. Pohl, H. Hauser, and J. Nicolics, Giant magneto-impedance magnetic field sensor with surface acoustic wave technology, *Proc. Eurosensors 1999*, Delft, The Netherlands, pp. 301–302, 1999.
72. L. Reindl, C. C. W. Ruppel, A. Kirmayr, N. Stockhausen, M. A. Hilhorst, and J. Balendonck, Radio requestable passive SAWwater content sensor, *IEEE Trans. Microwave Theory Tech.* **MTT-49**:803–808 (2000).
73. G. Schimetta, F. Dollinger, G. Scholl, and R. Weigel, Optimized design and fabrication of a wireless pressure and temperature sensor unit based on SAWtransponder technology, *Proc. IEEE Int. Microwave Symp.*, Phoenix, AZ, 2001, pp. 355–358.

SURFACE ACOUSTIC WAVE DEVICES

D. P. MORGAN
Impulse Consulting
Northampton, United Kingdom

1. INTRODUCTION

Surface acoustic wave (SAW) devices were first considered for electronics in the 1960s, and since then a vast array of devices has emerged, with wide-ranging applications. Like

other acoustic waves, SAWs have the advantage of a low velocity, around 3500 m/s, so that large delays are obtainable in a small space, and in suitable materials they can give very low propagation loss. A familiar device exploiting these properties is the quartz crystal oscillator, found almost everywhere in clocks and wristwatches as well as in many professional systems. The oscillator relies on propagation of a bulk acoustic wave in a quartz crystal, with reflections from the two major parallel faces so that a resonant cavity is formed. Surface wave devices exploit the same two advantages, low velocity and low loss, but with an additional feature. Because the wave travels along a surface it is accessible throughout its propagation path to components for generation, reflection, waveguiding, and so on, so that substantial versatility is obtained. The versatility is well illustrated by the enormous range of devices developed since the inception of the subject.

This subject developed initially in response to a demand for dispersive delay lines (chirp filters) for pulse compression radar. In this application the SAW filters perform a signal processing function, giving an improvement in signal-to-noise ratio and increasing the range capability of the radar. Other devices perform a similar function for spread-spectrum signals in communication systems. Another type of device is the bandpass filter, initially developed for I.F. filtering in domestic TV receivers. This has been an outstanding success for SAW, with practically all TV sets now having a SAW filter. The bandpass filter has also been widely used in professional systems such as radar, and more recently the demand for filters has increased greatly with the growth of wireless telecommunications, particularly mobile telephones. Many different types of SAW bandpass filter, suitable for different applications, have been developed, and a typical present-day mobile phone handset will contain 6–10 SAW filters. Another type of SAW device is the oscillator, in which a SAW delay line or resonator is used as a feedback element to control the frequency of an oscillating circuit. Compared with a bulk-wave oscillator, the SAW device can operate at higher frequencies, up to 500 MHz, though its stability is not quite as good. The popularity of SAW devices, particularly for wireless communications, is demonstrated by the worldwide production quantities of around 3 billion devices annually.

1.1. Nature of Surface Waves

In a solid material, acoustic waves (or “elastic” waves) are associated with distortions of the material, such that distances between particular atoms are changed. These distortions, formally expressed as “strains,” are accompanied by internal forces known as “stresses.” In an acoustic wave, energy is continuously exchanged between elastic and kinetic forms. An infinite material can support propagation of a bulk wave, that is, a freely propagating wave unaffected by boundaries. Bulk acoustic waves are of two basic types: (a) *longitudinal waves*, in which the particle motion is along the wavevector, and (b) *transverse* (or shear) *waves*, with particle motion normal to the wavevector. Typical velocities are 6000 m/s for longitudinal waves and 3000 m/s for transverse waves.

61. A. Pohl, G. Ostermayer, L. Reindl, and F. Seifert, Monitoring the tire pressure at cars using passive SAWsensors, *Proc. IEEE Ultrasonics Symp.*, Toronto, 1997, pp. 471–474.
62. H. Scherr, G. Scholl, F. Seifert, and R. Weigel, Quartz pressure sensor based on SAWreflective delay line, *Proc. 1996 IEEE Ultrasonics Symp.*, 1996, pp. 347–350.
63. A. Pohl, R. Steindl, and L. Reindl, Measurements of vibration and acceleration utilizing SAWsensors, *Proc. SENSOR'99*, Germany, 1999, Vol. 2, pp. 53–58.
64. A. Pohl, R. Steindl, and L. Reindl, The “intelligent tire” utilizing passive SAWsensors—measurement of tire friction, *IEEE Trans. Instrum. Meas.* **48**(6):1041–1046 (Dec. 1999).
65. T. Sachs, R. Grossmann, J. Michel, and E. Schröder, Remote sensing using quartz sensors, *Proc. SPIE 1996 Symp. Smart Structures and Materials*, 1996, SPIE Vol. 2718, pp. 47–58.
66. U. Wolff, F. Schmidt, G. Scholl, and V. Magori, Radio accessible SAWsensors for simultaneous noncontact measurement of torque and temperature, *Proc. 1996 IEEE Ultrasonics Symp.*, 1996, pp. 359–362.
67. L. Reindl, U. Rösler, C. Ruppel, R. Obertreis, and R. Weigel, Chirped SAWdevices for wireless passive sensors, *Proc. IEEE Ultrasonics Symp.*, 1997, pp. 343–348.
68. T. Pankratz, H. Scherr, L. Reindl, C. Ruppel, and R. Weigel, Low TB radio SAWsensors incorporating chirped transducers and reflectors for wireless pressure sensing applications, *Proc. 1998 IEEE MTT-S Int. Microwave Symp.*, 1998, pp. 845–848.
69. R. Steindl, A. Pohl, L. Reindl, and F. Seifert, SAWdelay lines for wirelessly requestable conventional sensors, *Proc. 1998 IEEE Ultrasonics Symp.*, 1998, pp. 351–354.
70. R. Steindl, A. Pohl, and F. Seifert, Impedance loaded SAWsensors offer a wide range of measurement opportunities, *Proc. IEEE MTT-S 1999*, Anaheim, CA, 1999, pp. 1453–1456.
71. R. Steindl, C. Hausleitner, A. Pohl, H. Hauser, and J. Nicolics, Giant magneto-impedance magnetic field sensor with surface acoustic wave technology, *Proc. Eurosensors 1999*, Delft, The Netherlands, pp. 301–302, 1999.
72. L. Reindl, C. C. W. Ruppel, A. Kirmayr, N. Stockhausen, M. A. Hilhorst, and J. Balendonck, Radio requestable passive SAWwater content sensor, *IEEE Trans. Microwave Theory Tech.* **MTT-49**:803–808 (2000).
73. G. Schimetta, F. Dollinger, G. Scholl, and R. Weigel, Optimized design and fabrication of a wireless pressure and temperature sensor unit based on SAWtransponder technology, *Proc. IEEE Int. Microwave Symp.*, Phoenix, AZ, 2001, pp. 355–358.

SURFACE ACOUSTIC WAVE DEVICES

D. P. MORGAN
Impulse Consulting
Northampton, United Kingdom

1. INTRODUCTION

Surface acoustic wave (SAW) devices were first considered for electronics in the 1960s, and since then a vast array of devices has emerged, with wide-ranging applications. Like

other acoustic waves, SAWs have the advantage of a low velocity, around 3500 m/s, so that large delays are obtainable in a small space, and in suitable materials they can give very low propagation loss. A familiar device exploiting these properties is the quartz crystal oscillator, found almost everywhere in clocks and wristwatches as well as in many professional systems. The oscillator relies on propagation of a bulk acoustic wave in a quartz crystal, with reflections from the two major parallel faces so that a resonant cavity is formed. Surface wave devices exploit the same two advantages, low velocity and low loss, but with an additional feature. Because the wave travels along a surface it is accessible throughout its propagation path to components for generation, reflection, waveguiding, and so on, so that substantial versatility is obtained. The versatility is well illustrated by the enormous range of devices developed since the inception of the subject.

This subject developed initially in response to a demand for dispersive delay lines (chirp filters) for pulse compression radar. In this application the SAW filters perform a signal processing function, giving an improvement in signal-to-noise ratio and increasing the range capability of the radar. Other devices perform a similar function for spread-spectrum signals in communication systems. Another type of device is the bandpass filter, initially developed for I.F. filtering in domestic TV receivers. This has been an outstanding success for SAW, with practically all TV sets now having a SAW filter. The bandpass filter has also been widely used in professional systems such as radar, and more recently the demand for filters has increased greatly with the growth of wireless telecommunications, particularly mobile telephones. Many different types of SAW bandpass filter, suitable for different applications, have been developed, and a typical present-day mobile phone handset will contain 6–10 SAW filters. Another type of SAW device is the oscillator, in which a SAW delay line or resonator is used as a feedback element to control the frequency of an oscillating circuit. Compared with a bulk-wave oscillator, the SAW device can operate at higher frequencies, up to 500 MHz, though its stability is not quite as good. The popularity of SAW devices, particularly for wireless communications, is demonstrated by the worldwide production quantities of around 3 billion devices annually.

1.1. Nature of Surface Waves

In a solid material, acoustic waves (or “elastic” waves) are associated with distortions of the material, such that distances between particular atoms are changed. These distortions, formally expressed as “strains,” are accompanied by internal forces known as “stresses.” In an acoustic wave, energy is continuously exchanged between elastic and kinetic forms. An infinite material can support propagation of a bulk wave, that is, a freely propagating wave unaffected by boundaries. Bulk acoustic waves are of two basic types: (a) *longitudinal waves*, in which the particle motion is along the wavevector, and (b) *transverse* (or shear) *waves*, with particle motion normal to the wavevector. Typical velocities are 6000 m/s for longitudinal waves and 3000 m/s for transverse waves.

The surface-wave solution in an isotropic material was found by Lord Rayleigh in 1885 [1], and is often called a *Rayleigh wave*. Here, the material is assumed to have a planar surface, free of mechanical forces. Rayleigh found a propagating-wave solution, essentially a sum of longitudinal and transverse components, with amplitude decaying exponentially away from the surface. Typically, most of the energy is within a depth equal to one wavelength. The wave is of seismological interest because it explains a component of the signal detected by a seismograph following a ground shock. It travels somewhat more slowly than transverse bulk waves and is nondispersive, with velocity independent of frequency. The motion of the material is in the *sagittal plane*: the plane containing the surface normal and the propagation direction.

1.2. Piezoelectric Materials

As will become clear later, SAW devices always use piezoelectric materials. The meaning of this term is that stresses and strains within the material are accompanied by electric fields, which arise from fundamental interactions at the atomic level. The electric fields are central to the operation of the majority of SAW components, particularly transducers for generation and detection of the waves. The presence of piezoelectricity complicates the nature of the wave, which is now (in most cases) accompanied by an electric field. But there is another complication in that to be piezoelectric a material has to be anisotropic, so that its macroscopic properties depend on the orientation of the internal structure. Usually crystalline materials are chosen because they can give low losses. The wave properties depend on the orientation of the crystal lattice relative to the macroscopic object. In contrast to the isotropic case considered by Rayleigh, anisotropy and piezoelectricity introduce immense complications when investigating properties of SAWs. As a consequence, the search for materials and orientations suitable for SAW devices has been an ongoing activity throughout the development of SAW.

In general, a numerical investigation of a piezoelectric crystal usually yields surface-wave solutions similar to the isotropic case except for the associated electric field. This is often called a *piezoelectric Rayleigh wave*. Various properties relevant to SAW usage are considered, in order to find a suitable orientation. As a result, a variety of “standard” materials and orientations have been established. In particular, crystals of quartz, lithium niobate, and lithium tantalate are used. Owing to anisotropy, it is essential to quote the orientation when specifying a SAW material.

In some cases other types of wave are found, in particular various types of “leaky wave.” Some of these can be used for SAW-type devices, although their behavior is somewhat different. In this article, the “wave” is assumed to be a piezoelectric Rayleigh wave unless otherwise stated; other types of wave are considered later.

1.3. Basic SAW Device

Piezoelectricity enables SAWs to be generated conveniently by *interdigital transducers* (IDTs) placed on the surface of the material, which is often called the *substrate* (Fig. 1). The IDT consists of a set of interleaved metal electrodes,

alternately connected to two bus bars. When a voltage is applied, this sets up a spatially alternating electric field at the surface, coupled to acoustic stresses by the piezoelectric effect. A surface wave is generated if the frequency is such that the SAW wavelength is similar to the transducer periodicity. The IDT is most effective for a frequency such that its periodicity equals the SAW wavelength. At other frequencies the waves generated in different regions of the transducer are subject to progressive phase differences, so that the total wave amplitude is smaller. The IDT is therefore frequency-selective. A similar IDT can be used to detect an incident SAW, producing an electrical output signal. Thus, the device has electrical input and output signals, with electroacoustic conversion at both transducers.

The wave propagation inside the device is almost ideal in that propagation loss is low, diffraction effects are small (because the beam of surface waves is typically more than 20 wavelengths wide), and dispersion is negligible. For typical power levels the material behaves linearly, so that harmonic generation and intermodulation products are negligible. Hence for many purposes second-order effects such as these can be ignored. However, they do need to be considered, and sometimes compensated for, when an exacting specification is to be satisfied.

Because of the selectivity of the IDTs, this device can be regarded as a bandpass filter. It can also be regarded as a delay line, with delay determined by the velocity and the distance between transducer centres, typically $3\ \mu\text{s}/\text{cm}$. As a delay line, it is suitable for signals whose spectrum is within the frequency band of the transducers. The input transducer generates SAWs traveling in both directions, and it is often necessary to add absorbing material to suppress reflections of waves from the ends of the substrate. The basic design is capable of a huge range of variations for special purposes. In particular, bandpass filters employ modifications to ensure good suppression in the stopband, a flat response in the passband, narrow skirts separating these regions, and minimal group delay variation within the passband.

1.4. Fabrication and Performance

The device basically consists of a piezoelectric substrate with a specially shaped metal film (usually of aluminium) on the surface. This structure is well suited to fabrication by established photolithographic techniques, similar to those used in semiconductor device processing. Many patterns can be made simultaneously by exposing a layer of photoresist on a large circular wafer (or “slice”), followed by development and chemical etching. The patterns are separated by cutting them into the individual devices, then known as “chips,” which are sealed into hermetic packages to protect them from moisture and contamination. This process is well established in the semiconductor industry and well suited to production of large quantities of devices, thus giving economy of scale. For large quantities, costs can be less than U.S. \$1.00 per device. Moreover, the method is very versatile since almost arbitrary geometries can be produced.

The fabrication process sets some limits on device performance. The linewidth of the basic IDT (Fig. 1) is a

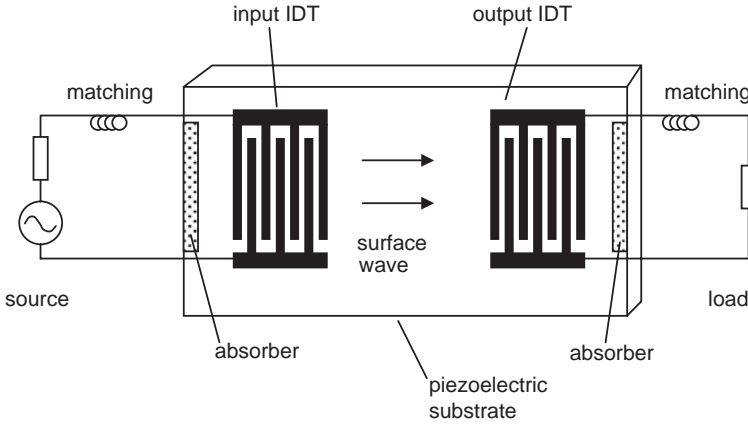


Figure 1. Basic SAW delay line.

quarter of the center-frequency wavelength, and the minimum linewidth usable in commercial production is around $0.4\ \mu\text{m}$. For a typical SAW velocity of $3500\ \text{m/s}$, this sets the maximum center frequency at about $2\ \text{GHz}$, although special techniques can increase this number a little. The minimum frequency is in the region of $10\ \text{MHz}$, simply because in this region the devices become rather clumsy and expensive. The velocity determines the delay for a given length. A device $2\ \text{cm}$ long gives about $6\ \mu\text{s}$ delay, and lengths of $15\ \text{cm}$ are quite feasible but become expensive because they are not suited for large-quantity production. Bandwidths range substantially, from 0.1% to 50% of the center frequency.

Generally, internal losses in the device are small, so one might expect a small insertion loss to be obtainable. However, in practice this is limited by distortion arising from multiple SAW transits. To give low loss, the device of Fig. 1 would need good electrical matching between the transducers and the source and load, normally involving inductors to tune out the transducer capacitances. For this case, the acoustoelectric conversion loss is ideally $3\ \text{dB}$ (because half of the energy applied to a transducer emerges as a wave generated in the unwanted direction). Hence a device insertion loss of $6\ \text{dB}$ is expected. This is indeed close to reality, but unfortunately there is also an unwanted signal because the transducers reflect the waves. This signal, called the *triple transit signal*, occurs after three transits of the device, involving a reflection from each transducer. When electrically matched, the transducer reflection coefficient is $-6\ \text{dB}$, and hence the triple-transit signal is $12\ \text{dB}$ below the main signal. This level is quite unacceptable for most applications, and often it is reduced by deliberately mismatching the transducers (e.g., omitting the inductors). For this reason, early types of SAW device often have relatively high insertion losses, $15\text{--}30\ \text{dB}$. However, a wide range of techniques have been applied to this problem, yielding a variety of low-loss types of bandpass filter.

Some general accounts of the subject will be found in Refs. 2–6.

2. INTERDIGITAL TRANSDUCERS

The *interdigital transducer* (IDT) is a basic component in all SAW devices. As explained earlier, a simple IDT

consists of a set of electrodes alternately connected to two busbars, as shown in Fig. 2a. The electrodes are regular, that is, they have constant width a and pitch p .

The operation of the IDT can be described approximately by a simple delta-function model [7]. Suppose initially that a voltage V is applied to only one electrode, with the others grounded. Surface waves will be generated with amplitude proportional to an element factor denoted by $E(\omega)$. The SAW amplitude is expressed in terms of the associated surface potential $\phi_s(x)$, which is thus given by $V E(\omega) \exp[\pm jk(x - x_n)]$, where k is SAW wavenumber and x_n is the location of the electrode center. Here k is related to the velocity v by $k = \omega/v$. In Fig. 2a we take the lower busbar to be grounded and apply the preceding formula to each live electrode, adding the waves generated. We define a polarity \hat{P}_n for electrode n , such that $\hat{P}_n = 1$ or zero for a live or grounded electrode, respectively. The potential of the wave emerging at the left is thus

$$\phi_s(\omega) = VE(\omega) e^{jkx} \sum_{n=1}^N \hat{P}_n \exp(-jkx_n) = VE(\omega) e^{jkx} A(\omega) \quad (1)$$

where N is the number of electrodes centred at x_n . The summation is denoted by $A(\omega)$, which is known as the *array factor*. Usually the array factor varies with ω much faster than the element factor $E(\omega)$, so the array factor is essentially the frequency response. Fourier transformation of $A(\omega)$ into the time domain gives the function $a(t) = \sum_{n=1}^N \hat{P}_n \delta(t - x_n/v)$, which is a series of delta functions at times corresponding to the centers of the live electrodes.

For the transducer of Fig. 2a the electrode positions are regular, and we can take $x_n = np$, where p is the electrode pitch. Also, the polarity sequence is $\hat{P}_n = 1, 0, 1, 0, \dots$, since the electrode voltages alternate between V and 0 . Substituting these, $A(\omega)$ becomes a simple geometrical progression that is easily summed. Its magnitude is

$$|A(\omega)| = \left| \frac{\sin(N_p \theta/2)}{\sin(\theta/2)} \right| \quad (2)$$

where $\theta = 2kp$ and N_p is the number of live electrodes (equal to the number of transducer periods). This equation predicts a series of peaks. The fundamental response, at which the transducer pitch equals the SAW wavelength,

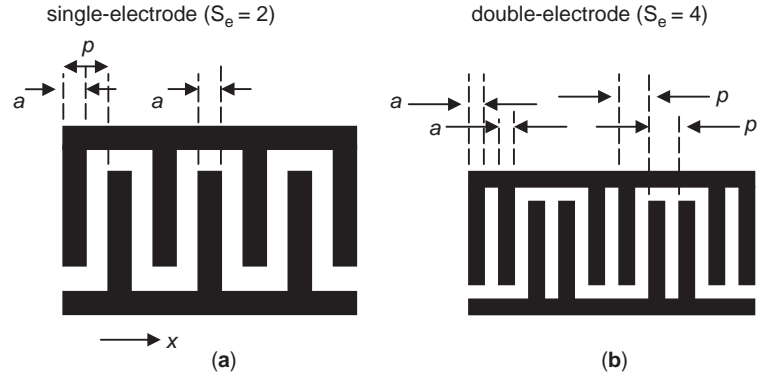


Figure 2. Transducer types: (a) single-electrode configuration; (b) double-electrode configuration.

occurs for $\theta = 2\pi$. The formula remains unchanged if we replace θ by $\phi = \theta - 2\pi$. In the region of the fundamental passband, ϕ is small and the function becomes $|A(\omega)| \approx N_p |\sin(X)/X|$, with $X = N_p \phi/2$; and X can be written as $X = \pi N_p (f/f_0 - 1)$, where $f_0 = v/(2p)$ is the center frequency. From this it follows that the 4-dB points are approximately at $\phi = \pm \pi/N_p$, giving a fractional bandwidth of $\Delta f/f_0 = 1/N_p$. The bandwidth is $\Delta f = 1/T$, where $T = 2pN_p/v$ is the transducer length in time units.

This delta-function model is applicable because in practice the wave propagation is almost ideal. Provided suitable materials are chosen for the substrate and the electrodes (usually aluminium), the waves propagate with very little loss or dispersion. Also, diffraction effects are usually small, although this often needs consideration, and we return to it in later.

In addition, we have assumed that the electrodes don't affect the waves, in particular, that they don't reflect the waves. This assumption is usually invalid for the transducer of Fig. 2a. Individual electrodes have a small reflection coefficient, typically 1 or 2%. However, the reflections add coherently at the center frequency, because the electrode pitch is $\lambda_0/2$ (where λ_0 is the centre-frequency wavelength). This problem can be avoided by using a *double-electrode transducer*, as in Fig. 2b, where each electrode is split into two. The electrode spacing is now $\lambda_0/4$, so reflections from adjacent electrodes are cancelled at f_0 . The main penalty is that the electrode width is $\lambda_0/8$ instead of $\lambda_0/4$, so that fabrication becomes more difficult. The original transducer of Fig. 2a is, in contrast, called a *single-electrode transducer*. The analysis in Eq. (1) applies for both types of transducer; it is necessary to change only the polarity sequence \hat{P}_n .

The transducer admittance Y_t , defined assuming that no waves are incident, is important when electrical matching is considered. Often the admittance is dominated by a capacitance C_t , so this is usually written explicitly. Y_t can be written as $Y_t = G_a(\omega) + jB_a(\omega) + j\omega C_t$, where G_a and B_a are the acoustic conductance and susceptance, due to the excitation of surface waves. For a uniform transducer such as those in Fig. 2, these terms have the approximate forms

$$\begin{aligned} G_a(\omega) &\approx G_a(\omega_0) \left[\frac{\sin X}{X} \right]^2; \\ B_a(\omega) &\approx G_a(\omega_0) \frac{\sin(2X) - 2X}{2X^2} \end{aligned} \quad (3)$$

These formulas assume that electrode reflections are not significant. The formula for B_a is deduced from G_a by using causality. This implies that B_a must be the Hilbert transform of G_a for any transducer.

For a two-transducer device, such as that in Fig. 1, the terminal admittances Y_{11} and Y_{22} are just the transducer admittances Y_t . This follows because Y_{11} is the admittance seen at one transducer when the other is shorted, and we have assumed that a short-circuited transducer does not reflect SAWs. Also, the transadmittance Y_{12} can be shown to have magnitude given by $|Y_{12}| = G_{a1}G_{a2}$, where G_{a1} and G_{a2} are the two transducer conductances.

As noted above, electrode reflections are eliminated by using a double-electrode transducer. However, these transducers still have a finite SAW reflection coefficient when connected to finite electrical loads, thus giving rise to the unwanted triple-transit signal. Special methods can be applied to deal with this, notably the use of specially designed internal reflections in SPUDTs, described later.

3. PROPAGATION EFFECTS

The choice of suitable materials for SAW devices is intimately concerned with a variety of propagation effects, particularly piezoelectric coupling, diffraction, and temperature effects. The choice of material is a vital part of the design procedure because the material properties have a strong bearing on the performance obtainable.

3.1. SAW Solutions and Velocities

Many of the required SAW properties of a material can be deduced from the SAW velocity, and the velocity itself is important, of course. The SAW solution is found starting from the bulk-material constants: the stiffness c_{ijkl} , piezoelectric d_{ijk} and dielectric ϵ_{ij} constants, together with the mass density ρ . The values originate from bulk measurements on the crystals, and large amounts of data are given by Slobodnik et al. [8] and Gualtieri et al. [9]. Kovacs et al. [10] give values for lithium niobate and tantalate.

The calculation of SAW solutions in an anisotropic piezoelectric material is a complex numerical process [11] that will not be described in detail here. Because of the anisotropy, the assessment of a material for SAW applications involves calculation of its SAW properties for all possible orientations, and since the orientation is governed by

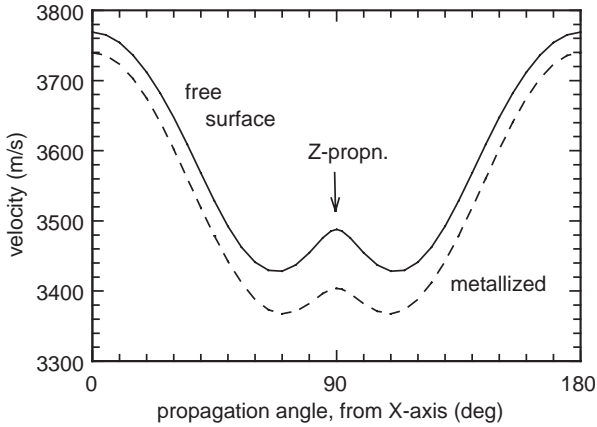


Figure 3. SAW velocities on Y-cut lithium niobate, as functions of propagation direction.

three angles, this task is very extensive. The substantial literature on these topics includes Slobodnik’s handbook [8] and a review [12].

The SAW solution for a free surface has velocity denoted here by v_f . It is also common to examine a “metallized” surface, meaning that an idealised metal film is assumed to be on the surface, short-circuiting the parallel electric field but thin enough to have no mechanical effect. In this case the velocity is v_m . The fractional difference between the two velocities is defined as

$$\frac{\Delta v}{v} \equiv \frac{v_f - v_m}{v_f} \quad (4)$$

and this indicates the strength of electrical coupling to the SAW. The element factor $E(\omega)$ mentioned earlier is proportional to $\Delta v/v$, so this governs the conversion efficiency of an IDT. Figure 3 shows velocities for Y-cut lithium niobate, as functions of propagation direction. The coupling is strongest for propagation in the Z direction and this orientation, known as “Y-Z lithium niobate,” is a popular choice. For this case, a 100-MHz wave on a free surface, with power density of 1 mW/mm, gives a surface potential of about 0.8 V. The particle displacements at the surface are about 0.08 nm (0.8 Å), which is comparable with interatomic distances and far less than the SAW wavelength of 35 μm . It is also common to define a coupling constant $k^2 = 2 \Delta v/v$.

3.2. Diffraction

SAW diffraction can be analyzed by a method similar to that often used in optics, using a scalar to represent the wave amplitude [12]. Perturbations due to components such as transducers and gratings are ignored in this method. Except for the most sophisticated devices, these approximations are usually adequate. The analysis may then be done on the basis of data for the SAW velocity. As in conventional optics, SAW diffraction gives a near-field (Fresnel) region, in which the amplitude distribution is similar to that of the source, and a far-field (Fraunhofer) region, where the amplitude corresponds to the Fourier transform of the source. Several complications occur, how-

ever, because of the anisotropy of the substrate material. In summary:

1. *Beamsteering.* In beamsteering, the energy flow direction \mathbf{E} in a wide beam of SAWs is not parallel to the wave vector \mathbf{k} . The angle γ between \mathbf{E} and \mathbf{k} is the beamsteering angle (or “power flow angle”), given by $\tan \gamma = (1/v) dv/d\theta$, where $v(\theta)$ is the SAW velocity at an angle θ . Usually the substrate is chosen such that $\gamma = 0$, but the effect can still occur as a result of misalignment.
2. *Minimal-Diffraction Orientations.* For some substrates, notably Y-Z lithium niobate, the anisotropy is such that diffraction spreading is substantially reduced. This occurs when $d\gamma/d\theta \approx -1$. This condition can be very helpful when designing high-performance devices, because it eliminates the need to compensate for diffraction.
3. *Parabolic Approximation and Scaling.* In many cases the SAW velocity variation $v(\theta)$ can be approximated by writing k_x as a quadratic function of k_y (where x is the principal propagation direction). Assuming no beamsteering, we can write $k_x(k_y) = k_x(0) - 0.5bk_y^2/k_x(0)$. The constant b is unity for an isotropic material and zero for a minimal-diffraction orientation and is given by $b = 1 + d\gamma/d\theta$. If the approximation is valid, the wave amplitude distribution is simply scaled in the x direction. Specifically, if $\psi_i(x,y)$ is the distribution for the isotropic case, the anisotropic case gives a distribution $\psi(x,y) = \psi_i(bx,y) \exp[j(b-1)xk_x(0)]$.

As in optics, the amplitude distribution for the isotropic case is given by formulas involving Fresnel integrals. When the parabolic approximation is invalid, it is necessary to use a more fundamental approach, commonly the angular spectrum of plane waves (ASoPW) method. For this method, the source is represented as a sum of plane-wave elements, with distribution determined by a Fourier transform. Each plane wave propagates according to the known velocity $v(\theta)$. The statements given above can all be deduced from the ASoPW formulation.

In SAW devices, diffraction is usually a second-order effect; that is, the receiving transducer is in the near-field region of the transmitter. However, in an apodized band-pass filter, described below, diffraction can cause some unacceptable signals in the stopband above the passband. These can be reduced by sophisticated design techniques that compensate for the diffraction.

3.3. Temperature Effects

Temperature stability is usually of vital interest when designing a SAW device. Temperature changes cause SAW velocity changes and also thermal expansion, and both these factors affect the delay given by a device. The velocity variation can be calculated using the temperature coefficients of the bulk piezoelectric constants, and with the expansion coefficient this gives the temperature coefficient of delay (TCD). In most cases the delay varies approximately linearly with temperature. However, for some

cases the velocity and expansion effects cancel, at one temperature. The delay $T(\theta)$ then has the quadratic form $T(\theta) = T(\theta_0)[1 + c(\theta - \theta_0)^2]$, where θ is the temperature and θ_0 is the “turn-over temperature,” at which the TCD is zero. In particular, for ST-X quartz, $\theta_0 = 21^\circ\text{C}$ and $c = 32 \times 10^{-9} (\text{C}^\circ)^{-2}$. This orientation is a rotated Y cut, with propagation along the crystal X axis and a rotation angle of 42.75° . It is commonly used for temperature-stable devices, although the rotation angle is usually reduced a little, increasing θ_0 . This is done because the center of the operational temperature range is usually higher than 21°C . It also compensates for a reduction of θ_0 associated with the crystal mounting and the presence of transducers.

The effect of a temperature change is to scale the device impulse response $h(t)$, which changes to $h'(t) = h[t/(1 + \varepsilon)]$, where ε is a small quantity. Correspondingly, the frequency response changes from $H(\omega)$ to $H'(\omega) = H[(1 + \varepsilon)\omega]$. Hence the center frequency is scaled by a factor $\Delta f_0/f_0 = -\Delta T/T = -\varepsilon$, and the bandwidth is also scaled by the same factor.

3.4. Other Propagation Effects

For standard SAW materials, propagation loss is usually small provided the crystals are well polished. For example, at 1 GHz the loss for a free surface is about 1 dB/ μs for Y-Z lithium niobate, and 3 dB/ μs for ST-X quartz [12]. These figures are approximately proportional to f^2 , and they are increased a little when transducers are present. Nonlinear effects are usually negligible in practical devices. Theoretically a free surface gives no dispersion, but in practice there is a little dispersion due to transducers and gratings. However, these effects are not usually of practical significance.

A more significant effect is waveguiding, which can occur because the SAW velocity in components such as transducers is slightly lower than the free-surface velocity outside. In relatively long devices the waves propagate as a series of modes, with some dispersion. For moderate apertures there is often a dominant fundamental mode plus some unwanted higher modes. The unwanted modes cause small perturbations, usually at frequencies somewhat higher than the center frequency. These distortions are seldom significant in devices with wide apertures, greater than typically 20 wavelengths.

4. MATERIALS

A considerable variety of suitable materials has been established, bearing in mind the above propagation effects and the strength of piezoelectric coupling ($\Delta v/v$). The orientation is often specified by two axes. For example, Y-Z lithium niobate indicates a Y-cut crystal with SAW propagation along the crystal X axis. An example of a rotated Y-cut crystal is ST-X quartz, which can be written as 42.75°Y-X quartz. This has propagation along the crystal X axis (in the surface). Looking down the X axis, toward the origin, the crystal Y axis is rotated by 42.74° clockwise from the surface normal.

For more general cases, it is common to use Euler angles, λ , μ , and θ . We define X, Y and Z as crystal axes

and x , y , and z as device axes, with x as the SAW propagation direction and z as the outward-directed normal to the surface. Initially the angles are zero and x,y,z are the same as X,Y,Z. There are three rotations, as follows:

1. Rotate the x , y , and z axes anticlockwise about z through an angle λ (as seen by an observer looking down the z axis toward the origin). Call the new axes x_1, y_1, z_1 .
2. Rotate the x_1, y_1, z_1 axes anticlockwise about x_1 through an angle μ . Call the new axes x_2, y_2, z_2 .
3. Rotate the x_2, y_2, z_2 axes anticlockwise about z_2 through an angle θ . Call the new axes x_3, y_3, z_3 .

In the final orientation, z_3 is the surface normal and x_3 is the propagation direction. For a rotated Y-cut crystal, with cut angle ψ , we have $\lambda = \theta = 0$ and $\mu = \psi - 90^\circ$.

Table 1 gives data for some common SAW materials. Y-Z lithium niobate (LiNbO₃) has strong piezoelectric coupling and minimal-diffraction properties, advantageous for wideband and low-loss devices, but its temperature stability is poor. This material generates unwanted bulk waves rather strongly. The 128° rotated cut minimizes bulk-wave generation, but this is not a minimal-diffraction orientation. ST-X quartz (SiO₂) has weak piezoelectric coupling and is generally limited to narrowband devices, but its good temperature stability is attractive for narrowband filters and resonators. X-112°Y lithium tantalate (LiTaO₃) is an intermediate case, as is lithium tetraborate (Li₂B₄O₇). Zinc oxide (ZnO) films on glass substrates have been used for TV IF filters, for reasons of economy. This film has also been used on sapphire substrates to give a high-velocity combination, and 1.5-GHz filters have been produced [13]. Langasite (La₃Ga₅SiO₁₄) has recently become available for SAW applications, giving properties quite similar to quartz but with stronger piezoelectric coupling [14]. A variety of other new crystals with similar properties, including langatate and langatite, are also becoming available.

The leaky SAW and STW cases will be described later.

Table 1. Data for Common Materials

Material	v_f (m/s)	$\Delta v/v$ (%)	$\varepsilon_\infty/\varepsilon_0$	TCD (ppm/°C)
Y-Z LiNbO ₃	3488	2.4	46	94
128°Y-X LiNbO ₃	3979	2.7	56	75
ST-X quartz	3159	0.06	5.6	0
X-112°Y LiTaO ₃	3300	0.35	48	18
45°X-Z Li ₂ B ₄ O ₇	3350	0.45	11	0
La ₃ Ga ₅ SiO ₁₄ ^a	2747	0.18	—	−1
ZnO on glass ^b				
(fundamental mode)	2576	0.7	—	11
36°Y-X LiTaO ₃ (LSAW) ^c	4212	2.4	50	32
64°Y-X LiNbO ₃ (LSAW)	4742	5.5	52	80
Quartz, $36^\circ\text{Y-X} + 90^\circ$ (STW)	5100	—	5.6	0

^aLangasite data are for Euler angles 0, 140, 25.5° . This is a minimal-diffraction orientation.

^bData depend on film thickness; typical data are shown.

^cLeaky surface acoustic wave.

5. BASIC SAW DEVICES

5.1. Bandpass Filtering

This is one of the commonest applications of SAW devices, and apodization is a fundamental method of achieving this.

5.1.1. Apodized Transducers. *Apodization*, that is, variation of the electrode lengths, is a common method for weighting SAW IDTs. The principle is illustrated in Fig. 4, which shows a device with two transducers, one apodized and the other unapodized. In the apodized transducer, at each x_n there are electrodes extending from both busbars, with a small break at a position that determines the apodization. The SAW sources can be taken to be the live electrodes, or alternatively the gaps between electrodes with different voltages. The figure shows single-electrode transducers for clarity, although in practice they are more commonly the double-electrode type to avoid the electrode reflection problem described above.

To appreciate the operation, it is first necessary to consider reception of waves by the unapodized transducer at the left. For the moment, we will simply state that the frequency response, for waves incident from the right, is essentially the same as the response when the transducer generates waves to the right. This is a result of reciprocity, considered later. For a transducer receiving SAWs, the response is defined by assuming the transducer to be short-circuited, and considering the current I_{sc} in the short circuit when a wave with specified potential ϕ_s is incident. The ratio I_{sc}/ϕ_s is almost the same as Eq. (1), except that a slightly different element factor is used.

The argument presented above applies if the surface-wave beamwidth is the same as the transducer aperture. When dealing with an apodized launching transducer, this is no longer true. To simplify, consider a voltage applied to only one electrode of the apodized transducer. The electrode extends a distance u_n , say, from the live busbar. Now, the short-circuit current induced in the left transducer will be proportional to u_n . To see this, note that apodization has not affected the amplitude of the wave or the charge density that the wave induces on the receiving transducer. However, the charges exist only within the SAW beamwidth, and this width is u_n . Hence, when integrated to obtain the short-circuit current, the result will

be proportional to u_n . The response of the apodized transducer is thus similar to an unapodized one [Eq. (1)], except that the source strength is proportional to u_n . To maintain the units, we use u_n/W , where W is the total aperture, so the response has the form

$$H_{ap}(\omega) = E(\omega) \sum_{n=1}^N \frac{u_n}{W} \exp(-jkx_n) \quad (5)$$

The device response is basically $H_{ap}(\omega)H_{un}(\omega)$, where $H_{un}(\omega)$ is the response of the unapodized transducer Eq. (1). To be more specific, this gives the transadmittance Y_{12} , which is the current obtained when the output transducer is short-circuited and unit voltage is applied to the input transducer. This formulation is valid only if one of the two transducers is unapodized. If we ignore the slow frequency variation of $E(\omega)$, the Fourier transform of Eq. (5) gives a series of impulses with amplitude proportional to u_n . Hence the *time-domain* response is directly related to the *spatial* variation of the electrode lengths, that is, by the apodization.

In practice the observed response is affected by the electrical source and load impedances, and to allow for these we also need the remaining Y -matrix components Y_{11} and Y_{22} . Since electrode reflections are assumed here to be negligible, these Y components are just the transducer admittances.

A general technique for analyzing an apodized device is to divide it into imaginary parallel “channels,” extending in the x direction [7]. Each channel can be regarded as an unapodized device, connected electrically in parallel with the others. However, provided there are no electrode reflections, the analysis can be done without channeling.

5.1.2. Transversal Filtering. If we ignore the slowly varying function $E(\omega)$, Eq. (5) has the form

$$H(\omega) = \sum_{n=1}^N A_n \exp(-j\omega n\tau) \quad (6)$$

where A_n are real constants and $\tau = p/v$ is the electrode spacing in time units. This is the response of a *transversal filter*, which can be thought of as a tapped delay line with taps spaced in time by τ and connected to an output via

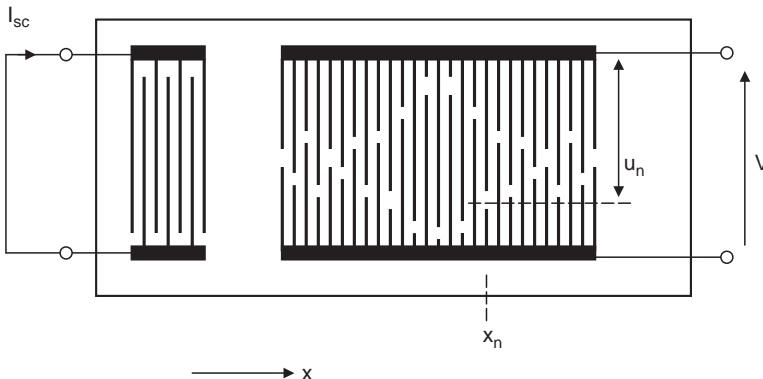


Figure 4. Transversal bandpass filter using an apodized transducer.

circuits with amplitude response A_n . The response could have been arrived at by considering a continuous waveform and then sampling it with a sampling frequency $f_s = 1/\tau$. In this context we can apply the sampling theorem, which states that any bandlimited waveform can be reproduced by sampling at a sufficiently high rate, and then filtering to eliminate some high-frequency components introduced by the sampling process. Hence, *any* required frequency response can be synthesized by appropriate choice of the real constants A_n , provided (1) f_s is high enough, (2) the original time-domain waveform is of finite length, and (3) technological constraints are satisfied (maximum frequency, device length etc.). It is a property of transversal filters that the amplitude response is symmetric about frequency $f_s/2$, and this is the center frequency of a single-electrode transducer. Hence, for the general case we need more than two electrodes per center-frequency wavelength; four is quite common. This actually provides a benefit in that electrode reflections are minimized, as discussed earlier.

Another realisation of the transversal filter is the digital finite impulse response (FIR) filter. This comparison is of great value because the design of FIR filters has been considered in great detail. A simple design method is to Fourier-transform the required frequency response to the time domain and then, in order to obtain finite length, multiply by a finite-length window function such as the Hamming function or the Kaiser function [3]. A very effective design method is provided by the Remez algorithm, which can be used to design a filter with an amplitude response of arbitrary shape, subject to a tolerance expressed as an arbitrary function of frequency [15]. Alternatively, linear programming can be used [16].

In practice, the design procedure needs to compensate for a variety of second-order effects, particularly distortion associated with the terminating impedances (the “circuit effect”) and diffraction. These can be compensated by recursive methods; it is even possible to compensate for distortions of unknown physical origin, provided experimental results are sufficiently repeatable.

Sometimes a transversal filter will incorporate a *multistrip coupler* (MSC). This consists of a sequence of disconnected metal strips perpendicular to the SAW wavevector and spanning two SAW tracks. The MSC can couple SAWs from one track to the other with high efficiency and with wide bandwidth. In the transversal bandpass filter, it has been widely used in order to minimize interference from unwanted bulk waves. The MSC is often used when the substrate is Y-Z lithium niobate;

this material gives significant bulk-wave generation but is otherwise attractive because it minimizes diffraction effects. The coupler also enables two apodized transducers to be used, giving improved flexibility. The number of strips needed for a full transfer of the SAWs is in the region of $2.5/(\Delta v/v)$. This prohibits use of the coupler on weakly piezoelectric substrates such as quartz, since the number of strips would be unrealistic.

5.1.3. Withdrawal Weighting. In this technique, selected SAW sources are withdrawn from a uniform transducer, in such a way that the density of remaining sources mimics the amplitude variation of an apodized transducer [17]. This is shown in Fig. 5. Withdrawal-weighted transducers are suitable for filters with small bandwidths, less than, say, 5%, and they have the merit of being insensitive to diffraction effects. The electrodes can still be regular, so the response is still governed by the simple delta-function analysis described earlier.

The two weighted transducers shown in Figs. 4 and 5 have rather different impulse responses, since the withdrawal-weighted transducer response has a sequence of steps. However, the latter can easily be designed such that the *integral* of its impulse response is similar to the *integral* of the impulse response of the apodized transducer. When this is done, the frequency responses of the two transducers will be similar. The main difference is that the stepped nature of the withdrawal-weighted transducer introduces unwanted sidelobes at some distance from the passband of the filter. For this reason, the technique is applicable only for narrowband devices.

5.1.4. Performance of Transversal Bandpass Filters. Filters of the types described here can give excellent performance because their behavior is well understood and the devices are very reproducible, so that small errors can be corrected by redesigning. The main limitation is that insertion losses must be high in order to minimize the triple-transit signal. For the best results, single-electrode transducers are avoided and great care is taken in the design—errors due to the circuit effect, diffraction, and other second-order effects are compensated for [18]. The apodization pattern is often “sloped,” because the presence of several sidelobes in line causes distortion in the conductance G_a and hence in the device response. Special techniques are used to minimize reflections from the ends of the transducers. Filters for vestigial sideband (VSB) applications in TV are made with 6 MHz bandwidth

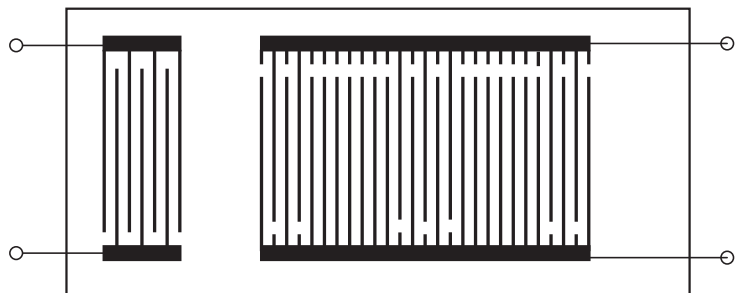


Figure 5. Transversal filter using a withdrawal-weighted transducer.

centred at 40 MHz, in-band variations of only ± 0.2 dB in amplitude and ± 20 ns in delay, and skirt width 500 kHz. Ganss-Puchstein et al. [19] developed filters for digital radio with 64-QAM (quadrature amplitude modulation), with 20 MHz bandwidth and an amplitude ripple of only ± 0.05 dB. Peach [16] shows filters at 160 MHz, with a shape factor (ratio of 40 and 3 dB bandwidths) of 1.04, and with an in-band ripple of ± 0.15 dB.

5.2. Correlation

In the context of SAW devices, “correlation” refers to the process of applying a complex waveform to a linear device whose impulse response is the time reverse of the input waveform. The device is known as a “matched filter.” The output waveform has a prominent peak called the *correlation peak*. If the input waveform is accompanied by noise, as is always the case for a radio receiver, the correlation process increases the signal-to-noise ratio (SNR), giving the maximum SNR obtainable by linear signal processing. Several types of SAW device have been developed for this purpose.

5.2.1. Pulse Compression. This technique, used in radar systems, increases the maximum range at which a target can be detected without needing an increase in the peak transmitted power. In principle any type of complex waveform is applicable, provided the time–bandwidth product (TB) is large, where T is the waveform duration and B is its bandwidth. The matched filter increases the signal-to-noise power ratio by a factor TB, equivalent to increasing the transmitted peak power by this factor. For radar systems, TB is typically 50–500.

In practice the transmitted waveform is usually a chirp, that is, a waveform whose frequency varies monotonically with time. The echo due to a point target has the same form. The matched filter needs to have its impulse response as the time reverse of this, another chirp, and this can be regarded as a dispersive delay line. In essence, the filter applies a delay dependent on frequency, such that all frequency components arrive at the output at the same time. Figure 6 shows a typical arrangement, where the right transducer has graded periodicity. For a single-frequency SAW, the transducer responds most strongly where its pitch corresponds to the SAW wavelength, so that different delays are obtained for different frequencies.

The left transducer can be uniform, as shown, or it could be another graded-periodicity transducer.

In the radar receiver, the device usually has one transducer apodized in order to give the impulse response a humped envelope. This reduces the sidelobes of the output signal, which need to be small so that they are not falsely interpreted as extra targets. The sidelobes can be 35 dB below the main peak. Typically, bandwidths are in the region 10–100 MHz and durations (T) are 5–20 μ s. For the longer devices quartz is the preferred material because temperature stability is needed, while shorter devices use strong piezoelectrics (lithium niobate or tantalate) to obtain acceptable losses.

Interdigital devices generally give larger insertion losses as the TB product is increased. This limitation is overcome in the reflective array compressor (RAC), which has two arrays of inclined grooves, each reflecting the waves through 90° . The groove arrays reflect strongly when the pitch corresponds to the wavelength, and the RAC has graded pitch so that different frequencies are subject to different pathlengths and hence delays. With this technique, devices with TB products up to 16,000 have been produced [20].

5.2.2. PSK Filters. While chirp waveforms are common in radar systems, communication systems often use phase-shift-keyed (PSK) waveforms, or other related waveforms. A PSK waveform consists of a sequence of contiguous pulses of carrier, with relative phase 0 or 180° . In spread-spectrum communications, each bit of data can be represented by a sequence of this type, and correlation is needed to optimise the SNR. This can be achieved using a SAW tapped delay line, with taps corresponding to the pulses; the taps are connected in a polarity sequence corresponding to the coding.

5.2.3. Convolver. Another type of correlator is the nonlinear convolver, shown in Fig. 7. In this device, RF signals are introduced at both ends of a lithium niobate substrate, so that they propagate towards each other. Where they overlap, a weak nonlinear mechanism causes mixing and a sum-frequency signal is produced, with amplitude proportional to the product of the input wave amplitudes. The non-linearity is an intrinsic property of the material. The product signal appears as an electric field which can be sensed by a uniform metal electrode (the

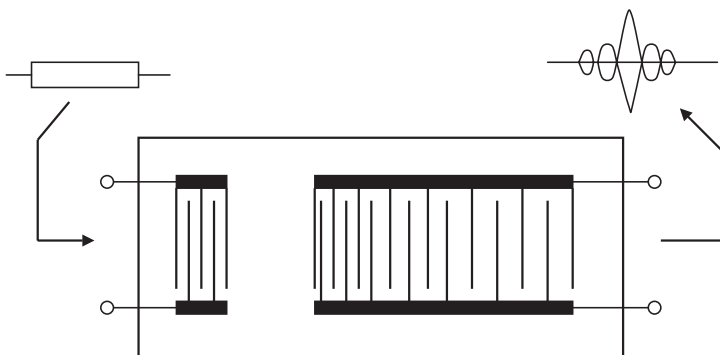


Figure 6. Interdigital pulse compression filter.

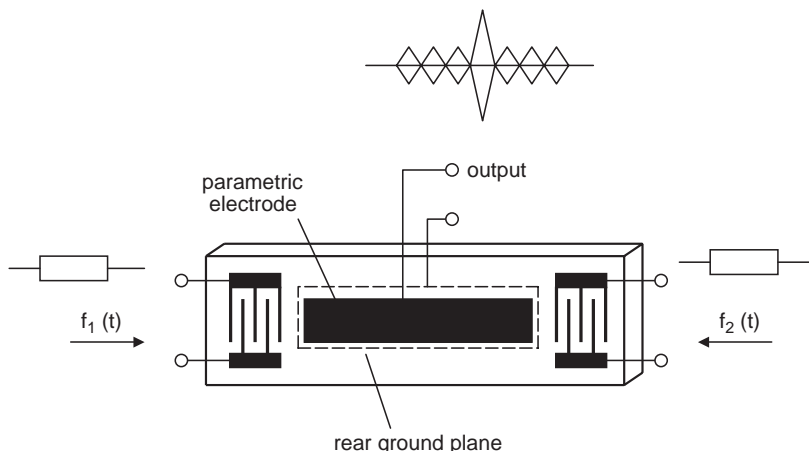


Figure 7. SAW convolver.

parametric electrode) extending over most of the area between the input transducers.

If the input waveforms are $f_1(t)$ and $f_2(t)$, the wave amplitudes within the device have the forms $f_1(t - x/v)$ and $f_2(t + x/v)$ (ignoring some delays). The output waveform $g(t)$ is proportional to the integrated product of these, so that

$$g(t) \propto \int f_1\left(t - \frac{x}{v}\right) f_2\left(t + \frac{x}{v}\right) dx = \frac{1}{v} \int f_1(2t - \tau) f_2(\tau) d\tau \tag{7}$$

where $\tau = t + x/v$. It is assumed here that the traveling SAW signals have finite length and that they overlap only under the parametric electrode. With this assumption, the integrals in Eq. (7) can have limits $\pm \infty$. The second form in Eq. (7) is a standard convolution integral, except that t is replaced by $2t$ because of the relative motion of the two waveforms—and, as is well known from systems theory, convolution describes mathematically the process performed by any linear device. Hence the convolver acts as a *linear* filter, but with one of the input waveforms acting as the impulse response. In particular, it can correlate any type of coded waveform, including the chirp and PSK waveforms considered above, and the coding can be changed instantaneously.

For the configuration of Fig. 7 the device produces a very weak output signal. To improve the efficiency, convolvers have been developed with the SAW beam compressed to a narrow width, typically 3 wavelengths, thus increasing the power density. Typically, the output power for CW signals is $P_O = P_1 + P_2 - 70$ dBm, where P_1 and P_2 are input powers and all powers are measured in dBm (decibels referenced to 1 mW). Although input signal levels of 25 dBm are feasible, the interaction is obviously very weak; nevertheless it is strong enough for practical signal processing. Practical devices can have parametric lengths of 20 μ s and bandwidths of 100 MHz. Interactions in semiconductors have also been used to improve the efficiency.

The convolver shows exceptional versatility. However, it is limited by the need to provide an input “reference” waveform to act as the impulse response, and it has not found widespread application.

5.3. Resonators

As for microwave devices, SAW resonators can be used either for stabilization of oscillators or as the basis for low-loss bandpass filters. A basic difference is that in SAW there is no effective localized reflection mechanism—a single strip, for example, gives mode conversion as well as reflection and is therefore unsuitable for a resonator. However, strong reflectivity can be obtained from a grating consisting of an array of strips, with period equal to $\lambda/2$ at the center frequency. Typically, each strip has a reflection coefficient in the region of 1%, and there may be, say, 200 strips. The strips are commonly short-circuited metal electrodes, although grooves are often used for oscillators because they give lower losses. The grating may be analyzed using the CoM equations given later.

As shown in Fig. 8, a resonant cavity can be formed by two reflecting gratings [21]. The waves penetrate some distance into the gratings, so that the cavity length is effectively larger than the separation of the gratings. Consequently, the frequency spacing of the resonances can be

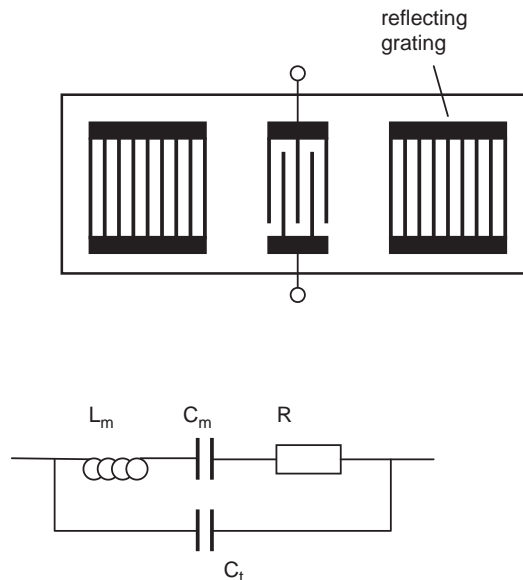


Figure 8. One-port resonator and its equivalent circuit.

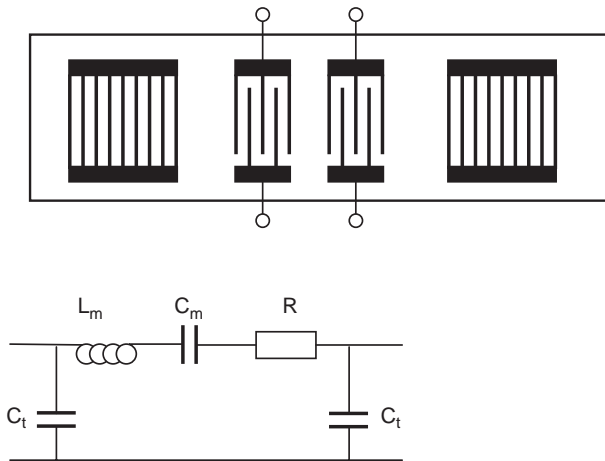


Figure 9. Two-port resonator and its equivalent circuit.

quite small, for example, 1% of the center frequency. The gratings reflect strongly only over a narrow bandwidth, and the device can be designed such that only one resonance appears.

The addition of one or two transducers between the gratings provides coupling to one electrical port (Fig. 8) or two electrical ports (Fig. 9). The transducers are often designed to have negligible electrode reflections. In high- Q devices for oscillator applications, this condition can be obtained by recessing the electrodes into grooves on the surface. Alternatively, it is possible to use double-electrode transducers. Such transducers have little effect on the cavity resonances. The substrate is usually ST-X quartz, because the high Q value implies that temperature stability is important. Experimental Q factors can be up to 10^5 at 100 MHz, or 10^4 at 1000 MHz [21].

Properly designed resonators behave approximately as the equivalent circuits shown in Figs. 8 and 9, with a series resonant branch connected to capacitances equal to the transducer capacitances C_t . The one-port device has a resonance frequency $\omega_r = [L_m C_m]^{-1/2}$, at which the admittance is maximized. There is also an antiresonance frequency ω_a at which the admittance is zero, related to the capacitance ratio by $(\omega_a - \omega_r)/\omega_r \approx 0.5 C_m/C_t$.

An alternative type of two-port resonator uses single-electrode transducers with the electrode pattern made as an extension of the adjacent grating pattern. In this case the device can be made entirely from a single metal film, and it is not necessary to recess the electrodes. This “synchronous” resonator is much easier to make, especially at high frequencies, and Q values of 2250 have been obtained at 2.6 GHz [22].

5.4. Oscillators

A two-port resonator can be used to realize an oscillator by connecting one port to the other via an amplifying feedback circuit, with the amplifier gain exceeding the resonator loss [21]. Alternatively, a SAW delay line can be used [23]. The delay line is designed with one or both transducers long enough to enable it to oscillate at only one frequency. It is also possible to use a one-port resonator, with a special type of circuit [21].

The frequency stability of the oscillator is a crucial issue. Short-term stability relates to fluctuations associated with noise in the loop, causing the output signal to have a spectrum of finite width. Lewis’ analysis [23] showed that for a delay line, the 3 dB width of the spectrum is $\Delta\omega \approx 4k\theta (\text{NF}) G^2 \omega_0^2 / [Q^2 P_0]$, where k = Boltzmann’s constant, θ = absolute temperature, and $Q = \omega_0 \tau$ is the Q factor of the delay line, with delay τ ; G , P_0 , and NF are respectively the amplitude gain, output power, and noise figure of the amplifier, when saturated as in the oscillation condition. This formula also applies for a resonator, although it does not include flicker noise. A delay line needs to be physically much larger than a resonator to obtain the same Q . On the other hand, the maximum input power for a resonator is less than that of a delay line because of the magnification associated with the resonance.

Medium-term stability is associated with the temperature stability of the quartz, discussed elsewhere. Long-term stability refers to frequency drift over periods of months or years, and the mechanisms determining this are not clear. However, Parker and Montress [21] have shown that use of a package made of quartz can enable the ageing rate to be 0.1 ppm per year or less.

Improved results are obtainable using the surface transverse wave (STW) on quartz. This orientation gives high velocity, which is attractive for high-frequency devices, and can tolerate higher power levels than ST-X quartz, leading to better short-term stability [24].

5.5. Wireless Interrogation: Sensors and Tags

The temperature sensitivity of SAW devices is usually seen as a limitation. However, it can be exploited to measure temperature. Many other quantities can also be measured, and related devices are used as identification tags. A typical device is shown in Fig. 10 [25]. An interdigital transducer is connected directly to an antenna, generating SAWs when a RF pulse signal is received. A series of reflectors, usually short gratings, generates a characteristic pattern of reflected waves, and these are received by the transducer and radiated by the antenna. Typically, the 2.4-GHz ISM band is used. The delay in the SAW device helps to distinguish the return signal from the transmitted signal.

The return signal generated by this device is dependent on environmental factors such as temperature or stress, so these can be measured. It is also characteristic of the device design, and can therefore be used for identification. Identity tags can be made by using a sequence of reflectors

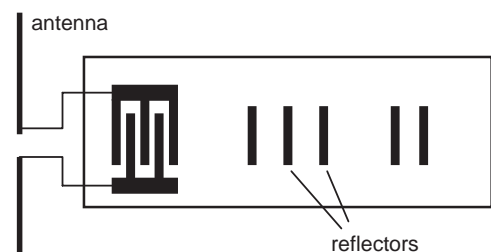


Figure 10. Reflective delay line for wireless tag or sensor.

coded in some way. For example, they might be in a regular sequence except that selected reflectors are omitted. Such devices potentially have wide-ranging applications. The number of possible codes is envisaged to be up to 10^{19} [26].

Temperature can be measured by comparing the phases of waves from individual reflectors. Strain can also be measured, and with the device mounted on a sealed cavity this can also indicate pressure. Chemicals can be detected by coating the device with a film that absorbs the target chemical, causing a change of density and hence SAW velocity. As an alternative to the delay line of Fig. 10, one-port resonators can be used.

6. LOW-LOSS BANDPASS FILTERS

Since the early 1980s, the rapid expansion of wireless systems, particularly mobile telephony, has led to a strong demand for bandpass filters with low insertion losses. Losses often need to be less than 10 dB for IF filters, and 2 dB for RF filters. As discussed above, this requirement cannot be met using traditional transversal filters because of the triple-transit problem, and consequently a variety of new devices have been developed. There are many approaches for this problem [27], but here we consider only the main ones. They can be classified as follows:

1. Use a unidirectional transducer, which generates waves more strongly in one direction than the other. With this feature, triple-transit signals can be reduced while still maintaining low losses. It can be shown that the transducer must have internal reflectivity to satisfy this condition.
2. Develop filters based on SAW resonators, analogous to microwave resonator filters. In effect, an infinity of multiple-transit signals are used here.

6.1. Single-Phase Unidirectional Transducers (SPUDTs)

This term describes a class of unidirectional transducers; the term “single-phase” distinguishes them from some earlier types that are of little interest now. The dominant type of SPUDT is known as the *distributed-array reflective*

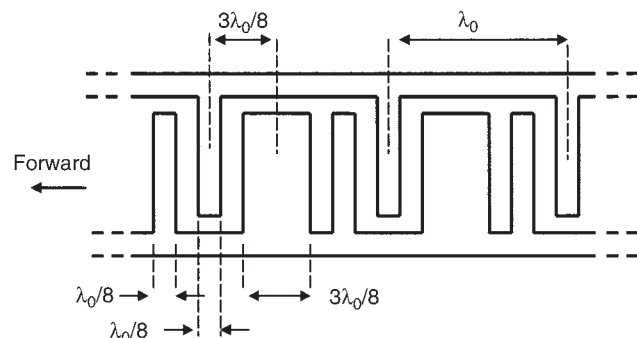


Figure 11. Structure of DART transducer.

transducer (DART), illustrated in Fig. 11. Each cell of this transducer has two narrow electrodes of width $\lambda_0/8$ and a wide electrode of width $3\lambda_0/8$, and the interelectrode gaps are all $\lambda_0/8$. Here λ_0 is the cell length, equal to the center-frequency wavelength. Reflections from the narrow electrodes are negligible because they occur in pairs with spacing $\lambda_0/4$, so that reflections cancel at the center frequency. Hence, in effect, only the wide electrodes act as SAW reflectors. The waves are effectively generated at the centers of the live electrodes. In general, it can be shown that for best directivity the distance between a generation center and a reflection center needs to be $(n/2 \pm 1/8)\lambda_0$, where the factor $1/8$ appears because the reflection coefficient is known to be imaginary. In the DART, the distance between the two centres is $3\lambda_0/8$ and therefore satisfies this requirement [28].

Like any other transducer, a SPUDT gives optimum acoustoelectric conversion if it is electrically matched. If it has enough directivity, it can be shown that this is also close to the condition that minimizes the acoustic reflection. Thus, low loss and good triple-transit suppression are obtained simultaneously. In practical DARTs it is common to have a directivity of 6 dB or more, and this is sufficient for these purposes. However, this is limited by the electrode reflectivity obtainable, and for this reason the DART needs to be fairly long, $100\lambda_0$ or more. Hence the bandwidth is quite small, and the substrate is a temperature-stable material such as quartz.

Weighting can be applied to modify the response. The transduction in one cell can be removed by connecting the second electrode to the ground bus instead of the live one. Reflection can be removed by replacing the wide electrode by two narrow ones (each $\lambda_0/8$ wide, with a $\lambda_0/8$ space). Moreover, the transduction and reflection can be regarded as smooth functions of position, using withdrawal weighting to obtain the actual designs for individual cells. In this way, the design can satisfy performance criteria such as bandwidth, ripple, skirt width, and stopband rejection. A considerable advance was made when it was realized that the reflection and transduction functions can also change sign; these changes are realized by displacing the corresponding electrodes. The use of differently signed reflectors is equivalent to incorporation of resonators into the structure, so the transducer became known as a *resonant SPUDT* (R-SPUDT) [28]. The resonances enable the device length to be substantially reduced, for a given specification. A further reduction was obtained by using a two-track arrangement, in which each track consists of two R-SPUDTs connected in parallel with the R-SPUDTs in the other track [29]. These size reductions have been very significant in the main application area, which is for IF filtering in CDMA mobile phones, with bandwidth around 1 MHz. The design process is an extremely sophisticated “global” optimization procedure, taking account of the amplitude and phase ripple requirements as well as the amplitude response and tolerances. These devices can actually exploit the triple-transit effect, using it to reduce the skirt widths; in the passband, the triple transit is usually minimized. This represents a considerable extension of the initial objective of the SPUDT, which was simply to reduce the triple-transit level.

6.2. Resonator Filters

As in microwave technology, SAW resonators can be coupled in order to realize a bandpass function. However, a SAW device behaves as a resonator only within the reflection band of the gratings. The width of this band is approximately $\Delta f/f \approx 2|r_s|/\pi$. Here $|r_s|$ is the strip reflection coefficient, typically a few percent, so the filter bandwidth obtainable is quite small.

An example is the *longitudinally coupled resonator* (LCR) filter, also called the *dual-mode SAW* (DMS) filter [30]. As shown in Fig. 12, this has three transducers between two reflecting gratings, with the outer two transducers connected together. In effect, each outer transducer plus its adjacent grating serves to act as a SPUDT, launching SAWs toward the center of the device when a voltage is applied. The device as a whole behaves as a cavity with two resonances. This arrangement is often used for RF filters, with center frequency 900 MHz or more, in which case the transducers are usually the single-electrode type. The response is typical of a two-pole filter, giving a flat passband with low loss when electrically matched. It is common to cascade two devices electrically in order to improve the stopband rejection. The device can give low loss and good stopband rejection, but the skirt width is relatively wide because of complications arising from reflections within the device.

Another resonator filter is known as the *impedance element filter* (IEF). This consists of a sequence of SAW resonators connected as an electrical circuit, without any acoustic coupling between them. Resonant behavior can be obtained simply by using long single-electrode transducers. It is known that, for a sufficiently large number of electrodes, the reflections can cause the transducer to behave as a resonator, with equivalent circuit approximately as in Fig. 8 [31]. Usually, reflecting gratings are also added at the ends to increase the Q factor. The IEF uses a sequence of series and parallel resonators (Fig. 13), where the former have higher resonant frequencies. The filter center frequency is at the antiresonance of the parallel resonator (where $Y \rightarrow 0$) and at the resonance of the series resonator (where $Z \rightarrow 0$), so that the signal is transmitted with little attenuation. Outside the passband there are deep nulls due to the resonance of the parallel resonator and the antiresonance of the series one. Beyond that are the stopbands where there is little acoustic activity, and here the response is determined mainly by the static capacitances and the electrical loading.

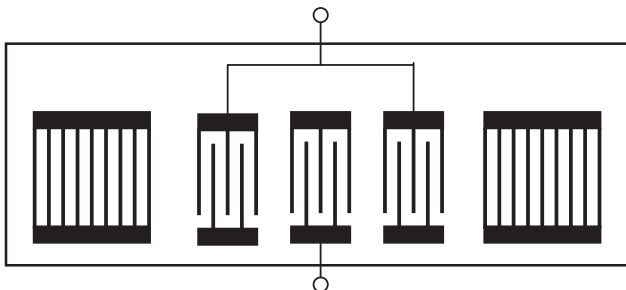


Figure 12. Longitudinally coupled resonator (LCR) filter. Bus-bars shown without connections are grounded.

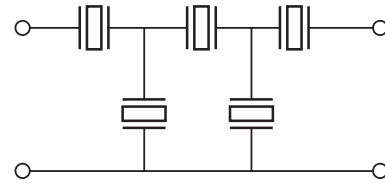


Figure 13. Typical configuration for impedance element filter (IEF). Usually each resonator is a single-electrode transducer with a grating on each side.

Like the LCR filter, the IEF can provide very low loss (1 dB) at RF frequencies (900 MHz and above) [32]. Its stopband rejection is not so good, but the skirts can be narrower. There is also the key advantage that quite high power levels can be tolerated, around 2 W. This ability is essential for some mobile phone transmitter filters. Many systems use a duplexer consisting of two IEFs, both connected to the antenna. One of these IEFs is at the transmitter output, and the other is at the receiver input. These devices normally use leaky waves on lithium tantalate, a subject described later.

The transverse-coupled resonator (TCR) filter is another resonant device, although it operates on entirely different principles [33]. As shown in Fig. 14, it has two identical tracks, each containing a single-electrode transducer with a grating on either side. Coupling between the tracks occurs because the device behaves as a waveguide that supports two waveguide modes, one symmetric and one antisymmetric. This behavior is associated with the narrow width, typically 6λ . Excitation of one transducer causes generation of both modes, and because of the different mode velocities, a signal appears in the other track. For each mode the device behaves as a conventional resonator. The presence of two modes gives the device a two-pole response. The pole frequencies correspond to the wave velocities of the modes, and because these are very close together, the fractional bandwidth of the filter is very small, typically 0.1%. Using a ST-X quartz substrate, this filter has been widely used in the IF circuit of GSM mobile phone handsets, with typically 200 kHz bandwidth and 200 MHz center frequency.

6.3. Capabilities of Bandpass Filters

Table 2 summarizes the capabilities of the various types of filter. When considering a particular requirement, the

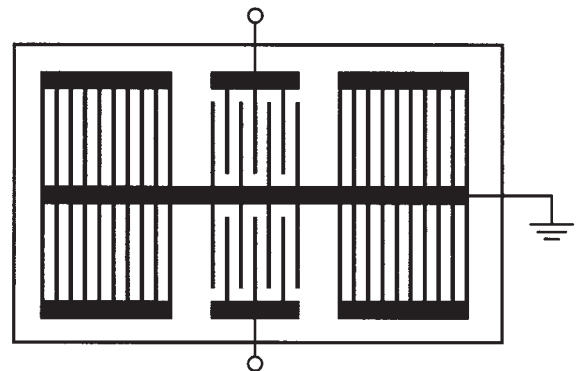


Figure 14. Transverse-coupled resonator (TCR) filter.

Table 2. Typical Performance for Main Types of Bandpass Filter

Type	Transversal	DART	LCR	IEF	TCR
Substrate	Various	ST-X quartz	42°Y-X LiTaO ₃	42°Y-X LiTaO ₃	ST-X quartz
Center frequency (MHz)	50–500	80–500	500–2000	600–3000	50–200
Bandwidth (%)	1–50	1–3	1–3	1–4	0.05–0.15
Insertion loss (dB)	15–40	6–10	1–3	1–3	5–7
Maximum rejection (dB)	60	45	55	45	50
Minimum shape factor ^a	1.1	1.5	3.0	1.5	2.0

^aShape factor = ratio of 40-dB and 3-dB bandwidths.

different capabilities of the various devices need to be considered, including the temperature stability. A variety of packages are used, including metal and surface-mount ceramic types. Flip-chip mounting is often used to minimize the size, which may be as small as $2 \times 2 \text{ mm}^2$ for GHz-range devices. The frequency response depends on the external terminating impedances, often specified as 50Ω , and often the transducer capacitances need to be tuned out using inductors. It is also common to use two-component circuits to transform the impedances. Other factors, especially important at high frequencies, are stray capacitance or inductance, and electromagnetic feedthrough.

Many filters can be arranged in a balanced form, that is, at each port there are two live terminals designed to accept voltages with opposite polarities. This is needed for operation with some modern communication circuitry. It is also possible to have one port balanced and the other unbalanced, so that the device acts as a balun transformer in addition to its filtering function.

7. LEAKY SURFACE WAVES

In addition to the Rayleigh-type surface wave described earlier, some devices use alternative wave types that behave in a somewhat similar manner. A particular case occurs on 36°Y-X lithium tantalate. The wave is rather like a Rayleigh wave, but the particle displacement is approximately in the transverse direction (parallel to the surface) instead of being in or near the sagittal plane. This wave is not a true surface wave, as shown by the fact that it can radiate some energy into the bulk of the material. Hence the wave is called a “leaky wave”. It is related to a bulk shear wave. A numerical search for wave solutions gives a wavenumber with a small imaginary part, and hence there is some attenuation. The attenuation depends on rotation angle, and becomes small, negligible for practical purposes, at an angle of 36° . For this angle, devices analogous to SAW devices behave in a similar manner. There are significant differences, however, notably that the leaky-wave material gives rise to substantial bulk-wave generation at frequencies above the passband.

This leaky wave has the advantage that, compared with SAWs on lithium tantalate, it gives stronger piezoelectric coupling without an increased TCD (in contrast, the SAW on Y-Z lithium niobate gives stronger coupling but the TCD is larger). In addition, the leaky wave can tolerate higher power levels, because the wave penetrates more deeply in to the substrate. It also has a higher velocity, increasing the electrode widths needed for a

specified frequency. All these features are attractive for low-loss RF filters, and hence IEF and LCR filters for these applications often use this wave. A modified orientation of 42° is now preferred because it is found to give less loss when in the presence of transducers and gratings.

A similar case occurs in 36°Y-cut quartz, with propagation normal to X. Again, this is related to a bulk shear wave, giving a high velocity with some attenuation. This was originally known as a *surface-skimming bulk wave* (SSBW). In practical applications the wave is trapped at the surface by transducers and gratings, and it is then known as a *surface transverse wave* (STW). The high velocity (5000 m/s) is attractive for high-frequency devices and losses can be small, as shown by high-Q resonators at 1 GHz [24].

Leaky waves have been found in a substantial variety of materials, often giving elevated piezoelectric coupling [34]. In addition to waves related to shear waves, as in the abovementioned cases, there are also wave related to longitudinal waves. These give even higher velocities. For example, in $47^\circ\text{Y-X} + 90^\circ$ lithium tetraborate, the longitudinal leaky wave has velocity 7000 m/s and $\Delta v/v = 0.7\%$.

8. ANALYSIS METHODS

Analysis techniques for SAW devices vary greatly in sophistication. The simple delta-function model is very effective for illustrating some basic features, and it can provide the basis for optimized design methods such as the Remez algorithm. At the other extreme, numerical techniques can take account of complicated wave behavior, together with effects due to the mechanical vibration of the electrodes. Such methods can simulate very complex second-order effects and can be beneficial when demanding requirements are to be met, even though the analysis may take many hours on a modern computer. The following presents some notes on methods for unapodized devices, omitting derivations.

8.1. SAW Analysis for Thin Films: Effective Permittivity

The electrodes in a SAW device perturb the waves as a result of electrical and mechanical effects. For practical purposes, electrical effects are independent of the film thickness. Mechanical effects do depend on thickness, causing reflections of the waves. However, these are not important if the film is thin enough, or if electrode reflections are canceled as in the double-electrode transducer.

Assuming initially that mechanical effects can be ignored, an excellent basis for analysis is provided by the effective permittivity $\varepsilon_s(\beta)$. We define this by assuming a surface potential of the form $\bar{\phi}(\beta)\exp(j\beta x)$ and a charge density of the form $\bar{\sigma}(\beta)\exp(j\beta x)$. A factor $\exp(j\omega t)$ is omitted from the equations. We then write

$$\bar{\sigma}(\beta) = \varepsilon_s(\beta)|\beta|\bar{\phi}(\beta) \quad (8)$$

It can be shown that $\varepsilon_s(\beta)$ is actually a function of the slowness β/ω . It can be calculated numerically using the electromechanical constants of the material and its orientation. Applying appropriate boundary conditions, this leads to an analysis allowing for electrode reflections and different wave modes (including bulk waves, e.g.) [35]. However, for many cases it is adequate to ignore bulk-wave generation. Noting that $\varepsilon_s(\beta)$ must be zero for a free surface and infinite for a metallized surface, we can approximate it by using first-order Taylor expansions, leading to Ingebrigtsen's form

$$\varepsilon_s(\beta) \approx \varepsilon_\infty \frac{\beta^2 - k_f^2}{\beta^2 - k_m^2} \quad (9)$$

where $k_f = \omega/v_f$ and $k_m = \omega/v_m$ are respectively the wavenumbers for a free surface and a metallized surface. Also, ε_∞ is an abbreviation for $\varepsilon_s(\infty)$. This formulation can also be written in terms of a Green function $G(x)$, relating potential $\phi(x)$ to charge density $\sigma(x)$, such that

$$\phi(x) = G(x) * \sigma(x) = \int_{-\infty}^{\infty} G(x-x')\sigma(x')dx' \quad (10)$$

where the asterisk indicates convolution. It can be shown that the Green function is the sum of an electrostatic term $G_e(x) = -\ln|x|/[\pi\varepsilon_\infty]$ and a surface-wave term $G_s(x) = j\Gamma_s \exp(-j k_f|x|)$, so that $G(x) \approx G_e(x) + G_s(x)$. Here Γ_s is given by

$$\Gamma_s \approx \frac{(v_f - v_m)/v_f}{\varepsilon_\infty} = \frac{\Delta v/v}{\varepsilon_\infty} \quad (11)$$

When a voltage is applied to a transducer, the surface wave generated in the $-x$ direction has surface potential $\phi_s(x) = j\Gamma_s \bar{\sigma}(k_f) \exp(jk_f x)$, where $\bar{\sigma}(\beta)$ is the Fourier transform of the charge density $\sigma(x)$. This arises from the SAW Green function $G_s(x)$. For the same transducer receiving SAWs, with potential ϕ_i , the short-circuit current is given by the reciprocity relation

$$\left[\frac{I_{sc}}{\phi_i} \right]_{\text{receive}} = - \left(\frac{\omega W}{\Gamma_s} \right) \left[\frac{\phi_s}{V} \right]_{\text{launch}} \quad (12)$$

provided the two potentials are evaluated at the same location. Here W is the beamwidth.

8.1.1. Quasistatic Solution. The formulation above leads to complex solutions because it includes the effects of electrode reflections. However, it can be shown that these reflections can be eliminated from the analysis if the

charge density $\sigma(x)$ is replaced by the electrostatic charge density $\sigma_e(x)$, that is, the charge density for the non-piezoelectric case $\Gamma_s = 0$. The SAW potential generated is then $\phi_s(x) = j\Gamma_s \bar{\sigma}_e(k_f) \exp(jk_f x)$. This is a much simpler formulation because $\sigma_e(x)$ is independent of frequency. Integration of $\sigma_e(x)$ over individual electrodes also gives the transducer capacitance C_t . Established numerical techniques [36] can be used to calculate this function.

In many transducers (including withdrawal-weighted transducers) the electrodes are regular, that is, they have constant width and spacing. In this case there is a simple algebraic method. First, imagine an infinite array of electrodes with width a and pitch p , and suppose that unit voltage is applied to one electrode, centered at $x=0$, with all other electrodes grounded. The electrostatic charge density for this case is denoted by $\rho_f(x)$ (which is finite on all electrodes). The total charge density on a transducer can be obtained simply by superposition, using $\rho_f(x)$ for each live electrode. The potential of the SAW generated is simply $\phi_s = j\Gamma_s \sum_n \bar{\rho}_f(k_f) \exp[jk_f(x-x_n)]$, where the sum is over the live electrodes, which are centered at x_n . Here $\bar{\rho}_f(\beta)$ is the Fourier transform of $\rho_f(x)$, given by the formula

$$\bar{\rho}_f(\beta) = \frac{2\varepsilon_\infty \sin(\pi s) P_m(\cos \Delta)}{P_{-s}(-\cos \Delta)} \quad \text{for } 0 < s < 1 \quad (13)$$

where $\Delta = \pi a/p$, $s = \beta p/(2\pi) - m$, and the integer m is chosen such that $0 < s < 1$. $P_\mu(x)$ is a Legendre function given by $P_\mu(x) = \sum_{n=0}^{\infty} a_n$, with $a_0 = 1$ and

$$\frac{a_n}{a_{n-1}} = \frac{(n-1-\mu)(n+\mu)(1-x)}{2n^2} \quad (14)$$

When μ is an integer, the Legendre function becomes a polynomial. This formulation provides a simple way of analyzing electrostatic phenomena, including the effect of the electrode width a on the fundamental and harmonic responses. For example, it shows that the third harmonic of a single-electrode transducer vanishes when $a/p = 0.5$.

The capacitance of the transducer is obtained by integrating the electrostatic charges on the live electrodes. To facilitate this, we define Q_n as the integral of $\rho_f(x)$ over electrode n . Generally, this requires a numerical integration, but for the special case $a/p = 0.5$, it is found that $Q_n = 4\varepsilon_\infty/[\pi(1-4n^2)]$. With this formula, the transducer capacitance is easily calculated using $C_t = W \sum_n \sum_m \hat{P}_n \hat{P}_m Q_{m-n}$, where \hat{P}_n are electrode polarities, equal to 1 for a live electrode and 0 for a grounded electrode. We find $C_t = \alpha \varepsilon_\infty W N_p$, where W is the aperture, N_p is the number of periods, and $\alpha = 1$ for a single-electrode transducer and 1.414 for a double-electrode transducer.

8.1.2. Electrode Reflections in Regular Arrays. Reflections are particularly relevant in reflective gratings and single-electrode transducers. They arise from electrical and mechanical loading of the surface, and to first order these effects can be analyzed separately and then added. Electrical loading is usually negligible in weakly piezoelectric materials such as quartz.

Electrical reflections can be deduced from Eq. (10) [2], giving a formula involving Legendre functions. For $a/p = 0.5$ and a frequency such that $\lambda = 2p$, the reflection coefficient of one electrode is $r_e \approx \pm 0.72j (\Delta v/v)$. Here the $+$ ($-$) sign is used for open-circuit (short-circuited) electrodes. This takes account of the influence of neighboring electrodes. The phase of r_e is defined by referring it to the center of the electrode. The fact that r_e is imaginary is a consequence of power conservation.

For mechanical loading, a first-order analysis based on perturbation theory [2] gives $r_e = jCh/(2p)$ for $a/p = 0.5$, where h = film thickness. The constant C is typically in the range -0.5 to -0.3 for common SAW materials, although for 128°Y-X lithium niobate $C = +0.8$. For grooves on Y-Z lithium niobate or ST-X quartz, $C \approx +0.6$.

For transducer analysis including electrode reflections, the quasistatic method described above can be adapted, giving the *reflective array model* (RAM) [37]. Alternatively, the CoM equations below can be used.

8.1.3. P-Matrix Description. For general purposes it is common to specify a transducer behavior in terms of a matrix P_{ij} , defined by

$$[A_{t1}, A_{t2}, I]^T = [P][A_{i1}, A_{i2}, V]^T \quad (15)$$

where superscript T indicates a transpose. Here I and V are the transducer current and voltage, respectively. The A s are SAW amplitudes, with subscript $i(t)$ indicating waves incident on (leaving) the transducer. These have additional subscripts 1 or 2 to indicate the acoustic port. The ports are imaginary lines near the edges of the transducer, and their precise location is unimportant. The amplitudes are defined such that $|A|^2/2$ equals the power of the surface wave, and the phase of A is the same as that of the surface potential ϕ_s . This requires the relation $A = \phi_s [\omega W/(2\Gamma_s)]^{1/2}$. Reciprocity leads to the relations $P_{21} = P_{12}$, $P_{31} = -2P_{13}$, and $P_{32} = -2P_{23}$. For a grating, the P_{ij} with i or $j = 3$ are not used.

The P matrix can be applied quite generally, although it is not valid if more than one type of wave is present. For example, it cannot be applied to a SAW device that is also generating bulk waves. However, it is very useful for analysing devices with several components, such as two-port resonators. Simple formulas [38] can be applied to cascade components together, leading to a device Y matrix.

8.1.4. Coupled-Mode Equations. These equations, also called *coupling-of-modes* (CoM) equations, are often used for unapodized components with internal electrode reflections. They are written in the form [38,39]

$$\begin{aligned} \frac{dC(x)}{dx} &= -j\delta C(x) + c_{12}B(x) + \alpha_1 V \\ \frac{dB(x)}{dx} &= j\delta B(x) + c_{12}^*C(x) + \alpha_1^* V \\ \frac{dI(x)}{dx} &= 2\alpha_1^*C(x) - 2\alpha_1 B(x) + j\omega C_t \end{aligned} \quad (16)$$

where $\delta = k - k_0$ and k_0 is the wavenumber at the Bragg frequency, determined by the structure. For example, at the first stopband of a grating with electrode pitch p we have $k_0 = \pi/p$. $C(x)$ and $B(x)$ are slowly varying wave amplitudes defined such that the “real” amplitudes are $c(x) = C(x) \exp(-jk_0x)$ and $b(x) = B(x) \exp(jk_0x)$. The parameters c_{12} and α_1 give the reflection and transduction per unit length, and their presence in different places is needed to satisfy reciprocity. $I(x)$ is the busbar current, which needs to be integrated to obtain the transducer current. C_t is the capacitance per unit length.

For a single-electrode transducer, the parameters are given by

$$c_{12} = \frac{-r_s^*}{p}; \quad \alpha_1 = \frac{j\bar{\rho}_t(k)[2\omega W\Gamma_s]^{1/2}}{4p} \quad (17)$$

assuming that the acoustic ports are taken at the center of the end electrodes. Here c_{12} and α_1 are independent of x , and the CoM equations have an algebraic solution. We first consider the case $V = 0$, which applies for a grating or a short-circuited transducer. We look for a “grating mode,” in which $C(x)$ and $B(x)$ are both proportional to $\exp(-jsx)$. Equations (16) give

$$s^2 = \delta^2 - |c_{12}|^2 \quad (18)$$

When there are no losses, δ is real. Then s is also real, except for a stopband with edges at $\delta = \pm |c_{12}|$. The stopband has a fractional width $\Delta f/f = 2|r_s|/\pi$. Equations (16) can also be solved to find the P matrix of a uniform transducer, assumed to extend from $x = 0$ to L . Defining $D = s \cos(sL) + j\delta \sin(sL)$, this is found to be

$$P_{11} = \frac{-c_{12}^* \sin(sL)}{D}$$

$$P_{12} = P_{21} = \frac{s \exp(-jk_0L)}{D}$$

$$P_{22} = \frac{c_{12} \sin(sL) \exp(-2jk_0L)}{D}$$

$$DP_{31} = 2\alpha_1^* \sin(sL) - 2sK_2[\cos(sL) - 1]$$

$$DP_{32} = \{-2\alpha_1 \sin(sL) + 2sK_1[1 - \cos(sL)]\} \exp(-jk_0L)$$

$$P_{33} = -K_1P_{31} - K_2P_{32} \exp(jk_0L) + 2(\alpha_1^*K_1 - \alpha_1K_2)L + j\omega C_t \quad (19)$$

where C_t is the transducer capacitance, $K_1 = (\alpha_1^*c_{12} - j\delta\alpha_1)/s^2$, and $K_2 = (\alpha_1c_{12}^* + j\delta\alpha_1^*)/s^2$. In Eqs. (19), the first three equations apply for a grating as well as a transducer. We also find $P_{13} = -P_{31}/2$ and $P_{23} = -P_{32}/2$, as required by reciprocity.

To use the CoM equations, c_{12} and α_1 must be known. Equation (17) gives approximate formulas for a single-electrode transducer, but it is also common to use values derived from more accurate analysis, or from experimental measurements. The equations are valid for a wide variety of devices. For example, they can also be used for

SPUDTs, with appropriate values for c_{12} and α_1 . For DARTs, approximate formulas are available [37].

The CoM equations can predict directivity (i.e., $|P_{23}| \neq |P_{13}|$), depending on the phases θ of c_{12} and ϕ of α_1 . Maximum directivity occurs when $2\theta - \phi = n\pi$. The transducer is bidirectional ($|P_{23}| = |P_{13}|$) if $2\theta - \phi = (2n + 1)\pi/2$. Usually the transducer geometry is designed to give directivity if needed, as in the DART. However, a symmetric transducer, which may be the single-electrode type, can give directivity because of asymmetry in the substrate properties. This is known as the *natural SPUDT effect*. It occurs in many materials to some extent, but for common SAW materials and orientations it is absent or negligible.

8.1.5. Accurate Analysis Methods. Although the methods described above are often adequate, many situations call for more detailed techniques. This is the case when better accuracy is needed, such as when the electrodes are relatively thick or have nonuniform geometry as in the DART. For such cases, numerical methods based on finite-element (FEM) or boundary-element (BEM) methods have been developed [40–43]. For long transducers, such methods can be very time-consuming. In this case, a possible approach is to use an accurate analysis for a short transducer and use it to deduce the CoM parameters; the latter can then be used to analyze a long transducer. Another approach is to use FEM to analyze infinite gratings corresponding to the transducer under short-circuit and open-circuit conditions. From the stopband edge frequencies, the CoM parameters c_{12} and α_1 can be deduced [44,45].

Accurate analysis of leaky-wave and STW devices call for different approaches, because these waves are fundamentally different from Rayleigh SAWs. The waves are substantially affected by surface gratings and transducers. For example, a grating can serve to trap the wave at the surface, thus reducing the attenuation. However, at frequencies above the stopband it can cause bulk-wave radiation and thus have the opposite effect. In transducers, the coupling parameter α_1 is known to increase with the film thickness of the electrodes. For these reasons, analysis of these waves is best done with the grating included a priori. Because of these complications, analysis of these waves has been confined mostly to uniform transducers and gratings. For leaky waves, center-frequency CoM parameters (dependent on film thickness) have been deduced from FEM analysis of gratings [44]. Hashimoto and Yamaguchi [46] analyzed a metal grating starting from the effective permittivity and adding mechanical loading using FEM analysis. The numerical results were fitted to an empirical formula due to Plessky [47]. This enabled frequency-dependent CoM parameters to be deduced, including the simulation of loss due to bulk-wave generation. This approach was used for leaky waves on 36°Y-X lithium tantalate [48] and STWs on quartz [49].

BIBLIOGRAPHY

1. Lord Rayleigh (John Strutt). On waves propagated along the plane surface of an elastic solid, *Proc. Lond. Math. Soc.* **17**:4–11 (1885).
2. S. Datta, *Surface Acoustic Wave Devices*, Prentice-Hall, 1986.
3. D. P. Morgan, *Surface-Wave Devices for Signal Processing*, Elsevier, 1991.
4. C. K. Campbell, *Surface Acoustic Wave Devices for Mobile and Wireless Communications*, Academic Press, 1998.
5. K.-Y. Hashimoto, *Surface Acoustic Wave Devices in Telecommunications*, Springer, 2000.
6. C. C. W. Ruppel and T. Fjeldy, eds., *Advances in Surface Acoustic Wave Technology, Systems and Applications*, World Scientific Publishing, 2000 (Vol. 1), 2001 (Vol. 2).
7. R. H. Tancrill and M. G. Holland, Acoustic surface wave filters, *Proc. IEEE* **59**:393–409 (1971).
8. A. J. Slobodnik, E. D. Conway, and R. T. Demonic, *Microwave Acoustics Handbook*, Vol. 1A, *Surface Wave Velocities*, U.S. Air Force Cambridge Research Labs., Report AFCRL-TR-73-0-597, 1973, Accession AD 780172.
9. J. G. Gualtieri, J. A. Kosinski, and A. Ballato, Piezoelectric materials for acoustic wave applications, *IEEE Trans. Ultrason. Ferroelec. Freq. Control*, **41**:53–59 (1994).
10. G. Kovacs et al., Improved material constants for LiNbO_3 and LiTaO_3 , *Proc. IEEE Ultrasonics Symp.*, 1990, pp. 435–438.
11. G. W. Farnell, Elastic surface waves, in H. Matthews, ed., *Surface Wave Filters*, Wiley, 1977, pp. 1–53.
12. A. J. Slobodnik, Materials and their influence on performance, in A. A. Oliner, ed., *Acoustic Surface Waves*, Springer, 1978, pp. 225–303.
13. J. Koike, K. Shimoe, and H. Ieki, 1.5 GHz low-loss SAW filter using ZnO /sapphire substrate, *Jpn. J. Appl. Phys.* **32**:2337–2340 (1993).
14. N. Naumenko and L. Solie, Optimal cuts of langasite, $\text{La}_3\text{Ga}_5\text{SiO}_{14}$ for SAW devices, *IEEE Trans. Ultrason. Ferroelec. Freq. Control* **48**:530–537 (2001).
15. L. R. Rabiner and B. Gold, *Theory and Application of Digital Signal Processing*, Prentice-Hall, 1975.
16. R. Peach, The use of linear programming for the design of SAW filters and filterbanks, *IEEE Trans. Ultrason. Ferroelec. Freq. Control* **41**:532–541 (1994).
17. C. S. Hartmann, Weighting interdigital surface wave transducers by selective withdrawal of electrodes, *Proc. IEEE Ultrasonics Symp.*, 1973, pp. 423–426.
18. G. Visintini, C. Kappacher, and C. C. W. Ruppel, Modular two-dimensional analysis of surface-acoustic-wave filters—Part II, *IEEE Trans. Ultrason. Ferroelec. Freq. Control* **39**:73–81 (1992).
19. R. Ganss-Puchstein, C. Ruppel, and H. R. Stocker, Spectrum shaping SAW filters for high bit rate digital radio, *IEEE Trans. Ultrason. Ferroelec. Freq. Control* **35**:673–684 (1988).
20. H. M. Gerard, P. S. Yao, and O. W. Otto, Performance of a programmable radar pulse compression filter based on a chirp transformation with RAC filters, *Proc. IEEE Ultrasonics Symp.*, 1977, pp. 947–951.
21. T. E. Parker and G. K. Montress, Precision surface-acoustic-wave (SAW) oscillators, *IEEE Trans. Ultrason. Ferroelec. Freq. Control* **35**:342–364 (1988).
22. L. L. Pendergrass and L. G. Studebaker, SAW resonator design and fabrication for 2.0, 2.6 and 3.3 GHz, *IEEE Trans. Ultrason. Ferroelec. Freq. Control* **35**:372–379 (1988).
23. M. Lewis, The surface acoustic wave oscillator—a natural and timely development of the quartz crystal oscillator, *Proc. 28th Annual Frequency Control Symp.* (NTIS), 1974, pp. 304–314.
24. I. D. Avramov et al., Extremely low thermal noise floor high power oscillators using surface transverse wave devices,

- IEEE Trans. Ultrason. Ferroelec. Freq. Control* **43**:20–29 (1996).
25. A. Pohl, A review of wireless SAW sensors, *IEEE Trans. Ultrason. Ferroelec. Freq. Control* **47**:317–332 (2000).
 26. C. S. Hartmann, A global SAW ID tage with large data capacity, *Proc. IEEE Ultrasonics Symp.*, 2002, pp. 65–69.
 27. C. C. W. Ruppel et al., SAW devices for consumer applications, *IEEE Trans. Ultrason. Ferroelec. Freq. Control* **40**:438–452 (1993).
 28. J. M. Hode et al., SPUDT-based filters: Design principles and optimization, *Proc. IEEE Ultrasonics Symp.*, 1995, pp. 39–50.
 29. M. Solal et al., Advanced design techniques for high-performance IF and RF SAW filters, *Int. Symp. Acoustic Devices for Future Mobile Communication Systems*, Chiba University, Chiba, Japan, 2001, Paper 3A-1.
 30. T. Morita et al., Wideband low loss double mode SAW filters, *Proc. IEEE Ultrasonics Symp.*, 1992, pp. 95–104.
 31. V. P. Plessky, SAW impedance elements, *IEEE Trans. Ultrason. Ferroelec. Freq. Control* **42**:870–875 (1995).
 32. X. Perois et al., An accurate design and modeling tool for the design of RF SAW filters, *Proc. IEEE Ultrasonics Symp.*, 2001, pp. 75–80.
 33. S. V. Biryukov et al., Consistent generalisation of COM equations to three-dimensional structures and the theory of the SAW transversely coupled waveguide resonator filter, *IEEE Trans. Ultrason. Ferroelec. Freq. Control* **42**:612–618 (1995).
 34. M. P. daCunha, Pseudo and high-velocity pseudo SAWs, in C. C. W. Ruppel and T. Fjeldy, eds., *Advances in Surface Acoustic Wave Technology, Systems and Applications*, Vol. 2, World Scientific Publishing, 2001, pp. 203–243.
 35. R. F. Milsom, N. H. C. Reilly, and M. Redwood, Analysis of generation and detection of surface and bulk acoustic waves by interdigital transducers, *IEEE Trans. Sonics Ultrasonics* **SU-24**:147–166 (1977).
 36. S. V. Biryukov and V. G. Polevoi, The electrostatic problem for the SAW interdigital transducer in an external electric field, *IEEE Trans. Ultrason. Ferroelec. Freq. Control* **43** (Part 1): 1150–1159, **43**(Part 2): 1160–1170 (1996).
 37. D. P. Morgan, Reflective array modelling for reflective and directional SAW transducers, *IEEE Trans. Ultrason. Ferroelec. Freq. Control* **45**:152–157 (1998).
 38. V. Plessky and J. Koskela, Coupling-of-modes analysis of SAW devices, in C. C. W. Ruppel and T. Fjeldy, eds., *Advances in Surface Acoustic Wave Technology, Systems and Applications*, Vol. 2, World Scientific Publishing, 2001, pp. 1–81.
 39. D. P. Chen and H. A. Haus, Analysis of metal-strip SAW gratings and transducers, *IEEE Trans. Sonics Ultrasonics* **SU-32**:395–408 (1985).
 40. P. Ventura, Full strip reflectivity study on quartz, *Proc. IEEE Ultrasonics Symp.*, 1994, pp. 245–248.
 41. K. Hashimoto and M. Yamaguchi, Derivation of coupling-of-modes parameters for SAW device analysis by means of boundary element method, *Proc. IEEE Ultrasonics Symp.*, 1991, pp. 21–26.
 42. P. Ventura, J. M. Hodé, and B. Lopes, Rigorous analysis of finite SAW devices with arbitrary electrode geometries, *Proc. IEEE Ultrasonics Symp.*, 1995, pp. 257–262.
 43. P. Ventura, J. M. Hodé, and M. Solal, A new efficient combined FEM and periodic Green's function formalism for the analysis of periodic SAW structures, *Proc. IEEE Ultrasonics Symp.*, 1995, pp. 263–268.
 44. Y. Suzuki et al., Coupled-mode theory of SAW periodic structures, *Electron. Commun. Jap.* **76**(Part 3): 87–98 (1993).
 45. Z. H. Chen, M. Takeuchi, and K. Yamanouchi, Analysis of the film thickness dependence of a single-phase unidirectional transducer using the coupling-of-modes theory and the finite-element method, *IEEE Trans. Ultrason. Ferroelec. Freq. Control* **39**: 82–94 (1992).
 46. K. Hashimoto and M. Yamaguchi, Precise simulation of surface transverse wave devices by discrete Green function theory, *Proc. IEEE Ultrasonics Symp.*, 1994, pp. 253–258.
 47. V. P. Plessky, A two parameter coupling-of-modes model for shear horizontal type SAW propagation in periodic gratings, *Proc. IEEE Ultrasonics Symp.*, 1993, pp. 195–200.
 48. K. Hashimoto and M. Yamaguchi, General-purpose simulator for leaky surface acoustic wave devices based on coupling-of-modes theory, *Proc. IEEE Ultrasonics Symp.*, 1996, pp. 117–122.
 49. B. I. Boyanov et al., COM—theory analysis of STW resonator structures, *Proc. IEEE Ultrasonics Symp.*, 1995, pp. 317–320.

SURFACE ACOUSTIC WAVE FILTERS

KEN-YA HASHIMOTO
MASATSUNE YAMAGUCHI
Chiba University
Chiba, Japan

1. SAW TRANSVERSAL FILTERS

In 1965, White and Voltmer showed that surface acoustic waves (SAWs) are excited and detected efficiently by an interdigital transducer (IDT) placed on a piezoelectric substrate [1]. Since precise and fine IDT patterns can be generated by means of photolithography, the IDT invention stimulated worldwide research in the development of various SAW-based signal processing devices in VHF-UHF ranges.

One typical device configuration is the so-called SAW transversal filter shown in Fig. 1. If an impulse signal is

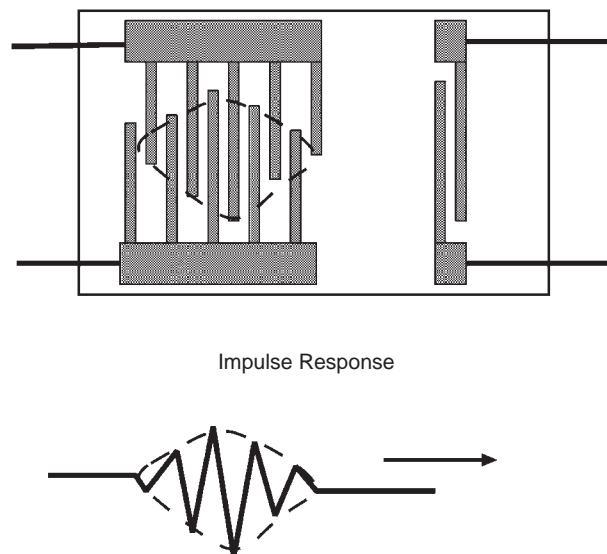


Figure 1. Basic configuration of SAW transversal filter.

applied to one IDT, SAWs are excited through piezoelectricity, and detected by another IDT, on the electrodes of which electrical charges are induced.

Since the delay time is determined simply by the propagation pathlength, the spatial distribution of the excited SAW amplitude determines the impulse response of the device output (see Fig. 1). This suggests that specified impulse responses could be synthesized by designing the IDT pattern; the excitation profile can be controlled by the electrode overlap length [2].

It is clear that the SAW response becomes strong when the SAW wavelength λ is close to the periodicity p_1 of IDT electrodes; that is, the SAW synchronous frequency ω_r is given by V_S/p_1 , where V_S is the SAW velocity.

Denoting the envelope of the weighting function for an IDT by $W(x)$, one obtains the transfer function $H(\Delta\omega)$ of this filter as

$$H(\Delta\omega) \propto \int_{-\infty}^{+\infty} W(x) \exp(+j\Delta\beta x) dx \quad (1)$$

as a function of the deviation $\Delta\omega$ of the frequency ω from ω_r , where $\Delta\beta = \Delta\omega/V_S$. Equation (1) indicates that $H(\Delta\omega)$ is proportional to the Fourier transform of $W(x)$; when $W(x)$ is uniform, $H(\Delta\omega) \propto \text{sinc}(\Delta\beta L_1/2)$, where L_1 is the IDT acoustic length (IDT length in the SAW propagation direction). If a rectangular passband is specified, $W(x)$ should be of the shape of $\text{sinc}(ax)$.

This operation is equivalent to that of finite impulse response (FIR) filters in the digital signal processing. The FIR filter is known to be flexible for designing both amplitude and phase responses, and various design techniques developed for them [3,4] could be adopted. For these reasons, the SAW transversal filters have been widely used in various communication systems and consumer products such as mobile phones, TV sets, and VCRs [4].

It may be understood from the discussion above that IDTs excite SAWs toward both left- and right-hand directions with equal amplitude, which is referred to as *bidirectionality*. Hence, the 3 dB power loss, which is usually called the *bidirectional loss*, is always unavoidable; half of the SAW power launched from the left-hand IDT never reaches the right-hand IDT. At the right-hand (receiving) IDT, the bidirectionality again causes the 3 dB bidirectional loss due to SAW regeneration (reflection) associated with detection. Adding to this bidirectional loss of 6 dB, the impedance mismatching with peripheral circuits should also be taken into account for the evaluation of the total device insertion loss.

In IDTs with the minimized mismatching loss, significant SAW reflection simultaneously occurs as a result of SAW regeneration. This means that multiple echoes are superimposed on the output of the original signal, which result in strong ripples in both amplitude and phase responses in the output signal. One possible and pessimistic countermeasure for suppressing the multiple echoes is to increase the device insertion loss. For this reason, conventional SAW transversal filters exhibit relatively large insertion loss (i.e. ≥ 10 dB). Detailed discussions on the IDT design can be seen in the article SURFACE ACOUSTIC WAVE DEVICES.

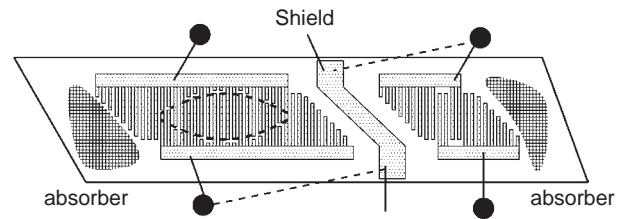


Figure 2. Typical configuration of SAW transversal filter.

Figure 2 shows a typical layout of an SAW transversal filter. A shield is placed between the input and output IDTs, earthing the static capacitance between the two IDTs. SAW reflection within the IDTs is suppressed by employing a double-electrode-type IDT (four electrodes per wavelength). The effect of SAW reflection at the IDT edges is minimized by placing grounded electrodes at both sides of the IDTs and cutting them obliquely. Acoustic absorbers are also placed to suppress SAW reflection from the substrate edges as shown in the figure.

Figure 3 shows, as an example, the frequency response of a TV-IF filter prepared on a X-112°Y-LiTaO₃ substrate for Japanese NTSC TV systems (Fujitsu FAR-F4SA-58M750-A008). It is seen that a very complex amplitude response is skillfully synthesized. With a moderate insertion loss of 16 dB, a superior out-of-band rejection of 45 dB and small group delay deviation of 25 ns (typical) are simultaneously realized.

Figure 4 shows the frequency response of an IF filter prepared on a 128°Y-X-LiNbO₃ substrate for U.S. CATV (cable TV) (Fujitsu SBF0406TPL). It is seen that very flat amplitude and group delay responses are obtained throughout the passband of 6 MHz width. The parameters are as follows: insertion loss of 15 dB, amplitude ripple of 0.3 dB, out-of-band rejection of 45 dB, and group delay deviation of 35 ns (typical).

It may be of interest to note that electrode periodicities as well as overlap lengths do not have to be uniform in transversal filters. An interesting application of this is SAW dispersive delay lines for the pulse compression in

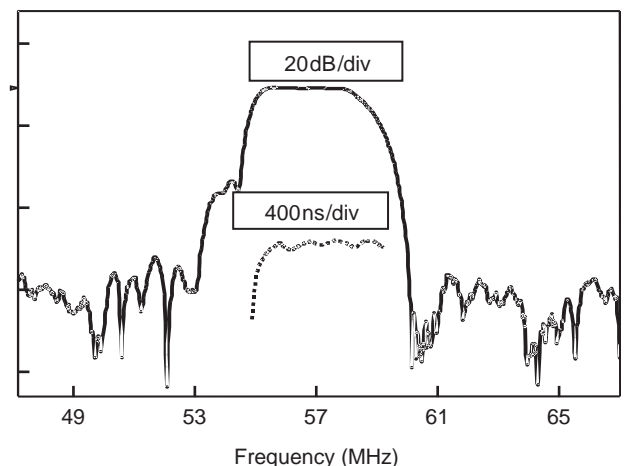


Figure 3. Frequency response of TV-IF filter for Japanese NTSC TV systems. (Courtesy of Fujitsu Media Devices, Ltd.)

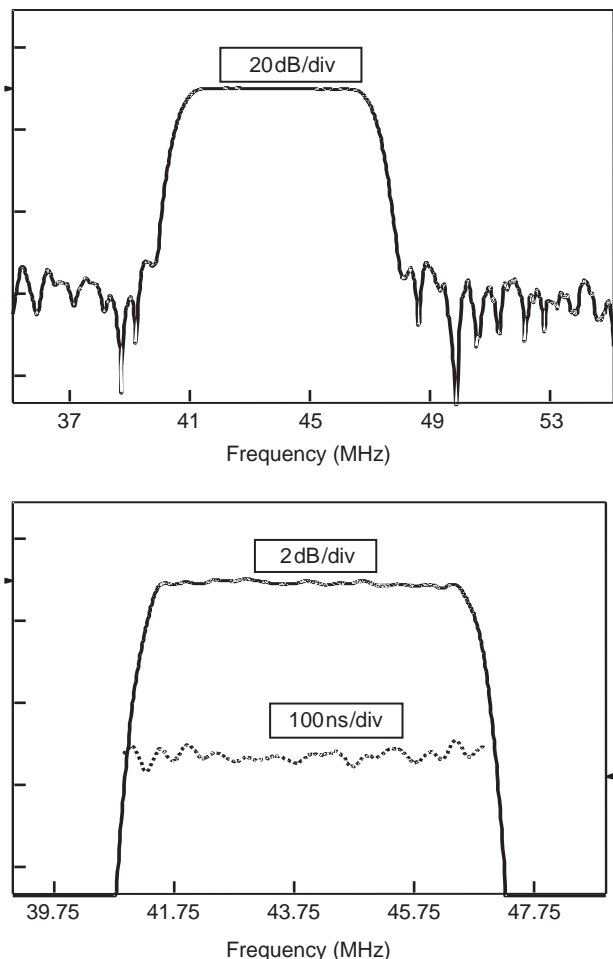


Figure 4. Frequency response of IF filter for U.S. CATV. (Courtesy of Fujitsu Media Devices, Ltd.)

radar systems [5]. Figure 5 shows the typical configuration.

In the structure shown in Fig. 5, the electrode periodicity gradually changes within each IDT, although all the electrodes are aligned in parallel; the inner electrodes possess larger periodicity, whereas outer ones have smaller periodicity. This means that the inner electrodes are responsible for signal transmission at lower frequencies, and outer ones become active at higher frequencies. As can be seen, due to the difference in the pathlength, the signal delay at lower frequencies is smaller than that at higher frequencies.

Consider an RF burst signal, called the “downchirp signal,” where the instantaneous frequency decreases

Figure 5. Typical configuration of SAW dispersive delay line.

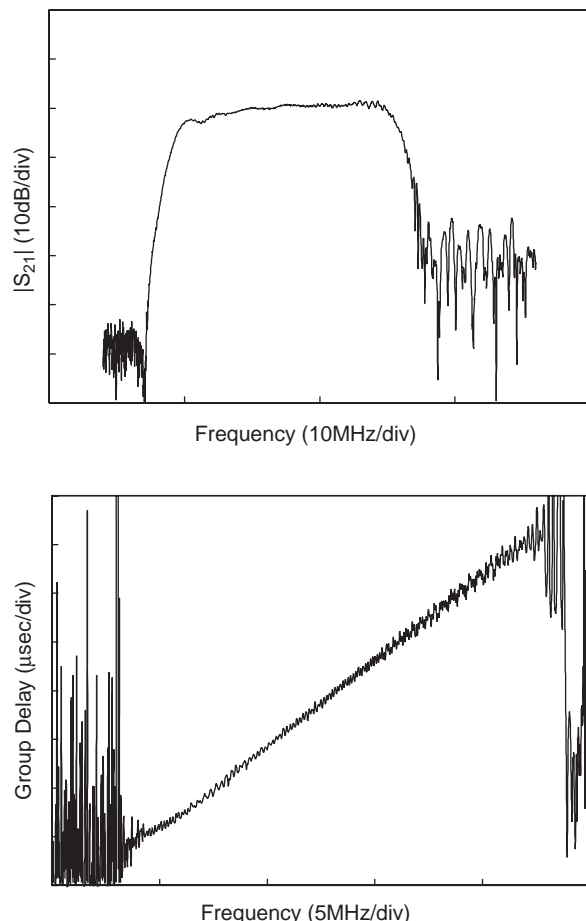
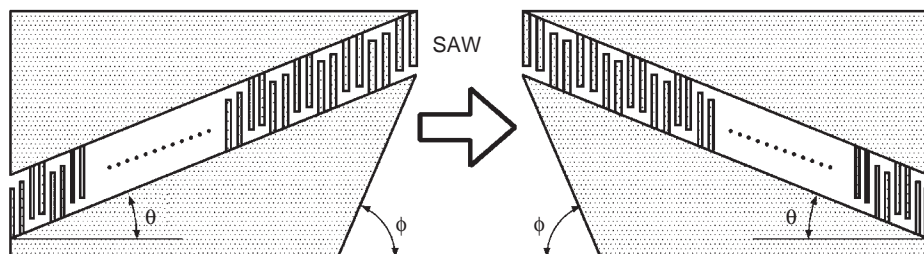


Figure 6. Frequency response of SAW dispersive delay line. (Courtesy of Mitsubishi Electric Co. Ltd.)

linearly with time, while the amplitude is almost constant. When this downchirp signal is applied to the delay line, the signal is compressed and an impulselike signal is obtained as the output.

This function is categorized by the matched filter whose impulse response is the time reversal of the specified input signal. Detailed discussion on this function is given in the article entitled SURFACE ACOUSTIC WAVE DELAY LINES.

In Fig. 5, the IDT electrodes are displaced laterally by an angle θ to reduce SAW internal reflection, and the metal edges are cut obliquely by an angle ϕ , by which the deflection caused at the boundaries between IDT electrode and uniformly-metallised regions is well compensated.

Figure 6 shows the frequency response of a typical SAW dispersive delay line on a YZ-LiNbO₃ substrate with $\theta = 5^\circ$

and $\phi = 22.9^\circ$ [6]. It is seen that the amplitude response is flat throughout the passband of 15 MHz width. The group delay changes linearly with frequency and its variation within the passband is $5 \mu\text{s}$.

2. SELECTION OF SUBSTRATE MATERIALS

Selection of substrate materials determines upper bounds of achievable SAW device performance. Since piezoelectric materials are inherently anisotropic, their properties depend on both crystal-cut angles and SAW propagation directions. In addition, anisotropic materials occasionally support unusual SAWs exhibiting interesting features. Since new substrate materials, waves, structures, and/or crystal cuts may expand the range of SAW device application, investigation of these agents has been one of the most important research topics for more than three decades.

Several important properties are listed here, and their impacts on SAW device performances are described:

1. *SAW Velocity.* The SAW velocity determines the center frequency of devices. Hence, for a given available photolithographic resolution, materials with high SAW velocities can be used to produce appropriately high-frequency devices. On the other hand, materials with low SAW velocities are needed to reduce the size of devices.

2. *Electromechanical Coupling Factor.* The maximum fractional bandwidth of devices is practically limited by the electromechanical coupling factor K^2 . If wideband SAW filters are designed using a substrate material with small K^2 , the electrical mismatching loss is unavoidable and the device insertion loss increases. Conversely, if one attempts to cancel the mismatching loss by peripheral circuits, this results in the reduction of passband width of devices because of large circuit Q .

3. *Temperature Stability.* The SAW characteristics are required to be invariant against temperature variation. The temperature dependence of the resonance frequency f_r is called the *temperature coefficient of frequency* (TCF), which can be estimated by

$$\text{TCF} = \text{TCV} - \alpha \quad (2)$$

where α is the thermal expansion coefficient in the SAW propagation direction and TCV is the temperature coefficient of the SAW velocity. The temperature coefficient of delay (TCD) is also often used and is defined by $-\text{TCF}$. It may be true that materials with large K^2 usually possess poor TCF; large K^2 implies that mechanical properties are very sensitive to perturbations.

4. *Propagation Loss.* Materials with small propagation loss are desirable because propagation loss is directly reflected in increased insertion loss of devices. An intrinsic loss of the order of $10^{-4} \text{ dB}/\lambda$ always exists as a result of thermal lattice vibration, surface roughness, SAW leakage into air, and other factors. Roughly speaking, materials with higher SAW velocities usually possess propagation loss smaller than that of materials having

Table 1. SAW Substrate Materials in Practical Use

Material	K^2	TCF	Notes
YZ-LiNbO ₃ [7]	○	×	Small diffraction
ST-cut Quartz [8]	×	⊙	
128° YX-LiNbO ₃ [9]	○	×	Weak spurious
X-112° Y-LiTaO ₃ [10]	◦	◦	Weak spurious
45° XZ-Li ₂ B ₄ O ₇ [11]	◦	○	
64(41)° YX-LiNbO ₃ [12]	⊙	×	Leaky
42(36)° YX-LiTaO ₃ [13,14]	○	◦	Leaky but low loss
ZnO/Glass [15]	◦	◦	Low cost
ZnO/Quartz [16]	◦	⊙	Weak spurious
ZnO/Sapphire [17]	○	◦	High velocity
SiO ₂ /ZnO/Diamond [18]	◦	⊙	Very high velocity

smaller SAW velocities. Leaky SAWs possess additional propagation loss due to coupling with bulk waves. Should materials, crystal cuts, and/or SAW propagation direction with very small coupling be found, however, the propagation loss becomes negligible.

5. *Spurious Responses.* Unwanted modes launched from IDTs, such as bulk waves propagating along the surface, deteriorate the frequency response of devices. One of the most practical countermeasures is to choose substrates from materials exciting very small spurious (unwanted) modes.

For resonators that will be described in Section 4, the effect of bulk waves is not significant because they do not strongly resonate.

Table 1 shows SAW substrate materials currently used for mass production of SAW devices.

3. ADVANCED SAW TRANSVERSAL FILTERS

3.1. IIDT Filters

It was pointed out in Section 1 that one of the most significant drawbacks of SAW transversal filters is their relatively large insertion loss originating in the bidirectionality of IDTs. A simple countermeasure is to increase the number of IDTs [19,20].

Figure 7 shows an example employing three IDTs [19], two of which have the identical patterns on both sides, and the middle IDT is symmetric with respect to the geometric center. If the middle IDT is impedance-matched with the load, it can receive all the SAW power launched from the

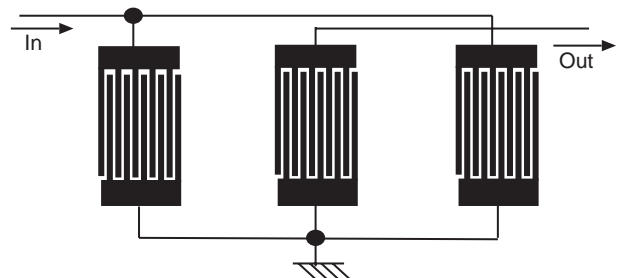


Figure 7. SAW transversal filter using three IDTs.

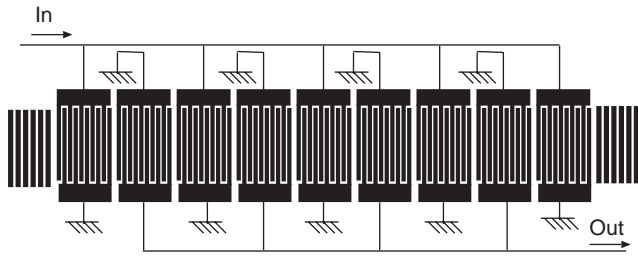


Figure 8. IIDT-type SAW filter.

two outer IDTs and propagated toward the middle IDT. Therefore, SAW reflection does not occur and the multiple echoes are suppressed. Since all the IDTs can be impedance-matched, low-loss filters are realized with suppressed multiple-echo responses. However, it should be noted that the SAW power launched from the two outer IDTs and propagated toward the outside are useless, which still results in the bidirectional loss of 3 dB.

If the number of IDTs is increased as shown in Fig. 8, the bidirectional loss can be decreased further. This structure is called an *interdigitated interdigital transducer* (IIDT) [20]. With an increase in the number of IDTs, the mutual interaction among the IDTs becomes strong and the device behaves like a resonator filter rather than a transversal filter.

Figure 9 shows the frequency response of an IIDT filter employing leaky SAWs on 36°YX-LiTaO₃ (Fujitsu FAR-F5CB-836M50-G201) [21]. When impedance-matched, the device performance achieved an insertion loss of 2.8 dB, a -3 dB bandwidth at 37 MHz, and an out-of-band rejection of 30 dB.

3.2. Filters Employing Unidirectional IDTs

Another simple solution to avoid the bidirectionality problem is to use unidirectional transducers (UDTs). Various UDTs have been proposed and are categorized into two groups.

The first type employs multiphase electrical input and/or output [22]. Although obtainable performance is ideal, interconnection among electrodes is troublesome in device

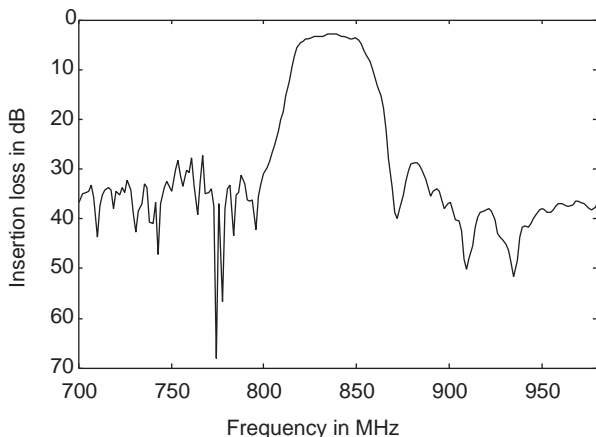


Figure 9. Frequency response of IIDT filter on 36°YX-LiTaO₃. (Courtesy of Fujitsu Media Devices, Ltd.)

fabrication. Although all the electrodes themselves are fabricated by a single-step photolithography, their series connection or an airgap structure is needed for the interconnection with the third electrodes. The former results in an increased ohmic loss, while the latter needs complicated fabrication processes.

Another type of UDT employs asymmetric electrode geometries that create the directionality even when the single-phase input and/or output are applied. This type of UDT is called the *single-phase unidirectional transducer* (SPUDT) [23]. Figure 10 shows the distributed acoustic reflection transducer (DART) [24]. For SAW propagation, the structure is symmetric with respect to the center of the wide electrode. This position is referred to as the *reflection center* C_r . On the other hand, when SAW reflection is ignored, SAWs are regarded as being excited from the center of the electrode connected to the upper busbar. This equivalent excitation point is called the excitation center C_e . It is seen, therefore, that the excitation center is displaced by $3p_1/8$ from the reflection center to the right.

Let the distance between C_e and C_r be Δ . SAWs excited at C_e toward $-x$ are reflected at C_r and return to C_e . Throughout the propagation, SAWs experience a phase shift of $\angle\Gamma - 2\beta_s\Delta$ (Γ is the reflectivity) and interfere with those excited directly toward $+x$. Similarly, SAWs excited toward $+x$ are reflected at C_r and return to C_e . For this case, the phase shift is $\angle\Gamma - 2\beta_s(p_1 - \Delta)$.

Since the structure is symmetric with respect to C_r , the phase of Γ is $\pm\pi/2$. So, if $\Delta = \pm 3\lambda/8$ and $\angle\Gamma = -\pi/2$, two SAWs propagating toward $\pm x$ are in phase and added up, whereas SAWs propagating toward $\mp x$ are antiphase and cancel out each other. When $\Delta = \pm\lambda/8$ or $\angle\Gamma = +\pi/2$, the situation is opposite.

Due to the periodicity of the structure, effects of the addition and cancellation are magnified when $\lambda \cong p_1$; the directivity is the function of frequency, and perfect unidirectionality is obtained when $\Delta = \pm\lambda(2n + 1)/8$.

The DART structure shown in Fig. 10 is almost optimal in this sense near the SAW resonance frequency. When this condition is not fulfilled, its performance is limited.

The unidirectionality is also realized by placing a reflector at either side of a bidirectional IDT. Although the structure is very simple, the bandwidth becomes much narrower than that of the IDT itself.

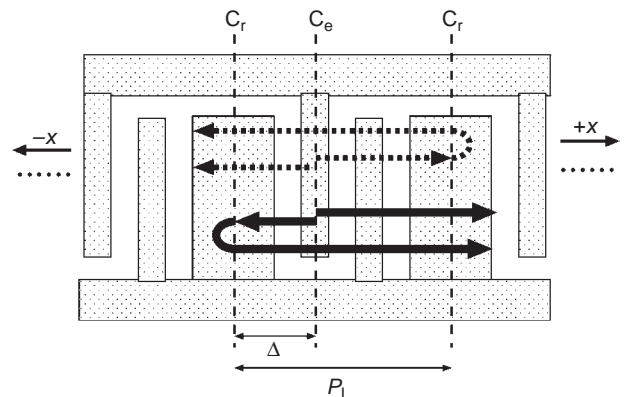


Figure 10. DART structure.

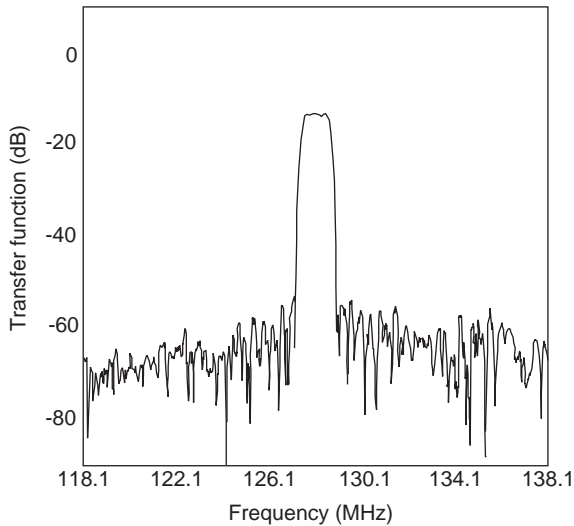


Figure 11. Frequency response of transversal SAW filter employing SPUDTs of DART structure. (Courtesy of Fujitsu Media Devices, Ltd.)

Figure 11 shows the frequency response of a transversal filter employing two SPUDTs of DART structure (Fujitsu SBF1301AC6) on a ST-cut quartz substrate for CDMA IF applications. At the center frequency of 128 MHz, a minimum insertion loss of 13 dB is achieved. By using SPUDTs with a long acoustic length, very flat and steep passband shape is achieved with superior out-of-band rejection of about 40 dB. However, the size of the device considerably increases ($19 \times 6.5 \text{ mm}^2$).

3.3. Resonant SPUDT Filters

For the SPUDT filters discussed above, mechanical reflection is used to cancel electrical regeneration [25]. This means that the frequency response is almost governed by the excitation profile of the SPUDT, and that the length of the impulse response is approximately determined by the physical size of the SPUDT.

Ventura et al. reported that if the directivity is partially reversed within an SPUDT, this causes a local resonance due to the internal multiple reflection, which results in expansion of the impulse response length [26]. This suggests that when both excitation and reflection profiles are properly designed, miniaturized low-loss filters can be realized with little deterioration of phase linearity. This configuration is called the *resonant SPUDT* (R-SPUDT). Although its design is not straightforward and computer aided optimization is essential, current computers are powerful enough for the purpose [28].

Figure 12 shows the frequency response of a 157-MHz R-SPUDT filter (Fujitsu SRF157WAC10) for U.S. TDMA IF applications [27]. Sharp passband shape and small insertion loss of 4.5 dB are simultaneously realized in spite of the limited package size of $5 \times 7 \text{ mm}^2$. As a substrate, $45^\circ\text{XZ-Li}_2\text{B}_4\text{O}_7$ was employed. Bulk-wave spurious responses inherent to this substrate are suppressed skillfully by the device design [27], and an out-of-band rejection of more than 50 dB is achieved at 185–500 MHz.

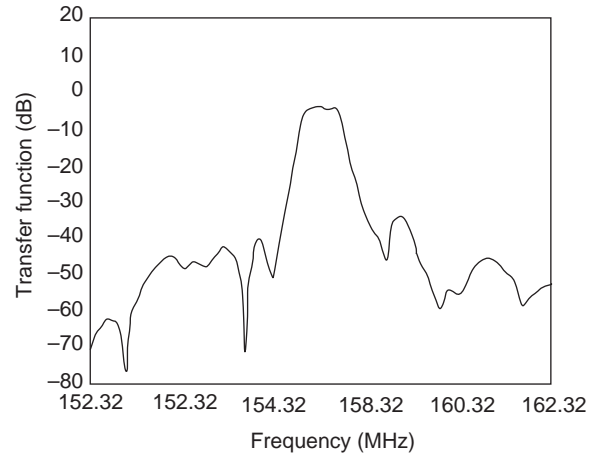


Figure 12. Frequency response of R-SPUDT filter. (Courtesy of Fujitsu Media Devices, Ltd.)

3.4. Z-Path Filters

Figure 13 shows a filter consisting of two oblique reflectors and two SPUDTs, which is called the *Z-path filter* [29]. It is clear that the folded structure offers substantial reduction in the size of devices without reducing IDT acoustic length. The idea of the R-SPUDT is also applicable to this configuration, and its modification has resulted in further reduction in the size of devices [30].

Figure 14 shows the frequency response of Z-path filter for the CDMA handsets in 1900-MHz band. Quartz was employed as a substrate. It is seen that very sharp passband shape is obtained in spite of the limited package size ($5 \times 5 \text{ mm}^2$), and the shape factor and out-of-band rejection obtained are 1.4 (5–30 dB) and 39 dB (typical), respectively. Because of the suppressed multiple echoes, the amplitude ripple of 0.6 dB (typical) is realized within $f_0 \pm 0.3 \text{ MHz}$. Associated with this, the phase ripple is low and its value is 2.3° RMS (typical) within $f_0 \pm 0.63 \text{ MHz}$.

3.5. Dual-Track Filters

A properly designed SPUDT acts as a perfect reflector when the electrical port is short-circuited.

Let us consider parallel-connected transversal filters, called the *dual-track filter* [31], where a reflector is sandwiched between two SPUDTs (see Fig. 15) and the upper

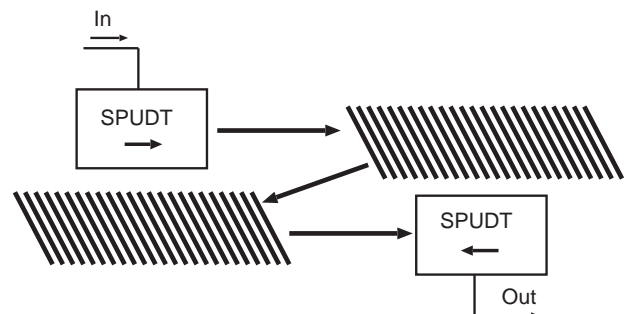


Figure 13. Configuration of Z-path filter.

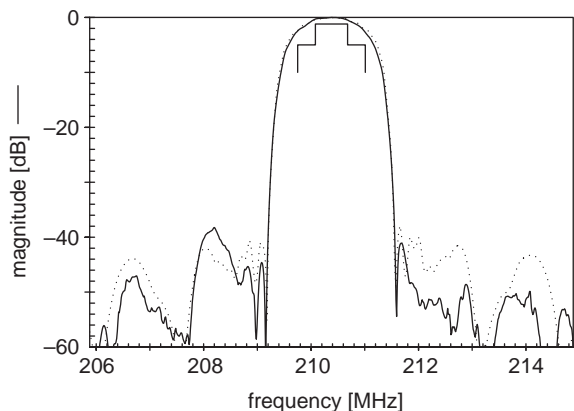


Figure 14. Frequency response of Z-path filter for CDMA. Solid line—experiment; and broken line—simulation. The minimum insertion loss is 8.2 dB. (Courtesy of EPCOS AG.)

track has $2 \times \lambda/4$ shorter propagation path than that in the lower track.

Now consider SAWs that are excited by the SPUDT and directly propagated toward the detecting SPUDTs without being reflected by the reflectors. Due to the $2 \times \lambda/4$ difference in the propagation pathlength, the outputs of the detecting SPUDTs cancel each other; the net output is unavailable and all the received SAW power is regenerated or reflected. On the other hand, SAWs arriving at the detecting SPUDTs and being reflected m times (where m is the odd number) by the reflector are in phase, and the net SAW power appears as the output. Since the frequency response is governed by the product of the excitation and the reflection characteristics of the input and output SPUDTs and of the reflector, this configuration offers a steeper response in transition bands with reasonable physical device size.

In addition, the device performances can be improved by designing each track with a different configuration. Furthermore, the idea of the R-SPUDT is also applicable to this configuration. This approach is useful in designing filters with wide fractional bandwidth, where simple R-SPUDT filters are not practical [28].

Figure 16 shows the frequency response of a dual-track R-SPUDT filter for CDMA IF at 183.6 MHz, which was installed in a $9.1 \times 4.8 \text{ mm}^2$ SMT package. The achieved performances are an insertion loss of 8.9 dB, amplitude ripples of less than 0.5 dB_{pp} (decibel peak to peak),

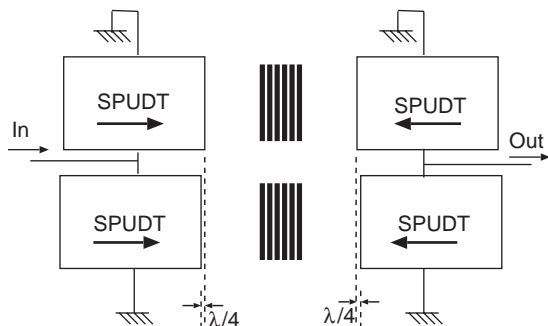


Figure 15. Configuration of dual-track filter.

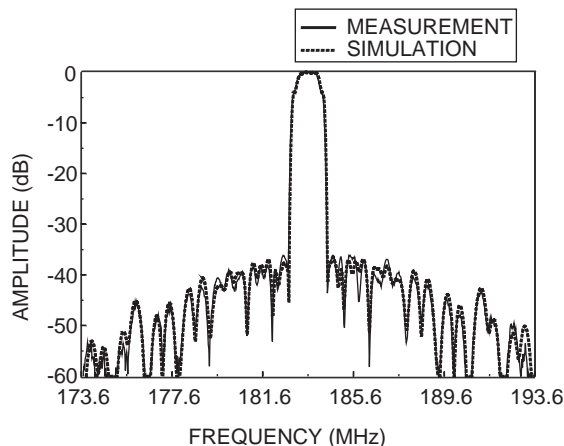
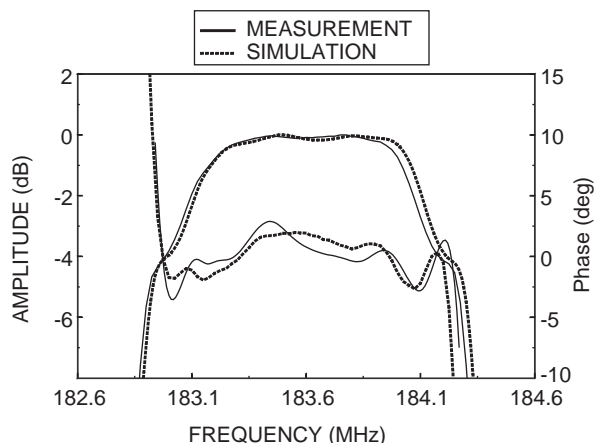


Figure 16. Frequency response of 183.6 MHz dual-track R-SPUDT filter. (Courtesy of Temex.)

phase ripple of 1.5° RMS, and out-of-band rejection of $> 35 \text{ dB}$.

3.6. Filters Using Tapered IDTs

For wideband IF filters with small shape factors, the fan-shaped (or tapered) IDTs shown in Fig. 17 are effective. In Fig. 17, the structure is subdivided into a number of tracks, where each track has the different center frequency and all the tracks are connected electrically in parallel.

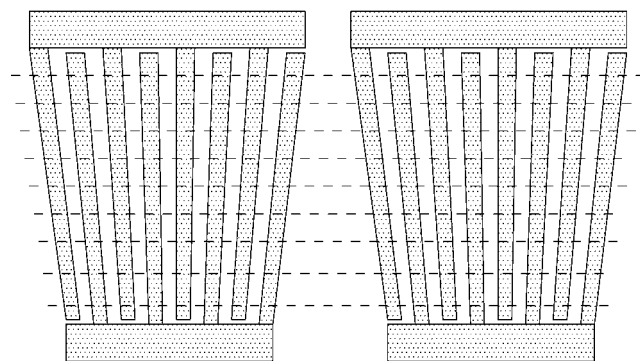


Figure 17. Transversal SAW filter employing fan-shaped (or tapered) IDTs.

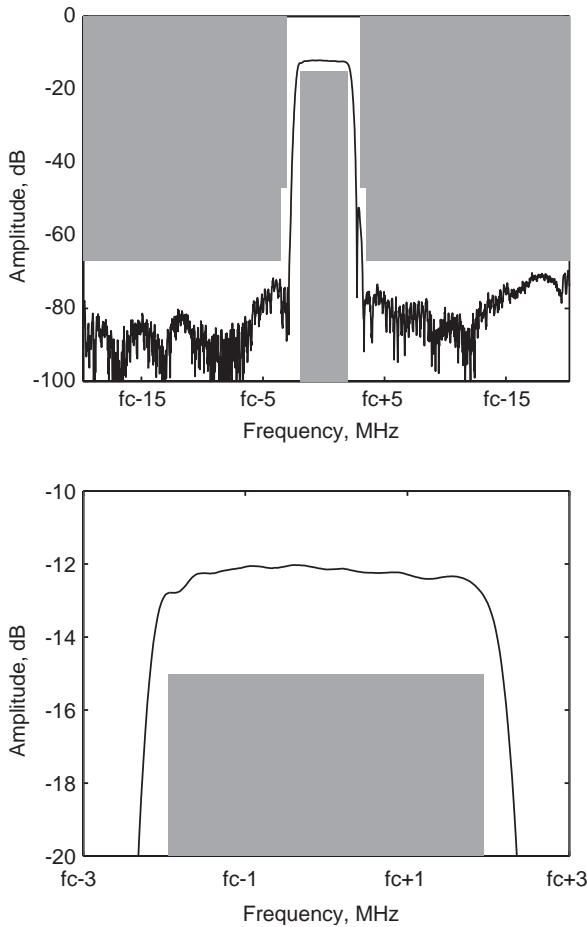


Figure 18. Frequency response of tapered SPUDT filter for 3G base station. (Courtesy of SAWTEK Inc.)

Since each track is equivalent to a very thin but a laterally long nonweighted transversal filter, its individual passband width is very narrow. Hence, as a sum of all the individual responses, the entire structure exhibits a very flat and wide passband with steep shoulder characteristics.

Giving the unidirectionality is also useful for the tapered IDTs to reduce insertion loss avoiding the multiple echo problem. Figure 18 shows the frequency response of an IF filter employing the tapered SPUDTs [32] for a third-generation (3G) base station, where a zero TCF cut of langasite [33] was used as a substrate. The filter exhibits a very flat passband and excellent shape factor around the center frequency about 400 MHz.

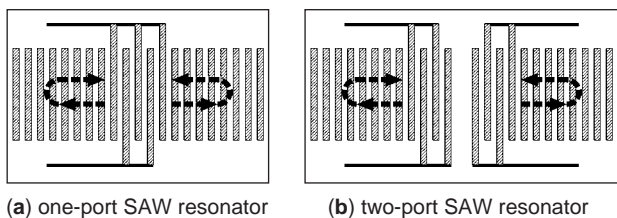


Figure 19. Basic configuration of SAW resonator: (a) one- and (b) two-port SAW resonators.

4. SAW RESONATOR FILTERS

4.1. SAW Resonators

In 1970, Ash suggested that SAW resonators could be realized by the configuration shown in Fig. 19, where IDT(s) are sandwiched by grating reflectors [34]. Although multiple resonant modes may exist as a result of a relatively long acoustic path, the number of possible resonant modes is limited by the frequency selectivity of the grating reflectors.

Similar to the invention of IDTs in 1965, the idea of SAW resonators again opened new applications to sophisticated signal processing devices at high frequencies.

Since the basic properties of SAW resonators are very similar to those of quartz bulk-wave resonators, their equivalent circuit shown in Fig. 20 is often used for one-port SAW resonators.

This circuit shows that the one-port SAW resonator exhibits the series resonance at frequency ω_r , where the conductance takes the maximum value. Just above this, the parallel resonance occurs at the (antiresonance) frequency ω_a , where the resistance takes the maximum value. From the equivalent circuit, these frequencies are given by

$$\omega_r = \frac{1}{\sqrt{L_m C_m}} \tag{3}$$

and

$$\omega_a = \frac{1}{\sqrt{L_m (C_m^{-1} + C_0^{-1})^{-1}}} \tag{4}$$

respectively. The capacitance ratio γ is frequently used as a measure of the resonator performance and given by

$$\gamma = \frac{C_0}{C_m} = \frac{1}{(\omega_a/\omega_r)^2 - 1} \tag{5}$$

which corresponds to the inverse of the effective electro-mechanical coupling factor.

The quality factor Q at $\omega = \omega_r$ is called the resonance Q and is denoted by Q_r . This is also an important measure, which is given by

$$Q_r = \frac{\omega_r L_m}{R_m} = \frac{1}{\omega_r C_m R_m} \tag{6}$$

Roughly speaking, the obtainable passband width and insertion loss of filters based on SAW resonators are limited by $1/\gamma$ and Q/γ , respectively.

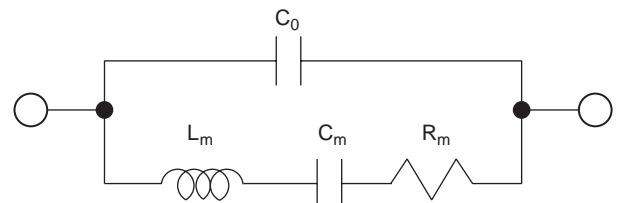


Figure 20. Equivalent circuit for one-port SAW resonator.

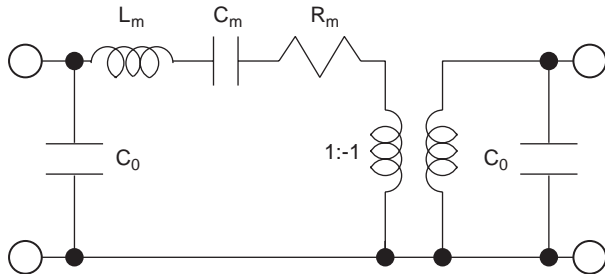


Figure 21. Equivalent circuit for two-port SAW resonator.

Figure 21 shows the equivalent circuit for two-port SAW resonators, where the resonance circuit is involved as a shunt element between two IDTs. This is because the structure is equivalent to a one-port SAW resonator and a simple capacitor if two IDTs are driven in phase and antiphase. This circuit shows that the two-port SAW resonator possesses a strong peak in the transmission response at $\omega \cong \omega_r$.

Figure 22 shows the frequency response of a two-port SAW resonator for the retiming filter in the OC-96 system [35]. A very sharp resonance peak is observed at 4.978 GHz. Thanks to very high SAW velocity ($\cong 10,000$ m/s) on an SiO₂/ZnO/diamond structure, the line resolution of 0.5 μ m is sufficient for the IDT patterning. The following parameters are obtained: an insertion loss of 13 dB, $Q_r = 650$, and a temperature deviation of 150 ppm from -40 to $+85^\circ\text{C}$.

By the way, it has been known that SAWs only with shear horizontal (SH) wave motion raise the total reflection at straight edges. This may be successfully employed to realize ultraminiaturized SAW resonators without grating reflectors [36] (see Fig. 23). However, this idea has not been applied to mass production for various reasons, including (1) difficulties in fabricating precise and fine straight edges, and (2) spurious resonances due to lack of frequency selectivity of the straight-edge reflectors.

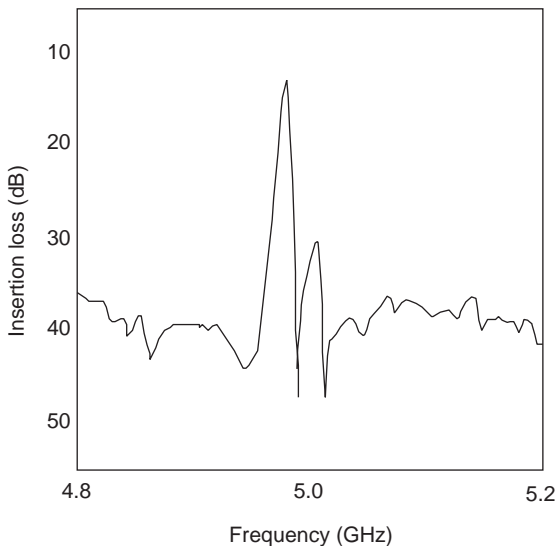


Figure 22. A 5-GHz retiming SAW filter on SiO₂/ZnO/diamond structure. (Courtesy of Sumitomo Electric industries, Inc.)

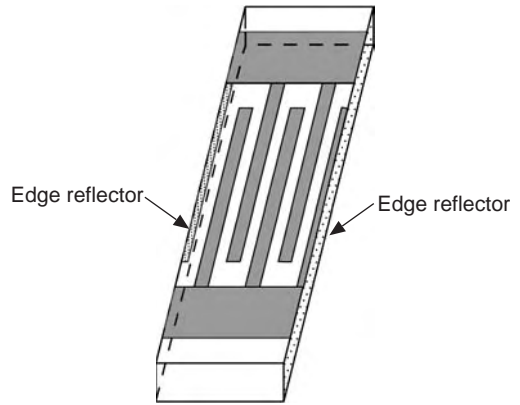


Figure 23. Device configuration of edge-reflection-type SAW resonator.

Kadota et al. showed that the precise and fine straight edges can be realized by using sophisticated dicing saw machines, and very compact SAW resonators were developed and mass-produced based on SH-type SAWs on a laterally polarized piezoelectric ceramic (PZT) substrate [37]. They also showed that various problems such as spurious resonance can be solved by proper device design, and that acoustically coupled resonators, discussed in Section 4.2, are realizable [38].

Figure 24 shows the frequency response of a first IF filter based on this technology for wideband CDMA (Rx) [38]. The filter consists of cascaded-connected two resonator filters, each of which employs a 36°YX-LiTaO₃ substrate and the longitudinally coupled configuration. The filter was specifically designed to attenuate the signal transmission at 190 ± 5 MHz. The filter parameters are as follows: an insertion loss of 4.7 dB, 3 dB bandwidth at 4.1 MHz, attenuation of > 50 dB at 185 MHz and 195 MHz, and group delay deviation of ≤ 50 ns. The chip size and package dimensions are only 0.9×1.7 mm² and $3 \times 3 \times 1.03$ mm³, respectively.

4.2. Double-Mode Filter

Figure 25 shows a configuration called the transversely coupled SAW resonator filter [39], where two identical

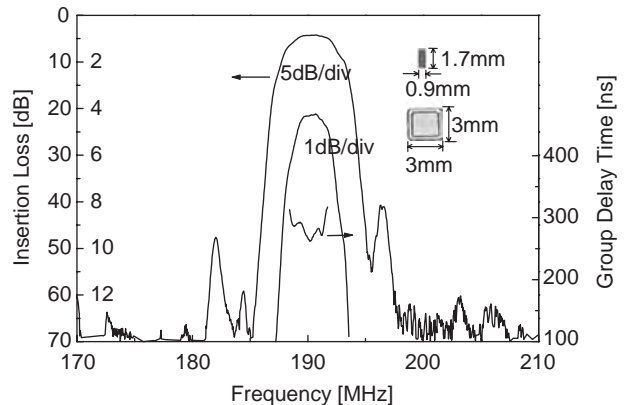


Figure 24. Frequency response of edge-reflection-type SAW resonator for W-CDMA IF. (Courtesy of Murata MFG Ltd.)

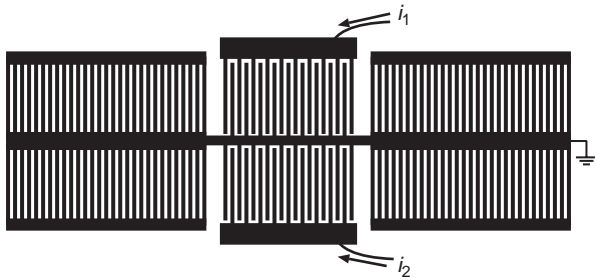


Figure 25. Configuration of transversely coupled SAW resonator filter.

one-port SAW resonators are placed in close proximity. Their lateral coupling raises two resonance modes. The field motions in the upper and lower resonators are in phase for the first mode but antiphase for the second one. Here, due to the lateral coupling, the resonance frequencies for these two modes are slightly different from each other.

Tanaka et al. [39] suggested that flat passband shape, high out-of-band rejection, and sharp skirt characteristics could simultaneously be achieved by the double-mode resonator filter, should the location of two resonance peaks be adjusted to partially overlap each other in the frequency domain. However, the bandwidth is intrinsically limited because of weak lateral coupling of the two modes. From its operation, it is called the *transversely coupled dual-mode SAW (DMS) filter*.

Figure 26 shows the frequency response of the transversely coupled DMS filter (TOYOCOM TQS-663AA-7R) for AMPS IF, where ST-cut quartz was employed as a substrate. Low spurious and superior out-of-band rejections are achieved. The insertion loss and -3 dB bandwidth were 4.5 dB and 60 kHz, respectively.

Incidentally the two-port SAW resonator shown in Fig. 19b can also support multiple resonances when the bandwidth of the reflectors is sufficiently wide. This is called the *longitudinally coupled DMS filter* [40]. Similar to the transversally coupled filter, this offers flat passband shape, sharp skirt characteristics, and good out-of-band

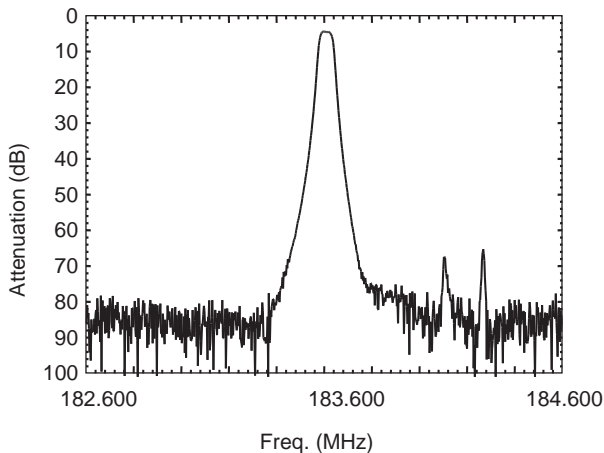


Figure 26. Frequency response of transversely coupled DMS filter for AMPS IF. (Courtesy of TOYOCOM, Co. Ltd.)

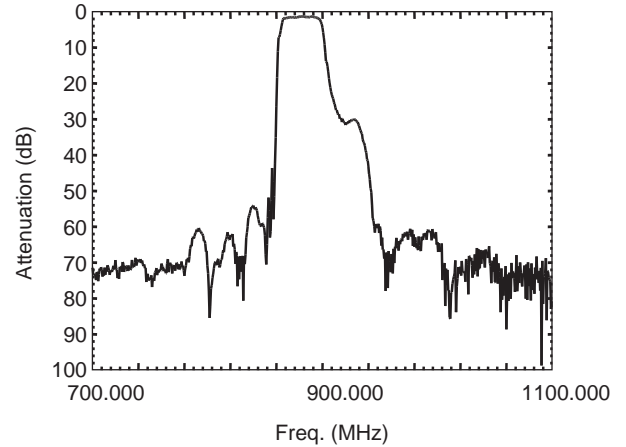


Figure 27. Frequency response of longitudinally coupled DMS filter for CDMA-Rx. (Courtesy of TOYOCOM, Co. Ltd.)

rejection. In addition, the passband width of this filter can be made relatively larger than that of the transversally coupled filter. This is because the difference in the resonance frequencies is determined simply by the device design.

Figure 27 shows the frequency response of the longitudinally coupled DMS filter composed of three IDTs [40] for CDMA-Rx (TOYOCOM TQS-516EA-7G). An insertion loss of 1.5 dB and a -3 dB bandwidth at 35 MHz are obtained with good out-of-band rejection.

At the upper shoulder of the passband, a relatively strong spurious response is seen. This is called the *transversal response*, which is caused by the direct SAW transmission between two IDTs.

In the DMS filters, the input and output ports are coupled acoustically but isolated electrically. This enables the implementation of various functions of the DMS filters such as balanced-to-unbalanced conversion and impedance conversion. In the current mobile phones, this sort of multifunctional DMS filters are widely used [41].

4.3. Ladder-Type Filter

The ladder-type configuration is historically well known for filter device applications at low frequencies. However, recent technologies have made it possible to apply SAW resonators to ladder-type filters working above GHz ranges. Figure 28 shows an example for the ladder-type SAW filter [42]. This type of filter offers low insertion loss and

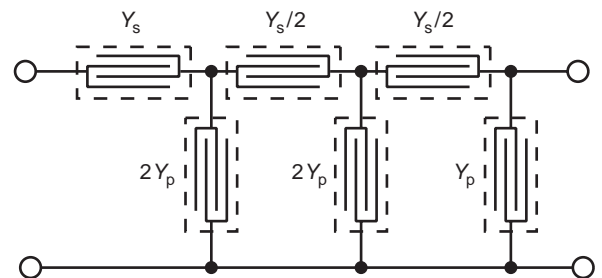


Figure 28. Ladder-type filter consisting of five SAW resonators.

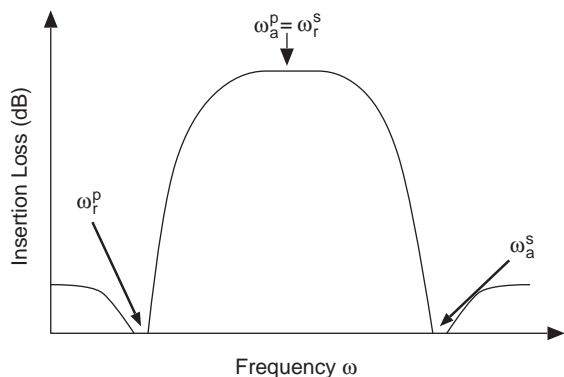


Figure 29. Frequency response of ladder-type SAW filters.

high power durability compared with the acoustically coupled SAW resonator filters described above [43].

The basic idea is to design the resonance frequency ω_r^s of Y_s at the series arms to coincide with the antiresonance frequency ω_a^p of Y_p at the parallel arms. Since $Y_s^{-1} \cong 0$ and $Y_p \cong 0$ near these resonance and antiresonance frequencies, the input signal passes through the filter with small attenuation. On the other hand, at the antiresonance frequency ω_a^s of Y_s and resonance frequency of ω_r^p of Y_p , respectively, the series arms become electrically open-circuited and the parallel arms become short-circuited. This results in no transmitted signals at the output. Consequently, the frequency response shown in Fig. 29 is obtained. According to the traditional electric circuit theory, the out-of-band rejection can be improved with an increase in the number of the resonators shown in Fig. 28 at the expense of the increased insertion loss.

Figure 30 shows, for example, the latest ladder-type SAW filters (Fujitsu FAR-F6CP-2G1400-L21M) for a W-CDMA Rx channel, where $42^\circ\text{YX-LiTaO}_3$ [14] was employed as a substrate. It is seen that in addition to good signal rejection of 36 dB (typical) in the Tx band (1920–1980 MHz), a very low insertion loss of 2.4 dB (typical) (the minimum loss of 1.4 dB) is achieved over the Rx band (2110–2170 MHz).

4.4. Antenna Duplexer

Since mobile phones use the same antenna for both the transmission and reception, a circuit element to separate

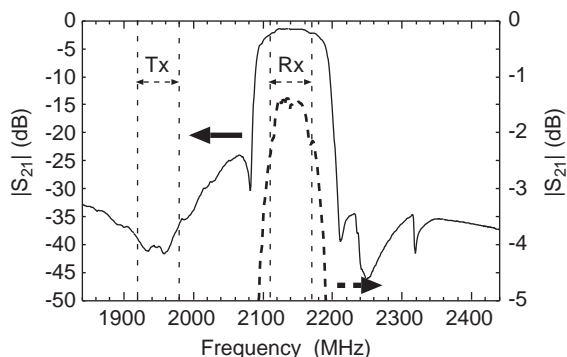


Figure 30. Frequency response of ladder-type filter for W-CDMA Rx channel. (Courtesy of Fujitsu Media Devices, Ltd.)

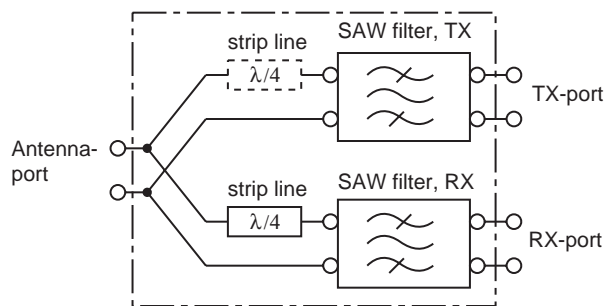


Figure 31. Configuration of SAW duplexer.

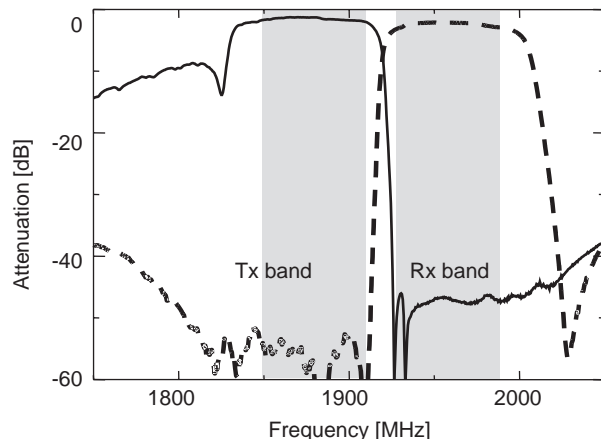


Figure 32. Frequency response of PCS duplexer. (Courtesy of Fujitsu Media Devices, Ltd.)

incoming and outgoing signals is necessary. In some systems, the separation is carried out in the frequency domain (frequency-domain duplex) and the SAW antenna duplexer is applied for this purpose [43]. Its basic configuration is shown in Fig. 31.

The Tx and Rx SAW filters are connected in parallel via two $\lambda/4$ striplines (see Fig. 31), in order to reduce electrical interference caused by the parallel connection. Usually the striplines are embedded in the ceramic package for the SAW duplexer.

Figure 32 shows the frequency response of the latest SAW duplexer for a personal communication system (PCS) mounted in a $5 \times 5 \text{ mm}^2$ surface mount package [44]. It employs the ladder-type and longitudinally coupled DMS filters for Tx and Rx channels, respectively, and the stripline for the Tx filter was removed to minimize insertion loss.

Adding to very low loss ($< 1 \text{ dB}$), very narrow transition bandwidths are realized in both the Rx and Tx filters. High isolation of 55 dB (at Tx band) and 48 dB (at Rx band) is obtained.

Acknowledgements

The authors express their thanks to Dr. Y. Satoh of Fujitsu Laboratories, Ltd., Dr. Y. Ebata, Mr. M. Koshino, Mr. M. Ueda, Mr. O. Ikata, and Mr. K. Ichikawa of Fujitsu Media Devices, Ltd.; Mr. K. Misu of Mitsubishi Electric Co. Ltd.; Dr. C. C. W. Ruppel of EPCOS AG; Dr. M. Solal of Temex;

Dr. B. Abbott of SAWTEK, Inc.; Mr. Shikata of Sumitomo Electric Industries, Inc.; Dr. M. Kadota of Murata MFG, Ltd.; and Mr. T. Morita of TOYOCOM, Ltd. for supplying their valuable device data.

BIBLIOGRAPHY

- R. M. White and F. W. Voltmer, Direct piezoelectric coupling to surface elastic waves, *Appl. Phys. Lett.* **17**:314–316 (1965).
- R. H. Tancrell and M. G. Holland, Acoustic surface wave filters, *Proc. IEEE* **59**:393–409 (1971).
- J. H. McClellan, T. M. Parks, and L. R. Rabiner, A computer program for designing optimum FIR linear phase digital filters, *IEEE Trans. Audio Electroacoust.* **AU-21**:506–526 (1973).
- C. K. Campbell, *Surface Acoustic Wave Devices and Their Signal Processing Applications*, Academic Press, Boston, 1989.
- D. P. Morgan, *Surface-Wave Devices for Signal Processing*, Elsevier, Amsterdam, 1985.
- K. Ibata and K. Misu, A study of slant angle of IDT for SAW dispersive delay line, *Proc. 32nd EM Symp.* 2002, pp. 123–126 (in Japanese).
- J. J. Campbell and W. R. Jones, A method for optimal crystal cuts and propagation directions for excitation of piezoelectric surface waves, *IEEE Trans. Sonics Ultrason.* **SU-15**:209–217 (1968).
- M. B. Schulz, M. J. Matsinger, and M. G. Holland, Temperature dependence of surface acoustic wave velocity on α -quartz, *J. Appl. Phys.* **41**:2755–2765 (1970).
- K. Shibayama, K. Yamanouchi, H. Sato, and T. Meguro, Optimal cut for rotated Y-cut LiNbO₃ crystal used as the substrate of acoustic-surface-wave filters, *Proc. IEEE* **64**:595–597 (1976).
- S. Takahashi, H. Hirano, T. Kodama, F. Miyashiro, B. Suzuki, A. Onoe, T. Adachi, and K. Fujinuma, SAW IF filter on LiTaO₃ for color TV receivers, *IEEE Trans. Consum. Electron.* **CE-24**(3):337–346 (1978).
- S. Matsumura, T. Omri, N. Yamaji, and Y. Ebata, A 45° X cut Li₂B₄O₇ single crystal substrate for SAW resonators, *Proc. IEEE Ultrason. Symp.* 247–252 (1987).
- K. Yamanouchi and K. Shibayama, Propagation and amplification of Rayleigh waves and piezo-electric leaky surface waves in LiNbO₃, *J. Appl. Phys.* **43**:856–862 (1970).
- K. Nakamura, M. Kazumi, and H. Shimizu, SH-type and Rayleigh-type surface waves on rotated Y-cut LiTaO₃, *Proc. IEEE Ultrason. Symp.* 819–822 (1977).
- O. Kawachi, G. Endoh, M. Ueda, O. Ikata, K. Hashimoto, and M. Yamaguchi, Optimum cut of LiTaO₃ for high performance leaky surface acoustic wave filters, *Proc. IEEE Ultrason. Symp.* 71–76 (1996).
- S. Fujishima, H. Ishiyama, A. Inoue, and H. Ieki, Surface acoustic wave VIF filters for TV using ZnO sputtered film, *Proc. Freq. Contr. Symp.* 119–122 (1976).
- M. Kadota and H. Kando, Small and low-loss IF SAW filters with excellent temperature coefficient consisting of zinc oxide film on quartz substrate, *Proc. IEEE Ultrason. Symp.* 161–165 (2002).
- J. Koike, H. Tanaka, and H. Ieki, Quasi-microwave and longitudinally coupled surface acoustic wave resonator filters using ZnO/sapphire substrate, *Jpn. J. Appl. Phys.* **34**(Part 1, 5B): 2678–2682 (1995).
- H. Nakahata, K. Higaki, S. Fujii, A. Hachigo, H. Kitabayashi, K. Tanabe, Y. Seki, and S. Shikata, SAW devices on diamond, *Proc. IEEE Ultrason. Symp.* 361–370 (1995).
- M. F. Lewis, Triple-Tansit echo suppression in surface-acoustic-wave devices, *Electron. Lett.* **8**:553–554 (1972).
- M. F. Lewis, SAW filters employing interdigitated interdigital transducer IIDT, *Proc. IEEE Ultrason. Symp.* 12–17 (1982).
- O. Ikata, Y. Satoh, T. Miyashita, T. Matsuda, and Y. Fujiwara, Development of 800 MHz band SAW filters using weighting for the number of finger pairs, *Proc. IEEE Ultrason. Symp.* 83–86 (1990).
- R. C. Rosenfeld, R. B. Brown, and C. S. Hartmann, Unidirectional acoustic surface wave filters with 2 dB insertion loss, *Proc. IEEE Ultrason. Symp.* 425–428 (1974).
- C. S. Hartmann, P. V. Wright, R. J. Kansy, and E. M. Garber, Analysis of SAW interdigital transducer with internal reflections and the application to the design of single-phase unidirectional transducers, *Proc. IEEE Ultrason. Symp.* 40–45 (1982).
- T. Kodama, H. Kawabata, Y. Yasuhara, and H. Sato, Design of low-loss SAW filters employing distributed acoustic reflection transducers, *Proc. IEEE Ultrason. Symp.* 313–324 (1986).
- C. S. Hartmann and B. P. Abott, Overview of design challenges for single phase unidirectional SAW filters, *Proc. IEEE Ultrason. Symp.* 79–89 (1989).
- P. Ventura, M. Solal, P. Dufilié, J. M. Hodé, and F. Roux, A new concept in SPUDT design, *Proc. IEEE Ultrason. Symp.* 1–76 (1994).
- S. Ichikawa, T. Tanaka, K. Kawaguchi, S. Mitobe, M. Koshino, and Y. Ebata, A bulk suppressed low loss TDMA-IF filter using LBO substrate, *Proc. IEEE Ultrason. Symp.* 28–32 (2002).
- M. Solal, P. B. Beonon, S. Chmaly, J. Desbois, M. Doisy, P. Duffilie, J. M. Hodé, L. Penavaire, X. Perois, V. Plessky, and P. Ventura, Advanced design techniques for high performance IF and RF SAW filters, *Proc. Int. Symp. Acoustic Wave Devices for Future Mobile Communication Systems*, 2001, pp. 151–168.
- J. Machui and W. Ruile, Z-Path IF-filters for mobile telephones, *Proc. IEEE Ultrason. Symp.* 147–150 (1992).
- S. Freisleben, A. Bergmann, U. Bauernschmitt, J. Gerster, C. Ruppel, and J. Franz, A highly miniaturized recursive Z-path SAW filter, *Proc. IEEE Ultrason. Symp.* 347–350 (1999).
- M. Solal and J. M. Hodé, A new compact SAW filter for mobile radio, *Proc. IEEE Ultrason. Symp.* 105–109 (1993).
- B. P. Abbott, S. M. Knapp, S. Krasnikova, and L. P. Solie, Linear phase SAW filters, *Proc. Int. Symp. Acoustic Wave Devices for Future Mobile Communication Systems*, 2001, pp. 117–124.
- N. F. Naumenko and L. P. Solie, Optimal cut of langasite for high performance SAW devices, *Proc. IEEE Ultrason. Symp.* 243–248 (1999).
- E. A. Ash, Surface wave grating reflectors and resonators, *Proc. IEEE MTT Symp.* 385–386 (1970).
- S. Shikata, H. Nakahata, S. Fujii, A. Hachigo, H. Kitabayashi, Y. Seki, K. Itakura, T. Uemura, H. Toyoda, and N. Fujimori, High frequency SAW devices using SiO₂/ZnO/diamond, *Proc. Int. Symp. Acoustic Wave Devices for Future Mobile Communication Systems*, 2001, pp. 227–234.
- A. Suzuki, H. Shimizu, M. Takeuchi, K. Nakamura, and A. Yamada, Some study on SAW resonators and multiple-mode filters, *Proc. IEEE Ultrason. Symp.* 297–302 (1976).

37. M. Kadota, K. Morozumi, T. Ikeda, and T. Kasanami, Ceramic resonators using BGS waves, *Jpn. J. Appl. Phys.* **30**(Suppl. 31):219–222 (1992).
38. M. Kadota, J. Ago, H. Horiuchi, and M. Ikeura, Very small IF resonator filters using reflection of shear horizontal wave at free edges of substrate, *IEEE Trans. Ultrason. Ferroelectric. Freq. Control* **49**(9):1269–1279 (2002).
39. M. Tanaka, T. Morita, K. Ono, and Y. Nakazawa, Narrowband bandpass filter using double-mode SAW resonators on quartz, *Proc. IEEE Frequency Control Symp.*, 1984, pp. 286–293.
40. T. Morita, Y. Watanabe, M. Tanaka, and Y. Nakazawa, Wide-band low loss double mode SAW filters, *Proc. IEEE Ultrason. Symp.* 95–104 (1992).
41. H. Meier, Th. Baier, and G. Riha, Miniaturization and advanced functionalities of SAW devices, *Proc. IEEE Ultrason. Symp.* 395–401 (2000).
42. O. Ikata, T. Miyashita, T. Matsuda, T. Nishikawa, and Y. Satoh, Development of low-loss band-pass filters using SAW resonators for portable telephone, *Proc. IEEE Ultrason. Symp.* 112–115, (1992).
43. Y. Satoh, O. Ikata, T. Miyashita, and H. Ohmori, RF SAW filters, *Proc. Int. Symp. Acoustic Wave Devices for Future Mobile Communication Systems*, 2001, pp. 145–150.
44. J. Tsutsumi, S. Inoue, Y. Iwamoto, T. Matsuda, M. Miura, Y. Satoh, M. Ueda, and O. Ikata, Extremely low-loss SAW filter and its application to antenna duplexer for the 1.9 GHz PCS full-band, *Proc. IEEE Frequency Control Symp.*, 2003, pp. 861–867.

SURFACE MOUNT TECHNOLOGY

WALTER J. TRYBULA
Austin, Texas,
MICHAEL TRYBULA
Cyber Optics Corp.
Minneapolis, Minnesota

Surface mount assembly (SMA) is the description of a technology that incorporates the electrical and mechanical of components to printed wiring boards (PWBs) or a similar type of circuit substrate. The term *surface mount* comes from the methodology of attaching the components. Surface mount places the components on the surface of the supporting media, the PWBs, or other type of substrate. There are two types of connections between the discrete packages and the supporting board material: those with leads, which require plated through-hole (PTH), and others with leads of pads for surface mounting the devices. The surface mount packages with connections that are significantly below those available for through-hole components. This yields a more compact design that reduces the area required and provides a more dense circuit.

Many categories of packages can be employed in surface mount assembly. They can be identified into two categories: leadless devices and leaded chip carriers. The leadless devices include leadless chip carriers, surface mount arrays, capacitors, resistors, and inductors. Leaded devices include packages for active devices, of either plastic or ceramic, and having a particular lead configura-

tion. The resistors, capacitors, inductors, and various types of semiconductor circuits can come in two configurations, leaded and chip. The leaded components are traditionally employed in through-hole mounting and seldom employed in SMA. The chip components are available in protected and unprotected states. The chip is a minimum configuration for the particular device. In the case of capacitors, it may be the actual device that is provided in the leaded package. The bare device has connection points that may be solder plated.

Semiconductors are typically manufactured in a multileaded ceramic or plastic packages, which can be with leads extending from the package or leadless (connections are on the package). (This provides the capability of testing the devices to ensure conformance to specifications.) The specifications for the devices conform to a Joint Electronic Development Engineering Council (JEDEC) standard so that the design of the PWB for attachment can be standardized. Bare chip circuits are also employed in special circumstances. One arrangement, chip-on-board (CoB), requires the application of wire attachment from the chip (semiconductor device) to the PWB. The other configuration is flip-chip. Flip-chip employs the bare semiconductor die (chip) with special solder placement on the surface to provide connection pads (bumps) for the semiconductor device. The chip is mounted circuitry toward the PWB. The processing of the assembly causes the bumps to reflow and attach the chip to the PWB.

Printed wiring boards (PWBs), also known as *printed circuit boards* (PCBs), are the most common interconnect mechanism to complete circuitry. The pattern of electrical circuitry, also known as *paths* or *traces*, is manufactured to provide the appropriate connections between various devices. Surface mount is a card assembly method that relies on a solder connection for both physical and electrical connections as well as package-to-board connections. The plated through holes (PTH) joining method employs a close mechanical fit between the components and the board via hole for location of the component, and the solder provides the final bond as well as the electrical connections. PWBs are manufactured from nonconductive, stable materials. These materials can be employed for the manufacture of single-sided, two-sided, or multilayer PWBs. The single-sided PWB has circuitry on only one side. The components are inserted through the boards and solder to the bottom side, which contains the circuitry. Two-sided boards have circuitry on both sides, and either side or both sides can be employed for soldering components in place. Multilayer boards are constructed of many levels of circuitry that are laminated to form many layers of interconnections. Most PWBs are designed on a grid pattern, which specifies the minimum dimension between different circuit elements. The standard package of the mid-1980s contained a lead pitch, with center-to-center distance between the individual leads of 0.1 in. or 100 mils. Applying the design of complex circuitry with traces of 20 mils provided adequate space to connect the circuit elements. As the circuitry became more complex, the need for more connections witnessed the manufacture of multilayer circuits that could provide more interconnects at the expense of additional processing layers. Also, work is

being done on packages with spacing of less than 20 mils to provide more dense packing. The smaller dimensions provide challenges for both the designer and the manufacturer. As the density of the interconnects increases, the manufacturing tolerances decrease. Decreasing tolerances has a direct impact on yields. The better the design, the greater the manufacturing tolerances. The miniaturization of circuitry causes a greater need for a complete “design for manufacturing” concept. (See the text by Boothroy et al. in the Further Reading list at the end of this article for more details.) The advantage of miniaturization is a decrease in the package size, a decrease in product volume, a decrease in cost, and an increase in the reliability due to better manufacturing control.

1. HISTORY

Surface mount assembly has evolved in response to the manufacturing need for increased miniaturization, for more complex products. Surface mount technology began with the development of thick-film hybrid techniques. The first attempts to manufacture thick-film hybrids were during World War II. Variable resistors were produced by printing a resistive paste on a carrier and firing the circuit. The design of the circuit was such that a movable contact provided the ability to change position on the printed resistor and consequently change the resistance in the circuit. The application of hybrid circuits came into widespread application in the 1960s. The need for military applications, which required more stringent operating environments than the conventional PWBs, required a radical solution. The development of ceramic substrates and conductive pastes provided the ability to develop a stable circuit. Populating the circuit with devices required providing holes in the ceramic substrate, which made the substrate more expensive and weakened it, or developing a means of mounting components directly onto the substrate. The development of the integrated circuit provided another impetus to mount devices to the substrate.

Hybrid circuits have two configurations: thick and thin film. Thick-film circuits are produced by printing conductive and resistive pastes and subsequently firing the pastes to stabilize the material and provide the operational characteristics. Thin-film circuits were similar to thick-film circuits except that the conductors and resistors were vacuum-deposited. This process provides for finer geometries, but cannot handle large amounts of power. Both types of circuits needed additional components to complete their functionality. There was a need to provide a means of mounting and connecting the additional components. Devices can be connected to this circuitry by soldering, eutectic and lower temperature materials, or by epoxy, both conductive and nonconductive. The start of these technologies led to the development of other surface mount techniques.

The early application of high-performance circuitry required a good thermal and electrical contact with the semiconductor. Through a combination of heating and mechanical motion, a eutectic bond can be produced. This was normally a gold-silicon interface that required pro-

cessing temperatures in excess of 400°C. As less stringent circuits were developed, the application of tin-lead solders was employed to attach prepackaged circuits. These were lower-cost devices. As miniaturization of devices accelerated, the drive to produce low-cost devices provided a rationale for experimenting with new approaches to circuit assembly. Prepackaged plastic devices could be attached to the substrate inexpensively, resulting in less expensive products. The driving force behind the initial development of surface mount assembly was high-volume, low-cost consumer products. In the late 1970s, the Japanese were investigating high-volume manufacturing of consumer electronics. The cost of the ceramic substrate was too high for the consumer market. Conventional PWBs were made and components attached to the surface. Since the surface mount component is smaller than the corresponding leaded one, the corresponding package, a SMT assembly, is smaller than a discrete assembly. (This is very understandable since the leaded component can contain the entire surface mount one.) While the initial surface mount assemblies were very elementary circuits, the potential cost savings provided the push needed to look at automating the process. During the early 1980s, assembly equipment manufacturers in the United States emphasized the development of equipment for placing through-hole components, while the Japanese were developing high-speed chip placement equipment. The requirements for high-speed placement equipment necessitated tighter tolerances and fewer selections of dimensions for devices. Those volumes, which were required for the consumer market, caught the attention of the component suppliers. The result was that in the early 1980s, the manufacturers of chip capacitors went from almost 20 different sizes to only 3. This change precipitated lower prices and an increased ease of manufacture. With the availability of inexpensive production, the application of surface mount technology increased. The mid-1980s witnessed the expansion of surface mount technology into higher-quality products. As the reliability of the devices improved, this acceptance increased even more.

The late 1980s witnessed a broad acceptance of surface mount technology in a large number of consumer applications. The development of the multichip module (MCM) during this time provided a highly reliable package that could apply the automated surface mount placement equipment. Successful high-reliability applications, like the fully automated digital electronics module (FADEC) that General Electric developed for the jet engine controls, proved that surface mount assembly in modules provided a packaging technology that could withstand almost any environment. As microprocessors kept shrinking and the functionality kept increasing, the personal computer (PC) market applied surface mount technology to increase reliability and reduce costs.

2. TERMINOLOGY

The terminology employed with surface mount assembly is derived from the two affiliated technologies: PWB assembly and device manufacturing.

2.1. Package Types

The development of packaging standards provided the basis of uniformity and the ability to develop high-speed manufacturing equipment. The Joint Electronic Development Engineering Council (JEDEC) develops the packaging standards. Various packaging types are shown in Fig. 1.

2.2. Three-Letter Acronyms (TLAs)

As with any technology, there develops a code language that simplifies communication within the industry. These acronyms are usually contain two to four letters but are classified as three-letter acronyms. Some of the more typical ones are given below:

- AOI—automated optical inspection: the process of using a machine to look for defects on the circuit board.
- CC—chip carrier: refers to the packaging of an electronic device, usually a semiconductor, into a package that protects the device and provides for electrical contact and mechanical mounting to a more complex circuit. The package can have leads extending from the device or be leadless.
- CoB—chip on board: refers to a packaging technique where bare semiconductor die are epoxied to PWBs and wire-bonded to the conductive paths on the PWB. (Wire bonding is the traditional method for attaching semiconductors to their packages.) The resulting interconnection is then protected by a hard epoxy that provides a thermal expansion match for the PWB and the wirebonds.
- CLCC—ceramic leadless chip carrier: refers to the package type shown in Fig. 1 that contains the device in a ceramic package.
- LCC—leadless chip carrier: a packaging technique that incorporates a device into a carrier that does not have external leads extending from the package. The

leads are actually on the package's periphery and are an integral part of the package.

- MCM—multichip module: a more complex arrangement than the chip carrier in that any number of devices can be interconnected with the package. This is a larger package that provides complex functionality. The advantage of the higher-level package is that more complex functionality can be verified.
- MELF—metallized electrode face: a packaging technique for cylindrical parts without leads. Both ends of the cylinder will have metallized terminations.
- PCB—printed circuit board: the basic building block of electronic circuitry. The printed circuit board is also known as the *printed wiring board* (PWB).
- PLCC—plastic leaded chip carrier: the plastic equivalent of the CLCC. This part will have leads coming off all four sides that wrap underneath the part in a “J” shape.
- PWB—printed wiring board: the material that provides both the platform for supporting the electronic devices and the means of interconnection for these devices. Typically, the material is resin-based and capable of withstanding high-stress environments. The fabrication of the circuitry results in the type of circuit: single-sided, two-sided, or multilayer. *Single-sided* refers to material with the circuitry on only one side. *Double-* or *two-sided* refers to material with the circuitry on both the top and bottom. *Multilayer* refers to material that has more than one level on one of the sides.
- QFJ—quad flatpack J lead: a quad flatpack with “J” leads extending from the package. The leads provide both electrical conductivity and mechanical mounting.
- QFP—quad flatpack: a package that typically is square with contacts on all four sides. The configuration of this package is either leaded or without leads.
- RA—rosin activated: a term referring to agents that are added to solder that increase the ability of the solder to adhere to the circuitry and the device leads. There are potential problems with the use of this activation, which requires especially thorough cleaning of any residues after the solder process.
- RMA—rosin mildly activated: less active than the RA; less aggressive in chemical reactions with the devices or circuitry.
- SMA—surface mount assembly: refers to a process that employs electronic components that are attached to the surface of the circuitry.
- SMT—surface mount technology: refers to the technology that involves any portion of the surface mount assembly process.
- SOIC—small-outline integrated circuit: generic term for parts with multiple leads on two opposing sides and no leads on the other two sides. Typically there will be the same number of leads on both sides of the part, and the lead spacing will be consistent throughout the part, although the center leads may be missing.

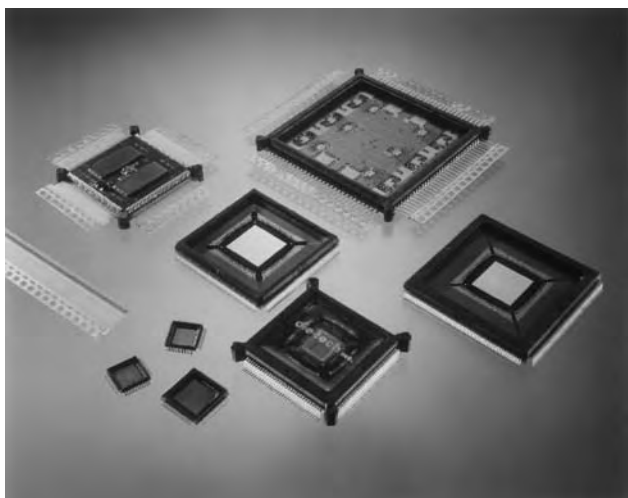


Figure 1. Complex surface mount packages that contain smaller surface mount devices. (Courtesy of Die Tech, Inc.)

- SOJ—small-outline J lead: a special case of the SOIC in which all the leads are bent in a “J” shape.
- SOP—small-outline package: frequently a part of the term referring to various types of SOICs (e.g., Q = quarter, S = shrink, T = thin, and V = very).
- SOT—small-outline transistor: rectangular plastic packages that house transistors or diodes. Typically these will have three or four leads.

3. SURFACE MOUNT PROCESSES

The critical element in surface mount assembly is provision of the proper mechanism for attaching the components to the substrates. The process of attaching the components to the circuitry involves either solder attachment or epoxy mount.

3.1. Solder

The process of attaching components by soldering involves raising the temperature of the solder until it becomes molten, and cooling the circuitry until the solder hardens. The solder consists of metals that have a relatively low melting point—usually below 315°C. This liquid metal composition is structured to adhere to both the components and the conductive material on the substrate. The ability of the material to adhere to the surfaces is a function of its wettability. Properly prepared surfaces show good adhesion. Because of the nature of the alloys involved, inorganic materials and metallic oxides can inhibit the formation of the bonds. In cases like these, there are chemicals, fluxes that can be employed to enhance the bondability of the materials.

3.2. Fluxes

The function of the flux is to provide an untarnished surface that is capable of easily spreading the liquid metal to cover the desired surfaces. Since there are varying degrees of contamination and different solubilities of materials, the characteristics of the fluxes have been tailored for specific circumstances. In general three types of fluxes are employed in electronics manufacturing: activated, nonactivated, and mildly activated rosin fluxes. Water white rosin flux is a chemically inactive and electrically insulating flux. When heated above its melting point, it becomes active and will react with some metals. Activated fluxes have additives introduced that exhibit more aggressive behavior that promote solderability in more difficult conditions. The mildly activated fluxes are more aggressive than nonactivated ones but do not have the residue problem of the activated fluxes. The activated fluxes require thorough cleaning to ensure removal of the flux, which can cause damage to the components if left on the circuit.

3.3. Composition

The main constituents of solders have been tin and lead in various compositions. Other materials have been incorporated into the metallurgy more recently in order to reduce the amount of lead employed in the products. *Eutectic*

solder refers to the composition of the material that has either a solid or a liquid state and no plastic state. For tin-lead, this composition is 63/37%. The melting point is 183°C. Other percentages provide melting points that differ slightly according to the percentages of the metals, but they exhibit a transition state where the solder becomes plastic and moldable before melting. Many different compounds are being used in production according to the constraints of the product or the environmental considerations of employing lead in products.

3.4. Adhesives

Two types of adhesives are employed in surface mount assemblies: epoxies and acrylics. The epoxies are further subdivided into thermosetting, thermoplastic, elastomeric, or alloy. Thermosetting involve a chemical or thermally induced reaction. Single-part epoxies normally require thermal elevation to initiate the chemical reaction. Two-part epoxies provide the catalyst by the combination of the two elements. Elastomer is named after material with elongation properties that can be employed in situations where a degree of stress relief is required. The alloy is a combination of material from the proceeding three categories.

3.5. Cleaning

The application of solder has the potential of leaving an undesirable residue after the solder process. Cleaning is a critical element in the process. The application of water white rosin should leave minimal residue and has been employed without cleaning. The slightly more active flux, mildly activated, should always be cleaned from assemblies. Activated flux must be cleaned because the residue is still active and can cause contamination and corrosion. There is a direct correlation between cleanliness and circuit reliability.

4. SURFACE MOUNT ASSEMBLY

In the development of a product, the capabilities of the manufacturing process as well as the functionality of the circuit determine the configuration of the design and the components that are required for the manufacturing process. The production of a high-volume, high-reliability product, such as a digital cellular phone, has constraints different from those for a portable, digital clock. The purpose of this section is not to develop the methodology of design for manufacturing but to overview the processes required for manufacturing. For small-volume or prototype quantities, manual assembly can be employed to produce working product. The potential problem with small-quantity manual assemblies is that the learning required to produce good-quality manual assembly is not immediately available. Consequently, the application and testing of prototype product should not be expected to approach that of a “debugged” assembly process.

For this article, assume that the product being introduced into production has been through a prototyping process that eliminated any design flaws that would

require revision of the assembly. The revision process will not be considered. Finally, we will assume that the design and manufacturing teams have been working together to develop a manufacturable product that does not require modifications or changes to achieve a shippable product. The selection and application of equipment is dependent on the desired volumes. The descriptions below cover manual, semiautomatic, and automatic assembly tools. The selection of the appropriate equipment is left to the reader.

4.1. Selection of Equipment

Once the type of board that will be built is identified, it is necessary to select the equipment that will be used to build the product. This article considers the more common methods of assembly and identifies the equipment that would be typically involved in each stage. The steps discussed will follow the typical order in which a board is built. There are many reasons for deviating from this model. Some of these are discussed in Section 5.

4.1.1. Solder Paste Application. Frequently when building a board, the topside is built first. The topside assembly normally starts by placing solder paste on the board. The paste serves many functions; it holds the part in place during assembly, provides the material to clean the contacts on the part, and provides the material to form the solder joints.

Solder paste is made up of two key components: flux and solder. The flux has the job of holding the compound together and, when the compound is heated, cleaning the pads on the board, the terminations on the components, and the solder particles. The solder has the job of forming the electrical connections when it is melted and cooled.

Because of these functions, the paste must be put on the board in the correct quantities and aligned on the pads. Too much solder, and there might be short circuits; too little solder, and the mechanical bond may not be sufficiently strong to hold the components. There are two basic ways of putting the paste on the board: dispensing and screening.

4.1.1.1. Dispensing Solder Paste. Solder paste dispensing involves having the paste delivered in a syringe (typically 10 or 30 mL). The paste is then forced out onto the PWB at the desired locations. (The methods of forcing the paste out are the same as dispensing glue). There are many machines available to do the dispensing.

The simplest machine is a very simple pump with a handheld syringe that the operator moves from location to location. The operator usually activates a foot switch that will start the dispensing process. At the other extreme, a gantry-style robot moves the dispensing head to the desired location, and the controller dispenses the paste. The advantage of the robots is that they are faster and more repeatable. The advantages and disadvantages of the various dispensing techniques are discussed in Section 4.1.2.

Dispensing solder paste offers some advantages: flexibility, no custom tooling required, and easy cleanup. The machines that dispense paste are normally programmable to allow for quick changes. These machines seldom require

creation of custom tooling per each assembly. Cleanup normally includes cleaning only the nozzle, which is one small piece. For these reasons paste is frequently dispensed for prototype boards.

Dispensing also has its disadvantages; it is slow, requires low-viscosity paste, and lacks repeatability. Because each location on a board must have the paste forced onto it one location at a time, dispensing a board can take a long time, since most assemblies contain multiple locations. To be dispensed, the paste must be thin enough to be forced through the needle. This means that the paste will not want to stay standing on the pads but will slump, leading to potential shorts. Depending on the dispensing method, the volume and the location of the paste may be difficult to repeat. For these reasons, dispensing paste is seldom not used in production.

4.1.1.2. Screen Printing Solder Paste. Screen printing is a simple process where a template is held over the substrate and a viscous fluid is then forced through. In electronics manufacturing the substrate is the PWB, and the viscous fluid is frequently solder paste. The template is either a stencil or a screen.

A stencil is a metal plate, of the same thickness as the desired paste height, with holes cut out in it where the paste is desired. The metal used may be almost any type, although stainless steel is the most common material used currently. The holes may be formed in any number of methods; chemical etching and laser cutting are among the most common. The holes are made in the same size and shape as the desired pattern of paste on the board.

A screen is a mesh, typically made of steel threads closely spaced, that is covered with a coating. (The gauge of the mesh indicates the number of wires per inch; so the higher numbers provide the ability to make thinner coating; e.g., 325-mesh is finer than 200.) The coating is removed from the areas where the paste is desired (the mesh is still there). Each location where paste is desired is actually formed of many smaller openings forcing the screen to thicken to achieve the same volume of paste. Because of the many smaller opening, the choice of paste to use with the screen must be thought out very carefully and may limit the applications that can be used. A screen, while cheaper than a stencil, is rarely used because it does not last as long, gives less desirable results, and is harder to clean.

The viscous fluid, typically paste, is moved along the top of the stencil or screen from one end to the other by a squeegee, which also pushes the paste downward through the openings in the stencil or screen. Typically three variables concerning the squeegee are controlled: hardness, pressure, and speed. The hardness of the squeegee determines how it will react when it is used. Pressure and speed are inversely related to each other. Increasing pressure will have effects similar to those of decreasing speed. The objective with these two variables is to find the right balance that yields good coverage on the board.

Up until now, we have not mentioned a machine. A machine is not required for this process. Many companies use an operator to do the screening. However, this method has several drawbacks, the largest of which is the lack of

consistency. Typically a machine will be used to improve the process. The machines range from semiautomatic to fully automatic. The semiautomatic printers require the operator to place the boards on the machine, verify and align the board and stencil, tell the machine to print, and then remove the board. The automatic machines will perform all the tasks automatically, including passing the board to the next machine.

For all the reasons mentioned above, screen printing has many advantages: repeatable results, speed, choice of pastes, and ease of use. The disadvantages of screen printing are few, related mostly to the cost of the stencil or screen. For these reasons screen printing is usually the preferred choice for placing solder paste on the board for production runs.

4.1.2. Glue Application. Glue is applied to the board to hold the components in place for the rest of manufacturing and for certain user requirements. The bottomside surface mounted devices (SMD) components are typically glued while the top side of the board is usually not. The choice of the glue must be carefully considered, as the glue must be sufficiently strong for manufacturing, easily broken for rework, not harmful to the components or board, and easily worked with and cleaned. There are several ways to put the glue on the board: dispensing, pin transfer, and screen printing.

4.1.2.1. Dispensing. *Dispensing* refers to taking the glue from a container (typically a syringe) and forcing the desired amount through a needle onto the desired location. There are two basic categories for dispensing: time-based and positive displacement. Each has its advantages.

4.1.2.1.1. Time-Based Dispensing. Time-based dispensing involves applying pressure for a certain amount of time to dispense the glue. Air is usually applied to the back of the syringe to supply the pressure to dispense the material. This system is usually referred to as *airover*. *Airover* is inexpensive, easy to maintain, and easy to clean. Unfortunately, the lower in the syringe the glue is, the more time that is required to achieve the same volume of glue. However, this can be compensated for through various machine controls.

4.1.2.1.2. Positive Displacement. In order to overcome the disadvantages of time-based dispensing, various methods of positive displacement have been created. The two most common are piston and screw.

An extremely common method of positive displacement is using a piston to force an exact amount of adhesive out the end of the dispensing tip. This is accomplished by keeping a steady pressure on the syringe and pulling the piston up high enough to allow the adhesive to enter the dispensing chamber. The piston is then brought down to force an amount of glue (equal to the volume of the chamber that the piston then occupies) out onto the substrate.

The screw method utilizes a screw that, when turned forces an amount of adhesive out the chamber that is proportional to the degree to which the screw is turned. This format is very similar to that for many pumps used for

other applications. This method is easy to vary as the more the screw is turned, the more glue that comes out the end.

Positive-displacement systems provide reliable consistent glue dot sizes. With this advantage come a few disadvantages; it is more expensive and more complex.

4.1.2.2. Pin Transfer. The methods of dispensing adhesive mentioned so far are extremely flexible but can require a long time to apply all the adhesive required on the board. There are several industries that do not need the flexibility mentioned above but need very quick cycle times (<8 s to apply all the adhesive). In order to meet this need, pin transfer was created. Pin transfer allows the whole board to be covered at once and allows reloading while the board is being transferred. A die is made for each different type of board and has pins sticking down from it at each locations where adhesive is desired. The die is "loaded" by dipping the pins in a tub of adhesive. A small amount of adhesive will stick to each pin; the quantity varies depending on the size of the pin. The die is then brought over to the substrate, and when contact is made, the adhesive transfers to the substrate. Pin transfer is fast but also expensive because of the tooling and requires long cleanup times.

4.1.2.3. Stencil Printing. Many manufacturers attempting to make use of their current equipment consider another method of adhesive application: stencil printing. Stencil printing adhesive is very similar to stencil printing paste. The advantages are that no new equipment needs to be purchased, but the board must be flat with nothing sticking out on its sides. This limits the number of options that are available in the order of manufacture.

4.2. Placement Equipment

After the material that is to hold the parts on the substrate during assembly is applied, the next step is to start populating the substrate. This requires that the parts be placed on the substrate in the correct location and the correct orientation. There are many standards designed to define what is acceptable and what is not. The standards are a compromise between perfect placements, production speeds required, and requirements of the finished product. Whatever standard is used, the process used must be capable of building to that standard in an efficient and timely manner. There are three basic ways to place parts on a substrate, each with its unique advantages.

4.2.1. Manual. Placing parts manually involves setting up an operator with a picking tool and all the parts to be placed. A machine is optional for this type of placement. The machines can provide instructions and even some assistance in picking and holding the parts. The operator follows a set of directions to determine where each part goes on the board. This is the least expensive and slowest way to build boards, but it is appropriate for prototype work. While this method can be used for production, it relies completely on the operator skills.

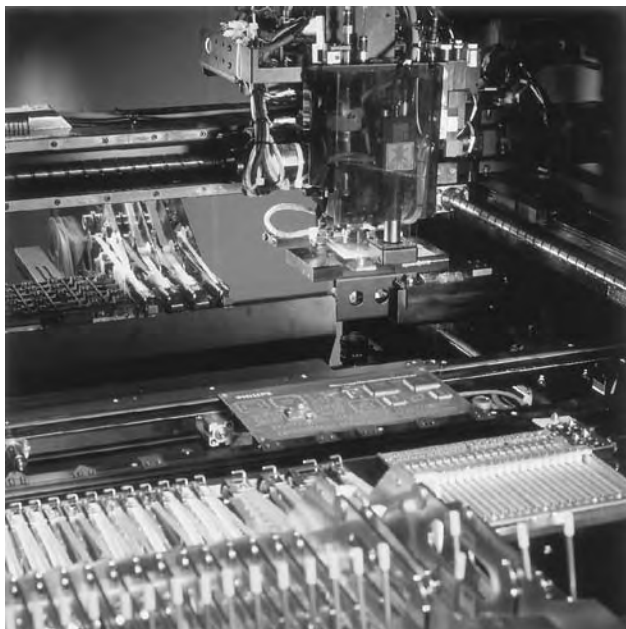


Figure 2. Example of placement mechanism of fine-pitch equipment with flexible placement head. (Figure of Philips Eclipse courtesy of North American Philips.)

4.2.2. Semiautomatic. Many machines fall into the semiautomatic range. The machines assist the operator in many ways. The machines may require the operator to place the parts individually in a location that the machine can reach and then tell the machine to go. The other extreme for this class of machines requires the operator only to place the substrate in the machine, let the machine place all the parts, and then remove the board. The machines require less precision from the operator since the operator does not actually place the parts. This class of machine is frequently used in contract manufacturing and other environments where batch processing of the substrates is preferred.



Figure 3. Example of high-speed chip placement equipment with placement rates in excess of 60,000 devices per hour. (Figure of Philips FCM courtesy of North American Philips.)



Figure 4. Example of medium-speed flexible placement machine with placement rates in excess of 14,000 devices per hour. (Figure of Philips Topaz courtesy of North American Philips.)

4.2.3. Automatic. The automatic machines require the least amount of operator intervention. These machines automatically bring the substrates in, populate them, and then pass them to the next machine (Fig. 2). This type of machine is used in environments where the continuous building of product is required. The machines in this class frequently are specialized in order to gain more speed. The machines are typically divided into two categories: chip shooters and fine pitch placers. The chip shooters are designed to put down the small parts (typically resistors, capacitors, and diodes) very quickly. The chip shooters (Fig. 3) typically use tape and reel parts expedite the feed action. These machines are designed so that the operator only has to replenish the parts as the machine uses them up. The fine-pitch placers (Figs. 4 and 5) usually take many types of inputs as the parts frequently come on trays or in sticks. These machines are very flexible and can do just about any type of part but are much slower than the chip shooters. A typical line would consist of a chip shooter and a fine-pitch placer. The automatic machines are usually the most expensive to buy, but are frequently the most cost-effective solution for placing parts.



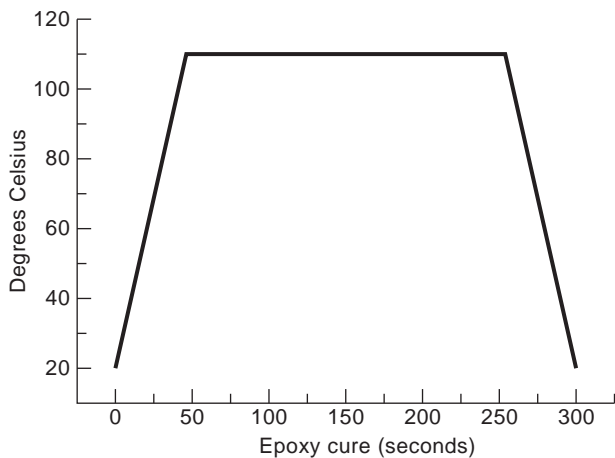
Figure 5. Example of flexible placement machine. (Figure of Philips Eclipse courtesy of North American Philips.)

4.3. Reflow/Curing Equipment

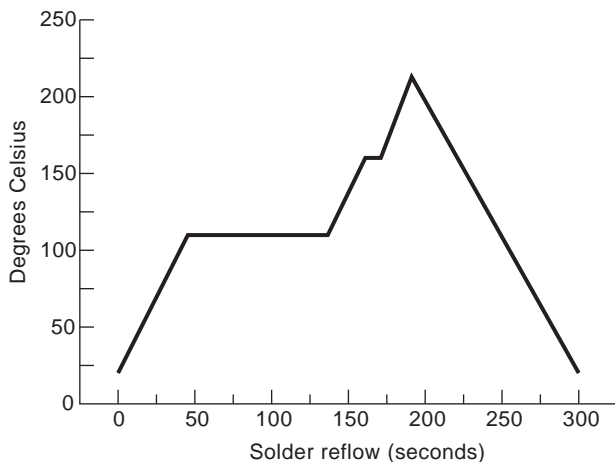
Once the parts have been placed on either adhesive or solder paste, it will be necessary to process the boards through an oven. In the case of adhesive the oven cures the adhesive so that the parts will stay put through the rest of the process (see Fig. 6a). For solder paste the oven has to activate the flux and allow the flux to eliminate oxidation, and then to melt the solder and allow it to form the solder joints between the board and the parts (see Fig. 6b). In both cases the oven temperature must be carefully controlled so as not to throw the boards and parts into thermal shock. Most surface mount parts can withstand temperature changes up to 4°C/s, but it is not recommended to exceed 2°C/s of heating or cooling.

The ovens fall into in two basic categories: batch and flowline. Batch ovens can work only on one group at a time. The flowline ovens are designed for the continuous introduction and removal of work. Each has its unique advantage.

Batch ovens typically have a sealed chamber to do their work. Because the chamber is sealed, control of the



(a)



(b)

Figure 6. Time-temperature plots for epoxy curing.

environment is easy to maintain. This makes it easier to achieve the ideal profile for the work desired. Batch ovens expose the whole board to the same temperatures at the same time so that the board will not be subjected to two different extremes in temperature at the same time. These ovens are used primarily for small batches of work and are frequently used in prototype environments where workflow may be erratic.

Flowline ovens are designed for the continuous introduction of boards into the process cavity. This means that the entry and exit points are not completely sealed (various techniques are implemented to achieve some degree of isolation). Flowline ovens will have several zones that control the amount of energy is being put into the board to heat it up as it goes through the various phases. By controlling the speed with which the board passes through these phases and the amount of energy applied in these zones, the desired profile can be achieved. Flowline ovens are typically used in production environments.

Regardless of the choice of batch or flowline oven, there are four main types of energy transfer that occurs inside the oven. Infra-Red (IR), convection, vapor phase, and Ultra-Violet (UV) are the main techniques.

Infrared ovens, which are used to cure adhesive and reflow solder paste, rely on IR transmitters to input energy into the oven cavity. As this IR energy is absorbed, it will heat up the object and, through conduction, whatever the object is touching. The choice of IR was made because the green printed wiring boards (typical color) absorb the infrared light. This technique was very common some years ago, but as the process cavity oven became better sealed, the energy transfer method started to become half convection and half IR. Because of the sensitivity of IR ovens to the color of the substrate (prototypes are typically reddish in color), these ovens lost favor with many people.

Convection ovens, which are used to cure adhesive and reflow solder paste, rely on hot gases to provide the transfer of energy to the substrate. The gases in a convection oven are either nitrogen or air. This transfer of energy is not dependent on the color of the substrate. Many different techniques are used to generate the heat and distribute it throughout the various parts of the oven. This technique for energy transfer is very stable and will work well in a wide variety of situations, making it a popular choice for ovens today.

Vapor-phase ovens, both batch and continuous-belt, are used to reflow solder paste. Vapor-phase ovens rely on a combination of fluids (fluorocarbons) brought to boiling temperature. The combination will have two separate boiling temperatures, and each will be used and kept in place by cooling coils. This results in vapors at two separate temperatures. The substrates will then be passed (lowered in batch ovens) through these gases, and the gases will efficiently heat up anything that they come in contact with. The substrates will then be cooled (removed in batch ovens) slowly to allow the solder to gradually solidify. Vapor-phase ovens are used primarily for high-reliability (military) applications and design-critical applications. This technique is no longer popular mainly because of the expense of the chemicals and the potential of these chemicals to damage the environment.

Ultraviolet (UV) ovens, which are used for curing adhesive, rely on UV light to transfer the energy to the adhesive. Several different adhesives may be used in electronics manufacturing that will cure only if exposed to strong UV light for a period of time. Consequently, there is a better control of the curing process, because it will not start without the UV energy. A second reason for using UV adhesives is that few substrates absorb UV light well, so this does not heat the substrate significantly.

4.4. Wave Solder Equipment

If through-hole parts are used, it is necessary to solder the parts in place and form the electrical connections. The parts may be soldered by hand, or more commonly by processing in a wave solder machine. A typical wave solder machine will consist of a fluxer, preheaters, and a solder wave. The fluxer will apply flux to the bottom of the substrate by spraying or foam. The only requirement is that the whole area be covered to ensure that the flux will contact all the surface area to be soldered. After the substrate is fluxed, it moves to the preheaters. The preheaters will activate the flux, enabling it to remove oxidation from the components and the substrate. The preheaters also elevate the substrate temperature to prevent the solder temperatures from providing a thermal shock when the substrate encounters the solder wave. When the soldering takes place, the substrate is moved across a wave of solder so that only a small line of solder is in contact with the substrate at a time. Depending on the system, a second wave may also be used. The waves are generated by pumping molten solder into a pot and allowing it to spill over, or are generated directly from a pump pushing the solder upward.

4.5. Cleaning Equipment

After assembly it may be necessary to clean the substrate. Cleaning is required if the flux residue is corrosive or if the cosmetic appearance of the substrate is critical. The chemicals used will vary depending on the type of flux used. The substrate will be exposed to various washing stages in order to remove all the corrosive material. Some of the newer fluxes available permit the elimination of this step.

4.6. Inspection Equipment

As the devices get smaller and the pin count increases, it is becoming more important to build the boards properly in the first place. This has led to equipment being used to perform the inspection process, and the inspection may take place in many places in the line: inspection of solder paste, postplacement component inspection, and postsolder inspection. Each has its proper place in the overall inspection process. When setting up a line and deciding on the inspection strategy, the costs associated with failure must be analyzed.

4.6.1. Solder Paste Inspection Equipment. The goal of solder paste inspection is to make sure that the correct volume of solder is available for the solder joint to be formed during the reflow process. There are a variety of

methods out there, ranging from fully automated 3D inspections systems to offline sampling processes that involve a lot of human intervention. The goal of all of the systems is simple: to control the process so that good solder joints can be made.

4.6.2. Postplacement Inspection. The goal of inspection after the components are placed on the board and prior to reflow is to troubleshoot production errors while they are still easy and inexpensive to fix. At this point measurements can be taken to verify how well the placement machines are doing their job (accuracy). Additionally, catching mistakes at this point means that not too many boards are in process yet and incorrect parts can be found because of some physical characteristic of the component without waiting until hundreds of them are built. The machines used for this inspection process are collectively referred to as *automated optical inspection* (AOI) equipment.

4.6.3. Postsoldering Inspection. Many companies are performing inspection after the solder joint is formed. In addition to determining whether the correct component is present, inspection done here can also ensure that the solder joints have the correct characteristics. This is difficult to do as many people disagree on what is and what is not a good solder joint. Many different machines are used to perform this inspection process and vary in strategy depending on what the manufacturer perceives to be the most important defects. Many companies use AOI machines to inspect the visible joints and do not worry about the hidden joints [J lead and ball grid array (BGA), for example]. For companies concerned about the internal solder joint integrity or hidden solder joint, X-ray inspection will be incorporated; however, XRD has the disadvantage of inability to isolate the individual sides of the board, and features from the second side may interfere with the solder joint inspection.

4.7. Testing Equipment

After all the assembly steps are completed, it will be necessary to test the assembly. At this point the assembly will be hooked up to various pieces of equipment to find out if it works and what is wrong with it. The testers may test each component separately (using a bed of nails to probe every node of the circuit) or use a functional test (plugging it in and see if it works). All the nonconforming boards are then separated out and are reworked or scrapped.

4.8. Rework Equipment

If the assembly is to be repaired, an operator will remove the problem parts and replace them. The equipment needed to do this may be as simple as a soldering iron, or complex enough to have robotic arms to help solder the parts and hold them in place. The choice is dependent on the parts to be replaced.

5. CONCLUSIONS

Surface mount assembly is a very dynamic field. The cost, size, and reliability advantages of surface mount implies

that this technology will be around for some time. There are many publications that address this field as well as many organizations. Additional information can be obtained from both IEEE/CPMT and IMAPS. Webpage information is provided in the Further Reading Section (below) as a starting point for further investigation. Because there are so many different challenges to implementing surface mount, the authors are not providing details about research on only one part of the process, such as using cobalt composite solder, as too many areas are being worked on. The recommendation is to investigate the publications and Websites to find the latest information.

Acknowledgments

Photographs are courtesy of Philips ESD, Norcross, Georgia.

FURTHER READING

- G. Boothroyd, P. Dewhurst, and W. Knight, *Product Design for Manufacture and Assembly*, Marcel Dekker, New York, 1994.
- C. Capillo, *Surface Mount Technology*, McGraw-Hill, New York, 1990.
- H. H. Manko, *Solders and Soldering*, McGraw-Hill, New York, 1992.
- IEEE/CPMT, available online at <http://www.cpm.org>.
- IMAPS, available online at <http://www.imaps>.
- R. Prasad, *Surface Mount Technology*, Prentice-Hall, Englewood Cliffs, NJ, 1997.
- R. Tummala and E. Rymaszewski, *Microelectronics Packaging Handbook*, Van Nostrand-Reinhold, New York, 1989.

SYNTHETIC APERTURE RADAR

CANER OZDEMIR
Mersin University
Mersin, Turkey

Synthetic aperture radar (SAR) is a high-resolution airborne and spaceborne remote sensing technique for imaging remote targets on a terrain or, more generally, on a scene. In 1951, Carl Wiley realized that if the echo signal is collected when the radar is moving along a straight path, the Doppler spectrum of the received signal can synthesize a much longer aperture so that very close targets in the along-track dimension can be resolved [1]. In 1953, the first measured SAR image was formed when a C-46 aircraft mapped a section of Key West, Florida [2,3]. The first onboard satellite SAR system was developed by NASA researchers and put on Seasat in 1978. This remarkable satellite provided so much data for oceanographic applications. Since Seasat, several satellites carrying SAR systems have been launched by different countries. Russian Almaz (1987), European ERS-1 (1991), ERS-2 (1995), and Canadian Radarsat (1995) were among some of them. The first space shuttle mission that has a

SAR module was SIR-A (Shuttle Imaging Radar). After SIR-A was launched aboard the space shuttle *Columbia* in 1981, other spaceborne SAR missions were followed. SIR-B (1984) and SIR-C/X-SAR (1994) acquired SAR images in multiple frequencies and polarizations for more advanced applications such as interferometric and polarimetric mapping of terrains.

Although the primary practices of SAR have been for surveillance applications such as detection of opponents' territories, airplanes, and tanks, it has also found many real-world applications from geophysics to archeology. Since the first measured SAR data was collected in 1953 [3], several air and space vehicles have been mapping Earth's surface to help better understand and interpret terrains and associated geological events. The use of SAR by scientists in predicting volcano eruption, coseismic displacement field, and glacier motions are some of the various applications in different sciences. In agriculture, it is mainly used by scientists for crop monitoring. SAR has also been used by environmental scientists for forest classification, deforest monitoring, hazard monitoring, oil spill, detection of squatters in the cities, and so on. With the help of SAR-based subsurface imaging techniques, it is possible to detect mines and unexploded ordnances. Similarly, these techniques have been very helpful in detecting archeological substances.

Synthetic aperture radar has gathered its fame because it can provide fine resolutions both in range and cross-range dimensions. The term *range* (*slant-range*) corresponds to the line-of-sight distance from radar to the target to be imaged. The term *cross-range* (*transverse-range*, *azimuth*, *along-track*) is the dimension that is perpendicular to range or parallel to the radar's along-track axis. High resolution in range is obtained by a wide bandwidth transmitted signal, usually a frequency-modulated "chirp" waveform. Fine resolution in the cross-range dimension is achieved by coherently processing the target's electromagnetic (EM) scattering measured at different aspects while radar moves along a straight path. With this construct, SAR can provide images that have comparable resolutions with optic imaging systems. In fact, SAR can do even better because it can operate day and night or at cloudy and rainy conditions. Furthermore, unlike photographic images that contain only amplitude information of the target's reflectivity of light, SAR provides both the amplitude and the phase information of the scattered electromagnetic field from a scene, which leads to form *interferometric* SAR images, as will be shown in Section 4.2.

1. BASIC THEORY OF SAR

To understand the physics behind the SAR, it is better to first take a look at the operation of conventional radar: Radar transmits an electromagnetic wave; the wave hits the target and its surroundings and scatters in all directions in space. Then, the backscattered signal is collected by the radar that measures the time delay: τ_d between the transmitted and received signals. As EM waves travels with the speed of light, c , it is possible to calculate the range distance of the target as $R = (c \cdot \tau_d)/2$. The number

“2” accounts for the two-way propagation between the radar and the target. As in the case of conventional radar, the SAR sensor also applies this equation in obtaining the range information. The minimum distance to distinguish two close targets in the range or simply the *range resolution* is equal to $\Delta r = (c \cdot \Delta\tau_d)/2$, where $\Delta\tau_d$ is the duration of the transmitted pulse. For instance, if the radar operates at 10 GHz and applies pulses of 1 μ s long, the resolution in range becomes 150 m. Although this number may be sufficient for imaging large portions of the Earth’s surface such as mountains and deserts, it is clearly not enough to image smaller targets. The Fourier theory states that the frequency bandwidth of a time signal whose time duration is $\Delta\tau_d$ is given by $BW_f = 1/\Delta\tau_d$. Therefore, the range resolution of conventional or synthetic aperture radar becomes $\Delta r = c/(2 \cdot BW_f)$. For the conventional radar, sensing two close targets that are in the same range distance is difficult, because the angular beamwidth of any single radar antenna is equal to $\Delta\theta = \lambda/D$, where λ is the wavelength for the operating frequency and D is the maximum physical length of the antenna. As two objects that are at the same range distance R can only be distinguished if they are at different radar beams, then the *cross-range resolution* is equal to one arc length of the radar beam as $\Delta x = \text{arc length} = R \cdot \Delta\theta = R \cdot \lambda/D$, as illustrated in Fig. 1(a). For example, a 2 m long, X-band (at 10 GHz) radar antenna can provide an azimuth resolution of 150 m at a range distance of 10 km. This amount of resolution is again not enough for imaging small targets and for capturing the details of a terrain. However, it is obvious that when the radar is moving, the distance between the radar and the target is changing. As a result, a frequency shift occurs in the returned EM wave because radar pulses experience different travel distances because of motion. This shift in frequency is called *Doppler shift*. In fact, we use

this Doppler effect in a SAR system to enhance the cross-range resolution, as will be explained in Section 1.3.2.

1.1. Range and Cross-Range Resolutions in SAR

We use the term *synthetic aperture* because the idea behind SAR is to synthesize the effect of a large, real aperture radar (RAR) by means of a collection of small-size aperture radars, which is accomplished by moving the small aperture radar along with the imaginary aperture axis to emulate a much larger aperture, as depicted in Fig. 1(b). Typically, the radar is put on an airborne or a spaceborne vehicle and the ground’s EM reflectivity is measured at different time instants while the radar vehicle is moving along-track path (see Fig. 2). Coherent processing of electromagnetic echoes from the illuminated area at different frequencies and apertures makes it possible to form a two- (or three-) dimensional image of the terrain.

The range resolution in SAR, $\Delta r = c/(2 \cdot BW_f)$, is the same as the conventional radar, as explained in Section 1. However, the frequency bandwidth of pulse in SAR is much longer to achieve finer resolutions. According to the Fourier theory, the time duration of the pulse is then required to be very short. On the other hand, it is hard to put enough energy into a very short pulse. As a very small portion of the transmitted power scatters back to radar, it will be almost impossible to sense the received signal above the noise floor for such a short pulse. To circumvent this problem, we use a linear frequency-modulated (LFM) *chirp* signal that has an instantaneous frequency of $f_i(t) = f_c + BW_f \cdot t/T_o$. Here, f_c is a fixed frequency, T_o is the pulse duration, and BW_f is the total bandwidth. Chirp signal has the suited property of providing required bandwidth with longer pulse duration. An X-band, 1 μ s duration chirp pulse with 1 GHz bandwidth can provide a range resolution of 30 cm that is attractive.

A good cross-range resolution in SAR is achieved by forming a synthetic line antenna of length D_{SA} by moving the radar antenna along a straight path [see Fig. 1(b)]. As will be shown in Section 1.3.2, the cross-range resolution in SAR then becomes $\Delta x = R \cdot \lambda/(2D_{SA})$. For example, if SAR platform collects the scattered EM wave at the center frequency of 10 GHz from a target of 10 km away and for a synthetic aperture of 1 km, then the cross-range resolution is 30 cm, which is much better than the RAR case.

Two main modes for SAR operation exist. As illustrated in Fig. 3(a), when the radar collects the EM reflectivity of the alongside region when it travels, observing a strip of a terrain parallel to the flight path, this is called *side-looking SAR*. When the radar focuses its illumination to a fixed, particular area of interest, this mode is called *spot-light SAR*, as shown in Fig. 3(b).

1.2. Range Ambiguity and Pulse Repetition Frequency (PRF)

A SAR system sends out many pulses to the scene. The reason that in SAR, we use discrete pulses instead of a continuous waveform is that very little of transmitted power scatters back to radar. If a continuous wave is used, the leakage from the transmitting unit to the receiving unit would jam and probably dominate the actual

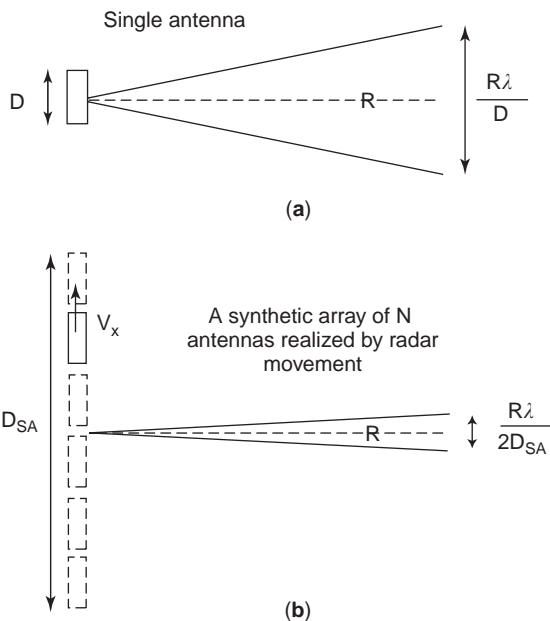


Figure 1. (a) A real aperture single antenna and (b) a synthetic aperture of N antennas.

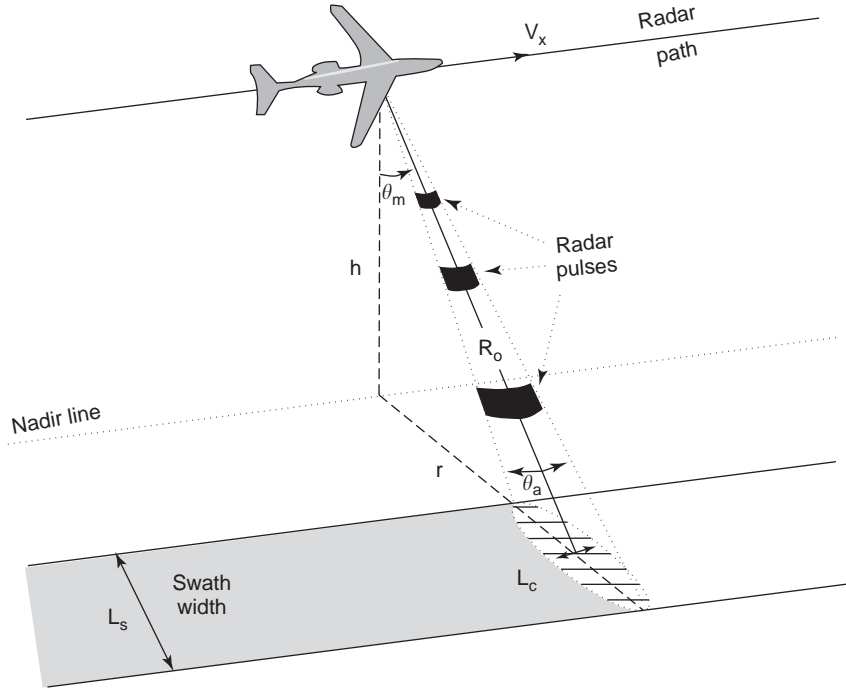


Figure 2. SAR operation: Radar platform is moving to synthesize the effect of a long real aperture radar.

received power. To avoid this, therefore, SAR first sends out a pulse to the scene, then turns off the transmitter, and listens the echo signal via its receiving unit. However, a limit is placed on the number of pulses that can be involved in a SAR. Suppose that a point target is at R distance away from the radar. For a pulse duration of T_o , the time delay of the returned pulse is $t_d = 2R/c$. Therefore, if a second pulse is sent before the first one arrives back, a phase ambiguity may exist such that the second pulse's echo from the nearest range point may arrive earlier than the first pulse's echo from the farthest range point. Of course, this ambiguity makes it difficult to resolve the points in the range. This situation is named *Range Ambiguity*. To prevent it, a lower limit must be placed on the number of pulses that can be transmitted in 1 second, i.e., *Pulse Repetition Frequency* (PRF), as follows:

$$PRF \leq \frac{1}{T_o + 2(R_F - R_N)/c} \quad (1)$$

where R_F and R_N are the farthest and the nearest range distances inside the swath and under the illumination of the radar beam [4].

1.3. SAR Image Formation

SAR imagery is based on successive signal processing algorithms called range and azimuth compression. The usual raw SAR data are in the form of a two-dimensional (2-D) multifrequency, multiaspect (or multispatial) scattered field data, as shown in Fig. 4. The range compression and azimuth compression are usually applied independently to obtain the ultimate SAR image (see Fig. 4).

1.3.1. Range Compression. As mentioned, we usually use a linear FM chirp waveform in range compression. The word *compression* refers to the frequency content of the chirp signal that is changing rapidly such that the full bandwidth BW_f corresponds to a time duration of $T_p = 1/BW_f$, which is much shorter than the actual pulse duration, T_o . A typical chirp waveform is plotted in Fig. 5(a). The instantaneous frequency of chirp signal is equal to $f_i(t) = f_c + \beta \cdot t/\pi$, where f_c is the initial frequency and β is related to the frequency bandwidth as $\beta = 2\pi BW_f/T_o$. Then, the transmitted signal will have the phase term of

$$p(t) = \exp[j(2\pi f_c t + \beta t^2)] \quad |t| \leq T_o/2 \quad (2)$$

A time-frequency transform of the signal is taken via spectrogram to show how the frequency increases linearly with respect to time in Fig. 5(b). When the range compression is applied, the output signal is depicted in Fig 5(c). The range-compressed one-dimensional (1-D) data, also known as *range profile*, contains distinct peaks corresponding to distinct scatterers along this particular range-bin. The locations of these peaks; t_i 's correspond to range distances: R_i 's of the scattering centers via $R_i = c \cdot t_i/2$. Therefore, the received signal will have the following phase term that contains the time delay of $t_d = 2R/c$:

$$s(t) = \exp[j(2\pi f'_c(t - t_d) + \beta(t - t_d)^2)] \quad (3)$$

Here, f'_c is a shifted version of f_c caused by Doppler shift of amount Δf . After collecting the received signal, it is then

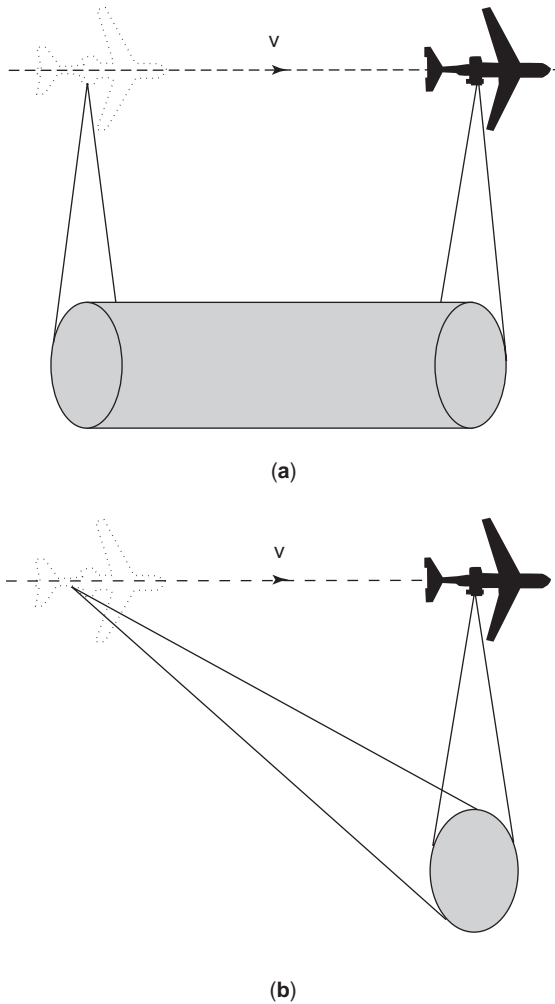


Figure 3. Modes of SAR: (a) side-looking SAR and (b) spotlight SAR.

passed to a *matched filter* whose filter characteristic is the same as the chirp signal:

$$h(t) = \exp[j(2\pi f_c t + \beta t^2)] \quad |t| \leq T_o/2 \quad (4)$$

The matched filter output is just the cross-correlation between the received signal and the filter impulse response

over the pulse duration as

$$\begin{aligned} y(t) &= \frac{1}{T_o} \int_{-T_o/2}^{T_o/2} s(t + \tau)h(\tau)d\tau \\ &= \frac{1}{T_o} \int_{-T_o/2}^{T_o/2} \exp[j(2\pi f'_c(t + \tau - t_d) \\ &\quad + \beta(t + \tau - t_d)^2)] \\ &\quad \cdot \exp[-j(2\pi f_c \tau + \beta \tau^2)]d\tau \\ &\cong \frac{\sin(\beta T_o(t - t_d) + \pi T_o \Delta f)}{\beta T_o(t - t_d) + \pi T_o \Delta f} \\ &\quad \cdot \exp[j(2\pi f'_c(t - t_d) + \beta(t - t_d)^2)] \end{aligned} \quad (5)$$

As the final process of the pulse compression, the high-frequency phase term at f_c is filtered by the following manner:

$$\begin{aligned} r(t) &= y(t) \cdot \exp[-j(2\pi f_c t)] \\ &= \frac{\sin(\beta T_o(t - t_d) + \pi T_o \Delta f)}{\beta T_o(t - t_d) + \pi T_o \Delta f} \\ &\quad \cdot \exp[-j(2\pi f_c t_d - 2\pi \Delta f(t - t_d) \\ &\quad - \beta(t - t_d)^2)] \end{aligned} \quad (6)$$

Here, the Doppler shift Δf depends on the position of the scatterer with respect to radar as well as to the ground velocity of the scatterer if the target is moving. Assuming that the scatterer is stationary, the Doppler shift term both in the amplitude and the phase terms of Eq. (6) produces a minor effect compared with the nominal values of SAR bandwidth. So, it can be ignored. Furthermore, the quadratic phase term in the last part of Eq. (6) also provides very small phase value in comparison with the first phase term, and so it can also be neglected. As a result, the range compressed signal can be approximately reduced to

$$\begin{aligned} r(t) &\cong \text{sinc}[\beta T(t - t_d)] \\ &\quad \cdot \exp[-j(2\pi f_c t_d)] \end{aligned} \quad (7)$$

The amplitude term in Eq. (7) is a *sinc* (sinus cardinalis or $\sin(x)/x$) function centered at $t = t_d$ that is clearly related to the scattered position as $R = t_d \cdot c/2$. The first nulls bandwidth of this sinc function is equal to $\Delta t_d = 1/BW_f$.

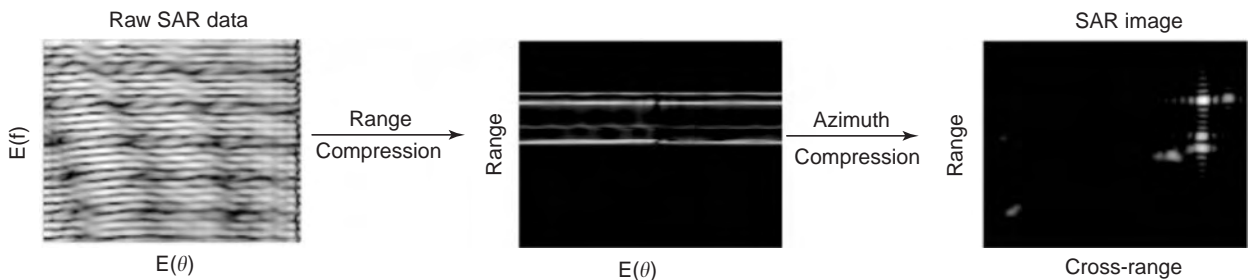


Figure 4. SAR image formation via signal processing.

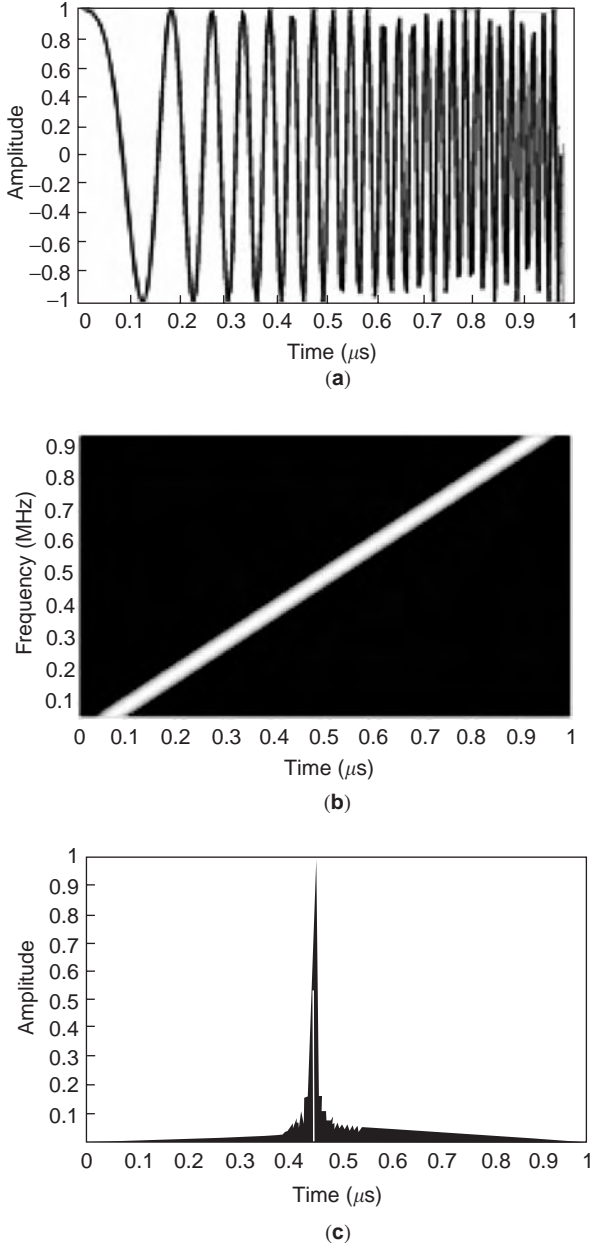


Figure 5. (a) Chirp signal, (b) time-frequency display of the chirp signal, and (c) output of the matched filter: range-compressed data.

Therefore, the range resolution is given by $\Delta r = \Delta t_d \cdot c / 2 = c / (2 \cdot BW_f)$.

1.3.2. Azimuth Compression. The compression in azimuth (or cross-range) is reached by a long synthetic antenna that is achieved by the radar motion. The geometry for SAR azimuth processing is drawn in Fig. 6. Assume that a point scatterer at R_o is away from the center of the synthetic aperture and the radar platform moves with a constant speed of V_x . When the radar travels a distance of $x = V_x \cdot t$ along the aperture, the scatterer's distance from the radar becomes $R = (R_o^2 + x^2)^{1/2}$. Assuming that $x \ll R_o$, the following approximation to the second order can be

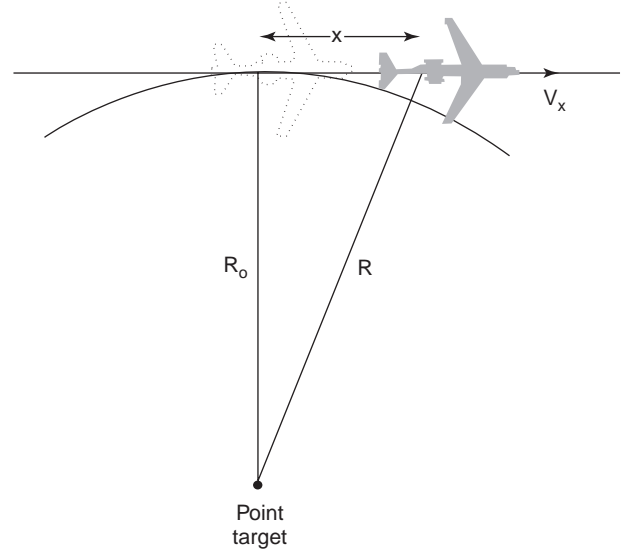


Figure 6. Geometry for SAR.

made:

$$R = R_o \left(1 + \frac{x^2}{R_o^2} \right)^{1/2} \approx R_o + \frac{x^2}{2R_o} \quad (8)$$

Therefore, the EM wave that possesses two-way propagation has a phase term

$$\begin{aligned} \Phi(x) &= \exp(-j2kR) = \exp \left[-j \left(\frac{4\pi}{\lambda} \right) \left(R_o + \frac{x^2}{2R_o} \right) \right] \\ &= \text{const.} \times \exp \left(-j \frac{2\pi x^2}{\lambda R_o} \right) \end{aligned} \quad (9)$$

By neglecting the phase term that has no time dependency, we can write the phase term of the received signal as

$$\Phi(t) = \exp \left(-j \frac{2\pi V_x^2 t^2}{\lambda R_o} \right) = \exp(-j\gamma t^2) \quad (10)$$

where $\gamma = 2\pi V_x^2 / (\lambda R_o)$. Then, the Doppler shift in frequency can be found by taking a time derivative of the phase:

$$f_d(t) = \frac{1}{2\pi} \frac{\partial}{\partial t} \left(-\frac{2\pi V_x^2 t^2}{\lambda R_o} \right) = -\frac{2V_x^2 t}{\lambda R_o} \quad (11)$$

The processing in cross-range dimension can be done by integrating all aperture return over an integration time T_s . This method is called *unfocused-SAR*. Then, the output signal of the azimuth SAR processing is obtained via the following averaging integral:

$$y(t) = \frac{1}{T_s} \int_{-T_s/2}^{T_s/2} \exp(-j\gamma t^2) d\tau \quad (12)$$

In fact, Eq. (12) is in the form of a *Fresnel* integral, which can only be solved numerically [5]. Therefore, the cross-range compressed data can be obtained numerically by solving the Fresnel integral in Eq. (12) in unfocused-SAR imaging. On the other hand, notice that the signal in

Eq. (10) is in the similar form as the chirp signal. Therefore, the processing in azimuth can also be carried out in a similar manner as range. In unfocused-SAR, the path lengths from different aperture points differ, which leads to a resolution mismatch as the radar moves. In photography, a lens focuses the rays from object to image plane. In SAR, this movement is achieved by adjusting the path lengths from all apertures to be the same by applying a matched filter. This process is called *focused-SAR* operation. So, if we can apply matched filter processing to the azimuth SAR data in a similar manner, then the output of the filter can be found via

$$\begin{aligned}
 E_x(t) &= \frac{1}{T_s} \int_{-T_s/2}^{T_s/2} \exp[-j(\gamma(t+\tau)^2)] \\
 &\quad \cdot \exp[j(\gamma\tau^2)] d\tau \\
 &= \sin c(\gamma T_s t) \cdot \exp(-j\gamma t^2) \\
 &= \sin c\left(\frac{2V_x^2 T_s t}{\lambda R_o}\right) \cdot \exp\left(-j\frac{2V_x^2 t}{\lambda R_o}\right)
 \end{aligned} \tag{13}$$

The second term in Eq. (13) is just the phase term. Therefore, only the first term represents the envelope of the azimuth-compressed SAR data. The first nulls bandwidth of the sinc function in Eq. (13) is equal to $\Delta t_x = \frac{\lambda R_o}{2V_x^2 T_s}$. Therefore, the cross-range resolution is equal to $\Delta x = V_x \cdot \Delta t_x$. After some calculation, it reduces to

$$\begin{aligned}
 \Delta x &= V_x \cdot \frac{\lambda R_o}{2V_x^2 T_s} = \frac{\lambda R_o}{2(V_x T_s)} = \frac{\lambda R_o}{2D_{SA}} \\
 &= \frac{\lambda R_o}{2(\lambda R_o/D)} = \frac{D}{2}
 \end{aligned} \tag{14}$$

where D_{SA} is the length of the synthetic aperture and D is the longest dimension of the radar antenna. Therefore, the cross-range resolution is independent of target distance R_o and the wavelength λ and depends only on antenna size for focused-SAR.

Generally, processing in range and cross-range is computationally intensive, because the correlation integral has to be calculated for every pixel of the 2-D SAR data. However, SAR image formation can be accelerated by the convolution theorem that makes it possible for us to use the Fourier transform (FT). In this regard, range or azimuth compressed data can be written in the form of a convolution as follows:

$$E(t) = \int_{-\infty}^{\infty} s(\tau)h(t+\tau)d\tau = s(t) \otimes h(-t) \tag{15}$$

where $s(t)$ is the chirp pulse in range or azimuth SAR signal in Eq. (10) and $h(t)$ is the matched filter impulse response. According to Fourier theory, convolution in time corresponds to multiplication in frequency. Therefore, the convolution in Eq. (15) can easily be sped up via Fourier transforms as shown below:

$$E(t) = IFT\{FT\{s(t)\} \times FT\{h(-t)\}\} \tag{16}$$

where FT and IFT are the forward and inverse Fourier transform operations, respectively. Therefore, clearly the shape of the resulting image response is determined by the Fourier transform of the pulse shape. When it is a rectangular pulse, the image response comes out to be a sinc function. This response is also known as point spread function (PSF) in radar imaging. As the SAR data have to be finite, the limits in the Fourier integral become finite. Therefore, the spreading effect is always unavoidable in SAR imagery. In some cases, a sinc-type PSF can be problematic when a weak scatterer happens to be located very near to a strong scatterer. As the first sidelobe level of the sinc function is only 13 dB lower than the main beam, the weak scatterer may not be detected because of high sidelobes of the strong scatterer. Therefore, we usually use smooth weightings such as Hanning, Hamming, or Kaiser-type windowing whose Fourier transform provide much smaller sidelobe levels. Figure 7 shows the compressed signal for a Hanning weighted chirp signal. It is clear that the sidelobes are well suppressed compared with the sinc response. Therefore, such weightings provide better peak-to-sidelobe ratio (PSLR) at the price of increased mainlobe beamwidth, i.e., worse resolution.

An example of a measured SAR imagery is given in Fig. 8. This image shows the space shuttle SAR image of San Francisco, California. The raw SAR data were collected by the SIR-C/X-SAR when it flew aboard the space shuttle *Endeavor* in 1994. The SAR system on SIR-C/X collected L-, C-, and X-band raw SAR data over 225 km above Earth's surface for multiple frequencies and polarizations to better understand the global environment and how it is changing. The SIR-C/X-SAR system was designed to provide surface resolutions of 30 m both in range and cross-range dimensions. The particular image in Fig. 8 shows the most general features of a typical SAR image. For instance, rough surfaces such as mountain terrains show up in the SAR image as the mixture of bright and dark spots because they experience scattering in all directions. On the other hand, smooth surfaces and regions of calm water such as sea or lake surfaces seen to be black. Because these surfaces behave like mirrors and scatter EM energy according to the Snell's law, almost no energy scatters back in the direction of radar. Hills and other large-scale targets tend to appear bright on the side where illuminated and dark on the other side where there is no EM illumination (shadowing). Man made objects such as

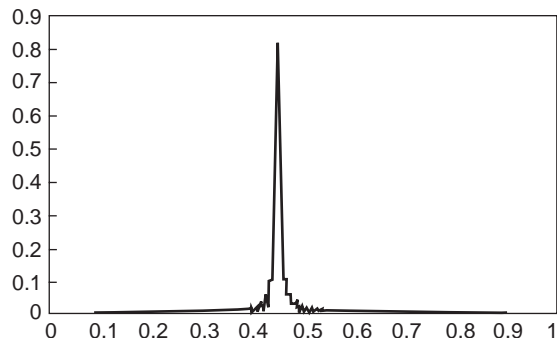


Figure 7. Hanning windowed range-compressed data.



Figure 8. SIR-C/X-SAR image of San Francisco, California. (Courtesy NASA/JPL-Caltech.) (This figure is available in full color at <http://www.mrw.interscience.wiley.com/erfme>.)

buildings and vehicles behave like corner reflectors, and they appear as brighter spots. When a very strong point scatterer exists (e.g., specular point), it shows up as a very bright cross in the image because of strong sidelobes in range and cross-range dimensions. Most of these features can be observed from the SAR image in Fig. 8.

2. COMMON PROBLEMS IN SAR IMAGERY

2.1. Range Migration

During the SAR operation, the radar platform first approaches and then moves away from any scatterer that is entering its main antenna beam. Therefore, the range distance of any scatterer depicts a parabolic curve called *range curvature* while it is illuminated by the radar beam. This ambiguity in range distance may result in shifting of scatters to the nearby range cells while integrating the raw SAR data over the synthetic aperture time interval. This phenomenon is called *range migration*. For spaceborne SAR, this curvature can be significant because the range extent and the integration time is longer compared with airborne SAR. On the other hand, the antenna's footprint on the ground is much shorter for the airborne SAR. Therefore, the range-delay shift of the scatterer may be less than the range resolution, which may cause no migration in the range. Another cause of range migration

occurs from the phenomena called *range walk*. When the integration time is long, the rotation of earth causes shifting of the position of the scatterer with respect to radar. The same effect happens when the ground target is moving. These reasons result in migration of the scatters in the image cells. To have a focused image, range migration correction is required in the Doppler frequency domain [6–8].

Both range curvature and range walk possess a parabolic track within the real beam of the radar. If the range error resulted by these effects is δR , the total range can be written as

$$R + \delta R = \left(R^2 + \left(\frac{V_p \cdot T_s}{2} \right)^2 \right)^{1/2} \quad (17)$$

Here, V_p is the velocity of the scatterer and T_s is the integration time in SAR azimuth processing. In fact, the integration time can also be written for the target's velocity V_p and the single-look angular extend θ_e as $T_s = R \cdot \theta_e / V_p$. After substituting this formula into Eq. (17) and taking the binomial expansion of the range error, we can get

$$\begin{aligned} \delta R &= \left(R^2 + \left(\frac{R \cdot \theta_e}{2} \right)^2 \right)^{1/2} - R = R \left(1 + \left(\frac{\theta_e}{2} \right)^2 \right)^{1/2} - R \\ &= R \left(1 - \frac{1}{2} \left(\frac{\theta_e}{2} \right)^2 + H.O.T. \right)^{1/2} - R \cong \frac{R \cdot \theta_e^2}{8} \end{aligned} \quad (18)$$

Then, Δr being the range resolution, the migration in the range cell can be found by

$$N \approx \frac{\delta R}{\Delta r} = \frac{R \cdot \theta_e^2}{8 \Delta r} \quad (19)$$

If this number turns out to be more than 1, the range migration correction has to be performed accordingly. If not, no correction is needed.

2.2. Motion Errors

The basic theory of SAR relies on the assumption that the scene or the target is stationary. If a scatterer in the scene is moving, the Doppler shift posed by the scatterer's line-of-sight velocity sets the "incorrect" distance information about the position of the scatterer to the phase of the received EM wave. When the scatterer is moving so fast, it occupies several pixels in the image during the integration interval of SAR. Therefore, the image of the scatterer is blurred like a comet in the sky, which is analogous to optical photography when the object is moving so fast that it occupies larger space until the lens is closed. When the scatterer is in slow motion, the SAR image may not be blurred. However, the location of the scatterer will still not be correct because of Doppler shift. To minimize these

motion errors, *motion compensation* techniques have to be applied (see Section 4.1).

2.3. Speckle Noise

The size of one SAR resolution cell (i.e., a pixel) can vary from a few centimeters to tens of meters depending on the size of the synthetic aperture and the bandwidth in frequency. Generally, Earth’s surface is uneven within one resolution cell. Therefore, one pixel of SAR may not resolve the detailed features of Earth’s surface. As the EM energy diffracted from such uneven patches will have various phase values, the net effect on the image pixel can be constructive or destructive. The resulting noise-like behavior is known as *ground clutter* or *speckle noise*. One way we can reduce speckle noise in SAR imaging is to use multi-look processing [4]. Another method is for us to apply statistical filtering of speckle noise by using proper probability distribution models such as Rayleigh distribution [9,10].

3. INVERSE SYNTHETIC APERTURE RADAR

3.1. SAR versus ISAR

Inverse synthetic aperture radar (ISAR) is a powerful signal processing technique for imaging moving targets in range and cross-range domains. SAR generally refers to the case when radar platform is moving while the target stays stationary. The required spatial (or angular) bandwidth is achieved by the movement of radar around the target or terrain. We use the term *inverse synthetic aperture radar* for scenarios when the radar is standing still and the target is in motion like airplanes, ships, and tanks, as illustrated in Fig. 9. For the ISAR case, stationary radar collects the angular data through the target movement. For the collected echo dataset, ISAR geometry, in fact, can also be thought as the same as spotlight SAR geometry with circular flight path (see Fig. 9).

3.2. Basic Theory of ISAR Imaging

Usually two-dimensional ISAR images in range and cross-range are generated with frequency and aspect diversity of the backscattered signal. Therefore, the echoed data are collected for various frequencies and angles in a two-

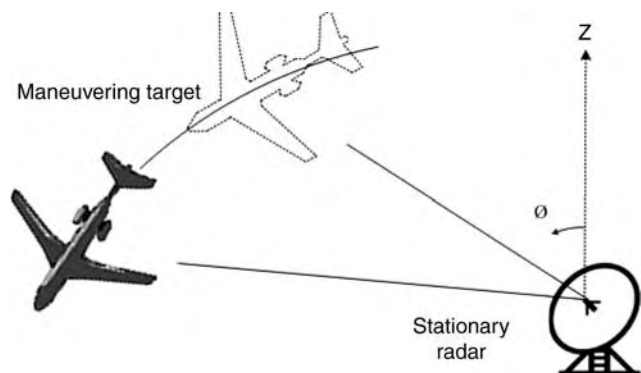


Figure 9. ISAR.

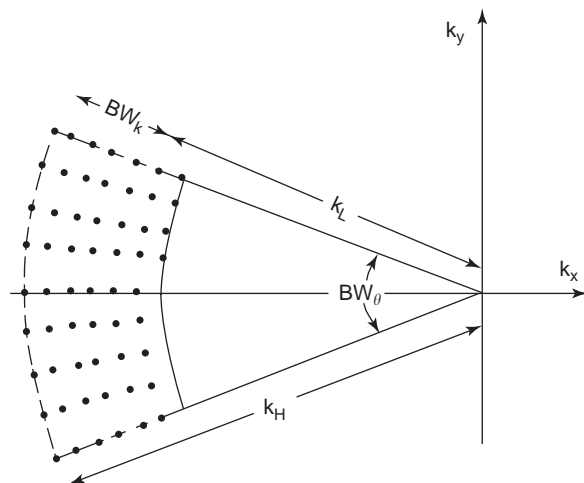


Figure 10. Collection of ISAR raw data in Fourier space for the monostatic case.

dimensional data grid as shown in Fig. 10. For *bistatic ISAR*, the transmitter and the receiver are at different locations in space. If the radar operates as both the transmitter and the receiver, this scenario is called *monostatic ISAR*. A simplified ISAR imaging theory for the monostatic case is summarized as follows. As illustrated in Fig. 11, $P(x_o, y_o)$ is a point scatterer situated on the target. Taking the origin as the phase center, the far-field back-scattered field from a point scatterer P at an azimuth angle ϕ can be written as

$$E_s(k, \phi) = A_o \exp(j2\mathbf{k} \cdot \mathbf{r}_o) \tag{20}$$

Here, A_o is the amplitude of the backscattered electric field intensity, \mathbf{k} is the vector wavenumber in propagation direction, and \mathbf{r}_o is the vector from origin to point P . The multiplier “2” in the exponential accounts for the two-way propagation between the radar and the scatterer. \mathbf{k} vector can be written for the wavenumbers in x - and y -directions

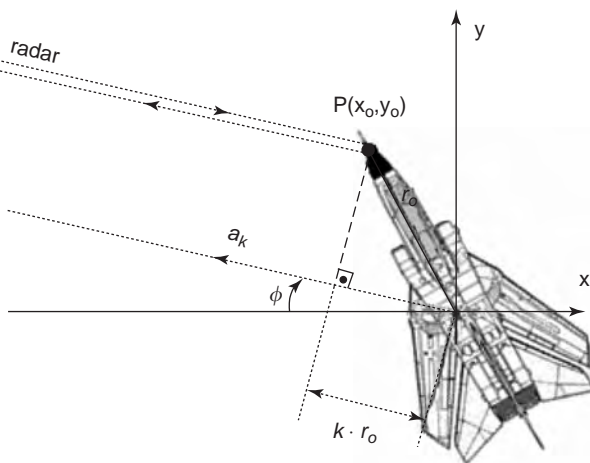


Figure 11. Geometry for monostatic ISAR imaging.

as follows:

$$\begin{aligned} \mathbf{k} &= k \cdot \mathbf{a}_k = k_x \cdot \mathbf{a}_x + k_y \cdot \mathbf{a}_y \\ &= k(\mathbf{a}_x \cdot \cos \phi + \mathbf{a}_y \cdot \sin \phi) \end{aligned} \quad (21)$$

where \mathbf{a}_k , \mathbf{a}_x , and \mathbf{a}_y are the unit vectors in k -, x -, and y -directions, respectively. Then, the argument in the phase term of Eq. (1) can be reorganized to give

$$\begin{aligned} \mathbf{k} \cdot \mathbf{r}_o &= k(\cos \phi \cdot \mathbf{a}_x + \sin \phi \cdot \mathbf{a}_y) \\ &\quad \cdot (x_o \cdot \mathbf{a}_x + y_o \cdot \mathbf{a}_y) \\ &= k \cos \phi \cdot x_o + k \sin \phi \cdot y_o \end{aligned} \quad (22)$$

Therefore, we can rewrite Eq. (20) as

$$\begin{aligned} E_s(k, \phi) &= A_o \cdot \exp(j2k \cos \phi \cdot x_o) \\ &\quad \cdot \exp(j2k \sin \phi \cdot y_o) \end{aligned} \quad (23)$$

It is obvious from Eq. (23) that Fourier relationships exist between $2k \cos \phi$ -and- x_o and $2k \sin \phi$ -and- y_o . Therefore, the ISAR image can be generated in range and cross-range domains by the convenience of the 2-D Fourier transform.

3.2.1. Small Bandwidth, Small-Angle ISAR Imaging. This procedure is standard where practical ISAR imaging is concerned. Assume that the frequency bandwidth, BW_f , is small compared with center frequency of operation f_c . Then, the wavenumber in the second phase term of Eq. (23) can be approximated as $k \approx k_c$, where k_c is the wavenumber corresponding to the center frequency. Furthermore, the synthetic aperture angular bandwidth, BW_ϕ , is also selected as small in most of the ISAR applications. Therefore, the following approximations for the angles within the specified angular bandwidth hold true:

$$\begin{aligned} \cos \phi &\approx 1 \\ \sin \phi &\approx \phi \end{aligned} \quad (24)$$

Then, the scattered electric field from point P can be approximated to

$$\begin{aligned} E_s(k, \phi) &\cong A_o \cdot \exp(j2k \cdot x_o) \\ &\quad \cdot \exp(j2k_c \phi \cdot y_o) \end{aligned} \quad (25)$$

With this construct, the two-dimensional polar data in Fig. 10 forms nearly a rectangular grid that makes it possible for us to use discrete Fourier transform (DFT). Then, it is easy for us to take the two-dimensional Fourier transform of Eq. (25) with respect to k and ϕ to get the image of the point scatterer at P in the range and cross-range domains as follows:

$$\begin{aligned} IFT_2\{E_s(k, \phi)\} &= A_o \cdot IFT_1\{\exp(j2k \cdot x_o)\} \\ &\quad \cdot IFT_1\{\exp(j2k_c \phi \cdot y_o)\} \end{aligned} \quad (26)$$

$$E_s(x, y) = A_o \cdot \delta(x - x_o) \cdot \delta(y - y_o)$$

Here $\delta(\cdot)$ represents the impulse (or dirac delta) function. Therefore, the point P manifests itself in the image as a two-dimensional impulse function located at (x_o, y_o) . In summary, a two-dimensional ISAR image of a target is obtained by the following Fourier integral of the scattered field:

$$\begin{aligned} ISAR(x, y) &= \int_{-\infty}^{\infty} \int_{-\infty}^{\infty} E_s(k, \phi) \cdot e^{j2k \cdot x} \\ &\quad \cdot e^{j2k_c \phi \cdot y} d(k) \cdot d(k_c \phi) \end{aligned} \quad (27)$$

Of course, the limits of the integral in Eq. (27) have to be finite in practice because the field data can be collected within a finite bandwidth for frequencies and angles. Therefore, the image response distorts from the impulse function to the sinc function.

3.2.1.1. Resolution, Bandwidth, and Sampling in ISAR. As is obvious from the first phase term in Eq. (25), the Fourier requirement exposes the following for the range resolution of ISAR:

$$\Delta r = \frac{2\pi}{2BW_k} = \frac{c}{2BW_f} \quad (28)$$

Looking at the second phase term in Eq. (25), the cross-range resolution, Δx , can be obtained with a similar manner as follows:

$$\Delta x = \frac{2\pi}{2k_c BW_\phi} = \frac{c}{2f_c BW_\phi} = \frac{\lambda_c}{2BW_\phi} \quad (29)$$

Therefore, a wide frequency bandwidth provides fine range resolution and a wide angular bandwidth assures good cross-range resolution. For example, if the target's EM reflectivity is collected for an angular bandwidth of 11.5 degrees with a frequency range changing from 9.5 GHz to 10.5 GHz, both the range and the cross range resolutions become 15 cm.

Having found resolutions in range and cross-range domains, the choice of number of sampling points determines the bandwidths in these domains (i.e., the image size). If the frequency range is sampled by N times and the angular range is sampled by M times, corresponding image domain bandwidths are given as

$$\begin{aligned} BW_r &= N \cdot \Delta r = \frac{N \cdot c}{2 \cdot BW_f} \\ BW_x &= M \cdot \Delta x = \frac{M \cdot c}{2 \cdot BW_\phi} \end{aligned} \quad (30)$$

For Eq. (30), if the two-dimensional frequency-aspect data are collected over 128 sampling points in each domain, the image size becomes 19.2 m by 19.2 m.

3.2.2. Wide Bandwidth, Wide-Angle ISAR Imaging. If the small bandwidth and small angle approximations are not valid, the ISAR imaging integration in Eq. (27) becomes in

its general format

$$\begin{aligned}
 E_s(x,y) &= \int_{-\infty}^{\infty} \int_{-\infty}^{\infty} E_s(k, \phi) \cdot e^{j2k \cdot r} d(k) \cdot d(\phi) \\
 &= \int_{-\infty}^{\infty} \int_{-\infty}^{\infty} E_s(k, \phi) \cdot e^{j2k \cos \phi \cdot x} \\
 &\quad \cdot e^{j2k \sin \phi \cdot y} d(k) \cdot d(\phi)
 \end{aligned}
 \tag{31}$$

Notice that collected Fourier space data are in polar format. For us to use DFT while forming the ISAR image, the data have to be in a discrete, uniformly spaced rectangular form. Therefore, the data should be reformatted from polar coordinates to Cartesian coordinates as depicted in Fig. 12. This process is known as *polar reformatting*. To minimize the error associated with this reformatting, several interpolation schemes such as four nearest neighbor approximation [11] are employed. After putting these data in their proper formats, the ISAR image can be generated similarly by applying the two-dimensional discrete Fourier transform operation as explained in Section 3.2.1. An example of ISAR imagery is shown in Fig. 13. The raw ISAR data were measured from a ground radar, and the target was an aircraft in flight [12].

4. SOME ADVANCED CONCEPTS IN SAR

4.1. Motion Compensation

As stated, the SAR theory is based on the assumption that the scene is stationary and the SAR platform travels along a straight path with a constant speed. If these assumptions are not valid, some degradation in SAR images is unavoidable. After radar sends an EM wave to the scene and the wave hits the target, the leading edge and then the trailing edge of the wave have different trip distances for a moving target. Therefore, the phase of the backscattered wave is altered such that the resultant image is mislocated in cross-range and defocused in both range and cross-range domains.

As illustrated in Fig. 14, we assume a scatterer point $P(x_c + x_o, y_c + y_o)$ on a target that has both translational and rotational motion. $Q(x_c, y_c)$ in Fig. 14 represents the center point of the target. We would like to estimate the phase error associated with the motion of the target. If the radar is situated at the far field of the target, the point

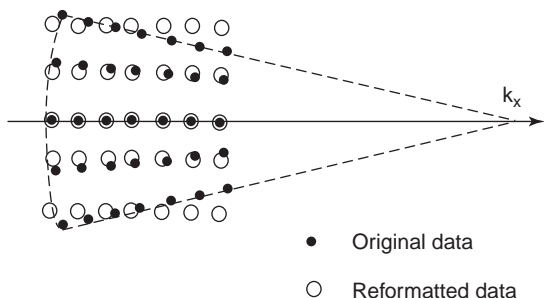


Figure 12. Rectangular reformatting of polar ISAR data.

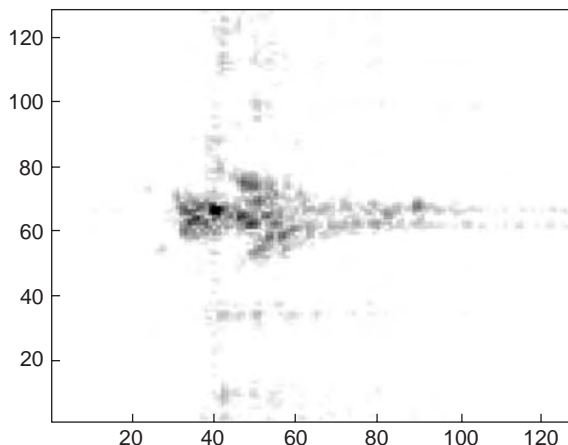


Figure 13. ISAR image of an aircraft from the measured data. (Source [12] © 1999 SPIE.)

P has a distance from the target as

$$R = R_c + x_o \cdot \cos(\phi_o - \phi) - y_o \cdot \sin(\phi_o - \phi) \tag{32}$$

Here, R_c is the distance between the radar and the center of the target. If the target has only linear translational velocity V_t and a linear rotational velocity ϕ_r , then the time-varying range distance and the rotation angle can be written as

$$\begin{aligned}
 R_c(t) &= R_o + V_t \cdot t \\
 \phi(t) &= \phi_o + \phi_r \cdot t
 \end{aligned}
 \tag{33}$$

where R_o and ϕ_o are the initial values for the target's distance from radar and the orientation of the target with respect to x -axis, respectively. The phase of the backscattered signal from point P is equal to

$$\Phi(t) = -j2kR(t) = -j2\pi f \frac{2R(t)}{c} \tag{34}$$

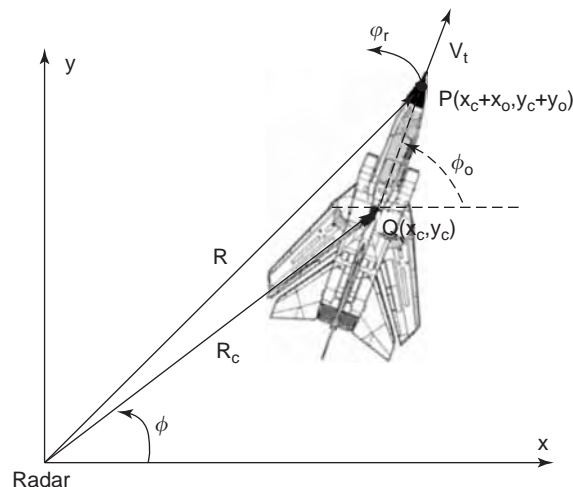


Figure 14. Geometry for imaging a target with motion.

Therefore, the Doppler shift caused by motion can be calculated by taking the time derivative of this phase as

$$\begin{aligned} f_D &= \frac{1}{2\pi} \frac{\partial}{\partial t} \Phi(t) = -\frac{2f}{c} \frac{\partial}{\partial t} R(t) \\ &= -\frac{2f}{c} V_t + \frac{2f\varphi_r}{c} [x_o \cdot \sin(\phi_o + \varphi_r t - \phi) \\ &\quad + y_o \cdot \cos(\phi_o + \varphi_r t - \phi)] \end{aligned} \quad (35)$$

Here, the first term represents the translational Doppler frequency shift, $f_D^{Trans} = -\frac{2f}{c} V_t$, and the second term corresponds to the rotational Doppler frequency shift, $f_D^{Rot} = \frac{2f\varphi_r}{c} [x_o \cdot \sin(\phi(t)) + y_o \cdot \cos(\phi(t))]$, where $\phi(t) = \phi_o + \varphi_r t - \phi$.

When the SAR is considered, the backscattered signal can be written as the integration of the returned signals from all scatterers inside the radar beam:

$$g(t) = \int_{-\infty}^{\infty} \int_{-\infty}^{\infty} \int_{-\infty}^{\infty} \Gamma(x, y, z) \cdot \exp\left(-j \frac{4\pi f}{c} R(t)\right) \cdot dzdydx \quad (36)$$

Here $\Gamma(x, y, z)$ is the backscattered signal intensity from point (x, y, z) . Substituting the range equation in Eq. (35) into Eq. (36), we can get the following:

$$\begin{aligned} g(t) &= \exp\left(-j \frac{4\pi f}{c} R_c(t)\right) \\ &\times \int_{-\infty}^{\infty} \int_{-\infty}^{\infty} \int_{-\infty}^{\infty} \Gamma(x, y, z) \\ &\cdot \exp\left(-j \frac{4\pi f}{c} (x_o \cdot \sin(\phi(t)) + y_o \cdot \cos(\phi(t)))\right) \cdot dzdydx \end{aligned} \quad (37)$$

If the target's initial range R_o and the linear translational velocity V_t is known, the phase term before the above integral can be removed by multiplying Eq. (37) by $\exp\left(j \frac{4\pi f}{c} R_c(t)\right)$ for every pixel in the SAR data. This process is called *range tracking*, and it is the basic procedure for the standard motion compensation. After obtaining the phase-compensated backscattered signal, a Fourier transform operation can be applied to image the backscattered signal intensity function $\Gamma(x, y, z)$ [13]. This process is the coarse motion compensation approach. If the scatterers pass different range cells during the coherent integration, the resultant phase-compensated image will still be defocused. Therefore, a finer compensation called *Doppler tracking* that tries to make the Doppler shifts constant is required [14–16].

An example of motion compensation is depicted in Fig. 15 where an ISAR image of Boeing-727 data with motion compensation is illustrated. In Fig. 15(a), a 2-D ISAR image of the original data is shown. As easily observed from the figure, the image is blurred because of motion errors. In Fig. 15(b), the motion errors are suppressed by applying both translational and rotational motion compensation

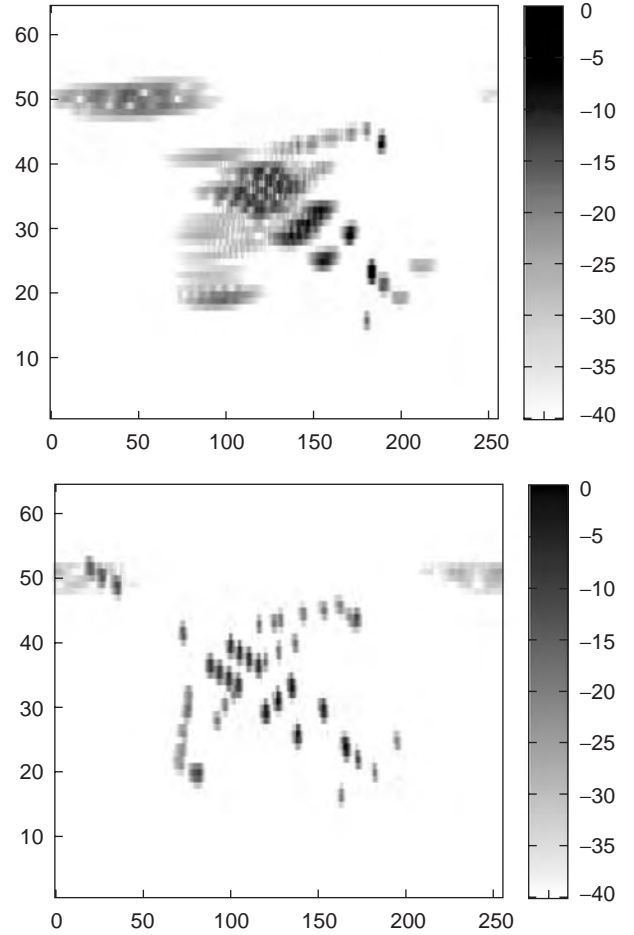


Figure 15. ISAR image of simulated B727 data (a) before and (b) after motion compensation. (Source [17] © 1998 IEEE.)

algorithms [17]. Therefore, the image is well focused and the motion errors in range are also mitigated.

4.2. SAR Interferometry

This application of SAR imagery is one of the most unique. When compared with optical imaging that has only the amplitude information of the reflected light, SAR images contain both the amplitude and the phase information of the backscattered electromagnetic energy. Therefore, if the multilook images of the scene from different elevations are obtained, the comparison of the phases can lead to the third dimension (i.e., height) having interferometric images. The first demonstrated interferometric SAR (IFSAR) was presented by Graham when he configured a cross-track interferometer in 1974 [18]. Goldstein and Zebker used an along-track SAR interferometry configuration to measure radial velocity of moving targets in 1987 [19]. In 1988, Gabriel and Goldstein obtained an elevation map of a terrain with the data collected by SIR-B by means of a single antenna with repeat pass [20].

In IFSAR, a second image of the same scene extracts the third dimension, which can be achieved either by an airborne/spaceborne vehicle carrying a two-radar system or by a single-antenna vehicle with repeat passes over the

same scene. For the latter situation, suppose that the vehicle is moving in the x -direction with a speed of V_x and an altitude of h from a reference scatterer point on the scene. Therefore, the phase of the roundtrip EM wave that is reflected from the reference point is

$$\vartheta_1 = \exp[-j2k(x^2 + y^2 + (z - h)^2)^{1/2}] \quad (38)$$

On the next pass, the vehicle keeps the same height and speed, but its track is shifted by a distance of d in the y -direction. Therefore, the phase of the backscattered EM wave from the same reference point becomes

$$\vartheta_2 = \exp[-j2k(x^2 + (y - d)^2 + (z - h)^2)^{1/2}] \quad (39)$$

Multiplying the first phase with the complex conjugate of the second phase and expanding the difference to the first order of d yields

$$\vartheta_2 \times \vartheta_1^* \cong \exp\left(j \frac{4\pi y d}{\lambda R}\right) \quad (40)$$

where $R = (x^2 + y^2 + (z - h)^2)^{1/2}$. In this equation, R , y , and x are already known after applying the range and azimuth compression and the Doppler processing. If the separation d between two passes is known, the only unknown parameter z (i.e., height) can easily be calculated from Eq. (40). This process is the basic approach for IFSAR. An example of interferometric SAR is shown in Fig. 16. This image of Mt. Etna, Italy was obtained by the SIR-C/X-SAR in 1994. The image covers an area of $51.2 \text{ km} \times 22.6 \text{ km}$. Different elevation regions surrounding the volcanic Etna are illustrated with different color values.

4.3. SAR Polarimetry

For a conventional SAR, both the receiver and the transmitter are designed to have only one polarization, i.e., horizontal (H) or vertical (V). However, to extract the full scattering feature of a scene, all polarization signatures, HH, HV, VH, and VV, have to be known. When identical polarizations are used by scientists for transmit and receive, the SAR system is said to be at *copolarization*. When the radar collects the received field at orthogonal polarization to that of the transmitted field, then the SAR system is *cross-polarized*. The images obtained by these two

polarization cases may differ because of the different scattering features of the terrain. For smooth surfaces such as oceans, lakes, and deserts, the copolarized SAR image differs significantly from the cross-polarized one. However, both co- and cross-polarized SAR setups produce almost similar images for rough surfaces like mountains and forests. Manmade objects are always found to appear in the image for any type of polarization because most of them have the feature of a corner reflector. Therefore, identifying the features and material types of terrain structure such as rock type may be possible with the help of SAR polarimetry. Good polarimetric SAR images were presented by Held et al. [21] and Sullivan et al. [22].

4.4. Three-Dimensional SAR/ISAR

Conventional SAR/ISAR provides a 2-D image of a scene/target. For SAR, a 3-D image can be obtained with interferometric/polarimetric techniques as explained in Sections 4.2 and 4.3. For 3-D ISAR, the scattered data are collected in a two-dimensional aperture in angles. Under small bandwidth and small aspect constructs, if BW_f , BW_ϕ , and BW_θ are the bandwidths in frequency, azimuth, and elevation, respectively, then the corresponding image resolutions in range and two cross-range dimensions are given by

$$\Delta x = \frac{c}{2 \cdot BW_f} \quad \Delta y = \frac{\lambda_c}{2 \cdot BW_\phi} \quad \Delta z = \frac{\lambda_c}{2 \cdot BW_\theta} \quad (41)$$

where λ_c is the wavelength corresponding the center frequency. The rest of the imaging process is similar to what is outlined in the ISAR imaging algorithm in Section 3.2. Therefore, a 3-D image can be obtained by taking the following 3-D Fourier integral:

$$\begin{aligned} ISAR_{3D}(x, y, z) = & \int_{-\infty}^{\infty} \int_{-\infty}^{\infty} \int_{-\infty}^{\infty} \mathbf{E}_s(k, \phi, \theta) \cdot e^{j2k \cdot x} \cdot e^{j2k_c \phi \cdot y} \\ & \cdot e^{j2k_c \theta \cdot z} d(k) \cdot d(k_c \phi) \cdot d(k_c \theta) \end{aligned} \quad (42)$$

Recently, new SAR algorithms called antenna SAR (ASAR) [23] and antenna coupling SAR (ACSAR) [24] to image antenna–platform interaction have been developed. Unlike conventional ISAR imaging that uses backscattered field data from a target, these algorithms use



Figure 16. (SIR-C/X-SAR) Interferometric image of Mount Etna, Italy. (Courtesy NASA/JPL-Caltech.) (This figure is available in full color at <http://www.mrw.interscience.wiley.com/erfme>.)

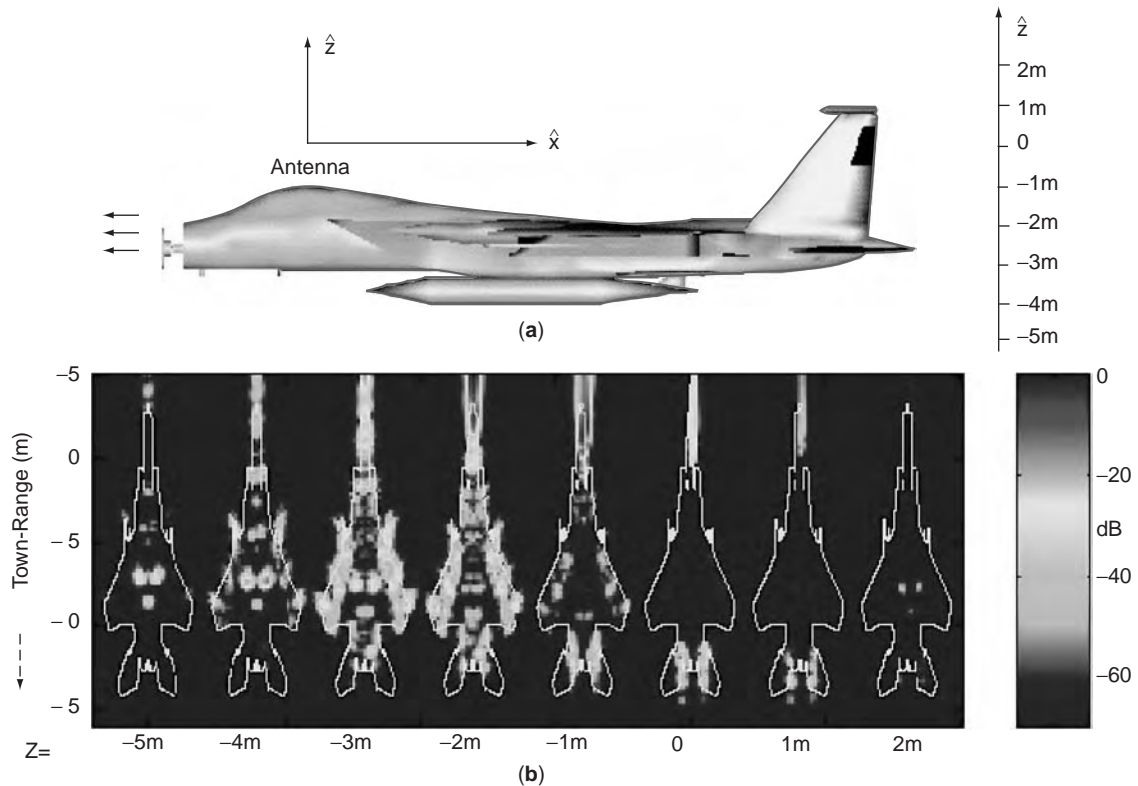


Figure 17. (a) An aircraft model and (b) simulated 2-D slices of 3-D ASAR image of the aircraft. (Source [23] © 1998 IEEE.) (This figure is available in full color at <http://www.mrw.interscience.wiley.com/erfme>.)

radiation field data off the antenna–platform pair. Both ASAR and ACSAR provide good-quality 3-D images of the antenna–platform interaction. An example of 3-D ASAR imagery is shown in Fig. 17. In this example, a monopole antenna operating at X-band is placed above the cockpit of the model aircraft. Three-dimensional multifrequency, multispect radiation data from the antenna–aircraft pair is collected at the far field from the nose-on. Figure 17 demonstrates eight different 2-D ASAR images corresponding to eight different slices of the target [23].

5. CONCLUSION

Synthetic aperture radar is a powerful and useful remote sensing technique primarily used by scientists for imaging Earth's surface. In this article, we mentioned many other applications of SAR from topographic imaging to mine detection. Some limitations and problems may occur while applying the SAR imaging process. For example, both range curvature and range walk may cause migration of the scatterers in the image. Furthermore, any moving target or nonlinear radar motion results in undesired Doppler shifts that lead various degradations (e.g., defocusing, shifting) in the resultant SAR image. Ground clutter or speckle is also a common problem in SAR imagery. Researchers are putting significant effort toward solving these challenging problems. Developments on SAR processing bring out many emerging SAR technologies in different fields. SAR-based *subsurface imaging* techniques

are the alternative approaches for detecting buried objects beneath Earth's surface or situated interior to a visually opaque medium [25–27]. Another interesting application is the *differential interferometry* [28–30]. In this method, SAR platform passes over the scene three times. If a change in the scene (like glacier motion or earthquake movement) occurs, the differential phases between the passes produce a value different than zero. Then, these changes can be detected and imaged. A similar technology is so-called *polarimetric interferometry* [31,32]. The idea in this method is to get the full scattering matrix (i.e., HH, HV, VH, and VV polarizations) at each end of the interferometric baseline. Once the full scattering matrix is acquired, optimum polarization orientation can be solved to maximize the interferometric coherence. In return, it becomes possible to measure interferometric differences at centimeter levels. Compensating induced errors caused by complex aircraft/target motions including 3-D movements has been a challenging topic since the invention of SAR. By applying joint-time frequency (JTF) processing to SAR/ISAR data, it is possible to compensate both the translational and the rotational motion errors that cause shifting and defocusing of scatterers in the resulting image [12].

BIBLIOGRAPHY

1. C. Wiley, *Pulsed Doppler Radar Method and Means*, U.S. Patent 3,196,436 (1954).

2. C. W. Sherwin, J. P. Ruina, and R. D. Rawcliffe, Some early developments in synthetic aperture radar systems, *IRE Trans. Military Electronics*, **6**(2):111–115 (1962).
3. L. J. Cutrona, et al., Optical data processing and filtering systems, *IRE Trans. Information Theory*, **6**:386–400 (1960).
4. R. J. Sullivan, *Microwave Radar Imaging and Advanced Concepts*, Norwood, MA: Artech House, 2000.
5. D. Wehner, *High Resolution Radar*, Norwood, MA: Artech House, 1987.
6. N. Levanon, *Radar Principles*, New York: Wiley-Interscience, 1988.
7. J. M. Lopez-Sanchez and J. Fortuny-Guasch, 3-D radar imaging using range migration techniques, *IEEE Trans. Antennas Propagat.*, **48**(5):728–737 (2000).
8. J. Fortuny-Guasch and J. M. Lopez-Sanchez, Extension of the 3-D range migration algorithm to cylindrical and spherical scanning geometries, *IEEE Trans. Antennas Propagat.*, **49**(10):1434–1444 (2001).
9. C. Oliver and S. Quegan, *Understanding Synthetic Aperture Radar Images*, Boston, MA: Artech House, 1998.
10. F. N. S. Medeiros, N. D. A. Mascarenhas, L. F. Costa, Evaluation of speckle noise MAP filtering algorithms applied to SAR images, *Intern. J. Remote Sensing*, **24**:5197–5218 (2003).
11. R. Bhalla and H. Ling, ISAR image formation using bistatic data computed from the shooting and bouncing ray technique, *J. Electromag. Waves App.*, **7**(9):1271–1287 (1993).
12. J. Li, et al., Comparison of high-resolution ISAR imageries from measurement data and synthetic signatures, *SPIE Pro. Radar Process., Techn., Applicat. IV*, **3810**:170–179 (1999).
13. V. C. Chen and H. Ling, *Time-Frequency Transforms for Radar Imaging and Signal Processing*, Norwood, MA: Artech House, 2002.
14. J. C. Kirk, Motion compensation for synthetic aperture radar, *IEEE Trans. Aerospace Electronic Sys.*, **11**:338–348 (1975).
15. J. Walker, Range-Doppler imaging of rotating objects, *IEEE Trans. Aerospace Electronic Sys.*, **16**:23–52 (1980).
16. H. Wu, et al., Translational motion compensation in ISAR image processing, *IEEE Trans. Image Processing*, **14**(11):1561–1571 (1995).
17. Y. Wang, H. Ling, and V. C. Chen, ISAR motion compensation via adaptive joint time-frequency technique, *IEEE Trans. Aerospace Electronic Sys.*, **34**:670–677 (1998).
18. L. C. Graham, Synthetic Interferometer radar for topographic mapping, *Proc. IEEE*, **62**(2):763–768 (1974).
19. R. M. Goldstein and H. A. Zebker, Interferometric radar measurements of ocean surface currents, *Nature*, **328**(20):707–709 (1987).
20. A. K. Gabriel and R. M. Goldstein, Crossed orbit interferometry: theory and experimental results from SIR-B, *Int. J. Remote Sens.*, **9**(5):857–872 (1988).
21. D. N. Held, W. E. Brown, and T. W. Miller, Preliminary results from the NASA/JPL multifrequency multipolarization SAR, *Proc. 1988 IEEE National Radar Conf.*, pp. 7–8, 1988.
22. R. J. Sullivan, et al., Polarimetric X/L/C band SAR, *Proc. 1988 IEEE National Radar Conf.*, pp. 9–14, 1988.
23. C. Ozdemir, et al., ASAR—Antenna synthetic aperture radar imaging, *IEEE Trans. Antennas Propagat.*, **46**(12):1845–1852 (1998).
24. C. Ozdemir and H. Ling, ACSAR—Antenna coupling synthetic aperture radar (ACSAR) imaging algorithm, *J. Electromag. Waves App.*, **13**(3):285–306 (1999).
25. J. I. Halman, K. A. Shubert, and G. T. Ruck, SAR processing of ground-penetrating radar data for buried UXO detection: results from a surface-based system, *IEEE Trans. Antennas Propagat.*, **46**:1023–1027 (1998).
26. A. Sullivan, et al., Ultra wide-band synthetic aperture radar for detection of unexploded ordnance: modeling and measurements, *IEEE Trans. Antennas Propagat.*, **48**:1306–1315 (2000).
27. C. Ozdemir, S. Lim, and H. Ling, A synthetic aperture algorithm for ground-penetrating radar imaging, *Microwave Opt. Tech. Letters*, **42**(5) (2004).
28. A. K. Gabriel, R. M. Goldstein, and H. A. Zebker, Mapping small elevation changes over large areas: differential radar interferometry, *J. Geophys. Res.*, **94**(7):9183–9191 (1989).
29. H. A. Zebker, et al., On the derivation of coseismic displacement field using differential radar interferometry: the Landers earthquake, *J. Geophys. Res.*, **99**(10):19617–19634 (1994).
30. D. Massonnet, et al., The displacement field of the Landers earthquake mapped by radar interferometry, *Nature*, **364**:138–142 (1993).
31. J. J. Van Zyl, H. A. Zebker, and C. Elachi, Polarimetric SAR Applications, F. T. Ulaby and C. Elachi, eds., *Radar Polarimetry for Geoscience Applications*, Norwood, MA: Artech House, 1990.
32. S. R. Cloude and K. P. Papathanassiou, Polarimetric SAR interferometry, *IEEE Trans. Geosci. Remote Sensing (TGARS)*, **36**(5):1551–1565 (1998).

TARGET TRACKING

OLIVER E. DRUMMOND
Consulting Engineer
Culver City, CA

1. TYPES OF TARGET TRACKING

Target-tracking problems can be broadly categorized into four generic classes, as follows:

1. Sensor tracking of a single (bright) target
2. Tracking of targets that are large
3. Tracking of targets that are medium-sized
4. Tracking of targets that are small

The target sizes indicated in this list are in terms of the number of resolution elements or pixels. The primary differences in each of these problems are the algorithms used in the signal, image, and track processing. The algorithms and processing methods used for each of these problems are substantially different. Of course, the system and its hardware must be designed to be compatible with and take advantage of the appropriate processing methods for an application. These methods depend on the types of algorithms used in the processing.

1.1. Sensor Tracking of a Single Target

Examples of the Class 1 tracking problem above are a gimbal-mounted telescope following a planet and an interceptor pursuing a target. Tracking is achieved typically through signal processing to locate the target in the field of view (FOV) and then guiding gimbals of the telescope (or seeker of an interceptor) to drive the target near the center of the FOV. This type of tracker is sometimes referred to as a closed-loop tracker. The signal from the signal processor is typically temporally filtered before it is sent to the telescope gimbal driver, and this filter may be fairly simple compared with a Kalman filter. For some applications in this class, the target may be small initially and then grow in size, such as with an interceptor sensor. Note that for this class of tracking problem, there is often only a single target in the FOV, and it is bright (high contrast) relative to any false signals or background objects. As a consequence, uncertainty about which are the target pixels and which are not is not a major issue. Thus, using sensor data obtained from a sequence of measurements over timepoints is fairly straightforward. In the future, however, as these systems are required to operate under more challenging conditions, the tracking algorithms developed for the other three tracking categories may be required. More challenging conditions might include initially tracking a dim target or a target with accompanying debris or countermeasures.

1.2. Tracking Large Targets

An example of a Class 2 tracking problem is the use of low-altitude surveillance sensors for locating or tracking ground targets. For that example, the target extent could cover many resolution elements that provide extensive detailed information about each target of interest and the other objects in the scene. With a large target, the components of the target might be identified such as wheels, tank treads, or airplane wings. Tracking and target recognition for this class of target are typically achieved through image-processing or possibly image-understanding methods. With a large target, image-processing methods could be used to determine the details of construction as well as shape of the target from only a single frame of data. With that information, normally a good probability of correctly identifying the target type for each target in the FOV with only a single frame of data is achievable. Furthermore, normally enough information exists to simply sort out and track each target over time. That is, no confusion exists about which target in one frame of data is the same target in another frame of data. Typically, image-understanding processing can be more complex than traditional image processing, but should be more versatile in handling various types of targets, including their shadows and obscurations caused by objects such as trees.

1.3. Tracking Medium-Sized Targets

An example of the Class 3 problem is use of medium altitude surveillance sensors for tracking ground vehicles. Tracking is typically achieved using either a correlation tracker or a centroid tracker. These methods are needed to deal with and possibly take advantage of the extent of the target. A target in this class might be 20 pixels in diameter. Typically, with a target of that size, not enough information useful for image processing is available, yet the extent should be taken into account. For example, for each timepoint, the location of the target needs to be established relative to some point on the target. That point on the target is then used to track the target over time. Thus a consistent point is needed on the target so that the estimated motion is not corrupted by use of different points on the target over time. With a *correlation tracker*, the processor finds the location that maximizes the correlation between the current image of the target and a reference target image. The appearance of the target can depend on the aspect angles, which can change over time, and that complicates the processing. The algorithms for correlation tracking usually are designed to accommodate all possible values of the aspect angles. A *centroid tracker* uses the shape and possibly the signal amplitude profile to establish a point on the target each time it is observed. For this type of target, the size and shape of the target helps in determining which target in one frame of data is the same target in another frame of data. This information can be corrupted by false signals, obscurations by other objects,

similar nearby objects, and random motions of the sensor line of sight.

1.4. Tracking Small Targets

An example of the Class 4 tracking problem is the use of ground-based surveillance sensors for tracking aircraft, cruise missiles, or ballistic missiles. Tracking small targets is achieved using what is commonly referred to as multiple target tracking methods. This class of problem is often referred to as *multiple target tracking*, even though it includes both single, small target tracking with persistent clutter or false signals and the tracking of multiple small targets that may be close or crossing and with possibly persistent clutter or false signals. For this class of tracking problem, uncertainty can exist as to which target is responsible for a measurement, because of closely spaced measurements. This uncertainty greatly complicates the processing. The processing function that decides how to relate the current measurements to the existing target tracks or prior data is called *data association* (sometimes referred to as correlation). The data-association function deals with the ambiguity of which measurement comes from each target that was observed earlier. In most small target tracking, there is not enough information in a sensor measurement to know which target (if any) was the source of the measurement. As a consequence, the wrong measurement might be used to update a target track, and this type of error is often referred to as a *misassociation*.

1.5. Impact of Target Conditions on Processing Methods

Not only does each of these classes of target-tracking problems call for different processing algorithms, but also the processing concepts and the algorithm development methodologies can be very different. For example, for the development of the small target-tracking algorithms, typically a simulation is used to generate data to test the algorithms. Many runs (instances) of a Monte Carlo simulation can then be used to obtain performance with reasonable confidence (given a sufficiently detailed simulation). On the other hand, to test image-processing algorithms for tracking large targets, usually a set of images of real scenes containing targets is used. Because typically it is difficult to obtain and test many hundreds of images, the methodology for algorithm development and performance evaluation of large target-tracking algorithms is very different from that for small targets. Also, the type of algorithms used for image processing are very different from those used for tracking small targets.

The track-processing methods used also depend on the type of sensor or suite of sensors that provide the data for a system application. The phenomena encountered for each type of sensor can have a significant impact on the type of processing required. For example, there are methods that can be used with an active sensor, such as radar, that cannot be used with a passive sensor, such as an electrooptical sensor. As a consequence, some specialized tracking techniques have been developed for some sensors that are not useful for others. Also, multiple-sensor systems require special considerations beyond those tracking

approaches used for single-sensor tracking. The type of target and its environment also have a major impact on the selection of the appropriate algorithms and the sequence of functions. The sequence of processing functions is often referred to as the *processing chain* or *algorithm architecture*. The algorithm architecture and specific algorithms appropriate to tracking ground targets can be very different from those used for surveillance of ballistic missiles.

2. INTRODUCTION TO SMALL TARGET TRACKING

Because each class of tracking problem poses different algorithm development issues, this article will concentrate on only one class of tracking, namely, tracking of small targets using multiple target-tracking methods. Multiple target tracking is a relatively new field. The first book dedicated exclusively to multiple target tracking was published in 1986 [1] and a number of books have been published since then [2–7]. In addition to the numerous papers and reports in the open literature (too numerous to be listed here), there is an on-going series of annual SPIE conferences concerned exclusively with signal and data processing of small targets that started in 1989 [8]. This article freely extracts and paraphrases material from some of the author's prior documents [9–15] and view graphs [16,17].

For this discussion, a *small target* is characterized as one that does not provide enough data for traditional automatic target recognition (ATR) using a single frame of data [9]. In contrast, a target large enough for ATR typically extends beyond a diameter of about 10 resolution elements, for example, larger than 10 by 10 pixels. Note that it is not uncommon to refer to all objects as targets whether they are of interest or not. Small targets include:

- Point source targets
- Small extended targets, including unresolved closely spaced objects
- Clusters (groups) of point source and small extended targets

The width of a typical point source target in the field of view is from 1 pixel to about 12 pixels (resolution elements), depending on the sensor design, for instance, the sensor spread function. Although the processing of point targets has been studied extensively, there are still many interesting challenges in this field. In contrast, the state of the art for processing small extended objects and clusters is far less mature, but interest is growing. Small targets that are not point-source objects include both small extended objects and unresolved closely spaced objects, sometimes called clumps. An *unresolved closely spaced object* (UCSO) refers to a measurement caused by a number of targets for which the location of each individual target could not be established by the signal processor because they were all too close relative to the resolution of the sensor. In many current systems, the data forwarded by the signal processor to the tracker do not give any indication of which measurement is probably a UCSO.

Although UCSOs and small extended targets provide little detailed information useful for ATR, they do exhibit some shape and size information that might be useful in tracking. Also, an extended object may partially obscure rather than add to the background or be partially obscured. The apparent size and shape of the target can differ from sensor to sensor and over time; this may have to be taken into account. Similarly, cluster processing offers significant advantages and challenges.

Developing a tracker to follow a single small target without false signals or persistent clutter is not particularly difficult. In contrast, developing a tracker is difficult for challenging conditions with resolved or unresolved closely spaced measurements caused by false signal, persistent clutter, or close targets plus possibly countermeasures or abrupt target maneuvers. Distributed multiple sensors that exhibit platform location uncertainty and residual sensor measurement biases pose additional challenges as do multiple sensors that exhibit different sensor phenomena, such as fusing data from radars and IR sensors.

There have been many advancements in small target processing algorithms in recent years. These advancements are, in part, because of opportunities to implement more advanced and complex algorithms because of the greatly increased capabilities of processors. Ongoing development of algorithms for new systems and upgrading existing systems is driven by improved sensors, increasingly demanding system requirements, processor and communications hardware limitations, severe operating environments, efficacious countermeasures, and challenging threat scenarios. There is growing interest in the ability to track dim targets or in a moderate to dense population of threshold exceedances caused by clutter, false signals, or targets that are close or crossing.

A common approach for processing target data from a single sensor is to partition the processing into the two major functions of signal processing and data processing, as shown in Fig. 1. The *signal processing* usually converts the sensor data into digital form, processes and thresholds the data to detect potential targets, and establishes the parameters of the measurement vector for each threshold exceedance. The type of signal processing algorithm used is highly specialized, based on the type of sensor. For systems that require detection of dim targets, multispectral sensor processing and the more complex multiple frame processing should be considered, such as the so-called

track-before-detect and the velocity filter approaches. The signal processor forwards the measurements to the data processor. Measurements are sometimes referred to as reports, returns, observations, hits, plots, or threshold exceedances, depending on the type of sensor. Typically, the signal processor forwards the measurements to the data processor in the form of a sequence of frames of data. A *frame of data* is simply a collection of measurements. For radar, a frame might consist of all the measurements from a single dwell, and for an IR imaging sensor, a frame of data might be all the measurements from a single look of the imager. Note in Fig. 1 the possible use of track data at the signal processing level. There is a growing recognition of the importance of using all available information in every stage of the processing and in the feedback of information [9].

The primary functions of the *data processing* of sensor data are tracking and target classification or discrimination; however, estimation of sensor registration biases, sensor resource management, situation assessment, combat identification, target weapon assignment, and other functions may also be included. Typically, a target evolves through the three processing stages of (1) track initiation, (2) track maintenance, and (3) track termination, see Fig. 2. The basic tracking functions for each stage are data association, filtering, and the track promotion and demotion logic. As mentioned earlier, the data-association function deals with the ambiguity of which measurement is from the same target as that of a track or a sequence of prior measurements.

The *filter* uses the measurement vector to update the target state estimate, its error covariance matrix, and possibly additional information. The elements of the target state typically consist of the target position and velocity in each direction plus possibly higher derivatives and other information, such as signal signature information or target features. For this discussion, the filter is assumed to be a Kalman filter or its mathematical equivalent [1,2,5]. Usually, process noise can be used in the filter model to accommodate gradual target maneuvers. If a target can make abrupt maneuvers, then a bank of Kalman filters might be used as with the interacting multiple model filters [5,18], which accommodates switching from one model to another. A bank of Kalman filters can also be used for multiple model problems that do not exhibit switching, sometimes called static multiple models [19,20]. An example

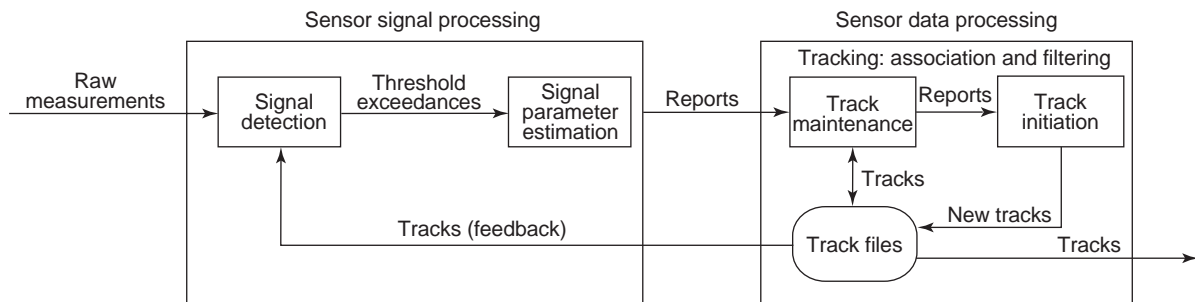


Figure 1. Block diagram of the major sensor processing functions of signal processing and data processing [9].

of the use of static multiple models is for tracking a single-stage booster that might be one of a number of different types of boosters.

Note that the Kalman filter equations are not very difficult to implement; it is the selection of the structure of the model and its parameter values used to design the filter that require pertinent background and experience. In addition, most target-sensor mathematical models are neither linear nor Gaussian, and thus some variant of an extended Kalman filter is typically used [2,5]. Nonlinearities can introduce biases in the estimation errors [6] and, in addition, unexpected results caused by the approximations used to deal with the nonlinearities are not uncommon.

For target tracking, the accuracy of both the target state estimate and its error covariance matrix (or mean square error matrix) are important. For many filtering problems other than for tracking, the accuracy of the state estimate is more important than the consistency of the error covariance matrix. Consistency in this context refers to how well the filter computed error covariance matrix reflects the actual covariance matrix of the state estimation errors. In addition, the state estimate is somewhat adaptive to model errors, but the error covariance matrix is not, which is because the computation of the state estimate is a function of the measurements that depend on the target location and motion. As a consequence, even with model errors, the computed state estimate is influenced by the true target trajectory. In contrast, the covariance matrix depends on the mathematical model used for the filter design, and in a linear system, for example, the computed filter error covariance matrix is not a function of the measurements.

In most tracking systems, the data-association function performance depends on the consistency of the computed filter covariance matrix. Hence the consistency of the error covariance consistency is substantially more important in tracking than in many other types of filtering applications and should be evaluated during the algorithm development process. Note that because the track error covariance matrix indicates how accurate a track is, this information might be useful for the functions downstream of the tracker. The consistency of the error covariance matrix is degraded by not only the filter design model errors but also by misassociations and more so with some data-association algorithms than others.

A fundamental characteristic of small target tracking is that optimal tracking is not practical. The algorithms that would provide optimal tracking performance are too complex primarily because of the data-association function but also because most systems are neither linear nor Gaussian. For *optimal tracking* performance, each possible combination of all target tracks with all the measurements obtained up to the current time must be enumerated, and that is not practical. As a consequence, a wide variety of suboptimal methods have been devised. In algorithm development, the major trade is between tracking performance and the processor loading plus, if applicable, communications loading. This is the major tradeoff, because improved performance can be obtained by more complex algorithms that are more hardware resource intensive.

Another fundamental characteristic of small target tracking is that it involves both discrete and continuous random variables or parameters. The measurement-track ambiguities introduce discrete random variables or hypotheses. Each *hypothesis* represents one combination that accounts for all the apparent targets and all the measurements. The continuous random variables are the elements of the target state vectors. Most estimation theory deals with random variables from a continuous sample space and decision theory deals primarily with random variables from discrete sample space. The combination of continuous and discrete random variables can lead to unusual results compared with the more classic estimation problems. The hypotheses can cause the *a posteriori* state probability density function to be multimodal, which can lead to unexpected tracking performance and estimation errors that clearly do not exhibit a Gaussian distribution.

As a consequence of the resulting complex nature of the estimation errors, multiple target-tracking performance evaluation and prediction are not very amenable to analysis. Therefore, usually performance is evaluated through Monte Carlo simulations followed by field testing. Monte Carlo runs are needed because tracker performance is data dependent because of misassociations and system nonlinearities. In addition, low-probability events might cause surprisingly poor performance that might not be uncovered with only one or a few Monte Carlo runs. The need for a simulation poses a dilemma because the performance evaluation results of simplistic simulation can be misleading and not reveal realistically all the phenomena or anomalies that will occur in the ultimate system. On the other hand, a more credible simulation of the targets, sensors, and signal processing characteristic can be very costly, and the simulation can be complex and difficult to manage. Typically, the simulation used to design and develop a system evolves, starting from simple simulations for preliminary evaluation of well selected critical functions to a complex high-fidelity simulation of the entire tracking system. The simulation environment needs to be flexible enough to easily accept major revisions to the tracker algorithms and the algorithms architecture, as well as new or modified sensor designs and targets.

Because optimal tracking methods are too complex to be practical, ad hoc algorithms are typically devised that take advantage of the particular targets, sensors, and related conditions of the system for which the tracker is designed. As a consequence, there is no universal tracker, although there might be a tracker that is developed for a particular type of scenario. Trackers are continually being developed to accommodate new requirements or target threat characteristics and to take advantage of increases in processor and communications capability as well as new or improved sensors.

Algorithm development of a tracker for a system is typically an experimental and iterative process, which is because of the undesirable performance that results from misassociations and unexpected operating conditions that are revealed through high-fidelity simulations and hardware in the loop testing. Each stage of the algorithm development spiral typically includes a reevaluation of the requirements and performance obtained during the

prior stage, algorithm redesign or replacement, performance evaluation testing, and study of the results. During algorithm development, it is not uncommon to have to replace some algorithms (or make major modifications to them) because of unexpected operating conditions or performance results. Thus care is needed in undertaking software development of the deliverable code before the algorithm development process is complete.

In describing the various target-tracking methods, tracking with data from a single sensor is discussed before discussing tracking with multiple sensors, which is more complex. Also, single target tracking is discussed before multiple target tracking because the tracking of multiple targets is substantially more complex than tracking a single target. The major emphasis in this article is on the data-association function, because that is the process that is unique to small target tracking relative to most other estimation tasks. The targets are assumed to be noncooperative in that, typically, they do not purposely communicate to the trackers their identity or location as is done for air-traffic control.

3. SINGLE TARGET TRACKING WITH FALSE SIGNALS

The methods used to track a single target can be useful also for tracking multiple targets, provided they are far apart. Targets that are far apart are sometimes referred to as isolated targets [16,17]. *Isolated targets* are far enough apart so that all of the measurements in the immediate neighborhood of a target track have a very low probability of being caused by another target. In both single and multiple target tracking, a processing function is used to compute a track gate that defines the immediate neighborhood of measurement for a track. The processing functions for tracking isolated targets are shown in Fig. 2.

3.1. Track Gate

A *track gate* is also called a validation region or correlation window [1,2,6]. For most tracking methods the gate function simply serves to reduce the processing load and has

little impact on performance if the track gate is big enough. To compute a simple yet practical gate, the filter function computes the expected location of the measurement for a target, which establishes the center of the gate. Then it establishes the extent of the track gate by computing the region around the predicted measurement in which the measurement caused by the target is expected to be located with a prescribed probability (given that the target is detected). A practical value is 0.99 for the prescribed probability that the correct measurement is in the track gate [17].

The size of the target gate region is computed using the innovations covariance matrix. The *innovations vector* is the difference between the measurement vector and the predicted measurement computed from the predicted target state vector. Thus the innovations covariance matrix takes into account the error in the prior target state estimate, the prediction error, and the measurement errors. The innovations are sometimes called the residuals, which is not to be confused with the measurement residuals. The *measurement residual* vector is the difference between the measurement vector and the estimated measurement computed from the estimated target state vector after being updated using that measurement.

The use of two gates each with a different shape can help reduce the processing load. For two-dimensional measurements such as with a passive sensor, for example, the first gate is a rectangle that is sized to include the second gate, which is an ellipse. The rectangular gate is less computationally intensive but is not as effective. The rectangular gate eliminates most of the measurements that will not be in the elliptical gate. The elliptical gate requires more computations, but is more effective in that it produces fewer measurements in a gate for a given probability that the correct measurement is in the gate [1,17]. An elliptical gate involves the computation of a chi-square static. In contrast, determining if a measurement is in a rectangular gate requires the computation of only a few comparisons, each preceded by the computation of the absolute value of a difference. There are other methods of computing a track gate, but for brevity they are not discussed here.

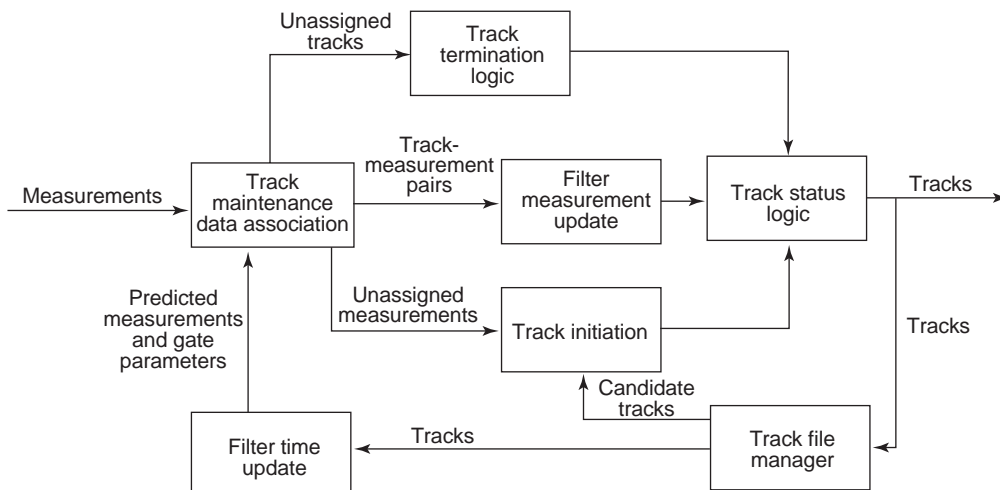


Figure 2. Block diagram of the processing functions for tracking isolated targets [17].

3.2. Data-Association Methods

For simplicity, consider single target-track maintenance, that is, assume that the target track has already been established. The tracking methods for multiple isolated targets is very similar, and track initiation, which is more complex, will be addressed later. The gate computation is the first function of the data-association process. Then, given the track gate, identify the measurements in the track gate by testing each measurement to determine first if it is in the rectangular gate and, if so, determine if it is in the elliptical gate. For a measurement vector that contains more than two elements, the rectangular and elliptical gates are replaced by their higher dimensioned counterparts. How the measurements that are in the track gate are subsequently processed depends on the chosen data-association method.

Data-association approaches can be classified as single-frame and multiple-frame methods [10,16,17]. For single target tracking, a measurement in a track gate is either a false signal or the detected target. (Note that a measurement could be because of persistent clutter. An estimate of the location of persistent clutter should be maintained because the target might pass through its neighborhood. Accordingly, persistent clutter is equivalent to a target that is not of interest and hence is in the multiple target tracking category rather than single target tracking.) Two single-frame approaches are described for single target tracking, whereas discussion of the multiple-frame data association methods are deferred to the multiple target-tracking section.

A *single-frame association* approach typically enumerates most or all the possible hypothesis tracks for a frame of data. The hypotheses are generated based on a single prior track that remains after completing the processing for the prior frame of data. For single target tracking with M measurements in the track gate, there are $M+1$ hypotheses, one for each measurement in the gate and one for the null hypothesis that the target was not detected in the gate for that frame of data. After the hypotheses are enumerated, the number of tracks is reduced to, at most, one track per apparent target for use with the next frame of data. Typically, the number of tracks of the current hypotheses is reduced to a single track by eliminating some, combining some, or both. The resulting single-state estimate will be referred to as the *composite state estimate*, and the composite state estimate and its covariance matrix (plus possibly additional information) will be referred to as the *composite track* [11].

A single-frame data-association algorithm does not reprocess sensor data from prior frames, does not update the prior probabilities of the hypotheses, and carries forward in time at most one track per apparent target. As a consequence, multiple-frame data-association approaches, described later, typically perform better than single-frame approaches. To their advantage, single-frame data-association algorithms are not as complex or processing intensive as multiple-frame methods and do not require as extensive an algorithm development effort.

The two best known single-target, single-frame data-association approaches are the nearest neighbor and the

probabilistic data-association filter. These approaches illustrate two very different types of decisions. The nearest neighbor approach makes *hard decisions*, that is, the association weight used for each measurement in a track gate is either zero or one. By contrast, the probabilistic data-association filter makes *soft decisions*, that is, the association weight used for each measurement in a track gate is usually between zero and one. With soft decisions, typically the sum of the weights for a track is one. The weights for a track include a weight for the possibility that none of the measurements in a gate are caused by the target.

3.2.1. Nearest Neighbor Tracking. The nearest neighbor (NN) algorithm is designed for tracking a single target, and only one track is carried forward for processing the next frame of data. This algorithm is sometimes referred to as the independent nearest neighbor (INN) algorithm to emphasize that each track is processed without regard to any other track. It *trims* (prunes) the hypotheses down to a single hypothesis by eliminating all but one hypothesis [1,2,6,16,17]. For each frame of data, the NN algorithm assigns the (statistically) nearest measurement to the track. The statistical distance measure used is typically the same chi-square value that is computed for the elliptical (or hyperellipsoidal) track gate. If the gate extent is sized appropriately, then an empty gate corresponds to the hypothesis that every measurement outside the gate is more probably a false signal than a detection of the target. Essentially, this is equivalent to finding the most probable hypothesis for each frame of data constrained by the decisions of the prior frames.

The NN algorithm is easily understood and implemented. It does not perform well, however, except with a low measurement density, such as up to an average of about 0.1 false signals in a 0.99 gate [1,2,16,17]. (A 0.99 gate means that there is a 0.99 probability that the measurement caused by the target will be in the gate given that it is detected.) Note that the average number of false signals in a 0.99 track gate is a relative measure of density, not absolute, because it depends on the gate size that depends, in turn, on the accuracy of the track and measurements. With the NN algorithm, how dense the measurements can be and still provide adequate performance depends on the specific application and its characteristics, such as probability of detection and number of elements in the measurement vector. The error covariance matrix for the resulting composite track is the covariance matrix of the most probable hypothesis track. The error covariance matrix of the composite track does not take into account the possibility that the most probable hypothesis track is the wrong track. In effect, this is equivalent to neglecting the possibility that the selected hypothesis is not the correct one. Thus the error covariance matrix for the NN track is optimistic, that is, the variance elements of the filter computed error covariance matrix are frequently smaller than the corresponding actual variances exhibited by the estimation errors.

3.2.2. Probabilistic Data-Association Filter. With the probabilistic data-association filter (PDAF) approach, all

current hypotheses are computed and then *combined* to obtain a single track for the apparent target [1,2,6,16,17]. Conceptually, the target state estimate and its error covariance matrix are computed for each hypothesis. Then the target state estimates of the hypotheses are combined into a single-composite target state estimate by computing their average using a weighted average. The weights are the probabilities of each of the hypotheses. The probabilities are a function of the same chi-square values that are used in track gating.

The error covariance matrix of the resulting composite state estimate is the sum over the hypotheses of the probability of each hypothesis times the error covariance matrix for the hypothesis plus the outer product of the difference between the hypothesis estimate and the composite state estimate. The equations for these computations are a special case of the ones discussed later in the multiple target-tracking section. However, if the measurement error covariance matrix is the same for all measurements and only one track is brought forward from the prior frame of data, the computations can be simplified [1,2,6]. The composite track is then provided to the user, and it consists of the composite estimated state and its error covariance matrix for the apparent target. (The term *apparent target* is used because a track might not be following a target, but instead can be based on mostly, or exclusively, false signals.) This track is also used for processing the next frame of data, that is, the composite track is used instead of the hypotheses tracks as a basis to enumerate the hypotheses for the next frame of data. Accordingly, the number of hypotheses that must be enumerated for the next frame of data is greatly reduced.

Typically, the PDAF exhibits better tracking accuracy and fewer lost tracks than does an NN tracker if more than an occasional false signal in the track gate occurs [2,6]. A *lost track* is one that was following a target but later was not following any single target. The mean-squared estimation errors are typically smaller for the PDAF than for the NN tracker because the weighted averaging using the association weights tends to “hedge the bets.” A disadvantage of the PDAF tracker is that it is more processor intensive than the NN tracker and soft decisions might degrade features or attributes used for target classification or by the battle manager.

The PDAF-computed composite error covariance matrix is usually more realistic than that of the NN tracker. The error covariance matrix of the PDAF composite estimate adapts to the sensor data because it depends on the number of measurements in the gate and how they are distributed. The variance elements of the error covariance matrix of the composite track usually will be small when there has been a sequence of frames with few false signals and large when there have been many false signals. Also, the value of the variance elements in the covariance matrix will increase when the track gate is empty. Thus both the PDAF composite state estimate and its covariance matrix are data dependent. The actual (true) error covariance matrix of a composite estimation problem is usually data dependent and the covariance matrix computed by the PDAF is also because it is an approximation to the actual error covariance matrix. Note that this is

very different from a traditional linear, Gaussian estimation problem, for which a single Kalman filter can be used, and both the actual and computed state estimation error covariance matrix do not depend on the values of the measurements.

In some tracking systems, single target-tracking approaches are used to track multiple targets. For example, the NN algorithm or the PDAF might be used to track multiple targets. As a result, each apparent target is tracked independent of the other apparent targets, that is, without the aid of information from tracks of the other apparent targets. Independent target tracking is justified with isolated targets. If some targets are closely spaced, improved performance will be obtained by using a multiple target-tracking approach that coordinates the processing of the tracks by using the prior multiple track data more effectively rather than using an isolated target-tracking approach.

4. MULTIPLE TARGET TRACKING

A variety of single-frame and multiple-frame data-association methods have been devised for tracking multiple targets with data from a single sensor. In discussing some of these methods, it is assumed that false signals and closely spaced targets can occur. Furthermore, it is assumed that persistent clutter points are treated as targets; however, to simplify the discussion, the assumption is that no UCSOs occur. When discussing hypotheses for multiple target tracking, the term *hypothesis* refers to a multiple-target hypothesis; that is, each hypothesis accounts for all target tracks and all measurements in the applicable sensor data.

In multiple target tracking, a frame of data will normally contain measurements from many targets. Most tracking algorithms assume that the signal processor provides measurements in a sequence of proper frames of data. A *proper frame of data* is a collection of measurements wherein no two measurements are from the same target. Performance is expected to degrade if the frames of data are smaller than is practical or are not proper frames.

Before discussing some of these suboptimal tracking methods, it is instructive to first discuss optimal tracking. It is useful to discuss optimal tracking for at least two reasons. First, the equations of optimal tracking are also used in suboptimal tracking but in a different way. Second, optimal tracking displays important properties that are helpful in understanding the characteristics of practical, suboptimal multiple target-tracking methods and in designing those methods.

4.1. Optimal Tracking of Multiple Targets

There is no single method for optimal tracking because different optimization criteria lead to different optimal tracking algorithms even for a linear, Gaussian problem [15]. This characteristic of target tracking is very different from the more traditional linear, Gaussian estimation problem, for which the Kalman filter is optimal for most optimization criteria. Other complexities unique to the multiple target estimation task also exist that muddy the

issue of what is meant by the optimal estimate, but that issue need not be explored here [15]. To limit this discussion, a simple scenario is addressed and with but two optimization criteria.

Suppose that at time zero the tracking system receives a handoff of tracks from another system that has (somehow) established a set of tracks for all the targets that includes credible error covariance matrices for all the target tracks. Furthermore, the handoff estimation errors for each target exhibit a Gaussian probability distribution and are not cross-correlated from target to target. The system has a linear sensor with measurement errors that exhibit a Gaussian probability distribution. Furthermore, the target motion is described by linear vector state equation and, if process (state) noise is applicable, it exhibits a Gaussian probability distribution. Note that this is not only a “nice” linear, Gaussian problem, but the number of targets is known, which greatly simplifies the problem.

In optimal tracking, all hypotheses and all their tracks must be retained for use in processing the subsequent frames of data. A bank of Kalman filters can be used to compute the state estimates for each target track for each hypothesis. Fortunately, a target track based on a specific sequence of measurements is used in more than one hypothesis so that some economy of processing is obtained by taking advantage of that fact. Equations for computing the probability for each hypothesis are given in Table 1. These equations apply to optimal multiple target tracking

for most optimization criteria. The notation used here is consistent with typical Kalman filter notation, except that the estimates are also conditioned on the hypothesis, as can be seen from Eq. (1d). The optimization criterion determines how the estimates of the hypotheses are processed to establish the single best track for each target. For the minimum mean-square error (MMSE) criterion, the equations for the optimal composite estimate are given in Table 2. Table 3 amplifies on the equations used to compute the probability of the innovations used to compute the probability of each hypothesis. All the current hypotheses are retained and used as a basis for computing the hypotheses’ tracks when the next frame of data becomes available. In contrast, the composite tracks are re-computed after every frame of data becomes available, based on the tracks of all the current hypotheses and their probabilities.

Note that the equations in Table 1 permit the targets’ state vectors to be handled in two different ways. If any of the random variables related to one target are cross-correlated with those of another target, then state vectors of all the targets are concatenated into a single “system state vector,” which consists of all the state vectors for all the targets. The equations of Table 2 are treated this way. Note from Eq. (2d) of Table 2 that the individual target tracks of the composite estimate are cross-correlated because of the last term, that is, the outer product in that equation. The second method for handling the target

Table 1. Block 2 Optimal Multiple Target Estimation Equations [16,17]

Block 2	
Compute $\hat{x}_{k_n}(n), P_{k_n}(n), S_{k_n}^{-1}(n)$, and $v_{k_n}(n)$ using Kalman filters	(1a)
$\omega_{k_n}^*(n) = p[v_{k_n}(n)]\omega_{k_{n-1}}(n-1)(P_D)^{nD}(1-P_D P_G)^{nT-nD} \beta_F^{nF} \beta_{NT}^{nNT}$	(1b)
$\omega_{k_n}^*(n) \propto p[k_n, z(n) Z(n-1)]$	(1c)
$\hat{x}_{k_n}(n) = E[x(n) k_n, Z(n)] =$ hypothesis estimate	(1d)
$P_{k_n}(n) =$ hypothesis estimate covariance	(1e)
$v_{k_n}(n) =$ hypothesis innovations	(1f)
$S_{k_n}(n) =$ hypothesis innovations covariance	(1g)
$k_n =$ hypothesis index	(1h)
$\beta_F = P_{FP}/A_P$	(1i)
$\beta_F =$ false signal density	(1j)
$P_{FP} =$ probability of false signal in a pixel (resolution element)	(1k)
$A_P =$ area (volume) of a pixel (resolution element)	(1l)
$P_D =$ probability of target signal detection	(1m)
$P_G =$ probability that target is in gate	(1n)
$n_F =$ number of false signals in gate	(1o)
$\beta_{NT} = P_{NT}/A_P$	(1p)
$\beta_{NT} =$ new target density	(1q)
$P_{NT} =$ Probability of new target in a pixel (resolution element)	(1r)
$A_P =$ area (volume) of a pixel (resolution element)	(1s)
$n_D =$ number of targets detected	(1t)
$n_T =$ number of targets	(1u)
$n_{NT} =$ number of new targets	(1v)
If the random variables are independent from target to target, that is, the system innovations covariance matrix is target, block diagonal, then:	
$p[v_{k_n}(n)] = \prod_i p[v_{ij}(n)]$	(1w)
where:	
$i =$ index of target tracks	(1x)
$j =$ index of measurements, a function of i and k_n	(1y)
$v_{ij}(n) =$ innovations vector for track i and measurement j	(1z)

Table 2. Block 1 Multiple Target Equations for optimal MMSE Estimation [15–17]

Block 1	
$p[z(n) Z(n-1)] = \sum_{k_n} \omega_{k_n}^*(n)$	(2a)
$\omega_{k_n}(n) = \omega_{k_n}^*(n) / \sum_{k_n} \omega_{k_n}^*(n)$	(2b)
$\hat{\mathbf{x}}(n) = \sum_{k_n} \omega_{k_n}(n) \hat{\mathbf{x}}_{k_n}(n)$	(2c)
$P(n) = \sum_{k_n} \omega_{k_n}(n) [P_{k_n}(n) + [\hat{\mathbf{x}}_{k_n}(n) - \hat{\mathbf{x}}(n)] [\hat{\mathbf{x}}_{k_n}(n) - \hat{\mathbf{x}}(n)]^T]$	(2d)
where	
$\omega_{k_n}(n) = p[k_n Z(n)] = \text{hypothesis probability}$	(3a)
$\hat{\mathbf{x}}(n) = E[\mathbf{x}(n) Z(n)] = \text{composite estimate}$	(3b)
$P(n) = \text{composite estimate covariance}$	(3c)

states applies if no target-to-target cross-correlation exists [see Eq. (1w)].

To illustrate that two different optimization criteria lead to different optimal multiple target-tracking algorithms, Table 4 provides the optimal composite estimate for the joint maximum a posteriori probability (JMAP) criterion [11,15–17]. Note that Eq. (2d) in Table 4 shows that any estimate that is not the same as optimal MMSE estimate will have a larger actual error covariance matrix [11,16,17]. Also note from that equation that any suboptimal hypothesis estimate will exhibit cross-correlations between the individual target hypothesis tracks because of the outer product term.

The optimal single track (in the minimum mean square sense) for an apparent target at any one time is a composite track that is the appropriately weighted sum of tracks for that apparent target contained in all the multiple-target hypotheses. To illustrate the magnitude of the complexity for optimal tracking without missed signals or false signals, N_T targets and N_F frames of data would require the enumeration of $(N_T!)^{N_F-1}$ hypotheses (assuming no tracks based on prior data are available).

It is the retention of all the hypotheses and all their tracks that makes optimal tracking impractical. Clearly, optimal tracking is a multiple-frame data-association approach with the number of frames in the data association equal to number of frames of data available. The so-called “gated optimal” tracking is optimal tracking except that gates are used to eliminate unlikely track-measure-

Table 3. Hypothesis Innovations Probability Equations for Optimal Multiple-Target Estimation [15–17]

For linear, Gaussian conditions:	
$p[v(n)] = \frac{e^{-\chi^2/2}}{(2\pi)^{M/2} \sqrt{ S }}$ for $\chi_{k_n}^2$ or χ_{ij}^2	(1)
$\chi^2 = \hat{\mathbf{v}}^T(n) R^{-1} \hat{\mathbf{v}}(n) + [\hat{\mathbf{x}}(n n-1) - \hat{\mathbf{x}}(n)]^T P^{-1} (n n-1) [\hat{\mathbf{x}}(n n-1) - \hat{\mathbf{x}}(n)]$	(2a)
$\chi^2 = \mathbf{v}^T(n) S^{-1} \mathbf{v}(n)$, $\mathbf{v}(n) = \mathbf{z}(n) - H(n) \hat{\mathbf{x}}(n n-1)$	(2b)
$S^{-1} = R^{-1}(n) - R^{-1}(n) H(n) P(n) H^T(n) R^{-1}(n)$	(3)
$S = H(n) P(n n-1) H^T(n) + R(n)$	(4)
where	
$S \triangleq E[\mathbf{v}(n) \mathbf{v}^T(n)]$, $M = \text{length} [v(n)]$	(5)
$\hat{\mathbf{v}}(n) = \mathbf{z}(n) - H(n) \hat{\mathbf{x}}(n)$	(6)

Table 4. Block 1 Multiple-Target Equations for Optimal JMAP Estimation [15–17]

Block 1. Maximum joint a posteriori estimate (JMAP estimate)	
For $\text{Max}_{x, k_n} \{p[x, k_n Z(n)]\}$; $\hat{k}_n = \text{Arg} \left\{ \text{Max}_{k_n} [W_{k_n}(n)] \right\}$	(2a)
$w_{k_n}(n) = \omega_{k_n}(n) / [(2\pi)^{M/2} \sqrt{ P_{k_n}(n) }]$	(2b)
$\hat{\mathbf{x}}_{\text{JMAP}}(n) = \hat{\mathbf{x}}_{k_n}(n)$	(2c)
$P_{\text{JMAP}}(n) = P_{\text{MS}}(n) + [\hat{\mathbf{x}}_{\text{JMAP}}(n) - \hat{\mathbf{x}}_{\text{MS}}(n)] [\hat{\mathbf{x}}_{\text{JMAP}}(n) - \hat{\mathbf{x}}_{\text{MS}}(n)]^T$	(2d)
where	
$\hat{k}_n = \text{JMAP hypothesis decision}$	(3a)
$\hat{\mathbf{x}}_{\text{JMAP}}(n) = \text{JMAP estimate}$	(3b)
$P_{\text{JMAP}}(n) = \text{JMAP mean square error matrix}$	(3c)
$\hat{\mathbf{x}}_{\text{MS}}(n) = \text{MMSE estimate}$	(3d)
$P_{\text{MS}}(n) = \text{MMSE mean square error matrix}$	(3e)

ment pairs [16,17]. The gating process reduces processing complexity, but, because it is a trimming process, the results are suboptimal.

4.2. Single-Frame Data-Association for Track Maintenance

Single-frame data-association approaches for multiple target-track maintenance include the global nearest neighbor algorithm and joint probabilistic data association.

4.2.1. Global Nearest Neighbor Tracking. The global nearest neighbor (GNN) tracker uses a single-frame data-association algorithm that makes hard decisions. It is an extension of the INN tracker for use with multiple targets. There is a number of different implementation approaches to GNN tracking. One version of the GNN finds the most probable (multiple-target) hypothesis for each frame of data constrained by the decisions of the prior frames. This version will be referred to as (multiple-target) single-frame most probable hypothesis (SF-MPH) tracking. Only one track per apparent target is carried forward for processing the next frame of data. Rather than enumerate all the hypotheses, typically an *optimal, unique, 2-D assignment algorithm* is used to find the most probable hypothesis, and that greatly reduces the amount of computations [1]. The assignment algorithm assigns measurements to tracks. The term *unique* in this context means that no track is assigned to more than one measurement and no measurement is assigned to more than one track. The 2-D qualifier refers to two dimensions because there are two data sets that are involved, namely, measurements and tracks, and therefore the assignment cost array is a matrix. Note that although finding the optimal (minimum cost) solution to a two-dimensional assignment problem is tractable, it turns out that a higher dimensional assignment problem is not. Also note that an optimal unique assignment algorithm does not provide optimal tracking.

In the past, suboptimal assignment algorithms were used to further reduce the amount of computations. However, there is little advantage to using a suboptimal assignment algorithm because now very fast optimal 2-D assignment algorithms are available. These

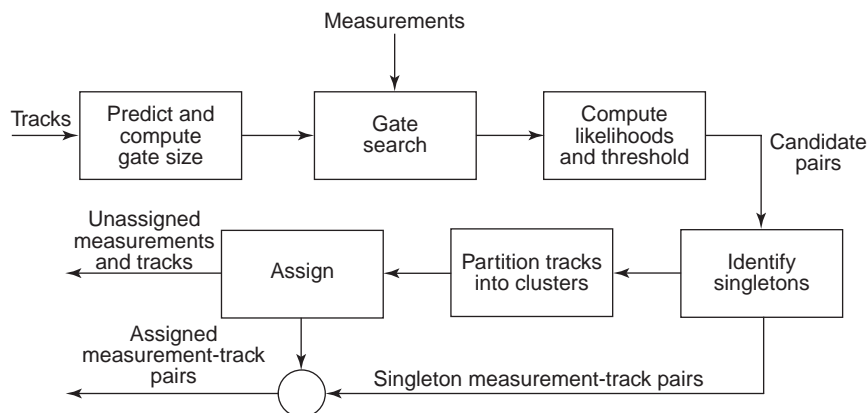


Figure 3. Typical block diagram of functions for single-frame data association [16,17].

algorithms are fast because they take advantage of the sparseness of the cost matrix. The sparseness occurs because not every measurement is in every track gate. A unique assignment algorithm is able to find the most probable hypothesis because of the basic structure of the equation for the probability of a hypothesis, provided the target-track-to-target-track cross-correlations are neglected.

Figure 3 displays a block diagram of the data-association functions for use of a 2-D assignment algorithm. The gate search function determines which measurements are in the rectangular track gates (or its higher dimensioned version). A simplistic algorithm should not be used for this function if many targets occur in any one region. For example, if two loops were used (one for measurements and one for tracks) for the gate search function, then 100 targets and 100 measurements would require 10,000 evaluations to determine which measurements are in each track gate. More ingenious methods will greatly reduce this number. The likelihood function serves to perform the elliptical (or hyperellipsoidal) gate process and also to compute the cost value for use in the assignment matrix. The chi-square calculation of Eq. (2) in Table 3 is often used for the cost in the assignment matrix [1,16,17]. *Singletons* are simply obvious measurement-track pairs for which there is no contention and thus need not be included in the assignment algorithm [16,17]. If many targets occur, then there may be an advantage to partitioning the tracks into what are called track clusters may exist. Tracks are partitioned so that no measurement in the gate of a track in one cluster is also in the gate of a track that is in another cluster. Track clusters should not be confused with target clusters, which are groups of targets whose state vectors are approximately the same. The purpose of partitioning tracks is to reduce the processing load but will not necessarily reduce processing if a state-of-the-art assignment algorithm is used.

The last function in Fig. 3 is the assignment algorithm, which uniquely assigns measurements to tracks. This block diagram is applicable with modification to other data-association approaches. The unassigned measurements are normally forwarded to the track-initiation function, and the unassigned tracks are tested for possible termination (see Fig. 2). The advantage of the GNN approach is that it does take into account multiple tar-

gets by using the multiple tracks and all the measurements in a frame of data (or partition). Also, it is relatively easy to implement, compared with other data-association methods and is not very processing intensive. In addition, this approach tends to adjust for shifts in the data from frame to frame because of interframe jitter. The disadvantage is that false signals and new targets tend to degrade performance. This might be an appropriate tracking approach for implementation early in the algorithm development stage for a new system and then followed later by a more advanced and complex tracking approach, if needed, when the system characteristics are better understood and established.

4.2.2. Joint Probabilistic Data Association. The joint probabilistic data-association (JPDA) tracker uses a single-frame data-association approach that makes soft decisions. It is an extension of the PDAF tracker for use with multiple targets [1,2,6]. In the JPDA approach, all current hypotheses are computed and then combined to obtain a single composite track for each apparent target. These composite tracks are used to provide to the user the estimated state and its covariance matrix for each apparent target. Also, for processing the next frame of data, the composite tracks are used instead of the hypotheses' tracks. Accordingly, the number of hypotheses that must be enumerated for the next frame of data is greatly reduced compared with optimal tracking. The equations of Table 1 are applicable to JPDA, but normally the target-track-to-target-track cross-correlations are neglected. A JPDA tracker is expected to perform better than the GNN tracker as the number of false signals or new targets increases. The JPDA is more processing intensive and requires more complex computer programming and algorithm development effort than the GNN approach. In addition, the soft decisions of the JPDA tracker might degrade features or attributes used for target classification or by the battle manager. Fortunately, the computed composite error covariance matrix of a JPDA tracker is usually more realistic than that of the GNN tracker.

A unique feature of the JPDA approach is that it permits the computation of the probability that a specific measurement is caused by because of the same target that a specific track is following. Similarly, the probability that a

measurement is a false signal or caused by a new target can also be computed. These probabilities can be used for a variety of purposes beyond simply computing the composite state estimate and the error covariance matrix for each track. These probabilities are sometimes referred to as marginal association probabilities, and the details for computing them depend in part on a number of assumptions, such as the mathematical model used for the false signals [1,2,6].

4.3. Multiple-Frame Data Association for Track Maintenance

Multiple-frame data-association approaches include the algorithm by Singer, Sea, and Housewright, multiple-hypothesis tracking, Poore's tracker, and other algorithms [10,11]. Typically multiple-frame data-association approaches enumerate (and also carry forward to the next frame) more candidate tracks than do single-frame approaches. Consequently, multiple-frame data-association approaches typically provide better estimation accuracy and fewer false and missed tracks than single-frame approaches. However, multiple-frame data-association algorithms are more complex and processing intensive, and they require substantially more effort in design, development, and test.

4.3.1. Singer, Sea, and Housewright Tracker. The Singer, Sea, and Housewright (SSH) tracker was designed for tracking a single target with false signals [21], but has been extended to multiple target tracking. It is sometimes referred to as the " n -scan back" approach [2] and is similar to the JPDA approach, except that it maintains more than one track per target for processing the next frame of data. The algorithm uses local combining to reduce the number of tracks. Tracks are selected to be combined if they use the same measurements in the latest N frames of data and the same target track $N + 1$ scans back. The number of frames, N , used in the combining process is a design parameter. Although the SSH algorithm can be classified as a multiple-frame, probabilistic data-association approach, it uses local rather than global combining and uses measurements as the criteria for forming local composite tracks. Because it usually retains more than one candidate track per target from frame to frame, it should perform better than JPDA but increases the processor load and requires more extensive algorithm and software development.

4.3.2. Multiple-Hypothesis Tracking. Multiple-hypothesis tracking (MHT) typically carries more than one hypothesis track per apparent target forward for processing the next frame of data. Many different versions of MHT have been developed since its original conception [22]. In MHT, for practical reasons the number of hypotheses is limited by both eliminating and combining some hypotheses and tracks [1,7,22]. In the original MHT, the typical combining (merging) process is local rather than global. Given four hypotheses' tracks for a single apparent target, for example, two similar hypotheses tracks might be combined (merged) to form one hypothesis track, a "local" composite. As a result, the four hypotheses tracks would be reduced to three. Then

one of these three, the one with the smallest hypothesis probability, might be eliminated so that only two tracks would be forwarded for processing with the next frame of data for that apparent target. In order to compute the needed probabilities, all the current hypotheses are enumerated and the (multiple target) hypotheses' probabilities computed. The computations for these probabilities are similar to those in Table 1.

MHT should perform better than the other tracking approaches just discussed. Improved performance is obtained at the expense of an increase in processing load, computer programming, and algorithm-development effort. Many organizations either have developed or are developing MHT or similar trackers and some are on their second- or third-generation (incarnation) multiple-frame tracker. Some of the more recent MHT approaches use a sliding window of multiple frames of data, which is similar to the method discussed in Section 4.3.3. In MHT, however, there is additional pruning of unlikely candidate tracks and combining of similar candidate tracks for a target to reduce the number of multiple target hypotheses that must be enumerated.

4.3.3. Multiple-Frame Most Probable Hypothesis Tracker.

Poore's tracker is similar to MHT but does not use any local combining or trimming; it uses deferred global trimming. His tracker employs a sliding window of $M - 1$ frames of data [23]. The window also includes tracks based on data up to and including M frames back, that is, the tracks are based on all data except the latest $M - 1$ frames of data. The tracker then uses an M -D assignment algorithm to seek the most probable hypothesis for the $M - 1$ frames of data given the tracks M frames back. This is a multiple-frame most probable hypothesis (MF-MPH) tracker. The M frames back tracks are then updated just one frame of data using the measurements in frame $M - 1$ back that are paired with those tracks in the most probable hypothesis.

It is not practical for most systems, however, to find the optimal solution to the M -D assignment algorithm with M greater than 2. To circumvent this problem, search for the optimal solution in Poore's M -D assignment algorithm is stopped when the current solution is close enough to the optimal assignment solution relative to the uncertainty caused by the random variables. His assignment algorithm is able to determine bounds on how close the current solution is to the optimal solution. This tracker makes a firm decision on the measurements in $M - 1$ frames back and tentative decisions on all subsequent measurements so that the current target state estimates can be computed for all apparent targets. A *firm decision* is an irreversible decision and a *tentative decision* is one that may be revisited and changed at a later time. After this processing is completed, the window is moved forward one frame of data and the process repeated.

4.3.4. Related Comments. There are also other multiple-frame data-association algorithms that have been devised, and some employ *retrodicted probabilities* [10,11], which are "smooth" decisions that are analogous to smoothing of continuous random variables in Kalman

filtering. (Note that in Kalman filtering, it seems that it might be more appropriate to refer to a “smoothed” estimate as a *retrodicted estimate*, i.e., an estimate of the state for a specific time given subsequent measurements.) More complex track processing can be expected in the future as the processing capabilities of computers continue to improve and thus permit tracking to approach optimal performance more closely.

Note that the hypotheses’ probabilities of all the sub-optimal tracking approaches discussed above, that is, except for optimal tracking, are not truly probabilities but “pseudoprobabilities.” A pseudoprobability is an approximation to the probability that the measurements assigned to the tracks for a hypothesis are the correct ones. The pseudoprobabilities are approximations because all previous hypotheses have not been maintained and used in the computations. The pseudoprobabilities are usually computed as if the deleted hypotheses were not possible and that no loss of information results from combining hypotheses.

Some target-tracking approaches partition the processing into the three major stages of (1) track initiation (formation), (2) track maintenance (extension or continuation), and (3) track termination, as in Fig. 2. Each track is started in the track-initiation processing and then continued in track-maintenance processing until terminated by the track-termination logic. The optimal, MHT, and MF-MPH approaches typically integrate all three phases in the process of enumerating hypotheses and generating tracks. In contrast, the NN, PDAF, JPDA, GNN, and SSH approaches are typically track-maintenance approaches that must be augmented by separate track-initiation and track-termination processing functions [1–4,17]. The algorithm for the track-termination function might be as simple as to terminate tracks that are not updated L frames in a row, or possibly not updated L frames out of J frames, where L and J are selected using Markov chain analysis. Markov chain analysis can be used to trade off the number of tracks incorrectly terminated versus the number of false tracks that are not terminated soon enough. This type of analysis can be used also to establish parameters for track initiation [1].

4.4. Track Initiation

Typically a sequence of more than two measurements is needed to initiate a track. Fortunately, tracks do not have to be initiated very often. The measurements not used by track maintenance are usually forwarded for use by the track-initiation function. In some approaches, all measurements are also used by the track-initiation function [3,4]. With a very sparse population of measurements, it may be sufficient to initiate tracks by using the same NN algorithm as used in track maintenance. The first measurement used to start a new track is called an *initiator*. An initiator starts a candidate initial track that is updated using the NN algorithm as appropriate measurements are provided to the track-initiation function. A score based on chi-square statistics can be updated as a candidate track is updated. When the score exceeds a prescribed threshold, the candidate initial track is promoted to a

mature track and processed by the track-maintenance function thereafter.

Note that in track initiation, not enough information exists to compute the first gate using only one measurement. After an initiator is identified, the first gate (and possibly more) is computed using *a priori* information on the velocity (and possibly higher derivatives) because the data of the initiator does not include complete velocity information, if any.

If more than just a few measurements exist in a region that are forwarded to the track-initiation function, there can be contention for measurements by a number of different candidate initial tracks. One approach that addresses this issue is to use binary linear programming or an optimal, unique M - D assignment algorithm to resolve the contentions and find all the appropriate sequences of measurements for promotion to mature tracks [24]. If this is too processing intensive, then it might be sufficient to use a unique suboptimal M - D assignment algorithm, such as the so-called greedy algorithm. A variety of other methods have been developed for track initiation. Track initiation is complex because usually more than just a few frames of data are needed to initiate tracks with reasonable confidence.

5. MULTIPLE-SENSOR ALGORITHM ARCHITECTURES

There are many different ways that data from multiple sensors can be combined. The differences between the various multiple sensor approaches may not be important with respect to performance for tracking with a sparse population of measurements. With challenging conditions of a moderate to dense population of measurements, the difference between the various tracking approaches can have a significant impact on both performance and hardware loading. In designing an algorithm architecture for multiple-sensor tracking, ultimately, the major considerations are typically cost, communication load, processor load, survivability, and performance. Performance considerations typically include estimation accuracy, number of false tracks, number of missed tracks, covariance matrix credibility, and robustness. There is virtually an infinite number of possible algorithm architectures for multiple target tracking with multiple sensors. One view of the different types of algorithm architectures is summarized in this section and then compared.

5.1. Alternative Fusion Algorithm Architectures

Four pure generic types of algorithm architectures for track maintenance and for track initiation have been identified. This classification of algorithm architectures is based primarily on how the association processing is performed over time and over the ensemble of sensors [10,12,17]. The four types of track maintenance algorithm architectures are as follows:

- *Type I:* Independent sensor algorithm architecture
- *Type II:* Track fusion algorithm architecture

- *Type III*: Composite measurement fusion algorithm architecture
- *Type IV*: Central measurement fusion algorithm architecture

In the *independent sensor algorithm architecture* (Type I), the tracks are processed for each sensor without use of the data from the other sensors. Frame-to-frame data association and filtering are performed without any sensor-to-sensor processing. Each user obtains tracks based on a single sensor. Note that each measurement is subjected to only one association process, but single-sensor tracks need to be retained in track files for each sensor. Also, there is no improvement in the track quality because of the existence of multiple-sensor data.

In the *track fusion algorithm architecture* (Type II), tracks are first processed for each sensor without use of data from the other sensors. Single-sensor frame-to-frame association and filtering are followed by sensor-to-sensor processing. Single-sensor tracks are fused using track-to-track association followed by filtering to form multiple-sensor (global) tracks. Note that each measurement is subjected to two association processes. Multiple-sensor tracks as well as single-sensor tracks for each sensor are retained in track files. This process is sometimes called hierarchical or distributed algorithm architecture and is complicated by the property that typically sensor-level tracks are cross-correlated with the global-level tracks. Feedback of the multiple-sensor global tracks to the single-sensor track processing can be employed. The vanilla architecture without feedback to the lower levels is designated Type IIa. Feedback to the lower levels usually improves the track accuracy at both that level and the higher levels, and that architecture is designated Type IIb. In systems where there are multiple sensors on each platform and each platform is at a different location, it is common to have three processing levels: (1) sensor-level tracking, (2) platform-level tracking, and (3) global-level tracking.

There are a number of methods for dealing with the track-to-track error cross-correlation in track fusion. In some methods, the track data are distributed in the form of a tracklet. A *tracklet* is a track computed so that its errors are not cross-correlated with any other data distributed in the system for the same target [12]. Tracklets can be computed by decorrelating the sensor tracks [25] or formed from a sequence of measurements [12]. One of the major benefits of track fusion compared with the other types of fusion is that the communications load can be greatly reduced by not distributing the track data after every measurement is obtained for a target. The *tracklet interval*, the time between when tracklets are distributed by a sensor for a target, can often be from 5 to 30 measurement sampling periods, depending on the application. Thus data compression is obtained with little loss of information. The original tracklet methods were designed for nonmaneuvering targets, and those methods might not provide adequate performance if the targets are maneuvering, because with maneuvers they do not provide lossless information [26]. If the possibility of misassociations exist at the local or fusion level, then a number of

considerations need to be addressed in deciding whether to distribute target tracks or tracklets [27].

In the *composite measurement fusion algorithm architecture* (Type III), multiple-sensor processing of the measurements from all sensors is first employed. The processing of measurements consists of associating measurements from one frame of data from all sensors and computing an improved estimate of a projection of the state vector for each target, such as estimated position. Note that normally for accurate fusion with this approach, either the sensors must obtain measurements at the same time or the targets and sensors must be moving slowly relative to the frame period. These composite measurements are then used in frame-to-frame association and filtering. Sensor-to-sensor processing precedes frame-to-frame processing. Note that each measurement is subjected to two association processes, but only one set of multiple-sensor tracks need be retained in track files.

In the *central measurement fusion algorithm architecture* (Type IV), measurement-to-track association is followed by filtering using the prior multiple-sensor tracks. This architecture is sometimes referred to as measurement fusion or central-level fusion [1,7]. In its simpler form, the data-association processing uses the multiple-sensor tracks and one frame of data from a sensor; the tracks are updated and then a frame of data from another sensor along with the updated multiple-sensor tracks is processed. Note that each measurement is subjected to only one association process and only one set of multiple-sensor tracks need be retained in track files.

In addition to the pure generic methods for track maintenance is one more type of fusion approach that is not a pure approach, namely, a hybrid approach. One devised hybrid approach is flexible and adaptive because it permits the distribution of tracklets, composite measurements, or measurements for each apparent target, depending on the needs of the system for data on that target at the current time [12].

Report responsibility is a multiple-sensor, multiple target-tracking algorithm architecture that is popular in the radar community. This approach might be viewed as a special case of the Type II, track fusion algorithm architecture. However, in report responsibility, data from more than one sensor are not combined to form a multiple-sensor track, and so it could be considered in a class by itself. It is discussed here for completeness in preparation for a qualitative comparison of algorithm architectures.

In report responsibility, each sensor tracker is responsible for providing the tracks for a subset of all the targets. The intent is for one and only one sensor tracker to broadcast a track for a target. The sensor tracker that provides the best track for a target is responsible for broadcasting the track for that target on the network to the users and all the other sensor trackers; no other sensor tracker is supposed to broadcast a track for that target. Consequently, the issue of track cross-correlation does not apply to this approach. A number of approaches on how to coordinate the decisions to achieve the intent of report responsibility exist. Depending on how report responsibility is coordinated, transients can exist with more than one sensor tracker broadcasting a track for a

target. Some advantages of report responsibility include very low communications rate and use of the best sensor track. In report responsibility, however, the sensor tracks for a target from multiple sensors are *not* combined, so that the full advantage is not taken of the capabilities of fusion and so-called “geographic diversity.”

5.2. Comparison of Fusion Algorithm Architectures

It would be very desirable to be able to compare algorithm architectures rigorously. The state of the art of target tracking and target typing is such that apparently no one can afford the cost of a comprehensive comparison of algorithm architectures or of the algorithms for each of the tracking functions. Performance is data dependent and requires simulations for evaluation. Comparing the fault tolerance of the various possible system designs is certainly not easy, and a comparison of the hardware required for alternative system designs can be extremely complex.

In lieu of an extensive quantitative comparison, a subjective qualitative comparison of some algorithm architectures has been made [12]. This comparison, shown in Table 5, is only an initial effort, assumes no process noise, and compares only five algorithm architectures. It must be stressed that this is a qualitative comparison in that a rating of 4 might be substantially better than a rating of 3 or only slightly better than a rating of 3 if measured quantitatively. Also, this comparison does not explicitly include all the dimensions or trade issues listed in the beginning of this section. The comparison of Table 5 is only intended to indicate some of the critical issues in selecting an algorithm architecture. This table is more applicable to track maintenance than to track initiation because the properties of some sensor combinations require special consideration for track initiation. For example, two sensors may not have much information in common with only a few frames of data, such as an active sensor with relatively inaccurate angle data and an accurate passive sensor with no range data.

A big influence in Table 5 is the relative location of the sensors. With all sensors at one location (on one platform), the communications load is not an issue and central fusion might be preferred. Communication between distant

participating units is a major consideration and, so with distributed platforms, track fusion might be preferred in order to reduce the communications load. Also, registration and sensor measurement biases are extremely important in the fusion of multiple-sensor data and typically must be estimated. The residual biases appear to cause more misassociations with central fusion than with track fusion.

The asterisks in Table 5 indicate that for best tracking accuracy, the selection of the best algorithm architecture depends heavily on how different the participating sensor characteristics are, the size of the residual biases, and the types of targets. For example, for best tracking accuracy, very similar sensors may make central fusion preferred whereas track fusion may be preferred for disparate sensors. Two benefits of central fusion is its data timeliness, which is critical for highly maneuverable targets and the aspect that each measurement goes through one association process. However, the number of misassociations exhibited by track fusion and central fusion can be very different. With diverse sensors and a very different number of targets observed by each sensor, central fusion might introduce many more misassociations than would track fusion.

Another consideration in the selection of a fusion approach is the impact on the existing hardware. Some sensor processors provide only sensor tracks and do not provide measurements. If a central fusion approach were chosen, then the processors would have to be changed, which could be expensive. Also, some existing trackers do not provide the track error covariance matrices. The error covariance matrices are not needed for some approaches to report responsibility, but are required to compute the tracklet if the tracks are to be decorrelated for track fusion, and the expense of this hardware change should be considered. Hybrid fusion that distributes tracklets or measurement data exhibits the best characteristics of both central fusion and track fusion because the choice of what is distributed can be based on the needs at any one time.

A clear distinction should be made between the functional (logical) algorithm architecture (discussed in Section 5.2) and the physical distribution of the processing. With multiple platforms and onboard processing, each function

Table 5. Qualitative Comparison of Fusion Algorithm Architectures [12]

	Report Responsibility	Track Fusion without Feedback	Track Fusion with Feedback	Measurement Fusion	Hybrid Fusion
Track accuracy, false/missed tracks	1	2	3.5*	3.5*	5
• Increase effective sampling rate	1	2.5	2.5	5	4
• Utilize diversity-geometrical/accuracy	1	3.5	3.5	3.5	3.5
Extend detection range	3	3	3	3	3
Extend field of view (FOV)	3	3	3	3	3
Communication load	5	4	2	1	3
Inaccuracy and misassociations due to residual registration biases	3	4	4	1	3
Need changes to sensor processor	5	2.5	2.5	1	4
For single-platform tracking	1	2	3.5*	3.5*	5
For multiple-platform tracking	2	3	4	1	5

Key: 5 (or Largest Number) Best.

Note: In ordering, values adjusted so that the sum of each row is 15.

of an algorithm architecture can be physically distributed in many ways over the sensor platforms and a central processing station, if applicable. Also, each of the generic algorithm architectures can be implemented in many ways.

An important example of a specific combination of both the algorithm architecture and the physical distribution of the processing is what could be called measurement fusion with distributed data association. Consider distributed sensor platforms with a fusion processor on each platform. For track maintenance, each platform is responsible for the assignment of its measurements to the fusion (network) tracks, and then each measurement is tagged with its assigned fusion track number. Each measurement with its fusion track tag is distributed to all the other platforms. When a platform receives a tagged measurement from another platform, the data-association function can be bypassed and the measurement is sent to the filter function for use to update the track with the track number as indicated by the measurement's tag. The track initiation function assigns new track numbers to new tracks, and processing is needed to attempt to identify and eliminate redundant tracks from being proliferated.

There are also four track-initiation architectures that are conceptually the same as the track-maintenance architectures summarized above. The type of track-initiation architecture need not be the same as the selected type of track maintenance. Note that for a number of fusion approaches, no simple obvious approach exists for upgrading from single-frame data association to multiple-frame data association as exists for tracking with data from a single sensor. One exception to this challenge is measurement fusion at a single ground station because it is very similar to processing with data from a single sensor.

6. PERFORMANCE EVALUATION

Ultimately, the performance of tracking algorithms is judged by the success of the system that they support. Evaluation of tracking performance serves as an intermediate measure of system effectiveness, to diagnose the algorithms, and to predict performance for use in system studies. However, ambiguities can occur in evaluating performance because of misassociations [13]. Misassociations can cause missed targets and false tracks such as redundant, spurious, and lost tracks. As a result, it may not be clear which target a track is following, if any. Measures of performance cannot be evaluated with the aid of a

simulation (or through field tests) without first designating which target a track is following. There are a number of evaluation methodologies that have been proposed to address this problem [28]. Care is needed not to use a methodology that gives unfair advantage to one tracking approach over another.

One methodology for resolving these ambiguities is to use an assignment algorithm to uniquely assign the tracks to targets [13,15]. The use of the statistical distances between targets and tracks for the cost elements in the assignment matrix tends to treat the alternative tracking algorithms fairly. Then the tracking errors and other measures of performance can be computed given these unique track-target assignments. This two-stage methodology is shown in Fig. 4. Some of the common measures of performance include the error biases, the mean sum square of the position errors and the velocity errors, covariance consistency, the number of misassociations, track purity, track duration, average time to initiate tracks, and the number of missed and false tracks [29]. If the system involves multiple platforms, then performance metrics may also be needed to determine if all platforms exhibit the same information about the threat and friendly forces. This property is sometimes called *single integrated air picture* (SIAP). For most tracking applications, no single critical performance metric exists that can be used to evaluate one or more trackers. For one reason, a collection of metrics are needed because usually the tracker parameters could be adjusted to favor one metric at the expense of others.

Both tracking performance and hardware loading should be evaluated. As mentioned earlier, choices of the algorithm architecture, algorithms for each function, and the algorithm parameters will impact both performance and required processor capacity (and communications load, if applicable). An example of this tradeoff between performance and required hardware resources is shown in Fig. 5. This figure summarizes results of the simulation of tracking a single target with passive sensor data that included false signals. The results are shown after seven frames of data have been processed. Two algorithms were evaluated. One algorithm was optimal for the MMSE criterion. The other was similar to a single-target version of Poore's tracker. The number of frames in the sliding window was varied from 1 to 6 so that the curve in the figure was obtained. The values for the horizontal and vertical axes have been normalized by dividing by the corresponding value that is exhibited by tracking without false signals. Note that the results for the NN algorithm is at the left end of each of the two curves. This figure illustrates

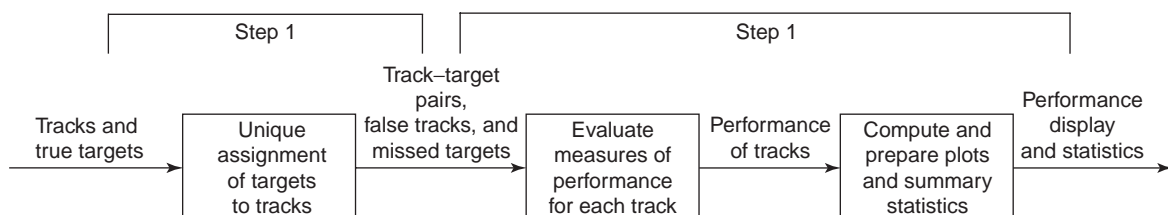


Figure 4. Diagram of a two-stage performance-evaluation methodology [17].

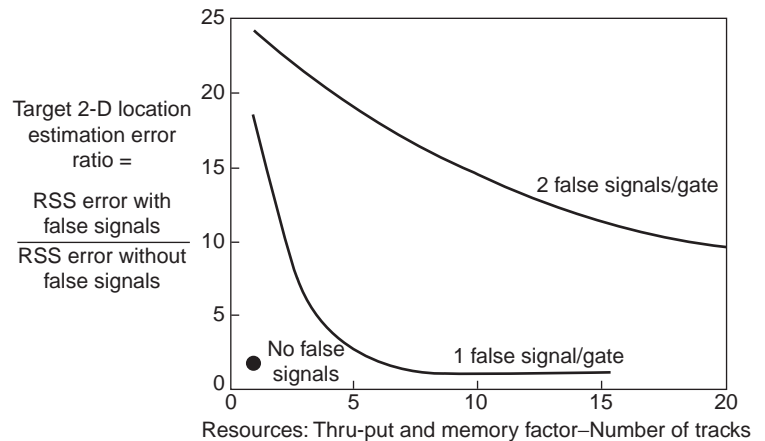


Figure 5. Illustration of major trade-off parameters for single-target tracking [14].

the major tradeoff between performance and required processor capacity (processing time or required memory).

BIBLIOGRAPHY

1. S. S. Blackman, *Multiple Target Tracking With Radar Applications*, Denham, MA: Artech House, 1986.
2. Y. Bar-Shalom and T. E. Fortmann, *Tracking and Data Association*, San Diego, CA: Academic Press, 1987.
3. Y. Bar-Shalom, ed., *Multitarget-Multisensor Tracking: Advanced Applications*, Norwood, MA: Artech House, 1990.
4. Y. Bar-Shalom, ed., *Multitarget-Multisensor Tracking: Applications and Advances*, Vol. 2, Norwood, MA: Artech House, 1992.
5. Y. Bar-Shalom and X. R. Li, *Estimation and Tracking: Principles, Techniques and Software*, Boston, MA: Artech House, 1993.
6. Y. Bar-Shalom and X. R. Li, *Multitarget-Multisensor Tracking: Principles and Techniques*, Los Angeles, CA: OPAMP Tech. Books, 1995.
7. S. S. Blackman and R. F. Popoli, *Design and Analysis of Modern Tracking Systems*, Norwood, MA: Artech House, 1999.
8. O. E. Drummond, ed., *Signal and Data Processing of Small Targets 1997, Proc. SPIE*, **3163** (1997).
9. O. E. Drummond, ed., Introduction, *Signal and Data Processing of Small Targets 1997, Proc. SPIE*, **3163**:ix (1997).
10. O. E. Drummond, Multiple sensor tracking with multiple frame, probabilistic data association, *Signal and Data Processing of Small Targets 1995, Proc. SPIE*, **2561**:322–336 (1995).
11. O. E. Drummond, Target tracking with retrodicted discrete probabilities, *Signal and Data Processing of Small Targets 1997, Proc. SPIE*, **3163**:249–268 (1997).
12. O. E. Drummond, A hybrid sensor fusion algorithm architecture and tracklets, *Signal and Data Processing of Small Targets 1997, Proc. SPIE*, **3163**:485–502 (1997).
13. O. E. Drummond and B. E. Fridling, Ambiguities in evaluating performance of multiple target tracking algorithms, *Signal and Data Processing of Small Targets 1992, Proc. SPIE*, **1096**:326–337 (1992).
14. O. E. Drummond and S. S. Blackman, Challenges of developing algorithms for multiple sensor, multiple target tracking, *Signal and Data Processing of Small Targets 1989, Proc. SPIE*, **1096**:244–256 (1989).
15. O. E. Drummond, *Multiple-object Estimation*, Ph.D. dissertation, Univ. of California at Los Angeles, Los Angeles, CA, 1975, Xerox Univ. Microfilms No. 75-26,954.
16. O. E. Drummond, Multiple Sensor, Multiple Target Tracking, SPIE Short Course SC56, April 1998 and earlier versions, SPIE, Bellingham, WA.
17. O. E. Drummond, *Multiple Target Tracking Lecture Notes*, Los Angeles, CA: Technical Book Company, 1998.
18. H. A. P. Blom and Y. Bar-Shalom, The interacting multiple model algorithm for systems with Markovian switching coefficients, *IEEE Trans. Autom. Control*, **33**:780–783 (1988).
19. D. T. Magill, Optimal adaptive estimation of sampled stochastic processes, *IEEE Trans. Autom. Control*, **10**:434–439 (1965).
20. F. L. Sims and D. G. Lainiotis, Recursive algorithm for the calculation of the adaptive Kalman filter weighting coefficients, *IEEE Trans. Autom. Control*, **14**:215–217 (1969).
21. R. A. Singer, R. G. Sea, and K. Housewright, Derivation and evaluation of improved tracking filters for use in dense multitarget environments, *IEEE Trans. Inf. Theory*, **20**:423–432 (1974).
22. D. B. Reid, An algorithm for tracking multiple targets, *IEEE Trans. Autom. Control*, **24**:843–854 (1979).
23. A. B. Poore and N. Rijavec, Multitarget and multidimensional assignment problems, *Signal and Data Processing of Small Targets 1991, Proc. SPIE*, **1481**:345–356 (1991).
24. C. L. Morefield, Application of 0–1 integer programming to multi-target tracking problems, *IEEE Trans. Autom. Control*, **22**:302–312 (1977).
25. G. Frenkel, Multisensor tracking of ballistic targets, *Signal and Data Processing of Small Targets 1995, Proc. SPIE*, **2561**:337–346 (1995).
26. O. E. Drummond, et al., Performance Assessment and Comparison of Various Tracklet Methods for Maneuvering Targets, *Signal Processing, Sensor Fusion, and Target Recognition XII, Proc. SPIE*, **5096**:514–539 (2003).
27. O. E. Drummond, Track and Tracklet Fusion Filtering, *Signal and Data Processing of Small Targets 2002, Proc. SPIE*, **4728**:176–195 (2002).
28. O. E. Drummond, Methodologies for Performance Evaluation of Multitarget Multisensor, *Signal and Data Processing of Small Targets 1999, Proc. SPIE*, **3809**:355–369 (1999).

29. R. L. Rothrock and O. E. Drummond, Performance Metrics for Multiple-Sensor, Multiple-Target Tracking, *Signal and Data Processing of Small Targets 2000, Proc. SPIE*, **4048**: 521–531 (2000).

TELEMEDICINE

CHANG WEN CHEN
University of Missouri-Columbia

Applications of information and communications technologies have become increasingly widespread because of the rapid development of microelectronics and computers. One of the most important applications is the use of advanced telecommunications and computer technologies to improve healthcare services and systems. Telemedicine—which combines many innovative information technologies that integrate research areas in human–computer interaction, data storage, processing, and compression with communications networking to improve health-care—has been recognized as a way to provide an effective and versatile solution to many of the intransigent problems in healthcare delivery.

A formal definition for telemedicine has recently been adopted by the Institute of Medicine (IOM), Washington, D.C. In the report developed by a 15-member committee of the Institute of Medicine, the term *telemedicine* is defined as “the use of electronic information and communication technologies to provide and support health care when distance separates the participants” [1]. The committee adopted this definition of telemedicine after consulting several suggested definitions. A list of these definitions is

shown in Table 1 [2–13]. The committee identified three common elements in these definitions: (1) information or telecommunications technologies, (2) distance between participants, and (3) health or medical uses.

The adopted definition of telemedicine includes all three common elements and covers a broad context in terms of both technologies employed and application areas considered. Traditionally, video conferencing is perceived as the defining technology for telemedicine, and the clinical application is considered as the defining mode for telemedicine. However, the adopted definition encompasses a wide variety of forms of communication, including telephone conversation, still-image transmission, and medical file electronic access. The definition of technologies also includes computer-based capturing, manipulating, analyzing, retrieving, and displaying of the related data and information. Both clinical and nonclinical uses of telemedicine are considered in the definition. In general, clinical applications of telemedicine involve patient care such as diagnosis, treatment, and other medical decisions and services. Nonclinical applications of telemedicine involve non-decision-making processes such as continuing medical education and management meetings. The boundary for clinical and nonclinical applications often cannot be clearly defined, because remote learning and consultation by participants will result in the application of acquired knowledge to future diagnostic and treatment decision-making processes. The third element, the geographic separation or distance between the participants, is the defining characteristic for telemedicine. In many cases, it is the separation of participants, not the distance between the participants, that requires telemedicine to overcome problems associated with patient care.

The concept of healthcare services performed over a distance first appeared in 1924 in an imaginative cover for

Table 1. Definitions of Telemedicine Consulted by the Institute of Medicine Committee

Proposer and Reference	Definition
Van Goord and Christensen [2], cited in Gott [3], p. 10 Weis [4], p. 151	The investigation, monitoring, and management of patients, and the education of patients and staff using systems that allow ready access to expert advice, no matter where the patient is located The use of telecommunications techniques at remote sites for the purpose of enhancing diagnosis, expediting research, and improving treatment of illnesses
Kansas Telemedicine Policy Group [5], p. 1.6 Grigsby et al. [6], p. 1.3	The practice of healthcare delivery, diagnosis, consultation, treatment, transfer of medical data, and education using . . . audio, visual, and data communications The use of telecommunication technology as a medium for providing healthcare services for persons that are at some distance from the provider
Council on Competitiveness [7], p. 6 Perednia and Allen [8], p. 483 Bashshur [9], p. 19	The use of two-way, interactive telecommunications video systems to examine patients from remote locations, to facilitate medical consultations, and to train healthcare professionals The use of telecommunications technologies to provide medical information and services An integrated system of healthcare delivery and education that employs telecommunications and computer technology as a substitute for face-to-face contact between provider and client
Office of Technology Assessment (OTA) [10], p. 224 Physician Payment Review Commission (PPRC) [11], p.135	The use of information technology to deliver medical services and information from one location to another An infrastructure for furnishing an array of individual services that are performed using telecommunication technologies
Lipson and Henderson [12], p. I-1–4 Puskin et al. [13]	Telemedicine encompasses all of the healthcare, education, information, and administrative services that can be transmitted over distances by telecommunications technologies The use of modern telecommunications and information technologies for the provision of clinical care to individuals at a distance and the transmission of information to provide that care

the magazine *Radio News*. The cover showed a "radio doctor" who could talk with the patient by a live picture through radio links [1]. However, the technology to support such a visionary concept, namely, television transmission, was not developed until three years later, in 1927. According to a recent review, the first reference to telemedicine in medical literature appeared in 1950 [14] and described the transmission of radiological images by telephone over a distance of 24 miles. The interactive practice of telemedicine began during the 1960s when two-way, closed-circuit microwave televisions were used for psychiatric consultation by clinicians at the Nebraska Psychiatric Institute [15]. Following the Nebraska program, several other telemedicine programs were developed in the 1960s. Some of these early programs aimed at improving health services in remote populations that traditionally had limited access to quality healthcare. One such early attempt was sponsored by the U.S. Department of Health, Education and Welfare, the National Aeronautics and Space Administration (NASA), and the Lockheed Company and was called the Space Technology Applied to Rural Papago Advanced Health Care (STARPAHC) program [16]. The program offered medical care through a mobile health unit (MHU), a medically equipped van that traveled over a prescribed route through the Papago Indian Reservation in the Sonora Desert, west of Tucson and south of Phoenix, Arizona. The MHU clinic and a fixed clinic at Santa Rosa, Arizona were linked via telemedicine facilities to a hospital in Phoenix. Other programs aimed to improve health services in urban emergency and urgent situations [17,18]. Although these pioneering telemedicine efforts demonstrated both technical and medical feasibility and received enthusiastic appraisal from the healthcare recipients [16], the issue of cost-effectiveness was debated at a premature stage by telemedicine authorities, especially the major funding agencies. The prevailing fear was that as the technologies for telemedicine became sophisticated, the cost of telemedicine would increase [15]. Such fear has been proven to be unfounded. Many applications of telemedicine are considered to have the potential to reduce healthcare costs or to reduce the rate of cost escalation [1]. The rapid advances of modern communications and information technologies during the 1990s have been a major driving force for the strong revival of telemedicine today.

The development of telemedicine has depended on the associated enabling technologies. One of the reasons that first-generation telemedicine projects did not succeed is that the technologies available at the time were, by today's standard, relatively primitive. The rapid advances in digital compression, fiber optics, and computer miniaturization and portability and their application to telemedicine systems were not even predicted during the early stage of telemedicine system development. In the case of communications, dedicated telephone lines were used in many telemedicine projects. However, such lines could only transmit slow-scan analog images, and digital compression techniques were not incorporated into the first generation of telemedicine systems. The recent rapid advances in digital communications, computer technology, and information science have provided a much broader

range of enabling technologies for today's telemedicine systems. For example, the original telephone-based communications mode has now reached very high capacity because of the revolutionary development in computer modem design. The transmission bandwidth of the telephone line is now more than 10 times greater than it was during the 1960s [19]. Other modes of modern communications, such as the integrated services digital network (ISDN) and asynchronous transfer mode (ATM), have been playing increasing roles in telemedicine systems. These new communications technologies enable the telemedicine system to operate with more flexibility and at a higher efficiency. In addition to these more advanced communication technologies, developments in digital compression (especially digital audio and video compression), and computer networking (in particular the Internet), have injected much needed versatility into the design of today's telemedicine systems. These greatly improved technologies and, more important, the decreasing cost of these technologies have allowed a wide-scale implementation of telemedicine.

The clinical applications of telemedicine have been adapted by a wide range of medical specialties and healthcare disciplines. Many of the current telemedicine applications involve the transmission of medical images for diagnosis and treatment. Two such primary image-related applications are teleradiology and telepathology. *Teleradiology* can be defined as the practice of radiology from a distance, and the initial interest in teleradiology as a practical cost-effective method of providing professional radiology services to underserved areas began some 30 years ago. Early teleradiology was considered as an alternative to recruiting radiologists for remote and isolated communities; it facilitated local patient care and avoided the unnecessary transport of patients to distant hospitals. However, until recently, technical deficiencies in the hardware, software, and telecommunications links have hindered the acceptance of teleradiology by radiologists and other physicians [20,21]. *Telepathology*, on the other hand, was developed more recently, during the late 1980s, and is still in its infancy compared with teleradiology. Two significantly different and competing techniques are currently used in telepathology: dynamic imaging and static imaging. *Dynamic imaging systems* provide real-time video imaging capability via a remotely controlled light microscope and a broadband communications link. With dynamic imaging systems, telepathologists are able to operate the microscope remotely via a keypad, mouse, or other input device so that the systems approximate the usual techniques of pathological examination. *Static imaging systems* are usually based on less expensive conventional telephone lines to transmit a limited number of still images. In this case, the consulting telepathologists are virtually excluded from the process of selecting the microscope fields for imaging. Other clinical applications of telemedicine include teledermatology, teleoncology, telepsychiatry, and more generally, the delivery of quality primary medical care to remote and isolated populations.

The nonclinical applications of telemedicine have received increased attention because of rapid developments in the telecommunications industry and the deployment of the National Information Infrastructure

(NII). In such cases, telemedicine systems are often employed to enhance educational and management activities through video conferencing and multimedia presentations. It has been recognized that nonclinical uses of telemedicine for educational and administrative activities will also contribute to the effectiveness of many clinical applications, especially when the clinicians gain greater familiarity with the telemedicine technologies through nonclinical uses. Examples of nonclinical uses of telemedicine include continuing medical education, online health-care information resources, coordinating research at multiple sites, and video conferencing for administrative meetings [1]. With Internet and World Wide Web resources, health-care information can be readily obtained for the formal and informal provision of medical advice, and continuing medical education can be implemented at multiple sites with effective multimedia presentations. Health-related research may also be conducted over telemedicine systems based on the patients' data collected and distributed at multiple sites to maximize the use of all available data. For health-care administrations, video conferencing for managers of integrated health-care systems allows such meetings to combine evaluation with quality monitoring.

More recently, public health has been identified as another nonclinical application of telemedicine with great potential. Public health for the most part is massive information transfer, teaching people how to find clean water, wash, and change lifestyles as well as disease monitoring. Telemedicine systems in the future will be able to provide the connectivity needed for mass education on disease prevention and the global network needed for disease monitoring. Such nonclinical applications of telemedicine can contribute to the improvement of human health on a global scale.

1. TECHNOLOGIES FOR TELEMEDICINE

As defined previously, telemedicine is the application of information and communications technologies to health-care. As a result, the development of telemedicine has largely been constrained by the balance of the supply and demand of technologies applicable to various telemedicine applications. The degree to which a particular telemedicine application is able to develop depends greatly on the development of appropriate technologies associated with the application. In general, the development of telemedicine applications are constrained by three fundamental aspects of information and communications technologies: information-carrying capacity, communications media, and information processing and digital technologies. These technologies determine the availability, quality, and affordability of many telemedicine applications.

The information-carrying capacity of a communications system is called *bandwidth*. Bandwidth measures the amount of information that can be carried at one time through the communications system. The advances in digital communications have offered various possibilities to transmit health-care-related information over communications systems with very high information-carrying

capacities. Usually, however, a communications system with higher bandwidth tends to be more expensive to install and maintain. Therefore, the demand for information-carrying capability, or bandwidth, depends on the needs and resources of the telemedicine users. Many recent advances in information and communications technologies have sought to increase the capacity of various communications systems by improving transmission media and by configuring the information in such a way as to reduce bandwidth requirements. The core modern information and communication technologies applicable to telemedicine are digital communications, digital video and video compression, digital imaging, and multimedia integration.

1.1. Digital Communication

The telecommunications industry is moving rapidly toward digital systems for various applications. This is because digital systems can easily facilitate more efficient transmission, more accurate signal reproduction, and more flexible information multiplexing. These characteristics of digital communications will benefit the further development of telemedicine systems. The more efficient transmission of a digital communications system can reduce the cost of transmission and therefore may spawn new applications in telemedicine. More accurate reproduction of the digital transmission will improve the quality of the received information and hence the quality of the telemedicine services. More flexible information multiplexing offers the integration of audio, video, and data signals into multimedia information so that more greatly enhanced telemedicine services can be made possible.

Historically, telemedicine was developed to overcome health-care problems arising from geographic separation between people who needed health-care and those who could provide it. Naturally, telemedicine applications have relied on existing telecommunications networks and technologies to resolve the geographic-separation issues. Depending on the nature of the telemedicine information to be transmitted, a particular type of communications media and network may be selected so that a tradeoff between the costs of and the need for timely connection can be achieved. Many telemedicine applications have depended on the public switched telephone network (PSTN) to transmit both time-critical and non-time-critical health-care information from one place to another. The carrier systems for such information transmission may include traditional telephone service, T-1 carrier systems, and ISDN.

The telephone network has several major advantages over the other two, more advanced technologies for some telemedicine applications. These advantages include ubiquity, relatively low cost for installation, and low cost per use. In addition, modern telephone systems offer a range of flexible services that have emerged during the past decade. Among them, telephone conferencing offers the opportunity for relatively large numbers of people who are geographically dispersed to meet together by phone. Voice mail enables the transmission of voice messages when instant response is not required. Fax service

facilitates the transmission of material on paper via the telephone system. With currently available computer modems, the exchange of electronic mail, data, documents, and even images can now be easily accomplished through the telephone system. In the near future, the videophone will provide more versatile and low-cost communications services for telemedicine participants.

The T-1 carrier system was the first successful system designed to use digitized voice transmission over the telephone network [19]. It was first developed to resolve the problems with the old analog telephone systems so that the system would be able to increase call-carrying capability and improve transmission quality. The first step of development was the deployment of mixed analog and digital transmission capabilities so that end users could use analog transmission through the twisted pair cable on the local loop, while the interoffice trunks were operating through digital carriers with digital switching systems. As the T-1 system evolved from the old analog telephone system, some of the features of the old telephone system remained compatible, such as the four-wire circuits in the local loop and full-duplex capability. However, many digital characteristics have been introduced in the T-1 carrier system. These characteristics include pulse-coded modulation (PCM), time-division multiplexing, framed format, bipolar format, byte-synchronous transmission, and channelized or nonchannelized services. With these digital technologies, the T-1 carrier system is able to provide a basic rate of digital transmission at 1.5444 Mbps, the rate of the digital signal level 1 (DS1) as defined by the time-division multiplexing hierarchy. This rate of the digital link is the result of multiplexing 24 standard 64-kbps PCM signals, also known as DS0 digital signals. With these higher capacity transmission links, many telemedicine applications are now able to transmit time-critical high-bandwidth requirement information, such as live video signals, over the telephone network via T-1 carrier systems.

The original motivation for the development of the T-carrier system was to provide lower cost and better quality dial-up telephone services. However, the technologies that evolved from such developments form the basis for a full end-to-end digital network, (ISDN), to support the simultaneous transmission of voice, data, video, image, text, and graphics information. ISDN provides a wide range of services using a limited set of connection types and multipurpose user-network interface arrangements [19,22]. ISDN is intended to be a single worldwide public telecommunications network to replace existing public telecommunications networks that are currently not totally compatible among various countries [23]. There are two major types of ISDN with different capacities: narrowband ISDN and broadband ISDN (BISDN). Narrowband ISDN is based on the use of a 64 kbps channel as the basic unit of switching with primarily a circuit-switching mode of transmission supported by frame-relay protocols. BISDN offers very high data rates at the order of hundreds of megabits per second with primarily a packet-switching mode of transmission supported by asynchronous transfer mode (ATM) protocols. Narrowband ISDN provides the transmission bandwidth ranging from

64 kbps to 1.544 Mbps, while BISDN provides broader transmission bandwidth, ranging from 44.736 Mbps, or DS3 in the digital signal hierarchy, to 2.48832 Gbps, or OC-48 in the optical carrier hierarchy in the synchronous optical network (SONET). Narrowband ISDN offers these services: (1) speech, (2) 3.1 kHz audio, (3) 3 kHz audio, (4) highspeed end-to-end digital channels at a rate between the basic rate of 64 kbps and the super-rate of 384 kbps, and (5) packet-mode transmission [24]. BISDN offers a variety of interactive and distribution services, including (1) broadband video telephony and video conferencing, (2) video surveillance, (3) highspeed file transfer, (4) video and document retrieval service, (5) television distribution, and (6) potentially many more future services [24]. Depending on a particular application and cost-effective consideration, a telemedicine system may employ either narrowband ISDN or BISDN to accomplish desired healthcare tasks. The development of ISDN enables a telemedicine system to encompass a much wider variety of applications, ranging from interactive videoconferencing-based diagnosis and treatment to the transfer of patient records and other healthcare-related documents for consultation and management.

1.2. Digital Video and Video Compression

As noted, video conferencing is considered the defining technology for telemedicine. Recent rapid development of video technologies, especially digital video and video compression, have enabled telemedicine to continue its strong revival.

Video refers to visual or pictorial information, which includes both still images and image sequences. Most common examples of video include television and motion pictures. The recording, storage, and transmission of video signals has traditionally been handled in analog form. Rapid advances in computer and communications technology, however, have exposed the limitations of traditional analog video. In particular, the analog video lacks interactivity and is difficult to be integrated with computer systems that accept and process digitized information and modern communications systems that transmit digital signals. As a result, efficient digital representation of the video signal has been extensively studied to take full advantage of the remarkable developments in digital communications and computer systems. Digital video is a coded sequence of data that represent the intensity and color of successive discrete points along the scan lines. Details in the digital representations of video signal are beyond the scope of this article and can be found in Refs. 25 and 26.

Digital video offers many advantages over its analog counterpart. Digital video allows the existence of video at multiple resolutions in the spatial and temporal domains, interactivity suitable for search and retrieval of video databases, variable-rate transmission based on user demand, and more important, integration of digital video with other digital media, such as digital audio, text, and graphics, for true multimedia computing and communications. These benefits of digital video create new opportunities for a telemedicine system to integrate a high level of

interactivity and flexibility into routine healthcare activities, such as efficient patient-information gathering, computerized therapy management, and automatic patient follow-up. These new opportunities are not possible with telemedicine systems that are based on analog communications. Because digital video typically requires huge storage and transmission bandwidth capacities, however, a fundamental issue is the development of video compression algorithms and the implementation of compression in hardware. For example, digital video requires a much higher data rate and transmission bandwidth than digital audio. For compact disk (CD)-quality digital audio, the data rate is about 700 kbps, whereas for a high-definition television (HDTV) signal, the data rate will be about 550 Mbps. Without appropriate compression, the sheer size of digital video will overwhelm many current storage and transmission systems. Therefore, video compression is a key technology that determines the cost and the quality of the interactive video transmission, which, in many cases, can determine the quality of the healthcare service in a specific telemedicine system. The temporal, spatial, intensity, and color resolutions required by specific telemedicine applications along with available communications channel bandwidth often dictate the desired compression performance. For example, the ISDN line with a data rate of 384 kbps may be adequate for face-to-face discussion among healthcare providers. However, remote real-time high-fidelity display of cardiological ultrasound image sequences would need a 45 Mbps communications channel. The video-compression requirements for these two applications would be quite different.

Compatibility among applications and manufacturers is often essential for the exchange and successful transmission of video data among different systems. As a result, several video-compression standards have recently been developed. Two major categories of such standards are reviewed here: (1) Standards H.261 and H.263 for video conferencing applications and (2) the MPEG series, including MPEG-1 for CD read-only memory (ROM) access, MPEG-2 for HDTV, and MPEG-4 for the true multimedia communications standard that encompasses audio coding, video coding, multiplexing of coded data, coding of text and graphics, and audiovisual scene composition.

An understanding of these video-compression standards starts with JPEG, a standard for coding single-frame color images developed by the International Standardization Organization (ISO) Joint Photographic Experts Group (JPEG). Compression of image data without significant degradation of the visual quality is usually possible because images often exhibit a high degree of spatial, spectral, and psychovisual redundancies. Spatial redundancy is due to the correlation among neighboring pixels. Spectral redundancy is due to the correlation among color components. Psychovisual redundancy is due to perceptual properties of the human visual system. For video signals, the compression algorithms also take advantage of the temporal redundancy due to usually very high correlation between neighboring frames. For the compression of still-frame images, the process is generally composed of three steps: (1) transformation, (2) quantization, and (3) symbol coding. The transforma-

tion in the JPEG standard is the discrete cosine transform (DCT), which is employed to pack the energy of the image signal to a small number of coefficients. As a result, the image can be well approximated by a small number of DCT coefficients. The quantization is needed to generate a finite number of symbols from originally continuously valued coefficients, whereas the symbol coding assigns a code word, or a binary bit stream, to each symbol generated by the quantization step. Intuitively, the coarser the quantization, the fewer the number of symbols. Higher compression can be used for coarser quantization; however, there is more degradation in the visual quality of the compressed image. In the case of symbol coding, variable length codes are usually employed to minimize the average length of the binary bitstream by assigning short codewords to more probable symbols. Huffman and arithmetic coding techniques are used as variable length coding in the JPEG standard [27].

In the compression of video signals, motion compensation is a basic technique to reduce the temporal redundancy of the image sequences. This is also the major difference between image compression and video compression. The temporal redundancy is due to the fact that there usually exists certain portion of an image that changes little from one image frame to the next. In the H.261 standard, which is the video-compression standard developed for video conferencing by the International Telecommunication Union-Telecommunication Standardization Sector (ITU-T), block-based motion compensation is performed to compute interframe differences. In this case, image data in the previous frame are used to predict the image blocks in the current frame. Only differences, typically of small magnitude, between the displaced previous block and the current block need to be coded. As in the case of JPEG, DCT and variable-length coding techniques are employed. However, interframe differences, instead of the frame itself in the case of JPEG, are transformed with DCT and coded with variable-length coding. The development of the H.261 standard began in 1984 and was completed in late 1989. This video-compression standard was developed for the application of video conferencing over low-bit-rate ISDN lines with target bit rate of p times 64 kbps, where p is between 1 and 30. Only two image formats are assumed: common intermediate format (CIF) and quarter-CIF (QCIF). CIF images consist of three components: luminance Y and color differences C_B and C_R . The size of a CIF image is 352 pixels per line by 244 lines per frame. As the H.261 standard is designed for real-time communication, it uses only the closest previous frames as a prediction to reduce the coding delay. In summary, the H.261 standard is a compromise among coding performance, real-time requirements, implementation complexity, and system robustness. This standard has been implemented in various video conferencing products. Many telemedicine systems with interactive video services are based on real-time video conferencing system over ISDN lines with the H.261 standard.

Standard H.263 was defined by the same group that developed the H.261 standard. The activities of the H.263 standard started in 1993 and were adopted in 1996. The main goal of Standard H.263 was to design a video coding

standard for applications with bit rates of less than 64 kbps. Examples of such applications include video data transmission over the public service telephone network and the mobile network in which the video bit rates range from 10 kbps to 24 kbps. As Standard H.263 was built on top of Standard H.261, the main structure is essentially the same. However, Standard H.263 offers several enhanced techniques over Standard H.261. These enhancements include the support of more image formats, the use of half-pel motion compensation, three-dimensional variable length coding, and a variable quantization step at each microblock. With the H.263 standard, telemedicine systems will have extended options in the choice of video transmission channels, the selection of image formats, and a much-improved picture quality at low-bit-rate transmission. It also opens up a new opportunity for telemedicine to use mobile communications, which may be very much desired in emergency and battlefield situations.

In parallel to the efforts by the ITU-T standards, the ISO Moving Picture Experts Group (MPEG) has developed both audio and video compression standards that can compress many types of video sources for storage and transmission on various digital media, including compact disk, remote video database, video-on-demand, digital television, and network video. The MPEG committee started its activities in 1988, and the MPEG-1 standard was approved by the end of 1992 [27]. The MPEG-1 standard has been developed for the storage of digital video and its associated audio at about 1.5 Mbps on various digital storage media. The target application for the MPEG-1 standard is the interactive multimedia system, in which video data can be decoded in real time to allow random access and fastforward/reverse with reasonable coding/decoding delays. In some telemedicine applications, in which interactive access to the desired video database is required, the MPEG-1 standard will be able to play a very important role. To reach the target bit rate of 1.5 Mbps, the input video is usually downsampled to MPEG standard input format (SIF) before compression. The SIF consists of noninterlaced frames of 352 pixels by 240 lines at a frame rate of 30 frames per second, with a 2:1 color subsampling both horizontally and vertically. The compression approach of the MPEG-1 standard uses a combination of JPEG and H.261 standards. In particular, the MPEG-1 standard also employs a block-based two-dimensional DCT to exploit spatial redundancy as in the JPEG and H.261 standards. However, the MPEG-1 standard uses bidirectional temporal prediction to achieve higher compression than the H.261 standard, which employs only forward prediction.

The second phase of the ISO MPEG standard, MPEG-2, began in 1990 and was approved as an international standard in 1994. Standard MPEG-2 provides a video coding solution for applications not originally covered or envisaged by the MPEG-1 standard. Specifically, the MPEG-2 standard was given the charter to code interlaced video at a bit rate of 4 Mbps to 9 Mbps and provide video quality not lower than National Television Systems Committee (NTSC)/Phase Alternation Line (PAL) and up to that of International Radio Consultative Committee (CCIR) 601

[26]. Emerging applications, such as digital cable TV distribution, networked database services via ATM, digital video tape recorder (VTR) applications, and satellite and terrestrial digital broadcasting distribution, were seen to benefit from the increased quality expected from the MPEG-2 standardization phase. Work was carried out in collaboration with the ITU-T SG 15 Experts Group for ATM video coding, and in 1994, the MPEG-2 Draft International Standard (which is identical to the ITU-T H.262 recommendation) was released. The specification of the standard is intended to be generic—hence, the standard aims to facilitate the bitstream interchange among different applications, transmissions, and storage media.

Basically the MPEG-2 standard can be seen as a superset of the MPEG-1 coding standard and was designed to be compatible with MPEG-1: Every MPEG-2-compatible decoder can decode a valid MPEG-1 bitstream. Many video coding algorithms were integrated into a single syntax to meet the diverse application requirements: Prediction modes were developed to support efficient coding of interlaced video, and scalable video coding extensions were introduced to provide such additional functions as embedded coding of digital TV and HDTV and graceful quality degradation in the presence of transmission errors.

The MPEG-2 standard offers enhanced capability of many telemedicine applications. At the higher bit rate of MPEG-2, a telemedicine system can take advantage of emerging video communications services to provide more flexible services and expand some remote medical consultation services over ATM, satellite, and terrestrial digital broadcasting distributions. As the MPEG-2 standard targets mainly HDTV and digital TV applications, telemedicine applications will benefit greatly the superior video quality in terms of both spatial and temporal resolution. Such high-quality video will enable telemedicine to tap many new applications that otherwise cannot be explored, among them real-time transmission of some high-resolution teleradiology images and telepathology images.

Anticipating the rapid convergence of telecommunications industries, computer, TV, and film industries, the MPEG group officially initiated a new MPEG-4 standardization phase in 1994—with the mandate to standardize algorithms and tools for coding and flexible representation of audiovisual data that are able to meet the challenges of future multimedia applications [28]. Four major future needs are identified and addressed in the development of the MPEG-4 standard: (1) universal accessibility and robustness in error-prone environments, (2) high interactive capability, (3) coding of natural and synthetic data, and (4) high compression efficiency. Bit rates targeted for the MPEG-4 video standard are between 5 kbps and 64 kbps for mobile or PSTN video applications and up to 2 Mbps for TV and film applications. The release of the MPEG-4 International Standard was targeted for late 1998.

Although the MPEG-4 standard encompasses a much wider scope of applications than telemedicine systems intended to accommodate, it will have a great impact on the quality of many telemedicine applications. These applications may include (1) video-based telemedicine services over the Internet and Intranets; (2) telemedicine video

transmission over wireless channels, such as an in-hospital mobile network and combat-field wireless links; (3) a video database search in heterogeneous network environments, including various medical image storage facilities and hospital medical record management environments; and (4) virtual-reality applications in healthcare such as remote visualization and image-guided surgery. As the demand for more sophisticated multimedia applications in healthcare grows and computer and communications systems integration continues, various video coding standards that have been developed or are currently under development are expected to facilitate enhanced telemedicine systems as well as improved healthcare services.

1.3. Digital Imaging

Imaging devices have been an integral part of healthcare service, especially diagnosis, since its very beginning. Many imaging devices have actually been invented primarily for medical applications. Traditional media used to record static diagnosis images include sheet and roll film for radiography and photography, whereas traditional media used to record dynamic images include movie film and videotapes. Modern medical imaging devices often create digital images directly. These digital imaging modalities include computer tomography (CT), magnetic resonance imaging (MRI), single-photon emission computer tomography (SPECT), and positron emission tomography (PET). For the images and videos acquired with traditional media to be exchanged over the telemedicine network, they must be converted into digital format by an appropriate digitization process to preserve the required image quality for diagnosis. A typical 11 in. \times 17 in. chest film requires at least 2000×2000 pixels and an optical dynamic range of at least 4000 to 1 (12 bits) to represent the image adequately [15]. The compression of medical images is often needed for telemedicine applications to reduce the storage and transmission costs and to reduce access time. Various image and video compression techniques and standards have been discussed previously. However, many of these generic compression techniques cannot be directly applied to diagnostic images as they employ lossy compression schemes.

The American College of Radiologists and the National Electrical Manufacturers Association (ACR-NEMA) sponsored and developed the Digital Imaging and Communications in Medicine (DICOM) Standard to meet the needs of manufacturers and users of medical imaging equipment, particularly computer radiography (CR), CT, MRI, and picture archiving and communication systems (PACS) for interconnection of devices on standard networks. The DICOM standard also provides a means by which users of imaging equipment may assess whether two devices claiming conformance are able to exchange meaningful information. As the DICOM is a standard for the transmission of radiological images from one location to another for the purpose of interpretation or consultation [29], it will have a great impact on development of telemedicine systems. In addition to personnel qualifications, licensing, and quality control, the standard includes equipment guidelines for digitization of both small and large matrix

images, display capabilities, and patient database requirements.

The DICOM standard allows digital communications between diagnostic and therapeutic equipment and systems from various manufacturers. Such connectivity is important to cost effectiveness in healthcare and therefore is crucial to the development of cost-effective telemedicine systems. Telemedicine systems with the DICOM standard can provide radiology services within facilities as well as across geographic regions. Therefore, they gain maximum benefit from existing resources and keep costs down through compatibility of new equipment and systems. For example, workstations, CT scanners, MR imagers, film digitizers, shared archives, laser printers, and computers from multiple vendors and located at one site or many sites can talk to one another by means of the DICOM standard across an open-system network. As a result, medical images can be captured and communicated more quickly and the healthcare providers in a telemedicine system can make diagnoses and treatment decisions more quickly. In summary, digital imaging and the related DICOM standard are able to facilitate an improved quality of healthcare through a networked telemedicine system.

1.4. Multimedia Integration

Today's telemedicine systems have evolved from simple video conferencing between the service provider and participant to integrating multiple types of media into a coherent medical information system for the service provider to optimize decision making in the diagnosis and treatment process. In general, multimedia resources enable telemedicine system developers to integrate a high level of interactivity into routine healthcare activities, such as patient-information gathering, problem solving, therapy management, and treatment follow-up. The integration of multimedia in a telemedicine system is characterized by computer-controlled production, manipulation, presentation, storage, and communications of several types of different media. Such integration enhances the value of the telemedicine system in that the traditional audiovisual world has been augmented by the processing of a variety of healthcare-related information to reinforce the diagnostic and treatment decision. It creates new opportunities for home-based multimedia integrated telemedicine systems, in which patients are able to monitor, treat, and learn more about their own health problems through the manipulation of a wide variety of health-related information. A telemedicine system with multimedia integration capability offers additional opportunities for healthcare providers to explore medical options that cannot be accomplished through traditional face-to-face healthcare services.

One specific area in which multimedia integration can play an important role is the coherent interpretation of patient data obtained from either direct or indirect patient observations. Direct observation of a patient may produce the data obtained from senses such as sight, sound, touch, and smell and through interaction with the patient. Indirect observations of a patient may be accomplished

through diagnostic instruments, including many medical imaging devices. These observations may be compared with the patient's health history to derive the progression of changes for a specific health problem. In the conventional healthcare setting, the clinician usually makes verbal notes and marks some sketches to characterize the observations. With multimedia integration tools, quantification of the patient data, such as computational analysis of the diagnostic images, becomes possible. Such quantification allows objective comparisons of the patient data at the follow-up examination and enables consistent treatment protocols even when the patient is assigned to a different healthcare provider at the follow-up examination.

Another application for multimedia integration is the management of the electronic medical record. With multimedia integration, electronic patient medical records, including those acquired at a remote site, can be shared online in a telemedicine system among physicians, patients, and specialists, as well as offline to facilitate consultation and second opinions. The management of the electronic medical records through multimedia integration has been made possible because, in a telemedicine system, the primary patient data can be electronically captured as images, videos, sounds, graphics, and text. In addition, the networked telemedicine systems allow sharing of patient data that may be located away from the service site or distributed at several sites.

Finally, multimedia integration is the key to access to Internet resources, including continuing medical education and case consultation. As the Internet offers hyperlinked multimedia information for either public or restricted access, it may be an integral part of a telemedicine system to provide access for the general public to medical education or for a restricted pool of participants to provide sharing of specific medical information. It is anticipated that the potential for multimedia integration will be further expanded in many information systems, including various telemedicine applications.

In summary, the convergence of communications and computer technologies has shaped a wide range of new telemedicine applications. As the technologies advance to new levels, new applications will transform the daily routine of a healthcare provider and offer enhanced service quality.

2. HUMAN AND POLICY CONTEXTS OF TELEMEDICINE

The success of the telemedicine system does not depend exclusively on technological infrastructures. Technological infrastructures are necessary conditions for the implementation of telemedicine systems. However, they are not sufficient conditions for implementation. An important factor that influences the success of a telemedicine system is the human infrastructure, which can be complex [30]. In fact, it has been reported that most failures of telemedicine programs are associated with the human aspects of implementation [31]. Several factors have been identified that could impede the acceptance and adoption of telemedicine, including the documentation of benefits

for clinicians and patients, incorporation of telemedicine with existing practices, operation of the equipment by participants, assessment of needs and preferences [32], and government policies [1]. As telemedicine practice involves both patients and healthcare providers, the success of an advanced system will eventually be determined by human participants, not the technologies that support the system.

The documentation of benefits for clinicians and patients is in fact a cultural and social factor. The benefits for the clinician may include professional image and healthcare quality improvement. In terms of professional image, the adoption of relatively new technology such as telemedicine by the clinicians may be regarded poorly by their peers, even though in many cases, the quality of the care has indeed been improved. Documentation on how telemedicine can help improve professional image and quality of healthcare service is greatly needed. The benefits for patients have been better documented, especially in the case of enhancing rural healthcare through telemedicine. However, more efforts are needed to educate patients and customers about the benefits of a well-staffed and well-equipped central hospital in a telemedicine system. Such benefits are evident when multimedia integration of patients' data can be made possible by a telemedicine system so that an optimal medical decision can be derived.

The next three issues are human factors. First, it is often difficult to incorporate telemedicine with existing practices. Interactive applications require primary-care and consulting practitioners at different locations to be present simultaneously to take advantage of a real-time system. This is quite different from the existing practice, in which consulting by peers is usually performed asynchronously. Many telemedicine systems are centrally located, requiring healthcare providers to travel from their traditional location of practice to use the systems. With practical and affordable multimedia desktop workstations soon to be widely available, it will be easier to incorporate telemedicine into the existing mode of healthcare practice.

Second, the operation of telemedicine equipment is usually not user friendly. The difficulties associated with this issue include the initial installation of the telemedicine system and continual maintenance and upgrading. In general, healthcare providers lack sufficient time to learn how to use complicated hardware and software, which usually require quite extensive training. This problem is further complicated by many information technology products that are designed from the perspective of the technology developer rather than that of the end user. As a result, users can find it very difficult to operate telemedicine equipment, and such problems can affect the quality of healthcare in a telemedicine system.

Third, the assessment of needs and preferences is inadequate. The needs of patients and medical practitioners are often not well communicated to the developer of a specific telemedicine system. The needs of patients include health status and problems, whereas the needs of practitioners include individual and organization characteristics, capacities, and objectives. The preferences are

related mostly to healthcare providers. Often, a practitioner would prefer a certain form of presentation of patient data to make a comfortable decision. Those preferences, however, may not be possible as a result of technical limitations and financial considerations. As such needs and preferences are usually individual, it will be a challenge to develop effective methods and tools for assessing them and to provide technology that can incorporate them. A continual exchange between the users and designers of telemedicine systems is critical to their success.

In addition to these human factors, the success of telemedicine also depends on public policies at both federal and state levels. One recent federal policy that will shape the future of telemedicine is the Telecommunication Bill of 1996. The part of the policy most relevant to telemedicine is the assurance of universal communication services at affordable rates for rural, high-cost, or low-income areas. Even though the National Information Infrastructure initiative includes more elements than just telemedicine, such a policy presents an incentive for the development of telemedicine systems, especially when many telemedicine systems are designed to enhance healthcare services for rural and underserved areas. State policies provide mixed incentives for the development of telemedicine. For example, policies regarding professional licensure have been greatly challenged by telemedicine. In particular, the medical practice through telemedicine complicates the decision as to whether the practitioner should be licensed if the practitioner and the patient are located across state lines. Existing state laws usually require that any out-of-state physician who evaluates and treats a patient in the state to be licensed in that state. Most states also provide an exception that allows physicians licensed in that state to consult with physicians from other states or even other countries, and this exception could be applied to some telemedicine applications. State policies of consultation exception are not uniform, however, and many of them limit the exception to one-time or occasional consultations. Furthermore, some states even have amended or are considering amending physician licensure to prohibit out-of-state physicians from practicing without a license in that state [33,34]. The inflexible or over-restrictive licensing policies of many states have a negative impact on the development of telemedicine systems. A national legislation that would create a national telemedicine license seems unlikely, unless telemedicine can prove itself despite regulatory obstacles. Several other policy issues also have impact on the development of telemedicine. These include policies on privacy, confidentiality, and security; payment policies for telemedicine practice; and policies on the regulation of medical devices. Privacy and confidentiality issues also exist in conventional healthcare practice, but the electronic recording, storage, transmission, and retrieval of patient data in a telemedicine system increase opportunities for infringing on patients' privacy and confidentiality rights. Payment policies for telemedicine practice must also be addressed. In fact, insurer and healthcare restrictions on fee-for-service payments to physicians for telemedicine consultations could hinder the growth of telemedicine development. Issues include lack of information on the value of telemedicine compared with

conventional service and uncertainty about whether telemedicine would cause excess service use or increase inappropriate use. The policies on the regulation of medical devices have been handled by the U.S. Food and Drug Administration (FDA) mainly through the Center for Devices and Radiological Health (CDRH). Many of the devices used in telemedicine have been regulated by CDRH to ensure that these devices are safe, effective, and properly manufactured. Most devices are hardware equipment such as medical imaging devices and can be appropriately regulated. However, the regulation of software used to transmit, store, process, display, and copy medical images is more complicated. The FDA is currently still exploring new policies that can better regulate software.

3. CONCLUSION

Telemedicine applications can expand the availability and accessibility of healthcare and improve the quality of medical services. Telemedicine is not a single technology or a small group of related technologies. Instead, it is an integration of many communications and information technologies. Key technologies in telemedicine include digital communications, digital video and video compression, digital imaging, and multimedia integration. In addition to technical infrastructure, human factors will also have a profound influence on the success of telemedicine.

Telemedicine will continue to evolve; the development of communications, computer, and information technologies is still moving forward at an unprecedented pace. There are great opportunities for telemedicine to improve diagnostics, therapeutics, and education in healthcare. However, great challenges remain. In particular, social, cultural, and legal obstacles must be overcome to achieve the maximum potential of telemedicine.

BIBLIOGRAPHY

1. M. J. Field, *Telemedicine: A Guide to Assessing Telecommunications in Health Care*, Washington, D.C.: National Academy Press, 1996.
2. J. N. Van Goord and J. P. Christensen, *Advances in Medical Informatics: Results of the AIM Exploratory Action*, Amsterdam: IOS Press, 1992.
3. M. Gott, *Telematics for Health: The Role of Telehealth and Telemedicine in Homes and Communities*, Luxembourg: Office for Official Publications of the European Community, 1995.
4. A. H. Weis, Telemedicine: A network view—usage and trends, *Proc. Mayo Telemed. Symp.*, 1993, p. 151.
5. Kansas Telemedicine Policy Group, *Telemedicine: Assessing the Kansas Environment*, Vol. 1, Topeka, KS: Kansas Department of Health and Environment, 1993.
6. J. Grigsby et al., *Analysis of Expansion of Access to Care Through Use of Telemedicine and Mobile Health Services. Report 1. Literature Review and Analytic Framework*, Denver, CO: Center for Health Policy Research, 1993.

7. Council on Competitiveness, *Breaking the Barriers to the National Informatics Infrastructure*, Washington, D.C.: Council on Competitiveness, 1994.
8. D. A. Perednia and A. Allen, Telemedicine technology and clinical applications, *JAMA, J. Amer. Med. Assoc.*, **273**: 483-487 (1995).
9. R. L. Bashshur, On the definition and evaluation of telemedicine, *Telemed. J.*, **1**:19-30 (1995).
10. Office of Technology Assessment (OTA), *Bringing Health Care Online*. Washington, D.C.: U.S. Government Printing Office, 1994.
11. Physician Payment Review Commission (PPRC), *Annual Report*. Washington, D.C.: U.S. Government Printing Office, 1988, 1989, 1995.
12. L. Lipson and T. Henderson, *State Initiatives to Promote Telemedicine*, Washington, D.C.: Intergovernmental Health Policy Project, 1995.
13. D. H. Puskin et al., Joint federal initiative for creating a telemedicine evaluation framework. Letter to the editor, *Telemed. J.*, **1**:393-397 (1995).
14. K. M. Zundel, Telemedicine: History, applications, and impact on librarianship, *Bull. Med. Libr. Assoc.*, **84**(1):71-79 (1996).
15. R. L. Bashshur, P. A. Armstrong, and Z. I. Youssef, *Telemedicine: Explorations in the Use of Telecommunications in Health Care*, Springfield, IL: Thomas, 1975.
16. R. Allan, Coming: The era of telemedicine, *IEEE Spectrum*, **13**(12):31-35 (1976).
17. E. L. Nagel et al., Telemetry of physiologic data: An aid to fire-rescue personnel in a metropolitan area, *South. Med. J.*, **61**:598-601 (1968).
18. K. Y. Bird, Cardiopulmonary frontiers: Quality health care via interactive television, *Chest*, **61**:204-205 (1972).
19. B. Bates and D. Gregory, *Voice and Data Communications Handbook*, New York: McGraw-Hill, 1995.
20. B. W. Gayler et al., A laboratory evaluation of teleradiology, *Proc. 6th Conf. Comput. Appl. Radiol.*, 1979, pp. 26-30.
21. J. N. Gitlin, Teleradiology, *Radiol. Clin. North Am.*, **24**(1): 55-68 (1986).
22. W. Stallings, *ISDN and Broadband ISDN with Frame Relay and ATM*, 3rd ed., Upper Saddle River, NJ: Prentice-Hall, 1995.
23. W. Stallings, *Data and Computer Communications*, 5th ed., Upper Saddle River, NJ: Prentice-Hall, 1997.
24. D. Minoli, *Telecommunications Technology Handbook*, Boston, MA: Artech House, 1991.
25. A. N. Netravali and B. G. Haskell, *Digital Pictures—Representation and Compression*, New York: Plenum, 1989.
26. A. M. Tekalp, *Digital Video Processing*, Upper Saddle River, NJ: Prentice-Hall, 1995.
27. H. M. Hang and J. W. Woods, *Handbook of Visual Communications*, San Diego, CA: Academic Press, 1995.
28. L. Chiariglione, MPEG and multimedia communications, *IEEE Trans. Circuits Syst. Video Technol.*, **7**:5-18 (1997).
29. American College of Radiology (ACR), *Standards for Teleradiology*, Reston, VA: ACR, 1994.
30. J. H. Sanders, *IOM Comm. Eval. Clin. Appl. Telemed.*, 1995.
31. A. Allen, Teleradiology I: Introduction, *Telemed. Today*, **4**(1):24 (1996).
32. J. S. Scott and N. Neuberger, Background paper, *IOM Comm. Eval. Clin. Appl. Telemed.*, 1996.
33. F. Gilbert, Licensure and credentialing barriers to the practice of telemedicine, in *Telemedicine Action Report: Background Papers*, Denver, CO: Western Governors' Association, 1995, pp. 27-35.
34. H. Young and R. Waters, License barriers to the interstate use of telemedicine, in *Health Information System and Telemedicine Newsletter*, Washington, D.C.: Arent Fox Kintner Plotkin & Kahn, 1995, pp. 1-4.

TELEMETRY

VICTOR BOYADZHIAN
Jet Propulsion Laboratory

The purpose of a telemetry system is to convey measurement information reliably and transparently from a remotely located data generating source to users located in space or on earth. Typically, data generators are scientific sensors, science housekeeping sensors, engineering sensors, and other subsystems on board a spacecraft.

The advent of capable microprocessor-based hardware will result in data systems with demands for greater throughput and a requirement for corresponding increases in spacecraft autonomy and mission complexity. These facts, along with the current technical and fiscal environments, create a need for greater telemetering capability and efficiency with reduced costs.

The telemetry link is the voice of the spacecraft, providing two basic types of information: performance and experimental information. By performance measurement, we mean spacecraft operating conditions consisting of temperature, pressure, voltage, current, subsystem monitoring, and so forth. The experimental measurements are related to scientific objectives of the mission, like investigations of solar plasma, magnetic fields, and micrometeorites. Because of the large number of measurements to be performed, it is necessary to time-multiplex them according to some priority.

Telemetry data can be categorized into three basic forms: *engineering parameter data*, *attitude*, and *payload*.

Engineering parameter data, also known as housekeeping data, keep check on the operating status and health of the spacecraft's onboard equipment. The following are a few forms and examples:

1. *Temperature*. Thermistors are usually used to convert temperature data into their voltage analog. In case of high temperatures, thermocouples are used to detect the temperature whose output does not exceed more than a few millivolts. This voltage signal corresponding to temperature is dc amplified to a level more suitable for the telemetry encoder.
2. *Pressure*. Various forms of pressure transducers are used to monitor pressure in fuel tanks and plenum chambers.
3. *Operating Status*. The operating status of a particular piece of equipment is represented by a single bit that indicates a function mode is enabled (Logic

Hi) or disabled (Logic Low). For proportional status information, such as amplifier gain setting, the bits are grouped into words of appropriate length.

4. *Redundancy Status*. The redundant status indicates which redundant side of equipment is in use. This is monitored by a status bit (either Logic Hi or Logic Low).
5. *Deployment of Mechanisms*. A microswitch is used to provide a status bit of separation from the launcher.
6. *Voltages and Currents of Equipment and Power Supplies*. Usually, these voltages are scaled to a common full-scale range. Current monitoring may involve a few signal processing circuits.

These are just a few examples of engineering parameter data to be monitored on a modern satellite payload. The result of every command is checked via the telemetry. Typical sampling and updating of these data are performed from every few seconds to every few minutes and hence require small bandwidths, which makes the engineering parameter data bit rate a few hundred per second for sufficient transmittal of total information.

Attitude data develop from a variety of sensors, such as gyroscopes, star mappers, accelerometers, and sun and earth sensors. The data can be analog, digital, or both.

During the transfer and intermediate orbit phase, the attitude and velocity will change rapidly, and frequent sampling is needed (i.e., one to four times per second). High sampling rates needed during some mission phases may lead to a bandwidth that exceeds that which can be provided conveniently by a standard PCM data system.

Payload data are variable and require individual consideration. For example, applications and scientific payloads are likely to need only few channels of data, but their rates may be high. Data compression may be required to reduce the downlink rate.

After launch, the command link is required in conjunction with telemetry link to supply information needed by the various spacecraft subsystems. Many commands are necessary for the routine operation and control of spacecraft functions; some are provided for changing the mission emphasis if unusual or unexpected conditions are encountered, whereas others are required to correct erratic operations or to salvage the mission if a spacecraft failure occurs. Command operation varies in complexity from simple on-off operations to trajectory-correction factors (based on tracking) for maneuvers. Usually, all of the commands will fall into two classes: (1) the discrete command for switching functions, which requires only an address for identification and execution, and (2) the quantitative command, which requires a magnitude in addition to the address.

1. TELEMETRY DATA ENCODING

All data considered develop from three basic forms: analog, digital bilevel, and digital serial. In conditioning *analog data*, the first step is scaling it to a common full-scale range; 0 V to 5 V is the usual range. The frequency

components greater than half the sampling frequency are then removed by a low-pass filter to prevent aliasing errors. Filtering channels are then sampled and converted to a digital word. An overall accuracy of about 1% is sufficient, and an 8 bit A/D converter is used to achieve this.

In *digital bilevel* data, the OFF state is represented by zero voltage and the ON state by +5 V for complementary metal-oxide semiconductor (CMOS) and 2.4 V for transistor-transistor logic (TTL). Individual groups are then arranged into 8 bit words and sampled by logic gates whose outputs are serialized and mixed with the main PCM data stream.

Digital data are usually acquired in serial form for reasons of simplifying the spacecraft's cable harness. Such data are initially stored as an 8 bit or 16 bit word in the shift register located in the equipment generating the data.

The usual spacecraft telemetry system is broken down into two major conceptual categories: a packet telemetry concept [1] and a telemetry channel coding concept [2].

Packet telemetry is a concept that facilitates the transmission of space-acquired data from source to user in a standardized and highly automated manner. Packet telemetry provides a mechanism for implementing common data structures and protocols that can enhance the development and operation of space mission systems. Packet telemetry addresses the following two processes:

1. The end-to-end transport of space mission data sets from source application processes located in space to distributed user application processes located in space or on earth.
2. The intermediate transfer of these data sets through space data networks; more specifically, those elements that contain spacecraft, radiolinks, tracking station, and mission control centers as some of their components.

Packet telemetry along with telemetry channel coding services provide the user reliable and transparent delivery of telemetry information.

2. TELEMETRY SYSTEM CONCEPT

The system design technique known as layering was found to be a very useful tool for transforming the telemetry system concept into sets of operational and formatting procedures. The layering approach is patterned after the International Organization for Standardization's Open Systems Interconnection layered network model, which is a seven-layer architecture that groups functions logically and provides conventions for connecting functions at each layer. Layering allows a complex procedure such as the telemetering of spacecraft data to the users to be decomposed into sets of peer functions residing in common architectural strata.

Within each layer, the functions exchange data according to established standard rules, or protocols. Each layer

draws on a well-defined set of services provided by the layer below and provides a similarly well-defined set of services to the layer above. As long as these service interfaces are preserved, the internal operations within a layer are unconstrained and transparent to other layers. Therefore, an entire layer within a system may be removed and replaced as dictated by user or technological requirements without destroying the integrity of the rest of the system. Furthermore, as long as the appropriate interface protocol is satisfied, users can interact with the system/service at any of the component layers. Layering is therefore a powerful tool for designing structured systems that change because of the evolution of requirements or technology.

A companion standardization technique that is conceptually simple, yet very robust, is the encapsulation of data within an envelope or header. The header contains the identifying information needed by the layer to provide its service while maintaining the integrity of the envelope contents.

2.1. Packetization Layer

Within packet telemetry, spacecraft-generated application data are formatted into end-to-end transportable data units called TM (transfer frame) source packets. These data are encapsulated within a primary header that contains identification, sequence control, and packet length information and an optional trailing error control field. A TM source packet is the basic data unit teleme-tered to the user by the spacecraft and generally contains a meaningful quantity of related measurements from a particular source.

2.2. Segmentation Layer

To provide assistance with data flow control, the Packet Telemetry Recommendation provides the capability to segment large packetized transportable data units into smaller communication-oriented TM source packets (Version 1 format) or TM segments (Version 2 format) for transfer through the space data channel. Consequently, the TM source packets and/or TM segments are of proper size for placement into the data field of the data unit of the next lower layer.

2.3. Transfer Frame Layer

In spacecraft communication, the TM (transfer frame) is used to transport source packets and segments through the telemetry channel to the receiving telecommunica-tions network. TM transfer frame protocols offer a range of delivery service options. An example of such a service option is the multiplexing of TM transfer frames into virtual channels (VCs).

The TM transfer frame begins with an attached frame synchronization marker and is followed by a primary header. The primary header contains frame identification, channel frame count information, and frame data field status information. The transfer frame data field may be followed by an optional trailer contain-ing an operational control field and/or a frame error

control field. The first of these fields provides a standard mechanism for incorporating a small number of real-time functions (e.g., telecommand verification or spacecraft clock calibration). The error control field provides the capability for detecting that which may have been introduced into the frame during the data handling process. The delivery of transfer frames requires the services provided by the lower layers (e.g., carrier, modulation/detection, and coding/decoding) to accomplish its role.

2.4. Channel Coding Layer

As a basic system requirement is the error-free delivery of the transfer frames, telemetry channel coding is used to protect the transfer frames against telemetry channel noise-induced errors. Reference 2 describes the Consultative Committee for Space Data Systems (CCSDS) Recommendation for Telemetry Channel Coding, includ-ing specification of a convolutionally encoded inner chan-nel concatenated with a Reed–Solomon block-oriented outer code [4]. The basic data units of the CCSDS Telemetry Channel Coding that interface with the layer below are the channel symbols output by the convolutional encoder. These are the information bits representing one or more transfer frames as parity-protected channel symbols.

The RF channel physically modulates the channel symbols into signal patterns interpretable as bit repre-sentations. Within the error detecting and correcting capability of the channel code chosen, errors that occur as a result of the physical transmission process may be detected and corrected by the receiving entity.

Telemetry source packets may be segmented and placed into the data field of telemetry segments, which are preceded by a header. The source packets and/or the segments are placed into the data field of the transfer frame, which is preceded by a transfer frame header. If the specified Reed–Solomon code is used in the channel coding scheme, the transfer frame is placed into the Reed–Solomon data space of the Reed–Solomon codeblock, and the codeblock is preceded by an attached synchronization marker.

2.5. Relationship Between Telemetry and Telecommand Systems

A different level of understanding is revealed by consider-ing interactions between the telemetry system and other systems in the operational environment. There is a balanced relationship between the telemetry system and the uplink telecommand system. The two systems work hand-in-hand to ensure the transfer of user directives from the sending end (traditionally on the ground) to the receiving end (controlled process, device, or instrument). Of course, the telemetry system does a great deal more than simply returning command receipt status informa-tion to the sender: Its usual function is to provide reliable, efficient transfer of all spacecraft data (housekeeping, sensor readings, etc.) back to users.

3. TELEMETRY DATA FORMATTING

The baseband data $d_i(t)$ can have different formats, as illustrated in Fig. 1. With a nonreturn to zero-level (NRZ-L) data format, a logical one is represented by one level and a logical zero by the other. With NRZ-M (mark), a logical one is represented by a change in level and a logical zero by no change. Two other formats, biphase and Miller, are also defined in Fig. 1.

Referring to Fig. 1 and assuming that binary waveform levels are $\pm A$, the NRZ signaling format falls into the class of signals [5] whose spectrum is given by

$$S_m(f) = \frac{1}{T} p(1-p) |S_1(f) - S_2(f)|^2 + \frac{1}{T^2} \sum_{n=-\infty}^{\infty} \left| pS_1\left(\frac{n}{T}\right) + (1-p)S_2\left(\frac{n}{T}\right) \right|^2 \delta\left(f - \frac{n}{T}\right) \quad (1)$$

As the elementary signal is a rectangular pulse of width T , its Fourier transform is

$$S_1(f) = -S_2(f)AT \exp(-j\pi fT) \frac{\sin(\pi fT)}{\pi fT} \quad (2)$$

Substituting Eq. (2) into Eq. (1), and letting $E = A^2T$, we get

$$\frac{S_m(f)}{E} = \frac{1}{T} (1-2p)^2 \delta(f) + 4p(1-p) \left[\frac{\sin^2(\pi fT)}{(\pi fT)^2} \right] \quad (3)$$

When $p = 1/2$, the dc spike at the origin disappears and the NRZ signaling format falls into the noise equivalent power (NEP) class with

$$\frac{S_m(f)}{E} = \left[\frac{\sin^2(\pi fT)}{(\pi fT)^2} \right] \quad (4)$$

3.1. RZ Baseband Signaling

In the RZ case, we have $S_1(f) = 0$, and $S_2(f)$ corresponds to the Fourier transform of a half-symbol-wide pulse; that is,

$$S_2(f) = \frac{AT}{2} \exp\left(\frac{-j\pi fT}{2}\right) \left[\frac{\sin\left(\frac{\pi fT}{2}\right)}{\left(\frac{\pi fT}{2}\right)} \right] \quad (5)$$

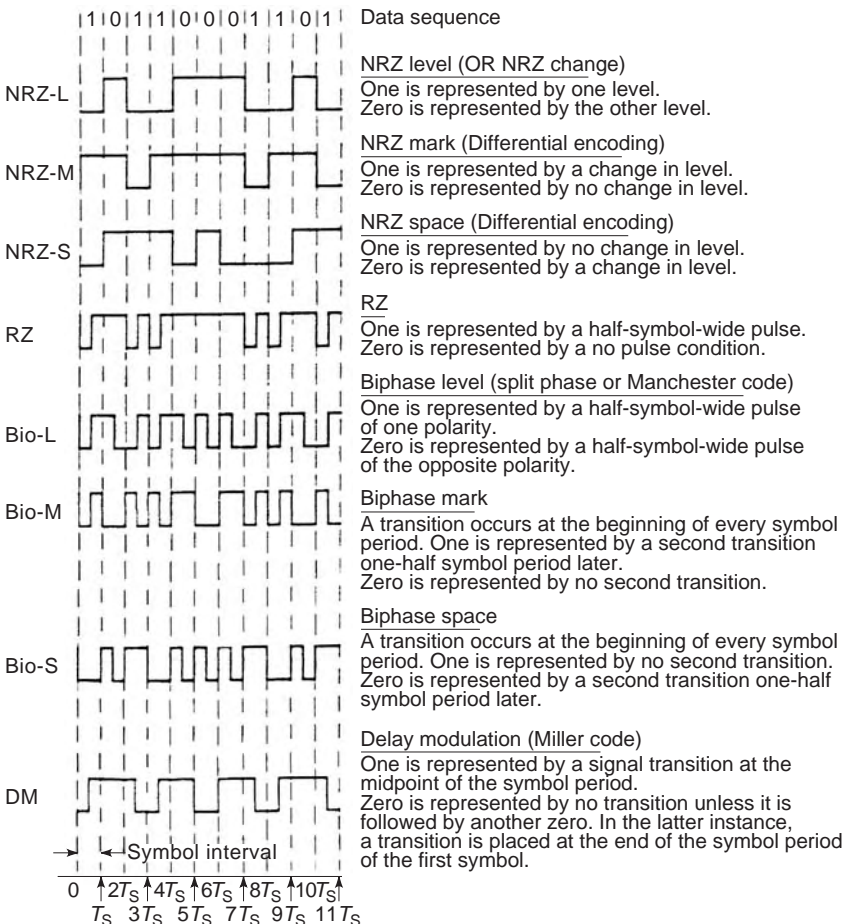


Figure 1. Various binary PCM waveforms.

As the source is again purely random, substituting Eq. (5) into Eq. (1) gives

$$\begin{aligned} \frac{S_m(f)}{E} &= \frac{1}{4T}(1-p)^2\delta(f) + \frac{1}{4T}(1-p)^2 \\ &\times \sum_{\substack{n=-\infty \\ n \neq 0}}^{\infty} \left(\frac{2}{n\pi}\right)^2 \delta\left(f - \frac{n}{T}\right) \\ &+ \frac{1}{4}p(1-p) \left[\frac{\sin^2\left(\frac{\pi f T}{2}\right)}{\left(\frac{\pi f T}{2}\right)^2} \right] \end{aligned} \quad (6)$$

3.2. Biphase (Manchester) Baseband Signaling

Two rudimentary signals in Manchester baseband signaling are defined by

$$\begin{aligned} s_1(t) &= A; \quad 0 < t < T/2 \quad \text{and} \quad -A; \quad T/2 < t < T \\ s_2(t) &= -s_1(t) \end{aligned} \quad (7)$$

Replacing the Fourier transform of Eq. (7) into Eq. (1) will yield

$$\begin{aligned} \frac{S_m(f)}{E} &= \frac{1}{T}(1-2p)^2 \sum_{\substack{n=-\infty \\ n \neq 0}}^{\infty} \left(\frac{2}{n\pi}\right)^2 \delta\left(f - \frac{n}{T}\right) \\ &+ 4p(1-p) \left[\frac{\sin^4\left(\frac{\pi f T}{2}\right)}{\left(\frac{\pi f T}{2}\right)^2} \right] \end{aligned} \quad (8)$$

for $p = 1/2$, the line spectrum disappears, and

$$\frac{S_m(f)}{E} = \left[\frac{\sin^4\left(\frac{\pi f T}{2}\right)}{\left(\frac{\pi f T}{2}\right)^2} \right] \quad (9)$$

The Miller coding scheme can be modeled as a Markov source with four states whose stationary probabilities all equal 1/4 and whose transition matrix is given by

$$P = \begin{bmatrix} 0 & 1/2 & 0 & 1/2 \\ 0 & 0 & 1/2 & 1/2 \\ 1/2 & 1/2 & 0 & 0 \\ 1/2 & 0 & 1/2 & 0 \end{bmatrix} \quad (10)$$

Another property of the Miller code is that it satisfies the recursion relation

$$P^{4+i}\Gamma = -\frac{1}{4}P^i\Gamma, \quad i \geq 0 \quad (11)$$

where Γ is the signal correlation matrix whose ik th is defined by

$$\gamma_{ik} \equiv \frac{1}{\sqrt{E_i E_j}} \int_0^T s_i(t)s_k(t)dt \quad i, k = 1, 2, 3, 4 \quad (12)$$

For the Miller code, the four rudimentary signals are defined as

$$\begin{aligned} s_1(t) &= -s_4(t) = A; & 0 \leq t \leq T \\ s_2(t) &= -s_3(t) = A; & 0 \leq t \leq T/2 \\ s_2(t) &= -s_3(t) = -A; & T/2 \leq t \leq T \\ \text{and } E_i &= A^2T; & i = 1, 2, 3, 4 \end{aligned} \quad (13)$$

Substituting Eq. (13) into Eq. (12), and putting the results in the form of a matrix,

$$\Gamma = \begin{bmatrix} 1 & 0 & 0 & -1 \\ 0 & 1 & -1 & 0 \\ 0 & -1 & 1 & 0 \\ -1 & 0 & 0 & 1 \end{bmatrix} \quad (14)$$

Finally, using Eqs. (10), (11), and (14) in the general PSD result, which is

$$\begin{aligned} S_m(f) &= \frac{1}{T} \sum_{i=1}^M p_i |s'_i(f)|^2 + \frac{1}{T^2} \sum_{n=-\infty}^{\infty} \left| \sum_{i=1}^M p_i s_i\left(\frac{n}{T}\right) \right|^2 \delta\left(f - \frac{n}{T}\right) \\ &+ \frac{2}{T} \text{Re} \left[\sum_{i=1}^M \sum_{k=1}^M p_i s_i^*(f) P_{ik} (e^{-j2\pi f T}) \right] \end{aligned} \quad (15)$$

where $S_i(f)$ is the Fourier transform of the i th elementary signal $s_i(t)$ and

$$P_{ik}(z) \equiv \sum_{n=1}^{\infty} P_{ik}^{(n)} z^n \quad (16)$$

$$s'_i(t) = s_i(t) - \sum_{k=1}^N p_k s_k(t) \quad (17)$$

yields the result of Miller code [5]

$$\begin{aligned} \frac{S_m(f)}{E} &= \frac{1}{2\theta^2(17 + 8 \cos \theta)} (23 - 2 \cos \theta - 22 \cos 2\theta \\ &- 12 \cos 3\theta + 5 \cos 4\theta + 12 \cos 5\theta \\ &+ 2 \cos 6\theta - 8 \cos 7\theta + 2 \cos 8\theta) \end{aligned} \quad (18)$$

where

$$\theta \equiv \pi f T \quad (19)$$

Spectral properties of the Miller code that make it valuable are as follows:

1. The majority of the signaling energy lies in frequencies less than one-half of the data rate, $R = 1/T$.
2. The spectrum is small, in the vicinity of $f = 0$. This spectral minimum facilitates carrier tracking, which can also be more efficiently achieved than Manchester coding.

3. The Miller coding is insensitive to the 180° phase ambiguity common to NRZ-L and Manchester coding.
4. Bandwidth requirements are approximately one-half those needed by Manchester coding.

When the data pulse stream experiences data asymmetry, distortion of the continuous component of the PSD as well as the presence of a line spectrum in PSD occurs. This problem obviously degrades the error probability of the receiving system. Let us look at the PSD of NRZ and Manchester streams when data asymmetry is present.

3.2.1. NRZ Data. Let us assume that +1 NRZ symbols are elongated by $\Delta T/2$ (relative to their nominal value of T -s) when a negative-going data transition occurs and -1 symbols are shortened by the same amount when a positive-going data transition occurs. During the absence of data transition, the symbols maintain their nominal T -s value.

Using generalized M -ary source model, where $M = 4$ with

$$\begin{aligned}
 s_1(t) &= A; & -T/2 \leq t \leq T(1 + \Delta)/2 \\
 s_1(t) &= 0; & \text{otherwise} \\
 s_2(t) &= -A; & -T/2 \leq t \leq T(1 - \Delta)/2 \\
 s_2(t) &= 0; & \text{otherwise} \\
 s_3(t) &= A; & -T/2 \leq t \leq T/2 \\
 s_3(t) &= 0; & \text{otherwise} \\
 s_4(t) &= -A; & -T/2 \leq t \leq T/2 \\
 s_4(t) &= 0; & \text{otherwise}
 \end{aligned} \tag{20}$$

The stationary probabilities associated with those four waveforms are

$$\begin{aligned}
 p_1 &= pp_t; & p_2 &= (1 - p)p_t; \\
 p_3 &= p(1 - p_t); & p_4 &= (1 - p)(1 - p_t)
 \end{aligned} \tag{21}$$

where p refers to the transition probability, which is related to the priori probability of the +1 NRZ symbol, p , by

$$p_t = 2p(1 - p) \tag{22}$$

Taking the Fourier transform of Eq. (20) and substituting the results in Eq. (1), with a great detail of simplification we get

$$\begin{aligned}
 S_m(f) &= A^2 T \frac{\sin^2(\pi f T)}{(\pi f T)^2} [A_1(p_t) + A_2(p, p_t, \eta)] \\
 &+ A^2 T \frac{\sin^2(\pi f T \eta)}{(\pi f T)^2} A^3 T \frac{\sin^2(\pi f T \eta)}{(\pi f T)^2} A^3(p_t, \eta) \\
 &+ A^2 T \frac{\sin(2\pi f T)}{(\pi f T)^2} [A_4(p, p_t, \eta) - A_5(p, p_t)] \\
 &+ A^2 [2p - (1 - \eta p_t)]^2 \delta(f) \\
 &+ \frac{2A^2}{\pi^2} p_t^2 \sum_{n=1}^{\infty} \frac{1}{n^2} C(n, p, \eta) \delta\left(f \frac{n}{T}\right)
 \end{aligned} \tag{23}$$

where

$$\begin{aligned}
 A_1(p_t) &= p_t(1 - p_t)[1 + 2(1 - p_t)] - p_t^3 \\
 A_2(p, p_t, \eta) &= (3p_t^3 + p_t(1 - p_t)[1 + 2(1 - 2p)]) \cos^2(\pi f T \eta) \\
 A_3(p_t, \eta) &= p_t^t(1 + p_t^2 - p_t) \cos^2(\pi f t) + p_t^3 \cos(2\pi f T \eta) \\
 A_4(p, p_t, \eta) &= (p_t(1 - p_t)(1 - 2p) \left[\frac{1}{2} \cos(2\pi f T \eta) \right. \\
 &\quad \left. - p \sin(2\pi f T \eta) \right]) \\
 A_5(p, p_t) &= \frac{1}{2} p_t(1 - p_t)(1 - 2p) \\
 C(n, p, \eta) &= \sin^2(n\pi\eta) [\cos^2(n\pi\eta) + (1 - 2p)^2 \sin^2(n\pi\eta)] \\
 \eta &= \frac{\Delta}{2}
 \end{aligned} \tag{24}$$

3.2.2. Manchester Data. Let us assume that for +1 data bit, the first half of the Manchester symbol is elongated by $\Delta T/4$ (relative to its nominal value of $T/2$). The same will extend to the -1 symbol—the first half of the Manchester symbol shortened by the same amount. When no data transition occurs, the second half of the Manchester symbol retains its T -s value. In view of the preceding asymmetry model, we can use the generalized M -ary source model, where $M = 4$, with

$$\begin{aligned}
 s_1(t) &= A; & -T/2 \leq t \leq \Delta T/4 \\
 s_1(t) &= -A; & \Delta T/4 \leq t \leq (T/2)(1 + \Delta/2) \\
 s_1(t) &= 0; & \text{otherwise} \\
 s_2(t) &= -A; & -T/2 \leq t \leq -\Delta T/4 \\
 s_1(t) &= A; & \Delta T/4 \leq t \leq (T/2)(1 - \Delta/2) \\
 s_2(t) &= 0; & \text{otherwise} \\
 s_3(t) &= A; & -T/2 \leq t \leq \Delta T/4 \\
 s_3(t) &= -A; & \Delta T/4 \leq t \leq (T/2) \\
 s_3(t) &= 0; & \text{otherwise} \\
 s_4(t) &= -A; & -T/2 \leq t \leq -\Delta T/4 \\
 s_4(t) &= A; & \Delta T/4 \leq t \leq (T/2) \\
 s_4(t) &= 0; & \text{otherwise}
 \end{aligned} \tag{25}$$

As before, the stationary probabilities are associated with Eq. (21). Taking Fourier transforms of Eq. (25), and substituting the results in Eq. (1), we get

$$S_m(f) = (S_m(f))_c + (s_m(f))_d \tag{26}$$

where for $p = p_t = 1/2$ the discrete component $(S_m(f))_d$ is given by

$$(s_m(f))_d = \frac{9}{4}A^2\eta^2\delta(f) + \frac{2A^2}{\pi^2} \sum_{m=1}^{\infty} \frac{1}{m^2} [H_1(m, \eta) + H_2(m, \eta) + H_3(m, \eta)]\delta\left(f - \frac{m}{T}\right) \tag{27}$$

with

$$\begin{aligned} \eta &= \frac{\Lambda}{4} \\ H_1(m, \eta) &= \frac{\sin^2(m\pi\eta)[1 + 2h_1(m, \eta)]^2}{4} \\ H_2(m, \eta) &= \sin^2(2m\pi\eta) \\ H_3(m, \eta) &= 2 \sin^2(m\pi\eta)(\cos m\pi\eta)[1 + 2h_1(m, \eta)] \end{aligned} \tag{28}$$

where

$$h_1(m, \eta) = \cos^2\left(\frac{m\pi\eta}{2}\right); \text{ for } m \text{ odd} \tag{29}$$

and

$$h_1(m, \eta) = \sin^2\left(\frac{m\pi\eta}{2}\right); \text{ for } m \text{ even}$$

Likewise, for $p = p_t = 1/2$, the continuous component of Eq. (26) is given by

$$\begin{aligned} (S_m(f))_c &= \frac{A^2T^4 \sin^4\left(\frac{\pi f T}{4}\right)}{\left(\frac{\pi f T}{4}\right)^2} \\ &- A^2T[c_1(\eta) + c_2(\eta) + c_3] \frac{\sin^2(\pi f T \eta)}{\left(\frac{\pi f T}{2}\right)^2} \\ &- A^2TC_4(\eta) \frac{\sin^2\left(\frac{\pi f T \eta}{2}\right)}{\left(\frac{\pi f T}{2}\right)^2} \\ &+ A^2TC_5(\eta) \frac{\sin^2\left(\frac{\pi f T(1 + \eta)}{2}\right)}{\left(\frac{\pi f T}{2}\right)^2} \\ &+ A^2TC_6(\eta) \frac{\sin^2\left(\frac{\pi f T(1 - \eta)}{2}\right)}{\left(\frac{\pi f T}{2}\right)^2} \end{aligned} \tag{30}$$

where

$$\begin{aligned} C_1(\eta) &= \frac{1}{4} \sin^2\left[\frac{\pi f T(1 + \eta)}{2}\right] \left\{ \sin^2\left[\frac{\pi f T(1 - \eta)}{2}\right] + \cos \pi f T \eta \right\} \\ C_2(\eta) &= \frac{1}{8} \cos \pi f T \eta \left\{ 2 \sin^2\left[\frac{\pi f T(1 - \eta)}{2}\right] - \sin^2\left[\frac{\pi f T \eta}{2}\right] \right\} \\ C_3(\eta) &= \frac{1}{8} \left[1 - 4 \cos\left(\frac{\pi f \eta}{4}\right) \right] \\ C_4(\eta) &= \frac{\sin \pi f T \eta}{8} \left\{ \sin\left(\frac{\pi f T \eta}{2}\right) \right. \\ &\quad \left. + \sin\left(\frac{5\pi f T \eta}{2}\right) [1 - \cos \pi f T \cos \pi f T \eta] - \right. \\ &\quad \left. - \frac{3}{8} \sin\left(\frac{\pi f T}{4}\right) \sin\left(\frac{\pi f T \eta}{4}\right) \right. \\ &\quad \left. + \frac{1}{8} [2 \cos 3\pi f T \eta + \cos 2\pi f T \eta] \right\} \\ C_5(\eta) &= \frac{1}{8} \left\{ \sin^2\left(\frac{\pi f T(1 - \eta)}{2}\right) - \frac{3}{2} \sin^2\left[\frac{\pi f T(1 + \eta)}{2}\right] \right\} \\ C_6(\eta) &= \frac{3}{16} \sin^2\left(\frac{\pi f T(1 - \eta)}{2}\right) + \frac{1}{4} \sin^2\left(\frac{\pi f T}{2}\right) \cos \pi f T \eta \end{aligned} \tag{31}$$

4. TELEMETRY SYSTEM DESCRIPTION AND RATIONALE

4.1. Packet Telemetry

The traditional way of transmitting scientific applications and engineering data has been the time-division multiplexing (TDM) method. Packet telemetry represents an evolutionary step from the traditional TDM method. The packet telemetry process conceptually involves:

1. Encapsulating, at the source, observational data (to which may be added ancillary data to then interpret the observational data), thus forming an autonomous packet of information in real time on the spacecraft
2. Providing a standardized mechanism whereby autonomous packets from multiple data sources on the spacecraft can be inserted into a common frame structure for transfer to another space vehicle or to earth through noisy data channels and delivered to facilities where the packet may be extracted for delivery to the user

The packet telemetry process has the following conceptual attributes:

1. Facilitating the acquisition and transmission of instrument data at a rate appropriate for the phenomenon being observed

2. Defining a logical interface and protocol between an instrument and its associated ground support equipment that remains constant throughout the life cycle of the instrument (bench test, integration, flight, and possible reuse)
3. Simplifying overall system design by allowing microprocessor-based symmetric design of the instrument control and data paths (telecommand packets in, telemetry packets out) compatible with commercially available components and interconnection protocol standards
4. Eliminating the need for mission-dependent hardware and/or software at intermediate points within the distribution networks through which space data flow; in particular, enabling the multimission components of these networks to be designed and operated in highly automated fashion, with consequent cost and performance advantages
5. Facilitating interoperability of spacecraft whose telemetry interfaces conform to CCSDS guidelines (i.e., allowing very simple cross strapping of spacecraft and network capabilities between space agencies)
6. Enabling the delivery of high-quality data products to the user community in a mode that is faster and

less expensive than would be possible with conventional telemetry

Figure 2 shows a functional diagram of the telemetry data flow from the creation of a dataset by an application process operating within a spacecraft “source” (instrument or subsystem), through to the delivery of the same data to a user “sink” (application process) on the ground. As many of the elements of this flow are currently mission unique, a primary objective of packet telemetry is to define stable, mission-independent interface standards for the communications path within the flow.

4.2. Telemetry Source Packet

A telemetry source packet is a data unit that encapsulates a block of observational data that may include ancillary data and that may be directly interpreted by the receiving end application process. Detailed discussion of the format specification for the telemetry source packet is specified in Ref. 1. The source packet format (Version 1), with the addition of a secondary header and packet error control field, is reproduced in Fig. 3 for the convenience of the reader.

From the viewpoint of data processing efficiency, the CCSDS strongly recommends that all major fields of all

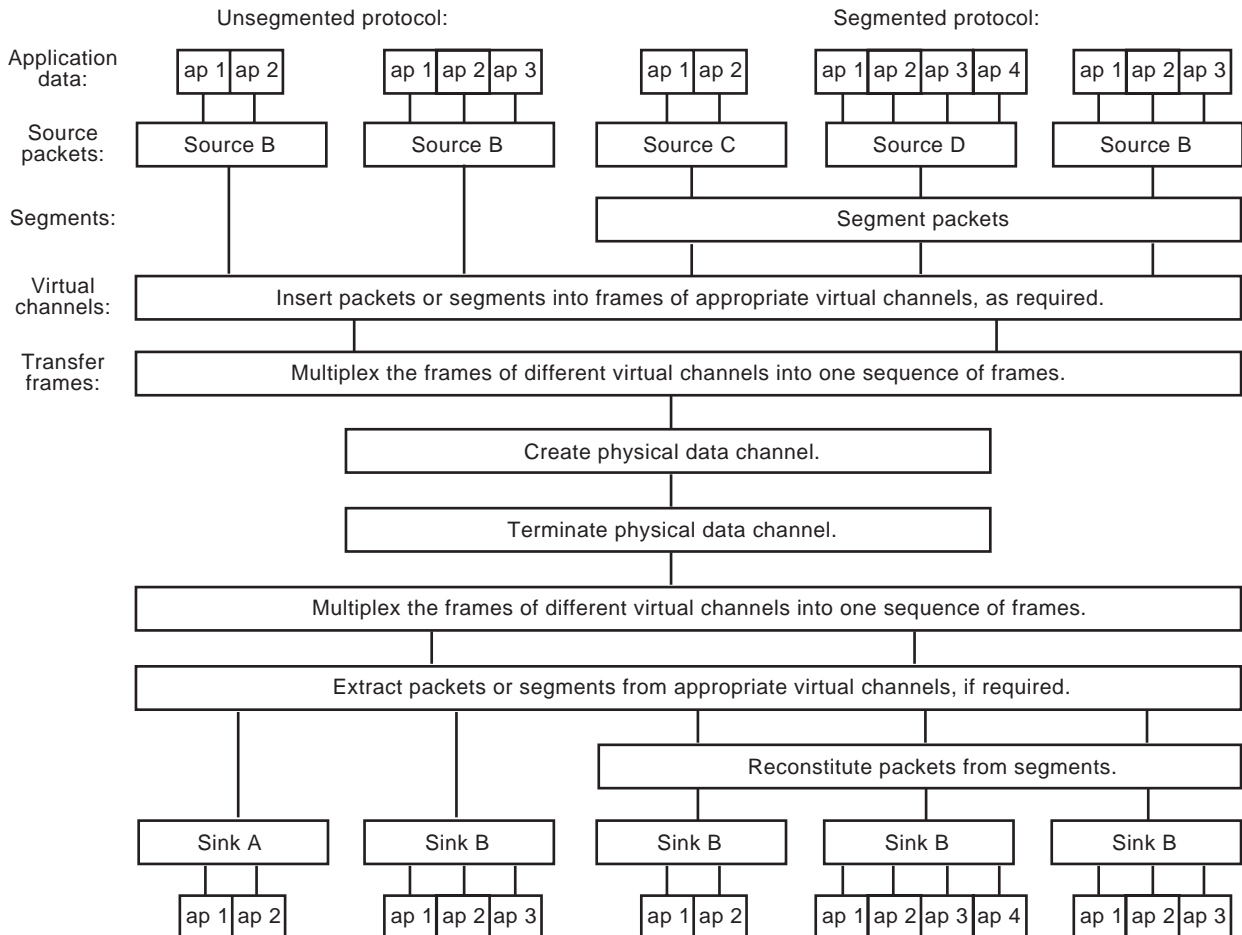


Figure 2. Telemetry data flow.

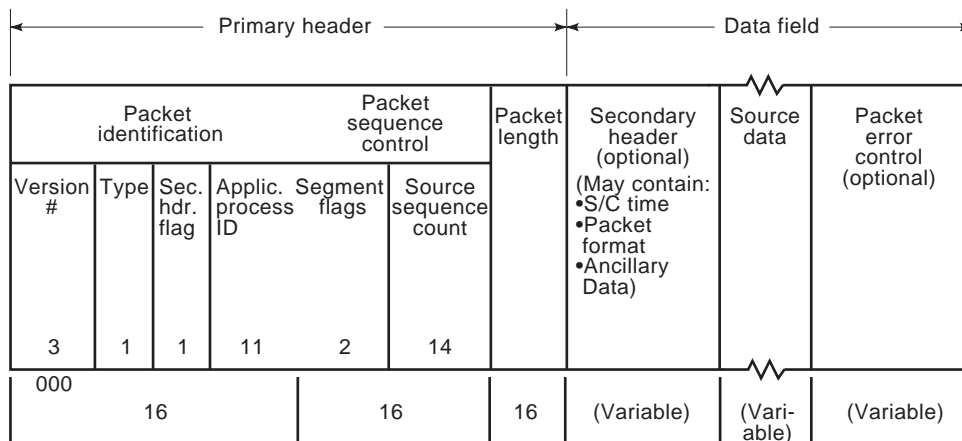


Figure 3. Source packet.

telemetry formats should be an even number of octets. This facilitates efficient internal processing within 16 bit or 32 bit computers, which are anticipated to be widely used in application processes.

User application data are encapsulated within a packet by prefacing them with a standard label or primary header, which is used by the data transport system to route the data through the system and to allow the user to reconstruct the original data set. The primary header consists of three main fields: packet identification, packet sequence control, and packet length.

4.3. Packet Identification

4.3.1. Version Number. The version number is the first of four subfields of packet identification. This subfield explicitly indicates the version of the formatted packet, and its length of 3 bits allows eight different versions to be identified. Although only two versions are currently defined, this arrangement allows a reasonable growth capability to support future needs. However, in the interest of constraining the proliferation of standards, additional versions will be discouraged unless it can be demonstrated that the current versions are truly inadequate.

4.3.2. Type. The second subfield is a 1 bit identifier to signal that this packet is a telemetry packet and not a telecommand packet. It is always set to zero for telemetry packets. (In the first issue of Ref. 1 [May 1984], this field was described as a “reserved spare” and was, by convention, set to zero for telemetry. In Issue 2 [January 1987], the value of the field had not changed, but its function had been established.)

4.3.3. Secondary Header Flag. The third subfield is a 1 bit secondary header flag. The CCSDS recognizes that users may need a means of encapsulating ancillary data (such as time, internal data field format, spacecraft position/attitude), which may be necessary for the interpretation of the information contained within the packet. Therefore, this flag, when set to one, indicates that a secondary header follows the primary header.

4.3.4. Application Process ID. The last subfield in the packet identification field is used to identify the originating source packet application process. In conventional free flyer spacecraft, source data (packets) are traditionally routed to the corresponding user application process on earth; this field could then also be used as a destination ID. (As such, the need for separate destination ID does not seem apparent. However, if users require one or more different destination IDs, these could be placed in the secondary header.) Eleven bits are allocated to the application process ID, permitting identification of up to 2048 separate application processes per spacecraft, sufficient for any envisioned free flyer spacecraft. For positive identification, one can consider this subfield an extension of the spacecraft ID, which is in the transfer frame primary header (see Fig. 5).

4.4. Packet Sequence Control

4.4.1. Segmentation Flags. The first subfield of the packet sequence control field is called segmentation flags and provides for a logical representation of four types of segmentation status. These flags identify whether the source data field contains the first, continuing, or last segment of a source packet, or if it contains no segment (meaning it contains a complete set of source application data).

4.4.2. Source Sequence Count. This second subfield provides for each packet to be numbered in a sequential manner, thus providing a method of checking the order of source application data at the receiving end of the system. It is normally used for ground accounting purposes to measure the quantity, continuity, and completeness of the data received from the source. The field provides a straight sequential count to modulo 16,384. Longer-term unambiguous ordering (beyond 16,384 packets) may be accomplished by associating the measurement time code contained within the packet with the source sequence count.

4.4.3. Packet Length. The last major field of the primary header delimits the boundaries of the packet. It is a count of the number of octets in the packet, beginning with the first octet after the 48 bit primary header and ending with the last octet of the packet. The 16 bit field allows packet lengths up to 65,536 octets (not counting the 48 bit primary header). This packet limit was a compromise between the majority of users (who produce medium-size packets) and the few users who may produce exceptionally long packets. Placing a reasonable limit on packet size helps avoid the flow control problems associated with very long packets and eliminates the overhead penalty of a larger-length field for the great majority of packet producers.

4.4.4. Data Field. The remainder of the packet may consist of any data desired, although some suggestions are provided by the Recommendation. The total length of all subsequent data should be an even number of octets (a multiple of 16 bits) for efficiency in computer processing. In addition, Fig. 3 indicates three possible subfields: secondary header, source application data, and a packet error control field.

4.4.5. Secondary Header. A secondary header may be desirable for providing any ancillary data generated by another application process (time, spacecraft position/attitude) or for providing an internal data field format. The CCSDS has not developed a recommendation for the format, but in order to allow for the future standardization of the secondary header, the most significant bit (bit 0) of the first octet of each secondary header shall be set to 0 to signify a non-CCSDS-defined secondary header.

4.4.6. Source Data. Following the secondary header, the source data subfield contains source application data generated by the application process identified in the primary header. For efficiency in computer processing, this subfield should be a multiple of 16 bits.

4.4.7. Packet Error Control. At the discretion of the user, an optional error detection code may be included at the end of the packet to verify that the overall integrity of the message has been preserved during the transport process. The particular implementation of such an error detection code, including the selection of the encoding polynomial and the length of the field, is left to the user or to the local agency.

4.5. Flow Control Mechanisms

Space telecommunications systems are usually constrained by the capacity or the bandwidth of the telecommunications channel that connects the spacecraft to the data capture element located in space or on earth. Flow control becomes crucial when multiple users must share the same telecommunications channel. The telemetry system must ensure that all sources have proper access to this common resource frequently enough to ensure timely delivery as well as to control the need to buffer data while other sources are being serviced. Long source

packets may present flow control problems if they monopolize the data channel for unacceptable periods of time while forcing other sources to implement unreasonably large local buffering of their data. Several alternative solutions to the problem of flow control are presented in the Recommendation.

4.5.1. Virtual Channelization. One solution to the flow control problem is to assign each source (which generates long packets) its own virtual channel. This is accomplished by inserting these packets into specially identified transfer frames. These dedicated frames form a virtual channel and may be interleaved with other frames containing data from other users.

4.5.2. Source-Internal Segmentation: Source Packet (Version 1). Another solution to the flow control problem is accomplished entirely within the source, whereby it manipulates its own segmentation flags when producing packets. That is, if the source is producing a very long message or data unit, it breaks the unit into segments that can fit into working-size Version 1 packets. This way, the spacecraft data system and ground see and handle normal packets whose data fields actually contain segments of a long message whose reassembly by the application can be assured by use of the packet sequence control.

4.5.3. Packet Identification. Except for the secondary header flag, the packet identification fields of each of the source packets created from the original very long message are identical. For example, the secondary header flag may indicate a secondary header present in the first packet of the sequence and not in subsequent packets of the sequence.

4.5.4. Packet Sequence Control. The packet containing the first segment of the original very long message is identified by setting the segmentation flags in the primary header to 0,1. The source sequence count value is incremented by one for each packet of the sequence. The actual value for the first segment depends on the running count at the time the first segment is to appear. Packets containing continuation segments are identified by setting the segmentation flags to 0,0. The sequence of packets is identified by incrementing the source sequence count for each packet. The packet containing the last segment of the original very long message is identified by setting its segmentation flags to 1, 0.

4.5.5. Packet Length. As the packet length field is used to point to the beginning of the next packet for purposes of extraction from the transfer frame, the packet length must always refer to the length of the source packet being handled. The total length of the original very long message can be provided by the user through private, internal message labeling.

4.5.6. Spacecraft Segmentation: Source Packet (Version 1). Instead of source-internal segmentation, another alternative is a more centralized approach to dataflow control wherein the spacecraft data system performs the segmentation.

Spacecraft segmentation is accomplished by breaking up a completely formed original long source packet and inserting the pieces into newly generated, shorter Version 1 source packets; but in this case, the shorter source packets are created by the spacecraft data system instead of the source itself and carry the “S/C data system” application process ID.

4.5.7. Packet Identification. The application process ID in the packet identification field indicates that the spacecraft data system is generating the source packets containing the segments.

4.5.8. Packet Sequence Control. The segmentation flags are set as described in section 4.5.7. The source sequence count subfield contains the count value generated by the spacecraft data system and is incremented for each segment produced. (The original long packet sequence count value remains hidden in the data field of the first packet generated by the spacecraft data system.)

4.5.9. Packet Length. As in section 4.5.8, the packet length field indicates the length of the newly generated packet.

4.5.10. Spacecraft Segmentation: Telemetry Segment (Version 2). The segmentation options discussed previously utilize the source packet (Version 1) format, in which the length is always based on the length, in octets, of the data field (packet or segment) that is transmitted, and the sequence count increments once per packet generated by a given application process. When a long packet (Version 1) requires segmentation, the monotonically increasing nature of the source sequence count, during the source packet generation process, may be disrupted.

For those missions that require the source sequence count for a given application process to increase without any gaps in the sequence, another formatting option exists. Version 2 of the packet format, called a telemetry segment, is a format within which the length field in the data unit defines the length of an original packet that remains to be transmitted, and the sequence count field remains static because it refers to the numbering of the

original source packet generated by its application process. The length and sequence count of the data unit being transmitted are, therefore, semantically different between the two versions.

It is assumed that telemetry segments (Version 2) are always generated by an application process other than the original application process. In most cases, such telemetry segments will be generated by the spacecraft data system.

The telemetry segment (Version 2) structure is shown in Fig. 4.

4.5.11. Segment Identification. When a long source packet (Version 1) is segmented using the telemetry segment protocol, the packet ID field is modified only by changing the version number subfield to indicate Version 2. This implies that a separate application process is doing the segmentation, and therefore, the application process ID subfield contains the value of the original application process.

4.5.12. Segment Sequence Control. The protocol for the segmentation flags subfield is the same as for the Version 1 format except that the sequence count subfield indicates the count of the original long packet being segmented and is not incremented for each segment generated. As such, it would seem as though each segment cannot be uniquely identified, but in fact, the following fields do provide a mechanism for assigning a serial number to each segment. The serial number may then be used to recombine segments should their natural order be disturbed during transmission or the data handling process.

4.5.13. Segment Length. Instead of indicating the length of the segment, the Version 2 format segment length field is based on the length of data (in octets) from the original long packet (including that contained within the segment) that remains to be transmitted. The length of the segment is a fixed value (256, 512, or 1024 octets) for each virtual channel and is specified in the transfer frame header.

As the fixed segment lengths are defined to be binary values of octets, by utilizing the decrementing length approach, the value of the segment length field will

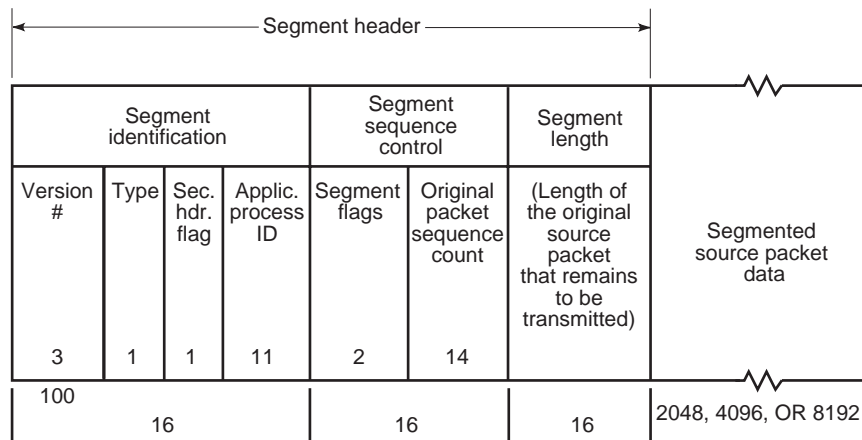


Figure 4. Telemetry segment.

decrease in binary countdown fashion as successive segments are transmitted. This information provides a “serial number” for the segment that may be used to recombine segments should their natural order be disturbed during transmission.

4.6. Telemetry Transfer Frame

The source packet data structures described in the previous sections are unsuitable for transmission directly through the communication links that interconnect the spacecraft and data capture element in space or on earth. They must be embedded within a data transfer structure that provides reliable, error-controlled transfer through the media. The CCSDS has developed such a data structure, the telemetry transfer frame, which has a fixed length for a given mission or spacecraft. The attributes of the transfer frame and its supporting rationale will follow during the discussion of the transfer frame format. Figure 5 illustrates the telemetry transfer frame format.

4.6.1. Synchronization Marker. Attached to the beginning of the transfer frame primary header is a 32 bit frame synchronization marker that is used by the receiving network to acquire synchronization with the frame boundaries after transmission through the data channel. A 32 bit synchronization pattern is selected because it provides good synchronization qualities in a noisy channel environment. The 32 bit pattern is also double-octet compatible

with 32 bit computers. The particular bit pattern and its performance characteristics are found in Refs. 1 and 6.

In conjunction with the selection of the 32 bit marker, the recommendations currently require that all transfer frames in a single physical data channel in a given mission be of constant length. When the frame is of fixed length, conventional “flywheeling” techniques may be used to maintain frame synchronization in a noisy environment.

The maximum distance from one attached sync marker to the next when using the maximum-length transfer frame (8920 bits), Reed–Solomon check symbols (1280 bits), and sync marker (32 bits) is 10,232 bits.

4.6.2. Frame Identification. The first major field of the transfer frame primary header is the frame identification field.

4.6.3. Version Number. Only one version of the transfer frame has been defined by the CCSDS, although this 2 bit field allows growth to four. The version refers to the frame structuring principles, which are described in this section. Given the small number of tracking networks, as opposed to the number of end users (packet creators), and the flexibility built into this version to meet future needs, the size of the field is considered adequate.

4.6.4. Spacecraft ID. The spacecraft identification field provides for positive identification of the spacecraft that generated the transfer frame. The 10 bits assigned to

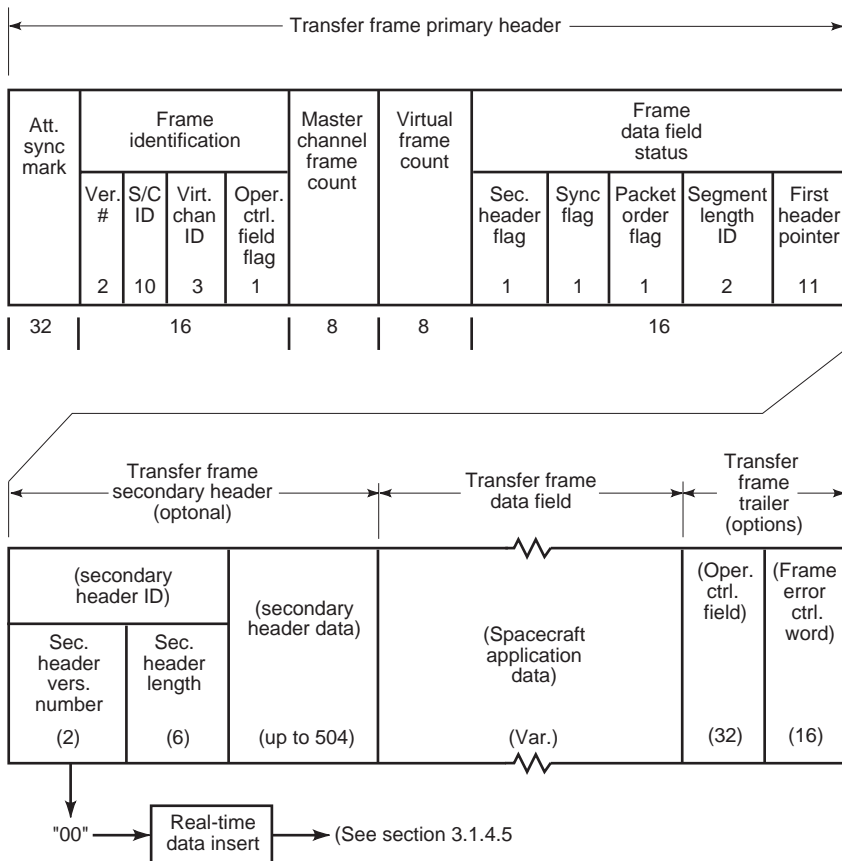


Figure 5. Telemetry transfer frame format.

spacecraft identification allow up to 1024 separate positive IDs. Spacecraft IDs are assigned per the procedures in Ref. 7 by the CCSDS, and analysis [8] has shown that under those procedures, 1024 is an adequate number for future needs.

4.6.5. Virtual Channel ID. This 3 bit subfield allows up to eight virtual channels to be run concurrently on a particular physical data channel. Frames from different virtual channels are multiplexed together on the telecommunications channel, and, with this identifier in each frame, can be easily split apart after receipt at the ground. Virtual channels can be used for a variety of purposes, such as flow control to prevent long packets from “hogging” the channel and selecting different types of data for stream splitting at the ground. Eight virtual channels are considered sufficient to provide adequate flexibility for envisioned future free flyer spacecraft.

4.6.6. Operational Control Field Flag. The last bit of the frame identification field, when set to one, signals the presence of the 32 bit operational control field, which is contained within the frame trailer. The information in this field is defined to provide a standardized spacecraft reporting mechanism for spacecraft telecommanding.

4.6.7. Master Channel and Virtual Channel Frame Count. The next two fields provide a running count of the number of frames transmitted. These counters provide a degree of data accountability (for short-duration data outages); the ambiguity level is defined by the field lengths.

4.6.8. Master Channel Frame Count. This 8 bit field provides a sequential count (modulo 256) of the number of frames transmitted by a single physical spacecraft data channel. The counter is long enough to provide a reasonable probability of detecting a discontinuity, in a sequence of frames, when the physical channel is briefly interrupted. If such a discontinuity does occur, the virtual channel accounting process can provide a greater probability of detecting the number of missing frames.

4.6.9. Virtual Channel Frame Count. This 8 bit field provides accountability for each of the eight independent virtual channels. This field is used with the virtual channel ID subfield to provide accountability via a sequential count (modulo 256). The rationale for the counter ambiguity level is the same as for the master channel frame counter. If only one virtual channel is incorporated for a given mission, both the virtual channel frame counter and the master channel frame counter must increment once per generated transfer frame (i.e., the two fields should not be concatenated into a master frame counter). This is because the ground facilities would normally be designed to handle the general case of spacecraft with multiple virtual channels.

4.6.10. Frame Data Field Status. The frame data field status field provides control information that allows the

receiving end to extract and reconstitute packets and/or segments.

4.6.11. Secondary Header Flag. The first subfield indicates the presence or absence of the optional secondary header. If its presence is so indicated, the secondary header must appear in every frame transmitted through a physical data channel, and its length must also be fixed. Rationale for this requirement is provided later in the discussion about the secondary header.

4.6.12. Synchronization Flag. This flag indicates whether the packet or segment data units are inserted into the transfer frame data field on octet boundaries. If they are, then they are said to be synchronously inserted (packet octet boundaries align with frame octet boundaries), and the extraction technique (pointing to specific octet) is valid. If the flag indicates asynchronous data insertion (i.e., unstructured [nonpacketized] data contents or packets are inserted without regard to octet boundaries), then the transfer frame layer at the receiving end will not be able to reconstitute the original data sets without additional knowledge.

4.6.13. Packet Order Flag. This flag indicates whether the sequence count order of the contained packet or segment is increasing (forward) or decreasing (reverse). This has important implications when tape recorded data are played back opposite to their recorded direction. When this is the case, the spacecraft electronics rejustify the bit direction of each packet/segment so each packet or segment individually flows in the forward direction and its header can be read to allow proper packet extraction from the transfer frame. Even though the playback packets appear individually to flow the same as the rest of the data, the sequence of packets will be running backward in time, as indicated by the decreasing sequence counter.

4.6.14. Segment Length ID. The segment length identifier subfield identifies which of three fixed segment lengths are contained within the data field of the standard Version 2 telemetry segment. The lengths are fixed in order to provide a method of serializing each telemetry segment, as explained in Section 4.3.1 in Ref. 1. The 2 bit flag allows for indication of three different lengths (2048, 4096, or 8192 bits) or an indication that the Version 2 telemetry segment is not being used on this virtual channel. Three lengths provide efficient flow control for the types of data and missions envisioned. Shorter lengths are not considered because the overhead becomes unacceptably large, whereas higher values are not considered because virtual channelization becomes a more effective flow control method.

4.6.15. First Header Pointer. The first header pointer subfield points directly to the location of the starting octet of the first packet or segment header structure within the frame data field. It counts from the end of the primary header (secondary header if present) and effectively delimits the beginning of the first packet/segment. The

packet/segment length field, in turn, delimits the beginning of the next packet/segment, and so on.

As the pointer counts octets, this feature works only when the headers are aligned with octet boundaries (i.e., when the packet/segment data are synchronously inserted [data field synchronization flag set to zero]). The 11 bits allocated to the pointer allow for a count to 2048 octets, which exceeds the count required to point to an octet at the end of the data field. Special pointer values are used to denote the following:

1. No packet/segment header is contained in this frame, but there is valid data.
2. No valid data are contained in this frame (“idle channel”).

4.6.16. Frame Secondary Header (Optional). An optional secondary header is provided for users who desire a means for deterministically inserting real-time data (e.g., time-division multiplexed data) that may be required for spacecraft monitoring and control applications.

When the secondary header presence is indicated by the secondary header flag, its length must be of a fixed value and must appear in every frame transmitted through a physical channel. Given the requirement for fixed transfer frame length, a fixed secondary header length simplifies data processing and packet extraction at the receiving end.

4.6.17. Secondary Header ID. The first part of the secondary header has two subfields. The first is the secondary header version number, a 2 bit field allowing four versions (or structuring rules). Only one version is currently defined by the CCSDS. This provides for a reasonable future growth capability.

The second subfield, secondary header length, indicates what length has been selected for the secondary header. This 6 bit subfield provides a binary count of the total number of octets contained within the entire transfer frame secondary header (including the ID field itself, which is one octet in length). This limits the total secondary header length to 64 octets (512 bits), which is considered adequate for currently understood applications.

4.6.18. Secondary Header Data. This subfield contains up to 504 bits of user-specified data.

4.6.19. Transfer Frame Data Field. The transfer frame data field contains an integral number of octets of data (e.g., source packets and/or telemetry segments) to be transmitted from the spacecraft to the receiving element. The maximum length of this field depends on which optional fields are implemented. As discussed in Ref. 2, if frame lengths shorter than the 8920 bit maximum are implemented and the frame is encoded using the recommended Reed–Solomon algorithm, then the length of the frame data field must be selected, bearing in mind the constraint that virtual fill (see the glossary at the end of this article) must occur in fixed increments. This is

necessary to simplify data processing at the receiving end. This field may also accommodate an unstructured bit stream (not necessarily packetized) as its data contents. In such a case, standard data extraction services would not be provided.

4.6.20. Transfer Frame Trailer (Optional). An optional transfer frame trailer is provided and is divided into two main fields, each of which is optional.

4.6.21. Operational Control Field. The presence or absence of the operational control field is indicated by a flag located in the frame identification field of the primary header. When present, this field facilitates closed-loop reporting of standardized real-time functions. The first bit (bit 0) of this field indicates the type of report and is currently set to zero, which signifies that this field contains a command link control word, which is used for acceptance reporting of spacecraft command activity and certain other front-end telecommunication status. This reporting mechanism is fundamental to the automated telecommand system, which is summarized in Ref. 9. The standardized internal format of the command link control word is fully defined in Ref. 10.

4.6.22. Frame Error Control Word. When present, this field occupies the two trailing octets of the transfer frame. Its presence or absence is implicitly defined from the spacecraft identifier and, thus, must or must not appear in all frames of a given spacecraft ID. It provides the capability for detecting errors that may have been introduced into the frame during the data handling processes. Its presence is mandatory if the transfer frame is *not* Reed–Solomon encoded but is optional if the frame is synchronously contained within the data space of a Reed–Solomon codeblock.

A cyclic redundancy code (CRC) has been selected for this purpose because of its effectiveness and simplicity and is defined and specified in Ref. 1, Section 5.5.2. Parity is generated over the entire transfer frame (less the final 16 bits), and the 16 bits of parity checks are then appended to complete the frame. To maintain compatibility with already built systems, it was necessary to allow for two options over which the CRC is applied; that is, it may include the sync marker or it may exclude it. As the marker pattern is always known, the preferred choice is to omit the marker when encoding. This is explained in Ref. 1, Section 5.5.2.

5. TELEMETRY CHANNEL CODING

Channel coding is a method by which data can be sent from a source to a destination by processing data so that distinct messages are easily distinguishable from one another. This allows reconstruction of the data with low error probability. In spacecraft, the data source is usually digital, with the data represented as a string of zeroes and ones. A channel encoder is a device that takes this string of binary data and produces a modulating waveform as output. If the channel code is chosen correctly for the

particular channel in question, then a properly designed decoder will be able to reconstruct the original binary data even if the waveforms have been corrupted by channel noise. If the characteristics of the channel are well understood and an appropriate coding scheme is chosen, then channel coding provides higher overall data throughput at the same overall quality (bit error rate) as uncoded transmission—but with less energy expended per information bit. Equivalently, channel coding allows a lower overall bit error rate than the uncoded system using the same energy per information bit.

There are other benefits that may be expected from coding. First, the resulting “clean” channel can benefit the transmission of compressed data. The purpose of data compression schemes is to map a large amount of data into a smaller number of bits. Adaptive compressors will continually send information to direct a ground decompressor in how to treat the data that follow. An error in these bits could result in improper handling of subsequent data. Consequently, compressed data are generally far more sensitive to communication errors than uncompressed data. The combination of efficient low error rate channel coding and sophisticated adaptive data compression can result in significant improvement in overall performance [11–14].

Second, a low bit error rate is also required when adaptive telemetry is used. Adaptive telemetry is much like adaptive data compression in that information on how various ground processors should treat the transmitted data is included as part of the data. An error in these

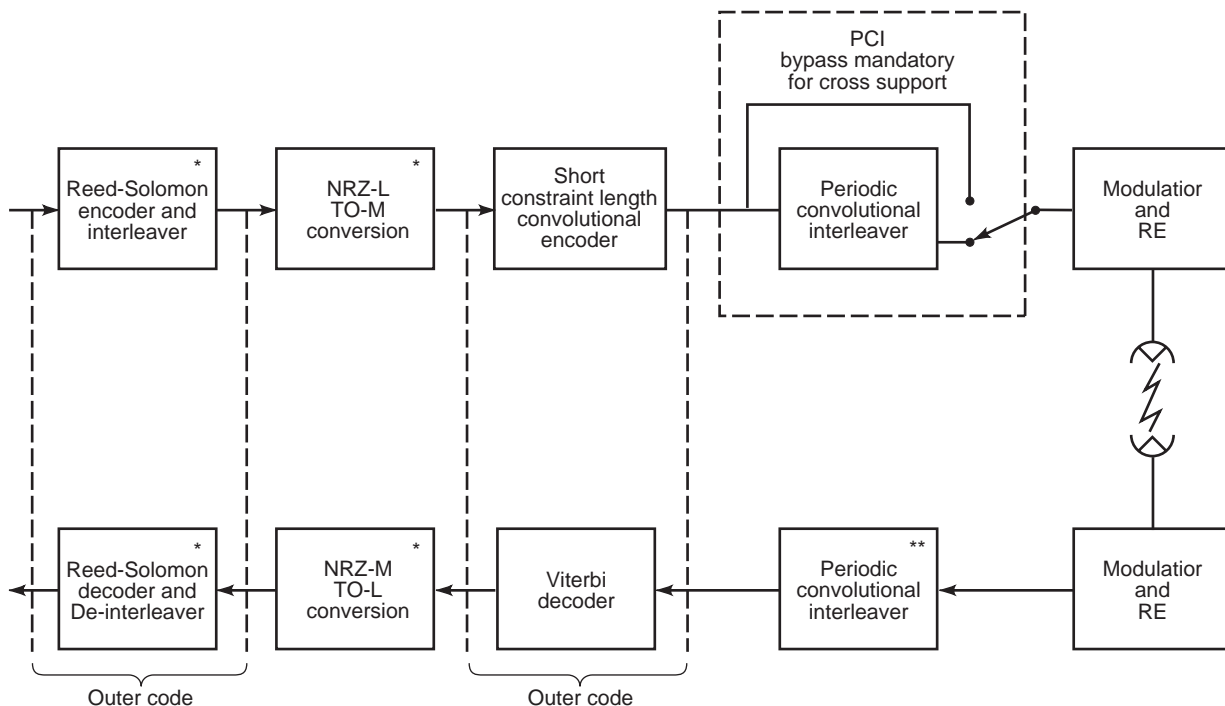
instructions could cause improper handling of subsequent data and the possible loss of much information.

Third, low error probability telemetry may allow a certain amount of unattended mission operations. This is principally because the operations systems will know that any anomalies detected in the downlink data are extremely likely to be real and not caused by channel errors. Thus, operators may not be required to try to distinguish erroneous data from genuine spacecraft anomalies.

In a typical space channel, the principal signal degradations are because of the loss of signal energy with distance and the thermal noise in the receiving system. The codes described in Ref. 2 can usually provide good communication over this channel. An additional degradation, caused by interference from earth-based pulse radars, may occur for users of the Tracking and Data Relay Satellite System (TDRSS). Such users may consider adding periodic convolutional interleaving (PCI) to their coding system; in this case, they should carefully analyze the effects of the PCI on their systems.

If interagency cross support requires one agency to decode the telemetry of another, then the codes recommended in Ref. 2 should be used. A block diagram of the recommended coding system appears in Fig. 6.

The relative performance of the various codes in a Gaussian channel is shown in Fig. 7. Here, the input is constrained to be chosen from between two levels, because biphase modulation is assumed throughout this Recommendation. These performance data were obtained by software simulation and assume that there are no



*Optional (may be bypassed)

**At White Sands Ground Station only

Figure 6. Block diagram of recommended coding system.

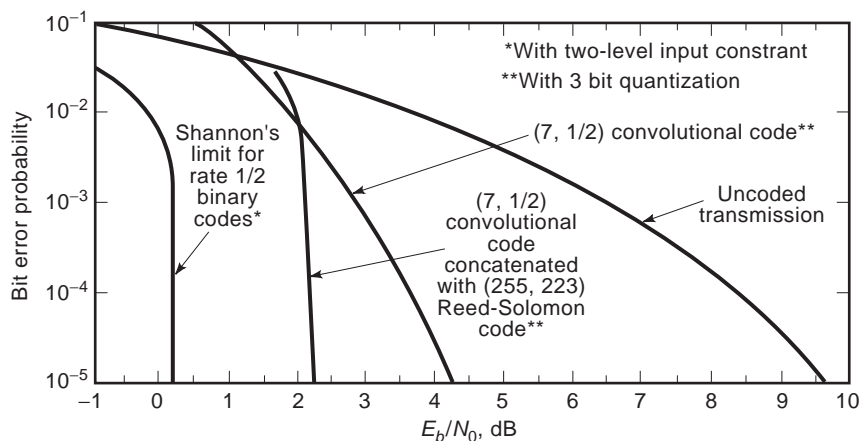


Figure 7. Performance of various codes in a Gaussian channel.

synchronization losses. The channel symbol errors were assumed to be independent. This is a good assumption for the deep-space channel. Also, infinite interleaving was assumed in the Reed–Solomon code. The use of the outer Reed–Solomon code results in an additional 2.0 dB of coding gain. Note that Fig. 7 does not necessarily represent the performance of the TDRSS channel.

These codes are included in the CCSDS Recommendation because they represent state-of-the-art coding technology and provide substantial coding gain over an uncoded system. They have already been incorporated, or are planned to be incorporated, into missions of member agencies of the CCSDS.

Sections 5.1–5.3 explain the choice of the codes and the parameters of each code in more detail.

5.1. Convolutional Code

A rate 1/2, constraint length 7 convolutional code with Viterbi (maximum likelihood) decoding is already a standard for both NASA and the European Space Administration (ESA). It has been used in several missions and has demonstrated the expected coding gain.

The encoder for this code is extremely simple. It consists of a shift register of length six and some exclusive OR gates that implement the two parity checks. The two checks are then multiplexed into one line. This means that the encoder can be made small and that it dissipates very little power. These are good attributes for spacecraft hardware. It has been customary to invert one or the other parity check in the encoder. This is to ensure that there are sufficient transitions in the channel stream for the symbol synchronizer to work in the case of a steady-state (all zeroes or all ones) input to the encoder.

Historically, ESA, NASA-Goddard Space Flight Center (GSFC), and NASA-Jet Propulsion Laboratory (JPL) have each used a different ordering of the two parity checks or inverted a different parity check. Performance is not affected by these minor differences. Although interim cross support of these different conventions may require minor differences in ground station equipment, all agencies are encouraged to adopt for all facilities the single convention described in Ref. 2, which is the NASA-GSFC convention.

5.2. Periodic Convolutional Interleaving

Low earth-orbiting spacecraft sending telemetry to the ground using the services of the TDRSS S-band single-access (SSA) channel when symbol rates exceed 300 kilosymbols/second (ks/s) may experience pulsed radio interference, which is expected to degrade the link performance severely during certain portions of the user orbit. To be able to maintain specified performance on this link at all times, the user satellite must employ an interleaving technique in conjunction with the convolutional coding and must increase the effective isotropic radiated power (EIRP). These techniques will ensure that no more than one of the dependent symbol errors because of a single radiofrequency interference (RFI) pulse is within the path memory length of the decoder at any given time, and that the signal energy has been increased sufficiently to offset the increased symbol error probability [15]. The interleaving parameters have been selected to achieve this goal for a particular worst-case pulse interference signature and the maximum symbol rate (6 Ms/s) of the SSA channel. Deinterleaving must take place before convolutional decoding and therefore is accomplished at the White Sands Ground Terminal.

5.3. Reed–Solomon Code

As a result of the nature of Viterbi decoding, the decoded bit errors of the (7, 1/2) convolutional code tend to clump together in bursts. For this reason, in a concatenated coding system that uses a convolutional inner code, the outer code should be tailored to a burst error environment. The code that is recommended as the outer code is a (255, 223) Reed–Solomon code. This is a nonbinary code. Each member of its coding alphabet is one of 256 elements of a finite field rather than zero or one. A string of 8 bits is used to represent elements in the field so that the output of the encoder still looks like binary data.

Reed–Solomon codes are block codes. This means that a fixed block of input data is processed into a fixed block of output data. In the case of the (255, 223) code, 223 Reed–Solomon input symbols (each 8 bits long) are encoded into 255 output symbols. The Reed–Solomon code in the Recommendation is systematic. This means that some portion of

the codeword contains the input data in unalterable form. In this case, the first 223 symbols are the input data. The Reed–Solomon decoder almost always knows when there are too many errors to correct a word. In the event that this happens, the decoder can inform the user of this fact.

A Reed–Solomon symbol size of 8 bits was chosen because the decoders for larger symbol sizes would be difficult to implement with current technology. This choice forces the longest codeword length to be 255 symbols. A 16 Reed–Solomon symbol error correction capability was chosen, as this was shown to have the best performance when concatenated with the (7, 1/2) convolutional inner code [11,14,16]. As two check symbols are required for each error to be corrected, this results in a total of 32 check symbols and 223 information symbols per codeword.

The (255, 223) Reed–Solomon code is capable of correcting up to 16 Reed–Solomon symbol errors in each codeword. As each symbol is actually 8 bits, this means that the code can correct up to 16 short bursts of error because of the inner convolutional decoder.

In addition, the Reed–Solomon codewords can be interleaved on a symbol basis before being convolutionally encoded. As this separates the symbols in a codeword, it becomes less likely that a burst from the Viterbi decoder disturbs more than one Reed–Solomon symbol in any one codeword. This improves the performance of the Reed–Solomon code. An interleaving depth of five was chosen for two reasons [14]: A depth of five results in performance that is virtually indistinguishable from a depth of infinity. Also, a depth of five results in a frame length (a set of five codewords that, together with the check symbol field, constitutes a codeblock) that is a good compromise considering ease of handling, data outages (quality, quantity, and continuity), and frame synchronization rate.

The same encoding and decoding hardware can implement a shortened (n , $n - 32$) Reed–Solomon code, where $n = 33, 34, \dots, 254$. This is accomplished by assuming that the remaining symbols are fixed: In the case of the Recommendation, they are assumed to be all zero. This virtual zero fill allows the frame length to be tailored, if necessary, to suit a particular mission or situation.

The method currently recommended for synchronizing the codeblock is by synchronization of the transfer frame, which contains a frame synchronization marker of 32 bits. However, advanced approaches being studied (e.g., self-synchronizing Reed–Solomon codes) may enable these two functions to be separately synchronized in the future.

The Reed–Solomon code, like the convolutional code, is a transparent code. This means that if the channel symbols have been inverted somewhere along the line, the decoders will still operate. The result will be the complement of the original data. However, the Reed–Solomon code loses its transparency if virtual zero fill is used. For this reason it is mandatory that the sense of the data (i.e., true or complemented) be resolved before Reed–Solomon decoding.

The two polynomials that define the Reed–Solomon code [Sections 4.2(4) and 4.2(5) in Ref. 2, and Ref. 17] were chosen to minimize the encoder hardware. The code generator polynomial is a palindrome (self-reciprocal poly-

nomial) so that only half as many multipliers are required in the encoder circuit. The particular primitive element “a” (and hence the field generator polynomial) was chosen to make these multipliers as simple as possible. An encoder using the “dual basis” representation requires for implementation only a small number of integrated circuits or a single VLSI chip.

GLOSSARY

- Block encoding = A one-to-one transformation of sequences of length k of elements of a source alphabet to sequences of length n of elements of a code alphabet $n > k$.
- Channel symbol = The unit of output of the innermost encoder that is a serial representation of bits, or binary digits, that have been encoded to protect against transmission-induced errors.
- Clean data (bits) = Data (bits) that are error free within the error detection and optional error correction capabilities of the TM system.
- Codeblock = A codeblock of an (n , k) block code is a sequence of n channel symbols that were produced as a unit by encoding a sequence of k information symbols and will be decoded as a unit.
- Code rate = The average ratio of the number of binary digits at the input of an encoder to the number binary digits at its output.
- Codeword = In a block code, one of the sequences in the range of the one-to-one transformation (see *block encoding*).
- Command link control word = The telecommand system transfer layer protocol data unit for telecommand reporting via the TM transfer frame operational control field.
- Concatenation = The use of two or more codes to process data sequentially with the output of one encoder used as the input of the next.
- Constraint length = In convolutional coding, the number of consecutive input bits that are needed to determine the value of the output symbols at any time.
- Convolutional code = As used in this article, a code in which a number of output symbols are produced for each input information bit. Each output symbol is a linear combination of the current input bit as well as some or all of the previous $k-1$ bits, where k is the constraint length of the code.
- Fill bit(s) = Additional bit(s) appended to enable a data entity to fit exactly an integer number of octets or symbols.

Inner code	= In a concatenated coding system, the last encoding algorithm that is applied to the datastream. The datastream here consists of the codewords generated by the outer decoder.	Transparent	= The invisible and seemingly direct (virtual) transfer of measurement information from the spacecraft source application process to the user (receiving application process).
Modulating waveform	= A way of representing databits (1 and 0) by a particular waveform.	Transparent code	= A code that has the property that complementing the input of the encoder or decoder results in complementing the output.
NRZ-L	= A modulating waveform in which a data one is represented by one of two levels, and a data zero is represented by the other level.	User	= A human or machine-intelligent process that directs and analyzes the progress of a space mission.
NRZ-M	= A modulating waveform in which a data one is represented by a change in level and a data zero is represented by no change in level.	Virtual channel	= A given sequence of transfer frames that are assigned a common identification code (in the transfer frame header), enabling all transfer frames who are members of that sequence to be uniquely identified. This allows a technique for multiple source application processes to share the finite capacity of the physical link (i.e., through multiplexing).
Octet	= An 8 bit word consisting of eight contiguous bits.	Virtual fill	= In a systematic block code, a codeword can be divided into an information part and a parity (check) part. Suppose that the information part is N symbols long (<i>symbol</i> is defined here to be an element of the code's alphabet) and that the parity part is M symbols long. A "shortened" code is created by taking only S ($S < N$) information symbols as input, appending a fixed string of length $N - S$ and then encoding in the normal way. This fixed string is called fill. As the fill is a predetermined sequence of symbols, it need not be transmitted over the channel. Instead, the decoder appends the same fill sequence before decoding. In this case, the fill is called virtual fill.
Outer code	= In a concatenated coding system, the first encoding algorithm that is applied to the datastream.		
Packet	= An efficient application-oriented protocol data unit that facilitates the transfer of source data to users located in space or on earth.		
Protocol	= A set of procedures and their enabling format conventions that define the orderly exchange of information between entities within a given layer of the TM system.		
Reed–Solomon (R-S) symbol	= A set of J bits that represents an element in the Galois field $GF(2^J)$, the code alphabet of a J -bit Reed–Solomon code.		
Reliable	= Meets the quality, quantity, continuity, and completeness criteria that are specified by the TM system.		
Segment	= A protocol data unit that facilitates telemetry flow control through the breaking of long source packets into communication-oriented data structures.		
Systematic code	= A code in which the input information sequence appears in unaltered form as part of the output codeword.		
Telemetry system	= The end-to-end system of layered data handling services that exist to enable a spacecraft to send measurement information, in an error-controlled environment, to receiving elements (application processes) in space or on earth.		
Transfer frame	= A communication-oriented protocol data unit that facilitates the transfer of application-oriented protocol data units through the space-to-ground link.		

BIBLIOGRAPHY

1. Packet Telemetry, Recommendations CCSDS 102.0-B-2, Issue 2, Blue Book, Consultative Committee for Space Data Systems, January 1987 or later issue.
2. Telemetry Channel Coding, Recommendations CCSDS 101.0-B-2, Issue 2, Blue Book, Consultative Committee for Space Data Systems, January 1987 or later issue.
3. Reference Model of Open Systems Interconnection, International Organization for Standardization, Draft International Standard DIS-7498, February 1982 or later issue.
4. R. F. Rice and E. Hilbert, U.S. Patent 3,988,677 (1976).
5. M. K. Simon, S. M. Hinedi, and W. C. Lindsey, *Digital Communication Techniques: Signal Design and Detection*, Upper Saddle River, NJ: Prentice-Hall, 1995.

6. J. C. Morakis, Discussion of synchronization words, NASA Tech. Memo. 86222, Greenbelt, MD: NASA-Goddard Space Flight Center, May 15, 1985.
7. Procedures Manual for the Consultative Committee for Space Data Systems, Issue 1, Consultative Committee for Space Data Systems, August 1985 or later issue.
8. R. Cager, Spacecraft Identification Requirements Analysis, CCSDS Panel 1-C Telecommand Action Item 6.26, June 3–7, 1985.
9. Telecommand: Summary of Concept and Service, Report CCSDS 200.0-G-6, Issue 6, Green Book, Consultative Committee for Space Data Systems, January 1987 or later issue.
10. Telecommand, Part 2: Data Routing Service, Architectural Specification, Recommendation CCSDS 202.0-B-1, Issue 1, Blue Book, Consultative Committee for Space Data Systems, January 1987 or later issue.
11. R. F. Rice, Channel coding and data compression system considerations for efficient communication of planetary imaging data, Tech. Memo. 33-695, Pasadena, CA: NASA-Jet Propulsion Laboratory, June 15, 1974.
12. R. F. Rice, End-to-end imaging rate advantages of various alternative communication systems, JPL Publication 82-61, Pasadena, CA: NASA-Jet Propulsion Laboratory, September 1, 1982.
13. R. F. Rice, Mission science value/cost savings from the advanced imaging communications system, JPL Publication 84-33, Pasadena, CA: NASA-Jet Propulsion Laboratory, July 15, 1984.
14. J. P. Odenwalder, Concatenated Reed-Solomon/Viterbi channel coding for advanced planetary missions, Final Rep., Contract 953866, December 1, 1974.
15. Tracking and Data Relay Satellite System (TDRSS) Users' Guide, STDN 101.2, Rev. 5, Greenbelt, MD: NASA-Goddard Space Flight Center, September 1984.
16. J. P. Odenwalder et al., Hybrid coding systems study, Final Rep., NASA-Ames Research Center Contract NAS2-6722, San Diego, CA: Linkabit Corporation, September 1972.
17. M. Perlman and J. J. Lee, Reed-Solomon encoders—Conventional vs Berlekamp's architecture, JPL Publication 82-71, Pasadena, CA: NASA-Jet Propulsion Laboratory, December 1, 1982.

TELEVISION AND FM BROADCASTING ANTENNAS

O. BENDOV
Dielectric Communications

1. BASICS FOR TV AND FM ANTENNAS

Antennas for television and FM broadcasting are usually installed on tall towers to maximize the service area. The maximum allowable tower height everywhere in the United States is 2000 ft aboveground. The distance to the horizon from a height of 2000 ft over flat terrain is 63 miles. The average tower height in the United States is 1200 ft, and the corresponding distance to the horizon is 49 miles.

A high-power transmitter feeds the broadcast antenna to provide “passable” picture and sound at distances approaching 70 m. In the UHF range (TV channels 14 to 69), the transmitter's peak power could be as high as 280 kW. In the VHF range (TV channels 2 to 13 and FM), a transmitter's peak power of 70 kW is not unusual. In this article, references made to channels and bands (VHF, FM, and UHF) are based on the U.S. designation.

In addition to high power-handling capability, broadcast antennas must continue to perform under severe weather conditions, such as ice storms and hurricane winds. As a protection against adverse weather conditions, broadcast antennas are supplied with a protective radome or with electrical deicing heaters. Because downtime due to antenna failure would result in severe financial loss, TV and FM broadcast antennas must be designed with extremely high reliability.

The radiation pattern of broadcast antennas is shaped in the elevation and azimuthal planes to provide service for as many households as possible. When the tower is geographically located near the population center, an omnidirectional azimuthal pattern is common. When the tower is geographically separated from the area served, a directional azimuthal pattern is more desirable.

Antennas, especially for television broadcasting, must be designed to accept and radiate all of the power delivered by the transmitter. Even a small percentage of the delivered power reflected back toward the transmitter is a cause for concern. In analog television, if 0.1% of the delivered power is reflected back by the antenna and then radiated by a second reflection at the transmitter, an annoying picture “ghost” appears on an average size TV screen.

After years of experimentation, transition from analog to digital television broadcasting in the United States was scheduled to begin in late 1998. Antennas for digital television must be designed to meet more stringent specifications than those for antennas for analog television. In analog TV, poor specifications translate into degradation of picture quality. In digital television, picture quality remains unaffected by poorly designed antennas. Instead, poor antenna design for digital television broadcasting results in loss of coverage area.

1.1. Elevation and Azimuthal Radiation Patterns

Broadcast antennas are designed to focus power toward the radio horizon. The radiation is described by two patterns, one in the elevation plane and one in the azimuthal plane. The elevation pattern depicts the relative field strength radiated at various depression angles above and below the horizon. Figure 1 shows a typical elevation pattern before and after shaping. The purpose of radiation pattern shaping is to direct maximum power toward the radio horizon and to provide essentially equal field strength to all users from the base of the tower to the radio horizon.

1.2. Null Fill and Beam Tilt

Pointing maximum power toward the horizon is accomplished by tilting the elevation pattern, usually less than

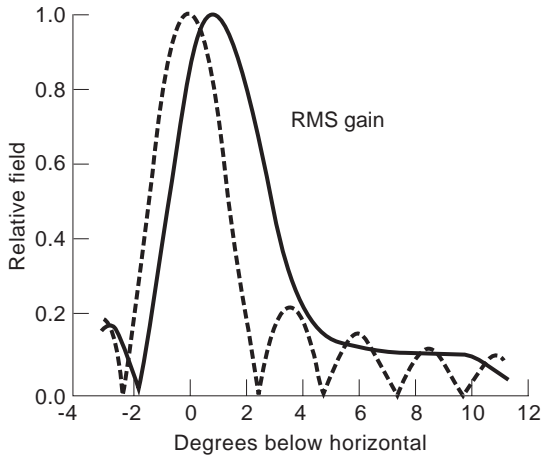


Figure 1. Elevation pattern.

2° below the horizontal plane. In Fig. 1, the tilt angle of the shaped pattern is 1°. Typically, the tilt angle corresponds to the depression angle Θ toward the horizon, which can be calculated from the formula

$$\Theta = 0.0153\sqrt{H} \text{ degrees}$$

where H is the height of the antenna above the average terrain in feet as defined by the Federal Communications Commission (FCC).

The shaping of the elevation pattern to provide essentially equal field strength to all viewers requires that all nulls in the elevation pattern are filled at depression angles below the horizon. The ideal shape of the elevation pattern before and after shaping, when applied to angles below the horizon, can be expressed as

$$\frac{\sin x}{x}$$

before shaping and

$$\frac{1}{\sin x}$$

after shaping

The azimuthal pattern depicts the relative field strength radiated at various angles around the horizontal plane. Figure 2 shows a typical omnidirectional pattern and an example of a directional pattern.

A broadcast antenna is an array of individual radiators, such as dipoles, slots, or helices. The number of individual radiators varies between 2 and 24 in a VHF array and, between 8 and 180 in a UHF array. Pattern shaping, such as shown in Figs. 1 and 2, is accomplished by nonuniform distribution of the phase and current feeding individual radiators in the array.

1.3. Gain and ERP

The gain of an antenna is a figure of merit that describes the antenna's ability to focus the input power within

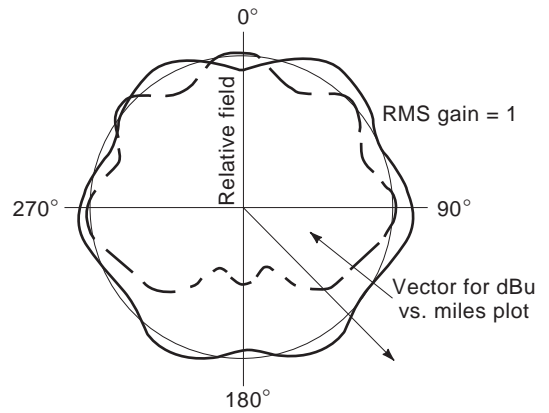


Figure 2. Azimuthal pattern.

a certain angular sector. For example, referring to Fig. 1, most of the power in the elevation plane is contained within $\pm 2^\circ$ around the peak of the elevation pattern.

The gain of broadcast antennas is specified relative to a half-wave dipole rather than relative to an isotropic radiator. Because the gain of a half-wave dipole relative to an isotropic radiator is 1.64, the peak gain of a broadcast antenna is given by

$$G_P = g_A g_E = 4\pi\eta \frac{|E(\theta, \phi)|^2}{1.64 \iint |E(\theta, \phi)|^2 \sin \theta d\theta d\phi}$$

where $E(\theta, \phi)$ is the electric field strength in the direction (θ, ϕ) at which the gain is desired and η is the power transfer efficiency of the array's distribution system. The peak gain is calculated in the direction of the peak of the elevation and azimuthal patterns.

It is customary to assume that the elevation pattern is not a function of azimuth. With that assumption, the double integral is separable into a product of two integrals, and the peak gain becomes the product of the azimuthal pattern gain g_A and the elevation pattern g_E .

The effective radiated power (ERP) is the product of the antenna's gain and the power delivered to the antenna. The maximum allowable ERP is set by each country's regulatory agency so as to maximize the service to consumers and to minimize the interference to and from all broadcast stations and other services. In the United States, the maximum allowable ERP for analog TV service is 100 kW for VHF channels 2 to 6, 316 kW for VHF channels 7 to 13, and 5,000 kW for UHF channels 14 to 69.

1.4. Coverage and Service

Passable picture and good sound quality require that a minimum level of field strength be available at the receiver. In the United States, the defining field strengths for analog TV broadcasting are shown in Table 1.

The coverage contour is described by the maximum radii beyond which, for a given transmitter power and

Table 1. Field Strengths for Analog TV Broadcasting

TV Channel	2-6	7-13	14-69
dBu ^a	47.00	56.00	64.0
mV/meter	0.22	0.63	1.6

^aAssuming an outdoor antenna 30 ft aboveground. dBμ = dB above 1 μV/m. dBu = dBμV/m is an 0 term.

antenna height aboveground, the field strength falls at or below the minimum level. Coverage contours are thermal-noise-limited. Where unacceptable interference from another station penetrates the thermal-noise-limited coverage contour, the coverage contour is modified into a service contour.

As an example, consider the UHF antenna described by the elevation patterns of Fig. 1 and the azimuthal patterns of Fig. 2. The antenna gain and input power were set to radiate ERP equal to 1000 kW. The field strength versus distance from the transmitter is shown in Fig. 3 in the direction of N135°E, as marked on Fig. 2. One of the two curves in Fig. 3 is for the omnidirectional antenna without elevation pattern shaping, and the other is for the directional antenna with a shaped elevation pattern. As shown in Fig. 3, both antennas can provide a passable picture (64 dBu) for at least 53 m, but the antenna without beam shaping will not deliver a usable signal at 5.5, 2.7, and 1.8 m from the transmitting tower.

The curves of Fig. 3 were obtained with US-FCC's F(50,50) propagation curves that translate the known ERP and antenna height into dBu versus distance. The 50,50 designation refers to the field strength that will be exceeded "at least 50% of the time at the best 50% of the locations."

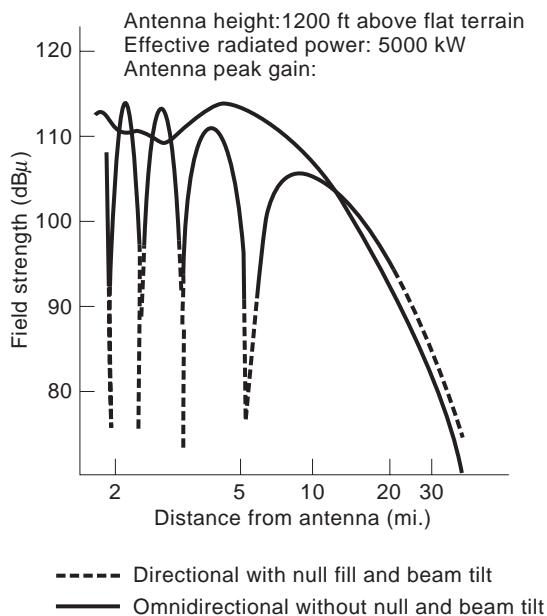


Figure 3. F(50,50) Field strength.

1.5. Polarization

For most TV stations, the electric field of the radiated power is polarized so that its vector lies in the horizontal plane, essentially parallel to the ground. Horizontal polarization was originally selected for broadcasting because its propagation is least affected by vertical obstructions, such as trees and utility poles and because measurements, conducted during the early stages of television development, showed that the polarization of man-made noise is more pronounced in the vertical than in the horizontal plane.

Circular polarization for broadcasting was introduced in the United States during the 1960s, first to FM and later to TV. Circular polarization allows for substantially improved reception of FM and TV with small receiving antennas of arbitrary physical orientation, such as those in automobiles or on top of portable TV sets.

By definition, circular polarization requires that equal power be radiated in the horizontal and vertical planes and that the two electric fields be phase-shifted 90° relative to each other. In practical antennas, the conditions for circular polarization cannot be met in all directions. The improved reception of circular and elliptical polarization broadcasting is best explained with the aid of Fig. 4.

Figure 4(a) shows the relative voltage delivered by a small, rotating dipole in any direction from the transmitting antenna when facing an essentially circularly polarized incoming signal. In the azimuthal direction of 40°, rotation of the receiving antenna varies the voltage available to the set by 1.4 dB at most. In contrast, if the incoming signal was horizontally polarized and the receiving dipole was positioned perpendicularly to the ground, the available voltage would drop to zero.

Figure 4(b) shows the relative voltage delivered by the same dipole when facing an essentially elliptically polarized incoming signal. In the azimuthal direction of 40°, rotating the receiving antenna causes the voltage delivered to the set to vary by as much as 7.6 dB, not as stable as the voltage available from a circularly polarized signal.

The gain of broadcast antennas for circular or elliptical polarization is normally specified in either the horizontal polarization plane or the vertical polarization plane. Because the two planes are orthogonal, it can be shown that

$$\text{Gain of horizontal polarization} = \frac{G_h}{1 + (G_h/G_v)|P|^2}$$

and

$$\text{Gain of vertical polarization} = \frac{G_v}{1 + (G_v/G_h)|P|^2}$$

where G_h is the gain in the absence of vertical polarization, G_v is the gain in the absence of horizontal polarization, and $P = E_v/E_h$ is the ratio of the vertical component of the electric field to the horizontal component of the electric field in the direction in which the gain is calculated.

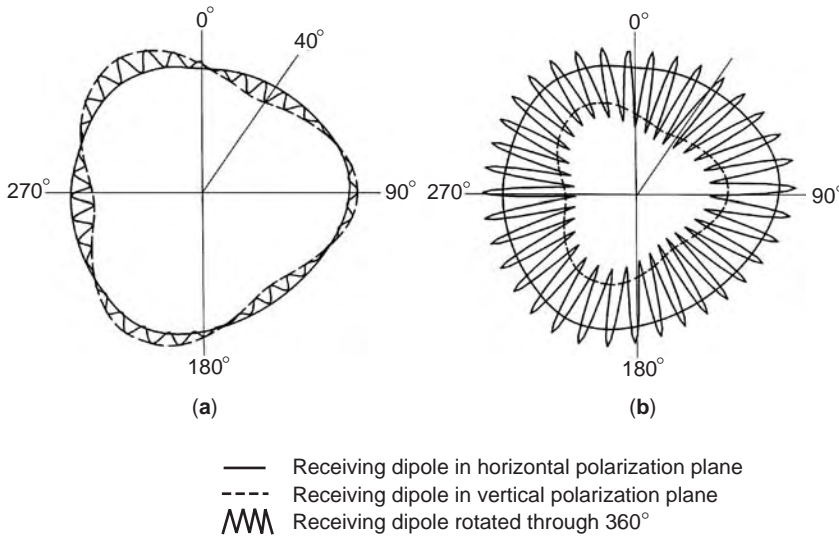


Figure 4. Voltage induced at the output terminals of a linear dipole receiving antenna: (a) Circularly polarized transmission; (b) Elliptically polarized transmission.

1.6. Coaxial and Waveguide Transmission Lines

The output power of the transmitter is delivered to the antenna via a coaxial or waveguide transmission line. A coaxial line is made of a circular pipe with a circular inner conductor. A waveguide is made of a hollow pipe of circular, elliptical, or rectangular cross section. For VHF channels 2 to 13, coaxial lines with outside diameters from 3 in. to 8 in. are used. For UHF channels 14 to 69, either coaxial lines or waveguides of various sizes are used, depending primarily on channel and power requirements. The widest cross section of waveguides for UHF broadcasting varies from 11.5 in. to 18 in. depending on the TV channel.

The main attribute of a waveguide transmission line is the high power-carrying capacity. Because of its large size with a typical vertical run of a 1000 ft up the tower, a waveguide is a major contributor to wind-load stresses on the tower. For a given cross section, a waveguide is limited to carrying only those UHF channels that propagate in its dominant mode. In contrast, for diameters not exceeding 7 in., a coaxial line accommodates any broadcast channel from 2 to 69.

In transferring the power from the transmitter to the antenna, some loss of power due to surface heating of the transmission line is inevitable. The power-transfer efficiency of a transmission line is defined by

$$\eta(\%) = 100 \frac{\text{Input Power}}{\text{Output Power}} = \frac{100}{\text{Antilog}(\alpha l / 100)}$$

where α is the attenuation in decibels/100 ft and l is the transmission line's length in feet.

2. ANTENNAS FOR TELEVISION BROADCASTING

2.1. Single-Station VHF Antennas

Most VHF antennas designed to accommodate a single TV station fall into the three distinct categories shown in Fig. 5.

The most popular category worldwide is an antenna made of a central support pole with a multiplicity of dipoles wrapped around the pole. One version of such an antenna, designed for circular polarization transmission, is shown in Fig. 5(a). This antenna accommodates any TV or FM channel. A typical gain of such an antenna is

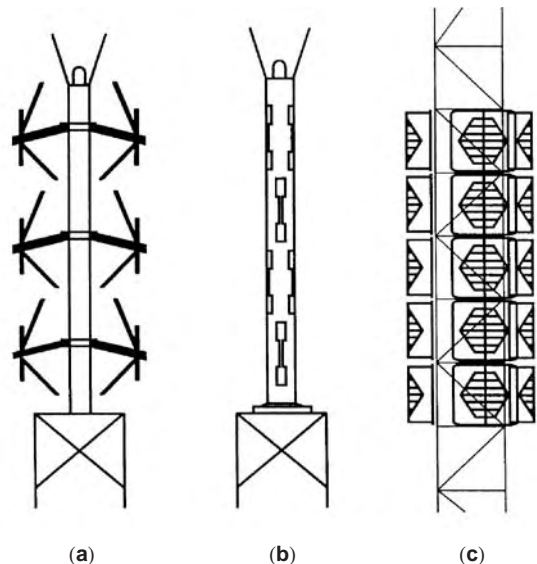


Figure 5. Single-station VHF antennas: (a) channels 2-6; (b) channels 7-13; (c) panel antenna.

3.0 in either the horizontal polarization plane or the vertical polarization plane. The height and weight of the antenna vary from 68 ft and 5.7 tons for channel 6 (United States) to 97 ft and 9.9 tons for channel 2 (United States).

A second category, popular mostly in the United States, is the slotted-pipe traveling-wave antenna, the horizontal-polarization version of which is shown in Fig. 5(b). The radiofrequency power enters this antenna at its bottom and continues to travel toward the beacon at the top. While traveling upward, power leaks outward through the slots, decaying exponentially. The remainder of the power is forced out of the top slot.

The panel antenna shown in Fig. 5(c) is composed of an array of dipoles, each placed approximately one quarter-wavelength in front of a reflecting screen. Then the array is wrapped around a support spine, which is often the tower itself. The panel antenna is popular mostly outside the United States because it is easily installed. In the United States, VHF panel antennas are used primarily where a directional pattern is required, if the top of the tower is unavailable, or as a support structure for one or more antennas stacked over the panel antenna.

2.2. Single-Station UHF Antennas

Most UHF antennas for TV broadcasting in the United States are the slotted pipe variety shown in Fig. 6(a) (horizontal polarization) and Fig. 6(b) (circular polarization). In the circular polarization version of the slotted-pipe antenna, a parasitic Z-shaped dipole is placed approximately one eighth of a wavelength in front of each slot. The Z-shaped dipole intercepts some of the horizontal polarization power emitted by the slot and radiates the intercepted power as vertical polarization, phase-shifted -90° relative to the horizontal polarization. The Z-shaped dipole

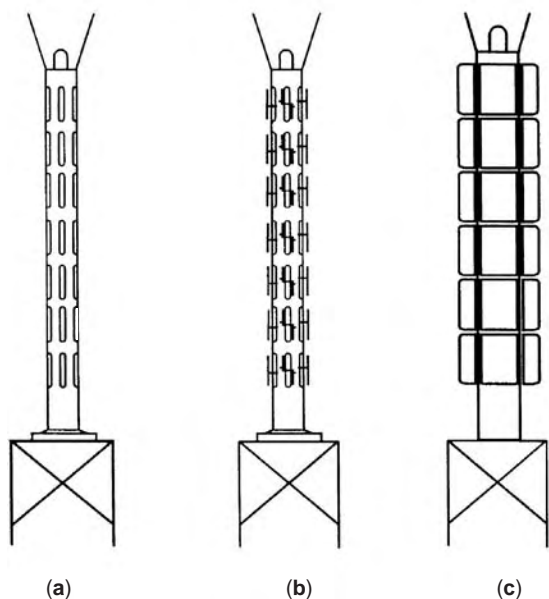


Figure 6. Single-station UHF antennas: (a) horizontal polarization; (b) circular polarization; (c) panel antenna.

can be adjusted for any power ratio of horizontal to vertical polarization. When the power ratio is one, the polarization is circular. For an unequal ratio, the result is elliptical polarization. Both elliptical and circular polarization provide superior analog TV reception on sets equipped with small indoor antennas, such as loops or monopoles.

In contrast, most UHF antennas for TV broadcasting outside the United States are made of an array of panels as shown in Fig. 6(c) (horizontal polarization). The panel antenna is relatively inexpensive, and its azimuthal pattern is easily shaped for directional antenna application. The panel antenna exhibits some drawbacks. The most noticeable drawbacks are large aerodynamic area and multiplicity of pressurized components, which adversely affect the long-term reliability and maintainability of the panel antenna.

2.3. Broadband VHF and UHF Panel Antennas

One of the most vexing problems for TV and FM broadcasters is the scarcity of tower space, especially at locations that permit maximum service. This problem is especially acute due to safety, legal, and environmental regulations in major metropolitan areas. Because of the scarcity of tower space and to save construction costs, broadcasters have been using antennas designed to accommodate multiple channels on single antennas. These so-called “broadband” panel antennas are used for VHF and UHF channels. A stack of two such antennas is shown in Fig. 7. The top antenna accommodates a multiplicity of UHF channels in the range from 450 MHz to 800 MHz, subject to average and peak power limitations.

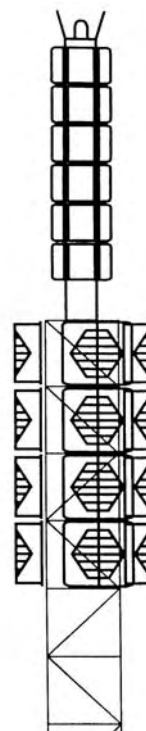


Figure 7. Broadband panel antennas.

The bottom antenna accommodates a multiplicity of VHF channels in any one of three bands. These bands (United States) are 54 MHz to 66 MHz (Low-V), 66 MHz to 88 MHz (Mid-V), and 174 MHz to 216 MHz (Hi-V).

2.4. Multistation Master Tower

Another solution to the problem of tower scarcity is deploying a master TV/FM tower that supports all the antennas necessary to serve the market, and placing it near the center of population. Master towers are either in the form of candelabras, where several antennas are installed side-by-side on a platform at the top of the tower, or a stack of several antennas installed one on top of another beginning at the top of the tower.

Two examples of a master tower, a candelabra and a stack are shown in Fig. 8. The stack shows all of the analog TV antennas on top of the north tower of the World Trade Center in New York City. This stack has been in operation since the 1970s. The height of the stack is 350 ft above the roof. The second master tower is a proposed design of a candelabra to be constructed early in the twenty-first century to support future digital TV service on channels 2 to 51 in New York City. The triangular top platform of the candelabra has a corner-to-corner width of 45 ft. A stack of three, slotted-pipe UHF antennas occupies each corner of the platform. One of the nine antennas designed to serve two multiplexed channels has a total tower capacity of ten digital TV stations.

2.5. Radiation Pattern Distortion

When an antenna is positioned close to other antennas or side-mounted on the support tower, undesired scattering of the intercepted primary radiation by nearby obstructions results. This undesired scattering combines vectori-

ally with the primary radiation to produce a new pattern that could significantly differ from the desired primary radiation pattern.

For example, when a perfectly omnidirectional antenna is mounted on top of the support tower without any nearby obstructions, its primary azimuthal pattern remains undistorted, as shown in Fig. 9. When side-mounted 8 ft from the center of a triangular tower with a 10-ft side, the same antenna shows a marked distortion in its pattern. Further, the distorted pattern shows significant variation in some directions when swept over the 6 MHz of the TV channel. Such a distorted pattern causes a significant reduction in the picture quality of analog TV in many directions. In the case of digital TV, total loss of picture and sound can be expected in the directions where the signal power is low or where power variation over the channel width of 6 MHz is significant. Depending on the country, the channel width could be 6, 7, or 8 MHz. In North America, it is 6 MHz.

In contrast, a directional antenna properly mounted close to a support tower, exhibits relatively small distortion of its primary pattern, as shown in Fig. 10. By judiciously mounting the antenna so that the minimum of its primary pattern points in the direction of the largest obstruction, the level of significant pattern distortion due to scattering is limited to an angular sector of 90° to 120° behind the support tower.

3. ANTENNAS FOR FM BROADCASTING

3.1. Single-Station Antennas

FM antennas for single-channel broadcasting are designed to be inexpensive relative to TV antennas. They are also designed to add a minimum of aerodynamic stress

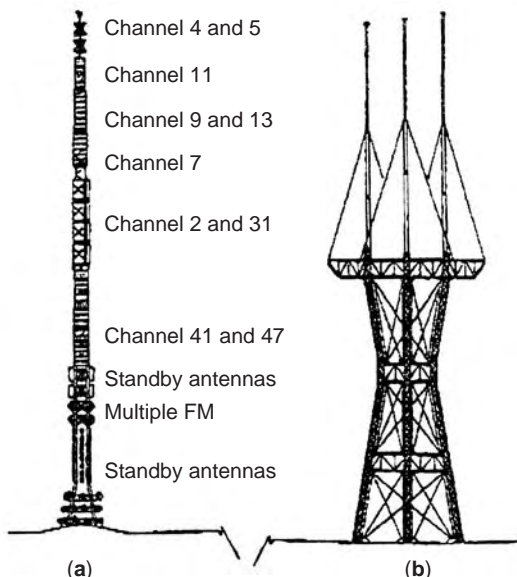


Figure 8. Multistation master antennas in New York: (a) present stack on World Trade Center 1; (b) future candelabra on World Trade Center 2.

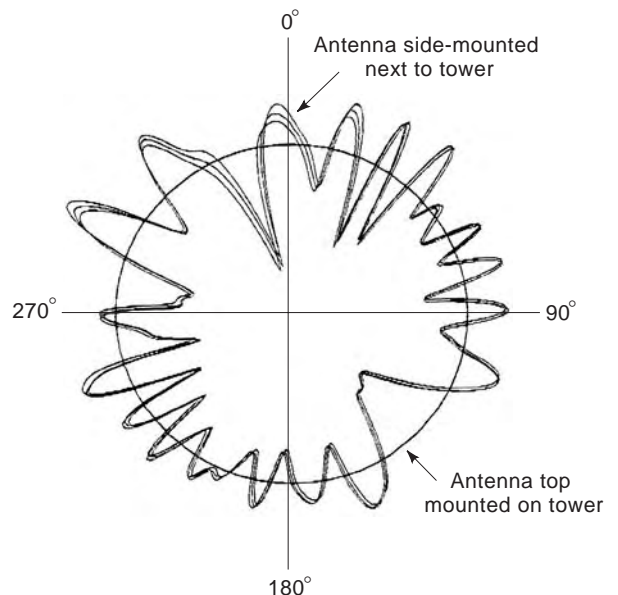


Figure 9. Tower distortion over 6 MHz for omnidirectional antenna.

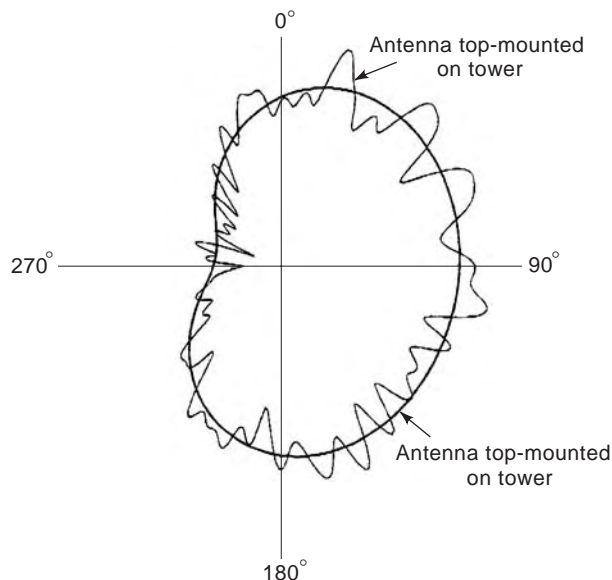


Figure 10. Tower distortion of directional antenna pattern.

on the support tower. These two objectives are relatively easy to meet because of the narrow bandwidth of the FM channel. The FM channel width in North America is 200 kHz, in Europe 100 kHz, and in Africa 86 kHz.

FM broadcasting was originally planned for reception by an outdoor antenna, and the polarization of the electric vector was linear, polarized either in the horizontal or vertical plane. Since the introduction of low-cost, portable, solid-state radios for automobiles and homes, polarization of the FM signal has gradually shifted worldwide to circular polarization.

The most popular implementation of the single-channel, low-cost, circular polarization FM antenna is shown in Fig 11. The antenna is an array of 1 to 12 radiators or “bays.” Each radiator consists of two to four interwoven, bent, half-wave dipoles. The dipoles are typically bent around a circular form approximately 20 in. in diameter. In another implementation of this design, the interwoven dipoles are bent in a V-shape. The radiators are mounted along a pipe, the diameter of which depends on the number of radiators and on whether the antenna is to be top-mounted or side-mounted on the tower.

Several disadvantages are associated with the single-channel antenna shown in Fig. 11. The antenna is designed to be omnidirectional and to radiate circular polarization in the absence of the pipe supporting the “bays.” When mounted on the pipe as shown, the antenna radiates elliptical polarization, and the vertical component of the electric field is substantially attenuated in the shadow of the support pipe. If the antenna with the support pipe is then side-mounted on the transmission tower, as is often the case, the radiation patterns in the elevation and azimuthal planes are further severely distorted. Another difficulty due to the physically small radiator of this antenna is a somewhat excessive downward radiation that may raise the level of the RF power density near the ground above the allowable protective limit. The

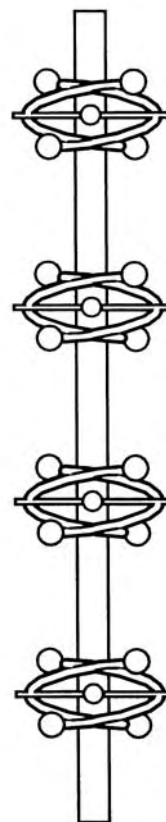


Figure 11. Single-station FM antenna.

downward radiation level can be reduced by spacing the array elements at half-wavelength intervals.

3.2. Multistation Master Antennas

The master FM antenna, capable of supporting multiple FM stations on a single antenna, is gradually replacing single-station antennas in major cities worldwide. Such a master antenna, made of multiple broad-band panels, is shown in Fig. 12. The master FM antenna does not exhibit any of the disadvantages of the single-station antenna and is ideal where tower space is scarce. Master FM antenna construction is similar to that of VHF-TV panel antennas with a high price to match. The installation cost is sometimes shared by the individual FM channels, which are multiplexed on the master antenna, making the antenna affordable.

4. ADVANCED TOPICS: ANALOG VERSUS DIGITAL TV

4.1. Spectral Distribution

Fundamental differences exist in the performance specifications of antennas for analog and digital TV broadcasting.

Reception of analog TV is subject to fading, manmade noise, and picture degradation in poor reception areas. In contrast, the reception of digital TV yields a perfect picture and sound all of the time or not at all. The same sources that cause poor reception of analog TV combine to reduce

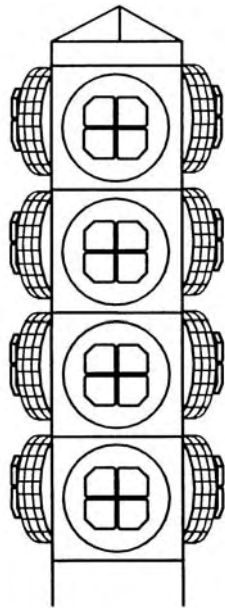


Figure 12. Multistation master FM antenna.

the coverage area of digital TV. Some of the coverage area of analog TV is traded off for the higher picture and sound quality of digital TV much as the long range and poor sound quality of AM radio are traded off for the shorter range and higher quality sound of FM radio.

An understanding of the specifications required for digital TV can be gained by comparing the spectra of analog TV and digital TV at the transmitter and at the receiver. Figure 13(a) shows the flat (except for the pilot) power distribution of the digital signal over 6 MHz, superimposed over the analog signal at the transmitter output. As shown in Figure 13(b), poor antenna response and undesired reflections at the receiver have significantly distorted the digital spectrum. Having most of the power centered near the picture and sound carrier hardly affects the analog spectrum.

From these spectra, it is clear that the antenna specifications in analog TV are critical only around the three carriers. In contrast, antenna specifications for digital TV are equally critical throughout the TV channel.

4.2. Voltage Standing-Wave Ratio

The magnitude of the voltage standing-wave ratio (VSWR) inside the transmission line, which connects the antenna to the transmitter, is an example of an antenna specification that depends on the spectral distribution. In analog TV, the VSWR must be minimized around the picture carrier to a value of 1.025, as shown in Fig. 14, to avoid an echo that appears as a “ghost” image. In other portions of the channel, the VSWR can be higher, up to 1.10 at band edges. In contrast, the VSWR must be minimized and equalized across the digital channel to a value not exceeding 1.05.

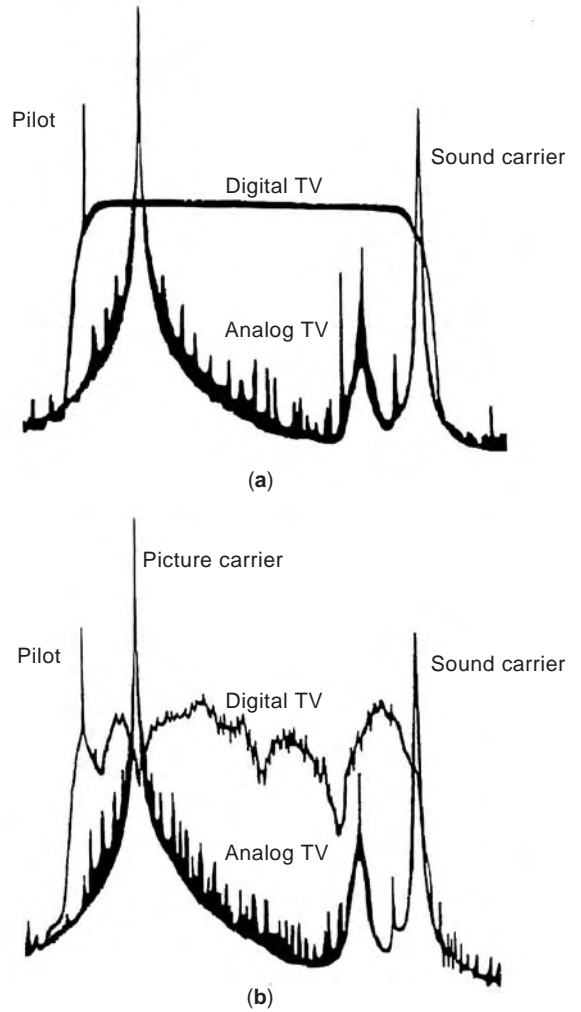


Figure 13. Analog and digital spectra: (a) at the transmitter; (b) at the receiver.

4.3. Effective Radiated Power

The ERP is a product of the antenna gain and the total input power to the antenna at the picture carrier frequency. For analog transmission, the total input power may include undesirable power components, such as intermodulation products and internal reflections. The undesirable components affect the picture quality of analog TV but not

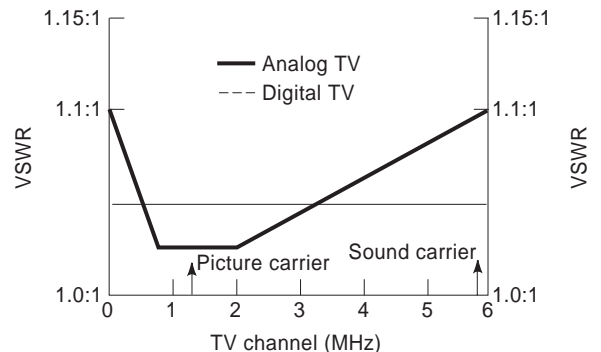


Figure 14. Antenna VSWR for a 6 MHz channel.

its range. The same undesirable power components affect the range of digital TV but not its picture quality. Therefore, the calculation of the ERP of digital TV must be based on the net useful power, rather than on the total available power.

4.4. Gain

In analog TV, antenna gain is specified at the picture carrier frequency around which most of the power is concentrated. In digital TV, where the power out of the antenna may be unevenly spread across the channel due to distortion, the electric field in the gain equation must be replaced by its value averaged over the operating channel bandwidth.

4.5. Pattern and Polarization Bandwidth

The same reasoning that was applied to the VSWR, ERP, and gain specifications requires that the antenna's transfer characteristics be specified across the digital TV channel rather than at a single frequency, as with analog TV. In particular, knowledge of the radiation pattern's behavior, including the polarization behavior across the TV channel, is fundamental to proper specification of broadcast antennas for digital TV.

4.6. Peak and Average Power

In analog TV, the peak-of-sync power is the significant parameter. It is used for ERP, coverage, and interference calculations. The peak-of-sync is defined by the root-mean-square amplitude of the carrier during the horizontal and vertical sync periods.

The average power of analog TV is not constant, unlike the peak-of-sync power during synchronization pulses. It depends on the picture being transmitted. Measurements over long periods indicate that the average picture power is 4.32 dB below peak-of-sync. With total blanking, the average picture (black) power is constant and is 2.2 dB below peak-of-sync. For analog TV, the peak-of-sync, the peak instantaneous, and the average power are given by the following:

$$P_{\text{SYNC}} = \frac{V_{\text{RMS}}^2}{Z_0} = \frac{V_{\text{PEAK}}^2}{2Z_0}$$

$$P_{\text{PEAK}} = \frac{V_{\text{PEAK}}^2}{Z_0} = 2(\sqrt{P_{\text{AURAL}}} + \sqrt{P_{\text{SYNC}}})^2$$

and

$$P_{\text{AVG}} = P_{\text{SYNC}}\text{APL} + P_{\text{AURAL}}$$

where Z_0 is the characteristic impedance of the transmission line and APL is the average picture level that is 0.6 during blanking and 0.37 during program transmission.

During program transmission (APL = 0.37) and with $P_{\text{AURAL}}/P_{\text{SYNC}} = 0.1$ (typical for UHF channels),

$$\frac{P_{\text{PEAK}}}{P_{\text{AVG}}} = 8.68 \text{ dB}$$

In digital TV, the average power is the significant parameter. It is independent of the content of the image being transmitted, and unlike analog TV, it has a constant value. The average power of digital TV is used for ERP, coverage, and interference calculations.

The average and peak instantaneous powers of digital TV are related by

$$P_{\text{PEAK}} = \frac{V_{\text{PEAK}}^2}{Z_0} = R_{\text{PA}}P_{\text{AVG}}$$

where R_{PA} is the ratio of peak instantaneous power to average power at the transmitter output.

Depending on the modulation scheme and channel filters, the peak instantaneous power of the digital TV signal can reach 7 dB to 13 dB above the average power, and 7 dB peaks occur as often as 0.01% of the time.

Acknowledgment

Manuscript review and many of the illustrations were kindly provided by Andre Skalina, Director of Antenna Engineering, Dielectric Communications.

TELEVISION ANTENNAS

HARUO KAWAKAMI
Antenna Giken Corporation

At the present time, the superturnstile antenna (of which the batwing antenna is a radiating element) [1], the supergain antenna (dipole antennas with a reflector plate), invented in the United States, and the Vierergruppe antenna, invented in Germany and sometimes called the *two-dipole antenna* in Japan, are widely used for very high-frequency television (VHF-TV) broadcasting around the world. The superturnstile antenna [2] is used in Japan, as well as in the United States.

Figure 1 shows the appearance of the original batwing antenna, when it was first made public by Masters [1]. The secret lies in its complex shape. It is called a *batwing antenna* in the United States and *Schmetterlings Antenne* (butterfly antenna) in Germany, in view of this shape.

The characteristics of the batwing antenna were calculated using the moment method proposed by Harrington [3], and experiments were conducted on this antenna. The model antenna was approximately two-fifths the size of a full-scale batwing antenna, with its design center frequency at 500 MHz.

It has been reported that for thick cylindrical antennas, a substantial effect on the current distribution appears because of nonzero current on the flat end faces. The assumption of zero current at the flat end face is appropriate for a thin cylindrical antenna; however, in the case of a thick cylindrical antenna, this assumption is, not valid.

Specifically, this article applies the moment method to a full-wave dipole antenna, with a reflector plate supported

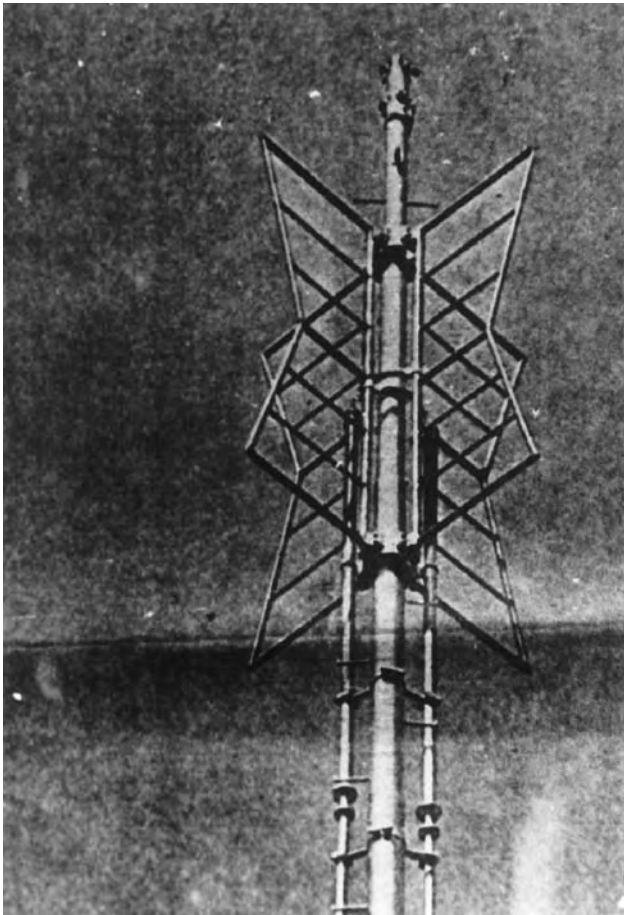
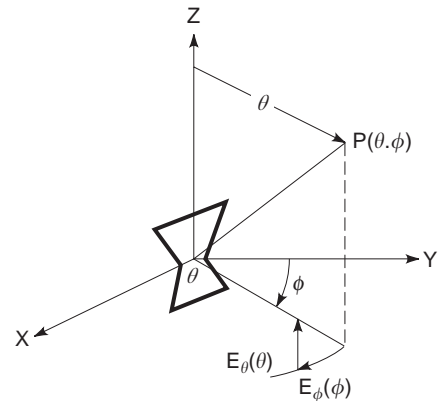


Figure 1. Historical shape of the batwing radiator.

1. THE BATWING ANTENNA ELEMENT

The antenna is installed around a support mast, as shown in Fig. 2, and fed from points f and f' , through a jumper from a branch cable with a characteristic impedance of 72Ω . The conducting support mast is idealized by an infinite, thin mast. The batwing antenna element is divided into 397 segments for the original type, with triangular functions as the weighting and expansion functions, and the analysis of the batwing antenna elements carried out using the Galerkin's method. The batwing antenna is fed with unit voltage. The currents flowing in each antenna conductor are calculated over a frequency range of 300–700 MHz.

Figure 3 illustrates these current distributions $I_i(i = 1 \sim 12)$ on the conductors at frequencies of 300,



by a metal bar, such as those widely used for TV and frequency modulated (FM) broadcasting [4]. In the present study, the analysis is made by including the flat end-face currents. As a result, it is found that the calculated and measured values agree well, and satisfactory wideband characteristics are obtained.

Next, the twin-loop antennas, most widely used for ultra high-frequency (UHF)-TV broadcasting, are considered. Previous researchers analyzed them by assuming a sinusoidal current distribution. Others adopted the higher order expansions (Fourier series) of the current distribution; however, their analyses did not sufficiently explain the wideband characteristics of this antenna.

This article applies the moment method to a twin-loop antenna with a reflector plate or a wire screen-type reflector plate. As for the input impedance, 2-L-type twin-loop antennas have reactance near zero [in the case where $l_1 = 0.15 \lambda_0$, that is, where the voltage standing-wave ratio (VSWR) is nearly equal to unity]. Also, satisfactory wideband characteristics are obtained. The agreement between the measurement and the theory is quite good. Thus, it may become possible in the future to improve practical antenna characteristics, based on the results obtained. Several popular television (transmitting) antennas [5,6] were mentioned, such as slot array, normal mode helix, and V-dipole antennas.

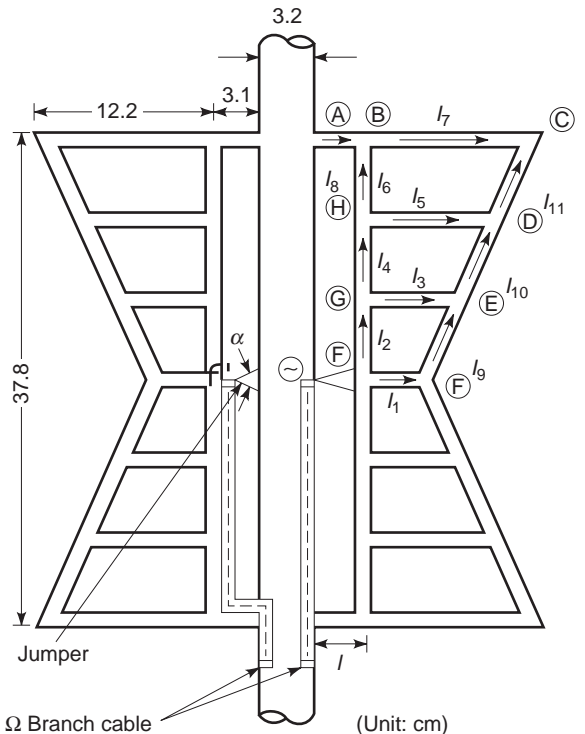


Figure 2. Construction of the model batwing antenna and its coordinate system.

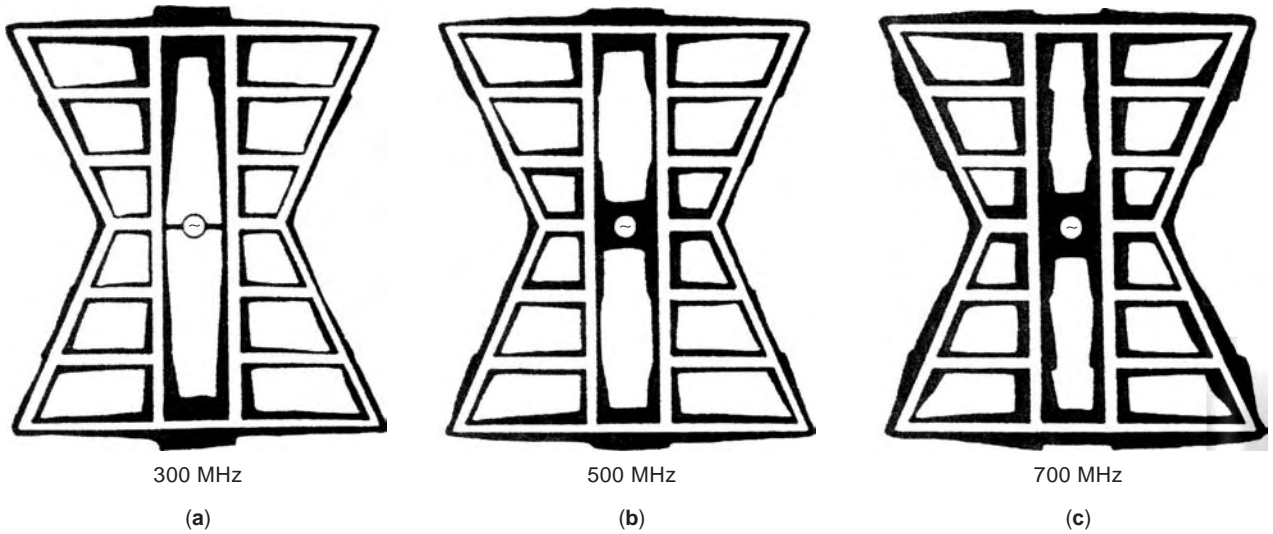


Figure 3. Amplitude characteristics of current distribution for frequency range from 300, 500, 700 MHz of shaded areas.

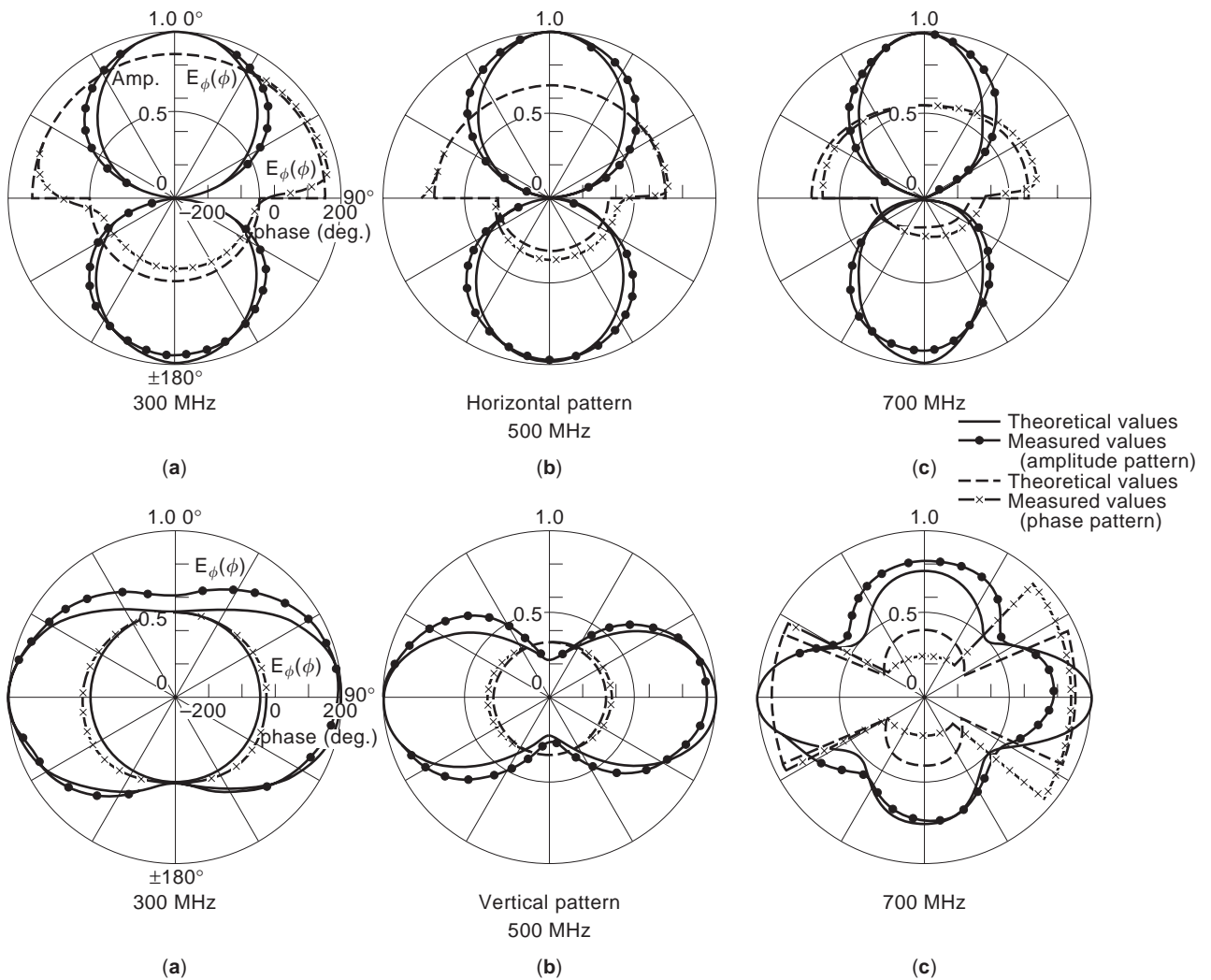


Figure 4. Amplitude and phase characteristics of radiation patterns at 300, 500, 700 MHz (with support mast).

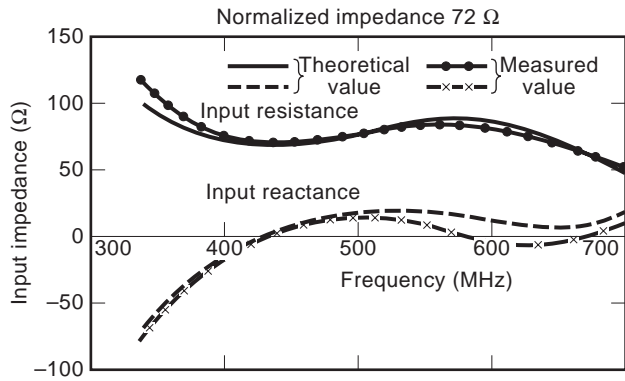


Figure 5. Theoretical and measured values of the input impedance as function of frequency (mast is infinite thin $\alpha = 0^\circ$).

500, and 700 MHz. As the distribution of currents along each conductor is calculated, this allows calculation of the radiation characteristics. Figure 4 illustrates the amplitude and phase characteristics of radiation patterns in the horizontal and vertical planes. It is seen from this figure that the theoretical values agree well with the measurements.

Figure 5 illustrates the theoretical and measured input impedance of a batwing antenna mounted on an aluminum plate, $3\text{ m} \times 3\text{ m}$. Both curves coincide closely with each other, with the input impedance having a value close to $72\ \Omega$, which is the proper match to the characteristic impedance of the branch cable. Vernier impedance matching is carried out in practice by connecting a metal jumper between the end of the branch cable and the feed point of the antenna element or the support mast. The feed strap's length, width, or form is varied to derive VSWR values below 1.10.

The power gain of the antenna at 500 MHz is calculated to be 3.3 dB. Figure 6 shows the gain of the antenna in the $\phi = 0^\circ$ direction as a function of the frequency, referenced to a half-wavelength dipole. Figure 7 illustrates three-dimensional amplitude characteristics of radiation patterns in the horizontal and vertical planes at each frequency.

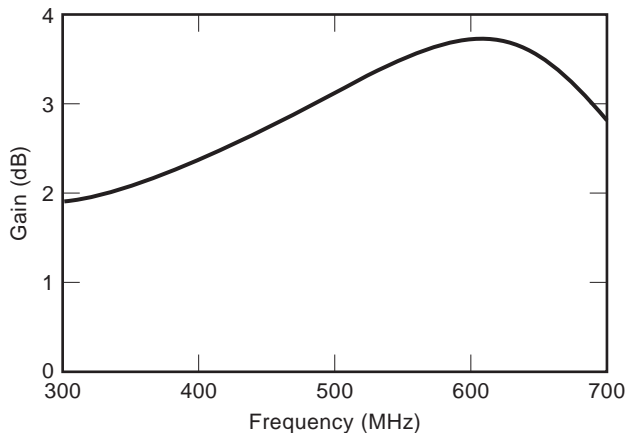


Figure 6. Batwing antenna gain with $\lambda/2$ dipole.

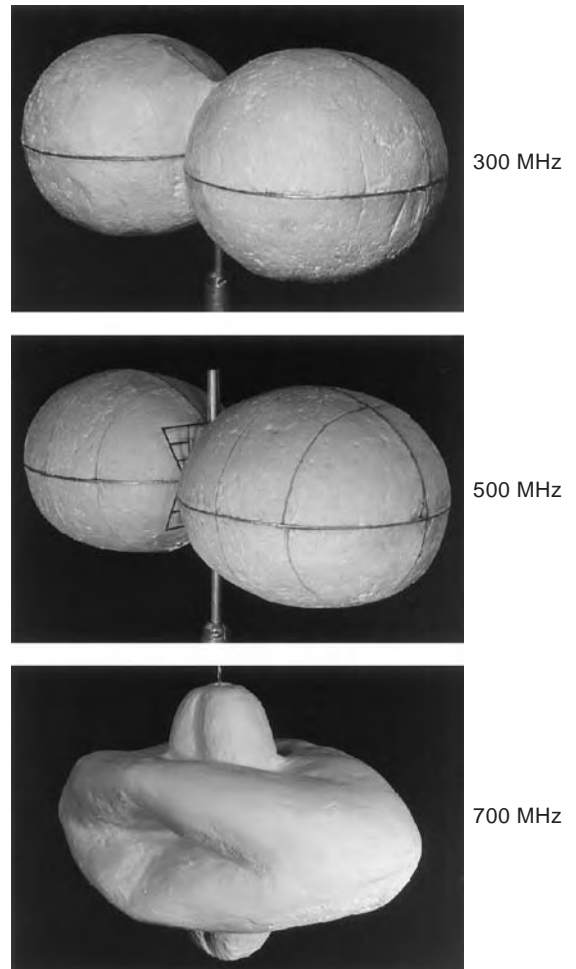


Figure 7. Three-dimension amplitude characteristics of radiation patterns at 300, 500, 700 MHz.

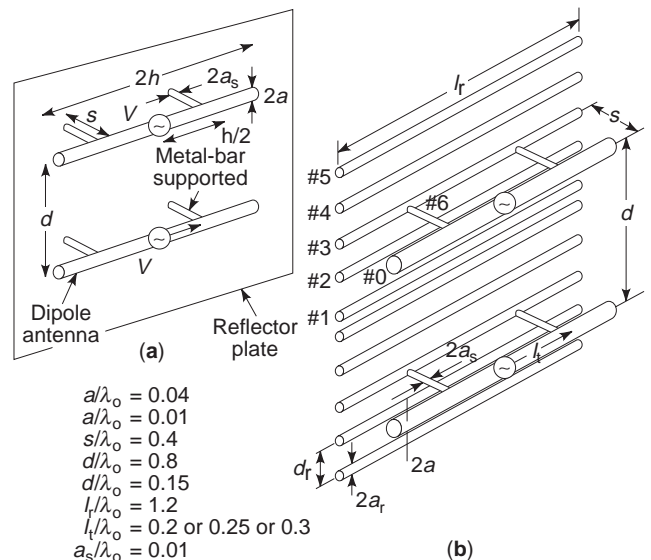


Figure 8. Metal-bar supported wideband full-wave dipole antennas with a reflector plate.

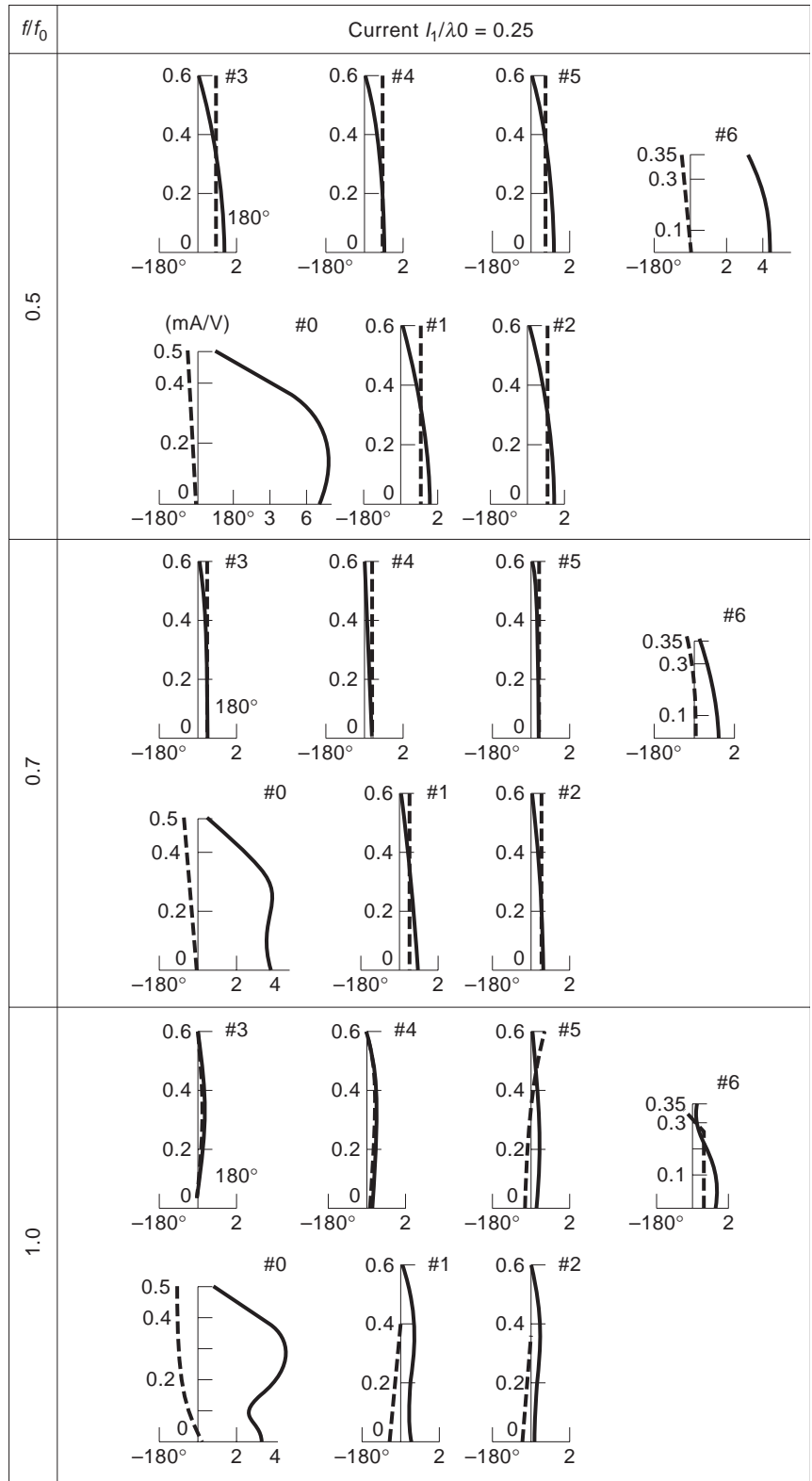


Figure 9. Current distribution of metal-bar supported full-wave dipole antennas (two-bay) with a wire screen-type reflector plate.

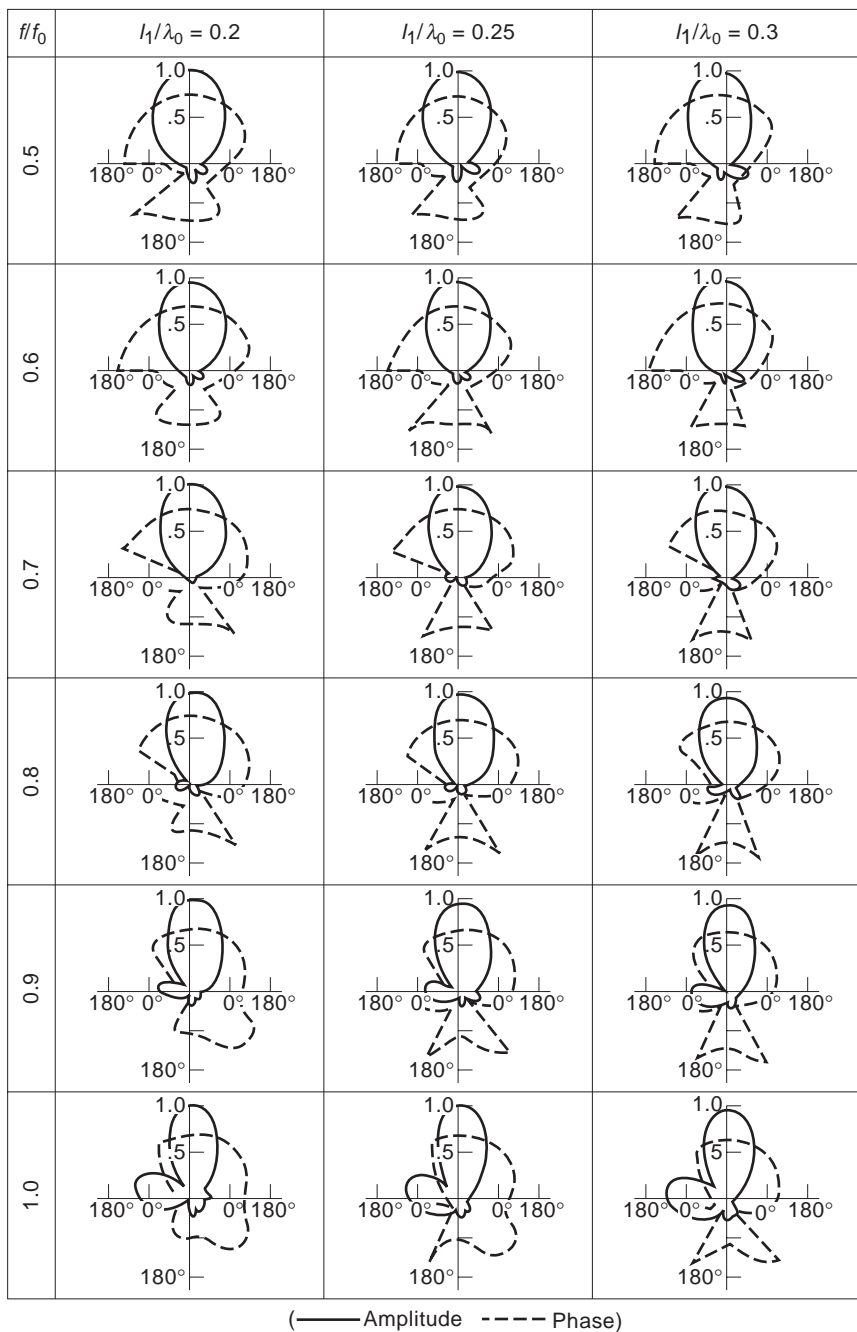


Figure 10. Radiation pattern of metal-bar supported full-wave dipole antennas (two-bay) with a wire screen-type reflector plate.

2. THEORETICAL ANALYSIS OF METAL-BAR-SUPPORTED WIDEBAND FULL-WAVE DIPOLE ANTENNAS WITH A REFLECTOR PLATE

Wideband full-wave dipole antennas with a reflector plate supported by metal bars were invented in Germany. The construction is shown in Fig. 8. A full-wave dipole antenna is located in front of a reflector, and supported directly by a metal bar attached to a reflector. This antenna was also analyzed by the moment method described previously.

As the supporting bar (see Fig. 8) is metallic, leakage currents may cause degradation of the radiation characteristics. To calculate these effects, the radial component of field, E_ρ , must be taken into consideration. In other words, E_ρ is needed for the calculation of $Z_{m,n}$, as defined by inner products of the expansion functions on the supporting bar and weighting functions on the antenna element or on the parallel conductors. We assume the supporting bar to be separated from the feed point by a distance l_1 . Also, the radius of the supporting bar is fixed at one-fourth of the radius of the antenna element (i.e., at $\lambda_0/100$), and then is

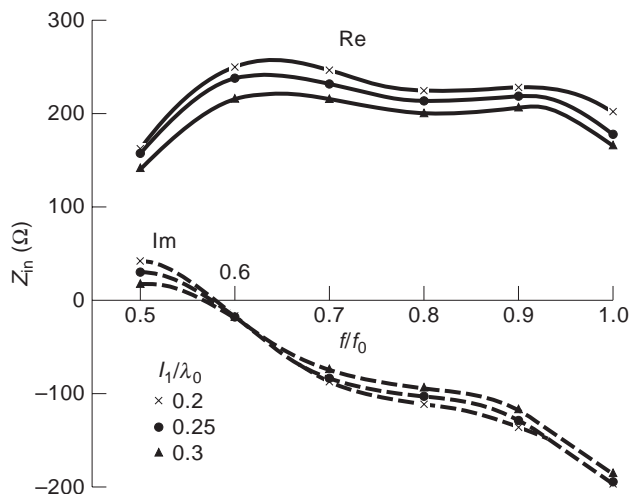


Figure 11. Input impedance characteristics of metal-bar supported full-wave dipole antennas (two-bay) with a wire screen-type reflector plate.

varied to be $0.2 \lambda_0$, $0.25 \lambda_0$, and $0.3 \lambda_0$. Figures 9–12 indicate various calculated performance characteristics. Note that the leakage current of the supporting bar is minimized for $f/f_0 = 0.7$, and that this current is substantial at other frequencies. The current distribution is shown only for the case of $l_1 = 0.25 \lambda_0$.

3. CHARACTERISTICS OF 2L TWIN-LOOP ANTENNAS WITH INFINITE REFLECTOR

As shown in Fig. 13, a twin-loop antenna has the loops connected by a parallel line: The 2L-type, 4L-type, and 6L-type are used, according to the number of loops. For actual use, a reactive load is provided by the trap at the top end, which also serves as the antenna support. The dimensions used for this article are as follows: center frequency $f_0 = 750$ MHz (wavelength $\lambda_0 = 40$ cm), length of the parallel line part $2l_1 = \lambda_0/2$ ($l_1 = 10$ cm), $12 = \lambda_0/2$ ($l_2 = 20$ cm),

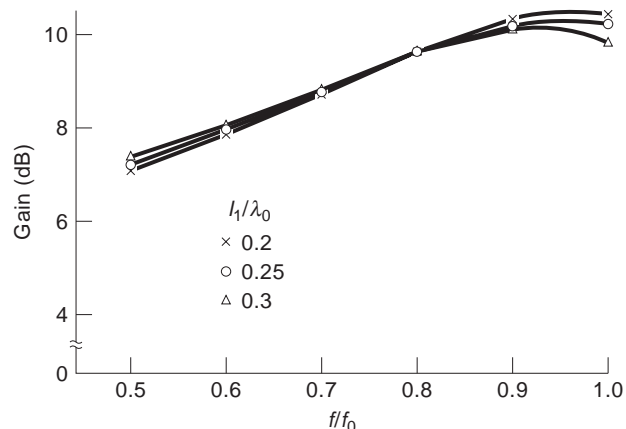


Figure 12. Gain of metal-bar supported full-wave dipole antennas (two-bay) with a wire screen-type reflector plate.

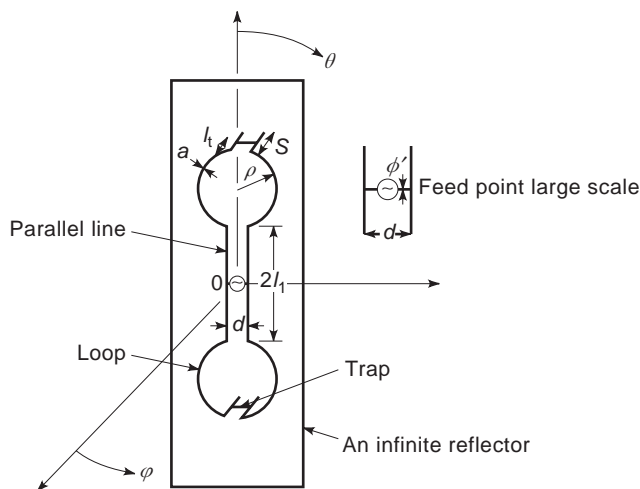


Figure 13. Structure of 2L-type twin-loop antenna and its coordinate system for analysis.

interval of the parallel line part, $d = \lambda_0/20$ ($d = 2$ cm), loop radius $b = \lambda_0/2\pi$ ($b = 6.366$ cm), distance from the reflector to the antenna $l_3 = \lambda_0/4$ ($l_3 = 10$ cm), conductor diameter $\phi = 10$ mm, and top-end trap $l_t = 0$ to $\lambda_0/4$, changed in intervals of $\lambda_0/16$. 2L twin-loop antennas were arranged in front of an infinite reflector, and calculations were executed in regard to the frequency characteristics of the trap length.

The radiation pattern of the type 2L antenna is shown in Fig. 14. Up to $l_t = \lambda_0/8$, the main beam gradually becomes sharper with increasing frequency, and it can be seen that the sidelobes increase. When l_t increases in this way to $\lambda_0/8$ and $\lambda_0/4$, the directivity becomes disturbed.

Figure 14 shows $l_1 = 0.15 \lambda_0$ and $l_1 = 0.25 \lambda_0$ characteristics of the radiation pattern in a polar display. The antenna gain for both lengths ($l_1 = 0.15 \lambda_0$ and $l_1 = 0.25 \lambda_0$) shows a small change of approximately 9.5–8.5 dB.

The input impedance has a value very close to 50Ω , essentially the same as the characteristic impedance of the feed cable. As for the input impedance, the 2L twin-loop antenna has reactance nearest zero (for the case where $l_1 = 0.15 \lambda_0$), that is, the VSWR is nearly equal to unity.

In the above calculation, the reflector was considered to be an infinite reflector, and the effect of the reflector on the antenna elements was treated by the image method. In the case of practical antennas, however, it is the usual practice to make the reflector finite, or consisting of several parallel conductors. Therefore, a calculation was executed for a reflector in which 21 linear conductors replaced the infinite reflector, as shown in Fig. 15.

The results are shown along with those for the infinite-reflector case. Based on these results, it was concluded that no significant difference was observed in input impedance and gain between the infinite reflector case and the case where the reflector consisted of parallel conductors.

The wire screen-type of reflector plate had a height of $3 \lambda_0$ (120 cm), a width of λ_0 (40 cm), and a wire interval of

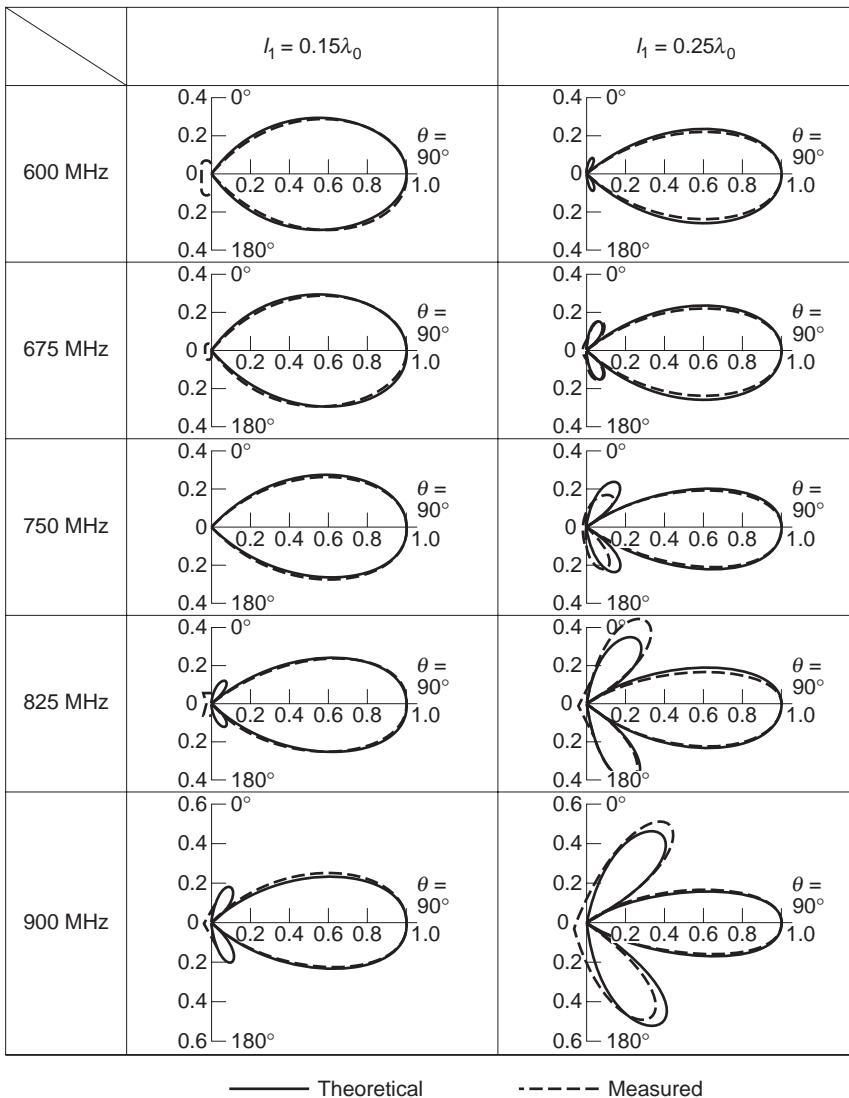


Figure 14. Vertical radiation pattern of 2L-type twin-loop antenna.

0.15λ₀ (6 cm). The radiation pattern is shown in Fig. 16. With regard to the pattern in the horizontal plane, no difference was found in comparison with an infinite reflector, but a backlobe of approximately -16 dB exists to the rear of the reflector. The same figure also shows the phase characteristics. With regard to the pattern in the vertical plane, the phase shows a large change where the pattern shows a cut.

4. SEVERAL POPULAR TRANSMITTING ANTENNAS

4.1. Slot Antennas

Both resonant and nonresonant end-fed arrays of slots are used for TV broadcasting. The resonant arrays are restricted to UHF applications because of their limited bandwidth. The traveling-wave slot antenna illustrated in Fig. 17 is a large end-fed coaxial transmission line with a slotted outer conductor. The slots are arranged in pairs at each layer, with the pairs separated by a quarter wave-

length along the length of the antenna. Adjacent pairs occupy planes at right angles to each other. The slot pairs, which are approximately one-half wavelength long, are fed out of phase by the coaxial line by capacitive probes projecting radially inward from one side of each slot so as to produce a figure-eight pattern. The probes are placed on opposite sides of adjacent inline slots that are spaced one-half wavelength to provide in-phase excitation. The quarter-wavelength separation of layers in conjunction with the space-quadrature arrangement of successive layers of slots effects a turnstile-type feed that produces a horizontally polarized azimuth pattern with a circularity of ±1 dB for VHF applications. An equal percentage of the power in the coaxial line is fed to each layer of slots, which results in an exponential aperture distribution that provides null fill.

Reflections from adjacent layers tend to cancel, which allows the traveling-wave operation. The top slots are strongly coupled to the line to reduce reflections. For high-gain applications, one-half of the slots may be

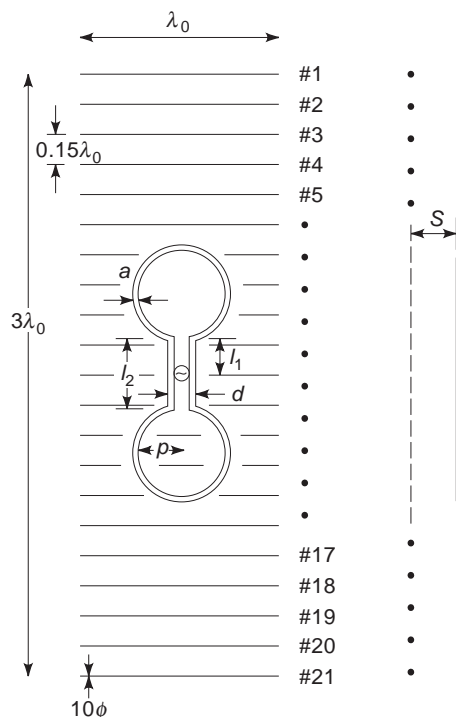


Figure 15. Structure of 2L-type twin-loop antenna with a wire screen-type reflector plate.

eliminated, resulting in a one-wavelength spacing of in-line slots. The standing-wave antenna consists of layers or bays of one or more axial slots spaced by one wavelength and fed by a coaxial line with the slotted pipe forming the outer conductor. Azimuth patterns are controlled by the number of slots per bay. One slot per bay produces a skull-shaped pattern, two slots a peanut-shaped pattern, and three slots a trilobe pattern. Four or more slots per bay are usually required for an omnidirectional pattern with a circularity of ± 1 dB. A typical omnidirectional pattern is shown in Fig. 18.

4.2. Helix Antennas

Figure 19 shows a single bay of a single-arm right-hand and left-hand helix fed in phase at the center so that the vertically polarized components of the two helices cancel in the broadside direction. The pitch angle is about 12° so that the vertically polarized radiation from each helix is about 10 dB down from the horizontally polarized radiation, which produces about 0.5 dB loss in gain because of cross-polarization radiation. As the beam of each helix scans about 2.7° per 1% change in frequency, the bay length is limited to about six wavelengths. Sidefire helical antenna pattern is shown in Fig. 20.

4.3. V-Shaped Antennas

The multi-V antenna has been designed especially to mount on the side of existing towers that are used for standard broadcast radiators or TV supporting towers. The multi-V antenna array (Fig. 21) consists of a number

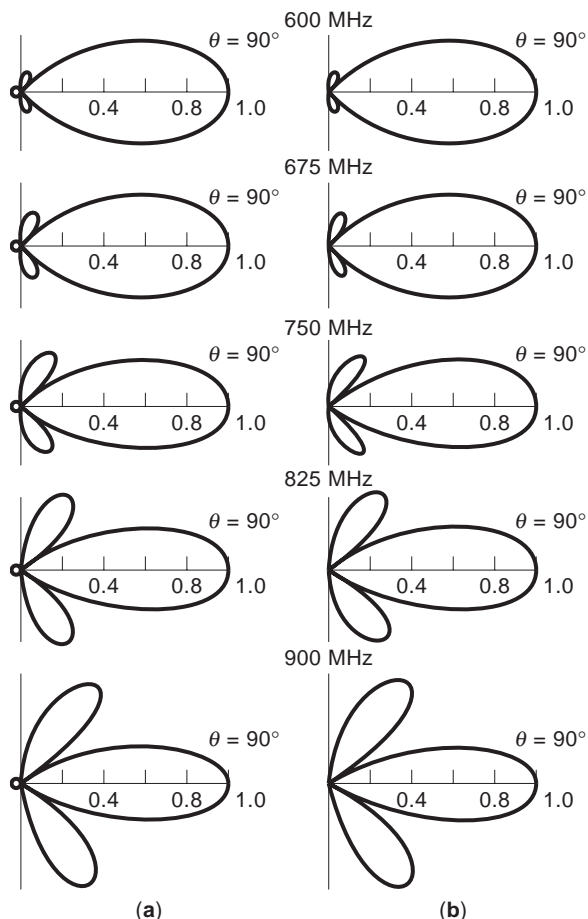


Figure 16. Comparison between characteristics of 2L-type twin-loop antenna with a wire screen-type reflector and with an infinite reflector.

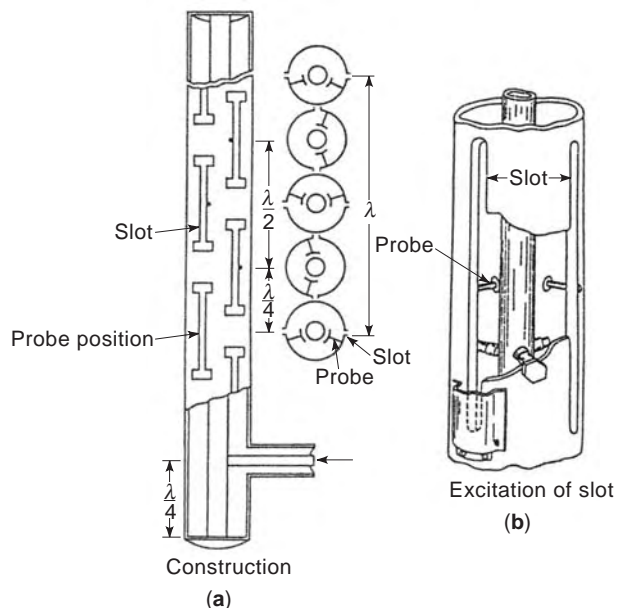


Figure 17. The traveling-wave slot antenna.

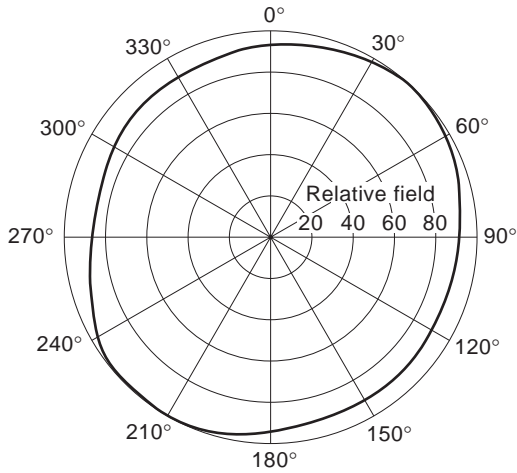


Figure 18. A typical omnidirectional pattern.

of V elements stacked vertically to provide power gain in the horizontal plane and vertical directivity. The resulting horizontal radiation pattern is essentially omnidirectional. The pattern remains approximately circular when side-mounted on a tower having a uniform cross section with 2 ft on a side.

The bays, or V's, are so designed that the input impedance of each pair is 50Ω , enabling them to be fed by standard coaxial transmission lines. The feed system enables an even number of bays from two to eight to be employed to obtain power gains ranging from 1.6 to 7.3. The design is such that it is necessary to tune the antenna at the factory for the desired frequency. It is very simple, with one feed point per bay and a maximum of four power-dividing elements for an eight-bay array. The radiating elements are grounded for maximum lightning protection.

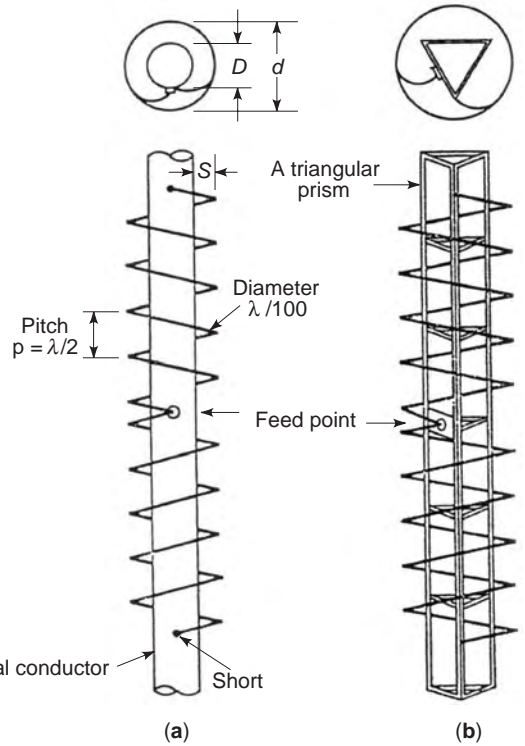


Figure 19. A sidefire helical antenna.

Figure 22 shows the four-bay V antenna pattern for various values of space.

5. CONCLUSION

Previous researchers [1,2] have analyzed batwing antennas by approximating the current distribution as a sinusoidal

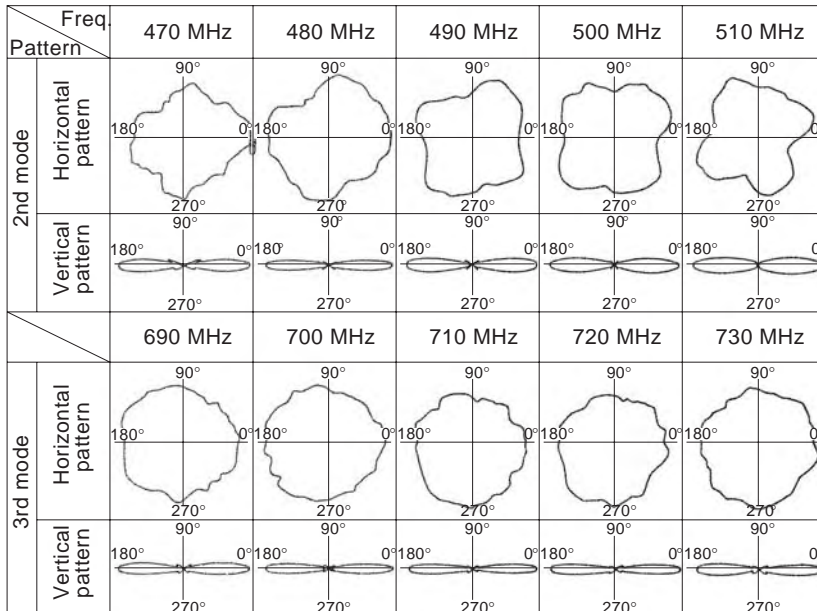


Figure 20. The horizontal and vertical pattern of sidefire helical antenna.

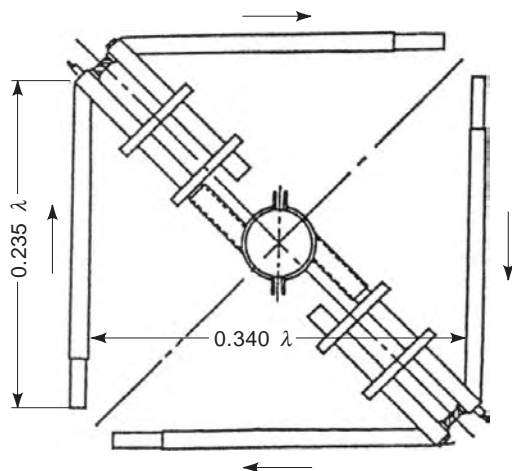


Figure 21. The construction of V-shaped antenna.

distribution. Wideband characteristics are not obtained with a sinusoidal current distribution. In this article, various types of modified batwing antennas, as the central form of the superturnstile antenna system, were analyzed theoretically with the aid of the moment method. The results were compared with measurements in order to examine the performance of the antenna elements in detail.

It is also evident from this research that the shape of the jumper has a remarkable effect on the reactance of the input impedance, and that the distance between the support mast and the antenna element also markedly influences the resistance of this impedance. Thus, a satisfactory explanation is given with regard to the matching conditions. As a result, it was found that the calculated and measured values agree well, and satisfactory wideband characteristics are obtained.

Next, an analytic method and calculated results for the performance characteristics of a thick cylindrical antenna were presented. The analysis used the moment method and takes the end face currents into account. The calculated results were compared with measured values, demonstrating the accuracy of the analytic method.

Using this method, a full-wave dipole antenna with a reflector supported by a metal bar was analyzed. The input impedance was measured for particular cases, thus obtaining the antenna dimensions for which the antenna input impedance permits broadband operation. In conclusion, wideband characteristics are not obtained with a one-bay antenna. The wideband characteristic is obtained by means of the mutual impedance of the two-bay arrangement. In the frequency region of $f/f_0 = 0.7$, the resistance of the input impedance is considered to be constant. In this case, the leakage current to the support bar is small. With regard to the radiation pattern, it was seen that a degradation of characteristics was caused by the metal support bar.

It is noted that the present method should be similarly useful for analyzing antennas of other forms where the end face effect is not negligible.

Next, the twin-loop antennas were considered for use as wideband antennas. The analysis results for $2L$ type

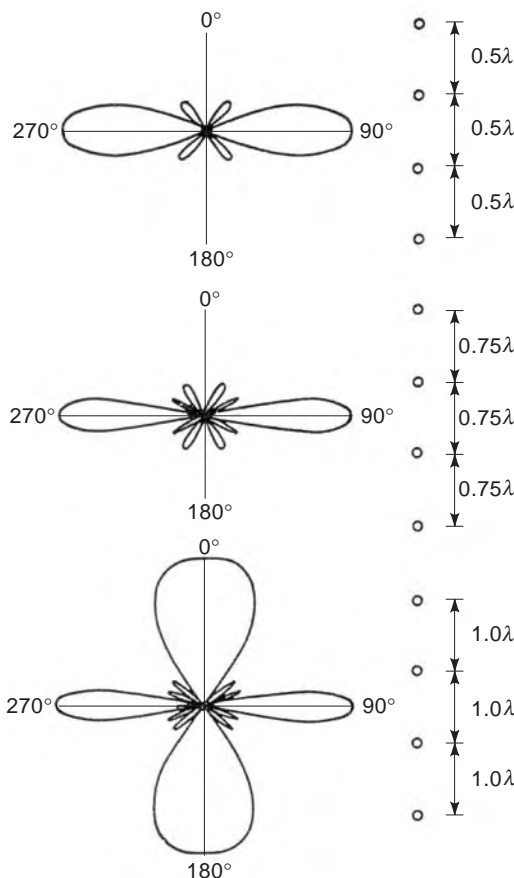
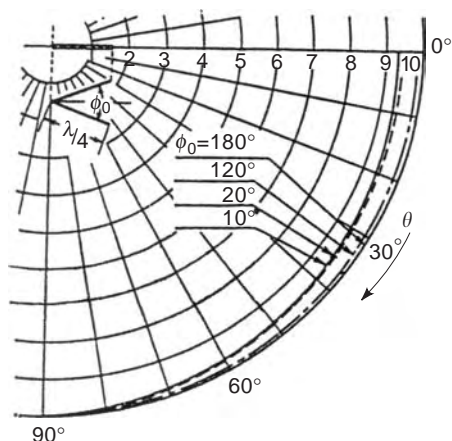


Figure 22. Vertical and horizontal pattern of V-shaped antenna.

showed that the change in the characteristics with a change in frequency becomes more severe with increasing trap length l_t , and the bandwidth becomes small, whereas a short trap length l_t shows a small change and a tendency for the bandwidth to become wide. For $l_t = 0$, a wide bandwidth for pattern and gain was obtained for the $2L$ type. The input impedance has a value very close to 50Ω , essentially the same as the characteristic impedance of the feed cable over a very wide frequency range. Thus, a

satisfactory explanation was given with regard to the matching conditions. Popular television antennas cover the properties of many basic types of antennas that are the mainstream of antenna technology. It has been reported here that a rigorous theoretical analysis has been achieved almost 30 years after the invention of these VHF-UHF antennas.

BIBLIOGRAPHY

1. R. W. Masters, The super turnstile, *Broadcast News*, **42**: (1946).
2. Y. Mushiake, ed., *Antenna Engineering Handbook*, The OHM-Sha, Ltd., 1980 (in Japanese).
3. R. F. Harrington, *Field Computation By Moment Method*, New York: Macmillan, 1968.
4. W. Berndt, Kombinierte Sendeantennen Fur Fernseh- und UKW-runfunk (Teil II), *Telefunken-Zeitung, Jahrgang, Heft. 26*, **101**:268 (1953).
5. Y. T. Lo and S. W. Lee, *Antenna Handbook*, New York: Van Nostrand Reinhold, 1988.
6. R. C. Johnson and H. Jasik, *Antenna Engineering Handbook*, New York: McGraw Hill, 1984.

TELEVISION BROADCAST TRANSMISSION STANDARDS

ALAN S. GODBER
 JAMES R. REDFORD
 IEEE BTS Audio-Video
 Techniques Standards
 Committee

Since the invention of television, images and sound have been captured, processed, transmitted, received, and displayed using analog technology, where the picture and sound elements are represented by signals that are proportional to the image amplitude and sound volume.

In more recent years, as solid-state technology has developed, spurred primarily by the development of computers, digital technology has gradually been introduced into the handling of the television signal, both for image and sound. The digital electric signal representing the various elements of the image and sound is composed of binary numbers that represent the image intensity, color, and so on, and the sound characteristics.

Many portions of television systems are now hybrid combinations of analog and digital, and it is expected that eventually all television equipment will be fully digital, except for the transducers, cameras, and microphones (whose inputs are analog) and the television displays and loudspeakers (whose outputs are analog).

The currently used broadcast television transmission standards [National Television Systems Committee (NTSC), phase alternate line (PAL), and sequential and memory (SECAM)] for 525- and 625-line systems were

designed around analog technology; although significant portions of those broadcast systems are now hybrid analog/digital or digital, the "over the air" transmission system is still analog. Furthermore, other than for "component" processed portions of the system, the video signals take the same "encoded" form from studio camera to receiver and conform to the same standard.

The recently developed ATSC Digital Television Standard, however, uses digital technology for "over the air" transmission, and the digital signals used from the studio camera to the receiver, although they represent the same image and sound, differ in form in portions of the transmission system. This variation is such that in the studio, maximum image and sound information is coded digitally; but during recording, special effects processing, distribution around a broadcast facility, and transmission, the digital signal is "compressed" to an increasing extent as it approaches its final destination at the home. This permits practical and economical handling of the signal.

1. ANALOG TELEVISION SYSTEMS

1.1. Black-and-White Television

It is the purpose of all conventional broadcast television systems to provide instantaneous vision beyond human sight, a window into which the viewer may peer to see activity at another place. Not surprisingly, all of the modern systems evolved to have similar characteristics. Basically, a sampling structure is used to convert a three-dimensional image (horizontal, vertical, and temporal variations) into a continuous time-varying broad-band electrical signal. This modulates a high-frequency carrier with the accompanying sound, and it is broadcast over the airwaves. Reasonably inexpensive consumer television sets are capable of recovering the picture and sound in the viewer's home.

1.1.1. Image Representation. The sampling structure first divides the motion into a series of still pictures to be sequenced rapidly enough to restore an illusion of movement. Next, each individual picture is divided vertically into sufficient segments so that enough definition can be retrieved in this dimension at the receiver. This process is called *scanning*. The individual pictures generated are known as *frames*, each of which contains *scanning lines* from top to bottom.

The number of scanning lines necessary was derived from typical room dimensions and practical display size. Based on the acuity of human vision, a viewing distance of four to six picture heights is intended. The scanning lines must be capable of enough transitions to resolve comparable definition horizontally. The image *aspect ratio* (width/height) of all conventional systems is 4:3, from the motion picture industry "academy aperture." All systems sample the picture from the top left to bottom right.

In professional cinema, the projection rate of 48 Hz is sufficient to make flicker practically invisible. Long-distance electric power distribution networks throughout the world use slightly higher rates of 50 Hz to 60 Hz alternating current. To minimize the movement of vertical "hum"

satisfactory explanation was given with regard to the matching conditions. Popular television antennas cover the properties of many basic types of antennas that are the mainstream of antenna technology. It has been reported here that a rigorous theoretical analysis has been achieved almost 30 years after the invention of these VHF-UHF antennas.

BIBLIOGRAPHY

1. R. W. Masters, The super turnstile, *Broadcast News*, **42**: (1946).
2. Y. Mushiake, ed., *Antenna Engineering Handbook*, The OHM-Sha, Ltd., 1980 (in Japanese).
3. R. F. Harrington, *Field Computation By Moment Method*, New York: Macmillan, 1968.
4. W. Berndt, Kombinierte Sendeantennen Fur Fernseh-und UKW-runfunk (Teil II), *Telefunken-Zeitung, Jahrgang, Heft. 26*, **101**:268 (1953).
5. Y. T. Lo and S. W. Lee, *Antenna Handbook*, New York: Van Nostrand Reinhold, 1988.
6. R. C. Johnson and H. Jasik, *Antenna Engineering Handbook*, New York: McGraw Hill, 1984.

TELEVISION BROADCAST TRANSMISSION STANDARDS

ALAN S. GODBER
 JAMES R. REDFORD
 IEEE BTS Audio-Video
 Techniques Standards
 Committee

Since the invention of television, images and sound have been captured, processed, transmitted, received, and displayed using analog technology, where the picture and sound elements are represented by signals that are proportional to the image amplitude and sound volume.

In more recent years, as solid-state technology has developed, spurred primarily by the development of computers, digital technology has gradually been introduced into the handling of the television signal, both for image and sound. The digital electric signal representing the various elements of the image and sound is composed of binary numbers that represent the image intensity, color, and so on, and the sound characteristics.

Many portions of television systems are now hybrid combinations of analog and digital, and it is expected that eventually all television equipment will be fully digital, except for the transducers, cameras, and microphones (whose inputs are analog) and the television displays and loudspeakers (whose outputs are analog).

The currently used broadcast television transmission standards [National Television Systems Committee (NTSC), phase alternate line (PAL), and sequential and memory (SECAM)] for 525- and 625-line systems were

designed around analog technology; although significant portions of those broadcast systems are now hybrid analog/digital or digital, the "over the air" transmission system is still analog. Furthermore, other than for "component" processed portions of the system, the video signals take the same "encoded" form from studio camera to receiver and conform to the same standard.

The recently developed ATSC Digital Television Standard, however, uses digital technology for "over the air" transmission, and the digital signals used from the studio camera to the receiver, although they represent the same image and sound, differ in form in portions of the transmission system. This variation is such that in the studio, maximum image and sound information is coded digitally; but during recording, special effects processing, distribution around a broadcast facility, and transmission, the digital signal is "compressed" to an increasing extent as it approaches its final destination at the home. This permits practical and economical handling of the signal.

1. ANALOG TELEVISION SYSTEMS

1.1. Black-and-White Television

It is the purpose of all conventional broadcast television systems to provide instantaneous vision beyond human sight, a window into which the viewer may peer to see activity at another place. Not surprisingly, all of the modern systems evolved to have similar characteristics. Basically, a sampling structure is used to convert a three-dimensional image (horizontal, vertical, and temporal variations) into a continuous time-varying broad-band electrical signal. This modulates a high-frequency carrier with the accompanying sound, and it is broadcast over the airwaves. Reasonably inexpensive consumer television sets are capable of recovering the picture and sound in the viewer's home.

1.1.1. Image Representation. The sampling structure first divides the motion into a series of still pictures to be sequenced rapidly enough to restore an illusion of movement. Next, each individual picture is divided vertically into sufficient segments so that enough definition can be retrieved in this dimension at the receiver. This process is called *scanning*. The individual pictures generated are known as *frames*, each of which contains *scanning lines* from top to bottom.

The number of scanning lines necessary was derived from typical room dimensions and practical display size. Based on the acuity of human vision, a viewing distance of four to six picture heights is intended. The scanning lines must be capable of enough transitions to resolve comparable definition horizontally. The image *aspect ratio* (width/height) of all conventional systems is 4:3, from the motion picture industry "academy aperture." All systems sample the picture from the top left to bottom right.

In professional cinema, the projection rate of 48 Hz is sufficient to make flicker practically invisible. Long-distance electric power distribution networks throughout the world use slightly higher rates of 50 Hz to 60 Hz alternating current. To minimize the movement of vertical "hum"

in the picture caused by marginal filtering in direct current power supplies, the picture repetition rate was made to equal the power line frequency.

A variation of this process used by all conventional systems is *interlaced scanning*, whereby every other line is scanned to produce a picture with half the vertical resolution, known as a *field*. The following field “fills in” the missing lines to form the complete frame. Each field illuminates a sufficient portion of the display so that flicker is practically invisible; yet only half the information is being generated. This conserves bandwidth in transmission. For both fields to start and stop at the same point vertically, one field must have a half scanning line at the top, and the other field must have a half scanning line at the bottom of the picture. This results in an odd number of scanning lines for the entire frame.

Mechanical systems using rotating disks with spiral holes to scan the image were investigated in the 1920s and 1930s, but these efforts gave way to “all electronic” television. Prior to World War II, developers in the United States experimented with 343-line and 441-line systems. Developers in Great Britain began a 405-line service, and after the war, the French developed an 819-line system, but these are no longer in use.

1.1.2. Synchronization. In most of North and South America and the Far East, where the power line frequency is 60 Hz, a 525-line system became the norm. This results in an interlaced scanning line rate of 15.750 kHz. The development of color television in Europe led to standardization of 625 lines in much of the rest of the world. The resulting line frequency with a 50 Hz field rate is 15.625 kHz. The similar line and field rates enable the use of similar picture tube deflection circuitry and components.

Horizontal and vertical frequencies must be synchronous and phase-locked, so they are derived from a common oscillator.

Synchronization pulses are inserted between each scanning line (Fig. 1) and between each field to enable the television receiver to present the picture details with the same spatial orientation as that of the camera. The *sync* pulses are of opposite polarity from the picture information, permitting easy differentiation in the receiver. The line sync pulses, occurring at a faster rate, are narrower than the field sync pulses, which typically are the duration of several lines. Sync separation circuitry in the receiver discriminates between the two time constants. Sync pulses cause the scanning to rapidly *retrace* from right to left and from bottom to top.

1.1.3. Blanking. To provide time for the scanning circuits to reposition and stabilize at the start of a line or field, the picture signal is *blanked*, or turned off. This occurs just before (front porch) and for a short time after (back porch) the horizontal sync pulse, as well as for several lines before and after vertical sync. During vertical sync, *serrations* are inserted to maintain horizontal synchronization. Shorter *equalizing pulses* are added in the several blanked lines before and after vertical sync (Fig. 2). All these pulses occur at twice the rate of normal sync pulses so that the vertical interval of both fields (which are offset by one-half line) can be identical, simplifying circuit design.

Additional scanning lines are blanked before the active picture begins; typically there is a total of 25 blanked lines per field in 625-line systems and 21 blanked lines per field for the 525-line system M. Modern television receivers complete the vertical retrace very soon after the vertical

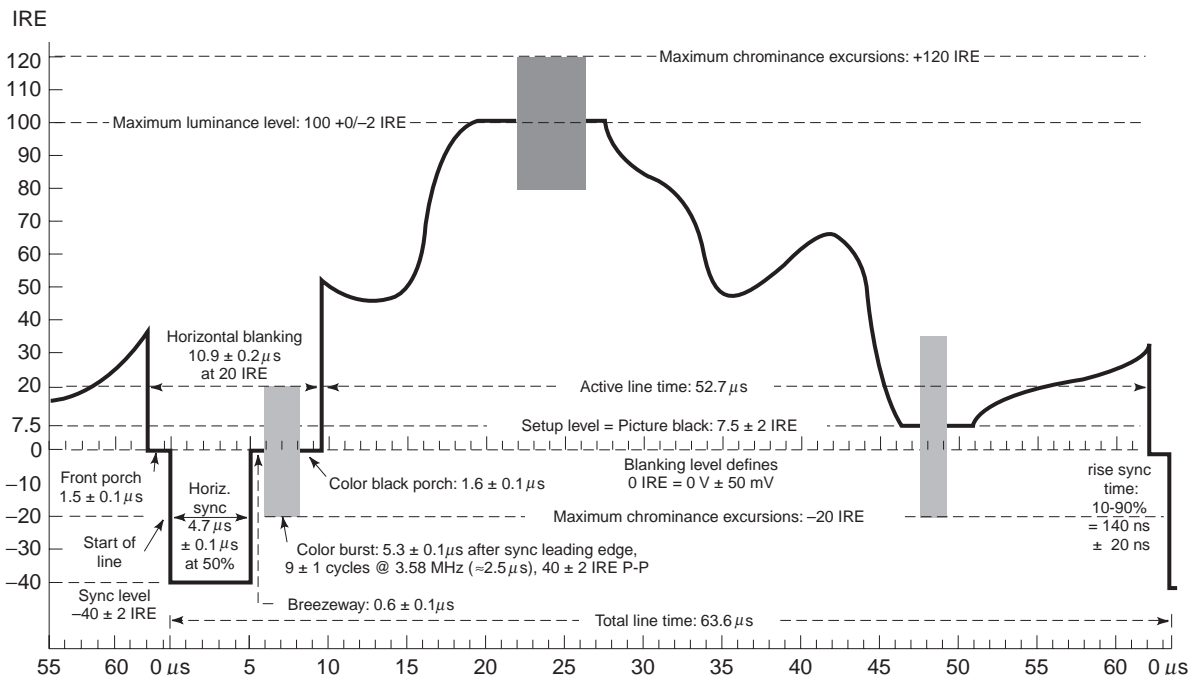


Figure 1. 525-line system M: Line-time signal specifications.

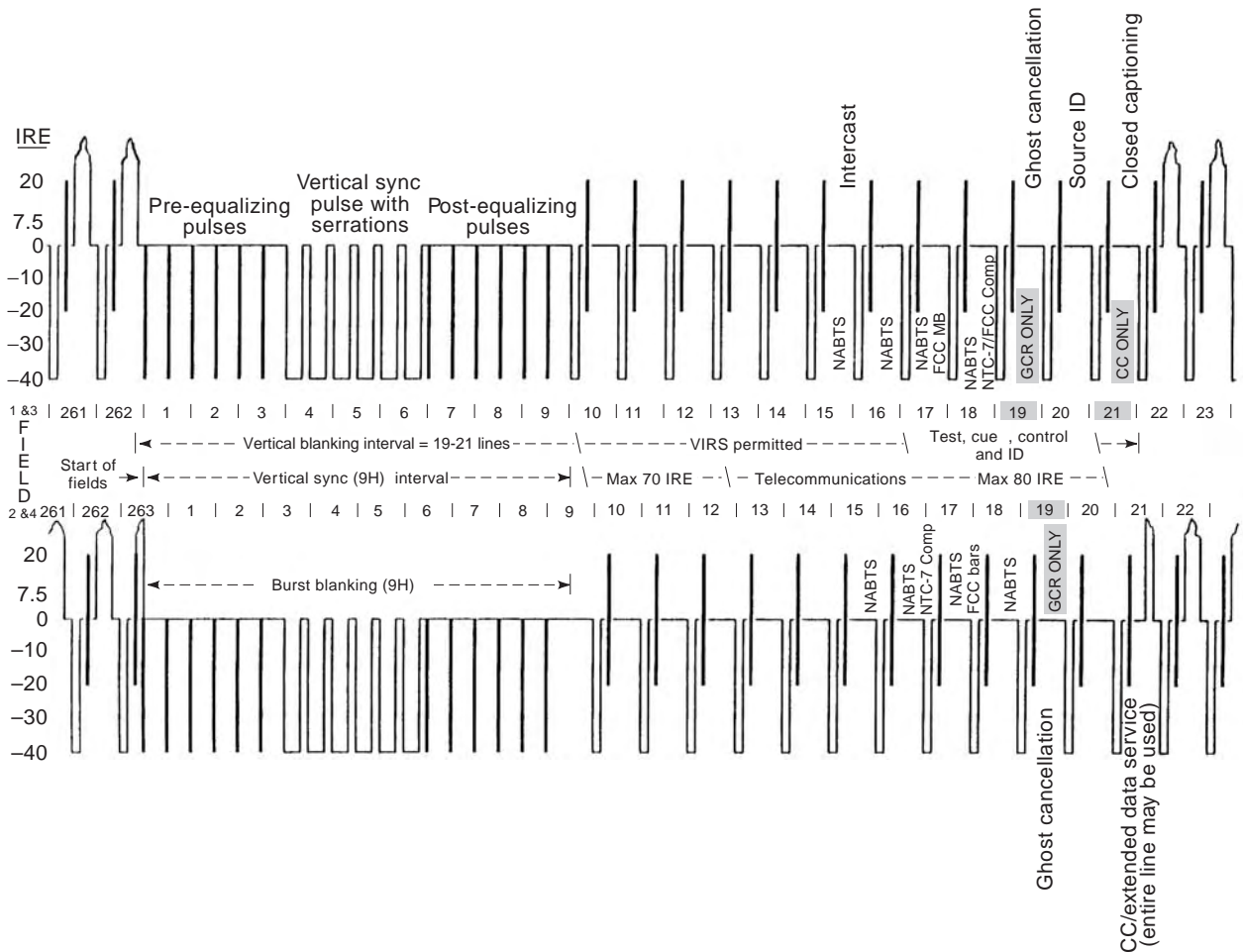


Figure 2. 525-line system M: field-time and vertical interval signal specifications.

sync pulse is received. The extra blanked lines now contain various ancillary signals, such as for short-time and line-time distortion and noise measurement, ghost cancellation, source identification, closed captioning, and teletext.

Fields and lines of each frame are numbered for technical convenience. In the 625-line systems, field 1 is that which begins the active picture with a half line of video. In the 525-line system M, the active picture of field 1 begins with a full line of video. Lines are numbered sequentially throughout the frame, beginning at the vertical sync pulse in the 625-line systems. For the 525-line system M, the line numbering begins at the first complete line of blanking for each field. Field 1 continues halfway through line 263, and then field 2 continues through line 262.

1.1.4. Signal Levels. During blanking, the video signal is at 0 V, the reference used to measure picture (positive-going) and sync (negative-going) levels. Signal amplitudes are measured directly in millivolts, except, because of changes made during the conversion to color, the 525-line system uses *IRE units*. A specialized oscilloscope is used to monitor characteristics of the signal amplitude and period. The *waveform monitor* has its voltage scale calibrated in millivolts (or IRE units for 525-line applica-

tions), and its time base is calibrated to scanning line and picture field rates, as well as in microseconds (Fig. 3).

Originally, the 525-line system used an amplitude of 1 V peak-to-peak (p-p) for the picture information, and it

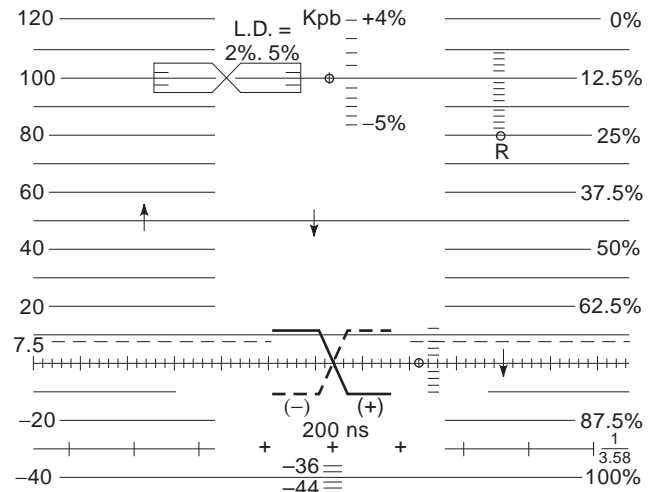


Figure 3. Typical NTSC-M waveform monitor graticule. Several additional markings are for measurement of various signal distortions.

used 0.4 V for sync. So that color information (modulated onto a *subcarrier* which can extend above peak white level) could be accommodated within the same dynamic range of existing equipment, the 1.4 V p-p scaling was compressed in amplitude to 1 V p-p. This created fractional voltage levels for peak white (714.3 mV) and sync (−286.7 mV), so a 1 V scale of 140 IRE units was adopted to simplify measurement. The 625-line standards did not have this historical complication. The peak white level is 700 mV, and the sync level is −300 mV.

Another anachronism of the 525-line system is the use of a direct-current (dc) offset of the picture black from blanking level. This was done to ensure that during retrace, the electron beam in the display tube was completely cut off, so *retrace lines* did not appear in the picture. This *setup level* originally varied between 5 and 10 IRE units above blanking, but it was standardized at 7.5 IRE for color TV, although it has been discarded altogether in Japan. Setup, or “lift,” was used to some extent in earlier systems but abandoned by the advent of 625-line services.

The electrical-to-optical transfer characteristic (*gamma*) of the cathode-ray picture tube is nonlinear. Doubling the video signal level applied to the control grid of the picture tube does not cause the light output to double; rather, it follows a power law of approximately 2.5. To correct for this, the video signal itself is made nonlinear, with an opposite transfer characteristic of about 0.4. This correction is applied at the camera in all systems.

1.1.5. Resolution. Resolution in the vertical direction is determined by taking the total number of scanning lines and subtracting those used for vertical blanking. This is multiplied by 0.7, the *Kell factor*, a correction for slight overlap between adjacent lines and the effect of imperfect interlace. By convention, television resolution is expressed in *television (TV) lines per picture height*, in contrast to photographic “line pairs per millimeter.” As the resolution is fixed by the scanning system, picture size is immaterial. Note that a vertical “line pair” in television requires two scanning lines.

To compute the bandwidth necessary for equal horizontal resolution, the vertical resolution is multiplied by the aspect ratio of 4/3 and is divided by the ratio of total scanning line time to active picture (unblanked) line time. This number is halved because an electric cycle defines a line pair, whereas a “TV line of resolution” is really only one transition. Multiplying the number of cycles per scanning line by the total number of scanning lines in a field, and then multiplying the number of fields per second, gives the bandwidth of the baseband video signal.

1.1.6. Broadcasting Standards. The various systems have been assigned letter designations by the International Telecommunications Union (ITU). The letters were assigned as the systems were registered, so alphabetical order bears no relation to system differences (Table 1), but a rearrangement highlights similarities (Table 2). Only scanning parameters and radiofrequency (RF) characteristics are defined; color encoding is not specified. Systems A, C, E, and F are no longer used.

Portions of the very-high-frequency (VHF) and ultra-high-frequency (UHF) RF spectrum are divided into *channels* for television broadcast. Modern channel assignments are 6 MHz wide in the Americas and the Far East. Elsewhere, they are generally 7 MHz in VHF and 8 MHz in UHF, with the carrier a fixed distance from one edge. As, in most systems, the picture carrier is near the lower edge and the audio signals are at the upper end, when the opposite is true, the channels are called *inverted*.

As a bandwidth-saving technique, the amplitude-modulated RF signal is filtered so that only one sideband is fully emitted; the other sideband is *vestigial*, or partially suppressed, which aids in fine-tuning to the correct carrier frequency at the receiver. The full sideband, which represents the video bandwidth, extends in the direction of the audio carrier(s), but sufficient guard band is included to prevent interference.

Bandwidth of the vestigial sideband varies among systems as does the placement of the audio carrier in relation to the picture carrier (Fig. 4). These factors complicate receiver design in areas where signals of two or more systems may exist. The main audio signal is sent via an amplitude-modulated or, more commonly, frequency-modulated carrier. Peak deviation in frequency modulation (FM) is ± 50 kHz, with 50 μ s preemphasis, except ± 25 kHz and 75 μ s for systems M and N. Preemphasis for improving the signal-to-noise ratio is common in FM systems; its use in some amplitude-modulation (AM) systems was to simplify receivers that could accommodate both modulation schemes.

Amplitude modulation is used in all systems for the video waveform, which, unlike audio, is not sinusoidal. Most systems employ a *negative sense of modulation*, such that negative excursions of the baseband signal produce an increase in the amplitude of the modulated carrier. This allows the constant amplitude sync pulses to serve as an indication of the received RF signal level for automatic gain control. Also, interfering electric energy tends to produce less noticeable black flashes in the received picture, and the duty cycle of the signal is reduced, which consumes less power at the transmitter.

1.2. Multichannel Sound

Early attempts to provide stereo sound for special TV events involved *simulcasting*, whereby an FM radio station in the same coverage area broadcast the stereo audio for the program. Due to the high profitability of FM radio today, this scheme is becoming impractical. For the 525-line system M, with channels of only 6 MHz bandwidth, a multiplexing scheme is used on the existing single audio carrier. Due to the wider channel bandwidths in 625-line systems, multiple sound carriers emerged as the solution.

1.2.1. Multiplex Sound Systems. In the United States, Zenith Electronics developed multichannel television sound (MTS), a pilot-tone system in which the sum of the two stereo channels (L+R) modulates the main TV audio FM carrier, providing a monophonic signal to conventional receivers. A difference signal (L−R) is dbx-TV suppressed-carrier amplitude-modulated onto an audio

Table 2. Survey of World Television Systems

Standard	Field	Lines	Bandwidth		Vestigial Sideband	Polarity	Audio	Standard	VHF	UHF	NTSC	PAL	SECAM																
			Channel	Video																									
M	60	525	┌	┌	┌	┌	┌	M	✓	✓	✓	✓																	
N			6	4.2										-0.75	Neg.	FM	✓	✓		✓									
D			┌	┌																		+1.25	Pos.	┌	K		✓		✓
K			┌	┌																									
L'	┌	┌	┌	┌	┌	L	✓	✓		✓																			
L	┌	┌									┌	┌	┌	K'	✓	✓		✓											
K'	┌	┌																	┌	┌	┌	I	✓	✓		✓			
I	50	625																									┌	┌	┌
H			6	5.5	-1.25	Neg.	┌	G	✓	✓																	✓	✓	
G			┌	┌							┌	┌	┌	B	✓	✓	✓	✓											
B			┌	┌															┌	┌	┌	C	✓	✓	✓	✓			
C	┌	┌	┌	┌																									┌
F	┌	┌			┌	┌	┌	E	✓	✓																	}	Obsolete Standard	
E	┌	┌									┌	┌	┌	A	✓	✓	}	Obsolete Standard											
A	┌	┌																	┌	┌	┌	A	✓	✓	}	Obsolete Standard			
	405	5	3.0	+0.75																									┌

subcarrier at twice the line scanning frequency ($2f_H$), whereas a pilot is sent at the line frequency as a reference for demodulation. A second audio program (SAP) may be frequency modulated at $5f_H$, and nonpublic voice or data may be included at $6.5f_H$.

Japan's NHK developed a similar *FM/FM* stereo system using FM of the L – R subchannel at $2f_H$. A control subcarrier at $3.5f_H$ is tone-modulated to indicate whether stereo or second audio programming is being broadcast.

1.2.2. Multiple Carrier Systems. In Germany, IRT introduced *Zweiton*, a dual-carrier system for transmission standards B and G. In both standards, the main carrier is frequency-modulated at 5.5 MHz above the vision carrier. For stereo, this carrier conveys the sum of the two channels (L + R). The second frequency-modulated sound carrier is placed 15.5 times the line scanning frequency above the main carrier, or 5.742 MHz above the vision carrier. For transmission system D, a similar relationship exists to the 6.0 MHz main channel. For stereo, this carrier conveys the right audio channel only.

A reference carrier at $3f_H$ is tone-modulated, and the particular tone frequency switches receivers for stereo or second audio channel sound. A variant is used in Korea where the second carrier is placed at 4.72 MHz above the vision carrier and conveys L – R information.

The British Broadcasting Corporation (BBC) in Britain developed near-instantaneous companded audio multiplex (NICAM), a digital sound carrier system. Both audio channels are sampled at 32 kHz with 14-bit resolution. Each sample is compressed to 10 bits and then arranged into frame packages of 728-bit length. These are rearranged, and then the data are scrambled to disperse the effect of noise at the receiver. Finally, two bits at a time are fed to a QPSK modulator for transmission.

Either stereo or two independent sound signals may be transmitted. Other possible combinations are (1) one

sound and one data channel or (2) two data channels. The original analog-modulated single-channel sound carrier is retained for older receivers. The digital carrier is 6.552 MHz above the vision carrier for transmission system I, or 5.85 MHz for systems B, G, and L.

1.3. NTSC Color Television

It has long been recognized that color vision in humans results from three types of photoreceptors in the eye, each sensitive to a different portion of the visible spectrum. The ratio of excitation creates the perception of hue and saturation, whereas the aggregate evokes the sensation of brightness. Stimulating the three types of photoreceptors using three wavelengths of light can produce the impression of a wide gamut of colors. For television, the image is optically divided into three primary color images, and this information is delivered to the receiver, which spatially integrates the three pictures, something like tripack color film and printing.

1.3.1. Sequential Color Systems. The first attempts at commercial color TV involved transmitting the three color images in a *sequential* fashion. Compatibility with existing transmitters was essential from an economic standpoint. Because line-sequential transmission caused crawl patterning, field-sequential was preferred. However, there was no separate *luminance* signal for existing black-and-white receivers to use.

To reduce flicker caused by the apparent brightness difference between the three primary colors, the field rate had to be increased, and maintaining an equivalent channel bandwidth required the number of scanning lines to be reduced. These changes aggravated the compatibility problem with existing sets. A field-sequential system developed by the Columbia Broadcasting System (CBS)

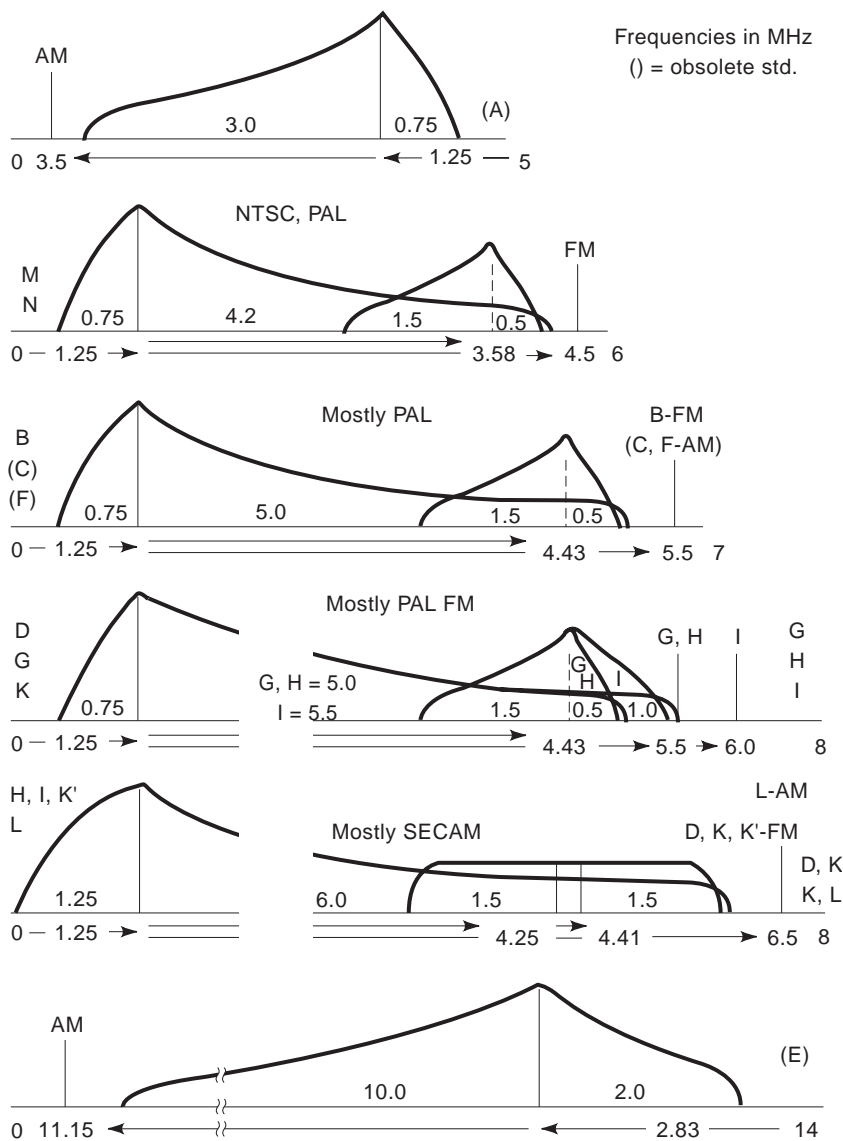


Figure 4. Television RF channel spectra for the various world television systems. For simplicity, only a single illustration of the lower and upper portions of the channel spectra is shown for the 8 MHz wide channels. Therefore, for systems D, H, I, and K, the lower and upper illustrations are not adjacent to each other.

network was briefly commissioned in the United States during 1951.

To be *compatible*, a color television system must have the same channel bandwidth as existing monochrome transmitters and receivers, use equivalent scanning parameters, and supply the same luminance signal, as if the picture were black and white. An all-industry body, the NTSC, was set up in the United States to devise such a color TV system.

1.3.2. Separate Luminance and Mixed Highs. The human visual system senses shapes and edges from brightness variations. Color only fills in the larger areas, much like a child's coloring book. At the suggestion of Hazeltine Electronics, the existing wide-bandwidth luminance signal of black-and-white television was retained. The color information is limited to a much narrower bandwidth, on the

order of 1 MHz, restricting its resolution in the horizontal direction.

This first led to a dot-sequential system that sampled the three colors many times along each scanning line to form a high-frequency chrominance signal. The frequency of sampling may be likened to a *subcarrier* signal whose amplitude and phase are changing according to color variations along the line. At the receiver, the "dot" patterns of each primary resulting from sampling are averaged in lowpass frequency filters. The result is a continuous but low-resolution full-color signal. Equal amounts of their higher frequency components are summed to form a *mixed-highs* signal for fine luminance detail ($Y = \frac{1}{3} R + \frac{1}{3} sG + \frac{1}{3} B$), an idea from Philco.

1.3.3. Quadrature Modulation. The dot-sequential concept formed the basis for a more sophisticated simultaneous system. The luminance signal contains both

high- and low-frequency components. Only two lower resolution color signals are needed (the third can be derived by subtracting their sum from the low-frequency portion of luminance). The spectral composition of green is nearest to that of luminance, so transmitting the red and blue signals improves the signal-to-noise performance. These low-frequency color signals are sampled using a time-multiplexing technique proposed by Philco, known as *quadrature modulation*.

The chrominance signal is formed by the addition of two subcarriers, which are locked at the same frequency but differ in phase by 90°. The two subcarriers are modulated by separate baseband signals such that each is sampled when the other carrier is at a null. This results in the subcarrier being modulated in both amplitude and phase. The amplitude relates to the saturation of the color, whereas the phase component corresponds to the hue (Fig. 5).

1.3.4. Frequency Multiplexing. The sampling rate is more than twice the highest frequency of the color signals after lowpass filtering, so the chrominance information shares the upper part of the video spectrum with luminance. This frequency-multiplexing scheme was put forward by General Electric. The scanning process involves sampling the image at line and field rates; therefore, energy in the video signal is concentrated at intervals of the line and field frequencies. These *sidebands* leave pockets between them where very little energy exists.

The exact subcarrier frequency was made an odd multiple of one half the line scanning frequency. This causes sidebands containing the color information to likewise fall

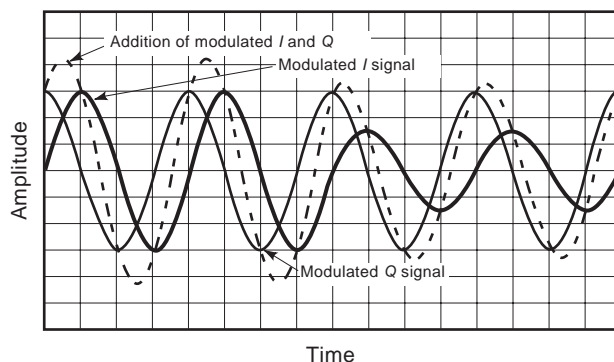


Figure 5. Quadrature modulation. Addition of two amplitude-modulated signals whose carrier frequencies are in phase quadrature (same frequency but offset in phase by 90°) produces an output signal whose carrier is modulated in both amplitude (AM) and phase (PM) simultaneously. This method of combining two baseband signals onto a single carrier is called quadrature modulation. In the case of NTSC or PAL encoding for color television, the two baseband components represent the two chrominance signals (I and Q for NTSC, U and V for PAL). The resulting amplitude of the subcarrier relates to the saturation, whereas the phase conveys the hue information. The frequency of the subcarrier is unchanged.

in between those of the existing luminance signal (Fig. 6). Therefore, the phase of the subcarrier signal is opposite line-to-line. This prevents the positive and negative excursions of the subcarrier from lining up vertically in the picture, and it results in a less-objectionable “dot” interference pattern between the subcarrier and luminance signal. Comb filtering to separate luminance and

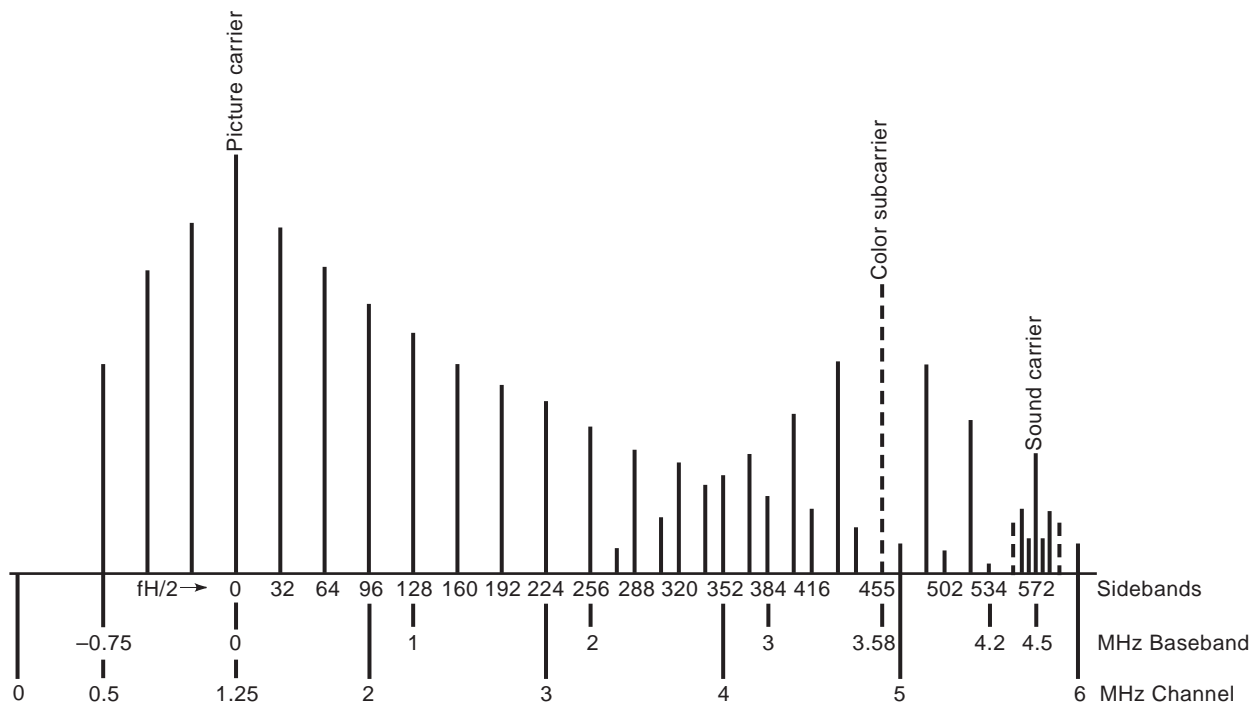


Figure 6. Frequency spectrum of composite NTSC-M color television signal showing relationships between the baseband and channel spectra and between sidebands of the picture carrier and color subcarrier.

chrominance may be employed by examining the phase of information around the subcarrier frequency on adjacent lines. The dot pattern is further concealed because the subcarrier phase is also opposite frame-to-frame.

A *four-field sequence* is established whereby the two interlaced picture fields, together with the alternating phase of subcarrier on sequential frames, requires the proper sequence to be maintained. Sources to be intercut or mixed must be properly timed, and editing points must be chosen to preserve the sequence of the four color fields.

A slight modification was necessary to the line and field scanning frequencies because one of the sidebands of the new color subcarrier fell right at the rest frequency of the FM sound carrier for system M, 4.5 MHz. Existing black-and-white receivers did not have adequate filtering to prevent an annoying buzz when the program sound was low and color saturation was high. By reducing the scanning frequencies by a mere 0.1%, the sidebands of luminance and chrominance remained interleaved, but shifted to eliminate the problem. Hence, the field frequency became 59.94 Hz, and the line frequency became 15.734 kHz.

1.3.5. Color-Difference Signals. Another suggestion came from Philco: Interference with the luminance signal is minimized by forming the two color signals as the difference between their respective primary and luminance (i.e., $R - Y$, $B - Y$). This makes the color-difference signals smaller in amplitude because most scenes have predominantly pale colors.

The subcarrier is suppressed, so that only the sidebands are formed. When there is no color in the picture, the subcarrier vanishes. This necessitates a local oscillator at the receiver. A *color-burst* reference is inserted on the back porch of the horizontal sync pulse, which synchronizes the reference oscillator and provides an amplitude reference for color saturation automatic gain control.

1.3.6. Constant Luminance. With the constant-amplitude formulation ($Y = \frac{1}{3}R + \frac{1}{3}G + \frac{1}{3}B$), the luminance signal does not represent the exact scene brightness. Part of the brightness information is carried by the chrominance channels, so unwanted irregularities in them, such as noise and interference, produce brightness variations. Also, the gray-scale rendition of a color broadcast on a black-and-white receiver is not correct.

Hazeltine Electronics suggested weighting the contributions of the primaries to the luminance signal according to their actual addition to the displayed brightness. The color-difference signals will then represent only variations in hue and saturation, because they are “minus” the true brightness ($R - Y$, $B - Y$). A design based on this principle is called a *constant-luminance* system. For the display phosphors and white point originally specified, the luminance composition is $Y = 30\% R + 59\% G + 11\% B$.

1.3.7. Scaling Factors. The two low-bandwidth color-difference signals modulate a relatively high-frequency subcarrier superimposed onto the signal level representing luminance. However, the peak subcarrier excursions for some hues could reach far beyond the original black-and-white limits, where the complete picture signal is

restricted between levels representing blanking and peak white picture information. Over-modulation at the transmitter may produce periodic suppression of the RF carrier and/or interference with the synchronizing signals. If the overall amplitude of the composite (luminance level plus superimposed subcarrier amplitude) signal was simply lowered, the effective power of the transmitted signal would be significantly reduced.

A better solution was to reduce the overall amplitude of only the modulated subcarrier signal. However, such an arbitrary reduction would severely impair the signal-to-noise ratio of the chrominance information. The best solution proved to be selective reduction of each of the baseband $R - Y$ and $B - Y$ signal amplitudes to restrict the resulting modulated subcarrier excursions to $\pm\frac{4}{3}$ of the luminance signal levels. The $R - Y$ signal is divided by 1.14, and $B - Y$ is divided by 2.03. The resulting 33.3% overmodulation beyond both peak white and blanking levels was found to be an acceptable compromise, because the incidence of highly saturated colors is slight (Fig. 7).

1.3.8. Proportioned Bandwidths. RCA proposed that the axes of modulation be shifted from $R - Y$, $B - Y$ to conform to the greater and lesser acuity of human vision for certain colors. The new coordinates, called I and Q, are along the orange/cyan and purple/yellow-green axes. This was done so that the bandwidths of the two color signals could be proportioned to minimize crosstalk (Fig. 8).

Early receivers made use of the wider bandwidth of the I signal; however, it became evident that a very acceptable color picture could be reproduced with the I bandwidth restricted to the same as that of the Q channel. Virtually all NTSC receivers now employ “narrowband” I channel decoding. A block diagram of NTSC color encoding is shown in Fig. 9. These recommendations were adopted by the American Federal Communications Commission in late 1953, and commercial color broadcasting was begun in early 1954.

1.4. Sequential and Memory (SECAM)

Economic devastation of World War II delayed the introduction of color television to Europe and other regions. As differences between 525- and 625-line scanning standards made videotapes incompatible anyway, and satellite transmission was unheard of, there seemed little reason not to explore possible improvements to the NTSC process.

1.4.1. Sequential Frequency Modulation. The most tenuous characteristic of NTSC proved to be its sensitivity to distortion of the phase component of the modulated subcarrier. As the phase component imparts color hue information, errors are noticeable, especially in skin tones. Also of concern was variations in the subcarrier amplitude, which affects the color saturation. Most long-distance transmission circuits in Europe did not have the phase and gain linearity to cope with the added color subcarrier requirements.

A solution to these drawbacks was devised by the Campagnie Française de Télévision in Paris. By employing a one-line delay in the receiver, quadrature

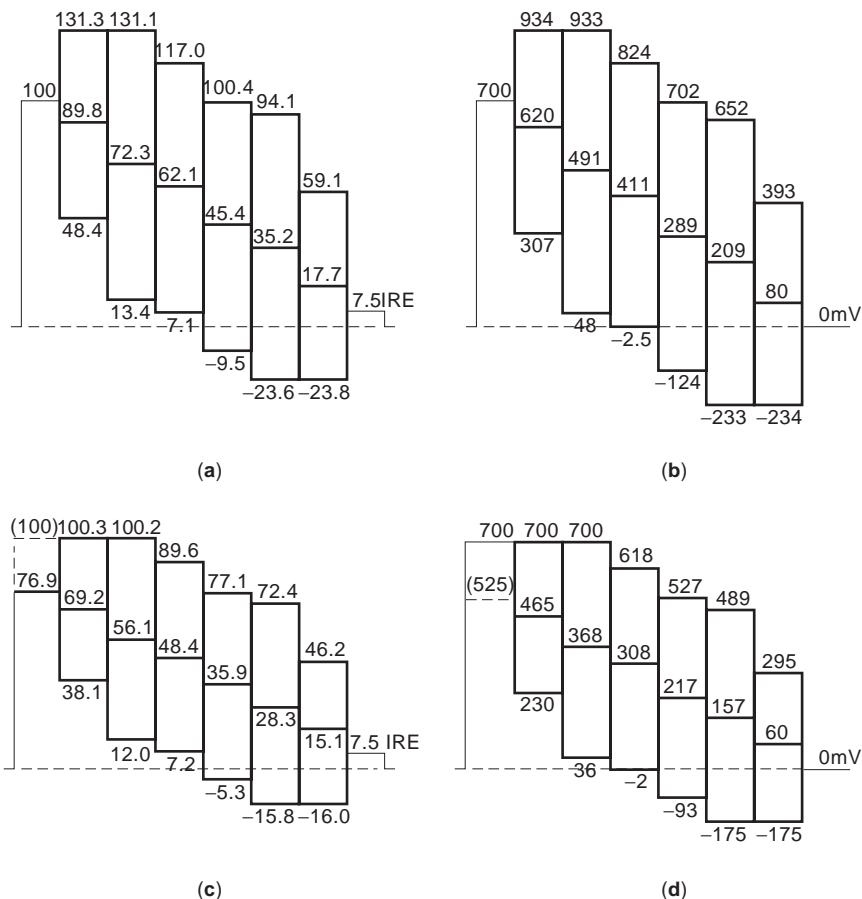


Figure 7. (a) 100% NTSC color bars (100/7.5/100/7.5). (b) 100% PAL color bars (100/0/100/0). (c) Standard 75% “EIA” color bars (75/7.5/75/7.5). (d) Standard 75% “EBU” color bars (100/0/75/0).

modulation of the subcarrier could be discarded, and the color-difference signals (called D_R and D_B in SECAM) sent sequentially, on alternate lines. This reduces vertical resolution in color by half; however, it is sufficient to provide only coarse detail vertically, as is already the case horizontally.

In early development, AM was contemplated; however, the use of FM also eliminated the effects of subcarrier amplitude distortion. In addition, FM allowed the composite signal to be recorded on conventional black-and-white tape machines because precise time base correction, required by phase modulation, was not necessary.

1.4.2. Compatibility. With FM, the subcarrier is always present, superimposed on the luminance signal at constant amplitude (unlike NTSC, in which the subcarrier produces noticeable interference with the luminance only on highly saturated colors). To reduce its visibility, several techniques are employed.

First, preemphasis is applied to the baseband color-difference signals to lessen their amplitudes at lower saturation, but preserve adequate signal-to-noise ratio (low-level preemphasis; see Fig. 10). Second, different subcarrier frequencies are employed, which are integral multiples of the scanning line frequency; f_{oB} is 4.25 MHz (272 H), and f_{oR} is 4.40625 MHz (282 H). The f_{oR} signal is

inverted before modulation so that the maximum deviation is toward a lower frequency, reducing the bandwidth required for the dual subcarriers.

Third, another level of preemphasis is applied to the modulated subcarrier around a point between the two rest frequencies, known as the “cloche” frequency of 4.286 MHz (high-level preemphasis, the so-called “anti-bell” shaping shown in Fig. 11). Finally, the phase of the modulated subcarrier is reversed on consecutive fields and, additionally, on every third scanning line, or, alternately, every three lines.

1.4.3. Line Identification. Synchronizing the receiver to the alternating lines of color-difference signals is provided in one of two ways. Earlier specifications called for nine lines of vertical blanking to contain a field identification sequence formed by truncated sawteeth of the color-difference signals from the white point to the limiting frequency (so-called “bottles”; see Fig. 12). This method is referred to as “SECAM-V.”

As use of the vertical interval increased for ancillary signals, receiver demodulators were fashioned to sample the unblanked subcarrier immediately following the horizontal sync pulse, providing an indication of line sequence from the rest frequency. Where this method is employed, it is called “SECAM-H.” An advantage of this

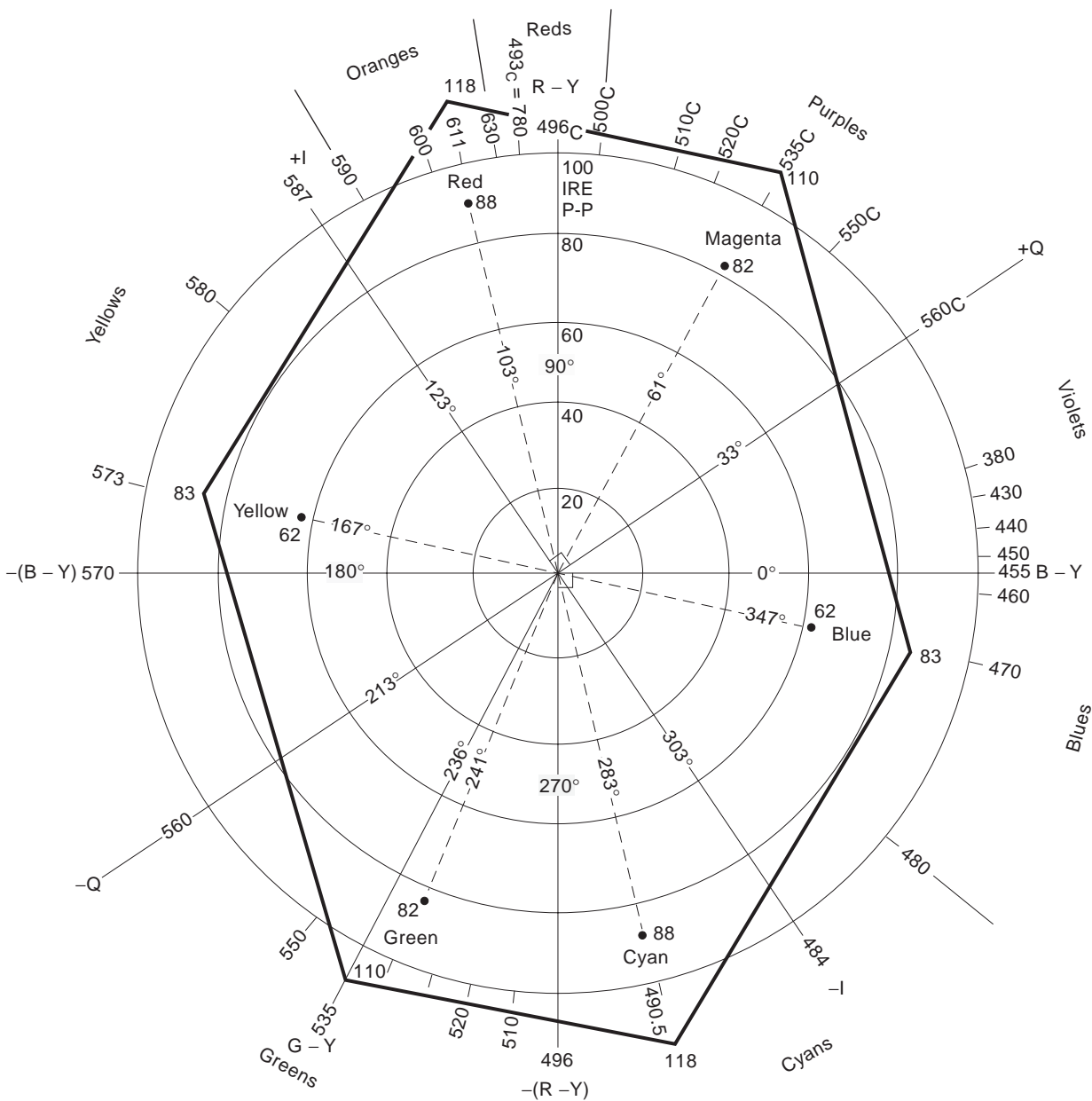


Figure 8. Vector relationship among chrominance components and corresponding dominant wavelengths. 75% Color bars with 7.5% setup. Linear NTSC system, NTSC luminophors, illuminant C. Hexagon defines maximum chrominance subcarrier amplitudes as defined by 100% color bars with 7.5% setup. *Caution:* The outer calibration circle on vectorscopes does not represent exactly 100 IRE P-P.

method is near-instantaneous recovery from momentary color field sequence errors, whereas SECAM-V receivers must wait until the next vertical interval.

1.4.4. Issues in Program Production. High-level preemphasis causes the chrominance subcarrier envelope to increase in amplitude at horizontal transitions, as can be seen on a waveform monitor (Fig. 13). Unlike NTSC, the subcarrier amplitude bears no relation to saturation, so, except for testing purposes, a luminance lowpass filter is employed on the waveform monitor. A vectorscope presen-

tation of the saturation and hue is implemented by decoding the FM subcarrier into baseband color-difference signals and applying them to an X-Y display.

Unfortunately, the choice of FM for the color subcarrier means that conventional studio production switchers cannot be employed for effects such as mixing or fading from one scene to another because reducing the amplitude of the sub-carrier does not reduce the saturation. This necessitates using a component switcher and then using encoding afterwards. In cases where the signal has already been encoded to SECAM (such as from a prerecorded video

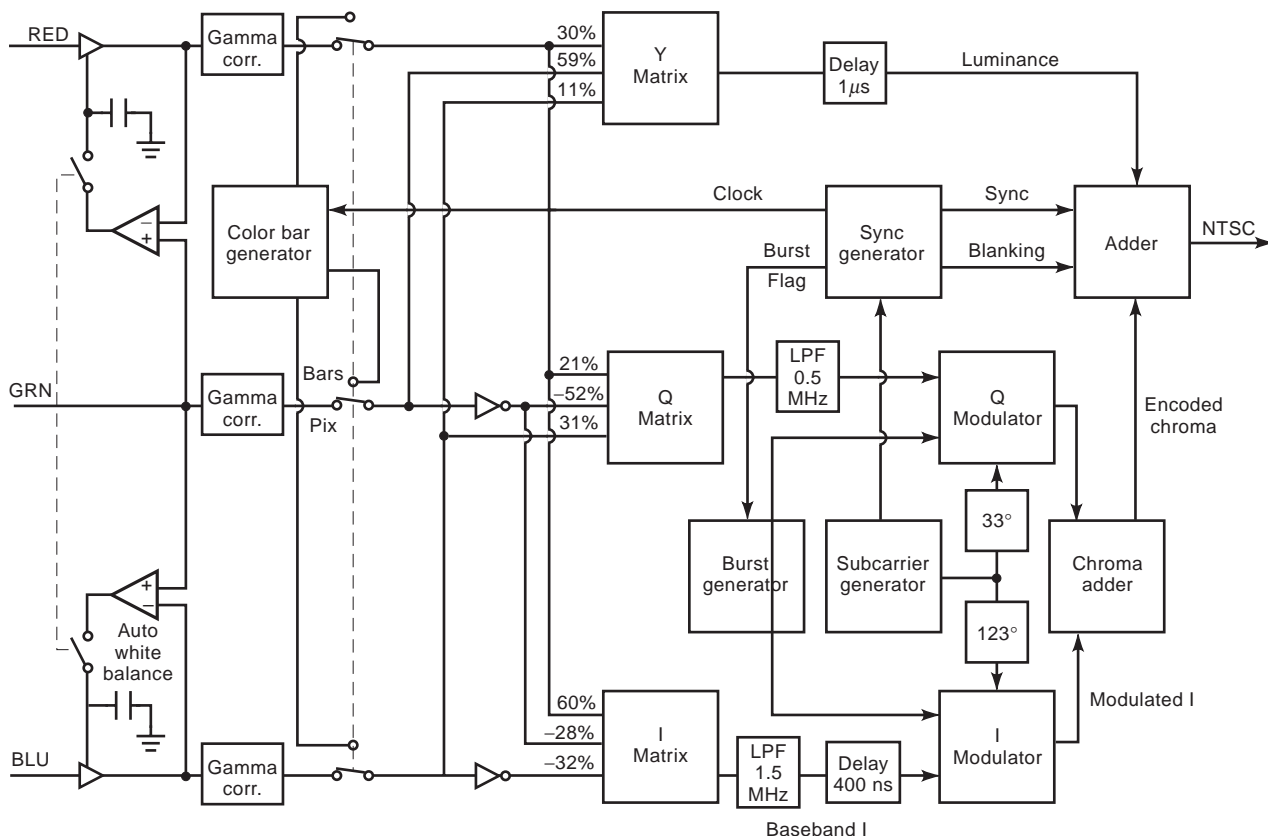


Figure 9. Block diagram of RGB to NTSC encoding (and related circuitry).

tape), it must be decoded prior to the component switcher and then reencoded.

Like NTSC, program editing must be done in two-frame increments. Although the subcarrier phase is reversed on a field-and-line basis, establishing a “12-field sequence,” it is the instantaneous frequency—not phase—which defines the hue. However, the line-by-line sequence of the

color-difference signals must be maintained. The odd number of scanning lines means that each successive frame begins with the opposite color-difference signal. As described above, mixes or fades are never done with composite signals.

Since the instantaneous frequency of the subcarrier is not related to the line scanning frequency, it is impossible

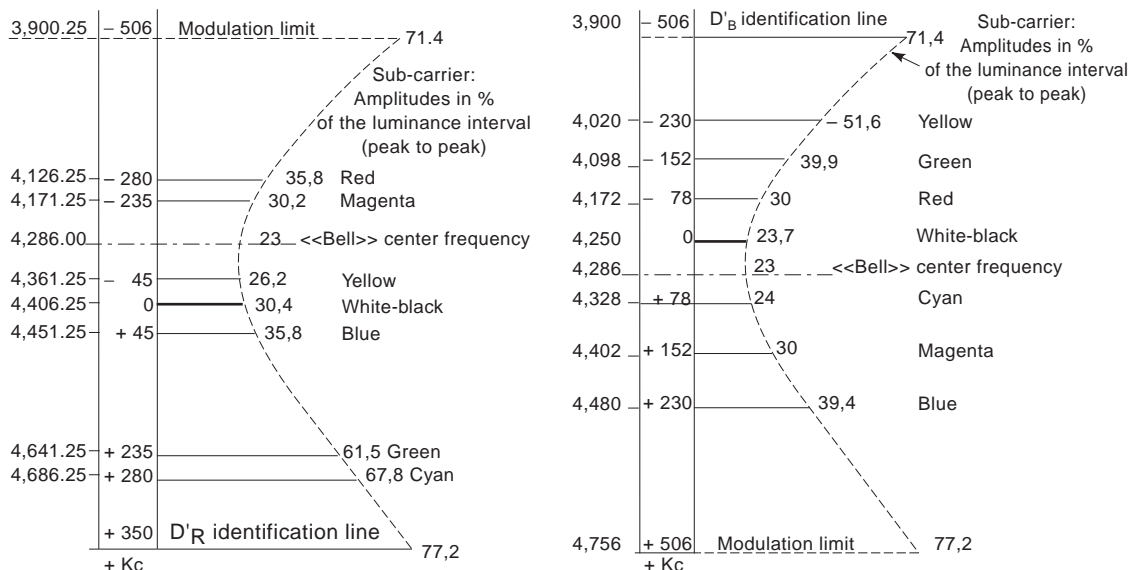


Figure 10. SECAM baseband (low-level) preemphasis.

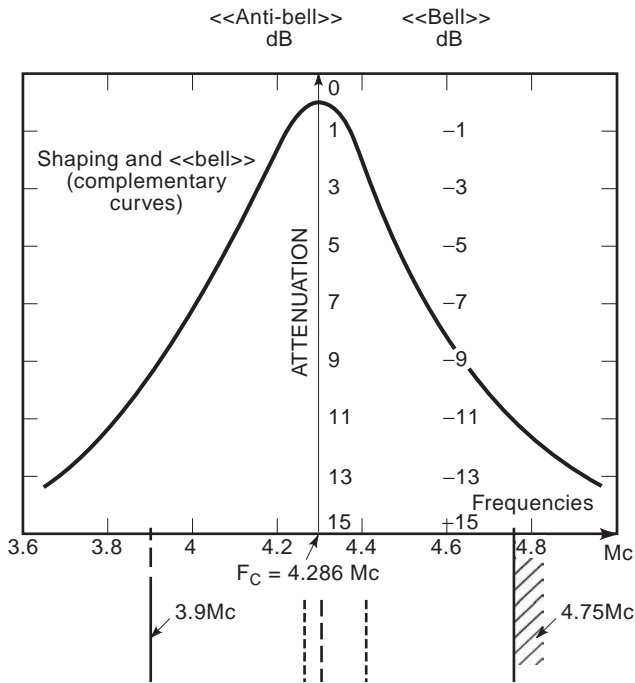


Figure 11. SECAM RF (high-level) preemphasis.

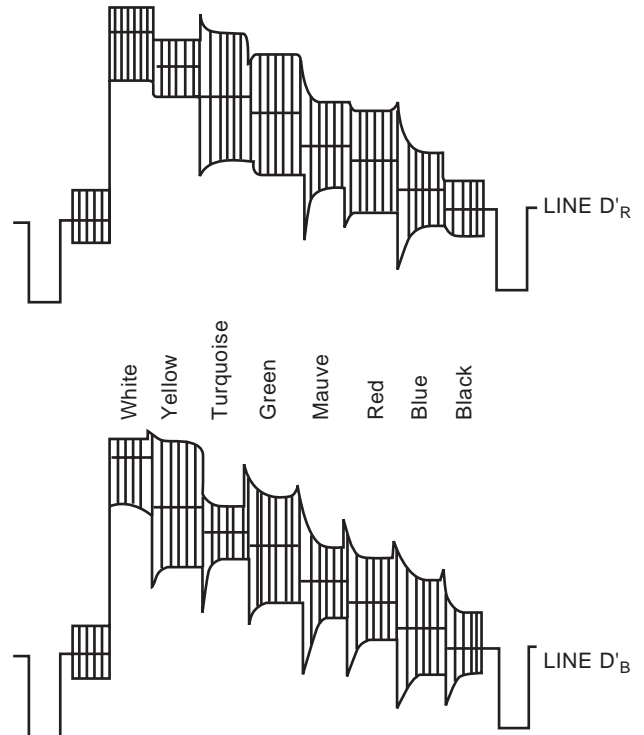


Figure 13. SECAM color bar waveforms.

to employ modern comb-filtering techniques to separate the chrominance and luminance in decoding. Increasingly, special effects devices rely on decoding the composite TV signal to components for manipulation, then reencoding. Every operation of this sort impairs luminance resolution because a notch filter must be used around the subcarrier frequency. These concerns have led many countries which formerly adopted SECAM to switch to PAL for program production, transcoding to SECAM only for RF broadcasting.

1.5. Phase Alternate Line (PAL)

To retain the ease in program production of NTSC, yet correct for phase errors, the German Telefunken Company developed a system more comparable with NTSC that retains quadrature modulation. Because of the wider channel bandwidth associated with 625-line systems, the color subcarrier could be positioned so that the sidebands from

both color-difference signals have the same bandwidth. This means that R-Y and B-Y signals could be used directly, rather than I and Q as in NTSC. Identical scaling factors are used, and the signals are known as V and U, respectively.

1.5.1. Color Phase Alternation. In the PAL system, the phase of the modulated V component of the chrominance signal is reversed on alternate lines to cancel chrominance phase distortion acquired in equipment or transmission. Any phase shift encountered will have the opposite effect on the displayed hue on adjacent lines in the picture. If the phase error is limited to just a few degrees, the eye integrates the error, because, in the vertical direction, more chrominance detail is provided than can be perceived at normal viewing distances. Receivers based on this principle are said to have "simple PAL" decoders.

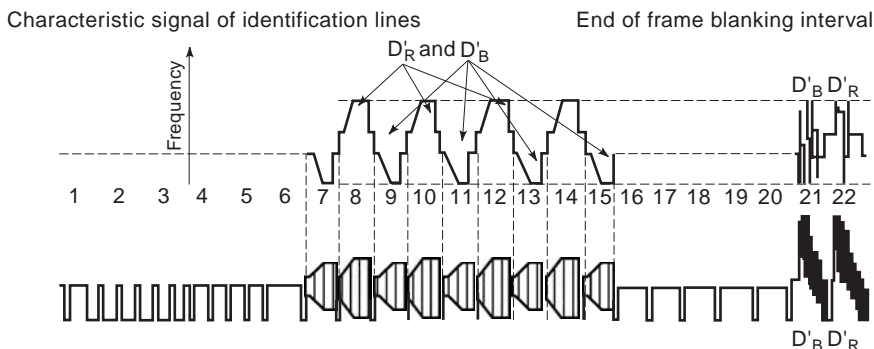


Figure 12. SECAM field identification "bottles."

If the phase error is more than a few degrees, the difference in hue produces a venetian-blind effect, called *Hanover bars*. Adding a one-line delay permits integrating chrominance information from adjacent scanning lines electrically, with a slight reduction in the saturation for large errors. Color resolution is reduced by half in the vertical direction but more closely matches horizontal resolution due to band-limiting in the encoder. This technique of decoding is called “deluxe PAL.” A reference is provided to indicate which lines have +V or -V phase by also shifting the phase of the color burst signal by $\pm 45^\circ$ on alternate lines.

1.5.2. Compatibility. The line-by-line phase reversal results in identical phase on alternate lines for hues on or near the V axis. To sustain a low-visibility interference pattern in PAL, the subcarrier frequency is made an odd multiple of one quarter of the line frequency (creating eight distinct color fields). This effectively offsets the excursions of the V component by 90° line-to-line and offsets those of the U component by 270° . As this 180° difference would cause the excursions of one component to line up vertically with those of the other in the next frame, an additional 25 Hz offset ($f_v/2$) is added to the PAL subcarrier frequency to further reduce its visibility.

In early subcarrier oscillator designs, the reference was derived from the mean phase of the alternating burst signal. Interlaced scanning causes a half-line offset between fields with respect to the vertical position so that the number of bursts actually blanked during the $7\frac{1}{2}$ H vertical interval would be different for the odd versus even fields. As the phase of burst alternates line-to-line, the mean phase would then appear to vary in this region, causing disturbances at the top of the picture.

This is remedied by a technique known as “Bruch blanking.” The burst blanking is increased to a total of

nine lines and repositioned in a four-field progression to include the $7\frac{1}{2}$ H interval, such that the first and last burst of every field has a phase corresponding to $(-U + V)$, or $+135^\circ$. The burst signal is said to “meander” so that color fields 3 and 7 have the earliest bursts.

1.5.3. Issues In Program Production. In PAL, because the subcarrier frequency is an odd multiple of one quarter the line frequency, each line ends on a quarter-cycle. This, coupled with the whole number plus one-half lines per field, causes the phase of the subcarrier to be offset each field by 45° . Thus, in PAL, the subcarrier phase repeats only every eight fields, creating an “eight-field sequence.” This complicates program editing, because edit points occur only every four frames, which is slightly less than 1/10 s in time.

Comb filtering to separate chrominance and luminance in decoding is somewhat more complicated in PAL; however, it has become essential for special picture effects. On a waveform monitor, the composite PAL signal looks very much like NTSC, except that the 25 Hz offset causes a slight phase shift from line to line, so that when viewing the entire field, the sine wave pattern is blurred. Because of the reversal in phase of the V component on alternate lines, the vectorscope presentation has a mirror image about the V axis (Fig. 14).

1.5.4. Variations of PAL. The differences between most 625-line transmission standards involve only RF parameters (such as sound-to-picture carrier spacing). For 625-line PAL program production, a common set of technical specifications may be used. These standards are routinely referred to in the production environment as “PAL-B,” although the baseband signals may be used with any 625-line transmission standard.

Several countries in South America have adopted the PAL system. The 6 MHz channel allocations in that region

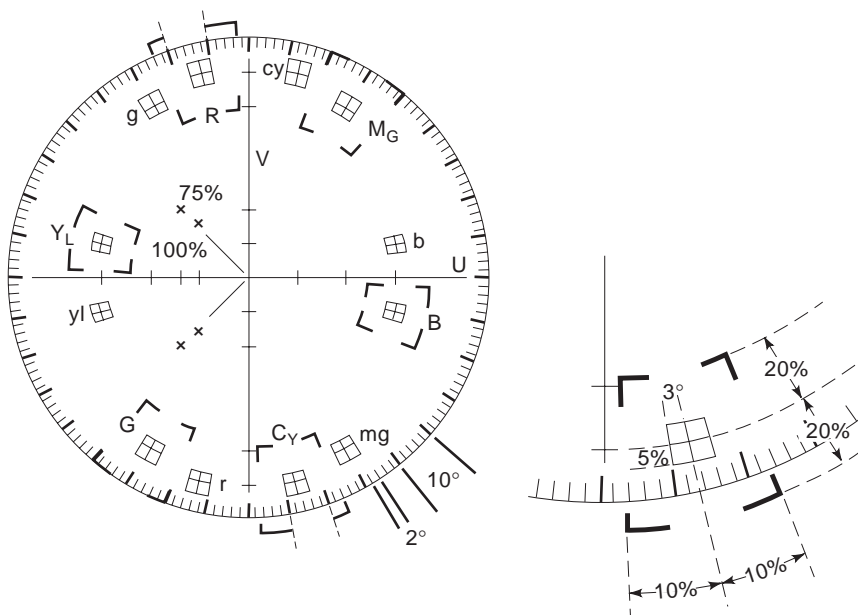


Figure 14. Typical PAL vectorscope graticule.

meant that the color subcarrier frequency had to be suitably located, about 1 MHz lower in frequency than for 7 MHz or 8 MHz channels. The exact frequencies are close to, but not the same as, those for NTSC. The 625-line system is known as PAL-N. Studio production for this standard is done in conventional “PAL-B,” then converted to PAL-N at the transmitter.

The 525-line PAL is known as PAL-M, and it requires studio equipment unique to this standard, although the trend is toward using conventional NTSC-M equipment and transcoding to PAL-M at the transmitter. PAL-M does not employ a 25 Hz offset of the subcarrier frequency, as is done in all other PAL systems.

1.6. Similarities of Color Encoding Systems

The similarities of the three basic color television encoding systems are notable (see Table 3). They all rely on the concept of a separate luminance signal that provides compatibility with black-and-white television receivers. The “mixed-highs” principle combines high-frequency information from the three color primaries into luminance, where the eye is sensitive to fine detail; only the relatively low-frequency information is used for the chrominance channels. All three systems use the concept of a subcarrier, located in the upper frequency spectrum of luminance, to convey the chrominance information (Fig. 15).

All systems use color-difference signals, rather than the color primaries directly, to minimize crosstalk with the luminance signal, and all derive the third color signal by subtracting the other two from luminance. The constant luminance principle is applied in all systems, based on the original NTSC picture tube phosphors, so the matrix formulations for luminance and color-difference signals are identical (some recent NTSC encoders use equal-bandwidth R–Y and B–Y signals, instead of proportioned-bandwidth I and Q signals).

All of the systems use scaling factors to limit excessive subcarrier amplitude (NTSC/PAL) or deviation (SECAM) excursions. Finally, all three systems use an unmodulated subcarrier sample on the back porch of the horizontal sync pulse for reference information in the decoding process.

Because of these similarities, conversion of signals between standards for international program distribution is possible. Early *standards converters* were optical in nature, essentially using a camera of the target standard focused on a picture tube operating at the source standard. Later, especially for color, electronic conversion became practical.

The most serious issue in standards conversion involves motion artifacts, owing to the different field rates between 525- and 625-line systems. Simply dropping or repeating fields and lines creates disturbing discontinuities, so interpolation must be done. In modern units, the composite signals are decoded into components, using up to three-dimensional adaptive comb filtering, converted using motion prediction, and then reencoded to the new standard. Table 4 lists the transmission and color standards used in various territories throughout the world.

1.7. Component Analog Video (CAV)

The advent of small-format videotape machines that recorded luminance and chrominance on separate tracks led to interest in component interconnection. Increasingly, new equipment decoded and reencoded the composite signal to perform manipulations that would be impossible or cause significant distortions if done in the composite environment. It was reasoned that if component signals (Y, R–Y, B–Y) could be taken from the camera and if encoding to NTSC, PAL, or SECAM could be done just before transmission, then technical quality would be greatly improved.

However, component signal distribution required some equipment, such as switchers and distribution amplifiers, to have three times the circuitry, and interconnection required three times the cable and connections as composite systems. This brought about consideration of *multiplexed analog component* (MAC) standards, whereby the luminance and chrominance signals are time-multiplexed into a single, higher bandwidth signal. No single standard for component signal levels emerged (Table 5), and the idea was not widely popular. Interest soon shifted to the possibility of digital signal distribution.

1.8. Digital Video

Devices such as time-base correctors, frame synchronizers, and standards converters process the TV signal in the digital realm but with analog interfaces. The advent of digital videotape recording set standards for signal sampling and quantization to the extent that digital interconnection became practical.

1.8.1. Component Digital. The European Broadcasting Union (EBU) and Society of Motion Picture and Television Engineers (SMPTE) coordinated research and conducted demonstrations in search of a component digital video standard that would lend itself to the exchange of programs on a worldwide basis. A *common data rate* of 13.5 Mbps based on line-locked sampling of both 525- and 625-line standards was chosen. This allows analog video frequencies of better than 5.5 MHz to be recovered and is an exact harmonic of the scanning line rate for both standards, enabling great commonality in equipment.

A *common image format* of static orthogonal shape is also employed, whereby the sampling instants on every line coincide with those on previous lines and fields and overlay the samples from previous frames. There are 858 total luminance samples per line for the 525-line system, 864 samples for the 625-line system, but 720 samples during the picture portion for both systems. This image structure facilitates filter design, special effects, compression, and conversion between standards.

For studio applications, the color-difference signals are sampled at half the rate of luminance, or 6.75 MHz, co-sited with every odd luminance sample, yielding a total data rate of 27 Mbps. This provides additional resolution for the chrominance signals, enabling good special effects keying from color detail. The sampling ratio for luminance and the two chrominance channels is designated “4 : 2 : 2.” Other related ratios are possible (Table 6).

Table 3. Principal Characteristics of Color Television Encoding Systems

System	NTSC	PAL	SECAM
Display primaries	FCC	EBU	EBU
White reference	CIE III C	CIE III D ₆₅	CIE III C
Display gamma	2.2	2.8	2.8
Luminance	$E'_Y = +0.30E'_R + 0.59E'_G + 0.11E'_B$		$E'_Y = +0.299E'_R + 0.587E'_G + 0.114E'_B$
Chrominance signals	$Q = +0.41 (B - Y) + 0.48 (R - Y)$ $I = -0.27 (B - Y) + 0.74 (R - Y)$	$U = 0.493 (B - Y)$ $V = 0.877 (R - Y)$	$D_B = +1.505 (B - Y)$ $D_R = -1.902 (R - Y)$
Chrominance baseband video preemphasis (kHz)	—	—	$D * _B = A \times D_R$ $D * _R = A \times D_B$ $A = \frac{1 + j \times \frac{f_B/f_R}{85}}{1 + j \times \frac{f_B/f_R}{255}}$
Modulation method	Amplitude modulation of two suppressed subcarriers in quadrature		Frequency modulation of two sequential subcarriers
Axes of modulation	$Q = 33^\circ, I = 123^\circ$	$U = 0^\circ, V = \pm 90^\circ$	—
Chroma BW/Deviation (kHz)	$Q = 620, I = 1300$	$U + V = 1300$	$\Delta f_{oB} = \pm 230 + 276 / - 120,$ $\Delta f_{oR} = \pm 280 + 70 / - 226$
Vestigial sideband (kHz)	+ 620	+ 570(PAL-B, G, H), + 1070(PAL-I), + 620(PAL-M, N)	—
Composite color video signal (CCVS)	$E_M = E'_Y + E'_Q (\sin \omega t + 33^\circ)$ $+ E'_I (\cos \omega t + 33^\circ)$	$E_M = E'_Y + E'_U \sin \omega t$ $\pm E'_V \cos \omega t$	$E_M = E'_Y + G_{sc} \times \cos 2\pi(f_{oB} + D * _B \Delta f_{oB}) t$ $+ G_{sc} \times \cos 2\pi(f_{oR} + D * _B \Delta f_{oR}) t$
Modulated subcarrier amplitude/pre-emphasis	$G_{sc} = \sqrt{E'_{Q^2} + E'_{I^2}}$	$G_{sc} = \sqrt{E'_{U^2} + E'_{V^2}}$	$G_{sc} = D * _B / D * _R \times 0.115E'_Y (P - P) \times \left \frac{1 + j(16)F}{1 + j(1.26)F} \right $
SC/H frequency relationship	$f_{sc} = (455/2)f_H$	$f_{sc} = (1135/4)f_H + f_{v/2}$ (PAL-B, G, H, I) $= (909/4)f_H$ (PAL-M) $= (917/4)f_H + f_{v/2}$ (PAL-N)	$F = \frac{f_B/f_R}{f_0} - \frac{f_0}{f_B/f_R}$ ($f_0 = 4.286 \pm 0.02\text{MHz}$) $f_{oB} = 272f_H f_{oR} = 282f_H$ $f_{oB} = 4.250000 \pm 2 \text{ kHz},$ $f_{oR} = 4.406250 \pm 2 \text{ kHz}$
Subcarrier frequency (MHz)	$3.579545 \pm 10 \text{ Hz}$	$4.43361875 \pm 5 \text{ Hz}$ (PAL-B, G, H, I); $\pm 1\text{Hz}$ (PAL-I) $3.57561149 \pm 10 \text{ Hz}$ (PAL-M)	
Phase/Deviation of SC reference	180°	$3.58205625 \pm 5 \text{ Hz}$ (PAL-N) $+ V = + 135^\circ, -V = - 135^\circ$	$D_B = - 350 \text{ kHz}, D_R = + 350 \text{ kHz}$
Start of SC reference (μs)	5.3 ± 0.1	5.6 ± 0.1 (PAL-B, G, H, I, N); 5.2 ± 0.5 (PAL-M)	5.7 ± 0.3
SC reference width (cycles)	9 ± 1	10 ± 1 (PAL-B, G, H, I,); 9 ± 1 (PAL-M, N)	—
SC reference amplitude (mV)	$286(40 \text{ IRE} \pm 4)$	300 ± 30	$D_B = 167, D_R = 215$

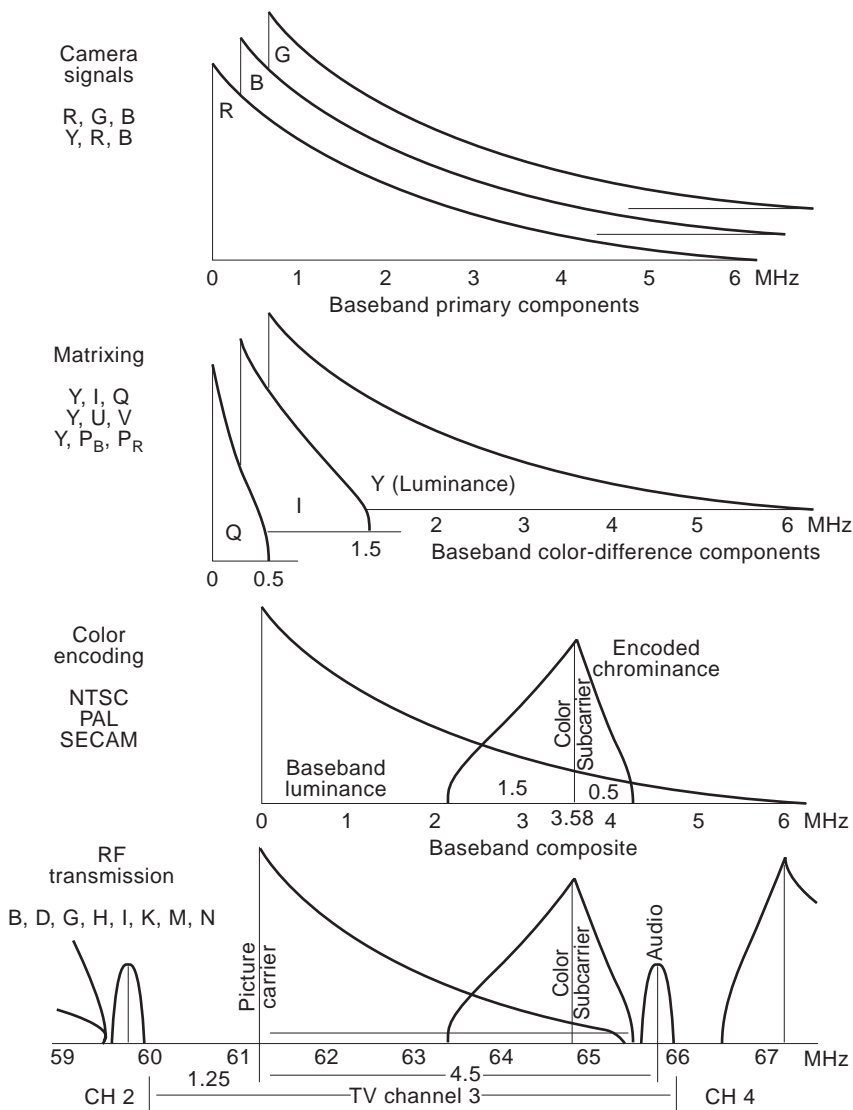


Figure 15. Four-stage color television frequency spectrum showing the compression of three wideband color-separation signals from the camera through bandwidth limiting and frequency multiplexing into the same channel bandwidth used for black-and-white television.

Quantization is uniform (not logarithmic) for both luminance and color-difference channels. Eight-bit quantization, providing 256 discrete levels, was found to provide adequate signal-to-noise ratio for videotape applications. However, the 25-pin parallel interface selected can accommodate two extra bits, because 10-bit quantization was foreseen as desirable in the future. Only the active picture information is sampled and quantized, allowing better resolution of the signal amplitude. Sync and blanking are coded by special signals (Figs. 16 and 17).

These specifications were standardized in ITU-R BT.601— hence the abbreviated reference, “601 Video.” The first component digital tape machine standard was designated “D1” by SMPTE. This term has come to be used in place of more correct designations. For widescreen applications, a 360 Mbps standard scales up the number of sampling points for 16:9 aspect ratio.

Interconnecting digital video equipment is vastly simplified by using a serial interface. Originally, an 8/9 block code was devised to facilitate clock recovery by preventing long strings of ones or zeros in the code. This would have

resulted in a serial data rate of 243 Mbps. To permit 10-bit data to be serialized, scrambling is employed, with complementary descrambling at the receiver. NRZI coding is used, so the fundamental frequency is half the bit-rate of 270 MHz.

1.8.2. Composite Digital. Time-base correctors for composite 1 in. videotape recorders had been developed with several lines of storage capability. Some early devices sampled at three times the color subcarrier frequency ($3f_{sc}$); however, better filter response could be obtained with $4f_{sc}$ sampling. The sampling instants correspond with peak excursions of the I and Q subcarrier components in NTSC. The total number of samples per scanning line is 910 for NTSC and is 1135 for PAL. To accommodate the 25 Hz offset in PAL, lines 313 and 625 each have 1137 samples. The active picture portion of a line consists of 768 samples in NTSC and 948 samples in PAL. These specifications are standardized as SMPTE 244 M (NTSC) and EBU Tech. 3280 (PAL).

Table 4. National Television Transmission Standards

Territory	VHF	UHF	Color	Territory	VHF	UHF	Color	Territory	VHF	UHF	Color
Afars and Isaas = Djibouti				Georgia	D	K	SECAM	Niger	K'		SECAM
Afghanistan	D		PAL	Germany	B	G	PAL	Nigeria	B		PAL
Albania	B	G	PAL	Ghana	B		PAL	Norway	B		PAL
Algeria	B		PAL	Gibraltar	B	G	PAL	Oman	B	G	PAL
Andorra	B		PAL	Greece	B	G	SECAM	Pakistan	B		PAL
Angola	I		PAL	Greenland	B		PAL	Palau	M		NTSC
Antigua and Barbuda	M		NTSC	Grenada	M		NTSC	Panama	M		NTSC
Argentina	N		PAL	Guadeloupe	K'		SECAM	Papua New Guinea	B	G	PAL
Armenia	D	K	SECAM	Guam	M	M	NTSC	Paraguay	N		PAL
Ascension Islands	I			Guatemala	M		NTSC	Peru	M	M	NTSC
Australia	B	B	PAL	Guinea	K'		PAL	Philippines	M		NTSC
Austria	B	G	PAL	Guinea-Bissau	I			Poland	D	K	P & S
Azerbaijan	D	K	SECAM	Guyana, Republic of	M		NTSC	Portugal	B	G	PAL
Azores	B		PAL	Haiti	M		NTSC	Puerto Rico	M	M	NTSC
Bahamas	M		NTSC	Honduras	M		NTSC	Qatar	B	G	PAL
Bahrain	B	G	PAL	Hong Kong		I		Reunion	K'		SECAM
Bangladesh	B		PAL	Hungary	D	K	P & S	Romania	D	G/K	PAL
Barbados	M		NTSC	Iceland	B	G	PAL	Russia	D	K	SECAM
Belarus	D	K	SECAM	India	B		PAL	Rwanda	K'		
Belgium	B	H	PAL	Indonesia	B		PAL	St. Helena	I		
Benin	K'		SECAM	Iran	B		SECAM	St. Pierre et Miquelon	K'	K'	SECAM
Bermuda	M		NTSC	Iraq	B		SECAM	St. Kitts and Nevis	M		NTSC
Bolivia	M	M	NTSC	Ireland	I	I	PAL	Samoa (American)	M		NTSC
Bosnia and Herzegovina	B	G	PAL	Israel	B	G	PAL	Samoa (Western)	B		PAL
Botswana	I		PAL	Italy	B	G	PAL	So Tomé e Príncipe	B		PAL
Brazil	M		PAL	Ivory Coast = Côte d'Ivoire				San Andres Islands	M		NTSC
Brunei Darussalam	B		PAL	Jamaica	M		NTSC	San Marino	B	G	PAL
Bulgaria	D	K	P & S	Japan	M	M	NTSC	Saudi Arabia	B	G	S/P S
Burkina Faso	K'		SECAM	Johnston Islands	M		NTSC	Senegal	K'		SECAM
Burma = Myanmar				Jordan	B	G	PAL	Serbia	B	G	PAL
Burundi		K'	SECAM	Kampuchea = Cambodia				Seychelles	B		PAL
Cambodia	B		PAL	Kazakhstan	D	K	SECAM	Sierra Leone	B		PAL
Cameroon	B		PAL	Kenya	B		PAL	Singapore	B		PAL
Canada	M	M	NTSC	Korea, Democracy of (N)				Slovakia	B	G/K	PAL
Canary Islands	B	G	PAL	Korea, Republic of (S)	M	M	NTSC	Slovenia	B	G	PAL
Cape Verde Islands	I		PAL	Kuwait	B	G	PAL	Society Islands = French Polynesia			
Cayman Islands	M		NTSC	Kyrgyzstan	D	K	SECAM	Somalia	B		PAL
Central African Republic	K'		SECAM	Laos	B		PAL	South Africa	I	I	PAL
Ceylon = Sri Lanka				Latvia	D	K	SECAM	S. West Africa = Namibia			
Chad	K'		SECAM	Lebanon	B	G	SECAM	Spain	B	G	PAL
Channel Islands		I	PAL	Leeward Islands = Antigua				Sri Lanka	B		PAL
Chile	M		NTSC	Lesotho	I		PAL	Sudan	B		PAL
China	D	D	PAL	Liberia	B		PAL	Suriname	M		NTSC
Colombia	M		NTSC	Libya	B		SECAM	Swaziland	B	G	PAL
Commonwealth of Independent States: see state				Lichtenstein	B	G	PAL	Sweden	B	G	PAL
Comores	K'			Lithuania	D	K	SECAM	Switzerland	B	G	PAL
Congo	K'		SECAM	Luxembourg	B	G/L	PP/S	Syria	B	G	P & S
Costa Rica	M		NTSC	Macao	I		PAL	Tahiti = French Polynesia			
Côte d'Ivoire	K'		SECAM	Macedonia	B	G	PAL	Taiwan	M	M	NTSC
Croatia	B	G	PAL	Madagascar	K'		SECAM	Tajikistan	D	K	SECAM
Cuba	M		NTSC	Madeira	B		PAL	Tanzania	B	I	PAL
Curaco	M	M	NTSC	Malawi	B		PAL	Thailand	B	M	PN
Cyprus	B	G	P & S	Malaysia	B		PAL	Togo	K'		SECAM
Czech Republic	D	K	SP	Maldives	B		PAL	Trinidad and Tobago	M	M	NTSC
Dahomey = Benin				Mali	K'		SECAM	Tunisia	B	G	P S
Denmark	B	G	PAL	Malta	B		PAL	Turks and Caicos	M		NTSC
Diego Garcia	M		NTSC	Martinique	K'		SECAM	Turkey	B	G	PAL
Djibouti	K'		SECAM	Mauritania	B		SECAM	Turkmenistan	D	K	SECAM
Dominican Republic	M		NTSC	Mauritius	B		SECAM	Uganda	B		PAL
Ecuador	M		NTSC	Mayotte	K'		SECAM	Ukraine	D	K'	SECAM
Equatorial Guinea = Fernando Po				Mexico	M	M	NTSC	USSR: see independent state			
Egypt	B	G	P & S	Micronesia	M		NTSC	United Arab Emirates	B	G	PAL
El Salvador	M		NTSC	Moldovia	D	K	SECAM	United Kingdom		I	PAL
Eritrea	B		PAL	Monaco	L	G/L	S P/S	United States	M	M	NTSC
Estonia	D	K	SECAM	Mongolia	D		SECAM	Upper Volta = Burkina Faso			
Ethiopia	B		PAL	Montserrat	M		NTSC	Uruguay	N		PAL
Faeroe Islands	B	G	PAL	Morocco	B		SECAM	Uzbekistan	D	K	SECAM
Falkland Islands	I		PAL	Mozambique		B	PAL	Venezuela	M		NTSC
Fernando Po	B		PAL	Myanmar	M		NTSC	Vietnam	D/M		S/N
Fiji	M		NTSC	Namibia	I		PAL	Virgin Islands	M		NTSC
Finland	B	G	PAL	Nepal	B		PAL	Yemen	B		PAL
France	L'	L	SECAM	Netherlands	B	G	PAL	Yugoslavia: see new state			
French Guyana	K'		SECAM	Netherlands Antilles	M		NTSC	Zaire	K'		SECAM
French Polynesia	K'		SECAM	New Caledonia	K'		SECAM	Zambia	B		PAL
Gabon	K'		SECAM	New Zealand	B	G	PAL	Zanzibar = Tanzania			
Gambia	B		PAL	Nicaragua	M		NTSC	Zimbabwe	B		PAL

Table 5. Component Analog Video Format Summary

Format	Color Bar Amplitudes (mV)						Peak Excursions (mV)		Setup
	Channel 1		Channel 2		Channel 3		Synchronization Channels/Signals		
	100%	75%	100%	75%	100%	75%			
R/G/B/S ^a	+1 V/ +750		+1 V/ +750		+1 V/ +750		S = -4 V		No
G/B/R	+700/ +525		+700/ +525		+700/ +525		G, B, R = -300		No
Y/I/Q (NTSC)	+714/ +549		±393/±295		±345/±259		Y = -286		Yes
Y/Q/I (M _I)	+934/ +714		±476/±357		±476/±357		Y = -286	I = -600	Yes
Y/R - Y/B - Y*	+700/ +525		±491/±368		±620/±465		Y = -300		No
Y/U/V (PAL)	+700/ +525		±306/±229		±430/±323		Y = -300		No
Betacam 525	+714/ +549		±467/±350		±467/±350		Y = -286		Yes
2 CH Y/CTDM	+714/ +549		±467/±350				Y = ±286	C = -420	
Betacam 625	+700/ +525		±467/±350		±467/±350		Y = -300		No
2 CH Y/CTDM	+700/ +525		±467/±350				Y = ±300	C = -420	
M _{II} 525	+700/ +538		±324/±243		±324/±243		Y = -300		Yes
2 CH Y/CTCM	+714/ +549		±350/±263				Y = -286	C = -650	
M _{II} 525	+700/ +525		±350/±263		±350/±263		Y = -300		No
2 CH Y/CTCM	+700/ +525		±350/±263				Y = -300	C = -650	
SMPTE/EBU (Y/P _B /P _R)	+700/ +525		±350/±263		±350/±263		Y = -300		No

^aOther levels possible with this generic designation.

Unlike component digital, nearly the entire horizontal and vertical blanking intervals are sampled and quantized, which degrades the amplitude resolution (Fig. 18). However, in PAL, no headroom is provided for sync level, and the sampling instants are specified at 45° from the peak excursions of the V and U components of subcarrier (Fig. 19). This allows a “negative headroom” in the positive direction. Thus, an improvement of about 0.5 dB in signal-to-noise ratio is obtained.

Rate conversion between component and composite digital television signals involves different sampling points

and quantizing levels. Each conversion degrades the picture, because exact levels cannot be reproduced in each pass. An important advantage of digital coding is thereby lost. In addition, decoding composite signals requires filtering to prevent cross-luminance and cross-color effects. This forever removes a part of the information; therefore, this process must be severely limited in its use.

Ancillary data may be added to digital component and composite video signals. AES/EBU-encoded digital audio can be multiplexed into the serial bit stream. Four channels are possible with the composite format, and 16 channels are possible with component digital video.

Table 6. Sampling Structures for Component Systemes

Sample/Pixel						Sample/Pixel													
1		2		3		4		5		1		2		3		4		5	
Line	YCbCr	YCbCr	YCbCr	YCbCr	YCbCr	Line	YCbCr	Y	YCbCr	Y	YCbCr	Y	YCbCr	Y	YCbCr	Y	YCbCr	Y	YCbCr
	YCbCr	YCbCr	YCbCr	YCbCr	YCbCr		YCbCr	Y	YCbCr	Y	YCbCr	Y	YCbCr	Y	YCbCr	Y	YCbCr	Y	YCbCr
	YCbCr	YCbCr	YCbCr	YCbCr	YCbCr		YCbCr	Y	YCbCr	Y	YCbCr	Y	YCbCr	Y	YCbCr	Y	YCbCr	Y	YCbCr
	YCbCr	YCbCr	YCbCr	YCbCr	YCbCr		YCbCr	Y	YCbCr	Y	YCbCr	Y	YCbCr	Y	YCbCr	Y	YCbCr	Y	YCbCr
4:4:4						4:2:2													
Sample/Pixel						Sample/Pixel													
1		2		3		4		5		1		2		3		4		5	
Line	YCbCr	Y	Y	Y	YCbCr	Line	Y	Y	Y	Y	Y	Y	Y	Y	Y	Y	Y	Y	Y
	YCbCr	Y	Y	Y	YCbCr		C_bC_r	Y	C_bC_r	Y	C_bC_r	Y	C_bC_r	Y	C_bC_r	Y	C_bC_r	Y	C_bC_r
	YCbCr	Y	Y	Y	YCbCr		Y	Y	Y	Y	Y	Y	Y	Y	Y	Y	Y	Y	Y
	YCbCr	Y	Y	Y	YCbCr		C_bC_r	Y	C_bC_r	Y	C_bC_r	Y	C_bC_r	Y	C_bC_r	Y	C_bC_r	Y	C_bC_r
4:1:1						4:2:0													

Y=luminance sample; C_bC_r=chrominance samples; YCbCr=pixels so shown are co-sited. Boldfaced type indicates bottom field, if interlaced.

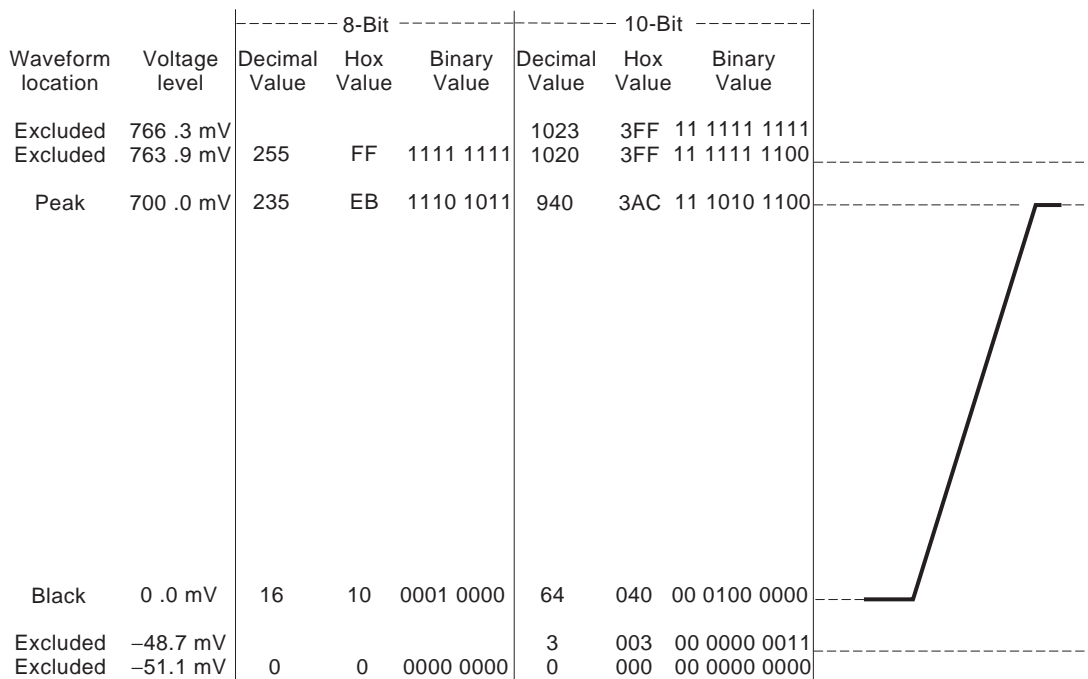


Figure 16.

1.9. Component Video Standards

The video signals from a camera before encoding to NTSC, PAL, SECAM, or the ATSC Digital Standard are normally green (G), blue (B), and red (R). These are described as

component signals because they are parts or components of the whole video signal. It has been found more efficient of band-width use for distribution and sometimes for processing to convert these signals into a luminance signal (Y), and two color-difference signals, blue minus lumi-

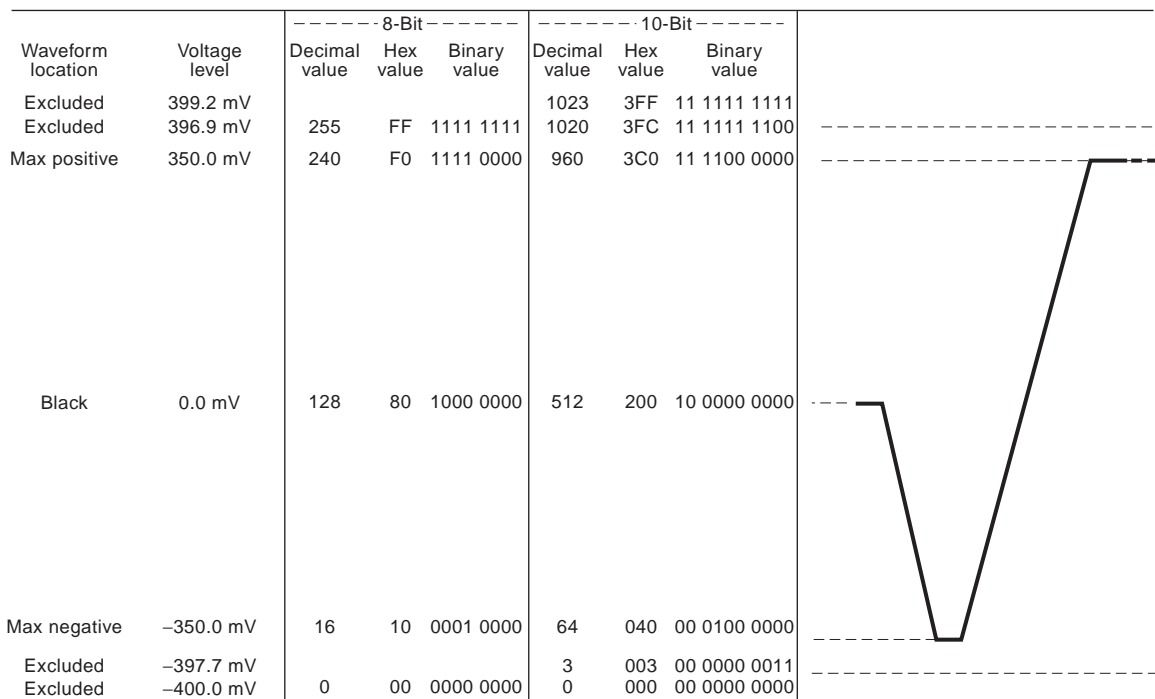


Figure 17. Quantizing levels for component digital color difference.

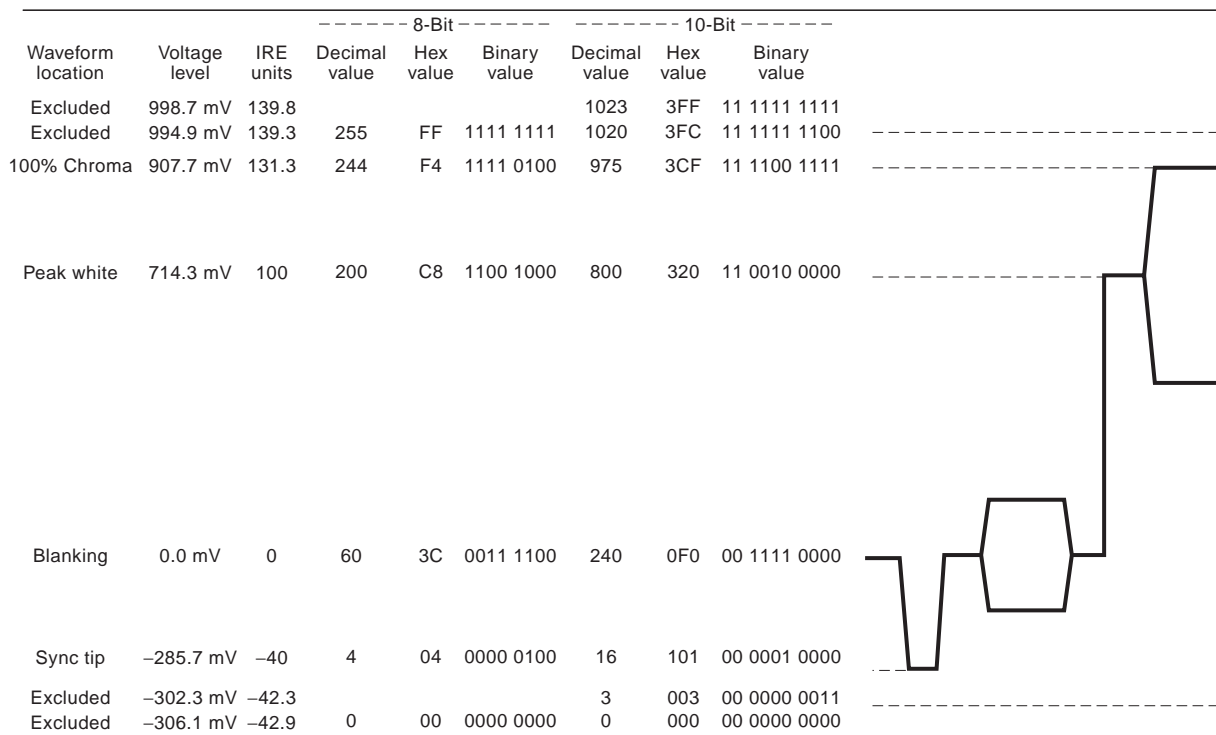


Figure 18. Quantizing levels for composite digital NTSC.

nance (B–Y) and red minus luminance (R–Y), where the color difference signals use one half or one quarter of the bandwidth of the luminance signal. The SMPTE/EBU Standard N10 has been adopted that has a uniform sig-

nal specification for all 525/60 and 625/50 television systems. The color difference signals in this standard, when they are digitally formatted, are termed C_b and C_r , respectively. At the same time, due to the lower sensitivity of

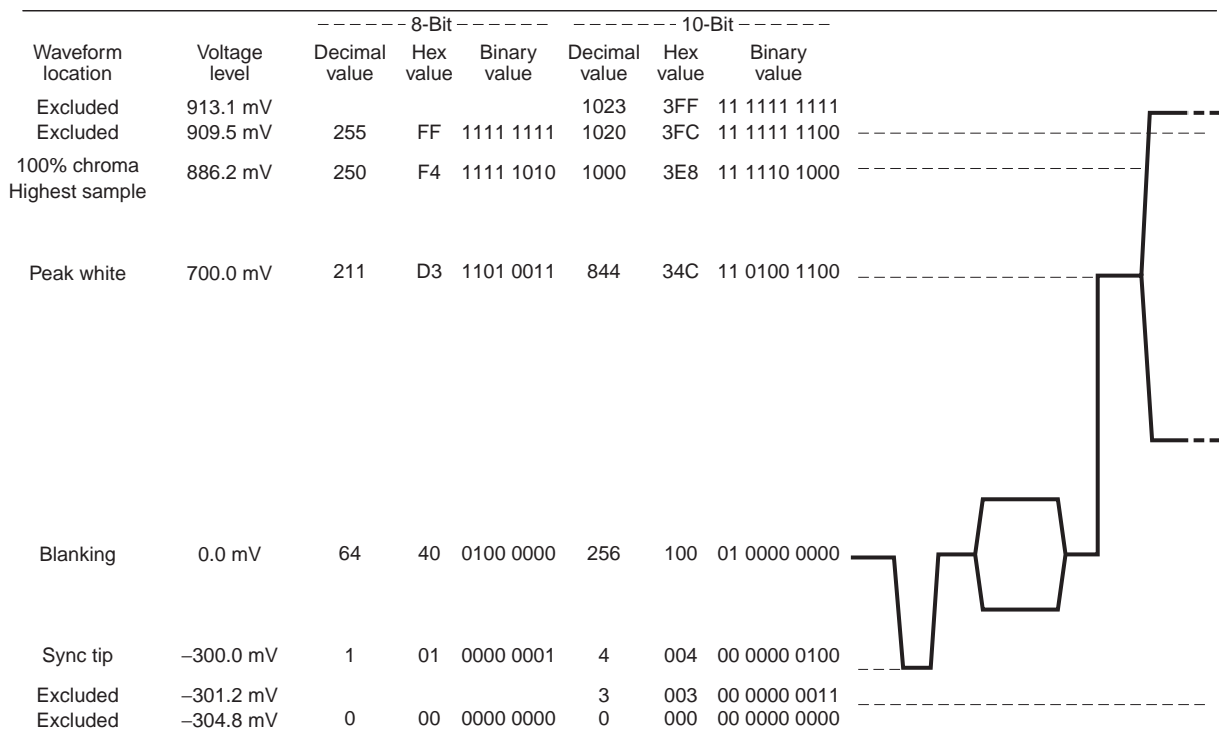


Figure 19. Quantizing levels for composite digital PAL.

the human eye to fine detail in color, it is possible to reduce the bandwidth of the color difference signals compared with that of the luminance signal.

When these signals are digitized according to International Telecommunication Union, Radiocommunication Sector, (ITU-R) Recommendation 601, for both 525/60 and 625/50 systems, there are several modes of transmission that may be used, all based on multiples of a 3.75 MHz sampling rate. For the ATSC standard, 4:2:0 is used (see below and the ATSC digital television standard). Either 8, or more frequently, 10 bits per sample are used.

1.9.1. 4:4:4 Mode. The G, B, R or Y, C_b , C_r signal with an equal sampling rate of 13.5 MHz for each channel is termed the 4:4:4 mode of operation, and it yields 720 active samples per line for both 525/60 and 625/50 standards. This mode is frequently used for postproduction. If a (full-bandwidth) key signal is also required to be carried with the video, this combination is known as a 4:4:4:4 signal.

1.9.2. 4:2:2 Mode. More frequently used for distribution is the 4:2:2 mode, where Y is sampled at 13.5 MHz, and the color difference signals are sampled at 6.25 MHz rate, corresponding to 360 active samples per line.

1.9.3. 4:1:1 Mode. The 4:1:1 mode is used where bandwidth is at a premium, and the color difference signals are each sampled at 3.75 MHz rate, corresponding to 180 samples per line.

1.9.4. 4:2:0 Mode. A further alternative, 4:2:0 mode, whose structure is not self-evident, is derived from a 4:2:2 sampling structure but reduces the vertical resolution of the color difference information by 2:1 to match the reduced color difference horizontal resolution. Four line (and field sequential if interlaced) co-sited C_b , C_r samples are vertically interpolated weighted toward the closest samples, and the resultant sample is located in between two adjacent scanning lines. This mode is used in MPEG bit-rate reduced digital signal distribution formats, and hence in the ATSC digital television standard.

The above four modes are illustrated in Table 6.

2. ADVANCED TELEVISION SYSTEMS, CURRENT AND FUTURE

2.1. ATSC Digital Television Standard

2.1.1. Overview. The Advisory Committee on Advanced Television Service (ACATS) to the Federal Communications Commission, with support from Canada and Mexico, from 1987 to 1995 developed a recommendation for an Advanced Television Service for North America. The ACATS enlisted the cooperation of the best minds in the television industry, manufacturers, broadcasters, cable industry, film industry, and federal regulators in its organization to develop an advanced television system that would produce a substantial improvement in video images and in audio performance over the existing NTSC, 525-line system. The primary video goal was at least a

doubling of horizontal and vertical resolution with a widening in picture aspect ratio from current 4 (W) \times 3 (H) to 16 (W) \times 9 (H), and this was named "high-definition television." Also included was a digital audio system consisting of five channels plus a low-frequency channel (5.1).

Twenty-one proposals were made for terrestrial transmission systems for extended-definition television (EDTV) or high-definition television (HDTV), using varying amounts of RF spectrum. Some systems augmented the existing NTSC system, with an additional channel of 3 MHz or 6 MHz, some used a separate simulcast channel of 6 MHz or 9 MHz bandwidth, and all of the early systems used hybrid analog/digital technology in the signal processing with an analog RF transmission system. Later proposals changed the RF transmission system to digital along with all-digital signal processing.

It was also decided that the signal would be transmitted in a 6 MHz RF channel, one for each current broadcaster of the (6 MHz channel) NTSC system, and that this new channel would eventually replace the NTSC channels. The additional channels were created within the existing UHF spectrum by improved design of TV receivers so that the previously taboo channels, of which there were many, could now be used.

In parallel with this effort, the Advanced Television Systems Committee (ATSC) documented and developed the standard known as the ATSC Digital Television Standard, and it is subsequently developing related implementation standards.

In countries currently using 625-line, 4:3 aspect ratio television systems, plans are being developed to eventually use a 1250-line, 16:9 aspect ratio system, and the ITU-R has worked successfully on harmonizing and providing interoperability between the ATSC and 1250-line systems.

Figure 20 shows the choices by which the signals of the various television standards will reach the consumer. Other articles detail satellite, cable TV, and asynchronous transfer mode (ATM) common carrier networks.

The ATSC and the ITU-R have agreed on a digital terrestrial broadcasting model, which is shown in Fig. 21. Video and audio sources are coded and compressed in separate video and audio subsystems. The compressed video and audio are then combined with ancillary data and control data in a service multiplex and transport, in which form the combined signals are distributed to the terrestrial transmitter. The signal is then channel-coded, modulated, and fed at appropriate power to the transmission antenna. The receiver reverses the process, demodulating the RF signal to the transport stream, and then demultiplexing the audio, video, ancillary, and control data into their separate but compressed modes; and the individual subsystems then decompress the bit streams into video and audio signals that are fed to display screen and speakers, and the ancillary and control data are used if and as appropriate within the receiver.

2.1.2. Information Service Multiplex and Transport System. These subsystems provide the foundation for the digital communication system. The raw digital data are first formatted into *elementary bit streams*, representing image data, sound data, and ancillary data. The elementary

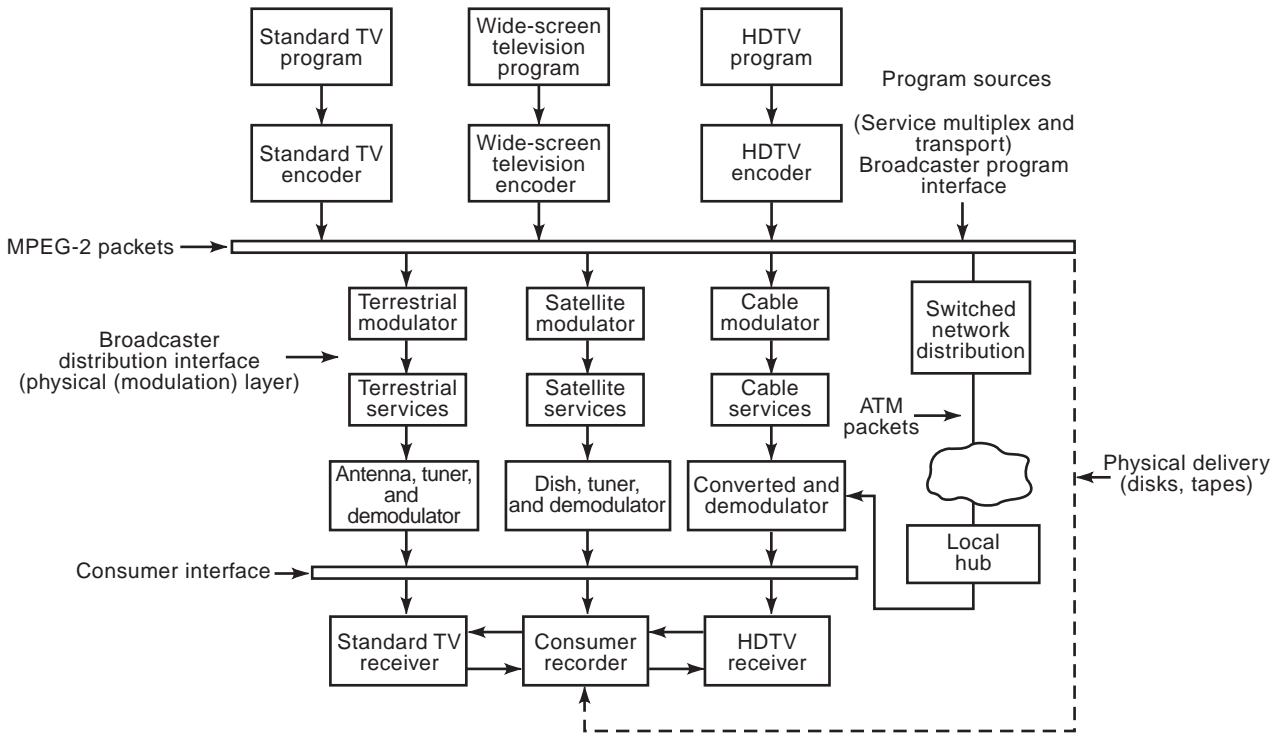


Figure 20. Television service model.

bit streams are then formed into manageable packets of information (*packetized elementary stream, PES*), and a mechanism is provided to indicate the start of a packet (synchronization) and assign an appropriate identification code (*packet identifier, PID*) within a header to each packet. The packetized data are then multiplexed into a *program transport stream* that contains all the information for a single (television) program. Multiple program transport streams may then be multiplexed to form a *system level multiplex transport stream*.

Figure 22 illustrates the functions of the multiplex and transport system and shows its location between the application (e.g., audio or video) encoding function and the

transmission subsystem. The transport and demultiplex subsystem functions in the receiver in the reverse manner, being situated between the RF modem and the individual application decoders.

2.1.2.1. Fixed-Length Packets. The transport system employs the fixed-length transportation stream packetization approach defined by the Moving Picture Experts Group (MPEG), which is well suited to the needs of terrestrial broadcast and cable television transmission of digital television. The use of moderately long, fixed-length packets matches well with the needs for error protection, and it provides great flexibility for initial needs of the ser-

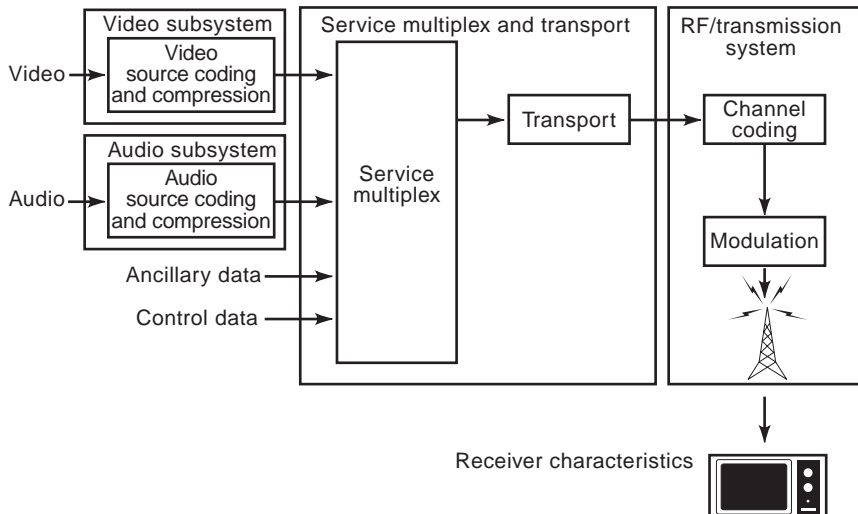


Figure 21. Block diagram showing ATSC and ITU-R terrestrial television broadcasting model.

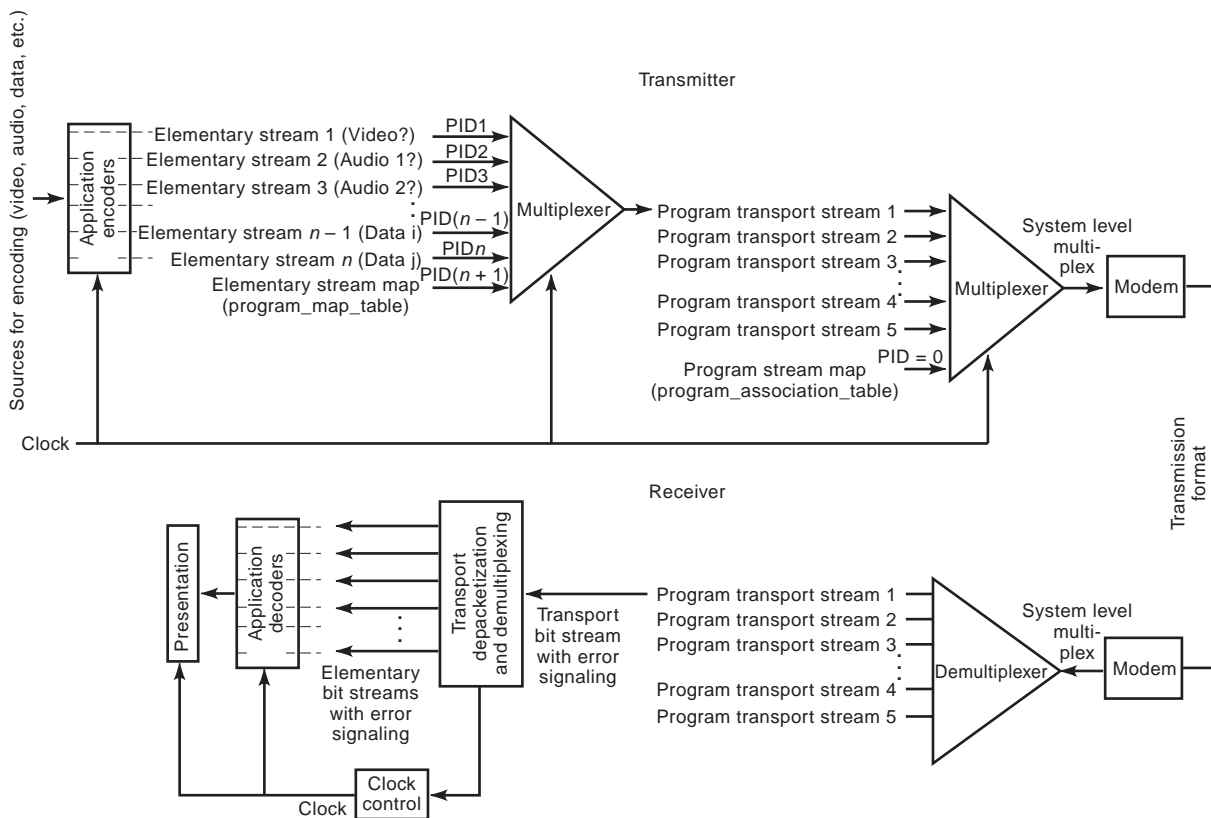


Figure 22. Organization of functionality within a transport system for digital TV programs.

vice to multiplex audio, video, and data, while providing backward compatibility for the future and maximum interoperability with other media (MPEG-based).

2.1.2.2. Packet Identifier. The use of a PID in each packet header to identify the bit stream makes it possible to have a mix of audio, video, and auxiliary data that is not specified in advance.

2.1.2.3. Scalability and Extensibility. The transport format is scalable in that more elementary bit streams may be added at the input of the multiplexer, or at a second

multiplexer. Extensibility for the future could be achieved with no hardware modification by assigning new PIDs for additional elementary bit streams.

2.1.2.4. Robustness. After detecting errors during transmission, the data bit stream is recovered starting with the first good packet. This approach ensures that recovery is independent of the properties of each elementary bit stream.

2.1.2.5. Transport Packet Format. The data transport packet format, as shown in Fig. 23, is based on fixed

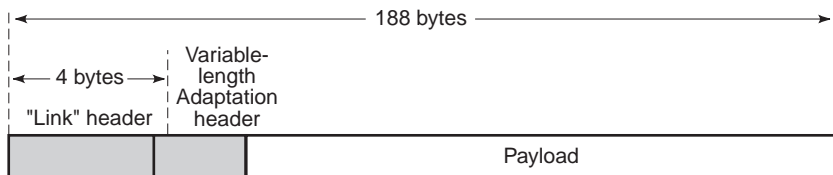


Figure 23. Transport packet format.

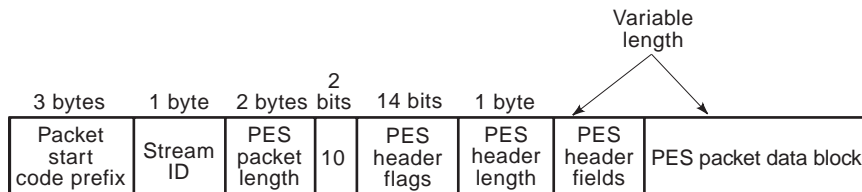


Figure 24. Structural overview of packetized elementary stream (PES) packet.

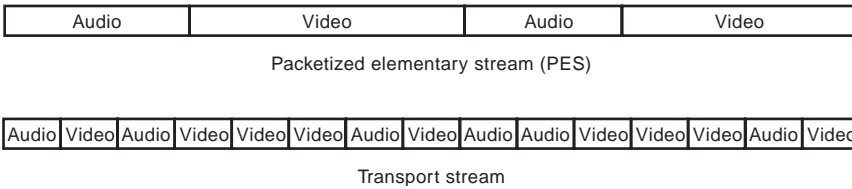


Figure 25. Variable-length PES packets and fixed-length transport packets.

length packets (188 bytes) identified by a variable-length header including a sync byte and the PID. Each header identifies a particular application bit stream (elementary bit stream) that forms the payload of the packet. Applications include audio, video, auxiliary data, program and system control information, and so on.

2.1.2.6. PES Packet Format. The elementary bit streams are themselves wrapped in a variable-length packet structure called the packetized elementary stream (PES) before transport processing. See Fig. 24. Each PES packet for a particular elementary bit stream then occupies a variable number of transport packets, and data from the various elementary bit streams are interleaved with each other at the (fixed length) transport packet layer. New PES packets always start a new transport packet, and stuffing bytes (i.e., null bytes) are used to fill partially filled transport packets.

2.1.2.7. Channel Capacity Allocation. The entire channel capacity can be reallocated to meet immediate service needs. As an example, ancillary data can be assigned fixed amounts depending on a decision made as to how much to allocate to video; or if the data transmission time is not

critical, then it can be sent as *opportunistic data* during periods when the video channel is not fully loaded.

Figure 25 illustrates how the variable-length PES packets relate to the fixed-length transport packets.

The transport system provides other features, including decoder synchronization, conditional access, and local program insertion. Also, issues relating to the storage and playback of programs are addressed, and the appropriate hooks are provided to support the design of consumer digital products based on recording and playback of these bitstreams, including the use of “trick modes” such as slow motion and still frame, typical of current analog video cassette recorders (VCRs).

2.1.2.8. Local Program Insertion. This feature is extremely important to permit local broadcast stations to insert video, audio, or data that is unique to that station. As shown in Fig. 26 to splice local programs, it is necessary to extract (by demultiplexing) the transport packets, identified by the PIDs of the individual elementary bit streams, which make up the program that is to be replaced, including the *program map table*, which identifies the individual bit streams that make up the program. Program insertion can then take place on an individual PID basis, using the fixed-length transport packets.

2.1.2.9. Presentation Time Stamp and Decoding Time Stamp. These time stamps both occur within the header of the PES packet, and they are used to determine when the data within the packet should be read out of the decoder. This process ensures the correct relative timing of the various elementary streams at the decoder relative to the timing at which they were encoded.

2.1.2.10. Interoperability With ATM. The MPEG-2 transport packet size (188 bytes) is such that it can easily be partitioned for transfer in a link layer, which supports asynchronous transfer mode (ATM) transmission (53 bytes per cell). The MPEG-2 transport layer solves MPEG-2 presentation problems and performs the multimedia multiplexing function, whereas the ATM layer solves switching and network adaptation problems.

2.1.3. Video Systems

2.1.3.1. Compressed Video. Compression in a digital HDTV system is required because the bit rate required for an uncompressed HDTV signal approximates 1 Gbps (with the luminance/chrominance sampling already compressed to 4:2:2 mode). The total transmitted data rate in the ATSC digital television standard over a 6 MHz channel is approximately 19.4 Mbps. A compression ratio of 50:1 or greater is therefore required.

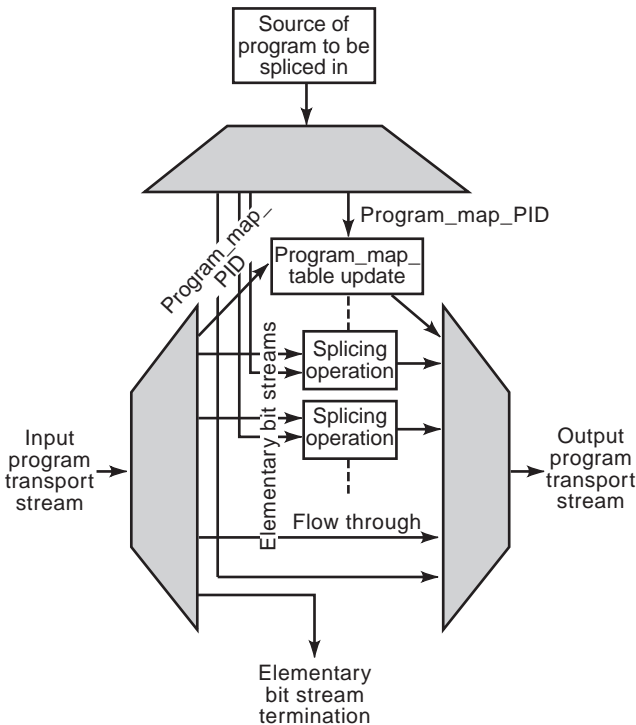


Figure 26. Example of program insertion architecture.

The ATSC Digital Television Standard specifies video compression using a combination of compression techniques that for compatibility conform to the algorithms of MPEG-2 Main Profile, High Level.

The goal of the compression and decompression process is to produce an approximate version of the original image sequence, such that the reconstructed approximation is imperceptibly different from the original for most viewers, for most images, and for most of the time.

2.1.3.2. Production Formats. A range of production format video inputs may be used. These include the current NTSC format of 483 active lines, 720 active samples/line, 60 fields, 2:1 interlaced scan (60I), the Standard Definition format of 480 active lines, 720 active samples/line, 60 frames progressive scan (60P), and high-definition formats of 720 active lines, 1280 active samples/line, 60P, or 1080 active lines, 1920 active samples/line, 60I.

2.1.3.3. Compression Formats. A large range of 18 compression formats is included to accommodate all of the above production formats. The 30P and 24P formats are included primarily to provide efficient transmission of film images, associated with the above production formats. The VGA graphics format is also included at 480 lines and 640 pixels (see below for pixel definition). Details of these compression formats are found in Table 7.

2.1.3.4. Colorimetry. The Digital Television Standard specifies SMPTE 274 M colorimetry (same as ITU-R BT.709, 1990) as the default, and preferred, colorimetry. This defines the color primaries, transfer characteristics, and matrix coefficients.

2.1.3.5. Sample Precision. After preprocessing, the various luminance and chrominance samples will typically be represented using 8 bits per sample of each component.

2.1.3.6. Film Mode. In the case of 24 fps film that is sent at 60 Hz rate using a 3:2 pull-down operation, the processor may detect the sequences of three nearly identical pictures followed by two nearly identical pictures and may only encode the 24 unique pictures per second that existed in the original film sequence. This avoids sending redundant information and permits higher quality transmission. The processor may detect similar sequencing for

30 fps film and may only encode the 30 unique pictures per second.

2.1.3.7. Color Component Separation and Processing. The input video source to the video compression system is in the form of RGB components matrixed into luminance (Y) (intensity or black-and-white picture) and chrominance (C_b and C_r) color-difference components, using a linear transformation. The Y, C_b , and C_r signals have less correlation with each other than R, G, and B and are thus easier to code. The human visual system is less sensitive to high frequencies in the chrominance components than in the luminance components. The chrominance components are lowpass-filtered and subsampled by a factor of two in both horizontal and vertical dimensions (4:2:0 mode) (see Section 1.9).

2.1.3.8. Representation of Picture Data. Digital television uses digital representation of the image data. The process of digitization involves sampling of the analog signals and their components, in a sequence corresponding to the scanning raster of the television format, representing each sample with a digital code.

2.1.3.9. Pixels. The individual samples of digital data are referred to as picture elements, or “pixels” or “pels.” When the ratio of active pixels per line to active pixels per frame is the same as the aspect ratio, the format is said to have “square pixels.” The term refers to the spacing of samples, not to the shape of the pixel.

2.1.3.10. Blocks, Macroblocks, and Slices. For further processing, pixels are organized into blocks of 8×8 , representing either luminance or chrominance information. Macroblocks consist of four blocks of luminance (Y) and one each of C_b and C_r . Slices consist of one or more macroblocks in the same row, and they begin with a slice start code. The number of slices affects compression efficiency; a larger number of slices provides for better error recovery but uses bits that could otherwise be used to improve picture quality. The slice is the minimum unit for resynchronization after an error.

2.1.4. Removal of Temporal Information Redundancy: Motion Estimation and Compensation. A video sequence is a series of still pictures shown in rapid succession to give

Table 7. ATSC Compression Formats: A Hierarchy of Pixels and Bits

Active Lines	Pixels per Line	Total Pixels per Frame	Uncompressed Payload Bit Rate in Mbps (8-bit 4:2:2 sampling) at Picture (Frame) Rate				Aspect Ratio and Notes
			60P	60I	30P	24P	
1080	1920	2,073,600	Future	995	995	796	16:9 only
720	1280	921,600	885	—	442	334	16:9 only
480	704	337,920	324	162	162	130	16:9 & 4:3
480	640	307,200	295	148	148	118	4:3 only (VGA)
Vertical Resolution	Horizontal Resolution	Higher	← → Temporal Resolution		Lower		

Source: Data courtesy of Patrick Griffis, Panasonic, NAB, 1998.

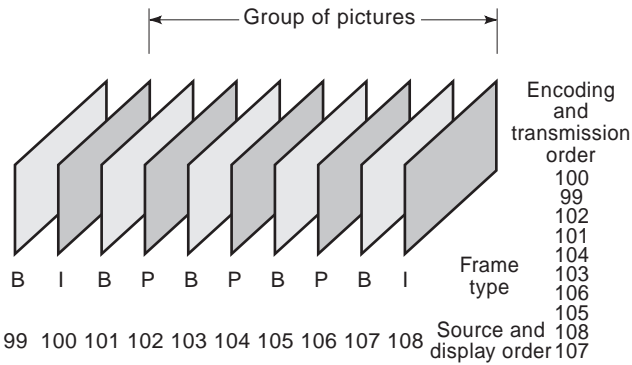


Figure 27. Video frame order, group of pictures, and typical I-frames, P-frames, and B-frames.

the impression of continuous motion. This usually results in much temporal redundancy (picture sameness) among the adjacent pictures. Motion compensation attempts to delete this temporal redundancy from the information transmitted. In the standard, the current picture is predicted from the previously encoded picture, estimating the motion between the two adjacent pictures and compensating for the motion. This “motion-compensated residual” is encoded rather than the complete picture, eliminating repetition of the redundant information.

2.1.4.1. Pictures, Groups of Pictures, and Sequences. The primary coding unit of a video sequence is the individual video frame or picture, which consists of the collection of slices constituting the active picture area. A video sequence consists of one or more consecutive pictures, and it commences with a sequence header, which can serve as an entry point.

One or more pictures or frames in sequence may be combined into a group of pictures (GOP), optional within MPEG-2 and the ATSC Standard, to provide boundaries for interpicture coding and registration of time code.

Figure 27 illustrates a time sequence of video frames consisting of intracoded pictures (I-frames), predictive coded pictures (P-frames), and bidirectionally predictive coded pictures (B-frames).

2.1.4.2. I-, P-, and B-Frames. Frames that do not use any interframe coding are referred to as I-frames (where I

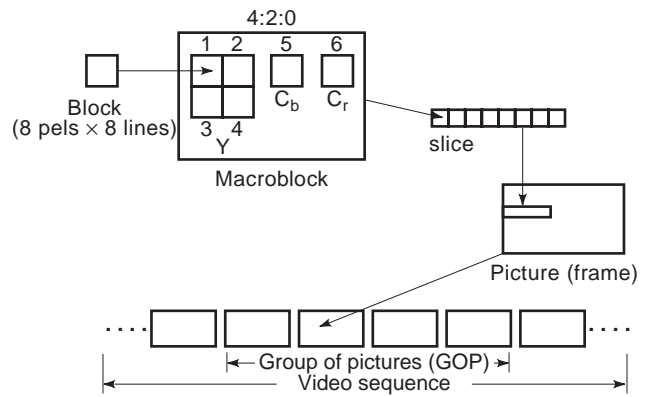


Figure 28. Video structure hierarchy.

denotes intraframe coded). All the information for a complete image is contained within an I-frame, and the image can be displayed without reference to any other frame. (The preceding frames may not be present or complete for initialization or acquisition, and the preceding or following frames may not be present or complete when noncorrectable channel errors occur.)

P-frames (where P denotes predicted) are frames where the temporal prediction is in the forward direction only (formed only from pixels in the most recently decoded I- or P-frame). Interframe coding techniques improve the overall compression efficiency and picture quality. P-frames may include portions that are only intraframe-coded.

B-frames (where B denotes bidirectionally predicted) include prediction from a future frame as well as from a previous frame (always I- or P-frames). Some of the consequences of using future frames in the prediction are as follows: The transmission order of frames is different from the displayed order of frames, and the encoder and decoder must reorder the video frames, thus increasing the total latency. B-frames are used for increasing compression efficiency and perceived picture quality.

Figure 28 illustrates the components of pictures as discussed above.

2.1.5. Removal of Spatial Information Redundancy: The Discrete Cosine Transform. As shown in Fig. 29, 8 × 8 blocks of spatial intensity showing variations of luminance and chrominance pel information are converted

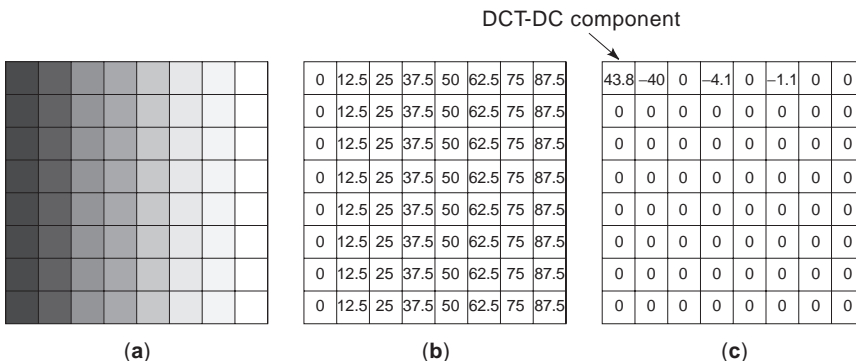


Figure 29. Discrete cosine transform.

into 8×8 arrays of coefficients relating to the spatial frequency content of the original intensity information. The transformation method used is the discrete cosine transform (DCT).

As an example, in Fig. 29(a), an 8×8 pel array representing a black-to-white transition is shown as increasing levels of a gray scale. In Fig. 29(b), the gray-scale steps have been digitized and are represented by pel amplitude numerical values. In Fig. 29(c), the gray-scale block is represented by its frequency transformation coefficients, appropriately scaled. The DCT compacts most of the energy into only a small number of the transform coefficients. To achieve a higher decorrelation of the picture content, two-dimensional (along two axes) DCT coding is applied. The (0,0) array position (top left) represents the DC coefficient or average value of the array.

2.1.6. Quantizing the Coefficients. The goal of video compression is to maximize the video quality for a given bit rate. Quantization is a process of dividing the coefficients by a value of N , which is greater than 1, and rounding the answer to the nearest integer value. This allows scaling the coefficient values according to their importance in the overall image. Thus high-resolution detail to which the human eye is less sensitive may be more heavily scaled (coarsely coded). The quantizer may also include a dead zone (enlarged interval around zero) to core to zero small noise-like perturbations of the element value. Quantization in the compression algorithm is a lossy step (information is discarded that cannot be recovered).

2.1.7. Variable Length Coding, Codeword Assignment. The quantized values could be represented using fixed-length codewords. However, greater efficiency can be achieved in terms of bit rate, by employing what is known as entropy coding. This attempts to exploit the statistical properties of the signal to be encoded. It is possible to assign a shorter codeword to those values occurring more frequently and a longer codeword to those occurring less frequently. The Morse code is an example of this method.

One optimal codeword design method, the Huffman Code, is used in the Standard. It will be noted that many zero-value coefficients are produced, and these may be prioritized into long runs of zeros by zigzag scanning or a similar method.

2.1.8. Channel Buffer. Motion compensation, adaptive quantization, and variable-length coding produce highly variable amounts of compressed video data as a function of time. A buffer is used to regulate the variable-input bit rate into a fixed-output bit rate for transmission. The fullness of the buffer is controlled by adjusting the amount of quantization error in each image block (a rate controller driven by a buffer state sensor adjusts the quantization level). Buffer size is constrained by maximum tolerable delay through the system and by cost.

2.1.9. Audio

2.1.9.1. System Overview. The audio subsystem used in the ATSC Digital Television Standard is based on the AC-3 digital audio compression standard. The subsystem can encode from one to six channels of source audio from a pulse-code modulation (PCM) representation (requiring 5.184 Mbps for the 5.1 channel mode) into a serial bit stream at a normal data rate of 384 kbps. The 5.1 channels are left (front), center (front), right (front), left surround (rear), right surround (rear) (all 3 Hz to 20 kHz), and low-frequency subwoofer (normally placed centrally) (which represents the 0.1 channel, 3 Hz to 120 Hz). The system conveys digital audio sampled at a frequency of 48 kHz, locked to the 27 MHz system clock.

In addition to the 5.1 channel input, monophonic and stereophonic inputs and outputs can be handled. Monophonic and stereophonic outputs can also be derived from a 5.1 channel input, permitting backward compatibility.

The audio subsystem, as illustrated in Fig. 30, comprises the audio encoding/decoding function and resides between the audio inputs/outputs and the transport system. The audio encoder(s) is (are) responsible

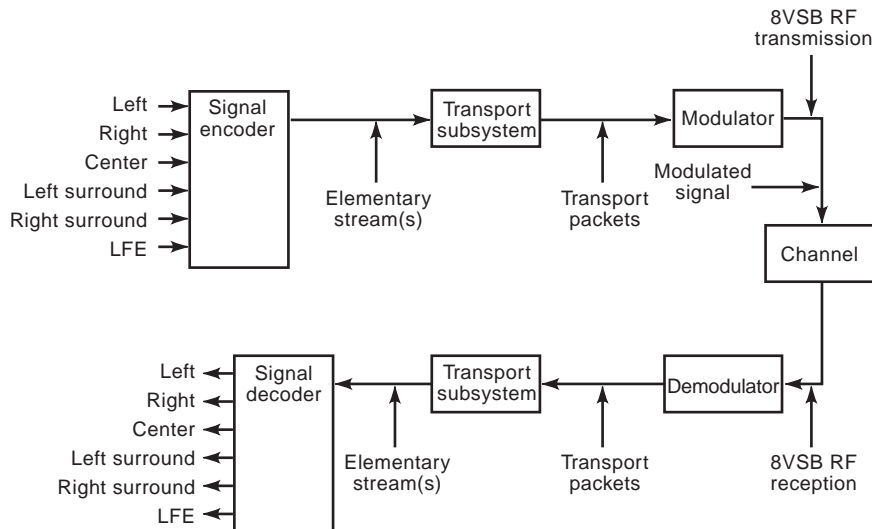


Figure 30. Audio subsystem within the digital television system.

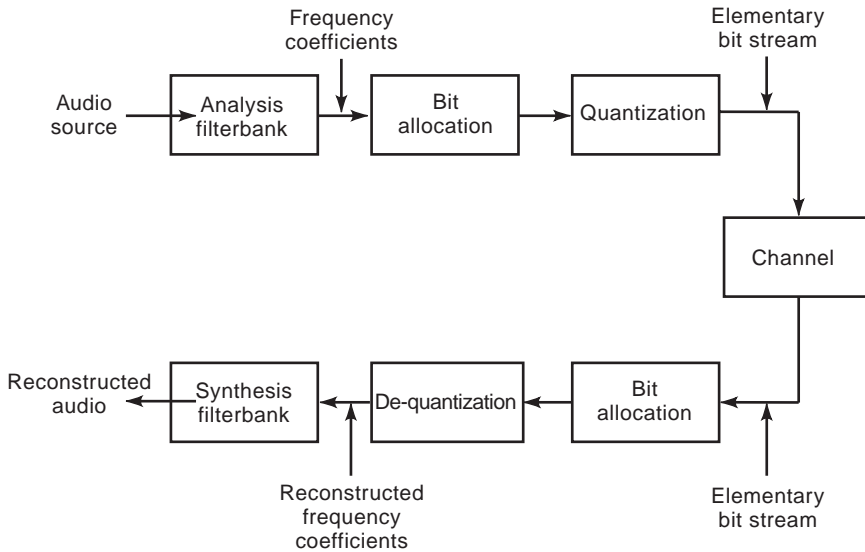


Figure 31. Overview of audio compression system.

for generating the *audio elementary stream(s)*, which are encoded representations of the baseband audio input signals.

The transport subsystem packetizes the audio data into PES packets that are then further packetized into (fixed length) transport packets. The transmission subsystem converts the transport packets into a modulated RF signal for transmission to the receiver. Transport system flexibility allows multiple audio elementary streams to be transmitted.

In the receiver, the encoding, packetization, and modulation process is reversed to produce reconstructed audio.

2.1.9.2. Audio Compression. Two mechanisms are available for reducing the bit rate of sound signals. The first uses statistical correlation to remove redundancy from the bit stream. The second uses the psychoacoustical characteristics of the human hearing system such as spectral and temporal masking to reduce the number of bits required to recreate the original sounds.

The audio compression system consists of three basic operations, as shown in Fig. 31. In the first stage, the representation of the audio signal is changed from the time domain to the frequency domain, which is more efficient in order to perform psychoacoustically based audio compression. The frequency domain coefficients may be coarsely quantized because the resulting quantizing noise will be at the same frequency as the audio signal, and relatively low signal-to-noise ratios (SNRs) are acceptable due to the phenomena of psychoacoustic masking. The bit allocation operation determines what actual SNR is acceptable for each individual frequency coefficient. Finally, the frequency coefficients are coarsely quantized to the necessary precision and formatted into the audio elementary stream.

The basic unit of encoded audio is the AC-3 sync frame, which represents six audio blocks of 256 frequency coefficient samples (derived from 512 time samples), a total of 1536 samples. The AC-3 bit stream is a sequence of AC-3 sync frames.

2.1.9.3. Additional Audio Services. Additional features are provided by the AC-3 subsystem. These include loudness normalization, dynamic range compression with an override for the listener, and several associated services, namely, dialogue, commentary, emergency, voice-over, help for the visually impaired and hearing-impaired (captioning), and multiple languages. Some of these services are mutually exclusive, and multilanguage service requires up to an extra full 5.1 channel service for each language (up to an additional 384 kbps).

2.2. Ancillary Data Services

Several data services have been included in the ATSC Standard. Other services can be added in the future. Currently included are program subtitles (similar to closed captioning in NTSC), emergency messages (mixed into baseband video in NTSC), and program guide information.

2.2.1. Possible Future Data Services. Information data related to the following may be desired: conditional access, picture structure, colorimetry, scene changes, local program insertion, field/frame rate and film pull-down, pan/scan, multiprogram, and stereoscopic image.

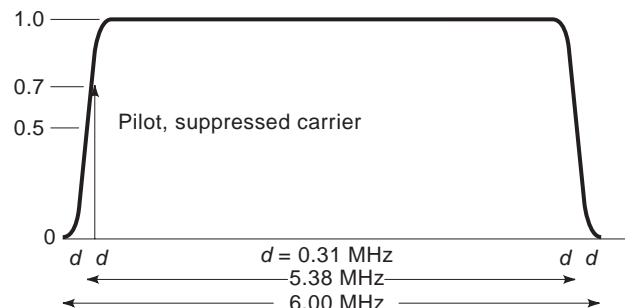


Figure 32. Vestigial sideband (VSB) in 6 MHz channel for digital transmission.

2.2.2. Transmission Characteristics. The transmission subsystem uses a vestigial sideband (VSB) method: (1) 8-VSB for simulcast terrestrial broadcast mode and (2) a 16-VSB high data rate mode. VSB includes a small part of the lower sideband with the full upper sideband. Sloped filtering at the transmitter and/or the receiver attenuates the lower end of the band. The 8-VSB coding maps three bits into one of eight signal levels. The system uses a symbol rate of 10.76 Msymbols/s, capable of supporting a data stream payload of 19.39 Mbits/s. See Fig. 32 VSB in 6-MHz channel.

Modulation techniques for some other planned broadcast systems use orthogonal frequency division multiplexing (OFDM) or coded OFDM (COFDM), which is a form of multicarrier modulation where the carrier spacing is selected, so that each subcarrier within the channel is orthogonal to the other subcarriers, which mathematically ensures that during the sampling time for one carrier, all other carriers are at a zero point.

The 8-VSB subsystem takes advantage of a pilot, segment sync, and a training sequence for robust acquisition and operation. In order to maximize service area, an NTSC rejection filter (in the receiver) and trellis coding are used. The system can operate in a signal-to-additive-white-Gaussian noise (S/N) environment of 14.9 dB. The transient peak power to average power ratio as measured on a low-power transmitted signal with no nonlinearities is no more than 6.3 dB for 99.9% of the time.

A block diagram of a generic transmitter subsystem is shown in Fig. 33. The incoming data (19.39 MB/s) are randomized and then processed for forward error correction (FEC) in the form of Reed–Solomon coding (20 RS parity bits are added to each packet, known as outer error correction). Data interleaving, to reorganize the data stream so that it is less vulnerable to bursts of errors, then interleaves to a depth of about one sixth of a data field (4 ms deep).

The second stage, called inner error correction, consists of a two-thirds rate trellis coding. This encodes one bit of a two-bit pair into two output bits, using a one-half convolutional code, whereas the other input bit is retained as precoded. Along with the Trellis Encoder, the data packets are precoded into data frames and mapped into a signaling waveform using an 8-level (3 bit), one-dimensional constellation (8 VSB). Data Segment Sync (4 symbols = 1 byte) at the beginning of a segment of 828 data

plus parity symbols, and Data Field Sync at the beginning of a data field of 313 segments (24.2 ms), are then added. Data Field Sync includes the training signal, used for setting the receiver equalizer.

A small in-phase pilot is then added to the data signal at a power of 11.3 dB below the average data signal power. The data is then modulated onto an IF carrier, which is the same frequency for all channels. The RF Up-Converter then translates the filtered, flat IF data signal spectrum to the desired RF channel. It is then amplified to the appropriate power for the transmitting antenna.

For the same approximate coverage as an NTSC transmitter (at the same frequency), the average power of the ATV signal is approximately 12 dB less than the NTSC peak sync power.

The frequency of the RF upconverter oscillator will typically be the same as for NTSC (except for offsets). For extreme co-channel situations, precise RF carrier frequency offsets with respect to the NTSC co-channel carrier may be used to reduce interference into the ATV signal. The ATV signal is noise-like, and its interference into NTSC does not change with precise offset.

The ATV co-channel pilot should be offset in the RF upconverter from the dominant NTSC picture carrier by an odd multiple of half the data segment rate. An additional offset of 0, +10 kHz, or –10 kHz is required to track the principal NTSC interferer.

For ATV-into-ATV co-channel interference, precise carrier offset prevents the adaptive equalizer from misinterpreting the interference as a ghost.

2.3. The Japanese High-Definition Television Production System

This television production system was developed by the Japanese Broadcasting Corporation (NHK). It was standardized in 1987 by the Broadcast Technology Association (BTA), now renamed the Association of Radio Industries and Business (ARIB), in Japan and in the United States by SMPTE (240 M and 260 M Standards). It uses a total of 1125 lines (1035 active lines), is interlaced at a field rate of 60 Hz, and has an aspect ratio of 16:9. It requires a bandwidth of 30 MHz for the luminance signal (Y), and 15 MHz for each of the two color difference signals (P_B and P_R). When digitized at 8 bits per sample, it uses 1920 pixels per

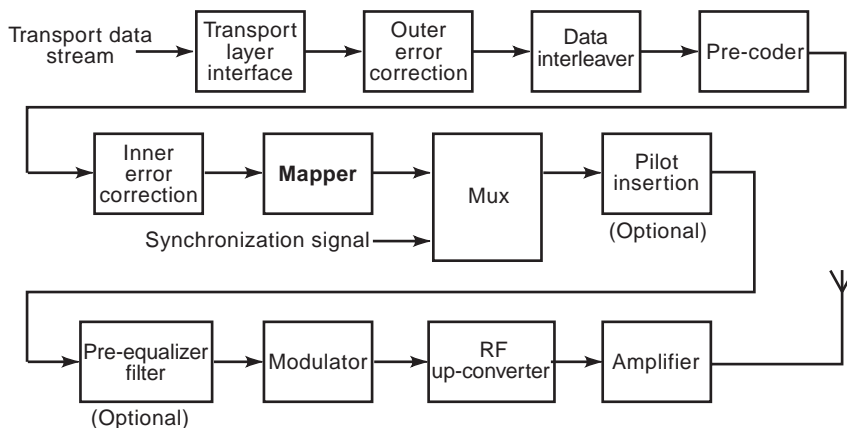


Figure 33. 8-VSB transmitter subsystem block diagram.

Table 8. MUSE Transmission Systems

Transmission System	Type of Transmission	Bandwidth	Channel Compatible	Compatible with NTSC
MUSE	Direct Broadcast by Satellite (DBS)	8.1 MHz	NA	No
MUSE-T	Satellite	16.2 MHz	NA	No
MUSE-6	Terrestrial Broadcast	6 MHz	Yes	Yes
MUSE-9	Terrestrial Broadcast	6 + 3 MHz Augmentation	Yes, with 2nd 3 MHz channel	Yes
MUSE-E	Terrestrial Broadcast	8.1 MHz	No	No

line and it requires a total bit rate of 1.2 Gbps. Note that this production system is similar to the interlaced system used in the ATSC standard, except that the latter uses 1080 active lines.

2.4. Japanese MUSE Transmission Systems

A range of transmission systems were developed by NHK based on the Multiple Sub-Nyquist Encoding (MUSE) transmission scheme (see Table 8). MUSE (8.1 MHz bandwidth) was developed for DBS broadcasting and MUSE-T (16.2 MHz bandwidth) was developed for satellite transmission. MUSE-6 was designed to be compatible with a 6 MHz channel and NTSC receivers. MUSE-9 uses a 3 MHz augmentation channel in addition to the standard 6 MHz channel and is NTSC receiver-compatible.

2.5. Japanese Hi-Vision System

This system incorporates the 1920×1035 television production system and the MUSE-E transmission system. MUSE-E uses an 8.1 MHz bandwidth and is incompatible with standard NTSC receivers and channel allocations. Four audio channels are time-division-multiplexed with the video signals, in the blanking intervals. The encoding and decoding processes are both very complex and require many very large-scale integration (VLSI) chips. This system requires a MUSE-E receiver, or a set-top box equipped with a MUSE decoder feeding either a 16:9 display or a 4:3 aspect ratio conventional receiver. In the near-term, NHK will use simultaneous Hi-Vision/NTSC program production.

The MUSE systems are not receiver-compatible with either the North-American ATSC system or the European DVB system (see below).

2.6. The Japanese Enhanced Definition Television System (EDTV-II)

EDTV-II is an NTSC-compatible letter-box analog transmission system standardized by the ARIB in Japan. The input signal is 525-line, 60-frame progressive scan (525P) with 16:9 aspect ratio. 525-line, 30-frame interlaced scan (525I) can be upconverted as an input signal. Note that the 525P signal is one of the SDTV signal formats defined in the ATSC Standard (720×480 at 60P). It is also defined as a production format in SMPTE 293 M and SMPTE 294 M standards documents.

Compared with the current 525I standard, the frame rate has been doubled from 30 to 60. The sampling frequency in the format has been doubled to 27 MHz, compared with 525I, and the aspect ratio has been changed from 4:3 to 16:9. This increase of sampling frequency permits comparable resolution in H and V axes to be maintained. The production system is effectively an 8:4:4 digital system with production interfaces at 540 Mbps. 4:2:0 can also be used in production and would require interfacing at 360 Mbps. Horizontal blanking is shrunk to achieve this bit rate.

The EDTV-II analog transmission system is used for both terrestrial and satellite broadcasting. It requires the same bandwidth as the NTSC system, and no changes are needed in transmitter implementations. The image is displayed on an EDTV-II receiver in a progressive manner with 480 lines and a 16:9 aspect ratio. It is compatible with existing NTSC receivers, except that the display image is a 16:9 aspect ratio and so appears in a letter-box format with black bars at top and bottom. The 525P signal requires a video bandwidth of approximately 6.2 MHz. The EDTV-II system creates three enhancement signals in addition to an NTSC signal, with which they are then frequency-domain-multiplexed.

2.6.1. Main Picture (MP). The 525P 16:9 signal is reduced from 6.2 MHz to 4.2 MHz bandwidth, and the 480 lines are decimated to 360 lines to produce a letter-box display on the NTSC 4:3 receiver. Black bars, at top and bottom, are each 60 lines wide. Thus, horizontal and vertical resolution are reduced to conform to the NTSC format, but to maintain the 16:9 aspect ratio.

2.6.2. Horizontal High (HH 4.2 MHz to 6.2 MHz). A frequency enhancement signal is extracted from the original 525P image and is multiplexed into the MP signal to increase the horizontal bandwidth to 6.2 MHz in the EDTV-II receiver. For transmission, the HH signal is downshifted to 2 to 4 MHz and frequency-division-multiplexed into an unused vertical temporal frequency domain in the conventional NTSC system called the Fukinuki hole. The Fukinuki hole may only be used for correlated video information, which applies in this case.

In the EDTV-II receiver, a motion detector multiplexes the HH signal only onto the still parts of the picture where there is more need for high resolution to satisfy human vision characteristics. Two enhancement signals are frequency-division-multiplexed together into the top and

bottom panels, which together occupy one third as much area as the main picture. As these are generated in a 360-line format, they must be compressed by a 3 to 1 pixel downsampling decimation process to fit into the 120 lines of the top and bottom panels.

2.6.3. Vertical High Frequency (VH). The VH signal enhances the vertical still picture resolution back up to 480 lines. The signal is transmitted only for stationary areas of the image, and temporal averaging is applied.

2.6.4. Vertical Temporal Frequency (VT). The VT enhancement signal is derived from the progressive-to-interlace scan conversion at the encoder and improves the interlace-to-progressive scan (360/2:1 to 360/1:1) conversion in the receiver.

The EDTV-II receiver performs the reverse of the encoding process. The NTSC receiver uses the MP signal directly.

2.7. The European DVB System

The Digital Video Broadcast (DVB) system has been designed for MPEG-2-based digital delivery systems for satellite, cable, community cable, multichannel multipoint distribution (MMDS), and terrestrial broadcasting. Service information, conditional access, and teletext functions are also available. All DVB systems are compatible.

DVB-T, the terrestrial broadcasting standard, is similar in many respects to the ATSC standard. However, there are several significant differences. DVB-T uses Coded Orthogonal Frequency Division Multiplexing (COFDM). This technique is already being used for Direct Audio Broadcast (DAB). A total of 1704 (2k) or 6816 (8k) individual carriers may be used. The 8k system is more robust, but increases receiver complexity and cost. Some broadcasters have already adopted the 2k system, although it will not be compatible with the 8k system. DVB-T uses the MPEG-2 Layer II Musicam audio standard, a 50 Hz frame rate, and aspect ratios of 4:3, 16:9, or 20:9.

2.8. The European PALplus System

This is an analog delivery system that uses a current TV channel to transmit an enhanced widescreen version of the PAL signal. A conventional receiver displays the PALplus picture as a letter-box in a 4:3 aspect ratio. A widescreen receiver shows the same transmitted picture in a 16:9 format with higher resolution. European broadcasters are divided on whether to use this format. The PALplus concept is closely similar to the Japanese EDTV-II format, described above.

Acknowledgment

The authors wish to sincerely thank the following for permission to use portions of their work in this article:

- The Advanced Television Systems Committee (ATSC) and its Executive Director, Craig Tanner, for text and figures from Standards A/52, A/53, and A/54.

- Mr. Stanley N. Baron, for text and figures from his book *Digital Image and Audio Communications, Toward a Global Information Infrastructure*.
- Mr. Patrick Griffis, for the data in a figure from his article Bits = Bucks, Panasonic, paper presented at NAB, 1998, unpublished.

FURTHER READING

- M. Ashibe and H. Honma, A wide-aspect NTSC compatible EDTV system, *J. SMPTE*, :130 (1992).
- ATSC Digital Television Standard, Advanced Television Systems Committee, Doc. A/53, September, 1995.
- S. N. Baron, ed., *Composite Digital Television: A Primer*, White Plains, NY: Soc. of Motion Picture and Television Eng., 1996.
- S. N. Baron and M. I. Krivocheev, *Digital Image and Audio Communications, Toward a Global Information Infrastructure*, New York: Van Nostrand Reinhold, 1996.
- K. B. Benson, ed., *Television Engineering Handbook*, revised by J. Whitaker, New York: McGraw-Hill, 1992.
- Digital Audio Compression Standard (AC-3), Advanced Television Systems Committee, Doc. A/52, December, 1995.
- A. Dubec, *The SECAM Colour Television System*, Paris: Compagnie Française de Télévision, 1976.
- P. Griffis, Bits = Bucks, Panasonic, paper at NAB, 1998.
- Guide to the Use of the ATSC Digital Television Standard, Advanced Television Systems Committee, Doc. A/54, October, 1995.
- A. Itoh, 525 line progressive scan signal digital interface standard and system, *J. SMPTE*, :768 (1997).
- R. W. G. Hunt, *The Reproduction of Colour*, 5th ed., Kingston-upon-Thames: Fountain Press, 1995.
- G. Hutson, P. Shepherd, and J. Brice, *Colour Television*, London: McGraw-Hill, 1990.
- A. F. Inglis and A. C. Luther, *Video Engineering*, 2nd ed., New York: McGraw-Hill, 1996.
- ISO/IEC IS 13818-1, International Standard MPEG-2 Systems, 1994.
- ISO/IEC IS 13818-2, International Standard MPEG-2 Video, 1994.
- ISO/IEC IS 13818-2, Section 8, 1994.
- ITU-R BT.470-4, Characteristics of television systems, Geneva: International Telecommunications Union, 1995.
- ITU-R Document/(com), 11-3/15, MPEG digital compression systems, August, 1994.
- K. Jack, *Video Demystified*, 2nd ed., San Diego, CA: HighText Interactive, 1996.
- K. Jackson and B. Townsend, eds., *TV & Video Engineer's Reference Book*, Oxford, UK: Butterworth-Heinemann, 1991.
- H. Y. Kim and S. Naimpally, Digital EDTV, compatible HDTV, *J. SMPTE*, :119(1993).
- B. Marti et al., Problems and perspectives of digital terrestrial TV in Europe, *J. SMPTE*, :708(1993).
- R. Mäusl, *Refresher Topics—Television Technology*, Munich: Rohde & Schwarz, 1992.
- R. S. O'Brien, ed., *Color Television, Selections from the Journal of the SMPTE*, New York: Society of Motion Picture and Television Engineers, 1970.
- G. Pensing, ed., *4:2:2 Digital Video Background and Implementation*, White Plains, NY: Society of Motion Picture and Television Engineers, 1989.

- D. H. Pritchard and J. J. Gibson, Worldwide color television standards—similarities and differences, *J. Soc. Motion Picture and Television Eng.*, **89**:111–120, (1980).
- Proc. IRE, Color Television Issue*, **39**(10):(1951).
- V. Reimer, Advanced TV systems, Germany and Central Europe, *J. SMPTE*, :398 (1995).
- M. Robin, Addendum to Worldwide color television standards—similarities and differences, *J. Soc. Motion Picture and Television Eng.*, **89**:948–949 (1980).
- M. Robin and M. Poulin, *Digital Television Fundamentals*, New York: McGraw-Hill, 1997.
- T. Rzeszewski, ed., *Color Television*, New York: IEEE Press, 1983.
- T. S. Rzeszewski, ed., *Television Technology Today*, New York: IEEE Press, 1984.
- H. V. Sims, *Principles of PAL Colour Television and Related Systems*, London: Newnes Technical Books, 1969.
- SMPTE 274 M Standard for Television, 1920 × 1080 Scanning and Interface, 1995.
- SMPTE S17.392 Proposed Standard for Television, 1280 × 720 Scanning and Interface, 1995.
- V. Steinberg, *Video Standards, Signals, Formats, and Interfaces*, Durford Mill, UK: Snell & Wilcox, 1997.
- N. Suzuki et al., Matrix conversion VT resolution in letterbox, *J. SMPTE*, :104 (1991).
- N. Suzuki et al., Experiments on proposed multiplexing scheme for vertical-temporal and vertical high helper signals in EDTV-II, *J. SMPTE*, :728 (1994).
- Television Operating and Interface Standards, Society of Motion Picture and Television Engineers, 595 W. Hartsdale Ave., New York, NY 10607-1824.
- Television Measurements Standards, Institute of Electrical and Electronic Engineers, Inc., Broadcast Technology Society, c/o IEEE Service Center, 445 Hoes Lane, Box 1331, Piscataway, NJ 08855.
- J. Watkinson, *Television Fundamentals*, Oxford, UK: Focal Press, 1996.

represent a fusion of ones commonly used in each realm, thus allowing the possibility to take the best of both. This common feature appears time and again in the Terahertz domain where technologists selectively adopt concepts from the optical community and use them alongside those taken from the microwave world.

Since we have become accustomed to think of waves of electrical energy and light waves as forming parts of a common spectrum, the attempt has often been made to extend our knowledge over the wide region which has separated the two phenomena, and to bring them closer together... [1]

This seminal statement characterizes precisely a revolution that is taking place now, more than 100 years after the recognition by Rubens and Nichols of a fundamental quandary [2]: Electromagnetic waves form a continuous spectrum, starting at the microwave region through the optical, ultraviolet, and X-ray region. Nevertheless, our possibilities to access certain regions of this spectrum are limited by fundamental and technological reasons, which leads to “gaps,” i.e., restrictions, for the widespread and practical use of radiation with certain frequencies. One such breach is associated with the transition region from microwave to optics, now recognized as the Terahertz region.

This long-standing gap in the spectrum is loosely defined as that between 100 GHz and 10 THz, which is equivalent to radiation with a wavelength of 30–3000 μm, associated with energies in the range of 0.4–40 meV. In this region of the electromagnetic spectrum, a fundamental change occurs in the way electromagnetic waves are generated and detected.

Electromagnetic radiation is associated with coupled and temporally varying electric $\vec{E}(t)$ and magnetic fields $\vec{H}(t)$. Analyzing Maxwell’s second equation, i.e., Ampere’s law [3]:

$$\nabla \times \vec{H} = \vec{j} + \frac{\partial \vec{D}}{\partial t}, \quad (1)$$

it can be seen that temporally varying magnetic fields can only be driven by two types of fundamentally different source terms, as evident from the two right-hand terms, which are the electric current density \vec{j} and the electric displacement \vec{D} . They represent different approaches to the generation of electromagnetic radiation. The first term is the dominant approach used at low “microwave” frequencies using the motion of electronic charges to generate radiation. This method was adopted already in the early days of electromagnetism [4]. By creating temporally varying currents, it was possible to produce the emission of electromagnetic radiation. Alternatively, at optical and infrared wavelengths, sources of radiation are associated with dipolar transitions [5], specifically electronic transitions, occurring within atoms or molecules. In modern times, interest in Terahertz photonics has increased, because inverted dipolar transitions make stimulated emission possible and so allow amplification of optical radiation, which, in turn, leads to the realization of coherent electromagnetic sources or, as they are better known, lasers [6].

These two fundamentally different approaches to the generation of electromagnetic radiation have led to

TERAHERTZ SCIENCE, ENGINEERING AND SYSTEMS—FROM SPACE TO EARTH APPLICATIONS

PETER DE MAAGT
European Space Research and
Technology Centre (ESTEC)
The Netherlands

PETER HARING BOLIVAR
University of Siegen
Germany

CHRIS MANN
Rutherford Appleton Laboratory
United Kingdom

Terahertz (THz), or 10^{12} Hz electromagnetic radiation lies between the infrared and microwave regions of the electromagnetic spectrum. The THz domain comprised the millimeter wave, submillimeter wave, and far infrared regions. Because this frequency range falls in between the more established domains of microwave and optics, the technologies used to access the THz frequency range

mature technology for diverse applications at both microwave (electrical) and infrared (optical) frequencies; however, both encounter fundamental difficulties when accessing the Terahertz range of the electromagnetic spectrum.

From the microwave perspective, the generation of high-frequency time-varying currents becomes difficult to control because of the parasitic effects of the miniature circuit structures combined with the exponential increase in electrical loss as the electrical current becomes restricted to the skin depth. For Terahertz circuitry to operate successfully, a simple rule holds true. As the frequency is increased, the area of the circuit must decrease as the square of the increase in frequency and the cube in volume. Consequently, from a power perspective, levels available rapidly drop with the increase in frequency from watts in the millimeter region to milliwatts in the Terahertz region.

Fortunately, this rule of thumb does not affect detector sensitivity to the same extent. In general, the size of the intrinsic detector is small compared with the wavelength of operation, and only small currents exist within the device. As a result, a relatively moderate degradation is experienced with increasing frequency.

In spite of the difficulties encountered in realizing microwave Terahertz circuits, many advances have recently occurred, which have been mainly achieved with the adoption of improved semiconductor processing capability, use of accurate design tools, and novel Micro-Electro-Mechanical Systems (MEMS) circuit engineering. As a result, increasing levels of power and bandwidth have been achieved from solid-state sources. Similarly, broad-band, very high sensitivity detectors have been demonstrated by a number of workers.

From the optical viewpoint, efficient sources of radiation are traditionally associated with solid-state lasers, which require the population inversion of an electronic transition, i.e., more electrons in an upper state than in a lower lying state of a dipolar transition. For Terahertz wavelengths, where a comparatively small energy spacing exists between lasing transitions, inversion is much harder to achieve. It is therefore difficult to realize Terahertz lasers and alternative methods to generate Terahertz radiation by optical means, like photomixing, have been necessary to circumvent this problem. Recently, however, the first quantum cascade lasers operating in the Terahertz frequency range have been realized but only at low temperatures. Complex materials processing (molecular beam epitaxy) is required to manufacture the artificial bandgap structures required to achieve population inversion. Although the fabrication process is complex, it provides many degrees of freedom for optimization, and rapid progress is to be expected.

As a result of these and other breakthroughs in technology, the Terahertz region is finally finding applications outside the traditional heartland of remote sensing and radio astronomy. Extensive research in the last few years has identified many attractive new application areas (see Fig. 1) and paved the technological path toward broadly usable Terahertz systems for everyday applications. Consequently, the Terahertz gap may be close to being bridged.

1. DRIVING FORCE

Research has been carried out in the Terahertz region for several decades (for an historical overview see [2]). However, until recently, work was limited to basic research or applications such as radio astronomy, planetary/cometary science, and atmospheric science. In the terrestrial domain, plasma diagnostics provided a thrust. In fact, without these driving influences, it is unlikely that many of the recent technological breakthroughs would have occurred.

Astronomy and remote sensing of the earth's atmosphere has provided a powerful incentive for the development of Terahertz technology. The photon energy level associated with Terahertz radiation is low when compared with optical photons. Optical photons are emitted when electrons change energy states during relaxation, e.g., from a conduction band to a valence band in a semiconductor or between atomic states in atoms. By comparison, Terahertz photons are emitted when a molecule change its thermal, rotational, or bending state. Correspondingly, the energies involved are 100–1500 times smaller, making their detection that much more difficult. However, although optical spectroscopy provides information as to the atomic composition of materials, Terahertz spectroscopy provides information regarding the molecular concentration as well as its physical condition, i.e., heat, pressure, speed, etc., in the region being measured. It is for this reason that radio astronomers, planetologists, and atmospheric scientists have undertaken so much work. By studying the Terahertz radiation emitted or absorbed by a gaseous region, it is possible to investigate chemical and physical processes in places where instrumentation cannot be sent and thereby obtain valuable insight into the processes and mechanisms involved.

Although space-based remote sensing still remains the dominant scientific application, Terahertz technology is also now expanding its usage into more everyday areas. Extensive research in the last years has identified numerous potential applications, and this paved the technological path toward more readily usable Terahertz systems.

2. APPLICATIONS PAST AND PRESENT

2.1. Space Applications

The requirements of the radiometric measurements desired for astronomy and remote environmental sensing has, in general, meant that space instrumentation has pushed technology toward operation at the highest frequencies and sensitivities. It is therefore sensible to start the applications sections with an overview of space-related developments.

Several Earth observation and space science missions, employing Terahertz frequency instruments, have been developed in the past and many more are planned for the future [13,14]. These instruments have many commonal-

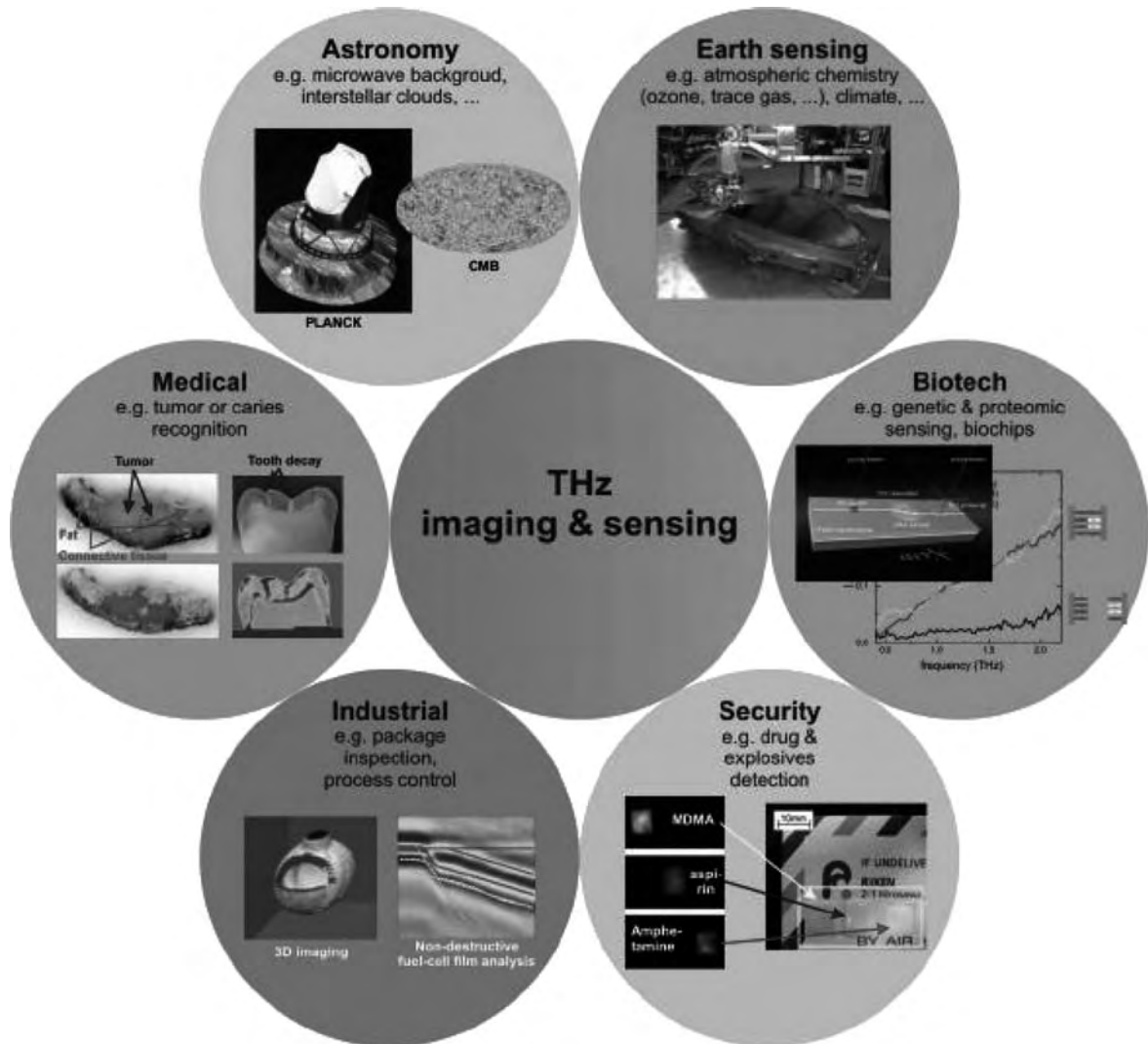


Figure 1. Illustration of some exemplary applications of Terahertz radiation. Illustrations taken from work performed at European Space Agency (astronomy and earth sensing), at Univ. of Frankfurt and Teraview Ltd. [7,8], RWTH Aachen and Rensselaer Polytechnic Inst. (industrial; [9,10]), Riken (security;[11]) and RWTH Aachen [12]. (This figure is available in full color at <http://www.mrw.interscience.wiley.com/erfme>.)

ities in their design and construction techniques, and they all make use of state-of-the-art Terahertz technology to achieve the ambitious goals of future missions in terms of resolution, sensitivity, and frequency of operation. Added to this is the requirement for low mass, power, and reliability.

Although the basic architectures of the instruments are similar, applications and status of technologies vary widely over the frequency range: The lower end of the spectrum is routinely used for communications, including satellite communications, and several commercial and military (terrestrial) applications have emerged at millimeter waves up to 100 GHz. In contrast, the highest frequencies are used mainly for scientific programs, in both space and terrestrial applications.

As a consequence, the maturity and availability of technologies in this frequency range decreases directly with the wavelength.

As a result of the potential commercial applications at lower Terahertz frequencies, all the technological ingredients are rapidly becoming available, and cost effectiveness becomes a driver. This is in contrast to the higher frequencies, where many of the technology elements may be missing or immature.

The emergence of large-volume markets (such as secure communications links, radars, anticollision car radars, short-distance radiolinks, and wireless local area networks) has provided the market pull for the development of mm-wave electronics. Although their suitability for space applications still needs to be demonstrated,

semiconductor devices and MMICs are commercially available at frequencies below 100 GHz, which can be considered today as the upper frequency limit of “commercial” microwave electronics.

However, changes will occur in the near future because of technology needs of optical communications. Globally, an ever-increasing need exists for more bandwidth. Even during the present slowdown in the telecommunications markets, Internet traffic is growing by 100% per year. This need for bandwidth can be satisfied with optical fiber in fixed networks. A single fiber can carry a bandwidth of over 1 THz (using Wavelength-Division Multiplex), but the bandwidth of the electronic interface creates the bottleneck. Consequently, faster mm-wave circuits are being developed. Optical systems at 40 Gbit/s are commercially available, 80 Gbit/s systems are under development, and 160 Gbit/s systems are being planned. As a result, this development will drive mm-wave technologies, including semiconductor devices, to frequencies well above 100 GHz, offering new prospects also for the space applications of millimeter-wave electronics.

Radio astronomy has also been a major driver for the development of Terahertz technology [15–18]. Here, however, the absolute requirement for the lowest noise receivers has led to the development of superconducting systems. Observations over the whole electromagnetic spectrum are required, e.g., in order to test different cosmological theories of the evolution of the Universe (see Fig. 2). As a result of the masking effect of the atmosphere, space observatories are considered as being of prime importance. Future planned instruments will open up this virtually unexplored part of the spectrum that cannot be observed from the ground.

Another space application for Terahertz sensors is in planetary and small-body (asteroids, moons, and comets) observations. To date, little heritage in planetary and cometary instruments and space-based observations utilizing (sub)millimeter-wave frequencies exists. However, planetary and cometary targets have been identified for which this type of instrument offers the opportunity for

significant scientific progress in the medium term. Surface-based (landers) or orbital remote sensing observations of gaseous species in the Venutian, Martian, and Jovian atmospheres, as well as around Europa and Titan, have all been proposed. The instruments should be able to provide information on composition, temperature, pressure, and gas velocity (winds) that will provide a wealth of information.

It has also resulted in the first such instrument: MIRO (Microwave Instrument for the Rosetta Orbiter) [19], launched on the ESA cornerstone mission Rosetta [20] in March 2004, and scheduled to reach its target comet (Churyumov–Gerasimenko) nucleus and of the cruise target asteroids in 2014.

In Earth observation, Terahertz instruments are often used in synergy with optical and infrared sensors. Vertical profiles of temperature and humidity of the atmosphere are conveniently determined from meteorological satellites using passive millimeter-wave sounders operating at specific spectral lines of high atmospheric attenuation (e.g., at 60 and 183 GHz). Remote sensing of the surface of the Earth is possible from a satellite even under cloudy or foggy conditions at window frequencies, which are not affected by the atmosphere or adverse weather conditions. Millimeter waves are especially useful for the imaging of ocean winds, sea ice, and snow, whereas ice clouds are best observed with sub-mm instruments.

Furthermore, there are several very important processes taking place in the atmosphere, [21,22] such as the greenhouse effect and ozone depletion. A growing need exists to better understand the possible detrimental effects of man’s activities on climate. The most effective way to correlate these interactions is to perform high-precision spaceborne global measurements of the composition of the atmosphere. Spectral lines at millimeter and sub-millimeter frequencies allow the use of radiometers for the determination of concentrations of, e.g., Ozone and other trace gases, such as CFCs, that are affecting its concentration.

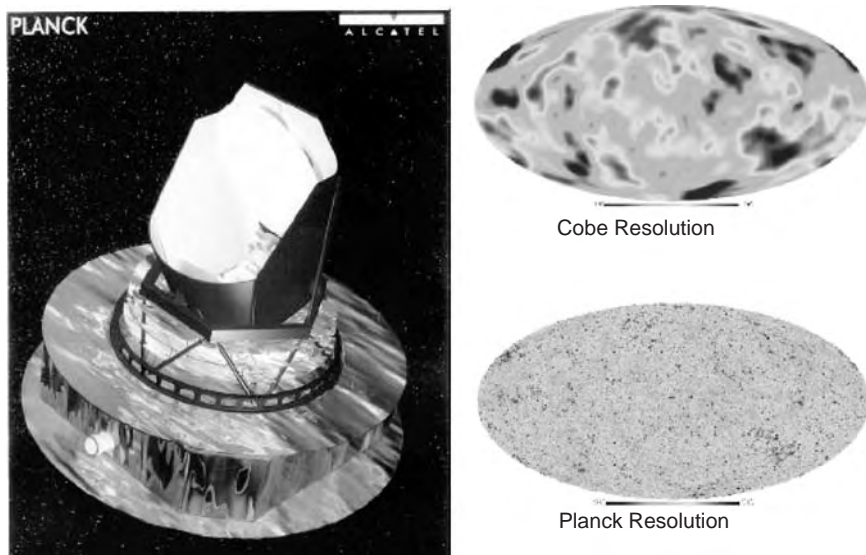


Figure 2. Terahertz space applications for the observation of the cosmic microwave background.

2.2. Plasma Diagnostics

Since the early days of fusion research in the late 1950s, intense efforts were devoted to the precise monitoring of a plasma, because an accurate determination of the spatial density and temperature profile of a hot and dense plasma is critical to enable a stable plasma confinement and steady operation conditions in a fusion reactor. Initially, the cyclotron emission was observed, like, e.g., experiments of the hot plasma emission in the wavelength range from 100 μm –1.6 mm (i.e., 0.18–3 THz) [23]. These experiments were conducted as early as 1961 in the framework of the first British fusion device attempt termed ZETA (Zero Energy Thermonuclear Assembly). Meanwhile, several nonperturbing techniques for measuring the electron density distribution of a hot plasma have been developed based on Thomson scattering, interferometry, or reflectometry. Most of the techniques operate at the low-frequency end of the Terahertz spectrum. Actually, complex heterodyne imaging and spectroscopy systems have been developed that allow monitoring and resolution in two and potentially even in three dimensions, the relevant properties of the plasma, in order to observe, e.g., plasma profiles, turbulence, and/or fluctuations [24–26]. In fact, it is accepted in the plasma community that these or similar measurement techniques will certainly be necessary for the next generation prototype fusion reactor device ITER. Apart from plasma diagnostics, high-power gyrotrons operating at the low-frequency edge of the Terahertz frequency are regularly used for RF-plasma production, heating, noninductive current drive, and plasma stabilization [27]. Ample efforts targeting high-power Terahertz sources were mainly determined by this application area.

2.3. Medical Imaging

Terahertz technology in the medical imaging field is currently in a crucial phase and may soon expand our ana-

lytic capabilities. Here, interest in Terahertz imaging comes from a combination of two intrinsic characteristics of Terahertz radiation. First, Terahertz radiation is non-ionizing and therefore intrinsically safe for biomedical sensing and imaging. Given the increasing awareness of the damaging effects of ionizing radiation, an intense interest in alternative techniques to X-ray diagnosis exists. Secondly, Terahertz analysis has indicated to be able to distinguish cancerous tissue from normal tissue (see Fig. 3, [28]). Although the precise reason for the observed different Terahertz response from healthy tissue and tumors is still unknown, it appears extremely attractive to have a nonionizing spectroscopic imaging technique that can directly identify and localize tumors.

Despite of a limited penetration depth for Terahertz waves in tissue on the order of several millimeters to a centimeter, a great interest in the technique for medical applications has emerged. Another potential medical application is checking how injuries are healing underneath surgical bandages without the need of taking off the bandage. A related imaging application also appears particularly suitable in the field of dental imaging (see Fig. 3). Here, a high interest in nonionizing radiation imaging also exists, and several analyses have demonstrated the capabilities of Terahertz radiation to image teeth and to identify early stages of caries or to monitor dental enamel thickness, which is necessary to quantify problems associated with enamel erosion [30].

2.4. Molecular Sensing for Environmental, Biotechnological, and Pharmaceutical Applications

Further sensing applications develop from the fact that specific molecular rotations, vibrations, or librations of molecules and molecular aggregates occur in this frequency range, which enables a large variety of applications for the detection and/or identification of molecules in diverse areas.

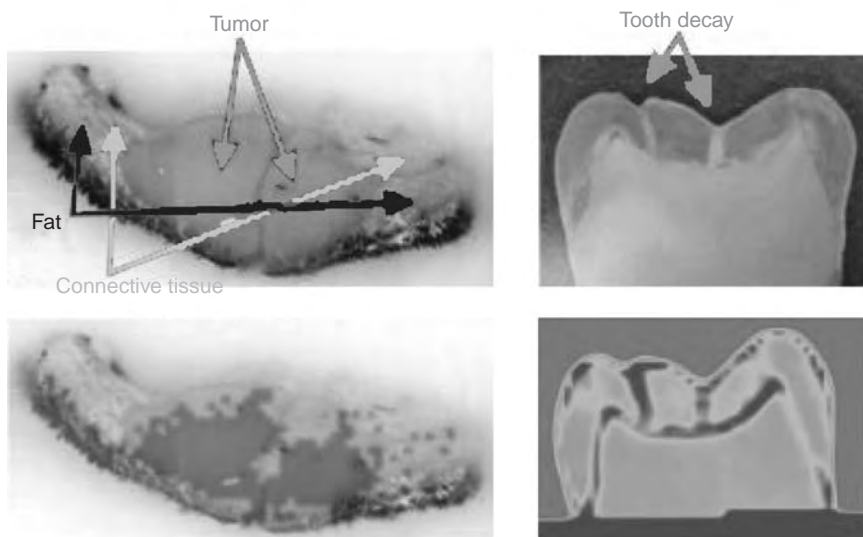


Figure 3. Exemplary Terahertz medical applications, illustrating the potential capability to distinguish tumors (left) and the early diagnosis of tooth decay (right). Figures from [7,29]. (This figure is available in full color at <http://www.mrw.interscience.wiley.com/erfme>.)

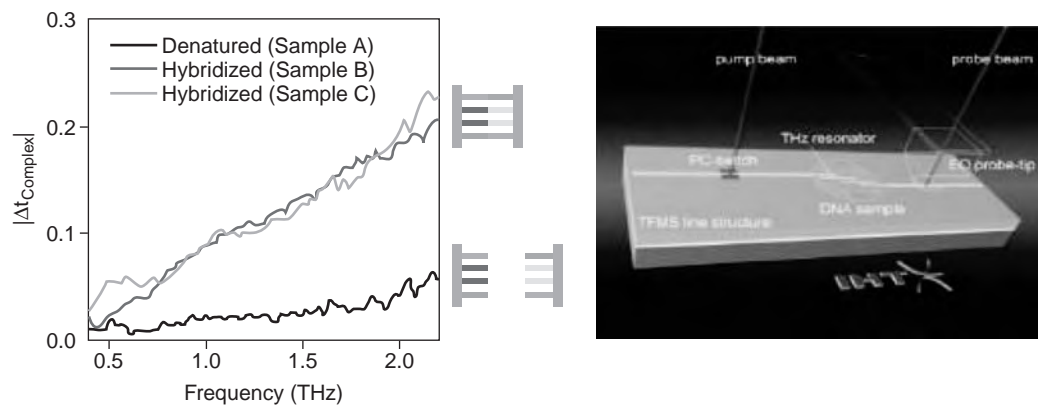


Figure 4. Exemplary illustration of Terahertz sensing of genes. The left figure illustrates spectral distinction of genes via binding state dependencies (adapted from [35]), and an integrated biosensing system (adapted from [37]). (This figure is available in full color at <http://www.mrw.interscience.wiley.com/erfme>.)

For environmental sensing, it appears very attractive that the rotational transitions of gases are highly dependent on the particular gas species. Broad-band Terahertz analysis can therefore trace complete gas compositions simultaneously with one device. Related applications for gas sensing are, e.g., monitoring of combustion processes [31,32], or plasma sensing [33], e.g., to control plasma etching processes.

Numerous applications in the field of biomolecular sensing are emerging. Here, a direct resonant probing of biomolecules of biomolecular binding events is crucial to detect and understand the function of biomolecules. Usual approaches are based on indirect probing by labeling the analyzed biomolecules, which is an additional costly process and also has a detrimental effect on the quality of the analysis.

A huge interest in label-free direct probing of biomolecules and their interactions exists. Terahertz spectroscopy has demonstrated that it allows to sense biomolecules like DNA and proteins [34–36] directly, without requiring labels. These basic observations are now being brought closer to application by the development of integrated Terahertz biochips (Fig. 4, [37], [38]). Many more molecular sensing applications have been identified, e.g., for monitoring chemicals or active ingredients in medicine during pharmaceutical manufacturing [39] or sensing chemical spatial distributions in objects [40].

2.5. Security

A great interest in the detection of drugs and explosives by Terahertz techniques has emerged, given the currently higher critical perception of security issues. Here, Terahertz techniques could also have a high potential, as resonant states seem to allow the spectroscopic distinction of explosives [41] and drugs [11]. One of the unique properties of longer wavelength Terahertz radiation is its ability to pass through many materials that are opaque in the visible region. Materials such as clothing, plastics, glass, and paper are transparent or have relatively low loss to frequencies as high as 1 THz. Above 1 THz,

most materials are relatively absorptive but can nevertheless be imaged through using active techniques. Below 1 THz, it becomes possible to image hidden objects through clothing passively [42] or to sense their corresponding molecules spectroscopically. Consequently, much interest at present exists in the use of Terahertz imagery and sensing for security purposes. Applications include intercepting foreign objects hidden within mail (see Fig. 5) and concealed weapons (see Fig. 6) at airports. Both applications are in their infancy and have yet to prove their superiority over existing techniques.

Work has also been undertaken to investigate the possibility of remotely detecting chemical and biological agents [43]. This problem has many challenges to overcome, but initial results show it to be possible.

2.6. Material Inspection and Quality Control

Already, from the early days of Terahertz technology, it was clearly recognized that Terahertz radiation could find applications in materials analysis and quality control, particularly for electronic materials (see Fig. 7). Wide-ranging demonstrations of these capabilities have been

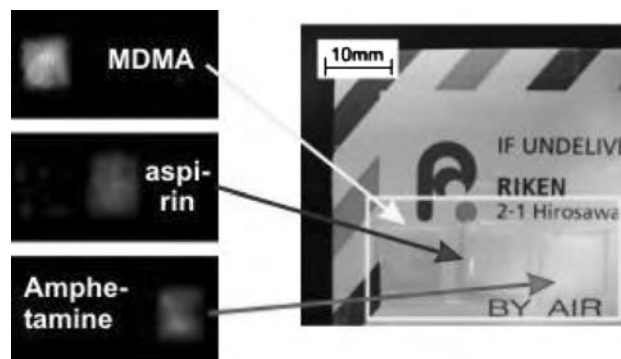


Figure 5. Exemplary illustration of Terahertz identification of drugs (adapted from [11]), using multispectral transillumination and component spatial pattern analysis. (This figure is available in full color at <http://www.mrw.interscience.wiley.com/erfme>.)



Figure 6. Exemplary illustration of Terahertz identification of concealed weapons (adapted from [42]).

performed to date, starting from the simple analysis of dielectrics and semiconductors [45,46]. Important work has been performed for the analysis of superconductors [47], including imaging at low temperatures [48]. Other examples of analyzed materials are ceramic materials for solid-oxide fuel cells (Fig. 8, [9]), manganites relevant for spintronics [49], and many more materials, like ferroelectrics, incommensurate crystals, dielectrics, magnets, low-

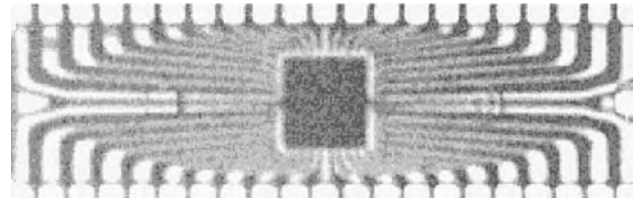


Figure 7. Terahertz image through a semiconductor chip (from [44]).

dimensional conductors and superconductors (for an overview, see [50]). Recent work in the field has been directed particularly to analysis in nanostructures that play a vital role for future photonic and electronic components (see, e.g., [51]).

Terahertz technology has a broad application perspective in this field. First commercial systems (e.g., Nikon) are emerging precisely in this field.

A further interesting application field of Terahertz technology is based on the long wavelength of this type of radiation in comparison with optics. The longer wavelength implies that Terahertz waves exhibit less scattering in comparison with optics. Imaging and vision systems in this frequency range can therefore tolerate harsh environmental conditions that are necessary in diverse application areas, like, e.g., package inspection [52] or industrial process monitoring [7]. Here, a higher resolution than what is available with conventional millimeter-wave imaging systems is often desired, while at the same time, optical imaging cannot provide a solution because of scattering.

3. BASIC TECHNOLOGY

3.1. Microwave Terahertz Detectors, Sources, and Systems

Whereas photonic-based Terahertz systems appeared relatively suddenly, quickly demonstrating their usefulness in the applications described previously, microwave

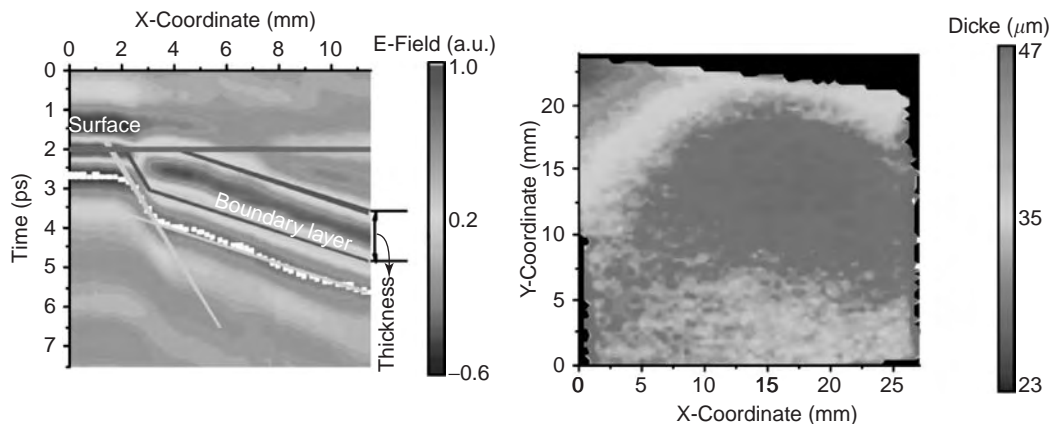


Figure 8. Material inspection analysis with Terahertz waves. Here, tomographic imaging allows cross sections and determines deposited film thickness of the active layers of solid-oxide fuel cells (adapted from [9]). (This figure is available in full color at <http://www.mrw.interscience.wiley.com/erfme>.)

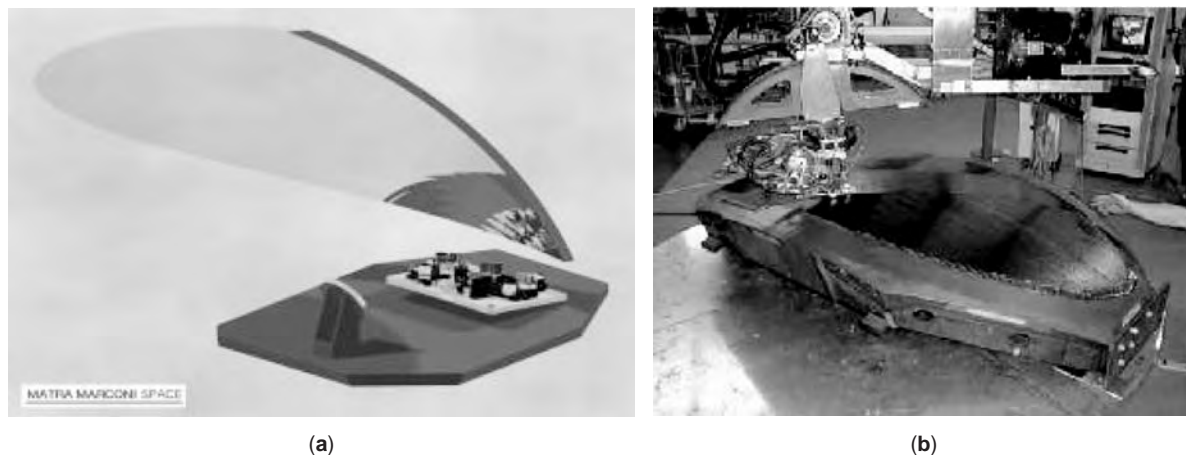


Figure 9. ADMIRALS (a) Artist view of the ADMIRALS antenna. (b) CFRP face skin manufacturing of the ADMIRALS antenna breadboard.

Terahertz systems evolved slowly over several decades. The broad-band solid-state radiometers used on current space missions and quantum noise limited cryogenic receivers used on ground and spaced-based radio telescopes find their origin in the humble cat's whisker detector [53] used in the earliest radios. The design rules governing the performance of microwave Terahertz detectors, sources, and systems have been understood for many years, and apart from the development of certain types of cooled detector progress, no groundbreaking discoveries have occurred since the Gunn diode [54]. Consequently, workers have resorted to better system engineering, new materials, and refining their design tools and manufacturing techniques to simultaneously improve performance and achieve operation at ever-higher frequencies. This section attempts to describe some of the techniques and technologies that have been developed for realizing the “microwave” instruments that operate in the Terahertz frequency range today. Such instruments have some commonalities. First, the basic building blocks are common: antenna, reflectors, waveguide and feed-systems, and receiver and the corresponding sub-systems. Second, semiconductor devices and device technologies are a key element for the construction of any (sub)millimeter-wave instrument.

These building blocks are discussed in the following sections and are categorized according to the way sub-systems would be positioned in a typical system, i.e., from the top down (antenna, feed, receiver, etc.).

3.1.1. Microwave Terahertz Technology: Antenna and Feed Systems. The antenna sub-system is a key element for most Terahertz instruments. In order to image or analyze the information gathered by a remote sensing instrument, knowledge of the instruments “field of view” is vital. Consequently, the instrument’s antenna performance is critical because it largely determines the resolution and accuracy with which, e.g., the concentration profiles of atmospheric species can be retrieved. Antenna performance is also of prime concern for astronomical and planetary missions. For pointed observatories, which seek to map point-like or not very extended objects, the emphasis is on beam efficiency and the control of main beam

shapes. For survey missions, the level of far side lobes also becomes very important, and in some cases (such as the PLANCK mission [15,16]) this exerts a critical influence on the success of the mission.

Terahertz reflectors and the corresponding sub-systems relevant to ambitious scientific and earth observation satellite programs lead to high-precision, stable reflectors, high-performance lightweight materials, and low-loss RF components [55,56]. The requirements of future missions outrange those of more classical telescopes working in the microwave frequency range by a few orders of magnitude in terms of surface accuracy and stability. Furthermore, the tolerances on relative positioning lead to near optical accuracies. In addition, the temperature range that the instruments must work reliably over add system complexity to the manufacturing, integration, and testing. Considerable effort has been taken to ensure antenna performance, and dedicated Terahertz antenna technology studies have been performed (e.g., the ADMIRALS activity [13]: Antenna Development in Millimeter/sub-millimeter-wave Range for Astronomy and Limb Sounding, Fig. 9).

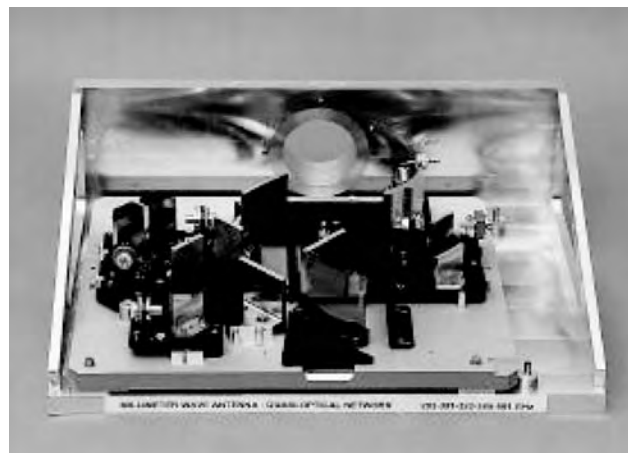


Figure 10. Breadboarded 5-frequency quasioptical demultiplexer.

Over the past years, several activities have been started in the field of quasi-optical feed systems (Fig. 10, [57]) in terms of controlling the observed signals, which has led to low-loss compact systems. Low-loss frequency selective structures (FSS) [58] are being considered because present receiver systems are limited by losses. Significant losses in high-Q multilayer beamsplitters occur because of the absorption in the substrate material that is required to support the individual printed arrays of resonant FSS elements. A radical approach for improvement is the removal of the dielectric backing and interlayer spacer material to form air-spaced self-supporting FSS structures [59].

Most of the instruments that have been mentioned in the previous sections have receivers that utilize waveguide horn antennas as the initial receiving elements. They have traditionally been the most common microwave antenna feed types and although the attenuation of fundamental-mode waveguides at (sub)millimeter-wave frequencies is high and both the effect of metal tolerances and misalignments becomes more severe, horns and waveguides have been produced for these wavelengths with great success [60].

However, the small size can be turned into an advantage when the dimensions and tolerances required become compatible with those achieved by lithography or micromachining. In recent years, the advancement of photolithographic and micromachining techniques has resulted in a very reliable and repeatable process for creating structures on dielectric substrates, and the fabrication of complex electronic structures with a high yield is now

possible, which means that a viable alternative for waveguide-based front ends has emerged.

An important advantage of the integrated planar technology [61] is that the antenna, mixer, local oscillator, and all peripheral circuitry can be realized on a single substrate, thereby eliminating the transmission lines between the separate devices (see Fig. 11, [62]).

However, some problems related to planar antennas may exist because of efficiency problems associated with the dielectric substrates on which these antennas are fabricated. If the dielectric is thick in terms of wavelength, substrate and surface wavemodes can be excited. Two basic approaches have been used to increase the efficiency; dielectric lenses or electromagnetic bandgap crystals (EBG) [63,64].

The electromagnetic bandgap antenna is still a relatively new concept, and with respect to the antenna performance, the EBG technology is still in an experimental stage [65]. On the contrary, research on integrated lens antennas has already shown that the radiation characteristics are very promising and the integrated lens designs have already reached some level of maturity. Several activities on the above technologies have been initiated with very good results [66,67].

Although this approach has offered competing performance, micromachining in a general sense is not restricted to planar structures. It is also possible to manufacture more traditional “waveguide-like” structures. The advantages of these come from the fact that it is possible to form a waveguide section in which the active semiconductor can be integrated directly into it, which allows more familiar design approaches to be applied [68].

Also, in the world of filters and windows (see Fig. 12) for submillimeter and Terahertz direct detection instruments, much work is being performed [69]. Metal mesh filter technology [70] has become the prime source of Terahertz filters for most space and sub-orbital instruments in both the astronomical and Earth Observation communities. These filters can be either embedded in a dielectric (hot-pressed filters [71]) or as airgap devices [72].

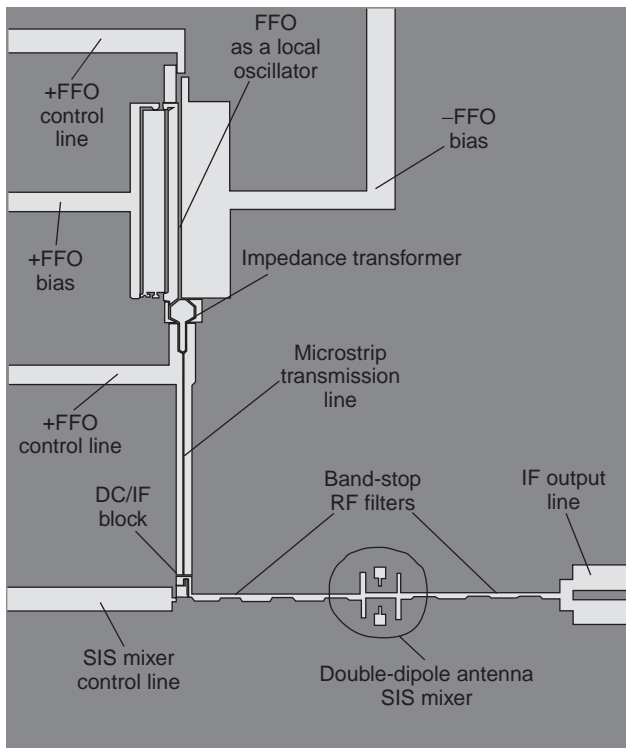


Figure 11. Integrated antenna with peripheral circuitry.



Figure 12. Metal mesh and dielectric filters.

The successful development of broad-band antireflection coatings [73] for high refractive index dielectrics (germanium, sapphire, silicon, quartz) serves as an enabling technology for the development of refracting optics for instruments operating at Terahertz wavelengths. Excellent performance of these coatings with low reflective losses has recently been demonstrated in windows, filters in windows, and filters at these wavelengths.

3.1.2. Microwave Terahertz Technology: Superconducting Detectors. One of the most powerful characteristics of the microwave Terahertz approach is the ability to realize sensors that are so sensitive they can detect the naturally occurring background Terahertz radiation. At this present time, an equivalent photonic technique that can achieve the required sensitivity without the use of an external signal seemingly does not exist. For certain applications, like radio astronomy and atmospheric sensing, the main aim is to observe the naturally occurring radiation purely by passive means. Consequently, the technology developed for this purpose follows a completely different path to the photonic route.

To an astronomer, detector performance is the main priority. Capturing an image of a distant extended source, such as a nebula, can take hours, days, or even weeks. The smallest signal that can be detected is directly proportional to the receiver noise temperature and inversely proportional to the square root of the product of the bandwidth of the radiometer and the time spent viewing the object. Observing time on the few radio telescopes that can operate up to 1 THz is very limited, and so astronomers want to make the most of the time they have. They will, therefore, go to extraordinary lengths to build radio receivers with sensitivities that approach to quantum limit. For the systems they use, two predominant methods of detection exist; direct and heterodyne detection.

Direct detection generally involves a bolometric device. This device acts like a very sensitive thermometer. The signal is coupled to the device and either the resistance, charge, or current of the device is monitored, and any observed change indicates that the incident power has varied. Such bolometers have traditionally been fabricated from InSb [74]. To achieve ultimate performance, such bolometers are generally actively cooled using a cryostat operating at a few tens of milliKelvin. The main advantage of the bolometer is that it is an intrinsically simple structure. This device, coupled with recent advances in MEMs-derived fabrication techniques, has provided the means to accurately control the thermal environment of the bolometer, increasing its sensitivity and speed while simultaneously providing the means to assemble large imaging arrays of uniform devices, which provides the means to dramatically reduce the time required to observe. Examples of such arrays are SCUBA [72], used on the James Clerk Maxwell Telescope in Hawaii, or BOLOCAM (Fig. 13 [75]).

With such arrays it is possible to detect the presence of planets around stars, hence the interest. Future bolometric arrays will have sensitivities that are two orders of magnitude higher, allowing images to be captured in minutes that would have taken weeks before. A new type of

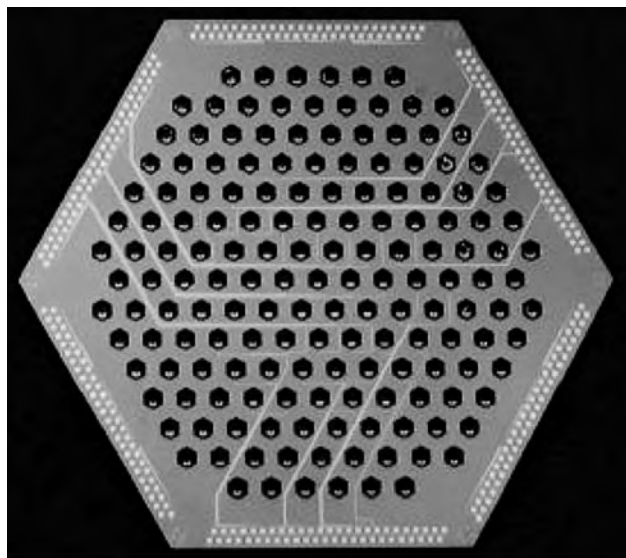


Figure 13. BOLOCAM Bolometer array.

bolometer, the transition edge bolometer [76] is potentially offering superior performance compared with previous devices, and the next generation of arrays could be implementing this emerging technology.

One disadvantage of such direct detection methods is the fact that the detector will also respond to power from signals at wavelengths other than those desired. Band-pass filters are therefore required to block unwanted signals, and the finesse of these filters effectively dictates the frequency being observed.

As the spectral resolution of bolometers is limited, a technique known as heterodyne mixing is used to provide spectral information. In heterodyne mixing, detection of the signal occurs when it is coupled into a nonlinear device and combined or “mixed” with a coherent spectrally pure second signal, the Local Oscillator, or LO. The LO is arranged so that it is close in frequency to the signal being observed. As the detection device is nonlinear, new signals are generated at various frequencies. One of these signals is the difference frequency (or intermediate frequency, IF), which is sufficiently low in frequency that it can then be amplified and detected using conventional low-frequency “base-band” electronics.

For radio astronomy, in order to add as little noise to the signal to be detected as possible, a very sensitive superconducting device known as an SIS (superconductor insulator superconductor) junction [76] is used as the mixing detector. This device is cooled to below its superconducting transition temperature. Most radio astronomy heterodyne systems use SIS mixers, but at around 1 THz the sensitivity, the SIS detector degrades. Above this frequency the energy of the received photons is above the bandgap of the superconducting material, and the losses within the junction become high. Consequently, the performance drops rapidly. In response to this fundamental problem, a relatively new device that operates using a combination of the bolometric and mixer effect has been developed. This device is known as the

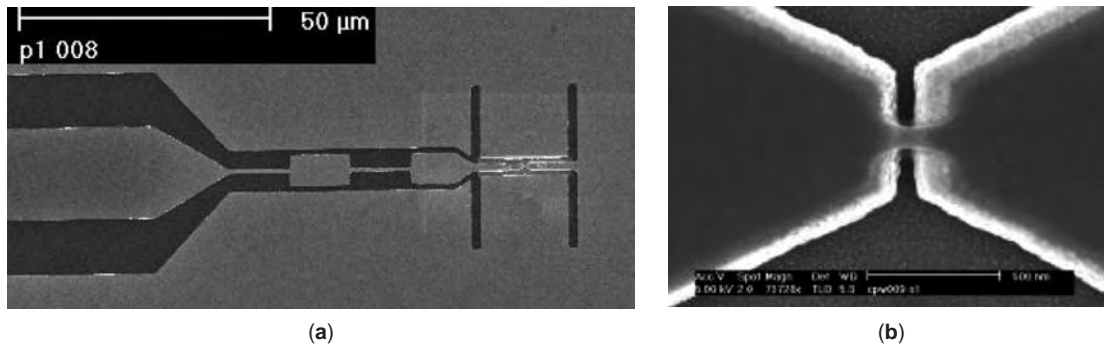


Figure 14. (a) 2.5 THz Nb HEB device. (b) Zoom of the 60 nm microbridge.

Hot Electron Bolometer (see Fig. 14), or HEB [77]. The HEB consists of a very small length of superconducting metal sandwiched between two normal metal electrodes. The device still needs to be cooled below the transition temperature, but unlike a conventional bolometer, the HEB temperature can be modulated very quickly. Like the SIS junction, an LO signal (at least an order of magnitude lower) is introduced, which is mixed with the signal to be observed and again an IF signal is created. However, in case of the HEB, it is the junction temperature that is modulated at the IF frequency. As a result of the fast cooling mechanisms involved, the responsivity of the HEB device is in the picosecond range [78].

3.1.3. Microwave Terahertz Technology: Room Temperature Detectors. The detectors described in Section 3.1.2 probably provide the highest sensitivity, but they have one serious disadvantage: they need to be cooled to very low temperatures. Some applications do not require maximum sensitivity but need to provide solutions at a reduced cost and complexity or are required to operate in hostile environments such as aircraft or satellites for extended periods. The measurements of interest may require an IF bandwidth much higher than can be achieved by superconducting receivers. Consequently, when weight, power, and longevity are paramount parameters, then room temperature Schottky-based heterodyne mixers [79] have been deployed.

By arranging Schottky diodes in particular configurations, the system complexity can be further simplified. One favored arrangement is the antiparallel configuration [80]. By arranging the diodes in this way, the mixer is able to operate in subharmonic mode [81], for which the LO can be at approximately half the signal frequency, which becomes evermore important as the available LO power drops at higher frequencies. Other benefits of the antiparallel configuration include increased RF and IF bandwidth, inherent amplitude noise immunity, and finally allows the LO signal to be fed into the mixer by a completely separate port to the signal, which greatly simplifies the system as a diplexer to combine the signal with the LO frequency, which is no longer required. It is for these reasons that the

subharmonic mixer has become the favorite solution for heterodyne detection on space- or aircraft-based remote sensing instruments [82].

The only real disadvantage of the subharmonic mixer is that it typically requires 2–3 mW of LO power. Consequently, as the signal frequency encroaches 1 THz, current source technology is unable to meet the LO requirement. At this point, the only option for room temperature heterodyne detection is the fundamental Schottky mixer [83] that typically requires only 0.5–1 mW of LO power, albeit at the signal frequency. These have been successfully demonstrated up to 2.5 THz using FIR gas lasers as the LO source [84]. An example of the kind of circuitry required to operate at these wavelengths is shown in Fig. 15.

At this frequency, the circuit dimensions that are required become truly microscopic in order to avoid the parasitic capacitances and inductances that are generated by the tiniest physical features. These can effectively short out the signal if the circuit is not designed carefully. Consequently, novel techniques have been developed to minimize circuit parasitics such

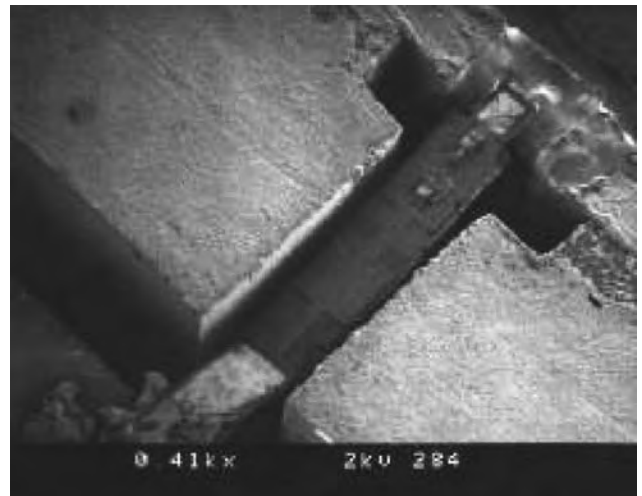


Figure 15. The internal Terahertz circuitry of a 2.5 THz mixer.

as the use of airbridged contacting fingers and substrate removal [85].

3.1.4. Microwave Terahertz Technology: Generation of Terahertz Waves. Detector technology has moved to a sufficient level of maturity that most future advances will come from improved engineering rather than new breakthroughs. In contrast, solid-state generation of sufficient Terahertz power is still a largely unsolved problem. To date, an efficient broad-band room temperature 1 THz (or above) source has eluded workers.

Vacuum devices have been demonstrated up to 1 THz in the form of Backward Wave Oscillators [86], but these have a number of disadvantages for most applications. Primarily they are expensive, require high power, are inefficient, and lifetime is also an issue.

This lack of a simple source is currently impeding commercialization of the Terahertz region. At lower microwave frequencies, complex applications have emerged such as radar and communications. Similar systems could be realized at Terahertz frequencies were a suitable source available.

FIR gas lasers can provide high powers and have recently demonstrated the required reliability, lifetime, and efficiency to fly on a space mission [87]. However, they are still far from ideal.

At present, the most convenient source of RF power at the lower end of the Terahertz region is the indium phosphide (InP) Gunn oscillator. Excellent performance has been demonstrated at room temperature to 150 GHz [88]. More importantly, the InP Gunn oscillator has a very modest DC power requirement of a few Watts. To obtain higher output power levels (several Watts), around 100 GHz power combining power amplifiers, which are now becoming available, have been used [89].

Although sufficient LO power levels for most applications is available to approximately 150 GHz to obtain LO at higher frequencies, it is necessary to frequency multiply, which is achieved by using a nonlinear element to generate higher order harmonics from a pump source. Whereas in a heterodyne mixer, a nonlinear resistance is used to mix frequencies, a frequency multiplier uses a nonlinear capacitance or varactor to generate higher harmonics of the pump frequency. These multipliers generally take the form of doublers (X2) or triplers (X3), or combinations with secondary multipliers to achieve higher multiplication factors. Again, various configurations of diodes are used to realize balanced multipliers. Frequency multipliers have moved forward rapidly recently with the adoption of MEMS-like circuits [90] and the implementation of accurate design tools. The result is that fixed tuned multipliers are now able to provide the LO requirement for SIS and HEB receivers up to 1.5 THz. Unfortunately, it may be some time before they can provide the LO requirement for a Schottky-based system, which would open up true commercialization possibilities with the eradication of the cooling requirement. The reason for the dropoff in performance is because of a fundamental problem in the frequency multiplication process. With each multiplication step, a low efficiency of conversion exists (typically 5–30% [91]), and consequently, power

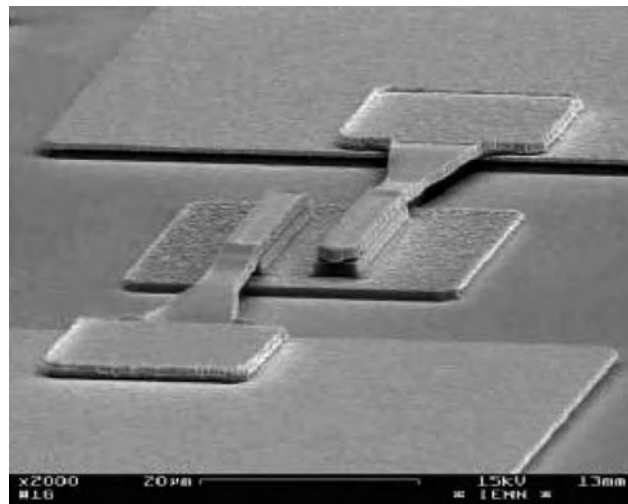


Figure 16. Close-up of an HBV device.

levels drop exponentially with the increase in frequency. An increase in pump power can be considered but power handling and thermal issues must then be considered. The standard route is to use balanced doublers that share the input power between several diodes. These devices have shown efficiencies in excess of 50% [92], but the low multiplication factor requires a number of stages before 1 THz is reached. The complex matching requirement between successive stages effectively limits the bandwidth of the complete chain.

A relatively new type of nonlinear element, the Heterostructure barrier varactor (see Fig. 16), or HBV, has demonstrated excellent performance [93]. As they have a symmetrical CV characteristic, these devices can greatly simplify the circuit design by canceling even harmonics and thus allowing higher harmonics, such as the 5th and 7th to be generated, which is achieved at the expense of complex material processing. The HBV provides an additional degree of freedom over the varactor because it can be tailored to handle high powers. Heating of the device again can become a problem, so that integral heatsinks and careful material engineering is required.

A Gunn or Transferred Electron Oscillator (TEO) device manufactured from new materials such as GaN has been shown theoretically to offer high powers at frequencies approaching 1 THz [94]. However, there are many manufacturing and design issues to overcome before such devices are realized.

3.1.5. Microwave Terahertz Technology: Integration Technologies. An area that has advanced rapidly is that of Terahertz circuit architecture. Deep lithographic techniques developed for the MEMS industry now offer an alternative to conventional machining of the low-loss waveguide cavities [95]. These techniques offer not only greatly reduced cost but also allow more complex systems to be realized. An example of such technology is shown in Fig. 17.

The image on the left shows the internal features of a 500 GHz subharmonic mixer. The image on the right gives an idea of scale with the finger tips shown holding the

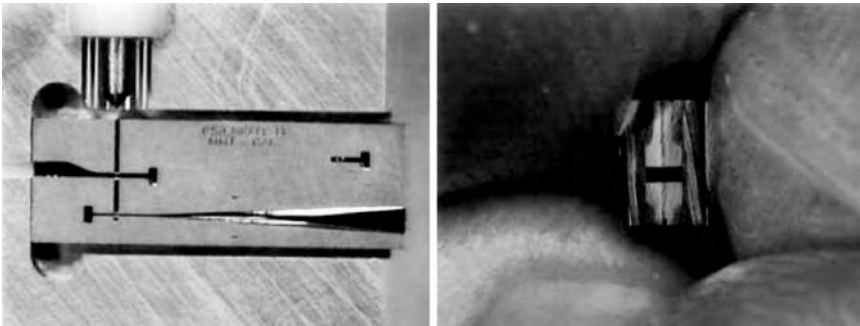


Figure 17. A 500 GHz micromachined sub-harmonic mixer.

complete mixer. The rectangular aperture is the LO input waveguide, which is approximately 800×400 microns in dimension; the signal waveguide is approximately half this size. A recent trend for Terahertz components is to remove as much of the dielectric material from the circuit as possible, which not only provides lower loss but also allows larger circuits to be implemented for the same frequency without the corresponding increase in parasitics. As the circuits have such little mass, it is usually possible to integrate supporting leads into the microstrip or coplanar waveguide circuit [96]. This approach greatly aids assembly, which can become challenging as the frequency increases.

3.1.6. Microwave Terahertz Technology: Design Tools. In the development of components and systems for high millimeter and sub-millimeter waves, the design tools have to cover both quasioptical and “microwave-like” components. This frequency range falls in between the more established domains of microwave and optical design, and considerable debate still exists as to which of the many electromagnetic analysis techniques and physical assumptions should be used for the correct design and analysis. Also, considerable effort is placed on speeding up calculation of large structures using quasioptical techniques while preserving accuracy.

Specific modelling efforts are needed for periodic structures [FSS, EBG, left-handed materials (LHM)] and sub-millimeter components like wiregrids and polarizers. More importantly, however, specific problems exist associated with modeling the complex interactions of these components and little measured data exist to date. To address this deficiency, validation becomes of prime importance.

A similar problem exists in the modeling of active devices. Linear and nonlinear simulation methods for active circuits and MMICs are fairly well established at microwave frequencies. Accurate modeling becomes more difficult with increasing frequency, and the upper frequency limit, where models can be validated, is determined by the available measurement equipment, currently 110 GHz or less. Development of MMICs for frequencies above 110 GHz will require considerable modeling efforts, not only with active devices, but also in constructing and validating the models for passive components, including transmission lines and their discontinuities.

The need for accurate design tools grows with the level of integration. The change from whiskered devices to pla-

nar discrete components creates a “generation gap,” as the change is more fundamental than simply replacing one component with another, and requires a change in the whole design process. A similar gap is encountered in the change from hybrid structures (that use discrete components) to monolithic circuits. Bridging the gap and taking full benefit of the potentials of a new technology requires that the CAD tools develop at a similar pace. For example, circuits at high mm and sub-mm wave frequencies have traditionally suffered from relatively narrow bandwidth, because of the largely empirical design and tuning approach used in their development. Monolithic structures allow broad-band, “tuner-less” operation, but only if a CAD tool is available that can analyze the complete structure, and if the models are valid and sufficiently accurate. A number of commercially available finite element simulation tools are presently on the market, and comparison between simulations and measurements have shown them to have some degree of accuracy providing the exact geometry is known along with the material properties being simulated. As more and more complex Terahertz systems are required, such tools will naturally evolve to fill the need.

3.2. Photonic Terahertz Technologies

Photonic Terahertz technologies have emerged since the late 1980s and are currently the most adaptable and broad-band-based approach to develop active Terahertz systems. The ample capabilities of photonic Terahertz technologies have resulted in a rapid proliferation of this technique from a handful of laser experts to a wide variety of researchers in various disciplines and to the emergence of first commercial systems based on these technologies. Several dedicated overviews have been published on photonic Terahertz technologies [44,97,98] so that only a very condensed summary of this approach is presented here. Although microwave Terahertz technologies clearly evolved from space application oriented device developments (for an overview, see [99]), photonic Terahertz technologies emerged independently as a research tool for the spectroscopic investigation of materials, trying to extend the analytic observation window of existing techniques like Fourier-Transform Infrared (FTIR) spectroscopy to longer and longer wavelengths. At the same time, an important motivator for these developments was the wish to

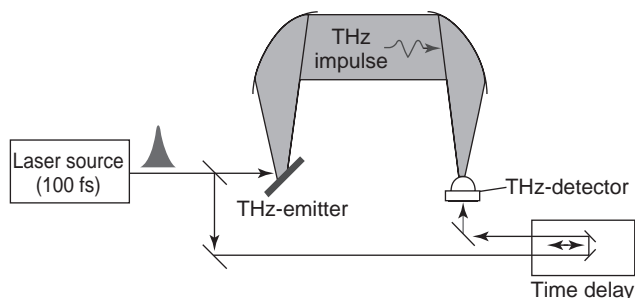


Figure 18. Scheme of the basic operation principle of an impulsive optical or time-domain Terahertz system.

provide broad-band photonic-based analytical tools for high-frequency electronic developments.

To date, most photonic Terahertz technologies are based on impulsive optical approaches for the generation and detection of electromagnetic radiation in the Terahertz frequency range (see Fig. 18). The general idea of this “time-domain THz spectroscopy” was to make use of ultrafast laser pulses, with a duration of typically less than 100 femtoseconds ($1 \text{ fs} = 10^{-15} \text{ s}$), to enable the optoelectronic activation of emitters and detectors of radiation for a brief moment in time. This concept hence allows sensing or “scanning” the real-time evolution of Terahertz waves by delaying the time-point of the detection event relative to that of the emission, which is easily done by delaying the respective optical laser pulses. This approach facilitates the implementation of coherent (phase-sensitive) detection schemes, which is relevant in terms of noise reduction in order to automatically suppress the unwanted thermal background radiation. Coherence also opens the way to a full range of appealing possibilities, as direct temporal or material thickness information can be derived from measured Terahertz transients, and modern image and object reconstruction algorithms can be implemented.

Two main principles (see Fig. 19) are currently used for the optoelectronic impulsive generation or detection of Terahertz waves. The first approach is based on using photoconductive structures in semiconductors to generate rapid current pulses to emit radiation or to sense Terahertz fields. This concept was initially demonstrated in [100] and allows generation of subpicosecond pulses of radiation with a very broad spectrum and coherent detec-

tion by converting impinging field amplitudes to currents at the time-point the detecting photoconductive structures are activated by a second femtosecond laser. The second concept is based on using nonlinear optical effects to mix electromagnetic fields. This concept was initially derived from Cerenkov radiation experiments and evolved to a first sub-picosecond system [101]. Since these early days, a significant improvement of these more or less “standard” femtosecond (fs) laser-based approaches has been achieved. Although detection efficiency is excellent, much research and improvement is dedicated to increase the efficiency of the emission process (see, e.g., [102]). Time-averaged power levels on the order of $40 \mu\text{W}$ and 1 mW are achieved by using appropriately conceived photoconductive structures with standard fs lasers [103], or amplified fs-laser systems, respectively [2]. Huge bandwidths have been demonstrated with exceptional achievements showing an emission and detection bandwidth extending from a few hundred Gigahertz up to 120 THz [103]. Broad-band analytic systems with a dynamic range of 110 dB in 20 ms have been reported by Brodschelm et al. [104], as well as systems with a 90 dB resolution [105].

Impulsive optical Terahertz technology has given rise to numerous system developments. Specifically, it has allowed the development of active Terahertz imaging systems [52], which have attracted great attention in diverse application fields. Currently, this development has reached a maturity that facilitates the increase in the complexity of Terahertz imaging in diverse areas. Major developments have been directed to enable 3-D spatially resolved analysis [106], and to adapt more sophisticated imaging concepts known from optical imaging, like near-field imaging [107], dark-field imaging [7], microscopic imaging [108] and synthetic phased arrays to increase resolution [109].

Despite the attraction of the developed time-domain Terahertz systems, significant developments have still to be made before video-rate systems for everyday applications can be provided by photonic Terahertz technologies. The essential problem of this approach is the high cost and significant complexity of the underlying femtosecond optical lasers that are used to drive these systems. Several approaches are therefore studied to develop alternatives to standard femtosecond laser-based systems. One evident approach is to minimize the complexity of femtosecond lasers used to drive Terahertz systems. Such approaches are

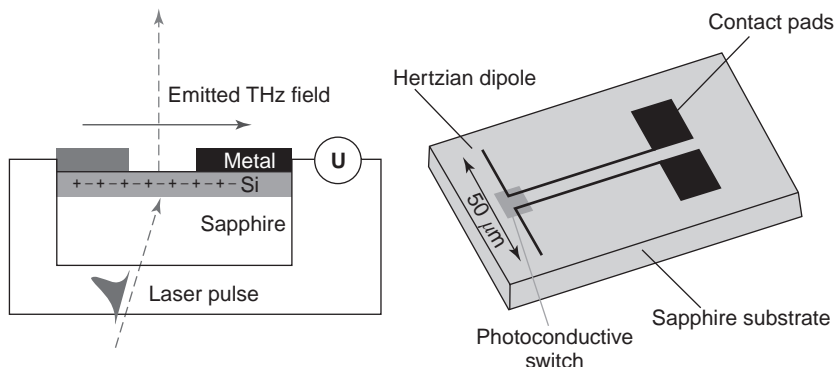


Figure 19. Schematic of a photoconductive Terahertz emitter/detector structure consisting of a dipole with an integrated metal-semiconductor-metal contact (Auston switch), coplanar waveguides, and contact pads. The left part of the figure depicts a cross section of the Auston switch, when the antenna is operated as a Terahertz emitter.

followed by industry and academia and are either directed at fabricating more compact femtosecond laser systems, or to increase the power output of fiber laser-based concepts.

Another photonic Terahertz technology alternative is to mix two continuous wave (cw) lasers to generate narrow, tunable Terahertz radiation. This approach adopted, e.g., in [110], has reached a remarkable complexity by demonstrating even cw-imaging systems (for an overview, see, e.g., [7]). It is highly attractive to follow this cw-photomixing route, as this concept can be transferred to use standard optical laser diodes, which have a high performance at low costs. Nevertheless, complex stabilization procedures of one laser wavelength with respect to the other have to be implemented to maintain and tune the generated and detected Terahertz radiation. Significant room for improvement in this area still exists, especially in view of the restricted power output of photonic cw-Terahertz sources, as typically more than an order of magnitude less power output is observed in comparison with pulsed sources. Improvements with regard to improved heat dissipation and prevention of charge carrier accumulation by heterostructures appear promising.

Another field that has matured is the development of optical parametric oscillators (OPOs) operating at Terahertz frequencies. Here, the traditional problem is the significant Terahertz absorption of adequate mixing crystals and the difficulty of achieving phase matching over extended crystal lengths. Nevertheless, using nanosecond high-power pulses at low repetition rates, OPOs with remarkable characteristics have been demonstrated [111]. Using parametric oscillation of LiNbO_3 crystals pumped by Q-switched Nd:YAG lasers, widely tunable coherent Terahertz sources in the range between 0.7 and 3 THz with output power levels in the range of 0.9 nJ/pulse have been realized.

A focus of attention in the recent past is the development of solid-state Terahertz lasers based on quantum cascade laser (QCL) approaches (Fig. 20). The initial demonstration of a Terahertz QCL is very recent [112], nevertheless extraordinarily rapid improvements of this technology have been achieved. The most recent progress

in this field is a 3.8 THz QCL working at a temperature of 137 K [113]. Such a high-temperature operation only 2 years after the first realization of Terahertz QCL was not foreseen and gives substantial hope that operation close to room temperature can be achieved. It is interesting to note that the first photonic Terahertz detectors have been demonstrated, inverting the operation regime of similar QCL structures [114].

4. REQUIREMENTS FOR FUTURE APPLICATIONS

4.1. General Requirements of Future Space Applications

The first part of this section identifies the “market pull,” for (sub)millimeter-wave technologies, generated by the future Earth observation and space science missions.

In the area of Earth observation, operational and atmospheric composition missions can be identified, with different levels of certainty.

For the operational missions like Post-EUMETSAT Polar System (Post-EPS) and Post-Meteosat Second Generation (Post-MSG), it seems clear that continuity of the observation data will be required, i.e., the new generation of instruments on polar orbit will cover at least the same frequencies (up to approximately 200 GHz), with a probable extension to higher frequencies.

The main function of current atmospheric sounders is the measurement of the vertical profiles of temperature and water vapor in the troposphere using multiple receivers around the spectral lines of oxygen and water vapor.

Sub-millimeter-wave imagers up to 875 GHz are considered as a potential part of the payload of the follow-up satellites. The main task of these instruments will be the observation of clouds, in particular cirrus clouds, which are one of the major unknowns in the radiative balance of the Earth’s atmosphere.

Atmospheric sounders and imagers will require low-noise instruments operating at multiple frequencies. Increased resolution will lead to the need for low-mass large-diameter reflector systems. The most important change in receiver technology with respect to the first generation sounders is that low-noise amplifiers and MMICs will become available in the near future for frequencies up to 220 GHz.

As low-noise amplifiers are not expected to be available for sub-millimeter-wave frequencies in the near future, heterodyne receivers will be needed. High-performance Schottky mixers operating at or close to room temperature and local oscillators (LO) are required.

Further requirements for sub-millimeter-wave instruments originate from the need to better understand the long-term climatological effects of the chemistry of the atmosphere. It seems likely that future Earth observation missions will include instruments for measuring the various trace gases that have spectral lines at sub-mm-wave frequencies up to 3.5 THz. Device technologies become very critical in low-noise receivers for Terahertz frequencies, especially in the LO generation.

With respect to space science, the most likely sub-millimeter-wave missions are Post-Herschel and Post-Planck.

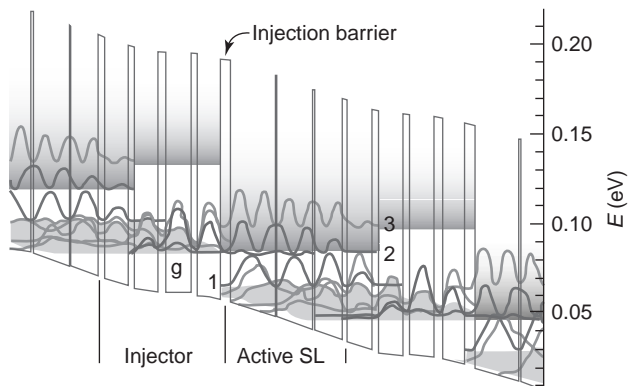


Figure 20. Semiconductor heterostructure and electronic wave-functions of the first electrically driven quantum cascade laser operating in the Terahertz frequency range [111]. (This figure is available in full color at <http://www.mrw.interscience.wiley.com/erfme>.)

It can be expected that a follow-up mission to Planck will occur, because of the key role the observations of Cosmic Microwave Background (CMB) has in increasing our understanding of the evolution of the universe. Such follow up would require measurement of the polarization properties of CMB radiation, requiring significant improvements in polarimetric antenna architectures and receivers, because of the extremely low level of the polarized signals.

Herschel has been an important driver for the development of sub-millimeter technologies for over 15 years, both in Europe and in the United States. Significant advances in superconducting device technologies (SIS, HEB) have allowed the development of sensitive heterodyne receivers for frequencies up to 1.9 THz. This development work also allows identification of the LO chain as the critical area where continuing efforts are essential for any future mission involving sub-mm receivers.

American and European astronomers are presently considering options for future Terahertz wavespace astronomy missions. Extrapolating from the past and present projects (space, airborne, and ground-based), and taking into account the still missing areas in observing capabilities (spectral, spatial, and imaging), several model missions have been proposed. Submillimeter-wave polarimetry, interferometry, and imaging systems will be reviewed for their scientific merits, feasibility status, and technical development needs in the frame of post-Planck and Post-Herschel.

The identified technology needs of future missions, and the foreseen missions themselves, are often extrapolations of the existing status, and thus represent “incremental” improvements. It is also important to follow the emergence of new breakthrough technologies (technology push), which may allow completely new solutions. Some candidates for such technologies, ranging from system-level solutions down to novel devices, are listed in the following:

- Interferometry allows resolution essentially better than that achievable by a single aperture. A commendable long-range goal is to achieve Hubble Space Telescope-class resolution in the sub-millimeter-wave range, which would require an imaging interferometer with at least 1 km maximum baseline.
- Imaging arrays are of great interest for space astronomy and for atmospheric research. In astronomy, most of the spectral line emitting regions are usually spatially extended over many observing beams in the sky, and mapping is required to astrophysically understand the regions under study. In atmospheric research, multiple beams would allow push-broom measurements, e.g., in-limb scanning experiments.
- Large arrays of superconducting bolometers (100 × 100 pixels).
- Improve LO power to sufficiently drive mixers.
- Novel artificial materials (EBG, metamaterials) are emerging, and initial studies have shown very promising results. EBG and LHM technology offers promising alternatives to overcome the limitations of the

current technology, and it is envisaged that many new structures will evolve.

- Micro-System Technologies and specifically RF MEMS will allow developing innovative functional concepts to demonstrate adjustability and tunability, which may represent a fundamental change in the way systems are being designed today when the design itself (and the technology) will probably allow compensation for design and fabrication process inaccuracy by the addition of MEMS devices to optimize the structure geometry and therefore its parameters.

4.2. Everyday Applications

In analogy to space applications, also for the everyday use of Terahertz technology, a “market pull” and “technology push” situation is observed.

Starting with the “market pull” emphasis on the application areas identified is given by the intrinsic benefits of Terahertz radiation. Interest is high, especially for imaging and sensing applications in niches where traditional analytic methods have difficulties, although no broad market exists to date. Some of the Terahertz sensing and imaging applications identified by exploratory work are:

- Gas sensing for environmental sensing or combustion/plasma process control [115,116].
- Material characterization, for example, analysis of dielectrics, semiconductors, metals, and – more exotic materials like superconductors [45,47].
- Biomolecular sensing chips for biotechnology and pharmaceutical research [36,37].
- Monitoring chemical content or composition, e.g., during medicament production [39].
- Process monitoring and quality control, e.g., for steel manufacturing [117].
- Imaging through packages or clothes for security issues and drug detection [11].
- Medical imaging, e.g., for early carcinoma detection [28].
- Cellular level imaging, e.g., for analysis of metabolic processes [108].
- Nonionizing dental imaging [29].
- Tomographic imaging, surface reconstruction [10,118].

In general, the fields where Terahertz technology has generated interests are very wide. However, it must be emphasized that many of these applications are currently still at the proof of principle stage and that they still have to meet market-relevant criteria such as cost, reliability, integration, etc., before a broad market penetration can be expected. In contrast to space applications, where Terahertz techniques are regularly used and it is widely accepted that most future scientific breakthroughs in astronomy will stem from Terahertz missions, Terahertz technology for everyday applications has still to meet technological issues before wider acceptance is achieved. Therefore, the “technology push” for everyday applica-

tions is not only a way to optimize or expand solutions, as is the case for space missions. For everyday applications it is imperative and obligatory to enhance the performance, lower the cost, and increase the integration of existing Terahertz technologies to meet the broad market expectations. Areas where crucial technological improvement is expected and required are:

- Compact and efficient Terahertz sources, like quantum cascade Terahertz lasers and quantum optoelectronic cw sources. Here efficiency increase has a two-fold positive implication: Higher efficiency enables the higher output powers that are required for fast high-throughput imaging and sensing solutions. Higher efficiency also enables more compact pump lasers or electronics, which reduce the cost and size of systems solutions.
- Room temperature sensitive detectors are necessary to cope with compact and cost efficient solutions in everyday applications.
- Detection arrays are decisive to enable fast imaging systems in various fields like security scanning, medical imaging, etc.
- Terahertz sensors and sensing elements, e.g., for biomolecular detection, are scarcely available, but necessary in order to realize integrated sensing systems like biochips.

Fundamental system integration technologies need improvement. Here, a close connection to the achieved advances and future expectations of space Terahertz technologies is given, including e.g., interest in emerging artificial materials (EBG, LHM) or the implementation of RF-MEMS.

At the system level, engineering improvements and data acquisition and processing improvements are desired to enable high-throughput sensing and imaging systems. For this purpose also, efficient parallel detection concepts seem promising.

5. SUMMARY/FUTURE

The Terahertz gap appears close to being bridged, which has come about through combined effort from both sides, the photonic side coming down in frequency and the microwave side going up. There is now little to stop Terahertz technology reaching the commercial sector. Many of the key technology requirements are now in place. High-sensitivity detectors exist in both cooled and room temperature form. The mass manufacturability fabrication technology is in place and the design tools necessary for more complex system integration are becoming commercially available. The main missing element is a convenient source of Terahertz power. Cooled lasers have been demonstrated and room temperature solid-state sources have been demonstrated to 1.4 THz, but relatively low powers have been achieved. To some extent, further progress may be realized by scaling up existing technology, but a quantum breakthrough is required before a practical solid-state Terahertz source is realized. The importance of this final step cannot be

understated, the arrival of the Gunn oscillator into the microwave allowed the rapid commercialization of the many applications, and such a simple solution for the Terahertz region would have a similar effect.

BIBLIOGRAPHY

1. H. Rubens and E. Nichols, Heat waves of great wavelength, *Phys. Rev. (Series I)*, **4**:314 (1897).
2. J. M. Chamberlain, Recent progress in decreasing the THz gap, *Phil. Trans. Roy. Soc. Lond. A*, **362**:199–213 (2004).
3. J. Maxwell, On a dynamical theory of the electromagnetic field, *Phil. Trans.*, **155**:459 (1865).
4. H. Hertz, Ueber die Ausbreitungsgeschwindigkeit der electrodynamischen Wirkungen, *Annalen der Physik und Chemie*, **34**:551–569 (1888).
5. P. Selenyi, Wide-angle interferences and the nature of the elementary light sources, *Phys. Rev.*, **56**:477 (1939).
6. A. Schawlow and C. Townes, Infrared and optical masers, *Phys. Rev.*, **112**(6):1940–1949 (1958).
7. T. Löffler, K. J. Siebert, H. Quast, N. Hasegawa, G. Loata, R. Wipf, T. Hahn, M. Thomson, R. Leonhardt, and H. G. Roskos, All-electronic continuous-wave terahertz systems, *Phil. Trans. Roy. Soc. Lond. A*, **362**:263–281 (2004).
8. D. Arnone and C. Ciesla, Applications of terahertz technology to medical imaging, *Proc. SPIE*, **3828**:209–219 (1999).
9. M. Brucherseifer, P. Haring Bolívar, H. Klingenberg, and H. Kurz, Angle dependent THz tomography—Characterization of thin ceramic oxide films for fuel cell applications, *Appl. Phys. B*, **72**:361 (2001).
10. Wang and X. C. Zhang, Pulsed terahertz tomography, *J. Phys. D: Appl. Phys.*, **37**:R1–R36 (2004).
11. K. Kawase, Y. Ogawa, and Y. Watanabe, Non-destructive terahertz imaging of illicit drugs using spectral fingerprints, *Opt. Expr.*, **11**:2549 (2003).
12. P. Haring Bolivar, M. Nagel, F. Richter, M. Brucherseifer, H. Kurz, A. Bosserhoff, and R. Büttner, Label-free THz sensing of genetic sequences: towards THz biochips, *Phil. Trans. Roy. Soc. Lond. A*, **362**:323–335 (2004).
13. P. de Maagt, (Sub)millimetre wave antenna technology for upcoming ESA missions, AP-2000 Millenium Conf. Ant. & Prop., April, 9–14, 2000, Davos, Switzerland, CD-ROM, pdf 233.
14. M. Gaidis, Space-based Applications of far-Infrared systems, *8th Int. Conference on Terahertz Electronics*, September 28–29, 2000, Darmstadt, Germany, pp. 125–128.
15. M. Salamone and J. Tauber, *PLANCK, A Mission to Understand the Origin and Evolution of our Universe*, ESA Publications Division, ESA BR-159, July 2000.
16. J. A. Tauber, The Planck mission, The extragalactic infrared background and its cosmological implications, *Proc. IAU Symp.*, **204**:493 (2001).
17. M. Salomone and G. Pilbratt, *Exploring the Formation of Galaxies and Stars—the FIRST Brochure*, ESA Publications Division, ESA BR-158, July 2000.
18. G. L. Pilbratt, The Herschel Mission, Scientific Objectives, and this Meeting, *Proc. Promise Herschel Space Observ.*, December 12–15, 2001, Toledo, Spain, ESA SP-460, pp. 13–20, 2001.
19. S. Gulkis, M. Frerking, G. Beaudin, P. Hartogh, M. Janssen, C. Kahn, T. Koch, and Y. Salinas, *Microwave Instrument for*

- the Rosetta Orbiter (MIRO) (Special Publication)*, Noordwijk, The Netherlands: ESA SP-1165, 2002.
20. P. Bond, *Rosetta's Comet Chaser*, ESA Publications Division, ESA BR-179, 2001.
 21. D. Lamarre, J. Langen, C-C. Lin, L. Marchand, P. de Maagt, and T. Narhi, Technological needs for ESA microwave limb-sounders, *Proc. 8th Int. Conf. Terahertz Electron.*, September 28-29, 2000, Darmstadt, Germany, pp. 103-108.
 22. B. Moyna, E. Allouis, R. Brunt, U. Cortesi, B. N. Ellison, J. Eskell, T. Forward, T. Jones, D. Lamarre, J. Langen, P. J. de Maagt, D. I. Morgan, M. Oldfield, J. Reburn, and R. Siddans, MARSCHALS: Development of an airborne millimeter wave limb sounder, *Proc. SPIE*, **4540**, International Symposium on Remote Sensing, September 17-21, 2001, Toulouse, France, pp. 221-228.
 23. G. N. Harding, M. F. Kimmitt, J. H. Ludlow, P. Porteous, A. C. Prior, and V. Roberts, Emission of sub-millimetre electromagnetic radiation from hot plasma in ZETA, *Proc. Phys. Soc.*, **77**:1069-1075 (1961).
 24. O. Tudisco, F. Berton, P. Buratti, E. Grilli, and S. Mantovani, A submillimeter polychromator for plasma spectroscopy, *Rev. Sci. Instr.*, **67**:3108-3116 (1996).
 25. D. L. Brower, K. W. Kim, L. Zeng, Y. Jiang, E. J. Doyle, and W. A. Peebles, Integrated reflectometer-interferometer system for plasma density profile measurement, *Plasma Phys. Control. Fusion*, **40**:1575-1584 (1998).
 26. S. Bäumel, G. Michel, H. J. Hartfuss, M. R. G. Arbolí, and H. L. Hartnagel, Two-dimensional correlation measurements of electron cyclotron emission fluctuations on the stellarator Wendelstein 7-AS, *Rev. Sci. Instr.*, **74**:1441-1444 (2003).
 27. M. Thumm, Novel applications of millimeter and submillimeter wave gyrodevices, *Intl. J. Infrared Millimeter Waves*, **22**:337-386 (2001).
 28. R. M. Woodward, B. Cole, V. P. Wallace, D. D. Arnone, R. Pye, E. H. Linfield, M. Pepper, and A. G. Davies, Terahertz pulse imaging of in-vitro basal cell carcinoma samples, *OSA TOPS*, **56**:329 (2001).
 29. N. N. Zinov'ev, C. D. Sudworth, E. Berry, S. M. Strafford, D. J. Wood, F. A. Carmichael, R. E. Miles, M. A. Smith, and J. M. Chamberlain, Identification of tooth abnormalities using THz imaging and spectroscopy, *Proc. SPIE*, **5141**:196-201 (2003).
 30. D. Crawley, C. Longbottom, V. P. Wallace, B. Cole, D. Arnone, and M. Pepper, Three-dimensional terahertz pulse imaging of dental tissue, *J. Biomol. Opt.*, **8**:303-307 (2003).
 31. R. A. Cheville and D. Grischkowsky, Far-infrared terahertz time-domain spectroscopy of flames, *Opt. Lett.*, **20**(15):1646-1648 (1995).
 32. D. M. Mittleman, S. Hunsche, L. Boivin, and M. C. Nuss, T-ray tomography, *Opt. Lett.*, **22**:904 (1997).
 33. S. P. Jamison, J. Shen, D. R. Jones, R. C. Issac, B. Ersfeld, D. Clark, and D. A. Jaroszynski, Plasma characterization with terahertz time-domain measurements, *J. Appl. Phys.*, **93**(7):4334 (2003).
 34. A. G. Markelz, A. Roitberg, and E. J. Heilweil, Pulsed terahertz spectroscopy of DNA, bovine serum albumin and collagen between 0.1 and 2.0 THz, *Chem. Phys. Lett.*, **320**:42 (2000).
 35. M. Brucherseifer, M. Nagel, P. Haring Bolívar, H. Kurz, A. Bosserhoff, and R. Büttner, Label-free probing of the binding state of DNA by time-domain terahertz sensing, *Appl. Phys. Lett.*, **77**:4049-4052 (2000).
 36. S. P. Mickan, A. Menikh, H. Liu, C. A. Mannella, R. MacColl, D. Abbott, J. Munch, and X-C. Zhang, Label-free bioaffinity detection using terahertz technology, *Phys. Med. Biol.*, **47**:3789-3795 (2002).
 37. M. Nagel, P. Haring Bolívar, M. Brucherseifer, H. Kurz, A. Bosserhoff, and R. Büttner, Integrated THz technology for label-free genetic diagnostics, *Appl. Phys. Lett.*, **80**:154-157 (2002).
 38. P. Haring Bolivar, M. Nagel, F. Richter, M. Brucherseifer, H. Kurz, A. Bosserhoff, and R. Büttner, Label-free THz sensing of genetic sequences: towards THz biochips, *Phil. Trans. Roy. Soc. Lond. A*, **362**:323-335 (2004).
 39. P. F. Taday, Applications of terahertz spectroscopy to pharmaceutical sciences, *Phil. Trans. Roy. Soc. Lond. A*, **362**:351-364 (2004).
 40. Y. Watanabe, K. Kawase, T. Ikari, H. Ito, Y. Ishikawa, and H. Minamide, Component spatial pattern analysis of chemicals using terahertz spectroscopic imaging, *Appl. Phys. Lett.*, **83**(4):800-802 (2003).
 41. M. C. Kemp, P. F. Taday, B. Cole, J. A. Cluff, A. J. Fitzgerald, and W. R. Tribe, *Proc. SPIE*, **5000**:44 (2003).
 42. R. Appleby, Passive millimetre-wave imaging and how it differs from terahertz imaging, *Phil. Trans. R. Soc. Lond. A*, **362**:379-394 (2004).
 43. D. Woolard, R. Kaul, R. Suenram, A. H. Walker, T. Globus, and A. Samuels, Terahertz electronics for chemical and biological warfare agent detection, *IEEE MTT-S Int. Microwave Symp. Dig.*, June 13-19:925-928 (1999).
 44. M. C. Nuss and J. Orenstein, THz time-domain spectroscopy, in *Millimeter and Sub-Millimeter Waves*, G. Gruener, ed., Heidelberg: Springer-Verlag, 1998.
 45. D. Grischkowsky, S. Keiding, M. van Exter, and Ch. Fattering, Far-infrared time-domain spectroscopy with terahertz beams of dielectrics and semiconductors, *JOSA B*, **7**(10):2006 (1990).
 46. P. Haring Bolivar, M. Brucherseifer, J. Gómez Rivas, R. Gonzalo, I. Ederra, A. Reynolds, M. Holker and P. de Maagt, Measurement of the dielectric constant and loss tangent of high dielectric constant materials at terahertz frequencies, *IEEE Trans. Microw. Th. Tech.*, **51**:1062-1065 (2003).
 47. M. C. Nuss and K. W. Goossen, Investigation of high-temperature superconductors with terahertz-bandwidth electrical pulses, *IEEE J. Quant. Electr.*, **25**(12):2596-2607 (1989).
 48. M. Brucherseifer, A. Meltzow-Altmeier, P. Haring Bolívar, H. Kurz, and P. Seidel, Low-temperature THz imaging of thin high-temperature superconductor films, *Physica C: Superconduct.*, **399**(1-2):53-60 (2003).
 49. R. D. Averitt, A. I. Lobad, C. Kwon, S. A. Trugman, V. K. Thorsmole, and A. J. Taylor, Ultrafast conductivity dynamics in colossal magnetoresistance manganites, *Phys. Rev. Lett.*, **87**(1):017401 (2001).
 50. G. Kozlov and A. Volkov, Coherent source submillimetre wave spectroscopy, in *Millimeter and Sub-Millimeter Waves*, G. Gruener, ed., Heidelberg, Germany: Springer-Verlag, 1998.
 51. T-I. Jeon, K-J. Kim, C. Kang, S-J. Oh, J-H. Son, K. H. An, D. J. Bae, and Y. H. Lee, Terahertz conductivity of anisotropic single walled carbon nanotube films, *Appl. Phys. Lett.*, **80**(18):2403-2406 (2002).
 52. B. B. Hu and M. C. Nuss, Imaging with terahertz waves, *Opt. Lett.*, **20**(16):1716 (1995).
 53. A. F. Harvey, *Microwave Engineering*, New York: Academic Press, 1963.
 54. J. B. Gunn, Microwave Oscillation of Current in III-V Semiconductors, *Solid State Commun.*, **1**:88 (1963).
 55. E. Sein, Y. Toulemont, F. Safa, M. Duran, P. Deny, D. de Chambure, Th. Passvogel, and G. Pilbratt, A 3.5 m

- diameter SiC telescope for Herschel mission, *Proc. SPIE*, **4850** (IR Space Telescopes and Instruments):606–618 (2003).
56. T. Stute, G. Wulz, and D. Scheulen, Recent developments of advanced structures for space optics at astrum germany, *Proc. SPIE*, **5179** (Optical Materials and Structures Technologies): 292–302 (2003).
 57. R. Jorgensen, G. Padovan, P. de Maagt, D. Lamarre, and L. Coste, A five frequency mm-wave antenna for a spaceborne limb sounding instrument, *IEEE Trans. Ant. Prop.*, **49**(5):703–714 (2001).
 58. C. Antonopoulos, R. Cahill, E. A. Parker, and I. M. Sturland, Multilayer frequency-selective surfaces for millimetre and submillimetre wave applications, *IEE Proc. Microwav. Ant. Prop.*, **144**(6):415–420 (1997).
 59. R. Dickie, R. Cahill, H. Gamble, V. Fusco, N. Grant, and C. Philpot, Multilayer mesh filters for quasi-optical beamsplitting applications in meteorological and Science Space instrumentation, *3rd ESA Workshop on Millimetre Wave Technology and Applications: Circuits, Systems, and Measurement techniques*, May 21–23, 2003, Millilab, Espoo, Finland, pp. 343–347.
 60. B. N. Ellison, M. L. Oldfield, D. N. Matheson, B. J. Maddison, C. M. Mann, and A. F. Smith, Corrugated feedhorns at terahertz frequencies—preliminary results, *5th Int. Symp. Space Terahertz Technol.*, May 1994, Ann Arbor, Michigan, pp. 851–860.
 61. G. Rebeiz, Millimeter-wave and terahertz integrated circuit antennas, *Proc. IEEE*, **80**(11):1748–1770 (1992).
 62. V. P. Koshelets and S. V. Shitov, Integrated superconducting receivers, *Supercond. Sci. Technol.*, **13**:R53–R69 (2000).
 63. E. Yablonovitch, Inhibited spontaneous emission in solid state physics and electronics, *Phys. Rev. Lett.*, **58**:2059–2062 (1987).
 64. S. John, Strong localization of photons in certain disordered dielectric superlattices, *Phys. Rev. Lett.*, **58**:2486–2489 (1987).
 65. R. Gonzalo, I. Ederra, C. M. Mann, and P. de Maagt, Radiation properties of terahertz dipole antenna mounted on photonic crystal, *Electron. Lett.*, **37**(10):613–614 (2001).
 66. M. van der Vorst, P. de Maagt, and M. Herben, Effect of internal reflections on the radiation properties and input admittance of integrated lens antennas, *IEEE Trans. Micr. Theory Techn.*, **47**(9):1696–1704 (1999).
 67. M. van der Vorst, P. de Maagt, A. Neto, A. Reynolds, R. Heeres, W. Luinge, and M. Herben, Effect of internal reflections on the radiation properties and input impedance of integrated lens antennas-comparison between theory and measurements, *IEEE Trans. Micr. Theory. Techn.*, **49**(6 Part 1):1118–1125 (2001).
 68. D. A. Brown, A. S. Treen, and N. J. Cronin, Micromachining of terahertz waveguide components with integrated active devices, *19th International Conference on Infrared and Millimetre Waves*, Sendai, Japan, pp. 359–360, 1994.
 69. D. A. Naylor, B. G. Gom, P. A. R. Ade, and J. E. Davis, Design and performance of a dual polarization detector system for broadband astronomical spectroscopy at submillimetre wavelengths, *Rev. Sci. Instrum.*, **70**:4097 (1999).
 70. C. V. Haynes and P. A. R. Ade, Low pass filters for the far infrared, *18th International Conference on IR and mm Waves*, Colchester, United Kingdom, September 1993.
 71. C. Lee, P. A. R. Ade, and C. V. Haynes, Self supporting filters for compact focal plane designs, *Proc. 30th ESLAB Symp.*, September 1996, Noordwijk, The Netherlands: ESTEC, pp. 81–83.
 72. W. S. Holland, E. I. Robson, W. K. Gear, C. R. Cunningham, J. F. Lightfoot, T. Jenness, R. J. Ivison, J. A. Stevens, P. A. R. Ade, M. J. Griffin, W. D. Duncan, J. A. Murphy, and D. A. Naylor, SCUBA: A common-user submillimetre camera operating on the James Clerk Maxwell Telescope, *MNRAS*, **303**:659 (1999).
 73. A. G. Murray, P. A. R. Ade, and M. J. Griffin, Development of achromatic waveplates for submillimetre polarimetry, in *Polarimetry of the Interstellar Medium*, W. Roberge and D. Whittet, eds., ASP Conference Series Vol. 97, 1996.
 74. T. G. Phillips and K. B. Jefferts, A low temperature bolometer heterodyne receiver for millimeter wave astronomy, *Rev. Sci. Instrum.*, **44**:1009–1014 (1973).
 75. P. Mauskopf, P. Ade, J. Bock, S. Edgington, S. Golwala, A. Goldin, J. Glenn, D. Haig, V. Hristov, B. Knowles, A. Lange, H. Nguyen, and B. Rownd, Results from the first engineering run of BOLOCAM and plans for the future, *AIP Conf. Proc.*, **616**(1):107–115 (2002).
 76. B. S. Karasik, W. R. McGrath, H. G. LeDuc, and M. E. Gershenson, A hot electron direct detector for radioastronomy, *Superconduct. Sci. Technol.*, **12**:745–747 (1999).
 77. A. D. Semenov, Yu. P. Gousev, R. S. Nebosis, K. F. Renk, P. Yagoubov, B. M. Voronov, G. N. Gol'tsman, V. D. Syomash, and E. M. Gershenson, Heterodyne detection of THz radiation with a superconducting hot-electron bolometer mixer, *Appl. Phys. Lett.*, **69**(2):1–3 (1996).
 78. W. R. McGrath, B. S. Karasik, A. Skalare, R. Wyss, B. Bumble, and H. G. LeDuc, Hot-electron superconductive mixers for THz frequencies, in *SPIE Terahertz Spectroscopy Applicat. Conf.*, **3617**:80–88 (1999).
 79. I. Mehdi, T. Lee, D. Humphrey, S. Martin, R. J. Dengler, J. E. Oswald, A. Pease, R. P. Smith, and P. H. Siegel, 600 GHz planar-Schottky-diode subharmonic waveguide mixers, *Proc. IEEE MTT-S Int. Microwave Symp.*, San Francisco, CA, June 17–21, 1996, Paper TU4-E3.
 80. S. A. Maas, *The RF and Microwave Circuit Design Cookbook (Microwave Library)*, ISBN: 0890069735.
 81. P. H. Siegel, R. J. Dengler, I. Mehdi, J. E. Oswald, W. L. Bishop, T. W. Crowe, and R. J. Mattauch, Measurements on a 215-GHz Subharmonically Pumped Waveguide Mixer Using Planar Back-to-Back Air-Bridge Schottky Diodes, *Trans. Microwave Theory Techn.*, **41**:1913–1921 (1993).
 82. B. P. Moyna, C. M. Mann, M. L. Oldfield, M. Beardsley, B. N. Ellison, D. N. Matheson, I. Cartmell, and T. W. Crowe, Broadband space-qualified subharmonic mixers at 183 GHz with low local oscillator power requirements, *The 2nd ESA Workshop on Millimetre Wave Technology and Applications: Antennas, Circuits and Systems*, May 27–29, 1998, MilliLab, Espoo, Finland, pp. 314–320.
 83. D. T. Young, and J. C. Irwin, Millimeter frequency conversion using Au-n-type GaAs Schottky barrier epitaxial diodes with a novel contacting technique, *Proc. IEEE*, **53**:2130–2131 (1965).
 84. E. R. Mueller, W. E. Robotham, R. Meisner, R. Hart, J. Kennedy, and L. Newman, 2.5 THz laser local oscillator for the EOS chem 1 satellite, *The 9th International Conference on Space Terahertz Technology*, Pasadena, CA, March 17–19, 1998, pp. 563–572.
 85. W. Bishop, K. McKinney, R. Mattauch, T. Crowe, and G. Green, A novel whiskerless diode for millimeter and submillimeter wave applications, *Proc. IEEE MTT-S Int. Microwave Symp.*, Las Vegas, NV, June 9–11, 1987, pp. 607–610.
 86. S. H. Gold and G. S. Nusinovich, Review of high-power microwave source research, *Rev. Sci. Instrum.*, **68**(11):3945–3974 (1997).
 87. J. W. Waters, et al., The UARS and EOS Microwave Limb Sounder (MLS) experiments, *J. Atmos. Sci.*, **56**(2):194–218 (1999).

88. H. Eisele and G. Haddad, Two terminal millimeter-wave sources, *IEEE Trans. Microwave Theory Tech.*, **46**:739–746 (1998).
89. P. Stenger, M. Sarantos, E. Niehenke, H. Fudem, C. Schwerdt, F. Kuss, D. Strack, G. Hall, and J. Masti, A miniature, MMIC one watt W-band solid-state transmitter, *Proc. MTT-S Int. Microwave Symp., Denver, CO*, **2**:431–434 (1997).
90. S. Martin, B. Nakamura, A. Fung, P. Smith, J. Bruston, A. Maestrini, F. Maiwald, P. H. Siegel, E. Schlecht, and I. Mehdi, Fabrication of 200 to 2700 GHz multiplier devices using GaAs and metal membranes, *Proc. IEEE MTT-S Int. Microwave Symp. Dig., Phoenix, AZ*, **3**:1641–1644 (2001).
91. A. V. Raisanen, Frequency multipliers for millimeter and sub-millimeter wavelengths, *Proc. IEEE*, **80**:1842–1852 (1992).
92. D. Porterfield, J. Hesler, T. Crowe, W. Bishop, and D. Woolard, Integrated Terahertz Transmit/Receive Modules, European Microwave Conference, Munich, Germany, October 2003, pp. 1319–1322.
93. X. Mélique, C. Mann, P. Mounaix, J. Thornton, O. Vanbésien, F. Molot, and D. Lippens, *IEEE Microwave Guided Wave Lett.*, **8**:384 (1998).
94. E. Alekseev, A. Eisenbach, D. Pavlidis, S. M. Hubbard, and W. Sutton, Development of GaN-based Gunn-Effect Millimeter-Wave Sources WOCSDICE 2000, Aegean Sea, Greece, May 29–June 02, 2000.
95. C. M. Mann, D. N. Matheson, M. L. Oldfield, P. J. Koh, T. W. Crowe, W. L. Bishop, R. M. Weikle, and J. L. Hesler, A simple micromachining technique for millimetre and submillimetre wavelengths, *Proc. 2nd ESA Workshop on Millimetre Wave Technology and Applications*, Espoo, Finland, pp. 144–150, 1998.
96. M. C. Gaidis, H. M. Pickett, C. D. Smith, R. P. Smith, S. C. Martin, and P. H. Siegel, A 2.5 THz receiver front-end for spaceborne applications, *IEEE Trans. Microwave Theory Tech.*, **48**:733–739 (2000).
97. P. Haring Bolívar, Coherent THz spectroscopy, in *Semiconductor Quantum Optoelectronics: From Quantum Physics to Smart Devices*, A. Miller, M. Ebrahimzadeh, and D. M. Finlayson, eds., Bristol, UK: Institute of Physics Publishing, pp. 151–192, 1999.
98. D. Dragoman and M. Dragoman, THz fields and applications, *Progress in Quantum Electron.*, **28**: 1–66 (2004).
99. P. H. Siegel, Terahertz technology, *IEEE Trans. Micr. Th. Techn.*, **50**:910–928 (2002).
100. P. R. Smith, D. H. Auston, and M. C. Nuss, Subpicosecond photoconductive antennas, *IEEE J. Quant. Electr.*, **24**: 255–260 (1988).
101. D. H. Auston and M. C. Nuss, Electrooptic generation and detection of femtosecond transients, *IEEE J. Quant. Electr.*, **24**:184–197 (1988).
102. C. Janke, P. Haring Bolívar, A. Bartels, H. Kurz, and H. Künzel, Inversionless amplification of coherent terahertz radiation, *Phys. Rev. B*, **67**:155206 (2003).
103. G. Zhao, R. N. Schouten, N. van der Valk, W. Th. Wenkebach, and P. C. M. Planken, Design and performance of a THz emission and detection setup based on a semi-insulating GaAs emitter, *Rev. Sci. Instr.*, **73**:1715 (2002).
104. A. Brodschelm, F. Tausser, R. Huber, J. Y. Sohn, and A. Leitenstorfer, Detection of tunable femtosecond pulses with frequency components beyond 100 THz, *Springer Series in Chemical Physics*, **66**:215 (2000).
105. M. Brucherseifer, P. Haring Bolívar, and H. Kurz, Combined optical and spatial modulation THz-spectroscopy for the analysis of thin-layered systems, *Appl. Phys. Lett.*, **81**:1791–1793 (2002).
106. X. C. Zhang, Three-dimensional terahertz wave imaging, *Phil. Trans. Roy. Soc. Lond. A*, **362**:283–300 (2004).
107. S. Hunsche, M. Koch, I. Brener, and M. C. Nuss, THz near-field imaging, *Opt. Comm.*, **150**:22–26 (1998).
108. N. C. J. van der Valk and P. C. M. Planken, Electro-optic detection of subwavelength terahertz spot sizes in the near field of a metal tip, *Appl. Phys. Lett.*, **81**:1558 (2002).
109. J. O'Hara and D. Grischkowsky, Synthetic phased-array terahertz imaging, *Opt. Lett.*, **27**:1070 (2002).
110. S. Verghese, K. A. McIntosh, S. Calawa, W. F. Dinatale, E. K. Duerr, and K. A. Molvar, Generation and detection of coherent terahertz waves using two photomixers, *Appl. Phys. Lett.*, **73**:3824 (1998).
111. K. Kawase, J. Shikata, and H. Ito, Terahertz wave parametric source, *J. Phys. D: Appl. Phys.*, **34**:R1–R14 (2001).
112. R. Köhler, A. Tredicucci, F. Beltram, H. Beere, E. Linfield, A. Davies, D. Ritchie, R. Iotti, and F. Rossi, Terahertz semiconductor-heterostructure laser, *Nature*, **417**:(6885): 156–159 (2002).
113. B. S. Williams, S. Kumar, H. Callebaut, Q. Hu, and J. L. Reno, THz quantum-cascade laser operating up to 137 K, *Appl. Phys. Lett.* **83**:5142 (2003).
114. M. Graf, G. Scalari, D. Hofstetter, J. Faist, H. Beere, E. Linfield, D. Ritchie, and G. Davies, Terahertz range quantum well infrared photodetector, *Appl. Phys. Lett.*, **84**(4):475 (2004).
115. D. M. Mittleman, R. H. Jacobsen, and M. C. Nuss, IT-ray imaging, *IEEE J. Sel. Top. Quan. Electron.*, **2**:679 (1996).
116. M. van Exter and D. R. Grischkowsky, *IEEE Trans. Microwave Th. Tech.*, **38**:1684 (1990).
117. N. Hasegawa, T. Löffler, M. Thomson, and H. G. Roskos, Remote identification of protrusions and dents on surfaces by THz reflectometry with spatial beam filtering and out-of-focus detection, *Appl. Phys. Lett.*, **83**:3996 (2003).
118. D. M. Mittleman, R. H. Jacobsen, R. Neelamani, R. G. Baraniuk, and M. C. Nuss, Gas sensing using terahertz time-domain spectroscopy, *Appl. Phys. B*, **67**:379–390 (1998).

THERMAL ANALYSIS AND DESIGN OF ELECTRONIC SYSTEMS

ALLAN D. KRAUS
Allan D. Kraus Associates
AVRAM BAR-COHEN
KARL J. GEISLER
University of Minnesota-Twin
Cities

1. TRENDS AND NEEDS IN THERMAL MANAGEMENT

1.1. Thermal Packaging Roadmaps

The challenges posed by high chip heat fluxes and ever more stringent performance and reliability constraints make thermal management a key enabling technology in the development of microelectronic systems for the

Table 1. SIA/NEMI Roadmap Product Categories

Product	Description
Low cost— <\$300	Commodity consumer products, disk drives, displays, and microcontrollers
Hand held— <\$1000	Battery-powered products, PDAs, and cellular telephones
Cost/performance— <\$3000	Notebooks, desktop computers, and telecommunications
High performance— >\$3000	High-end workstations, servers, and supercomputers
Harsh environments	Under-the-hood automotive, mining, and resource exploration
Memory	DRAMs and SRAMs

twenty-first century. Thus, thermal packaging efforts must be performed in the context of the salient trends and parameters that characterize the IC technology and the electronic products industry.

Recent road-mapping efforts, including the Semiconductor Industry Association's (SIAs) National Technology Roadmap for Semiconductors [1] and NEMI's National Electronics Manufacturing Technology Roadmap [2], have affirmed the expectation that improvements in CMOS semiconductor technology will continue unabated into the early part of the twenty-first century. Exploiting the potential of this IC technology, with the attendant increase in chip size, switching speed, and transistor density, will necessitate significant improvements in packaging technology. Furthermore, under the influence of growing product complexity, packaging is evolving from an IC technology enabler to a primary electronic product/system differentiator. Consequently, future packaging technology may well be driven primarily by market application requirements, with reduced cost per function providing the major technology development and execution challenges.

The SIA and NEMI roadmaps recognize the six categories of market applications listed in Table 1. Together these categories encompass the majority of the product stream of the semiconductor industry. It is anticipated that system costs will remain fixed in each of these categories, despite ever increasing functionality. It is also assumed that power, voltage, operating, and chip junction temperatures, as well as package thickness, will be determined by market requirements, whereas all other needs are derived from scaling laws or physics-based extrapolations.

Table 2 summarizes the range expected to prevail in the salient IC device characteristics, across the six categories. As may be seen in Table 2, by the year 2006, at the leading edge, chip frequency is expected to reach 1250 MHz with a chip size of 900 mm² and a chip power 140 W. In assessing the technology needed for each of these categories, emphasis was placed on the revenue "center-of-gravity."

Based on these considerations, the NEMI Packaging Working Group determined that the following research and development issues needed to be addressed:

- Arriving innovation with aggressive cost-reduction targets, for all but the Cost-Performance segment
- Achieving the breakthroughs needed for 0.2mm chip thinning and handling
- EMI and noise margin management, for high-speed, low-voltage applications

Integration of design, chip fabrication, assembly and packaging, and test technologies beyond 2001

Anticipation of an accelerating shift from peripheral to area array chip interconnects

The NEMI Working Groups also concluded that significant improvements in thermal management are required to support power-cost targets and that automotive needs ($T_j > 185^\circ\text{C}$) will require new quality and reliability techniques and packaging.

It may thus be seen that the challenges posed by high chip heat fluxes and ever more stringent performance and reliability constraints make thermal management one of the key enabling technologies for microelectronic systems in the twenty-first century. Focusing more specifically on cooling needs, the NEMI Working Groups proposed the following topology for thermal packaging technology:

Commodity products—natural convection

Handheld products—natural convection with heat spreaders

Cost and performance products—forced convection with heatsinks

High-performance products—forced convection, aggressive heatsinking, heat pipes, impingement cooling, and liquid cooling

1.2. Thermal packaging options

When the heat flux is dissipated by an electronic component, device, or assembly and the local ambient temperatures are known and the allowable temperature is specified, the equations of the following sections can be used to determine which heat transfer process or combination of processes (if any) can be employed to meet the desired performance goals. Figure 1 shows the variation of

Table 2. SIA National Technology Roadmap—Parameter Range for 2006

Parameter	Value
Chip frequency	300 to 1250 MHz
Chip size	75 to 900 mm ²
Package inputs/outputs	400 to 2200
Chip power	1 to 28 to 140 W
Junction temperature	100 to 195°C
Ambient temperature	45 to 170°C
Voltage	0.90 to 3.30 V

Source: Semiconductor Industry Association [1].

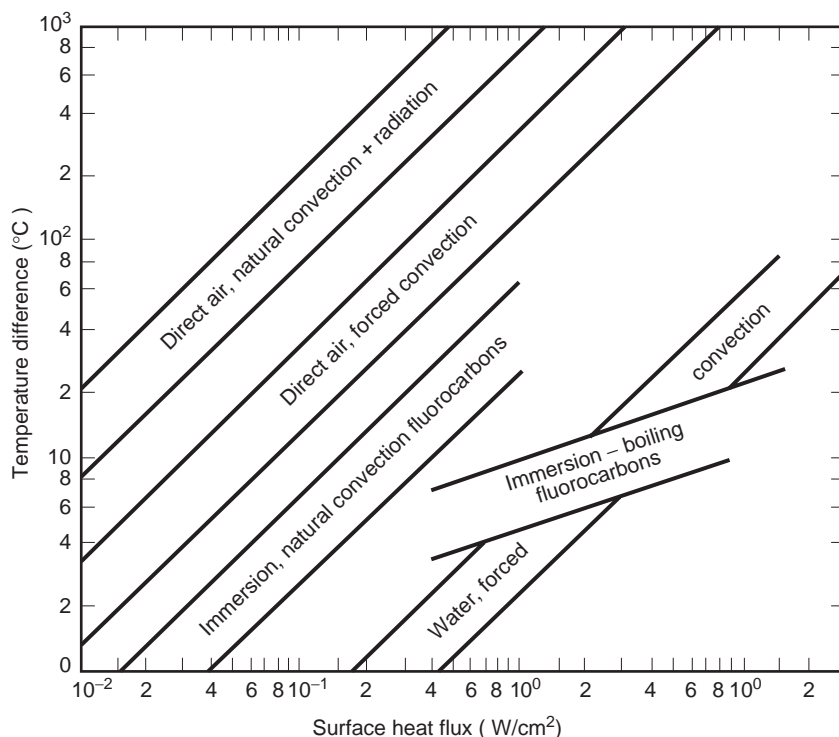


Figure 1. Temperature differences attainable as a function of heat flux for various heat transfer modes and various coolant fluids [3].

attainable temperature differences with surface heat flux for a variety of heat transfer modes and coolant fluids.

Examination of Fig. 1 reveals that for a typical allowable temperature difference of 60°C between the component surface and the ambient, natural cooling in air, relying on both free convection and radiation, is effective only for heat fluxes below approximately 0.05 W/cm^2 . Although forced convection cooling in air offers approximately an order-of-magnitude improvement in the heat transfer coefficient, this thermal configuration is unlikely to provide heat removal capability in excess of 1 W/cm^2 even at an allowable temperature difference of 100°C .

To facilitate the transfer of moderate and high heat fluxes from component surfaces, the thermal designer must choose between the use of finned air-cooled heatsinks and direct or indirect liquid cooling. Finned arrays and sophisticated techniques for improving convective heat transfer coefficients can extend the effectiveness of air cooling to progressively higher component heat fluxes but often at ever-increasing weight, cost, and volume penalties. Alternatively, reliance on heat transfer to liquids flowing at high velocity through so-called cold plates can offer a dramatic improvement in the transferrable heat flux even at temperature differences as low as 10°C , when the conduction resistance in the cold plate wall is negligible.

A similarly high heat flux capability is offered by boiling heat transfer to fluorochemical liquids. The high dielectric properties of these liquids make it possible to immerse most components. This direct liquid contact allows the removal of component heat fluxes in excess of 10 W/cm^2 with saturated pool boiling at temperature differences typically less than 20°C . Immersion cooling can also offer significant advantages and, as seen in Fig. 1 [3],

serves to bridge the gap between direct air cooling and cold plate technology.

Unfortunately, when addressed within stringent cost targets, the cooling requirements of twenty-first century microelectronic components cannot be met by today's thermal packaging technology. Rather, ways must be sought to improve on currently available technology, to leverage and combine the best features of existing thermal packaging hardware, and to introduce unconventional, perhaps even radical, thermal solutions into the electronic product family. In so doing, attention must be devoted to three primary issues:

1. *Highly Effective Air Cooling.* Removing dissipated power from one or several advanced chips within minimal volumes and with low air-side pressure drops.
2. *Heat Spreading.* Transporting heat from a relatively small area contiguous with the chip to a relatively large heatsink or cold plate base.
3. *Interfacial Heat Transfer.* Thermal resistances between the chip and the next level of thermal packaging.

Attention now turns to a detailed discussion of basic heat transfer and the determination of the various types of thermal resistances often encountered in electronic equipment.

2. THERMAL MODELING

To determine the temperature differences encountered in the flow of heat within electronic systems, it is necessary

to recognize the relevant heat transfer mechanisms and their governing relations. In a typical system, heat removal from the active regions of the microcircuit(s) or chip(s) may require the use of several mechanisms, some operating in series and others in parallel, to transport the generated heat to the coolant or ultimate heatsink. Practitioners of the thermal arts and sciences generally deal with four basic thermal transport modes: conduction, convection, phase change, and radiation.

2.1. Conduction Heat Transfer

2.1.1. One-dimensional Conduction. Steady thermal transport through solids is governed by the Fourier equation, which, in one-dimensional form, is expressible as

$$q = -kA \frac{dT}{dx} \quad (1)$$

where q is the heat flow, k is the thermal conductivity of the medium, A is the cross-sectional area for the heat-flow, and dT/dx is the temperature gradient. As depicted in Fig. 2 [4], heat-flow produced by a negative temperature gradient is considered positive. This convention requires the insertion of the minus sign in Eq. (1) to assure a positive heat flow, q . The temperature difference resulting from the steady-state diffusion of heat is thus related to the thermal conductivity of the material, the cross-sectional area, and the path length, L , according to

$$(T_1 - T_2)_{cd} = q \frac{L}{kA} \quad (2)$$

The form of Eq. (2) suggests that, by analogy to Ohm's Law governing electric current flow through a resistance, it is possible to define a thermal resistance for conduction, R_{cd} , as

$$R_{cd} \equiv \frac{(T_1 - T_2)}{q} = \frac{L}{kA}$$

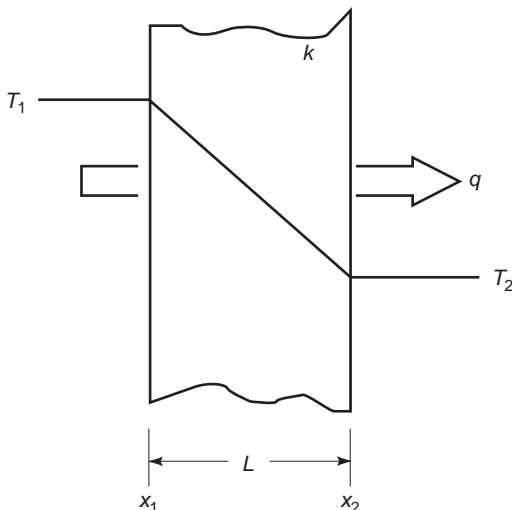


Figure 2. One-dimensional conduction through a slab [4].

2.1.2. One-Dimensional Conduction with Internal Heat Generation. Situations in which a solid experiences internal heat generation, such as that produced by the flow of an electric current, give rise to more complex governing equations and require greater care in obtaining the appropriate temperature differences. The axial temperature variation in a slim, internally heated conductor subjected to a constant and uniform internal heat generation and whose edges (ends) are held at a temperature T_0 , is found to equal

$$T = T_0 + q_g \frac{L^2}{2k} \left[\left(\frac{x}{L} \right) - \left(\frac{x}{L} \right)^2 \right]$$

When the volumetric heat generation rate, q_g , in watts per cubic meter, is uniform throughout, the peak temperature is developed at the center of the solid and is given by

$$T_{\max} = T_0 + q_g \frac{L^2}{8k}$$

Alternatively, because q_g is the volumetric heat generation, $q_g = q/LW\delta$, the center-edge temperature difference can be expressed as

$$T_{\max} - T_0 = q \frac{L^2}{8kLW\delta} = q \frac{L}{8kA} \quad (3)$$

where the cross-sectional area, A , is the product of the width, W , and the thickness, δ . An examination of Eq. (3) reveals that the thermal resistance of a conductor with a distributed heat input is only one quarter that of a structure in which all of the heat is generated at the center.

In the design of airborne electronic systems and equipment to be operated in a corrosive or damaging environment, it is often necessary to conduct the heat dissipated by the components down into the substrate or printed circuit board (PCB) and, as shown in Fig. 3, across the substrate-PCB to a cold plate or sealed heat exchanger. For a symmetrically cooled substrate-PCB with approximately uniform heat dissipation on the surface, a first estimate of the peak temperature at the center of the board can be obtained by use of Eq. (3).

This relation can be used effectively in the determination of the temperatures experienced by conductively cooled substrates and conventional PCBs, as well as PCB's with copper lattices on the surface, metal cores, or heatsink plates in the center. In each case, it is necessary to evaluate or obtain the effective thermal conductivity of the conducting layer. As an example, consider an alumina substrate, 0.20 m long, 0.15 m wide, and 0.005 m thick with a thermal conductivity of 20 W/mK, whose edges are cooled to 35°C by a cold plate. Assuming that the substrate is populated by 30 components, each dissipating 1 W, the substrate center temperature will equal 85°C when calculated using Eq. (3).

2.1.3. Spreading Resistance. In chip packages that provide for lateral spreading of the heat generated in the chip, the increasing cross-sectional area for heat flow at

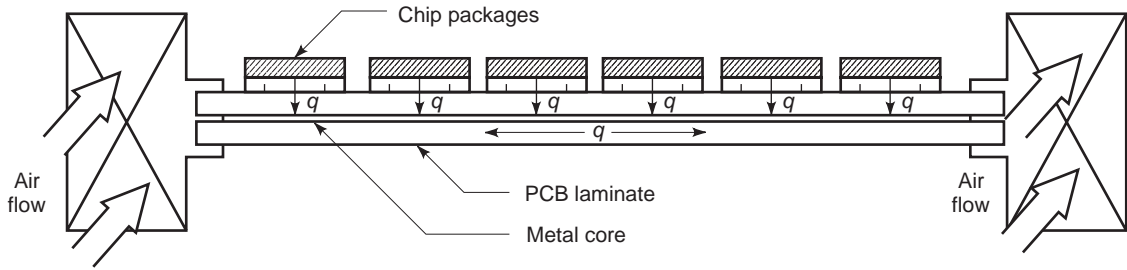


Figure 3. Edge-cooled printed circuit board populated with components [4].

successive layers below the chip reduces the internal thermal resistance. Unfortunately, however, there is an additional resistance associated with this lateral flow of heat. This, of course, must be taken into account in the determination of the overall chip package temperature difference.

For the circular and square geometries common in microelectronic applications, Negus et al. [5] provided an engineering approximation for the spreading resistance for a small heatsource on a thick substrate or heat spreader (required to be three to five times thicker than the square root of the heatsource area) can be expressed as

$$R_{sp} = \frac{0.475 - 0.62\varepsilon + 0.13\varepsilon^2}{k\sqrt{A_c}} \quad (4)$$

where ε is the ratio of the heatsource area to the substrate area, k is the thermal conductivity of the substrate, and A_c is the area of the heatsource.

For relatively thin layers on thicker substrates, such as encountered in the use of thin lead frames, or heat spreaders interposed between the chip and substrate, Eq. (4) cannot provide an acceptable prediction of R_{sp} . Instead, use can be made of the numerical results plotted in Fig. 4 to obtain the requisite value of the spreading resistance.

2.1.4. Interface and Contact Resistance. Heat transfer across the interface between two solids is generally accompanied by a measurable temperature difference, which can be ascribed to a contact or interface thermal resistance. For perfectly adhering solids, geometrical differences in the crystal structure (lattice mismatch) can impede the flow of phonons and electrons across the interface, but this resistance is generally negligible in engineering design. When dealing with real interfaces, the asperities present on each of the surfaces, as shown in an artist's conception in Fig. 5, limit actual contact between the two solids to a very small fraction of the apparent interface area. The flow of heat across the gap between two solids in nominal contact is, thus, seen to involve solid conduction in the areas of actual contact and fluid conduction across the open spaces. Radiation across the gap is of increasing importance for elevated surface temperatures and in a vacuum environment when convective and conductive mechanisms are suppressed.

The total contact conductance, h_{co} , is taken as the sum of the solid-to-solid conductance, h_c , and the gap conductance, h_g

$$h_{co} = h_c + h_g \quad (5)$$

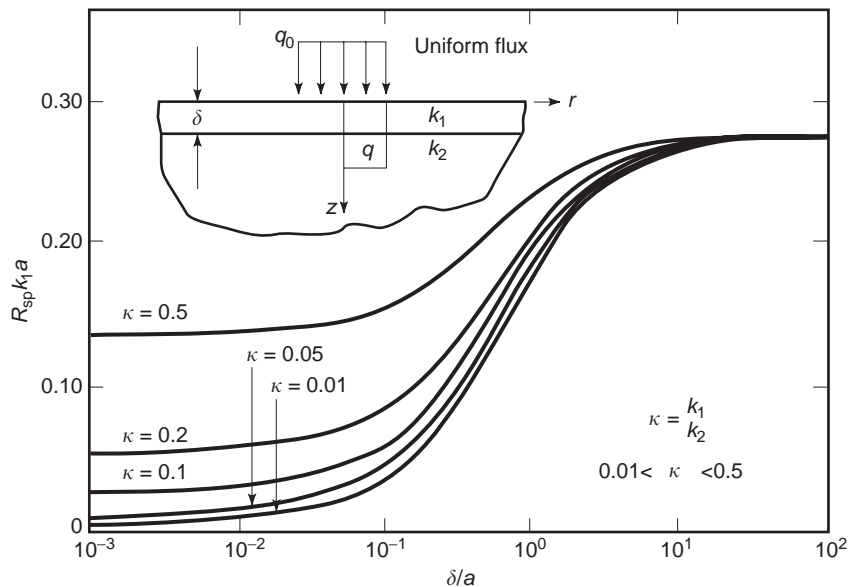


Figure 4. The thermal resistance for a circular heatsource on a two-layer substrate [6].

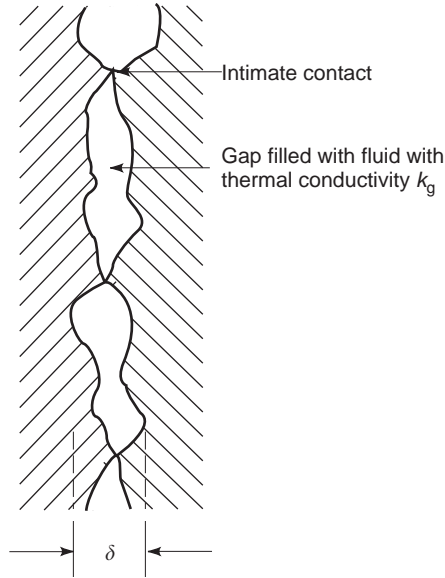


Figure 5. Physical contact between two nonideal surfaces [4].

and the contact resistance based on the apparent contact area, A_a may be defined as

$$R_{co} \equiv \frac{1}{h_{co}A_a} \quad (6)$$

In Eq. (5), h_c is given by Yovanovich and Antonetti [6] as

$$h_c = 1.25k_s \left(\frac{m}{\sigma} \right) \left(\frac{P}{H} \right)^{0.95} \quad (7)$$

where P is the contact pressure and H is the microhardness of the softer material (both in Pa), k_s is the harmonic mean thermal conductivity for the two solids with thermal conductivities, k_1 and k_2 ,

$$k_s = \frac{2k_1k_2}{k_1 + k_2}$$

σ is the effective rms surface roughness developed from the surface roughnesses of the two materials, σ_1 and σ_2 ,

$$\sigma = \sqrt{\sigma_1^2 + \sigma_2^2}$$

and m is the effective absolute surface slope composed of the individual slopes of the two materials, m_1 and m_2 ,

$$m = \sqrt{m_1^2 + m_2^2}$$

In the absence of detailed information, the σ/m ratio can be taken equal to 5–9 μm for relatively smooth surfaces [7].

For normal interstitial gases near atmospheric pressure, h_g in Eq. (5) is given by

$$h_g = \frac{k_g}{Y} \quad (8)$$

where k_g is the thermal conductivity of the gap fluid and Y is the distance between the mean planes given by

$$Y = 1.185 \left[-\ln \left(3.132 \frac{P}{H} \right) \right]^{0.547} \sigma$$

Equations (7) and (8) can be added and, in accordance with Eq. (6), the total contact resistance becomes

$$R_{co} = \left\{ \left[1.25k_s \left(\frac{m}{\sigma} \right) \left(\frac{P}{H} \right)^{0.95} + \frac{k_g}{Y} \right] A_a \right\}^{-1} \quad (9)$$

2.1.5. Transient Heating or Cooling. An internally heated solid, of relatively high thermal conductivity, which is experiencing no external cooling, will undergo a constant rise in temperature according to

$$\frac{dT}{dx} = \frac{q}{mc} \quad (10)$$

where q is the rate of internal heat generation, m is the mass of the solid, and c is the specific heat of the solid. Equation (10) assumes that all of the mass can be represented by a single temperature, and this relation is frequently termed the *lumped capacity* solution for transient heating.

Expanding on the analogy between thermal and electric resistances, the product of mass and specific heat can be viewed as analagous to electric capacitance and thus to constitute the thermal capacitance.

When the same solid is externally cooled, the temperature rises asymptotically toward the steady-state temperature, which is itself determined by the external resistance to the heat flow, R_{ex} . Consequently, the time variation of the temperature of the solid is expressible as

$$T(t) = T(t-0) + qR_{ex}[1 - e^{-t/mcR_{ex}}]$$

The lumped capacitance model is accurate when the ratio of the internal conduction resistance of a solid to the external thermal resistance is small. This ratio is represented by the Biot number (Bi), and the criterion for applicability of the lumped capacitance model is typically given as

$$\text{Bi} = \frac{hL_c}{k} < 0.1$$

where the characteristic length, L_c , is typically defined as the ratio of the solid's volume to its surface area. More generally, L_c should be taken as the distance over

which the solid experiences its maximum temperature difference [8].

2.2. Convective Heat Transfer

2.2.1. The Heat Transfer Coefficient. Convective thermal transport from a surface to a fluid in motion can be related to the heat transfer coefficient, h , the surface-to-fluid temperature difference, and the wetted surface area, S , in the form

$$q = hS(T_s - T_{fl}) \quad (11)$$

The differences among convection to a rapidly moving fluid, a slowly flowing or stagnant fluid, and variations in the convective heat transfer rate for various fluids are reflected in the values of h . For a particular geometry and flow regime, h may be found from available empirical correlations and/or theoretical relations. Use of Eq. (11) makes it possible to define the convective thermal resistance as

$$R_{cv} \equiv \frac{1}{hS}$$

2.2.2. Dimensionless Parameters. Common dimensionless quantities that are used in the correlation of heat transfer data are the *Nusselt number*, Nu , which relates the convective heat transfer coefficient to the conduction in the fluid where the subscript, fl , pertains to a fluid property,

$$Nu \equiv \frac{h}{k_{fl}/L} = \frac{hL}{k_{fl}}$$

the *Prandtl number*, Pr , which is a fluid property parameter relating the diffusion of momentum to the conduction of heat,

$$Pr \equiv \frac{c_p \mu}{k_{fl}}$$

the *Grashof number*, Gr , which accounts for the buoyancy effect produced by the volumetric expansion of the fluid,

$$Gr \equiv \frac{\rho^2 \beta g L^3 \Delta T}{\mu^2}$$

and the *Reynolds number*, Re , which relates the momentum in the flow to the viscous dissipation,

$$Re \equiv \frac{\rho VL}{\mu}$$

2.2.3. Natural Convection. Despite increasing performance demands and advances in thermal management technology, direct air-cooling of electronic equipments continues to command substantial attention. Natural convection is the quietest, least expensive, and most reliable

implementation of direct fluid cooling. In more demanding systems, natural convection cooling with air is often investigated as a baseline design to justify the application of more sophisticated techniques.

In natural convection, fluid motion is induced by density differences resulting from temperature gradients in the fluid. The heat transfer coefficient for this regime can be related to the buoyancy and the thermal properties of the fluid through the *Rayleigh number*, Ra , which is the product of the Grashof and Prandtl numbers,

$$Ra = \frac{\rho^2 \beta g c_p}{\mu k_{fl}} L^3 \Delta T$$

where the fluid properties, ρ , β , c_p , μ , and k , are evaluated at the fluid bulk temperature, and ΔT is the temperature difference between the surface and the fluid.

Empirical correlations for the natural convection heat transfer coefficient generally take the form

$$Nu \equiv C(Ra)^n$$

where n is found to be approximately 0.25 for $10^3 < Ra < 10^9$, representing laminar flow, 0.33 for $10^9 < Ra < 10^{12}$, the region associated with the transition to turbulent flow, and 0.4 for $Ra > 10^{12}$, when strong turbulent flow prevails. The precise value of the correlating coefficient, C , depends on fluid, the geometry of the surface, and the Rayleigh number range. Nevertheless, for common plate, cylinder, and sphere configurations, it has been found to vary in the relatively narrow range of 0.45 to 0.65 for laminar flow and 0.11 to 0.15 for turbulent flow past the heated surface [3].

2.2.4. Vertical Channels. Vertical channels formed by parallel PCBs or longitudinal fins are a frequently encountered configuration in natural convection cooling of electronic equipment. The historical work of Elenbaas [9], a milestone of experimental results and empirical correlations, was the first to document a detailed study of natural convection in smooth, isothermal parallel plate channels. In subsequent years, this work was confirmed and expanded both experimentally and numerically by a number of researchers, including Bodia and Osterle [10], Sobel et al. [11], Aung [12], Aung et al. [13], Miyatake and Fujii [14], and Miyatake et al. [15].

These studies have revealed that the value of the Nusselt number lies between two extremes associated with the separation between the plates or the channel width. For wide spacing, the plates appear to have little influence on one another and the Nusselt number in this case achieves its *isolated plate limit*. On the other hand, for closely spaced plates or for relatively long channels, the fluid attains its *fully developed* value and the Nusselt number reaches its *fully developed limit*. Intermediate values of the Nusselt number can be obtained from a composite expression for smoothly varying processes and have been verified by the detailed experimental and numerical studies of BarCohen and Rohsenow [16].

For an isothermal channel, at the fully developed limit, the Nusselt number takes the form

$$\text{Nu} = \frac{\text{El}}{C_1 \mathcal{A}} \quad (12)$$

where El is the Elenbaas number, defined as

$$\text{El} \equiv \frac{c_p \rho^2 g \beta (T_w - T_{\text{amb}}) H^4}{\mu k l}$$

where H is the channel spacing, l is the channel length, and $(T_w - T_{\text{amb}})$ is the temperature difference between the channel wall and the ambient, or channel, inlet. For an asymmetric channel, or one in which one wall is heated and the other is insulated, the appropriate value of C_1 is 12, whereas for a symmetrically heated channel, $C_1 = 24$.

For an isoflux channel, at the fully developed limit, the Nusselt number has been shown to take the form

$$\text{Nu} = \sqrt{\frac{\text{El}'}{C_1}} \quad (13)$$

where the modified Elenbaas number, El' , is defined as

$$\text{El}' \equiv \frac{c_p \rho^2 g \beta q'' H^5}{\mu K^2 l}$$

where q'' is the heat flux leaving the channel wall(s). When this Nusselt number is based on the maximum wall temperature ($x=l$), the appropriate values of C_1 are 24 and 48 for the asymmetric and symmetric cases, respectively. When based on the midheight ($x=l/2$) wall temperature, the asymmetric and symmetric C_1 values are 6 and 12, respectively.

In the limit where the channel spacing is very large, the opposing channel walls do not influence each other either hydrodynamically or thermally. This situation may be accurately modeled as heat transfer from an isolated vertical surface in an infinite medium. Natural convection from an isothermal plate can be expressed as

$$\text{Nu} = C_2 \text{El}^{1/4} \quad (14)$$

where McAdams [17] suggests a C_2 value of 0.59. Natural convection from an isoflux plate is typically expressed as

$$\text{Nu} = C_2 \text{El}^{1/5} \quad (15)$$

with a leading coefficient of 0.631 when the Nusselt number is based on the maximum ($x=l$) wall temperature and 0.73 when the Nusselt number is based on the midheight ($x=l/2$) wall temperature.

2.2.5. Composite Equations. When a function is expected to vary smoothly between two limiting expressions, which are themselves well defined, and when intermediate values are difficult to obtain, an approximate composite relation can be obtained by appropriately summing the

two limiting expressions. Using the Churchill and Usagi [18] method, BarCohen and Rohsenow [19] developed composite Nusselt number relations for natural convection in parallel plate channels of the form

$$\text{Nu} = [(\text{Nu}_{\text{fd}})^{-n} + (\text{Nu}_{\text{ip}})^{-n}]^{-1/n} \quad (16)$$

where Nu_{fd} and Nu_{ip} are Nusselt numbers for the fully developed and isolated plate limits, respectively. The correlating exponent n was given a value of 2 to offer good agreement with Elenbaas's [9] experimental results.

For an isothermal channel, combining Eqs. (12) and (14) yields a composite relation of the form

$$\text{Nu}_{\text{comp}} = \left[\frac{C_3}{\text{El}^2} + \frac{C_4}{\sqrt{\text{El}}} \right]^{-1/2} \quad (17)$$

whereas for an isoflux channel, Eqs. (13) and (15) yield a result of the form

$$\text{Nu}_{\text{comp}} = \left[\frac{C_3}{\text{El}'} + \frac{C_4}{\text{El}'^{2/5}} \right]^{-1/2} \quad (18)$$

Values of the coefficients C_3 and C_4 appropriate to various cases of interest appear in Table 3.

In electronic cooling applications where volumetric concerns are not an issue, it is desirable to space the PCBs far enough apart that the isolated plate Nusselt number prevails along the surface. In lieu of choosing an infinite plate spacing, the composite Nusselt number may be set equal to 99%, or some other high fraction, of its associated isolated plate value. The composite Nusselt number relation may then be solved for the appropriate channel spacing.

For an isothermal channel, the channel spacing that maximizes the rate of heat transfer from individual PCBs takes the form

$$H_{\text{max}} = \frac{C_5}{P^{1/4}} \quad (19)$$

where

$$P = \frac{c_p \rho^2 g \beta (T_w - T_{\text{amb}})}{\mu k l} = \frac{\text{El}}{H^4}$$

whereas for an isoflux channel, the channel spacing that minimizes the PCB temperature for a given heat flux takes the form

$$H_{\text{max}} = \frac{C_5}{R^{1/5}} \quad (20)$$

where

$$R = \frac{c_p \rho^2 g \beta q''}{\mu k^2 l} = \frac{\text{El}'}{H^5}$$

Values of the coefficient C_5 appropriate to various cases of interest appear in Table 3.

Table 3. Appropriate Values of the C_i Coefficients Appearing in Eqs. (12)–(25)

Case	C_1	C_2	C_3	C_4	C_5	C_6	C_7
<i>Isothermal</i>							
In general	X	Y	X^2	Y^{-2}	$\left(\frac{X^2Y^2(0.99)^2}{1 - (0.99)^2}\right)^{1/6}$	$\frac{1}{(XY)^2}$	$(\sqrt{2XY})^{1/3}$
Symmetric heating	24	0.59	576	2.87	4.63	0.0050	2.72
Asymmetric heating	12	0.59	144	2.87	3.68	0.0199	2.16
<i>Isoflux</i>							
In general	X	Y	X	Y^{-2}	$\left(\frac{XY^2(0.99)^2}{1 - (0.99)^2}\right)^{1/3}$	$\frac{2}{(XY)^2}$	$\left(\frac{XY^2}{2}\right)^{1/3}$
Symmetric heating							
maximum temp.	48	0.63	48	2.52	9.79	0.105	2.12
midheight temp.	12	0.73	12	1.88	6.80	0.313	1.47
Asymmetric heating							
maximum temp.	24	0.63	24	2.52	7.77	0.210	1.68
midheight temp.	6	0.73	6	1.88	5.40	0.626	1.17

2.2.6. Optimum Spacing. In addition to being used to predict heat transfer coefficients, the composite relations presented may be used in optimizing the spacing between PCBs. For isothermal arrays, the optimum spacing maximizes the total heat transfer from a given base area or the volume assigned to an array of PCBs. In the case of isoflux parallel plate arrays, the total array heat transfer for a given base area may be maximized by increasing the number of plates indefinitely. Thus, it is more practical to define the optimum channel spacing for an array of isoflux plates as that spacing that will yield the maximum volumetric heat dissipation rate per unit temperature difference. Despite this distinction, the optimum spacing is found in the same manner.

The total heat transfer rate from an array of vertical, single-sided plates can be written as

$$\frac{Q_T}{l_s W k \Delta T} = \left(\frac{Nu}{H(H+d)} \right) \tag{21}$$

where the number of plates, $m = W/(H+d)$, d is the plate thickness, W is the width of the entire array, and s is the depth of the channel. The optimum spacing may be found by substituting the appropriate composite Nusselt number equation into Eq. (21), taking the derivative of the resulting expression with respect to H , and setting the result equal to zero. Use of the isothermal composite Nusselt number of Eq. (21) yields a relation of the form

$$(2b + 3d - C_6 P^{3/2} b^7)_{opt} = 0 \tag{22}$$

or

$$b_{opt} = \frac{C_7}{P^{1/4}} \tag{23}$$

when d , the PCB thickness, is negligible. Use of an isoflux composite Nusselt number yields

$$(b + 3d - C_6 R^{3/5} b^4)_{opt} = 0 \tag{24}$$

or

$$b_{opt} = \frac{C_7}{R^{1/5}} \quad (d=0) \tag{25}$$

Values of the coefficients C_6 and C_7 appropriate to various cases of interest appear in Table 3.

2.2.7. Limitations. These smooth plate relations have proven useful in a wide variety of applications and have been shown to yield very good agreement with measured empirical results for heat transfer from arrays of PCBs. However, when applied to closely spaced PCBs, these equations tend to underpredict heat transfer in the channel because of the presence of between-package wall flow and the nonsmooth nature of the channel surfaces [20].

2.2.8. Forced Convection. For forced laminar flow in long, or very narrow, parallel-plate channels, the heat transfer coefficient attains an asymptotic value (a fully developed limit), which for symmetrically heated channel surfaces is equal approximately to

$$h = \frac{4k_f}{d_e}$$

where d_e is the *hydraulic diameter* defined in terms of the flow area, A , and the wetted perimeter of the channel, P_w

$$d_e \equiv \frac{4A}{P_w}$$

In the inlet zones of such parallel-plate channels and along isolated plates, the heat transfer coefficient varies with the distance from the leading edge. The low-velocity or laminar flow average convective heat transfer coefficient for $Re < 2 \times 10^5$ is given by [3]

$$h = 0.664 \left(\frac{k}{L} \right) Re^{1/2} Pr^{1/3} \tag{26}$$

where k is the fluid thermal conductivity and L is the characteristic dimension of the surface.

A similar relation applies to flow in tubes, pipes, ducts, channels, and/or annuli with the equivalent diameter, d_e , serving as the characteristic dimension in both the Nusselt and Reynolds numbers. For laminar flow, $Re \leq 2100$

$$\frac{hd_e}{k} = 1.86 \left[\text{Re Pr} \left(\frac{d_e}{L} \right) \right]^{1/3} \left(\frac{\mu}{\mu_w} \right)$$

which is attributed to Sieder and Tate [21] and where μ_w is the viscosity of the convective medium at the wall temperature. Observe that this relationship shows that the heat transfer coefficient attains its maximum value for short channels and decreases as L increases.

In higher velocity turbulent flow, the dependence of the convective heat transfer coefficient on the Reynolds number increases and, in the range $Re \geq 3 \times 10^5$, is typically given by [3]

$$h = 0.036 \left(\frac{k}{L} \right) (\text{Re})^{0.80} (\text{Pr})^{1/3} \quad (27)$$

In pipes, tubes, channels, ducts, and/or annuli, turbulent flow occurs at an equivalent diameter based Reynolds number of 10,000 with the flow regime bracketed by

$$2110 \leq \text{Re} \leq 10,000$$

usually referred to as the transition region. Hausen [22] has provided the correlation

$$\frac{hd_e}{k} = 0.116[\text{Re} - 125](\text{Pr})^{1/3} \left(1 + \frac{d_e}{L} \right)^{2/3} \left(\frac{\mu}{\mu_w} \right)$$

and Sieder and Tate [21] give for turbulent flow

$$\frac{hd_e}{k} = 0.23(\text{Re})^{0.80} (\text{Pr})^{1/3} \left(\frac{\mu}{\mu_w} \right)$$

Additional correlations for the coefficient of heat transfer in forced convection for various configurations may be found in the heat transfer textbooks [8,23–25].

2.2.9. Phase Change Heat Transfer. When heat exchange is accompanied by evaporation of a liquid or condensation of a vapor, the resulting flow of vapor toward or away from the heat transfer surface and the high rates of thermal transport associated with the latent heat of the fluid can provide significantly higher heat transfer rates than single phase heat transfer alone.

2.2.10. Boiling. Boiling heat transfer displays a complex dependence on the temperature difference between the heated surface and the saturation temperature (boiling point) of the liquid. In nucleate boiling, the primary region of interest, the ebullient heat transfer rate is typically expressed in the form of the Rohsenow [26] equation

$$q = \mu_f h_{fg} \sqrt{\frac{g(\rho_f - \rho_g)}{\sigma}} \left[\frac{c_{pf}}{C_{sf} \text{Pr}_f^{1.7} h_{fg}} \right]^{1/r} (T_s - T_{\text{sat}})^{1/r} \quad (28)$$

where $1/r$ is typically correlated with a value of three, and C_{sf} is a function of characteristics of the surface–fluid combination. Rohsenow recommended that the fluid properties in Eq. (28) be evaluated at the liquid saturation temperature.

For pool boiling of the dielectric liquid FC-72 ($T_{\text{sat}} = 56^\circ\text{C}$ at 101.3 kPa) on a plastic-pin-grid-array (PPGA) chip package, Watwe [27] obtained values of 7.47 for $1/r$ and 0.0075 for C_{sf} . At a surface heat flux of 10 W/cm^2 , the wall superheat at 101.3 kPa is nearly 30°C , corresponding to a average surface temperature of approximately 86°C .

The departure from nucleate boiling, or critical heat flux (CHF), places an upper limit on the use of the highly efficient boiling heat transfer mechanism. CHF can be significantly influenced by system parameters such as pressure, subcooling, heater thickness and properties, and dissolved gas content. Watwe et al. [28] presented the following equation to predict the pool boiling critical heat flux of dielectric coolants on a horizontal surface and under a variety of parametric conditions.

$$\begin{aligned} \text{CHF} = & \left\{ \frac{\pi}{24} h_{fg} \sqrt{\rho_g} [\sigma_f g (\rho_f - \rho_g)]^{1/4} \right\} \left(\frac{\delta \sqrt{\rho_h c_{ph} k_h}}{\delta \sqrt{\rho_h c_{ph} k_h} + 0.1} \right) \\ & \times \{ 1 + [0.3014 - 0.01507L/P] \} \\ & \times \left\{ 1 + 0.03 \left[\left(\frac{\rho/f}{\rho/g} \right)^{0.75} \frac{c_{pf}}{h_{fg}} \Delta T_{\text{sub}} \right] \right\} \quad (29) \end{aligned}$$

The first term on the right-hand side of Eq. (29) is the classical Kutateladze–Zuber prediction, which is in the upper limit on the saturation value of CHF on very large heaters. The second term represents the effects of heater thickness and thermal properties on the critical heat flux. The third term in Eq. (29) accounts for the influence of the length scale. The last term is an equation representing the best-fit line through the experimental data of Watwe et al. [28] and represents the influence of subcooling on CHF. The pressure effect on CHF is embodied in the Kutateladze–Zuber and the subcooling model predictions, which make up Eq. (29), via the thermophysical properties. Thus, it can be used to estimate the combined influences of various system and heater parameters on CHF. The critical heat flux, under saturation conditions at atmospheric pressure, for a typical dielectric coolant like FC-72 is approximately 17 W/cm^2 .

2.2.11. Condensation. Closed systems involving an evaporative process must also include some capability for vapor condensation. Gerstmann and Griffith [29] correlated film condensation on a downward-facing flat plate as

$$\text{Nu} = 0.81 \text{Ra}^{0.193} \quad 10^{10} > \text{Ra} > 10^8$$

$$\text{Nu} = 0.69 \text{Ra}^{0.20} \quad 10^8 > \text{Ra} > 10^6$$

where

$$\text{Nu} \equiv \frac{h}{k} \left(\frac{\sigma}{g(\rho_f - \rho_g)} \right)^{1/2}$$

$$\text{Ra} \equiv \frac{g\rho_f(\rho_f - \rho_g)h_{fg}}{k\mu\Delta T} \left(\frac{\sigma}{g(\rho_f - \rho_g)} \right)^{3/2}$$

The Nusselt number for laminar film condensation on vertical surfaces was correlated by Nusselt [30] and later modified by Sadasivan and Lienhard [31] as

$$\text{Nu} = \frac{hL}{k_f} = 0.943 \left[\frac{g\Delta\rho_{fg}L^3h'_{fg}}{k_f\nu_f(T_{\text{sat}} - T_c)} \right]^{1/4}$$

where

$$h'_{fg} = h_{fg}(1 + C_c Ja)$$

$$C_c = 0.683 - \frac{0.228}{\text{Pr}_l}$$

$$Ja = \frac{c_{\text{pf}}(T_{\text{sat}} - T_c)}{h_{fg}}$$

2.2.12. Flow Resistance. The transfer of heat to a flowing gas or liquid that is not undergoing a phase change results in an increase in the coolant temperature from an inlet temperature of T_{in} to an outlet temperature of T_{out} , according to

$$T_{\text{out}} - T_{\text{in}} = \frac{q}{\dot{m}c_p}$$

To facilitate the use of a resistance network representation for the analysis of convectively cooled packaging configurations, it is possible to use the above equation to define an effective flow resistance, R_{f1} , as

$$R_{f1} \equiv \frac{1}{\dot{m}c_p} \quad (30)$$

where \dot{m} , the mass flowrate, is given in kilograms per second.

In multicomponent systems, determination of individual component temperatures requires knowledge of the fluid temperature adjacent to the component. The rise in fluid temperature relative to the inlet value can be expressed in a flow thermal resistance, as in Eq. (30). When the coolant flow path traverses many individual components, care must be taken to use R_{f1} with the total heat absorbed by the coolant along its path, rather than the heat dissipated by an individual component. For system-level calculations aimed at determining the average component temperature, it is common to base the flow resistance on the average rise in fluid temperature, that is, one-half the value indicated by Eq. (30).

2.3. Radiative Heat Transfer

Unlike conduction and convection, radiative heat transfer between two surfaces or between a surface and its

surroundings is not linearly dependent on the temperature difference and is expressed instead as

$$q = \sigma S \mathcal{F} (T_1^4 - T_2^4)$$

where \mathcal{F} includes the effects of surface properties and geometry and σ is the Stefan–Boltzmann constant, $\sigma = 5.67 \times 10^{-8} \text{ W/m}^2 \cdot \text{K}^4$. For modest temperature differences, this equation can be linearized to the form

$$q = h_r S (T_1 - T_2) \quad (31)$$

where h_r is the effective radiation heat transfer coefficient

$$h_r = \sigma \mathcal{F} (T_1^2 + T_2^2)(T_1 + T_2)$$

and, for small $\Delta T = T_1 - T_2$, h_r is approximately equal to

$$h_r = 4\sigma \mathcal{F} (T_1 T_2)^{3/2}$$

It is of interest to note that for temperature differences of the order of 10 K with absolute temperatures around room temperature, the radiative heat transfer coefficient, h_r , for an ideal (or black) surface in an absorbing environment, is approximately equal to the heat transfer coefficient in natural convection of air.

Noting the form of Eq. (31), the radiation thermal resistance, analogous to the convective resistance, is seen to equal

$$R_r = \frac{1}{h_r S}$$

3. THERMAL RESISTANCE NETWORKS

The expression of the governing heat transfer relations in the form of thermal resistances greatly simplifies the first-order thermal analysis of electronic systems. Following the established rules for resistance networks, thermal resistances that occur sequentially along a thermal path can be simply summed to establish the overall thermal resistance for that path. In similar fashion, the reciprocal of the effective overall resistance of several parallel heat transfer paths can be found by summing the reciprocals of the individual resistances. In refining the thermal design of an electronic system, prime attention should be devoted to reducing the largest resistances along a specified thermal path and/or providing parallel paths for heat removal from a critical area.

Although the thermal resistances associated with various paths and thermal transport mechanisms constitute the building blocks in performing a detailed thermal analysis, they have also found widespread application as figures of merit in evaluating and comparing the thermal efficacy of various packaging techniques and thermal management strategies.

3.1. Chip Module Thermal Resistances

3.1.1. Definition. The thermal performance of alternative chip and packaging techniques is commonly compared on the basis of the overall (junction-to-coolant) thermal resistance, R_T . This packaging figure-of-merit is generally defined in a purely empirical fashion,

$$R_T \equiv \frac{T_j - T_{f1}}{q_c}$$

where T_j and T_{f1} are the junction and coolant (fluid) temperatures, respectively, and q_c is the chip heat dissipation.

Unfortunately, however, most measurement techniques are incapable of detecting the actual junction temperature, that is, the temperature of the small volume at the interface of p -type and n -type semiconductors. Hence, this term generally refers to the average temperature or a representative temperature on the chip.

Examination of various packaging techniques reveals that the junction-to-coolant thermal resistance is, in fact, composed of an internal, largely conductive, resistance and an external, primarily convective, resistance. As shown in Fig. 6, the internal resistance, R_{jc} , is encountered in the flow of dissipated heat from the active chip surface through the materials used to support and bond the chip and onto the case of the integrated circuit package. The flow of heat from the case directly to the coolant, or indirectly through a fin structure and then to the coolant, must overcome the external resistance, R_{ex} .

3.1.2. Internal Thermal Resistance. As previously discussed, conductive thermal transport is governed by the Fourier equation, which can be used to define a conduction thermal resistance, as in Eq. (3). In flowing from the chip to the package surface or case, the heat encounters a series of resistances associated with individual layers of materials such as silicon, solder, copper, alumina, and epoxy, as well as the contact resistances that occur at the interfaces between pairs of materials. Although the actual

heat-flow paths within a chip package are rather complex and may shift to accommodate varying external cooling situations, it is possible to obtain a first-order estimate of the internal resistance by assuming that power is dissipated uniformly across the chip surface and that heat flow is largely one-dimensional. To the accuracy of these assumptions, Eq. (32)

$$R_{jc} = \frac{T_j - T_c}{q_c} = \sum \frac{x}{kA} \tag{32}$$

can be used to determine the internal chip module resistance, where the summed terms represent the conduction thermal resistances posed by the individual layers, each with thickness x . As the thickness of each layer decreases and/or the thermal conductivity and cross-sectional area increase, the resistance of the individual layers decreases. Values of R_{cd} for packaging materials with typical dimensions can be found using Eq. (32) or Fig. 7, to range from 2 K/W for a 1000 mm² by 1 mm thick layer of epoxy encapsulant to 0.0006 K/W for a 100 mm² by 25 μm (1 mil) thick layer of copper. Similarly, the values of conduction resistance for typical soft bonding materials are found to lie in the range of approximately 0.1 K/W for solders and 1 K/W–3 K/W for epoxies and thermal pastes for typical x/A ratios of 0.25 to 1.0.

Comparison of theoretical and experimental values of R_{jc} reveals that the resistances associated with compliant, low thermal conductivity bonding materials, and the spreading resistances, as well as the contact resistances at the lightly loaded interfaces within the package, often dominate the internal thermal resistance of the chip package. Thus, it is not only necessary to correctly determine the bond resistance but to also add the values of R_{sp} , obtained from Eq. (4) and/or Fig. 4, and R_{co} from Eqs. (6) or (9) to the junction-to-case resistance calculated from Eq. (32). Unfortunately, the absence of detailed information on the void in the die-bonding and heatsink attach layers and the present inability to determine, with precision,

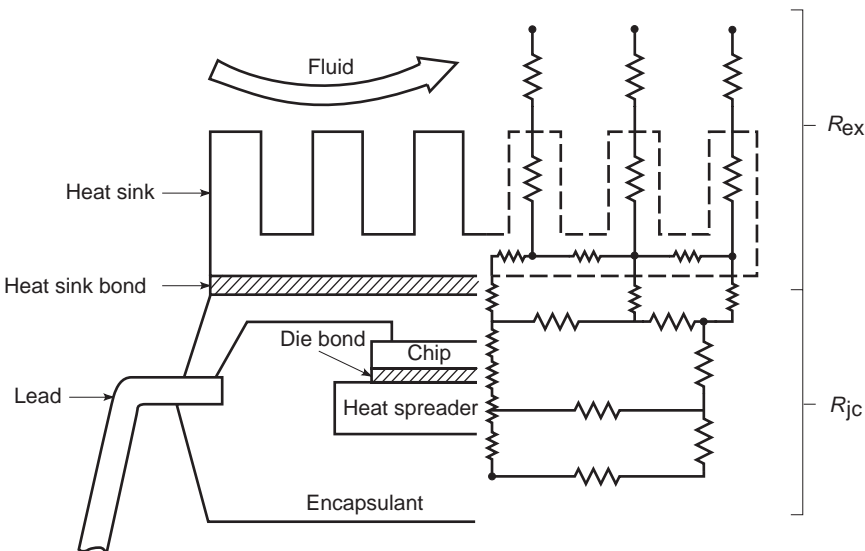


Figure 6. Primary thermal resistances in a single-chip package [4].

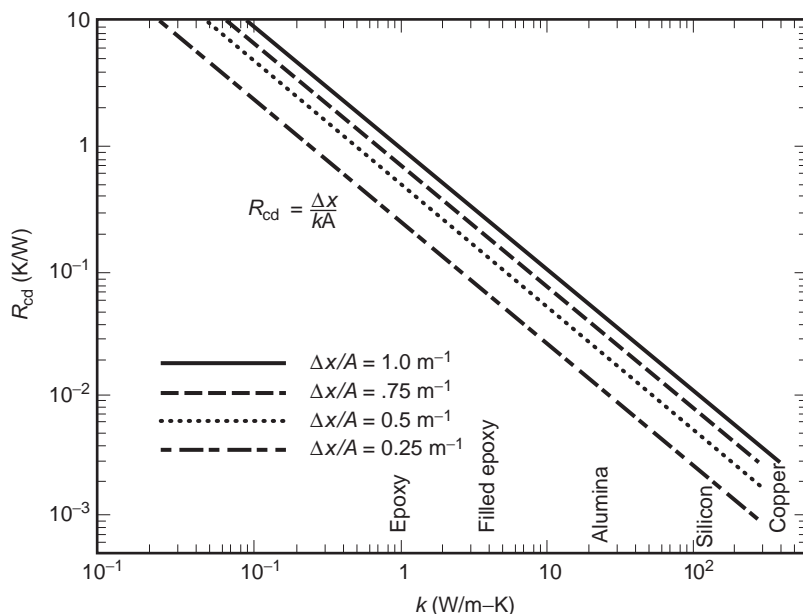


Figure 7. Conductive thermal resistances for packaging materials [4].

the contact pressure at the relevant interfaces, conspire to limit the accuracy of this calculation.

3.1.3. External Resistance. An application of Eqs. (26) or (27) to the transfer of heat from the case of a chip module to the coolant shows that the external resistance, $R_{ex} = 1/hS$, is inversely proportional to the wetted surface area and to the coolant velocity to the 0.5 to 0.8 power and directly proportional to the length scale in the flow direction to the 0.5 to 0.2 power. It may, thus, be observed that the external resistance can be strongly influenced by the fluid velocity and package dimensions and that these factors must be addressed in any meaningful evaluation of the external thermal resistances offered by various packaging technologies.

Values of the external resistance, for a variety of coolants and heat transfer mechanisms, are shown in Fig. 8 for a typical component wetted area of 10cm^2 and a velocity range of 2m/s to 8m/s. They are seen to vary from a nominal 100 K/W for natural convection in air, to 33 K/W for forced convection in air, to 1 K/W in fluorocarbon liquid forced convection, and to less than 0.5 K/W for boiling in fluorocarbon liquids. Clearly, larger chip packages will experience proportionately lower external resistances than the displayed values. Moreover, conduction of heat through the leads and package base into the PCB or substrate will serve to further reduce the effective thermal resistance.

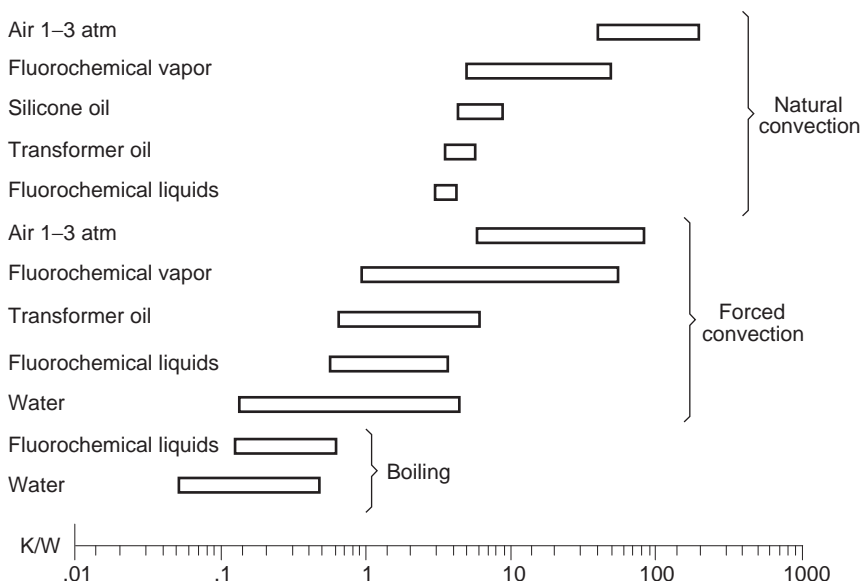


Figure 8. Typical external (convective) thermal resistances for various coolants and cooling modes [4].

In the event that the direct cooling of the package surface is inadequate to maintain the desired chip temperature, it is common to attach finned heatsinks, or compact heat exchangers, to the chip package. These heatsinks can considerably increase the wetted surface area but may act to reduce the convective heat transfer coefficient by obstructing the flow channel. Similarly, the attachment of a heatsink to the package can be expected to introduce additional conductive resistances in the adhesive used to bond the heatsink and in the body of the heatsink. Typical air-cooled heatsinks can reduce the external resistance to approximately 10 K/W to 15 K/W in natural convection and to as low as 3 K/W to 5 K/W for moderate forced convection velocities.

When a heatsink or compact heat exchanger is attached to the package, the external resistance accounting for the bond-layer conduction and the total resistance of the heatsink, R_{sk} , can be expressed as

$$R_{ex} = \frac{T_c - T_{fl}}{q_c} = \sum \left(\frac{x}{kA} \right)_b + R_{sk} \quad (33)$$

where R_{sk}

$$R_{sk} = \left[\frac{1}{nhS_f\eta} + \frac{1}{h_bS_b} \right]^{-1}$$

is the parallel combination of the resistance of the n fins

$$R_f = \frac{1}{nhS_f\eta}$$

and the *bare* or base surface not occupied by the fins

$$R_b = \frac{1}{h_bS_b}$$

Here, the base surface is $S_b = S - S_f$ and the heat transfer coefficient, h_b , is used because the heat transfer coefficient that is applied to the base surfaces is not necessarily equal to that applied to the fins.

An alternative expression for R_{sk} involves an *overall surface efficiency*, η_0 , defined by

$$\eta_0 = 1 - \frac{nS_f}{S}(1 - \eta)$$

where S is the total surface composed of the base surface and the finned surfaces of n fins

$$S = S_b + nS_f$$

In this case, it is presumed that $h_b = h$, so that

$$R_{sk} = \frac{1}{h\eta_0S}$$

In an optimally designed fin structure, η can be expected to fall in the range of 0.50 to 0.70 [4]. Relatively thick fins in a low velocity flow of gas are likely to yield fin

efficiencies approaching unity. This same unity value would be appropriate, as well, for an unfinned surface and, thus, serve to generalize the use of Eq. (33) to all package configurations.

3.1.4. Total Resistance of Single-Chip Packages. To the accuracy of the assumptions employed in the preceding development, the overall single-chip package resistance, relating the chip temperature to the inlet temperature of the coolant, can be found by summing the internal, external, and flow resistances to yield

$$\begin{aligned} R_T &= R_{jc} + R_{ex} + R_{fl} \\ &= \sum \frac{x}{kA} + R_{int} + R_{sp} \frac{1}{\eta h A} + \left(\frac{Q}{q} \right) \left(\frac{1}{2\rho Q c_p} \right) \end{aligned} \quad (34)$$

In evaluating the thermal resistance by this relationship, care must be taken to determine the effective cross-sectional area for heat flow at each layer in the module and to consider possible voids in any solder and adhesive layers.

As previously noted in the development of the relationships for the external and internal resistances, Eq. (34) shows R_T to be a strong function of the convective heat transfer coefficient, the flowing heat capacity of the coolant, and their geometric parameters (thickness and cross-sectional area of each layer). Thus, the introduction of a superior coolant, use of thermal enhancement techniques that increase the local heat transfer coefficient, or selection of a heat transfer mode with inherently high heat transfer coefficients (boiling, for example) will all be reflected in appropriately lower external and total thermal resistances. Similarly, improvements in the thermal conductivity and reduction in the thickness of the relatively low conductivity bonding materials (such as soft solder, epoxy, or silicone) would act to reduce the internal and total thermal resistances.

3.1.5. Applications of R_{jc} . The commonly used junction-to-case thermal resistance, relying on just a single case temperature, can be used with confidence only in the relatively unlikely circumstance that the package case is isothermal. In a more typical packaging configuration, when substantial temperature variations are encountered among and along the external surfaces of the package, Andrews [32], Furkay [33], and Wilson [34], among others, showed that the use of the reported R_{jc} can lead to grossly erroneous chip temperature predictions, which is especially of concern in the analysis and design of plastic chip packages, because of the inherently high thermal resistance of the plastic encapsulant and the package anisotropies introduced by the large differences in the conductivity and the resulting conductance between the lead frame and/or heat spreader and the plastic encapsulant. Although the use of R_{ja} is best suited to the determination of the actual chip temperature, not only does it contain the drawbacks of R_{jc} , but the variability of the convective (external) component in R_{ja} makes this an inappropriate parameter for the thermal characterization of the chip package itself.

Despite these limitations, the persistent demand for chip temperature prediction and control has sustained the use of the R_{ja} and R_{jc} metrics in the thermal characterization of chip packages. As an alternative, it is possible to model a chip package with a resistor network, in which each of the primary thermal paths is represented by a single thermal resistor, typically connecting the chip to one of the external package surfaces. This compact model approach was discussed and illustrated by Krueger and Bar-Cohen [35] and Bar-Cohen and Krueger [36] and was implemented by the French Telecom Research Centre (CNET) in creating a databank for thermal characteristics of electronic components used in the telecommunication industry [37]. When calibrated with empirical data, such a resistor network model could provide a universal thermal representation of a chip package, which is nearly independent of the package attachment and cooling configuration. Using this model, the design engineer could then determine the chip temperature as a function of known temperatures and/or heat transfer relations at each of the exposed surfaces.

Recognition of the popularity and longevity of the single-valued, junction-to-case thermal resistance leads to a recasting of the chip package thermal network model in the form of surface-weighting factors, which could be used to obtain the appropriate average case temperature for various thermal packaging configurations. This approach makes it possible to extend the use of the conventional R_{jc} to situations in which the exterior case is highly nonisothermal, including thermal insulation of one or more surfaces.

3.2. R_{jc} with Weighted Average Case Temperature

As R_{jc} is strictly valid only for an isothermal package surface, a method must be found to address the individual contributions of the various surface segments according to their influence on the junction temperature. In Section 3.2.1., the theory and assumptions underpinning this approach and the derivation of the relevant “thermal

influence coefficients” as well as evaluation of the accuracy attained will be presented. It will be shown that the use of the junction-to-case thermal resistance can be extended to nonisothermal packages by defining an appropriately weighted, average surface temperature based on numerically derived thermal influence coefficients for each package surface (or segment) of interest.

3.2.1. Expanded R_{jc} Methodology. It is convenient to introduce the expanded R_{jc} methodology with a thermal model of a chip package that can be approximated by a network of three thermal resistances connected in parallel from the chip to the top, sides, and bottom of the package, respectively. This type of compact model is commonly referred to as a star network and, in this model, the heat flow from the chip is

$$q = q_1 + q_2 + q_3$$

or

$$q = \frac{T_j - T_1}{R_1} + \frac{T_j - T_2}{R_2} + \frac{T_j - T_3}{R_3} \tag{35}$$

This compact model of an electronic device is shown schematically in Fig. 9.

Equation (35) can be rearranged to yield the dependence of the chip (or junction) temperature on the temperature of the three surface segments as

$$T_j = \left(\frac{R_2 R_3}{R_s}\right) T_1 + \left(\frac{R_3 R_1}{R_s}\right) T_2 + \left(\frac{R_1 R_2}{R_s}\right) T_3 + \left(\frac{R_1 R_2 R_3}{R_s}\right) q \tag{36}$$

where $R_s = R_1 R_2 + R_1 R_3 + R_2 R_3$

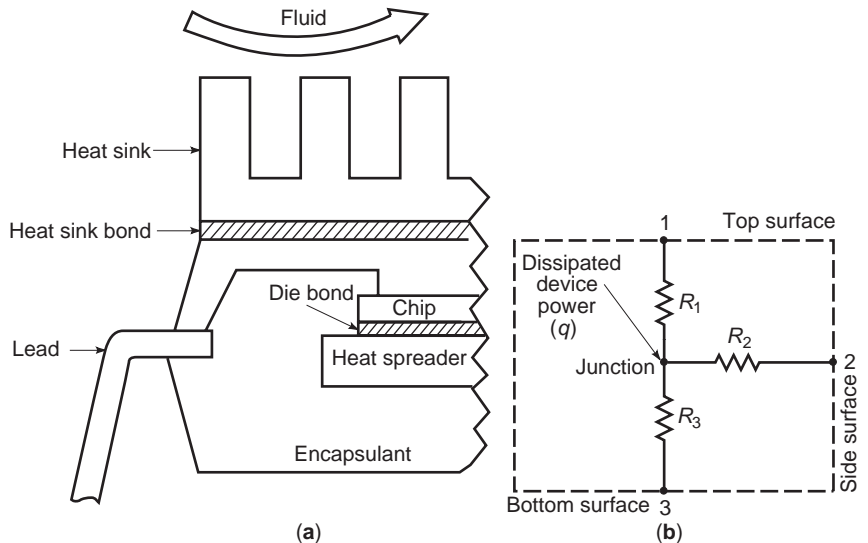


Figure 9. Geometry of a 28-lead PLCC device. (a) The compact model schematic and (b) the actual device cross section [37].

Equation (36) may be generalized to admit n distinct elements along the package surface, or

$$T_j = \sum_{k=1}^n A_k T_k + A_{n+1} q \quad (37)$$

A comparison of Eqs. (36) and (37) shows that the coefficients of the specified surface temperatures, the A_k 's, are totally determined by the internal resistances of the chip package

$$A_1 = \frac{R_2 R_3}{R_s} \quad A_2 = \frac{R_3 R_1}{R_s}$$

$$A_3 = \frac{R_1 R_2}{R_s} \quad A_4 = \frac{R_1 R_2 R_3}{R_s}$$

The temperature coefficients needed to generate a junction temperature relation of the form shown in Eq. (37) can thus be determined from previously calculated internal resistances or, in the absence of such values, by extraction from empirical data or numerical results for the junction temperature. Furthermore, inspection of Eq. (36) reveals that the sum of the coefficients of the various surface temperatures, whether expressed in terms of the directional, internal resistances, as in Eq. (36), or in terms of influence coefficients, as in Eq. (37), is identically equal to unity for all boundary conditions. Alternatively, as shown by Furkay [33], the power dissipation coefficient, $A_{n+1} q$, is, in fact, the familiar R_{jc} , the isothermal, junction-to-case thermal resistance. Consequently, Eq. (37) may be rewritten as

$$T_j = \sum_{k=1}^n A_k T_k + R_{jc} q \quad (38)$$

or, returning to R_{jc}

$$R_{jc} = T_j - \frac{\sum_{k=1}^n A_k T_k}{q} = \frac{T_j - \bar{T}_c}{q} \quad (39)$$

where \bar{T}_c is the average case temperature

$$\bar{T}_c = \frac{\sum_{k=1}^n S_k}{S_T} T_k \quad (40)$$

where S_k is the surface area of the k th surface and S_T is the surface area of the entire package.

Equation (39) can be viewed as a generalized and expanded junction-to-case thermal resistance, based on an appropriately weighted, average case temperature. As previously noted, several different approaches may be taken in determining the average temperature of a nonisothermal chip package or case. The most basic approach involves calculating a simple average of, for example, the top, bottom, and fourside surface temperature. A somewhat better value can be found by surface area averaging of these temperatures in accordance with Eq. (40).

In a package with anisotropic conduction, the simple average and area average approaches yield an erroneous

case temperature by neglecting the variation in resistance to heat flow from the chip to the surface element. This shortcoming is addressed by this approach, which provides an improved weighted average temperature based on the importance to heat transfer of the various package surfaces. The average case temperature should be found in the prescribed manner, that is, by

$$\bar{T}_c = \sum_{k=1}^n A_k T_{k,1} \quad (41)$$

With this particular value of \bar{T}_c , the conventional R_{jc} , obtained empirically or numerically from isothermal case results, can be used to find T_j for all operating conditions, subject to the assumption that each surface segment is itself isothermal. When necessary, a single surface may be divided into several zones, each of which is more nearly isothermal than the entire surface and is recognized with its own index in Eq. (41). It should be noted that the weighting imposed by this equation on the average case temperature addresses variations in the size of the surface segments, as well as variations in the internal thermal paths between the chip and each of the surface elements.

3.2.2. The Insulated Surface. In many applications, chip packages are cooled selectively along particular exposed surfaces. One such example is a package cooled from the top and side surfaces while the bottom surface is insulated. The thermally active surfaces may vary from application to application, and the thermal analyst needs to quantify the effect of thermally insulating one or more areas on a package of known thermal resistance. For the assumptions used in the development of the expanded R_{jc} model, insulation of surface m results in zero heat flow through resistance, R_m . This causes the temperature of surface m to equal the chip temperature. With this in mind, the junction temperature for a package with a single insulated surface given by Eq. (38) is found to equal

$$T_j = \sum_{k \neq m} \left(\frac{A_k}{1 - A_m} \right) T_k + (R_{jc}^*) q \quad (42)$$

The weighted-average case temperature for this thermal configuration is found to equal

$$\bar{T}_c = \sum_{k \neq m} \left(\frac{A_k}{1 - A_m} \right) T_k \quad (43)$$

and the modified junction to case resistance, R_{jc}^* is

$$R_{jc}^* = \frac{R_{jc}}{1 - A_m} \quad (44)$$

3.2.3. Implementation. To thermally characterize any electronic package by relations of the form of Eqs. (40) and (42), it is necessary to compute or measure the relevant influence coefficients or the equivalent set of internal

resistances. Several difficult issues will develop undertaking such an effort. Fundamentally, a strictly experimental approach to thermal characterization of electronic devices would suffer from measurement errors and nonlinearities. Even more esoteric, is a precise experimental definition of what temperatures must be measured on the electronic component. Precise measurement of the p - n junction operating temperature is usually not practical. Approximations using signal characteristics, or implanted temperature sensors are generally used for experimental purposes.

Numerical simulation of the thermal behavior of a finite element (or finite difference) model of a chip package can provide the necessary temperatures and heat flows for a variety of operating conditions. Such a model can properly represent the conduction temperature field in each of the solid elements constituting the package but unfortunately cannot yet faithfully reproduce the thermal resistances at the interfaces (the so-called contact thermal resistances) between these elements. Regrettably, these contact resistances, and especially the values along the chip surfaces where the heat fluxes are highest, can account for a significant fraction of the package resistance [38]. Thus, in the near term, empirical contact resistance data must be used in generating an accurate finite element or finite difference thermal model of an integrated circuit package. For typical contact resistance values, the reader is referred to Refs. 6 and 30.

4. ADVANCED TOPICS

4.1. Convection Between Populated Printed Circuit Boards

The relations presented previously for natural convection in vertical channels have proved useful in a wide variety of applications and have been shown to yield very good agreement with measured empirical results for heat transfer from arrays of PCBs. However, these traditional models, employing smooth-walled channel relations and based on the free channel spacing, underestimate heat transfer for narrowly spaced PCB configurations and overestimate optimum PCB spacings. Furthermore, when an attempt is made to maximize volumetric heat dissipation in an array of PCBs, the optimum PCB spacing is overestimated and, as a result, the maximum array dissipation is underestimated.

Teertstra et al. [39] proposed an analytical friction factor correlation for fully developed flow through an idealized array of uniformly sized and spaced cuboid blocks on one side of a parallel-plate channel.

$$f_{2H} = \left[\left(\frac{96\mathcal{A}}{Re_{2H}} \right)^3 + \left(\frac{0.347\mathcal{B}}{Re_{2H}^{1/4}} \right)^3 \right]^{1/3} \quad (45)$$

This composite equation connects the laminar and turbulent limiting cases and is applicable for a full range of Reynolds numbers, $1 \leq Re_{2H} = 2HV/v \leq 100000$.

The \mathcal{A} and \mathcal{B} factors appearing in Eq. (45) are expressed solely in terms of the component array geometry

$$\mathcal{A} = \frac{\gamma^2}{\zeta^3 \chi} \quad (46)$$

$$\mathcal{B} = \frac{\gamma^{5/4}}{\zeta^3 \xi} \quad (47)$$

where

$$\gamma = \left[1 + \frac{B}{H} \frac{H}{L} \frac{1}{1+S/L} \right] \quad (48)$$

$$\zeta = \left[1 - \frac{B}{H} \frac{1}{1+S/L} \right] \quad (49)$$

$$\chi = \left[\frac{B}{H} + \left(1 - \frac{B}{H} \right) \left(1 + \frac{2B}{H} \frac{H}{L} \frac{1}{1+S/L} \right) \right] \quad (50)$$

and

$$\xi = \left[\frac{B}{H} + \left(1 - \frac{B}{H} \right) \frac{1}{1+S/L} \right] \quad (51)$$

Figure 10 illustrates the definitions of the geometrical parameters B , H , S , and L appearing in Eqs. (48)–(51). The groupings B/H and S/L represent the nondimensional package array height and spacing, respectively, where H/L provides the needed link between them.

Despite the complexity of the dependence, it is clear that as the package size shrinks (i.e., $B/H \rightarrow 0$) and/or as the spacing increases (i.e., $S/L \rightarrow \infty$) \mathcal{A} and \mathcal{B} approach unity, and the associated laminar and turbulent friction factors reduce to appropriate smooth plate values. With finite package size, however, \mathcal{A} and \mathcal{B} increase steeply with increasing package size. As \mathcal{A} and \mathcal{B} increase, the friction factor associated with the channel also increases, leading to deteriorated channel flow with increased protuberance size. Thus, by representing the actual populated PCB by

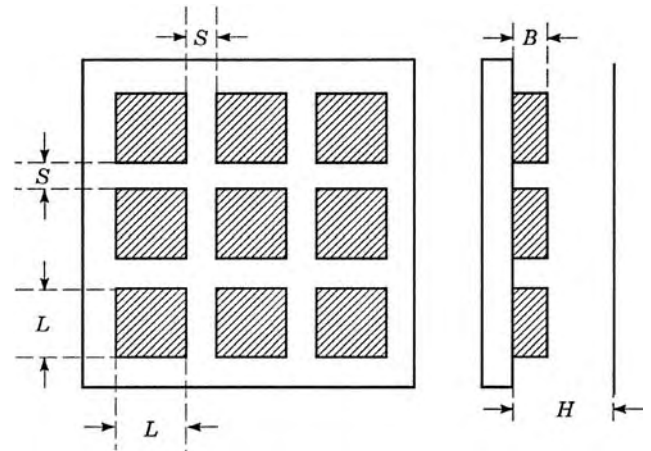


Figure 10. Definition of the various geometrical parameters used in Eqs. (48) through (51).

an equivalent array of cuboid blocks mounted on a flat plate, the package-corrected friction factor for the PCB channel may be predicted using Eq. (45).

Knowledge of the friction factor may be used to calculate the pressure loss and flowrate in the channel.

$$\left. \frac{\partial P}{\partial x} \right|_{\text{loss}} = \frac{-f_{2H} \rho Re_{2H}^2 v^2}{16H^3} \quad (52)$$

This flowrate may then be used in standard forced convection correlations to obtain a heat transfer coefficient.

In an approach to a real situation, the deviation of the friction factor characteristics of an actual PCB channel from that of an idealized smooth channel could be obtained and used to more accurately predict the flowrate and thus the convective heat transfer in the channel.

4.2. Air-Cooled Heatsinks

The simplicity and cost effectiveness of air-cooled heatsinks continue to expand the design space for this most ubiquitous of all thermal management hardware in the electronic industry. When attached to modules, chip packages, or directly to chips, heatsinks can enhance both the reliability and functional performance of electronic, telecommunication, and power conversion systems. However, rapidly increasing chip power dissipation and concerns over weight, cost, acoustic noise, and time-to-market are constraining the successful application of these thermal devices. Greater attention to the underlying thermal, fluid, and structural interactions, as well as an appreciation for the cost and limits of available materials and fabrication processes, will be needed to maintain the viability of this cooling technique.

Extended surface heat transfer relations, which describe the thermal performance of individual fins and fin arrays, can be manipulated to provide criteria for the selection of fin geometries that will minimize the volume and mass required to meet a target dissipation. Attention must also be devoted to the impact of the fluid dynamic design on the pressure drop, dissipated pumping power, and acoustic noise generated by the heatsink. All three of these penalty quantities vary non-linearly with velocity, and a desire for quiet operation may lead to the selection of higher airflow rates at lower pressures.

Use of a large, high-performance heatsink to cool a single chip requires that the base of the heatsink serve as a heat spreader. The tradeoffs involved in optimizing the base in terms of volume, mass, and performance suggest that one consider the use of new, engineered materials, such as ceramics, composite materials, and embedded heat pipes.

Although the use of a heatsink is intended to improve the reliability of an individual electronic component, potential failure modes of the material layer or coating used to attach the heatsink may compromise this goal. Thermally induced stresses may lead to cracking, delamination, and rupture of the heatsink bond. Unfortunately, although thermal stress considerations favor a relatively thick interfacial layer, thermal performance demands that this low thermal conductivity layer be as thin as possible.

In the design and selection of high-performance, compact heatsinks, attention must be paid to the immediate physical surroundings. Neglecting the potential for air-flow bypassing the heatsink and leaking out can lead to serious overpredictions in heatsink performance. Moreover, care must often be taken to minimize the volume occupied by the thermal solution and its impact on the form and shape of the packaged product. Although analysis and testing can provide guidelines for dealing with these issues, today's commercial computational fluid dynamics (CFD) software is most effective in identifying solutions and optimization opportunities early in the design cycle and can be used successfully to tailor the thermal solution to the specified physical and performance envelope.

Air-cooled, least-material optimum fin arrays are typically characterized by large aspect ratio fins and interfin spacings that are beyond the range of conventional casting, extrusion, and machining operations. The design of cost-effective heatsinks requires that attention be devoted to manufacturing considerations. The performance and manufacturing costs of various suboptimal (thermal) configurations must be sufficiently well understood to perform a more generalized optimization.

Using the present as prologue, it appears clear that future heatsink design will need to address the myriad of concerns and constraints that define the electronic product envelope. In the coming era, the limits on heatsink performance will be established not by thermal performance alone but by the cost effectiveness of the thermal design, including material and manufacturing/fabrication costs, as well as the less visible costs of reliability, acoustic noise, space utilization, and time-to-market. To assist in this multidimensional design process, it can be expected that, in the future, automated design will play a far greater role in heatsink development. Such second-generation CAD tools can be expected to provide sophisticated inverse-design capability, which will help define the optimal configurations to offer virtual reality displays—this will aid the designer in tailoring the heatsink to the size and shape of the available space and to afford easy access to rapid prototyping tools that generate heatsink samples for rapid evaluation of proposed solutions.

For a thorough treatment of heatsink design and analysis, the reader is referred to Ref. 4.

4.3. Passive Immersion Modules

The challenges posed by high chip heat fluxes make direct liquid cooling a leading candidate for future thermal packaging systems. Passive immersion modules (PIMs) consist of active microelectronic components encapsulated in a liquid-filled enclosure. The dielectric liquid wets the surface of the component, and heat is removed by convection and/or boiling. As liquid circulates within the enclosure, heat is spread to the module walls. The external surfaces of the module are then cooled by the ambient air. The module walls may be internally finned, externally finned, or both [40].

The circulation of the liquid within a PIM, including the formation, collapse, and additional buoyancy of vapor bubbles generated through boiling, may be used to

overcome the barriers posed by thermal conduction through solids and across solid-to-solid interfaces (a dominant concern in the application of conventional heatsink technology). Although high-velocity-flow boiling, liquid jet impingement, and liquid sprays could all be used to cool the anticipated high flux chips of 2006, the SIA/NEMI cost constraints appear to favor development of modules that passively reject the generated heat to air.

A PIM consists of heat-dissipating microelectronics enclosed in a liquid-filled module. In such PIMs, high heat fluxes may lead to boiling on the component surfaces. Vapor bubbles generated in the module rise, coalesce, and condense in the liquid, inducing considerable circulation and bubble pumped convection along the module walls that serve as submerged condensers. The thermal performance of such a PIM is constrained by the departure from nucleate boiling or critical heat flux (CHF) on the surface of the components and the maximum attainable heat transfer rate at the submerged condenser surfaces.

Markowitz and Bergles [41] proposed that the complex phenomena occurring within a PIM could be effectively represented in a performance map, similar to that depicted in Fig. 11, relating the heat dissipation, Q , to the temperature difference, ΔT_{hc} , between the chips (heaters) and the condenser. In creating a theoretical performance map for a PIM, the lower bound of the performance envelope is defined by natural convection on both the chip and condenser surfaces. In modules in which the condenser surface is at the top of the module where vapor can collect, the upper bound for the performance envelope is vapor-space condensation. However, for tall, narrow modules in which the majority of the heat is removed from side-wall submerged condenser, vapor-space condensation does not represent a realistic upper limit for the performance of the condenser. A more realistic upper bound may be that of bubble pumped convection with noncondensing bubbles. A semi-empirical correlation by Bar-Cohen et al. [42] for this maximal bubble pumped convection on a vertical plate, is given by

$$Nu = (1 + \lambda Z)^{1/3} Nu_{nc} \quad (53)$$

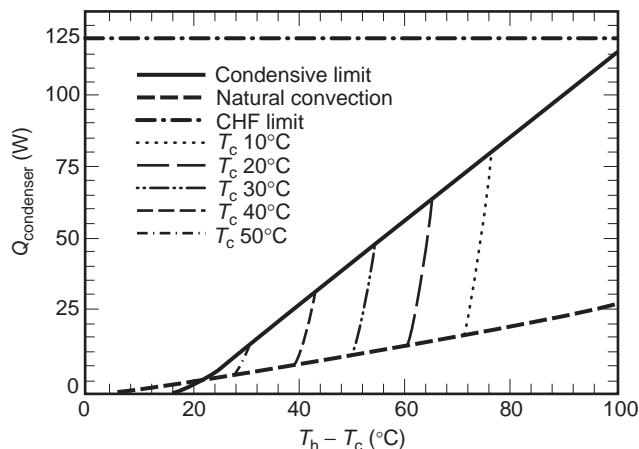


Figure 11. Theoretical performance map for a PIM.

where

$$Z = \frac{(\rho_f - \rho_g)QW}{\sqrt{gD_0\rho_f\rho_g}h_{fg}\beta(T_{sat} - T_s)V} \quad (54)$$

and Nu_{nc} is the appropriate single-phase natural convection Nusselt number. In Eq. (53), λ is an empirically determined factor that depends on the heater and condenser configuration of the module, typically ranging in value from 2 to 9.

Between the lower bound of natural convection and the upper bound of vapor-space condensation, the temperature difference between the chips and the submerged condenser surface is governed primarily by nucleate boiling on the chips and bubble pumped convection on the condenser. With sufficient condenser capacity, the performance of the PIM may be limited by the critical heat flux at the chip surfaces, which is accompanied by vapor blanketing of the surface and a large increase in surface temperature.

Kitching et al. [40] studied the thermal characteristics of a prototype, air-cooled PIM and addressed the upper-bound and bubble pumped augmentation on the finned submerged condenser surface. The experimental observations and supporting modeling studies revealed that thermal performance maps could be used to represent the behavior of finned, submerged condenser PIMs. Moreover, in this study, a two- to threefold improvement in the convective heat transfer coefficient was attained along a horizontal, submerged condenser surface, consisting of square pin fins. This augmentation was achieved with a relatively modest bubble (void) fraction of 2% to 3% in the enclosed liquid. Condensation on the exposed fin surfaces represents the upper bound for operation of a horizontal PIM.

BIBLIOGRAPHY

1. Semiconductor Industry Association, *National Technology Roadmap for Semiconductors*, Washington, DC: SIA, 1994.
2. National Electronics Manufacturing Initiative, *National Electronics Manufacturing Technology Roadmap*, Herndon, VA: NEMI, 1996.
3. A. D. Kraus and A. Bar-Cohen, *Thermal Analysis and Control of Electronic Equipment*, New York: McGraw-Hill, 1983.
4. A. D. Kraus and A. Bar-Cohen, *Design and Analysis of Heat Sinks*, New York: Wiley, 1995.
5. K. J. Negus, M. M. Yovanovich, and J. V. Beck, On the non-dimensionalization of constriction resistance for semi-infinite heat flux tubes, *J. Heat Transfer*, **111**:804–807 (1989).
6. M. M. Yovanovich and V. W. Antonetti, Application of thermal contact resistance theory to electronic packages, in A. Bar-Cohen and A. D. Kraus, eds., *Advances in Thermal Modeling of Electronic Components and Systems*, Vol. 1, New York: Hemisphere, 1988.
7. M. M. Yovanovich, personal communication, 1990.
8. F. P. Incropera and D. P. Dewitt, *Introduction to Heat Transfer*, New York: Wiley, 1996.
9. W. Elenbaas, Heat dissipation of parallel plates by free convection, *Physica*, **9**(1):665–671 (1942).

10. J. R. Bodia and J. F. Osterle, The development of free convection between heated vertical plates, *J. Heat Transfer*, **84**:40–44 (1964).
11. N. Sobel, F. Landis, and W. K. Mueller, Natural convection heat transfer in short vertical channels including the effect of stagger, *Proc. 3rd Int. Heat Transfer Conf.*, Vol. 2, Chicago, IL, 1966, pp. 121–125.
12. W. Aung, Fully developed laminar free convection between vertical plates heated asymmetrically, *Int. J. Heat Mass Transfer*, **15**:40–44 (1972).
13. W. Aung, L. S. Fletcher, and V. Sernas, Developing laminar free convection between vertical flat plates with asymmetric heating, *Int. J. Heat Mass Transfer*, **15**:2293–2308 (1972).
14. O. Miyatake and T. Fujii, Free convection heat transfer between vertical parallel plates—one plate isothermally heated and the other thermally insulated, *Heat Transfer Jpn. Res.*, **3**:30–38 (1972).
15. O. Miyatake et al., Natural convection heat transfer between vertical parallel plates—one plate with a uniform heat flux and the other thermally insulated, *Heat Transfer Jpn. Res.*, **4**: 25–33 (1973).
16. A. Bar-Cohen and W. M. Rohsenow, Thermally optimum spacing of vertical, natural convection cooled, vertical plates, *J. Heat Transfer*, **106**:116–122 (1984).
17. W. H. McAdams, *Heat Transmission*, New York: McGraw-Hill, 1954.
18. S. W. Churchill and R. Usagi, A general expression for the correlation of rates of transfer and other phenomena, *AIChE J.*, **18**:1121–1138 (1972).
19. A. Bar-Cohen and W. M. Rohsenow, Thermally optimum spacing of vertical, natural convection cooled, parallel plates, *Heat Transfer Electron. Equip.*, ASME HTD, Vol. 20, Washington, DC, 1981, pp. 11–18.
20. A. Bar-Cohen, Bounding relations for natural convection heat transfer from vertical printed circuit boards, *Proc. IEEE*, **73**(9):1388–1395 (1985).
21. E. N. Sieder and G. E. Tate, Heat transfer and pressure drops of liquids in tubes, *Ind. Eng. Chem.*, **28**:1429–1435 (1936).
22. H. Hausen, Darstellend des wärmeüberganges in röhren durch verallgemeinerte potenzbeziehungen, *VDI-Z.*, **4**:91–98 (1943).
23. A. Bejan, *Heat Transfer*, New York: Wiley, 1993.
24. J. P. Holman, *Heat Transfer*, New York: McGraw-Hill, 1990.
25. J. H. Lienhard, *A Heat Transfer Textbook*, Englewood Cliffs, NJ: Prentice-Hall, 1987.
26. W. M. Rohsenow, A method of correlating heat transfer data for surface boiling of liquids, *Trans. ASME*, **74**:969–976 (1951); reprinted in *3rd ASME/JSME Therm. Eng. Jt. Conf.*, Vol. 1, pp. 503–512.
27. A. A. Watwe, *Measurement and Prediction of Pool Boiling Heat Flux in Highly Wetting Liquids*, PhD Thesis, Department of Mechanical Engineering, University of Minnesota, 1996.
28. A. A. Watwe, A. Bar-Cohen, and A. McNeil, Combined pressure and subcooling effects on pool boiling from a PPGA chip package, *ASME J. Electron. Packag.*, **119**(2):95–105 (1997).
29. F. Gertsmann and P. Griffith, Laminar film condensation on the underside of horizontal and inclined surfaces, *Int. J. Heat Mass Transfer*, **10**:567–580 (1966).
30. W. Z. Nusselt, Die oberflächencondensation der was-serdampfes, *VDI-Z.*, **60**:541–569 (1916).
31. P. Sadasivan and J. H. Lienhard, Sensible heat correction in laminar film boiling and condensation, *J. Heat Transfer*, **109**:545–546 (1987).
32. J. A. Andrews, Package thermal resistance model dependency on equipment design, *IEEE Trans. Compon. Hybrids Manuf. Technol.*, **11**:528–537 (1988).
33. S. S. Furkay, Thermal characterization of plastic and surface mount components, *IEEE Trans. Compon. Hybrids Manuf. Technol.*, **11**:521–527 (1988).
34. E. A. Wilson, Factors influencing the interdependence of R_{jc} and R_{ca} , *Proc. 2nd Int. Electron. Packag. Soc. Meet.*, 1981, pp. 247–255.
35. W. B. Krueger and A. Bar-Cohen, Thermal characterization of a PLCC-expanded R_{jc} methodology, *IEEE Trans. Compon. Hybrids Manuf. Technol.*, **15**:691–698 (1992).
36. A. Bar-Cohen and W. B. Krueger, Determination of weighted average case temperature for a single chip package, in S. Kakac, H. Yuncu, and K. Hijikata, eds., *Cooling of Electronic Systems*, NATO ASI Ser., Dordrecht, The Netherlands: Kluwer, 1993.
37. J. P. LeJannou and Y. Huon, Representation of thermal behavior of electronic behaviour of electronic components for the creation of a databank, *IEEE Trans. Compon. Hybrids Manuf. Technol.*, **14**:366–373 (1994).
38. W. S. Childres and P. G. Peterson, Quantification of thermal contact in electronic packages, *IEEE Trans. Compon. Hybrids Manuf. Technol.*, **12**:717–723 (1989).
39. P. Teertstra, M. M. Yovanovich, and J. R. Culham, Pressure loss modeling for surface mounted cuboid-shaped packages in channel flow, *Proc. 13th IEEE Semi-Therm. Symp.*, 1997, pp. 238–246.
40. D. Kitching, T. Ogata, and A. Bar-Cohen, Thermal performance of a passive immersion-cooling multichip module, *J. Enhanced Heat Transfer*, **2**(1–2):95–103 (1995).
41. A. Markowitz and A. E. Bergles, Operational limits of submerged condenser, *Prog. Heat Mass Transfer*, **6**:701–716 (1972).
42. A. Bar-Cohen, G. Perelman, and A. Sabag, Bubble pumped convective augmentation on vertical submerged condenser surfaces, *Proc. ASME / JSME Therm. Eng. Jt. Conf.*, Vol. 3, 1987, pp. 431–440.

THIN FILM RESISTORS

F. M. COLLINS
Ohmcraft, Inc.
W. A. ANDERSON
State University of New York at
Buffalo
E. M. MA
Cypress Semiconductor Inc.
(Minnesota)

1. HISTORICAL DEVELOPMENT

The earliest forms of thin film resistors were developed in Germany during World War II based on “cracked-carbon,” which was deposited onto ceramic cores during a high-temperature chemical vapor deposition (CVD) process.

The resistor was brought to value by removing material in a spiral pattern by grinding. A cap-and-lead termination was followed by polymeric encapsulation.

The performance characteristics of these carbon-film resistors were an order of magnitude improvement over prior resistors consisting of a carbon composition product. These exhibit sizable changes in value when subjected to fluctuations in temperature or humidity because of large dimensional changes in the resin matrix. By contrast, film resistors were far more stable and the inline procedure for adjusting them to value enabled production in high yield of close-tolerance (1%) components.

The next evolutionary step was adopting the low-temperature-coefficient metal alloys that were used in wire-wound resistor construction. They were deposited as films using nickel-chromium carbonyl in a CVD process. Subsequent manufacturing steps were similar to the carbon film product. These "precision" metal film resistors had a much lower temperature coefficient of resistance (TCR) and greater overall endurance than the carbon film product. TCR is defined as the unit change of resistance per unit change in temperature, expressed as parts per million per degree centigrade (ppm/°C) and discussed in Section 6.

During the 1960s, the techniques for fabricating integrated circuits were also applied to manufacturing resistive components. At that time, the only substrate material that could be made with a sufficiently uniform surface was a very low-alkali-content borosilicate glass. Nichrome alloys were evaporated in high vacuum onto flat substrates. Patterns were produced by photolithography, resulting in very fine features. The techniques used for resistance adjustment by selective removal of the film, including chemical thinning and diamond grinding, were slow and clumsy. The development of laser trimming resolved those issues, but difficulty was encountered with microcracks in the glass substrate. Soon, however, an appropriate ceramic material in wafer form was developed. This had a flaw-free surface, chemical resistance, high thermal conductivity, and sufficient strength to survive the rigors of automatic equipment handling. This material, smooth, fine-grained, high-purity alumina, represented an important step in advancing thin film technology.

The problem of maintaining compositional consistency during evaporation of multicomponent alloys, such as nickel-chromium, was eventually resolved by adopting cathodic sputtering. However, it was soon discovered that nichrome in thin film form is subject to electromigration under high humidity. This corrosion resulted in occasional catastrophic failure. For this reason, another material, tantalum nitride, which had been developed during thin film capacitor research at Bell Labs, came into use.

Resistive materials in thin film form required greater attention to the nature of the termination than had bulk materials. For instance, the deposition of gold directly onto a thin film of nichrome results in thinning of the resistor in the critical region adjacent to the termination by absorption of the nickel constituent by the gold. It was therefore necessary to interpose barrier layer materials

between the resistive film and the overlaying termination to minimize adverse metallurgical interactions.

The adaptation of integrated circuit manufacturing techniques had enormous impact on passive component manufacture. As distinct from discrete resistors, it facilitated fabricating resistor *networks* within which all the elements were uniformly matched. Good tracking was an intrinsic property of integrated multielement networks. In addition, whereas the achievement of high precision had placed strict demands on the manufacture of discrete resistors for maximum *absolute* performance, integrated network construction allowed focusing the emphasis on unprecedented *relative* performance. In addition, the small size of single chip networks allowed economic packaging in hermetic enclosures using familiar chip and wire technology. Of course, the economy of simultaneously manufacturing hundreds or even thousands of resistors per wafer significantly reduced the unit cost.

2. DESIGN CONCEPTS

In choosing a resistor technology, consideration must be given to requirements for (1) the range of resistance values, (2) their precision, and (3) the physical size in terms of power or voltage demands.

Different resistance values are obtained, in general, by selecting a material with appropriate specific resistivity, by arranging a given material in an appropriate geometrical configuration, and/or by a combination of both. For example, wire-wound resistors are composed of alloy compositions with exceptionally low TCRs. Differing values are obtained by using wires of different cross-sectional area and length. This is an exclusively geometric, mostly one-dimensional, approach.

By contrast, carbon composition resistors and thick film resistors are produced in a limited number of physical configurations in which the resistance value is varied by changing the resistivity of the material. In particular, thick film materials consist of a two-phase mixture of a conducting oxide particulate dispersed throughout a glass matrix. By varying the proportions of the two ingredients, the resistivity and, thereby, the resistance are adjusted controllably over a range of seven decades or so. The discontinuous nature of the conducting phase in composites, however, presents difficulties. It is not easy to obtain lower resistivities. Composites are also characterized by higher noise and greater voltage and temperature dependence. Nevertheless, composite materials attain resistivities far higher than those of any other technology. A comparison of thick and thin film resistor technologies is given in Table 1.

Thin film resistors are made from materials with a limited resistivity range, and different values are obtained primarily by geometric means. The most common materials, nichrome and tantalum nitride, have a resistivity of about $500 \mu\Omega \cdot \text{cm}$ (this falls in the semimetallic category, characterized by a weak dependence of resistivity on temperature). The film thickness is varied in a practical manner only from a few hundred to a few thousand angstroms.

Table 1. A Comparison of Resistor Technologies

	Thick Film	Thin Film
Manufacturing process	Screen print	Vacuum deposit and photolithography
Film thickness	10 μm	0.1 μm
Line width	30 mils	0.3 mils
Material resistivity range	6 + decades	1 decade
Typical aspect ratio	20:1	2000:1
Resistance tolerance	1%	0.01%
TCR	250 ppm/ $^{\circ}\text{C}$	25 ppm/ $^{\circ}\text{C}$
TCR tracking	50 ppm/ $^{\circ}\text{C}$	5 ppm/ $^{\circ}\text{C}$
High-voltage capability	Yes	No
Current/Voltage linearity	Poor	Excellent
Current noise	-5 dB	-30 dB
Corrosion	Never	Sometimes
Custom tooling	Hard	Hard
Cost	Lower	Higher

The principal means of achieving different values is by varying the length and width of the conducting trace.

To facilitate design calculations, practitioners have rearranged the customary relationship describing the dependence of resistance R on resistivity ρ , length L , and cross-sectional area A into one that involves “sheet resistance” ρ_{sh} and “number of unit squares” n as shown in Fig. 1:

$$R = \frac{\rho L}{A} = \left(\frac{\rho}{t}\right) \left(\frac{L}{W}\right) = \rho_{\text{sh}} n \quad (1)$$

For example, a film of material with a resistivity of 500 $\mu\Omega \cdot \text{cm}$ and 50 nm thick has a sheet resistance of 100 Ω/\square . The usefulness of this concept is based on the fact that the resistance across a square area is independent of its size, unlike one- and three-dimensional geometries. The sheet resistance must be multiplied by the number of unit squares in series, which is given by the length/width ratio of the design trace, otherwise known as the aspect ratio.

The maximum resistance value attainable with a given film is determined by the highest aspect ratio that can be generated in a given area, which, in turn, is determined by the lower limit of line and space width achievable via the patterning technique employed. The optimum pattern for this is serpentine, as shown in Fig. 2. Following are the relationships among the various parameters:

$$R = \rho_s n = \rho_s \left(\frac{L_1}{\ell}\right) \left(\frac{L_2}{\ell + s}\right) = \rho_s \left(\frac{A}{\ell(\ell + s)}\right) \quad (2)$$

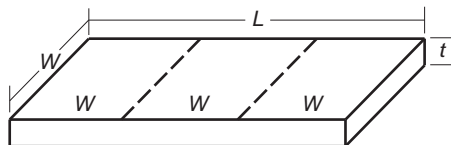


Figure 1. Simple rectangular resistor structure showing the basic concept.

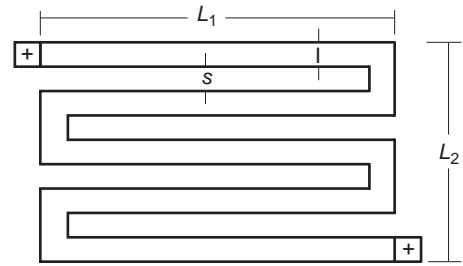


Figure 2. Typical serpentine resistor pattern to conserve space.

For equal line/space width,

$$R = \frac{\rho_s A}{2l^2} \quad (3)$$

For example, with a film of sheet resistivity 100 Ω/\square and minimum attainable line/space width of 0.5 mil, the maximum resistance value attainable in a 50 \times 100 mil area is 1 m Ω . To achieve higher values, a film of higher sheet resistivity would be necessary, or greater substrate area, or narrower line/space width, or a combination.

Very low resistance values are not easily obtained with thin films. The lowest sheet resistivity directly obtainable is about 10 Ω/\square . Low values are therefore often designed with fractional aspect ratios. This is done with interleaving termination traces, but the performance characteristics are compromised, because of the proportionately increasing roles of the conductor itself and the resistor-conductor interface.

The potential contribution of conductor traces within networks must be minimized even with midvalue resistors, where precision tolerances or ratios are required. This is done through appropriate design by keeping the aspect ratio of the conductor as small as possible and by reducing its sheet resistance, which is commonly done by electroplating to a thickness much greater than practical with vacuum deposition. The form of the external lead must also be taken into consideration, especially with chip-and-wire assembly, where the resistance of a typical wire lead is 0.1 Ω . That amount adds significantly to the total resistance and affects the TCR, as shown in Table 2. The effect of lead resistance is minimized by using alternative packaging techniques, such as direct soldering of lead wires in a single-in-line style. Fortunately, the circuit requirements for resistance networks are more often on voltage ratio output; in which case, interconnection resistance is less important.

Table 2. Effect of 0.1 Ω Lead Resistance on Resistance Value and TCR

	Total Resistance	Temperature Coefficient ^a
10 W	1.00%	40.0
100 W	0.10%	4.0
1000 W	0.01%	0.4

^aAssuming a TCR of gold of +4000 ppm/ $^{\circ}\text{C}$.

The design of thin film resistors must also allow for adjustment to a value. Modern laser systems are capable of adjusting resistors to very close tolerances at very high speed. However, the closer the required tolerance, the more carefully the resistor must be designed for both trimming efficiency and to minimize the amount of physical damage done to the remaining active area of the resistor by the laser beam. This is done by the use of special trim geometries, which allow for sequential steps from large to small increments of resistance change. These special geometries occupy a significant amount of substrate area. An example of such a design is shown in Fig. 3.

3. WAFER-SCALE FABRICATION

The process of fabricating thin film resistors and networks is comparatively simple relative to that for active devices, but considerable variety is still possible along with much art. A typical sequence is described below.

The surface of the substrate is given some type of cleaning and/or conditioning to ensure good adhesion of the thin film. This is accomplished before deposition by chemical cleaning in ultrasonic baths followed by transport through a vaporphase solvent system. Further conditioning is accomplished by plasma treatment during the initial stage of the vacuum deposition process. This is often done within a load-lock entry chamber, a system that allows maintaining the cathode within a controlled, non-reactive atmosphere. Film deposition is accomplished by dc sputtering in a controlled atmosphere across a gap of

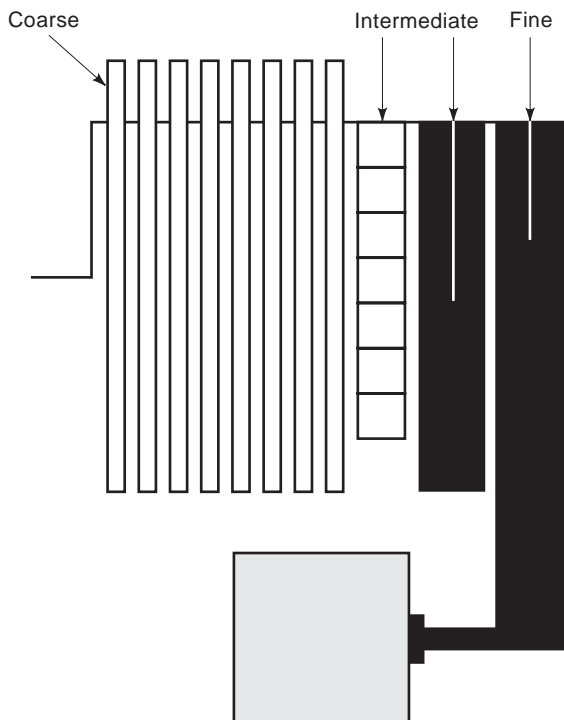


Figure 3. Special resistor design feature. A multitude of different designs are possible.

the order of 1 in. The substrates are often periodically cycled under the cathode. The atmosphere employed is usually 10 μm of argon containing a partial pressure of either oxygen or nitrogen. Deposition is done at rates ranging from 1 nm/min to 10 nm/min.

Most deposition systems accommodate multiple cathodes to deposit several different materials sequentially without breaking vacuum. This provides efficient operation, assures intimate contact between layers, and allows for the deposition of composite resistive films. The design and placement of physical shields, located in the cathodic dark-space region, govern the uniformity of deposition across a wafer. It is possible to attain uniformity of sheet resistance to within $\pm 10\%$ of a design value.

The general order of deposition is (1) resistive film, (2) barrier layer, and (3) conductive film. The barrier layer is included to minimize metallurgical interaction between the resistive and conductive layers, especially during subsequent high-temperature stabilization. It usually consists of nickel in the case of the nichrome/gold system and palladium in the case of the tantalum nitride/gold system.

After film deposition, the appropriate resistor and conductor patterns are formed by photolithographic techniques, often in conjunction with an electroplating operation as noted earlier. An example of such a sequence is shown in Fig. 4 in idealized form. The first photoresist layer is applied, exposed in the termination pattern, and developed. Then the wafer is electroplated, thickening the conductor traces within the openings in the photoresist layer. After stripping the photoresist, the remaining thin film conductor/barrier is etched away. Then the photolithographic patterning process is repeated with the resistive film.

It is common practice to employ a positive photoresist that stands up in electroplating solutions. The conductive layers are removed with cyanide solutions, and resistive materials are dissolved in potassium iodide or hydrogen fluoride solution.

Although there are many variants in the sequence of these steps, they always include stabilizing the resistive film by baking at high temperature in air, typically for several hours at temperatures in the 300–450°C range. This renders the material metallurgically stable and chemically inert. The precise conditions during stabilization are often adjusted slightly to bring the TCR within a required specification.

The resistors are adjusted to their required value by laser machining with automatic, specially designed high-speed operating systems. The choice of electrical probes for online measurement is critical, involving a balance between requirements for good electrical contact and optimum physical wear. Laser beam (YAG) parameters must be carefully chosen to provide clean, efficient removal of resistive film but with minimum disturbance of the remaining film and substrate. In the case of precision tolerances, a two-step trim procedure is frequently employed that includes an intermediate annealing step.

The final step in wafer-scale fabrication is dicing. This is done by laser scoring or diamond-wheel sawing. With a ceramic substrate, scoring is normally done with a CO_2

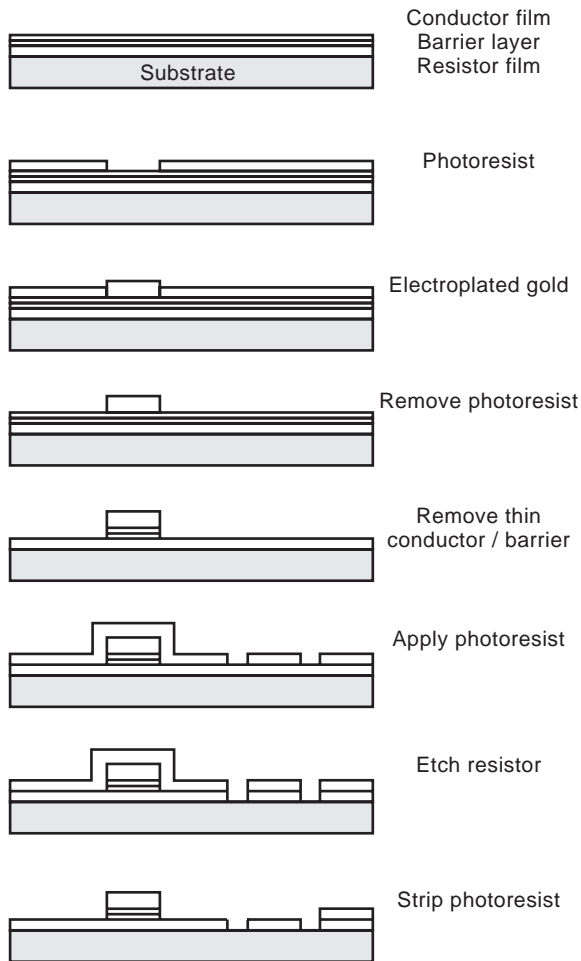


Figure 4. Typical resistor processing sequence. This is just one example of resistor fabrication.

laser system and usually in the postage-stamp mode, followed by breakage. Alternatively, high-speed diamond-sawing is done with ceramic or silicon substrates.

Chip networks are usually assembled into one of many available types of package formats, including conformably coated single-inline, hermetic dual-inline, flatpack, or several molded small-outline package styles.

4. MATERIALS

4.1. Substrates

One of the most widely used substrate materials for thin film resistors is high-alumina ceramic. This is available from many suppliers in a variety of thicknesses ranging from 10 to 40 mils. It is manufactured by a green-tape process in sizes up to 6 in. In finished form, it consists of 99.6% alumina and has a surface finish generally better than 1 microinch/inch. It provides excellent adhesion of the deposited film. Its high strength is essential for withstanding the rigors of handling by manufacturing equipment. It is reasonable in cost, and its comparatively high

thermal conductivity is important for dissipating power and reducing thermal gradients within a chip network.

High-alumina does not saw easily, but with the proper composite diamond blades and high-speed equipment, reasonable rates are achieved. Pulsed-laser scoring and subsequent breaking is done much more rapidly but with attendant risk to higher precision network tolerances.

Ceramic substrate was not always available with consistent surface characteristics, and during its evolution, the use of oxide passivated silicon wafers became, and has remained, popular for fabricating film resistance networks. This material is readily available in large sizes with consistent surface characteristics. With it, much finer circuit features can be successfully imaged. It dissipates internally generated power very adequately.

Silicon substrates are favored in applications involving highly automated assembly equipment because of the superior pattern visibility in autoalignment systems and the relative ease and speed with which they can be singulated by diamond-blade sawing. However, because of the inherent electrical conductivity of silicon and the relatively large capacitive reactance involved, it performs more poorly at higher signal frequencies than do similar networks on ceramic. On the other hand, the combination of the conductive silicon base and its overlying dielectric layer provides the basis for fabricating integrated resistor-capacitor networks.

Experience with both high-alumina and silicon substrates indicates that better stability is generally obtained on ceramic, making it the preferred choice for precision network applications. Substrates of thin sapphire wafers (single crystal alumina) were used in high reliability applications when ceramic quality was still inconsistent. It is still employed occasionally in applications for which its superior thermal conductivity is critical.

4.2. Resistive Films

The use of nickel-chromium alloys [1] for fabricating thin film resistor networks was a natural extension of their use in manufacturing wire-wound resistors. Nichrome wire was made in compositions with a very low TCR for instruments and the endurance of red heat for power applications. Compositional control of early film depositions by thermal evaporation of nichrome in high vacuum was difficult because of the different partial pressures of the constituents. This problem is resolved by high-voltage sputtering, which after an initial break-in period, delivers a film whose composition is identical to that of the cathode. Sputtering provides excellent control of the film deposition process.

The composition of nickel-chromium alloys for thin films generally falls within the range 80/20 to 40/60. The as-deposited film is uniform in composition with varying degrees of microcrystallinity, depending on the temperature at which the substrate is maintained during deposition. During thermal annealing, however, stratification occurs, with chromium migrating to the surface where it is oxidized, leaving a nickel-rich underlayer. The chromium oxide layer is etch-resistant. The deposition is also done

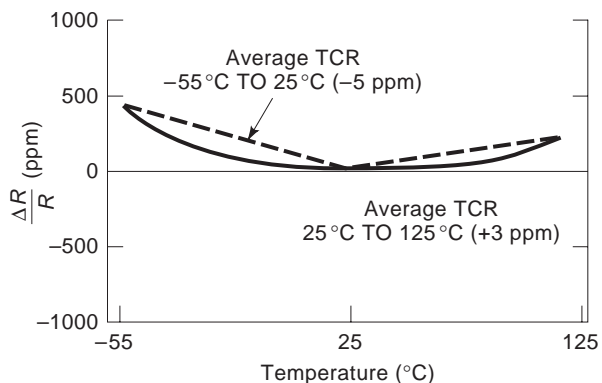


Figure 5. Example of nonlinear TCR. It is usually desired that TCR be linear.

using a partial pressure of oxygen, which modifies the behavior during subsequent processing.

Nichrome is made in sheet resistance ranging from 25 to 1000 Ω/■ or so, and in that range, the TCR is maintained to within ±50 ppm/°C. However, within the commonly employed narrower range of 100–200 Ω/■, the TCR is held to a very low value, less than 10 ppm/°C, by exercising careful control of critical process steps. It remains the material of choice for high-precision applications.

The TCR of the as-deposited film is generally negative and moves to a more (metallic) positive value during thermal stabilization. A near-zero TCR is attained by critical control of the process parameters. However, this is compromised by the significant nonlinearity of the resistance-temperature relationship, as shown in Fig. 5. Even with films with an incremental TCR of zero near room temperature, the slope of the curve at lower and higher temperatures may range between -5 and +5 ppm/°C.

Properly manufactured nichrome thin films on ceramic substrates are exceptionally stable. The small resistance changes that occur in circuit operation are entirely a function of substrate temperature, induced by power loading or ambient. The rate of change of resistance measured at higher temperatures can be extrapolated to lower temperatures and longer times by classic kinetic equations, as in Fig. 6 and Table 3.

Nichrome thin films are often provided with deposited gold terminations for wire-bonding. If the gold is laid directly on the nichrome, however, it absorbs chromium from the nichrome nearby, resulting in a region of high resistance and circuit vulnerability. This interaction is blocked by adding an intermediate nickel layer between the nichrome and the gold.

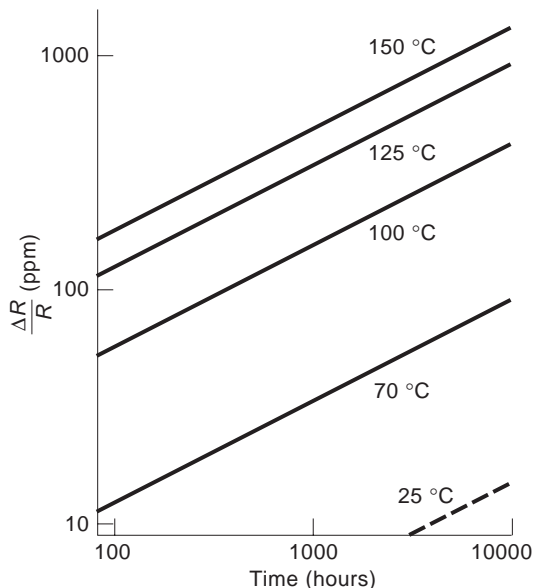


Figure 6. Change in TCR with time and temperature to show prediction of performance.

Unlike its bulk forms, thin film nichrome is subject to catastrophic failure by electromigration from dc voltage under high humidity, which permits a condensed water layer to form. This phenomenon resulted in dramatic field failures before it was recognized and dealt with by hermetic packaging or by applying an insulating material to the nichrome surface.

To overcome moisture difficulties associated with nichrome, thin film resistors of tantalum nitride are employed. These are deposited on ceramic substrates by dc sputtering from a tantalum cathode at a pressure of about 10 μm with a partial pressure of nitrogen, appropriate for obtaining the film in the form Ta₂N [2]. These films usually have an interdiffusional barrier layer of palladium and gold termination. They are photolithographically imaged and thermally stabilized.

Tantalum nitride is made in a range of film thickness and sheet resistance similar to that of nichrome. It is regarded as having superior reliability. The disadvantage of tantalum nitride, compared with nichrome, is that it has an intrinsic TCR of -120 ppm/°C.

Efforts to combine the best features of nichrome and tantalum nitride in a single system have been made by way of a composite, two-layer film. A film of nichrome is covered with a thin film of tantalum, which is subsequently

Table 3. Extrapolated Stability Data for Nichrome Films

Film Temp, °C Time, h	25 ΔR/R, ppm		70 ΔR/R, ppm		125 ΔR/R, ppm	
	Absolute	Ratio	Absolute	Ratio	Absolute	Ratio
1,000	—	—	50	10	500	100
2,000	—	—	70	15	700	150
10,000	15 ^a	3 ^a	150	30	1500	300
100,000	50 ^a	10 ^a	500 ^a	100 ^a	5000 ^a	1000 ^a

^aExtrapolated data.

converted by thermal treatment to an oxynitride. The resultant composite can be made with a very low and nearly linear TCR along with greatly increased resistance to electromigration.

Still another class of vacuum-deposited thin films used in resistor products are composites of mixed chromium and silicon oxides. Historically, these are obtained as vacuum evaporated mixtures, but serious process control was almost impossible. Now such films produced by sputtering from cathodes formed of chrome-silicon in an atmosphere with oxygen. High sheet resistance is obtained with these films, to values up to 10,000–20,000 Ω/\square . The TCR of these films is more suitable for general-purpose applications, and the films exhibit higher levels of current noise and less stability than homogenous film materials. For situations requiring very high resistance and/or minimum size, these film materials fulfill a real need. A comparison of film materials is given in Table 4.

5. FINISHED FORMATS

5.1. Through-Hole Assembly

Regardless of the end product, all wafers in a given facility are processed in pretty much the same way. After singulation, however, the chips are packaged in a variety of formats. For through-hole circuit-based assembly with 100 mil pin spacing, the choice is between dual-inline and single-inline and styles. The former may be hermetic or molded plastic. Both involve chip-and-wire assembly technology, which requires that a significant amount of additional electrical resistance must be taken into account in designing and trimming precision networks. This is more critical in networks with lower value resistors.

Dual-inline construction imposes limits on chip size and thereby on the total amount of resistance that can be accommodated. However, a hermetic seal provides an added measure of reliability/stability.

An alternative format for through-hole assembly is single-inline. These are nonhermetic, usually with a conformal resin encapsulation. Single-inline format involves a much larger “chip” than does dual-inline, but this added size allows much higher total resistance values. An advantage of single-inline construction is that the external leads are connected directly to the chip, by soldering or thermocompression bonding.

The stability of thin film resistor networks is impacted by mechanical stress introduced within the chip during assembly, such as by mechanical contraction of a molding compound during curing or through the interaction of materials with a different coefficient of thermal expansion.

Where the development of such stress is unavoidable, the effects are reversed or moderated by thermal annealing. It is also possible to allow for a final “tweak” of resistance value to close tolerances by laser matching just before the final assembly step.

5.2. Surface-Mount Format

In the case of surface-mount assembly, a greater number of formats are available, beginning with individual chip resistors. These are available on ceramic in a variety of standard sizes and standard values to tolerances of 0.1%. The solderable, wraparound end termination may be a thick film or thin film.

Another form of individual chip resistor is the square silicon chip, usually either 20 or 30 mil meant primarily for hybrid circuit application, with terminal pads for wire-bond connection. A major advantage of this product is that it is usually supplied as a two-element, three-terminal version, which allows adjustment to close ratio tolerance.

Other forms of surface mount packaging for chip networks include:

1. Hermetic flatpack, with chip-and-wire internal connection and 50 mil pin spacing.
2. Leadless chip carrier, with solderable, wraparound terminals on two or four edges in 50 mil pin spacing.
3. Small-outline (50) formats, primarily of molded construction with chip-and-wire assembly, in 50 and 25 mil gull-wing lead spacing on two edges. The popular RC networks are supplied in this format.
4. Lead-frame-bonded directly to a ceramic chip in gull-wing style.

Most surface-mount networks are designed for general purpose (1% tolerance) networks to attain maximum component onboard density.

6. PERFORMANCE CHARACTERISTICS

6.1. Integrated Construction

An important aspect of integrated, thin film resistor construction is that all resistors on a given wafer close to one another are exposed to nearly identical conditions during manufacturing, which results in matching their electrical characteristics very closely. This ensures that the relative values of resistance remain virtually unchanged throughout a variety of operational conditions. During the lifetime of the circuit, the resistors within a given network are said to track one another closely.

Table 4. A Comparison of Resistive Film Materials

	NiCr	Ta ₂ N	Poly. Chrom.	Multilayer
Sheet resistivity range, Ω/\square	50–500	50–500	to 10,000	50–500
TCR ppm/ $^{\circ}$ C	10–50	– 120	< 300	5–25
Thermal stability	Excellent	Excellent	Fair	Excellent
Reliability	Marginal	Excellent	?	Excellent

The difference in TCR between a seemingly matched pair of *discrete* resistors may be as great as twice the specified absolute TCR. For example, for a TCR of $0 \pm 2.5 \text{ ppm}/^\circ\text{C}$, the tracking between a pair may be as much as $5 \text{ ppm}/^\circ\text{C}$. With integrated film networks, the tracking is independent of the absolute TCR and usually an order-of-magnitude better. For instance, even with an absolute TCR of $\pm 25 \text{ ppm}/^\circ\text{C}$, the internal tracking is generally less than $2 \text{ ppm}/^\circ\text{C}$.

An additional advantage of integrated construction is that serpentine patterns are essentially noninductive compared with discrete, spiraled resistors. Further, the interconnections between resistors in a network at the chip level are inherently more reliable than are those made with external lead connections, greatly improving the overall reliability of the network.

Thermoelectric voltages are generated if the terminations of a resistor are at different temperatures. This is a real problem with discrete precision resistors where measurable thermal gradients easily exist over the relatively large dimensions of conventional circuit boards. In thin film integrated networks, all resistors are at nearly the same temperature as a result of the small chip size, proximity, and the heat-spreading effect of the thermally conducting substrate. It is not surprising, therefore, that there are no reported thermoelectric effects in thin-film networks.

6.2. Temperature Coefficient of Resistance

The temperature coefficient of resistance is the measure of resistance change with a change in ambient temperature. It is defined as the unit change of resistance per unit change in temperature, and it is commonly expressed as parts per million per degree centigrade. It is the property by which different types of resistors are most often characterized or differentiated. In practice, the TCR is usually determined experimentally by measuring the resistance value at several temperatures and calculating the rate of change over the specific temperature interval, as indicated later. If the resistance changes linearly with temperature, the TCR is constant, regardless of the temperature interval. However, when it is not linear, the TCR varies according to the exact temperature interval over which the measurement is made. For this reason, it is critical that the interval is specified:

$$\text{TCR} = \left[\frac{R_2 - R_1}{R_1(T_2 - T_1)} \right] \times 10^6 \quad (4)$$

where TCR = temperature coefficient of resistance ($\text{ppm}/^\circ\text{C}$), R_1 = resistance at room temperature (Ω), R_2 = resistance at operating temperature (Ω), T_1 = room temperature ($^\circ\text{C}$), and T_2 = operating temperature ($^\circ\text{C}$).

By adjusting processing conditions, it is possible to tailor the resistance versus temperature curve to produce a TCR with a negative slope below 25°C and a positive slope above it, with an incremental TCR of zero in the vicinity of room temperature, as shown in Fig. 5.

A zero absolute TCR is especially advantageous in circuit operation, whereby current is switched on and off in

one resistor that is matched to a reference resistor carrying a constant current. In this case, even though the two resistors are perfectly matched, they may differ in value because of differential self-heating, depending on the absolute TCR of the pair. In these situations, the absolute TCR should be as low as possible in the operating temperature region.

6.3. TCR Tracking

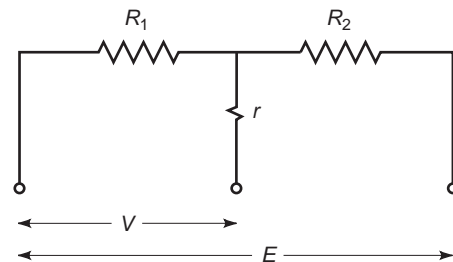
TCR tracking is defined as the difference between the TCR of a pair of resistors over a given temperature interval. Close tracking is difficult to achieve among discrete components, but it is intrinsic to integrated construction. TCR tracking among neighboring resistors on the same wafer is usually no more than a few tenths of a parts per million per degree centigrade. However, an “apparent” TCR tracking is sometimes found that is higher than the “true” TCR tracking because of the contribution of terminations with a small but measurable resistance r and a large metallic TCR. The contribution of the common lead disappears when critical ratios are specified and measured according to voltage division rather than to resistance ratio.

6.4. Voltage Ratios

Frequently when resistors are employed as voltage dividers, it is more appropriate to deal with voltage ratio specifications than with resistance ratios. Ideally, the voltage drop across a pair of resistors is determined by the ratio of resistance values: $R_1/(R_1 + R_2)$ as shown in Fig. 7. When the resistance values are not equal, however, the voltage ratio differs from that calculated from the apparent (measured) resistance values by an amount governed by the resistance of the common lead. This deviation can be quite significant, especially with low-value resistors. For a $10 \text{ k}\Omega$ resistor in series with a $1 \text{ k}\Omega$ resistor with a common “tap” lead of $100 \text{ m}\Omega$ resistance, the two ratios differ by 75 ppm :

Voltage Ratio Calculated Using Apparent Resistance:

$$\frac{1000.1}{1000.1 + 10,000.1} = 0.0909165$$



$$\frac{V}{E} = \frac{R_1}{R_1 + R_2} \neq \frac{(R_1 + r)}{(R_1 + r) + (R_2 + r)}$$

Figure 7. Voltage ratio versus apparent resistance ratio.

Voltage Ratio Measured Directly:

$$\frac{1000}{1000 + 10,000} = 0.0909090$$

Voltage ratio tracking over temperature is always less (better) than TCR tracking.

6.5. Thermal Stability

The effects described in the previous sections are reversible. The changes are not permanent and disappear when the temperature reverts to its initial point. Irreversible changes, however, are brought about by holding the components at an elevated temperature for extended intervals. The advantage of integrated construction again becomes evident. All resistors in a given film network exhibit very similar absolute changes during life testing, and the changes in resistance ratio or voltage ratio are an order-of-magnitude smaller.

6.6. Power Rating

Because thin film networks are not generally used in high-power applications, methods for establishing maximum power ratings are not as formalized as for discrete resistors. However, because chip size is quite small, internally generated power *density* may reach significant levels.

Rated power is generally accepted as that power which is sustained without raising the surface temperature of a part above a specified maximum operating temperature, commonly 150°C. The designer must, therefore, consider the power density developed at the chip surface. For more precise tolerances, a limit of 25 W/in² is appropriate. More general tolerances sustain power density levels up to 200 W/in² without jeopardizing their integrity. Allowance must be made for the fact that different packaging formats vary greatly in their ability to dissipate heat and thereby lower the chip surface temperature.

6.7. Voltage Coefficient of Resistance and Current Noise

These two characteristics, which can be a serious drawback in resistors made from composite materials, such as cermets or polymers, are inconsequential in thin film networks. Voltage coefficient of resistance is the unit change in resistance per unit change in voltage expressed as parts per million per volt. It is a measure of the nonohmic behavior and, in thin films, reaches identifiable levels only in the megohm range, where it has been measured at about 0.1 ppm/V. Current noise is characterized and measured by an industry standard instrument. Typical values for thin film elements are less than -35 dB.

7. SUMMARY OF THE ADVANTAGES OF THIN FILM, INTEGRATED RESISTOR CONSTRUCTION

- Very small, high-density, multielement networks.
- Extremely close matching of all elements in a network, ensuring close tracking over temperature and throughout life.

- The small chip size enables hermetic construction in a variety of standard, contemporary formats.
- Repeatable and consistent characteristics part-to-part and lot-to-lot.
- Very low inductance.
- Outstanding reliability—fewer manmade interconnections.
- No discernible thermoelectric effects on voltage coefficient.
- Very low current noise.
- Installed costs are usually less than for discrete resistors.

8. NiCr THIN FILM RESISTORS

8.1. Background

Studies of NiCr TFRs have used resistance variation with annealing of different elemental ratios of Ni and Cr to achieve low values of the TCR [3]. Nucleation and growth of microcrystalline particles occur with annealing in air or vacuum [4,5]. Vacuum annealing may positively increase the TCR because of grain growth, whereas air annealing forms surface oxides of Cr with a negative TCR, which compensates for the effect of grain growth. Grain growth and intermetallic phases were observed [6] for SiO_x protected films, and selective oxidation of Cr on the top of unprotected films led to the development of an in-depth concentration gradient.

NiCr TFRs may be optimally developed [7] by annealing to minimize the TCR, by stability testing for various annealing conditions, and by identifying the annealing mechanism by secondary ion mass spectrometry (SIMS), electron spectroscopy for chemical analysis (ESCA), scanning electron microscopy (SEM), energy dispersive X-ray (EDAX), and transmission electron microscopy (TEM).

8.2. Fabrication Techniques

A thorough study of the NiCr TFR was conducted in a joint project by the State University of New York (SUNY) at Buffalo and Ohmtek, Inc. [8]. NiCr thin film resistors used RF sputter deposition from a 40/60 NiCr:Si target on alumina substrates to a thickness of 300–700 Å. Sheet resistivities ρ_s of 10, 100, 150, 191, 212, 280, 500, and 1000 Ω/\square were studied. The TCR was determined for both air and vacuum annealing, as in Table 5, in the range -180°C to +100°C. The TCR of 10, 500, and 1000 Ω/\square samples was not improved satisfactorily by annealing. Films within the range of 100–200 Ω/\square were successfully annealed, except for the vacuum annealing of the 191 Ω/\square case. Vacuum annealing for 100 Ω/\square samples required higher temperature to achieve the same TCR improvement as air annealing. The 150 Ω/\square sample attained the lowest TCR with less range span. For the 191 Ω/\square case, only air annealing improved the TCR. As shown in Fig. 8, air annealing flattens the TCR versus T increases, but an opposite effect was observed for vacuum annealing.

Samples were tested for stability after 1 month using repeated temperature cycling between 40 and 150°C for

Table 5. Result of TCR Measurements on NiCr TFRs

Sheet Resistivity, ohm/sq	Annealing Environment	Temperature, °C	Typical As-Deposited TCR, ppm/°C	Typical Annealed TCR, ppm/°C
10	Air	300	+70 ± 20	+90 ± 50
100	Air	337	-40 ± 20	+5 ± 5
100	Vacuum	400	-40 ± 20	+5 ± 5
150	Air	360	-45 ± 10	+3 ± 1
191	Air	350	-45 ± 8	+5 ± 4
191	Vacuum	340	-45 ± 8	-40 ± 10
500	Vacuum	300	-55 ± 10	-50 ± 8
1000	Air	200	-70 ± 27	-110 ± 20
1000	Vacuum	400	-70 ± 27	-50 ± 15
1000	Vacuum	500	-70 ± 27	-80 ± 20

8 h; elevated temperature at 150°C for 4 h; humidity >90% for 4 h and then 8 h. During a 1-month storage period, before stability tests, air annealed 100 Ω/□ samples retained the low TCR, whereas the vacuum annealed 100 Ω/□ and air annealed 191 Ω/□ samples had a TCR change from 5 to 17 ppm/°C. In 100 Ω/□ and 191 Ω/□ samples, the TCR was undisturbed by the previously described stability tests.

8.3. Mechanisms of Stabilization

SIMS analysis reveals that annealing enhances the Cr oxide to the same level as Si oxide. ESCA and TEM analyses confirm this in that an elemental Cr peak for the as-deposited film is replaced by a Cr oxide peak. The absence of Ni in the ESCA spectrum for annealed samples indicates segregation of Cr to the surface. SIMS reveals that the oxide ratio of Cr to Si in the bulk is lower for the samples with improved TCR. The lack of a Cr-Si structure in the unimproved samples, evidenced from the electron diffraction patterns, and the limited range of sheet resistivity showing a TCR improvement, suggests that the bulk Cr oxides, then coordinated with Si, are important in achieving a low TCR; that is, Si is the medium for CrO and Ni

interaction. After optimal annealing of samples consisting of enough Si-Cr structure in the 100–200 Ω/□ range, the amount of bulk oxide with a negative TCR balances the positive TCR contributed by the nucleation of segregated Ni. Thus, NiCr TFRs have a low and stable TCR after annealing because new compounds form and a balance occurs between negative and positive TCR components in the film. However, NiCr is not easily tuned to a TCR of ±5 ppm/°C and degrades in a harsh environment.

9. TANTALUM NITRIDE THIN FILM RESISTORS

9.1. Fabrication Techniques

The linear TCR and physiochemical inertness make Ta-N superior to the more popular NiCr for thin film resistors. The mass production of Ta₂N TFRs, deposited at 450°C by magnetron sputtering, with sheet resistivity of 50 to 100 Ω/sq and TCR of about -80 ppm/°C, was announced in 1982 [9]. A slow annealing process under vacuum [10] might produce a near-zero TCR.

A thorough study of Ta₂N-TFRs was jointly conducted by SUNY at Buffalo and Ohmtek, Inc. [11,12]. The Ta-N films were deposited on SiO₂/Si or alumina from a pure Ta target by either dc diode or magnetron reactive sputtering, without substrate heating, on stationary or rotating substrates for better uniformity. The end contact materials consisted of Au on an interlayer of NiCr, TiW, or Tamelex (the tradename for the Ta/NiCr), for adhesion and a diffusion barrier.

Optimal air annealing was at 425°C for 15 min followed by 375°C for 1 h. The result in Fig. 9 shows a linear TCR, better than -20 ppm/°C for the temperature range of -150 to +100°C. Air annealing effectiveness was a strong function of sheet resistance and the initial TCR. As for vacuum annealing, both high and low sheet resistivity films (25–140 Ω/sq) were effectively improved in TCR. Ten 140 Ω/sq resistors with an initial TCR = -140 ppm/°C were improved to close to zero TCR (±5 ppm/°C) by annealing at 700°C for 2 min. Figure 10 shows a linear and very low TCR resulting from vacuum annealing. Air annealing would not be successful for such high sheet resistivity films. A summary of annealing effects is listed in Table 6. The 25 Ω/sq films are extremely temperature sensitive, resulting in a wider TCR range after vacuum annealing.

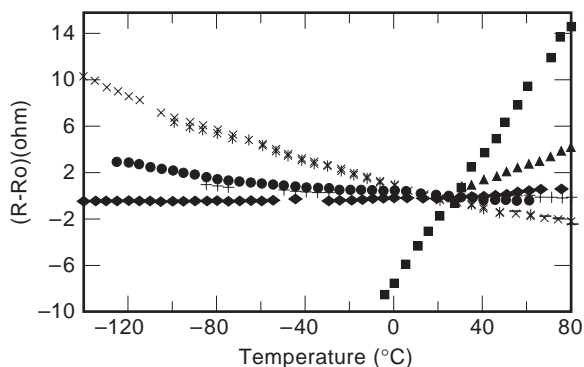


Figure 8. Resistance variation versus ambient temperature for 191 Ω/□ films of NiCr. The change in resistance decreases as air annealing temperature increases from 250°C to 350°C [7]. * = 250°C in air, 1 h; ● = 330°C in air, 1 h; + = 340°C in air, 1 h; ◆ = 350°C in air, 1 h; ■ = 380°C in air, 1 h; ▲ = 340°C in air, 2 h; × = 340°C in vac, 2 h.

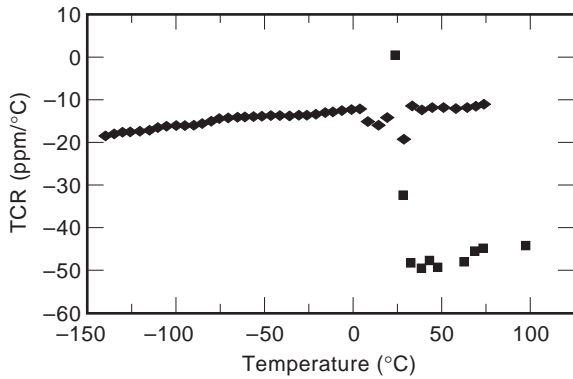


Figure 9. Typical TCR behavior after air annealing Ta-N TFRs, $>70\ \Omega/\square$ [12], ■ as deposited; ◆ annealed at 400°C in air, 1 h.

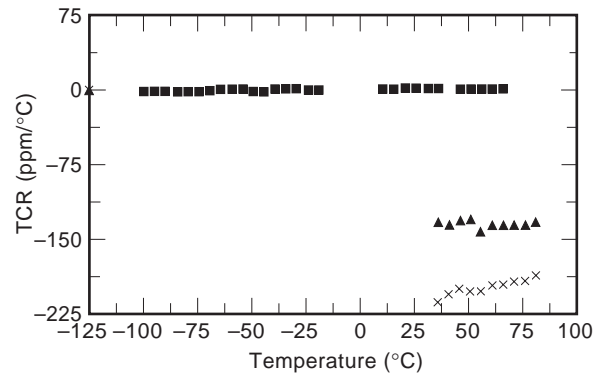


Figure 10. Typical TCR behavior after vacuum annealing Ta-N TFRs [12]. ▲ as deposited; × annealed at 400°C in air, 1 h. ■; annealed at 650°C in vacuum plus 250°C in air.

An aging test (or burn-in) may be conducted at 250°C and an accelerated lifetime test at 150°C. Because the Ta₂N material possesses a very high free energy of formation (−457 kcal/mol) [13], no aging would occur at a lower temperature. It is desired to maintain the change in resistance, for resistors held at 150°C, to less than 0.02% after 1000 h.

Annealing at 680–700°C in vacuum followed by 250°C in air for 100 h is effective in stabilizing TFRs with a wide range of initial values of R . Contacts of TiW or Tanelox are superior to Au/NiCr contacts. Data in Table 7 indicate results of a stability study at 150°C after air annealing at 250°C. Degradation is seen after 600 h, but this is attributed to the contacts and not to the resistor.

9.2. Mechanisms of Stabilization

TEM reveals little crystallinity in as-deposited Ta-N. Elevated temperature annealing produces Ta-N interaction and grain growth. Vacuum annealing produces Ta₂N regardless of the initial resistivity, whereas air annealing is effective for high resistivity films. Stabilized grain size is about 150 nm. Analysis by ESCA indicates a competing mechanism between oxide or nitride formation. Vacuum annealing promotes nitride formation and reduces the oxygen signal. The gradually aggregated Ta₂N crystallites follow the predicted activated tunneling conduction mechanism. As the amorphous Ta-N matrix is consumed, the exposed substrate participates in the conduction mechanism. This phenomenon happens only when the films are excessively annealed. The Ta₂N structure remains intact after overannealing, and the TCR remains around +80 ppm/°C in the vacuum annealing temperature range

from 750 to 850°C. In high-frequency applications, substrate selection is the most important factor. It has been shown that Al₂O₃ is five orders of magnitude better than the SiO₂/Si substrate.

Ta₂N thin film resistors are electrically and physically superior to NiCr. The linearity of the TCR behavior, the low TCR, high recrystallization temperature, and resistance to strong acidic medium are positive attributes. Ta-N is prepared with a TCR ranging from −150 ppm/°C to almost zero. Convenient and inexpensive air annealing is used with TCR stabilized from as low as −150 ppm/°C. For high-precision applications, a vacuum annealing process is used, with a resulting TCR within ± 5 ppm/°C. After 400 h at 150°C, the Ta₂N resistors are stable within 0.02%. Aging at 250°C is by a bulk diffusion mechanism. With confident extrapolation, the resistors would be stable at 150°C within 0.05% for 1000 h if a stable contact like TiW is used.

10. RUTHENIUM OXIDE THIN FILM RESISTORS

10.1. Background

RuO₂ TFRs represent a further improvement over presently available materials [14]. Transition-metal oxides with rutile structures, such as RuO₂, may be a very attractive metallization option in a variety of very large-scale integrated circuit applications. RuO₂ is a good diffusion barrier in silicon contact metallizations with an aluminum overlayer [15–18]. RuO₂ thick film resistors find wide application in hybrid circuits [19–22].

Table 6. Result of TCR Measurements on Ta₂N TFRs

Sheet Resistivity, Ω/\square	As-Deposited TCR, ppm/°C	Annealing Condition	After annealing TCR, ppm/°C	Comments
30–90	< −60	Air	−20	—
80	< −60	Air	−120	Not improved
25	−140	Vacuum	± 30	Extremely sensitive to condition
140	−140	Vacuum	± 5	Highly reproducible results

Table 7. Stability after Optimized Air Treatment for Ta₂N TFRs

Annealing Condition	Avg. $\Delta R/R$ Environment	Avg. TCR, ppm/°C
After vacuum annealing	—	-4.5
After air annealing (0 h)	—	-1.3
After air annealing (160 h)	0.014	0.4
After air annealing (390 h)	0.016	—
After air annealing (610 h)	0.111	—
After air annealing (1400 h)	0.363	+0.8

10.2. Fabrication Techniques

Thin RuO₂ films with thicknesses of 20–200 nm are reactively sputtered by a dc magnetron. Using a target of Ru with a purity of 99.9% and diameter 5 cm, RuO₂ thin-film resistors are deposited onto SiO₂/Si substrates, directly patterned with a shadow mask during sputtering to be 1 mm wide and 10 mm long [23]. Sputtering is done with the substrate temperature ranging from 25 to 500°C, O₂ pressure from 5×10^{-5} – 1×10^{-3} Torr, total pressure (Ar + O₂) of 10 mTorr, distance between substrate and target of 7.5 cm, and sputtering rate of approximately 50 nm min⁻¹.

The TCR is controlled by a combination of substrate temperature and oxygen pressure. Films deposited at relatively low temperature give a negative TCR. A positive TCR is obtained with films deposited at relatively high temperature. Clearly, the films undergo a change in microstructure and/or chemical composition as the TCR changes from semiconductor-like to metal-like. A critical substrate temperature T_{cs} during sputtering exists, at which the TCR changes signs from negative to positive, as shown in Fig. 11, where the O₂ pressure was 5×10^{-4} Torr. The critical temperature from a simple curve fitting of experimental data is about 85°C. A TCR as low as -30 ppm °C⁻¹ to -80 ppm °C⁻¹ may result for thin film resistors deposited at a substrate temperature of 80°C and an oxygen pressure of 5×10^{-4} Torr. The TCR is further improved to 0 ± 3 ppm °C⁻¹ by heating the sample at 150°C in air for several hours.

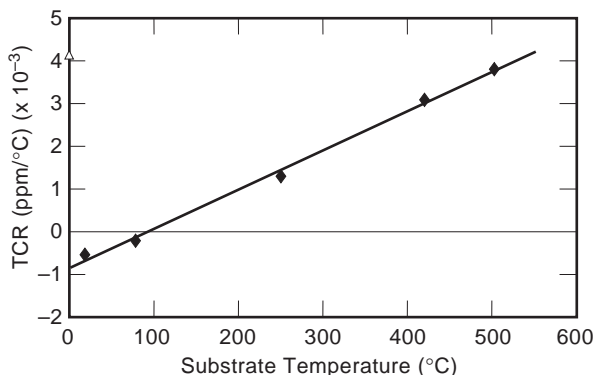


Figure 11. Dependence of TCR on the substrate temperature during sputtering for RuO₂ thin films with oxygen pressure of 5×10^{-4} Torr [14]. Symbols represent data points.

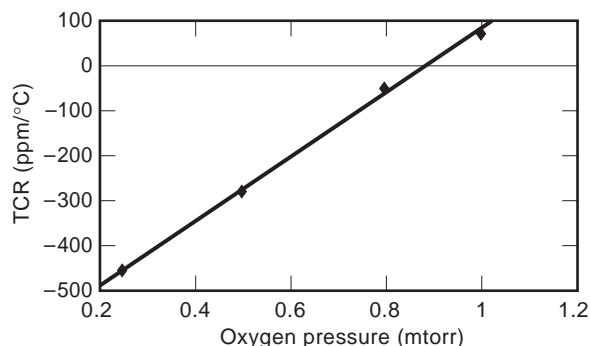


Figure 12. Dependence of TCR on the oxygen pressure during sputtering for RuO₂ thin films with the substrate temperature of 80°C [14]. Symbols represent data points.

Figure 12 shows that the positive or negative TCR of the film is controlled by changing the oxygen pressure during sputtering. However, the resistance becomes unstable for oxygen pressure lower than 1×10^{-4} Torr. From a practical viewpoint, the substrate temperature during sputtering rather than oxygen pressure should be used to control the TCR.

10.3. Mechanism of Stabilization

Using SEM and XRD, the films are amorphous or have a very fine grain size when deposited at lower substrate temperatures. The grain size of the film becomes much larger with increasing substrate temperature during sputtering. XRD patterns show that the films undergo a structure change when the substrate temperature changes from room temperature to 500°C during sputtering. From the viewpoint of material structure, amorphous RuO₂ gives a negative TCR, whereas polycrystalline thin films have a positive TCR [22–25].

Using in situ annealing, it is possible to routinely fabricate near-zero TCR resistors. Resistors annealed in such a way have a layer-like structure, automatically formed during the in situ annealing in oxygen. The TCR of the resistors is mainly controlled by the oxygen content in the film. The top layer, which contains more stoichiometric RuO₂, has a positive TCR, but the bottom layer, which shows oxygen deficiency, has a negative TCR. This can be clearly seen from the AES depth profiling shown in Fig. 13. The in situ technique is very controllable and reproducible.

11. DOUBLE-LAYER RuO₂/Ta₂N THIN FILM RESISTORS

A resistor design that overcomes potentially weak areas of the single-layer structure of NiCr, Ta₂N, or RuO₂ uses a layered structure of RuO₂/Ta₂N. This design combines the best characteristics of the two different materials Ta₂N and RuO₂ in one system. Thin film Ta₂N has a negative TCR, whereas RuO₂ has a positive TCR. Near-zero-TCR resistors are fabricated by layering Ta₂N and RuO₂. Because the resistance of RuO₂ decreases with time and that of Ta₂N increases with time, the layered design is expected

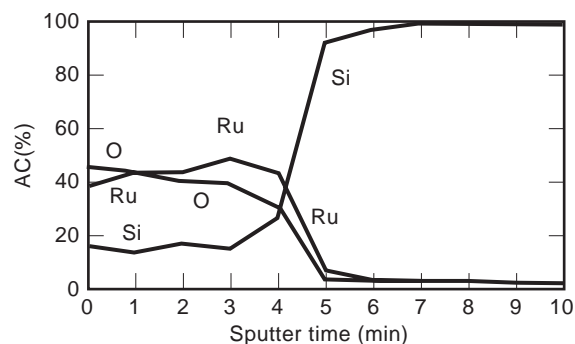


Figure 13. AES depth profiling of a resistor with a near-zero TCR deposited at room temperature followed by annealing in situ at 250°C in oxygen for 60 min (oxygen pressure of 0.5 m Torr during film deposition). AC = atomic concentration [23].

to be unchanged with time. The high thermal stability and acidic or environmental hardness of RuO_2 make it a perfect capping layer in this system. The use of highly conductive RuO_2 as a capping layer also provides a very easy way to form an ohmic contact in the resistor termination. More versatile techniques and materials for packaging and assembly become possible because of the unique barrier properties of RuO_2 and its resistance to acids [27–29].

12. CONCLUSION

In order of use today, TFRs are made from NiCr, Ta_2N , RuO_2 , or multilayers. Performance quality is improved in the same order. Fabrication consists of reactive sputtering, annealing in situ or ex situ, patterning, contact formation, longterm burn-in to establish R and TCR, and finally, stability testing. A near-zero TCR ($< \pm 5$ ppm/°C) is achieved with longterm stability. Each material system has a different mechanism of stabilization that includes oxidation, nitridation, grain growth, and layering. As applications become more demanding, RuO_2 or $\text{RuO}_2/\text{Ta}_2\text{N}$ TFRs may become materials of choice.

BIBLIOGRAPHY

1. M. A. Bayne, On nichrome film resistor technology, nickel-chromium for hybrid thin film resistors, *IEEE Proc. 36th Elect. Comp. Conf.*, 1986, pp. 48–52.
2. R. W. Berry, P. M. Hall, and M. T. Harris, Thin Film Technology, in *Tantalum Nitride Resistor Technology*, Princeton, NJ: VanNostrand, 1968.
3. M. I. Birjega et al., Structural transformations induced during the annealing of thin Ni-Cr films, *Thin Solid Films*, **57**:337–341 (1979).
4. K. Ramachandran and E. Giani, Ni-Cr thin film resistors, *Int. J. Hybrid Microelectron.*, **4**:269–274 (1981).
5. J. Rolke, Nichrome thin film technology and its application, *Electrocomponent Sci. Technol.*, **57**:51–57 (1981).
6. L. Toth, A. Barna, and P. B. Barna, Electron microscopic and AES studies on thin layers of NiCr, *Vacuum*, **33**:111–115 (1983).

7. C. L. Au, M. A. Jackson, and W. A. Anderson, Structural and electrical properties of stable Ni/Cr thin films, *J. Electron. Mater.*, **16**(4):301–306 (1987).
8. C. L. Au, *Temperature coefficient of resistance study on nickel-chrome thin film resistors*, M.S. Thesis, SUNY at Buffalo, 1986.
9. S. Yoshida, T. Shirakawa, and A. Aritoma, Mass production of HCP tantalum nitride film resistors sputtered by planar magnetron, *Proc. 32nd Electron. Compon. Conf.*, San Diego, CA: XII, IEEE, 1982, pp. 530–535.
10. W. D. Westwood, N. Waterhouse, and P. S. Wilcox, *Tantalum Thin Films*, New York: Academic Press, 1975, pp. 253–256.
11. C. L. Au, *Post Deposition Annealing Study of Tantalum Nitride Thin Film Resistors*, Ph.D. Dissertation, SUNY at Buffalo, 1989.
12. C. L. Au et al., Stability of tantalum nitride thin film resistors, *J. Mater. Res.*, **5**:1224–1232 (1990).
13. T. Yasar and N. Puri, Thin Film Resistors and Capacitors for Hybrid Circuits, *Electron. Packaging Production*, November 1979, pp. 108–116.
14. Q. X. Jia et al., Reactively sputtered RuO_2 thin film resistor with near zero temperature coefficient of resistance, *Thin Solid Films*, **196**:29–34 (1991).
15. M. L. Green et al., Chemical vapor deposition of ruthenium and ruthenium dioxide films, *J. Electrochem. Soc.*, **132**:2677 (1985).
16. E. Kolawa et al., Reactively sputtered RuO_2 diffusion barriers, *Appl. Phys. Lett.*, **50**:854 (1987).
17. L. Krusin-Elbaum, M. Wittmer, and D. S. Yee, Characterization of reactively sputtered ruthenium dioxide for very large scale integrated metallization, *Appl. Phys. Lett.*, **50**:1879 (1987).
18. E. Kolawa et al., Microstructure of reactively sputtered oxide diffusion barriers, *A. J. Electron. Mater.*, **17**:425 (1988).
19. G. E. Pike and C. H. Seager, Electrical properties and conduction mechanisms of ru-based thick film resistors, *J. Appl. Phys.*, **48**:5152 (1977).
20. T. M. Chen, S. F. Su, and D. Smith, $1/f$ noise in ru-based thick film resistors, *Solid State Electron.*, **25**:821 (1982).
21. N. C. Halder, Electron tunneling and hopping possibilities in RuO_2 thick films, *Electrocompo. Sci. Technol.*, **11**:21 (1983).
22. N. C. Halder and R. J. Snyder, Measurement of the tunneling and hopping parameters in ruthenium dioxide thick films, *Electrocompo. Sci. Technol.*, **11**:123 (1984).
23. Q. X. Jia, K. L. Jiao, and W. A. Anderson, Microstructural analysis and modeling of RuO_2 thin film resistors, *Mater. Sci. Eng.*, **B20**:301–307 (1993).
24. K. L. Jiao, Q. X. Jia, and W. A. Anderson, Stability of RuO_2 thin film resistors, *Thin Solid Films*, **227**:59–65 (1993).
25. Q. X. Jia et al., Development and fabrication of RuO_2 thin film resistors, *Mater. Sci. Eng.*, **B18**:220–225 (1993).
26. Q. X. Jia et al., Stable thin film resistors using double layer structure, *J. Mater. Res.*, **10**:1523–1528 (1995).
27. Q. X. Jia et al., Microstructural analysis and modeling of RuO_2 thin film resistors, *Mater. Sci. Eng.*, **B1320**:301–307 (1993).
28. E. Ma, R. L. Wallace, and W. A. Anderson, Microstructure and Interfacial Reaction in $\text{RuO}_2/\text{Ta}_2\text{N}$ Precision Thin Film Resistors, *MRS Symp. Proc.*, Boston, MA: 1994, pp. 355, 471.
29. E. Ma and W. A. Anderson, Mechanism of stabilizing $\text{RuO}_2/\text{Ta}_2\text{N}$ double layer thin film resistors, *Mater. Sci. Eng.*, **B47**:161–166 (1997).

THIN FILMS

KIYOTAKA WASA
Yokohama City University
KENTARO SETSUNE
Matsushita Electric
Industrial Co.

1. THIN FILM MATERIALS

Thin film ferroelectric materials and hexagonal piezoelectric materials are essential for fabrication of electronic and/or photonic devices. Historically ferroelectric materials were discovered in a form of bulk single crystals of Rochelle salt in 1920. Since then, a number of ferroelectric materials, including $\text{NH}_4\text{H}_2\text{PO}_4$ (ADP), KH_2PO_4 (KDP), LiNbO_3 (LN), LiTaO_3 (LT), BaTiO_3 (BT), PbTiO_3 (PT), and $\text{Pb}(\text{Zr},\text{Ti})\text{O}_3$ (PZT), were developed in a form of bulk single crystals or bulk ceramics. Among these ferroelectric materials, perovskite (ABO_3) with oxygen octahedral structures has become an important ferroelectric material.

Ferroelectric materials are dielectrics that have a spontaneous polarization with nonlinear hysteretic properties and show several unique properties including high dielectric permittivity, high piezoelectricity, high pyroelectricity, and high electrooptic characteristics.

Bulk ferroelectric materials were widely used to manufacture discrete electronic components including ceramics capacitors, bandpass filters, resonators, ultrasonic transducers, and positive temperature coefficient (PTC) thermistors. Novel ferroelectric materials such as optical transparent ferroelectric $(\text{Pb},\text{La})(\text{Zr},\text{Ti})\text{O}_3$ (PLZT) ceramics were developed by Haertling and Land in 1971. A high-speed electrooptical shutter was realized using hot-pressed transparent PLZT ceramics. The bulk-type ferroelectric devices, however, could not meet recent requirements of miniaturization and/or integration with Si and/or GaAs semiconductive devices.

Thin film ferroelectric materials have a high potential for miniaturization and/or integration with the semiconductive devices. Thin films are also important to the understanding of ferroelectricity. Thin films are commonly fabricated by depositing individual atoms on a substrate. The film thickness is typically less than several micrometers. The structure of thin films is essentially homogeneous on an atomic scale. Thin films exhibit the following useful aspects including thin film effects:

1. Unique material properties resulting from the atomic scale growth
2. Size effects at ultrathin films
3. Unique functional properties at layered structure including human-made superlattice and tailored ferroelectric materials

Polycrystal and/or single-crystal thin films of ferroelectric/piezoelectric materials are used for the fabri-

cation of thin film devices. The polycrystal thin films are commonly deposited on a noncrystalline substrate such as fused quartz, borosilicate glass, and passivated Si substrates. The single-crystal thin films are heteroepitaxially grown on a foreign single-crystal substrate such as sapphire, MgO , SrTiO_3 (ST), LaAlO_3 , and YSZ substrates. At the early stage, the ferroelectric thin films were considered to be a simple substitution of bulk dielectric materials by thin films, such as a fabrication of thin film discrete capacitor for an electronics system.

Since the 1970s, several kinds of thin film ferroelectric and/or piezoelectric films were developed for a fabrication of bulk acoustic wave (BAW) devices, surface acoustic wave (SAW) devices, thin film ferroelectric memory, acoustooptical (AO) devices, and electrooptical (EO) devices. Among these thin films, piezoelectric ZnO and CdS thin films of hexagonal structure were extensively studied for a fabrication of the thin film SAW devices and the thin film AO devices, although the piezoelectric hexagonal ZnO and/or CdS were not ferroelectric materials. The technology for a production of ZnO thin film SAW devices was established, and the ZnO thin film SAW devices are used in practice. Since the 1980s, much attention has been paid to the application of ferroelectric thin films such as PZT and $(\text{Pb},\text{La})\text{TiO}_3$ (PLT) to thin film optical waveguide devices, an integrated pyroelectric sensor, a memory capacitor of high dielectric permittivity at megabit dynamic random access memory (DRAM), the ferroelectric random access memory (FERAM) combined with Si and/or GaAs integrated circuits, and a thin film microactuator. Two-dimensional integrated optical devices are made by electrooptic thin films. The multilayer structures tailor SAW materials with designed acoustic velocity, electromechanical coupling, and temperature stability. The electromechanical coupling for the generation of SAW is enhanced at the layered structures. High electromechanical coupling with zero temperature coefficient of delay time (TCD) could be achieved at the layered structure of ZnO/glass substrate. The electrostrictive properties are also of interest for making a microelectromechanical system (MEMS). A MEMS provides integration of sensors, actuators, and electronic circuits in a single chip. Table 1 shows typical thin film ferroelectric materials and their devices including hexagonal piezoelectric thin films [1–3].

2. THIN FILM FABRICATION

Thin films of ferroelectric materials are fabricated by a thin film deposition process including physical vapor deposition (PVD), chemical vapor deposition (CVD), and chemical solvent deposition, as shown in Table 2.

Thin films of ferroelectric materials were first fabricated by Feldman in 1955 for BaTiO_3 by PVD using a simple vacuum evaporation. In the 1960s, others tried to deposit thin films of PbTiO_3 by cylindrical magnetron sputtering. The controlled deposition of the perovskite

Table 1. Ferroelectric Thin Films and Devices

Function	Devices: Materials	Miscellaneous
Ferroelectricity	FEDRAM: PZT, PLZT FESRAM: BPZT, SBT FEMFET: BMF	Nonvolatile High Ps, Pr PZT > 20 μm/cm ²
High Permittivity	Capacitor for high count	High permittivity
Pyroelectricity	DRAM: SBT, ST, PZT, PLT IR detector: PT, PLT	PZT: 500–2000 Sensitive/low noise PLT: $\gamma = 5.5 \times 10^{-4} \text{ C/m}^2\text{K}$
Piezoelectricity	BAW/SAW: ZnO, AlN Filter PZT, PLT Resonator Oscillator Delay line	High coupling for SAW ZnO/sapphire: $k^2 = 5\%$ High temperature stability ZnO/glass: TCD = 0
Electrostriction	Actuator: PLT, PZT, ZnO MEMS	High sensitive
Acousto-optics	Integrated optics: ZnO, LN Channel switch PLT, PLZT Modulator	Low working voltage High-speed operation
Electro-optics	Integrated optics: LT, LN, BTO Coupler PLT, PLZT Channel switch Modulator Optical shutter EO disk memory	Pockels effect (linear EO) LN, LT, BTO, PLZT Kerr effect (quadratic EO) PLT, PLZT: $R = 1 \times 10^{-16} \text{ m}^2/\text{V}^2$ (6328 Å)

BPZT:BaTiO₃-PbZrO₃; SBT:SrBi₂Ta₂O₉, BST: (Ba,Sr)/TiO₃; BTO:Bi₄Ti₃O₁₂; LN:LiNbO₃; LT:LiTaO₃; BMF:BaMgF₄

ferroelectric materials of ABO₃ and A(B1,B2)O₃ structure could not be attained because of their complex chemical composition. Since the middle of the 1970s, rapid progress has been observed in the thin film deposition processes, including planar magnetron sputtering, molecular beam epitaxy (MBE), and metal organic chemical vapor deposi-

tion (MOCVD). After the discovery of high-Tc superconductors of layered perovskite in 1986, rapid progress has been seen in the development of the deposition process for complex perovskite with atomically controlled crystal structure using sputtering, MBE, laser ablation, and MOCVD.

Table 2. Thin Film Deposition Process

Classification	Deposition System	Source Materials	Film Structure
<i>Vapor phase deposition</i>			
PVD	Thermal evaporation	Individual metals Individual oxides Multisource	Uniaxial crystal by epitaxial growth (poly/single)
	Laser ablation	FE compounds Individual oxides Multitarget	Tailoring FE by layer-by-layer deposition <i>In situ</i> poling
	Sputtering	FE compounds Individual metals Individual oxides Multitarget	
CVD	Low-pressure CVD	Individual halide	Uniaxial crystal by epitaxial growth (poly/single)
	MOCVD	Metal organic gas	<i>In situ</i> poling
	Plasma-assisted MOCVD		
<i>Chemical solvent deposition</i>			
	MOD	Individual	Multiaxial (polycrystal)
	Sol-gel deposition	Metal organic gas	<i>Ex situ</i> poling (porous)

Typical configuration of deposition systems are shown in Fig. 1. A conventional thermal evaporation process provides inhomogeneous and nonstoichiometric thin films. A multisource MBE system is used for the deposition. The laser ablation is carried out by the direct evaporation of source ferroelectric materials resulting from the irradiation of high-intensity pulsed excimer laser. The mechanism of laser ablation includes photo and thermal evaporation. The pulsed evaporation by high-intensity laser improves the inhomogeneity and/or nonstoichiometry, although the laser ablation includes the thermal evaporation process. The phenomenon of sputtering consists of a nonthermal evaporation. The sputtering process essentially provides homogeneous and stoichiometric thin films of complex ferroelectric materials because the sputtering mechanism consists of removing source materials (target) on an atomic scale by an impact of energetic ions through the momentum transfer mechanism. Multitarget magnetron sputtering is used for the deposition of layered structures and/or human-made superlattices. The sputtering process has a high potential for the fabrication of complex ferroelectric thin films. In the plasma-assisted MOCVD, energetic electron in gas plasma enhances the chemical reaction. At present, these thin film processes provide the thin films of perovskite with an accuracy of 1 nm corresponding to two or three of their crystal units. The chemical solvent deposition provides a simple fabrication process. However, the deposited thin films are essentially porous because the growth process is governed by

a conventional thick film technology including dipping and/or spinning of sol-gel precursor solution followed by annealing for sintering.

The deposition, chiefly by sputtering, of transducer quality ZnO thin films has been studied since the 1970s. The technology to fabricate ZnO thin films has already been established. The *c*-axis-oriented polycrystalline thin films are deposited on a glass substrate by direct sputtering from the ZnO target. The *c*-axis orientation on the glass substrate is quite reasonable because the film growth of a hexagonal structure is governed by Bravis's empirical law for crystal growth, where the most densely packed plane (*c*-plane) will be the most preferable surface of crystal growth. Single-crystal ZnO thin films are epitaxially grown on a sapphire substrate. The *a*-axis-oriented ZnO thin films are epitaxially grown on *R*-plane sapphire.

It is particularly important to understand the structure of thin films because it can have a profound influence on the operation of the thin film devices.

Thin films of polycrystalline phase comprise a column geometry with an interfacial layer between the thin films and a substrate. Low dielectric permittivity of the interfacial layer apparently reduces the permittivity of the ferroelectric thin films and/or increases a coercive field (extrinsic thickness effect). The decrease of dielectric permittivity for ferroelectric thin films with the decrease of their film thickness is also governed by the depolarization phenomenon (intrinsic thickness effect).

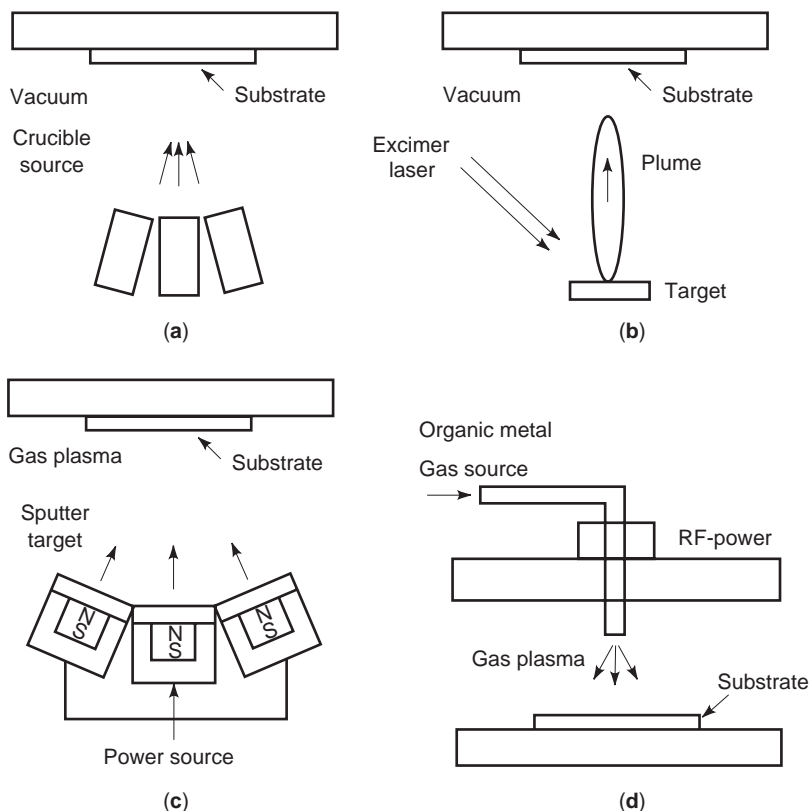


Figure 1. Typical configuration of thin film deposition systems: (a) multisource MBE, (b) laser ablation, (c) multitarget sputtering, (d) plasma-assisted MOCVD.

The epitaxial ferroelectric thin films show different microstructures depending on the degree of lattice match between the thin films and substrates. It is generally believed that, under an excellent lattice match, the thin films such as PT on ST show a single domain; under a poor lattice match for both *a*- and *c*-axes, the thin films such as PT on MgO show a multi-axial crystal structure; and under a fairly good lattice match, the thin films such as PT on KTaO₃ (KTO) constitute a periodic domain structure. These microstructures are grown primarily to minimize the total energy of the heterostructure. The phenomena are understood by linear-elasticity theory and a Landau–Ginzburg–Devonshire type phenomenological theory.

The actual epitaxial thin films of ferroelectric materials commonly constitute inhomogeneous microstructures including an interfacial layer that resembles polycrystalline thin films on a glass substrate as a result of the inhomogeneous nucleation at the initial stage of film growth. A selection of substrate materials is important for the control of thin film growth. Typical structural properties of substrates are shown in Table 3 [4–6].

3. THIN FILM DEVICES

3.1. Thin Film SAW Devices

The use of thin film SAW devices is an example of a successful application using piezoelectricity of hexagonal thin films and perovskite ferroelectric thin films. In the quasistatic approximation, the acoustic fields associated with plane waves in a piezoelectric medium are obtained by solving the stiffened Christoffel equation. In the case of a half-space medium with a free boundary surface, the boundary conditions must be satisfied and the mechanical stress and electric displacement must be calculated from the piezoelectric constitutive equations. These procedures give the solution as a SAW, which acoustic vibration energy concentrates near the surface of elastic solid materials. The Rayleigh wave and Love wave are obtained as the typical solutions of SAWs. The particle displacement of the former is in the sagittal plane, which is

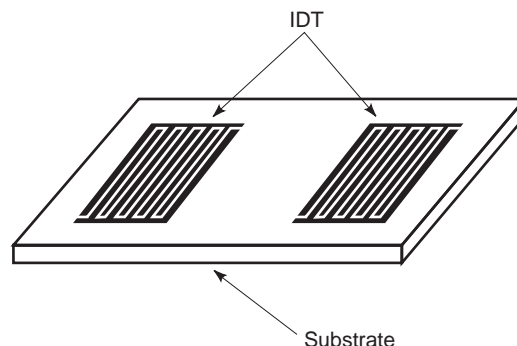


Figure 2. Interdigital transducer formed on the surface of the piezoelectric substrate.

perpendicular to the surface and parallel to the wave-propagation direction, and that of the latter is parallel to the surface and perpendicular to the direction of propagation. The SAW makes possible acoustoelectronic devices including the SAW filter for cellular phone/PCS/pager.

3.1.1. Generation of SAWs. The SAW modes can be generated by an interdigital transducer (IDT) formed on the surface of the piezoelectric substrate shown in Fig. 2. In the bulk SAW devices, bulk single crystals such as the LiNbO₃ and/or LiTaO₃ are adopted as the piezoelectric substrate. Whereas in the thin film SAW devices, a layered structure consisting of a piezoelectric thin film on the nonpiezoelectric medium is used as the piezoelectric substrate. Figure 3 shows the calculated result of an effective electromechanical coupling constant k^2 for four types of electrode configurations of a *c*-axis-oriented ZnO film on fused quartz. These electrode configurations for a thin film SAW transducer are also illustrated in Fig. 7. Each configuration consists of an IDT with or without a counter electrode. The value of k^2 is determined by the relation $k^2 = \Delta V_p / V_p$ where ΔV_p is the variation of SAW phase velocity V_p by the short condition of the surface electric field. The k^2 is simply evaluated by the equation $k^2 = \pi \omega_0 C_T / 4NG_a$, the inline model of Smith’s equivalent circuit model for electromechanical bulk wave, where ω_0 ,

Table 3. Lattice Parameters of Typical Single-Crystal Substrates

	Crystal System	Structure	Lattice Constant (Å)	Coefficient of Expansion (10 ⁻⁶ /K)
Sapphire	Trigonal	Corundum	<i>a</i> = 4.7630	7.5–8.0
MgO	Cubic	NaCl	<i>a</i> = 4.2030	13.8
SrTiO ₃	Cubic	Perovskite	<i>a</i> = 3.9050	10.8
LaAlO ₃	Pseudo cubic	Perovskite	<i>a</i> = 3.7920	10.0
YSZ	Cubic	Fluoride	<i>a</i> = 5.1600	10.0
KTaO ₃	Cubic	Perovskite	<i>a</i> = 3.9890	6.7
PbTiO ₃	Tetragonal	Perovskite	<i>a</i> = 3.8890	16.1
			<i>c</i> = 4.1532	–54.2
	Cubic		<i>a</i> = 3.9610	

epitaxial relations:

- (111)PT//(001)sapphire (0001)ZnO//(0001)sapphire
- (100)PT//(100)ST (1120) ZnO//(0112) sapphire (*R*-plane)
- (100)PLZT//(100)MgO (0001)LN//(0001)sapphire
- (111)PLZT//(0001)sapphire (0001)LN//(0001)LT
- (100)PLZT//(100)ST

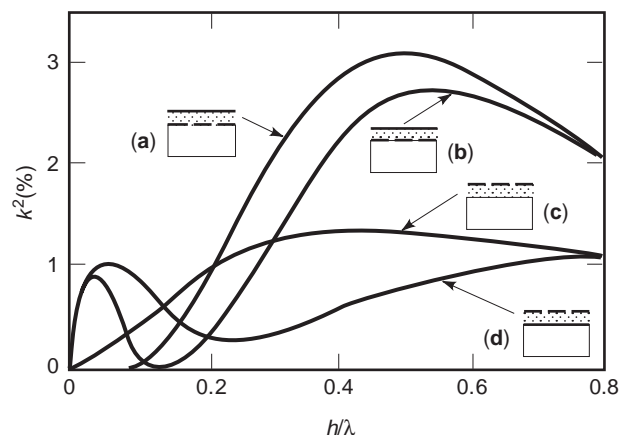
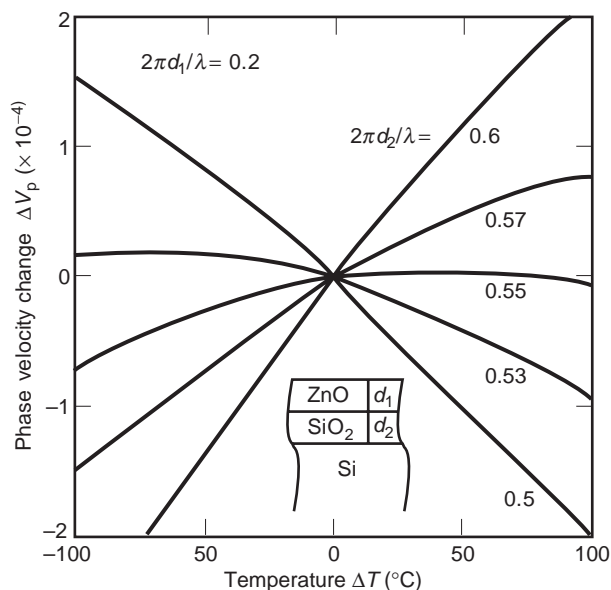


Figure 3. Calculated result of an effective electromechanical coupling constant k^2 for each configuration in the case of c -axis-oriented ZnO film on fused quartz. Four types of thin film electrode configurations are illustrated [7].

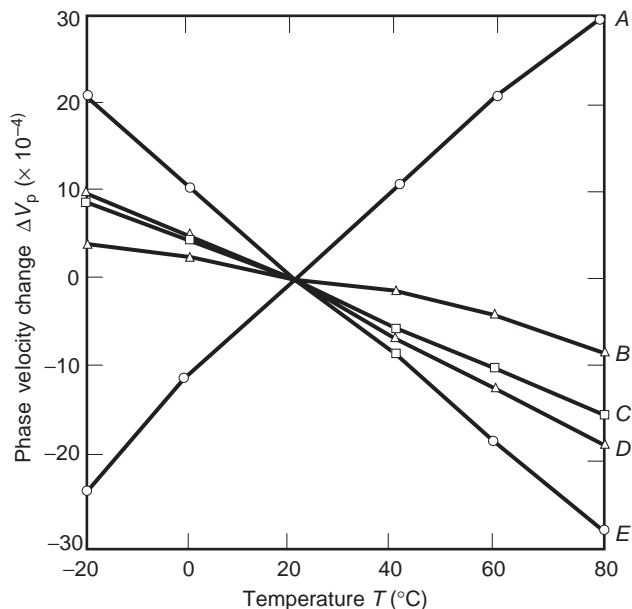
C_T , G_a , and N are the synchronous frequency, capacitance, radiation conductance, and number of finger pairs of IDT, respectively. The inline model (the major electric field component is parallel to the surface) becomes almost equal to the crossed-field model (the major electric field component is perpendicular to the surface) under the rough condition of $k^2 N > 1$. Figure 3 shows that k^2 varies with the ZnO film thickness, and the variations show a double-peaked character for the IDT structures including the counter electrodes. Note that the k^2 for thin films is higher than the bulk value at optimum film thickness.

3.1.2. Temperature Stability. SAW-layered structures have flexibility in that substrate materials can be chosen to adjust the temperature coefficient of a center frequency (TCF) and a delay time (TCD). The temperature stability of TCF or TCD is given by the equation, $(1/f)(dt/dT) = (1/t)(dt/dT) = (1/v)(dv/dT) - \beta$, where β denotes the thermal expansion coefficient of the substrate. The tendency of the phase velocity change $(1/v)(dv/dT)$ varies with the layered film thickness and elastic properties of the substrate materials. A suitable film thickness and a pertinent selection of substrate materials result in a zero TCD. Figure 4(a) shows one example of such a temperature deviation of the center frequency of the SAW IDT, which consists of the ZnO thin film, the SiO₂ or fused quartz layer, and the Si substrate. In this structure, the TCF of ZnO has a negative value of about -30 ppm/°C, and that of fused quartz has a positive value of $+60$ ppm/°C. These opposite values cancel the TCF while controlling the thickness of the SiO₂-layered film. Another example is shown in Fig. 4(b). Here the borosilicate-glass substrate can control TCF by controlling the composition ratio of the elements added to the glass.

3.1.3. SAW in Layered Media. The Rayleigh wave and Love wave are the solutions for a half-space medium with a free boundary surface. In layered structures, which



(a)



(b)

Figure 4. Temperature deviation of the center frequency of the SAW IDT constructed by the ZnO thin film: (a) the SiO₂ or fused quartz layer and the Si substrate; (b) the borosilicate-glass substrate [8].

include the thin plate rigidly bonded to the half-space (or substrate) having different material properties, the solutions for propagating waves must satisfy the appropriate wave equation in the layer and in the substrate as well as the boundary conditions imposed by the interface and the free surface. We know that fundamental and higher order modes of both Rayleigh and Love waves can propagate when the bulk shear wave velocity of the layer is lower than that of the substrate. This condition corresponds to that of the heavier and less stiff layer loads on

the substrate and will tend to confine the propagation energy to the layer. In this case, the propagating wave nodes are regarded as the modified plate modes. Sezawa discovered that a second fundamental mode may also exist in layered media. The Rayleigh modes and Sezawa modes correspond to symmetric and antisymmetric modes of a free plate modified by the contact of the surface with the substrate. In addition to these, the layer on an infinite half-space is open on one side, and there is a possibility of radiation or energy leakage out of the layer into the half-space. This condition gives the leaky wave solution for SAW.

The particle displacement of the SAW in the sagittal plane degrades with the depth from the surface. Also in the case of the layered substrate, almost the same situation exists in the half-space substrate. However, the degradation of that area in or near the top layer is different from the monotonous degradation of the zeroth Rayleigh mode. The amplitude distribution of the particle displacement is calculated for each propagating mode. Figure 5 shows the depth profiles of the particle displacement in the sagittal plane for the fundamental mode and higher four modes of the Rayleigh-type wave. More complex profiles and deeper penetration are shown for the particle displacement of higher order modes. Moreover, Fig. 5 shows that the higher order modes have a large displacement component in the substrate. So, it can be understood qualitatively that the higher order modes have a higher phase velocity because the phase velocity of the substrate is higher than that of the layer.

In Fig. 6, the solid lines and broken lines show the phase velocity V_p and the effective coupling coefficient k^2 of the Rayleigh-type and Love-type wave modes as a function of h/λ , respectively, where h is the layer thickness. These numerical results were obtained for the SAW directed to [1000] ZnO axes in the layered structure with the ZnO layer on the R -plane sapphire substrate. The first mode of the Rayleigh-type (zero Sezawa mode) shows an exceedingly large maximum value of k^2 with very high phase velocity at relatively small h/λ . These computer solutions were experimentally confirmed. For higher Rayleigh-type

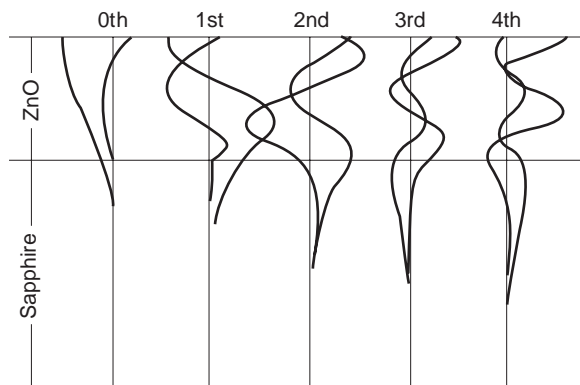


Figure 5. Depth profiles of the particle displacement in the sagittal plane for the fundamental mode and higher four modes of the Rayleigh-type wave.

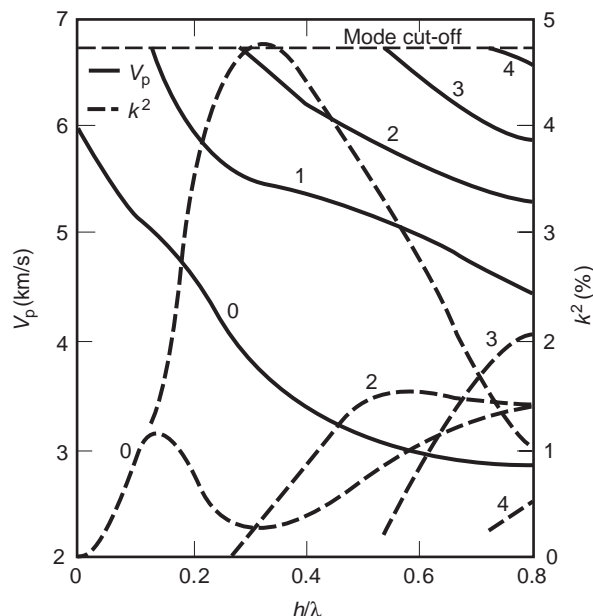


Figure 6. Rayleigh-type and Love-type wave mode solutions as a function of h/λ on the [1000] direction of the single-crystal (11 $\bar{2}$ 0) ZnO thin film epitaxially grown on the (01 $\bar{1}$ 2) sapphire surface. Solid lines and broken lines show the phase velocity V_p and the effective coupling coefficient k^2 [9].

modes, responses were still observed above the mode cutoff frequency as leaky mode responses.

3.1.4. Thin Film SAW Filters. Thin film SAW devices are constructed by the thin film IDTs on nonpiezoelectric substrates, by high-frequency propagation of the higher order modes of layered SAW, the substrate selected for the temperature stability, and so on. These distinguishing characteristics can realize the high performance of bandpass filters, resonators, delay lines, convolvers, integrated devices, and acoustooptic devices. The video intermediate frequency (VIF) filters for color TV sets were the first thin film mass-production devices. The frequency range of a VIF filter of 50–60 MHz is low enough for the SAW propagation loss of polycrystalline piezoelectric thin films such as c -axis-oriented ZnO films on a borosilicate-glass substrate. The thin film SAW filter shows excellent long-term stability. The long-term drift of the center frequency is less than 100 ppm after 1000 hours of exposure to 125°C in the air. The long-term stability of the ZnO thin film SAW filter is higher than that of bulk single-crystal LiNbO₃ SAW filters because of the absence of subsurface damage inflicted during sawing and polishing, which is unavoidable for bulk SAW devices. Figure 7 shows one example of the configuration of SAW VIF filters with two normal output IDTs and one apodized input IDT.

Another example is the high-frequency filter of epitaxially grown single-crystal thin film, which has low propagation loss of higher order Rayleigh wave modes in the gigahertz range. The ZnO single-crystal film on sapphire substrate is the typical construction of devices that

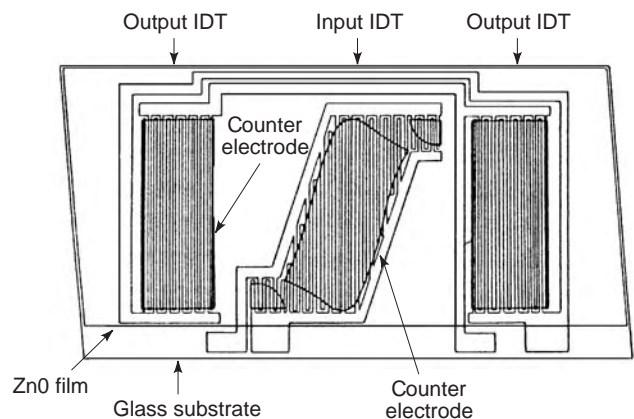


Figure 7. IDT configuration of SAW VIF filters with two normal output IDTs and one apodized input IDT on the layered substrate.

provide 4.37 GHz filters with a phase velocity of 5327 m/s and an insertion loss of 16 dB by 0.27 μm thick ZnO film, 3-IDT of 50 nm thick Al electrodes, and third-order response of double electrode-type IDTs. These excellent properties of thin film SAW filters are able to provide the high performance of information communication systems [7–17].

3.2. Ferroelectric Nonvolatile Memory

The basic operation of ferroelectric nonvolatile memory is switching of polarization states in a ferroelectric ABO_3 structure. Figure 8 shows a typical configuration and

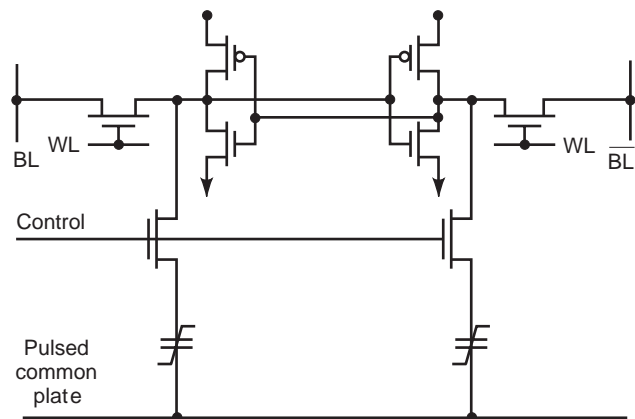


Figure 9. Schematic circuit of 256-bit FESRAM (Ramtron Corp. [18]).

schematic circuit of ferroelectric nonvolatile memories, dynamic random access memory (FEDRAM). The FEDRAM resembles a conventional dynamic random access memory (DRAM). The memory capacitor C_s of DRAM is replaced by a ferroelectric thin film capacitor. The C_s is in series with a MOS (metal-oxide-semiconductor) transistor whose source is connected to the bit line, the gate to the word line, and the drain to the pulsed 5 V common plate. In the FEDRAM, the polarization of the ferroelectric thin films switches to the opposite polarity on application of an electrical field higher than the coercive force when the MOS transistor is turned on by the appropriate voltage on

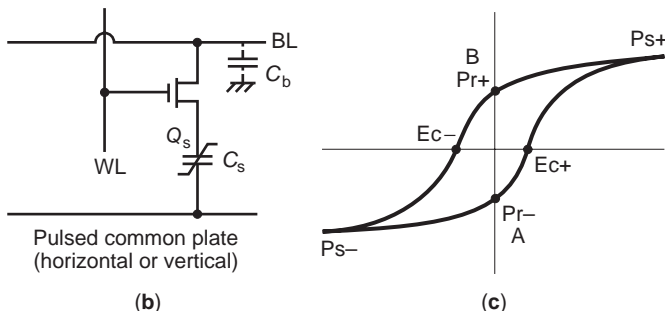
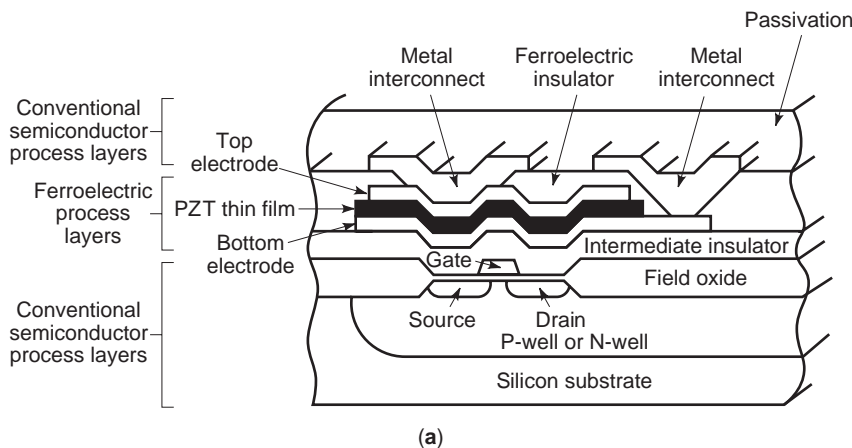


Figure 8. (a) Cross-sectional view of FEDRAM with (b) a schematic circuit and (c) a hysteresis loop of ferroelectric thin films (Ramtron Corp. [4]).

Type	Conventional ceramics (PbTiO ₃)	New thin film (c-axis oriented PLT)
Structure		
Pyroelectric coefficient γ	1.8×10^{-8} [C/cm ² K]	5.5×10^{-8} [C/cm ² K]
Figure of merit F_m	4.4×10^{-9} [Ccm/J]	14×10^{-9} [Ccm/J]
Merits		High S/N ($\times 10$) High responsivity Small size

Figure 10. Structure and pyroelectric properties of La-doped PT (PLT) thin films and conventional bulk PT ceramics [20].

the gate. In the hysteresis loop of memory capacitor C_s , the position *A* is taken to be a bit 1 state and *B*, a bit 2 state. The switching signal is detected by the voltage change at the bit line V_b . The V_b is given by $V_b = Q_s/C_b$, where Q_s denotes change of charge at switching on the capacitor C_s and C_b denotes the storage capacitor at the bit line. The Q_s is given by $Q_s = 2P_r$, where P_r denotes remanent polarization for ideal ferroelectric thin films having a symmetric hysteresis loop. For memory capacitors, PZT thin films are widely used. The P_r is 20–30 $\mu\text{C}/\text{cm}^2$ for typical PZT thin films. The value of Q_s for each memory cell is 400–600 fC for a cell area of $1 \mu\text{m}^2$, which is enough for the switch

memory operation because the minimum detectable value of Q_s for each cell is 20–30 fC at the conventional DRAM. The switching speed is essentially governed by the switching time of polarization reversal. The switching time is 1 ns for typical ferroelectric materials. The FEDRAM has some definite advantages, including a permanent memory and radiation hard characteristics. However, there are disadvantages of switch fatigue resulting from domain switching. Historically, the ferroelectric memory was proposed in the first part of the 1970s and first developed in 1987 by Ramtron Corp., Colorado Springs, and Krysails Corp., Albuquerque. The first developed ferroelectric

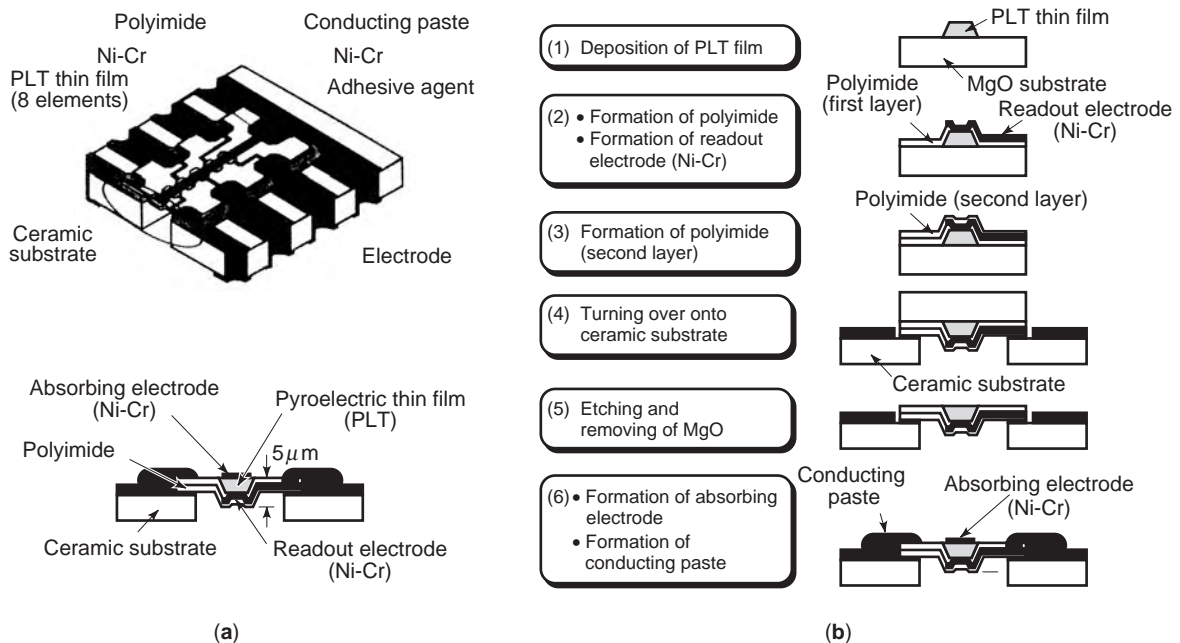


Figure 11. Schematic configuration of a linear array IR sensor for (a) a smart air conditioner and (b) its fabrication process [20].

memories look like the six-transistor static random access memory (SRAM) except that they include an additional pair of ferroelectric thin film capacitors, as shown in Fig. 9. Presently, the FEDRAM with a single transistor, where the ferroelectric thin films make a conventional DRAM nonvolatile, has been extensively studied to improve long-term stability. The ferroelectric thin films placed in the gate area of a MOS transistor provide another type of ferroelectric memory—the ferroelectric memory field effect transistor (FEMFET). Depending on the polarization of the gate materials, the source-to-drain current is increased or decreased significantly. The 1 or 0 state is detected by monitoring the source-to-drain current without switching the remanent polarization. This type of switch gives a nondestructive read out. This type of memory is under research because the interface control between the ferroelectric thin film and semiconductor is not completed.

Apart from the FEDRAM, the high dielectric permittivity of ferroelectric films is used for the local capacitor in highcount DRAM to reduce the area of the memory capacitor and/or eliminate the complex trenching and/or corrugation structures for the increased capacitive area. The high permittivity of the ferroelectric thin films achieves the flat structure of the memory cell. In the mega-/gigabit DRAM, the requirement for ferroelectric thin films is a permittivity of 200–2,000 at a film thickness of 100 nm

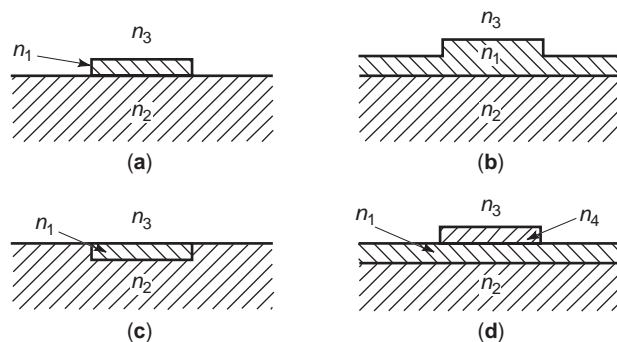


Figure 12. Cross-sectional view of thin film optical channel waveguide: (a) raised-strip type, (b) ridge type, (c) embedded type, and (d) strip-loaded type. n_1, n_2, n_3, n_4 are refractive index of waveguide, substrate, environment, and loaded strip, respectively.

without remanent polarization. The ferroelectric thin films should be used above their Curie temperature. If ferroelectric thin films are used, their operating coercive field should be large [18,19].

3.3. Thin Film Pyroelectric Infrared Detectors

Ferroelectric materials have been used for making pyroelectric infrared detectors by measuring the pyroelectric

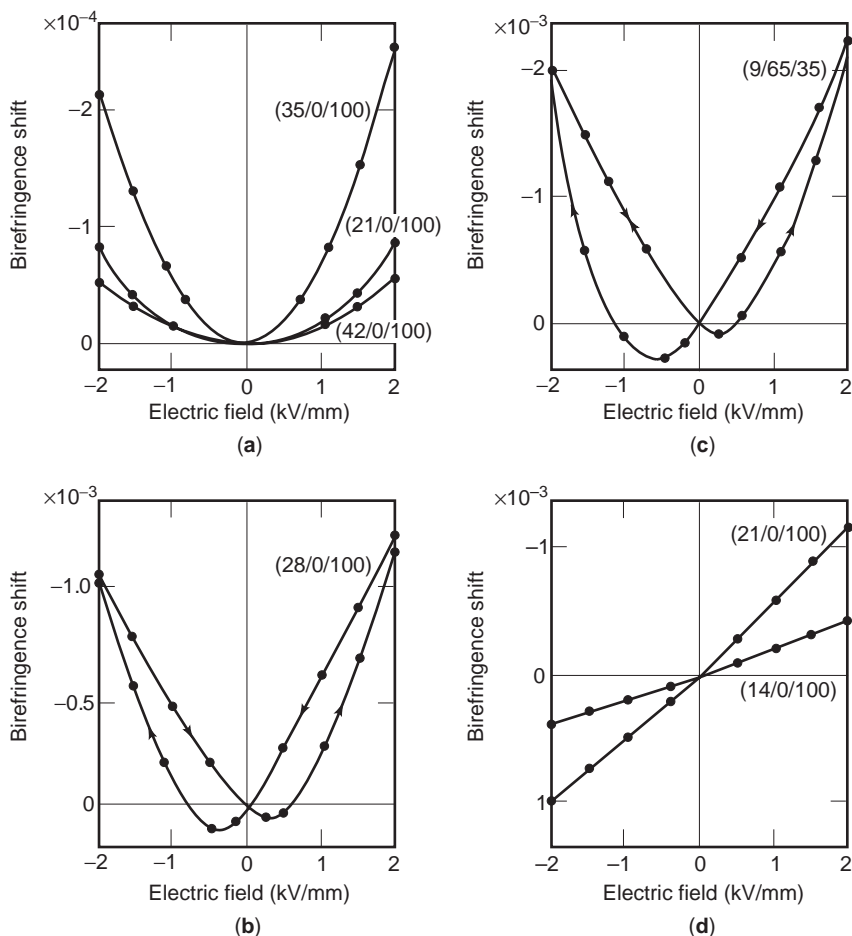


Figure 13. The effective birefringence shift as a function of transverse electric field for PLZT thin film of 0.4 mm in thickness [22].

current because they exhibit a large pyroelectric effect. The pyroelectric effect is described by the pyroelectric coefficient γ , which relates the change of polarization to the change in temperature. Pyroelectric current i_p will be detected by the temperature change of the detector materials generated by absorbed infrared radiation. The i_p is given by $i_p = \gamma(dT/dt)$. Bulk ferroelectric single crystals TGS (triglycine-sulphate) and LT, ferroelectric polymer PVDF (polyvinyl-di-fluoride), and ferroelectric ceramics PT and PbZrO_3 (PZ) are widely used for making pyroelectric infrared detectors. The pyroelectric materials are evaluated by figures of merit; $F_1 = \gamma/C_v$, $F_v = \gamma/C_v \cdot \varepsilon$, $F_M = \gamma/C_v (\varepsilon \cdot \tan \delta)^{1/2}$, where C_v denotes a volume-specific heat, ε denotes a dielectric constant, and F_1 , F_v , and F_m denote the figure-of-merit related to a current response, an output voltage response, and a detectivity, respectively. Perovskite thin films of PT and/or PLT are epitaxially grown on a Pt-metallized MgO substrate. The MgO substrate is removed after deposition of perovskite thin films. The as-deposited thin films show a highly oriented structure, which results in excellent pyroelectric properties without poling treatment after deposition. The single-domain structure with a low dielectric constant in the c -axis direction improves the figure-of-merit of conventional ceramic pyroelectric materials. Figure 10 shows the typical pyroelectric properties of bulk and thin film PLT. The integrated infrared sensor array shown in Fig. 11 was created using thin film infrared detector technology. The sensor array, manufactured by Matsushita Elec. Ind., Osaka, Japan, is used for a room air conditioner. The array detects the position and number of persons and their body temperatures to create a comfortable space [20,21].

3.4. Thin Film Optical Waveguide Devices

Thin film optical waveguide devices commonly consist of a sandwich structure of a thin film waveguide and a substrate. The refractive index of the thin film waveguide is larger than the substrate value so that a guided light beam propagates in the thin film waveguide. The direction of a propagated light beam is controlled by the channel waveguide shown in Fig. 12. The waveguide thin films comprise functional materials including EO or AO materials such as LN, PLZT, and ZnO. The PLZT thin films exhibit a linear EO effect or a quadratic EO effect depending on their composition. Typical EO properties of PLZT thin films are shown in Fig. 13. The birefringence shift $\delta\Delta n$ is several times larger than for conventional LN crystals. The linear EO coefficient r is given by the relation $\delta\Delta n = -\frac{1}{2} \times n^3 r E$ and the quadratic E/O coefficient R is given by the relation $\delta\Delta n = -\frac{1}{2} \times n^3 R E^2$, where n is the refractive index and E is the applied electric field. The value of R is $0.6 \times 10^{-16} (\text{m/V})^2$ and r is $0.81 \times 10^{-10} \text{m/V}$. The light beam is introduced using an optical coupler such as a prism, micrograting coupler, and microlens directly connected to the optical fiber. The thin film waveguide is fabricated by deposition of the functional thin films on a substrate followed by microfabrication. The surface treatment, such as doping of a foreign element on the functional crystal substrate (i.e., Ti doping on LN),

is also used for the fabrication of thin film waveguides. Typical thin film waveguide devices are shown in Figs. 14–16.

Figure 14(a) shows the Mach–Zehnder interferometric modulator. The input light signal is equally divided into two waves by the branching guide and fed through two parallel arms of guide. In each arm, the waves are electrooptically modulated by the applied field. The intensity of guided light of TE_0 mode is strongly modulated because of a large EO effect. A typical sinusoidal pattern is observed as the applied electrical field is varied as shown in Fig. 14(b). The Bragg diffraction switches comprise PLZT epitaxial thin films on sapphire for the EO switch and ZnO epitaxial thin films on sapphire for the AO switch, respectively. The guided light, chiefly TE_0 mode, is diffracted as a result of a periodic grating with refractive index by applying a periodical electrical field for the EO switch using an interdigital electrode and by applying SAW for the AO switch using an interdigital SAW transducer. The angle of diffraction is governed by the Bragg diffraction, and the diffraction angle 2θ is given by $2\theta = \lambda_0/n\lambda_s$, where θ denotes the Bragg angle, λ_0 denotes

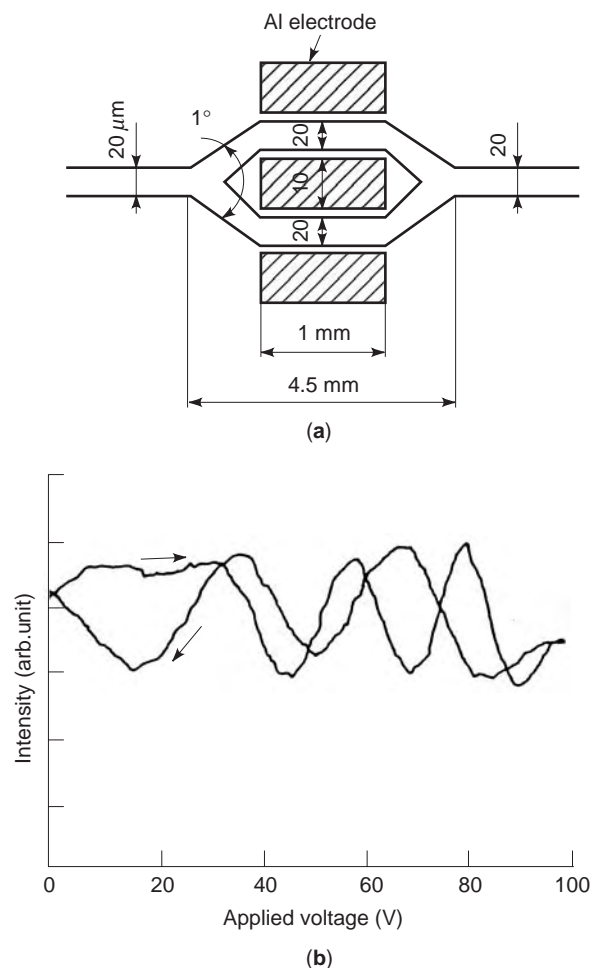


Figure 14. (a) Configuration of a thin film Mach–Zehnder interferometer using PLZT thin film on sapphire and (b) the variation of output light intensity with applied voltage [23].

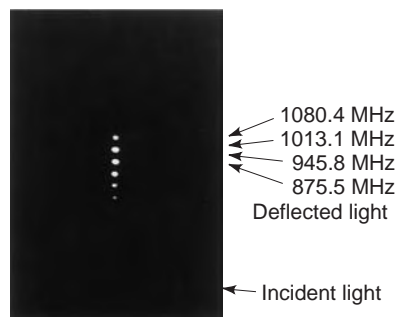
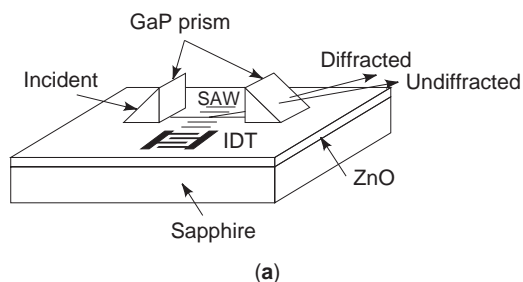


Figure 15. (a) Configuration of thin film AO Bragg deflector using ZnO thin film waveguide on sapphire and (b) a deflected light beam as a function of applied frequency at IDT driven by the first-order Sezawa mode of SAW [24].

the wavelength of light, n denotes the effective refractive index of the waveguide, and λ_s denotes the wavelength of the interdigital electrode. Figure 15 shows a typical operation of the ZnO thin film AO deflector. The Bragg deflector is driven by the first-order mode of SAW (Sezawa mode) with a phase velocity of 5700 m/s. The IDT is designed for 2 GHz operation. The TE_0 mode of a guided He–Ne laser beam is effectively deflected by the high-frequency SAW.

The total internal reflection (TIR) switch, which was first proposed by C. S. Tsai, is composed of a pair of crossed channel PLZT (20/0/100) waveguides, quadratic EO, with four terminals on sapphire as shown in Fig. 16(a). The intersecting angle of the channel waveguide θ satisfies the relation, $\theta < 90 - \theta_c$, $\theta_c = 1/\sin(1 - \frac{1}{2}n^2RE^2)$, where θ_c denotes the critical angle of total reflection, R denotes the quadratic EO coefficient, and E denotes the electrical field at the crossed area. At the crossed area, a pair of control electrodes are deposited to apply a control electrical field. Figure 16(b) shows a typical operation of the PLZT TIR switch. The TE_0 mode of the guided He–Ne laser beam directly coupled from port 1 propagates to port 3 without applying a control voltage, but the guided light is switched to port 4 as a result of the decreased refractive index at the interaction area under the application of control voltages. The switching voltage is less than 5 V because of the high EO coefficient of PLZT. The switching speed is expected to be as high as 100 GHz.

Thin film waveguide devices are flourishing. A number of promising devices are proposed for optical communication systems and integrated optical circuits, including optical computing [22–29].

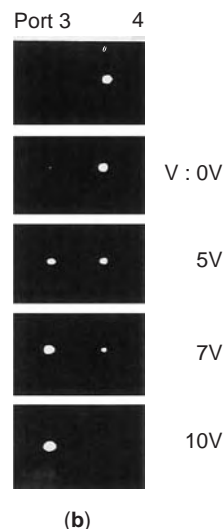
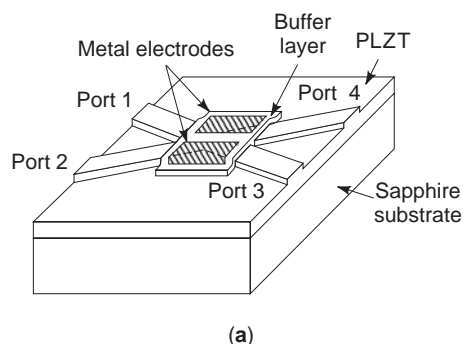


Figure 16. (a) Configuration of thin film TIR optical waveguide switch using PLZT thin film on sapphire and (b) the light intensity output at port 3 and 4 for various applied voltages [25].

BIBLIOGRAPHY

1. L. E. Cross, Ferroelectric ceramics, in N. Setter and E. L. Colla, eds., *Ferroelectric Ceramics*, Berlin: Birkhauser, 1993.
2. G. H. Haertling and C. E. Land, Hot-pressed (Pb,La)(Zr,Ti)O₃ ferroelectric ceramics, *J. Amer. Ceram. Soc.*, **54**:1 (1971).
3. K. L. Chopra, *Thin Film Phenomena*, New York: McGraw-Hill, 1969.
4. G. H. Haertling, Ferroelectric thin films for electronic applications, *J. Vac. Sci. Technol.*, **A9**(3):414 (1991).
5. R. F. Bunshah, *Deposition Technologies for Films and Coatings*, Park Ridge, NJ: Noyes, 1982.
6. K. Wasa and S. Hayakawa, *Handbook of Sputter Deposition Technology*, Park Ridge, NJ: Noyes, 1992.
7. G. S. Kino and R. S. Wagers, Theory of interdigital couplers on nonpiezoelectric substrates, *J. Appl. Phys.*, **44**:1480 (1973).
8. S. Ono, K. Wasa, and S. Hayakawa, Surface-acoustic wave properties in ZnO-SiO₂-Si layered structure, *Wave Electron.*, **3**:35 (1977).
9. T. Mitsuyu, O. Yamazaki, and K. Wasa, A 4.4 GHz SAW filter using a single-crystal ZnO film on sapphire, *1981 IEEE Ultrason. Symp. Proc.*, 1983, p.74.
10. W. R. Smith et al., Analysis of interdigital surface wave transducers by use of an equivalent circuit model, *IEEE Trans. Microwave Theory Tech.*, **MTT-17**(11):856 (1969).

11. G. W. Farnell and E. L. Adler, *Physical Acoustics*, Vols. 9, 35, New York: Academic Press, 1972.
12. K. Sezawa and K. Kanai, *Bull. Earth. Res. Inst. Tokyo*, **13**:237 (1935).
13. F. S. Hickernell, DC triode sputtered zinc oxide surface elastic wave transducers, *J. Appl. Phys.*, **44**:1061 (1973).
14. S. Ono et al., SAW resonators using rf-sputtered ZnO films on glass substrates, *Appl. Phys. Lett.*, **33**:217 (1978).
15. K. Setsune et al., Preparation and application of ZnO thin film by cylindrical magnetron sputter—ZnO thin film SAW long delay line, *Jpn. J. Appl. Phys.*, **20**:137 (1981).
16. K. L. Davis, Properties of the MZOS surface wave convolver configuration, *IEEE Trans. Electron Devices*, **ED-23**:554 (1976).
17. F. Hickernell et al., An integrated ZnO/Si-MOSFET programmable matched filter, *IEEE Ultrason. Symp. Proc.*, 1975, p. 223.
18. S. S. Eaton et al., A ferroelectric nonvolatile memory, *Tech. Dig. IEEE Int. Solid-State Circuit Conf.*, 1988, p. 130.
19. D. W. Bondurant and F. P. Gnadinger, Ferroelectrics for nonvolatile RAMS, *IEEE Spectrum*, **26**(7):30 (1989).
20. T. Kamada et al., Pyroelectric infrared sensors made of La-modified PbTiO₃ thin films and their applications, *Integrated Ferroelectrics*, **11**:15 (1995).
21. W. Wersing, Ferroelectric device, in N. Setter and E. L. Colla, eds., *Ferroelectric Ceramics*, Berlin: Birkhauser, 1993.
22. H. Adachi et al., Ferroelectric (Pb,La)(Zr,Ti)O₃ epitaxial thin films on sapphire grown by rf-planar magnetron sputtering, *J. Appl. Phys.*, **60**:736 (1986).
23. T. Kawaguchi et al., Optical PLZT thin film waveguides, *Appl. Opt.*, **20**:2187 (1984).
24. K. Setsune et al., Discrete frequency Bragg deflector in 2 GHz range using ZnO/sapphire substrate, *IEEE Ultrason. Symp. Proc.*, 1983, p. 467.
25. K. Wasa et al., Optical TIR switches using PLZT thin-film waveguides on sapphire, *J. Lightwave Technol.*, **LT-2**(5):710 (1984).
26. C. E. Land, New devices using ferroelectric thin films, *Proc. Int. Electron Devices Meeting*, Washington, DC, Dec. 1989, p. 10.1.1.
27. D. Botez and G. J. Herskowitz, Components for optical communications systems, *Proc. IEEE*, **68**:689 (1980).
28. C. S. Tsai, B. Kim, and F. Akkari, Optical channel waveguide switch and coupler using total internal reflection, *IEEE J. Quantum Electron.*, **QE-14**:513 (1978).
29. C. S. Tsai, Integrated acoustooptic and magneto optic devices for optical information processing, *Proc. IEEE*, **84**:853 (1996).

III-V SEMICONDUCTORS

CHRISTOPHER M. SNOWDEN
 Filtronic plc and University of
 Leeds
 West Yorkshire, United
 Kingdom

1. INTRODUCTION

The study of III-V compounds dates back to the dawn of semiconductor technology, when in 1952 Welker [1] suggested that gallium arsenide (GaAs) showed potential as a semiconductor material. The key aspect of this class of

materials that makes them of particular interest is their properties, which make them particularly suitable for high-frequency electronic and photonic devices. In the case of GaAs the electron velocity of bulk material, which determines the frequency limits of devices, is significantly higher than that found in silicon (Si). Furthermore, the low field mobility of electrons in many III-V materials is higher than that of Si. Diodes fabricated from III-V materials have demonstrated cutoff frequencies of several terahertz; transistors have demonstrated cutoff frequencies (f_T) higher than 300 GHz [2] and monolithic microwave integrated circuits (MMICs) operating above 200 GHz [3]. This has led to the use of GaAs and InP in a wide variety of high-frequency semiconductor devices operating in applications as diverse as low-noise amplifiers, mixers, power amplifiers, RF switches, and oscillators at frequencies up to 240 GHz. The wide operating temperature range of III-V semiconductors, typically from -200 to 300°C, coupled with superior radiation hardness compared to Si, led to GaAs and InP becoming key materials for space and defence requirements. In more recent years the photonic properties of III-V materials, arising from their direct bandgap energy band structures, have been extensively exploited for solid-state lasers, light-emitting diodes, photodetectors, and optical modulators, with the potential for fully integrated optoelectronic integrated circuits. To date these properties are unrivalled by Si, which is an indirect bandgap semiconductor.

Although many III-V materials are routinely used in microwave and optoelectronic semiconductor devices today, it wasn't until the early 1970s that the first semiconductor devices became widely available, and even then it was restricted to two terminal devices and simple transistors. The relatively slow progress in developing commercially viable technologies was partly due to the challenging problems in establishing high-quality material growth and the development of processing techniques that allow reliable devices to be fabricated. The key step to achieving volume production and widespread use of cost-effective devices is the availability of larger-diameter wafers, from which the semiconductor devices are fabricated. Early work was restricted to very small samples (parts of wafers) or small-diameter wafers of 2 in. or less. Gradually, high-quality 3- and 4-in.-diameter wafers became available and discrete devices and integrated circuits were introduced for military and commercial applications. Significant advances since the early 1980s have led to the introduction of 6-in. (150-mm) very-high-quality GaAs substrates and epitaxy suitable for high-volume production of semiconductor devices. Similarly, other materials such as InP are now well established and production is supported by 4-in.-diameter substrates.

The advent of high-quality reproducible epitaxy, provided by molecular-beam epitaxy (MBE) and organic metal vapor-phase epitaxy (OMVPE, MOCVD), led to a shift in interest from bulk III-V devices to heterostructure semiconductor devices, based on bandgap engineering, which allow higher performance to be obtained. In particular, the development of ternary and quaternary compounds, such as AlGaAs, GaInAs, and GaInAsP, were key steps forward for new transistor technologies,

Table 1. III-V Semiconductor Materials

Compound Type	III-V Material
Binary	BAs, BP, AlSb, BN, GaSb, AlAs, AlP, GaAs, InSb, GaP, InAs, InP, AlN, GaN
Ternary	AlGaAs, AlGaIn, InGaAs, InGaP, GaAsP, InAsP, GaInSb, GaInAs
Quaternary	InAlGaAs, GaInAsP, InAlGaP, InAlGaSb, AlGaAsSb

high-electron-mobility transistors (HEMTs), heterojunction bipolar transistors (HBTs), and long wavelength optoelectronic devices. The exploitation of lattice-matched (usually to InP) and strained (usually to GaAs) crystal structures using these compounds is an essential element of today's III-V technology. More recently the use of material systems such as GaN/AlGaN for high-voltage, high-power-density transistors has led to increased interest in examining the growth on nonnative layers using epitaxy to create III-V active layers on SiC, sapphire, or more recently silicon substrates. Record performance power density levels are being achieved with GaN HEMTs, reporting over 30 W/mm gate periphery, compared with less than 1 W/mm from conventional MES-FETs and HEMTs [4].

In the mid-1980s GaAs integrated circuit technology was costly and reserved only for the most demanding system requirements. Contemporary III-V semiconductor device technology is able to provide microwave monolithic integrated circuits (MMICs) at a cost of less than 20 cents per square millimeter in some very high volumes, supporting a market approaching a billion die per annum. III-V transistor technology is the foundation of high-efficiency power amplifier and low-loss RF switch MMICs in today's cellular handsets. The advent of heterostructure technologies using Si, notably SiGe, which have demonstrated the potential for very fast devices, is likely to displace III-V in some very-high-volume RF and microwave applications.

This article aims to provide a basic introduction and an overview of contemporary III-V semiconductors. Many of the topics touched on in these pages are expanded in detail elsewhere in this encyclopedia, but the reader is encouraged to explore the wealth of material available in this exciting area of semiconductor technology.

2. III-V SEMICONDUCTOR MATERIAL PROPERTIES

III-V semiconductor materials are alloys formed from elements in group III and group V of the periodic table. They are grown as single crystals and as either binary, ternary, or quaternary alloys (Table 1).

2.1. Crystal Structure

All III-V semiconductors are alloys, and unlike the elemental semiconductors silicon (Si) and germanium (Ge), which exhibit diamond cubic crystal structures, generally crystallize in more complex structures. GaAs and InP have cubic zincblende structures (sphalerite structures), with a tetrahedral arrangement of the atoms, with each group III atom bonded to four group V atoms (Fig. 1). The tetrahedral structure is characteristic of directional covalent

bonding in semiconductors, with eight valence electrons per pair of atoms (in sp^3 -hybridized orbitals). In the case of GaAs and InP, unlike diamond cubic semiconductors, there is some charge transfer between the two types of atom giving rise to the partial ionic character of the bond. Generally speaking, these partly heteropolar bonds are stronger than homopolar bonds such as those found in Si. Heteropolar bonds also tend to be associated with lower amplitude lattice vibrations and wider energy bandgaps.

The properties of crystal structures, including their electrical behavior, vary according to the plane considered. The most commonly used method of defining planes in crystals is the use of Miller indices [5], which are obtained by determining the intercepts of each plane on the three Cartesian coordinates in terms of the lattice constant and then taking their reciprocals and reducing them to the smallest three integers having the same ratio (Fig. 2). The lattice parameter is usually denoted a , for sphalerite structures. The resulting Miller indices are expressed in parentheses (hkl). For example, a plane that intercepts the x axis on the negative side of the origin is (100) . Extensions of this notation allow for planes of equivalent symmetry, defined as $\{hkl\}$; for example, $\{100\}$ for cubic symmetry. Crystal direction is defined using the notation $\langle hkl \rangle$; for example, $\langle 100 \rangle$ for the equivalent set of directions $[100], [010], [001], [100], [010], [001]$. Crystal direction is used to define the orientation of wafers for the

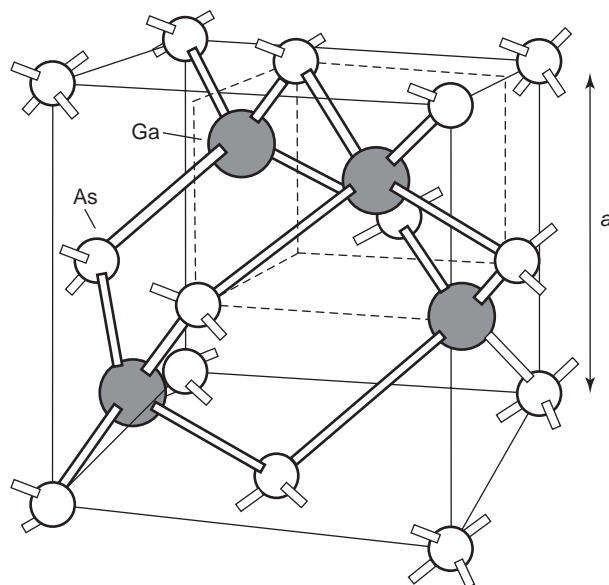


Figure 1. Cubic zincblende (sphalerite) crystal structure of GaAs [based on diagram from S. M. Sze, *Physics of Semiconductor Devices*, Wiley-Interscience (1981)].

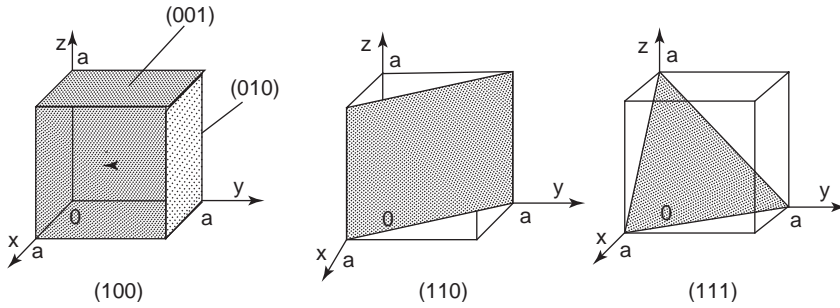


Figure 2. Miller indices [based on diagram from S. M. Sze, *Physics of Semiconductor Devices*, Wiley-Interscience (1981)].

fabrication purposes, since the electrical properties and chemical etching properties differ according to orientation. Notches or “flats” are created on the edge of wafers to precisely indicate the orientation of the wafer with respect to the crystal structure.

In the case of GaAs cleaved along the (111) plane, the surface consists of either Ga atoms, which have three bonds with the crystal or As atoms that have one bond with the crystal. In fact, the bonds between the nearest Ga and As atoms are in the $\langle 111 \rangle$ directions. Gallium nitride GaN has a wurtzite crystal structure, which has two lattice parameters a and c .

2.2. Energy Band Structure

The electronic and vibrational states in crystals are usually described in reciprocal space or k space. The smallest unit cell in reciprocal space is called the *first Brillouin zone*. The first Brillouin zone in cubic semiconductors is a truncated octahedron with symmetry points and lines denoted Γ , X , L , K , U ($K=U$), W , Δ , Λ , and Σ . A very good detailed description is given in Ref. 6. The Γ point at $k=0,0,0$ in Cartesian coordinates is the point of highest symmetry in the Brillouin zone.

The energy band theory of semiconductors assumes that the lattice features perfect translational symmetry, that one electron at a time is considered, and that the influence of all electrons is represented by the average over their wavefunctions. The Schrödinger equation for the one-electron case is used to define the functional dependence of energy $E(k)$ on the wavevector k for the various bands. This model is modified to form the Sommerfeld free-electron model by introducing the idea of effective mass. The nearly free-electron approximation provides a basis for developing energy band theory, and the origin of the energy bandgap between the valence and conduction bands. It also introduces the concept of effective mass, which is defined as the reciprocal of the curvature of the E - k diagram. The band structure for a semiconductor is calculated using the well-known **k.p.** method [7]. The **k.p.** representation results from the complete set of eigen functions that are obtained from the substitution of Bloch functions [6] in the one-electron Schrödinger equation. Spin-orbit interaction is also included in the full definition of the energy-wavevector relationship, which leads to a formulation based on a series of Hamiltonians.

Valence band maxima occur at the Γ point for semiconductors with tetrahedral structure. Many semiconductors with this structure, such as GaAs and InP, also have conduction band minima at this point. In GaAs and similar semiconductors, the conduction band structure close to Γ is essentially parabolic. The lowest conduction band minimum occurs at $k=0$ with further minima in the Δ $\langle 100 \rangle$ and Λ $\langle 111 \rangle$ directions. Other important conduction and minima occur at 0.31 and 0.52 eV above the first Γ minima for X and L . The valence band structure has heavy hole and light hole bands that degenerate at $k=0$ and spin-orbit split bands at 0.34 eV below this level. The energy band structure for GaAs are shown in Fig. 3. The direct energy bandgap is the difference in energy between the conduction band minima and the valence band maxima.

The energy band structure of other III-V semiconductors such as ternary and quaternary alloys is dependent on the mole fractions x and y (e.g., $\text{Al}_x\text{Ga}_{1-x}\text{As}$ and $\text{Ga}_x\text{In}_{1-x}\text{As}_y\text{P}_{1-y}$). The direct energy bandgap $E_0(x,y)$ is usually expressed as a quadratic function of the mole fraction, characterized by the coefficient of the second-order term, also known as the “bowing parameter.” The

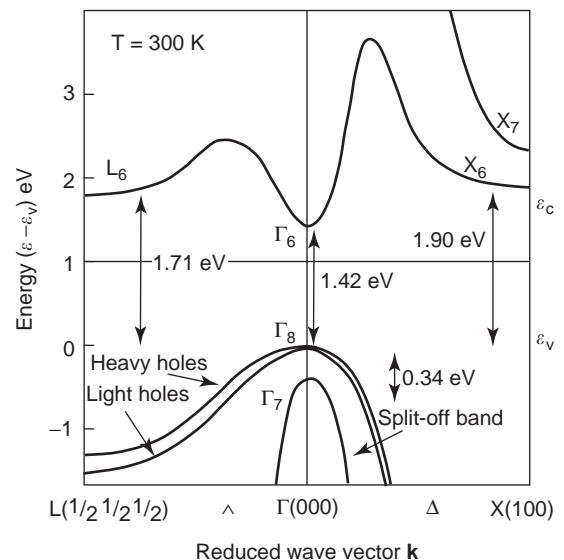


Figure 3. Energy band structure, showing variation of energy with wavevector for gallium arsenide [based on diagram from J. S. Blakemore, *Key Papers in Physics—Gallium Arsenide* (1987)].

Table 2. Physical Properties of III-V Binary Semiconductor Materials

Material	Lattice Constant (Å)	Direct Energy Bandgap ^a (eV)	Indirect Bandgap ^b (eV)	Density ($\times 10^9$ kg/m ³)	Melting Point K	Thermal Conductivity ^a (W m ⁻¹ K ⁻¹)	Dielectric Constant ^c
AlAs	5.660	3.03	2.15	3.76	2013	80	10.1
GaP	5.450	2.78	2.27	4.14	1735	77	11.1
GaAs	5.653	1.42	1.80	5.32	1513	46	12.8
GaN	3.19/5.19	3.44	—	6.09	—	120	10.4
AlN	3.11/4.98	6.20	—	3.28	—	300	9.1
InP	5.869	1.34	2.74	4.81	1335	68	12.6
InAs	6.058	0.36	—	5.67	1215	27	15.2

^aValues at 300 K.

^bIndirect energy bandgap is the difference between the first X minima and the valance band maximum at 300 K.

^cIn units of free-space permittivity ϵ_0 8.85×10^{-12} F/m.

bowing parameter typically varies from 0.2 for AlGaAs to 0.88 for GaInP. Positive bowing parameters imply that the energy band bows downward. In contrast to the energy bandgap, the lattice constant of ternary alloy semiconductors generally varies linearly with composition. The lattice constant behavior for quaternary compounds is more complex with a higher-order dependence on the mole fractions. The energy bandgap, lattice constant, and other parameters of binary III-V semiconductors are shown in Table 2.

The energy bandgap is a very important parameter in device design. The temperature dependence of the bandgap E_g , which decreases with increasing temperature, is generally expressed as

$$E_g(T) = E_g(0) - \frac{\alpha T^2}{T + \beta}$$

where $E_g(0)$ is the energy bandgap at 0 K and α and β are constants; α typically lies in the range $2.5\text{--}6 \times 10^{-4}$ eV K⁻¹, β in the range 75–600. In the case of GaAs $E_g(0)$, α and β have the values 1.519, 5.405×10^{-4} eV/K, and 204.

The bandgap of ternary and quaternary III-V alloys depends on their composition and mole fraction [8]. The lattice matching criteria and compositional factors (Vegard's law) limits the range of mole fractions. In the case of $\text{Al}_x\text{Ga}_{1-x}\text{As}$ and $\text{In}_x\text{Ga}_{1-x}\text{As}$ the bandgap dependence on mole fraction x (at 300 K) is described by simple quadratic equations:

$$\text{Al}_x\text{Ga}_{1-x}\text{As} : E_g = 1.424 + 1.429x - 0.14x^2 \text{ eV}$$

$$\text{In}_x\text{Ga}_{1-x}\text{As} : E_g = 1.425 - 1.501x + 0.436x^2 \text{ eV}$$

In the case of ternary compounds such as InAlGaAs, the energy bandgap is a function of two mole fractions x and y such that at 300 K:

$$\begin{aligned} \text{In}_{1-x-y}\text{Al}_x\text{Ga}_y\text{As} : E_g(x, y) = & 0.360 + 2.093x + 0.629y + 0.577x^2 \\ & + 0.436y^2 + 1.013xy - 2.0xy \\ & (1 - x - y)\text{eV} \end{aligned}$$

Additionally in the case of InAlGaAs, it is necessary to account for the lattice-matching condition $0.98x + y = 0.47$ and the compositional parameter z where $x = 0.48z$ and

$$E_g(z) = 0.76 + 0.49z + 0.20z^2 \text{ eV}$$

The range of mole fraction compositions in III-V ternary and quaternary semiconductors is limited by the requirement to achieve lattice matching to GaAs, InP or GaSb substrates. Figure 4 shows the variation in lattice parameter with energy bandgap for a range of III-V semiconductors [6]. The shaded regions show the range of parameters for quaternary alloys $\text{Ga}_x\text{In}_{1-x}\text{As}_y\text{Sb}_{1-y}$ and $\text{Ga}_x\text{In}_{1-x}\text{As}_y\text{P}_{1-y}$.

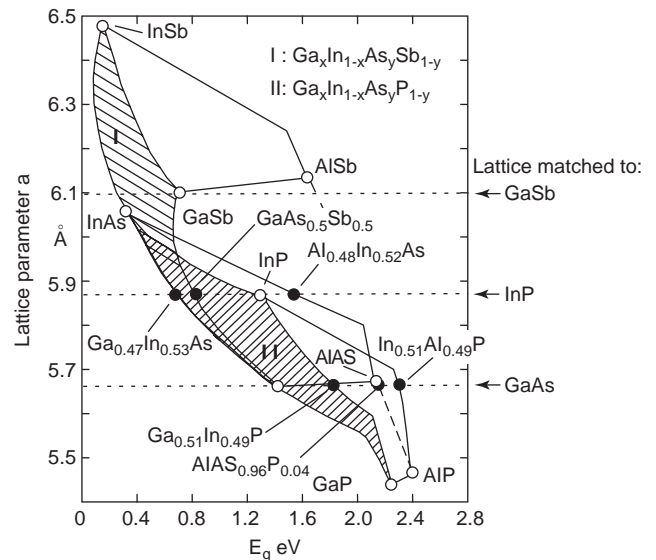


Figure 4. Variation of lattice parameter with energy bandgap associated with a variety of III-V semiconductors at 300 K [Landolt-Bornstein, “Numerical Data and Functional Relationships” in *Science and Technology*, Vol. 22, *Semiconductors*, Subvol. A., O. Madelung and M. Schulz, eds., Springer, New York (1987)].

2.3. Crystal Growth

Ideally, integrated circuits require an insulating substrate to provide electrical isolation between the various circuit elements. Silicon does not have a native insulating or semiinsulating state, although the more recent silicon-on-insulator (SoI) technology facilitates a suitable substrate for silicon RF and microwave integrated circuits. On the other hand GaAs and many other III-V semiconductors can be grown as semiinsulating materials. The active (conductive) regions of the circuit are defined by combinations of epitaxy, ion implantation, and mesa etching (or isolation by ion implantation).

Active devices and integrated circuits are fabricated on semiinsulating wafers that may have epitaxial layers grown on the surface. Some devices such as diodes may use bulk doped substrates. The wafers are obtained by sawing single-crystal boules along predetermined planes. These single crystal boules may be grown using a variety of techniques, including horizontal or vertical Bridgman, Czochralski, liquid-encapsulated Czochralski (LEC), magnetic LEC, liquid-encapsulated Kryopoulos (LEK), horizontal gradient freeze, or by float-, horizontal- or vertical-zone melting [9]. Bridgman techniques are the most commonly used methods of growing semiinsulating substrates.

The horizontal Bridgman technique involves the progressive crystallization of a molten bar of material as it is passed through a carefully controlled temperature gradient. The semiconductor crystal is grown in a quartz boat using a seed crystal and the constituent materials. In the case of GaAs, the boat containing the GaAs seed crystal and Ga is placed in a sealed quartz ampoule, with an overpressure of arsenic produced from a separate charge of arsenic at the opposite end of the ampoule. A temperature difference is produced along the tube, ensuring that one end of the boat is at the melting point (1238°C for Ga) while the arsenic, at the other end of the ampoule, is maintained at 614°C. Stoichiometry is ensured by precise control of the temperature and by accurate weighing of the Ga and As. Precise temperature control is required, ensuring horizontal thermal uniformity within 0.1°C. Long crystals of up to 1 m in length have been produced using this method. Very-good-quality material is produced using the horizontal Bridgman technique, and dislocation densities approaching 10^5 m^{-3} have been achieved for low-chromium-doped GaAs. The horizontal gradient freeze technique is similar to the horizontal Bridgman method; the main difference is that the former method induces crystallization from the seed by carefully controlled cooling of a melt. Both the Bridgman and gradient freeze techniques tend to have Si as impurities in the finished GaAs crystal as a consequence of the quartz boat.

The Czochralski technique is often used to grow large-diameter boules, suitable for wafers up to 6-in. in diameter. This pulling method uses a chamber with heated walls to maintain the required arsenic pressure. The LEC method is the more common than the basic Czochralski approach since it avoids arsenic loss and atmospheric contamination. The LEC system consists of a growth chamber housing a vertical puller with a seed crystal at

the tip of a rotating tip, which, in the case of GaAs growth, is immersed in a Ga melt, which in turn is fed with arsenic vapor from a separately heated quartz ampoule of arsenic. The susceptor containing the crucible with the Ga melt is heated with an RF coil. A molten B_2O_3 encapsulating layer on the surface of a Ga melt is used to prevent arsenic loss and contamination. An inert gas, such as nitrogen, is used to pressurize the growth chamber to a level higher than the As partial pressure. The rotating seed crystal is slowly withdrawn vertically upward, and the GaAs crystal boule is grown from the melt. The magnetic LEC method is a variation on the LEC technique that reduces the thermal convection currents found in the conventional LEC approach, improving the boule's homogeneity.

2.4. Epitaxy and Implantation

Semiinsulating substrates, available as wafers usually in the region of 600 μm thickness, are usually used as the basis for fabricating devices and integrated circuits in most III-V technologies. The conductive regions required for the active devices are formed using either epitaxial layers grown on the surface of the semiinsulating substrate, or by selective ion implantation.

Ion implantation techniques, which are used widely in Si technology to define conductive regions, were used widely to form the channel regions for MESFETs, bipolar junction transistors, varactor diodes, and IMPATT diode structures, especially in earlier integrated circuit designs. This low-cost approach, which is still widely in use today, can provide devices with moderate low-field channel mobilities ($0.35 \text{ m}^2 \text{ V}^{-1} \text{ s}^{-1}$) associated with channel doping densities of up to the mid- 10^{23} m^{-3} range for GaAs. High doping densities of up to $2 \times 10^{25} \text{ m}^{-3}$ are achievable for ohmic contacts, but have very low mobilities ($0.03 \text{ m}^2 \text{ V}^{-1} \text{ s}^{-1}$) [10].

Ion implantation is achieved by bombarding the semiconductor substrate with high-energy ions of the required dopant species. These ions displace semiconductor atoms from their sites in the crystal structure. In order to avoid extreme surface damage, which would render the surface amorphous, GaAs substrates are usually heated to 150°C during implantation. Fabrication of FETs and diodes with ion-implanted active profiles usually requires several implantations with energies tailored to produce the required doping profile. Each implantation produces an almost Gaussian profile of implanted ions as a function of depth from the semiconductor surface. This allows a selective three-dimensional doping profile to be produced in planar devices with localized highly doped regions for ohmic contacts. The wafers require annealing at a temperature in the range 800–950°C (for GaAs) after implantation to reduce the damage (defects) caused by the high-energy ion bombardments and achieve activation of the donor species. The doping efficiency is a function of the type of ion, implantation dose, and annealing temperature. Annealing is performed using either annealing furnaces, infrared radiation from halogen lamps, pulsed laser beam or electron-beam, techniques. The surface of GaAs loses arsenic at temperatures above 600°C, and hence annealing is performed either under arsenic overpressure

(“capless” annealing) or encapsulated using Si_3N_4 or AlN . The implanted dopants diffuse during annealing. Implantation can be used to produce either n- or p-type materials. Materials such as S, Se, Te, Si, and Sn are used to produce n-type GaAs. Dopants for p-type GaAs include Be, Zn, Cd, Mg, and C.

Ion implantation is widely used as an alternative to etched mesa isolation in integrated circuit designs to isolate the active regions of individual devices, allowing a more planar fabrication technology. In this scenario, semiinsulating material is produced locally by ion induced damage using proton bombardment or oxygen implantation, followed by annealing at a temperature between 650 and 800°C.

The advent of heterostructure devices, including high-electron-mobility transistors (HEMTs) and heterojunction bipolar transistors (HBTs), coupled with the demand for higher mobilities, higher channel carrier densities, lower-noise-figure FETs, and higher power densities from existing devices, has led to widespread use of epitaxial layer growth techniques. Although there are four potential candidates, vapor-phase epitaxy (VPE), liquid-phase epitaxy (LPE), molecular-beam epitaxy (MBE), and metallorganic chemical vapor deposition (MOCVD, also known as OMVPE), only the latter two techniques provide the necessary abruptness of interface and quality of growth necessary for most contemporary III-V semiconductor devices. MBE allows precise thickness and dopant control and is widely used as the basis of material for HEMTs, while the thicker layers found in HBTs are normally grown using MOCVD. Both techniques have been shown to produce very-high-quality material on high-quality semiinsulating substrates, achieving high mobilities and low defect densities [11].

MBE requires an ultra-high-vacuum growth chamber in a system that has multiple ultra-high-purity sources, achieving stoichiometric growth [12]. The growth rate is relatively slow, achieving 0.1–10 $\mu\text{m}/\text{h}$, but allowing very precise control of the film thickness, material composition, and dopant density. Highly abrupt interfaces are easily achieved and pulse (or delta) doping layers are readily grown, with layer thicknesses as thin as 5 Å. Heated crucibles, known as *Knudsen cells*, containing the elements or compounds used to form the various material layers are used as the sources. Contemporary multiwafer MBE production systems are capable of simultaneously growing high-quality material, with excellent uniformity on up to seven 6-in.-diameter wafer substrates (or a larger number of smaller-diameter substrates). This has led to widespread use of MBE grown wafers in modern III-V fabrication facilities. A wide range of compound semiconductor material systems can be grown using MBE and the same system can contain a range of Knudsen cells with ultra-high-purity Ga, In, Al, As, P, and Sb, as well as smaller cells for doping such as Si. It is common practice to have the most heavily used cells, such as Ga, duplicated. Growth is carried out on a single-crystal substrate—most commonly GaAs, which is heated to a temperature in the range 540–650°C. Faster growth rates tend to occur at the higher temperatures, and require careful control of the ratio of arsenic to gallium. The upper limit on growth

temperature is generally limited by the availability of the group V element over pressure.

MBE is used to grow highly complex multilayer heterostructures such as those found in quantum-well lasers and optical guides. Indeed, it is common for over 10 layers to be grown to form the active region of HEMTs, pseudomorphic HEMTs (PHEMTs), and metamorphic HEMTs (MHEMTs). MBE is used to produce the epitaxial material for a wide range of other microwave devices, including HBTs, MESFETs and resonant tunneling diodes. Superlattices, consisting of alternating layers of wide- and narrower-bandgap materials, are often used in these structures, and MBE is ideally suited to forming these abrupt interfaces [13].

The basic configuration of an MBE system requires a stainless-steel growth chamber, analysis chamber, and a load lock for transporting wafers into and out of the system (Fig. 4). The growth chamber is maintained at an ultrahigh vacuum and requires extreme cleanliness to ensure low defect densities during crystal growth. In addition to the Knudsen cells, the growth chamber houses shutters, substrate-handling equipment (which is robotic in many production systems), cryoshrouds, and surface analysis equipment to monitor growth. The effusion cell shutters regulate the emission of material from the cells. Normally, an additional “main” shutter is placed in front of the rotating substrate. The substrate is mounted on a heated holder, which rotates at speeds of up to 150 rpm for smaller holders, although lower rates of 5 rpm are normally used. This rotation and heating assist in maintaining uniformity in doping and thickness. The cryoshroud, which requires liquid nitrogen, encloses the entire growth area and minimizes water vapor and other unwanted gases during growth. Cooling of the regions surrounding the Knudsen cells also ensures that cross-contamination is minimized. In addition, each cell is usually water-cooled. The cells themselves, which are contained in stainless-steel housings, are made of graphite or boron nitride. The flux emitted from the cells is regulated by the shutters and monitored by an ion gauge behind the wafer holder. In more recent times, many systems use additional “cracker cells” placed between the Knudsen cells and the substrate. The cracker cells operate a high temperature (850–1000°C), and as effusion beams of arsenic or phosphorus pass through the region occupied by these cells, the As_4 and P_4 tetramers form As_2 and P_2 dimers. Dimer sources have been shown to reduce the density of deep levels and have a higher “sticking” coefficient, reducing the arsenic flux required during growth. Finally, surface analysis tools are normally incorporated into the system, including a scanning electron microscope (SEM), reflective high-energy electron diffraction (RHEED), Auger electron spectroscopy, secondary-ion mass spectroscopy (SIMS), and X-ray photoelectron spectroscopy. The RHEED analysis instrument plays a crucial role in determining substrate quality, growth condition and monitoring the thickness of the layer growth.

The molecular-beam epitaxial growth process (Fig. 5) for III-V materials requires precise control of the beam fluxes from the Knudsen cells and careful control of the surface temperature on which crystal growth is required.

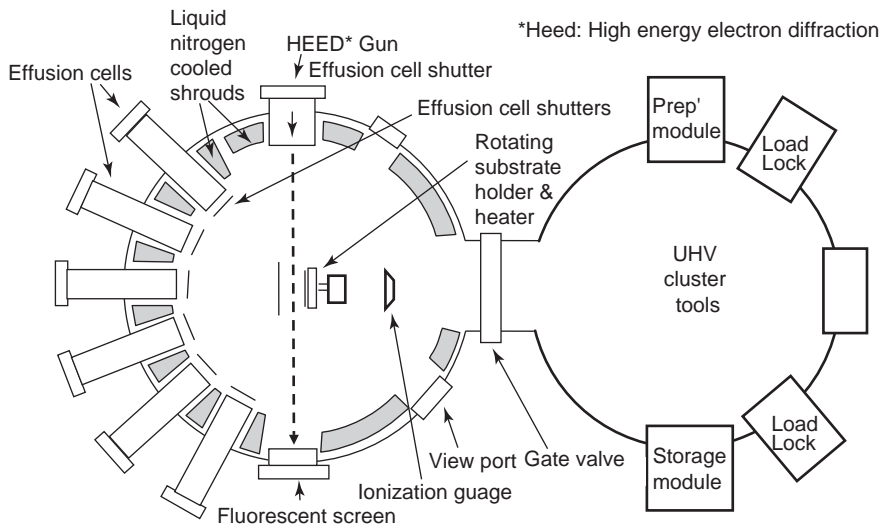


Figure 5. Schematic diagram of a molecular-beam epitaxy system [based on A. Y. Cho, *Molecular Beam Epitaxy and Heterostructures*, L. L. Chang and K. Ploog, eds., Kluwer, Academic Press (1985)].

Prior to initiating III-V growth, the substrate is heated to absorb the oxide layer on the surface, to ensure that the surface is atomically clean. This occurs at temperatures in the region of 590°C for GaAs and 520°C for InP. The process itself involves adsorption of the constituent atoms and molecules, surface migration and dissociation of the adsorbed molecules and incorporation of the atoms into the substrate, leading to nucleation and growth. In the case of GaAs, stoichiometric growth requires that an excess of arsenic be available at the growing surface, and that any excess that does not incorporate with gallium reevaporate. The growth of ternary (e.g., $\text{Ga}_x\text{In}_{1-x}\text{As}$) and quaternary compounds (e.g., $\text{Al}_x\text{In}_{1-x}\text{As}_y\text{P}_{1-y}$) is achieved with MBE using precise control of the ratios of the beam fluxes to ensure that growth occurs with the required mole fractions. A high-volume multiwafer MBE system for production purposes is shown in Fig. 6.

In contrast to the MBE, the metallorganic chemical vapor deposition growth (MOCVD) technique involves chemical reactions between gases that occur at tempera-

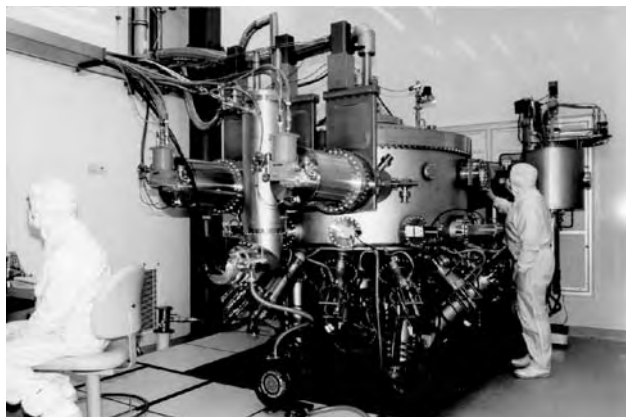


Figure 6. High-volume MBE production system capable of simultaneously growing epitaxial layers on seven 150-mm wafers (Veeco Applied Epitaxy GEN2000 system at Filtronic plc).

tures far below the melting point of the growing material. A typical MOCVD process involves a pyrolysis reaction between a metal alkyl vapor, such as trimethylgallium (TMGa), trimethylindium (TMIIn), or trimethylaluminum (TMAI), and a hydride such as arsine (AsH_3) or phosphine (PH_3), in proximity to a heated substrate (Fig. 7). Epitaxial growth occurs on the crystal surface of the substrate as a result of the deposition. Common substrates used for growth include semiinsulating GaAs and InP. In MOCVD, all the constituents of the process are in the vapor phase. This allows for easy control of gas flowrates and partial pressures in the vicinity of the growth surface. Also since the pyrolysis reaction is relatively insensitive to growth temperature, MOCVD achieves highly reproducible deposition of thin layers and can also produce very good abrupt interfaces between the various deposited layers.

MOCVD systems are available in a range of configurations, including high-volume 150-mm substrate growth systems. The hydrides, including arsine and phosphine are highly toxic and require special handling. The choice of source material is critical to the efficient operation of the MOCVD process. In particular, the group V sources must possess high vapor pressures, pyrolysis at temperatures above 395°C, and low temperature stability. They must also be available with very high purity and not prone to parasitic reactions with the group III sources. Group V sources used in MOCVD include the elemental, hydride, trimethyl, triethyl, and tertiarybutyl materials; As, AsH_3 , TMAs, TEAs, TBAs, P, PH_3 , TMP, TEP, IBP, and TBP. Although arsenic and phosphorus require heating to be used as sources, arsine and phosphine have high vapor pressures of 760 torr at -55 and -88°C, respectively. TMAs and TMP have vapor pressures of >250 torr at room temperature, but both these sources have the disadvantage of requiring high pyrolysis temperatures. Similarly, TEP is not an effective phosphorus source since it is stable at normal growth temperatures and TEA has a relatively low vapor pressure, despite its ability to pyrolyze at normal growth temperatures. Metallorganic sources used for MOCVD typically have the lowest molecular

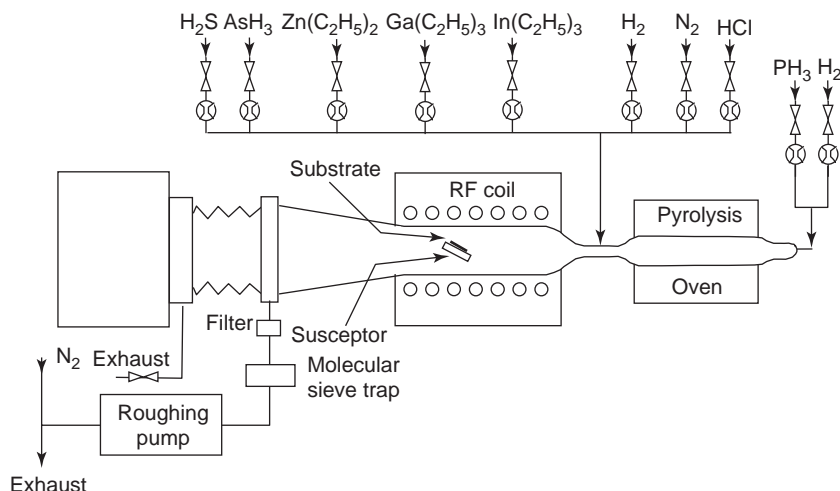


Figure 7. Schematic of a typical horizontal MOCVD system [derived from J. P. Hintz, M. Razeghi, M. Bonnet, and J. P. Duchemin, *GaInAsP Alloy Semiconductors*, T. P. Pearsall, ed., Wiley (1982)].

weights possible with vapor pressures in the region of 1–100 torr at temperatures from -25 to 25°C , and decompose thermally at the required growth temperatures of 550 – 800°C [14]. Generally, trimethyl compounds are used in preference to triethyl materials because of their higher vapor pressures promoting faster growth rates. Typical group III organometallic sources used in MOCVD include TMGa, TMAI, TMIIn, and TMSb. Group III alkyls used in MOCVD readily pyrolyze at low or atmospheric pressures.

The purity of III–V material grown using MOCVD is dependent on the quality of the substrate and the purity of the starting materials (the metal alkyls and hydrides), growth temperature, and the ratio of the constituents in the reactor. In the case of GaAs grown using TMGa and AsH_3 , the purity decreases with increasing growth temperature, probably due to the incorporation of carbon and silicon at higher temperatures. Carbon impurities usually take the form of acceptors, and Stringfellow has shown that a large increase in carbon incorporation occurs at higher growth temperatures [14]. In the case of AlGaAs growth, carbon contamination can lead to significant degradation in mobility, especially with increasing aluminum mole fraction. Doping of MOCVD grown material is usually performed using either Si, Ge, Se, S, or Te for donor impurities and Zn, Cd, Mg, and Be as acceptor impurities. Zinc (p-type) and selenium, tellurium or silicon (n-type) are the most common dopants. Hydrogen selenide H_2Se , SiH_4 , or DETe are used as sources for the donors, and dimethyl or diethyl zinc (DMZn or DEZn) as the p-type dopants.

2.5. Defects and Traps

Semiconductor crystals contain three types of defect: dislocations (or line defects), point defects, and volume defects (precipitates). Line defects occur as the melt crystallizes and shortly after solidification, and are associated with polygonization and slip interactions. The dislocation density is nonuniform and typically lies in the range 10^5 – 10^9 m^{-2} . High values of dislocation density

are detrimental to device performance and are extremely undesirable. Point defects are due to either native defects or chemical impurities. Native defects are usually associated with energy levels deep in the bandgap (known as deep levels) [15,16]. Chemical impurities often originate from the crucible or B_2O_3 encapsulant in LEC material and may include Si, C, or B. Other unwanted impurities, including Fe, Mg, Mn, S, Se, Te, and Zn, may also be found at concentrations of up to 10^{21} m^{-3} . Impurities, such as Cr, may be added to increase the resistivity of the semi-insulating material, with densities in the region of 10^{19} m^{-3} . Volume defects are often found in association with dislocations. Hexagonal precipitates of arsenic and GaAs microparticles create volume defects in some circumstances. Heat treatment of ingots reduces the effect of volume defects.

Point defects are usually characterized as either electron or hole traps. A particularly important point defect is the EL2 deep donor level, common in LEC grown GaAs. Traps play a key role in producing semi-insulating behavior in GaAs substrates [15]. Semi-insulating GaAs has intrinsic behavior in addition to high-resistivity properties, and is remarkably tolerant of small variations in impurity concentrations, retaining good uniformity throughout the ingot. It is important to appreciate that the presence of the deep donor (acceptor) and an excess of shallow acceptors (donors) are required for semi-insulating behavior. If these conditions are not satisfied, it is extremely difficult to achieve semi-insulating behavior [15]. In order to significantly reduce the concentrations of deep traps required to produce semi-insulating material, the concentrations of shallow donors and acceptors must be reduced, requiring material of very high chemical purity. In the case of bulk material, this is most easily achieved for LEC bulk material where the dominant shallow levels are acceptors, possibly due to Zn, Mg, Be, and carbon introduced in the growth process. These compensate the deep donor EL2. Bridgman material tends to be n-type, probably attributable to silicon introduced during growth. Semi-insulating material can be obtained from Bridgman by adding acceptors to compensate

the deep-level EL2 or adding chromium to introduce a deep acceptor, which, along with compensation with excess shallow donors, behaves in a manner analogous to EL2 [15].

Semiinsulating GaAs substrates (undoped and lightly Cr-doped) are often characterized using only one or two deep level traps: the EL2 midgap trap around 0.72 eV, dominant for LEC undoped substrates, and a shallower trap with an activation energy of approximately 0.39 eV. The EL2 level has been found to have an emission time constant that has a strong dependence on electric field [17]. The ionisation of the EL2 level produces an ionized EL2 center and an electron in the conduction band. Spectra associated with hole-type trap behavior have been observed bulk GaAs substrates [18].

The presence of the EL2 level, located near the middle of the bandgap, is essential to avoid nonuniformity and to ensure semiintrinsic behavior. The presence of the EL2 level and its concentration in GaAs ingots is dependent on the melt stoichiometry, and is minimized by having a slightly arsenic-rich content. The arsenic atom fraction in the melt stoichiometry during growth of the ingot determines whether the material is semiinsulating, for fractions in the range 0.475–0.535 with resistivity typically above $10^5 \Omega \cdot \text{m}$, or whether it is p-type in behavior for fractions in the range 0.43–0.47 with resistivities of the order of $10^{-2} \Omega \cdot \text{m}$. The association of semiinsulating behavior with the EL2 level suggests that the electrical properties of the material are due to the deep donor EL2 level and additional residual compensating acceptors, such as carbon.

A comprehensive survey of electron and hole traps was published in Refs. 18 and 19, in which over 33 electron and 22 hole trap levels were tabulated from various sources. It was suggested that some of these observations related to the same traps levels in differing materials. Even so, if this is the case, over 20 separate electron and 11 separate hole trap energies exist. A number of different transient spectroscopy methods have been developed to characterize traps in GaAs; the most commonly used is deep-level transient spectroscopy (DLTS) [10]. These include voltage-pulsed stimulated current and capacitive DLTS [e.g., 18,20], thermally stimulated current and capacitance techniques TSC, TSCAP [e.g., 21], and optically stimulated methods.

The presence of traps in active-device structures can have a profound effect on their transient electrical behavior. Many III–V devices suffer from adverse transient effects such as “gate and drain lag” in FETs, where the drain current responds with a transient of typically many hundreds of microseconds in response to a step excitation in the gate or drain voltages, respectively. The origin of these effects is associated with combinations of surface, bulk, and substrate traps. Surface traps, which are responsible for surface charge, play a particularly important role in determining the transient response of planar devices such as FETs. The transient behavior of these traps gives rise to dispersion phenomena in the drain current, transconductance, output resistance, and gate–drain capacitance. Surface charge can also have a profound impact on the breakdown voltage of these

transistors (which can consequently be a time-dependent phenomena). Ladbroke [22] provides a detailed insight into the impact of surface charge effects and dispersion in III–V MESFETs.

2.6. Substrates and Wafers

Although doped (and unintentionally doped) substrates were commonly grown in the past, for vertically oriented devices such as diodes, today the majority of substrates are semiinsulating. In 2003 over 13 million III–V substrates were manufactured worldwide. The rapid growth in III–V technology demand over the period 2001–2006 is expected to see a threefold increase in substrate supplies with a shift to increase wafer diameter [23].

As in all semiconductor technologies, wafer diameter plays a key role in the economics of manufacturing III–V devices. Since it is proportionately cheaper to fabricate devices on larger wafers than on smaller wafers, there has been a progression over the years from 1-in.-diameter wafers through to the current 6-in.-diameter wafers used for GaAs technologies. Up until 2000, 3- and 4-in.-diameter wafer processes dominated the industry. However, with the successful introduction of 6-in. semiinsulating substrates and associated epitaxial processes (MBE initially, followed by MOCVD), by 2004 there were over 10 large-scale 6-in. fabrication facilities worldwide, gradually displacing the less cost-effective smaller diameter fabrication facilities. This migration to larger wafer sizes can be compared with the movement from 2- through to 12-in.-diameter silicon wafers. The prospect of larger-diameter wafers for GaAs needs to be considered in the context of the level of demand and return on investment in the fabrication equipment as well as the fact that boules of GaAs have a density of more than double that of Si, presenting substantial challenges for growing boules for wafers of over 150 mm (6 in.) diameter.

Generally speaking, in applications where very low defect densities are required (e.g., laser diodes), or for more specialised materials, smaller diameter wafers are used. For example, at the time of writing high-quality GaN is usually grown on 2-in. wafers, and while GaAs is well established on 6-in. wafers, InP technology is still based on 3-in.- and more rarely 4-in.-diameter wafers. Continual improvements in epitaxy have led to dramatic improvements in defect density and epitaxial wafer quality, and this is reflected in the impressive yields, of over 95%, which can be achieved routinely on 150-mm (6-in.-) diameter GaAs wafers [24].

The quality of substrates and epitaxial layers is examined using a range of material characterization techniques, including X ray, photoluminescence, SEM/EDAX, and classical Hall mobility and sheet resistance measurements. In the case of epitaxial layers, the aim is to determine layer thicknesses, uniformity, surface morphology, chemical composition, carrier mobility, Hall factor, defect density, doping profile, and sheet carrier densities. A wide variety of techniques are used and cannot be covered in this article; the reader should consult Refs. 10 and 25. Surface and layer analysis is performed using a

range of spectrometry systems, including X-ray spectroscopy, secondary-ion mass spectrometry, Auger electron spectrometry, and X-ray photoelectron spectroscopy. Defect density and trap density and type are investigated using X-ray spectrometry systems, supported by DLTS. Sheet resistance and Hall mobility are often determined using van der Pauw measurements, based on Schottky gate patterns [26] and magnetoresistance measurements [27]. The doping density and in some cases the doping profile is determined for bulk doped materials, using tests such as C - V profiling, or evaluation from a combination of C - V and I - V data on long-gate length FETs. In the case of heterostructure layers, such as those used in HEMTs, the material is also characterized in terms of its sheet carrier concentration.

3. CARRIER TRANSPORT PROPERTIES

The carrier transport properties of materials determine a material's electrical behavior. The key properties that characterize carrier transport in semiconductor materials are the mobility and velocity of the electrons and holes, which are dependent on the scattering mechanisms in the particular material. The main scattering processes, which influence the mobility of electrons and holes, are acoustic phonon, nonpolar optical mode, polar mode, and ionized impurity scattering. Ionized impurity scattering dominates at low temperatures (< 100 K). Alloy scattering is a limiting process at room temperature in some material systems, such as in AlGaIn/GaN used in HEMTs. The bulk electrical conductivity is then expressed in terms of the mobilities and carrier densities in the bulk material. The low field mobilities of electrons and holes are a strong function of lattice temperature, carrier, and doping density. The transport properties have fundamental dependence on the electric field within the device structure, and are further modified by nonequilibrium behavior in small-scale structures, where rapid changes in the electric field can occur quickly changing the energy of the carriers leading to "hot" carrier transport phenomena.

The mobility in III-V semiconductor samples is normally determined from Hall effect measurements [5], where bulk samples of the material are characterized under the influence of a strong magnetic field. The hole mobility μ_p for p-type material in a small electric field is determined from the Hall mobility μ_H according to the relationship,

$$\mu_H = \sigma R_H = r_H \mu_p$$

where σ is the conductivity, R_H is the Hall constant, and r_H is the Hall factor, which tends to unity for strong magnetic field conditions ($B\mu_p \gg 1$). Similarly for electrons mobility μ_n for n-type material in a small electric field is determined from the Hall mobility μ_H according to the relationship

$$\mu_H = |\sigma R_H| = r_H \mu_n$$

where the Hall factor r_H is close to unity for strong magnetic fields and greater than 1 for medium or weak magnetic fields. Electron and hole mobilities are strongly temperature-dependent, showing approximately $(300/T)^{2.3}$ behavior above 100 K for GaAs. Below 70 K ionized impurity scattering reduces the mobility with decreasing temperature. Mobilities are also a function of carrier density. Typical values of hall mobility for p-type GaAs are in the region of $0.04 \text{ m}^2 \text{ V}^{-1} \text{ s}^{-1}$ for hole densities below 10^{22} m^{-3} , falling to $0.005 \text{ m}^2 \text{ V}^{-1} \text{ s}^{-1}$ for densities above 10^{25} m^{-3} . The Hall mobility of the electrons in GaN/AlGaIn HEMTs at 300 K has been found to be as high as $0.14 \text{ m}^2 \text{ V}^{-1} \text{ s}^{-1}$ in high-quality material for sheet carrier concentrations of 10^{17} m^{-2} .

The electron and hole drift velocities are defined by the product of the mobility and electric field \mathbf{E} . Hence, for electrons, the drift velocity v_d is given by $\mu_n \mathbf{E}$. In the case of low doped n-type GaAs μ_n is in the region of $0.8 \text{ m}^2 \text{ V}^{-1} \text{ s}^{-1}$ at 300 K for low values of electric field. At low values of electric field the velocity increases with increasing electric field. However, as the electric field increases and the electrons gain energy, the mobility decreases slightly. Increasing the electric field still further results in the most energetic electrons transferring from the central Γ valley to the first satellite valley X , which has a higher effective mass and reduced mobility. Eventually, a value of electric field is reached where the velocity attains a peak value, in the region of $2 \times 10^5 \text{ m/s}$ for GaAs. Beyond this value the drift velocity decreases with increasing electric field, asymptotically approaching the saturated value of $7 \times 10^5 \text{ m/s}$ at very high values of electric field. The steady-state electron velocity-electric field characteristics for several III-V semiconductors compared with silicon at 300 K are shown in Fig. 8 [28–32]. The region of negative-differential mobility beyond the peak velocity in each characteristic, where the velocity decreases with increasing electric field, is due to the transferred electron effect where electrons are transferring from the high-mobility central (Γ) valley to the low-mobility satellite (X) valley in the energy band structure. This phenomenon can give rise to oscillations in samples of InP and GaAs, and forms the basis of the Gunn diode (transferred electron device) [5].

The transient (nonequilibrium) carrier transport properties of semiconductors may be markedly different from their steady-state (equilibrium) characteristics [33,34]. In the case of many III-V semiconductors, the change in velocity experienced by electrons entering a high-electric-field region can lead to a phenomenon known as "velocity overshoot," where the electron is accelerated in the electric field, rapidly gaining energy, to a velocity significantly higher than the peak steady-state value, for a short interval (usually less than 0.1 ps). In the case of GaAs the transient velocity of these hot electrons may reach values in excess of $5 \times 10^5 \text{ m/s}$ over a short distance ($< 0.1 \mu\text{m}$) until scattering, energy, and momentum relaxation lead to a reduction in velocity that subsequently approaches the steady-state value over a short interval in time and distance [33,34]. Velocity overshoot in III-V devices can enhance their high-frequency performance

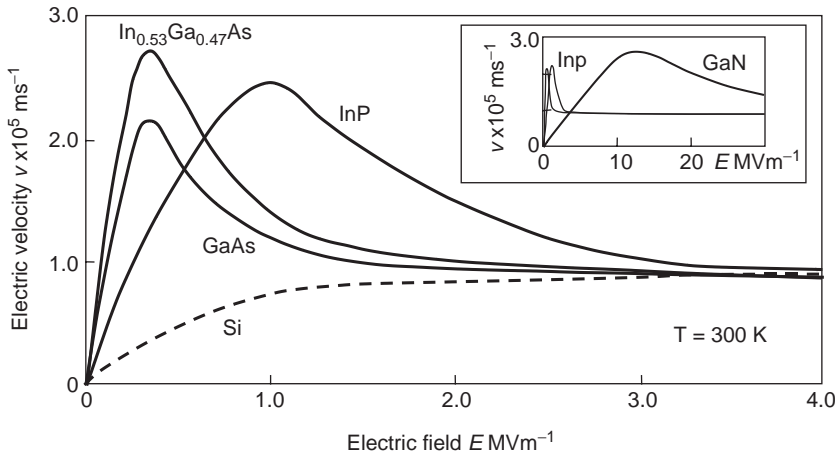


Figure 8. Steady-state velocity–electric field characteristics for GaAs, InP, $\text{In}_{0.53}\text{Ga}_{0.47}\text{As}$, and GaN, compared with Si at 300 K.

and is significant for short-gate (submicrometer)-length FETs.

The conductivity of semiconductors is given by

$$\sigma = \sigma_n + \sigma_p = q(n\mu_n + p\mu_p)$$

where n and p are the electron and hole densities (n_0, p_0 for intrinsic condition). In the case of GaAs doped with shallow donors or acceptors, the ratio of n/p is far from unity at 300 K, and the conduction is essentially unipolar depending on the dopant type. GaAs can be engineered to achieve a high value of resistivity, close to the intrinsic state, by the use of chromium doping, which introduces EL2 centers (see Section 2.5), creating semiinsulating GaAs. The room temperature resistivity of semiinsulating GaAs is typically in the range 10^3 – $10^7 \Omega \cdot \text{m}$, which makes an ideal substrate for integrated circuits.

4. PROCESSING AND DEVICE FABRICATION

The fabrication of semiconductor devices using either semiinsulating wafers with ion implantation of epitaxial layered wafers requires several stages of lithography, selective etching, deposition, and passivation, finishing with die separation, final test, and packaging. It is not possible to provide a detailed description of processing in this article, but an outline is a useful aid in understanding the design constraints and properties of the finished semiconductor devices. Williams provides a useful introductory text for GaAs processing [11].

4.1. Lithography

One of the most fundamental elements of device processing is the definition of the active and passive regions of the device, electrical contacts, bondpads, implantation regions, passivation areas, and interconnecting lines. This process of transferring patterns, made up of geometric shapes, to a thin layer of radiation sensitive material (*resist*) deposited on the surface of a semiconductor wafer is known as *lithography*. The resist is usually

deposited on the wafer by spinning a few drops of resist fluid into thin film at very high speeds, on to the surface of the wafer. The resist is then patterned (exposed) using photolithography, ultraviolet light lithography, electron-beam lithography, or in special cases X-ray or ion-beam lithography. The resist is then developed, selectively removing either the exposed or unexposed areas. The remaining pattern is then used to define areas for etching, deposition, or implantation. The resists are classified as either positive or negative depending on whether the exposed region is removed (positive) or whether the unexposed regions are removed (negative). An additional technique is based on image-reversal, which can provide enhanced resolution, which is particularly useful for submicrometer photolithography.

The photolithography techniques used in III–V processing include contact printing, proximity printing, projection printing, and stepping. Contact printing, which is frequently used for initial research development and for backside processing, is a straightforward process where the mask is aligned on the wafer and the resist exposed using a beam of ultraviolet light. Resolutions down to the region of one micrometer are possible as a result of the direct contact between the mask and the wafer. The two main disadvantages of this approach are (1) abrasion of the mask through direct contact, which reduces mask lifetime, and (2) *runout* due to any lack of planarity between the mask and wafer, preventing contact. Runout, due to curvature in either the mask or wafer, results in misalignment in areas of the pattern. Contact printing systems are significantly lower in cost than steppers or other precision lithography systems. Proximity printing places the mask in close proximity to the wafer, but avoids direct contact. Diffraction at edges in the pattern produces a slightly blurred image. This technique cannot achieve high resolutions and is not widely used in modern fabrication processes.

Optical steppers are the mainstay of silicon fabrication and are becoming widely used in III–V fabrication. The mask consists of the patterning for device and integrated circuit designs and is known as a *reticule*. The reticule is projected onto the wafer, which has previously been coated

in resist. A typical reticle is 20×20 mm. Many reticle patterns can be accommodated on a wafer. After the first reticle pattern is exposed, the wafer is moved very precisely and a second image is created. This process repeats across the wafer until the whole wafer is exposed. This step and repeat process is well established and is precisely indexed to allow multiple mask sets to be used, achieving precise alignment between layers. Steppers normally allow reduction of the reticle pattern on the mask by factors of 5 or 10, although in some circumstances unity reduction is used. Steppers achieve optical imaging using either lenses (refractive optics) or mirrors (reflective optics). The limitations of the optics are constrained by diffraction, where the optical surfaces must be accurate to within a quarter-wavelength. Steppers achieve a highly repeatable pattern, where any runout or misalignment is generally confined to the reticle. As a result, steppers have become established as a key element of high-yield processing, producing very-high-quality, highly repeatable lithographic patterning. Contemporary steppers for III-V lithography are available that achieve feature sizes of 0.35, 0.18, and 0.12 μm ; the cost of the system increases with increased resolution. Excimer laser (KrF) sources are used for the high-resolution steppers in the 0.18 μm range. Even higher resolutions are possible today, but the cost of the stepper is prohibitive for anything other than very-high-volume Si applications (microprocessors and memory). More recently there has been increased interest in using phase-shifting masks [35], which improve optical resolution by using interference to cancel diffraction effects. Steppers are available for 3, 4, 6, 8, and 12 in. wafer sizes.

Electron-beam (e-beam) lithography is widely used in III-V processing, as a means of both precisely patterning the masks used in photolithography and directly exposing (direct *writing*) patterns on wafers. Submicrometer gates were first written on GaAs using e-beam systems, although more recently, gate lengths above 0.35 μm are more routinely written using steppers, and it can be expected that 0.25- and 0.15- μm gates will in due course be written using steppers. At the heart of e-beam systems is the electron gun, which operates continuously, and beam-blanking plates that turn the beam on and off. The beam is moved over the surface of the wafer, within the scanned region, using deflection coils. The wafer is coated in a resist such as polymethylmethacrylate (PMMA). The wafer is positioned using a precision mechanism to move from one scanning field to the next. The pattern is generated in e-beam systems using computer controlled raster or vector scanning techniques. Electron-beam systems can achieve very high resolutions (currently below 70 nm), excellent registration, and great flexibility and do not require masks. Wafer flatness is not a problem for e-beam systems as they have a greater depth of field than do steppers. However, the throughput of e-beam systems is significantly slower than steppers at present. Also, on larger wafers e-beam systems can suffer from degradation of alignment accuracy, especially toward the edge of the wafers, away from the initial scanning fields. E-beam systems for III-V processing are available that will handle wafer sizes up to 6 in. (150 mm).

III-V processing has a number of significant differences to silicon device fabrication and in some respects is simpler — generally requiring fewer steps for monolithic microwave integrated circuits (MMICs) than for silicon ICs. A key stage in semiconductor device fabrication is the metal patterning, where, following evaporation of the required metal, the unwanted metal regions are removed. The metals used with silicon processing (typically Al) are usually fairly easy to etch, whereas the metallization schemes used in III-V processing (frequently TiPtAu, AuGeNi) are often difficult to etch. In silicon, this is achieved by depositing the metal first and then coating the metal with resist and lithographically defining the pattern. The unwanted metal, which is not protected by resist, is then removed by etching after developing the resist pattern. The resist is then removed using a solvent. In the case of III-V semiconductors a process known as “lift-off” is normally used, where the resist pattern is produced using lithography prior to evaporation of the metal. The desired metal pattern is then obtained by removing (“lifting off”) the resist (with metal evaporated on its surface) using a solvent, leaving the metal deposited on the semiconductor surface in the regions where the resist was originally removed following the development stage. The liftoff process is very sensitive to the pattern defined by the resist and an undercut in the resist profile is usually used to help define the desired metal regions.

It is convention to include a process control monitor (PCM) site in the reticle. This important element of the patterning includes a range of test devices, such as simple contact structures, transistors, and diodes and if it is a MMIC, a small range of transmission-line structures resistors, capacitors, and inductors. The purpose of these structures is to monitor the key parameters against the expected values as the wafer goes through each stage of the processing. This allows the quality of the processing to be closely monitored and assists in process control and yield optimization. The PCM sites are usually tested after each processing stage or at suitable intervals. The PCM site usually occupies only a small area of the reticle — often less than 1%.

4.2. Etching Techniques

III-V semiconductors can be etched using either wet- or dry-etch techniques or a combination of both. Prior to processing and at stages during the fabrication, it is necessary to clean the wafer surfaces. Exposure of GaAs to the atmosphere leaves an oxide layer on the exposed surface of the material, which can be 50 Å thick, which is removed using a highly diluted acid such as HCl. Highly pure deionized water is used extensively in processing to avoid contamination. Wet and dry etchings are used as a means of forming patterns and defining features in the surface of the semiconductor wafer, and for polishing (e.g., after thinning of wafers during backside processing).

Wet etching techniques have been established since the early days of fabrication and normally have the properties of providing selective and preferential etching depending on the crystallographic orientation of the wafer. In the case of Si, this allows distinctive etching that is exploited

in MEMs, and, for example, allows “V” grooves to be readily defined. Etching of III-V compounds is usually crystallographic, and key features and critical dimensions can be defined by ensuring proper alignment with the lattice planes. In the case of GaAs, (111) Ga faces etch up to 5 times slower than do (100), (110), and (111) As faces. Wet etches are categorized either as electrolytic or nonelectrolytic. Electrolytic etches require an electrical contact to the wafer and in the case of GaAs have an anodic oxidation mechanism. One advantage of electrolytic etches is that they can be used to provide accurate technical depth control. Nonelectrolytic etching rates are either diffusion or chemical-reaction-limited. Diffusion-limited etches are generally isotropic and are well suited for polishing wafers after mechanical grinding. Chemical-reaction-limited etches are often anisotropic are particularly suitable for defining patterns. Wet etches generally contain an oxidizing agent, such as Br_2 or HNO_3 , a complexing agent, such as NH_4OH , NaOH , HC , citric acid, or H_2SO_4 and water. The complexing agent ensures that the relatively insoluble oxidized layer is dissolved in the water. The etch is chosen to remove areas of the wafer that are not protected by the exposed resist pattern.

Dry etching techniques have become increasingly popular for use in III-V device fabrication in more recent years. They are widely used in III-V processing to produce recesses (e.g., single- and double-gate recesses), mesas for isolation, and via holes through the substrate that are metallized to connect the top surface to the metallized back surface of the wafer. These reactive plasma etching techniques have several important advantages over wet-etch methods, including better directional control of the etch and improved anisotropy of the etch. Specifically, the laterals etch rates in plasma etching are very low indeed, preventing undesirable undercutting of the resist pattern. Dry etching utilizes an ionized gas to achieve plasma-driven chemical reactions or use highly energetic ion beams to remove material that is not protected by the resist pattern. Dry etching can be classified as plasma etching, reactive-ion etching (RIE), ion milling, or reactive-ion-beam etching (RIBE). Inductively coupled plasma etching is also widely used in III-V device fabrication. Control of the plasma by varying the system electrode configuration, gas composition, pressure, and bias voltages allows the characteristics of the etching process to be tailored to the particular semiconductor material and the required shape of the etched region.

Plasma etching systems often use chlorine, HCL , PCl_3 as sources of chlorine ions. O_2 and Ar are often added. CH_4/H_2 systems have been used for InP and GaAs. The system itself in its basic form consists of two parallel plates with a DC and RF ionizing source (100–600 V at 13 MHz) attached to the top plate and the wafers clamped to the lower water-cooled plate. The plasma is formed between the plates and energetic ions perpendicularly impact the surface of the exposed semiconductor material. The resist prevents the ions penetrating the unexposed surface of the semiconductor. Plasma etching can give rise to radiation damage and in some circumstances leaves residues that require subsequent removal (often using a light wet etch). RIE is in many ways similar to plasma

etching, with the reactive species generated from the plasma, but with greater directionality of the ions. RIE systems typically operate at low pressures and the substrates are mounted on the powered electrode. Reactive-ion etching is usually used to etch GaN/AlGaIn because of the difficulty in finding suitable wet etches. BCl_3/Ar is found to produce surfaces smoother than those obtained with Cl_2/Ar for GaN/AlGaIn. Finally, the electrodes themselves are often asymmetric with the chamber forming the grounded electrode. In RIE the semiconductor is etched through a combination of chemical reaction and sputtering. Similar ion species can be used to plasma etching, but a smoother surface is obtained using H_2 , BCl_3 , or CCl_3F . Again O_2 is added to CCl_3F and CCl_4 to increase etch rates, and Ar to increase anisotropy.

Ion-beam milling is a high-energy (~ 1000 eV) etching process, where inert ions (Ar) are allowed to impinge on the target substrates in a uniform beam. Ion-beam milling can achieve relatively high resolutions, and can be used to define structures smaller than $0.01\ \mu\text{m}$. It is a highly anisotropic process, and the profile of the etched sidewall can be determined by positioning the relative angle of the substrate and by using shadow masking. Ion-beam milling can be used to etch metals, including Ti, Pt, and Au metallization layers and will etch materials that are challenging for plasma or wet-etch systems. The main disadvantages are damage from ion bombardment, poor sensitivity, and redeposition of materials. Focused ion-beam etching can be used to define small-scale structures. The final dry etching process, reactive-ion-beam etching (RIBE) takes advantage of both chemical reaction and ion bombardment to etch material. Unlike ion beam milling it uses a reactive gas although the etch characteristic are very similar. Redeposition of the etched material is avoided in RIBE by using a vacuum removal system.

4.3. Deposition and Metallization

It is usually necessary to provide insulating coatings on the surface of semiconductors at various stages in processing, either to planarize the surface for additional processing (e.g., metallization) or as a dielectric for capacitors in integrated circuits, or as a passivation to protect the surface of the semiconductor. The type of materials deposited can be either inorganic, such as silicon nitride or silicon dioxide, or organic, such as BCP. Plasma-enhanced chemical vapor deposition (PECVD) techniques, which use RF excited plasmas, are often used to deposit these films, as they can achieve this at relatively low temperatures (typically $250\text{--}350^\circ\text{C}$). This low temperature capability is very important for III-V processing, where higher temperatures would lead to changes or decomposition of the semiconductor material. PECVD films are amorphous, and the density and quality of the material depend strongly on growth conditions. In particular, the frequency of the RF stimulated discharge, which may lie between 50 kHz and 13 MHz, directly influences the stress in the film (the higher the frequency, the lower the compressive stress). PECVD layers are usually deposited in thickness between $1000\ \text{\AA}$ and $1\ \mu\text{m}$, with growth rates typically of the order of $300\ \text{\AA}/\text{min}$.

Plasma deposition is usually carried out in either a planar (parallel-plate) or barrel (tubular) reactor. The best uniformity is achieved in radial flow planar reactors, where the substrates are positioned on the lower electrode of the two parallel plates. Deposition is performed under a vacuum to minimize contamination, and a wide variety of highly reactive chemical species are used, including chlorine, fluorine, hydrogen, oxygen, silane (SiH_4), and ammonia. Silicon nitride, which is one of the most frequently used insulating materials, is often deposited using electron cyclotron resonance systems, which operate at 2.45 GHz.

Silicon nitride Si_3N_4 is used widely in III-V processing as a dielectric layer in capacitors, an encapsulant (to prevent diffusion) or for passivation to protect the surface of the semiconductor or die from the environment. It is normally grown using silane as a source of silicon and ammonia (or nitrogen in some cases) as the nitrogen source. The silane is mixed with an inert gas (argon). The dielectric constant of the amorphous silicon nitride is a function of film thickness and silane concentration. The film thickness dependence is due to the impact of stress and nonuniform growth of the layer. Thin films (below 1000 Å) can achieve relative dielectric constants of up to 11, whereas thicker films typically have dielectric constants in the region of 8. Silicon dioxide has a lower dielectric constant than silicon nitride and is often used as a spacer layer in metal cross-overs to minimize parasitic capacitance. Again, silane is usually used as the silicon source, and the oxygen source is selected from CO , O_2 , or N_2O .

Some III-V processes utilize aluminium nitride as an insulator or passivation layer. AlN for these purposes is grown either by sputtering, vapor phase, or MBE. Single-crystal films may be grown at temperatures in the region of 1150°C, although amorphous AlN films can be grown at lower temperatures or using plasma CVD. Other dielectric films such as silicon oxynitride are used in some circumstances.

The final element in processing is the provision of metallization on the surface of the semiconductor to act either as contacts or interconnections. Two types of metal-semiconductor contact can be fabricated in III-V devices: ohmic contacts and Schottky contacts. Ohmic contacts have the property that they possess very low resistances across the metal-semiconductor interface, while Schottky barrier contacts have a more complex rectifying contact behavior, representative of a diode, where in reverse bias the interface demonstrates very high resistance (ideally no current flow) and capacitance associated with the charge developed in the depletion region below the contact. In contrast in forward bias, the interface behaves like a diode, with the potential for significant current flow, but only supporting relatively low forward voltages across the interface. In addition to the contacts, first- and second-level metallization is used to interconnect the various elements of the active devices, and circuits, where the metal is chosen to possess high conductivity, excellent adherence, and conformal coating, coupled with compatibility with the Schottky and ohmic contacts. Additionally, via holes that connect between levels or between the top and backside metallized surfaces of the substrate.

Schottky contacts can be formed with III-V semiconductors using sputter or evaporation deposited multi-layer metal contact structures such as TiPtAu, TiW, TiWSi, Pt, Al, WSi, WAl, and TiPdAu. Metal silicides, such as tungsten silicide, widely used in silicon VLSI, can achieve low contact resistances for III-V devices when annealed at high temperatures and may be deposited using RF cosputtering. Schottky contacts on AlGaN can be achieved using Ni/Au. The barrier height of the Schottky barrier varies with the semiconductor material composition, crystal orientation, and the contact metal. In the case of GaAs and gold, for example, the barrier height varies from 0.82 eV for (100) orientation to 0.97 eV for (110) crystal orientation at the interface [36]. The range of barrier height for Schottky contacts on several III-V binary semiconductors is shown in Table 3 [5,36,37].

Ohmic contacts are formed with III-V semiconductors using n^+ or p^+ layers immediately below the contact metallization. Very high doping levels above $5 \times 10^{24} \text{ m}^{-3}$ are used with multilevel metal-alloyed contacts. In the case of GaAs, alloys based on Au or Ag are popular choices. In the case of contacts made on p-type material, zinc is usually added to the alloy, which acts as a dopant in the semiconductor. In the case of n-type contacts germanium and tin are used in the alloy. AuGeNi contacts provide among the lowest contact resistances and high reliability in III-V devices. Other GaAs metal alloy ohmic systems include Au-Zn, Au-Zn-Sb, Au-Be, and Au-Be-Ni. Ohmic contacts to InP are achieved using Au-Ge-Ni, Au-Sn, Ag-Sn-In, In-Zn, Au-Mg, and Au-Be. AlGaAs ohmic contacts are made with Al, Au-Zn, and Au-Ge-Ni; GaInAs, with Au-Zn, Au-Sn, and Au-Ge-Ni. Ohmic contacts to AlGaN/GaN devices are usually made with alloys based on Ti/Al annealed at 850–875°C. Rapid thermal annealing is usually employed for ohmic contacts. “Balling” of the metals on the contact surface can be avoided by including a thin cover layer of Ni/Au over the Ti/Al prior to annealing at 900°C. It should be noted that it is hard to form ohmic contacts to AlGaN when the mole fraction exceeds 33%.

A first-level metal used as part of the interconnection metallization has the characteristic of good adhesion to ohmic and Schottky barrier metals. Gold-based alloys are generally used for interconnection first metallization — the most common are TiPtAu and TiPdAu, using e-beam deposition systems. Copper, with its very high conductivity, which is used with silicon, diffuses in several III-V semiconductor materials and cannot be used. Aluminum

Table 3. Schottky Barrier Heights for n-Type III-V Semiconductors

Material	Barrier Heights (eV)						
	Ag	Al	Au	Ni	Pt	Ti	W
GaAs	0.88	0.80	0.90	0.79	0.85	0.82	0.79
GaP	1.20	1.07	1.30	1.27	1.45	1.12	—
AlAs	—	—	1.20	—	1.00	—	—
InAs	—	—	0.47	—	—	—	—
InP	0.65	—	0.65	—	—	—	—
$\text{Al}_{0.14}\text{Ga}_{0.86}\text{As}$	—	0.90	1.02	—	—	—	—
$\text{Al}_{0.32}\text{Ga}_{0.68}\text{As}$	—	1.09	1.10	—	—	—	—
$\text{In}_{0.53}\text{Ga}_{0.47}\text{As}$	0.20	—	0.20	0.20	—	0.15	—

interacts adversely with gold, with high-resistance intermetallic products. Silver is very reactive and is rarely used in III-V devices. First metallization is usually in the region of $0.5\ \mu\text{m}$ thickness. Second-level metallization is usually based on gold (Ti/Au), due to its low tendency to electromigration [38] and ability to handle very high current densities. Airbridges are also formed in the second-level metal. Metallization is achieved using sputtering, evaporation or electroplating. An evaporation system for 150-mm-diameter wafers is shown in Fig. 9. Thicker layers ($> 1\ \mu\text{m}$) are usually deposited using RF sputtering systems. Via holes may be plated using either electroplating or electroless plating (based on gold–cyanide solutions) or magnetron sputtering or by evaporation of TiAu.

4.4. Backside Processing

The final stage of the fabrication process is backside processing and die separation. After completing the frontside with the devices, metallization, contacts, and circuit elements, the reverse side of the wafer is processed. At this stage the wafer is usually thinned to its final thickness, which usually lies in the range $30\ \mu\text{m}$ (for high power) to $150\ \mu\text{m}$ (Fig. 10). A mechanical grinding process is used to remove the bulk of the material, which is then finished with a chemical etch. If there is a requirement for via holes to connect the top surface to the backside, vias will be etched, usually using dry etching techniques (Fig. 11). If a ground plane is required, the backside is metallized with gold (as in the case of vias). After completion of processing, the wafer may be attached to a film frame to facilitate temporary die retention during the on-wafer test and die separation processes. The die on the wafer are then subject to visual inspection and electrical testing. The process control monitor (PCM) sites receive their final electrical tests to complete the process data for the wafer. The die may be probed using DC and RF testing to determine whether they meet the specification (and hence determine the final yield). After on-wafer testing the final stage is to separate the die, which is achieved using either a diamond scribe (“scribe and break”) or a



Figure 9. Evaporation system for metallizing semiconductor wafers.

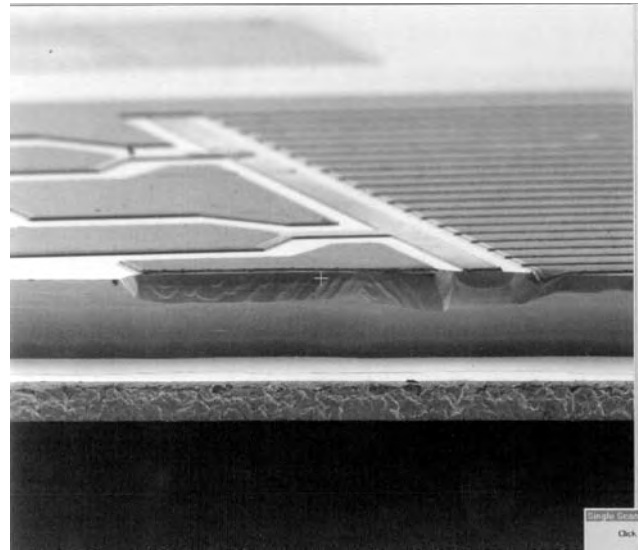


Figure 10. Cross section of a die, showing thinning of the GaAs to $30\ \mu\text{m}$ and gold metallization of the backside ($\sim 10\ \mu\text{m}$). The FET structure can be seen on the frontside (Filtronic plc).

diamond saw. Laser separation techniques are beginning to appear that also show promise. The die are retained on the film in preparation for packaging using robotic pick-and-place instruments.

5. RF AND MICROWAVE DEVICE TECHNOLOGY

III-V RF and microwave devices may be fabricated as unipolar or bipolar designs. The early interest in GaAs and InP centred around the properties of these materials that demonstrated negative-differential resistance as a consequence of their velocity–electric field relationships. J. B. Gunn demonstrated microwave oscillations in 1963, using a simple GaAs two-terminal structure. This phenomena forms the basis of the *transferred electron effect*

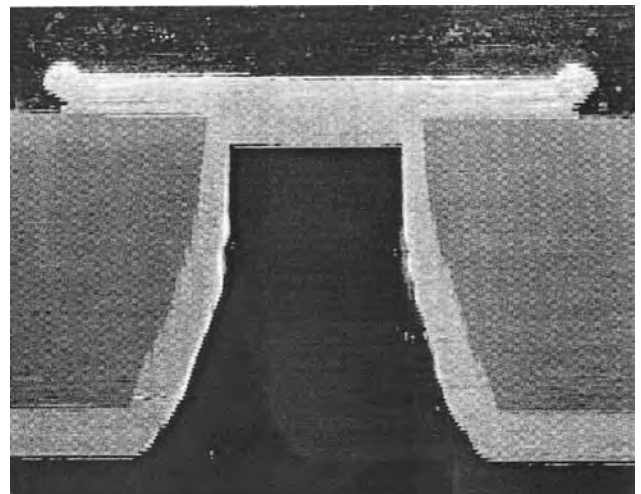


Figure 11. A via hole etched in a $125\text{-}\mu\text{m}$ substrate and plated in gold (light color) (Filtronic plc).

[5], which is characterized by the behavior of the Gunn diode. GaAs and InP Gunn diodes have found widespread application as the active devices in microwave oscillators ranging from 1–100 GHz.

The most common transistor technologies in use today are based on unipolar field-effect transistor (FET) or heterojunction bipolar transistor technologies [39,40]. GaAs and Si bipolar transistors were widely used prior to the advent of higher-frequency FETs [41]. In 1971 Turner reported a 1- μm -gate-length FET with gain of ≤ 18 GHz [42]. By 1980, GaAs metal semiconductor field-effect transistors (MESFETs) were established as the device of choice in microwave low-noise and medium-power amplifiers, achieving noise figures of less than 1 dB at 4 GHz and output powers of up to 25 W [43]. Although MESFETs were employed in oscillator designs, especially varactor tuned designs, from their introduction in the mid-1970s [44], relatively poor $1/f$ noise performance in early MESFETs led to the continued use of bipolar junction transistors in low-noise oscillators up to 6 GHz. The advent of AlGaAs/GaAs high-electron-mobility transistors (HEMTs), also known as *modulation-doped FETs* (MODFETs), in the 1980s with their improved noise performance displaced MESFETs in low-noise amplifiers and wider use in oscillators and mixers, although still with some remaining $1/f$ noise limitations. AlGaAs/GaAs heterojunction bipolar transistors (HBTs) were introduced in the early 1980s, but were not widely used until the advent of mobile communications and the widespread development of low-voltage, high-efficiency power amplifiers for cellular handsets. By 2000 pseudomorphic HEMTs (PHEMTs) had become the established high-frequency transistor, operating at frequencies up to 200 GHz and achieving noise figures below 0.2 dB at 2 GHz. HBTs based on AlGaAs/InGaAs/GaAs, and InGaP structures demonstrating maximum frequencies of oscillation f_{max} above 100 GHz, are now readily available. GaAs-based PHEMTs have demonstrated high power and high efficiency operation up to X band [45]. The state of the art is now occupied by gallium nitride transistors, with AlGaN/GaN FETs achieving power densities above 10 W/mm gate periphery and capable of over 170 W at high efficiencies [46], and power densities of over 4 W/mm at 30 GHz [47]. Similarly, GaN/AlGaN HBTs show potential for high-power high-frequency operation and demonstrate high emitter injection efficiencies.

6. APPLICATION OF TRANSISTOR TECHNOLOGIES

Up until 1985, the MESFET dominated as the preferred choice of microwave transistor, with some usage of silicon bipolar remaining for niche applications below 8 GHz (such as low-noise oscillators). By 1990, the PHEMT had begun to displace MESFETs for low noise amplifiers, and the AlGaAs/GaAs HBT had begun to emerge as a candidate for low-voltage power amplifier applications (such as in the emerging cellular handset market). Up until this time, MESFET technology had been dominated by ion-implanted designs, utilizing semiinsulating GaAs substrates. Improvements in epitaxial growth (MBE and MOCVD/OMVPE) allowed higher performance FETs to be designed, with improved gain, current, and power handling. By 2000, MESFET technology was being displaced in many applications by PHEMT and HBT, because of the superior gain and power handling of these technologies. Nevertheless, the simpler fabrication technology MESFETs remains attractive for low-cost applications where the performance is undemanding. At the present time, HBTs are the most common choice for power amplifiers in cellular handsets, while PHEMTs power FETs are being introduced in many microwave and millimeter-wave power amplifier applications and are even challenging silicon LDMOS in some specialized applications at 2 GHz. By 2006 GaAs-based HEMTs are expected to be found in over 35% of microwave applications, while HBTs provide another 30%, with MESFETs falling to around 20%.

The maximum electric field sustainable before the material breakdown determines the maximum voltage sustainable across the device, which in turn directly influences the power handling of the device. The electron and hole mobilities impact the resistivity, frequency limit, and current handling (and thus power handling) of the device. The saturation velocity determines the current handling and frequency limitations. The thermal conductivity limits the temperature of operation and thus the power-handling and frequency limits. Table 4 lists these parameters for a range of semiconductors used or potentially available for power devices. The potential for newer materials such as GaN, SiC, and diamond is still being evaluated. It should be noted that the reported data for more recent materials varies in the literature. The Johnson and Baliga figures of merit are frequently used to compare the potential of materials for power device applications [48,49]. Baliga's figure of merit is a measure of the

Table 4. Material Properties for Power Devices at 300 K

Property	GaAs	InP	GaN	Si	4 HSiC	Diamond	Units
Energy bandgap	1.42	1.34	3.44	1.12	3.26	5.47	eV
Relative permittivity	12.8	12.6	9.5	11.8	10.1	5.7	—
Breakdown field	48	53	330	31	300	2000	MV/m
Electron mobility	0.86	0.54	0.15	0.15	0.08	0.28	$\text{m}^2 \text{V}^{-1} \text{s}^{-1}$
Hole mobility	0.04	0.02	0.02	0.04	0.01	0.20	$\text{m}^2 \text{V}^{-1} \text{s}^{-1}$
Saturation velocity	0.8	0.8	1.3	0.9	2.0	2.7	$\times 10^5 \text{ m/s}$
Peak velocity ^a	2.1	2.3	2.6	1.0	2.0	2.7	$\times 10^5 \text{ m/s}$
Thermal conductivity	46	68	130	150	490	2200	$\text{W m}^{-1} \text{K}^{-1}$

^aNontransient (steady-state).

Table 5. Johnson Figure of Merit Normalised to Silicon

Material	Johnson Figure of Merit
Si	1.0
GaAs	1.9
InP	2.3
GaN	233.0
4 HSiC	455.0
Diamond	37,000.0

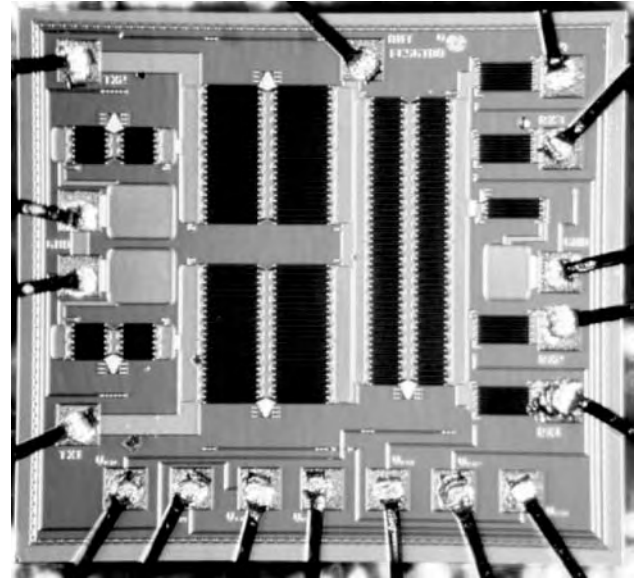
ON resistance of the drift region of a transistor (usually applied to vertical FETs) [50]. The Johnson figure of merit (JFM) is a measure of the ultimate high frequency capability of the material and is given by the product of critical breakdown field E_{Br} and saturated electron drift velocity v_{sat} :

$$JFM = \left(\frac{E_{Br} v_{sat}}{2\pi} \right)^2$$

The Johnson figure of merit is shown for a range of power semiconductors in Table 5. It should be noted that practical limitations encountered in fabricating power transistors limits the actual performance of devices, although the more mature technologies of Si and GaAs can approach these limits in some applications. InP has demonstrated excellent performance in applications, including MMICs, above 100 GHz, although it is still mainly applied to small-signal transistor applications and a limited range of relatively low-power millimeter-wave devices such as Gunn diodes (75 mW at 94 GHz).

7. APPLICATIONS AND MARKETS FOR MMICs AND DIGITAL ICs

Historically, the market for III-V integrated circuits grew steadily up until 2000, without the cyclical behavior often seen in the silicon digital IC market. In 2000 over \$2 billion MMICs and digital GaAs ICs were sold and despite the technology recession observed in 2001/02, the market for these products is expected to grow to over \$4 billion by 2006. Wireless communications represented over 70% of this market in 2000, but by 2006 this is expected to fall to around 60% as the use of MMICs in automotive applications increases. Interestingly, despite the intense interest in optoelectronics, the total share of the GaAs IC market in this application (for modulators, switches, driver ICs, detectors, and high-speed processing) is not expected to exceed 12% in the foreseeable future (indeed, its market share fell to 8% in 2002). Although digital GaAs was originally seen as a major growth element of the industry in the late 1990s, the collapse in the optoelectronic market in 2000 and the increase in CMOS Si and SiGe capabilities, have seen the GaAs largely displaced for digital applications below 2.5 Gbps. Analogue applications now dominate for III-V MMICs with increased usage in mobile terminal products (cellular handsets, personal digital assistants wireless LANs, etc.), principally for power amplifiers and low-loss RF switches (Fig. 12). The emer-

**Figure 12.** A microwave switch MMIC (1 × 1 mm) (Filtronic plc).

gence of automotive radar applications has led to forecasts of significant growth for chipsets at 17, 24 and 77 GHz, possibly reaching 5 million chipsets per annum by 2007.

BIBLIOGRAPHY

1. H. Welker, Über neue halbleitende Verbindungen (New semiconductor compounds), *Z. Naturforsch.* **79**:744–749 (1952).
2. M. Ida, K. Kurishima, and N. Watanabe, Over 300 GHz f_T and f_{max} InP/InGaAs double heterojunction bipolar transistors with a thin pseudomorphic base, *IEEE Electron. Device Lett.* **23**(12):694–696 (Dec. 2002).
3. J. W. Archer, R. Lai, R. Grundbacher, M. Barsky, R. Tsai, and P. Reid, An indium phosphide MMIC amplifier for 180 to 205 GHz, *IEEE Microwave Wireless Compon. Lett.* **11**(1):4–6 (Jan. 2001).
4. Y.-F. Wu, A. Saxler, M. Moore, R. P. Smith, S. Sheppard, P. M. Chavarkar, T. Wisleder, U. K. Mishra, and P. Parikh, 30-W/mm GaN HEMTs by field plate optimization, *IEEE Electron. Device Lett.* **25**(3):117–119 (March 2004).
5. S. Sze, *Physics of Semiconductors*, Wiley-Interscience, 1981.
6. V. Swaminathan and A. T. Macrander, *Materials Aspects of GaAs and InP Based Structures*, Prentice-Hall, Englewood Cliffs, NJ, 1991.
7. E. O. Kane, in W. Paul, ed., *Handbook on Semiconductors*, Vol. 1, North Holland, Amsterdam, 1982, Chap. 4.
8. O. Madelung, *Semiconductors—Basic Data*, Springer, 1996.
9. C. Y. Chang and F. Kai, *GaAs High-Speed Devices*, Wiley, 1994.
10. M. Shur, *GaAs Devices and Circuits*, Plenum Press, 1986.
11. R. Williams, *Modern GaAs Processing Methods*, Artech House, 1990.
12. M. A. Herman and H. Sitter, *Molecular Beam Epitaxy*, Springer-Verlag, 1988.
13. L. L. Chang and K. Ploog, *Molecular Beam Epitaxy and Heterostructure*, Martinus Nijhoff, 1985.
14. G. B. Stringfellow, *Organometallic Vapour-Phase Epitaxy*, Academic Press, 1989.

15. E. J. Johnson, J. A. Kafalas, and R. W. Davies, The role of deep level centers and compensation in producing semi-insulating GaAs, *J. Appl. Phys.* **54**(1):204–207 (Jan. 1983).
16. S. T. Pantelides, ed., *Deep Centres in Semiconductors A State of the Art Approach*, Gordon & Breach Science Publishers, 1992.
17. S. Sriram and M. Das, Characterization of electron traps in ion-implanted GaAs MESFETs on undoped and Cr-doped LEC semi-insulating substrates, *IEEE Trans. Electron. Devices* **ED-30**(6):588–592 (June 1983).
18. A. Mitonneau, G. M. Martin, and A. Mircea, Hole traps in bulk and epitaxial GaAs crystals, *Electron. Lett.* **13**(22):666–668 (Oct. 27, 1977).
19. G. M. Martin, A. Mitonneau, and A. Mircea, Electron traps in bulk and epitaxial GaAs crystals, *Electron. Lett.* **13**(7):191–193 (March 31, 1977).
20. D. Lang, Deep-level transient spectroscopy: A new method to characterize traps in semiconductors, *J. Appl. Phys.* **45**:3023–3032 (1974).
21. D. K. Chen and M. B. Das, Characterization of deep levels using unconventional zero-bias thermally stimulated current in ion-implanted semi-insulating GaAs substrates, *IEEE Trans. Electron. Devices* **ED-32**(11):2506–2507 (Nov. 1985).
22. P. Ladbroke, *MMIC Design: GaAs FETs and HEMT*, Artech House, 1989.
23. M. Telford, GaAs boosted by WLAN and auto radar, *III–V Rev.* **17**(1):32–35 (2004).
24. M. F. O’Keefe, J. S. Atherton, W. Bösch, P. Burgess, N. I. Cameron, and C. M. Snowden, GaAs pHEMT based technology for microwave applications in a volume MMIC production environment on 150 mm wafers, *IEEE Trans. Semicond. Manuf.* **16**(3):376–383 (Aug. 2003).
25. D. K. Schroder, *Semiconductor Material and Device Characterization*, Wiley-Interscience, 1990.
26. L. J. Van der Pauw, A method of measuring specific resistivity and Hall effect of disc of arbitrary shape, *Philips Res. Rep.* **13**:1–9 (1958).
27. J. S. Sites and H. H. Wider, Magnetoresistance mobility profiling of MESFET channels, *IEEE Trans. Electron. Devices* **ED-27**(12):2277–2281 (Dec. 1980).
28. P. Bhattacharya, *Indium Gallium Arsenide*, IEE INSPEC, 1993.
29. S. Adachi, *Aluminium Gallium Arsenide*, IEE INSPEC, 1993.
30. M. R. Brozel and G. E. Stillman, *Properties of Gallium Arsenide*, 3rd ed., IEE INSPEC, 1996.
31. S. Adachi and J. Brice, *Properties of Indium Phosphide*, IEE INSPEC, 1991.
32. S. Sze, *High Speed Semiconductor Devices*, Wiley-Interscience, 1990.
33. C. M. Snowden, *Semiconductor Device Modelling*, IEE Peter Peregrinus, 1988.
34. C. M. Snowden and R. E. Miles, eds., *Compound Semiconductor Device Modelling*, Springer-Verlag, 1993.
35. G. E. Flores and B. Kirkpatrick, Optical lithography stalls X-rays, *IEEE Spectrum* 24–27 (Oct. 1991).
36. D. C. Northrop and E. H. Rhoderick, The physics of Schottky barriers, in M. J. Howes and D. V. Morgan, eds., *Variable Impedance Devices*, Wiley, New York, 1978.
37. C. J. Palmstrom and D. V. Morgan, Metallizations for GaAs devices and circuits, in M. J. Howes and D. V. Morgan, eds., *Gallium Arsenide Materials, Devices and Circuits*, Wiley, 1985.
38. A. Christou, *Reliability of Gallium Arsenide MMICs*, Wiley, Chichester, UK, 1992.
39. J. M. Golio, *Microwave MESFETs and HEMTs*, Artech House, 1991.
40. F. Ali and A. Gupta, *HEMTs and HBTs*, Artech House, 1991.
41. C. M. Snowden, Active microwave devices, in D. V. Morgan and M. J. Howes, eds., *Microwave Solid-State Component and Subsystem Design*, Leeds Univ. Press, 1983.
42. J. Turner, A. Waller, R. Bennett, and D. Parker, *Proc. 9th Institute of Physics Conf.*, London, 1971, pp. 234–239.
43. J. V. Dilozenzo and D. D. Khandelwal, eds., *GaAs FET Principles and Technology*, Artech House, 1982.
44. R. S. Pengelly, *Microwave Field Effect Transistors—Theory, Design and Applications*, Research Studies Press, 1986.
45. C. M. Snowden, Recent developments in compound semiconductor microwave power transistor technology, *IEE Proc. Circuits and Systems*, April 2004.
46. K. Joshin, T. Kikkawa, H. Hayashi, T. Maniwa, S. Yokokawa, M. Yokoyama, N. Adachi, and M. Takikawa, A 174 W high efficiency GaN HEMT power amplifier for WCDMA base station applications, *Proc. IEEE Int. Electron Devices Meeting Technical Digest*, Dec. 2003, pp. 12.6.1–12.6.3.
47. F. Raay, R. Quay, R. Kiefer, M. Schlechtweg, and G. Weimann, Large-signal modelling of AlGaIn/GaN HEMTs with $P_{\text{sat}} > 4 \text{ W/mm}$ at 30 GHz suitable for power applications, *Proc. IEEE MTT-S Int. Microwave Symp. Digest*, June 2003, Vol. 1, pp. 451–455.
48. T. P. Chow and R. Tyagi, Wide bandgap compound semiconductors for superior high voltage unipolar power devices, *IEEE Trans. Electron. Devices* **41**:1481–1483 (Aug. 1994).
49. E. O. Johnson, Physical limitations on frequency and power parameters of transistors, *RCA Rev.* **26**:163–177 (1965).
50. B. J. Baliga, Power semiconductor device figure of merit for high-frequency applications, *IEEE Electron. Device Lett.* **10**:455–457 (1989).

FURTHER READING

- H. Morkoç, H. Unlu, and G. Ji, *Principles and Technology of MODFETS*, Vol. 1, Wiley, 1991.
- H. Morkoç, H. Unlu, and G. Ji, *Principles and Technology of MODFETS*, Vol. 2, Wiley, 1991.
- W. Liu, *Handbook of III–V Heterojunction Bipolar Transistors*, Wiley-Interscience, 1998.
- D. Haigh and J. Everard, *GaAs Technology and Its Impact on Circuits and Systems*, IEE Peter Peregrinus, 1989.
- J. J. Liou, *Advanced Semiconductor Device Physics and Modeling*, Artech House, 1994.

TRANSCIEVERS

FRANCIS DOMINIQUE
Lucent Technologies

1. COMMUNICATION SYSTEMS

The ability of electromagnetic radiation to provide almost instantaneous communication without any interconnecting wires has been a major factor in the explosive growth

of mobile communications, especially cellular and personal communications during the latter half of the twentieth century. The vacuum tube made the radio practical and affordable during the earlier half of the twentieth century. The invention of the transistor and highly complex yet cheap integrated circuits have allowed the development of ever complex digital communication systems that operate quite close to theoretical limits on channel capacity, spectrum efficiency, and so on.

The word *transceiver* is actually a combination of two words, *transmitter* and *receiver*. Figure 1 shows the block diagram of a general radio transceiver. Below each system block is a list of some of the popular techniques used. A modern digital transceiver uses most, if not all, of the system blocks in Fig. 1. Based on the direction of information transfer, radio systems are of three general types: simplex, half-duplex, and full-duplex systems. A *simplex* system transmits information in only one direction from a transmitter to a receiver. Examples of simplex systems are commercial audio and television broadcast systems organized in a *star* configuration. A *half-duplex* system is one in which transmission is bidirectional but only one transmitter at a time can transmit. A *full-duplex* or duplex system is one in which bidirectional communication can occur at any time. Although all communication systems are either some kind of simplex or duplex system, a variety of communications architectures exist dependent on the end application.

Section 2 points out the important characteristics of radio transceivers. Section 3 is devoted to the evolution of transceiver architecture. The characteristics of various different architectures are discussed in detail. Section 4 describes the implementation of important transceiver components with special emphasis on digital processing. Section 5 concludes by looking at the future.

2. TRANSCIEVER CHARACTERISTICS

2.1. Radio Transmitter Characteristics

This section details the important characteristics and performance issues for a transmitter.

2.1.1. Out-of-Band Emissions. There are stringent requirements as part of the standards for out-of-band power emissions. For example, the interim standard IS-54 for digital cellular radio specifies that power emission in adjacent and alternate channels must be 26 dB and 45 dB below the mean output power, respectively. Spectral shaping to maintain out-of-band emissions below those required by the standards is usually achieved through a combination of baseband pulse shaping, IF/RF filtering, and proper operation of the radiofrequency (RF) power amplifier.

2.1.2. Output Power, Distortion, and Efficiency of the Power Amplifier. In the early days of radio, power was amplified by vacuum tubes. With the invention of the transistor, solid state circuits have replaced vacuum tubes. The power amplifier should provide adequate output power with the least distortion and maximum possible efficiency [1]. The gain, efficiency, distortion, and power of the transistors typically used in solid-state power amplifiers depend on the choice of the bias point and the drive mechanism through the familiar designation of the operating class (Class A, B, AB, C, or E). The distortion introduced by the amplifier is specified by its AM-AM and AM-PM transfer characteristics.

The two most important parameters of the power amplifier, namely, efficiency and distortion, are incompatible with one another. Linear power amplifiers provide the least distortion but have quite large quiescent currents, resulting in poor efficiency. Nonlinear amplifiers, like

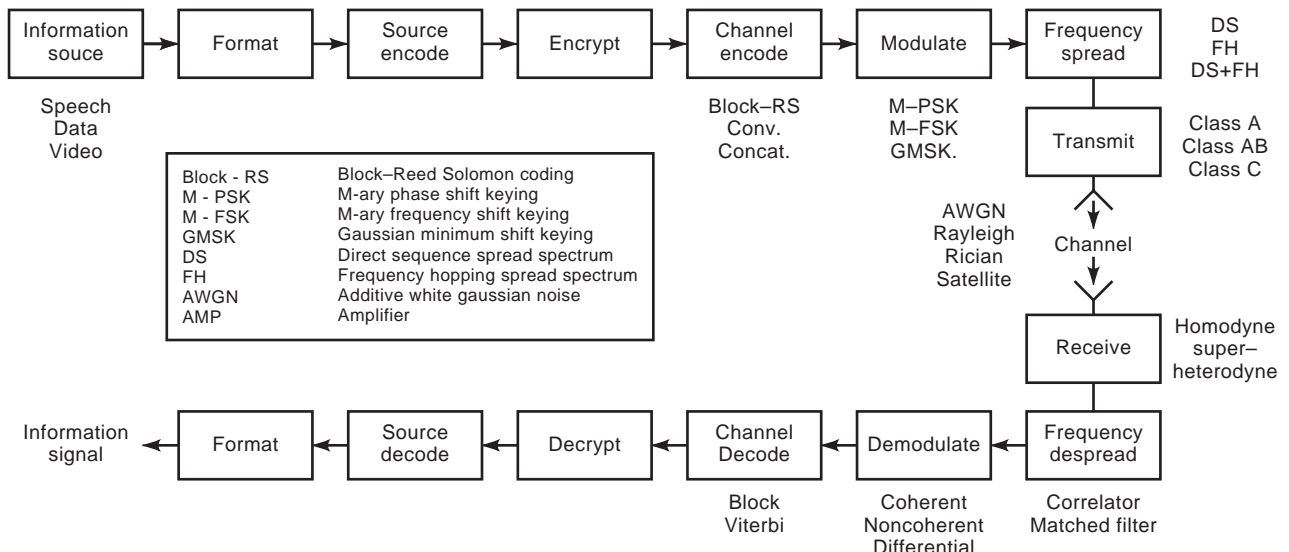


Figure 1. General block diagram of a modern transceiver. Abbreviations are listed at the end of the article.

Class C amplifiers, are highly efficient but cannot be used for linear modulation because of the distortion introduced by the amplifier. The type of power amplifier used depends on the requirements of the modulation used. Constant envelope modulation like frequency modulation (FM) can be amplified with nonlinear Class C amplifiers. However, in recent years, increasing demand for RF spectrum usage is forcing the use of spectrally efficient linear modulation techniques. These signals have a fluctuating envelope, and nonlinear amplification results in spectral spreading and intermodulation products. Therefore highly linear power amplifiers are required. One way to achieve linear amplification is to back off the amplifier from saturation and operate in the linear region of its transfer function. However, such amplifiers have poor dc-to-RF conversion efficiency. A major challenge in designing a high-power amplifier is to maintain linearity without compromising power efficiency [2].

2.2. Radio Receiver Characteristics

This section details the important characteristics and performance issues for a receiver.

2.2.1. Antenna and Input Characteristics. The main function of a radio receiver is to pick up electromagnetic radio energy at the antenna and transfer it efficiently to the processing section of the receiver. The important characteristics of an antenna are its efficiency, impedance, 3 dB beam width, bandwidth, and gain. Other characteristics are null-fill, upper sidelobe suppression, and performance versus specification. All antenna characteristics are functions of the physical antenna dimensions relative to the operating wavelength. Another important component is the coupler between the antenna and the input circuit of the receiver, which typically is a filter or an amplifier. Maximum energy is transferred if the impedance of the input circuit matches that of the antenna throughout the band of interest. Some of the antenna matching problems in a radio receiver are as follows:

1. The problem of matching the antennas at certain frequencies may be limited by component availability.
2. The impedance of antennas used in mobile applications or in locations where the environment changes with time due to foliage or traffic.

The problem of antenna matching is often solved by the system designer taking into account and compensating for a range of mismatch losses that might occur in practice. Other input characteristics that need to be taken into account are as follows:

1. The input RF circuits may be balanced, unbalanced, or both.
2. Protection from high-voltage discharges due to lightning.
3. Ability to handle high-power cochannel and adjacent channel transmissions

2.2.2. Gain and Sensitivity. Radio receivers typically process signals with a wide range of powers. The extent to which the signals can be received and processed usefully depends on the noise levels received at the antenna and those generated by the circuits within the receiver itself. The receiver is also required to produce a certain level of output power suitable for the application. Receivers are designed so that the gain is distributed among the various stages as required. Modern receivers are usually not gain-limited, and the weakest signal that can be processed is usually noise-limited. This signal level is known as the *sensitivity* of the receiver. A measure of sensitivity is the *minimum detectable signal* (MDS), which is the power of a sinusoidal signal that just equals the noise power at the intermediate frequency (IF) output of the receiver. MDS [1] can be expressed in decibels as

$$\text{MDS} = KTB_n F$$

where K is Boltzmann's constant (1.38×10^{-20} mW/°K), T is the reference temperature (typically 290°K), B_n is the noise bandwidth of the receiver, and F is the noise figure.

2.2.3. Noise Figure. The noise figure compares the total receiver noise with the noise that would be present if the receiver generated no noise. This ratio is called the *noise factor* F , and, when expressed in decibels, the noise figure (NF). It is thus a measure of the amount of noise introduced by the circuits within the receiver itself.

$$F = \frac{(S/N)_{\text{input}}}{(S/N)_{\text{output}}}$$

where (S/N) is the signal-to-noise ratio.

2.2.4. Selectivity. Selectivity is the ability of a receiver to separate a signal at one frequency from signals at other frequencies. Selectivity is defined as the bandwidth for which a signal x dB stronger than the minimum acceptable signal at a nominal frequency is reduced to the level of that minimum acceptable signal. Two important characteristics are required in establishing the selectivity of a receiver. One is that the selective components of the receiver must be sufficiently sharp to suppress unwanted interference from adjacent channel transmissions and spurious responses. The other is that the components must be sufficiently broad to pass the highest frequency of interest with acceptable gain and phase distortion.

2.2.5. Dynamic Range. Dynamic range is used to indicate the ratio between the strongest and weakest signals that a receiver can handle with acceptable noise or distortion. The weakest signal commonly considered is the minimum detectable signal. This definition is of limited value especially when the desired signal is surrounded by other signals with varying signal power. The selectivity of a receiver provides protection against many of the unwanted signals. The strong unwanted signals, however, can still cause degradation because of nonlinearities in the receiver chain. Therefore it is important to consider the

definition of the strongest signal component when determining the dynamic range of the receiver.

2.2.6. Characterization of Spurious Outputs. A modern receiver typically has a synthesizer and possibly several local oscillators, especially if superheterodyne architecture is used. It is possible for these frequencies to interact and produce spurious outputs without any inputs present. The following are other sources of spurious signals:

1. Parasitic oscillations in amplifiers because of parasitic feedback
2. Intermediate frequency subharmonics
3. Power supply harmonics

2.2.7. Frequency/Clock Generator Characteristics

2.2.7.1. Accuracy and Stability. Modern transceivers have a frequency synthesizer to which all other local oscillators are slaves. Earlier radios had free running oscillators that have largely been replaced by digital synthesizers because of the superior frequency accuracy, stability, flexibility, and cost performance of digital circuitry. Once the synthesizer has been set to operate at a specified frequency, its frequency must remain unchanged for a period sufficient for nominal operation despite temperature and environmental changes. Modern transceivers use temperature-compensated crystal oscillators as clocks for their digital circuitry. These oscillators typically are accurate to about 1 part per million. Higher accuracies are provided by oven-stabilized crystal oscillators and rubidium oscillators when sufficient power is available. In certain applications, such as mobile handsets where cost and power are at a premium, less expensive clocks with accuracies of approximately 3 to 10 parts per million are used.

2.2.7.2. Settling Time. Modern receivers typically span large frequency ranges and might be required to retune to a different frequency of operation. Because the frequency synthesizer used is typically based on a phase-locked loop, the loop goes out of lock for a short period whenever the receiver retunes. The settling time of the loop is important as any loss of lock results in degraded receiver performance.

2.2.8. Digital Receiver Characteristics. In addition to the characteristics previously mentioned, these are other important characteristics useful for systems using digital modulation.

2.2.8.1. Eye Diagram. The eye diagram [3], the traditional way of displaying digital data, is obtained by displaying the received demodulated digital data signal in successive symbol intervals on top of each other. The eye pattern provides the following wealth of information:

1. The width of the eye opening defines the time interval over which the received signal can be sampled without error from intersymbol interference.

2. The sensitivity of the system to timing error is determined by the rate of closure of the eye, as the sampling time instant is varied.
3. The height of the eye opening at any specified time defines the margin over channel noise.

2.2.8.2. Bit Error Rate (BER). The BER [1] is the primary measure of the quality of a digital communication system. The BER is defined as

$$\text{BER} = \frac{N_E}{N}$$

where N_E is the number of bit errors and N is the total number of bits transmitted.

3. RADIO ARCHITECTURES

3.1. Evolution

Radio architectures have remained relatively unchanged since the invention of the homodyne and superheterodyne receivers in the early part of the twentieth century. With the advent of integrated processors during the 1970s and 1980s, there was a migration from analog to digital processing in almost every aspect of radio systems engineering. The only radio system block that survived this migration was the RF front end, which by its function has to be analog. However, the basic radio architecture has remained the same. The word *digital* in digital radio has a double meaning. First, it refers to the fact that information is carried in digital form and second that the radio uses digital processing to recover the transmitted signal after it has been downconverted by an analog front end. The following are the advantages of using digital processing [1,4]:

1. The repeatability and temperature stability of digital processing are substantially better than analog processing.
2. Certain functions that cannot be or are difficult to implement in analog hardware, such as sharp rolloff linear phase filters, can easily be implemented with digital processing.
3. Once engineered, digitally implemented system functions do not require the tuning or tweaking typically required in analog systems.

The software radio [5] can be thought of as the next logical evolution of the digital radio, where software control of radio functions is pushed as close as possible to the antenna in the conventional digital radio architecture. Here, the entire RF band of interest is digitized right at the operating RF band by high-speed analog-to-digital converters (ADCs). The rest of the radio functions, such as downconversion, equalization, demodulation, and decoding, would be carried out by reprogrammable logic, typically digital signal processors (DSPs).

Software radio architecture has the following advantages over conventional hardwired digital radio architecture:

1. A highly flexible and reconfigurable transceiver can be implemented.
2. The transceiver can be easily adapted to any particular environment by changing the modulation, filtering, demodulation, and so on.
3. Because of open architecture, future upgrades can easily be made without reengineering the entire radio.
4. Software radio architecture benefits readily from concentration, where multiple radio channels share the same RF front end, whereas analog systems need a separate RF front end for each channel.

Applications that already use or are likely to use digital/software radio architectures include cellular and personal communications systems, satellite communications, digital television, digital audio broadcasting, navigation and position location systems, and test equipment.

3.2. Transmitter Architectures

The earliest analog radio transmitter architecture was the direct conversion transmitter. Figure 2 shows the general block diagram of an analog direct conversion architecture. Although this architecture is simple, it has the following disadvantages [6].

1. The analog implementation of precise modulators at the operating RF is difficult.
2. When used as an analog quadrature modulator, gain and phase imbalances between the mixers require compensation because unwanted sidebands are generated.
3. The filtering required to reduce out-of-band emissions to conform to government-mandated spectral masks must be carried out completely at the RF

band of interest. Designing high rolloff RF filters that introduce minimal amplitude and phase distortion across the frequency band of interest is difficult.

The superheterodyne architecture shown in Fig. 3 was intended to overcome some of the disadvantages of the direct conversion architecture. Here, modulation is carried out at a low IF. Then the desired signal band is filtered to conform to the desired spectral mask, and the filtered signal is upconverted to the desired RF band. The main disadvantage of the superheterodyne architecture is that the one or more IF stages used increase power consumption, space, and cost.

The advent of digital modulation and digital integrated circuits has resulted in the ever increasing use of digital processing in the transmitter chain. Digital processing can alleviate most of the problems associated with analog direct conversion transmitters, and as a result there is a resurgence of interest, especially for low-power mobile handsets where space and power are at a premium. Following are the advantages of digital architecture [7]:

1. Design and implementation are flexible.
2. Digital implementation overcomes the problems of gain and phase, dc offsets, and performance drifts in analog implementations.
3. Multichannel digital IFs especially at base stations eliminate the multiple analog IF chains required in analog architecture. With digital upconversion, all digital IF signals can be combined in a digital summer and then transformed into a single analog signal by a digital-to-analog converter (DAC).
4. Manufacturing is reliable.

Some of these combined analog-digital architectures are shown in Fig. 4.

The advent of software radio architecture will result in almost complete replacement of the RF system by programmable digital processing. Figure 5 shows the block diagram of an ideal software radio. In this ideal architecture, except for the final RF power amplifier and filter, the

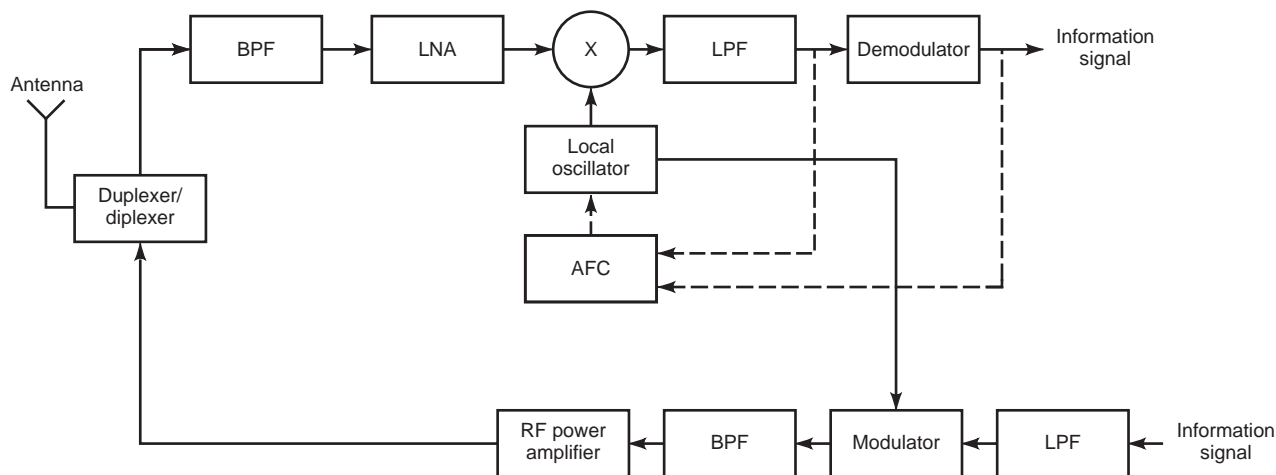


Figure 2. General block diagram of an analog homodyne transceiver.

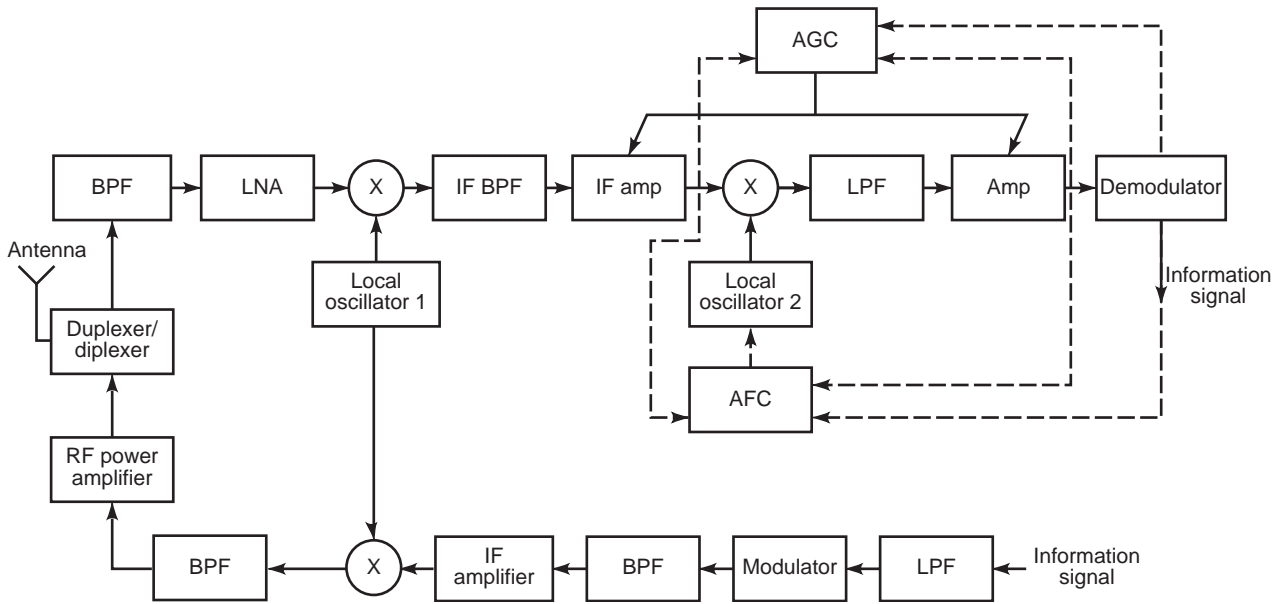


Figure 3. General block diagram of an analog superheterodyne transceiver.

analog upconversion chain has been replaced by digital IF upconversion. Limitations on the maximum sampling rate by currently available technology, however, permits replacing only the first analog IF strip.

3.3. Receiver Architectures

The earliest analog receiver architecture was the homodyne or the direct conversion architecture, as seen in Fig. 2. The receiver consists of a bandpass filter (BPF) following the antenna for noise and interference rejection

followed by a low-noise amplifier (LNA). Then the signal is downconverted to baseband by a pair of analog mixers. The in-phase and quadrature components are low-pass filtered to remove the mixer products and are demodulated. Following are the advantages of direct conversion architecture:

1. Reduced hardware complexity as there are no IF stages
2. No image frequencies

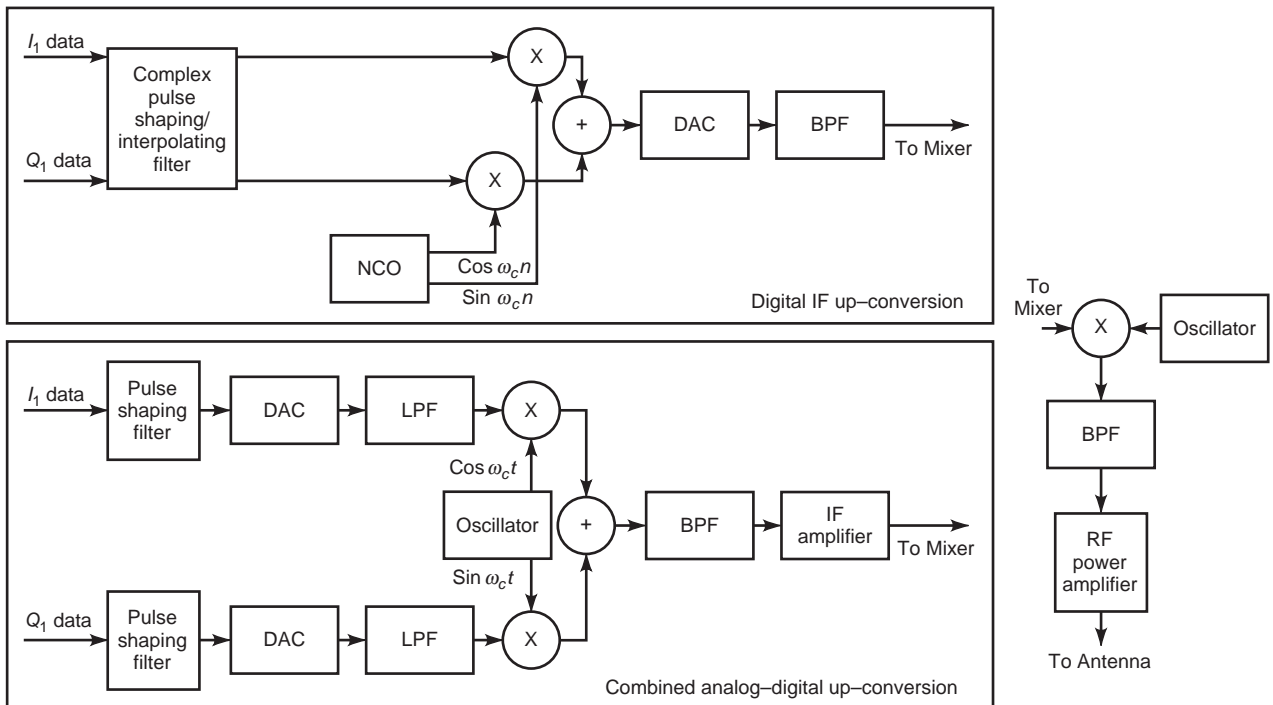


Figure 4. General block diagram of combined analog-digital upconversion architectures.

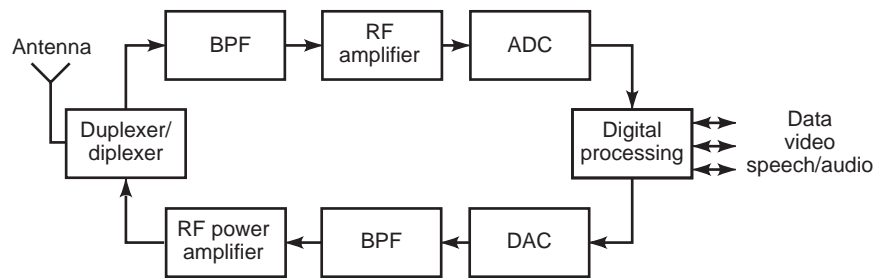


Figure 5. General block diagram of an ideal software radio architecture.

Following are the disadvantages of the direct conversion receiver, *especially* with an analog implementation:

1. Amplitude and phase mismatches between the mixers distort the signal.
2. Sharp rolloff analog low-pass filters (LPF) also distort the desired signal.
3. Carrier leakage, $1/f$ noise in the mixers, and bias in the filters all contribute to an unpredictable time-varying dc offset in the recovered signal.
4. All signal amplification has to be done at the carrier frequency. Building high-gain RF amplifiers at such high frequencies is difficult and expensive.
5. Carrier recovery for coherent reception has to be carried out at the carrier frequency. Precise control of high-frequency oscillators is difficult.

The superheterodyne receiver shown in Fig. 3 was developed to alleviate some of the disadvantages of the direct conversion receiver. In this architecture, the RF signal is downconverted to an intermediate frequency before being downconverted to baseband. This is known as the single IF stage superheterodyne receiver. Various versions of this general architecture with multiple IF stages have been developed. The most common version is the dual IF stage architecture. Following are the advantages of superheterodyne architecture compared with the direct conversion receiver:

1. Most of the signal amplification is done at relatively lower IFs, where it is easier to build high-gain amplifiers.
2. Automatic frequency control is usually carried out at the lower IFs and hence is easier to implement.

With the advent of digital modulation, high-speed ADCs, and digital integrated circuits, digital processing started to replace segments of the analog receiver architecture especially in demodulation and baseband processing. This led to the development of digital radio architecture. Both direct conversion and superheterodyne RF front-end architectures have been used in digital radios. The direct conversion digital radio requires two ADCs to digitize the in-phase and quadrature components of the downconverted signal. Superheterodyne digital radios have used both low-pass and bandpass digitization. The advantage of bandpass digitization is that it can replace the last analog downconversion stage. In addition, because the final

downconversion to center the chosen spectral image around dc is done digitally, all problems associated with quadrature analog downconversion disappear. Some of the digital receiver architectures are shown in Fig. 6.

Although the digital radio provides superior performance, its architecture is still based on the direct conversion or the superheterodyne architectures. Recently, a more fundamental change in receiver architecture occurred with the advent of software radio architecture, made possible by technological advances in ADC technology, computing technology, and software engineering. The software radio architecture looks similar to that of the digital radio with one crucial difference. In software radio architecture, programmable digital processing is pushed as close to the antenna as technology permits. The block diagram of an ideal software radio architecture is shown in Fig. 5. In this architecture, the only analog RF components are the preselection bandpass RF filter and the low-noise RF amplifier. Then the RF signal is directly digitized using bandpass subsampling, and the rest of the receiver functions are carried out in embedded software modules running on high-speed DSPs. This architecture is still a few years away from commercial implementation because high-speed ADCs that operate with sufficient resolution at the desired RF band are unavailable. Current software radio architectures use at least one IF stage.

4. TRANSCIEVER IMPLEMENTATION

4.1. Transmitter

The design and implementation of transmitters involves the following:

1. Filtering
2. Modulation and frequency upconversion
3. Power amplification

4.1.1. Filtering. In analog radios, analog filters are the only way to achieve frequency selectivity and to limit out-of-band emissions. In digital radios, digital filters in addition to analog filters are used to shape the spectrum of the transmitted signal. Analog filters are discussed in detail later. Some of the popular digital filters used for pulse shaping to achieve a compact modulated spectrum are the raised cosine and Gaussian filters [8]. The advantages of using digital filters are discussed in Section 4.2.7.2.

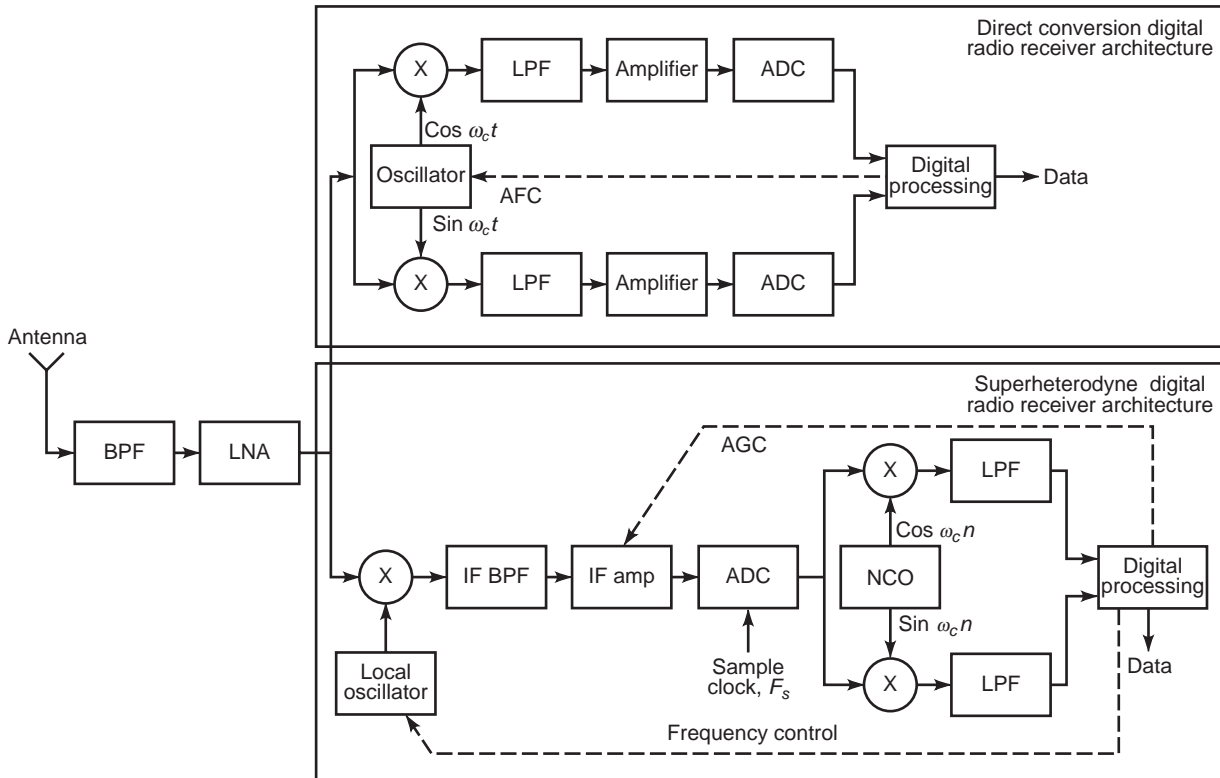


Figure 6. Some digital receiver architectures.

4.1.2. Modulation. Modulation [8] is the process of encoding information from a message source onto a format suitable for transmission. The process involves translating the baseband message signal, called the modulating signal, onto a bandpass signal at a much higher frequency, called the carrier. This process is called modulation. Modulation is usually carried out by varying the amplitude, frequency, phase, or any combinations of these three parameters of a carrier signal. Based on whether the message information signal is analog or digital, modulation is classified as analog or digital modulation.

4.1.2.1. Analog Modulation. In analog modulation, the modulating signal is analog and can assume an infinite number of amplitude values. Analog modulation is broadly classified into two categories, amplitude modulation and angle modulation.

In amplitude modulation (AM), the amplitude of a high-frequency carrier signal is varied in accordance with the instantaneous amplitude of the modulating information signal [3,8]. The amplitude-modulated signal is expressed as

$$S(t) = A_C[1 + m(t)] \cos 2\pi f_C t$$

where A_C is the amplitude of the carrier, f_C is its frequency, $m(t)$ is the modulating information signal, and $S(t)$ is the modulated signal. The spectrum of an AM signal contains a component at the carrier frequency and two sidebands that replicate the original information spectrum.

An AM signal is generated by a nonlinear device, such as a diode or transistor. Many variations of amplitude modulation exist based on what percentage of the sidebands is transmitted. Some of these variations are single-sideband AM (SSB-AM), pilot-tone-sideband AM, and vestigial-sideband AM (VSB-AM).

Angle modulation [3,8] varies the angle of the carrier signal according to the amplitude of the modulating signal. There are two important classes of angle modulation, FM and phase modulation (PM).

In FM, the instantaneous frequency of the carrier is varied with the information signal $m(t)$, as shown by the following equation:

$$S(t) = A_C \cos \left(2\pi f_C t + 2\pi k_f \int_{-\infty}^t m(l) dl \right)$$

where k_f is the frequency deviation constant measured in units of hertz per volt. There are two basic methods for generating an FM signal, the *direct method* and the *indirect method*. In the direct method, voltage-controlled oscillators vary the frequency of the carrier signal directly in accordance with the amplitude of the information signal. Such oscillators commonly use devices, such as varactor diodes, whose reactance can be varied in accordance with the modulating signal's voltage level. The indirect method is based on approximating a narrowband FM signal as the sum of a carrier signal and a single sideband signal where the sideband is 90° out of phase with the carrier.

PM is a form of angle modulation where the phase of the carrier is varied according to the information signal $m(t)$. A PM signal can be generated by first differentiating the information signal $m(t)$ and then outputting it to a frequency modulator.

4.1.2.2. Digital Modulation. Modern communication systems use digital modulation. In digital modulation, the modulating information signal is represented as a time sequence of symbols in which each symbol has m finite states. Each symbol represents n bits of information, where $n = \log_2 m$ bits/symbol. Digital modulation offers many advantages over analog modulation, including greater noise immunity, robustness to channel impairments, and easier multiplexing of various forms of information, such as voice, data, and video. Furthermore, digital transmissions use error-correcting codes and support complex signal conditioning and processing techniques, such as source coding/compression, encryption, and equalization to improve the performance of the communications. Advancements in very large-scale integration and digital signal processing technology have made it possible to implement digital modulators and demodulators easily. The use of embedded software to do most of the signal processing allows alterations without having to replace the hardware.

Some of the widely used digital modulation techniques are m -ary amplitude-shift keying (ASK), m -ary frequency-shift keying (FSK), m -ary phase shift keying (PSK), combined amplitude and phase modulation, combined coding and modulation, and multicarrier modulation.

In ASK, the amplitude of the carrier signal is varied in accordance with the instantaneous amplitude of the modulating information signal, which can take one of several discrete amplitudes. In FSK, the frequency of the carrier signal is varied in accordance with the instantaneous discrete amplitude of the modulating information signal. In PSK, the phase of the carrier signal is varied in accordance with the instantaneous discrete amplitude of the modulating information signal. In a general sense, ASK, FSK, and PSK can be thought of as special cases of AM, FM, and PM, respectively, where the modulating signal is discrete in amplitude. In combined amplitude and phase modulation, both the amplitude and phase of the carrier are varied according to the amplitude of the modulating signal. Ungerboeck [9] realized that error-correction coding and modulation can be combined at a fundamental level to realize performance gains greater than with the conventional method of coding and modulating separately. Combined coding and modulating is more commonly known as *trellis-coded modulation*. The basic concept of multi-carrier modulation is dividing a given RF bandwidth into many narrowband subchannels that are transmitted.

4.1.3. Frequency Upconversion. Frequency conversion is usually achieved by devices called *mixers*. A mixer is a component that acts as a frequency converter by mixing two input signals together to produce a desired signal. A mixer can be implemented by a variety of semiconductor devices, such as diodes (typically Schottky

diodes), bipolar-junction transistors, and field-effect transistors. Mixers are generally of two types, single-balanced and double-balanced. The single-balanced mixer improves port-to-port isolation and reduces the magnitude of some of the spurious signals. It consists of two single-ended mixers interconnected in a configuration that greatly reduces some spurious products. A double-balanced mixer further improves port-to-port isolation and suppresses spurious inter-modulation products even further.

4.1.4. Amplifiers. The triode vacuum tube amplifier was the mainstay for many communication systems before the transistor was invented. Because of transit time limitations, triodes were limited to VHF and UHF. For operation at higher microwave frequencies, the magnetron was invented in the early 1940s. The invention of the transistor was a boon for developing low-cost, reliable, handheld, low-power mobile communication systems. Since then, solid-state amplifiers have replaced vacuum tube amplifiers in almost all communication systems. Systems requiring extremely high power at microwave frequencies, such as deep space and radar systems, continue to use tube amplifiers.

All commercial communication systems use solid-state transistor amplifiers. Solid-state amplifiers come in four main types: discrete, hybrid, integrated (ICs), and application-specific IC (ASIC). A discrete amplifier is one built with discrete transistors and passive components. Hybrid modules, also known as microwave integrated circuits (MICs), have a substrate and discrete devices, including RF matching and bias circuitry. RF ICs, also known as microwave monolithic ICs (MMICs), have all bias and RF matching circuitry on the same substrate, whereas MICs use different materials to achieve optimum matching. The advantage of using a single substrate is that components can be closely matched in value. The difference between an IC and an ASIC is that an IC typically integrates only a few transistors together with transmission line filters and inductors, whereas ASICs, on the other hand, contain several hundred or thousands of transistors.

Several amplifier configurations are based on operating classes A, B, AB, C, D, E, or F. Silicon (Si) bipolar, heterojunction-bipolar, and field-effect transistors (FET) have been used most often to date in RF circuits. Gallium arsenide (GaAs) and complementary metal oxide semiconductor transistors have been gaining interest. GaAs amplifiers offer simple functionality with some biasing and matching components around a chain of transistors. One of the advantages of GaAs versus silicon is that GaAs is an insulator, whereas silicon is a conductor at RF frequencies. As a result, GaAs can integrate several RF components monolithically, facilitating closer components and better matching.

High-power amplification at microwave frequencies, especially those used for satellite communications, are usually handled by traveling-wave tube amplifiers (TWTAs). Other tube amplifiers are the magnetron, coupled-cavity TWT, continuous-wave TWT, helix TWT, klystron, and crossed-field amplifier (CFA).

4.2. Receiver

The main function of the receiver is to pick up the RF energy transmitted at its antenna and efficiently and effectively recover the original information signal transmitted. The design and implementation of receivers involves the following:

1. Antennas
2. Amplification
3. Filtering
4. Downconversion
5. Automatic gain control
6. Demodulation and other associated signal processing functions

Antennas, amplification, analog filtering, and downconversion are common to both analog and digital/software radios. The rest of the receiver functionality depends on its implementation, whether analog or digital. Because these implementations are quite different, they are discussed in different sections with special emphasis on digital implementation.

4.2.1. Antennas. The type of antenna used in a transceiver depends on its application. Handheld or backpacked transceivers require integral antenna structures. Vehicular transceivers must use antennas of limited size and relatively short wavelengths. Antennas that operate at frequencies substantially below their first resonance are called small antennas. Large point-to-point systems use large antennas. Some of the most popular antennas used in commercial communication systems are the vertical whip antenna, the loop antenna, and the dipole array.

4.2.1.1. Whip Antenna. For operating frequencies below the quarter-wave resonance of the antenna, the whip input impedance appears as a small capacitance in series with a resistance. The radiation resistance R_R of a short vertical whip is given by [1]

$$R_R = 40\pi^2 \left(\frac{h}{\lambda}\right)^2$$

where h is the antenna height and λ is the operating wavelength. The whip is also used as a quarter-wavelength monopole antenna for applications, such as cellular and PCS handsets. The whip antenna has an omnidirectional antenna pattern in azimuth.

4.2.1.2. Loop Antennas. Loop antennas have been used in portable broadcast receivers and radio direction finders. When the dimensions of the loop are small compared with the wavelength, the loop is said to be small and its impedance is an inductance in series with a resistance. The radiation resistance R_R for a loop with N turns is given by

$$R_R = 320\pi^4 \left(\frac{AN}{\lambda^2}\right)^2$$

where A is the area of the loop. The loop antenna responds as the cosine of the angle between its face and the arrival direction of the electromagnetic wave. This results in a figure-eight antenna pattern with the null for waves arriving perpendicularly to the loop face.

4.2.2. Amplification. The RF signal picked up by the antenna is very weak and has to be amplified before it can be processed. Typically the very first amplifier used is a specially designed, low-distortion, low-noise amplifier. The operating characteristics of the amplifier are important, as its noise performance dominates the noise figure of the receiver. Both bipolar-junction and FET amplifiers have been used. In recent years, the use of GaAs instead of Si has been gaining interest.

4.2.3. Analog Filters. The selectivity of an analog radio receiver is achieved solely by bandpass and low-pass analog filters. Even in digital and software radio architectures, the analog bandpass filter is an important component and is used both for preselection and antialiasing. Digital radios also use analog filters in their RF front end to implement some selectivity.

The most important characteristics of a filter are its amplitude and phase response. The various characteristics of a filter are interrelated because they are completely determined by the poles and zeros of the transfer function of the filter. Following are some of the common filter families:

1. Butterworth
2. Chebychev
3. Elliptic
4. Equiripple

Analog filters are implemented with a number of different resonators. Following are the available technologies:

1. Inductor–capacitor (LC) resonators
2. Mechanical resonators
3. Quartz crystal resonators

Another important filter implementation is the surface acoustic wave (SAW) filter, of interest because it can be implemented with integrated circuit techniques and can use finite impulse response designs, similar to those for digital filters.

4.2.4. Downconversion. Downconversion is the process of shifting the received RF signal to baseband. Both direct conversion and superheterodyne architectures are used. The basic components of downconversion are mixers, bandpass and low-pass filters, and oscillators.

4.2.5. Automatic Gain Control (AGC). The large dynamic range of signals that must be handled by radio receivers requires gain adjustment to prevent overload or intermodulation of the stages to adjust the demodulator input level for optimum operation. Gain control is generally distributed over several stages throughout the receiver architecture. AGC typically measures the signal level into the

demodulator and tries to keep the level in the desired range by a feedback control loop. The control should be smooth and cause a generally logarithmic variation with the input variable.

4.2.6. Other Analog Radio Receiver Functions. The remaining functionality of the analog radio receiver is demodulation. Double-sideband AM signals are usually detected by an envelope detector. An envelope detector is any rectifier circuit that produces a component at the modulating frequency that is then recovered by a low-pass filter. The rectifier is generally implemented by diodes and by bipolar and field effect transistors. Other AM transmissions, such as SSB-AM and VSB-AM, are demodulated by a coherent demodulator. The coherent demodulator uses a mixer circuit with a local oscillator signal synchronized to the AM input carrier. Carrier synchronization is achieved through a carrier recovery circuit, such as the Costas loop. Common FM demodulators are the slope detector, quadrature detector, phase-locked loop (PLL), demodulator, and zero-crossing detector. The slope detector uses linear circuits to convert the frequency variations to envelope variations that can then be detected by an envelope detector. The quadrature detector consists of a network that shifts the phase of the FM signal by an amount proportional to its instantaneous frequency and uses a phase detector to detect the phase difference between the original FM signal and the signal at the output of the phase shift network. The output of the phase detector is proportional to the instantaneous frequency of the FM signal. In this manner, a frequency-to-amplitude conversion is achieved and the FM signal is demodulated. Phase detectors are generally implemented by diode-based mixer circuits. Because a PM signal can be modeled as an FM signal where the modulating signal has first been differentiated, PM demodulation is achieved by passing the PM signal through an FM demodulator and integrating its output.

4.2.7. Other Digital/Software Radio Receiver Functions. The rest of the digital/software radio receiver can be split into two distinct segments: signal digitization and signal processing.

4.2.7.1. Signal Digitization. Signal digitization, implemented by ADCs, is a two-step process [10], signal sampling followed by quantization. The sampling process is critical in signal digitization. There are two types of sampling, uniform and nonuniform sampling. In uniform sampling, signal samples are taken at uniform intervals, whereas in nonuniform sampling, the samples are non-uniformly spaced. The ADCs in communication systems use uniform sampling, and so the rest of the discussion concentrates on uniform sampling ADCs. The sampling methods for uniform sampling are Nyquist sampling, oversampling, quadrature sampling, and bandpass sampling.

The general sampling theorem for a bandlimited analog signal with no spectral components above f_M Hz

requires that the sampling rate F_S satisfies

$$F_S \geq 2f_M$$

$F_S = 2f_M$ is known as Nyquist sampling, and at this rate, the replicas of the spectrum of the original analog signal do not overlap. Two practical problems develop when implementing Nyquist sampling. The first is defining what a truly bandlimited signal is, and the second is antialiasing filtering before the ADC. In general, an RF signal has components at all frequencies. It is desirable that the distortion of the desired signal be dominated by ADC nonlinearities, not by spectral overlap. This requires that signals higher in frequency than $F_S/2$ be lower in power than the largest spurious response of the ADC. Bandlimiting is usually carried out by the analog antialiasing filter before the ADC. Unfortunately, practical analog filters cannot provide the kind of "brickwall" filter response required. Also, as the steepness of the filter rolloff increases, the phase response of the filter becomes more nonlinear, introducing more distortion.

Sampling the signal at a rate higher than the Nyquist rate is called oversampling. The benefit of oversampling is that the spectral replicas of the original analog signal in the sampled signal spectrum become increasingly separated as the sampling rate is increased beyond the Nyquist rate. Hence, a simpler antialiasing analog filter with a more gradual transition band can be used.

In quadrature sampling, the signal to be digitized is split into two signals. One of the signals is multiplied by a sinusoid to downconvert the signal to a zero-center frequency and then filtered to form the in-phase component of the analog signal. The other signal is multiplied by a 90° phase-shifted version of the sinusoid and filtered to form the quadrature component. Because each of these two signals occupies only one half the bandwidth of the original RF signal, the sampling rate can be reduced by one half at the expense of requiring two ADCs.

Bandpass sampling is based on the bandpass sampling theorem, which states that a bandpass signal with no frequency components below f_L Hz and none above f_H Hz can be determined uniquely by sampling the signal at a rate F_S Hz, where

$$\frac{2f_H}{k} \leq F_S \leq \frac{2f_L}{k-1}$$

where k is restricted to integral values that satisfy

$$2 \leq k \leq \frac{f_H}{f_H - f_L}$$

and

$$(f_H - f_L) \leq f_L$$

Bandpass sampling provides an image of the desired signal at multiples of the sampling frequency, and the spectral replica of the original analog bandpass signal closest to dc is usually chosen for further processing.

Once sampling is over, the sampled analog signal with its infinite range of amplitudes has to be converted to a finite set of discrete amplitudes. This is known as quantization. There are two general quantization methods, uniform and nonuniform quantization. In uniform quantization, the voltage difference between each quantization level is the same. In nonuniform quantization, the quantization levels are nonlinearly spaced in voltage. The ADCs used in RF and IF digitization typically use uniform quantization. In uniform quantization, some error is introduced into the quantized signal because the analog signal cannot be represented exactly by a finite number of discrete amplitude levels. Statistically, it can be assumed that the error signal is uniformly distributed within a quantization level.

4.2.7.2. Signal Processing. Signal processing is the core of the radio receiver and is the segment where the original transmitted information signal is recovered. Many operations are carried out by this system. These operations are quite application specific and may include some or all of the following:

1. Downconversion
2. Filtering, either spatial or temporal or both
3. Equalization
4. Despreading
5. Synchronization
6. Demodulation
7. Automatic gain control
8. Carrier recovery
9. Error-correction decoding
10. Source decoding
11. Decryption
12. Timing recovery

Some of the most important signal processing functions of a receiver are examined here in further detail.

Downconversion. When bandpass subharmonic digitization is used, spectral replicas of the original analog signal are found at multiples of the sampling frequency. However, there is generally no spectral replica centered around the zero-center frequency. To generate the complex baseband signal centered around the zero-center frequency, the output of the ADC is sent to a pair of digital multipliers. The reference inputs for the digital multipliers come from a quadrature-output, numerically controlled oscillator (NCO). The multipliers shift the spectral replica to the zero-center frequency. Then the outputs of the multipliers are sent to low-pass digital filters, which are typically finite impulse response (FIR) filters, to recover the baseband signal and filter out the other mixer products.

Filtering. Digital filters [11] are widely used in communication signal processing for tasks, such as digital downconversion, equalization, interference suppression, and pulse shaping. Following are the advantages of digital filters:

1. Exact linear phase filters can be implemented easily.

2. Filters with almost any desired frequency and phase response can be designed and implemented easily.
3. Changes in filter responses due to component variations caused by aging are eliminated.
4. Changes to the filters can be carried out easily because most of the filtering is implemented in software running on programmable processors.

Digital filters are of two general types, FIR filters and infinite impulse response (IIR) filters. Finite impulse response filters are the most common digital filters in radio receivers mainly because of the following advantages:

1. Filters with exactly linear phases can be easily designed.
2. There are efficient recursive and nonrecursive realizations of FIR filters.
3. FIR filters realized nonrecursively are always stable.
4. Round-off noise inherent in finite precision arithmetic implementations are easily made small for non-recursive realizations.

Following are the disadvantages of FIR filters:

1. A large filter order is required for sharp cutoff filters.
2. The delay of linear phase FIR filters need not always be an integral number of samples.

The main advantage of IIR filters is that sharp cutoff filters can be realized in relatively small filter orders. Following are the main disadvantages:

1. IIR filters generally do not possess linear phases.
2. IIR filters are more prone to be unstable because of quantization and round-off noise.

Carrier Recovery. Coherent demodulation requires that the phase and frequency of the transmitted carrier be known. Carrier recovery is the process of estimating the phase and frequency of the carrier to establish a reference for demodulation at the receiver. Any error in estimating the phase and frequency of the carrier causes significantly degraded performance. The information signal may be modulated onto the RF carrier so that a residual component at the RF exists in the overall transmitted signal spectrum. This residual RF component can be easily tracked by a narrowband PLL and provides the desired reference signal. However, this residual component represents power unavailable to transmit the information. Techniques that conserve power are of interest especially in mobile applications where power is at a premium because batteries supply power to the radio. As such, suppressed carrier transmissions are widely used. Following are some of the popular suppressed carrier recovery techniques:

1. Squaring loop
2. Costas loop
3. Decision feedback loop

Demodulation. The ultimate function of the radio receiver is to recover the original information signal that modulated the transmitted carrier. This process is known as *demodulation*. The portion of the receiver system that implements demodulation is known as the *demodulator*.

Some of the popular FSK demodulators are the limiter-discriminator, the PLL, and noncoherent and coherent demodulators. Noncoherent demodulation is carried out by a bank of bandpass filters whose outputs are envelope-detected. The largest output is selected as the transmitted symbol. The bandpass filters used to detect the tones are implemented either as FIR or IIR filters. Coherent demodulation compares the received signal with all reference frequencies. The comparison is done by multiplying the received signal by all the reference signals and then low-pass filtering the outputs of the bank of multipliers. The largest output is selected as the demodulated symbol. The locally generated reference signals must be synchronized in phase and frequency to the transmitted signal states.

Common PSK demodulators are the coherent demodulator and the differential demodulator. PSK can also be demodulated by using a frequency demodulator, such as a limiter-discriminator or a PLL, and integrating the output before the decision stage. The block diagram of a coherent PSK demodulator is shown in Fig. 7. Differential demodulators determine the cosine and sine of the phase difference and then decide on the phase difference accordingly. Differential demodulation shown in Fig. 7 is implemented by taking the product of the signal and a delayed version of the same signal. The output of the multiplier is low-pass filtered, usually by a FIR filter, to recover the information symbol transmitted. The transmitted symbols need to be encoded differentially to use differential demodulation.

Differential demodulators are often used in highly mobile applications where fading in the channel makes it impossible to get a robust coherent estimate of the transmitted carrier.

Processing Implementation. The processing elements that implement the functions in a radio are crucial, especially in software radio architecture, as they implement virtually all of the functions of the radio transceiver except the frequency conversion and RF amplification. The main attraction of the software radio concept, namely, its flexibility and ease of adaptation, is possible because signal processing is implemented in software modules. The software requires a hardware platform to run on, and the capability of the hardware architecture of the processing platform is critical.

Typically digital signal processing functions are implemented on special digital processors called DSPs [12]. Although DSPs are also microprocessors, there are several crucial differences between general multipurpose microprocessors and DSPs. General microprocessors are typically built for a range of general functions and normally run large blocks of software. The DSP, on the other hand, is built for a small dedicated group of tasks, the most important being the multiply-accumulate arithmetic operation that forms the core of any digital filter. DSPs contain large, high-speed data busses and use direct memory access to transfer large amounts of data, thereby avoiding communication bottlenecks. In addition, DSPs contain dedicated hardware blocks, such as multipliers, to speed up the arithmetic-intensive signal processing steps.

Some of the signal processing functions are so complex that parallel and sequential partitioning of algorithms is required to get the required processing power. DSPs are getting faster but are currently incapable of implementing

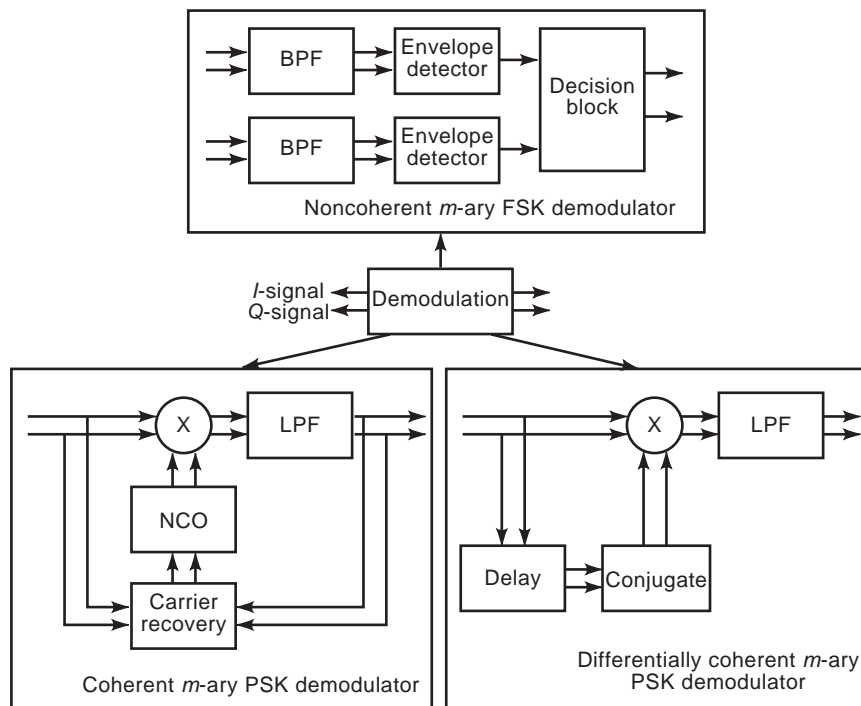


Figure 7. Some general demodulator architectures.

everything possible on a single chip. One approach has been to use multiprocessing to share the computational burden. The traditional approach to multiprocessing has been to integrate various DSPs on a board. Modern DSPs contain various hooks to simplify multiprocessing, such as simplified addressing across processors. A recent approach has been to integrate multiple processors within a single chip. This within-the-chip approach benefits from having closely coupled memory and cache, which improves communication efficiency.

To keep the flexibility of a programmable solution and the efficiency of a dedicated solution, field-programmable gate arrays (FPGAs) are increasingly becoming another viable option to implement highly complex signal processing functions. FPGAs are logic devices whose hardware architecture can be programmed before use. Techniques, such as distributed arithmetic for array multiplication, can increase the data bandwidth and throughput of an FPGA-based solution by orders of magnitude beyond those possible with general-purpose DSPs. It is projected that DSP cores will have onchip FPGA sections to provide configurable accelerators.

5. CONCLUSION

This article has presented an overview of the radio transceiver, its architecture, and the implementation of its most important system blocks. Several other specialized functions are not present in all transceivers and have not been discussed here. Some of these circuits are noise limiting and blanking, squelch, diversity reception, and adaptive antenna array processing.

Traditionally, transceivers have used analog circuits for implementation. The capabilities and advantages of digital processing have allowed replacing many of these analog functions. The movement of the digital portions of the processing closer to the antenna has resulted in the development of software radio architecture. The software radio is a powerful architectural framework that helps to deliver advanced radio services by leveraging the economics of contemporary micro-electronics and software technologies. Although much technological progress has been made in the field of digital processing, technology is not currently available to implement the ideal software radio. Following are some of the challenges and issues that face radio designers today:

1. To engineer low-cost, low-loss, and low-distortion wideband antennas
2. To engineer low-cost, low-loss, and low-distortion wideband RF front ends
3. To develop high-efficiency linear power amplifiers
4. To develop low-power integrated RF front ends
5. To develop low-cost, high-resolution (> 14 bits), and high-speed ADCs
6. To develop low-cost, high-speed reconfigurable digital processors

The development of the software radio transceiver is by no means over. Further technological advances are required,

especially in the hardware implementation of ADCs and reconfigurable processors. There will be further development toward integrating the analog RF front end into a single integrated circuit. The development of low-power RF and digital circuits is another challenge. The ultimate goal of implementing a radio on a chip, although not yet a practical reality, is not far away.

6. ABBREVIATIONS

ADC	= Analog-to-digital converter
AFC	= Automatic frequency control
AGC	= Automatic gain control
AM	= Amplitude modulation
ASIC	= Application-specific integrated circuit
BER	= Bit error rate
BPF	= Bandpass filter
DAC	= Digital-to-analog converter
DSP	= Digital signal processor
FET	= Field-effect transistor
FIR	= Finite impulse response
FM	= Frequency modulation
FPGA	= Field-programmable gate array
FSK	= Frequency-shift keying
GaAs	= Gallium arsenide
Hz	= Hertz
IC	= Integrated circuit
IF	= Intermediate frequency
IIR	= Infinite impulse response
LNA	= Low-noise amplifier
LPF	= Low-pass filter
MDS	= Minimum detectable signal
MIC	= Microwave integrated circuit
MMIC	= Microwave monolithic integrated circuit
NCO	= Numerically controlled oscillator
NF	= Noise figure
PLL	= Phase-locked loop
PM	= Phase modulation
PSK	= Phase-shift keying
RF	= Radiofrequency
SAW	= Surface acoustic wave
TWTA	= Traveling-wave tube amplifier

BIBLIOGRAPHY

1. U. L. Rohde, J. Whitaker, and T. T. Bucher, *Communications Receivers*, 2nd ed., New York: McGraw-Hill, 1996.
2. M. Faulkner and M. A. Briffa, Amplifier linearisation using RF feedback and feedforward techniques, *Proc. Veh. Technol. Conf. (VTC)*, 1995, pp. 525–529.
3. S. Haykin, *An Introduction to Analog and Digital Communications*, New York: Wiley, 1994.
4. H. Meyr, M. Moeneclaey, and S. A. Fechtel, *Digital Communication Receivers-Synchronization, Channel Estimation, and Signal Processing*, New York: Wiley, 1998.
5. J. Mitola, The software radio architecture, *IEEE Commun. Mag.*, **33**:26–38 (1995).

6. J. K. Cavers and S. P. Stapleton, A DSP-based alternative to direct conversion receiver for digital mobile communications, *Proc. Veh. Technol. Conf. (VTC)*, 1990.
7. D. B. Chester and J. Fakatselis, The architecture and benefits of digital IF up conversion implementations, *Proc. Int. Conf. Signal Process. Appl. Technol. (ICSPAT)*, 1995, pp. 356–360.
8. T. S. Rappaport, *Wireless Communications-Principles and Practice*, Upper Saddle River, NJ: Prentice Hall, 1996.
9. G. Ungerboeck, Trellis coded modulation with redundant signal sets, part 1: Introduction, *IEEE Commun. Mag.*, **25**:5–21 (1987).
10. J. A. Wepman, Analog-to-digital converters and their applications in radio receivers, *IEEE Commun. Mag.*, **33**:39–45 (1995).
11. J. G. Proakis and D. G. Manolakis, *Digital Signal Processing*, 2nd ed., New York: Macmillan, 1992.
12. R. Baines, The DSP bottleneck, *IEEE Commun. Mag.*, **33**: 46–54 (1995).

TRANSIENT ANALYSIS

ORLA FEELY
 BRIAN MULKEEN
 University College Dublin
 Dublin, Ireland

1. INTRODUCTION

Transient circuit analysis is used to find transient currents and voltages in a circuit. The word “transient” describes a quantity that is fleeting rather than permanent, and distinguishes this branch of circuit analysis from steady-state analysis, which is concerned with the long-term or settled behavior of a circuit. Transient circuit analysis asks not just “Where will my circuit end up?” but also “How will it get there?” The charging of a capacitor is one of the classic examples, but we might also consider what happens when a short pulse is applied to a transmission line (perhaps an interconnection on a high-speed digital integrated circuit), or when a burst of radiofrequency energy is applied to the antenna in a radar system. In this article, we review the basic principles of transient circuit analysis, which is a long-established branch of circuit theory with a wide range of applications. We will not consider the many techniques that are used in the simulation of transient behavior in circuits—these are an enormous topic in their own right, and are covered elsewhere.

Before proceeding, it should be noted that the circuits to be considered in this article in fact form only a subset of the universe of circuits—they are all linear and time-invariant. A linear circuit is one in which each element (except the sources that drive the circuit) is described by one or more linear equations involving its current(s) and voltage(s). For example, the resistor defined by $v = Ri$ is linear, but the diode defined by $i = I_s(e^{v/V_T} - 1)$ is nonlinear, and any circuit containing the diode is therefore nonlinear. Nonlinear circuits can exhibit highly complex behavior

and cannot be handled by the techniques described in this article. A time-invariant circuit is one in which the equations defining the elements (except the independent sources) do not change with time.

The equations describing a circuit arise from two sources: (1) Kirchhoff’s laws tell us how the elements in the circuit are interconnected, and then (2) each element in the circuit has an individual equation (or equations) describing its behavior. If all of the circuit elements are described by algebraic equations (i.e., ones in which no derivatives appear) involving their currents and voltages, these equations can be combined with Kirchhoff’s equations to give a set of algebraic equations that completely describe the circuit. These equations are linear equations in terms of the currents and/or voltages in the circuit, and can be solved by any of the techniques of linear algebra. The power of linear algebra means that these circuits, known as *resistive circuits*, are (relatively) easy to analyze. The behavior of these circuits is quite simple; if a linear resistive circuit is driven by a 1-V battery, then changing to a 2-V battery will cause all voltages and currents in the circuit to double. There is no time delay in this response—the doubling of voltages and currents occurs at the precise instant when the 2-V battery is inserted into the circuit. If the battery is replaced by a more complicated voltage source that varies with time, each voltage and current in the circuit will also vary with time as a scaled replica of the new voltage source.

Although easy to analyze, the limited behavior of a linear resistive circuit means that such circuits are not hugely useful. Instead of producing a scaled replica of the signal that drives them, most circuits are required to convert a signal into a more useful form. For example, the ignition circuit in a car is “driven” by a battery with almost constant voltage, but its output is a short, sharp spark; the circuits in a radio receiver are “driven” by a jumble of signals from many different sources, but must select the signal of interest and extract some information from it. These effects rely on the use of capacitors and/or inductors. These circuit elements are defined by equations involving not only their currents and voltages but also the rate of change (or derivative) of these quantities with time. Specifically, the current through a capacitor is proportional to the derivative of the capacitor’s voltage with respect to time, and the voltage across an inductor is proportional to the derivative of the inductor’s current with respect to time. Capacitors and inductors are known as *dynamic circuit elements*, conveying the importance to them of time variation, or energy storage elements, since they are capable of storing energy for later release.

Dynamic elements can be placed deliberately in a circuit, or they can be unwanted parasitic elements, modeling, for example, the capacitance between wires in the circuit. If a circuit contains even a single dynamic element, it is in general described no longer by a set of algebraic equations, but by one or more differential equations, in which the variables are not only the voltages and currents but also the derivatives of certain of these quantities with respect to time. A dynamic circuit is one that contains at least one dynamic element.

At higher frequencies, there is an additional complexity to consider in our circuit analysis, namely, the appearance of distributed circuit effects. Distributed circuits, unlike lumped circuits, have voltages and currents that vary not only with time but also with position within the circuit. The basic distributed circuit element is the transmission line, an incremental length of which is commonly modeled by a series resistance and inductance and a shunt capacitance and conductance. The inductance and capacitance in the model give rise to time derivatives in the equations that describe the line, while the distributed nature of the element gives rise to derivatives with respect to position along the line. Thus circuits of this nature are described by differential equations containing derivatives with respect to position as well as derivatives with respect to time. This gives rise to new forms of transient behavior in a circuit.

The goal of transient circuit analysis is to solve the differential equations that describe a dynamic circuit and thus to come up with expressions predicting the way in which the voltages and currents in the circuit will vary with time. It is often concerned in particular with the response of the circuit to changes, such as when a source is inserted, removed, or suddenly changed in some way, or a switch is closed and the makeup of the circuit thereby changed.

Dynamic circuits can exhibit more interesting behavior than resistive circuits, but they are also more difficult to analyze. One of the simplest dynamic circuits contains a single capacitor in series with a resistor and a constant voltage source that is switched on at some specified time. This circuit is described by an equation involving the capacitor voltage v_C and its derivative with respect to time dv_C/dt . The absence of any higher derivatives gives this equation the description “first order.” A circuit containing just a single dynamic element is described by a first-order differential equation and is called a *first-order circuit*.

The solution of a first-order differential equation will contain an unknown constant. To find this constant, it is necessary to apply some additional information about the value of the solution at a specified time instant. Since we are in general concerned with finding the response of the circuit to changes that occur at a certain time instant, we often know the state of the circuit just before the change occurs and can apply this information in order to find the unknown constant. The value of the capacitor voltage (or inductor current, if the circuit contains an inductor rather than a capacitor) just before the change occurs, is known as the *initial condition*.

Solving the first-order circuit just described yields the result shown in Fig. 1. The capacitor voltage plotted as a function of time is of exponential form, moving from its initial value toward the value of the constant voltage source and eventually settling there. (Certain assumptions have been made here, and are discussed in the next section.) This is intuitively plausible—once the voltage source has been inserted, the resistor voltage and capacitor voltage must sum to equal the voltage of the source. If the capacitor voltage does not initially equal that of the source, the voltage difference must be developed across the resistor by a current flowing through it. This current

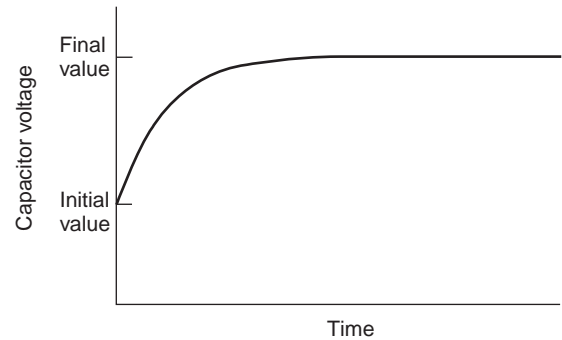


Figure 1. Capacitor voltage in a first-order circuit increasing exponentially from its initial value to its final value.

charges the capacitor, bringing its voltage closer to that of the source, and the net effect is to cause the capacitor voltage to approach that of the voltage source.

Already in this simple circuit we can see how dynamic circuits behave in ways that would be impossible for a resistive circuit. If the circuit described above had been resistive, all voltages and currents would have been scaled versions of the source. In this circuit, however, the capacitor voltage takes on a form quite unlike that of the source—it varies exponentially with time, whereas the source is constant. The action of the resistor and capacitor has processed the source signal, with the capacitor voltage resisting the sudden change when the source was inserted, but retaining the steady behavior of the source. The resistor voltage, on the other hand, captures the change in the source very well, but eventually dies away to include nothing of the steady behavior of the input. This behavior is an example of the filtering behavior of this simple resistor–capacitor combination, which is useful in a variety of communications applications.

The exponential nature of the voltage observed in this simple circuit is not unusual—in fact, as we shall see, exponential functions appear in various guises in the solution to linear differential equations. Possibly the most widely known example of an exponential function appears in the analysis of radioactive decay, where the rate of decay of a substance is proportional to the amount of the substance present, and so the amount remaining decays exponentially to zero at a rate depending on the half-life of the substance.

A circuit that contains two dynamic elements in general gives rise to a second-order differential equation (containing the second derivative of the variable with respect to time) and is termed a *second-order circuit*. If all sources in the circuit are DC (constant) sources, this equation can be solved by application of standard theory of linear differential equations, with the aid of two initial conditions, one for each dynamic element. Instead of the single exponential transient of the first-order circuit, this circuit contains two exponential transients that are added to give the overall transient. The relationship (via complex numbers) between the exponential and sinusoidal functions can give rise to new types of behavior arising from these transients, as shown in Fig. 2. If the arguments of these exponentials are complex, as may turn out to be the case, then they can

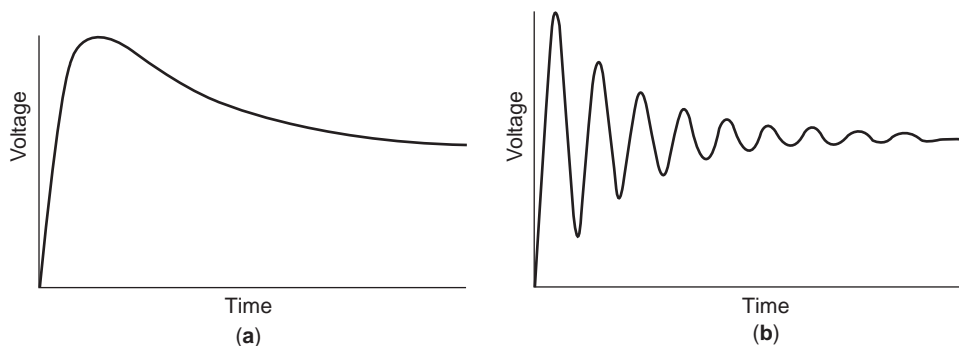


Figure 2. Two possible responses of a second-order circuit, made up of the sum of two exponentials.

be added to give a transient that oscillates sinusoidally. In most circuits the magnitude of this oscillation decays exponentially with time. A common example of such a decaying oscillation is produced when a tuning fork is struck or a child's swing given a single push. If there are no losses in the circuit (not a practical requirement), the oscillation could persist indefinitely without decaying, and if the circuit is unstable, it is possible that the oscillation can actually grow.

In a radiofrequency system, a circuit would normally be “driven” by a more complicated signal, but the same basic principles apply. We can consider a simple example, where a short burst of a sinusoidal signal is applied to a second-order system. Such a signal might arise in a radar system or in a digital communication system. The resulting transient, shown in Fig. 3, is essentially sinusoidal in form, but its amplitude changes with time in a way that is similar to the transients shown earlier, first increasing in response to the start of the burst of sinusoidal signal, eventually settling to a steady amplitude, and then decaying exponentially following the end of the burst.

While it is possible to analyze simple first- and second-order dynamic circuits by applying standard theory of differential equations, such solution becomes rapidly more difficult when the order of the circuit increases or when the sources become more complicated. When faced with

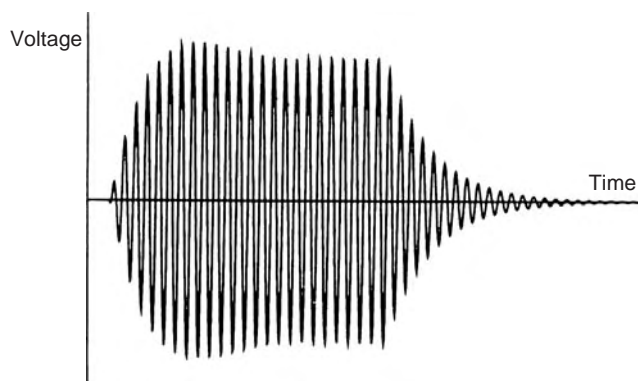


Figure 3. Example transient response of a second-order circuit in response to a short burst of a sinusoidal signal.

such a problem, one might look enviously back at the much simpler process of solving a resistive circuit. In fact, it is possible to apply techniques of resistive circuit analysis to dynamic circuits with the aid of a variety of transforms. A *transform* is a method of changing a problem into a different form, solving it in the new form (where the solution is easier to obtain) and then changing the solution back to the original form. For example, a student unfamiliar with binary arithmetic, when asked to add two binary numbers, might convert the numbers to decimal form (presumably with the aid of a table), add the decimal numbers, and then convert back to binary. The transforms to be applied in this context change a system of differential equations to a system of algebraic equations that are significantly easier to solve.

The most important and most widely used of these transforms in circuit analysis is the Laplace transform. A second transform, the Fourier transform, is particularly useful in analyzing circuits designed for applications in communication systems. These transforms convert a set of differential equations involving the time variable into a set of algebraic equations involving a new variable called the *frequency* (in the case of the Fourier transform) or the *complex frequency* (in the case of the Laplace transform). Application of these transforms allows us to analyze a circuit by transforming it into an equivalent form in the frequency domain, where its equations are purely algebraic, analyzing the circuit in this frequency domain using the techniques of linear algebra, and then applying the transform in reverse to convert the result of this analysis into a function of time. We will see how the Laplace transform can be applied to distributed circuits as well as lumped circuits.

Once again, Laplace transform analysis shows up the special role of the exponential function (and its complex cousin, the sinusoid) in the behavior of circuits. Every dynamic circuit favors certain exponential (including sinusoidal) modes of behavior whose rate of decay (and frequency of oscillation, if applicable) is governed by the so-called natural frequencies of the circuit. These natural frequencies tell us whether the currents and voltages in a circuit will, of their own accord, tend to exhibit exponential or oscillatory decay, constant behavior or steady oscillation, exponential or oscillatory growth, or some

combination thereof. When an input signal is applied to the circuit, the currents and voltages may contain components controlled by the natural frequencies as well as a component controlled by the input. In many practical circuits it is desirable for the output to depend on the input, and the prospect of a growing oscillation in the circuit is a designer's nightmare. (This effect is similar to that demonstrated by sound systems when a microphone is placed in the path of a loudspeaker and an unwanted tone appears and swamps the desired signal.) In other cases, a sustained oscillation is the objective, and the designer's aim is to fix the frequency and amplitude of this oscillation. The issue here is one of *stability*. An asymptotically stable system is one in which all exponential transients die away, leaving only the effect of the input signal. Laplace transform techniques allow us to analyze a system to determine whether it is asymptotically stable, or whether a sustained oscillation is possible.

The effects of transients are seen in a huge range of electronic and electrical engineering applications, from the transmission of tiny pulses between parts of a communication system to the behavior of an electrical power system struck by lightning. The techniques described in this article provide the reader with the ability to understand and analyze transient behavior in a wide variety of circuits.

2. TIME-DOMAIN ANALYSIS

2.1. Natural Response and Step Response of a First-Order Circuit

Consider the circuit shown in Fig. 4a. Until the time $t = 0$, the switch S is in position 1, and the resistor R and capacitor C are connected in a loop. At time $t = 0$ the switch is moved to position 2, connecting the DC voltage source E in series with R and C . We assume that the switch closes instantaneously and that it presents a short circuit between the terminals that it connects. Mathematically, we say that the voltage applied to the RC series combination is $EU(t)$, where $U(t)$ is the unit step function given by

$$U(t) = \begin{cases} 0 & \text{for } t < 0 \\ 1 & \text{for } t \geq 0 \end{cases} \quad (1)$$

The circuit of Fig. 4a can, therefore, also be drawn in the form shown in Fig. 4b.

The analysis of the circuit for $t \geq 0$ in Fig. 4 will require knowledge of the initial voltage across the capacitor just after the switch is thrown, $v_C(0^+)$, where $0^+ = \lim_{\epsilon \rightarrow 0} \epsilon$.

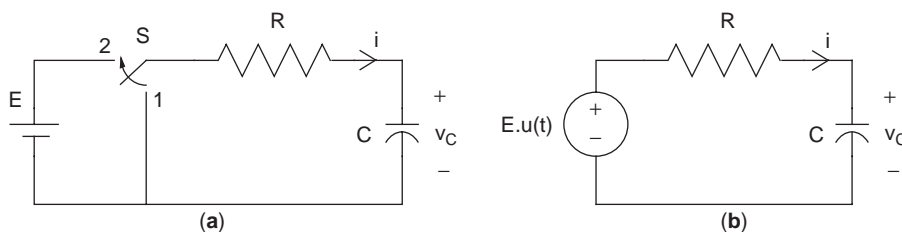


Figure 4. (a) The switch S moves from position 1 to position 2 at time $t = 0$, so the voltage applied to the RC series combination is 0 for $t < 0$ and E thereafter. The switch/voltage source combination is represented in (b) by the single voltage source $EU(t)$.

We generally know, or can find from analysis of a previous regime, $v_C(0^-)$, the voltage at the instant just before the switch is thrown: ($0^- = \lim_{\epsilon \rightarrow 0} -\epsilon$). If the capacitor current is finite, $v_C(0^+)$ must equal $v_C(0^-)$, and we can refer to both as $v_C(0)$. Similarly, if the voltage across an inductor is finite, its current waveform must be continuous. We will assume these continuity conditions throughout this analysis. The alternative case, where the capacitor current or inductor voltage can be infinite, is not practical but turns out to be mathematically interesting and useful in analysis. It can be handled by an extension of our analysis in this section (see Ref. 1 for details), but we will postpone consideration of this possibility until Section 3, where it can be handled more conveniently.

For $t \geq 0$, Kirchhoff's voltage law gives the equation

$$v_C(t) + i(t)R = E$$

or, applying the constitutive relation $i(t) = C \frac{dv_C(t)}{dt}$ for the capacitor

$$RC \frac{dv_C(t)}{dt} + v_C(t) = E \quad (2)$$

This is a first-order differential equation in the capacitor voltage v_C , and so this circuit is referred to as a *first-order circuit*. It can be solved by a number of methods to give an expression for v_C as a function of time. One such method is to recast the equation in the form

$$\frac{d(v_C(t) - E)}{dt} = -\frac{1}{RC}(v_C(t) - E)$$

This equation is of the familiar form

$$\frac{dx(t)}{dt} = ax(t)$$

which has the solution [2]

$$x(t) = x(0)e^{at}$$

where $x(0)$ is the value of x at time $t = 0$. This initial condition must be known if the equation is to be solved for $x(t)$. Thus Eq. (2) has the solution

$$v_C(t) - E = (v_C(0) - E)e^{-t/RC} \quad (3a)$$

or

$$v_C(t) = v_C(0)e^{-t/RC} + E(1 - e^{-t/RC}) \quad (3b)$$

The response of the series RC circuit with zero initial capacitor voltage to the application of a voltage source given

by the unit step function is known as the *step response* of the series RC circuit. (Note that we will use the word “response” to signify any current or voltage in the circuit, or any set thereof, including, for example, the set of all currents and voltages. Throughout this article the variables that constitute the response in any given instance will be clear from the context in which the term is used.)

It is clear from Eq. (3a) that the difference between v_C and E varies exponentially with time, and when the product RC is positive (a condition that will be assumed to hold unless otherwise stated), this difference tends to zero as t tends to infinity. v_C is plotted as a function of time in Fig. 5, where, as expected, v_C is seen to converge exponentially to E . The rate of this convergence is governed by the value of RC , which is termed the time constant of the waveform and denoted by the symbol τ . The smaller the time constant, the faster the rate of convergence. After one time constant has elapsed (i.e., at $t = \tau$), $v_C(t) - E$ has decreased to $e^{-1} = 36.8\%$ of its value at $t = 0$, and at time $t = 5\tau$ this difference has decreased to $e^{-5} = 0.7\%$ of its initial value. Although v_C does not reach E within any finite time (unless, of course, it started out at E), after five time constants have elapsed, the difference between v_C and E has been reduced to less than 1% of its initial value. The time constant is a useful measure of the response speed of a first-order circuit. For more general circuits, the risetime is used as a measure of response time. This is defined as the time taken for the step response to rise from 10% to 90% of the steady-state value. For the first-order circuit analysed in this section, the risetime can be found to be $\tau \ln 9 \approx 2.2\tau$.

The value E to which the capacitor voltage converges is termed the *steady-state value* of this voltage. It is the only value of capacitor voltage at which the circuit can settle, or in other words it is only when $v_C = E$ that all currents and voltages in the circuit cease to vary with time. Clearly, when a quantity ceases to vary with time, its derivative with respect to time is zero, and so the steady-state value of v_C can be found directly from the differential equation (2) by setting the term dv_C/dt to zero (or, in circuit terms, replacing the capacitor by an open circuit), yielding the

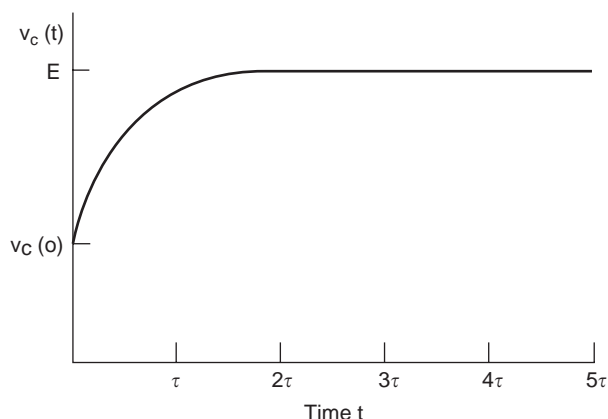


Figure 5. The capacitor voltage in the circuit of Figure 1 varies exponentially from its starting value $v_C(0)$ to its steady-state value E , with time constant $\tau = RC$.

equation $v_C = E$, as expected. The overall waveform $v_C(t)$ is the sum of this steady-state component and a second component that dies away with time. This second component is known as the transient component (or just the transient). The exponential form of the transient in this circuit is, as we will see later, particularly common in linear circuits and other linear systems.

Note, however, that the procedure just outlined yields the value of v_C at which the circuit variables (currents and voltages) can remain constant, but it does not guarantee that the circuit will actually converge to this state. For example, if $RC < 0$, Eq. (3a) implies that v_C will diverge exponentially away from E and the circuit has no steady-state response. [The only exception to this divergence is when $v_C(0) = E$, in which case it will theoretically remain fixed at E for all time. The word “theoretically” is important—in practice, any noise in the circuit that causes v_C to differ even infinitesimally from E will result in its diverging exponentially from E .] This distinction relates to the issue of the stability of equilibria of differential equations [2].

Another useful view of the solution waveform (3b) for $v_C(t)$ is that it is composed of two components: one caused by the initial condition $v_C(0)$, and the other caused by the voltage source E . If $E = 0$, the response (3) reduces to $v_C(t) = v_C(0)e^{-t/RC}$, which is termed the “natural” or “unforced” response of the circuit. This is a viewpoint to which we will return later.

Any circuit consisting of a single capacitor in an otherwise resistive circuit containing only DC sources is generally analyzed by transforming it to single-loop form by means of a Thévenin transformation [3], as shown in Fig. 6. The analysis described above is then applicable, where E is the Thévenin equivalent voltage source, and R the Thévenin equivalent resistance. (The small number of circuits that do not have a Thévenin equivalent can be handled separately.)

Before leaving the single-loop first-order circuit of Fig. 4, we note that the analysis of this section can be used to find the response of a first-order circuit to a voltage source that is piecewise-constant, that is, constant over certain time intervals with discontinuous jumps between these constant levels. One important such waveform is the pulse

$$p(t) = \begin{cases} 0 & \text{for } t < 0 \\ E & \text{for } 0 \leq t < t_0 \\ 0 & \text{for } t \geq t_0 \end{cases}$$

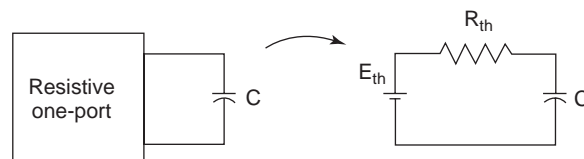


Figure 6. A circuit consisting of a single capacitor in an otherwise resistive circuit is simplified by replacing the resistive one-port seen by the capacitor by its Thévenin equivalent.

The response of the first-order RC circuit to this source waveform is found by an extension of the analysis just performed. For $0 \leq t < t_0$, the analysis proceeds as before and $v_C(t)$ is given by Eq. (3b):

$$v_C(t) = v_C(0)e^{-t/RC} + E(1 - e^{-t/RC}) \text{ for } 0 \leq t < t_0 \quad (3c)$$

For $t \geq t_0$, the response is just the natural response found previously; the only difference is that since this phase of the analysis commences at $t = t_0$ instead of $t = 0$, the initial condition is $v_C(t_0)$ instead of $v_C(0)$. Applying this initial condition in the usual way, we find that

$$v_C(t) = v_C(t_0)e^{-(t-t_0)/RC} \text{ for } t \geq t_0 \quad (4)$$

$v_C(t_0)$ is, by our assumption of bounded currents, equal to $v_C(t_0^-)$, the capacitor voltage just before the source waveform drops to zero. Since Eq. (3c) gives $v_C(t)$ for all times in the range $0 \leq t < t_0$, it can be used to find that

$$v_C(t_0^-) = v_C(0)e^{-t_0/RC} + E(1 - e^{-t_0/RC})$$

Substituting this value for $v_C(t_0)$ in (4) completes the analysis of the response of the series RC circuit to the voltage pulse. This response is plotted in Fig. 7 for two different values of the time constant. The response of a circuit to a pulse is particularly important in communication systems where such pulses are used to carry information and must be clearly identifiable at the receiver. An RC combination of the type studied here often occurs in such transmission systems, formed by the output resistance of the part of the system where the signal originates and the input capacitance of the part of the system into which the signal is fed, and thus exponential distortion will inevitably ensue. Clearly the “smearing” of the pulse evident in Fig. 7 when the time constant is large limits the rate at which pulses can be transmitted if they are to be separated at the receiver.

The response of the series RC circuit to any piecewise-constant source waveform is found by an extension of the

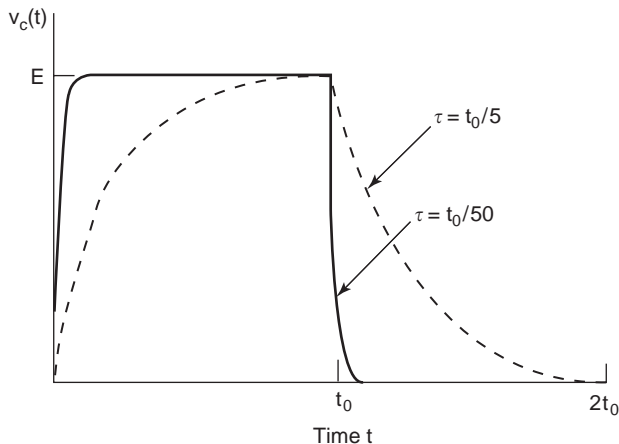


Figure 7. The response of a first-order RC circuit to a voltage pulse of amplitude E and duration t_0 . The solid line shows the response if $\tau = t_0/50$; the dashed line, the response if $\tau = t_0/5$.

analysis performed above. The circuit is analysed using the standard method over each of the time intervals in which the source is constant, starting with the first time interval. The initial condition for the n th time interval, commencing at time $t = t_n$, is found by evaluating the response from the previous time interval at time $t = t_n^-$.

The second type of first-order circuit is one in which the single energy storage element in the circuit is an inductor rather than a capacitor, and by application of a Norton transformation (where possible) is of the form shown in Fig. 8, where the constant current source I is connected in parallel with conductance G and inductance L for $t \geq 0$. Kirchhoff’s current law applied to this circuit gives the following differential equation in the inductor current i_L for $t \geq 0$

$$GL \frac{di_L(t)}{dt} + i_L(t) = I$$

which can be solved as before to find

$$i_L(t) - I = (i_L(0) - I)e^{-t/GL}$$

or

$$i_L(t) = i_L(0)e^{-t/GL} + I(1 - e^{-t/GL})$$

Thus the inductor current waveform for the circuit of Fig. 8 takes the same form as the capacitor voltage waveform for the circuit of Fig. 4b, with time constant GL and steady-state value I . This is a consequence of the fact that the circuit of Fig. 8 is the dual of that of Fig. 4b. The response to a piecewise-constant source waveform can be found by applying the method previously described for the series RC circuit.

2.2. Natural Response of Second-Order Circuits

The circuit in Fig. 9 consists of a resistor and two energy storage elements—a capacitor and an inductor. Kirchhoff’s voltage law gives the equation

$$v_C(t) + L \frac{di_L(t)}{dt} + Ri_L(t) = 0$$

which on application of the relation $i_L(t) = C[dv_C(t)/dt]$ becomes

$$LC \frac{d^2v_C(t)}{dt^2} + RC \frac{dv_C(t)}{dt} + v_C(t) = 0 \quad (5)$$

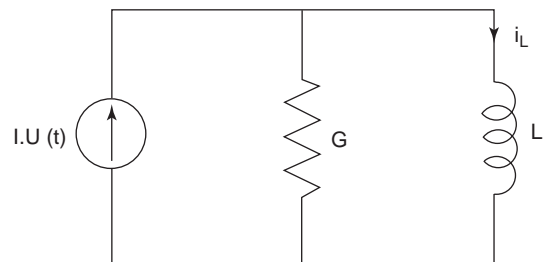


Figure 8. First-order circuit consisting of the parallel combination of current source $IU(t)$, conductance G , and inductor L .

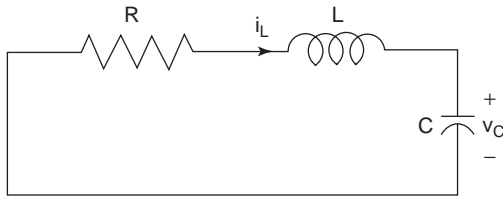


Figure 9. Second-order circuit consisting of resistor R , capacitor C and inductor L .

This is a second-order differential equation, and so the circuit is termed a *second-order circuit*. The exponential waveform

$$v_C(t) = Ae^{st}$$

is a solution to Eq. (5) provided

$$LCs^2 + RCs + 1 = 0$$

which yields

$$s = \frac{-R}{2L} \pm \sqrt{\frac{R^2}{4L^2} - \frac{1}{LC}}$$

If these two values, s_1 and s_2 , are distinct (i.e. $s_1 \neq s_2$), then the general solution of Eq. (5) is of the form

$$v_C(t) = A_1 e^{s_1 t} + A_2 e^{s_2 t} \quad (6)$$

Since there are no sources in the circuit, this is the natural or unforced response of the series RLC circuit. The constants A_1 and A_2 will be determined by applying the initial conditions $v_C(0)$ and $i_L(0)$ and solving the resulting simultaneous equations:

$$v_C(0) = A_1 + A_2$$

$$i_L(0) = C \left. \frac{dv_C}{dt} \right|_{t=0} = CA_1 s_1 + CA_2 s_2$$

We will now consider the nature of the natural or unforced voltage waveform represented by Eq. (6). We will use the following shorthand form for s_1 and s_2

$$s_1 = -\alpha + \sqrt{\alpha^2 - \omega_0^2} \quad \text{and} \quad s_2 = -\alpha - \sqrt{\alpha^2 - \omega_0^2}$$

where

$$\alpha = \frac{R}{2L} \quad \text{and} \quad \omega_0 = \frac{1}{\sqrt{LC}}$$

We will assume for now that $\alpha \geq 0$.

The first case to be considered is the case where $\omega_0^2 < \alpha^2$ and s_1 and s_2 are real and distinct. In this case the circuit is said to be overdamped and the response $v_C(t)$ is the sum of two exponentials with time constants $1/|s_1|$ and $1/|s_2|$.

An example of an overdamped response is plotted in Fig. 10a.

The second case occurs when $\omega_0^2 > \alpha^2$ and s_1 and s_2 are complex conjugates of the form $-\alpha \pm j\omega_d$, where $\omega_d = \sqrt{\omega_0^2 - \alpha^2}$. In this case the circuit is said to be underdamped. Equation (6) remains valid but can be expressed more clearly in the form

$$v_C(t) = e^{-\alpha t} [(A_1 + A_2) \cos \omega_d t + j(A_1 - A_2) \sin \omega_d t]$$

where A_1 and A_2 are complex conjugates, and so the coefficients $B_1 = (A_1 + A_2)$ and $B_2 = j(A_1 - A_2)$ are real and can once again be found from the initial conditions. The underdamped response takes the form of an oscillation of frequency ω_d multiplied by an exponential envelope $e^{-\alpha t}$. If $\alpha > 0$, the amplitude of the oscillation decreases exponentially with time, with the rate of this decrease, known as “damping”, controlled by α . If $\alpha = 0$, the response is an oscillation of constant amplitude and frequency $\omega_d = \omega_0 = 1/\sqrt{LC}$. This is the case of the well-known LC oscillator, which arises when $R = 0$ and there is no dissipation in the circuit. The underdamped response is plotted in Figs. 10b and 10c for the two cases $\alpha > 0$ and $\alpha = 0$. Note that the underdamped response is always characterized by oscillation, sometimes termed “ringing”.

If $\omega_0^2 = \alpha^2$, then $s_1 = s_2 = -\alpha = -R/2L$. In this case the general solution of Eq. (5) is no longer given by Eq. (6) but instead by [2]

$$v_C(t) = (D_1 + D_2 t) e^{-\alpha t}$$

and is said to be “critically damped”. The constants D_1 and D_2 are once again found by application of the initial conditions. An example of a critically damped response is plotted in Figure 10d.

2.3. Step Response of Second-Order Circuit

The circuit in Fig. 11 is identical to that of Fig. 9 but for the addition of the voltage source E at $t = 0$. Applying Kirchhoff’s voltage law for $t \geq 0$ gives the equation

$$v_C(t) + L \frac{di_L(t)}{dt} + Ri_L(t) = E$$

which on application of the relation $i_L(t) = C[dv_C(t)/dt]$ becomes

$$LC \frac{d^2 v_C(t)}{dt^2} + RC \frac{dv_C(t)}{dt} + v_C(t) = E \quad (7)$$

To solve this equation, we apply the fact that the general solution to a differential equation is the sum of two components, which are known in mathematics as the “homogeneous solution” and a “particular solution” [2]. The homogeneous solution is the solution to the differential equation obtained when all input terms (i.e., all terms not involving the variable or its derivatives) are set to zero. In circuit terms, this is just the response obtained when all independent voltage and current sources are removed, namely, the natural or unforced response. A particular

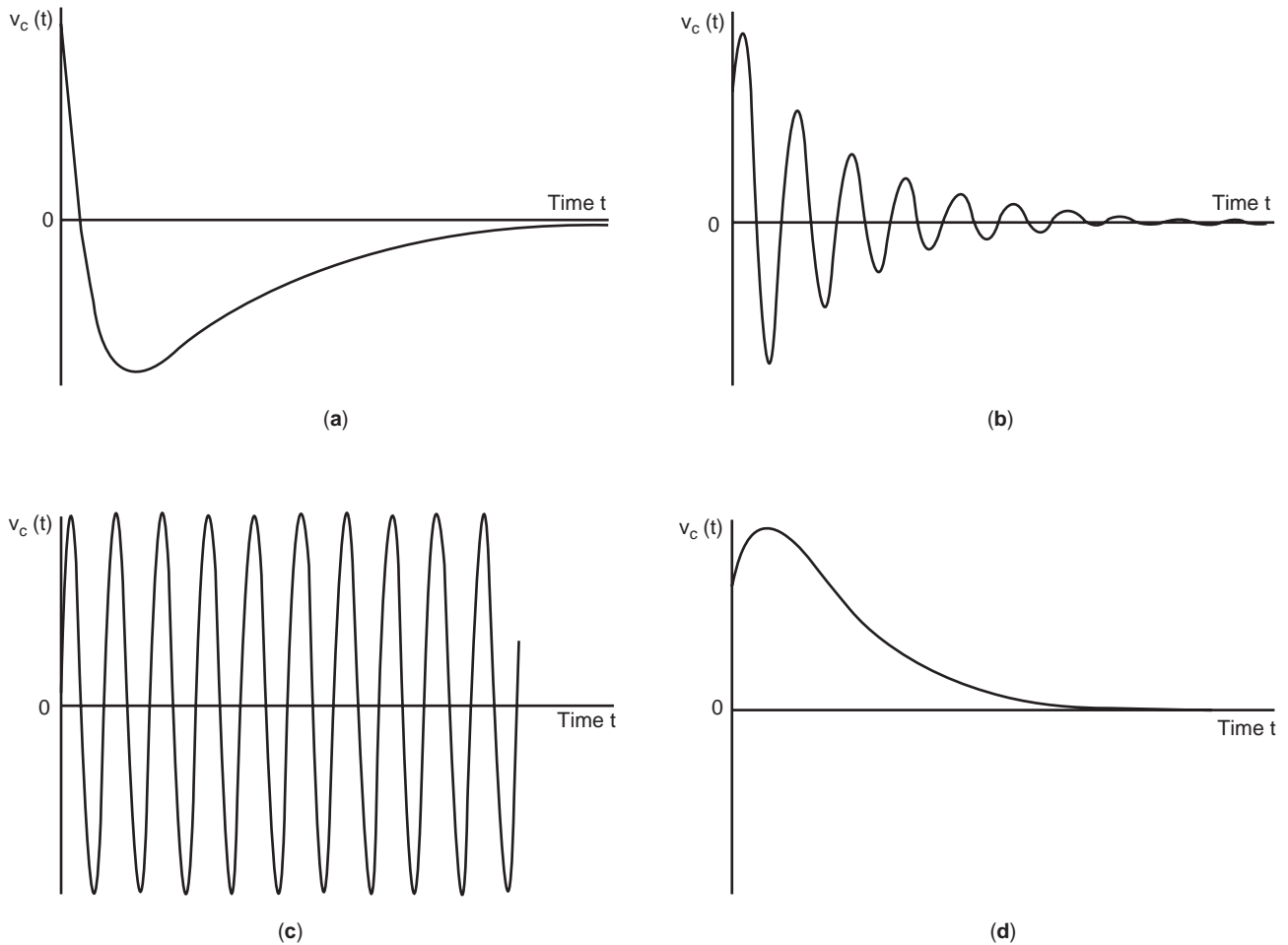


Figure 10. Examples of the natural response of the series *RLC* circuit: (a) overdamped; (b) underdamped; (c) underdamped and lossless; (d) critically damped.

solution is any solution to the differential equation. This decomposition may seem to be of no particular benefit, since it states that to solve the differential equation, one must obtain a solution to the differential equation. The benefit lies in the ability to choose a particularly simple form for the particular solution, which can then be extended to yield the general solution by the addition of the homogeneous solution. The simplest particular solution is the constant solution, which is obtained by setting all derivatives to zero.

The particular solution to Eq. (7) obtained by setting all derivatives to zero is $v_C(t) = E$. Adding this solution to the homogeneous solution that has already been found in Eq. (6) yields the general solution, which is of the form

$$v_C(t) = A_1 e^{s_1 t} + A_2 e^{s_2 t} + E \text{ if } \omega_0^2 < \alpha^2 \text{ (overdamped)} \quad (8a)$$

$$v_C(t) = e^{-\alpha t} [B_1 \cos \omega_d t + B_2 \sin \omega_d t] + E \text{ if } \omega_0^2 > \alpha^2 \quad (8b)$$

(underdamped)

$$v_C(t) = (D_1 + D_2 t) e^{-\alpha t} + E \text{ if } \omega_0^2 = \alpha^2 \text{ (critically damped)} \quad (8c)$$

The appropriate constants A_1 and A_2 , B_1 and B_2 , or D_1 and D_2 are found by applying the initial conditions. If the initial conditions are zero, Eqs. (8) represent the step response of the series *RLC* circuit, and are plotted in Fig. 12.

Depending on the system in which a circuit is to be used, different demands may be made of its step response. In some applications, for example, there may be a requirement that the voltage reach its steady-state value as soon as possible, while in others it may be necessary that the

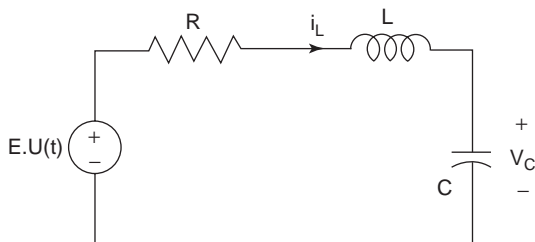


Figure 11. Second-order circuit consisting of resistor *R*, capacitor *C*, inductor *L*, and voltage source $EU(t)$.

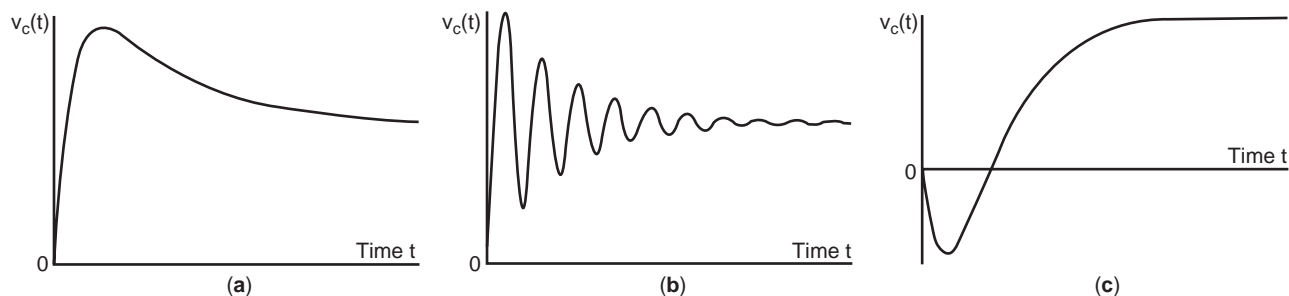


Figure 12. Examples of the step response of the series RLC circuit: (a) overdamped; (b) underdamped; (c) critically damped.

voltage never exceed its steady-state value by more than some specified percentage, to avoid driving circuit elements into saturation. A number of figures of merit have been defined to characterize the step response of a circuit in order to test its suitability for a given application [1]. The risetime has already been defined. The *settling time* is the time beyond which the step response does not differ from its steady-state value by more than 2%. The *delay time* is the time taken for the step response to reach 50% of its steady-state value. The *overshoot* is defined as the difference between the peak value and the steady-state value of the step response, expressed as a percentage of the steady state value.

3. LAPLACE TRANSFORM CIRCUIT ANALYSIS

The analyses described above have found the circuit variables as a function of time by directly solving the differential equations that describe the circuit. While such a procedure is reasonably straightforward for first- and second-order circuits with simple source waveforms, it becomes significantly more difficult as the order of the circuit increases and as the source waveforms become more complex. It is desirable, therefore, to have a more powerful method of finding a solution. In the special case where all sources in the circuit are sinusoidal of the same frequency, the transformation of circuit variables into phasor or complex number form [3–5] allows the circuit to be handled using purely algebraic equations instead of differential equations. Although extremely useful in certain circumstances, this is not a general circuit analysis method: it can handle only sinusoidal sources, it is applicable only if the circuit is stable, it finds only the steady-state component of the waveform and does not allow consideration of initial capacitor voltages and inductor currents.

3.1. The Laplace Transform

A more general transform than the phasor transform is the Laplace transform, named after the French mathematician Pierre-Simon Laplace (1749–1827) [3–6]. This transform method retains the fundamental advantage of the phasor transform, which is the ability to transform a system of differential equations into a system of algebraic equations, but has the additional advantages of being able to handle a much broader class of source waveforms

(including all that are of any practical interest), accommodating initial conditions, and yielding solutions that incorporate both transient and steady-state components without requiring that the circuit be stable.

The Laplace transform is discussed in the article on linear systems, and we will merely summarize its properties here. Given a function of time $f(t)$, its Laplace transform is

$$F(s) = \mathbf{L}\{f(t)\} = \int_{0^-}^{\infty} f(t)e^{-st} dt \quad (9)$$

where the variable s is complex and is termed the (*complex*) *frequency*. Thus the Laplace transform converts a function $f(t)$ from the time domain into a function $F(s)$ in the frequency domain. There exist functions that do not have a Laplace transform, since the integral in (9) fails to converge, but all functions of interest in circuit theory have a Laplace transform. Since the interval of integration is from 0^- to ∞ , the transform defined by Eq. (9) is sometimes called the “one-sided Laplace transform”, to distinguish it from another version in which the integration is from $-\infty$ to ∞ , but we will not need to draw this distinction here and will refer to it simply as the *Laplace transform*. The lower limit of integration of 0^- is chosen in order to accommodate functions with infinite spikes at $t=0$. Such functions will prove extremely useful in our analysis.

Some of the properties of the Laplace transform that make it so useful in circuit analysis are the following [3,6], where $F(s)$ denotes the Laplace transform of $f(t)$, $F_1(s)$ the Laplace transform of $f_1(t)$ and $F_2(s)$ the Laplace transform of $f_2(t)$:

Uniqueness: $f_1(t) = f_2(t)$ for all $t \geq 0 \Leftrightarrow F_1(s) = F_2(s)$ (More precisely, if $F_1(s) = F_2(s)$ then $\int_{0^-}^{\infty} |f_1(t) - f_2(t)| dt = 0$, but for our purposes it will suffice to assume that $F_1(s) = F_2(s) \Rightarrow f_1(t) = f_2(t)$ for all $t \geq 0$)

Linearity: $\mathbf{L}\{k_1 f_1(t) + k_2 f_2(t)\} = k_1 F_1(s) + k_2 F_2(s)$, where k_1 and k_2 are scalars.

Differentiation: $\mathbf{L}\{(d/dt)f(t)\} = sF(s) - f(0^-)$.

Integration: $\mathbf{L}\left\{\int_{0^-}^t f(\tau) d\tau\right\} = (1/s)F(s)$.

Time shift: $\mathbf{L}\{f(t - \tau)U(t - \tau)\} = e^{-s\tau}F(s)$, where $\tau > 0$ and $U(t)$ is the unit step function given by Eq. (1).

Frequency shift: $\mathbf{L}\{e^{-\alpha t}f(t)\} = F(s + \alpha)$.

The first three of these properties are particularly important. The uniqueness property guarantees that if a system of differential equations is solved by transforming to the frequency domain, solving in the frequency domain and transforming back to the time domain, the solution obtained will be the same as would have been obtained if the solution had been carried out entirely in the time domain. The linearity property guarantees that a system of linear equations in the time domain will remain linear in the frequency domain, allowing powerful linear analysis techniques to be applied in both domains. The differentiation property allows differentiation in the time domain to be replaced by multiplication in the frequency domain, together with the addition of a term related to the initial condition. It is this property that allows a system of differential equations in the time domain to be replaced by a system of algebraic equations in the frequency domain, which can be solved by a variety of powerful and elegant techniques. The Laplace transforms of some important functions are given in Table 1, in which $\delta(t)$ is the delta function defined by

$$\begin{aligned} \delta(t) &= 0 \text{ for } t \neq 0 \\ \int_{-\infty}^{\infty} \delta(t) dt &= 1 \end{aligned} \tag{10}$$

Three steps are to be taken in solving a set of differential equations using Laplace transform analysis: (1) the system of differential equations in the time domain is transformed to a set of algebraic equations in the frequency domain; (2) this set of algebraic equations is solved in the frequency domain, using standard linear techniques; and (3) the solution is transformed from the frequency domain back to the time domain. Step (1) involves application of the definition of the Laplace transform (9) together with certain of its properties (notably the differentiation property). Step (2) involves standard techniques from linear algebra. The third step involves the application of the inverse Laplace transform, which converts a function $F(s)$ in the frequency domain to a function of time $f(t) = \mathbf{L}^{-1}(F(s))$ in such a way that $\mathbf{L}(f(t)) = F(s)$. Note that the function $f(t)$ is unique only for $t \geq 0$, since two functions of time that

differ for $t < 0$ but are identical for $t \geq 0$ will have the same Laplace transform.

3.2. The Inverse Laplace Transform

There is a closed-form equation for the inverse Laplace transform (see Ref. 6 for details), but it is rather difficult to apply (involving contour integration) and is rarely used in circuit analysis applications. Instead, the inverse Laplace transform of a function is generally found by writing the function as the sum of simpler functions, each of whose inverse Laplace transform is known. A technique that is particularly useful here is the partial fraction expansion [2,6]. This is a technique that allows the decomposition of a function $F(s)$ that is the ratio of two real polynomials in s into the sum of simpler terms. It is assumed that the degree of the numerator of $F(s)$ is less than that of the denominator—if this is not the case, then $F(s)$ can be expressed in the form $F(s) = r(s) + \hat{n}(s)/\hat{d}(s)$, where $r(s)$ is a polynomial in s and the degree of $\hat{n}(s)$ is less than that of $\hat{d}(s)$. The inverse Laplace transform of $R(s)$ can be found from Table 1, leaving only the component $\hat{n}(s)/\hat{d}(s)$ to be handled by the partial fraction expansion. Thus, without loss of generality, we can assume that the degree of the numerator of $F(s)$ is less than that of the denominator. The first step in the partial fraction expansion is the factorization of the denominator polynomial:

$$F(s) = \frac{n(s)}{d(s)} = \frac{n(s)}{(s - p_1)^{\alpha_1} (s - p_2)^{\alpha_2} \cdots (s - p_m)^{\alpha_m}}$$

The quantities p_i , the zeros of the denominator $d(s)$ of $F(s)$, are known as the *poles* of $F(s)$, and the multiplicity of the pole p_i is the number of times α_i that it appears as a zero of $d(s)$. A pole of multiplicity 1 is called a *simple* pole. If all poles are simple, then

$$\begin{aligned} F(s) &= \frac{n(s)}{(s - p_1)(s - p_2) \cdots (s - p_m)} \\ &= \frac{k_1}{s - p_1} + \frac{k_2}{s - p_2} + \cdots + \frac{k_m}{s - p_m} \end{aligned}$$

where $k_i = [(s - p_i)F(s)]_{s=p_i}$.

The term k_i is the *residue* of $F(s)$ at the pole p_i . If $F(s)$ has a pole of multiplicity α_j at p_j , the partial fraction expansion takes the form

$$\begin{aligned} F(s) &= \frac{n(s)}{(s - p_j)^{\alpha_j} \hat{d}(s)} = \frac{k_{j1}}{s - p_j} \\ &+ \frac{k_{j2}}{(s - p_j)^2} + \cdots + \frac{k_{j\alpha_j}}{(s - p_j)^{\alpha_j}} + \frac{\hat{n}(s)}{\hat{d}(s)} \end{aligned}$$

where

$$k_{ji} = \left\{ \frac{1}{(\alpha_j - i)!} \frac{d^{\alpha_j - i}}{ds^{\alpha_j - i}} [(s - p_j)^{\alpha_j} F(s)] \right\} \Big|_{s=p_j}$$

Since the numerator and denominator of $F(s)$ are real polynomials in s , poles appear in complex conjugate pairs,

Table 1. Some Important Laplace Transforms

$f(t)$	$F(s) = \mathbf{L}(f(t))$
$\delta(t)$	1
$U(t)$	$\frac{1}{s}$
t^n	$n! \frac{1}{s^{n+1}} \quad n = 1, 2, \dots$
e^{-at}	$\frac{1}{s+a}$
$\sin \omega t$	$\frac{\omega}{s^2 + \omega^2}$
$\cos \omega t$	$\frac{s}{s^2 + \omega^2}$

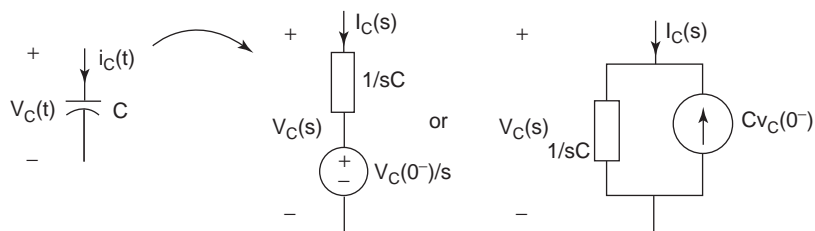


Figure 13. Transformation of a capacitor with initial voltage $v_C(0^-)$ into the frequency domain.

as do their residues. This allows the combination of any complex term in the expansion with its conjugate to give a real term.

The inverse Laplace transform of each of the terms in the partial fraction expansion is known:

$$\mathbf{L}^{-1}\left\{\frac{k_{j\alpha_j}}{(s-p_j)^{\alpha_j}}\right\} = k_{j\alpha_j} \frac{t^{\alpha_j-1}}{(\alpha_j-1)!} e^{p_j t}$$

In this way it is possible to find the inverse Laplace transform of any function consisting of the ratio of two polynomials in s by decomposing the function via the partial fraction expansion and taking the inverse Laplace transform of each of the constituent functions. This method relies fundamentally on the uniqueness and linearity properties of the Laplace transform. Clearly the method applies only to a restricted range of functions, those which can be expressed as the ratio of two polynomials in s . As will be seen, however, functions of this type are particularly important in circuit analysis, and so this is not a significant limitation.

3.3. Circuit Analysis

The first step in the Laplace transform analysis of a circuit is the transformation of the circuit from the time domain to the frequency domain. All branch voltages $v(t)$ and currents $i(t)$ that appear as variables in the differential equations describing the circuit will appear in the transformed equations as variables $V(s) = \mathbf{L}\{v(t)\}$ and $I(s) = \mathbf{L}\{i(t)\}$. Independent voltage and current sources are transformed from known functions of time $v_s(t)$ and $i_s(t)$ to known functions of frequency $V_s(s) = \mathbf{L}\{v_s(t)\}$ and $I_s(s) = \mathbf{L}\{i_s(t)\}$. A resistor is described in the time domain by the linear equation $v(t) = Ri(t)$ and so is defined in the transformed circuit by the relation $V(s) = RI(s)$. Similarly the linear equations describing all resistive two-ports (including ideal transformers, gyrators and controlled sources), and indeed resistive n -ports, are unchanged in the transformation from time domain to frequency domain. The

capacitor is defined in the time domain by the equation

$$i_C(t) = C \frac{dv_C(t)}{dt}$$

Applying the differentiation property of the Laplace transform yields the frequency-domain equation for the capacitor:

$$I_C(s) = sCV_C(s) - Cv_C(0^-)$$

Thus the capacitor C with initial voltage $v_C(0^-)$ appears in the transformed circuit as the parallel combination of the independent current source $Cv_C(0^-)$ and the linear element defined by the relation $V(s) = (1/sC)I(s)$. This second element can be regarded as a generalized resistance (known as an *impedance*) $1/sC$ and throughout the analysis in the frequency domain can be handled as if it were a resistance. Figure 13 shows the transformation of a capacitor from the time domain into the parallel combination of an impedance and an independent current source in the frequency domain or, by Thévenin's theorem, into the series combination of an impedance and an independent voltage source. In a similar manner, the inductor defined in the time domain by the relation

$$v_L(t) = L \frac{di_L(t)}{dt}$$

is defined in the frequency domain by the relation

$$V_L(s) = sLI_L(s) - Li_L(0^-)$$

Thus, as shown in Fig. 14, the inductor appears in the transformed circuit as the series combination of an impedance sL and voltage source $Li_L(0^-)$ or the parallel combination of the same impedance and current source $[i_L(0^-)]/s$. Note that once again this circuit transformation could have been obtained from Fig. 13 by application of the

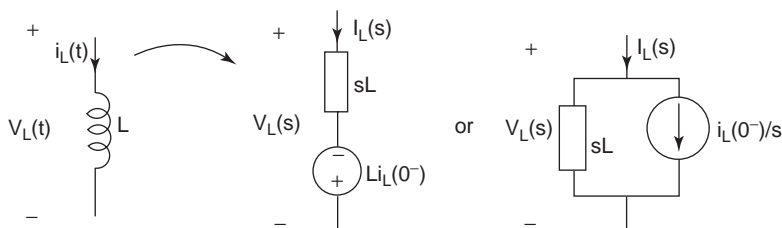


Figure 14. Transformation of an inductor with initial current $i_L(0^-)$ into the frequency domain.

principle of duality. Coupled inductors can be transformed in a similar manner.

When all the elements in the circuit have been transformed into the frequency domain, the first step of the analysis process is complete. The second step is to analyze the circuit in the frequency domain, employing any of a wide variety of techniques such as loop current analysis, node voltage analysis, modified nodal analysis, and sparse tableau analysis. The analysis of a circuit in the frequency domain is described in the article on frequency-domain circuit analysis, and also in most circuit theory textbooks, such as Refs. 3–5. The third step is then to transform the results of the analysis back to the time domain via the inverse Laplace transform.

Example 1. The circuit of Fig. 4 can be transformed into the Laplace transform domain, yielding the circuit of Fig. 15. Analysis in the frequency domain, followed by partial fraction expansion, yields the result that

$$V_C(s) = \frac{v_C(0^-)}{s + \frac{1}{RC}} + \frac{E}{s} \frac{1}{\left(s + \frac{1}{RC}\right)} = \frac{v_C(0^-)}{s + \frac{1}{RC}} + \frac{E}{s} - \frac{E}{s + \frac{1}{RC}}$$

The inverse Laplace transform is then applied to find

$$v_C(t) = v_C(0^-)e^{-t/RC} + E(1 - e^{-t/RC}) \text{ for } t \geq 0$$

which agrees with the time domain analysis performed earlier.

3.4. Laplace Transform Analysis of Distributed Circuits

Laplace transform techniques can also be applied to the analysis of distributed circuits. Consider the example of a transmission line modeled as in Fig. 16 by incremental series inductance L and resistance R and shunt capacitance C and conductance G , all per unit length. Applying Kirchhoff's laws and taking the limit of vanishing line length gives the telegrapher's equations

$$\begin{aligned} \frac{\partial i(x, t)}{\partial x} &= -Gv(x, t) - C \frac{\partial v(x, t)}{\partial t} \\ \frac{\partial v(x, t)}{\partial x} &= -Ri(x, t) - L \frac{\partial i(x, t)}{\partial t} \end{aligned}$$

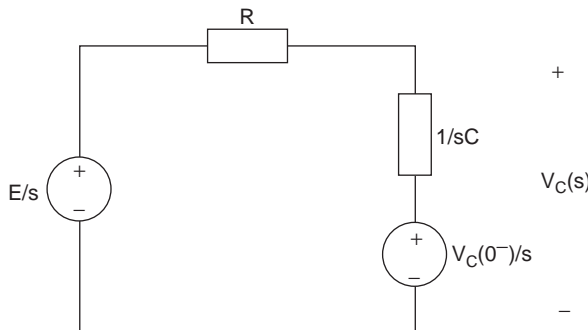


Figure 15. Laplace transform of the circuit of Figure 4.

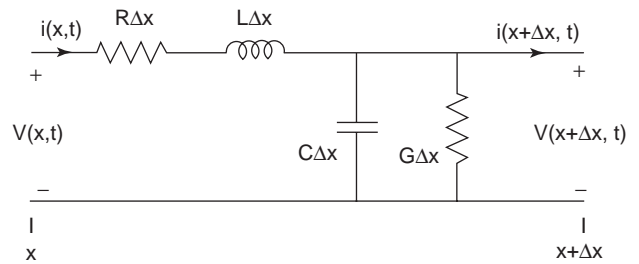


Figure 16. Basic model of a length Δx of transmission line.

The current and voltage now vary not only with time t but also with distance x along the line. The appearance of distance in this fashion, and also of the derivative with respect to distance, does not occur in lumped circuits.

The new parameter x can be shown explicitly in the definition of the Laplace transform:

$$\mathbf{L}[f(x, t)] = \int_0^\infty f(x, t)e^{-st} dt = F(x, s)$$

There is now a second differentiation property:

$$\mathbf{L} \left[\frac{\partial f(x, t)}{\partial x} \right] = \frac{\partial F(x, s)}{\partial x}$$

Then taking

$$I(x, s) = \mathbf{L}[i(x, t)]$$

$$V(x, s) = \mathbf{L}[v(x, t)]$$

the telegrapher's equations become

$$\begin{aligned} \frac{\partial I(x, s)}{\partial x} &= -GV(x, s) - sCV(x, s) + Cv(x, 0^-) \\ \frac{\partial V(x, s)}{\partial x} &= -RI(x, s) - sLI(x, s) + Li(x, 0^-) \end{aligned}$$

If, for simplicity, we assume zero initial voltage and current along the line, these equations can be solved for $V(x, s)$ and $I(x, s)$:

$$\begin{aligned} V(x, s) &= V^+(s)e^{-\gamma x} + V^-(s)e^{\gamma x} \\ \Rightarrow I(x, s) &= \frac{1}{Z_0} [V^+(s)e^{-\gamma x} - V^-(s)e^{\gamma x}] \end{aligned}$$

where $Z_0 = \sqrt{(R + sL)/(G + sC)}$, $\gamma = \sqrt{(R + sL)(G + sC)}$ and V^+ and V^- are as yet unknown constants of integration. Z_0 is called the characteristic impedance of the line, and γ is the propagation constant. If the line is lossless, $R = G = 0$, and so $Z_0 = \sqrt{L/C}$, which is purely real (generally denoted R_0) and $\gamma = s\sqrt{LC}$. We define $u = 1/\sqrt{LC}$, and so $\gamma = s/u$. (We shall shortly see the physical significance of this variable.)

Inserting typical terminations for a line of length L , consisting of the series combination of voltage source $V_0(s)$

and generator impedance Z_g at $x = 0$, and load impedance Z_L at $x = L$, we can solve these equations for V^+ and V^- to find

$$\frac{V^-}{V^+} e^{2\gamma L} = \frac{Z_L - Z_0}{Z_L + Z_0} = \Gamma_R$$

where Γ_R is the receiving end reflection coefficient, and in a similar manner we define the generating end reflection coefficient

$$\Gamma_g = \frac{Z_g - Z_0}{Z_g + Z_0}$$

We can substitute for V^+ and V^- to find the expressions for the voltage and current along the line in the frequency domain:

$$V(x, s) = \frac{Z_0 V_0}{Z_0 + Z_g} \left[\frac{e^{-\gamma x} + \Gamma_R e^{-\gamma(2L-x)}}{1 - \Gamma_R \Gamma_g e^{-2\gamma L}} \right]$$

$$I(x, s) = \frac{V_0}{Z_0 + Z_g} \left[\frac{e^{-\gamma x} - \Gamma_R e^{-\gamma(2L-x)}}{1 - \Gamma_R \Gamma_g e^{-2\gamma L}} \right]$$

In the important case of a lossless line, these equations can be rewritten as

$$V(x, s) = \frac{V_0 R_0}{R_0 + Z_g} \left[\frac{e^{-(sx/u)} + \Gamma_R e^{-s(2\tau - (x/u))}}{1 - \Gamma_R \Gamma_g e^{-2s\tau}} \right] \tag{11}$$

$$I(x, s) = \frac{V_0}{R_0 + Z_g} \left[\frac{e^{-(sx/u)} - \Gamma_R e^{-s(2\tau - (x/u))}}{1 - \Gamma_R \Gamma_g e^{-2s\tau}} \right]$$

where $\tau = L/u$ is the delay of the line. (Once again, we shall shortly see the physical significance of this variable).

We will now consider the solution of these equations in three cases of increasing complexity. It suffices to consider the voltage equation (11), since the current follows easily.

3.4.1. Matched Lossless Line. If the load impedance Z_L equals the characteristic impedance R_0 of the line, then $\Gamma_R = 0$ and Eq. (11) becomes

$$V(x, s) = \frac{V_0 R_0}{R_0 + Z_g} e^{-(sx/u)}$$

In the time domain, applying the time-shift property of the Laplace transform, we get

$$v(x, t) = \mathbf{L}^{-1}[V(x, s)] = f\left(t - \frac{x}{u}\right) U\left(t - \frac{x}{u}\right)$$

where $U(t)$ is the unit step function given by (1) and

$$f(t) = \mathbf{L}^{-1}\left[\frac{V_0 R_0}{R_0 + Z_g}\right]$$

The voltage at the generator end of the line, that is, at $x = 0$, is

$$\frac{V_0 R_0}{R_0 + Z_g}$$

which agrees with the result expected by voltage division. The voltage at any point x along the line is an undistorted

replica of the voltage at $x = 0$ delayed by the time interval x/u , where u is the velocity at which the waveform propagates along the line.

3.4.2. Lossless Line with Matched Source and Unmatched Load. If the lossless line is matched at the source end but unmatched at the load end (i.e., $\Gamma_g = 0$ and $\Gamma_R \neq 0$), the voltage in the frequency domain is given by

$$V(x, s) = \frac{V_0}{2} \left[e^{-(sx/u)} + \Gamma_R e^{-s(2\tau - (x/u))} \right]$$

The inverse Laplace transform gives the voltage in the time domain:

$$v(x, t) = f_1\left(t - \frac{x}{u}\right) U\left(t - \frac{x}{u}\right) + f_2\left(t - 2\tau + \frac{x}{u}\right) U\left(t - 2\tau + \frac{x}{u}\right) \tag{12}$$

where

$$\mathbf{L}^{-1}\left[\frac{V_0}{2}\right] = f_1(t) U(t)$$

and

$$\mathbf{L}^{-1}\left[\Gamma_R \frac{V_0}{2}\right] = f_2(t) U(t)$$

The voltage given by Eq. (12) is the sum of two terms. The first of these is a waveform that starts from the generator end of the line ($x = 0$) at $t = 0$ and travels along the line toward the load with velocity u . This waveform reached the load at time $L/u = \tau$. The second, or reflected, term originates at the load end of the line ($x = L$) at time $t = \tau$, and travels to the left with velocity u .

3.4.3. Lossless Line with Unmatched Source and Unmatched Load. The voltage equation (11) can be expanded to the form

$$V(x, s) = F(s) \sum_{n=0}^{\infty} \Gamma_R^n \Gamma_g^n e^{-s(2n\tau + (x/u))} + F(s) \sum_{n=0}^{\infty} \Gamma_R^{n+1} \Gamma_g^n e^{-s(2(n+1)\tau - (x/u))}$$

where

$$F(s) = \frac{V_0 R_0}{R_0 + Z_g}$$

Defining

$$F_1^{(n)}(s) = F(s) \Gamma_R^n \Gamma_g^n = \mathbf{L}\left[f_1^{(n)}(t) U(t)\right]$$

and

$$F_2^{(n)}(s) = F(s) \Gamma_R^{n+1} \Gamma_g^n = \mathbf{L}\left[f_2^{(n)}(t) U(t)\right]$$

we get

$$V(x, s) = \sum_{n=0}^{\infty} F_1^{(n)}(s) e^{-s(2n\tau + (x/u))} + \sum_{n=0}^{\infty} F_2^{(n)}(s) e^{-s(2(n+1)\tau + (x/u))}$$

Taking the inverse Laplace transform, we get the time-domain voltage

$$v(x, t) = \sum_{n=0}^{\infty} f_1^{(n)}\left(t - 2n\tau - \frac{x}{u}\right) U\left(t - 2n\tau - \frac{x}{u}\right) + \sum_{n=0}^{\infty} f_2^{(n)}\left(t - 2(n+1)\tau + \frac{x}{u}\right) U\left(t - 2(n+1)\tau + \frac{x}{u}\right)$$

Hence the voltage waveform consists of a sum of two types of terms. The first type has the form

$$f_1^{(n)}\left(t - 2n\tau - \frac{x}{u}\right) U\left(t - 2n\tau - \frac{x}{u}\right) \quad (13)$$

which represents a waveform traveling toward the load with velocity u . This expression is zero for $t < 2n\tau + (x/u)$. Since $0 \leq x \leq L$, $0 \leq x/u \leq \tau$, and so the term (13) is zero everywhere on the line if $t < 2n\tau$. Thus this term represents a waveform that starts at the generator end of the line at time $t = 2n\tau$ and travels to the load, reaching it at time $t = (2n+1)\tau$.

The second type has the form

$$f_2^{(n)}\left(t - 2(n+1)\tau + \frac{x}{u}\right) U\left(t - 2(n+1)\tau + \frac{x}{u}\right)$$

which represents a waveform traveling to the left with velocity u . This expression is zero for $t < 2(n+1)\tau - (x/u)$, and is zero everywhere on the line if $t < 2(n+1)\tau - x/u$. Thus this term represents a waveform that starts at the load at time $t = (2n+1)\tau$ and travels toward the generator end of the line, reaching it at time $t = (2n+2)\tau$.

4. NATURAL RESPONSE AND ZERO-STATE RESPONSE

When converted into the frequency domain, a (lumped or distributed) circuit contains independent sources of two types. The first are the transformed versions of the independent sources from the time domain. These sources drive the circuit in the time domain, and are often termed the “inputs” to the circuit, borrowing a viewpoint from system theory. The second group of independent sources in the frequency-domain circuit are those that are introduced during the transformation of energy storage elements and account for the initial conditions in the circuit, specifically, the capacitor voltages and inductor currents at time $t = 0^-$. We will call these sources the “initial” condition generators, to distinguish them from those sources that represent the independent sources from the time domain. By superposition, the response of the circuit to these sources (by which we mean any current or voltage in the circuit, or any collection thereof) is the sum of two components: one due to the independent sources acting alone, with the initial condition generators removed, and the

other due to the initial condition generators acting alone, with the independent sources removed. Since these two components of the response arise from different mechanisms, it is often useful to treat them separately. The component of the response due to the independent sources, with the initial conditions set to zero, is called the *zero-state response*, and the component due to the initial conditions, with the independent sources set to zero, is the *natural or unforced response* (also called the *zero-input response*).

4.1. Natural Response and Natural Frequencies

We will consider first the natural response of a circuit. Application of any of the standard frequency-domain analysis techniques will yield a matrix equation of the form [3]

$$\mathbf{M}(s)\mathbf{X}(s) = \mathbf{U}(s)$$

where $\mathbf{M}(s)$ is a matrix each element of which is a polynomial in s ; $\mathbf{X}(s)$ is a vector containing some subset of the unknown branch voltages, branch currents, node voltages, and loop currents; and $\mathbf{U}(s)$ is a vector, each nonzero element of which is a linear combination of the initial condition generators. If the circuit has a unique solution, that solution is given by [2]

$$\mathbf{X}(s) = \mathbf{M}^{-1}(s)\mathbf{U}(s) = \frac{1}{\det(\mathbf{M}(s))} \text{Adj}(\mathbf{M}(s)) \cdot \mathbf{U}(s)$$

where the existence of a unique solution guarantees that the determinant $\det(\mathbf{M}(s))$ is not identically zero. We assume, unless otherwise stated, that all zeros p_1, p_2, \dots, p_m of $\det(\mathbf{M}(s))$ are simple. Each component $X_i(s)$ of the vector $\mathbf{X}(s)$ is the ratio of two polynomials in s , and so the partial fraction expansion can be applied to yield the expression

$$X_i(s) = \frac{k_1}{s - p_1} + \frac{k_2}{s - p_2} + \dots + \frac{k_m}{s - p_m}$$

The time-domain response $x_i(t)$ is therefore

$$x_i(t) = k_1 e^{p_1 t} + k_2 e^{p_2 t} + \dots + k_m e^{p_m t}$$

for $t \geq 0$. [If some of the zeros of $\det(\mathbf{M}(s))$ have multiplicity greater than one, the time response will contain terms of the form $t^2 e^{p_i t}$.]

Clearly the zeros p_i of $\det(\mathbf{M}(s))$ play a crucial role in determining the natural response of the circuit. These quantities are known as the *natural frequencies* of the circuit. The number of natural frequencies in a circuit is less than or equal to the number of energy storage elements in the circuit. The contribution of each natural frequency to the natural response depends on its location in the complex plane. A natural frequency at zero contributes a constant term to the natural response. A real and positive natural frequency p_i contributes a term $k_i e^{p_i t}$ that grows exponentially with time. A real and negative natural frequency p_i contributes a term $k_i e^{p_i t}$ that decays exponentially with time. Complex natural frequencies occur in conjugate pairs, and their contributions add to make a

real contribution to the response waveform. If the natural frequencies in question lie on the imaginary axis at $\pm j\omega$, their composite contribution to the time response is of the form $k_i e^{j\omega t} + \bar{k}_i e^{-j\omega t} = 2|k_i| \cos(\omega t + \angle k_i)$, an oscillation of constant amplitude. If the complex natural frequencies lie in the right half-plane at $\alpha \pm j\omega$, their composite contribution is of the form $k_i e^{(\alpha + j\omega)t} + \bar{k}_i e^{(\alpha - j\omega)t} = 2|k_i| e^{\alpha t} \cos(\omega t + \angle k_i)$, an oscillation whose amplitude grows exponentially with time. Finally, if the complex natural frequencies lie in the left half-plane at $\alpha \pm j\omega$, their composite contribution is of the form $k_i e^{(\alpha + j\omega)t} + \bar{k}_i e^{(\alpha - j\omega)t} = 2|k_i| e^{\alpha t} \cos(\omega t + \angle k_i)$, an oscillation whose amplitude decays exponentially with time. (If some of the natural frequencies have multiplicity greater than one, their contribution to the time response will be more complicated, with polynomials times exponentials in place of exponentials, but can be handled by an extension of the preceding analysis.)

The preceding discussion leads to the important conclusion that if all natural frequencies of a circuit lie in the open left half-plane (i.e., if their real parts are less than 0), then for any set of initial conditions the natural or zero-input response of the circuit decays to zero as $t \rightarrow \infty$. This decay may be oscillatory, depending on the presence of complex natural frequencies. A circuit is said to be asymptotically stable or exponentially stable if all of its natural frequencies lie in the open left half-plane. If any natural frequency lies in the open right half-plane, then the initial conditions can cause certain currents and voltages to grow exponentially with time, which is clearly undesirable. Obviously in a real circuit this growth cannot continue indefinitely as the circuit elements will eventually cease to function, possibly in dramatic fashion. Also obvious is the fact that this behavior cannot occur in a circuit made up entirely of passive elements, since the exponential growth requires that energy be supplied to the circuit by an active element such as a controlled source or negative resistance.

While the natural frequencies determine the possible natural modes of behavior of a circuit, the actual response that will be observed in a circuit with zero input depends on the values of the initial conditions. Certain sets of initial conditions will excite one mode only, which means that all circuit variables will exhibit the same exponential or oscillatory behavior, but for most sets the response will be the combination of various modes. Also, not all modes can be observed in any given circuit variable—it may be that certain variables are not susceptible to the influence of one or more natural frequencies.

Example 2. To find the natural frequencies of the circuit of Fig. 17, the voltage source can be set to zero and the resulting circuit analyzed by any of the usual methods. In this case node voltage analysis is possible, yielding the matrix equation

$$\begin{pmatrix} \frac{1}{R_1} + sC_1 & 0 \\ -g_m & \frac{1}{R_2} + sC_2 \end{pmatrix} \begin{pmatrix} V_1(s) \\ V_2(s) \end{pmatrix} = \begin{pmatrix} C_1 v_1(0^-) \\ C_2 v_2(0^-) \end{pmatrix}$$

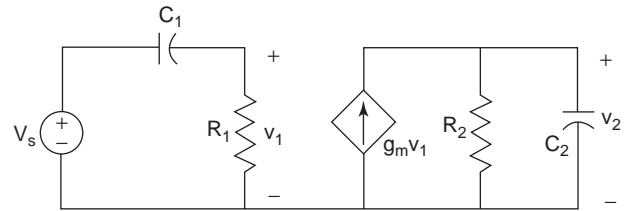


Figure 17. Circuit to be analyzed in Examples 2 and 3.

The natural frequencies are the values of s for which the determinant of the matrix in this equation is zero, and therefore equal $(-1)/R_1 C_1$ and $(-1)/R_2 C_2$. Solving explicitly for $V_1(s)$ and $V_2(s)$, we find that

$$V_1(s) = \frac{V_1(0^-)}{s + \frac{1}{R_1 C_1}} \quad \text{and} \quad V_2(s) = \frac{\frac{g_m}{C_2} V_1(0^-) + \frac{1}{C_1} V_2(0^-)}{\left(s + \frac{1}{R_1 C_1}\right) \left(s + \frac{1}{R_2 C_2}\right)}$$

Thus the voltage v_1 (natural or zero-input component) exhibits only the behavior controlled by the natural frequency at $(-1)/R_1 C_1$ and is unaffected by the natural frequency at $(-1)/R_2 C_2$.

4.2. The Zero-State Response and Transfer Functions

The zero-state response of a circuit is its response to one or more independent sources (inputs) with all initial capacitor voltages and inductor currents set to zero. It suffices to consider the response to a single input, since superposition can then be applied to calculate the response due to multiple inputs. Application of any of the standard frequency-domain analysis techniques to a single-input zero-state circuit will yield a matrix equation of the form

$$\mathbf{M}(s)\mathbf{X}(s) = \mathbf{U}(s)$$

where $\mathbf{M}(s)$ is a matrix, each element of which is a polynomial in s ; $\mathbf{X}(s)$ is a vector containing some subset of the unknown branch voltages, branch currents, node voltages, and loop currents; and $\mathbf{U}(s)$ is a vector, each nonzero element of which is a term involving the independent source, say, $V_s(s)$ (although the theory applies equally to the case where the input is a current source). It follows from linear algebra [2,3] that

$$X_i(s) = \frac{n(s)}{\det(\mathbf{M}(s))} V_s(s) = H(s) V_s(s) \quad (14)$$

where $n(s)$ is a polynomial in s and $\det(\mathbf{M}(s))$ is nonzero, by our standing assumption of unique solvability. Thus the zero-state response to a source $v_s(t)$ is obtained by multiplying its Laplace transform $V_s(s)$ by the appropriate function $H(s) = n(s)/\det(\mathbf{M}(s))$ and taking the inverse Laplace transform to return to the time domain. This function is known as a transfer function or network function. Note that the poles of a transfer function are zeros of $\det(\mathbf{M}(s))$ and are therefore natural frequencies of the circuit.

However, not all natural frequencies need show up as poles of a given transfer function, due to cancellations with numerator terms.

Once again we see that the natural frequencies play a crucial role in determining the response of the circuit—even, as in this case, when the initial conditions are zero. From (14) the poles of $X_i(s)$ will be some subset (determined by numerator cancellations) of the poles of $V_s(s)$ and the natural frequencies. Therefore, $x_i(t)$ will in general, contain terms related to the input together with exponential, constant, or oscillatory terms governed once again by the natural frequencies. If the circuit is asymptotically stable, the contributions governed by the natural frequencies will die away, leaving only the component governed by the input.

The simplest application of Eq. (14) occurs when $V_s(s) = 1$, that is, when the independent source $v_s(t)$ is the delta function or impulse function defined by (10). Although this function is physically unrealizable, it proves extremely useful in circuit and system analysis. When $v_s(t) = \delta(t)$, then $X_i(s) = H(s)\mathbf{L}\{\delta(t)\} = H(s)$, and so the zero-state response is $x_i(t) = h(t) = \mathbf{L}^{-1}\{H(s)\}$. The zero-state response to an impulse function is known as the *impulse response*, and so we have found that the Laplace transform of the impulse response equals the transfer function. The expression

$$X_i(s) = H(s)\mathbf{L}\{v_s(t)\}$$

giving the frequency-domain response of the system with transfer function $H(s)$ to an input $v_s(t)$ can be expressed in the time domain as

$$x_i(t) = h(t) * v_s(t) = \int_{0^-}^{t^+} h(t - \tau)v_s(\tau)d\tau$$

where $h(t) = \mathbf{L}^{-1}\{H(s)\}$ is the impulse response and the asterisk $*$ is the convolution operator [3,6].

If the input is the unit step function $U(t)$, which has Laplace transform $1/s$, that is, $X_i(s) = H(s) \cdot \mathbf{L}\{u(t)\} = H(s)/s$, and so the step response is $x_i(t) = \mathbf{L}^{-1}\{H(s)/s\}$. It is easy to see that the impulse response is the derivative of the step response.

Example 3. The transfer function $V_2(s)/V_s(s)$ of the circuit of Fig. 17 is

$$\begin{aligned} H(s) &= \frac{\frac{g_m s}{C_2}}{\left(s + \frac{1}{R_1 C_1}\right)\left(s + \frac{1}{R_2 C_2}\right)} \\ &= \frac{\frac{g_m}{C_2}}{R_2 C_2 - R_1 C_1} \left[\frac{R_2 C_2}{\left(s + \frac{1}{R_1 C_1}\right)} - \frac{R_1 C_1}{\left(s + \frac{1}{R_2 C_2}\right)} \right] \end{aligned}$$

and so the impulse response is

$$\begin{aligned} h(t) &= \frac{g_m R_2}{R_2 C_2 - R_1 C_1} e^{-t/R_1 C_1} \\ &\quad - \frac{g_m R_1 C_1 / C_2}{R_2 C_2 - R_1 C_1} e^{-t/R_2 C_2} \text{ for } t \geq 0 \end{aligned}$$

The step response is

$$\begin{aligned} &\mathbf{L}^{-1} \left\{ \frac{\frac{g_m}{C_2}}{\left(s + \frac{1}{R_1 C_1}\right)\left(s + \frac{1}{R_2 C_2}\right)} \right\} \\ &= \frac{g_m R_1 C_1 R_2}{R_2 C_2 - R_1 C_1} \left[-e^{-t/R_1 C_1} + e^{-t/R_2 C_2} \right] \text{ for } t \geq 0 \end{aligned}$$

Note the exponential modes corresponding to the natural frequencies in both the step response and the impulse response. Note also that the impulse response is the derivative of the step response.

5. FOURIER TRANSFORM CIRCUIT ANALYSIS

The power of the Laplace transform in finding the transient and steady-state response of a circuit, the variety of source waveforms that it can handle and its ability to accommodate initial conditions make it the method of choice in transient circuit analysis. Despite these advantages, another transform, closely related to the Laplace transform, is preferred in certain situations. This is the Fourier transform [4–6], named after the French mathematician Jean Baptiste Joseph Fourier (1768–1830). The close relationship between the Fourier transform of a signal and the frequency content of that signal make it particularly useful in applications such as communications and signal processing where this frequency content is of paramount importance. However, the Fourier transform is defined for a smaller class of source waveforms than the Laplace transform, and it cannot handle initial conditions. The latter condition in particular makes it poorly suited to transient circuit analysis and so we will merely give a brief discussion of its properties here, with the intention of (1) explaining why it is unsuited to transient circuit analysis and (2) providing a link to other forms of transient circuit analysis for circuits such as filters that are more usually handled using Fourier analysis.

The Fourier transform is closely related to the Fourier series [4–6], in which a periodic function with period T is decomposed into the weighted sum of sinusoids whose angular frequencies are integer multiples of $2\pi/T$. By superposition, the response of a circuit to a periodic function could be obtained by decomposing the function into the sum of sinusoids, finding the response to each of these sinusoids via phasor analysis, and summing these responses to find the overall response. The main disadvantage to this Fourier series method of analysis is that many source waveforms of interest are not periodic, and since the

method is based on phasor analysis, it finds only the steady-state component of the response. The fundamental idea underlying this method, however, namely, the idea of a sum of input sinusoids being processed (i.e., altered in magnitude and phase) in different ways by a circuit and then added to form the response, is a very useful one and underlies the more general Fourier transform analysis.

The Fourier transform is a generalization of the Fourier series to accommodate nonperiodic functions. A nonperiodic function can be viewed as the limit of a periodic function as the period T tends to infinity. The Fourier series of this periodic function consists of weighted sinusoids spaced in frequency at integer multiples of $2\pi/T$. As T tends to infinity, the separation of these sinusoidal frequency components tends to zero, and in the limit we have the nonperiodic function represented by a continuum or spectrum of sinusoidal components. This spectrum of sinusoidal components constitutes the Fourier transform of the function. The Fourier transform of a signal $f(t)$ is found, as in the preceding discussion, by taking the limit of the expression for the Fourier series of a periodic function as the period tends to infinity, which turns out to be

$$F(j\omega) = \mathbf{F}\{f(t)\} = \int_{-\infty}^{\infty} f(t)e^{-j\omega t} dt \tag{15}$$

and exists if the integral in (15) converges. Once again we say that the Fourier transform converts a function from the time domain into the frequency domain, with $F(j\omega)$ indicating the frequency content of the signal at frequency ω . If $f(t) = 0$ for $t < 0$ and the integral shown above converges, the Fourier transform of f is just the Laplace transform with $j\omega$ substituted for s . Given $F(j\omega)$, the function $f(t)$ such that $F(j\omega) = \mathbf{F}\{f(t)\}$ is found by application of the inverse Fourier transform

$$f(t) = \mathbf{F}^{-1}\{F(j\omega)\} = \frac{1}{2\pi} \int_{-\infty}^{\infty} F(j\omega)e^{j\omega t} d\omega$$

One important feature of the Fourier transform is the differentiation property, which states that differentiation in the time domain is equivalent to multiplication by $j\omega$ in the frequency domain. Thus the Fourier transform can, like the Laplace transform, be used to transform a system of differential equations in the time domain to a system of algebraic equations in the frequency domain.

In Fourier transform analysis a circuit is transformed into the frequency domain by replacing all independent sources by their Fourier transforms, replacing each inductor L by an impedance $j\omega L$ (and replacing any time-domain coupling M between inductors by the frequency-domain coupling $j\omega M$), replacing each capacitor C by an impedance $1/j\omega C$ and leaving resistive components unchanged. Note the lack of any initial condition generators—this is a consequence of the fact that the lower limit of integration in the definition of the Fourier transform is $-\infty$ rather than 0^- . Analysis in the frequency domain proceeds as described in the article on frequency-domain analysis or in Refs. 4 and 5, using the standard tools, and

the frequency-domain response is converted back to the time domain by application of the inverse Fourier transform. Once again there is a transfer function—in this case a function of frequency $H(j\omega)$ —relating input and output in the frequency domain. Note that the response obtained through Fourier transform analysis is the zero-state response only, since the method contains no provision for handling initial conditions.

Given a circuit with input $\sin(\omega_0 t)$ and transfer function $H(j\omega)$ [which is in general complex and, for the circuits in which we are interested, has the property that $H(-j\omega)$ is the complex conjugate of $H(j\omega)$], the output is obtained by taking the inverse Fourier transform of $H(j\omega) \cdot \mathbf{F}\{\sin(\omega_0 t)\}$, which turns out to be $|H(j\omega_0)| \sin(\omega_0 t + \angle H(j\omega_0))$. In other words, the sinusoidal input appears at the output as a sinusoid of the same frequency, with amplitude multiplied by the magnitude of the transfer function at that frequency and phase incremented by the phase of the transfer function at that frequency. If the input to the circuit is more general, it can be viewed as the finite or infinite sum of sinusoids, which will be altered in magnitude and phase by the action of the circuit and then recombined to form the output of the circuit. The magnitude and phase of the transfer function will generally vary with frequency, and when plotted against frequency are called the *amplitude* (or *magnitude*) *response* and *phase response* plots.

Frequency-selective circuits that pass certain ranges of frequencies from input to output while blocking other ranges are known as *filters* [7]. For example, an ideal low-pass filter would pass to the output all frequency components of its input up to a certain cutoff frequency, and pass no higher frequency components. This ideal lowpass filter cannot be realized and is therefore approximated by a variety of functions such as the Butterworth and Chebyshev approximations. Figure 18 plots the amplitude response of the ideal lowpass filter with cutoff frequency at 1 rad/s, together with the amplitude responses of the normalized Butterworth filters of orders 2,3,4,5. The amplitude response of each of these Butterworth filters is 0.7071 or -3 dB at $\omega = 1$ rad/s, which is to say that their 3 dB bandwidth is 1 rad/s.

In a communication system designed to transmit pulses, the step response of a filter is crucial. Too slow a risetime leads to neighboring pulses in a pulsetrain being smeared over one another, rendering them indistinguishable at the output. Too high an overshoot can drive circuit elements into saturation. The step response of a filter can be found by Fourier transform methods, by taking the inverse Fourier transform of the function $H(j\omega)\mathbf{F}\{u(t)\}$, but there is in general no reason to prefer the Fourier transform over the Laplace transform in this situation, and it is usual to take instead the inverse Laplace transform of the function $H(s)\mathbf{L}\{u(t)\}$. For example, the normalised third order Butterworth lowpass filter has transfer function $H(s) = 1/(s^3 + 2s^2 + 2s + 1)$, and so its step response is $\mathbf{L}^{-1}\{1/[s(s^3 + 2s^2 + 2s + 1)]\}$, which can be found by the partial fraction decomposition to be

$$1 - e^{-t} - \frac{2}{\sqrt{3}}e^{-t/2} \sin \frac{\sqrt{3}}{2}t \quad \text{for } t > 0$$

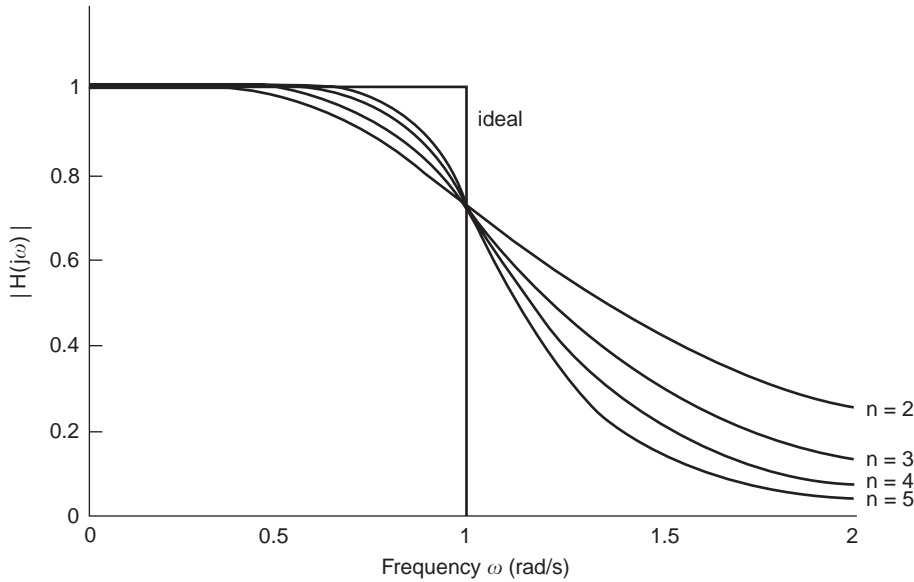


Figure 18. Amplitude response of the ideal lowpass filter with cutoff frequency at 1 rad/s, together with the amplitude responses of the normalized Butterworth filters of orders $n=2, 3, 4, 5$. Note that the approximation more closely matches the ideal as the order of the filter increases.

Figure 19 plots the step response of the normalised Butterworth filters of orders 2,3,4,5, as obtained by application of the Laplace transform. It can be seen that as the order increases (and the amplitude response more closely approximates the ideal) the overshoot, settling time and delay time of the filters all increase, but the risetime is approximately constant.

The procedure outlined above can be used to find the exact step response of a filter, allowing a designer to compare the suitability of various filters in pulse transmission applications. Designers should also have an intuitive understanding of the relationship between amplitude response and transient response of a filter. A lowpass filter allows low frequencies to pass to the output, but blocks high frequencies. Thus when the input is a step

function, the output will preserve the steady-state constant behavior of the input, but will act to block the high frequencies involved in the transition from 0 to 1. This can be seen in Fig. 19, where the high-order filters that are most effective at blocking high frequencies are least effective in capturing the discontinuity in the input. We now recognize the RC circuit of Fig. 4, with the output voltage taken across the capacitor, as a lowpass filter. If the output voltage were taken across the resistor, we would have a highpass filter whose step response captures the initial discontinuity in the step but then falls away to zero due to its inability to pass DC. Readers interested in a more detailed discussion of the relationship between frequency response and transient response of filters are referred to Refs. 1 and 7.

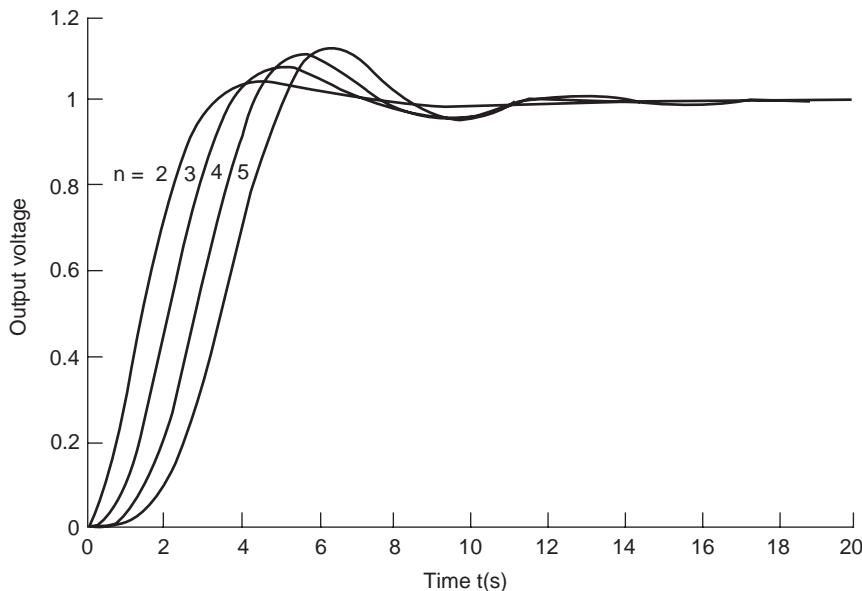


Figure 19. Step response of the normalized Butterworth filters of orders $n=2, 3, 4, 5$.

BIBLIOGRAPHY

1. F. F. Kuo, *Network Analysis and Synthesis*, 2nd ed., Wiley, New York, 1966.
2. E. Kreyszig, *Advanced Engineering Mathematics*, 6th ed., Wiley, New York, 1988.
3. L. O. Chua, C. A. Desoer, and E. S. Kuh, *Linear and Nonlinear Circuits*, McGraw-Hill, New York, 1987.
4. R. C. Dorf and J. A. Svoboda, *Introduction to Electric Circuits*, 3rd ed., Wiley, New York, 1996.
5. J. W. Nilsson and S. A. Riedel, *Electric Circuits*, 5th ed., Addison-Wesley, Reading, MA, 1996.
6. A. V. Oppenheim, A. S. Willsky, and I. T. Young, *Signals and Systems*, Prentice-Hall, London, 1983.
7. L. P. Huelsman, *Active and Passive Analog Filter Design*, McGraw-Hill, Singapore, 1993.

TRANSMISSION LINE MATRIX (TLM) METHOD

CHRISTOS CHRISTOPOULOS
 Director, George Green Institute
 for Electromagnetics Research
 University of Nottingham,
 Nottingham, United Kingdom

1. HISTORICAL BACKGROUND

The transmission-line modeling or matrix method, commonly referred by the acronym TLM, belongs to the class of differential equation methods and it is best known in its implementation in the time domain (TD-TLM). Implementations in the frequency domain are also available, but the method is known primarily as a time-domain method. It models electromagnetic field phenomena by analogy to pulse propagation in networks of transmission lines—hence its name. The idea of using circuits to model fields is not a new one. The foundation work in this area was done some time ago [1–3], but the difficulty at the time of solving such large networks precluded any useful implementation. This had to wait the advent of modern digital computers and the work of John and Beurle in 1971 [4], which set the scene for the rapid development of TLM into a versatile and general tool for EM simulation. The first developments were for models in two dimensions where an intuitive derivation of suitable network topologies is straightforward. The first three-dimensional structure appeared in 1975 [5]. There followed a period of development to obtain a circuit structure with good accuracy, efficiency, and versatility as described by Hofer [6]. The circuit structure (TLM node), which is the workhorse of TLM today, is described as the symmetric condensed node (SCN) and was developed in 1985 [7]. This marks the year when TLM entered its period of maturity. Many developments followed thereafter both improving the basic SCN and introducing complementary techniques that enhanced the power

of TLM. These are described in more detail in the following sections. More details of the TLM technique may be found in a large number of journal papers and in a number of texts that may be consulted for a fuller explanation of TLM and its applications [8–10]. The next section introduces the basics of TLM in a manner that should be accessible to all before more complex issues are addressed.

2. BASIC CONCEPTS

A basic introduction to the idea of TLM can proceed from an example of propagation in a transmission line and of one-dimensional field propagation. For a typical transmission line, as shown by two segments in Fig. 1, the differential equation describing the evolution of the current in space and in time is

$$\frac{\partial^2 i}{\partial x^2} = \frac{LC}{(\Delta x)^2} \frac{\partial^2 i}{\partial t^2} + \frac{GL}{(\Delta x)^2} \frac{\partial i}{\partial t} \quad (1)$$

where L and C are the inductance and capacitance, respectively, for a segment of the line of length Δx and G represents line losses.

In a similar way one can derive an equation for the current density j in one-dimensional field propagation

$$\frac{\partial^2 j}{\partial x^2} = \mu\epsilon \frac{\partial^2 j}{\partial t^2} + \mu\sigma \frac{\partial j}{\partial t} \quad (2)$$

where μ , ϵ , and σ respectively are the magnetic permeability, electric permittivity, and electrical conductivity of the medium.

One can see that Eq. (1) for the circuit and (2) for the field have the same structure. This isomorphism between the two equations means that field behavior may be understood by reference to circuit behavior. All that needs to be done is to establish appropriate circuit topologies in two and three dimensions and a formal equivalence between field and circuit quantities. This is possible to do. For the case of the one-dimensional example shown here, the equivalence is shown in Table 1.

Inspection of Eq. (2) shows that the two terms on the right-hand side represent wavelike behavior and diffusionlike behavior, respectively. By minimizing the wave term relative to the diffusion term, the models described

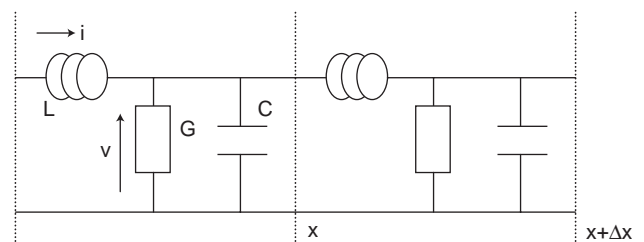


Figure 1. A simple one-dimensional transmission-line network to illustrate circuit-field analogies.

Table 1. Equivalence between Circuit and Field Quantities

Circuit	EM Field
I	j
$L/\Delta x$	μ
$C/\Delta x$	ϵ
$1/R \Delta x$	σ

thus may be used to study diffusion phenomena such as thermal conduction [9].

The lumped circuit shown in Fig. 1 can be replaced by transmission-line (TL) segments. Hence, in essence, in TLM models the field problem is reduced to lumped circuit models (space discretization), which in turn are reduced to TL models (time discretization). The art in TLM modeling is to devise TL interconnect topologies, in what are referred to as “nodes,” with each node describing a small block of space of dimensions $\Delta x \Delta y \Delta z$, such as there is an exact equivalence between the voltages and currents in each node and electric and magnetic fields. The TLM node is the equivalent of the computational element or molecule in other methods much like the Yee cell in FDTD.

A schematic arrangement in two dimensions is shown in Fig. 2a. Here, a mesh of transmission lines is shown, each line in the diagram representing a TL, namely, a line and its return conductor (not shown). One node is shown highlighted by a broken line. If a voltage pulse

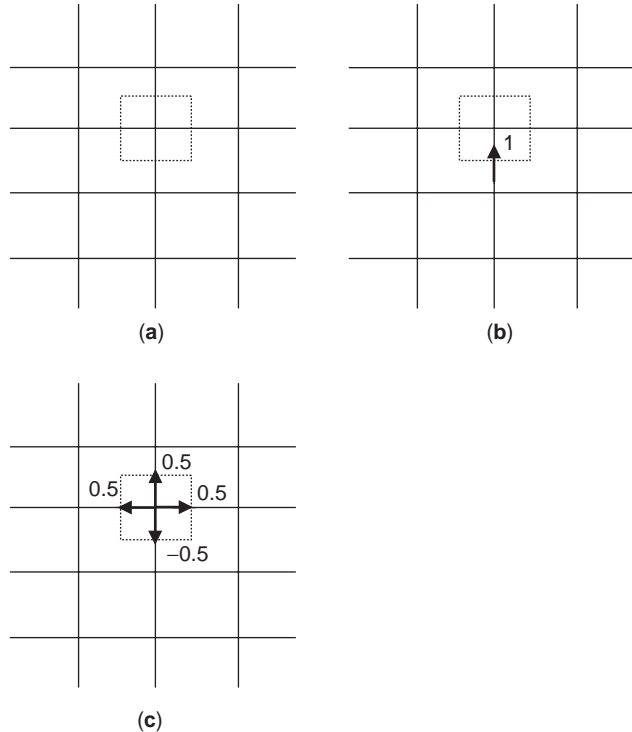


Figure 2. Schematic of a 2D TLM mesh: (a) 2D mesh with one node marked out; (b) impulse excitation at one port; (c) output after the first scattering event.

of magnitude 1 V is incident as shown in Fig. 2b, then this pulse will scatter at the node. If the TL characteristic impedance is Z , then at the node the pulse encounters three TLs in parallel (characteristic impedance $Z/3$) and scatters at this discontinuity with a reflection coefficient -0.5 and a transmission coefficient 0.5 . The scattered pulses are as shown in Fig. 2c. The reflected pulse of -0.5 V combines with the incident pulse of 1 V so that in total the pulse on this TL has a magnitude of 0.5 V. As a result of the scattering, a secondary isotropic wavefront is formed at the node in accordance with Huygens’ principle [11]. TLM can thus be viewed as a discrete implementation of the Huygens principle [12]. After the initial scattering, pulses propagate to adjacent nodes and the process repeats. The TLM algorithm consists of the process of “scattering” at each node; “connection,” that is, the exchange of pulses between nearest neighbors; followed by another “scattering”; and so on. Figure 3 illustrates the results of scattering and connection at the first two timesteps following the isotropic excitation of one node.

For TM modes the basic TLM node in two dimensions (2D) is described as a “shunt” node and is shown in Fig. 4. The dual of this node for TE modes is described as a “series” node. As an illustration, the scattering process in a shunt node is described below:

In order to proceed for the node shown in Fig. 4, we assume that four incident pulses travel toward the node at timestep k . These are labeled as

$${}_k V_j^i \quad j = 1, 2, 3, 4$$

where the superscript “i” stands for incident pulse (traveling toward the center of the node). We also assume that the characteristic impedance of each line segment is Z_{TL} . For each of the four line segments, a Thevenin equivalent circuit is derived and therefore each node is now represented as in Fig. 5. The total voltage at the center of the node can then be obtained directly:

$${}_k V_z = 0.5({}_k V_1^i + {}_k V_2^i + {}_k V_3^i + {}_k V_4^i) \quad (3)$$

The electric field component E_z and magnetic field components H_x, H_y are then directly obtained:

$${}_k E_z = -0.5 \frac{({}_k V_1^i + {}_k V_2^i + {}_k V_3^i + {}_k V_4^i)}{\Delta z} \quad (4)$$

$${}_k H_x = \frac{{}_k V_3^i - {}_k V_1^i}{Z_{TL} \Delta x}, \quad {}_k H_y = \frac{{}_k V_2^i - {}_k V_4^i}{Z_{TL} \Delta x} \quad (5)$$

Scattering is directly implemented as follows

$${}_k V_1^r = {}_k V_z - {}_k V_1^i = 0.5(-{}_k V_1^i + {}_k V_2^i + {}_k V_3^i + {}_k V_4^i) \quad (6)$$

and similarly for the other reflected components. These expressions can be put into a matrix form

$${}_k \mathbf{V}^r = S_k \mathbf{V}^i \quad (7)$$

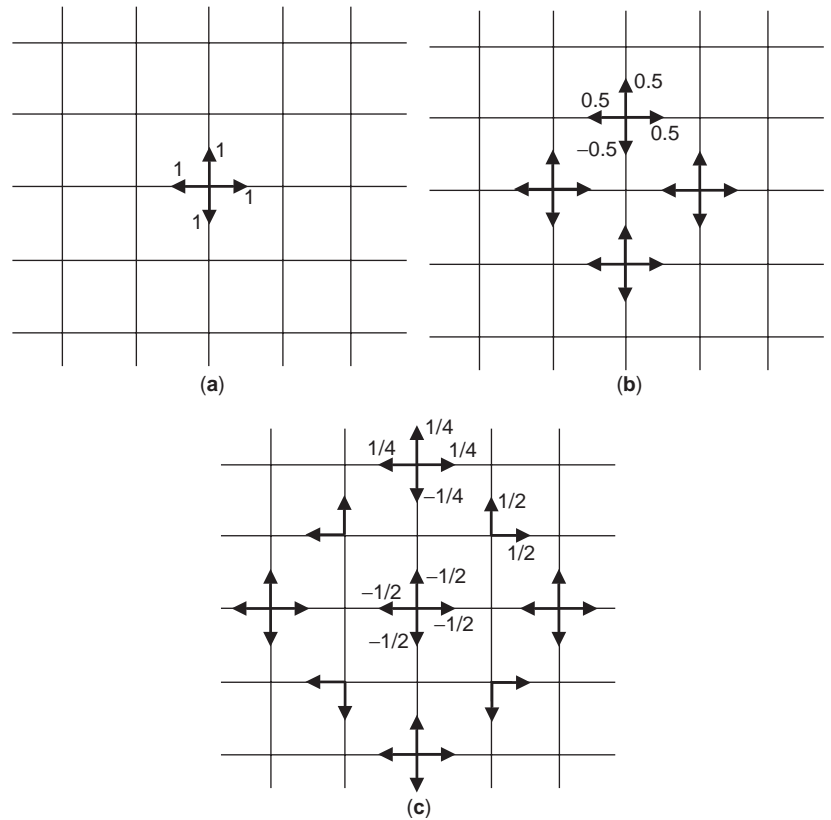


Figure 3. Scattering in a 2D TLM mesh: (a) symmetric excitation at one node; (b) output after the first timestep; (c) output after the second timestep.

where S is the scattering matrix, which for the case of the shunt node shown here is given by

$$S = 0.5 \begin{bmatrix} -1 & 1 & 1 & 1 \\ 1 & -1 & 1 & 1 \\ 1 & 1 & -1 & 1 \\ 1 & 1 & 1 & -1 \end{bmatrix} \quad (8)$$

Equations (7) and (8) show the process of scattering at each node. Scattered pulses are passed on to the adjacent ports of neighboring nodes to form the new incident voltages at timestep $k + 1$ in a process described as “connection.” This is expressed schematically as

$${}_{k+1}V^i = C_k V^r \quad (9)$$

where C is described as the “connection” matrix. The TLM algorithm consists of the repetition at each timestep of the processes of scattering and connection at each node with appropriate modifications to account for initial and boundary conditions. The same procedure applies to all TLM schemes, including those in three dimensions, but the form of the scattering matrix in (8) is different. It will be seen from this basic description of TLM that it is a

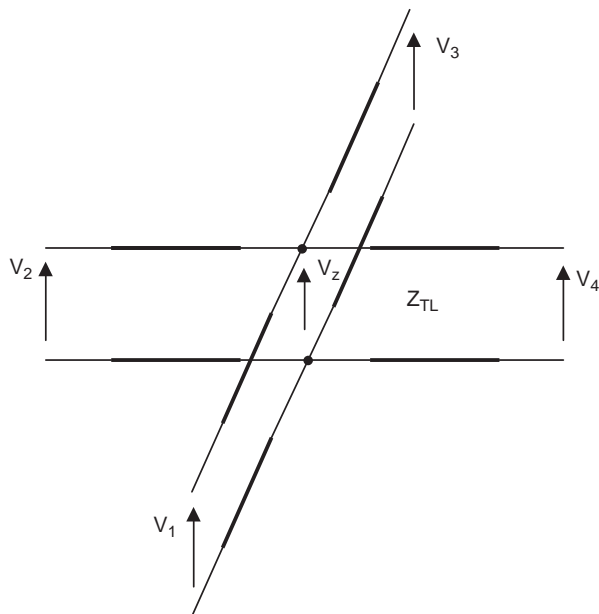


Figure 4. The shunt 2D TLM node for TM modes.

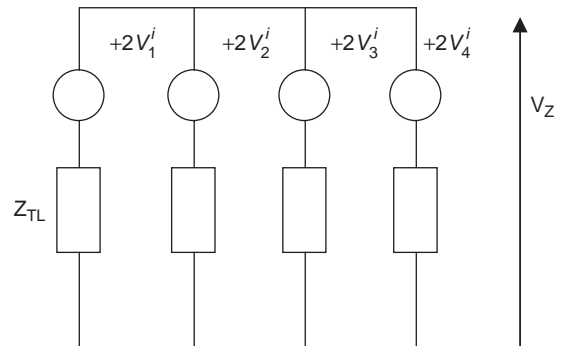


Figure 5. The Thevenin equivalent circuit of the shunt node.

scattering algorithm—energy goes in at each node (incident pulses) and comes out (reflected pulses). The scattering process is lossless (S is unitary). Because we have an exact solution of a passive network, unconditional stability is ensured. Accuracy is good as long as at least 10 segments per wavelength are used.

Several modifications can be made to this basic scheme to extend the applicability of the model in Fig. 4. Foremost among them is the inclusion of stubs to allow for the modeling of inhomogeneous lossy materials. A suitable node is shown in Fig. 6, where two stubs are included: an infinitely long stub (conductance G_s) and an open-circuit stub (admittance Y_s). This node can model TM propagation in a medium of relative dielectric constant ϵ_r and electrical conductivity σ . The choice of parameters is as follows:

$$u_{\text{TL}} = \frac{\Delta x}{\Delta t} = \sqrt{2} \frac{1}{\sqrt{\mu_0 \epsilon_0}}, \quad Z_{\text{TL}} = \sqrt{2} \sqrt{\frac{\mu_0}{\epsilon_0}} \quad (10)$$

$$Y_s = 4 \frac{(\epsilon_r - 1)}{Z_{\text{TL}}}, \quad G_s = \sigma \Delta x \quad (11)$$

In this case the scattering matrix is given by

$$S = \frac{1}{\hat{Y}} \begin{bmatrix} 2 - \hat{Y} & 2 & 2 & 2 & 2\hat{Y}_s \\ 2 & 2 - \hat{Y} & 2 & 2 & 2\hat{Y}_s \\ 2 & 2 & 2 - \hat{Y} & 2 & 2\hat{Y}_s \\ 2 & 2 & 2 & 2 - \hat{Y} & 2\hat{Y}_s \\ 2 & 2 & 2 & 2 & 2\hat{Y}_s - \hat{Y} \end{bmatrix} \quad (12)$$

where

$$\hat{Y} = 4 + \hat{Y}_s + \hat{G}_s, \quad \hat{Y}_s = Y_s Z_{\text{TL}}, \quad \hat{G}_s = G_s Z_{\text{TL}} \quad (13)$$

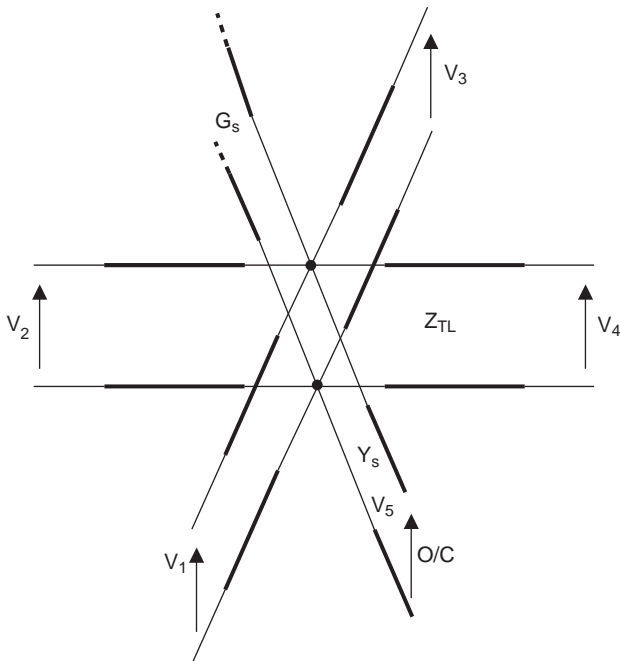


Figure 6. The shunt node with capacitive and lossy stubs added.

The inclusion of stubs permits the development of a model where all linklines have the same (free-space) parameters, hence ensuring the same timestep (synchronism) in the entire mesh. Stubs add capacitance to account for the presence of dielectric materials other than free space. Similar procedures apply to the dual node (series node). More detailed information may be found in the references already cited.

3. TLM IN THREE DIMENSIONS

In the previous section the rudiments of TLM were presented with reference to simple two-dimensional structures so that the basic modeling philosophy could be explained in simple physical terms. In this section the model is extended to three dimensions (3Ds) by presenting the *symmetric condensed node* (SCN), which is extensively used in 3D TLM models.

The structure best suited to general 3D models is the SCN described by Johns [7] and shown in Fig. 7. In this figure the traditional labeling of each port is shown (numbers 1–12) alongside an alternative labeling scheme introduced latter. This node describes the properties of EM propagation in a cuboidal block of space $\Delta x \Delta y \Delta z$. In a regular SCN, $\Delta x = \Delta y = \Delta z$. But with the addition of stubs, this restriction can be removed to form a more flexible structure for general modeling. For simplicity, the regular SCN is discussed first, which results in a uniform mesh.

At each of the six faces of the cube there are two ports polarized at 90° to each other to account for all possible wave polarizations. In total, therefore, there are 12 ports and the scattering matrix is a 12×12 . It is a sparse matrix, and its elements, which are nonzero, can be identified by physical intuition or by formal methods. The value of each element can be readily obtained by enforcing circuitual laws, charge, and energy conservation

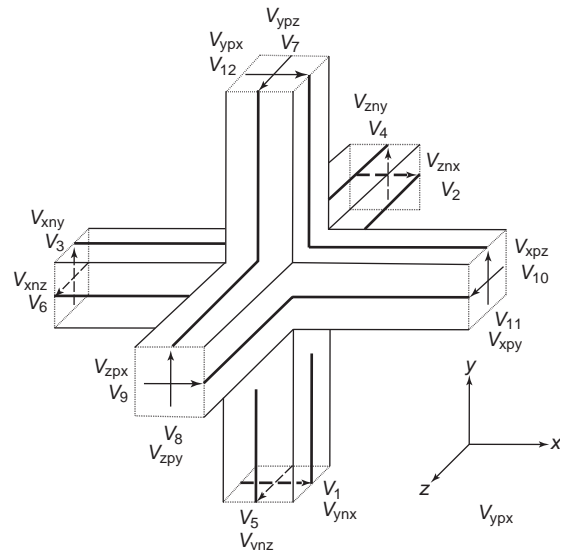


Figure 7. The three-dimensional symmetric condensed node (SCN).

(the scattering matrix must be unitary). A detailed discussion may be found in Refs. 7 and 9. For the stubless SCN, S is given by

$$S = 0.5 \begin{bmatrix} 0 & 1 & 1 & 0 & 0 & 0 & 0 & 0 & 1 & 0 & -1 & 0 \\ 1 & 0 & 0 & 0 & 0 & 1 & 0 & 0 & 0 & -1 & 0 & 1 \\ 1 & 0 & 0 & 1 & 0 & 0 & 0 & 1 & 0 & 0 & 0 & -1 \\ 0 & 0 & 1 & 0 & 1 & 0 & -1 & 0 & 0 & 0 & 1 & 0 \\ 0 & 0 & 0 & 1 & 0 & 1 & 0 & -1 & 0 & 1 & 0 & 0 \\ 0 & 1 & 0 & 0 & 1 & 0 & 1 & 0 & -1 & 0 & 0 & 0 \\ 0 & 0 & 0 & -1 & 0 & 1 & 0 & 1 & 0 & 1 & 0 & 0 \\ 0 & 0 & 1 & 0 & -1 & 0 & 1 & 0 & 0 & 0 & 1 & 0 \\ 1 & 0 & 0 & 0 & 0 & -1 & 0 & 0 & 0 & 1 & 0 & 1 \\ 0 & -1 & 0 & 0 & 1 & 0 & 1 & 0 & 1 & 0 & 0 & 0 \\ -1 & 0 & 0 & 1 & 0 & 0 & 0 & 1 & 0 & 0 & 0 & 1 \\ 0 & 1 & -1 & 0 & 0 & 0 & 0 & 0 & 1 & 0 & 1 & 0 \end{bmatrix} \quad (14)$$

It will be seen from (this matrix) that the scattering process is particularly simple, amounting to a simple averaging of four incident voltage pulses to obtain each scattered (reflected) pulse. There is no need for matrix inversion or matrix manipulation of any kind. The 3D TLM algorithm is then an implementation of the scheme described for 2D format in connection with Eqs. (7) and (9), where the scattering matrix is as given by (14). The connection matrix C is again very simple, codifying information for each node and its nearest ports in each coordinate direction. The correspondence between field and circuit quantities is again, as in the case of the 2D node, straightforward.

Fields may be calculated at the center of the node or at the boundaries between nodes. As an illustration the electric field component E_x at the center of the node is associated with port generating voltages in the x direction and is obtained as follows:

$$E_x = -\frac{V_x}{tax} = -\frac{V_1^i + V_2^i + V_9^i + V_{12}^i}{2tax} \quad (15)$$

Similarly, for the magnetic field component in the same direction, we obtain

$$H_x = \frac{I_x}{tax} = \frac{V_4^i + V_7^i - V_5^i - V_8^i}{2Ztax} \quad (16)$$

Fields at the boundary between nodes are also easily obtained as shown below for two field components at the boundary between nodes (x,y,z) and $(x+1,y,z)$:

$$E_y = -\frac{V_{11}^i(x,y,z) + V_3^i(x+1,y,z)}{tay} \quad (17)$$

$$H_z = \frac{V_3^i(x+1,y,z) - V_{11}^i(x,y,z)}{Ztaz}$$

Current and charge density may be obtained directly from the fields using Ampere and Gauss laws or with reference to the analogies between field and circuit quantities.

Excitation of the mesh is achieved by launching appropriate voltage pulses on the TL of particular nodes. As an illustration, to launch an electric field component $E_x = E_0$ at a particular node, the following voltage pulses must be applied:

$$V_1^i = V_2^i = V_9^i = V_{12}^i = -\frac{E_0 tax}{2} \quad (18)$$

Perfectly conducting boundaries are easily imposed on the mesh at the connection stage, at the boundaries between nodes, by specifying that the reflection coefficient there is equal to -1 . More complex boundaries (e.g., with frequency-dependent properties) can also be specified as explained in the following sections.

A variable mesh ($\Delta x \neq \Delta y \neq \Delta z$), or a mesh describing an inhomogeneous material, is established by adding stubs to the standard SCN described above, to maintain synchronism and account for values of permittivity and permeability larger than one. In the most general case, open-circuit, short-circuit, and infinitely long stubs are used to account for ϵ, μ, σ of the medium [7,9]. The structure thus obtained is referred to as the *stubbed SCN*. However, this is not the most efficient structure, and in most practical implementations of TLM the *hybrid SCN* is employed. In this node, synchronism is maintained, but the condition that all link lines have the same characteristic impedance is relaxed. This allows all the required inductance (μ in field terms) to be modeled by the linklines, and stubs are needed only to account for ϵ [13]. This results in a reduction of the storage required and in operating the mesh at a larger timestep compared with a stubbed SCN. Alternatively, all the required capacitance may be described by the linklines, and stubs then account for extra inductance. A general discussion of the properties of the hybrid SCN may be found in a paper by Trenkic et al. [14]. For problems with

cylindrical symmetry, non-Cartesian nodes are available to facilitate modeling [15].

Developments to increase the efficiency of TLM computation are described in the literature. A particular technique to speed up scattering is described in another paper by Trenkic et al. [16]. For each coordinate direction, total voltage and current are first calculated and the reflected voltages are then obtained from

$$V_{y\text{mx}}^r = V_x - ZI_z - V_{y\text{px}}^i \quad (19)$$

Similar equations apply for the y and z directions. The notation used to designate voltage pulses in (19) is as follows: superscripts “i” or “r” indicate incident or reflected voltages, the first subscript indicates direction of propagation (x , y , or z), the second subscript (“ n ” or “ p ”) indicates line segment along the negative or positive axis, and the third subscript indicates the polarization direction of the pulse (x , y , or z).

4. THEORETICAL FOUNDATIONS OF TLM

In this section some of the general concepts that underpin the foundation of TLM are discussed together with important features of the method such as dispersion and accuracy.

4.1. The General SCN TLM Node

A number of TLM nodes are available, many of them derivatives of the basic SCN, which appeared in the literature over the years. These may be unified under a general formulation described in Ref. 17. It accounts for a general anisotropic materials represented by ϵ_{ri} , μ_{ri} , $i = 1, 2, 3$ where the indices 1, 2, 3 refer to the coordinate directions x, y, z . In this node, for the i -directed, j -polarized link line, the capacitances and inductances per unit length are C_{ij}, L_{ij} . The i -directed stubs represent capacitance and inductance:

$$C_0^i, L_s^i$$

The TLM constitutive equations are (Δi is the node size in i direction)

$$\begin{aligned} C_{kitak} + C_{jitaj} + C_0^i &= \epsilon_{r0} \epsilon_{ri} \frac{t_j t_k t a k}{t a i} \\ L_{jktaj} + L_{kjtak} + L_s^i &= \mu_0 \mu_{ri} \frac{t_j t_k t a k}{t a i} \end{aligned} \quad (20)$$

Synchronism requires that the same timestep prevail throughout; therefore

$$t a t = t a i \sqrt{C_{ij} L_{ij}} \quad (21)$$

Using all possible permutations of $i, j, k \in \{x, y, z\}$, we obtain six equations from (20) and another six from (21). There

are 18 unknown parameters

$$C_{ij}, L_{ij}, C_0^i, L_s^i$$

and therefore there remain 6 degrees of freedom. By imposing additional restrictions on the linkline and stub parameters, several TLM nodes may be derived. According to Trenkic et al. [17], a classification of 3D TLM condensed nodes in the time domain is as follows:

- *Stub-loaded nodes*, which have the same characteristic impedance for all linklines (constant L/C ratio for all six lines giving the additional constraints).
- *Hybrid nodes*, which have either open- or short-circuit stubs (thus supplying three additional conditions), the other three conditions obtained by demanding that all the line impedances modeling the same magnetic or electric field components are the same.
- *Supercondensed nodes*, which have no stubs at all; therefore six conditions are imposed by demanding that all stub capacitances and inductances be equal to zero. The supercondensed node is described in Ref. 18.
- *General nodes*, which have a combination of linklines and stubs.

According to the constitutive equations above, a *general symmetric condensed node* (GSCN) may be derived where material properties may be shared between linklines and stubs. The advantage of this option is that an optimization is possible to achieve, for example, particular dispersion characteristics. This in general results in a node with six different characteristic impedances, six stubs, and six lossy elements. The general theory of the GSCN and its scattering properties may be found in Ref. 17.

4.2. Field-Theoretic Derivation of TLM

An elegant derivation of TLM SCN method is by applying the method of moments (MoM) to Maxwell's equations [19, 20]. The field components are expanded in a set of subdomain basis functions, as shown below for the x components,

$$\begin{aligned} E_x(\vec{x}, t) &= \sum \lim its_{k,l,m,n} k + (1/2) E_{l,m,n}^x F_{l,m,n}^x(\vec{x}) T_{k+(1/2)}(t) \\ &\quad + \sum \lim its_{k,l,m,n} k + (1/2) E_{l,m,n}^x F_{l,m,n}^x(\vec{x}) T_{k+(1/2)}(t) \\ H_x(\vec{x}, t) &= \sum \lim its_{k,l,m,n} k + (1/2) H_{l,m,n}^x F_{l,m,n}^x(\vec{x}) T_{k+(1/2)}(t) \\ &\quad + \sum \lim its_{k,l,m,n} k + (1/2) H_{l,m,n}^x F_{l,m,n}^x(\vec{x}) T_{k+(1/2)}(t) \end{aligned} \quad (22)$$

where

$$k + (1/2) E_{l,m,n}^\mu, \quad k + (1/2) H_{l,m,n}^\mu, \quad \mu = x, y, z$$

are the expansion coefficients. The other components are obtained by permutation of x, y, z and the corresponding

discrete coordinates l, m, n . The basis functions in time are defined as

$$T_{k\pm(1/2)}(t) = g\left(\frac{t}{\Delta t} - k \mp \frac{1}{2}\right)$$

where

$$g(x) = \begin{cases} \text{trix}1 - |x|, & |x| < 10, \\ |x|, & |x| \geq 1 \end{cases}$$

The spatial basis functions are defined as

$$F_{l,m,n}^{\mu}(\vec{x}) = H_l(x)F_{m\pm(1/2),n}(pa, \mu, v)$$

where H is a rectangular pulse function and F is a two-dimensional triangular basis function. This spatial basis functions provides a step approximation in the μ direction and a piecewise linear approximation in the diagonal directions of the plane perpendicular to the μ direction. Substituting these expansions into Maxwell's equations, sampling with delta functions and the derivatives of delta functions, and combining the 12 resulting equations gives the following form:

$$(M_1 + TM_2)\mathbf{b} = (M_3 + TM_4)\mathbf{a} \quad (23)$$

In this expression \mathbf{a} and \mathbf{b} are the incident and reflected wave amplitudes, respectively. Introducing the normal TLM choices for the timestep, one obtains, after some manipulation [19]

$$\mathbf{b} = TS\mathbf{a} \quad (24)$$

where S is the normal scattering matrix for the TLM SCN node, thus demonstrating that the TLM scattering scheme may be derived directly from MoM procedures. An interesting development, which stems from the theoretical foundation of TLM described above, is the derivation of the alternating TLM (ATLM) scheme, which reduces computational effort and removes spurious solutions at the expense of more complicated boundary conditions [20].

4.3. Dispersion Properties of TLM

A mesh consisting of a lattice of SCN TLM nodes is essentially a lowpass network, and therefore propagation properties are dependent on both frequency and propagation angle. At the interface between areas of the mesh with different spatial resolutions, waves encounter, effectively, a numerical discontinuity. These features are generally described as "dispersion" and are common to all numerical schemes such as FDTD. However, each particular scheme has its own unique dispersion characteristics, and a basic understanding is useful in applications where control of errors is important. A simple analysis of the 3D SCN based on circuit concepts may be done in certain cases [21], and results may be obtained using numerical means [22]. For propagation along the diagonal, the regular SCN exhibits no dispersion, but in other directions there is dispersion that increases with frequency. The best advice, which is common to all similar

numerical schemes, is to use a resolution of at least 10 segments per wavelength at the highest frequency of interest. If this is done, dispersion errors of a few percent under the worst circumstances should be expected. Studying dispersion properties by deriving dispersion relations in a closed analytical form is a much more demanding task, but some significant progress has been reported [23,24].

The problem of propagation behavior at the interface between different meshes is a difficult one, and no general analytical expressions are available that allow a rapid assessment of prevailing errors. Most studies are based on numerical work and the general advice is that abrupt changes in resolution should be avoided. A study that compares the behavior of TLM and FDTD for the same grading ratios across interfaces may be found in Ref. 25.

4.4. A Modal View of TLM

Another interesting insight into TLM is to examine its structure in terms of modal components.

At the surface of each mode there are 12 electric and 12 magnetic field components, which are related by an admittance operator Y :

$$\mathbf{H} = Y\mathbf{E} \quad (25)$$

Expressing field components in terms of incident and reflected voltages at the node gives

$$\mathbf{E} = \mathbf{V}^i + \mathbf{V}^r, \quad \mathbf{H} = y_0(\mathbf{V}^i - \mathbf{V}^r) \quad (26)$$

where y_0 is a scalar quantity. Combining these expressions, one obtains the scattering equation for the TLM node

$$\{y_0 I + Y\}\mathbf{V}^r = \{y_0 I - Y\}\mathbf{V}^i \quad (27)$$

where I is the identity matrix. The best way to solve Eq. (27) is to solve an eigenvalue problem

$$Y\mathbf{U}_n = \gamma_n \mathbf{U}_n \quad (28)$$

where \mathbf{U}_n and γ_n are the eigenvectors and eigenvalues of Y , respectively. Defining a matrix U with columns that are the eigenvector of Y , the voltage components incident and reflected at each node may be expressed in terms of modal components:

$$\mathbf{V}^i = U\mathbf{X}^i, \quad \mathbf{V}^r = U\mathbf{X}^r \quad (29)$$

Combining these expressions with (27) gives the following equation, after some manipulation:

$$X_n^r = \frac{y_0 - \gamma_n}{y_0 + \gamma_n} X_n^i \quad (30)$$

This expression shows that, effectively, the admittance seen into the node by each mode is the eigenvalue, as shown schematically in Fig. 8.

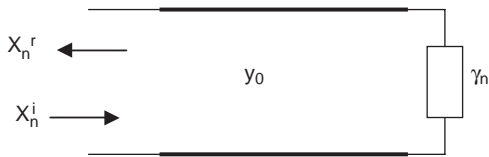


Figure 8. Admittance seen by each mode incident on a TLM node.

The structure of Y and its eigenvalues can be formally derived or obtained from physical intuition in terms of 12 cylindrical harmonics (two TE and two TM modes per coordinate direction). As an example for TM modes the field components are

$$\begin{aligned} E_{z,n} &= \frac{J_n(k_0 r)}{J_n(k_0 \Delta)} \cos(n\varphi) \\ H_{\varphi,n} &= \frac{1}{j\omega\mu} \frac{dJ_n(k_0 r)/dr}{J_n(k_0 \Delta)} \cos(n\varphi) \end{aligned} \quad (31)$$

where k_0 is the wavenumber and the fields were normalized at the edge of the node $r = \Delta$. The eigenvalues for this mode are

$$\gamma_n = \frac{H_{\varphi,n}}{E_{z,n}} = \frac{1}{j\omega\mu} \left. \frac{dJ_n(k_0 r)/dr}{J_n(k_0 r)} \right|_{r=\Delta} \quad (32)$$

Using a small argument expansion for the Bessel functions, the eigenvalue for the $n = 0$ TM_{z0} mode is obtained:

$$\gamma_0 = j \frac{\omega\epsilon\Delta}{2} \quad (33)$$

Hence the reflection coefficient for the TM_{z0} mode is

$$\Gamma = \frac{y_0 - \gamma_0}{y_0 + \gamma_0} \simeq e^{-jk\Delta} \quad (34)$$

This represents a simple phase shift on a lossless line segment. Similar expressions are obtained for the other modes. TLM therefore may be interpreted as a procedure for implementing in the time domain the process of analysis of total voltages into modes, the proper reflection of each mode at the node, and the recombination of modes to obtain total voltages for transmission to adjacent nodes. These ideas are useful in implementing schemes for embedding thin wires into TLM nodes. More details may be found in Ref. 26.

5. FURTHER DEVELOPMENTS AND SELECTED APPLICATIONS

5.1. Absorbing Boundary Conditions

All differential equation numerical techniques that are based on a volumetric discretization require special boundary conditions to deal with open-boundary problems.

Typically, at the extremities of the numerical mesh, where an open boundary exists, a termination must be

placed that mimics, as far as possible, the open boundary of the real physical problem. The simplest approach in TLM has been to use the “matched boundary condition,” which effectively terminates the line segments at the open boundary with the medium’s characteristic impedance. This is an inexpensive absorbing boundary condition to use and should be employed whenever possible. The resulting small reflections are acceptable in all except the most demanding problems.

In cases where a better absorbing boundary condition is required, two approaches have emerged for use in a TLM mesh. The first approach is based on the Johns matrix concept and is particularly suitable for terminating waveguide problems [27]. In time-domain diakoptics the impulse response of the TLM mesh at selected input points is in effect a discrete Green function, which is referred to as the “Johns matrix”. If this response is known, then the response to any excitation is obtained by convolving the excitation with its Johns matrix. At an interface marking an open boundary, the Johns matrix is in effect a reflection coefficient matrix such as impulses reflected at the interface are dependent on the impulses not only at a given time but also at previous times. This approach works well and efficiently on simple open boundaries such as those found in waveguide problems.

For terminating open boundaries in more general configurations, the computational cost of the Johns matrix approach is unacceptable and schemes based on the “perfectly absorbing layer” [also known as “perfectly matched layer” (PML)] are generally preferred. This effectively introduces a fictitious material as an absorber and is used extensively in FDTD schemes. An implementation of the PML boundary condition in TLM is described in Ref. 28. It should be noted that the PML schemes exhibit instabilities under certain conditions, notably when terminating waveguides contain irises, and hence in such cases the Johns matrix approach should be preferred.

5.2. Multigrid Schemes

Mesh refinement is necessary whenever fine features such as wires, wire looms, edges, and thin walls with perforations need to be described in the mesh. It would appear that the simplest way and the one resulting in the best accuracy is to use a finer mesh so that the finest feature can be accommodated by the resolution of the mesh. This would imply typically four sampling points per fine feature. The resulting size of the computation, however, would be excessively large. An alternative is to use a finer mesh only where it is required, thus resulting in a multigrid mesh.

Substantial effort has been expended in this area over many years as reviewed in Ref. 29. There are many difficulties to overcome, and it appears that an entirely satisfactory scheme is not available. Two schemes, that allow for a multigrid mesh in TLM are described in Refs. 30,31. Multigrid schemes are available mainly as research tools and should be used with caution and only for small resolution ratios between fine and coarse meshes.

5.3. The ADI TLM

Another development in TLM, which results in an implicit algorithm, is the alternate-direction-implicit TLM (ADI-TLM) or split-step TLM (SS-TLM) [32–34] scheme. These algorithms split sampling in time into two steps. As an example, for the x component of the electric field, two sub-equations are obtained:

$$\begin{aligned} \frac{1}{2} \left[\epsilon \frac{\partial E_x}{\partial t} + \sigma E_x \right] &= \frac{\partial H_z}{\partial y} \\ \frac{1}{2} \left[\epsilon \frac{\partial E_x}{\partial t} + \sigma E_x \right] &= -\frac{\partial H_y}{\partial z} \end{aligned} \tag{35}$$

The first step is implemented by approximating the first equation in (35) between times $(n - \frac{1}{2})\Delta t$ and $n \Delta t$ and the second equation between $n \Delta t$ and $(n + \frac{1}{2})\Delta t$. The second step is similarly obtained by approximating the second equation between $(n + \frac{1}{2})\Delta t$ and $(n + 1)\Delta t$, and the first between $(n + 1)\Delta t$ and $(n + \frac{3}{2})\Delta t$. This results in an implicit algorithm, but a larger timestep can be employed compared to nonsplit explicit TLM algorithms. The overall result is that in some circumstances a computational saving is achieved. It is not clear at present whether these benefits persist when dealing with general EM problems with inhomogeneous materials, embedded wires, or similar.

5.4. Modeling of General Materials with Frequency-Dependent Properties in the Time Domain

Simple materials with frequency independent properties are easily modeled in TLM by adjusting node parameters (dielectrics, losses) or reflection coefficients (perfect conductors). For more general materials, which may involve dependence on frequency, anisotropy, chirality, nonlinearity, and other properties, special techniques need to be developed for time-domain models. The simplest way to visualize the procedures to be followed in the development of such models, is to consider that in the frequency-domain material properties represent in effect the transfer function of an analog filter. By deriving an equivalent digital filter, which has the same frequency response as the analog filter, a time-domain procedure is readily obtained that can be directly embedded into the time-domain TLM model.

A simple yet important example is of propagation in a Debye material where

$$\epsilon(\omega) = \epsilon_\infty + \frac{\epsilon_s - \epsilon_\infty}{1 + j\omega\tau} \tag{36}$$

where $\epsilon_s, \epsilon_\infty, \tau$, are the static permittivity, permittivity at infinite frequencies, and relaxation time, respectively. Limiting, for simplicity, the discussion to 1D propagation in a Debye medium the calculation proceeds as follows.

The basic circuit equivalent for the problem is shown in Fig. 9. The TLM equivalent of this circuit is shown in

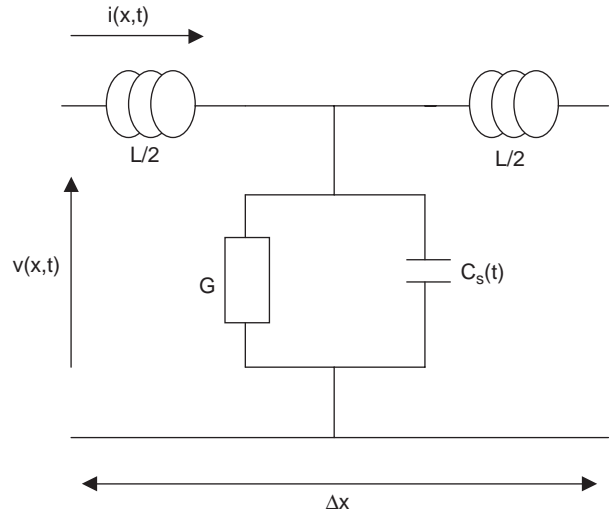


Figure 9. A segment of a model to describe 1D propagation in a Debye medium.

Fig. 10, where all impedances are normalized to

$$Z_0 = \frac{1}{Y_0} = \sqrt{\frac{\mu_0}{\epsilon_0}} \tag{37}$$

The timestep and the following parameters are calculated from

$$\begin{aligned} \Delta t &= \frac{\Delta x}{c} \\ \beta &= \exp\left(\frac{-\Delta t}{\tau}\right) \\ \alpha &= (\epsilon_s - \epsilon_\infty)(1 - \beta) \\ g &= \sigma \Delta x Z_0 \\ t &= \frac{2}{2\epsilon_\infty + g + 2\alpha} \\ t_s &= 2t(\epsilon_\infty + \alpha - 1) \\ t_f &= t\beta \end{aligned} \tag{38}$$

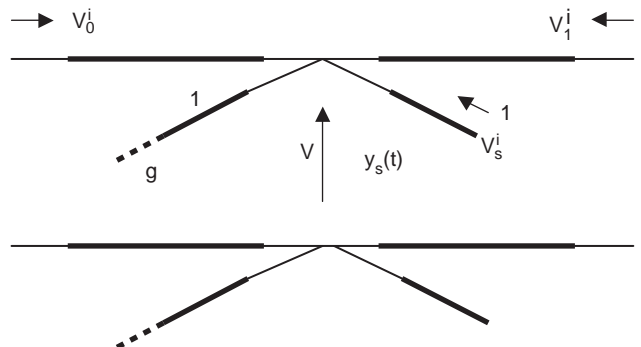


Figure 10. The normalized equivalent circuit of the circuit in Fig. 9, where lumped components were replaced by link and stub lines.

The total voltage is obtained from

$${}_k V = t({}_k V_0^i + {}_k V_1^i) + t_s {}_k V_s^i + t_f {}_{k-1} u \quad (39)$$

The quantity u is obtained by the procedure shown in Fig. 11. The reflected voltages are then calculated as follows:

$$\begin{aligned} {}_k V_0^r &= {}_k V - {}_k V_0^i \\ {}_k V_1^r &= {}_k V - {}_k V_1^i \\ {}_k V_s^r &= {}_k V - {}_k V_s^i \end{aligned} \quad (40)$$

The algorithm requires one backstore variable. Similar procedures are available to deal with material modeling in three dimensions and with a range of material parameters [35–39].

5.5. Multiscale Schemes

The problem of fine features in large computations and the need to deal effectively and efficiently with multiscale problems were already discussed [29]. Two examples are given here for two important practical problems: the simulation of coupling to wires and the simulation of the shielding effectiveness of cabinets.

For describing thin wires, the approach first described by Holland and Simpson [40] has been used for some time. It is based on the principle of calculating an in-cell capacitance to represent the wire and thus building an interface between the wire and the rest of the TLM mesh. Calculation of the parameters of this interface is based on the quasistatic assumption regarding the field around the wire. Several papers discuss in detail the nature of this interface for a wire placed between nodes [41], a wire placed at the node center [42], and multiconductor looms [43]. All these developments suffer from a number of assumptions and limitations.

An alternative technique is based on taking into account more than one modes for the field around the wire [modal expansion technique (MET)]. Because MET takes more modes into account (some of which are asymmetric), it is suited to placing the wire arbitrarily anywhere in the node. It is also accurate and removes several other restrictions inherent in the conventional approach. MET is based on the approach described in Section 4.4 for a node without a wire, with the important modification that more modes need now be taken into account, and, the imped-

ance seen by incoming pulses takes account of the presence of the wire. The complete field solution for a long wire is

$$\begin{aligned} E_z(r, \varphi) &= \sum_{n=-\infty}^{\infty} B_n e^{jn\varphi} \left[J_n(k_0 r) - \frac{J(k_0 a)}{N_n(k_0 a)} N_n(k_0 r) \right] \\ H_\varphi(r, \varphi) &= \frac{1}{j\omega\mu_0} \frac{\partial E_z}{\partial r} \end{aligned} \quad (41)$$

From this it can be seen that the static solution used in the conventional approach based on Holland and Simpson is only the first term in this expansion. Depending on the degrees of freedom available, several modes may be used. In two dimensions, where TLM nodes have four ports, four modes are employed. In three dimensions, for a z -directed wire, four modes (TE, TM, TEM odd, TEM even) and four angular instances are selected, making a total of 16 modes. Wires that are offset from the center of the node may also be described by exploiting as an example the addition theorems for Bessel functions. The approach of working out the eigenvalues, the impedance seen by each mode and for constructing suitable algorithms, may be found in Ref. 26.

Another problem of importance in many applications is the description of a thin wall with numerous perforations that is part of a resonant box (e.g., equipment cabinet). It is simply computationally far too expensive to generate a mesh with the necessary resolution to describe all relevant features. The simplest approach to this type of problem is to place the thin wall with perforations between nodes and to account for its properties by a frequency-dependent scattering matrix $S(\omega)$ implemented during the connection process in TLM. This technique is referred to as a *digital filter interface* (DFI) since it reduces to a time-domain algorithm as part of the connection process. Each coefficient of the scattering matrix is put into standard Padé form and then the frequency-domain Prony method is used to find its poles and zeros. The resulting expression is converted into the discrete time domain by application of the bilinear transformation. The resulting equations in state form relating incident and reflected voltages are of the form

$$\begin{aligned} V^i &= B_0 V^r + \mathbf{B}' X \\ X &= z^{-1} A' X + z^{-1} \mathbf{1}' V^r \end{aligned} \quad (42)$$

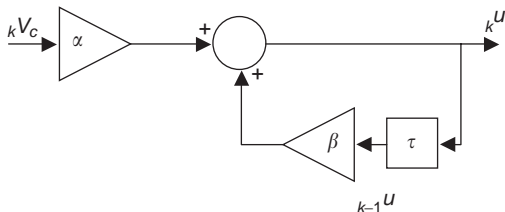


Figure 11. Signal flow diagram representing the algorithm for implementing the model for Debye materials.

In (42) the first equation is the output equation and the second is the state equation, and the computational procedure is shown in Fig. 12. Details may be found in Ref. 44. Using this approach, very substantial computational savings can be made. Moreover, the frequency-dependent scattering matrix may be obtained by numerical simulation, analytically or experimentally. The calculation of the poles and zeros is a preprocessing task and therefore is not an overhead on the main timestepping simulation.

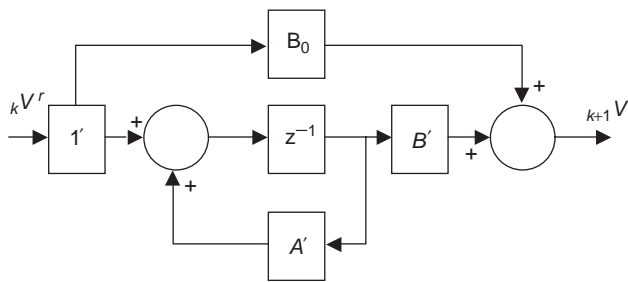


Figure 12. Signal flow diagram of the “connection” process to account for fine features using the DFI algorithm.

5.6. Frequency-Domain TLM (FD-TLM)

TLM is mainly used as a time-domain method but can also be implemented in the frequency domain. In FD-TLM time-harmonic variations are used and therefore discretization in space only is required. This considerably simplifies the modeling of materials and other features. However, the algorithm requires the inversion of a large matrix.

Several schemes are available in which either the characteristic impedance of each line is kept the same or phase constants are kept the same. Details may be found in the literature [45–48].

BIBLIOGRAPHY

- G. Kron, Equivalent circuit of the field equations of Maxwell, *Proc. IRE* **32**:289–299 (1944).
- J. R. Whinnery and S. Ramo, A new approach to the solution of high-frequency problems, *Proc. IRE* **32**:284–288 (1944).
- J. R. Whinnery et al., Network analyser studies of electromagnetic cavity resonators, *Proc. IRE* **32**:360–367 (1944).
- P. B. Johns and R. L. Beurle, Numerical solution of two-dimensional scattering problems using transmission-line matrix, *Proc. IEE* **118**:1203–1208 (1971).
- S. Akhtarzad and P. B. Johns, Solution of Maxwell’s equations in three space dimensions and time by the TLM method of numerical analysis, *Proc. IEE* **122**:1344–1348 (1975).
- W. J. R. Hoefer, The transmission-line matrix method-theory and applications, *IEEE Trans. Microwave Theory Tech.* **MTT-33**:882–893 (1985).
- P. B. Johns, A symmetrical condensed node for the TLM method, *IEEE Trans. Microwave Theory Tech.* **MTT-35**:370–377 (1987).
- W. J. R. Hoefer and P. P. M. So, *The Electromagnetic Wave Simulator—a Visual Electromagnetics Laboratory Based on the 2D TLM Method*, Wiley, New York, 1991.
- C. Christopoulos, *The Transmission-Line Modeling Method-TLM*, IEEE Press, New York; 1995.
- P. Russer and C. Christopoulos, Transmission-line method, Part IV, in N. K. Uzunoglu et al., eds., *Applied Computational Electromagnetics*, Springer-Verlag, Berlin, 1998.
- C. Huygens, *Traite de la Lumiere*, Leiden, Paris; 1690.
- P. B. Johns, A new mathematical model to describe the physics of propagation, *Radio Electron. Eng.* **44**:657–666 (1974).
- R. A. Scaramuzza and A. J. Lowery, Hybrid symmetrical condensed node for the TLM method, *Electron. Lett.* **26**:1947–1949 (1990).
- V. Trenkic et al., On the time step in hybrid symmetrical condensed nodes, *IEEE Trans. Microwave Theory Tech.* **MTT-43**:2172–2174 (1995).
- R. Allen and M. J. Clark, Application of the symmetrical TLM method to the cold modelling of magnetrons, *Int. J. Num. Model.* **1**:61–70 (1988).
- V. Trenkic et al., Simple and elegant formulation of scattering in TLM nodes, *Electron. Lett.* **29**:1651–1652 (1993).
- V. Trenkic et al., Development of a general symmetrical condensed node for the TLM method, *IEEE Trans. Microwave Theory Tech.* **MTT-44**:2129–2135 (1996).
- V. Trenkic et al., Theory of the symmetrical super-condensed node for the TLM method, *IEEE Trans. Microwave Theory Tech.* **MTT-43**:1342–1348 (1995).
- M. Krumpolz and P. Russer, A field theoretical derivation of TLM, *IEEE Trans. Microwave Theory Tech.* **MTT-42**:1660–1668 (1994).
- P. Russer and B. Bader, The alternating transmission-line matrix (ATLM) scheme, *Proc. IEEE Microwave Theory Tech.* **MTT-S**:19–22 (1995).
- W. J. R. Hoefer, The transmission-line matrix (TLM) method, in T. Itoh, ed., *Numerical Techniques for Microwave and Millimeter-Wave Passive Structures*, Wiley, New York, 1989.
- J. S. Nielsen and W. J. R. Hoefer, A complete dispersion analysis of the condensed node TLM mesh, *IEEE Trans. Magn.* **27**:3982–3985 (1991).
- M. Krumpolz and P. Russer, On the dispersion in TLM and FDTD, *IEEE Trans. Microwave Theory Tech.* **MTT-42**:1275–1279 (1994).
- V. Trenkic et al., Analytical expansion of the dispersion relation for TLM condensed nodes, *IEEE Trans. Microwave Theory Tech.* **MTT-44**:2223–2230 (1996).
- F. J. German et al., A numerical comparison of dispersion in irregularly graded TLM and FDTD meshes, *Proc. Annu. Rev. Prog. Appl. Computational Electromagn.* **12**:270–278 (1996).
- P. Sewell et al., An accurate thin-wire model for 3D TLM simulations, *IEEE Trans. Electromagnetic Compatibility*, **EMC-45**:207–217 (2003).
- W. J. R. Hoefer, The discrete time-domain Green’s function or Johns matrix—a new powerful concept in TLM, *Int. J. Num. Model.* **2**:215–225 (1989).
- S. Le Maguer and M. M. Ney, Extended PML-TLM: An efficient approach for full wave analysis of open structures, *Int. J. Num. Model.* **14**:129–144 (2001).
- C. Christopoulos, Multi-scale modelling in time-domain electromagnetics, *Int. J. Electron. Commun. (AEU)* **57**:100–110 (2003).
- J. L. Herring and C. Christopoulos, Solving EM problems using a multiple grid TLM method, *IEEE Trans. Antenn. Propag.* **AP-42**:1654–1658 (1994).
- J. Wlodarczyk, New multigrid interface for the TLM method, *Electron. Lett.* **32**:1111–1112 (1996).
- T. Namiki, A new FDTD algorithm based on alternating direction implicit method, *IEEE Trans. Microwave Theory Tech.* **MTT-47**:2003–2007 (1999).
- F. Zheng et al., Toward the development of a 3D unconditionally stable FDTD method, *IEEE Trans. Microwave Theory Tech.* **MTT-48**:1550–1558 (2000).

34. S. Le Maguer and M. M. Ney, Split step TLM (SS-TLM) for efficient electromagnetic simulation of small heterogeneous apertures, *Proc. Zurich Electromagnetic Compatibility Symp.*, 2003, pp. 275–278.
35. L. De Menezes and W. J. R. Hoefler, Modeling of general constitutive relationships using SCN TLM, *IEEE Trans. Microwave Theory Tech.* **MTT-44**:854–861 (1996).
36. J. Paul et al., Generalised material models in TLM—Part 1: Materials with frequency dependent properties, *IEEE Trans. Anten. Propag.* **AP-47**:1528–1534 (1999).
37. J. Paul et al., Generalised material models in TLM—Part 2: Materials with anisotropic properties, *IEEE Trans. Anten. Propag.* **AP-47**:1535–1542 (1999).
38. J. Paul et al., Generalised material models in TLM—Part 3: Materials with non-linear properties, *IEEE Trans. Anten. Propag.* **AP-50**:997–1004 (2002).
39. I. Barba et al., Multiresolution model of electromagnetic wave propagation in dispersive materials, *IEEE Trans. Microwave Theory Tech.* **MTT-S**:243–246 (2000).
40. R. Holland and J. W. Simpson, Finite-difference analysis of EMP coupling to thin struts and wires, *IEEE Trans. Electromagnetic Compatibility*, **23**:88–97 (1981).
41. J. Wlodarczyk and D. P. Johns, New wire interface for graded 3D TLM, *Electron. Lett.* **28**:728–729 (1992).
42. J. A. Porti et al., A comparison of thin wire models for the TLM method, *Electron. Lett.* **28**:1910–1911 (1992).
43. J. Wlodarczyk et al., A fully integrated multiconductor model for TLM, *IEEE Trans. Microwave Theory Tech.* **MTT-46**:2431–2437 (1998).
44. J. Paul et al., The use of digital filtering techniques for the simulation of fine features in EMC problems solved in the time-domain, *IEEE Trans. Electromagnetic Compatibility* **EMC-45**:238–244 (2003).
45. D. P. Johns et al., New TLM technique for steady-state field solutions in three dimensions, *Electron. Lett.* **28**:1692–1694 (1992).
46. H. Jin and R. Vahldieck, The frequency domain transmission-line matrix method—a new concept, *IEEE Trans. Microwave Theory Tech.* **MTT-40**:2207–2218 (1992).
47. D. P. Johns, An improved node for frequency-domain TLM—the distributed node, *Electron. Lett.* **30**:500–502 (1994).
48. P. Berini and K. Wu, A new frequency domain symmetrical condensed node, *IEEE Microwave Guided Wave Lett.* **4**:180–182 (1994).

TRANSMISSION LINE THEORY

RAGHU K. SETTALURI
Oregon State University
Corvallis, OR

A transmission line is a network that connects a generator circuit to a load for the purpose of transmitting electric energy or information from one point to another. Examples of transmission lines include cable connection between a service provider and your television set, telephone wires, interconnection between a transmitter and an antenna, and optic nerves and neural networks in human brain. The list can go on and on with the same essential purpose of transporting energy or information between

two points. In these examples, we can notice one important difference for each scenario. The choice of transmission line is different and depends on the purpose and application. For example, high-power transmission lines that are used to transport megawatts of electric energy need to be thicker and bulkier to accommodate the large power-handling capability and minimize power losses. On the other hand, a microminiaturized interconnect in the 4 GHz central processor of your desktop or laptop needs to be precisely designed to transfer the information in a densely packed circuit environment! In electrical engineering applications, the choice of a suitable transmission medium depends on a variety of factors including the frequency of operation, power handling, and the topology.

Many readers might be familiar with basic circuit analysis techniques for low-frequency electric circuits, which have been well developed over decades. At low frequencies, the physical size of the circuit is much smaller compared with the wavelength. This condition implies that when a load is connected to a voltage source via a length of transmission line, the voltage appears instantaneously at the load end without any time delay, which also implies that lumped elements such as inductors, capacitors, and resistors will have much smaller sizes compared with wavelength, and we can conveniently assume that the voltage across an element on one side of the circuit was exactly in phase with the voltage on the other side. Thus size or separation between elements was never an issue in the low-frequency circuit design!

When the size of an element is a considerable fraction of a wavelength or many wavelengths, the network becomes *distributed* in nature. In this case, aside from time variation, voltages and currents can vary in magnitude and phase as a function of distance. A transmission line may no longer be considered as a simple interconnecting mechanism between two points. It behaves like a distributed-parameter network, for which the transmission properties need to be considered as a part of the design process, which leads to electromagnetic wave propagation on transmission lines with possible standing wave formations.

1. PROPAGATION MODES

The orientation of electric and magnetic fields and their interaction along a transmission line is essentially decided by the geometry of the transmission line structure, which is generally characterized by the *mode* supported by the transmission line structure for the electromagnetic wave propagation. Figure 1 shows several commonly used transmission lines, which are broadly classified into three main categories. The two-wire line, coaxial line, and strip-line, shown Figs. 1a–1c, support transverse electromagnetic (TEM) mode, where the electric and magnetic fields are entirely transverse to the direction of propagation. Many of the characteristics of wave propagation in TEM supporting structures are the same as those for a uniform plane wave propagating in an unbounded dielectric medium.

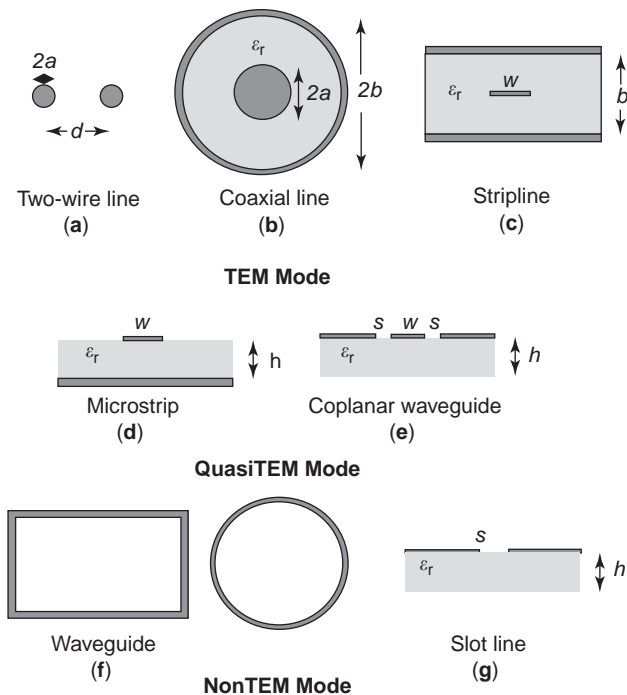


Figure 1. Commonly used transmission lines supporting different propagation modes.

A microstrip line and a coplanar waveguide (Figs. 1d and 1e) are two commonly used planar transmission lines at microwave frequencies. As a result of the presence of the air-dielectric interface, these structures are considered as inhomogeneous transmission lines. Here, the field lines between the conducting strip and the ground lines are not contained entirely in the substrate, and these structures support quasiTEM mode of propagation. However, because the nontransverse field components are considerably smaller compared with the transverse field components, for most practical applications, they can be included in the TEM class of transmission lines. A common feature among TEM and quasiTEM transmission line structures is that they require at least two conductors to support TEM mode and frequencies as low as DC can propagate along these lines.

Several other transmission lines exist that do not support TEM or quasiTEM mode of propagation. These include the rectangular and circular waveguides (Fig. 1f) and slotlines (Fig. 1g). Depending on the configuration, these structures support several higher order modes, such as transverse electric (TE) and transverse magnetic (TM), where the presence of a longitudinal field component cannot be ignored. The minimum frequency (also called the *cutoff* frequency) of the electromagnetic wave that can be supported in these structures depends on factors such as mode number and physical dimensions. Further, the transmission properties will have a strong frequency dependence. As transmission lines supporting TEM/quasiTEM wave propagation are more commonly used in practice, this article focuses on understanding

the wave propagation in the case of TEM supporting structures.

2. TRANSMISSION LINE EQUATIONS

As we have noticed in our earlier discussion, incorporating the spatial dependence of fields is important while addressing the characteristics of the transmission lines at high frequencies. For a given structural geometry, the transmission line characteristics can be determined by solving the Maxwell's equations [1] in various regions. This approach can provide a complete description of electric and magnetic fields at every point in the region. However, many times we are interested in terminal quantities such as voltage, current, impedance, and power, for which a discretized circuit representation of a distributed transmission line may offer simpler, yet adequately accurate solution.

Let us consider a transmission line connected to a source at one end and a load at the other end, as shown in Fig. 2a. If we choose a small section of the line with differential length Δz , it can be modeled as a discrete circuit, as shown in Fig. 2b and described by the following four basic parameters:

- R , resistance per unit length for both conductors, in Ω/m
- L , inductance per unit length for both conductors, in H/m
- G , conductance per unit length in S/m
- C , capacitance per unit length in F/m

The inductance L , represents the total series self inductance in both the conductors and the capacitance C , represents the capacitive coupling between the two conductors, which depends on the proximity between the conductors. R and G develop because of the conductor losses of both conductors and dielectric losses that exist in the medium between the conductors respectively. Thus R and G are essentially the *attenuation* or *loss* parameters of the transmission line. A finite length of transmission line can be considered as a cascade of several sections of infinitesimal length Δz , representing the distributed nature of the line.

The quantities $v(z, t)$ and $i(z, t)$ represent the instantaneous voltage and current at the input of the differential length section at node N . Similarly, $v(z + \Delta z, t)$ and $i(z + \Delta z, t)$ represent the same quantities on the output side at node $N + 1$. Applying Kirchhoff's voltage law, we obtain

$$v(z, t) - R\Delta z i(z, t) - L\Delta z \frac{\partial i(z, t)}{\partial t} - v(z + \Delta z, t) = 0 \quad (1a)$$

Rearranging the terms in Eq. (1a) leads to

$$-\frac{v(z + \Delta z, t) - v(z, t)}{\Delta z} = Ri(z, t) + L \frac{\partial i(z, t)}{\partial t} \quad (1b)$$

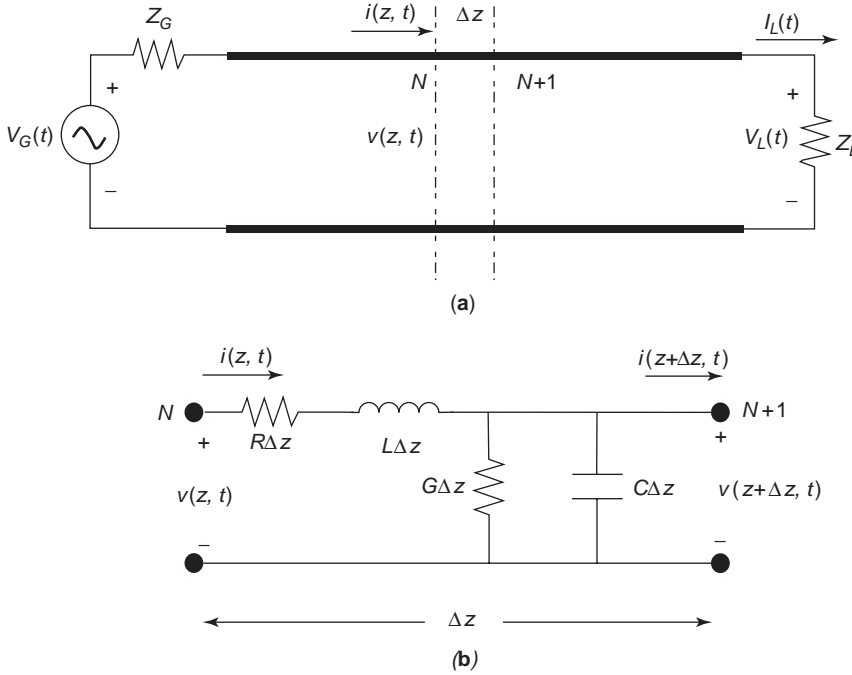


Figure 2. Transmission line and lumped-element representation for the purpose of deriving the Telegrapher's equations. (a) Definition of voltages and currents on a transmission line connected between a source and a load. (b) Lumped-element equivalent circuit for an elemental length of transmission line.

Similarly, applying Kirchhoff's current law to node $N+1$ in Fig. 2b leads to

$$i(z, t) - G\Delta z v(z + \Delta z, t) - C\Delta z \frac{\partial v(z + \Delta z, t)}{\partial t} - i(z + \Delta z, t) = 0 \quad (2a)$$

Again, rearranging the terms in Eq. (2a), we have

$$-\frac{i(z + \Delta z, t) - i(z, t)}{\Delta z} = Gv(z, t) + C \frac{\partial v(z, t)}{\partial t} \quad (2b)$$

In the limit, $\Delta z \rightarrow 0$, Eqs. (1b) and (2b) become

$$-\frac{\partial v(z, t)}{\partial z} = Ri(z, t) + L \frac{\partial i(z, t)}{\partial t} \quad (3a)$$

$$-\frac{\partial i(z, t)}{\partial z} = Gv(z, t) + C \frac{\partial v(z, t)}{\partial t} \quad (3b)$$

The first-order partial differential equations given in Eqs. (3) are the time-domain form of the transmission line equations, which are also called the *Telegrapher's* equations.

As we are primarily interested in sinusoidal steady-state conditions, we can apply the phasor notation with cosine reference to represent the time-domain equations given in Eqs. (3) in frequency-domain. For this, we define

$$v(z, t) = \text{Re}[V(z)e^{j\omega t}] \quad (4a)$$

$$i(z, t) = \text{Re}[I(z)e^{j\omega t}] \quad (4b)$$

where, $V(z)$ and $I(z)$ are phasor quantities dependent on space coordinate z only, and each of them could be real or

complex, and Re represents the real part of a complex quantity. Substituting Eqs. (4a) and (4b) in Eqs. (3) yields the following first-order ordinary differential equations in frequency-domain:

$$-\frac{dV(z)}{dz} = (R + j\omega L)I(z) \quad (5a)$$

$$-\frac{dI(z)}{dz} = (G + j\omega C)V(z) \quad (5b)$$

Eqs. (5) are called the *time-harmonic transmission line equations*.

3. WAVE PROPAGATION ON AN INFINITE TRANSMISSION LINE

The two coupled first-order time-harmonic transmission line equations given in Eqs. (5) can be combined to give two second-order uncoupled differential equations in $V(z)$ and $I(z)$ as

$$\frac{d^2V(z)}{dz^2} - \gamma^2 V(z) = 0 \quad (6a)$$

$$\frac{d^2I(z)}{dz^2} - \gamma^2 I(z) = 0 \quad (6b)$$

where

$$\gamma = \alpha + j\beta = \sqrt{(R + j\omega L)(G + j\omega C)} \quad (m^{-1}) \quad (7)$$

is the *complex propagation constant* of the transmission line, whose real and imaginary parts, α and β , represent

the *attenuation constant* (Np/m) and *phase constant* (rad/m) of the line, respectively. For all passive transmission lines, α will be either zero or a positive quantity.

The wave equations given in Eqs. (6) have solutions of the form

$$V(z) = V_0^+ e^{-\gamma z} + V_0^- e^{\gamma z} \tag{8a}$$

$$I(z) = I_0^+ e^{-\gamma z} + I_0^- e^{\gamma z} \tag{8b}$$

The terms $e^{-\gamma z}$ and $e^{\gamma z}$ represent the wave propagation in $+z$ and $-z$ directions, respectively. V_0^+ and I_0^+ are the wave amplitudes in the $+z$ direction, and V_0^- and I_0^- are the wave amplitudes in the $-z$ direction. These amplitudes are related via the expression

$$\frac{V_0^+}{I_0^+} = -\frac{V_0^-}{I_0^-} = \frac{R + j\omega L}{\gamma} \tag{9}$$

The ratio of the forward wave amplitudes or the negative of the backward wave amplitudes is also defined as *characteristic impedance*, Z_o , of the transmission line, where

$$Z_o = \frac{R + j\omega L}{\gamma} = \frac{\gamma}{G + j\omega C} = \sqrt{\frac{R + j\omega L}{G + j\omega C}} \tag{10}$$

Note that the parameters γ and Z_o can be complex and are independent of the length of the transmission line. As seen in Eqs. (7) and (10), these characteristic properties of the line are directly related to the line parameters R , L , G , and C , which are real in nature. These parameters are dependent on the geometry of the transmission line and material properties of the conductors and the dielectric medium. For example, the line parameters for coaxial line and a two-wire transmission line are given in Table 1.

3.1. Special Cases

3.1.1. Lossless transmission line. The transmission line equations derived in Section 3 are for a general transmission line taking the effect of finite conductivity of the conductors and dielectric losses into account. However, in many practical situations, transmission lines at radiofrequencies are designed to have conductors with high

conductivities and dielectric materials with small values of loss tangent, $\tan\delta$, which would result in values of $R \ll \omega L$ and $G \ll \omega C$. Therefore, if we approximate $R = 0 = G$ in Eqs. (7) and (10), we get

$$\gamma = \alpha + j\beta = j\omega\sqrt{LC} \tag{11a}$$

$$\alpha = 0 \tag{11b}$$

$$\beta = \omega\sqrt{LC} \tag{11c}$$

$$Z_o = \sqrt{\frac{L}{C}} \tag{11d}$$

Thus, the propagation constant, γ , for a lossless transmission line becomes purely imaginary, reasserting the fact that attenuation will be zero for ideal lines with no dielectric and conductor losses. From Eq. (11d), it can be seen that the characteristic impedance, Z_o , becomes real for a lossless line. Phase velocity v_p , which is defined as the velocity of propagation of an equiphase front on the transmission line, is given as

$$v_p = \frac{\omega}{\beta} = \frac{1}{\sqrt{LC}} \tag{12}$$

From Eq. (12), it can be seen that the phase velocity is independent of the frequency of the propagating wave. As any arbitrary signal can be composed of a combination of sinusoidal waves of different frequencies and amplitudes, a constant phase velocity for all frequencies will ensure that all these waves will travel with the same velocity along a lossless line without suffering any attenuation, thus preserving the shape of the signal. On the other hand, for a general lossy transmission line, from Eq. (7), it can be seen that the phase velocity, β , and attenuation, α , are functions of frequency. As different frequency components propagate with different velocities and attenuation factors, the signal suffers *dispersion* and gets *distorted* as it propagates along the line.

3.1.2. Distortionless line. The theory for distortionless line was first proposed by Oliver Heaviside, whose contributions to the electromagnetism were well described in [2]. Consider a general lossy transmission line, which

Table 1.

Structure	Transmission line parameters			
	R (Ω/m)	L (H/m)	G (S/m)	C (F/m)
Two-wire Line (Fig. 1a)	$\frac{R_s}{\pi a}$	$\frac{\mu}{\pi} \ln\left(\frac{d}{2a} + \sqrt{\left(\frac{d}{2a}\right)^2 - 1}\right)$	$\frac{\pi\sigma}{\ln\left(\frac{d}{2a} + \sqrt{\left(\frac{d}{2a}\right)^2 - 1}\right)}$	$\frac{\pi\epsilon}{\ln\left(\frac{d}{2a} + \sqrt{\left(\frac{d}{2a}\right)^2 - 1}\right)}$
Coaxial Line (Fig. 1b)	$\frac{R_s}{2\pi} \left[\frac{1}{a} + \frac{1}{b}\right]$	$\frac{\mu}{2\pi} \ln\left(\frac{b}{a}\right)$	$\frac{2\pi\sigma}{\ln\left(\frac{b}{a}\right)}$	$\frac{2\pi\epsilon}{\ln\left(\frac{b}{a}\right)}$

Notes:

a. μ , ϵ , and σ are the material properties of the dielectric medium.

b. R_s is the surface resistance of the conductors, which is related to the frequency and material properties of the conductor.

satisfies the condition

$$\frac{R}{L} = \frac{G}{C} \quad (13)$$

Substituting Eq. (13) in Eqs. (7) and (10), we get

$$\gamma = \alpha + j\beta = R\sqrt{\frac{C}{L}} + j\omega\sqrt{LC} \quad (14)$$

$$Z_o = \sqrt{\frac{L}{C}} \quad (15)$$

Phase velocity, v_p , is given by,

$$v_p = \frac{\omega}{\beta} = \frac{1}{\sqrt{LC}} \quad (16)$$

Comparing Eqs. (14)–(16) with Eqs. (11) and (12), it can be seen that, except for a nonzero value of attenuation constant, the distortionless line has same characteristics as that of a lossless line. Although the signal suffers attenuation as it propagates along the line, because of the constant phase velocity, waves of different frequency components will travel with the same velocity, thus preserving the shape of the signal, which is why it is called the *distortionless line*.

4. WAVE CHARACTERISTICS ON TERMINATED TRANSMISSION LINE

As you may recall, the general solution for transmission line wave equations given in Eqs. (8) consists of two types of wave propagation—the wave traveling in forward (+z) direction and the wave traveling in the backward (−z) direction. When a wave is incident at one end on an infinitely long transmission line, it continues to propagate in +z or −z direction depending on the direction of the incident wave. Thus, only one of the two terms consisting of either $e^{-\gamma z}$ or $e^{+\gamma z}$ exists. Let us now consider a transmission line of finite length l , terminated by an arbitrary load impedance Z_L , as shown in Fig. 3. It is assumed that the load is at $z=0$ and the source is connected at $z=-l$.

Using Eqs. (9) and (10), Eqs. (8a) and (8b) can be modified to contain only two unknown voltage amplitudes V_o^+ and V_o^- as

$$V(z) = V_o^+ e^{-\gamma z} + V_o^- e^{\gamma z} \quad (17a)$$

$$I(z) = \frac{V_o^+}{Z_o} e^{-\gamma z} - \frac{V_o^-}{Z_o} e^{\gamma z} \quad (17b)$$

At $z=0$, Eqs. (17a) and (17b) become

$$V_L = V(z=0) = V_o^+ + V_o^- \quad (18a)$$

$$I_L = I(z=0) = \frac{V_o^+}{Z_o} - \frac{V_o^-}{Z_o} \quad (18b)$$

Also, V_L and I_L are related via the load impedance, Z_L , as

$$Z_L = \frac{V_L}{I_L} \quad (19)$$

Using Eqs. (18a) and (18b) in Eq. (19) and rearranging terms, we get

$$V_o^- = \Gamma V_o^+ \quad (20a)$$

where

$$\Gamma = |\Gamma| e^{j\theta_r} = \left(\frac{Z_L - Z_o}{Z_L + Z_o} \right) \quad (20b)$$

Γ , which is the ratio of the reflected wave amplitude and the incident wave amplitude, is called the *voltage reflection coefficient*. As both Z_o and Z_L could be complex quantities, Γ can also be complex in general. It may be seen that, for all transmission lines, $|\Gamma| \leq 1$.

Using Eq. (20a) in Eqs. (17a) and (17b), we get

$$V(z) = V_o^+ (e^{-\gamma z} + \Gamma e^{\gamma z}) \quad (21a)$$

$$I(z) = \frac{V_o^+}{Z_o} (e^{-\gamma z} - \Gamma e^{\gamma z}) \quad (21b)$$

The ratio of $V(z)$ and $I(z)$ is called the *input impedance*, Z_{in} , and is given by

$$Z_{in}(z) = \frac{V(z)}{I(z)} = Z_o \left[\frac{1 + \Gamma e^{2\gamma z}}{1 - \Gamma e^{2\gamma z}} \right] \quad (\Omega) \quad (22)$$

At the input of the transmission line, the input impedance can be written as

$$Z_{in}(-l) = Z_o \left[\frac{1 + \Gamma e^{-2\gamma l}}{1 - \Gamma e^{-2\gamma l}} \right] \quad (\Omega) \quad (23)$$

Substituting Eq. (20b) in Eq. (23) and rearranging the terms, we get

$$Z_{in}(-l) = Z_o \left[\frac{Z_L + Z_o \tanh \gamma l}{Z_o + Z_L \tanh \gamma l} \right] \quad (\Omega) \quad (24)$$

Thus, Z_{in} is the impedance seen at the input of the transmission line, when the line is terminated with a load impedance Z_L . From the generator standpoint, the transmission line-load impedance combination can be replaced by a simple impedance Z_{in} , without disturbing the input voltage and current amplitudes, as shown in Fig. 3b. If the line is lossless, we can substitute for $\gamma = j\beta$ in Eq. (24) and get a modified expression for Z_{in} , as

$$Z_{in}(-l) = Z_o \left[\frac{Z_L + jZ_o \tan \beta l}{Z_o + jZ_L \tan \beta l} \right] \quad (\Omega) \quad (25)$$

4.1. Standing Wave Ratio

Consider a lossless transmission line of characteristic impedance Z_o , which is terminated by an arbitrary load impedance Z_L . From Eqs. (21a) and (21b), the expressions for

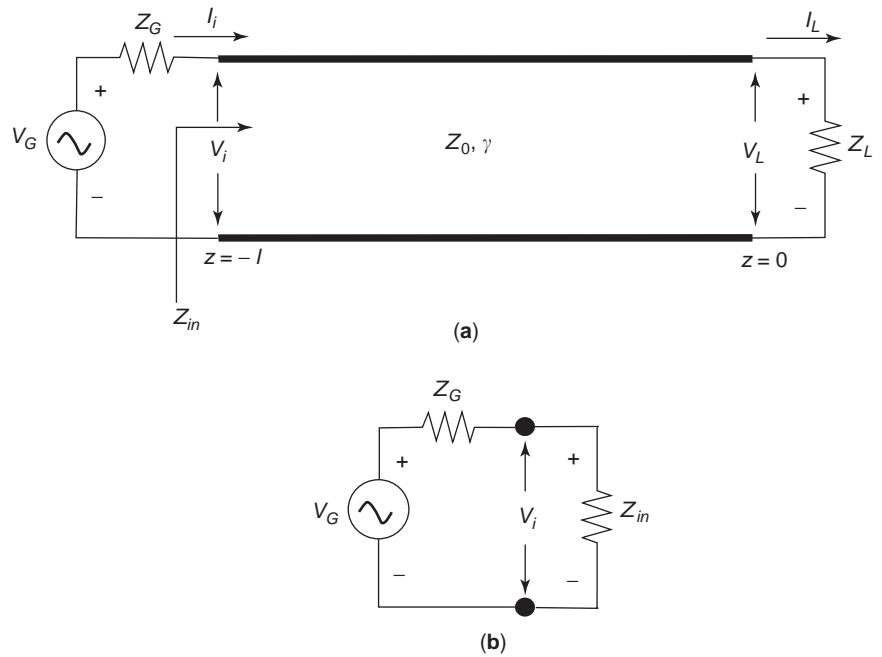


Figure 3. (a) A finite length transmission line terminated with a load impedance, Z_L . (b) Equivalent representation in terms of the input impedance, Z_{in} .

$V(z)$ and $I(z)$ for the lossy transmission line can be written as

$$V(z) = V_0^+ (e^{-j\beta z} + \Gamma e^{j\beta z}) \tag{26a}$$

$$I(z) = \frac{V_0^+}{Z_0} (e^{-j\beta z} - \Gamma e^{j\beta z}) \tag{26b}$$

The magnitude of the voltage, $|V(z)|$, will be

$$|V(z)| = |V_0^+| \cdot |1 + |\Gamma| e^{j(\theta_r + 2\beta z)}| \tag{27}$$

where, $\Gamma = |\Gamma|e^{j\theta_r}$ has been substituted.

Equation (27) shows that the voltage magnitude oscillates as a function of z , as shown in Fig. 4, indicating the standing wave formation. We can see that the voltage will be maximum when $e^{j(\theta_r + 2\beta z)} = 1$, and is given by

$$V_{\max} = |V_0^+| (1 + |\Gamma|) \tag{28a}$$

Similarly, voltage will be minimum when $e^{j(\theta_r + 2\beta z)} = -1$, and is given by

$$V_{\min} = |V_0^+| (1 - |\Gamma|) \tag{28b}$$

It may be noticed that when the load impedance is the same as the characteristic impedance of the line, the reflection coefficient $\Gamma = 0$, from Eq. (27), and we can see that $|V(z)| = |V_0^+|$, a constant value independent of z . As $|\Gamma|$ increases, the ratio of V_{\max} to V_{\min} increases, which leads us to define *voltage standing wave ratio (VSWR)*, or simply *standing wave ratio (SWR)*, as

$$SWR = \frac{V_{\max}}{V_{\min}} = \frac{1 + |\Gamma|}{1 - |\Gamma|} \tag{29}$$

SWR is always a real number such that $1 \leq SWR \leq \infty$. For a matched transmission line (when $Z_0 = Z_L$), $SWR = 1$. It may also be noted that the distance between two successive voltage maxima (or minima) is $\lambda/2$, where λ is the wavelength on the transmission line.

4.2. Special Cases of Terminated Lossless Transmission Lines

Often, we use lossless transmission lines with special terminations to give interesting characteristics. For example, in impedance tuning networks and microwave filter design we commonly use *stubs* (open- or short-circuited transmission lines) in series or shunt configuration as part of the design. Also, at microwave frequencies, the

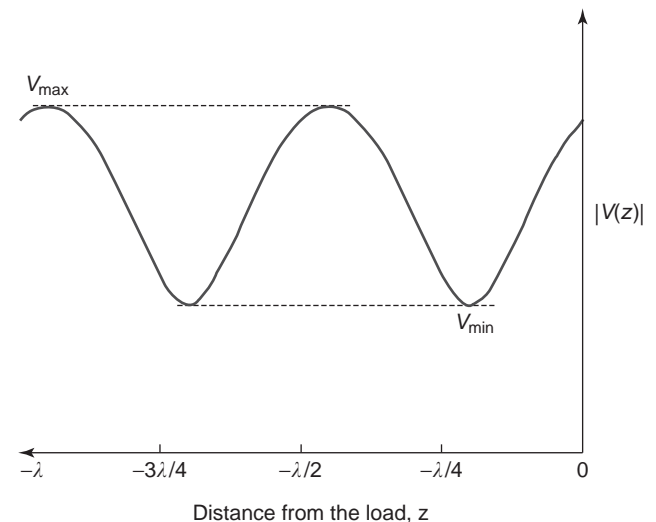


Figure 4. Standing wave formation on a lossless transmission line.

open- and short-circuited stubs can be used to replace lumped capacitors and inductors, which are otherwise impractical to realize. Similarly, we use lines with quarter wavelength for impedance transformation. Section 4.2.1 briefly describes the special properties of some of the lossless lines.

4.2.1. Open-Circuited Line. When a transmission line is open-circuited at one end, as shown in Fig. 5a, it sees an infinite load impedance ($Z_L = \infty$). From Eq. (20b), we can see that the voltage reflection coefficient $\Gamma = 1$, which means that the SWR becomes ∞ . From Eqs. (26a) and (26b), the voltage and current on an open-circuited loss-

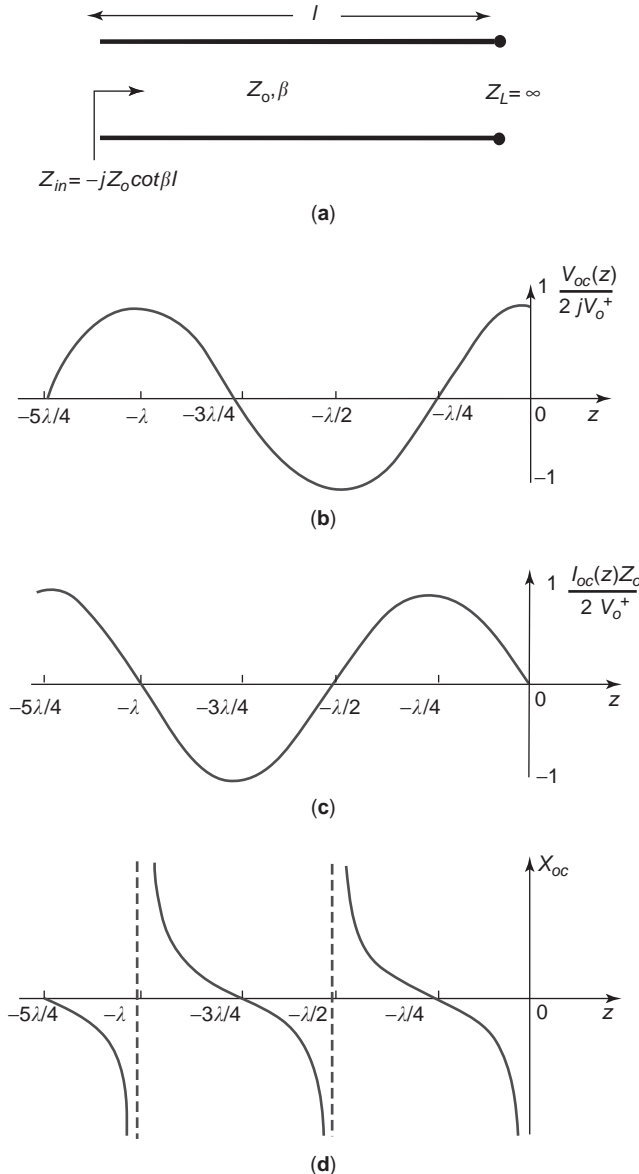


Figure 5. A lossless transmission line terminated with an (a) open circuit, (b) voltage distribution, (c) current distribution, and (d) input reactance as a function of the distance from the termination.

less transmission line are given by

$$V_{oc}(z) = V_0^+ (e^{-j\beta z} + e^{j\beta z}) = 2V_0^+ \cos \beta z \quad (30a)$$

$$I_{oc}(z) = \frac{V_0^+}{Z_0} (e^{-j\beta z} - e^{j\beta z}) = \frac{-2jV_0^+}{Z_0} \sin \beta z \quad (30b)$$

Both voltage and current are plotted as a function of the distance from the load location in Figs. 5b and 5c, respectively. As a result of the sinusoidal nature, both the quantities are periodic and repeat for multiples of λ .

Substituting $Z_L = \infty$ in Eq. (25) for the expression for input impedance, we get

$$Z_{oc} = Z_{in} = -jZ_0 \cot \beta z \quad (\Omega) \quad (31)$$

We can see from Eq. (30) that the input impedance Z_{oc} for the open-circuited line is always purely imaginary irrespective of length z . The variation of open-circuit reactance (imaginary part of Z_{oc}) is plotted as a function of z in Fig. 5d. The plot is again periodic and repeats for multiples of $\lambda/2$. The behavior varies between being inductive and capacitive as the length z is varied.

4.2.2. Short-circuited line. A lossless transmission line short circuited at the load end ($Z_L = 0$) is shown in Fig. 6a. Here, $\Gamma = -1$ and $SWR = \infty$. The voltage and current along the line can be given by

$$V_{sc}(z) = V_0^+ (e^{-j\beta z} - e^{j\beta z}) = -2jV_0^+ \sin \beta z \quad (32a)$$

$$I_{sc}(z) = \frac{V_0^+}{Z_0} (e^{-j\beta z} + e^{j\beta z}) = \frac{2V_0^+}{Z_0} \cos \beta z \quad (32b)$$

From Eq. (25), the input impedance for a short-circuited line can be given as

$$Z_{sc} = jZ_0 \tan \beta z \quad (\Omega) \quad (33)$$

The voltage, current, and the input reactance are plotted in Figs. 6b–6d as a function of the distance, z . As it can be seen, the input reactance for a shorted transmission line is also purely imaginary irrespective of the value of z . Comparing Figs. 5 and 6, we can see that in the range where X_{oc} is inductive, X_{sc} is capacitive, and vice versa. The input reactances of the short-circuited and open-circuited lossless transmission lines are essentially the same if their lengths differ by an odd multiple of $\lambda/4$.

Consider an open-circuited transmission line of length much smaller compared with a wavelength. As the electrical length of the line $\beta l \ll 1$, we can make the approximation that $\tan \beta l \cong \beta l$. From Eq. (31), at the input of the line, we have

$$Z_{oc} \cong \frac{Z_0}{j\beta l} = \frac{\sqrt{L/C}}{\omega \sqrt{LC}l} = \frac{1}{j\omega Cl} \quad (34)$$

This equation implies that an open-circuited lossless transmission line with a very short length will behave as a capacitance of Cl farads as shown in Fig. 7a. Similarly,

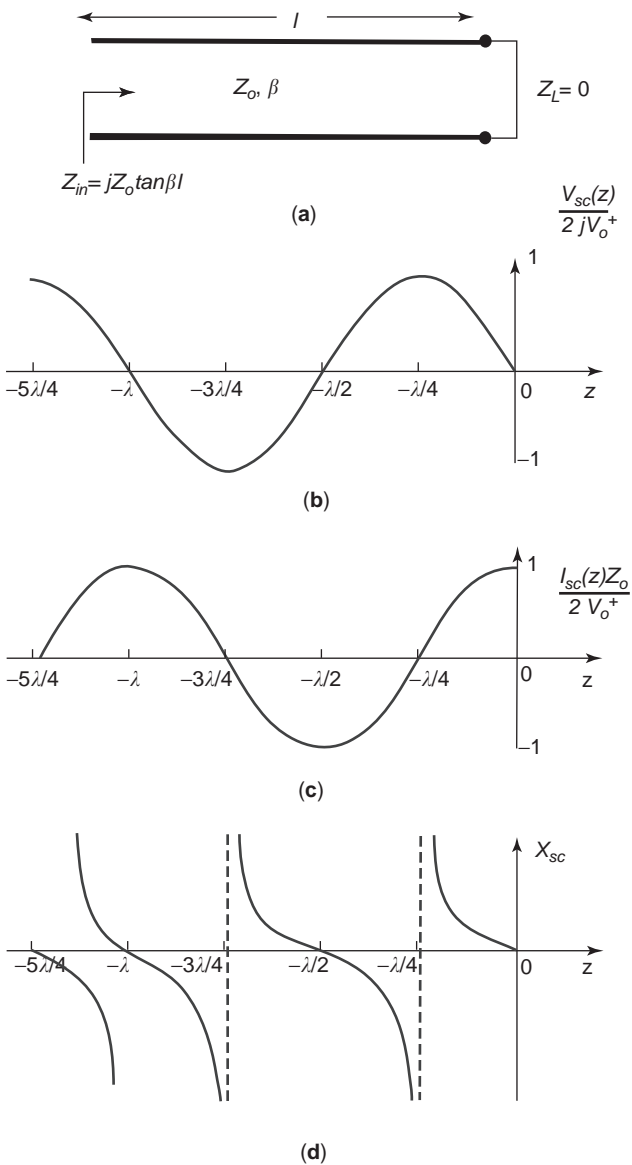


Figure 6. A lossless transmission line terminated with a (a) short circuit, (b) voltage distribution, (c) current distribution, and (d) input reactance as a function of the distance from the termination.

consider a short-circuited transmission line of small length. From Eq. (33), we get

$$Z_{sc} \approx Z_0 \cdot j\beta l = \sqrt{L/C} \cdot j\omega \sqrt{LC}l = j\omega Ll \quad (35)$$

Thus a short-circuited lossless transmission line with a short length can behave as an inductance of Ll henries, as shown in Fig. 7b.

This property of open- or short-circuited transmission lines behaving as lumped inductors or capacitors will be a useful feature at microwave frequencies, where discrete capacitor or inductor realization will be very difficult because of the parasitics associated with the structure. By proper choice, an open-circuited or short-circuited

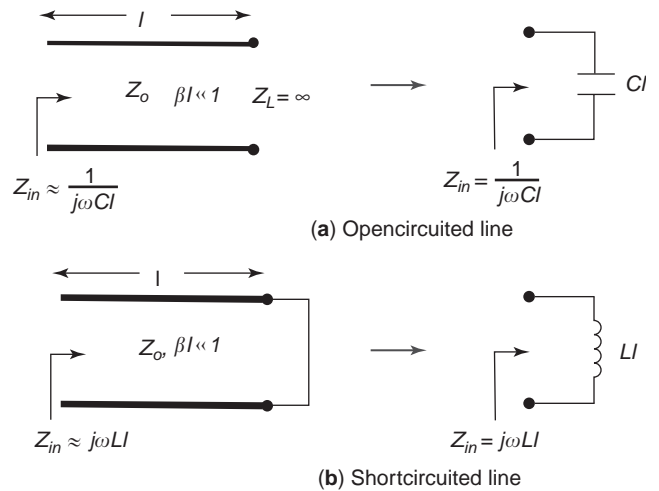


Figure 7. Transmission lines as circuit elements.

line can replace the lumped elements during circuit design.

4.2.3. Quarter-wave line. When the length of a transmission line is an odd multiple of $\lambda/4$, ($l = (2n - 1)\lambda/4$, n is a nonzero positive integer),

$$\beta l = \frac{2\pi}{\lambda} (2n - 1) \frac{\lambda}{4} = (2n - 1) \frac{\pi}{2} \Rightarrow \tan \beta l \rightarrow \pm\infty$$

and Eq. (25) becomes

$$Z_{in} = \frac{Z_0^2}{Z_L} \quad (36)$$

Hence, the load impedance connected at one end of a quarter-wave transmission line appears to be inverted at the other end. Thus, an open-circuited quarter-wave line appears to be short circuited at the input terminals and vice versa. This *impedance inverting* feature is used in many circuit design applications such as filters and impedance transformers.

4.2.4. Half-wave line. When the length of a lossless line is an integral multiple of $\lambda/2$ ($l = n\lambda/2$, n is a nonzero positive integer),

$$\beta l = \frac{2\pi}{\lambda} \cdot \frac{n\lambda}{2} = n\pi, \Rightarrow \tan \beta l \rightarrow 0$$

and Eq. (25) reduces to

$$Z_{in} = Z_L \quad (37)$$

which implies that a load impedance connected to a half-wave lossless transmission line appears to be the same without any change at the input terminals.

4.3. Transmission Line Characterization from Open- and Short-Circuit Measurements

A microwave network analyzer is an instrument, which can be used to measure the input impedance of any device connected to its input terminal. We can determine the characteristics of an unknown lossy transmission line of length less than or equal to $\lambda/2$, by measuring the input impedance under open-circuit and short-circuit conditions.

From Eq. (24), when $Z_L = \infty$,

$$Z_{oc} = Z_o \coth \gamma l \quad (\text{open-circuited line}) \quad (38)$$

when $Z_L = 0$,

$$Z_{sc} = Z_o \tanh \gamma l \quad (\text{short-circuited line}) \quad (39)$$

From Eqs. (38) and (39), we have

$$Z_o = \sqrt{Z_{oc} Z_{sc}} \quad (\Omega) \quad (40)$$

and

$$\gamma = \frac{1}{l} \tanh^{-1} \sqrt{\frac{Z_{sc}}{Z_{oc}}} \quad (\text{m}^{-1}) \quad (41)$$

where Z_o and γ are the characteristic impedance and propagation constant of the lossy line, respectively.

Example 1. A lossless transmission line of characteristic impedance of 50 ohms is connected to a load impedance of $60 \angle 60^\circ \Omega$. What is the load reflection coefficient? Find the input impedance and voltage reflection coefficient at $l = \lambda/8$ and $3\lambda/8$. Also, calculate the standing wave ratio of the line.

Solution: A simple schematic indicating input impedances at different locations is shown in Fig. 8a.

Load reflection coefficient,

$$\begin{aligned} \Gamma_L &= \frac{(Z_L - Z_o)}{(Z_L + Z_o)} = \frac{(30 + j51.96 - 50)}{(30 + j51.96 + 50)} \\ &= 0.1279 + j0.571 = 0.5837 \angle 78^\circ \end{aligned}$$

From Eq. (25), we have,

$$Z_{in} = Z_o \left[\frac{Z_L + jZ_o \tan \beta l}{Z_o + jZ_L \tan \beta l} \right]$$

Case (i) $l = \lambda/8$

$$\beta l = \frac{2\pi}{\lambda} \cdot \frac{\lambda}{8} = \frac{\pi}{4} \Rightarrow \tan \beta l = 1$$

$$(Z_{in})_{\lambda/8} = 50 \left[\frac{30 + j51.96 + j50}{50 + j(30 + j51.96)} \right]$$

$$= 165.96 - j60.85 \quad \Omega$$

$$\Gamma_{\lambda/8} = \left(\frac{165.96 - j60.85 - 50}{165.96 + j60.85 + 50} \right)$$

$$= 0.571 - j0.121 = 0.5837 \angle -12^\circ$$

Case (ii) $l = 3\lambda/8$

$$\beta l = \frac{2\pi}{\lambda} \cdot \frac{3\lambda}{8} = \frac{3\pi}{4} \Rightarrow \tan \beta l = -1$$

$$(Z_{in})_{3\lambda/8} = 50 \left[\frac{30 + j51.96 - j50}{50 - j(30 + j51.96)} \right]$$

$$= 13.28 + j4.87 \quad \Omega$$

The input impedance Z_{in} at $3\lambda/8$ can also be determined using a different procedure. Once we have calculated the input impedance at $\lambda/8$, that length of line terminated with the load can be replaced by the calculated input impedance at $\lambda/8$, as shown in Fig. 8b, which leaves with a line with length $3\lambda/8 - \lambda/8 = \lambda/4$. Thus, we have a quarter-

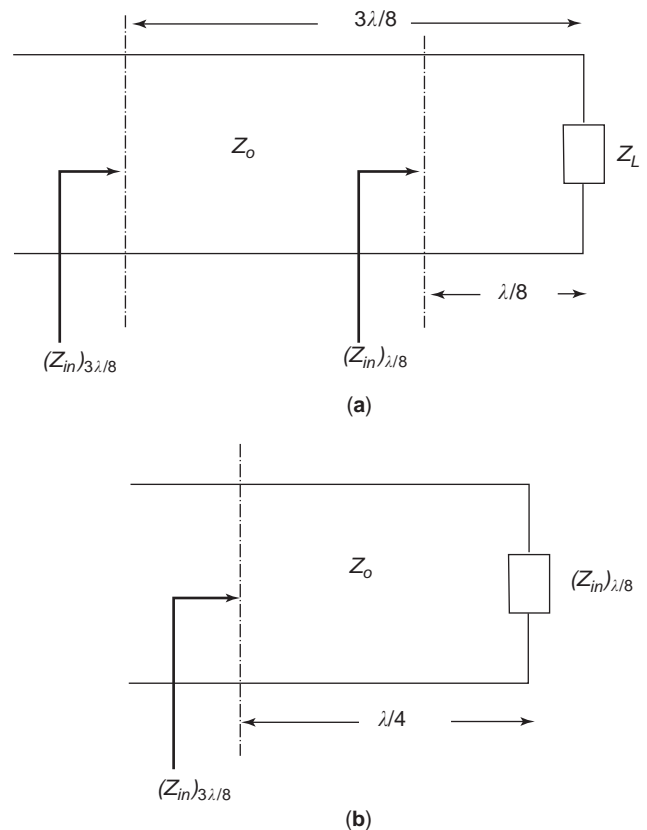


Figure 8. Transmission line problem in Example 1.

wave line of characteristic impedance 50Ω , terminated with a new load $(Z_{in})_{\lambda/8} = 165.96 - j60.85 \Omega$. From Eq. (36), we can calculate $(Z_{in})_{3\lambda/8}$ as

$$\begin{aligned} (Z_{in})_{3\lambda/8} &= \frac{Z_o^2}{(Z_{in})_{\lambda/8}} = \frac{50^2}{165.96 - j60.85} \\ &= 13.28 + j4.87 \Omega \end{aligned}$$

The reflection coefficient at $3\lambda/8$ can be calculated as

$$\begin{aligned} \Gamma_{3\lambda/8} &= \left(\frac{13.28 + j4.87 - 50}{13.28 + j4.87 + 50} \right) = -0.571 + j0.121 \\ &= 0.5837 \angle 168^\circ \end{aligned}$$

We can see that the magnitude of reflection coefficient at different locations is the same, and only the angle changes depending on the distance from the load.

The SWR for the line is

$$SWR = \frac{1 + |\Gamma|}{1 - |\Gamma|} = \frac{1 + 0.5837}{1 - 0.5837} = 3.804$$

5. SMITH CHART

Transmission line calculations, such as determination of input impedance and reflection coefficient, often involve manipulations with complex quantities making it tedious compared with dealing with real numbers. The *Smith chart*, which was developed by P.H. Smith [3,4], is considered to be the most widely used graphical technique for the analysis and design of transmission line circuits. Some readers may feel that in today’s world of powerful computers and modern scientific calculators, graphical ways of solving engineering problems may seem out of the ordinary. More than just being a graphical tool, the Smith chart provides a powerful way of visualizing the transmission line phenomenon, which is why many commercially available popular CAD software used for RF and microwave circuit design have integrated Smith chart calculations into the design stream.

The most common form of the Smith chart is shown in Fig. 9. First, it is important to understand that a Smith chart is essentially a polar plot of the voltage reflection coefficient, Γ . Therefore, we begin with expressing Γ as a complex quantity

$$\Gamma = |\Gamma|e^{j\theta_\Gamma} = \Gamma_r + j\Gamma_i \tag{42}$$

The right-hand side of the horizontal diameter in the chart represents the Γ_r axis, and the top side of the vertical diameter represents the Γ_i axis. $|\Gamma|$ is plotted as a radius ($|\Gamma| \leq 1$) from the center of the chart. The angle, θ_Γ ($-180^\circ \leq \theta_\Gamma \leq 180^\circ$) is measured from the Γ_r axis. We can also relate Γ to the load impedance as

$$\Gamma = \left(\frac{Z_L - Z_o}{Z_L + Z_o} \right) = \left(\frac{Z_L/Z_o - 1}{Z_L/Z_o + 1} \right) = \left(\frac{z_L - 1}{z_L + 1} \right) \tag{43}$$

where

$$z_L = r + jx = \frac{Z_L}{Z_o}$$

z_L is the *normalized* load impedance. In fact, all impedances we plot on the chart are normalized with respect to the characteristic impedance, Z_o .

From Eq. (43), we can write z_L in terms of Γ as

$$z_L = \left(\frac{1 + \Gamma}{1 - \Gamma} \right) \tag{44}$$

Thus, we can write

$$z_L = r + jx = \left(\frac{1 + \Gamma_r + j\Gamma_i}{1 - \Gamma_r - j\Gamma_i} \right) \tag{45}$$

The real and imaginary parts of this equation are

$$r = \frac{1 - \Gamma_r^2 - \Gamma_i^2}{(1 - \Gamma_r)^2 + \Gamma_i^2} \tag{46a}$$

$$x = \frac{2\Gamma_i}{(1 - \Gamma_r)^2 + \Gamma_i^2} \tag{46b}$$

Eqs. (46a) and (46b) can be rearranged as

$$\left(\Gamma_r - \frac{r}{1+r} \right)^2 + \Gamma_i^2 = \left(\frac{1}{1+r} \right)^2 \tag{47}$$

$$(\Gamma_r - 1)^2 + \left(\Gamma_i - \frac{1}{x} \right)^2 = \left(\frac{1}{x} \right)^2 \tag{48}$$

Equation (47) describes a family of circles called the *resistance circles*, where each circle is associated with a specific value of resistance, r . The resistance circles for different values of r are shown on the chart. We can notice that the centers of all r -circles lie on the horizontal axis. All circles pass through the $(\Gamma_r = 1, \Gamma_i = 0)$ point. The largest r -circle is the $r = 0$ circle with a unity radius.

Equation (48) represents the other family of circles called the *reactance circles*, which are also shown on the chart. Different values of x lead to circles of different radii with centers at different positions on the $\Gamma_r = 1$ line. These circles are always orthogonal to the resistance circles. Reactance circles with positive reactance ($x > 0$) lie in the upper half of the chart and those with $x < 0$ lie in the lower half. Intersection of a resistance and reactance circle represents the normalized load impedance, z_L .

One of the main advantages of the Smith chart is that it can be used directly to read the reflection coefficient for a given normalized load impedance and vice versa without having to calculate them. Another useful feature is that the value of the resistance passing through the intersection of the $|\Gamma|$ circle and the Γ_r axis (positive real axis) directly equals the standing wave ratio, SWR. Perhaps the most important feature of the Smith chart is that the angular motion on a constant $|\Gamma|$ circle in a clockwise or counterclockwise direction represents a corresponding movement on a terminated transmission line toward the generator or the load, respectively. Thus, a movement of half a wavelength in the line length on the transmission line corresponds to a complete 360° revolution on the $|\Gamma|$

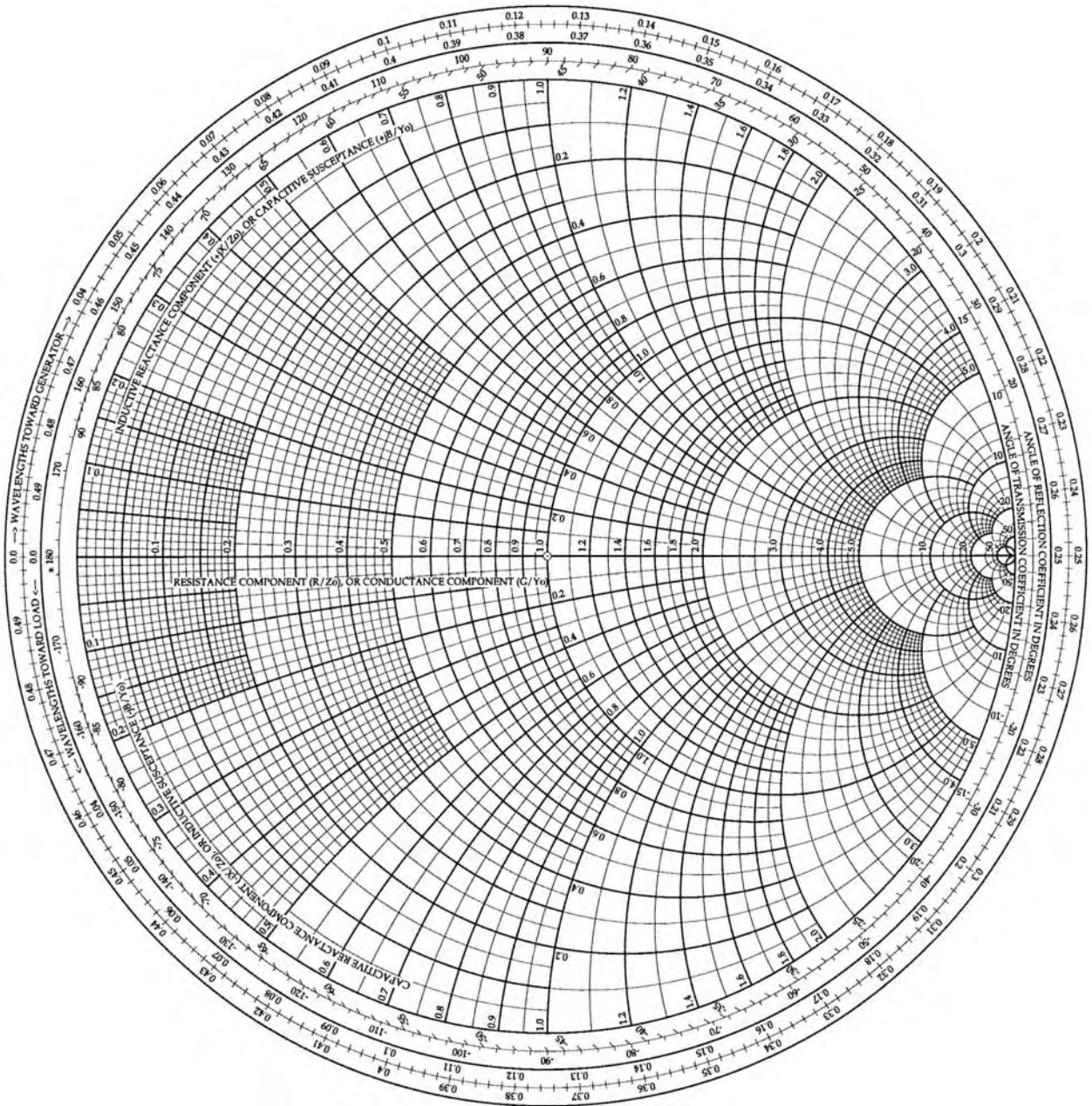


Figure 9. The Smith chart.

circle reaching the same normalized impedance (or reflection coefficient) point, which reasserts the fact we have seen earlier in the case of a half-wave line, where the input impedance is same as the load impedance. Thus the Smith chart takes into account the periodic behavior of the transmission line.

Example 2. Calculate the input impedance and reflection coefficient for the problem given in Example 1 at $\lambda/8$ and $3\lambda/8$ using the Smith chart. Also, find the SWR of the line.

Solution: The procedure for calculating the above parameters using the Smith chart is described in steps as shown below:

1. Calculate normalized $z_L = Z_L/Z_0 = 0.6 + j1.039$ and mark the same on the Smith chart as point A in Fig. 10.
2. With OA as the radius, draw a circle. Measure the radius and normalize it with respect to the radius of the largest r circle ($r = 0$ circle). Read $|\Gamma| = 0.58$.
3. Extend OA to intersect the angular scale given on the Smith chart for reflection coefficient. Mark the reading. This gives the angle of Γ in degrees. $\theta_r = 78^\circ$.
4. Mark the reading where the $|\Gamma|$ circle intersects the positive real axis. This gives $SWR = 3.8$.
5. From point A, move 0.125λ toward the generator to reach point B. Mark the reading on the angular scale of reflection coefficient. This gives angle of Γ at

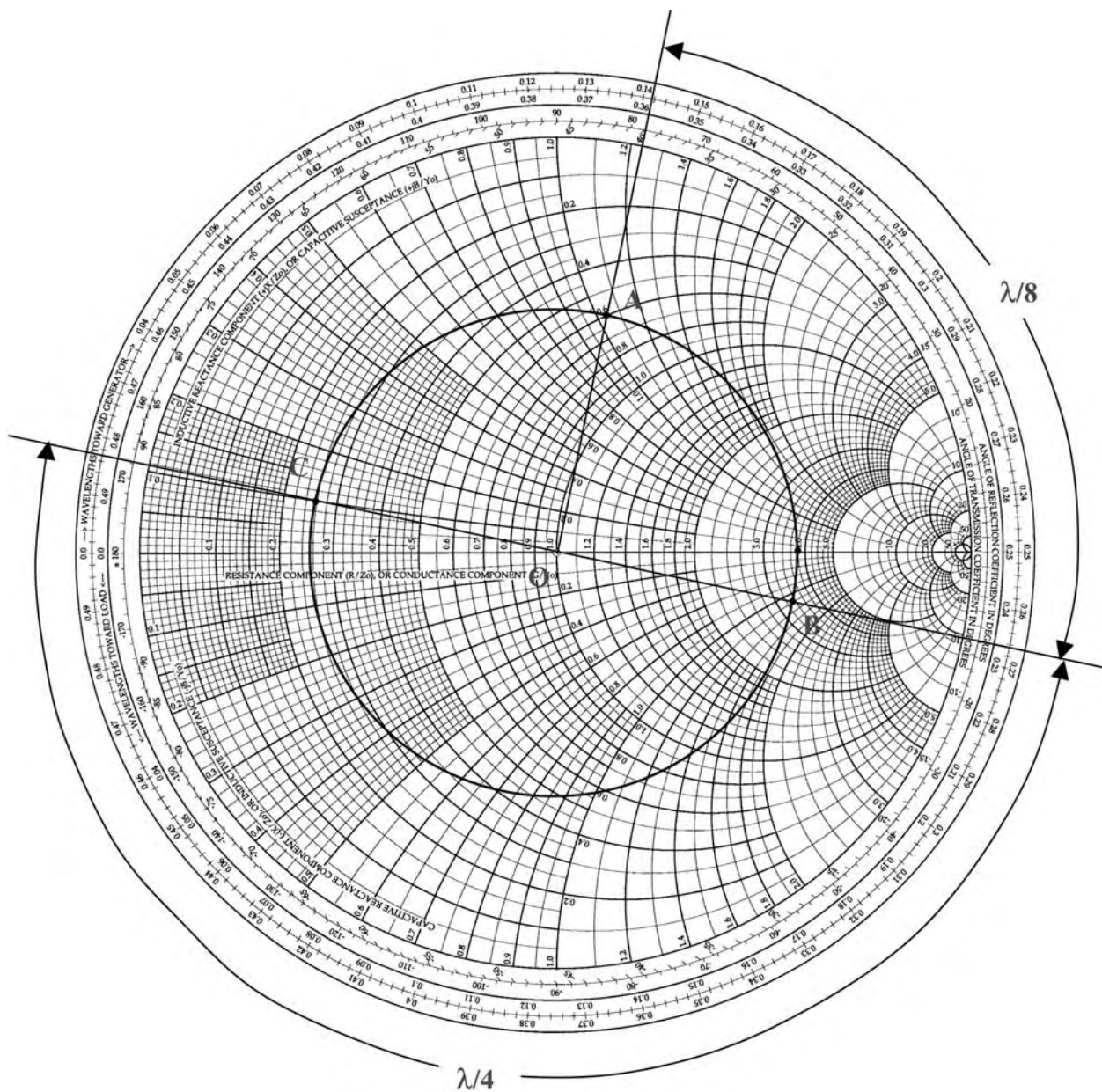


Figure 10. The Smith chart solution for Example 2.

$l = \lambda/8$. The magnitude of Γ remains the same. Measure $(\theta_\Gamma)_{\lambda/8}$ as -12° .

6. Mark the normalized impedance value by observing r and x values at B, where $\Gamma = 0.58 \angle -12^\circ$. We get

$$r = 3.3 \text{ and } x = -1.21$$

$$\begin{aligned} \therefore (Z_{in})_{\lambda/8} &= 50.(z_{in})_{\lambda/8} = 50.(3.3 - j1.21) \\ &= 165 - j60.5 \Omega \end{aligned}$$

7. From B, move $\lambda/4$ toward the generator to reach point C. Join OC and extend it to intersect the

angular scale for Γ at 168° . This gives $(\Gamma)_{3\lambda/8} = 0.58 \angle 168^\circ$.

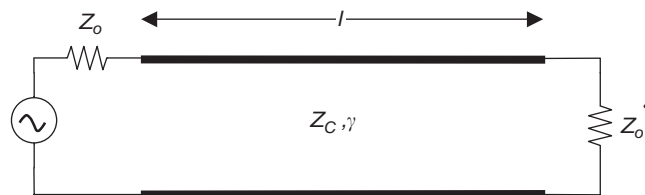
$$(z_{in})_{3\lambda/8} = r + jx = 0.265 + j0.1$$

$$\begin{aligned} (Z_{in})_{3\lambda/8} &= 50.(z_{in})_{\lambda/8} = 50.(0.265 + j0.1) \\ &= 13.25 + j5 \Omega \end{aligned}$$

6. NETWORK PARAMETERS OF A GENERAL LOSSY TRANSMISSION LINE

Transmission lines are used in every microwave network system design. When we look at various blocks of a

Table 2.



Type	Two-port Parameters	
ABCD	$A = \cosh(\gamma l)$ $C = Y_C \sinh(\gamma l)$	$B = Z_C \sinh(\gamma l)$ $D = \cosh(\gamma l)$
Z	$Z_{11} = Z_C \coth(\gamma l)$ $Z_{12} = Z_{21}$	$Z_{21} = Z_C \operatorname{cosech}(\gamma l)$ $Z_{22} = Z_{11}$
Y	$Y_{11} = Y_C \coth(\gamma l)$ $Y_{12} = Y_{21}$	$Y_{21} = -Y_C \operatorname{cosech}(\gamma l)$ $Y_{22} = Y_{11}$
S	$S_{11} = \frac{Z_C^2 - Z_o^2}{2Z_C Z_o \coth \gamma l + Z_C^2 + Z_o^2}$ $S_{12} = S_{21}$	$S_{21} = \frac{2Z_C Z_o}{2Z_C Z_o \cosh \gamma l + (Z_C^2 + Z_o^2) \sinh \gamma l}$ $S_{22} = S_{11}$

microwave system, such as a transceiver, we see components such as amplifiers, mixers, oscillators, and filters interconnected using transmission lines of different characteristic impedances, propagation constants, and lengths. Depending on the overall system requirement, these transmission lines could be realized in different configurations such as a microstrip line, coplanar waveguide, stripline, or waveguide among several variations. For a given physical geometry, the electrical characteristics, Z_o and γ for these transmission lines, can be obtained based on the available analytical/numerical approaches from the literature. Interested readers are encouraged to refer to [5–7].

A common approach in microwave network analysis is to represent each component as a two-port or multiport network and use the network analysis principles to calculate the overall characteristics of the larger network formed by interconnecting various components. In this procedure, each component is associated with a set of network parameters, such as impedance (Z), admittance (Y), transmission (ABCD) or scattering (S) parameters, and the voltage/current or wave amplitudes are interrelated at various junctions/interconnections to obtain the overall characteristics of the system. As with other components, transmission lines can also be treated as microwave networks, and the knowledge of network parameters will often be useful when they are used in a system.

Table 2 presents various commonly used network parameters of a general lossy transmission line. The line is assumed to have a characteristic impedance of Z_C , propagation constant, γ , and length l . The expressions for the scattering (S) parameters assume that the reference port impedance is considered to be Z_o , which is different from the characteristic impedance Z_C . The expressions for a lossless transmission line can be directly obtained from Table 2 by replacing γ with $j\beta$. In the case of scattering

parameters, when $Z_C = Z_o$, the line becomes a matched lossy transmission line of length l and the scattering matrix reduces to

$$S = \begin{bmatrix} 0 & e^{-\gamma l} \\ e^{-\gamma l} & 0 \end{bmatrix} \quad (49)$$

BIBLIOGRAPHY

1. J. C. Maxwell, *A Treatise on Electricity and Magnetism*, Dover, New York, 1954.
2. P. J. Nahin, *Oliver Heaviside: Sage in Solitude*, IEEE Press, New York, 1988.
3. P. H. Smith, Transmission-line calculator, *Electronics*, **12:29** (1939).
4. P. H. Smith, An improved transmission-line calculator, *Electronics*, **17:130** (1944).
5. D. M. Pozar, *Microwave Engineering*, 3rd ed., Wiley, New York, 2003.
6. K. C. Gupta, R. Garg, and I. J. Bahl, *Microstrip Lines and Slotlines*, Artech House Norwood, MA, 1979.
7. B. Bhat and S. K. Koul, *Strip-Line Like Transmission Lines for Microwave Integrated Circuits*, Wiley, New York, 1989.

FURTHER READING

- D. K. Cheng, *Field and Wave Electromagnetics*, 2nd ed., Addison-Wesley, Reading, MA, 1990.
- W. H. Hayt, Jr., *Engineering Electromagnetics*, 6th ed., McGraw-Hill, New York, 2001.
- F. T. Ulaby, *Fundamentals of Applied Electromagnetics*, Prentice-Hall, Englewood Cliffs, NJ, 2003.

TRANSMISSION LINES AND PARAMETERS

JI CHEN
 RICHARD L. CHEN
 University of Houston
 Houston, Texas

1. INTRODUCTION

In electromagnetic theory, the term *transmission line* usually refers to a structure that can guide TEM waves, such as parallel-plate waveguides or coaxial cables [1–3]. To support TEM waves, at least two conductors and a homogeneous medium in the propagation region are required [4]. Transmission lines are a special class of general electromagnetic waveguides, such as rectangular waveguides and dielectric waveguides. One of the most important properties of a TEM mode on transmission lines is that its voltage, current, and characteristic impedance can be uniquely defined by using the electromagnetic fields. In addition, transmission-line parameters, such as inductance per unit length and capacitance per unit length, can also be uniquely determined using electromagnetic field analyses. Hence transmission line theory bridges the specialized lumped-element electric circuits principles with the general and fundamental approach of electromagnetic theory [2,3,5].

For a TEM mode, only transverse electromagnetic components exist, and therefore electric and magnetic components can be obtained by solving two-dimensional Laplace’s equations in the cross section [2]. This approach is very similar to solving an electrostatic problem. For the simplest transmission line, which is a parallel-plate waveguide, solving Laplace’s equations is very straightforward. However, it is rather difficult to solve Laplace’s equations for transmission lines with more complex cross sections. Conformal transformation methods [6] are usually adopted to transform the complicated cross sections to simpler cases, such as a cross section of parallel-plate waveguides [1,7–14] whose analytical solutions are available. However, for some transmission-line structures, such as striplines, the procedure and results of the conformal transformation approach could be cumbersome [15]. In addition, for transmission lines with inhomogeneous media, such as microstrip lines, analytical solutions are impossible without approximations [16]. To obtain such a solution, quasi-TEM approximations [17–21] are often used. However, as the operating frequency increases due to the dispersive nature as well as the fringe effects, rigorous full-wave analyses, such as the spectral-domain approach [22,23], the integral equation method [24], and the method of lines [25], have to be considered.

This article starts with the derivation of the “telegrapher’s equations” by using the lumped-element circuit model. The transmission-line parameters will be defined and introduced during the derivation. Field analysis is then used to determine those parameters when a particular transmission line is introduced. Five typical transmission-line structures—parallel-plate waveguides,

coaxial cables, two-wire transmission lines, striplines, and microstrip lines—are studied, and their transmission-line parameters are derived on the basis of the results of field analysis. Finally, the transmission-line structures for the IC-level interconnects are introduced, and the challenges for future micro- and nanoscale transmission-line parameter extraction are discussed.

2. TELEGRAPHER’S EQUATIONS

Circuit analysis is the preferred technique when the physical dimensions of a network are much smaller than the wavelength of an electrical signal. However, at radiofrequency (RF) or microwave frequencies, the transmission-line dimension is usually comparable to or even greater than the electrical signal wavelength. The lumped-element circuit model is no longer valid for these types of applications. Under these circumstances, rigorous electromagnetic field analyses are required. To bridge the gap between the rigorous electromagnetic analysis and the circuit theory, a transmission line is modeled as a distributed-parameter network and the transmission-line theory is developed.

The theory starts with dividing the electrically long transmission line into many electrically small pieces, with a segment length Δz , within which region the lumped-circuit model can be applied. A segment of such a division is shown in Fig. 1, where L represents the inductance per unit length, C stands for the capacitance per unit length, R corresponds to the resistance per unit length due to the finite conductivity of the conductors, and G is the conductance per unit length due to the dielectric loss in the material between the two conductors. Both current and voltage are functions of position z and time t , as shown in the figure.

Applying Kirchhoff’s voltage law within each segment, we obtain

$$v(z, t) = v(z + \Delta z, t) + i(z, t)R \Delta z + L \Delta z \frac{\partial i(z + \Delta z, t)}{\partial t} \quad (1)$$

Similarly, applying Kirchhoff’s current law within each segment, we have

$$i(z, t) = i(z + \Delta z, t) + v(z + \Delta z, t)G \Delta z + C \Delta z \frac{\partial v(z + \Delta z, t)}{\partial t} \quad (2)$$

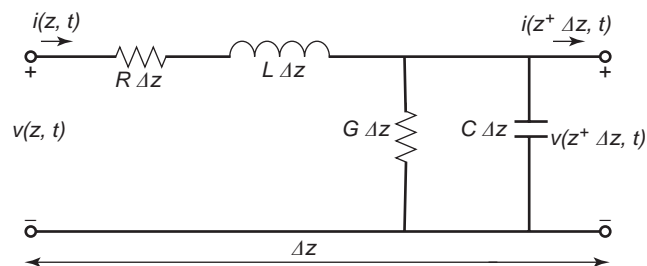


Figure 1. A segment of the divided transmission line.

Rewriting Eqs. (1) and (2) and letting $\Delta z \rightarrow 0$ yield the telegrapher's equations, we obtain

$$\frac{\partial v}{\partial z} = -Ri - L \frac{\partial i}{\partial t} \quad (3)$$

and

$$\frac{\partial i}{\partial z} = -Gv - C \frac{\partial v}{\partial t} \quad (4)$$

Then, combining (3) and (4) yields

$$\frac{\partial^2 v}{\partial z^2} - RGv - (RC + LG) \frac{\partial v}{\partial t} - LC \frac{\partial^2 v}{\partial t^2} = 0 \quad (5)$$

A similar differential equation can also be derived for the current. For time-harmonic cases, $v(z, t) = V(z)e^{j\omega t}$, (5) can be simplified as

$$\frac{d^2 V}{dz^2} - \gamma^2 V = 0 \quad (6)$$

where

$$\gamma = \alpha + j\beta = \sqrt{ZY} \quad (7)$$

In (7), γ is the complex propagation constant. Z and Y are series impedance and shunt admittance per unit length, written as

$$Z = R + j\omega L \quad (8)$$

and

$$Y = G + j\omega C \quad (9)$$

The general solution of (6) is

$$V(z) = V_0^+ e^{-\gamma z} + V_0^- e^{\gamma z} \quad (10)$$

Similarly, the general solution for the current distribution along the transmission can be written as

$$I(z) = I_0^+ e^{-\gamma z} + I_0^- e^{\gamma z} \quad (11)$$

In (10) and (11), the superscript + denotes the voltage/current that propagates along the +z direction and the superscript - denotes the voltage/current that propagates along the -z direction. The characteristic impedance of such transmission line is then defined as

$$Z_0 = \frac{V_0^+}{I_0^+} = -\frac{V_0^-}{I_0^-} = \sqrt{\frac{Z}{Y}} \quad (12)$$

For lossless cases, the transmission-line characteristic impedance can be simplified as follows:

$$Z_0 = \sqrt{\frac{L}{C}} \quad (13)$$

Another important parameter of the wave propagation along transmission lines is the phase velocity:

$$v_p = \frac{\omega}{\beta} \quad (14)$$

A lossless transmission line, can be expressed as follows:

$$v_p = \frac{1}{\sqrt{LC}} \quad (15)$$

The *phase velocity* is the quantity that describes the propagation speed of the constant wave front along the transmission line.

3. TRANSMISSION-LINE PARAMETERS

As shown in the previous section, an electrically long transmission line can be divided into many electrically small sections. Those small sections can be represented by lumped-circuit elements that are related to the per unit length transmission-line resistance, inductance, capacitance, and conductance. To accurately evaluate those parameters, rigorous electromagnetic analysis has to be used. Fortunately, the transmission-line theory discussed here is limited only to the TEM wave. Hence, the inductance, capacitance, and conductance per unit length can be determined from a static solution to a 2D Laplace equation in the cross section of transmission-line structures. The resistance per unit length can be obtained from electromagnetic field distribution inside the conductors.

The inductance per unit length is associated with the time-average stored magnetic energy for a 1-m section of the transmission line. If the transmission line structure is embedded in a homogeneous medium characterized by a permittivity of ϵ , a permeability of μ , and a loss tangent of $\tan \delta$, the inductance per unit length can be evaluated by [2]

$$L = \frac{4W_m}{|I_0|^2} = \frac{\mu}{|I_0|^2} \int_S \vec{H} \cdot \vec{H}^* ds \quad (16)$$

where the integration is carried out on the surface of a cross section S of the transmission line, W_m is the time-average stored magnetic energy, and I_0 is the total current on one of the conductors. The capacitance per unit length is related to the time-average stored electric energy for a 1-m section of the transmission line, which can be expressed as [2]

$$C = \frac{4W_e}{|V_0|^2} = \frac{\epsilon}{|V_0|^2} \int_S \vec{E} \cdot \vec{E}^* ds \quad (17)$$

where W_e is the time-average stored electric energy and V_0 is the potential difference between the two conductors. The conductance per unit length is related to the time-average power dissipated per unit length in the lossy dielectric medium. The per unit length conductance is given by [2]

$$G = \frac{2P_d}{|V_0|^2} = \frac{\omega\epsilon \tan \delta}{|V_0|^2} \int_S \vec{E} \cdot \vec{E}^* ds \quad (18)$$

where P_d is time-average power dissipated per unit length. Similarly, the resistance per unit length is related to the power loss per unit length due to the finite metal conductivity. For a good conductor with a conductivity of σ , the resistance per unit length is given by [2]

$$R = \frac{2P_c}{|I_0|^2} = \frac{R_s}{|I_0|^2} \int_{C_1+C_2} \vec{H} \cdot \vec{H}^* dl \quad (19)$$

where P_c is power loss per unit length due to the finite metal conductivity, $R_s = \sqrt{\omega\mu}/2\sigma$ is the surface resistance of the conductors, and C_1 and C_2 represent integral paths over the conductor boundaries.

With the parameters defined above, in the remainder of this section we discuss five typical transmission-line structures and derive their corresponding parameters.

3.1. Parallel-Plate Waveguide

A parallel-plate waveguide, shown in Fig. 2, is probably the simplest type of transmission-line structure that supports a TEM wave. It has two parallel metal plates with a width W and a separation h . A homogeneous medium characterized by a dielectric constant ϵ and a loss tangent $\tan \delta$ is filled in between. The strip width W is usually much greater than the separation h , so that fringing fields and field variations in the x direction can be ignored.

Assuming that the potential difference between the two plates is V_0 , the electric field can be obtained by solving Laplace's equations; hence

$$\vec{E} = -\hat{y} \frac{V_0}{h} e^{-jkz} \quad (20)$$

where k is the propagation constant along the z direction. The magnetic field is given by

$$\vec{H} = \frac{1}{\eta} \hat{z} \times \vec{E} = \hat{x} \frac{V_0}{\eta h} e^{-jkz} \quad (21)$$

where $\eta = \sqrt{\mu/\epsilon}$ is the intrinsic impedance in the medium.

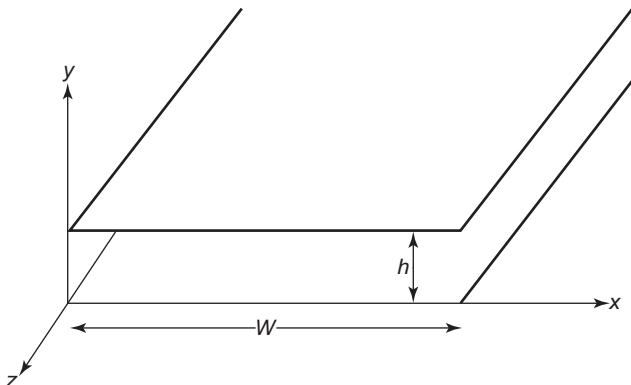


Figure 2. Geometry of a parallel-plate waveguide.

The total current on either the top or bottom plate can be found from the surface current density:

$$I_0 = \int_{x=0}^W \vec{J}_s \cdot \hat{z} dx = \int_{x=0}^W (-\hat{y} \times \vec{H}) \cdot \hat{z} dx = \frac{WV_0}{\eta h} \quad (22)$$

Substituting (21) and (22) into (16), we can obtain the inductance per unit length of a parallel-plate waveguide as follows:

$$L = \frac{\mu}{|I_0|^2} \int_0^h \int_0^W \frac{|V_0|^2}{\eta^2 h^2} dx dy = \frac{\mu h}{W} \quad (23)$$

Similarly, substituting (20) into (17), (20) into (18), and (21) and (22) into (19), we can obtain the capacitance, conductance, and resistance per unit length as

$$C = \frac{\epsilon}{|V_0|^2} \int_0^h \int_0^W \frac{|V_0|^2}{h^2} dx dy = \frac{W\epsilon}{h} \quad (24)$$

$$G = \frac{\omega\epsilon \tan \delta}{|V_0|^2} \int_0^h \int_0^W \frac{|V_0|^2}{h^2} dx dy = \frac{\omega\epsilon \tan \delta W}{h} \quad (25)$$

and

$$R = \frac{2R_s}{|I_0|^2} \int_0^h \int_0^W \frac{|V_0|^2}{\eta^2 h^2} dx dy = \frac{2R_s}{W} \quad (26)$$

Usually the conducting loss or the dielectric loss is negligible when we evaluate the characteristic impedance [2]. Hence, the characteristic impedance of a parallel-plate waveguide is given by [2]

$$Z_0 = \sqrt{\frac{L}{C}} = \frac{\eta h}{W} \quad (27)$$

3.2. Coaxial Cable

When the upper and lower conductors of a parallel-plate waveguide are folded into two concentric circles, a coaxial cable waveguide is formed. Coaxial cable transmission lines are widely used in many applications ranging from high-precision radiofrequency (RF) signal measurement to low-cost TV signal delivery. A typical cross section of a coaxial cable is shown in Fig. 3. It has an inner conductor with a radius a and an outer conductor with a radius b . A homogeneous medium, with a dielectric constant ϵ and a loss tangent $\tan \delta$, is filled between these two conductors.

The magnetic field between the inner and outer conductors can be derived by using Ampere's law:

$$\vec{H}(\rho) = \frac{I_0}{2\pi\rho} \hat{\phi} \quad (28)$$

Substituting (28) into (16), we can obtain the inductance per unit length as follows:

$$L = \frac{\mu}{|I_0|^2} \int_a^b \int_0^{2\pi} \frac{|I_0|^2}{(2\pi\rho)^2} d\phi \rho d\rho = \frac{\mu}{2\pi} \ln \frac{b}{a} \quad (29)$$

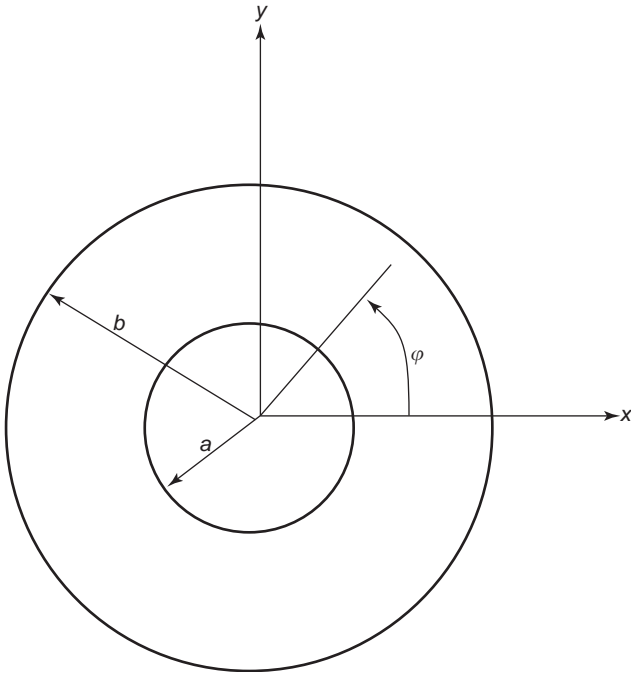


Figure 3. A cross section of a coaxial cable.

Also, applying Gauss' law in the region $a \leq \rho \leq b$ results in

$$E_\rho = \frac{\rho_l}{2\pi\epsilon\rho} \quad (30)$$

where ρ_l is the charge density per unit length. Integrating the electric field from the inner conductor to the outer conductor gives the voltage potential difference as

$$V_0 = - \int_b^a E_\rho d\rho = \frac{\rho_l}{2\pi\epsilon} \ln\left(\frac{b}{a}\right) \quad (31)$$

Substituting (30) and (31) into (17), we can obtain the capacitance per unit length:

$$C = \frac{2\pi\epsilon}{\ln(b/a)} \quad (32)$$

The conductance and resistance per unit length can be derived by substituting corresponding electric and magnetic fields into (18) and (19):

$$G = \frac{2\pi\omega\epsilon \tan \delta}{\ln(b/a)} \quad (33)$$

$$R = \frac{R_s}{2\pi} \left(\frac{1}{a} + \frac{1}{b} \right) \quad (34)$$

Neglecting the dielectric and conducting loss, we can obtain the characteristic impedance of a coaxial cable as

$$Z_0 = \eta \frac{1}{2\pi} \ln\left(\frac{b}{a}\right) \quad (35)$$

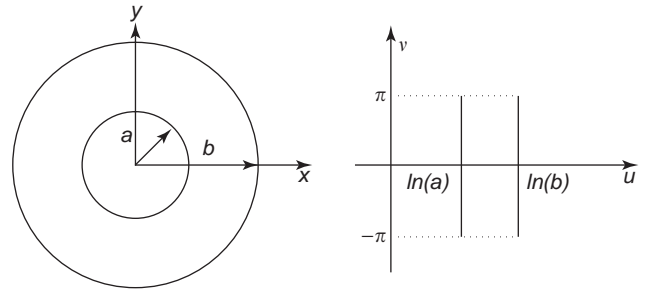


Figure 4. Conformal mapping from a cross section of coaxial cable to a cross section of a parallel-plate waveguide.

Alternatively, the parameters L , C , and G can also be obtained by using a conformal transformation, $w = \ln z$. After the transformation, the coaxial cable structure in the original complex plane z can be transformed to a parallel-plate waveguide in plane w , with a width 2π and a thickness $\ln(b/a)$, as shown in Fig. 4. Substituting the corresponding width and thickness into (23), (24), and (25), we can find that the parameters of L , C , and G are identical to those obtained from the direct electromagnetic analysis. However, the resistance per unit length cannot be derived from conformal transformation since this parameter depends on the electromagnetic field distribution inside the conductors rather than the electromagnetic fields between the conductors.

3.3. Two-Wire Transmission Line

Another kind of frequently used transmission-line structure is the two-wire transmission line. It is also referred to as a *twin-line structure*. This type of line is mostly used for powerlines, rural telephone lines, and telegraph lines. A cross section of a two-wire transmission-line structure is shown in Fig. 5. Both wires have a radius a , and the separation between these two wires is D . In general terms, we assume that the two-wire transmission line is embedded in a medium with a dielectric constant ϵ and a loss tangent $\tan \delta$. The effect of the wire conductivity can be represented by surface resistance R_s .

Since the electric and magnetic field solutions in the two-wire system have a more complex distribution than does either the parallel-plate waveguide or the coaxial cable structure, it is rather difficult to evaluate the transmission line parameters by simply integrating the electric or magnetic fields. However, by choosing an appropriate conformal mapping, we can transform the two-wire transmission line to a parallel-plate waveguide and hence the

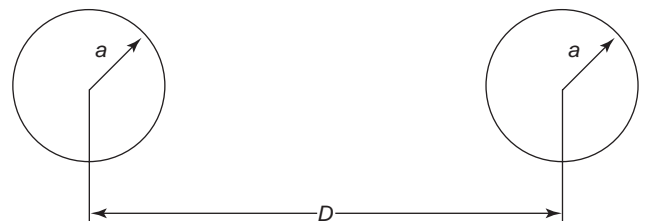


Figure 5. A cross section of a two-wire transmission line.

capacitance, inductance and conductance per unit length can be easily derived.

Using the conformal transformation, $w = \frac{1}{2} \ln[(1+z)/(1-z)]$, we can map the cross section of a two-wire transmission line in the complex z plane to the cross section of a parallel-plate waveguide in the complex w plane, as shown in Fig. 6. The parallel-plate waveguide has a width of π and a separation distance of $\cosh^{-1}(D/2a)$. Hence substituting $W = \pi$ and $h = \cosh^{-1}(D/2a)$ into (23), (24) and (25), we have

$$L = \frac{\mu}{\pi} \cosh^{-1}\left(\frac{D}{2a}\right) \tag{36}$$

$$C = \frac{\pi\epsilon}{\cosh^{-1}(D/2a)} \tag{37}$$

and

$$G = \frac{\pi\omega\epsilon \tan \delta}{\cosh^{-1}(D/2a)} \tag{38}$$

Typically, the spacing between wires D is much larger than the wire radius a , so that proximity effects can be neglected [10]. For the same reason, the induced magnetic field on one wire due to the current on the other wire can be ignored. As a result, the resistance per unit length can be obtained from (19)

$$R = \frac{2R_s}{|I_0|^2} \int_0^{2\pi} \frac{|I_0|^2}{4\pi^2 a^2} a d\varphi = \frac{R_s}{\pi a} \tag{39}$$

Neglecting the dielectric and conductor loss, the characteristic impedance of a two-wire transmission line is given by

$$Z_0 = \eta \frac{\cosh^{-1}(D/2a)}{\pi} \tag{40}$$

3.4. Striplines

Striplines are often used in wideband networks and devices because of their low radiation, dispersion and loss. The cross section of a stripline is shown in Fig. 7. It has two parallel outer conductors with a separation b and also

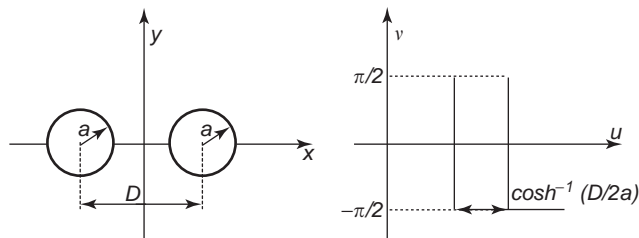


Figure 6. Conformal mapping of the cross section of a two-wire transmission line to the cross section of a parallel-plate waveguide.

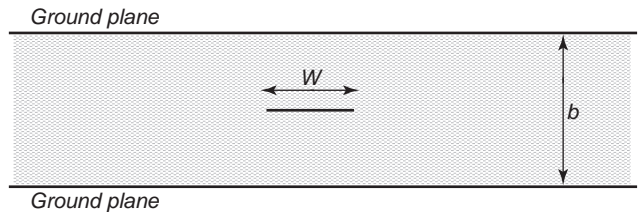


Figure 7. The cross section of a stripline transmission line.

a thin conducting strip with a width W , which is centered in between two conductors. The inner conductor is embedded in a homogeneous and isotropic dielectric with a relative dielectric constant ϵ_r and a loss tangent $\tan \delta$. Since a stripline structure has more than two conductors and a homogeneous dielectric, a TEM wave can be supported.

As in similar previous cases, we can apply the conformal transformation to map this complex structure into a parallel-plate waveguide [1]. Here, the Schwarz–Christoffel transformation needs to be applied twice. First, the cross section of a stripline in w plane is mapped to the real axis in z plane. Then another Schwarz–Christoffel transformation is used to map the real axis in the z plane to a cross section of the parallel-plate waveguide in the w' plane.

Due to the symmetry, we only need to consider a quarter of the structure, as shown in Fig. 8. Using a mapping function

$$w = -\frac{b}{\pi} \ln \left[z^{\frac{1}{2}} + (z+1)^{\frac{1}{2}} \right] + j \frac{b}{2}, \tag{41}$$

the structure in the w plane can be transformed to two flat strips in the z plane, as shown in Fig. 8. Note that five points, $w_0 = -W/2$, $w_1 \rightarrow -\infty$, $w_2 = 0$, $w_3 = jb/2$ and $w_4 \rightarrow -\infty + jb/2$ in the w plane are mapped to the points, $-x_0$, $x_1 \rightarrow -\infty$, $x_2 = -1$, $x_3 = 0$ and $x_4 \rightarrow \infty$ in the z plane correspondingly. As a result, the center strip and the ground plane in the w plane correspond to the short strip in the left half space and the half infinite strip in the z plane. The value of x_0 is

$$x_0 = \cosh^2 \left(\frac{\pi W}{2b} \right) \tag{42}$$

The new structure is still difficult to analyze. Therefore, a second Schwarz–Christoffel transformation is used to

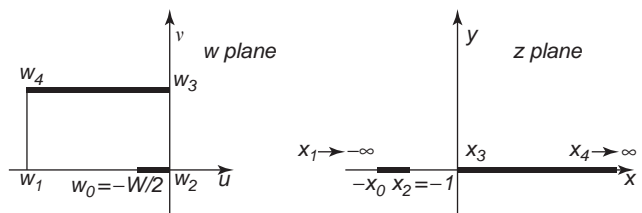


Figure 8. Conformal mapping for a symmetric stripline.

map the structure in the complex z plane to a parallel-plate waveguide in the w' plane, as shown in Fig. 9. Through the second transformation, the points $-x_0$, x_2 , x_3 , and x_4 in the z plane are mapped to the points $w'_0=0$, $w'_2=1$, $w'_3=1+jv_0$, and $w'_4=jv_0$ in the w' plane, respectively. Therefore the center strip and the ground plane in the w plane correspond to the bottom and top plates in the w' plane.

The transformation function of this second mapping is given by

$$w' = A_0 \text{Sn}^{-1}[(-z)^{1/2}, x_0^{(1/2)}] + B_0 \quad (43)$$

where $A_0 = -jv_0/\{\text{Sn}^{-1}[1, x_0^{(1/2)}]\}$, $B_0 = 1 + jv_0$, and

$$\text{Sn}^{-1}(x, k) = \int_0^x \frac{d\lambda}{[(1-\lambda^2)(1-k^2\lambda^2)]^{1/2}}$$

Also $\text{Sn}^{-1}(x, k)$ is called an *inverse elliptic function*, and the separation between the parallel plates is given by

$$v_0 = \frac{j\text{Sn}^{-1}(1, x_0^{(1/2)})}{\text{Sn}^{-1}(1, x_0^{(1/2)}) - \text{Sn}^{-1}(x_0^{(1/2)}, x_0^{(1/2)})} \quad (44)$$

Obviously, the capacitance per unit length of the stripline is 4 times that of the mapping of one-quarter section in the w' plane; therefore it is given by

$$C = \frac{4\epsilon}{v_0} \quad (45)$$

Furthermore, the characteristic impedance can be obtained as

$$Z_0 = \frac{\sqrt{\epsilon\mu}}{C} \quad (46)$$

Simpler forms have been developed based on the curve fitting of the exact solutions developed above [15,23]. For example, for the characteristics impedance, it can be

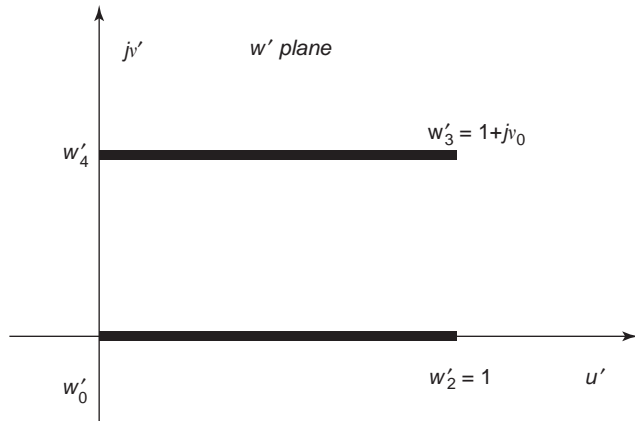


Figure 9. Conformal mapping from z plane to w' plane.

approximated by [2]

$$Z_0 = \frac{30\pi}{\sqrt{\epsilon_r}} \frac{b}{W_e + 0.441b} \quad (47)$$

where W_e is the effective width of the center conductor given by

$$\frac{W_e}{b} = \frac{W}{b} - \begin{cases} 0 & \text{for } W/b > 0.35 \\ (0.35 - W/b)^2 & \text{for } W/b < 0.35 \end{cases} \quad (48)$$

The inductance per unit length can be obtained by

$$L = Z_0^2 C \quad (49)$$

For this particular structure, the attenuation constant is often used to characterize the dielectric loss. The attenuation constant due to the dielectric loss is given by [2]

$$\alpha_d = \frac{k \tan \delta}{2} \quad (50)$$

and the attenuation constant due to the conductor loss can be found by the perturbation method or Wheeler's incremental inductance rule. An approximate result is [2]

$$\alpha_c = \begin{cases} \frac{2.7 \times 10^{-3} R_s \epsilon_r Z_0}{30\pi(b-t)} A & \text{for } \sqrt{\epsilon_r} Z_0 < 120 \\ \frac{0.16 R_s}{Z_0 b} B & \text{for } \sqrt{\epsilon_r} Z_0 > 120 \end{cases} \quad (51)$$

with

$$A = 1 + \frac{2W}{b-t} + \frac{1}{\pi} \frac{b+t}{b-t} \ln \left(\frac{2b-t}{t} \right) \quad (52)$$

$$B = 1 + \frac{b}{(0.5W + 0.7t)} \left(0.5 + \frac{0.414t}{W} + \frac{1}{2\pi} \ln \frac{4\pi W}{t} \right) \quad (53)$$

where t is the thickness of the strip.

3.5. Microstrip Lines

The microstrip line is the most popular planar transmission line in microwave integrated circuits (MIC). Figure 10 shows a typical microstrip-line configuration. It has a conducting strip, with a width W , residing on the top of a dielectric slab that has a thickness of h and a dielectric constant of ϵ_r . The microstrip configuration is not capable of supporting a pure TEM wave [2]. The propagation modes on microstrip lines need to be accurately characterized by hybrid transverse magnetic (TM)–transverse electric (TE) modes. However, the hybrid modes cannot be fully described in terms of static capacitances and inductances, like the previous transmission lines. Fortunately, the substrate thickness is usually electrically thin, and hence a quasi-TEM-mode assumption can be made.

In the quasi-TEM approximation, an artificial homogeneous dielectric, which has an effective dielectric constant ϵ_e , is assumed to fill the entire upper half-space above the

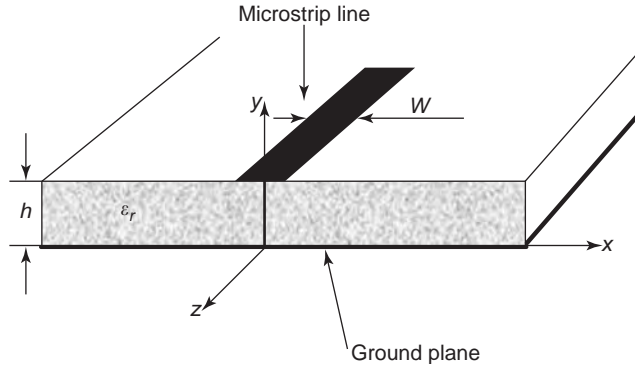


Figure 10. Configuration of a microstrip line.

ground plane. The effective dielectric constant and characteristic impedance can be obtained using curve-fitting approximations from rigorous quasistatic solutions as described in Refs. 2 and 16. The effective dielectric constant of a microstrip line is given by

$$\epsilon_e = \frac{\epsilon_r + 1}{2} + \frac{\epsilon_r - 1}{2} \frac{1}{\sqrt{1 + 12h/W}} \quad (54)$$

The characteristic impedance is given by

$$Z_0 = \begin{cases} \frac{60}{\sqrt{\epsilon_e}} \ln\left(\frac{8h}{W} + \frac{W}{4d}\right) & \text{for } \frac{h}{d} \leq 1 \\ \frac{120\pi}{\sqrt{\epsilon_e}[W/h + 1.393 + 0.667 \ln(W/h + 1.444)]} & \text{for } \frac{h}{d} \geq 1 \end{cases} \quad (55)$$

The capacitance per unit length is given by

$$C = \frac{\sqrt{\epsilon_e}}{cZ_0} \quad (56)$$

where c is the speed of light in free space. The inductance per unit length is given by

$$L = Z_0^2 C \quad (57)$$

The attenuation constant due to the dielectric loss is

$$\alpha_d = \frac{k_0 \epsilon_r (\epsilon_e - 1) \tan \delta}{2\sqrt{\epsilon_e} (\epsilon_r - 1)} \quad (58)$$

The attenuation constant due to the conductor loss is

$$\alpha_c = \frac{R_s}{Z_0 W} \quad (59)$$

where $R_s = \sqrt{\omega\mu_0/2\sigma}$ is the surface resistivity of the conductor.

In this section, we have derived the parameters of five commonly used transmission-line structures for RF and microwave applications. Driven by future system-on-chip (SoC) and system-on-packaging (SoP) applications,

transmission-line structures have been extended to the IC level [26].

4. TRANSMISSION LINE AT IC LEVEL

For SoC/SoP applications, RF circuits and GHz digital circuits often reside on the same substrate at very close spacing. The undesired interaction between transmission-line pairs plays a significant role in determining circuit performance [27–30]. To reduce the crosstalk between different transmission-line pairs, a dedicated return ground is often required. As a result of the manufacturing process, it is difficult to fabricate a dedicated global ground for all transmission-line structures. To guarantee the quality of signal transmission at the IC level, the often used transmission-line structure is the coplanar waveguide (CPW). Similar to microstrip-line structures, the CPW structure also cannot support a pure TEM mode. A quasistatic approximation must be made in order to apply the transmission-line theory to analyze this structure.

A CPW structure at the IC level is shown in Fig. 11 [26]. The center conductor is the signal trace while two neighboring traces are considered as the ground. In general, due to the conductor skin effect, the width-to-height ratio of the conductor, the high conductive loss in the substrate, and the strong dispersive effects, it is very difficult to extract the transmission-line parameters using analytical approaches [26,29]. Numerical techniques, such as the method of moments (MoM), the partial-element equivalent circuit (PEEC), the finite-difference time-domain (FDTD) method, or the finite-element method (FEM) are often required to extract these transmission-line parameters. Each numerical method has its advantages and disadvantages for different IC applications. For example, the PEEC method is very efficient when it is applied to model the transmission-line conductors, while the FDTD and FEM methods have their advantages if the effects of the IC substrate profile must be included. How to efficiently extract the parameters for multi-layered transmission line at the IC level is still an ongoing research topic [31,32].

5. CONCLUSIONS

The transmission line is one of the key devices in RF circuits, microwave circuits, and high-speed digital circuits.

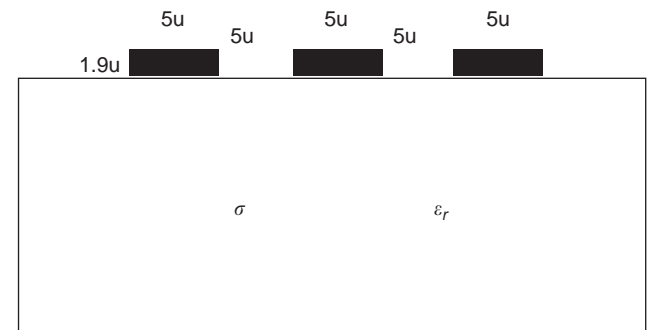


Figure 11. A common ground-signal-ground (GSG) transmission-line structure at IC level.

It is used to deliver signal or power from one device to other devices. Signal propagation behaviors on the transmission lines can be modeled using the telegrapher's equations. The electrical characteristics of different types of transmission lines can be described by using transmission-line parameters, such as the capacitance and the inductance per unit length for a lossless transmission line. If the conductor loss and the dielectric loss are considered, two more parameters, the resistance and the conductance per unit length, also need to be considered. This article starts with the derivation of the telegrapher's equations. Five commonly used transmission lines—parallel-plate waveguides, coaxial cables, two-wire transmission lines, striplines, and microstrip lines—are introduced and their transmission line parameters are derived. For the first three kinds of transmission line structures, four parameters, R , L , C , and G , as well as the characteristic impedance Z_0 , are derived from direct field analysis or conformal transformations. For stripline structures, a simple curve-fitting formula was developed for the capacitance per unit length. Then the inductance per unit length and the characteristic impedance were derived. The loss terms were described by the conductor loss constant and the dielectric loss constant, as shown earlier in the article. For microstrip lines, a quasi-TEM wave assumption was made to extract the transmission-line parameters Z_0 , C , and L . Similar to the striplines, the conductor loss constant and the dielectric loss constant were introduced.

As current technology allows us to develop transmission-line structures on ICs at high density, how to efficiently extract these transmission line parameters is still an ongoing research. As an example, an IC level CPW was discussed. With the development of new transmission-line structures at micrometer and nanometer scales, both the design of novel transmission-line structures and the techniques for their parameter extraction are topics currently being researched.

BIBLIOGRAPHY

1. R. E. Collin, *Field Theory of Guided Waves*, IEEE Press, New York, 1991.
2. D. M. Pozar, *Microwave Engineering*, Wiley, New York, 1998.
3. S. Ramo, J. R. Whinnery, and T. Van Duzer, *Fields and Waves in Communication Electronics*, Wiley, New York, 1994.
4. C. R. Paul, *Analysis of Multi-conductor Transmission Lines*, Wiley, New York, 1994.
5. R. W. P. King, *Transmission-line Theory*, Dover Publications, New York, 1965.
6. H. Kober, *Dictionary of Conformal Representations*, Dover Publications, New York, 1952.
7. W. X. Zhang, *Differential Equations for Radio Engineering*, National Defense Industry Press, Beijing, 1982 (in Chinese).
8. L. A. Pipes, *Applied Mathematics for Engineering and Physicists*, McGraw-Hill, New York, 1958.
9. W. R. Smythe, *Static and Dynamic Electricity*, McGraw-Hill, New York, 1939.
10. W. C. Johnson, *Transmission Lines and Networks*, McGraw-Hill, New York, 1950.
11. P. C. Magnusson, *Transmission Lines and Wave Propagation*, Allyn & Bacon, Boston, 1965.
12. S. B. Cohn, Shielded coupled strip transmission line, *IRE Trans. Microwave Theory Tech.* **3**:29–38 (Oct. 1955).
13. H. A. Wheeler, Transmission-line properties of parallel strips separated by a dielectric sheet, *IEEE Trans. Microwave Theory Tech.* **13**:172–185 (March 1965).
14. J. S. Rao and B. N. Das, Analysis of asymmetric stripline by conformal mapping, *IEEE Trans. Microwave Theory Tech.* **27**(4):299–303 (April 1979).
15. H. Howe, Jr., *Stripline Circuit Design*, Artech House, Dedham, MA, 1974.
16. K. C. Gupta, R. Garg, and I. J. Bahl, *Microstrip Lines and Slotlines*, Artech House, Dedham, MA, 1979.
17. H. A. Wheeler, Transmission-line properties of a strip on a dielectric sheet on a plane, *IEEE Trans. Microwave Theory Tech.* **25**(8): 631–647 (Aug. 1977).
18. H. E. Stinehefer, An accurate calculation of uniform microstrip transmission lines, *IEEE Trans. Microwave Theory Tech.* **16**:439–444 (July 1968).
19. H. E. Green, The numerical solution of some important transmission line problems, *IEEE Trans. Microwave Theory Tech.* **13**:676–692 (Sept. 1965).
20. P. Silverster, TEM properties of microstrip transmission lines, *Proc. IEE* **115**:42–49 (1968).
21. E. Yamashita, Variational method for the analysis of microstrip-like transmission lines, *IEEE Trans. Microwave Theory Tech.* **16**(8):529–535 (Aug. 1968).
22. T. Itoh, Spectral domain immittance approach for dispersion characteristics of generalized printed transmission lines, *IEEE Trans. Microwave Theory Tech.* **28**(7):733–736 (July 1980).
23. J. Knorr and A. Tufekcioglu, Spectral-domain calculation of microstrip characteristic impedance, *IEEE Trans. Microwave Theory Tech.* **23**(9):725–728 (Sept. 1975).
24. E. Yamashita and K. Atsuki, Analysis of microstrip-like transmission lines by nonuniform discretization of integral equations, *IEEE Trans. Microwave Theory Tech.* **24**(4):195–200 (April 1976).
25. U. Schulz and R. Pregla, A new technique for the analysis of the dispersion characteristics of planar waveguides, *AEU, International Journal of Electronics and Communications*, **34**(4):169–173 (1980).
26. C. K. Cheng, J. Lillis, S. Lin, and N. Chang, *Interconnect Analysis and Synthesis*, Wiley, New York, 2000.
27. J. Cong, An interconnect-concentric design flow for nanometer technologies, *Proc. IEEE* **89**(4):505–528 (April 2001).
28. J. Cong, ed., *Challenges and Opportunities in Giga-scale Integration for System-on-a-Chip*, Final report of NSF/NSC Int. Workshop, 1999.
29. A. Deutsch et al., Frequency-dependent losses on high-performance interconnects, *IEEE Trans. EMC* **43**(4):446–465 (Nov. 2001).
30. A. Deutsch, Electrical characteristics of interconnections for high-performance system, *Proc. IEEE* **86**:315–355 (Feb. 1998).
31. Semiconductor Industry Association, *International Technology Roadmap for Semiconductor*, 2001 ed.
32. D. Leenaerts, G. Gielen, and R. Rutenbar, CAD solutions and outstanding challenges for mixed-signal and RF IC design, *Proc. ICCAD 2001* San Jose, CA, 2001.

TRANSMITTERS FOR ANALOG TELEVISION

GERALD W. COLLINS
GW Collins Consulting,
Quincy, Illinois

Significant advances continue to be made in television (TV) transmitter technology. New technology has been introduced to provide high-quality TV signal transmission while improving reliability, reducing maintenance, and lowering overall cost of ownership. These new technologies include solid-state, high-power amplifiers and improvements in UHF tube transmitters. The FCC continues its policy of technical deregulation, which allows more flexibility in transmitter design and system operation. This article discusses the relevant technology and provides the information needed to understand the operation, design criteria, and some of the future developments of TV transmitters. Although this information is presented from the viewpoint of equipment used in the United States, the principles apply to analog TV broadcasting worldwide. Specific details and numerical constants may differ in other systems, but the fundamental principles are the same.

TV transmitters are composed of two essential components: the exciter and the RF power amplifier (PA). The exciter provides the signal processing functions to convert a baseband TV signal into a modulated RF signal on the assigned channel. These functions include baseband signal processing, modulation, precorrection, equalization, upconversion, bandlimiting, and amplification to a relatively low-power RF signal. Although different methods are used for different types of signals, all functions must be performed regardless of whether the baseband signal is video or audio. Because the output of the exciter is a modulated RF signal, most commercially available exciters are considered low-power transmitters.

The basic block diagram of a television transmitter that provides separate amplification of visual and aural signals is shown in Fig. 1. The visual portion of the exciter receives a video baseband signal, processes it, and converts it to a fully modulated vestigial sideband signal. Because intermediate-frequency (IF) modulation is used in all modern TV transmitters, most of the signal processing occurs in the video and IF stages. Similarly, the aural por-

tion of the exciter receives the audio baseband signal, processes it, and converts it to a frequency-modulated signal. The exciter includes all blocks through the upconverter.

For transparent transmission of video, it is important to optimize the incoming signal, which is done in the video processing section of the exciter. The following are the main functions of the exciter video processing circuitry:

- Assurance of proper sync:video ratio
- Removal of common mode signals
- Provision for overall video-level control
- DC restoration
- Prevention of overmodulation
- Frequency response correction

In nearly all IF-modulated transmitters, the visual modulator is a broadband, balanced, diode mixer. It is configured for maximum rejection of the local-oscillator signal and biased to provide excellent linearity, low noise, and capability to achieve carrier cutoff. The video signal is DC-offset to provide the proper modulation level. Peak of sync corresponds to maximum IF envelope output, and white corresponds to minimum IF output. The output signal of the modulator is a double-sideband AM signal that has a modulation depth of 12.5%. A surface acoustic wave (SAW) filter removes the lower sideband and produces vestigial sideband (VSB) modulation. This filter also bandlimits the upper sideband to within 4.75 MHz of the visual carrier.

In its most basic form, the aural exciter consists of an audio processor, a frequency-modulated IF oscillator, and an upconverter. To ensure that the transmitter is not the limiting factor in monaural and stereo audio reproduction, the transmitter must add as little distortion as possible to the incoming signal. Baseband audio of the BTSC multi-channel television sound (MTS) system may include monophonic or stereo, a second audio program (SAP), and professional channels. These signals may include frequency components out to 105 kHz. To achieve good stereo separation and minimum crosstalk between the stereo and the SAP channels, it is necessary to achieve good phase linearity, low distortion, and reduced amplitude ripples and rolloff over the stereo passband. Errors in phase linearity and amplitude response within the audio

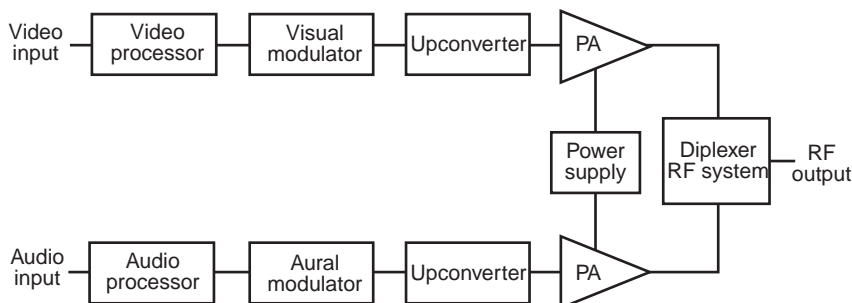


Figure 1. Block diagram of a basic television transmitter.

circuitry contribute to stereo separation degradation. As a general rule, amplitude rolloff should be less than 0.1 dB, and departure from phase linearity should be less than 1° for quality stereo.

Transmitters employing IF modulation generate visual IF, aural IF, and master oscillator signals for translating visual and aural IF to the final carrier frequencies. These signals are implemented with either digital synthesizers or crystal oscillators. An advantage of the synthesizer is that only one crystal is needed at a single standard frequency for all TV channels. Synthesized sources should be tested for spurious frequencies that may appear as FM noise. The crystal oscillator usually involves simpler circuitry.

The PA provides the “muscle” to amplify the modulated RF signal to the desired level for transmission. The type of power amplifier technology used to perform this function is key. Both solid-state and tube devices are available in commercial equipment. For VHF channels, solid-state devices predominate. For UHF, both solid-state and tube devices are used. TV transmitters are unique in that no other application requires such high levels of linear RF power generation while operating virtually uninterruptedly. This has led to the development of specialized techniques to assure highly efficient and reliable operation. The need for high efficiency has led to the near-universal use of partially saturated class AB final power amplifiers. This, in turn, has resulted in the development of precorrection and equalization techniques to compensate for residual nonlinearity inherent in this class of operation. To achieve the levels of reliability required, redundant system architectures that minimize single points of failure are used.

Traditionally, TV transmitters have used separate RF amplifier chains for the visual and aural signal paths. This is generally the most cost-effective approach for high-power, solid-state transmitters for both VHF and UHF. Many broadcast engineers believe that separate amplification provides the highest-quality transmitted video. With the introduction of inductive output tubes (IOTs) as final high-power UHF amplifiers, it has become popular to combine the visual and aural signals in the exciter and amplify them together in the stages that follow.

For visual signals in separate amplification and combined aural and visual signals in common amplification, it is important that the power amplifier have a linear transfer characteristic in amplitude and phase and flat, symmetric frequency response and minimum group delay variation across the modulation passband. For visual-only signals, the required bandwidth is 4.5 MHz. For common amplification and digital signals, 6 MHz is required.

Even though linear class AB amplifiers are used, some residual nonlinearity remains. With combined amplification, the visual, color subcarrier, and aural signals are mixed to produce in-band as well as the out-of-band intermodulation (IMD) and cross-modulation products. The out-of-band products sufficiently removed from the channel of operation may be eliminated by a high-level filter. However, in-band products can be reduced to acceptable

levels only by making the transmitter sufficiently linear. This requires highly effective precorrection circuits in the IF and/or RF signal paths. For example, the IMD within ± 920 kHz of the visual carrier can be precorrected by low-level IF circuitry.

For optimum stereo performance a nonlinear class C amplifier with flat response and group delay across the modulation passband may be used. Because frequency modulation and demodulation constitute a nonlinear process, there is no one-to-one correspondence between RF amplitude and phase response and baseband stereo separation and crosstalk. Generally, a 3 dB bandwidth of 1.5 MHz provides excellent stereo and SAP performance.

Other key functions in the PA, common to all amplifier technologies, include cooling and AC-to-DC power conversion. Proper cooling of the power amplifier, whether solid-state or tube is important for safe operation and high reliability. For example, it is generally acknowledged that the service life of a transistor doubles approximately for every 10°C reduction in junction temperature. Power amplifier cooling may employ either liquids or air. Distributed air-cooling systems using more than one fan offer good redundancy for solid-state amplifiers. Motor and fan technology has matured to the point where a single, large, direct drive fan is as reliable as many smaller fans. Because many RF power amplifiers modules may be employed in a solid-state transmitter, a large volume of air is needed to cool the heatsinks adequately. Low-pressure fans or blowers may be used if heatsink fin density is not high. This aids in reducing audible noise. The heat is distributed over a large volume of air, and the temperature rise is relatively low.

Cooling of most tube amplifiers requires large volumes of liquid. For example, cooling a 60-kW IOT, typically used for high-power UHF applications, requires about 25 gallons per minute of liquid for the collector under maximum ambient temperature conditions. The body of the tube is also liquid-cooled. A 50:50 water/glycol solution is typically used in cold climates without any special water purification. Input and output cavities are air-cooled. Lower-power IOTs may be air-cooled. Air cooling is also used to cool other transmitter components, such as the intermediate power amplifier (IPA).

Power supply design is critical to the performance and reliability of television transmitter power amplifiers, whether solid-state or tube. Because FET and bipolar devices are low-voltage devices, the power supplies that serve solid-state transmitters must provide low voltage and high current. High-reliability connections must be guaranteed in the DC distribution. Because the available power output from any amplifier varies with the square of the DC voltage applied, it is desirable that the supply remain very tightly controlled over incoming AC line variation. The amplifier current also changes with modulation, thus requiring videofrequency currents from the power supply. The supply must provide excellent regulation from no load (white picture) to full load (peak sync output) and a low source impedance for all videofrequencies. The efficiency of the power supply is important because dissipated power results in heat and unnecessarily high utility costs. Any voltage or current transients or

voltage sags at the AC input should be suppressed before reaching any solid-state device.

Television transmitters that employ separate amplification and use a common antenna and transmission line for visual and aural require a high level diplexer to combine the visual and aural signals before transmission. Other components required in the output RF system include harmonic filters and a color notch filter. If multiple transmitters or PA cabinets are combined, power combiners and RF switching devices are also required.

1. KEY PERFORMANCE FACTORS AND OPERATIONAL CONSIDERATIONS

The key performance factors for the visual portion of a television transmitter include power output, linearity, efficiency, and reliability. These factors are also important for the aural section except that linearity in separate amplification aural amplifiers is not needed.

The geographic separation and effective radiated power (ERP) of television stations are carefully specified by the FCC to assure reliable service within the coverage area and to avoid interference between stations operating on the same frequency, that is, cochannel interference. The visual transmitter power output (TPO) is determined from the ERP by using the antenna gain [1] *g* and the transmission-line efficiency η . Stated mathematically

$$TPO = \frac{ERP}{g\eta}$$

ERP is given in kilowatts (kW) of power at the peak of the synchronizing (sync) pulse so that the TPO is also in kW at the peak of sync. Table 1 relates TPO and ERP for typical lowband VHF, highband VHF, and UHF stations using the maximum allowable ERP for each band.

The transmission line efficiency varies depending on tower height and the type and size of line selected. The minimum line size is determined by the TPO and desired line efficiency.

Aural power may range from 5 to 20% of the visual peak sync value. Most stations transmit aural at 10%, although some UHF stations using common amplification reduce the aural power to as low as 5% to reduce IMD products.

Calibration of transmitter power is vitally important. ERP is specified by the FCC. Thus, maintaining TPO within tolerance assures that the ERP is in accordance with the allocation. If the power output is not accurately known, the amplifier dissipation and efficiency are equally

Table 1. Typical Transmitter Power Output (TPO) for VHS and UHF

Band	ERP (kW)	Antenna Gain	Line Efficiency (%)	TPO (kW)
Low VHF	100	6	85	19.6
High VHF	316	12	80	32.9
UHF	5000	30	76	219.3

unknown, and power amplifier device life may be shortened. In addition, linearity precorrection circuits must be set up at a known, stable power level to assure that system linearity is maintained. Calibration of power level is best done by using a calorimeter, especially for higher-power transmitters. In a calorimeter, the temperature rise of a known volume of water caused by the heat generated in a water-cooled load is used to determine the average power output. For the visual transmitter, this measurement is done with modulation at blanking level, or 75% of peak sync. The measured average power is converted to peak sync power by multiplying by the peak:average ratio (1.68). The formula for the power calculation is

$$P_o = (1.68)(0.264)(T_o - T_i)R_f$$

where T_o the temperature of the water exiting the load in degrees Celsius, T_i is the temperature of the water entering the load, and R_f is the flow rate in gallons per minute. The numeric factor 0.264 is the specific heat of water.

For aural output, the measurement technique may be similar. However, because the peak and average power for a frequency-modulated signal are the same, the peak:average factor is unity. Alternatively, the aural power may be set by observing the relative levels of the visual and aural signals on a spectrum analyzer. This is especially useful for measurements made after the signals are combined, as in common amplification.

Accurately calibrated couplers and low-level power meters located at the output of the transmitter RF system are also widely used for power measurement. Because the coupling factor is known, the reading of the power meter may be calibrated to the actual power output.

1.1. Efficiency

Because of environmental concerns and the high cost of electricity, TV transmitters must operate efficiently. Although efficient power conversion is important at VHF, it is unusually important for UHF transmitters because the transmitted power is almost always much higher and consequently much more expensive to generate. When considering the efficiency of TV transmitters, several factors must be understood. To determine total power consumed, the AC-to-RF conversion efficiency is the parameter of interest. For systems with unity power factor, determining the AC input power is relatively straightforward. For power factors less than unity, the relative phase of the AC fundamental voltage and current must be determined. In addition, in systems generating significant line harmonics, the relative level of these harmonics must be known [2]. Power factor is expressed either as displacement power factor or total power factor. The displacement power factor (DPF) is the cosine of the phase between the voltage and current at the fundamental frequency:

$$DPF = \cos(\phi_v - \phi_i)$$

The displacement power factor is equal to the total power factor only for undistorted sinusoidal voltage and current waveforms.

Total power factor is the ratio of total AC power input P_i to the apparent power VI :

$$PF = \frac{P_i}{VI}$$

Determining input power is simplified by considering only the DC-to-RF conversion process. In this case it is necessary to determine only the voltage and current provided by the power supply to the final amplifying devices. Although this is a useful tool for evaluating power amplifier performance, it has the disadvantage of ignoring the power consumed elsewhere in the transmitter, such as power supplies for drive stages, cooling systems, filament power, magnet power, and control system power. If these items are to be included in the efficiency calculation, they must be determined separately.

Determining output power for efficiency calculation is equally complex. As we have seen, transmitters are rated in terms of peak sync visual power. Exclusive use of this number neglects the aural output. Some amplifier technologies exhibit apparent efficiencies greater than 100% if visual peak power is used as the measure of output power. This has given rise to the use of a figure of merit (FoM) defined as

$$FoM = \frac{P_o}{P_{DC}}$$

where P_o is the visual peak sync output power and P_{DC} is the DC input power at 50% average picture level (APL). This definition is valid for transmitters using separate amplification. For common amplification, the aural input and output power must be added to the denominator and numerator, respectively. Typical values of the figure of merit for several tube amplifiers operating in separate amplification are shown in Table 2 [3].

The DC input power for a typical visual-only power amplifier is given by

$$P_i = V_b(I_s DF_s + I_v DF_v)$$

where V_b is the beam voltage, I_s is the beam current at peak sync, DF_s is the duty factor of the sync pulse (0.08), I_v is the beam current during video, and DF_v is the duty factor of the video (0.92). For a 60-kW-pulsed klystron, typical values are $V_b = 24$ kV, $I_s = 5.5$ A, and $I_v = 3.7$ A, so that

$$P_i = 24[(5.5 \times 0.08) + (3.7 \times 0.92)] = 92.2 \text{ kW}$$

Table 2. Figures of Merit for Commonly Used Tube Amplifiers

Amplifier Device	Figure of Merit
Tetrode	0.9–1.0
Integral cavity klystron	0.65–0.75
External cavity klystron	0.65–0.75
Klystrode or IOT	1.1–1.3
Depressed collector klystron	1.2–1.3

and

$$FoM = \frac{60}{92.2} = 0.65$$

Other important efficiency factors to consider include the power lost in the RF system and antenna transmission line. These losses can be considerable and represent added cost of operation after the full cost of generating the transmitter output power has been spent. Thus it is extremely important to minimize these losses. If losses are to be minimized, the largest coaxial transmission line or waveguide should be used consistent with avoiding higher-order modes and within the wind load capability of the transmission tower. At UHF, the choice is usually between $6\frac{1}{8}$ or $8\frac{3}{16}$ in. coaxial line or rectangular or circular waveguide. The larger the coaxial line, the lower the loss. However, at the higher UHF channels, $8\frac{3}{16}$ -inch line supports an evanescent waveguide mode. Rectangular and circular waveguides provide lower loss but are larger in cross section than coaxial lines. The larger the physical size of the line, the higher the wind load. Because of its cross-section, circular waveguide offers lower wind load than rectangular. Thus many factors must be considered when selecting transmission line type and size. The larger size coaxial lines and waveguides are more expensive to purchase and install. However, this is a one-time cost that should be carefully weighed against the long-term reduction in transmitter plant efficiency resulting from the use of a line with excessive loss.

1.2. Reliability

Many stations operate continuously unattended, making reliability a key requirement. There are many factors that affect the reliability of a TV transmitter. Overall design philosophy, device technology, module design, control architecture, power supplies, cooling, and cabinet design are critical areas, all of which must be considered. Consider a transmitter design that uses subsystems in series with no system redundancy. If one device fails, the entire transmitter fails; that is, each subsystem represents a critical point in the event of failure. This is illustrated in Fig. 2, which shows a system of three subsystems in series with no redundancy. This might represent a tube-type transmitter with a single exciter and IPA. If each device (a, b, c) has a reliability or probability of functioning until time t , the reliability of the system $R_s(t)$ is given by the product of each subsystem reliability:

$$R_s(t) = R_a R_b R_c$$

If three identical subsystems are operated in parallel, as in Fig. 3, and only one is required for on-air operation, there are no single points that may cause system failure. This represents a parallel arrangement of identical PAs,



Figure 2. Subsystems in series.

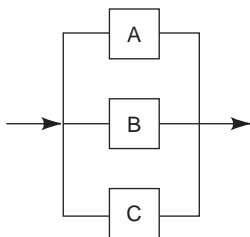


Figure 3. Subsystems in parallel.

each with their own IPA. In this case, the overall system reliability is given by

$$R_s(t) = R_a + R_b + R_c - R_a R_b - R_a R_c - R_b R_c + R_a R_b R_c$$

To illustrate, assume that each subsystem has a reliability of 0.5. In the series case, the system reliability is only 0.125. In the parallel case, the reliability is 0.875, an improvement by 8 times.

The reliability is related to failure rate λ as follows:

$$R(t) = e^{-\lambda t}$$

The mean time between failures (MTBF) is the reciprocal of the failure rate:

$$\text{MTBF} = \frac{1}{\lambda}$$

On-air availability is related to reliability but perhaps even more important. On-air availability is the percentage of time the transmitter is available for service, defined by the following equation

$$\text{Availability} = \frac{\text{MTBF}}{(\text{MTBF} + \text{MTTR} + \text{MPMT})} \times 100\%$$

where MTTR is the mean time to repair and MPMT is the mean preventive-maintenance time. All quantities are stated in hours (or other consistent time units).

There is little point in designing a transmitter that has a high MTBF figure if, because of poor design and mechanical packaging, it takes an inordinate length of time to make repairs, or if the transmitter has to be shut down frequently for routine preventive maintenance.

Many stations have very short signoff windows or operate 24 h a day. This often results in a less than optimum maintenance schedule, which can lead to premature failure or out-of-tolerance operation. One way to reduce the amount of off-air maintenance time is by making provisions for on-air maintenance or to have redundant transmitters. This significantly reduces the MPMT.

Several design factors should be considered for optimum on-air availability. These include high reliability of the fundamental circuits and provision for fast, easy access to all subassemblies. A subassembly, which can be readily removed, can be repaired by station personnel or returned to the manufacturer for exchange. Another

factor contributing to availability is the maximum use of common parts and subassemblies. If fewer items are needed, it is more economical for the station to maintain a full inventory of spares. If spares are on hand, the repair time may be much shorter.

1.3. Linearity

This parameter refers to the degree with which the transmitter output signal is directly proportional to the input. Common terms used to quantify the degree of transmitter nonlinearity include low frequency or luminance nonlinearity, differential gain, and AM-to-AM conversion. Output phase may also be a function of input level. The deviation from linear phase is often quantified as incidental-carrier phase modulation (ICPM), differential phase, and AM-to-PM conversion. These deviations from linearity are called *nonlinear distortions*, that is, distortions to the transmitted signal introduced by nonlinear components in the transmission path. A nonlinear component is any device whose complex output voltage is not directly proportional to input voltage. Power amplifiers operating near compression and intermediate power amplifiers (IPAs) are major contributors to nonlinear amplitude distortion. This process creates the frequency spectra of the lower sideband, usually called *lower-sideband reinsertion*. Filters are commonly used to reduce sideband spectral components, but these introduce phase distortions.

Differential gain is nonlinear chroma gain as a function of luminance level. A change in the picture color saturation results from differential gain. Differential phase is nonlinear chroma phase as a function of luminance level. A change in picture hue results from differential phase. Low-frequency or luminance nonlinearity is the change in luminance gain as a function of picture brightness level.

Precorrection is a technique to compensate for nonlinear distortion. The objective of precorrection is to provide a complementary transfer function that when operating on the nonlinear transfer function of the power amplifier, minimizes total system nonlinear distortion. Precorrection may be introduced in the baseband, IF or RF sections of the system and may be manually or adaptively adjusted.

IF linearity precorrection provides the correction for nonlinear distortions in the intermediate-frequency (IF) sections of the exciter. There are important advantages to correcting at IF. Because most distortions are caused in the high-power RF amplifiers after vestigial sideband (VSB) filter, a precorrector placed after the VSB filter can most accurately precorrect the modulated signal. Intermodulation products are caused by the nonlinear transfer function of the IPA and PA. As the power output increases toward saturation, amplitude compression and phase lag occur. The nonlinear transfer function gives rise to mixing products that occur at sum and difference frequencies around the visual carrier. Precorrection spectra generated at IF after the VSB filter produce energy components that can cancel intermodulation products generated in the amplifier stages. This is particularly important for pulsed klystron or common amplification transmitters.

An example of a basic gain expansion circuit used for precorrection is shown in Fig. 4. The signal is normally attenuated a fixed amount by using a resistive L-pad, R_1 and R_2 . The diodes, D_1 and D_2 , are normally reverse biased by equal but opposite DC voltages. Reducing the DC voltage permits the diodes to conduct on the signal peaks, inserting additional resistance in parallel with the series arm of the L-pad attenuator, thereby decreasing the attenuation. Varying the resistance in series with the diodes provides variable-gain expansion.

1.4. Incidental-Carrier Phase Modulation

Nonlinear phase distortions in high power amplifiers produce incidental-carrier phase modulation (ICPM) or spectral components in quadrature with the modulated signal. Fast video amplitude changes, such as a step or pulse, cause larger incidental-phase spectral components than slow changes. Receivers make this condition worse by attenuating the lower sidebands below 0.75 MHz. The receiver responds to the extra sidebands created by the phase modulation as if they were amplitude-modulated single sidebands, producing spikes. The faster the rise time of the signal, the more high-frequency energy is present, resulting in edge distortions in the picture.

The picture impairment due to ICPM is similar to simultaneous group delay and differential-phase errors in that edges are less sharp and the color hue changes with brightness. On a waveform monitor, overshoots are visible on trailing edges and as rounding of leading edges. These overshoots vary in severity depending on how far into saturation the power amplifier is driven.

Audio impairment is produced by ICPM in receivers employing intercarrier conversion. Intercarrier receivers use an AM or synchronous detector to produce a 4.5-HMz aural IF from the composite video IF. Any phase

modulation on the visual carrier is transferred to the aural carrier. For monoaural baseband audio, the effect of increasing amplitude versus frequency of ICPM is nullified to some degree by receiver deemphasis. With multi-channel sound, however, there is no deemphasis applied to the baseband stereo signal, and the distortion is more pronounced at the stereo subchannel and pilot frequencies. Audio companding is employed to counteract the effects of ICPM and other noise sources on the stereo subchannel. Although the audio companding process reduces some of the effects of ICPM, precorrection is essential for delivering clear, low-noise audio to intercarrier receivers.

There is no defined level of ICPM for a given stereo performance level because the signal-to-buzz ratio is highly dependent on the picture spectral components. Refer to the EIA recommended practices [4] for recommendations on ICPM limits.

ICPM precorrectors are grouped into two types: those using a phase modulator and those inserting a fixed phase directly on the signal. The phase modulator uses video to modulate the IF or a master oscillator with a phase characteristic opposite that of the nonlinear amplifier. A phase modulator can also operate directly on the IF signal using a video signal to set the amount of modulation. A block diagram of a master oscillator phase modulator is shown in Fig. 5.

ICPM precorrectors operating directly on the IF signal are implemented in several ways. Direct precorrection at IF is similar in concept to baseband differential phase precorrection. In both cases, the visual signal is split into two-phase quadrature paths, as shown in Fig. 6. In the IF corrector, the full video bandwidth is processed, whereas in the video precorrector only the chroma signal is affected. One method of implementation is to modify the quadrature signal gain function with level-dependent diode

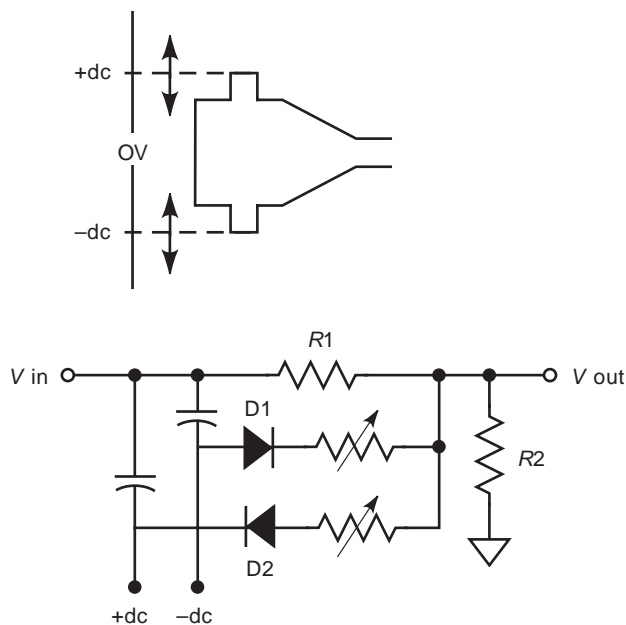


Figure 4. Basic gain expansion circuit.

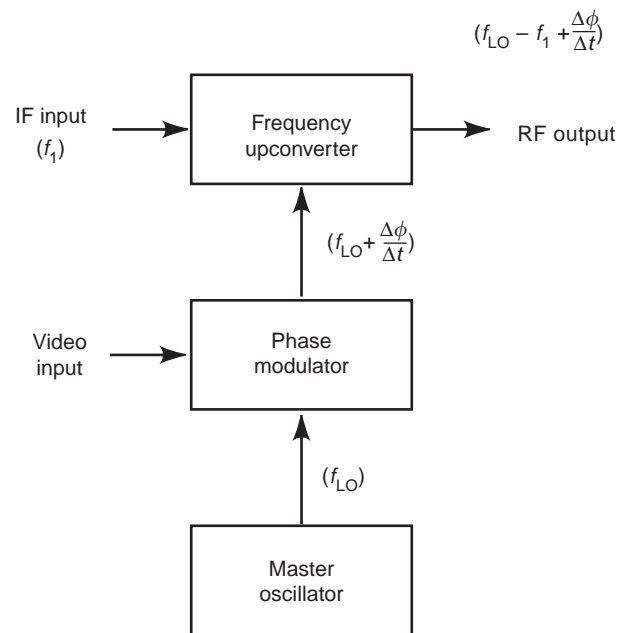


Figure 5. Block diagram of master oscillator phase modulator.

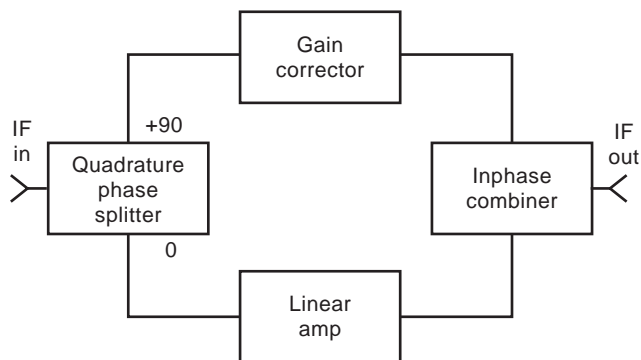


Figure 6. Direct ICPM corrector.

expansion or compression circuits. This can be done by the same techniques as in the linearity corrector.

The vector diagram shown in Fig. 7 illustrates the operating principles of the ICPM and linearity correctors. The input signal is represented by the vector on the left. Because of nonlinear distortions in the transmitter, the output signal is shifted in phase and compressed, producing the resultant distorted signal. To produce the correct output signal, it is necessary first to expand the in-phase signal and introduce an equal and opposite quadrature signal. When the resultant signal is amplified, the output signal is restored to the undistorted TV signal.

1.5. Linear Distortions

These are distortions to the transmitted signal that are not level-dependent. Unlike nonlinear distortions, linear distortions can be introduced by linear (as well as nonlinear) components in the transmission path. These components include any device with a nonconstant frequency response, such as matching networks, cavities, filters, diplexers, and other tuned circuits. Variations in both amplitude and phase are produced, that is, variations in both in-band amplitude response and group delay (GD) produce linear distortions.

Group or envelope delay is the nonuniform delay of different frequencies over the signal bandwidth, that is,

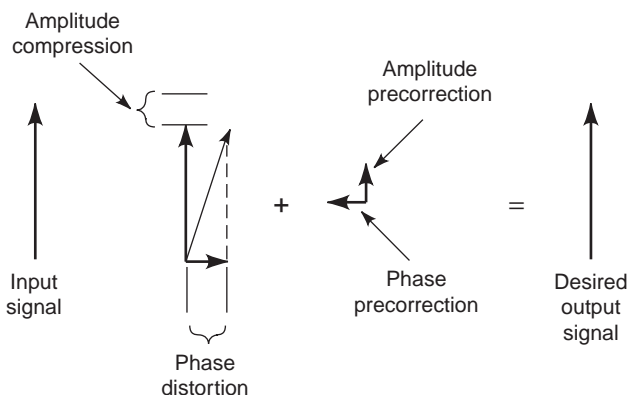


Figure 7. Vector representation of precorrection.

the first derivative of phase with respect to frequency:

$$GD = \frac{d\phi}{d\omega}$$

Group delay is caused by nonlinear phase as a function of frequency inherent in RF amplifiers, filters, combiners, and other devices. In general, the closer the amplitude rolloff is to the passband of a tuned circuit, the higher the group delay distortion.

Equalization is the technique used to compensate for linear distortions. The objective is to provide a complementary transfer function that when operating on the frequency response function, minimizes linear distortion. Equalization may be introduced in the baseband, IF, or RF sections of the system and may be manually or adaptively adjusted.

Group delay equalization of the aural transmitter introduces group delay equalization in the IF section of the aural modulator, effectively correcting the group delay in the diplexer. The result is improved TV stereo separation. The notch diplexer is a passive device, but it can introduce significant linear distortions that degrade stereo separation because the FM stereo signal is most sensitive to the notch diplexer group delay and amplitude response over the occupied bandwidth of the FM signal. The group delay and amplitude response of a single-cavity diplexer optimized for minimum aural reject power is shown in Fig. 8. The bandpass is somewhat narrow, and the group delay is steep. Fortunately, the response curves have a high degree of symmetry, which makes equalization possible. Equalization of the FM bandpass allows using a lower cost, single-cavity notch diplexer. A stagger-tuned, dual-cavity, notch diplexer might be used to provide more bandwidth. However, a dual-cavity, notch diplexer introduces more group delay in the visual path and is more expensive than a single-cavity diplexer.

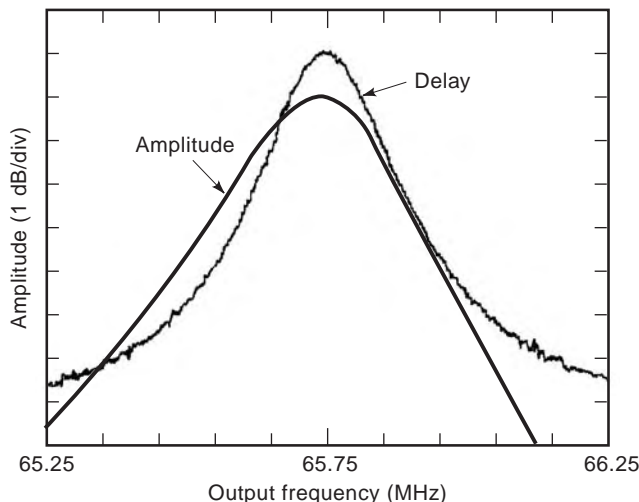


Figure 8. Single-cavity notch diplexer amplitude response and group delay.

1.6. Transmitter Control Systems

The transmitter control system provides the interface to the user. It provides control, monitoring, and protection for the transmitter. Essential control features include transmitter ON and OFF states, output power raising and lowering, remote or local control selection, and automatic gain or level control. Other automatic control features, such as VSWR foldback, are desirable. VSWR foldback reduces forward power when reflected power is high, such as in antenna icing, and restores RF power to normal when the reflected power returns to normal.

Easy-to-read status indicators are essential for quick fault diagnosis. Typical status conditions displayed include exciter fault, VSWR fault, VSWR foldback status, power supply fault, controller fault, loss of cooling air, door open, failsafe interlock open, AC phase loss, RF power module fault, visual drive fault, aural drive fault, and external interlock open.

If individual RF amplifier modules and power supplies are self-protecting, the system control and monitoring functions are relatively simple and straightforward. A most effective approach is to distribute the control system throughout the transmitter, as shown in Fig. 9. In the distributed control system, the failure of any individual controller component does not affect the operation of the others. For example, failure of any single cabinet controller would not affect the operation of the other cabinet controllers or the main controller. Failure of the main controller would not cause an off-air condition if the cabinet controllers operate independently of the main controller. Failure of monitoring and metering should not cause an off-air condition. It is also important that the controller have backup memory to restore the transmitter operating condition after AC power failure.

2. TRENDS IN TV TRANSMITTER DESIGN

Television broadcasting is a mature technology. In the half-century or so since the adoption of the color standard, there has been steady progress in transmission technology. The prospect is for improvements to continue. Many of

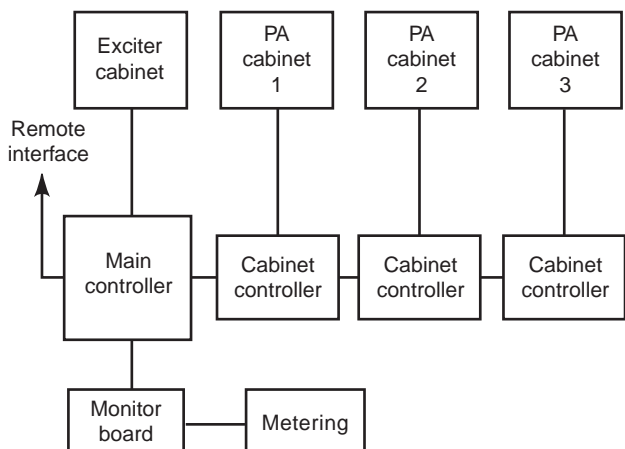


Figure 9. Distributed control and monitoring.

these will occur simply because TV transmitters involve such a wide range of electronics technology. Others will be driven by the implementation of digital television [8]. It may be expected that the analog transmission will benefit from many of the improvements created by the digital revolution. Improvements that reduce the cost of ownership, improve the human to transmitter interface, and simplify operation and maintenance are the areas in which the most progress can be expected. These will include steady improvements in high-power, solid-state devices and high-power UHF tubes, advances in digital signal processing and in microprocessor-based controls, and improved displays for monitoring functions. The pervasive use of digital technology will allow more and more functions that have traditionally been defined by the hardware design to be part of software.

3. SOLID-STATE DEVELOPMENTS

Technological advances in bipolar and field-effect transistors (FETs) have made the development of solid-state, high-power, linear amplifier modules for TV applications both practical and cost-effective. By combining RF modules, it is practical to create transmitters at any power range up to 75 kW. This is especially true for the VHF bands and is becoming increasingly true for UHF. The trend in solid-state technology is toward devices that produce higher power at higher frequencies and lower cost. As costs are reduced, the feasibility of higher power transmitters at UHF is enhanced. Solid-state power amplifiers are operated in class AB for the best tradeoff of efficiency, linearity, reliability, and cost. Driver stages usually contain class A amplifiers.

There are several advantages to high-power, solid-state technology. Solid-state transmitters maintain their performance over extended periods of time because of the absence of tuning controls and degradation of filament emissions. No warmup time is required. Solid-state transmitters produce full-rated power within seconds of activation. Solid-state transmitters most often are air-cooled. This has the advantage of eliminating any chance of coolant spills and concern for cooling system freeze up in cold climates. There have been some attempts to develop liquid-cooled solid-state transmitters. The advantages of liquid cooling include somewhat quieter operation and improved cooling efficiency. Safety is also enhanced in solid-state systems. Operating voltages are usually 65 V or lower compared to tens of kilovolts for tube amplifiers. There is no need for crowbars to protect solid-state devices in the event of a short circuit. However, protection against lightning and static-induced transients is required. Maintenance is also eased. Solid-state transmitters employ modular architectures in which a large number of RF and power supplies modules operate in parallel. Failure of any one of these units has only a minor effect on TPO. Thus immediate corrective action is not as critical as in tube transmitters in which there may be only a single output tube. Simple diagnostic displays make the identification of the failed unit easy. Hot pluggable designs and a minimum of spare modules make it possible to remove and

replace the failed unit while the transmitter remains on air. Repair of the failed unit may be done offline.

Both bipolar and field effect transistors (FETs) are used today as RF amplification devices. Vertical metal oxide silicon field-effect transistors (MOSFETs) are the devices of choice for VHF transmitters. Both bipolar transistors and MOSFETs have been available for UHF. However, UHF vertical MOSFETs are not as linear and therefore not as cost-effective as bipolar devices. Recently, laterally diffused metal oxide silicon field effect transistors (LDMOSFETs) have developed cost-effective linear power for UHF. This has enabled producing cost-effective, solid-state transmitters for UHF. Although both bipolar transistors and FETs have merit, FETs have some advantages over bipolar devices. FETs have an amplification factor higher than that in bipolar transistors, reducing the number of driver stages required. The fewer the drive stages, the lower the manufacturing cost, and the better the linearity because there are fewer parts contributing to cost and nonlinearity. The higher power supply voltage required by FETs reduces the current rating required for the power supply. Power supply cost is driven by current rating. Simple bias circuitry for FETs minimizes parts count and amplifier production cost.

New developments in high-power, solid-state devices are ahead. Silicon carbide (SiC) materials make it possible to produce a variety of devices. In addition to blue light-emitting diodes (LEDs) and switching transistors, linear high-power UHF transistors are under development [6]. These transistors promise to operate at voltages and temperatures higher than ordinary silicon devices, thereby increasing available power output, system efficiency, and cooling effectiveness while lowering transmitter system cost.

4. TRANSMITTER TUBES

Because higher transmitter power is needed, power consumption and efficiency are of utmost importance for UHF transmitters. Although solid-state transmitters offer many advantages to the broadcaster, many UHF stations find that the most cost-effective transmitter design is based on tube technology. Many of the advantages of solid-state transmitters may be adapted to tube-based designs. For the highest power multiple output tubes, each with its own drive chain, provide a minimum level of redundancy and the benefits of a soft-fail architecture. The high beam voltage required by tubes minimizes power supply cost. Liquid cooling for high-power tubes results in low acoustic noise within the transmitter plant. Some of the lower power and more efficient tubes are air-cooled. High-power tube designers have shown great ingenuity in improving operating efficiency and bandwidth, so that tubes remain a viable alternative for UHF transmitters [7].

A variety of tube technologies are available to address UHF requirements. These technologies include tetrodes, klystrons, multiple-stage depressed collector (MSDC) klystrons, and inductive output tubes (IOTs). Some are most suited for lower-power transmitter designs, and

others are more appropriate for the highest power requirements. Work has been reported on a constant-efficiency amplifier (CEA) that promises dramatic improvements in UHF transmitter efficiency. This tube combines the design of the IOT and the MSDC to achieve near-constant and high efficiency independent of drive level.

5. TETRODES

Tetrodes are a generic category of four-element tubes suitable for the linear amplification of RF signals [5]. The anode and screen grid are cooled with distilled water. Typical peak sync power ratings are up to 30 kW, although a "dual tetrode" design boasts a 60 kW rating. Tetrodes are biased for class AB operation and therefore, are more efficient than the class A klystron. The tetrode beam voltage is much lower than that of the klystron or inductive output tube. Tetrodes exhibit excellent linearity. The tradeoff for performance in these areas is power gain lower than most other amplifiers. The gain of a tetrode is only about 15 dB. Tetrode filament currents are high to minimize cathode current modulation of the cathode temperature. "Black heat" is used to reduce the time to on-air. This feature provides a lower than normal filament voltage and current to keep the filament warm when the transmitter is off-air. This reduces the thermal stress on the filament when going quickly to full power.

UHF power tetrodes combine visual and aural amplification. Ten percent aural power is the norm, and tubes are rated according to peak sync power with the aural carrier. For example, a typical UHF tetrode may be rated at 30 kW peak sync. With 10% aural power, the peak envelope power (PEP) is 52 kW.

6. KLYSTRONS

For a discussion of klystrons, refer to the article on this subject. See also Ref. 3.

7. INDUCTIVE OUTPUT TUBES (IOTS)

The IOT combines features of a tetrode and a klystron. The electron beam is constrained similarly to that of a klystron by using electromagnets. The mode of operation of the IOT is similar to that of a tetrode. However, there are significant differences because of differing geometry. An IOT, shown schematically in Fig. 10, is composed of an electron gun very similar to a klystron, a control grid, an input cavity, accelerating anode, drift tube, output cavity, and collector. The electrodes are arranged linearly unlike the concentric configuration of a tetrode. An IOT is physically smaller than a klystron. The electron beam is formed at the cathode. It is density-modulated by the input signal applied to the control grid via a resonant cavity and then accelerated through the anode aperture. The grid is biased negatively near cutoff. The first part of the tube may be thought of as a triode with a perforated anode through which the electron beam is guided by electric and magnetic fields. The beam is bunched at the radiofrequency and is accelerated

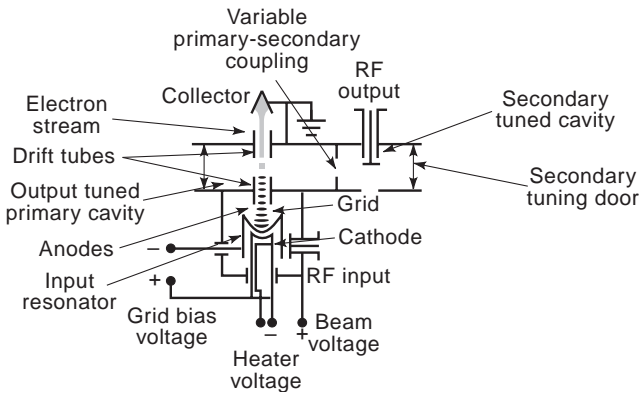


Figure 10. Inductive output tube schematic.

by the high anode potential. In its bunched form, the beam drifts through a field-free region (the anode extension cylinder, which is an electrostatic shield). Then the beam interacts with the RF field at the drift-tube gap in the output cavity. Power is extracted from the beam in the output cavity in the same manner as a klystron. The spent beam is dissipated in the collector, which is separate from the output RF interaction circuit. The grid may intercept some electrons, causing a small amount of grid current. This increases markedly if the tube is overdriven.

The fundamental benefit of the IOT is that it operates as a class AB amplifier, resulting in high efficiency. Thus the beam current I_b is proportional to the RF drive signal V_g and follows the modulation envelope according to the three-halves law

$$I_b = K(\mu V_g + V_a)^{3/2}$$

where μ is the amplification factor. The perveance K is proportional to the cathode area and inversely proportional to the square of the grid-to-cathode spacing. The drive voltage is not normally high enough to make the instantaneous grid voltage-positive.

In aural service, the IOT is tuned the same as for visual service. A single tube covers the entire UHF operating band, although two slightly different input cavities are required. Power gain in either visual or aural service is about 21 dB. Thus, drive power is about 500 W for the visual and 50 W for the aural, assuming 10% nominal aural power.

Acknowledgment

This article was adapted from material published in the *NAB Engineering Handbook*, 9th ed., Jerry C. Whitaker, Editor-in-Chief, used by permission.

BIBLIOGRAPHY

1. Y. T. Lo and S. W. Lee eds., *Antenna Handbook*, Van Nostrand-Reinhold, New York, 1988, Chap. 27.

2. R. Redl, P. Tenti, and J. Van Wyk, Power electronics' polluting effects, *IEEE Spectrum* 34(5):33-39 (1997).
 3. J. Whitaker, ed., *NAB Engineering Handbook*, 9th ed., The Association, Washington, DC, 1998, Chap. 6.
 4. Electronic Industries Association, BTSC system recommended practices, *EIA Syst. Bull.* 5 (1985).
 5. The original material on tetrodes was supplied by Timothy P. Hulick, Ph.D. of Acrodyne Industries, Inc., Blue Bell, PA 19422.
 6. C. Davis, J. Hawkins, and C. Einolf, Jr., Solid state DTV transmitters, *IEEE Trans. Broadcast* 43(3):252-260 (1997).
 7. R. S. Symons. Tubes: Still vital after all these years, *IEEE Spectrum* 35(4):52-63 (1998).
 8. B. Bhatt, D. Birks, and D. Hermreck, Digital television: making it work, *IEEE Spectrum* 34(10):19-28 (1997).

TRANSMITTERS FOR DIGITAL TELEVISION

ROBERT WEIRATHER
 Harris Corporation
 Quincy, Illinois

The television industry in the United States began the search to improve the quality of television images and sound as early as the 1970s, and the Federal Communication Commission (FCC) sought more spectrum in the 1990s. These two paths ultimately led to digital television (DTV). The desire was to put improved television (TV) in the same frequency bands allocated for existing TV channels. These frequencies are low VHF (55-88 MHz) channels 2-6, high VHF (176-225 MHz) channels 7-13, and UHF (476-860 MHz) channels 14-69. The DTV Standard (1998) allocated another complete set of digital TV stations that are frequency-compatible with the existing analog NTSC (National Television Systems Committee) TV channels. This requires that the new DTV channels be allocated between current channels and that neither service interfere with each other. As we shall see, this in-between (including adjacent) channel operation tightly restricts digital TV transmitters.

Paralleling the early development of DTV in the United States, other digital TV systems were being implemented worldwide. Nation after nation has adopted digital TV as a way of delivering more programming content with less spectrum. Better use of the spectrum is one driving force being development of digital RF technology. Digital has proved effective in cellular telephones, microwave telecommunication, and digital TV. Spectrum efficiency is not the only motivation for the use of digital RF means. Use of digital implies a possibility for multiple uses of the transmitted bit stream and thus the potential of serving more demands.

The design for practical digital television transmission systems began in the 1980s. These digital systems required a new approach to high-power over-the-air (OTA) TV broadcast. The television industry began to consider the use of OTA transmission of TV of such quality and function that new modulation and RF power schemes

evolved. The goal for producing significant digital TV signal power is to

- Create a digitally modulated RF signal (called the *modulator or exciter*)
- Reproduce the idealized signal suitable for demodulation (controllable linearity)
- Provide the highest efficiency (power out vs. power used)
- Deliver an RF signal that is reliable, practical, and thus useful

Over-the-air terrestrial digital TV requires high RF power, typically a few kilowatts to 100 kW. Compared with cable, wireless cable, or satellites, this is substantially different and deserves special attention. Whether the digital TV transmitter is used for the system in the United States or another digital system, as will be explained, the requirements are similar.

1. DIGITAL TV MODULATION

Currently analog systems use two separate signals to carry the TV signals. The visual information is carried by AM means, while the aural information is carried by FM means. When using two separate transmitters, class AB linear amplifiers amplify the visual RF carrier and class C nonlinear amplifiers typically provide the aural RF carrier. These two different carriers are combined and transmitted to form the RF TV signal.

Two digital modulation systems have been approved for use in terrestrial broadcast:

- Eight-level Vestigial Sideband (8VSB), often referred to as the Advanced Television System Committee (ATSC) standard. This system has been also termed *digital television (DTV)*.
- Coded orthogonal frequency division multiplex (COFDM), which is also referred to as *digital videobroadcasting—terrestrial (DVB-T)*.

8VSB uses a single modulated RF carrier to transport the digital information. 8VSB is 64 QAM with most of the lower sideband removed (vestigial). COFDM uses many RF carriers (thousands), each modulated with a portion of the digital information. These thousands of carriers are combined to create the transmitted digital RF signal. Both of these schemes (8VSB and OFDM) are required to reside compatibly within the RF channel allocated for analog.

Surprisingly, both 8VSB and COFDM exhibit similar spectra and time-varying waveforms. Both spectra are noiselike, while the time plots appear random in amplitude and duration (see Figs. 1 and 2).

The digital RF signals used for over-the-air (OTA) TV broadcast are a vector-modulated signal, thus containing amplitude modulation (AM) and phase modulation (PM). The RF digital signal is modulated with a bitstream of typically 30 Mbps (megabits per second). This results in a

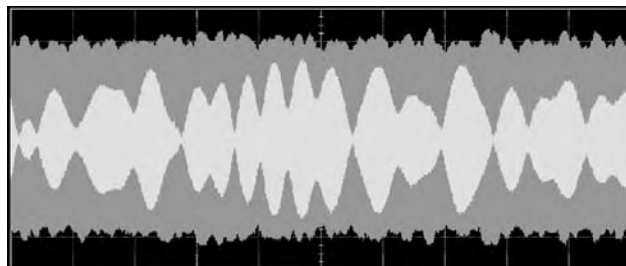


Figure 1. Time-domain capture of 8VSB. (This figure is available in full color at <http://www.mrw.interscience.wiley.com/erfme>.)

high bit/per hertz efficient scheme (~30 Mbps within 6 MHz bandwidth or 5 bits/Hz).

Many other digital modulation techniques are used in television services, and other types of digital modulation are in use. Television delivery such as cable TV (CATV), satellite direct to home, wireless cable, or the PC (personal computer) telephone modem may use a scheme different to optimize delivery versus transmission path characteristics and digital payload. But transmitters for terrestrial broadcast are the subjects of this article.

It is significant to note that digital terrestrial TV modulation is generally thought of in terms of AM. This is a result of the fact that the signal does go to zero at some time. However, it is similar to PM/FM in that the signal has no low-rate time-varying component. Comparisons of terrestrial analog TV and digital TV at RF are enlightening:

Analog TV at RF	Digital TV at RF
Peak to average varies	Peak to average constant
RF never goes to zero	RF goes to zero
Power changes with picture content	Power constant for any picture content
In-channel noise corrupts picture	Noise below threshold does not corrupt
Two RF carriers	One RF carrier

These differences require approaches to digital power amplifiers that may be compared to conventional analog

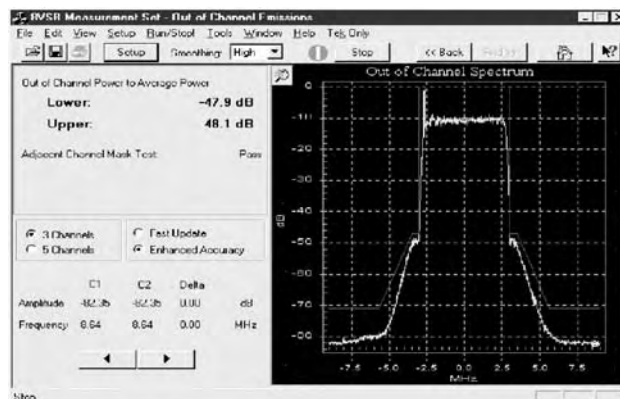


Figure 2. Spectrum capture of 8VSB. (This figure is available in full color at <http://www.mrw.interscience.wiley.com/erfme>.)

(NTSC/PAL/SECAM) RF amplifiers. As we shall see, the requirements for digital transmitters are sufficiently different enough to warrant specific considerations.

2. DIGITAL TV MODULATOR OR EXCITER

Generation of an 8VSB or COFDM RF signal can be best understood with the aid of block diagrams. A typical implementation for 8VSB is shown in Fig. 3.

3. DIGITAL RF MODULATION

Terrestrial digital TV such as 8VSB and COFDM signals are not symmetric and have both AM and PM components. Both system designs results in a signal that occupies the bandwidth with a noiselike signal. This noiselike characteristic requires the use of linear amplifiers for practical transmitter implementations.

3.1. Amplification of Digitally Modulated Signals

The most common way to increase the power of an RF signal is simple amplification. This is generally straightforward for signals of a few watts but becomes increasingly complicated as the power extends above several kilowatts. Cost is excessive to execute a linear amplifier at even a kilowatt. At high power the amplitude and phase linearity plus IMD (intermodulation distortion) of the amplifying chain dominate the details. Nonlinearity gives rise to bit error rates (BERs) that excessively degrade the digital signal.

3.2. Modulated Single-Carrier Systems: QAM, and 8VSB

The ATSC system is a modified quadrature amplitude-modulated (QAM) system generated by amplitude-modulating an RF carrier ($\sin \omega t$) and summing it with the same RF carrier 90° phase shifted [$\sin (\omega t + 90^\circ)$] that is modulated differently. By modulating these two carriers with multilevel digital signals, multilevel QAM is generated.

To create 8VSB, a 64-QAM signal can be generated and then filtered with a surface acoustic wave (SAW) to eliminate the lower sideband. In practice, 8VSB may be generated by all digital means using a combination of software and hardware.

3.3. Modulated Multicarrier Systems: DVB-T

To meet the needs of the European market, another digital modulation method was developed. European needs are different from those in the United States: multiple languages, more mountainous terrain, denser population, and single program coverage nationally, to name only a few. Today’s European analog systems, PAL (Phase Alternation Line) and SECAM (Sequential Couleur Avec Memoire), use lower-powered transmitters than in the United States. The system chosen for Europe, DVB-T or COFDM, uses many carriers (thousands), each digitally modulated and contained in a single TV channel (8-MHz in Europe vs 6 MHz in the United States). The carriers are each modulated with a portion of the digital information and thus spread the digital data across the 8 MHz spectrum. Spreading data across the spectrum improves the likelihood of lessened interference resulting from multipath propagation.

COFDM development has its roots in Europe but has spread worldwide. Many nations around the world have adopted the DVB standards for digital TV.

4. POWER AMPLIFIERS FOR TV

Power amplifiers are the last active element in the RF path before the antenna system. The power amplifier final amplifying stage is the most critical. This final stage determines several critical characteristics of the broadcast signal:

- Average power
- Peak power
- Distortion (intermodulation and harmonic)
- AC power (efficiency)
- Frequency response (bandlimiting and/or tilting)
- Signal quality (SNR, BER)
- Spectrum mask (compliance with standards, e.g., FCC)

The power of a digital transmitter is rated by its average power output. But digital TV signals have high peak-to-average time-varying envelopes. 8VSB exhibits a typical 7 dB peak-to-average values while DVB-T is closer to

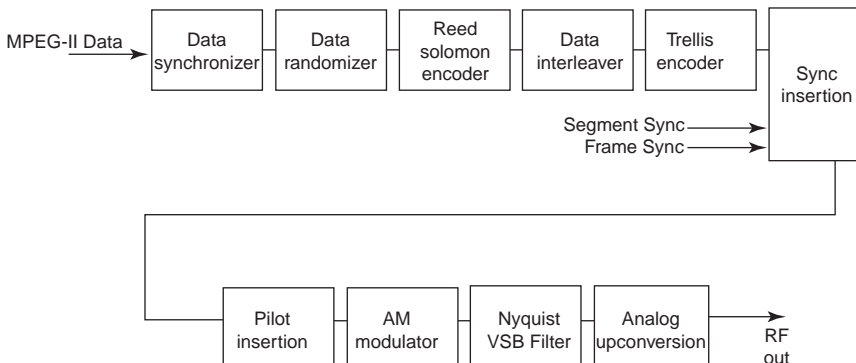


Figure 3. Block diagram of 8VSB exciter.

9 dB. Thus the peak power handling power and average power output are important factors for final PAs.

Power amplifiers are generally nonlinear and band-limiting, thus creating distortions of the input RF signal at the output. Power amplifier nonlinearity creates both in-band and out-of-band intermodulation distortion products within the amplifier. In-band products are important because the received bit error rate (BER) is affected and decoding errors will be produced if the intermodulation products (IPs) are too high.

Out-of-band nonlinearity (spectrum shoulders) must also be minimized to prevent interference with adjacent analog or digital services. In most transmitters, correction signals for amplitude and phase nonlinearities are applied to the input signal of the digital amplifier (feedforward), correcting both the in-band and out-of-band intermodulation distortions at the same time. Therefore, reductions in both the in-band and out-of-band IPs coincide. The only exception to this is when frequency response or group delay errors are present in the amplifier.

5. VACUUM-TUBE POWER DEVICES

Tubes have a unique place in high-frequency amplification; with a single device, they can amplify a signal to tens of kilowatts over a band from a few hundred megahertz to several gigahertz. Gridded tubes such as triodes, tetrodes, or pentodes modulate the electron beam with a small applied RF voltage to the grid. Other tubes such as klystrons use an applied RF voltage to bunch electrons generated from a gun, and these bunched electrons drift through additional cavities, creating additional bunching until reaching a final cavity that extracts energy from the formed beam.

Tube amplifiers usually are limited to 1–5% bandwidth. This is determined by the number of resonant circuits (usually cavities) and their loading (Q). This limited bandwidth is helpful to reduce IPs in adjacent channels but also causes group delay distortions at the channel band edges.

Other varieties of vacuum devices use a grid, a drift region, and an output cavity to form a tube called the *klystrode* or *inductive output tube* (IOT). The IOT (Fig. 4), which found favor with digital TV by providing peak powers in excess of 100 kW at a gain of over 20 dB with good linearity. Efficiencies of IOTs reach 30%.

The IOT has been integrated with a new collector: the depressed-voltage collector. This depressed collector IOT has many of the same characteristics of the IOT, except its efficiency can exceed 50%.

6. SOLID-STATE POWER DEVICES

The use of solid-state devices for amplifiers has an obvious attraction but comes with some limitations. Growth of solid-state devices has led to improvements and reduction in vacuum device usage. However, concentrated power (volts and amperes) and power density of RF transistors have



Figure 4. Inductive output tube.

limited the usage of transistors to combined configurations (Fig. 5). The RF transistors are frequently multicelled and multichip devices in a single package to reach a typical of 150 W peak power.

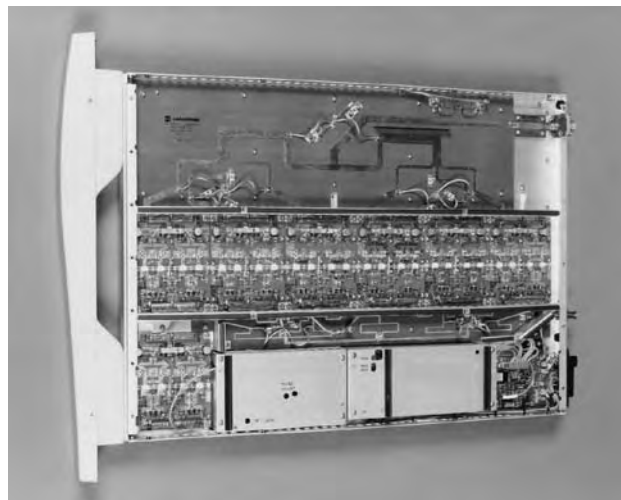


Figure 5. RF amplifier module.

6.1. Bipolar Transistors

Bipolar transistors are minority-carrier devices and as such exhibit several distinguishing characteristics. Bipolar transistors have moderate gain and reasonable linearity but suffer from thermal runaway.

6.2. Field-Effect Transistors

Generally, field-effect transistors (FETs) are majority carrier devices and can be characterized by properties inherent with this class of devices. FETs have higher gain and improved linearity and are tolerant of poor load VSWR without catastrophe.

6.3. Other Devices

Clearly, the FET and bipolar transistors are the most widely used semiconductor devices for power amplification. Other semiconductor technologies used for power generation include MOSFETs, lateral diffused MOSFETs (LDMOSFETs), HEMPT, and GaAs.

6.4. The Solid-State Amplifier

Transistors have one fundamental limit—they don't come with kilowatt power ratings at terrestrially delivered TV frequencies. Kilowatts (sometimes tens of kilowatts) of RF power are necessary for digital TV transmitters. To cover a substantial area with an antenna at a reasonable height, several tens of kilowatts of RF power may be required. A typical analog (NTSC) station has a coverage circle with radius of typically 55 mi. To duplicate this coverage with digital transmissions may take tens of kilowatts or even 100 kW of RF power radiated from an antenna placed 1000 ft or more in the air. Transistors cannot do this with one transistor in the final PA as can be done with a vacuum device.

A single large transistor can typically produce 150 W of peak power. This means that many transistors must be combined to generate a multikilowatt RF signal. The solid-state amplifier does exhibit a wider bandwidth than a tube version, thus reducing some degradation created by band limiting.

A single IOT can produce 25 kW average digital RF power (125 kW peak). To amplify equivalently to 25 kW with transistors would require almost 2000 transistors.

6.5. Amplifier Class of Operation

To amplify a signal with least distortion, current conduction over the 360° RF cycle (class A) is used. Class A operation is lowest in efficiency (same power supply draw regardless of amplifier power output) and thus preferred in lower-power stages where efficiency and dissipation are not of great concern. Class A may be either a small or large signal amplifier, depending on the scale of the design. Efficiency is limited to a theoretical maximum of 50% using class A. Generally this is optimistic, and efficiencies of 10–25% are far more typical.

Class B operation (180° Conduction) is ideally a linear mode of operation, but practically it is not used at high

Table 1. Efficiency for Various Classes of Operation

Class of Operation	Ideal Maximum Efficiency (%)
A	12.5
B	78
A/B	12–78
C	100
D	100

frequencies because of saturation and crossover distortions. Even with its more efficient operation, class B finds little use because of these limitations. Of more interest and practical use is class AB. Class AB biases the device (transistor or vacuum tube) with some idle current without RF drive and thus minimizes crossover distortions, but it retains the efficiency of class B at higher output power. Efficiency is limited to 78% for the class B amplifier. The class AB mode efficiency depends on bias conditions and thus can be bracketed somewhere between the class A and class B efficiencies.

Class C (less than 180° Conduction) and class D (switching or saturation mode) operation exhibit higher efficiencies but exhibit no linear amplification properties. Useful for FM or power supply modulated applications, class C amplifiers are rarely considered. Efficiency can theoretically approach 100% with class C or D. This efficiency is shown in Table 1.

6.6. Push-Pull Pairs

RF power amplification frequently employs the use of transistors in a push-pull configuration (Fig. 6). In a push-pull configuration, two parallel-driven transistors conduct on alternate halves of the RF cycle and then are summed. This approach simplifies the transistor combining, bias, and required circuit area.

7. THE FINAL POWER AMPLIFIER

Digital television transmitters for either DTV or DVB-T have only been in use since the mid-1990s. Digital TV

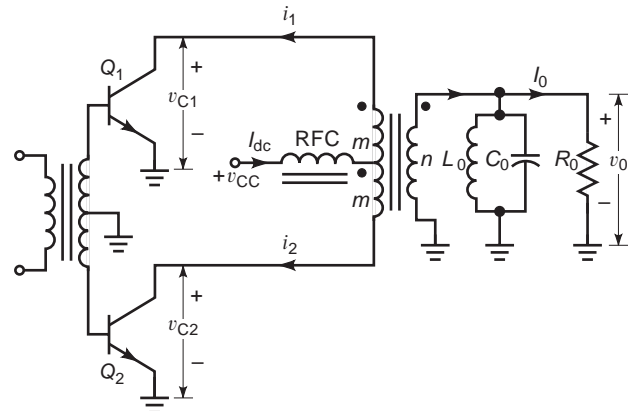


Figure 6. Simplified push-pull RF power amplifier.

transmitter characteristics aren't known as completely as those of other mature power amplifiers. Although the 8VSB and OFDM modulation schemes are very different, they have high peak-to-average ratios. The probability of peaks occurring varies as the difference between the average level and peak observed level increases. As may be expected, as the difference between the two increases, the probability of a peak reaching that amplitude decreases. With an 8000-carrier OFDM signal, the maximum theoretical peak level can be as high as 38 dB, but the probability of this occurring is very small. With both systems, the method of signal generation normally limits the peak-to-average ratio to 8 dB for 8VSB and 12 dB for OFDM without degrading performance (Fig. 7).

To amplify these signals transparently would require a perfectly linear amplifier with a power capability of 8–12 dB higher than the average power output. For example, to produce an average 1 kW output would require an amplifier of 6–16 kW peak.

7.1. Combiners

Power amplifiers, even those using vacuum devices of 100 kW or more, must sometimes be combined (external to the basic circuit power amplifier design). Various combiners of the following types are widely used:

- In-phase or star (impedance transformed to a single common point)
- Quadrature two-way [90°, hybrid, magic tee (also known as “magic T”)]
- Multiple input (bandwidth-limited)
- Isolated or nonisolated input ports (reject loads used or not)
- Constant impedance (independent of sources)
- Nonreciprocal (circulator/isolator used)

The choice of combiner is usually determined by minimum insertion loss and the need for isolation from other circuits or surroundings. At high power, it is wise to not waste precious RF watts generated in power amplifiers as

losses in combiners. Conductor losses prevail at higher powers, and thus air dielectric coax (coaxial cable)/stripline and waveguide are widely used to minimize losses.

By alternating both in-phase and quadrature combiners, arrangements that cancel certain intermodulation products can be made. This technique can be also used to divert RF that is intercepted by the antenna.

7.2. Control and Monitoring: Protection of the PA

High-power amplifiers need various controls and subsequent monitoring. Typically the monitor and control are focused on three broad areas:

1. RF path
 - Drive power
 - Output power
 - Load VSWR
 - RF signal phase
2. Power supply(ies)
 - Voltage
 - Current
 - Sequencing of supply turn on/off
3. Auxiliary
 - Dissipation
 - Temperature
 - Air/coolant flow
 - Arcing

The speed for the protection circuits in the power amplifier will depend on the robustness of the device. Very-high-power amplifiers will be operated near limits of performance, thus requiring fast and tight limit-setting circuits. Headroom in the PA is costly, and thus less costly protection circuits are preferred.

7.3. Peak and Average Power

RF power amplifiers are limited by several factors, but dynamic range of the RF signal governs much of the limitation. Generally, peak power determines the highest voltage/currents, whereas average power determines dissipation limit. The idealized digital signal has a higher peak-to-average ratio than is generally provided by many high-power PAs. If the highest peak were preserved, then the penalty would be an inefficient PA. By permitting some saturation and attendant nonlinearities, a nonideal but practical signal can be transmitted with reasonable cost and efficiency.

The 8VSB DTV signal has a peak-to-average ratio in excess of 8 dB. To observe the high state, peak cannot be captured and measured easily. To reach this peak may take a long time. Instrumentation used to measure ordinary highly repetitive signals will mislead the uninformed. This unusual phenomenon is caused by the number of combinations of digital states and the sequences that are possible. Finding that combination may take hours. As a result, the data lost by distorting these occa-

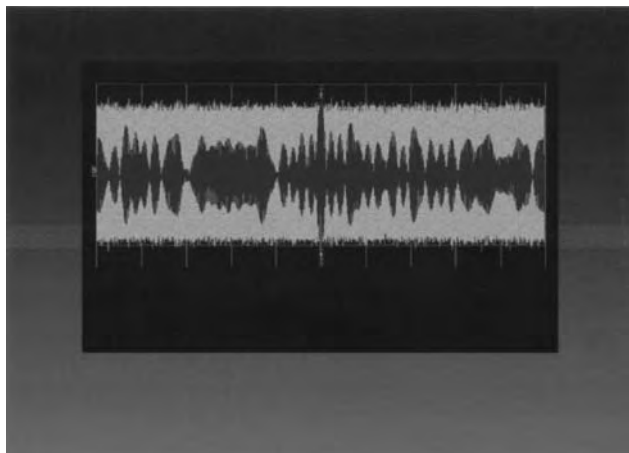


Figure 7. The DTV RF waveform.

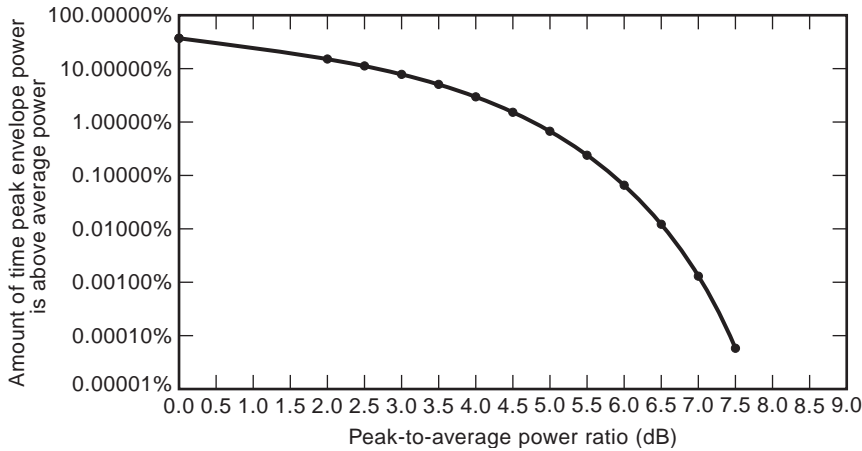


Figure 8. Distribution of peak power.

sional symbols can be corrected by the forward error correction (FEC) codes. Tests indicate that a transmitted signal limited to 6–7 dB peak-to-average power ratio (Fig. 8) does not generate excessively uncorrectable IPs, and the receiver FEC can correct these errors. Similarly, OFDM has an even higher peak-to-average ratio. Two varieties of OFDM systems employ either 2000 or 8000 carriers. On average, half of the carriers would be turned on, whereas the peak would be all carriers turned on. The dynamic range extends from all carriers on to all carriers turned off. This very wide dynamic RF range and high peak-to-average ratio can be improved by not allowing certain states to exist to give high peaks and to let the FEC handle those occasional peaks that get clipped.

7.4. Efficiency and Dissipation

Knowing the average power output and efficiency of a PA, one can compute the dissipation. This dissipation may be limited by the power output, the cooling mechanism, the device, or the peak-to-average ratio. Efficiency has been measured for both class AB vacuum and solid-state amplifiers (Table 2). Efficiency is typically 25–35% of average output power. (Note: Higher efficiencies have been measured but at intolerable distortions.) This means that as much as 3 times as much power may be dissipated in the power amplifier as is delivered

to the load. Misleading is the high peak-to-average power ratio, perhaps leading one to quickly predict a low dissipation. One view is to consider that the class AB amplifier signal dwells in the low-efficiency class A most of the time, thus creating the lowered efficiency; where the signal dwells briefly at the higher-efficiency, class B peaks.

8. PRECORRECTION CIRCUITS

Powerful amplifiers characteristically modify the input signal in undesirable ways. High-power stages with little effect on the RF signal can be built, but they are not practical in terms of cost or efficiency. By choosing the design of a PA with limited but known distortion characteristics, one can use a number of ways to precorrect or correct these problems.

8.1. Frequency

The PA may exhibit ripple, passband tilt, or band edge problems. This is most notable in tube amplifiers using tuned cavities to extract the RF beam energy. This is often corrected by complementary tuning in the low-power drive. As the power amplifier reaches saturation, the frequency response often changes, thus complicating the correction process.

Table 2. DTV Transmitter Comparisons

	IOT (UHF)	FET (UHF)	FET (VHF)
Average DTV power	25 kW	5.5 kW	5.0 kW
Main supply (V)	37 kW	32 VDC	50 VDC
Main supply (I)	1.9 A	560 A	490 A
Signal-to-noise ratio (SNR)	25 dB	25 dB	26 dB
Error vector magnitude (EVM)	5%	5%	4%
Power consumption	70.3 kW at 25 kW	25 kW at 5.5 kW	32 kW at 5.0 kW
Power amplifier efficiency	35%	31%	22%
Transmitter efficiency	27%	22%	15%
Cooling	Air and liquid	Air	Air

8.2. Amplitude

A PA can have multiple sources of deviations from linear (power in versus power out). These nonlinearities can include saturation/compression, class B crossover distortion, or feedback/neutralization. These problems may be corrected with complementary circuits using diodes with multiple amplitude breakpoints. These circuits are implemented at lower powers ahead of the PA.

8.3. Phase or Group Delay

Power amplifier characterizations that focus only on amplitude come up short. Digital TV is both amplitude- and phase-modulated, and thus PA phase distortions limit performance, too. Phase problems are corrected by using all pass networks that exhibit tunable delay variations without amplitude variations. Usually, several of these networks are inserted at IF and have tunable characteristics over the RF band.

8.4. Analog Feedback

One of the oldest forms of distortion reduction is feedback. By sampling the amplified output, inverting it, and applying it to the input, linearity can be improved. The most common feedback in solid-state amplifiers is to leave some unbypassed resistance in the emitter (or drain). This may be done inside the transistor package. Similar feedback may be done with vacuum tubes, but some reduction in gain is required with each analog feedback scheme. It is also possible to neutralize the reactive feedback mechanism to improve the linearity characteristics. These techniques call for identifying the feedback path element and determining the best way to compensate this element reactively.

8.5. Feedforward

Feedforward has become highly developed. This technique is widely used in smaller amplifiers where very high linearity is required. Widely used is a method of distortion reduction using feedforward. There are many novel ways to accomplish feedforward, depending on the performance required. The simple form of feedforward takes a sample of the output signal from the PA, subtracts a sample of the input signal, linearly amplifies the result, and reinserts this correction into the delayed output (Fig. 9). The result is a highly corrected, linear RF output but with a lower power than the original capability of the PA.

8.6. Digital Feedback

Digital feedback can be used if the output signal can be compared to the internally generated modulator signal and an error signal can be derived. This error signal is digitized and is then used to distort or precorrect the digital signal in a manner that linearizes the transmitter. Two general classes of errors are linear and nonlinear. Linear errors are those that do not vary with signal strength. The linear errors are frequency response and group delay. Nonlinear errors are those caused by

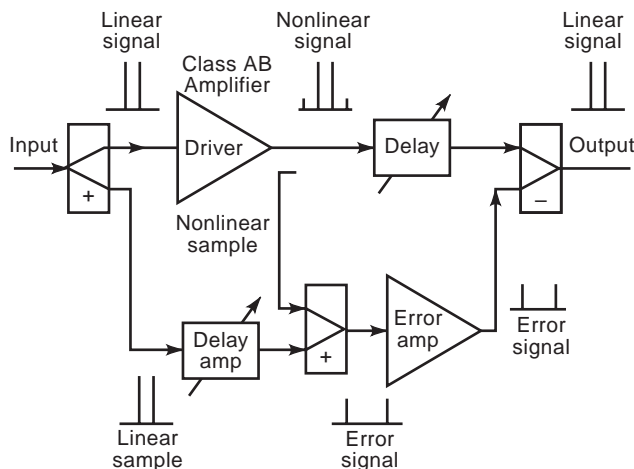


Figure 9. Feedforward block diagram.

the internal mixing action of nonlinear V_i/V_o response amplifiers.

Linear errors cause the digital constellation to be less defined, and hence demodulation uncertainties give rise to bit errors. This is shown in Fig. 10 for 8VSB.

- Phase shift (group delay) across the channel bandwidth and amplitude compression are common characteristics of power amplifiers. Similarly, filters with in-channel ripple responses and sharp cutoffs affect group delay, giving rise to linear errors.

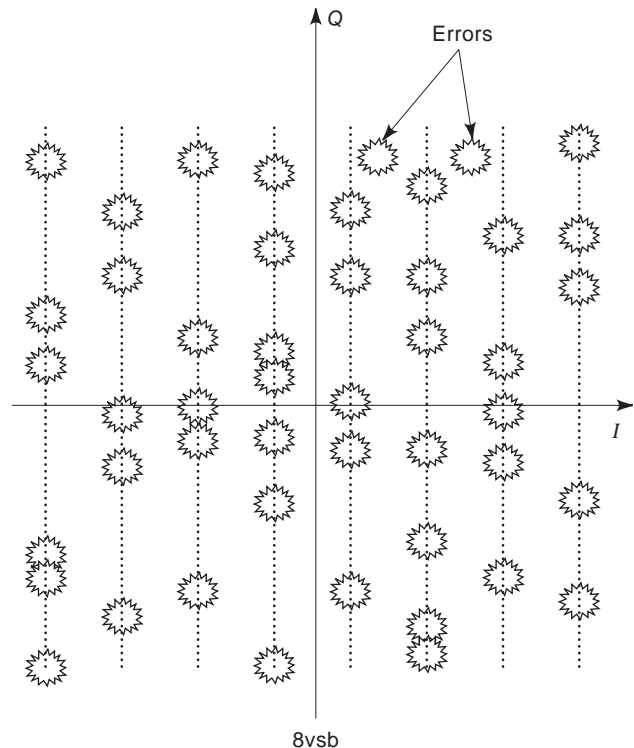


Figure 10. Constellation errors.

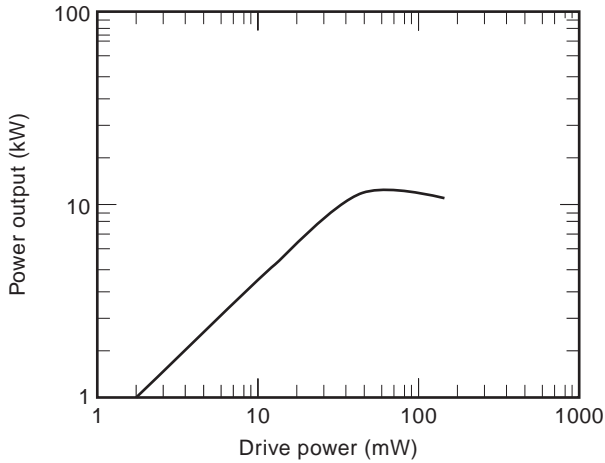


Figure 11. P_{in} versus P_{out} for a power amplifier.

- Nonlinear errors are typically caused by amplifiers with gain compression and crossover distortion. Response such as that shown in Fig. 11 are what may be present in a typical efficient power amplifier.
- These nonlinear errors generate IPs that may either degrade the desired signal or create interference with an adjacent service.

9. OUTPUT FILTER

The high-power amplifiers all generate significant IP levels that are both in and out of band. The in-band IPs act as noise to degrade the SNR of the system. The IPs that are adjacent to the occupied band interfere with other services such as other TV channels. To minimize out-of-band IPs and other interference problems, using an output bandpass filter can improve the IPs. These filters degrade the digital TV signal by adding amplitude and group delay distortions. These filters are generally sharp-skirted filters to effect the IPs within 1 MHz of the channel edge. These sharp skirts have more of an impact on group delay than amplitude, and thus additional pre-correction must be added for this high-power bandpass filter.

To achieve the needed response, a many-pole filter must be used. A demanding filter may have a response as shown in Fig. 12.

The need and use of these types of filters are shown in Fig. 13. Here the amplifier is solid-state and has little bandwidth narrowing at the output. Placing a filter (not that of Fig. 12) can limit adjacent channel IPs significantly.

10. PUTTING IT ALL TOGETHER

Digital television transmitters are generally linear amplifiers using frequencies that terrestrial analog TV uses today. Thus the transmission layer is used to deliver the

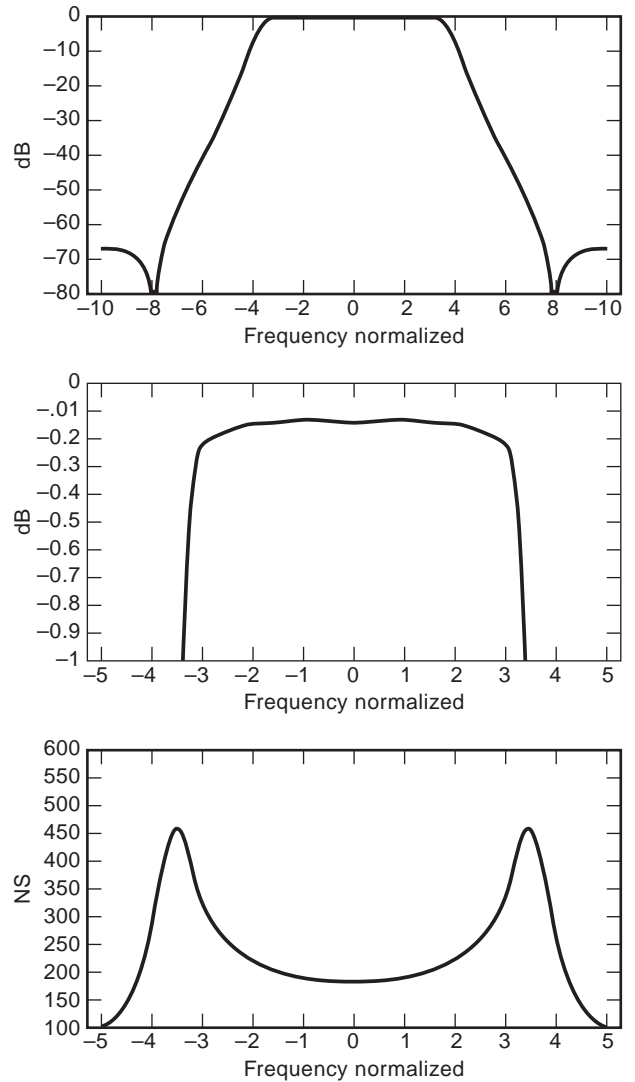


Figure 12. Bandpass filter response.

transport layer digital payload, MPEG2. After generating the RF signal (8VSB or OFDM) at some low power, it is necessary to provide linear amplification. Examples of this are the IOT PA and the solid-state PA. Results of 8VSB

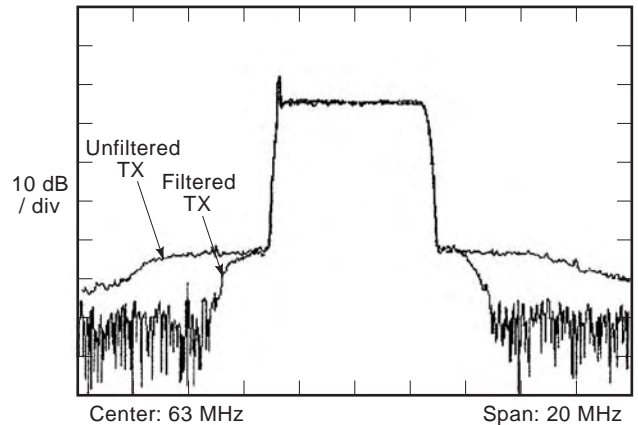


Figure 13. Filtered and unfiltered transmitter.



Figure 14. IOT power amplifier output without filtering.



Figure 15. Solid-state power amplifier output without filtering.

generation, precorrection, and filtering are shown in Figs. 14 and 15.

11. SUMMARY

Digital television has revolutionized our thinking about TV services to the home. Terrestrial digital TV delivery will be by means similar to analog TV, that is, by linearly amplifying a digital RF signal and then directing this power by antenna systems typically located 1000 ft above the served community. The purpose of the digital transmitter (power amplifiers and excitors) is to produce a digital signal faithfully and within the limits of broadcasters' financial means.

Acknowledgments

The author acknowledges the contributions of many colleagues from numerous parts of the industry for advancing digital television.

FURTHER READING

- Advanced Television Test Center, *Digital HDTV Grand Alliance System*, Advanced Television Test Center, 1995.
- Advanced Television Test Center, *Digital HDTV Grand Alliance System, Record of Test Results*, Advanced TVTest Center.
- K. B. Benson and D. G. Fink, *HDTV Advanced Television for the 1990s*, McGraw-Hill, New York, 1991.
- K. K. Clarke and D. T. Hess, *Communications Circuits: Analysis and Design*, Addison-Wesley, Reading, MA, 1971.
- G. W. Collins, *Fundamentals of Digital Television Transmission*, Wiley, New York, 2001.
- H. L. Krauss, C. W. Bostian, and F. H. Raab, *Solid State Radio Engineering*, Wiley, New York, 1980.
- National Association of Broadcasters, *Engineering Handbook*, 8th ed., Washington, DC, NAB, 1992.
- F. G. Stremmer, *Introduction to Communications Systems*, 3rd ed., Addison-Wesley, Reading, MA, 1990.
- M. Schwartz, *Information Transmission Modulation and Noise*, 4th ed., McGraw-Hill, New York, 1990.
- R. E. Ziemer and W. H. Tranter, *Principles of Communications*, 2nd ed., Houghton-Mifflin, Boston, 1985.
- W. Y. Zou and Y. Wu, COFDM: An overview, *IEEE Trans. Broadcast.* **41**: 1–8 (1995).

WEB SITES

- <http://www.atsc.org/>
- <http://www.fcc.gov/>
- <http://www.dvb.org/>
- <http://www.dtg.org.uk/>
- <http://www.broadcastpapers.com/>

TRANSMITTERS FOR FM BROADCASTING

GEOFFREY N. MENDENHALL
 P. E. Richard J. FRY
 Harris Corporation

1. THE FM BROADCAST TRANSMITTER

The purpose of the FM transmitter is to convert one or more audiofrequency (composite baseband) input signal or an AES3 serial digital audio data bit stream into a frequency-modulated, radiofrequency (RF) signal at the desired power output level to feed into the radiating antenna system. In its simplest form, the FM broadcast transmitter can be considered an FM modulator and an RF power amplifier packaged in one unit.

Actually the FM transmitter consists of a series of individual subsystems each having a specific function:

1. The FM exciter converts the analog audio baseband or serial digital audio data into frequency-modulated RF and determines the key qualities of the signal.
2. The intermediate power amplifier (IPA) is required in some transmitters to boost the RF power level up to a level sufficient to drive the final stage.
3. The final power amplifier further increases the signal level to the final value required to drive the antenna system.
4. The power supplies convert the input power from the ac line into the various dc or ac voltages and currents needed by each of these subsystems.
5. The transmitter control system monitors, protects, and provides commands to each of these subsystems so that they work together to provide the desired result.
6. The RF low-pass filter removes undesired harmonic frequencies from the transmitter's output, leaving only the fundamental output frequency.

7. The directional coupler provides an indication of the power being delivered to and reflected from the antenna system.

Figure 1 shows a simplified block diagram of a typical FM transmitter.

2. FM BROADCAST TRANSMITTER POWER OUTPUT REQUIREMENTS

The FCC regulates the power of FM broadcast stations in terms of effective radiated power (ERP), which is determined by the class of station and the antenna height above the average terrain. The authorized ERP applies only to the horizontally polarized component of radiation. Elliptical or circular polarization is also permitted where the ERP of the vertically polarized component may be as great as the authorized horizontal component. This means that twice as much total power is radiated and twice as much transmitter power is required.

The transmitter power requirement is reduced by increasing the gain of the antenna. There is, of course, an economic tradeoff between the cost of a higher gain antenna versus the cost of a larger transmitter and the added primary power costs. For a high ERP, it is common to use antennas with up to 12 elements that provide a power gain of about 12.6 (or 6.3 in each polarization).

The long transmission lines associated with the tall towers commonly used are a source of considerable power loss. For example, the efficiency of 2000 ft of 3 1/8 in. rigid coax at 100 MHz is only about 62%.

The required ERP is first determined. Then the transmitter power output (TPO) can be calculated taking into account the transmission line losses and the antenna array gain. Depending on the particular situation, the TPO could vary from as little as 50 W to as much as 70 kW.

FM transmitters are designed to operate over a wide range of power outputs so that any required power output can be furnished with a few basic sizes. Popular maximum ratings range from 250 W to 70 kW. Most installations use a maximum TPO of 30 kW or less because it is more

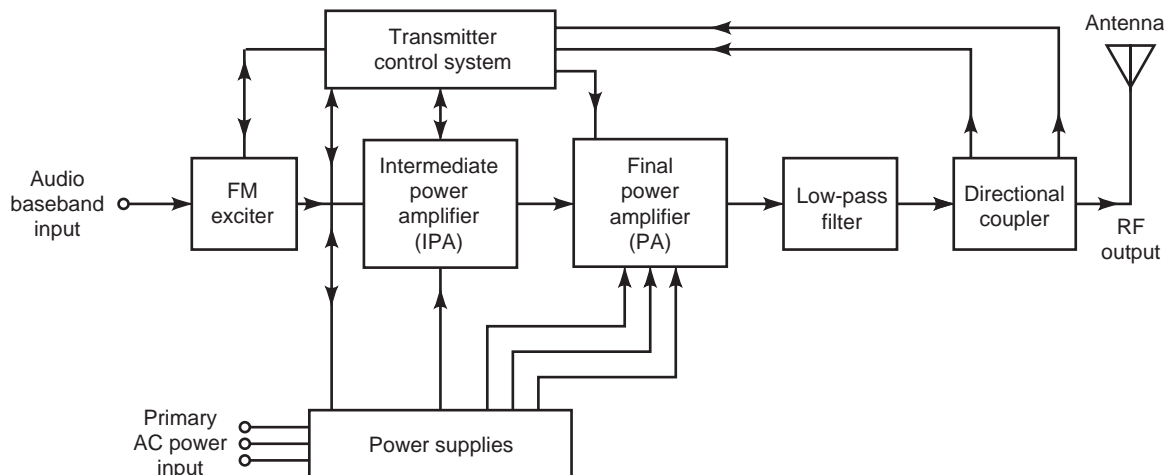


Figure 1. Simplified block diagram of an FM broadcast transmitter.

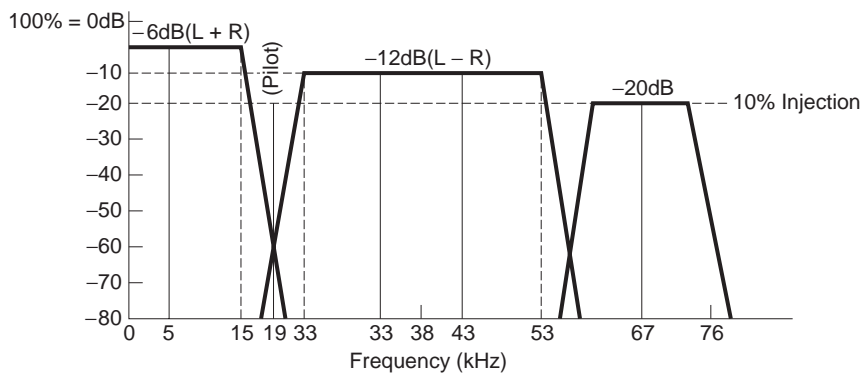


Figure 2. Stereo composite baseband with SCA subcarrier.

L or R only modulated 100% @ 5 kHz. Unmodulated SCA @ 10% injection

economical to achieve the maximum 100 kW of ERP with circular polarization by sufficient antenna gain.

2.1. FM exciters

The heart of an FM broadcast transmitter is its exciter. The function of the exciter is to generate and modulate the carrier wave with one or more inputs (mono, stereo, SCA) in accordance with the FCC standards. Then the FM carrier is amplified by a wideband amplifier to the level required by the transmitter’s following stage.

Stereo transmission places the most stringent performance requirements on the exciter. Because the exciter is the origin of the transmitter’s signal, it determines most of the signal’s technical characteristics, including signal-to-noise-ratio (SNR), distortion, amplitude response, phase response, and frequency stability. Waveform linearity, amplitude bandwidth, and phase linearity must be maintained within acceptable limits throughout the analog baseband chain from the stereo and subcarrier generators to the analog FM exciter’s modulated oscillator [1]. Figure 2 shows the frequency spectrum of the modulating baseband signal, including monaural, stereo pilot, stereo subchannel, and one SCA subcarrier. The recent introduction of AES3 (Audio Engineering Society Digital Audio Transport Standard) digital audio transport and all-digital

FM modulation techniques like direct digital synthesis (DDS) eliminate the distortions introduced by analog circuits. In a digital FM exciter, the left and right audio data are converted into a digital representation of stereo baseband by digital signal processing (DSP). Then these data are further converted into a frequency-modulated carrier by a DDS numerically controlled oscillator (NCO). From here, the FM carrier is usually amplified in a series of class C nonlinear power amplifiers, where any amplitude variation is removed. The amplitude and phase responses of all RF networks that follow the exciter must also be controlled to minimize degradation of the signal quality.

2.2. Direct FM

Direct FM is a modulation technique where the frequency of an oscillator can be made to change in proportion to an applied voltage. Such an oscillator, called a voltage tuned oscillator (VTO), was made possible by the development of varactor tuning diodes that change capacitance as their reverse bias voltage is varied (also known as a voltage-controlled oscillator or VCO).

If the composite baseband signal is applied to the tuning terminal of a VTO, the result is a *direct* FM modulated oscillator. Figure 3 is a block diagram that describes most of the modern direct FM exciters on the market.

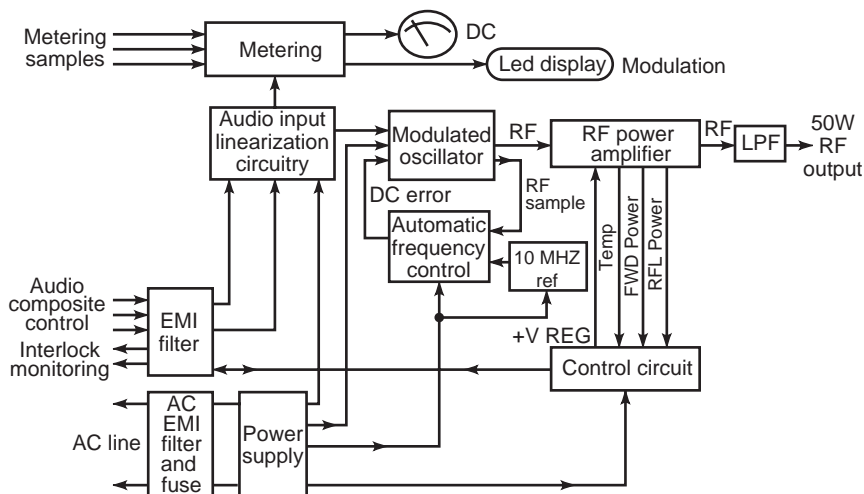


Figure 3. Analog FM exciter block diagram.

2.3. Automatic Frequency Control

The frequency stability of direct FM oscillators is not good enough to meet the FCC frequency tolerance of ± 2000 Hz. This requires an automatic frequency control system (AFC) that uses a stable crystal oscillator as the reference frequency.

The modulated oscillator need not have good long-term stability because the AFC feedback loop will correct for long-term drift to keep the average carrier frequency within limits. The modulated oscillator does need excellent short-term stability (less than 1 s) because the control-loop time constant must be long enough so that the AFC circuit does not try to remove desired low-frequency audio modulation. This means that the oscillator is essentially running open-loop at frequencies above a few hertz so that the noise performance of the modulator will also be determined by the short-term stability characteristics of the oscillator.

2.4. Phase-Locked-Loop Automatic Frequency Control

Phase-locked-loop (PLL) technology has provided a means of precisely controlling the carrier's average frequency while permitting wide deviation of the carrier frequency at baseband modulating frequencies. This implies that a PLL system behaves like an audio high-pass filter where higher modulating frequencies are ignored by the control loop, whereas lower frequencies are considered errors in the average frequency and are tracked out by the loop. An added advantage of the PLL is the ability to synthesize the desired frequency from a single reference oscillator, thereby eliminating the need to change crystals when changing the frequency of the exciter.

The block diagram shown in Fig. 4 includes the key elements in the PLL. The output of the modulated oscillator operating at the carrier frequency is digitally divided down to a frequency of a few kilohertz or even less, called the comparison frequency. Likewise, the reference crystal

oscillator is also digitally divided down to the reference frequency. The two frequencies are compared in a digital phase/frequency detector to develop an error voltage that corrects the carrier frequency of the modulated oscillator. The reason for dividing the modulated oscillator frequency so many times is to reduce the modulation index enough to limit the peak phase deviation at the reference frequency to a value that will not exceed the linear range of the phase/frequency detector. If the linear range is exceeded, the loop will lose lock. This is why some exciters may lose AFC lock in the presence of low-frequency modulation components [2].

The phase detector output is integrated and lowpass filtered to remove the comparison frequency and all other frequency components above a few hertz so that the AFC circuit does not try to track out low-frequency modulation. Some FM exciters use a dual-speed PLL to keep the loop-turnover frequency low enough to maintain good amplitude and phase response at 30 Hz, while also providing quick lock-up time. The PLL error correction circuitry must respond quickly during the initial frequency scan of the FM band to achieve lock-up to the precision reference oscillator in a few seconds. The loop bandwidth is wide during acquisition and lock-up. After lock is achieved, the bandwidth is reduced to provide the optimum modulation characteristic.

The reference oscillator is usually temperature compensated and requires no warm-up to maintain ± 3 PPM or better accuracy over the operating temperature range. A reference frequency of 10 MHz is often selected for convenient comparison with international frequency standards.

2.5. Digital FM Exciter using Direct Digital Synthesis

A new technology called direct digital synthesis (DDS) eliminates the need for a PLL in the FM modulation process by directly synthesizing the carrier frequency,

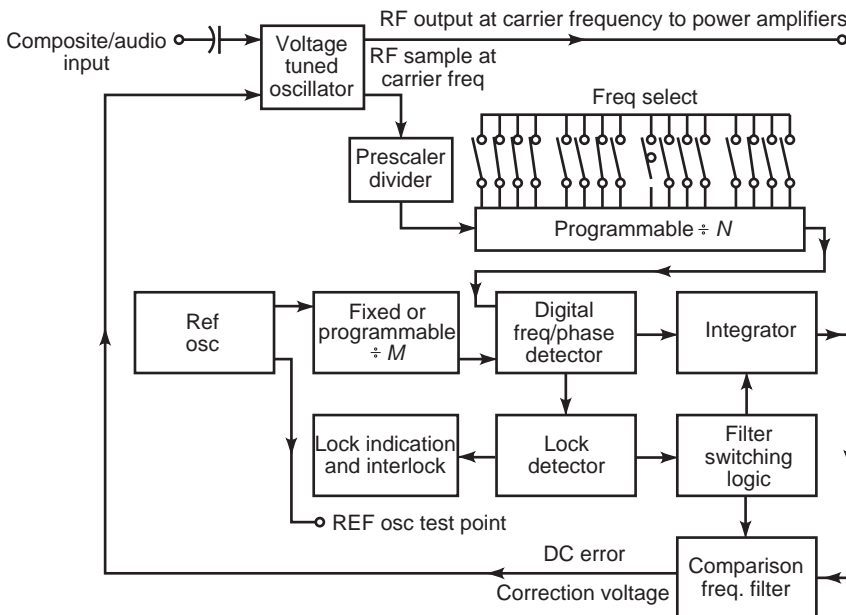


Figure 4. Phase-locked-loop frequency synthesizer.

including FM modulation, from a sine wave look-up table in a programmable read-only memory device (PROM) operating in conjunction with a digital phase accumulator and a fast digital-to-analog converter (DAC). When this technique is combined with digital signal processing (DSP) technology, the entire process of generating stereo baseband with SCAs (Subsidiary Communications Authorization) and FM modulating this baseband information onto the RF carrier can be done entirely in the digital domain. The cost-to-performance ratio of DDS/DSP technology has made it competitive with the analog technology in present excitors [3]. The full benefit of DDS/DSP technology requires digital transmission of audio information as an uncompressed, digital, bit stream all the way from the digital audio source through a digital console, digital audio processing, and an uncompressed, digital, studio-to-transmitter link (STL) to the AES3 digital input port of the DSP/DDS exciter [4]. This same technology is used in the fully digital audio broadcast (DAB) services with the European Eureka 147 (EU-147) transmission standard and other technical standards presently implemented worldwide [5].

2.6. Direct Digital Synthesis of the FM Waveform

Direct digital synthesis (DDS) is a technique in which the completely modulated FM waveform is generated totally in the digital domain. As digital modulation is an inherently linear process, no predistortion is required. The FM signal generated by a DDS device has extremely low noise and distortion, for true 16-bit digital audio quality (-96 dB FM signal-to-noise ratio and 0.0016% harmonic distortion for ± 75 kHz deviation and $75 \mu\text{s}$ preemphasis/deemphasis).

The current generation of DDS excitors use a 32-bit numerically controlled oscillator (NCO). The basic resting frequency of the NCO is set by a 32-bit tuning word. Frequency modulation occurs when modulation data varies the structure of the tuning word data within the phase accumulator section of the NCO. The modulated output of the NCO is converted to analog FM, upconverted, filtered, and amplified to become the RF excitation for a conven-

tional FM broadcast transmitter RF amplifier chain. A block diagram of a DDS digital FM exciter is shown in Fig. 5.

DDS FM excitors also eliminate several basic limitations found in analog excitors using direct FM via the modulation of a voltage-controlled oscillator (VCO). Very low audiofrequencies must be filtered from program signals to avoid affecting the automatic frequency control (AFC) circuits of the analog exciter, which see very low modulating frequencies as an off-frequency condition that needs correction. A DDS-based FM exciter has no such limitation, and modulation response extends virtually to dc (zero hertz). These lower octaves of program material are important for sonic realism and to preserve the phase correlation existing in the original program.

2.7. Digital Modulator

The digital modulator, which is the heart of a digital exciter, utilizes a 32-bit NCO to digitally generate the completely modulated FM waveform. Other supporting circuitry including a digital peak detector drives the front panel modulation display. The block diagram in Fig. 6 shows the functional subsystems of a digital modulator.

The input to the digital modulator is fed modulation data in the format and at the clock rate required. These data represent the stereo baseband created in the digital input module, which contains the DSP digital stereo generator and subcarrier input circuitry.

The digital modulator module includes a precise, digital peak detector to provide the drive for a peak modulation display. This circuit is driven by the same data as the NCO modulator. Therefore, the modulation indication on the front panel of the digital exciter has very high accuracy to within 0.25% of the true FM deviation value at any modulation index or frequency.

The output of the NCO is D/A converted to a precise, conventional FM signal at an intermediate frequency and bandpass filtered to remove the images produced in the DDS process [6].

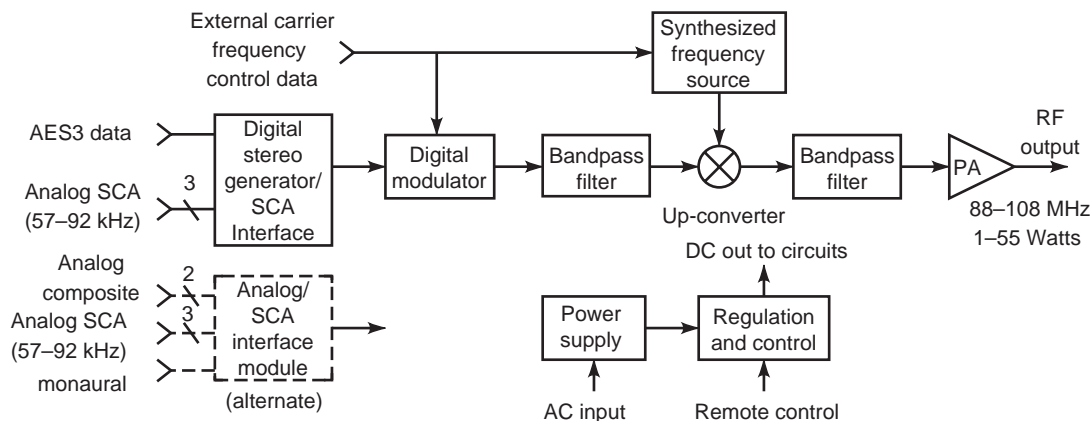


Figure 5. Harris DIGIT-CD DDS digital FM exciter.

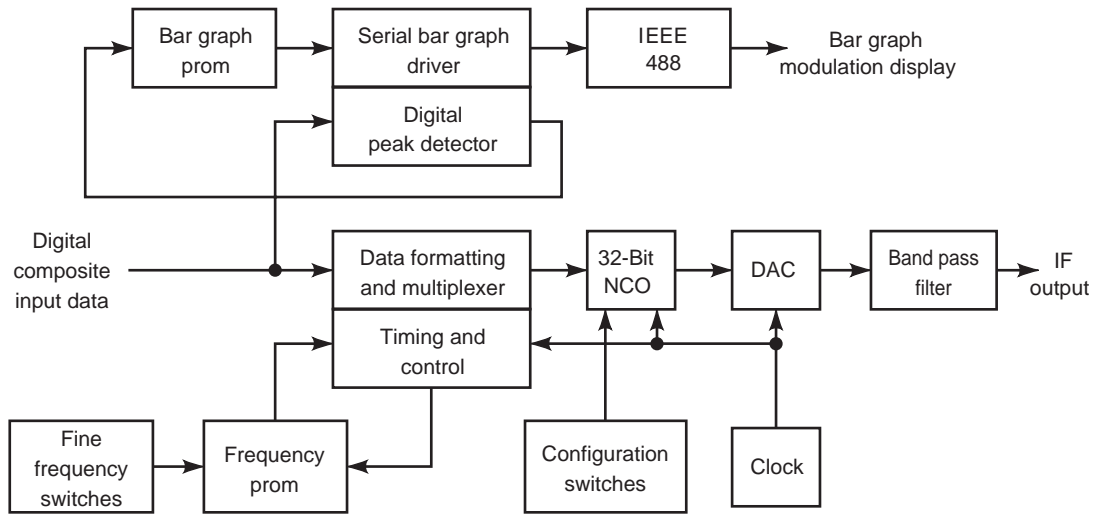


Figure 6. Digital modulator in the Harris DIGIT-CD FM exciter.

2.8. Digital Input and DSP Stereo Generator

DDS techniques are compatible with standard AES3 digital audio and provide the last link in maintaining a 100% digital audio path from the program source through the generation of the FM carrier with no intervening A/D or D/A conversions to add noise and distortion. The DDS exciter includes a built-in DSP stereo generator to convert the incoming AES3 digital stereo into the digital stereo modulation data needed for the NCO to generate FM stereo. Most DDS exciters also offer as an option a high-quality A/D converter that will convert the analog base-band output of an analog stereo generator into the digital data format needed by the NCO.

Auxiliary signals, such as SCA and RBDS/RDS (Radio Broadcast Data Service), are accepted as modulated analog waveforms from external devices, then A/D converted to digital data and applied to the NCO for simultaneous

transmission with normal stereo program material. Figure 7 shows the major signal blocks in the digital input module [7].

The digital input module provides the interface, monitoring, and control circuitry for these functions:

1. Accepts standard AES3 stereo digital data at any rate from 20.8 kHz to 56 kHz, normally 32 kHz. Rate conversion is automatic (self-clocking).
2. Accepts analog subcarriers in the range of 57 kHz to 92 KHz.
3. Converts all input signals to the composite digital format needed by the digital modulator.
4. Provides a 19 kHz output to synchronize an external RBDS/RDS generator.
5. Supplies digital composite limiting using *look ahead* digital technology.

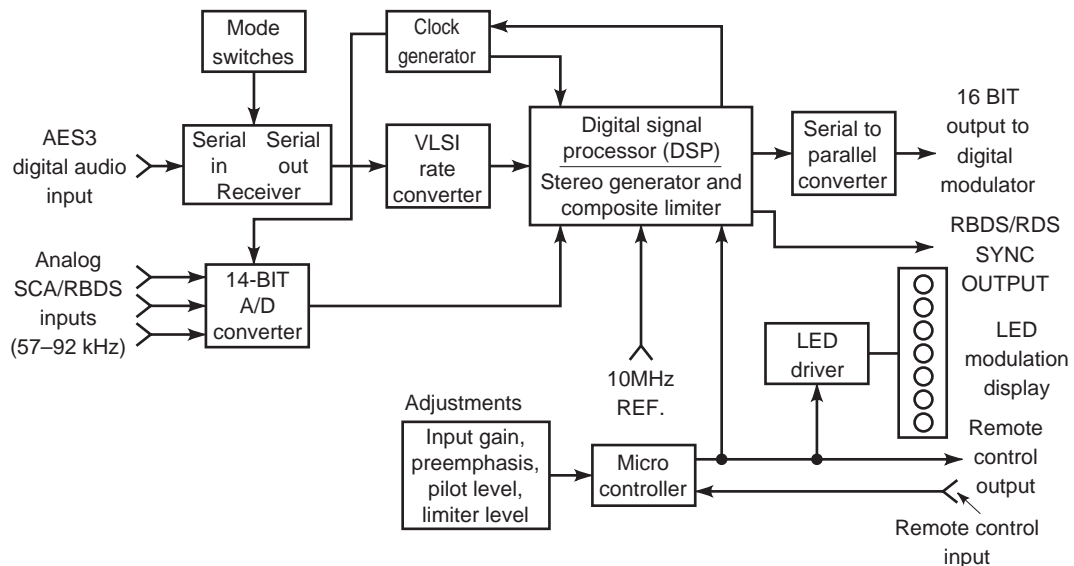


Figure 7. Harris DIGIT-CD digital input and DSP stereo generator.

6. Provides gain adjustment for SCA, overall deviation, limiting level, and pilot level.
7. Provides a switchable LED display showing either total peak deviation or limiting level.
8. Allows user selection of program channel mode (AES3/EBU or analog) (Audio Engineering Society/European Broadcast Union Digital Audio Transport Standard), preemphasis ON/OFF/time-constant, mono ON/OFF, and data error detection mode.

2.9. Exciter Metering

Metering of important operating parameters can be provided by a combination of analog metering and a digital LED display. Steady-state parameters are usually selected by a multi-position switch and displayed on an analog or LCD multimeter. Typical steady-state functions include regulated, preregulated, and unregulated supply voltages; the AFC control voltage; RF power amplifier collector voltage and current; forward output power; and reflected power.

A color-coded peak reading display is usually provided to constantly monitor the peak FM deviation. A high-speed peak detector gives accurate peak readings on signals from dc to 100 kHz. A one-shot multivibrator circuit provides a clear indication of short transient peaks exceeding 100% modulation. Digital exciters directly read the peak values of the modulation data producing the FM deviation in the NCO.

2.10. Exciter Output Stage

The broad-band RF amplifier in the exciter amplifies the output of the modulated oscillator from a power level of a few milliwatts up to an output level in the range of 5 W to 50 W. The output stage is usually protected against damage by an infinite VSWR at any phase angle.

The typical RF amplifier is designed to have a bandwidth of at least 20 MHz, using successive broadband impedance matching sections for each stage. Each group of matching sections consists of microstrip or lumped elements.

The broad-band performance of the RF amplifier eliminates the need for adjustments to any particular frequency within the FM band. The exciter output is transparent to the signal generated by the modulated oscillator, and the amplifier stability is enhanced under varying load conditions.

A microstrip directional coupler is often incorporated in the RF amplifier output network. This coupler supplies information to the exciter control circuitry that provides automatic control of power output level and provides protection against operation under high VSWR conditions.

All current generation FM exciters will produce at least 50 W of RF output so they can be used as complete transmitters for educational stations with the addition of a harmonic filter to the output. For higher power levels, the exciter is used to drive an external power amplifier.

3. RF POWER AMPLIFIERS

The remainder of the FM transmitter consists of a chain of power amplifiers, each having from 8 dB to 20 dB of power gain. Ideally, the transmitter should have as wide a bandwidth as practical with a minimum of tuned stages. Broad-band solid-state amplifiers are preferred to eliminate tuned networks in the RF path. Higher powered transmitters in the multikilowatt range may use multiple tube stages, each with fairly low gain, such as in the grounded-grid configuration or a single grid-driven PA stage with high gain and efficiency. The cost, redundancy, and wide bandwidth benefits of solid-state transmitters have made them attractive at power levels up to 20 kW. At higher power levels beyond 20 kW, the lower cost per watt of high-power, single-tube transmitters still make them attractive even though the modulation performance and reliability are less than those of a solid-state transmitter. Design improvements in tube-type power amplifiers have concentrated on improving bandwidth, reliability, and cost effectiveness, whereas design improvements in solid state amplifiers have focused on continuous cost reduction to make them competitive with tube technology at ever increasing power levels [8].

3.1. RF Power Amplifier Performance Requirements

The basic function of the power amplifier is to amplify the exciter output to the authorized transmitter power output level. Most of the overall performance characteristics of the transmitter are determined by the exciter, but a few are established or affected by the power amplifier characteristics:

1. The RF output level at harmonics of the carrier frequency is almost completely a function of the attenuation provided by the output matching circuit and output lowpass/notch filters. The FCC limit in decibels is $[43 \text{ dB} + 10(\log \text{ watts}) \text{ dB}]$ or 80 dB whichever is less (73 dB for 1 kW output or 80 dB for 5 kW and higher).
2. The major source of asynchronous AM noise usually originates in the last power amplifier stage. The FCC limit is 50 dB below 100% equivalent AM.
3. The RF power output control system that must keep the output within +5% and -10% of authorized output is usually achieved in the final power amplifier.
4. Inadequate power amplifier RF bandwidth, particularly with respect to phase linearity (constant time delay) across the signal bandwidth, can reduce stereo separation and cause SCA crosstalk.
5. The presence of standing waves on the transmission line to the antenna may also interact with the power amplifier to cause degraded stereo separation and SCA crosstalk.

The power amplifier should provide trouble-free service and be easy to maintain and repair. Good overall efficiency is also desirable to reduce the primary power consumption and heat load released into the transmitter room.

3.2. Power Amplifier Bandwidth Considerations

As mentioned earlier, the FM signal theoretically occupies infinite bandwidth. In practice, however, truncation of the insignificant sidebands (typically less than 1% of the carrier) makes the system practical by accepting a certain degree of signal degradation. The transmitter power amplifier bandwidth affects the modulation performance. Available bandwidth determines the amplitude response and group delay response. There is a tradeoff involved among the bandwidth, gain, and efficiency in the design of a power amplifier [9,10].

The bandwidth of an amplifier is determined by the load resistance across the tuned circuit and the output or input capacitance of the amplifier. For a single-tuned circuit, the bandwidth is proportional to the ratio of capacitive reactance to resistance:

$$BW \propto \frac{K}{2\pi f R_L C} = \frac{K X_C}{R_L} \quad (1)$$

where:

- BW = bandwidth between half-power points (BW3)
- K = proportionality constant
- R_L = load resistance (appearing across tuned circuit)
- C = total capacitance of tuned circuit (includes stray capacitances and output or input capacitances of the tube)
- X_C = capacitive reactance of C
- f = carrier frequency [11]

The load resistance is directly related to the RF voltage swing on the tube element. For the same power and efficiency, the bandwidth can be increased if the capacitance is reduced.

4. EFFECTS OF CIRCUIT TOPOLOGY AND TUNING ON FM MODULATION PERFORMANCE

FM broadcast transmitter RF power amplifiers are typically adjusted for minimum synchronous AM (incidental amplitude modulation with FM), which results in symmetrical amplitude response. This will assure that the transmitter's amplitude passband is properly centered on the FM channel. The upper and lower sidebands will be attenuated equally or symmetrically, which is *assumed* to result in optimum FM performance. This will be true if the RF power amplifier circuit topology results in simultaneous symmetry of amplitude and group delay responses.

Actually, symmetry of the group delay response has a much greater effect on FM distortion than has the amplitude response. Tuning for symmetrical group delay will cause the phase/time delay errors to affect the upper and lower sidebands equally or symmetrically. The group delay response is constant if the phase shift versus frequency is linear. All components of the signal are delayed equally in time, but no phase distortion occurs.

The tuning points for symmetrical amplitude response and symmetrical group delay response usually do *not*

coincide, depending on the circuit topology. Therefore, simply tuning for minimum synchronous AM (symmetrical amplitude response) does not necessarily result in the best FM performance [12].

Measurements taken on typical FM transmitters as well as computer simulations show that tuning the RF power amplifier for symmetrical group delay response results in minimum distortion and crosstalk. Group delay response asymmetry causes higher FM distortion and crosstalk than amplitude response asymmetry. The transmitter should be tuned for symmetrical group delay response, which results in the best FM performance, rather than for symmetrical amplitude response, which results in minimum synchronous AM [13].

4.1. Power Amplifier Output Source Impedance

At the milliwatt levels used in RF test equipment, it is customary to provide 50 Ω source and load impedances at both ends of a coaxial transmission line. This approach minimizes any reflections on the line because both the transmitter (source) and the termination (load) absorb reflected energy. A 50 Ω source impedance is usually provided by placing a 50 Ω build-out resistor in series with a low-impedance voltage source (Thevenin equivalent). The closed-circuit voltage with this configuration is exactly one half of the open-circuit voltage, meaning that half of the total available RF power is dissipated in the source resistance. The best possible efficiency for this system is 50% assuming that the voltage source is 100% efficient without the source resistance.

It becomes obvious that, although an FM transmitter is designed to drive a 50 Ω load, it does not have an output source impedance of 50 Ω . To achieve high efficiency, the transmitter must have a very low output source impedance so that nearly all of the power is delivered to the load. The plate dissipation indirectly represents some of the power lost within the low source resistance. Because the low source impedance of the transmitter provides a mismatch to reflected power from the load, this power is almost totally reflected back from the transmitter output stage toward the load again.

4.2. Intermediate Power Amplifiers

The intermediate power amplifier (IPA) is located between the exciter and the final amplifier in higher power transmitters that require more than about 50 W of drive to the final amplifier. The IPA may consist of one or more tubes or solid-state amplifier modules.

Most of the newer design, high-power transmitters with a tube in the final amplifier require between 150 W and 600 W of drive. This permits the use of solid-state, wideband, power amplifier modules to boost the exciter's power up to the level required to drive the grid of the final tube.

4.3. Interstage Coupling Circuits

The separate IPA output circuit and the final amplifier input circuit are often coupled together by a coaxial transmission line. Impedance matching is usually

accomplished at either end by one of the configurations shown in Fig. 8.

The interconnecting transmission line between the coupling circuits should be properly matched to avoid a high VSWR. Directional wattmeters are normally placed in the line to measure forward and reflected power from which a standing wave ratio can be established. The VSWR is established by the match at the load end of the transmission line.

Solid-state RF power devices possess a very low load impedance at the device output terminal, so that an impedance transformation that goes through the 50 Ω intermediate impedance level is required to couple these devices into the relatively high impedance of the final amplifier grid circuit. Therefore, virtually all solid-state IPA systems have a 50 Ω impedance point within the system that can be used to feed the antenna in an emergency.

4.4. Solid-State RF Power Amplifier Systems

A solid-state RF power amplifier almost always consists of a system of individual amplifier modules combined to provide the desired power output. Following are the advantages of using several lower power modules instead of a single high-power amplifier:

1. Redundancy is provided by isolating the input and output of each module, permitting uninterrupted

operation at reduced power if one or more of the modules fails.

2. The ability to repair or replace failed modules without having to go “off the air.”
3. More effective cooling of each power device junction by splitting the concentration of heat to be dissipated into several areas instead of one small area.
4. Better isolation between the amplifier modules and the input circuit of the final power amplifier or antenna is provided by the combiner/isolator.
5. Redundant power supplies and air cooling systems for each module improve overall reliability.

Each RF power amplifier module consists of one or more solid-state devices with broad-band impedance transformation networks for input and output matching. A new generation of class “C” MOSFET devices permits the design of broad-band amplifier stages with both high efficiency and the wide bandwidth necessary to cover the FM broadcast band.

The input impedance to the solid-state device is always lower than the desired 50 Ω input impedance, so a broad-band impedance transformation scheme is required. This is usually accomplished by a combination of coaxial baluns and push-pull coaxial line sections cross-coupled to provide 4:1 or higher transformation ratios over the FM band.

By operating two devices in push-pull, the input impedance (differential) is double that of a single-ended circuit, and the suppression of even order harmonics is enhanced. Two devices fed in this manner also provide some degree of redundancy within the module because partial RF output may be obtained when one device fails. Similarly, the low output impedance of these solid-state devices can be transformed up to the desired 50 Ω module output impedance where combining occurs. Figure 9(a) illustrates a simplified schematic of a broad-band, 350 W, MOSFET, RF amplifier module using the push-pull configuration. Figure 9(b) is a photograph of this RF amplifier module [14].

4.5. Solid-State Amplifier Splitting and Combining

The following are two frequently used types of splitting/combining schemes:

1. A 90° hybrid splitter or combiner ($N - 1$ hybrids are required to split or combine N inputs) (see section on transmitter output combining).
2. A Wilkinson N -way in-phase splitter or combiner.

Either type of splitter/combiner must provide isolation between the individual power amplifier modules and low-loss splitting or combining of the total power.

The cascaded 90° hybrid system shown in Fig. 10 provides double isolation between the power amplifiers and the load by first combining the two pairs of amplifiers and then combining the outputs of the first two combiners. A portion of the reflected power, caused by a mismatch at the output, will be dissipated in the reject loads so that the power amplifier modules will operate into a lower VSWR

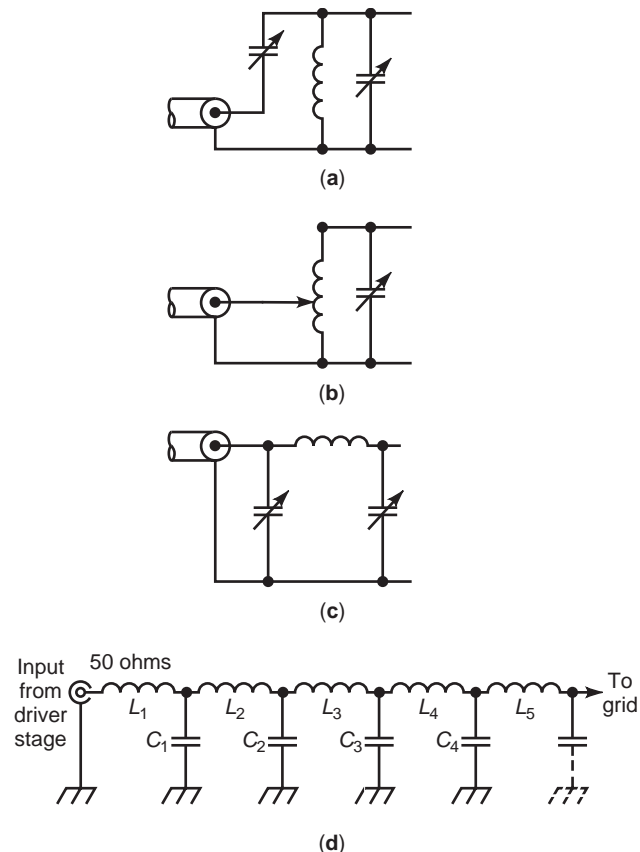
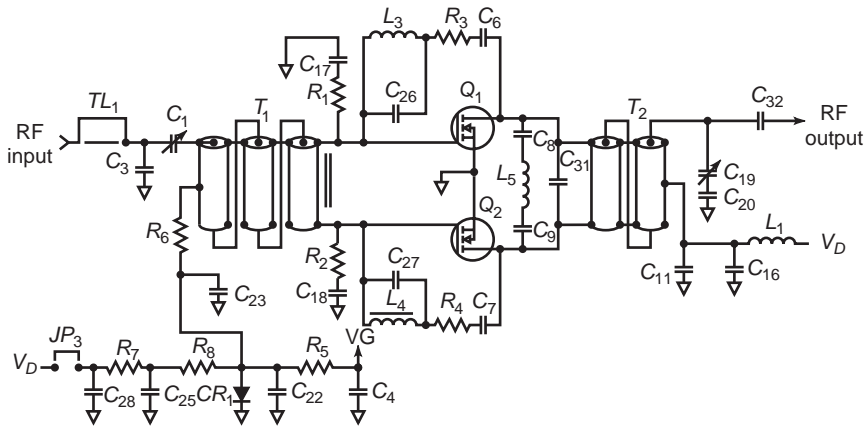
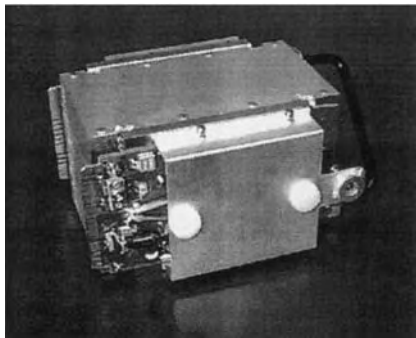


Figure 8. Interstage RF coupling circuits.



(a)



(b)

Figure 9. (a) Schematic of broad-band, 350 W, MOSFET, RF power amplifier module. (b) Broad-band, 350 W, MOSFET, RF power amplifier module.

than exists at the output. The unbalanced 50 Ω reject loads are accessible for monitoring of reject load power, which is useful in determining the balance of the system.

The Wilkinson system shown in Fig. 11 is a simple and effective way to split and combine modules operating in-phase but usually requires a balanced reject load that makes reject power measurements more difficult. By adding additional coaxial balun sections to the Wilkinson, it is

possible to use unbalanced reject loads [15]. This configuration is called Wilkinson–Gysel.

5. ADAPTIVE CONTROL OF THE COMBINER CONFIGURATION

Both the 90° hybrid and the Wilkinson combining systems require resistive RF power reject loads to provide isolation

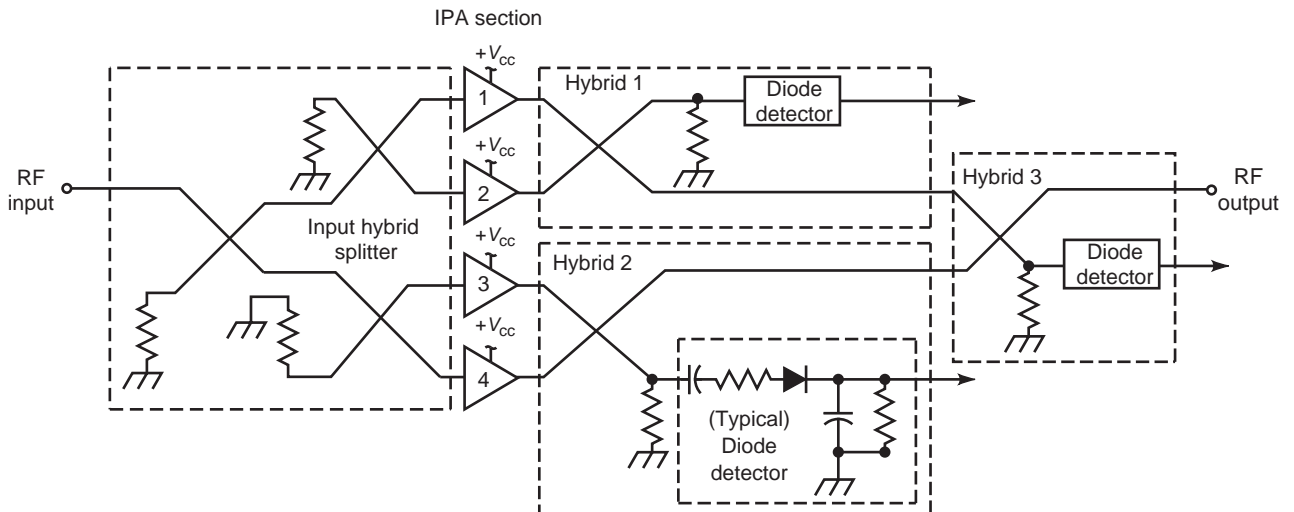


Figure 10. Cascaded 90° hybrid combiner.

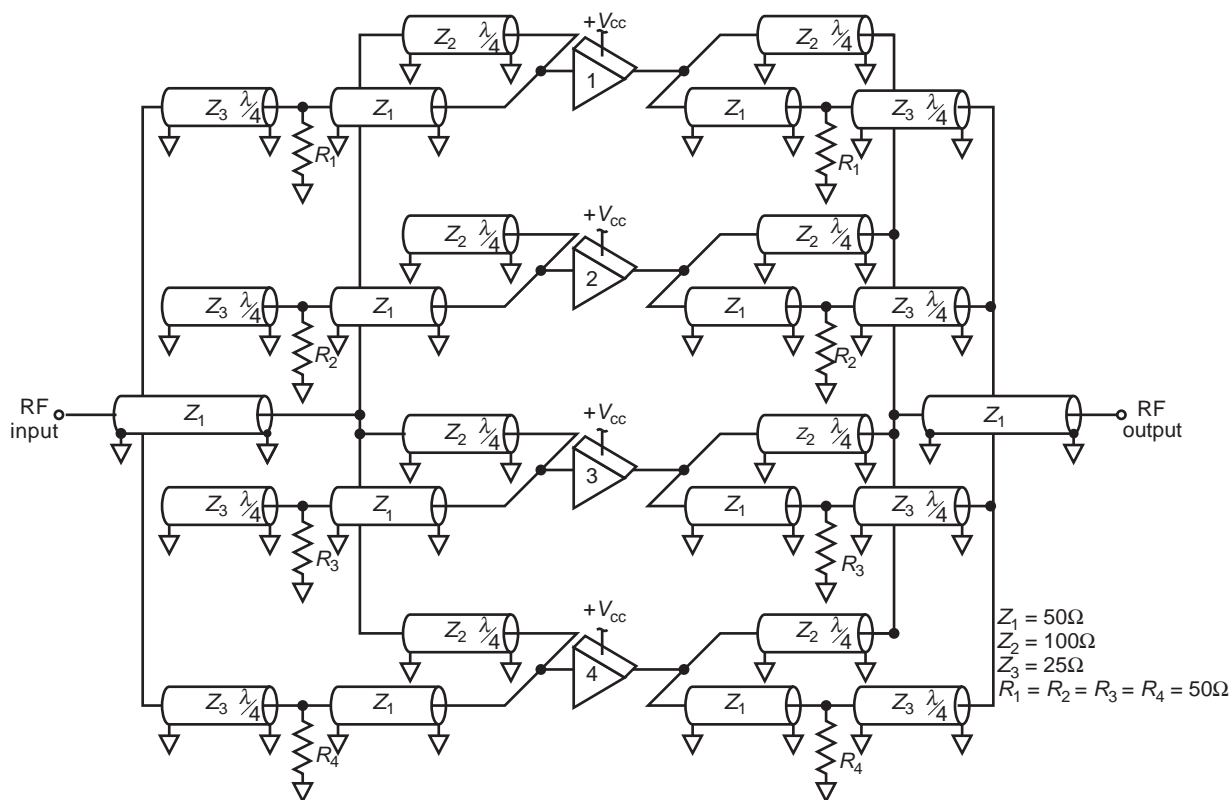


Figure 11. Wilkinson-Gysel in-phase splitting/combining system with unbalanced reject loads.

between the amplifier modules in the event that one or more of the modules fail. A portion of the RF power from the remaining modules is wasted in the reject loads instead of being delivered to the output. Recent developments have made it possible for a microcomputer to monitor the degree of imbalance in the system and adaptively change the configuration of the combiner to losslessly compensate for the failure of one or more power amplifier modules. This is accomplished by having the microcomputer substitute the appropriate reactances in place of the resistive reject loads to maintain enough isolation for the remaining power amplifiers to work efficiently. This technique is used in the Harris "Z" plane combiner.

Because most splitter/combiner systems are designed around a 50Ω input and output impedance level, these systems can be easily used as low-power standby transmitters by routing the output to the antenna system. An RF lowpass filter (LPF) is required only when directly feeding the antenna system. The harmonic suppression of the IPA is not as critical when driving a nonlinear power amplifier that also generates harmonics, because this stage will have its own LPF.

6. SOLID-STATE FM BROADCAST TRANSMITTERS

The techniques used to construct IPA systems can also be used to construct a completely solid-state transmitter using arrays of combined modules for the final output stage.

An additional RF lowpass filter is usually required to meet FCC emission requirements.

6.1. Advantages of Solid-State Transmitters

The primary advantages of a solid-state transmitter are the built-in amplifier and power supply redundancy, superior FM performance, the ability to cover the entire FM band without the need for retuning, and elimination of tube replacement costs. A tubeless transmitter is nearly maintenance free.

6.2. Solid-State Transmitter Design Considerations

Several manufacturers offer solid-state FM broadcast transmitters with power outputs ranging from 100 W up to 20 kW, but present economic factors still favor the single-tube FM transmitter for power levels above 20 kW. For a solid-state transmitter to be competitive in cost and power consumption with a single tube transmitter, the efficiency of the solid-state RF power amplifiers and combining system have to approach the 80% efficiency obtainable from tube type RF amplifiers. This high efficiency has recently been achieved with MOSFET solid-state devices at VHF frequencies.

Recent solid-state designs have provided higher efficiencies, up to 80% dc to RF efficiency at the MOSFET device level and over 62% overall efficiency, from ac line in to RF output. This is actually better ac to RF efficiency at the 5 kW level than a typical single-tube transmitter.

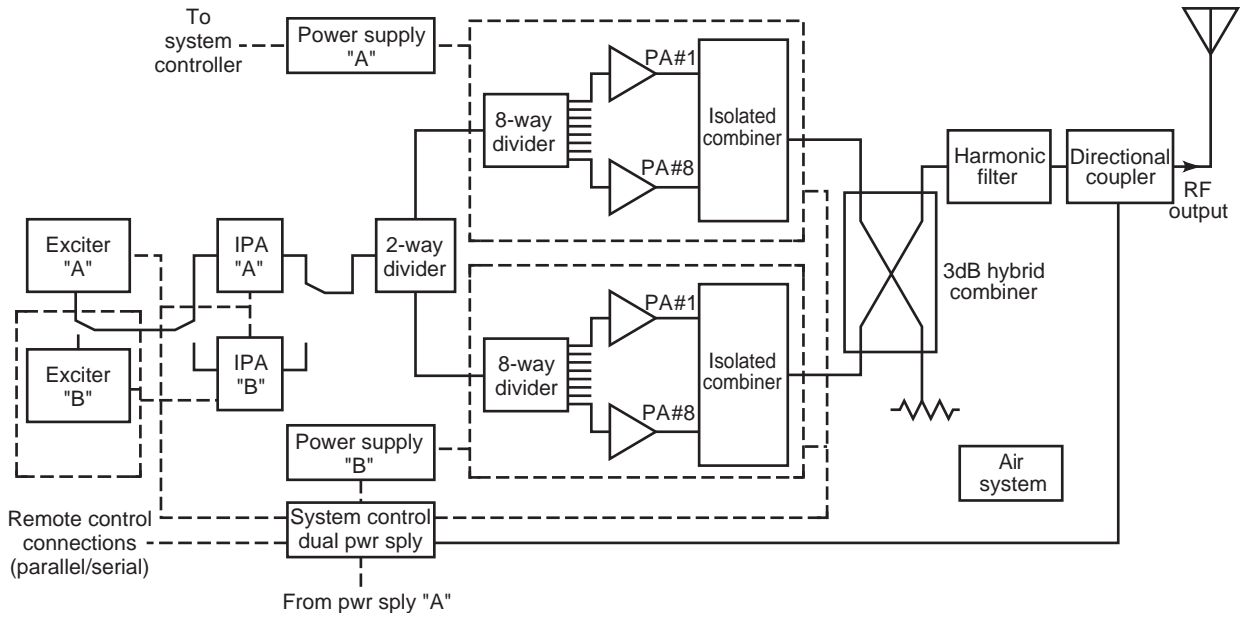


Figure 12. Harris Z 5 kW solid-state FM transmitter.

Some solid-state designs have added a few percent to their overall ac to RF efficiency by optimizing their RF circuits over narrowband sections of the FM band. This approach is beneficial to the user who is certain that there will be no need to change the transmitter's frequency or who is prepared to provide the transmitter modifications needed to do so.

Trends in the newest solid-state FM transmitters are to supply redundant RF, power supply, and control circuits so as to keep the transmitter on the air at reduced power in the event one or more components should fail. Identical and interchangeable IPA and PA modules offer additional redundancy. RF modules that can be removed and inserted in an operating transmitter also provide the advantage of not requiring an off-air period for some maintenance services.

Solid-state transmitter layouts with direct, cable-free connection of the RF modules to the RF combiner have also been introduced and further enhance transmitter reliability and stability. Another enhancement provided in some current solid-state FM transmitters is an advanced, microprocessor-based, control system that monitors detailed parameters within the transmitter and provides *intelligent control* of the transmitter system, including the RF combiner, so as to maximize output power and minimize reject load power under various combinations of active and inactive modules.

Figure 12 shows a block diagram of a 5 kW solid-state transmitter.

6.3. Vacuum-Tube Power Amplifier Circuits

The amplitude of an FM signal remains constant with modulation so that efficient, nonlinear, Class C, amplifiers can be used.

FM broadcast vacuum-tube power amplifier circuits have evolved into two basic types. One type uses a tetrode or pentode tube in a grid-driven circuit, whereas the other uses a high- μ triode in a cathode-driven (grounded grid) circuit.

6.3.1. Cathode-Driven Triode Amplifiers. The high- μ triodes being used in cathode-driven (grounded-grid) FM amplifiers were originally developed for linear SSB amplifiers. Their characteristics are well adapted to FM broadcast use because the circuit is very simple and no screen or grid bias power supplies are required. Figure 13 shows the basic circuit configuration. In this case, the grid is connected directly to chassis ground. Dc grid current is the difference between dc cathode current and dc plate current. The output tank circuit is a shorted coaxial cavity that is capacitively loaded by the tube output and stray circuit capacitance. A small capacitor is used for trimming

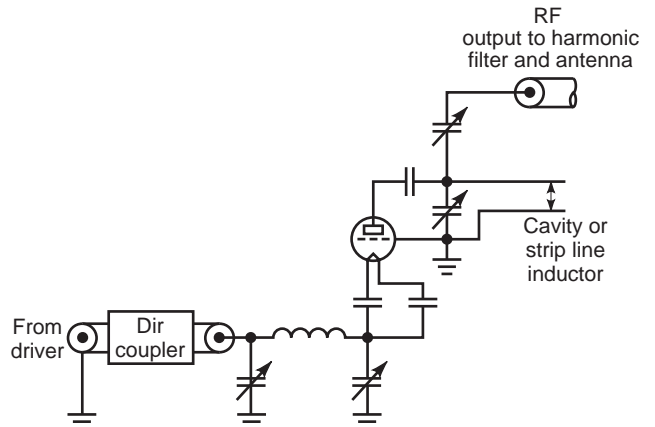


Figure 13. Cathode-driven, triode, power amplifier.

the tuning and another small variable capacitor is used to adjust the loading. A π -network matches the $50\ \Omega$ input to the tube cathode impedance.

The triodes are usually operated in the less efficient, class “B” mode to achieve maximum power gain, which is on the order of 20 (13 dB). They can be driven into high-efficiency, class “C” operation by providing negative grid bias. This increases the plate efficiency, but also requires increased drive power.

Most of the drive power into a grounded-grid amplifier is fed through the tube and appears in the stage’s output. This increases the apparent efficiency so that the efficiency factor given by the manufacturer may be higher than the actual plate efficiency of the tube. The true plate efficiency is determined by dividing the output power by the total input power, which includes both the dc plate input power ($I_p \times E_p$) and the RF drive power. Because most of the drive power is fed through the tube, any changes in loading of the output circuit also affect the input tuning and driver stage.

There is RF drive voltage on the cathode (filament) of the tube, so some means of decoupling must be used to block it from the filament transformer. One method employs high-current RF chokes because the inductance can be very low at this frequency range. The other commonly used method feeds the filament power through the input tank circuit inductor.

Cathode-driven stages are normally used only for the higher power stages. The first stage in a multitube transmitter is nearly always a tetrode because of its higher power gain.

6.3.2. Grid-Driven Tetrode and Pentode Amplifiers.

Transmitters with tetrode amplifiers throughout usually have one less stage than do those with triodes. Because tetrodes have higher power gain, they are driven into class “C” operation for high plate efficiency. Against these

advantages is the requirement for neutralization, along with screen and bias power supplies.

Figure 14 shows a schematic of a grid-driven tetrode amplifier. In this example, the screen is operated at dc ground potential and the cathode (filament) is operated below ground by the amount of screen voltage required. This is called grounded-screen operation. It has the advantage that stability problems due to undesired resonances in the screen-by-pass capacitors are eliminated. With directly heated tubes, it is necessary to use filament-bypass capacitors. During grounded-screen operation, these bypass capacitors need a higher breakdown voltage rating because they have the dc screen voltage across them. The filament transformer must have additional insulation to withstand the dc screen voltage.

The screen power supply provides a negative voltage in series with the cathode to ground and must have the additional capacity to handle the sum of the plate and screen currents. A coaxial cavity is used in the output circuit so that the circulating current is spread over large surfaces to keep the losses very low. This cavity is a shorted quarter-wavelength transmission line section that resonates the tube’s output capacitance. The quarter-wavelength cavity is actually shorter than a physical quarter-wavelength due to the electrical loading effect of the tube’s output capacitance across the open end of the transmission line. The length is preset to the desired carrier frequency, and then a small-value variable capacitor is used to trim the system to resonance. Capacitive output coupling is used to match from the high RF voltage point to the $50\ \Omega$ transmission line.

The $50\ \Omega$ input is capacitively coupled into the grid circuit inductor to provide the correct impedance match.

Pentode amplifiers have even higher gain than their tetrode counterparts. The circuit configuration and bias supply requirements for the pentode are similar to the tetrode because the third (suppressor) grid is tied directly to ground. The additional isolating effect of the (suppressor) grid eliminates the need for neutralization in the pentode amplifier [16].

6.3.3. Impedance Matching Into the Grid. The grid circuit is usually loaded (swamped) with added resistance. The purpose of this resistance is to broaden the bandwidth of the circuit by lowering the circuit Q and to provide a more constant load to the driver. It also makes neutralizing less critical so that the amplifier is less likely to become unstable.

Cathode or filament lead inductance from inside the tube through the socket and filament capacitors to ground can heavily load the input circuit. This is caused by RF current flowing from grid to filament through the tube capacitance and then through the filament lead inductance to ground. An RF voltage is developed on the filament, which in effect causes the tube to be partly cathode-driven. This undesirable extra drive power requirement can be minimized by series resonating the cathode return path with the filament bypass capacitors or by minimizing the cathode-to-ground inductance with a specially designed tube socket containing thin-film dielectric sandwich capacitors for coupling and bypassing.

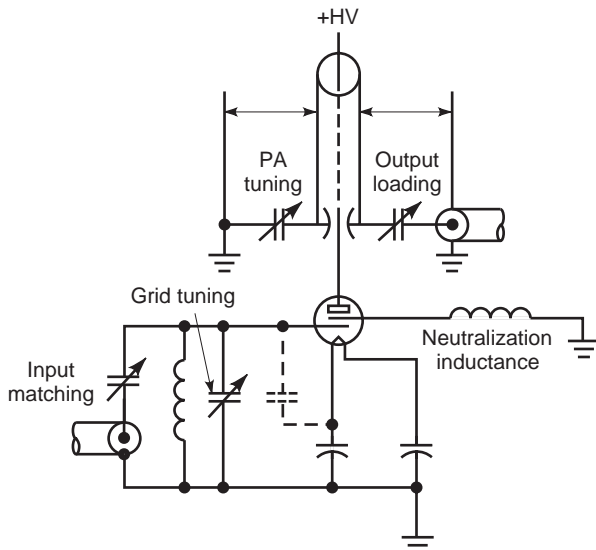


Figure 14. Grid-driven, grounded-screen, tetrode, power amplifier.

High-power, grid-driven, class “C” amplifiers require a swing of several hundred RF volts on the grid. To develop this high-voltage swing, the input impedance of the grid must be increased by the grid input matching circuit. Because the capacitance between the grid and the other tube elements may be 100 pF or more, the capacitive reactance at 100 MHz will be very low unless the input capacitance is resonated in parallel with an inductor. Figures 15(a) and 15(b) show two popular methods of resonating and matching into the grid of a high-power tube. Both methods can be analyzed by recognizing that the desired impedance transformation is produced by an equivalent L network.

In Fig. 15(a), a variable inductor L_{in} is used to raise the input reactance of the tube by bringing the tube input capacitance C_{in} almost to parallel resonance. Parallel resonance is not reached because a small amount of parallel capacitance C_p is required by the equivalent L network to transform the high impedance Z_{in} of the tube down to a lower value through the series matching inductor L_s . This configuration provides an L -network lowpass filter by using part of the tube’s input capacitance to form C_p .

Figure 15(b) uses variable inductor L_{in} to take the input capacitance C_{in} past parallel resonance so that the

tube’s input impedance becomes slightly inductive. The variable series matching capacitor C_s forms the rest of the equivalent L network. This configuration is a high-pass filter.

6.3.4. Neutralization. Cathode-driven, grounded-grid amplifiers using triodes do not require neutralization. It is necessary that the grid-to-ground inductance, both internal and external to the tube, be kept very low to maintain this advantage. Omission of neutralization allows a small amount of interaction between the output circuit and the input circuit through the plate-to-filament capacitance. This effect is not very noticeable because of the large coupling between the input and output circuits through the electron beam of the tube. Cathode-driven tetrodes have higher gain and therefore require some form of neutralization.

Grid-driven, high-gain tetrodes need accurate neutralization for best stability and performance. Self-neutralization can be accomplished very simply by placing a small amount of inductance between the tube screen grid and ground, usually in the form of several short, adjustable-length straps. The RF current flowing from plate to screen in the tube also flows through the screen lead inductance. This develops a small RF voltage on the screen, of the opposite phase, which cancels the voltage fed back through the plate-to-grid capacitance. This method of lowering the self-neutralizing frequency of the tube works only if the self-neutralizing frequency of the tube/socket combination is above the desired operating frequency before the inductance is added. Feedback neutralization uses a small coupling capacitor, usually in the form of a small plate located near the anode of the tube. The sample of the RF voltage from the anode intercepted by this plate is coupled through a 180° phase-shift network into the grid circuit. This technique has the advantage of providing neutralization over a very broad range of frequencies if implemented correctly, and stray reactances are minimized. Special attention must also be given to minimizing the inductances in the tube socket by integrating distributed bypass capacitors into the socket and cavity deck assembly. Pentodes normally do not require neutralization because the suppressor grid effectively isolates the plate from the grid.

6.3.5. Power Amplifier Output Circuits. Usually, the output circuit consists of a *high-Q* (low-loss) transmission line cavity, strip line, or a lumped inductor that resonates the tube output capacitance. A means of trimming the tuning and a means of adjusting the coupling to the output transmission line must also be provided by the output circuit. The tank circuit loaded Q is kept as low as practical to minimize circuit loss and to maintain as wide an RF bandwidth as possible.

6.3.6. The Power Amplifier Cavity. The vacuum-tube power amplifier is constructed in an enclosure containing distributed tank circuit elements for minimum loss. The efficiency of the PA depends on the RF plate voltage swing, the plate current conduction angle, and the cavity efficiency. The cavity efficiency is related to the ratio of the

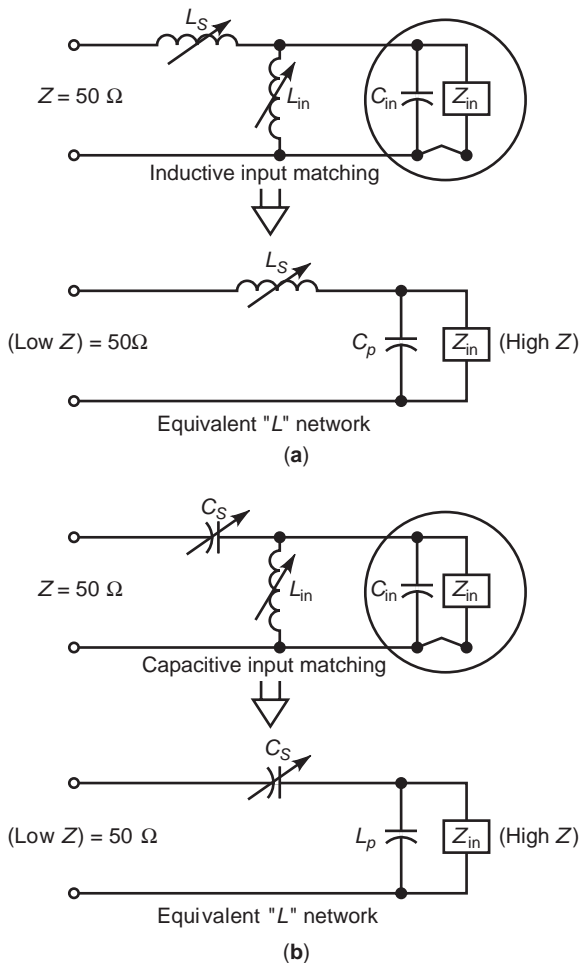


Figure 15. (a) Inductive input matching. (b) Capacitive input matching.

loaded to unloaded Q as follows:

$$N = 1 - \left(\frac{Q_L}{Q_U} \right) \times 100 \quad (2)$$

where N is the efficiency in percent, Q_L is the loaded Q of cavity, and Q_U is the unloaded Q of cavity.

The loaded Q depends on the plate load impedance and output circuit capacitance. Unloaded Q depends on the cavity volume and the RF resistivity of the conductors due to skin effects. A high unloaded Q is desirable, as is a low loaded Q , for best efficiency. As the loaded Q goes up, the bandwidth decreases. For a given tube output capacitance and power level, the loaded Q decreases with decreasing plate voltage and increasing plate current. The increase in bandwidth at reduced plate voltage occurs because the smaller load resistance is directly related to the RF voltage swing (for the same power) on the tube element. For the same power and efficiency, the bandwidth can also be increased if the output capacitance is reduced. Power tube selection and minimization of stray capacitance are areas of prime concern when designing for maximum bandwidth.

6.3.7. The Quarter-Wavelength Cavity. The “quarter-wavelength” coaxial cavity is the compact and popular output circuit illustrated in Fig. 16. The tube anode is coupled through a dc blocking capacitor to a shortened “quarter-wavelength” transmission line. The tube’s output capacitance is brought to resonance by the inductive component of the transmission line that is physically less than a quarter-wavelength long. Plate tuning is accomplished either by adding end-loading capacitance at the high-impedance end of the line with a variable capacitor or by changing the position of the ground plane at the low-

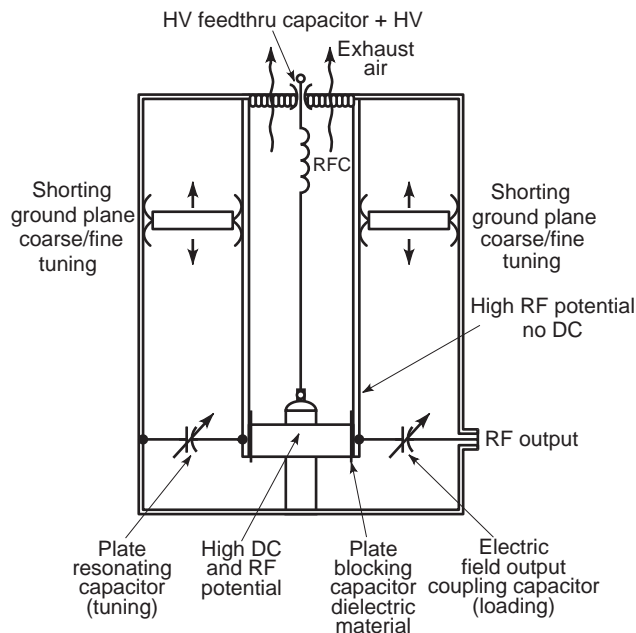


Figure 16. The quarter-wavelength cavity.

impedance end of the line. The plate-tuning capacitor may be a sliding or rotating plate near the anode of the tube. The center conductor of the transmission line (air exhaust chimney) is at dc ground, whereas the anode of the tube operates at a high RF and dc potential. Dc voltage is fed through an isolated “quarter-wavelength” decoupling network inside the chimney to the anode of the tube. The plate blocking capacitor prevents dc current flow from the anode into the chimney.

6.3.8. The Folded, Half-Wavelength Cavity. Another approach to VHF power amplification uses the reentrant, folded, “half-wavelength” cavity design illustrated in Fig. 17. The dc anode voltage is applied to the lower portion of the plate line through a choke at the RF voltage null point. The “half-wave-length” line is tuned by mechanically expanding or contracting the physical length of a flexible extension (bellows) on the end of the secondary transmission line stub, which is located concentrically within the primary transmission line (air exhaust chimney). Coarse frequency adjustment is accomplished by presetting the depth of the top secondary section of plate line into the tank cavity.

Other power amplifier configurations may use lumped components or hybrid combinations with distributed transmission line elements to achieve similar results. The discrete circuit elements are chosen for their individual inductance or capacitance, instead of being operated in a purely “quarter-wavelength” or “half-wavelength” mode. Stray inductance and capacitance add to the component values resulting in the hybrid nature of these circuits.

The RF voltage and current distributions for the “quarter-wavelength” and the folded, “half-wavelength” cavities are shown in Fig. 18.

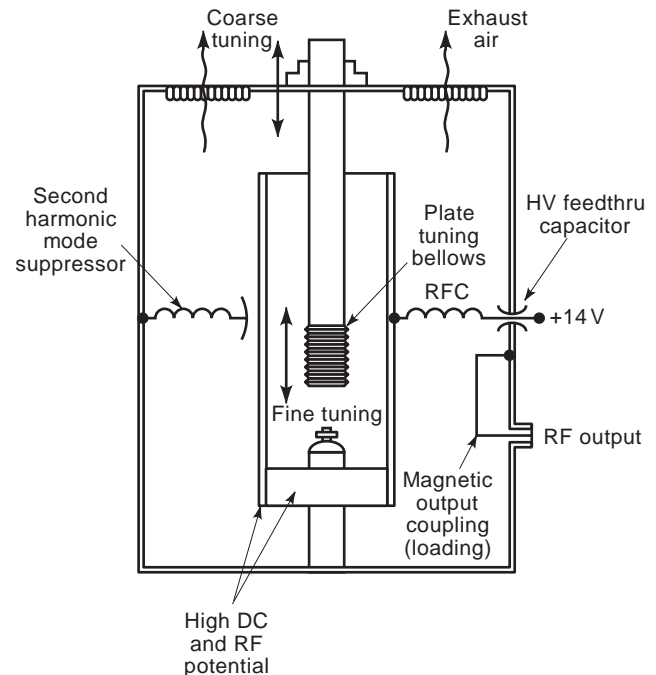


Figure 17. The folded, half-wavelength cavity.

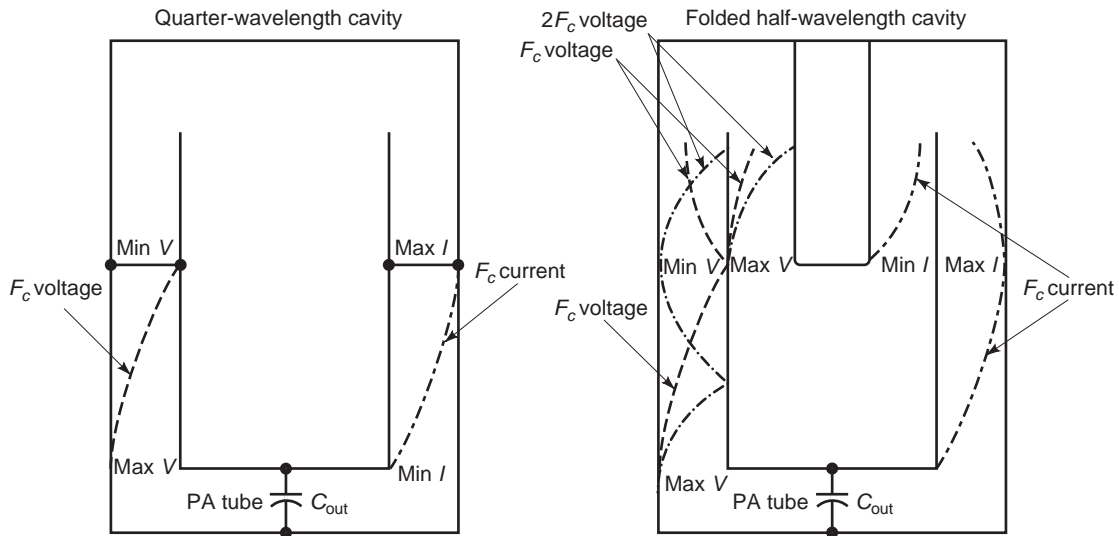


Figure 18. Cavity RF voltage and current distributions.

Regardless of the specific configuration, the output circuit must transform the high resonant plate impedance down to the output transmission line impedance of $50\ \Omega$. The bandwidth of a transmission line cavity is optimized by choosing the highest characteristic impedance mechanically and electrically allowable.

6.3.9. Output Coupling. Power may be coupled from a “quarter-wavelength” cavity to the transmission line by a capacitive probe located near the high RF voltage point located at the anode end of the “quarter-wave” line as shown in Fig. 16. The amount of output coupling capacitance is determined by the RF power output required. The loaded Q of this circuit varies with the degree of capacitive coupling. Another method of coupling power from the “quarter-wavelength” cavity uses a tuned loop located near the grounded (high current) end of the line. In this case, the tuned loop operates both as an inductive and a capacitive pickup device. Power may be coupled from the “half-wavelength” line by an inductive loop located in the strong fundamental magnetic field near the center of the cavity, as shown in Fig. 17.

6.3.10. RF Output Low-Pass Filters. The high-efficiency, nonlinear RF power amplifiers used in FM broadcast transmitters generate significant amounts of energy on frequencies that are integral multiples (harmonics) of the desired fundamental frequency. The output circuit alone does not provide enough harmonic attenuation to meet FCC regulations. To comply with Part 73 of the FCC rules and regulations and to prevent interference to other services, a lowpass filter must be installed in the transmission line at the output of the transmitter. The FM band is narrow enough that one lowpass filter design can be used for any FM channel carrier frequency. These filters usually consist of multiple LC sections arranged so that frequencies within the FM band are passed with little attenuation (typically 0.1 dB or less), whereas frequencies above the FM band are highly attenuated (60 dB or more).

The most common type of filter in this application is called a *reflective* filter, meaning that the frequency components outside the passband are reflected back out of the filter toward the source because it provides a mismatch at these undesired frequencies. The filter can be constructed using either *lumped* inductors and capacitors or a section of nonconstant impedance transmission line to form *distributed* inductors and capacitors. The filters designed for low-power transmitters often employ *lumped* elements (coils and capacitors) because they are compact and can be integrated into the transmitter cabinet. The distributed type of filter is most often used with high-power FM broadcast transmitters because of its simplicity, extreme ruggedness, and ability to handle higher power levels. The distributed filter does have the disadvantage of having larger physical dimensions than a similar lumped filter, which may necessitate mounting the filter outside of the transmitter cabinet. Figure 19 shows a cutaway view of a typical distributed lowpass filter. Note that the areas where the center conductor for the transmission line is smaller than that required for the input Z_0 are inductive, whereas the areas where the center conductor is larger in diameter are capacitive.

When two filters (such as the output cavity and the harmonic filter) are connected by a transmission line, the total harmonic attenuation varies with interconnecting line length. The attenuation characteristics of the harmonic filter are specified for the condition where both the source and load impedances are equal to the desired transmission line impedance.

In actual use, the source impedance at the output of the tank circuit is much less than the $50\ \Omega$ load impedance presented by a properly terminated filter. At the operating frequency, the output impedance of the power amplifier

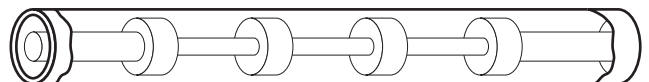


Figure 19. Cutaway view of a distributed lowpass filter.

and the input impedance of the lowpass filter become predominantly reactive at harmonic frequencies causing interaction between the two. If an unfortunate length of line is selected, the harmonic attenuation may be insufficient, and the transmitter tuning may be affected. This undesirable condition can be corrected by changing the line length by approximately one quarter-wavelength. At the operating frequency, the line length between the tank circuit and the harmonic filter is usually supplied precut to a value known to be satisfactory by the transmitter manufacturer.

6.3.11. Harmonic Notch Filters. In some cases, a second harmonic notch filter is required in addition to the lowpass filter because the second harmonic component from the amplifier is high and the cutoff slope of the lowpass filter is not steep enough to provide sufficient second harmonic attenuation. The additional attenuation required (typically 30 dB) can be provided by a notch filter that places a short circuit across the transmission line at the second harmonic while providing a high impedance at the fundamental. A one quarter-wavelength (at the fundamental frequency), shorted coaxial stub is often used for this function. The second harmonic energy is primarily reflected back toward the power amplifier and to a lesser extent dissipated in the equivalent series resistance of the series tuned circuit formed by the stub. This shorted stub provides a very low impedance and a dc path from the center conductor of the transmission line to ground providing a separate, protective, advantage by shunting static discharges, such as lightning, to ground.

7. COMBINED TRANSMITTERS

It is possible to combine the output of two RF power amplifiers for higher power levels. The important advantage is that the broadcast transmission is not interrupted if one amplifier fails. The radiated signal strength merely drops 6 dB until the failed amplifier is repaired and put back on the air. A dual-amplifier system costs more than a single amplifier for a given total power output, but there are the economic advantages of reducing lost air time and eliminating the need for a separate standby transmitter. Automatic or manual output switching can be used to route the full power of the remaining amplifier directly to the antenna, reducing the loss in radiated power from 6 dB to 3 dB.

Two methods may be used to bypass the output-combining hybrid to allow 100% of the power of the remaining transmitter to be sent to the antenna if one transmitter of a combined pair should fail.

The first method uses three motorized switches (or patch panels) to bypass the 3 dB hybrid while connecting the operating transmitter directly to the antenna and the failed transmitter directly to the test load. This allows recovery of the 50% power lost in the reject load when one transmitter is off the air. One disadvantage is that the system must be taken off the air for several seconds to operate the coax switches.

A second method provided by some transmitter suppliers uses a pair of 3 dB hybrids interconnected with one fixed and one variable RF phasing section. The phasing section is constructed to operate while under RF power and can redirect the full output of either transmitter directly to the antenna and place the other transmitter into the test load without taking the system off the air. A dedicated system controller allows automatic or manual control. This so-called *switchless* combiner offers the highest possible on-air availability for combined FM transmitters. With complete redundancy in the RF power amplifier chain, some stations go one step further and install dual exciters with automatic switching so that, if one exciter fails, the other unit is quickly switched into service.

7.1. 90° Hybrid Couplers

Hybrid couplers are reciprocal four-port devices used either for splitting or combining RF sources over a wide frequency range. Figure 20 shows an exploded view of a typical 3 dB, 90°, hybrid coupler. The coupler consists of two identical parallel transmission lines coupled over a distance of approximately one quarter-wavelength and are enclosed within a single outer conductor. Ports at the same end of the coupler are in phase, whereas ports at opposite ends of the coupler are in quadrature (90° phase shift) with respect to each other.

The phase shift between the two inputs or outputs is always 90° and is almost independent of frequency. If the coupler is being used to combine two signals into one output, these two signals must be fed to the hybrid coupler in phase quadrature. The reason this type of coupler is also called a 3 dB coupler is that when used as a power splitter, the split is equal or half-power (3 dB) between the two outputs.

7.2. 90° Hybrid Combiners

The output hybrid combiner effectively isolates the two amplifiers from each other. Tuning adjustments can be

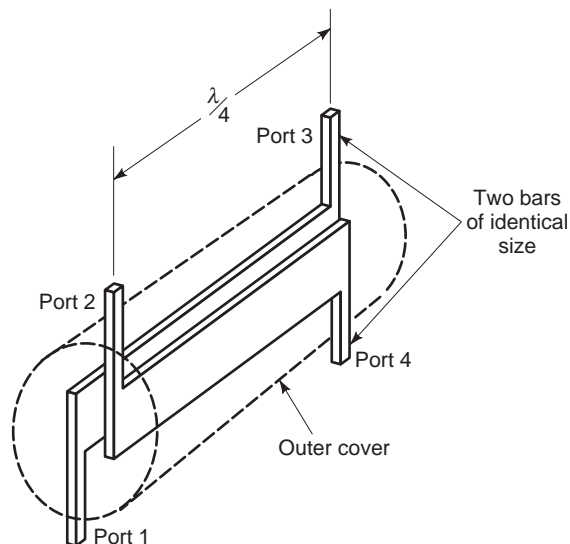


Figure 20. Physical model of a 90° hybrid coupler.

made on one amplifier including turning it on and off without appreciably affecting the operation of the other amplifier. Good isolation is necessary so that if one transmitter fails, the other continues to operate normally instead of in a mistuned condition. Two of the ports on the hybrid coupler are the inputs from the power amplifiers, the sum port is the antenna output terminal, and the difference port goes to a resistive dummy load called the *reject load* because only the rejected power caused by imbalance appears here. When the power fed to each of the two inputs is equal in amplitude with a phase difference of 90°, the total power is delivered to the sum port (antenna). Very little of the power appears at the reject load if the phase relationship and power balance are correct. If the phase relationship is reversed between the two amplifiers, all the power is delivered to the reject load, so care must be taken to ensure that the proper one of the two possible 90° phase relationships is used. When all the ports on the hybrid combiner are properly terminated, isolation of 30 dB or more can be achieved between the power amplifiers. For perfect isolation between the amplifiers, the load impedance on the sum and difference ports must be exactly the same. This is approached in practice by providing a 1.0:1 VSWR with a resistive 50 Ω load for the termination (reject load) on the difference port and then reducing the VSWR on the antenna transmission line as low as possible by trimming the antenna match. This keeps the input port impedances from changing very much when one amplifier is not operating.

The input ports will present a load to each transmitter with a VSWR that is lower than the VSWR on the output transmission line because part of the reflected power coming into the output port will be directed to the reject load and only a portion will be fed back into the transmitters. Figure 21 shows the effect of output port VSWR on the input port VSWR and on the isolation between ports.

If the two inputs from the separate amplifiers are not equal in amplitude or exactly in phase quadrature, some of the power will be dissipated in the difference port reject load. The match in input power and phase is not extremely critical as shown in Figs. 22 and 23. The power lost in the difference port reject load can be easily reduced to a

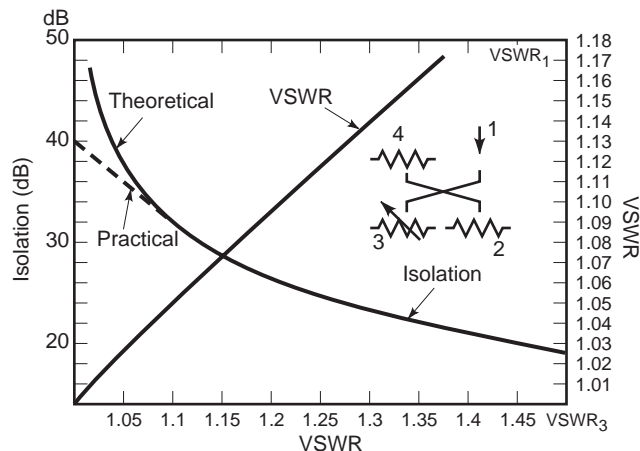


Figure 21. Isolation and VSWR of a 90° hybrid coupler.

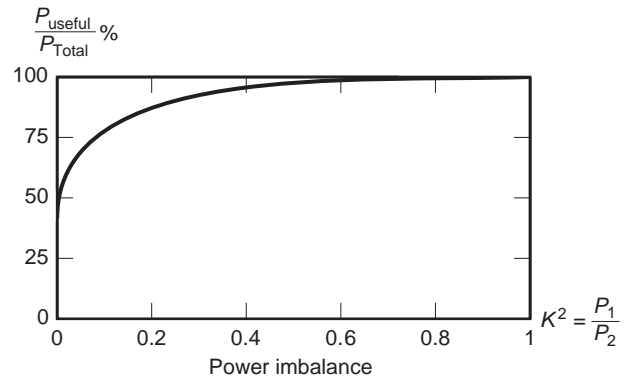


Figure 22. Loss due to power imbalance in 90° hybrid coupler.

negligible value by touching up the amplifier tuning and by adjusting the phase shift. For example, if one amplifier is delivering only half the power of the other amplifier, only about 3% of the total available power will be dissipated in the reject load and 97% is still fed to the output transmission line [17].

If one transmitter fails completely, half of the working amplifier’s output goes to the antenna, and the other half is dissipated in the difference port reject load. This is why the radiated output drops by 6 dB or to one fourth of the original combined power. The reject load must be rated to handle a minimum of one fourth of the total combined power, but often the reject load is rated to handle one half the total power, so that it can also be used a test load for one of the transmitters.

7.3. Hybrid Splitting of Exciter Power

Figure 24 shows a block diagram of a pair of combined amplifiers with dual exciters. The exciters cannot be operated in parallel like the amplifiers because their RF outputs would have to be on exactly the same carrier frequency and exactly in phase under all modulation conditions. An automatic or manual exciter switcher is used to direct the output of the desired exciter to the combined transmitter, and the other standby exciter is routed to a dummy load. The one exciter in use feeds a hybrid splitter/phase shifter, which transforms one 50 Ω input into two

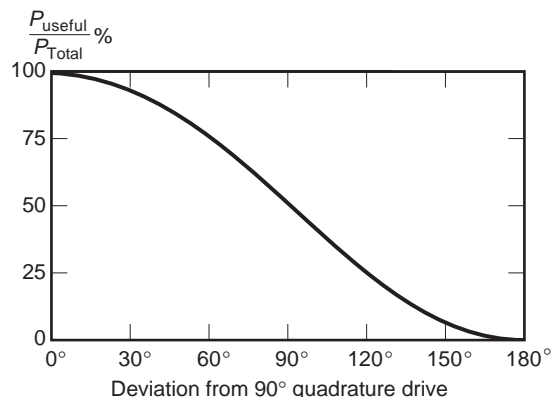


Figure 23. Phase sensitivity in a 90° hybrid coupler.

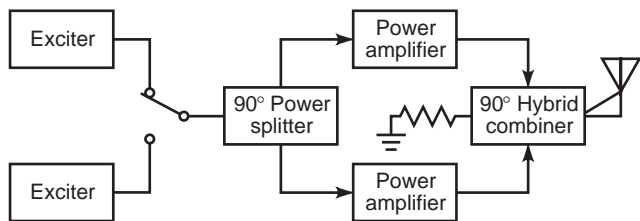


Figure 24. Block diagram of a transmitter with two power amplifiers, a 90° hybrid combiner, and dual exciters with 90° power splitter.

isolated 50 Ω outputs that have a 90° phase shift between them with half the power going to each output. The operation of this hybrid splitter is the reciprocal of the hybrid combiner described above. The exciter must have enough power output capability to drive both power amplifiers. In some cases, an additional IPA is required between the exciter and the splitter to boost the drive level. The length of coax from the power splitter to each amplifier input must be cut to a precise length so that the amplifiers will be fed in the proper phase relationship.

Each of the power amplifiers is assumed to have equal gain and phase shift. In practice, it may be difficult to tune the amplifiers so that their gains and phase shifts are equal at the same time. For this reason, a line stretcher or variable phase-shift network is usually included with the exciter splitter so that the station engineer can adjust phasing independent of amplifier tuning.

7.4. Filterplexing

The practice of having several FM stations share a single broad-band antenna system has become more popular in recent years. To connect several transmitters on different frequencies together onto one antenna system, a special device called a filterplexer is required. The purpose of the filterplexer is to provide isolation between the various transmitters while efficiently combining their power into a single transmission line. This is usually accomplished by a system of bandpass filters, band-reject filters, and hybrid combiners. The isolation is required to prevent power from one transmitter from entering another transmitter with resulting spurious emissions and to keep the rest of the system running in the event of the failure of one or more transmitters.

An important consideration in designing a filterplexing system is the effect on the phase response (group delay characteristic in the passband) of each of the signals passing through the system because of individual bandwidth limitations on each of the inputs.

7.5. RF Intermodulation Between FM Broadcast Transmitters

Interference with other stations within the FM broadcast band and with other services outside the broadcast band can be caused by RF intermodulation between two or more FM broadcast transmitters. Transmitter manufacturers have begun to characterize the susceptibility of their equipment to RF intermodulation so this information

Third-order intermodulation products

$f_1 = 100.3 \text{ MHz.} \quad f_2 = 101.1 \text{ MHz.}$

$2f_1 - f_2 = [2(100.3) - (101.1)] = [200.6 - 101.1] = 99.5 \text{ MHz.}$

$2f_2 - f_1 = [2(101.1) - (100.3)] = [202.2 - 100.3] = 101.9 \text{ MHz.}$

OR

$[f_1 - (f_2 - f_1)] = [100.3 - (101.1 - 100.3)] = [100.3 - 0.8] = 99.5 \text{ MHz.}$

$[f_2 + (f_2 - f_1)] = [101.1 + (101.1 - 100.3)] = [101.1 + 0.8] = 101.9 \text{ MHz.}$

Figure 25. Calculation of intermodulation product frequencies.

will be available to the designers of filterplexing equipment.

The degree of intermodulation interference generated within a given system can be accurately predicted before the system is built if the actual mixing loss of the transmitters is available when the system is designed. Accurate data on *mixing loss* or *turnaround-loss* speed the design of filterplexing equipment and result in higher performance and more cost-effective designs because the exact degree of isolation required is known before the system is designed. Filterplexer characteristics and antenna isolation requirements can be tailored to the specific requirements of the transmitters being used. The end user is assured in advance of construction that the system will perform to specification without fear of overdesign or underdesign of the components within the system.

7.6. Mechanisms Which Generate RF Intermodulation Products

When two or more transmitters are coupled to each other, new spectral components are produced by mixing the fundamental and harmonic terms of each of the desired output frequencies. For example, if only two transmitters are involved,

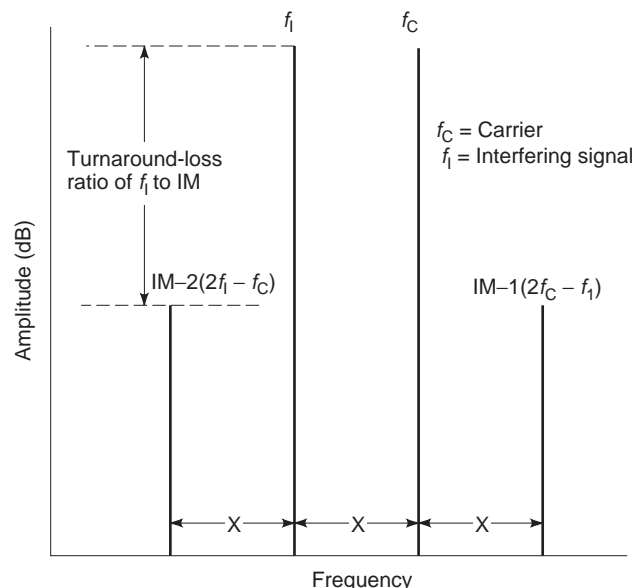


Figure 26. Frequency spectrum of third-order IM products with the interfering level equal to the carrier level.

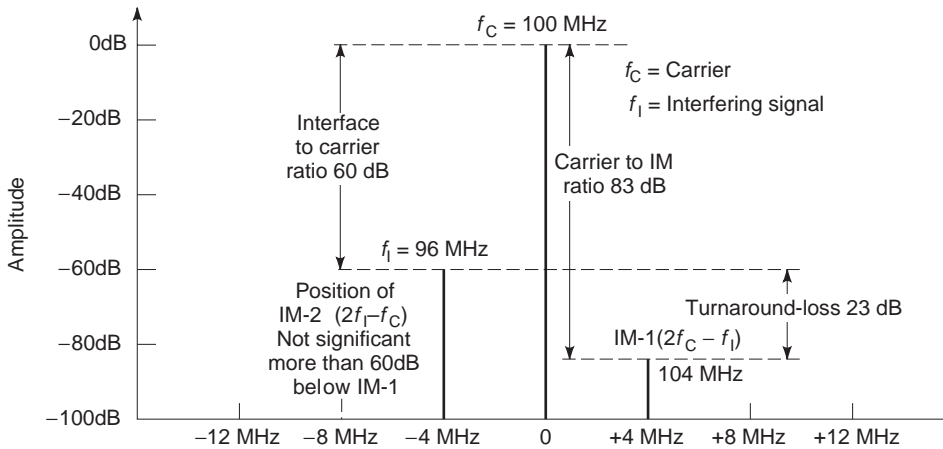


Figure 27. Typical frequency spectrum of third-order IM products of a broadcast FM transmitter.

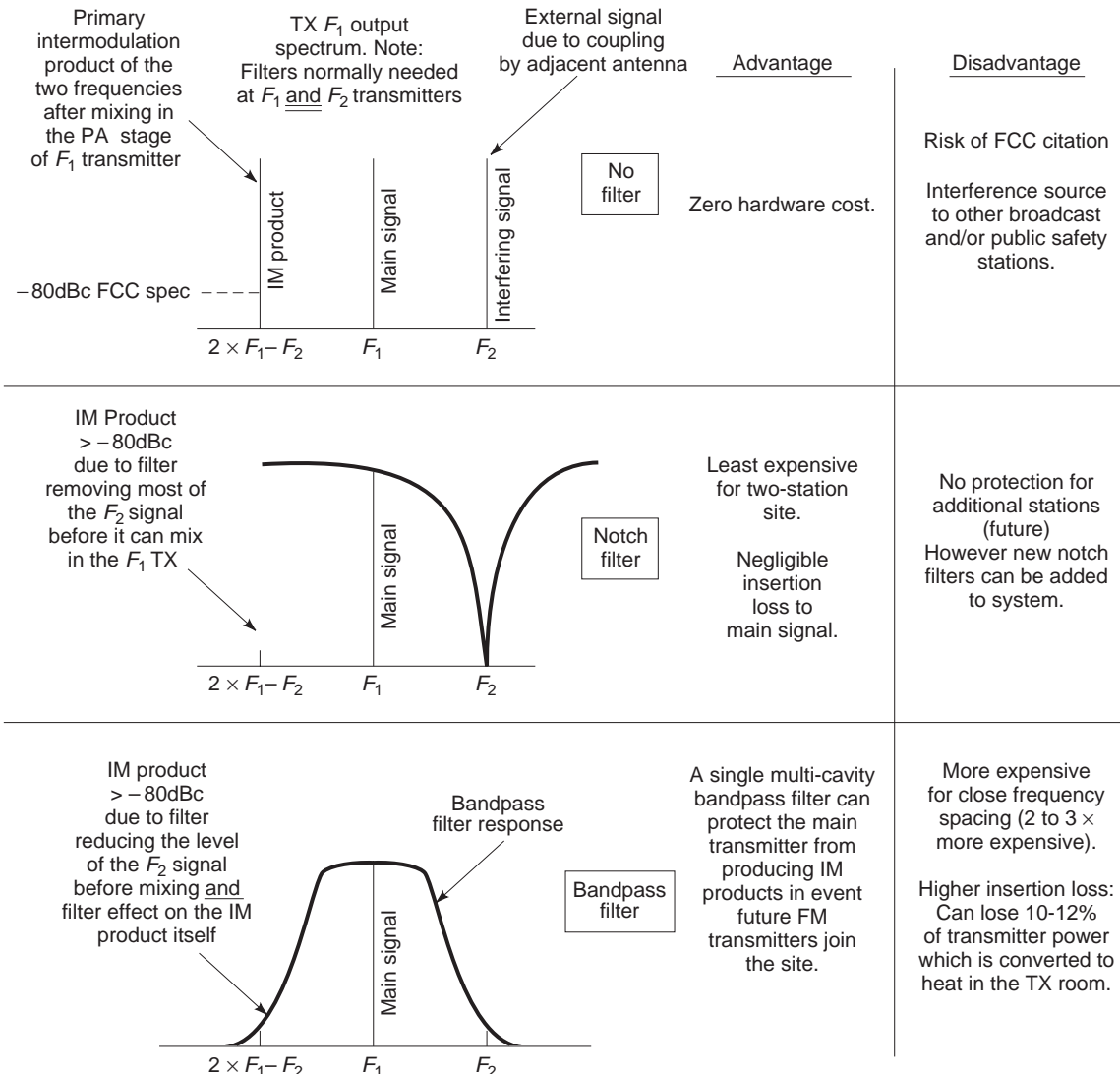


Figure 28. An overview of the various filtering options for preventing excessive IM3 products.

the third-order intermodulation (IM3) terms could be generated in the following way. The output of the first transmitter f_1 is coupled into the nonlinear output stage of the second transmitter f_2 because there is not complete isolation between the two output stages. f_1 will mix with the second harmonic of f_2 producing an in-band third-order term with a frequency of $[2(f_2) - (f_1)]$. Similarly, the other third-order term will be produced at a frequency of $[2(f_1) - (f_2)]$. This implies that the second harmonic content within each transmitter's output stage along with the specific nonlinear characteristics of the output stage will have an effect on the value of the mixing loss.

It is possible, however, to generate these same third-order terms in another way. If the difference frequency between the two transmitters $[(f_2) - (f_1)]$, which is an out-of-band frequency, remixes with either (f_1) or (f_2) , the same third-order intermodulation frequencies are produced.

Empirical measurements indicate that the $[2(f_2) - (f_1)]$ type of mechanism is the dominant mode generating third-order IM products in modern transmitters using a tuned cavity for the output network.

Figure 25 is an example of calculating intermodulation product frequencies. Figures 26 and 27 show the resulting frequency spectra.

7.7. Intermodulation As A Function of Turnaround Loss

Turnaround loss or *mixing loss* describes the phenomenon in which the interfering signal mixes with the fundamental and its harmonics within the nonlinear output device. This mixing occurs with a net conversion loss; hence, the term *turnaround loss* has become widely used to quantify the ratio of the interfering level to the resulting IM3 level. A *turnaround loss* of 10 dB means that the IM3 product fed back to the antenna system will be 10 dB below the interfering signal fed into the transmitter's output stage.

Turnaround loss increases if the interfering signal falls outside the passband of the transmitter's output circuit, varying with the frequency separation of the desired signal and the interfering signal because the interfering signal is first attenuated by the selectivity going into the nonlinear device and then the IM3 product is further attenuated as it comes back out through the frequency selective circuit.

Turnaround loss can be broken into three individual parts:

1. The basic in-band conversion loss of the nonlinear device.
2. The attenuation of the out-of-band interfering signal caused by the selectivity of the output stage.
3. The attenuation of the resulting out-of-band IMS products caused by the selectivity of the output stage.

As the *turnaround loss* increases, the level of undesirable intermodulation products is reduced, and the amount of isolation required between transmitters is also reduced.

The transmitter output circuit loading control directly affects the power amplifier source impedance and therefore

affects the efficiency of coupling the interfering signal into the output circuit where it mixes with the other frequencies present to produce IM3 products. Light loading reduces the amount of interference that enters the output circuit with a resulting increase in *turnaround loss*. In addition, the output loading control setting will change the output circuit bandwidth (loaded Q) and therefore affect the amount of attenuation that out-of-band signals will encounter passing *into* and *out of* the output circuit [18].

Second harmonic traps or lowpass filters in the transmission line of either transmitter have little effect on the generation of intermodulation products because the harmonic content of the interfering signal entering the output circuit of the transmitter has much less effect on IM3 generation than does the harmonic content within the nonlinear device. The resulting IM3 products fall within the passband of the lowpass filters and outside the reject band of the second harmonic traps. So these devices offer no attenuation to RF intermodulation products.

Figure 28 gives an overview of the various filtering options for preventing excessive IM3 products.

BIBLIOGRAPHY

1. G. N. Mendenhall, *The Composite Signal—Key to Quality FM Broadcasting*, Quincy, IL: Broadcast Electronics, 1981.
2. U. L. Rohde, *Digital PLL Synthesizers—Theory and Design*, Englewood Cliffs, NJ: Prentice-Hall, 1983.
3. E. R. Twitchell, A digital approach to an FM exciter, *IEEE Trans. Broadcast.*, 1991.
4. AES3 Technical Standard Audio Engineering Society, Inc., *AES Recommended practice for digital audio engineering—Serial transmission format for two-channel linearly represented digital audio data*. For more information, refer to: AES3-1992.
5. D. L. Bytheway, Charting a path through the maze of digital audio technology, *Broadcast Engineering Magazine*, July 1991.
6. T. W. Dittmer, *Advances in Digitally Modulated RF Systems*, Quincy, IL: Harris Corporation—Broadcast Division, 1997.
7. R. J. Fry, *Harris DIGIT FM Exciter Facts and Features*, Quincy, IL: Harris Corporation—Broadcast Division, 1995.
8. M. B. Shrestha, The Significance of RF Power Amplifier Circuit Topology on FM Modulation Performance, Quincy, IL: Broadcast Electronics, 1990.
9. E. J. Anthony, *Optimum Bandwidth for FM Transmission*, Quincy, IL: Broadcast Electronics, 1989.
10. D. Hershberger and R. Weirather, *Amplitude Bandwidth, Phase Bandwidth, Incidental AM, and Saturation Characteristics of Power Tube Cavity Amplifiers for FM*, Quincy, IL: Harris Corporation—Broadcast Division, 1982.
11. F. E. Terman, *Electronic and Radio Engineering*, 4th ed., New York: McGraw-Hill, 1955.
12. G. N. Mendenhall, *Improving FM Modulation Performance by Tuning for Symmetrical Group Delay*, Quincy, IL: Broadcast Electronics, 1991.
13. G. N. Mendenhall, *Techniques for Measuring Synchronous AM Noise in FM Transmitters*, Quincy, IL: Broadcast Electronics, 1988.
14. H. L. Krauss, C. W. Bostian, and F. H. Raab, *Solid State Radio Engineering*, New York: Wiley, 1980.

15. H. Howe, Jr., *Simplified Design of High Power, N-Way, In-Phase Power Divider/Combiners*, *Microw. J.*, December 1979.
16. Eimac, *Care and Feeding of Power Grid Tubes*, Eimac Division of Varian Corporation, San Carlos, CA, 1967.
17. A. G. Uyttendaele, *Design Requirements and Operational Features of the Gates Dualtran RF Switching System*, Quincy, IL: Harris Corporation—Broadcast Division.
18. G. N. Mendenhall, *A Study of RF Intermodulation Between FM Broadcast Transmitters Sharing Filterplexed or Co-located Antenna Systems*, Quincy, IL: Broadcast Electronics, 1983.

TRANSVERSE RESONANCE TECHNIQUES

ROBERTO SORRENTINO
 MAURO MONGIARDO
 University of Perugia
 Perugia, Italy

1. INTRODUCTION

The transverse resonance technique (TRT) can be regarded as an approach to the analysis, either rigorous or approximate, of guiding structures and their discontinuities, based on the simple idea of looking at the problem in the transverse rather than axial direction. This technique originated as an application of the microwave circuit formalism in the direction perpendicular to the actual power flow in a cylindrical waveguide, [1]. Over the years it has then been applied to evaluate the dispersion relation for the dominant mode of certain types of waveguides and also to evaluate the complete spectra of some nonseparable waveguides; more recent developments involve the modeling of discontinuities in closed or open transmission structures. Since the original concept of the TRT is now being used in a much broader sense, it is worth clarifying the basic ideas laying behind this technique.

As its name suggests, the TRT combines two different concepts. On one hand, the term *transverse* indicates, within a reference coordinate frame, a geometric direction to be preferred in contrast with the axial or longitudinal direction of propagation in a guiding structure (waveguide or other transmission line). The *resonance* concept, on the other hand, is associated with the stationary fields and the relevant reactive energy storage in a microwave structure. In the TRT, the structure under investigation may be a guiding structure, in which case its propagation characteristics are sought, or a discontinuity in a guiding structure, in which case the circuit characterization of the discontinuity (impedance, scattering parameters, etc.) are to be found. In either case, by expressing the resonance condition(s) in the transverse direction, the unknown parameters can be computed. For a number of practical geometries this approach proves to be computationally much more convenient than analyzing the structure in the axial direction.

The TRT concept will first be clarified in Section 2 with the example of simple guiding structures that can be treated analytically. The TRT will then be illustrated in

more involved cases in Section 3, where a certain degree of numerical processing becomes necessary. In the conventional formulation of TRT, a suitable transverse equivalent network is established to compute the cutoff frequencies and possibly some additional characteristics of the structure. An example of this procedure, making use of equivalent network representation of discontinuities, is illustrated in Section 3.1 by referring to a ridge waveguide. In a more elaborate and rigorous formulation, a full-wave analysis may be performed in order to find, via the dispersion equation, the modes of a nonseparable structure. Depending on whether the guiding structure is a closed or open one, different analytical formulations can be adopted. In the latter case, the approach will yield the bound (guided) modes of the waveguide, while in the former case the entire modal spectrum of the closed waveguide can be obtained. The procedure is illustrated in Section 3.2 for the computation of the slot-line spectrum.

As mentioned above, the TRT can also be applied for the characterization of discontinuities and junctions. In this case, the extraction of the discontinuity parameters is obtained by artificially inducing a resonance condition also in the longitudinal direction. The relevant procedure is briefly described in Section 4, where the characterization of circular posts in a rectangular waveguide using a hybrid mode-matching/FEM numerical technique is taken as an example.

2. TRANSVERSE RESONANCE TECHNIQUE: ANALYTICAL SOLUTIONS

2.1. Homogeneous Waveguides

To introduce the concept of transverse resonance, consider the cross section of a rectangular waveguide excited by the fundamental TE₁₀ mode (Fig. 1 depicts the wave propagation in this case); we remind the reader that the nonzero field components are E_y , H_x , and H_z . TE₁₀ mode propagation in the guide can be considered as a wave propagating with propagation constant β in the longitudinal z

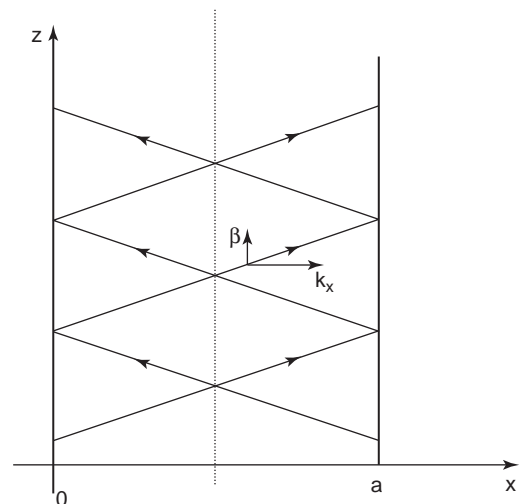


Figure 1. TE₁₀ wave propagation in a rectangular waveguide of width a .

direction, and at the same time bouncing back and forth between the sidewalls at $x=0, a$ with propagation constant k_x . Wavenumber conservation imposes that

$$k_x^2 + \beta^2 = k_0^2 \tag{1}$$

Because of the round-trip condition $k_x = n\pi/a$.

The same results for k_x can be obtained by applying the transverse resonance condition. Let us consider the network equivalent of the round-trip condition as illustrated in Fig. 2. A short circuit is located at $x=a$ and an open circuit, at the symmetry plane $x=a/2$, with a transmission-line section in between; the latter has propagation constant k_x . A TE wave propagating in the positive z direction has a characteristic impedance given by the ratio between the fields transverse to the propagation direction:

$$Z_0^z = \frac{E_y}{-H_x} = \frac{\omega\mu_0}{\beta} \tag{2}$$

This wave is also TE if we consider propagation in the x direction; the characteristic impedance of the line, in this case, is given by the following ratio:

$$Z_0^x = \frac{E_y}{H_z} = \frac{\omega\mu_0}{k_x} \tag{3}$$

In the following, unless otherwise stated, we will consider the propagation in the x direction and the x apex will be omitted in the corresponding impedance. Resonance of the transverse equivalent circuit of Fig. 2 implies that a finite voltage response V_r ensues from zero current excitation I_e

$$I_e = YV_r = 0 \tag{4}$$

or vice versa; that is, a finite current response I_r follows from zero voltage excitation V_e :

$$V_e = ZI_r = 0 \tag{5}$$

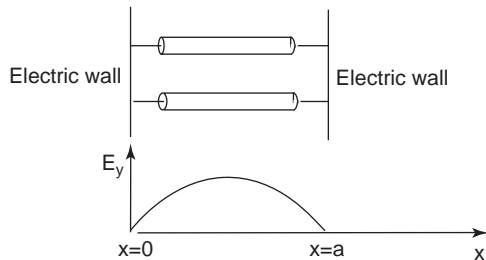


Figure 2. By symmetry, we may place a magnetic wall, namely, an open circuit, in the midplane of the guide, thus obtaining the transverse equivalent circuit for even modes in a rectangular waveguide. The transverse equivalent circuit for odd modes is obtained by replacing the magnetic wall with an electric wall. Also shown is the electric field component for the fundamental mode.

In the circuit of Fig. 3, the total impedance, calculated at the x section, is

$$\vec{Z}(x) = \vec{Z}(x) + \overleftarrow{Z}(x) \tag{6}$$

and similarly for the admittance. The arrow points according to whether we take the impedance to the left or right of the observation point. The resonance condition implies that, at any point x along the line, we must have

$$\vec{Z}(x) = \vec{Z}(x) + \overleftarrow{Z}(x) = 0 \tag{7}$$

or

$$\vec{Y}(x) = \vec{Y}(x) + \overleftarrow{Y}(x) = 0 \tag{8}$$

Observe that condition (7) implies Eq. (8) and vice versa. In fact, by noting that

$$\vec{Y}(x) + \overleftarrow{Y}(x) = \frac{\vec{Z}(x) + \overleftarrow{Z}(x)}{\vec{Z}(x)\overleftarrow{Z}(x)} \tag{9}$$

it follows that resonances occur either when (7) is satisfied, or at common poles of $\vec{Z}(x), \overleftarrow{Z}(x)$, that is, when $\vec{Z}(x) = \infty$ and $\overleftarrow{Z}(x) = \infty$.

With reference to Fig. 2, placing the observation point at $x=a$ yields

$$\vec{Z}(a) = 0 \tag{10}$$

because of the short circuit at $x=a$, while, on the left, we obtain

$$\overleftarrow{Z}(a) = \frac{j\omega\mu_0}{k_x} \tan k_x a \tag{11}$$

Hence the resonance condition implies $\tan k_x a = 0$ or

$$k_x a = n\pi \tag{12}$$

which is the same condition we found from the round-trip phase difference. This procedure, of course, can be applied

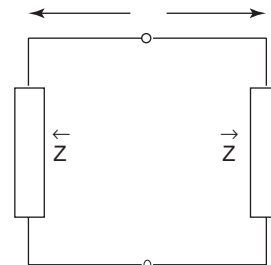


Figure 3. At any point along the line it is possible to define an impedance looking at the left side \overleftarrow{Z} and an impedance looking at the right side \vec{Z} . The zeros of the total impedance $Z = \overleftarrow{Z} + \vec{Z}$ provide the circuit resonances (in addition to the common poles of \overleftarrow{Z} and \vec{Z}).

in less trivial cases such as, for example, a waveguide filled with one or more dielectric layers or a slab waveguide, as shown in the next subsections.

2.2. Waveguides Filled with Layered Dielectrics

A rectangular waveguide loaded with one dielectric slab is sketched in Fig. 4. For such a geometry, the boundary conditions at the dielectric interface can be individually satisfied by TM^x and TE^x fields. This becomes evident if one considers the simple discontinuity due to an abrupt change in the z direction of the dielectric constant filling the guide. The cross-sectional distribution of the electromagnetic field is not altered by the change of the dielectric; the only change is in the impedance.

By adopting the transmission-line formalism to represent the field propagation along the x axis, the boundary conditions can be represented in a straightforward manner as shown in the lower part of Fig. 4. Let us recall that, for TE^x modes, the characteristic impedances of the i -th transmission line is

$$Z_0^{(i)} = \frac{j\omega\mu_0}{k_x^{(i)}} \quad (i = 1, 2) \quad (13)$$

while the wavenumber conservation imposes that

$$k_x^{(i)2} + \beta^2 = k_0^2 \epsilon_i \quad (14)$$

The total impedance seen at $x = a_1$ is given by Eq. (6), where

$$\overleftarrow{Z}(a_1) = Z_0^{(1)} \tan k_x^{(1)} a_1 \quad (15)$$

$$\overrightarrow{Z}(a_1) = Z_0^{(2)} \tan k_x^{(2)} a_2 \quad (16)$$

The resonance condition (7) $\overleftrightarrow{Z} = 0$, together with Eq. (14), provides the dispersion relation for the waveguide. The cutoff frequencies can be obtained by setting $\beta = 0$.

This approach can easily be extended to more complicated cases where several dielectric layers are present. In such cases the transmission-line formalism can highly

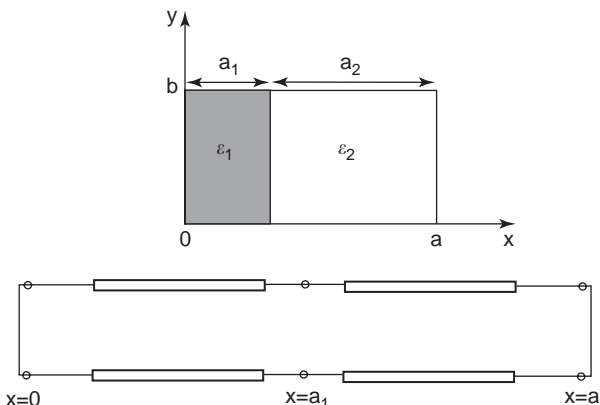


Figure 4. Sketch of a dielectric-loaded waveguide; in the lower part the transverse equivalent network is represented.

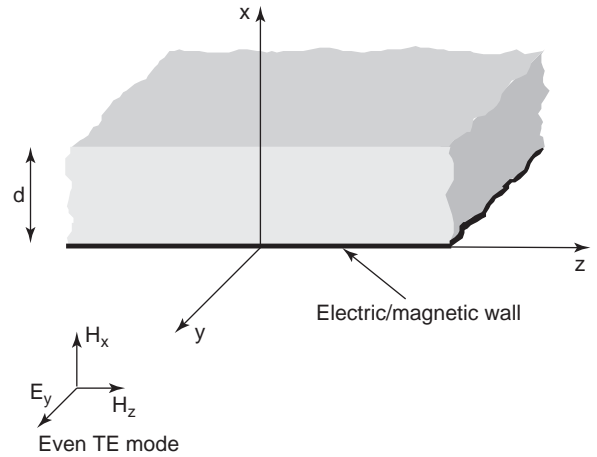


Figure 5. A TE even field for a slab waveguide. The original slab of width $2d$ has been replaced by a slab of width d over an electric/magnetic wall.

simplify the computations by adopting the ABCD representation.

2.3. Slab Waveguide

Another interesting case is the slab waveguide (Fig. 5). The equivalent network appropriate for this structure is shown in Fig. 6 for the TE mode. In the even case, a magnetic wall is placed at the symmetry plane $x = 0$. Looking from $x = d$, the impedance Z is that of a line section open-circuited at the opposite end, while \overleftarrow{Z} is that of a TE wave in free space. The transverse resonance condition (7) is thus given by

$$\overleftarrow{Z} + \overrightarrow{Z} = -j \frac{\omega\mu_0}{q_s} \cot(q_s d) + j \frac{\omega\mu_0}{\gamma_x} = 0 \quad (17)$$

where q_s and γ_x are the propagation constants in the x direction in the slab and in the air, respectively. Hence, we

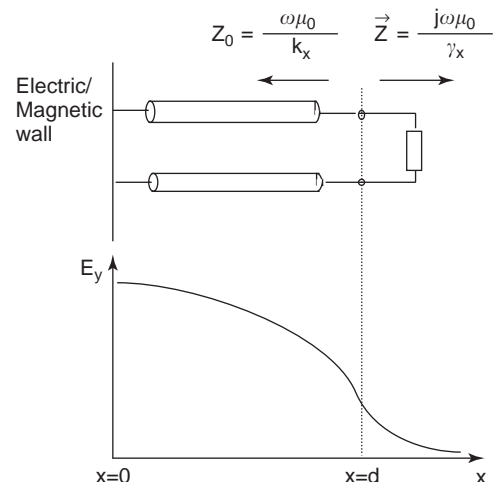


Figure 6. Equivalent network of a TE even field for a slab waveguide.

recover the dispersion relation

$$q_s \tan(q_s d) = \gamma_x \quad (18)$$

This equation is identical to that obtained by matching the fields.

Consider now the odd TE modes (electric wall at the symmetry plane $x=0$). Their x dependence is given by a sine function inside the slab and an exponential function outside. As a consequence, the total impedance seen at $x=d$ is

$$\vec{Z} = j \frac{\omega \mu_0}{q_s} \tan(q_s d) + j \frac{\omega \mu_0}{\gamma_x} = 0 \quad (19)$$

yielding the dispersion relation

$$q_s \cot q_s d = -\gamma_x \quad (20)$$

For a network interpretation of the cutoff it is instructive to consult Ref. 2, where the transverse resonance approach is also used to provide further insight into the nature of the continuous part of the spectrum.

3. TRANSVERSE RESONANCE TECHNIQUE FOR TRANSVERSELY DISCONTINUOUS WAVEGUIDES

The presence of any discontinuity in the transverse direction other than a dielectric interface perpendicular to the x or y direction would produce the coupling between different modal sets, that is, between TE^x and TM^x modes, so that the elementary solutions seen before cannot be obtained anymore. The presence of discontinuities normal to the transverse direction produces energy storage that can be taken into account by a proper lumped reactance. Once again the resonance condition of such networks provides the characteristic equation for the structure. Since the solutions for many practical discontinuity problems are available in classical textbook such as Ref. 3, the TRT proves extremely useful in providing the guide propagation properties with a minimal amount of computer effort. Naturally, this type of application of the TRT has some limitations: (1) the discontinuity must be noninteracting with the sidewall of the waveguide, (2) characterization of the discontinuity is typically available only for the fundamental mode incidence, and (3) this approach does not allow the field computation in the proximity of the discontinuity. These limitations are removed by the use of the *generalized TRT*. In Section 3.1 we will first describe the use of conventional TRT with equivalent circuits by means of the ridge waveguide example. In Section 3.2 we will describe the slotline hybrid spectrum computation by means of the generalized TRT.

3.1. Ridge Waveguide

Fig. 7 shows the cross-sectional geometry of a single-ridge waveguide whose dominant mode is a TE^z mode with even symmetry with respect to the plane $x=a/2$. Looking in the transverse x direction, the ridged waveguide is seen as a

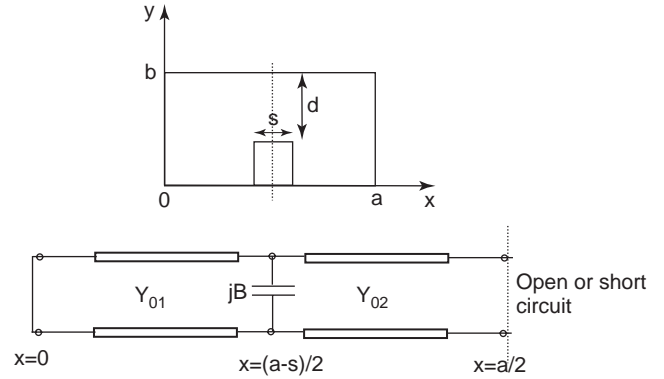


Figure 7. Single-ridge waveguide cross section and its transverse equivalent network. Use has been made of symmetry by placing an electric/magnetic wall in the midsection $x = a/2$.

composite structure consisting of waveguides of different heights. Transverse step discontinuities produce TE^x and TM^x higher-order mode excitation. In practical cases these are well below cutoff; hence they contribute only to the reactive energy stored in the proximity of the ridge edges. If characterization of these step discontinuities is possible, the TRT provides a very simple way to compute the characteristic (dispersion) equation of the structure.

For ease of explanation, let us reduce the problem to a more familiar one by assuming two dominant TE^z modes traveling in opposite directions, thus creating a standing-wave pattern. We may now insert two perfectly conducting planes normal to the z axis, spaced $\lambda_g/2$ apart, that do not alter the field distribution in the ridge waveguide. By looking in the x direction the same closed resonator is seen as the cascade of three rectangular waveguides; the central one is of reduced height. By using symmetry and an appropriate equivalent network representation for the step discontinuity, we can obtain the equivalent circuit shown in Fig. 7. The shunt capacitance (susceptance B) accounts for the reactive energy associated with stray field at the discontinuity; a simple expression for the susceptance B can be found in Ref. 3. The transmission-line sections correspond to TE_{10}^x modes in the two waveguide sections having the same width $\lambda_g/2 = \pi/\beta$ and are therefore characterized by the same propagation constant

$$k_x^2 = k_0^2 - \beta^2 \quad (21)$$

where β is the longitudinal propagation constant. Characteristic impedances are chosen to be proportional to the waveguide heights. Because of symmetry considerations, in the transverse equivalent circuit an open- or short-circuit condition is established at $x = a/2$. In particular, the open-circuit condition (magnetic wall) provides the lowest resonance (fundamental mode). The resonance condition can be simply obtained by equating to zero the sum of the three admittances seen at the connection $x = (a-s)/2$ between the lines:

$$-jY_{01} \cot \frac{k_x(a-s)}{2} + jB + jY_{02} \tan \frac{k_x s}{2} = 0 \quad (22)$$

By using the fact that $Y_{02}/Y_{01} = b/d$ we obtain the dispersion equation for the ridge waveguide

$$\frac{b}{d} \tan \frac{k_x s}{2} - \cot \frac{k_x(a-s)}{2} + \frac{B}{Y_{01}} = 0 \quad (23)$$

It is worth noting that the analysis above could also be carried out at cutoff condition, when $\beta = 0$. In this case the problem would be that of a parallel-plate waveguide discontinuity. This type of technique can be used for semi-open waveguiding structures, slotted rectangular and circular waveguides, open groove guides, or other structures of interest in leaky-wave antennas.

3.2. Slotline Hybrid Modes

The TRT can also be applied in a rigorous manner in order to determine the spectrum of closed or open waveguides with nonseparable cross sections. We can, in fact, expand the transverse field at an interface in terms of two components (in turn each component will be expanded on a suitable basis). In addition we can also set up a rigorous relationship between the electric and magnetic transverse fields, hence obtaining a rigorous formulation.

As an example, we consider the fully hybrid problem of slotline characterization by application of the generalized TRT. We refer the reader to Refs. 1 and 2 for the analytical details relative to the closed and open configurations, respectively. Here we provide only the general framework.

The slotline geometry is shown in Fig. 8. With reference to this figure, from the continuity of the transverse-to-y electric and magnetic fields across the slot, we obtain a pair of coupled integral equations for E_x and E_z on the slot aperture in the form:

$$\begin{bmatrix} H_z \\ H_x \end{bmatrix} = \begin{bmatrix} \hat{Y}_{11} & \hat{Y}_{12} \\ \hat{Y}_{21} & \hat{Y}_{22} \end{bmatrix} \cdot \begin{bmatrix} E_x(x, 0) \\ E_z(x, 0) \end{bmatrix} = 0 \quad (24)$$

The integral operators \hat{Y} , for instance, denote the sum of the admittance operators of the two half spaces

$$\hat{Y}_{11} = \hat{Y}_{11}^a + \hat{Y}_{11}^s$$

where the “a” superscript stands for air half-space ($y > 0$) and the “s” superscript stands for substrate region ($y < 0$). The relative kernels are obtained as described, for example,

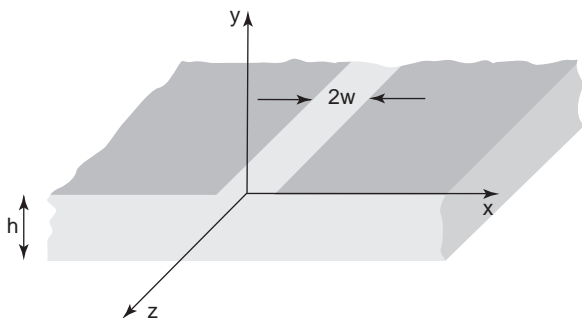


Figure 8. Slotline geometry and relative coordinate system.

in Ref. 2 for the open slotline. The integral operators \hat{Y}_{ij} play the same role as Y in Eq. (7). They represent the sum of the admittance operators of the two half-spaces \hat{Y}_{ij}^a and \hat{Y}_{ij}^s , which are the operator equivalent of Y and \hat{Y} in Eq. (7).

The integral equation (24) is the dispersion equation for the slotline discrete modes, which we solve by discretization in the space domain. By making use of the moment method approach, the integral equation (24) is reduced to the following matrix equation

$$\begin{bmatrix} \mathbf{Y}_{11}(\beta) & \mathbf{Y}_{12}(\beta) \\ \mathbf{Y}_{21}(\beta) & \mathbf{Y}_{22}(\beta) \end{bmatrix} \begin{bmatrix} \mathbf{X} \\ \mathbf{Z} \end{bmatrix} = 0 \quad (25)$$

where \mathbf{X} and \mathbf{Z} are vectors containing the electric field expansion coefficients. The vanishing of the determinant of (25) is therefore the generalization of Eq. (7); it gives the propagation constant β of the guide, whereas \mathbf{X} and \mathbf{Z} yield the transverse field distributions within a normalization constant that is fixed by the transverse normalization of the fields.

4. TRANSVERSE RESONANCE ANALYSIS FOR WAVEGUIDE DISCONTINUITIES AND JUNCTIONS

In the previous section we showed how to evaluate the propagation characteristics of a transversely discontinuous waveguide (e.g., a ridge waveguide): the resonant frequencies of a waveguide section are computed from knowledge of the equivalent transverse network and the network characterization of the discontinuity.

In this section we show how to derive the network characterization of a longitudinal discontinuity from the knowledge of the resonant frequencies of a waveguide section containing the discontinuity, using a transverse field formulation. Such a generalization of the TRT is a rigorous useful tool for characterization of a variety of discontinuity problems.

The method consists schematically of the following steps:

1. A resonant cavity is created by enclosing the discontinuity or junction by auxiliary reactive walls sufficiently apart from it.
2. A field analysis based on transverse field formulation is performed to compute the resonant frequencies and the corresponding field distributions.
3. The network matrix representation (scattering matrix, impedance matrix, etc.) of the discontinuity is evaluated by means of the resonant frequencies and/or field distributions.

It is noted that the determination of the equivalent circuit parameters of a two-port network via the resonant frequencies of the network inserted between two reactive terminations is equivalent to the experimental technique known as the tangent or Weissfloch method [3]. Analytical formulations based on a variational approach have also been presented [4].

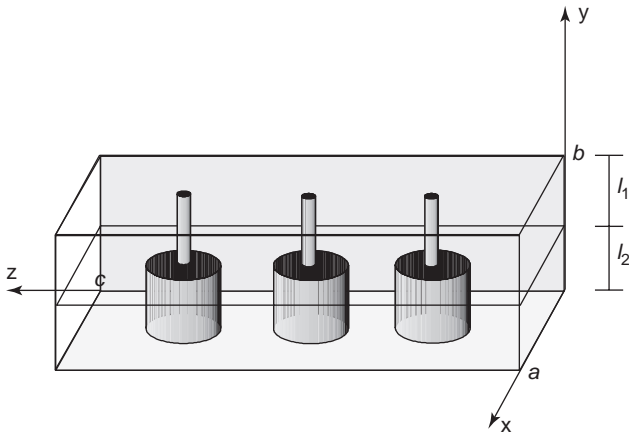


Figure 9. Example of a structure to be simulated. The propagation direction is along the x axis.

This technique was used in Ref. 5 for characterization of finline discontinuities and is reported with a detailed example also in Ref. 1.

A more recent development of the technique is shown next as an example, this time using a hybrid technique, namely, a FEM modal analysis, for the electromagnetic analysis of the structure.

4.1. Example Based on Finite-Element/Modal Analysis Computations

This method is based on the use of the hybrid finite-element/mode-matching analysis and application of the TRT for evaluating the frequency response of the device under analysis from its natural resonances. Let us consider the structure in Fig. 9, which consists of a rectangular waveguide containing three circular posts, each post having two different diameters. The direction of propagation is assumed along the z axis. In order to avoid a time-consuming three-dimensional analysis, we analyze such a structure along the transverse direction (y axis). Input and output ports ($z=0$ and $z=c$) are terminated by metallic walls, obtaining a resonant cavity. Referring to Fig. 10, such a resonator can be seen, in the transverse y direction, as a waveguide step in which ports at $y=0$ and $y=b$ are short-circuited. The scattering matrix of the

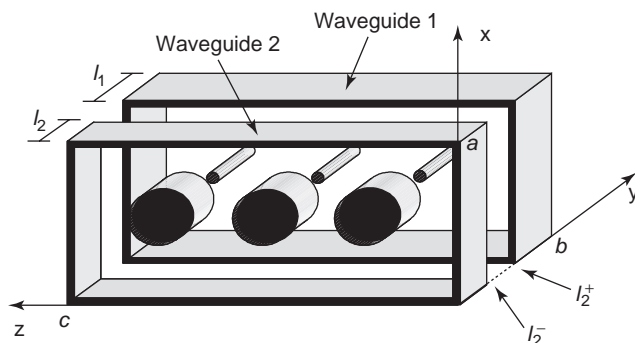


Figure 10. Example of a structure to be simulated. The direction of propagation is along the x axis, but we analyze such a structure with a mode matching along the z axis.

waveguide step at $y=l_2$ can be evaluated using the mode-matching technique. The application of the mode-matching technique requires the evaluation of the coupling integrals

$$g_{n,m} = \iint_{\mathcal{S}_2} \mathbf{e}_n^{(1)}(x,z) \cdot \mathbf{e}_m^{(2)}(x,z) dx dz \quad (26)$$

where $\mathbf{e}_k^{(i)}(x,z)$ represents the transverse normalized modal electric field of the k th mode in the i th waveguide, while \mathcal{S}_2 is the transverse section of the waveguide with smallest cross-sectional area (waveguide 2). As the waveguide cross sections are nonseparable, waveguide modes are evaluated by using a two-dimensional finite-element method. A step-by-step procedure is summarized as follows (see Ref. 6 for further details and Fig. 11 for reference planes):

1. Insert shorting planes at distances d_1 and d_2 away from the reference planes 1 and 2.
2. Evaluate the resonant modes and corresponding field distributions at the reference planes in the frequency range where only the waveguide fundamental mode is propagating. The resonant modes frequencies of the cavity are the frequencies of our analysis.
3. Evaluate the characteristic admittance y_c and the propagation constant β of the input and output waveguides at the abovementioned frequencies.
4. By using the computed modal voltages and currents, solve the following system:

$$\begin{aligned} \begin{bmatrix} I_1 \\ I_2 \end{bmatrix} &= \begin{bmatrix} Y_{11} & Y_{12} \\ Y_{12} & Y_{11} \end{bmatrix} \begin{bmatrix} V_1 \\ V_2 \end{bmatrix} \\ &= \begin{bmatrix} V_1 & V_2 \\ V_2 & V_1 \end{bmatrix} \begin{bmatrix} Y_{11} \\ Y_{12} \end{bmatrix} \end{aligned} \quad (27)$$

hence obtaining the sought values for Y_{11}, Y_{12} . Note that we have considered a symmetric and

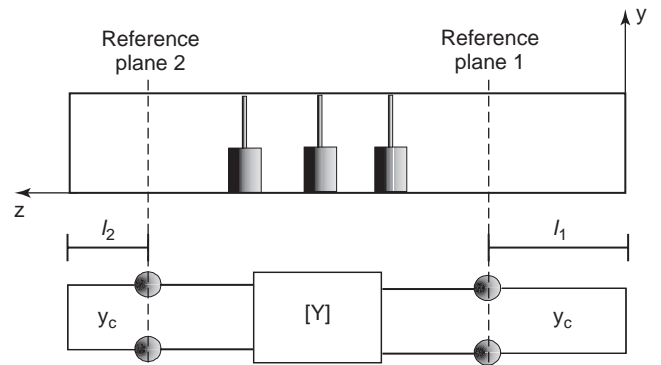


Figure 11. The device and its equivalent network (admittance representation) at the reference planes. Both device and equivalent circuit are short-circuited at distances d_1 and d_2 from ports 1 and 2, respectively.

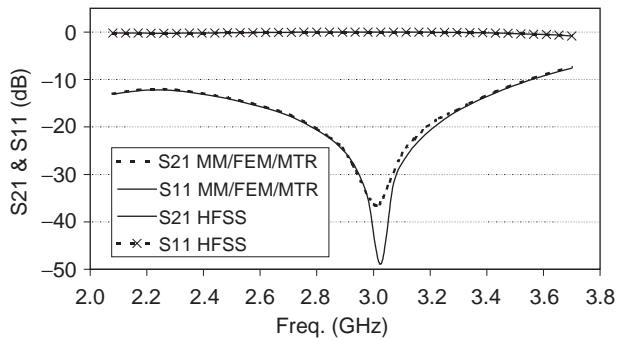


Figure 12. Scattering parameters of a circular post in rectangular waveguide. Comparison between our data and those obtained by a 3D FEM [high-frequency structure simulator (HFSS)] (MTR=modified transverse resonance) [7].

reciprocal component: $Y_{11} = Y_{22}$ and $Y_{21} = Y_{12}$. Also observe that we need $V_1 \neq V_2$ for solving the system in (27).

5. For other frequency points, repeat the whole procedure by performing another finite-element/modal analysis by changing d_1 or d_2 or both of them.

As an example of application of the method described above, consider a single circular metallic post of radius $r = 5.64$ mm and height $h = 30.6$ mm inside a rectangular waveguide with the broad wall $a = 80$ mm and the narrow wall $b = 40$ mm. Note that analysis of this structure requires, with the present method, only the solution of a two-dimensional problem: finding the modes of the waveguides. By contrast, a typical solver considers the structure as three-dimensional, hence significantly increasing the operation count. This fact becomes more relevant as the geometric dimensions of the structure are increased. In the present case a discretization with about 1200 triangles has been used in order to find the modes with sufficient accuracy. By performing just six analyses it was possible to generate the results in the frequency band shown in Fig. 12. Results obtained by TRT have been compared with those obtained by a 3D FEM, as obtained by about 40 frequency analyses, as illustrated in Fig. 12.

BIBLIOGRAPHY

1. R. Sorrentino, Transverse resonance technique, in T. Itoh, ed., *Numerical Techniques for Microwave and Millimeter-Wave Passive Structures*, Wiley, New York, 1989.
2. T. Rozzi and M. Mongiardo, *Open Electromagnetic Waveguides*, IEE, London, 1997.
3. N. Marcuvitz, *Waveguide Handbook*, McGraw-Hill, New York, 1951.
4. R. E. Collin, *Field Theory of Guided Waves*, IEEE Press, New York, 1991.
5. R. Sorrentino and T. Itoh, Transverse resonance analysis of finline discontinuities, *IEEE Trans. Microwave Theory Tech.* **32**:1633–1638 (Dec. 1984).
6. V. Crino, M. Mongiardo, and C. Tomassoni, Efficient CAD of a class of waveguide discontinuities via an hybrid finite-

element/mode-matching and modified transverse-resonance analysis, *Proc. Int. Microwave Theory and Techniques Symp.*, Philadelphia, 2003.

7. HFSS, in *Ansoft*, Pittsburgh, PA, 2002.

TRAVELING WAVE ANTENNAS

ROD B. WATERHOUSE
Pharad LLC

1. INTRODUCTION

Probably one of the most diversified styles of antennas is a traveling wave antenna. From the IEEE Standard Definitions of Terms for Antennas (IEEE Std 145-1983) [1], traveling wave antennas are defined as, “an antenna whose excitation has a quasi-uniform progressive phase, as a result of a single feeding wave traversing its length in one direction only.” Thus any antenna that relies on this mechanism to radiate falls into this class, and as you can imagine, a plethora of antennas exist that do so. Examples include beverage antennas, horn antennas, reflectors, tapered slot antennas, and lens antennas. A more simplified interpretation of the above IEEE standard definition, which is not necessarily valid for all forms of traveling wave antennas, is that this form of radiator converts guided electromagnetic energy into radiated energy in a gradual or smooth transition. An example of a traveling wave antenna, whose form is obviously compliant with this statement, is a horn antenna where the flange of the waveguide is gradually opened to effectively match the impedance/mode of the guided wave to that of free space. Thus expanding this postulation on the nature of traveling wave antennas, one can almost make the statement that two fundamental forms of antennas exist; resonant and nonresonant (traveling wave) styles. Resonant antennas (also referred to as standing wave antennas) include dipoles, monopoles, microstrip patches, and slots, and are defined as [1], “antennas whose excitation is essentially equiphase, as the result of two feeding waves which traverse its length in opposite directions, their combined effect being that of a standing wave.” So, using these definitions we can make some generalizations that may help distinguish these classes of antennas. Traveling antennas tend to be electrically large (the size with respect to the wavelength of operation), whereas resonant antennas tend to be much smaller, as these antenna are usually operated at their lowest resonant mode. Thus versions of resonant antennas tend to be incorporated into applications where size is an issue, for example mobile/wireless communication terminals and scanning arrays (where grating lobes need to be avoided to ensure a highly efficient solution). On the other hand, traveling wave antennas generally give a better electromagnetic solution than their resonant counterpart, whether it be higher gain, larger impedance bandwidth, or more linear phase, and

therefore are applied in the more “high end” problems where the electromagnetic performance cannot be compromised: radio astronomy, ground penetration radar, and wideband scanning arrays. One can almost think of the comparison between the two classes of radiators as comparing a Volkswagen to a Rolls Royce, or in today’s culture, a Jeep to a Hummer.

Of course, once you draw a line in the sand, a certain grey/blurred zone associated with the demarcation exists. This issue is evident here as many traveling wave antennas incorporate resonant style antennas within their structure. Reflector and lens antennas commonly use dipoles (and patches) as their feeding elements. Yagi Uda antennas (TV antennas before cable and satellite services) also use resonant elements to achieve their appropriate responses. Simplistically, all these antennas on the macroscale are traveling wave antennas in that they are compliant with the aforementioned definition, namely they have a single feeding wave traversing its length in one direction only; however, on the microscale they rely on a standing wave antenna to help perform this function. Log periodic and spiral antennas further blur this definition.

In this article, we will review traveling wave antennas. We will briefly investigate the general characteristics of several versions of this class of antenna. We will summarize the physical layout and performance of wire (Section 2), waveguide (Section 3), reflector and lens (Section 4) traveling wave antennas, in particular looking at the general responses and some design strategies. In Section 5, we will look at some printed versions of traveling wave antennas, focusing on tapered slots, printed beverage antennas, printed quasi Yagi Uda, antennas, and reflectarrays. The objective of this article is to give the reader an overview of this antenna technology. More detail on the various traveling wave antennas presented can be found in the given references, and the reader is encouraged to read these to obtain a more complete understanding on the topics.

2. WIRE ANTENNAS

Probably one of the easiest traveling wave antennas to visualize the above mentioned definition is the Beverage, or long wire or wave, antenna. The antenna was invented in the early 1920s by Harold Beverage and variations of this form of radiator are very common, in particular in the MF (300 KHz–3 MHz) and HF (3–30 MHz) ranges. A simple schematic of the long wire antenna is shown in Fig. 1. In Fig. 1, a long wire mounted above the ground is excited at its leftmost point and terminated at the other end. Here, the antenna is designed to have uniform patterns in both current and voltage. To achieve this pattern, the wire antenna must be appropriately terminated to ensure no reflections occur. The length of this antenna ranges from one to many wavelengths. Several design parameters of the Beverage antenna exist that impact its response: the characteristics and dimensions of the material used to create the wire, the height of the antenna above ground, and the termination of the antenna. To achieve an “ideal” traveling wave response, this termination must be

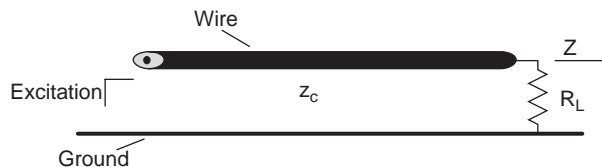


Figure 1. Schematic of a wire beverage antenna.

matched to that of the impedance of the transmission line, or the long wire. Doing so will prevent reflections at the end of the wire and thereby reduce the likelihood of standing wave effects in both the radiation patterns and the impedance response of the antenna. However, as a consequence, these antennas do suffer from relatively low efficiencies as power is dumped into the load. In some cases, if the antenna is long enough, then much of the injected power may have leaked from the wire by the time the wave reaches the end of the wire, and so a termination may not be required. For more detail on this form of antenna, please refer to [2,3].

A variation of the long wire antenna that can overcome several of its shortcomings is the V-antenna, which can be formed by using two wires each with one of their ends connected to a feedline. A schematic showing an aerial view of this concept is shown in Fig. 2a. To maximize the directivity of this antenna, smaller included angles (θ) are required for longer V’s (L). To ensure a traveling wave response for this antenna, once again proper termination is required. One way to achieve this is to attach a load (equal to the open-end characteristic impedance of the V-wire transmission line). Another option (shown in Fig. 2b) is to terminate each wire to ground via an impedance of half of that of the characteristic impedance. Typical θ ’s and L ’s range from 30–80° and 1–3 λ_0 , respectively. For more details on this form of wire traveling wave antenna, please refer to [2,4]. Two V antennas can be connected at their ends to form a rhombic antenna [2,5,6]. The antenna is typically terminated with a 600–800 Ω resistor to minimize reflections, as shown in Fig. 3a. A common version of the rhombic antenna is shown in Fig. 3b, the inverted V antenna. The inverted V antenna is connected to ground via a resistor. The patterns and responses of all these

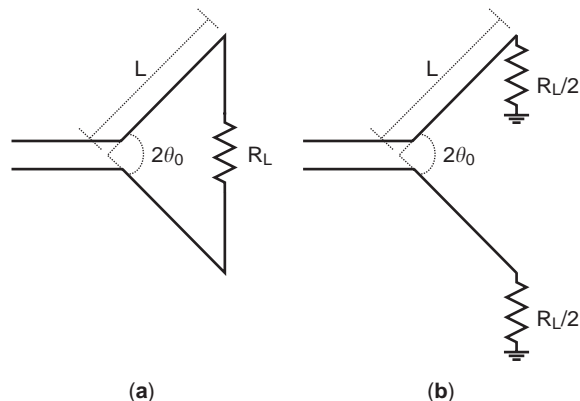


Figure 2. Schematic of terminated V antennas: (a) not grounded; (b) grounded.

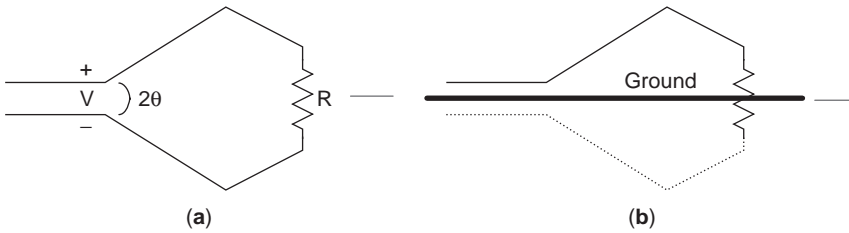


Figure 3. Schematic of rhombic antennas: (a) formed by 2V antennas; (b) inverted V antenna.

variations of the V antenna can be controlled by varying the element lengths and the angles between the elements.

A very well established traveling wave wire antenna is the endfire helix (for examples, see [2,7]). The helix is an antenna that can actually be both resonant and nonresonant, depending on its electrical length. Short helices (normal mode) are resonant in nature as opposed to endfire (or axial mode) helices, which are electrically long and can readily provide circular polarization over a wide bandwidth (VSWR <2:1). For this reason, endfire helix antennas are commonly used for satellite communications. A schematic of an endfire helix is shown in Fig. 4. Here, the wire antenna is fed by a coaxial cable where the inner conductor is extended beyond the edge of the outer conductor. The outer conductor is connected to a groundplane of the antenna that is typically $\lambda/2$ in diameter. The helix consists of N turns of diameter D and spacing S between each turn. The total length of the antenna is $L=NS$. Another important parameter of a helix is the pitch angle, α , which is the angle formed by a line tangent to the helix wire and a plane perpendicular to the helix axis. For the endfire helix, one major lobe exists and its maximum radiation intensity is directed along the axis of the helix. To ensure the helix works in this mode of operation, the D and S must be large fractions of the wavelength. To

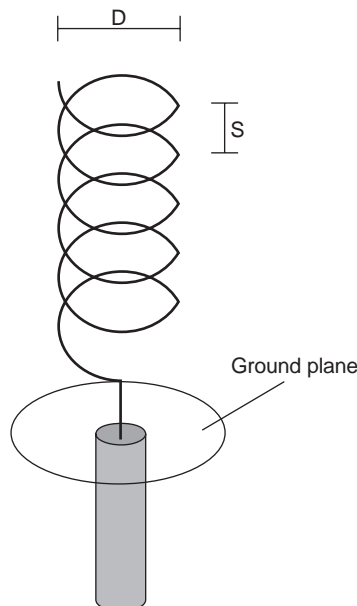


Figure 4. Schematic of an endfire helix antenna.

achieve circular polarization, the circumference of the helix with respect to wavelength should be near unity and S should be approximately quarter-wave. α should be approximately $12\text{--}14^\circ$.

Another very common traveling wave wire antenna is the Yagi Uda antenna [8]. These antennas are commonly used in the high frequency (HF), very high frequency (VHF), and ultra-high frequency (UHF) ranges. The antenna consists of a number of linear dipole elements, one of which is fed by a transmission line and the others act as parasitic radiators via mutual coupling. Figure 5 shows a schematic of a wire Yagi Uda antenna, where the parasitic elements in the forward direction (to the right of the driven element) act as directors and the elements in the rear behave as reflectors, and so the overall structure can be thought of as a traveling wave antenna. The driven element is typically of the order of 0.5λ . The director elements are usually $0.4\text{--}0.45 \lambda$ in length and can be of different size. The spacing between these elements is usually of the order of $0.3\text{--}0.4 \lambda$, although this may not always be the case. The length of the reflector element is greater than the fed element and is typically spaced approximately 0.25λ from the driven element. An excellent review of wire Yagi Uda antennas, including design procedures, can be found in [2].

3. WAVEGUIDE ANTENNAS

Probably the most widespread moderate gain traveling wave antenna in the microwave frequency range is the horn antenna [9]. Schematics depicting four types of horns

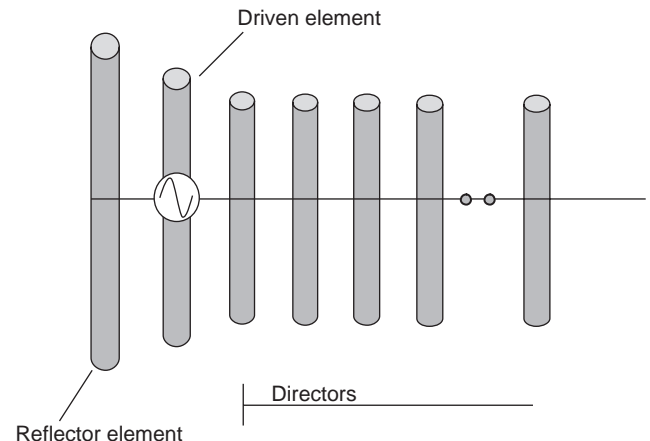


Figure 5. Schematic of a wire Yagi Uda antenna.

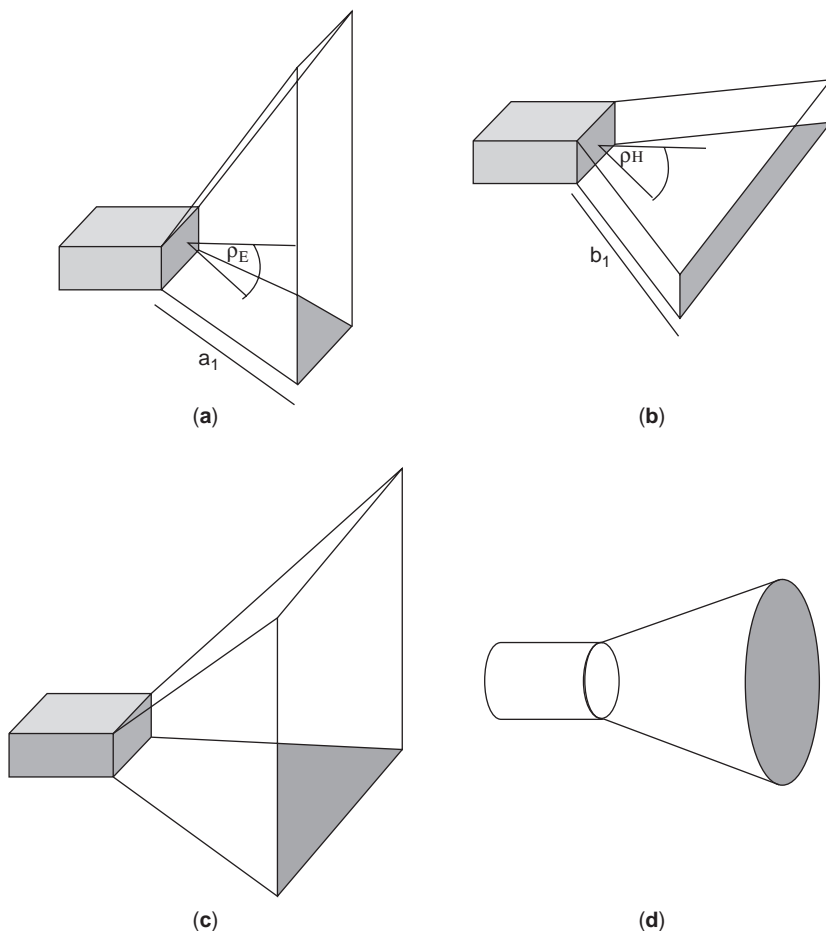


Figure 6. Schematics of conventional horn antennas: (a) E-plane; (b) H-plane; (c) Pyramidal, (d) Conical.

are shown in Fig. 6. As mentioned before, a horn antenna consists of a waveguide (typically rectangular or circular), which is then tapered (or flared) to a larger opening. The type, direction, and amount of flare can greatly impact the performance of the antenna. The four horns shown in Fig. 6 are: the E-plane horn, where the dimensions of the side walls of the waveguide remain constant whereas the top and bottom walls are flared to the appropriate angle; the H-plane horn, where the dimensions of the top and bottom walls are kept constant and the side walls are tapered; the pyramidal horn, a combination of the E-plane and H-plane horns; and the conical horn, where a circular waveguide is flared to a larger opening. Horn antennas became of intense interest in the late 1930s for radar applications because of their relative ease in design as well as their superior power handling capabilities. Nowadays, variations of the horn antenna are used in many applications ranging from feeds for radio astronomy to gain standards for accurate gain measurements of antennas.

Pyramidal horns are the most common form of horn antenna [2]. The design parameters of this antenna are the E- and H-plane aperture dimensions a_1 and b_1 , respectively) and the E- and H-plane axial horn lengths (ρ_E and ρ_H , respectively). Intuitively, as the a_1 and b_1 are increased (for constant lengths), the directivity of antenna should increase. The same should hold for increase of the

axial horn lengths while maintaining the aperture dimensions. These trends do hold to a degree until phase errors associated with the different path lengths the wave travels from the apex of the horn to the aperture distort the patterns. As the axial horn lengths increase (keeping the aperture dimensions constant), the phase errors decrease, whereas as the aperture dimensions increase (keeping the horn lengths constant), the phase errors increase. One means to mitigate the phase error issue is to use an exponential taper, as opposed to a linear taper. A photograph of such a pyramidal horn is shown in Fig. 7 [10].

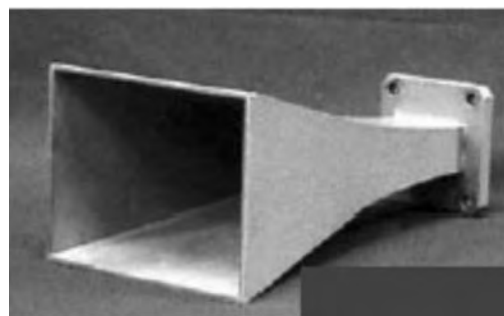


Figure 7. Photograph of a pyramidal horn antenna.

Another frequently used horn antenna is the conical horn [11], which, unlike the pyramidal horn antenna, is fed with a circular waveguide. One obvious feature of the conical horn is the ease in which this antenna can generate dual/circular polarization, essential for satellite communications. The performance of a conical horn is similar to that of a pyramidal horn: as the flare angle increases, the directivity for a given axial length increases until it reaches a maximum beyond which it starts to degrade. Once again the degradation is because of the dominance of the phase error at the aperture.

As the applications for horn antennas grew in the 1960s and 1970s, it was apparent that the overall performance of these waveguide-based antennas needed to be improved. In particular, horn antennas suffered from spillover loss, cross-polarization generation, and impedance mismatch with respect to the feeding waveguide. It was found that the origin of these problems stemmed from diffraction from the aperture of the antenna. Two techniques were proposed and successfully demonstrated to mitigate these issues: the corrugated horn antenna [12,13] and the aperture-matched horn antenna [14]. A corrugated horn applies the principal that a corrugated surface can produce the same boundary conditions for both the electric and magnetic fields, thereby making the radiation pattern symmetrical. A photograph of an array of circular aperture corrugated horns used to feed a radio astronomy reflector is shown in Fig. 8. An aperture-matched horn consists of a smooth curved surface section connected to

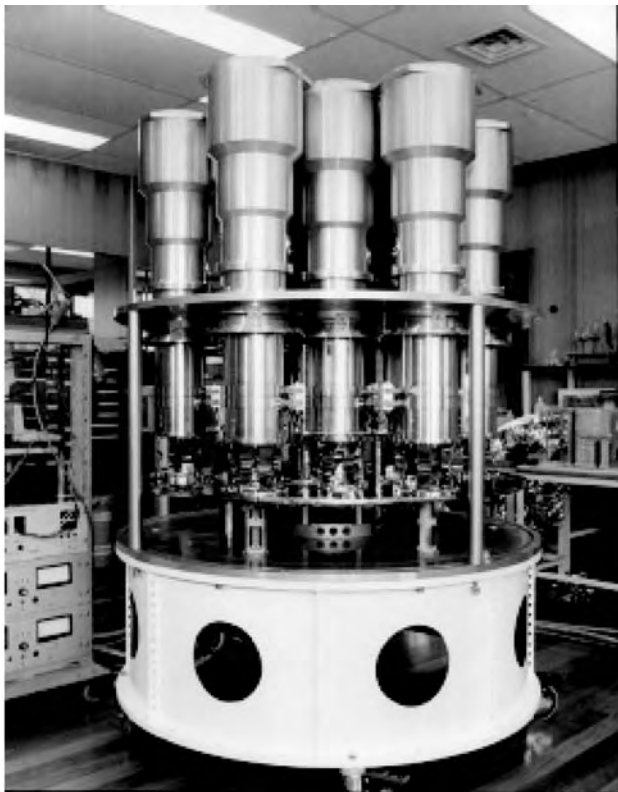


Figure 8. Photograph of an array of circular aperture corrugated horns.

the outside of the aperture. This section provides continuous matching sections between the horn modes and free-space radiation and therefore can reduce the previously encountered diffraction problems of conventional horn antennas. An excellent review on horn antennas, including the theory of operation, can be found in [2].

4. REFLECTORS AND LENS ANTENNAS

The previously considered traveling wave antennas (with the exception of the Yagi Uda antenna) have a guided medium excitation. There are two types of antennas that still have traveling wave antenna traits; however, they are typically excited by a feed radiator. The two types of antennas are reflectors [15–17] and lenses [18,19]. Reflector antennas are extremely prevalent in today's communications (both satellite and terrestrial) and radio astronomy solutions. Reflector antennas are typically used when a high-gain solution is required as large arrays of other forms of radiating elements suffer from feed losses when attempting to develop a high-gain antenna. Of the many different shapes a reflector may have, the parabolic reflector is probably the most prevalent. A schematic of this antenna (a front-fed parabolic reflector) is shown in Fig. 9, highlighting the important design parameters: the diameter of the reflector (D) and the f/D ratio (where f is the focal point). There are some very simple relationships that can be established here: as the diameter of the reflector increases, so does the gain; as the f/D ratio increases, the lower the amplitude taper loss and phase loss, however, the greater the spillover loss. These f/D ratio relationships will depend on the radiation characteristics of the feed antenna. A photograph of a millimeter-wave (mm-wave) front-fed parabolic reflector is shown in Fig. 10. The choice of D (and f/D for that matter) really depends on how much gain is required for the system and also how much space is available for the antenna platform. For example, for a gain of 35 dBi, a reflector of diameter $21 \lambda_0$ is required for an f/D of 0.44. A problem with the front-fed reflector is the decrease in efficiency because of blockage (and cross-polarization generation) created by the feed antenna and the subsequent transmitter and receiver circuitry. To reduce the blockage, the circuitry can be located behind the

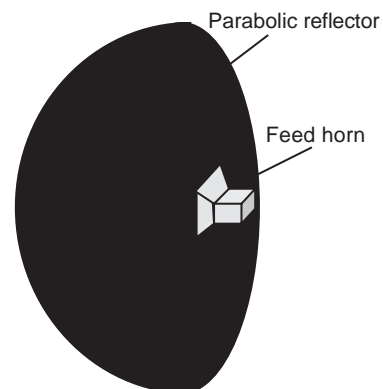


Figure 9. Schematic of a front-fed parabolic reflector.

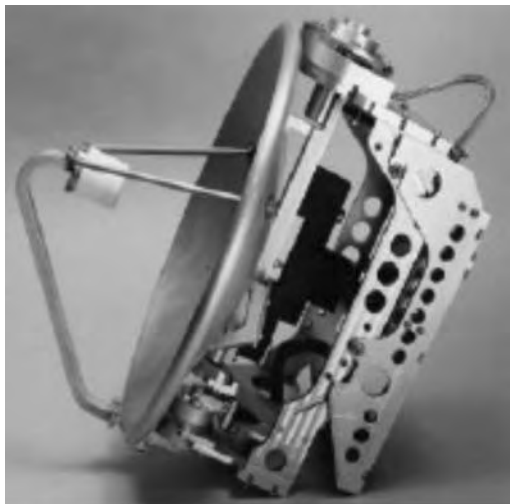


Figure 10. Photograph of a mm-wave front-fed parabolic reflector.

reflector; however, the loss in the transmission lines to the feed antenna located at the focal point can be an issue. To overcome this problem, Cassegrain feeds (named after the astronomer) were introduced. Here, a secondary reflector (or subreflector), typically hyperbola in shape, is illuminated by a conveniently located feed antenna, and then this reflector excites the parabolic reflector (see for example [20]). Cassegrain feeding techniques are typically 10% more efficient than the front-fed procedure. In fact, the Cassegrain arrangement has the following features: the ability to place the feed in a convenient location; the reduction of spillover and sidelobe radiation; the ability to obtain an equivalent focal length much greater than the physical length; and the capability for scanning the main beam by moving one of the reflecting surfaces. A photograph of a variation of a Cassegrain feed arrangement and parabolic reflector is shown in Fig. 11. There are numerous review articles on reflector-style antennas, and some can be found in [2,15–17].

Another traveling wave antenna with an optical origin is the lens antenna. Lens antennas are an alternative to reflector antennas, although they are only really practical at very high frequencies, well into the mm-wave frequency band and beyond. Below these frequencies the size and weight associated with the lens material become too large if a high-gain solution is required. Lens antennas have similar advantages as reflectors over large arrays, namely the feed loss can be very low. It is well known that elliptical shaped lenses can focus a planewave to a point; however, in practice, typically extended hemispherical lenses are used to synthesize an elliptical lens [19,21–23]. Figure 12 shows the parameters of an extended hemispherical lens, the radius of the hemisphere (R_L), and the length of the extension (L_L). These dimensions are dependent on the material used to realize the lens, however, in general, the larger the R_L and L_L , the more gain. For example, for a gain of 32 dBi, R_L is approximately $6 \lambda_0$ and L_L is approximately $8 \lambda_0$. In a lens



Figure 11. Photograph of a Cassegrain feed arrangement and parabolic reflectors.

antenna configuration, reflections from the lens/air interface can cause unwanted radiation in the form of increased cross-polarization levels as well as increased sidelobe levels. A coating can be used on the interface to help reduce this effect similar to what is used on Light Emitting Diodes; however, at microwave (and even millimeter-wave) frequencies, this is impractical. Figure 13 shows a photograph of a mm-wave lens antenna designed for operation between 26–40 GHz [24]. The traveling wave antenna is fed by an aperture stacked patch (ASP) of sufficient bandwidth. The layers used to develop the ASP have a similar dielectric constant to that used for the creation of the lens (polyethylene) to ensure the overall efficiency of the antenna is maximized. Several reported articles exist on lens antennas that are available in the literature (for example, [18]).

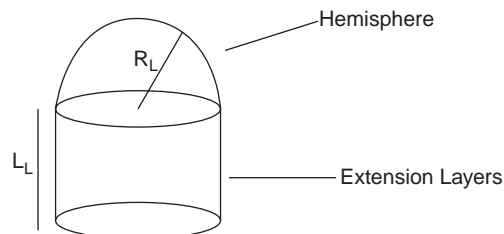


Figure 12. Schematic of an extended hemispherical lens.



Figure 13. Photograph of a mm-wave aperture stacked patch mounted on an extended hemispherical lens.

5. PRINTED ANTENNAS

In this section, we will look at a few examples of traveling wave printed antennas, in particular tapered slots, printed quasi Yagi Uda antennas, printed beverage antennas, and reflectarrays. Interestingly, all of these printed traveling wave antennas have their analogies that can be drawn from the previous sections. Also, the printed antennas presented here are all relatively new concepts with

the oldest (the tapered slots) dating back to the early/mid 1980s.

The tapered slot antenna is undoubtedly the most common printed traveling wave antenna (see [25–28] for examples). These antennas can operate over multioctave bandwidths and can operate well in a phased array environment. Effectively, one can think of this form of printed radiator in the same manner as a horn antenna where a waveguide is flared out to “match” the electromagnetic wave to free space, although in this case the transmission medium is a slotline. However, unlike a conventional horn antenna, the fundamental mode of the slotline is TEM in nature, and so some of the issues associated with the wave matching of a horn antenna are mitigated here. Having said that, the tapered slot is a relatively complicated radiating element with many degrees of freedom. As is the case for a horn antenna, the profile of the taper (or flare) contributes to the input impedance behavior as well as the radiation performance of this printed traveling wave antenna. Common profiles include linear, exponential, and piece-wise linear. One particular challenge with a tapered slot antenna is the transition from the slotline to a more common transmission media used in microwave circuitry design. Figure 14 shows a photograph of a tapered slot antenna with a Coplanar Waveguide (CPW) feed. Incorporated in this design is a wideband balun (part of which is the large slotline cavity in the top left-hand corner of the photograph), which efficiently transfers energy from an unbalanced transmission line (CPW) to the balanced slotline. Figure 15 shows the predicted and measured return loss of the developed traveling antenna, as well as a typical radiation pattern.

The Yagi Uda antenna as described in Section 2 is an endfire antenna. However, only limited success has been achieved at adapting this antenna to microwave/millimeter wave operation. Figure 16 shows a schematic of the uniplanar quasiYagi antenna [29,30]. The antenna is

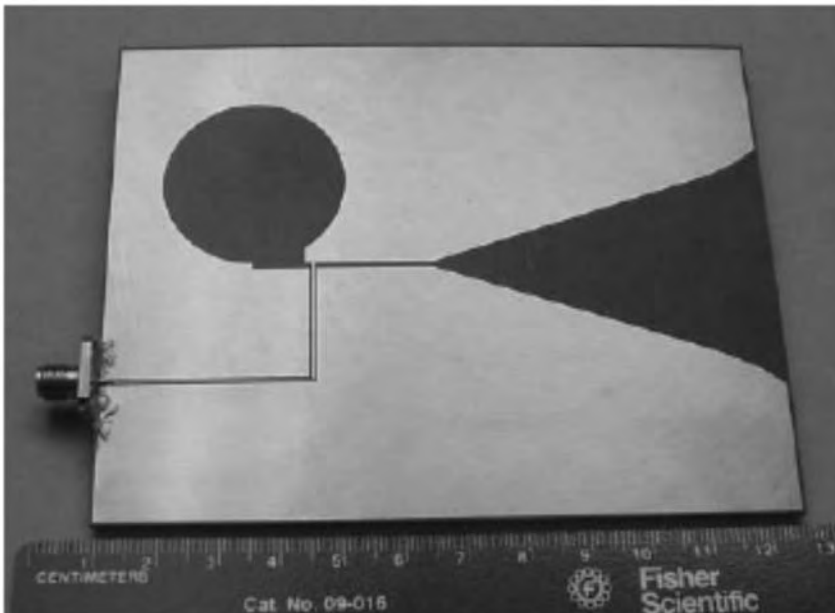


Figure 14. Photograph of a tapered slot antenna.

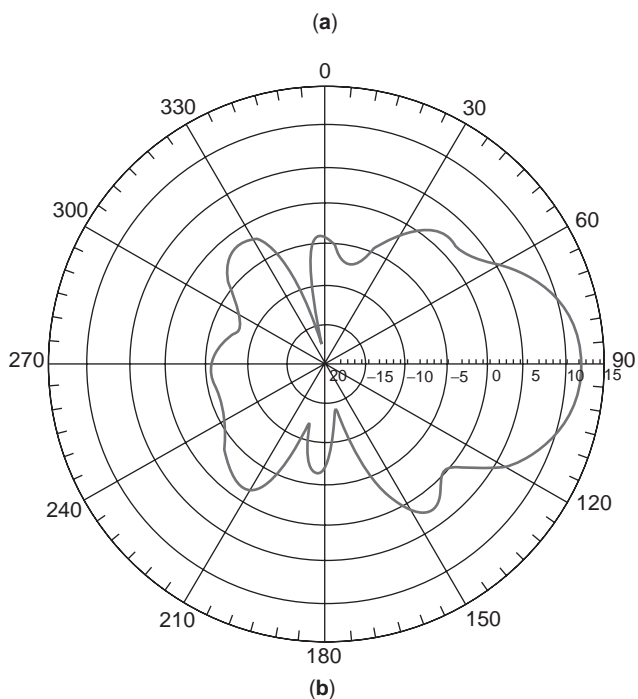
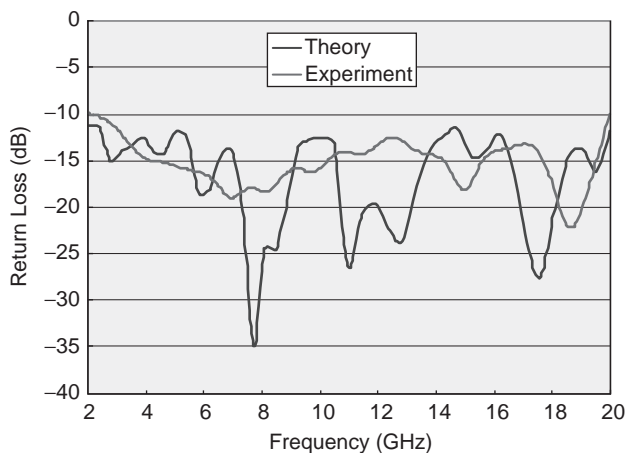


Figure 15. Characteristics of tapered slot antenna: (a) return loss; (b) radiation pattern at 10 GHz.

constructed on a single layer of microwave laminate with metallization on both sides. The top metallization consists of a microstrip feed, a broad-band microstrip-to-CPS (Coplanar Stripline) balun and two dipole elements, one of which is the driver element fed by CPS and the second dipole being the parasitic director. The metallization on the bottom plane is a truncated microstrip ground, which serves as the reflector element for the antenna. The parasitic director element on the top plane simultaneously directs the antenna propagation toward the endfire direction, and acts as an impedance matching element. Thus, the printed version of the Yagi Uda antenna in Fig. 16 is similar in operation to that of a wire version presented earlier. Figure 17 shows the return loss response and radiation patterns of a typical

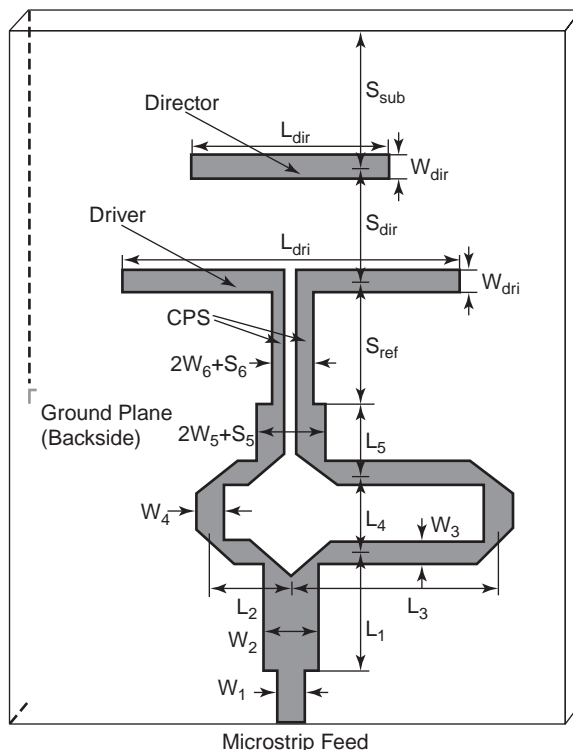


Figure 16. Schematic of a printed Yagi Uda antenna.

printed quasiYagi Uda antenna [30]. Recently, a modification of this traveling wave antenna was presented that greatly simplifies the feed arrangement of the printed antenna [31].

It is also possible to realize a printed version of a Beverage (or long wire) antenna. Figure 18 shows the cross-sectional view of such an antenna where microstrip is used as the transmission medium. For this particular configuration, a probe soldered to the microstrip line is used to excite the antenna, and the characteristic impedance of the transmission line is designed as 50Ω , and so the termination resistance is also this value. The antenna is well matched over a very wide bandwidth (in excess of a decade), and a typical radiation pattern (including gain) is shown in Fig. 19. This pattern is consistent with a wire version of the antenna (see, for example, [2]). The printed Beverage antenna radiates better when the height of the substrate is increased; however, doing so can compromise the input impedance response because of the discontinuity associated with the feeding mechanism as well as that associated with the load.

The microstrip reflectarray is a traveling wave antenna that combines the mechanical advantages of printed antenna technology with some of the robust electrical characteristics of reflector antennas [32–34]. Its main mechanical advantage is that the geometrical constraint of the parabolic reflector is eliminated, and that printed antenna technology is used, providing repeatable, low-cost manufacture of the antennas. The microstrip reflectarray resembles an ordinary array of microstrip elements printed on a grounded dielectric substrate with two notable

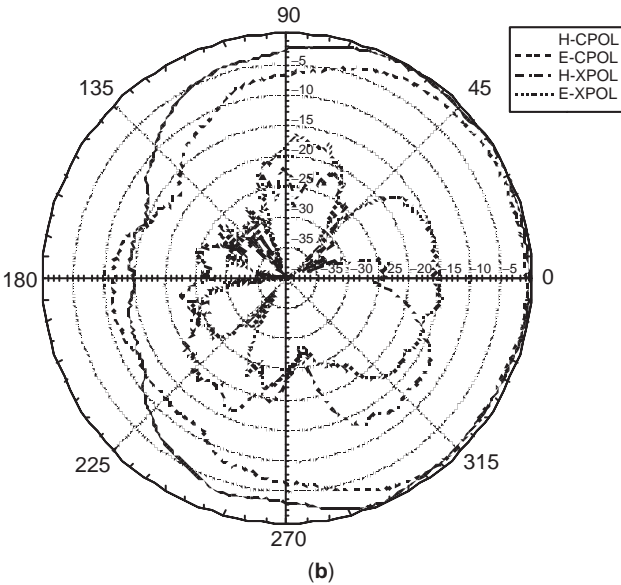
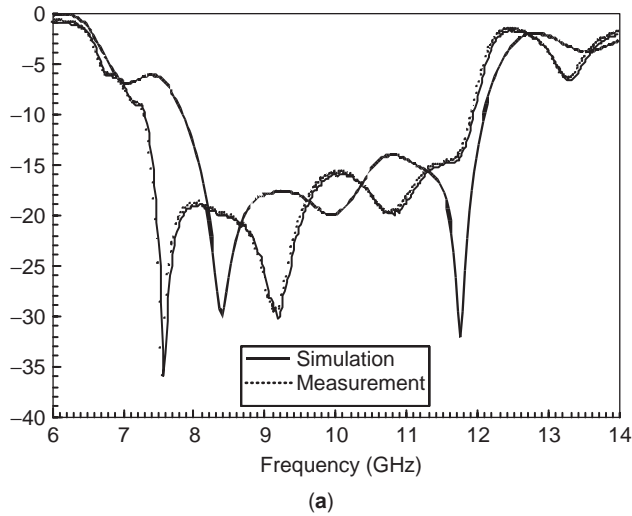


Figure 17. Typical characteristics of a printed Yagi Uda antenna: (a) return loss; (b) radiation patterns.

exceptions: the array elements are excited by a feed antenna, replacing the microstrip-line feed network commonly used in large arrays, and secondly, the resonant frequency of each element is tuned slightly off the center operating frequency of the reflectarray. The patches are tuned in order to adjust the scattering phase of each ele-

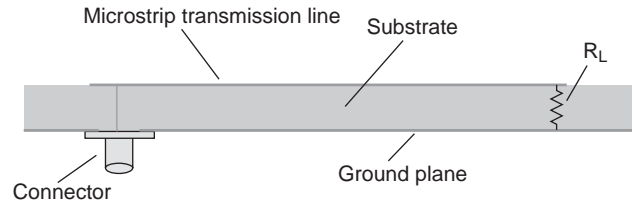


Figure 18. Schematic of a printed Beverage antenna.

ment and therefore produce a main beam at a predetermined angle. The elimination of the microstrip-line feed network produces an antenna with larger bandwidth and lower loss, especially at millimeter-wave frequencies. A photograph of a reflectarray (including its feed element and support structure) is shown in Fig. 20.

6. CONCLUSIONS

In this article we have reviewed some of the most common traveling wave antennas. In particular, we have looked at wire, waveguide, and printed versions of this concept as well as briefly examined reflectors and lens antennas. Traveling wave antennas play a very important role in a variety of wireless communications and radar systems, and it appears this fundamental form of radiator will continue to do so for a long time to come. Traveling wave antennas are typically more complicated in nature (both electromagnetically and structurally) than their resonant-style counterparts; however, their overall performance usually justifies the increase in complexity. A summary of some of the traveling wave antennas discussed is presented in Table 1. Here, typical gain, bandwidth, and overall dimensions are given. Also, the cost of implementation is provided and some applications where these antennas can be used are summarized. An important note should be added here, which is that several commercially available electromagnetic simulation software packages exist that can greatly assist in the design of traveling wave antennas (for example, Ansoft’s HFSS™). These are typically computationally intensive simply because the structures to be analyzed are either complicated or electrically large. Some useful and yet relatively simple design software packages also exists, which are included in some of the references given here (for example, [2]). Finally, another useful book highlighting design trends of some traveling wave antennas can be found in [35].

Table 1. Summary of Some Traveling Waves

Antenna	Gain	Bandwidth	Dimensions	Relative Cost	Applications
Beverage	< 3 dBi	< 10 : 1	< 10 λ ₀	cheap	Ham radio
Yagi Uda	4 dBi–14 dBi	(depends on gain requirement)	0.5 λ ₀ × 1 λ ₀ –0.8 λ ₀ × 10 λ ₀	cheap	TV, Radar
Horn	7–18 dBi	< 1.3 : 1	< 10 λ ₀	expensive	Radar
Tapered slot	6–12 dBi	> 4 : 1	< 5 λ ₀	moderate	Radar
Reflector	< 60 dBi	< octave (feed dependent)	< 30 λ ₀	moderate	Point-to-point links, radio astronomy
Lens	< 50 dBi	< octave (feed dependent)	< 10 λ ₀ × 10 λ ₀	moderate	Point-to-point links

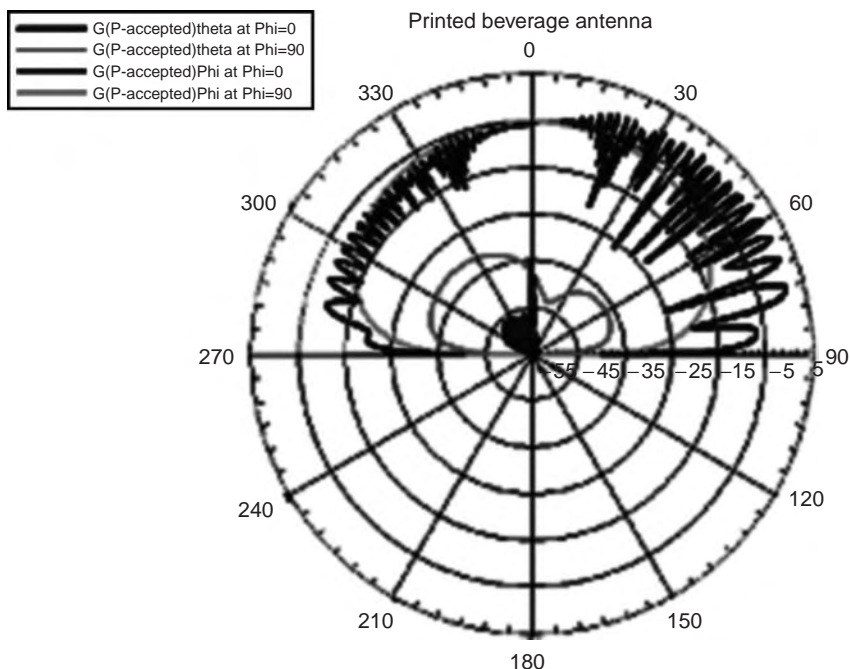


Figure 19. Typical radiation pattern of the printed Beverage antenna. (This figure is available in full color at <http://www.mrw.interscience.wiley.com/erfme>.)

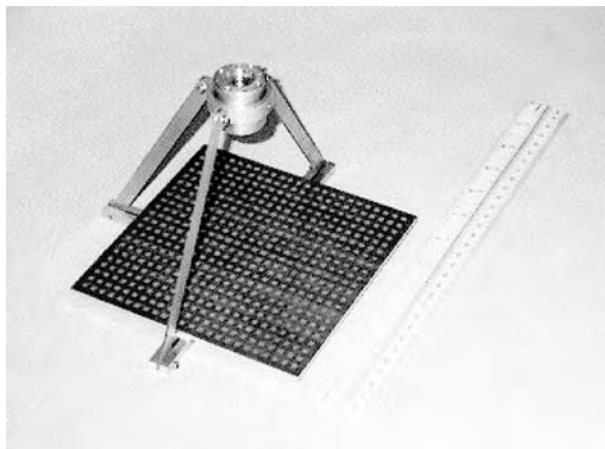


Figure 20. Photograph of a printed reflectarray.

Acknowledgments

The author would like to thank the staff at CSIRO, Australia for photographs of the array of corrugated horn antennas and the reflector and also Dr S. Targonski for the photograph of the reflectarray.

BIBLIOGRAPHY

1. IEEE Standard Definitions of Terms for Antennas, IEEE Std 145-1983, *IEEE Trans. Antennas Propagat.*, **31**: (1983).
2. C. A. Balanis, *Antenna Theory: Analysis and Design*, 2nd Ed., Wiley, New York, 1997.
3. R. W. P. King, The wire antenna for transmission and reception, *IEEE Trans. Antennas Propagat.*, **31**:956-965 (1983).
4. G. A. Thiele and E. P. Ekelman, Design formula for Vee dipole, *IEEE Trans. Antennas Propagat.*, **28**:588-590 (1980).
5. R. S. Elliot, *Antenna Theory and Design*, Prentice-Hall, Englewood Cliffs, NJ, 1981.
6. E. Bruce, A. C. Beck, and L. R. Lowry, Horizontal rhombic antennas, *Proc. IRE*, **23**:24-26 (1935).
7. J. D. Krauss, *Antennas*, McGraw-Hill, New York, 1983.
8. H. Yagi, Beam transmission of the ultra short waves, *Proc. IRE*, **16**:715-741 (1928).
9. A. W. Love, ed., *Electromagnetic Horn Antennas*, IEEE Press, New York, 1976.
10. (online), available at www.milpi.com/261main.html.
11. A. P. King, The radiation characteristics of a conical horn antenna, *Proc. IRE*, **38**:249-251 (1950).
12. B. MacA. Thomas, Design of corrugated conical horns, *IEEE Trans. Antennas Propagat.*, **26**:367-372 (1978).
13. B. MacA. Thomas, A review of the early development of circular-aperture hybrid-mode corrugated horns, *IEEE Trans. Antennas Propagat.*, **34**:930-935 (1986).
14. W. D. Burnside and C. W. Chuang, An aperture matched horn design, *IEEE Trans. Antennas Propagat.*, **30**:790-796 (1982).
15. A. W. Love, ed., *Reflector Antennas*, IEEE Press, Piscataway, NJ, 1978.
16. W. V. Rusch, The current state of reflector art, *IEEE Trans. Antennas Propagat.*, **32**:313-329 (1984).
17. W. V. T. Rusch, The current state of reflector antenna art - entering the 1990s, *Proc. IEEE*, **80**:113-126 (1992).
18. D. B. Rutledge, D. P. Neikirk, and D. P. Kasilingam, Integrated circuit antennas, in *Infrared and Millimeter-waves*, Vol. 10, Academic Press, New York, pp. 1-90, 1983.
19. G. Rebeiz, Millimeter-wave and Terahertz integrated circuit antennas, *Proc. IEEE*, **80**:1748-1770 (1992).
20. G. W. Collins, Shaping of subreflectors in Cassegrainian antennas for maximum antenna efficiency, *IEEE Trans. Antennas Propagat.*, **21**:309-313 (1973).

21. G. V. Eleftheriades, Y. Brand, J-F. Zurcher, and J. R. Mosig, ALPSS: A millimetre-wave aperture-coupled patch antenna on a substrate lens, *Electron. Lett.*, **33**:169–170 (1997).
22. P. Otero, G. V. Eleftheriades, and J. R. Mosig, Integrated modified rectangular loop slot antenna on substrate lenses for millimeter- and submillimeter-wave frequencies mixer applications, *IEEE Trans. Antennas Propagat.*, **46**:1489–1497 (1998).
23. L. Mall and R. B. Waterhouse, Millimeter-wave proximity-coupled microstrip antenna on an extended hemispherical dielectric lens, *IEEE Trans. Antennas Propagat.*, **49**:1769–1772 (2001).
24. R. B. Waterhouse, *Microstrip Patch Antennas: A Designer's Guide*, Kluwer, Boston, MA, 2003.
25. K. S. Yngvesson, et al., The tapered slot antenna - a new integrated element for millimeter-wave applications, *IEEE Trans. Microwave Theory Tech.*, **37**:365–374 (1989).
26. K. S. Yngvesson, et al., Endfire tapered slot antennas on dielectric substrates, *IEEE Trans. Antennas Propagat.*, **33**:1392–1400 (1985).
27. C. H. Chio and D. H. Schaubert, Parameter study and design of wide-band widescan dual-polarized tapered slot antenna arrays, *IEEE Trans. Antennas Propagat.*, **48**:879–886 (2000).
28. M. C. Greenberg, K. L. Virga, and C. L. Hammond, Performance characteristics of the dual exponentially tapered slot antenna (DE TSA) for wireless communications applications, *IEEE Trans. Vehicular Tech.*, **52**:305–312 (2003).
29. Y. Qian, W. R. Deal, N. Kaneda, and T. Itoh, A microstrip-fed quasi-Yagi antenna with broadband characteristics, *Electron. Lett.*, **34**:2194–2196 (1998).
30. N. Kaneda, W. R. Deal, Y. Qian, R. Waterhouse, and T. Itoh, A broadband planar quasi-yagi antenna, *IEEE Trans. Antennas Propagat.*, **50**:1158–1160 (2002).
31. G. Zheng, et al., Simplified feed for modified printed Yagi antenna, *Electron. Lett.*, **40**:464–466 (2004).
32. T. A. Metzler, Stub Loaded Microstrip Reflectarray, *IEEE AP-S Int. Sympos. Dig.*, 574–577 (1995).
33. D. M. Pozar, S. D. Targonski, and H. D. Syrigos, Design of millimeter-wave microstrip reflectarrays, *IEEE Trans. Antennas Propagat.*, **45**:287–296 (1997).
34. A. Kelkar, FLAPS: Conformal Phased Reflecting Surface, *Proc. IEEE National Radar Conf.* March 1991, pp. 58–62.
35. R. C. Johnson and H. Jasik, Eds., *Antenna Engineering Handbook*, 2nd ed., McGraw-Hill, New York, 1984.

TRAVELING WAVE TUBES

CAROL L. KORY
ANALEX Corporation

The traveling-wave tube (TWT) is a vacuum device invented in the early 1940s [1,2] used for amplification at microwave frequencies. Amplification is attained by surrendering kinetic energy from an electron beam to a radiofrequency (RF) electromagnetic wave. The demand for vacuum devices has been decreasing largely owing to the advent of solid-state devices. However, although solid state devices have replaced vacuum devices in many areas, there are still many applications such as radar, elec-

tronic countermeasures, and satellite communications that require operating characteristics such as high power (watts to megawatts), high frequency (below 1 GHz to over 100 GHz), high efficiency (65% efficient, 100 Watt, Ka-band TWTs are commonplace), and large bandwidth that only vacuum devices can provide. Vacuum devices are also deemed irreplaceable in the music industry where musicians treasure their tube-based amplifiers, claiming that the solid-state and digital counterparts could never provide the same “warmth” [3]. The term traveling-wave tube includes both fast-wave and slow-wave devices. This article will concentrate on slow-wave devices as the vast majority of TWTs in operation around the world fall into this category.

1. TRAVELING-WAVE TUBE PRINCIPAL COMPONENTS

The TWT possesses four major components as shown in Fig. 1 [4]

1. An electron gun that produces an electron beam
2. A slow-wave circuit that slows an RF electromagnetic wave to a speed synchronous with the electron beam
3. A collector that collects the spent electron beam
4. The TWT package that provides cooling, beam focusing, and access to the RF input and output

Amplification is obtained by feeding the RF signal to be amplified into the slow-wave circuit while the electron beam is moving along the TWT axis. The slow-wave structure reduces the electromagnetic wave phase velocity so that it propagates near synchronism with the electron beam resulting in interaction between the wave and the beam and thus amplification of the RF signal. The spent electron beam is collected at the end of the tube by the collector.

1.1. Electron Gun

The electron gun is used to produce the electron beam. The electron guns used for nearly all TWTs mimic a section of a spherical diode as first derived by Pierce [5] and are consequently referred to as Pierce guns. The major components of the gun are the cathode, heater, focus electrode, and one or more anodes. The type of cathode used in TWTs is the thermionic cathode where electron emission is achieved by using a heat source to supply the electrons near the surface of the cathode with enough energy to escape from the surface. Cathode operation is a complex subject, and the reader can consult [6] or the article on cathodes in this encyclopedia for further detail. In a simplified description, the higher the temperature of the cathode, the greater the emission (current density), but the shorter the life. Because of the limited lifetime of cathodes, the electron gun design must be consistent with the expected life of the application. For example, if a lifetime of 12 to 15 years is required, as in commercial space applications, cathode current densities of 1 A/cm² or less are usually specified for an M-type cathode [7].

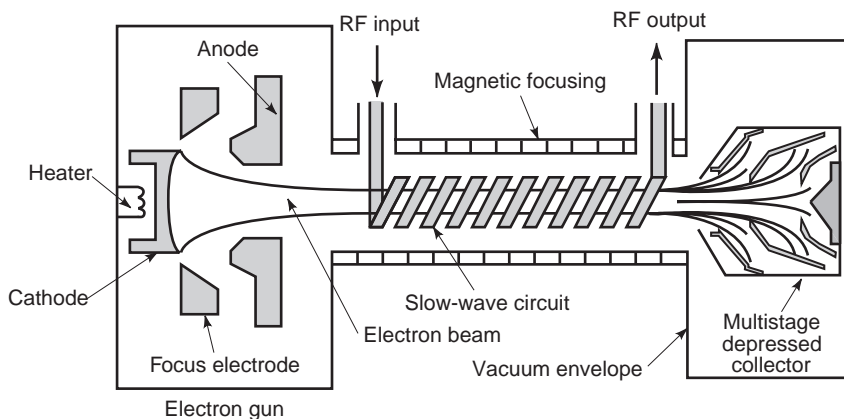


Figure 1. Basic TWT. The electron gun shown to the left encompasses the heater, cathode, focus electrode, and anode. A multistage depressed collector is shown on the right with electron beam trajectories.

A heater connected to a dc or ac power supply, consisting of a coil of tungsten or tungsten-rhenium wire adjacent to or embedded within the cathode body, is typically used to raise the temperature of the cathode to an adequate level for electron emission. The wire is formed into a contrawound coil to reduce the amount of magnetic field introduced into the electron gun by the current through the heater, thus reducing large perturbations in the electron trajectories that would make the beam difficult to focus or couple modulation onto the electron beam.

The anode is a positively charged electrode that attracts and accelerates the electrons emitted from the cathode. Because of electrostatic repulsion forces, the electrons are deflected as they are emitted so the focus electrode is used to produce equipotential lines with the same center of curvature as the cathode resulting in electron flow toward this center of curvature; therefore, the electrons are focused into a beam. TWTs used in pulsed applications often have a grid placed close to the cathode that permits the electron beam to be turned off and on with a small swing (relative to the cathode-to-ground potential drop) in the applied grid-to-cathode bias. The grid typically causes some perturbation of the electron beam so it is typically not used in high reliability devices.

1.2. Slow-Wave Circuit

The RF voltage to be amplified is fed into the slow-wave circuit through the input coupler. The purpose of the slow-wave circuit is to slow the axial velocity of the RF wave so that it propagates near synchronism with the electron beam. There are numerous possible slow-wave structures limited only by human inventiveness. Some of the more common are the helix, contrawound helix, coupled-cavity, ring-bar, cloverleaf, ladder, and grating circuits. The axial component of the electric field set up by the voltage on the circuit is somewhat sinusoidal in the vicinity of the electron beam so a force is directed to the left when the field is positive and to the right when the field is negative (see Fig. 1). This causes some of the electrons in the beam to decelerate (force is directed to the left) and others to accelerate (force is directed to the right), causing the electron beam to form bunches or be velocity modulated. The bunches drift into a decelerating region of the field, and

the electrons lose velocity and thus kinetic energy. The energy lost by the electrons is transferred to RF energy in the RF wave, thus amplifying the RF signal. Further down the length of the tube, the bunches become more compact leaving even more electrons in the decelerating region causing the RF wave to grow even more. As this continues, the electron velocities decrease and space-charge forces within the bunch increase. Eventually a portion of the bunch leaves the decelerating region of the circuit field and enters the accelerating region. These electrons extract energy from the circuit field. When the energy extracted from the circuit field becomes equal to the energy supplied, amplification of the RF wave stops and the interaction is said to reach saturation.

Backward wave oscillations (BWOs) can occur when power is reflected back to the input because of a mismatch in the slow-wave circuit, at the load or at the output coupler. Because of a mismatch at the input, a portion of the signal is again reflected to provide a feedback signal. To prevent these reflections, or backward waves, from reaching the input, it is common that a sever or distributed loss is added to the slow-wave circuit. A sever isolates the input wave from the output wave by physically separating the sections. Distributed loss usually consists of a lossy resistive coating that attenuates both forward and backward waves. Although the RF wave is severed or attenuated at this point in the slow-wave circuit, the bunching of the electrons has been established and will reestablish the RF wave on the circuit beyond the sever or region of attenuation, allowing interaction to continue.

A common method to increase efficiency by prolonging synchronism between the electron beam and the RF wave is to incorporate a velocity taper in the TWT design. A velocity taper is achieved by changing the dimensions of the slow-wave circuit near the output of the tube so that the RF wave velocity is slowed along with the electron beam. With this technique, even though the electron bunches are slowed as they lose energy to the circuit, they will remain in synchronism longer with the consecutively slowed RF wave and continue to deliver energy to the circuit fields. Velocity tapering has proved to significantly increase the efficiency of TWTs [8–10]. In addition, the technique can be used to enhance the linearity of the

power output versus power input [11] and to prevent BWOs [12–14].

1.2.1. Helix. The helix is the most common type of slow-wave structure. A typical modern helical structure embodies a metal tape wound into a helix supported by three or more dielectric support rods inside a conducting barrel. Figure 2 shows the cross-sectional view of a typical helical circuit and a three-dimensional view of the helical tape. Derived from a single-wire transmission line that has zero dispersion, the helix has a primarily constant phase velocity over a large bandwidth making it the widest bandwidth circuit of any structure available. This relatively low dispersion can be reduced further by incorporating dispersion shaping techniques into the circuit design. This is achieved by perturbing the circuit fields predominantly at low frequencies so that the phase velocity is decreased at the low frequency end while staying constant at high frequencies, thus reducing dispersion and increasing bandwidth. As the fields are concentrated between the helical turns at high frequencies and in the area extending from the helix to the barrel at low frequencies, this low-frequency perturbation is possible by including specially shaped dielectric support rods or longitudinally conducting metal vanes that anisotropically load the circuit [6,15]. Several loading methods are shown in Fig. 3.

1.2.2. Coupled-Cavity Circuit. Another common slow-wave structure is the coupled-cavity circuit that is used mostly for high-power applications. Because of its all-metal construction, it is able to dissipate a greater amount of heat compared with the helix, but can operate over only a comparatively narrow bandwidth. As shown in Fig. 4 for the cross-sectional and top views, the circuit includes a chain of cavities, typically made of copper, brazed together with a coupling slot alternating 180 degrees at adjacent

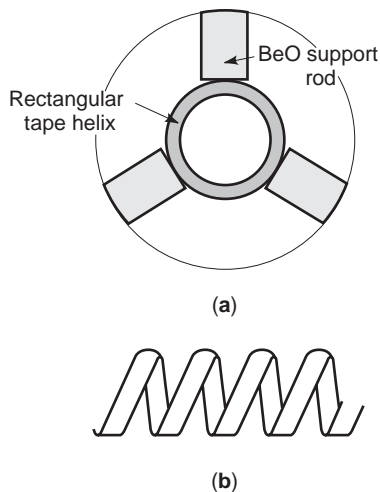


Figure 2. Cross-sectional view of typical helix slow-wave circuit and three-dimensional view of helical tape. The rectangular helical tape is supported by three rectangular dielectric support rods, all enclosed in a conducting barrel. The electron beam travels through the axial center ($r=0$) of the helical circuit.

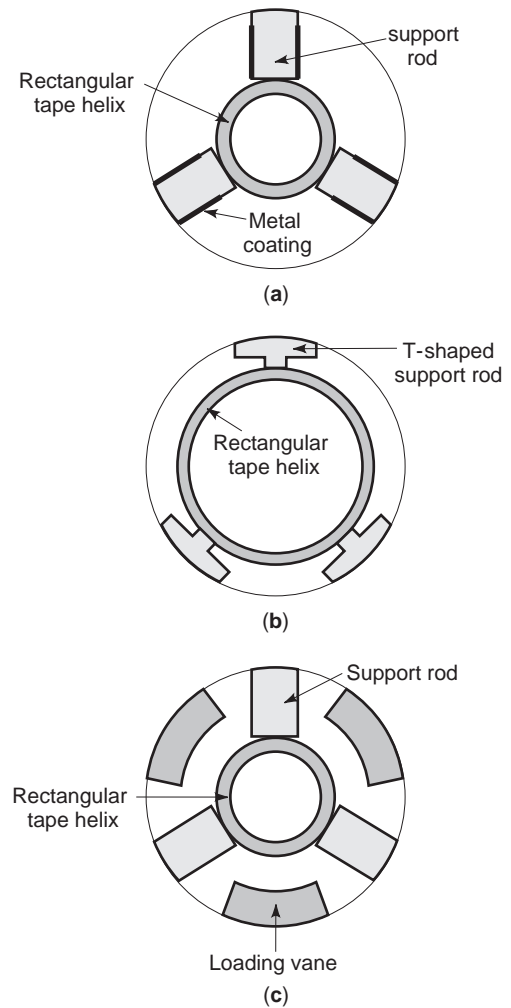


Figure 3. Various dispersion shaping techniques for broad-band helical TWTs. (a) A metal coating is applied to the dielectric support rods. (b) The support rods are formed into T-shapes. (c) Loading vanes are added between the support rods.

cavities. Ferrules may surround the beam hole to concentrate the RF electric field in the vicinity of the electron beam for increased interaction.

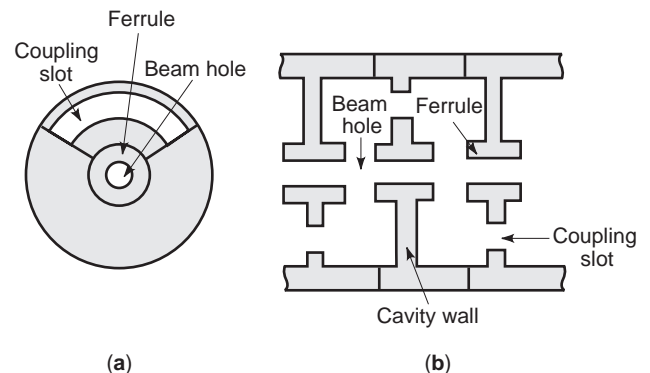


Figure 4. (a) Cross-sectional view, (b) top view of ferruled coupled-cavity circuit. The coupled-cavity circuit employs an all-metal construction suitable for high-power TWTs.

1.3. Collector

After the amplified RF output is removed from the TWT, the spent electron beam passes through the end of the beam focusing section, so space charge forces cause the beam to expand as it enters the collector. Upon entering the collector, the beam is highly disordered with a broad spectrum of energies. The electron beam at this point still possesses a great deal of kinetic energy as only about 5% to 30% is extracted during interaction with the RF wave [16]. If the collector was at the same potential as the body of the tube, this kinetic energy would be dissipated as heat on the collector surface. By operating the collector electrode at a potential below that of the RF circuit, the beam is decelerated before it hits the collector surface. Thus, some of the remaining kinetic energy from the electron beam is converted to electric potential energy. This negative potential operation is known as depressing the collector. The greater the amount of recovered power, the higher the total efficiency of the tube. The impact of an efficient collector is made clear by considering the efficiency formula. Overall efficiency can be expressed as the ratio of the output power to input power or

$$\eta_{0v} = \frac{P_{out}}{P_{in}} \tag{1}$$

where P_{out} is the RF power output and P_{in} is the sum of the heater power, P_h , beam power from the gun, P_o , RF input power, P_{RFin} , and power to the magnetic focusing system, P_m , minus the power recovered by the collector, P_{rec} , or

$$P_{in} = P_h + P_o + P_m + P_{RFin} - P_{rec} \tag{2}$$

Figure 5(a) plots the current to the collector versus the amount by which the collector is depressed below ground potential (the slow-wave circuit potential). Assuming zero loss and zero interception between the beam and the slow-wave circuit, the area under the curve represents the maximum power that could possibly be recovered by the collector. The beam power converted to RF power is represented by the area above the curve less the cross-hatched area for voltages greater than the beam voltage. The beam current and voltage are represented by I_o and V_o , respectively. For a single-stage collector depressed to voltage V_1 , the maximum power that can be recovered is represented graphically in Fig. 5(a) by the shaded area, which is the product of the magnitudes of the collector current and collector voltage or

$$P_{rec} = V_1 I_o$$

Several phenomena complicate the collector operation including space-charge effects of the electrons already in the collector repelling those electrons entering, secondary electron emission from the surface caused by incident electrons, and electrons having different amounts of kinetic energy, thus traveling with different velocities. Multistage depressed collectors (MDC), where several electrodes are used at different depressed potentials, in-

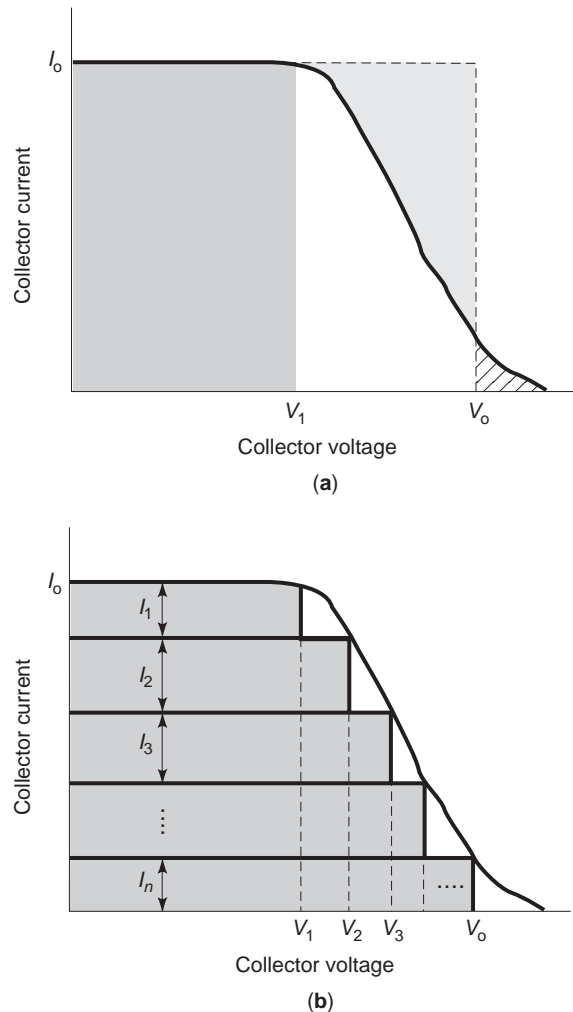


Figure 5. Collector current versus collector voltage. (a) The dark shaded area designates the maximum power that can be recovered by a single-stage collector. (b) The dark shaded area designates the maximum power that can be recovered by a multistage depressed collector with n stages.

corporate multiple velocity sorting stages. This directs high-velocity electrons to the stages having the greatest depression and the slow electrons to the stages with the least depression. This design has proven to greatly increase the overall efficiency of TWTs [17]. The reason for this becomes clear when the collector current versus voltage curve is again considered for the multistage collector. The total possible recoverable power for an n -stage MDC is represented by the shaded region in Fig. 5(b) where the n th electrode is at cathode potential, V_o . The possible recovered power is significantly greater compared with the single-stage collector given as

$$P_{rec} = \sum_{k=1}^n V_k I_k$$

In practice, this can never be exactly achieved because of secondary emission and imperfect energy sorting in the

collector. Considering Eqs. (1) and (2), it becomes obvious that the overall efficiency can be significantly increased. In practice, typical MDC designs incorporate no more than five collector stages as the law of diminishing returns starts to occur with regard to efficiency improvement versus fabrication and power supply complexity. A typical azimuthally symmetric four-stage MDC design is shown in two dimensions in Fig. 1.

1.4. Traveling-Wave Tube Package

The TWT package serves as a mechanical support structure for the TWT and RF input/output connectors, a thermal path for the conduction of waste heat, an electromagnetic interference (EMI) shield, and as a protective cover over the high-voltage connections and beam focusing magnets [4].

1.4.1. Beam Focusing. The electrons in the beam each possess negative charge; therefore, they repel one another causing the beam to diverge. To counteract this space charge effect and prevent the beam from diverging and being intercepted by the slow-wave structure as it flows through the length of the tube, external focusing is applied using an axial magnetic field. One way of doing this is to surround the TWT with a large solenoid that can be a permanent magnet or an electromagnet. Because of their size and large amount of stray magnetic field, solenoids are typically used only on very high-power (kilowatt level) TWTs with high current density beams.

A more commonly used method for focusing is to employ periodic permanent magnet (PPM) focusing that is lighter and more compact than an equivalent solenoidal magnet [18]. Alternating iron pole pieces and cylindrical magnets are placed side-by-side along the length of the tube, the polarity of adjacent magnets being reversed, as shown in Fig. 6. The PPM structure provides a nearly sinusoidal magnetic field at the beam axis with rms (root-mean-square) value about equal to the value of field required in a uniform field design.

1.4.2. Vacuum Envelope. It is necessary to operate the main components of the TWT under vacuum to ensure proper cathode operation and long cathode life, prevent formation of positive ions within the electron beam, and avoid high-voltage arcing at the electrodes. Thus, the gun, slow-wave structure, and collector are contained in a leak tight vacuum envelope. The beam focusing mechanism is usually mounted outside of the vacuum envelope, and this whole assembly is mounted in the TWT package.

2. BASIC FIELD THEORY

TWT gain is based on the surrender of energy from the electron beam to the RF electromagnetic wave. For this phenomena to occur, the phase velocity of the RF wave,* v , must be in near synchronism with the dc beam velocity, u_o ,

*The RF wave actually consists of space harmonics and the harmonic component of interest must be near synchronism with the dc beam velocity.

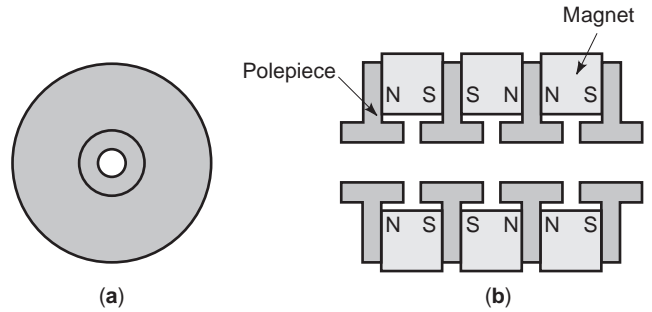


Figure 6. (a) Cross-sectional view, (b) top view of periodic permanent magnet focusing.

or

$$v = u_o \tag{3}$$

The gain of the tube depends on the strength of this interaction. A summary of the small-signal analysis for TWT gain is summarized by Gilmour [6], Gewartowski [19], and more succinctly by Wilson [20], based on the analysis done by Pierce [21]. The theory neglects space harmonics of the RF field other than that which is synchronous with the electron beam assuming these harmonics have no net effect.

First, the equation is derived for the ac current induced on the beam by the RF field (electronic equation). Next, the RF field resulting from the modulated beam is derived (circuit equation). These equations are solved simultaneously to determine the self-consistent relations for the circuit and beam quantities. The equations take on a neater form when several parameters are defined. Pierce's small-signal gain parameter C is defined as

$$C^3 = \frac{KI_o}{4V_o} \tag{4}$$

where K is the interaction impedance defined as

$$K = \frac{\int |E|^2 dS}{2\beta^2 PS} \tag{5}$$

where $|E|$ is the magnitude of the RF axial electric field, $\beta = \omega/\mu$ is the axial propagation constant, $\dagger P$ is the total RF power flow, and S is the cross-sectional surface area of the electron beam. I_o and V_o are the dc beam current and voltage, respectively. Pierce's space-charge parameter QC is defined as

$$QC = \frac{\omega_q^2}{4C^2 \omega^2} \tag{6}$$

where ω_q is the reduced plasma frequency and ω is the angular frequency ($2\pi f$), where f is the operating frequency.

A measure of synchronism between the electrons and the space harmonic wave is specified by Pierce's velocity

$\dagger K E$, and β are calculated for the space harmonic of interest.

parameter b defined as

$$b = \frac{u_o - v}{vC} = \frac{b_0 - N}{NC} \quad (7)$$

Pierce's loss parameter d is proportional to circuit attenuation and is defined as

$$d = \frac{\alpha\omega}{u_o C} \quad (8)$$

where α is the circuit attenuation including surface and attenuator losses. The various fields and beam quantities have a z dependence of the form

$$e^{-\Gamma z}$$

where Γ is the complex propagation constant for the circuit-beam coupled system. The allowed values for Γ are determined by simultaneously solving for the circuit and electronic equations. Doing so gives

$$\Gamma = j \frac{u_o}{\omega} (1 + jC\delta) \quad (9)$$

Making the appropriate substitutions and taking advantage of the fact that C is small,

$$\delta^2 = \frac{1}{-b + jd + j\delta} - 4QC \quad (10)$$

The solutions for Eq. (10) give three allowable propagation constants. Regardless of the values of d and QC , one will always obtain one growing wave that is responsible for the gain in the tube, one decaying wave, and one wave of nearly constant amplitude as long as the tube is operating near synchronism (small b).

The initial loss factor A_1 is defined as

$$A_1 = 20 \log \left| \frac{\delta_1^2}{(\delta_1 - \delta_2)(\delta_1 - \delta_3)} \right| \text{dB} \quad (11)$$

The space charge loss factor is defined as

$$A_2 = 20 \log \left| \frac{\delta_1^2 + 4QC}{\delta_1^2} \right| \text{dB} \quad (12)$$

Next we define

$$B = 54.6 \text{Re}(\delta_1) \quad (13)$$

and the electronic wavelength number N as

$$N = \frac{u_o l}{2\pi\omega} \quad (14)$$

where l is the length of the interaction circuit. The small-signal gain can now be expressed as

$$\text{Gain}_{s-s} = A_1 + A_2 + BCN - \text{sever loss dB} \quad (15)$$

The loss associated with each sever is typically about 6 dB. It should be noted that the small-signal gain analysis is valid only when the tube is operating well below saturation. Near or at saturation, the TWT behaves in a nonlinear manner and the small-signal theory is no longer valid.

3. TRAVELING-WAVE TUBE COMPUTER MODELING

Because of the complexity of operation, there are numerous codes that are used in the design, development, and analysis of TWTs. Some of the codes stand alone, and others are incorporated into the microwave and millimeter-wave advanced computational environment (MMACE), which is a vacuum electronics initiative directed at integrating existing codes into a compatible environment having a user-friendly interface [22]. A discussion of available codes follows that is grouped by TWT section. This is intended to point the reader to the appropriate references for each code.

3.1. Electron Gun

Numerous codes exist that will calculate electron trajectories in electrostatic and magnetostatic focusing systems. Electron gun (EGUN) is a widely used code that includes two-dimensional(2-D) fields and three-dimensional(3-D) particle trajectories [23]. In contrast to EGUN's rectangular mesh capability, DEMEOS uses a deformable triangular mesh that is efficient in modeling both the small and the relatively large dimensions of the electron gun [24]. The two-and-one-half-dimensional particle-in-cell (PIC) code MAGIC is also used in gun design [25].

3.2. Slow-Wave Structure

There is a large variety of codes available for the analysis of slow-wave structures. An important step in TWT design is to obtain the cold-test characteristics of the circuit. Cold-testing implies testing the circuit or a scale model of the circuit on the RF test bench without the electron beam to obtain dispersion, interaction impedance, and attenuation characteristics. Accurate results have been obtained in terms of cold-test parameters for several slow-wave circuits using codes like the 3-D electrodynamic PIC code MAFIA [26,27], the 3-D cold-test codes Micro-SOS [28,29] and ARGUS/ESP of MMACE [30], the 3-D cold-test code for helical structures TLM [31], and the 3-D cold-test code limited to axially symmetric cavities in cylindrical coordinates SUPERFISH [32].

It is also important to obtain information about the match from the slow-wave structure to the input/output couplers. Accurate results regarding the transmission characteristics of TWT couplers have been obtained using codes like Ansoft Eminence [33] and MAFIA [34].

3.3. Collector

There has been significant progress made in the computational modeling of collectors within the past several years. Typically an electron trajectory code such as EGUN was used to aid in collector design [35], but because it can simulate only azimuthally symmetric

structures with steady-state electron streams, three-dimensional codes that compute instantaneous conditions are also being used. Several 3-D codes have provided reasonably accurate results: the 3-D PIC code, MAFIA [36]; the 3-D PIC collector simulator integrated into the MMACE framework, C3D [37]; the 3-D PIC code, PIC3D [38]; and the 3-D electron trajectory collector simulator, LKOBRA [39].

3.4. Traveling-Wave Tube Interaction

As mentioned previously, the field theory for small-signal gain provides insight into TWT interaction, but when the tube is operated near or at saturation, this analysis is no longer valid. Near saturation the TWT behaves in a nonlinear manner referred to as large-signal operation. This means that when large-amplitude signals are present, higher order RF terms are no longer negligible as compared with the corresponding dc values. The analysis of the nonlinear system does not lend itself to neat solutions of closed-form equations, so computational modeling becomes crucial [40]. There are a number of codes available to simulate TWT interaction and thus provide characteristics such as gain, power transfer curves, and efficiency near and at saturation.

There are several codes devoted strictly to helical TWT interaction such as the one-dimensional (1-D) code, which predicts intermodulation distortion CHRISTINE [41], the 2-D code, which incorporates 3-D field vector components and beam velocities and which is part of the MMACE framework GATOR [42]; and the 2-D deformable disk model DDM HELIX TWT [43]. The NASA CC TWT code analyzes interaction between a 3-D electron beam and 2-D RF electromagnetic fields in coupled-cavity TWTs [44]. Fully three-dimensional PIC codes such as MAFIA, ARGUS, SOS, and 3DPIC offer the advantage of being able to simulate an entire TWT section in 3-D including modulation effects. Modeling the beam dynamics in just the TWT slow-wave section in 3-D has been accomplished with good accuracy [38,45] but an entire 3-D TWT model from gun to collector has not yet been accomplished because of the computational intensity of the problem.

4. FUTURE TRENDS

The microwave power module (MPM) is a recent development that has had a significant impact on microwave and millimeter-wave electronics system development by taking advantage of the best features of both vacuum electronics and solid-state devices. The MPM is a lightweight, miniaturized RF amplifier consisting of a low-noise, high-gain microwave monolithic integrated circuit preamplifier/signal conditioner, a high-efficiency vacuum power booster TWT, and a miniaturized high-efficiency integrated power conditioner. The MPM has proven to outperform conventional TWT technology in areas of power density (power per unit weight) and noise figure. Analyses also indicate improvement in reliability due to fewer components, lower typical operating temperatures, and improved interconnection technology [46], but data are not yet available to verify this.

Once thought to be a declining field, there is now a substantial opportunity for growth in the commercial demand for TWTs. Particularly, two types of systems are of interest, satellite communications and local multipoint distribution systems (LMDS) [47]. These commercial systems are close to turning the balance from a mostly military market to a commercial market. U.S. industry is proposing to invest more than U.S. \$35 billion in commercial Ka-Band satellite communications systems over the next 6 years, which will create a demand for thousands of TWT amplifiers. The LMDS concept would cover major metropolitan areas with a grid of cellular stations operating at Ka-Band and transmitting programming in competition with cable TV systems. One estimate suggests that 5000 to 6000 highly linear Ka-Band TWTs, probably operating at 28 GHz, would be required to implement LMDS in the continental United States [48].

BIBLIOGRAPHY

1. R. Kompfner, The invention of the traveling-wave tubes, *IEEE Trans. Electron Devices*, **ED-23**:730-738 (1976).
2. N. E. Lindenblad, U.S. Patent 2,300,052, filed May 4, 1940, issued October 27, 1942.
3. R. Wilson, Digital be damned! These days, for high-end audio...—Vacuum tubes are aglow again, *Electronic Engineering Times*, Issue 909, July 8, 1996.
4. TWT/TWTA Handbook, Hughes Aircraft Company, Electron Dynamics Division, Torrance, CA, 1992.
5. J. R. Pierce, *Theory and Design of Electron Guns*, 2nd ed., New York: Van Nostrand, 1954.
6. A. S. Gilmour, Jr., *Principles of Traveling-Wave Tubes*, Norwood, MA: Artech House, 1994, pp. 328-329.
7. J. A. Dayton, Jr., Traveling-wave tube amplifier reliability, *1995 IEEE MTT-S International Microwave Symposium/TWTA Workshop Proc.*, May 1995.
8. A. N. Curren et al., High-efficiency helical traveling-wave tube with dynamic velocity taper and advanced multistage depressed collector, *IEEE Int. Electron Devices Meet. Tech. Dig.*, 473-476, 1987.
9. J. D. Wilson et al., A high efficiency ferruleless coupled-cavity traveling-wave tube with phase-adjusted taper, *IEEE Trans. Electron Devices*, **ED-37**:2638-2643 (1990).
10. J. D. Wilson, A simulated annealing algorithm for optimizing RF power efficiency in coupled-cavity traveling-wave tubes. *IEEE Trans. Electron Devices*, (1997).
11. H. G. Kosmahl and J. C. Peterson, A TWT amplifier with a linear power transfer characteristic and improved efficiency, *NASA TM-83590*, March 1984.
12. G. I. Haddad and R. M. Bevensee, Start-oscillation conditions of tapered backward-wave oscillators, *IEEE Trans. Electron Devices*, **ED-10**:389-393 (1963).
13. B. Epsztein and G. Kantrowicz, Suppression of backward-wave oscillations in multikilowatt helix TWT's, *Proc. European Microwave Conf.*, 376-380, September 1973.
14. K. Tsutaki, Y. Yuasa, and Y. Morizumi, Numerical analysis and design for high-performance helix traveling-wave tubes. *IEEE Trans. Electron Devices*, **ED-32**:1842-1849 (1985).
15. J. L. Putz and M. J. Cascone, Effective use of dispersion shaping in broadband helix TWT circuits, *IEEE Int. Electron Devices Meet. Tech. Dig.*, 422-424, 1979.

16. J. W. Hansen, System Aspects of Communications TWTA's, Hughes Aircraft Company Electron Dynamics Division Applications Note, 1983.
17. H. G. Kosmahl, Modern multistage depressed collectors—A review. *Proc. IEEE Trans. Electron Devices*, **70**:1325–1334 (1982).
18. J. T. Mendel, C. F. Quate, and W. H. Yocom, Electron Beam focusing with periodic permanent magnet fields, *Proc. IRE*, pp. 800–810, May 1954.
19. J. W. Gewartowski and H. A. Watson, *Principles of Electron Tubes*, New York: Van Nostrand, 1965, pp. 349–370.
20. J. D. Wilson, Traveling-wave thermionic devices, in T. Koryu Ishii's *Handbook of Microwave Technology*, Vol.2, San Diego, CA: Academic Press, 1995, pp. 57–95.
21. J. R. Pierce, *Traveling-Wave Tubes*, New York: Van Nostrand, 1950, pp. 5–18.
22. B. Hantman et al., The MMACE framework: an integrated environment for power tube design and analysis, *Proc. Microwave Tubes for Space, Military and Commercial Applications Workshop*, Noordwijk, The Netherlands, April 1997.
23. W. B. Herrmannsfeldt, Electron trajectory program, Stanford Linear Accelerator Center Rep. 331, Stanford University, Stanford, CA, 1988.
24. R. True, Electron beam formation, focusing, and collection in microwave tubes, in T. Koryu Ishii's *Handbook of Microwave Technology*, Vol. 1, San Diego, CA: Academic Press, 1995, pp. 497–567.
25. K. Nguyen et al., Analysis of the 425-MHz klystrode, *IEEE Trans. Electron Devices*, **38**:2212–2220 (1991).
26. C. L. Kory and J. D. Wilson, Three-dimensional simulation of traveling-wave tube cold-test characteristics using MAFIA, *NASA TP-3513*, May 1995.
27. C. L. Kory, Three-dimensional simulation of helix traveling-wave tube cold-test characteristics using MAFIA, *IEEE Trans. Electron Devices*, **43**:1317–1319 (1996).
28. C. L. Kory, J. D. Wilson, and J. W. Maruschek, Simulation of cold-test dispersion and interaction impedance for coupled-cavity traveling-wave tube slow-wave circuits, *IEEE Int. Electron Devices Meet. Tech. Dig.*, 763–766, 1992.
29. B. Stockwell, K. Doniger, and F. Friedlander, Advanced software coldtest of electron devices with μ SOS, *IEEE Int. Electron Devices Meet. Tech. Dig.*, 207–210, 1989.
30. A. A. Mondelli, J. J. Petillo, and H. P. Freund, Cold-test and interaction models for helix TWT's in MMACE, *Proc. IEEE Int. Conf. on Plasma Science (ICOPS)*, 198–199, 1997.
31. K. D. Ward and J. Wlodarczyk, Transmission line modeling of helix slow-wave structures, *IEEE Int. Electron Devices Meet. Tech. Dig.*, 157–160, 1993.
32. K. Halbach and R. F. Holsinger, Superfish—A computer program for evaluation of RF cavities with cylindrical symmetry, *Part. Accel.*, **7**:213–222 (1976).
33. R. T. Benton et al., Efficiency improvements in KU-band space helix traveling-wave tubes, *Proc. Microwave Tubes for Space, Military and Commercial Applications Workshop*, Noordwijk, The Netherlands, April 1997.
34. C. L. Kory and A. H. Qureshi, Simulation of TunnelLadder traveling-wave tube input/output coupler characteristics using MAFIA, *NASA CR-198505*, September 1996.
35. J. A. Dayton, Jr. et al., Analytical prediction with multidimensional computer programs and experimental verification of the performance, at a variety of operating conditions, of two traveling-wave tubes with depressed collectors, *NASA TP-1449*, May 1979.
36. K. R. Vaden, V. O. Heinen, and J. A. Dayton, Jr., Three dimensional modeling of multistage depressed collectors, *Proc. IEEE Int. Conf. on Plasma Science (ICOPS)*, 198, 1997.
37. L. Ludeking and J. Geary, C3D, A three-dimensional tool for collector design, *Proc. 1996 Microwave Power-Tube Conference*, May 1996.
38. K. D. Ward, M. J. Duffield, and A. R. Wise, Power-booster traveling-wave tubes, *Proc. Microwave Tubes for Space, Military and Commercial Applications Workshop*, Noordwijk, The Netherlands, April 1997.
39. L. Kumar et al., Three-dimensional simulation of multistage depressed collectors on micro-computers, *IEEE Trans. Electron Devices*, **42**:1663–1673, (1995).
40. J. E. Rowe, *Nonlinear Electron-Wave Interaction Phenomena*, New York: Academic Press, 1965.
41. T. M. Antonsen and B. Levush, CHRISTINE, A multifrequency simulation code for traveling-wave tube amplifiers, *NRL Report*, 1996.
42. H. P. Freund and E. G. Zaidman, GATOR: A 3D time-dependent simulation code for helix TWT's, *Proc. IEEE Int. Conference on Plasma Science (ICOPS)*, 197, 1997.
43. H. K. Detweiler, Characteristics of magnetically focused large-signal traveling-wave amplifiers, Rome Air Development Center Tech. Rep. RADC-TR-68-433, Griffiss Air Force Base, NY, 1968.
44. J. D. Wilson, Revised NASA axially symmetric ring model for coupled-cavity traveling-wave tubes, *NASA TP-2675*, 1987.
45. F. Friedlander et al., Transient analysis of beam interaction with antisymmetric mode in truncated periodic structure using three-dimensional computer code "SOS", *IEEE Trans. Electron Devices*, **ED-33**:1896–1901 (1986).
46. C. Smith et al., MPM technology—The miniaturized transmitter solution, *Proc. Microwave Tubes for Space, Military and Commercial Applications Workshop*, Noordwijk, The Netherlands, April 1997.
47. R. L. Spence, Lewis investigates frequency sharing between future NASA space systems and local multipoint distribution systems in the 27-GHz band, Research and Technology 1996, *NASA TM-107350*, 130, 1997.
48. J. A. Dayton, Jr. and G. H. Stevens, Commercial Opportunities for Microwave Tubes, 1996 Crane Microwave Tube Conference, Bloomington, Indiana, November 1996.

TUNNEL DEVICES

EDWARD H. SARGENT
J. M. XU
University of Toronto

Tunnel devices take advantage of the wave-like properties of charge carriers in implementing a desired function. The term *tunneling* refers to the movement of matter from one side of an energetic barrier to the other even though it does not possess sufficient energy to overcome the potential barrier according to the laws of classical mechanics. Instead, the quantum-mechanical wave function of the particle penetrates inside the barrier and extends into the medium on the far side. Therefore, some probability exists for the particle to be on the other side. For these wave

properties of matter to be manifested, the particle mass and the tunneling distance must be small.

Tunnel devices typically possess nonlinear, nonmonotonic current-voltage characteristics and are characterized by very rapid fundamental propagation times. They find application in such diverse areas as microwave oscillators; multiple-level logic, switches, memory elements; and lasers. They are examples of functional devices whose underlying physical mechanisms are exploited and applied to meet a sophisticated demand simply. Often they replace a set of many interconnected devices in the form of a single device, which performs the desired function more naturally. In addition to playing an important role in modern electronics and optoelectronics, tunneling devices have played an important role in twentieth century science by offering direct, macroscopic evidence of microscopic quantum-mechanical phenomena.

1. TUNNELING CONCEPT

The quantum-mechanical concept of tunneling may be illustrated by a simple example. A particle with energy E impinges from the left on a potential barrier of height V , as illustrated in Fig. 1. The solution to the Schrödinger wave equation to the left of the barrier consists of traveling waves (the incident wave travels to the right and any reflected component travels to the left). As the particle energy is stated to be less than the barrier height, the wavevector inside the barrier is complex. The corresponding solution is a sum of decaying exponentials. To the right of the barrier, the solution is a wave traveling to the right. Continuity of the wave function and its derivative at the boundary specifies the overall solution to within a multiplicative constant. There is a nonzero probability of finding the particle on the far side of the barrier.

Associated with each particular choice of the energy E of the incident particle is a transmission coefficient $T(E)$, defined as the ratio of the current density of particles transmitted through the barrier to the current density of particles with energy E impinging on the barrier. As the wave function penetrating into the barrier decays expo-

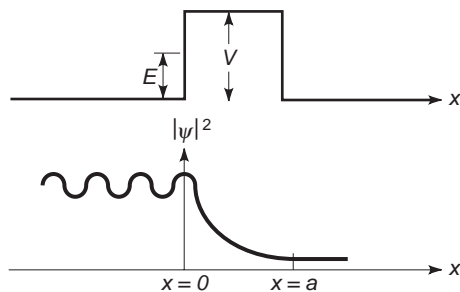


Figure 1. A particle with energy E impinges from the left on a potential barrier of height V and width a . In the case considered, $E < V$, and the wavefunction inside the barrier takes the form of a decaying exponential. The wavefunction penetrates all the way through the finite barrier and emerges in the form of a traveling wave on the far side, and it is possible for the tunneling probability to be appreciable.

nentially, T will also decay exponentially with increasing barrier width and also with increasing difference between the barrier height and the energy of the incident particle. If T is much less than unity, it may be approximated as

$$T \sim 4 \left(\frac{E}{V} \right) \left(1 - \frac{E}{V} \right) \exp \left[-\sqrt{\frac{8m(V-E)}{\hbar^2}} a \right] \quad (1)$$

where m is the particle mass and \hbar^2 is Planck's constant divided by 2π . In Fig. 2, the transmission coefficient is shown as a function of barrier width for a typical electron at room temperature with energy 40 meV and effective mass $m_e = 0.05 m_0$. For this realistic range of parameters, the barrier width should be on the order of nanometers for T to be appreciable.

2. FUNCTIONAL DEVICES

Before the advent of tunnel devices, electronic devices (e.g., diodes, transistors) were dominated by physical mechanisms that gave rise to a monotonic dependence of outputs on inputs.

In 1965, J. A. Morton [1] of Bell Labs popularized the term *functional devices*, a family of which tunneling devices are natural members. Morton described traditional electronic circuits as consisting of vast numbers of interconnected transistors and other devices with simple, monotonic relationships between inputs and outputs. The equations that describe these relationships are mathematical approximations that develop out of physical interactions within matter. The relative simplicity and monotonicity of the resulting equations allows for representation using classic network equations employed in circuit function synthesis.

Morton argued that substantial inroads could be made by abandoning classic circuit concepts and exploiting instead the most basic interactions between energy and matter. Such functional devices would be designed to perform a desired function as simply as possible. The aim

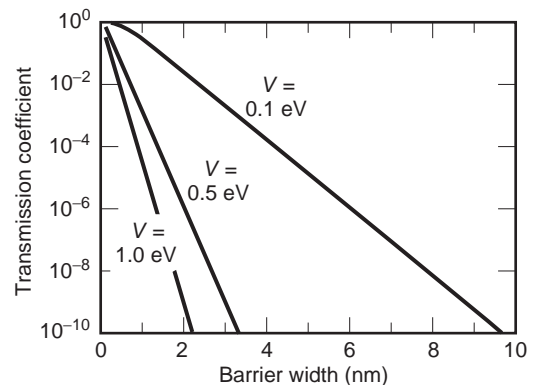


Figure 2. The transmission coefficient for a typical room temperature electron ($E = 40 \text{ meV}$) through a finite potential barrier of various widths (a) and heights (V).

would be to reduce greatly the number of elements and process steps per function:

... the aim of electronics should be not simply to reproduce physically the narrow elegance of classical circuit theory; rather, it should be to perform needed system functions as directly, as simply, and as economically as possible from the most relevant knowledge of energy–matter interactions [1].

Despite such arguments for a natural and elegant approach to device innovation, in the 1960s, functional devices had only gained acceptance in fulfilling niche applications. The slow rate of incorporating the devices at that time is the result of at least two important factors. First, it had been possible until that time and has been possible until recently to continue to extract additional functionalities by making larger, denser circuits by interconnecting simple *black boxes* of traditional circuit elements. Technological inertia contributed to the success of this brute force approach to a point. It is believed, however, that present-day technology is approaching the practical limits of simple-minded miniaturization and densification, and therefore a more elegant and fundamental approach is necessary. A related factor is human inertia, wherein designers who employ electronic devices in creating circuits can manage complexity by conceptualizing device behavior in terms of sets of monotonic curves. They are not trained to manipulate the complicated hypersurfaces that mathematically describe the characteristics of functional devices.

As the demand for sophisticated functionality from a small number of densely packed devices grows and the limitations of traditional device and circuit approaches become more apparent, there will necessarily be a cultural shift in the area of circuit design. The complexities of functional devices will be recognized as a source of opportunities and challenges.

3. TUNNELING: EARLY DEVELOPMENTS

Through the development of the theory discussed later in this section, Fowler and Nordheim [2] are generally credited with one of the early triumphs of the quantum theory: explaining the ejection of electrons from a cold metal in vacuo subjected to a high electric field. They invoked the *new wave mechanics of Schrodinger* to show how electrons could tunnel through a sufficiently thin energetic barrier and escape into the vacuum.

Although Fowler and Nordheim were indeed the first to apply the Schrodinger mechanics specifically to the metal-

vacuum system, it was Oppenheimer [3], in a work concerning the ionization of hydrogen atoms via the tunneling process, who stated

...[the] pulling of electrons out of metal by [large] fields ... is probably to be accounted for in this way.

The history of the study of electron emission from metals is the background against which the advances attributed to Fowler and Nordheim may be understood. Schottky [4] studied the escape of electrons from a conductor via the process of thermionic emission, a purely classic process wherein a fraction of the electrons in the metal have sufficient energy to overcome the metal-vacuum barrier (Fig. 3). At higher temperatures, the average energy of electrons and the breadth of their statistical energetic distribution is increased, leading to a strong temperature dependence of the resulting current. When a weak field is applied to the metal, the Schottky formula describes the temperature T and electric field F dependence of the thermionic emission current:

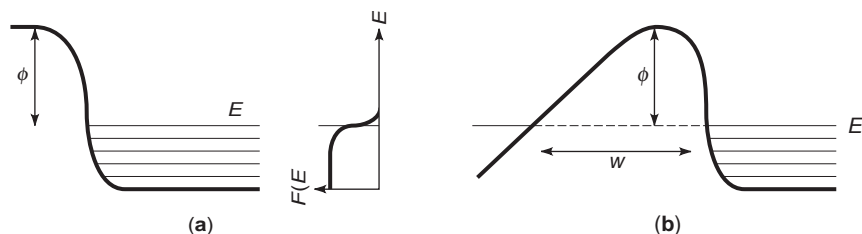
$$J(F, T) = A_R T^2 \exp \left[- \frac{\phi - (e^3 F)^{1/2}}{k_B T} \right] \quad (2)$$

where A_R is a material-dependent constant, ϕ is the metal-vacuum barrier height in the absence of an applied field, and $(e^3 F)^{1/2}$ accounts for the lowering of the barrier height brought about by the application of the field. In the case where no field is applied, Eq. (2) reduces to the Richardson–Laue–Dushman equation, often called the Richardson equation, from which the Richardson constant A_R derives its name.

Thermionic emission theory did not adequately explain the behavior of strong currents that could be obtained at low temperatures if very high electric fields were applied. A number of experiments had shown that the current was independent of temperature over a broad temperature range. This led to attempts to distinguish between electrons *pulled out by fields* and those of a *thermionic character* in a way that Fowler and Nordheim thought artificial. A new empirical relationship was proposed [5], which was correct under high fields and low temperatures (*field emission*) and also at high temperatures (*thermionic emission*) but untested in the transitional region between these mechanisms and not motivated by fundamental considerations.

Fowler and Nordheim posited that the escape of electrons from a cold conductor under application of a sufficiently high electric field could be explained by a

Figure 3. Mechanisms of thermionic and field emission. In the case of (a) thermionic emission, a fraction of the electrons have sufficient energy to escape classically. In the case of (b) field emission, electrons may not have sufficient energy to escape classically, but may tunnel out quantum-mechanically for small enough potential height and barrier width.



quantum-mechanical description: electrons could tunnel through the field-deformed potential energy barrier to generate a current of field-emitted electrons [Fig. 1(b)]. They invoked de Broglie's description wherein electrons could be viewed as having wave-like properties, with a characteristic wavelength λ given by

$$\lambda = \frac{h}{(2mE)^{1/2}} \quad (3)$$

where h is Planck's constant, m is the electron mass, and E is the electron energy. The wave-like properties of the electron allow it to pass through an energetic barrier at an appreciable rate if the barrier is lowered below the level E_F in a distance comparable with the electron wavelength λ .

Fowler and Nordheim treated the matter of field-emission tunneling by solving the Schrodinger wave equation on either side of the barrier with appropriate boundary conditions. They obtained an expression for the quantum-mechanical transmission of electrons through the barrier as a function of electron energy and linked this with the rate of electrons impinging on the barrier as a function of energy. They obtained an electron field-emission tunnel-

ing current density J of

$$J(T, F) = AF^2 \exp\left(-\frac{B\phi^{3/2}}{F}\right) \quad (4)$$

where F is the electric field strength, ϕ is the conductor work function, and A and B are weaker functions of F and ϕ . Thus a plot of $\ln(J/F^2)$ versus $1/F$, the Fowler-Nordheim plot, is predicted to be a straight line, a fact that is borne out experimentally. The temperature-independence of the measured field-emission current is also predicted and explained by the Fowler-Nordheim theory.

4. THE TUNNEL, OR ESAKI, DIODE

In 1958, Leo Esaki [6] observed a negative differential resistance in the forward current-voltage characteristic of a Zener diode (Fig. 4). The devices under study were germanium p - n junctions with heavy dopant concentrations on the order of 10^{19} cm^{-3} . From capacitance measurements, Esaki found that the junction width was approximately 150 \AA . He accounted for the observed current-voltage characteristic in terms of tunneling of electrons in the conduction band of the heavily doped n -side through the narrow junction (whose width was comparable with

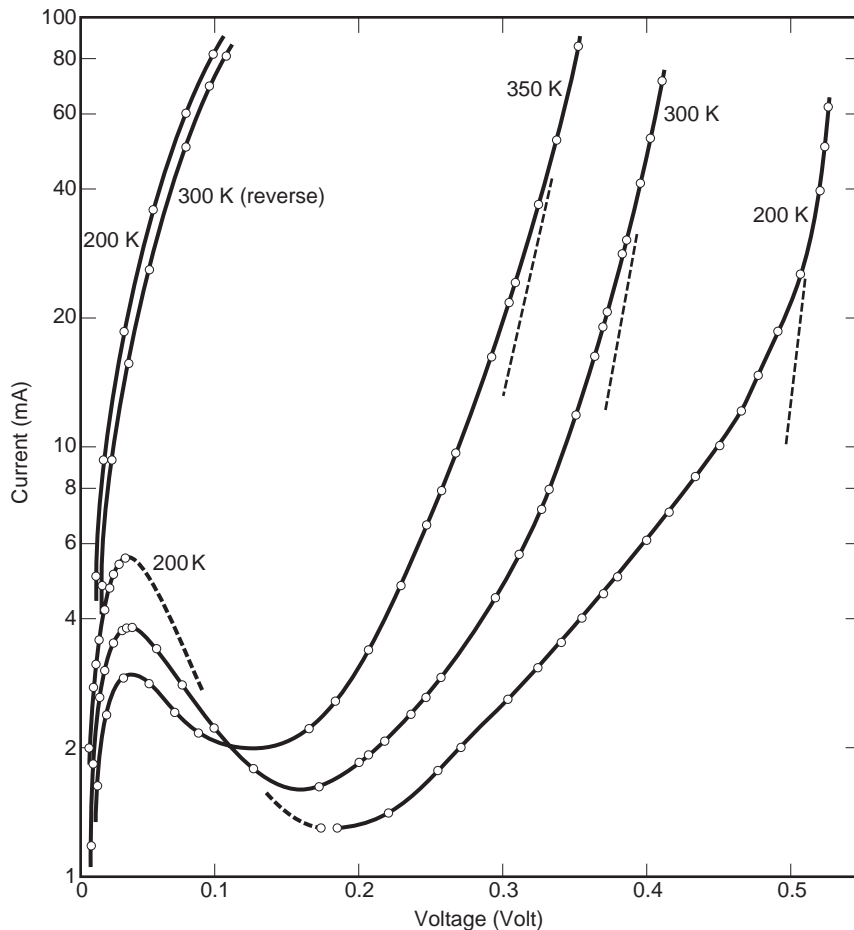


Figure 4. I - V characteristic of the tunnel diode of Leo Esaki's seminal work. The negative differential resistance characteristic—explained with the aid of Fig. 5—provides evidence of the importance of the tunneling mechanism and forms the basis for device applications of tunneling.

the electron wavelength, making the tunneling probability appreciable) into the valence band of the heavily doped p -type contact, and through the analogous process for holes.

To gain an understanding of the operation of the Esaki diode, one must consider the transmission coefficient for electrons and holes through the barrier as a function of their allowed energies and also the availability of states from which and into which to tunnel. Fermi's golden rule gives the transition rate from initial state i to final state m as

$$W_{i \rightarrow m} = \frac{2\pi}{\hbar} M_{im} \rho(E_m) \quad (5)$$

where M_{im} is called the matrix element for the transition and, in this case, is directly related to the tunneling transmission coefficient. The density of states $\rho(E_m)$ describes the availability of states into which the carriers may tunnel. To obtain the net tunneling current in a particular direction, the difference between $W_{c \rightarrow v}$ and $W_{v \rightarrow c}$ will be considered.

This concept and its consequences are illustrated schematically in Fig. 5. At zero bias [Fig. 5(a)], n -side electrons above the Fermi level can tunnel into vacant states on the p -side. However, because they do so at an equal rate in the opposite direction (and the same argument applies for holes), there is no net current. As a small forward bias is applied [Fig. 5(b)], electrons on the n -side become energetically aligned with unoccupied states on the p -side. As the bias is increased further [Fig. 5(c)], more of the electrons lie opposite the forbidden band on the p -side, so that tunneling (in this simple model) is not possible. At even higher biases [Fig. 5(c)], classic drift-diffusion processes dominate the I - V characteristic, and the diodes begin to obey the usual Shockley equation. It is essential that both sides of the junction be degenerately doped (i.e., that the Fermi level lie within the conduction band in the n -type contact and within the valence band in the p -type contact).

Esaki was a cowinner of the 1973 Nobel Prize for Physics for his experimental discovery regarding tunneling phenomena in semiconductors.

4.1. Excess Current

In many tunnel diode applications, a large ratio of peak current to valley current is required. For this reason, the *excess current*, the value of the current in the valley region of the I - V characteristic, where tunneling current is expected to drop to zero and before standard thermionic emission current takes over, is of practical significance. A number of hypotheses were put forth to explain this observation. Mechanisms whereby tunneling carriers could lose energy through photon, phonon, plasmon, or Auger processes were suggested but were not sufficiently important to explain the observed excess tunneling current. Starting from the hypothesis put forth by Esaki that electrons could not tunnel completely through the energy gap but only part of the way, making use of states in the energy gap, Chynoweth et al. [7] developed and experimentally corroborated a model for the excess current.

4.2. Desired Properties

One of the most prominent applications of the Esaki diode is as a high-speed component in oscillator circuits and switches. The preservation of the diode's negative resistance at high frequencies makes it a candidate for such applications. The switching speed is determined by the current available for charging the junction capacitance. To achieve high-speed performance, low capacitance is desired, and sufficient current must be supplied by the diode to charge the junction capacitance. Therefore, one simple figure-of-merit is the ratio of the peak current to the junction capacitance. Another important figure-of-merit is the ratio of the peak current to the valley current, known as the peak-to-valley ratio (P/V), which is related to the current gain obtainable. Maximizing the peak-to-valley ratio in Esaki diodes represents a compromise, primarily in the doping level. At lower (though still degenerate) dopings, the peak current is small because there is only a narrow energy range over which conduction-band electrons see unoccupied valence-band states (and analogously for holes in the valence band). At higher dopings, the density of bandgap states increases (as described above), and the valley current increases. The maximal P/V is found for some intermediate concentration. In either case, the

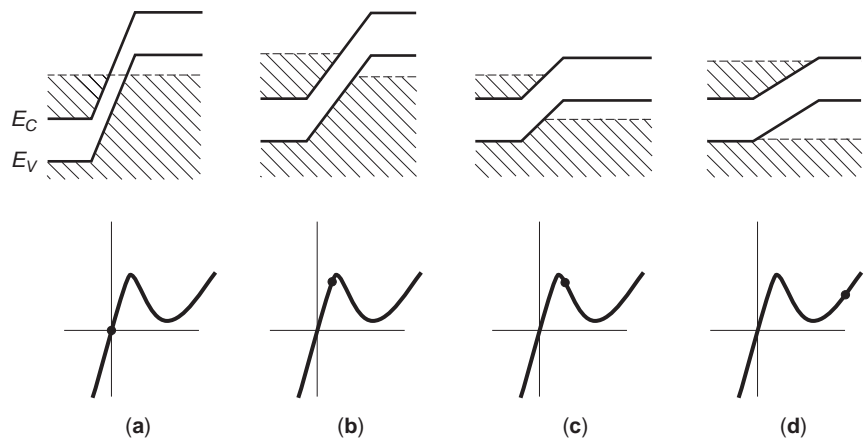


Figure 5. Schematic portrayal of the mechanism of Esaki diode negative resistance. Quantum-mechanical effects dominate the current at low forward bias (b); electrons and holes tunnel through the forbidden zone into the opposite band. As the bias is increased (c), fewer states are available into which carriers may tunnel, and the current decreases. The classic diode current takes over at higher biases (d).

requisite doping level is near the maximum level that can be activated in the semi-conductor, typically around 10^{19} cm^{-3} .

Although a remarkable device and one which provided a satisfying early example of engineering in the quantum domain the Esaki diode exhibits some intrinsic properties that limit its usefulness to certain regimes and application areas. Most importantly, the degenerate doping levels required to achieve a reasonable peak current give rise to a large shunt capacitance that limits high-speed performance and necessitates presenting the device with impedances properly matched to the capacitive reactance of the diode.

5. THE RESONANT TUNNELING DIODE

These fundamental limitations on the performance of the Esaki diode, taken together with the promising prospect that it demonstrated for devices based on tunneling, motivated the development of a structure whose performance was not fundamentally linked to heavy doping. This was first sought and realized in the form of the resonant (intra-band)-tunneling diode.

The history of resonant tunneling precedes the perception of its need in device implementations. The concept originally elaborated by Bohm [8] is illustrated in Fig. 6. The system of double barriers is characterized by a set of quantized energy states. If an incident particle impinges with energy equal to one of these bound-state energies, it is resonantly transmitted. If it differs substantially, it is resonantly reflected.

The first suggestions for resonant-tunneling devices were made by Davis and Hosack [9] and Ioganson [10]. Esaki and Tsu [11] proposed a superlattice implementation of the same basic concept and anticipated explicitly the negative differential resistance resulting from the strong energy dispersive effects that may develop in such a structure if the critical dimensions are on the order of the electron wavelength. In 1973, they extended their theoretical considerations [12] to the case of a multiple-barrier superlattice as opposed to a theoretically infinite one. In 1974, a superlattice was implemented using molecular beam epitaxy [13], with 45 Å GaAs wells clad by 40 Å AlAs barriers. The negative differential conductance characteristic of Fig. 7 was reported.

The mechanism of the intraband resonant-tunneling diode may be illustrated (Fig. 8) by considering one pair of barriers. The same principles apply in determining the conductance features of Fig. 7, the more complicated structure giving rise to the more intricate observed fea-

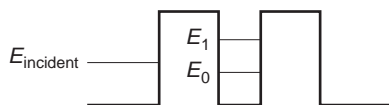


Figure 6. Resonant transmission in a double barrier system. The alignment of the incident particle energy relative to the energies of barrier-confined states determines the rate of transmission through the system.

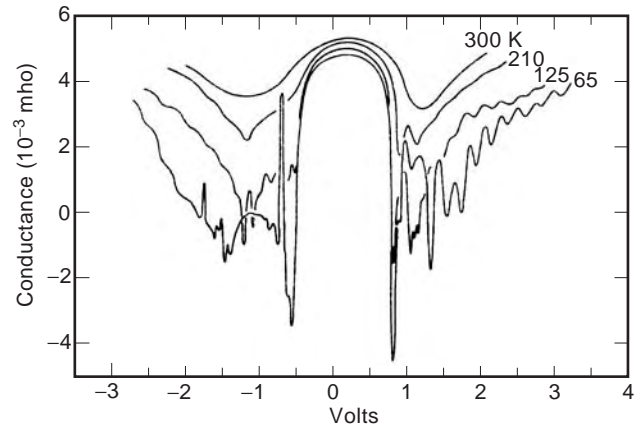


Figure 7. Differential conductance of the first resonant intra-band tunneling structure of Esaki and Chang, 1974 [14].

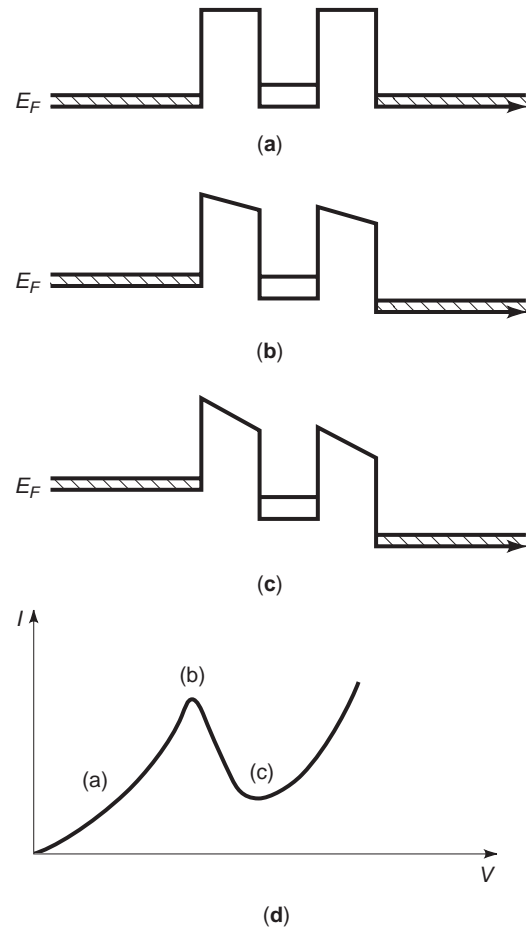


Figure 8. Mechanism of negative differential conductance in resonant-tunneling diodes. At zero bias (a), the electron energy is less than that of the confined barrier states. Under increased bias (b), the incident and confined energies become aligned, and the states at this same energy in the collector are almost completely unoccupied, so that resonant transmission is achieved. As bias is further increased (c), electrons in the injector and the double barrier fall out of resonance.

tures. At zero bias, the energy of conduction-band electrons in the emitter is less than that of quantum-confined electrons between the barriers [Fig. 8(a)], and they are not resonantly transmitted. As the bias is increased, these energies become aligned [Fig. 8(b)]. The states at this same energy in the collector are almost completely unoccupied, so that resonant transmission is achieved, and the conductance is increased. As bias is further increased, however, the energies of the electrons in the injector and inside the well are out of resonance and the conductance is reduced [Fig. 8(c)].

It was not until the observation of fast intrinsic response times by Sollner et al. [14] and soon thereafter of room temperature negative differential resistance [15,16] that the field of superlattices and quantum wells began to grow rapidly. Sollner et al. obtained a P/V ratio of 6:1 at low temperatures, and although the negative differential resistance characteristic was not manifested at room temperature, the effect of resonant tunneling was nevertheless apparent in the room temperature differential conductance characteristic. In addition, Sollner et al. reported one of the first experimental manifestations of the anticipated high-speed response of the room temperature device (RTD). The authors concluded that the charge transport mechanisms are characterized by a time of 6×10^{-14} s. The room temperature NDR of Shewchuck et al. [15] was one of many incremental steps of progress in the direction of acceptably high room temperature peak-to-valley ratios that came with gradual technological improvements in molecular beam epitaxy [17]. In particular, very thin (~ 1 nm) high barrier layers were eventually obtained with precise thickness control and uniformity. Double-barrier RTDs operating at room temperature have been achieved with peak-to-valley ratios as high as 50:1 at 300 K [17]. With the benefit of such incremental technological progress, the experimentally observed fundamental oscillation frequency has improved approximately linearly with time.

6. RESONANT INTERBAND TUNNELING

It is remarkable that, with the benefit of the high-quality atomic-layer engineering made possible by molecular beam epitaxy, resonant-tunneling diodes achieved room temperature peak-to-valley ratios no better than those of the original Esaki diodes of thirty years earlier, which used much less sophisticated material engineering techniques. Had the abrupt interfaces and high doping of modern epitaxial crystal growth techniques been possible at that time, the Esaki diode would likely have provided still more competitive performance.

On the other hand, the RTD held the clear advantage of a much lower capacitance and more manageable technological challenges. In the light of these observations, in 1989, Sweeny and Xu proposed [18] a structure operating on both interband and resonant-tunneling principles with the objective of preserving the attractive features of each one. Their resonant interband tunnel diode concept was an otherwise ordinary p - n diode with quantum wells in the conduction and valence bands. Thus, although it was a

bipolar interband-tunneling device like Esaki's, it incorporated the resonance features of the RTD through the use of coupled quantum wells. The device did not rely on heavy doping to ensure tunneling, but instead took advantage of quantum wells (grown or induced) and exploited the resonance tunneling phenomenon. The operation of one such device is illustrated in Fig. 9. Regions I and IV of Fig. 9 have opposite doping and need not be degenerate. The well regions II and III have a lower bandgap and are doped the same as their higher bandgap outer neighbors. As in previous tunneling devices, the barrier must be sufficiently thin that there is significant interpenetration of the carrier wave functions in II and III. Using bandgap engineering, high carrier concentrations may be achieved in the wells without requiring degenerate doping at any point in the structure. When a bias is applied so that the conduction-band density of states in the n -type quantum well (II) is energetically aligned with the valence-band density of states in the p -type quantum well (III), resonant transmission of carriers through the barrier occurs. As the bias is further increased, no states are available for tunneling until the conduction band of (II) and (III) are aligned. These possibilities and the resulting I - V characteristic are illustrated in Fig. 10. The type-II heterostructural version in their proposal was later suggested independently and demonstrated the same year [19]. This very first implementation of the RIT achieved a room temperature P/V ratio of 20. Within four years, a room temperature peak-to-valley current ratio of greater than 100 had been demonstrated by Day et al. [20].

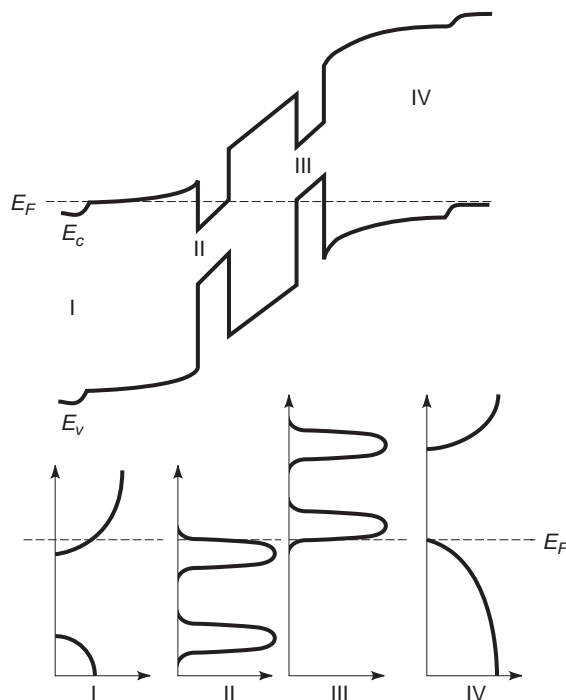


Figure 9. Resonant Interband Tunneling device operation. Resonant transmission occurs between the conduction to the valence bands, rather than within a single band as in earlier intraband tunneling devices.

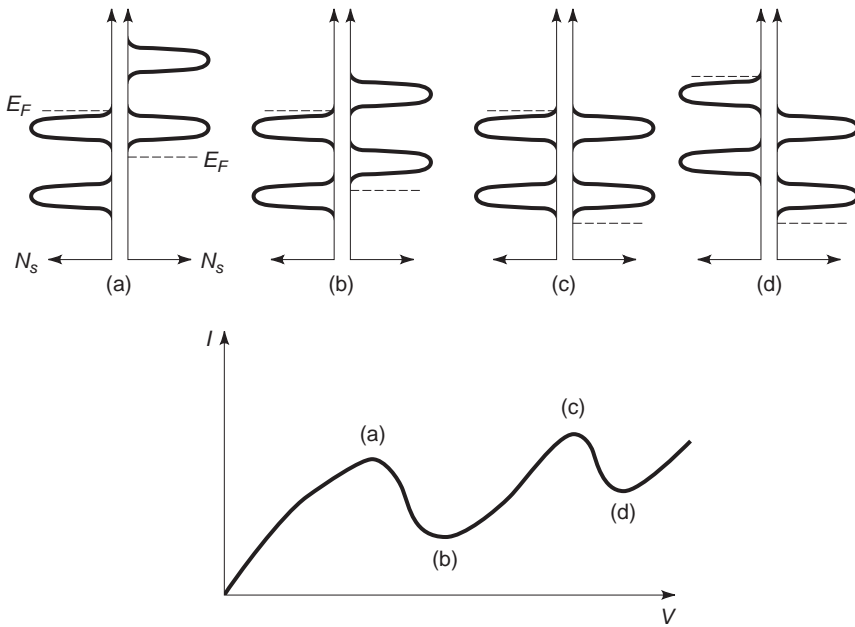


Figure 10. Mechanism of I - V characteristic of resonant intraband tunneling diode. The alignment of quantum-confined energetic states in the conduction and valence bands determines the rate of resonant transmission.

The two alternate implementations of the resonant interband tunneling concept work similarly [18]. The polytype heterostructural implementation exploits the fact that the conduction band of one material is below the valence band of the other in a type-II heterostructure. Resonant intraband tunneling could be realized in such a device [Fig. 11(a)] using very low doping, enabling ultra-high-speed performance not limited by significant contact capacitances. Another realization, a modulation-doped homostructure [Fig. 11(b)], also allows resonant intraband tunneling with a minimum of material doping.

7. SINGLE-ELECTRON TUNNELING: EFFECTS AND DEVICES

The preceding discussion centered around collective transport of many electrons through a system. Tunneling of individual electrons—known as single-electron tunneling—is difficult to observe and control, because thermal fluctuations in electron energy (of order kT) are typically larger than the Coulomb energy change of the system.

Substantial progress has nevertheless been made in this area [21–24]. The possibility of observing single-electron tunneling in very small systems was noted around the same time that Esaki observed the effects of macro-

scopic tunneling electron tunneling in semiconductors. To observe single-electron tunneling, it is not sufficient simply for the system to be small and to have a large effective capacitance, in turn giving rise to a large charging energy (much greater than kT). It must also be well isolated (electromagnetically decoupled) from the environment such that the electron is essentially localized within the system. This localization condition may be expressed in the requirement that the tunneling resistance (impedance) of the system be much greater than the quantum resistance.

Only recently—with the aid of technological advances and further important progress [25]—has broad interest been generated in this problem, and a wide range of investigations begun into single-electron tunneling effects. If the conditions described above are met, the effect may be observed in a number of ways. Because of the discrete nature of electrons, a staircase relation between system charge and voltage exists, so that conductance peaks may be observed at specified voltages. A Coulomb staircase I - V characteristic [25]—a dramatic manifestation of the effect of single-electron charging—develops in suitable structures in which one tunnel barrier is more strongly transmitting than the other [26]. One application area already demonstrated is in the use of controlled Coulomb blockade effects in realizing accurate current standards: by cycling tunneling barrier heights, individual electrons

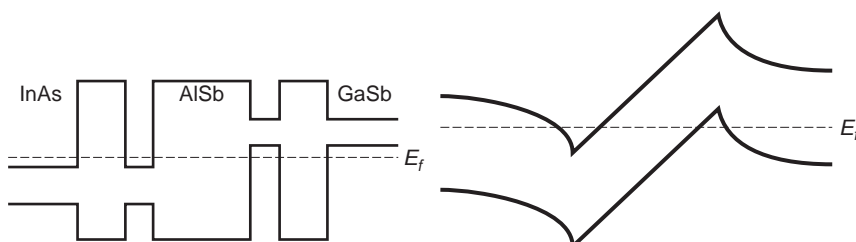


Figure 11. (a) Polytype heterostructure implementation of the resonant interband tunneling diode. (b) Modulation-doped homostructure implementation of the resonant interband tunneling diode.

can be made to pass through the confined system at the applied frequency—resulting in an “electronic turnstile” [27]—and producing a current $I = ef$ (where e is the electronic charge and f the frequency of modulation).

The introduction of further tunneling junctions and more complex connections and coupling provide a rich variety of externally observable single-electron tunneling phenomena. Foreseeable applications in conventional electronics include memory cells, D/A converters, and sensitive analog transistors.

8. TUNNELING IN OPTOELECTRONICS

Laser technology has also benefited from innovative solutions to problems posed by new applications. Conventional semiconductor lasers are bipolar devices that rely on band-to-band transitions between the conduction and valence bands. The energy associated with these interband transitions and consequently the energy of the emitted photons is largely determined by the properties of the semiconductor material. By introducing quantum wells in which spatially confined electrons and holes have ground-state energies above the semiconductor bandgap, it is possible to tailor somewhat the energy of photon emission.

For a number of applications, mid- or long-wavelength lasers with photon energies ranging from 2 to 12 μm are desired. One solution that reduces the dependence on material choice takes advantage of transitions in quantum wells within a particular band, typically the conduction band. In these intraband devices, the photon emission energy may be selected by careful tailoring of well and barrier widths.

One fundamental requirement in lasers is that of population inversion. If photons are emitted during the stimulated transition from state 2 to state 1, then the population of state 2 must exceed that of state 1. Two dominant approaches have been adopted in achieving population inversion in intraband lasers, both of them based on tunneling.

The group of Capasso [28] realized the first intrasubband laser. In this device, population inversion within the conduction band was achieved via very careful design of the active region, which consists of sets of wells and barriers for injection, relaxation, and removal of carriers. Electrons are injected by resonant tunneling into one of the higher states of the active region quantum wells. By simultaneously making the lower state depopulation mechanisms resonant with other phonon and tunneling processes, the lifetime of the lower state is made less than that of the upper state, and population inversion may be achieved. Using this tunneling-based mechanism, room temperature quantum cascade lasers have been achieved [29].

Another approach to achieving population inversion was proposed by Yang and Xu [30]. As illustrated in Fig. 12, intraband tunneling or simply intraband transport may be used to inject carriers into the upper state (from I–II in the figure), and interband tunneling to remove carriers from the lower state (from II–III) to invert the populations in the first two states of the conduction

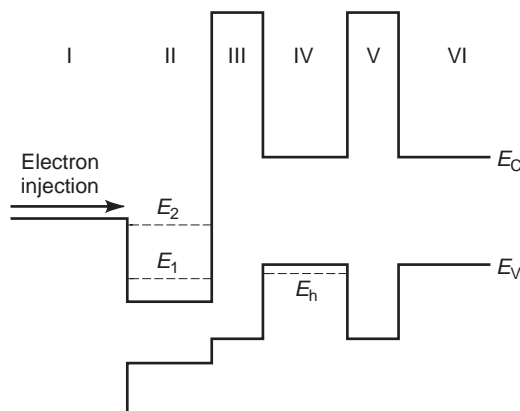


Figure 12. Illustration of resonant interband tunneling-assisted population inversion. Carriers are injected into the upper state (from I–II) and are removed from the lower state (from II–III) via interband tunneling. The population in the first two states of the conduction band is thereby inverted.

band. The structure is designed to prevent tunneling out of the upper state. Low-temperature operation of a device incorporating this concept was demonstrated by Yang et al. in 1997 [31].

9. TUNNEL DEVICE MODELING

Since the seminal work of Fowler and Nordheim [2], a variety of advances have been made in the accuracy of models of tunnel device operation [32]. An element common to these developments is the use of the effective mass approximation. In this approach, widely employed throughout condensed matter physics, an effective mass term (not generally equal to the true physical mass of the carrier) is used to account for the effects of the atomic potentials that the charge carrier encounters during its trajectory through a solid medium. The simplifications involved transform the modeling of interactions in a solid from what would be a daunting task, accounting individually for a large, complex set of potentials, into potentially tractable problems. The effective mass is used in an approximate Schrodinger equation, and the validity of the results vary according to structure and the region within a given structure.

The Bohm approximation (or the golden rule of Fermi) is usually invoked to quantify tunneling currents. Tunneling may be viewed as the scattering of an electron in an electric field in which the scattering potential is usually invariant in the transverse direction, so that the transverse momentum vector is conserved. (In more complex devices, one may take advantage of the transverse direction in further enhancing functionality.)

Although a number of simplifications have already been invoked to this point, further approximations are typically employed in modeling interband tunnel devices. In this case, the coupling between conduction and valence bands provides the central mechanism for device operation, and a singleband effective mass approximation does not yield physically correct results.

In such devices, interband coupling is strongest in the tunneling region. To a first-order approximation, the current-voltage relationship is obtained from a coupled-band effective mass equation. If spin is taken into consideration, there are two conduction-band contributions and six valence-band contributions. Within this eight-band framework, the $\vec{k} \cdot \vec{p}$ of Kane [33] is the most commonly employed and may also be the most exact. Altarelli [34] provides a review of the $\vec{k} \cdot \vec{p}$ treatment.

To gain physical insight into the problem without onerous computation, a two-band model is often used. By symmetry considerations of the Bloch functions, the conduction band and light-hole bands are most strongly coupled and must be retained. The other bands of the eight-band Luttinger–Kohn Hamiltonian [29] may be removed if the effective masses of the bands remaining are adjusted to ensure that their dispersion relationships agree reasonably with the known band structure over the energy of interest (for a review, see Datta [36]). Even this simplified two-band model provides coupling between the differential equations associated with different bands.

10. OVERVIEW, ASSESSMENT, AND OUTLOOK

Digital functional devices based on carrier tunneling take advantage of nonmonotonic I – V characteristics and fast intrinsic response times. Applications include high-speed analog-to-digital converters, parity bit generators, and multiple-valued logic elements. Three terminal devices, such as the resonant tunneling bipolar transistor proposed by Capasso and Kiehl in 1985 [37] have also been developed. This particular device, which uses a quantum well in the p -type base layer, exhibits a series of peaks in its collector current as a function of base-emitter voltage. For this device, applications include multiple-valued logic, parity generators, analog-to-digital converters, and multiple state memory, all implemented more naturally than using a collection of two-terminal devices. Three-terminal unipolar devices based on tunneling include the resonant hot electron transistor (RHET) of Yokoyama et al. [38] and the quantum wire transistor proposed in 1985 by Luryi and Capasso [39].

High-speed analog devices typically exploit the high-frequency negative differential conductance obtained from tunneling devices. Two-terminal oscillators are perhaps the simplest device examples, which take advantage of the fact that the negative differential conductance persists on timescales as short as the lifetime of the electron in the resonant state between the barriers of a resonant tunneling diode. RTDs may also be used as efficient mixers by exploiting the rapid variation in dynamic conductance with voltage near the negative differential resistance portion of the I – V characteristic.

RTDs find applications in switching when they are biased with a source resistance larger than the magnitude of their negative differential resistance. A stable bias point is no longer achievable in the NDR region, and switching occurs between the stable points outside of this region. Switching times as short as 2 ps have been measured [40,41].

The preceding list of applications covers those that could be thought of as niche roles for tunneling devices. They fulfill a specific role often very effectively but typically in isolation from general circuit applications. It has been argued that tunneling devices have a much more important role to play in the future.

Exponential improvements in circuit speed have been enabled by an exponential downward trend in minimum device geometries and switching power. This downscaling cannot continue indefinitely. Before fundamental physical limits are reached, ICs based on transistors will be rendered impossible or exorbitant by a combination of problems related to device technology, interconnection, noise, and reliability. A saturation in circuit density improvements is likely to imply a saturation in the historically downward trend in cost per bit or function.

Three-terminal devices based on tunneling would provide a means to continue this downward scaling and in fact to exploit it to the fullest. However, as argued previously, tunneling devices technologies will not gain acceptance if they cannot penetrate the culture of circuit design—if they do not become accessible to their users. This necessitates coordination between device creators and device users in matching physics with function, as per Morton’s vision of 1965.

Another possible trend is a further extrapolation of Morton’s functional device concept and of the desirability of device miniaturization. The inspiration is taken from biological systems and biochemical reactions and interactions, which possess the desired characteristics of being based on tunneling and, therefore are very fast; of being intrinsically multifunctional; and of possessing, in some instances, the potential to implement a *local learning function*. At least two approaches have been witnessed on this front. First, simple tunneling processes have been incorporated into otherwise standard bipolar transistors [42] and MOS transistors [43]. In the bipolar transistor, the large ratio of electron tunneling transmission to hole transmission (because of the large effective mass disparity in compound semiconductors) yields improved injected efficiency of homojunction BJTs with a more easily fabricated layer structure than traditional heterojunction BJTs. In the MOS case, tunneling into a floating gate structure enables functionality analogous to learning. A second approach, more revolutionary and therefore less mature in approach, involves developing devices that perform some of the basic electronic functions using human-engineered molecules, a field known as (bio)molecular electronics. Both approaches use tunneling, as a consequence of miniaturization and as a means for expanding and exploring new functionalities.

BIBLIOGRAPHY

1. J. A. Morton, From physics to function, *IEEE Spectrum*, **2**: 62–66 (1965).
2. R. H. Fowler and L. Nordheim, Electron emission in intense electric fields, *Proc. R. Soc. Lond.*, **119**:173–181 (1928).
3. J. R. Oppenheimer, Three notes on the quantum theory of aperiodic effects, *Phys. Rev.*, **13**:66–81 (1928).

4. W. Schottky, Über den einfluss von strukturwirkungen, besonders der Thomsonchen bildkrft, auf die electronemission der metalle, *Physikalische Zeitschrift*, **15**:872–878 (1914).
5. R. A. Millikan and C. C. Lauritsen, Relations of field currents to thermionic currents, *Proc. Natl. Acad. Sci.*, **14**:45–49 (1928).
6. L. Esaki, New phenomenon in narrow germanium p-n junctions, *Phys. Rev.*, **109**:603–604 (1958).
7. A. G. Chynoweth, W. L. Feldmann, and R. A. Logan, Excess tunnel current in silicon Esaki junctions, *Phys. Rev.*, **121**:684–694 (1961).
8. D. Bohn, *Quantum Theory*, Englewood Cliffs, NJ: Prentice-Hall, 1951.
9. R. H. Davis and H. H. Hosack, Double barrier in thin-film triodes, *J. Appl. Phys.*, **34**:864–866 (1963).
10. L. V. logansen, The possibility of resonance transmission of electrons in crystals through a system of barriers, *Soviet Phys. JETP*, **18**:146–150 (1964).
11. L. Esaki and R. Tsu, Superlattice and negative differential conductivity in semiconductors, *IBM J. Res. Develop.*, **14**(1):61–65 (1970).
12. L. Esaki and R. Tsu, Tunneling in a finite superlattice, *Appl. Phys. Lett.*, **22**: 562–564 (1973).
13. L. Esaki and L. L. Chang, New transport phenomenon in a Semi-conductor “superlattice,” *Phys. Rev. Lett.*, **33**:495–498 (1974).
14. T. C. L. G. Sollner et al., Resonant tunneling through quantum wells at frequencies up to 2.5 Thz, *Appl. Phys. Lett.*, **43**:588–590, (1983).
15. T. J. Shewchuk et al., Resonant tunneling oscillations in a GaAsAl_xGa_{1-x}As heterostructure at room temperature, *Appl. Phys. Lett.*, **46**:508–510 (1985).
16. M. Tsuchiya, H. Sakaki, and J. Yoshino, Room temperature observation of differential negative resistance in AlAs/GaAs/AlAs resonant tunneling diode, *Jpn. J. Appl. Phys.*, **24**:L466–L468 (1985).
17. J. Smet, T. P. E. Broekaert, and C. G. Fonstand, Peak-to-valley current ratios as high as 50:1 at room temperature in pseudomorphic In_{0.53}Ga_{0.47}As/AlAs/InAs resonant tunneling diodes, *J. Appl. Phys.*, **71**:2475–2477 (1992).
18. M. Sweeny and J. Xu, Resonant interband tunnel diodes, *Appl. Phys. Lett.*, **54**:546–548 (1989).
19. J. R. Soderstrom, D. H. Chow, and T. C. McGill, New negative differential resistance device based on resonant interband tunneling, *Appl. Phys. Lett.*, **55**:1094–1096 (1989).
20. D. J. Day et al., Experimental demonstration of resonant interband tunnel diode with room temperature peak-to-valley current ratio over 100, *J. Appl. Phys.*, **73**:1542–1544 (1993).
21. C. J. Gorter, *Physica*, **17**:777 (1951).
22. C. A. Neugebauer and M. B. Webb, *J. Appl. Phys.*, **33**:74 (1962).
23. I. Giaever and H. R. Zeller, *Phys. Rev. Lett.*, **20**:1504 (1968).
24. J. Lambe and R. C. Jaklevic, *Phys. Rev. Lett.*, **22**:1371 (1969).
25. K. K. Likharev, *IBM J. Res. Dev.*, **32**:144 (1988).
26. U. Meirav and E. B. Foxman, *Semiconductor Sci. Technol.*, **11**:255–284 (1996).
27. Y. Nagamune et al., *Appl. Phys. Lett.*, **64**:2379 (1994).
28. J. Faist et al., Quantum cascade laser: Temperature dependence of the performance characteristics and high T₀ operation, *Appl. Phys. Lett.*, **65**:2901–2903 (1994).
29. J. Faist et al., High power mid-infrared ($\lambda \sim 5 \mu\text{m}$) quantum cascade lasers operating above room temperature, *Appl. Phys. Lett.*, **68**:3680–3682 (1996).
30. R. Q. Yang and J. M. Xu, Population inversion through resonant interband tunneling, *Appl. Phys. Lett.*, **59**:181–183 (1991).
31. R. Q. Yang et al., High power mid-infrared interband cascade lasers band on type-II quantum wells, *Appl. Phys. Lett.*, **71**: 2409– 2411 (1997).
32. E. E. Mendez, J. Nocera, and W. I. Wang, Conservation of momentum and its consequences in interband resonant tunneling, *Phys. Rev. B*, **45**:3910–3913 (1992).
33. E. O. Kane, Band structure of indium antimonide, *J. Phys. Chem. Solids*, **1**:249–261 (1957).
34. M. Altarelli, in G. Allen et al., *Heterojunction and Semiconductor Superlattices*, Berlin: Springer-Verlag, 1986.
35. J. M. Luttinger and W. Kohn, Motion of electrons and holes in perturbed periodic fields, *Phys. Rev.* **97**:869–883 (1955).
36. S. Datta, *Quantum Phenomena*, Reading, MA: Addison-Wesley, 1989.
37. F. Capasso and R. A. Kiehl, Resonant tunnelling transistor with quantum well base and high-energy injection: A new negative differential resistance device, *J. Appl. Phys.*, **58**:1366 (1985).
38. N. Yokoyama et al., A new functional resonant tunnelling hot electron transistor (RHET), *Jpn. J. Appl. Phys.*, **24**:L853 (1985).
39. S. Luryi and F. Capasso, Resonant tunnelling of two-dimensional electrons through a quantum wire: A negative transconductance device, *Appl. Phys. Lett.*, **47**:1347 (1985).
40. J. F. Whitaker et al., Picosecond switching time measurement of a resonant tunneling diode, *Appl. Phys. Lett.*, **53**:385–387, (1988).
41. S. K. Diamond et al., Resonant tunneling diodes for switching applications, *Appl. Phys. Lett.*, **54**:153–155 (1989).
42. J. Xu and M. Shur, A tunneling emitter bipolar transistor, *IEEE Electron Device Lett.*, **EDL-7**:416–418 (1986).
43. C. Diorio et al., A single-transistor silicon synapse, *IEEE Trans. Electron Devices*, **43**:1972–1980 (1996).

FURTHER READING

- C. B. Duke, *Tunneling in Solids*, New York: Academic, 1969.
- H. C. Okean, Tunnel diodes, in *Semiconductors and Semimetals*, Vol. 7, Part B, R. K. Willardson and A. C. Beer, eds., New York: Academic, 1966.
- D. K. Roy, *Tunnelling and Negative Resistance Phenomena in Semiconductors*, New York: Pergamon, 1977.

UHF RECEIVERS

CHARLES W. BOSTLAN
DENNIS G. SWEENEY
Virginia Tech

An ultra-high frequency (UHF) receiver receives radio signals with input frequencies between 300 MHz and 3000 MHz. Radio waves in this part of the spectrum usually follow line-of-sight paths and penetrate buildings well. The natural radio environment is significantly quieter at UHF than at lower frequencies, making receiver noise performance more important. UHF antennas are small enough to be attractive for vehicular and handheld applications, but are not as directional or expensive as microwave antennas. Many radio services use UHF, including land mobile, TV broadcasting, and point-to-point. The point-to-point users are rapidly disappearing, and the greatest current interest in receiver design centers on cellular and personal communications system (PCS) applications in bands from 800 MHz to 950 MHz and 1850 MHz to 1990 MHz.

UHF receiver design was once a specialized field incorporating parts of the lumped-circuit techniques of radio-frequency (RF) engineering and the guided-wave approach of microwave engineering. Recent trends in circuit integration and packaging have extended RF techniques to the UHF region, and there are few qualitative distinctions between UHF receivers and those for lower frequencies. UHF receivers differ from their lower-frequency counterparts primarily by having better noise performance and by being built from components that perform well at UHF.

1. UHF RECEIVER OPERATION

1.1. The Role of a UHF Receiver in a Radio Communications System

Radiofrequency communications systems exist to transfer information from one source to a remote location. Figure 1 is a system block diagram of a simple radio communications system. A transmitter takes information from an

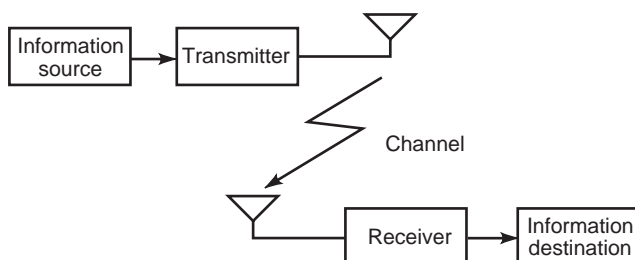


Figure 1. Block diagram of a UHF communications system showing the role of the receiver.

external source, modulates it onto an RF carrier, and radiates it into a radio channel. The radiated signal grows weaker with distance from the transmitter. The receiver must recover the transmitted signal, separate it from the noise and interference that are present in the radio channel, and recover the transmitted information at some level of fidelity. This fidelity is measured by a signal-to-noise ratio for analog information or by a bit error rate for digital information.

1.2. Receiver Characteristics

The following characteristics describe receiver performance:

- *Sensitivity* is a measure of the weakest signal that the receiver can detect. The ideal receiver should be capable of detecting very small signals. Internally generated noise and antenna performance are the primary factors limiting the sensitivity of UHF receivers.
- *Selectivity* describes the receiver's ability to recover the desired signal while rejecting others from transmitters operating on nearby frequencies.
- *Stability* is the receiver's ability to remain tuned to the desired frequency over time with variations in supply voltage, temperature, and vibration, among others.
- *Dynamic range* is a measure of the difference in power between the strongest signal and the weakest signal that the receiver can receive.
- *Image rejection* measures the receiver's ability to reject images, incoming signals at unwanted frequencies that can interfere with a wanted signal.
- *Spurious response protection* measures the receiver's freedom from internally generated unwanted signals that interfere with the desired signal.

1.3. The Superheterodyne Architecture

The most widely used receiver topology is the superheterodyne or superhet. A block diagram of this topology is shown in Fig. 2. It provides amplification both at the incoming radiofrequency and at one or more intermediate

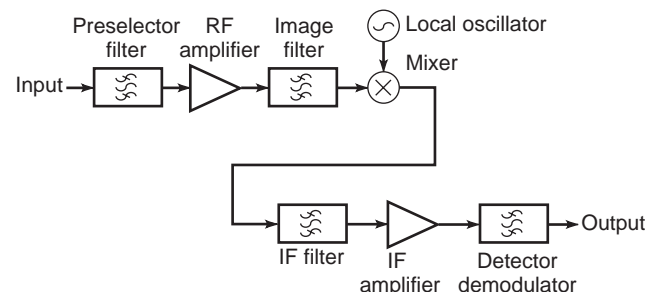


Figure 2. The architecture of a superheterodyne receiver.

THIN FILMS

KIYOTAKA WASA
Yokohama City University
KENTARO SETSUNE
Matsushita Electric
Industrial Co.

1. THIN FILM MATERIALS

Thin film ferroelectric materials and hexagonal piezoelectric materials are essential for fabrication of electronic and/or photonic devices. Historically ferroelectric materials were discovered in a form of bulk single crystals of Rochelle salt in 1920. Since then, a number of ferroelectric materials, including $\text{NH}_4\text{H}_2\text{PO}_4$ (ADP), KH_2PO_4 (KDP), LiNbO_3 (LN), LiTaO_3 (LT), BaTiO_3 (BT), PbTiO_3 (PT), and $\text{Pb}(\text{Zr},\text{Ti})\text{O}_3$ (PZT), were developed in a form of bulk single crystals or bulk ceramics. Among these ferroelectric materials, perovskite (ABO_3) with oxygen octahedral structures has become an important ferroelectric material.

Ferroelectric materials are dielectrics that have a spontaneous polarization with nonlinear hysteretic properties and show several unique properties including high dielectric permittivity, high piezoelectricity, high pyroelectricity, and high electrooptic characteristics.

Bulk ferroelectric materials were widely used to manufacture discrete electronic components including ceramics capacitors, bandpass filters, resonators, ultrasonic transducers, and positive temperature coefficient (PTC) thermistors. Novel ferroelectric materials such as optical transparent ferroelectric $(\text{Pb},\text{La})(\text{Zr},\text{Ti})\text{O}_3$ (PLZT) ceramics were developed by Haertling and Land in 1971. A high-speed electrooptical shutter was realized using hot-pressed transparent PLZT ceramics. The bulk-type ferroelectric devices, however, could not meet recent requirements of miniaturization and/or integration with Si and/or GaAs semiconductive devices.

Thin film ferroelectric materials have a high potential for miniaturization and/or integration with the semiconductive devices. Thin films are also important to the understanding of ferroelectricity. Thin films are commonly fabricated by depositing individual atoms on a substrate. The film thickness is typically less than several micrometers. The structure of thin films is essentially homogeneous on an atomic scale. Thin films exhibit the following useful aspects including thin film effects:

1. Unique material properties resulting from the atomic scale growth
2. Size effects at ultrathin films
3. Unique functional properties at layered structure including human-made superlattice and tailored ferroelectric materials

Polycrystal and/or single-crystal thin films of ferroelectric/piezoelectric materials are used for the fabri-

cation of thin film devices. The polycrystal thin films are commonly deposited on a noncrystalline substrate such as fused quartz, borosilicate glass, and passivated Si substrates. The single-crystal thin films are heteroepitaxially grown on a foreign single-crystal substrate such as sapphire, MgO , SrTiO_3 (ST), LaAlO_3 , and YSZ substrates. At the early stage, the ferroelectric thin films were considered to be a simple substitution of bulk dielectric materials by thin films, such as a fabrication of thin film discrete capacitor for an electronics system.

Since the 1970s, several kinds of thin film ferroelectric and/or piezoelectric films were developed for a fabrication of bulk acoustic wave (BAW) devices, surface acoustic wave (SAW) devices, thin film ferroelectric memory, acoustooptical (AO) devices, and electrooptical (EO) devices. Among these thin films, piezoelectric ZnO and CdS thin films of hexagonal structure were extensively studied for a fabrication of the thin film SAW devices and the thin film AO devices, although the piezoelectric hexagonal ZnO and/or CdS were not ferroelectric materials. The technology for a production of ZnO thin film SAW devices was established, and the ZnO thin film SAW devices are used in practice. Since the 1980s, much attention has been paid to the application of ferroelectric thin films such as PZT and $(\text{Pb},\text{La})\text{TiO}_3$ (PLT) to thin film optical waveguide devices, an integrated pyroelectric sensor, a memory capacitor of high dielectric permittivity at megabit dynamic random access memory (DRAM), the ferroelectric random access memory (FERAM) combined with Si and/or GaAs integrated circuits, and a thin film microactuator. Two-dimensional integrated optical devices are made by electrooptic thin films. The multilayer structures tailor SAW materials with designed acoustic velocity, electromechanical coupling, and temperature stability. The electromechanical coupling for the generation of SAW is enhanced at the layered structures. High electromechanical coupling with zero temperature coefficient of delay time (TCD) could be achieved at the layered structure of ZnO/glass substrate. The electrostrictive properties are also of interest for making a microelectromechanical system (MEMS). A MEMS provides integration of sensors, actuators, and electronic circuits in a single chip. Table 1 shows typical thin film ferroelectric materials and their devices including hexagonal piezoelectric thin films [1–3].

2. THIN FILM FABRICATION

Thin films of ferroelectric materials are fabricated by a thin film deposition process including physical vapor deposition (PVD), chemical vapor deposition (CVD), and chemical solvent deposition, as shown in Table 2.

Thin films of ferroelectric materials were first fabricated by Feldman in 1955 for BaTiO_3 by PVD using a simple vacuum evaporation. In the 1960s, others tried to deposit thin films of PbTiO_3 by cylindrical magnetron sputtering. The controlled deposition of the perovskite

Table 1. Ferroelectric Thin Films and Devices

Function	Devices: Materials	Miscellaneous
Ferroelectricity	FEDRAM: PZT, PLZT FESRAM: BPZT, SBT FEMFET: BMF	Nonvolatile High Ps, Pr PZT > 20 μm/cm ²
High Permittivity	Capacitor for high count	High permittivity
Pyroelectricity	DRAM: SBT, ST, PZT, PLT IR detector: PT, PLT	PZT: 500–2000 Sensitive/low noise PLT: $\gamma = 5.5 \times 10^{-4} \text{ C/m}^2\text{K}$
Piezoelectricity	BAW/SAW: ZnO, AlN Filter PZT, PLT Resonator Oscillator Delay line	High coupling for SAW ZnO/sapphire: $k^2 = 5\%$ High temperature stability ZnO/glass: TCD = 0
Electrostriction	Actuator: PLT, PZT, ZnO MEMS	High sensitive
Acousto-optics	Integrated optics: ZnO, LN Channel switch PLT, PLZT Modulator	Low working voltage High-speed operation
Electro-optics	Integrated optics: LT, LN, BTO Coupler PLT, PLZT Channel switch Modulator Optical shutter EO disk memory	Pockels effect (linear EO) LN, LT, BTO, PLZT Kerr effect (quadratic EO) PLT, PLZT: $R = 1 \times 10^{-16} \text{ m}^2/\text{V}^2$ (6328 Å)

BPZT:BaTiO₃-PbZrO₃; SBT:SrBi₂Ta₂O₉, BST: (Ba,Sr)/TiO₃; BTO:Bi₄Ti₃O₁₂; LN:LiNbO₃; LT:LiTaO₃; BMF:BaMgF₄

ferroelectric materials of ABO₃ and A(B1,B2)O₃ structure could not be attained because of their complex chemical composition. Since the middle of the 1970s, rapid progress has been observed in the thin film deposition processes, including planar magnetron sputtering, molecular beam epitaxy (MBE), and metal organic chemical vapor deposi-

tion (MOCVD). After the discovery of high-Tc superconductors of layered perovskite in 1986, rapid progress has been seen in the development of the deposition process for complex perovskite with atomically controlled crystal structure using sputtering, MBE, laser ablation, and MOCVD.

Table 2. Thin Film Deposition Process

Classification	Deposition System	Source Materials	Film Structure
<i>Vapor phase deposition</i>			
PVD	Thermal evaporation	Individual metals Individual oxides Multisource	Uniaxial crystal by epitaxial growth (poly/single)
	EB crucible MBE		
	Laser ablation	FE compounds Individual oxides Multitarget	Tailoring FE by layer-by-layer deposition <i>In situ</i> poling
CVD	Sputtering	FE compounds Individual metals Individual oxides Multitarget	
	Low-pressure CVD MOCVD Plasma-assisted MOCVD	Individual halide Metal organic gas	Uniaxial crystal by epitaxial growth (poly/single) <i>In situ</i> poling
	<i>Chemical solvent deposition</i>		
	MOD Sol-gel deposition	Individual Metal organic gas	Multiaxial (polycrystal) <i>Ex situ</i> poling (porous)

Typical configuration of deposition systems are shown in Fig. 1. A conventional thermal evaporation process provides inhomogeneous and nonstoichiometric thin films. A multisource MBE system is used for the deposition. The laser ablation is carried out by the direct evaporation of source ferroelectric materials resulting from the irradiation of high-intensity pulsed excimer laser. The mechanism of laser ablation includes photo and thermal evaporation. The pulsed evaporation by high-intensity laser improves the inhomogeneity and/or nonstoichiometry, although the laser ablation includes the thermal evaporation process. The phenomenon of sputtering consists of a nonthermal evaporation. The sputtering process essentially provides homogeneous and stoichiometric thin films of complex ferroelectric materials because the sputtering mechanism consists of removing source materials (target) on an atomic scale by an impact of energetic ions through the momentum transfer mechanism. Multitarget magnetron sputtering is used for the deposition of layered structures and/or human-made superlattices. The sputtering process has a high potential for the fabrication of complex ferroelectric thin films. In the plasma-assisted MOCVD, energetic electron in gas plasma enhances the chemical reaction. At present, these thin film processes provide the thin films of perovskite with an accuracy of 1 nm corresponding to two or three of their crystal units. The chemical solvent deposition provides a simple fabrication process. However, the deposited thin films are essentially porous because the growth process is governed by

a conventional thick film technology including dipping and/or spinning of sol-gel precursor solution followed by annealing for sintering.

The deposition, chiefly by sputtering, of transducer quality ZnO thin films has been studied since the 1970s. The technology to fabricate ZnO thin films has already been established. The *c*-axis-oriented polycrystalline thin films are deposited on a glass substrate by direct sputtering from the ZnO target. The *c*-axis orientation on the glass substrate is quite reasonable because the film growth of a hexagonal structure is governed by Bravis's empirical law for crystal growth, where the most densely packed plane (*c*-plane) will be the most preferable surface of crystal growth. Single-crystal ZnO thin films are epitaxially grown on a sapphire substrate. The *a*-axis-oriented ZnO thin films are epitaxially grown on *R*-plane sapphire.

It is particularly important to understand the structure of thin films because it can have a profound influence on the operation of the thin film devices.

Thin films of polycrystalline phase comprise a column geometry with an interfacial layer between the thin films and a substrate. Low dielectric permittivity of the interfacial layer apparently reduces the permittivity of the ferroelectric thin films and/or increases a coercive field (extrinsic thickness effect). The decrease of dielectric permittivity for ferroelectric thin films with the decrease of their film thickness is also governed by the depolarization phenomenon (intrinsic thickness effect).

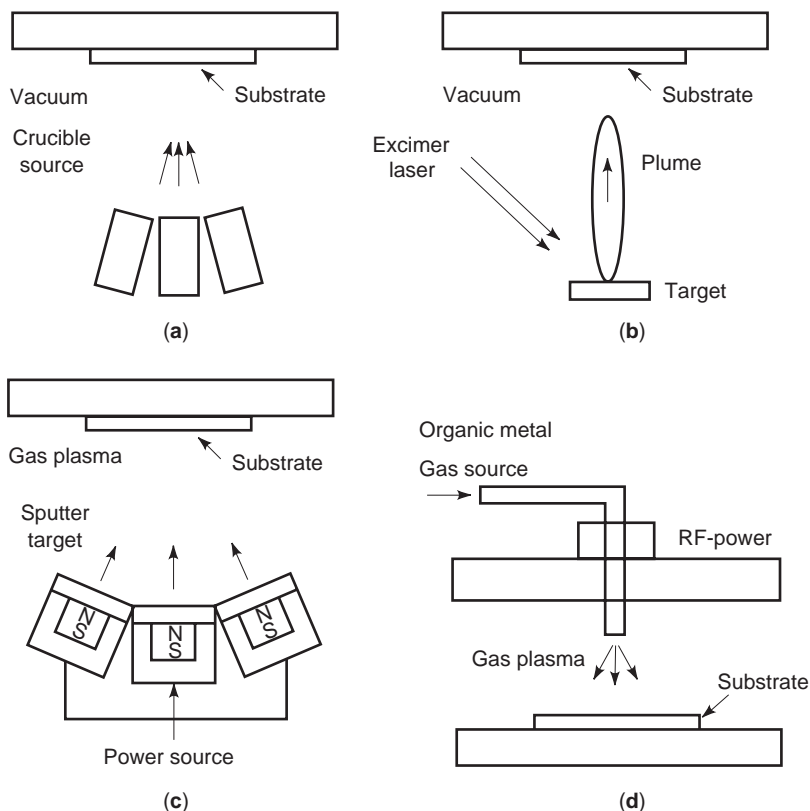


Figure 1. Typical configuration of thin film deposition systems: (a) multisource MBE, (b) laser ablation, (c) multitarget sputtering, (d) plasma-assisted MOCVD.

The epitaxial ferroelectric thin films show different microstructures depending on the degree of lattice match between the thin films and substrates. It is generally believed that, under an excellent lattice match, the thin films such as PT on ST show a single domain; under a poor lattice match for both *a*- and *c*-axes, the thin films such as PT on MgO show a multi-axial crystal structure; and under a fairly good lattice match, the thin films such as PT on KTaO₃ (KTO) constitute a periodic domain structure. These microstructures are grown primarily to minimize the total energy of the heterostructure. The phenomena are understood by linear-elasticity theory and a Landau–Ginzburg–Devonshire type phenomenological theory.

The actual epitaxial thin films of ferroelectric materials commonly constitute inhomogeneous microstructures including an interfacial layer that resembles polycrystalline thin films on a glass substrate as a result of the inhomogeneous nucleation at the initial stage of film growth. A selection of substrate materials is important for the control of thin film growth. Typical structural properties of substrates are shown in Table 3 [4–6].

3. THIN FILM DEVICES

3.1. Thin Film SAW Devices

The use of thin film SAW devices is an example of a successful application using piezoelectricity of hexagonal thin films and perovskite ferroelectric thin films. In the quasistatic approximation, the acoustic fields associated with plane waves in a piezoelectric medium are obtained by solving the stiffened Christoffel equation. In the case of a half-space medium with a free boundary surface, the boundary conditions must be satisfied and the mechanical stress and electric displacement must be calculated from the piezoelectric constitutive equations. These procedures give the solution as a SAW, which acoustic vibration energy concentrates near the surface of elastic solid materials. The Rayleigh wave and Love wave are obtained as the typical solutions of SAWs. The particle displacement of the former is in the sagittal plane, which is

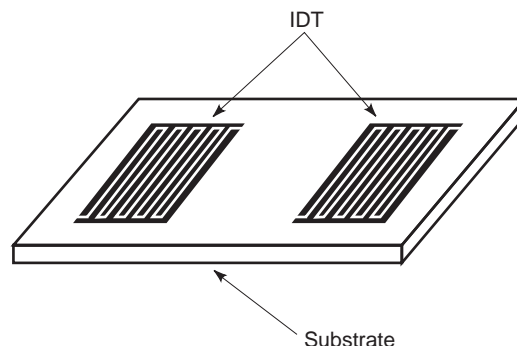


Figure 2. Interdigital transducer formed on the surface of the piezoelectric substrate.

perpendicular to the surface and parallel to the wave-propagation direction, and that of the latter is parallel to the surface and perpendicular to the direction of propagation. The SAW makes possible acoustoelectronic devices including the SAW filter for cellular phone/PCS/pager.

3.1.1. Generation of SAWs. The SAW modes can be generated by an interdigital transducer (IDT) formed on the surface of the piezoelectric substrate shown in Fig. 2. In the bulk SAW devices, bulk single crystals such as the LiNbO₃ and/or LiTaO₃ are adopted as the piezoelectric substrate. Whereas in the thin film SAW devices, a layered structure consisting of a piezoelectric thin film on the nonpiezoelectric medium is used as the piezoelectric substrate. Figure 3 shows the calculated result of an effective electromechanical coupling constant k^2 for four types of electrode configurations of a *c*-axis-oriented ZnO film on fused quartz. These electrode configurations for a thin film SAW transducer are also illustrated in Fig. 7. Each configuration consists of an IDT with or without a counter electrode. The value of k^2 is determined by the relation $k^2 = \Delta V_p / V_p$ where ΔV_p is the variation of SAW phase velocity V_p by the short condition of the surface electric field. The k^2 is simply evaluated by the equation $k^2 = \pi\omega_0 C_T / 4NG_a$, the inline model of Smith’s equivalent circuit model for electromechanical bulk wave, where ω_0 ,

Table 3. Lattice Parameters of Typical Single-Crystal Substrates

	Crystal System	Structure	Lattice Constant (Å)	Coefficient of Expansion (10 ⁻⁶ /K)
Sapphire	Trigonal	Corundum	<i>a</i> = 4.7630	7.5–8.0
MgO	Cubic	NaCl	<i>a</i> = 4.2030	13.8
SrTiO ₃	Cubic	Perovskite	<i>a</i> = 3.9050	10.8
LaAlO ₃	Pseudo cubic	Perovskite	<i>a</i> = 3.7920	10.0
YSZ	Cubic	Fluoride	<i>a</i> = 5.1600	10.0
KTaO ₃	Cubic	Perovskite	<i>a</i> = 3.9890	6.7
PbTiO ₃	Tetragonal	Perovskite	<i>a</i> = 3.8890	16.1
			<i>c</i> = 4.1532	–54.2
	Cubic		<i>a</i> = 3.9610	

epitaxial relations:

- (111)PT//(001)sapphire (0001)ZnO//(0001)sapphire
- (100)PT//(100)ST (1120) ZnO//(0112) sapphire (*R*-plane)
- (100)PLZT//(100)MgO (0001)LN//(0001)sapphire
- (111)PLZT//(0001)sapphire (0001)LN//(0001)LT
- (100)PLZT//(100)ST

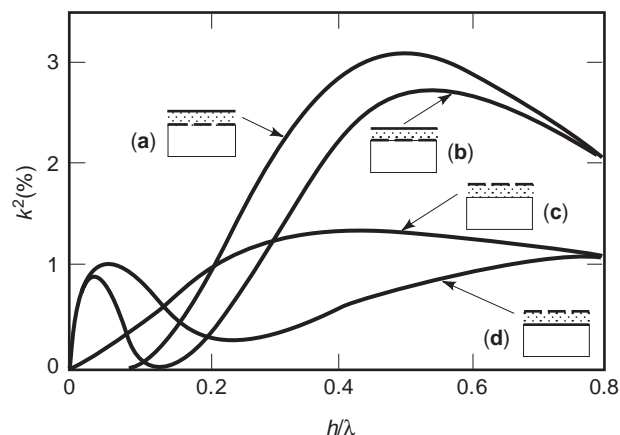
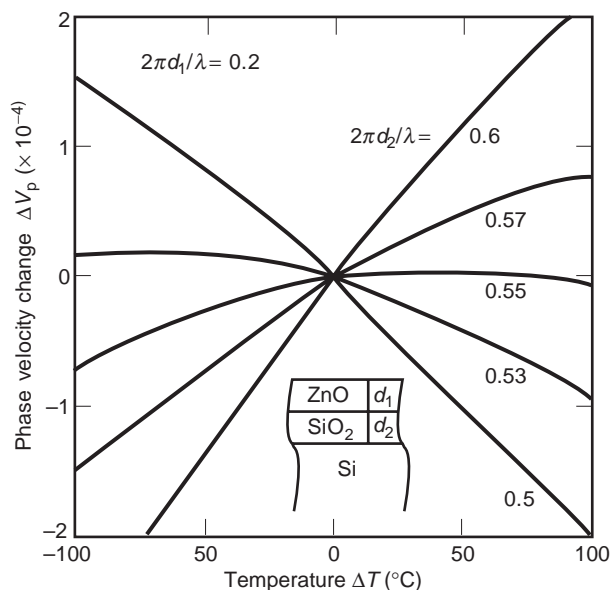


Figure 3. Calculated result of an effective electromechanical coupling constant k^2 for each configuration in the case of c -axis-oriented ZnO film on fused quartz. Four types of thin film electrode configurations are illustrated [7].

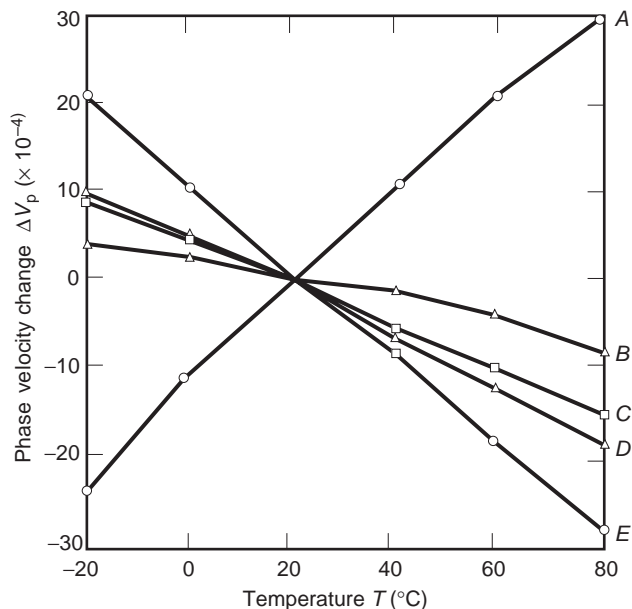
C_T , G_a , and N are the synchronous frequency, capacitance, radiation conductance, and number of finger pairs of IDT, respectively. The inline model (the major electric field component is parallel to the surface) becomes almost equal to the crossed-field model (the major electric field component is perpendicular to the surface) under the rough condition of $k^2 N > 1$. Figure 3 shows that k^2 varies with the ZnO film thickness, and the variations show a double-peaked character for the IDT structures including the counter electrodes. Note that the k^2 for thin films is higher than the bulk value at optimum film thickness.

3.1.2. Temperature Stability. SAW-layered structures have flexibility in that substrate materials can be chosen to adjust the temperature coefficient of a center frequency (TCF) and a delay time (TCD). The temperature stability of TCF or TCD is given by the equation, $(1/f)(dt/dT) = (1/t)(dt/dT) = (1/v)(dv/dT) - \beta$, where β denotes the thermal expansion coefficient of the substrate. The tendency of the phase velocity change $(1/v)(dv/dT)$ varies with the layered film thickness and elastic properties of the substrate materials. A suitable film thickness and a pertinent selection of substrate materials result in a zero TCD. Figure 4(a) shows one example of such a temperature deviation of the center frequency of the SAW IDT, which consists of the ZnO thin film, the SiO₂ or fused quartz layer, and the Si substrate. In this structure, the TCF of ZnO has a negative value of about -30 ppm/°C, and that of fused quartz has a positive value of $+60$ ppm/°C. These opposite values cancel the TCF while controlling the thickness of the SiO₂-layered film. Another example is shown in Fig. 4(b). Here the borosilicate-glass substrate can control TCF by controlling the composition ratio of the elements added to the glass.

3.1.3. SAW in Layered Media. The Rayleigh wave and Love wave are the solutions for a half-space medium with a free boundary surface. In layered structures, which



(a)



(b)

Figure 4. Temperature deviation of the center frequency of the SAW IDT constructed by the ZnO thin film: (a) the SiO₂ or fused quartz layer and the Si substrate; (b) the borosilicate-glass substrate [8].

include the thin plate rigidly bonded to the half-space (or substrate) having different material properties, the solutions for propagating waves must satisfy the appropriate wave equation in the layer and in the substrate as well as the boundary conditions imposed by the interface and the free surface. We know that fundamental and higher order modes of both Rayleigh and Love waves can propagate when the bulk shear wave velocity of the layer is lower than that of the substrate. This condition corresponds to that of the heavier and less stiff layer loads on

the substrate and will tend to confine the propagation energy to the layer. In this case, the propagating wave nodes are regarded as the modified plate modes. Sezawa discovered that a second fundamental mode may also exist in layered media. The Rayleigh modes and Sezawa modes correspond to symmetric and antisymmetric modes of a free plate modified by the contact of the surface with the substrate. In addition to these, the layer on an infinite half-space is open on one side, and there is a possibility of radiation or energy leakage out of the layer into the half-space. This condition gives the leaky wave solution for SAW.

The particle displacement of the SAW in the sagittal plane degrades with the depth from the surface. Also in the case of the layered substrate, almost the same situation exists in the half-space substrate. However, the degradation of that area in or near the top layer is different from the monotonous degradation of the zeroth Rayleigh mode. The amplitude distribution of the particle displacement is calculated for each propagating mode. Figure 5 shows the depth profiles of the particle displacement in the sagittal plane for the fundamental mode and higher four modes of the Rayleigh-type wave. More complex profiles and deeper penetration are shown for the particle displacement of higher order modes. Moreover, Fig. 5 shows that the higher order modes have a large displacement component in the substrate. So, it can be understood qualitatively that the higher order modes have a higher phase velocity because the phase velocity of the substrate is higher than that of the layer.

In Fig. 6, the solid lines and broken lines show the phase velocity V_p and the effective coupling coefficient k^2 of the Rayleigh-type and Love-type wave modes as a function of h/λ , respectively, where h is the layer thickness. These numerical results were obtained for the SAW directed to [1000] ZnO axes in the layered structure with the ZnO layer on the R -plane sapphire substrate. The first mode of the Rayleigh-type (zero Sezawa mode) shows an exceedingly large maximum value of k^2 with very high phase velocity at relatively small h/λ . These computer solutions were experimentally confirmed. For higher Rayleigh-type

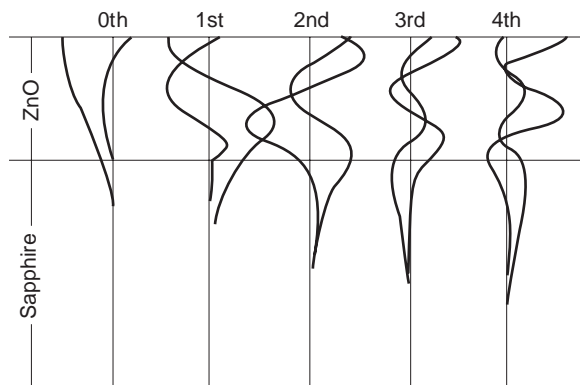


Figure 5. Depth profiles of the particle displacement in the sagittal plane for the fundamental mode and higher four modes of the Rayleigh-type wave.

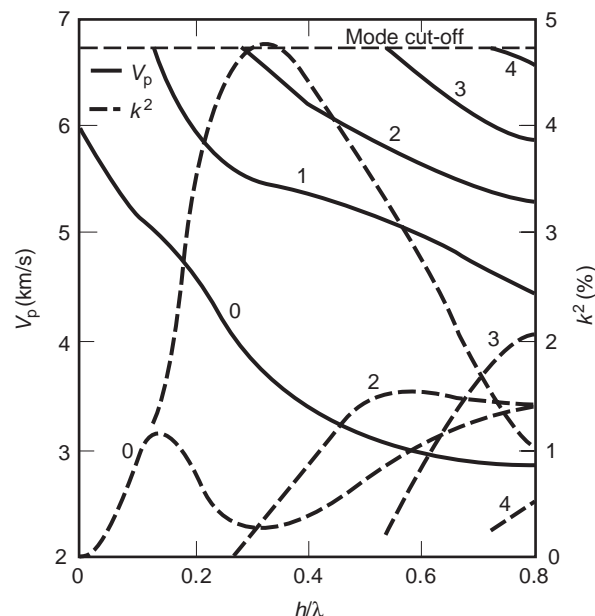


Figure 6. Rayleigh-type and Love-type wave mode solutions as a function of h/λ on the [1000] direction of the single-crystal (11 $\bar{2}$ 0) ZnO thin film epitaxially grown on the (01 $\bar{1}$ 2) sapphire surface. Solid lines and broken lines show the phase velocity V_p and the effective coupling coefficient k^2 [9].

modes, responses were still observed above the mode cutoff frequency as leaky mode responses.

3.1.4. Thin Film SAW Filters. Thin film SAW devices are constructed by the thin film IDTs on nonpiezoelectric substrates, by high-frequency propagation of the higher order modes of layered SAW, the substrate selected for the temperature stability, and so on. These distinguishing characteristics can realize the high performance of bandpass filters, resonators, delay lines, convolvers, integrated devices, and acoustooptic devices. The video intermediate frequency (VIF) filters for color TV sets were the first thin film mass-production devices. The frequency range of a VIF filter of 50–60 MHz is low enough for the SAW propagation loss of polycrystalline piezoelectric thin films such as c -axis-oriented ZnO films on a borosilicate-glass substrate. The thin film SAW filter shows excellent long-term stability. The long-term drift of the center frequency is less than 100 ppm after 1000 hours of exposure to 125°C in the air. The long-term stability of the ZnO thin film SAW filter is higher than that of bulk single-crystal LiNbO₃ SAW filters because of the absence of subsurface damage inflicted during sawing and polishing, which is unavoidable for bulk SAW devices. Figure 7 shows one example of the configuration of SAW VIF filters with two normal output IDTs and one apodized input IDT.

Another example is the high-frequency filter of epitaxially grown single-crystal thin film, which has low propagation loss of higher order Rayleigh wave modes in the gigahertz range. The ZnO single-crystal film on sapphire substrate is the typical construction of devices that

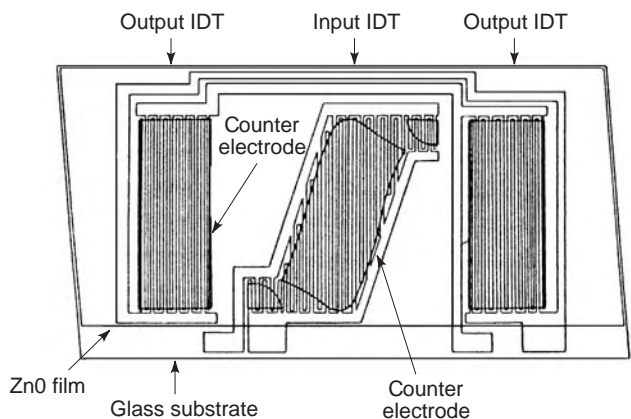


Figure 7. IDT configuration of SAW VIF filters with two normal output IDTs and one apodized input IDT on the layered substrate.

provide 4.37 GHz filters with a phase velocity of 5327 m/s and an insertion loss of 16 dB by 0.27 μm thick ZnO film, 3-IDT of 50 nm thick Al electrodes, and third-order response of double electrode-type IDTs. These excellent properties of thin film SAW filters are able to provide the high performance of information communication systems [7–17].

3.2. Ferroelectric Nonvolatile Memory

The basic operation of ferroelectric nonvolatile memory is switching of polarization states in a ferroelectric ABO_3 structure. Figure 8 shows a typical configuration and

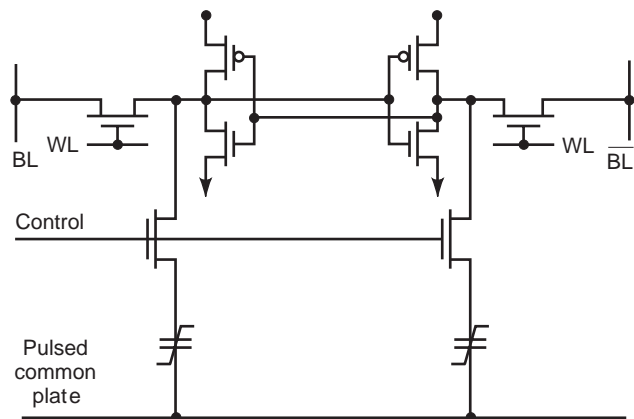


Figure 9. Schematic circuit of 256-bit FESRAM (Ramtron Corp. [18]).

schematic circuit of ferroelectric nonvolatile memories, dynamic random access memory (FEDRAM). The FEDRAM resembles a conventional dynamic random access memory (DRAM). The memory capacitor C_s of DRAM is replaced by a ferroelectric thin film capacitor. The C_s is in series with a MOS (metal-oxide-semiconductor) transistor whose source is connected to the bit line, the gate to the word line, and the drain to the pulsed 5 V common plate. In the FEDRAM, the polarization of the ferroelectric thin films switches to the opposite polarity on application of an electrical field higher than the coercive force when the MOS transistor is turned on by the appropriate voltage on

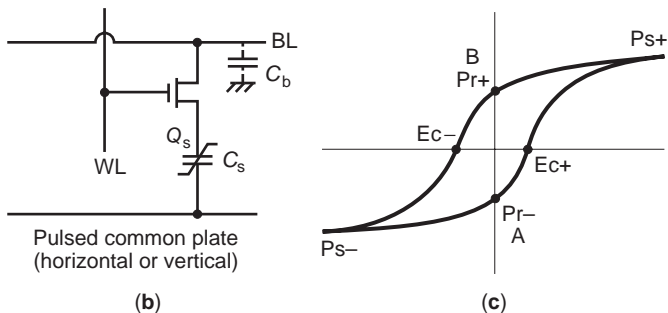
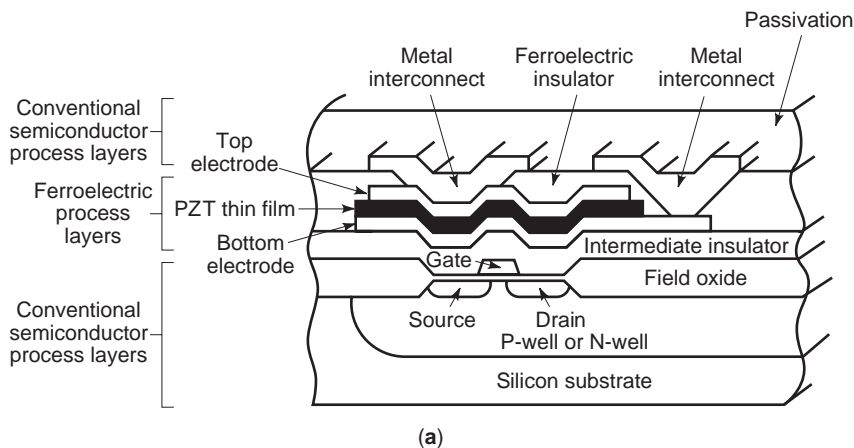


Figure 8. (a) Cross-sectional view of FEDRAM with (b) a schematic circuit and (c) a hysteresis loop of ferroelectric thin films (Ramtron Corp. [4]).

Type	Conventional ceramics (PbTiO ₃)	New thin film (c-axis oriented PLT)
Structure		
Pyroelectric coefficient γ	1.8×10^{-8} [C/cm ² K]	5.5×10^{-8} [C/cm ² K]
Figure of merit F_m	4.4×10^{-9} [Ccm/J]	14×10^{-9} [Ccm/J]
Merits		High S/N ($\times 10$) High responsivity Small size

Figure 10. Structure and pyroelectric properties of La-doped PT (PLT) thin films and conventional bulk PT ceramics [20].

the gate. In the hysteresis loop of memory capacitor C_s , the position *A* is taken to be a bit 1 state and *B*, a bit 2 state. The switching signal is detected by the voltage change at the bit line V_b . The V_b is given by $V_b = Q_s/C_b$, where Q_s denotes change of charge at switching on the capacitor C_s and C_b denotes the storage capacitor at the bit line. The Q_s is given by $Q_s = 2P_r$, where P_r denotes remanent polarization for ideal ferroelectric thin films having a symmetric hysteresis loop. For memory capacitors, PZT thin films are widely used. The P_r is 20–30 $\mu\text{C}/\text{cm}^2$ for typical PZT thin films. The value of Q_s for each memory cell is 400–600 fC for a cell area of $1 \mu\text{m}^2$, which is enough for the switch

memory operation because the minimum detectable value of Q_s for each cell is 20–30 fC at the conventional DRAM. The switching speed is essentially governed by the switching time of polarization reversal. The switching time is 1 ns for typical ferroelectric materials. The FEDRAM has some definite advantages, including a permanent memory and radiation hard characteristics. However, there are disadvantages of switch fatigue resulting from domain switching. Historically, the ferroelectric memory was proposed in the first part of the 1970s and first developed in 1987 by Ramtron Corp., Colorado Springs, and Krysails Corp., Albuquerque. The first developed ferroelectric

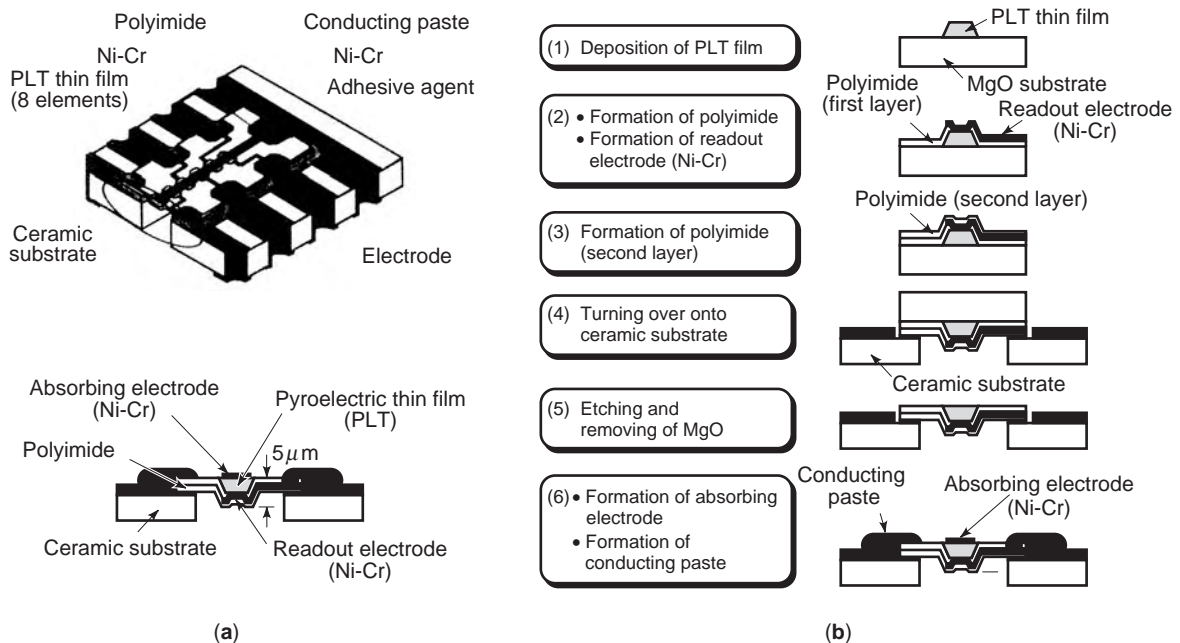


Figure 11. Schematic configuration of a linear array IR sensor for (a) a smart air conditioner and (b) its fabrication process [20].

memories look like the six-transistor static random access memory (SRAM) except that they include an additional pair of ferroelectric thin film capacitors, as shown in Fig. 9. Presently, the FEDRAM with a single transistor, where the ferroelectric thin films make a conventional DRAM nonvolatile, has been extensively studied to improve long-term stability. The ferroelectric thin films placed in the gate area of a MOS transistor provide another type of ferroelectric memory—the ferroelectric memory field effect transistor (FEMFET). Depending on the polarization of the gate materials, the source-to-drain current is increased or decreased significantly. The 1 or 0 state is detected by monitoring the source-to-drain current without switching the remanent polarization. This type of switch gives a nondestructive read out. This type of memory is under research because the interface control between the ferroelectric thin film and semiconductor is not completed.

Apart from the FEDRAM, the high dielectric permittivity of ferroelectric films is used for the local capacitor in highcount DRAM to reduce the area of the memory capacitor and/or eliminate the complex trenching and/or corrugation structures for the increased capacitive area. The high permittivity of the ferroelectric thin films achieves the flat structure of the memory cell. In the mega-/gigabit DRAM, the requirement for ferroelectric thin films is a permittivity of 200–2,000 at a film thickness of 100 nm

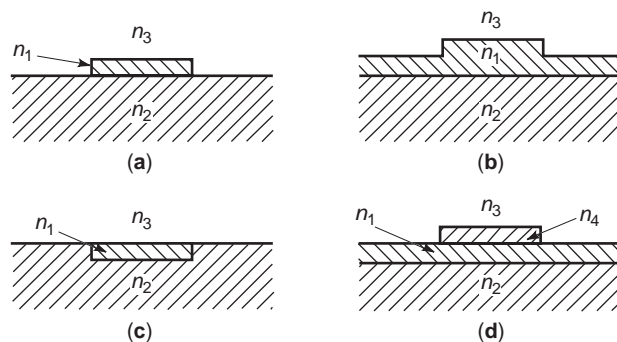


Figure 12. Cross-sectional view of thin film optical channel waveguide: (a) raised-strip type, (b) ridge type, (c) embedded type, and (d) strip-loaded type. n_1, n_2, n_3, n_4 are refractive index of waveguide, substrate, environment, and loaded strip, respectively.

without remanent polarization. The ferroelectric thin films should be used above their Curie temperature. If ferroelectric thin films are used, their operating coercive field should be large [18,19].

3.3. Thin Film Pyroelectric Infrared Detectors

Ferroelectric materials have been used for making pyroelectric infrared detectors by measuring the pyroelectric

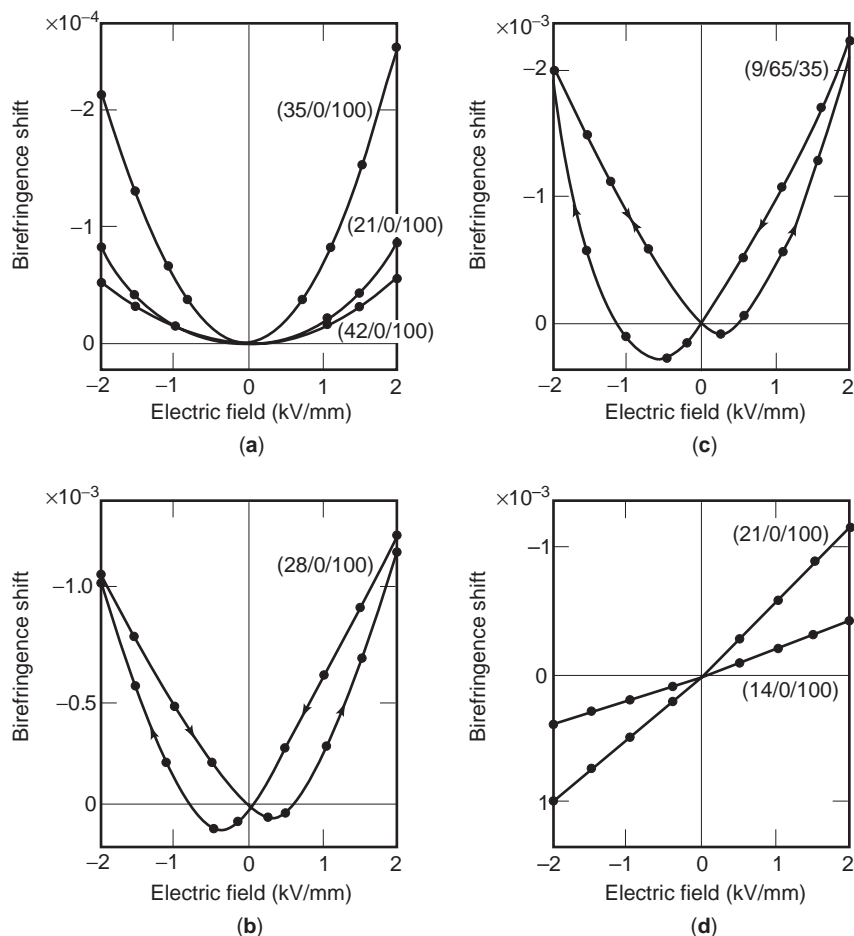


Figure 13. The effective birefringence shift as a function of transverse electric field for PLZT thin film of 0.4 mm in thickness [22].

current because they exhibit a large pyroelectric effect. The pyroelectric effect is described by the pyroelectric coefficient γ , which relates the change of polarization to the change in temperature. Pyroelectric current i_p will be detected by the temperature change of the detector materials generated by absorbed infrared radiation. The i_p is given by $i_p = \gamma(dT/dt)$. Bulk ferroelectric single crystals TGS (triglycine-sulphate) and LT, ferroelectric polymer PVDF (polyvinyl-di-fluoride), and ferroelectric ceramics PT and PbZrO_3 (PZ) are widely used for making pyroelectric infrared detectors. The pyroelectric materials are evaluated by figures of merit; $F_1 = \gamma/C_v$, $F_v = \gamma/C_v \cdot \varepsilon$, $F_M = \gamma/C_v(\varepsilon \cdot \tan \delta)^{1/2}$, where C_v denotes a volume-specific heat, ε denotes a dielectric constant, and F_1 , F_v , and F_m denote the figure-of-merit related to a current response, an output voltage response, and a detectivity, respectively. Perovskite thin films of PT and/or PLT are epitaxially grown on a Pt-metallized MgO substrate. The MgO substrate is removed after deposition of perovskite thin films. The as-deposited thin films show a highly oriented structure, which results in excellent pyroelectric properties without poling treatment after deposition. The single-domain structure with a low dielectric constant in the c -axis direction improves the figure-of-merit of conventional ceramic pyroelectric materials. Figure 10 shows the typical pyroelectric properties of bulk and thin film PLT. The integrated infrared sensor array shown in Fig. 11 was created using thin film infrared detector technology. The sensor array, manufactured by Matsushita Elec. Ind., Osaka, Japan, is used for a room air conditioner. The array detects the position and number of persons and their body temperatures to create a comfortable space [20,21].

3.4. Thin Film Optical Waveguide Devices

Thin film optical waveguide devices commonly consist of a sandwich structure of a thin film waveguide and a substrate. The refractive index of the thin film waveguide is larger than the substrate value so that a guided light beam propagates in the thin film waveguide. The direction of a propagated light beam is controlled by the channel waveguide shown in Fig. 12. The waveguide thin films comprise functional materials including EO or AO materials such as LN, PLZT, and ZnO. The PLZT thin films exhibit a linear EO effect or a quadratic EO effect depending on their composition. Typical EO properties of PLZT thin films are shown in Fig. 13. The birefringence shift $\delta\Delta n$ is several times larger than for conventional LN crystals. The linear EO coefficient r is given by the relation $\delta\Delta n = -\frac{1}{2} \times n^3 r E$ and the quadratic E/O coefficient R is given by the relation $\delta\Delta n = -\frac{1}{2} \times n^3 R E^2$, where n is the refractive index and E is the applied electric field. The value of R is $0.6 \times 10^{-16} (\text{m/V})^2$ and r is $0.81 \times 10^{-10} \text{ m/V}$. The light beam is introduced using an optical coupler such as a prism, micrograting coupler, and microlens directly connected to the optical fiber. The thin film waveguide is fabricated by deposition of the functional thin films on a substrate followed by microfabrication. The surface treatment, such as doping of a foreign element on the functional crystal substrate (i.e., Ti doping on LN),

is also used for the fabrication of thin film waveguides. Typical thin film waveguide devices are shown in Figs. 14–16.

Figure 14(a) shows the Mach–Zehnder interferometric modulator. The input light signal is equally divided into two waves by the branching guide and fed through two parallel arms of guide. In each arm, the waves are electrooptically modulated by the applied field. The intensity of guided light of TE_0 mode is strongly modulated because of a large EO effect. A typical sinusoidal pattern is observed as the applied electrical field is varied as shown in Fig. 14(b). The Bragg diffraction switches comprise PLZT epitaxial thin films on sapphire for the EO switch and ZnO epitaxial thin films on sapphire for the AO switch, respectively. The guided light, chiefly TE_0 mode, is diffracted as a result of a periodic grating with refractive index by applying a periodical electrical field for the EO switch using an interdigital electrode and by applying SAW for the AO switch using an interdigital SAW transducer. The angle of diffraction is governed by the Bragg diffraction, and the diffraction angle 2θ is given by $2\theta = \lambda_0/n\lambda_s$, where θ denotes the Bragg angle, λ_0 denotes

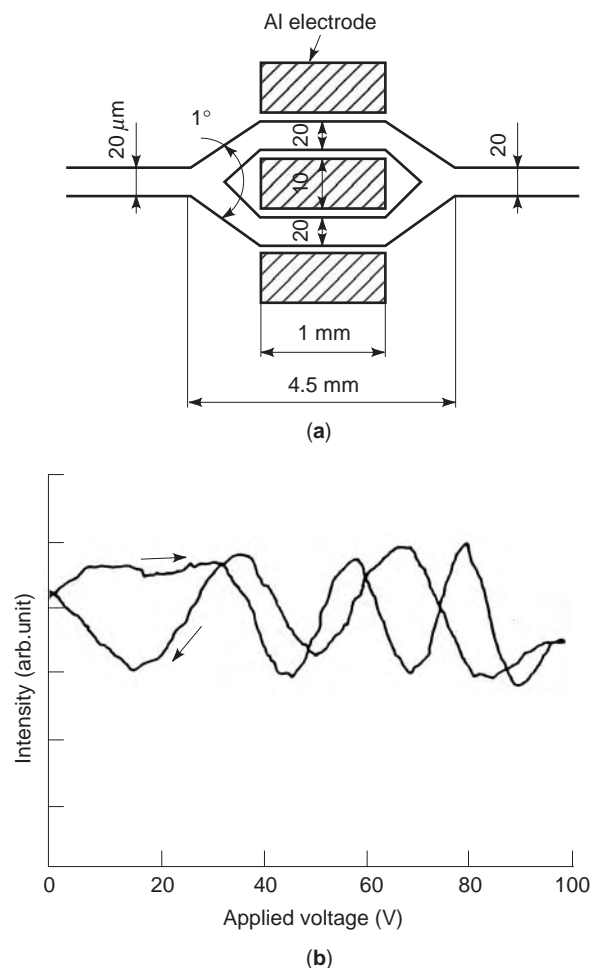


Figure 14. (a) Configuration of a thin film Mach–Zehnder interferometer using PLZT thin film on sapphire and (b) the variation of output light intensity with applied voltage [23].

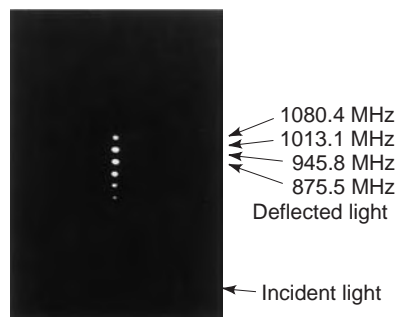
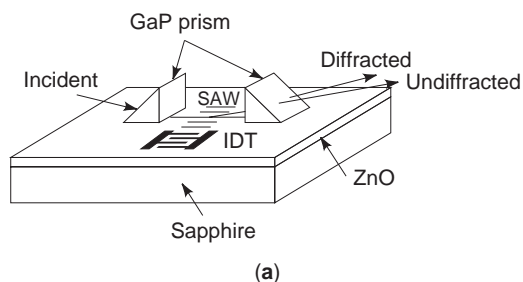


Figure 15. (a) Configuration of thin film AO Bragg deflector using ZnO thin film waveguide on sapphire and (b) a deflected light beam as a function of applied frequency at IDT driven by the first-order Sezawa mode of SAW [24].

the wavelength of light, n denotes the effective refractive index of the waveguide, and λ_s denotes the wavelength of the interdigital electrode. Figure 15 shows a typical operation of the ZnO thin film AO deflector. The Bragg deflector is driven by the first-order mode of SAW (Sezawa mode) with a phase velocity of 5700 m/s. The IDT is designed for 2 GHz operation. The TE_0 mode of a guided He–Ne laser beam is effectively deflected by the high-frequency SAW.

The total internal reflection (TIR) switch, which was first proposed by C. S. Tsai, is composed of a pair of crossed channel PLZT (20/0/100) waveguides, quadratic EO, with four terminals on sapphire as shown in Fig. 16(a). The intersecting angle of the channel waveguide θ satisfies the relation, $\theta < 90 - \theta_c$, $\theta_c = 1/\sin(1 - \frac{1}{2}n^2RE^2)$, where θ_c denotes the critical angle of total reflection, R denotes the quadratic EO coefficient, and E denotes the electrical field at the crossed area. At the crossed area, a pair of control electrodes are deposited to apply a control electrical field. Figure 16(b) shows a typical operation of the PLZT TIR switch. The TE_0 mode of the guided He–Ne laser beam directly coupled from port 1 propagates to port 3 without applying a control voltage, but the guided light is switched to port 4 as a result of the decreased refractive index at the interaction area under the application of control voltages. The switching voltage is less than 5 V because of the high EO coefficient of PLZT. The switching speed is expected to be as high as 100 GHz.

Thin film waveguide devices are flourishing. A number of promising devices are proposed for optical communication systems and integrated optical circuits, including optical computing [22–29].

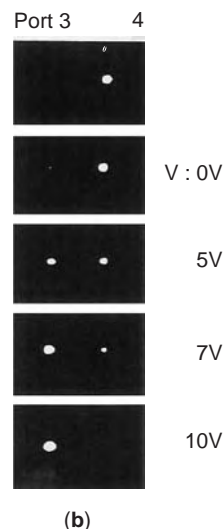
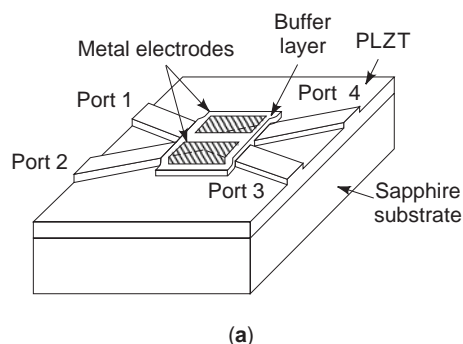


Figure 16. (a) Configuration of thin film TIR optical waveguide switch using PLZT thin film on sapphire and (b) the light intensity output at port 3 and 4 for various applied voltages [25].

BIBLIOGRAPHY

1. L. E. Cross, Ferroelectric ceramics, in N. Setter and E. L. Colla, eds., *Ferroelectric Ceramics*, Berlin: Birkhauser, 1993.
2. G. H. Haertling and C. E. Land, Hot-pressed (Pb,La)(Zr,Ti)O₃ ferroelectric ceramics, *J. Amer. Ceram. Soc.*, **54**:1 (1971).
3. K. L. Chopra, *Thin Film Phenomena*, New York: McGraw-Hill, 1969.
4. G. H. Haertling, Ferroelectric thin films for electronic applications, *J. Vac. Sci. Technol.*, **A9**(3):414 (1991).
5. R. F. Bunshah, *Deposition Technologies for Films and Coatings*, Park Ridge, NJ: Noyes, 1982.
6. K. Wasa and S. Hayakawa, *Handbook of Sputter Deposition Technology*, Park Ridge, NJ: Noyes, 1992.
7. G. S. Kino and R. S. Wagers, Theory of interdigital couplers on nonpiezoelectric substrates, *J. Appl. Phys.*, **44**:1480 (1973).
8. S. Ono, K. Wasa, and S. Hayakawa, Surface-acoustic wave properties in ZnO-SiO₂-Si layered structure, *Wave Electron.*, **3**:35 (1977).
9. T. Mitsuyu, O. Yamazaki, and K. Wasa, A 4.4 GHz SAW filter using a single-crystal ZnO film on sapphire, *1981 IEEE Ultrason. Symp. Proc.*, 1983, p.74.
10. W. R. Smith et al., Analysis of interdigital surface wave transducers by use of an equivalent circuit model, *IEEE Trans. Microwave Theory Tech.*, **MTT-17**(11):856 (1969).

11. G. W. Farnell and E. L. Adler, *Physical Acoustics*, Vols. 9, 35, New York: Academic Press, 1972.
12. K. Sezawa and K. Kanai, *Bull. Earth. Res. Inst. Tokyo*, **13**:237 (1935).
13. F. S. Hickernell, DC triode sputtered zinc oxide surface elastic wave transducers, *J. Appl. Phys.*, **44**:1061 (1973).
14. S. Ono et al., SAW resonators using rf-sputtered ZnO films on glass substrates, *Appl. Phys. Lett.*, **33**:217 (1978).
15. K. Setsune et al., Preparation and application of ZnO thin film by cylindrical magnetron sputter—ZnO thin film SAW long delay line, *Jpn. J. Appl. Phys.*, **20**:137 (1981).
16. K. L. Davis, Properties of the MZOS surface wave convolver configuration, *IEEE Trans. Electron Devices*, **ED-23**:554 (1976).
17. F. Hickernell et al., An integrated ZnO/Si-MOSFET programmable matched filter, *IEEE Ultrason. Symp. Proc.*, 1975, p. 223.
18. S. S. Eaton et al., A ferroelectric nonvolatile memory, *Tech. Dig. IEEE Int. Solid-State Circuit Conf.*, 1988, p. 130.
19. D. W. Bondurant and F. P. Gnadinger, Ferroelectrics for nonvolatile RAMS, *IEEE Spectrum*, **26**(7):30 (1989).
20. T. Kamada et al., Pyroelectric infrared sensors made of La-modified PbTiO₃ thin films and their applications, *Integrated Ferroelectrics*, **11**:15 (1995).
21. W. Wersing, Ferroelectric device, in N. Setter and E. L. Colla, eds., *Ferroelectric Ceramics*, Berlin: Birkhauser, 1993.
22. H. Adachi et al., Ferroelectric (Pb,La)(Zr,Ti)O₃ epitaxial thin films on sapphire grown by rf-planar magnetron sputtering, *J. Appl. Phys.*, **60**:736 (1986).
23. T. Kawaguchi et al., Optical PLZT thin film waveguides, *Appl. Opt.*, **20**:2187 (1984).
24. K. Setsune et al., Discrete frequency Bragg deflector in 2 GHz range using ZnO/sapphire substrate, *IEEE Ultrason. Symp. Proc.*, 1983, p. 467.
25. K. Wasa et al., Optical TIR switches using PLZT thin-film waveguides on sapphire, *J. Lightwave Technol.*, **LT-2**(5):710 (1984).
26. C. E. Land, New devices using ferroelectric thin films, *Proc. Int. Electron Devices Meeting*, Washington, DC, Dec. 1989, p. 10.1.1.
27. D. Botez and G. J. Herskowitz, Components for optical communications systems, *Proc. IEEE*, **68**:689 (1980).
28. C. S. Tsai, B. Kim, and F. Akkari, Optical channel waveguide switch and coupler using total internal reflection, *IEEE J. Quantum Electron.*, **QE-14**:513 (1978).
29. C. S. Tsai, Integrated acoustooptic and magneto optic devices for optical information processing, *Proc. IEEE*, **84**:853 (1996).

III-V SEMICONDUCTORS

CHRISTOPHER M. SNOWDEN
 Filtronic plc and University of
 Leeds
 West Yorkshire, United
 Kingdom

1. INTRODUCTION

The study of III-V compounds dates back to the dawn of semiconductor technology, when in 1952 Welker [1] suggested that gallium arsenide (GaAs) showed potential as a semiconductor material. The key aspect of this class of

materials that makes them of particular interest is their properties, which make them particularly suitable for high-frequency electronic and photonic devices. In the case of GaAs the electron velocity of bulk material, which determines the frequency limits of devices, is significantly higher than that found in silicon (Si). Furthermore, the low field mobility of electrons in many III-V materials is higher than that of Si. Diodes fabricated from III-V materials have demonstrated cutoff frequencies of several terahertz; transistors have demonstrated cutoff frequencies (f_T) higher than 300 GHz [2] and monolithic microwave integrated circuits (MMICs) operating above 200 GHz [3]. This has led to the use of GaAs and InP in a wide variety of high-frequency semiconductor devices operating in applications as diverse as low-noise amplifiers, mixers, power amplifiers, RF switches, and oscillators at frequencies up to 240 GHz. The wide operating temperature range of III-V semiconductors, typically from -200 to 300°C, coupled with superior radiation hardness compared to Si, led to GaAs and InP becoming key materials for space and defence requirements. In more recent years the photonic properties of III-V materials, arising from their direct bandgap energy band structures, have been extensively exploited for solid-state lasers, light-emitting diodes, photodetectors, and optical modulators, with the potential for fully integrated optoelectronic integrated circuits. To date these properties are unrivalled by Si, which is an indirect bandgap semiconductor.

Although many III-V materials are routinely used in microwave and optoelectronic semiconductor devices today, it wasn't until the early 1970s that the first semiconductor devices became widely available, and even then it was restricted to two terminal devices and simple transistors. The relatively slow progress in developing commercially viable technologies was partly due to the challenging problems in establishing high-quality material growth and the development of processing techniques that allow reliable devices to be fabricated. The key step to achieving volume production and widespread use of cost-effective devices is the availability of larger-diameter wafers, from which the semiconductor devices are fabricated. Early work was restricted to very small samples (parts of wafers) or small-diameter wafers of 2 in. or less. Gradually, high-quality 3- and 4-in.-diameter wafers became available and discrete devices and integrated circuits were introduced for military and commercial applications. Significant advances since the early 1980s have led to the introduction of 6-in. (150-mm) very-high-quality GaAs substrates and epitaxy suitable for high-volume production of semiconductor devices. Similarly, other materials such as InP are now well established and production is supported by 4-in.-diameter substrates.

The advent of high-quality reproducible epitaxy, provided by molecular-beam epitaxy (MBE) and organic metal vapor-phase epitaxy (OMVPE, MOCVD), led to a shift in interest from bulk III-V devices to heterostructure semiconductor devices, based on bandgap engineering, which allow higher performance to be obtained. In particular, the development of ternary and quaternary compounds, such as AlGaAs, GaInAs, and GaInAsP, were key steps forward for new transistor technologies,

Table 1. III-V Semiconductor Materials

Compound Type	III-V Material
Binary	BAs, BP, AlSb, BN, GaSb, AlAs, AlP, GaAs, InSb, GaP, InAs, InP, AlN, GaN
Ternary	AlGaAs, AlGaIn, InGaAs, InGaP, GaAsP, InAsP, GaInSb, GaInAs
Quaternary	InAlGaAs, GaInAsP, InAlGaP, InAlGaSb, AlGaAsSb

high-electron-mobility transistors (HEMTs), heterojunction bipolar transistors (HBTs), and long wavelength optoelectronic devices. The exploitation of lattice-matched (usually to InP) and strained (usually to GaAs) crystal structures using these compounds is an essential element of today's III-V technology. More recently the use of material systems such as GaN/AlGaN for high-voltage, high-power-density transistors has led to increased interest in examining the growth on nonnative layers using epitaxy to create III-V active layers on SiC, sapphire, or more recently silicon substrates. Record performance power density levels are being achieved with GaN HEMTs, reporting over 30 W/mm gate periphery, compared with less than 1 W/mm from conventional MES-FETs and HEMTs [4].

In the mid-1980s GaAs integrated circuit technology was costly and reserved only for the most demanding system requirements. Contemporary III-V semiconductor device technology is able to provide microwave monolithic integrated circuits (MMICs) at a cost of less than 20 cents per square millimeter in some very high volumes, supporting a market approaching a billion die per annum. III-V transistor technology is the foundation of high-efficiency power amplifier and low-loss RF switch MMICs in today's cellular handsets. The advent of heterostructure technologies using Si, notably SiGe, which have demonstrated the potential for very fast devices, is likely to displace III-V in some very-high-volume RF and microwave applications.

This article aims to provide a basic introduction and an overview of contemporary III-V semiconductors. Many of the topics touched on in these pages are expanded in detail elsewhere in this encyclopedia, but the reader is encouraged to explore the wealth of material available in this exciting area of semiconductor technology.

2. III-V SEMICONDUCTOR MATERIAL PROPERTIES

III-V semiconductor materials are alloys formed from elements in group III and group V of the periodic table. They are grown as single crystals and as either binary, ternary, or quaternary alloys (Table 1).

2.1. Crystal Structure

All III-V semiconductors are alloys, and unlike the elemental semiconductors silicon (Si) and germanium (Ge), which exhibit diamond cubic crystal structures, generally crystallize in more complex structures. GaAs and InP have cubic zincblende structures (sphalerite structures), with a tetrahedral arrangement of the atoms, with each group III atom bonded to four group V atoms (Fig. 1). The tetrahedral structure is characteristic of directional covalent

bonding in semiconductors, with eight valence electrons per pair of atoms (in sp^3 -hybridized orbitals). In the case of GaAs and InP, unlike diamond cubic semiconductors, there is some charge transfer between the two types of atom giving rise to the partial ionic character of the bond. Generally speaking, these partly heteropolar bonds are stronger than homopolar bonds such as those found in Si. Heteropolar bonds also tend to be associated with lower amplitude lattice vibrations and wider energy bandgaps.

The properties of crystal structures, including their electrical behavior, vary according to the plane considered. The most commonly used method of defining planes in crystals is the use of Miller indices [5], which are obtained by determining the intercepts of each plane on the three Cartesian coordinates in terms of the lattice constant and then taking their reciprocals and reducing them to the smallest three integers having the same ratio (Fig. 2). The lattice parameter is usually denoted a , for sphalerite structures. The resulting Miller indices are expressed in parentheses (hkl). For example, a plane that intercepts the x axis on the negative side of the origin is (100) . Extensions of this notation allow for planes of equivalent symmetry, defined as $\{hkl\}$; for example, $\{100\}$ for cubic symmetry. Crystal direction is defined using the notation $\langle hkl \rangle$; for example, $\langle 100 \rangle$ for the equivalent set of directions $[100], [010], [001], [100], [010], [001]$. Crystal direction is used to define the orientation of wafers for the

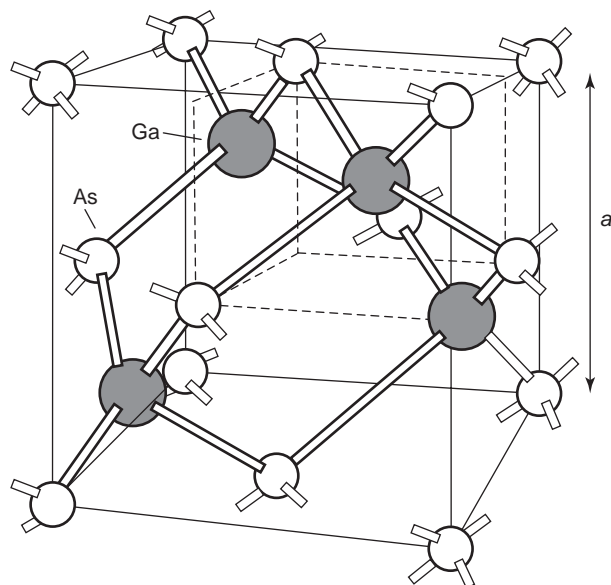


Figure 1. Cubic zincblende (sphalerite) crystal structure of GaAs [based on diagram from S. M. Sze, *Physics of Semiconductor Devices*, Wiley-Interscience (1981)].

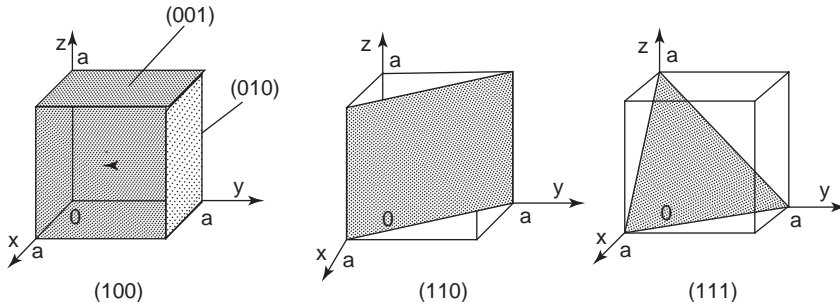


Figure 2. Miller indices [based on diagram from S. M. Sze, *Physics of Semiconductor Devices*, Wiley-Interscience (1981)].

fabrication purposes, since the electrical properties and chemical etching properties differ according to orientation. Notches or “flats” are created on the edge of wafers to precisely indicate the orientation of the wafer with respect to the crystal structure.

In the case of GaAs cleaved along the (111) plane, the surface consists of either Ga atoms, which have three bonds with the crystal or As atoms that have one bond with the crystal. In fact, the bonds between the nearest Ga and As atoms are in the $\langle 111 \rangle$ directions. Gallium nitride GaN has a wurtzite crystal structure, which has two lattice parameters a and c .

2.2. Energy Band Structure

The electronic and vibrational states in crystals are usually described in reciprocal space or k space. The smallest unit cell in reciprocal space is called the *first Brillouin zone*. The first Brillouin zone in cubic semiconductors is a truncated octahedron with symmetry points and lines denoted Γ , X , L , K , U ($K=U$), W , Δ , Λ , and Σ . A very good detailed description is given in Ref. 6. The Γ point at $k=0,0,0$ in Cartesian coordinates is the point of highest symmetry in the Brillouin zone.

The energy band theory of semiconductors assumes that the lattice features perfect translational symmetry, that one electron at a time is considered, and that the influence of all electrons is represented by the average over their wavefunctions. The Schrödinger equation for the one-electron case is used to define the functional dependence of energy $E(k)$ on the wavevector k for the various bands. This model is modified to form the Sommerfeld free-electron model by introducing the idea of effective mass. The nearly free-electron approximation provides a basis for developing energy band theory, and the origin of the energy bandgap between the valence and conduction bands. It also introduces the concept of effective mass, which is defined as the reciprocal of the curvature of the E - k diagram. The band structure for a semiconductor is calculated using the well-known $\mathbf{k}\cdot\mathbf{p}$ method [7]. The $\mathbf{k}\cdot\mathbf{p}$ representation results from the complete set of eigen functions that are obtained from the substitution of Bloch functions [6] in the one-electron Schrödinger equation. Spin-orbit interaction is also included in the full definition of the energy-wavevector relationship, which leads to a formulation based on a series of Hamiltonians.

Valence band maxima occur at the Γ point for semiconductors with tetrahedral structure. Many semiconductors with this structure, such as GaAs and InP, also have conduction band minima at this point. In GaAs and similar semiconductors, the conduction band structure close to Γ is essentially parabolic. The lowest conduction band minimum occurs at $k=0$ with further minima in the Δ $\langle 100 \rangle$ and Λ $\langle 111 \rangle$ directions. Other important conduction and minima occur at 0.31 and 0.52 eV above the first Γ minima for X and L . The valence band structure has heavy hole and light hole bands that degenerate at $k=0$ and spin-orbit split bands at 0.34 eV below this level. The energy band structure for GaAs are shown in Fig. 3. The direct energy bandgap is the difference in energy between the conduction band minima and the valence band maxima.

The energy band structure of other III-V semiconductors such as ternary and quaternary alloys is dependent on the mole fractions x and y (e.g., $\text{Al}_x\text{Ga}_{1-x}\text{As}$ and $\text{Ga}_x\text{In}_{1-x}\text{As}_y\text{P}_{1-y}$). The direct energy bandgap $E_0(x,y)$ is usually expressed as a quadratic function of the mole fraction, characterized by the coefficient of the second-order term, also known as the “bowing parameter.” The

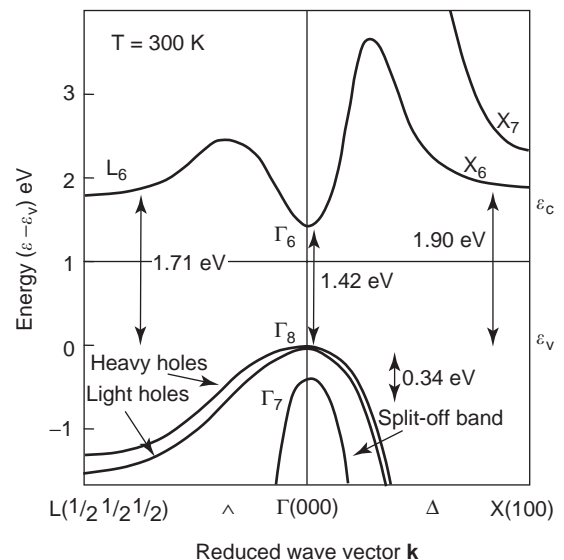


Figure 3. Energy band structure, showing variation of energy with wavevector for gallium arsenide [based on diagram from J. S. Blakemore, *Key Papers in Physics—Gallium Arsenide* (1987)].

Table 2. Physical Properties of III-V Binary Semiconductor Materials

Material	Lattice Constant (Å)	Direct Energy Bandgap ^a (eV)	Indirect Bandgap ^b (eV)	Density ($\times 10^9$ kg/m ³)	Melting Point K	Thermal Conductivity ^a (W m ⁻¹ K ⁻¹)	Dielectric Constant ^c
AlAs	5.660	3.03	2.15	3.76	2013	80	10.1
GaP	5.450	2.78	2.27	4.14	1735	77	11.1
GaAs	5.653	1.42	1.80	5.32	1513	46	12.8
GaN	3.19/5.19	3.44	—	6.09	—	120	10.4
AlN	3.11/4.98	6.20	—	3.28	—	300	9.1
InP	5.869	1.34	2.74	4.81	1335	68	12.6
InAs	6.058	0.36	—	5.67	1215	27	15.2

^aValues at 300 K.

^bIndirect energy bandgap is the difference between the first X minima and the valance band maximum at 300 K.

^cIn units of free-space permittivity ϵ_0 8.85×10^{-12} F/m.

bowing parameter typically varies from 0.2 for AlGaAs to 0.88 for GaInP. Positive bowing parameters imply that the energy band bows downward. In contrast to the energy bandgap, the lattice constant of ternary alloy semiconductors generally varies linearly with composition. The lattice constant behavior for quaternary compounds is more complex with a higher-order dependence on the mole fractions. The energy bandgap, lattice constant, and other parameters of binary III-V semiconductors are shown in Table 2.

The energy bandgap is a very important parameter in device design. The temperature dependence of the bandgap E_g , which decreases with increasing temperature, is generally expressed as

$$E_g(T) = E_g(0) - \frac{\alpha T^2}{T + \beta}$$

where $E_g(0)$ is the energy bandgap at 0 K and α and β are constants; α typically lies in the range $2.5\text{--}6 \times 10^{-4}$ eV K⁻¹, β in the range 75–600. In the case of GaAs $E_g(0)$, α and β have the values 1.519, 5.405×10^{-4} eV/K, and 204.

The bandgap of ternary and quaternary III-V alloys depends on their composition and mole fraction [8]. The lattice matching criteria and compositional factors (Vegard's law) limits the range of mole fractions. In the case of $\text{Al}_x\text{Ga}_{1-x}\text{As}$ and $\text{In}_x\text{Ga}_{1-x}\text{As}$ the bandgap dependence on mole fraction x (at 300 K) is described by simple quadratic equations:

$$\text{Al}_x\text{Ga}_{1-x}\text{As} : E_g = 1.424 + 1.429x - 0.14x^2 \text{ eV}$$

$$\text{In}_x\text{Ga}_{1-x}\text{As} : E_g = 1.425 - 1.501x + 0.436x^2 \text{ eV}$$

In the case of ternary compounds such as InAlGaAs, the energy bandgap is a function of two mole fractions x and y such that at 300 K:

$$\begin{aligned} \text{In}_{1-x-y}\text{Al}_x\text{Ga}_y\text{As} : E_g(x, y) = & 0.360 + 2.093x + 0.629y + 0.577x^2 \\ & + 0.436y^2 + 1.013xy - 2.0xy \\ & (1 - x - y)\text{eV} \end{aligned}$$

Additionally in the case of InAlGaAs, it is necessary to account for the lattice-matching condition $0.98x + y = 0.47$ and the compositional parameter z where $x = 0.48z$ and

$$E_g(z) = 0.76 + 0.49z + 0.20z^2 \text{ eV}$$

The range of mole fraction compositions in III-V ternary and quaternary semiconductors is limited by the requirement to achieve lattice matching to GaAs, InP or GaSb substrates. Figure 4 shows the variation in lattice parameter with energy bandgap for a range of III-V semiconductors [6]. The shaded regions show the range of parameters for quaternary alloys $\text{Ga}_x\text{In}_{1-x}\text{As}_y\text{Sb}_{1-y}$ and $\text{Ga}_x\text{In}_{1-x}\text{As}_y\text{P}_{1-y}$.

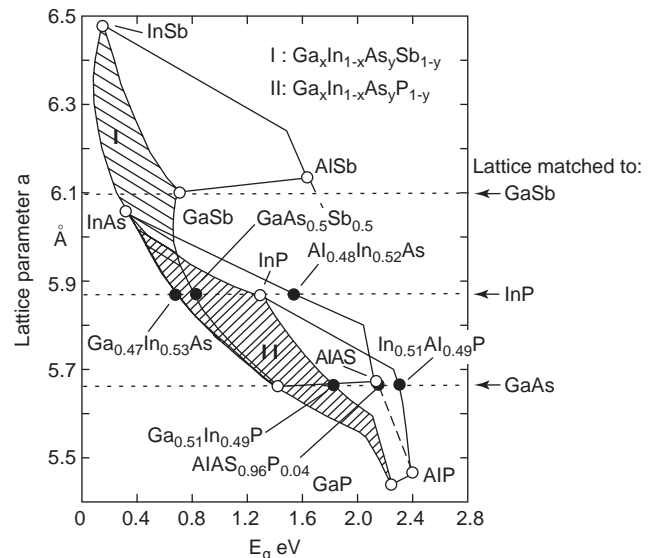


Figure 4. Variation of lattice parameter with energy bandgap associated with a variety of III-V semiconductors at 300 K [Landolt-Bornstein, “Numerical Data and Functional Relationships” in *Science and Technology*, Vol. 22, *Semiconductors*, Subvol. A., O. Madelung and M. Schulz, eds., Springer, New York (1987)].

2.3. Crystal Growth

Ideally, integrated circuits require an insulating substrate to provide electrical isolation between the various circuit elements. Silicon does not have a native insulating or semiinsulating state, although the more recent silicon-on-insulator (SoI) technology facilitates a suitable substrate for silicon RF and microwave integrated circuits. On the other hand GaAs and many other III-V semiconductors can be grown as semiinsulating materials. The active (conductive) regions of the circuit are defined by combinations of epitaxy, ion implantation, and mesa etching (or isolation by ion implantation).

Active devices and integrated circuits are fabricated on semiinsulating wafers that may have epitaxial layers grown on the surface. Some devices such as diodes may use bulk doped substrates. The wafers are obtained by sawing single-crystal boules along predetermined planes. These single crystal boules may be grown using a variety of techniques, including horizontal or vertical Bridgman, Czochralski, liquid-encapsulated Czochralski (LEC), magnetic LEC, liquid-encapsulated Kryopoulos (LEK), horizontal gradient freeze, or by float-, horizontal- or vertical-zone melting [9]. Bridgman techniques are the most commonly used methods of growing semiinsulating substrates.

The horizontal Bridgman technique involves the progressive crystallization of a molten bar of material as it is passed through a carefully controlled temperature gradient. The semiconductor crystal is grown in a quartz boat using a seed crystal and the constituent materials. In the case of GaAs, the boat containing the GaAs seed crystal and Ga is placed in a sealed quartz ampoule, with an overpressure of arsenic produced from a separate charge of arsenic at the opposite end of the ampoule. A temperature difference is produced along the tube, ensuring that one end of the boat is at the melting point (1238°C for Ga) while the arsenic, at the other end of the ampoule, is maintained at 614°C. Stoichiometry is ensured by precise control of the temperature and by accurate weighing of the Ga and As. Precise temperature control is required, ensuring horizontal thermal uniformity within 0.1°C. Long crystals of up to 1 m in length have been produced using this method. Very-good-quality material is produced using the horizontal Bridgman technique, and dislocation densities approaching 10^5 m^{-3} have been achieved for low-chromium-doped GaAs. The horizontal gradient freeze technique is similar to the horizontal Bridgman method; the main difference is that the former method induces crystallization from the seed by carefully controlled cooling of a melt. Both the Bridgman and gradient freeze techniques tend to have Si as impurities in the finished GaAs crystal as a consequence of the quartz boat.

The Czochralski technique is often used to grow large-diameter boules, suitable for wafers up to 6-in. in diameter. This pulling method uses a chamber with heated walls to maintain the required arsenic pressure. The LEC method is the more common than the basic Czochralski approach since it avoids arsenic loss and atmospheric contamination. The LEC system consists of a growth chamber housing a vertical puller with a seed crystal at

the tip of a rotating tip, which, in the case of GaAs growth, is immersed in a Ga melt, which in turn is fed with arsenic vapor from a separately heated quartz ampoule of arsenic. The susceptor containing the crucible with the Ga melt is heated with an RF coil. A molten B_2O_3 encapsulating layer on the surface of a Ga melt is used to prevent arsenic loss and contamination. An inert gas, such as nitrogen, is used to pressurize the growth chamber to a level higher than the As partial pressure. The rotating seed crystal is slowly withdrawn vertically upward, and the GaAs crystal boule is grown from the melt. The magnetic LEC method is a variation on the LEC technique that reduces the thermal convection currents found in the conventional LEC approach, improving the boule's homogeneity.

2.4. Epitaxy and Implantation

Semiinsulating substrates, available as wafers usually in the region of 600 μm thickness, are usually used as the basis for fabricating devices and integrated circuits in most III-V technologies. The conductive regions required for the active devices are formed using either epitaxial layers grown on the surface of the semiinsulating substrate, or by selective ion implantation.

Ion implantation techniques, which are used widely in Si technology to define conductive regions, were used widely to form the channel regions for MESFETs, bipolar junction transistors, varactor diodes, and IMPATT diode structures, especially in earlier integrated circuit designs. This low-cost approach, which is still widely in use today, can provide devices with moderate low-field channel mobilities ($0.35 \text{ m}^2 \text{ V}^{-1} \text{ s}^{-1}$) associated with channel doping densities of up to the mid- 10^{23} m^{-3} range for GaAs. High doping densities of up to $2 \times 10^{25} \text{ m}^{-3}$ are achievable for ohmic contacts, but have very low mobilities ($0.03 \text{ m}^2 \text{ V}^{-1} \text{ s}^{-1}$) [10].

Ion implantation is achieved by bombarding the semiconductor substrate with high-energy ions of the required dopant species. These ions displace semiconductor atoms from their sites in the crystal structure. In order to avoid extreme surface damage, which would render the surface amorphous, GaAs substrates are usually heated to 150°C during implantation. Fabrication of FETs and diodes with ion-implanted active profiles usually requires several implantations with energies tailored to produce the required doping profile. Each implantation produces an almost Gaussian profile of implanted ions as a function of depth from the semiconductor surface. This allows a selective three-dimensional doping profile to be produced in planar devices with localized highly doped regions for ohmic contacts. The wafers require annealing at a temperature in the range 800–950°C (for GaAs) after implantation to reduce the damage (defects) caused by the high-energy ion bombardments and achieve activation of the donor species. The doping efficiency is a function of the type of ion, implantation dose, and annealing temperature. Annealing is performed using either annealing furnaces, infrared radiation from halogen lamps, pulsed laser beam or electron-beam, techniques. The surface of GaAs loses arsenic at temperatures above 600°C, and hence annealing is performed either under arsenic overpressure

(“capless” annealing) or encapsulated using Si_3N_4 or AlN . The implanted dopants diffuse during annealing. Implantation can be used to produce either n- or p-type materials. Materials such as S, Se, Te, Si, and Sn are used to produce n-type GaAs. Dopants for p-type GaAs include Be, Zn, Cd, Mg, and C.

Ion implantation is widely used as an alternative to etched mesa isolation in integrated circuit designs to isolate the active regions of individual devices, allowing a more planar fabrication technology. In this scenario, semiinsulating material is produced locally by ion induced damage using proton bombardment or oxygen implantation, followed by annealing at a temperature between 650 and 800°C.

The advent of heterostructure devices, including high-electron-mobility transistors (HEMTs) and heterojunction bipolar transistors (HBTs), coupled with the demand for higher mobilities, higher channel carrier densities, lower-noise-figure FETs, and higher power densities from existing devices, has led to widespread use of epitaxial layer growth techniques. Although there are four potential candidates, vapor-phase epitaxy (VPE), liquid-phase epitaxy (LPE), molecular-beam epitaxy (MBE), and metallorganic chemical vapor deposition (MOCVD, also known as OMVPE), only the latter two techniques provide the necessary abruptness of interface and quality of growth necessary for most contemporary III-V semiconductor devices. MBE allows precise thickness and dopant control and is widely used as the basis of material for HEMTs, while the thicker layers found in HBTs are normally grown using MOCVD. Both techniques have been shown to produce very-high-quality material on high-quality semiinsulating substrates, achieving high mobilities and low defect densities [11].

MBE requires an ultra-high-vacuum growth chamber in a system that has multiple ultra-high-purity sources, achieving stoichiometric growth [12]. The growth rate is relatively slow, achieving 0.1–10 $\mu\text{m}/\text{h}$, but allowing very precise control of the film thickness, material composition, and dopant density. Highly abrupt interfaces are easily achieved and pulse (or delta) doping layers are readily grown, with layer thicknesses as thin as 5 Å. Heated crucibles, known as *Knudsen cells*, containing the elements or compounds used to form the various material layers are used as the sources. Contemporary multiwafer MBE production systems are capable of simultaneously growing high-quality material, with excellent uniformity on up to seven 6-in.-diameter wafer substrates (or a larger number of smaller-diameter substrates). This has led to widespread use of MBE grown wafers in modern III-V fabrication facilities. A wide range of compound semiconductor material systems can be grown using MBE and the same system can contain a range of Knudsen cells with ultra-high-purity Ga, In, Al, As, P, and Sb, as well as smaller cells for doping such as Si. It is common practice to have the most heavily used cells, such as Ga, duplicated. Growth is carried out on a single-crystal substrate—most commonly GaAs, which is heated to a temperature in the range 540–650°C. Faster growth rates tend to occur at the higher temperatures, and require careful control of the ratio of arsenic to gallium. The upper limit on growth

temperature is generally limited by the availability of the group V element over pressure.

MBE is used to grow highly complex multilayer heterostructures such as those found in quantum-well lasers and optical guides. Indeed, it is common for over 10 layers to be grown to form the active region of HEMTs, pseudomorphic HEMTs (PHEMTs), and metamorphic HEMTs (MHEMTs). MBE is used to produce the epitaxial material for a wide range of other microwave devices, including HBTs, MESFETs and resonant tunneling diodes. Superlattices, consisting of alternating layers of wide- and narrower-bandgap materials, are often used in these structures, and MBE is ideally suited to forming these abrupt interfaces [13].

The basic configuration of an MBE system requires a stainless-steel growth chamber, analysis chamber, and a load lock for transporting wafers into and out of the system (Fig. 4). The growth chamber is maintained at an ultrahigh vacuum and requires extreme cleanliness to ensure low defect densities during crystal growth. In addition to the Knudsen cells, the growth chamber houses shutters, substrate-handling equipment (which is robotic in many production systems), cryoshrouds, and surface analysis equipment to monitor growth. The effusion cell shutters regulate the emission of material from the cells. Normally, an additional “main” shutter is placed in front of the rotating substrate. The substrate is mounted on a heated holder, which rotates at speeds of up to 150 rpm for smaller holders, although lower rates of 5 rpm are normally used. This rotation and heating assist in maintaining uniformity in doping and thickness. The cryoshroud, which requires liquid nitrogen, encloses the entire growth area and minimizes water vapor and other unwanted gases during growth. Cooling of the regions surrounding the Knudsen cells also ensures that cross-contamination is minimized. In addition, each cell is usually water-cooled. The cells themselves, which are contained in stainless-steel housings, are made of graphite or boron nitride. The flux emitted from the cells is regulated by the shutters and monitored by an ion gauge behind the wafer holder. In more recent times, many systems use additional “cracker cells” placed between the Knudsen cells and the substrate. The cracker cells operate a high temperature (850–1000°C), and as effusion beams of arsenic or phosphorus pass through the region occupied by these cells, the As_4 and P_4 tetramers form As_2 and P_2 dimers. Dimer sources have been shown to reduce the density of deep levels and have a higher “sticking” coefficient, reducing the arsenic flux required during growth. Finally, surface analysis tools are normally incorporated into the system, including a scanning electron microscope (SEM), reflective high-energy electron diffraction (RHEED), Auger electron spectroscopy, secondary-ion mass spectroscopy (SIMS), and X-ray photoelectron spectroscopy. The RHEED analysis instrument plays a crucial role in determining substrate quality, growth condition and monitoring the thickness of the layer growth.

The molecular-beam epitaxial growth process (Fig. 5) for III-V materials requires precise control of the beam fluxes from the Knudsen cells and careful control of the surface temperature on which crystal growth is required.

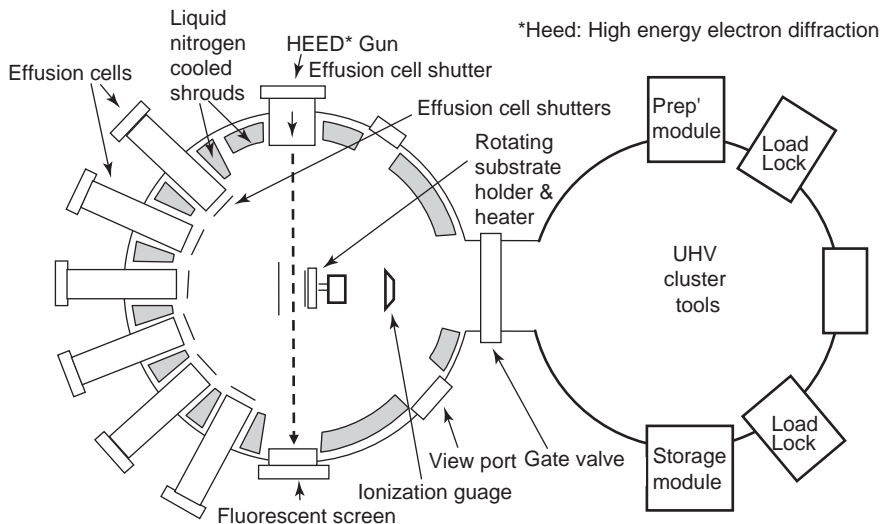


Figure 5. Schematic diagram of a molecular-beam epitaxy system [based on A. Y. Cho, *Molecular Beam Epitaxy and Heterostructures*, L. L. Chang and K. Ploog, eds., Kluwer, Academic Press (1985)].

Prior to initiating III-V growth, the substrate is heated to absorb the oxide layer on the surface, to ensure that the surface is atomically clean. This occurs at temperatures in the region of 590°C for GaAs and 520°C for InP. The process itself involves adsorption of the constituent atoms and molecules, surface migration and dissociation of the adsorbed molecules and incorporation of the atoms into the substrate, leading to nucleation and growth. In the case of GaAs, stoichiometric growth requires that an excess of arsenic be available at the growing surface, and that any excess that does not incorporate with gallium reevaporate. The growth of ternary (e.g., $\text{Ga}_x\text{In}_{1-x}\text{As}$) and quaternary compounds (e.g., $\text{Al}_x\text{In}_{1-x}\text{As}_y\text{P}_{1-y}$) is achieved with MBE using precise control of the ratios of the beam fluxes to ensure that growth occurs with the required mole fractions. A high-volume multiwafer MBE system for production purposes is shown in Fig. 6.

In contrast to the MBE, the metallorganic chemical vapor deposition growth (MOCVD) technique involves chemical reactions between gases that occur at tempera-

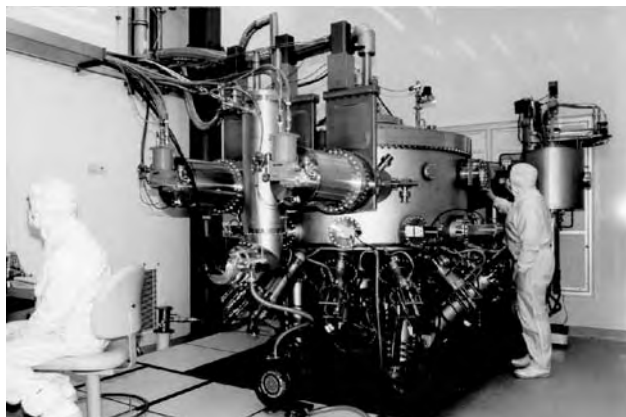


Figure 6. High-volume MBE production system capable of simultaneously growing epitaxial layers on seven 150-mm wafers (Veeco Applied Epitaxy GEN2000 system at Filtronic plc).

tures far below the melting point of the growing material. A typical MOCVD process involves a pyrolysis reaction between a metal alkyl vapor, such as trimethylgallium (TMGa), trimethylindium (TMIn), or trimethylaluminum (TMAI), and a hydride such as arsine (AsH_3) or phosphine (PH_3), in proximity to a heated substrate (Fig. 7). Epitaxial growth occurs on the crystal surface of the substrate as a result of the deposition. Common substrates used for growth include semiinsulating GaAs and InP. In MOCVD, all the constituents of the process are in the vapor phase. This allows for easy control of gas flowrates and partial pressures in the vicinity of the growth surface. Also since the pyrolysis reaction is relatively insensitive to growth temperature, MOCVD achieves highly reproducible deposition of thin layers and can also produce very good abrupt interfaces between the various deposited layers.

MOCVD systems are available in a range of configurations, including high-volume 150-mm substrate growth systems. The hydrides, including arsine and phosphine are highly toxic and require special handling. The choice of source material is critical to the efficient operation of the MOCVD process. In particular, the group V sources must possess high vapor pressures, pyrolysis at temperatures above 395°C, and low temperature stability. They must also be available with very high purity and not prone to parasitic reactions with the group III sources. Group V sources used in MOCVD include the elemental, hydride, trimethyl, triethyl, and tertiarybutyl materials; As, AsH_3 , TMAs, TEAs, TBAs, P, PH_3 , TMP, TEP, IBP, and TBP. Although arsenic and phosphorus require heating to be used as sources, arsine and phosphine have high vapor pressures of 760 torr at -55 and -88°C, respectively. TMAs and TMP have vapor pressures of >250 torr at room temperature, but both these sources have the disadvantage of requiring high pyrolysis temperatures. Similarly, TEP is not an effective phosphorus source since it is stable at normal growth temperatures and TEA has a relatively low vapor pressure, despite its ability to pyrolyze at normal growth temperatures. Metallorganic sources used for MOCVD typically have the lowest molecular

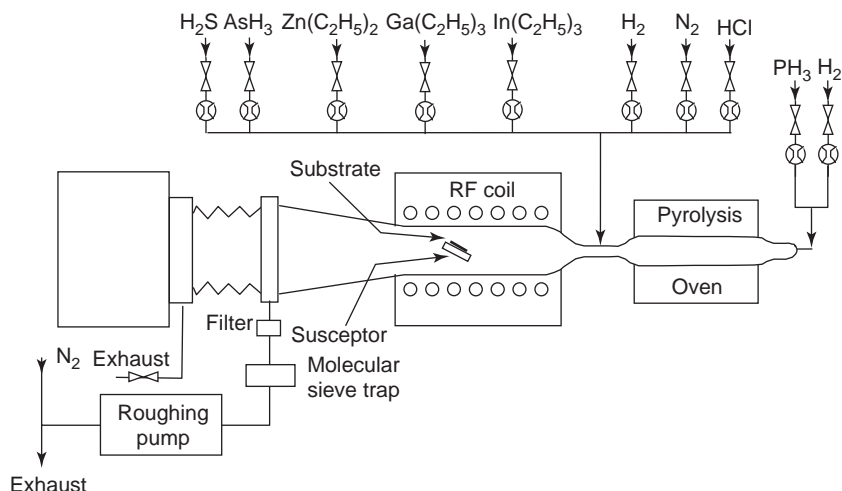


Figure 7. Schematic of a typical horizontal MOCVD system [derived from J. P. Hintz, M. Razeghi, M. Bonnet, and J. P. Duchemin, *GaInAsP Alloy Semiconductors*, T. P. Pearsall, ed., Wiley (1982)].

weights possible with vapor pressures in the region of 1–100 torr at temperatures from -25 to 25°C , and decompose thermally at the required growth temperatures of 550 – 800°C [14]. Generally, trimethyl compounds are used in preference to triethyl materials because of their higher vapor pressures promoting faster growth rates. Typical group III organometallic sources used in MOCVD include TMGa, TMAI, TMIIn, and TMSb. Group III alkyls used in MOCVD readily pyrolyze at low or atmospheric pressures.

The purity of III–V material grown using MOCVD is dependent on the quality of the substrate and the purity of the starting materials (the metal alkyls and hydrides), growth temperature, and the ratio of the constituents in the reactor. In the case of GaAs grown using TMGa and AsH_3 , the purity decreases with increasing growth temperature, probably due to the incorporation of carbon and silicon at higher temperatures. Carbon impurities usually take the form of acceptors, and Stringfellow has shown that a large increase in carbon incorporation occurs at higher growth temperatures [14]. In the case of AlGaAs growth, carbon contamination can lead to significant degradation in mobility, especially with increasing aluminum mole fraction. Doping of MOCVD grown material is usually performed using either Si, Ge, Se, S, or Te for donor impurities and Zn, Cd, Mg, and Be as acceptor impurities. Zinc (p-type) and selenium, tellurium or silicon (n-type) are the most common dopants. Hydrogen selenide H_2Se , SiH_4 , or DETe are used as sources for the donors, and dimethyl or diethyl zinc (DMZn or DEZn) as the p-type dopants.

2.5. Defects and Traps

Semiconductor crystals contain three types of defect: dislocations (or line defects), point defects, and volume defects (precipitates). Line defects occur as the melt crystallizes and shortly after solidification, and are associated with polygonization and slip interactions. The dislocation density is nonuniform and typically lies in the range 10^5 – 10^9 m^{-2} . High values of dislocation density

are detrimental to device performance and are extremely undesirable. Point defects are due to either native defects or chemical impurities. Native defects are usually associated with energy levels deep in the bandgap (known as deep levels) [15,16]. Chemical impurities often originate from the crucible or B_2O_3 encapsulant in LEC material and may include Si, C, or B. Other unwanted impurities, including Fe, Mg, Mn, S, Se, Te, and Zn, may also be found at concentrations of up to 10^{21} m^{-3} . Impurities, such as Cr, may be added to increase the resistivity of the semiinsulating material, with densities in the region of 10^{19} m^{-3} . Volume defects are often found in association with dislocations. Hexagonal precipitates of arsenic and GaAs microparticles create volume defects in some circumstances. Heat treatment of ingots reduces the effect of volume defects.

Point defects are usually characterized as either electron or hole traps. A particularly important point defect is the EL2 deep donor level, common in LEC grown GaAs. Traps play a key role in producing semiinsulating behavior in GaAs substrates [15]. Semiinsulating GaAs has intrinsic behavior in addition to high-resistivity properties, and is remarkably tolerant of small variations in impurity concentrations, retaining good uniformity throughout the ingot. It is important to appreciate that the presence of the deep donor (acceptor) and an excess of shallow acceptors (donors) are required for semiinsulating behavior. If these conditions are not satisfied, it is extremely difficult to achieve semiinsulating behavior [15]. In order to significantly reduce the concentrations of deep traps required to produce semiinsulating material, the concentrations of shallow donors and acceptors must be reduced, requiring material of very high chemical purity. In the case of bulk material, this is most easily achieved for LEC bulk material where the dominant shallow levels are acceptors, possibly due to Zn, Mg, Be, and carbon introduced in the growth process. These compensate the deep donor EL2. Bridgman material tends to be n-type, probably attributable to silicon introduced during growth. Semiinsulating material can be obtained from Bridgman by adding acceptors to compensate

the deep-level EL2 or adding chromium to introduce a deep acceptor, which, along with compensation with excess shallow donors, behaves in a manner analogous to EL2 [15].

Semiinsulating GaAs substrates (undoped and lightly Cr-doped) are often characterized using only one or two deep level traps: the EL2 midgap trap around 0.72 eV, dominant for LEC undoped substrates, and a shallower trap with an activation energy of approximately 0.39 eV. The EL2 level has been found to have an emission time constant that has a strong dependence on electric field [17]. The ionisation of the EL2 level produces an ionized EL2 center and an electron in the conduction band. Spectra associated with hole-type trap behavior have been observed bulk GaAs substrates [18].

The presence of the EL2 level, located near the middle of the bandgap, is essential to avoid nonuniformity and to ensure semiintrinsic behavior. The presence of the EL2 level and its concentration in GaAs ingots is dependent on the melt stoichiometry, and is minimized by having a slightly arsenic-rich content. The arsenic atom fraction in the melt stoichiometry during growth of the ingot determines whether the material is semiinsulating, for fractions in the range 0.475–0.535 with resistivity typically above $10^5 \Omega \cdot \text{m}$, or whether it is p-type in behavior for fractions in the range 0.43–0.47 with resistivities of the order of $10^{-2} \Omega \cdot \text{m}$. The association of semiinsulating behavior with the EL2 level suggests that the electrical properties of the material are due to the deep donor EL2 level and additional residual compensating acceptors, such as carbon.

A comprehensive survey of electron and hole traps was published in Refs. 18 and 19, in which over 33 electron and 22 hole trap levels were tabulated from various sources. It was suggested that some of these observations related to the same traps levels in differing materials. Even so, if this is the case, over 20 separate electron and 11 separate hole trap energies exist. A number of different transient spectroscopy methods have been developed to characterize traps in GaAs; the most commonly used is deep-level transient spectroscopy (DLTS) [10]. These include voltage-pulsed stimulated current and capacitive DLTS [e.g., 18,20], thermally stimulated current and capacitance techniques TSC, TSCAP [e.g., 21], and optically stimulated methods.

The presence of traps in active-device structures can have a profound effect on their transient electrical behavior. Many III–V devices suffer from adverse transient effects such as “gate and drain lag” in FETs, where the drain current responds with a transient of typically many hundreds of microseconds in response to a step excitation in the gate or drain voltages, respectively. The origin of these effects is associated with combinations of surface, bulk, and substrate traps. Surface traps, which are responsible for surface charge, play a particularly important role in determining the transient response of planar devices such as FETs. The transient behavior of these traps gives rise to dispersion phenomena in the drain current, transconductance, output resistance, and gate–drain capacitance. Surface charge can also have a profound impact on the breakdown voltage of these

transistors (which can consequently be a time-dependent phenomena). Ladbroke [22] provides a detailed insight into the impact of surface charge effects and dispersion in III–V MESFETs.

2.6. Substrates and Wafers

Although doped (and unintentionally doped) substrates were commonly grown in the past, for vertically oriented devices such as diodes, today the majority of substrates are semiinsulating. In 2003 over 13 million III–V substrates were manufactured worldwide. The rapid growth in III–V technology demand over the period 2001–2006 is expected to see a threefold increase in substrate supplies with a shift to increase wafer diameter [23].

As in all semiconductor technologies, wafer diameter plays a key role in the economics of manufacturing III–V devices. Since it is proportionately cheaper to fabricate devices on larger wafers than on smaller wafers, there has been a progression over the years from 1-in.-diameter wafers through to the current 6-in.-diameter wafers used for GaAs technologies. Up until 2000, 3- and 4-in.-diameter wafer processes dominated the industry. However, with the successful introduction of 6-in. semiinsulating substrates and associated epitaxial processes (MBE initially, followed by MOCVD), by 2004 there were over 10 large-scale 6-in. fabrication facilities worldwide, gradually displacing the less cost-effective smaller diameter fabrication facilities. This migration to larger wafer sizes can be compared with the movement from 2- through to 12-in.-diameter silicon wafers. The prospect of larger-diameter wafers for GaAs needs to be considered in the context of the level of demand and return on investment in the fabrication equipment as well as the fact that boules of GaAs have a density of more than double that of Si, presenting substantial challenges for growing boules for wafers of over 150 mm (6 in.) diameter.

Generally speaking, in applications where very low defect densities are required (e.g., laser diodes), or for more specialised materials, smaller diameter wafers are used. For example, at the time of writing high-quality GaN is usually grown on 2-in. wafers, and while GaAs is well established on 6-in. wafers, InP technology is still based on 3-in.- and more rarely 4-in.-diameter wafers. Continual improvements in epitaxy have led to dramatic improvements in defect density and epitaxial wafer quality, and this is reflected in the impressive yields, of over 95%, which can be achieved routinely on 150-mm (6-in.-) diameter GaAs wafers [24].

The quality of substrates and epitaxial layers is examined using a range of material characterization techniques, including X ray, photoluminescence, SEM/EDAX, and classical Hall mobility and sheet resistance measurements. In the case of epitaxial layers, the aim is to determine layer thicknesses, uniformity, surface morphology, chemical composition, carrier mobility, Hall factor, defect density, doping profile, and sheet carrier densities. A wide variety of techniques are used and cannot be covered in this article; the reader should consult Refs. 10 and 25. Surface and layer analysis is performed using a

range of spectrometry systems, including X-ray spectroscopy, secondary-ion mass spectrometry, Auger electron spectrometry, and X-ray photoelectron spectroscopy. Defect density and trap density and type are investigated using X-ray spectrometry systems, supported by DLTS. Sheet resistance and Hall mobility are often determined using van der Pauw measurements, based on Schottky gate patterns [26] and magnetoresistance measurements [27]. The doping density and in some cases the doping profile is determined for bulk doped materials, using tests such as C - V profiling, or evaluation from a combination of C - V and I - V data on long-gate length FETs. In the case of heterostructure layers, such as those used in HEMTs, the material is also characterized in terms of its sheet carrier concentration.

3. CARRIER TRANSPORT PROPERTIES

The carrier transport properties of materials determine a material's electrical behavior. The key properties that characterize carrier transport in semiconductor materials are the mobility and velocity of the electrons and holes, which are dependent on the scattering mechanisms in the particular material. The main scattering processes, which influence the mobility of electrons and holes, are acoustic phonon, nonpolar optical mode, polar mode, and ionized impurity scattering. Ionized impurity scattering dominates at low temperatures (< 100 K). Alloy scattering is a limiting process at room temperature in some material systems, such as in AlGaIn/GaN used in HEMTs. The bulk electrical conductivity is then expressed in terms of the mobilities and carrier densities in the bulk material. The low field mobilities of electrons and holes are a strong function of lattice temperature, carrier, and doping density. The transport properties have fundamental dependence on the electric field within the device structure, and are further modified by nonequilibrium behavior in small-scale structures, where rapid changes in the electric field can occur quickly changing the energy of the carriers leading to "hot" carrier transport phenomena.

The mobility in III-V semiconductor samples is normally determined from Hall effect measurements [5], where bulk samples of the material are characterized under the influence of a strong magnetic field. The hole mobility μ_p for p-type material in a small electric field is determined from the Hall mobility μ_H according to the relationship,

$$\mu_H = \sigma R_H = r_H \mu_p$$

where σ is the conductivity, R_H is the Hall constant, and r_H is the Hall factor, which tends to unity for strong magnetic field conditions ($B\mu_p \gg 1$). Similarly for electrons mobility μ_n for n-type material in a small electric field is determined from the Hall mobility μ_H according to the relationship

$$\mu_H = |\sigma R_H| = r_H \mu_n$$

where the Hall factor r_H is close to unity for strong magnetic fields and greater than 1 for medium or weak magnetic fields. Electron and hole mobilities are strongly temperature-dependent, showing approximately $(300/T)^{2.3}$ behavior above 100 K for GaAs. Below 70 K ionized impurity scattering reduces the mobility with decreasing temperature. Mobilities are also a function of carrier density. Typical values of hall mobility for p-type GaAs are in the region of $0.04 \text{ m}^2 \text{ V}^{-1} \text{ s}^{-1}$ for hole densities below 10^{22} m^{-3} , falling to $0.005 \text{ m}^2 \text{ V}^{-1} \text{ s}^{-1}$ for densities above 10^{25} m^{-3} . The Hall mobility of the electrons in GaN/AlGaIn HEMTs at 300 K has been found to be as high as $0.14 \text{ m}^2 \text{ V}^{-1} \text{ s}^{-1}$ in high-quality material for sheet carrier concentrations of 10^{17} m^{-2} .

The electron and hole drift velocities are defined by the product of the mobility and electric field \mathbf{E} . Hence, for electrons, the drift velocity v_d is given by $\mu_n \mathbf{E}$. In the case of low doped n-type GaAs μ_n is in the region of $0.8 \text{ m}^2 \text{ V}^{-1} \text{ s}^{-1}$ at 300 K for low values of electric field. At low values of electric field the velocity increases with increasing electric field. However, as the electric field increases and the electrons gain energy, the mobility decreases slightly. Increasing the electric field still further results in the most energetic electrons transferring from the central Γ valley to the first satellite valley X, which has a higher effective mass and reduced mobility. Eventually, a value of electric field is reached where the velocity attains a peak value, in the region of $2 \times 10^5 \text{ m/s}$ for GaAs. Beyond this value the drift velocity decreases with increasing electric field, asymptotically approaching the saturated value of $7 \times 10^5 \text{ m/s}$ at very high values of electric field. The steady-state electron velocity-electric field characteristics for several III-V semiconductors compared with silicon at 300 K are shown in Fig. 8 [28–32]. The region of negative-differential mobility beyond the peak velocity in each characteristic, where the velocity decreases with increasing electric field, is due to the transferred electron effect where electrons are transferring from the high-mobility central (Γ) valley to the low-mobility satellite (X) valley in the energy band structure. This phenomenon can give rise to oscillations in samples of InP and GaAs, and forms the basis of the Gunn diode (transferred electron device) [5].

The transient (nonequilibrium) carrier transport properties of semiconductors may be markedly different from their steady-state (equilibrium) characteristics [33,34]. In the case of many III-V semiconductors, the change in velocity experienced by electrons entering a high-electric-field region can lead to a phenomenon known as "velocity overshoot," where the electron is accelerated in the electric field, rapidly gaining energy, to a velocity significantly higher than the peak steady-state value, for a short interval (usually less than 0.1 ps). In the case of GaAs the transient velocity of these hot electrons may reach values in excess of $5 \times 10^5 \text{ m/s}$ over a short distance ($< 0.1 \mu\text{m}$) until scattering, energy, and momentum relaxation lead to a reduction in velocity that subsequently approaches the steady-state value over a short interval in time and distance [33,34]. Velocity overshoot in III-V devices can enhance their high-frequency performance

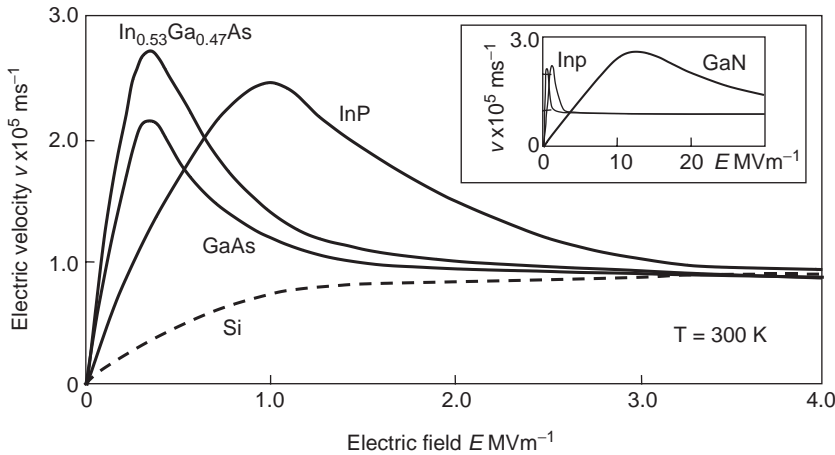


Figure 8. Steady-state velocity–electric field characteristics for GaAs, InP, $\text{In}_{0.53}\text{Ga}_{0.47}\text{As}$, and GaN, compared with Si at 300 K.

and is significant for short-gate (submicrometer)-length FETs.

The conductivity of semiconductors is given by

$$\sigma = \sigma_n + \sigma_p = q(n\mu_n + p\mu_p)$$

where n and p are the electron and hole densities (n_0, p_0 for intrinsic condition). In the case of GaAs doped with shallow donors or acceptors, the ratio of n/p is far from unity at 300 K, and the conduction is essentially unipolar depending on the dopant type. GaAs can be engineered to achieve a high value of resistivity, close to the intrinsic state, by the use of chromium doping, which introduces EL2 centers (see Section 2.5), creating semiinsulating GaAs. The room temperature resistivity of semiinsulating GaAs is typically in the range 10^3 – $10^7 \Omega \cdot \text{m}$, which makes an ideal substrate for integrated circuits.

4. PROCESSING AND DEVICE FABRICATION

The fabrication of semiconductor devices using either semiinsulating wafers with ion implantation of epitaxial layered wafers requires several stages of lithography, selective etching, deposition, and passivation, finishing with die separation, final test, and packaging. It is not possible to provide a detailed description of processing in this article, but an outline is a useful aid in understanding the design constraints and properties of the finished semiconductor devices. Williams provides a useful introductory text for GaAs processing [11].

4.1. Lithography

One of the most fundamental elements of device processing is the definition of the active and passive regions of the device, electrical contacts, bondpads, implantation regions, passivation areas, and interconnecting lines. This process of transferring patterns, made up of geometric shapes, to a thin layer of radiation sensitive material (*resist*) deposited on the surface of a semiconductor wafer is known as *lithography*. The resist is usually

deposited on the wafer by spinning a few drops of resist fluid into thin film at very high speeds, on to the surface of the wafer. The resist is then patterned (exposed) using photolithography, ultraviolet light lithography, electron-beam lithography, or in special cases X-ray or ion-beam lithography. The resist is then developed, selectively removing either the exposed or unexposed areas. The remaining pattern is then used to define areas for etching, deposition, or implantation. The resists are classified as either positive or negative depending on whether the exposed region is removed (positive) or whether the unexposed regions are removed (negative). An additional technique is based on image-reversal, which can provide enhanced resolution, which is particularly useful for submicrometer photolithography.

The photolithography techniques used in III–V processing include contact printing, proximity printing, projection printing, and stepping. Contact printing, which is frequently used for initial research development and for backside processing, is a straightforward process where the mask is aligned on the wafer and the resist exposed using a beam of ultraviolet light. Resolutions down to the region of one micrometer are possible as a result of the direct contact between the mask and the wafer. The two main disadvantages of this approach are (1) abrasion of the mask through direct contact, which reduces mask lifetime, and (2) *runout* due to any lack of planarity between the mask and wafer, preventing contact. Runout, due to curvature in either the mask or wafer, results in misalignment in areas of the pattern. Contact printing systems are significantly lower in cost than steppers or other precision lithography systems. Proximity printing places the mask in close proximity to the wafer, but avoids direct contact. Diffraction at edges in the pattern produces a slightly blurred image. This technique cannot achieve high resolutions and is not widely used in modern fabrication processes.

Optical steppers are the mainstay of silicon fabrication and are becoming widely used in III–V fabrication. The mask consists of the patterning for device and integrated circuit designs and is known as a *reticule*. The reticule is projected onto the wafer, which has previously been coated

in resist. A typical reticle is 20×20 mm. Many reticle patterns can be accommodated on a wafer. After the first reticle pattern is exposed, the wafer is moved very precisely and a second image is created. This process repeats across the wafer until the whole wafer is exposed. This step and repeat process is well established and is precisely indexed to allow multiple mask sets to be used, achieving precise alignment between layers. Steppers normally allow reduction of the reticle pattern on the mask by factors of 5 or 10, although in some circumstances unity reduction is used. Steppers achieve optical imaging using either lenses (refractive optics) or mirrors (reflective optics). The limitations of the optics are constrained by diffraction, where the optical surfaces must be accurate to within a quarter-wavelength. Steppers achieve a highly repeatable pattern, where any runout or misalignment is generally confined to the reticle. As a result, steppers have become established as a key element of high-yield processing, producing very-high-quality, highly repeatable lithographic patterning. Contemporary steppers for III-V lithography are available that achieve feature sizes of 0.35, 0.18, and 0.12 μm ; the cost of the system increases with increased resolution. Excimer laser (KrF) sources are used for the high-resolution steppers in the 0.18 μm range. Even higher resolutions are possible today, but the cost of the stepper is prohibitive for anything other than very-high-volume Si applications (microprocessors and memory). More recently there has been increased interest in using phase-shifting masks [35], which improve optical resolution by using interference to cancel diffraction effects. Steppers are available for 3, 4, 6, 8, and 12 in. wafer sizes.

Electron-beam (e-beam) lithography is widely used in III-V processing, as a means of both precisely patterning the masks used in photolithography and directly exposing (direct *writing*) patterns on wafers. Submicrometer gates were first written on GaAs using e-beam systems, although more recently, gate lengths above 0.35 μm are more routinely written using steppers, and it can be expected that 0.25- and 0.15- μm gates will in due course be written using steppers. At the heart of e-beam systems is the electron gun, which operates continuously, and beam-blanking plates that turn the beam on and off. The beam is moved over the surface of the wafer, within the scanned region, using deflection coils. The wafer is coated in a resist such as polymethylmethacrylate (PMMA). The wafer is positioned using a precision mechanism to move from one scanning field to the next. The pattern is generated in e-beam systems using computer controlled raster or vector scanning techniques. Electron-beam systems can achieve very high resolutions (currently below 70 nm), excellent registration, and great flexibility and do not require masks. Wafer flatness is not a problem for e-beam systems as they have a greater depth of field than do steppers. However, the throughput of e-beam systems is significantly slower than steppers at present. Also, on larger wafers e-beam systems can suffer from degradation of alignment accuracy, especially toward the edge of the wafers, away from the initial scanning fields. E-beam systems for III-V processing are available that will handle wafer sizes up to 6 in. (150 mm).

III-V processing has a number of significant differences to silicon device fabrication and in some respects is simpler — generally requiring fewer steps for monolithic microwave integrated circuits (MMICs) than for silicon ICs. A key stage in semiconductor device fabrication is the metal patterning, where, following evaporation of the required metal, the unwanted metal regions are removed. The metals used with silicon processing (typically Al) are usually fairly easy to etch, whereas the metallization schemes used in III-V processing (frequently TiPtAu, AuGeNi) are often difficult to etch. In silicon, this is achieved by depositing the metal first and then coating the metal with resist and lithographically defining the pattern. The unwanted metal, which is not protected by resist, is then removed by etching after developing the resist pattern. The resist is then removed using a solvent. In the case of III-V semiconductors a process known as “lift-off” is normally used, where the resist pattern is produced using lithography prior to evaporation of the metal. The desired metal pattern is then obtained by removing (“lifting off”) the resist (with metal evaporated on its surface) using a solvent, leaving the metal deposited on the semiconductor surface in the regions where the resist was originally removed following the development stage. The liftoff process is very sensitive to the pattern defined by the resist and an undercut in the resist profile is usually used to help define the desired metal regions.

It is convention to include a process control monitor (PCM) site in the reticle. This important element of the patterning includes a range of test devices, such as simple contact structures, transistors, and diodes and if it is a MMIC, a small range of transmission-line structures resistors, capacitors, and inductors. The purpose of these structures is to monitor the key parameters against the expected values as the wafer goes through each stage of the processing. This allows the quality of the processing to be closely monitored and assists in process control and yield optimization. The PCM sites are usually tested after each processing stage or at suitable intervals. The PCM site usually occupies only a small area of the reticle — often less than 1%.

4.2. Etching Techniques

III-V semiconductors can be etched using either wet- or dry-etch techniques or a combination of both. Prior to processing and at stages during the fabrication, it is necessary to clean the wafer surfaces. Exposure of GaAs to the atmosphere leaves an oxide layer on the exposed surface of the material, which can be 50 Å thick, which is removed using a highly diluted acid such as HCl. Highly pure deionized water is used extensively in processing to avoid contamination. Wet and dry etchings are used as a means of forming patterns and defining features in the surface of the semiconductor wafer, and for polishing (e.g., after thinning of wafers during backside processing).

Wet etching techniques have been established since the early days of fabrication and normally have the properties of providing selective and preferential etching depending on the crystallographic orientation of the wafer. In the case of Si, this allows distinctive etching that is exploited

in MEMs, and, for example, allows “V” grooves to be readily defined. Etching of III-V compounds is usually crystallographic, and key features and critical dimensions can be defined by ensuring proper alignment with the lattice planes. In the case of GaAs, (111) Ga faces etch up to 5 times slower than do (100), (110), and (111) As faces. Wet etches are categorized either as electrolytic or nonelectrolytic. Electrolytic etches require an electrical contact to the wafer and in the case of GaAs have an anodic oxidation mechanism. One advantage of electrolytic etches is that they can be used to provide accurate technical depth control. Nonelectrolytic etching rates are either diffusion or chemical-reaction-limited. Diffusion-limited etches are generally isotropic and are well suited for polishing wafers after mechanical grinding. Chemical-reaction-limited etches are often anisotropic are particularly suitable for defining patterns. Wet etches generally contain an oxidizing agent, such as Br_2 or HNO_3 , a complexing agent, such as NH_4OH , NaOH , HC , citric acid, or H_2SO_4 and water. The complexing agent ensures that the relatively insoluble oxidized layer is dissolved in the water. The etch is chosen to remove areas of the wafer that are not protected by the exposed resist pattern.

Dry etching techniques have become increasingly popular for use in III-V device fabrication in more recent years. They are widely used in III-V processing to produce recesses (e.g., single- and double-gate recesses), mesas for isolation, and via holes through the substrate that are metallized to connect the top surface to the metallized back surface of the wafer. These reactive plasma etching techniques have several important advantages over wet-etch methods, including better directional control of the etch and improved anisotropy of the etch. Specifically, the laterals etch rates in plasma etching are very low indeed, preventing undesirable undercutting of the resist pattern. Dry etching utilizes an ionized gas to achieve plasma-driven chemical reactions or use highly energetic ion beams to remove material that is not protected by the resist pattern. Dry etching can be classified as plasma etching, reactive-ion etching (RIE), ion milling, or reactive-ion-beam etching (RIBE). Inductively coupled plasma etching is also widely used in III-V device fabrication. Control of the plasma by varying the system electrode configuration, gas composition, pressure, and bias voltages allows the characteristics of the etching process to be tailored to the particular semiconductor material and the required shape of the etched region.

Plasma etching systems often use chlorine, HCL , PCl_3 as sources of chlorine ions. O_2 and Ar are often added. CH_4/H_2 systems have been used for InP and GaAs. The system itself in its basic form consists of two parallel plates with a DC and RF ionizing source (100–600 V at 13 MHz) attached to the top plate and the wafers clamped to the lower water-cooled plate. The plasma is formed between the plates and energetic ions perpendicularly impact the surface of the exposed semiconductor material. The resist prevents the ions penetrating the unexposed surface of the semiconductor. Plasma etching can give rise to radiation damage and in some circumstances leaves residues that require subsequent removal (often using a light wet etch). RIE is in many ways similar to plasma

etching, with the reactive species generated from the plasma, but with greater directionality of the ions. RIE systems typically operate at low pressures and the substrates are mounted on the powered electrode. Reactive-ion etching is usually used to etch GaN/AlGaN because of the difficulty in finding suitable wet etches. BCl_3/Ar is found to produce surfaces smoother than those obtained with Cl_2/Ar for GaN/AlGaN. Finally, the electrodes themselves are often asymmetric with the chamber forming the grounded electrode. In RIE the semiconductor is etched through a combination of chemical reaction and sputtering. Similar ion species can be used to plasma etching, but a smoother surface is obtained using H_2 , BCl_3 , or CCl_3F . Again O_2 is added to CCl_3F and CCl_4 to increase etch rates, and Ar to increase anisotropy.

Ion-beam milling is a high-energy (~ 1000 eV) etching process, where inert ions (Ar) are allowed to impinge on the target substrates in a uniform beam. Ion-beam milling can achieve relatively high resolutions, and can be used to define structures smaller than $0.01\ \mu\text{m}$. It is a highly anisotropic process, and the profile of the etched sidewall can be determined by positioning the relative angle of the substrate and by using shadow masking. Ion-beam milling can be used to etch metals, including Ti, Pt, and Au metallization layers and will etch materials that are challenging for plasma or wet-etch systems. The main disadvantages are damage from ion bombardment, poor sensitivity, and redeposition of materials. Focused ion-beam etching can be used to define small-scale structures. The final dry etching process, reactive-ion-beam etching (RIBE) takes advantage of both chemical reaction and ion bombardment to etch material. Unlike ion beam milling it uses a reactive gas although the etch characteristic are very similar. Redeposition of the etched material is avoided in RIBE by using a vacuum removal system.

4.3. Deposition and Metallization

It is usually necessary to provide insulating coatings on the surface of semiconductors at various stages in processing, either to planarize the surface for additional processing (e.g., metallization) or as a dielectric for capacitors in integrated circuits, or as a passivation to protect the surface of the semiconductor. The type of materials deposited can be either inorganic, such as silicon nitride or silicon dioxide, or organic, such as BCP. Plasma-enhanced chemical vapor deposition (PECVD) techniques, which use RF excited plasmas, are often used to deposit these films, as they can achieve this at relatively low temperatures (typically 250 – 350°C). This low temperature capability is very important for III-V processing, where higher temperatures would lead to changes or decomposition of the semiconductor material. PECVD films are amorphous, and the density and quality of the material depend strongly on growth conditions. In particular, the frequency of the RF stimulated discharge, which may lie between 50 kHz and 13 MHz, directly influences the stress in the film (the higher the frequency, the lower the compressive stress). PECVD layers are usually deposited in thickness between $1000\ \text{\AA}$ and $1\ \mu\text{m}$, with growth rates typically of the order of $300\ \text{\AA}/\text{min}$.

Plasma deposition is usually carried out in either a planar (parallel-plate) or barrel (tubular) reactor. The best uniformity is achieved in radial flow planar reactors, where the substrates are positioned on the lower electrode of the two parallel plates. Deposition is performed under a vacuum to minimize contamination, and a wide variety of highly reactive chemical species are used, including chlorine, fluorine, hydrogen, oxygen, silane (SiH_4), and ammonia. Silicon nitride, which is one of the most frequently used insulating materials, is often deposited using electron cyclotron resonance systems, which operate at 2.45 GHz.

Silicon nitride Si_3N_4 is used widely in III-V processing as a dielectric layer in capacitors, an encapsulant (to prevent diffusion) or for passivation to protect the surface of the semiconductor or die from the environment. It is normally grown using silane as a source of silicon and ammonia (or nitrogen in some cases) as the nitrogen source. The silane is mixed with an inert gas (argon). The dielectric constant of the amorphous silicon nitride is a function of film thickness and silane concentration. The film thickness dependence is due to the impact of stress and nonuniform growth of the layer. Thin films (below 1000 Å) can achieve relative dielectric constants of up to 11, whereas thicker films typically have dielectric constants in the region of 8. Silicon dioxide has a lower dielectric constant than silicon nitride and is often used as a spacer layer in metal cross-overs to minimize parasitic capacitance. Again, silane is usually used as the silicon source, and the oxygen source is selected from CO , O_2 , or N_2O .

Some III-V processes utilize aluminium nitride as an insulator or passivation layer. AlN for these purposes is grown either by sputtering, vapor phase, or MBE. Single-crystal films may be grown at temperatures in the region of 1150°C, although amorphous AlN films can be grown at lower temperatures or using plasma CVD. Other dielectric films such as silicon oxynitride are used in some circumstances.

The final element in processing is the provision of metallization on the surface of the semiconductor to act either as contacts or interconnections. Two types of metal-semiconductor contact can be fabricated in III-V devices: ohmic contacts and Schottky contacts. Ohmic contacts have the property that they possess very low resistances across the metal-semiconductor interface, while Schottky barrier contacts have a more complex rectifying contact behavior, representative of a diode, where in reverse bias the interface demonstrates very high resistance (ideally no current flow) and capacitance associated with the charge developed in the depletion region below the contact. In contrast in forward bias, the interface behaves like a diode, with the potential for significant current flow, but only supporting relatively low forward voltages across the interface. In addition to the contacts, first- and second-level metallization is used to interconnect the various elements of the active devices, and circuits, where the metal is chosen to possess high conductivity, excellent adherence, and conformal coating, coupled with compatibility with the Schottky and ohmic contacts. Additionally, via holes that connect between levels or between the top and backside metallized surfaces of the substrate.

Schottky contacts can be formed with III-V semiconductors using sputter or evaporation deposited multi-layer metal contact structures such as TiPtAu, TiW, TiWSi, Pt, Al, WSi, WAl, and TiPdAu. Metal silicides, such as tungsten silicide, widely used in silicon VLSI, can achieve low contact resistances for III-V devices when annealed at high temperatures and may be deposited using RF cosputtering. Schottky contacts on AlGaN can be achieved using Ni/Au. The barrier height of the Schottky barrier varies with the semiconductor material composition, crystal orientation, and the contact metal. In the case of GaAs and gold, for example, the barrier height varies from 0.82 eV for (100) orientation to 0.97 eV for (110) crystal orientation at the interface [36]. The range of barrier height for Schottky contacts on several III-V binary semiconductors is shown in Table 3 [5,36,37].

Ohmic contacts are formed with III-V semiconductors using n^+ or p^+ layers immediately below the contact metallization. Very high doping levels above $5 \times 10^{24} \text{ m}^{-3}$ are used with multilevel metal-alloyed contacts. In the case of GaAs, alloys based on Au or Ag are popular choices. In the case of contacts made on p-type material, zinc is usually added to the alloy, which acts as a dopant in the semiconductor. In the case of n-type contacts germanium and tin are used in the alloy. AuGeNi contacts provide among the lowest contact resistances and high reliability in III-V devices. Other GaAs metal alloy ohmic systems include Au-Zn, Au-Zn-Sb, Au-Be, and Au-Be-Ni. Ohmic contacts to InP are achieved using Au-Ge-Ni, Au-Sn, Ag-Sn-In, In-Zn, Au-Mg, and Au-Be. AlGaAs ohmic contacts are made with Al, Au-Zn, and Au-Ge-Ni; GaInAs, with Au-Zn, Au-Sn, and Au-Ge-Ni. Ohmic contacts to AlGaN/GaN devices are usually made with alloys based on Ti/Al annealed at 850–875°C. Rapid thermal annealing is usually employed for ohmic contacts. “Balling” of the metals on the contact surface can be avoided by including a thin cover layer of Ni/Au over the Ti/Al prior to annealing at 900°C. It should be noted that it is hard to form ohmic contacts to AlGaN when the mole fraction exceeds 33%.

A first-level metal used as part of the interconnection metallization has the characteristic of good adhesion to ohmic and Schottky barrier metals. Gold-based alloys are generally used for interconnection first metallization — the most common are TiPtAu and TiPdAu, using e-beam deposition systems. Copper, with its very high conductivity, which is used with silicon, diffuses in several III-V semiconductor materials and cannot be used. Aluminum

Table 3. Schottky Barrier Heights for n-Type III-V Semiconductors

Material	Barrier Heights (eV)						
	Ag	Al	Au	Ni	Pt	Ti	W
GaAs	0.88	0.80	0.90	0.79	0.85	0.82	0.79
GaP	1.20	1.07	1.30	1.27	1.45	1.12	—
AlAs	—	—	1.20	—	1.00	—	—
InAs	—	—	0.47	—	—	—	—
InP	0.65	—	0.65	—	—	—	—
$\text{Al}_{0.14}\text{Ga}_{0.86}\text{As}$	—	0.90	1.02	—	—	—	—
$\text{Al}_{0.32}\text{Ga}_{0.68}\text{As}$	—	1.09	1.10	—	—	—	—
$\text{In}_{0.53}\text{Ga}_{0.47}\text{As}$	0.20	—	0.20	0.20	—	0.15	—

interacts adversely with gold, with high-resistance intermetallic products. Silver is very reactive and is rarely used in III-V devices. First metallization is usually in the region of $0.5\ \mu\text{m}$ thickness. Second-level metallization is usually based on gold (Ti/Au), due to its low tendency to electromigration [38] and ability to handle very high current densities. Airbridges are also formed in the second-level metal. Metallization is achieved using sputtering, evaporation or electroplating. An evaporation system for 150-mm-diameter wafers is shown in Fig. 9. Thicker layers ($> 1\ \mu\text{m}$) are usually deposited using RF sputtering systems. Via holes may be plated using either electroplating or electroless plating (based on gold–cyanide solutions) or magnetron sputtering or by evaporation of TiAu.

4.4. Backside Processing

The final stage of the fabrication process is backside processing and die separation. After completing the frontside with the devices, metallization, contacts, and circuit elements, the reverse side of the wafer is processed. At this stage the wafer is usually thinned to its final thickness, which usually lies in the range $30\ \mu\text{m}$ (for high power) to $150\ \mu\text{m}$ (Fig. 10). A mechanical grinding process is used to remove the bulk of the material, which is then finished with a chemical etch. If there is a requirement for via holes to connect the top surface to the backside, vias will be etched, usually using dry etching techniques (Fig. 11). If a ground plane is required, the backside is metallized with gold (as in the case of vias). After completion of processing, the wafer may be attached to a film frame to facilitate temporary die retention during the on-wafer test and die separation processes. The die on the wafer are then subject to visual inspection and electrical testing. The process control monitor (PCM) sites receive their final electrical tests to complete the process data for the wafer. The die may be probed using DC and RF testing to determine whether they meet the specification (and hence determine the final yield). After on-wafer testing the final stage is to separate the die, which is achieved using either a diamond scribe (“scribe and break”) or a



Figure 9. Evaporation system for metallizing semiconductor wafers.

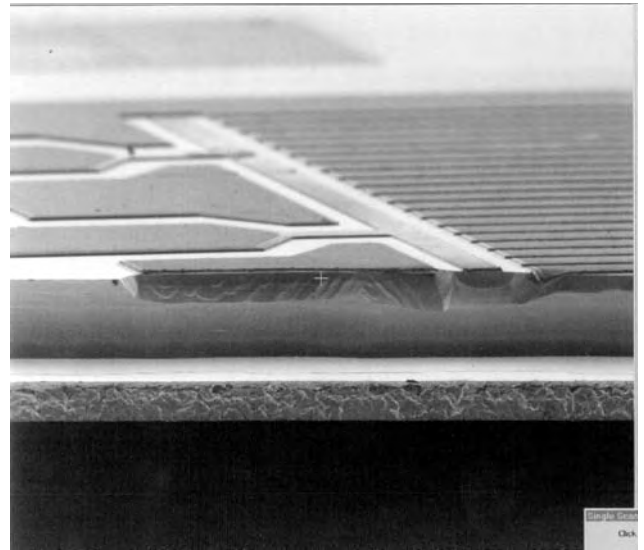


Figure 10. Cross section of a die, showing thinning of the GaAs to $30\ \mu\text{m}$ and gold metallization of the backside ($\sim 10\ \mu\text{m}$). The FET structure can be seen on the frontside (Filtronic plc).

diamond saw. Laser separation techniques are beginning to appear that also show promise. The die are retained on the film in preparation for packaging using robotic pick-and-place instruments.

5. RF AND MICROWAVE DEVICE TECHNOLOGY

III-V RF and microwave devices may be fabricated as unipolar or bipolar designs. The early interest in GaAs and InP centred around the properties of these materials that demonstrated negative-differential resistance as a consequence of their velocity–electric field relationships. J. B. Gunn demonstrated microwave oscillations in 1963, using a simple GaAs two-terminal structure. This phenomena forms the basis of the *transferred electron effect*

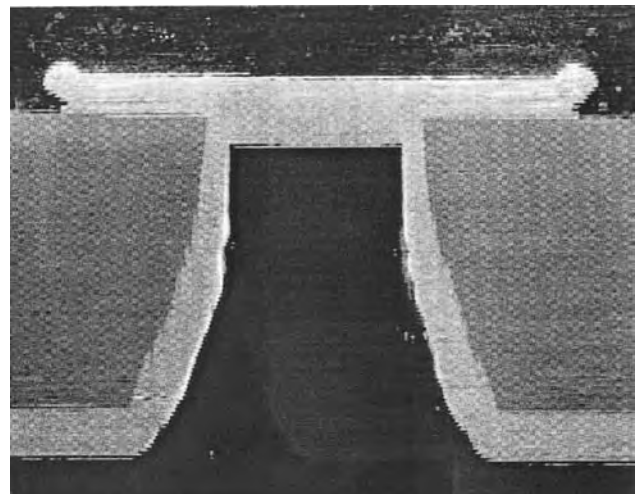


Figure 11. A via hole etched in a $125\text{-}\mu\text{m}$ substrate and plated in gold (light color) (Filtronic plc).

[5], which is characterized by the behavior of the Gunn diode. GaAs and InP Gunn diodes have found widespread application as the active devices in microwave oscillators ranging from 1–100 GHz.

The most common transistor technologies in use today are based on unipolar field-effect transistor (FET) or heterojunction bipolar transistor technologies [39,40]. GaAs and Si bipolar transistors were widely used prior to the advent of higher-frequency FETs [41]. In 1971 Turner reported a 1- μm -gate-length FET with gain of ≤ 18 GHz [42]. By 1980, GaAs metal semiconductor field-effect transistors (MESFETs) were established as the device of choice in microwave low-noise and medium-power amplifiers, achieving noise figures of less than 1 dB at 4 GHz and output powers of up to 25 W [43]. Although MESFETs were employed in oscillator designs, especially varactor tuned designs, from their introduction in the mid-1970s [44], relatively poor $1/f$ noise performance in early MESFETs led to the continued use of bipolar junction transistors in low-noise oscillators up to 6 GHz. The advent of AlGaAs/GaAs high-electron-mobility transistors (HEMTs), also known as *modulation-doped FETs* (MODFETs), in the 1980s with their improved noise performance displaced MESFETs in low-noise amplifiers and wider use in oscillators and mixers, although still with some remaining $1/f$ noise limitations. AlGaAs/GaAs heterojunction bipolar transistors (HBTs) were introduced in the early 1980s, but were not widely used until the advent of mobile communications and the widespread development of low-voltage, high-efficiency power amplifiers for cellular handsets. By 2000 pseudomorphic HEMTs (PHEMTs) had become the established high-frequency transistor, operating at frequencies up to 200 GHz and achieving noise figures below 0.2 dB at 2 GHz. HBTs based on AlGaAs/InGaAs/GaAs, and InGaP structures demonstrating maximum frequencies of oscillation f_{max} above 100 GHz, are now readily available. GaAs-based PHEMTs have demonstrated high power and high efficiency operation up to X band [45]. The state of the art is now occupied by gallium nitride transistors, with AlGaN/GaN FETs achieving power densities above 10 W/mm gate periphery and capable of over 170 W at high efficiencies [46], and power densities of over 4 W/mm at 30 GHz [47]. Similarly, GaN/AlGaN HBTs show potential for high-power high-frequency operation and demonstrate high emitter injection efficiencies.

6. APPLICATION OF TRANSISTOR TECHNOLOGIES

Up until 1985, the MESFET dominated as the preferred choice of microwave transistor, with some usage of silicon bipolar remaining for niche applications below 8 GHz (such as low-noise oscillators). By 1990, the PHEMT had begun to displace MESFETs for low noise amplifiers, and the AlGaAs/GaAs HBT had begun to emerge as a candidate for low-voltage power amplifier applications (such as in the emerging cellular handset market). Up until this time, MESFET technology had been dominated by ion-implanted designs, utilizing semiinsulating GaAs substrates. Improvements in epitaxial growth (MBE and MOCVD/OMVPE) allowed higher performance FETs to be designed, with improved gain, current, and power handling. By 2000, MESFET technology was being displaced in many applications by PHEMT and HBT, because of the superior gain and power handling of these technologies. Nevertheless, the simpler fabrication technology MESFETs remains attractive for low-cost applications where the performance is undemanding. At the present time, HBTs are the most common choice for power amplifiers in cellular handsets, while PHEMTs power FETs are being introduced in many microwave and millimeter-wave power amplifier applications and are even challenging silicon LDMOS in some specialized applications at 2 GHz. By 2006 GaAs-based HEMTs are expected to be found in over 35% of microwave applications, while HBTs provide another 30%, with MESFETs falling to around 20%.

The maximum electric field sustainable before the material breakdown determines the maximum voltage sustainable across the device, which in turn directly influences the power handling of the device. The electron and hole mobilities impact the resistivity, frequency limit, and current handling (and thus power handling) of the device. The saturation velocity determines the current handling and frequency limitations. The thermal conductivity limits the temperature of operation and thus the power-handling and frequency limits. Table 4 lists these parameters for a range of semiconductors used or potentially available for power devices. The potential for newer materials such as GaN, SiC, and diamond is still being evaluated. It should be noted that the reported data for more recent materials varies in the literature. The Johnson and Baliga figures of merit are frequently used to compare the potential of materials for power device applications [48,49]. Baliga's figure of merit is a measure of the

Table 4. Material Properties for Power Devices at 300 K

Property	GaAs	InP	GaN	Si	4 HSiC	Diamond	Units
Energy bandgap	1.42	1.34	3.44	1.12	3.26	5.47	eV
Relative permittivity	12.8	12.6	9.5	11.8	10.1	5.7	—
Breakdown field	48	53	330	31	300	2000	MV/m
Electron mobility	0.86	0.54	0.15	0.15	0.08	0.28	$\text{m}^2 \text{V}^{-1} \text{s}^{-1}$
Hole mobility	0.04	0.02	0.02	0.04	0.01	0.20	$\text{m}^2 \text{V}^{-1} \text{s}^{-1}$
Saturation velocity	0.8	0.8	1.3	0.9	2.0	2.7	$\times 10^5 \text{ m/s}$
Peak velocity ^a	2.1	2.3	2.6	1.0	2.0	2.7	$\times 10^5 \text{ m/s}$
Thermal conductivity	46	68	130	150	490	2200	$\text{W m}^{-1} \text{K}^{-1}$

^aNontransient (steady-state).

Table 5. Johnson Figure of Merit Normalised to Silicon

Material	Johnson Figure of Merit
Si	1.0
GaAs	1.9
InP	2.3
GaN	233.0
4 HSiC	455.0
Diamond	37,000.0

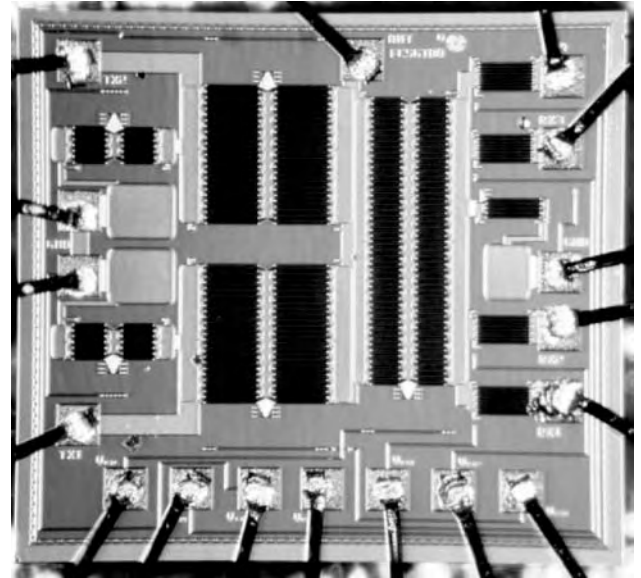
ON resistance of the drift region of a transistor (usually applied to vertical FETs) [50]. The Johnson figure of merit (JFM) is a measure of the ultimate high frequency capability of the material and is given by the product of critical breakdown field E_{Br} and saturated electron drift velocity v_{sat} :

$$JFM = \left(\frac{E_{Br} v_{sat}}{2\pi} \right)^2$$

The Johnson figure of merit is shown for a range of power semiconductors in Table 5. It should be noted that practical limitations encountered in fabricating power transistors limits the actual performance of devices, although the more mature technologies of Si and GaAs can approach these limits in some applications. InP has demonstrated excellent performance in applications, including MMICs, above 100 GHz, although it is still mainly applied to small-signal transistor applications and a limited range of relatively low-power millimeter-wave devices such as Gunn diodes (75 mW at 94 GHz).

7. APPLICATIONS AND MARKETS FOR MMICs AND DIGITAL ICs

Historically, the market for III-V integrated circuits grew steadily up until 2000, without the cyclical behavior often seen in the silicon digital IC market. In 2000 over \$2 billion MMICs and digital GaAs ICs were sold and despite the technology recession observed in 2001/02, the market for these products is expected to grow to over \$4 billion by 2006. Wireless communications represented over 70% of this market in 2000, but by 2006 this is expected to fall to around 60% as the use of MMICs in automotive applications increases. Interestingly, despite the intense interest in optoelectronics, the total share of the GaAs IC market in this application (for modulators, switches, driver ICs, detectors, and high-speed processing) is not expected to exceed 12% in the foreseeable future (indeed, its market share fell to 8% in 2002). Although digital GaAs was originally seen as a major growth element of the industry in the late 1990s, the collapse in the optoelectronic market in 2000 and the increase in CMOS Si and SiGe capabilities, have seen the GaAs largely displaced for digital applications below 2.5 Gbps. Analogue applications now dominate for III-V MMICs with increased usage in mobile terminal products (cellular handsets, personal digital assistants wireless LANs, etc.), principally for power amplifiers and low-loss RF switches (Fig. 12). The emer-

**Figure 12.** A microwave switch MMIC (1 × 1 mm) (Filtronic plc).

gence of automotive radar applications has led to forecasts of significant growth for chipsets at 17, 24 and 77 GHz, possibly reaching 5 million chipsets per annum by 2007.

BIBLIOGRAPHY

1. H. Welker, Über neue halbleitende Verbindungen (New semiconductor compounds), *Z. Naturforsch.* **79**:744–749 (1952).
2. M. Ida, K. Kurishima, and N. Watanabe, Over 300 GHz f_T and f_{max} InP/InGaAs double heterojunction bipolar transistors with a thin pseudomorphic base, *IEEE Electron. Device Lett.* **23**(12):694–696 (Dec. 2002).
3. J. W. Archer, R. Lai, R. Grundbacher, M. Barsky, R. Tsai, and P. Reid, An indium phosphide MMIC amplifier for 180 to 205 GHz, *IEEE Microwave Wireless Compon. Lett.* **11**(1):4–6 (Jan. 2001).
4. Y.-F. Wu, A. Saxler, M. Moore, R. P. Smith, S. Sheppard, P. M. Chavarkar, T. Wisleder, U. K. Mishra, and P. Parikh, 30-W/mm GaN HEMTs by field plate optimization, *IEEE Electron. Device Lett.* **25**(3):117–119 (March 2004).
5. S. Sze, *Physics of Semiconductors*, Wiley-Interscience, 1981.
6. V. Swaminathan and A. T. Macrander, *Materials Aspects of GaAs and InP Based Structures*, Prentice-Hall, Englewood Cliffs, NJ, 1991.
7. E. O. Kane, in W. Paul, ed., *Handbook on Semiconductors*, Vol. 1, North Holland, Amsterdam, 1982, Chap. 4.
8. O. Madelung, *Semiconductors—Basic Data*, Springer, 1996.
9. C. Y. Chang and F. Kai, *GaAs High-Speed Devices*, Wiley, 1994.
10. M. Shur, *GaAs Devices and Circuits*, Plenum Press, 1986.
11. R. Williams, *Modern GaAs Processing Methods*, Artech House, 1990.
12. M. A. Herman and H. Sitter, *Molecular Beam Epitaxy*, Springer-Verlag, 1988.
13. L. L. Chang and K. Ploog, *Molecular Beam Epitaxy and Heterostructure*, Martinus Nijhoff, 1985.
14. G. B. Stringfellow, *Organometallic Vapour-Phase Epitaxy*, Academic Press, 1989.

15. E. J. Johnson, J. A. Kafalas, and R. W. Davies, The role of deep level centers and compensation in producing semi-insulating GaAs, *J. Appl. Phys.* **54**(1):204–207 (Jan. 1983).
16. S. T. Pantelides, ed., *Deep Centres in Semiconductors A State of the Art Approach*, Gordon & Breach Science Publishers, 1992.
17. S. Sriram and M. Das, Characterization of electron traps in ion-implanted GaAs MESFETs on undoped and Cr-doped LEC semi-insulating substrates, *IEEE Trans. Electron. Devices* **ED-30**(6):588–592 (June 1983).
18. A. Mitonneau, G. M. Martin, and A. Mircea, Hole traps in bulk and epitaxial GaAs crystals, *Electron. Lett.* **13**(22):666–668 (Oct. 27, 1977).
19. G. M. Martin, A. Mitonneau, and A. Mircea, Electron traps in bulk and epitaxial GaAs crystals, *Electron. Lett.* **13**(7):191–193 (March 31, 1977).
20. D. Lang, Deep-level transient spectroscopy: A new method to characterize traps in semiconductors, *J. Appl. Phys.* **45**:3023–3032 (1974).
21. D. K. Chen and M. B. Das, Characterization of deep levels using unconventional zero-bias thermally stimulated current in ion-implanted semi-insulating GaAs substrates, *IEEE Trans. Electron. Devices* **ED-32**(11):2506–2507 (Nov. 1985).
22. P. Ladbroke, *MMIC Design: GaAs FETs and HEMT*, Artech House, 1989.
23. M. Telford, GaAs boosted by WLAN and auto radar, *III–V Rev.* **17**(1):32–35 (2004).
24. M. F. O’Keefe, J. S. Atherton, W. Bösch, P. Burgess, N. I. Cameron, and C. M. Snowden, GaAs pHEMT based technology for microwave applications in a volume MMIC production environment on 150 mm wafers, *IEEE Trans. Semicond. Manuf.* **16**(3):376–383 (Aug. 2003).
25. D. K. Schroder, *Semiconductor Material and Device Characterization*, Wiley-Interscience, 1990.
26. L. J. Van der Pauw, A method of measuring specific resistivity and Hall effect of disc of arbitrary shape, *Philips Res. Rep.* **13**:1–9 (1958).
27. J. S. Sites and H. H. Wider, Magnetoresistance mobility profiling of MESFET channels, *IEEE Trans. Electron. Devices* **ED-27**(12):2277–2281 (Dec. 1980).
28. P. Bhattacharya, *Indium Gallium Arsenide*, IEE INSPEC, 1993.
29. S. Adachi, *Aluminium Gallium Arsenide*, IEE INSPEC, 1993.
30. M. R. Brozel and G. E. Stillman, *Properties of Gallium Arsenide*, 3rd ed., IEE INSPEC, 1996.
31. S. Adachi and J. Brice, *Properties of Indium Phosphide*, IEE INSPEC, 1991.
32. S. Sze, *High Speed Semiconductor Devices*, Wiley-Interscience, 1990.
33. C. M. Snowden, *Semiconductor Device Modelling*, IEE Peter Peregrinus, 1988.
34. C. M. Snowden and R. E. Miles, eds., *Compound Semiconductor Device Modelling*, Springer-Verlag, 1993.
35. G. E. Flores and B. Kirkpatrick, Optical lithography stalls X-rays, *IEEE Spectrum* 24–27 (Oct. 1991).
36. D. C. Northrop and E. H. Rhoderick, The physics of Schottky barriers, in M. J. Howes and D. V. Morgan, eds., *Variable Impedance Devices*, Wiley, New York, 1978.
37. C. J. Palmstrom and D. V. Morgan, Metallizations for GaAs devices and circuits, in M. J. Howes and D. V. Morgan, eds., *Gallium Arsenide Materials, Devices and Circuits*, Wiley, 1985.
38. A. Christou, *Reliability of Gallium Arsenide MMICs*, Wiley, Chichester, UK, 1992.
39. J. M. Golio, *Microwave MESFETs and HEMTs*, Artech House, 1991.
40. F. Ali and A. Gupta, *HEMTs and HBTs*, Artech House, 1991.
41. C. M. Snowden, Active microwave devices, in D. V. Morgan and M. J. Howes, eds., *Microwave Solid-State Component and Subsystem Design*, Leeds Univ. Press, 1983.
42. J. Turner, A. Waller, R. Bennett, and D. Parker, *Proc. 9th Institute of Physics Conf.*, London, 1971, pp. 234–239.
43. J. V. Dilozenzo and D. D. Khandelwal, eds., *GaAs FET Principles and Technology*, Artech House, 1982.
44. R. S. Pengelly, *Microwave Field Effect Transistors—Theory, Design and Applications*, Research Studies Press, 1986.
45. C. M. Snowden, Recent developments in compound semiconductor microwave power transistor technology, *IEE Proc. Circuits and Systems*, April 2004.
46. K. Joshin, T. Kikkawa, H. Hayashi, T. Maniwa, S. Yokokawa, M. Yokoyama, N. Adachi, and M. Takikawa, A 174 W high efficiency GaN HEMT power amplifier for WCDMA base station applications, *Proc. IEEE Int. Electron Devices Meeting Technical Digest*, Dec. 2003, pp. 12.6.1–12.6.3.
47. F. Raay, R. Quay, R. Kiefer, M. Schlechtweg, and G. Weimann, Large-signal modelling of AlGaIn/GaN HEMTs with $P_{\text{sat}} > 4 \text{ W/mm}$ at 30 GHz suitable for power applications, *Proc. IEEE MTT-S Int. Microwave Symp. Digest*, June 2003, Vol. 1, pp. 451–455.
48. T. P. Chow and R. Tyagi, Wide bandgap compound semiconductors for superior high voltage unipolar power devices, *IEEE Trans. Electron. Devices* **41**:1481–1483 (Aug. 1994).
49. E. O. Johnson, Physical limitations on frequency and power parameters of transistors, *RCA Rev.* **26**:163–177 (1965).
50. B. J. Baliga, Power semiconductor device figure of merit for high-frequency applications, *IEEE Electron. Device Lett.* **10**:455–457 (1989).

FURTHER READING

- H. Morkoç, H. Unlu, and G. Ji, *Principles and Technology of MODFETS*, Vol. 1, Wiley, 1991.
- H. Morkoç, H. Unlu, and G. Ji, *Principles and Technology of MODFETS*, Vol. 2, Wiley, 1991.
- W. Liu, *Handbook of III–V Heterojunction Bipolar Transistors*, Wiley-Interscience, 1998.
- D. Haigh and J. Everard, *GaAs Technology and Its Impact on Circuits and Systems*, IEE Peter Peregrinus, 1989.
- J. J. Liou, *Advanced Semiconductor Device Physics and Modeling*, Artech House, 1994.

TRANSCIEVERS

FRANCIS DOMINIQUE
Lucent Technologies

1. COMMUNICATION SYSTEMS

The ability of electromagnetic radiation to provide almost instantaneous communication without any interconnecting wires has been a major factor in the explosive growth

of mobile communications, especially cellular and personal communications during the latter half of the twentieth century. The vacuum tube made the radio practical and affordable during the earlier half of the twentieth century. The invention of the transistor and highly complex yet cheap integrated circuits have allowed the development of ever complex digital communication systems that operate quite close to theoretical limits on channel capacity, spectrum efficiency, and so on.

The word *transceiver* is actually a combination of two words, *transmitter* and *receiver*. Figure 1 shows the block diagram of a general radio transceiver. Below each system block is a list of some of the popular techniques used. A modern digital transceiver uses most, if not all, of the system blocks in Fig. 1. Based on the direction of information transfer, radio systems are of three general types: simplex, half-duplex, and full-duplex systems. A *simplex* system transmits information in only one direction from a transmitter to a receiver. Examples of simplex systems are commercial audio and television broadcast systems organized in a *star* configuration. A *half-duplex* system is one in which transmission is bidirectional but only one transmitter at a time can transmit. A *full-duplex* or duplex system is one in which bidirectional communication can occur at any time. Although all communication systems are either some kind of simplex or duplex system, a variety of communications architectures exist dependent on the end application.

Section 2 points out the important characteristics of radio transceivers. Section 3 is devoted to the evolution of transceiver architecture. The characteristics of various different architectures are discussed in detail. Section 4 describes the implementation of important transceiver components with special emphasis on digital processing. Section 5 concludes by looking at the future.

2. TRANSCIEVER CHARACTERISTICS

2.1. Radio Transmitter Characteristics

This section details the important characteristics and performance issues for a transmitter.

2.1.1. Out-of-Band Emissions. There are stringent requirements as part of the standards for out-of-band power emissions. For example, the interim standard IS-54 for digital cellular radio specifies that power emission in adjacent and alternate channels must be 26 dB and 45 dB below the mean output power, respectively. Spectral shaping to maintain out-of-band emissions below those required by the standards is usually achieved through a combination of baseband pulse shaping, IF/RF filtering, and proper operation of the radiofrequency (RF) power amplifier.

2.1.2. Output Power, Distortion, and Efficiency of the Power Amplifier. In the early days of radio, power was amplified by vacuum tubes. With the invention of the transistor, solid state circuits have replaced vacuum tubes. The power amplifier should provide adequate output power with the least distortion and maximum possible efficiency [1]. The gain, efficiency, distortion, and power of the transistors typically used in solid-state power amplifiers depend on the choice of the bias point and the drive mechanism through the familiar designation of the operating class (Class A, B, AB, C, or E). The distortion introduced by the amplifier is specified by its AM-AM and AM-PM transfer characteristics.

The two most important parameters of the power amplifier, namely, efficiency and distortion, are incompatible with one another. Linear power amplifiers provide the least distortion but have quite large quiescent currents, resulting in poor efficiency. Nonlinear amplifiers, like

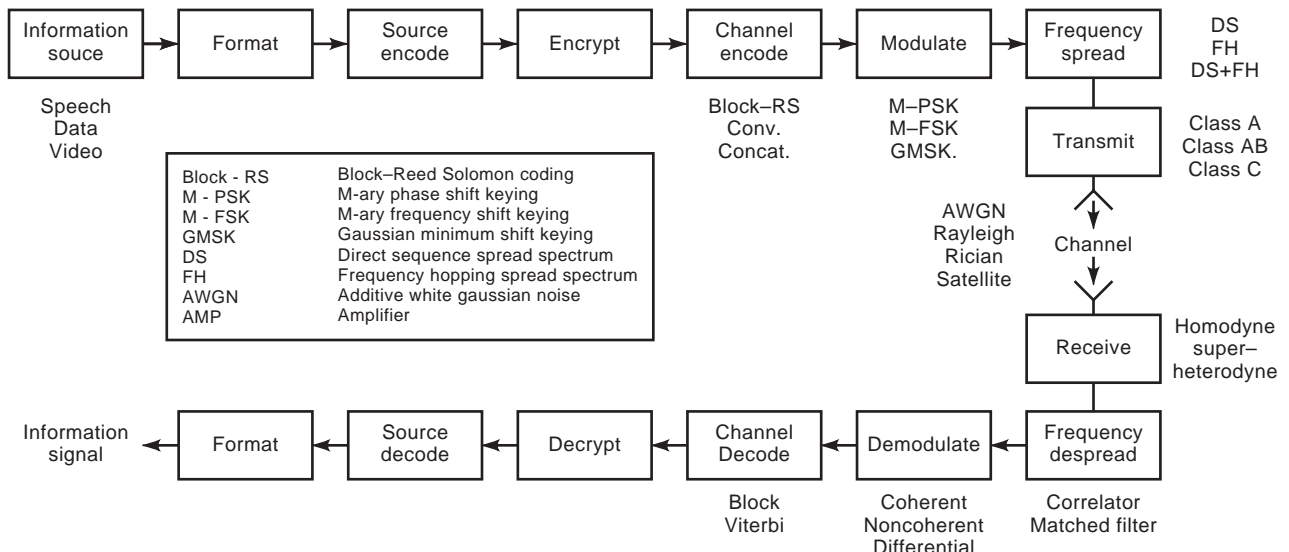


Figure 1. General block diagram of a modern transceiver. Abbreviations are listed at the end of the article.

Class C amplifiers, are highly efficient but cannot be used for linear modulation because of the distortion introduced by the amplifier. The type of power amplifier used depends on the requirements of the modulation used. Constant envelope modulation like frequency modulation (FM) can be amplified with nonlinear Class C amplifiers. However, in recent years, increasing demand for RF spectrum usage is forcing the use of spectrally efficient linear modulation techniques. These signals have a fluctuating envelope, and nonlinear amplification results in spectral spreading and intermodulation products. Therefore highly linear power amplifiers are required. One way to achieve linear amplification is to back off the amplifier from saturation and operate in the linear region of its transfer function. However, such amplifiers have poor dc-to-RF conversion efficiency. A major challenge in designing a high-power amplifier is to maintain linearity without compromising power efficiency [2].

2.2. Radio Receiver Characteristics

This section details the important characteristics and performance issues for a receiver.

2.2.1. Antenna and Input Characteristics. The main function of a radio receiver is to pick up electromagnetic radio energy at the antenna and transfer it efficiently to the processing section of the receiver. The important characteristics of an antenna are its efficiency, impedance, 3 dB beam width, bandwidth, and gain. Other characteristics are null-fill, upper sidelobe suppression, and performance versus specification. All antenna characteristics are functions of the physical antenna dimensions relative to the operating wavelength. Another important component is the coupler between the antenna and the input circuit of the receiver, which typically is a filter or an amplifier. Maximum energy is transferred if the impedance of the input circuit matches that of the antenna throughout the band of interest. Some of the antenna matching problems in a radio receiver are as follows:

1. The problem of matching the antennas at certain frequencies may be limited by component availability.
2. The impedance of antennas used in mobile applications or in locations where the environment changes with time due to foliage or traffic.

The problem of antenna matching is often solved by the system designer taking into account and compensating for a range of mismatch losses that might occur in practice. Other input characteristics that need to be taken into account are as follows:

1. The input RF circuits may be balanced, unbalanced, or both.
2. Protection from high-voltage discharges due to lightning.
3. Ability to handle high-power cochannel and adjacent channel transmissions

2.2.2. Gain and Sensitivity. Radio receivers typically process signals with a wide range of powers. The extent to which the signals can be received and processed usefully depends on the noise levels received at the antenna and those generated by the circuits within the receiver itself. The receiver is also required to produce a certain level of output power suitable for the application. Receivers are designed so that the gain is distributed among the various stages as required. Modern receivers are usually not gain-limited, and the weakest signal that can be processed is usually noise-limited. This signal level is known as the *sensitivity* of the receiver. A measure of sensitivity is the *minimum detectable signal* (MDS), which is the power of a sinusoidal signal that just equals the noise power at the intermediate frequency (IF) output of the receiver. MDS [1] can be expressed in decibels as

$$\text{MDS} = KTB_n F$$

where K is Boltzmann's constant (1.38×10^{-20} mW/°K), T is the reference temperature (typically 290°K), B_n is the noise bandwidth of the receiver, and F is the noise figure.

2.2.3. Noise Figure. The noise figure compares the total receiver noise with the noise that would be present if the receiver generated no noise. This ratio is called the *noise factor* F , and, when expressed in decibels, the noise figure (NF). It is thus a measure of the amount of noise introduced by the circuits within the receiver itself.

$$F = \frac{(S/N)_{\text{input}}}{(S/N)_{\text{output}}}$$

where (S/N) is the signal-to-noise ratio.

2.2.4. Selectivity. Selectivity is the ability of a receiver to separate a signal at one frequency from signals at other frequencies. Selectivity is defined as the bandwidth for which a signal x dB stronger than the minimum acceptable signal at a nominal frequency is reduced to the level of that minimum acceptable signal. Two important characteristics are required in establishing the selectivity of a receiver. One is that the selective components of the receiver must be sufficiently sharp to suppress unwanted interference from adjacent channel transmissions and spurious responses. The other is that the components must be sufficiently broad to pass the highest frequency of interest with acceptable gain and phase distortion.

2.2.5. Dynamic Range. Dynamic range is used to indicate the ratio between the strongest and weakest signals that a receiver can handle with acceptable noise or distortion. The weakest signal commonly considered is the minimum detectable signal. This definition is of limited value especially when the desired signal is surrounded by other signals with varying signal power. The selectivity of a receiver provides protection against many of the unwanted signals. The strong unwanted signals, however, can still cause degradation because of nonlinearities in the receiver chain. Therefore it is important to consider the

definition of the strongest signal component when determining the dynamic range of the receiver.

2.2.6. Characterization of Spurious Outputs. A modern receiver typically has a synthesizer and possibly several local oscillators, especially if superheterodyne architecture is used. It is possible for these frequencies to interact and produce spurious outputs without any inputs present. The following are other sources of spurious signals:

1. Parasitic oscillations in amplifiers because of parasitic feedback
2. Intermediate frequency subharmonics
3. Power supply harmonics

2.2.7. Frequency/Clock Generator Characteristics

2.2.7.1. Accuracy and Stability. Modern transceivers have a frequency synthesizer to which all other local oscillators are slaves. Earlier radios had free running oscillators that have largely been replaced by digital synthesizers because of the superior frequency accuracy, stability, flexibility, and cost performance of digital circuitry. Once the synthesizer has been set to operate at a specified frequency, its frequency must remain unchanged for a period sufficient for nominal operation despite temperature and environmental changes. Modern transceivers use temperature-compensated crystal oscillators as clocks for their digital circuitry. These oscillators typically are accurate to about 1 part per million. Higher accuracies are provided by oven-stabilized crystal oscillators and rubidium oscillators when sufficient power is available. In certain applications, such as mobile handsets where cost and power are at a premium, less expensive clocks with accuracies of approximately 3 to 10 parts per million are used.

2.2.7.2. Settling Time. Modern receivers typically span large frequency ranges and might be required to retune to a different frequency of operation. Because the frequency synthesizer used is typically based on a phase-locked loop, the loop goes out of lock for a short period whenever the receiver retunes. The settling time of the loop is important as any loss of lock results in degraded receiver performance.

2.2.8. Digital Receiver Characteristics. In addition to the characteristics previously mentioned, these are other important characteristics useful for systems using digital modulation.

2.2.8.1. Eye Diagram. The eye diagram [3], the traditional way of displaying digital data, is obtained by displaying the received demodulated digital data signal in successive symbol intervals on top of each other. The eye pattern provides the following wealth of information:

1. The width of the eye opening defines the time interval over which the received signal can be sampled without error from intersymbol interference.

2. The sensitivity of the system to timing error is determined by the rate of closure of the eye, as the sampling time instant is varied.
3. The height of the eye opening at any specified time defines the margin over channel noise.

2.2.8.2. Bit Error Rate (BER). The BER [1] is the primary measure of the quality of a digital communication system. The BER is defined as

$$\text{BER} = \frac{N_E}{N}$$

where N_E is the number of bit errors and N is the total number of bits transmitted.

3. RADIO ARCHITECTURES

3.1. Evolution

Radio architectures have remained relatively unchanged since the invention of the homodyne and superheterodyne receivers in the early part of the twentieth century. With the advent of integrated processors during the 1970s and 1980s, there was a migration from analog to digital processing in almost every aspect of radio systems engineering. The only radio system block that survived this migration was the RF front end, which by its function has to be analog. However, the basic radio architecture has remained the same. The word *digital* in digital radio has a double meaning. First, it refers to the fact that information is carried in digital form and second that the radio uses digital processing to recover the transmitted signal after it has been downconverted by an analog front end. The following are the advantages of using digital processing [1,4]:

1. The repeatability and temperature stability of digital processing are substantially better than analog processing.
2. Certain functions that cannot be or are difficult to implement in analog hardware, such as sharp rolloff linear phase filters, can easily be implemented with digital processing.
3. Once engineered, digitally implemented system functions do not require the tuning or tweaking typically required in analog systems.

The software radio [5] can be thought of as the next logical evolution of the digital radio, where software control of radio functions is pushed as close as possible to the antenna in the conventional digital radio architecture. Here, the entire RF band of interest is digitized right at the operating RF band by high-speed analog-to-digital converters (ADCs). The rest of the radio functions, such as downconversion, equalization, demodulation, and decoding, would be carried out by reprogrammable logic, typically digital signal processors (DSPs).

Software radio architecture has the following advantages over conventional hardwired digital radio architecture:

1. A highly flexible and reconfigurable transceiver can be implemented.
2. The transceiver can be easily adapted to any particular environment by changing the modulation, filtering, demodulation, and so on.
3. Because of open architecture, future upgrades can easily be made without reengineering the entire radio.
4. Software radio architecture benefits readily from concentration, where multiple radio channels share the same RF front end, whereas analog systems need a separate RF front end for each channel.

Applications that already use or are likely to use digital/software radio architectures include cellular and personal communications systems, satellite communications, digital television, digital audio broadcasting, navigation and position location systems, and test equipment.

3.2. Transmitter Architectures

The earliest analog radio transmitter architecture was the direct conversion transmitter. Figure 2 shows the general block diagram of an analog direct conversion architecture. Although this architecture is simple, it has the following disadvantages [6].

1. The analog implementation of precise modulators at the operating RF is difficult.
2. When used as an analog quadrature modulator, gain and phase imbalances between the mixers require compensation because unwanted sidebands are generated.
3. The filtering required to reduce out-of-band emissions to conform to government-mandated spectral masks must be carried out completely at the RF

band of interest. Designing high rolloff RF filters that introduce minimal amplitude and phase distortion across the frequency band of interest is difficult.

The superheterodyne architecture shown in Fig. 3 was intended to overcome some of the disadvantages of the direct conversion architecture. Here, modulation is carried out at a low IF. Then the desired signal band is filtered to conform to the desired spectral mask, and the filtered signal is upconverted to the desired RF band. The main disadvantage of the superheterodyne architecture is that the one or more IF stages used increase power consumption, space, and cost.

The advent of digital modulation and digital integrated circuits has resulted in the ever increasing use of digital processing in the transmitter chain. Digital processing can alleviate most of the problems associated with analog direct conversion transmitters, and as a result there is a resurgence of interest, especially for low-power mobile handsets where space and power are at a premium. Following are the advantages of digital architecture [7]:

1. Design and implementation are flexible.
2. Digital implementation overcomes the problems of gain and phase, dc offsets, and performance drifts in analog implementations.
3. Multichannel digital IFs especially at base stations eliminate the multiple analog IF chains required in analog architecture. With digital upconversion, all digital IF signals can be combined in a digital summer and then transformed into a single analog signal by a digital-to-analog converter (DAC).
4. Manufacturing is reliable.

Some of these combined analog-digital architectures are shown in Fig. 4.

The advent of software radio architecture will result in almost complete replacement of the RF system by programmable digital processing. Figure 5 shows the block diagram of an ideal software radio. In this ideal architecture, except for the final RF power amplifier and filter, the

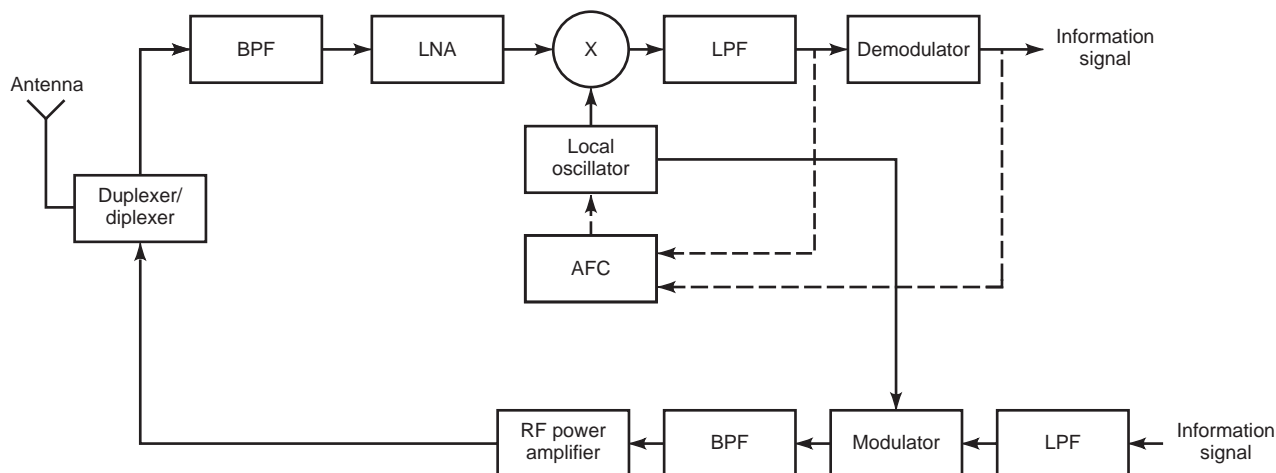


Figure 2. General block diagram of an analog homodyne transceiver.

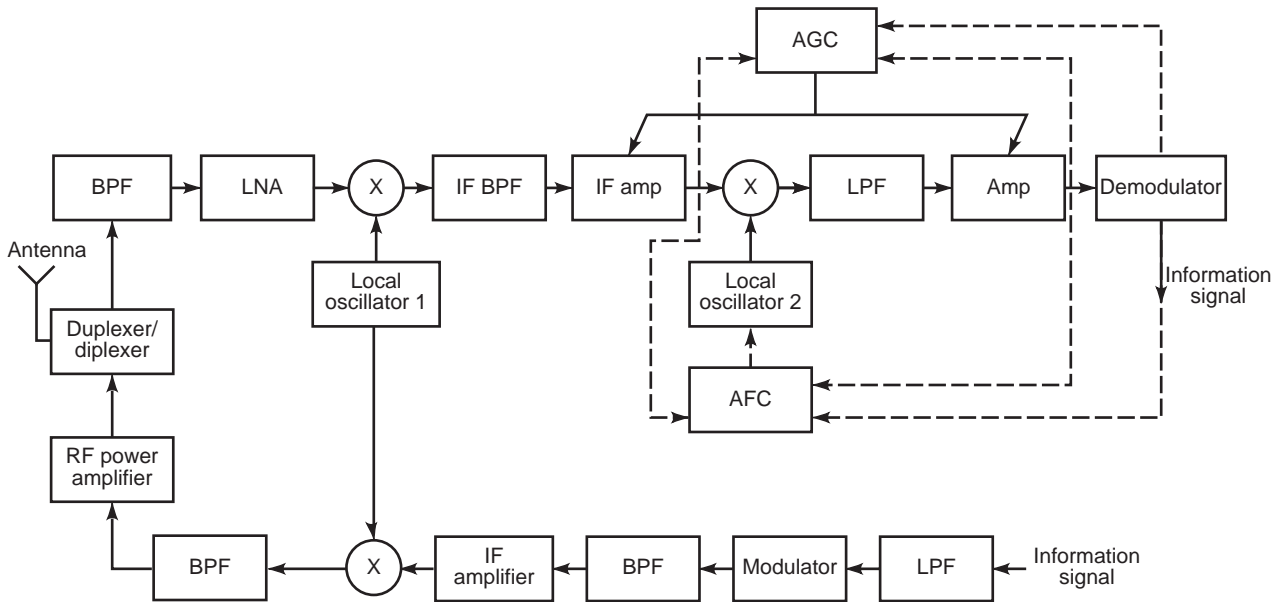


Figure 3. General block diagram of an analog superheterodyne transceiver.

analog upconversion chain has been replaced by digital IF upconversion. Limitations on the maximum sampling rate by currently available technology, however, permits replacing only the first analog IF strip.

3.3. Receiver Architectures

The earliest analog receiver architecture was the homodyne or the direct conversion architecture, as seen in Fig. 2. The receiver consists of a bandpass filter (BPF) following the antenna for noise and interference rejection

followed by a low-noise amplifier (LNA). Then the signal is downconverted to baseband by a pair of analog mixers. The in-phase and quadrature components are low-pass filtered to remove the mixer products and are demodulated. Following are the advantages of direct conversion architecture:

1. Reduced hardware complexity as there are no IF stages
2. No image frequencies

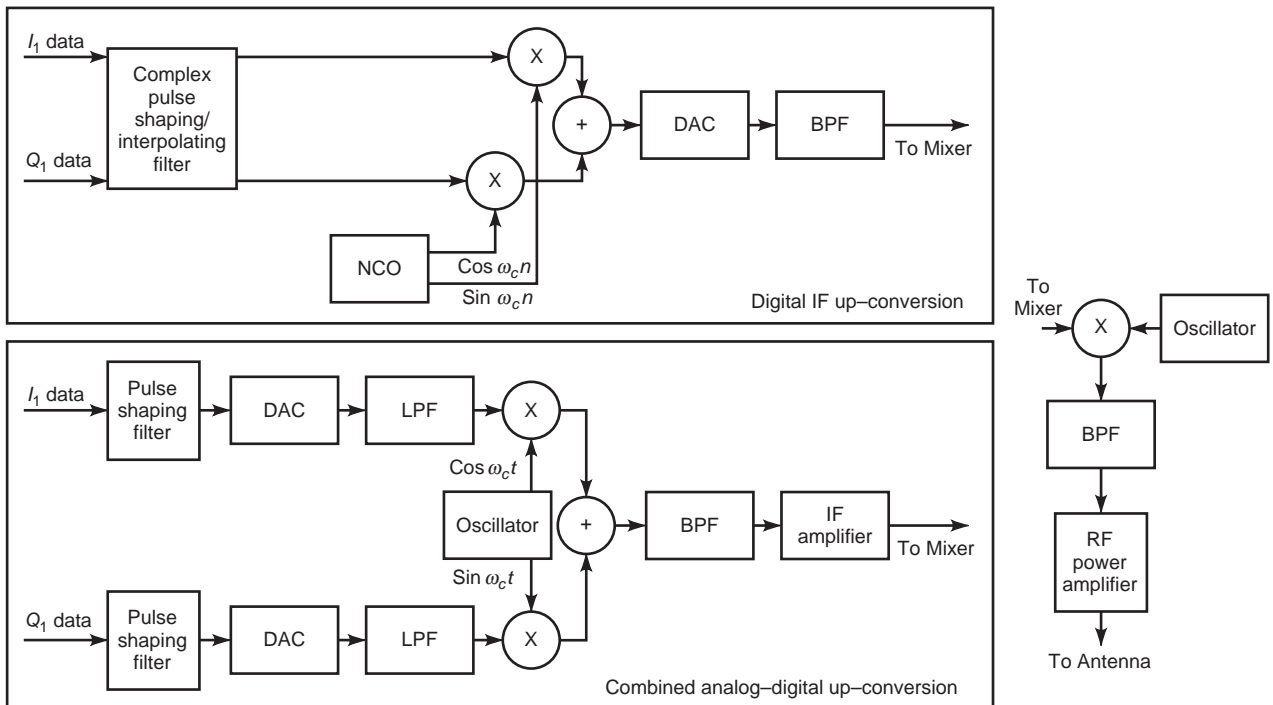


Figure 4. General block diagram of combined analog-digital upconversion architectures.

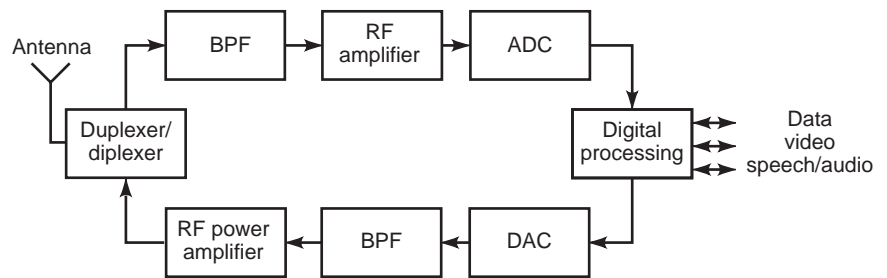


Figure 5. General block diagram of an ideal software radio architecture.

Following are the disadvantages of the direct conversion receiver, *especially* with an analog implementation:

1. Amplitude and phase mismatches between the mixers distort the signal.
2. Sharp rolloff analog low-pass filters (LPF) also distort the desired signal.
3. Carrier leakage, $1/f$ noise in the mixers, and bias in the filters all contribute to an unpredictable time-varying dc offset in the recovered signal.
4. All signal amplification has to be done at the carrier frequency. Building high-gain RF amplifiers at such high frequencies is difficult and expensive.
5. Carrier recovery for coherent reception has to be carried out at the carrier frequency. Precise control of high-frequency oscillators is difficult.

The superheterodyne receiver shown in Fig. 3 was developed to alleviate some of the disadvantages of the direct conversion receiver. In this architecture, the RF signal is downconverted to an intermediate frequency before being downconverted to baseband. This is known as the single IF stage superheterodyne receiver. Various versions of this general architecture with multiple IF stages have been developed. The most common version is the dual IF stage architecture. Following are the advantages of superheterodyne architecture compared with the direct conversion receiver:

1. Most of the signal amplification is done at relatively lower IFs, where it is easier to build high-gain amplifiers.
2. Automatic frequency control is usually carried out at the lower IFs and hence is easier to implement.

With the advent of digital modulation, high-speed ADCs, and digital integrated circuits, digital processing started to replace segments of the analog receiver architecture especially in demodulation and baseband processing. This led to the development of digital radio architecture. Both direct conversion and superheterodyne RF front-end architectures have been used in digital radios. The direct conversion digital radio requires two ADCs to digitize the in-phase and quadrature components of the downconverted signal. Superheterodyne digital radios have used both low-pass and bandpass digitization. The advantage of bandpass digitization is that it can replace the last analog downconversion stage. In addition, because the final

downconversion to center the chosen spectral image around dc is done digitally, all problems associated with quadrature analog downconversion disappear. Some of the digital receiver architectures are shown in Fig. 6.

Although the digital radio provides superior performance, its architecture is still based on the direct conversion or the superheterodyne architectures. Recently, a more fundamental change in receiver architecture occurred with the advent of software radio architecture, made possible by technological advances in ADC technology, computing technology, and software engineering. The software radio architecture looks similar to that of the digital radio with one crucial difference. In software radio architecture, programmable digital processing is pushed as close to the antenna as technology permits. The block diagram of an ideal software radio architecture is shown in Fig. 5. In this architecture, the only analog RF components are the preselection bandpass RF filter and the low-noise RF amplifier. Then the RF signal is directly digitized using bandpass subsampling, and the rest of the receiver functions are carried out in embedded software modules running on high-speed DSPs. This architecture is still a few years away from commercial implementation because high-speed ADCs that operate with sufficient resolution at the desired RF band are unavailable. Current software radio architectures use at least one IF stage.

4. TRANSCIEVER IMPLEMENTATION

4.1. Transmitter

The design and implementation of transmitters involves the following:

1. Filtering
2. Modulation and frequency upconversion
3. Power amplification

4.1.1. Filtering. In analog radios, analog filters are the only way to achieve frequency selectivity and to limit out-of-band emissions. In digital radios, digital filters in addition to analog filters are used to shape the spectrum of the transmitted signal. Analog filters are discussed in detail later. Some of the popular digital filters used for pulse shaping to achieve a compact modulated spectrum are the raised cosine and Gaussian filters [8]. The advantages of using digital filters are discussed in Section 4.2.7.2.

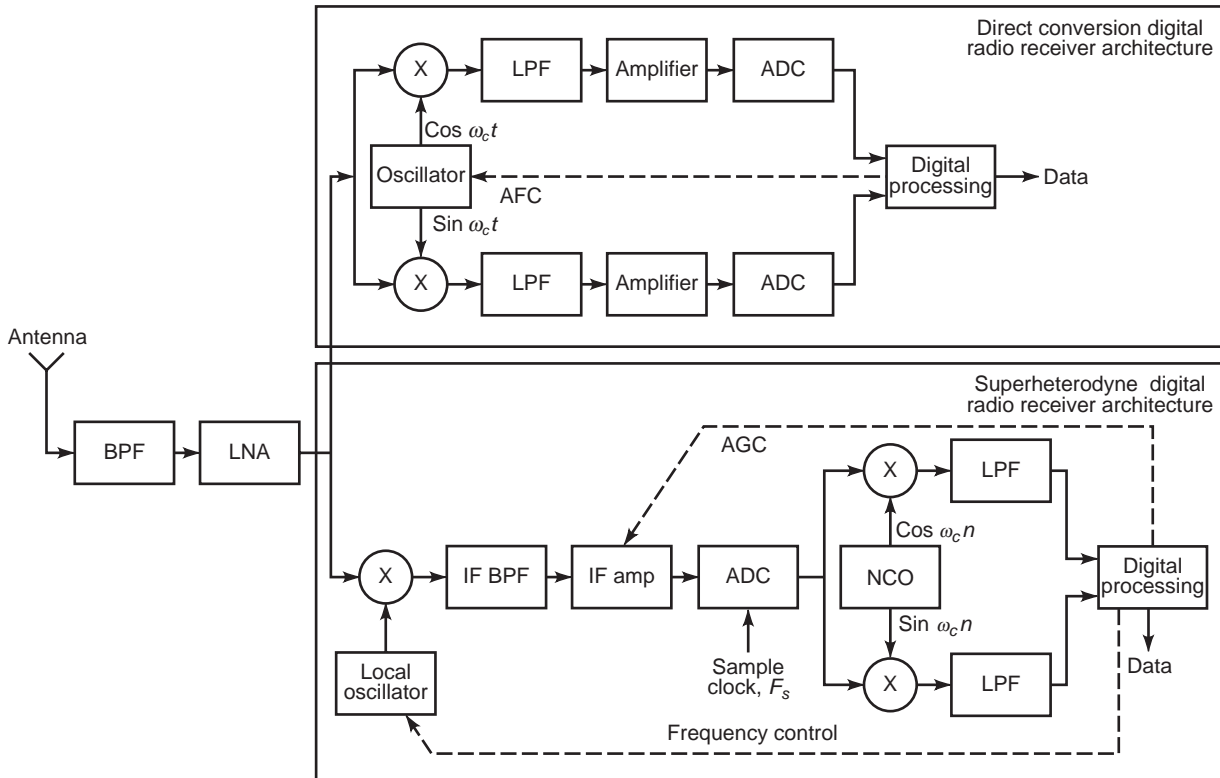


Figure 6. Some digital receiver architectures.

4.1.2. Modulation. Modulation [8] is the process of encoding information from a message source onto a format suitable for transmission. The process involves translating the baseband message signal, called the modulating signal, onto a bandpass signal at a much higher frequency, called the carrier. This process is called modulation. Modulation is usually carried out by varying the amplitude, frequency, phase, or any combinations of these three parameters of a carrier signal. Based on whether the message information signal is analog or digital, modulation is classified as analog or digital modulation.

4.1.2.1. Analog Modulation. In analog modulation, the modulating signal is analog and can assume an infinite number of amplitude values. Analog modulation is broadly classified into two categories, amplitude modulation and angle modulation.

In amplitude modulation (AM), the amplitude of a high-frequency carrier signal is varied in accordance with the instantaneous amplitude of the modulating information signal [3,8]. The amplitude-modulated signal is expressed as

$$S(t) = A_C[1 + m(t)] \cos 2\pi f_C t$$

where A_C is the amplitude of the carrier, f_C is its frequency, $m(t)$ is the modulating information signal, and $S(t)$ is the modulated signal. The spectrum of an AM signal contains a component at the carrier frequency and two sidebands that replicate the original information spectrum.

An AM signal is generated by a nonlinear device, such as a diode or transistor. Many variations of amplitude modulation exist based on what percentage of the sidebands is transmitted. Some of these variations are single-sideband AM (SSB-AM), pilot-tone-sideband AM, and vestigial-sideband AM (VSB-AM).

Angle modulation [3,8] varies the angle of the carrier signal according to the amplitude of the modulating signal. There are two important classes of angle modulation, FM and phase modulation (PM).

In FM, the instantaneous frequency of the carrier is varied with the information signal $m(t)$, as shown by the following equation:

$$S(t) = A_C \cos \left(2\pi f_C t + 2\pi k_f \int_{-\infty}^t m(l) dl \right)$$

where k_f is the frequency deviation constant measured in units of hertz per volt. There are two basic methods for generating an FM signal, the *direct method* and the *indirect method*. In the direct method, voltage-controlled oscillators vary the frequency of the carrier signal directly in accordance with the amplitude of the information signal. Such oscillators commonly use devices, such as varactor diodes, whose reactance can be varied in accordance with the modulating signal's voltage level. The indirect method is based on approximating a narrowband FM signal as the sum of a carrier signal and a single sideband signal where the sideband is 90° out of phase with the carrier.

PM is a form of angle modulation where the phase of the carrier is varied according to the information signal $m(t)$. A PM signal can be generated by first differentiating the information signal $m(t)$ and then outputting it to a frequency modulator.

4.1.2.2. Digital Modulation. Modern communication systems use digital modulation. In digital modulation, the modulating information signal is represented as a time sequence of symbols in which each symbol has m finite states. Each symbol represents n bits of information, where $n = \log_2 m$ bits/symbol. Digital modulation offers many advantages over analog modulation, including greater noise immunity, robustness to channel impairments, and easier multiplexing of various forms of information, such as voice, data, and video. Furthermore, digital transmissions use error-correcting codes and support complex signal conditioning and processing techniques, such as source coding/compression, encryption, and equalization to improve the performance of the communications. Advancements in very large-scale integration and digital signal processing technology have made it possible to implement digital modulators and demodulators easily. The use of embedded software to do most of the signal processing allows alterations without having to replace the hardware.

Some of the widely used digital modulation techniques are m -ary amplitude-shift keying (ASK), m -ary frequency-shift keying (FSK), m -ary phase shift keying (PSK), combined amplitude and phase modulation, combined coding and modulation, and multicarrier modulation.

In ASK, the amplitude of the carrier signal is varied in accordance with the instantaneous amplitude of the modulating information signal, which can take one of several discrete amplitudes. In FSK, the frequency of the carrier signal is varied in accordance with the instantaneous discrete amplitude of the modulating information signal. In PSK, the phase of the carrier signal is varied in accordance with the instantaneous discrete amplitude of the modulating information signal. In a general sense, ASK, FSK, and PSK can be thought of as special cases of AM, FM, and PM, respectively, where the modulating signal is discrete in amplitude. In combined amplitude and phase modulation, both the amplitude and phase of the carrier are varied according to the amplitude of the modulating signal. Ungerboeck [9] realized that error-correction coding and modulation can be combined at a fundamental level to realize performance gains greater than with the conventional method of coding and modulating separately. Combined coding and modulating is more commonly known as *trellis-coded modulation*. The basic concept of multi-carrier modulation is dividing a given RF bandwidth into many narrowband subchannels that are transmitted.

4.1.3. Frequency Upconversion. Frequency conversion is usually achieved by devices called *mixers*. A mixer is a component that acts as a frequency converter by mixing two input signals together to produce a desired signal. A mixer can be implemented by a variety of semiconductor devices, such as diodes (typically Schottky

diodes), bipolar-junction transistors, and field-effect transistors. Mixers are generally of two types, single-balanced and double-balanced. The single-balanced mixer improves port-to-port isolation and reduces the magnitude of some of the spurious signals. It consists of two single-ended mixers interconnected in a configuration that greatly reduces some spurious products. A double-balanced mixer further improves port-to-port isolation and suppresses spurious inter-modulation products even further.

4.1.4. Amplifiers. The triode vacuum tube amplifier was the mainstay for many communication systems before the transistor was invented. Because of transit time limitations, triodes were limited to VHF and UHF. For operation at higher microwave frequencies, the magnetron was invented in the early 1940s. The invention of the transistor was a boon for developing low-cost, reliable, handheld, low-power mobile communication systems. Since then, solid-state amplifiers have replaced vacuum tube amplifiers in almost all communication systems. Systems requiring extremely high power at microwave frequencies, such as deep space and radar systems, continue to use tube amplifiers.

All commercial communication systems use solid-state transistor amplifiers. Solid-state amplifiers come in four main types: discrete, hybrid, integrated (ICs), and application-specific IC (ASIC). A discrete amplifier is one built with discrete transistors and passive components. Hybrid modules, also known as microwave integrated circuits (MICs), have a substrate and discrete devices, including RF matching and bias circuitry. RF ICs, also known as microwave monolithic ICs (MMICs), have all bias and RF matching circuitry on the same substrate, whereas MICs use different materials to achieve optimum matching. The advantage of using a single substrate is that components can be closely matched in value. The difference between an IC and an ASIC is that an IC typically integrates only a few transistors together with transmission line filters and inductors, whereas ASICs, on the other hand, contain several hundred or thousands of transistors.

Several amplifier configurations are based on operating classes A, B, AB, C, D, E, or F. Silicon (Si) bipolar, heterojunction-bipolar, and field-effect transistors (FET) have been used most often to date in RF circuits. Gallium arsenide (GaAs) and complementary metal oxide semiconductor transistors have been gaining interest. GaAs amplifiers offer simple functionality with some biasing and matching components around a chain of transistors. One of the advantages of GaAs versus silicon is that GaAs is an insulator, whereas silicon is a conductor at RF frequencies. As a result, GaAs can integrate several RF components monolithically, facilitating closer components and better matching.

High-power amplification at microwave frequencies, especially those used for satellite communications, are usually handled by traveling-wave tube amplifiers (TWTAs). Other tube amplifiers are the magnetron, coupled-cavity TWT, continuous-wave TWT, helix TWT, klystron, and crossed-field amplifier (CFA).

4.2. Receiver

The main function of the receiver is to pick up the RF energy transmitted at its antenna and efficiently and effectively recover the original information signal transmitted. The design and implementation of receivers involves the following:

1. Antennas
2. Amplification
3. Filtering
4. Downconversion
5. Automatic gain control
6. Demodulation and other associated signal processing functions

Antennas, amplification, analog filtering, and downconversion are common to both analog and digital/software radios. The rest of the receiver functionality depends on its implementation, whether analog or digital. Because these implementations are quite different, they are discussed in different sections with special emphasis on digital implementation.

4.2.1. Antennas. The type of antenna used in a transceiver depends on its application. Handheld or backpacked transceivers require integral antenna structures. Vehicular transceivers must use antennas of limited size and relatively short wavelengths. Antennas that operate at frequencies substantially below their first resonance are called small antennas. Large point-to-point systems use large antennas. Some of the most popular antennas used in commercial communication systems are the vertical whip antenna, the loop antenna, and the dipole array.

4.2.1.1. Whip Antenna. For operating frequencies below the quarter-wave resonance of the antenna, the whip input impedance appears as a small capacitance in series with a resistance. The radiation resistance R_R of a short vertical whip is given by [1]

$$R_R = 40\pi^2 \left(\frac{h}{\lambda}\right)^2$$

where h is the antenna height and λ is the operating wavelength. The whip is also used as a quarter-wavelength monopole antenna for applications, such as cellular and PCS handsets. The whip antenna has an omnidirectional antenna pattern in azimuth.

4.2.1.2. Loop Antennas. Loop antennas have been used in portable broadcast receivers and radio direction finders. When the dimensions of the loop are small compared with the wavelength, the loop is said to be small and its impedance is an inductance in series with a resistance. The radiation resistance R_R for a loop with N turns is given by

$$R_R = 320\pi^4 \left(\frac{AN}{\lambda^2}\right)^2$$

where A is the area of the loop. The loop antenna responds as the cosine of the angle between its face and the arrival direction of the electromagnetic wave. This results in a figure-eight antenna pattern with the null for waves arriving perpendicularly to the loop face.

4.2.2. Amplification. The RF signal picked up by the antenna is very weak and has to be amplified before it can be processed. Typically the very first amplifier used is a specially designed, low-distortion, low-noise amplifier. The operating characteristics of the amplifier are important, as its noise performance dominates the noise figure of the receiver. Both bipolar-junction and FET amplifiers have been used. In recent years, the use of GaAs instead of Si has been gaining interest.

4.2.3. Analog Filters. The selectivity of an analog radio receiver is achieved solely by bandpass and low-pass analog filters. Even in digital and software radio architectures, the analog bandpass filter is an important component and is used both for preselection and antialiasing. Digital radios also use analog filters in their RF front end to implement some selectivity.

The most important characteristics of a filter are its amplitude and phase response. The various characteristics of a filter are interrelated because they are completely determined by the poles and zeros of the transfer function of the filter. Following are some of the common filter families:

1. Butterworth
2. Chebychev
3. Elliptic
4. Equiripple

Analog filters are implemented with a number of different resonators. Following are the available technologies:

1. Inductor–capacitor (LC) resonators
2. Mechanical resonators
3. Quartz crystal resonators

Another important filter implementation is the surface acoustic wave (SAW) filter, of interest because it can be implemented with integrated circuit techniques and can use finite impulse response designs, similar to those for digital filters.

4.2.4. Downconversion. Downconversion is the process of shifting the received RF signal to baseband. Both direct conversion and superheterodyne architectures are used. The basic components of downconversion are mixers, bandpass and low-pass filters, and oscillators.

4.2.5. Automatic Gain Control (AGC). The large dynamic range of signals that must be handled by radio receivers requires gain adjustment to prevent overload or intermodulation of the stages to adjust the demodulator input level for optimum operation. Gain control is generally distributed over several stages throughout the receiver architecture. AGC typically measures the signal level into the

demodulator and tries to keep the level in the desired range by a feedback control loop. The control should be smooth and cause a generally logarithmic variation with the input variable.

4.2.6. Other Analog Radio Receiver Functions. The remaining functionality of the analog radio receiver is demodulation. Double-sideband AM signals are usually detected by an envelope detector. An envelope detector is any rectifier circuit that produces a component at the modulating frequency that is then recovered by a low-pass filter. The rectifier is generally implemented by diodes and by bipolar and field effect transistors. Other AM transmissions, such as SSB-AM and VSB-AM, are demodulated by a coherent demodulator. The coherent demodulator uses a mixer circuit with a local oscillator signal synchronized to the AM input carrier. Carrier synchronization is achieved through a carrier recovery circuit, such as the Costas loop. Common FM demodulators are the slope detector, quadrature detector, phase-locked loop (PLL), demodulator, and zero-crossing detector. The slope detector uses linear circuits to convert the frequency variations to envelope variations that can then be detected by an envelope detector. The quadrature detector consists of a network that shifts the phase of the FM signal by an amount proportional to its instantaneous frequency and uses a phase detector to detect the phase difference between the original FM signal and the signal at the output of the phase shift network. The output of the phase detector is proportional to the instantaneous frequency of the FM signal. In this manner, a frequency-to-amplitude conversion is achieved and the FM signal is demodulated. Phase detectors are generally implemented by diode-based mixer circuits. Because a PM signal can be modeled as an FM signal where the modulating signal has first been differentiated, PM demodulation is achieved by passing the PM signal through an FM demodulator and integrating its output.

4.2.7. Other Digital/Software Radio Receiver Functions. The rest of the digital/software radio receiver can be split into two distinct segments: signal digitization and signal processing.

4.2.7.1. Signal Digitization. Signal digitization, implemented by ADCs, is a two-step process [10], signal sampling followed by quantization. The sampling process is critical in signal digitization. There are two types of sampling, uniform and nonuniform sampling. In uniform sampling, signal samples are taken at uniform intervals, whereas in nonuniform sampling, the samples are non-uniformly spaced. The ADCs in communication systems use uniform sampling, and so the rest of the discussion concentrates on uniform sampling ADCs. The sampling methods for uniform sampling are Nyquist sampling, oversampling, quadrature sampling, and bandpass sampling.

The general sampling theorem for a bandlimited analog signal with no spectral components above f_M Hz

requires that the sampling rate F_S satisfies

$$F_S \geq 2f_M$$

$F_S = 2f_M$ is known as Nyquist sampling, and at this rate, the replicas of the spectrum of the original analog signal do not overlap. Two practical problems develop when implementing Nyquist sampling. The first is defining what a truly bandlimited signal is, and the second is antialiasing filtering before the ADC. In general, an RF signal has components at all frequencies. It is desirable that the distortion of the desired signal be dominated by ADC nonlinearities, not by spectral overlap. This requires that signals higher in frequency than $F_S/2$ be lower in power than the largest spurious response of the ADC. Bandlimiting is usually carried out by the analog antialiasing filter before the ADC. Unfortunately, practical analog filters cannot provide the kind of "brickwall" filter response required. Also, as the steepness of the filter rolloff increases, the phase response of the filter becomes more nonlinear, introducing more distortion.

Sampling the signal at a rate higher than the Nyquist rate is called oversampling. The benefit of oversampling is that the spectral replicas of the original analog signal in the sampled signal spectrum become increasingly separated as the sampling rate is increased beyond the Nyquist rate. Hence, a simpler antialiasing analog filter with a more gradual transition band can be used.

In quadrature sampling, the signal to be digitized is split into two signals. One of the signals is multiplied by a sinusoid to downconvert the signal to a zero-center frequency and then filtered to form the in-phase component of the analog signal. The other signal is multiplied by a 90° phase-shifted version of the sinusoid and filtered to form the quadrature component. Because each of these two signals occupies only one half the bandwidth of the original RF signal, the sampling rate can be reduced by one half at the expense of requiring two ADCs.

Bandpass sampling is based on the bandpass sampling theorem, which states that a bandpass signal with no frequency components below f_L Hz and none above f_H Hz can be determined uniquely by sampling the signal at a rate F_S Hz, where

$$\frac{2f_H}{k} \leq F_S \leq \frac{2f_L}{k-1}$$

where k is restricted to integral values that satisfy

$$2 \leq k \leq \frac{f_H}{f_H - f_L}$$

and

$$(f_H - f_L) \leq f_L$$

Bandpass sampling provides an image of the desired signal at multiples of the sampling frequency, and the spectral replica of the original analog bandpass signal closest to dc is usually chosen for further processing.

Once sampling is over, the sampled analog signal with its infinite range of amplitudes has to be converted to a finite set of discrete amplitudes. This is known as quantization. There are two general quantization methods, uniform and nonuniform quantization. In uniform quantization, the voltage difference between each quantization level is the same. In nonuniform quantization, the quantization levels are nonlinearly spaced in voltage. The ADCs used in RF and IF digitization typically use uniform quantization. In uniform quantization, some error is introduced into the quantized signal because the analog signal cannot be represented exactly by a finite number of discrete amplitude levels. Statistically, it can be assumed that the error signal is uniformly distributed within a quantization level.

4.2.7.2. Signal Processing. Signal processing is the core of the radio receiver and is the segment where the original transmitted information signal is recovered. Many operations are carried out by this system. These operations are quite application specific and may include some or all of the following:

1. Downconversion
2. Filtering, either spatial or temporal or both
3. Equalization
4. Despreading
5. Synchronization
6. Demodulation
7. Automatic gain control
8. Carrier recovery
9. Error-correction decoding
10. Source decoding
11. Decryption
12. Timing recovery

Some of the most important signal processing functions of a receiver are examined here in further detail.

Downconversion. When bandpass subharmonic digitization is used, spectral replicas of the original analog signal are found at multiples of the sampling frequency. However, there is generally no spectral replica centered around the zero-center frequency. To generate the complex baseband signal centered around the zero-center frequency, the output of the ADC is sent to a pair of digital multipliers. The reference inputs for the digital multipliers come from a quadrature-output, numerically controlled oscillator (NCO). The multipliers shift the spectral replica to the zero-center frequency. Then the outputs of the multipliers are sent to low-pass digital filters, which are typically finite impulse response (FIR) filters, to recover the baseband signal and filter out the other mixer products.

Filtering. Digital filters [11] are widely used in communication signal processing for tasks, such as digital downconversion, equalization, interference suppression, and pulse shaping. Following are the advantages of digital filters:

1. Exact linear phase filters can be implemented easily.

2. Filters with almost any desired frequency and phase response can be designed and implemented easily.
3. Changes in filter responses due to component variations caused by aging are eliminated.
4. Changes to the filters can be carried out easily because most of the filtering is implemented in software running on programmable processors.

Digital filters are of two general types, FIR filters and infinite impulse response (IIR) filters. Finite impulse response filters are the most common digital filters in radio receivers mainly because of the following advantages:

1. Filters with exactly linear phases can be easily designed.
2. There are efficient recursive and nonrecursive realizations of FIR filters.
3. FIR filters realized nonrecursively are always stable.
4. Round-off noise inherent in finite precision arithmetic implementations are easily made small for non-recursive realizations.

Following are the disadvantages of FIR filters:

1. A large filter order is required for sharp cutoff filters.
2. The delay of linear phase FIR filters need not always be an integral number of samples.

The main advantage of IIR filters is that sharp cutoff filters can be realized in relatively small filter orders. Following are the main disadvantages:

1. IIR filters generally do not possess linear phases.
2. IIR filters are more prone to be unstable because of quantization and round-off noise.

Carrier Recovery. Coherent demodulation requires that the phase and frequency of the transmitted carrier be known. Carrier recovery is the process of estimating the phase and frequency of the carrier to establish a reference for demodulation at the receiver. Any error in estimating the phase and frequency of the carrier causes significantly degraded performance. The information signal may be modulated onto the RF carrier so that a residual component at the RF exists in the overall transmitted signal spectrum. This residual RF component can be easily tracked by a narrowband PLL and provides the desired reference signal. However, this residual component represents power unavailable to transmit the information. Techniques that conserve power are of interest especially in mobile applications where power is at a premium because batteries supply power to the radio. As such, suppressed carrier transmissions are widely used. Following are some of the popular suppressed carrier recovery techniques:

1. Squaring loop
2. Costas loop
3. Decision feedback loop

Demodulation. The ultimate function of the radio receiver is to recover the original information signal that modulated the transmitted carrier. This process is known as *demodulation*. The portion of the receiver system that implements demodulation is known as the *demodulator*.

Some of the popular FSK demodulators are the limiter-discriminator, the PLL, and noncoherent and coherent demodulators. Noncoherent demodulation is carried out by a bank of bandpass filters whose outputs are envelope-detected. The largest output is selected as the transmitted symbol. The bandpass filters used to detect the tones are implemented either as FIR or IIR filters. Coherent demodulation compares the received signal with all reference frequencies. The comparison is done by multiplying the received signal by all the reference signals and then low-pass filtering the outputs of the bank of multipliers. The largest output is selected as the demodulated symbol. The locally generated reference signals must be synchronized in phase and frequency to the transmitted signal states.

Common PSK demodulators are the coherent demodulator and the differential demodulator. PSK can also be demodulated by using a frequency demodulator, such as a limiter-discriminator or a PLL, and integrating the output before the decision stage. The block diagram of a coherent PSK demodulator is shown in Fig. 7. Differential demodulators determine the cosine and sine of the phase difference and then decide on the phase difference accordingly. Differential demodulation shown in Fig. 7 is implemented by taking the product of the signal and a delayed version of the same signal. The output of the multiplier is low-pass filtered, usually by a FIR filter, to recover the information symbol transmitted. The transmitted symbols need to be encoded differentially to use differential demodulation.

Differential demodulators are often used in highly mobile applications where fading in the channel makes it impossible to get a robust coherent estimate of the transmitted carrier.

Processing Implementation. The processing elements that implement the functions in a radio are crucial, especially in software radio architecture, as they implement virtually all of the functions of the radio transceiver except the frequency conversion and RF amplification. The main attraction of the software radio concept, namely, its flexibility and ease of adaptation, is possible because signal processing is implemented in software modules. The software requires a hardware platform to run on, and the capability of the hardware architecture of the processing platform is critical.

Typically digital signal processing functions are implemented on special digital processors called DSPs [12]. Although DSPs are also microprocessors, there are several crucial differences between general multipurpose microprocessors and DSPs. General microprocessors are typically built for a range of general functions and normally run large blocks of software. The DSP, on the other hand, is built for a small dedicated group of tasks, the most important being the multiply-accumulate arithmetic operation that forms the core of any digital filter. DSPs contain large, high-speed data busses and use direct memory access to transfer large amounts of data, thereby avoiding communication bottlenecks. In addition, DSPs contain dedicated hardware blocks, such as multipliers, to speed up the arithmetic-intensive signal processing steps.

Some of the signal processing functions are so complex that parallel and sequential partitioning of algorithms is required to get the required processing power. DSPs are getting faster but are currently incapable of implementing

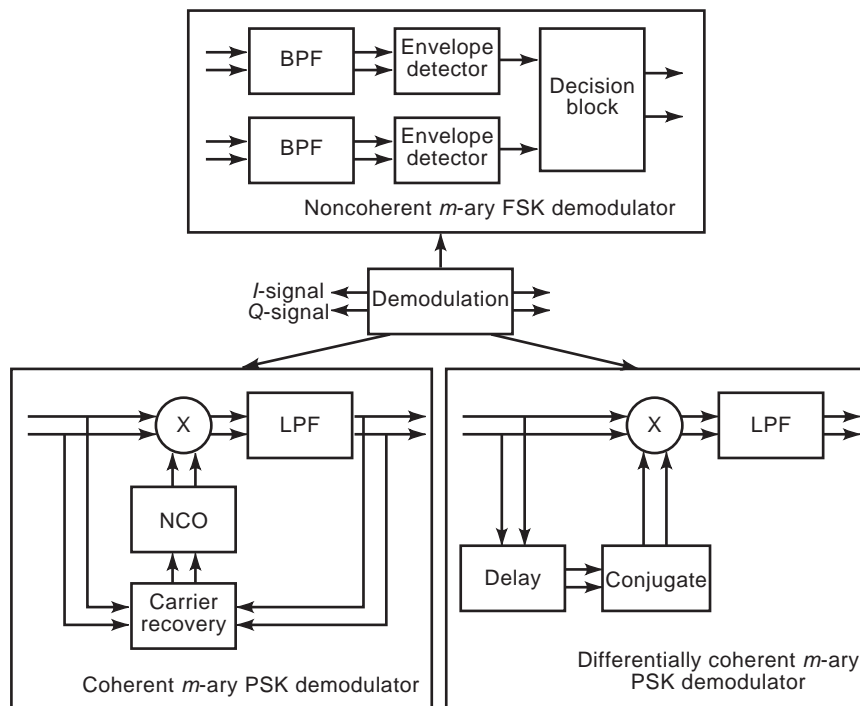


Figure 7. Some general demodulator architectures.

everything possible on a single chip. One approach has been to use multiprocessing to share the computational burden. The traditional approach to multiprocessing has been to integrate various DSPs on a board. Modern DSPs contain various hooks to simplify multiprocessing, such as simplified addressing across processors. A recent approach has been to integrate multiple processors within a single chip. This within-the-chip approach benefits from having closely coupled memory and cache, which improves communication efficiency.

To keep the flexibility of a programmable solution and the efficiency of a dedicated solution, field-programmable gate arrays (FPGAs) are increasingly becoming another viable option to implement highly complex signal processing functions. FPGAs are logic devices whose hardware architecture can be programmed before use. Techniques, such as distributed arithmetic for array multiplication, can increase the data bandwidth and throughput of an FPGA-based solution by orders of magnitude beyond those possible with general-purpose DSPs. It is projected that DSP cores will have onchip FPGA sections to provide configurable accelerators.

5. CONCLUSION

This article has presented an overview of the radio transceiver, its architecture, and the implementation of its most important system blocks. Several other specialized functions are not present in all transceivers and have not been discussed here. Some of these circuits are noise limiting and blanking, squelch, diversity reception, and adaptive antenna array processing.

Traditionally, transceivers have used analog circuits for implementation. The capabilities and advantages of digital processing have allowed replacing many of these analog functions. The movement of the digital portions of the processing closer to the antenna has resulted in the development of software radio architecture. The software radio is a powerful architectural framework that helps to deliver advanced radio services by leveraging the economics of contemporary micro-electronics and software technologies. Although much technological progress has been made in the field of digital processing, technology is not currently available to implement the ideal software radio. Following are some of the challenges and issues that face radio designers today:

1. To engineer low-cost, low-loss, and low-distortion wideband antennas
2. To engineer low-cost, low-loss, and low-distortion wideband RF front ends
3. To develop high-efficiency linear power amplifiers
4. To develop low-power integrated RF front ends
5. To develop low-cost, high-resolution (> 14 bits), and high-speed ADCs
6. To develop low-cost, high-speed reconfigurable digital processors

The development of the software radio transceiver is by no means over. Further technological advances are required,

especially in the hardware implementation of ADCs and reconfigurable processors. There will be further development toward integrating the analog RF front end into a single integrated circuit. The development of low-power RF and digital circuits is another challenge. The ultimate goal of implementing a radio on a chip, although not yet a practical reality, is not far away.

6. ABBREVIATIONS

ADC	= Analog-to-digital converter
AFC	= Automatic frequency control
AGC	= Automatic gain control
AM	= Amplitude modulation
ASIC	= Application-specific integrated circuit
BER	= Bit error rate
BPF	= Bandpass filter
DAC	= Digital-to-analog converter
DSP	= Digital signal processor
FET	= Field-effect transistor
FIR	= Finite impulse response
FM	= Frequency modulation
FPGA	= Field-programmable gate array
FSK	= Frequency-shift keying
GaAs	= Gallium arsenide
Hz	= Hertz
IC	= Integrated circuit
IF	= Intermediate frequency
IIR	= Infinite impulse response
LNA	= Low-noise amplifier
LPF	= Low-pass filter
MDS	= Minimum detectable signal
MIC	= Microwave integrated circuit
MMIC	= Microwave monolithic integrated circuit
NCO	= Numerically controlled oscillator
NF	= Noise figure
PLL	= Phase-locked loop
PM	= Phase modulation
PSK	= Phase-shift keying
RF	= Radiofrequency
SAW	= Surface acoustic wave
TWTA	= Traveling-wave tube amplifier

BIBLIOGRAPHY

1. U. L. Rohde, J. Whitaker, and T. T. Bucher, *Communications Receivers*, 2nd ed., New York: McGraw-Hill, 1996.
2. M. Faulkner and M. A. Briffa, Amplifier linearisation using RF feedback and feedforward techniques, *Proc. Veh. Technol. Conf. (VTC)*, 1995, pp. 525–529.
3. S. Haykin, *An Introduction to Analog and Digital Communications*, New York: Wiley, 1994.
4. H. Meyr, M. Moeneclaey, and S. A. Fechtel, *Digital Communication Receivers-Synchronization, Channel Estimation, and Signal Processing*, New York: Wiley, 1998.
5. J. Mitola, The software radio architecture, *IEEE Commun. Mag.*, **33**:26–38 (1995).

6. J. K. Cavers and S. P. Stapleton, A DSP-based alternative to direct conversion receiver for digital mobile communications, *Proc. Veh. Technol. Conf. (VTC)*, 1990.
7. D. B. Chester and J. Fakatselis, The architecture and benefits of digital IF up conversion implementations, *Proc. Int. Conf. Signal Process. Appl. Technol. (ICSPAT)*, 1995, pp. 356–360.
8. T. S. Rappaport, *Wireless Communications-Principles and Practice*, Upper Saddle River, NJ: Prentice Hall, 1996.
9. G. Ungerboeck, Trellis coded modulation with redundant signal sets, part 1: Introduction, *IEEE Commun. Mag.*, **25**:5–21 (1987).
10. J. A. Wepman, Analog-to-digital converters and their applications in radio receivers, *IEEE Commun. Mag.*, **33**:39–45 (1995).
11. J. G. Proakis and D. G. Manolakis, *Digital Signal Processing*, 2nd ed., New York: Macmillan, 1992.
12. R. Baines, The DSP bottleneck, *IEEE Commun. Mag.*, **33**: 46–54 (1995).

TRANSIENT ANALYSIS

ORLA FEELY
 BRIAN MULKEEN
 University College Dublin
 Dublin, Ireland

1. INTRODUCTION

Transient circuit analysis is used to find transient currents and voltages in a circuit. The word “transient” describes a quantity that is fleeting rather than permanent, and distinguishes this branch of circuit analysis from steady-state analysis, which is concerned with the long-term or settled behavior of a circuit. Transient circuit analysis asks not just “Where will my circuit end up?” but also “How will it get there?” The charging of a capacitor is one of the classic examples, but we might also consider what happens when a short pulse is applied to a transmission line (perhaps an interconnection on a high-speed digital integrated circuit), or when a burst of radiofrequency energy is applied to the antenna in a radar system. In this article, we review the basic principles of transient circuit analysis, which is a long-established branch of circuit theory with a wide range of applications. We will not consider the many techniques that are used in the simulation of transient behavior in circuits—these are an enormous topic in their own right, and are covered elsewhere.

Before proceeding, it should be noted that the circuits to be considered in this article in fact form only a subset of the universe of circuits—they are all linear and time-invariant. A linear circuit is one in which each element (except the sources that drive the circuit) is described by one or more linear equations involving its current(s) and voltage(s). For example, the resistor defined by $v = Ri$ is linear, but the diode defined by $i = I_s(e^{v/V_T} - 1)$ is nonlinear, and any circuit containing the diode is therefore nonlinear. Nonlinear circuits can exhibit highly complex behavior

and cannot be handled by the techniques described in this article. A time-invariant circuit is one in which the equations defining the elements (except the independent sources) do not change with time.

The equations describing a circuit arise from two sources: (1) Kirchhoff’s laws tell us how the elements in the circuit are interconnected, and then (2) each element in the circuit has an individual equation (or equations) describing its behavior. If all of the circuit elements are described by algebraic equations (i.e., ones in which no derivatives appear) involving their currents and voltages, these equations can be combined with Kirchhoff’s equations to give a set of algebraic equations that completely describe the circuit. These equations are linear equations in terms of the currents and/or voltages in the circuit, and can be solved by any of the techniques of linear algebra. The power of linear algebra means that these circuits, known as *resistive circuits*, are (relatively) easy to analyze. The behavior of these circuits is quite simple; if a linear resistive circuit is driven by a 1-V battery, then changing to a 2-V battery will cause all voltages and currents in the circuit to double. There is no time delay in this response—the doubling of voltages and currents occurs at the precise instant when the 2-V battery is inserted into the circuit. If the battery is replaced by a more complicated voltage source that varies with time, each voltage and current in the circuit will also vary with time as a scaled replica of the new voltage source.

Although easy to analyze, the limited behavior of a linear resistive circuit means that such circuits are not hugely useful. Instead of producing a scaled replica of the signal that drives them, most circuits are required to convert a signal into a more useful form. For example, the ignition circuit in a car is “driven” by a battery with almost constant voltage, but its output is a short, sharp spark; the circuits in a radio receiver are “driven” by a jumble of signals from many different sources, but must select the signal of interest and extract some information from it. These effects rely on the use of capacitors and/or inductors. These circuit elements are defined by equations involving not only their currents and voltages but also the rate of change (or derivative) of these quantities with time. Specifically, the current through a capacitor is proportional to the derivative of the capacitor’s voltage with respect to time, and the voltage across an inductor is proportional to the derivative of the inductor’s current with respect to time. Capacitors and inductors are known as *dynamic circuit elements*, conveying the importance to them of time variation, or energy storage elements, since they are capable of storing energy for later release.

Dynamic elements can be placed deliberately in a circuit, or they can be unwanted parasitic elements, modeling, for example, the capacitance between wires in the circuit. If a circuit contains even a single dynamic element, it is in general described no longer by a set of algebraic equations, but by one or more differential equations, in which the variables are not only the voltages and currents but also the derivatives of certain of these quantities with respect to time. A dynamic circuit is one that contains at least one dynamic element.

At higher frequencies, there is an additional complexity to consider in our circuit analysis, namely, the appearance of distributed circuit effects. Distributed circuits, unlike lumped circuits, have voltages and currents that vary not only with time but also with position within the circuit. The basic distributed circuit element is the transmission line, an incremental length of which is commonly modeled by a series resistance and inductance and a shunt capacitance and conductance. The inductance and capacitance in the model give rise to time derivatives in the equations that describe the line, while the distributed nature of the element gives rise to derivatives with respect to position along the line. Thus circuits of this nature are described by differential equations containing derivatives with respect to position as well as derivatives with respect to time. This gives rise to new forms of transient behavior in a circuit.

The goal of transient circuit analysis is to solve the differential equations that describe a dynamic circuit and thus to come up with expressions predicting the way in which the voltages and currents in the circuit will vary with time. It is often concerned in particular with the response of the circuit to changes, such as when a source is inserted, removed, or suddenly changed in some way, or a switch is closed and the makeup of the circuit thereby changed.

Dynamic circuits can exhibit more interesting behavior than resistive circuits, but they are also more difficult to analyze. One of the simplest dynamic circuits contains a single capacitor in series with a resistor and a constant voltage source that is switched on at some specified time. This circuit is described by an equation involving the capacitor voltage v_C and its derivative with respect to time dv_C/dt . The absence of any higher derivatives gives this equation the description “first order.” A circuit containing just a single dynamic element is described by a first-order differential equation and is called a *first-order circuit*.

The solution of a first-order differential equation will contain an unknown constant. To find this constant, it is necessary to apply some additional information about the value of the solution at a specified time instant. Since we are in general concerned with finding the response of the circuit to changes that occur at a certain time instant, we often know the state of the circuit just before the change occurs and can apply this information in order to find the unknown constant. The value of the capacitor voltage (or inductor current, if the circuit contains an inductor rather than a capacitor) just before the change occurs, is known as the *initial condition*.

Solving the first-order circuit just described yields the result shown in Fig. 1. The capacitor voltage plotted as a function of time is of exponential form, moving from its initial value toward the value of the constant voltage source and eventually settling there. (Certain assumptions have been made here, and are discussed in the next section.) This is intuitively plausible—once the voltage source has been inserted, the resistor voltage and capacitor voltage must sum to equal the voltage of the source. If the capacitor voltage does not initially equal that of the source, the voltage difference must be developed across the resistor by a current flowing through it. This current

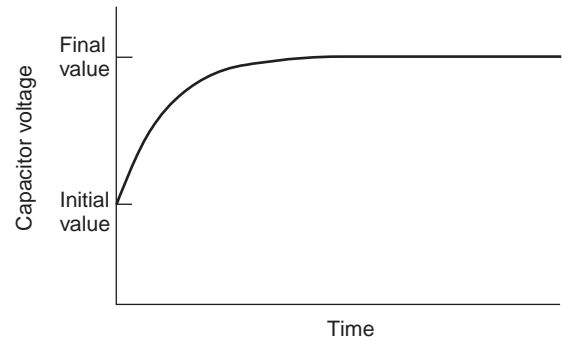


Figure 1. Capacitor voltage in a first-order circuit increasing exponentially from its initial value to its final value.

charges the capacitor, bringing its voltage closer to that of the source, and the net effect is to cause the capacitor voltage to approach that of the voltage source.

Already in this simple circuit we can see how dynamic circuits behave in ways that would be impossible for a resistive circuit. If the circuit described above had been resistive, all voltages and currents would have been scaled versions of the source. In this circuit, however, the capacitor voltage takes on a form quite unlike that of the source—it varies exponentially with time, whereas the source is constant. The action of the resistor and capacitor has processed the source signal, with the capacitor voltage resisting the sudden change when the source was inserted, but retaining the steady behavior of the source. The resistor voltage, on the other hand, captures the change in the source very well, but eventually dies away to include nothing of the steady behavior of the input. This behavior is an example of the filtering behavior of this simple resistor–capacitor combination, which is useful in a variety of communications applications.

The exponential nature of the voltage observed in this simple circuit is not unusual—in fact, as we shall see, exponential functions appear in various guises in the solution to linear differential equations. Possibly the most widely known example of an exponential function appears in the analysis of radioactive decay, where the rate of decay of a substance is proportional to the amount of the substance present, and so the amount remaining decays exponentially to zero at a rate depending on the half-life of the substance.

A circuit that contains two dynamic elements in general gives rise to a second-order differential equation (containing the second derivative of the variable with respect to time) and is termed a *second-order circuit*. If all sources in the circuit are DC (constant) sources, this equation can be solved by application of standard theory of linear differential equations, with the aid of two initial conditions, one for each dynamic element. Instead of the single exponential transient of the first-order circuit, this circuit contains two exponential transients that are added to give the overall transient. The relationship (via complex numbers) between the exponential and sinusoidal functions can give rise to new types of behavior arising from these transients, as shown in Fig. 2. If the arguments of these exponentials are complex, as may turn out to be the case, then they can

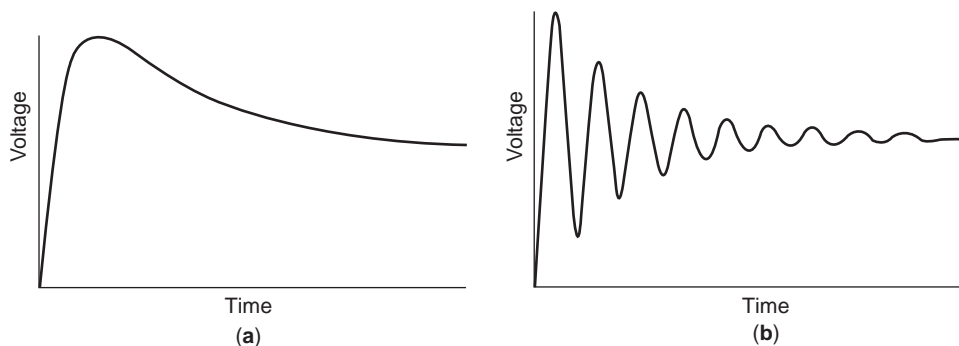


Figure 2. Two possible responses of a second-order circuit, made up of the sum of two exponentials.

be added to give a transient that oscillates sinusoidally. In most circuits the magnitude of this oscillation decays exponentially with time. A common example of such a decaying oscillation is produced when a tuning fork is struck or a child's swing given a single push. If there are no losses in the circuit (not a practical requirement), the oscillation could persist indefinitely without decaying, and if the circuit is unstable, it is possible that the oscillation can actually grow.

In a radiofrequency system, a circuit would normally be “driven” by a more complicated signal, but the same basic principles apply. We can consider a simple example, where a short burst of a sinusoidal signal is applied to a second-order system. Such a signal might arise in a radar system or in a digital communication system. The resulting transient, shown in Fig. 3, is essentially sinusoidal in form, but its amplitude changes with time in a way that is similar to the transients shown earlier, first increasing in response to the start of the burst of sinusoidal signal, eventually settling to a steady amplitude, and then decaying exponentially following the end of the burst.

While it is possible to analyze simple first- and second-order dynamic circuits by applying standard theory of differential equations, such solution becomes rapidly more difficult when the order of the circuit increases or when the sources become more complicated. When faced with

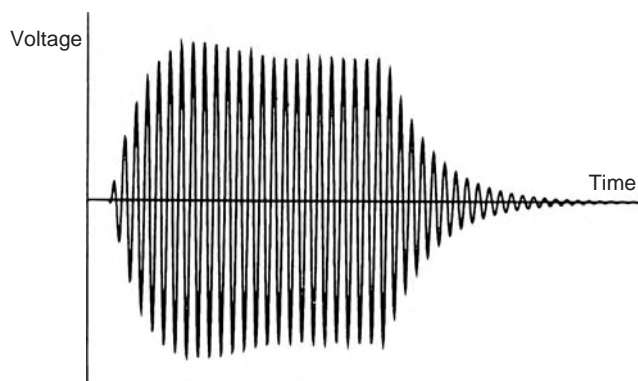


Figure 3. Example transient response of a second-order circuit in response to a short burst of a sinusoidal signal.

such a problem, one might look enviously back at the much simpler process of solving a resistive circuit. In fact, it is possible to apply techniques of resistive circuit analysis to dynamic circuits with the aid of a variety of transforms. A *transform* is a method of changing a problem into a different form, solving it in the new form (where the solution is easier to obtain) and then changing the solution back to the original form. For example, a student unfamiliar with binary arithmetic, when asked to add two binary numbers, might convert the numbers to decimal form (presumably with the aid of a table), add the decimal numbers, and then convert back to binary. The transforms to be applied in this context change a system of differential equations to a system of algebraic equations that are significantly easier to solve.

The most important and most widely used of these transforms in circuit analysis is the Laplace transform. A second transform, the Fourier transform, is particularly useful in analyzing circuits designed for applications in communication systems. These transforms convert a set of differential equations involving the time variable into a set of algebraic equations involving a new variable called the *frequency* (in the case of the Fourier transform) or the *complex frequency* (in the case of the Laplace transform). Application of these transforms allows us to analyze a circuit by transforming it into an equivalent form in the frequency domain, where its equations are purely algebraic, analyzing the circuit in this frequency domain using the techniques of linear algebra, and then applying the transform in reverse to convert the result of this analysis into a function of time. We will see how the Laplace transform can be applied to distributed circuits as well as lumped circuits.

Once again, Laplace transform analysis shows up the special role of the exponential function (and its complex cousin, the sinusoid) in the behavior of circuits. Every dynamic circuit favors certain exponential (including sinusoidal) modes of behavior whose rate of decay (and frequency of oscillation, if applicable) is governed by the so-called natural frequencies of the circuit. These natural frequencies tell us whether the currents and voltages in a circuit will, of their own accord, tend to exhibit exponential or oscillatory decay, constant behavior or steady oscillation, exponential or oscillatory growth, or some

combination thereof. When an input signal is applied to the circuit, the currents and voltages may contain components controlled by the natural frequencies as well as a component controlled by the input. In many practical circuits it is desirable for the output to depend on the input, and the prospect of a growing oscillation in the circuit is a designer's nightmare. (This effect is similar to that demonstrated by sound systems when a microphone is placed in the path of a loudspeaker and an unwanted tone appears and swamps the desired signal.) In other cases, a sustained oscillation is the objective, and the designer's aim is to fix the frequency and amplitude of this oscillation. The issue here is one of *stability*. An asymptotically stable system is one in which all exponential transients die away, leaving only the effect of the input signal. Laplace transform techniques allow us to analyze a system to determine whether it is asymptotically stable, or whether a sustained oscillation is possible.

The effects of transients are seen in a huge range of electronic and electrical engineering applications, from the transmission of tiny pulses between parts of a communication system to the behavior of an electrical power system struck by lightning. The techniques described in this article provide the reader with the ability to understand and analyze transient behavior in a wide variety of circuits.

2. TIME-DOMAIN ANALYSIS

2.1. Natural Response and Step Response of a First-Order Circuit

Consider the circuit shown in Fig. 4a. Until the time $t = 0$, the switch S is in position 1, and the resistor R and capacitor C are connected in a loop. At time $t = 0$ the switch is moved to position 2, connecting the DC voltage source E in series with R and C . We assume that the switch closes instantaneously and that it presents a short circuit between the terminals that it connects. Mathematically, we say that the voltage applied to the RC series combination is $EU(t)$, where $U(t)$ is the unit step function given by

$$U(t) = \begin{cases} 0 & \text{for } t < 0 \\ 1 & \text{for } t \geq 0 \end{cases} \quad (1)$$

The circuit of Fig. 4a can, therefore, also be drawn in the form shown in Fig. 4b.

The analysis of the circuit for $t \geq 0$ in Fig. 4 will require knowledge of the initial voltage across the capacitor just after the switch is thrown, $v_C(0^+)$, where $0^+ = \lim_{\epsilon \rightarrow 0} \epsilon$.

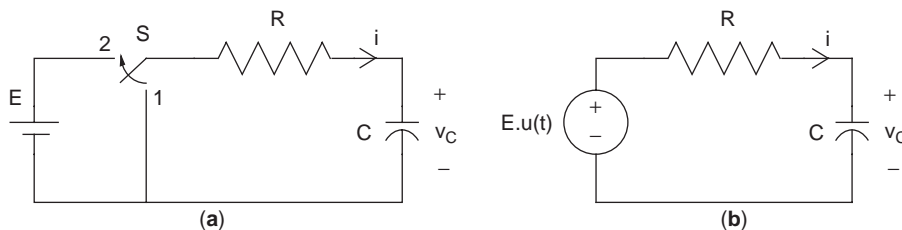


Figure 4. (a) The switch S moves from position 1 to position 2 at time $t = 0$, so the voltage applied to the RC series combination is 0 for $t < 0$ and E thereafter. The switch/voltage source combination is represented in (b) by the single voltage source $EU(t)$.

We generally know, or can find from analysis of a previous regime, $v_C(0^-)$, the voltage at the instant just before the switch is thrown: ($0^- = \lim_{\epsilon \rightarrow 0} -\epsilon$). If the capacitor current is finite, $v_C(0^+)$ must equal $v_C(0^-)$, and we can refer to both as $v_C(0)$. Similarly, if the voltage across an inductor is finite, its current waveform must be continuous. We will assume these continuity conditions throughout this analysis. The alternative case, where the capacitor current or inductor voltage can be infinite, is not practical but turns out to be mathematically interesting and useful in analysis. It can be handled by an extension of our analysis in this section (see Ref. 1 for details), but we will postpone consideration of this possibility until Section 3, where it can be handled more conveniently.

For $t \geq 0$, Kirchhoff's voltage law gives the equation

$$v_C(t) + i(t)R = E$$

or, applying the constitutive relation $i(t) = C \frac{dv_C(t)}{dt}$ for the capacitor

$$RC \frac{dv_C(t)}{dt} + v_C(t) = E \quad (2)$$

This is a first-order differential equation in the capacitor voltage v_C , and so this circuit is referred to as a *first-order circuit*. It can be solved by a number of methods to give an expression for v_C as a function of time. One such method is to recast the equation in the form

$$\frac{d(v_C(t) - E)}{dt} = -\frac{1}{RC}(v_C(t) - E)$$

This equation is of the familiar form

$$\frac{dx(t)}{dt} = ax(t)$$

which has the solution [2]

$$x(t) = x(0)e^{at}$$

where $x(0)$ is the value of x at time $t = 0$. This initial condition must be known if the equation is to be solved for $x(t)$. Thus Eq. (2) has the solution

$$v_C(t) - E = (v_C(0) - E)e^{-t/RC} \quad (3a)$$

or

$$v_C(t) = v_C(0)e^{-t/RC} + E(1 - e^{-t/RC}) \quad (3b)$$

The response of the series RC circuit with zero initial capacitor voltage to the application of a voltage source given

by the unit step function is known as the *step response* of the series RC circuit. (Note that we will use the word “response” to signify any current or voltage in the circuit, or any set thereof, including, for example, the set of all currents and voltages. Throughout this article the variables that constitute the response in any given instance will be clear from the context in which the term is used.)

It is clear from Eq. (3a) that the difference between v_C and E varies exponentially with time, and when the product RC is positive (a condition that will be assumed to hold unless otherwise stated), this difference tends to zero as t tends to infinity. v_C is plotted as a function of time in Fig. 5, where, as expected, v_C is seen to converge exponentially to E . The rate of this convergence is governed by the value of RC , which is termed the time constant of the waveform and denoted by the symbol τ . The smaller the time constant, the faster the rate of convergence. After one time constant has elapsed (i.e., at $t = \tau$), $v_C(t) - E$ has decreased to $e^{-1} = 36.8\%$ of its value at $t = 0$, and at time $t = 5\tau$ this difference has decreased to $e^{-5} = 0.7\%$ of its initial value. Although v_C does not reach E within any finite time (unless, of course, it started out at E), after five time constants have elapsed, the difference between v_C and E has been reduced to less than 1% of its initial value. The time constant is a useful measure of the response speed of a first-order circuit. For more general circuits, the risetime is used as a measure of response time. This is defined as the time taken for the step response to rise from 10% to 90% of the steady-state value. For the first-order circuit analysed in this section, the risetime can be found to be $\tau \ln 9 \approx 2.2\tau$.

The value E to which the capacitor voltage converges is termed the *steady-state value* of this voltage. It is the only value of capacitor voltage at which the circuit can settle, or in other words it is only when $v_C = E$ that all currents and voltages in the circuit cease to vary with time. Clearly, when a quantity ceases to vary with time, its derivative with respect to time is zero, and so the steady-state value of v_C can be found directly from the differential equation (2) by setting the term dv_C/dt to zero (or, in circuit terms, replacing the capacitor by an open circuit), yielding the

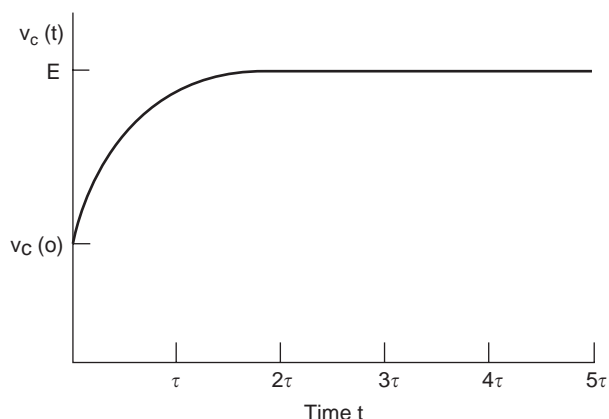


Figure 5. The capacitor voltage in the circuit of Figure 1 varies exponentially from its starting value $v_C(0)$ to its steady-state value E , with time constant $\tau = RC$.

equation $v_C = E$, as expected. The overall waveform $v_C(t)$ is the sum of this steady-state component and a second component that dies away with time. This second component is known as the transient component (or just the transient). The exponential form of the transient in this circuit is, as we will see later, particularly common in linear circuits and other linear systems.

Note, however, that the procedure just outlined yields the value of v_C at which the circuit variables (currents and voltages) can remain constant, but it does not guarantee that the circuit will actually converge to this state. For example, if $RC < 0$, Eq. (3a) implies that v_C will diverge exponentially away from E and the circuit has no steady-state response. [The only exception to this divergence is when $v_C(0) = E$, in which case it will theoretically remain fixed at E for all time. The word “theoretically” is important—in practice, any noise in the circuit that causes v_C to differ even infinitesimally from E will result in its diverging exponentially from E .] This distinction relates to the issue of the stability of equilibria of differential equations [2].

Another useful view of the solution waveform (3b) for $v_C(t)$ is that it is composed of two components: one caused by the initial condition $v_C(0)$, and the other caused by the voltage source E . If $E = 0$, the response (3) reduces to $v_C(t) = v_C(0)e^{-t/RC}$, which is termed the “natural” or “unforced” response of the circuit. This is a viewpoint to which we will return later.

Any circuit consisting of a single capacitor in an otherwise resistive circuit containing only DC sources is generally analyzed by transforming it to single-loop form by means of a Thévenin transformation [3], as shown in Fig. 6. The analysis described above is then applicable, where E is the Thévenin equivalent voltage source, and R the Thévenin equivalent resistance. (The small number of circuits that do not have a Thévenin equivalent can be handled separately.)

Before leaving the single-loop first-order circuit of Fig. 4, we note that the analysis of this section can be used to find the response of a first-order circuit to a voltage source that is piecewise-constant, that is, constant over certain time intervals with discontinuous jumps between these constant levels. One important such waveform is the pulse

$$p(t) = \begin{cases} 0 & \text{for } t < 0 \\ E & \text{for } 0 \leq t < t_0 \\ 0 & \text{for } t \geq t_0 \end{cases}$$

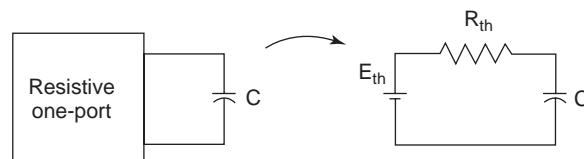


Figure 6. A circuit consisting of a single capacitor in an otherwise resistive circuit is simplified by replacing the resistive one-port seen by the capacitor by its Thévenin equivalent.

The response of the first-order RC circuit to this source waveform is found by an extension of the analysis just performed. For $0 \leq t < t_0$, the analysis proceeds as before and $v_C(t)$ is given by Eq. (3b):

$$v_C(t) = v_C(0)e^{-t/RC} + E(1 - e^{-t/RC}) \text{ for } 0 \leq t < t_0 \quad (3c)$$

For $t \geq t_0$, the response is just the natural response found previously; the only difference is that since this phase of the analysis commences at $t = t_0$ instead of $t = 0$, the initial condition is $v_C(t_0)$ instead of $v_C(0)$. Applying this initial condition in the usual way, we find that

$$v_C(t) = v_C(t_0)e^{-(t-t_0)/RC} \text{ for } t \geq t_0 \quad (4)$$

$v_C(t_0)$ is, by our assumption of bounded currents, equal to $v_C(t_0^-)$, the capacitor voltage just before the source waveform drops to zero. Since Eq. (3c) gives $v_C(t)$ for all times in the range $0 \leq t < t_0$, it can be used to find that

$$v_C(t_0^-) = v_C(0)e^{-t_0/RC} + E(1 - e^{-t_0/RC})$$

Substituting this value for $v_C(t_0)$ in (4) completes the analysis of the response of the series RC circuit to the voltage pulse. This response is plotted in Fig. 7 for two different values of the time constant. The response of a circuit to a pulse is particularly important in communication systems where such pulses are used to carry information and must be clearly identifiable at the receiver. An RC combination of the type studied here often occurs in such transmission systems, formed by the output resistance of the part of the system where the signal originates and the input capacitance of the part of the system into which the signal is fed, and thus exponential distortion will inevitably ensue. Clearly the “smearing” of the pulse evident in Fig. 7 when the time constant is large limits the rate at which pulses can be transmitted if they are to be separated at the receiver.

The response of the series RC circuit to any piecewise-constant source waveform is found by an extension of the

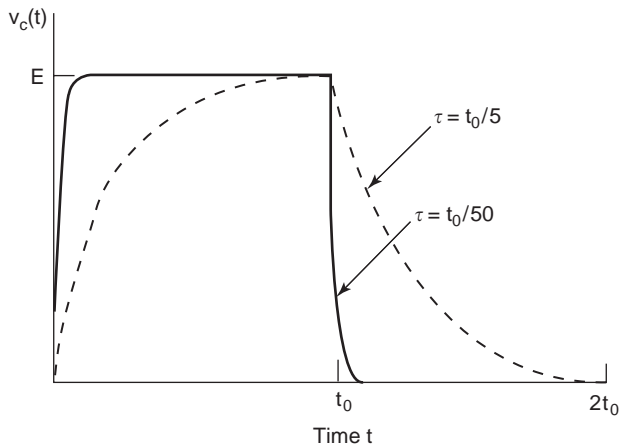


Figure 7. The response of a first-order RC circuit to a voltage pulse of amplitude E and duration t_0 . The solid line shows the response if $\tau = t_0/50$; the dashed line, the response if $\tau = t_0/5$.

analysis performed above. The circuit is analysed using the standard method over each of the time intervals in which the source is constant, starting with the first time interval. The initial condition for the n th time interval, commencing at time $t = t_n$, is found by evaluating the response from the previous time interval at time $t = t_n^-$.

The second type of first-order circuit is one in which the single energy storage element in the circuit is an inductor rather than a capacitor, and by application of a Norton transformation (where possible) is of the form shown in Fig. 8, where the constant current source I is connected in parallel with conductance G and inductance L for $t \geq 0$. Kirchhoff’s current law applied to this circuit gives the following differential equation in the inductor current i_L for $t \geq 0$

$$GL \frac{di_L(t)}{dt} + i_L(t) = I$$

which can be solved as before to find

$$i_L(t) - I = (i_L(0) - I)e^{-t/GL}$$

or

$$i_L(t) = i_L(0)e^{-t/GL} + I(1 - e^{-t/GL})$$

Thus the inductor current waveform for the circuit of Fig. 8 takes the same form as the capacitor voltage waveform for the circuit of Fig. 4b, with time constant GL and steady-state value I . This is a consequence of the fact that the circuit of Fig. 8 is the dual of that of Fig. 4b. The response to a piecewise-constant source waveform can be found by applying the method previously described for the series RC circuit.

2.2. Natural Response of Second-Order Circuits

The circuit in Fig. 9 consists of a resistor and two energy storage elements—a capacitor and an inductor. Kirchhoff’s voltage law gives the equation

$$v_C(t) + L \frac{di_L(t)}{dt} + Ri_L(t) = 0$$

which on application of the relation $i_L(t) = C[dv_C(t)/dt]$ becomes

$$LC \frac{d^2v_C(t)}{dt^2} + RC \frac{dv_C(t)}{dt} + v_C(t) = 0 \quad (5)$$

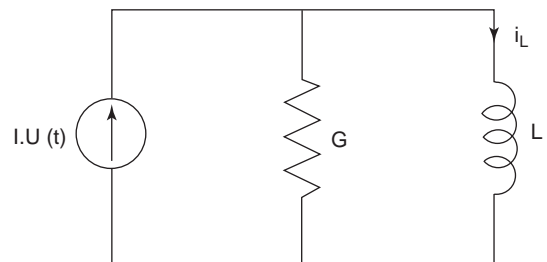


Figure 8. First-order circuit consisting of the parallel combination of current source $IU(t)$, conductance G , and inductor L .

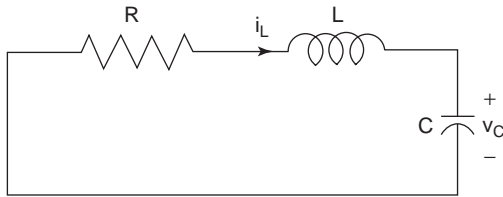


Figure 9. Second-order circuit consisting of resistor R , capacitor C and inductor L .

This is a second-order differential equation, and so the circuit is termed a *second-order circuit*. The exponential waveform

$$v_C(t) = Ae^{st}$$

is a solution to Eq. (5) provided

$$LCs^2 + RCs + 1 = 0$$

which yields

$$s = \frac{-R}{2L} \pm \sqrt{\frac{R^2}{4L^2} - \frac{1}{LC}}$$

If these two values, s_1 and s_2 , are distinct (i.e. $s_1 \neq s_2$), then the general solution of Eq. (5) is of the form

$$v_C(t) = A_1 e^{s_1 t} + A_2 e^{s_2 t} \quad (6)$$

Since there are no sources in the circuit, this is the natural or unforced response of the series RLC circuit. The constants A_1 and A_2 will be determined by applying the initial conditions $v_C(0)$ and $i_L(0)$ and solving the resulting simultaneous equations:

$$v_C(0) = A_1 + A_2$$

$$i_L(0) = C \left. \frac{dv_C}{dt} \right|_{t=0} = CA_1 s_1 + CA_2 s_2$$

We will now consider the nature of the natural or unforced voltage waveform represented by Eq. (6). We will use the following shorthand form for s_1 and s_2

$$s_1 = -\alpha + \sqrt{\alpha^2 - \omega_0^2} \quad \text{and} \quad s_2 = -\alpha - \sqrt{\alpha^2 - \omega_0^2}$$

where

$$\alpha = \frac{R}{2L} \quad \text{and} \quad \omega_0 = \frac{1}{\sqrt{LC}}$$

We will assume for now that $\alpha \geq 0$.

The first case to be considered is the case where $\omega_0^2 < \alpha^2$ and s_1 and s_2 are real and distinct. In this case the circuit is said to be overdamped and the response $v_C(t)$ is the sum of two exponentials with time constants $1/|s_1|$ and $1/|s_2|$.

An example of an overdamped response is plotted in Fig. 10a.

The second case occurs when $\omega_0^2 > \alpha^2$ and s_1 and s_2 are complex conjugates of the form $-\alpha \pm j\omega_d$, where $\omega_d = \sqrt{\omega_0^2 - \alpha^2}$. In this case the circuit is said to be underdamped. Equation (6) remains valid but can be expressed more clearly in the form

$$v_C(t) = e^{-\alpha t} [(A_1 + A_2) \cos \omega_d t + j(A_1 - A_2) \sin \omega_d t]$$

where A_1 and A_2 are complex conjugates, and so the coefficients $B_1 = (A_1 + A_2)$ and $B_2 = j(A_1 - A_2)$ are real and can once again be found from the initial conditions. The underdamped response takes the form of an oscillation of frequency ω_d multiplied by an exponential envelope $e^{-\alpha t}$. If $\alpha > 0$, the amplitude of the oscillation decreases exponentially with time, with the rate of this decrease, known as “damping”, controlled by α . If $\alpha = 0$, the response is an oscillation of constant amplitude and frequency $\omega_d = \omega_0 = 1/\sqrt{LC}$. This is the case of the well-known LC oscillator, which arises when $R = 0$ and there is no dissipation in the circuit. The underdamped response is plotted in Figs. 10b and 10c for the two cases $\alpha > 0$ and $\alpha = 0$. Note that the underdamped response is always characterized by oscillation, sometimes termed “ringing”.

If $\omega_0^2 = \alpha^2$, then $s_1 = s_2 = -\alpha = -R/2L$. In this case the general solution of Eq. (5) is no longer given by Eq. (6) but instead by [2]

$$v_C(t) = (D_1 + D_2 t) e^{-\alpha t}$$

and is said to be “critically damped”. The constants D_1 and D_2 are once again found by application of the initial conditions. An example of a critically damped response is plotted in Figure 10d.

2.3. Step Response of Second-Order Circuit

The circuit in Fig. 11 is identical to that of Fig. 9 but for the addition of the voltage source E at $t = 0$. Applying Kirchhoff’s voltage law for $t \geq 0$ gives the equation

$$v_C(t) + L \frac{di_L(t)}{dt} + Ri_L(t) = E$$

which on application of the relation $i_L(t) = C[dv_C(t)/dt]$ becomes

$$LC \frac{d^2 v_C(t)}{dt^2} + RC \frac{dv_C(t)}{dt} + v_C(t) = E \quad (7)$$

To solve this equation, we apply the fact that the general solution to a differential equation is the sum of two components, which are known in mathematics as the “homogeneous solution” and a “particular solution” [2]. The homogeneous solution is the solution to the differential equation obtained when all input terms (i.e., all terms not involving the variable or its derivatives) are set to zero. In circuit terms, this is just the response obtained when all independent voltage and current sources are removed, namely, the natural or unforced response. A particular

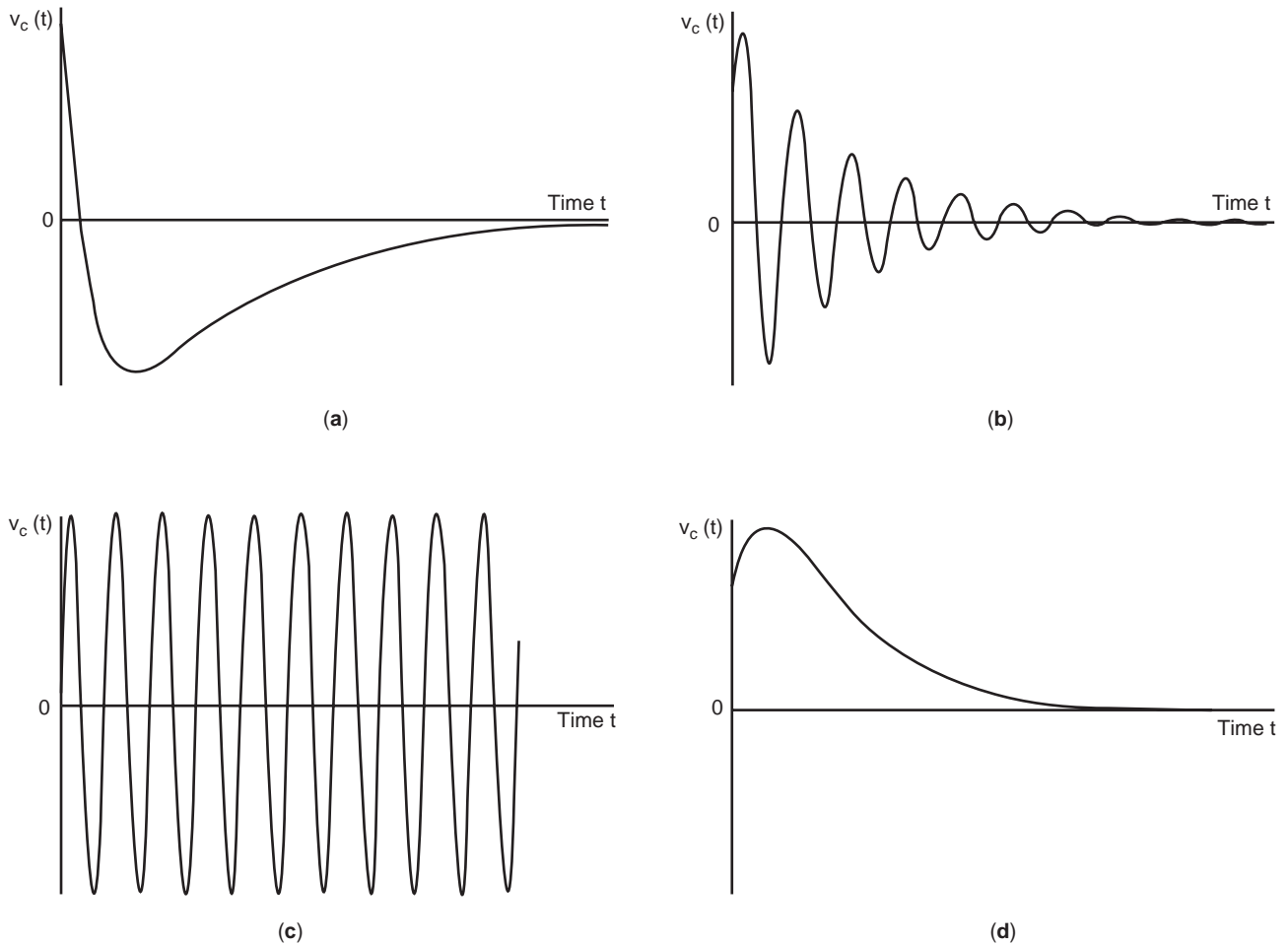


Figure 10. Examples of the natural response of the series *RLC* circuit: (a) overdamped; (b) underdamped; (c) underdamped and lossless; (d) critically damped.

solution is any solution to the differential equation. This decomposition may seem to be of no particular benefit, since it states that to solve the differential equation, one must obtain a solution to the differential equation. The benefit lies in the ability to choose a particularly simple form for the particular solution, which can then be extended to yield the general solution by the addition of the homogeneous solution. The simplest particular solution is the constant solution, which is obtained by setting all derivatives to zero.

The particular solution to Eq. (7) obtained by setting all derivatives to zero is $v_C(t) = E$. Adding this solution to the homogeneous solution that has already been found in Eq. (6) yields the general solution, which is of the form

$$v_C(t) = A_1 e^{s_1 t} + A_2 e^{s_2 t} + E \text{ if } \omega_0^2 < \alpha^2 \text{ (overdamped)} \quad (8a)$$

$$v_C(t) = e^{-\alpha t} [B_1 \cos \omega_d t + B_2 \sin \omega_d t] + E \text{ if } \omega_0^2 > \alpha^2 \quad (8b)$$

(underdamped)

$$v_C(t) = (D_1 + D_2 t) e^{-\alpha t} + E \text{ if } \omega_0^2 = \alpha^2 \text{ (critically damped)} \quad (8c)$$

The appropriate constants A_1 and A_2 , B_1 and B_2 , or D_1 and D_2 are found by applying the initial conditions. If the initial conditions are zero, Eqs. (8) represent the step response of the series *RLC* circuit, and are plotted in Fig. 12.

Depending on the system in which a circuit is to be used, different demands may be made of its step response. In some applications, for example, there may be a requirement that the voltage reach its steady-state value as soon as possible, while in others it may be necessary that the

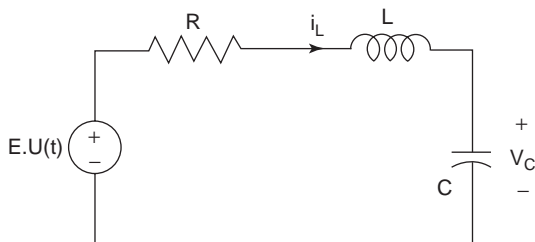


Figure 11. Second-order circuit consisting of resistor *R*, capacitor *C*, inductor *L*, and voltage source $EU(t)$.

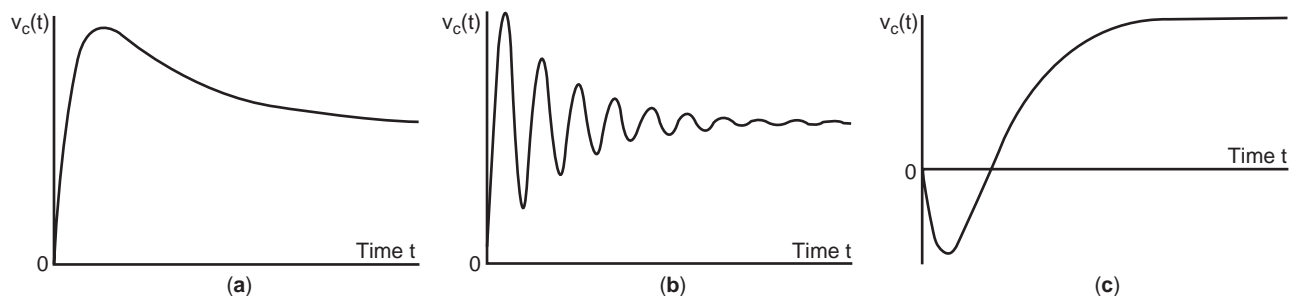


Figure 12. Examples of the step response of the series RLC circuit: (a) overdamped; (b) underdamped; (c) critically damped.

voltage never exceed its steady-state value by more than some specified percentage, to avoid driving circuit elements into saturation. A number of figures of merit have been defined to characterize the step response of a circuit in order to test its suitability for a given application [1]. The risetime has already been defined. The *settling time* is the time beyond which the step response does not differ from its steady-state value by more than 2%. The *delay time* is the time taken for the step response to reach 50% of its steady-state value. The *overshoot* is defined as the difference between the peak value and the steady-state value of the step response, expressed as a percentage of the steady state value.

3. LAPLACE TRANSFORM CIRCUIT ANALYSIS

The analyses described above have found the circuit variables as a function of time by directly solving the differential equations that describe the circuit. While such a procedure is reasonably straightforward for first- and second-order circuits with simple source waveforms, it becomes significantly more difficult as the order of the circuit increases and as the source waveforms become more complex. It is desirable, therefore, to have a more powerful method of finding a solution. In the special case where all sources in the circuit are sinusoidal of the same frequency, the transformation of circuit variables into phasor or complex number form [3–5] allows the circuit to be handled using purely algebraic equations instead of differential equations. Although extremely useful in certain circumstances, this is not a general circuit analysis method: it can handle only sinusoidal sources, it is applicable only if the circuit is stable, it finds only the steady-state component of the waveform and does not allow consideration of initial capacitor voltages and inductor currents.

3.1. The Laplace Transform

A more general transform than the phasor transform is the Laplace transform, named after the French mathematician Pierre-Simon Laplace (1749–1827) [3–6]. This transform method retains the fundamental advantage of the phasor transform, which is the ability to transform a system of differential equations into a system of algebraic equations, but has the additional advantages of being able to handle a much broader class of source waveforms

(including all that are of any practical interest), accommodating initial conditions, and yielding solutions that incorporate both transient and steady-state components without requiring that the circuit be stable.

The Laplace transform is discussed in the article on linear systems, and we will merely summarize its properties here. Given a function of time $f(t)$, its Laplace transform is

$$F(s) = \mathbf{L}\{f(t)\} = \int_{0^-}^{\infty} f(t)e^{-st} dt \quad (9)$$

where the variable s is complex and is termed the (*complex*) *frequency*. Thus the Laplace transform converts a function $f(t)$ from the time domain into a function $F(s)$ in the frequency domain. There exist functions that do not have a Laplace transform, since the integral in (9) fails to converge, but all functions of interest in circuit theory have a Laplace transform. Since the interval of integration is from 0^- to ∞ , the transform defined by Eq. (9) is sometimes called the “one-sided Laplace transform”, to distinguish it from another version in which the integration is from $-\infty$ to ∞ , but we will not need to draw this distinction here and will refer to it simply as the *Laplace transform*. The lower limit of integration of 0^- is chosen in order to accommodate functions with infinite spikes at $t = 0$. Such functions will prove extremely useful in our analysis.

Some of the properties of the Laplace transform that make it so useful in circuit analysis are the following [3,6], where $F(s)$ denotes the Laplace transform of $f(t)$, $F_1(s)$ the Laplace transform of $f_1(t)$ and $F_2(s)$ the Laplace transform of $f_2(t)$:

Uniqueness: $f_1(t) = f_2(t)$ for all $t \geq 0 \Leftrightarrow F_1(s) = F_2(s)$ (More precisely, if $F_1(s) = F_2(s)$ then $\int_{0^-}^{\infty} |f_1(t) - f_2(t)| dt = 0$, but for our purposes it will suffice to assume that $F_1(s) = F_2(s) \Rightarrow f_1(t) = f_2(t)$ for all $t \geq 0$)

Linearity: $\mathbf{L}\{k_1 f_1(t) + k_2 f_2(t)\} = k_1 F_1(s) + k_2 F_2(s)$, where k_1 and k_2 are scalars.

Differentiation: $\mathbf{L}\{(d/dt)f(t)\} = sF(s) - f(0^-)$.

Integration: $\mathbf{L}\left\{\int_{0^-}^t f(\tau) d\tau\right\} = (1/s)F(s)$.

Time shift: $\mathbf{L}\{f(t - \tau)U(t - \tau)\} = e^{-s\tau}F(s)$, where $\tau > 0$ and $U(t)$ is the unit step function given by Eq. (1).

Frequency shift: $\mathbf{L}\{e^{-\alpha t}f(t)\} = F(s + \alpha)$.

The first three of these properties are particularly important. The uniqueness property guarantees that if a system of differential equations is solved by transforming to the frequency domain, solving in the frequency domain and transforming back to the time domain, the solution obtained will be the same as would have been obtained if the solution had been carried out entirely in the time domain. The linearity property guarantees that a system of linear equations in the time domain will remain linear in the frequency domain, allowing powerful linear analysis techniques to be applied in both domains. The differentiation property allows differentiation in the time domain to be replaced by multiplication in the frequency domain, together with the addition of a term related to the initial condition. It is this property that allows a system of differential equations in the time domain to be replaced by a system of algebraic equations in the frequency domain, which can be solved by a variety of powerful and elegant techniques. The Laplace transforms of some important functions are given in Table 1, in which $\delta(t)$ is the delta function defined by

$$\begin{aligned} \delta(t) &= 0 \text{ for } t \neq 0 \\ \int_{-\infty}^{\infty} \delta(t) dt &= 1 \end{aligned} \tag{10}$$

Three steps are to be taken in solving a set of differential equations using Laplace transform analysis: (1) the system of differential equations in the time domain is transformed to a set of algebraic equations in the frequency domain; (2) this set of algebraic equations is solved in the frequency domain, using standard linear techniques; and (3) the solution is transformed from the frequency domain back to the time domain. Step (1) involves application of the definition of the Laplace transform (9) together with certain of its properties (notably the differentiation property). Step (2) involves standard techniques from linear algebra. The third step involves the application of the inverse Laplace transform, which converts a function $F(s)$ in the frequency domain to a function of time $f(t) = \mathbf{L}^{-1}(F(s))$ in such a way that $\mathbf{L}(f(t)) = F(s)$. Note that the function $f(t)$ is unique only for $t \geq 0$, since two functions of time that

differ for $t < 0$ but are identical for $t \geq 0$ will have the same Laplace transform.

3.2. The Inverse Laplace Transform

There is a closed-form equation for the inverse Laplace transform (see Ref. 6 for details), but it is rather difficult to apply (involving contour integration) and is rarely used in circuit analysis applications. Instead, the inverse Laplace transform of a function is generally found by writing the function as the sum of simpler functions, each of whose inverse Laplace transform is known. A technique that is particularly useful here is the partial fraction expansion [2,6]. This is a technique that allows the decomposition of a function $F(s)$ that is the ratio of two real polynomials in s into the sum of simpler terms. It is assumed that the degree of the numerator of $F(s)$ is less than that of the denominator—if this is not the case, then $F(s)$ can be expressed in the form $F(s) = r(s) + \hat{n}(s)/\hat{d}(s)$, where $r(s)$ is a polynomial in s and the degree of $\hat{n}(s)$ is less than that of $\hat{d}(s)$. The inverse Laplace transform of $R(s)$ can be found from Table 1, leaving only the component $\hat{n}(s)/\hat{d}(s)$ to be handled by the partial fraction expansion. Thus, without loss of generality, we can assume that the degree of the numerator of $F(s)$ is less than that of the denominator. The first step in the partial fraction expansion is the factorization of the denominator polynomial:

$$F(s) = \frac{n(s)}{d(s)} = \frac{n(s)}{(s - p_1)^{\alpha_1} (s - p_2)^{\alpha_2} \cdots (s - p_m)^{\alpha_m}}$$

The quantities p_i , the zeros of the denominator $d(s)$ of $F(s)$, are known as the *poles* of $F(s)$, and the multiplicity of the pole p_i is the number of times α_i that it appears as a zero of $d(s)$. A pole of multiplicity 1 is called a *simple* pole. If all poles are simple, then

$$\begin{aligned} F(s) &= \frac{n(s)}{(s - p_1)(s - p_2) \cdots (s - p_m)} \\ &= \frac{k_1}{s - p_1} + \frac{k_2}{s - p_2} + \cdots + \frac{k_m}{s - p_m} \end{aligned}$$

where $k_i = [(s - p_i)F(s)]_{s=p_i}$.

The term k_i is the *residue* of $F(s)$ at the pole p_i . If $F(s)$ has a pole of multiplicity α_j at p_j , the partial fraction expansion takes the form

$$\begin{aligned} F(s) &= \frac{n(s)}{(s - p_j)^{\alpha_j} \hat{d}(s)} = \frac{k_{j1}}{s - p_j} \\ &\quad + \frac{k_{j2}}{(s - p_j)^2} + \cdots + \frac{k_{j\alpha_j}}{(s - p_j)^{\alpha_j}} + \frac{\hat{n}(s)}{\hat{d}(s)} \end{aligned}$$

where

$$k_{ji} = \left\{ \frac{1}{(\alpha_j - i)!} \frac{d^{\alpha_j - i}}{ds^{\alpha_j - i}} [(s - p_j)^{\alpha_j} F(s)] \right\} \Big|_{s=p_j}$$

Since the numerator and denominator of $F(s)$ are real polynomials in s , poles appear in complex conjugate pairs,

Table 1. Some Important Laplace Transforms

$f(t)$	$F(s) = \mathbf{L}(f(t))$
$\delta(t)$	1
$U(t)$	$\frac{1}{s}$
t^n	$n! \frac{1}{s^{n+1}} \quad n = 1, 2, \dots$
e^{-at}	$\frac{1}{s+a}$
$\sin \omega t$	$\frac{\omega}{s^2 + \omega^2}$
$\cos \omega t$	$\frac{s}{s^2 + \omega^2}$

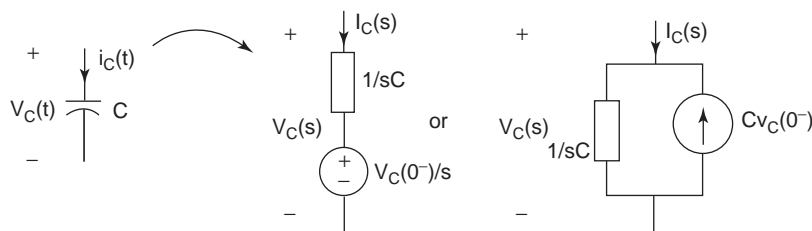


Figure 13. Transformation of a capacitor with initial voltage $v_C(0^-)$ into the frequency domain.

as do their residues. This allows the combination of any complex term in the expansion with its conjugate to give a real term.

The inverse Laplace transform of each of the terms in the partial fraction expansion is known:

$$\mathbf{L}^{-1}\left\{\frac{k_{j\alpha_j}}{(s-p_j)^{\alpha_j}}\right\} = k_{j\alpha_j} \frac{t^{\alpha_j-1}}{(\alpha_j-1)!} e^{p_j t}$$

In this way it is possible to find the inverse Laplace transform of any function consisting of the ratio of two polynomials in s by decomposing the function via the partial fraction expansion and taking the inverse Laplace transform of each of the constituent functions. This method relies fundamentally on the uniqueness and linearity properties of the Laplace transform. Clearly the method applies only to a restricted range of functions, those which can be expressed as the ratio of two polynomials in s . As will be seen, however, functions of this type are particularly important in circuit analysis, and so this is not a significant limitation.

3.3. Circuit Analysis

The first step in the Laplace transform analysis of a circuit is the transformation of the circuit from the time domain to the frequency domain. All branch voltages $v(t)$ and currents $i(t)$ that appear as variables in the differential equations describing the circuit will appear in the transformed equations as variables $V(s) = \mathbf{L}\{v(t)\}$ and $I(s) = \mathbf{L}\{i(t)\}$. Independent voltage and current sources are transformed from known functions of time $v_s(t)$ and $i_s(t)$ to known functions of frequency $V_s(s) = \mathbf{L}\{v_s(t)\}$ and $I_s(s) = \mathbf{L}\{i_s(t)\}$. A resistor is described in the time domain by the linear equation $v(t) = Ri(t)$ and so is defined in the transformed circuit by the relation $V(s) = RI(s)$. Similarly the linear equations describing all resistive two-ports (including ideal transformers, gyrators and controlled sources), and indeed resistive n -ports, are unchanged in the transformation from time domain to frequency domain. The

capacitor is defined in the time domain by the equation

$$i_C(t) = C \frac{dv_C(t)}{dt}$$

Applying the differentiation property of the Laplace transform yields the frequency-domain equation for the capacitor:

$$I_C(s) = sCV_C(s) - Cv_C(0^-)$$

Thus the capacitor C with initial voltage $v_C(0^-)$ appears in the transformed circuit as the parallel combination of the independent current source $Cv_C(0^-)$ and the linear element defined by the relation $V(s) = (1/sC)I(s)$. This second element can be regarded as a generalized resistance (known as an *impedance*) $1/sC$ and throughout the analysis in the frequency domain can be handled as if it were a resistance. Figure 13 shows the transformation of a capacitor from the time domain into the parallel combination of an impedance and an independent current source in the frequency domain or, by Thévenin's theorem, into the series combination of an impedance and an independent voltage source. In a similar manner, the inductor defined in the time domain by the relation

$$v_L(t) = L \frac{di_L(t)}{dt}$$

is defined in the frequency domain by the relation

$$V_L(s) = sLI_L(s) - Li_L(0^-)$$

Thus, as shown in Fig. 14, the inductor appears in the transformed circuit as the series combination of an impedance sL and voltage source $Li_L(0^-)$ or the parallel combination of the same impedance and current source $[i_L(0^-)]/s$. Note that once again this circuit transformation could have been obtained from Fig. 13 by application of the

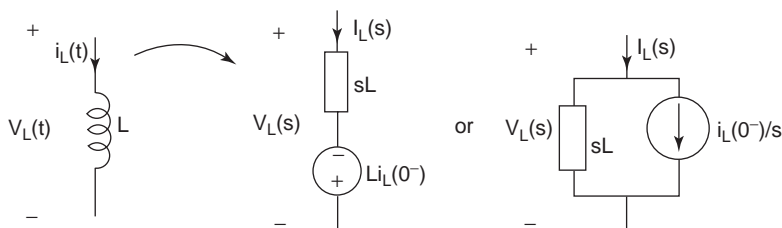


Figure 14. Transformation of an inductor with initial current $i_L(0^-)$ into the frequency domain.

principle of duality. Coupled inductors can be transformed in a similar manner.

When all the elements in the circuit have been transformed into the frequency domain, the first step of the analysis process is complete. The second step is to analyze the circuit in the frequency domain, employing any of a wide variety of techniques such as loop current analysis, node voltage analysis, modified nodal analysis, and sparse tableau analysis. The analysis of a circuit in the frequency domain is described in the article on frequency-domain circuit analysis, and also in most circuit theory textbooks, such as Refs. 3–5. The third step is then to transform the results of the analysis back to the time domain via the inverse Laplace transform.

Example 1. The circuit of Fig. 4 can be transformed into the Laplace transform domain, yielding the circuit of Fig. 15. Analysis in the frequency domain, followed by partial fraction expansion, yields the result that

$$V_C(s) = \frac{v_C(0^-)}{s + \frac{1}{RC}} + \frac{E}{s} \frac{1}{\left(s + \frac{1}{RC}\right)} = \frac{v_C(0^-)}{s + \frac{1}{RC}} + \frac{E}{s} - \frac{E}{s + \frac{1}{RC}}$$

The inverse Laplace transform is then applied to find

$$v_C(t) = v_C(0^-)e^{-t/RC} + E(1 - e^{-t/RC}) \text{ for } t \geq 0$$

which agrees with the time domain analysis performed earlier.

3.4. Laplace Transform Analysis of Distributed Circuits

Laplace transform techniques can also be applied to the analysis of distributed circuits. Consider the example of a transmission line modeled as in Fig. 16 by incremental series inductance L and resistance R and shunt capacitance C and conductance G , all per unit length. Applying Kirchhoff's laws and taking the limit of vanishing line length gives the telegrapher's equations

$$\begin{aligned} \frac{\partial i(x, t)}{\partial x} &= -Gv(x, t) - C \frac{\partial v(x, t)}{\partial t} \\ \frac{\partial v(x, t)}{\partial x} &= -Ri(x, t) - L \frac{\partial i(x, t)}{\partial t} \end{aligned}$$

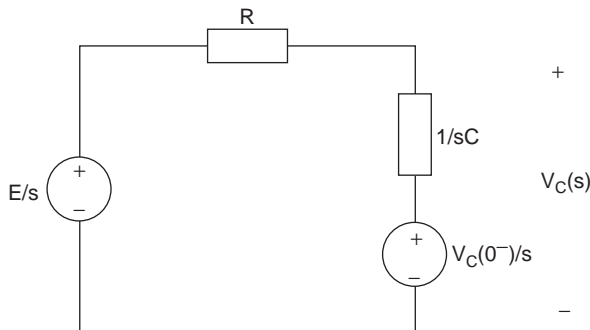


Figure 15. Laplace transform of the circuit of Figure 4.

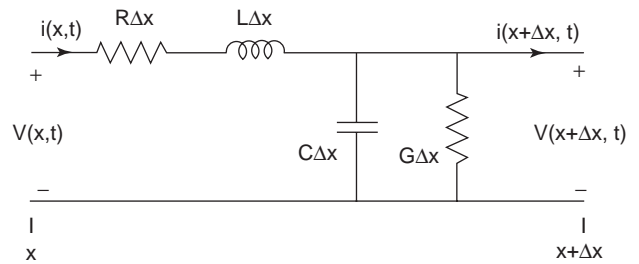


Figure 16. Basic model of a length Δx of transmission line.

The current and voltage now vary not only with time t but also with distance x along the line. The appearance of distance in this fashion, and also of the derivative with respect to distance, does not occur in lumped circuits.

The new parameter x can be shown explicitly in the definition of the Laplace transform:

$$\mathbf{L}[f(x, t)] = \int_0^\infty f(x, t)e^{-st} dt = F(x, s)$$

There is now a second differentiation property:

$$\mathbf{L}\left[\frac{\partial f(x, t)}{\partial x}\right] = \frac{\partial F(x, s)}{\partial x}$$

Then taking

$$I(x, s) = \mathbf{L}[i(x, t)]$$

$$V(x, s) = \mathbf{L}[v(x, t)]$$

the telegrapher's equations become

$$\begin{aligned} \frac{\partial I(x, s)}{\partial x} &= -GV(x, s) - sCV(x, s) + Cv(x, 0^-) \\ \frac{\partial V(x, s)}{\partial x} &= -RI(x, s) - sLI(x, s) + Li(x, 0^-) \end{aligned}$$

If, for simplicity, we assume zero initial voltage and current along the line, these equations can be solved for $V(x, s)$ and $I(x, s)$:

$$\begin{aligned} V(x, s) &= V^+(s)e^{-\gamma x} + V^-(s)e^{\gamma x} \\ \Rightarrow I(x, s) &= \frac{1}{Z_0} [V^+(s)e^{-\gamma x} - V^-(s)e^{\gamma x}] \end{aligned}$$

where $Z_0 = \sqrt{(R + sL)/(G + sC)}$, $\gamma = \sqrt{(R + sL)(G + sC)}$ and V^+ and V^- are as yet unknown constants of integration. Z_0 is called the characteristic impedance of the line, and γ is the propagation constant. If the line is lossless, $R = G = 0$, and so $Z_0 = \sqrt{L/C}$, which is purely real (generally denoted R_0) and $\gamma = s\sqrt{LC}$. We define $u = 1/\sqrt{LC}$, and so $\gamma = s/u$. (We shall shortly see the physical significance of this variable.)

Inserting typical terminations for a line of length L , consisting of the series combination of voltage source $V_0(s)$

and generator impedance Z_g at $x = 0$, and load impedance Z_L at $x = L$, we can solve these equations for V^+ and V^- to find

$$\frac{V^-}{V^+} e^{2\gamma L} = \frac{Z_L - Z_0}{Z_L + Z_0} = \Gamma_R$$

where Γ_R is the receiving end reflection coefficient, and in a similar manner we define the generating end reflection coefficient

$$\Gamma_g = \frac{Z_g - Z_0}{Z_g + Z_0}$$

We can substitute for V^+ and V^- to find the expressions for the voltage and current along the line in the frequency domain:

$$V(x, s) = \frac{Z_0 V_0}{Z_0 + Z_g} \left[\frac{e^{-\gamma x} + \Gamma_R e^{-\gamma(2L-x)}}{1 - \Gamma_R \Gamma_g e^{-2\gamma L}} \right]$$

$$I(x, s) = \frac{V_0}{Z_0 + Z_g} \left[\frac{e^{-\gamma x} - \Gamma_R e^{-\gamma(2L-x)}}{1 - \Gamma_R \Gamma_g e^{-2\gamma L}} \right]$$

In the important case of a lossless line, these equations can be rewritten as

$$V(x, s) = \frac{V_0 R_0}{R_0 + Z_g} \left[\frac{e^{-(sx/u)} + \Gamma_R e^{-s(2\tau - (x/u))}}{1 - \Gamma_R \Gamma_g e^{-2s\tau}} \right] \tag{11}$$

$$I(x, s) = \frac{V_0}{R_0 + Z_g} \left[\frac{e^{-(sx/u)} - \Gamma_R e^{-s(2\tau - (x/u))}}{1 - \Gamma_R \Gamma_g e^{-2s\tau}} \right]$$

where $\tau = L/u$ is the delay of the line. (Once again, we shall shortly see the physical significance of this variable).

We will now consider the solution of these equations in three cases of increasing complexity. It suffices to consider the voltage equation (11), since the current follows easily.

3.4.1. Matched Lossless Line. If the load impedance Z_L equals the characteristic impedance R_0 of the line, then $\Gamma_R = 0$ and Eq. (11) becomes

$$V(x, s) = \frac{V_0 R_0}{R_0 + Z_g} e^{-(sx/u)}$$

In the time domain, applying the time-shift property of the Laplace transform, we get

$$v(x, t) = \mathbf{L}^{-1}[V(x, s)] = f\left(t - \frac{x}{u}\right) U\left(t - \frac{x}{u}\right)$$

where $U(t)$ is the unit step function given by (1) and

$$f(t) = \mathbf{L}^{-1}\left[\frac{V_0 R_0}{R_0 + Z_g}\right]$$

The voltage at the generator end of the line, that is, at $x = 0$, is

$$\frac{V_0 R_0}{R_0 + Z_g}$$

which agrees with the result expected by voltage division. The voltage at any point x along the line is an undistorted

replica of the voltage at $x = 0$ delayed by the time interval x/u , where u is the velocity at which the waveform propagates along the line.

3.4.2. Lossless Line with Matched Source and Unmatched Load. If the lossless line is matched at the source end but unmatched at the load end (i.e., $\Gamma_g = 0$ and $\Gamma_R \neq 0$), the voltage in the frequency domain is given by

$$V(x, s) = \frac{V_0}{2} \left[e^{-(sx/u)} + \Gamma_R e^{-s(2\tau - (x/u))} \right]$$

The inverse Laplace transform gives the voltage in the time domain:

$$v(x, t) = f_1\left(t - \frac{x}{u}\right) U\left(t - \frac{x}{u}\right) + f_2\left(t - 2\tau + \frac{x}{u}\right) U\left(t - 2\tau + \frac{x}{u}\right) \tag{12}$$

where

$$\mathbf{L}^{-1}\left[\frac{V_0}{2}\right] = f_1(t) U(t)$$

and

$$\mathbf{L}^{-1}\left[\Gamma_R \frac{V_0}{2}\right] = f_2(t) U(t)$$

The voltage given by Eq. (12) is the sum of two terms. The first of these is a waveform that starts from the generator end of the line ($x = 0$) at $t = 0$ and travels along the line toward the load with velocity u . This waveform reached the load at time $L/u = \tau$. The second, or reflected, term originates at the load end of the line ($x = L$) at time $t = \tau$, and travels to the left with velocity u .

3.4.3. Lossless Line with Unmatched Source and Unmatched Load. The voltage equation (11) can be expanded to the form

$$V(x, s) = F(s) \sum_{n=0}^{\infty} \Gamma_R^n \Gamma_g^n e^{-s(2n\tau + (x/u))} + F(s) \sum_{n=0}^{\infty} \Gamma_R^{n+1} \Gamma_g^n e^{-s(2(n+1)\tau - (x/u))}$$

where

$$F(s) = \frac{V_0 R_0}{R_0 + Z_g}$$

Defining

$$F_1^{(n)}(s) = F(s) \Gamma_R^n \Gamma_g^n = \mathbf{L}\left[f_1^{(n)}(t) U(t)\right]$$

and

$$F_2^{(n)}(s) = F(s) \Gamma_R^{n+1} \Gamma_g^n = \mathbf{L}\left[f_2^{(n)}(t) U(t)\right]$$

we get

$$V(x, s) = \sum_{n=0}^{\infty} F_1^{(n)}(s)e^{-s(2n\tau + (x/u))} + \sum_{n=0}^{\infty} F_2^{(n)}(s)e^{-s(2(n+1)\tau + (x/u))}$$

Taking the inverse Laplace transform, we get the time-domain voltage

$$v(x, t) = \sum_{n=0}^{\infty} f_1^{(n)}\left(t - 2n\tau - \frac{x}{u}\right)U\left(t - 2n\tau - \frac{x}{u}\right) + \sum_{n=0}^{\infty} f_2^{(n)}\left(t - 2(n+1)\tau + \frac{x}{u}\right)U\left(t - 2(n+1)\tau + \frac{x}{u}\right)$$

Hence the voltage waveform consists of a sum of two types of terms. The first type has the form

$$f_1^{(n)}\left(t - 2n\tau - \frac{x}{u}\right)U\left(t - 2n\tau - \frac{x}{u}\right) \tag{13}$$

which represents a waveform traveling toward the load with velocity u . This expression is zero for $t < 2n\tau + (x/u)$. Since $0 \leq x \leq L$, $0 \leq x/u \leq \tau$, and so the term (13) is zero everywhere on the line if $t < 2n\tau$. Thus this term represents a waveform that starts at the generator end of the line at time $t = 2n\tau$ and travels to the load, reaching it at time $t = (2n + 1)\tau$.

The second type has the form

$$f_2^{(n)}\left(t - 2(n+1)\tau + \frac{x}{u}\right)U\left(t - 2(n+1)\tau + \frac{x}{u}\right)$$

which represents a waveform traveling to the left with velocity u . This expression is zero for $t < 2(n+1)\tau - (x/u)$, and is zero everywhere on the line if $t < 2(n+1)\tau - x/u$. Thus this term represents a waveform that starts at the load at time $t = (2n + 1)\tau$ and travels toward the generator end of the line, reaching it at time $t = (2n + 2)\tau$.

4. NATURAL RESPONSE AND ZERO-STATE RESPONSE

When converted into the frequency domain, a (lumped or distributed) circuit contains independent sources of two types. The first are the transformed versions of the independent sources from the time domain. These sources drive the circuit in the time domain, and are often termed the “inputs” to the circuit, borrowing a viewpoint from system theory. The second group of independent sources in the frequency-domain circuit are those that are introduced during the transformation of energy storage elements and account for the initial conditions in the circuit, specifically, the capacitor voltages and inductor currents at time $t = 0^-$. We will call these sources the “initial” condition generators, to distinguish them from those sources that represent the independent sources from the time domain. By superposition, the response of the circuit to these sources (by which we mean any current or voltage in the circuit, or any collection thereof) is the sum of two components: one due to the independent sources acting alone, with the initial condition generators removed, and the

other due to the initial condition generators acting alone, with the independent sources removed. Since these two components of the response arise from different mechanisms, it is often useful to treat them separately. The component of the response due to the independent sources, with the initial conditions set to zero, is called the *zero-state response*, and the component due to the initial conditions, with the independent sources set to zero, is the *natural or unforced response* (also called the *zero-input response*).

4.1. Natural Response and Natural Frequencies

We will consider first the natural response of a circuit. Application of any of the standard frequency-domain analysis techniques will yield a matrix equation of the form [3]

$$\mathbf{M}(s)\mathbf{X}(s) = \mathbf{U}(s)$$

where $\mathbf{M}(s)$ is a matrix each element of which is a polynomial in s ; $\mathbf{X}(s)$ is a vector containing some subset of the unknown branch voltages, branch currents, node voltages, and loop currents; and $\mathbf{U}(s)$ is a vector, each nonzero element of which is a linear combination of the initial condition generators. If the circuit has a unique solution, that solution is given by [2]

$$\mathbf{X}(s) = \mathbf{M}^{-1}(s)\mathbf{U}(s) = \frac{1}{\det(\mathbf{M}(s))} \text{Adj}(\mathbf{M}(s)) \cdot \mathbf{U}(s)$$

where the existence of a unique solution guarantees that the determinant $\det(\mathbf{M}(s))$ is not identically zero. We assume, unless otherwise stated, that all zeros p_1, p_2, \dots, p_m of $\det(\mathbf{M}(s))$ are simple. Each component $X_i(s)$ of the vector $\mathbf{X}(s)$ is the ratio of two polynomials in s , and so the partial fraction expansion can be applied to yield the expression

$$X_i(s) = \frac{k_1}{s - p_1} + \frac{k_2}{s - p_2} + \dots + \frac{k_m}{s - p_m}$$

The time-domain response $x_i(t)$ is therefore

$$x_i(t) = k_1e^{p_1t} + k_2e^{p_2t} + \dots + k_me^{p_mt}$$

for $t \geq 0$. [If some of the zeros of $\det(\mathbf{M}(s))$ have multiplicity greater than one, the time response will contain terms of the form $t^2e^{p_it}$.]

Clearly the zeros p_i of $\det(\mathbf{M}(s))$ play a crucial role in determining the natural response of the circuit. These quantities are known as the *natural frequencies* of the circuit. The number of natural frequencies in a circuit is less than or equal to the number of energy storage elements in the circuit. The contribution of each natural frequency to the natural response depends on its location in the complex plane. A natural frequency at zero contributes a constant term to the natural response. A real and positive natural frequency p_i contributes a term $k_ie^{p_it}$ that grows exponentially with time. A real and negative natural frequency p_i contributes a term $k_ie^{p_it}$ that decays exponentially with time. Complex natural frequencies occur in conjugate pairs, and their contributions add to make a

real contribution to the response waveform. If the natural frequencies in question lie on the imaginary axis at $\pm j\omega$, their composite contribution to the time response is of the form $k_i e^{j\omega t} + \bar{k}_i e^{-j\omega t} = 2|k_i| \cos(\omega t + \angle k_i)$, an oscillation of constant amplitude. If the complex natural frequencies lie in the right half-plane at $\alpha \pm j\omega$, their composite contribution is of the form $k_i e^{(\alpha + j\omega)t} + \bar{k}_i e^{(\alpha - j\omega)t} = 2|k_i| e^{\alpha t} \cos(\omega t + \angle k_i)$, an oscillation whose amplitude grows exponentially with time. Finally, if the complex natural frequencies lie in the left half-plane at $\alpha \pm j\omega$, their composite contribution is of the form $k_i e^{(\alpha + j\omega)t} + \bar{k}_i e^{(\alpha - j\omega)t} = 2|k_i| e^{\alpha t} \cos(\omega t + \angle k_i)$, an oscillation whose amplitude decays exponentially with time. (If some of the natural frequencies have multiplicity greater than one, their contribution to the time response will be more complicated, with polynomials times exponentials in place of exponentials, but can be handled by an extension of the preceding analysis.)

The preceding discussion leads to the important conclusion that if all natural frequencies of a circuit lie in the open left half-plane (i.e., if their real parts are less than 0), then for any set of initial conditions the natural or zero-input response of the circuit decays to zero as $t \rightarrow \infty$. This decay may be oscillatory, depending on the presence of complex natural frequencies. A circuit is said to be asymptotically stable or exponentially stable if all of its natural frequencies lie in the open left half-plane. If any natural frequency lies in the open right half-plane, then the initial conditions can cause certain currents and voltages to grow exponentially with time, which is clearly undesirable. Obviously in a real circuit this growth cannot continue indefinitely as the circuit elements will eventually cease to function, possibly in dramatic fashion. Also obvious is the fact that this behavior cannot occur in a circuit made up entirely of passive elements, since the exponential growth requires that energy be supplied to the circuit by an active element such as a controlled source or negative resistance.

While the natural frequencies determine the possible natural modes of behavior of a circuit, the actual response that will be observed in a circuit with zero input depends on the values of the initial conditions. Certain sets of initial conditions will excite one mode only, which means that all circuit variables will exhibit the same exponential or oscillatory behavior, but for most sets the response will be the combination of various modes. Also, not all modes can be observed in any given circuit variable—it may be that certain variables are not susceptible to the influence of one or more natural frequencies.

Example 2. To find the natural frequencies of the circuit of Fig. 17, the voltage source can be set to zero and the resulting circuit analyzed by any of the usual methods. In this case node voltage analysis is possible, yielding the matrix equation

$$\begin{pmatrix} \frac{1}{R_1} + sC_1 & 0 \\ -g_m & \frac{1}{R_2} + sC_2 \end{pmatrix} \begin{pmatrix} V_1(s) \\ V_2(s) \end{pmatrix} = \begin{pmatrix} C_1 v_1(0^-) \\ C_2 v_2(0^-) \end{pmatrix}$$

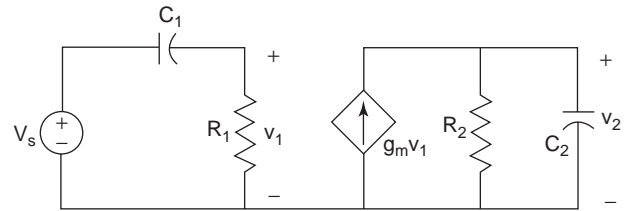


Figure 17. Circuit to be analyzed in Examples 2 and 3.

The natural frequencies are the values of s for which the determinant of the matrix in this equation is zero, and therefore equal $(-1)/R_1 C_1$ and $(-1)/R_2 C_2$. Solving explicitly for $V_1(s)$ and $V_2(s)$, we find that

$$V_1(s) = \frac{V_1(0^-)}{s + \frac{1}{R_1 C_1}} \quad \text{and} \quad V_2(s) = \frac{\frac{g_m}{C_2} V_1(0^-) + \frac{1}{C_1} V_2(0^-)}{\left(s + \frac{1}{R_1 C_1}\right) \left(s + \frac{1}{R_2 C_2}\right)}$$

Thus the voltage v_1 (natural or zero-input component) exhibits only the behavior controlled by the natural frequency at $(-1)/R_1 C_1$ and is unaffected by the natural frequency at $(-1)/R_2 C_2$.

4.2. The Zero-State Response and Transfer Functions

The zero-state response of a circuit is its response to one or more independent sources (inputs) with all initial capacitor voltages and inductor currents set to zero. It suffices to consider the response to a single input, since superposition can then be applied to calculate the response due to multiple inputs. Application of any of the standard frequency-domain analysis techniques to a single-input zero-state circuit will yield a matrix equation of the form

$$\mathbf{M}(s)\mathbf{X}(s) = \mathbf{U}(s)$$

where $\mathbf{M}(s)$ is a matrix, each element of which is a polynomial in s ; $\mathbf{X}(s)$ is a vector containing some subset of the unknown branch voltages, branch currents, node voltages, and loop currents; and $\mathbf{U}(s)$ is a vector, each nonzero element of which is a term involving the independent source, say, $V_s(s)$ (although the theory applies equally to the case where the input is a current source). It follows from linear algebra [2,3] that

$$X_i(s) = \frac{n(s)}{\det(\mathbf{M}(s))} V_s(s) = H(s) V_s(s) \quad (14)$$

where $n(s)$ is a polynomial in s and $\det(\mathbf{M}(s))$ is nonzero, by our standing assumption of unique solvability. Thus the zero-state response to a source $v_s(t)$ is obtained by multiplying its Laplace transform $V_s(s)$ by the appropriate function $H(s) = n(s)/\det(\mathbf{M}(s))$ and taking the inverse Laplace transform to return to the time domain. This function is known as a transfer function or network function. Note that the poles of a transfer function are zeros of $\det(\mathbf{M}(s))$ and are therefore natural frequencies of the circuit.

However, not all natural frequencies need show up as poles of a given transfer function, due to cancellations with numerator terms.

Once again we see that the natural frequencies play a crucial role in determining the response of the circuit—even, as in this case, when the initial conditions are zero. From (14) the poles of $X_i(s)$ will be some subset (determined by numerator cancellations) of the poles of $V_s(s)$ and the natural frequencies. Therefore, $x_i(t)$ will in general, contain terms related to the input together with exponential, constant, or oscillatory terms governed once again by the natural frequencies. If the circuit is asymptotically stable, the contributions governed by the natural frequencies will die away, leaving only the component governed by the input.

The simplest application of Eq. (14) occurs when $V_s(s) = 1$, that is, when the independent source $v_s(t)$ is the delta function or impulse function defined by (10). Although this function is physically unrealizable, it proves extremely useful in circuit and system analysis. When $v_s(t) = \delta(t)$, then $X_i(s) = H(s)\mathbf{L}\{\delta(t)\} = H(s)$, and so the zero-state response is $x_i(t) = h(t) = \mathbf{L}^{-1}\{H(s)\}$. The zero-state response to an impulse function is known as the *impulse response*, and so we have found that the Laplace transform of the impulse response equals the transfer function. The expression

$$X_i(s) = H(s)\mathbf{L}\{v_s(t)\}$$

giving the frequency-domain response of the system with transfer function $H(s)$ to an input $v_s(t)$ can be expressed in the time domain as

$$x_i(t) = h(t) * v_s(t) = \int_{0^-}^{t^+} h(t - \tau)v_s(\tau)d\tau$$

where $h(t) = \mathbf{L}^{-1}\{H(s)\}$ is the impulse response and the asterisk $*$ is the convolution operator [3,6].

If the input is the unit step function $U(t)$, which has Laplace transform $1/s$, that is, $X_i(s) = H(s) \cdot \mathbf{L}\{u(t)\} = H(s)/s$, and so the step response is $x_i(t) = \mathbf{L}^{-1}\{H(s)/s\}$. It is easy to see that the impulse response is the derivative of the step response.

Example 3. The transfer function $V_2(s)/V_s(s)$ of the circuit of Fig. 17 is

$$\begin{aligned} H(s) &= \frac{\frac{g_m}{C_2}}{\left(s + \frac{1}{R_1 C_1}\right)\left(s + \frac{1}{R_2 C_2}\right)} \\ &= \frac{\frac{g_m}{C_2}}{R_2 C_2 - R_1 C_1} \left[\frac{R_2 C_2}{\left(s + \frac{1}{R_1 C_1}\right)} - \frac{R_1 C_1}{\left(s + \frac{1}{R_2 C_2}\right)} \right] \end{aligned}$$

and so the impulse response is

$$\begin{aligned} h(t) &= \frac{g_m R_2}{R_2 C_2 - R_1 C_1} e^{-t/R_1 C_1} \\ &\quad - \frac{g_m R_1 C_1 / C_2}{R_2 C_2 - R_1 C_1} e^{-t/R_2 C_2} \text{ for } t \geq 0 \end{aligned}$$

The step response is

$$\begin{aligned} \mathbf{L}^{-1} \left\{ \frac{\frac{g_m}{C_2}}{\left(s + \frac{1}{R_1 C_1}\right)\left(s + \frac{1}{R_2 C_2}\right)} \right\} \\ = \frac{g_m R_1 C_1 R_2}{R_2 C_2 - R_1 C_1} \left[-e^{-t/R_1 C_1} + e^{-t/R_2 C_2} \right] \text{ for } t \geq 0 \end{aligned}$$

Note the exponential modes corresponding to the natural frequencies in both the step response and the impulse response. Note also that the impulse response is the derivative of the step response.

5. FOURIER TRANSFORM CIRCUIT ANALYSIS

The power of the Laplace transform in finding the transient and steady-state response of a circuit, the variety of source waveforms that it can handle and its ability to accommodate initial conditions make it the method of choice in transient circuit analysis. Despite these advantages, another transform, closely related to the Laplace transform, is preferred in certain situations. This is the Fourier transform [4–6], named after the French mathematician Jean Baptiste Joseph Fourier (1768–1830). The close relationship between the Fourier transform of a signal and the frequency content of that signal make it particularly useful in applications such as communications and signal processing where this frequency content is of paramount importance. However, the Fourier transform is defined for a smaller class of source waveforms than the Laplace transform, and it cannot handle initial conditions. The latter condition in particular makes it poorly suited to transient circuit analysis and so we will merely give a brief discussion of its properties here, with the intention of (1) explaining why it is unsuited to transient circuit analysis and (2) providing a link to other forms of transient circuit analysis for circuits such as filters that are more usually handled using Fourier analysis.

The Fourier transform is closely related to the Fourier series [4–6], in which a periodic function with period T is decomposed into the weighted sum of sinusoids whose angular frequencies are integer multiples of $2\pi/T$. By superposition, the response of a circuit to a periodic function could be obtained by decomposing the function into the sum of sinusoids, finding the response to each of these sinusoids via phasor analysis, and summing these responses to find the overall response. The main disadvantage to this Fourier series method of analysis is that many source waveforms of interest are not periodic, and since the

method is based on phasor analysis, it finds only the steady-state component of the response. The fundamental idea underlying this method, however, namely, the idea of a sum of input sinusoids being processed (i.e., altered in magnitude and phase) in different ways by a circuit and then added to form the response, is a very useful one and underlies the more general Fourier transform analysis.

The Fourier transform is a generalization of the Fourier series to accommodate nonperiodic functions. A nonperiodic function can be viewed as the limit of a periodic function as the period T tends to infinity. The Fourier series of this periodic function consists of weighted sinusoids spaced in frequency at integer multiples of $2\pi/T$. As T tends to infinity, the separation of these sinusoidal frequency components tends to zero, and in the limit we have the nonperiodic function represented by a continuum or spectrum of sinusoidal components. This spectrum of sinusoidal components constitutes the Fourier transform of the function. The Fourier transform of a signal $f(t)$ is found, as in the preceding discussion, by taking the limit of the expression for the Fourier series of a periodic function as the period tends to infinity, which turns out to be

$$F(j\omega) = \mathbf{F}\{f(t)\} = \int_{-\infty}^{\infty} f(t)e^{-j\omega t} dt \tag{15}$$

and exists if the integral in (15) converges. Once again we say that the Fourier transform converts a function from the time domain into the frequency domain, with $F(j\omega)$ indicating the frequency content of the signal at frequency ω . If $f(t) = 0$ for $t < 0$ and the integral shown above converges, the Fourier transform of f is just the Laplace transform with $j\omega$ substituted for s . Given $F(j\omega)$, the function $f(t)$ such that $F(j\omega) = \mathbf{F}\{f(t)\}$ is found by application of the inverse Fourier transform

$$f(t) = \mathbf{F}^{-1}\{F(j\omega)\} = \frac{1}{2\pi} \int_{-\infty}^{\infty} F(j\omega)e^{j\omega t} d\omega$$

One important feature of the Fourier transform is the differentiation property, which states that differentiation in the time domain is equivalent to multiplication by $j\omega$ in the frequency domain. Thus the Fourier transform can, like the Laplace transform, be used to transform a system of differential equations in the time domain to a system of algebraic equations in the frequency domain.

In Fourier transform analysis a circuit is transformed into the frequency domain by replacing all independent sources by their Fourier transforms, replacing each inductor L by an impedance $j\omega L$ (and replacing any time-domain coupling M between inductors by the frequency-domain coupling $j\omega M$), replacing each capacitor C by an impedance $1/j\omega C$ and leaving resistive components unchanged. Note the lack of any initial condition generators—this is a consequence of the fact that the lower limit of integration in the definition of the Fourier transform is $-\infty$ rather than 0^- . Analysis in the frequency domain proceeds as described in the article on frequency-domain analysis or in Refs. 4 and 5, using the standard tools, and

the frequency-domain response is converted back to the time domain by application of the inverse Fourier transform. Once again there is a transfer function—in this case a function of frequency $H(j\omega)$ —relating input and output in the frequency domain. Note that the response obtained through Fourier transform analysis is the zero-state response only, since the method contains no provision for handling initial conditions.

Given a circuit with input $\sin(\omega_0 t)$ and transfer function $H(j\omega)$ [which is in general complex and, for the circuits in which we are interested, has the property that $H(-j\omega)$ is the complex conjugate of $H(j\omega)$], the output is obtained by taking the inverse Fourier transform of $H(j\omega) \cdot \mathbf{F}\{\sin(\omega_0 t)\}$, which turns out to be $|H(j\omega_0)| \sin(\omega_0 t + \angle H(j\omega_0))$. In other words, the sinusoidal input appears at the output as a sinusoid of the same frequency, with amplitude multiplied by the magnitude of the transfer function at that frequency and phase incremented by the phase of the transfer function at that frequency. If the input to the circuit is more general, it can be viewed as the finite or infinite sum of sinusoids, which will be altered in magnitude and phase by the action of the circuit and then recombined to form the output of the circuit. The magnitude and phase of the transfer function will generally vary with frequency, and when plotted against frequency are called the *amplitude* (or *magnitude*) *response* and *phase response* plots.

Frequency-selective circuits that pass certain ranges of frequencies from input to output while blocking other ranges are known as *filters* [7]. For example, an ideal low-pass filter would pass to the output all frequency components of its input up to a certain cutoff frequency, and pass no higher frequency components. This ideal lowpass filter cannot be realized and is therefore approximated by a variety of functions such as the Butterworth and Chebyshev approximations. Figure 18 plots the amplitude response of the ideal lowpass filter with cutoff frequency at 1 rad/s, together with the amplitude responses of the normalized Butterworth filters of orders 2,3,4,5. The amplitude response of each of these Butterworth filters is 0.7071 or -3 dB at $\omega = 1$ rad/s, which is to say that their 3 dB bandwidth is 1 rad/s.

In a communication system designed to transmit pulses, the step response of a filter is crucial. Too slow a risetime leads to neighboring pulses in a pulsetrain being smeared over one another, rendering them indistinguishable at the output. Too high an overshoot can drive circuit elements into saturation. The step response of a filter can be found by Fourier transform methods, by taking the inverse Fourier transform of the function $H(j\omega)\mathbf{F}\{u(t)\}$, but there is in general no reason to prefer the Fourier transform over the Laplace transform in this situation, and it is usual to take instead the inverse Laplace transform of the function $H(s)\mathbf{L}\{u(t)\}$. For example, the normalised third order Butterworth lowpass filter has transfer function $H(s) = 1/(s^3 + 2s^2 + 2s + 1)$, and so its step response is $\mathbf{L}^{-1}\{1/[s(s^3 + 2s^2 + 2s + 1)]\}$, which can be found by the partial fraction decomposition to be

$$1 - e^{-t} - \frac{2}{\sqrt{3}}e^{-t/2} \sin \frac{\sqrt{3}}{2}t \quad \text{for } t > 0$$

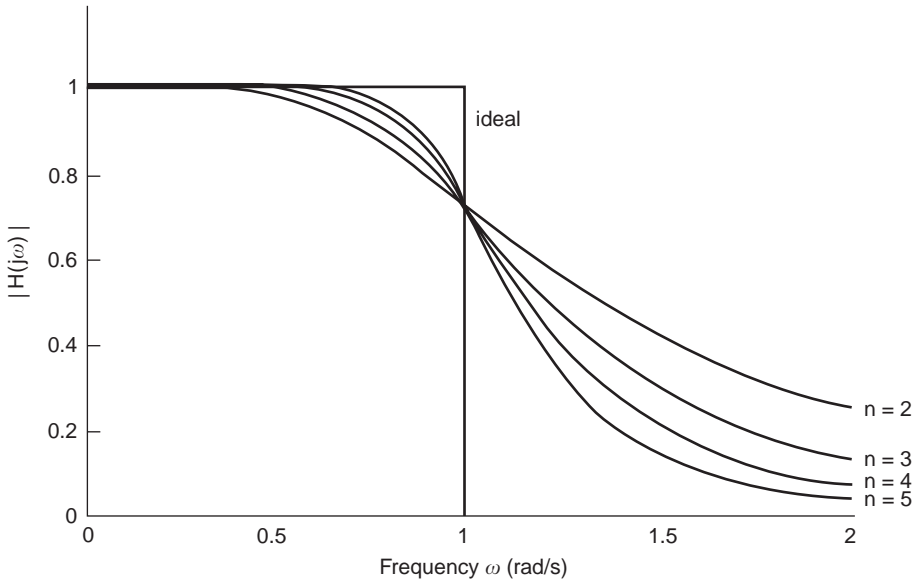


Figure 18. Amplitude response of the ideal lowpass filter with cutoff frequency at 1 rad/s, together with the amplitude responses of the normalized Butterworth filters of orders $n=2, 3, 4, 5$. Note that the approximation more closely matches the ideal as the order of the filter increases.

Figure 19 plots the step response of the normalised Butterworth filters of orders 2,3,4,5, as obtained by application of the Laplace transform. It can be seen that as the order increases (and the amplitude response more closely approximates the ideal) the overshoot, settling time and delay time of the filters all increase, but the risetime is approximately constant.

The procedure outlined above can be used to find the exact step response of a filter, allowing a designer to compare the suitability of various filters in pulse transmission applications. Designers should also have an intuitive understanding of the relationship between amplitude response and transient response of a filter. A lowpass filter allows low frequencies to pass to the output, but blocks high frequencies. Thus when the input is a step

function, the output will preserve the steady-state constant behavior of the input, but will act to block the high frequencies involved in the transition from 0 to 1. This can be seen in Fig. 19, where the high-order filters that are most effective at blocking high frequencies are least effective in capturing the discontinuity in the input. We now recognize the RC circuit of Fig. 4, with the output voltage taken across the capacitor, as a lowpass filter. If the output voltage were taken across the resistor, we would have a highpass filter whose step response captures the initial discontinuity in the step but then falls away to zero due to its inability to pass DC. Readers interested in a more detailed discussion of the relationship between frequency response and transient response of filters are referred to Refs. 1 and 7.

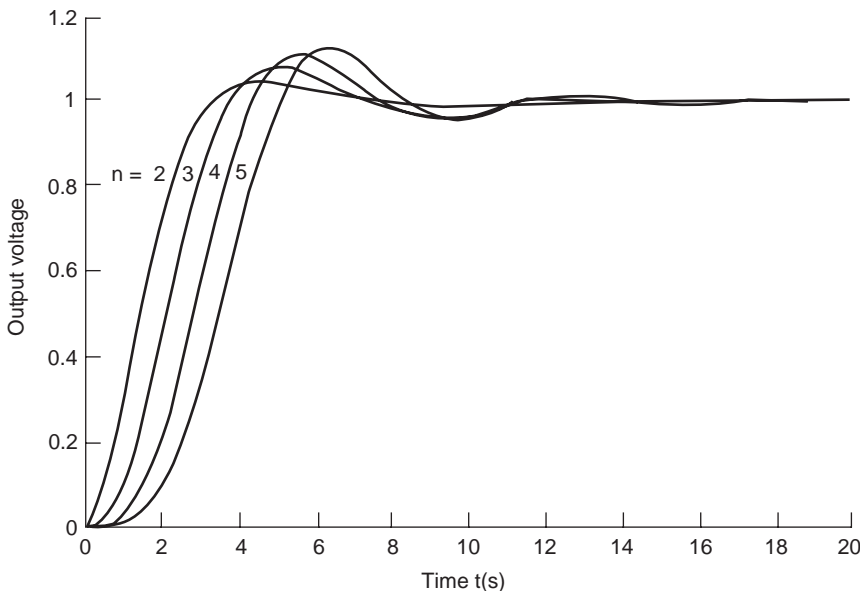


Figure 19. Step response of the normalized Butterworth filters of orders $n=2, 3, 4, 5$.

BIBLIOGRAPHY

1. F. F. Kuo, *Network Analysis and Synthesis*, 2nd ed., Wiley, New York, 1966.
2. E. Kreyszig, *Advanced Engineering Mathematics*, 6th ed., Wiley, New York, 1988.
3. L. O. Chua, C. A. Desoer, and E. S. Kuh, *Linear and Nonlinear Circuits*, McGraw-Hill, New York, 1987.
4. R. C. Dorf and J. A. Svoboda, *Introduction to Electric Circuits*, 3rd ed., Wiley, New York, 1996.
5. J. W. Nilsson and S. A. Riedel, *Electric Circuits*, 5th ed., Addison-Wesley, Reading, MA, 1996.
6. A. V. Oppenheim, A. S. Willsky, and I. T. Young, *Signals and Systems*, Prentice-Hall, London, 1983.
7. L. P. Huelsman, *Active and Passive Analog Filter Design*, McGraw-Hill, Singapore, 1993.

TRANSMISSION LINE MATRIX (TLM) METHOD

CHRISTOS CHRISTOPOULOS
 Director, George Green Institute
 for Electromagnetics Research
 University of Nottingham,
 Nottingham, United Kingdom

1. HISTORICAL BACKGROUND

The transmission-line modeling or matrix method, commonly referred by the acronym TLM, belongs to the class of differential equation methods and it is best known in its implementation in the time domain (TD-TLM). Implementations in the frequency domain are also available, but the method is known primarily as a time-domain method. It models electromagnetic field phenomena by analogy to pulse propagation in networks of transmission lines—hence its name. The idea of using circuits to model fields is not a new one. The foundation work in this area was done some time ago [1–3], but the difficulty at the time of solving such large networks precluded any useful implementation. This had to wait the advent of modern digital computers and the work of John and Beurle in 1971 [4], which set the scene for the rapid development of TLM into a versatile and general tool for EM simulation. The first developments were for models in two dimensions where an intuitive derivation of suitable network topologies is straightforward. The first three-dimensional structure appeared in 1975 [5]. There followed a period of development to obtain a circuit structure with good accuracy, efficiency, and versatility as described by Hofer [6]. The circuit structure (TLM node), which is the workhorse of TLM today, is described as the symmetric condensed node (SCN) and was developed in 1985 [7]. This marks the year when TLM entered its period of maturity. Many developments followed thereafter both improving the basic SCN and introducing complementary techniques that enhanced the power

of TLM. These are described in more detail in the following sections. More details of the TLM technique may be found in a large number of journal papers and in a number of texts that may be consulted for a fuller explanation of TLM and its applications [8–10]. The next section introduces the basics of TLM in a manner that should be accessible to all before more complex issues are addressed.

2. BASIC CONCEPTS

A basic introduction to the idea of TLM can proceed from an example of propagation in a transmission line and of one-dimensional field propagation. For a typical transmission line, as shown by two segments in Fig. 1, the differential equation describing the evolution of the current in space and in time is

$$\frac{\partial^2 i}{\partial x^2} = \frac{LC}{(\Delta x)^2} \frac{\partial^2 i}{\partial t^2} + \frac{GL}{(\Delta x)^2} \frac{\partial i}{\partial t} \quad (1)$$

where L and C are the inductance and capacitance, respectively, for a segment of the line of length Δx and G represents line losses.

In a similar way one can derive an equation for the current density j in one-dimensional field propagation

$$\frac{\partial^2 j}{\partial x^2} = \mu\epsilon \frac{\partial^2 j}{\partial t^2} + \mu\sigma \frac{\partial j}{\partial t} \quad (2)$$

where μ , ϵ , and σ respectively are the magnetic permeability, electric permittivity, and electrical conductivity of the medium.

One can see that Eq. (1) for the circuit and (2) for the field have the same structure. This isomorphism between the two equations means that field behavior may be understood by reference to circuit behavior. All that needs to be done is to establish appropriate circuit topologies in two and three dimensions and a formal equivalence between field and circuit quantities. This is possible to do. For the case of the one-dimensional example shown here, the equivalence is shown in Table 1.

Inspection of Eq. (2) shows that the two terms on the right-hand side represent wavelike behavior and diffusionlike behavior, respectively. By minimizing the wave term relative to the diffusion term, the models described

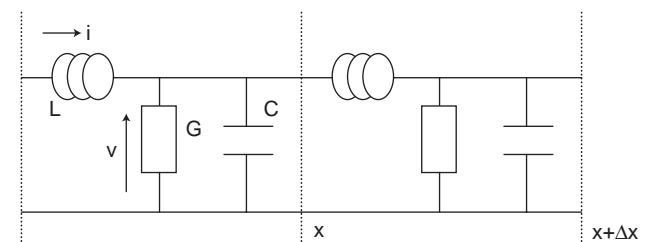


Figure 1. A simple one-dimensional transmission-line network to illustrate circuit-field analogies.

Table 1. Equivalence between Circuit and Field Quantities

Circuit	EM Field
I	j
$L/\Delta x$	μ
$C/\Delta x$	ϵ
$1/R \Delta x$	σ

thus may be used to study diffusion phenomena such as thermal conduction [9].

The lumped circuit shown in Fig. 1 can be replaced by transmission-line (TL) segments. Hence, in essence, in TLM models the field problem is reduced to lumped circuit models (space discretization), which in turn are reduced to TL models (time discretization). The art in TLM modeling is to devise TL interconnect topologies, in what are referred to as “nodes,” with each node describing a small block of space of dimensions $\Delta x \Delta y \Delta z$, such as there is an exact equivalence between the voltages and currents in each node and electric and magnetic fields. The TLM node is the equivalent of the computational element or molecule in other methods much like the Yee cell in FDTD.

A schematic arrangement in two dimensions is shown in Fig. 2a. Here, a mesh of transmission lines is shown, each line in the diagram representing a TL, namely, a line and its return conductor (not shown). One node is shown highlighted by a broken line. If a voltage pulse

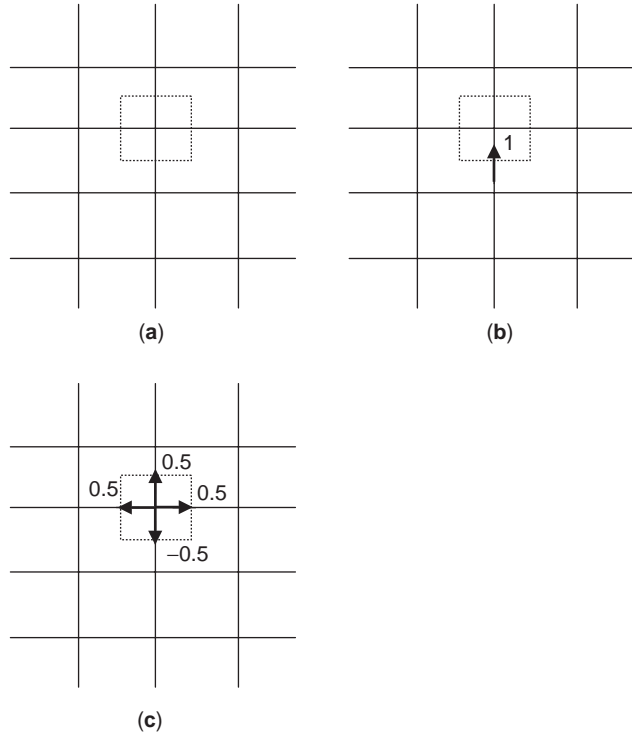


Figure 2. Schematic of a 2D TLM mesh: (a) 2D mesh with one node marked out; (b) impulse excitation at one port; (c) output after the first scattering event.

of magnitude 1 V is incident as shown in Fig. 2b, then this pulse will scatter at the node. If the TL characteristic impedance is Z , then at the node the pulse encounters three TLs in parallel (characteristic impedance $Z/3$) and scatters at this discontinuity with a reflection coefficient -0.5 and a transmission coefficient 0.5 . The scattered pulses are as shown in Fig. 2c. The reflected pulse of -0.5 V combines with the incident pulse of 1 V so that in total the pulse on this TL has a magnitude of 0.5 V. As a result of the scattering, a secondary isotropic wavefront is formed at the node in accordance with Huygens’ principle [11]. TLM can thus be viewed as a discrete implementation of the Huygens principle [12]. After the initial scattering, pulses propagate to adjacent nodes and the process repeats. The TLM algorithm consists of the process of “scattering” at each node; “connection,” that is, the exchange of pulses between nearest neighbors; followed by another “scattering”; and so on. Figure 3 illustrates the results of scattering and connection at the first two timesteps following the isotropic excitation of one node.

For TM modes the basic TLM node in two dimensions (2D) is described as a “shunt” node and is shown in Fig. 4. The dual of this node for TE modes is described as a “series” node. As an illustration, the scattering process in a shunt node is described below:

In order to proceed for the node shown in Fig. 4, we assume that four incident pulses travel toward the node at timestep k . These are labeled as

$${}_k V_j^i \quad j = 1, 2, 3, 4$$

where the superscript “i” stands for incident pulse (traveling toward the center of the node). We also assume that the characteristic impedance of each line segment is Z_{TL} . For each of the four line segments, a Thevenin equivalent circuit is derived and therefore each node is now represented as in Fig. 5. The total voltage at the center of the node can then be obtained directly:

$${}_k V_z = 0.5({}_k V_1^i + {}_k V_2^i + {}_k V_3^i + {}_k V_4^i) \quad (3)$$

The electric field component E_z and magnetic field components H_x, H_y are then directly obtained:

$${}_k E_z = -0.5 \frac{({}_k V_1^i + {}_k V_2^i + {}_k V_3^i + {}_k V_4^i)}{\Delta z} \quad (4)$$

$${}_k H_x = \frac{{}_k V_3^i - {}_k V_1^i}{Z_{TL} \Delta x}, \quad {}_k H_y = \frac{{}_k V_2^i - {}_k V_4^i}{Z_{TL} \Delta x} \quad (5)$$

Scattering is directly implemented as follows

$${}_k V_1^r = {}_k V_z - {}_k V_1^i = 0.5(-{}_k V_1^i + {}_k V_2^i + {}_k V_3^i + {}_k V_4^i) \quad (6)$$

and similarly for the other reflected components. These expressions can be put into a matrix form

$${}_k \mathbf{V}^r = \mathbf{S}_k \mathbf{V}^i \quad (7)$$

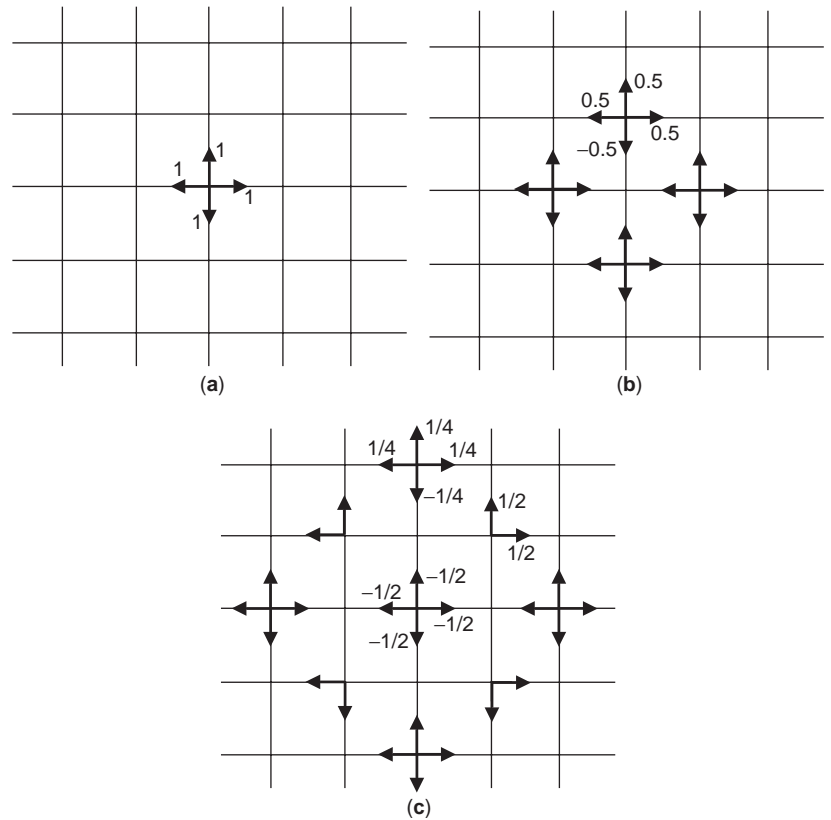


Figure 3. Scattering in a 2D TLM mesh: (a) symmetric excitation at one node; (b) output after the first timestep; (c) output after the second timestep.

where S is the scattering matrix, which for the case of the shunt node shown here is given by

$$S = 0.5 \begin{bmatrix} -1 & 1 & 1 & 1 \\ 1 & -1 & 1 & 1 \\ 1 & 1 & -1 & 1 \\ 1 & 1 & 1 & -1 \end{bmatrix} \quad (8)$$

Equations (7) and (8) show the process of scattering at each node. Scattered pulses are passed on to the adjacent ports of neighboring nodes to form the new incident voltages at timestep $k + 1$ in a process described as “connection.” This is expressed schematically as

$${}_{k+1}V^i = C_k V^r \quad (9)$$

where C is described as the “connection” matrix. The TLM algorithm consists of the repetition at each timestep of the processes of scattering and connection at each node with appropriate modifications to account for initial and boundary conditions. The same procedure applies to all TLM schemes, including those in three dimensions, but the form of the scattering matrix in (8) is different. It will be seen from this basic description of TLM that it is a

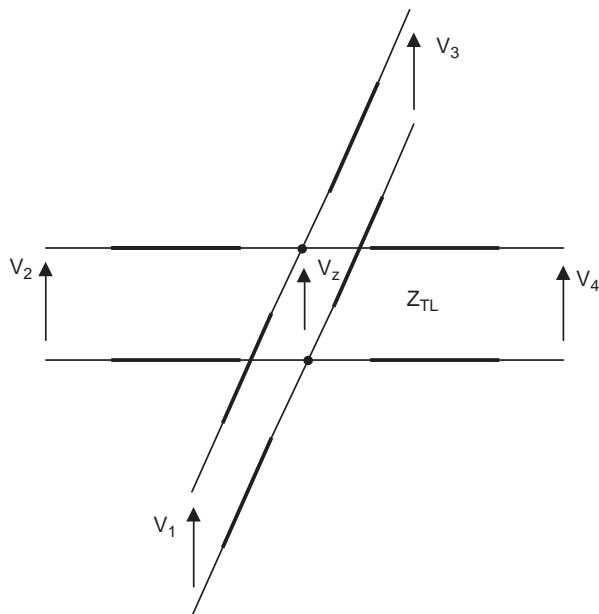


Figure 4. The shunt 2D TLM node for TM modes.

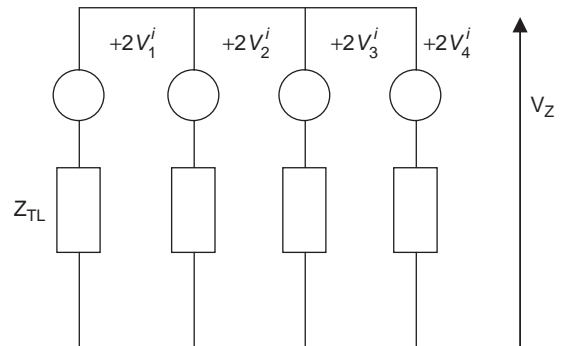


Figure 5. The Thevenin equivalent circuit of the shunt node.

scattering algorithm—energy goes in at each node (incident pulses) and comes out (reflected pulses). The scattering process is lossless (S is unitary). Because we have an exact solution of a passive network, unconditional stability is ensured. Accuracy is good as long as at least 10 segments per wavelength are used.

Several modifications can be made to this basic scheme to extend the applicability of the model in Fig. 4. Foremost among them is the inclusion of stubs to allow for the modeling of inhomogeneous lossy materials. A suitable node is shown in Fig. 6, where two stubs are included: an infinitely long stub (conductance G_s) and an open-circuit stub (admittance Y_s). This node can model TM propagation in a medium of relative dielectric constant ϵ_r and electrical conductivity σ . The choice of parameters is as follows:

$$u_{\text{TL}} = \frac{\Delta x}{\Delta t} = \sqrt{2} \frac{1}{\sqrt{\mu_0 \epsilon_0}}, \quad Z_{\text{TL}} = \sqrt{2} \sqrt{\frac{\mu_0}{\epsilon_0}} \quad (10)$$

$$Y_s = 4 \frac{(\epsilon_r - 1)}{Z_{\text{TL}}}, \quad G_s = \sigma \Delta x \quad (11)$$

In this case the scattering matrix is given by

$$S = \frac{1}{\hat{Y}} \begin{bmatrix} 2 - \hat{Y} & 2 & 2 & 2 & 2\hat{Y}_s \\ 2 & 2 - \hat{Y} & 2 & 2 & 2\hat{Y}_s \\ 2 & 2 & 2 - \hat{Y} & 2 & 2\hat{Y}_s \\ 2 & 2 & 2 & 2 - \hat{Y} & 2\hat{Y}_s \\ 2 & 2 & 2 & 2 & 2\hat{Y}_s - \hat{Y} \end{bmatrix} \quad (12)$$

where

$$\hat{Y} = 4 + \hat{Y}_s + \hat{G}_s, \quad \hat{Y}_s = Y_s Z_{\text{TL}}, \quad \hat{G}_s = G_s Z_{\text{TL}} \quad (13)$$

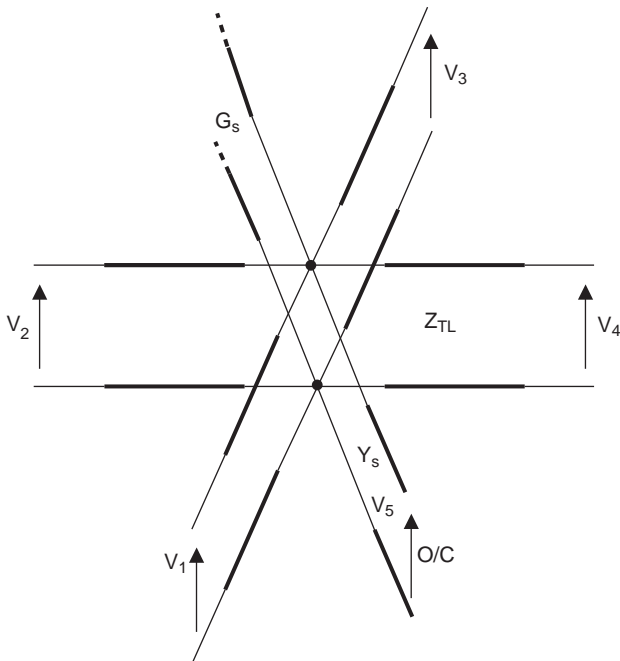


Figure 6. The shunt node with capacitive and lossy stubs added.

The inclusion of stubs permits the development of a model where all linklines have the same (free-space) parameters, hence ensuring the same timestep (synchronism) in the entire mesh. Stubs add capacitance to account for the presence of dielectric materials other than free space. Similar procedures apply to the dual node (series node). More detailed information may be found in the references already cited.

3. TLM IN THREE DIMENSIONS

In the previous section the rudiments of TLM were presented with reference to simple two-dimensional structures so that the basic modeling philosophy could be explained in simple physical terms. In this section the model is extended to three dimensions (3Ds) by presenting the *symmetric condensed node* (SCN), which is extensively used in 3D TLM models.

The structure best suited to general 3D models is the SCN described by Johns [7] and shown in Fig. 7. In this figure the traditional labeling of each port is shown (numbers 1–12) alongside an alternative labeling scheme introduced latter. This node describes the properties of EM propagation in a cuboidal block of space $\Delta x \Delta y \Delta z$. In a regular SCN, $\Delta x = \Delta y = \Delta z$. But with the addition of stubs, this restriction can be removed to form a more flexible structure for general modeling. For simplicity, the regular SCN is discussed first, which results in a uniform mesh.

At each of the six faces of the cube there are two ports polarized at 90° to each other to account for all possible wave polarizations. In total, therefore, there are 12 ports and the scattering matrix is a 12×12 . It is a sparse matrix, and its elements, which are nonzero, can be identified by physical intuition or by formal methods. The value of each element can be readily obtained by enforcing circuitual laws, charge, and energy conservation

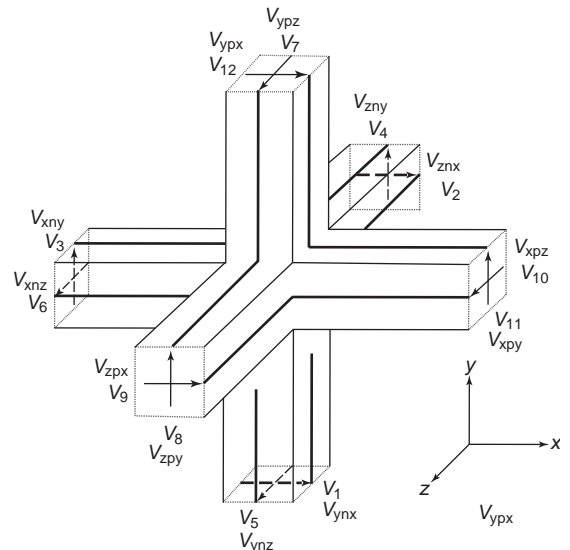


Figure 7. The three-dimensional symmetric condensed node (SCN).

(the scattering matrix must be unitary). A detailed discussion may be found in Refs. 7 and 9. For the stubless SCN, S is given by

$$S = 0.5 \begin{bmatrix} 0 & 1 & 1 & 0 & 0 & 0 & 0 & 0 & 1 & 0 & -1 & 0 \\ 1 & 0 & 0 & 0 & 0 & 1 & 0 & 0 & 0 & -1 & 0 & 1 \\ 1 & 0 & 0 & 1 & 0 & 0 & 0 & 1 & 0 & 0 & 0 & -1 \\ 0 & 0 & 1 & 0 & 1 & 0 & -1 & 0 & 0 & 0 & 1 & 0 \\ 0 & 0 & 0 & 1 & 0 & 1 & 0 & -1 & 0 & 1 & 0 & 0 \\ 0 & 1 & 0 & 0 & 1 & 0 & 1 & 0 & -1 & 0 & 0 & 0 \\ 0 & 0 & 0 & -1 & 0 & 1 & 0 & 1 & 0 & 1 & 0 & 0 \\ 0 & 0 & 1 & 0 & -1 & 0 & 1 & 0 & 0 & 0 & 1 & 0 \\ 1 & 0 & 0 & 0 & 0 & -1 & 0 & 0 & 0 & 1 & 0 & 1 \\ 0 & -1 & 0 & 0 & 1 & 0 & 1 & 0 & 1 & 0 & 0 & 0 \\ -1 & 0 & 0 & 1 & 0 & 0 & 0 & 1 & 0 & 0 & 0 & 1 \\ 0 & 1 & -1 & 0 & 0 & 0 & 0 & 0 & 1 & 0 & 1 & 0 \end{bmatrix} \quad (14)$$

It will be seen from (this matrix) that the scattering process is particularly simple, amounting to a simple averaging of four incident voltage pulses to obtain each scattered (reflected) pulse. There is no need for matrix inversion or matrix manipulation of any kind. The 3D TLM algorithm is then an implementation of the scheme described for 2D format in connection with Eqs. (7) and (9), where the scattering matrix is as given by (14). The connection matrix C is again very simple, codifying information for each node and its nearest ports in each coordinate direction. The correspondence between field and circuit quantities is again, as in the case of the 2D node, straightforward.

Fields may be calculated at the center of the node or at the boundaries between nodes. As an illustration the electric field component E_x at the center of the node is associated with port generating voltages in the x direction and is obtained as follows:

$$E_x = -\frac{V_x}{tax} = -\frac{V_1^i + V_2^i + V_9^i + V_{12}^i}{2tax} \quad (15)$$

Similarly, for the magnetic field component in the same direction, we obtain

$$H_x = \frac{I_x}{tax} = \frac{V_4^i + V_7^i - V_5^i - V_8^i}{2Ztax} \quad (16)$$

Fields at the boundary between nodes are also easily obtained as shown below for two field components at the boundary between nodes (x,y,z) and $(x+1,y,z)$:

$$E_y = -\frac{V_{11}^i(x,y,z) + V_3^i(x+1,y,z)}{tay} \quad (17)$$

$$H_z = \frac{V_3^i(x+1,y,z) - V_{11}^i(x,y,z)}{Ztaz}$$

Current and charge density may be obtained directly from the fields using Ampere and Gauss laws or with reference to the analogies between field and circuit quantities.

Excitation of the mesh is achieved by launching appropriate voltage pulses on the TL of particular nodes. As an illustration, to launch an electric field component $E_x = E_0$ at a particular node, the following voltage pulses must be applied:

$$V_1^i = V_2^i = V_9^i = V_{12}^i = -\frac{E_0 tax}{2} \quad (18)$$

Perfectly conducting boundaries are easily imposed on the mesh at the connection stage, at the boundaries between nodes, by specifying that the reflection coefficient there is equal to -1 . More complex boundaries (e.g., with frequency-dependent properties) can also be specified as explained in the following sections.

A variable mesh ($\Delta x \neq \Delta y \neq \Delta z$), or a mesh describing an inhomogeneous material, is established by adding stubs to the standard SCN described above, to maintain synchronism and account for values of permittivity and permeability larger than one. In the most general case, open-circuit, short-circuit, and infinitely long stubs are used to account for ϵ, μ, σ of the medium [7,9]. The structure thus obtained is referred to as the *stuffed SCN*. However, this is not the most efficient structure, and in most practical implementations of TLM the *hybrid SCN* is employed. In this node, synchronism is maintained, but the condition that all link lines have the same characteristic impedance is relaxed. This allows all the required inductance (μ in field terms) to be modeled by the linklines, and stubs are needed only to account for ϵ [13]. This results in a reduction of the storage required and in operating the mesh at a larger timestep compared with a stuffed SCN. Alternatively, all the required capacitance may be described by the linklines, and stubs then account for extra inductance. A general discussion of the properties of the hybrid SCN may be found in a paper by Trenkic et al. [14]. For problems with

cylindrical symmetry, non-Cartesian nodes are available to facilitate modeling [15].

Developments to increase the efficiency of TLM computation are described in the literature. A particular technique to speed up scattering is described in another paper by Trenkic et al. [16]. For each coordinate direction, total voltage and current are first calculated and the reflected voltages are then obtained from

$$V_{y\text{mx}}^r = V_x - ZI_z - V_{y\text{px}}^i \quad (19)$$

Similar equations apply for the y and z directions. The notation used to designate voltage pulses in (19) is as follows: superscripts “i” or “r” indicate incident or reflected voltages, the first subscript indicates direction of propagation (x , y , or z), the second subscript (“ n ” or “ p ”) indicates line segment along the negative or positive axis, and the third subscript indicates the polarization direction of the pulse (x , y , or z).

4. THEORETICAL FOUNDATIONS OF TLM

In this section some of the general concepts that underpin the foundation of TLM are discussed together with important features of the method such as dispersion and accuracy.

4.1. The General SCN TLM Node

A number of TLM nodes are available, many of them derivatives of the basic SCN, which appeared in the literature over the years. These may be unified under a general formulation described in Ref. 17. It accounts for a general anisotropic materials represented by ϵ_{ri} , μ_{ri} , $i = 1, 2, 3$ where the indices 1, 2, 3 refer to the coordinate directions x, y, z . In this node, for the i -directed, j -polarized link line, the capacitances and inductances per unit length are C_{ij}, L_{ij} . The i -directed stubs represent capacitance and inductance:

$$C_0^i, L_s^i$$

The TLM constitutive equations are (Δi is the node size in i direction)

$$\begin{aligned} C_{kitak} + C_{jitaj} + C_0^i &= \epsilon_{r0} \epsilon_{ri} \frac{t_j t_k}{t_i} \\ L_{jktaj} + L_{kjtak} + L_s^i &= \mu_0 \mu_{ri} \frac{t_j t_k}{t_i} \end{aligned} \quad (20)$$

Synchronism requires that the same timestep prevail throughout; therefore

$$t_j t_k = t_i \sqrt{C_{ij} L_{ij}} \quad (21)$$

Using all possible permutations of $i, j, k \in \{x, y, z\}$, we obtain six equations from (20) and another six from (21). There

are 18 unknown parameters

$$C_{ij}, L_{ij}, C_0^i, L_s^i$$

and therefore there remain 6 degrees of freedom. By imposing additional restrictions on the linkline and stub parameters, several TLM nodes may be derived. According to Trenkic et al. [17], a classification of 3D TLM condensed nodes in the time domain is as follows:

- *Stub-loaded nodes*, which have the same characteristic impedance for all linklines (constant L/C ratio for all six lines giving the additional constraints).
- *Hybrid nodes*, which have either open- or short-circuit stubs (thus supplying three additional conditions), the other three conditions obtained by demanding that all the line impedances modeling the same magnetic or electric field components are the same.
- *Supercondensed nodes*, which have no stubs at all; therefore six conditions are imposed by demanding that all stub capacitances and inductances be equal to zero. The supercondensed node is described in Ref. 18.
- *General nodes*, which have a combination of linklines and stubs.

According to the constitutive equations above, a *general symmetric condensed node* (GSCN) may be derived where material properties may be shared between linklines and stubs. The advantage of this option is that an optimization is possible to achieve, for example, particular dispersion characteristics. This in general results in a node with six different characteristic impedances, six stubs, and six lossy elements. The general theory of the GSCN and its scattering properties may be found in Ref. 17.

4.2. Field-Theoretic Derivation of TLM

An elegant derivation of TLM SCN method is by applying the method of moments (MoM) to Maxwell's equations [19, 20]. The field components are expanded in a set of subdomain basis functions, as shown below for the x components,

$$\begin{aligned} E_x(\vec{x}, t) &= \sum \lim its_{k,l,m,n} k + (1/2) E_{l,m}^x H_{l,m,n}^x(\vec{x}) T_{k+(1/2)}(t) \\ &\quad + \sum \lim its_{k,l,m,n} k + (1/2) E_{l,m,n}^x F_{l,m,n}^x(\vec{x}) T_{k+(1/2)}(t) \\ H_x(\vec{x}, t) &= \sum \lim its_{k,l,m,n} k + (1/2) H_{l,m,n}^x F_{l,m,n}^x(\vec{x}) T_{k+(1/2)}(t) \\ &\quad + \sum \lim its_{k,l,m,n} k + (1/2) H_{l,m,n}^x F_{l,m,n}^x(\vec{x}) T_{k+(1/2)}(t) \end{aligned} \quad (22)$$

where

$$k + (1/2) E_{l,m,n}^\mu, \quad k + (1/2) H_{l,m,n}^\mu, \quad \mu = x, y, z$$

are the expansion coefficients. The other components are obtained by permutation of x, y, z and the corresponding

discrete coordinates l, m, n . The basis functions in time are defined as

$$T_{k\pm(1/2)}(t) = g\left(\frac{t}{\Delta t} - k \mp \frac{1}{2}\right)$$

where

$$g(x) = \begin{cases} \text{trix}1 - |x|, & |x| < 10, \\ |x| \geq 1 \end{cases}$$

The spatial basis functions are defined as

$$F_{l,m,n}^{\mu}(\vec{x}) = H_l(x)F_{m\pm(1/2),n}(pa, \mu, v)$$

where H is a rectangular pulse function and F is a two-dimensional triangular basis function. This spatial basis functions provides a step approximation in the μ direction and a piecewise linear approximation in the diagonal directions of the plane perpendicular to the μ direction. Substituting these expansions into Maxwell's equations, sampling with delta functions and the derivatives of delta functions, and combining the 12 resulting equations gives the following form:

$$(M_1 + TM_2)\mathbf{b} = (M_3 + TM_4)\mathbf{a} \quad (23)$$

In this expression \mathbf{a} and \mathbf{b} are the incident and reflected wave amplitudes, respectively. Introducing the normal TLM choices for the timestep, one obtains, after some manipulation [19]

$$\mathbf{b} = TS\mathbf{a} \quad (24)$$

where S is the normal scattering matrix for the TLM SCN node, thus demonstrating that the TLM scattering scheme may be derived directly from MoM procedures. An interesting development, which stems from the theoretical foundation of TLM described above, is the derivation of the alternating TLM (ATLM) scheme, which reduces computational effort and removes spurious solutions at the expense of more complicated boundary conditions [20].

4.3. Dispersion Properties of TLM

A mesh consisting of a lattice of SCN TLM nodes is essentially a lowpass network, and therefore propagation properties are dependent on both frequency and propagation angle. At the interface between areas of the mesh with different spatial resolutions, waves encounter, effectively, a numerical discontinuity. These features are generally described as "dispersion" and are common to all numerical schemes such as FDTD. However, each particular scheme has its own unique dispersion characteristics, and a basic understanding is useful in applications where control of errors is important. A simple analysis of the 3D SCN based on circuit concepts may be done in certain cases [21], and results may be obtained using numerical means [22]. For propagation along the diagonal, the regular SCN exhibits no dispersion, but in other directions there is dispersion that increases with frequency. The best advice, which is common to all similar

numerical schemes, is to use a resolution of at least 10 segments per wavelength at the highest frequency of interest. If this is done, dispersion errors of a few percent under the worst circumstances should be expected. Studying dispersion properties by deriving dispersion relations in a closed analytical form is a much more demanding task, but some significant progress has been reported [23,24].

The problem of propagation behavior at the interface between different meshes is a difficult one, and no general analytical expressions are available that allow a rapid assessment of prevailing errors. Most studies are based on numerical work and the general advice is that abrupt changes in resolution should be avoided. A study that compares the behavior of TLM and FDTD for the same grading ratios across interfaces may be found in Ref. 25.

4.4. A Modal View of TLM

Another interesting insight into TLM is to examine its structure in terms of modal components.

At the surface of each mode there are 12 electric and 12 magnetic field components, which are related by an admittance operator Y :

$$\mathbf{H} = Y\mathbf{E} \quad (25)$$

Expressing field components in terms of incident and reflected voltages at the node gives

$$\mathbf{E} = \mathbf{V}^i + \mathbf{V}^r, \quad \mathbf{H} = y_0(\mathbf{V}^i - \mathbf{V}^r) \quad (26)$$

where y_0 is a scalar quantity. Combining these expressions, one obtains the scattering equation for the TLM node

$$\{y_0 I + Y\}\mathbf{V}^r = \{y_0 I - Y\}\mathbf{V}^i \quad (27)$$

where I is the identity matrix. The best way to solve Eq. (27) is to solve an eigenvalue problem

$$Y\mathbf{U}_n = \gamma_n \mathbf{U}_n \quad (28)$$

where \mathbf{U}_n and γ_n are the eigenvectors and eigenvalues of Y , respectively. Defining a matrix U with columns that are the eigenvector of Y , the voltage components incident and reflected at each node may be expressed in terms of modal components:

$$\mathbf{V}^i = U\mathbf{X}^i, \quad \mathbf{V}^r = U\mathbf{X}^r \quad (29)$$

Combining these expressions with (27) gives the following equation, after some manipulation:

$$X_n^r = \frac{y_0 - \gamma_n}{y_0 + \gamma_n} X_n^i \quad (30)$$

This expression shows that, effectively, the admittance seen into the node by each mode is the eigenvalue, as shown schematically in Fig. 8.

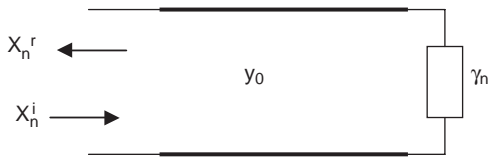


Figure 8. Admittance seen by each mode incident on a TLM node.

The structure of Y and its eigenvalues can be formally derived or obtained from physical intuition in terms of 12 cylindrical harmonics (two TE and two TM modes per coordinate direction). As an example for TM modes the field components are

$$\begin{aligned} E_{z,n} &= \frac{J_n(k_0 r)}{J_n(k_0 \Delta)} \cos(n\varphi) \\ H_{\varphi,n} &= \frac{1}{j\omega\mu} \frac{dJ_n(k_0 r)/dr}{J_n(k_0 \Delta)} \cos(n\varphi) \end{aligned} \quad (31)$$

where k_0 is the wavenumber and the fields were normalized at the edge of the node $r = \Delta$. The eigenvalues for this mode are

$$\gamma_n = \frac{H_{\varphi,n}}{E_{z,n}} = \frac{1}{j\omega\mu} \left. \frac{dJ_n(k_0 r)/dr}{J_n(k_0 r)} \right|_{r=\Delta} \quad (32)$$

Using a small argument expansion for the Bessel functions, the eigenvalue for the $n = 0$ TM_{z0} mode is obtained:

$$\gamma_0 = j \frac{\omega\epsilon\Delta}{2} \quad (33)$$

Hence the reflection coefficient for the TM_{z0} mode is

$$\Gamma = \frac{Y_0 - \gamma_0}{Y_0 + \gamma_0} \simeq e^{-jk\Delta} \quad (34)$$

This represents a simple phase shift on a lossless line segment. Similar expressions are obtained for the other modes. TLM therefore may be interpreted as a procedure for implementing in the time domain the process of analysis of total voltages into modes, the proper reflection of each mode at the node, and the recombination of modes to obtain total voltages for transmission to adjacent nodes. These ideas are useful in implementing schemes for embedding thin wires into TLM nodes. More details may be found in Ref. 26.

5. FURTHER DEVELOPMENTS AND SELECTED APPLICATIONS

5.1. Absorbing Boundary Conditions

All differential equation numerical techniques that are based on a volumetric discretization require special boundary conditions to deal with open-boundary problems.

Typically, at the extremities of the numerical mesh, where an open boundary exists, a termination must be

placed that mimics, as far as possible, the open boundary of the real physical problem. The simplest approach in TLM has been to use the “matched boundary condition,” which effectively terminates the line segments at the open boundary with the medium’s characteristic impedance. This is an inexpensive absorbing boundary condition to use and should be employed whenever possible. The resulting small reflections are acceptable in all except the most demanding problems.

In cases where a better absorbing boundary condition is required, two approaches have emerged for use in a TLM mesh. The first approach is based on the Johns matrix concept and is particularly suitable for terminating waveguide problems [27]. In time-domain diakoptics the impulse response of the TLM mesh at selected input points is in effect a discrete Green function, which is referred to as the “Johns matrix”. If this response is known, then the response to any excitation is obtained by convolving the excitation with its Johns matrix. At an interface marking an open boundary, the Johns matrix is in effect a reflection coefficient matrix such as impulses reflected at the interface are dependent on the impulses not only at a given time but also at previous times. This approach works well and efficiently on simple open boundaries such as those found in waveguide problems.

For terminating open boundaries in more general configurations, the computational cost of the Johns matrix approach is unacceptable and schemes based on the “perfectly absorbing layer” [also known as “perfectly matched layer” (PML)] are generally preferred. This effectively introduces a fictitious material as an absorber and is used extensively in FDTD schemes. An implementation of the PML boundary condition in TLM is described in Ref. 28. It should be noted that the PML schemes exhibit instabilities under certain conditions, notably when terminating waveguides contain irises, and hence in such cases the Johns matrix approach should be preferred.

5.2. Multigrid Schemes

Mesh refinement is necessary whenever fine features such as wires, wire looms, edges, and thin walls with perforations need to be described in the mesh. It would appear that the simplest way and the one resulting in the best accuracy is to use a finer mesh so that the finest feature can be accommodated by the resolution of the mesh. This would imply typically four sampling points per fine feature. The resulting size of the computation, however, would be excessively large. An alternative is to use a finer mesh only where it is required, thus resulting in a multigrid mesh.

Substantial effort has been expended in this area over many years as reviewed in Ref. 29. There are many difficulties to overcome, and it appears that an entirely satisfactory scheme is not available. Two schemes, that allow for a multigrid mesh in TLM are described in Refs. 30,31. Multigrid schemes are available mainly as research tools and should be used with caution and only for small resolution ratios between fine and coarse meshes.

5.3. The ADI TLM

Another development in TLM, which results in an implicit algorithm, is the alternate-direction-implicit TLM (ADI-TLM) or split-step TLM (SS-TLM) [32–34] scheme. These algorithms split sampling in time into two steps. As an example, for the x component of the electric field, two sub-equations are obtained:

$$\begin{aligned} \frac{1}{2} \left[\epsilon \frac{\partial E_x}{\partial t} + \sigma E_x \right] &= \frac{\partial H_z}{\partial y} \\ \frac{1}{2} \left[\epsilon \frac{\partial E_x}{\partial t} + \sigma E_x \right] &= -\frac{\partial H_y}{\partial z} \end{aligned} \tag{35}$$

The first step is implemented by approximating the first equation in (35) between times $(n - \frac{1}{2})\Delta t$ and $n \Delta t$ and the second equation between $n \Delta t$ and $(n + \frac{1}{2})\Delta t$. The second step is similarly obtained by approximating the second equation between $(n + \frac{1}{2})\Delta t$ and $(n + 1)\Delta t$, and the first between $(n + 1)\Delta t$ and $(n + \frac{3}{2})\Delta t$. This results in an implicit algorithm, but a larger timestep can be employed compared to nonsplit explicit TLM algorithms. The overall result is that in some circumstances a computational saving is achieved. It is not clear at present whether these benefits persist when dealing with general EM problems with inhomogeneous materials, embedded wires, or similar.

5.4. Modeling of General Materials with Frequency-Dependent Properties in the Time Domain

Simple materials with frequency independent properties are easily modeled in TLM by adjusting node parameters (dielectrics, losses) or reflection coefficients (perfect conductors). For more general materials, which may involve dependence on frequency, anisotropy, chirality, nonlinearity, and other properties, special techniques need to be developed for time-domain models. The simplest way to visualize the procedures to be followed in the development of such models, is to consider that in the frequency-domain material properties represent in effect the transfer function of an analog filter. By deriving an equivalent digital filter, which has the same frequency response as the analog filter, a time-domain procedure is readily obtained that can be directly embedded into the time-domain TLM model.

A simple yet important example is of propagation in a Debye material where

$$\epsilon(\omega) = \epsilon_\infty + \frac{\epsilon_s - \epsilon_\infty}{1 + j\omega\tau} \tag{36}$$

where $\epsilon_s, \epsilon_\infty, \tau$, are the static permittivity, permittivity at infinite frequencies, and relaxation time, respectively. Limiting, for simplicity, the discussion to 1D propagation in a Debye medium the calculation proceeds as follows.

The basic circuit equivalent for the problem is shown in Fig. 9. The TLM equivalent of this circuit is shown in

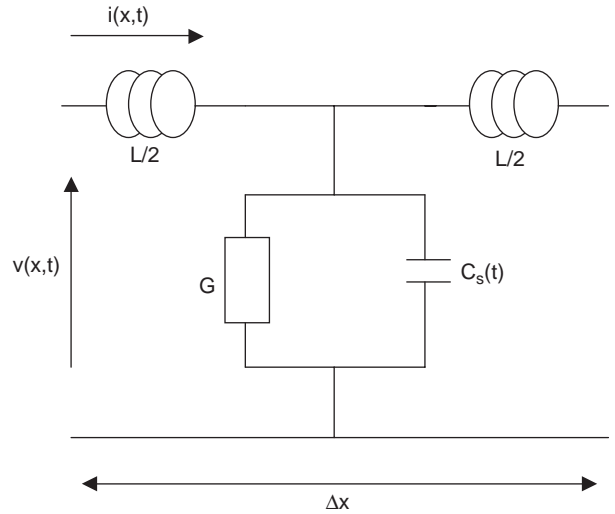


Figure 9. A segment of a model to describe 1D propagation in a Debye medium.

Fig. 10, where all impedances are normalized to

$$Z_0 = \frac{1}{Y_0} = \sqrt{\frac{\mu_0}{\epsilon_0}} \tag{37}$$

The timestep and the following parameters are calculated from

$$\begin{aligned} \Delta t &= \frac{\Delta x}{c} \\ \beta &= \exp\left(\frac{-\Delta t}{\tau}\right) \\ \alpha &= (\epsilon_s - \epsilon_\infty)(1 - \beta) \\ g &= \sigma \Delta x Z_0 \\ t &= \frac{2}{2\epsilon_\infty + g + 2\alpha} \\ t_s &= 2t(\epsilon_\infty + \alpha - 1) \\ t_f &= t\beta \end{aligned} \tag{38}$$

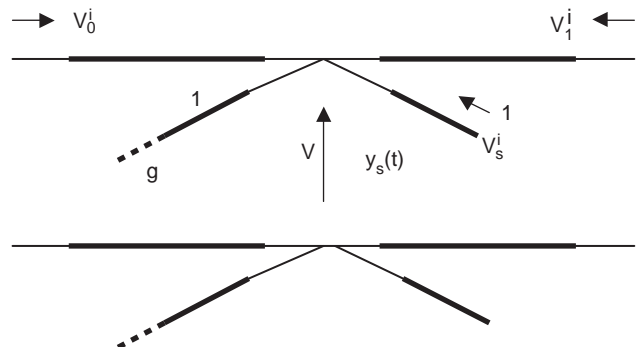


Figure 10. The normalized equivalent circuit of the circuit in Fig. 9, where lumped components were replaced by link and stub lines.

The total voltage is obtained from

$${}_k V = t({}_k V_0^i + {}_k V_1^i) + t_s {}_k V_s^i + t_f {}_{k-1} u \quad (39)$$

The quantity u is obtained by the procedure shown in Fig. 11. The reflected voltages are then calculated as follows:

$$\begin{aligned} {}_k V_0^r &= {}_k V - {}_k V_0^i \\ {}_k V_1^r &= {}_k V - {}_k V_1^i \\ {}_k V_s^r &= {}_k V - {}_k V_s^i \end{aligned} \quad (40)$$

The algorithm requires one backstore variable. Similar procedures are available to deal with material modeling in three dimensions and with a range of material parameters [35–39].

5.5. Multiscale Schemes

The problem of fine features in large computations and the need to deal effectively and efficiently with multiscale problems were already discussed [29]. Two examples are given here for two important practical problems: the simulation of coupling to wires and the simulation of the shielding effectiveness of cabinets.

For describing thin wires, the approach first described by Holland and Simpson [40] has been used for some time. It is based on the principle of calculating an in-cell capacitance to represent the wire and thus building an interface between the wire and the rest of the TLM mesh. Calculation of the parameters of this interface is based on the quasistatic assumption regarding the field around the wire. Several papers discuss in detail the nature of this interface for a wire placed between nodes [41], a wire placed at the node center [42], and multiconductor looms [43]. All these developments suffer from a number of assumptions and limitations.

An alternative technique is based on taking into account more than one modes for the field around the wire [modal expansion technique (MET)]. Because MET takes more modes into account (some of which are asymmetric), it is suited to placing the wire arbitrarily anywhere in the node. It is also accurate and removes several other restrictions inherent in the conventional approach. MET is based on the approach described in Section 4.4 for a node without a wire, with the important modification that more modes need now be taken into account, and, the imped-

ance seen by incoming pulses takes account of the presence of the wire. The complete field solution for a long wire is

$$\begin{aligned} E_z(r, \varphi) &= \sum_{n=-\infty}^{\infty} B_n e^{jn\varphi} \left[J_n(k_0 r) - \frac{J(k_0 a)}{N_n(k_0 a)} N_n(k_0 r) \right] \\ H_\varphi(r, \varphi) &= \frac{1}{j\omega\mu_0} \frac{\partial E_z}{\partial r} \end{aligned} \quad (41)$$

From this it can be seen that the static solution used in the conventional approach based on Holland and Simpson is only the first term in this expansion. Depending on the degrees of freedom available, several modes may be used. In two dimensions, where TLM nodes have four ports, four modes are employed. In three dimensions, for a z -directed wire, four modes (TE, TM, TEM odd, TEM even) and four angular instances are selected, making a total of 16 modes. Wires that are offset from the center of the node may also be described by exploiting as an example the addition theorems for Bessel functions. The approach of working out the eigenvalues, the impedance seen by each mode and for constructing suitable algorithms, may be found in Ref. 26.

Another problem of importance in many applications is the description of a thin wall with numerous perforations that is part of a resonant box (e.g., equipment cabinet). It is simply computationally far too expensive to generate a mesh with the necessary resolution to describe all relevant features. The simplest approach to this type of problem is to place the thin wall with perforations between nodes and to account for its properties by a frequency-dependent scattering matrix $S(\omega)$ implemented during the connection process in TLM. This technique is referred to as a *digital filter interface* (DFI) since it reduces to a time-domain algorithm as part of the connection process. Each coefficient of the scattering matrix is put into standard Padé form and then the frequency-domain Prony method is used to find its poles and zeros. The resulting expression is converted into the discrete time domain by application of the bilinear transformation. The resulting equations in state form relating incident and reflected voltages are of the form

$$\begin{aligned} V^i &= B_0 V^r + \mathbf{B}' X \\ X &= z^{-1} A' X + z^{-1} \mathbf{1}' V^r \end{aligned} \quad (42)$$

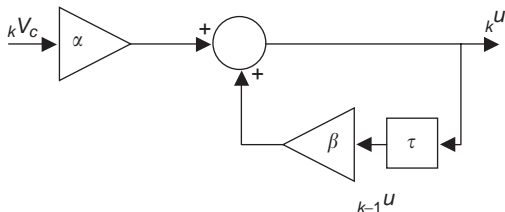


Figure 11. Signal flow diagram representing the algorithm for implementing the model for Debye materials.

In (42) the first equation is the output equation and the second is the state equation, and the computational procedure is shown in Fig. 12. Details may be found in Ref. 44. Using this approach, very substantial computational savings can be made. Moreover, the frequency-dependent scattering matrix may be obtained by numerical simulation, analytically or experimentally. The calculation of the poles and zeros is a preprocessing task and therefore is not an overhead on the main timestepping simulation.

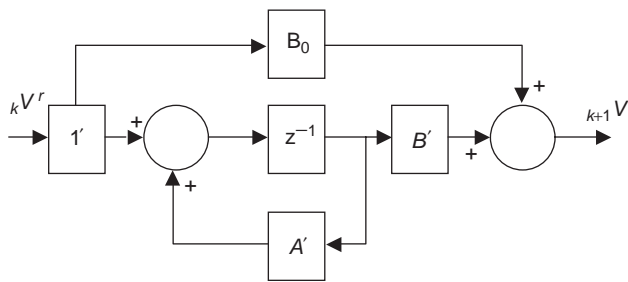


Figure 12. Signal flow diagram of the “connection” process to account for fine features using the DFI algorithm.

5.6. Frequency-Domain TLM (FD-TLM)

TLM is mainly used as a time-domain method but can also be implemented in the frequency domain. In FD-TLM time-harmonic variations are used and therefore discretization in space only is required. This considerably simplifies the modeling of materials and other features. However, the algorithm requires the inversion of a large matrix.

Several schemes are available in which either the characteristic impedance of each line is kept the same or phase constants are kept the same. Details may be found in the literature [45–48].

BIBLIOGRAPHY

- G. Kron, Equivalent circuit of the field equations of Maxwell, *Proc. IRE* **32**:289–299 (1944).
- J. R. Whinnery and S. Ramo, A new approach to the solution of high-frequency problems, *Proc. IRE* **32**:284–288 (1944).
- J. R. Whinnery et al., Network analyser studies of electromagnetic cavity resonators, *Proc. IRE* **32**:360–367 (1944).
- P. B. Johns and R. L. Beurle, Numerical solution of two-dimensional scattering problems using transmission-line matrix, *Proc. IEE* **118**:1203–1208 (1971).
- S. Akhtarzad and P. B. Johns, Solution of Maxwell’s equations in three space dimensions and time by the TLM method of numerical analysis, *Proc. IEE* **122**:1344–1348 (1975).
- W. J. R. Hoefer, The transmission-line matrix method-theory and applications, *IEEE Trans. Microwave Theory Tech.* **MTT-33**:882–893 (1985).
- P. B. Johns, A symmetrical condensed node for the TLM method, *IEEE Trans. Microwave Theory Tech.* **MTT-35**:370–377 (1987).
- W. J. R. Hoefer and P. P. M. So, *The Electromagnetic Wave Simulator—a Visual Electromagnetics Laboratory Based on the 2D TLM Method*, Wiley, New York, 1991.
- C. Christopoulos, *The Transmission-Line Modeling Method-TLM*, IEEE Press, New York; 1995.
- P. Russer and C. Christopoulos, Transmission-line method, Part IV, in N. K. Uzunoglu et al., eds., *Applied Computational Electromagnetics*, Springer-Verlag, Berlin, 1998.
- C. Huygens, *Traite de la Lumiere*, Leiden, Paris; 1690.
- P. B. Johns, A new mathematical model to describe the physics of propagation, *Radio Electron. Eng.* **44**:657–666 (1974).
- R. A. Scaramuzza and A. J. Lowery, Hybrid symmetrical condensed node for the TLM method, *Electron. Lett.* **26**:1947–1949 (1990).
- V. Trenkic et al., On the time step in hybrid symmetrical condensed nodes, *IEEE Trans. Microwave Theory Tech.* **MTT-43**:2172–2174 (1995).
- R. Allen and M. J. Clark, Application of the symmetrical TLM method to the cold modelling of magnetrons, *Int. J. Num. Model.* **1**:61–70 (1988).
- V. Trenkic et al., Simple and elegant formulation of scattering in TLM nodes, *Electron. Lett.* **29**:1651–1652 (1993).
- V. Trenkic et al., Development of a general symmetrical condensed node for the TLM method, *IEEE Trans. Microwave Theory Tech.* **MTT-44**:2129–2135 (1996).
- V. Trenkic et al., Theory of the symmetrical super-condensed node for the TLM method, *IEEE Trans. Microwave Theory Tech.* **MTT-43**:1342–1348 (1995).
- M. Krumpolz and P. Russer, A field theoretical derivation of TLM, *IEEE Trans. Microwave Theory Tech.* **MTT-42**:1660–1668 (1994).
- P. Russer and B. Bader, The alternating transmission-line matrix (ATLM) scheme, *Proc. IEEE Microwave Theory Tech.* **MTT-S**:19–22 (1995).
- W. J. R. Hoefer, The transmission-line matrix (TLM) method, in T. Itoh, ed., *Numerical Techniques for Microwave and Millimeter-Wave Passive Structures*, Wiley, New York, 1989.
- J. S. Nielsen and W. J. R. Hoefer, A complete dispersion analysis of the condensed node TLM mesh, *IEEE Trans. Magn.* **27**:3982–3985 (1991).
- M. Krumpolz and P. Russer, On the dispersion in TLM and FDTD, *IEEE Trans. Microwave Theory Tech.* **MTT-42**:1275–1279 (1994).
- V. Trenkic et al., Analytical expansion of the dispersion relation for TLM condensed nodes, *IEEE Trans. Microwave Theory Tech.* **MTT-44**:2223–2230 (1996).
- F. J. German et al., A numerical comparison of dispersion in irregularly graded TLM and FDTD meshes, *Proc. Annu. Rev. Prog. Appl. Computational Electromagn.* **12**:270–278 (1996).
- P. Sewell et al., An accurate thin-wire model for 3D TLM simulations, *IEEE Trans. Electromagnetic Compatibility*, **EMC-45**:207–217 (2003).
- W. J. R. Hoefer, The discrete time-domain Green’s function or Johns matrix—a new powerful concept in TLM, *Int. J. Num. Model.* **2**:215–225 (1989).
- S. Le Maguer and M. M. Ney, Extended PML-TLM: An efficient approach for full wave analysis of open structures, *Int. J. Num. Model.* **14**:129–144 (2001).
- C. Christopoulos, Multi-scale modelling in time-domain electromagnetics, *Int. J. Electron. Commun. (AEU)* **57**:100–110 (2003).
- J. L. Herring and C. Christopoulos, Solving EM problems using a multiple grid TLM method, *IEEE Trans. Antenn. Propag.* **AP-42**:1654–1658 (1994).
- J. Wlodarczyk, New multigrid interface for the TLM method, *Electron. Lett.* **32**:1111–1112 (1996).
- T. Namiki, A new FDTD algorithm based on alternating direction implicit method, *IEEE Trans. Microwave Theory Tech.* **MTT-47**:2003–2007 (1999).
- F. Zheng et al., Toward the development of a 3D unconditionally stable FDTD method, *IEEE Trans. Microwave Theory Tech.* **MTT-48**:1550–1558 (2000).

34. S. Le Maguer and M. M. Ney, Split step TLM (SS-TLM) for efficient electromagnetic simulation of small heterogeneous apertures, *Proc. Zurich Electromagnetic Compatibility Symp.*, 2003, pp. 275–278.
35. L. De Menezes and W. J. R. Hoefer, Modeling of general constitutive relationships using SCN TLM, *IEEE Trans. Microwave Theory Tech.* **MTT-44**:854–861 (1996).
36. J. Paul et al., Generalised material models in TLM—Part 1: Materials with frequency dependent properties, *IEEE Trans. Anten. Propag.* **AP-47**:1528–1534 (1999).
37. J. Paul et al., Generalised material models in TLM—Part 2: Materials with anisotropic properties, *IEEE Trans. Anten. Propag.* **AP-47**:1535–1542 (1999).
38. J. Paul et al., Generalised material models in TLM—Part 3: Materials with non-linear properties, *IEEE Trans. Anten. Propag.* **AP-50**:997–1004 (2002).
39. I. Barba et al., Multiresolution model of electromagnetic wave propagation in dispersive materials, *IEEE Trans. Microwave Theory Tech.* **MTT-S**:243–246 (2000).
40. R. Holland and J. W. Simpson, Finite-difference analysis of EMP coupling to thin struts and wires, *IEEE Trans. Electromagnetic Compatibility*, **23**:88–97 (1981).
41. J. Włodarczyk and D. P. Johns, New wire interface for graded 3D TLM, *Electron. Lett.* **28**:728–729 (1992).
42. J. A. Porti et al., A comparison of thin wire models for the TLM method, *Electron. Lett.* **28**:1910–1911 (1992).
43. J. Włodarczyk et al., A fully integrated multiconductor model for TLM, *IEEE Trans. Microwave Theory Tech.* **MTT-46**:2431–2437 (1998).
44. J. Paul et al., The use of digital filtering techniques for the simulation of fine features in EMC problems solved in the time-domain, *IEEE Trans. Electromagnetic Compatibility* **EMC-45**:238–244 (2003).
45. D. P. Johns et al., New TLM technique for steady-state field solutions in three dimensions, *Electron. Lett.* **28**:1692–1694 (1992).
46. H. Jin and R. Vahldieck, The frequency domain transmission-line matrix method—a new concept, *IEEE Trans. Microwave Theory Tech.* **MTT-40**:2207–2218 (1992).
47. D. P. Johns, An improved node for frequency-domain TLM—the distributed node, *Electron. Lett.* **30**:500–502 (1994).
48. P. Berini and K. Wu, A new frequency domain symmetrical condensed node, *IEEE Microwave Guided Wave Lett.* **4**:180–182 (1994).

TRANSMISSION LINE THEORY

RAGHU K. SETTALURI
Oregon State University
Corvallis, OR

A transmission line is a network that connects a generator circuit to a load for the purpose of transmitting electric energy or information from one point to another. Examples of transmission lines include cable connection between a service provider and your television set, telephone wires, interconnection between a transmitter and an antenna, and optic nerves and neural networks in human brain. The list can go on and on with the same essential purpose of transporting energy or information between

two points. In these examples, we can notice one important difference for each scenario. The choice of transmission line is different and depends on the purpose and application. For example, high-power transmission lines that are used to transport megawatts of electric energy need to be thicker and bulkier to accommodate the large power-handling capability and minimize power losses. On the other hand, a microminiaturized interconnect in the 4 GHz central processor of your desktop or laptop needs to be precisely designed to transfer the information in a densely packed circuit environment! In electrical engineering applications, the choice of a suitable transmission medium depends on a variety of factors including the frequency of operation, power handling, and the topology.

Many readers might be familiar with basic circuit analysis techniques for low-frequency electric circuits, which have been well developed over decades. At low frequencies, the physical size of the circuit is much smaller compared with the wavelength. This condition implies that when a load is connected to a voltage source via a length of transmission line, the voltage appears instantaneously at the load end without any time delay, which also implies that lumped elements such as inductors, capacitors, and resistors will have much smaller sizes compared with wavelength, and we can conveniently assume that the voltage across an element on one side of the circuit was exactly in phase with the voltage on the other side. Thus size or separation between elements was never an issue in the low-frequency circuit design!

When the size of an element is a considerable fraction of a wavelength or many wavelengths, the network becomes *distributed* in nature. In this case, aside from time variation, voltages and currents can vary in magnitude and phase as a function of distance. A transmission line may no longer be considered as a simple interconnecting mechanism between two points. It behaves like a distributed-parameter network, for which the transmission properties need to be considered as a part of the design process, which leads to electromagnetic wave propagation on transmission lines with possible standing wave formations.

1. PROPAGATION MODES

The orientation of electric and magnetic fields and their interaction along a transmission line is essentially decided by the geometry of the transmission line structure, which is generally characterized by the *mode* supported by the transmission line structure for the electromagnetic wave propagation. Figure 1 shows several commonly used transmission lines, which are broadly classified into three main categories. The two-wire line, coaxial line, and strip-line, shown Figs. 1a–1c, support transverse electromagnetic (TEM) mode, where the electric and magnetic fields are entirely transverse to the direction of propagation. Many of the characteristics of wave propagation in TEM supporting structures are the same as those for a uniform plane wave propagating in an unbounded dielectric medium.

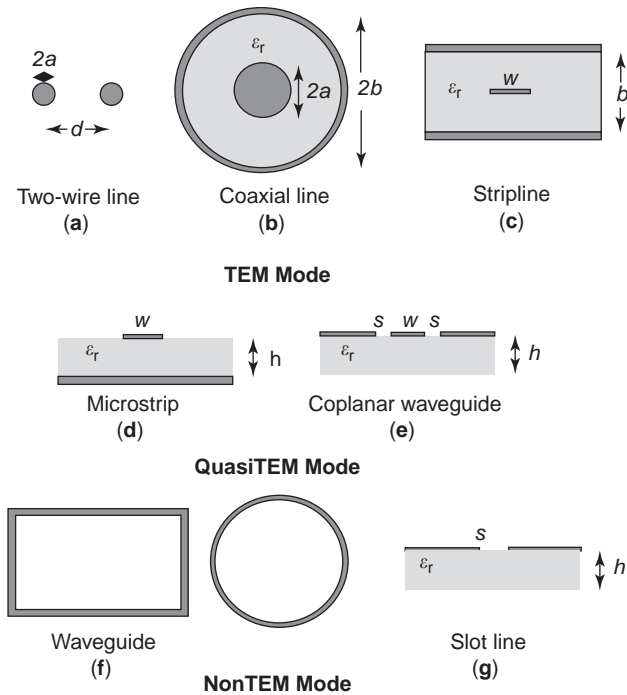


Figure 1. Commonly used transmission lines supporting different propagation modes.

A microstrip line and a coplanar waveguide (Figs. 1d and 1e) are two commonly used planar transmission lines at microwave frequencies. As a result of the presence of the air-dielectric interface, these structures are considered as inhomogeneous transmission lines. Here, the field lines between the conducting strip and the ground lines are not contained entirely in the substrate, and these structures support quasiTEM mode of propagation. However, because the nontransverse field components are considerably smaller compared with the transverse field components, for most practical applications, they can be included in the TEM class of transmission lines. A common feature among TEM and quasiTEM transmission line structures is that they require at least two conductors to support TEM mode and frequencies as low as DC can propagate along these lines.

Several other transmission lines exist that do not support TEM or quasiTEM mode of propagation. These include the rectangular and circular waveguides (Fig. 1f) and slotlines (Fig. 1g). Depending on the configuration, these structures support several higher order modes, such as transverse electric (TE) and transverse magnetic (TM), where the presence of a longitudinal field component cannot be ignored. The minimum frequency (also called the *cutoff* frequency) of the electromagnetic wave that can be supported in these structures depends on factors such as mode number and physical dimensions. Further, the transmission properties will have a strong frequency dependence. As transmission lines supporting TEM/quasiTEM wave propagation are more commonly used in practice, this article focuses on understanding

the wave propagation in the case of TEM supporting structures.

2. TRANSMISSION LINE EQUATIONS

As we have noticed in our earlier discussion, incorporating the spatial dependence of fields is important while addressing the characteristics of the transmission lines at high frequencies. For a given structural geometry, the transmission line characteristics can be determined by solving the Maxwell's equations [1] in various regions. This approach can provide a complete description of electric and magnetic fields at every point in the region. However, many times we are interested in terminal quantities such as voltage, current, impedance, and power, for which a discretized circuit representation of a distributed transmission line may offer simpler, yet adequately accurate solution.

Let us consider a transmission line connected to a source at one end and a load at the other end, as shown in Fig. 2a. If we choose a small section of the line with differential length Δz , it can be modeled as a discrete circuit, as shown in Fig. 2b and described by the following four basic parameters:

- R , resistance per unit length for both conductors, in Ω/m
- L , inductance per unit length for both conductors, in H/m
- G , conductance per unit length in S/m
- C , capacitance per unit length in F/m

The inductance L , represents the total series self inductance in both the conductors and the capacitance C , represents the capacitive coupling between the two conductors, which depends on the proximity between the conductors. R and G develop because of the conductor losses of both conductors and dielectric losses that exist in the medium between the conductors respectively. Thus R and G are essentially the *attenuation* or *loss* parameters of the transmission line. A finite length of transmission line can be considered as a cascade of several sections of infinitesimal length Δz , representing the distributed nature of the line.

The quantities $v(z, t)$ and $i(z, t)$ represent the instantaneous voltage and current at the input of the differential length section at node N . Similarly, $v(z + \Delta z, t)$ and $i(z + \Delta z, t)$ represent the same quantities on the output side at node $N + 1$. Applying Kirchhoff's voltage law, we obtain

$$v(z, t) - R\Delta z i(z, t) - L\Delta z \frac{\partial i(z, t)}{\partial t} - v(z + \Delta z, t) = 0 \quad (1a)$$

Rearranging the terms in Eq. (1a) leads to

$$-\frac{v(z + \Delta z, t) - v(z, t)}{\Delta z} = Ri(z, t) + L \frac{\partial i(z, t)}{\partial t} \quad (1b)$$

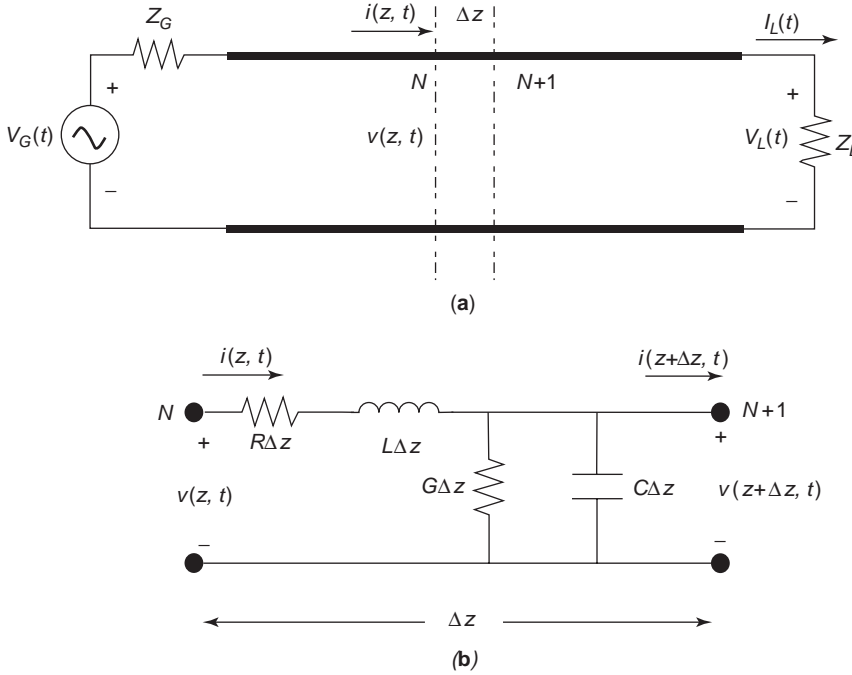


Figure 2. Transmission line and lumped-element representation for the purpose of deriving the Telegrapher's equations. (a) Definition of voltages and currents on a transmission line connected between a source and a load. (b) Lumped-element equivalent circuit for an elemental length of transmission line.

Similarly, applying Kirchhoff's current law to node $N+1$ in Fig. 2b leads to

$$i(z, t) - G\Delta z v(z + \Delta z, t) - C\Delta z \frac{\partial v(z + \Delta z, t)}{\partial t} - i(z + \Delta z, t) = 0 \quad (2a)$$

Again, rearranging the terms in Eq. (2a), we have

$$-\frac{i(z + \Delta z, t) - i(z, t)}{\Delta z} = Gv(z, t) + C \frac{\partial v(z, t)}{\partial t} \quad (2b)$$

In the limit, $\Delta z \rightarrow 0$, Eqs. (1b) and (2b) become

$$-\frac{\partial v(z, t)}{\partial z} = Ri(z, t) + L \frac{\partial i(z, t)}{\partial t} \quad (3a)$$

$$-\frac{\partial i(z, t)}{\partial z} = Gv(z, t) + C \frac{\partial v(z, t)}{\partial t} \quad (3b)$$

The first-order partial differential equations given in Eqs. (3) are the time-domain form of the transmission line equations, which are also called the *Telegrapher's* equations.

As we are primarily interested in sinusoidal steady-state conditions, we can apply the phasor notation with cosine reference to represent the time-domain equations given in Eqs. (3) in frequency-domain. For this, we define

$$v(z, t) = \text{Re}[V(z)e^{j\omega t}] \quad (4a)$$

$$i(z, t) = \text{Re}[I(z)e^{j\omega t}] \quad (4b)$$

where, $V(z)$ and $I(z)$ are phasor quantities dependent on space coordinate z only, and each of them could be real or

complex, and Re represents the real part of a complex quantity. Substituting Eqs. (4a) and (4b) in Eqs. (3) yields the following first-order ordinary differential equations in frequency-domain:

$$-\frac{dV(z)}{dz} = (R + j\omega L)I(z) \quad (5a)$$

$$-\frac{dI(z)}{dz} = (G + j\omega C)V(z) \quad (5b)$$

Eqs. (5) are called the *time-harmonic transmission line equations*.

3. WAVE PROPAGATION ON AN INFINITE TRANSMISSION LINE

The two coupled first-order time-harmonic transmission line equations given in Eqs. (5) can be combined to give two second-order uncoupled differential equations in $V(z)$ and $I(z)$ as

$$\frac{d^2V(z)}{dz^2} - \gamma^2 V(z) = 0 \quad (6a)$$

$$\frac{d^2I(z)}{dz^2} - \gamma^2 I(z) = 0 \quad (6b)$$

where

$$\gamma = \alpha + j\beta = \sqrt{(R + j\omega L)(G + j\omega C)} \quad (m^{-1}) \quad (7)$$

is the *complex propagation constant* of the transmission line, whose real and imaginary parts, α and β , represent

the *attenuation constant* (Np/m) and *phase constant* (rad/m) of the line, respectively. For all passive transmission lines, α will be either zero or a positive quantity.

The wave equations given in Eqs. (6) have solutions of the form

$$V(z) = V_0^+ e^{-\gamma z} + V_0^- e^{\gamma z} \tag{8a}$$

$$I(z) = I_0^+ e^{-\gamma z} + I_0^- e^{\gamma z} \tag{8b}$$

The terms $e^{-\gamma z}$ and $e^{\gamma z}$ represent the wave propagation in $+z$ and $-z$ directions, respectively. V_0^+ and I_0^+ are the wave amplitudes in the $+z$ direction, and V_0^- and I_0^- are the wave amplitudes in the $-z$ direction. These amplitudes are related via the expression

$$\frac{V_0^+}{I_0^+} = -\frac{V_0^-}{I_0^-} = \frac{R + j\omega L}{\gamma} \tag{9}$$

The ratio of the forward wave amplitudes or the negative of the backward wave amplitudes is also defined as *characteristic impedance*, Z_o , of the transmission line, where

$$Z_o = \frac{R + j\omega L}{\gamma} = \frac{\gamma}{G + j\omega C} = \sqrt{\frac{R + j\omega L}{G + j\omega C}} \tag{10}$$

Note that the parameters γ and Z_o can be complex and are independent of the length of the transmission line. As seen in Eqs. (7) and (10), these characteristic properties of the line are directly related to the line parameters $R, L, G,$ and C , which are real in nature. These parameters are dependent on the geometry of the transmission line and material properties of the conductors and the dielectric medium. For example, the line parameters for coaxial line and a two-wire transmission line are given in Table 1.

3.1. Special Cases

3.1.1. Lossless transmission line. The transmission line equations derived in Section 3 are for a general transmission line taking the effect of finite conductivity of the conductors and dielectric losses into account. However, in many practical situations, transmission lines at radiofrequencies are designed to have conductors with high

conductivities and dielectric materials with small values of loss tangent, $\tan\delta$, which would result in values of $R \ll \omega L$ and $G \ll \omega C$. Therefore, if we approximate $R = 0 = G$ in Eqs. (7) and (10), we get

$$\gamma = \alpha + j\beta = j\omega\sqrt{LC} \tag{11a}$$

$$\alpha = 0 \tag{11b}$$

$$\beta = \omega\sqrt{LC} \tag{11c}$$

$$Z_o = \sqrt{\frac{L}{C}} \tag{11d}$$

Thus, the propagation constant, γ , for a lossless transmission line becomes purely imaginary, reasserting the fact that attenuation will be zero for ideal lines with no dielectric and conductor losses. From Eq. (11d), it can be seen that the characteristic impedance, Z_o , becomes real for a lossless line. Phase velocity v_p , which is defined as the velocity of propagation of an equiphase front on the transmission line, is given as

$$v_p = \frac{\omega}{\beta} = \frac{1}{\sqrt{LC}} \tag{12}$$

From Eq. (12), it can be seen that the phase velocity is independent of the frequency of the propagating wave. As any arbitrary signal can be composed of a combination of sinusoidal waves of different frequencies and amplitudes, a constant phase velocity for all frequencies will ensure that all these waves will travel with the same velocity along a lossless line without suffering any attenuation, thus preserving the shape of the signal. On the other hand, for a general lossy transmission line, from Eq. (7), it can be seen that the phase velocity, β , and attenuation, α , are functions of frequency. As different frequency components propagate with different velocities and attenuation factors, the signal suffers *dispersion* and gets *distorted* as it propagates along the line.

3.1.2. Distortionless line. The theory for distortionless line was first proposed by Oliver Heaviside, whose contributions to the electromagnetism were well described in [2]. Consider a general lossy transmission line, which

Table 1.

Structure	Transmission line parameters			
	R (Ω/m)	L (H/m)	G (S/m)	C (F/m)
Two-wire Line (Fig. 1a)	$\frac{R_s}{\pi a}$	$\frac{\mu}{\pi} \ln\left(\frac{d}{2a} + \sqrt{\left(\frac{d}{2a}\right)^2 - 1}\right)$	$\frac{\pi\sigma}{\ln\left(\frac{d}{2a} + \sqrt{\left(\frac{d}{2a}\right)^2 - 1}\right)}$	$\frac{\pi\epsilon}{\ln\left(\frac{d}{2a} + \sqrt{\left(\frac{d}{2a}\right)^2 - 1}\right)}$
Coaxial Line (Fig. 1b)	$\frac{R_s}{2\pi} \left[\frac{1}{a} + \frac{1}{b}\right]$	$\frac{\mu}{2\pi} \ln\left(\frac{b}{a}\right)$	$\frac{2\pi\sigma}{\ln\left(\frac{b}{a}\right)}$	$\frac{2\pi\epsilon}{\ln\left(\frac{b}{a}\right)}$

Notes:

a. $\mu, \epsilon,$ and σ are the material properties of the dielectric medium.

b. R_s is the surface resistance of the conductors, which is related to the frequency and material properties of the conductor.

satisfies the condition

$$\frac{R}{L} = \frac{G}{C} \quad (13)$$

Substituting Eq. (13) in Eqs. (7) and (10), we get

$$\gamma = \alpha + j\beta = R\sqrt{\frac{C}{L}} + j\omega\sqrt{LC} \quad (14)$$

$$Z_o = \sqrt{\frac{L}{C}} \quad (15)$$

Phase velocity, v_p , is given by,

$$v_p = \frac{\omega}{\beta} = \frac{1}{\sqrt{LC}} \quad (16)$$

Comparing Eqs. (14)–(16) with Eqs. (11) and (12), it can be seen that, except for a nonzero value of attenuation constant, the distortionless line has same characteristics as that of a lossless line. Although the signal suffers attenuation as it propagates along the line, because of the constant phase velocity, waves of different frequency components will travel with the same velocity, thus preserving the shape of the signal, which is why it is called the *distortionless line*.

4. WAVE CHARACTERISTICS ON TERMINATED TRANSMISSION LINE

As you may recall, the general solution for transmission line wave equations given in Eqs. (8) consists of two types of wave propagation—the wave traveling in forward (+z) direction and the wave traveling in the backward (−z) direction. When a wave is incident at one end on an infinitely long transmission line, it continues to propagate in +z or −z direction depending on the direction of the incident wave. Thus, only one of the two terms consisting of either $e^{-\gamma z}$ or $e^{+\gamma z}$ exists. Let us now consider a transmission line of finite length l , terminated by an arbitrary load impedance Z_L , as shown in Fig. 3. It is assumed that the load is at $z=0$ and the source is connected at $z=-l$.

Using Eqs. (9) and (10), Eqs. (8a) and (8b) can be modified to contain only two unknown voltage amplitudes V_o^+ and V_o^- as

$$V(z) = V_o^+ e^{-\gamma z} + V_o^- e^{\gamma z} \quad (17a)$$

$$I(z) = \frac{V_o^+}{Z_o} e^{-\gamma z} - \frac{V_o^-}{Z_o} e^{\gamma z} \quad (17b)$$

At $z=0$, Eqs. (17a) and (17b) become

$$V_L = V(z=0) = V_o^+ + V_o^- \quad (18a)$$

$$I_L = I(z=0) = \frac{V_o^+}{Z_o} - \frac{V_o^-}{Z_o} \quad (18b)$$

Also, V_L and I_L are related via the load impedance, Z_L , as

$$Z_L = \frac{V_L}{I_L} \quad (19)$$

Using Eqs. (18a) and (18b) in Eq. (19) and rearranging terms, we get

$$V_o^- = \Gamma V_o^+ \quad (20a)$$

where

$$\Gamma = |\Gamma| e^{j\theta_r} = \left(\frac{Z_L - Z_o}{Z_L + Z_o} \right) \quad (20b)$$

Γ , which is the ratio of the reflected wave amplitude and the incident wave amplitude, is called the *voltage reflection coefficient*. As both Z_o and Z_L could be complex quantities, Γ can also be complex in general. It may be seen that, for all transmission lines, $|\Gamma| \leq 1$.

Using Eq. (20a) in Eqs. (17a) and (17b), we get

$$V(z) = V_o^+ (e^{-\gamma z} + \Gamma e^{\gamma z}) \quad (21a)$$

$$I(z) = \frac{V_o^+}{Z_o} (e^{-\gamma z} - \Gamma e^{\gamma z}) \quad (21b)$$

The ratio of $V(z)$ and $I(z)$ is called the *input impedance*, Z_{in} , and is given by

$$Z_{in}(z) = \frac{V(z)}{I(z)} = Z_o \left[\frac{1 + \Gamma e^{2\gamma z}}{1 - \Gamma e^{2\gamma z}} \right] \quad (\Omega) \quad (22)$$

At the input of the transmission line, the input impedance can be written as

$$Z_{in}(-l) = Z_o \left[\frac{1 + \Gamma e^{-2\gamma l}}{1 - \Gamma e^{-2\gamma l}} \right] \quad (\Omega) \quad (23)$$

Substituting Eq. (20b) in Eq. (23) and rearranging the terms, we get

$$Z_{in}(-l) = Z_o \left[\frac{Z_L + Z_o \tanh \gamma l}{Z_o + Z_L \tanh \gamma l} \right] \quad (\Omega) \quad (24)$$

Thus, Z_{in} is the impedance seen at the input of the transmission line, when the line is terminated with a load impedance Z_L . From the generator standpoint, the transmission line-load impedance combination can be replaced by a simple impedance Z_{in} , without disturbing the input voltage and current amplitudes, as shown in Fig. 3b. If the line is lossless, we can substitute for $\gamma = j\beta$ in Eq. (24) and get a modified expression for Z_{in} , as

$$Z_{in}(-l) = Z_o \left[\frac{Z_L + jZ_o \tan \beta l}{Z_o + jZ_L \tan \beta l} \right] \quad (\Omega) \quad (25)$$

4.1. Standing Wave Ratio

Consider a lossless transmission line of characteristic impedance Z_o , which is terminated by an arbitrary load impedance Z_L . From Eqs. (21a) and (21b), the expressions for

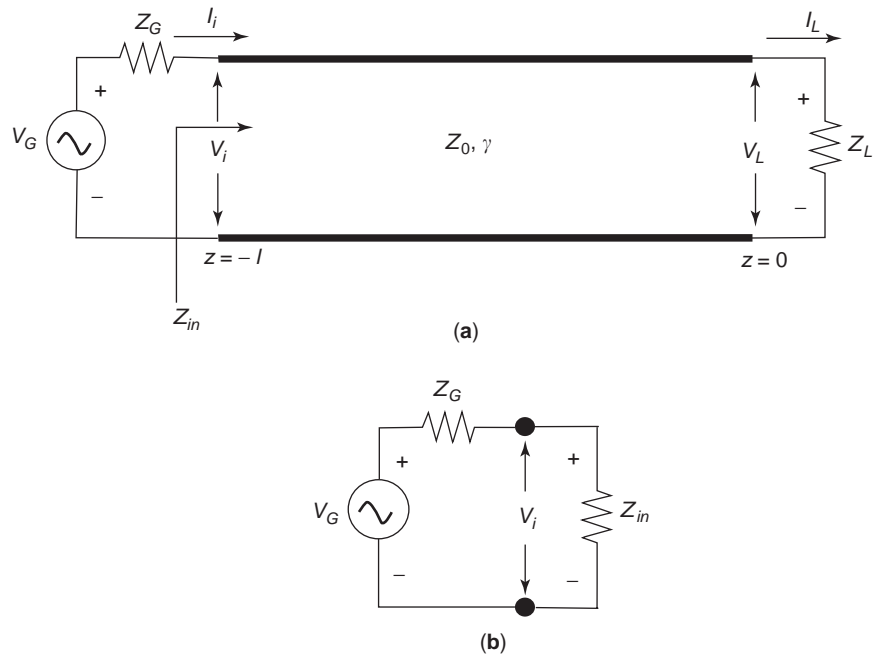


Figure 3. (a) A finite length transmission line terminated with a load impedance, Z_L . (b) Equivalent representation in terms of the input impedance, Z_{in} .

$V(z)$ and $I(z)$ for the lossy transmission line can be written as

$$V(z) = V_0^+ (e^{-j\beta z} + \Gamma e^{j\beta z}) \tag{26a}$$

$$I(z) = \frac{V_0^+}{Z_0} (e^{-j\beta z} - \Gamma e^{j\beta z}) \tag{26b}$$

The magnitude of the voltage, $|V(z)|$, will be

$$|V(z)| = |V_0^+| \cdot |1 + |\Gamma| e^{j(\theta_r + 2\beta z)}| \tag{27}$$

where, $\Gamma = |\Gamma| e^{j\theta_r}$ has been substituted.

Equation (27) shows that the voltage magnitude oscillates as a function of z , as shown in Fig. 4, indicating the standing wave formation. We can see that the voltage will be maximum when $e^{j(\theta_r + 2\beta z)} = 1$, and is given by

$$V_{\max} = |V_0^+| (1 + |\Gamma|) \tag{28a}$$

Similarly, voltage will be minimum when $e^{j(\theta_r + 2\beta z)} = -1$, and is given by

$$V_{\min} = |V_0^+| (1 - |\Gamma|) \tag{28b}$$

It may be noticed that when the load impedance is the same as the characteristic impedance of the line, the reflection coefficient $\Gamma = 0$, from Eq. (27), and we can see that $|V(z)| = |V_0^+|$, a constant value independent of z . As $|\Gamma|$ increases, the ratio of V_{\max} to V_{\min} increases, which leads us to define *voltage standing wave ratio (VSWR)*, or simply *standing wave ratio (SWR)*, as

$$SWR = \frac{V_{\max}}{V_{\min}} = \frac{1 + |\Gamma|}{1 - |\Gamma|} \tag{29}$$

SWR is always a real number such that $1 \leq SWR \leq \infty$. For a matched transmission line (when $Z_o = Z_L$), $SWR = 1$. It may also be noted that the distance between two successive voltage maxima (or minima) is $\lambda/2$, where λ is the wavelength on the transmission line.

4.2. Special Cases of Terminated Lossless Transmission Lines

Often, we use lossless transmission lines with special terminations to give interesting characteristics. For example, in impedance tuning networks and microwave filter design we commonly use *stubs* (open- or short-circuited transmission lines) in series or shunt configuration as part of the design. Also, at microwave frequencies, the

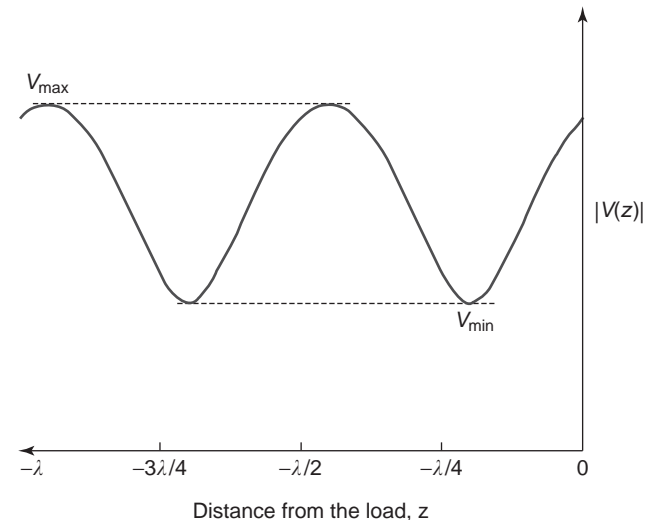


Figure 4. Standing wave formation on a lossless transmission line.

open- and short-circuited stubs can be used to replace lumped capacitors and inductors, which are otherwise impractical to realize. Similarly, we use lines with quarter wavelength for impedance transformation. Section 4.2.1 briefly describes the special properties of some of the lossless lines.

4.2.1. Open-Circuited Line. When a transmission line is open-circuited at one end, as shown in Fig. 5a, it sees an infinite load impedance ($Z_L = \infty$). From Eq. (20b), we can see that the voltage reflection coefficient $\Gamma = 1$, which means that the SWR becomes ∞ . From Eqs. (26a) and (26b), the voltage and current on an open-circuited loss-

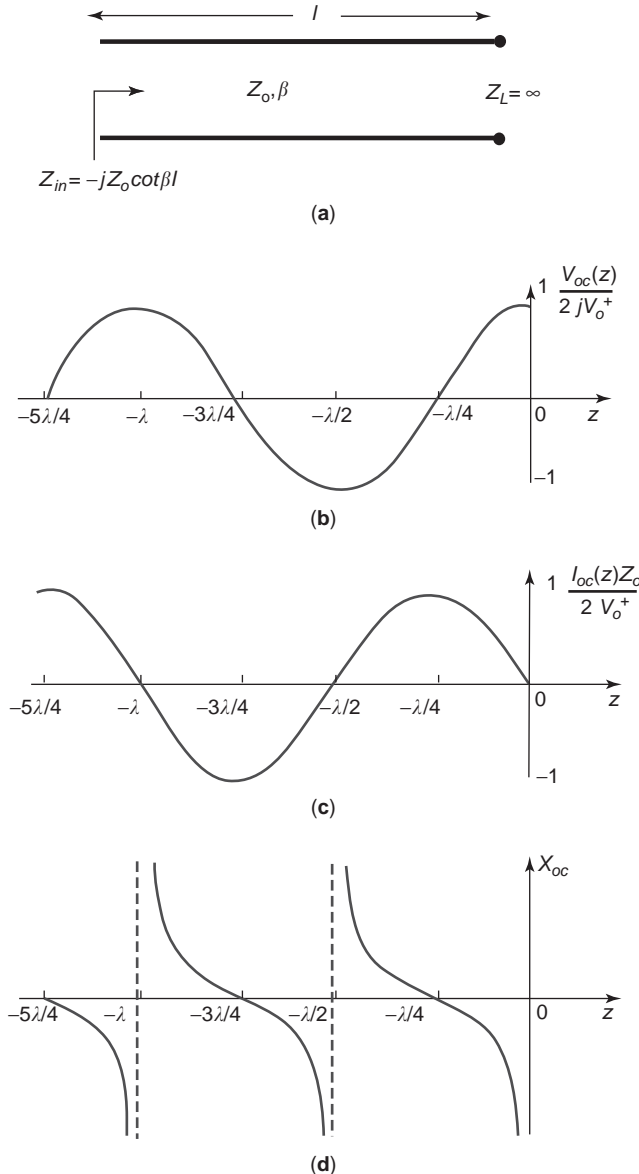


Figure 5. A lossless transmission line terminated with an (a) open circuit, (b) voltage distribution, (c) current distribution, and (d) input reactance as a function of the distance from the termination.

less transmission line are given by

$$V_{oc}(z) = V_0^+ (e^{-j\beta z} + e^{j\beta z}) = 2V_0^+ \cos \beta z \quad (30a)$$

$$I_{oc}(z) = \frac{V_0^+}{Z_0} (e^{-j\beta z} - e^{j\beta z}) = \frac{-2jV_0^+}{Z_0} \sin \beta z \quad (30b)$$

Both voltage and current are plotted as a function of the distance from the load location in Figs. 5b and 5c, respectively. As a result of the sinusoidal nature, both the quantities are periodic and repeat for multiples of λ .

Substituting $Z_L = \infty$ in Eq. (25) for the expression for input impedance, we get

$$Z_{oc} = Z_{in} = -jZ_0 \cot \beta z \quad (\Omega) \quad (31)$$

We can see from Eq. (30) that the input impedance Z_{oc} for the open-circuited line is always purely imaginary irrespective of length z . The variation of open-circuit reactance (imaginary part of Z_{oc}) is plotted as a function of z in Fig. 5d. The plot is again periodic and repeats for multiples of $\lambda/2$. The behavior varies between being inductive and capacitive as the length z is varied.

4.2.2. Short-circuited line. A lossless transmission line short circuited at the load end ($Z_L = 0$) is shown in Fig. 6a. Here, $\Gamma = -1$ and $SWR = \infty$. The voltage and current along the line can be given by

$$V_{sc}(z) = V_0^+ (e^{-j\beta z} - e^{j\beta z}) = -2jV_0^+ \sin \beta z \quad (32a)$$

$$I_{sc}(z) = \frac{V_0^+}{Z_0} (e^{-j\beta z} + e^{j\beta z}) = \frac{2V_0^+}{Z_0} \cos \beta z \quad (32b)$$

From Eq. (25), the input impedance for a short-circuited line can be given as

$$Z_{sc} = jZ_0 \tan \beta z \quad (\Omega) \quad (33)$$

The voltage, current, and the input reactance are plotted in Figs. 6b–6d as a function of the distance, z . As it can be seen, the input reactance for a shorted transmission line is also purely imaginary irrespective of the value of z . Comparing Figs. 5 and 6, we can see that in the range where X_{oc} is inductive, X_{sc} is capacitive, and vice versa. The input reactances of the short-circuited and open-circuited lossless transmission lines are essentially the same if their lengths differ by an odd multiple of $\lambda/4$.

Consider an open-circuited transmission line of length much smaller compared with a wavelength. As the electrical length of the line $\beta l \ll 1$, we can make the approximation that $\tan \beta l \cong \beta l$. From Eq. (31), at the input of the line, we have

$$Z_{oc} \cong \frac{Z_0}{j\beta l} = \frac{\sqrt{L/C}}{\omega \sqrt{LC}l} = \frac{1}{j\omega Cl} \quad (34)$$

This equation implies that an open-circuited lossless transmission line with a very short length will behave as a capacitance of Cl farads as shown in Fig. 7a. Similarly,

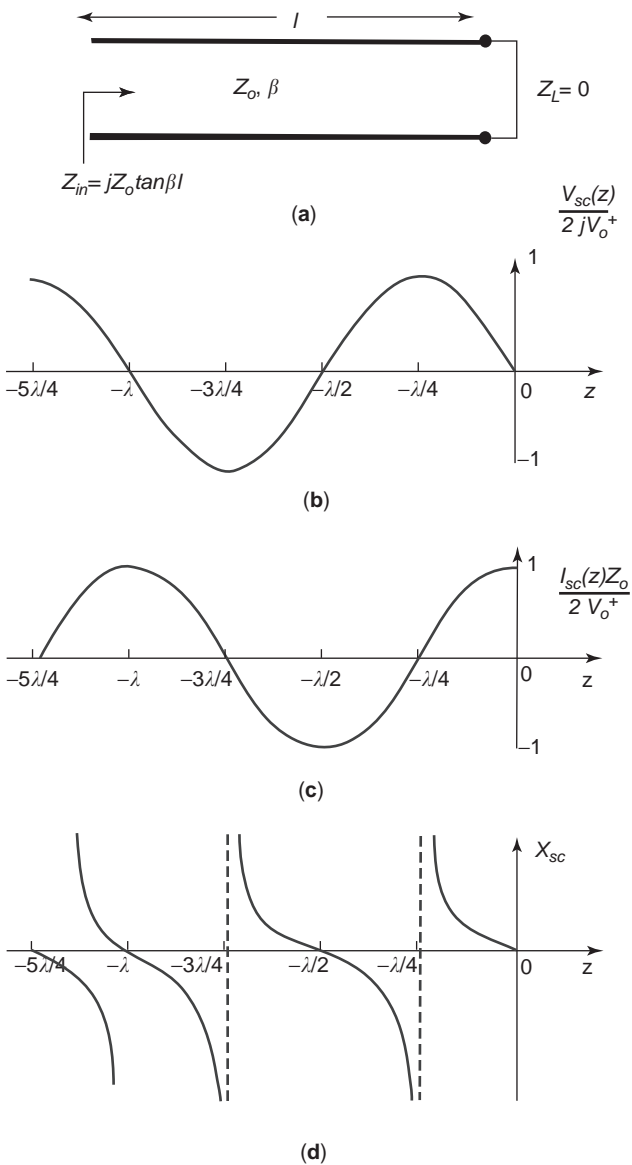


Figure 6. A lossless transmission line terminated with a (a) short circuit, (b) voltage distribution, (c) current distribution, and (d) input reactance as a function of the distance from the termination.

consider a short-circuited transmission line of small length. From Eq. (33), we get

$$Z_{sc} \approx Z_0 \cdot j\beta l = \sqrt{L/C} \cdot j\omega \sqrt{LC}l = j\omega Ll \quad (35)$$

Thus a short-circuited lossless transmission line with a short length can behave as an inductance of Ll henries, as shown in Fig. 7b.

This property of open- or short-circuited transmission lines behaving as lumped inductors or capacitors will be a useful feature at microwave frequencies, where discrete capacitor or inductor realization will be very difficult because of the parasitics associated with the structure. By proper choice, an open-circuited or short-circuited

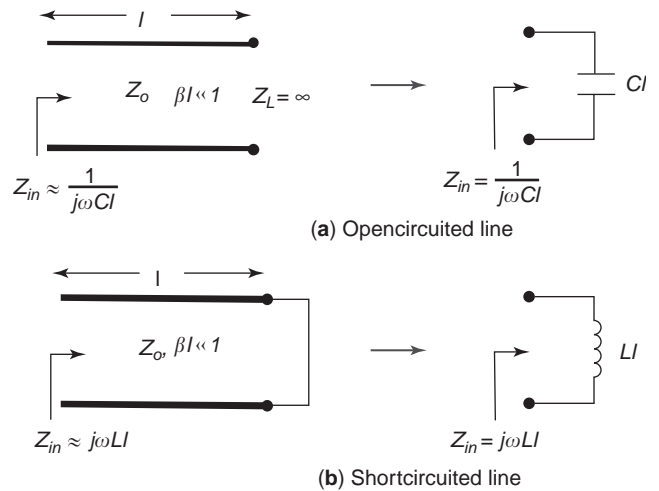


Figure 7. Transmission lines as circuit elements.

line can replace the lumped elements during circuit design.

4.2.3. Quarter-wave line. When the length of a transmission line is an odd multiple of $\lambda/4$, ($l = (2n - 1)\lambda/4$, n is a nonzero positive integer),

$$\beta l = \frac{2\pi}{\lambda} (2n - 1) \frac{\lambda}{4} = (2n - 1) \frac{\pi}{2} \Rightarrow \tan \beta l \rightarrow \pm\infty$$

and Eq. (25) becomes

$$Z_{in} = \frac{Z_0^2}{Z_L} \quad (36)$$

Hence, the load impedance connected at one end of a quarter-wave transmission line appears to be inverted at the other end. Thus, an open-circuited quarter-wave line appears to be short circuited at the input terminals and vice versa. This *impedance inverting* feature is used in many circuit design applications such as filters and impedance transformers.

4.2.4. Half-wave line. When the length of a lossless line is an integral multiple of $\lambda/2$ ($l = n\lambda/2$, n is a nonzero positive integer),

$$\beta l = \frac{2\pi}{\lambda} \cdot \frac{n\lambda}{2} = n\pi, \Rightarrow \tan \beta l \rightarrow 0$$

and Eq. (25) reduces to

$$Z_{in} = Z_L \quad (37)$$

which implies that a load impedance connected to a half-wave lossless transmission line appears to be the same without any change at the input terminals.

4.3. Transmission Line Characterization from Open- and Short-Circuit Measurements

A microwave network analyzer is an instrument, which can be used to measure the input impedance of any device connected to its input terminal. We can determine the characteristics of an unknown lossy transmission line of length less than or equal to $\lambda/2$, by measuring the input impedance under open-circuit and short-circuit conditions.

From Eq. (24), when $Z_L = \infty$,

$$Z_{oc} = Z_o \coth \gamma l \quad (\text{open-circuited line}) \quad (38)$$

when $Z_L = 0$,

$$Z_{sc} = Z_o \tanh \gamma l \quad (\text{short-circuited line}) \quad (39)$$

From Eqs. (38) and (39), we have

$$Z_o = \sqrt{Z_{oc} Z_{sc}} \quad (\Omega) \quad (40)$$

and

$$\gamma = \frac{1}{l} \tanh^{-1} \sqrt{\frac{Z_{sc}}{Z_{oc}}} \quad (\text{m}^{-1}) \quad (41)$$

where Z_o and γ are the characteristic impedance and propagation constant of the lossy line, respectively.

Example 1. A lossless transmission line of characteristic impedance of 50 ohms is connected to a load impedance of $60 \angle 60^\circ \Omega$. What is the load reflection coefficient? Find the input impedance and voltage reflection coefficient at $l = \lambda/8$ and $3\lambda/8$. Also, calculate the standing wave ratio of the line.

Solution: A simple schematic indicating input impedances at different locations is shown in Fig. 8a.

Load reflection coefficient,

$$\begin{aligned} \Gamma_L &= \frac{(Z_L - Z_o)}{(Z_L + Z_o)} = \frac{(30 + j51.96 - 50)}{(30 + j51.96 + 50)} \\ &= 0.1279 + j0.571 = 0.5837 \angle 78^\circ \end{aligned}$$

From Eq. (25), we have,

$$Z_{in} = Z_o \left[\frac{Z_L + jZ_o \tan \beta l}{Z_o + jZ_L \tan \beta l} \right]$$

Case (i) $l = \lambda/8$

$$\beta l = \frac{2\pi}{\lambda} \cdot \frac{\lambda}{8} = \frac{\pi}{4} \Rightarrow \tan \beta l = 1$$

$$(Z_{in})_{\lambda/8} = 50 \left[\frac{30 + j51.96 + j50}{50 + j(30 + j51.96)} \right]$$

$$= 165.96 - j60.85 \quad \Omega$$

$$\Gamma_{\lambda/8} = \left(\frac{165.96 - j60.85 - 50}{165.96 + j60.85 + 50} \right)$$

$$= 0.571 - j0.121 = 0.5837 \angle -12^\circ$$

Case (ii) $l = 3\lambda/8$

$$\beta l = \frac{2\pi}{\lambda} \cdot \frac{3\lambda}{8} = \frac{3\pi}{4} \Rightarrow \tan \beta l = -1$$

$$(Z_{in})_{3\lambda/8} = 50 \left[\frac{30 + j51.96 - j50}{50 - j(30 + j51.96)} \right]$$

$$= 13.28 + j4.87 \quad \Omega$$

The input impedance Z_{in} at $3\lambda/8$ can also be determined using a different procedure. Once we have calculated the input impedance at $\lambda/8$, that length of line terminated with the load can be replaced by the calculated input impedance at $\lambda/8$, as shown in Fig. 8b, which leaves with a line with length $3\lambda/8 - \lambda/8 = \lambda/4$. Thus, we have a quarter-

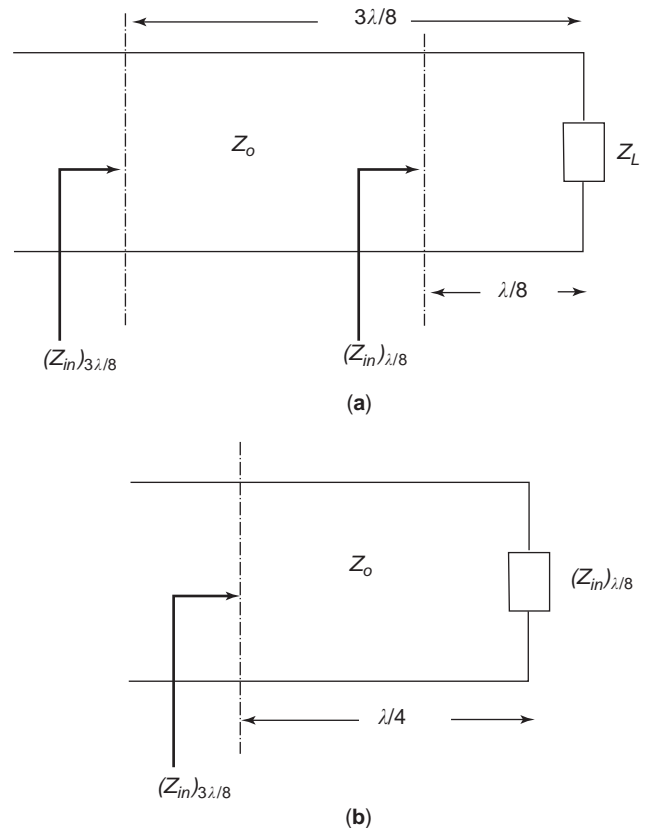


Figure 8. Transmission line problem in Example 1.

wave line of characteristic impedance $50\ \Omega$, terminated with a new load $(Z_{in})_{\lambda/8} = 165.96 - j60.85\ \Omega$. From Eq. (36), we can calculate $(Z_{in})_{3\lambda/8}$ as

$$\begin{aligned} (Z_{in})_{3\lambda/8} &= \frac{Z_o^2}{(Z_{in})_{\lambda/8}} = \frac{50^2}{165.96 - j60.85} \\ &= 13.28 + j4.87\ \Omega \end{aligned}$$

The reflection coefficient at $3\lambda/8$ can be calculated as

$$\begin{aligned} \Gamma_{3\lambda/8} &= \left(\frac{13.28 + j4.87 - 50}{13.28 + j4.87 + 50} \right) = -0.571 + j0.121 \\ &= 0.5837 \angle 168^\circ \end{aligned}$$

We can see that the magnitude of reflection coefficient at different locations is the same, and only the angle changes depending on the distance from the load.

The SWR for the line is

$$SWR = \frac{1 + |\Gamma|}{1 - |\Gamma|} = \frac{1 + 0.5837}{1 - 0.5837} = 3.804$$

5. SMITH CHART

Transmission line calculations, such as determination of input impedance and reflection coefficient, often involve manipulations with complex quantities making it tedious compared with dealing with real numbers. The *Smith chart*, which was developed by P.H. Smith [3,4], is considered to be the most widely used graphical technique for the analysis and design of transmission line circuits. Some readers may feel that in today’s world of powerful computers and modern scientific calculators, graphical ways of solving engineering problems may seem out of the ordinary. More than just being a graphical tool, the Smith chart provides a powerful way of visualizing the transmission line phenomenon, which is why many commercially available popular CAD software used for RF and microwave circuit design have integrated Smith chart calculations into the design stream.

The most common form of the Smith chart is shown in Fig. 9. First, it is important to understand that a Smith chart is essentially a polar plot of the voltage reflection coefficient, Γ . Therefore, we begin with expressing Γ as a complex quantity

$$\Gamma = |\Gamma|e^{j\theta_\Gamma} = \Gamma_r + j\Gamma_i \tag{42}$$

The right-hand side of the horizontal diameter in the chart represents the Γ_r axis, and the top side of the vertical diameter represents the Γ_i axis. $|\Gamma|$ is plotted as a radius ($|\Gamma| \leq 1$) from the center of the chart. The angle, θ_Γ ($-180^\circ \leq \theta_\Gamma \leq 180^\circ$) is measured from the Γ_r axis. We can also relate Γ to the load impedance as

$$\Gamma = \left(\frac{Z_L - Z_o}{Z_L + Z_o} \right) = \left(\frac{Z_L/Z_o - 1}{Z_L/Z_o + 1} \right) = \left(\frac{z_L - 1}{z_L + 1} \right) \tag{43}$$

where

$$z_L = r + jx = \frac{Z_L}{Z_o}$$

z_L is the *normalized* load impedance. In fact, all impedances we plot on the chart are normalized with respect to the characteristic impedance, Z_o .

From Eq. (43), we can write z_L in terms of Γ as

$$z_L = \left(\frac{1 + \Gamma}{1 - \Gamma} \right) \tag{44}$$

Thus, we can write

$$z_L = r + jx = \left(\frac{1 + \Gamma_r + j\Gamma_i}{1 - \Gamma_r - j\Gamma_i} \right) \tag{45}$$

The real and imaginary parts of this equation are

$$r = \frac{1 - \Gamma_r^2 - \Gamma_i^2}{(1 - \Gamma_r)^2 + \Gamma_i^2} \tag{46a}$$

$$x = \frac{2\Gamma_i}{(1 - \Gamma_r)^2 + \Gamma_i^2} \tag{46b}$$

Eqs. (46a) and (46b) can be rearranged as

$$\left(\Gamma_r - \frac{r}{1+r} \right)^2 + \Gamma_i^2 = \left(\frac{1}{1+r} \right)^2 \tag{47}$$

$$(\Gamma_r - 1)^2 + \left(\Gamma_i - \frac{1}{x} \right)^2 = \left(\frac{1}{x} \right)^2 \tag{48}$$

Equation (47) describes a family of circles called the *resistance circles*, where each circle is associated with a specific value of resistance, r . The resistance circles for different values of r are shown on the chart. We can notice that the centers of all r -circles lie on the horizontal axis. All circles pass through the $(\Gamma_r = 1, \Gamma_i = 0)$ point. The largest r -circle is the $r = 0$ circle with a unity radius.

Equation (48) represents the other family of circles called the *reactance circles*, which are also shown on the chart. Different values of x lead to circles of different radii with centers at different positions on the $\Gamma_r = 1$ line. These circles are always orthogonal to the resistance circles. Reactance circles with positive reactance ($x > 0$) lie in the upper half of the chart and those with $x < 0$ lie in the lower half. Intersection of a resistance and reactance circle represents the normalized load impedance, z_L .

One of the main advantages of the Smith chart is that it can be used directly to read the reflection coefficient for a given normalized load impedance and vice versa without having to calculate them. Another useful feature is that the value of the resistance passing through the intersection of the $|\Gamma|$ circle and the Γ_r axis (positive real axis) directly equals the standing wave ratio, SWR. Perhaps the most important feature of the Smith chart is that the angular motion on a constant $|\Gamma|$ circle in a clockwise or counterclockwise direction represents a corresponding movement on a terminated transmission line toward the generator or the load, respectively. Thus, a movement of half a wavelength in the line length on the transmission line corresponds to a complete 360° revolution on the $|\Gamma|$

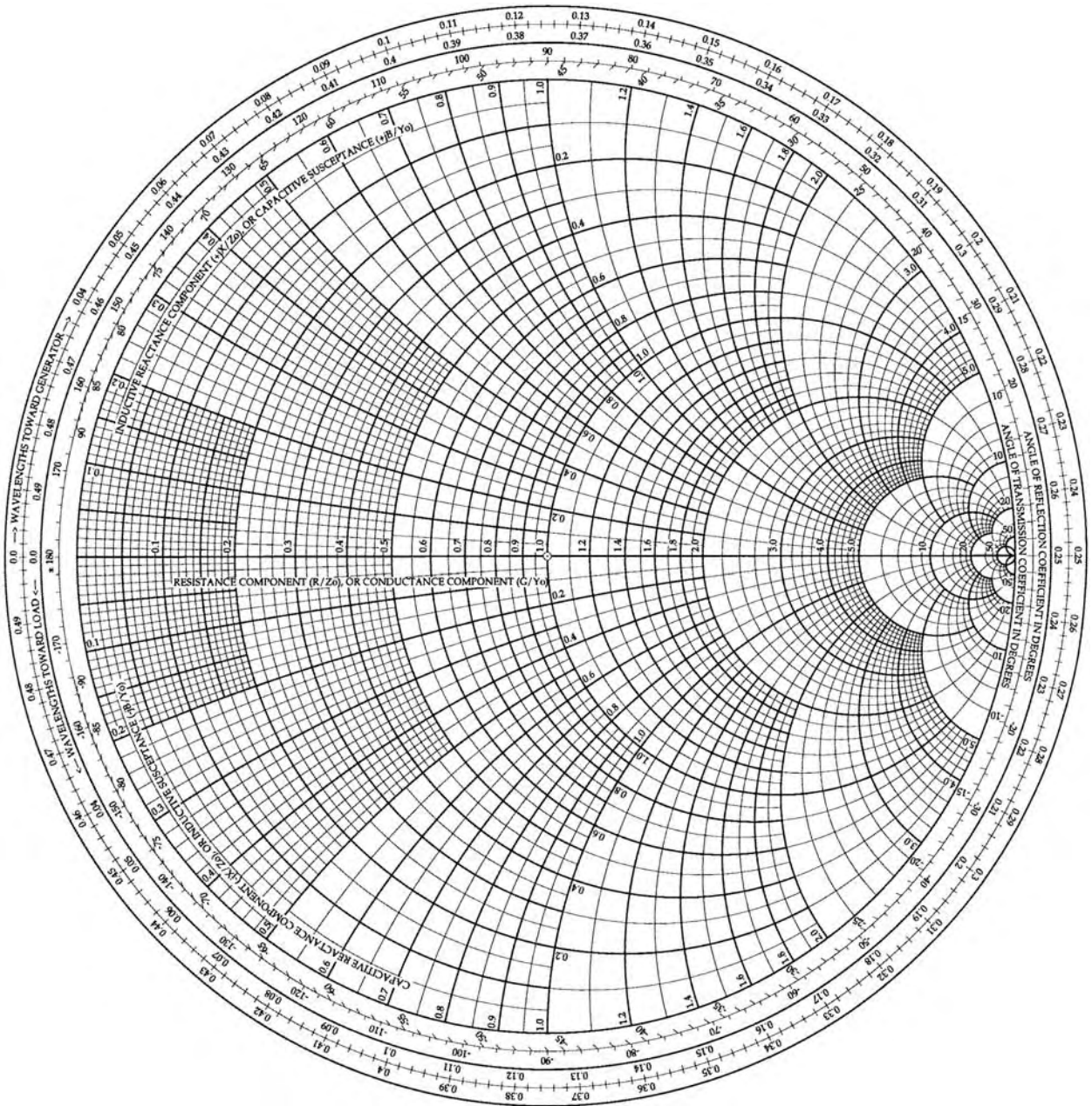


Figure 9. The Smith chart.

circle reaching the same normalized impedance (or reflection coefficient) point, which reasserts the fact we have seen earlier in the case of a half-wave line, where the input impedance is same as the load impedance. Thus the Smith chart takes into account the periodic behavior of the transmission line.

Example 2. Calculate the input impedance and reflection coefficient for the problem given in Example 1 at $\lambda/8$ and $3\lambda/8$ using the Smith chart. Also, find the SWR of the line.

Solution: The procedure for calculating the above parameters using the Smith chart is described in steps as shown below:

1. Calculate normalized $z_L = Z_L/Z_o = 0.6 + j1.039$ and mark the same on the Smith chart as point A in Fig. 10.
2. With OA as the radius, draw a circle. Measure the radius and normalize it with respect to the radius of the largest r circle ($r = 0$ circle). Read $|\Gamma| = 0.58$.
3. Extend OA to intersect the angular scale given on the Smith chart for reflection coefficient. Mark the reading. This gives the angle of Γ in degrees. $\theta_r = 78^\circ$.
4. Mark the reading where the $|\Gamma|$ circle intersects the positive real axis. This gives $SWR = 3.8$.
5. From point A, move 0.125λ toward the generator to reach point B. Mark the reading on the angular scale of reflection coefficient. This gives angle of Γ at

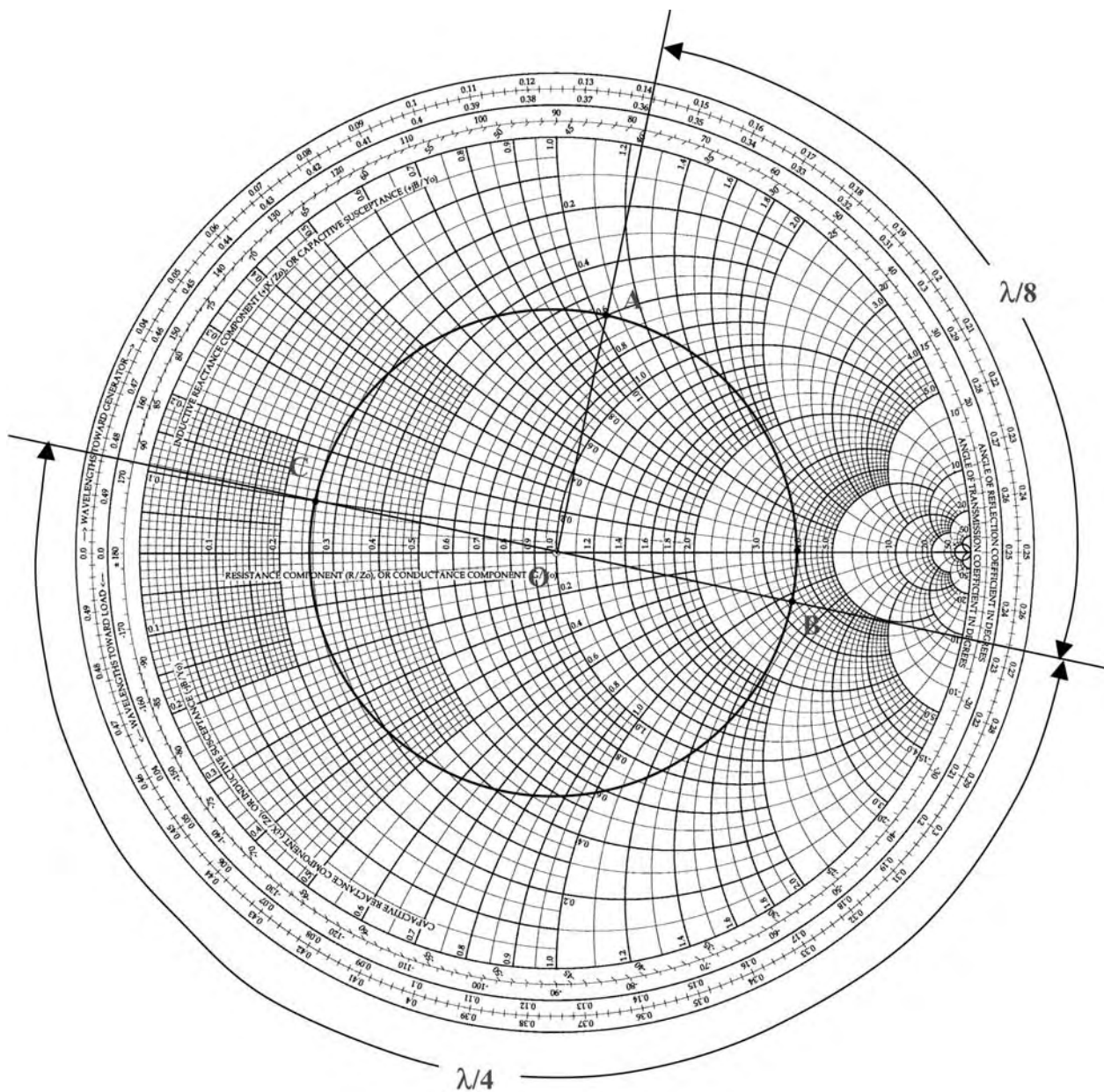


Figure 10. The Smith chart solution for Example 2.

$l = \lambda/8$. The magnitude of Γ remains the same. Measure $(\theta_\Gamma)_{\lambda/8}$ as -12° .

6. Mark the normalized impedance value by observing r and x values at B, where $\Gamma = 0.58 \angle -12^\circ$. We get

$$r = 3.3 \text{ and } x = -1.21$$

$$\begin{aligned} \therefore (Z_{in})_{\lambda/8} &= 50.(z_{in})_{\lambda/8} = 50.(3.3 - j1.21) \\ &= 165 - j60.5 \Omega \end{aligned}$$

7. From B, move $\lambda/4$ toward the generator to reach point C. Join OC and extend it to intersect the

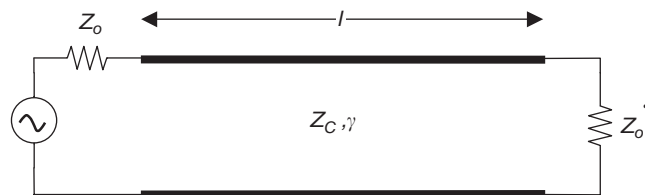
angular scale for Γ at 168° . This gives $(\Gamma)_{3\lambda/8} = 0.58 \angle 168^\circ$.

$$\begin{aligned} (z_{in})_{3\lambda/8} &= r + jx = 0.265 + j0.1 \\ (Z_{in})_{3\lambda/8} &= 50.(z_{in})_{\lambda/8} = 50.(0.265 + j0.1) \\ &= 13.25 + j5 \Omega \end{aligned}$$

6. NETWORK PARAMETERS OF A GENERAL LOSSY TRANSMISSION LINE

Transmission lines are used in every microwave network system design. When we look at various blocks of a

Table 2.



Type	Two-port Parameters	
ABCD	$A = \cosh(\gamma l)$ $C = Y_C \sinh(\gamma l)$	$B = Z_C \sinh(\gamma l)$ $D = \cosh(\gamma l)$
Z	$Z_{11} = Z_C \coth(\gamma l)$ $Z_{12} = Z_{21}$	$Z_{21} = Z_C \operatorname{cosech}(\gamma l)$ $Z_{22} = Z_{11}$
Y	$Y_{11} = Y_C \coth(\gamma l)$ $Y_{12} = Y_{21}$	$Y_{21} = -Y_C \operatorname{cosech}(\gamma l)$ $Y_{22} = Y_{11}$
S	$S_{11} = \frac{Z_C^2 - Z_o^2}{2Z_C Z_o \coth \gamma l + Z_C^2 + Z_o^2}$ $S_{12} = S_{21}$	$S_{21} = \frac{2Z_C Z_o}{2Z_C Z_o \cosh \gamma l + (Z_C^2 + Z_o^2) \sinh \gamma l}$ $S_{22} = S_{11}$

microwave system, such as a transceiver, we see components such as amplifiers, mixers, oscillators, and filters interconnected using transmission lines of different characteristic impedances, propagation constants, and lengths. Depending on the overall system requirement, these transmission lines could be realized in different configurations such as a microstrip line, coplanar waveguide, stripline, or waveguide among several variations. For a given physical geometry, the electrical characteristics, Z_o and γ for these transmission lines, can be obtained based on the available analytical/numerical approaches from the literature. Interested readers are encouraged to refer to [5–7].

A common approach in microwave network analysis is to represent each component as a two-port or multiport network and use the network analysis principles to calculate the overall characteristics of the larger network formed by interconnecting various components. In this procedure, each component is associated with a set of network parameters, such as impedance (Z), admittance (Y), transmission (ABCD) or scattering (S) parameters, and the voltage/current or wave amplitudes are interrelated at various junctions/interconnections to obtain the overall characteristics of the system. As with other components, transmission lines can also be treated as microwave networks, and the knowledge of network parameters will often be useful when they are used in a system.

Table 2 presents various commonly used network parameters of a general lossy transmission line. The line is assumed to have a characteristic impedance of Z_C , propagation constant, γ , and length l . The expressions for the scattering (S) parameters assume that the reference port impedance is considered to be Z_o , which is different from the characteristic impedance Z_C . The expressions for a lossless transmission line can be directly obtained from Table 2 by replacing γ with $j\beta$. In the case of scattering

parameters, when $Z_C = Z_o$, the line becomes a matched lossy transmission line of length l and the scattering matrix reduces to

$$S = \begin{bmatrix} 0 & e^{-\gamma l} \\ e^{-\gamma l} & 0 \end{bmatrix} \quad (49)$$

BIBLIOGRAPHY

1. J. C. Maxwell, *A Treatise on Electricity and Magnetism*, Dover, New York, 1954.
2. P. J. Nahin, *Oliver Heaviside: Sage in Solitude*, IEEE Press, New York, 1988.
3. P. H. Smith, Transmission-line calculator, *Electronics*, **12:29** (1939).
4. P. H. Smith, An improved transmission-line calculator, *Electronics*, **17:130** (1944).
5. D. M. Pozar, *Microwave Engineering*, 3rd ed., Wiley, New York, 2003.
6. K. C. Gupta, R. Garg, and I. J. Bahl, *Microstrip Lines and Slotlines*, Artech House Norwood, MA, 1979.
7. B. Bhat and S. K. Koul, *Strip-Line Like Transmission Lines for Microwave Integrated Circuits*, Wiley, New York, 1989.

FURTHER READING

1. D. K. Cheng, *Field and Wave Electromagnetics*, 2nd ed., Addison-Wesley, Reading, MA, 1990.
2. W. H. Hayt, Jr., *Engineering Electromagnetics*, 6th ed., McGraw-Hill, New York, 2001.
3. F. T. Ulaby, *Fundamentals of Applied Electromagnetics*, Prentice-Hall, Englewood Cliffs, NJ, 2003.

frequencies. The incoming signal from the channel passes through the preselector filter, RF amplifier, and image filter, where it is applied to the mixer. The mixer combines the incoming signal with the local oscillator (LO) waveform to generate output at the sum and difference of the signal and LO frequencies. The LO frequency can be above or below the signal frequency. If the LO frequency is above the signal frequency, the receiver uses high-side injection. If the LO frequency is below the signal frequency, the receiver uses low-side injection. The intermediate frequency (IF) filter selects either the sum or the difference and rejects the other. The selected frequency is termed the intermediate frequency (IF), and the IF amplifier provides additional gain at this frequency. The detector/demodulator extracts the transmitted information from the IF waveform. Some superhet architectures use two or more intermediate frequencies in succession to simplify the requirements placed on the filters. The mixing process is sometimes called *conversion*. A receiver with one intermediate frequency is a single-conversion receiver, and a receiver with two intermediate frequencies is a dual-conversion receiver. Unless explicitly stated otherwise, examples in this article refer to single-conversion receivers.

Although other receiver architectures exist, the superheterodyne has many advantages. Distributing the amplifier gain between the RF and IF frequencies makes it less difficult to prevent unwanted oscillation. The receiver is tuned to a wanted input frequency by selecting the frequency of the LO. The IF filter can have a fixed center frequency, so its characteristics like bandwidth and delay can be optimized. It does not have to be retuned when the receiver is tuned to a new channel.

1.3.1. Weak Signal Performance. At UHF, internally generated noise limits the weakest signal that can be detected. The noise generated by the RF amplifier is amplified by all the stages in the receiver so that it determines the receiver sensitivity. Low-noise, high-gain RF amplifiers produce the greatest sensitivity. There is often a trade-off between sensitivity and strong signal performance, because a high-gain RF amplifier can overload the mixer with a strong signal.

1.4. Images

The mixing or frequency conversion process introduces unwanted and spurious responses. The most important unwanted response is called an image. The image frequency and the wanted frequency are symmetrical about the LO frequency. Any unwanted signal at the image frequency that gets into the mixer will be amplified and demodulated essentially as if it came in at the wanted frequency. Consider a simple example. A TV broadcast receiver is tuned to 561.25 MHz, the video carrier frequency for television channel 29. The receiver has an IF of 45 MHz, so the LO runs at 516.25 MHz. A difference frequency of 45 MHz is generated by mixing 561.25 MHz and 516.25 MHz. Suppose there is a nearby transmitter on channel 14. When the 471.25 MHz channel 14 video mixes with the 516.25 MHz LO output, the difference is also

45 MHz. The receiver is tuned to channel 29, but it will also pick up channel 14 if the channel 14 signal reaches the mixer. The preselector and image filters must pass the desired signal but reject the image. Figure 3 shows the frequency relationship among the desired signal, the image, and the LO for a single-conversion receiver. Note that the image and the wanted response are separated by twice the IF frequency. A dual-conversion superhet would have three images.

Images are the key drawback to the superheterodyne architecture. Their elimination requires filters, and image rejection is easier with high IF frequencies. The higher the IF frequency, the more difficult it is to make narrowband filters. Filters are the major impediment to fully integrated UHF receivers. They are usually separate discrete components.

1.5. Spurious Responses

The image is only one of many possible unwanted mixer outputs. The mixer is an inherently nonlinear device that generates and combines harmonics of the LO and signal frequencies. Continuing with the numbers from the previous example, the second harmonic of the 516.25 MHz LO appears at 1032.5 MHz. If a 538.75 MHz signal reaches the mixer, the mixer generates a second harmonic at 1077.5 MHz. The mixer also generates the sum and the difference of the harmonics. One of these products is at the 45 MHz IF frequency, and the receiver has a spurious response at 538.75 MHz. This response is sometimes called the half IF spur because it appears 22.5 MHz or one-half the IF frequency from the desired response. Two times the IF, in this case 90 MHz, separates the image from the wanted signal. It is much easier to design the image and the preselector filters to remove the image than the half IF spur.

Other spurious products are a serious problem in superhet receivers. Mixers generate not only the second harmonic but higher order harmonics as well. Balanced mixers, which suppress the even-order harmonics, are widely used to eliminate some of the spurious mixing products. UHF receivers may have multiple mixers and intermediate frequencies, and predicting all the spurious mixing products can be difficult. Software for this purpose is commercially available to help the designer select mixers.

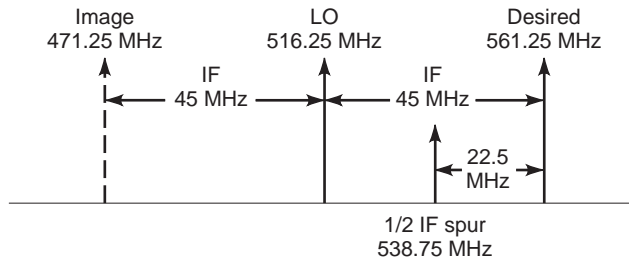


Figure 3. The frequency relationship between the desired signal, the local oscillator signal, and the image signal for a TV receiver with a 45 MHz intermediate frequency. Note that the image and the desired signal frequencies are symmetric about the local oscillator frequency.

1.5.1. Strong Signal Behavior. At UHF frequencies, it is difficult to build a preselector filter narrow enough to pass a single channel of information. It may not be desirable to build very narrowband filters if the receiver is to be tuned over a range of frequencies. If the range of desired signal frequencies cannot pass through the preselector filters, then these filters must be retuned when the LO is tuned to the new frequency. This process, called tracking, increases the complexity of the receiver. For these reasons the receiver's ultimate bandwidth is usually set at IF, and a number of unwanted signals can reach the mixer.

All of the unwanted signals that reach the mixer will produce sum and difference frequency products with the LO. The RF amplifier may generate some of the unwanted signals. RF amplifiers are not perfectly linear; strong signals can cause them to saturate. This nonlinearity generates harmonics, which combine either in the amplifier itself or in the mixer.

The nonlinear behavior of amplifiers and mixers is specified in terms of third-order mixing products. Figure 4 shows a test setup for measuring these products. The output for an ideal amplifier would be only at the input frequencies f_1 and f_2 . Amplifier nonlinearities generate harmonics of f_1 and f_2 plus the mixing products of these harmonics. These mixing products are specified in terms of the harmonic number of the signals that generate them. Particularly important are the third-order products $2f_1 - f_2$ and $2f_2 - f_1$. Figure 5 shows the output of a nonideal amplifier. The third-order products are the most problematic because their frequencies fall close to the desired signal and are difficult to filter.

As an example, consider a handheld analog cellular telephone receiver. Channel 1 is 870.030 MHz, channel 2 is 870.060 MHz, channel 3 is 870.090 MHz, and channel 4 is 870.120 MHz. The second harmonic of channel 2 is 1740.12 MHz. If this mixes with channel 3, the difference is 870.030 MHz, which is channel 1. Similarly, the second harmonic of channel 3 mixes with channel 2 to produce a signal at 870.12 MHz, which is channel 4. Figure 5 shows that third-order mixing of channels 2 and 3 creates signals on channels 1 and 4. If the receiver is tuned to channel 1 or 4 and strong channel 2 and 3 signals are present, then nonlinear RF amplifier or mixer products will interfere with channel 1 or 4, limiting the receiver's ability to detect a weak signal on these channels.

The nonlinear products increase with increasing signal levels. The power in the third-order products increases three times faster than the power of the desired signals. The point where the power in the third-order products

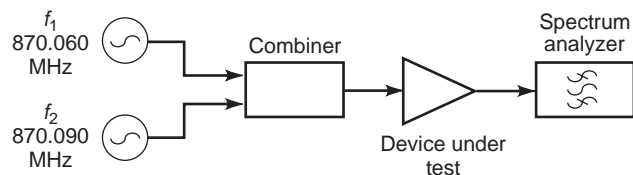


Figure 4. A test setup for measuring third-order products. The frequencies shown are for the example presented in the text.

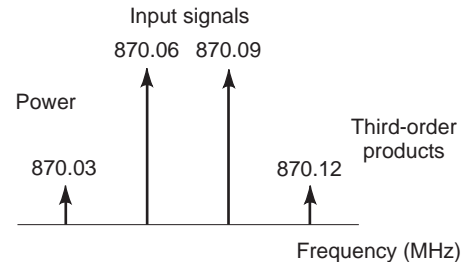


Figure 5. Sketch of a spectrum analyzer display showing the output of a nonideal amplifier with strong input signals at 870.06 and 870.09 MHz. The amplifier generates unwanted third-order products at 870.03 and 870.12 MHz.

would be equal to the power in the desired signal is called the third-order intercept point.

1.5.2. Spurious Free Dynamic Range. The weakest signal the receiver can detect is limited by the internally generated noise. The equivalent power of this noise is the noise floor. The strongest signals the receiver can tolerate without internally generated interference are those that create a third-order mixing product that equals the noise floor. The ratio of the strongest signal power to the noise floor power is the spurious free dynamic range (SFDR).

High-gain, low-noise RF amplifiers maximize sensitivity. Maximizing SFDR requires a careful tradeoff among the gain, noise performance, and third-order intercept of all the stages prior to the narrowest filter in the system. Building a sensitive receiver is relatively easy; building a sensitive receiver that can handle strong signals can be a challenge.

1.6. Other Receiver Topologies

1.6.1. Direct Conversion Receivers. The superhet receiver converts the incoming signal to an intermediate frequency, but it is possible to convert the radio signal directly to the original baseband of the transmitted information. This requires the LO to be tuned to the frequency of the incoming signal. If the signal and LO frequencies are equal, their difference is zero. The mixer output is the original information, which was contained in modulation sidebands, about the carrier frequency. A receiver that works this way is called a direct conversion (DC), homodyne, or zero IF receiver (see Fig. 6).

Direct conversion receivers offer a simpler design and fewer components than superhets. High-gain amplifiers are easier to build at baseband than at the signal or IF frequency, so a DC receiver can be as sensitive as a superhet. This topology minimizes the number of components at the RF and IF frequencies. On the other hand, mixer imbalance and LO leakage (LO feedthrough) into the antenna can cause large DC offsets. Local oscillator phase noise is highest close to the LO frequency, and the mixer translates this noise directly to baseband. Low-frequency noise in mixers and high-gain baseband amplifiers can limit sensitivity. Depending on the choice of mixer, DC receivers have spurious responses at integer multiples of the input frequency, so a preselector filter is

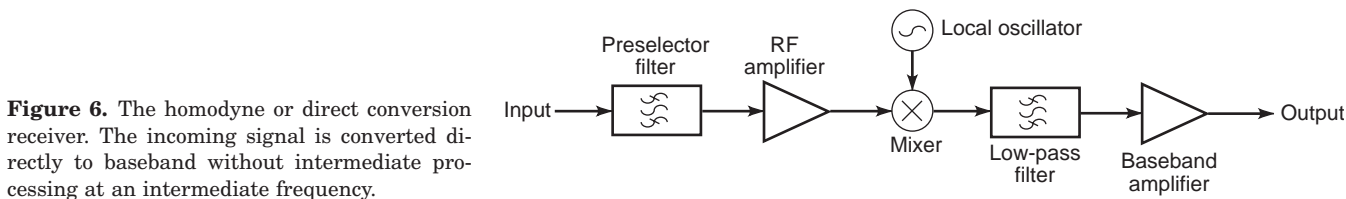


Figure 6. The homodyne or direct conversion receiver. The incoming signal is converted directly to baseband without intermediate processing at an intermediate frequency.

still required. As all the signal processing occurs at baseband, it is possible to integrate the entire receiver, including the mixer. This is attractive for small low-power receivers like those found in pagers. DC receivers cannot be used for narrowband FM without extra signal processing.

1.6.2. Tuned Radiofrequency Receivers. The tuned radiofrequency (TRF) receiver of Fig. 7 is an old design that offers great simplicity. The signal passes through a preselector filter and is amplified by an RF amplifier at the signal frequency. The classic TRF receiver consists of a cascade of tuned amplifiers. The filtering and amplifying functions are combined. The amplified signal goes directly to the detector, which is typically a simple diode amplitude demodulator. TRF receivers work well with amplitude modulation or on-off keyed digital signals. They are not used for narrowband phase or frequency modulation, because these waveforms are difficult to demodulate at UHF. The simplicity of the TRF is attractive for low-current, low-cost applications. As the TRF receiver has no oscillators, there is no oscillator radiation. TRF receivers escape the government regulations that limit RF emissions. They have none of the spurious mixing responses that are a problem in superhet receivers. As TRF receivers contain no mixers, they have no images and can reproduce exactly the frequency or phase information in the original signal.

TRF receivers have several disadvantages. They are not frequency agile and thus are useful only for single-frequency systems. TRF receivers cannot use standard low-cost filters like those available at common IFs for superhets. Narrowband filters, which match modulation bandwidths, are difficult to build at UHF, and tuning a TRF receiver to a new frequency requires retuning or replacing the filters. TRF receiver sensitivity is limited because of the difficulty of building stable high-gain amplifiers at UHF. For these reasons, the UHF applications for TRF receivers tend to be limited to low-cost, short-range devices.

1.6.3. Regenerative and Superregenerative Receivers. Regenerative receivers come from the earliest days of radio and are capable of very high sensitivity with only a

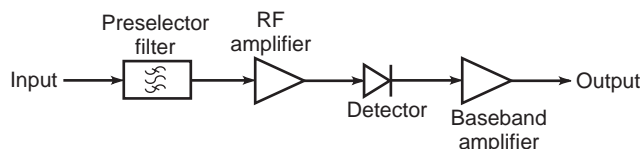


Figure 7. The tuned radiofrequency receiver. The incoming signal is amplified and detected without frequency conversion.

single active device. A regenerative receiver is an amplifier to which frequency selective positive feedback has been applied. If the feedback is adjusted below the point of oscillation, the receiver acts as a square law detector. It is suitable for amplitude-modulated signals. The feedback can be advanced to the point where oscillation occurs. The regenerative receiver then acts as a self-oscillating direct conversion receiver. In this mode, it will demodulate single sideband (SSB) or continuous wave signals.

The superregenerative receiver is a variation on the regenerative theme. The positive feedback is advanced beyond the point where oscillations begin. This increases the gain. It takes a finite amount of time for the oscillation amplitude to buildup because of energy storage in the oscillator-tuned circuit. Before the oscillation amplitude reaches a significant level, the oscillating amplifier is shut off or “quenched.” The process of oscillation buildup and quenching is repeated. Injecting a signal close to the oscillation frequency speeds the buildup of oscillations. The envelope of any amplitude modulation on the injected signal can be extracted from the amplitude of the oscillations in the superregenerative detector.

Superregenerative receivers find application in short-range, low-cost devices such as radio-controlled toys and garage door openers. They work well at UHF, and their high sensitivity and extreme simplicity make them attractive for such applications.

The major drawbacks of a superregenerative receiver are poor selectivity and the potential to create interference. They can be easily overloaded by strong adjacent channel signals, and, if not properly designed, they can radiate a potent signal of their own. The use of positive feedback results in very high gain, but it accentuates any variations in amplifier gain because of temperature, voltage, aging, or other effects. Stable performance is difficult to obtain, and receiver bandwidth will vary inversely with gain. It is very difficult to meet emission specifications with regenerative and superregenerative receivers.

2. DESIGNING SUPERHETERODYNE RECEIVERS FOR UHF

2.1. Weak Signal Behavior

2.1.1. Noise Temperature and Receiver Sensitivity. Sensitivity is a measure of a receiver’s weak signal performance. Depending on the particular application, sensitivity may be expressed in terms of [1] the receiver’s noise floor, [2] the minimum detectable signal, or [3] the minimum input signal level necessary to achieve a useful output. However defined, sensitivity is closely related to the irreducible noise level at the receiver’s output.

Noise is generated within all electronic components, active or passive. The noise power that a resistor at physical temperature T would deliver to an ideal power meter whose response is frequency independent over a measurement bandwidth B is given by

$$P_N = kTB \quad (1)$$

where k is Boltzmann's constant (1.38×10^{-23} J/K).

Any other one-port noise source can be described by an equivalent noise temperature T_N such that the noise delivered to an ideal power meter with measurement bandwidth B is

$$P_N = kT_N B \quad (2)$$

Now imagine a two-port device with gain g connected between an antenna or other noise source with noise temperature T_A and a load. The noise power delivered to the load will consist of amplified input noise plus additional noise that is generated inside the two-port device:

$$p_N = gkT_A B + \Delta p \quad (3)$$

where Δp is the internally generated noise (see Fig. 8).

For analysis, it is convenient to represent the internally generated noise as if it came from a fictitious noise source at the input of a noiseless equivalent circuit of the two-port device. This noise temperature T_e of this fictitious noise source is the effective input noise temperature of the device (see Fig. 9):

$$p_N = gkT_A B + \Delta p = gkT_A B + gkT_e B = gk(T_A + T_e)B \quad (4)$$

If a receiver with effective input noise temperature T_e is connected to an antenna with equivalent noise temperature T_A , the resulting system noise temperature T_S is given by

$$T_S = T_A + T_e \quad (5)$$

The receiver noise floor is $kT_S B$, where B is the overall receiver bandwidth (usually set by the IF filter). The minimum detectable signal (MDS) is usually specified as the noise floor. Depending on the application, the receiver sensitivity may be defined as the noise floor or as the

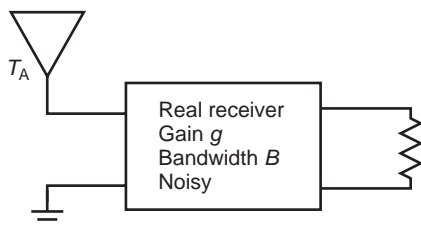


Figure 8. Representation of a real receiver. It amplifies thermal noise from the antenna and adds its own internally generated noise.

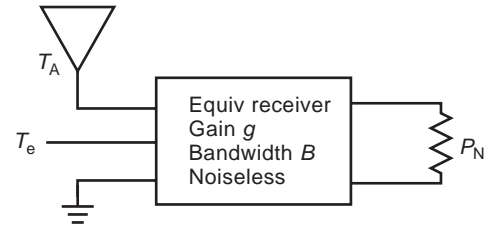


Figure 9. The noiseless equivalent receiver. Internally generated noise is represented as if it came from a fictitious input at temperature T_e .

minimum signal necessary to produce a specified output signal-to-noise ratio (SNR). The noise floor is sometimes specified with a bandwidth B of 1 Hz. At room temperature, this corresponds to -174 dBm.

2.1.2. Noise Figure. Although noise temperature is perhaps a more immediately useful quantity, the noise figure of a UHF receiver is more commonly specified. The noise figure of a two-port device was originally defined as the ratio of the input SNR to the output SNR. This definition is quite useful for “back of the envelope” calculations for point-to-point microwave systems, but it suffers from a lack of uniqueness (because it depends on the antenna noise temperature) and universal applicability. Officially, noise figure is “the ratio of (A) the total noise power per unit bandwidth (at a corresponding output frequency) delivered by the system into an output termination to (B) the portion thereof engendered at the input frequency by the input termination, whose noise temperature is standard (290 K at all frequencies)” [1].

Mathematically, the noise figure is given as a ratio by nf and in decibels by NF :

$$nf = 1 + \frac{T_e}{290} \quad (6)$$

$$NF = 10 \log_{10}(nf) \quad (7)$$

Although some authors argue rather vehemently that noise figure is not a meaningful concept, it is well established as a specification for UHF receivers and their components. Overall values of 2 dB are achievable. Most calculations ultimately require the noise temperature, conveniently obtained from the noise figure by

$$T_e = 290(nf - 1) \quad (8)$$

The noise figure as defined in Eq. (6) is the standard noise figure, based on an assumed standard source noise temperature of 290 K. This is the one that manufacturers measure and quote. An actual noise figure, based on the true source temperature, is often used to calculate the minimum detectable signal or SNR degradation. See Ref. 2 for an excellent discussion of noise figure issues.

2.1.3. Determining Receiver Noise Temperature and Noise Figure. Most analyses of receiver performance assume that bandwidth narrows as one moves from the

RF input to the IF output. The last stage has the narrowest bandwidth, and it effectively determines the overall bandwidth. Thus, if the preselector, RF amplifier, mixer, and so on, have bandwidths $B_1, B_2, B_3 \dots B_N$, and if B_N is much less than any of the others, then the overall bandwidth B is given by

$$B \approx \min\{B_1, B_2, B_3 \dots B_N\} = B_N \quad (9)$$

Under these conditions, the overall noise temperature and noise figure are given by

$$T_e = T_1 + \frac{T_2}{g_1} + \frac{T_3}{g_1 g_2} + \dots + T_N \prod_{m=1}^{N-1} \frac{1}{g_m} \quad (10)$$

$$\text{nf}_o = \text{nf}_1 + \frac{\text{nf}_2 - 1}{g_1} + \frac{\text{nf}_3 - 1}{g_1 g_2} + \dots + (\text{nf}_N - 1) \prod_{m=1}^{N-1} \frac{1}{g_m} \quad (11)$$

where T_i, g_i , and B_i , are the noise temperature, gain, and bandwidth of the i th stage. It is important to note that the gains and noise figures in the preceding equations are ratios, not decibel values.

If one bandwidth dominates but is not the bandwidth of the last block in the chain, it is still possible to calculate T_e and NF_o . This situation occurs in some modern receiver designs that put most of their gain in a wideband amplifier at the end of the IF chain. A narrowband low-gain amplifier precedes the mixer. This architecture leads to better dynamic range performance. Under these conditions, let B_1 and g_1 be the bandwidth and gain of the low gain and narrowband part of the receiver, and let B_2 and g_2 be the bandwidth and gain of the subsequent high gain and wideband part of the receiver. The corresponding noise temperatures and noise figures are T_1 and nf_1 and T_2 and nf_2 . Under these conditions, the output noise power is given by Eq. (12) and the overall noise temperature and noise figure by Eqs. (13) and (14).

$$p_o = g_1 g_2 k T_A B_1 + g_1 g_2 k T_1 B_1 + g_2 k T_2 B_2 \quad (12)$$

$$= g_1 g_2 k T_A B_1 + g_1 g_2 k T_e B_1$$

$$T_e = T_1 + T_2 \frac{B_2}{g_1 B_1} \quad (13)$$

$$\text{nf}_o = 1 + \frac{T_e}{T_o} = \text{nf}_1 + (\text{nf}_2 - 1) \frac{B_2}{g_1 B_1} \quad (14)$$

It is possible for the wideband IF stage to dominate the receiver's noise performance in this topology. Additional filters are sometimes added just prior to the detector, or as part of the detector, effectively narrowing B_2 .

2.1.4. Mixer Noise Performance. Like all two-port devices, mixers both process incoming noise and add to it their own internally generated noise. The situation is more complicated in mixers because the input noise is translated in frequency from two places in the spectrum. Noise coming in at the wanted signal frequency and at the unwanted image frequency appears at the IF frequency.

Depending on how the total output noise power is interpreted, a mixer can be described by both a double sideband (DSB) noise figure and a single sideband (SSB) noise figure. A single sideband noise temperature corresponds to the single sideband noise figure, and a double sideband noise temperature corresponds to the double sideband noise figure. The SSB quantities are twice as large (or 3 dB larger if expressed in decibels) as the DSB quantities, which seems backward.

This confusion develops largely because SSB and DSB apply to the NF measurement technique rather than to the way in which the mixer is used. In an NF measurement, the input to the mixer is connected to a broad-band noise source, and the noise power at the mixer output is compared with the noise power at the mixer input. The noise figure so measured is called the DSB NF because noise got into the mixer through both the wanted signal frequency and the unwanted image frequency. Noise at the two frequencies is analogous to the two sidebands that surround a carrier in some modulation schemes. For the given output power, there is twice as much input noise power as there would be in an SSB noise measurement. Thus, the signal-to-noise ratio is 3 dB better than it would be in an SSB noise measurement, and the DSB noise figure is 3 dB better than the SSB noise figure. See Refs. 3 and 4 for a detailed discussion of the measurement issues.

A double set of parameters with the SSB quantities larger than the DSB quantities leads to a great deal of confusion about which noise figure should be used for a particular application. See Ref. 2 for a detailed discussion of this point. The rule of thumb is if, for a particular application, the mixer input sees equal incoming noise powers at the signal and image frequencies, the mixer is described by the SSB noise temperature and noise figure. If the input noise level at the signal frequency is much greater than the input noise level at the image frequency, then the frequency-translated image noise has little effect on the output noise power, and the mixer is described by the DSB noise temperature and noise figure.

The last situation is attractive because it allows the lower noise figure to be used. The reader should note that its application does require that the mixer see insignificant input noise in the image band. If the stage immediately ahead of the mixer is an image rejection filter, its noise output in the image band should be checked. The filter could look like a noise source at the ambient temperature.

2.1.5. LO Phase Noise. Local oscillator noise can be a significant contributor to the overall receiver noise level. Oscillator noise takes two forms: amplitude and phase noise. In well-designed oscillators, the effect of amplitude noise can be neglected [5], but phase noise effectively phase-modulates the oscillator frequency. Oscillator performance is measured in terms of the power spectral density of the resulting modulation sidebands. The spectral density can be predicted from the Q of the oscillator resonator and from the noise power generated by the active device in the oscillator [6]. Figure 10 shows the phase noise in a typical oscillator output spectrum.

Phase noise degrades receiver dynamic range through what is called "reciprocal mixing." Figure 11 shows the

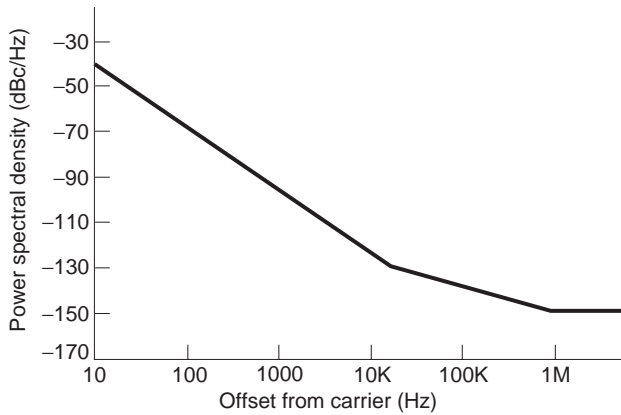


Figure 10. The phase noise spectrum of a typical local oscillator.

effect of reciprocal mixing in a receiver containing a noisy LO and a strong adjacent channel signal that is outside the IF bandwidth. Without the LO noise, this signal would be rejected by the IF filter. With LO noise the strong adjacent channel signal acts as a “local oscillator” for the oscillator noise. The oscillator noise appears as signals adjacent to the LO, and those noise frequencies separated by the IF from the interfering signal will be mixed into the IF. The noise floor is increased by the oscillator phase noise, and it obscures the desired weak signal.

Phase noise produces an additional receiver impairment in systems where information is carried in signal frequency (frequency modulation, FM) or phase (phase modulation, PM). In digital phase shift keyed (PSK) systems, it is necessary to regenerate the phase of the carrier signal as a demodulation reference. Mixing transfers the phase noise of the receiver’s LO to the incoming signal. This increases the phase uncertainty of the demodulation reference and leads to bit errors.

2.2. Strong Signal Behavior

2.2.1. Nonlinear Operation and Intermodulation Products.

In ideal linear components, superposition holds, and the output waveform is linearly proportional to the input waveform. No frequencies appear in the output waveform that were not present in the input waveform. Any real two-port device will, when driven hard enough, become nonlinear. Nonlinear operation in receivers creates unwanted signals called intermodulation products that interfere with the

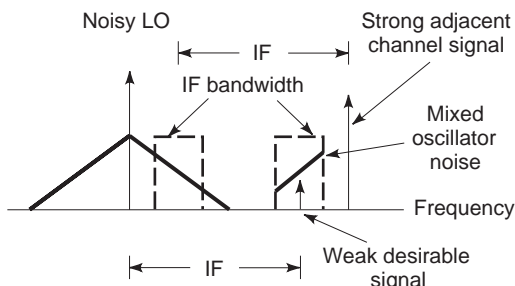


Figure 11. An illustration of reciprocal mixing, the process by which local oscillator phase noise combines with an adjacent channel signal to raise the receiver noise floor.

wanted signals. It also can cause a loss of sensitivity when an unwanted strong signal is close in frequency to a wanted weak signal.

To illustrate nonlinearity, consider an RF amplifier with a sinusoidal input at frequency f_1 . A typical plot of input power versus the output power delivered at frequency f_1 would appear as shown in Fig. 12.

At low power levels, the relationship between output and input powers is linear. At high levels of input power, the slope decreases and the input-output relationship becomes nonlinear. This onset of nonlinearity is called gain compression (or just compression). A common measure of large-signal handling ability is the input 1 dB compression point, the input power level at which the output power falls 1 dB below the extrapolation of the linear relationship. Gain compression in a receiver results in an effect called desensitizing. If a receiver is tuned to a weak signal and a strong signal appears in the RF amplifier’s pass-band, the strong signal can reduce the RF amplifier gain. The gain reduction can make the weak signal disappear even though the strong signal is not translated into the IF passband and never reaches the demodulator. Desensitizing is a problem in large-signal handling that is distinct from intermodulation products.

Increasing the input power beyond the 1 dB compression point causes the plot to fall farther below a linear relationship. This part of the curve is called the compression region. The output power reaches a peak and then decreases. The peak is called saturation, and the region beyond the peak is the overdrive region.

Output power falls below the linear value after compression begins because output is developed at frequencies other than the input frequency. As long as the input is a sinusoid at frequency f_1 , these frequencies are harmonics of f_1 (i.e., $2f_1, 3f_1 \dots$) and easy to filter. If the input contains two or more frequencies, then the resulting intermodulation products can interfere with and distort the wanted output signal.

Intermodulation products are usually described in terms of a two-tone test, where the input signal is two equal-amplitude sinusoids at closely spaced frequencies f_1 and f_2 . These represent a wanted signal and an equal-amplitude adjacent-channel interferer. Nonlinearities cause

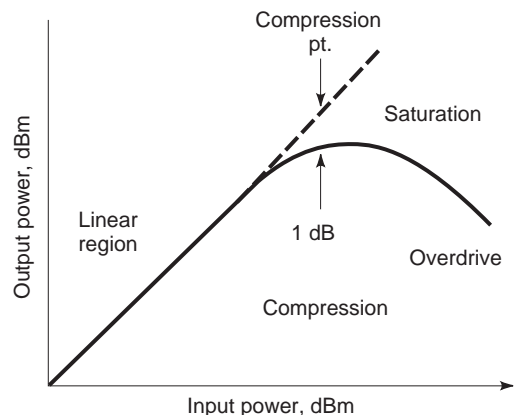


Figure 12. Nonlinear behavior of an amplifier. As the input power level increases, the gain decreases below its linear value.

outputs to appear at all the sums and positive differences of integer combinations of f_1 and f_2 . The most important are the third-order products at frequencies $2f_1 - f_2$ and $2f_2 - f_1$, described earlier (see Fig. 13).

To quantify the process, one should plot the output power P_{o3} at one of the third-order frequencies ($2f_1 - f_2$ or $2f_2 - f_1$) versus the input power P_{o1} at f_1 or f_2 . On a dBm or dBW scale, the curve will be a straight line with a slope of 3, at least for reasonable values of input power [7]. On the same graph, we can also plot output power at one of the input frequencies. Below the compression region, this will be the straight line. If we extrapolate the straight line far enough, it will cross the third-order curve at the third-order intercept point. The corresponding input power is called the third-order input intercept point IIP3, and the corresponding output power is called the third-order output intercept point OIP3 (see Fig. 14). IIP3 and OIP3 measure the strong-signal handling capabilities of an amplifier, mixer, or other two-port device. Note that the third-order intercept point is a graphical construction. No real device operates at that point.

To measure the intercept points, one can drive the device at a level where the third-order products are measurable and view the output on a spectrum analyzer. Figure 13 sketches the resulting display. If P_{o1} and P_{o3} are the output powers in dBm at one of the wanted frequencies and one of the third-order frequencies, then the rejection R is given by

$$R = P_{o1} - P_{o3} \text{ dB} \tag{15}$$

P_{o1} is related to the input power P_i at one of the wanted frequencies (f_1 or f_2) by the gain, G , of the device.

$$P_{o1} = P_i + G \text{ dBm} \tag{16}$$

The input and output intercept points can be calculated from

$$IIP_3 = \frac{R}{2} + P_i \text{ dBm} \tag{17}$$

$$OIP_3 = \frac{R}{2} + P_{o1} \text{ dBm} \tag{18}$$

$$OIP_3 = IIP_3 + G \text{ dBm} \tag{19}$$

2.2.2. Determining Receiver Third-Order Intercept Point. Consider a receiver that consists of a cascaded system of M stages with dB gains G_i and dBm input intercept points IIP_i . The corresponding linear values are g_i and iip_i .

Following Ref. 8, we assume that (1) the interfaces between stages are all at 50Ω and (2) the third-order products add in-phase. Assumption (1) is realistic, and assumption (2) leads to a worst-case analysis. Under these conditions, we can project the output intercept points of the individual stages through to the output of the last stage and add the projected values reciprocally. For 1, 2, 3, and M stages, the overall output intercept point in milli-

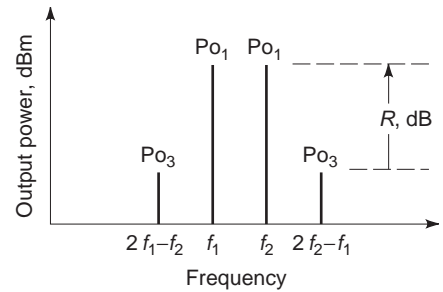


Figure 13. The spectrum of the output of a nonlinear amplifier with inputs at frequencies f_1 and f_2 . The amplifier creates unwanted third-order products at frequencies $2f_1 - f_2$ and $2f_2 - f_1$. The wanted output signals are at power level P_{o1} and the unwanted products are at power level P_{o3} .

watts is given by

$$oip_o = \frac{1}{\frac{1}{oip_1}} \text{ for 1 stage} \tag{20}$$

$$oip_o = \frac{1}{\frac{1}{oip_2} + \frac{1}{g_2 \times oip_1}} \text{ for 2 stages} \tag{21}$$

$$oip_o = \frac{1}{\frac{1}{oip_3} + \frac{1}{g_3 \times oip_2} + \frac{1}{g_3 \times g_2 \times oip_1}} \text{ for 3 stages} \tag{22}$$

$$oip_o = \frac{1}{\frac{1}{oip_M} + \sum_{i=1}^{M-1} \frac{1}{oip_i \times \prod_{k=i+1}^M g_k}} \text{ for } M \text{ stages} \tag{23}$$

This formula can be written in a simpler form to yield OIP_o directly in dBm:

$$OIP_o = -10 \log_{10} \left[\sum_{i=1}^M \frac{1}{oip_i g_i + 1 g_{i+2} \dots g_M} \right] \tag{24}$$

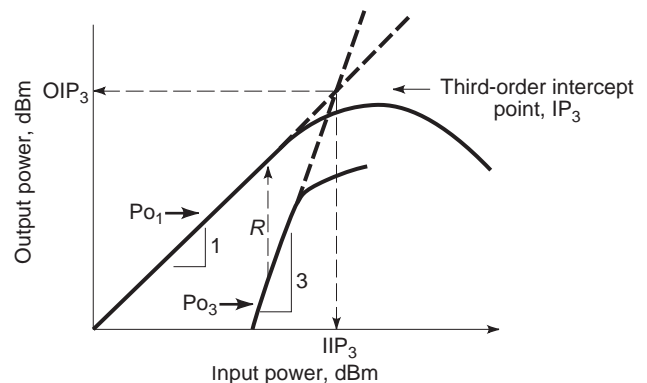


Figure 14. An illustration of how first-order (P_{o1}) and third-order (P_{o3}) output power increase with increasing input power in a nonlinear device. The straight-line extrapolations of the two curves cross at the third-order intercept point.

The overall input intercept point is the overall output intercept point divided by the total gain.

$$iip_o = \frac{oip_o}{\prod_{i=1}^M g_i} \tag{25}$$

Expressed in dBm,

$$IIP_o = OIP_o - \sum_{i=1}^M G_i \tag{26}$$

2.3. Dynamic Range

The dynamic range of a receiver is the decibel difference between the strongest signal and the weakest signal that the receiver can handle. There are multiple definitions of dynamic range, depending on how the strongest signal and the weakest signal are defined.

2.3.1. Spurious Free Dynamic Range. Spurious free dynamic range makes the weakest signal the MDS (receiver noise floor $kT_S B$), where T_S is the system noise temperature and B is the bandwidth. T_S is the sum of the antenna noise temperature T_A and the effective input noise temperature of the receiver T_e :

$$T_S = T_A + T_e \tag{27}$$

so this definition describes the receiver when it is used with an antenna having a specified noise temperature.

The strongest signal used in the SFDR definition is the input power that, in a two-tone intermodulation test, makes the power in either of the third-order products at the receiver output equal to the noise power (see Fig. 15). Mathematically,

$$SFDR = \frac{2}{3}(IIP_3 - MDS) \text{ dB} \tag{28}$$

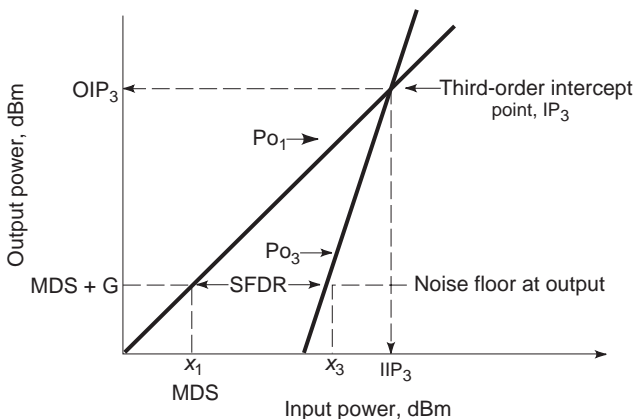


Figure 15. The spurious free dynamic range of a receiver is the decibel difference between the noise floor and the input signal level that would bring third-order products to the noise floor.

2.3.2. Other Definitions of Dynamic Range. In practice, third-order products may be tolerated at levels somewhat higher than the noise floor. The maximum permissible signal may be the input power for which the rejection R in Eq. (17) reaches a specified level.

2.4. UHF Receiver Design

2.4.1. LO and IF Frequency Selection. There are several standard IF frequencies (10.7 MHz and 45 MHz are two examples commonly used in UHF radios), and the selected IF frequency should be one for which appropriately priced components are available. The higher the IF frequency, the farther images will lie from the wanted frequency and the easier it will be to filter them out. Beyond these general guidelines, the IF and LO frequencies should be selected so that no high-level inter-modulation products fall within the IF passband.

To illustrate the process, consider a mixer with input signal f_S , local oscillator signal f_L , and wanted IF output signal f_I . Depending on whether the LO frequency is above (high-side injection) or below (low-side injection) the signal frequency, the mixer will produce a wanted output at either

$$f_i = f_L - f_R \tag{29}$$

or

$$f_i = f_R - f_L \tag{30}$$

The mixer will also produce unwanted outputs at all positive values of

$$f_o(m, n) = \pm(mf_L \mp nf_R) \tag{31}$$

where m and n are positive integers. If any of these spurious responses (“spurs”) fall within the IF passband—that is, if

$$f_o(m, n) = f_i \pm \frac{B}{2} \tag{32}$$

where B is the IF bandwidth—they can interfere with wanted signals. The frequencies f_i , f_R , and f_L , must be chosen so that this either does not occur or any spurs within the IF passband are at negligible power levels. The process, described later, is outlined in Ref. 9. The amplitudes of the spurs depend on the nature of the mixer’s nonlinearity. Typical values are found in Ref. 10 and in most mixer manufacturer’s catalogs.

We began by treating the frequencies as parameters and m and n as positive real variables. The relationship between m and n is

$$n = \pm \frac{f_i}{f_R} \pm m \frac{f_L}{f_R} \tag{33}$$

All solutions to Eq. (33) that yield integer values of m and n correspond to spurious responses that may fall within the IF passband of the receiver.

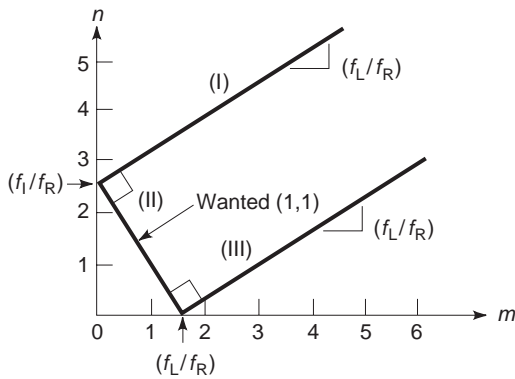


Figure 16. A graphical technique to check for mixer spurious responses in a receiver. The three straight lines are plotted from Eq. (34). In an ideal receiver design, the lines would not cross any points corresponding to integer values of both m and n except (1, 1).

Plotting these equations on a set of n versus m axes (Fig. 16) yields three straight lines whose equations are

$$\begin{aligned} n &= \frac{f_I}{f_R} + m \frac{f_L}{f_R} \text{ (curve I)} \\ n &= \frac{f_I}{f_R} - m \frac{f_L}{f_R} \text{ (curve II)} \\ n &= -\frac{f_I}{f_R} + m \frac{f_L}{f_R} \text{ (curve III)} \end{aligned} \quad (34)$$

We plot these for f_R and f_L corresponding to the upper and lower limits of the receiver's tuning range. The needed lines are easy to draw from the known intercepts (f_I/f_R) and (f_I/f_L) and the slope (f_L/f_R). Ideally, only the line representing the wanted response should pass through a point corresponding to integer values of m and n . That should be the (1, 1) point.

If one of the plotted curves comes close to an integer-valued point, we can determine if the corresponding spur lies within the passband by plotting the appropriate line with f_I replaced by $f_I \pm B/2$.

With properly chosen IF and LO frequencies, no high-level spurs will fall within the IF passband. Usually, a high LO frequency gives better performance.

2.4.2. Mixer Selection [11]. Almost any nonlinear device can serve as a mixer. Mixers can be active or passive, and they can rely on filters or cancellation or on some combination of both to provide needed isolation between their RF, IF, and LO ports. Figures-of-merit for mixers include conversion gain, noise figure, third-order intercept point, required LO drive, and relative levels of intermodulation products. Some mixer types are more sensitive to impedance mismatches than others.

Active mixers require dc power, less amplifier gain, and less LO drive than passive mixers. Passive mixers do not need dc, but they require more LO drive and more amplifier gain than active mixers. Which type of mixer requires less total dc power for the whole receiver depends on the overall design. Manufacturing factors (cost, ease of auto-

mated assembly, etc.) may be more important in mixer selection than small differences in RF characteristics or power consumption.

Mixers may be unbalanced, single balanced, or double balanced. An unbalanced mixer usually has a single active component (a diode or a transistor) and relies on filters to provide LO-RF and LO-IF isolation. Single-balanced mixers use cancellation to achieve LO-RF isolation and filters for LO-IF isolation. Double-balanced mixers use cancellation to achieve both LO-RF and LO-IF isolation. Usually (but not always), whether a mixer is unbalanced, single balanced, or double balanced can be determined by counting the balun transformers. An unbalanced mixer has none, a single-balanced mixer usually has one, and a double-balanced mixer usually has two.

Diode mixers operate as switches and chop the RF waveform at the LO frequency. As proper operation depends on the LO rather than the RF signal turning the diodes on and off, the maximum RF power that a diode mixer can handle without unacceptable distortion is somewhere between 10 and 6 dB below the LO level. Switching-diode mixers usually offer a larger dynamic range but higher conversion loss and noise figure than mixers whose operation is based on device nonlinearity.

Low-cost double-balanced diode mixers are widely available. They are inherently broad-band and offer conversion gains typically between -6 and -8 dB. Required RF drive levels are fairly high— $+5$ dBm is typical.

Passive field-effect transistor (FET) mixers apply the LO directly to the gate of an unbiased FET. The LO drive modulates the channel resistance at the LO frequency, and the RF signal applied to the drain sees this modulation. As their operation is based on this resistance modulation, passive FET mixers are often called FET resistive mixers. Their primary advantage over diode mixers is that they offer very good intermodulation distortion performance; third-order input intercept points of $+30$ dBm or better are possible. FET resistive mixers can be made with single devices or in single-balanced and double-balanced configurations.

Active FET mixers can consist of single devices. In the past, dual-gate active FET mixers were common, but these have largely disappeared. Gilbert cell multipliers offer uniformly good performance.

An image-canceling mixer contains two internal mixers whose LO drives are 90° out of phase. The RF amplifier output is divided and fed to both mixers in phase. The output of one internal mixer is phase shifted by an additional 90° . The resulting waveforms may be added or subtracted to cancel the unwanted (image) response. (See Ref. 2.) Successful operation of an image-canceling mixer depends on maintaining the required power levels and phase shifts over the IF bandwidth for the expected signal amplitudes and operating temperature ranges. Typical image suppression is in the 28 to 45 dB range.

2.4.3. RF and IF Amplifiers. RF amplifiers for UHF receivers are selected to give the desired overall noise figure and dynamic range. IF amplifiers are selected to present a particular desired signal level at the demodulator. To keep the demodulator from being overdriven at high-input

signal levels, IF amplifiers may incorporate limiting or automatic gain control (AGC), depending on whether signal amplitude information is important. Both RF and IF amplifiers are available as separate components for all standard frequency bands, chips combining IF and mixing or RF and mixing functions are widely available. These typically incorporate Gilbert cell multipliers. One current example is the Motorola MC13156 wideband IF system that may be used as the basis for a complete radio or IF system for frequencies up to 500 MHz. Another is the RF Micro-Devices RF2411, covering 500 MHz to 1900 MHz.

2.4.4. RF and IF Filters. The first stage of most receivers is a band-pass filter (often called a preselector) that rejects noise and unwanted signals (particularly unwanted signals at image frequencies) outside of the desired tuning range. Bandpass filters at IF keep unwanted mixer products out of the demodulator, select the desired channel, and determine the overall noise bandwidth of the receiver. The IF filter usually determines the selectivity of a super-het receiver.

Selecting RF and IF filters is similar to selecting mixers. There are many competing types and usually no immediately obvious best choice for a given application. RF filter design and manufacturing are so specialized that receiver designers usually select filters from catalogs and data sheets instead of building their own. Selection is based on technical characteristics, price, and manufacturing considerations.

Filters for IF include crystal, ceramic, and SAW (surface acoustic wave). RF filters can be made with SAW, dielectric, helical resonator, and transmission line technologies. *LC* filters tend to be too lossy for these applications. Active filters are usually not available or not cost effective at RF and IF frequencies.

Filter specifications are based on treating the filter as a two-port device driven by a source with a specified resistance R_i and feeding a load resistance R_o . The values of R_i and R_o depend on the filter type and frequency range. For example, ceramic filters for 10.7 MHz IF applications expect to see 330 Ω , whereas values between 1 and 2.5 k Ω are common for 455 kHz ceramic filters.

Let V_o and V_i be the phasor output and input voltages for a filter operating at frequency f . The complex transfer function $H(f)$ of the filter is given by

$$H(f) = \frac{V_o(f)}{V_i(f)} = |H(f)|e^{-j\phi(f)} \quad (35)$$

The filter attenuation A in dB is given by

$$A(f) = -20 \log_{10}|H(f)| \quad (36)$$

Insertion loss (IL) is the value of A at the filter's center frequency f_0 .

$$\text{IL} = A(f_0) \quad (37)$$

Manufacturers normally provide plots of A versus f . A variety of bandwidths are often specified in addition to the

expected 3 dB value. The shape factor of a filter is the ratio of one of these larger bandwidths (for example, the 60 dB bandwidth) to the 3 dB bandwidth. An ideal "brick wall" filter would have a shape factor of 1.

The phase response $\phi(f)$ of a filter is also important, but it is plotted far less frequently. Ideally, $\phi(f)$ should be a linear function of frequency. In that case, the spectral components of a complex waveform would pass through the filter without changing their relative phases. Phase distortion is particularly important in analog FM and in digital applications.

Phase distortion is measured by group delay, T , which has units of time and is given by

$$T = \frac{\partial\phi}{\partial\omega} = \frac{1}{2\pi} \frac{\partial\phi}{\partial f} \quad (38)$$

Relating receiver performance to filter group delays usually requires computer simulation. No simple formulas are available.

Some mixers (diode mixers in particular) are sensitive to the impedance presented at the IF port at frequencies outside of the passband. Some crystal filters are particularly troubling in this regard. Diplexer circuits are available to isolate the mixer from the filter's impedance variations. See Ref. 2 for a further discussion of this issue.

2.4.5. Demodulators. The choice of demodulator for a given receiver design depends on the modulation that is to be received. For a given application, demodulators differ in fidelity, dynamic range, and input and output signal levels.

2.4.6. RF Integrated Circuits for UHF Receivers. The level of integration available in receivers and receiver subsystems is increasing rapidly, particularly for consumer applications. For further information, see Refs. 12–14.

BIBLIOGRAPHY

1. F. Jay, ed., *IEEE Standard Dictionary of Electrical and Electronics Terms*, 3rd ed., New York: IEEE Press; 1984.
2. S. Maus, *Microwave Mixers*, 2nd ed., Norwood, MA: Artech House, 1993.
3. D. Cheadle, Measure noise power with your power meter, in *RF Signal Processing Components*, Palo Alto, CA: Watkins-Johnson Company, 1980.
4. *Fundamentals of RF and Microwave Noise Figure Measurements*, Application Note 57-1, Palo Alto, CA: Hewlett-Packard, 1983.
5. U. Rohde, *Microwave and Wireless Synthesizers: Theory and Design*, New York: Wiley, 1997.
6. W. Robins, *Phase Noise in Signal Sources*, London: Peregrinus, 1984.
7. D. Heknes and S. Kwok, Intermodulation: Concepts and calculations, *Appl. Microw. Wireless*, **9**(4):38–43 1997.
8. S. Wilson, Evaluate the distortion of modular cascades, *Microwaves*, **21**(3):67–70 1981.

9. W. A. Davis, *Radio and Microwave Engineering* (EE4605 Class Notes), Blacksburg, VA: Virginia Polytechnic Institute, State University, 1996.
10. U. Rohde, *Digital PLL Frequency Synthesizers Theory and Design*, Englewood Cliffs, NJ: Prentice-Hall, 1983.
11. S. Maas, Mixers for wireless applications, in L. Larson, ed., *RF and Microwave Circuit Design for Wireless Communications*, Norwood, MA: Artech House, 1996.
12. B. Razavi, *RF Microelectronics*, Upper Saddle River, NJ: Prentice-Hall, 1998.
13. T. H. Lee, *The Design of CMOS Radio Frequency Circuits*, New York: Cambridge University Press, 1998.
14. A. Abadi and P. Gray, *Integrated Circuits for Wireless Communications*, Piscataway, NJ: IEEE Press, 1998.

ULTRA-WIDEBAND RADIO

KAZIMIERZ SIWIAK
TimeDerivative, Inc.
Coral Springs, Florida

1. INTRODUCTION

Ultra-wideband signaling is essentially the art of generating, modulating, emitting, and detecting impulse wavelet signals that inherently occupy large bandwidths. Impulse transmissions date back to the infancy of wireless technology. They include the experiments of Heinrich Hertz in the 1880s, and the 100-year-old sparkgap “impulse” transmissions of Guglielmo Marconi, who in 1901 sent the first ever over-the-horizon wireless transmission from the Isle of Wight to Cornwall on the British mainland. Early radio circuits consisted solely of passive electrical components, without tubes or transistors, and hence lacked the means to efficiently receive the short transient impulse energy. Therefore radio subsequently developed along narrowband frequency-selective analog techniques. This led to voice broadcasting and telephony—and more recently to digital telephony and wireless data. Through the years, a small cadre of scientists have worked to develop and refine impulse technologies. The origin of modern UWB technology stems from work in time-domain electromagnetics begun in the early 1960s to fully describe the transient behavior of certain classes of microwave networks. By 1970 the primary focus in impulse radio research was on impulse radar techniques and government-sponsored projects. Through the late 1980s, the technology was alternately referred to as “baseband,” “carrier-free,” or “impulse”—the term “ultrawideband” was not applied until approximately 1989 by the U.S. Department of Defense. By that time UWB theory, techniques, and many hardware approaches had experienced nearly 30 years of extensive development [1] culminating in today’s UWB technology [2]. In the late 1980s digital techniques began to mature to the point where the commercial practicality of modern low-power impulse radiocommunications and precision radar could be demonstrated using

an impulse time coding–time modulation approach. Digital impulse radio [3–12], the modern echo of Hertz’s century-old transmissions, now emerges under the banner “ultrawideband” radio.

An FCC Report and Order legalized unlicensed UWB emission in the United States on February 14, 2002, with a full report issued on April 22, 2002 [13] and the subsequent publication of U.S. 47 *Code of Federal Regulations* (CFR) Part 15(f) spelling out the rules for UWB emissions in the United States. Five categories of UWB devices are summarized in Table 1. The rules do not spell out either the signaling or the waveforms. To access the UWB spectra, the intentionally radiated EIRP levels must be below –41.3 dBm/MHz. The measurement method specifies the use of a metal ground plane, or else EIRP must be below –46 dBm/MHz if measured in an anechoic chamber. A *UWB transmitter* is defined as one that emits a UWB signal with bandwidth of the lesser of 500 MHz or 20% bandwidth, as measured at the –10-dB point.

UWB wavelets or pulses are bursts of electromagnetic energy. Normally, the wavelet duration in time is inversely related to its occupied bandwidth. For example, a 1-ns wavelet occupies 1 GHz of spectrum, a 2-ns pulse occupies 500 MHz, while a 133-ps pulse instantaneously occupies 7.5 GHz of spectrum. The “zero crossing” rate of a wavelet determines where in the spectrum that wavelet bandwidth will appear. Finally the envelope shape of the wavelet (and to some extent the zero-crossing structure) determine the detail of the distribution of the energy in the spectrum. Conventional technologies like OFDM (orthogonal frequency division multiplexing) can be configured so that the signal meets the UWB spectrum access rules, and hence might also appear in the UWB bands. OFDM in the UWB spectrum does not employ short pulses, but rather constitutes a symbol wavelet that is an ensemble of modulated sinusoidal carriers spanning at least 500 MHz. The OFDM wavelet is a long burst equal to the OFDM symbol duration, where the symbol duration defines the OFDM carrier spacing, while the total OFDM bandwidth results from the aggregation of those carriers. For example, 122 carriers spaced every 4.125 MHz span at total of 504 MHz, and the OFDM symbol wavelet duration is approximately 0.25 ms.

2. UWB RADIO TECHNOLOGIES

A UWB radio physical layer standard is under development within the IEEE 802 LAN/MAN Standards Committee. The IEEE 802.15.3a, *Wireless Personal Area Networks* (W-PAN)¹ task group are tackling the definition of an alternative UWB radio physical layer for the 802.15.3 W-PAN standard [14]. The IEEE 802.15.4 project in a new group 4a are considering a new physical layer that is to include positioning and distancing capabilities. UWB proposals within 4a are inevitable because of the demonstrated positioning capabilities of UWB systems [5].

¹W-PAN is a trademark of IEEE, Piscataway, NJ; generic acronym is WPAN (wireless personal-area network).

Table 1. Classes of UWB Devices Authorized under U.S. FCC Rules

Class/Application	UWB Spectra for Operation at Part 15 Limits	User Limitations
Communications and measurement systems	3.1–10.6 GHz (different out-of-band emission limits for indoor and handheld devices)	No
Imaging: ground-penetrating radar, wall, medical imaging	<960 MHz <i>or</i> 3.1–10.6 GHz	Yes
Imaging: through-wall	<960 MHz <i>or</i> 1.99–10.6 GHz	Yes
Imaging: surveillance	1.99–10.6 GHz	Yes
Vehicular	22–29 GHz	No

The IEEE Project 802.15.3a task group provides us with examples of three very different UWB radio systems. All three systems described here evolved from the Project 802.15a UWB PHY (physical layer) proposal. As of this writing, the approach to a standard has not been chosen, and perhaps this reflects the abundance of good choices! The three implementations show how differently a physical description of a radio can become while conforming to the same broad regulatory requirements. One method is based on orthogonal frequency-division multiplexing (OFDM), and another is based on direct-sequence code-division multiple access (DSUWB). A third method is a time-division/frequency division multiple access (TD/FDMA) pulse approach. Of these, the TD/FDMA is closest to an impulse radio. Additionally time-modulated (TM-UWB²) and transmitted delayed reference (TDR-UWB) examples are shown in Table 2.

The 802.15.3a process has exposed several viable techniques to access the UWB spectrum, as summarized in Table 2. All three systems access a minimum of about 1.5 GHz in the simplest mode of operation. OFDM and TD/FDMA systems hop among at least three channels of about 500 MHz width within the 3.1–5 GHz range. DSUWB uses one channel of 1.4 GHz bandwidth. All three have a way of utilizing the segment of spectrum between 3.1 and approximately 5 GHz with similar performance. Each, additionally, has ways of increasing performance, again essentially by similar amounts, by utilizing the rest of the UWB band up to 10.6 GHz. Table 2 shows that each method delivers more than 100 Mbps (megabits per second) at 10 m distance and well over 400 Mbps at shorter distances. All of the methods were crafted to meet the regulatory criteria for access to the UWB spectrum. Time-modulated ultrawideband (TM-UWB) and transmitted delay reference (TDR-UWB) are also represented in Table 2.

Modulation efficiency is the needed energy per bit : noise density ratio for achieving a bit error rate (BER) no greater than a specified value. A BER less than 10^{-3} is used for comparison in the table. Table 3 lists various modulations that have been applied to UWB systems. System designers wishing to estimate performance in realistic environments should consider the additional propagation losses usually encountered in practical environments. Performance in multipath and shadowing conditions should also be considered.

²The proprietary (capitalized) term Time Modulated UWB and acronym TM-UWB are trademarks of Time Domain Corporation, Huntsville, AL.

2.1. An OFDM Approach to UWB

The OFDM approach to UWB meets the “500 MHz bandwidth” requirement by using 122 carriers that are modulated with a quadrature phase shift keying (QPSK) constellation. The composite signal occupies a 504-MHz-wide channel and persists on a channel for the information length of 242.42 ns plus the 60.61 ns cyclic prefix time, and then switches to another channel within a 9.5 ns guard time. The long symbol interval, approximately 242 ns, means that multipath fading is effectively viewed through a narrow band (approximately 4 MHz) filter. This OFDM system will encounter full Rayleigh fading in multipath channels. Because the UWB emission regulations limit power per megahertz, a larger utilized bandwidth will result in a larger total emitted average power. The three time-frequency hopping OFDM signals occupy 1.5 GHz. Frequency hopping is used in this OFDM approach as a way of having this system occupy a large total bandwidth for the purpose of increasing the total radiated power.

The system parameters for an OFDM system are shown in Table 4. At least three data rates are supported: 110, 200, and 480 Mbps, with additional data rates possible. QPSK modulation is used on the OFDM tones, and a 128-point Fourier transform generates the OFDM tones. Different data rates are supported by different combinations of error correction coding rates, numbers of tones carrying data, and the spreading rate on each tone. Additional channels spaced 528 MHz all the way up to the bandlimit at 10.6 GHz provide additional system capacity, more available power, and combinations of power and capacity to further improve performance. This OFDM approach uses conventional radio techniques to access the 7500 MHz of unlicensed spectrum under the UWB rules. The performance of this OFDM will resemble that of 122 narrowband radios, each occupying about 4 MHz of spectrum. Multipath manifests itself as full Rayleigh fading and is dealt with by spreading the forward error correction code across the frequency bands.

2.2. A DS-UWB Approach to UWB

Direct-sequence spread spectrum (DSSS) has roots in secure and military communications systems. It also appears in the IEEE 802.11b wireless local area network standard. In this UWB implementation, summarized in the DS-UWB column of Table 2, we see a direct sequence approach designed to occupy at least 1.5 GHz bandwidth in the 3.1–5.15 GHz range and 3.7 GHz bandwidth in the

Table 2. Three UWB Systems Crafted to Meet U.S. Regulatory Requirements

	OFDM	DS-UWB	TD/FDMA Pulses	TM-UWB	TDR-UWB
Bands	3–13	2	3–13	1	1
Bandwidths	3–13 × 504 MHz	1.5 and 3.6 GHz	3 × 550–13 × 528 MHz	2 GHz	2 GHz
Frequency ranges (GHz)	3.1–4.8 4.8–10.6	3.1–5.15 5.825–10.6	3.1–5.0 4.9–10.6	3.1–5.2	3.1–5.2
Modulation	OFDM-QPSK	<i>M</i> -BOK, BPSK	<i>M</i> -BOK, QPSK	TM-PPM	DPSK
Modulation efficiency 10 ⁻³ BER	6.8 dB	4.1–6.8 dB	6.1–6.8 dB	7–10 dB	9–12 dB
Error correction codes	Convolutional	Convolutional and Reed–Solomon	Convolutional and Reed–Solomon	Various	Various
Capabilities	10 m at 110 Mbps 7 m at 200 Mbps 3 m at 480 Mbps	10 m at 112 Mbps 7 m at 224 Mbps 2 m at 1.3 Gbps	10 m at 108 Mbps 7 m at 288 Mbps 3 m at 577 Mbps	40 m at 10 Mbps 10 m at 40 Mbps	30 m at 10 Mbps

Table 3. UWB Modulation Efficiencies

Modulation	Modulation Efficiency e_b (dB)		
	BER = 10 ⁻²	BER = 10 ⁻³	BER = 10 ⁻⁵
64-BOK	2.4	4.1	6.1
16-BOK	3.0	4.9	7.1
8-BOK	3.4	5.4	7.8
4-BOK	3.8	6.1	8.6
2-BOK/2-PAM/BPSK	4.3	6.8	9.6
PPM/OOK	7.3	9.8	12.6
<i>N</i> -TDR	5.9	7.9	10.3
2-TDR	8.9	10.9	13.3
4-PAM	8.3	10.8	13.5
16-QAM	8.9	11.2	13.8
8-PAM	12.8	15.2	18.0
64-QAM	13.5	15.7	18.3
16-PAM	17.6	20.1	22.9
256-QAM	18.4	20.6	23.2

Table 4. OFDM System Parameters for a UWB System

Information Data Rate:	110 Mbps	200 Mbps	480 Mbps
Modulation/Constellation:	OFDM/QPSK	OFDM/QPSK	OFDM/QPSK
FFT size	128	128	128
Coding rate	$\frac{11}{32}$	$\frac{5}{8}$	$\frac{3}{4}$
Spreading rate	2	2	1
Information tones	50	50	100
Data tones	100	100	100
Information length	242.42 ns	242.42 ns	242.42 ns
Cyclic prefix	$32/528 = 60.61$ ns	60.61 ns	60.61 ns
Guard interval	$5/528 = 9.47$ ns	9.47 ns	9.47 ns
Symbol interval	312.5 ns	312.5 ns	312.5 ns
Channel bit rate	640 Mbps	640 Mbps	640 Mbps
Symbol period	937.5 ns	937.5 ns	937.5 ns

Table 5. A DS-UWB System for the 3.1–5.1 GHz Band

Information Data Rate:	112 Mbps	224 Mbps	1.368 Gbps
Modulation/Constellation:	64-BOK	QPSK/64-BOK	BPSK
Symbol rate (Msym/s)	42.75	42.75	1,368
Coding rate	0.44	0.44	1
Code length (chips/s)	32	32	1
Channel chip rate (Gchips/s)	1.368	1.368	1.368

5.8–10.6 GHz range. The DS-UWB parameters are listed in Table 5. Unlike a traditional carrier based DSSS system, this UWB approach uses nonsinusoidal wavelets tailored to occupy the desired spectrum in an efficient manner. Figure 1 shows a sample wavelet along with its spectral content in the 3.1–5.1 GHz band. Figure 2 shows another sample wavelet that occupies the 5.8–10.6 GHz band. The lowest-cost systems are envisioned to use the lower frequency band. The two bands can be used independently, or together to provide a range of options for system deployment. This system uses a multilevel biorthogonal keying (*M*-BOK) modulation or *M*-BOK in combination with QPSK depending on the required data rate.

The UWB bandwidth spreading is accomplished by sending the wavelets shown in Figs. 1 and 2 at the 1.368 Gchip/s chip rate. Modulation of the sequence of wavelets “whitens” the spectrum, which means that it disrupts regularities that would otherwise result in spectral lines. *M*-BOK modulation comprises 24/32-length ternary orthogonal sequences (−1, 0, +1) of wavelets. The ternary codes simultaneously provide the DS spreading as well as the *M*-BOK modulation symbol set. Either 1, 2, 3,

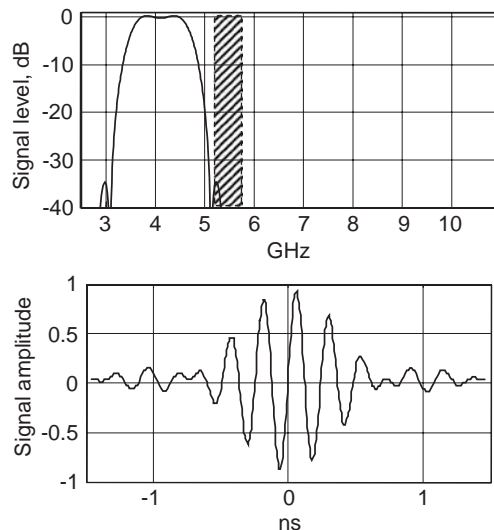


Figure 1. UWB wavelet and its spectrum in the 3.1–5 GHz range.

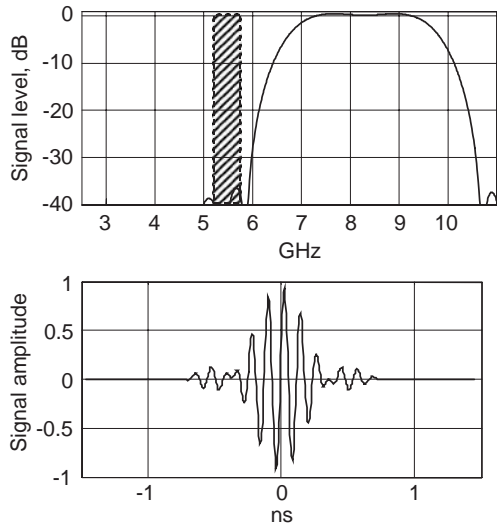


Figure 2. UWB wavelet and its spectrum in the 6–10.6 GHz range.

or 6 bits are sent with each code symbol. For example, 64-BOK modulation takes 6 chips at a time ($2^6 = 64$ BOK combinations) to form a symbol. The 24-length ternary codes are used with 2-BOK, 4-BOK, and 8-BOK, while 32-length codes are used with 64-BOK. *M*-BOK modulation has the property that as *M* increases without bound the modulation efficiency approaches the Shannon-limited value of -1.59 dB.

Symbols are sent at 42.75 Msym/s, resulting in a channel bit rate of 256.5 Mbps. The data are encoded with a rate 0.44 error correction code resulting in the 112 Mbps information data rate seen in Tables 1 and 4. A second set of wavelets that have orthogonal properties to the wavelets depicted in Figs. 1 and 2 are sent on top of the original wavelets in a manner analogous to quadrature phase shift keying (QPSK) in carrier-based radio systems. With QPSK there are up to 12 bits per symbol. This doubles the data information rate to 224 Mbps. Finally, moving from a 0.87 rate to a 0.44 rate error correcting code, and using QPSK, a 448 Mbps data information rate is achieved. Many other combinations of modulation depths (*M*-BOK) and coding rates are possible including a 1.368 Gbps mode at 1 bit per chip with error correction omitted. The *M*-BOK codes along with forward error correction are especially effective in multipath propagation. This example of a UWB system uses wavelets that are approximately 1.5 and 3.6 GHz, respectively, when measured at the points 10 dB down from the peak level. They resemble an impulse approach where the impulses are sent with minimal spacing between them. The design and characteristics of wavelet impulses are given in Ref. 2.

2.3. A TD/FDMA Approach to UWB

The time-division/frequency-division multiple-access approach (TD/FDMA) uses impulses that are centered at frequencies spaced by 550 MHz. Here the impulses are 3 ns long and occupy a 700 MHz bandwidth when measured at points 10 dB below the peak value. The

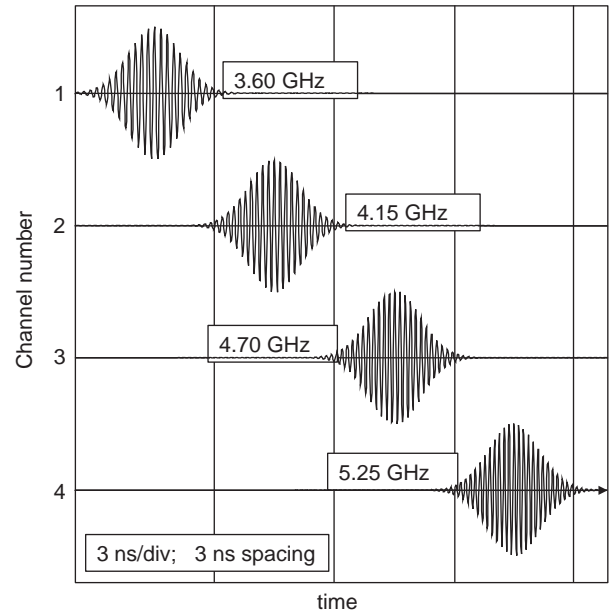


Figure 3. Impulse wavelets for a TD/FDMA UWB system.

impulse wavelets for the lower four bands are shown in Fig. 3. The corresponding spectral occupancy is portrayed in Fig. 4.

Multipath is mitigated by the time interval between pulses that appear on the same channel. The TD/FDMA system used impulses that are separated in time.

2.4. TM-UWB Technology

A TM-UWB system is introduced in Table 2. TM-UWB transmitters emit ultrashort pulses with tightly controlled pulse-to-pulse intervals. The waveform pulsewidths are typically less than 1 ns in duration, and are centered near 4 GHz, with pulse-to-pulse intervals of 25–1000 ns. The pulse-to-pulse interval is varied on a pulse-by-pulse basis

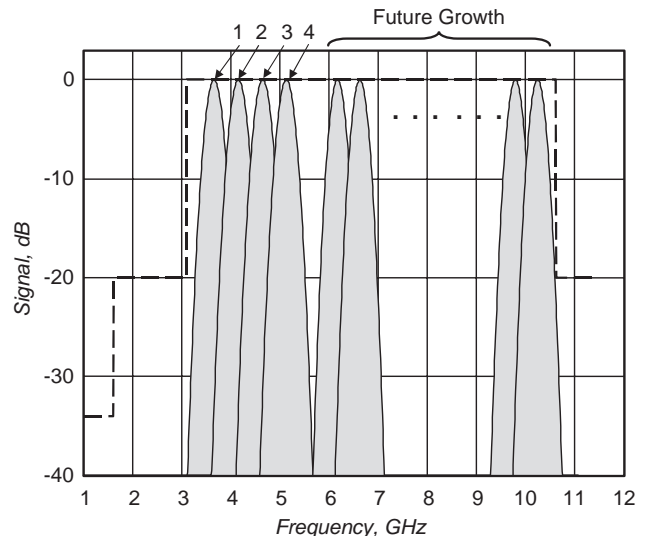


Figure 4. Spectrum occupancy of the TD/FDMA UWB system.

in accordance with two components: an information signal and a channel code. The TM-UWB receiver directly converts the received RF signal into a baseband digital or analog output signal. A receiver correlator coherently converts the electromagnetic pulsetrain to a baseband signal in one stage. A single bit of information may be spread over multiple wavelets, providing a way of scaling the energy content of a data bit with the data rate. The receiver coherently sums the proper number of pulses to recover the transmitted information.

TM-UWB systems use a fine pulse shift modulation by positioning the pulse one quarter-cycle early or late relative to the nominal PN-coded location (Fig. 5), or by pulse polarity. Furthermore, multilevel pulse position modulation may be used to provide enhanced bit-energy:noise ratio performance. The error probability for fine-shift modulation in additive white Gaussian noise (AWGN) follows the same behavior as conventional orthogonal or ON/OFF keying (OOK), while the error probability of pulse polarity modulation in AWGN follows the same behavior as that of conventional BPSK or antipodal signaling. Because TM-UWB modulation is based on accurate timing, the method is especially suitable for accurate distance determination. FCC-certified TM-UWB devices demonstrating communications, distancing, and 2D radar are commercially available [5].

2.5. TRD-UWB Technology

A method of transmitting and receiving impulses that can implement an efficient rake receiver is exemplified by TRD-UWB, [15]. The method employs differentially encoded impulse pairs sent at a precise spacing D . The system is shown in the simplified block diagram of Fig. 6. The transmitter sends a pair of pulses separated by a delay D , and differentially encoded by pulse polarity. The pulses, including propagation induced multipath replicas, are received and detected using a correlator with one input fed directly and another input delayed by D . The receiver resembles a conventional DPSK receiver that in AWGN exhibits an error probability P_D [16] of

$$P_D = \frac{1}{2} \exp\left(-\gamma_b \frac{N-1}{N}\right) \tag{1}$$

where $N > 1$ is the number of differentially encoded pulses in a sequence and γ_b is the SNR per bit. The integration interval is sufficiently long to rake in some multipath

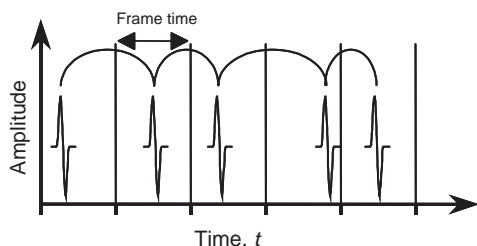


Figure 5. PN-coded UWB waveform sequence in time.

energy. TRD-UWB modulation performance is compared with other modulations in Table 3.

One channelization method employing TRD-UWB, [15], has $N = 2$ and employs a family of delays D_i . Impulse pair sequences of these delay combinations constitute the channels. Table 3 compares the error probability P_D of TRD-UWB with N arbitrarily large to the performance of other modulations.

3. UWB SHORT PULSE RADIATION AND RECEPTION

Solving for the radiated fields of pulses applied to antennas involves finding solutions to Maxwell’s equations in space and time. We begin by defining the geometry of a dipole antenna that supports surface currents $\mathbf{J}(\mathbf{r}', \tau)$ at points described by a vector \mathbf{r}' pointing from the coordinate origin to the current density point, and by a retarded time variable $\tau = t - R/c$. The solution to the dipole current density on an arbitrarily shaped antenna is well beyond the scope of this work, and approximations will be given on the basis of Ref. 2. Numerical solutions for specific antenna shapes can be found using the FDTD numerical method, as described in Ref. 18. The solutions given below are general, that is, they apply to narrowband signals as well as UWB wavelets. Narrowband solutions are always approximated by sinusoids; hence narrowband solutions are always sine waves.

3.1. UWB Wavelet Fields

The vector \mathbf{r}' in Fig. 7 points to the antenna current vector \mathbf{J} , and the radiated field point is \mathbf{r}_a . An additional vector \mathbf{R} with magnitude R points from the current point to the field point. A general expression for the magnetic far-zone field for the geometry in Fig. 7 using the space-time

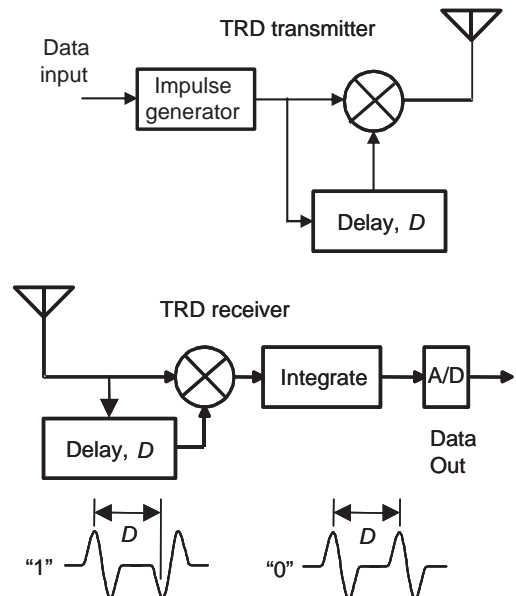


Figure 6. A TRD-UWB transmitter and receiver.

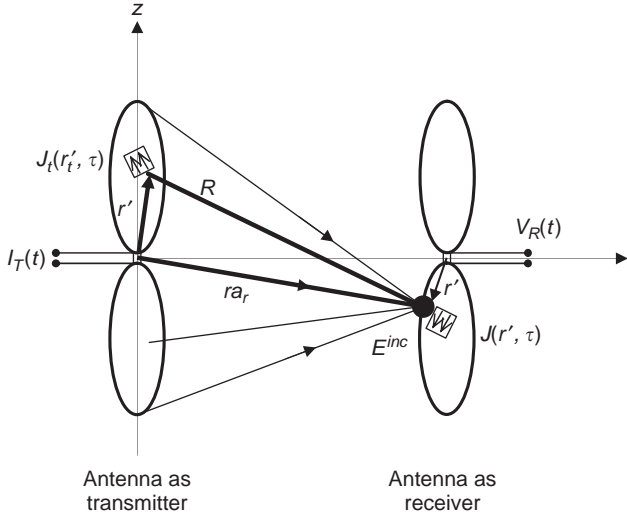


Figure 7. A wideband dipole.

integral equation (STIE) formulation [17] is

$$\mathbf{H}(\mathbf{r}, t) = \frac{1}{4\pi rc} \int_V \frac{\partial}{\partial \tau} \mathbf{J}(\mathbf{r}', \tau) \times \mathbf{a}_r dV' \quad (2)$$

The integral over volume V reduces to an integration over the surface current density \mathbf{J} , the *retarded time variable* is $\tau = t - R/c$, where c is the speed of propagation and \mathbf{a}_r is a unit vector pointing in the direction of radiation. A key factor in Eq. (2) is the appearance of the partial derivative in τ , which includes both time *and* delay. The radiated magnetic field \mathbf{H} and hence the electric field \mathbf{E} are related to a time and delay derivative of the antenna current density; that is, to the acceleration of charges on the antenna. Thus, the radiated field signal shapes will be different from the signal shape supplied to the feedpoint of the antenna. *This is a key difference from narrowband solutions where the signal shape everywhere is sinusoidal.* We note that this time-delay derivative is not always present, as for example in some traveling-wave antennas, which are not consider here.

An approximate solution for the magnetic fields radiated from the dipole aligned with the z axis and having effective length $2h_a$ is given in Ref. 2.

$$H_\phi(r, t) = \frac{\sin(\theta) h_a}{4\pi rc} \frac{\partial}{\partial t} \{ I_z(t) + I_z(t - [1 - \cos(\theta)]h_a/c) + I_z(t - [1 + \cos(\theta)]h_a/c) \} \quad (3)$$

where $I_z(t)$ is the dipole feedpoint current. The usual spherical (r, θ, ϕ) coordinates are employed, and the $\sin(\theta)$ term is the projection of the z -directed current density on the θ direction at the observation point. The electric far field is

$$\mathbf{E}_\theta(r, t) = -\eta_0 \mathbf{H}_\phi(r, t) \quad (4)$$

The fields in Eq. (3) appear to emanate from three sources (see Fig. 7): one at the feedpoint and one at each dipole end. The total magnetic field comprises time derivative compo-

nents that are delayed by t as well as by $\cos(\theta)h_a/c$. Thus two processes contribute to the field signal shape, a time and distance delay. *Both processes tend to lengthen the signal in time; hence both processes will contribute to a narrowing of the radiated bandwidth compared to the bandwidth of the signal supplied to the antenna.* Furthermore, and more generally, the delay term $[1 \pm \cos(\theta)]h_a/c$ in Eq. (3) means that the radiated signal shape as a function of time will vary depending on where the observation point is, measured by the observation angle θ relative to the antenna axis.

3.2. Receiving UWB Wavelets

Antennas, for example dipoles, receive signals by a process of impressing incident fields onto the receiving antenna surface. These fields are weighted and summed up to appear as a voltage across the feedpoint terminals of the receiving antenna. The receiving process can be derived from the *principle of reciprocity in electromagnetic theory* applied to the receiver antenna problem as shown in Ref. 2. Alternatively, and perhaps in a clearer fashion, the Lorentz force law can be used to relate the force \mathbf{F} exerted on a charge q by the incident electric \mathbf{E} and magnetic \mathbf{H} fields on an antenna having length Δh . For the infinitesimal antenna

$$\mathbf{F} = \mathbf{E}q + q\mu_0 \mathbf{v} \times \mathbf{H} \quad (5)$$

The antenna velocity \mathbf{v} here is zero acting over the incremental antenna length here, so the magnetic field term drops out. The force per charge, has the units of voltage, so

$$V_R(t) = - \int_{-\Delta h/2}^{\Delta h/2} \frac{1}{q} \mathbf{F} \cdot d\mathbf{l} = - \int_{-\Delta h/2}^{\Delta h/2} \mathbf{E}^{\text{inc}} \cdot d\mathbf{l} = - \mathbf{E}^{\text{inc}}(t) \Delta h \quad (6)$$

giving the result that the open circuit received voltage on a point antenna is proportional to the electric field incident on it. For finite-size wideband dipole antennas, the received voltage signal V_R is related to the transmitted current signal I_T through several processes that can alter the shape of the signal. First, I_T gives rise to a current density distribution \mathbf{J} on the transmitting antenna. This current density has time delays associated with it depending on the transmitter antenna dimensions. The current densities produce the electric field \mathbf{E}^{inc} at the field point on the receiving antenna that is proportional to the time-delay derivative of the transmitting antenna current density. Finally, the received open circuit voltage V_R is a summation of weighted electric field points, and another set of signal time delays is encountered in this summation due to the physical dimensions of the receiving antenna. A reasonable approximation for the voltage received by a wideband dipole is

$$V_R(t) = -h_a(E_z(t) + E_z(t - [1 - \cos(\theta)]h_a/c) + E_z(t - [1 + \cos(\theta)]h_a/c)) \quad (7)$$

Thus, the received signal V_R comprises weighted sum of and time-delayed derivatives of the transmitted current I_T . If the antenna is small, then there are no time-delay components in the received-signal shape.

4. PROPAGATION OF UWB SIGNALS

Wavelets, both UWB and narrowband, propagate in free space as expanding spherical waves. Thus, the inverse square law applies. In buildings and in cluttered environments the wavelets additionally shed energy to multipath dispersion. Thus we expect a propagation phenomenon that has a free-space term multiplied by a dispersion term. It is easy to show theoretically and from measurements [19] that the dispersion term gives rise to a term that increases the propagation law (to approximately inverse third power inside buildings). The dispersion term is also related to the maximum energy available for rake receiver gain.

4.1. The SBY Median Multipath Propagation Model

A propagation model in multipath, the SBY model [2], for the strongest impulse is based on theory and measurements given in Ref. 19. The path gain P_G between 0 dBi antennas is weighted by receiver antenna aperture ($c^2/4\pi f_m^2$), where f_m is the geometric mean of the low- and high-frequency band edges of the UWB pulse and c is the velocity of propagation. The SBY path gain model is

$$P_G = 10 \log\{[c/4\pi df_m]^2 [1 - \exp(-(d_t/d)^{n-2})]\} \quad (8)$$

where n is the propagation law beyond a breakpoint distance d_t . Nominally, based on measurements, $n = 3$. The term in brackets represents wavelet (including sinusoidal waves) attenuation due to the time dispersion of multipath occurring beyond the breakpoint distance d_t . Using a small argument approximation to the terms in the brackets, the resulting $(d_t/d)^{n-2}$ term, with $n = 3$, gives rise to an overall inverse third-power propagation law inside buildings. Equation (8) is especially useful for modeling propagation in short range indoor personal area networks as exemplified by the IEEE 802.15.3 standard.

4.2. Relation to Maximum Rake Gain

The maximum average rake gain is defined by the ratio of "total energy density" to "single-impulse energy density," which is the term in brackets in Eq. (8), and on average is

$$G_{\max} = 10 \log[1 - \exp(-(d_t/d)^{n-2})] \quad (9)$$

Based on some indoor measurements, $d_t = 1$ and $n = 3$, so $G_{\max} = 10 \log(d/d_t)$, so that G_{\max} increases with d as $10 \log(d)$. This means that on average, the maximum rake gain possible results from the total collection of all the multipath dispersed energy, and is given by Eq. (9).

5. RECOVERING UWB IMPULSE ENERGY

UWB signals are detected in a correlation-type receiver. A filter with impulse response $h(t)$ is optionally placed between signal $s(t)$ at the receiver antenna load and the correlator input. The locally generated correlation template pulse $p(t)$ multiplies the received data pulse and is integrated and sampled at the correlator output. The receiver implementation efficiency e_c is

$$e_c = 10 \log \left[\frac{\left| \iint s(\tau) h(\tau - t) d\tau p(t) dt \right|^2}{\int s(t)^2 dt \int \left| \int p(\tau) h(\tau - t) d\tau \right|^2 dt} \right] \quad (10)$$

and is maximized when

$$C \int p(\tau) h(\tau - t) d\tau = s(t) \quad (11)$$

provided $h(t)$ is causal and where C is the RMS value of $s(t)$. Solutions to Eq. (11) range from the matched template, $h(t) = \delta(t)$ (the Dirac delta function) with $p(t) = s(t)$, to the matched filter, $h(t) = s(-t)$ with $p(t) = \delta(t)$. The correlator efficiency depends strongly on the shape of the signal $s(t)$ and its relationship to $h(t)$ and $p(t)$. The efficiency e_c can typically range from -6 to -2 dB for simple rectangular templates, to a fraction of a decibel in some receiver implementations.

6. A UWB LINK PERFORMANCE

The UWB link specifies a transmitter and antenna providing an EIRP of P_{TX} , a receiver with sensitivity S_{RX} , and a propagation factor P_L determined at a convenient distance. A transmitter operating over an equivalent bandwidth of about 1.3 GHz emits $P_{TX} = -10$ dBm. A companion UWB receiver operating in AWGN (-174 dBm/Hz), referenced to a data bandwidth W Hz, with noise figure, implementation loss and margin totaling L dB, and operating at an SNR dB signal-to-noise ratio per bit, has a sensitivity

$$S_{RX} = -174 + 10 \log(W) + L + \text{SNR dBm} \quad (12)$$

The propagation term P_L is evaluated at a distance $d = 1$ m using Eq. (8), and the resulting system gain SG, including a receiver antenna gain of G_{RX} dBi, is

$$\text{SG} = P_{TX} - S_{RX} + P_L + G_{RX} \quad \text{dB} \quad (13)$$

When $f_c = 4$ GHz, then $P_L = -45$ dB, and using a data bandwidth of $W = 40$ MHz, losses $L = 10$ dB, SNR = 7 dB, and $G_{RX} = 5$ dBi, the receiver sensitivity is $S_{RX} = -81$ dBm, and the system gain at one meter is SG = 31 dB.

Using Eq. (8), a 31 dB system gain at 1 m permits a median range of approximately 11 m without rake gain. A "perfect rake" receiver would permit a median range of more than 31 meters. Practical implementations would result in a median-range performance between 10 and 30 m at a 40 Mbps throughput data rate.

7. APPLICATIONS AND MARKETS OF UWB SYSTEMS

UWB technology uniquely harnesses an ultra wideband of spectrum to provide high-bandwidth communications, but in certain implementations also enables indoor precision tracking and radar sensing on top of communications.

7.1. UWB Applications

The unique capabilities of UWB driving it into application space markets include

- Communications and sensors
- Position location and tracking
- Radar

UWB has characteristic attributes that make it especially attractive in those three categories. These include

- *Stealth*—in many varieties of UWB the signal appears to be very-low-level background noise to an unintended narrow band receiver
- *Local-area networks*—the exceptionally large available bandwidth can be used as the basis for a short-range wireless local-area network with data rates approaching 1 Gbps
- *Position location*—some UWB systems are capable of determining the 3D location of any of its transponders to within a few centimeters
- *Radar imaging*—UWB systems can be used as an open-air, through-wall, or ground-penetrating radar imager
- *Security bubble*—some UWB systems can be configured to create a security “bubble” in the fashion of a bistatic radar to detect penetration of the bubble walls
- *Vehicular radar systems*—UWB has an available vehicular radar band in the frequency range 22–29 GHz for use in collision avoidance and parking aids.

7.2. The Role of UWB in Wireless Markets

Advancements in UWB radio technology promise the opportunity of creating unique solutions meeting emerging market needs. There are essentially three basic market spaces in which UWB plays a role.

7.2.1. Wireless Communications. As available bandwidth to users increases, applications will continue to evolve to fill the available bandwidth and demand further increases. On top of this increasing demand for bandwidth, the increase in mobile telephony and travel has spurred demand for bandwidth mobility, implying wireless technology. Initial applications of UWB will evolve from the existing market needs for higher-speed data transmission, but demand for multimedia-capable wireless is already driving multiple initiatives in the wireless standards bodies. UWB solutions will emerge that are tailored for these applications because of the available high bandwidth. In particular, high-density multimedia applications, such as multimedia streaming in “hotspots” such as airports or shopping centers or even in multidwelling

units, will require bandwidths not currently enabled by continuous-wave “narrowband” technologies. The ability to tightly pack high-bandwidth UWB “cells” into these areas without degrading performance will further drive the development of UWB solutions. UWB radio systems using microwatts of power have already been demonstrated with data rates up to hundreds of Mbps at useful ranges in home and office environments.

7.2.2. Precision Tracking. As the mobility of people and objects increases, up-to-date and precise information about their location becomes a relevant market need. While GPS and some E911 technologies promise to deliver some level of accuracy outdoors, current indoor tracking technologies remain relatively scarce and have accuracies on the order of 3–10 m. UWB implementations are an adjunct to GPS and E911 that allow the precise determination of location and the tracking of moving objects within an indoor space to an accuracy of a few centimeters or less. This, in turn, enables the delivery of location-specific content and information to individuals on the move, and the tracking of high-value assets for security and efficient utilization. While this is an emerging market segment, the accuracy provided by UWB will accelerate market growth and the development of new applications in this area. UWB technology is uniquely positioned to provide distancing and location capabilities to wireless sensor networks. The popularity of wireless sensor networks is expected to grow dramatically in the near future because they provide practical machine-to-machine communication at a very low cost. The growth is expected to duplicate the recent explosion of wireless LANs [20]. Accurate distance measuring using UWB has been demonstrated adequately in recent years, and several corporations have developed chip sets as early as 1993 demonstrating distance measuring capabilities [5,21]. Aether Wire & Location, Inc., chose a direct-sequence spread-spectrum (DSSS) approach to measure distance using UWB. Time Domain Corporation pioneered a time-modulated impulse approach, which not only measured position but also fused data communications within the same protocol. In the IEEE 802 organization, a new group, 4a, has begun work to propose a new radio physical layer for the 802.15.4 standard. Because of the unique capabilities of UWB to satisfy the need for positioning, low data rates at longer distances, and high system capacities, UWB proposal are inevitable.

7.2.3. Radar. Finally, UWB signals enable inexpensive high-definition radar. With the new radar capability created by the addition of UWB, the radar market will grow dramatically and radar will be used in areas currently unthinkable. Some of the key new radar applications where UWB is likely to have a strong impact include automotive sensors, collision avoidance sensors, smart airbags, intelligent highway initiatives, personal security sensors, precision surveying, and through-wall public safety applications. Through-wall radar is already being tested to assist law enforcement and public safety personnel in clearing and securing buildings more quickly and with less risk by providing the capability to detect human presence and movement through walls. Radar enhanced security

domes based on precision radar have already demonstrated the capability to detect motion near protected areas, such as high-value assets, personnel, or restricted areas. The dome is software configurable to detect movement passing through the edge of the dome, but can disregard movement within or beyond the dome edge. Operation of vehicular radar in the 22–29 GHz band is permitted under the UWB rules using directional antennas on automobiles. These devices are able to detect the location and movement of objects near a vehicle, enabling features such as near collision avoidance, improved airbag activation, and suspension systems that better respond to road conditions.

7.3. UWB over Wires

UWB technology can be delivered over wirelines and cables. This could effectively double the bandwidth available to cable television (CATV) systems without modification to the existing infrastructure [22]. Over-wire technology for coax cable can provide up to 1.2 Gbps downstream and up to 480 Mbps upstream of additional bandwidth, at low cost, on differing CATV architectures. The UWB signals can be introduced at the cable headend and extracted at the customer premises. The wireline UWB technology does not interfere with or degrade television, high-speed internet, voice, or other services already provided by the CATV infrastructure. This will give operators the ability to leverage existing infrastructure to deliver greater functionality in the pursuit of additional revenues. As shown in Fig. 8, the system uses innovative techniques to seamlessly integrate the UWB-wireless and UWB-wired communications.

This integrated wireline and wireless technology provides tremendous wireless networking bandwidth but that also extends content security all the way from the cable provider's headend offices out to a variety of wirelessly networked devices. The concept turns the home entertainment center into a wireless hub and networking gateway.

8. ADDRESSING THE WIRELESS SPECTRUM SQUEEZE WITH UWB

UWB operates at ultralow power, transmitting impulses over multiple gigahertz of bandwidth. Each pulse, or pulse

sequence, is randomized by modulation, thus appears as incremental “white noise” to other narrowband radiofrequency devices. UWB operates with emission levels commensurate with levels of unintentional emissions from common digital devices such as laptop computers and pocket calculators. Today we have a “spectrum drought” in which there is a finite amount of available spectrum, yet there is a rapidly increasing demand for spectrum to accommodate new commercial wireless services. Even the defense community continues to find itself defending its spectrum allocations from the competing demands of commercial users and other government users. UWB exhibits incredible spectral efficiency that takes advantage of underutilized spectrum, effectively creating “new” spectrum for existing and future services by making productive use of what appears as the “noise floor” in conventional receiver bandwidths. The best applications for UWB are for indoor use in high-clutter environments. UWB technology enables not only communication devices but also positioning capabilities of exceptional performance. The fusion of positioning and data capabilities in a single technology opens the door to exciting and new technological developments.

BIBLIOGRAPHY

1. R. J. Fontana, A history of UWB, (online) <<http://www.multispectral.com/history.html>> (Jan. 30, 2004).
2. K. Siwiak and D. McKeown, *Ultra-Wideband Radio Technology*, Wiley, Chichester, UK, 2004.
3. K. Siwiak and L. L. Huckabee, An introduction to ultra-wide band wireless technology, in B. Bing, ed., *Wireless Local Area Networks—the New Wireless Revolution*, Wiley, New York, 2001.
4. M. Z. Win and R. A. Scholtz, Impulse radio: How it works, *IEEE Commun. Lett.*, **2**(1) (Jan. 1998).
5. Time Domain Corporation, Huntsville, AL (online), <<http://www.timedomain.com>> (Jan. 30, 2004).
6. K. Siwiak, Ultra-wide band radio: Introducing a new technology, invited plenary paper, *Proc. IEEE Vehicular Technology Conf. 2001*, Rhodes, Greece, May 2001.
7. H. L. Bertoni, L. Carin, and L. B. Felson, eds., *Ultra-Wideband Short-Pulse Electromagnetics*, Plenum Press, New York, 1993.
8. L. Carin, and L. B. Felson, eds., *Ultra-Wideband Short-Pulse Electromagnetics*, 2nd ed., Plenum Press, New York, 1995.
9. C. E. Baum, L. Carin, and A. P. Stone, eds., *Ultra-Wideband Short-Pulse Electromagnetics*, 3rd ed., Plenum Press, New York, 1997.
10. E. Heyman, B. Mandelbaum, and J. Shiloh, eds., *Ultra-Wideband Short-Pulse Electromagnetics*, 4th ed., Plenum Press, New York, 1999.
11. P. D. Smith and S. R. Cloude, eds., *Ultra-Wideband Short-Pulse Electromagnetics*, 5th ed., Kluwer Academic/Plenum Publishers, New York, 2002.
12. E. L. Mokole, M. Kragalott, and K. R. Gerlach, eds., *Ultra-Wideband Short-Pulse Electromagnetics*, 6th ed., Kluwer Academic/Plenum Publishers, New York, 2003.
13. US 47 CFR Part 15, *Ultra-Wideband Operations*, FCC Report and Order, April 22, 2002.
14. J. K. Gilb, *Wireless Multimedia: A Guide to the IEEE 802.15.3 Standard*, IEEE Press, Piscataway, NJ, 2003.

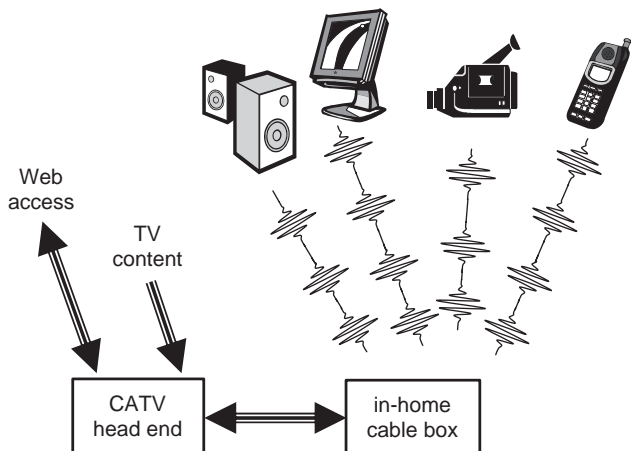


Figure 8. Integrated wireline and wireless UWB technology.

15. R. Hoxtor, Transmitted-reference, Delay-hopped ultra-wideband communications, *Forum on Ultra-Wide Band*, Hillsboro, OR (online), <<http://www.ieee.or.com/IEEEProgramCommittee/uwb/uwb.html>> (Oct. 11–12, 2001).
16. J. G. Proakis, *Digital Communications*, McGraw-Hill, New York, 1983.
17. C. L. Bennett and G. F. Ross, Time-domain electromagnetics and its applications, *Proc. IEEE* **66**(3):299–318 (March 1978).
18. K. Siwiak, T. M. Babij, and Z. Yang, FDTD simulations of ultra-wideband impulse transmissions, *Proc. IEEE Radio and Wireless Conf. (RAWCON 2001)*, Boston, Aug. 19–22, 2001.
19. K. Siwiak, H. Bertoni, and S. Yano, On the relation between multipath and wave propagation attenuation, *Electron. Lett.* **39**(1):142–143 (Jan. 9, 2003).
20. E. H. Callaway, *Wireless Sensor Networks: Architectures and Protocols*, Auerbach Publications (CRC Press), New York, 2003.
21. Aether Wire & Location, Inc. (online), <<http://www.aetherwire.com/>> (Feb. 21, 2004).
22. Pulse~LINK Inc. (online), <<http://www.pulselink.net/>> (Feb. 21, 2004).

ULTRA-WIDEBAND WIRELESS SYSTEMS

BRIAN M. DONLAN
 R. MICHAEL BUEHRER
 JEFFERY H. REED
 Virginia Tech
 Blacksburg, Virginia

1. INTRODUCTION

The concept of ultra-wideband (UWB) has been in existence since the early 1960s when short subnanosecond pulses were applied to the characterization of microwave networks. Impulses were used to probe the network, which allowed the system's impulse response to be determined. In the late 1960s, this impulse excitation technique was eventually applied to the design of wideband antennas and, as a natural consequence, led to the beginnings of pulse-based radar and communications systems [1]. Soon after, the first UWB communications patent was awarded in 1973 to Sperry [1], whose system focused on the transmission and reception of short subnanosecond pulses. However, until 1994, the majority of the research in the United States was conducted under the umbrella of classified U.S. government projects [1]. Research continued into what is now referred to as Impulse Radio and was primarily propelled in the academic realm by the work of Scholtz and Win [2–6] during the 1990s. Since the Federal Communications Commission (FCC) approved a First Report and Order in February 2002, allowing for the development, production, and operation of unlicensed commercial UWB devices, research efforts have increased dramatically and interest in UWB remains strong.

This article focuses on the different aspects of UWB as they relate to the research and development of future UWB applications and places emphasis on pulse-based UWB. First, a brief discussion of the FCC's First Report and Order is provided because it will directly impact the

development and production of UWB devices. A general introduction into UWB follows, and the remainder of the article focuses on possible UWB applications, including the current IEEE standardization efforts for wireless personal area networks (WPANs).

2. FCC GUIDELINES AND REGULATIONS

On February 14, 2002, the FCC approved a First Report and Order allowing the development and operation of unlicensed UWB devices in the United States, a milestone for the commercial development of UWB technology. (At the time this article was being written, regulation efforts were underway in both Europe and Asia.) Much effort was expended to characterize UWB and to determine the operating limitations that should be imposed on these devices. The result was a description of several target applications along with their allowable operating frequency ranges and power emission limits. The specific applications of interest to the FCC fall into three categories: imaging systems, vehicular radar systems, and communications and measurement systems. The imaging systems are subcategorized into ground-penetrating radar (GPR), wall imaging, through-wall imaging, medical, and surveillance systems. (Surveillance systems are not imaging systems but are regulated as such [7].)

Currently, all communications and imaging systems are allowed to operate in the 3.1–10.6 GHz range (high-frequency range). However, some additional spectrum has been allocated for certain imaging applications. GPR, wall imaging, and through-wall imaging can currently also operate below 960 MHz (low-frequency range). From 1.99–3.1 GHz (mid-frequency range), through-wall imaging and surveillance systems are permitted as well. The final application area, vehicular radar, must operate in the 24 GHz band with the stipulation that the center frequency is 24.075 GHz. Figures 1–3 provide the imposed limits on the spectral emissions allowed for each type of device. Furthermore, the regulations restrict the physical operation of

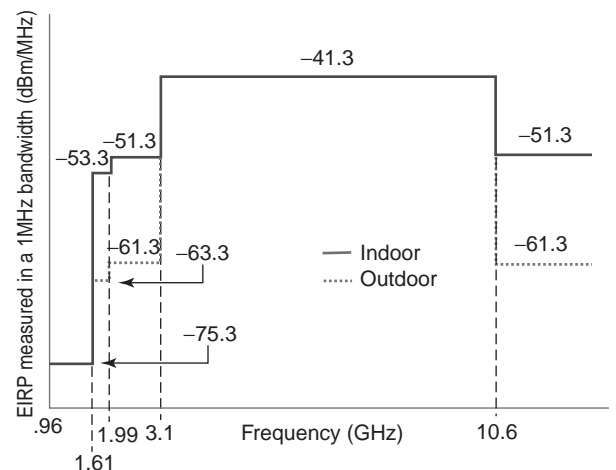


Figure 1. FCC spectral mask for communications and measurement systems. (This figure is available in full color at <http://www.mrw.interscience.wiley.com/erfme>.)

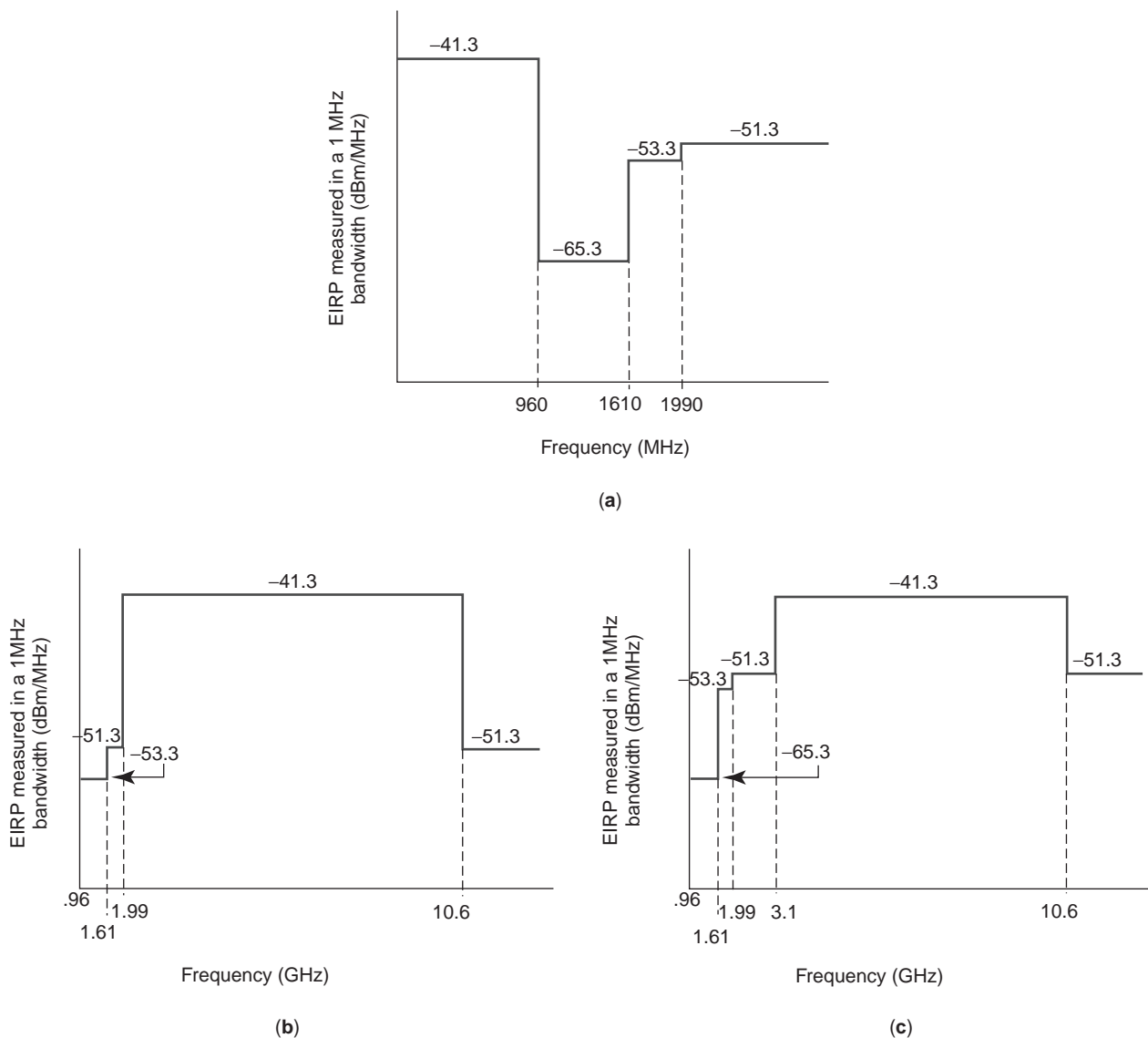


Figure 2. FCC mask for imaging systems for (a) low (b) mid and (c) high frequency.

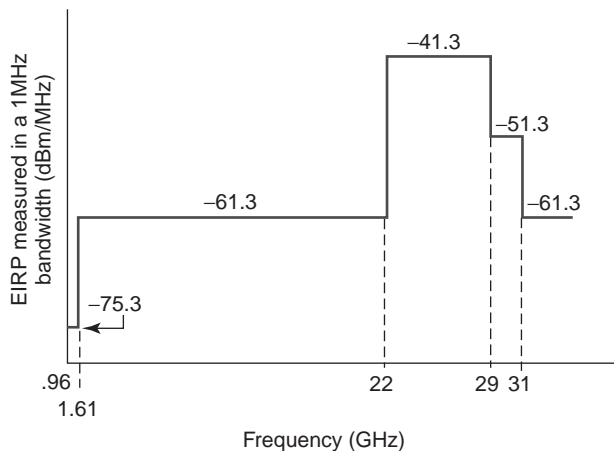


Figure 3. FCC spectral mask for vehicular radar systems.

the devices and the individuals who may operate them. For instance, GPR must be operated only within close proximity to the ground. Use of GPR and wall imaging systems is limited to law enforcement, fire and rescue, scientific research organizations, commercial mining companies, and construction companies. Through-wall imaging systems may be operated by only law enforcement and fire and rescue entities. Medical systems are restricted to medical professionals, and surveillance systems may be used by law enforcement, fire and rescue, public entities, and industrial entities [7]. The imaging devices, therefore, will target only specific markets and are unavailable to the general public. The largest and most recognizable application in the general consumer market will be communications devices. Specifically, UWB is being targeted for high-speed home and business networking, and the first devices will most likely be for wireless personal area networks (WPANs). Vehicular

radar may also appear in the consumer automobile market for applications such as collision avoidance.

For any device designed for the previously mentioned applications to be considered UWB, it must also adhere to the guidelines set forth by the FCC. The commission defines a UWB signal as one that has a fractional bandwidth of 0.20 or greater when operating below 2.5 GHz or a bandwidth exceeding 500 MHz when operating above 2.5 GHz (both measured at the -10 dB emission point). The fractional bandwidth is defined as $2(f_H - f_L)/(f_H + f_L)$, where f_H is the upper frequency and f_L is the lower frequency, each measured at the -10 dB emission point [7]. As a point of reference, narrowband systems typically have a fractional bandwidth of less than 0.01.

3. PROPERTIES OF UWB

For the United States, the FCC currently defines UWB for commercial regulation. This definition allows for the possible use of many different waveform types as long as they can adhere to the regulatory restrictions. Historically, however, UWB refers to the use of pulses with ultra-short time durations, typically subnanosecond, which consequently have extremely large bandwidths, which is sometimes referred to as carrier-free or impulse radio/radar. The ensuing discussion will focus on the properties of UWB as they relate to impulse radio.

3.1. Pulses

Many researchers typically consider a Gaussian pulse or a derivative of the Gaussian pulse as the pulse used in UWB systems. Several pulse generation techniques use transistors or diodes to create Gaussian pulses [8], but these are not discussed here. A Gaussian pulse can be simply described by the waveform

$$p(t) = e^{-\frac{1}{2}(t/t_p)^2} \quad -\infty < t < \infty \quad (1)$$

where t_p is approximately the width of the pulse in seconds. Figure 4 provides an example of a Gaussian pulse with $t_p = 1$ ns and its corresponding magnitude spectrum. The -10 dB bandwidth of this signal is approximately 2 GHz. Note that all -10 dB bandwidth measurements are with respect to power.

Considering the derivatives of the Gaussian pulse is also of interest. Producing these pulses by filtering the original Gaussian pulse is possible, but more importantly, the antennas employed in a UWB system can largely impact the shape of the pulse, and many times the antenna results in the differentiation of the generated pulse on transmission. Antennas are an extremely important component of a UWB system and deserve a great deal of consideration when designing a UWB system. (Schantz [9] offers a detailed introduction.) Here we simply provide the first and second derivatives of the Gaussian pulse, which are given by

$$\frac{d}{dt} p(t) = \frac{t}{t_p} e^{-\frac{1}{2}(t/t_p)^2} \quad (2)$$

and

$$\frac{d^2}{dt^2} p(t) = \frac{1}{t_p^2} e^{-\frac{1}{2}(t/t_p)^2} - \frac{t^2}{t_p^3} e^{-\frac{1}{2}(t/t_p)^2} \quad (3)$$

Figures 5 and 6 provide example plots of the first and second derivatives with their corresponding spectra, again for $t_p = 1$ ns. Here, the -10 dB bandwidths are approximately 2.5 GHz and 2.7 GHz, respectively.

As mentioned earlier and shown in Figs. 1–3, the FCC specifies both the frequency range and the power limitations for UWB emissions. Therefore, the baseband pulses previously mentioned could not be used for the mid- and high-frequency imaging, vehicular radar, or communications applications. Thus, it may be desirable to modulate a sinusoid using the Gaussian pulse in order to shift the pulse into the proper frequency range. Such an RF pulse could be described by

$$p(t) = e^{-\frac{1}{2}(t/t_p)^2} \cdot \sin(2\pi f_{c,UWB} t) \quad (4)$$

where $f_{c,UWB}$ is the center frequency of the RF pulse. Figure 7 provides an example of such an RF pulse, along with its corresponding spectrum, for $t_p = 1$ ns and $f_{c,UWB} = 6$ GHz. The -10 dB bandwidth for this pulse is approximately 4 GHz with the signal centered at 6 GHz.

These RF pulses, however, use the allotted spectrum inefficiently. Examining Figs 1 and 7 shows that the amplitude must be reduced for the sides of the spectrum to fit

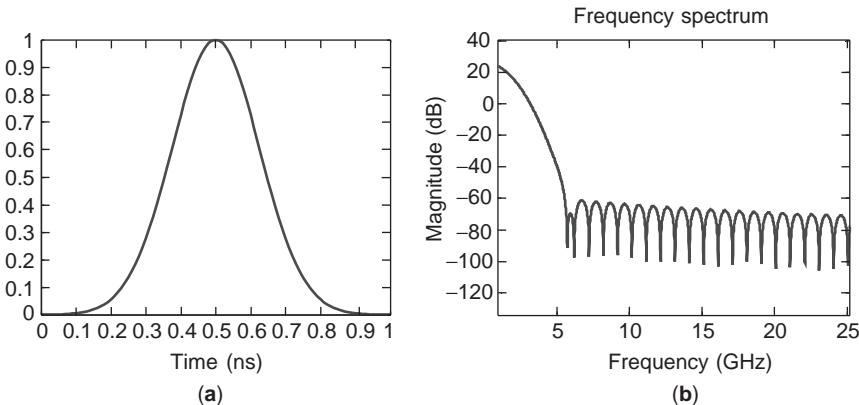


Figure 4. (a) Gaussian pulse and (b) spectrum.

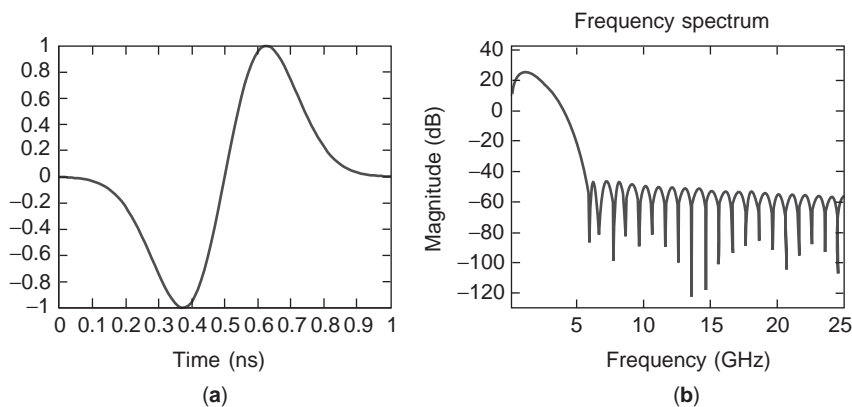


Figure 5. (a) First derivative of a Gaussian pulse and (b) spectrum.

under the spectral mask, which leaves portions of the spectrum significantly underutilized. Recent works have approached this as a filter design problem, designing a pulse's spectrum to more closely match the spectral mask [10,11].

These impulse-like signals provide some inherent advantages that make them appealing for use in communications and radar systems (including imaging systems). First, because of the short duration and quick “rise” and “fall” times of these signals, the energy contained within the pulse is spread over a large bandwidth, resulting in a low-power spectral density, which makes UWB appealing as an overlay technology, making coexistence with regulated narrowband devices possible. This possibility could partially ease the spectrum shortage in the United States and is likely largely responsible for the FCC's consideration of UWB. The “spreading” of energy could also present the possibility for low-probability-of-detection/interception (LPD/I) communications and could be extremely beneficial in a military setting. Several advantages in the time-domain exist as well. In terms of radar, the pulses can be used in a low-duty cycle system to provide precise timing information and can, therefore, improve a radar's ranging precision. For communications, the narrow pulses provide multipath immunity because paths arriving at the receiver are much less likely to interfere with one another. Consequently, a UWB system would experience much less fading than a traditional narrowband system. However, it is difficult to exploit this diversity. A large number of resolvable

paths arrive at the receiver, and searching for these paths and performing channel estimation is very computationally intensive, which remains a significant research challenge.

3.2. Channel

The characterization of the wireless UWB channel is extremely important and will help ensure the success of future UWB systems. Much of the recent UWB research has focused on this characterization by trying to determine the large- and small-scale effects of the indoor UWB channel, ultimately creating a representative channel model that would be applicable to system design. Channel measurement campaigns have been conducted using both time-domain and frequency-domain measurement systems [12–19]. Frequency-domain measurements are typically conducted using a vector network analyzer (VNA). Time-domain measurement systems probe the channel using pulses like those previously described and using a digital sampling oscilloscope. The following describes both the large- and small-scale modeling aspects of the channel.

The large-scale effects of the channel refer to the expected received power (i.e., path loss) seen at a receiver. The power is expressed as a function of distance, obstacles, and the channel properties in general. The modeling aspects do not differ in principle from traditional narrowband path loss, but some differences should be noted. The

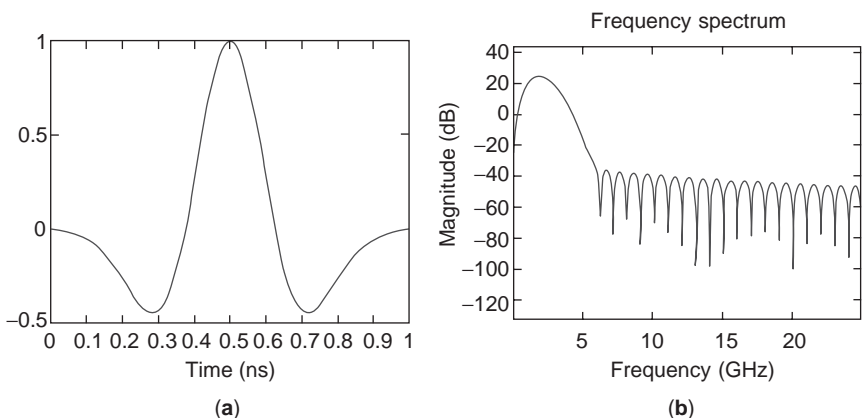


Figure 6. (a) Second derivative of a Gaussian pulse and (b) spectrum.

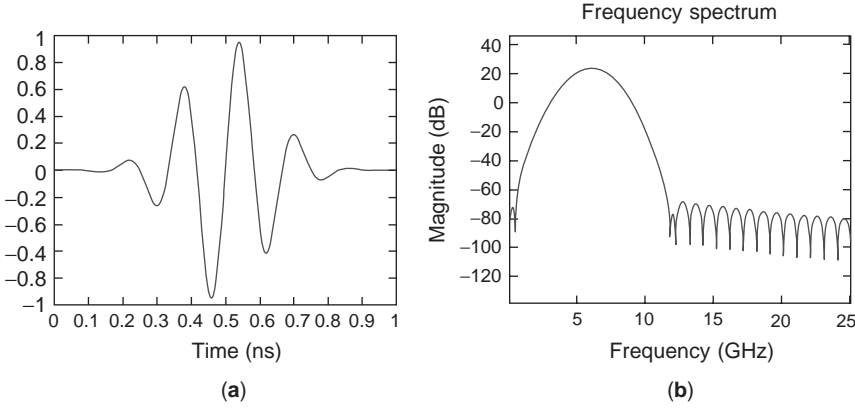


Figure 7. (a) Gaussian modulated RF pulse and (b) spectrum.

calculation of path loss is still performed relative to a reference measurement, and the standard narrowband path loss equation still applies, which is given by

$$P_r(d)_{dBm} = \bar{P}_r(d_0)_{dBm} - 10n \log_{10}\left(\frac{d}{d_0}\right) + X_\sigma \quad (5)$$

where $P_r(d)_{dBm}$ represents the received power at a distance d computed relative to a reference distance d_0 . X_σ is the shadowing term and is a log-normal random variable with a standard deviation σ . However, the Friis transmission formula, which traditionally provides a means for predicting received power in free space, is no longer applicable. The Friis transmission formula is given by

$$P_r = \frac{P_t G_t G_r \lambda^2}{(4\pi d)^2} \quad (6)$$

where P_t is the transmit power, G_t is the transmit antenna gain, G_r is the receive antenna gain, λ is the wavelength of interest, and d is the separation in meters between the transmitter and receiver [19,20]. Several issues develop when applying Eq. (6) to a UWB signal. First, the formulation of the equation assumes constant gain antennas, which is sufficient for calculating values for narrowband signals. However, for UWB signals, the antennas used will not likely be constant gain over the entire bandwidth of the UWB signal. Second, even if the antennas were constant gain, no single wavelength could be associated with the UWB signal. In general, the impact of the antennas on the UWB pulses makes the theoretical calculations of the received power extremely problematic. Such calculations could be performed using an integral equation that takes into account the antenna gains, but more practically, the calculations would most likely have to be facilitated through the use of a reference measurement. Note that Eq. (6) can be restated similar to Eq. (5) as

$$P_r(d) = P_r(d_0) \left(\frac{d_0}{d}\right)^2$$

where $P_r(d_0)$ contains all the antennas effects.

The small-scale effects of the channel refer to the arrival of multipath components at the receiver. These

effects are typically modeled as a time-invariant linear filter with the channel impulse response, $h(t)$, given by

$$h(t) = \sum_{k=0}^{N-1} a_k \delta(t - t_k) \quad (7)$$

where a_k is a random amplitude whose polarity is determined by a binary random variable [2]. This equation can be recognized as the classic narrowband model with the phase replaced by polarity. Therefore, the traditional definitions for the small-scale statistics still apply. The mean excess delay, $\bar{\tau}$, is given by

$$\bar{\tau} = \frac{\sum a_k^2 \tau_k}{\sum a_k^2} \quad (8)$$

where a_k^2 represents the power in the path at a time delay, τ_k [20]. The RMS delay spread, σ_τ , is given by

$$\sigma_\tau = \sqrt{\bar{\tau}^2 - (\bar{\tau})^2}, \quad \text{where } \bar{\tau}^2 = \frac{\sum a_k^2 \tau_k^2}{\sum a_k^2} \quad (9)$$

using the same notation [20]. The goal is to then create a statistical tap delay model matching the statistics of the measured environment [18,21]. In practice, matching additional statistics, such as the number of paths and the max excess delay, is also helpful. Note that Eqs. (8) and (9) refer to the average statistics of the data. To make the best match possible, comparing the statistics cumulative distribution functions (CDFs) is also a good idea [22,23].

Creating such models can be facilitated through the use of a time-domain measurement system, which probes the environment using very short time duration pulses, which results in the channel “impulse” response being received at the receiver. Obviously, this is an approximation, and the narrower the pulse, the better the resolution of the system. However, techniques exist, most notably the CLEAN algorithm, that allow one to extract an approximate tapped delay line channel model, like the one described in Eq. (7) [24].

Much research has focused on the small-scale characterization of the indoor UWB channel for both residential and office environments. Foerster and Li propose that the

UWB channel can be modeled using a modified Saleh–Valenzuela model for both the line-of-sight (LOS) and non-line-of-sight (NLOS) channels [25,26], and this modified Saleh–Valenzuela model has been adopted by the 802.15.3 standards body. This modified model and the Saleh–Valenzuela model both assume that multipath arrives in clusters, with a cluster and the paths within a cluster both arriving according to a Poisson distribution. The energy decay of the cluster and paths are both considered to occur exponentially. According to this model, the channel impulse response can be given as

$$h(t) = \sum_{l=0}^L \sum_{k=0}^K \alpha_{k,l} \delta(t - T_l - \tau_{k,l}) \quad (10)$$

where $\alpha_{k,l}$ is the path amplitude, T_l is the arrival time of the l th cluster, and $\tau_{k,l}$ is the delay of the k th multipath component relative to the l th cluster arrival time. Note that unlike the Saleh–Valenzuela model, the magnitude of the path amplitudes, $\alpha_{k,l}$, are considered to vary according to a log-normal distribution instead of a Rayleigh distribution. Also, a path is modeled as being real instead of complex, with its polarity being determined by an equally likely binary random variable. The cluster and path distributions can then be given by

$$p(T_l | T_{l-1}) = \Lambda \exp[-\Lambda(T_l - T_{l-1})], \quad l > 0$$

$$p(\tau_{k,l} | \tau_{(k-1),l}) = \lambda \exp[-\lambda(\tau_{k,l} - \tau_{(k-1),l})], \quad k > 0 \quad (11)$$

where Λ is the cluster arrival rate, and λ is the ray arrival rate.

McKinstry found that, for his particular set of measurement data, the indoor LOS channel was best modeled using a modified single Poisson model [24]. The channel model, which uses a single cluster with paths arriving according to a Poisson distribution, was modified to include a few dominant early paths. This model was found to match nicely in terms of BER performance and average statistics.

Using McKinstry’s measurement set, Venkatesh et al. suggest a two-cluster NLOS channel model. This channel model is very similar to the Saleh–Valenzuela model, but rather than having a random number of arriving multipath clusters, this model defines only two clusters because of the characteristics of the measurement set. The model was found to match the data quite well in terms of BER performance, average statistics, and cumulative distribution of those statistics. A good discussion of UWB channel measurements and modeling can be found in [21].

It should be noted that how well a channel model fits a particular environment will certainly vary from environment to environment. However, in general, the UWB channel may be statistically modeled as having paths that arrive according to a Poisson distribution, with the path amplitudes decaying exponentially.

A strong advantage of UWB signals for communication applications is that, because of the resolvability of the multipath components in Eq. (10), the total received energy shows very little fluctuation. However, the receiver must capture the entire available signal. Simple struc-

tures may be unable to capture all of the multipath components, leading to increased fading and lower average energy [4,5].

3.3. Communications

As wireless devices continue to proliferate and we head more and more toward a completely wireless world, UWB may make its largest immediate impact in communications. The following discussion describes the digital modulation techniques typically considered for UWB, which mirror those for sinusoidal carrier modulation [27].

Any of the pulses described previously could be incorporated into several different M -ary or binary modulation schemes. Of the several modulation techniques, two are predominately considered in research and industry: pulse position modulation (PPM) and biphase modulation. (Note that biphase is an antipodal modulation scheme, and “biphase” is somewhat of a misnomer because a baseband pulse has no phase parameter associated with it. However, the technique is still commonly referred to as biphase modulation.)

PPM is an M -ary modulation format that conveys information by placing pulses at specified time delays. This modulation scheme is typically orthogonal in time, and, in the binary case, its performance in Additive White Gaussian Noise (AWGN) is identical to binary frequency shift keying (BFSK). Consider Fig. 8, which illustrates 4-ary PPM modulation. Here, T_c is associated with the amount time used to transmit one UWB pulse. T_c is then accordingly divided into M (in this case, 4) different timeslots of width δ . The bit or symbol being transmitted then determines within which timeslot the pulse is placed. Demodulation is performed at the receiver by correlating a template with each of the four timeslots to determine the most likely transmitted symbol. Note that the demodulation requires precise synchronization, making the issue of delay spread extremely important. Depending on the pulse width and the delay spread of the channel (i.e., pulse interaction), synchronization could be difficult, rendering the system ineffective.

Biphase modulation is strictly a binary scheme by which information is encoded into the polarity of the pulse. Biphase is therefore antipodal and has identical performance in AWGN to binary phase shift keying (BPSK). Figure 9 provides an illustration of biphase modulation where a negative pulse represents a 0 and a positive pulse represents a 1.

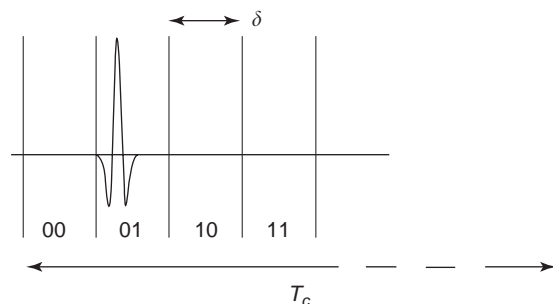


Figure 8. 4-ary pulse position modulation.

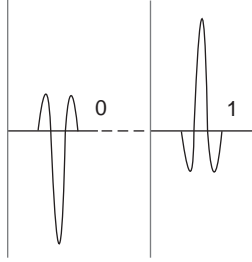


Figure 9. Biphase modulation.

Other modulation techniques are also possible with UWB. These techniques include pulse amplitude modulation (PAM) and on-off keying (OOK). PAM is an M -ary modulation format that encodes the information in the amplitude of the pulse. Figure 10 gives an example of a 4-ary PAM scenario. PAM, however, is not a particularly attractive modulation scheme because UWB systems are typically power limited and PAM is increasingly energy inefficient with increasing M . With every doubling of M , approximately 6 dB/bit of additional signal-to-noise ratio (SNR) is required to achieve equivalent performance. (Proakis provides the relevant derivations [27].) OOK is a binary scheme. In this case, the presence or absence of a pulse determines whether a 1 or a 0 was transmitted. This technique is also energy inefficient but may be attractive for a low-cost, low-complexity system. Figure 11 provides an example of OOK.

Some UWB system designs also include the use of time hopping for the purpose of multiple access. (Time hopping also provides some other advantages discussed later.) As UWB is a target technology for WPANs, multiple access will be a very important issue. Any of the previously discussed modulation types could be used in conjunction with time hopping, but PPM is typically considered in the literature and will be the basis of the following discussion. Scholtz first presented time hopping PPM (TH-PPM) for UWB [28], and it has been discussed in many other works [24,29]. Such a system can be described by

$$s^{(k)}(t) = \sum_j A p(t - jT_f - c_j^{(k)}T_c - \delta d_{\lfloor j/N_s \rfloor}^{(k)}) \quad (12)$$

where

- $s^{(k)}(t)$ is the transmitted signal for the k th user
- A is the amplitude of the pulse, equal to $\sqrt{E_p}$, where E_p is the energy per pulse

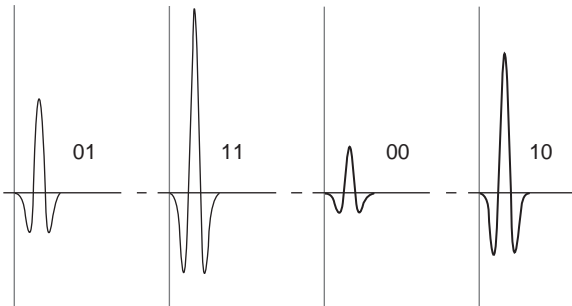


Figure 10. 4-ary pulse amplitude modulation.



Figure 11. On-Off keying modulation.

- N_s is the number of pulses used to represent one data symbol, i.e., the pulse repetition number
- $p()$ is the transmitted pulse shape with normalized energy
- T_f is the frame repetition time (a UWB frame is defined as the time interval in which one pulse is transmitted)
- $c_j^{(k)}$ is the time hopping sequence, often pseudorandom and/or repetitive
- T_c is the granularity of the time hop delay (together $c_j^{(k)}$ and T_c determine the “coarse” time dithering)
- δ is the PPM time delay parameter
- $d_{\lfloor \cdot \rfloor}^{(k)}$ is a function of the data sequence (the notation $\lfloor \cdot \rfloor$ represents the integer portion of the argument)

The total received signal is given by

$$r(t) = \sum_k s^{(k)}(t) * h^{(k)}(t) \quad (13)$$

where $h^{(k)}(t)$ is the channel impulse response between the k th user and the receiver and $*$ denotes the convolution operation [28].

Figure 12 provides a depiction of an unmodulated pulse train without time hopping. The frame, T_f , represents the time between pulses, and T_p represents the pulse width.

In contrast, Fig. 13 provides an example of a time hopped signal where a frame, T_f , is considered to be the time in which one pulse is sent. The frame is divided into several timeslots of period T_c . Referring to the discussion on PPM, T_c represents the same timeslot given in Fig. 8. A pulse is then transmitted in any one of the timeslots. In a multiple access scenario, the k th user would have a unique code, $c_j^{(k)}$, which is usually pseudorandom, and it would specify the time hopping location of the pulse from frame to frame. Modulation then occurs independently within the timeslot. In regards to modulation, the variable N_s specifies the number of pulses used to transmit one symbol or bit. Using $N_s > 1$ introduces time diversity over the period of one symbol, which provides the system with a processing or spreading gain proportional to N_s , in turn improving the ability to properly detect a symbol (for a constant transmit power) at the cost of reducing the data rate.

Several research issues must be addressed for UWB to reach its full potential as a communications technology. For example, the successful exploitation of the favorable qualities of UWB signals is highly dependent on the receiver structure. However, detector and channel estimation approaches that can provide both high energy capture

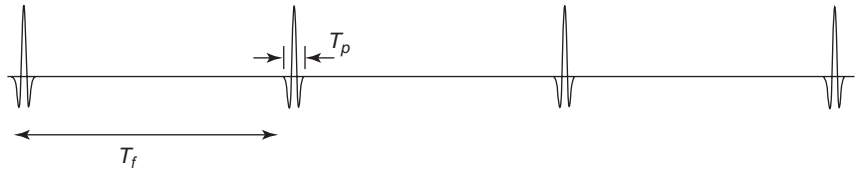


Figure 12. UWB pulse train (no modulation and no time hopping).

[4,5] and low complexity are nontrivial. The problem is further complicated by the difficulty of predicting the pulse shape because of the channel or even the antenna itself. This item highlights the need for a different approach for UWB than for traditional communication system design. Second, the low-power spectral density and dense multipath structure of the received signal make synchronization particularly difficult. Third, data networks have traditionally relied on carrier sense mechanisms for medium access control (MAC), which will be particularly difficult with UWB signals in dense multipath. Finally, because UWB signals are to be overlaid on existing systems, narrowband interference will exacerbate an already difficult detection and synchronization problem. Many interference mitigation algorithms assume acquisition has occurred, which ignores the difficulty in achieving acquisition in the presence of strong interference. Research is currently ongoing to address each of these concerns.

3.4. Radar

All radar, whether it is imaging or target recognition, can benefit from the use of UWB pulses. From a spectral standpoint, the bandwidth of the signal directly relates to the resolution of the radar, and, from a temporal standpoint, the ability to periodically send very short pulses allows for accurate timing and therefore improved ranging precision. These characteristics make UWB an ideal candidate for radar.

Consider again the Gaussian pulses mentioned in Eqs. (1)–(3). These pulses could be transmitted singularly, but a method using a group of pulses offers some advantages, which is sometimes referred to as pulse compression. It involves sending a series of successive pulses that are modulated by a pseudorandom (PN) binary sequence, b_n . Note that this technique could also be used in communications and is sometimes referred to as direct sequence UWB (DS-UWB). The transmitted signal $s(t)$ could then be given by

$$s(t) = \sum_{n=0}^{N-1} b_n p(t - nt_p) \quad (14)$$

where $p(t)$ is a single pulse, N is the length of the PN sequence, and b_n takes on the values -1 and $+1$ [30]. The advantages for radar are two-fold. First, by sending a series of pulses, the average power of the radar “pulse” is increased. This increase is beneficial because the ability to detect a target directly relates to the available signal energy. Second, the accurate range resolution may still be attained by using a code matched filter for the pulse sequence. Doing so produces a spike when the sequence is properly aligned in the matched filter, compressing the sequence into one pulse, and like DS-SS, it also offers some interference suppression. The performance of the radar is then directly related to the autocorrelation of the group of UWB pulses [30]. Also, although UWB does not suffer from the effects of Doppler, like traditional sinusoidal radar, motion-induced effects still exist. Motion can contribute to pulse distortion causing individual pulse shapes to vary as pulses interact with each other and different materials. This distortion can cause the compressed pulse to broaden, degrading the resolution of the system.

Another important aspect for radar is target recognition, which directly relates to the interaction of the signal with an object. One of the differences between UWB and sinusoidal signals is that the interaction of UWB pulses with certain objects and materials will result in a change in the parameters of the pulse, causing a transformation in the pulse’s shape. On the other hand, a sinusoidal signal’s interactions, such as subtractions, additions, differentiations, and integrations, all result in a change in signal parameters, specifically the magnitude and the phase, but the shape of the signal remains the same. The association of a specific pulse shape with a target provides UWB with a distinct advantage in this area [31].

The interaction of a Gaussian pulse with a complex target can be considered a linear time invariant system (similar to the UWB channel) [30]. Thus each target will have a unique impulse response that is a function of the target’s material make-up, shape, size, and the signal’s angle of arrival. The impulse response, $h_s(t)$, is given by

$$h_s(t) = \sum_{i=0}^{N-1} E_i e^{-a_i^2(t-t_i)^2} \quad (15)$$

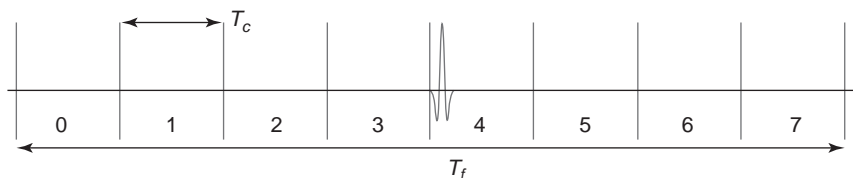


Figure 13. Example frame for time hopping UWB.

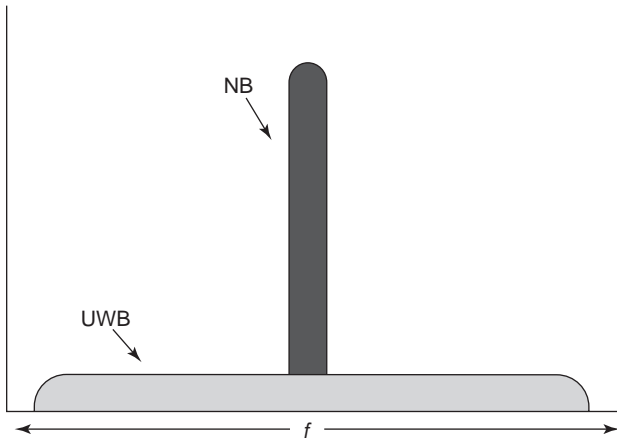


Figure 14. UWB versus narrowband signals.

and is a series of time-shifted Gaussian pulses representing a complex target with N scattering centers, where E_i weights the Gaussian pulse and a_i controls the shape of the Gaussian impulse [30]. The response of a Gaussian pulse to a target is then given as

$$s(t) = p(t) * h_s(t) \tag{16}$$

where $*$ denotes the convolution operation.

The received signal, $s(t)$, then contains specific information regarding the target’s location and structure and is often referred to as the “target image.” It should be noted that this profile is sensitive to the location of the radar with respect to the target; more specifically, the relative angle between the two is of importance because the target’s response will change with different angles of arrival [30].

3.5. Interference

As a result of the extremely wide bandwidth of a UWB signal, the interference a UWB system both inflicts and observes is a concern. The spectral limits proposed by the FCC are, by their own consent, conservative estimates of the acceptable emission levels for UWB devices. This provision is mainly to protect the legacy narrowband government systems from interference caused by UWB devices. One major concern is the impact of UWB on the operation of GPS systems, especially because of air traffic’s depen-

dence on this technology. Therefore, UWB transmissions are not allowed in the spectrum allocated for GPS. The following provides some comments on interference from both perspectives.

The intent of the FCC is to eventually amend the imposed limits once the interference that UWB systems inflict can be sufficiently characterized. The initial thinking is that UWB will cause little interference to in-band narrowband systems. Consider the illustration given in Fig. 14. Even if the two signals are received with equal power, a UWB signal should add little noise to the narrowband signal because a very small fraction of the UWB signal’s power is in the narrowband signal’s bandwidth. Several research efforts have investigated the impact of a UWB signal on existing systems. Light presents test results examining the effects of UWB signals on many different legacy military systems [32]. Light found that UWB transmissions did interfere with some devices more than others and that many factors impact the level of interference, including pulse shape and pulse repetition frequency. This work also reports that some devices were susceptible to interference at transmit powers even below the FCC spectral mask. Giuliano et al. analyzes the effects of UWB on UMTS [33]. Using simulation, they conclude that UWB poses no threat to the operation of UMTS. The effects of aggregation are also a concern because, especially for communications applications, many colocated devices may be operating simultaneously. This issue requires much more investigation.

In the context of UWB-based interference, it is important to consider the effect of a stream of pulses. Consider again the pulse train represented in Fig. 12. As a result of the periodic nature of the pulse train, transmitting a signal of this nature would produce spectral lines in the pulse’s spectrum. Figure 15 provides an example of such a signal’s spectrum. As previously stated, time hopping actually serves a dual purpose: besides multiple access, it can also be used to smooth the spectrum of the UWB signal. In contrast, Fig. 16 shows the spectrum with time hopping using a random hopping sequence with sixteen different time-slots. Comparing Fig. 15(a) and Fig. 16, a noticeable difference exists between the magnitudes of the two signals’ spectra. By employing time hopping, the periodicities are greatly reduced, which smoothes the spectrum by reducing the spectral lines. Note that it is also possible to combat spectral lines by using biphas modulation.

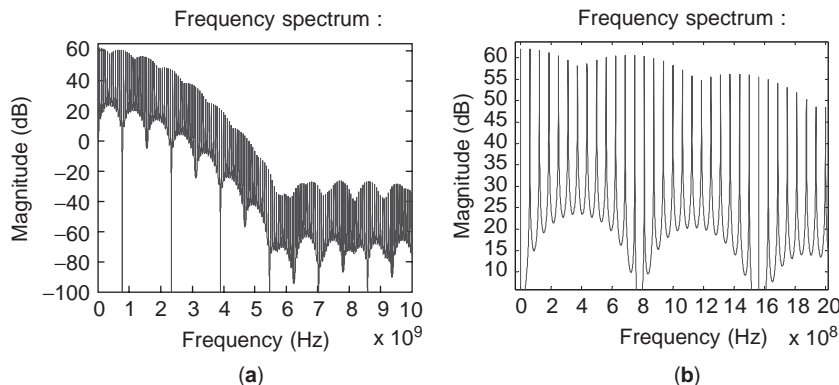


Figure 15. (a) Spectrum of unmodulated pulse train and (b) a magnified portion. (This figure is available in full color at <http://www.mrw.interscience.wiley.com/erfme>.)

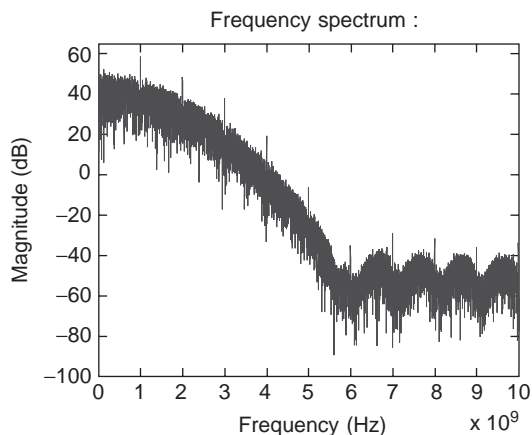


Figure 16. Spectrum of time hopped pulse train. (This figure is available in full color at <http://www.mrw.interscience.wiley.com/erfme>.)

Regardless of any future changes in the FCC's spectral mask, UWB will most likely continue to suffer from interference caused by in-band narrowband systems, which will limit a system's range. Firoozbakhsh et al. analyzed the performance of a UWB system in the presence of an 802.11a network [34]. Through simulation, they found that 802.11a could cause significant interference and greatly degrades the UWB system's performance, which will likely be true of many narrowband systems. It will therefore be necessary to apply advanced signal processing techniques to perform interference cancellation. As the problem is similar to that of spread spectrum, ideally some crossover will occur from previous spread spectrum front-end interference cancellation techniques. Unfortunately, techniques such as linear prediction filters, which are purely digital, are not yet viable solutions because the current state-of-the-art does not allow for an entirely digital cost-effective UWB system. Some possible solutions include the use of transform domain processing, a combination analog-digital cancellation circuit, and the use of a Rake receiver to exploit the temporal diversity of the UWB channel. Such research is beginning to emerge and will probably garner considerable attention in the near future.

4. UWB APPLICATIONS

The extremely large bandwidth of UWB provides the potential for high-data rate communications, and accurate ranging devices (e.g., radar). These characteristics make UWB attractive for a variety of interesting applications, from digital communication to imaging. These applications include ground-penetrating radar, through-wall imaging, medical imaging, WPANs, and vehicular radar. The following provides introductions and examples for these UWB wireless applications. Please see [35] for additional information.

4.1. Ground-Penetrating Radar Systems

Ground-penetrating radar (GPR) systems will provide the ability to locate objects that are beneath the ground,

beneath rubble, and so forth. The capabilities of GPR are affected by the range of frequencies used in the system. The characteristics of the object, its location, and the medium in which it is buried in part determine which frequency band is most suited for detection. For instance, higher frequencies allow for more accurate depth resolution. However, the soil will introduce greater attenuation at higher frequencies, and therefore deep objects may not be detected. In this case, lower frequencies would be more beneficial. The use of large bandwidth, baseband pulses are therefore very attractive for this application as they incorporate a wide range of frequencies [36,37].

Park et al. demonstrate the viability of such a device by demonstrating its ability to find metal objects buried in the ground at varied depths [37]. The GPR system employed used separate transmit and receive antennas and a 2.5 ns pulse. A 5 G/s digital sampling scope was used to digitize the signal and a 2-D image signal processing algorithm was used to interpret the results. An additional study also investigated the use of GPR for the detection of plastic landmines, another extremely important application [37].

4.2. Through-Wall Imaging Systems

Through-wall imaging systems use UWB radar to monitor the movements of people through a wall. Time Domain Corporation (www.timedomain.com) has a working through-wall imaging system called RadarVision. The device transmits pulses at ten million pulses per second and has a range of thirty feet. It has been demonstrated to penetrate reinforced concrete, concrete block, sheetrock, brick, wood and wood composites, plaster, tile, and fiberglass. Many situations can be envisioned where a device of this nature would be extremely beneficial. Consider a hostage situation where it would be extremely advantageous to know the locations and movements of the people within the room. Also, consider a burning building where a fire fighter could determine if anyone was still trapped within a room. Many other scenarios can be envisioned, and this could be an extremely useful device in the near future.

4.3. Medical Systems

Medical imaging radar systems present much promise for the ability to provide noninvasive medical monitoring. For instance, UWB radar has been demonstrated to provide the ability to monitor the movements of the heart wall. Much like what was described in the radar section, the pulses will respond differently to different materials (in this case, the heart tissue and blood). Specifically, an impedance difference exists between the blood and heart muscle, which provides different reflection magnitudes and allows the heart to be monitored [38]. Using this idea, a UWB radar prototype was developed at La Sapienza University in Rome. The device operates at 800 MHz and has the ability to detect heart and body movements [38]. This concept could be extended to applications involving other parts of the body because the pulse will react uniquely to different fluids, organs, and tissues in the body. Besides heart monitoring, the applications could possibly extend to respiratory monitoring and fetal monitoring (an ultrasound replacement). At some point, it

could even extend to actual imaging of the brain, heart, chest, and so forth. Nevertheless, many challenges still lay ahead, most notably characterizing the response of certain pulses to bodily tissues and organs.

4.4. Communications Systems

UWB communications systems have recently received the most attention of any UWB area, with visions of low-power, high-data rate wireless devices being available in the near future. Multispectral Solutions, Inc., (www.multispectral.com) has long been involved with the development of UWB radios and has many working UWB communications products [1]. These devices include transceivers for both voice and data and even a tactical ad hoc wireless network. However, most of these devices were developed for the U.S. military rather than as part of the current FCC regulations.

The current push for wireless UWB communications devices among industry, however, is in WPANs, groups of interconnected wireless devices within one's own personal operating space. These devices can communicate among each other and with an already existing network, a wireless local area network (WLAN) for instance. The devices include laptop computers, mobile phones, PDAs, digital cameras, and other handheld devices. The IEEE 802.15.3 working group is responsible for developing a standard for high-data rate WPANs that would provide low-cost, low-power solutions for wireless digital and multimedia applications. Within this working group, a task group, 802.15.3a, was formed to investigate UWB as an alternative physical layer technology for the standard. There has been much debate within the task group over which technology to use, and they have yet to reach a conclusion. Two possibilities are being considered: a MultiBand OFDM approach and a direct sequence approach using pulses (DS-UWB). (DS-UWB was mentioned in the Section 3.4.)

The MultiBand OFDM supporters formed the MultiBand OFDM Alliance (MBOA, www.multibandofdm.org), which is comprised of many industry leaders, and has created its own specifications and standards for UWB wireless devices. Staccato Communications (www.staccato.com), a member of MBOA, has developed a MultiBand OFDM Transceiver and MAC PCI card, which they have integrated into an MBOA UWB Development Platform based on the MBOA specifications. Many more MultiBand OFDM (MB-OFDM) devices will likely begin to emerge in the near future.

MB-OFDM divides the available spectrum into subbands, with each subband having a bandwidth of 528 MHz. Using OFDM symbols, the information is transmitted by interleaving these symbols across the specified subbands. A time-frequency code is then used to determine which particular frequency and timeslot will be used for a given symbol [39]. These subbands provide the capability to avoid interferers, simply by avoiding a particular band, and also facilitate more effective use of spectrum. Compared with pulse-based systems, MB-OFDM requires less precise timing and can easily be designed to meet the FCC spectral mask.

Even so, some commercially available communications products are based on the traditional pulse-based UWB. Specifically, XtremeSpectrum, recently acquired by Motorola, offers its Trinity Chipset (www.xtremespectrum.com), which includes a medium access controller, a baseband processor, an RF transceiver, an RF front end, and an antenna. The MAC protocol adheres to the 802.15.3 standard. Trinity includes selected data rates of 25, 50, 75, and 100 Mbps and uses biphase modulation. In a demonstration for the FCC, the chipset was used to simultaneously stream multiple high-definition television (HDTV) feeds.

The IEEE is also considering creating another standard, 802.15.4, where UWB is also a potential technology. In general, 802.15.4 would be a standard for low-data rate, low-complexity devices that have an extended battery life. These devices could possibly be used for sensors, interactive toys, smart badges, remote controls, and home automation. (Please visit www.ieee.org for the latest news concerning 802.15.4.)

The Time Domain Corporation provides evaluation and analysis kits based on their PulsON 200 chipset, which includes timing, correlator, and digital baseband chips. These devices are not intended for wireless multimedia or WPAN devices but as investigative tools. The systems are capable of data rates from 75 kbps to 9.6 Mbps. The devices are FCC compliant and have a center frequency of 4.7 GHz with a bandwidth of 3.2 GHz.

Aether Wire & Location, Inc., (www.aetherwire.com/) is developing devices called localizers. These localizers are approximately pager-sized units that transmit a unique pulse waveform as a result of the antennas used in their systems. A single pulse is actually represented by a series of two pulses, in which case the transmission of a 1 is represented by a positive pulse followed by a negative pulse, and the transmission of a 0 is the inverse of this. These devices can provide centimeter accuracy over large distances and are targeted for a variety of applications generally centered around position location. Unlike GPS, which uses triangulation and fixed satellites to locate objects, these localizers are capable of defining their position relative to other localizers. Some of the possible applications for these devices include the location of persons, possibly for military, law enforcement, fire and rescue, or even personal situations, sensor networks, smart homes, smart highways, and inventory control [40].

4.5. Vehicular Radar Systems

Vehicular radar is a promising application for improving driver safety. Sensors can be placed throughout a vehicle, creating a network for collecting valuable information. This information could be used to sense driving conditions, aid in parking, avoid collisions, detect objects in blind spots, aid cruise control, and aid airbag deployment. However, the current frequency range and spectral emissions limits will place constraints on the sensors' operation. As always, a tradeoff will occur between the bandwidth and the range resolution. The closer ranging applications will need a much larger bandwidth (narrower pulses) than the longer ranging applications. For close-range systems, it

would be possible to use PN-coded waveforms for improved ranging [41] (like that described in the radar section). However, in this instance, the ability to isolate the transmit and receive antennas is a concern because it will impact the dynamic range of the system. However, for longer ranging applications, a pulsed-based system with a low duty cycle could be used, which would help with the isolation of the transmit and receive antennas.

As a note, Multispectral Solutions, Inc., has developed a UWB backup sensor that can detect objects from one foot to thirty feet. It has a 500 MHz bandwidth and operates in the 5.4–5.9 GHz band [1], but unfortunately this falls outside of the frequency range specified by the FCC.

5. CONCLUSION

This article provided an introduction into the basic principles of UWB, mainly in the context of impulse radio. Modulation formats, pulse types, the channel, and interference considerations were all discussed in terms of radar and communications systems. The final section of the chapter introduced possible UWB applications as defined by the FCC. UWB presents many exciting possibilities and many technical challenges must still be overcome.

BIBLIOGRAPHY

- R. J. Fontana, *Recent Applications of Ultra Wideband Radar and Communications Systems*, Kluwer Academic/Plenum Publishers, New York, 2000. available at www.multispectral.com/presentations/UWB%20Applications/index.htm.
- R. A. Scholtz and M. Z. Win, Impulse radio, *Personal Indoor Mobile Radio Conference*, September 1997.
- M. Z. Win and R. A. Scholtz, Impulse radio: how it works, *IEEE Commun. Lett.*, **2**:36–38 (1998).
- M. Z. Win and R. A. Scholtz, On the energy capture of ultra-wide bandwidth signals in dense multipath environments, *IEEE Commun. Lett.*, **2**(9):245–247 (1998).
- M. Z. Win and R. A. Scholtz, Energy capture vs. correlator resources in ultra-wide bandwidth indoor wireless communications channels, *MILCOM Proc.*, **3**(2–5):1277–1281 (1997).
- M. Z. Win and R. A. Scholtz, Characterization of ultra-wide bandwidth wireless indoor channels: a communication-theoretic view, *IEEE J. Selected Areas Commun.*, **20**(9):1613–1627 (2002).
- Federal Communications Commission, First report and order, ET Docket 98-153, April 2002.
- T. W. Barret, History of ultrawideband communications and radar: Part 1, UWB communications, *Microwave J.*, **44**(2): 22–56 (2001).
- H. G. Schantz, Introduction to ultra-wideband antennas, *IEEE Conf. Ultra Wideband Syst. Technol.*, pp. 1–9, 2003.
- D. Zeng, A. Annamalai, and A. I. Zaghoul, Pulse shaping filter design in UWB system, *IEEE Conf. Ultra Wideband Syst. Technol.*, pp. 66–70, November 2003.
- X. Luo, L. Yang, and G. B. Giannakis, Designing optimal pulse-shapers for ultra-wideband radios, *IEEE Conf. Ultra Wideband Syst. Technol.*, pp. 349–353, November 2003.
- S. S. Ghassemzadeh and V. Tarokh, UWB path loss characterization in residential environments, *IEEE Radio Frequency Intergrated Circuits Symposium*, pp. 501–504, 2003.
- D. Cassioli, M. Z. Win, and A. F. Molisch, The ultra-wide bandwidth indoor channel: from statistical study to simulation, *IEEE J. Selected Areas Commun.*, **20**:1247–1257 (2002).
- J. Keignart and N. Daniele, Subnanosecond UWB channel sounding in frequency and temporal domain, *IEEE Conf. Ultra Wideband Syst. Technol.*, pp. 21–23, 2002.
- J. Kunisch and J. Pamp, Measurement results and modeling aspects for the UWB radio channel, *IEEE Conf. Ultra Wideband Syst. Technol.*, pp. 19–23, 2002.
- S. M. Yano, Investigating the ultra-wideband wireless channel, *IEEE Vehicular Technol. Conf.*, pp. 1200–1204, 2002.
- A. H. Muqaibel, A. Safaai-Jazi, A. M. Attiya, A. Bayram, and S. M. Riad, Measurements and characterization of indoor ultra-wideband propagation, *IEEE Conf. Ultra Wideband Syst. Technol.*, pp. 295–299, 2003.
- B. M. Donlan, S. Venkatesh, V. Bharadwaj, R. M. Buehrer, and J-A. Tsai, The ultra-wideband indoor channel, *IEEE Vehicular Technol. Conf.*, 2004.
- R. M. Buehrer, W. A. Davis, A. Safaai-Jazi, and D. Sweeney, Characterization of the ultra-wideband channel, *IEEE Conf. Ultra-Wideband Syst. Technol.*, pp. 26–31, 2003.
- T. S. Rappaport, *Wireless Communications: Principles and Practice*, 2nd ed., Prentice Hall, Upper Saddle River, NJ, 2002.
- A. F. Molisch, J. R. Foerster, and M. P. Grass, Channel models for ultrawideband personal area networks, *IEEE Wireless Commun.*, **6**:14–21 (2003).
- D. R. McKinstry and R. M. Buehrer, UWB small scale channel modeling and system performance, *IEEE Vehicular Technol. Conf.*, pp. 6–10, 2003.
- S. Venkatesh, J. Ibrahim, and R. Michael Buehrer, A new 2-cluster model for indoor UWB channel measurements, *IEEE Int. Sympos. Antennas and Propagat.*, pp. 946–949, 2004.
- D. R. McKinstry, *Ultra-Wideband Small Scale Channel Modeling and its Application to Receiver Design*, Master's Thesis, Dept. of Electrical and Computer Engineering, Virginia Tech, Blacksburg, VA, 2003.
- J. Foerster and Q. Li, "UWB Channel Modeling Contribution from Intel (doc: IEEE P802.15-02/279-SG3a)," submitted to IEEE P802.15 Working Group for Wireless Personal Area Networks (WPANs), June 2002, available at grouper.ieee.org/groups/802/15/pub/2002/Jul02/.
- A. Saleh and R. Valenzuela, A statistical model for indoor multipath propagation, *IEEE J. Selected Areas Commun.*, **5**(2):128–137 (1987).
- J. G. Proakis, *Digital Communications*, McGraw Hill, New York, 2001.
- R. Scholtz, Multiple access with time-hopping impulse modulation, *IEEE Military Commun. Conf.*, **2**:447–450 (1993).
- C. J. Le Martret and G. B. Giannakis, All-Digital impulse radio with multiuser detection for wireless cellular systems, *IEEE Trans. Commun.*, **50**(9):1440–1450 (2002).
- M. G. M. Hussain, Ultra-Wideband impulse radar—an overview of the principles, *IEEE Aerospace Electron. Syst. Mag.*, **13**(9):9–14 (1998).
- I. I. Immoreev, P. G. S. Dmitry, and V. Fedotov, Ultra wide-band radar systems: advantages and disadvantages, *IEEE Conf. Ultra Wideband Syst. Technol.*, pp. 201–205, 2002.
- A. H. Light, NETEX task 1: measured effects of ultrawideband (UWB) emitters on existing narrowband military receivers, *IEEE Conf. Ultra Wideband Syst. Technol.*, pp. 10–14, November 2003.

33. R. Giuliano, F. Mazzenga, and F. Vatalaro, On the interference between UMTS and UWB systems, *IEEE Conf. Ultra Wideband Syst. Technol.*, pp. 339–343, November 2003.
34. B. Firoozbakhsh, T. Pratt, and N. Jayant, Analysis of IEEE 802.11a interference on UWB systems, *IEEE Conf. Ultra Wideband Syst. Technol.*, pp. 473–477, November 2003.
35. J. H. Reed, ed., *An Introduction to Ultra Wideband Communication Systems*, Prentice-Hall, Englewood Cliffs, NJ, in press.
36. Y.-J. Park, K.-H. Kim, S.-B. Cho, D.-W. Yoo, D. G. Youn, and Y.-K. Jeong, Development of a UWB GPR system for detecting small objects buried underground, *IEEE Conf. Ultra Wideband Syst. Technol.*, pp. 384–388, 2003.
37. B. Scheers, M. Piette, and A. Vander Vorst, The detection of AP mines using UWB GPR, *Second Int. Conf. Detection Land Mines*, **458**:50–54 (1998).
38. E. M. Staderini, UWB radars in medicine, *IEEE Aerospace Electron. Syst. Mag.*, **17**(1):13–18, January 2002.
39. J. Balakrishnan, A. Batra, and A. Dabak, A multi-band OFDM system for UWB communication, *IEEE Conf. Ultra Wideband Syst. Technol.*, pp. 354–358, November 2003.
40. R. Fleming and C. Kushner, Low-Power, miniature, distributed position location and communication devices using ultra-wideband nonsinusoidal communication technology, Semi-Annual Technical Report, ARPA Contract J-FBI-94-058, July 1995, available at www.aetherwire.com/PI_Report_95/awl_pi95.pdf.
41. I. Gresham, A. Jenkins, R. Egri, C. Eswarappa, R. Kolak, R. Wohler, J. Bennett, and J.-P. Lanteri, Ultra wide band 24 GHz automotive radar front-end, *IEEE Radio Frequency Integrated Circuits Symposium*, pp. 505–508, 2003.

UNDERGROUND PROPAGATION

Y. P. ZHANG
Nanyang Technological
University
Singapore

Underground structures such as subway networks and subterranean cities play important roles in our daily life. Everyday millions of passengers travel through subway networks or thousands of people go shopping in subterranean cities worldwide. Obviously, radio systems are needed in underground structures for normal and emergency operations. Underground structures are either constructed in tunnels or linked with tunnels. To design radio systems for underground structures, the understanding of the propagation of radiowaves in tunnels is essential. Substantial research efforts have been made on this topic and a good knowledge of the involved propagation mechanisms is now available [1]. In the following sections, we introduce underground propagation by considering a straight circular tunnel with axial conductors. We assume that only one axial conductor such as the high-voltage cable is suspended in the tunnel and other axial conductors such as rails and pipes are on the tunnel wall. Despite the mediocre conductivity of the tunnel wall, we can already obtain a good picture of the propagation phenomena by comparing the

tunnel with a coaxial cable, the inner and outer conductors of which are the axial conductor and the tunnel wall. The structure supports the propagation of the coaxial mode that has current flowing along the axial conductor and returning along the tunnel wall. Figure 1 shows the attenuation constant of the coaxial mode as a function of frequency and distance from the axial conductor to the tunnel wall [2]. Note that the attenuation constant of the coaxial mode generally increases with frequency and decreases with the distance from the axial conductor to the tunnel wall. As the attenuation constant of the coaxial mode takes on relatively low values at lower frequencies, radio systems using the coaxial mode propagation at frequencies lower than a few hundred kilohertz have been exploited successfully in various underground mines across the world.

In addition to the coaxial mode, the structure also supports the propagation of waveguide modes when the frequency exceeds the cutoff frequency determined by the tunnel shape and size. The cutoff frequency occurs approximately at tens of MHz for most tunnels. Figure 2 shows the attenuation constant of the fundamental waveguide mode in the tunnel as a function of frequency [3]. As shown, the attenuation constant of the fundamental waveguide mode generally decreases with frequency. It should be mentioned that the axial conductor has no effect whatsoever on the propagation of the fundamental waveguide mode because the electric field has only a circular component. As the attenuation constant of the fundamental waveguide mode takes on relatively low values above the cutoff, it is possible to communicate in the tunnel using the fundamental waveguide mode propagation in the ultra-high frequency (UHF) range. In this process, the antennas of radio systems are mainly coupled to the electromagnetic field of the fundamental waveguide mode. A problem with the propagation of waveguide modes is the disastrous additional attenuation caused by tunnel bends, corners, and crossings, and of vehicles obstructing a large part of the tunnel cross section.

An important but fortuitous discovery in underground propagation was that a coaxial cable with an imperfect

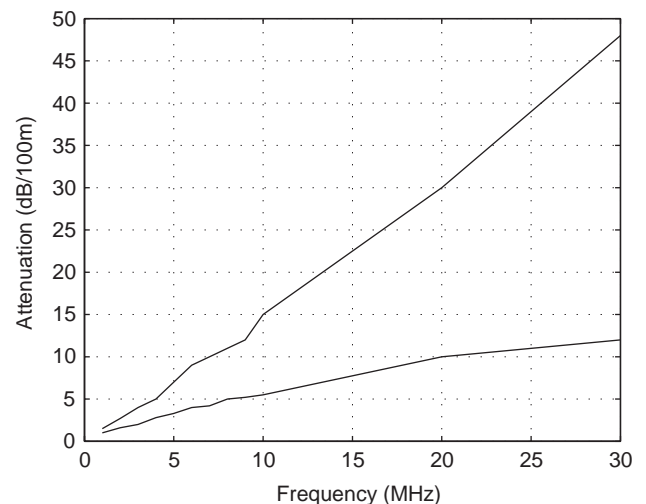


Figure 1. Attenuation constant of the coaxial mode for a single conductor of diameter 1 cm and conductivity 10^9 S/m in the circular tunnel of radius 2 m, $\epsilon_{r1} = 10$, $\sigma = 10^{-2}$ S/m.

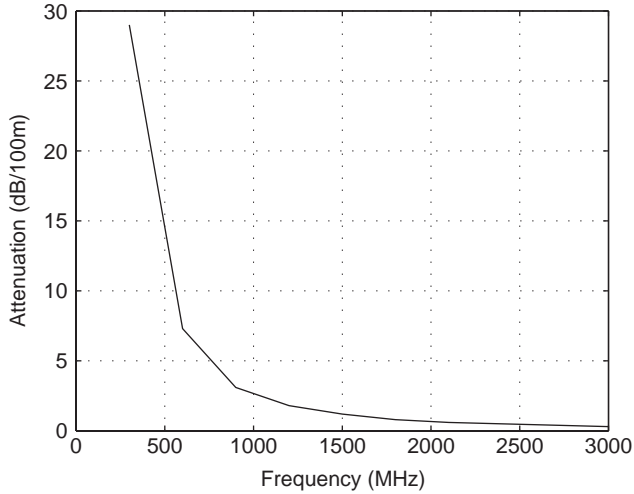


Figure 2. Attenuation constant of the fundamental TE_{01} waveguide mode in the circular tunnel of radius 2 m, $\epsilon_{r1} = 10$, $\sigma = 10^{-2}$ S/m.

shield seemed to guide radiowaves continuously in the tunnel [4]. This was the origin of leaky feeder techniques. The leaky feeder supports two coaxial modes in the tunnel. One is between the inner and outer conductors of the leaky feeder and the other between the outer conductor of the leaky feeder and the tunnel wall. Figure 3 shows the attenuation constant of the leaky feeder as a function of frequency. The leaky feeder techniques take advantage of the relatively low attenuation of the coaxial mode of the coaxial leaky feeder itself. Furthermore, the leaky feeder techniques are not sensitive to tunnel bends, corners, and crossings as well as to the presence of local obstacles. As a result, the leaky feeder techniques are widely used to construct radio systems in underground structures.

The propagation of waveguide modes in underground structures is called natural propagation, whereas the propagation of coaxial modes in underground structures is called guided propagation. We focus on natural propagation in

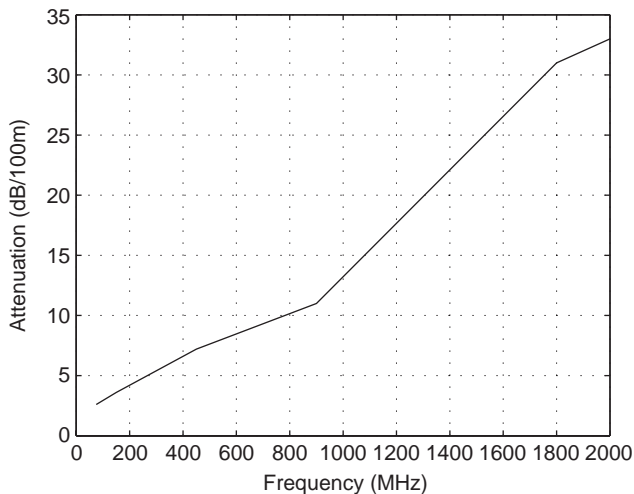


Figure 3. Attenuation constant of the leaky feeder RLC 4.4/11.1.

Section 1 and guided propagation in Section 2. Finally, we summarize the conclusions in Section 3.

1. NATURAL PROPAGATION

By natural propagation we mean that no special-purpose cables are strung in the tunnel to guide radiowaves. Propagation is then that of waveguide modes. Unintentional axial conductors in the tunnel may influence these modes, but this effect is considered as of second order at the frequencies considered here at UHF or above [1].

1.1. Imperfect Waveguide Model

The ambient media of a tunnel at UHF or above behaves as dielectrics with the relative permittivity in the range 5–10. Under these conditions, the tunnel can reasonably be treated as an oversized imperfect waveguide. Therefore, natural propagation will be possible only above a cutoff frequency determined by the tunnel size and shape. As the frequencies of UHF radio signals are higher than the cutoff frequency of the tunnel oversized imperfect waveguide model, the natural propagation of UHF radiowaves is realized through a fundamental and infinite number of higher order waveguide modes. All of these waveguide modes are hybrid and lossy modes because of the tunnel electromagnetic imperfectness. An exact analytical solution to the problem of natural propagation in the rectangular or arched tunnel would lead to extreme complexity. The difficulty lies in the matching of the tangential components of electromagnetic fields on the tunnel walls. Approximate methods are obviously required. Emslie et al. studied natural propagation in the rectangular tunnel and Yamaguchi et al. in the arched tunnel [4,5]. Common to these studies is the fact that the boundary conditions are satisfied approximately because the fields in the corner regions do not enter the derivation of the solutions. We adopt the approach similar to Emslie et al. However, we start with the construction of more general expressions for two scalar components of Hertz electric and magnetic vectors.

The imperfect waveguide model of a straight empty rectangular tunnel is shown in Fig. 4, with its rectangular cross section of sides a and b . The ambient media, assumed to be lossy nonmagnetic homogeneous, have complex wavenumbers

$$K_1 = \omega \sqrt{\mu_1 \epsilon_0 \epsilon_{r1}^*} = \omega \sqrt{\mu_1 \epsilon_0 \left(\epsilon_{r1} - j \frac{\sigma_1}{\omega \epsilon_0} \right)} \quad (1)$$

for the top and bottom walls and

$$K_2 = \omega \sqrt{\mu_2 \epsilon_0 \epsilon_{r2}^*} = \omega \sqrt{\mu_2 \epsilon_0 \left(\epsilon_{r2} - j \frac{\sigma_2}{\omega \epsilon_0} \right)} \quad (2)$$

for the left and right walls. The enclosed space of the imperfect waveguide model of the straight empty rectangular tunnel is filled with air of constitutive parameters μ_0 and ϵ_0 . The rigorous analytical solution to the natural propagation of UHF radiowaves in this imperfect

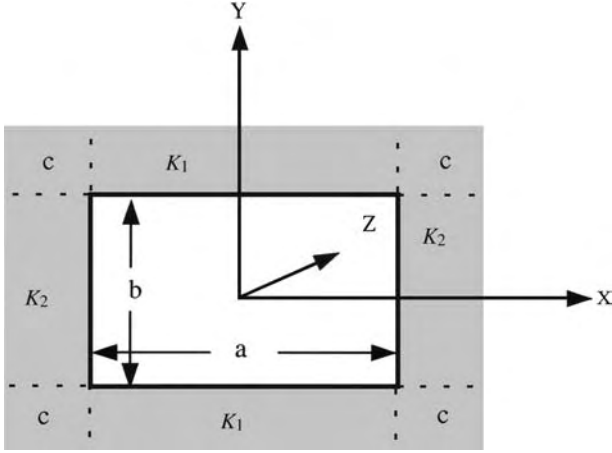


Figure 4. The imperfect waveguide model of a straight empty rectangular tunnel.

waveguide model of the straight empty rectangular tunnel would be extremely complex. However, the approximate analytical solution can be obtained if the transverse dimensions are much larger than the free space wavelength. This condition is usually satisfied in actual tunnels for UHF radiowaves. Thus, most of the power travels in the model interior region, a small part travels in regions K_1 and K_2 , and even less travels in the four-corner regions. Consequently, only a tolerable error will be introduced into the solution of the propagation when we neglect the fields in the corner regions.

For the present problem, it is convenient to describe the fields in terms of y components of electric Π_y^e and magnetic Π_y^m Hertz vectors. Except the source, the Hertz vectors satisfy the Helmholtz equation.

$$\nabla^2 \Pi_y^e + K_i^2 \Pi_y^e = 0 \quad (3)$$

$$\nabla^2 \Pi_y^m + K_i^2 \Pi_y^m = 0 \quad (4)$$

where K_i is complex wavenumber.

Once the Π_y^e and Π_y^m are determined, the related electromagnetic fields can be described as follows [1]:

$$E_x = \frac{\partial^2 \Pi_y^e}{\partial y \partial x} + j\omega\mu_i \frac{\partial \Pi_y^m}{\partial z} \quad (5)$$

$$E_y = \left(K_i^2 + \frac{\partial^2}{\partial y^2} \right) \Pi_y^e \quad (6)$$

$$E_z = \frac{\partial^2 \Pi_y^e}{\partial y \partial z} - j\omega\mu_i \frac{\partial \Pi_y^m}{\partial x} \quad (7)$$

$$H_x = \frac{\partial^2 \Pi_y^m}{\partial x \partial y} - j\omega\epsilon_i \frac{\partial \Pi_y^e}{\partial z} \quad (8)$$

$$H_y = \left(K_i^2 + \frac{\partial^2}{\partial y^2} \right) \Pi_y^m \quad (9)$$

$$H_z = \frac{\partial^2 \Pi_y^m}{\partial y \partial z} + j\omega\epsilon_i \frac{\partial \Pi_y^e}{\partial x} \quad (10)$$

We will first deal with the interior region of the imperfect waveguide model of the straight empty rectangular tunnel. The required forms for the y components of Hertz vectors are

$$\Pi_y^e = \sum_{m=1}^{\infty} \sum_{n=1}^{\infty} A_{mn} \text{Sin}(k_{xm}x) \text{Sin}(k_{yn}y) \exp(-\Gamma_{mn}z) \quad (11)$$

$$\Pi_y^m = \sum_{m=1}^{\infty} \sum_{n=1}^{\infty} A_{mn}^* \text{Cos}(k_{xm}x) \text{Cos}(k_{yn}y) \exp(-\Gamma_{mn}z) \quad (12)$$

For the region ($x \geq \frac{a}{2}$), expressions for the y components of Hertz vectors are thus

$$\Pi_y^e = \sum_{m=1}^{\infty} \sum_{n=1}^{\infty} B_{mn} \exp(\gamma_{xm}x) \text{Sin}(k_{yn}y) \exp(-\Gamma_{mn}z) \quad (13)$$

$$\Pi_y^m = \sum_{m=1}^{\infty} \sum_{n=1}^{\infty} B_{mn}^* \exp(\gamma_{xm}x) \text{Cos}(k_{yn}y) \exp(-\Gamma_{mn}z) \quad (14)$$

whereas for the region ($y \geq \frac{b}{2}$),

$$\Pi_y^e = \sum_{m=1}^{\infty} \sum_{n=1}^{\infty} C_{mn} \text{Sin}(k_{xm}x) \exp(\gamma_{yn}y) \exp(-\Gamma_{mn}z) \quad (15)$$

$$\Pi_y^m = \sum_{m=1}^{\infty} \sum_{n=1}^{\infty} C_{mn}^* \text{Cos}(k_{xm}x) \exp(\gamma_{yn}y) \exp(-\Gamma_{mn}z) \quad (16)$$

where the above y components of Hertz vectors are functions of Γ_{mn} , which appears in the following equations:

$$k_{xm}^2 + k_{yn}^2 - \Gamma_{mn}^2 = K_0^2 \quad (17)$$

$$k_{xm}^2 + \gamma_{yn}^2 - \Gamma_{mn}^2 = K_1^2 \quad (18)$$

$$\gamma_{xm}^2 + k_{yn}^2 - \Gamma_{mn}^2 = K_2^2 \quad (19)$$

where $K_0 = \omega\sqrt{\mu_0\epsilon_0}$. Matching the tangential field components on the walls of the imperfect waveguide model of the straight empty rectangular tunnel, we can derive

$$\begin{aligned} k_{xm} \text{tg} \left(\frac{k_{xm}a}{2} \right) &= -\frac{\gamma_{xm}(\Gamma_{mn}^2 - k_{xm}^2)\mu_1}{(\Gamma_{mn}^2 + k_{xm}^2)\mu_0} \\ &\approx -\frac{jK_0\mu_1\sqrt{\epsilon_{r1}^* - 1}}{\epsilon_{r1}^*\mu_0} \end{aligned} \quad (20)$$

$$\begin{aligned} k_{xm} \text{Ctg} \left(\frac{k_{xm}a}{2} \right) &= -\frac{\gamma_{xm}(\Gamma_{mn}^2 - k_{xm}^2)\epsilon_1}{(\Gamma_{mn}^2 + k_{xm}^2)\epsilon_0} \\ &\approx -\frac{jK_0\epsilon_1\sqrt{\epsilon_{r1}^* - 1}}{\epsilon_{r1}^*\epsilon_0} \end{aligned} \quad (21)$$

$$k_{yn} \text{tg} \left(\frac{k_{yn}b}{2} \right) = -\frac{\gamma_{yn}\mu_0}{\mu_2} \approx -\frac{jK_0\mu_0\sqrt{\epsilon_{r2}^* - 1}}{\mu_2} \quad (22)$$

$$k_{yn} \text{Ctg} \left(\frac{k_{yn}b}{2} \right) = -\frac{\gamma_{yn}\epsilon_0}{\epsilon_2} \approx -\frac{jK_0\epsilon_0\sqrt{\epsilon_{r2}^* - 1}}{\epsilon_2} \quad (23)$$

Equations (20) and (22) are the propagation modal equations for E_{mn}^h modes. For these types of modes, the main electric field component is the horizontal E_x , whereas the vertical electric field component E_y is zero. Similarly, Equations (21) and (23) are the propagation modal equations for E_{mn}^v modes. For these types of modes, the main electric field component is the vertical E_y , whereas the horizontal electric field component E_x is zero.

Both analytical and numerical solutions can be obtained for the propagation modal Equations (20)–(22), and (23). Using the procedures given in [6], we get

$$k_{xm} \approx \frac{m\pi}{a} + j \frac{2\pi m \epsilon_{r1}^*}{K_0 a^2 \sqrt{\epsilon_{r1}^* - 1}} \tag{24}$$

$$k_{yn} \approx \frac{n\pi}{b} + j \frac{2\pi n}{K_0 b^2 \sqrt{\epsilon_{r2}^* - 1}} \tag{25}$$

for E_{mn}^h modes, and

$$k_{xm} \approx \frac{m\pi}{a} + j \frac{2\pi m}{K_0 a^2 \sqrt{\epsilon_{r1}^* - 1}} \tag{26}$$

$$k_{yn} \approx \frac{n\pi}{b} + j \frac{2\pi n \epsilon_{r2}^*}{K_0 b^2 \sqrt{\epsilon_{r2}^* - 1}} \tag{27}$$

for E_{mn}^v modes. These results show that k_{xm} and k_{yn} are complex. The first terms are the same as for a waveguide with perfect electric walls. The small second terms account for the energy loss absorbed by the walls of the imperfect waveguide model of the straight empty rectangular tunnel.

Substituting Eqs. (24) and (25) into Eq. (17), we obtain the propagation constants for E_{mn}^h modes as

$$\begin{aligned} \Gamma_{mn}^h &= \alpha_{mn}^h + j\beta_{mn}^h \\ &\approx \sqrt{m^2 \left[\frac{\pi}{a} + j \frac{2\pi \epsilon_{r1}^*}{K_0 a^2 \sqrt{\epsilon_{r1}^* - 1}} \right]^2 + n^2 \left[\frac{\pi}{b} + j \frac{2\pi}{K_0 b^2 \sqrt{\epsilon_{r2}^* - 1}} \right]^2} - K_0^2 \end{aligned} \tag{28}$$

$$\begin{aligned} \alpha_{mn}^h &\approx \frac{2(m\pi)^2}{K_0^2 a^3} \operatorname{Re} \left(\frac{\epsilon_{r1}^*}{\sqrt{\epsilon_{r1}^* - 1}} \right) \\ &\quad + \frac{2(n\pi)^2}{K_0^2 b^3} \operatorname{Re} \left(\frac{1}{\sqrt{\epsilon_{r2}^* - 1}} \right) \text{ Np/m} \end{aligned} \tag{29}$$

$$\beta_{mn}^h \approx \sqrt{K_0^2 - \left(\frac{m\pi}{a} \right)^2 - \left(\frac{n\pi}{b} \right)^2} \tag{30}$$

Similarly, substituting Eqs. (26) and (27) into Eq. (17) gives the propagation constants for E_{mn}^v modes as

$$\begin{aligned} \Gamma_{mn}^v &= \alpha_{mn}^v + j\beta_{mn}^h \\ &\approx \sqrt{m^2 \left[\frac{\pi}{a} + j \frac{2\pi}{K_0 a^2 \sqrt{\epsilon_{r1}^* - 1}} \right]^2 + n^2 \left[\frac{\pi}{b} + j \frac{2\pi \epsilon_{r2}^*}{K_0 b^2 \sqrt{\epsilon_{r2}^* - 1}} \right]^2} - K_0^2 \end{aligned} \tag{31}$$

$$\begin{aligned} \alpha_{mn}^v &\approx \frac{2(m\pi)^2}{K_0^2 a^3} \operatorname{Re} \left(\frac{1}{\sqrt{\epsilon_{r1}^* - 1}} \right) \\ &\quad + \frac{2(n\pi)^2}{K_0^2 b^3} \operatorname{Re} \left(\frac{\epsilon_{r2}^*}{\sqrt{\epsilon_{r2}^* - 1}} \right) \text{ Np/m} \end{aligned} \tag{32}$$

$$\beta_{mn}^v \approx \sqrt{K_0^2 - \left(\frac{m\pi}{a} \right)^2 - \left(\frac{n\pi}{b} \right)^2} \tag{33}$$

These analytical results show that the attenuation constants of both E_{mn}^h and E_{mn}^v modes are directly proportional to the square of the mode order and are inversely proportional to the square of frequency and to the cube of the imperfect waveguide model size of the straight empty rectangular tunnel, and the phase constants are almost identical to those of the perfect conducting waveguide. Now assuming that the complex wavenumbers of the ambient media of the imperfect waveguide model of the straight empty rectangular tunnel are the same $K_1 = K_2$, we note from Eqs. (29) and (32) that E_{11}^h and E_{11}^v modes have the minimum attenuation for the case of $a > b$ and $b > a$, respectively. Thus, let an electric type transmit antenna oriented in the X direction excite the natural propagation of the imperfect waveguide model of the straight empty rectangular tunnel, the E_{11}^h mode will represent the field distribution in the far region of the imperfect waveguide model of the straight empty rectangular tunnel as a is larger than b for most tunnels. The E_{11}^h wave is the fundamental mode of the imperfect waveguide model of the straight empty rectangular tunnel.

Knowing the propagation of waveguide modes does not allow a calculation of the strength of radio signals in the imperfect waveguide model of the straight empty rectangular tunnel. We also need to know the excitation of the transmit antenna and the reception of the receive antenna to these modes. The excitation or reception of an antenna to these modes can be calculated as follows. Consider the antenna located at point (x, y) in the cross section of the imperfect waveguide model of the straight empty rectangular tunnel. The power that the antenna receives or transmits is given by

$$P_{mn} = A_e S_{mn}(x, y) \tag{34}$$

where A_e is the effective area of the antenna and $S_{mn}(x, y)$ is Poynting's vector. One can express A_e as

$$A_e = \frac{G\lambda^2}{4\pi} \tag{35}$$

and $S(x,y)$ as

$$S_{mn}(x,y) = \frac{1}{2} \eta_0 \text{Cos}^2\left(\frac{m\pi x}{a}\right) \text{Cos}^2\left(\frac{n\pi y}{b}\right) \quad (36)$$

where G is the antenna gain, λ is the wavelength, and η_0 is the free space characteristic impedance. The power, calculated as the flux of this vector through the cross section of the imperfect waveguide model of the straight empty rectangular tunnel, is given by

$$P_{mn} = \frac{\eta_0 ab}{4} \quad (37)$$

The excitation or reception loss of the antenna is defined as

$$\frac{P_{mn}}{P} = \frac{2\pi ab}{\lambda^2 G} \text{Cos}^{-2}\left(\frac{m\pi x}{a}\right) \text{Cos}^{-2}\left(\frac{n\pi y}{b}\right) \quad (38)$$

It should be mentioned that Eq. (38) does not remain accurate when the antenna is located close to the tunnel wall. Figure 5 shows the measured natural propagation together with the calculated one from the imperfect waveguide model. The measurement was made at 900 MHz in a tunnel of 4 m wide and 3.5 m high. As shown, the imperfect waveguide model predicts the general trend of the strength of the radio signal.

It is thus, in principle, easy to design radio systems for unobstructed straight tunnels. A safety margin should be included to account for standing waves. These cannot be avoided in practice: they are because of the existence of several modes traveling with different phase velocities [1]. It is far more difficult to predict the undesirable mode conversion caused by discontinuities such as bends, corners, and vehicles in tunnels and changes in cross sections. It is found that they increase the propagation loss of waveguide modes. The calculation of this additional propagation loss is extremely difficult by the imperfect waveguide theory.

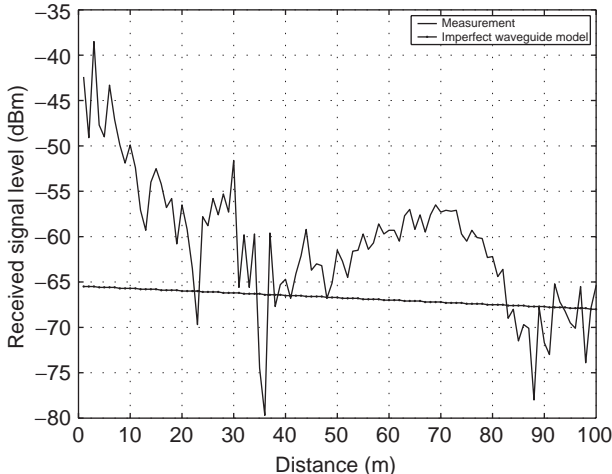


Figure 5. Measured natural propagation together with the calculated from the imperfect waveguide model.

1.2. Geometrical Optical Model

The problem of the natural propagation of radiowaves at UHF or above can also be solved with the geometrical optics. The geometrical optical model has been developed by Mahmoud and Wait for a straight empty rectangular tunnel [7]. Hwang et al. and Zhang et al. extended the geometrical optical approach to branched tunnels [8,9] and Didascalou et al. to arbitrarily shaped tunnels [10]. Chen and Jeng considered the effects of traffic vehicles in tunnels [11] and Pallares et al. the transition from land propagation to tunnel propagation [12]. By assuming that the radiowaves are locally plane waves, the Fresnel reflection coefficients of vertically and horizontally polarized plane waves incident on the tunnel walls can be used. Thus, the natural propagation is achieved via a direct ray and many reflected rays caused by the tunnel walls. The tunnel wall reflection points of the rays can be easily determined by adopting the image principle of geometrical optics. As the contribution of a reflected ray to the propagation is weighted by its reflection coefficient, it will become weaker as the reflected ray undergoes multiple reflections. In other words, only those images in the vicinity of the tunnel walls are significant for the propagation in the far-field region. The fields are obtainable from any two suitable scalar potentials. Based on the problem to be solved, we choose Π_x^e , Π_y^e as two scalar functions, where Π_x^e and Π_y^e are x and y components of Hertz electric vectors, respectively [7]. They are given by

$$\begin{aligned} & \begin{bmatrix} \Pi_x^e(x,y,z) \\ \Pi_y^e(x,y,z) \end{bmatrix} \\ &= \left(\frac{1}{4\pi j \omega \epsilon_0} \right) \sum_l \cdot \sum_i \left[\frac{\exp(-jK_0 r_{li})}{r_{li}} \right] [M_{li}] \begin{bmatrix} S_x \\ S_y \end{bmatrix} \end{aligned} \quad (39)$$

where S_x and S_y are the horizontal and vertical dipole moments of the source located at $(x_s, y_s, 0)$, l and i are integers representing the multiple images of the source in any arbitrary manner, and M_{li} is the product of the reflection coefficients of the images taking into account the coupling between the horizontally and vertically polarized rays. Equation (39) is an exact equation provided that the geometrical ray approximation is valid.

$$r_{li} = [z^2 + (x - x_l)^2 + (y - y_i)^2]^{1/2} \quad (40)$$

(x_l, y_i) are the coordinates of the $l - i$ image, where

$$x_l = 2ma \pm x_0, \quad m = -\infty \text{ to } \infty \quad (41)$$

$$y_i = 2nb \pm y_0, \quad m = -\infty \text{ to } \infty \quad (42)$$

and $[M_{li}]$ is the product of all the reflection coefficient matrices involved in producing the $l - i$ image. If only the field components of major polarization are of interest, the coupling between the horizontally and vertically polarized rays can be neglected, as a result, Equation (39) is

approximated as

$$\begin{aligned} \begin{bmatrix} \Pi_x^e(x, y, z) \\ \Pi_y^e(x, y, z) \end{bmatrix} &\cong \left(\frac{1}{4\pi j\omega\epsilon_0} \right) \sum_l \cdot \sum_i \frac{\exp(-jK_0 r_{li})}{r_{li}} \\ &\times \begin{bmatrix} R_H^{n_l} & R_V^{n_l} \\ R_V^{n_l} & R_H^{n_l} \end{bmatrix} \begin{bmatrix} S_x \\ S_y \end{bmatrix} \end{aligned} \quad (43)$$

where R_H and R_V are the Fresnel reflection coefficients for horizontal and vertical polarizations, respectively, n_l and n_i are the numbers of reflection on the vertical and horizontal tunnel walls, respectively, involved in forming the $(l - i)$ image of the antenna. The respective horizontal and vertical electric field components are then obtained by

$$E_x(x, y, z) = \left(K_0^2 + \frac{\partial^2}{\partial x^2} \right) \Pi_x^e + \frac{\partial^2 \Pi_y^e}{\partial x \partial y} \quad (44)$$

$$E_y(x, y, z) = \left(K_0^2 + \frac{\partial^2}{\partial x^2} \right) \Pi_y^e + \frac{\partial^2 \Pi_x^e}{\partial x \partial y} \quad (45)$$

Modern radio systems measure the strength of radio signals in power. Knowing that the antenna radiates P_t power in the tunnel space, the dipole moments of the antenna are given by

$$\begin{aligned} \begin{bmatrix} S_x \\ S_y \end{bmatrix} &= I \frac{\cos(\omega t + \phi)}{\omega} L \begin{bmatrix} \hat{x} \\ \hat{y} \end{bmatrix} \\ &= \sqrt{\frac{P_t}{60\pi}} \frac{\cos(\omega t + \phi)}{\omega} \begin{bmatrix} \hat{x} \\ \hat{y} \end{bmatrix} \end{aligned} \quad (46)$$

where L is the length of the antenna. For half-wavelength dipoles used as both the distributed and received antennas, the received power for horizontal and vertical polarization can be expressed as

$$\begin{aligned} \begin{bmatrix} P_{rH}(x, y, z) \\ P_{rV}(x, y, z) \end{bmatrix} \\ = \left(\frac{\lambda}{4\pi} \right)^2 \left| \sum_l \cdot \sum_i \left[\frac{\exp(-jK_0 r_{li})}{r_{li}} \right] \begin{bmatrix} R_H^{n_l} & R_V^{n_l} \\ R_V^{n_l} & R_H^{n_l} \end{bmatrix} \right|^2 \sqrt{P_t} \end{aligned} \quad (47)$$

If directional antennas are used, antenna gain must be taken into consideration. Generally, the geometrical optical approach will give the propagation attenuation constant in a numerical form. Figure 6 shows the measured natural propagation together with the calculated one from the geometrical optical model. The measurement was made at 900 MHz in a tunnel of 9 m wide and 5 m high. As shown, the geometrical optical model predicts not only

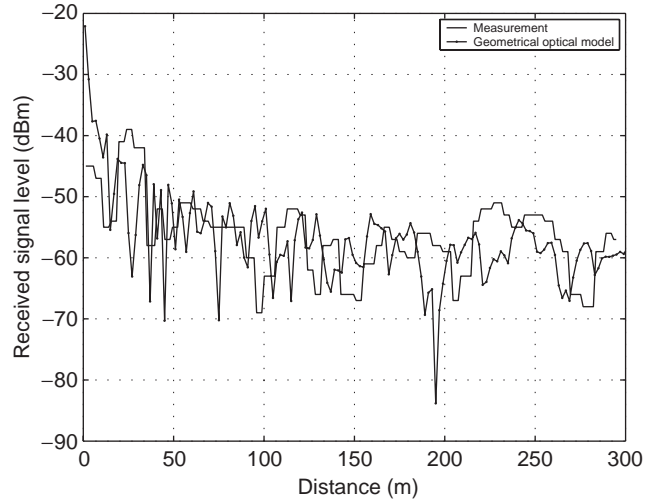


Figure 6. Measured natural propagation together with the calculated from the geometrical optical model.

the general trend but also the rapid variation of the strength of the radio signal.

1.3. Statistical Model

Natural propagation of multiple waveguide modes in underground structures produces the random signal fluctuations [13]. The signal fluctuations can be decomposed into the slow fading engendered by the global mode variations and the fast fading caused by the interference of local modes. The slow fading in many propagation environments has been found to follow theoretical lognormal distribution. The lognormal probability density on dB terms is given in function of the mean η and of the standard deviation δ as

$$P(r) = \frac{1}{\delta\sqrt{2\pi}} \exp\left(-\frac{(r - \eta)^2}{2\delta^2}\right) \quad (48)$$

The fast fading has been found to follow Rician or Rayleigh. The Rice probability density on dB terms is given by

$$\begin{aligned} P(r) &= \frac{1}{8.68\alpha^2} \exp\left(\frac{r}{4.34} - \frac{(d^2 + \exp(r/4.34))}{2\alpha^2}\right) \\ &\times I_0\left(\frac{d}{\alpha^2} \exp\left(\frac{r}{4.34}\right)\right) \end{aligned} \quad (49)$$

where $I_0(x)$ is a modified Bessel function of order zero and d is the fundamental mode signal. This fundamental mode signal can decrease the standard deviation of the received signal envelope if it increases relative to higher order mode signals. When $d=0$, Equation (49) becomes the Rayleigh probability density. The mean of the Rice probability density is expressed as

$$\eta = \exp(-y)\alpha\sqrt{\frac{\pi}{2}}[(1+2y)I_0(y) + 2yI_1(y)] \quad (50)$$

where $I_1(y)$ is a modified Bessel function of order 1 and $y = d^2/4x^2$. The standard deviation is expressed as

$$\delta = \sqrt{d^2 + 2x^2 - 1} \quad (51)$$

In Equations (50) and (51), η and δ are known after we have statistically analyzed the experimental data files. Hence, simultaneous solution to Equations (50) and (51) will find the parameters α and d of the theoretical Rice probability density. The impact of conversion of higher order modes to the fundamental mode signal can be described by the ratio of the fundamental mode signal to higher order mode signals as

$$K = 10 \log(d^2/2\delta^2) \quad (52)$$

In addition, another key parameter to describe the slow fading is power loss that generally is represented by z^n . z is the separation between the transmit and receive antennas, and n is the loss exponent to be determined experimentally. The analysis of natural propagation measurements shows $n < 2$ for line-of-sight paths and $n > 2$ for non-line-of-sight paths in underground structures.

The slow fading statistics deals with the remaining slow variation after removal of the power distance dependence. It is a useful indicator of estimate of the coverage and cochannel interference. Many radio propagation environments predicted that the slow fading would follow the lognormal probability distribution as expressed in Equation (48). However, our measurements conducted in various underground structures show a consistent deviation from the lognormal probability distribution as presented in Fig. 7. The standard deviation is 4.7 dB. This deviation becomes worse when the signal level is moved further away from its median value. It indicates that the fundamental mode and the higher order modes are closely associated in an enclosed space of underground structures

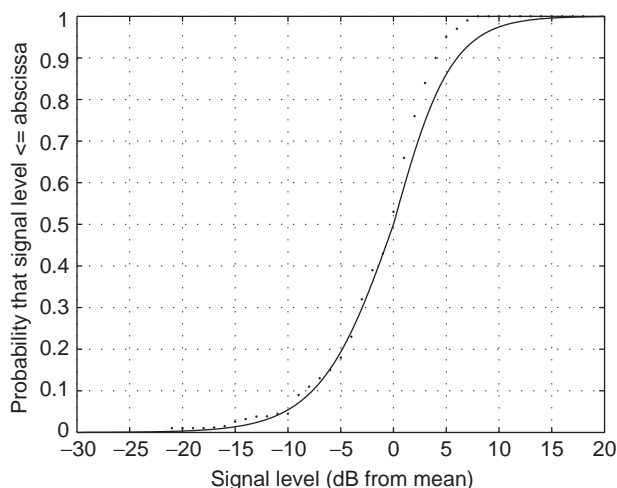


Figure 7. Cumulative distribution of natural propagation slow fading.

and are not randomly independent as in other radio propagation environments.

The fast fading statistics deals with the remaining rapid variation after removal of the slow fading. It is useful to determine the safety margin for link budget calculation. Our measurements indicate that the fast fading occurs in all regions. However, within the short-distance region where the receive antenna is near the transmit antenna, the received signal consistently shows more rapid and deeper fluctuations. The fast fading is strongly related to the structure dimensions and the frequency. The fast and deep fading cover a longer distance for either the case of larger dimensional underground structure or higher frequency. These results can be explained as follows. In the short-distance region, there are more significant higher order modes that cause large fluctuations. In the long-distance region, as the higher order modes become less significant, only the fundamental mode, the direct incident signal, contributes the most to the received signal. Therefore, the fast fading diminishes as the receiver is moving farther away from the transmitter. Higher frequencies and larger dimensions will generate more significant higher order modes. As a result, the fading region will extend farther. Figure 8 shows that the fast fading in the straight empty sections of a tunnel is correlated well to Rician distribution. Figure 9 shows that the fast fading in the curved empty sections does not closely fit Rayleigh distribution. Further analysis also revealed that there was some correlation between Tx-Rx separation and the fast fading distribution in the straight empty sections of tunnels.

2. GUIDED PROPAGATION

By guided propagation we mean that special-purpose cables such as leaky feeders are strung in the tunnel to guide radiowaves. Leaky feeders can be classified into coupled and radiated types. A coupled-type coaxial leaky

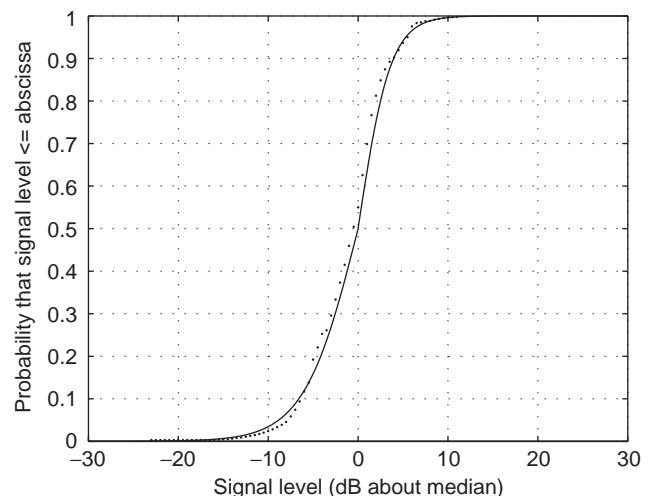


Figure 8. Cumulative distribution of natural propagation fast fading in straight sections of a tunnel.

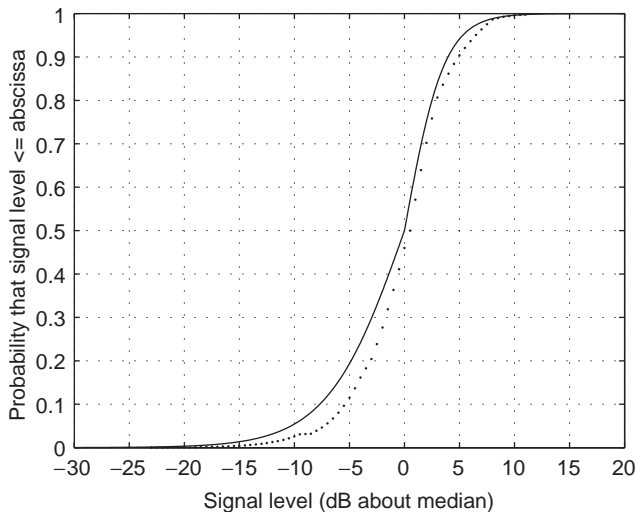


Figure 9. Cumulative distribution of natural propagation fast fading in curved sections of a tunnel.

feeder has either a longitudinal slot or small apertures in the outer conductor with spacing much smaller than the operating wavelength, whereas a radiated-type coaxial leaky feeder has periodic apertures in the outer conductor with spacing comparable with the operating wavelength.

2.1. Diffuse Model

A coupled-type leaky feeder is shown in Fig. 10, in which there are small apertures situated in the leaky feeder outer conductor. The interval distance d between two adjacent apertures is much smaller than the operational wavelength λ . For the coupled-type leaky feeder, radiation depends on scattering of the local fields by nearby random objects. To look for a detailed model of scattering from the leakage fields of the coupled-type leaky feeder is not promising because underground structures are so varied. Instead, we can assume heuristically that each small aperture radiates diffusely through a cylindrical surface of some radius larger than the physical radius of the coupled-type leaky feeder, but small compared with the distance to the receiver [14]. The mean power flow per unit solid angle in a given direction from a surface element is proportional to $\text{Cos } \gamma$, where γ is the angle of emission with respect to the normal. In photometry, this assumption is called *Lambert's cosine law*, and it is satisfied approximately by many diffusely emitting surfaces. We use it here with no further justification than analytic convenience. The diffuse model undertakes to calculate the median power level over a region whose dimensions are comparable with a wavelength. Local fluctuations in the field amplitude are expected to be Rayleigh distributed, as would

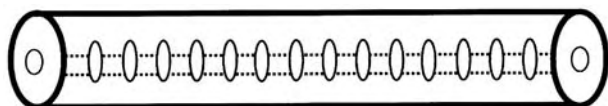


Figure 10. A coupled-type leaky feeder.

result from scattering of leakage fields by nearby inhomogeneities located randomly along the couple-type leaky feeder.

The diffuse model follows that the power flow per unit solid angle from a thin, Lambert's law coupled-type leaky feeder element is proportional to

$$\Phi_1(\theta) = \text{Sin}(\theta) \tag{53}$$

where θ is the angle between the viewing direction and the coupled-type leaky feeder axis. The equivalent electric field generated at distance r by a thin coupled-type leaky feeder element is proportional to

$$E = \frac{\sqrt{\text{Sin}\theta}}{r} \tag{54}$$

The standard coupling loss C of a leaky feeder is defined as

$$C = 10 \log_{10}(P_{\text{feeder}}/P_{\text{dipole}}) \tag{55}$$

where P_{dipole} is the median power received by a half-wave dipole moved along a path parallel to and at a distance D from a long straight leaky feeder carrying power P_{feeder} . The distance D is conventionally 2 m. It is easy to relate the standard coupling loss to the power radiated per unit length of the diffuse model. Let P_{dipole} be the power received by a half-wave dipole parallel to and at a distance D from the axis of a long diffuse radiator having negligible attenuation over distances comparable with D . Let H be the power radiated per unit length in the polarization to which the dipole responds (typically a diffuse source radiates equal power in both polarizations). The power-transmitting pattern $\Phi_1(\theta)$ of an element of the coupled-type leaky feeder is given by Equation (65), and the power-receiving pattern of the half-wave dipole is

$$\Phi_2(\theta) = \frac{\text{Cos}^2[(\pi/2)\text{Sin}\theta]}{\text{Sin}^2\theta} \tag{56}$$

The power received by the dipole is

$$P_{\text{dipole}} = \frac{\Pi\lambda^2}{N_1N_2} \int_{-\infty}^{\infty} \frac{\Phi_1\Phi_2}{r^2} dx \tag{57}$$

where $x = DCot\theta$, $r = DCsc\theta$, and the normalized constants are

$$N_{1,2} = 2\pi \int_0^\pi \Phi_{1,2}(\theta)\text{Sin}\theta d\theta \tag{58}$$

A straight calculation gives

$$P_{\text{dipole}} = (8\Pi/\pi D)(\lambda/4\pi)^2 \tag{59}$$

Equations (55) and (59) relate the feeder power, the standard coupling loss, and the effective radiated power per unit length. If the input power to the leaky feeder is P_{input} and the leaky feeder has a matched termination, then the

radiated power per unit length is

$$\Pi = (\pi D/8)(4\pi/\lambda)^2 10^{-C/10} \exp(-2\alpha z) P_{input} \quad (60)$$

at a distance z from the feed point, where α is the attenuation constant in Np/m. Note that in the diffuse model, the coupling loss depends on the orientation of the receiving dipole. If “axial” denotes the orientation in which the dipole parallels to the leaky feeder axis, “radial” denotes the orientation in which the dipole points directly toward the leaky feeder axis, and “transverse” denotes the orientation perpendicular to both of these, it turns out that

$$\frac{P_{radial}}{P_{axial}} = \frac{\int_0^{2\pi} \text{Cos}^2[(\pi/2)\text{Sin}\theta](\text{Sin}\theta/\text{Cos}^2\theta) d\theta}{\int_0^{2\pi} \text{Cos}^2[(\pi/2)\text{Cos}\theta](\text{Sin}\theta/\text{Sin}^2\theta) d\theta} \quad (61)$$

$$= 0.456 \text{ or } -3.41 \text{ dB}$$

and

$$\frac{P_{transversel}}{P_{axial}} = \frac{\int_0^{2\pi} \text{Sin}\theta d\theta}{\int_0^{2\pi} \text{Cos}^2[(\pi/2)\text{Cos}\theta](\text{Sin}\theta/\text{Sin}^2\theta) d\theta} \quad (62)$$

$$= 1.64 \text{ or } 2.15 \text{ dB}$$

We shall use the axial dipole as a reference and assume that the dependence on orientation is less than the other uncertainties of the diffuse model.

2.2. Geometrical Optical Model

A radiated-type leaky feeder is shown in Fig. 11. It is seen that periodic slots situated in the leaky feeder outer conductor exist. The interval distance d between two adjacent slots is comparable with the operational wavelength λ . The frequency band, where the radiated mode exists, is given by the inequality

$$(\sqrt{\epsilon_r} - 1)d \leq \lambda \leq (\sqrt{\epsilon_r} + 1)d \quad (63)$$

where ϵ_r is the relative permittivity of the dielectric material inside the leaky feeder. Within this band, the radiation mechanism is comparable with the radiation of an array of magnetic dipoles oriented along the leaky feeder axis [15]. The azimuthal component of the electric field radiated by the leaky feeder in free space is given by

$$E_\phi = \sum_{i=1}^N E_i \text{Sin}(\theta_i) \frac{\exp(-jK_0 r_i - jK_0 \sqrt{\epsilon_r}(i-1)d)}{r_i} \quad (64)$$

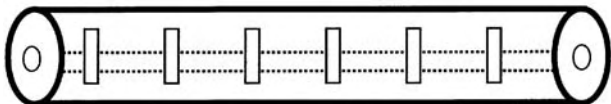


Figure 11. A radiated-type leaky feeder.

where E_i is the field amplitude of the i th slot and r_i is the distance from the i th slot to the observation point. As for the leaky feeder installed in an underground structure, the electric field produced by the leaky feeder will be modified by the existence of the structure walls. The effects of the structure walls on the electric field are calculated according to the image principle.

2.3. Statistical Model

Guided propagation of leaky feeders in underground structures involves the random mechanism. We have to resort to a statistical model for measurements. Guided propagation from a leaky feeder in underground structures can be expressed by the equation

$$P_r = P_t - \alpha z - L_c - L_v - L_b - 10n \log_{10}(D) \quad (65)$$

where P_r is the received power, P_t is the transmitted power, z is the distance along the leaky feeder to the point nearest the receiver, α is the attenuation constant of the leaky feeder, L_c is the coupling loss referenced to 1 m radial distance from the cable, L_v is the variability in coupling loss, L_b is the loss factor because of blockage, D is the distance between the cable and the receiver, and n is the loss exponent. The aim of the measurements has been to quantify the unknown parameters in this equation.

Typical plots of guided propagation by the coupled-type leaky feeder 512RC8R at 2 GHz are shown in Figs. 12 and 13 for the measurements in the corridor and room of a basement, respectively. In both cases, the received signal levels fluctuate over the whole routes. Also, the received signal levels are stronger in the corridor than those in the room, which is because the received signal traveled a shorter radial distance in the corridor, whereas the received signal not only propagated a longer radial distance but also underwent the wall penetration loss into the room. For the corridor case, it is noted that the received signal levels appear stronger along the middle route than those along the side routes. The route-dependent difference in the received signal levels is mainly attributed to the coupling pattern of the leaky feeder. As the slot of the

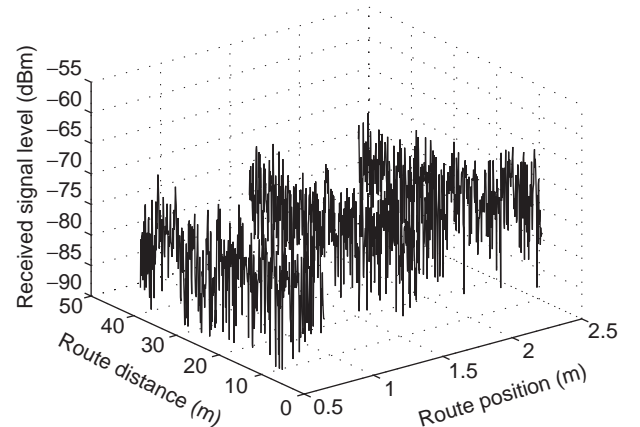


Figure 12. Guided propagation by the coupled-type leaky feeder 512RC8R at 2 GHz in the corridor of a basement.

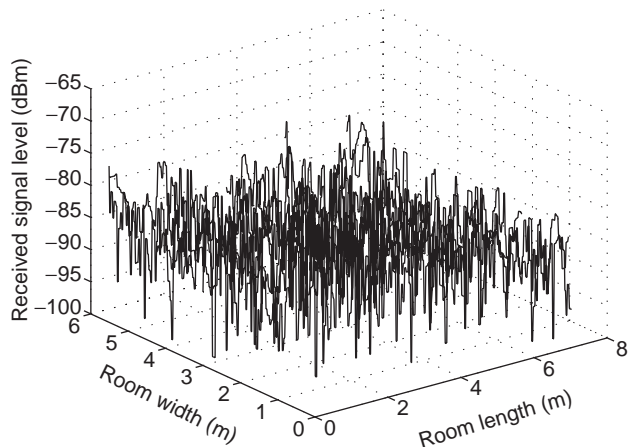


Figure 13. Guided propagation by the coupled-type leaky feeder 512RC8R at 2 GHz in the room of a basement.

leaky feeder was installed facing downward, it resulted in the occurrence of the downward maximum coupling; therefore, the received signal levels were observed stronger along the middle route. For the room case, it is evident that a slight decrease exists in the received signal levels along a route parallel to the axis of the leaky feeder; however, a considerable decay exists in the received signal levels along a route radial to the axis of the leaky feeder. The quantified parameters for Equation (65) from the measurements are listed in Table 1.

The fading statistics are examined. Analysis of the slow fading components of the measurements shows that they basically fit the lognormal distribution in both directions, parallel and radial, to the leaky feeder, which can be seen from Fig. 14. The solid and dot curves represent the lognormal and experimental distributions with the mean of 0.0 dB and the standard deviation of 1.8 dB for the direction parallel to the leaky feeder. The dash-dot and asterisk curves stand for the lognormal and experimental distributions with the mean of -0.06 dB and the standard deviation of 2.5 dB for the direction radial to the leaky feeder. Analysis of the fast fading components of the measurements shows that they follow the Rayleigh distribution in the direction parallel to the cable and the Rician distribution in the direction radial to the leaky feeder, which can be seen from Fig. 15. The solid and dot curves express the Rayleigh and experimental distributions with the mean value of -0.02 dB and the standard deviation of 6.0 dB for the direction parallel to the leaky feeder. The dash-dot and asterisk curves depict the Rician and experimental distributions with a K value of 4.0 dB for the room case.

Table 1. The Parameters Obtained from the Measurement

L_c (dB)	L_v (dB)	L_b (dB)	α (dB/100m)	n
89.2	Min. -6.10	8.6	16	Min. 0.51
	Max. 6.80 (brick wall)			Max. 1.15
	Mean -0.06			Mean 0.90
	Std. 2.52			Std. 0.24

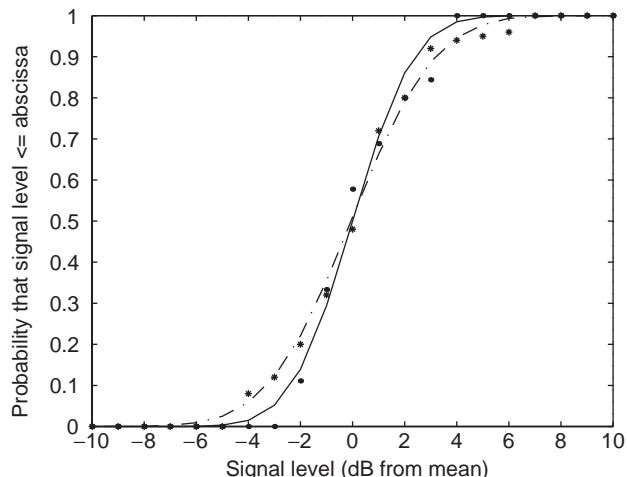


Figure 14. Cumulative distribution of guided propagation slow fading.

3. CONCLUSIONS

Both natural and guided propagation in underground structures have been covered in this article. Natural propagation is that of waveguide modes or multiple rays. The fundamental mode is important for long-distance propagation as it suffers the least attenuation, whereas higher order modes are problematic as they cause fluctuation because of addition or subtraction of these modes. As the contribution of a reflected ray to the propagation is weighted by its reflection coefficient, and will become weaker as the reflected ray undergoes multiple reflections. Thus, only the direct ray and those rays with fewer reflections are significant for long-distance propagation. Natural propagation suffers from the disastrous additional attenuation caused by bends, corners, and crossings, and vehicles in underground structures. Guided propagation is that of

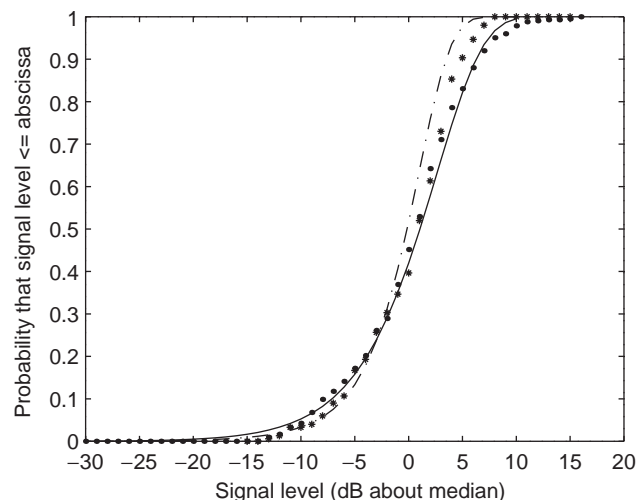


Figure 15. Cumulative distribution of guided propagation fast fading.

coaxial modes, and mode conversion plays an important role. Guided propagation takes advantage of the relatively low attenuation of the coaxial mode of the leaky feeder itself. Furthermore, guided propagation is not sensitive to bends, corners, and crossings as well as to the presence of local obstacles. As a result, guided propagation finds wide application in underground structures to construct radio systems.

BIBLIOGRAPHY

1. P. Delogne, *Leaky Feeders and Subsurface Radio Communications*, Stevenage, UK: Peregrinus, 1982.
2. J. R. Wait and D. A. Hill, Guided electromagnetic waves along an axial conductor in a circular tunnel, *IEEE Trans. Antennas Propagat.*, **22**:627–630 (1974).
3. J. Chiba, T. Inaba, Y. Kuwamoto, O. Banno, and R. Sato, Radio communication in tunnels, *IEEE Trans. Microwave Theory Tech.*, **26**:439–443 (1978).
4. A. G. Emslie, R. L. Lagace, and P. F. Strong, Theory of the propagation of UHF radio waves in coal mine tunnels, *IEEE Trans. Antennas Propagat.*, **23**:192–205 (1975).
5. Y. Yamaguchi, T. Abe, T. Sekiguchi, and J. Chiba, Attenuation constants of UHF radio waves in arched tunnels, *IEEE Trans. Microwave Theory Tech.*, **33**:714–718 (1985).
6. Y. P. Zhang and Y. Hwang, Theory of the radio wave propagation in railway tunnels, *IEEE Trans. Vehicular Technol.*, **47**:1027–1036 (1998).
7. S. F. Mahmoud and J. R. Wait, Geometrical optical approach for electromagnetic wave propagation in rectangular mine tunnels, *Radio Sci.*, **9**:1147–1158 (1974).
8. Y. Hwang, Y. P. Zhang, and R. G. Kouyoumjian, Ray-optical prediction of radio wave propagation characteristics in tunnel environments, Part one: Theory, *IEEE Trans. Antennas Propagat.*, **46**:1328–1336 (1998).
9. Y. P. Zhang, Y. Hwang, and R. G. Kouyoumjian, Ray-optical prediction of radio wave propagation characteristics in tunnel environments, Part two: Analysis and measurements, *IEEE Trans. Antennas Propagat.*, **46**:1337–1345 (1998).
10. D. Didascalou, J. Maurer, and W. Wiesbeck, Subway tunnel guided electromagnetic wave propagation at mobile communications frequencies, *IEEE Trans. Antennas Propagat.*, **49**:1590–1596 (2001).
11. S. H. Chen and S. K. Jeng, SBR image approach for radio wave propagation in tunnels with and without traffics, *IEEE Trans. Vehicular Technol.*, **45**:570–578 (1996).
12. F. M. Pallares, F. J. P. Juan, and J. L. Leandro, Analysis of path loss and delay spread at 900 MHz and 2.1 GHz while entering tunnels, *IEEE Trans. Vehicular Technol.*, **50**:767–775 (2001).
13. Y. P. Zhang and Y. Hwang, Characterization of UHF radio propagation channels in tunnel environments for microcellular and personal communications, *IEEE Trans. Vehicular Technol.*, **47**:283–296 (1998).
14. S. P. Morgan, Prediction of indoor wireless coverage by leaky coaxial cable using ray tracing, *IEEE Trans. Vehicular Technol.*, **48**:2005–2014 (1999).
15. M. Lienard, P. Mariage, J. Vandamme, and P. Degauque, Radiowave retransmission in confined areas using radiating cable: theoretical and experimental study, *Proc. Annu. Int. Conf. IEEE Vehicular Technol. Soc.*, **44**:938–941 (1994).

UNIFORM GEOMETRICAL THEORY OF DIFFRACTION

PRABHAKAR H. PATHAK
The Ohio State University
Columbus, Ohio

1. INTRODUCTION

Keller's geometrical theory of diffraction (GTD) [1,2] constitutes a major breakthrough for solving problems of electromagnetic (EM) radiation and scattering at high frequencies. The GTD can also be applied to solving acoustic and elastic wave problems; however, only the EM case is discussed here. At high frequencies (or short wavelengths), the radiating/scattering object becomes large in terms of the wavelength, and as a result, conventional numerical solution methods, as well as convergent eigenfunction expansion-based solutions, respectively, which are best suited for low to moderately high frequencies, become highly inefficient and even intractable for treating electrically large problems. The reason for the latter difficulties stems from the fact that such convergent expansions and numerical methods are generally based on exact formulations that must satisfy EM field conditions of self-consistency in a global sense, i.e., over the entire radiating/scattering object at once, rather than in a highly local sense as done in the high-frequency approximation. It is noted that the property of localization of EM radiation, propagation, scattering, and diffraction phenomena at high frequencies will become more apparent later in Section 2.

Recently, the development of fast solvers for significantly increasing the efficiency of numerical methods in solving large problems has met with some success. However, for truly large problems, asymptotic high-frequency methods in general, and especially ray methods such as the GTD and its uniform version, still remain the most useful analysis tools. More importantly, asymptotic high-frequency methods, and in particular the GTD, are probably the only methods that can directly provide a valuable physical insight into the radiation and scattering mechanisms. The latter property of the GTD is extremely important not only for gaining a clear physical understanding of the wave radiation and scattering phenomena, but it, in turn, is important for providing useful design information in dealing with problems of radiation and scattering in engineering applications. The latter physical insight is provided by the GTD because it describes the phenomena of wave radiation/scattering locally in terms of rays that arrive at the observer after originating from certain localized or critical points (or flash points) on a radiating/scattering object. In most practical applications, such objects can be quite complex. These GTD rays are associated firstly with the incident, reflected and transmitted rays of classic geometrical optics (GO), and secondly with an additional new class of diffracted rays that have been introduced by Keller [1] into the GTD via a generalization of Fermat's principle.

The GTD [1,3] explained, for the first time, the phenomena of high-frequency diffraction systematically in terms of rays. Prior to Keller's GTD, which he introduced in the 1950s, it was Thomas Young [4] who in 1802 attempted to explain light diffraction by a slit in terms of rays that actually originated at the edges of the slit. However, the early ideas of Young on the use of rays to explain diffraction by a slit were eventually superseded in 1816 by Fresnel's approach [5] in which he employed a wave theory (or Huygen-Fresnel principle) that explained slit diffraction more accurately. Thus, Keller's GTD revives Young's ideas, and it provides a very systematic and modern treatment of diffraction by including diffracted rays that exist in addition to the rays of classic GO.

The above GTD rays may be visualized through a simple example in Fig. 1 as follows. The primary source at Q' in Fig. 1 launches rays radially from Q' in all directions. Only for simplicity, this source is assumed to be a point source; however, the ideas presented below can be directly extended to a source of finite extent. When such a point source radiates in the presence of an impenetrable object as shown in Fig. 1, then the GO rays incident from Q' , which directly impinge on the smooth part of the objects, but which do not graze the object, are transformed into a set of GO reflected rays. For an observer at $P=P_1$ or $P=P_2$ in the lit region, where the source is directly visible, the field radiated by the source arrives at P_1 via the direct (or incident) and reflected GO ray paths, respectively. The reflected ray at P_1 is generated by an incident ray path, which is transformed into a reflected path at an appropriate point of reflection Q_R on the lit (or directly illuminated) portion of the surface. The point Q_R is such that the incident and reflected ray directions at this point satisfy Snell's law of reflection (which is a consequence of Fermat's principle for reflected rays). This law of reflection simply implies that the incident ray, the reflected ray, and the surface normal at Q_R all lie in the same plane, which is usually defined as the incidence plane; furthermore, the angles that the incident and reflected rays make with the surface normal at Q_R must be the same ($\theta^i = \theta^r$ in Fig. 2). It is noted that the EM point source at Q' , which launches rays radially outward from Q' , generates a

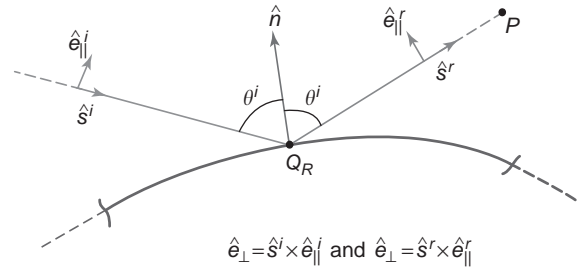


Figure 2. Unit vectors fixed in the incident and reflected rays.

spherical wave, i.e., it generates a spherical wavefront at a sufficient distance from Q' . The family of rays is always perpendicular to their associated wavefront surface in an isotropic medium, and the rays are straight lines in a homogeneous medium, as shown in Fig. 3. The following development is restricted to rays in a homogeneous isotropic medium. The wavefront is defined as an equiphase surface, and the phase here refers to the phase delay along a ray path; this delay, which increases linearly with increase in distance along the ray, results from the finite speed of propagation of the wave field associated with any ray. This wave speed, or phase velocity, is given by ω/k for a single frequency, time harmonic (or continuous wave) field. In this development, the source and the fields are assumed to satisfy an $e^{i\omega t'}$ time harmonic variation, where ω is $2\pi f$ with f being the wave frequency and t' denotes the time.

The source at Q' excites GO incident and reflected rays that exist only in a limited region of space surrounding the radiating/scattering object. In particular, the incident rays do not exist beyond the edge induced geometrical shadow boundary, because the edge geometry serves as a screen to block or shadow a portion of the incident GO rays. This incident shadow boundary (ISB) is shown in Fig. 1, and it is an extension of the incident ray past the edge at Q_E . Likewise, the incident ray, which grazes a smooth part of the object, defines a surface shadow boundary (SSB), as also shown in Fig. 1. The SSB is formed by an extension of the incident ray past the point of grazing incidence on the smooth portion of the object; here, again, the smooth portion of the object blocks or shadows the incident rays past grazing. Furthermore, the reflected rays cannot exist past the edge induced reflection shadow boundary (RSB) as at a point P_3 in Fig. 1, because a surface does not exist past the edge to produce reflection. In the case of the reflection of the incident ray, which grazes a smooth convex surface, one may visualize the coalescing of ISB and RSB into a

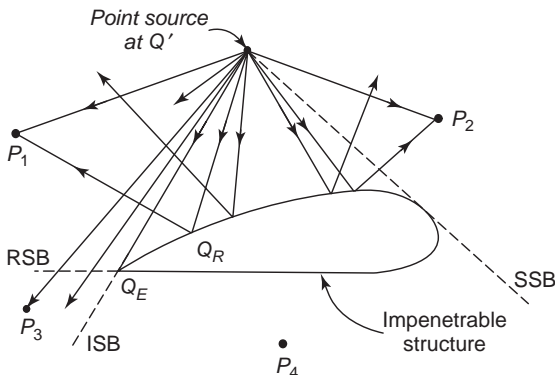


Figure 1. Geometrical optics (GO) incident and reflected rays produced by an electromagnetic point source radiating in the presence of an impenetrable structure.

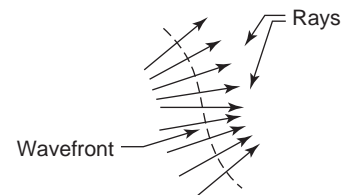


Figure 3. Wavefront surface and associated family of rays.

single SSB. It is clear from the above discussion that the classic GO incident and reflected rays do not penetrate into the shadow region; hence, the GO field vanishes completely in the geometrical shadow cast by the object illuminated from the source at Q' . The latter is seen clearly in Fig. 1, where no GO rays exist at any point P_4 in the shadow region where the source at Q' is not directly visible. This failure of the GO field in the shadow zone behind an object, where the source and its image are not directly visible, was overcome by Keller's GTD [1]. In contrast to the situation in Fig. 1, the diffracted rays of the GTD now develop at Q_E and Q_S , as shown in Fig. 4, to reach an observer at P_4 in the shadow zone. The existence of these diffracted rays can be verified via the asymptotic high-frequency solutions to appropriate canonical problems, which also indicate that the asymptotic solutions to problems of radiation, scattering, and diffraction exhibit highly local properties. Moreover, such asymptotic analysis serves to identify the so-called large parameters relevant to various diffraction mechanisms. Asymptotic high-frequency (HF) solutions become increasingly accurate with increase in the size of their large parameters. Typically, a large parameter in an asymptotic HF analysis involves a product of the wavenumber k and some characteristic distance L pertaining to any diffraction mechanism. For example, for a point source excited impenetrable half screen, the large parameter kL is given by $k \frac{s's}{s'+s} \sin^2 \beta_0$, where β_0 is the angle between the incident ray and the edge tangent at the point of edge diffraction Q_E . Also, s and s' are the distances from Q_E to the observer at P and from Q_E to the source at Q' , respectively. Although asymptotic HF solutions become increasingly accurate with increasing wave frequency, they remain surprisingly accurate even for moderately high frequencies for which the radiating/scattering object is only a few wavelengths in extent (rather than tens or hundreds of wavelengths in extent).

Some of the diffracted rays that develop from Keller's generalization of Fermat's principle are illustrated below in Fig. 5. The diffracted rays shown in Fig. 5(a) and 5(e) are present in Fig. 4. In general, diffracted rays develop whenever an incident ray field impinges on a surface

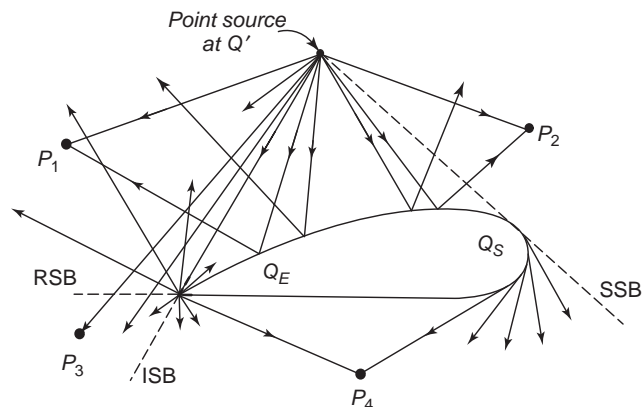


Figure 4. Edge diffracted rays originating from the edge Q_E and rays diffracted tangentially from the surface ray excited at the point of grazing Q_S .

discontinuity on a radiating/scattering object, or on a discontinuity in surface boundary conditions, or both. Diffracted rays are also initiated at grazing incidence on a smooth convex surface.

The initial values of the diffracted field are given in terms of a diffraction coefficient, exactly analogous to a reflection or transmission coefficient, which provides the initial values of the reflected and transmitted fields of classic GO. These diffraction coefficients indicate how the diffracted fields are launched into space surrounding a diffracting object. As mentioned previously, the local nature of the high-frequency diffraction phenomena allows one to find the diffraction coefficients, once and for all, from the asymptotic high-frequency solution to appropriate simpler canonical problems. The latter model the local geometrical and electrical properties in the neighborhood of the point of diffraction as in the original problem. As such, the GTD provides an efficient analytical high-frequency solution to large complex problems for which exact analytical solutions are not possible. Consequently, a GTD analysis of the radiation/scattering from complex structures (e.g., aircraft, spacecraft, ships, etc.) can be developed by simulating such objects with simpler shapes that only locally need to provide a sufficiently accurate description of all the dominant reflection and diffraction effects. It is for this reason that the GTD can provide information on ways to control the radiation/scattering as indicated previously. Although the GTD is not a rigorous method, it generally yields the leading terms in the asymptotic high-frequency solutions of diffraction problems.

It is noted that because GTD is a purely ray optical method, it fails at and near the ray shadow boundaries, i.e., the GTD fails within the so-called "transition regions" adjacent to ISB, RSB, and SSB. Transition regions are those through which the high-frequency fields must undergo a rapid change from one ray optical form to another across the shadow boundaries. Typically, the GTD field predicts an erroneous infinite field value for the diffracted fields at these shadow boundaries. The failure of the GTD at shadow boundaries can be overcome via the use of a uniform version of the GTD, such as the UTD [6–8] or the UAT [9–11], respectively. The uniform version basically patches up the GTD where it fails in the shadow boundary transition regions, because the high-frequency fields depart from a strictly ray optical behavior in these regions, and it automatically recovers the purely ray optical GTD behavior, which is valid outside these transition regions. In particular, the UTD contains Fresnel-type functions for describing the proper behavior within the ISB and RSB transition regions produced by edges [6]. On the other hand, one requires the Fock-type transition function for describing the behavior of the fields within the SSB transition regions associated with diffraction by smooth convex objects. For the sake of simplicity, the discussion in this work is restricted to impenetrable or perfectly conducting diffracting structures. Actually, only a limited amount of work has been done to date for describing HF diffraction by penetrable structures; the latter is a more complex problem [12,13]. Also, not much work has been done to describe high-frequency diffraction by objects in lossy media, or in anisotropic media, or the high-frequency diffraction by

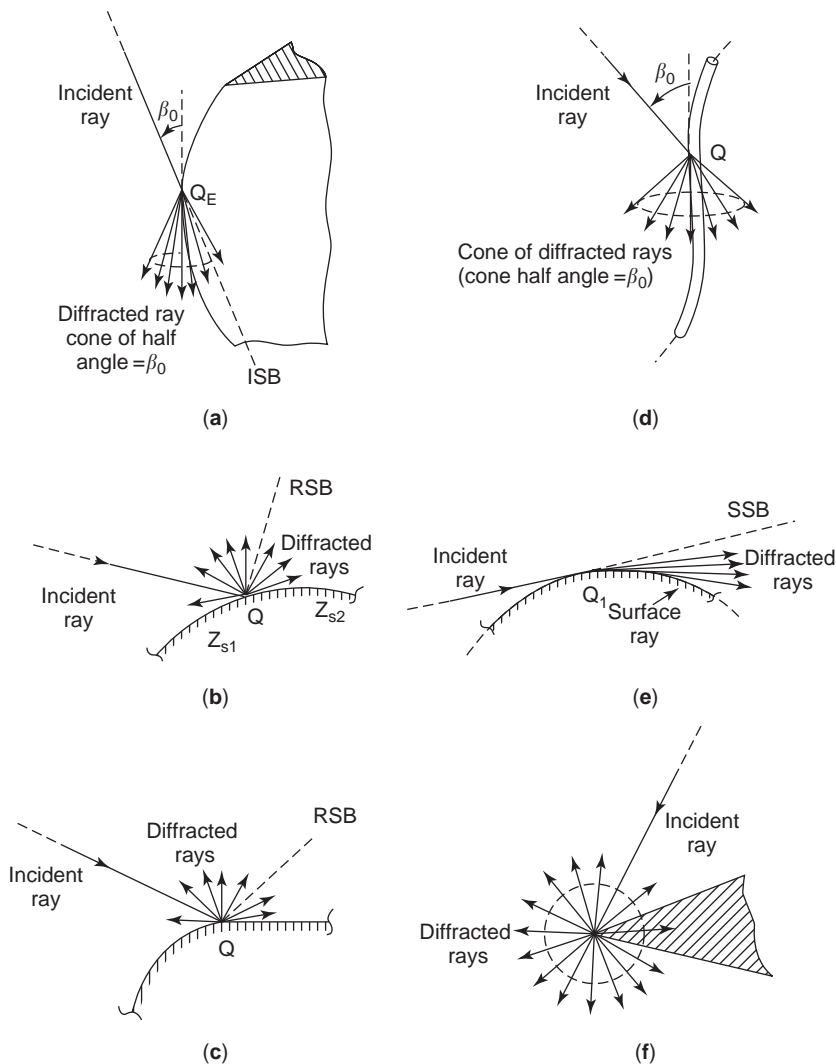


Figure 5. Examples of diffracted rays: (a) diffraction by a curved wedge, (b) diffraction at a discontinuity in surface impedance (Z_{s1} and Z_{s2}), (c) diffraction at a discontinuity in surface curvature, (d) diffraction by a thin curved wedge, (e) diffraction by a smooth convex surface, (f) diffraction by a corner in a plane screen.

anisotropic structures; nevertheless, some references to such work are available in the literature [12,14].

The GTD and its uniform versions, UTD and UAT, fail within regions of GO and diffracted ray caustics. Ray caustics are present whenever a family of rays merge or intersect to form a focal point, line, or surface, respectively. In some of these cases, the solutions can be patched up by Airy integral-type caustic transition functions [15,16], or in other cases by the equivalent current method (ECM) [17–24], or by methods of Physical Optics (PO) and its modifications such as the Physical Theory of Diffraction (PTD) [20,25,26]. The PTD may be regarded as an integral version of the GTD; it was developed by Ufimtsev at about the same time as Keller’s GTD. The PTD corrects PO, whereas GTD corrects GO; likewise, PO is a part of PTD analogous to the fact that GO is a part of the GTD. As such, the PO/PTD requires an integration of the known asymptotic currents over the radiating/scattering object. Therefore, the PO/PTD does not scale with frequency, i.e., the number of samples for integration increases rapidly with frequency making it more cumbersome even though it is more robust for applications. The GTD or UTD, on the other hand, does not require any integration on the

radiating/scattering object, and the ray paths generally remain independent of frequency making it more efficient. However, it may be less robust in some cases than the PO/PTD because one needs to find the ray paths; this fact may become somewhat complicated for arbitrary, smooth convex surfaces on which rays follow the surface geodesics, or for calculating rays associated with multiple wave interactions if they are important. Progress is being made to find such ray paths very efficiently, and work continues in this area of GTD/UTD applications. An alternative to PTD is the relatively more recent incremental theory of diffraction (ITD), which offers some advantages and is presented in [24]. It is noted, however, that the PO/PTD and ITD methods, unlike UTD, are not sufficiently developed as yet to adequately account for diffraction around smooth convex objects. It is noted that, in practical applications, it is the UTD and not GTD that must be used to obtain nonsingular and continuous fields across ray shadow boundaries. Only for far-zone calculations, the UTD may reduce to GTD in most cases if the illumination is uniform.

In Section 2, explicit UTD expressions are given for the two main mechanisms of diffraction, namely for the problems of diffraction by perfectly conducting wedges and

smooth convex surfaces, respectively. Some other commonly encountered diffraction problems are also listed. Additionally, some future research directions in the GTD/UTD area are mentioned briefly. In Section 3, several applications of UTD are provided to illustrate the utility and accuracy of this method for solving electrically large EM problems of practical interest.

Before proceeding further, to provide some expressions for the GTD/UTD field that propagate along GTD/UTD rays, it is useful to introduce the notation that will be used for dealing with time harmonic (or single frequency) fields. As EM waves exhibit polarization properties, it is essential to describe EM fields and sources as vector quantities. The vector field or source can be denoted here, in general, by $\overline{\mathcal{F}}(\bar{r}, t'')$, where \bar{r} is a vector to some observation point. For a time harmonic field,

$$\overline{\mathcal{F}}(\bar{r}, t'') = \text{Re} \overline{F}(\bar{r}, \omega) e^{j\omega t''} \quad (1)$$

where $\overline{F}(\bar{r}, \omega)$ is a phasor field that has direction (polarization) \hat{u} , and a magnitude $|\overline{F}(\bar{r}, \omega)| = \sqrt{\overline{F} \cdot \overline{F}^*}$. The preceding relations for $|\overline{F}|$ contains a scalar or dot product between \overline{F} and its complex conjugate \overline{F}^* (with asterisk denoting the conjugate operator). In the development to follow, the time harmonic factor $e^{j\omega t''}$ will be suppressed and the field/source expressions will be given in the phasor domain, i.e., in terms of the \overline{F} type quantity. Once \overline{F} is known, the time-dependent field/source quantity $\overline{\mathcal{F}}$ can be found trivially from it. The wavenumber k , in the expression for the wave speed (ω/k), is given by $\omega/\sqrt{\mu\epsilon}$, where μ and ϵ are the electrical permeability and permittivity of the isotropic, homogeneous medium in which the rays propagate.

2. GTD/UTD FIELDS

In this section, expressions for the UTD fields are presented in some detail for describing the diffraction by perfectly conducting wedges and smooth convex surfaces. As the UTD reduces to the ray optical GTD fields outside the shadow boundary transition regions, a separate discussion of GTD fields is not given. Also, only the uniform version of GTD corresponding to UTD is presented rather than discussing both UTD and UAT, which is primarily because of space limitations. A very brief discussion is also provided for other diffraction problems. As the leading terms in the GTD/UTD high-frequency asymptotic approximation are in the GO fields, the present discussion will begin with a description of the GO fields that are ray optical fields.

2.1. GO Fields

The classic GO field description can be obtained in several ways. A solution to Maxwell's equations in terms of an asymptotic expansion in inverse powers of the wavenumber, k , referred to as the Luneberg Kline expansion, yields the GO field as the leading term [3]. One can also evaluate the GO field by asymptotically evaluating the radiation integral in terms of known equivalent source distributions

(in the representation based on the equivalence theorem or the corresponding Green's theorem) over a wavefront (or equiphase surface) patch. The latter asymptotic evaluation of the radiation integral is done via the double stationary phase method in which the large parameter is ks , where s is the distance along the ray measured to the observation point from a stationary point O on the wavefront; it is noted that \bar{s} is normal to the wavefront/phasefront at O . Alternatively, the GO fields emerge from asymptotic solutions to appropriate canonical scattering and diffraction problems, and they again constitute the leading terms in the resulting asymptotic expansion. It is noted that asymptotic expansions are, in general, semi-convergent; hence, the convergence is based on retaining only a fixed number of terms in the expansion (usually only a few dominant terms) and allowing the large parameter of the asymptotic solution to increase until the resulting field converges to within some prescribed error bounds. In contrast, convergent expansions are evaluated for a fixed value of the parameter and by allowing the number of terms to increase until the result converges to within some prescribed error criterion; a tight control on the error bound is possible for convergent expansions. Nevertheless asymptotic high-frequency solutions generally remain very accurate within their domain of validity (determined primarily by the minimum value that the largeness parameter must assume in the asymptotic development in which a fixed number of dominant terms are retained). The accuracy of the asymptotic solutions can be established by comparison with known exact solutions where possible, or corresponding measured results, respectively. In the following development, the classic GO field expressions are obtained via simple, heuristic arguments based on geometrical considerations.

In GO, the field propagates along ray paths determined by Fermat's principle. As energy is transported along rays within the ray optical framework for GO fields, it follows that power must be conserved in a narrow tube of rays, i.e., in an astigmatic ray tube or a ray pencil as in Fig. 6. Consider an axial (central) ray in that tube denoted by the path \overline{OP} , where P is the observation point on the ray and O is some previous point along this ray path. Let $|\overline{OP}| = s$, which is the distance from O to P . It is then of interest to find the GO field at P if its field value is known at an earlier point O .

In order to find the continuation of the electric field $\overline{E}(O)$ at O to its value $\overline{E}(P)$ at P , one makes the usual assumption that power is conserved in a ray tube, i.e., the power $\Delta P(O)$ crossing the surface dA_o of the ray tube at O must be the same as the power $\Delta P(P)$ crossing the surface dA of that same tube at P . From Fig. 6, one observes that

$$dA_o \approx |(\rho_1 d\psi_1)(\rho_2 d\psi_2)| \quad (1a)$$

and

$$dA \approx |[(\rho_1 + s)d\psi_1][(\rho_2 + s)d\psi_2]| \quad (2)$$

where ρ_1 and ρ_2 are the principle of wavefront radii of curvature at O . Consequently, the power $\Delta P(O)$ and $\Delta P(P)$,

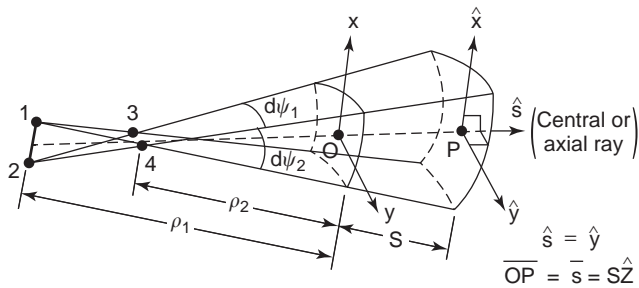


Figure 6. Astigmatic GO ray tube corresponding to Eq. (4).

which is transferred across the ray tube surfaces at O and P , are given by $\frac{|\bar{E}(O)|^2}{2Z_o} dA_o$ and $\frac{|\bar{E}(P)|^2}{2Z_o} dA$, respectively, where Z_o is the wave impedance for the homogeneous isotropic medium in which the rays propagate. Conservation of power in a ray tube therefore requires $\Delta P(O) = \Delta P(P)$ or

$$|\bar{E}(P)| = |\bar{E}(O)| \sqrt{\frac{\rho_1 \rho_2}{(\rho_1 + s)(\rho_2 + s)}} \quad (3)$$

via Eqs. (1a) and (2). One next heuristically incorporates the local plane wave polarization and phase into the expression in Eq. (2) to arrive at the GO expression for the electric field intensity at P

$$\bar{E}(P) = \bar{E}(O) \sqrt{\frac{\rho_1 \rho_2}{(\rho_1 + s)(\rho_2 + s)}} e^{-jks} \quad (4)$$

The polarization is unchanged from O to P because the medium is homogeneous and isotropic. Rays can bend in an inhomogeneous medium and, in that case, the polarization can change from O to P . The local plane wave phase and polarization in Eq. (4) is associated with the central ray from O to P in Eq. (4). The GO field in Eq. (4) is referred to as an arbitrary ray optical field. The ray tube in Fig. 6 is referred to as an astigmatic ray tube, or a quadratic ray tube, because ρ_1 and ρ_2 , the principle wavefront radii of curvature at O , are assumed to be different in general. If $\rho_1 = \rho_2 = \rho$, then the ray optical field becomes a simple spherical wave. If $\rho_1 = \rho_2 = \rho \rightarrow \infty$, then the ray optical field is everywhere a plane wave. If $\rho_1 = \rho$, where ρ is bounded and $\rho_2 \rightarrow \infty$, then one gets a cylindrical wave. Thus, it can be observed that plane, cylindrical, conical, and spherical waves are all special cases of the general GO astigmatic wavefield in Eq. (4). The ray congruencies or intersections at 1-2 and 3-4 for the ray pencil (or tube) in Fig. 6 form a ray caustic corresponding to the centers of the wavefront radii of curvatures ρ_1 and ρ_2 . The accepted sign convention is that the distances, ρ_1 and ρ_2 , are respectively positive if the ray caustics, or ray foci, at 1-2 and 3-4 occur along the ray path (in the direction \hat{s}) before reaching the reference point O , as is seen to be the case in Fig. 6; otherwise they are negative. The distance s is positive in the ray propagation direction. Also, the positive branch of the square root is chosen in Eq. (4). Indeed, if

one crosses a caustic along a ray path, then

$$\sqrt{\frac{\rho_i}{\rho_i + s}} = \left| \sqrt{\frac{\rho_i}{\rho_i + s}} \right| e^{j\frac{\pi}{2}}, \text{ if } \rho_i = -|\rho_i| \text{ and } s > -|\rho_i|, \text{ for } i = 1 \text{ or } 2 \quad (5)$$

It is noted that Eq. (4) becomes singular at the caustic locations 1-2 and 3-4 of Fig. 5. Hence, the GO field in Eq. (4) is not valid at and near these caustics. As the astigmatic ray field is locally plane with phase being tracked locally as a plane wave along the ray path direction \hat{s} , the magnetic field intensity, \bar{H} , is given via the plane wave condition

$$\bar{H} = Z_o^{-1} \hat{s} \times \bar{E}$$

along the ray, i.e., at O or P or any other point on that ray. Note that $Z_o = (Y_o)^{-1}$ is the plane wave impedance in the medium.

The general GO field expression in Eq. (4) can be associated with the incident, reflected, or transmitted GO fields, respectively. As the discussion is restricted to impenetrable objects for simplicity, no transmitted waves will be discussed explicitly. Outside the shadow boundary transition regions, the GTD field, as postulated by Keller, is also a ray optical field of the type in Eq. (4). Hence,

$$\bar{E}^p(P) = \bar{E}^p(O) \sqrt{\frac{\rho_1^p}{\rho_1^p + s^p}} \sqrt{\frac{\rho_2^p}{\rho_2^p + s^p}} e^{-jks^p} \quad (6a)$$

with

$$p = i, r, \text{ or } d \quad (6b)$$

to represent the incident ($p = i$), reflected ($p = r$) or diffracted ($p = d$) fields, respectively.

2.2. Incident GO Ray Field Expression

Incident GO ray field is given by (6a) with $p = i$ in (6b), namely

$$\bar{E}^i(P) = \bar{E}^i(O) \sqrt{\frac{\rho_1^i}{\rho_1^i + s^i}} \cdot \frac{\rho_2^i}{\rho_2^i + s^i} e^{-jks^i} U_i \quad (7)$$

in which U_i is a step function that has a value of unity within the lit region where the incident field is directly visible, and $U_i = 0$ in the shadow region behind an obstacle that blocks the incident ray system (see Fig. 1).

2.3. Reflected GO Ray Field Expression

It is shown in Fig. 6 how an incident ray tube is transformed into a reflected ray tube at the point of reflection Q_R on a smooth, perfectly conducting surface. The incident ray direction \hat{s}^i and the unit normal vector to the surface at the point of reflection Q_R define the plane of incidence. From Fermat's principle, the reflected ray (along \hat{s}^r) must also lie in this plane of incidence, namely, $\hat{n} \cdot (\hat{s}^i \times \hat{s}^r) = 0$. Also, Fermat's principle implies Snell's law, which simply states that the angles of incidence and reflection are the

same with respect to the surface normal at Q_R , as in Fig. 2. The field $\overline{E}^r(P)$ at P , which is reflected from a smooth surface when an astigmatic ray field $\overline{E}^i(Q_R)$ is incident at any point of reflection Q_R has the ray optical form

$$\overline{E}^r(P) = \overline{E}^i(Q_R) \sqrt{\frac{\rho_1^r}{\rho_1^r + s^r} \cdot \frac{\rho_2^r}{\rho_2^r + s^r}} e^{-jks^r} \quad (8)$$

The above results directly from (6a) with $p = r$ as in (6b). It is clear from Fig. 6 that the geometry of the reflected astigmatic ray tube depicts Q_R as the reference point on that tube, and the principle wavefront radii of curvatures ρ_1^r and ρ_2^r of reflected field are measured from this reference at Q_R ; the reflected ray distance s^r is also measured from Q_R . A reflection coefficient $\overline{R}(Q_R)$ at Q_R is introduced, which indicates how much of the field incident at any point of reflection Q_R is transformed into a reflected field at that point and in the direction \hat{s}^r of the reflected ray. Thus, $\overline{R}(Q_R)$ is simply defined by

$$\overline{E}^r(Q_R) = \overline{E}^i(Q_R) \cdot \overline{R}(Q_R) \quad (9)$$

Hence, $\overline{E}^r(P)$ in Eq. (8) becomes via Eq. (9) the following:

$$\overline{E}^r(Q_R) = \overline{E}^i(Q_R) \cdot \overline{R}(Q_R) \sqrt{\frac{\rho_1^r \rho_2^r}{(\rho_1^r + s^r)(\rho_2^r + s^r)}} e^{-jks^r} U_r \quad (10)$$

where U_r is a step function whose value is unity in the region only where the reflected GO field exists and is zero elsewhere. It is useful to express $\overline{E}^i(Q_R)$ and $\overline{E}^r(P)$ in terms of unit vectors $(\hat{e}_{||}^i, \hat{e}_{\perp}^i)$ and $(\hat{e}_{||}^r, \hat{e}_{\perp}^r)$ that are fixed in the incident and reflected rays, respectively, as shown in Fig. 2. The set of unit vectors $(\hat{s}^i, \hat{e}_{||}^i, \hat{e}_{\perp}^i)$ and $(\hat{s}^r, \hat{e}_{||}^r, \hat{e}_{\perp}^r)$ form an orthogonal triad, namely

$$\hat{e}_{\perp}^i = \hat{s}^i \times \hat{e}_{||}^i \quad \text{and} \quad \hat{e}_{\perp}^r = \hat{s}^r \times \hat{e}_{||}^r \quad (11)$$

The $\hat{e}_{||}^i$ and $\hat{e}_{||}^r$ are unit vectors that lie in the plane of incidence [defined by \hat{s}^i and $\hat{n}(Q_R)$]. On the other hand, \hat{e}_{\perp}^i is perpendicular to the plane of incidence (and hence of reflection). In the ray coordinates $(\hat{s}^i, \hat{e}_{||}^i, \hat{e}_{\perp}^i)$ and $(\hat{s}^r, \hat{e}_{||}^r, \hat{e}_{\perp}^r)$, the $\overline{R}(Q_R)$ may be expressed as

$$\overline{R}(Q_R) = \hat{e}_{||}^i R_h(Q_R) \hat{e}_{||}^r + \hat{e}_{\perp}^i R_s(Q_R) \hat{e}_{\perp}^r \quad (12)$$

For a perfectly conducting surface, the boundary condition that the total tangential electric field vanishes on such a surface leads to

$$\hat{n}(Q_R) \times [\overline{E}^i(Q_R) + \overline{E}^r(Q_R)] = 0 \quad (13)$$

It follows for a perfect electric conductor (PEC) that R_h and R_s in Eq. (12) are given by

$$R_h = \mp 1 \quad (14)$$

For a nonperfectly conducting surface with radii of curvature large in terms of the wavelength, the R_h and R_s can

be found from the canonical problem of electromagnetic plane wave reflection from a plane surface with the same local electrical properties as those of the original surface at Q_R . The original surface at Q_R is assumed to be ‘‘locally’’ flat for the purpose of calculating \overline{R} from an appropriate canonical problem. The incident astigmatic GO ray field at Q_R is also assumed to satisfy ‘‘local’’ plane wave conditions in this high-frequency approximation. The subscripts h and s in Eq. (12) denote the commonly used nomenclature assigned to the ‘‘vertical’’ and ‘‘horizontal’’ field polarizations. However, the subscripts s and h actually correspond to the acoustic soft and hard cases indicating the strong connection between \overline{EM} and acoustics for high-frequency reflection. Clearly, \overline{R} is polarization-dependent. The effect of surface curvature at Q_R on the field reflected to P is contained in ρ_1^r and ρ_2^r of Eq. (10). These $\rho_{1,2}^r$ may be found as discussed in [6,27]. The phase of the reflected field along the reflected ray path $\overline{Q_R P} = |\overline{Q_R P}| \hat{s}^r$ is contained in e^{-jks^r} of Eq. (10).

A convenient matrix notation for Eq. (10) is given by

$$\begin{pmatrix} E_{||}^r(P) \\ E_{\perp}^r(P) \end{pmatrix} = \begin{pmatrix} R_h & 0 \\ 0 & R_s \end{pmatrix} \begin{pmatrix} E_{||}^i(Q_R) \\ E_{\perp}^i(Q_R) \end{pmatrix} \sqrt{\frac{\rho_1^r \rho_2^r}{(\rho_1^r + s^r)(\rho_2^r + s^r)}} e^{-jks^r} \quad (15)$$

It is noted that Eq. (10) [and Eq. (15)] fails at caustics, i.e., when P moves to the paraxial ray tube intersections where $(\rho_1^r + s^r) = 0$ or $(\rho_2^r + s^r) = 0$ at 1'-2' or 3'-4', respectively, in Fig. 7. If $\rho_{1,2}^r > 0$, then $s^r = -|\rho_{1,2}^r|$ in virtual space inside the reflecting surface. On the other hand, if the caustics ρ_1^r or ρ_2^r are in physical space, then ρ_1^r or ρ_2^r are negative, i.e., $s^r = -|\rho_1^r|$ or $s^r = -|\rho_2^r|$, respectively, at the caustic. Whenever a ray crosses a caustic, then $\frac{\rho_{1,2}^r}{\rho_{1,2}^r + s^r}$ changes sign, and $\sqrt{\frac{\rho_{1,2}^r}{\rho_{1,2}^r + s^r}} = \left| \frac{\rho_{1,2}^r}{\rho_{1,2}^r + s^r} \right| e^{j\pi/2}$ for an $e^{+j\omega t}$ time harmonic dependence.

A uniform asymptotic solution is required to patch up fields near caustics, see, for example [15,16,28]. Also, the

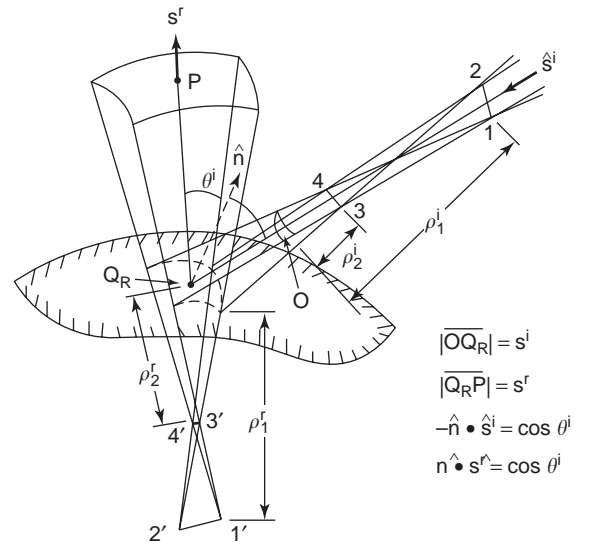


Figure 7. Reflected ray tube geometry.

simple GO ray representation fails for reflection from a smooth surface near grazing incidence; this failure can be overcome using the uniform GTD (or UTD) solution for the lit zone pertaining to the problem of EM of an incident GO ray field by a smooth PEC convex surface, as discussed later in Section 2.4.2. It is important to note that near the SSB (i.e., as $\theta^i \rightarrow \pi/2$), the ρ_1^r and ρ_2^r approach the following limiting values:

$$\rho_2^r \rightarrow \frac{\rho_g(Q_R) \cos \theta^i}{2} \rightarrow 0 \text{ for } \theta^i \rightarrow \pi/2 \quad (16a)$$

$$\rho_2^r \rightarrow \rho_b^i \quad (16b)$$

where $\rho_g(Q_R)$ is the surface radius of curvature in the plane of incidence at Q_R and ρ_b^i is the radius of curvature of the incident wavefront in the plane tangent to the surface at Q_R for $\theta^i \rightarrow \pi/2$. The total GO electric field E^{GO} at a point P_L in the lit region is the sum of the fields of the incident and reflected rays; hence,

$$\begin{aligned} \bar{E}^{GO}(P_L) = & \bar{E}^i(P_L)U_i + \bar{E}^r(Q_R) \\ & \cdot \bar{R} \sqrt{\frac{\rho_1^r \rho_2^r}{(\rho_1^r + s^r)(\rho_2^r + s^r)}} e^{-jks^r} U_r \end{aligned} \quad (17)$$

In summary, it is noted that the GO incident and reflected fields are discontinuous across their associated shadow boundaries such as ISB, RSB, and SSB in Figs. 1 and 4. The failure of GO to account for a proper nonzero field within the shadow zone behind an impenetrable obstacle can be overcome through the GTD/UTD. Nevertheless, GO generally yields the dominant contribution to the total high-frequency fields, and it constitutes the leading term in the GTD/UTD solution.

The reflected GO field $\bar{E}^r(P_L)$ for the two-dimensional (2-D) case can be deduced directly from the 3-D case by allowing ρ_1^r or ρ_2^r to approach infinity. Thus, one may let $\rho_1^r \equiv \rho^r$ and $\rho_2^r \rightarrow \infty$ in Eq. (17) to arrive at the 2-D reflected GO field $\bar{E}^r(P_L)$ as

$$\bar{E}^r(P_L) = \bar{E}^i(Q_R) \cdot \bar{R} \sqrt{\frac{\rho^r}{\rho^r + s^r}} e^{-jks^r} U_r \quad (18)$$

in which the incident ray optical field $\bar{E}^i(Q_R)$ is now a cylindrical wave at Q_R and the caustic distance ρ^r in Eq. (18) for the 2-D case is given by

$$\frac{1}{\rho^r} = \frac{1}{s^i} + \frac{2}{\rho_g(Q_R) \cos \theta^i} \quad (19)$$

where θ^i has the same meaning as before and s^i is the radius of curvature of the incident cylindrical wavefront at Q_R . If the cylindrical wave is produced by a 2-D line source, then s^i can be chosen to be the distance from that line source to the point of reflection Q_R on the 2-D boundary. The quantity $\rho_g(Q_R)$ denotes the radius of curvature of the 2-D boundary at the point of reflection Q_R .

2.4. Diffracted Ray Fields

As mentioned previously, diffracted rays are introduced in the GTD via a generalization of Fermat’s principle. The initial value of the diffracted ray field is given in terms of a diffraction coefficient. Away from the point of diffraction, the diffracted rays behave according to the laws of GO. The phenomenon of edge diffraction will be discussed first, and it will be followed by a discussion on the phenomenon of diffraction at a smooth convex surface. The latter phenomenon is more complicated to describe mathematically than edge diffraction.

2.4.1. Edge Diffraction. When a ray is incident on an edge in an otherwise smooth surface, it produces diffracted rays that lie on a cone about the tangent to the edge at the point of diffraction such that the angle β_0 between the incident ray and the edge tangent equals the half angle of the diffracted ray cone, as shown in Fig. 5(a). This cone of diffracted rays is referred to as the “Keller cone,” and it results from the generalization of Fermat’s principle to describe rays diffracted by an edge.

Let an arbitrarily plane polarized astigmatic ray optical field be incident on a perfectly conducting curved wedge, as shown in Fig. 8. The point O , and the edge tangent at the point of diffraction Q_E , define a plane; then ρ_e^i is the radius of curvature of the incident astigmatic wavefront in that plane. The resultant total HF electric field $\bar{E}(P)$ at any point P exterior to the wedge is given by

$$\bar{E}(P) \sim \bar{E}^{GO}(P) + \bar{E}^d(P) \quad (20)$$

where the symbol \sim denotes “asymptotically equals to.” As before, the GO field component $\bar{E}^{GO}(P)$ is given as

$$\bar{E}^{GO}(P) = \bar{E}^i(P)U_i + \bar{E}^r(P)U_r \quad (21)$$

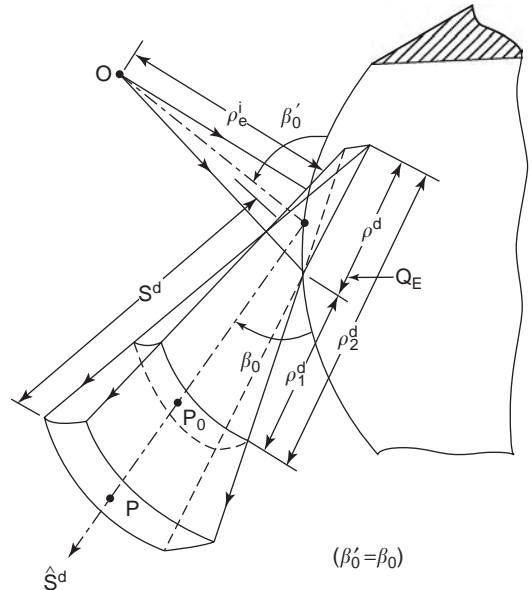


Figure 8. Edge-diffracted ray tube.

The domains of existence of the incident and reflected ray fields $\overline{E}^i(P)$ and $\overline{E}^r(P)$ are indicated by the step functions U_i and U_r , respectively, which are defined for a wedge as

$$U_i = \begin{cases} 1, & \text{if } 0 < \phi < \pi + \phi' \\ 0, & \text{if } \pi + \phi' < \phi < n\pi \end{cases} \quad (22)$$

and

$$U_r = \begin{cases} 1, & \text{if } 0 < \phi < \pi - \phi' \\ 0, & \text{if } \pi - \phi' < \phi < n\pi \end{cases} \quad (23)$$

The wedge faces make the angles 0 and $n\pi$, respectively, so that the wedge angle is $(2-n)\pi$, as in Fig. 9(b). The azimuthal angles ϕ and ϕ' are made by the projections

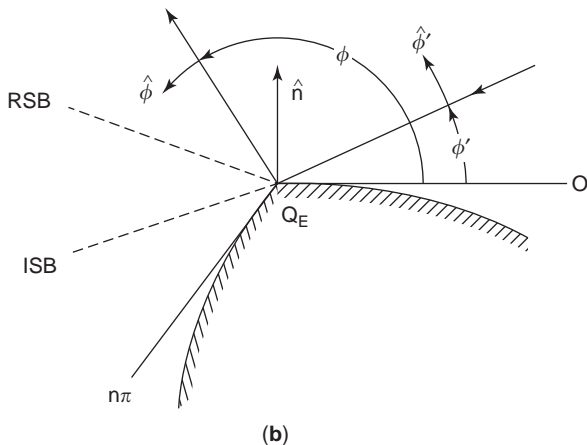
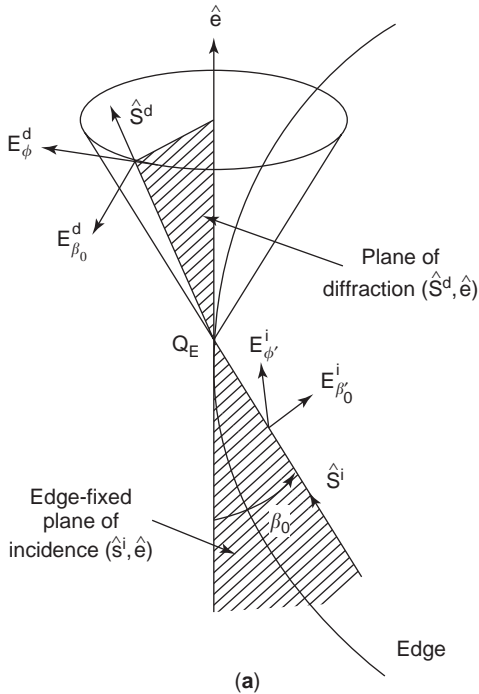


Figure 9. Edge fixed planes of incidence and diffraction.

of the directions of incidence and observation on a plane perpendicular to the edge at the point of diffraction Q_E . These angles are measured from a plane tangent to the “0” face of the wedge at Q_E , as shown in Fig. 9(b).

The expressions for the GO incident and reflected fields have been discussed previously. The diffracted field \overline{E}^d exists exterior to the wedge (i.e., for $0 < \phi < n\pi$). From (6a) and (6b), one may write the general field expression for the ray diffracted in the direction \hat{s}^d from Q_E as

$$\overline{E}^d(P) \sim \overline{E}^d(P_o) \sqrt{\frac{\rho_1^d \rho_2^d}{(\rho_1^d + s_o^d)(\rho_2^d + s_o^d)}} e^{-jks_o^d} \quad (24)$$

The diffracted ray tube corresponding to Eq. (24) is shown in Fig. 8. The superscript “d” on $\rho_{1,2}^d$ and s_o^d denotes that these quantities are associated with the diffracted ray field component. In order to relate $\overline{E}^d(P)$ to the incident field at the point of edge diffraction Q_E , one moves the reference P_o in Fig. 8 to the point of edge diffraction Q_E by letting $\rho_1^d \rightarrow 0$, so that

$$\overline{E}^d(P) = \lim_{\rho_1^d \rightarrow 0} [\sqrt{\rho_1^d} \overline{E}^d(P_o)] \sqrt{\frac{\rho_2^d}{(\rho_1^d + s_o^d)(\rho_2^d + s_o^d)}} e^{-jks_o^d} \quad (25)$$

As $\overline{E}^d(P)$ is independent of the reference point P_o , the above limit exists, and it is defined as

$$\lim_{\rho_1^d \rightarrow 0} \sqrt{\rho_1^d} \overline{E}^d(P_o) \equiv \overline{E}^i(Q_E) \cdot \overline{D}_e^k \quad (26)$$

where $\overline{D}_e^k = \overline{D}_e^k(\phi, \phi', \beta_0; k)$ is Keller’s “dyadic edge diffraction coefficient” at Q_E , which indicates how the energy is distributed in the diffracted field as a function of the angles ϕ , ϕ' , and β_0 ; \overline{D}_e^k also depends on n and the wave-number k . From Eqs. (25) and (26), it is clear that

$$\overline{E}^d(P) \sim \overline{E}^i(Q_E) \cdot \overline{D}_e^k(\phi, \phi', \beta_0; k) \sqrt{\frac{\rho_e}{s^d(\rho_e + s^d)}} e^{-jks^d} \quad (27)$$

where $\lim_{\rho_1^d \rightarrow 0} \rho_2^d \equiv \rho_e$ (edge diffracted ray caustic distance), and likewise $\lim_{\rho_1^d \rightarrow 0} s_o^d \equiv s^d$, as shown in Fig. 8. $\overline{E}^d(P)$ is polarized transverse to the diffracted ray direction \hat{s}^d because the field $\overline{E}^d(P)$ is ray optical; hence, the associated magnetic field can be expressed via local plane wave conditions at P as

$$\overline{H}^d(P) \sim Y_0 \hat{s}^d \times \overline{E}^d(P) \quad (28)$$

If the incident field $\overline{E}^i(Q_E)$ exhibits a rapid spatial variation at the point of edge diffraction Q_E , then an additional term referred to as a slope diffracted field must be added to Eq. (27) to describe the diffraction effects accurately; however, that slope diffracted field will not be described here. An expression for finding the diffracted ray caustic distance ρ_e is given later in Eq. (47).

It is convenient to express the dyadic edge diffraction coefficient \overline{D}_e^k in terms of unit vectors fixed in the incident and diffracted ray as follows. Let \hat{s}^i and \hat{e} define an edge

fixed plane of incidence where \hat{e} is the edge tangent at Q_E . Likewise, let \hat{s}^d and \hat{e} define the edge fixed plane of diffraction. The law of diffraction that defines the Keller cone is $\hat{s}^i \cdot \hat{e} = \hat{s}^d \cdot \hat{e}$. Thus, $\beta'_0 = \beta_0$. Let $\hat{\beta}'_0$ and $\hat{\beta}_0$ be parallel to the edge fixed planes of incidence and diffraction, respectively, as in Fig. 9(a), and let

$$\hat{\beta}'_0 = \hat{s}^i \times \hat{\phi}' \quad \hat{\beta}_0 = \hat{s}^d \times \hat{\phi} \quad (29)$$

Here, $\hat{\phi}$ and $\hat{\phi}'$ point in the direction of increasing ϕ and ϕ' angles, respectively. The incident field $\vec{E}^i(Q_E)$ can be expressed in terms of the triad of unit vectors $(\hat{s}^i, \hat{\beta}'_0, \hat{\phi}')$ fixed in the incident ray; likewise, the edge diffracted field $\vec{E}^d(P)$ can be expressed in terms of $(\hat{s}^d, \hat{\beta}_0, \hat{\phi})$ fixed in the diffracted ray. Then in the ray coordinates, one writes

$$\vec{E}^i(Q_E) = \hat{\beta}'_0 E_{\beta'_0}^i + \hat{\phi}' E_{\phi'}^i \quad (30)$$

and

$$\vec{E}^d(P) = \hat{\beta}_0 E_{\beta_0}^d + \hat{\phi} E_{\phi}^d \quad (31)$$

One can relate \vec{E}^d to \vec{E}^i through the previously introduced dyadic diffraction coefficient \overline{D}_e in Eq. (26), where

$$\overline{D}_e^k = -\hat{\beta}'_0 \hat{\beta}_0 D_{es}^k - \hat{\phi}' \hat{\phi} D_{eh}^k \quad (32)$$

The scalar components of the dyadic diffraction coefficient, namely, D_{es}^k and D_{eh}^k , can be found from the asymptotic solutions of appropriate canonical wedge diffraction problems; they are given by

$$D_{es}^k(\phi, \phi'; \beta_0) = \frac{-e^{-j\frac{\pi}{4}} \sin \frac{\pi}{n}}{n\sqrt{2\pi k} \sin \beta_0} \left[\frac{1}{\cos \frac{\pi}{n} - \cos\left(\frac{\phi - \phi'}{n}\right)} \mp \frac{1}{\cos \frac{\pi}{n} - \cos\left(\frac{\phi + \phi'}{n}\right)} \right] \quad (33)$$

The subscripts s and h in Eqs. (32) and (33) refer again to acoustic soft and hard boundary conditions indicating the intimate connection between EM and acoustics for explaining high-frequency diffraction. It is clear that the Keller edge diffraction coefficient in Eq. (33) becomes singular at the incident shadow boundary (ISB) and the reflection shadow boundary (RSB), which occur when $\phi = \pi + \phi'$ and $\phi = \pi - \phi'$, respectively. Thus, the result in Eq. (27) together with Eqs. (32) and (33) is not valid at and near the GO incident and reflection shadow boundaries. This deficiency of GTD can be overcome via the use of uniform geometrical theory of diffraction (UTD). According to the UTD [6,8], the total HF field exterior to the wedge is still given by Eq. (27) as in Keller's original GTD; however, the \vec{E}^d in Eqs. (27), (32), and (33) is modified such that \overline{D}_e of Eq. (32) is now replaced by the UTD edge

diffraction coefficient \overline{D}_e , so that

$$\vec{E}^d(P) = \vec{E}^i(Q_E) \cdot \overline{D}_e(\phi, \phi'; \beta_0; k) \sqrt{\frac{\rho_e}{s^d(\rho_e + s^d)}} e^{-jks^d} \quad (34)$$

The \overline{D}_e in Eq. (34) can also be expressed as

$$\overline{D}_e = -\hat{\beta}'_0 \hat{\beta}_0 D_{es} - \hat{\phi}' \hat{\phi} D_{eh} \quad (35)$$

In matrix notation, Eq. (34) becomes

$$\begin{bmatrix} E_{\beta_0}^d \\ E_{\phi}^d \end{bmatrix} = \begin{bmatrix} -D_{es} & 0 \\ 0 & -D_{eh} \end{bmatrix} \begin{bmatrix} E_{\beta'_0}^i \\ E_{\phi'}^i \end{bmatrix} \sqrt{\frac{\rho_e}{s^d(\rho_e + s^d)}} e^{-jks^d} \quad (36)$$

in which the D_{es} and D_{eh} are [6,8]

$$D_{eh}(\phi, \phi'; \beta_0) = \frac{-e^{-j\frac{\pi}{4}}}{2n\sqrt{2\pi k} \sin \beta_0} \left[\cot\left(\frac{\pi + (\phi - \phi')}{2n}\right) \cdot F[kL^i a^+(\phi - \phi')] + \cot\left(\frac{\pi - (\phi - \phi')}{2n}\right) \cdot F[kL^i a^-(\phi - \phi')] \mp \left[\cot\left(\frac{\pi + (\phi + \phi')}{2n}\right) \cdot F[kL^{rn} a^+(\phi + \phi')] + \cot\left(\frac{\pi - (\phi + \phi')}{2n}\right) \cdot F[kL^{ro} a^-(\phi + \phi')] \right] \right] \quad (37)$$

where the asymptotic large parameter kL (with the superscripts i, rn, ro , on L omitted for convenience) is required to be sufficiently large (generally greater than 3) and

$$a^\pm(\beta) = 2 \cos^2\left(\frac{2n\pi N^\pm - \beta}{2n}\right) \quad (38)$$

The N^\pm are the integers that most nearly satisfy the equation

$$2\pi n N^\pm - \beta = \pm \pi \quad (39)$$

with

$$\beta = \phi \pm \phi' \quad (40)$$

Note that $n=2$ for a half plane or a semiinfinite curved screen. Also, $n=3/2$ for an exterior right angled wedge, etc. For a point source (or spherical wave) type illumination, the distance parameter L^i is

$$L^i = \frac{s^i s^d}{s^i + s^d} \sin^2 \beta_0 \quad (41)$$

in which s^i and s^d are the distances from the point of edge diffraction at Q_E to the source and observation points, respectively. Only for a straight wedge with planar faces

that is illuminated by a point source does

$$L^{r0} = L^{rn} = L^i = \frac{s^i s^d}{s^i + s^d} \sin^2 \beta_0 \quad (42)$$

as in Eq. (41). For a general astigmatic ray optical illumination that is characterized by two distinct principal wavefront radii of curvature, ρ_1^i and ρ_2^i , the above L^i must be modified as shown below in the general expressions for L^{r0} and L^{rn} pertaining to a curved wedge; thus,

$$L^i = \left[\frac{s^d(\rho_e^i + s^d)\rho_1^i\rho_2^i \sin^2 \beta_0}{\rho_e^i(\rho_1^i + s^d)(\rho_2^i + s^d)} \right]_{\text{at ISB}} \quad (43)$$

$$L^r = \left[\frac{s^d(\rho_e^r + s^d)\rho_1^r\rho_2^r \sin^2 \beta_0}{\rho_e^r(\rho_1^r + s^d)(\rho_2^r + s^d)} \right]_{\text{at RSB}} \quad (44)$$

Here, L^{r0} and L^{rn} are the values of L^r associated with the “0” and “n” faces of the wedge, respectively. Furthermore, ρ_e^r is given by

$$\frac{1}{\rho_e^r} = \frac{1}{\rho_e^i} - \frac{2(\hat{n} \cdot \hat{n}_e)(\hat{s}^i \cdot \hat{n})}{a \sin^2 \beta_0} \quad (45)$$

Also, ρ_e is given by

$$\frac{1}{\rho_e} = \frac{1}{\rho_e^i} - \frac{\hat{n}_e \cdot (\hat{s}^i - \hat{s}^d)}{a \sin^2 \beta_0} \quad (46)$$

The unit vector \hat{n} is defined in Fig. 9(b), whereas \hat{n}_e is a unit vector normal to the edge that is directed away from the center of edge curvature at Q_E . The radius of edge curvature is denoted locally by “ a ” in Eqs. (45) and (46). ρ_e^i is the radius of curvature of the incident wavefront at Q_E that lies in the edge fixed plane of incidence. In the far zone, when $s^d \gg \rho_{1,2}^i$, $s^d \gg \rho_{1,2}^r$, and $s^d \gg \rho_e$, then the L^i and L^r in Eqs. (43) and (44) simplify to $L \approx \frac{\rho_1 \rho_2 \sin^2 \beta_0}{\rho_e}$, in which the superscripts on L , ρ_1 , and ρ_2 are omitted for convenience. It is noted that L^i and L^r in Eqs. (43) and (44) are calculated on the appropriate shadow boundaries. The transition function, F , which appears in Eq. (37), contains a

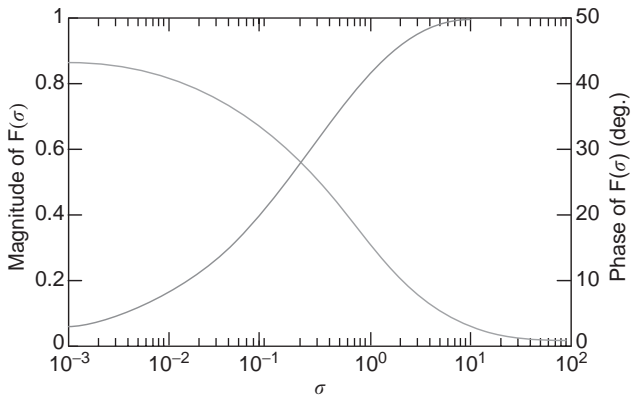


Figure 10. Plot of $F(\sigma)$ versus σ .

Fresnel integral; it is defined by

$$F(x) = 2j\sqrt{x}e^{jx} \int_{\sqrt{x}}^{\infty} d\tau e^{-j\tau^2} \quad (47)$$

A plot of the above UTD transition function $F(x)$ is illustrated in Fig. 10. In Eq. (47), $\sqrt{x} = |\sqrt{x}|$ if $x > 0$ and $\sqrt{x} = -j|\sqrt{x}|$ if $x < 0$. If $x < 0$, then $F(x)|_{x < 0} = F^*(|x|)$, where * denotes the complex conjugate. Exterior to the (ISB/RSB) transition regions, x becomes large and $F(x) \rightarrow 1$, so that the uniform D_{es}^{eh} in Eq. (37) then reduces to Keller’s form as it should; namely,

$$\bar{D}_e \rightarrow \bar{D}_e^h \text{ outside the transition region} \quad (48)$$

Near the (ISB and RSB) boundaries, the small argument approximation for $F(x)$ may be employed (because $x = 0$ on ISB and RSB); namely,

$$F(x) \xrightarrow{x \rightarrow 0} \sqrt{\pi x} e^{j(\frac{\pi}{4} + x)} \quad (49)$$

Using the above limit into Eq. (37) yields the following result for the diffracted field \bar{E}^d at ISB or RSB:

$$\bar{E}^d|_{\text{ISB;RSB}} = \left[\mp \frac{1}{2} \bar{E}^{i;r} + \begin{pmatrix} \text{continuous} \\ \text{higher order} \\ \text{terms} \end{pmatrix} \right]; \quad (50)$$

$$\text{if } \left\{ \begin{array}{l} \text{on lit side of ISB; RSB} \\ \text{on shadow side of ISB; RSB} \end{array} \right\}$$

The result in Eq. (50) ensures the continuity of the total HF field in Eq. (20) across ISB and RSB. The field contribution developing from the edge excited “surface diffracted rays” is not included in Eq. (37); it may be important for observation points close to the surface shadow boundaries (SSB) associated with the tangent to the “0” and “n” faces of a curved wedge at Q_E if the “0” and “n” faces are convex boundaries. The result in Eqs. (34) and (36) along with Eq. (37) is valid away from any diffracted ray caustics and away from the edge caustic at Q_E .

For grazing angles of incidence on a perfectly conducting wedge with planar faces, $D_{es} = 0$, and D_{eh} must be replaced by $D_{eh}/2$. The reason for the one-half factor in the latter case is explained as follows. The incident and reflected GO fields tend to combine into a single “total incident field” as one approaches grazing angles of incidence; consequently, only half of this “total field” is the incident field. The illumination at grazing angles of incidence at an edge in a curved surface cannot be handled as easily as the case of a wedge with planar faces. Presently, one can only treat angles of incidence that are greater than $\left[\frac{2}{k\rho_g(Q_E)} \right]^{1/3}$, where $\rho_g(Q_E)$ is the radius of curvature of the surface in the direction of

the incident ray at the point of edge diffraction Q_E . Under the above restrictions, the result in Eq. (37) for D_{eh}^{es} simplifies in the case of a plane or curved screen ($n = 2$ case) to

$$D_{eh}^{es}(\phi, \phi', \beta_0) = \frac{-e^{-j\frac{\pi}{4}}}{2\sqrt{2\pi k} \sin \beta_0} \left[\sec\left(\frac{\phi - \phi'}{2}\right) F[kL^i a(\phi - \phi')] \mp \sec\left(\frac{\phi + \phi'}{2}\right) F[kL^r a(\phi + \phi')] \right] \quad (51)$$

where $a(\beta) = 2 \cos^2(\beta/2)$ and $L^{i,r}$ are as in Eqs. (43) and (44) with the understanding that L^r is evaluated at the RSB corresponding to the face that is illuminated; hence the superscripts “o” and “n” in L^r are dropped for this $n = 2$ case.

The UTD edge diffracted field $\bar{E}^d(P)$ for the 2-D situation can be obtained from Eq. (34) by allowing ρ_e to approach infinity and by requiring $\beta_0 = \pi/2$; thus, for the 2-D case,

$$\bar{E}^d(P) = \bar{E}^i(Q_E) \bullet \bar{D}_e(\phi, \phi', \pi/2; k) \frac{e^{-jks^d}}{\sqrt{s^d}} \quad (52)$$

The \bar{D}_e in Eq. (52) for the 2-D case is available from Eqs. (36) and (51) with $\beta_0 = \pi/2$ (or $\sin \beta_0 = 1$). Also, L^i for the 2-D case is given by Eq. (44) with $\beta_0 = \pi/2$; in particular,

$$L^i = \frac{s^i s^d}{s^i + s^d} \quad (53)$$

Likewise, L^r is obtained from Eq. (44) with $\beta_0 = \pi/2$, $\rho_1^r \rightarrow \infty$, $\rho_2^r \equiv \rho^r$ [as in Eq. (19)], and $\rho_e^r \rightarrow \infty$; therefore, in the 2-D case,

$$L^r = \frac{\rho^r s^d}{\rho^r + s^d} \quad (54)$$

Note that ρ^r in Eq. (54) is the same as the one in Eq. (19), as indicated above; however, ρ^r is, in general, different for the “o” and “n” faces of the wedge, with L^{ro} and L^{rn} denoting the values of L^r for these two different faces. Although the expression for L^r in Eq. (44) is fixed to its value on the RSB for convenience, the one in Eq. (54) can be evaluated as a function of the observation point with almost the same ease as if one had approximated the value of L^r by its value at the RSB. The values of L^i and L^r for the 3-D case involve various caustic distances, as is evident from Eqs. (43) and (44). These distances are generally slowly varying within the ISB and RSB transition regions, and it is therefore convenient to approximate L^i and L^r throughout the transition regions by their values fixed at the ISB and RSB, as done in Eqs. (43) and (44). Outside the respective transition regions, the F functions containing L^i and L^r approach unity and are thus unaffected by the above approximation.

It is noted that the comment below Eq. (50) in regard to grazing incidence is also valid for the 2-D case. It is important to note that the difference between \bar{D}_e and \bar{D}_e^k is that the former is range dependent whereas the latter is not. As a

result, Eq. (37) is not strictly ray optical within the ISB and RSB transition regions; exterior to these regions, $\bar{D}_e \rightarrow \bar{D}_e^k$, as indicated before. Figure 11 illustrates the diffraction of a plane wave by a perfectly conducting half-plane. It is noted that the geometrical optics field is discontinuous; however, the UTD diffracted field compensates the GO discontinuity to yield a total UTD field that is continuous.

2.4.2. Diffraction at a Smooth Convex Surface. The geometry associated with the problem of the diffraction by a smooth convex surface is shown in Fig. 12 (and also Fig. 1(e)). The total high-frequency field $\bar{E}(P)$ for the situation in Fig. 12 can be expressed as [8,29,30]

$$\bar{E}(P) = \begin{cases} \bar{E}^i(P_L)U + \bar{E}^r(P_L)U + \bar{E}^d(P_L), & \text{if } P = P_L \text{ in the lit zone} \\ \bar{E}^d(P_S)[1 - U], & \text{if } P = P_S \text{ in the shadow zone} \end{cases} \quad (55)$$

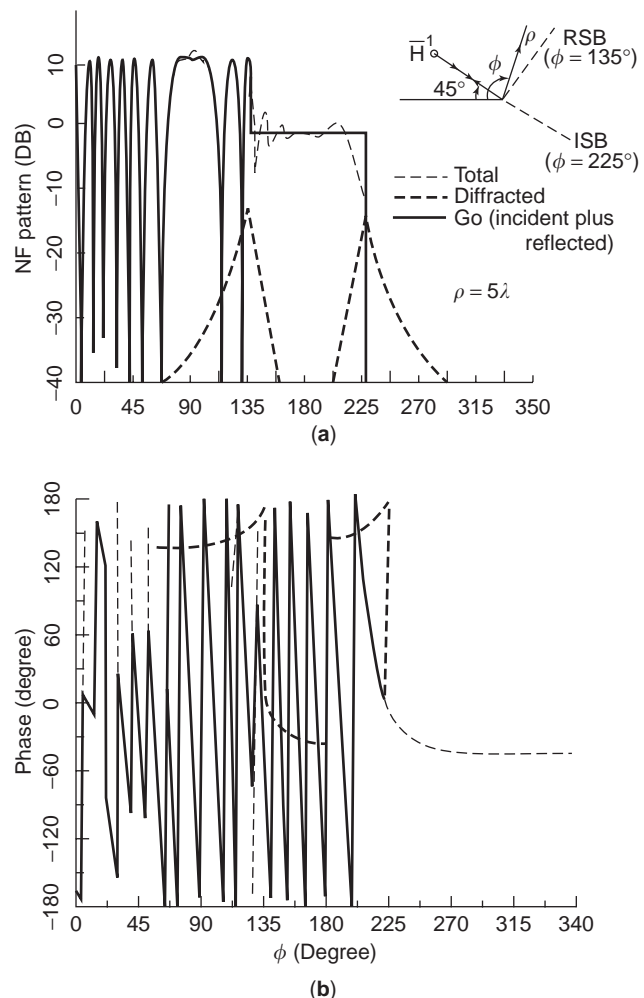


Figure 11. Continuity of the total UTD field surrounding a perfectly conducting half-plane excited by a plane wave.

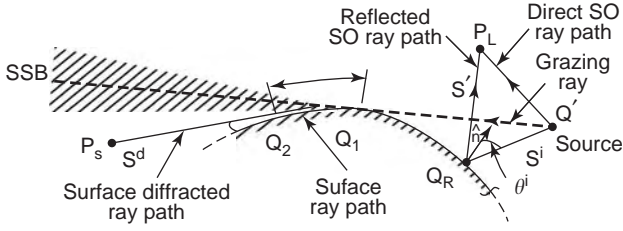


Figure 12. Diffraction at a convex surface.

The incident and reflected fields, \vec{E}^i and \vec{E}^r , are associated with the incident (direct) and reflected GO rays shown in Fig. 12. The step function U in Eq. (55) is defined below with respect to the surface shadow boundary (SSB) as

$$U = \begin{cases} 1, & \text{in the lit region which lies above} \\ & \text{the SSB where source is visible} \\ 0, & \text{in the shadow region which lies} \\ & \text{below the SSB where source is invisible} \end{cases} \quad (56)$$

The surface diffracted field $\vec{E}^d(P_S)$ follows the surface diffracted ray path into the shadow region, as in Figure 12; whereas, the field $\vec{E}^d(P_L)$, which is diffracted into the lit region, follows the reflected ray path (of \vec{E}^r) in this solution. Therefore, it is convenient here to combine the GO reflected field $\vec{E}^r(P_L)U$ and the diffracted field $\vec{E}^d(P_L)$ into a single ‘‘generalized reflected field,’’ $\vec{E}^{gr}(P_L)U$ in the lit region, so that Eq. (55) becomes

$$\vec{E}(P) = \begin{cases} \vec{E}^i(P_L)U + \vec{E}^{gr}(P_L)U, & \text{if } P = P_L \text{ in the lit zone} \\ \vec{E}^d(P_S)[1 - U], & \text{if } P = P_S \text{ in the shadow zone} \end{cases} \quad (57)$$

The fields $\vec{E}^{gr}(P_L)$ and $\vec{E}^d(P_S)$ are given symbolically by

$$\vec{E}^{gr}(P_L) \sim \vec{E}^i(Q_R) [\hat{R}_s \hat{e}_\perp \hat{e}_\perp + \hat{R}_h \hat{e}_\parallel^i \hat{e}_\parallel^r] \cdot \sqrt{\frac{\rho_1^r \rho_2^r}{(\rho_1^r + s^r)(\rho_2^r + s^r)}} e^{-jks^r} \quad (58)$$

$$\vec{E}^d(P_S) \sim \vec{E}^i(Q_1) [\hat{D}_s \hat{b}_1 \hat{b}_2 + \hat{D}_h \hat{n}_1 \hat{n}_2] \cdot \sqrt{\frac{\rho_S}{s^d(\rho_S + s^d)}} e^{-jks^d} \quad (59)$$

where the points Q_R and Q_1 and the distances s^r and s^d are indicated in Fig. 12. The surface diffracted ray caustic distance ρ_S is shown in Fig. 13. The quantities within brackets involving \hat{R}_s and \hat{D}_h in Eqs. (58) and (59) may be viewed as the generalized dyadic coefficients for surface

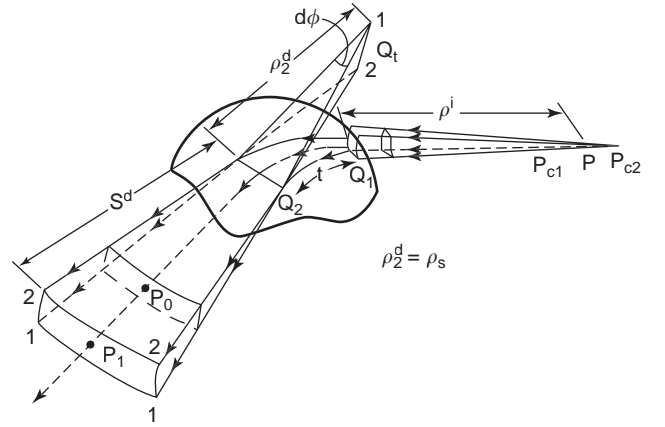


Figure 13. Surface-diffracted ray path.

reflection and diffraction, respectively. The subscripts s and h in Eq. (59) once again denote the acoustic soft and hard contributions to diffraction, respectively, as in Eqs. (34) and (37). It is noted that Eqs. (58) and (59) are expressed invariantly in terms of the unit vectors fixed in the reflected and surface diffracted ray coordinates. The unit vectors \hat{e}_\parallel^i , \hat{e}_\parallel^r , and \hat{e}_\perp in Eq. (58) have been defined earlier in connection with the reflected field. It can be shown that cross terms actually exist in the above generalized dyadic reflection coefficient; but, in general, their effect is seen to be weak within the SSB transition region. Also, these cross terms vanish in the deep lit region and on the SSB, hence, they have been ignored in Eq. (58).

At Q_1 , let \hat{t}_1 be the unit vector in the direction of incidence, \hat{n}_1 be the unit outward normal vector to the surface, and $\hat{b}_1 = \hat{t}_1 \times \hat{n}_1$; likewise, at Q_2 , let a similar set of unit vectors ($\hat{t}_2, \hat{n}_2, \hat{b}_2$) be defined with \hat{t}_2 in the direction of the diffracted ray as in Fig. 14. In the case of surface rays with zero torsion, $\hat{b}_1 = \hat{b}_2$. It is clear from Fig. 13 that ρ_S in Eq. (59) is the wavefront radius of curvature of the surface diffracted ray evaluated in the \hat{b}_2 direction at Q_2 . First, the UTD expressions for \hat{R}_s and \hat{D}_h in Eqs. (58) and (59) will be given below; it will be shown that these expressions are valid within the transition region adjacent to the SSB. Subsequently, it will be shown how these expressions automatically simplify outside the SSB transition region to

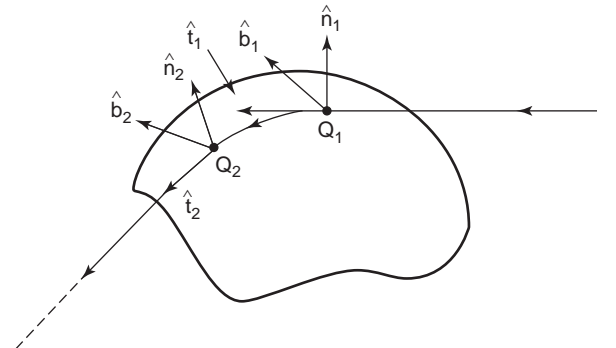


Figure 14. Unit vectors fixed in the surface ray.

reduce to those obtained by Keller in his GTD representation. The R_h and D_h in Eqs. (58) and (59) are

$$\tilde{R}_h = - \left[\sqrt{\frac{-4}{\zeta^L}} e^{-j(\zeta^L)^3/12} \left[\frac{e^{-j\pi/4}}{2\sqrt{\pi}\zeta^L} [1 - F(x^L)] + \tilde{P}_h(\zeta^L) \right] \right] \quad (60)$$

for the lit region

and

$$\begin{aligned} \tilde{D}_h = & - \left[\sqrt{m(Q_1)m(Q_2)} \sqrt{\frac{2}{k}} \frac{e^{-j\pi/4}}{2\sqrt{\pi}\zeta} [1 - F(x^d)] + \tilde{P}_h(\zeta) \right] \\ & \cdot \sqrt{\frac{d\eta(Q_1)}{d\eta(Q_2)}} e^{-jkt} \text{ for the shadow region} \end{aligned} \quad (61)$$

The function F appearing above has been defined earlier in Eq. (47). The Fock-type surface reflection function \tilde{P}_h is related to the (soft) Pekeris function (p^*) by

$$\tilde{P}_h(\delta) = \left\{ \begin{matrix} p^*(\delta) \\ q^*(\delta) \end{matrix} \right\} e^{-j\frac{\pi}{4}} - \frac{e^{-j\frac{\pi}{4}}}{2\sqrt{\pi}\delta} \quad (62)$$

(Note that $\delta = 0$ at SSB)

where p^* and q^* are finite and well behaved even when $\delta = 0$; these universal functions are plotted in Figs 15 and 16. Also,

$$\begin{aligned} \tilde{P}_h(\delta) &= \frac{e^{-j\frac{\pi}{4}}}{\sqrt{\pi}} \int_{-\infty}^{\infty} d\tau \frac{\tilde{Q}V(\tau)}{\tilde{Q}W_2(\tau)} e^{-j\delta\tau} \\ \tilde{Q} &= \left\{ \begin{matrix} 1, & \text{soft case (h)} \\ \frac{\partial}{\partial\tau}, & \text{hard case (v)} \end{matrix} \right\} \end{aligned} \quad (63)$$

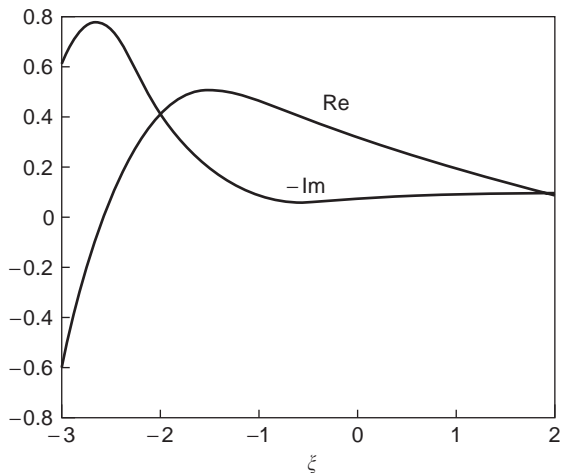


Figure 15. Plot of $e^{-j\pi/4}p^*(\zeta)$ versus ζ .

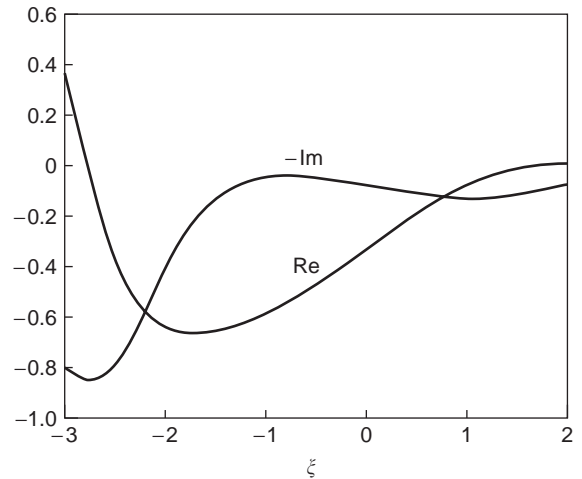


Figure 16. Plot of $e^{-j\pi/4}q^*(\zeta)$ versus ζ .

in which the Fock-type Airy functions are

$$\begin{aligned} 2jV(\tau) &= W_1(\tau) - W_2(\tau); \\ W_1(\tau) &= \frac{1}{\sqrt{\pi}} \int_{\infty e^{-j2\pi/3}}^{\infty} e^{t\tau - t^3/3} dt \end{aligned} \quad (64)$$

$$W_2(\tau) = \frac{1}{\sqrt{\pi}} \int_{\infty e^{j2\pi/3}}^{\infty} e^{t\tau - t^3/3} dt \quad (65)$$

The rest of the quantities occurring in Eqs. (60) and (61) are

$$\zeta^L = -2m(Q_R) \cos \theta^i; \quad \zeta = \int_{Q_1}^{Q_2} dt' \frac{m(t')}{\rho_g(t')} \quad (66)$$

$$m(\bullet) = \left[\frac{k\rho_g(\bullet)}{2} \right]^{1/3}$$

$$t = \int_{Q_1}^{Q_2} dt'; \quad X^L = 2kL \cos^2 \theta^i; \quad X^d = \frac{kL\zeta^2}{2m(Q_1)m(Q_2)} \quad (67)$$

The quantity $\rho_g(Q_R)$ in $m(Q_R)$ denotes the surface radius of curvature at Q_R in the plane of incidence; whereas, $\rho_g(Q_{1,2})$ is the surface radius of curvature at $Q_{1,2}$ in the $\hat{t}_{1,2}$ direction. The dt' in Eqs. (66) and (67) is an incremental arc length along the surface ray path that must be a surface geodesic in accordance with Keller's generalization of Fermat's principle for diffracted rays. The angle of incidence θ^i is shown in Fig. 12. Also, the $d\eta(Q_1)$ and $d\eta(Q_2)$ in Eq. (61) denote the widths of the surface ray tube at Q_1 and Q_2 , respectively; the surface ray tube is formed by considering a pair of rays adjacent to the central ray, as in Fig. 13. The geodesic surface ray paths are easy to find on cylinders, spheres, and cones. For example, they are helical paths on cylinders and great circles on spheres. For arbitrary convex surfaces, the geodesic surface ray paths must be found numerically. The distance

parameter L in Eq. (67) is given by

$$L = \frac{\rho_1^i(Q_1)\rho_2^i(Q_1)}{(\rho_1^i(Q_1) + s)(\rho_2^i(Q_1) + s)} \cdot \frac{s(\rho_b^i(Q_1) + s)}{\rho_b^i(Q_1)} \quad (68)$$

where

$$s \equiv (s^r|_{SSB} = s^d|_{SSB});$$

$$\rho_b^i(Q_1) = \left\{ \begin{array}{l} \text{incident wavefront radius of curvature} \\ \text{in the } \hat{b}_1 \text{ direction at } Q_1 \end{array} \right\} \quad (69)$$

The distance s in Eq. (69) may be obtained by projecting $(s^r|_{SSB})$ on the SSB if the observation point within the ($\text{lit}_{\text{shadow}}$) side of the SSB transition region does not move in a predetermined manner. If the observation point moves across the SSB in a predetermined fashion, then it is clear that s in Eq. (69) can be found unambiguously. The $\rho_1^i(Q_1)$ and $\rho_2^i(Q_1)$ in Eq. (68) denote the principal radii of curvature of the incident wavefront at Q_1 , and ρ_b^i , which is defined in Eq. (69), has been mentioned previously in Eq. (16b). For the special case of point source or spherical wave illumination, the L in Eq. (67) simplifies to

$$L = \frac{s's}{s' + s} \text{ for spherical wave illumination} \quad (70)$$

where

$$s' \equiv (\rho_1^i(Q_1) = \rho_2^i(Q_1) = \rho_b^i(Q_1))$$

$$= \left\{ \begin{array}{l} \text{distance from the point source to} \\ \text{the point of grazing incidence at } Q_1 \end{array} \right\} \quad (71)$$

For the case of plane wave illumination, $s' \rightarrow \infty$, and hence Eq. (70) simplifies to

$$L = s \text{ for plane wave illumination} \quad (72)$$

If the incident wavefront is of the converging type ($\rho_{1,2}^i < 0$), or converging-diverging type ($\rho_1^i \geq 0; \rho_2^i \leq 0$), then the parameter L in Eq. (67) can become negative. It has not been fully investigated how the general solution can be completed if L becomes negative. On the other hand, if one of the principle directions of the incident wavefront coincides with one of the principal planes of surface at grazing, then one can treat a converging, or converging-diverging (saddle) type wavefront for which $L < 0$ by replacing $F(X^{L,d})$ with $F^*(|X^{L,d}|)$. Note that the asterisk in F^* denotes the complex conjugate operator. The use of $F^*(|X^{L,d}|)$ when $L < 0$ leads to a continuous total field at SSB in this case.

The above UTD result is valid outside the paraxial (i.e., near axial) regions of quasicylindrical or elongated convex

surfaces; a different solution is required in the paraxial region, and it has not yet been completed. It is assumed that the source and observation points are not too close to the surface. Also, it is assumed that any caustics of the incident ray system are not too close to the surface. Furthermore, the amplitude of the incident field is assumed to be slowly varying at Q_R and Q_1 ; otherwise, it is necessary to add a slope diffraction contribution. The UTD solution described above remains accurate if kL and m are sufficiently large. Typically, kL should be larger than 3, although, in some cases, kL can be made smaller. Also, m should be such that $2m^3 > 5$ or so; however, the results generally lose their accuracy slowly as $2m^3$ becomes smaller. It is noted that the angular extent of the SSB transition region is of order m^{-1} radians.

A surface diffracted field of the type $\bar{E}^d(P_S)$ can also be present in the lit zone if the surface is closed; this may be seen noting that the field of the type \bar{E}^d can propagate around the closed surface. Also, additional contributions to $\bar{E}^d(P_S)$ can be present in the shadow zone for a closed surface because surface diffracted rays can be initiated at all points of grazing incidence on that closed surface; furthermore, these surface rays can undergo multiple encirclements around a closed body. However, these additional surface diffracted ray contributions are generally quite weak in comparison with the \bar{E}^{gr} contribution within the lit zone for surfaces that are quite large in terms of the wavelength; hence their contribution may be neglected in such cases.

The parameters ζ^L , ξ , X^L , and X^d become small as one approaches the surface shadow boundary, SSB, from both the lit and shadow regions. As one approaches the SSB, the small argument limiting form of the transition function $F(x)$, which has been introduced previously in Eq. (49), becomes helpful for verifying the continuity of the total high-frequency field at the SSB. On the other hand, the above parameters become large as one moves outside the SSB transition region; in this case, \hat{R}_s reduces to $R_s = \mp 1$ outside the SSB transition region, so that $\bar{E}^{gr}(\hat{P}_L) \rightarrow \bar{E}^r(P_L)$ of GO, and likewise $\bar{E}^d(P_S) \rightarrow \bar{E}_k^d(P_S)$ therein, respectively, in which the Keller surfaced diffracted ray field $\bar{E}_k^d(P_S)$ is given by [1,3,31]

$$\bar{E}_k^d(s) \sim \bar{E}^i(Q_1) \cdot \bar{T}^k(Q_1, Q_2) e^{-jkt}$$

$$\cdot \sqrt{\frac{d\eta(Q_1)}{d\eta(Q_2)}} \sqrt{\frac{\rho_s}{s^d(\rho_s + s^d)}} e^{-jks^d} \quad (73)$$

$$\bar{T}^k(Q_1, Q_2) = [\hat{b}_1 \hat{b}_2 T_s + \hat{n}_1 \hat{n}_2 T_h] \quad (74)$$

where

$$T_{s,h} = \sum_{n=1}^N D_n^{s,h}(Q_1) e^{-\int_{Q_1}^{Q_2} \alpha_n^{s,h}(t') dt'} D_n^{s,h}(Q_2) \quad (75)$$

The D_n^s and α_n^s are the Keller's GTD diffraction coefficients and attenuation constants for the n th soft (s) or hard (h)

surface ray mode. Thus, in the GTD, the surface ray field consists of surface ray modes that propagate independently of one another. Also, this surface ray field is not the true field on the surface; it is a boundary layer field. The GTD result of Eq. (73) in terms of Eqs. (74) and (75) is not valid within the SSB transition region. On the other hand, the UTD result of Eqs. (58) and (59) in terms of Eqs. (60) and (61) is indeed valid and continuous across the SSB.

The UTD result for the 3-D configuration can be simply modified to recover the corresponding UTD result for the 2-D case by allowing the caustic distances ρ_1^r and ρ_s in Eqs. (58) and (59) to recede to infinity. Then, let

$$\rho_2^r \equiv \rho^r \text{ if } \rho_1^r \rightarrow \infty \text{ and } \rho_s \rightarrow \infty \quad (76)$$

so that

$$\vec{E}^{gr}(P_L) \approx \vec{E}^i(Q_R) \cdot [\vec{R}_s \hat{e}_\perp \hat{e}_\perp + \vec{R}_h \hat{e}_\parallel^i \hat{e}_\parallel^r] \sqrt{\frac{\rho^r}{\rho^r + s^r}} e^{-jks^r} \quad (77)$$

in which ρ^r is as in Eq. (19), and

$$\vec{E}^d(P_s) \approx \vec{E}^i(Q_1) \cdot [\vec{D}_s \hat{b} \hat{b} + \vec{D}_h \hat{n}_1 \hat{n}_2] \frac{e^{-jks^d}}{\sqrt{s^d}} \quad (78)$$

because $[\hat{b}_1 = \hat{b}_2 \equiv \hat{b}$ for the 2-D case (note: $\hat{b} = \hat{e}_\perp$)]. The \vec{R}_s and \vec{D}_s in Eqs. (77) and (78) are as defined earlier, respectively; only the L appearing in Eq. (67) is given by

$$L = \frac{s' s^d}{s' + s^d} \text{ for the 2-D case} \quad (79)$$

where s' is the distance from the 2-D line source to the point of grazing incidence at Q_1 and $s \equiv s^d|_{SSB}$ as before. A comparison of the UTD and GTD solutions for a 2-D circular cylinder illuminated by a nearby line source is

illustrated in Figs. 17(a) and 17(b); those UTD solutions are then compared with the corresponding exact (Eigenfunction) solutions in Figs. 18(a) and 18(b).

2.4.3. Some Additional Diffraction Problems. Sections 2.4.1 and 2.4.2 focused on the important problems of diffraction by edges and smooth convex surfaces (with source and observer both off the surface). Also important are the problems of radiation and mutual coupling associated with conformal antennas and arrays located directly on a smooth convex metallic surface. In the convex surface problem of Section 2.4.2, the source and observer must be at least a few wavelengths away from the surface. On the other hand, either the source or the observer must lie on the convex boundary for the conformal antenna radiation(transmitting)/receiving cases, respectively, whereas both the source and the observer must lie on the convex boundary for the calculation of the mutual coupling between a pair of conformal antenna elements. The rays encountered in the radiation and mutual coupling associated with antennas located conformally on a convex surface are shown in [32,33]. The UTD ray field expressions for the latter two cases are available in [8,32–35]. It is noted that surface rays in general exhibit torsion (or twist) giving rise to interesting polarization effects. The problem of scattering by a smooth convex surface discussed earlier in Section 2.4.2, where neither the source nor the observer lies on the surface, does not contain such torsional ray effects in terms of an explicit torsion factor in the solution even though the surface rays may be torsional. However, the solutions to the problems of radiation and mutual coupling where either the source or observer lies on the surface, and where both the source and observer lie on the surface, respectively, contain explicit torsion factors [8,32,33].

The HF diffraction by the tip of a metallic plane angular sector, as in Fig. 19, or by the tip of a metallic

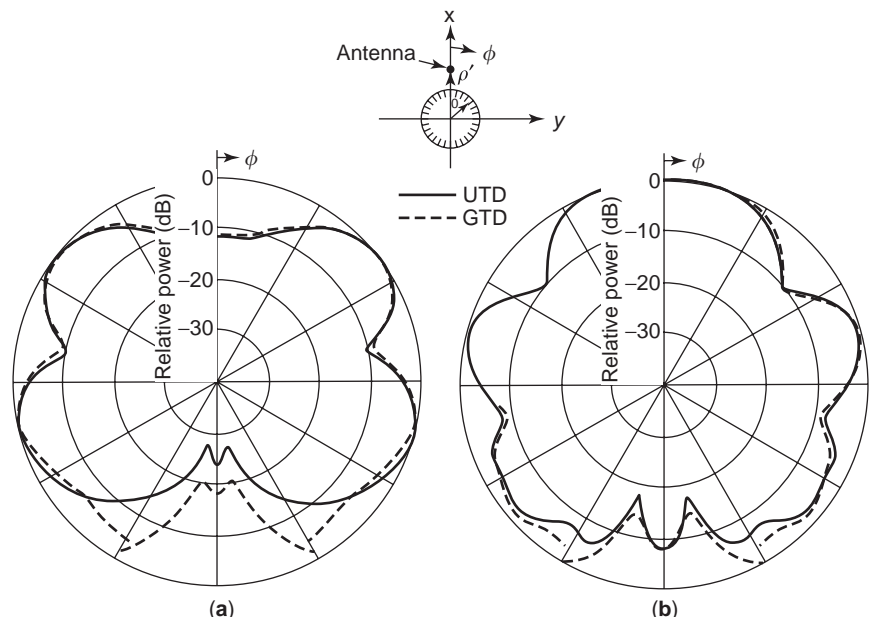


Figure 17. Comparison between GTD and UTD solutions for the radiation by electric (a) and magnetic (b) line sources in the presence of a circular cylinder. Here, $a = 1\lambda$ and $\rho' = 2\lambda$.

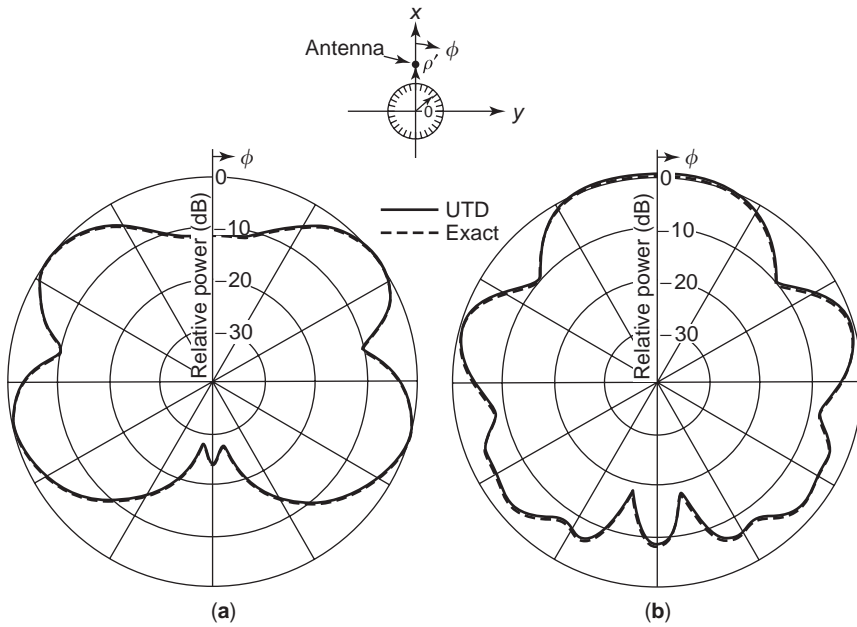


Figure 18. Comparison of UTD solutions of Fig. 16 with exact (eigenfunction) solutions.

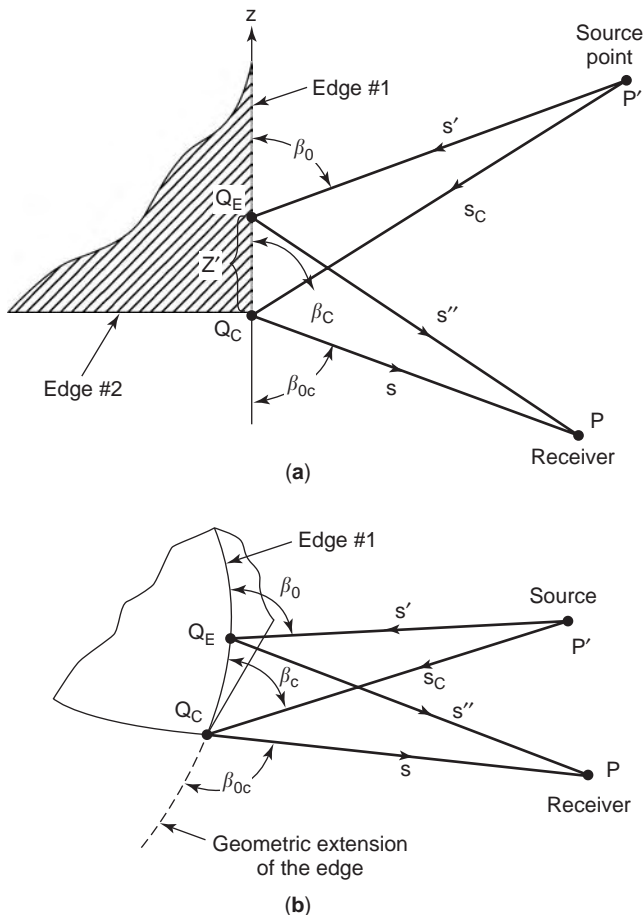


Figure 19. Geometry for the corner diffraction case (a) Corner in a planar surface (b) Corner in a nonplanar surface. (After Sikta, Burnside, Chu and Peters, ©1983 IEEE Trans AP.)

cone, as in Fig. 20, respectively, have been addressed with some limited success to date. Such problems are far more complex to solve. However, tip diffraction problems including the diffraction by the tip of a metallic pyramidal or other complex surfaces remain to be attacked for providing useful UTD solutions in a fairly accurate and tractable manner for all aspects of incidence and scattering. Some interesting work in this area of high-frequency tip diffraction can be found in [36–47]. One notes that tip diffraction is generally not as strong as edge diffraction except in the shadow boundary transition regions that develop when an edge or surface terminates at a tip.

Although all of the above work discussed thus far in Sections 2.4.1, 2.4.2 and 2.4.3 is limited to perfectly conducting structures, far less work has been performed to date on developing sufficiently general UTD or uniform asymptotic HF solutions for nonperfectly conducting (i.e., nonmetallic) surfaces. Some work in this area involves the diffraction by wedges and cylinders with impedance boundary conditions [12,48–52]. The impedance boundary

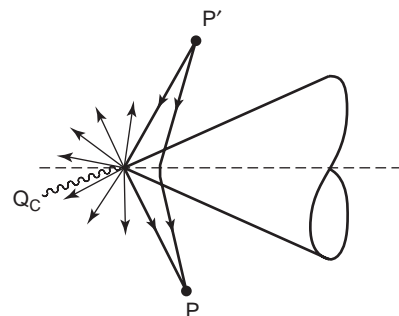


Figure 20. Rays diffracted by a cone.

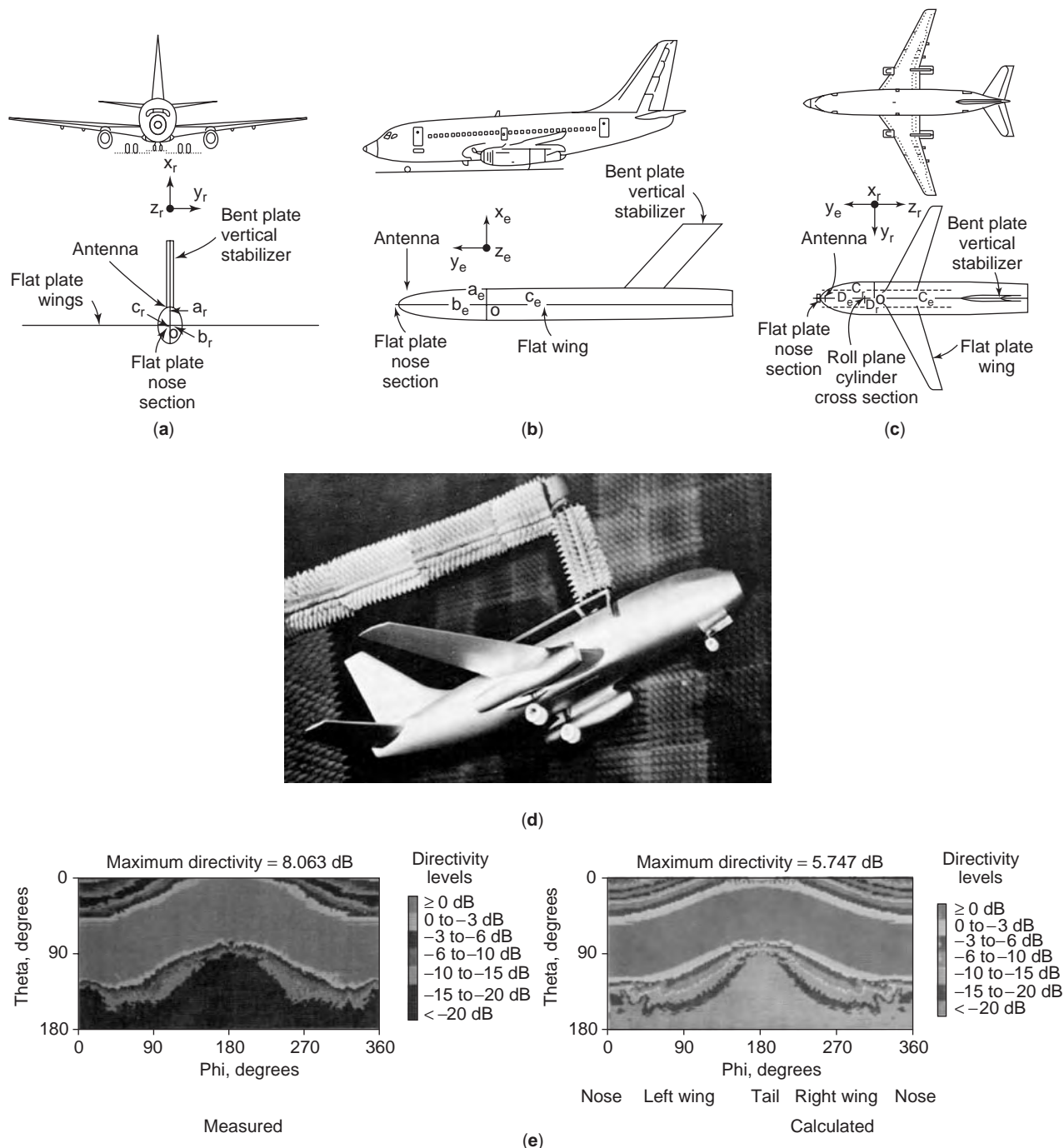


Figure 21. Modeling of Boeing 737 aircraft for radiation pattern simulations using OSU’s aircraft pattern prediction code. UTD calculations are validated using scale model measurements. The aircraft geometry is approximated to meet UTD assumptions. (a) Roll Plane Simulation, (b) Elevation plane simulation, (c) Azimuthal plane simulation, (d) 1:11 Scale model of Boeing 737, (e) Volumetric directive gain pattern of a monopole at station 220 a Boeing 737.

conditions simulate the effect of thin material coatings on metallic structures. Clearly, more work needs to be done in developing more rigorous and more general UTD solutions for nonmetallic canonical problems to further extend the applicability of the UTD ray technique for solving an even larger class of practical EM problems.

More recently, the development of GTD/UTD has been extended to treat the HF radiation from large, finite planar periodic arrays of antenna elements and frequency selective surface (FSS) elements, as well as similar large conformal periodic arrays on even larger cylindrical host structures, where the radiation from the entire large,

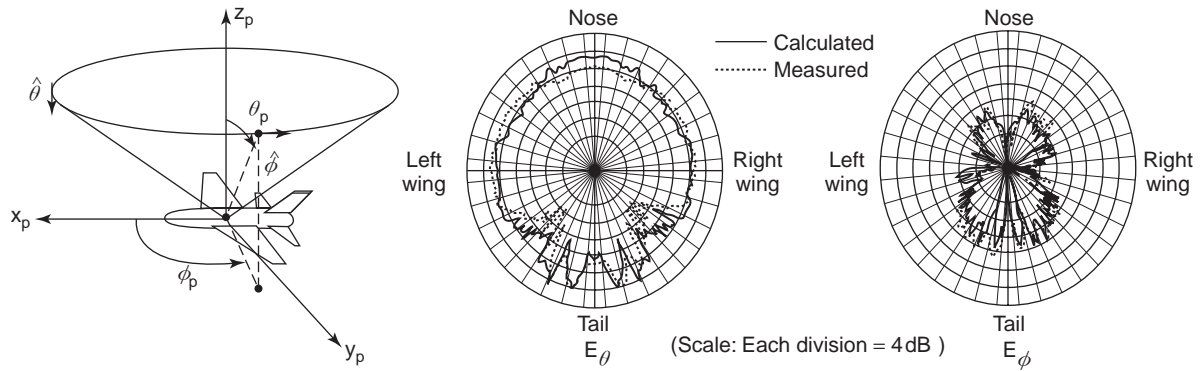


Figure 22. Radiation Pattern of F-16 Monopole antenna mounted on fuselage just behind the cockpit. Again here the plane geometry is approximated to meet UTD assumptions.

finite array can be described in terms of just a few rays [53–56], thus providing a useful picture for array radiation/scattering. In contrast, conventional approaches employ an array element by element field summation method

that, besides being inefficient, hides any physical insights into the large array radiation mechanisms.

Some references to related work on UTD for interior waveguide discontinuity problems may be found in

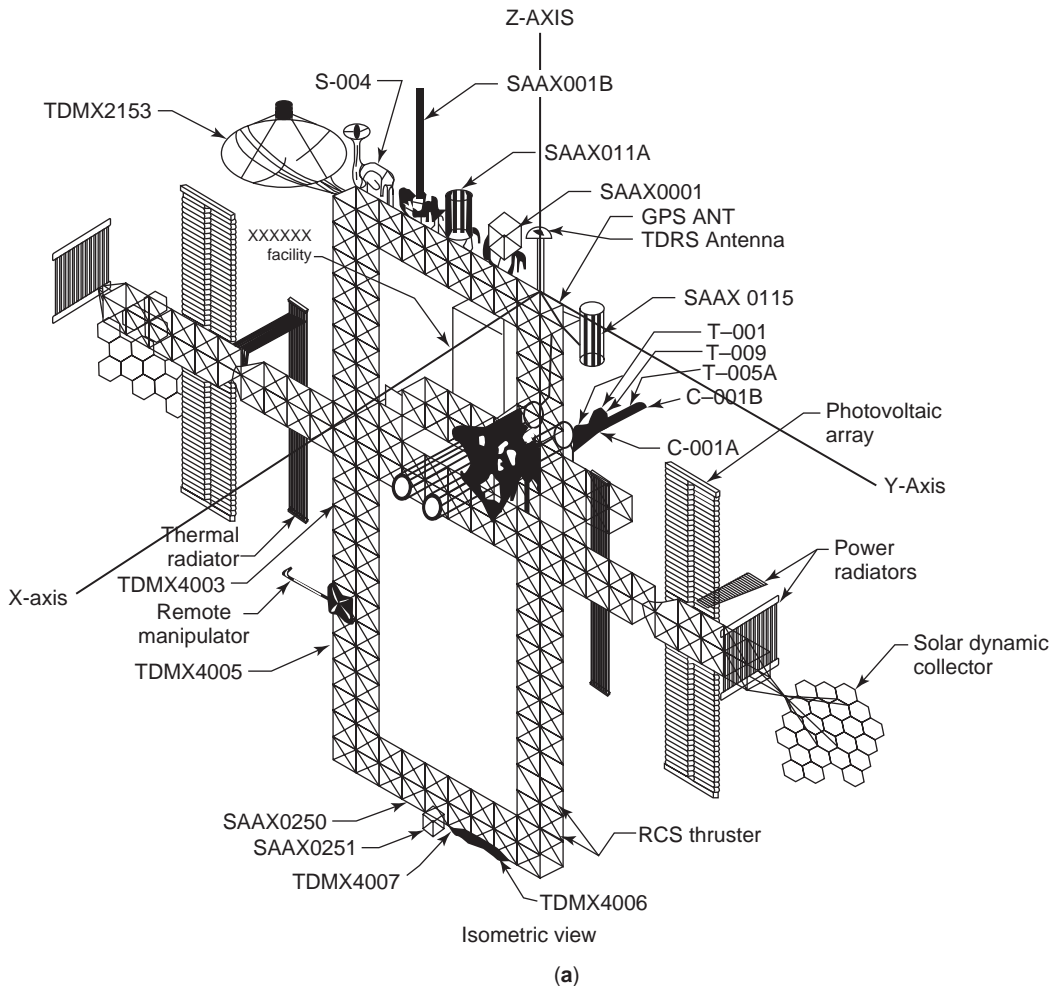


Figure 23. GPS antenna patterns with space station structure located on upper boom near TDRS ant. support boom. (a) International Space Station, (b) GPS Antenna and local UTD model of the International Space Station, (c) Measured and calculated patterns.

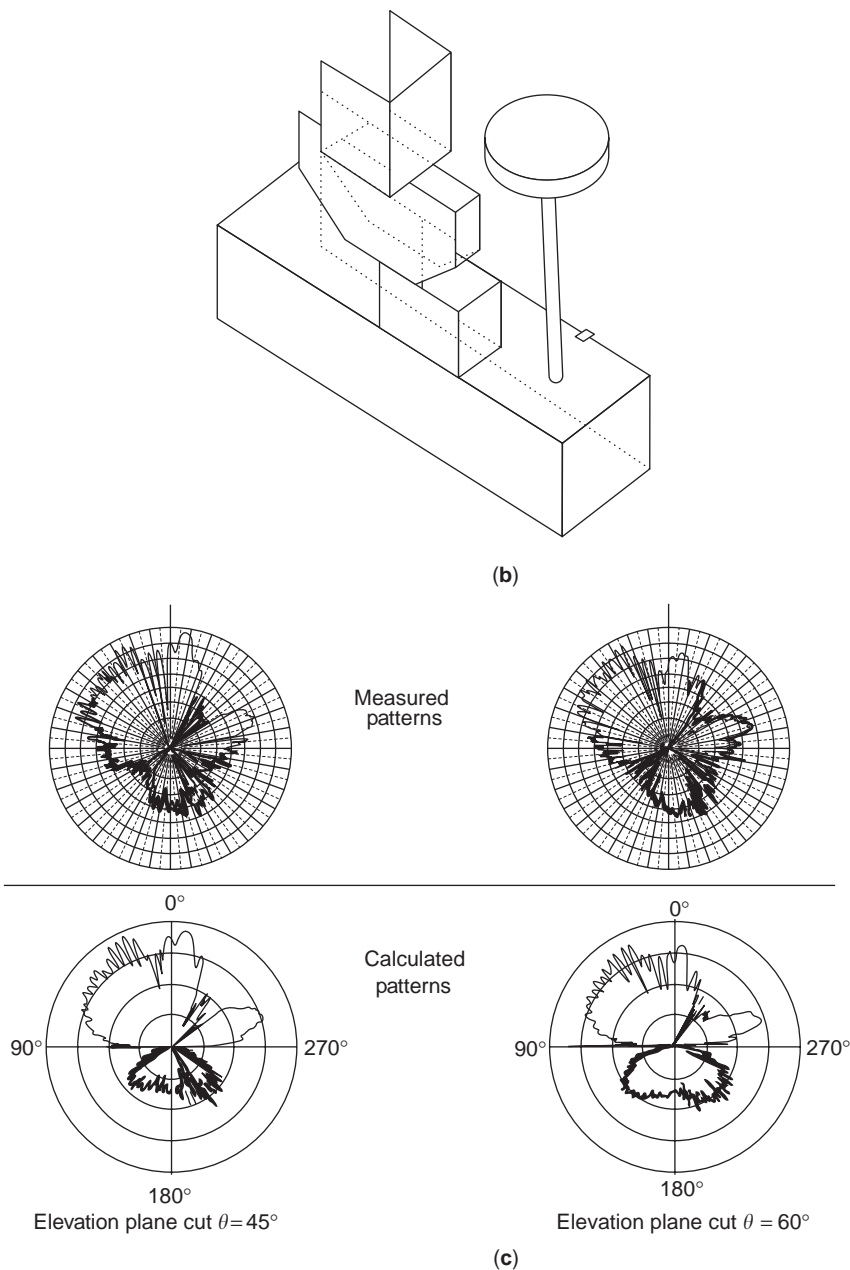


Figure 23. (Continued).

[57–61]. Also, additional general references to ray methods, such as GO, UTD, and other high-frequency methods such as the equivalent current method (ECM) and PO/PTD, are included [62–79]. Finally, some books that discuss specific HF methods, or HF methods in general, may be found in [28,80–88].

3. SOME ADDITIONAL NUMERICAL EXAMPLES

In Section 2, some simple examples were indicated to illustrate the accuracy of the GTD/UTD. The application of UTD to deal with a slightly more complex antenna problem of how its pattern is affected by a finite ground

plane is available in [89]. More complex problems of radiation by horn and large reflector antennas have been treated successfully by the UTD; these are summarized in [90–92]. Reference [91] also contains examples illustrating the accurate prediction of the pattern of antennas on aircraft in a relatively efficient manner by the UTD, as given in [93,94]. An example of the radiation by a monopole antenna placed just behind the cockpit on a Boeing 737 aircraft and as predicted by the UTD is shown in Fig. 21. The UTD result is compared with a model measurement in Fig. 21. This latter work [94] is based on the NEWAIR code written at the Ohio State University ElectroScience Laboratory by Prof. Burnside and his coworkers; the NEWAIR aircraft antenna code [95] is based on the

UTD. The good agreement between the predicted and measured patterns is readily evident in Fig. 21. Another example is that of the UTD analysis of an antenna on an F-16 fighter plane; the results are shown in Fig. 22 and are taken from [93]. The next example deals with the UTD analysis of an antenna near a space station model. This latter work is based on the NEC-BSC code [96] written by Dr. Marhefka and his coworkers at the Ohio State University ElectroScience Laboratory. The agreement between the UTD analysis of the space station antenna pattern and the corresponding model measurement [97] is also very good, as seen from Fig. 23.

NOTE: Some relevant references may have been left out inadvertently. The author regrets any oversight.

BIBLIOGRAPHY

- J. B. Keller, Geometrical theory of diffraction, *J. Opt. Soc. Am.*, **52**:116–130 (1962).
- J. B. Keller, A geometrical theory of diffraction, in L. M. Graves, ed., *Calculus of Variations and Its Applications*, McGraw-Hill, New York, 1958, pp. 2–52.
- R. G. Kouyoumjian, Asymptotic high-frequency methods, *Proc. IEEE*, **53**:864–876 (1965).
- T. Young, *Phil. Trans. Royal Soc.*, **20**:26 (1802).
- A. Fresnel, *Ann. Chim. Et Phys.*, **1**:239 (1816).
- R. G. Kouyoumjian and P. H. Pathak, A uniform geometrical theory of diffraction for an edge in a perfectly conducting surface, *Proc. IEEE*, **62**:1448–1461 (1974).
- R. G. Kouyoumjian and P. H. Pathak, A uniform GTD approach to EM scattering and radiation, in V. J. Varadan and V. V. Varadan, eds., *Acoustic, Electromagnetic and Elastic Wave Scattering—High and Low Frequency Asymptotics*, Vol. 2, North Holland, Amsterdam, The Netherlands, 1986.
- P. H. Pathak, Techniques for high frequency problems, in Y. T. Lo and S. W. Lee, eds., *Antenna Handbook, Theory Application and Design*, Van Nostrand Reinhold, New York, 1988.
- D. S. Ahluwalia, R. M. Lewis, and J. Boersma, Uniform asymptotic theory of diffraction by a plane screen, *SIAM J. Appl. Math.*, **16**:783–807 (1968).
- S. W. Lee and G. A. Deschamps, A uniform asymptotic theory of EM diffraction by a curved wedge, *IEEE Trans. Ant. Prop.*, **24**:25–34 (1976).
- S. W. Lee, Ray theory of diffraction by open-ended waveguides: applications, *J. Math. Phys.*, **13**:656–664 (1972).
- T. B. A. Senior and J. L. Volakis, Approximate boundary conditions in electromagnetics, *IEE Electromagn. Wave Ser.*, **41**:1995.
- L. M. Brekhovskikh, *Waves in Layered Media*, sec. 21–23, Academic Press, New York, 1960.
- F. Bertocini, R. Kouyoumjian, G. Manara, and P. Nepa, High-frequency scattering by objects buried in lossy media, *IEEE Trans. Ant. Prop.*, **49**:1649–1656 (2001).
- P. H. Pathak and M. C. Liang, On a uniform asymptotic solution valid across smooth caustics of rays reflected by smoothly indented boundaries, *IEEE Trans. Ant. Prop.*, **38**:1192–1203 (1990).
- E. D. Constantinides and R. J. Marhefka, A UGO/EUTD solution for the scattering and diffraction from cubic polynomial strips, *IEEE Trans. Ant. Prop.*, **41**:1088–1098 (1993).
- R. F. Millar, An approximate theory of the diffraction of an electromagnetic wave by an aperture in a plane screen, *Proc. Inst. Elect. Eng.*, **103C**:177–185 (1956).
- C. E. Ryan Jr. and L. Peters Jr., Evaluation of edge diffracted fields including equivalent currents for caustic regions, *IEEE Trans. Ant. Prop.*, **17**:292–299 (1969). Correction, *IEEE Trans. Ant. Prop.*, **18**:275 (1970).
- E. F. Knott and T. B. A. Senior, Comparison of three high-frequency diffraction techniques, *Proc. IEEE*, **22**:1468–1478 (1974).
- K. M. Mitzner, *Incremental Length Diffraction Coefficients*, Aircraft Div., Northrop Corp. Tech. Rep. AFAL-TR-73-296 1974.
- A. Michaeli, Elimination of infinities in equivalent edge currents, part I, *IEEE Trans. Ant. Prop.*, **34**:912–918 (1986).
- A. Michaeli, Elimination of infinities in equivalent edge currents, part II, *IEEE Trans. Ant. Prop.*, **34**:1034–1037 (1986).
- R. A. Shore and A. D. Yaghjian, Incremental diffraction coefficients for planar surfaces, *IEEE Trans. Ant. Prop.*, **36**:55–70 (1988).
- R. Tiberio, S. Maci, and A. Toccafondi, An incremental theory of diffraction: electromagnetic formulation, *IEEE Trans. Ant. Prop.*, **43**:87–96 (1995).
- P. Ya. Ufimtsev, Method of edge waves in the physical theory of diffraction, *Izd-Vo Sov. Radio*, **1**:243 (1962) [In Russian: translation prepared by the U.S. Air Force Foreign Technology Division, Wright Patterson AFB, Ohio; released for public distribution Sep. 7, 1971.]
- D. I. Butorin and P. Ya. Ufimtsev, *Sov. Phys. Acoust.*, **32**: (1986).
- G. A. Deschamps, Ray techniques in electromagnetics, *Proc. IEEE*, **60**:1022–1035 (1972).
- L. B. Felsen and N. Marcuvitz, *Radiation and Scattering of Waves*, Prentice-Hall, Englewood Cliffs, NJ, 1973.
- P. H. Pathak, An asymptotic analysis of the scattering of plane waves by a smooth convex cylinder, *Radio Sci.*, **14**:419–435 (1979).
- P. H. Pathak, W. D. Burnside, and R. J. Marhefka, A uniform UTD analysis of the diffraction of electromagnetic waves by a smooth convex surface, *IEEE Trans. Ant. Prop.*, **28**:609–622 (1980).
- B. R. Levy and J. B. Keller, Diffraction by a smooth object, *Commun. Pure Appl. Math.*, **12**:159–209 (1959).
- P. H. Pathak, N. Wang, W. D. Burnside, and R. G. Kouyoumjian, A uniform GTD solution for the radiation from sources on a convex surface, *IEEE Trans. Ant. Prop.*, **29**:609–621 (1981).
- P. H. Pathak and N. Wang, Ray analysis of mutual coupling between antennas on a convex surface, *IEEE Trans. Ant. Prop.*, **29**:911–922 (1981).
- S. W. Lee, Mutual admittance of slots on a cone: solution by ray technique, *IEEE Trans. Ant. Prop.*, **26**:768–773 (1978).
- P. H. Pathak, A. Ghantous, C. W. Chuang, and O. M. Buyukdura, *A Preliminary Investigation of Conformal Antenna Phased Arrays on Perfectly-Conducting Convex Surfaces*, The Ohio State Univ. ElectroScience Laboratory, Tech. Rep. 717060-2, 1985.
- K. C. Hill, *A UTD solution to the EM Scattering by the Vertex of a Perfectly Conducting Plane Angular Sector*, Ph.D. dissertation, Dept. of Electrical Engineering, Ohio State University, 1990.
- L. B. Felsen, Alternative representations in regions bounded by spheres, cones and planes, *IRE Trans. Ant. Prop.*, **5**:109–121 (1957).

38. L. B. Felsen, Plane wave scattering by small angle cones, *IRE Trans. Ant. Prop.*, **5**:121–129 (1957).
39. L. B. Felsen, Asymptotic expansion of the diffracted wave for a semi-infinite cone, *IRE Trans. Ant. Prop.*, **5**:402–404 (1957).
40. K. E. Golden, G. E. Stewart, and D. C. Pridmore-Brown, Approximation techniques for the mutual admittance of slot antennas on metallic cones, *IEEE Trans. Ant. Prop.*, **22**:43–48 (1974).
41. A. S. Goryainov, Diffraction of a plane electromagnetic wave propagating along the axis of a cone, *Radio Eng. Electron.*, **6**: (1961).
42. K. D. Trott, P. H. Pathak, and F. A. Molinet, A UTD type analysis of the plane wave scattering by a fully illuminated perfectly conducting cone, *IEEE Trans. Ant. Prop.*, **38**: 1150–1160 (1990).
43. V. Babich, D. Dement'ev, and B. Samokish, On the diffraction of high-frequency waves by a cone of arbitrary shape, *Wave Motion*, **21**:203–207 (1995).
44. V. M. Babich, V. P. Smyshlyaev, D. B. Dement'ev, and B. A. Samokish, Numerical calculation of the diffraction coefficients for an arbitrary shaped perfectly conducting cone, *IEEE Trans. Ant. Prop.*, **44**:740–747 (1996).
45. T. Brinkley, *Current near the Vertex of a Perfectly Conducting Angular Sector*, Ph.D. dissertation, Dept. of Electrical Engineering, Ohio State University, 1991.
46. F. Capolino and S. Maci, Uniform high-frequency description of singly, doubly, and vertex diffracted rays for a plane angular sector, *J. EM Waves Appl.*, **10**:1175–1197 (1996).
47. D. C. Pridmore-Brown and G. E. Stewart, Radiation from slot antennas on cones, *IEEE Trans. Ant. Prop.*, **20**:36–39 (1972).
48. R. G. Rojas, Electromagnetic diffraction of an obliquely incident plane wave field by a wedge with impedance faces, *IEEE Trans. Ant. Prop.*, **36**:956–970 (1988).
49. R. G. Rojas and P. H. Pathak, Diffraction of EM waves by a dielectric/ferrite half-plane and related configurations, *IEEE Trans. Ant. Prop.*, **37**:751–763 (1989).
50. J. L. Volakis and T. B. A. Senior, Diffraction by a thin dielectric half plane, *IEEE Trans. Ant. Prop.*, **35**:1483–1487 (1987).
51. R. Tiberio, G. Pelosi, G. Manara, and P. H. Pathak, High frequency scattering from a wedge with impedance faces illuminated by a line source: Part I diffraction, *IEEE Trans. Ant. Prop.*, **37**:212–218 (1989).
52. G. Manara, R. Tiberio, G. Pelosi, and P. H. Pathak, High frequency scattering from a wedge with impedance faces illuminated by a line source: Part II surface wave, *IEEE Trans. Ant. Prop.*, **41**:877–883 (1993).
53. L. Carin and L. B. Felsen, Time harmonic and transient scattering by finite periodic flat strip arrays: hybrid(ray)-(Floquet mode)-(MOM) algorithm, *IEEE Trans. Ant. Prop.*, **41**:412–421 (1993).
54. F. Capolino, S. Maci, and L. B. Felsen, Asymptotic high-frequency Green's function for a planar phased sectoral array of dipoles, *Radio Sci.*, **35**:579–593 (2000).
55. O. A. Civi, P. H. Pathak, H. -T. Chou, and P. Nepa, A hybrid UTD-MoM for efficient analysis of electromagnetic radiation/scattering from large finite planar arrays, *Radio Sci.*, **35**: (2000).
56. J. Janpugdee and P. H. Pathak, A novel GTD ray analysis for the collective radiation from large finite cylindrical conformal antenna arrays, *Proc. AP-S/URSI Int. Sympos.*, 2004.
57. H. Y. Yee, L. B. Felsen, and J. B. Keller, Ray theory of reflection from the open end of a waveguide, *SIAM J. Appl. Math.*, **16**:268–300 (1968).
58. J. Boersma, Ray-optical analysis of reflections in an open ended parallel plane waveguide: TM case, *SIAM J. Appl. Math.*, **29**:164–195 (1975).
59. R. C. Rudduck and L. L. Tsai, Aperture reflection coefficients for TEM and TE₁₀ mode parallel-plate waveguides, *IEEE Trans. Ant. Prop.*, **16**:83–89 (1968).
60. P. H. Pathak and A. Altintas, An efficient high-frequency analysis of modal reflection and transmission coefficients for a class of waveguide discontinuities, *Radio Sci.*, **23**:107–1119 (1988).
61. C. W. Chuang and P. H. Pathak, Ray analysis of modal reflection for three-dimensional open-ended waveguides, *IEEE Trans. Ant. Prop.*, **37**:339–346 (1989).
62. M. Kline, An asymptotic solution of Maxwell's equation, *Commun. Pure Appl. Math.*, **4**:225–263 (1951).
63. R. K. Luneberg, *Mathematical Theory of Optics*. Brown University Press, Providence, RI, 1964
64. H. Ikuno and L. B. Felsen, Complex ray interpretation of reflection from concave-convex surfaces, *IEEE Trans. Ant. Prop.*, **36**:1206–1271 (1988).
65. M. C. Liang, P. H. Pathak, and C. W. Chuang, A generalized UTD analysis for the diffraction by a wedge with convex faces to include surface ray effects and grazing angles of incidence/diffraction, *Proc. Int. IEEE APS/Radio Science Meeting*, Syracuse, NY, 1988. (Also see Ohio State Univ. Dept. of Electrical Engineering, Ph.D. dissertation by Liang, M.C., 1988.)
66. W. D. Burnside and K. S. Burgener, High-frequency scattering by a thin lossless dielectric slab, *IEEE Trans. Ant. Prop.*, **31**:318–327 (1983).
67. A. Michaeli, Transition function for high frequency diffraction by a curved perfectly conducting wedge—parts I, II and III, *IEEE Trans. Ant. Prop.*, **37**:1073–1092 (1989).
68. R. Tiberio, G. Manara, G. Pelosi, and R. G. Kouyoumjian, High-frequency electromagnetic scattering of plane waves from double wedges, *IEEE Trans. Ant. Prop.*, **37**:1172–1180 (1989).
69. M. Idemen and L. B. Felsen, Diffraction of a whispering gallery mode by the edge of a thin concave cylindrically curved surface, *IEEE Trans. Ant. Prop.*, **29**:571–579 (1981).
70. E. F. Knott, The relationship between Mitzner's ILDC and Michaeli's equivalent currents, *IEEE Trans. Ant. Prop.*, **33**:112–114 (1985).
71. S. W. Lee, Comparison of uniform asymptotic theory and Ufimtsev's theory of EM edge diffraction, *IEEE Trans. Ant. Prop.*, **25**:162–170 (1977).
72. I. J. Gupta, C. W. I. Pistorius, and W. D. Burnside, An efficient method to compute spurious endpoint contributions in PO solutions, *IEEE Trans. Ant. Prop.*, **35**:1426–1435 (1987).
73. F. Obelleiro, J. L. Rodriguez, and R. J. Burkholder, An iterative physical optics approach for analyzing the electromagnetic scattering by large open-ended cavities, *IEEE Trans. Ant. Prop.*, **43**:356–361 (1995).
74. H. Ling, R. C. Chou, and S. W. Lee, Shooting and bouncing rays: Calculating the RCS of an arbitrarily shaped cavity, *IEEE Trans. Ant. Prop.*, **37**:194–205 (1989).
75. Y. Rahmat-Samii and R. Mittra, A spectral domain interpretation of high frequency phenomena, *IEEE Trans. Ant. Prop.*, **25**:676–687 (1977).
76. F. A. Sikta, W. D. Burnside, T. T. Chu, and L. Peters Jr., First-order equivalent current and corner-diffraction scattering from flat-plate structures, *IEEE Trans. Ant. Prop.*, **31**: 584–589 (1983).

77. K. K. Chan and L. B. Felsen, Transient and time harmonic diffraction by a semi-infinite cone, *IEEE Trans. Ant. Prop.*, **25**:802–804 (1977).
78. A. Aktas and R. J. Marhefka, An approximate UTD coefficient for material plate junctions, *1998 International IEEE/AP-S Symposium and URSI Radio Science Meeting*, Atlanta, Georgia, June 21–26, 1998.
79. A. Aktas and R. J. Marhefka, An approximate slope diffraction coefficient for material plate junctions, *1999 International IEEE/AP-S Symposium and URSI Radio Science Meeting*, Orlando, Florida, July 11–16, 1999.
80. R. C. Hansen, ed., *Geometrical Theory of Diffraction*, IEEE Press, New York, 1981.
81. G. L. James, *Geometrical Theory of Diffraction for Electromagnetic Waves*, IEE EM Waves Series 1, Peter Peregrinus, Stevenage, UK, 1976.
82. D. A. McNamara, C. W. I. Pistorius, and J. A. G. Malherbe, *Introduction to the Uniform Geometrical Theory of Diffraction*, Artech House, New York, 1990.
83. V. A. Fock, *Electromagnetic Diffraction and Propagation Problems*, Pergamon, New York, 1965.
84. N. A. Logan and K. S. Yee, A mathematical model for diffraction by convex surfaces, in R. Langer, ed., *Electromagnetic Waves*, Univ. Wisconsin Press, Madison, WI, 1962, pp. 139–180.
85. C. A. Balanis, *Advanced Engineering Electromagnetics*, Wiley, New York, 1989.
86. D. Bouche, F. Molinet, and R. Mittra, *Asymptotic Methods in Electromagnetics*, Springer-Verlag, New York, 1997.
87. E. V. Jull, *Aperture Antennas and Diffraction Theory*, IEE EM Waves Series 10, Peter Peregrinus, Stevenage, UK, 1981.
88. J. J. Bowman, T. B. A. Senior, and P. L. E. Uslenghi, eds., *Electromagnetic and Acoustic Scattering by Simple Shapes*, Chap. 18, North-Holland, Amsterdam, 1969.
89. C. R. Cockrell and P. H. Pathak, Diffraction theory techniques applied to aperture antennas on finite circular and square ground planes, *IEEE Trans. Ant. Prop.*, **22**:443–448 (1974).
90. M. S. Narasimhan and K. M. Prasad, GTD analysis of near field patterns of a prime focus symmetric parabolic reflector antenna, *IEEE Trans. Ant. Prop.*, **29**:959–961 (1981).
91. P. H. Pathak, High-frequency techniques for antenna analysis, *Proc. IEEE*, **80**:44–65 (1992).
92. C. A. Mentzer, L. Peters Jr., and R. C. Rudduck, Slope diffraction and its application to horns, *IEEE Trans. Ant. Prop.*, **23**:153–159 (1975).
93. J. J. Kim and W. D. Burnside, Simulation and analysis of antennas radiating in a complex environment, *IEEE Trans. Ant. Prop.*, **34**:554–562 (1986).
94. C. L. Yu, W. D. Burnside, and M. C. Gilreath, Volumetric pattern analysis of airborne antennas, *IEEE Trans. Ant. Prop.*, **26**:636–641 (1978).
95. W. D. Burnside, J. J. Kim, B. Grandchamp, R. G. Rojas, and P. Law, Airborne antenna radiation pattern code user's manual, Technical Report 716199-4, The Ohio State University, ElectroScience Laboratory for National Aeronautics & Space Administration, Langley Research Center, September 1985.
96. R. J. Marhefka and J. W. Silvestro, Near zone—basic scattering code user's manual with space station applications, Technical Report 716199-13, The Ohio State University, ElectroScience Laboratory for National Aeronautics & Space Administration, Langley Research Center, March 1989.
97. E. M. Bracalente and J. Sweet, Personal communications with R. J. Marhefka relating to measured results, National Aeronautics & Space Administration, Langley Research Center, 1989.

VAN ATTA ARRAY REFLECTOR

SHYH-JUNG CHUNG
TAN-HSIUNG HO
National Chiao-Tung University
Hsinchu, Taiwan, Republic of
China

1. INTRODUCTION

Retrodirective array reflectors have found many applications in wireless communications, RF identification (RFID), and intelligent transportation systems (ITSs). These reflectors have the characteristic of reflecting an incident wave toward the source direction without any prior information on the source location. Two types of the retrodirective antenna arrays are usually used. One contains the phase-conjugate elements, and the other uses the Van Atta arrangement [1]. In a phase-conjugate retrodirective array [2], each antenna is connected to a mixer, which in turn is pumped by a local oscillator (LO) with double the frequency of the incident wave. When an incident wave (RF signal) is caught by the antenna, it is mixed with the LO signal, leading to an IF signal reradiated out from the same antenna. The IF signal has an approximate frequency as to the incident wave, but with a conjugated phase (opposite in sign). Due to the phase conjugation, all the IF signals from the antennas would thus coherently reach a remote receiver in the wave incident direction, resulting in an array reradiation beam in the direction. This type of retrodirective array has the advantage that the array elements can be arbitrarily located, not necessarily with equal interelement spacing, nor in the same plane; thus it easily conforms to the object surface. (Nevertheless, a large interelement spacing may cause grating reradiating beams in other directions.) Another advantage is that, by changing the LO frequency, the reradiation wave can be easily frequency-modulated. On the contrary, the phase-conjugated array suffers from the disadvantage that it needs a mixer circuit with a large-frequency difference between RF and LO signals for each array element. Also, an LO with double the system frequency and a corresponding distribution network from the LO to the entire array elements are required. These may make the array complicated, bulky, and costly.

The Van Atta retrodirective array, which was first proposed by L. C. Van Atta [1] in 1959, has a much simpler configuration than the phase-conjugated array does. The antennas of the Van Atta array are paired and connected by transmission lines with equal length or length differences equal to multiples of the guided wavelength. The two antennas of each pair are located symmetrically with respect to the array center. Every antenna serves as both receiving and transmitting antennas. The field received by each antenna is, through the connecting transmission line, reradiated from the corresponding paired antenna. Therefore, the phase distribution for the reradiated fields

at the antennas becomes reversal to that for the receiving fields at antennas, thus producing a reradiation beam in the wave incidence direction. Unlike the phase-conjugated array where active devices are always needed, the Van Atta array can be designed with a passive or active type.

Since the Van Atta array has the simplest form of retrodirective array, it has received a great deal of attention in basic theories and various applications after the report of Van Atta. Sharp made an experimental investigation about the backscattering characteristics of the Van Atta array by forming a planar reflector consisting of 16 dipoles [3,4]. He observed that the backscattering of the Van Atta array may have a minimum at normal incidence and suggested that the scattering of dipole antennas may influence the reradiated fields. Researchers such as Appel-Hansen [5] and Fusca [6] also conducted experimental work on the dipole reflectors, and Walther [7] studied an acoustic horn reflector. Other investigators such as Larsen [8] and Nielsen [9] addressed the theoretical basis of Van Atta dipole reflectors. Another field of research regarding the Van Atta reflector emphasized the use of auxiliary active devices in the interconnection transmission line of Van Atta reflectors and its applications. The idea of making Van Atta reflector active by inserting active components in the transmission line was first proposed by Bauer [10], who suggested using modulating phase shifters in the transmission lines and accomplished an amplitude modulation in the reradiated field. Hansen [11] then suggested adding amplifiers in the transmission lines to enhance the backscattering field strength. In the meantime, Davies [12] proposed a way to vary the angle of the radiation field by introducing a mixer in the delay path for a frequency shift. This idea was later applied by Whithers [13].

Numerous applications of the Van Atta reflector were discussed in 1960s because of the conspicuous superiority of the reflector. One proposed application of the Van Atta reflector is in the satellite communications. Passive, active, and semipassive systems have been discussed [11,14,15]. Another possible application of the Van Atta reflector is as a navigation aid, to strengthen the reflected radar signal from a small boat or airplane toward the searching radar, which was discussed mainly by Davies [12]. By the same feature of reflected-signal enhancement, Fusca suggested an ECM (electronic countermeasures) system [6] for military applications based on the idea that the artificial enhanced signal will confuse the enemy radars. Bauer then discussed an IFF (identify friend or foe) system [10] using code modulation in the reflector.

The generous investigation of Van Atta reflectors continued for about 10 years after Van Atta's proposal. In this period, most of the research focused on Van Atta reflectors using bulky antennas such as dipoles and horns. It was not until the early 1990s, when the intelligent transportation system (ITS) [16] became widely discussed, that the study of Van Atta reflectors began afresh. The retrodirective reflectors were developed mostly by using the low-cost printed antennas, including microstrip antennas, slot

antennas, and printed dipoles. ITS-related applications, such as collision warning radars and vehicle communications, were considered when developing these printed Van Atta reflectors. Cohn [17] first proposed a retrodirective transponder based on the Van Atta array for automotive collision avoidance application in 1993. Chung and Chang [18,19] conducted the methods for predicting the scattering field patterns of the printed Van Atta reflectors in both analytical and numerical aspects. Many planar Van Atta reflectors, including those of passive, active, and quasiactive arrays, were developed [20–24]. Others such as Fujita [25] also studied the depolarizing characteristics of the retrodirective reflectors.

The theoretical analysis of Van Atta arrays is introduced in Section 2, where important formulas regarding the reradiation fields of the arrays are derived. Various design examples of planar Van Atta array reflectors, including passive and active types, are described in Section 3. Section 4 depicts the applications of the vehicle-mounting Van Atta reflectors associated with the ITS, and Section 5 gives a brief summary.

2. THEORY OF THE VAN ATTA ARRAY

As shown in Fig. 1, the Van Atta reflector array consists of a number of antenna elements arranged in pairs. The elements in each pair are placed symmetrically about a conveniently selected center, which is common for all pairs. Transmission lines of equal length, or of multiple-wavelength difference, connect the elements of each pair. An antenna element may be placed at the selected array center and connected to an open-circuited transmission line with a length equal to half the length of other lines. Also, the elements may be arranged as a two-dimensional Van Atta reflector array as illustrated in Fig. 2, where the elements located symmetrically to the center of the two-dimensional array are paired by transmission lines with equal length or of multiple-wavelength difference.

To understand how the reflector array operates, consider an N -element linear Van Atta array illuminated by a plane wave incident at an angle θ , as shown in Fig. 3a. Assume that the N elements form M antenna pairs with $M = N/2$. Antennas 1 and N are paired by a transmission line of length l_1 , antennas 2 and $N - 1$ are paired by a transmission line of length l_2 , and so on. The incident field received by the array elements has a phase distribution of $[0, -\Delta, 2\Delta - (N - 2)\Delta, -(N - 1)\Delta]$. Here $\Delta = k_0 d \sin \theta$ is the incident field phase lag between adjacent antennas, $k_0 = 2\pi/\lambda_0$ is the free-space propagation constant, and d is

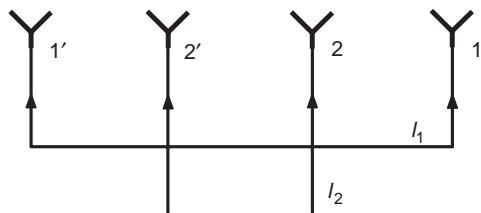


Figure 1. A four-element Van Atta array reflector.

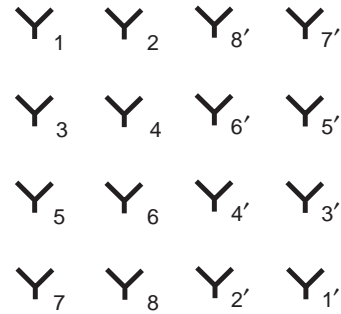


Figure 2. Antenna arrangement of a two-dimensional Van Atta array reflector.

the interelement spacing. Now consider the m th ($m = 1, 2, \dots, M$) antenna pair. The signal S_m^r received by the m th antenna can be expressed as

$$S_m^r = C_f E_0 G(\theta) e^{-j(m-1)\Delta} \tag{1}$$

where C_f is a feed factor depending on the configuration of the antenna feed, E_0 is the amplitude of the incident field, and $G(\theta)$ is antenna gain at the incident angle θ . This signal, after traveling through the m th transmission line

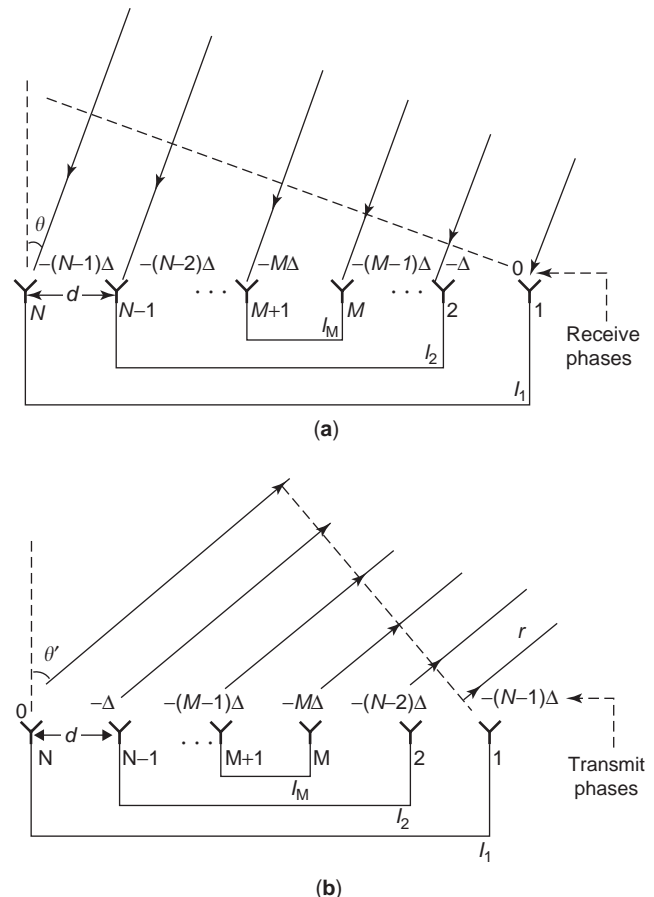


Figure 3. An N -element Van Atta array reflector with (a) receiving phase distribution and (b) transmitting phase distribution.

of length l_m , is fed to the corresponding paired antenna $(N - m + 1)$ and will be radiated out from this antenna. Similarly, through the same transmission line, the signal S_{N-m+1} received by antenna $(N - m + 1)$ is fed to antenna m and will also be radiated out. The signal S_m^f fed to the m th antenna is thus written as

$$S_m^f = S_{N-m+1}^r e^{-jk_g l_m} \quad (2)$$

where k_g is the propagation constant of the transmission line. Using (1) with m replaced by $N - m + 1$, the feeding signal is rewritten as

$$S_m^f = C_f E_0 G(\theta) e^{-jk_g l_m} e^{-j(N-m)\Delta} \quad (3)$$

Since the connecting transmission lines are of equal length or of multiple-wavelength difference, the propagation phase delays $\exp[-jk_g l_m]$ in the transmission lines are the same and equal to $\exp[-jk_g l_1]$. Thus, one obtains

$$S_m^f = C_f E_0 G(\theta) e^{-jk_g l_1} e^{-j(N-m)\Delta} \quad (4)$$

It is seen from (4) that, as shown in Fig. 3b, the signals fed to the array elements have a phase distribution of $[-(N - 1)\Delta, -(N - 2)\Delta \dots -2\Delta, -\Delta, 0]$, which is the reversal of the phase distribution of the incident field received by the array elements. The total reradiation field $E_{\text{rerad}}(\theta', \theta)$ from the array at an observation angle of θ' can be calculated using the antenna array theory [26]

$$E_{\text{rerad}}(\theta', \theta) = \frac{e^{-jk_0 r}}{r} G(\theta') \sum_{n=1}^N S_n^f e^{-j(n-1)\Delta'} \quad (5)$$

with $\Delta' = k_0 d \sin \theta'$. Substituting (4) into (5), one obtains

$$E_{\text{rerad}}(\theta', \theta) = \left\{ \frac{e^{-jk_0 r}}{r} e^{-j(N-1)\Delta} C_f E_0 \right\} e^{-jk_g l_1} \times G(\theta) G(\theta') \sum_{n=1}^N e^{j(n-1)(\Delta-\Delta')} \quad (6)$$

This equation is the bistatic scattering field pattern of the Van Atta array reflector. It is actually a radiation field pattern of the antenna array with excitation from the incident wave. For a given incidence angle θ , the scattering field level varies with the change of the observation angle θ' . As the observation angle coincides with the incidence angle, the scattering field attains a maximum level. The resultant monostatic backscattering field pattern is obtained by letting θ' equal to θ in (6)

$$E_{\text{rerad}}(\theta) = N \left\{ \frac{e^{-jk_0 r}}{r} e^{-j(N-1)\Delta} C_f E_0 \right\} e^{-jk_g l_1} G^2(\theta) \quad (7)$$

where the relationship $\Delta' = \Delta$, when $\theta' = \theta$, has been used. Note that the backscattering field is proportional to the element number N and to the square of the radiation pattern

$G(\theta)$ of the array element. Also, its phase is controlled by the length l_1 of the connecting transmission lines.

To obtain a higher level of backscattering field, more antenna elements may be used in the Van Atta array, which, however, would complicate the layout of the connecting transmission lines, especially for a large planar array. Another way to increase the responding field level is to use the active Van Atta array. The active array may be implemented by inserting an ordinary unilateral amplifier or a bidirectional amplifier on the midway of each transmission line. Figure 4 shows an N -element active Van Atta array with embedded unilateral amplifiers. The N antennas are divided into two groups, one for receiving and one for transmitting. Each group contains M ($= N/2$) elements. Transmission lines of equal length, or of multiple-wavelength difference, are used to pair the antennas in the two groups. Unilateral amplifiers with field gain of A_m , $m = 1, 2, \dots, M$, are implemented in the direction from the receiving antennas to the transmitting antennas. The incident field received by each antenna in the receiving group will travel along the connecting transmission line, be enlarged by the amplifier, and then be fed to the corresponding transmitting antenna. Following the analysis above, the signal S_m^f fed to the m th transmitting antenna is

$$S_m^f = C_f E_0 G_r(\theta) e^{-j(m-1)\Delta} e^{-jk_g l_1} A_m \quad (8)$$

As shown in Fig. 4, these signals have a phase distribution reverse that of the incident fields at the receiving antennas. The total bistatic scattering field is derived as

$$E_{\text{rerad}}(\theta', \theta) = \frac{e^{-jk_0 r}}{r} G_r(\theta') \sum_{m=1}^M S_m^f e^{j(m-1)\Delta'} \quad (9)$$

or

$$E_{\text{rerad}}(\theta', \theta) = \left\{ \frac{e^{-jk_0 r}}{r} C_f E_0 \right\} e^{-jk_g l_1} \times G_r(\theta) G_t(\theta') \sum_{m=1}^M A_m e^{-j(m-1)(\Delta-\Delta')} \quad (10)$$

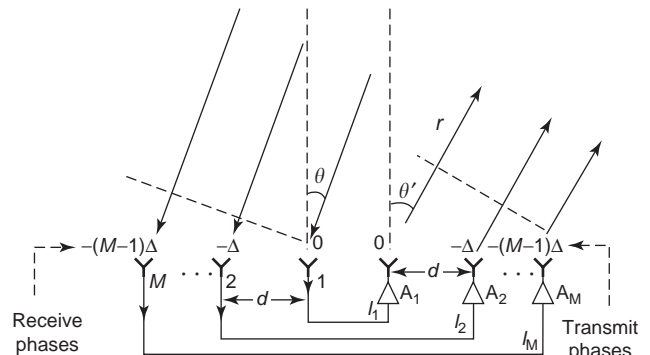


Figure 4. An N -element active Van Atta array with embedded unilateral amplifiers.

Here $G_r(\theta)$ and $G_t(\theta')$ are the radiation patterns of the receiving and transmitting antennas, respectively. For the active array with identical antennas and amplifiers, $G_r(\theta) = G_t(\theta) = G(\theta)$ and $A_m = A$, the monostatic backscattering field $E_{\text{rerad}}(\theta)$ may be written as

$$E_{\text{rerad}}(\theta) = \frac{N}{2} A \left\{ \frac{e^{-jk_0 r}}{r} C_f E_0 \right\} e^{-jk_g l_1} G^2(\theta) \quad (11)$$

Comparing (11) and (7), it is observed that for a given number of antennas, the backscattering field level of the active Van Atta array using unilateral amplifiers is $A/2$ times higher than that of the passive one, although amplifiers with a gain of A are used. This is because that only the fields received by half of the antennas are amplified by the unilateral amplifiers. To get the merit of the active array, the amplifier's field gain should be greater than 2, or 6 dB. Otherwise, one may use the configuration of active Van Atta array with bidirectional amplifiers. The bidirectional amplifier possesses the characteristic of simultaneously amplifying the signal from both I/O ports with the same gain. As illustrated in Fig. 5, the active Van Atta array is similar to a passive array, but with a bidirectional amplifier embedded midway along each connecting transmission line. Following the procedure from (1) to (6), the bistatic scattering field $E_{\text{rerad}}(\theta', \theta)$ of this active array can be easily derived as

$$E_{\text{rerad}}(\theta', \theta) = \left\{ \frac{e^{-jk_0 r}}{r} e^{-j(N-1)\Delta} C_f E_0 \right\} e^{-jk_g l_1} \times G(\theta) G(\theta') \sum_{n=1}^N A_n e^{j(n-1)(\Delta-\Delta')} \quad (12)$$

where $A_n = A_{N+1-n}$, $n = M+1, M+2, \dots, N$. The corresponding monostatic backscattering field $E_{\text{rerad}}(\theta)$ for the array with identical bidirectional amplifiers is

$$E_{\text{rerad}}(\theta) = NA \left\{ \frac{e^{-jk_0 r}}{r} e^{-j(N-1)\Delta} C_f E_0 \right\} \times e^{-jk_g l_1} G^2(\theta). \quad (13)$$

It is seen that the ratio of the backscattering field level of the active array over that of a passive one is exactly equal to the amplifiers' gain. Also, the active Van Atta

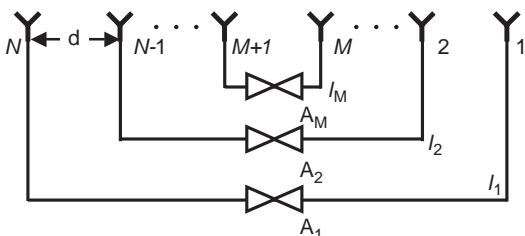


Figure 5. An N -element active Van Atta array with embedded bi-directional amplifiers.

array using bidirectional amplifiers possesses the backscattering field level 6 dB higher than that using unilateral amplifiers. In other words, to get the same field level, only half the number of antennas or amplifiers with 6 dB lower gain are needed in the array of bidirectional amplifiers.

The Van Atta array reflector is usually built on a large metal plate because of antenna design requirements or to shield the transmission lines so as to reduce their scattering. This metal plate, however, would produce an extra strong, varying scattering field and thus deteriorate the retrodirectivity property of the Van Atta reflector, especially in the metal's specular direction. Another mechanism that would influence the reflection characteristic of the Van Atta array is the scattering due to the individual array antennas. Figure 6 illustrates these scattering phenomena for a Van Atta reflector designed using the aperture-coupled microstrip antennas. The total scattering field is composed primarily of three parts: the *reradiated field from the antenna* (RFA), the *scattered field from the terminated antennas* (SFA), and the *scattered field from the partially covered ground plane* (SFG). When a wave is incident the array, some of the power is captured by the antennas and reradiated from corresponding antennas of the same pairs. This is the RFA. In addition, some of the power is scattered by the microstrip antennas and by the partially covered ground plane, corresponding to the SFA and SFG, respectively. The RFA is the dominant contribution of the scattering field for a Van Atta array, and, as derived above, it is proportional to the square of the radiation pattern of the individual array element. The scattered field from the antennas comes from the antenna current induced by the incident wave, which may be calculated by using a numerical method such as the method of moments (MoM) [19]. Finally, the scattered field from the ground plane can be obtained by using the physical optics (PO) method together with the method of equivalent currents (MEC) [18,26]. Figure 7 depicts the theoretical results for the reradiated field (RFA), scattered field (SFA + SFG), and total field (RFA + SFA + SFG) of a common Van Atta array reflector. It is seen that the reradiation

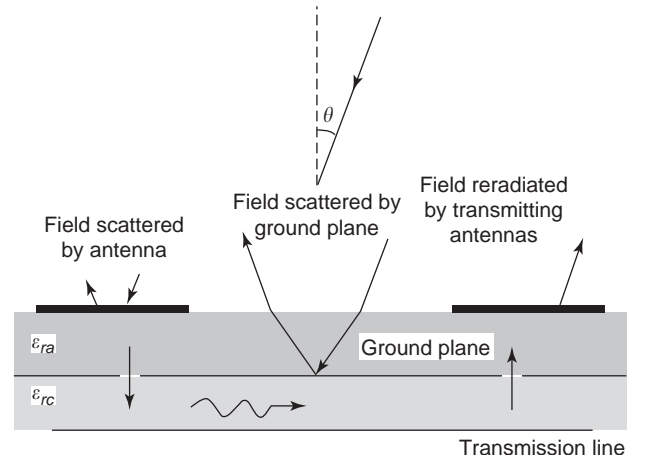


Figure 6. Illustration of the scattering field components from a Van Atta array reflector.

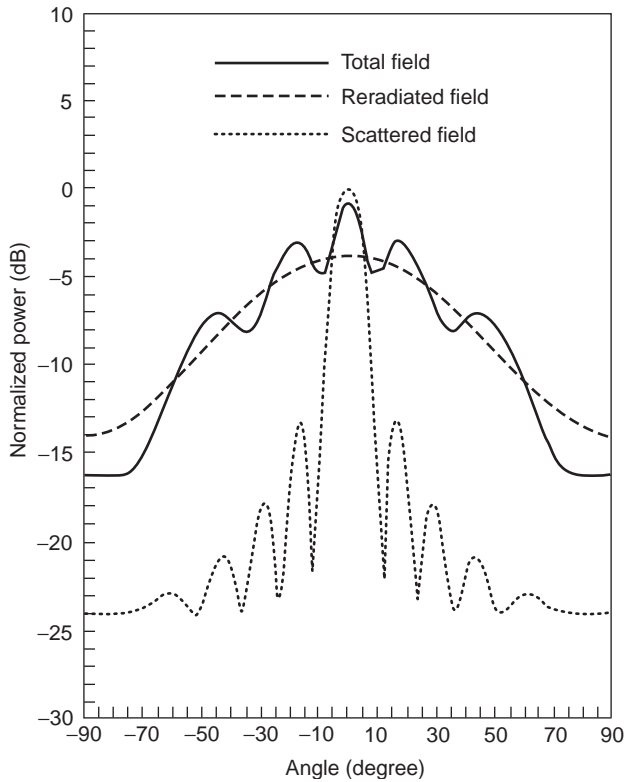


Figure 7. Theoretical backscattering field patterns of a common Van Atta reflector.

field is a slowly varying function of the angle θ , which is the principal contribution to the retrodirectivity of the array reflector. On the contrary, both the amplitude and the phase of the scattered field change quickly with the angle, leading to an oscillatory behavior of the total backscattering field. Since the scattered fields at angles away from the normal of the reflector are much less than the reradiated fields, they can cause only small ripples at these angles. But when the incidence angle is near the reflector normal direction, the scattered field becomes comparable to, if not larger than, the reradiation field. Finally, it is noted that, since the phase of the reradiation field depends on the phase delays in the connecting transmission lines, the total field pattern may be smoothed out by adjusting the lengths of the connecting lines.

3. DESIGN EXAMPLES

In the following text, several Van Atta array reflectors designed using planar antennas and printed transmission lines will be introduced. Since using the printed circuit board (PcB) technique, these reflectors have the advantages of easy fabrication, low cost, and superior conformability to a given body surface, which greatly enhance the merits and extend the application field of the Van Atta array. Passive Van Atta reflectors with one-dimensional and two-dimensional retrodirectivities and active reflectors with unilateral amplifiers and bidirectional amplifiers are described.

Figure 8 shows a printed Van Atta reflector using aperture-coupled microstrip antennas [18]. This two-layer structure creates the antenna and feeding network in two sides separated by the ground plane, leading to a comfort in routing of the feeding network. Three identical *E*-plane subarrays are made to enhance the echo of the reflector. Each linear subarray contains two pairs (four elements) of aperture-coupled microstrip antennas fed by two equal-length microstrip lines ($l_1=l_2=l$) on the reverse side of the ground plane. The distance between subarrays (*s*) and between subarray elements (*d*) are set as $0.7\lambda_0$ and $0.6\lambda_0$, respectively, for a frequency of 10 GHz. The total area of the reflector is $76 \times 68 \text{ mm}^2$. Figure 9 shows the measured pattern of the backscattering field for a retrodirective reflector with $l = 64 \text{ mm}$; that of a plate reflector of the same size is also shown for comparison. It is seen that the retrodirective reflector has quite a smooth pattern. The variation of the field stays within 8 dB in a very wide range of angles (from $\theta = -60^\circ$ to $\theta = +60^\circ$). On the other hand, the plate reflector contributes high returning fields only in the range within $\theta = \pm 5^\circ$. Outside this range, its fields are strongly oscillatory and are much less than those of the retrodirective reflector. As stated above, the phase of the reradiation field depends on the length *l* of the connecting transmission lines. Thus, because of interference between the reradiation field and the scattered field, the pattern of the total backscattering field will change when the length (*l*) of the microstrip lines is varied. To verify this, another reflector with shorter connecting microstrip lines ($l = 62 \text{ mm}$) was measured and compared to the theoretical pattern (see Fig. 10). As predicted by the theory, the total backscattering field near the reflector normal should decrease when the microstrip-line length is reduced. This did happen in the measured field pattern, as can be observed in the figure.

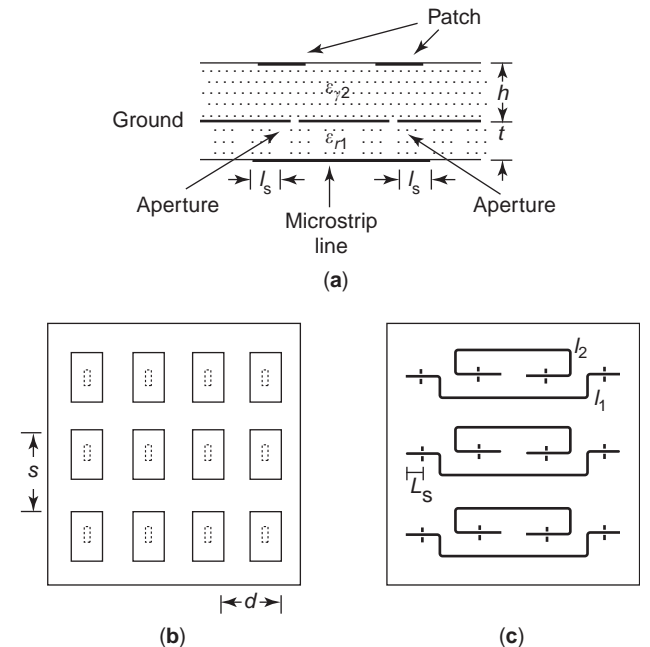


Figure 8. (a) Partial side view, (b) top view, and (c) bottom view of a Van Atta aperture-coupled microstrip antenna array.

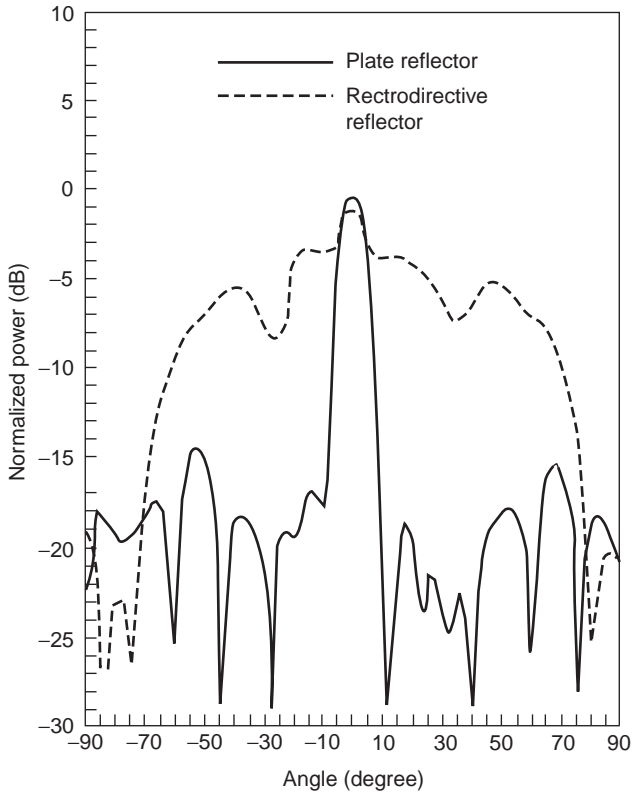


Figure 9. Measured backscattering field patterns for a metal plate reflector and a Van Atta aperture-coupled microstrip array of $l = 64$ mm.

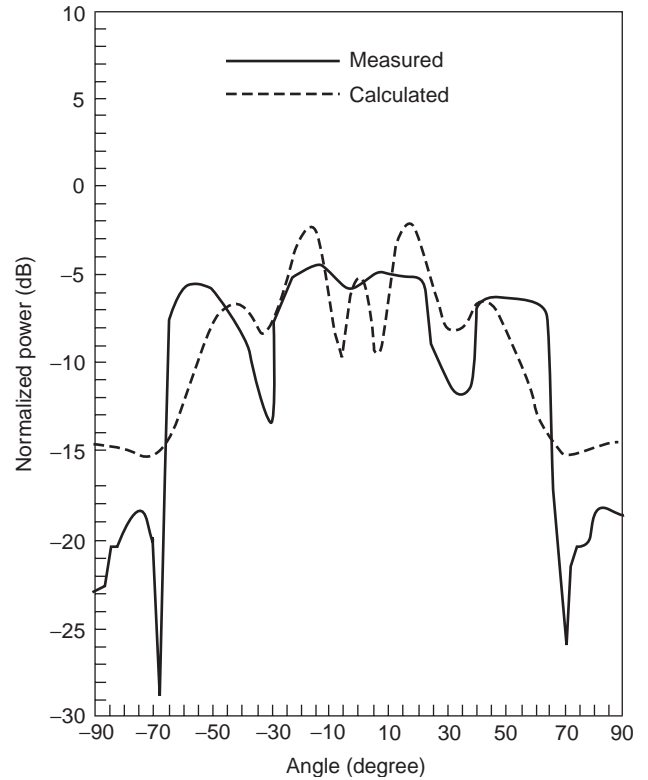


Figure 10. Comparison between measured and calculated backscattering field patterns for the Van Atta aperture-coupled microstrip array of $l = 62$ mm.

Although the aperture-coupled patch antenna has been shown to be a good candidate of the planar Van Atta array element, other planar antennas such as slot antenna and printed dipole antenna can be used to construct the Van Atta array. Figure 11 shows an example of the dual-slot antenna used in a Van Atta reflector [20]. The reflector contains four antenna subarrays, each with six dual-slot antennas appropriately fed and paired by microstrip lines on the backside of the substrate. The dual-slot antenna is formed by cascading two radiating slots via a connecting microstrip line. Owing to the characteristic of the slot antenna that half of the power is radiated backward, a metal plate is placed behind the antenna to enhance the forward radiating power. The two slots are chosen to have the same dimensions and the length l_m of the connecting microstrip line is designed as one guided wavelength λ_g , so that the antenna possesses broadside and symmetric radiation. The measured and calculated E -plane backscattering patterns of the 4×6 retrodirective array reflector at 10 GHz are shown in Fig. 12. The calculated pattern using the method of moments agreed quite well with the measured one. The mainlobe at 0° of the total field pattern is due to the high scattering field from the ground plane. Outside the mainlobe, the variations in the total field pattern eventually follow those of the reradiation field pattern. The small ripples come from the interference of the ground-plane scattering field. It has been suggested [27] that the peak of the backscattering field pattern can be avoided if, when measuring or in applications, the array

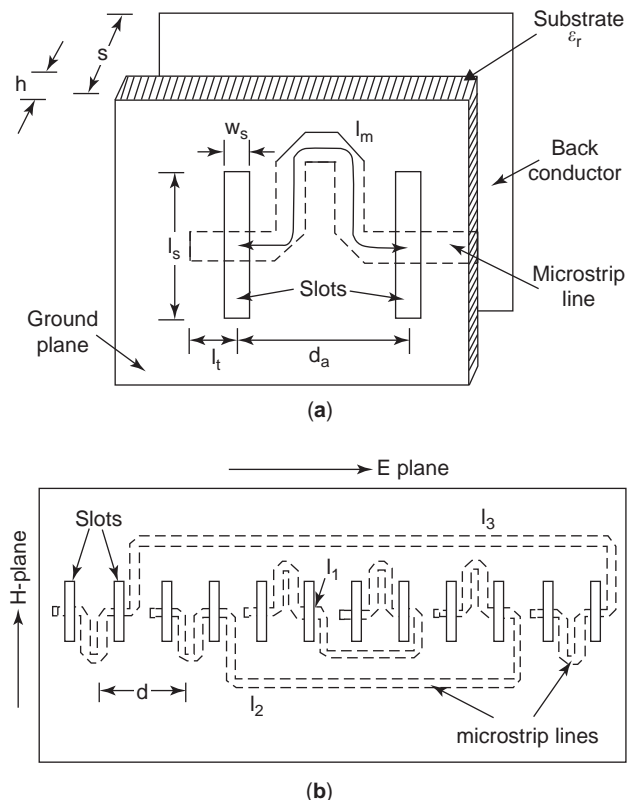


Figure 11. Geometry of dual-slot antenna and top view of six-element linear Van Atta reflector subarray.

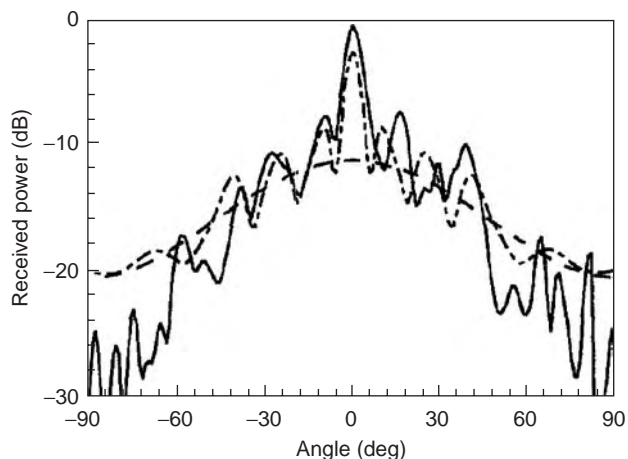


Figure 12. Comparison between the measured and calculated field patterns of 4×6 Van Atta dual-slot antenna array.

reflector is tilted several degrees in the H plane to avoid exposure to the specular reflection of the ground plane. Another way to reduce the peak scattering near the broadside direction is to arrange half of the array elements with a quarter-wavelength displacement relative to the other elements, so that the directly scattering field from the first half elements will cancel with that from the other half near the broadside direction [28].

The planar array reflectors described above are retro-directivity in one dimension. They could reflect high fields

only to the source points in the E plane or the H plane of the antenna array. Figure 13 presents a configuration of the two-dimensional Van Atta reflector with retro-directivity in both E plane and H plane [19]. The reflector includes six aperture-coupled microstrip antenna pairs on the antenna substrate (Fig. 13a) linked by $50\text{-}\Omega$ microstrip lines of lengths ranging from l_1 to l_6 on the circuit substrate (Fig. 13b). The lengths l_5 and l_6 are the same and l_1 – l_4 , with differences of multiples of a microstrip-line wavelength. As a result of the opposite feed orientations at the two ends of l_5 (l_6), the differences between l_5 (l_6) and other lines (l_1 to l_4) are odd multiples of half a wavelength. The interelement distances in the E plane and H plane are both chosen as $0.6\lambda_0$ at 10 GHz. Figure 14 shows the measured backscattering field patterns of the reflector in the E plane and H plane. The calculated patterns using the method of moments and the measured patterns of a metal plate of the same size are also shown for comparison. It is seen that the measured patterns agree well with the calculated ones. The relative 10 dB beamwidth is about 130° in both planes, which is much wider than that (18°) of the metal plate. Outside the angles near the normal direction, the reflected fields produced by the Van Atta reflector are, on average, 9 dB higher than those by the metal plate.

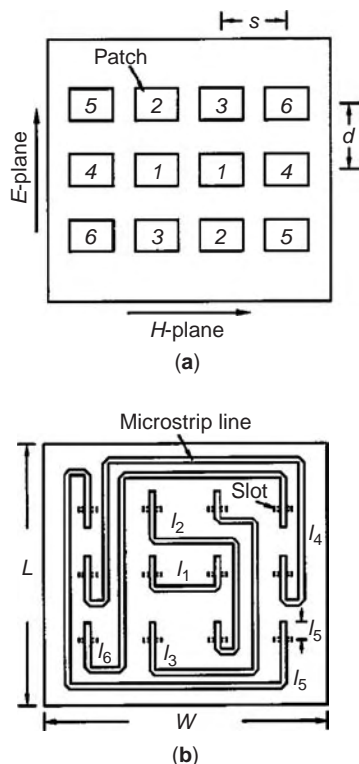


Figure 13. (a) Top view and (b) bottom view of a 2D Van Atta reflector using six pairs of aperture-coupled microstrip antennas.

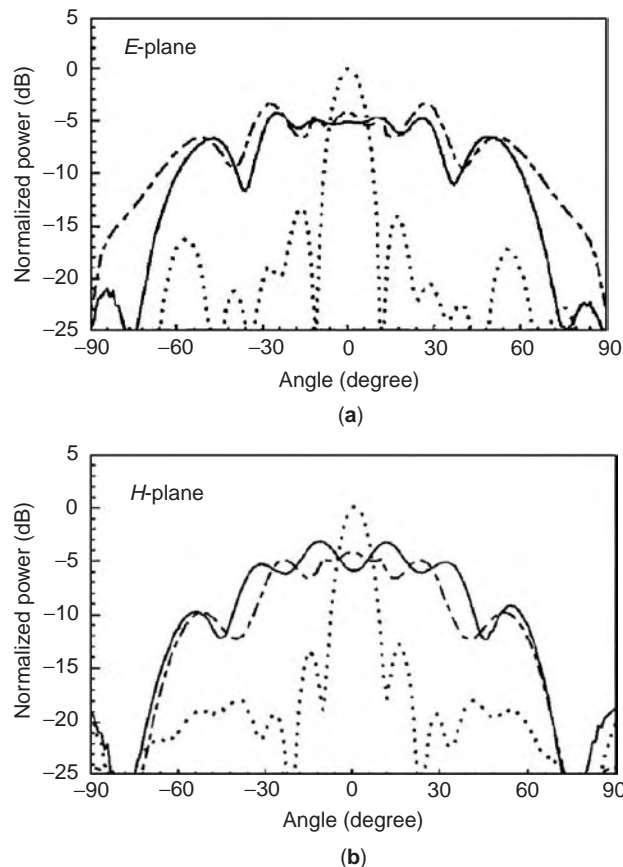


Figure 14. Measured (—) and calculated (---) backscattering field patterns of the Van Atta array of Fig. 13 in (a) E plane and (b) H plane. Dotted lines (•••) represent the measured reflect pattern of a metal plate reflector of the same size.

An important characteristic of retrodirective arrays is the isolation between the incident wave and the backscattering wave at the source position. One way to increase the isolation is by use of different polarizations for those waves. The basic configuration of such a depolarizing Van Atta reflector is shown in Fig. 15a [29]. It consists of several pairs of dual-polarized antennas. For each pair, the vertical polarization (V-pol) port of one antenna is connected to the horizontal polarization (H-pol) port of the paired antenna, and the H-pol port of the former antenna is connected to the V-pol port of the latter, using transmission lines of equal length or of multiple-wavelength difference. In this configuration, an H-pol (V-pol) beam is automatically formed toward an incoming direction of a V-pol (H-pol) wave. The isolation between the polarization diverse signals ensures minimum interference between received and transmitted signals at the receiving end. A planar depolarizing Van Atta array with retrodirectivity in both *E* and *H* planes is illustrated in Fig. 15b [30], which contains four microstrip antennas operating in two linear orthogonal modes. Figure 16 depicts the measured backscattering field patterns in *E* and *H* planes. For both planes, the backscattering pattern has a 3 dB beamwidth of about 80°. It is noted that by using the depolarizing configuration, the scattering interference from the ground plane is reduced, if not eliminated, to the minimum.

The Van Atta array may be configured as an active reflector by embedded solid-state amplifiers in the interconnection transmission lines. Figure 17 illustrates a four-pair Van Atta aperture-coupled microstrip antenna array with inserted unilateral amplifiers [22]. The transmitting antennas (4',3',2',1') were designed with polarization

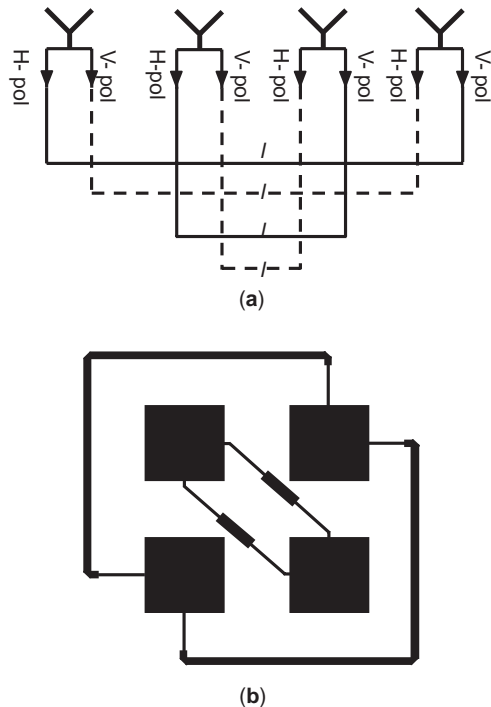


Figure 15. (a) Configuration and (b) layout of a 2D depolarizing microstrip Van Atta array reflector.

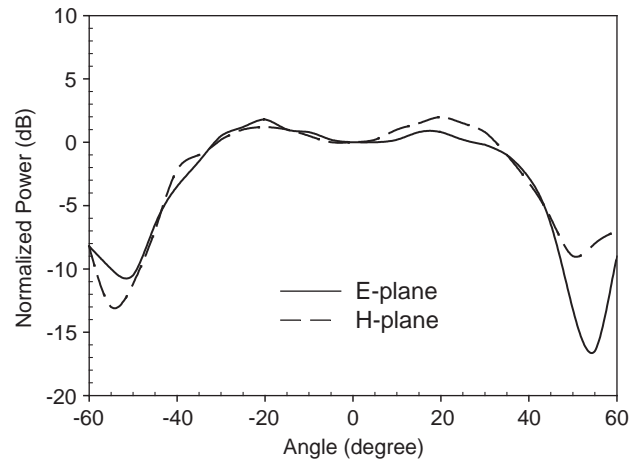


Figure 16. Measured depolarized field patterns in both *E* plane and *H* plane of the Van Atta array shown in Fig. 15b.

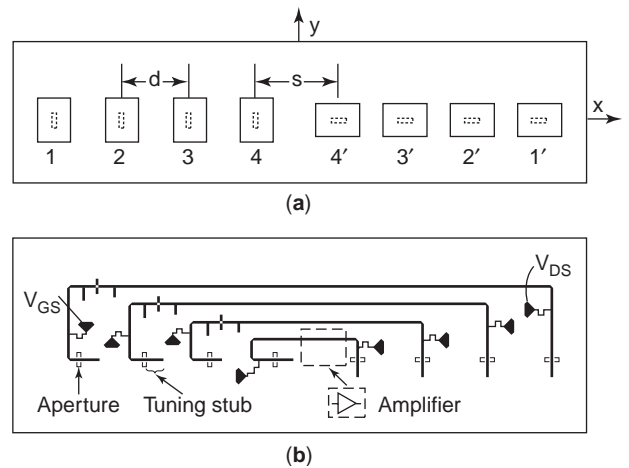


Figure 17. (a) Top view and (b) bottom view of a planar active Van Atta array.

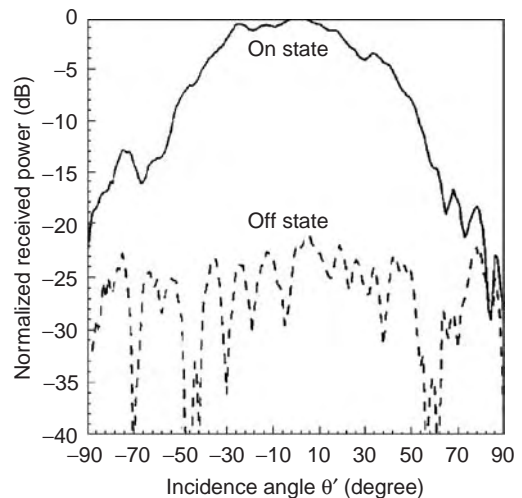


Figure 18. Cross-polarized backscattering field patterns of the Van Atta array shown in Fig. 17 with amplifiers turned on and off.

orthogonal (linear) to (with) that of the receiving antennas (1,2,3,4). The interelement distance d between the receiving (transmitting) antennas was chosen as $0.6\lambda_0$, and the distance between antennas 4 and 4' was $0.7\lambda_0$ at 10 GHz. Before being designed into the reflector, a separate unilateral amplifier was made with a measured gain of 11 dB and return loss of -18 dB. The fabricated active Van Atta array had a cross-polarized backscattering field pattern as shown in Fig. 19. This pattern eventually follows the theoretical one, with a 5 dB beamwidth of 80° achieved. Since the cross-polarized reradiated field with amplifier gain is large relative to the copolarized scattering field from the antennas and ground plane, the latter is obviously negligible. Measurement results show that the cross-polarized backscattering fields of a metal plate of the same size are, on average, -25 dB lower than those of the active Van Atta array. The active retrodirective reflector may also be adopted as a transponder. A digital code can be used to control the bias conditions of the amplifiers so that identification or communication messages are produced. It is seen from Fig. 18 that in the range of angles of interest, the backscattering field pattern with amplifiers in OFF state is at least 20 dB down as compared to that with amplifiers in ON state.

Figure 19 presents another demonstration of active Van Atta array designed at 24 GHz [21]. The array contains two linear subarrays, each, in turn, composed of four receiving and four transmitting inset-fed microstrip antennas. Contrary to the previous design, the transmitting antennas have the same polarization as the receiving ones. The embedded HEMT amplifiers have a gain of 10 dB and return loss of -23 dB. Figure 20 shows the backscattering field pattern of the active reflector, compared to that of a metal plate. The reflector's pattern exhibits a narrow peak at 0° , which is due to the strong specular reflection of the array substrate ground. With the exception of this peak, the backscattering pattern of the array in the range from -40° to 40° has variation less than 3 dB and is 10 dB higher than that of the metal plate.

As mentioned earlier, when embedded with unilateral amplifiers, the resultant active Van Atta array can benefit from only half the amplifiers' gain as compared to a passive array. This is because only the fields received by half of the antennas are amplified by the unilateral amplifiers.

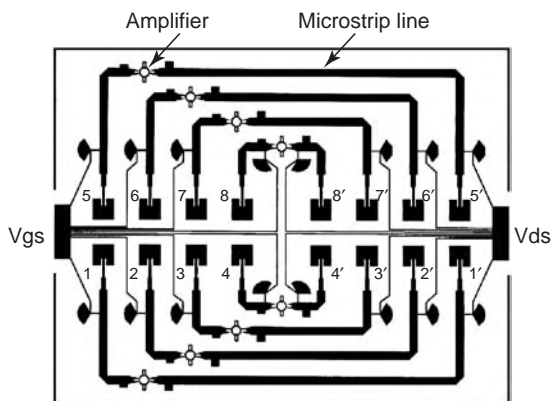


Figure 19. A 24-GHz active Van Atta microstrip antenna array.

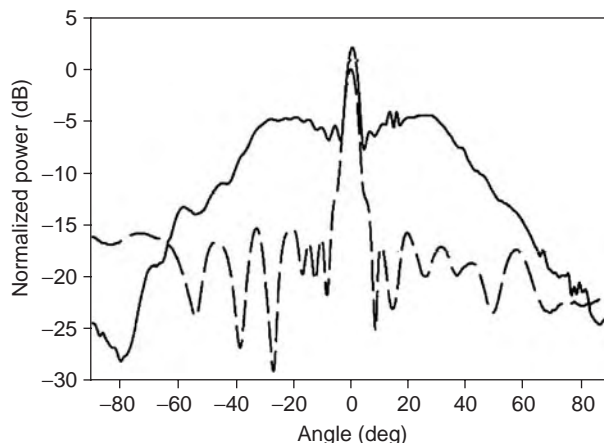


Figure 20. Measured backscattering field patterns of the 24-GHz active Van Atta array (—) and a metal plate (---).

To get the full merit of amplifiers' gain, the field received by each antenna should be amplified and then transmitted. One way to achieve this goal is to insert bidirectional amplifiers in the Van Atta array as shown in Fig. 5. Figure 21 depicts the configuration of a bidirectional amplifier proposed by Chung et al. [24], which is constructed by two identical reflection-type amplifiers and a 3-dB 90° hybrid. This bidirectional amplifier possesses the same gain as that of the reflection-type amplifiers, and, due to the symmetry of the configuration, may perform for waves coming from both I/O ports. The measured results of the fabricated bidirectional amplifier show that it provides the transmission gain over the frequency band from 5.76 to 6.88 GHz. At 6.04 GHz, this gain reaches a maximum value of 9.1 dB. Figure 22 is a photograph of a two-element active Van Atta array using the developed bidirectional amplifiers. Printed Yagi antennas with antenna gain of 7.4 dBi and half-power-beamwidth of 55° are used as the radiators in the array. Figure 23 shows its measured backscattering field pattern; that of a four-element passive Van Atta array using the same antennas is also shown for comparison. It is seen that both the patterns are wide. The 3 dB beamwidth of the active array is 74° and that of the passive array is 65° . The backscattering field level of the active array is, on average, 4.5 dB higher than that of the passive one, although the antenna number of the former array is only half that of the latter one.

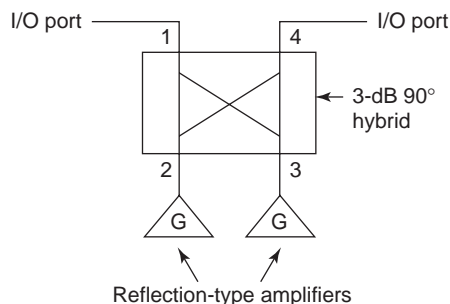


Figure 21. Configuration of a microwave bidirectional amplifier.

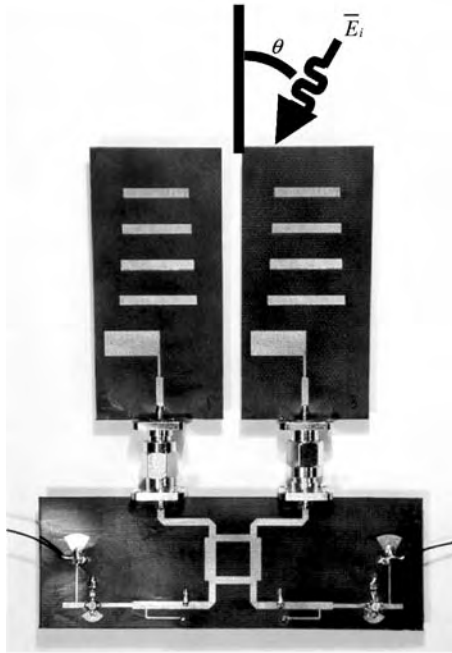


Figure 22. Photograph of a two-element active Van Atta array with bidirectional amplifiers.

Another way to have all the antennas' receiving fields amplified is by using the depolarizing Van Atta array. Figure 24 illustrates such an active retrodirective array with incidence field of V-pol and scattering field of H-pol. Two unilateral amplifiers, one for each direction, are used for the bidirectional amplification in each antenna pair. The field level received by the V-pol port of an antenna is enhanced by the amplifier and then fed to the H-pol port of the corresponding paired antenna. To achieve retrodirectivity of the array, the total phase delay of the transmission line and the amplifier in any path of the same direction should be the same.

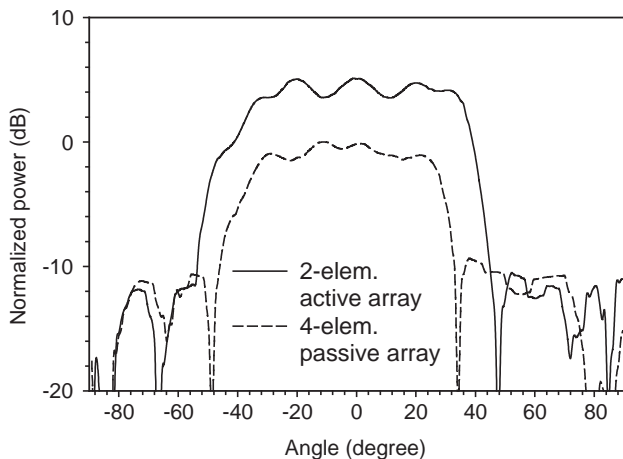


Figure 23. Measured backscattering-field patterns of the active Van Atta array shown in Fig. 22 and a four-element passive one.

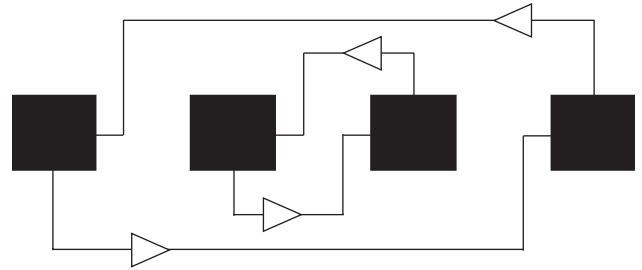


Figure 24. Diagram of an active retrodirective array with incidence field of V-pol and scattering field of H-pol.

4. APPLICATIONS OF THE VAN ATTA ARRAY

Applications of the Van Atta array were widely discussed only a day after Van Atta array was proposed in the 1960s. Since the 1990s, the movements of vehicle safety and intelligent transportation systems (ITSs) have attracted much attention. Collision warning radars and many wireless communication systems are used in moving vehicles. Collision warning radars encounter problems such as clutter from the roadway or roadside objects, which may be more hazardous for smaller cars. This may result in many sources of false alarms. One solution to this problem is to increase the vehicle's effective radar cross section (RCS), which may be achieved by mounting the Van Atta reflectors on a vehicle to increase the scattering beamwidth and thus enhance their "visibility." The Van Atta reflector can also be placed on a potential hazard to increase its echo to an interrogating vehicle radar, thus preventing a possible collision with it. When implemented with modulation circuits, Van Atta reflectors would play a much greater role in these automotive applications. For example, the reflectors mounted at the front and rear of a vehicle would have different modulation codes so that an interrogating vehicle can distinguish between approaching vehicles and those traveling in the same direction. The speed of the Van Atta reflector-bearing vehicle would be included in the modulated return, and thus the interrogating vehicle can distinguish a hazardous closing situation from a normal following situation in which the gap between vehicles is constant or increasing. In essence, the information can be incorporated as part of an intelligent cruise control system. Similarly obstacles and hazards such as bends in the road can be unambiguously identified by the Van Atta reflectors that are coded to indicate the type of fixed obstacle being marked [17].

On the other hand, in ITS applications, various types of information can be exchanged between the system centers and the vehicles by using the wireless communication systems. Among these communication systems, the dedicated short-range communication (DSRC), in which information is exchanged between roadside units (RSUs) and onboard units (OBUs), is one that can fulfill many of the requirements in ITS, and has been widely used for the electronic toll collection (ETC) system. Depending on whether a microwave oscillator is incorporated in the OBU, DSRC can be classified as either an active or a passive system. Although, the active system possesses the advantages of higher sensitivity and wider communication zone, the passive one has transponders with simple

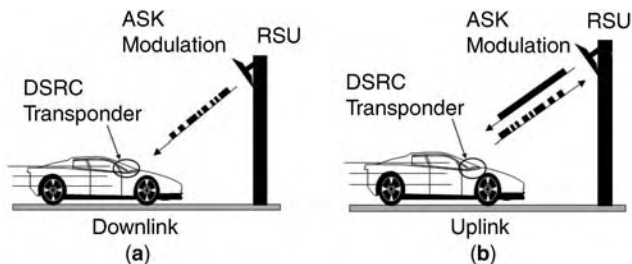


Figure 25. (a) Downlink and (b) uplink of data transmission in DSRC.

circuitry, low consumption power, and low cost. As shown in Fig. 25, the data transmission in the passive DSRC is half-duplex. In the downlink mode, the RSU emits an ASK-modulated left-hand circular polarization (LHCP) wave to the transponder. A detector circuit is established in the transponder to decode the downlink information. In the uplink mode, the RSU simply emit an LHCP continuous wave. The wave is received by the antenna in the transponder, modulated with an ASK or PSK code (containing the uplink information), and then reradiated by the transponder antenna to the RSU. Most of transponders use only one elementary antenna to reradiate the uplink signal, which are limited by the responding signal level. Although the signal level can be increased by using an array antenna in the transponder, it suffers from the drawback of narrow radiation beam, which thus constricts the responding angles of the transponder.

To reduce or eliminate these limitations, the Van Atta array was proposed for use in the transponder design [23]. Figures 26 and 27 show the functional block diagram and the photograph, respectively, of the Van Atta transponder. This card-type transponder has a two-sided configuration, with an area of $12.5 \times 5.5 \text{ cm}^2$. The frontside consists of four LHCP corner-trimmed square microstrip antennas

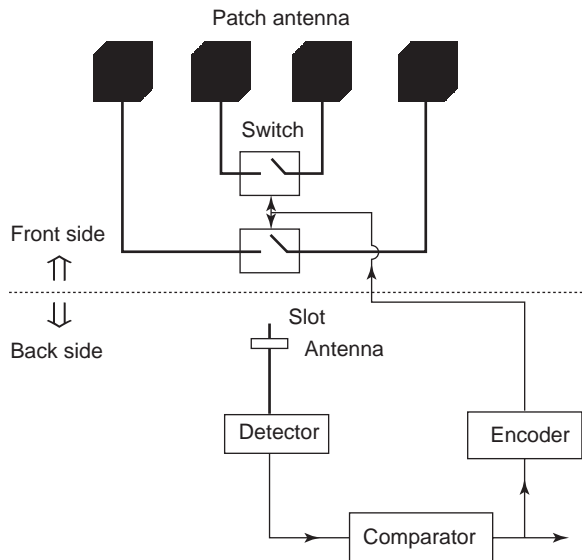


Figure 26. Function blocks of a passive transponder using the Van Atta microstrip antenna array.

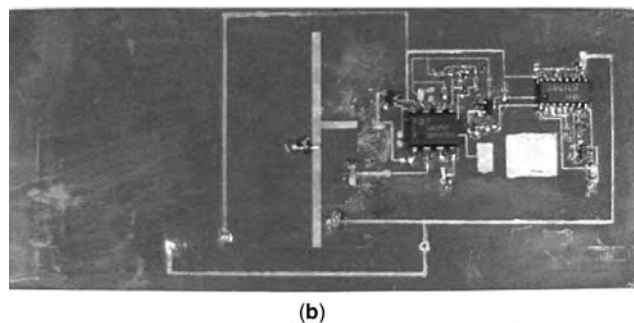
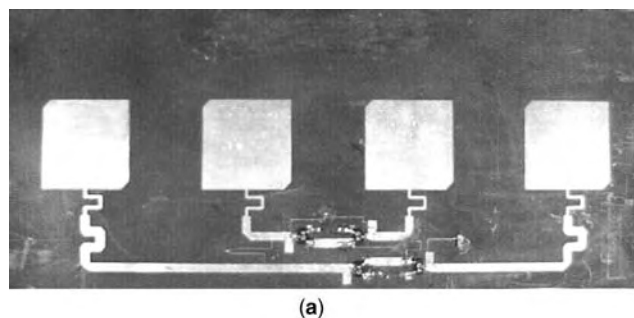


Figure 27. (a) Frontside photo and (b) backside photo of the fabricated card-type 5.8-GHz transponder.

and two pin (positive–intrinsic–negative) diode switches. The two edge antennas and the two middle ones are separately connected by two $50\text{-}\Omega$ microstrip lines, and the switches are embedded midway along the lines. The backside circuit contains a Schottky diode detector and a binary encoder circuit to control the switches on the frontside. A receiving slot antenna is built on the ground plane between the two substrates of the circuits. The slot output signal is connected to the diode detector through a microstrip line on the backside. In the downlink mode, the ASK-modulated wave from the RSU is received by the slot antenna and fed to the diode detector. The detected binary signal is then sent to a voltage comparator to reshape the signal and filter out the noise. In the uplink mode, a continuous wave is received by the slot antenna so that the output from the detector is a small DC voltage. After passing the comparator, this DC voltage will trigger the following encoder circuit to produce a binary voltage code containing the uplink information. This voltage code is then used to control the pin diode switches on the transponder’s frontside so that an ASK/PSK-modulated responding wave is produced. The only power source in the transponder is a 1.5-V-DC standby battery attached on the transponder backside. Only when the communication happens will the battery deliver power to the encoder and switch circuits.

In measuring the transponder performance, a fixed 8-bit binary code of “10101011” as shown in Fig. 28a was designed in the transponder’s encoder circuit. The clock rate for the encoder circuit was set as 16.4 kbps (kilobits per second). In the uplink communication mode, this code was carried by the responding wave to the RSU and detected from the mixing circuit. The detected signal at a distance of 1.5 m is shown in Fig. 28b, which exhibits

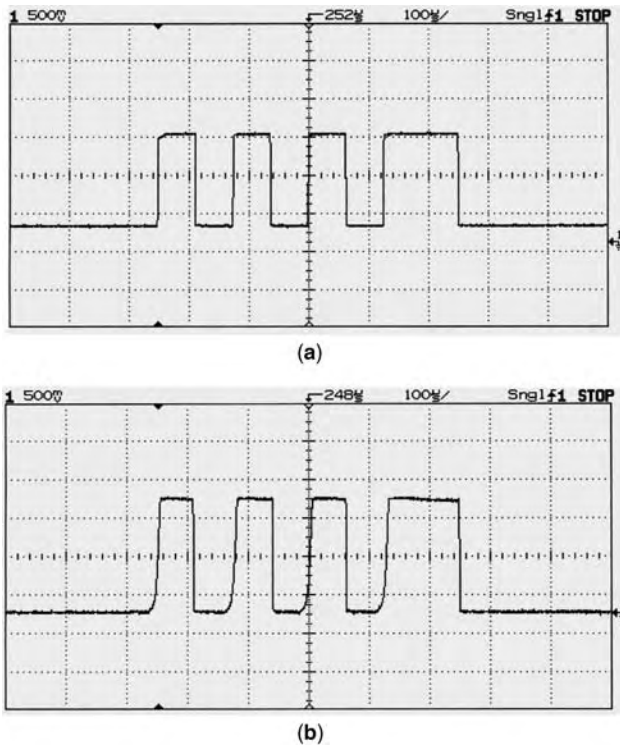


Figure 28. (a) Binary code incorporated in the encoder circuit of the transponder for the uplink measurement; (b) signal detected at the RSU in the uplink measurement.

exactly the same code as the original one. For the downlink measurement, a binary code of “10110101” with clock rate of 23 kbps was embedded in the encoder circuit of the RSU and was added to the 5.8-GHz continuous wave. The modulated wave, after being transmitted to the transponder, was then decoded in the transponder’s detector circuit. Although not shown here, the decoded signal did present the same code as that in the RSU.

The Van Atta reflector can also be used to design the OBU of an active DSRC system, where a microwave

source is required. Figure 29 illustrates the circuit diagram of such an active transponder proposed by Luxey and Laheurte [31] for use in a half-duplex communication system. The transponder is a two-element active Van Atta array containing depolarizing antennas, injection-locked oscillators, and amplifiers. The uplink signal is produced in the injection-locked oscillators and fed to the V-pol ports of the antennas for transmitting, and the downlink signal is received by the H-pol ports of the antennas. For retrodirectivity, the two phase delays from the receiving port of one antenna, through the amplifier and oscillator, to the transmitting port of the other antenna should be the same. The operation principle for the downlink mode is similar to that of the passive Van Atta transponder described above. For the uplink mode, an H-pol continuous wave is emitted from the RSU to the transponder and, after received by the antenna and enlarged by the amplifier, is injected to the oscillator of the corresponding element. If its frequency is within the injection-locking bandwidth of the oscillator, the frequency and the phase of the wave from the injection locked oscillator will follow those of the incoming wave [32]. Therefore, the waves produced by the two injection-locked oscillators can radiate with a maximal combination in the wave incoming direction. A PSK modulation can be implemented in the locking signal by tuning the bias voltages of the oscillators, or, an ASK modulation can be obtained by ON/OFF-switching the bias. Using the injection-locked oscillators, this active transponder design has the advantage of simplicity and inexpensiveness, as compared to a conventional transceiver design where a stable and exact microwave source is needed. Also, due to the Van Atta arrangement, this transponder may produce an output signal with higher effective isotropic radiated power (EIRP).

5. SUMMARY

A brief literature survey of the Van Atta retrodirective reflector was discussed initially in this article. The progress of the investigation comprises two main stages, one from 1960 to the early 1970s, and the other from the early 1990s until the present. In the first stage, the reflectors were built by bulky antennas such as dipoles and horns, with proposed application areas in satellite communications, military ECM systems, and small-boat or airplane navigation aids. The second-stage research dealt with planar Van Atta arrays using printed antennas with vehicle-mounting applications such as vehicle communications and collision warning systems. The theory of the Van Atta array was then described, which illustrated that the backscattering field pattern is primarily proportional to the array element number and the square of the element’s radiation pattern. Also pointed out is that the phase delays of the connecting transmission lines may be adjusted to smooth out the backscattering field pattern and to increase the beamwidth. Many design examples using PCB techniques were presented following introduction of the theory. These include Van Atta microstrip antenna arrays with retrodirectivity in one or two incidence planes, and active Van Atta reflectors with

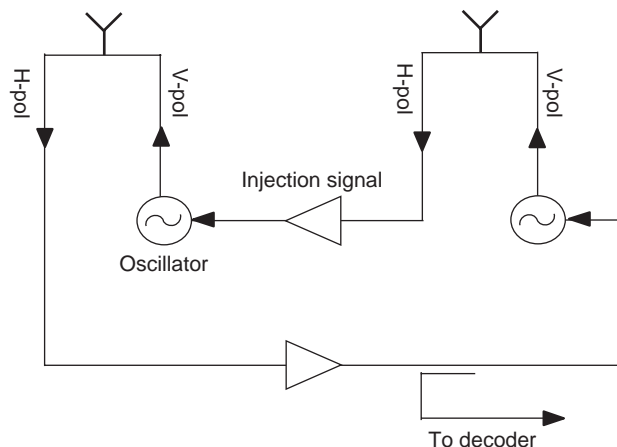


Figure 29. Circuit diagram of an active DSRC transponder using the Van Atta array.

unilateral amplifiers or bidirectional amplifiers. Finally, we have depicted the reflector's applications in the intelligent transportation system, focusing mostly on vehicle collision warning systems and the roadside-to-vehicle dedicated short-range communications.

BIBLIOGRAPHY

1. L. C. Van Atta, *Electromagnetic Reflector*, US Patent 2, 908, 002 (Oct. 1959).
2. C. Y. Pon, Retrodirective array using the heterodyne technique, *IEE Trans. Anten. Propag.* **AP-12**:176–180 (March 1964).
3. E. D. Sharp, *Properties of the Van Atta Reflector*, Rome Air Development Center, Technical Report. RADC-TR-58-53, ASTIADocument AD-148 684, Rome, NY, April 1958.
4. E. D. Sharp and M. A. Diab, Van Atta reflector array, *IRE Trans. Anten. Propag.* **AP-8**:436–438 (July 1960).
5. J. Appel-Hansen, A Van Atta reflector consisting of half-wave dipoles, *IEE Trans. Anten. Propag.* **AP-14**:694–700 (Nov. 1966).
6. J. A. Fusca, Compact reflector has E.C.M. potential, *Aviation Week* **70**:66–69 (Jan. 1959).
7. K. Walther, Model experiments with acoustic Van Atta reflectors, *J. Acoust. Soc. Am.* **34**:665–674 (May 1962).
8. T. Larsen, Reflector arrays, *IEE Trans. Anten. Propag.* **AP-14**:689–693 (Nov. 1966).
9. E. D. Nielsen, Square Van Atta reflector with conducting mounting plane, *IEEE Trans. Anten. Propag.* **AP-18**:48–54 (Jan. 1970).
10. L. H. Bauer, Technique for amplitude modulating a Van Atta radar reflector, *Proc. IRE* (correspondence) **49**:634–635 (March 1961).
11. R. C. Hansen, Communications satellites using arrays, *Proc. IRE.* **49**:1066–1074 (June 1961).
12. D. E. N. Davies, Some properties of Van Atta arrays and the use of 2-way amplification in the delay paths, *Proc. IEE* **110**:507–512 (March 1963).
13. M. J. Whithers, An active Van Atta array, *Proc. IEE* **111**:982 (May–June 1964).
14. J. L. Ryerson, Passive satellite communication, *Proc. IRE* **48**:613–619 (April 1960).
15. J. Kaiser and I. Kay, Passive and active reflectors, (Part 4.4 of the US Natl. Committee Report for Committee 6 of URSI), *Radio Sci.* **68D**:515–517 (April 1964).
16. B. McQueen and J. McQueen, *Intelligent Transportation Systems Architectures*, Artech House, Boston, 1999.
17. M. Cohn, A millimeter wave retrodirective transponder for collision/obstacle avoidance and navigation/location, *Vehicle Navigation and Information System conf.*, Oct. 1993, pp. 534–538.
18. S.-J. Chung and K. Chang, A retrodirective microstrip antenna array, *IEEE Trans. Anten. Propag.* **46**:1802–1809 (Dec. 1998).
19. W.-J. Tseng, S.-J. Chung, and K. Chang, A planar Van Atta array reflector with retrodirectivity in both E-plane and H-plane, *IEEE Trans. Anten. Propag.* **48**:173–175 (Feb. 2000).
20. W.-J. Tseng, C.-S. Hu, and S.-J. Chung, Planar retrodirective array reflector using dual-slot antennas, *Electron. Lett.* **34**:1374–1376 (July 1998).
21. T.-J. Hong and S.-J. Chung, 24GHz active retro-directive antenna array, *Electron. Lett.* **35**:1785–1786 (Oct. 1999).
22. H.-T. Chen and S.-J. Chung, Design of a planar array transponder with broad responding beam, *IEEE Microwave Guided Wave Lett.* **7**:297–299 (Sept. 1997).
23. S.-J. Chung, T.-C. Chou, and Y.-N. Chiu, A novel card-type transponder designed using retrodirective antenna array, *IEEE MTT-S, Microwave Symp. Digest*, May 2001, Vol. 2, pp. 1123–1126.
24. S.-J. Chung, S.-M. Chen, and Y.-C. Lee, A novel bi-directional amplifier with applications in active Van Atta retrodirective arrays, *IEEE Trans. Microwave Theory Tech.* **51**:542–547 (Feb. 2003).
25. M. Fujita, Development of a retrodirective PARCfor ALOS/PALSAR calibration, *IEEE Trans. Geosci. Remote Sens.* **41**:2177–2186 (Oct. 2003).
26. W. L. Stutzman and G. A. Thiele, *Antenna Theory and Design*, Wiley, New York, 1981.
27. C. Cavello, B. Baertlein, and J. Young, Radar retro-directive patch for vehicle convoying applications, *Proc. IEEE Conf. Intelligent Transportation Systems*, Nov. 1997, pp. 667–671.
28. M. Fujita and C. Murakami, Experimental study of a polarization-rotating Van Atta array with reduced co-polarized radar cross-section, *Geoscience and Remote Sensing Symp. paper INT_F26_03*, July 2003.
29. M. Fujita, A depolarizing reflector of Van Atta array design for polarimetric calibration, *Proc. Geoscience and Remote Sensing Symp.* July 2000, Vol. 6, pp. 2721–2723.
30. M. G. Christodoulou and D. P. Chirssoulidis, 2D Van Atta retrodirective array using dual polarized two-port square microstrip patches, *Proc. IEEE Conf. Antennas and Propagation*, April 2001, Vol. 2, pp. 814–816.
31. C. Luxey, and J. M. Laheurte, A retrodirective transponder with polarization duplexing for dedicated short-range communication, *IEEE Trans. Microwave Theory Tech.* **47**:1910–1915 (Sept. 1999).
32. V. F. Fusco, S. Drew, and D. S. McDowall, Injection locking phenomena in an active microstrip antenna, *Proc. IEEE Conf. Antennas and Propagation*, 1993, Vol. 1, pp. 295–298.

VARIABLE-FREQUENCY OSCILLATORS

GERMÁN GUTIERREZ
Centellax, Inc.
Carlsbad, California

An *oscillator* is defined as anything that swings back and forth like a pendulum (vibrates) or travels back and forth between two points. An *electronic oscillator* is a device used for producing alternating current (e.g., a radiofrequency or audiofrequency generator). *Frequency* is the number of times that a periodic function repeats the same sequence of values during a unit of time or the number of complete oscillations of a wave per second.

Oscillators are abundant all around us: light, sound, the rotation of Earth, electric AC power, heartbeats, musical instruments, motors, microprocessor clocks, and so on. Some of these oscillatory systems have variable frequency, and some have fixed frequency. We will first

describe all the different types of electronic oscillators to appreciate what determines their operating frequency and how it can be varied.

1. TYPES OF OSCILLATORS

There are two basic kinds of oscillators: sinusoidal and relaxation. The mechanisms that produce these two types of oscillations are different, as are the required conditions for oscillation. Sinusoidal oscillations are represented by RC- and LC-tuned circuits. Their oscillations are continuous and relatively sinusoidal. Relaxation oscillators are represented by multivibrators and ring oscillators. Their oscillations are discontinuous and nonsinusoidal.

Sinusoidal oscillations are created when energy stored in one form is allowed to change uniformly into another form, going back and forth between the two without stopping. Because energy may be transferred between states with minimum loss, some sinusoidal oscillators can be energy-efficient because only small amounts of energy need to be supplied externally to keep the action going. This type of oscillator is associated with linear systems. Sinusoidal oscillators are of two types: feedback and negative resistance.

Relaxation oscillations are characterized by the sequential accumulation and release of energy in one or several storage elements. Energy is accumulated up to a certain level (threshold) and then quickly released (usually dissipated as heat), and then another element (or the same element) in the system begins to accumulate energy until the cycle repeats. The action exhibits positive feedback during reset or relaxation, reinforcing itself and occurring rapidly. This type of oscillator is associated with nonlinear systems. Because all the accumulated energy is periodically dissipated, relaxation oscillators are very energy-inefficient.

This article does not cover chaotic oscillators. Chaotic oscillators do not have a periodic sequence of events that repeat in a unit of time. Related to nonlinear systems, chaotic oscillators occur, for example, in turbulent flows of liquids or in noiselike random signals generated in certain electronic systems.

2. MECHANICAL EXAMPLES

The most elementary types of mechanical oscillators are the spring and mass, and the pendulum, as shown in Fig. 1. In the spring and mass the energy is alternately changing from the spring to the potential and kinetic energy in the mass. At the top of its swing, all the energy is potential energy related to the elevation of the mass. Midway down are kinetic, potential, and spring energies. The pendulum is a well-known example of the oscillation between potential and kinetic energies.

Both systems will slow down because of the friction in the air. The spring also dissipates energy as a result of the internal friction of its metal grains. The pendulum has friction at the hinge. Rather than being strictly oscillators, these mechanical arrangements are examples of damped oscillators. An energy input is necessary to compensate for

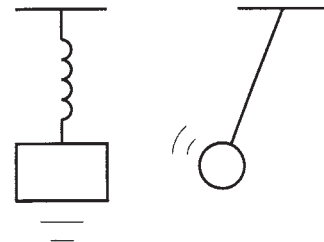


Figure 1. Simple mechanical damped oscillators.

the losses and to deliver power to outside loads, for example, to synchronize other mechanical devices.

The windmill is an interesting example of an oscillator (Fig. 2). Its frequency is proportional to the drive level (e.g., the wind strength). The amplitude of the oscillation is, however, fixed. This is the opposite of electronic oscillators, which increase their signal swing in response to more supplied power. However, if we think of the windmill as driving a load, like an AC voltage generator, then there is a relationship between its energy output and the available wind energy. The paddles seem to rotate with the same magnitude, but they deliver changing amounts of energy at varying frequencies.

An example of an oscillatory system that is not sinusoidal, like the pendulum or the windmill, is shown in Fig. 3. The waterdrops accumulate in the glass until the surface tension can no longer hold any more liquid, the water spills over the edge, and the cycle repeats. It is called a *relaxation oscillator* because the energy accumulates in a certain form up to the level that causes the system to relax and let go of the accumulation; then the system resets and restarts the sequence.

3. ELECTRICAL RESONATORS

The electrical equivalents of the mechanical resonator are the series and parallel resonant tanks shown in Fig. 4. They are composed ideally of just an inductor and a capacitor, but there are always losses that are modeled by resistors. The energy is alternatively stored in the capacitor (as an electric field of potential energy) and in the inductor (as magnetic energy). When the capacitor is at full charge, the voltage across the parallel arrangement is at its peak, and when the current through the inductor is at its peak, then the voltage across the tank is zero.

Other popular resonators are transmission line, dielectric, yttrium-iron-garnet (YIG), crystal, and surface acoustic wave (SAW). Resonant tank equivalent circuits at different frequencies of operation can represent all of these.

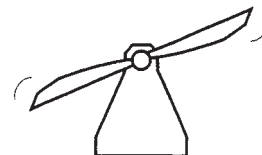


Figure 2. A windmill produces oscillations of varying frequency in response to the wind force.

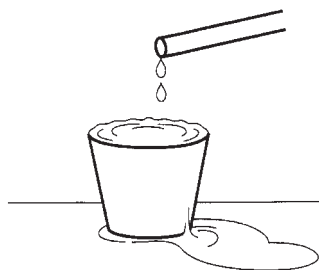


Figure 3. Mechanical example of a relaxation oscillator.

4. QUALITY FACTOR (Q)

The Q of a resonator is a useful number to calculate. It is defined as 2 times the ratio of the energy stored in the system to the energy dissipated per cycle [1]. It turns out that Q has two other useful interpretations. It is a measure of how many cycles it takes a damped oscillatory system to decay [2], and it defines the 3 dB bandwidth of a second-order resonator [3]. Q also describes how rapidly the phase changes with frequency near the resonant frequency, indicating how little the frequency will shift with changes that affect a delay in an oscillator loop [4]. Finally, for a series-resonant circuit, Q is the ratio of impedance in L or C divided by R [5]; for the parallel-resonant circuit, Q is the inverse of this equation.

$$Q = 2\pi \frac{\text{peak energy stored in } L \text{ or } C}{\text{energy dissipated per cycle}} \quad (1)$$

$$Q = \pi(\text{number of cycles to decay to } 1/e) \quad (2)$$

$$Q = \frac{\text{resonant frequency}}{3 \text{ dB bandwidth of resonator}} \quad (3)$$

$$Q = \frac{\omega}{2} \times \frac{d\phi}{d\omega} = \frac{\omega}{2} \times \text{rate of phase change with frequency} \quad (4)$$

$$Q = \omega \frac{L}{R} \quad (5)$$

5. SINUSOIDAL OSCILLATORS

5.1. Feedback Oscillators

A general way of thinking about an oscillator is in terms of an amplifier that feeds its output back to its own input

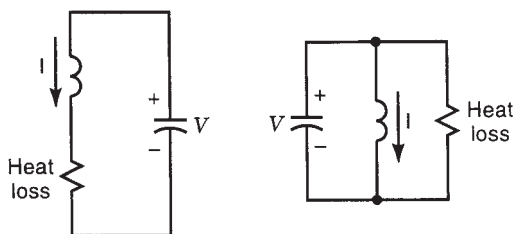


Figure 4. Electrical damped oscillatory systems: series and parallel resonators with loss.

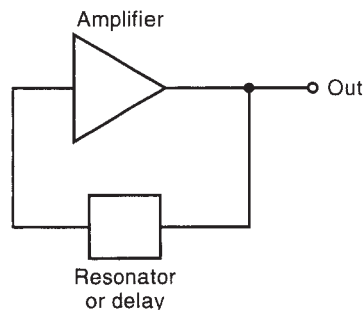


Figure 5. An oscillator viewed as a feedback system in which the output provides its own input.

(Fig. 5). The feedback is controlled by a resonator or a delay element in such a way that the desired frequency and amplitude of oscillation are achieved. Note that the resonator or delay box is still indicated as a two-terminal box with another two-terminal amplifying box connected across it. This could be viewed as a negative-resistance oscillator, as will be discussed later.

5.2. Conditions for Oscillation

Normally, for oscillation to start, the active device provides more energy than is being dissipated in the resonator. This causes the amplitude of the oscillation to grow until it is limited by changes in the active device that reduce its gain. The losses in a system may be linearly related to its amplitude over a limited region, but they grow more rapidly (nonlinearly) over an extended region of amplitude, until they eventually hardlimit the amplitude (e.g., when a barrier is reached).

The requirements for oscillation are that the amplitude of the signal being fed back be large enough to produce an output that can reproduce the feedback (greater than unity loop gain) and that the relative phase between the input and the fed-back input be near zero (so that the feedback reinforces the output). More simply said, the one-way trip around the loop needs to have gain greater than one and zero phase. However, these conditions should not be met at DC; otherwise, the oscillator will latch into a limit state, and no AC oscillation will develop. Additionally, stable oscillations develop only if disturbances in amplitude or phase cause the oscillator to respond by moving back to the unstable point. Finally, reliable oscillators need to have only one frequency at which the conditions for oscillation are met; otherwise, frequency jumps could occur.

5.3. RC Delay Oscillator (Phase Shift Oscillator)

The circuit shown in Fig. 6 is known as the RC (resistor-capacitor) delay oscillator. Three stages of RC delay are used in the feedback path. If the amplifier is inverting, then the RC network needs to produce 180° of phase shift at the frequency of oscillation. Stated differently, the oscillation will occur at that frequency at which the feedback has a phase delay of 180° and the gain is greater than one. Other possibilities to realize the phase delays are to RL (resistor-inductor) delay or lossy transmission-line

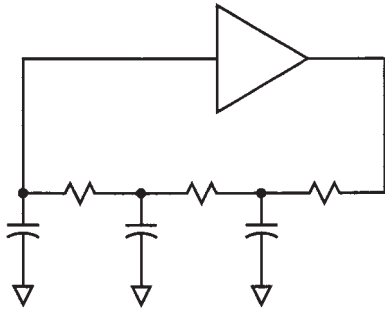


Figure 6. RC delay oscillator. For an inverting amplifier, there must be 180° of phase shift in the RC feedback path.

delay. A transmission line is just a distributed RLC delay element. LC delay elements and lossless transmission lines will be covered next.

5.4. LC-Tuned Oscillators

When a tuned circuit is used to define the oscillation frequency, it is desirable to preserve its frequency-selective properties Q . To prevent loading a resonator by the input of an amplifier, a transformer is necessary. Several types of impedance transformation are possible by using coupled inductors, inductive division, or capacitive division. Another possibility is to use another amplifier as a buffer; the input impedance of the buffer is high, and the loading on the resonator is light.

Figure 7 shows two ways of looking at how an amplifier can be connected across a tank circuit using capacitive division of voltage. The arrangement shown on the right is known as the *Colpitts circuit*. Capacitors C_1 and C_2 in series form part of the resonator, and the input loading by the amplifier is reduced by their ratio. The circuit on the left uses the capacitors as a way of getting 180° of phase shift at resonance, while internally completing the loop with an additional 180° resulting from signal inversion. However, the two capacitors are still connected in series to each other and across the inductor, and voltage division takes place across this tank. The advantage of capacitive division over inductive division is that it is easier to realize in an integrated circuit. Split inductors or transformers are more complicated to build than simple inductors.

The arrangements shown in Fig. 8 are known as *Hartley* and *Armstrong oscillators*, respectively. Inductive divi-

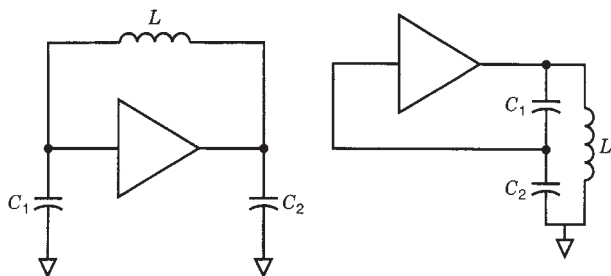


Figure 7. Oscillators with capacitive division of voltage, also known as *Colpitts arrangements*.

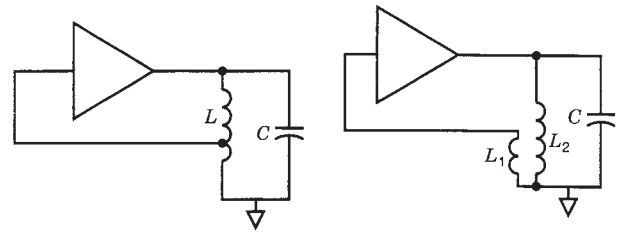


Figure 8. Inductive division of voltage in Armstrong and Hartley oscillators.

sion, using two inductors or a single inductor with a tap connection, provides the feedback in the Hartley circuit. The input loading is therefore decreased. The Armstrong circuit uses two inductors, L_1 and L_2 , with inductive coupling between them. This may be attractive if the objective is to keep the input and output biases isolated from each other. Moreover, the amount of coupling between the coils can be varied without changing the values of the inductors.

A single-transistor implementation of the capacitively divided tank circuit is depicted in Fig. 9. This circuit is simple because the base bias is provided through the inductor. The value of the collector load resistor needs to be large enough to prevent decreasing the Q of the resonant circuit. The coil and the series connection of the two capacitors make up the resonant circuit. This arrangement can be modified by placing a capacitor in series with the coil (and providing base bias). The series resonant frequency of the coil and the added capacitor can dominate the oscillation frequency, making the circuit less sensitive to variations in the transistor and in the other two capacitors. This modification is known as the *Clapp oscillator*.

The DC-coupled LC oscillator in Fig. 10 is based on a differential amplifier. It has a single-ended tank and a single-ended output. Its output is directly coupled to its noninverting input, and therefore the feedback needs to provide 0° of phase delay because 360° would be impossible with the circuit shown. At resonance, the LC tank presents a purely resistive load to the collector output, and therefore it has no phase delay. Any internal delay through the device will need to be canceled by adjusting the oscillation frequency slightly out of resonance. Using a

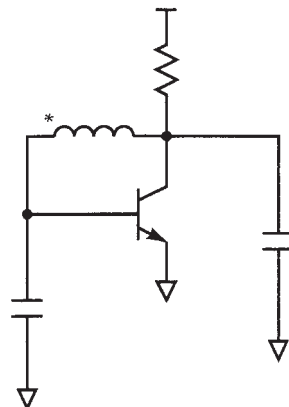


Figure 9. Single-transistor implementation of a capacitive division oscillator.

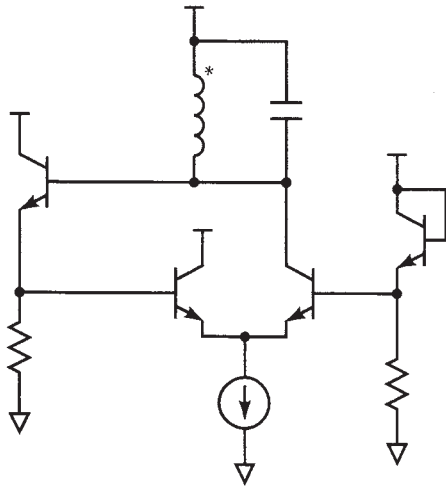


Figure 10. Differential amplifier LC-tuned oscillator with single-ended output. The emitter-follower provides DC-coupled impedance transformation.

variable capacitor would normally control the frequency of this oscillator. A small change in frequency can also be obtained by changing the bias on the differential amplifier.

Tuned oscillators may also use transmission lines, cavities, dielectric resonators, crystals, or YIG resonators to determine their operating frequency. These resonators have equivalent circuits of very high Q . For example, because of the interaction between voltage and mechanical resonance, piezoelectric quartz crystals are much more stable and of higher Q than are LC resonators.

5.5. Use of Varactors

Varactors are used to vary the frequency of resonant LC circuits (Fig. 11). The combined symbol of a capacitor with a diode arrow is used to indicate that they are diodes whose junction depletion capacitance varies. This happens in response to a change in the reverse voltage applied across them. The types of varactor diodes that have the most change of capacitance with voltage are called *hyperabrupt*. The junction between the n region and the p region is made very sharp, and the doping concentrations are very different. This causes the depletion layer on the lightly doped side to move considerably with applied voltage. Since varactors also have loss, they must be selected or designed to minimize the degradation of the resonator's Q .

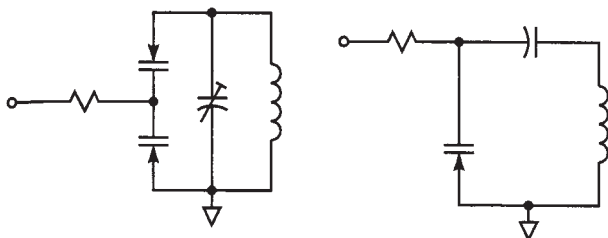


Figure 11. Resonator arrangements using varactor diodes to tune the center frequency.

The drawing on the left side of Fig. 11 shows a common back-to-back connection of two varactors. Because the voltage that develops in a tank circuit is large, this arrangement offers some cancellation of the variation of the capacitance as a function of the tank voltage. Even-order distortion products are canceled, and the voltage at which the diodes would conduct is increased. The simpler arrangement on the right requires a capacitor to AC-couple the varactor to the inductor so that the inductor does not short-circuit the bias voltage. This circuit is adequate when the signal level is small or when there is no concern about generating harmonics of the tank's fundamental frequency.

5.6. Negative-Resistance Oscillators

Negative-resistance oscillators also can be viewed as one-port oscillators, as opposed to the two-port oscillators used in feedback arrangements. Some electronic devices (e.g., microwave diodes) are two-terminal devices and can be operated only as a one-port device. Therefore, negative-resistance oscillator analysis is the most general in that it includes two- and three-terminal (or more) electronic devices.

To compensate for the losses in a resonant circuit, an active circuit needs to supply power to cancel them. This can be regarded as paralleling the resonator with a negative resistor (Fig. 12). It turns out that most oscillator arrangements can be simplified to this type of model, and an equivalent value for negative R can be calculated. If the negative-resistance "blackbox" is a two-port, which is common, then the other port can be tuned to deliver power to a load.

One possible single-transistor version of a negative resistance oscillator is shown in Fig. 13. The capacitor from emitter to ground makes the input impedance at the base partly negative real and partly capacitive. The inductor at the base can be either series- or parallel-resonated with the input capacitor and with other tuning capacitors or varactors. Note that one could use the collector to deliver power to a load instead of connecting it to the power supply.

6. RELAXATION OSCILLATORS

6.1. Ring Oscillators

Ring oscillators are a popular topology for variable-frequency oscillators used in integrated circuits because they have broad tuning range and require no resonators. They consist of a number of amplifiers or delay stages that may be inverting or noninverting, connected in such a way that

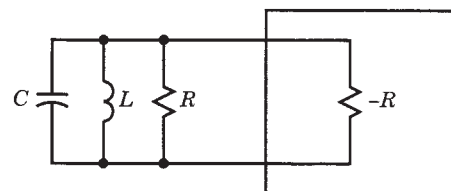


Figure 12. Negative resistance compensates for the losses in a parallel tank resonator.

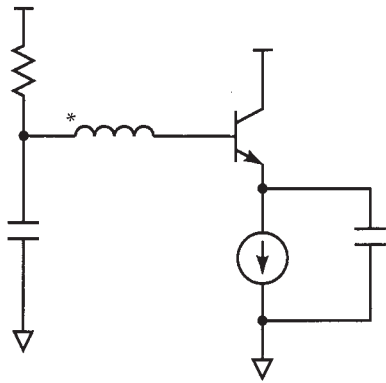


Figure 13. Negative-resistance oscillator with series resonant tuning.

an odd number of inversions exist around the loop (Fig. 14). The loop is therefore never “happy,” and the result is that an “edge” propagates around the loop. Loops with as little as two buffers are possible, but for large number of stages it is customary to choose prime numbers to prevent the occurrence of multiple modes of oscillation. For example, if we used six buffers, we could have three edges running around the loop, with the result that the frequency would sometimes be 3 times higher. This would happen at random after powering up the circuit.

The frequency of a ring oscillator can be varied in several ways. One popular way is to change the internal delay of each buffer by adjusting the amount of current available to charge and discharge the circuit capacitances. Another way is to vary the amount of load presented at the output of each buffer.

6.2. Astable Multivibrators

Figure 15 shows the main features of an astable multivibrator. It consists of an amplifier with a positive-feedback connection that causes hysteresis in the multivibrator. When one of the inputs causes the output to swing in one direction, the positive feedback changes the switching threshold, reinforcing the input so that there is no hesitation if the input begins to change back. It behaves like a comparator with a moving input threshold. This prevents noisy outputs when the inputs are changing too slowly or when they sit too close to the threshold. In the case of this oscillator, the hysteresis allows the operation of the circuit, which would not occur otherwise. The R and C connected to the inverting input cause this point to vary

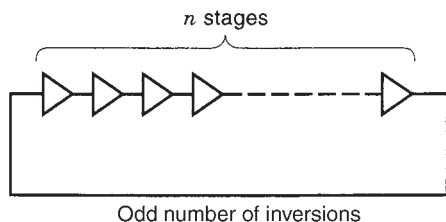


Figure 14. A ring oscillator consists of a number of buffers connected in a loop.

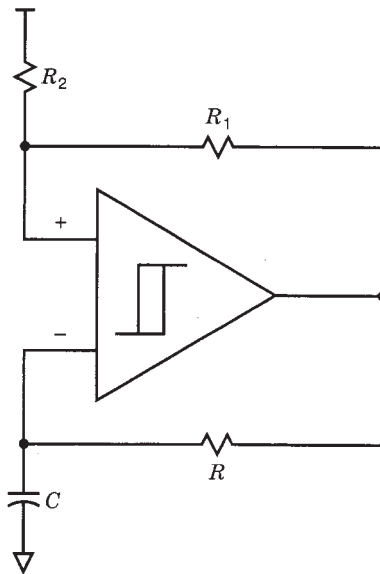


Figure 15. Diagram of a bistable oscillator.

exponentially up and down around the hysteresis voltage region. Multivibrators have a broad tuning range.

The astable multivibrator in Fig. 16 is a popular oscillator circuit that is often built in university engineering laboratories and by hobbyists. It is fairly nonlinear because the two transistors take turns being on and off, without spending much time midway. When transistor Q_1 turns on, its collector pulls the base of Q_2 down, through C_2 , keeping it off. Resistor R_3 will in time recharge C_2 and turn Q_2 back on. When this happens, there is positive feedback. As Q_2 turns on, it will turn Q_1 off, and as the collector of Q_1 goes high, it will reinforce Q_2 being on. Next, R_2 will begin to recharge C_1 until Q_1 is turned back on. The RC time constants (R_2C_1 and R_3C_2) need not be the same, and nonsymmetric oscillations can be designed with this circuit. For example, a narrow pulse can be produced. The frequency of oscillation can be varied by changing the value of the resistors (most commonly R_2 and R_3) or by switching different values for the capacitors and using the resistors for fine adjustment. Other possibilities

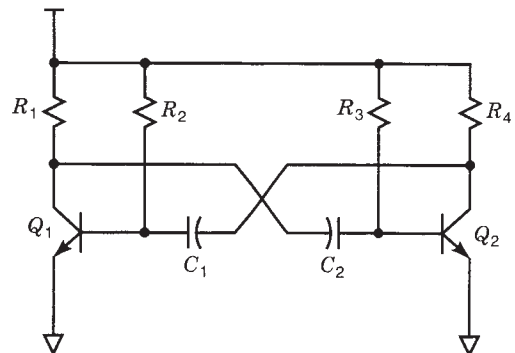


Figure 16. Example of common multivibrator. The system has two stable points: when Q_1 is on and when Q_1 is off (and Q_2 is therefore on).

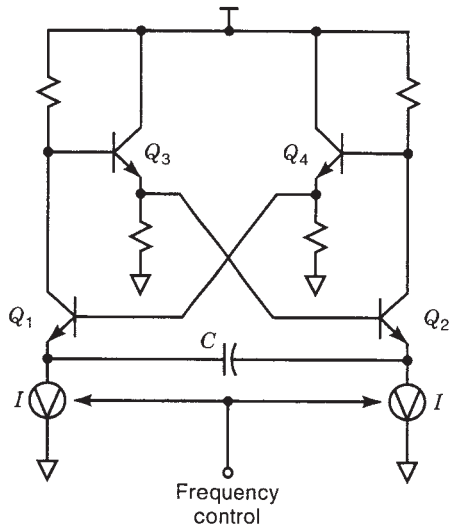


Figure 17. Another multivibrator or astable oscillator that needs only one capacitor.

are changing the power supply voltage or the value of the collector load resistors, which are typically smaller than R_2 and R_3 .

Another popular astable multivibrator circuit has a single timing capacitor (Fig. 17). Its frequency is adjusted by changing the value of the current sources. Transistors Q_1 and Q_2 form a cross-coupled pair through Q_3 and Q_4 that acts like an emitter-follower buffer. In this configuration, when one of the two bottom transistors is on, it forces the other transistor off and vice versa, in a latching arrangement with large hysteresis. For example, Q_1 being on forces Q_2 off, which reinforces the state of Q_1 being on. The transistor that is on must supply current to both current sources I and therefore will begin to charge capacitor C until the voltage at its own emitter rises and turns itself off. This happens quickly. The other transistor begins to

charge the capacitor in the opposite direction, and the cycle repeats itself. The frequency of oscillation is linearly proportional to the value of the current in the sources because the capacitor is charged linearly by current and not through a resistor. The waveforms at the emitters of Q_1 and Q_2 are linear sawtooth waves.

The Schmitt trigger oscillator shown in Fig. 18 is also known as the *grounded-timing-capacitor oscillator*. The differential amplifier and two emitter-followers on the right are connected in positive feedback. When the transistor directly on top of the timing capacitor is turned on, it quickly charges it to near the power supply voltage and forces the trigger to switch states. This turns off the top transistor, and the current source begins to discharge the capacitor linearly. When the capacitor voltage is low enough, the trigger switches, and the process repeats. The output waveforms of this oscillator consist of narrow complementary pulses, whereas the voltage across the timing capacitor is a linear sawtooth waveform.

6.3. Voltage-to-Frequency Converters

Voltage-to-frequency converter circuits are used not so much to produce oscillations but rather to measure voltages precisely. They achieve very linear transfer characteristics from voltage to frequency and allow a frequency counter (a digital circuit of high repeatability) to measure the input voltage level. However, as an example of a variable-frequency oscillator, this is the most linear of all.

In the schematic drawn in Fig. 19, the input voltage V_{in} causes current to flow into the precision integrator circuit containing or including C_i . The comparator with hysteresis periodically switches capacitor C_f from the voltage reference V_{ref} to the input terminal of the integrator, discharging it fully. This achieves the transfer of a measure of charge in a way that is independent of the waveform driving the switch, as long as capacitor C_f is given enough time to discharge fully. Note that the polarity of

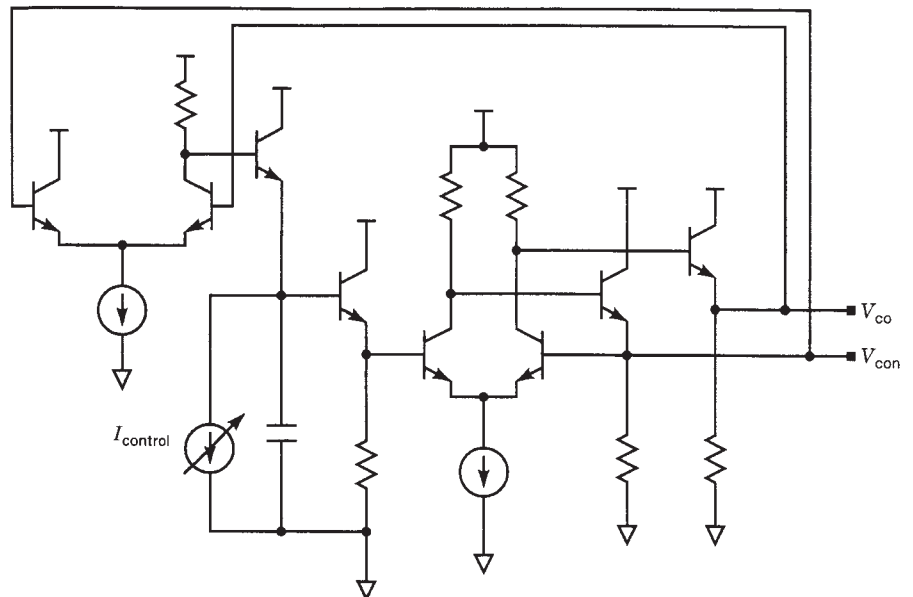


Figure 18. Detailed schematic of a Schmitt trigger oscillator with the single timing capacitor tied to ground.

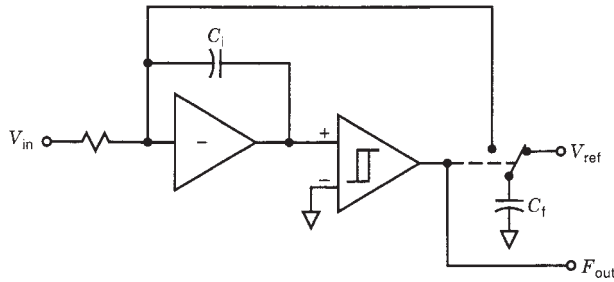


Figure 19. Voltage-to-frequency converters are used to measure voltages.

V_{ref} needs to be opposite that of V_{in} , or the capacitor needs to be discharged-inverted. This can be done by connecting the topside of the capacitor to the input and the switch, to the bottom side.

7. PROGRAMMABILITY DESIGN STYLES: HOW TO VARY THE FREQUENCY

Most variable-frequency oscillators are voltage-controlled [i.e., voltage-controlled oscillators (VCOs)]. This is a desirable feature because producing a variable voltage is usually easier than producing a variable current. Even if the frequency control is by variable capacitance, varactors that require a control voltage can be used. In cases where the control variable is naturally current, as in relaxation oscillators or in some ring oscillators, a voltage-to-current converter can be added to make the circuit a VCO.

For sinusoidal oscillators, the presence of a resonant circuit imposes a limited tuning range. Frequency change in these circuits usually uses variable capacitors—or variable resistors in an RC oscillator. In the past, mechanically tuned air dielectric capacitors and even variable inductors were used. Modern designs prefer using varactor diodes. However, the tuning range is limited to less than an octave in a resonant circuit that uses variable components.

To increase the tuning range, different component values can be switched around for different ranges. Usually the inductance is switched, while the capacitance is continuously varied. Mechanical switches have been used in the past, but today switching diodes are preferred because of their small size, lower cost, and higher frequency performance (less parasitics). A popular switching diode is known as *positive-intrinsic-negative* (p-i-n). It consists of three layers of p-type (undoped or intrinsic) and n-type semiconductors. When no current flows through the p-i-n diode, the i (intrinsic) layer acts like a thick dielectric, and

the diode’s capacitance is low. When current is forced through the diode, it exhibits low series resistance. It therefore approximates an ideal switch.

Although their frequency can be varied over only a very small range, crystal oscillators can change frequencies dramatically by switching the crystal element. In some radios, channels are changed by switching crystal values in several oscillators, and their outputs are multiplied or mixed together to produce the desired frequency.

Relaxation and ring oscillators have wide tuning ranges in spite of their poor stability and noise performance. It is easy to tune them over a 10:1 ratio, and with careful circuit design, more than two decades of frequency control are possible. Voltage-to-frequency converters are also easy to tune over broad ranges, although they are relatively slow oscillators.

Table 1 highlights the features of the different oscillators covered. Depending on speed, tuning range, and method of tuning required, a variable-frequency oscillator that meets the required needs can be found. Of course, no single oscillator can simultaneously satisfy all possible needs, and other variables like available materials and cost need to be evaluated.

8. ADVANCED CIRCUITS

Further examples of more sophisticated circuits will be described shortly. The first three examples are differential versions of previously discussed arrangements. Their advantages in rejecting power supply noise and in reducing even-order distortion more than offset the added complexity. Particularly in integrated circuit design, trading the number of components for enhanced response is always a winning strategy. The last circuit shown is an elegant arrangement for a crystal oscillator that has improved output buffering.

A differential LC oscillator with delay tuning has frequency control by varying the delay of the feedback signal (Fig. 20). This works well for low- Q tank circuits that are realized in monolithic implementations. The outputs are directly coupled to the inputs without inversion. The resonant circuit is composed of the series sum of the two inductors and the capacitance across them. The two collectors connected to the tank are operating 180° out of phase. The current at the bottom of the two emitter-followers, which connect to the tank inductors, is varied to change the oscillation frequency. This is done by using another differential amplifier with two output transistors. Less current results in more delay, which the loop compensates for by lowering the frequency of oscillation.

Table 1. Main Features of Variable-Frequency Oscillators

Type	Frequency	Tuning Range	Tuning Means
RC oscillator	Low to medium	Medium	Resistor or capacitor
LC -tuned oscillator	Medium to high	Narrow	Capacitor, switch inductor
Crystal oscillator	Medium	Very small	Voltage, switch crystals
Ring oscillator	Low to high	Wide	Current or capacitor
Astable multivibrator	Low to medium	Wide	Current
Voltage-to-frequency convertor	Low	Very wide	Voltage

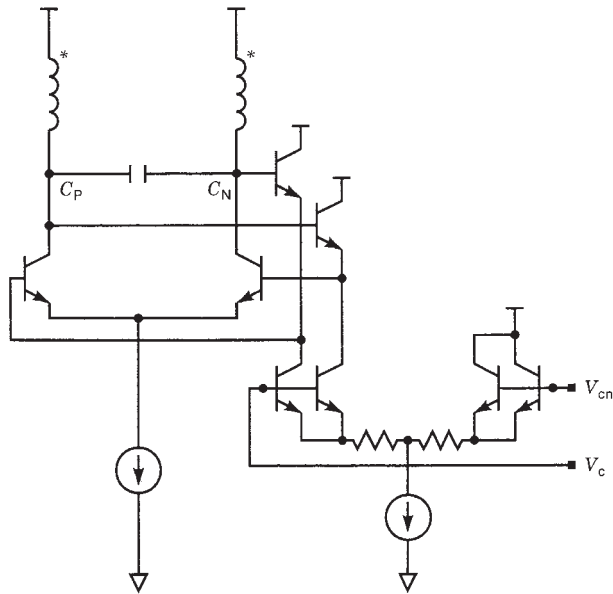


Figure 20. Fully differential LC oscillator with delay tuning.

Because of large emitter degeneration, the control voltage produces a near-linear change in the current going into the emitter-followers. For a tank with a Q of less than 10, this circuit achieves a tuning range of over 20% of the central frequency. The inductor is often a planar spiral layout of thin metal sitting on a lightly conductive substrate. The series resistive loss in the inductor and the field-absorbing loss in the substrate dominate the Q of the tank.

A differential version of the negative resistance oscillators is shown in Fig. 21. During operation, transistors Q_1 and Q_2 alternatively turn on and off. The inductor series resonates with the capacitor and with the capacitive input impedance of the two transistors. They present a negative real input impedance when they are on; however, they alternatively turn off, and the real part of the input impedance goes from negative to positive. This simple arrangement provides differential outputs that are useful in several applications in integrated circuit design.

A high-speed, two-stage ring oscillator is depicted in Fig. 22. The buffers consist of slow and fast amplifiers connected in parallel and sitting on top of a differential amplifier. The control voltage allows us to interpolate

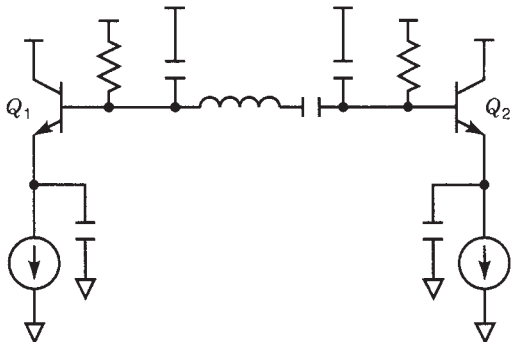


Figure 21. Differential version of negative-resistance oscillator.

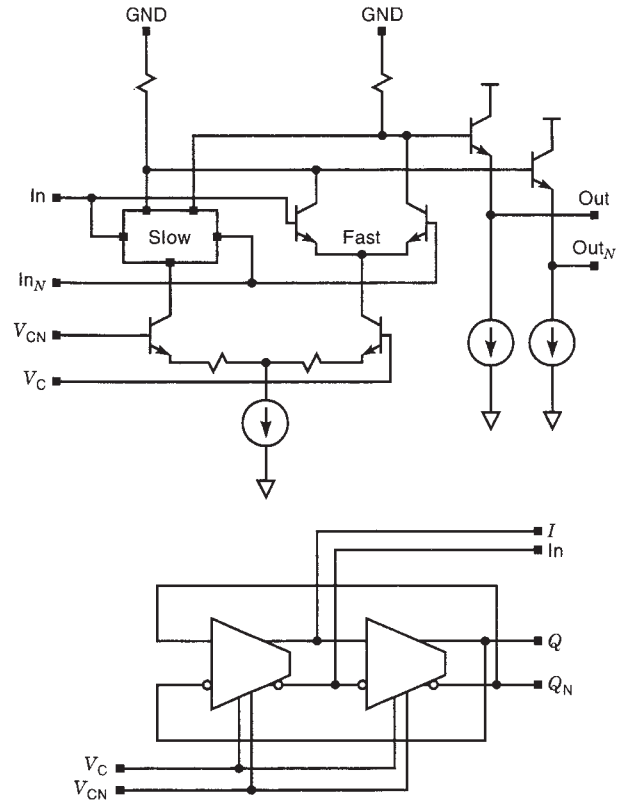


Figure 22. High-speed, two-stage ring oscillator. The frequency is controlled by interpolating the delay of the buffer stages between fast and slow paths.

between slow and fast by splitting the amount of current available at the current source. The differential amplifier has emitter degeneration resistors to linearize the current partitioning as a function of the differential voltage. Two emitter-followers buffer the outputs between stages and improve jitter by improving the voltage transition time. Both the control and the input/output signals are fully differential, resulting in a circuit that is very tolerant to common-mode disturbances. Fully differential oscillators do not depend on reference voltage generators or intrinsic device voltage thresholds to set their operating points. Furthermore, they give us complementary outputs, at twice the differential voltage swing compared to single-ended implementations.

The crystal oscillator with buffered output in Fig. 23 uses two transistors, connected as emitter-followers, in a Darlington arrangement. The input bias current is small, and the resistive loading on the crystal is light. Capacitors C_1 and C_2 connected across the Darlington pair make the input impedance have a negative real part. This arrangement can therefore be viewed as a negative-resistance or one-port oscillator. The oscillation amplitude will be limited by the voltage increase at the emitter of transistor Q_2 , which debiases the transistor and limits the maximum current flowing through it. However, the amplitude at the base of transistor Q_1 should not be so large that it saturates it. The output is taken at the collector of

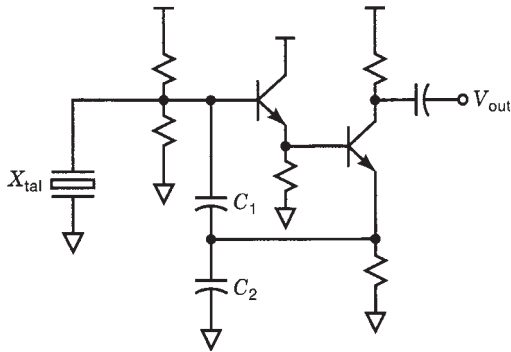


Figure 23. Crystal oscillator based on Darlington pair used in negative-resistance circuit.

transistor Q_2 , and the load is elegantly isolated from the core of the oscillator.

9. SUMMARY AND SUGGESTIONS FOR FUTURE STUDY

The design of variable-frequency oscillators requires knowledge of the main topologies, the limits of frequency-selective arrangements, the conditions for reliable oscillation, and the available means of tuning, to name the main variables. This article has tried to organize the types of oscillators into two main groups—sinusoidal and relaxation—and has described how their frequencies are changed. A good understanding of a system requires a model of the system. A sinusoidal oscillator can be modeled in two different ways: using feedback and using negative resistance. Relaxation oscillators operating at high frequency can sometimes be modeled in the same way, but in general they are described by their states and their time constants. Simple equivalent circuits and equations for the resonators were presented, attempting to highlight the most intuitive representations.

The variety of oscillators in existence offers many choices, but it also emphasizes the fact that there are unexplored combinations. Particularly because so much of society is influenced by the advances in electronic engineering, and especially integrated circuit engineering, the design of smaller, faster, and cheaper circuits is a very important activity. Variable-frequency oscillators of improved quality are needed today in telecommunications, data transmission, and instrumentation. The components available to design oscillators are constantly undergoing change, most particularly in integrated circuits.

BIBLIOGRAPHY

1. A. P. French, *Vibrations and Waves*, Norton, New York, 1971.
2. J. Williams, ed., *Analog Circuit Design: Art, Science and Personalities*, Butterworth-Heinemann, Stoneham, MA, 1991.
3. The American Radio Relay League, *The ARRL Handbook for Radio Amateurs*, American Radio Relay League, Newington, CT, 1995.
4. J. J. DeFrance, *Communications Electronics Circuits*, 2nd ed., Rinehart Press, Corte Madera, CA, 1972.
5. L. E. Larson, ed., *RF and Microwave Circuit Design for Wireless Communications*, Artech House, Norwood, MA, 1996.

FURTHER READING

- J. Millman, *Microelectronics: Digital and Analog Circuits and Systems*, McGraw-Hill, New York, 1979.
- G. Gonzalez, *Microwave Transistor Amplifiers*, Prentice-Hall, Englewood Cliffs, NJ, 1984.
- G. D. Vendelin, *Design of Amplifiers and Oscillators by the S-Parameter Method*, Wiley, New York, 1982.
- M. J. Howes, and D. V. Morgan, eds., *Microwave Devices*, Wiley, New York, 1976.
- R. Meyer, *Advanced Integrated Circuits for Communications*, Univ. California, Berkeley, Course ECE242 Notes, 1994.
- B. Razavi, *RF Microelectronics*, Prentice-Hall, Upper Saddle River, NJ, 1998.
- U. L. Rohde, J. C. Whitaker, and T. T. Bucher, *Communications Receivers: Principles and Design*, McGraw-Hill, New York, 1996.

VERY HIGH FREQUENCY RANGE

RICHARD L. CAMPBELL
 Cascade Microtech, Inc.
 Beaverton, OR

1. TIME, FREQUENCY, AND WAVELENGTH

The Very High Frequency (VHF) range extends from 30 MHz to 300 MHz, which means that when a VHF sine-wave signal is observed on an oscilloscope, the trace completes from 30 to 300 million cycles each second. Each cycle takes from 3.3 to 33 nanoseconds. When a VHF signal is radiated into the air by an antenna, it travels at the speed of light. If you could watch the signals travel, like water waves radiating from a stone dropped in a pond, you would observe that the wavelength of 30 MHz signals is 10 meters, and the wavelength of 3 MHz signals is 1 meter. The wavelength and frequency of VHF signals has a profound impact on the hardware we build to use these frequencies.

2. UNIQUE CAPABILITIES OF VHF

2.1. Compact, Effective Antennas

The 30 to 300 MHz frequency range has been popular since radio engineers first discovered how to reliably generate and amplify VHF signals during the 1930s. The VHF range has significant advantages for some common applications over higher and lower frequency ranges. Many of these advantages are related to the size of effective antennas. Antennas interact with radiofrequency waves according to the wavelength of the signals. Antennas for low frequencies (long wavelength) are large, and antennas for high frequencies (short wavelength) are small. For example, the Navy's ELF (extremely low frequency) antenna at 72 Hz covers several counties in the state of Wisconsin, and the EHF (extremely high frequency) 10 GHz

radar that opens the door at the grocery store has an antenna several centimeters across. Neither of these antennas is particularly effective: the 72 Hz antenna in Wisconsin is filled with lossy rocks, dirt, animals, and people, and the little grocery store door-opener antenna is too small to collect much signal.

Nondirectional antennas can be built with dimensions from about 0.1 wavelength to 0.5 wavelength. Antennas that radiate and collect radio energy from a particular direction have larger dimensions from about 0.5 to 5 wavelengths, and highly directional antennas (sometimes called “Pencil Beam” antennas) have dimensions larger than 5 wavelengths. The VHF range, with wavelengths from 1 to 10 meters, allows us to build effective, nondirectional wire or rod antennas with lengths from 10 cm to 5 meters, and directional antennas with dimensions from about 1 meter to 50 meters. Pencil Beam directive antennas for VHF are large and expensive. If a very narrow antenna beam is needed, for example, for a radar system, it usually makes sense to select a frequency above VHF. Some of the first radar systems developed during WWII used VHF bands because engineers had not yet figured out how to generate high power at microwave frequencies.

With effective nondirectional whip antennas less than 1 meter long, and directional antennas with dimensions a little larger than 1 meter, the VHF range is in demand for a number of different radio services. It is very convenient to build good, inexpensive, lightweight nondirectional antennas that may be carried around or mounted on a moving automobile, train, boat, or airplane. The most common type of nondirectional antenna is the vertical whip, as seen on automobiles. Directional VHF antennas, mounted on an antenna rotator or fixed in a particular direction, are often seen on the roofs of buildings. The most common type of VHF directional antenna is the yagi television antenna (named for Yagi and Uda, early twentieth century Japanese inventors).

2.2. Reliable Local Signal Propagation

The convenient size of effective antennas is not the only advantage of the VHF range. Lower frequencies are much more strongly effected by the highly variable electron densities in Earth’s ionosphere. These electron densities vary with height above the earth, position around the earth, from day to night, from day to day, summer to winter, over the 28 day solar rotation period, and over an 11 year cycle related to solar activity. The high frequency or shortwave bands from 3 to 30 MHz are famous for providing worldwide but unreliable radio coverage that varies with the whims of ionospheric weather. Ionospheric effects occur much less frequently at VHF. Television Channel 2 at 54 MHz might experience ionospheric reflected interference from TV stations 1000 km away 10 days a year, and FM broadcast signals near 100 MHz experience long distance propagation even less often.

2.3. Bandwidth

Even if the 3 to 30 MHz range were not susceptible to highly variable ionospheric propagation, it could still only accommodate 4 TV channels, each 6 MHz wide. The VHF

range from 30 to 300 MHz includes 12 TV channels and still has almost 200 MHz left for other services. Almost all of the services permitted to operate below 30 MHz are required to use very narrow bandwidth—typically 6 kHz or less. AM broadcast channels are 10 kHz apart, and high-frequency SSB voice channels may be spaced every 3 kHz. It is possible to send pictures over a 3 kHz channel, but the number of frames per minute is very small. To transmit moving pictures requires much more bandwidth. VHF Television channels are 6 MHz wide. Bandwidth may also be used to improve signal-to-noise ratio and audio fidelity when signals are strong. FM broadcasting, which operates from 88–108 MHz, has 150 kHz wide channels spaced every 200 kHz.

3. RADIO SERVICES ON THE VHF BANDS

With many useful radio activities competing for frequencies in the VHF range, government agencies have assigned frequency bands to a large number of different services. Here is an abbreviated list of frequencies and some of the different services assigned to the VHF spectrum:

- 30–40 MHz Police and Fire
- 46–49 MHz Cordless Telephones, Radio Controlled toys
- 50–54 MHz Amateur Radio
- 54–72 MHz TV channels 2,3,4
- 72–76 MHz Radio Control
- 76–88 MHz TV channels 5,6
- 88–108 MHz FM broadcasting
- 108–135 MHz Aircraft
- 136–144 MHz Space, Weather Satellites
- 144–148 MHz Amateur Radio
- 148–160 MHz Police and Fire
- 162–166 MHz Weather radio and Boats
- 166–216 MHz TV channels 7–13
- 222–225 MHz Amateur Radio
- 225–300 MHz Military

All of these different services operate at once in the VHF range. Some of them operate continuously, like TV stations, some of them occasionally, like cordless phones, and some of them only in emergencies. Government regulations, antennas, and, particularly, VHF radios are all designed to allow these different services to share the VHF range without interfering with each other.

4. VHF RADIO TECHNOLOGY

4.1. Radio Systems

VHF radio systems consist of transmitters, transmitting antennas, the path signals follow between transmitter and receiver, receiving antennas, and receivers. In FM and TV broadcasting, the transmitters and transmitting antennas are large, expensive, and owned by corporations, whereas the receivers are inexpensive and available at the local department store. Communication services usually have a transmitter and receiver sharing the same box (called a transceiver) connected to the same antenna. Handheld transceivers include a battery pack and an antenna all in one common unit.

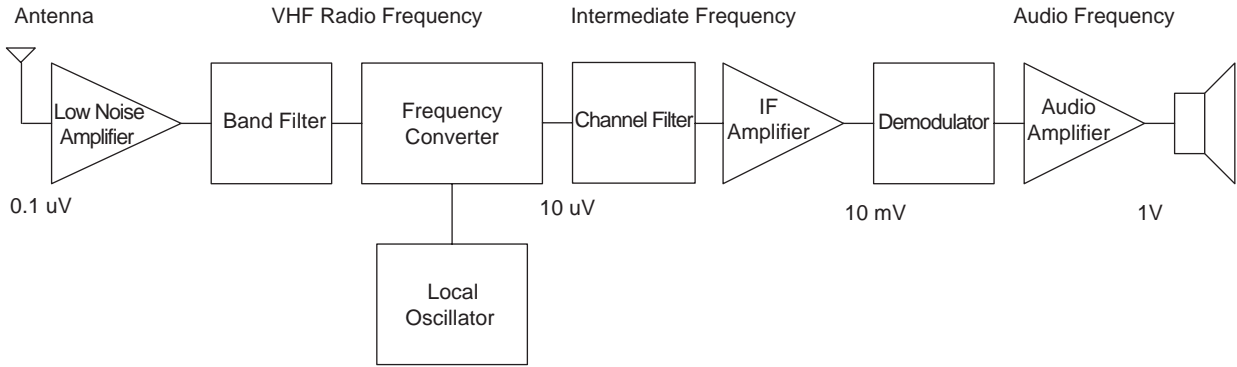


Figure 1. Block diagram of typical VHF receiver.

Figure 1 is the block diagram of a typical VHF receiver, and Fig. 2 is a block diagram of a transmitter. A number of common blocks exist: amplifiers, local oscillators, frequency converters (usually called mixers), filters, modulators, and demodulators. Audio amplifiers operate at much lower frequencies, and intermediate frequency (IF) amplifiers, filters, and demodulators operate in the high-frequency range—often at 10.7 MHz or 21.4 MHz in VHF radio systems. All of the electronic circuits at frequencies below 30 MHz operate within the range of common laboratory instruments, such as oscilloscopes, and use technology familiar to both analog and radiofrequency (RF) designers. In addition, the clock speeds of Digital Signal Processing (DSP) systems continue to increase, and much of the IF signal processing, including modulation and demodulation, is now commonly done in DSP.

The electronic blocks that must operate above 30 MHz in a VHF radio include low noise amplifiers (LNA), mixers, local oscillators, power amplifiers (PA), switches, and RF filters. Above 30 MHz, components and interconnecting wires are large enough that their dimensions have significant impact of circuit operation.

4.2. The Inductance of Interconnecting Wires

VHF electronic design includes some peculiarities, but it is a mature art, and many successful designs have resulted from following a few basic rules. One rule for building

VHF radios, often quoted in 1960s era Amateur Radio VHF Handbooks, is that if component leads are visible, they are too long. The LNA input circuit schematic and sketch in Fig. 3 will illustrate the need for short leads. The circuit includes a 10 nH (nanohenry) inductor, a 46 nH inductor, and a 22 pF capacitor. The 10 nH inductor is just 1 cm of bare copper wire soldered directly from the input connector to ground. At low frequencies, this wire is a short circuit, but at 144 MHz, its inductive reactance is exactly cancelled by the reactance presented by the 46 nH inductor and 22 pF capacitor, so no signal is lost. However, this only happens at 144 MHz if the other inductor in the circuit is 46 nH. What if the 46 nH inductor were soldered into the circuit with a 1 cm lead on each end? Then the inductance would be approximately 10 nH + 46 nH + 10 nH = 66 nH, and the input circuit would resonate at about 130 MHz. Suppose the 22 pF capacitor had 1 cm leads. Each capacitor lead would have about 10 nH, or 10 ohms of inductive reactance at 144 MHz. The 22 pF capacitor has about 50 ohms capacitive reactance at 144 MHz, so the 22 pF capacitor in series with two 10 nH leads would have a reactance of +j10 - j50 + j10 = -j30 ohms. So the 22 pF capacitor looks about 40 percent larger with 1 cm leads at 144 MHz—it looks like about 30 pF. It still looks like 22 pF at low frequencies. However, at some frequency around 250 MHz, a 22 pF capacitor with 1 cm leads stops behaving like a capacitor and acts like a perfect short circuit. Above that series resonant frequency,

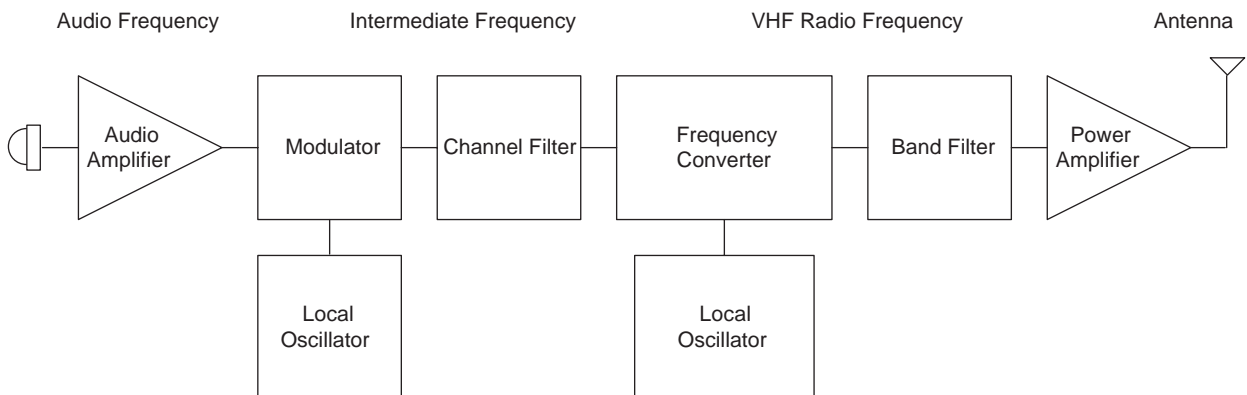


Figure 2. Block diagram of typical VHF transmitter.

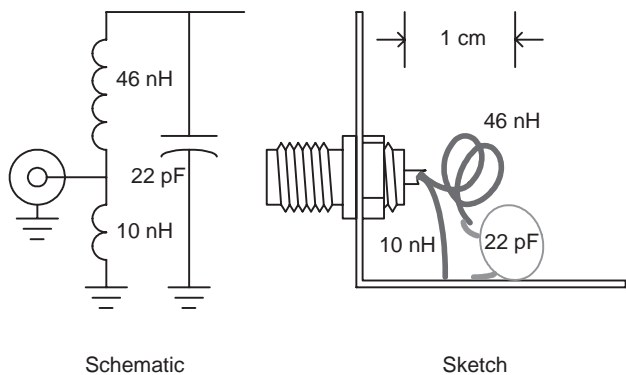


Figure 3. Schematic of LNA input circuit.

the capacitor, and its leads, behaves like an inductor, except that it does not pass DC.

Several generations of VHF design engineers struggled with the problem of undesired inductance in both component leads and interconnecting printed circuit board traces, but much of that difficulty is avoided by using surface mount components. A useful rule of thumb is that every surface mount component has about 1 nH of series inductance, as does each millimeter of printed circuit trace. Wise VHF designers minimize the extra inductance in the circuit by keeping the components and layout small, incorporate the extra inductance in the design, and choose circuitry that tolerates small amounts of additional inductance. A common approach to building VHF systems is to design physically small circuit blocks with signal connections that have an impedance of 50 ohms, and interconnect them with 50 ohm characteristic impedance transmission lines.

4.3. The 50 Ohm Environment

VHF circuit blocks are designed to operate in a 50 ohm environment for several very good reasons, including controlling the amplitude and phase of signals, preventing radiation, and compatibility with test equipment. Recall that the wavelength of VHF signals is between 1 and 10 meters. Even 300 MHz signals at the top of the VHF band have 1 meter wavelength, which is likely to be larger than the boxes that radio blocks are mounted inside. However, when it is important to maintain control of the phase of signals between different circuit blocks, a few electrical degrees of phase difference may be significant. An electrical degree is 1/360 of a wavelength, or only 3.3 mm at 300 MHz. Typical components have dimensions of about one electrical degree at 300 MHz. Phase is particularly important in balanced systems, in filters, in oscillators, and when the output of a circuit block is connected through a length of wire to the input of another circuit block. Balance is used to cancel noise and distortion in radio amplifiers and mixers. Perfect balance occurs when signals are 180 electrical degrees apart. A few extra electrical degrees can result in significant degradation of noise and distortion performance. Filters and oscillators depend on well-defined phase relationships to select or generate

one frequency while rejecting others. The need for a well-defined impedance environment becomes clear when we study interconnections between circuit blocks, because signals reflect from boundaries between different impedances, whether the signals are waves in space or waves traveling on transmission lines. Reflected signals result in standing waves.

Figure 4 shows an electromagnetic wave striking a partially reflecting surface. Some of the wave is reflected and some is transmitted. This experiment is easily done with a flashlight and a glass window. The window reflects some of the incident wave because it has a different impedance than air. In space, impedance is the ratio of the magnitude of the E and H fields. Air has an impedance of about 377 ohms, and window glass has an impedance of about 100 ohms. It is possible to get more of the flashlight energy into the glass by matching the impedances using an impedance transformer. Camera and binocular lenses, and some eyeglasses do this by using a coating on the glass. If the same flashlight is shined on a camera lens, much less light is reflected. In an electric circuit, impedance is defined as the ratio of voltage to current. A high-impedance circuit has high voltage and low current, and a low-impedance circuit has low voltage and high current. The standard impedance for radiofrequency instruments and cables is 50 ohms. If a 50 ohm cable connected to a 50 ohm load has a 1 volt rms sine-wave voltage, 20 mA rms current will flow. If this cable is connected to a load with a different impedance, some of the signal will be reflected.

Consider the case illustrated in Fig. 5. To an analog designer at low frequencies, a low-impedance source is considered ideal. Similarly, a high-impedance input is ideal. The low-impedance source in Fig. 5 drives a 30 cm coax cable connected to the high-impedance input of the amplifier. This arrangement works well and is commonly used at audio and low radiofrequencies. Now observe what happens at 144 MHz, in the middle of the VHF band. The signal leaves the low-impedance generator and travels toward the high-impedance amplifier input. The phase velocity of the signal in the cable is about two-thirds the speed of light, so the cable is about a quarter wavelength, or 90 electrical degrees long. Some of the signal power goes

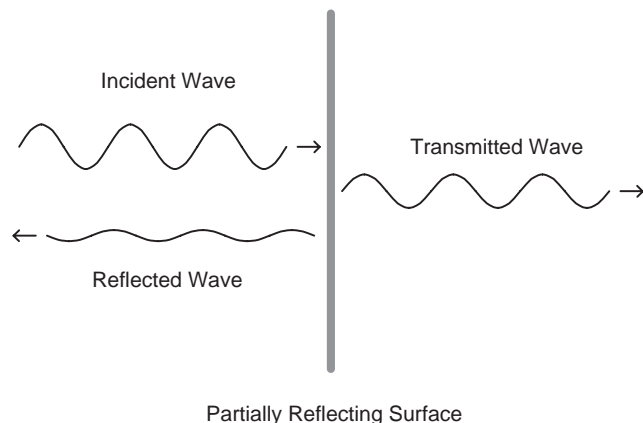


Figure 4. Electromagnetic wave striking a partially reflecting surface.

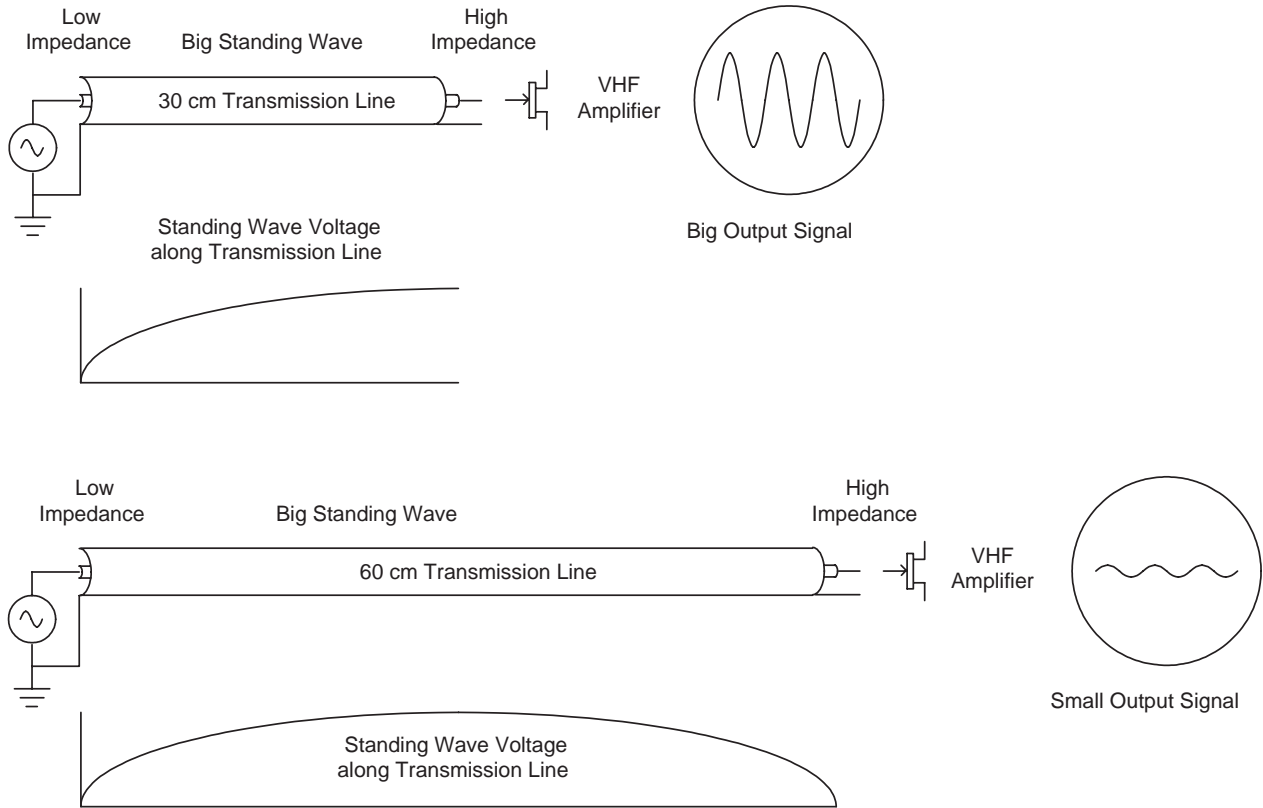


Figure 5. 50 ohm transmission line connected between a voltage source and a high impedance.

into the amplifier, but most of it is reflected. Signals reflected from a high impedance are in phase with the incident signal. The reflected signal travels another 90 electrical degrees back toward the generator, and reflects off the low-impedance generator. Signals reflected from a low impedance experience a 180 degree phase shift. The signal reflected from the generator travels back toward the amplifier input, where it adds to the original signal. The signal at the input of the amplifier is larger than it was, because it has arrived after 180 electrical degrees of travel and 180 degrees of reflection phase shift, for a total of 360 degrees. It adds in-phase with the original signal. The length of transmission line has performed an impedance transformation from the low-impedance source to the high-impedance amplifier input, and the output of the amplifier is large.

Now suppose that the 30 cm cable mysteriously disappears from the bench and a 60 cm cable is borrowed from a nearby lab setup and used to connect the generator to the amplifier. The reflected signal now experiences 360 degrees of travel, plus 180 degrees of reflection phase shift, and it is now out-of-phase with the original signal at the input of the amplifier. The two signals subtract, leaving a very small voltage at the input of the amplifier. The output of the amplifier is now small.

Systems that operate very differently with different lengths of interconnecting cable are a common source of frustration for technicians and engineers with little experience at VHF.

As different blocks in a VHF radio system must be interconnected, and because the length of the interconnecting cables will be a significant number of electrical degrees at VHF, we need a way to control signal reflections. Standard practice at VHF and above is to design system blocks, and even individual components, to present 50 ohm impedances at their terminals, and then interconnect all of the pieces with 50 ohm coax and microstrip transmission lines. Even components designed for 50 ohm terminations must be used with care. Amplifiers and mixers have impedance that changes with frequency, and most filters reflect signals outside the passband. Figure 6 illustrates the passband response and reflection coefficient of a typical narrow bandpass filter. One common technique used to optimize VHF systems with filters is to try different lengths of transmission line while measuring an important system performance characteristic.

Another reason for using coax and microstrip transmission lines to interconnect VHF circuit blocks is that coax and microstrip define the electric and magnetic fields of the traveling signal in a way that prevents radiation. In contrast, antennas configure the electric and magnetic fields to encourage radiation. If VHF circuit blocks are interconnected with simple wires, those wires can become incidental antennas, and radiate most of the signal off into space. Even worse, if an amplifier has wires on both the input and output, the output wire can radiate the signal into space, where it will be picked up by the input wire, and instead of an amplifier, the circuit will be an oscillator.

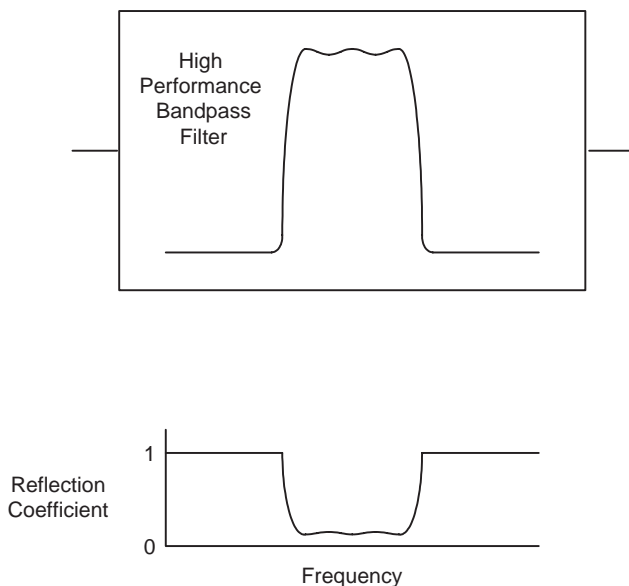


Figure 6. Bandpass filter with termination impedance plot.

Recall that under the right conditions, a tenth wavelength wire can be an effective antenna. A tenth wavelength at 150 MHz is only 20 cm.

5. NOISE AT VHF

Less atmospheric and Earth noise exist at VHF than at lower frequencies. Often a VHF receiver connected to an antenna through a length of transmission line will hear more internal noise from the losses in the transmission line and the input stage of the LNA than from external sources picked up by the antenna. Receiver sensitivity is thus limited directly by the noise in the receiver input stages and losses in transmission lines. Attention paid to LNA design, and moving the LNA to a location near the antenna (instead of inside the receiver box) can greatly improve receiver sensitivity. Amateur VHF stations with directive antennas aimed at the horizon and well-designed LNAs may hear the increase in background noise as the sun rises.

6. POWER, MODULATION, AND SIGNAL PROPAGATION

The VHF bands are normally used for local coverage, out to about 100 km. Handheld radios may communicate directly with each other out to about 10 km, or over longer distances by using repeater stations located on towers, tall buildings, or hilltops. The effective range of VHF communications systems is highly dependent on local terrain, obstructions near the receiver or transmitter, and the type of antennas used. Most voice communications at VHF use narrowband frequency modulation (FM), with channel bandwidths of about 15 kHz. FM broadcasting uses 150 kHz wide channels for better audio fidelity, and better audio signal-to-noise ratio when the received signals are strong. Stereo and other information is modulated

onto the FM broadcast signal using subcarriers. FM receivers exhibit a capture effect, where the strongest signal captures the receiver and weaker interfering signals are not heard at all, which improves the fidelity of received audio in the presence of interference. VHF Aircraft radios use amplitude modulation (AM) for historical reasons, and because AM receivers do not have a capture effect. If a distant aircraft with a weak signal is calling the tower, it is important for the air traffic controller to know it is there so that stronger stations may be asked to stand by. Amateur Radio Morse code and Single Sideband voice stations with medium-sized yagi antennas and 150 watt amplifiers routinely communicate to about 500 km on a daily basis. These long distance communications are supported by scattering the VHF signals off anomalies in the troposphere. More power and larger antennas allow worldwide VHF communications by bouncing signals off the moon.

7. VHF MEASUREMENTS

At low frequencies, measurements of voltage and current are commonly used to determine whether circuits are working as expected (by engineers and technicians) or hoped (by designers). Although some oscilloscopes are capable of making measurements at VHF, the standard tools on a VHF radio bench include the spectrum analyzer, power meter, signal generators, forward and reflected power meter, noise figure meter, and network analyzer. All of these instruments have 50 ohm ports and standard connectors. The network analyzer measures how well inputs and outputs are matched to the 50 ohm standard, filter passbands and reflections, and amplifier small-signal gain, frequency response, and reverse isolation. Reverse isolation determines how much of what occurs at the amplifier output appears at the input. If reverse isolation is very poor, the amplifier will oscillate when connected to certain loads. If reverse isolation is good enough to prevent oscillation but not much better, loads connected to the output will affect the input impedance of the amplifier, which is significant for LNAs, because they are typically connected to a narrow bandpass filter on the output, and if reverse isolation is only modest, the LNA input impedance will change rapidly at near the edges of the bandpass filter response, which commonly causes the system gain to vary across the desired frequency range. System performance can often be improved by selecting a different length of 50 ohm cable between the LNA and bandpass filter.

8. THE SMITH CHART AT VHF

Simple VHF matching circuits, lumped element transmission lines, reflections and transmissions at boundaries with different impedances, and the effect of different lengths of transmission lines on system performance may be conveniently studied using the Smith Chart. The Smith Chart is a polar plot of reflection coefficient, with curve scales to read impedances. Figure 7 is a simplified Smith Chart with two points plotted. The round point is a reflection coefficient of 0.7 at an angle of 45 degrees, and

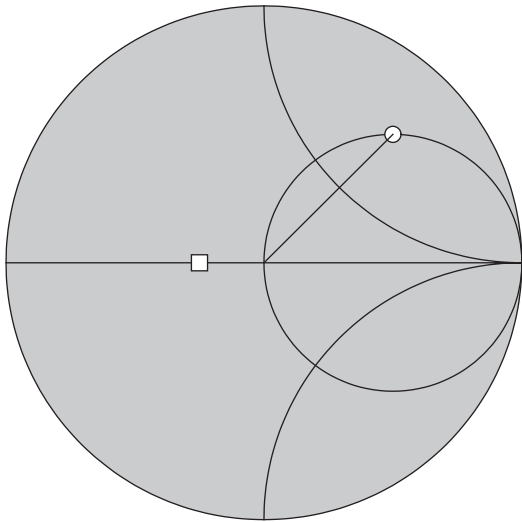


Figure 7. Smith Chart.

the square point is a reflection coefficient of 0.25 at an angle of 180 degrees. The Smith Chart is a powerful graphic calculator, and may be used with a pocket calculator (originally a slide rule) to solve a large class of transmission line problems. The Smith Chart approach is so fundamental to the field of radiofrequency engineering that even when it is not used as a calculator, it is used to display the results of radiofrequency measurements and computer simulations. Both the modern network analyzer and RF engineering software packages provide Smith Chart graphical output. The Smith Chart is covered in detail elsewhere in this encyclopedia. As the VHF frequencies were pioneered during the same era that Phil Smith invented his useful chart, VHF technology and the use of the Smith Chart have matured together. More than any other group of technologists, VHF workers are likely to analyze problems and present their results using Smith Charts.

9. VHF COMPONENTS

In 50 ohm systems at VHF, the most common reactive components (inductors and capacitors) have reactive impedance between about 5 and 500 ohms. At 144 MHz, a $-j50$ ohm inductor is 56 nH and a $-j50$ ohm capacitor is 22 pF. We can easily scale from these values to find that a $-j500$ ohm capacitor is 2.2 pF and a $-j5$ ohm capacitor is 220 pF. Similarly, a $+j500$ ohm inductor is 560 nH and a $+j5$ ohm inductor is 5.6 nH. Clearly we need to be very careful using these components at VHF if they have wire leads, because the lead inductance is roughly 1 nH per mm of lead length. If a 5.6 nH inductor with wire leads is mounted on a standard 0.062 inch thick FR-4 printed circuit board, the leads will add several nH to the inductance. Similarly, capacitor lead inductance will increase the effective value of capacitor (decreasing its capacitive reactance). Furthermore, it is wise to recall that inductance is a numerical representation of the ratio of energy in a magnetic field to the current that caused it. It is not the

wire that determines inductance, it is the volume containing the wire and resulting magnetic field. An inductor will behave differently depending on how it is mounted on the printed circuit board. Chip inductors usually have a marking that permits production circuits to be built with the inductor in the same orientation as the working prototype. Capacitance is a numerical representation of the ratio of the amount of energy in an electric field to the voltage that caused it. Chip capacitors are relatively good at containing the electric field within a volume not much bigger than the component. The fact that capacitor leads add inductive reactance to capacitors means that, above a certain value, capacitors stop behaving like capacitors. VHF designers often use the self-resonance of a capacitor and its wire leads or PC board traces to obtain a virtual short circuit at RF that blocks DC. A 220 pF capacitor ($-j5$ ohms at 144 MHz) with a total wire lead and capacitor body inductance of $+j5$ ohms (about 6 mm) has an impedance of $-j5 + j5 = 0$ ohms, which makes a good bypass capacitor, or coupling capacitor between matched amplifier stages.

It is not just the inductance of wire leads that makes components behave differently than expected at VHF. The capacitance between turns of an inductor will make an inductor appear larger than its marked value, which is particularly true for inductors with many turns. It is good practice to avoid capacitors with reactance less than $-j5$ ohms and inductors with reactance greater than about $+j500$ ohms if it is important for their behavior to coincide with their marked value.

Many VHF engineers memorize a set of 50 ohm components at one frequency (i.e., 22 pF and 56 nH at 144 MHz) because it is then easy to scale to different frequencies and impedances. At 48 MHz (one-third of 144 MHz) 50 ohms is 66 pF and 168 nH. At 288 MHz, 50 ohms is 11 pF and 28 nH. For the whole VHF range from 30 to 300 MHz, the most common capacitors will be between 1 pF and 1000 pF (1 nF). 1 pF is about 500 ohms at 300 MHz, and 1 nF is about 5 ohms at 30 MHz. The most common inductors will be between 2.5 nH (5 ohms at 300 MHz) and 2.5 uH (500 ohms at 30 MHz).

9.1. VHF Inductors

Many different configurations of inductors are useful at VHF. In the several hundred nH range, simple self-supporting coils of enameled wire mounted with their own leads above a printed circuit board are particularly effective, and often used in small volume, hand assembled electronics. They are difficult to handle by machine, so small wire coils on a polyethylene form are common in mass produced VHF circuitry. Inductors may be made tunable by moving a threaded powdered iron slug in and out of the polyethylene form. The magnetic field lines around a solenoid coil extend well beyond the dimensions of the coil. Other circuitry, and in particular other inductors in the vicinity of a solenoid, will couple energy out of the magnetic field. Such inductor coupling may be intentional, but often it is not, and the circuit does not perform as expected. Inductor coupling to nearby circuitry may be reduced by shielding the inductors with small metal cans. Subcircuits containing inductors are often surrounded

with metal shields. A shield around an inductor modifies the magnetic field, and usually reduces the energy stored for a given amount of wire and current. As the resistance in the wire is not reduced by the shield, the inductor quality factor Q is degraded. Small shielded inductors typically have about 70% of the Q of the same inductors without shields. Q is improved by using larger shield cans that have less effect on the inductor magnetic field. One way to obtain both high Q and shielding in a compact inductor is by using toroid inductor cores. The magnetic material in the toroid core and the configuration of the winding forces the magnetic field lines into a closed ring shape. Little magnetic field exist outside the physical dimensions of the toroid, and the Q is determined by losses in the wire and toroid core. Several types of inductors are illustrated in Fig. 8.

9.2. Inductor Q

Q is a measure of how much energy is lost (to heat or radiation) per sinusoidal cycle. A bell that rings for a long time has high Q . A cardboard box that goes “thud” when you hit it has very low Q . A useful approximate definition of Q for inductors is the ratio of inductive reactance to series resistance. This definition neglects losses because of radiation or heating of the inductor core. If inductor Q is measured using a Q meter at the desired operating frequency, an inductor model using a larger series resistance may be used. Typical Q s for the inductors used at VHF are from about 30 for small, inexpensive chip inductors, around 100 for small polyethylene core slug-tuned inductors, up to 250 for toroids and large air-core inductors without shields, to about 1000 for silver-plated #12 wire helical resonators. High Q is not necessary or desirable in inductors used to provide DC to a circuit, but they often use large low-resistance wire for current capacity.

Filter circuits need as much Q as possible in the available space. Filter designers trade Q , filter bandwidth, and

loss. Resonator loss is approximately

$$\text{Filter Loss} \sim 20 \log[1 - QL/Qu]$$

Unloaded Qu is the Q of the components used to build the resonator. Usually at VHF, inductor Q is much lower than capacitor Q , so the unloaded Q is approximately the Q of the inductor. Loaded QL is the operating frequency divided by the 3 dB bandwidth of the resonant circuit. For example, a 150 MHz single resonator filter with a 3 dB bandwidth of 15 MHz has a loaded Q of 10. If we built this filter with an inductor with Q of 100, the loss would be

$$20 \log[1 - .1] \sim 1 \text{ dB}$$

which would be a useful filter except at the input to a very sensitive receiver. A filter with three of these resonators would have roughly 3 dB loss. Now if the same filter were built using inductors with a Q of 30, the loss per resonator would be

$$20 \log[1 - .3] \sim 3 \text{ dB}$$

Often we want to build much narrower filters. The 144 MHz amateur band is 4 MHz wide. A three resonator, 4 MHz filter with 3 dB loss has a loaded Q of 36, and would need resonators with an unloaded Q of about 360 to have 1 dB loss per resonator. Small helical resonators can achieve this. For still lower loss, physically larger resonators and thick wire are needed. The highest Q resonators used at VHF are quarter wave sections of large coaxial transmission line. The outer conductors may be 10 cm across, and these cavity resonators are tuned by adjusting the length of the center conductor.

9.3. Capacitors

Fixed capacitors for VHF are usually metal plated on opposite sides of a ceramic or mica wafer. In the past, these capacitors usually had wire leads, but most present day VHF circuitry uses surface-mount ceramic chip capacitors. These capacitors are available in various temperature coefficients. NP0 or COG capacitors have capacitance that changes less than about 50 ppm/degree C. N750 capacitors have a negative 750 ppm temperature coefficient. Electrolytic, tantalum, and many polystyrene and polyethylene capacitors have too much lead inductance to be useful at VHF.

It is convenient to build variable capacitors with air, ceramic, or polyethylene dielectric in capacitance ranges from a few pF to a few hundred pF. Each year physically smaller variable capacitors are introduced, and several manufacturers have variable chip capacitors on the market. Variable capacitors are useful in prototype and small production circuits because it is difficult to consider all of the printed circuit board traces and component lead inductance and interwinding capacitance when designing the circuit. A few variable circuit elements allow the designer to tune out the unknown deviations from ideal behavior.

For precision circuitry like narrow filters and oscillators, it is useful to have precision adjustable capacitors.

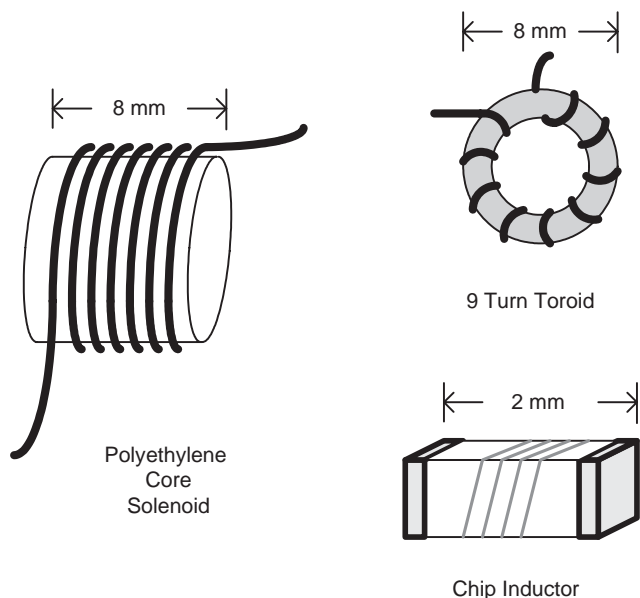


Figure 8. Different types of inductors.

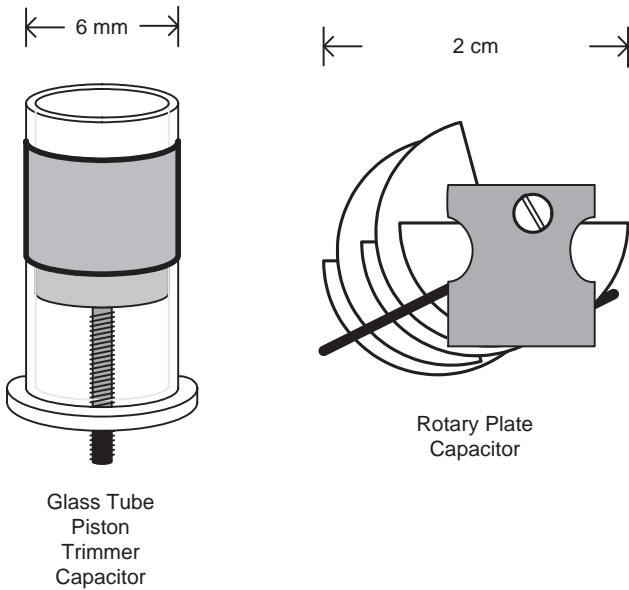


Figure 9. Two types of VHF variable capacitors.

Several manufacturers produce air or glass dielectric piston trimmer capacitors with a ceramic or glass body and a moving, cylindrical capacitor piston driven in and out of an insulating cylinder with an outer conductor or second internal plate by a precision lead screw mechanism. Figure 9 is a drawing of two types of VHF variable capacitors.

One type of capacitor that has been used at VHF for at least a half century is the gimmick, illustrated in Fig. 10. It is simply two wires twisted together. Gimmick capacitors are typically 0.5 pF to about 5 pF, and may be easily adjusted by clipping them shorter or twisting the turns tighter. The gimmick capacitor is a useful reminder that capacitors are not just a component that one selects from a catalog, but a device that behaves in a certain way because of the electric field between two conductors.

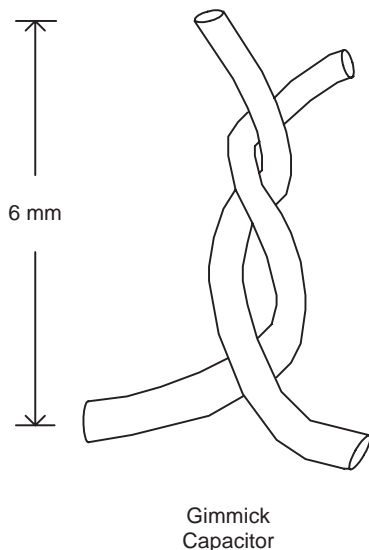


Figure 10. Gimmick capacitor.

9.4. Resistors

The rules for using resistors at VHF are the same as for lower and higher frequencies: Observe the power rating and be aware of inductance. Some resistors have a cylindrical body with a resistive coat. The precise value of resistance is obtained by making a spiral cut in the resistive coat. Such resistors may have much higher series inductance than expected from their physical size. Other resistors for high power have spiral windings of nichrome wire. Such resistors are inappropriate for radiofrequency use. Chip resistors are the best choice for VHF, as long as their power ratings are observed.

9.5. Transformers, Baluns, Splitters

The VHF frequency range is ideal for building transformers, baluns, splitters, and couplers using small ferrite cores and multiconductor windings of enameled wire. The low-frequency limit of such devices is determined by the permeability of the ferrite core, and the upper frequency limit occurs when the length of the winding becomes a significant fraction of a wavelength. With tiny ferrite cores a few mm in diameter or smaller, it is possible to have many turns on the core with much less than a wavelength of wire, even at 300 MHz. Several manufacturers have extensive product lines of transformers, baluns, splitters, and couplers that approach ideal performance in the VHF range.

A large class of useful device may be constructed from transmission line transformers formed from parallel turns of wire through a small ferrite core or bead. The transmission line transformer has very low resistance to differential currents, and very high impedance to common mode currents. Figure 11 illustrates a simple transmission line transformer constructed of a pair of enameled wires and a ferrite bead and several useful components that may be built by connecting the windings in different ways. Like the gimmick capacitor, it is a reminder that VHF components are just applications of basic physics.

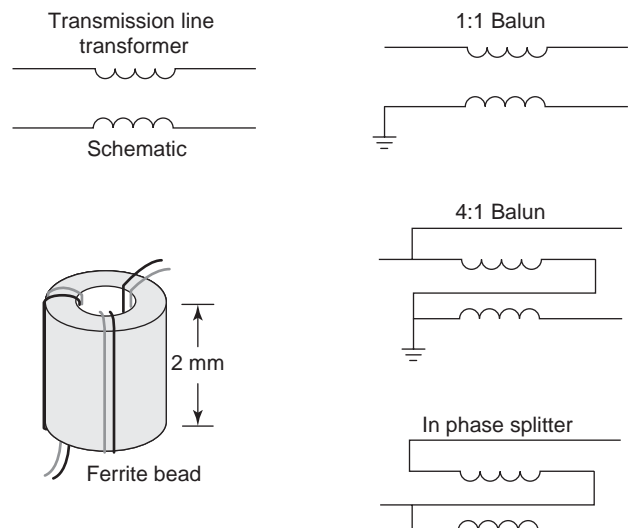


Figure 11. Transmission line transformers.

9.6. Two-Terminal Solid-State Devices

Silicon switching diodes, i.e., the ubiquitous 1N4148, have small enough internal capacitance to be useful for non-critical signal processing at VHF. Schottkey barrier diodes like the HP 5082-2835 have much lower capacitance and well-defined characteristics and are a better choice for repeatable performance and critical circuits. Capacitance is low enough and switching fast enough that small-signal Schottkey diodes have nearly ideal behavior at VHF. PIN diodes are widely used to replace mechanical relays for signal switching at VHF. Variable capacitance diodes are used for tuning filters and voltage-controlled oscillators. Other two-terminal solid-state devices like step recovery diodes and tunnel diodes are occasionally seen in specialized VHF circuitry.

9.7. Frequency Doublers and Diode Ring Mixers

With nearly ideal transformers and diodes, it is easy to build very good diode frequency doublers and mixers over the whole VHF range. Figure 12 is the schematic of a frequency doubler, which is the same schematic as a full-wave rectifier power supply, only in this case it is the double frequency component and not the DC that is of interest. The DC voltage is connected to ground in the circuit shown, but it may also be used as an indicator of drive and output level. If the diodes are reversed, it is a

negative voltage, which might be useful for biasing circuits elsewhere in the VHF radio. The output power is typically between 6 and 10 dB lower than the drive level, over a very wide frequency range. Both doubler ports are reasonably well matched to 50 ohms. If the waveforms are sketched (or reviewed in a book on DC power supply design), it is clear that the input signal needs to be a good sine-wave for frequency doubling to occur. Figure 13 is the standard diode ring double balanced mixer. This mixer works well with 50ohm terminations on all ports, requires about 5 milliwatts of local oscillator drive, and can be built for any frequency from audio to 1 GHz by selecting the appropriate transformers. At VHF, it typically has conversion loss of about 6 dB, port-to-port isolations of around 40 dB, and an input third-order intercept of +17 dBm.

Diode ring mixer and frequency double transformers may be hand wound using small toroid cores for the lower VHF frequency range, but much smaller cores are useful to obtain the best performance at frequencies above 200 MHz. Commercial transformers are available in a wide range of sizes and configurations. Other mixers using passive FETs and integrated Gilbert Cell mixers are commonly used at VHF.

9.8. Three-Terminal Active Devices

Many silicon NPN transistors such as the common 2N5179 work well as oscillators and amplifiers through

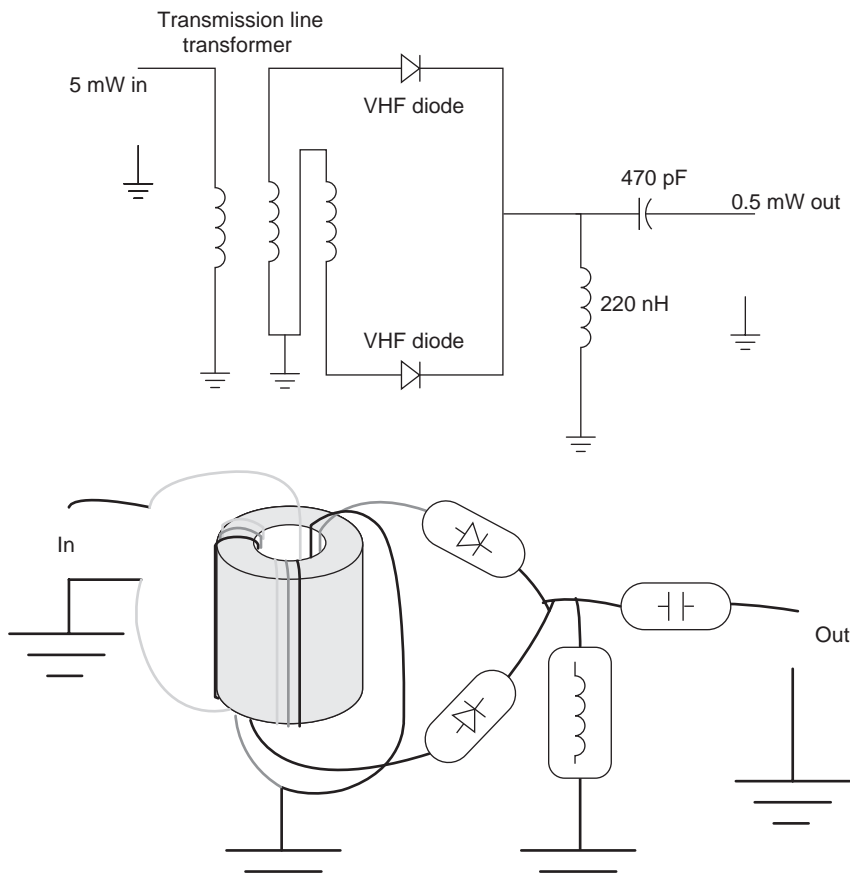


Figure 12. Diode frequency doubler.

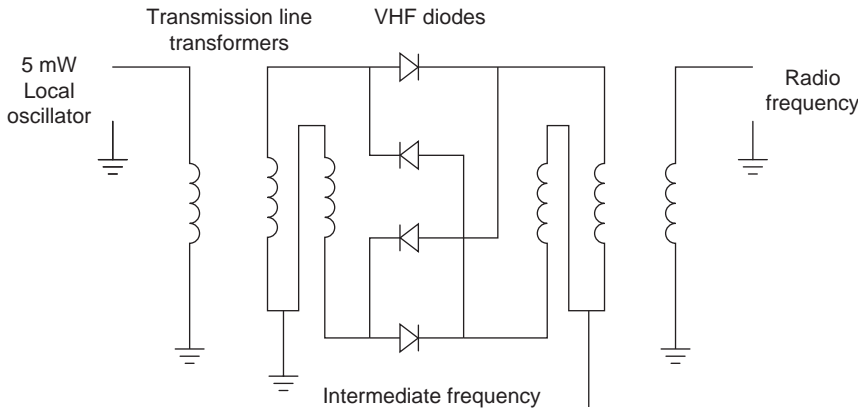


Figure 13. Diode ring mixer.

the entire VHF range. Discrete amplifier designs permit the designer to tailor the circuitry to exactly the needs of the system and make most efficient use of power supplies by using RF inductors instead of resistors as collector loads. JFETs, such as the J310, are also very useful throughout the VHF range. Figure 14 is a typical amplifier using the U310, the metal can version of the J310. The metal can is internally connected to the device gate, and the can is soldered to the printed circuit ground plane to build a common gate amplifier.

9.9. MMICS

A family of silicon monolithic microwave integrated circuits is available that operates from DC to past 1 GHz. Several of these devices, including the MAR-2 and MAV-11, are particularly useful at VHF. The MAR-2, in addition to providing gain, a modest noise figure, and a few milliwatts of output power, has nearly perfect 50 ohm match on both input and output ports, so it is very useful as a basic gain

element in systems with filters and other ill behaved impedances. The MAV-11 had a good enough noise figure to be used as an LNA in modes VHF receiver systems, and 50 milliwatts of output power capability. The disadvantage of these MMIC amplifiers is that half of the power is dissipated in the collector bias resistor, so they are less efficient than well-designed discrete amplifiers and less attractive for battery operated equipment. Their broad bandwidth also requires that bypassing, shielding, and filtering extend to cover the entire gain range of the MMIC, even if the radio is being designed only for a narrow sliver of the VHF spectrum.

9.10. Packaged Filters

Bandpass, highpass, lowpass, and allpass filters may be built in the VHF range using several different technologies including inductors and capacitors, helical resonators, quartz crystals, and surface acoustic wave devices. Bandpass filters for commercially important frequencies

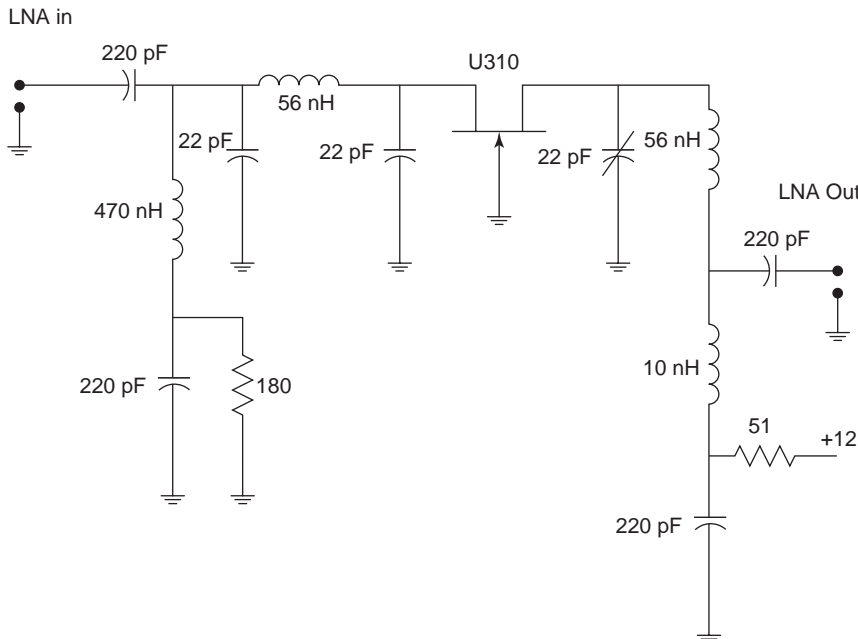


Figure 14. 144 MHz LNA.

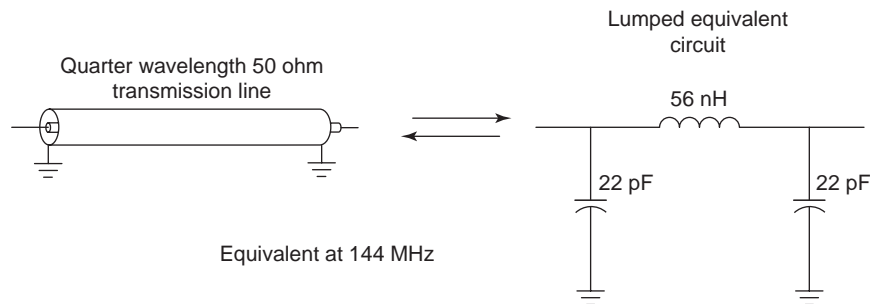


Figure 15. Lumped equivalent transmission line.

are available from a number of sources. If the desired filter is not available in the catalog, an analog circuit simulator can be used to design filters using standard slug tuned inductors and chip capacitors. When the percentage bandwidth is modest (filter bandwidth is between 5% and 20% of the center frequency), these filter simulations tend to agree fairly well with measured performance.

9.11. Power Amplifiers

VHF amplifiers for a few watts through about 50 watts may be designed and built using discrete bipolar or FET power devices, or complete amplifier modules may be purchased for many different VHF frequency ranges. Broadband low-distortion amplifiers are used to distribute cable TV signals. From 50 watts to a few hundred watts, discrete transistor amplifiers are often combined using power splitters and combiners. Above a few hundred watts, vacuum tubes become practical and compete with large solid-state amplifiers.

9.12. Lumped Element Transmission Lines

A radiofrequency designer often needs a transmission line with a particular electrical length to obtain a specific phase shift. In the VHF range, lengths of coax cable are short enough that they are sometimes used in circuits. In very small circuits, and at the low end of the VHF range, coax cables may be too long to fit in the available space. A lumped element equivalent transmission line may be made using pi network sections of alternating inductors and capacitors. Figure 15 shows a quarter wavelength 50 ohm coaxial line at 144 MHz and its equivalent lumped element circuit. At VHF, lumped element equivalent transmission lines made up of surface-mount components are much smaller than coax cables, and much less expensive.

9.13. VHF Circuitry

VHF circuits operate at a high enough frequency that it is important to minimize lead lengths and pay attention to making layouts compact, but are not so high that completely different circuit techniques must be developed. A VHF amplifier schematic and circuit might look just like one for 10 MHz, but with a more compact layout. In contrast, an Ultra High Frequency (UHF) amplifier circuit is often distributed along a length of 50 ohm microstrip transmission line, with the interconnecting line lengths

just as important as the component values. Microstrip transmission line circuits are also common at the upper frequency end of the VHF range, and for power amplifiers. VHF circuits often employ a mix of components with wire leads and chip components, mounted on opposite sides of the same circuit board.

9.14. Shielding

As VHF circuit board layouts occupy a significant fraction of a wavelength, they radiate more RF energy than radio circuits at lower frequencies. VHF designers often include metal shield cans around VHF amplifier, filter, and oscillator circuits to keep the desired signals inside and undesired signals out. A VHF filter with an ultimate stop-band rejection of 60 dB when connected to measurement equipment on the bench may have only 40 dB when mounted on a radio printed circuit board. Metal shields soldered over the input and output circuits can improve isolation.

10. FURTHER INFORMATION

VHF Engineering is a mature art that forms a bridge between high-frequency radio design and microwave technology. Many professional VHF engineers are also active as amateur radio designer/builders, and the amateur radio literature provides a good catalog of accepted and proven VHF circuits and techniques. Both the American Radio Relay League (ARRL) and Radio Society of Great Britain (RSGB) publish extensive handbooks on practical HF and VHF technology. A recent copy of the ARRL Handbook for the Radio Amateur is often found on the HF and VHF engineer's bookshelf. More specialized, very practical VHF information is available in the Proceedings of the Central States VHF Conference, also published by ARRL. Much of the emphasis in professional radio engineering for the past several decades has been focused on high-volume consumer microwave electronics like cell phones and wireless local area networks, so it may not be easy to find practical applied VHF engineering information in the recent professional literature. Several journals, including RF Design and High Frequency Electronics, offer a good selection of articles on practical VHF technology. Committee MTT-17 of the Institute for Electrical and Electronic Engineers has a Website devoted to HF, VHF, and UHF Technology.

FURTHER READING

- D. Biddulph, MOCGN, ed., VHF/UHF Handbook, Radio Society of Great Britain, Hertfordshire, UK, 2002.
- W. Hayward, R. Campbell and R. Larkin, Experimental Methods in RF Design, American Radio Relay League, Newington, CT, 2003.
- G. R. Jessop, G6JP, VHF/UHF Manual, Radio Society of Great Britain, Hertfordshire, UK, 1983. Proc. 38th Conf. Central States VHF Society, American Radio Relay League, Inc, Newington, CT, 2004.
- D. G. Reed, W1LC, ed., The ARRL Handbook for Radio Communications 2004, American Radio Relay League, Inc, Newington, CT 2003.

VOLTAGE-TO-FREQUENCY CONVERTERS

FERNANDO VIDAL-VERDÚ
RAFAEL NAVAS-GONZÁLEZ
University of Málaga
Málaga, Spain

ANGEL RODRIGUEZ-VÁZQUEZ
University of Seville
Seville, Spain

1. INTRODUCTION

The *voltage-to-frequency converters* (VFCs) belong to the category of the *oscillator* circuits. The function of an oscillator is to produce periodic time-varying signals with only DC excitations.¹ These signals may have quite diverse waveform shapes such as triangular, square, impulsive, exponential, and sinusoidal. For some oscillator applications, the shape of the generated signal is an important design criterion, for instance, in the production of periodic sweep voltages for display systems or in the generation of quasisinusoidal signals for testing and instrumentation purposes. In other applications, the most important design criterion is the signal *frequency*, while the spectral purity of the signal remains secondary. This is, for instance, the case for oscillators used to generate clock signals for timing purposes and also for VFCs.

The function of VFCs is to convert the value of an analog *input* voltage or current into an *output* frequency; that is, they must generate signals of any shape whose frequency is a faithful representation of the analog input data. Thus, they also belong to the category of the *data converter* circuits, whose function is to convert the information among different domains with minimum degradation of the information itself. From this point of view, the VFCs have some similarities with the analog-to-digital converters (ADCs), whose function is to convert an analog data into a digital word with the minimum error possible.

¹In practice, the excitations may not strictly be DC, but AC signals whose frequency is smaller, commonly much smaller, than that of the signal generated by the circuit.

In the case of VFCs the domain of the transformed information is the frequency of a signal, instead of a digital word, and the aim is to obtain the smallest possible error in the voltage-to-frequency mapping. The design criteria for VFCs include the following [14]:

- *Dynamic range*, the range of input voltage values where the transformation takes place. A related magnitude is the *frequency range*—the range of output frequencies that corresponds to the input voltage range; 60 dB and larger dynamic ranges² are commonplace.
- *Linearity* of the voltage-to-frequency map, $f_0 = F(v_{in})$. This map is required to be highly linear,

$$F(v_{in}) = k \cdot v_{in} + E(v_{in}) \quad (1)$$

with error $E(v_{in})$ much smaller than 1% of full scale.

- *Scale factor accuracy and stability*. The parameter k in Eq. (1) must be externally set for given voltage-to-frequency gain. After its setting, the gain must remain stable with temperature (≤ 100 ppm/ $^{\circ}$ C), aging, and changes of the power supply ($\leq 0.1\%$ /V).

Such requirements are related to the main application area of the VFCs, namely, the encoding of information for telemetry or remote control. In these applications, the analog data are converted into frequency at the emitter front end using a VFC. The generated signal is then transmitted through an optical or radiolink—a process in which the signal frequency remains essentially unchanged. Then, at the receiver front end, the analog data are recovered from the signal frequency by using a *frequency-to-voltage converter* (FVC).

From the construction point of view, the VFCs are in the same category as the so-called voltage-controlled-oscillators (VCOs), in the sense that the circuit structures employed to realize VFCs and VCOs are actually quite similar. However, the typical applications of VCOs usually demand low precision in the voltage-to-frequency map and, in some cases, high spectral purity. In this article, we will start by presenting a broad overview of the different circuit structures that qualify to generate periodic signals with voltage-controlled frequency. Then, we will focus on structures that are better suited to achieve accuracy in the voltage-to-frequency mapping.

2. BASIC CONCEPTS AND MODELS FOR OSCILLATOR DESIGN

Circuit synthesis is the process of interconnecting circuit components so as to realize some targeted behavior. The first step for systematic circuit synthesis is to identify mathematical descriptions for the targeted behavior. In the case of oscillators, the target is to obtain a steady-state

²The dynamic range (DR) can be expressed in a number of equivalent bits b by using the expression $DR = 6.02 \cdot b + 1.76$. Thus, 60 dB dynamic range corresponds to an equivalent resolution of 9.7 bits.

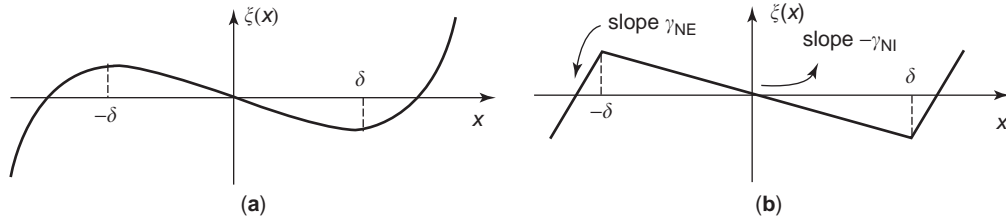


Figure 1. *N*-shaped characteristics necessary to implement oscillator circuits and associated piecewise-linear approximation.

cyclic solution with only DC excitations. For VCOs and VFCs, the timing of these cyclic solutions must also be electronically controllable.

“The simpler, the better” is a basic motto for electronic circuit design. In the case of oscillators, two ineludible (inevitable) ingredients are dynamics and nonlinearity. Thus, oscillator circuits must contain capacitors and/or inductors together with nonlinear elements. Strictly speaking, the dynamics must be at least of second-order type—meaning that the corresponding circuit requires at least two energy storage elements. With regard to the nonlinearity, the simplest one is the *N*-like shape of Fig. 1a, which can be approximated by a series expansion

$$\zeta(x) = -\eta_{\text{NI}} \cdot x + \eta_{\text{NE}} \cdot x^3 \quad (2)$$

where η_{NI} and η_{NE} are real parameters that can be used to fit the required function shape. Alternatively, Fig. 1a can be approximated by the *piecewise-linear* curve depicted in Fig. 1b, where the fitting is realized through the real parameters γ_{NI} and γ_{NE} .

2.1. Basic Oscillator Model

The basic oscillator model is built by combining the ingredients above into

$$\begin{aligned} \tau_x \frac{dx}{dt} &= -y - \zeta(x) \\ \tau_y \frac{dy}{dt} &= x \end{aligned} \quad (3)$$

Figure 2a shows a conceptual realization of this equation using two integrators, one adder and one block with nonlinear transfer function $\zeta(x)$ —all realizable in electronic form. Figures 2b and 2c show realizations using capacitors, inductors, and nonlinear resistors; it is easy to confirm that Fig. 2b maps onto Eq. (3) for $x = v$, $y = Ri_L$, $\tau_x = RC$, $\tau_y = L/R$, and assuming that the resistor has a voltage-controlled characteristic $iR = \zeta(v)$; similarly, Fig. 2c maps onto Eq. (3) for $x = Ri_L$, $y = v_C$, $\tau_x = L/R$, $\tau_y = CR$ and assuming that the resistor has a current-controlled characteristic $v = \zeta(iR)$.

The model of Eq. (3) generates stable oscillations—called *limit cycles*—due to the dynamic *equilibrium* between two opposite forces: one *expansive*, the other *contractive*. The expansive force occurs for $|x| < \delta$ because of the negative slope of the nonlinearity in this region (see

Fig. 1b).³ This negative slope can be realized only through an active element that injects energy into the system, thereby causing $|x|$ to increase with time. On the other hand, the contractive force occurs for $|x| > \delta$ as a result of the positive slope of the nonlinearity in this region. Because of this positive slope, the system dissipates energy and, consequently, $|x|$ decreases with time.

The actual trajectories in the transient evolution toward the limit cycle depend on the values of the parameters τ_x , τ_y , γ_{NI} , γ_{NE} , and δ . The shape of the limit cycle orbit and the frequency of the motion are also dependent on these values. Finding closed relationships among the shape and frequency, on one side, and the parameter values, on the other, is not even possible in the more general case. However, for our purposes here it suffices to study the approximated solutions in two particular cases. First, we find it convenient to rewrite Eq. (3) in terms of a normalized time variable $\tau = t/\tau_0$ with $\tau_0 \equiv \sqrt{\tau_x \tau_y}$. It yields

$$\begin{aligned} \frac{dx}{d\tau} &= \alpha[-y - \zeta(x)] \\ \frac{dy}{d\tau} &= \frac{1}{\alpha}x \end{aligned} \quad (4)$$

where $\alpha = \sqrt{\tau_y/\tau_x}$. The two particular cases of interest occur for extreme values of the parameter α ; they are respectively called the *harmonic oscillator case*, corresponding to $\alpha \ll 1$, and the *relaxation oscillator case*, corresponding to $\alpha \gg 1$.

2.2. Harmonic Oscillator Case

This corresponds to $\alpha \ll 1$, namely, to $\tau_y \ll \tau_x$. For a better understanding of what happens in this case, it is

³In the electronic implementation of Figs. 2b and 2c, the negative slope is caused by a negative resistance. This negative resistance injects energy into the two other circuit components, namely, the inductor and the capacitor. Because these latter elements do not dissipate energy, but simply store it, the total energy increases and this manifests itself as an increase of the signal amplitude. On the other hand, the positive slope is caused by a positive resistance that dissipates part of the energy stored in the energy storage part of the circuit. At the equilibrium there is balance between the energy injected and the energy dissipated, the circuit energy remains unchanged, and the movement is due to a continuous interchange of this energy between the inductor and the capacitor.

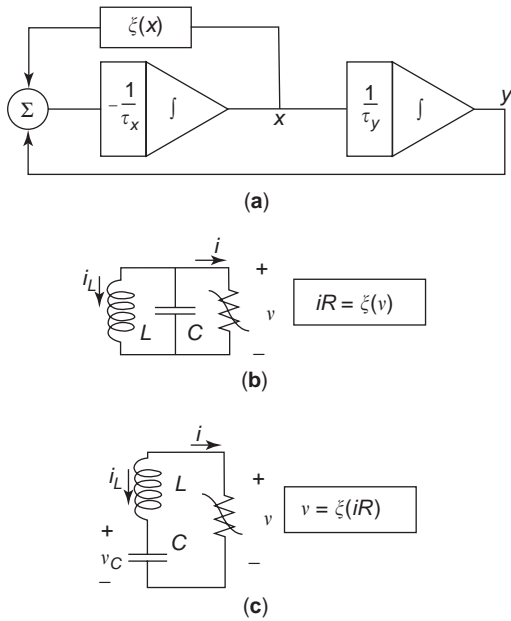


Figure 2. Conceptual realization of the basic oscillator model in Eq. (3) (a) and LC realizations for $x = v, y = Ri_L, \tau_x = RC, \tau_y = L/R$ (b) and for $x = Ri_L, y = v_C, \tau_x = L/R, \tau_y = CR$ (c).

convenient to recast Eq. (4) into the following scalar form

$$\frac{d^2x}{d\tau^2} + \alpha \frac{d\xi}{dx} \frac{dx}{d\tau} + x = 0 \quad (5)$$

obtained after differentiating the top expression in Eq. (4) and using the bottom expression to substitute $dy/d\tau$.

Assume first that the nonlinearity is null. Then $d\xi/dx = 0$ and the solution of Eq. (5) for initial conditions $x(0) = x_0$ and $dx/d\tau|_{\tau=0} = 0$ is $x(\tau) = x_0 \cos(\tau)$, and hence

$$x(t) = x_0 \cos(\omega_0 t) \quad (6)$$

where $\omega_0 \equiv 1/\tau_0$. Obviously, such a solution could not be maintained in practice because of the unavoidable energy dissipation, which is why nonlinearity is needed for practical oscillator design. However, because $\alpha \ll 1$, the second term in Eq. (5) is negligible and at the limit cycle $x(t)$ is quas sinusoidal; $x(t) \approx \rho \cos(\omega_0 t)$ with the amplitude for fixed α and τ_0 depending on γ_{NI}, γ_{NE} , and δ .

The set of drawings in Fig. 3 illustrate the harmonic oscillation case. On one hand, they are intended to highlight the dynamic equilibrium process underlying the onset of oscillations. On the other, they give insight on the influence of the model parameters. All the drawings are for $\tau_x = 10, \tau_y = 0.1$, and $\delta = 1$. The three drawings at the top are for $\gamma_{NE} = 1$ and $\gamma_{NI} = 1$. The one on the left in this subset shows the solution trajectories in the x - y plane for different initial conditions. The opposed expansive and contractive forces are highlighted by this figure. Their equilibrium results in the system evolving toward a limit cycle from any initial condition located either inside or outside it. The waveform at the center in the top set of figures shows $x(t)$ at the steady state. Because this steady

state is obtained as the result of a nonlinear equilibrium process, this waveform is not a pure sinusoidal, but contains harmonics. The spectrum on the right shows these harmonics. The three drawings in the center row in Fig. 3 are for $\gamma_{NE} = 1$ and $\gamma_{NI} = 0.2$. Here the frequency is practically the same as in the previous case, although the amplitude and distortion of $x(t)$ are now smaller. On the other hand, the evolution from inside the limit cycle toward the limit cycle itself is much slower. However, the last set of drawings, for $\gamma_{NE} = 1$ and $\gamma_{NI} = 3$, again display practically the same frequency but much larger amplitude and distortion, and a very fast evolution to the limit cycle.

The following observations on the influence of parameters can be made regarding the harmonic oscillator case:

- The oscillation frequency is basically set by $\tau_0 = \sqrt{\tau_x \tau_y}$. The voltage control of this frequency is hence achieved through electronic tuning of the time constants τ_x and τ_y . For the LC circuits of Figs. 2b and 2c, the frequency can be made voltage-controlled by resorting to the use of tunable capacitors or inductors [15,17,25].
- On one hand, for given values of $\tau_x, \tau_y, \gamma_{NE}$, and δ , the larger γ_{NI} , the larger the signal amplitude and the signal distortion; also, the faster the dynamic evolution toward the limit cycle from the inside. On the other hand, for given values of $\tau_x, \tau_y, \gamma_{NI}$, and δ , the smaller γ_{NE} , the smaller the signal distortion, although the speed of the dynamic evolution towards the limit cycle from the inside does not change with γ_{NE} . Finally, the value of δ influences the signal amplitude, but has no influence on either the signal distortion or the speed of the evolution towards the limit cycle.

2.3. General Harmonic Oscillator Model

Figure 2a can be redrawn as depicted in Fig. 4a, consisting of the interconnection of a linear dynamic block with transfer function in the s domain given by

$$H(s) = \frac{X(s)}{Z(s)} = \frac{s \frac{1}{\tau_x}}{s^2 + s \frac{\gamma_{NE}}{\tau_x} + \frac{1}{\tau_x \tau_y}} \quad (7)$$

and a nonlinear block with transfer characteristics $\zeta(x)$. Note that the linear block acts as a bandpass filter with resonant frequency $\omega_0 \equiv 1/\tau_0$ and quality factor $Q = 1/(\gamma_{NE}\alpha)$. Note also that the gain of this filter at the resonant frequency is $1/\gamma_{NE}$; and that the nonlinear block gains $\gamma_{NE} + \gamma_{NI}$ inside its inner linear region.

Assume $x(t) \approx \rho \cos(\omega t)$. The system can oscillate, provided the amplitude and the phase of this signal are maintained while the signal is being transmitted across the loop. Consider first the phase. On one hand, the nonlinearity is static, and does not produce any phase shift. On the other hand, the phase of the linear block is null only for $\omega = \omega_0$, which is why the oscillation actually occurs at this frequency. Now consider the amplitude. On one hand,

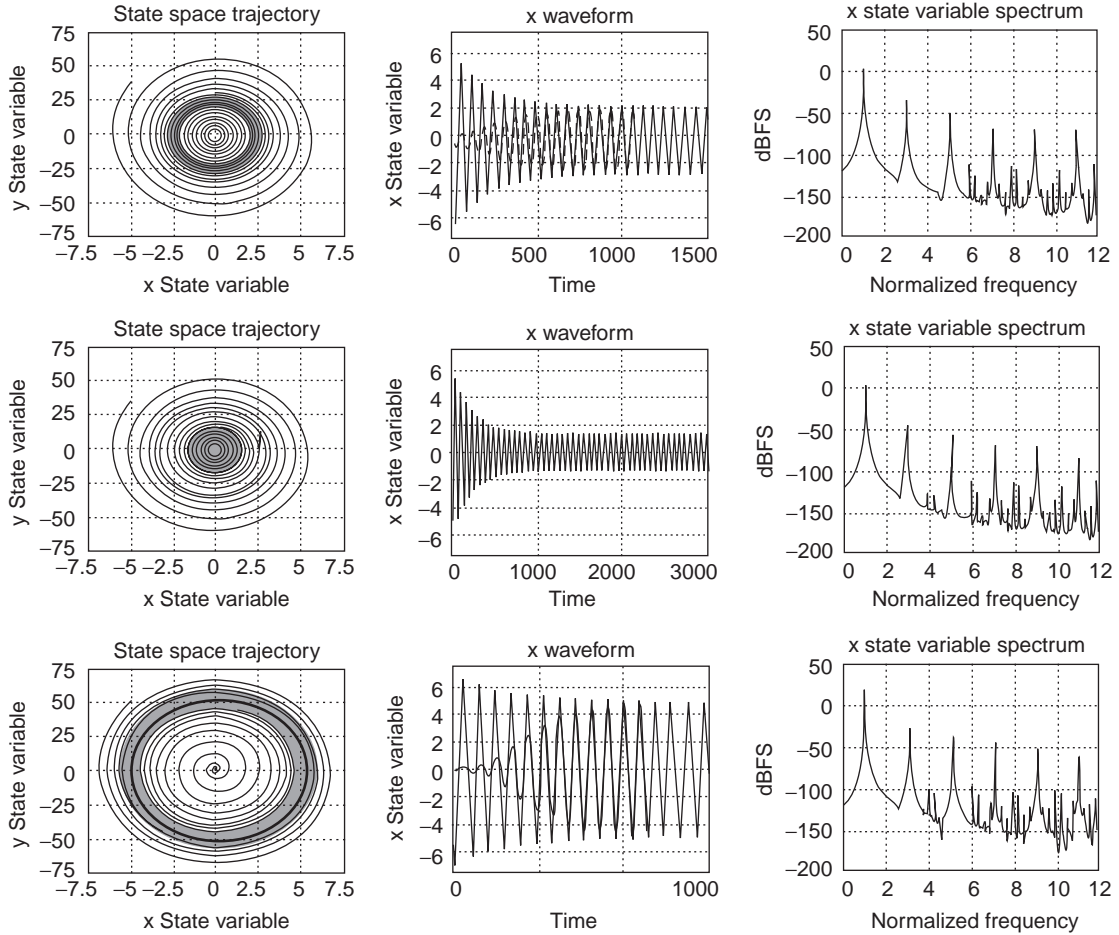


Figure 3. Trajectories, signals, and spectrum for the oscillator model in the harmonic oscillation case for $\tau_x = 10$, $\tau_y = 0.1$, and $\delta = 1$. The three drawings at the top are for $\gamma_{NE} = 1$ and $\gamma_{NI} = 1$; those in the center row are for $\gamma_{NE} = 1$ and $\gamma_{NI} = 0.2$, and the drawings at the bottom were obtained for $\gamma_{NE} = 1$ and $\gamma_{NI} = 3$. We see that the oscillation frequency is practically the same in the three cases (basically set by $\tau_0 = \sqrt{\tau_x \tau_y}$). We also observe that the larger γ_{NI} , the larger the signal amplitude and distortion, while the dynamic evolution toward the limit cycle is faster.

for $\rho < \delta$ the loop has a gain of $1 + \gamma_{NI}/\gamma_{NE}$, larger than unity, so that the amplitude grows while the signal transverse the loop. On the other hand, for $\rho > \delta$, the gain is compressed because of the saturation nonlinearity. The compression increases with ρ until a critical amplitude value ρ_0 is reached where the effective gain is unity.

Figure 4b shows the block diagram of a generic harmonic oscillator model. On the basis of the explanations given for Fig. 4a, the following statements are made for this generic model:

- The phase shift of the linear block must be frequency-dependent and null at a single frequency $\omega = \omega_0$, which is the oscillation frequency. The sharper the phase-versus-frequency characteristics of the linear block around this zero-phase frequency, the higher the accuracy of the oscillation frequency setting.
- Now consider the oscillation amplitude. On one hand, the loop gain at the zero-phase frequency must be larger than unity for low amplitudes. This ensures

that the oscillations will start. On the other hand, the compression exercised by the nonlinear block must render the loop gain smaller than unity for large amplitude values. The oscillation occurs at the amplitude for which the compressed loop gain at the zero-phase frequency is just unity.

This can be applied to the *ring oscillator* structure of Fig. 5a, commonly employed in VCOs. It is composed of N identical stages, each with linearized transfer function [23]

$$F(s) = \frac{-G_m R}{1 + sRC} \quad (8)$$

connected into a feedback loop. On one hand, note that each stage produces a phase shift of $\pi - \text{atan}(\omega RC)$; the zero-phase frequency is hence readily calculated as

$$f_0 = \frac{1}{2\pi RC} \tan \frac{\pi}{2N} \{3 + (-1)^N\} \quad (9)$$

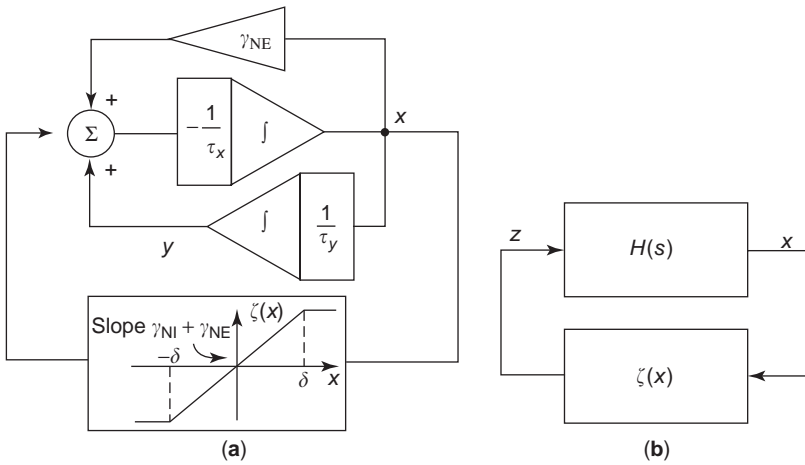


Figure 4. (a) Representation of the basic oscillator model in Fig. 2a as the interconnection of a linear dynamic block and a nonlinear block and (b) general harmonic oscillator model with these blocks. The phase shift of the linear block is null at the oscillation frequency, and the oscillation occurs at the amplitude for which the loop gain is just unity.

On the other hand, the nonlinearity, and hence the control of the oscillation amplitude, is inherent to the active devices used to realize the transconductors. For the simple circuits typically employed in these transconductors, such as, for instance, those in Fig. 5b, the transconductance decreases with the signal amplitude. Hence the condition for the generation of oscillations is $G_m R > 1$.

2.4. Relaxation Oscillator Case

This case corresponds to α in Eq. (4) being much larger than unity, namely, to $\tau_x \ll \tau_y$. In the limit, as $\alpha \rightarrow \infty$, its factor in the top equation of Eq. (4) becomes negligible and hence

$$y = -\zeta(x) \tag{10}$$

meaning that the shape of the limit cycle fits with the nonlinear function $-\zeta(x)$, drawn with a thick solid trace in Fig. 6a.

This piece of information has to be complemented with analysis of the solution trajectories of Eq. (4) for the different linear pieces of $-\zeta(x)$. Let us consider first the inner piece, where $y = \gamma_{NI}x$. Analysis obtains

$$x(\tau) \approx -\frac{1}{\gamma_{NI}} [y(0) - \gamma_{NI}x(0)] e^{\alpha \gamma_{NI} \tau}$$

$$y(\tau) \approx [y(0)] e^{\alpha \gamma_{NI} \tau} \tag{11}$$

valid for $|x| < \delta$. Note that in the limit for $\alpha \rightarrow \infty$, $y(\tau)$ remains practically constant while the system evolves in this inner region. Quite on the contrary, $x(t)$ changes at very high speed; either decreasing, for $y(0) > \gamma_{NI}x(0)$, or increasing, for $y(0) < \gamma_{NI}x(0)$. The arrows drawn with thin solid lines in Fig. 6a indicate the direction and sense of the trajectories in this inner region. From this picture, it is readily inferred that the nonlinearity inner piece is not part of the limit cycle.

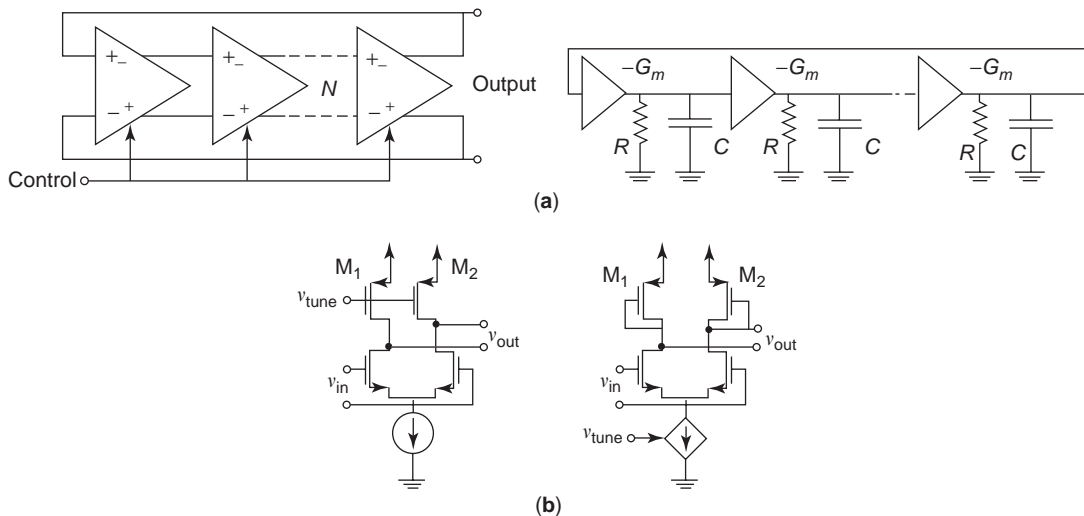


Figure 5. (a) Ring oscillator structure and its linearized model as a specific example of Fig. 4; (b) simple typical circuit realizations for the tunable transconductors.

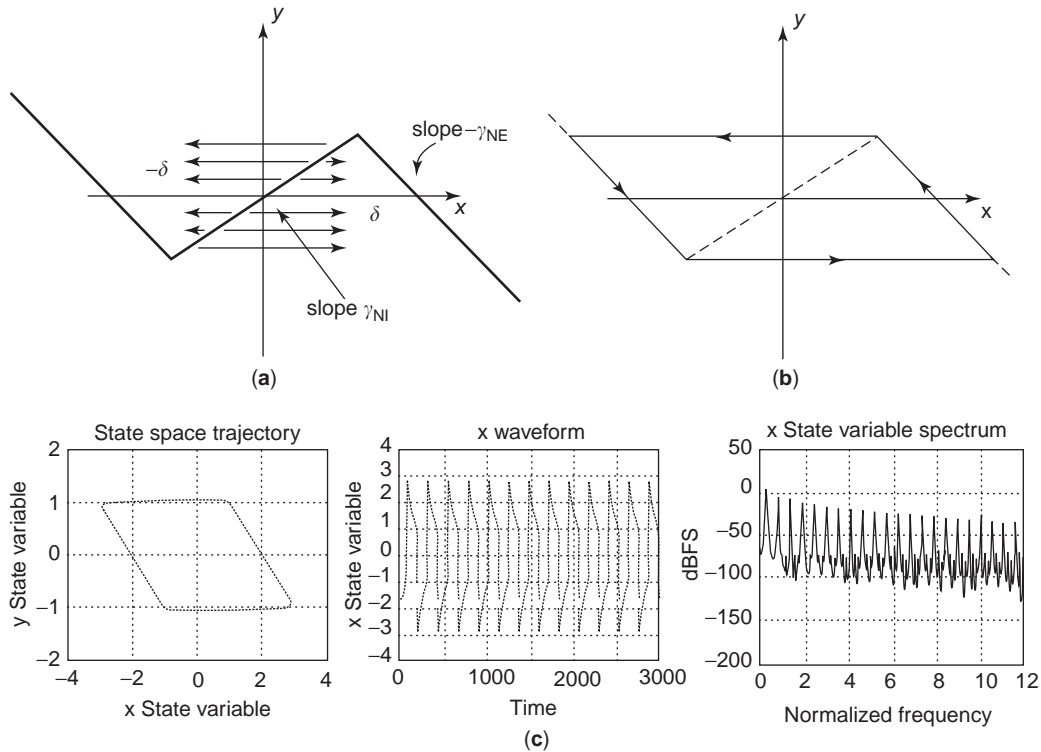


Figure 6. The limit cycle in the relaxation case fits with the nonlinear function $\zeta(x)$ in (a) as depicted in (b), where we assume that the horizontal transitions occur instantaneously. The bottom drawing (c) shows the limit cycle, the $x(t)$ waveform, and its spectrum for $\tau_x = 0.1$, $\tau_y = 10$, $\delta = 1$ and $\gamma_{NE} = \gamma_{NI} = 1$.

Let us now consider the outer pieces, where $y = -\gamma_{NE}x \mp \beta$, where the minus sign is for the left-hand piece; the plus sign, for the right-hand one; and β is the absolute value of the ordinate at the origin. Analysis obtains a fast transient across a quasihorizontal trajectory followed by a slow asymptotic behavior whose trajectory is described by

$$x(\tau) \approx -\frac{1}{\gamma_{NE}} [y(0) - (\mp\beta)] e^{-(1/\gamma_{NE})\tau} \tag{12}$$

$$y(\tau) \approx [y(0) - (\mp\beta)] e^{-(1/\gamma_{NE})\tau} \mp \beta$$

Note that this slow asymptotic behavior results in trajectories that fit exactly with the corresponding outer piece of the nonlinear function.

Summarizing these considerations, the limit cycle can be built as shown in Fig. 6b, where we assume that the horizontal transitions occur instantaneously. Thus, the oscillation frequency is basically determined by the time invested in making the asymptotic evolutions on the outer pieces of the nonlinearity, which can be calculated from Eq. (12) as

$$T_c = 2\tau_y \gamma_{NE} \ln \frac{\beta + \gamma_{NI}\delta}{\beta - \gamma_{NI}\delta} \tag{13}$$

These summary considerations are confirmed by the simulations depicted in Fig. 6c, which shows the limit cycle,

the $x(t)$ waveform, and its spectrum for $\tau_x = 0.1$, $\tau_y = 10$, $\delta = 1$ and $\gamma_{NE} = \gamma_{NI} = 1$.

At this point let us explore the implications of the conditions leading to the relaxation oscillator case on the LC circuits of Figs. 2b and 2c. These conditions are met by making $C \rightarrow 0$ in the former case; and by making $L \rightarrow 0$ in the latter. For circuit implementation purposes, these negligible elements can be considered parasitics and, hence, the relaxation oscillator can be built by simply connecting either an inductor or a capacitor to a nonlinear resistor. Figure 7 shows these realizations, where the nonlinear resistor is N-shaped for Fig. 7a and S-shaped for Fig. 7b.

3. CONVERTERS BASED ON MULTIVIBRATORS

Since the frequency in oscillators can be controlled by means of tunable capacitors, resistors, or inductors, any oscillator can be used to translate a voltage into a frequency, provided that the voltage to be converted is that used to tune the devices [15,17,25]. However, in the case of harmonic oscillators, these mechanisms do not provide a good enough linear dependence of the output frequency on the input voltage, nor temperature stability for most voltage-to-frequency applications. They are used instead in PLL (phase-locked loop) applications, many allowing nonlinearities up to several tens of percent and temperature-induced variations as long as the tuning range accommodates them [24]. The jitter in these circuits is

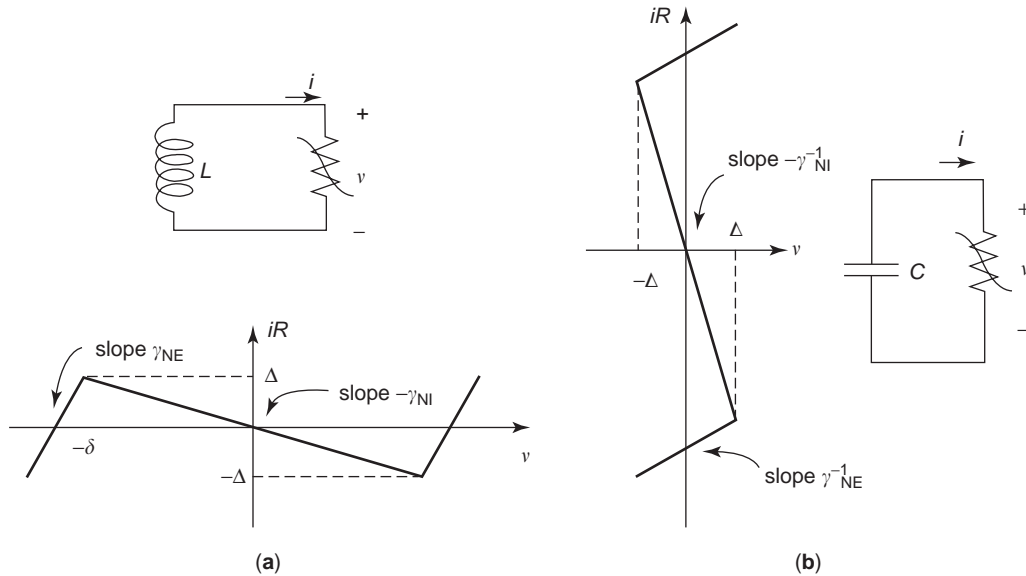


Figure 7. Simplified first-order abstractions for a relaxation oscillator. The conditions leading to the relaxation oscillator case on the LC circuits of Figs. 2b and 2c are met by making $C \rightarrow 0$ in the former case (a) and $L \rightarrow 0$ in the latter (b).

also lower than in relaxation oscillators, which make them more appropriate for timing applications [11]. Multivibrators usually have poor timing accuracy for frequencies above a few hundred kilohertz because of the random fluctuations of the threshold levels and charging and discharging currents and their increasing importance with respect to shorter clock periods [1], but they provide the best linearity and temperature and supply stability at medium to low frequencies, as well as wide control and

signal ranges [8]. Since the latter are features required for voltage-to-frequency conversion, most VFCs on the market are based on multivibrators; thus we will focus our approach on the following.

Implementations of VFCs are usually based on capacitors as energy storage elements, and the nonlinear resistor in Fig. 7b is commonly implemented as depicted in Fig. 8a. The current switches in Fig. 8a are set to the Ch or Dh position by the reversal block, corresponding to the

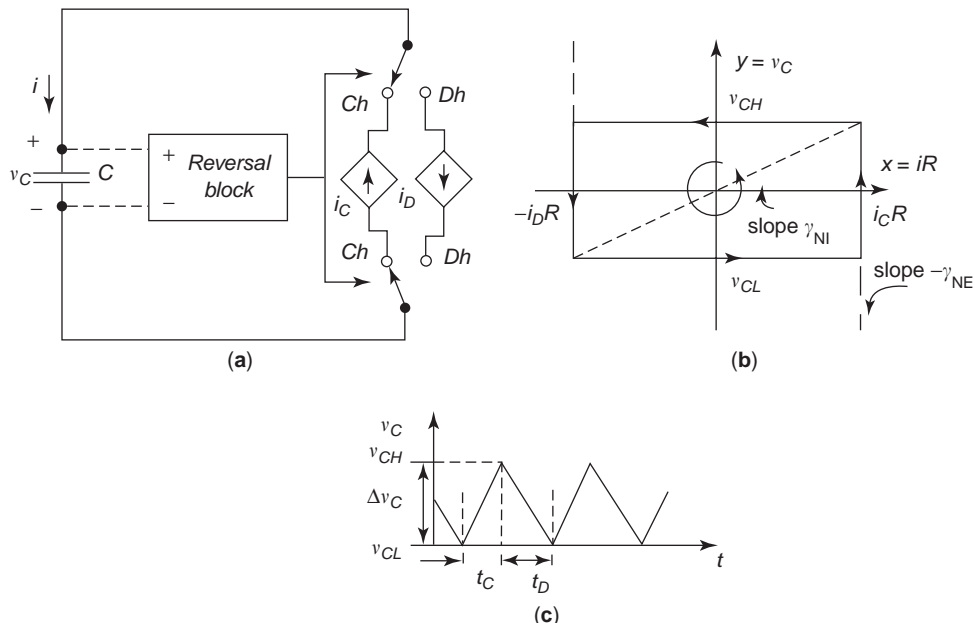


Figure 8. Realization of relaxation oscillators based on Fig. 7b. The reversal block controls the switches to alternatively charge and discharge the capacitor (a). The associated cyclic diagram corresponding to the general case in Fig. 6 is shown in (b), while (c) depicts the resultant waveform.

charging phase and the *discharging phase*, respectively. During the charging phase, the current i_C enters the capacitor input node (+) and the voltage v_C grows, while it decreases during the discharging phase, wherein the current i_D leaves the capacitor input node. The circuit operation consists in the succession of these two phases in a cyclic behavior. The period of the cycle is determined by (1) the value of i_C and i_D and the capacitance C associated with the *timing capacitor*, which set the rate for the voltage v_C to change inside each phase, and (2) the reversal block, which senses v_C and turns the switches to the *Ch* or *Dh* positions. Assuming constant values for the currents i_C and i_D , the time intervals corresponding to the charging and discharging phases are (see Fig. 8c)

$$t_C = \frac{C(v_{CH} - v_{CL})}{i_C} \quad t_D = \frac{C(v_{CH} - v_{CL})}{i_D} \quad (14)$$

where v_{CH} and v_{CL} are the top and bottom limits, respectively, of the voltage swing in the capacitor terminals. In the specific case of having $i = i_C = i_D$, the time invested in a cycle is

$$T_c = t_C + t_D = \frac{2C(v_{CH} - v_{CL})}{i} \quad (15)$$

where we have supposed that the delay associated with the reversal block and the current switches is negligible, which corresponds to the assumption $\tau_x \ll \tau_y$ in the previous section. Actually, the expression for T_c above is also derived from Eq. (13) by making $\gamma_{NE} \rightarrow \infty$, which provides

$$T_c = 4\tau_y\gamma_{NI} \quad (16)$$

for the time invested in completing the cyclic diagram in Fig. 8b (see also Fig. 6). Note that Eq. (16) yields Eq. (15) if γ_{NI} is obtained from Fig. 8a as

$$\gamma_{NI} = \frac{v_{CH} - v_{CL}}{2iR} \quad (17)$$

and taking into account that $\tau_y = RC$.

The VFCs currently on the market can be classified into two major types that follow the previous approach: the *Schmitt trigger converters* and the *charge balancing converters*. The main difference between both types lies in the role that the reversal block plays. In the former, the reversal block works like a Schmitt trigger, which senses $v_C(t)$ and turns the current switch to the position *Ch* or *Dh* any time it reaches the low v_{CL} and high v_{CH} threshold values, respectively. Thus, the reversal block imposes the thresholds v_{CH} and v_{CL} , and sets directly the voltage swing ($v_{CH} - v_{CL}$) in the capacitor during the circuit operation. Equation (14) applies here, and the frequency of the waveform associated with v_C is determined by means of voltage-controlled current sources, thus causing $i_C = K_C v_{in}$ and $i_D = K_D v_{in}$ to obtain

$$f = \frac{1}{t_C + t_D} = \frac{K_C K_D v_{in}}{(K_C + K_D)C(v_{CH} - v_{CL})} \quad (18)$$

where v_{in} is the input voltage that is converted into the frequency f . In the particular case of having $K_C = K_D$, we get a symmetric triangle-shaped periodic signal.

On the other hand, in charge-balancing-type converters, the reversal block does not impose lower and upper limits or thresholds to the voltage drop in the capacitor, but a fixed duration of the charging phase T_0 . These circuits also are built to fulfill $i_C = i_0 - i_D$, where i_0 is a constant current. The basic working principles are similar to those in the Schmitt trigger converters, and the circuit evolves in a cycle with successive charging and discharging phases. Let us begin in a certain point inside the discharging phase. The voltage v_C ramps down until it equals a lower threshold v_{CL} . At this time, the switch is turned to *Ch* by the reversal block and the capacitor is charged but now for a fixed period T_0 . Thus, the voltage v_C changes by an amount given as

$$\Delta v_C = \frac{i_C T_0}{C} = \frac{(i_0 - i_D) T_0}{C} \quad (19)$$

Once this charging phase is concluded, the switch is set to *Dh* by the reversal block and the capacitor is discharged by i_D until the lower threshold is reached again; hence the voltage v_C falls an amount of Δv_C and the duration of this phase is

$$t_D = \frac{C \Delta v_C}{i_D} = \left(\frac{i_0}{i_D} - 1 \right) T_0 \quad (20)$$

Since T_0 and i_0 are constant values, the frequency is changed by tuning i_D in Eq. (20). If $i_D = K_D v_{in}$, we obtain the following expression for the frequency of $v_C(t)$:

$$f = \frac{1}{t_C + t_D} = \frac{i_D}{i_0 T_0} = \frac{K_D v_{in}}{i_0 T_0} \quad (21)$$

In the following section we will show implementations of these two classes of converters and discuss design issues and nonidealities.

4. SCHMITT TRIGGER CONVERTERS

4.1. Direct Implementation

Figure 9a shows a straightforward implementation of a Schmitt trigger type converter with a grounded capacitor. Two possible realizations of the Schmitt trigger block are also depicted in Fig. 9b [14]. In the single-comparator-type Schmitt trigger on the left of Fig. 9b, for very low values of v_i the comparator output is low and the current switch is open; thus the voltage reference at the inverting input is

$$v_{iH} = V_{CC} \frac{R_2 + R_3}{R_1 + R_2 + R_3} \quad (22)$$

For increasing values of the input voltage, eventually the reference in Eq. (22) is crossed and the comparator output changes and turns the switch on; thus the resistor R_3 is short-circuited. Hence, if the input voltage decreases at

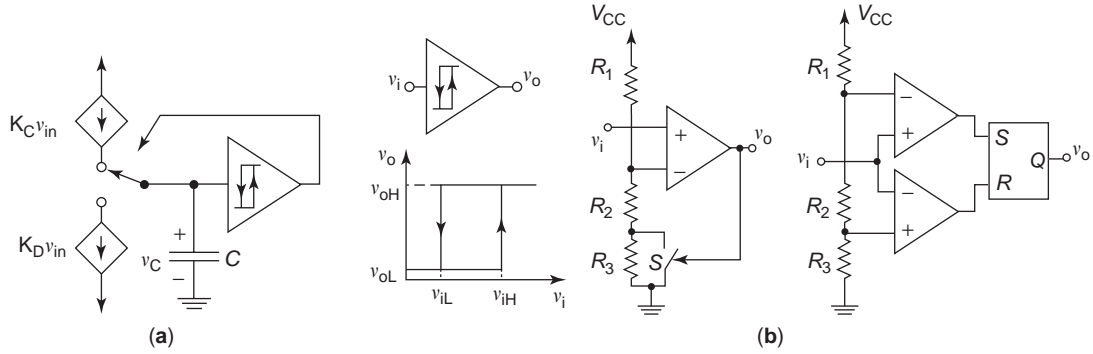


Figure 9. (a) Direct implementation of a Schmitt trigger VFC converter, where the reversal block in Fig. 8 is implemented by a Schmitt trigger circuit; (b) two realizations of the Schmitt trigger block.

this point, the new reference voltage at the inverting input of the comparator is

$$v_{iL} = V_{CC} \frac{R_2}{R_1 + R_2} \quad (23)$$

Note that Eqs. (22) and (23) constitute the high and low threshold voltages, respectively, of the single-comparator Schmitt trigger. The main drawback of this circuit is that the parasitic capacitors at the nodes between the resistors have to be charged and discharged every time the switch is closed or opened, which is a time-consuming task and causes errors that limit the high-frequency capability of the circuit. A better behavior is obtained by using two comparators and fixed voltage references to define the threshold values. The right part of Fig. 9b shows the dual-comparator Schmitt trigger, which is based on this approach and whose threshold voltages are determined by the resistor ladder as

$$v_{iL} = V_{CC} \frac{R_3}{R_1 + R_2 + R_3} \quad v_{iH} = V_{CC} \frac{R_2 + R_3}{R_1 + R_2 + R_3} \quad (24)$$

Besides other general limitations that will be seen later, the basic disadvantage of this strategy is the poor supply voltage stability, due to the dependence of the threshold values on V_{CC} . Table 1 shows the typical performance parameters associated to the NE566 [19], which follows the direct approach in Fig. 9a and whose maximum drift with supply voltage is 2%/V.

4.2. Emitter-Coupled Multivibrator

Instead of a grounded capacitor, the circuit in Fig. 10 uses a floating one that is charged and discharged by means of the bias current sources i_C and i_D . Basically, the circuit

fixes the voltage at one terminal of the capacitor, for instance, the emitter of Q_3 , to a nearly constant voltage V_M , while the other terminal is connected to the current source i_C that charges it. Eventually, the voltage in the latter drops enough to allow the base-to-emitter voltage of Q_2 to reach the transistor threshold, which causes the voltage at the base of Q_3 to fall and the transistor is turned off. The voltage at the emitter of Q_2 is now fixed to two base-to-emitter drops below the supply voltage and the capacitor is being discharged by i_D . Since the circuit is symmetric, the process is repeated periodically. Let us split the cycle in periods related to important events in order to derive the expression of the output wave frequency:

- Figure 10b shows the circuit working somewhere in the cycle with the transistor Q_2 and the diode D_1 in the cutoff region, which is indicated by using a white trace. Consider the clamping block in Fig. 10a formed by one diode and one resistor in parallel. The voltage drop across this block is depicted in Fig. 10a, as well as the response to a step in the current I_D . As long as Q_2 is off, the voltage across the block equals zero if we neglect the base and leakage currents. Since Q_1 and Q_3 are on, the voltage at node B is clamped to $V_M = V_{CC} - 2V_{BEon}$ approximately. On the other hand, the current source i_C is charging the capacitor with a constant current; thus the voltage at the emitter of Q_2 falls to a lower threshold V_L beyond which Q_2 is no longer cut off. Since D_2 and Q_4 are on, such a limit is given by the equation

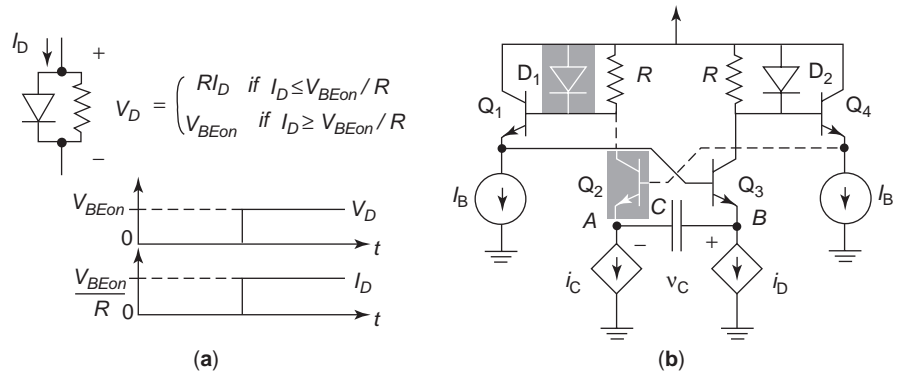
$$V_L = V_{CC} - (V_{D2} + V_{BEQ4} + V_{BEQ2}) \approx V_{CC} - 3V_{BEon} \quad (25)$$

- Once the voltage at node A reaches V_L , the transistor Q_2 turns on and its collector current makes the voltage drop across the left clamping block rise to V_{BEon} ; thus the base of Q_1 drops to $V_{CC} - V_{BEon}$ and the emitter of Q_1 follows this voltage, and hence the voltage at the base of Q_3 is now $V_{CC} - 2V_{BEon}$. Since its emitter was fixed to the same voltage, the transistor Q_3 turns off. Note that at this point, the voltage drop across the capacitor is $v_C = V_B - V_A = V_{BEon}$.

Table 1. Typical Performance Parameters of the NE566

Maximum operating frequency	1 MHz
Sweep range	10–1
Frequency drift with supply voltage	0.2%/V
Frequency drift with temperature	600 ppm/°C
FM distortion ($\pm 10\%$ deviation)	0.4%

Figure 10. Emitter-coupled multivibrator. The clamping block in (a) causes a voltage drop of value V_{BEon} for a current $I_D \geq V_{BEon}/R$, that makes the basis voltage of Q_2 fall, thus it is cut off and the capacitor is charged through i_C . The situation remains until the voltage drop at the emitter of Q_2 is low enough to turn on Q_2 , thus the clamping block at the top-left corner cuts off Q_3 and the situation is reversed. The process is repeated cyclically.



- Since Q_3 is cut off, its collector current vanishes and the voltage drop across the right clamping block goes down to zero. As a consequence, the voltage at node A is pulled up to the value $V_{CC} - 2V_{BEon}$. On the other hand, since the switching time is very short, the capacitor remains charged and the voltage increment is translated into an increment in the voltage at node B, which reaches the value

$$V_H = V_{CC} - V_{BEon} \tag{26}$$

- Note that the situation is symmetric to that in the first point, but now the voltage at node A remains constant while the current source i_D discharges the capacitor, which is equivalent to the initial point above.

From the previous discussion we conclude that in each charging or discharging phase, the voltage at one capacitor terminal A or B remains constant, while the other changes from the voltage V_H to V_L . It is then easy to derive the voltage increment in the capacitor:

$$\Delta v_C = v_{CH} - v_{CL} = (V_H - V_M) - (V_L - V_M) = 2V_{BEon} \tag{27}$$

Since the problem is equivalent to that treated in the previous section, Eq. (18) is also valid here and the frequency of oscillation is given by the expression

$$f = \frac{Kv_{in}}{4CV_{BEon}} \tag{28}$$

where $K_C = K_D = K$.

4.3. Improved Emitter-Coupled Multivibrator

Since the base-to-emitter voltage has a strong temperature coefficient, the circuit in Fig. 10 has as a main drawback: the dependence of Eq. (28) on temperature. One strategy to compensate this dependence consists of making sure that the current that charges and discharges the capacitor is dependent on the temperature for canceling the global dependence [14]. Such an approach achieves circuits whose output frequency does not change with temperature for $v_{in} = 0$, while there is a dependence for values of v_{in} different from zero. Another strategy tries to

make $\Delta v_C = v_{CH} - v_{CL}$ equal to a quantity very stable under temperature variations. That is the strategy followed in the circuit of Fig. 11, which basically works in the same way as the previous one in Fig. 10. The main difference consists in the change of the voltage values used to clamp the collectors of Q_1 and Q_2 . For this purpose, the simple diodes in Fig. 10 are substituted by a more complex circuitry depicted at the top of Fig. 11. In addition to the current sources, the circuit uses two reference voltages to implement the strategy: a very stable voltage reference V_R and the reference voltage $V_{CC} - 2V_{BEon}$ generated by D_5 and D_6 . In addition, one diode bridge derives the voltages at the collectors of Q_1 and Q_2 from these references.

Figure 11 illustrates the same situation as in Fig. 10, where Q_1 was cut off, the voltage at node B was fixed, and the capacitor was being charged by i_C . The same process continues in Fig. 11, where the devices in white are off, but the voltages at the collectors of Q_1 and Q_2 are set to $V_{CC} - V_{BEon}$ and $V_{CC} - V_R - V_{BEon}$, respectively, by the top circuitry referred to above. Taking into account the voltage drops across the emitter-followers as well as that

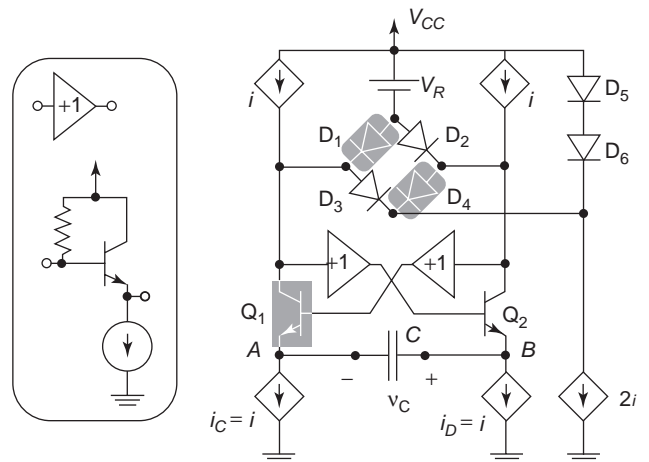


Figure 11. Improved emitter-coupled multivibrator. The clamping circuitry is redesigned to make the voltage variations at the capacitor depend on a voltage (V_R) very stable against temperature change; thus the frequency drift with temperature is improved.

in Q_2 , the voltage at B is

$$V_M = V_{CC} - 3V_{BEon} \quad (29)$$

and the voltage at A beyond which Q_1 is no longer off is

$$V_L = V_{CC} - V_R - 3V_{BEon} \quad (30)$$

When this limit is reached, the situation is reversed, Q_1 is turned on, and Q_2 is turned off. At this point, the voltage across the capacitor is $v_C = V_B - V_A = V_M - V_L = V_R$, and the final voltage at B after the switching will be

$$V_H = V_M + V_R = V_{CC} - 3V_{BEon} + V_R \quad (31)$$

Now, from Eqs. (29)–(31), $\Delta v_C = v_{CH} - v_{CL} = (V_H - V_M) - (V_L - V_M) = 2V_R$, and Eq. (18) reduces to

$$f = \frac{KV_{in}}{4CV_R} \quad (32)$$

The frequency of oscillation can now be stable if V_R is designed carefully to have a low temperature coefficient, which is described later. Table 2 shows some typical parameters of the AD537 [2]. The data refer to the current-to-frequency converter block without accounting for the deviations introduced by the voltage-to-current converter at input.

5. CHARGE-BALANCING CONVERTERS

The other major class of commercial voltage-to-frequency converters are based on a charge balancing system. As mentioned in Section 3, these circuits are characterized by having a fixed length in time in the charging phase. We can classify them into two major categories, those based on one-shot timers and those synchronized to a clock signal.

5.1. Charge-Balancing Converters Based on One-Shot Timers

Figure 12 illustrates a typical implementation of these converters, whose working principle we now describe. Suppose that $v_C \leq v_{in}$; then the comparator provides a high output. As a consequence, the one-shot timer output rises and the current switch is set to the Ch position. This behavior of the one-shot continues under the startup conditions or in the case of a change in the input voltage, and the frequency of the timer output signal is zero. Once the condition $v_C > v_{in}$ is reached, the one-shot (timer) is reset and the current switch is set to the Dh position; thus the capacitor is discharged through R . However, as soon as the condition $v_C \leq v_{in}$ is fulfilled again, the timer is triggered and the switch is turned to Ch again to allow the current

flow into the integrator. This time the one-shot timer operates as usual and generates a pulse of fixed duration t_{os} ; thus a packet of charge is injected in the RC integrator and v_C ramps upward by an amount

$$\Delta v_C = t_{os} \frac{dv_C}{dt} = t_{os} \frac{(i_0 - i_D)}{C} \quad (33)$$

which is enough to make $v_C > v_{in}$; thus the one-shot is reset and the capacitor is discharged again until v_C reaches v_{in} . If $\Delta v_C \ll v_C$, we can approximate $i_D \approx v_{in}/R$, which is a constant current that discharges C ; thus the time t_D is given by

$$t_D \approx \frac{|\Delta v_C|}{\left| \frac{dv_C}{dt} \right|} = \frac{t_{os}((i_0 - i_D))/C}{\frac{i_D}{C}} = t_{os} \left(\frac{i_0 R}{v_{in}} - 1 \right) \quad (34)$$

The cycle is repeated again as soon as v_C equals v_{in} ; thus the output of the one-shot timer is a periodic signal whose frequency is

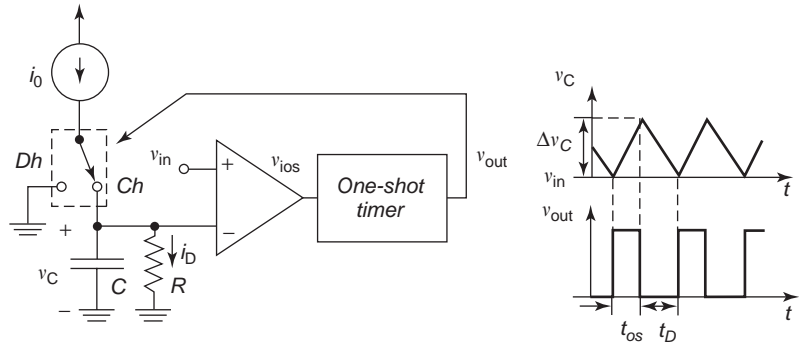
$$f = \frac{1}{t_{os} + t_D} = \frac{v_{in}}{t_{os} i_0 R} \quad (35)$$

Note that this coincides with Eq. (21) for $K_D = 1/R$ and $T_0 = t_{os}$. The circuit in Fig. 12 has two main drawbacks: (1) the change of v_C causes an error in the charging current due to the finite output impedance of the current source that generates it, as well as in the discharging current i_D , which is not constant as supposed above; and (2) the passive RC integrator is very slow, especially for large input voltage changes, which require a large amount of charge to be injected in or extracted from the capacitor. Both aspects can be improved by using an active integrator, as Fig. 13 depicts for two possible and similar approaches [3,26]. The negative feedback provides low impedance at the inverting input terminal of the integrator, whose voltage remains nearly constant; thus the error in the charging and discharging currents is reduced. Equations (33)–(35) are valid in Fig. 13b, but now $i_D = v_{in}/R$ “exactly.” With respect to Fig. 13a, v_C diminishes in the reset mode; thus the derivative in Eq. (33) is negative, as is the voltage increment, but Eqs. (34) and (35) are valid. In both cases, the output current of the op amp (operational amplifier) in the integrator is the same for the charging and the discharging modes, which improves the dynamic response because this minimizes the transients. In addition, Fig. 13a provides high impedance for the input terminal, which can be useful for applications with low load requirements. Finally, note that the capacitance of the integrating capacitor does not appear in Eq. (35) and thus does not directly influence the output frequency. However, it certainly influences the shape of $v_C(t)$, because if C is too small, Δv_C in Eq. (33) could become too large and exceed the linear range of the integrator. In Ref. 16, a nonlinearity error of $\pm 0.024\%$ FS ($f = 10$ – 11 kHz) is reported for the approach in Fig. 12, while it is reduced to 0.006% FS for the improved converter in Fig. 13b.

Table 2. Typical Performance Parameters of the AD537

Frequency range	0–150 kHz
Nonlinearity ($f_{max} = 100$ kHz)	0.25% max
Error drift with temperature (0–70°C)	30 ppm/°C
Error drift with supply voltage	0.01%/V

Figure 12. Basic diagram of a charge-balancing converter based on a one-shot timer. The charging phase has fixed length in time, which is the width of the pulse generated by the one-shot timer (t_{os}) when it is triggered by the comparator. For $\Delta v_C \ll v_C$, the average voltage at the comparator inverting input is v_{in} , thus $i_D \approx v_{in}/R$. The average current injected in the bottom integrator must equal i_D and depends on the rate the one-shot timer is triggered with; hence this rate depends on v_{in} .



The input voltage offset V_{off} of the comparator in Fig. 12 and the integrators in Fig. 13 introduce an error

$$\epsilon_f = \left| \frac{V_{off}}{t_{os} i_0 R} \right|$$

in the expected output frequency—an effect that can be significant, especially for low frequencies, in terms of relative error. On the other hand, precision and low-temperature coefficient current sources to derive i_0 are generated on-chip by means of a voltage bandgap reference and a precision voltage-to-current conversion circuit (see Section 8), while further reflections and replications should also be carried out by cascode current mirrors. Nevertheless, accuracy as well as high-frequency capability of these converters is determined primarily by the precision of the one-shot section.

Figure 14 shows the simplest form of an exponential-ramp-type one-shot timer [14]. The principle of operation is as follows. As long as the flip-flop is reset (low input), the voltage at the output \bar{Q} is high and the current switch (which can be implemented in the simplest way by a grounded transistor) is open; thus the voltage drop in the capacitor is zero. If the circuit is triggered by a high input, the outputs Q and \bar{Q} of the flip-flop are set to a high voltage and a low voltage, respectively; thus the switch is turned off and the capacitor is charged through R , and $v_{C_{os}}$

grows exponentially with a time constant of RC_{os} . However, as soon as the reference voltage at the noninverting input (which is determined by the voltage divider formed by R_a and R_b) is reached, the comparator output changes to a low voltage value and the flip-flop is reset; hence the switch is closed and the capacitor is discharged quickly. Simple calculations on the circuit formed by the supply voltage source, R , and C_{os} provides

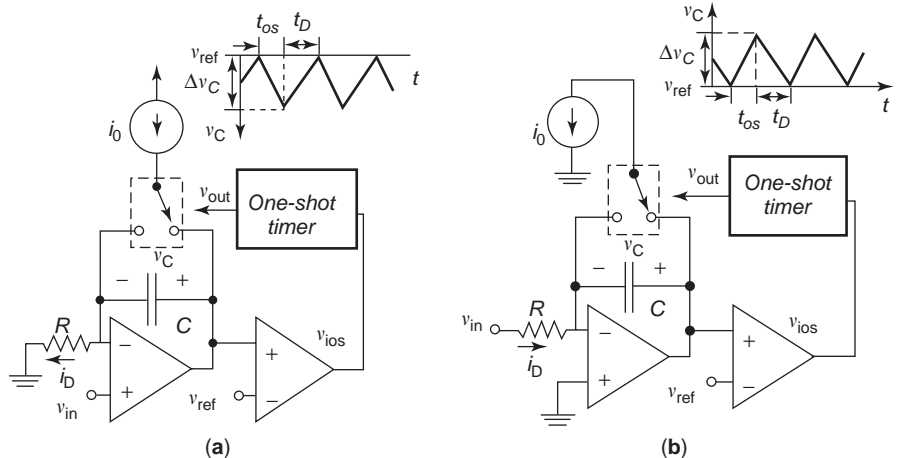
$$t_{os} = RC_{os} \ln \left(1 + \frac{R_a}{R_b} \right) \tag{36}$$

The voltage divider formed by R_a and R_b is usually implemented on-chip and the accuracy obtained for the ratio R_a/R_b is within $\pm 1\%$, and does not depend on the temperature. Thus, the precision, as well as the temperature stability in the expected t_{os} , are determined mainly by the resistor R and the capacitor. However, for small values of t_{os} , the time delays in the input comparator, the flip-flop, and the switch limit the accuracy. In addition, for low frequencies the leakage currents in the capacitor and the switch introduce an error in the timing prediction.

5.2. Synchronized Charge-Balancing-Type Converters

Further improvements can be achieved by replacing the one-shot timer by circuitry clocked by a precise oscillator, usually a crystal one, which determines the charging

Figure 13. Improved converters based on one-shot timers. The use of active integrators instead of the passive one in Fig. 12 achieves smaller errors and improves the dynamic response.



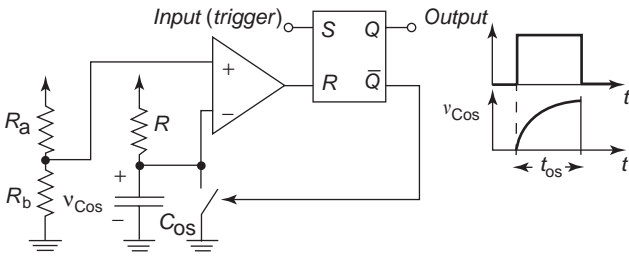


Figure 14. Exponential-ramp-type one-shot timer.

phase duration [4,27]. Figure 15 shows the circuit which results from substituting the one-shot timer with a block composed of one bistable and one AND logic gate, which works as follows. If the integrator output crosses the threshold v_{ref} , the comparator places a high value at the bistable input (suppose that \bar{Q} is high). However, the output does not follow it immediately as in Fig. 13b, but is synchronized with the clock by the flip-flop and changes at the next clock rising edge. At the same time, the output complement (low value) is put at the flip-flop input by the feed-back loop; thus the output, will go back down at the next rising edge of the clock, and the duration of the output pulse will be just one clock cycle. Note that the circuit operates in the charging phase as long as the output is high, thus T_{CLK} replaces t_{os} in Eqs. (33)–(35), which remain valid. However, since the output is now synchronized, its frequency must be a multiple of the clock frequency

$$f = \frac{1}{T_{CLK} + T_{CLK} \times i_S \left(\frac{t_D}{T_{CLK}} \right)} = \frac{1}{T_{CLK} \left[1 + i_S \left(\frac{i_0 R}{v_{in}} - 1 \right) \right]} \quad (37)$$

where i_S means the next superior integer of the argument. Table 3 shows some typical performance parameters of the synchronized converter AD652 [4].

In addition to other design issues that will be discussed in the next section, Fig. 15 has a specific problem to solve due to the lack of synchronism between the input voltage and the clock. The latter could cause the comparator

Table 3. Typical Performance Parameters of the AD652JP

Gain temperature coefficient	
$f_{\text{CLOCK}} = 200 \text{ kHz}$	$\pm 25 \text{ ppm}/^\circ\text{C}$
$f_{\text{CLOCK}} = 4 \text{ MHz}$	$\pm 25 \text{ ppm}/^\circ\text{C}$
Linearity error	
$f_{\text{CLOCK}} = 200 \text{ kHz}$	$\pm 0.002\%$
$f_{\text{CLOCK}} = 4 \text{ MHz}$	$\pm 0.02\%$
Power supply rejection ratio	$0.001\%/V$

output to change at the same time as the clock arrives at the D flip-flop. Since the latter are usually designed to work synchronously, a setup time must be respected for the input signal to change before the clock edge, otherwise there could be metastability problems that do not guarantee a correct value of the flop output; thus t_C can be shorter or larger and the circuit does not work properly. Is it possible to avoid this problem by building the D flip-flop with two flip-flops in cascade or with a flip-flop and a latch in cascade [4], as shown in the right part of Fig. 15, where the clock edge for both flops is delayed. The simplest way to have delayed edges for both flops consists in using the clock falling edge to trigger the first flip-flop, while the second flop is triggered by the rising edge; thus they are delayed half a clock cycle. With this strategy, the metastability of the first flip-flop has ended by the time the second flip-flop is clocked, and the pulsewidth of the output is a clock cycle; thus there is not error in t_C .

5.3. Sigma-Delta Modulators

Figure 16 shows a first-order sigma-delta modulator. It basically consists in a loop with a 1-bit analog-to-digital converter, which is the latched comparator, and a 1-bit digital-to-analog converter in the feedback path. Provided the loop has enough gain, the difference between the analog input and the D/A converter output is minimized and the average value of the D/A output must approach that of the input signal. Similarly, the averaging of the comparator output provides a digital word that represents the analog input. This averaging is described later as part of

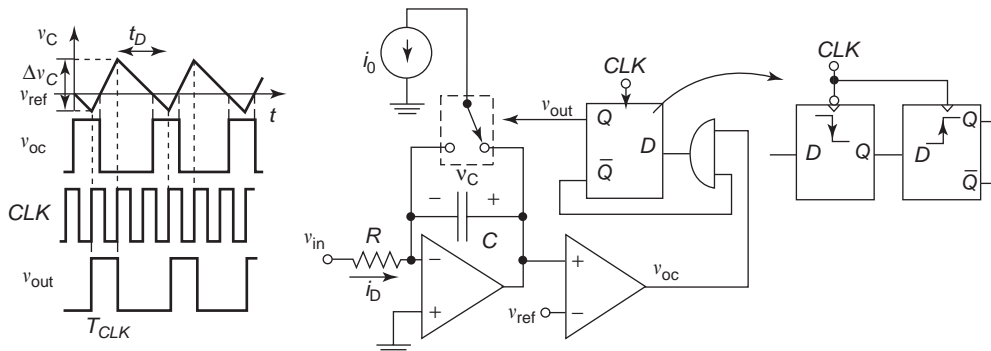


Figure 15. Synchronized charge-balancing converter. The one-shot timer is replaced by externally clocked circuitry. The charging phase length is now fixed by the clock period, which is supposedly very accurate.

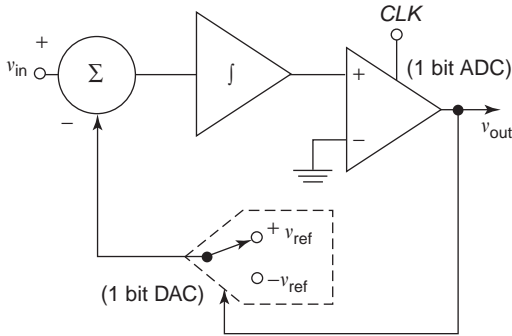


Figure 16. Sigma-delta modulator as synchronized charge-balancing voltage to frequency converter.

the processing required to obtain a digital word from the frequency output of a VFC (digital processing discussed in Section 8); thus sigma-delta modulators can be viewed as synchronized charge-balancing voltage-to-frequency converters (where the charge is injected into or removed from the integrator for the DAC output to track the input voltage). In fact, the transfer function of the AD7740 [5] is $f = 0.1f_{\text{CLK}} + 0.8(v_{\text{in}}/v_{\text{ref}})f_{\text{CLK}}$.

Since sigma-delta modulators can be built currently with cheap CMOS technology, the main advantage of this approach is the cost. The AD7741 [7] with 2.76 MHz at 0.024% of *FoutMax at Nonlinearity* costs 5 times less than the synchronous AD652 with 2 MHz at 0.01% of *FoutMax at Nonlinearity*. In addition, they need fewer external components.

6. DESIGN ISSUES AND LIMITATIONS OF CONVERTERS BASED ON MULTIVIBRATORS

Although some design aspects relative to the design and nonidealities have already been discussed in previous sections, for more clarity, some others regarding all the converters based on relaxation oscillators are examined here. Specifically, note that Eqs. (15) and (18) have been derived without taking into account the deviations from the ideal case. Let us now show some real implementations of formerly ideal blocks and discuss deviations from the ideal case and their consequences in the output wave shape.

6.1. Implementation of the Voltage-Controlled Current Sources

Many VFCs described above use voltage-controlled current sources to implement the charging and discharging currents in Fig. 8, where $i_C = K_C v_{\text{in}}$ and $i_D = K_D v_{\text{in}}$. Such a proportional relationship is obtained readily with a resistor, but a transistor is needed to isolate the control node from the output, which is depicted in Fig. 17a. Such a circuit provides the reference current

$$i_{\text{ref}} = \frac{v_{\text{in}} - v_{\text{BEon}}}{R} - i_B \quad (38)$$

which acts as charging or discharging current. However, note that this circuit provides a current that is not

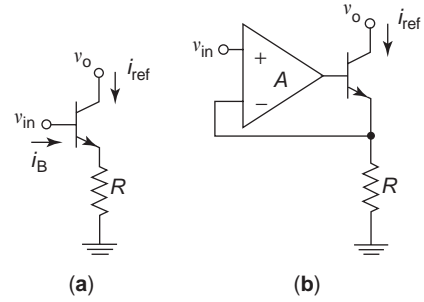


Figure 17. Controlled current source implementation.

proportional to v_{in} , but contains an offset that equals $-(v_{\text{BEon}}/R + i_B)$. Besides modifying the intended proportional relationship, the added term has a strong temperature coefficient, since the base to emitter voltage varies with the temperature as $-2 \text{ mV}/^\circ\text{C}$.

A common alternative for eliminating the dependence of i_{ref} on V_{BEon} places the transistor in a negative-feedback loop as shown in Fig. 17b. If we neglect the base current, the output reference current for this circuit is

$$i_{\text{ref}} = \frac{A}{(A+1)R} v_{\text{in}} - \frac{v_{\text{BEon}}}{(A+1)R} \quad (39)$$

Note that for $A \gg 1$ the term depending on V_{BEon} vanishes and the reference current equals

$$i_{\text{ref}} \approx \frac{v_{\text{in}}}{R} \quad (40)$$

which is proportional to v_{in} . The higher the value of the input amplifier A , the larger the accuracy of Eq. (40). In addition, a MOS transistor can replace the bipolar one in Fig. 17b to reduce the error introduced by neglecting the base current, due to the high impedance associated with the gate of MOS transistors.

6.2. Finite Output Resistance of the Constant Currents

The current source depicted in Fig. 17b still has a nonideal behavior that can introduce deviations in the expected output current. Specifically, since the collector current depends on the collector-to-emitter voltage drop because of the BJT baselength modulation, the current i_{ref} varies with v_o , and this causes an error if the output node directly drives the terminals of the capacitor in Fig. 8, because the voltage drop in the capacitor changes as a consequence of the circuit operation. We can model this dependence on the output node voltage by means of a resistor in parallel with an ideal current source whose value is the expected one. This is illustrated in Fig. 18, where the Thévenin equivalent is also depicted. If the circuit is now connected to the timing capacitor, the voltage v_C does not follow a linear behavior with t , but a well-known exponential behavior. As a consequence, the time to charge or discharge the capacitor an amount Δv_C is longer than expected, which is indicated in Fig. 18a by means of the error ε_t . For the circuits described above, this means longer

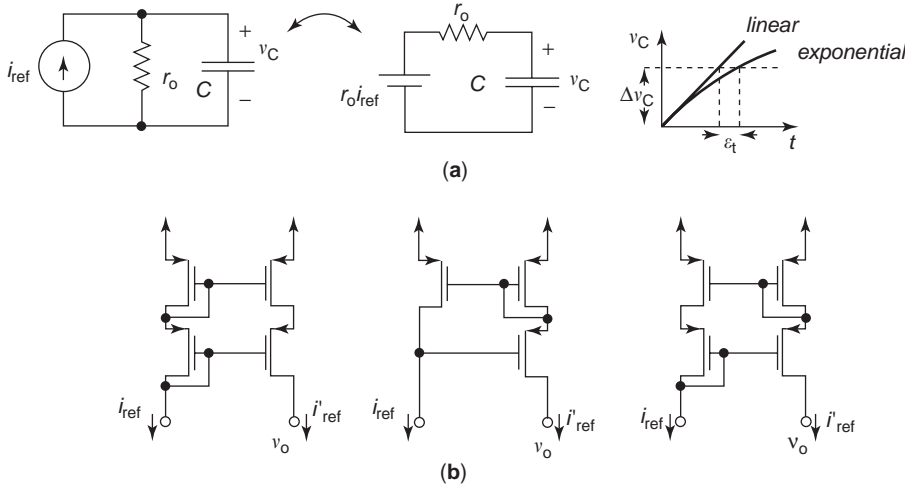


Figure 18. Current source finite output resistance: timing error (a) and common cascode strategies to increase the output resistance (b).

periods or lower frequencies than those in the ideal case. In order to improve the output impedance of the current source, several cascode configurations have been reported [13]. Some common ones are depicted in Fig. 18b, where the current i'_{ref} equals i_{ref} but the output resistance $\partial v_o / \partial i'_{\text{ref}}$ is much higher than $\partial v_o / \partial i_{\text{ref}}$ of circuit in Fig. 17.

6.3. Dependence of Frequency on Temperature and Voltage Supply Variations

The temperature stability of the converter output frequency depends on many factors, some of which have already been discussed. First, in order to improve the temperature stability, we should avoid circuits like that in Fig. 10, whose output frequency depends directly on parameters such as V_{BEon} , which has a large temperature coefficient. Other circuits described above must still be designed carefully to avoid drift.

First, voltage references and charging currents have a large influence on temperature stability. For instance, the voltage source V_R in Eq. (32) must be designed to compensate the temperature dependence. Figure 19a shows an example circuit capable of generating a reference

voltage V_R with a low-temperature coefficient [13]. Such a circuit utilizes the different sign of the temperature coefficients associated with the voltage-to-emitter drop in a BJT and the thermal voltage V_T . The inset box in Fig. 19b encloses a circuit capable of generating a current that is proportional to V_T . As long as the voltage at both output terminals A_1 and A_2 is the same (i.e. $V_{A1} = V_{A2}$), the current I_2 is given by the equation

$$I_2 = \frac{(V_{\text{BE,Q1}} - V_{\text{BE,Q2}})}{R_2} = \frac{V_T}{R_2} \ln\left(\frac{nI_1}{I_2}\right) \quad (41)$$

Two possible approaches to force $V_{A1} = V_{A2}$ are illustrated in Fig. 19b. The circuit at the top of Fig. 19b uses a negative-feedback loop with an operational amplifier that ensures zero differential input; thus $V_{A1} = V_{A2}$. Since the voltage drop across resistors R_1 and R_3 is the same, we can derive the following expression for V_R in Fig. 19b:

$$V_R = V_{\text{BE,Q1}} + \frac{R_3 V_T}{R_2} \ln\left(\frac{nR_3}{R_1}\right) \quad (42)$$

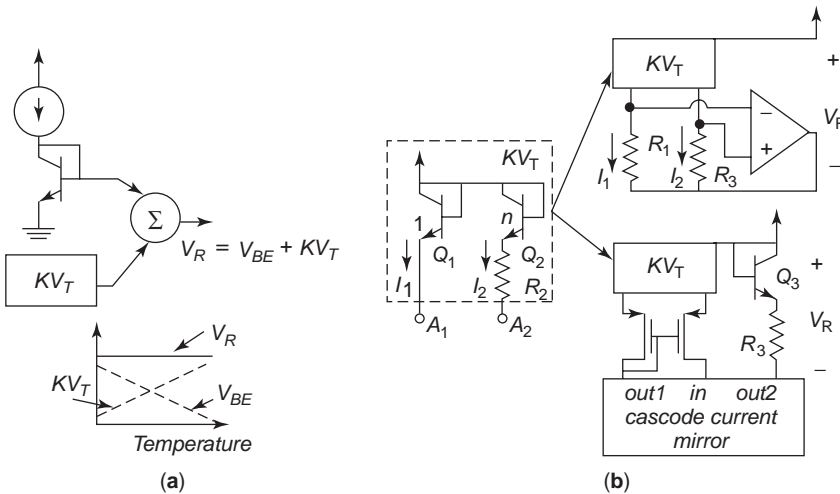


Figure 19. Bandgap reference voltage: (a) the voltages V_{BE} and V_T temperature coefficients of opposite sign, thus they compensate the global dependence of V_R ; (b) two realizations of this approach.

Another strategy uses cascode transistors to get $V_{A1} = V_{A2}$. This is the approach followed by the circuit at the bottom of Fig. 19b, where the reference voltage is

$$V_R = V_{BE,Q3} + \frac{R_3 V_T}{R_2} \ln(n) \quad (43)$$

The reference voltage in Eq. (42) and Eq. (43) is made independent of the temperature variations by choosing properly the circuit and device parameters to achieve

$$\left. \frac{dV_R}{dT} \right|_{T=T_0} = 0$$

(see Ref. 13 for more details).

On the other hand, stable current sources can be obtained by driving the circuit in Fig. 17b with a stable voltage source like that in Fig. 19, which is the strategy followed by many commercial VFCs like the AD537 [2]. Another element that affects the temperature stability is the dependence on the temperature of the Schmitt trigger thresholds, specifically that of the difference $\Delta v_C = v_{CH} - v_{CL}$ in Eq. (15). We have already discussed the particular case of the emitter-coupled circuit in Fig. 11. With regard to the direct implementation in Fig. 9, the reference voltages and the comparator offsets are the main sources of drift. In both cases contributions to global drift are a few tens of ppm $^\circ$ C.

In the case of the charge-balancing converters, note that Δv_C is determined mainly by the charging and discharging currents and by the parameter T_0 in Eq. (21). The drift of T_0 in converters based on one-shot timers is due mainly to the resistance R and the capacitance C_{os} in Eq. (36) and Fig. 14, which are usually external in most commercial VFCs. Finally, the stability of T_0 is obviously improved when such a parameter is determined by a precise external clock as in the synchronous converters.

On the other hand, frequency drift with the supply voltage is also due mainly to variations of the charging and discharging currents as well as that of Δv_C . Bandgap references like those described above also provide supply independent biasing.

6.4. Finite Sensing Node Impedance and Leakage Currents

Note that Fig. 8 assumes infinite impedance in the reversal block-sensing input nodes. Real implementations, however, seldom present such a feature. Specifically, if the reversal block is built with bipolar transistors in the input stage, bias currents have to be provided from the input to the sensing nodes. Such currents are usually in the range of a few hundred nanoamperes and add to or subtract from charging and discharging currents. MOS transistors can be used instead, to implement almost infinite input impedance, thanks to the isolation provided by the gate oxide. In addition, junction leakage or dielectric absorption currents can also be added to or subtracted from charging currents, thus also affecting the output frequency. However, these currents are commonly at a low nanoampere range. Hence, errors due to these base and leakage currents can be usually tolerated as long as the

charging and discharging currents are in the range of $\geq 10 \mu\text{A}$ [14].

6.5. Finite Switching Times

The switching times in Fig. 8 have been neglected in computation of the output frequency in Eq. (18). However, they are not zero in real implementations and limit the frequency capability of the converter. The elements that contribute to the delay in switching are mainly the length of the feedback path and the delays of the blocks along it, while the gain of the active devices, the parasitic capacitances, and the internal current levels determine such delays.

6.6. Output Interfacing

The output stage of the commercial VFCs is designed to allow easy interfacing to all digital logic families. Hence, BJT open collector or both uncommitted collector and emitter interfaces are provided. External pullup resistors and proper biasing complete the interface and determine the risetimes and output logic levels that are adequate for each specific application. Internally, some interface circuitry is needed to drive the base of the output BJT for circuits like that on the right in Fig. 11 [2], while it is not necessary in one-shot-based converters like those described in Refs. 3 and 26, whose one-shot output drives it directly. Synchronous converters also may use a one-shot timer to drive the output transistor, which allows the pulsewidth of the frequency output to be controlled by means of an external capacitor.

6.7. External-Component Selection

Timing capacitors in the converters described above, as well as resistors in Figs. 12, 14 and 15, are usually external components in commercially available VFCs. Special care must be taken to select these components in order to preserve performance. High linearity and low temperature coefficients for the resistors and the capacitors are required. In addition, the latter should not leak, since dielectric absorption can affect the linearity and offset of the transfer function.

7. FREQUENCY-TO-VOLTAGE CONVERSION

The complementary operation of that carried out by the voltage to frequency converters is the frequency to voltage conversion, which is performed by the *frequency-to-voltage converters* (FVCs). This task can be often implemented by the same ICs that perform the V/F conversion, and it is applicable in areas such as telemetry, motor speed control, as well as to build interfaces for sensors whose output is in the form of a variable frequency or pulsetrain [14,20]. Figure 20a shows how this conversion can be accomplished by means of an integrator and a current switch that is driven by the frequency signal in the so-called pulse-integrating FVCs. The switch can also be driven by the output of a one-shot timer (see Fig. 20a), which reduces the integration time, thus allowing small increments in the output voltage without needing too large capacitors. The average

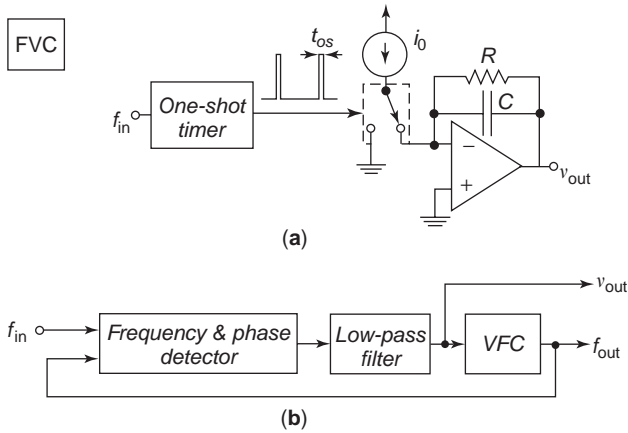


Figure 20. Frequency-to-voltage converters: (a) pulse-integrating converters, where the charge packets are injected in the integrator at a rate determined by the input frequency; (b) phase-locked-loop-type converters, where the lowpass filter output voltage in a PLL is proportional to the deviations of the input signal frequency.

output voltage in Fig. 20a can be calculated by assuming that in the steady state the whole current will flow through the resistor R thus

$$v_{out} = -Ri_0t_{os}f_{in} \quad (44)$$

where $i_0t_{os}f_{in}$ is the average current injected by the top current source in the integrator. A simpler passive integrator could be used instead of the active one in Fig. 20a, but the latter reduces the error caused by the finite output impedance of the current source (this can also be accomplished by means of cascode transistors [21]) and speeds up the converter response time. Since the current is injected in the integrator in packets of size i_0t_{os} , the output voltage has an AC ripple riding on it whose peak-to-peak value is

$$(\Delta v_{out})_{pp} = \frac{i_0t_{os}}{C} \quad (45)$$

It is possible to reduce the ripple by increasing the capacitance C in Eq. (45), but it also will enlarge the time constant associated to the integrator $\tau=RC$; thus the

response time is slow. This is a common tradeoff in the design of these circuits. One strategy to reduce the ripple while keeping the dynamic response consists in filtering the output. As reported in Ref. 22, a passive RC filter exhibits low ripple at all frequencies, but it is slow. The lowest ripple at high frequencies is achieved by an active filter, which also provides much faster step response than does the RC filter. Finally, is it possible to cascade a second active filter on the converter’s output to reduce the ripple at moderate frequencies.

Another approach to convert a frequency into a voltage is implemented by the phase-locked-type FVCs [22]. Figure 20b shows a phase-locked loop (PLL), which basically works as follows. The frequency–phase detector provides an output voltage that is proportional to the difference between the output and input signal phases. After filtering, this voltage is converted back into the output frequency by a V/F converter. The feedback loop locks the phase difference between both input and output signals. The filter output voltage is proportional to the deviations of the frequency of the input signal; thus the circuit also performs a frequency-to-voltage conversion. This converter operates over a wide frequency range of 1 or 2 or 3 decades and responds quickly to frequency changes while it does not have any inherent ripple.

Finally, pulse-integrating converters are open-loop versions of the charge-balancing-type converters described in Section 5; thus their accuracy, linearity, and stability are basically the same as those obtainable from their related VFCs. With respect to Fig. 20b, the high linearity provided by the VFC, which is not required for most PLL applications, is exploited here to ensure an ultralinear FVC.

8. APPLICATIONS

This section describes some typical applications of the voltage-to-frequency converters, which we classify in five major fields: telemetry and remote control, isolation, digital processing, communication and signal processing, and artificial neural networks.

8.1. Telemetry and Remote Control

Data acquisition of remote sensors is seldom possible without transforming the DC sensor output signal, because it is physically unreachable or because of the

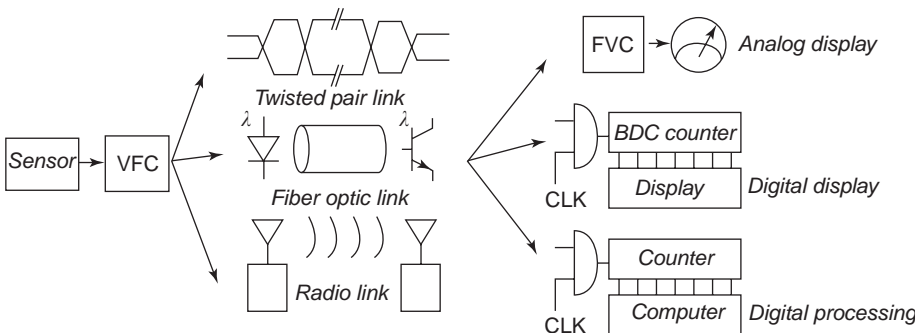
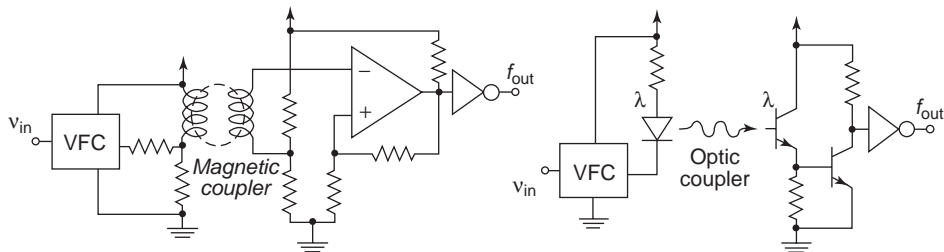


Figure 21. Telemetry with VFC. The voltage signal from a sensor is translated into a frequency signal to be transmitted through twisted-pair or fiber optic links or radiolinks. On the other side, the signal can be converted back into a voltage to drive an analog display or an actuator, or can be processed digitally.

Figure 22. Isolation with VFCs. The frequency signal from a VFC can be transmitted through magnetic (a) or optic (b) couplers to implement galvanic isolation, thus preventing damage due to high bias voltages, or unreasonable current leakage.



vulnerability of DC signals to be degraded when they have to travel long distances through noisy channels [10,12,17,20]. Once converted to frequency signals, they can be transmitted by wires, radio links, or fiberoptic links and processed digitally or converted back into a DC signal to drive an actuator. The latter is performed by a frequency-to-voltage converter, as shown in Fig. 21.

8.2. Isolation

Some applications require galvanic isolation of the sensor and the data-processing unit in order to prevent unreasonable current leakage, or to prevent damage due to high bias voltages, which are often of several volts. Typical isolation interfaces use magnetic or optical couplers [10,17] like those depicted in Fig. 22.

8.3. Digital Processing

The output frequency signal from a VFC can be easily translated into a digital code in order to be processed, stored, or displayed by conventional digital circuits and systems [9,18,20,28]. Actually, this procedure implements an A/D converter while transforming the DC input of the VFC into a digital word. Figure 23a shows the simplest way to carry out this A/D conversion, where a counter, which is only enabled for a given interval T_G termed *gate time*, counts the transitions of the input signal. Thus, after this known period, the counter stores the decimal value $N = f \times T_G$, which encodes the input voltage in a binary number. Another approach is illustrated in Fig. 23b and

uses two counters, one to count the transitions of the input signal and the other to act as a timer that generates an interruption to a microcomputer that reads the content of the first counter and resets it. In both cases, if $FS = f_{max} - f_{min}$ is the full-scale frequency range, the resolution of the A/D converters will be

$$n = \log_2(FS \times T_G) \tag{46}$$

where n is the number of bits of the output digital word. Hence, the larger the gate time, the larger the resolution, which is also limited by the resolution of the VFC. Commercial VFCs provide resolutions as high as 13 bits. Note that the input frequency must remain constant during the gate time for proper conversion; otherwise an average of the input frequency is computed. In addition, since the input signal and the clock are not synchronized, one cycle of the frequency signal can be lost or counted if the transition is just after or before the edge of the clock signal, which causes an error of ± 1 in the result stored in the counter.

8.4. Communication and Signal Processing

Since voltage-to-frequency converters are actually VCOs, they can be used in phase-locked loops in applications such as jitter reduction, skew suppression, frequency synthesis, clock recovery, or FM modulation [24]. However, special care must be taken in order to reduce the jitter and enhance the spectral purity of the output signal, such as use of the differential mode in signal and control paths and guard rings to isolate the noise sources. High linearity is not a key issue in PLL applications, except that described in the Section 7, where nonlinearity degrades the loop stability but can be of several tens of percent. Higher linearity is required for FM modulation, where distortion in the detected signal must be below 1%. Figure 20b depicts a PLL that uses a voltage-to-frequency converter as a voltage controlled oscillator.

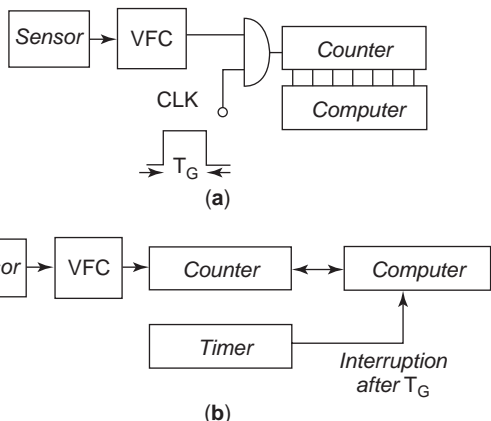


Figure 23. Digital processing of the output frequency signal of a VFC. The transitions in a fixed time interval T_G are counted and the average frequency is computed.

Acknowledgment

This work was supported in part by the spanish government under contract TIC 2003-09817-C02-02.

BIBLIOGRAPHY

1. A. A. Abidi and R. G. Meyer, Noise in relaxation oscillators, *IEEE J. Solid-State Circuits* **CS-18**:794–802 (Dec. 1983).

2. AD537, Integrated circuits voltage-to-frequency converter, *Analog Devices Product Catalogue*, available online at http://www.analog.com/Analog_Root/productPage/productHome/0,2121,AD537,00.html.
3. AD650, Voltage-to-frequency and frequency-to-voltage converter, *Analog Devices Product Catalogue*, available online at http://www.analog.com/Analog_Root/productPage/productHome/0%2C2121%2CAD650%2C00.html.
4. AD652, Monolithic synchronous voltage-to-frequency converter, *Analog Devices Product Catalogue*, available online at http://www.analog.com/Analog_Root/productPage/productHome/0,2121,AD652,00.html.
5. AD7740, 3V/5V low power, synchronous voltage-to-frequency converter, available online at <http://www.analog.com>.
6. AD7741/AD7742, Single and multichannel, synchronous voltage-to-frequency converters, available online at <http://www.analog.com>.
7. M. Banu, MOS oscillators with multi-decade tuning range and gigahertz maximum speed, *IEEE J. Solid-State Circuits* **CS-23**:474–479 (April 1988).
8. L. N. Beard, Use of a voltage-to-frequency converter to measure the integral $\int Edt$, *Am. J. Phys.* **57**(5):457–476 (1989).
9. R. Carr and J. Yang, Current-to-frequency converter for electron multipliers, *Rev. Sci. Instrum.* **60**(7):2321–2323 (1989).
10. L. M. DeVito, A versatile clock recovery architecture and monolithic implementation, in B. Razavi, ed., *Monolithic Phase-Locked Loops and Clock Recovery Circuits*, IEEE Press, New York, 1996.
11. S. W. Glowacki, A current-to-frequency converter, *Nucl. Instrum. Meth.* (186):549–551 (1981).
12. P. R. Gray and R. G. Meyer, *Analysis and Design of Analog Integrated Circuits*, 2nd ed., Wiley, Singapore, 1984.
13. A. B. Grebene, *Bipolar and MOS Analog Integrated Circuit Design*, Wiley, New York, 1984.
14. K. W. Kobayashi et al., A novel self-oscillating HEMT-HBT cascode VCO-Mixer using an active tunable inductor, *IEEE J. Solid-State Circuits* **33**(6) (June 1998).
15. LM131A/LM131, LM231A/LM231, LM331A/LM331, Precision voltage-to-frequency converters, *National Semiconductor Digital Product Catalogue*, available online at http://www.national.com/catalog/AnalogDataAcquisition_VoltageToFrequencyConverter.html.
16. J.-F. Loude, Current-to-frequency isolation converter, *J. Phys. E—Sci. Instrum.* **18**(10):824–826 (1985).
17. T. D. Moore, S. Turner, and C. C. Speake, A capacitance displacement transducer with large dynamic-range, good linearity and frequency read-out, *Meas. Sci. Technol.* **4**(12):1519–1521 (1993).
18. NE/SE566, Function generator, *Philips Semiconductor Product Catalogue*, available online at http://www.semiconductors.philips.com/pip/NE_SE566.html.
19. R. Pallás-Areny and J. G. Webster, *Sensors and Signal Conditioning*, Wiley, New York, 1991.
20. R. A. Pease, Application Note C: V/F converter ICs handle frequency-to-voltage needs, *National Semiconductor Application Notes*, available online at <http://www.national.com/search/search.cgi/apnotes>.
21. R. A. Pease, Application Note 210: New phase-locked-loops have advantages as frequency to voltage converters (and more), *National Semiconductor Application Notes*, available online at <http://www.national.com/search/search.cgi/apnotes>.
22. B. Razavi, Analysis, modeling and simulation of phase noise in monolithic voltage-controlled oscillator, *Proc. CICC*. 323–326 (May 1995).
23. B. Razavi, Design of monolithic phase-locked loops and clock recovery circuits—a tutorial, in B. Razavi, ed., *Monolithic Phase-Locked Loops and Clock Recovery Circuits*, IEEE Press, New York, 1996.
24. M. Soyuer and R. G. Meyer, High-frequency phase-locked loops in monolithic bipolar technology, *IEEE J. Solid-State Circuits*. **CS-24**:787–795 (June 1989).
25. VFC32, Voltage-to-frequency and frequency-to-voltage converter, *Texas Instruments Analog & Mixed-Signal Product Catalogue*, available online at <http://www.ti.com>.
26. VFC100, High-frequency voltage-to-frequency converter, *Texas Instruments Analog & Mixed-Signal Product Catalogue*, available online at <http://www.ti.com>.
27. W. S. Wilburn, A high-accuracy beam current integrator for fast spin-flip experiments, *Nucl. Instrum. Meth. Phys. Res. A—Accel. Spectrom. Detect. Assoc. Equip.* **394**(1/2):257–260 (1997).

VOLTERRA MODELING IN ANALOG, RF AND MICROWAVE ENGINEERING

MICHAEL B. STEER
 KHALED M. GHARAIBEH
 North Carolina State University

1. INTRODUCTION

Volterra techniques are used in radiofrequency (RF) and Microwave engineering primarily in modeling the input-output characteristics of nonlinear circuits and systems that operate with limited bandwidth signals. Volterra models capture frequency-dependent effects within the band. Two forms of the Volterra model exist; one being in the time-domain invoking Volterra kernels in what is in effect a multidimensional convolution; and the other being a frequency-domain form with what are called Volterra nonlinear transfer function akin to the transfer functions of linear circuits but, of course, extended to handle nonlinearities. The mathematics of Volterra links the kernels and the nonlinear transfer functions, so provides a mathematically rigorous way of modeling circuits in the frequency-domain even though the underlying nonlinear processes are in the time-domain.

When dealing with RF and microwave circuits, it is most convenient to work in the frequency-domain. In the case of communication circuits, many of the important performance parameters are specified in the frequency-domain such as maximum allowable intermodulation distortion and spectral regrowth levels. In the frequency-domain we have a well established set of tools—including Fourier analysis, phasors, and linear transfer functions—essential to the design of linear analog circuits and systems. Volterra analysis builds on these established tools and extends them to handle nonlinearities.

Volterra behavioral modeling coupled with system-level simulation tools can be used to predict the system performance, provide insight into the sources of performance-limiting elements, enable system-level tradeoffs, and lead to the development of predistortion techniques. Volterra nonlinear transfer functions are used in their full generality only for weakly nonlinear circuits because of the difficulty of extracting higher order elements of the Volterra model. Instead, various levels of simplification are used relating to particular characteristics of the stages being modeled and the availability of an extraction procedure.

The fundamentals of Volterra modeling are contained in Volterra's book, *Theory of Functionals and of Integral and Integro-Differential Equations* [1], published in 1930. Volterra series-based methods can model input-output systems that, in the time-domain, are described by the nonlinear differential equation

$$f \left[\frac{d^p y(t)}{dt^p}, \dots, \frac{dy(t)}{dt}, y(t), \right. \\ \left. \frac{d^p w(t)}{dt^p}, \dots, \frac{dw(t)}{dt}, w(t) \right] = 0 \quad (1)$$

where $w(t)$ is the input and $y(t)$ is the output. The above relationship describes an expansion of the input-output characteristics at a single time t . Thus the inherent assumption is that past events are captured by the expansion around the present timepoint. That is, with enough derivatives, the effect of past events can be captured. Thus, a range of effects can be captured including causality, stability, continuity, and limited memory. Chaos, subharmonic generation, hysteresis, and hard limiting can not be so represented. Thus, Volterra methods are best suited to modeling weak to moderately nonlinear circuits. However, the key is that Volterra methods provide a theoretical underpinning for the use of other basis function expansions that extend the range of applicability.

Following the chronological order by jumping into Volterra series analysis is too great a step to make. The discussion here begins with the power series analysis of nonlinear systems, which is used to introduce the concept of intermodulation products and relating time- and frequency-domain descriptions.

2. POWER SERIES BEHAVIORAL MODELING

Now consider the unilateral memoryless nonlinear system of Fig. 1 described by the memoryless polynomial model

$$y(t) = \sum_{l=1}^{\infty} a_l w(t)^l \quad (2)$$

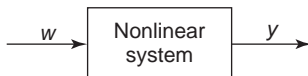


Figure 1. A unilateral nonlinear system.

where the input $w(t)$ is the sum of three sinusoids:

$$w(t) = c_1 \cos(\omega_1 t + \phi_1) + c_2 \cos(\omega_2 t + \phi_2) \\ + c_3 \cos(\omega_3 t + \phi_3) \quad (3)$$

To simplify the trigonometry that follows, let $\alpha_1 = \omega_1 t + \phi_1$, $\alpha_2 = \omega_2 t + \phi_2$, and $\alpha_3 = \omega_3 t + \phi_3$, so that

$$w(t)^l = [c_1 \cos(\alpha_1) + c_2 \cos(\alpha_2) + c_3 \cos(\alpha_3)]^l \\ = \sum_{p=0}^l \sum_{k=0}^p \binom{p}{k} \binom{l}{p} c_1^k c_2^{p-k} c_3^{l-p} \\ (\cos \alpha_1)^k (\cos \alpha_2)^{p-k} (\cos \alpha_3)^{l-p} \quad (4)$$

This equation includes a large number of components, the radian frequencies of which are the sum and differences of ω_1 , ω_2 , and ω_3 . These result from multiplying out the term $(\cos \alpha_1)^k (\cos \alpha_2)^{p-k} (\cos \alpha_3)^{l-p}$. In general, the frequencies of the components of y are $n_1 \omega_1 + n_2 \omega_2 + n_3 \omega_3$ and the order of intermodulation $n = |n_1| + |n_2| + |n_3|$. The total output is the sum of all individual intermodulation products. Volterra nonlinear transfer function analysis is based on exactly the same concepts.

3. VOLTERRA SERIES ANALYSIS

A general Volterra series model of a nonlinear system is described by the following functional expansion of continuous functions:

$$y(t) = \sum_{n=0}^{\infty} F_n(w(t)) = \sum_{n=0}^{\infty} y_n(t) \quad (5)$$

where $F_n(w(t))$ is the Volterra functional. If the nonlinear system is time invariant, then it can be expressed as

$$F_n(w(t)) = \int_{-\infty}^{\infty} \dots \int_{-\infty}^{\infty} h_n(\lambda_1, \dots, \lambda_n) \\ \prod_{i=1}^n w(t - \lambda_i) d\lambda_i \quad (6)$$

where $h_n(\lambda_1, \dots, \lambda_n)$ is the n -dimensional Volterra kernel, which can be made symmetric (with respect to its arguments) without loss of generality and leads to a unique set of Volterra kernels. Thus, Fig. 2 shows a graphical representation of the Volterra model in the time-domain with Volterra kernels, whereas Fig. 3 shows the model in the frequency-domain with Volterra nonlinear transfer functions.

The n th order kernel, h_n , is called the nonlinear impulse response of the circuit of order n . Equation (6) is then interpreted as an n -dimensional convolution of an n th order impulse response (h_n) and the input signal (w). The total response $G(w)$ is the summation of the different order responses $F_n(w)$. For a linear system, only a first-order response exists, so that the total response of the

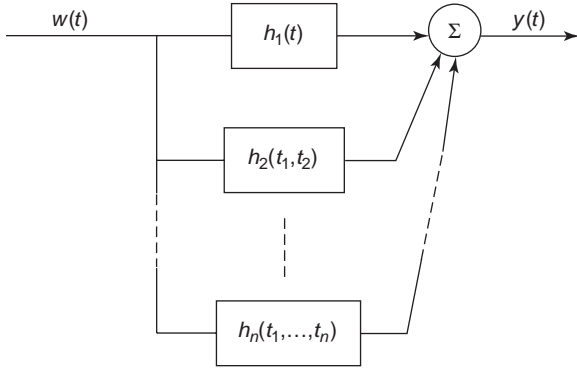


Figure 2. A block diagram of the general Volterra model.

system is the conventional convolution integral

$$y(t) = F_0 + \int_{-\infty}^{\infty} h_1(\tau)w(t - \tau) d\tau \quad (7)$$

where F_0 is just a DC offset.

It is more convenient to write Eq. (6) in terms of the n -dimensional Volterra transfer functions because these functions are usually easier to extract than their corresponding time kernels. Therefore $y_n(t)$ can be expressed as

$$y_n(t) = F_n(w(t)) = \int_{-\infty}^{\infty} \dots \int_{-\infty}^{\infty} H_n(f_1, \dots, f_n) \times \prod_{i=1}^n W(f_i) e^{j2\pi f_i t} df_i \quad (8)$$

where $H_n(f_1, \dots, f_n)$ is the n -dimensional Volterra Transfer Function (TF), which results from the n -dimensional Fourier transform of $h_n(\lambda_1, \dots, \lambda_n)$:

$$H_n(f_1, \dots, f_n) = \int_{-\infty}^{\infty} \dots \int_{-\infty}^{\infty} h_n(\lambda_1, \dots, \lambda_n) \times e^{-j2\pi(f_1\lambda_1 + \dots + f_n\lambda_n)} d\lambda_1 \dots d\lambda_n \quad (9)$$

and consequently

$$h_n(\lambda_1, \dots, \lambda_n) = \int_{-\infty}^{\infty} \dots \int_{-\infty}^{\infty} H_n(f_1, \dots, f_n) \times e^{j2\pi(f_1\lambda_1 + \dots + f_n\lambda_n)} d\lambda_1 \dots d\lambda_n \quad (10)$$

and therefore, the frequency-domain description of the n th order response can be expressed as

$$Y_n(f) = \int_{-\infty}^{\infty} \dots \int_{-\infty}^{\infty} H_n(f_1, \dots, f_n) \times \delta(f - f_1 - \dots - f_n) \prod_{i=1}^n W(f_i) df_i \quad (11)$$

This frequency-domain form is the form in which the Volterra model is most frequently used in modeling RF and

microwave circuits. The important concept here is that the total response of a signal is the summation of a number of responses of different order. This scheme only works as the order n increases, the contribution to the response gets smaller and eventually insignificant. The reason this works for many RF and microwave circuits is that the overall response is close to linear, and nonlinear behavior is a departure from linearity. This insight was provided by Wiener who applied this type of functional series to the analysis of nonlinear systems in 1942 [2]. He suggested that a weak nonlinearity could be represented with just the first few terms of such a series. His ideas have subsequently been developed by many researchers including milestones described by Bedrosian and Rice [3]; by Bussgang, Ehrman, and Graham [4]; and by Wiener and Spina [5].

4. BEHAVIORAL MODELING IN THE FREQUENCY-DOMAIN

Central to application of the Volterra methods is extraction of the Volterra nonlinear transfer functions, which can be derived algebraically [3,6,7], experimentally [8–10], or numerically [11]. This process is called system identification, and most of what is published on Volterra modeling of circuits and systems is about the choice of functionals that describe the physical process and the appropriate parameter extraction procedure. Therefore, if the input to a nonlinear system can be described by a multifrequency input of the form

$$w(t) = \sum_{k=0}^K w_k(t) = \sum_{k=0}^K |W_k| \cos(\omega_k t + \phi_k) = \sum_{k=-K}^K W_k e^{j\omega_k t}$$

then the n th order output can be written as

$$y_n(t) = \sum_{q_1=-K}^K \dots \sum_{q_n=-K}^K H_n(f_{q_1}, \dots, f_{q_n}) \prod_{i=1}^n W_{q_i} e^{j2\pi f_{q_i} t} df_i \quad (12)$$

The term $H_n(f_{q_1}, \dots, f_{q_n})W_{q_1} \dots W_{q_n}$ is an n th order intermodulation product of frequency $(f_{q_1} + \dots + f_{q_n})$, and $f = \sum_{k=1}^N n_k f_k = \sum_{i=1}^N f_{q_i}$ is the output frequency. In Wiener analysis, the relationship between positive and negative frequencies ($f_{-q} = -f_q$) is defined by $W_{-q} = W_q^*$. The set of q_k 's describes an intermodulation product to calculate a response of a certain order, all intermodulation products of that order are summed. Each intermodulation product is a product of the input phasors and the appropriate nonlinear transfer function. The nonlinear transfer functions (the H_n) do not depend on the input and are only determined by the nonlinearity. Thus, if $n=4$ and $q_1=1$, $q_2=-2$, $q_3=-2$, and $q_4=3$, the intermodulation product

so defined has frequency $(f_1 + f_{-2} + f_{-2} + f_3)$, or $(f_1 + -2f_2 + f_3)$, and is given by

$$H_4(f_1, -f_2, -f_2, f_3)(\hat{W}_2^*)^2 \hat{W}_1 \hat{W}_3 \quad (13)$$

The intermodulation product of Eq. (13) is only one of the fourth-order intermodulation products. To obtain the total response of the nonlinear system, all intermodulation products of a particular order and for all orders must be summed as illustrated in Fig. 3.

5. RELATIONSHIP BETWEEN VOLTERRA AND POWER SERIES

Power series expansion analysis of a nonlinear subsystem is straightforward and is a convenient way to introduce the basic principles of Volterra nonlinear transfer function analysis. A Generalized Power Series (GPS) model was pioneered by Steer [12] and is used to determine the steady-state frequency-domain description of the output of a nonlinear system. Therefore, if the input to a nonlinear system can be described by a multifrequency input of the form (13), then the output can be represented by a GPS as [13]

$$y(t) = A \sum_{n=0}^{\infty} a_n \left[\sum_{k=0}^K b_k w_k(t - \tau_{n,k}) \right]^n \quad (14)$$

where b_k are real coefficients, a_n are complex coefficients, and $\tau_{n,k}$ is a time delay that depends on the power series order and the index of the input frequency component.

The inclusion of complex coefficients and frequency-dependent time delays allows a variety of systems to be modeled. The GPS was proved to be equivalent to the single-frequency approximation of the Volterra series in [13,14]. Parameter extraction can be done by measuring the response to a multifrequency input. In fact, the equivalence of Volterra and GPS series makes the multifrequency

excitation suitable to developing the Volterra transfer functions in the frequency-domain of the form

$$H_n(f_{q_1}, \dots, f_{q_n}) = A a_n \prod_{i=0}^n b_{q_i} e^{j2\pi f_{q_i} \tau_{n,q_i}} \quad (15)$$

Instantaneous model, as provided by a power series model, leads to a straightforward way of handling nonlinearities in the frequency-domain. Combining an instantaneous model with linear filters creates complex models suitable for modeling RF and microwave circuits. Instantaneous models have both meaning in the time-domain and in the frequency-domain, and a number of mapping techniques have been developed to calculate the phasors of a signal at the output of an instantaneous model given the phasors at the input of the model. For example, with power series, an elegant input-output phasor mapping exists [15], for any analytic function an arithmetic mapping exists [16], and for any instantaneous function an inverse Fourier transform of a set of input phasors yields a time-domain signal that can be applied to the instantaneous functional and the output then Fourier transformed to obtain the output phasors.

6. BEHAVIORAL MODELING OF RF AND MICROWAVE CIRCUITS—THE BLACK BOX APPROACH

In modeling RF and microwave circuits, a priori knowledge is available because nonlinearity originates from active devices. Therefore, this nonlinearity takes input-output characteristics that are well known a priori, and then the modeling problem reduces to estimating system parameters using classic parameter estimation theory such as least squares and its variants.

Lee and Schetzen [17], developed an approach for measuring Volterra kernels leading to the complete identification process of a Volterra system. Wang and Brazil [18] developed a discrete time-frequency approach for the estimation of Volterra model kernels. However, these methods become inefficient and even computationally prohibitive for high-order kernels, and so are limited to third-order nonlinearity. Provided the system is weakly nonlinear, these methods are powerful and comprehensive approaches.

A wide variety of Volterra model variants have been developed in the literature to overcome the computational complexity of developing Volterra kernels when the system has finite memory. The structural classification of nonlinear systems was based on a theory developed by Korenberg [19], which states that any finite memory nonlinear system can be represented by a finite number of parallel Linear-Nonlinear (L-N) or Nonlinear-Linear (N-L) cascades of alternating linear and nonlinear operators. Boyd and Chua [21] showed that the I-O measurements alone are sufficient to classify these structures because of the unique I-O mappings. Therefore, dependent on the measured data, a certain structure can be accepted or rejected based on satisfying the kernel relationships constituting a sufficient and necessary condition for a system to have a given structure. Parameter estimation of these

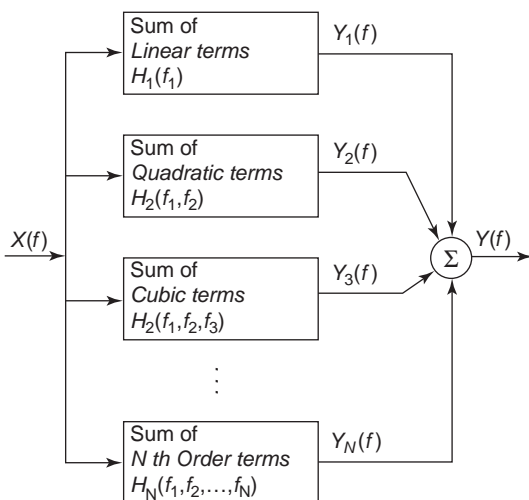


Figure 3. Architecture of Volterra nonlinear transfer function analysis.

structures is usually based on measuring the first- and second-order Volterra or Wiener kernels, which are used to define the linear filters incorporated in the given structure. In the following, the major approaches for nonlinear amplifier modeling are reviewed with emphasis on their parameter estimation techniques.

6.1. Single Frequency Volterra Models

Single frequency Volterra models represent a simplified version of a Volterra system by simplifying the branches of the general model, see Fig. 2, into cascades of L-N or N-L subsystems. These configurations simplify parameter estimation and reduce computational complexity because all spectral calculations required involve only a single frequency variable instead of several [22]. Single frequency Volterra models take one of the following topologies: filter-nonlinearity (FN) model and nonlinearity-filter (NF).

A single frequency FN Volterra model is shown in Fig. 4 and is characterized by a Volterra kernel that has the property

$$\begin{aligned} h_n(\lambda_1, \dots, \lambda_n) &= a_n h_n(\lambda_1) h_n(\lambda_2) \dots h_n(\lambda_n) \\ &= a_n \prod_{i=1}^n h_n(\lambda_i) \end{aligned} \quad (16)$$

which can be contrasted to the general form in Eq. (6), and it follows that the Volterra transfer function is

$$H_n(f_1, \dots, f_n) = a_n \prod_{i=1}^n H_n(f_i) \quad (17)$$

For the NF Volterra model shown in Fig. 5, the Volterra kernel has the property

$$\begin{aligned} h_n(\lambda_1, \dots, \lambda_n) &= h_n(\lambda_1) \\ &\times \delta(\lambda_1 - \lambda_2) \dots \delta(\lambda_{n-1} - \lambda_n) \end{aligned} \quad (18)$$

and it follows that

$$H_n(f_1, \dots, f_n) = H(f_1 + \dots + f_n) \quad (19)$$

The primary advantage of the single frequency Volterra model is the simplicity of its parameter extraction. However, it does not represent the broad variety of systems that the general Volterra model does, single frequency

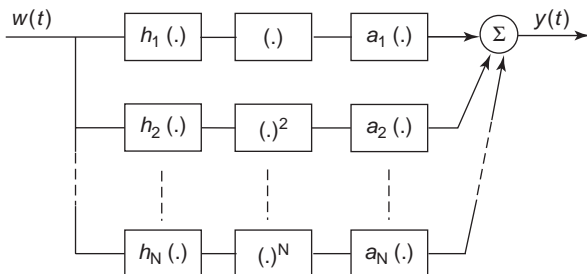


Figure 4. Filter-nonlinearity Volterra model.

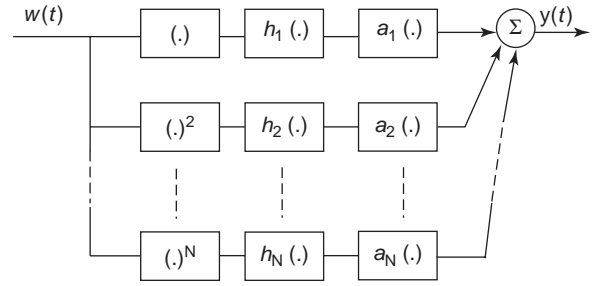


Figure 5. Nonlinearity-filter Volterra model.

model offers a significant simplicity of nonlinear system analysis.

Parameter extraction for the single frequency Volterra model was discussed in [22] using cross-correlation spectral analysis performed on time-domain measured data. These models are regarded as polyspectral models and they showed good performance for TWT high-power amplifiers [22]. A detailed analysis of the identification process can be found in [22,23]. Model parameters were also extracted using multifrequency excitation [24], but only third-order nonlinearity was considered.

6.2. Block Models

Block models refer to a class of models where a system is represented by a single cascade of linear and nonlinear elements. These models are popular because of the simplicity of their parameter extraction using either direct Vector Network Analyzer (VNA) measurements or cross correlation of time-domain measured data [22]. These models, although intuitively reasonable, are theoretically special cases of the Volterra model and therefore kernel relationships can be developed.

6.2.1. The Two-Box and Three-Box Models. A simplified version of the Volterra model is the two-box structure, which takes the following form of the Volterra kernel in the frequency-domain:

$$H_n(f_1, \dots, f_n) = a_n H_1(f_1) \dots H_1(f_n) \dots \quad (20)$$

and for the three box model:

$$\begin{aligned} H_n(f_1, \dots, f_n) &= a_n H_1(f_1) \dots H_1(f_n) \\ &\times H_2(f_1 + \dots + f_n) \end{aligned} \quad (21)$$

These forms of the Volterra kernels, Eqs. (20) and (21), provide a great simplification over the general form because they can be realized by the models shown in Fig. 6. These structures have been successful in representing a wide class of nonlinear systems where the nonlinear operation can be modeled as a cascade of linear operations that represent the finite memory of the system and of a memoryless nonlinearity. These models are called Wiener-Hammerstein models and are used to model a wide variety of nonlinear systems [19,25–28]. Parameter

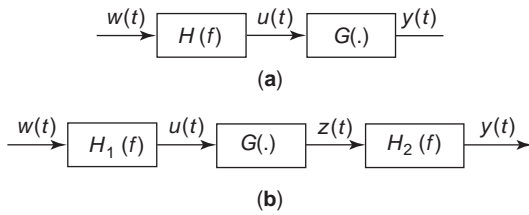


Figure 6. Block models: (a) two-box model; and (b) three-box model.

extraction of such models are usually based on measuring first- and second-order Volterra kernels [29].

6.2.2. Parallel Cascade Model. The parallel cascade model takes the following form of the Volterra kernel in the frequency-domain:

$$H_n(f_1, \dots, f_n) = \sum_{p=1}^P a_n H_{1,p}(f_1) \dots H_{1,p}(f_n) \times H_{2,p}(f_1 + \dots + f_n) \tag{22}$$

Here, p is the number of branches and it represents the memory depth. The above kernel relationship enables the realization of the Volterra model as a parallel cascade of linear and nonlinear elements, as shown in Fig. 7 [19,20,29], which enables the reformulation of the system equations in the time-domain [29], as

$$y(t) = \sum_{p=1}^P y_p(t) \tag{23}$$

where

$$y_p(t) = z_p(t) * h_{2,p}$$

and

$$z_p(t) = \sum_{r=0}^{N_p} a_{r,p} u_p^r(t)$$

$$u_p(t) = h_{1,p}(t) * w(t)$$

where $*$ is the convolution operator and N_p is the maximum order of the polynomial in branch p .

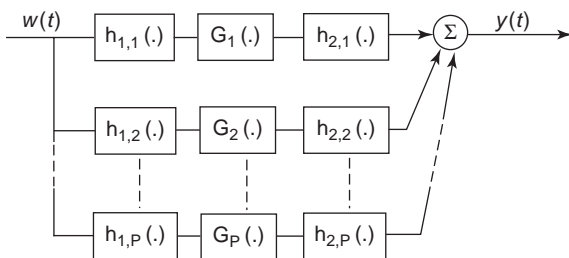


Figure 7. Parallel cascade Volterra model.

Note that the parallel cascade model represents the system by a finite number of branches with polynomials of finite order. This model was proven adequate for modeling a finite-memory Volterra model having a finite order. In [19], Korenberg derived an upper bound for the number of cascades required for representing a finite-memory system. Parameter extraction of this model was discussed in [19] using time-domain measurements. In a recent work [20], system parameters were developed using measured two-tone test with varying frequency separation.

6.3. Memoryless and Quasimemoryless Models

Perhaps the most commonly used model for modeling distortion in power amplifiers is the memoryless model. This model is characterized by a constant Volterra transfer function over frequency, i.e.,

$$H_n(\underline{f}) = H_n(\underline{0}) = a_n \tag{24}$$

where the under bals indicate an n -dimensional vector, and it follows that the corresponding Volterra kernel is

$$h_n(\lambda_1, \dots, \lambda_n) = a_n \delta(\lambda_1) \delta(\lambda_2) \dots \delta(\lambda_n) \tag{25}$$

Therefore, the model reduces to a power series model with either real or complex coefficients of the form

$$y(t) = \sum_{n=1}^N a_n w^n(t) \tag{26}$$

The system is called memoryless if the coefficients a_n are real. These coefficients can be developed from AM-AM power sweep measurements of single tones using a VNA. The system is called quasimemoryless if the coefficients are obtained from AM-AM and AM-PM measurements where polynomial fitting yields a complex power series. The quasimemoryless system takes into account short-term memory effects, which are manifested as a phase shift in the output waveform that is a function of the input power level. The power series model obtained is popular for its simplicity and the fact that distortion can be directly related to its parameters (coefficients), as will be seen in the following chapter. However, it has its limitations because it does not take into account the long-term memory effects, which makes it inadequate for modeling wideband and multichannel systems.

7. CIRCUIT SIMULATION USING VOLTERRA METHODS

It is also possible to use Volterra methods to analyze nonlinear circuits in the frequency-domain using Volterra-based methods.

The so-called method of nonlinear currents, most recently described by Crosmun and Maas [11], has applicability to nonlinear circuits with large signals. In this method, a circuit is first solved for its linearized response described by zero- and first-order Volterra nonlinear transfer functions. Considering only the linearized response allows standard linear circuit nodal admittance

matrix techniques to be used. The second-order response, described by the second-order Volterra nonlinear transfer functions, can then be represented by controlled current sources. Thus, the second-order sources are used as excitations again enabling linear nodal admittance techniques to be used. The process is repeated for the third- and higher order node voltages and is easily automated in a general purpose microwave simulator. The process is terminated at some specified order of the Volterra nonlinear transfer functions, which is a noniterative technique but relies on rapid convergence of the Volterra series.

Volterra techniques can also be used in a spectral balance procedure [30,31]. With the advent of powerFul and well developed harmonic balance procedures, little incentive exists to use Volterra techniques to model RF and microwave circuits.

One more technique exists that is becoming important. In many situations, a small signal interacts with a large signal. Derivation of the large-signal waveform permits a weakly nonlinear time-varying Volterra series description of the circuit [6,32], which is an extension of the linear conversion matrix concept [33] to include nonlinear dependencies on the level of the small signal but special condition on the LO waveform, such as being sinusoidal current, are typically required.

8. CONCLUSION

Volterra series provide the theoretical underpinning of behavioral modeling in RF and microwave engineering. The classic Volterra model is limited to weakly nonlinear systems because of the difficulty in extracting the Volterra nonlinear transfer functions of order higher than third order. Volterra modeling theory illustrates that nonlinear RF and microwave circuits can be modeled as a sequence of cascaded linear frequency variant blocks and nonlinear instantaneous blocks represented by frequency independent functionals. It is easy to handle the linear blocks in the frequency-domain and a variety of instantaneous functional descriptions are used to model the nonlinear block. Various schemes have been developed for evaluating the functionals in the frequency-domain so that an output set of phasors can be calculated from an input set of phasors.

BIBLIOGRAPHY

1. V. Volterra, *Theory of Functionals and of Integral and Integro-Differential Equations*, Blackie & Sons, London, 1930; or Dover, New York, 1959.
2. N. Wiener, Response of a nonlinear device to noise, *M.I.T. Radiation Lab. Report V-16S*, Apr. 1942.
3. E. Bedrosian and S. O. Rice, The output properties of Volterra systems (nonlinear systems with memory) driven by harmonic and Gaussian inputs, *Proc. IEEE*, **59**:1688–1707 (1971).
4. J. J. Busgang, L. Ehrman, and J. W. Graham, Analysis of nonlinear systems with multiple inputs, *Proc. IEEE*, **62**:1088–1119 (1974).
5. D. D. Weiner and J. F. Spina, *Sinusoidal Analysis and Modeling of Weakly Nonlinear Circuits*, Van Nostrand Reinhold Co., New York, 1980.
6. J. W. Graham and L. Ehrman, *Nonlinear System Modeling and Analysis With Applications to Communications Receivers*, Rome Air Development Center, Rome, NY, 1973.
7. R. A. Minasian, Intermodulation distortion analysis of MESFET amplifiers using Volterra series representation, *IEEE Trans. Microwave Theory Tech.*, **28**:1–8 (1980).
8. V. Krozer, K. Fricke, and H. L. Hartnagel, A novel analytical approach for the nonlinear microwave circuits and experimental characterization of the nonlinear behaviour of a new MESFET device structure, *1989 IEEE MTT-S Int. Microwave Symp. Dig.*, June 1989, pp. 351–354.
9. S. Boyd, Y. S. Tang, and L. O. Chua, Measuring Volterra kernels, *IEEE Trans. Circuits Syst.* **30**:571–577 (1987).
10. L. O. Chua and Y. Liao, Measuring Volterra kernels (II), *Int. J. Circuits Theory Applications*, **17**:151–190 (1989).
11. A. M. Crossmun and S. A. Maas, Minimization of intermodulation distortion in GaAs MESFET small-signal amplifiers, *IEEE Trans. Microwave Theory Tech.*, **37**:1411–1417 (1989).
12. G. W. Rhyne and M. B. Steer, Generalized power series analysis of intermodulation distortion in a MESFET amplifier: simulation and experiment, *IEEE Trans. Microwave Theory Techn.*, **35**:1248–1255 (1987).
13. P. J. Lunsford, II, *The Frequency Domain Behavioral Modeling and Simulation of Nonlinear Analogue Circuits and Systems*, Ph.D. dissertation, North Carolina State University, Raleigh, NC, 1993.
14. M. B. Steer, P. J. Khan, and R. S. Tucker, Relationship of Volterra series and generalized power series, *Proc. IEEE*, **1453**–1454 (1983).
15. M. B. Steer and P. J. Khan, An algebraic formula for the complex output of a system with multi-frequency excitation, *Proc. IEEE*, **177**–179 (1983).
16. F. P. Hart, D. G. Stephenson, C. R. Chang, K. M. Gharaibeh, R. G. Johnson, and M. B. Steer, Mathematical foundations of frequency domain modeling of nonlinear circuit and systems using the Arithmetic Operator Method, *Int. J. RF Microwave Comp. Aided Engin.*, **473**–495 (2003).
17. M. Schetzen, Nonlinear System Modeling based on the Wiener theory, *Proc. IEEE*, **69**:1557–1573 (1981).
18. T. Wang and T. J. Brazil, Volterra-mapping-based behavioral modeling of nonlinear circuits and systems for high frequencies, *IEEE Trans. Microwave Theory Tech.*, **51**:1433–1440 (2003).
19. M. Korenberg, Parallel cascade identification and kernel estimation for nonlinear systems, *Ann. Biomed. Engin.*, **19**:429–455 (1991).
20. H. Ku, M. D. McKinley, and J. S. Kenney, Quantifying memory effects in RF power amplifiers, *IEEE Trans. Microwave Theory Techn.*, **50**:2843–2849 (2002).
21. S. Boyd, S. and L. Uniqueness of a basic nonlinear structure, *IEEE Trans. Circuits Syst.*, **30**:648–651 (1983).
22. C. P. Silva, A. A. Moulthrop, and M. S. Muha, Polyspectral techniques for nonlinear system modeling and distortion compensation, *IEEE Int. Vacuum Electron. Conf.*, April 2002, pp. 314–315.
23. M. S. Muha, C. J. Clark, A. A. Moulthrop, and C. P. Silva, Validation of power amplifier nonlinear block models, *1999 IEEE MTT-S Int. Microwave. Symp. Dig.*, **2**:759–762 (1999).
24. M. Maqusi, Characterization of nonlinear distortion in HRC multiplexed cable television systems, *IEEE Trans. Circuits Syst.*, **32**:605–609 (1985).

25. P. Crama and J. Schoukens, Initial estimates of Wiener and Hammerstein systems using multisine excitation, *IEEE Trans. Instrument. Measure.*, **50**:1791–1795 (2001).
26. J. Shi and H. H. Sun, Nonlinear system identification for cascaded block model: an application to electrode polarization impedance, *IEEE Trans. Biomed. Engin.*, **37**:574–587 (1990).
27. D. T. Westwick and R. E. Kearney, Identification of a Hammerstein model of the stretch reflex EMG using separable least squares, *22nd Annual Int. Conf. IEEE Engineering Med. Biol. Soc.*, **3**:1901–1904 (2000).
28. I. Scott and B. Mulgrew, Nonlinear system identification and prediction using orthogonal functions, *IEEE Trans. Signal Proc.*, **45**:1842–1853 (1997).
29. H. W. Chen, Modeling and identification of parallel nonlinear systems: structural classification and parameter estimation methods, *Proc. IEEE*, **83**:39–66 (1995).
30. E. Van den Eijnde and J. Schoukens, Steady-state analysis of a periodically excited nonlinear system, *IEEE Trans. Circuits Syst.*, **37**:232–242 (1990).
31. L. O. Chua and C. Y. Ng, Frequency-domain analysis of nonlinear systems: general theory, *Electron. Circuits Syst.*, **3**:165–185 (1979).
32. R. B. Swerdlow, Analysis of intermodulation noise in frequency converters by Volterra series, *IEEE Trans. Microwave Theory Tech.*, **26**:305–313 (1978).
33. D. N. Held and A. R. Kerr, Conversion loss and noise of microwave and millimeter-wave mixers: Part 1 — Theory and Part 2 — Experiment, *IEEE Trans. Microwave Theory Tech.*, **26**:49–61 (1978).
34. R. S. Tucker and C. Rauscher, Modeling the 3rd-order intermodulation-distortion properties of a GaAs FET, *Electron. Lett.*, **13**:508–509 (1977).
35. R. S. Tucker, Third-order intermodulation distortion and gain compression in GaAs FETs, *IEEE Trans. Microwave Theory Tech.*, **27**:400–408 (1979).
36. M. B. Steer, C. R. Chang, and G. W. Rhyne, Computer aided analysis of nonlinear microwave circuits using frequency domain spectral balance techniques: the state of the art, *Int. J. Microwave Millimeter Wave Comp. Aided Engineer.*, **1**:181–200 (1991).
37. B. S. Troitskiy, Analysis and design of nonlinear circuits by the method of power series inversion, *Elektosvyaz*, **8**:50–52 (1987).
38. M. B. Steer, Multifrequency analysis of nonlinear circuits, *IEEE Southeastcon Convention Dig.*, 116–120 (1985).
39. V. D. Dmitriev and A. I. Silyutin, A method of designing broadband nonlinear circuits based on a modification of the nonlinear current method, amplifiers, *Radioelectron Commun. Syst.*, **29**(11):50–55 (1986).
40. R. J. Gilmore and M. B. Steer, Nonlinear circuit analysis using the method of harmonic balance—a review of the art: part II, *Int. J. Microwave Millimeter Wave Comp. Aided Engineer.*, **1**(2).
41. P. B. Kenington, *High Linearity Amplifier Design*, Artech House, Norwood, MA, 2000.
42. S. C. Cripps, *RF Power Amplifiers for Wireless Communications*, Artech House, Norwood, MA, 2000.
43. M. Schetzen, *The Volterra and Wiener Theories of Nonlinear Systems*, Wiley, New York, 1980.
44. J. S. Bendat, *Nonlinear System Analysis and Identification*, Wiley, New York, 1990.
45. M. Jeruchim, P. Balaban, and S. Shanmugan, *Simulation of Communication Systems*, Kluwer Academic/Plenum Publishers, New York, 2000.
46. J. S. Bendat and A. G. Piersol, *Engineering Applications of Correlation and Spectral Analysis*, Wiley, New York, 1993.
47. J. C. Pedro and N. B. Carvalho, On the use of multi-tone techniques for assessing RF components' intermodulation distortion, *1999 IEEE Trans. Microwave Theory Techn.*, **47**:2393–2402 (1999).
48. G. W. Rhyne and M. B. Steer, A new frequency domain approach to the analysis of nonlinear microwave circuits, *1985 IEEE MTT-S Int. Microwave Symp. Dig.*, **85**:401–404 (1985).
49. P. J. Lunsford and M. B. Steer, The relationship between bivariate Volterra analysis and power series analysis with application to behavioral modeling of microwave circuits, *Int. J. Microwave Millimeter-wave Comp. Aided Engin.*, **1**:253–262 (1991).
50. P. Crama and Y. Rolain, Broad-band measurement and identification of a Wiener-Hammerstein model for an RF amplifier, *ARFTG Conf. Dig.*, 49–57 (2002).

WAVEGUIDE ANTENNAS

WINIFRED E. KUMMER
Raytheon Systems Company

Waveguide antennas are useful for a variety of airborne, ground-based, space, and missile applications in the microwave frequency band because they offer high radiating efficiency, a high degree of control over the radiation pattern, compact architecture, and low weight. The high radiating efficiency and compact architecture, namely, the small depth compared with a parabolic reflector antenna with equivalent gain, combine to optimize the use of the available aperture area. Accurate control of the radiation pattern allows designing arrays with a radiation pattern envelope tailored to the specific application. The low weight minimizes the impact on the installation and allows mounting the antenna on a mechanical gimbal assembly to scan the radiation pattern. A waveguide slot array designed to mount on a gimbal for an airborne radar application is shown in Fig. 1.

In waveguide slot arrays the radiating and transmission structures are inexorably intertwined, thus it is appropriate to treat the history of the waveguides together with that of slot radiators. In the 1930s, G. C. Southworth [1] at Bell Telephone Laboratories investigated electromagnetic propagation in hollow waveguides. Carson, Mead, and Schelkunoff performed the accompanying theoretical analysis [2]. Independent work by Barrow of MIT [3] was published at about the same time [4]. The analysis of waveguides and slot radiators in terms of transmission

lines is also because of Schelkunoff [5]. Another aspect of array work is the need for pattern synthesis. S. A. Schelkunoff's classic 1943 paper [6] and the subsequent C. L. Dolph [7] paper on the synthesis of equal sidelobe levels were used by T. T. Taylor [8] to achieve practical array designs. The major work on waveguide slot arrays during World War II was carried out in Canada at McGill University by W. H. Watson and his colleagues [9]. The basis of their work included A. F. Stevenson's [10] analysis of the behavior of radiating slots in waveguides. Significant advances were made at the MIT Radiation Lab and are summarized in S. Silver's book [11]. Further work was carried out by members of this group and others at Hughes Aircraft Co. in Culver City, CA [12]. A. A. Oliner [13,14] and others refined Stevenson's theory at Polytechnic Institute of Brooklyn. R. S. Elliott and his students at UCLA, and numerous other researchers worked to further refine the design process.

The rectangular waveguide is the guide geometry used for most waveguide slot arrays because it provides a compact, low-loss transmission line that contributes to the high efficiencies achievable with these arrays. The basic radiating element, a single rectangular slot located in an infinite ground plane, is the complement to a dipole radiator [15] and, like the dipole, produces a broad radiation pattern. The radiating slot in the rectangular waveguide is realized in a variety of configurations, thus providing flexibility for the designer. The slot radiation characteristics are controlled by adjusting the slot location on the waveguide and the slot length and width.

An array of slots with a specified aperture distribution generates a highly directive or specially shaped radiation pattern. Arrays of slots are created by placing slot radiators in a waveguide to create a linear array and by joining a number of these waveguides with a power-divider network to create a planar array. Slots are used to couple energy between waveguides, and these coupling slots provide a compact way to realize the power-divider network. The closed-feed network eliminates the spillover loss suffered in horn-fed reflectors and other space-fed antennas. The aperture distribution is determined by the radiating slot characteristics and the power dividers in the feed network. The designer adjusts these parameters to achieve a high degree of control of the aperture distribution and thereby achieves a low-sidelobe or shaped-beam radiation pattern. The design process for these arrays is complex because of the need to accurately characterize the relationship between the slot geometry and performance and also because of interactions between the various elements of the array. The characteristics of the individual elements are derived from the interaction of the slot with the modes in the waveguide, and a simple lumped-circuit model is used to approximate the slot characteristics. The initial array design approach uses these lumped circuit elements to approximate array performance. The lumped-circuit model neglects interactions between the elements created by radiated and internal electromagnetic coupling.

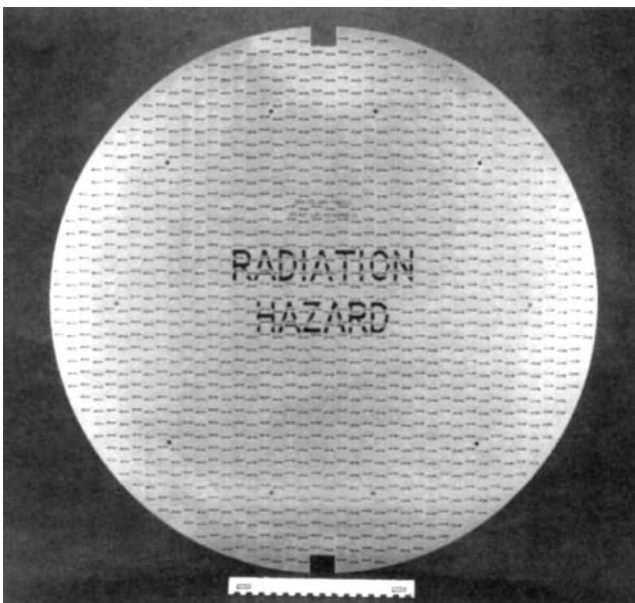


Figure 1. Waveguide slot array for an airborne radar application. (Courtesy of Raytheon Systems Co.)

Refinement of the design to compensate for the interactions is done with experimental hardware or sophisticated electromagnetic simulation software.

1. WAVEGUIDE RADIATING SLOTS

A rectangular slot cut into a metallic ground plane radiates when an electric field is excited across the slot. The electric field distribution in the slot must meet the boundary condition that the tangential electric field at the slot boundary is zero. The lowest mode that meets the boundary conditions has a constant electric field directed across the width of the slot with a cosinusoidal distribution along the length of the slot:

$$E^s(x, z) = \hat{x} \frac{V^s}{w} \cos(\pi z/l) \text{ for} \quad (1)$$

$$-w/2 < x < w/2, \quad -l/2 < z < l/2$$

where V^s is the peak voltage across the slot. The far-field radiation pattern of the slot located in an infinite ground plane is calculated by using Babinet's principle [15] (or image theory). For a slot located in the $x-z$ plane, this results in a radiation pattern given by

$$E_\phi = E_\phi(\theta, \phi) \frac{e^{-jkR}}{R} \quad (2)$$

$$E_\phi(\theta, \phi) = \frac{-jV^s k \sin \theta \cos(kl/2 \cos \theta)}{l (\pi/l)^2 - k^2 \cos^2 \theta}$$

If the slot size is adjusted to the lowest resonance, the loss because of reactive energy is minimized, and the slot coupling is enhanced. At resonance, when the slot is assumed to be equal to one-half the free space wavelength, the radiation pattern becomes

$$E_\phi(\theta, \phi) = \frac{-jV^s \cos(\pi/2 \cos \theta)}{\pi \sin \theta} \quad (3)$$

The directivity for a radiator measures the focusing effect of the radiator and is defined as the directivity relative to that for an isotropic radiator:

$$D(\theta, \phi) = \frac{4\pi P(\theta, \phi)}{\int_0^{2\pi} \int_0^\pi P(\theta, \phi) \sin \theta d\theta d\phi} \quad (4)$$

and the power is given by

$$P(\theta, \phi) = \frac{1}{2} \sqrt{\frac{\epsilon}{\mu}} |\mathbf{E}(\theta, \phi)|^2 \quad (5)$$

The gain of the element is given by the directivity minus any losses in the antenna. The directivity and gain are typically quoted in decibels. For a resonant slot, assuming that radiation occurs only above the ground plane, the peak directivity is 5.6 dB above that of an isotropic radiator.

1.1. Rectangular Waveguide Modes

The field in a waveguide slot is created by a displacement current caused by disruption of the currents generated on the waveguide walls by the energy in the waveguide modes. A metal-walled rectangular waveguide has a set of waveguide modes that satisfy the boundary conditions imposed on the fields by the metallic walls. These modes are classified into two types: the transverse electric (TE), which has only a magnetic field component in the direction of propagation, and the transverse magnetic (TM), which has an electric field component only in the direction of propagation. The complete sets of field components for these modes for a lossless waveguide are as follows [16]: for the TE_{mn} modes,

$$H_z = \cos\left(\frac{m\pi x}{a}\right) \cos\left(\frac{n\pi y}{b}\right) e^{-\gamma_{mn}z}$$

$$H_x = -\frac{\gamma_{mn}}{j\omega\mu} E_y = \frac{m\pi\gamma_{mn}}{k_{mn}^2 a} \sin\left(\frac{m\pi x}{a}\right) \cos\left(\frac{n\pi y}{b}\right) e^{-\gamma_{mn}z}$$

$$H_y = \frac{\gamma_{mn}}{j\omega\mu} E_x = \frac{n\pi\gamma_{mn}}{k_{mn}^2 b} \cos\left(\frac{m\pi x}{a}\right) \sin\left(\frac{n\pi y}{b}\right) e^{-\gamma_{mn}z}$$

$$k^2 = \left(\frac{m\pi}{a}\right)^2 + \left(\frac{n\pi}{b}\right)^2 \quad (6)$$

and for the TM_{mn} modes,

$$E_z = \sin\left(\frac{m\pi x}{a}\right) \sin\left(\frac{n\pi y}{b}\right) e^{-\gamma_{mn}z}$$

$$E_x = -\frac{\gamma_{mn}}{j\omega\mu} H_y = -\frac{m\pi\gamma_{mn}}{k_{mn}^2 a} \cos\left(\frac{m\pi x}{a}\right) \sin\left(\frac{n\pi y}{b}\right) e^{-\gamma_{mn}z} \quad (7)$$

$$E_y = \frac{-\gamma_{mn}}{j\omega\mu} H_x = \frac{n\pi\gamma_{mn}}{k_{mn}^2 b} \sin\left(\frac{m\pi x}{a}\right) \cos\left(\frac{n\pi y}{b}\right) e^{-\gamma_{mn}z}$$

The waveguide mode propagates unattenuated, except for ohmic losses, for frequencies where the propagation constant

$$\gamma_{mn} = \sqrt{\left(\frac{m\pi}{a}\right)^2 + \left(\frac{n\pi}{b}\right)^2 - k^2} \quad (8)$$

is imaginary. The wavelength at which this first occurs, the cutoff wavelength, is given by

$$\lambda = 2\sqrt{(m/a)^2 + (n/b)^2} \quad (9)$$

For almost all applications, it is desirable to operate with only a single propagating mode. The mode with the lowest cutoff frequency, the TE_{10} mode, is used. The guide dimensions are chosen to allow only this mode to propagate over the desired frequency range. The ohmic losses increase as the frequency approaches the cutoff frequency, therefore it is generally desirable to operate at least 20% above the waveguide cutoff frequency. It is also preferable to operate a similar amount below the onset of the next propagating mode. The waveguide fields for the dominant TE_{10} mode

are given by

$$\begin{aligned} H_z &= j \cos\left(\frac{\pi x}{a}\right) e^{\mp j\beta_{10}z} \\ H_x &= \mp \frac{\beta_{10}}{\pi/a} \sin\left(\frac{\pi x}{a}\right) e^{\mp j\beta_{10}z} \\ E_y &= \frac{\omega\mu_0}{\pi/a} \sin\left(\frac{\pi x}{a}\right) e^{\mp j\beta_{10}z} \end{aligned} \quad (10)$$

where the upper sign denotes a wave traveling in the $+z$ -direction and the lower sign denotes a wave traveling in the $-z$ -direction. The propagation constant for this mode is given by

$$\gamma_{10} = j\beta_{10} = j\sqrt{k^2 - \left(\frac{\pi}{a}\right)^2} \quad (11)$$

and the wavelength in the guide is given by

$$\lambda_g = \frac{\lambda}{\sqrt{1 - \left(\frac{\lambda}{2a}\right)^2}} \quad (12)$$

The relationship $\mathbf{J} = \mathbf{1}_n \times \mathbf{H}$ gives the electric currents flowing on the broadwall surface of the waveguide for this mode as

$$\begin{aligned} J_x &= j \cos\left(\frac{\pi x}{a}\right) e^{-j\beta_{10}z} \\ J_z &= \frac{-\beta_{10}}{\pi/a} \sin\left(\frac{\pi x}{a}\right) e^{-j\beta_{10}z} \end{aligned} \quad (13)$$

1.2. Waveguide Slot Radiation Mechanism

If slots are cut into the waveguide in locations where they interrupt the current flow, shown in Fig. 2, a displacement current is setup across the slot and radiation occurs. The amount of radiation is determined by the amount of current intercepted and is controlled by adjusting the slot position on the waveguide and its length and width. A variety of locations create slots with significant amounts of radiation. Slots are also made to radiate by introducing

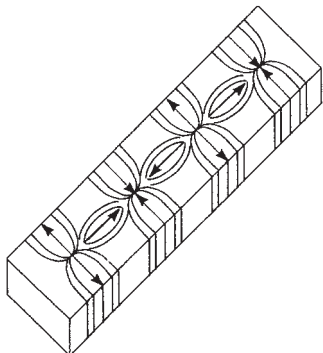


Figure 2. Rectangular waveguide current distribution for the TE_{10} mode.

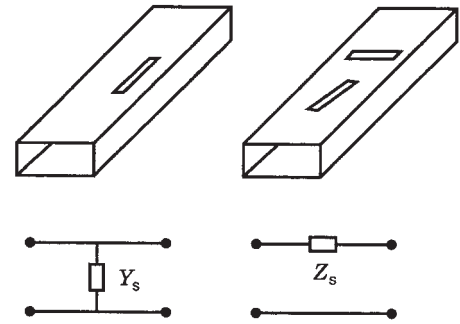


Figure 3. Waveguide radiating slots and their lumped-element circuit models: offset longitudinal shunt slot, and angled and transverse series slot.

discontinuities into the waveguide, such as probes, wires, posts, and irises.

The slot scatters energy in the waveguide in addition to radiating energy. The slot acts as an obstacle in the equivalent transmission line, and it is modeled as a lumped-circuit element in a two-wire transmission line [15]. The lumped-circuit model has a resistive component representing the power lost to the radiated fields and a reactive component representing the stored energy. The backward and forward scattered waves for a slot in the waveguide wall are calculated from [10].

$$\begin{aligned} B_{10} &= \frac{1}{2S_a} \int_{\text{Slot}} (jE_t K_t + E_z K_z) e^{-j\beta_{10}z} dS \\ A_{10} &= \frac{1}{2S_a} \int_{\text{Slot}} (jE_t K_t - E_z K_z) e^{+j\beta_{10}z} dS \end{aligned} \quad (14)$$

where S_a is twice the Poynting energy flux for the dominant mode, \mathbf{E} is the electric field in the slot, and \mathbf{K} is the surface current density on the waveguide wall if the slot were not present. The scattering characteristics are used to compute the equivalent circuit characteristics and their dependence on the slot location and geometry. The slots are characterized by their location and orientation in the waveguide and by their equivalent circuit characteristics. Several slot geometries and their equivalent circuit models are shown in Fig. 3.

1.3. Waveguide Radiating-Slot Geometries

1.3.1. Offset Longitudinal Shunt Slot. A narrow slot located along the waveguide broadwall centerline does not radiate a significant amount of energy because it causes minimal disruption to the current flow on the waveguide walls. As the slot is offset from the waveguide centerline, it intercepts more of the waveguide currents, and the amount of power radiated becomes significant. The phase of the radiated field is reversed if the slot is located on the opposite side of the waveguide centerline. For an offset slot, it is a reasonable approximation to assume that the fields in the slot are symmetrical, and it can be shown that the scattering from the slot in the waveguide is also symmetrical. This symmetrical scattering corresponds to a shunt obstacle for the lumped-circuit model. The scattering

for the slot is given by [17].

$$B_{10} = A_{10} = \frac{j2V^s(\pi/a)^2(\pi/l)}{\omega\mu_0 ab\beta_{10}[(\pi/l)^2 - \beta_{10}^2]} \cos\left(\frac{\beta_{10}l}{2}\right) \sin\left(\frac{\pi x}{a}\right) \quad (15)$$

This assumes a narrow offset slot with only an E_x component that has the cosinusoidal distribution given in Eq. (1). This can be related to the modes in a two-wire transmission line to calculate the conductance of the lumped-circuit element:

$$\frac{Y}{G_0} = K_1 f(x, l) \frac{V^s}{V}$$

where

$$K_1 = \frac{2\pi}{ja} \sqrt{\frac{2}{kG_0\eta\beta_{10}ab}} \quad (16)$$

and

$$f(x, l) = \frac{(\pi/l) \cos(\beta_{10}l/2)}{(\pi/l)^2 - \beta_{10}^2} \sin N(\pi x/a)$$

where x is the slot offset from the centerline and G_0 is the characteristic conductance of the guide. At resonance, when the slot length is one-half a free-space wavelength, the scattering coefficient is given by

$$B_{10} = \frac{j2V^s}{\omega\mu_0(\beta_{10}/k)ab} \cos\left(\frac{\pi\beta_{10}}{2k}\right) \sin\left(\frac{\pi x}{a}\right) \quad (17)$$

and the slot is represented by a shunt conductance. The conductance value is a function of the slot offset and the waveguide dimensions. The dependence of the conductance on the slot offset is given by [10,18]

$$\begin{aligned} \frac{G}{G_0} &= g = g_1 \sin^2 \frac{\pi x}{a} \\ g_1 &= 2.09 \frac{\lambda_g a}{\lambda b} \cos^2 \left(\frac{\pi \lambda}{2\lambda_g} \right) \end{aligned} \quad (18)$$

These equations are useful for understanding the slot characteristics but are not accurate enough for many design applications. The amount of radiation from the slot is controlled primarily by the offset and length as expressed previously but also depends on the slot width and the thickness of the wall in which the slot is cut. The slot resonant frequency must also be determined accurately. The slot is defined to be resonant when the phase of the scattered field is 180° out of phase with the incident wave. The resonant frequency occurs when the slot length is approximately one-half of a free-space wavelength, but the exact frequency is also a function of the slot offset, width, and thickness. The characteristics of the slot are determined more accurately by using an electromagnetic simulation technique, such as the method of moments [19], or by

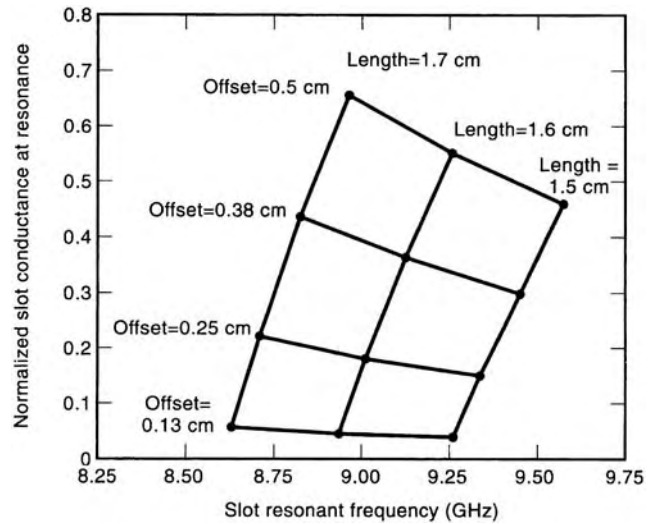


Figure 4. Offset shunt-slot resonant frequency and conductance for various slot lengths and offsets.

careful measurements. Figure 4 shows the variation of the slot conductance and resonant frequency as the offset and length are varied. The slot characteristics were calculated by using a computer simulation based on the method of moments formulation described in Khac [20], with slot thickness effects added. The variation of the slot admittance normalized to the peak conductance values versus frequency relative to the resonant frequency for a slot in full height ($2.3 \text{ cm} \times 1.0 \text{ cm}$) X-band (8 GHz to 12 GHz) waveguide is shown in Fig. 5. Away from the resonant frequency, the slot becomes reactive, and the radiation is reduced. The variation with frequency is relatively insensitive to the slot offset and length, so the curves are applicable over a wide range of offset and length values. If the slot offset is large or the waveguide height is reduced

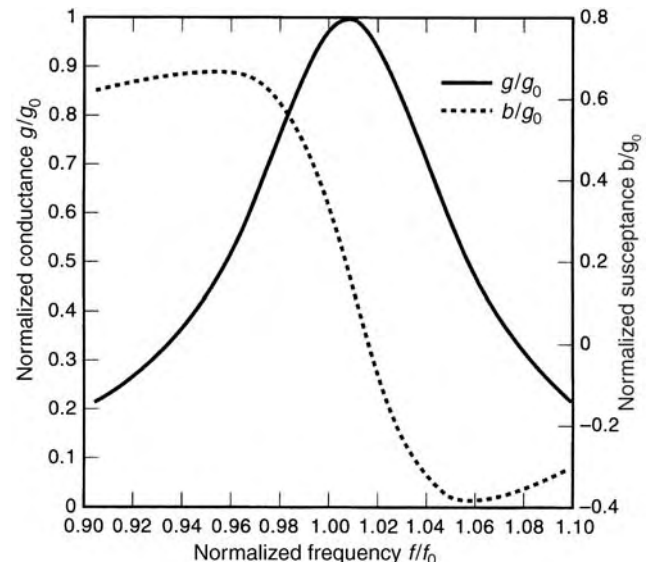


Figure 5. Variation of normalized conductance and admittance for an offset-shunt slot relative to the resonant frequency.

considerably, $b < a/4$, the fields in the slot are less symmetrical, and the slot behaves less like a pure shunt element [21]. For these cases a more complicated circuit model is required, or the scattering matrix description should be used instead of a lumped-circuit model.

1.3.2. Broadwall Series Slots. A slot cut transversely across the waveguide broadwall radiates when centered in the waveguide, and the amount of radiation is controlled by adjusting the offset. For this element, the forward scattered field is opposite in sign to that of the backscattered field, so this slot is modeled as a series element. The normalized series resistance for this element is given by

$$\frac{R}{R_0} = r = r_1 \cos^2\left(\frac{\pi x_1}{2}\right) \quad (19)$$

$$r_1 = 0.523 \left(\frac{\lambda_g}{\lambda}\right)^3 \frac{\lambda^2}{ab} \cos^2\left(\frac{\pi \lambda}{4a}\right)$$

The maximum coupling for this element occurs when the slot is centered. This slot has a high coupling value, but the range of coupling attainable is limited because the slot length restricts the range of offsets, and the slot is confined to the broadwall.

A slot located along the waveguide centerline also radiates when rotated at an angle relative to the centerline. The forward scattering from this element is opposite in phase to that of the backscattered field, and hence it is modeled as a series lumped element. The amount of power coupled is controlled primarily by the slot angle and is adjustable over a wide range of coupling values.

$$\frac{R}{R_0} = r = 0.131 \left(\frac{\lambda}{\lambda_g}\right) \frac{\lambda^2}{ab} \left[I(\theta) \sin \theta + \frac{\lambda_g}{2a} J(\theta) \cos \theta \right]^2$$

$$\left. \begin{aligned} I(\theta) \\ J(\theta) \end{aligned} \right\} = \frac{\cos\left(\frac{\pi \zeta}{2}\right)}{1 - \zeta^2} \pm \frac{\cos\left(\frac{\pi \eta}{2}\right)}{1 - \eta^2} \quad (20)$$

$$\left. \begin{aligned} \zeta \\ \eta \end{aligned} \right\} = \frac{\lambda}{\lambda_g} \cos \theta \mp \frac{\lambda}{2a} \sin \theta$$

The resonant frequency for this slot is relatively insensitive to the slot angle. The polarization characteristics of the slot rotate with the slot orientation and generate a cross-polarization component that limits its usefulness in systems where polarization purity is required.

1.3.3. Narrow-Wall and End-Wall Slots. Transverse angle slots located in the narrow wall of the waveguide are also used as radiating elements. The height of the narrow wall is typically less than the half free-space wavelength required for a resonant slot. So to achieve resonance, the ends of the slot are extended into the broadwall. The coupling is controlled by the slot angle and the depth to which the slot extends into the broadwall. This slot exhibits a

cross-polarization component that varies with the slot angle. This geometry is difficult to model accurately.

Slots located in the shorted end of a waveguide are used for phased-array applications. The slot radiation is created by the disruption of the currents in the terminating short of the waveguide. For most phased-array applications, the slot characteristics are chosen to provide the best match in the array environment, and the power to the slot is controlled by the feed network. Open-ended waveguides are frequently used for scanned-array applications.

2. WAVEGUIDE COUPLING SLOTS

In addition to their function as radiating elements, slots are also used to couple energy between waveguides. The electric field excited in the slot by the incident mode at the input port excites fields in the coupled waveguide. In conjunction with linear radiating slot arrays, the coupling slots provide the building blocks for the planar slot array. The slot configurations described for the radiating elements are also applied as coupling elements. Coupling between the broadwalls is useful to create arrays with minimal depth, and coupling is achieved with the waveguides parallel or perpendicular to each other.

The coupling slots can be modeled by using lumped-circuit elements. For these elements, a transformer between two sets of two-wire lines models the coupling characteristics, and a reactive element models the stored energy in the slot. The slot-coupling ratio determines the turns ratio for the transformer model. The slot is described in terms of its lumped-element characteristics in each of the lines. The element may be a series-series, shunt-shunt, or shunt-series element depending on its orientation in the two waveguides.

2.1. Coupling-Slot Characterization

The characteristics of these elements are determined by a method similar to that for the radiating elements. The forward and backward scattering components are the same as those for the radiating slot given in Eq. (14). Now they are applied in both the input and coupled guides to give the backscattered, forward scattered, and coupled fields. The coupling coefficient between the waveguides is a function of the slot characteristics in the two waveguides and the characteristic impedances of the two guides. The power balance requirement is applied to the junction to show that the coupling coefficient can be calculated from the ratio of the scattered fields and characteristic impedances in the two guides. The scattered-field terms are the same as those derived for the radiating slot except for the value of the coefficient of the field in the slot. For the coupling slot, the ratio of the scattered fields in the two guides is independent of the value of the coefficient, so it need not be determined. The coupling ratio for the slot is given by [22]

$$M = \frac{a_1 b_1 Y_1 |B_1|^2}{a_2 b_2 Y_2 |B_2|^2} \quad (21)$$

where Y_1 and Y_2 are the characteristic impedances in the input and coupling guides, respectively, and B_1 and B_2 are the backscattered fields in the two guides. The value of $1/\sqrt{M}$ gives the turns ratio for the transformer in the lumped-circuit model.

2.2. Coupling-Slot Geometries

The series-series angle slot is a convenient element for broadwall coupling between transverse waveguides because the coupling is controlled by adjusting the slot angle without changing the relative locations of the waveguides and a wide range of coupling values is attainable. This slot and its equivalent circuit model are shown in Fig. 6. The coupling value for this element at resonance, assuming a narrow rectangular slot with zero thickness, is given by

$$M = \frac{a_2 b_2 \lambda_{g_2}}{a_1 b_1 \lambda_{g_1}} \left[\frac{I_1(\theta) \sin \theta + \frac{\lambda_{g_1}}{2a_1} J_1(\theta) \cos \theta}{I_2(\theta) \sin \theta + \frac{\lambda_{g_2}}{2a_2} J_2(\theta) \cos \theta} \right]^2 \tag{22}$$

where the expressions in the equation are the same as those defined in Eq. (20) for the angled radiating slot. The transverse series-series slot, which is the limiting case for the angled series-series slot, provides large coupling values between the guides.

The offset shunt-series coupling slot provides coupling between transverse waveguides. The slot is oriented as an offset shunt slot in one waveguide and a transverse series slot in the other. The coupling values are adjusted by changing the slot offset that is equivalent to moving the location of the shunt waveguide relative to the slot. The

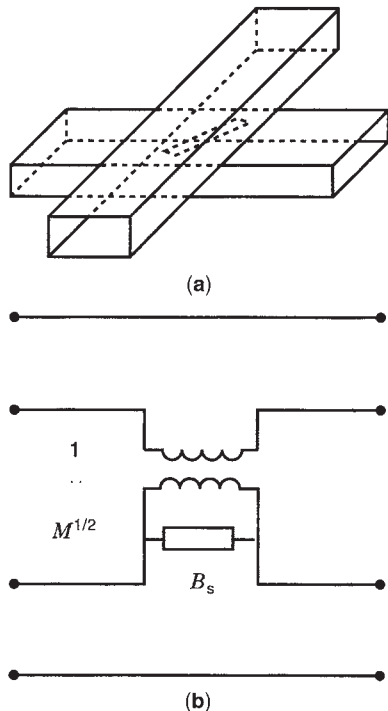


Figure 6. Series-series angle slot coupling element and its lumped-element circuit model.

coupling value for this slot at resonance is given by

$$M = \frac{1}{4} \frac{a_2 b_2 \lambda_{g_1} \lambda_{g_2}}{a_1^3 b_1} \left[\frac{1 - (l/a_2)^2}{1 - (2l/\lambda_{g_1})^2} \right]^2 \frac{\cos^2(\beta_1 l/2) \sin^2(\pi x_1/a_1)}{\cos^2(\pi l/2a_2) \cos^2(\pi x_2/a_2)} \tag{23}$$

where waveguide 1 contains the shunt-slot orientation.

These approximate values for the slot coupling depend on the accuracy of the assumption made for the field in the slot and neglect effects, such as slot thickness and the reactive component of the slot, as the frequency departs from the resonant frequency. More accurate models for the slot are derived by the method of moments [23]. Computer simulation tools based on the finite-element method [24] are also suitable for modeling coupling slots because they operate in a closed structure. This differs from the radiating slot case, which does not lend itself well to this type of model because the problem is unbounded.

3. LINEAR SLOT ARRAYS

A linear array of slots serves alone as an antenna or as a building block for a planar array. The far-field radiation pattern for a linear array of N elements located along the z -axis is given by

$$S(\phi, \theta) = A(\phi, \theta) \sum_{n=1}^N V_n e^{jkz_n \cos \theta} \tag{24}$$

The $A(\phi, \theta)$ term is the radiation pattern of a single radiating element, which is assumed to be the same for all elements in the array. The element pattern is similar to that given in Eq. (2), but it is modified by the array environment. The summation term represents the array factor where V_n are the excitation values and z_n are the element locations. The excitation values of the elements are chosen to generate a specified array radiation pattern. Slot-radiating elements allow controlling the excitations to achieve the desired pattern characteristics.

Linear arrays are divided into two categories: the standing-wave array (or resonant array) and the traveling-wave array (or nonresonant array). The antenna and system performance requirements dictate the choice between the two configurations. In the standing-wave array, the slot locations are chosen to maximize the coupling at the design frequency, and the waveguide is terminated with a short circuit. This creates an efficient antenna, but the bandwidth is limited. In the traveling-wave array, the slot spacings are nonresonant, and the waveguide is terminated with an absorptive load. The traveling-wave array operates over a larger frequency bandwidth than the standing-wave array, but the power absorbed by the load reduces the radiating efficiency. It is difficult to generate a beam perpendicular to the guide with the traveling-wave array, and it also exhibits beam scan with frequency.

3.1. Standing-Wave Arrays

For the resonant array, standing-wave fields are created in the waveguide by terminating the waveguide with a metal

wall to create a short circuit. The slot locations relative to the short circuit are chosen to maximize the array radiation coupling. For series elements, such as the angled series slot, the slots are located multiples of a half guide wavelength from the short circuit. For shunt elements, such as the offset-shunt slot, the maximum coupling locations are multiples of a half guide wavelength from an open circuit, which is achieved by locating a short circuit at one-quarter guide wavelength from the nearest slot. For broadside operation, the slots are located in the guide to achieve a uniform phase distribution. A uniform phase distribution is achieved by locating the slots at one guide-wavelength intervals. However, this results in an array spacing greater than one free-space wavelength, which creates multiple main beams and reduces the antenna gain and performance. The spacing can be reduced to one-half guide-wavelength intervals by alternating the slot offsets to compensate for the 180° phase reversal in the guide.

3.1.1. Circuit Model for Resonant Linear Array. A circuit model of the array provides a good starting point for predicting the array performance and for determining the slot dimensions. The array is modeled by using the lumped-circuit elements for the individual slots, transmission line sections representing the waveguide sections, and a short circuit termination. An offset-shunt-slot linear array and its circuit model are shown in Fig. 7. The transmission matrix is defined as [25]

$$\begin{bmatrix} V_i \\ I_i \end{bmatrix} = \begin{bmatrix} A & B \\ C & D \end{bmatrix} \begin{bmatrix} V_{i+1} \\ I_{i+1} \end{bmatrix} \quad (25)$$

A section of transmission line of length d with a propagation constant β and a characteristic impedance Z_0 has a transmission matrix

$$\begin{bmatrix} \cos(\beta d) & jZ_0 \sin(\beta d) \\ \frac{j}{Z_0} \sin(\beta d) & \cos(\beta d) \end{bmatrix} \quad (26)$$

The transmission matrices for the shunt element with admittance Y and series element with impedance Z are

$$\begin{bmatrix} 1 & 0 \\ Y & 1 \end{bmatrix} \text{ and } \begin{bmatrix} 1 & Z \\ 0 & 1 \end{bmatrix} \quad (27)$$

To achieve a satisfactory design, the coupling values for the individual slots must be chosen so that the reflection coefficient at the array input achieves the required value, and so that the relative coupling from the slots generates the desired radiated phase and amplitude distribution for the array. The input match to the array and its variation with frequency is modeled by cascading the transmission matrices for the slots and the waveguide sections. At the array resonant frequency the normalized input conductance or resistance for an array of N shunt or series slots

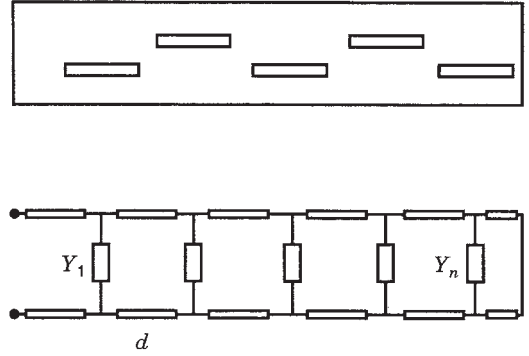


Figure 7. Waveguide linear array of offset longitudinal shunt-slot radiators and its transmission line circuit model.

reduces to

$$\frac{Y_i}{Y_0} = \sum_{n=1}^N \frac{Y_n}{Y_0}$$

or

$$\frac{Z_i}{Z_0} = \sum_{n=1}^N \frac{Z_n}{Z_0} \quad (28)$$

The input reflection coefficient is given by

$$\Gamma_i = \frac{1 - Y_i/Y_0}{1 + Y_i/Y_0} = \frac{Z_i/Z_0 - 1}{Z_i/Z_0 + 1} \quad (29)$$

To achieve an input match for an end-fed standing-wave array, the slot parameters should be chosen so that the slot conductances or impedances sum to one. The slot conductances must also be selected to obtain the amplitude distribution required to achieve the desired radiation pattern. If the slots are all assumed to be resonant and the desired distribution is all equiphase, the ratios of the slot conductances are proportional to the relative slot radiated powers. This gives a set of N equations that can be solved to give the required slot conductances for a shunt-slot array:

$$\frac{G_i}{G_0} = \frac{G_1}{G_0} \sum_{n=1}^N \frac{P_n^r}{P_1^r}$$

$$\frac{G_n}{G_0} = \frac{G_m}{G_0} \frac{P_n^r}{P_m^r}$$

The offset-shunt slot is a commonly used element for linear arrays. It offers a wide range of conductance values and linear polarization. The slot offsets and length can be computed using the equations for the offset shunt slot given earlier, or interpolated from a graph, such as Fig. 4.

3.1.2. Array Mutual-Coupling Effects. The simple circuit model design is useful for understanding the slot array or for determining a set of initial design values, but it is not accurate enough for most applications. The assumption was made that the slots in the array have the characteristics of an isolated slot. In the array environment, the slots are affected by the presence of the other slots, and slots at the edge of the array exhibit behavior that differs

significantly from that of slots in the center of the array. If neglected, these effects result in an array where the input reflection coefficient and radiation pattern depart significantly from the desired values. The characteristics of the isolated slot were determined by using a single source of excitation for the slot: the incident waveguide mode. Multiple sources in the array environment excite the slot: the incident field, the fields scattered in the waveguide by the other slots in the guide, and the radiated fields from all the other slots. The characteristics for each slot are influenced by all the other slots in the array to some extent, so a slot's configuration cannot be determined independently. A series of simultaneous equations is required to perform the array design. Elliott [17] has developed a series of design equations that account for the internal and external mutual coupling effects:

$$\frac{Y_p^a/G_0}{Y_n^a/G_0} = \frac{f_p}{f_n} \frac{V_p^s}{V_n^s} \frac{V_n}{V_p} \quad (30)$$

$$\frac{Y_n^a}{G_0} = \frac{2f_n^2}{\frac{2f_n^2}{Y/G_0} + j(\beta_{10}/k)(k_0b)(a/\lambda)^3 \sum_{m=1}^{N'} \frac{V_m^s}{V_n^s} g_{mn}}$$

$$f_n(x_n, l_n) = \frac{(\pi/l) \cos(\beta_{10}l_n)}{(\pi/l_n)^2 - \beta_{10}^2} \sin\left(\frac{\pi x_n}{a}\right)$$

$$g_{mn}(x_n, l_n, x_m, l_m) = \int_{-l_m/2}^{l_m/2} \cos(\pi \zeta'_m/l_m) \int_{-l_n/2}^{l_n/2} \cos(\pi \zeta'_n/l_n) \left[\frac{\partial^2}{\partial \zeta_n'^2} + k_0^2 \right] \frac{e^{-jk_0R}}{R} d\zeta_n' d\zeta_m' \quad (31)$$

The Y_n^a/G_0 are the active slot admittances in the array environment, the V_n^s, V_n are the slot and the waveguide mode voltages, and the g_{mn} terms represent the external mutual coupling effects between the slots. The set of equations is applied iteratively along with the equation for the required input impedance to determine the slot offsets and lengths. These equations assume an ideal cosinusoidal distribution in a narrow slot, and may not be accurate enough for some applications. A more thorough analysis, where the field distribution in the slots are unknowns that must be determined, provides a more accurate model of the impact of element mutual coupling on array performance [26]. The computational requirements for a rigorous analysis may limit the size of the array for which it is applicable. A good approximation to the final design should be found first by using an approximate method to reduce the number of iterations required.

3.1.3. Variation of Performance with Frequency. The design achieves the desired input match at the design frequency, but the input match of the linear array degrades as the frequency moves away from resonance. This effect is modeled using the transmission matrices by adjusting the propagation constant in the transmission line sections and including the variation of the slot admittance with frequency. The bandwidth is generally defined as the

frequency range over which the input reflection coefficient remains below a specified level. The bandwidth is determined primarily by the number of elements in the array, and it degrades as the number of elements in the array increases. Watson [9] derived an approximate expression for the variation of the input reflection coefficient that neglects the multiple reflections:

$$\Gamma = \frac{2 - \sum_{n=1}^N Y_n/Y_0 - e^{j2N\beta d} \sum_{n=1}^N Y_n/Y_0 e^{-j2n\beta d}}{\left(2 + \sum_{n=1}^N Y_n/Y_0\right) e^{j2N\beta d} + \sum_{n=1}^N Y_n/Y_0 e^{j2n\beta d}} \quad (32)$$

The array excitations also change away from the center frequency because the slot locations relative to the standing wave in the guide are no longer optimum and the slot radiation characteristics also exhibit frequency variation. This causes pattern degradation and main-beam distortion. The effects are modeled by using the circuit model to determine the slot excitations and computing the far-field pattern generated by these excitations.

3.2. Traveling-Wave (Nonresonant) Arrays

For the nonresonant array, the array distribution is generated by progressively coupling energy from the waveguide mode as it travels down the guide. The element spacings are chosen to be nonresonant, and the waveguide is terminated with a matched load. The design process differs from that of the standing-wave array because the reflections from the slots do not add coherently at the input. The input reflection is controlled by the destructive interference because of the nonresonant spacing, and the reflection coefficients of the individual elements are kept small to minimize the reflection. The traveling-array input-match bandwidth does not decrease as the array size increases, unlike that of the resonant array. The resonant slot spacing case for a broadside beam is avoided because the summation of the individual reflections creates a large reflection. The traveling wave generates a linear phase slope across the aperture that corresponds to a scanned beam with the beam pointing direction given by [27]

$$\cos \theta_0 = \lambda/\lambda_g - \lambda/2d \quad (33)$$

for an array with alternating slot offsets. The beam scans with frequency because of the change in the guide wavelength. This frequency-scanning effect is often exploited by making the waveguide path length between the slots greater than the array spacing to enhance the amount of scan for a given frequency change [28]. The beam position for this case is given by

$$\cos \theta_0 = d_g \lambda/d\lambda_g - \lambda/2d \quad (34)$$

3.2.1. Circuit Model for Nonresonant Arrays. The circuit model for the traveling-wave array is similar to that used for the resonant array, but a matched-load termination

replaces the terminating short, and the line lengths are adjusted to reflect the nonresonant spacing. The initial design is simplified by assuming that the scattering from each slot is small, and hence multiple reflections are neglected. With this assumption and a perfect load termination, the reflection coefficient at the waveguide input is given by

$$\Gamma_i = \sum_{n=1}^N \rho_n e^{-j2n\beta d} \quad (35)$$

where the reflection coefficient for a resonant slot

$$\rho_n = \frac{-2G/G_0}{2 + G/G_0} \quad (36)$$

Neglecting the slot reflections, the ratios of the slot radiated powers for a traveling-wave array of resonant shunt elements are given by

$$\frac{P_n^r}{P_1^r} = \frac{G_n/G_0}{G_1/G_0} \prod_{i=1}^{n-1} \left(1 - \frac{G_i}{G_0}\right) \quad (37)$$

where the product term gives the decrease in the power along the guide caused by radiated energy. The ratio of the power remaining after the final element is absorbed in the load termination relative to the input power is given by

$$\frac{P_l}{P_i} = \prod_{n=1}^N \left(1 - \frac{G_n}{G_0}\right) \quad (38)$$

If the waveguide loss is significant, the attenuation factor $e^{-\alpha z}$ should be included in the power calculation. The initial design process requires solving these equations to achieve both the desired amplitude distribution and an acceptable value for the power lost to the load. For the traveling-wave array, it is advantageous to have a longer array because this reduces the amount of power that must be absorbed in the load termination. The range of coupling values available for the radiating elements also affects the amount of power that will be lost in the load. The circuit models can be cascaded to account for the multiple reflections and frequency effects. The design process for the array including mutual coupling effects is similar to that for the resonant array. However, the variation of the mode voltage along the array must be included in the model [29].

4. WAVEGUIDE PLANAR ARRAY

The waveguide planar array is constructed by joining a number of linear arrays via a feed network. The planar aperture provides the area required to achieve high gain, which is a critical parameter for most designs as it determines the effective range of system operations. The rectangular waveguide exhibits low loss values over a wide range of frequencies (up to the millimeter waveband), which makes the waveguide slot array desirable for high-gain applications. The sidelobe distribution is also important for many applications as high sidelobes may

result in unwanted interference between adjacent installations or false returns off scatterers located in the sidelobe region. For the planar-slot array, the aperture distribution is achieved by controlling the characteristics of the individual radiating elements and the coupling characteristics of the feed network. The ability to accurately control the excitation across the aperture allows the designer to set the radiation pattern sidelobes.

4.1. Planar-Array Far-Field Patterns

The equation to compute the far-field pattern of a planar array located in the $x-y$ plane is

$$S(\theta, \phi) = A(\theta, \phi) \sum_{m=1}^M \sum_{n=1}^N V_{mn} e^{jk(x_{mn} \sin \theta \cos \phi + y_{mn} \sin \theta \sin \phi)} \quad (39)$$

The array elements are assumed to have identical element patterns that are similar to Eq. (2) with the appropriate coordinate transformation to match the element orientation. The array factor is given by the summation term where V_{mn} is the excitation of each element. If the array elements are on a rectangular grid, the equation simplifies to

$$S(\theta, \phi) = A(\theta, \phi) \sum_{m=1}^M \sum_{n=1}^N V_{mn} e^{jk(md_x \sin \theta \cos \phi + nd_y \sin \theta \sin \phi)} \quad (40)$$

This formulation is in the form of a Fourier transform, and with appropriate manipulations fast Fourier transform [30] computer routines are used to reduce computation time greatly. For a rectangular, separable array, the distribution is chosen to be of the form

$$V_{mn} = V_m V_n$$

Now the resulting planar-array equation is the product of the two linear-array distributions. This results in a dramatic reduction in computation time:

$$S(\theta, \phi) = A(\theta, \phi) \sum_{m=1}^M V_m e^{jkm d_x \sin \theta \cos \phi} \sum_{n=1}^M V_n e^{jkn d_y \sin \theta \sin \phi} \quad (41)$$

For arrays with separable distributions, the desired linear-array distributions are selected, and then the products are used to determine the individual element distributions. The cardinal plane patterns of the array match the linear-array patterns, and the intercardinal planes have sidelobes that are the product of the two linear-array distributions. For circular apertures, there are a variety of circular distributions available that are sampled to generate the array distribution [31]. More complex distributions are synthesized for specific applications. The planar-array directivity is computed by using the array far-field pattern in the directivity expression, Eq. (4). The

directivity is reduced by the losses in the antenna system to determine the array gain.

4.2. Resonant Planar-Array Design

A common architecture for a resonant planar array, shown in Fig. 8, uses broadwall offset-shunt slots as the radiating elements. The linear arrays are attached along the sidewalls, and common sidewalls are used to reduce the weight. Different lengths are used for the linear arrays to fit the array within a specified area. Power is fed to the individual linear arrays via a waveguide network beneath the radiating aperture. A compact feed network is formed with a linear array of broadwall coupling slots to distribute power to the radiating waveguides. Angled series-series slots provide a convenient coupling mechanism because the power to each linear array is controlled by adjusting the slot angle. Offset shunt-series slots are also used as coupling elements, but they have the disadvantage that the linear arrays must be offset to maintain the proper feed point and compensate for the staggered offsets of the coupling slot.

The radiating slots and feed network are designed together to provide the desired input match and to achieve the aperture radiating distribution. The design values for the radiating slots and the coupling slots must be chosen together to meet the performance goals as the input impedance and the slot radiation are functions of both the radiating slot values and the coupling values of slots in the feed waveguide. The array spacings to achieve resonance in both the radiating and feed planes are related because the radiating guide width determines the spacing in the feed plane. The spacings and the waveguide dimensions must be chosen as a set to achieve the correct resonant frequency in each plane of the array.

4.2.1. Planar-Array Circuit Models. The lumped-circuit models used for the linear-array design combine with the coupling-slot models to provide a simple model for the planar array. The impedance at resonance of a series-series slot coupling to a linear array of M radiating slots is

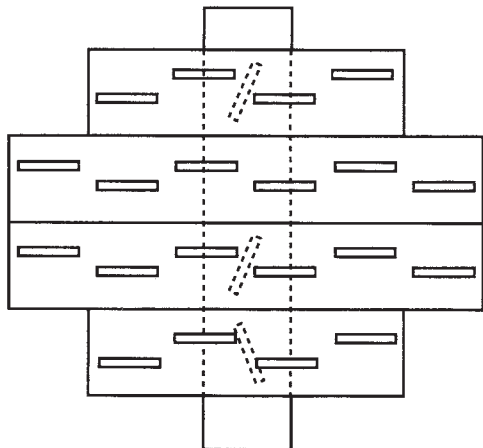


Figure 8. Waveguide planar array with offset longitudinal shunt-slot radiators and series-series angle-slot coupling elements.

given by

$$R_n/R_0 = \frac{1}{M_n} \sum_{m=1}^{M(n)} G_{mn}/G_0 \tag{42}$$

The coupling elements form a linear array of N slots in the feed waveguide with an input impedance at resonance of

$$Z_i/Z_0 = \sum_{n=1}^N \frac{1}{M_n} \sum_{m=1}^{M(n)} G_{mn}/G_0 \tag{43}$$

The ratios of the slot conductance and coupling values must be chosen to provide the correct ratios for the radiating-slot voltages. The slot conductance values within each radiating guide are given by

$$G_{mn} = G_{1n} \frac{P_{mn}^r}{P_{1n}^r} \tag{44}$$

and the coupling ratio for each series-series slot is given by

$$M_n = M_1 \frac{\sum_{m=1}^{M(n)} G_{mn}/G_0 \sum_{m=1}^{M(1)} P_{m1}^r}{\sum_{m=1}^{M(1)} G_{m1}/G_0 \sum_{m=1}^{M(n)} P_{mn}^r} \tag{45}$$

The values for the G_{1n} and M_1 must be chosen to create the desired input impedance value. For compactness and improved bandwidth characteristics, it may be desirable to feed the array at the center of the feed waveguide using an additional feed layer with a coupling slot. For a shunt-series coupling element where the waveguide terminated by a short at one-quarter guide wavelength, the input admittance to the array is given by

$$Y_i = \frac{Z'}{\mathcal{M}_0} \tag{46}$$

where Z' is the impedance in the feed waveguide and \mathcal{M}_0 is the input slot coupling ratio. The values for the series-series coupling slots must be chosen to account for the power division between the elements to each side of the input slot.

4.2.2. Mutual-Coupling Effects. As in the linear array, the simple-circuit model neglects effects, such as mutual coupling between the slots, that perturb the performance. The mutual-coupling effects between the radiating elements are handled as described for the linear array with a separate input admittance requirement for each radiating waveguide. The external mutual-coupling effects are generally more significant in the E -plane of the slots than in the H -plane. Additional coupling mechanisms that impact the array performance include coupling-slot interaction with the radiating slots and with the other coupling slots in the feed guide. The radiating slots closest to the coupling slots in each guide are significantly affected by these

interactions, which are modeled by the method of moments [32].

4.2.3. Large Resonant Arrays. The array bandwidth decreases as the size increases because of the increased number of elements in the radiating and feed linear arrays. To avoid the bandwidth reduction for a large array, the array is subdivided into a number of subarrays or modules with shorter radiating and feed arrays. The array power is distributed to the individual modules via a feed network made up of a series of waveguide power dividers. The configurations of the modules are dictated by the required array bandwidth, the available aperture area, and the packaging limitations for the feed network. It is desirable to minimize the modular size to improve the array bandwidth, but this requires more modules and complicates the feed network. Dividing the array into subarrays is fairly straightforward for rectangular arrays. The choice of modular layouts is more complex for arrays with elliptical or irregular boundaries. The available range of coupling values for the slots and the feed network limits the choice of modular configurations. Systems requirements, such as the need to provide both sum and difference patterns, which necessitates dividing the array into equal quadrants, also determine the available configurations.

A typical configuration for a resonant planar array is built up of several modules with offset-shunt radiating slots and angled series-series coupling slots. Offset-shunt series slots are used to couple power from a waveguide corporate feed network made up of reactive H -plane waveguide three-port power dividers. For an array with difference pattern requirements, the power is distributed to the quadrants of the array by a network of waveguide magic-tee four-port power dividers. This architecture provides some inherent mechanical advantages because of the box-like structure of the radiating aperture, and, depending on the array size, is packaged so that the depth of the array is as small as three times the waveguide b dimensions. Numerous other variations of array architecture are also used.

To begin the design of an array of this type, the desired gain, sidelobe performance, and frequency bandwidth must be specified. The size of the array is driven by the array gain. The area is chosen so that the area directivity minus the taper loss, all losses in the aperture and feed networks, and any of the return loss at the array input meets the required gain value with some margin. Because of variations, the required aperture distribution is selected to meet the sidelobe requirements with some margin. The array slot spacings are chosen to meet the frequency requirements and make the most effective use of the available area. The aperture distribution is discretized to give the required value at each slot. Then the array is subdivided into modules whose size is based on the required frequency bandwidth. The design of individual modules is similar to that described previously with the additional complication that now the external mutual coupling includes both the slots within the module and all slots in the other modules.

The feed network is a multiport power-dividing network with an output port for each module. The relative power to each port is calculated by summing the specified powers of the slots in each module. For most applications, a corporate feed structure with equal path lengths to each module is required to meet the bandwidth requirements. A reactive H -plane tee in a rectangular waveguide provides a low-loss, low-profile, power-dividing network. The individual tees are matched, and the power splits are controlled by adjusting inductive-tuning irises at the tee input and the length and position of a septum on the back wall of the tee. The performance of the reactive-feed network is sensitive to the loads placed on the feed by the modules. To reduce this sensitivity and provide broader band performance, matched power dividers are used even though they have higher loss and larger sizes.

4.2.4. Frequency and Power-Handling Effects. As the operating frequency of a resonant array moves away from the design frequency, the input match degrades and the pattern performance suffers. For arrays whose radiating guide and feed waveguides are fed near or at their centers, the amplitude and phase of elements at the ends of the guide diverge from those near the center. For a single module, this broadens the main beam and increases the sidelobe level. For an array of modules, this creates an error across the array with a period equal to the modular spacing, which creates error lobes in the far-field pattern and reduces the array directivity. These effects are modeled by using a circuit model for the modules and feed network.

The amount of power that the array is required to handle also influences the design. The waveguide power-handling capability is reduced as the waveguide b dimension is decreased, so for high-power applications, full-height waveguide should be used. For arrays that must operate at high altitudes, the waveguides are pressurized. Care should be taken to avoid any obstacles that protrude into the guide in the b dimension, and mismatches should be minimized to reduce the standing-wave effect. The amount of power is reduced as it divides through the feed network and subarrays, so the power-handling problem is less severe at the aperture.

4.3. Nonresonant Planar Arrays

The traveling-wave planar array is created by joining a set of linear, traveling-wave arrays with a feed network. The sidewall edge-slot array is frequently chosen, particularly for applications where the array is scanned in the feed plane, because the linear arrays can be packed closely together. The radiating arrays are designed similarly to the linear array, but mutual coupling between the linear arrays must be taken into account. It is generally preferable not to subdivide the array and to end feed the radiating aperture to minimize the power lost to the loads. The feed network can be traveling wave or standing wave depending on the application. A linear array of coupling slots provides a compact feed network for many applications. Where beam squint in the feed plane is not desired, a corporate feed network of waveguide power dividers is used.

4.4. Effects of Manufacturing Variations

Array performance is influenced by how accurately the design is realized in manufacturing. For arrays with stringent sidelobe requirements, the effects of manufacturing deviations from the design values significantly alter the performance, and the deviations must be carefully controlled. The potential impacts of the manufacturing process should be accounted for in the design. Where possible, the design values should be chosen to minimize sensitivity to the variations. The acceptable limits for process variations should be set on the basis of acceptable performance limits; the processes should be chosen for compatibility with these limits. The relative locations of the features and the geometry of the individual features must be controlled. The potential cost impacts of overly tight tolerances must be weighed against the performance impacts. The operating frequency of the array is a major factor in the allowable tolerances and hence the preferred manufacturing technique. Typical manufacturing processes for slot arrays include machined metal assemblies joined either by brazing or bonding, stamped or punched slots, etched slots on metal clad dielectric, molded metallized plastic assemblies, or cast parts.

For slots manufactured by conventional machining techniques, it is more convenient and cost effective to machine the slots with a rounded end that matches the diameter of the endmill rather than create a true rectangular slot. For narrow slots, the main effect of the rounded end is a change in the slot resonant frequency. The effect is modeled and compensated for by assuming that a rounded end slot has the same resonant frequency as a square-ended slot of equal area [14].

For large arrays, errors that are randomly distributed across the array face result primarily in increased average sidelobe level and a decreased array gain. The effects of these errors are estimated by statistical techniques [33,34] or by a Monte Carlo simulation of the array pattern. The variation in the element excitation must be estimated from the tolerances on the element features, and then these values are used to estimate the change in array performance. The sensitivity of the characteristics of the individual slots to a given variation in slot dimensions is determined by using the slot design equations or design curves such as those shown in Fig. 4.

Systematic errors have more significant impacts. A consistent change in the waveguide a dimension shifts the resonant frequency of the standing-wave array and alters the beam-pointing angle in the traveling-wave array. A systematic error in the slot locations creates undesirable sidelobes. In the traveling-wave array, if the slot coupling or the waveguide losses are consistently higher or lower than the design value, the error in the array excitation accumulates along the array because the mode amplitude is increasingly perturbed. If the coupling is significantly lower than the design value, excess power is lost in the load. Periodic errors raise the sidelobe at the position where a grating lobe would occur for an array whose spacing is equal to the spacing of the periodic error. Feed network or other errors that affect large portions of the array have significant impacts on the array sidelobe and

gain performance. An array with a difference pattern requirement is sensitive to asymmetrical errors across the array because any imbalance affects the cancellation that occurs at the difference pattern null.

Acknowledgments

The author wishes to thank W. H. Kummer for his assistance with the manuscript and historical background, R. C. Hansen for providing historical material, G. R. Kulakowski for his assistance with the figures, and the reviewers for their helpful comments.

BIBLIOGRAPHY

1. G. C. Southworth, Hyper-frequency wave-guides—General considerations and experimental results, *Bell Syst. Tech. J.*, **15**:284–309 (1936).
2. J. R. Carson, S. M. Mead, and S. A. Schelkunoff, Hyper-frequency wave guides—Mathematical theory, *Bell Syst. Tech. J.*, **15**:310–333 (1936).
3. W. L. Barrow, Transmission of electromagnetic waves in hollow tubes of metal, *Proc. IRE*, **24**:1298–1398 (1936).
4. K. S. Packard, The origin of waveguides: A case of multiple rediscovery, *IEEE Trans. Microw. Theory Tech.*, **MTT-32**:961–969 (1984).
5. S. A. Schelkunoff, The impedance concept and its application to problems of reflection, refraction, shielding, and power absorption, *Bell Syst. Tech. J.*, **17**:17–48 (1938).
6. S. A. Schelkunoff, A mathematical theory of linear arrays, *Bell Syst. Tech. J.*, **22**:80–107 (1943).
7. C. L. Dolph, A current distribution for broadside arrays which optimizes the relation between beamwidth and sidelobe levels, *Proc. IRE*, **34**:335–348 (1946).
8. T. T. Taylor, Design of line source antennas for narrow beamwidth and low sidelobe, *IRE Trans. Antennas Propag.*, **AP-7**:15–28 (1955).
9. W. H. Watson, *The Physical Principles of Wave Guide Transmission and Antenna Systems*, Oxford, UK: Clarendon Press, 1947.
10. A. F. Stevenson, Theory of slots in rectangular waveguides, *J. Appl. Phys.*, **18**:24–38 (1948).
11. S. Silver, *Microwave Antenna Theory and Design*, Vol. 12, MIT Rad Lab Series, New York: McGraw-Hill, 1949.
12. I. P. Kaminow and R. J. Stegen, *Waveguide slot array design*, Tech. Memo. No. 348, Hughes Aircraft Co., July 1954.
13. A. A. Oliner, The impedance properties of narrow radiating slots in the broad face of rectangular waveguide—Part I—theory, Part II—comparison with measurement, *IEEE Trans. Antennas Propag.*, **AP-5**:4–20 (1957).
14. A. A. Oliner, Historical perspectives on microwave field theory, *IEEE Trans. Microw. Theory Tech.*, **MTT-32**:1022–1045 (1984).
15. H. G. Booker, Slot aerials and their relations to complementary wire aerials (Babinet's principle), *J.I.E.E. (London)*, **93**, part IIIA:620–626 (1946).
16. Ref. 11, pp. 226–229.
17. R. S. Elliott, An improved design procedure for small arrays of shunt slots, *IEEE Trans. Antennas Propag.*, **AP-31**:48–53 (1983).
18. Ref. 11, pp. 286–299.

19. R. F. Harrington, *Field Computation by Moment Methods*, New York: Macmillan, 1968.
20. V. T. Khac, A study of some slot discontinuities in rectangular waveguides, Ph.D. Dissertation, Monash University, Australia, November 1974.
21. G. J. Stern, R. S. Elliott, Resonant length of longitudinal slots and validity of circuit representation: Theory and experiment, *IEEE Trans. Antennas Propag.*, **AP-33**: 1264–1271 (1985).
22. D. J. Lewis, *Waveguide Coupling Slots*, Internal memo., Hughes Aircraft Co.
23. S. R. Rengarajan, Analysis of a centered-inclined waveguide slot coupler, *IEEE Trans. Microw. Theory Tech.*, **37**:884–889 (1989).
24. P. P. Silvester, *Finite Elements in Electrical and Magnetic Field Problems*, New York: Wiley, 1980.
25. J. L. Altman, *Microwave Circuits*, New York: Van Nostrand, 1964, pp. 399–406.
26. J. J. Gulick and R. S. Elliott, The design of linear and planar arrays of waveguide-fed longitudinal slots, *Electromagnetics*, **10**(4):327–347 (1990).
27. R. S. Elliott, *Microwave Antenna Theory and Design*, Englewood Cliffs, NJ: Prentice-Hall, 1981.
28. N. A. Begovich, Frequency scanning, in R. C. Hansen, ed., *Microwave Scanning Antennas*, Vol. 3, New York: Academic Press, 1964, Chap. 2.
29. R. S. Elliott, on the design of traveling-wave-fed longitudinal shunt slot arrays, *IEEE Trans. Antennas Propag.*, **AP-27**: 717–720 (1979).
30. E. O. Brigham, *The Fast Fourier Transform*, Englewood Cliffs, NJ: Prentice-Hall, 1974.
31. T. T. Taylor, Design of circular apertures for narrow beamwidth and low sidelobes, *IRE Trans. Antennas Propag.*, **8**: 17–22 (1960).
32. D. C. Senior, Higher order mode coupling effects in a shunt-series coupling junction in a planar slot array antenna, Ph.D. Dissertation, University of California at Los Angeles, 1986.
33. J. Ruze, The effects of aperture errors on the radiation pattern, *Nouvo Cimento*, **9**(Suppl. No. 3):364–380 (1952).
34. R. S. Elliott, Mechanical and electrical tolerances for two-dimensional scanning antenna arrays, *IRE Trans. Antennas Propag.*, **10**:114–120 (1958).

WAVEGUIDE COMPONENTS

D. BUDIMIR
University of Westminster
London, United Kingdom

1. INTRODUCTION

Waveguide components such as waveguides as transmission lines, mode transducers, terminations, discontinuities, attenuators, nonreciprocal devices (isolators and circulators), TR cells, phase shifters, power measuring

devices (bolometers), crystal detectors, junctions devices (the magic “tee”), directional couplers, mixers, periodic structures (disk-loaded slow-wave structures), resonators, filters, diplexers, and multiplexers are extensively employed in industry to produce waveguide subsystems for a wide variety of microwave and millimeter-wave applications. Waveguide components, in general, are constructed from elements of transmission structures and it is therefore essential to understand the theory of electromagnetic waveguides. This article attempts to illustrate the basic considerations by referring to a few of the more important rectangular waveguide components employed in microwave and millimeter-wave systems. It is hoped that the references included at the end of this article will direct the interested reader to sources of more detailed information on particular subjects.

2. WAVEGUIDE AS TRANSMISSION LINES

In this section we will summarize the information for waveguides as transmission lines that is most often needed in waveguide component design. Waveguides have a relatively low loss and a large power-handling capability for a given operating frequency. They are used in a wide variety of applications, including precision instrumentation equipment, specifically, the network analyzer. Waveguides are also useful in some millimeter-wave systems, very-low-loss transmission systems, very-low-loss filters (very-high- Q filters), and high-power transmission (e.g., kW–MW range).

2.1. Rectangular Waveguides

Probably the most widely used elements in high-power and very-low-loss microwave and millimeter-wave filters are the rectangular waveguides (see Fig. 1). Additional details on waveguides and their applications may be found in the literature [1–23].

The waveguide supports TE (transverse electric) and TM (transverse magnetic) modes. TE modes have a magnetic field (H_z) but no electric field (E_z) in the direction of propagation. They have also been referred to as H modes, or modes of magnetic type.

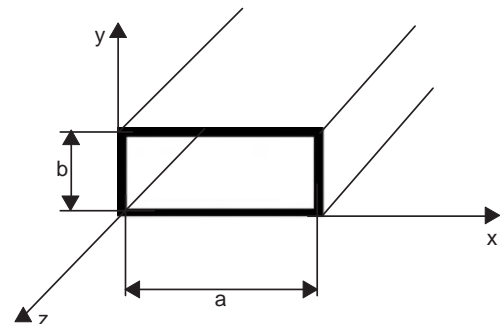


Figure 1. The rectangular waveguide structure.

For TE_{mn} modes, the electromagnetic field components are given by

$$E_x = \frac{jk_0\eta_0 n\pi}{b} A_{mn} \cos\left(\frac{m\pi x}{a}\right) \sin\left(\frac{n\pi y}{b}\right) \quad (1)$$

$$E_y = \frac{jk_0\eta_0 m\pi}{a} A_{mn} \sin\left(\frac{m\pi x}{a}\right) \cos\left(\frac{n\pi y}{b}\right) \quad (2)$$

$$E_z = 0 \quad (3)$$

$$H_x = \frac{j\beta_{mn} m\pi}{a} A_{mn} \sin\left(\frac{m\pi x}{a}\right) \cos\left(\frac{n\pi y}{b}\right) \quad (4)$$

$$H_y = \frac{j\beta_{mn} n\pi}{b} A_{mn} \cos\left(\frac{m\pi x}{a}\right) \sin\left(\frac{n\pi y}{b}\right) \quad (5)$$

$$H_z = k_c^2 A_{mn} \cos\left(\frac{m\pi x}{a}\right) \cos\left(\frac{n\pi y}{b}\right) \quad (6)$$

Modes that have an electric field (E_z) but no magnetic field (H_z) in the direction of propagation are known as *TM*, and have also been referred to as *E modes* or modes of electric type.

The electromagnetic field components of TM_{mn} modes are given by

$$E_x = \frac{-j\beta_{mn} m\pi}{a} B_{mn} \cos\left(\frac{m\pi x}{a}\right) \sin\left(\frac{n\pi y}{b}\right) \quad (7)$$

$$E_y = \frac{-j\beta_{mn} n\pi}{b} B_{mn} \sin\left(\frac{m\pi x}{a}\right) \cos\left(\frac{n\pi y}{b}\right) \quad (8)$$

$$E_z = k_c B_{mn} \sin\left(\frac{m\pi x}{a}\right) \sin\left(\frac{n\pi y}{b}\right) \quad (9)$$

$$H_x = \frac{jk_0 n\pi}{b\eta_0} B_{mn} \sin\left(\frac{m\pi x}{a}\right) \cos\left(\frac{n\pi y}{b}\right) \quad (10)$$

$$H_y = \frac{-jk_0 m\pi}{a\eta_0} B_{mn} \cos\left(\frac{m\pi x}{a}\right) \sin\left(\frac{n\pi y}{b}\right) \quad (11)$$

$$H_z = 0 \quad (12)$$

where A_{mn} and B_{mn} are amplitude coefficients, and

$$k_0 = \omega\sqrt{\mu_0\epsilon_0} \quad (13)$$

$$\eta_0 = \sqrt{\frac{\mu_0}{\epsilon_0}} \quad (14)$$

$$k_c = \sqrt{\left(\frac{m\pi}{a}\right)^2 + \left(\frac{n\pi}{b}\right)^2} \quad (15)$$

The phase constant of the waveguide is related to λ_g by

$$\beta = \frac{2\pi}{\lambda_g} \quad \text{with} \quad \lambda_g = \frac{\lambda_0}{\sqrt{1 - \left(\frac{\lambda_0}{\lambda_c}\right)^2}} \quad (16)$$

where λ_0 is the free-space wavelength:

$$\lambda_0 = \frac{c}{f} \quad \text{and} \quad \lambda_c = \frac{2\pi}{k_c} \quad (17)$$

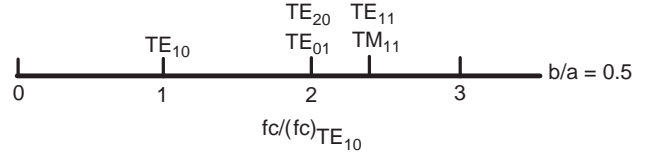


Figure 2. Relative cutoff frequencies of waves in a rectangular waveguide.

The modes that enable single-mode operation in the natural state are usually referred to as *dominant* or *fundamental*, while all other modes are known as *high-order* modes. The TE_{10} is the dominant mode of the rectangular waveguide. It has the lowest cutoff frequency of all possible rectangular waveguide modes. Figure 2 shows the line diagram that indicates the cutoff frequencies of a few of the lowest-order modes in a rectangular waveguide for a ratio of width a to height b of 0.5. The properties of standard air-filled rectangular waveguides are summarized in Table 1.

2.1.1. Dominant TE_{10} Mode in Rectangular Waveguides. For TE_{10} modes, the electromagnetic field components are given by

$$E_x = 0 \quad (18)$$

$$E_y = E_{y0} \sin\left(\frac{\pi x}{a}\right) \quad (19)$$

$$E_z = 0 \quad (20)$$

$$H_x = H_{x0} \sin\left(\frac{\pi x}{a}\right) \quad (21)$$

$$H_y = 0 \quad (22)$$

$$H_z = H_{z0} \cos\left(\frac{\pi x}{a}\right) \quad (23)$$

2.1.2. Characteristic Impedance (Z_0) in Waveguides. There are a few commonly used definitions, as follows. The *voltage-current* definition:

$$Z_0 = \frac{V}{I} = \frac{\pi}{2} \frac{b}{a} Z_{TE}$$

The *power-current* definition:

$$Z_0 = \frac{P}{I^2} = \frac{\pi^2}{8} \frac{b}{a} Z_{TE}$$

The *power-voltage* definition:

$$Z_0 = \frac{V^2}{P} = 2 \frac{b}{a} Z_{TE}$$

The modified *power-voltage* definition:

$$Z_0 = \frac{V^2}{P} = \frac{b}{a} Z_{TE}$$

Table 1. Rectangular Waveguide Properties [57]

EIA WG Designation WR (WG in parentheses)	Recommended Operating Range for TE ₁₀ Mode (GHz)	Cutoff Frequency for TE ₁₀ Mode (GHz)	Theoretical CW Power Rating Lowest to Highest Frequency (MW)	Inside Dimensions in Millimeters (Inches in Parentheses)
650 (6)	1.12–1.70	0.908	11.90–17.20	165.100–82.550 (6.500–3.250)
510 (7)	1.45–2.20	1.157	7.50–10.70	129.540–64.770 (5.100–2.550)
430 (8)	1.70–2.60	1.372	5.20–7.50	109.220–54.610 (4.300–2.150)
340 (9A)	2.20–3.30	1.736	3.10–4.50	86.360–43.180 (3.400–1.700)
284 (10)	2.60–3.95	2.078	2.20–3.20	72.140–34.040 (2.840–1.340)
229 (11A)	3.30–4.90	2.570	1.60–2.20	58.170–29.083 (2.290–1.145)
187 (12)	3.95–5.85	3.152	1.40–2.00	47.550–22.149 (1.872–0.872)
159 (13)	4.90–7.05	3.711	0.79–1.00	40.390–20.193 (1.590–0.795)
137 (14)	5.85–8.20	4.301	0.56–0.71	34.850–15.799 (1.372–0.622)
112 (15)	7.05–10.00	5.259	0.35–0.46	28.499–12.624 (1.122–0.497)
90 (16)	8.20–12.40	6.557	0.20–0.29	22.860–10.160 (0.900–0.400)
75 (17)	10.00–15.00	7.868	0.17–0.23	19.050–9.525 (0.750–0.375)
62 (18)	12.40–18.00	9.486	0.12–0.16	15.799–7.899 (0.622–0.311)
51 (19)	15.00–22.00	11.574	0.08–0.107	12.954–6.477 (0.510–0.255)
42 (20)	18.00–26.50	14.047	0.043–0.058	10.666–4.318 (0.420–0.170)
34 (21)	22.00–33.00	17.328	0.034–0.048	8.636–4.318 (0.340–0.170)
28 (22)	26.50–40.00	21.081	0.022–0.031	7.112–3.556 (0.280–0.140)
22 (23)	33.00–50.00	26.342	0.014–0.020	5.690–2.845 (0.224–0.112)
19 (24)	40.00–60.00	31.357	0.011–0.015	4.775–2.388 (0.188–0.094)
15 (25)	50.00–75.00	39.863	0.0063–0.0090	3.759–1.880 (0.148–0.074)
12 (26)	60.00–90.00	48.350	0.0042–0.0060	3.099–1.549 (0.122–0.061)
10 (27)	75.00–110.00	59.010	0.0030–0.0041	2.540–1.270 (0.100–0.050)
8 (28)	90.00–140.00	73.840	0.0018–0.0026	2.032–1.016 (0.080–0.040)
7 (136)	110.00–170.00	90.840	0.0012–0.0017	1.651–0.8255 (0.065–0.0325)
5 (135)	140.00–220.00	115.750	0.00071–0.00107	1.2954–0.6477 (0.051–0.0255)
4 (137)	170.00–260.00	137.520	0.00052–0.00075	1.0922–0.5461 (0.043–0.0215)
3 (139)	220.00–325.00	173.280	0.00035–0.00047	0.8636–0.4318 (0.034–0.0170)

The wave impedance for the TE_{mn} mode is given by

$$Z_{TE} = \frac{E_y}{H_x} = \frac{\omega\mu}{\beta} = \eta_0 \left(\frac{\lambda_g}{\lambda_0} \right)$$

2.2. Ridged Waveguides

Ridged waveguides are commonly used in some communication systems for wideband operation. The cross section of a ridged waveguide is given in Fig. 3. The introduction of a ridge to the waveguide reduces the

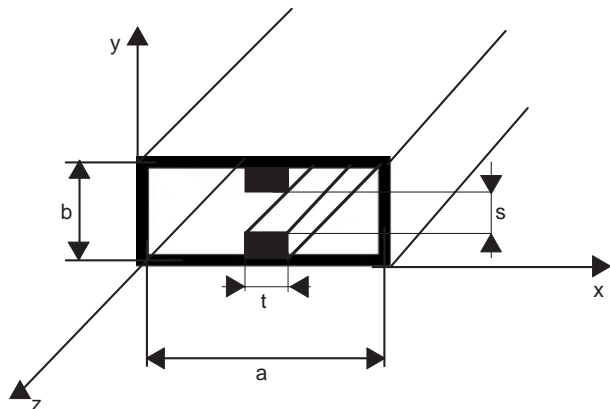


Figure 3. The ridged waveguide structure.

cutoff frequency of the fundamental mode more than the cutoff of the first higher-order mode. Thus, the bandwidth of single-mode operation in such a waveguide can be expanded. By suitable selection of the geometry of the ridge, the bandwidth of the ridged waveguide can be controlled. For more information about these lines the reader is referred to the literature [1,5,6,23,24,56,57,59].

2.3. Circular Waveguides

The cross section of a circular waveguide is given in Fig. 4. Like the rectangular waveguide, the circular waveguide

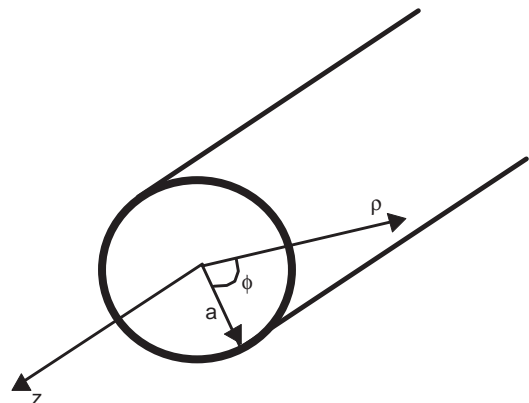


Figure 4. Geometry of a circular waveguide.

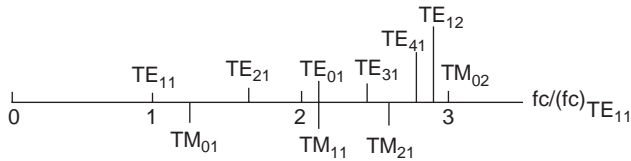


Figure 5. Relative cutoff frequencies of waves in a circular waveguide.

supports TE and TM modes. In the circular waveguide the *dominant* mode is the TE₁₁ since it has the lowest cutoff frequency. The circular waveguide is well suited for application in long-distance communication at frequencies between 40 and 110 GHz because it has, if oversized and excited in the TE₀₁ mode, extremely low attenuation. However, the TE₀₁ is not a dominant mode, thus necessitating the incorporation of mode filters. Figure 5 shows the line diagram that indicates the cutoff frequencies of a few of the lowest-order modes in a circular waveguide. The line diagrams shown in Figs. 2 and 5, respectively, in which the mode numbers refer to a particular field structure, are very important because they provide information about the relative frequency range over which only a single mode will propagate in a particular waveguide. For more details, the reader is referred to references the literature [1–5,56,58].

For the TE₁₁ mode, the electromagnetic field components are given by

$$H_z = \left(\frac{pr}{a}\right)BJ_1(\cos \phi + \sin \phi)e^{j(\omega t - \gamma z)} \quad (24)$$

$$E_r = \frac{jf\eta}{2\pi r f_c^2 \sqrt{\mu\epsilon}} \left(\frac{pr}{a}\right)BJ_1(\sin \phi - \cos \phi)e^{j(\omega t - \gamma z)} \quad (25)$$

$$E_\phi = \frac{jf\eta}{f_c} \left(\frac{pr}{a}\right)BJ'_1(\cos \phi - \sin \phi)e^{j(\omega t - \gamma z)} \quad (26)$$

$$H_\phi = \frac{E_r}{Z} \quad (27)$$

$$H_r = -\frac{E_\phi}{Z} \quad (28)$$

where

$$Z = \frac{\eta}{\sqrt{1 - \left(\frac{f_c}{f}\right)^2}}, \quad \eta = \sqrt{\frac{\mu}{\epsilon}}, \quad f_c = \frac{p}{2\pi a \sqrt{\mu\epsilon}} \quad (29)$$

and p is the first root of $J'_1(x) = 0$.

2.4. Some Special Waveguide Configurations

2.4.1. Rectangular Dielectric-Loaded Waveguides. The rectangular dielectric-loaded waveguide is basically a form of capacitively loaded rectangular waveguide. Figure 6 shows a cross-sectional view of this waveguide used in some communication systems for wideband operation. As with the ridged waveguide, the usable bandwidth of the dielectric-loaded waveguide is greater than that of an ordinary rectangular waveguide. However, this waveguide

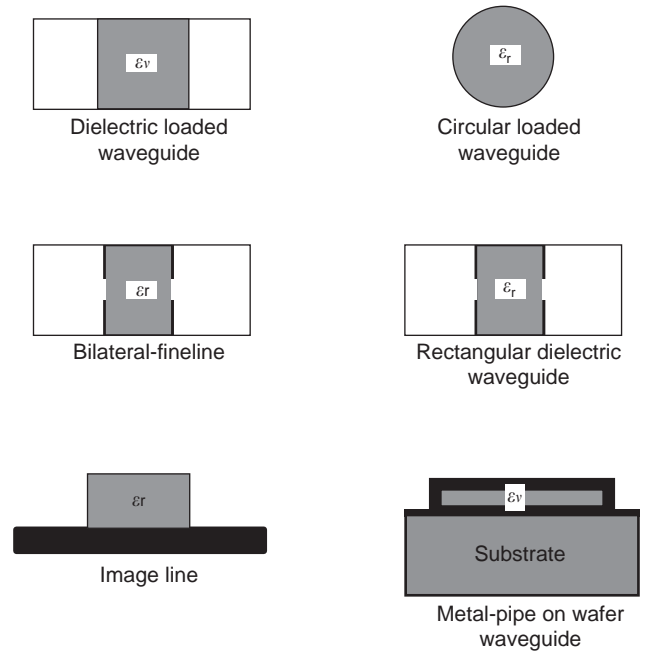


Figure 6. Transmission-line structures for microwave, millimeter, submillimeter, and terahertz frequency applications.

has higher conductor losses and lower power-handling capacity than does an ordinary rectangular waveguide. By suitable selection of geometry of the dielectric slab, the bandwidth of the dielectric-loaded waveguide can be controlled. For more details, the reader is referred to the literature [1,25,26].

2.4.2. E-Plane Circuits (Finlines). A dielectric-loaded waveguide with fins is called a “printed E -plane circuit”. It can also be viewed as a slotline inserted in the E plane of a rectangular waveguide, or as a ridged waveguide, with thin ridges backed by dielectric substrate or all-metal E -plane circuits and finlines (see Fig. 6). The advantages of low insertion loss, simple fabrication, and wide single-mode bandwidth have made this circuit widely utilized in low- and medium-power millimeter-wave applications. The mode of propagation is a hybrid mode consisting of a combination of TE and TM modes. In Ref. 25 the line parameters of these waveguides are determined numerically as well as experimentally for the first time considering the metallization thickness and the influence of the longitudinal slits in the mount groove. A substantial amount of work on these structures has been reported in the literature [26–28].

2.4.3. Dielectric Waveguides. At millimeter-wave frequencies (up to ~ 140 GHz), where precise fabrication of ordinary rectangular waveguides, suspended striplines, and finlines becomes extremely difficult, dielectric waveguide structures offer an alternative approach with the potential for lower losses and relaxed tolerances. There are several different dielectric waveguide structures such as dielectric rod, dielectric slab (image line), trapped image line, insulated image line, or inverted stripline. Cross-sectional views of a dielectric rod waveguide and an image

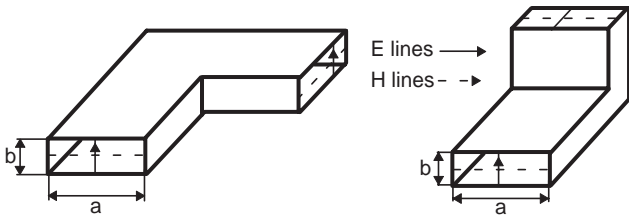


Figure 7. *H*-plane and *E*-plane waveguide bends.

line are shown in Fig. 6. The dielectric rod waveguide consists of a rectangular dielectric rod surrounded by an infinite air medium. The dominant mode of a dielectric rod waveguide has no cutoff frequency, so its operational bandwidth is unlimited in theory. The image line consists of a rectangular dielectric slab placed on a backing sheet of a perfectly conducting ground plane. This structure behaves like a dielectric rod waveguide that supports hybrid modes. The main drawback of these structures is the radiation loss at junctions, discontinuities, and bends. Also the dielectric/metal adhesives are very lossy, and this reduces the practical, loaded *Q* factor. Because of these difficulties, some further low-cost contenders have been considered for operation at frequencies around and exceeding 100 GHz. A detailed discussion about these structures has been reported in the literature [25,26,29,30].

2.4.4. MMIC Waveguides. Monolithic transmission lines for sub-millimeter-wave and terahertz frequency applications may be realized by considering variants of the early dielectric waveguides. Metal pipe on-wafer waveguides are constructed from dielectric materials and structures that are available in monolithic technology, enabling their use in integrated circuits. A cross-sectional view of this transmission line is shown in Fig. 6. These structures may be used not only as transmission lines but also as filter elements. For more information about these lines the reader is referred to Refs. 31–34.

3. MODE TRANSDUCERS

In order to change the mode, direction, or polarization of wave transmission in microwave and millimeter-wave systems, mode transducers should be used. The most popular mode transformers are coaxial-to-rectangular waveguide transitions, rectangular-waveguide-to-rectangular-waveguide transitions, rectangular-waveguide-to-ridged-waveguide transitions, stepped transformers in rectangular waveguides, impedance transformers in a circular waveguide, stepped dielectric slab transformers, waveguide bends, and waveguide circular polarizers. Figure 7 shows

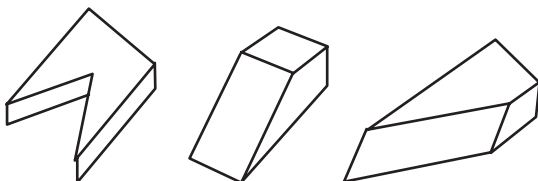


Figure 8. Waveguide terminations with low VSWR.

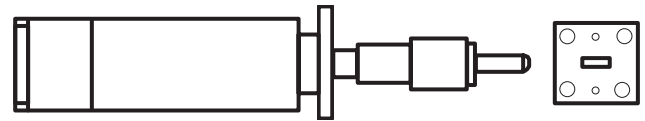


Figure 9. Adjustable waveguide load.

the *H*-plane and *E*-plane waveguide bends. For more details about mode transducers, the reader is referred to the literature [3,37,38,56].

4. TERMINATIONS AND ATTENUATORS

The most commonly used waveguide terminations are the matched loads, the standard mismatches, and the adjustable short circuits. The matched loads are of either the stepped or tapered variety. Some of them are shown in Fig. 8. Figure 9 shows the adjustable waveguide load used to provide a variable reactance in waveguide systems. This section presents a brief description of the terminations and attenuators commonly used in microwave systems.

Some of the methods used to control the amplitude of microwave transmission in waveguides will be illustrated in this subsection. These include the resistive card attenuator, and the be either variable of fixed, the rotary-vane attenuator, and the cutoff waveguide attenuator, which are shown in Figs. 10, 11 and 12, respectively. The latter is particularly useful in signal generators, where large attenuation is required. The cutoff attenuator is based on a section of circular waveguide operating at a frequency below cutoff. The attenuation is frequency-independent at frequencies well below cutoff and is not dissipative (reactive). The lowest mode (TE_{11}) suffers the least attenuation, and operation is usually viewed in terms of this mode. For more information about terminations and attenuators, the reader is referred to Ref. 3.

5. WAVEGUIDE RESONATORS AND FILTERS

Resonant structures are used extensively as filter elements in the realization of various bandpass and band-stop filters. At low frequencies, resonant structures are invariably composed of lumped elements. At higher frequencies, however, lumped elements in general cannot be employed because of low *Q* and difficulties in realizing inductances and capacitances at high frequencies. Distributed

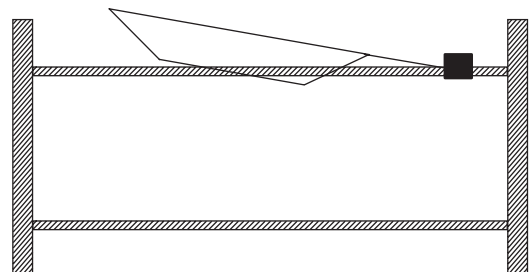


Figure 10. Variable resistive card waveguide attenuator.

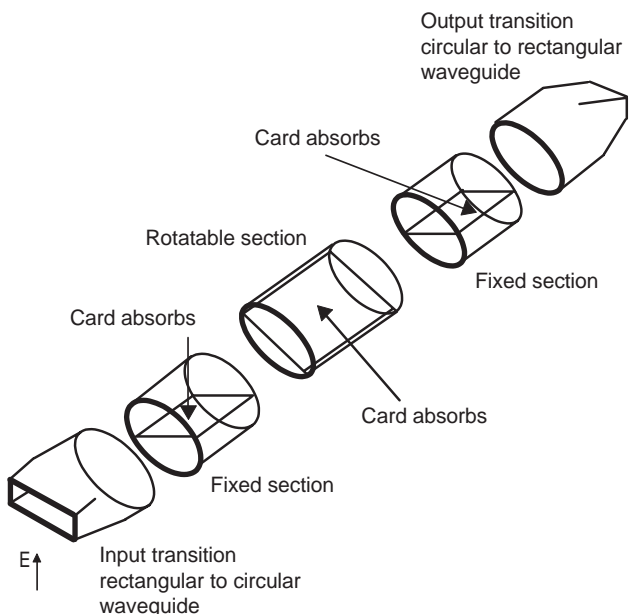


Figure 11. The rotary-vane waveguide attenuator.

elements, that is, transmission-line and waveguide sections, are widely used to overcome these limitations. The resonant structures commonly used in various bandpass and bandstop filters can be realized in several forms, such as lumped-element resonators, cavity resonators, planar resonators, and dielectric resonators. The choice of structure depends on the mechanical size of the resonator at the resonant frequency, the unloaded Q , and the temperature stability and electrical tunability of the frequency. This section presents a brief description of the waveguide filters commonly used in microwave and millimeter-wave systems. Inductive elements such as posts, transverse strips, and transverse diaphragms (irises) are extensively employed in industry to produce waveguide bandpass filters for a wide variety of applications. However, they are difficult to make cheaply and to put into mass production because of their complicated structure. To solve this problem, E -plane metal insert filters have been proposed by Y. Konishi [40]. The normal construction for E -plane bandpass filters is to place inductive obstacles, typically metal septa, in the E plane of a rectangular waveguide, at spacings close to a half-guide wavelength apart (see Fig. 13a). The size and number of the metal septa are the parameters that vary the filter bandwidth,

while the longitudinal spacing determines the center frequency of the E -plane filter.

A common feature of these filters is that the performance is determined essentially by the metallization pattern of the insert. The most important point, however, is that the insert can be fabricated very accurately by spark erosion or photolithographic metal-etching techniques, which allows low-cost mass fabrication. Finally, the insert is clamped between the two halves of a split block housing, which simplifies assembly and reduces machining cost to a minimum. E -plane filters can offer an unloaded Q factor of about 2000–2500 at X band, and can be used at frequencies up to 140 GHz. The CAD of these filters has received considerable attention in the literature [57].

However, the problem with the use of these filters in many applications (e.g., for diplexers and multiplexers) is that the attainable stopband attenuation and edge steepness may be too low. Several different solutions have been proposed to alleviate the latter problem [39]. Although most of these solutions lead to a higher passband insertion loss, this is at the expense of increased manufacturing complexity. Therefore, new E -plane filter structures are proposed, in order to improve performance in the second stopband. The main characteristics of the new filter structures are the use of a conventional rectangular waveguide housing and the use of a metal insert that when mounted introduces ridges in the resonators. The proposed filter structures relate to microwave filters employing sections of ridged waveguide in which all the waveguide sections are resonant at a single fundamental frequency but are not simultaneously resonant at any higher frequency because of different guide wavelengths in the different filter sections (see Fig. 13b). A detailed description of waveguide resonant structures and waveguide filters may be found in the literature [35,36,39–42,55–59].

6. WAVEGUIDE DIPLEXERS AND MULTIPLEXERS

Point-to-point and point-to-multipoint digital communication systems are a rapidly expanding market. Such systems commonly employ filters and diplexers in microwave and millimeter-wave transceivers as channel separators. Hence there is an increasing demand for low-cost, low-dissipation-loss, low-insertion-loss, low-return-loss (see Fig. 14), and compact filters and diplexers. The designed diplexer offers broadband operation and improved selectivity without introducing any further complexity over that involved in the fabrication of standard E -plane

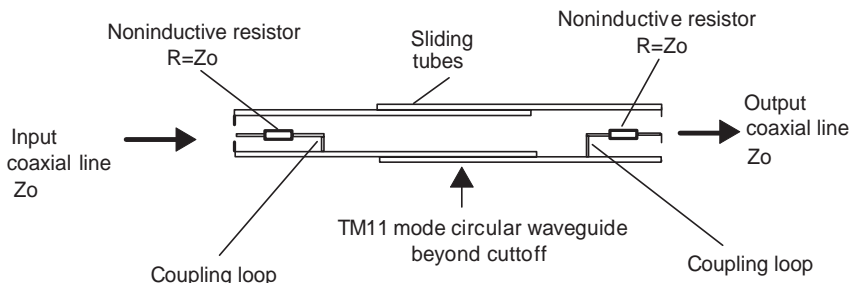


Figure 12. Below-cutoff waveguide attenuator.

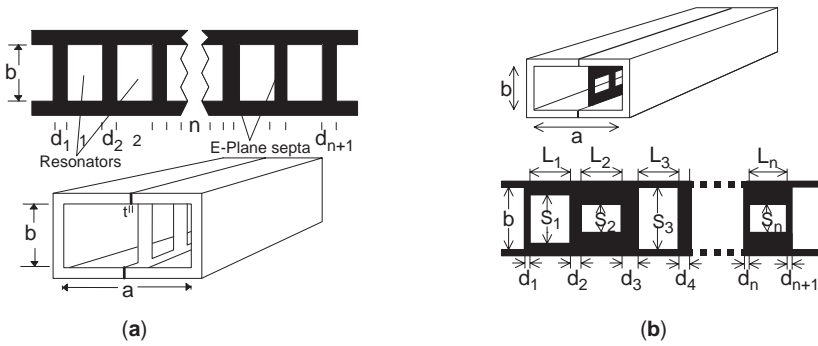


Figure 13. *E*-plane filter structures: (a) standard and (b) ridged waveguide filters.

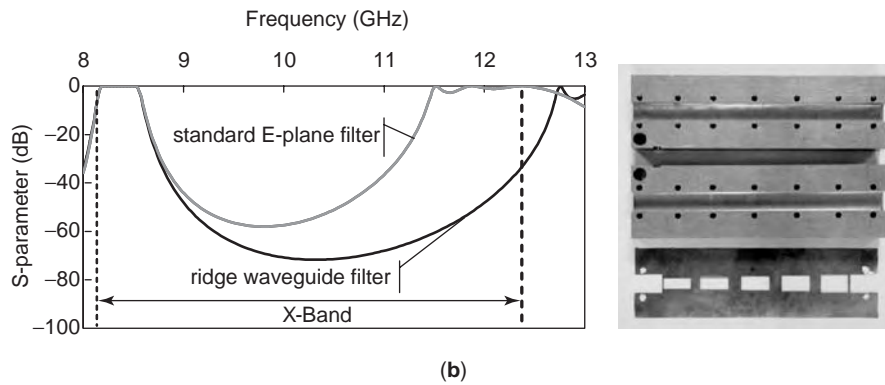
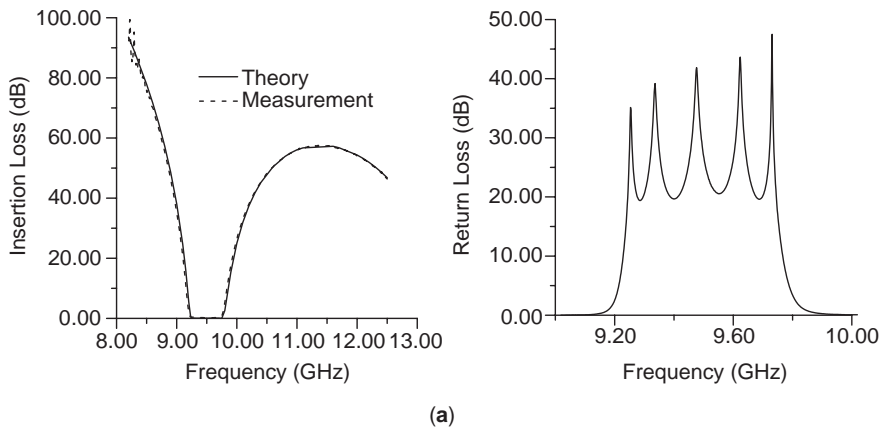


Figure 14. Measured and calculated insertion loss and measured return loss of standard *E*-plane filter Stopband performance of standard and ridged waveguide *E*-plane filters and photograph of fabricated ridged waveguide filter.

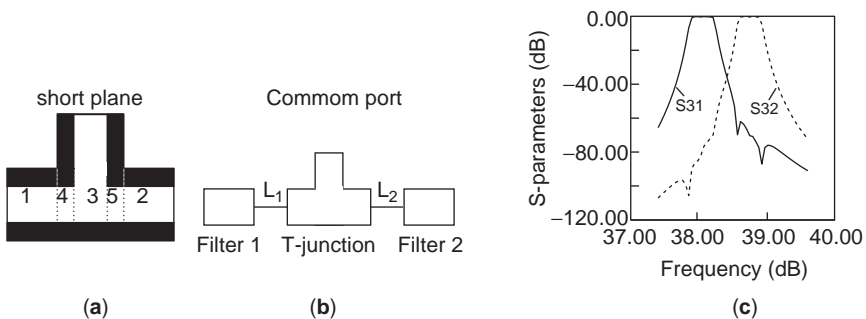


Figure 15. (a) Cross section of a double-ridge waveguide T junction; (b) configuration of the designed diplexer; (c) simulated *S* parameters of a double-ridge waveguide diplexer.

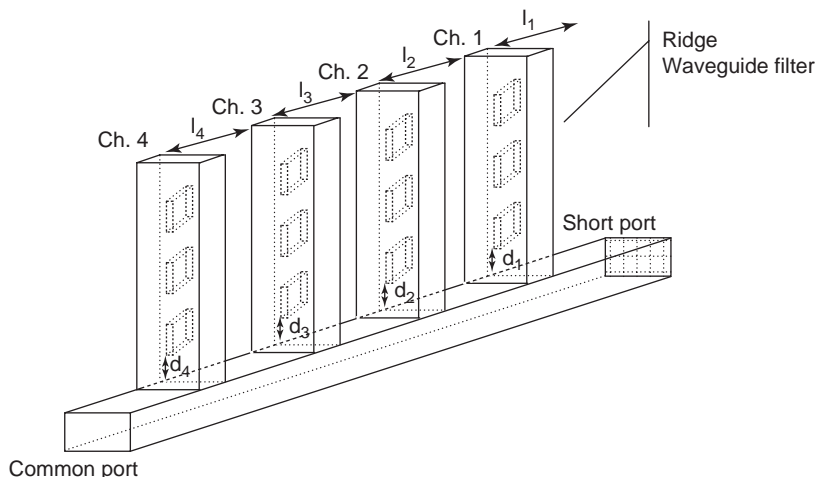
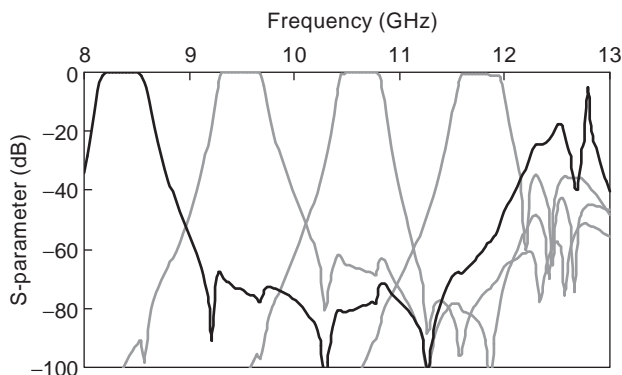


Figure 16. Layout of a Four-channel *E*-plane manifold multiplexer and performance of the Four-channel multiplexer using a ridged waveguide Filter.



diplexers. Figure 15 shows the cross section of a double-ridge waveguide T junction, the configuration of the designed diplexer, and the simulated *S* parameters of a double-ridge waveguide diplexer.

Waveguide manifold multiplexers have been widely used in wireless applications that require high power-handling capability and low insertion loss in the passband of each channel. *E*-plane integrated quasiplanar printed-circuit technology is a well-established technology for realizing microwave and millimeter-wave circuits and offers a convenient low-cost solution for waveguide manifold multiplexers [56]. Since the waveguide housing dimensions have been standardized in bands, the available bandwidth for a particular system is generally determined as the width of the corresponding microwave or millimeter-wave waveguide band. Conventional *E*-plane filters exhibit a spurious harmonic passband at a frequency roughly 1.4 times their center frequency. For such a filter centered at the lower part of a standardized band, the harmonic behavior is exhibited within the upper part of the same band. Hence, in order to avoid significant crosstalk between the channels at the lower and higher frequency ranges of a band, the available bandwidth for the multiplexer is reduced to the stopband of the lowest frequency filter. Improvement in the stopband performance of an *E*-plane filter may be met by introducing ridges in the resonators of a conventional *E*-plane filter. Such a

configuration, without involving any further complexity in the fabrication process, could shift the spurious harmonic passband of the filter farther away from its centre frequency, out of the waveguide band, increasing at the same time the isolation between the channels. Incorporating ridge waveguide filters in *E*-plane manifold multiplexers can thus maximize the available multiplexer bandwidth to that of the waveguide band. This contribution demonstrates the bandwidth limitation imposed by the poor stopband performance of standard *E*-plane filters on the bandwidth of a multiplexer. A four-channel X-band multiplexer is used as an example. It shows how ridged waveguide filters help to overcome this limitation. Figure 16 shows the layout of Four-channel *E*-plane manifold multiplexer and the performance of the Four-channel multiplexer using a ridged waveguide filter. A detailed description of waveguide diplexers and multiplexers may be found in the literature [43–57].

BIBLIOGRAPHY

1. S. Ramo, J. R. Whinnery, and T. Van Duzer, *Fields and Waves in Communication Electronics*, 3rd ed., J Wiley, New York, 1994.
2. R. E. Collin, *Foundations for Microwave Engineering*, 2nd ed., McGraw-Hill, New York, 1992.

3. P. A. Rizzi, *Microwave Engineering Passive Circuits*, Prentice-Hall, Englewood Cliffs, NJ, 1988.
4. D. M. Pozar, *Microwave Engineering*, Addison-Wesley, Reading, MA, 1990.
5. N. Marcuvitz, *Waveguide Handbook*, McGraw-Hill, New York, 1951; also Peter Peregrinus, London, 1985.
6. T. S. Saad, *Microwave Engineers Handbook*, Vol. 1, Artech House, Dedham, MA, 1971.
7. J. C. Slater, *Microwave Transmission*, McGraw-Hill, New York, 1942.
8. C. G. Montgomery, R. H. Dicke, and E. M. Purcell, eds., *Principles of Microwave Circuits*, Radiation Laboratory Series, Vol. 8, McGraw-Hill, New York, 1948.
9. G. L. Ragan, *Microwave Transmission Circuits*, Radiation Laboratory Series, Vol. 9, McGraw-Hill, New York, 1948.
10. L. D. Smullin, and C. G. Montgomery, *Microwave Duplexers*, Radiation Laboratory Series, Vol. 14, McGraw-Hill, New York, 1948.
11. G. C. Southworth, *Principles and Applications of Waveguide Transmission*, Van Nostrand, Princeton, NJ, 1950.
12. L. Lewin, *Advanced Theory of Waveguides*, Iliffe, London, 1951.
13. L. Lewin, *Theory of Waveguides*, Newnes-Butterworth, London, 1975.
14. R. N. Chose, *Microwave Circuit Theory and Analysis*, McGraw-Hill, New York, 1963.
15. G. J. Wheeler, *Introduction to Microwaves*, Prentice-Hall, Englewood Cliffs, NJ, 1963.
16. J. L. Altman, *Microwave Circuits*, Van Nostrand, Princeton, NJ, 1964.
17. R. Levy, Directional couplers, in L. Young, ed., *Advances in Microwaves*, Vol. 1, Academic Press, New York, 1966.
18. I. V. Blake, *Transmission Lines and Waveguides*, Wiley, New York, 1969.
19. F. E. Gardiol, *Introduction to Microwaves*, Artech House, Norwood, MA, 1984.
20. J. Schwinger, and D. Saxon, *Discontinuities in Wave Guide*, Documents on Modern Physics Series, Gordon & Breach, New York, 1968.
21. R. Mittra, and S. W. Lee, *Analytical Techniques in the Theory of Guided Waves*, Macmillan, New York, 1971.
22. R. E. Collin, *Field Theory of Guided Waves*, 2nd ed, IEEE Press; Piscataway, NJ, 1990.
23. S. B. Cohn, Properties of ridge waveguide, *Proc. IRE* **35**: 783–788 (Aug. 1947).
24. S. Hopfer, The design of ridged waveguide, *IRE Trans. Microwave Theory Tech.* **MTT-3**:20–29 (Oct. 1955).
25. A. Beyer, Analysis of the characteristics on an earthed fin line, *IEEE Trans. Microwave Theory Tech.* **MTT-29**: 676–680 (July 1981).
26. P. Bhartia, and I. J. Bahl, *Millimeter Wave Engineering and Applications*, J Wiley, New York, 1984.
27. F. A. Benson, and F. J. Tischer, Some guiding structures for millimetre waves, *IEE Proc.* **131**(7): 429–449 (Sept. 1984).
28. T. Itoh, Overview of quasi-planar transmission lines, *IEEE Trans. Microwave Theory Tech.* **MTT-37**:275–280 (Feb. 1989).
29. R. Knox, Dielectric waveguide microwave integrated circuits—an overview, *IEEE Trans. Microwave Theory Tech.* **MTT-24** (11): 806–814 (Nov. 1976).
30. K. Solbach, The fabrication of dielectric image lines using casting resins and the properties of the lines in the millimeter wave range, *IEEE Trans. Microwave Theory Tech.* **MTT-24**: 879–881 (Nov. 1976).
31. A. G. Engel, and L. P. B. Katehi, Low-loss monolithic transmission lines for submillimeter and terahertz frequency applications, *IEEE Trans. Microwave Theory Tech.* **MTT-39**: 1847–1854 (Nov. 1991).
32. D. A. Brown, A. S. Treen, and N. J. Cronin, Micromachining of terahertz waveguide components with integrated active devices, *Proc. 19th Int. Conf. Infrared and Millimetre-waves*, Sendai, Japan, 1994.
33. A. S. Treen and N. J. Cronin, Terahertz metal-pipe waveguides, *Proc. 18th Int. Conf. on Infrared and Millimetre-waves*, Essex, UK, 1993, pp. 470–471.
34. S. Lucyszyn, D. Budimir, Q. H. Wang, and I. D. Robertson, Design of compact monolithic dielectric filled metal-pipe rectangular waveguide for millimetre-wave applications, *IEE Proc. Microwave Anten. Propag. H* 143(5) (Oct. 1996).
35. D. Deslandes and K. Wu, Integrated microstrip and rectangular waveguide in planar form, *IEEE Microwave Wireless Compon. Lett.* **11**(2) (Feb. 2001).
36. A. Shelkovich and D. Budimir, Novel waveguide E-plane bandpass filters in planar form, *Asia-Pacific Microwave Conference (APMC '03)*, Nov. 2003.
37. H. Patzelt and F. Arndt, Double-plane steps in rectangular waveguide and their application for transformers, irises and filters, *IEEE Trans. Microwave Theory Tech.* **MTT-30**: 771–776 (May 1982).
38. J. Bornemann and F. Arndt, Modal S-matrix design of optimum stepped ridged and finned waveguide transformers, *IEEE Trans. Microwave Theory Tech.* **MTT-35**:561–567 (June 1987).
39. F. Arndt, The status of rigorous design of millimeter wave low insertion loss fin-line and metallic E-plane filters, *J. Inst. Electron. Telecommun. Eng.* **34**(2): 107–119 (1988).
40. Y. Konishi and K. Uenakada, The design of a band-pass filter with inductive strip-planar circuit mounted in waveguide, *IEEE Trans. Microwave Theory Tech.* **MTT-22**:869–873 (Oct. 1974).
41. D. Budimir, Optimized E-plane bandpass filters with improved stopband performance, *IEEE MTT Trans. Microwave Theory Tech.* (Feb. 1997).
42. D. Budimir and G. Goussetis, Design of asymmetrical RF and microwave bandpass filters by computer optimization, *IEEE MTT Trans. Microwave Theory Tech.* **51**(4):1174–1178 (April 2003).
43. F. Arndt, J. Bornemann, D. Grauerholtz, D. Fasold, and N. Schroeder, Waveguide E-plane integrated-circuit diplexer, *Electron. Lett.* **21**:615–617 (July 4, 1985).
44. A. Kirilenko, S. Senkevich, V. Tkachenko, and B. Tysik, Waveguide diplexer and multiplexer design, *IEEE Trans. Microwave Theory Tech.* **MTT-42**(7): 1393–1396 (July 1994).
45. C. Wang and K. Zaki, Full-wave modelling of generalised double ridge waveguide T-junctions, *IEEE Trans. Microwave Theory Tech.* **MTT-44**(12):2536–2542 (Dec. 1996).
46. Y. Rong, H. Yao, K. Zaki, and T. Dolan, Millimeter wave H-plane diplexers, *Proc. IEEE MTT-S Int. Microwave Symp.*, 1999, pp. 1347–1350.
47. G. Goussetis and D. Budimir, E-plane double ridge waveguide filters and diplexers for communication systems, *Proc. 31th European Microwave Conf.* London, UK, Sept. 24–29, 2001.
48. A. Shelkovich and D. Budimir, Novel E-plane filters and diplexers using rectangular waveguide in planar form, *Proc. Asia-Pacific Microwave Conf. (APMC '03)*, Nov. 2003.

49. A. Gebauer and F. Hernandez-Gil, Analysis and design of waveguide multiplexers using the finite element method, *Proc. 18th European Microwave Conf.*, 1988, pp. 521–524.
50. X.-P. Linag, K. A. Zaki, and A. E. Atia, A rigorous three plane mode-matching technique for characterizing waveguide T-junctions, and its application in multiplexer design, *IEEE Trans. Microwave Theory Tech.* **MTT-39**(12):2138–2147 (Dec. 1991).
51. C. Kudsia, R. Cameron, and W. C. Tang, Innovations in microwave filters and multiplexing networks for communications satellite systems, *IEEE Trans. Microwave Theory Tech.* **MTT-40**(6):1133–1149 (June 1992).
52. A. Morini, T. Rozzi, and M. Morelli, New formulae for the initial design in the optimization of T-junction manifold multiplexers, *Proc. IEEE MTT-S Int. Microwave Symp.*, 1997, pp. 1025–1028.
53. M. Guglielmi, Simple CAD procedure for microwave filters and multiplexers, *IEEE Trans. Microwave Theory Tech.* **MTT-42**(7):1347–1352 (July 1994).
54. G. Goussetis and D. Budimir, E-plane manifold multiplexers with improved bandwidth, *Proc. 31th European Microwave Conf.*, London, Sept. 24–28, 2001.
55. G. Matthaei, L. Young, and E. M. T. Yones, *Microwave Filters, Impedance Matching Networks, and Coupling Structures*, 2nd ed., Artech House, Norwood, MA, 1980.
56. J. Uher, J. Bornemann, and U. Rosenberg, *Waveguide Components for Antenna Feed Systems: Theory and CAD*, Artech House, Norwood, MA, 1993.
57. D. Budimir, *Generalized Filter Design by Computer Optimization*, Artech House, Norwood, MA, 1998.
58. I. Hunter, *Theory and Design of Microwave Filters*, The IEE, London, 2001.
59. J. Helszajn, *Ridge Waveguides and Passive Microwave Components*, The IEE, London, 2001.

WAVEGUIDE DIRECTIONAL COUPLERS

RALPH LEVY
R. Levy Associates
La Jolla, California

1. INTRODUCTION

A directional coupler is a four-port circuit having the schematic shown in Fig. 1, where transmission lines 1–4 and 2–3 are mutually coupled by means of some type of cou-

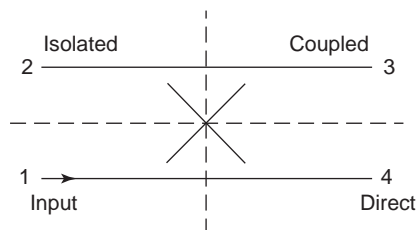


Figure 1. Directional coupler showing port nomenclature and symmetry planes.

pling mechanism or mechanisms indicated by the central cross. An electromagnetic wave incident at port 1 is partly coupled to port 3, and the remaining power is transmitted to port 4. In an ideal directional coupler no energy is coupled to port 2, which is termed the *isolated port*. In this article the transmission lines to be considered are waveguides, but similar theory and design principles may apply to other types of transmission lines, such as coaxial, strip-line, or microstrip lines.

Directional couplers have several applications, such as a device for monitoring the power along the mainline (1–4 in Fig. 1). Since the device is directional, the power at the coupled port 3 will be proportional to the power propagating in the 1–4 direction. Power propagating in the 4–1 direction will be coupled to port 2 and will not be detected by a detector mounted on port 3. This forms the basis of another application, known as a *reflectometer*, where detectors at ports 3 and 2 may be used to measure both the incident and reflected waves on the main 1–4 transmission line. In practice it is simpler to use two directional couplers connected in tandem, one for the incident and one for the reflected wave, since this device, known as a *dual-directional coupler*, is simpler to “match” over a broad frequency bandwidth, avoiding having very well-matched detectors.

A very common type of directional coupler is designed to couple half of the power to port 3 with the remaining half directed to port 4. Here the coupling is 3.01 dB (or 3 dB for conciseness), and such a coupler is also known as a “hybrid coupler” or simply as a “hybrid”. It has many applications in microwave technology, including use as a component of a balanced mixer with detectors mounted on ports 3 and 4. The main signal is applied to port 1 and a local oscillator signal to port 2. Hybrids are used in the design of duplexers or diplexers, and their advantageous phase properties make them ideal as power dividers for balanced amplifiers or as components in feed networks for antenna arrays. The phase property alluded to here refers to the fact that in a well-matched hybrid the phase difference between the main (or through) line and coupled port signals is either 0°, 90°, or 180°, depending on the type of coupler. The proofs of these phase properties are given by fundamental theory from geometric considerations (i.e., the type of network symmetry) and will be discussed further in Section 2.

2. BASIC PROPERTIES OF DIRECTIONAL COUPLERS

Early work in the field of directional couplers with the basic theory together with numerous references is discussed in Refs. 1 and 2. The most fundamental theory states that all reciprocal four-port junctions having a perfect match at all four ports are directional couplers. This simplifies the conceptual design of directional couplers since one need obtain only a matched condition, knowing that there will always be an isolated port. The theorem may be proved by application of the unitary condition to the scattering matrix of the matched four-port [3]

$$SS^* = I \quad (1)$$

where S^* is the complex conjugate transposed matrix and I is the unit matrix. (Since the network is reciprocal, the transposed matrix is identical to the original matrix.)

In all types of couplers considered here there is symmetry about the plane indicated by the horizontal dotted line shown in Fig. 1; thus the coupled waveguides are identical. This condition is by far the most common case, but couplers between nonidentical waveguides have been described in the literature for special rare applications. The symmetric case simplifies the analysis and synthesis (i.e., the design) of directional couplers since the four-port may be split into odd and even mode two-port circuits [1, p. 125]. In the even mode the symmetry plane becomes a magnetic wall or open circuit, and in the odd mode it becomes an electric wall or short circuit.

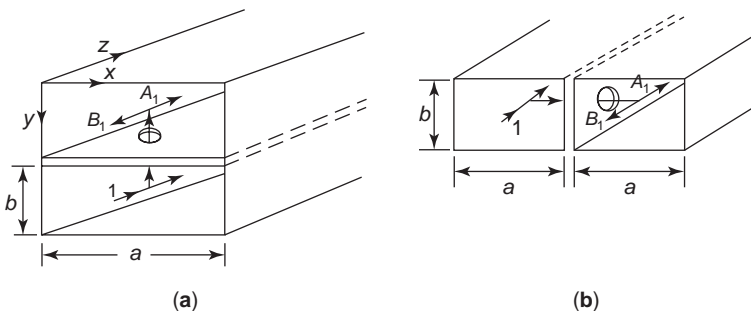
In the case where there are symmetry planes at both the horizontal and vertical planes indicated by the dotted lines in Fig. 1, then the coupler has complete symmetry and the four ports are indistinguishable. This will be the case for all the couplers to be described here, and almost all waveguide couplers fall into this category. An important property of all such couplers is that the phase difference between the two signals at the direct and coupled ports is always 90° . The proof involves writing down the unitary condition (1) on the scattering matrix—see details presented in [Ref. 1 (pp. 121–122)]. The phase difference is exactly 90° only if the coupler has perfect match and isolation. The deviation from 90° may be estimated using the same scattering matrix theory for a slightly imperfect coupler, and is surprisingly small. In the case of a nominal 3-dB coupler or hybrid, the phase difference between the waves coupled to ports 3 and 4 is given by [1, pp. 122–125]

$$\cos(\theta_3 - \theta_4) = 2 \times 10^{-I/10} \quad (2)$$

where I represents the isolation in decibels. Thus for 30 dB isolation we obtain a phase difference of 89.885° and for 20 dB isolation this becomes 88.854° . We may conclude that there is no need to worry about the phase performance of any symmetric coupler that is well matched and isolated.

3. TYPES OF WAVEGUIDE DIRECTIONAL COUPLERS

The most widely used types of waveguide directional couplers are multiaperture couplers, cross-guide couplers, sidewall and topwall hybrids, and branch-guide couplers.



Some of the very early couplers designed during the 1930s and 1940s are no longer or rarely used; examples are the Bethe hole and Schwinger couplers, and are omitted here. The theory for many couplers as presented in Ref. 1 have been superseded by more accurate theories, including those by the present author who realized that there were deficiencies in the previous theories while preparing the 1966 survey [1].

3.1. Waveguide Multiaperture Couplers

The design initially evolves from Bethe's small-aperture coupling theory [4], whose main result may be applied to the case of a pair of waveguides propagating in the dominant TE_{10} mode with a single aperture, as shown in Fig. 2. The amplitudes of the forward coupled wave A_1 and the backward wave B_1 are given by

$$A_1 = j \frac{2\pi}{ab\lambda_g} [M_x H_x^2 + M_z H_z^2 - P E_y^2] \quad (3)$$

$$B_1 = j \frac{2\pi}{ab\lambda_g} [-M_x H_x^2 + M_z H_z^2 - P E_y^2] \quad (4)$$

where the two identical waveguides have broad and narrow dimensions a and b , respectively; M_x and M_y are the components of the magnetic polarizability of the aperture in the x and y directions; and P is the electric polarizability. The polarizabilities are functions of the aperture shape and size having the dimensions of volume, and expressions for these will be presented. H_x , H_z , and E_y are amplitudes of the magnetic and electric fields evaluated at the center of the aperture, and are given by

$$\begin{aligned} H_x &= -\sin \frac{\pi x}{a} e^{-jy z}; \\ H_z &= j \frac{\lambda_g}{2a} \cos \frac{\pi x}{a} e^{-jy z}; \\ E_y &= \frac{\lambda_g}{\lambda} \sin \frac{\pi x}{a} e^{-jy z} \end{aligned} \quad (5)$$

In the case of narrow-wall coupling as shown in Fig. 2b, at the hole location we have $x = 0$ so that the only field component is H_z . The coupled waves as given by Eqs. (3) and (4) become

$$A_1 = B_1 = \frac{-j\lambda_g M_z}{2a^3 b} \quad (6)$$

Figure 2. (a) Broad-wall coupling aperture; (b) narrow-wall coupling aperture.

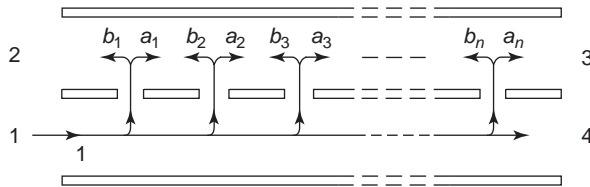


Figure 3. Loose coupling theory for a multiaperture coupler.

Now the polarizability M_z possesses only a slow variation with frequency (this will be shown later), and hence the coupling is closely proportional to the guide wavelength λ_g . This implies that the coupling of a narrow-wall coupler, consisting of several apertures spaced at $\lambda_g/4$ intervals to give some directivity, will vary considerably over a moderate to broad bandwidth. The broadwall coupler case is far different since all three components of the field with their varying frequency dependence are present, and by judicious choice of x , the distance from the sidewall, couplers may be designed with flat coupling over very broad bandwidths [1, pp. 136–138]. However, narrow-wall couplers find application when the power is very high since there is no component of the electric field, which is mainly responsible for power breakdown in broad-wall couplers, at the apertures located on the sidewalls.

In order to obtain high directivity in directional couplers consisting of parallel waveguides and also reasonably tight coupling values, several apertures must be used to cancel out the backward waves, specifically, the B_1 terms of Eq. (3). The standard theory given in all textbooks to date [e.g., 1, pp. 140–144] is based on an approximate coupling theory as indicated in Fig. 3. In the forward direction the coupled waves add in phase, and the total coupled wave is given by

$$A = e^{-j(n-1)\phi} \sum a_r \tag{7}$$

where the summation is taken from $r = 1$ to n . Note that errors in sign in Ref. 1 have been corrected, and also here we consider the more general case with the forward and backward coupled waves of each aperture being unequal, but the final results are affected only marginally.

In the case of the backward wave the opposite situation occurs; specifically, the individual waves tend to cancel since they are out of phase by multiples of 180° , at least at midband. The total wave coupled in the backward direction is

$$B = b_1 + b_2 e^{-2j\phi} + b_3 e^{-4j\phi} + \dots + b_n e^{-2(n-1)j\phi} \tag{8}$$

When the array is symmetric, we have $b_1 = b_n$, $b_2 = b_{n-1}$, and so on, and (8) simplifies to give

$$B = [2b_1 \cos(n-1)\phi + 2b_2 \cos(n-2)\phi + \dots + 2b_{n/2} \cos \phi] e^{-(n-1)j\phi} \quad (\text{n even}) \tag{9}$$

$$B = [2b_1 \cos(n-1)\phi + 2b_2 \cos(n-2)\phi + \dots + b_{(n+1)/2}] e^{-(n-1)j\phi} \quad (\text{n odd}) \tag{10}$$

If the apertures are of equal size, $b_i = b_1$, then B in (8) becomes a geometric progression with n terms and a multiplication factor of $e^{-2j\phi}$, which may be summed to give

$$B = \frac{b_1 \sin(n\phi)}{\sin \phi} e^{-(n-1)j\phi} \tag{11}$$

The directivity D is defined as the ratio of this backward wave to the forward wave given by (7). In the case of equal coupling apertures, $a_i = a_1$, and the ratio of (11) to (7) becomes

$$D = \frac{b_1 \sin(n\phi)}{a_1 n \sin \phi} \tag{12}$$

The angle ϕ deviates from 90° by perhaps $\pm 20^\circ$ over a fairly wide bandwidth of about 30% and Eq. (12) varies considerably over this band, having maximums equal to $b_1/(na_1)$ which is of the order $1/n$. Thus, for a 10-aperture coupler, the directivity would be expected to oscillate between infinity and approximately 20 dB, and this is considered to represent a rather poor performance. In practice a tapered distribution of the coupling apertures is used to obtain much better directivity. Similar techniques are employed in the design of multielement antenna arrays to give low sidelobe levels, such as in the well-known Dolph–Chebyshev array. The simplest tapered distribution is the binomial one, where for three apertures the relative amplitudes of the b_i in (9) or (10) are given by the series 1,2,1; for four apertures, 1,3,3,1; for five apertures, 1,4,6,4,1, and so on. However, a much better result is obtained using a Chebyshev amplitude taper, where the amplitude distribution for three apertures is

$$1, 2(1 - c^2), 1 \tag{13}$$

For four apertures, the distribution is

$$1, 3(1 - c^2), 3(1 - c^2), 1 \tag{14}$$

and for five apertures

$$1, 4(1 - c^2), 6(1 - c^2)(1 - c^2/3), 4(1 - c^2), 1 \tag{15}$$

Here $c = \cos \phi_0$, where the design band extends from ϕ_0 to $(\pi - \phi_0)$. Hence the Chebyshev taper is less steep than the corresponding binomial taper and also has much better directivity [1, p. 141–143]. The latter reference also gives a simple formula to calculate the relative couplings of the various apertures in the array [1, Eq. (88), etc.].

When the number of apertures becomes large, it is more convenient to use the concept of superimposed arrays. Here two or more smaller Chebyshev arrays are staggered along the length of the coupler, and are actually superimposed. An example is given in Ref. 1 (p. 144) but is not convenient since the central apertures are unequal and the array distribution is nonmonotonic. A possibly better and certainly well tested set of superimposed arrays is to combine $n = 5$ arrays as follows. We take a Chebyshev array with $\phi_0 = 72^\circ$ and $c_0 = \cos(72^\circ) = 0.309$, and

substituting in the general formula [15] above, the series is 1, 3.618, 5.254, 3.618, 1. Superimposing two such arrays gives

$$\text{Total : } \frac{1 \quad 3.618 \quad 5.254 \quad 3.618 \quad 1}{1 \quad 3.618 \quad 6.254 \quad 7.236 \quad 6.254 \quad 3.618 \quad 1}$$

Rather than continuing this process by adding extra arrays, which causes oscillatory behavior of the central values, it is simpler merely to repeat the central value of 7.236 as many times as required. This is convenient and practical since all apertures have the same size except for three at each end, and such arrays have been found to give excellent performance when applied to the design of multiaperture couplers for operation over complete recommended waveguide operating bandwidths.

The simple theory outlined above is applicable only to the design of couplers having loose coupling values, since the series representation of the coupled waves given by Eqs. (7)–(10) assume very small couplings, and the uncoupled wave is assumed to be unattenuated. In particular, it has been found that the directivity is not well predicted if this technique is used, and the prediction of coupling is often quite poor. A considerably improved method is to form the equivalent circuit of the aperture and then to analyze the coupler using circuit theory, for instance, by multiplication of transfer matrices for the even- and odd-mode subnetworks as described in Ref. 5, with extensions and improvements given in Ref. 6. The concept of the equivalent circuit of a coupling aperture was described much earlier by Oliner [7], but without much in the way of detail for the design of waveguide directional couplers. However, this contribution was key in formulation of the later developments [5,6]. One form of the equivalent circuit of an aperture having all three field components as designated in Eqs. (3) and (4) is given in Ref. 1 (Fig. 4 there) and is derived by substituting the field expressions given in Eq. (5) into Eqs. (3) and (4), leading to the equivalent circuit shown in Fig. 4 (here). The proof is somewhat lengthy, and interested readers will find this detailed in Ref. 5. Another lengthy argument is given there to derive equations for the coupling. These are based on the multi-section quarter-wave transformer circuit [8] or alternatively the equivalent lowpass prototype circuit [9]. An

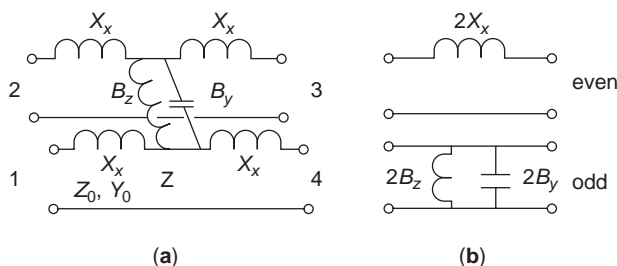


Figure 4. (a) Equivalent circuit for an aperture; (b) even and odd mode equivalent circuits; $X_x/Z_0 = 4\pi M_x \sin^2(\pi x/a)/(ab\lambda_g)$, $B_z/Y_0 = -\pi\lambda_g M_z \cos^2(\pi x/a)/(a^3b)$, $B_y/Z_0 = 4\pi\lambda_g P_y \sin^2(\pi x/a)/(ab\lambda^2)$.

appropriate prototype is chosen to give a value for the quantity R , which is the product of all the junction VSWRs (i.e., the ratios of the impedances > 1 at each junction) of the prototype. R is also equal to the impedance ratio of the quarter-wave transformer prototype. Defining an angle

$$\psi = \frac{2}{n} \sin^{-1} k \tag{16}$$

where k is the coupling coefficient, then the value of R is

$$R = \left(\frac{1 + \sin \psi}{1 - \sin \psi} \right)^n \tag{17}$$

In these equations n is the number of coupling apertures, equal to the number of step junctions of the prototype, which therefore has $n - 1$ steps.

Rather than using a complete distributed prototype, which, although giving the ultimate in directivity performance, means that all the apertures up to the centerline are different, the superimposed array method may be used, in almost all cases giving an insignificant degradation in directivity. The junction VSWRs V_i are calculated using the method outlined in Ref. 10 (pp. 284–290)

$$\log(V_i) = \frac{Z_i \log(R)}{\Sigma(Z_i)} \tag{18}$$

where Z_i is the i th step impedance of the distributed prototype and the summation is from $i = 1$ to n .

The final step in the theory is to relate the aperture polarizabilities to dimensions, with the correct frequency dependencies. The most commonly used apertures are circular holes, usually with two holes transversely arranged on the broad wall as indicated in Fig. 5, or longitudinal and transverse slots as shown in Fig. 6. Bethe's theory [4] assumes that the apertures are small, and direct application of simple formulas for the electric and magnetic polarizabilities leads to considerable deviations from measured results. The most complete account of the correction factors for large apertures is given in Ref. 6. In addition to the aperture resonance effect and wave attenuation due to finite wall thickness, the fields are averaged over the areas of the apertures. The resulting theory has given agreement of coupling with measurements of the order of 0.2 dB over complete waveguide operating

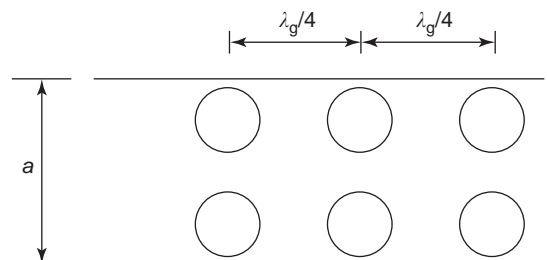


Figure 5. Common wall of broad-wall coupler using circular apertures.

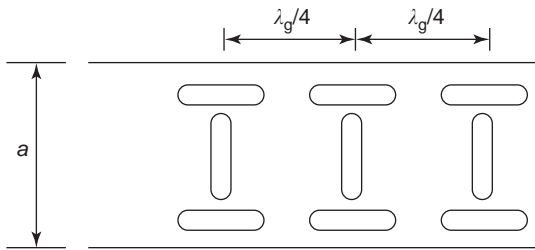


Figure 6. Common wall of broad-wall coupler using slot apertures.

bandwidths, and such a figure is within errors caused by tolerances.

3.2. Cross-Guide Directional Couplers

These are closely related to multiaperture couplers; the difference is that since the waveguides are crossed as shown in Fig. 7, only one or two sets of coupling apertures are feasible. Hence the coupling is limited to rather loose values, although tight values of the order of 5 dB may be obtained using reduced-height crossed waveguides [11]. Since the narrow coupling slots have negligible electric polarizabilities, using the generalized form of Bethe's coupling equations [Eqs. (3) and (4)], where H_x^2 and H_y^2 are replaced by products of the fields in the two waveguides, the equations for the coupled waves become

$$A_1 = j \frac{2\pi}{ab\lambda_g} [M_1 H_x H_z + M_2 H_z H_x] \tag{19}$$

$$B_1 = j \frac{2\pi}{ab\lambda_g} [-M_1 H_x H_z + M_2 H_z H_x] \tag{20}$$

where M_1 and M_2 are the polarizabilities of the individual slots in the cross or crosses. When these coupling slots have equal dimensions, then $M_1 = M_2$ and (23) gives $B_1 = 0$; thus we obtain perfect directivity. In the case of a

single-cross aperture, the coupling becomes

$$A_1 = j \frac{\pi}{a^2 b} M_1 \sin \frac{2\pi x_0}{a} \tag{21}$$

where the only frequency sensitive term is M_1 . Hence cross-guide couplers have very good coupling flatness over entire waveguide recommended operating bandwidths. The directivity in practice is not as good as implied above (i.e., $B_1 = 0$), since it relies on perfect cancellation of only two coupled waves, one from each slot in the cross. However, the theory has ignored the finite width of the slots that introduces small terms in the coupled waves due to the electric polarizability, as indicated in Eqs. (3) and (4). Much better directivity is obtained with multiaperture couplers where there are many such backward waves.

In the case of two cross slot apertures the theory for loosely coupled waves may be applied, taking the phase difference of the line lengths $2d$ between the two coupled waves into account. This gives a total coupled wave

$$A_1 = j \frac{\pi}{a^2 b} M_1 \sin \frac{2\pi x_0}{a} (1 + e^{-2j\phi}) \tag{22}$$

which has an amplitude of

$$A_1 = \frac{2\pi}{a^2 b} M_1 \sin \frac{2\pi x_0}{a} \sin(\phi); \quad \phi = \frac{2\pi d}{\lambda_g} \tag{23}$$

3.3. Sidewall and Topwall Directional Couplers and Hybrids

The sidewall or short-slot coupler was initially described by Riblet [12], and became the most commonly employed 90° hybrid junction used in the microwave industry. The representation of Fig. 8 shows a view looking down on the broad walls of the waveguides. The coupling slot is the full height of the narrow dimension. An analysis of the coupler uses the even/odd-mode concept, where the reflected and transmitted wave amplitudes for the even mode are Γ_e

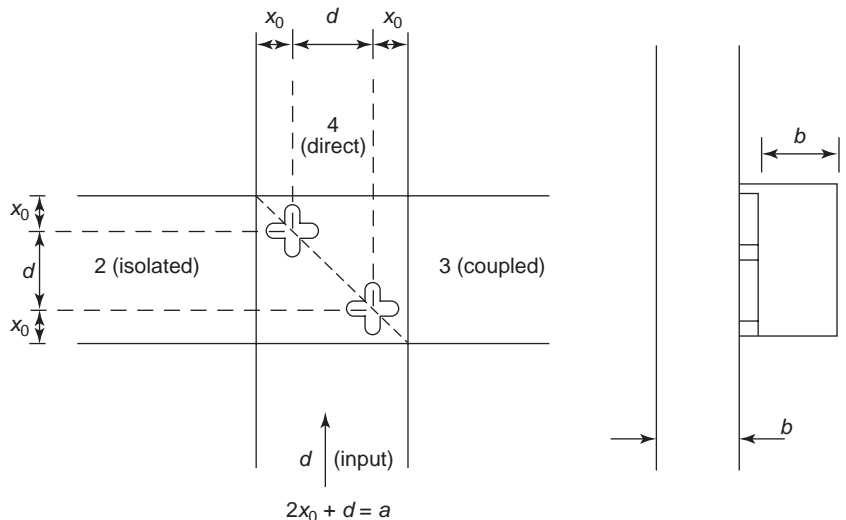


Figure 7. Cross-guide directional coupler.

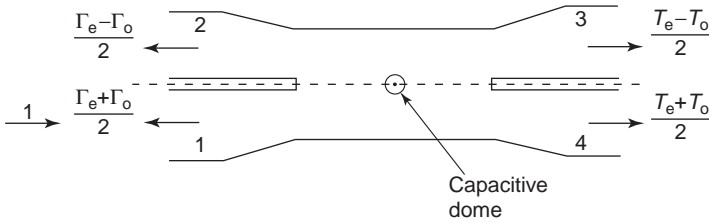


Figure 8. Short-slot or narrow-wall directional coupler.

and T_e and for the odd mode Γ_o and T_o , respectively [1, pp. 125–126]. In the odd-mode case we can see that the match may be very good for an infinitesimally thin common wall thickness since then we have straight waveguides with only minor discontinuities due to a pair of small steps and the end tapers. The design of the coupler then hinges on the analysis of the even-mode circuit, and then forcing the condition for good match and directivity, specifically, that $\Gamma_e = 0$.

This was a rather empirical procedure for many years until the advent of 3D field analysis programs made possible a better understanding of the role of the higher-order modes in the coupling region. It was always somewhat of a mystery why the coupling of the short-slot hybrid could be so flat over relatively broad bandwidths. The author [13,14] has shown that this is due solely to the presence of the evanescent TE_{30} mode, which is cutoff only slightly above the operating band of the coupler. An equivalent circuit of the even-mode two-port is given in Fig. 5 of Ref. 13, which leads to good physical understanding of the operation of this mode. Ref. 14 describes how a central capacitive matching probe is necessary to give good performance in 3-dB hybrids, but for looser coupling values this is not required because of the stronger effect of the TE_{30} mode for shorter slot lengths.

The topwall coupler [15] shown in Fig. 9 has a pair of short slots in the common broad wall, and the E -field patterns of the even and odd modes are given in Fig. 10. Here it is seen that the even mode is fairly trivial, being simply a TE_{10} mode with a central floating strip. The odd-mode circuit is also amenable to straightforward analysis since

it is a commonly used thick stripline TEM line with side-walls.

3.4. Branch-Guide Couplers

A schematic representation is shown in Fig. 11, where the view is of the side walls of the waveguide, and the broad dimensions of the main and coupling branches are all equal. Such couplers are very useful for coupling values in the range 0 dB to about 15 dB, since for looser couplings the branches become too thin (i.e., small b dimensions.) The bandwidths are not as broad as those of multiaperture couplers, but for bandwidths typically half of the recommended waveguide operating ranges they are very useful because in general they are both shorter in length and less expensive to manufacture than multiaperture couplers.

The couplers may be manufactured in two halves split down the centerline of the broad walls. In addition, the spacing between the input and coupled waveguides means that access to the ports may not require special bends, and the flange hole patterns may be machined directly into the blocks constituting the two halves, avoiding the expense of separate brazed flanges.

A number of original approximate theories were used to design branch-guide couplers, but they have been superseded by exact synthesis techniques [16,17]. The even- and odd-mode circuits are shown in Fig. 12 for an ideal branch-guide coupler; thus junction discontinuities are disregarded initially. In both circuits the stubs are half the length of the connecting mainlines. The transfer matrices of the a series stub of characteristic admittance a_i is given by

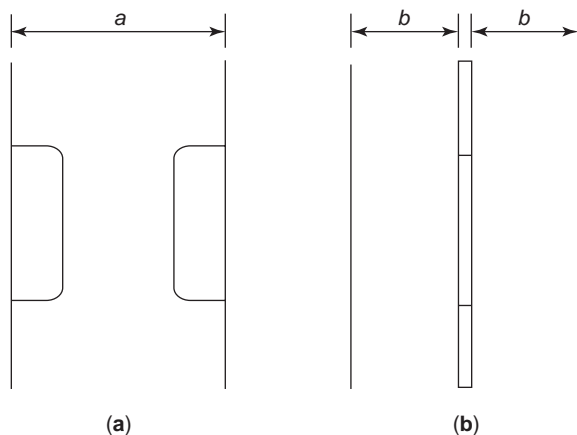


Figure 9. Topwall directional coupler or hybrid: (a) top view; (b) side view.

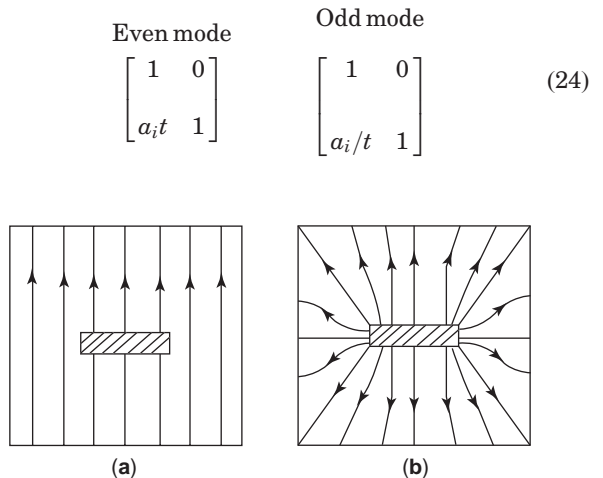


Figure 10. Electric field patterns of the topwall coupler: (a) even mode; (b) odd mode.

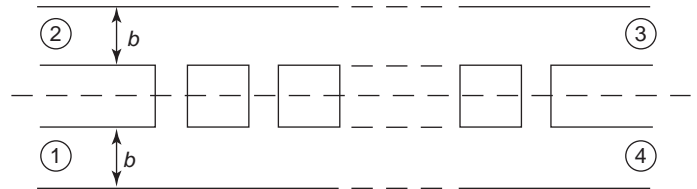


Figure 11. Cross section of a branch-guide directional coupler (uniform in the broad dimension).

where t is the Richards variable:

$$t = j \tan \theta \tag{25}$$

The transfer matrix of a connecting line of admittance b_i is

$$\begin{bmatrix} \cos 2\theta & \sin 2\theta/b_i \\ b_i \sin 2\theta & \cos 2\theta \end{bmatrix} = \frac{1}{1-t^2} \begin{bmatrix} 1+t^2 & 2t/b_i \\ 2tb_i & 1+t^2 \end{bmatrix} \tag{26}$$

Note that apart from an unimportant change of sign, Eq. (26) is invariant to the transformation

$$t \rightarrow \frac{1}{t} \tag{27}$$

Since the transfer matrices of the series stub networks of the even- and odd-mode series stubs of (24) are related by this same transformation (27), the overall transfer matrices of the even- and odd-mode networks are similarly related. Hence, if either network is synthesized to give a match between band edges where the electrical lengths of the commensurate stubs are θ_c and $\pi - \theta_c$, then the other network will also be matched over the same passband. This reduces the synthesis problem from that of a four-port to that of a two-port, but the question then arises, as to how the unit elements of the mainlines can be extracted from a transfer function to have twice the length of the series stubs. The answer is related to the fact that both the even- and odd-mode circuits have redundant series stubs; specifically, the nonredundant transfer function is that of

one series stub and $2(n - 1)$ unit elements, which are transmission lines of electrical length θ . It is possible therefore to extract the first series stub such that two unit elements may then be extracted in cascade having equal admittances. Starting from a transfer matrix $[A,B,C,D]$ where the matrix elements are polynomials in t , it can be shown that the admittance of the extracted series stub is

$$a = \frac{A(1)}{C(1)} = \frac{B(1)}{D(1)} \tag{28}$$

This relationship holds for the extraction of the first $n - 1$ series stubs with the associated double-length unit elements, with the final stub given by the remainder matrix.

The final steps in the design process are concerned with the choice of suitable equiripple functions in the t variable, followed by the synthesis. In the original paper [16] the insertion loss function is

$$\frac{1}{|S_{12}|^2} = 1 + \frac{K^2 P_{n-1}^2(x/x_c)}{(1-x^2)} \tag{29}$$

where

$$x = \cos(2\theta), \quad x_c = \cos(2\theta_c) \tag{30}$$

or in terms of t

$$x = \frac{1+t^2}{1-t^2} \tag{31}$$

The function $P_{n-1}(x/x_c)$ gives equiripple performance in the range of x from $-x_c$ to x_c when it takes the following form [16]:

$$P_{n-1} \frac{x}{x_c} = 0.5[1 + (1-x_c^2)^{1/2}]T_{n-1} \frac{x}{x_c} - 0.5[1 - (1-x_c^2)^{1/2}]T_{n-3} \frac{x}{x_c} \tag{32}$$

The original paper [16] includes design tables for Chebyshev couplers having three to eight branches, coupling values from 3 to 20 dB, and for a wide range of bandwidths. From these data it becomes evident that there is a drawback for tight values of coupling of less than 6 dB; namely, the mainline immittances (actually impedances for waveguide branch-guide couplers) become somewhat larger than the desired value of unity. A solution to this problem is to select a different insertion loss function, and this is described in Ref. 17, where the Zolotarev

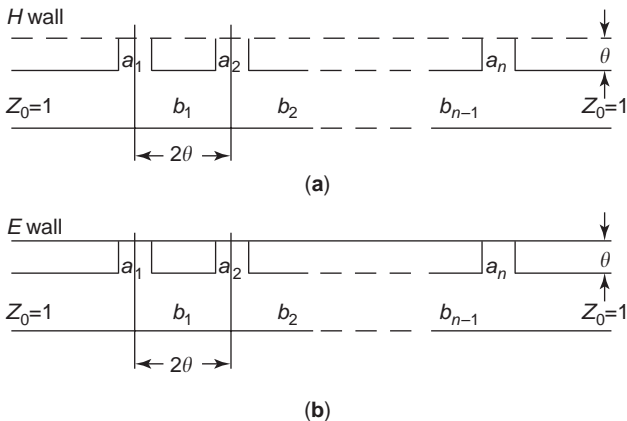


Figure 12. Even (a) and odd (b) modes for the branch-guide coupler.

branch-guide coupler is introduced. The Zolotarev function has a free parameter that controls the lower band edge of the equiripple function, and this has a very significant effect on the internal impedance levels of the coupler, where the mainline impedances are close to unity and the branch-guide impedances have much more favorable values with much less spread of impedances compared with the simple Chebyshev designs. Examples are given in Table 1 of Ref. 17 for 3-dB couplers of five branches indicating the tremendous range of design possibilities. Note that it is not absolutely necessary to work with the complicated formal theory, involving elliptic functions and integrals, to derive the Zolotarev functions in order to obtain these results. The Zolotarev polynomials, which have one large zero above $x = 0$ and the rest of equal ripple, may be easily generated using simple computer optimization.

4. COMPUTER-AIDED DESIGN TECHNIQUES

There are numerous papers describing the design of waveguide couplers of the types described in this article using computer-aided design (CAD), but considering the precision of the latest purely theoretical techniques, CAD may be considered to be mainly unnecessary, at least as a primary design methodology. It tends to be cumbersome, and with standard optimization packages, convergence to a good design may be a very slow process. However, computer analysis programs are useful in checking the accuracy of the theoretical designs. There are several general analysis programs available based either on three-dimensional field theory using the finite-element method or mode matching. Rather than using them to design a complicated multisection waveguide coupler ab initio, it is recommended that they be used in conjunction with analytical theory. For example, in the case of a branch-guide coupler of the type described in Section 3.4, the CAD program may be used to analyze the performance of a theoretical design. The initial design may then be adjusted to compensate for slight discrepancies in the coupling, which are typically up to about 0.3 dB. It has been found that some designs require no adjustments.

In some cases CAD has proved very useful as a design tool. Thus the design of the short-slot hybrid described in Section 3.3 relies on results obtained from 3D field theory. However, even in this case, the field analysis is used as a method for obtaining equivalent circuits for the even mode, which are then used in a circuit theory design approach, not simply and solely as a CAD technique. Similar design approaches may be applied to the design of other single- or multiaperture directional couplers. As an example, in the case of multiaperture couplers (Section 3.1) the field theory could be used to check the equivalent circuits for single apertures, and to investigate any interaction effects between closely spaced apertures.

BIBLIOGRAPHY

1. R. Levy, Directional couplers, in L. Young, ed., *Advances in Microwaves*, Academic Press, New York, 1966, Vol. 1, pp. 115–209.

2. S. B. Cohn and R. Levy, History of microwave passive components with particular attention to directional couplers, *IEEE Trans. Microwave Theory Tech.* **32**:1046–1054 (Sept. 1984).
3. R. H. Dicke, in C. G. Montgomery et al., eds., *Principles of Microwave Circuits*, McGraw-Hill, New York, 1948, pp. 301–303.
4. H. A. Bethe, Theory of diffraction by small holes, *Phys. Rev.* **66**:163–182 (Oct. 1944).
5. R. Levy, Analysis and synthesis of waveguide multiaperture directional couplers, *IEEE Trans. Microwave Theory Tech.* **16**:995–1006 (Dec. 1968).
6. R. Levy, Improved single and multiaperture waveguide coupling theory, including explanation of mutual interactions, *IEEE Trans. Microwave Theory Tech.* **28**:331–338 (April 1980).
7. A. A. Oliner, Equivalent circuits for small symmetrical longitudinal apertures and obstacles, *IRE Trans. Microwave Theory Tech.* **8**:72–80 (Jan. 1960).
8. L. Young, The quarter-wave transformer prototype circuit, *IRE Trans. Microwave Theory Tech.* **8**:483–489 (Sept. 1960).
9. R. Levy, Tables of element values for the distributed low-pass prototype filter, *IEEE Trans. Microwave Theory Tech.* **5**:514–536 (Sept. 1965).
10. G. L. Matthaei, L. Young, and E. M. T. Jones, *Microwave Filters, Impedance-Matching Networks, and Coupling Structures*, McGraw-Hill, New York, 1964.
11. P. Meyer and J. C. Kruger, Wideband crossed-guide waveguide directional couplers, *1998 Int. Microwave Symp. Digest*, 1998, Vol. 1, pp. 253–256.
12. H. J. Riblet, The short-slot hybrid junction, *Proc. IRE* **40**:180–184 (Feb. 1952).
13. R. Levy, Determination of simple equivalent circuits of interacting discontinuities in waveguides or transmission lines, *IEEE Trans. Microwave Theory Tech.* **48**:1712–1716 (Oct. 2000).
14. L. W. Hendrick and R. Levy, Design of waveguide narrow-wall short-slot couplers, *IEEE Trans. Microwave Theory Tech.* **48**:1771–1774 (Oct. 2000).
15. E. Hodge, Compact top-wall hybrid junction, *IRE Trans. Microwave Theory Tech.* **1**:29–30 (Jan. 1953).
16. R. Levy and L. F. Lind, Synthesis of symmetrical branch-guide directional couplers, *IEEE Trans. Microwave Theory Tech.* **16**:80–89 (Feb. 1968).
17. R. Levy, Zolotarev branch-guide couplers, *IEEE Trans. Microwave Theory Tech.* **21**:95–99 (Feb. 1973).

WAVEGUIDE DISCONTINUITIES

R. SORRENTINO
F. ALIMENTI
University of Perugia
Perugia, Italy

1. INTRODUCTION

Any deviation from uniformity along the longitudinal axis of a waveguide constitutes a discontinuity. Discontinuities

are unavoidably present in any microwave circuit either unintentionally or to the purpose of performing a prescribed function. In the former case one usually tries to minimize the unwanted mismatching due to the presence of the discontinuity, while in the latter case the discontinuity is instrumental in the design of a specific component. Typical example of the former category is a waveguide bend, while a metal diaphragm is representative of the latter.

The electromagnetic (EM) field incident onto a discontinuity is partly reflected and partly transmitted, while reactive energy is stored in the proximity of the discontinuity. If lossy materials are present, some power may be lost and, in case of open structures, some power may be radiated.

The electromagnetic analysis of a discontinuity involves the solution of Maxwell's equations with the appropriate boundary conditions. Analytical techniques for the solution of boundary-value problems in electromagnetics are presented and discussed in a number of classical textbooks such as, for instance, Refs. 1–4. Extensive discussion on waveguide discontinuities and their general properties can be found in Refs. 5 and 6. With the exception of a few simple cases, for which an analytical solution can be found, some sort of approximation, either analytical or numerical, is necessary to express the solution of the electromagnetic problem.

The problem can be attacked using either rigorous or approximate approaches. Rigorous approaches differ from approximate ones in that the exact solution can, in principle, be obtained with any degree of accuracy. On the contrary, the accuracy obtainable with approximate approaches cannot be pushed beyond intrinsic limits.

Although a number of rigorous methods have been developed for the solution of electromagnetic structures and available computational resources are extremely powerful, rigorous solutions are often too heavy for many practical purposes. Approximate solutions, although less accurate, may result more advantageous as they are much simpler to achieve.

Numerical methods for the analysis of waveguide discontinuities and, more generally, for the solution of microwave boundary-value problems have been presented in large amount of papers and books Refs. 7–10.

One of the most powerful and popular methods used to solve waveguide discontinuities is the modal analysis or mode-matching technique Refs. 11–13. Besides being a rigorous approach, it lends itself to a physical interpretation of the electromagnetic field behavior due to the presence of the discontinuity and leads to the so-called microwave network formalism. By virtue of the equivalence between waveguide modes and transmission lines, the electromagnetic description of the discontinuity can be translated in terms of an equivalent network. Observe that the full computation of the electromagnetic field in the structure is more than is usually required. A terminal description of the discontinuity as seen from the waveguides connected to it is all that is necessary. This makes it possible to express a complicated electromagnetic problem in terms of a more familiar circuit theory model.

In Section 2 the description of waveguide discontinuities is introduced on the basis of the modal analysis approach. This leads to the generalized description of the discontinuity as a multiport network using impedance, admittance, or scattering matrix (or other matrix descriptions). General properties of waveguide discontinuities are presented in Section 3, while Section 4 categorizes various classes of waveguide discontinuities. The concept of interacting and isolated discontinuities, which is familiar to the microwave engineer, but has no counterpart in the conventional circuit theory, is illustrated in Section 5 by a specific example.

2. DESCRIPTION OF WAVEGUIDE DISCONTINUITIES

Figure 1a depicts a generic discontinuity with two outputs. The structure consists of a central region bounded by metallic walls, connected to two uniform waveguides. In the present discussion, the structure of Fig. 1a is taken as an example; the extension to more general cases, such as multiple outputs and magnetic walls, is straightforward. Two reference planes, T_1 and T_2 , define the boundary between the discontinuity region and the input and output waveguides. Various types of obstacles, either lossless (perfectly conducting or perfect dielectric materials) or lossy, isotropic or anisotropic may be present in the discontinuity region.

When an electromagnetic field impinges onto the discontinuity from one or both waveguides, part of the associated energy is reflected, part is dissipated within the discontinuity, and part is transmitted to the other waveguide. In case of open discontinuities (see Section 4.5), part of the energy can be radiated into outer space. Reactive energy is stored in the discontinuity region and in the waveguide region close to it.

In most practical cases, rather than a detailed knowledge of the electromagnetic field distribution within the discontinuity, what is required is just a terminal description of the discontinuity. It is worth recalling here that the field distribution in a waveguide results from the superposition of its normal modes. Under normal operating conditions, the dominant mode is the only propagating mode, while all higher-order modes, excited at the discontinuity, are exponentially decaying. The terminal planes are usually, placed far enough from the discontinuity in such a way that only the dominant modes have nonnegligible amplitudes. In such conditions, a terminal description of the discontinuity can be obtained by writing the equations relating the field quantities at the two terminal planes. Such relations may take the form of a 2×2 impedance matrix if the electric fields are expressed in terms of the magnetic fields, or the form of an admittance matrix if the magnetic fields are expressed in terms of the electric fields, and so on. As will be specified below, in fact, electric and magnetic fields can be replaced by equivalent voltage and current amplitudes. In a number of important cases, however, the terminal planes must be placed near the discontinuity region, so that the field distribution cannot be reduced to the only dominant modes. This typically happens when multiple discontinuities are cascaded

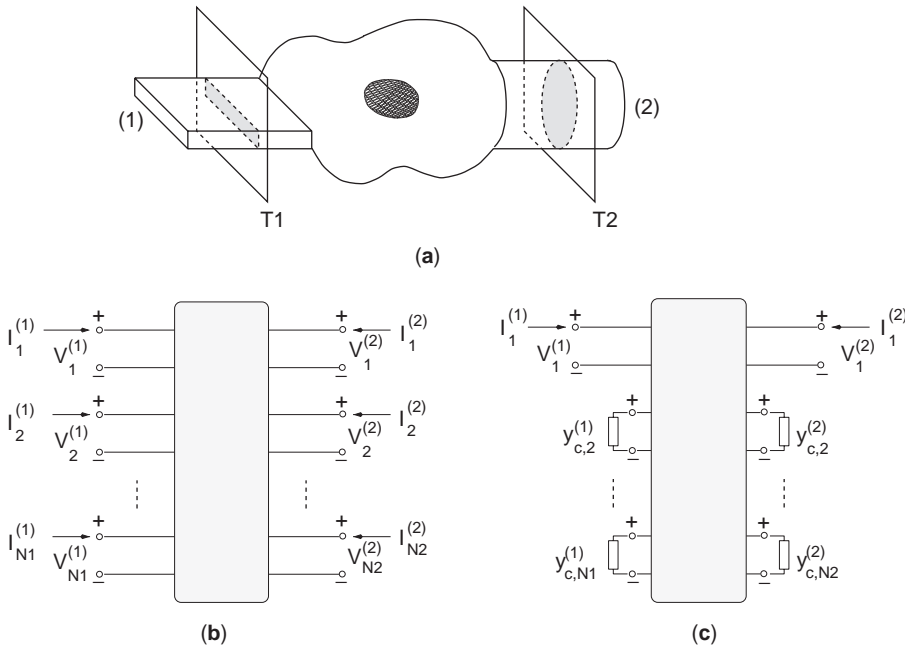


Figure 1. Generic, two-port, waveguide discontinuity and its network representations: (a) waveguide discontinuity; (b) multiport description; (c) reduced two-port description.

together at short distances. In higher-order modes interaction takes place between adjacent discontinuities, in such a way that active power may be carried by these higher-order modes. In such cases, a more general description of the discontinuity is needed.

In order to obtain a terminal description of the discontinuity in the general case, it is worth recalling that each waveguide mode can be represented by an equivalent transmission line, where the voltage and current amplitudes are proportional to the modal electric and magnetic field amplitudes, respectively:

$$\mathbf{E}_t^{(i)}(x, y, z) = \sum_m V_m^{(i)}(z) \mathbf{e}_m^{(i)}(x, y) \quad (1)$$

$$\mathbf{H}_t^{(i)}(x, y, z) = \sum_m I_m^{(i)}(z) \mathbf{h}_m^{(i)}(x, y) \quad (2)$$

where z is the longitudinal axis of the waveguide, $\mathbf{E}_t^{(i)}$ and $\mathbf{H}_t^{(i)}$ are the transverse electric and magnetic fields, $V_m^{(i)}$ and $I_m^{(i)}$ are the voltage and current of the transmission line equivalent to the m th mode of the i th waveguide, and $\mathbf{e}_m^{(i)}$ and $\mathbf{h}_m^{(i)}$ are the transverse and magnetic modal vectors, respectively.

Although in principle an infinite series of modes is involved in the electromagnetic field representation, in practice only a finite number of modes need to be taken into account to achieve a prescribed accuracy. As a consequence, the electromagnetic field distribution over each terminal plane is expressed in terms of a finite number of voltage and current amplitudes. Letting N_i be the number of modes taken into account in the field description at the i th terminal plane ($i = 1, 2$), the terminal description of the discontinuity will involve $N_1 + N_2$ voltages and the same number of currents. Because of the linearity of Maxwell's

equations, these quantities are related by a linear set of $N_1 + N_2$ equations. One can easily realize that Maxwell's equations lead to $N_1 + N_2$ equations by the following reasoning. By virtue of the unicity theorem for electromagnetic fields, the entire electromagnetic field distribution in the structure is determined by the knowledge of tangential electric (or magnetic) field at the two terminal planes, thus by the knowledge of the whole set of $N_1 + N_2$ voltages (or currents) over such planes. In other words, from the knowledge of $N_1 + N_2$ voltages (currents), one can compute the $N_1 + N_2$ currents (voltages). This implies that the linear system consists of $N_1 + N_2$ equations relating the $N_1 + N_2$ voltages to the $N_1 + N_2$ currents.

The modal approach lends itself to the so-called microwave network formalism. The discontinuity, rather than in terms of electric and magnetic field distributions, is described in terms of voltages and currents, namely, as a multiport circuit. This is described with the equivalent circuit of Fig. 1b, where each port corresponds to a mode excited at one of the terminal planes of the discontinuity. The system can be put in many different forms. One of the most convenient approach consists of expressing currents in terms of voltages. In matrix form this corresponds to writing

$$[I] = [Y] \cdot [V] \quad (3)$$

where $[I]$ is the vector of the currents, $[V]$ that of the voltages, and $[Y]$ the admittance matrix. For the case of the two-terminal-plane network of Fig. 1a the vector of the currents is

$$[I] = \begin{bmatrix} [I^{(1)}] \\ [I^{(2)}] \end{bmatrix} \quad (4)$$

The subvector of the currents at the i th terminal plane ($i = 1, 2$) is

$$[I^{(i)}] = [I_1^{(i)}, I_2^{(i)}, \dots, I_{N_i}^{(i)}]^T \quad (5)$$

where N_i is the number of modes (or electrical ports) considered at the i th plane. The voltage vector is similar to the current vector, and the admittance matrix is composed by four submatrices as follows:

$$[Y] = \begin{bmatrix} [Y^{(11)}] & [Y^{(12)}] \\ [Y^{(21)}] & [Y^{(22)}] \end{bmatrix} \quad (6)$$

Observe that while the electromagnetic structure has two outputs (or two apertures), the equivalent circuit has $N_1 + N_2$ electric ports.

In most practical cases the terminal planes are chosen far enough from the discontinuity in such a way that higher-order modes have vanished. This is possible whenever the discontinuity is isolated, that is, if there are no other discontinuities close to it. The electromagnetic field at the terminal planes is that of the dominant modes of the respective waveguides, while higher-order modes have died out. In the multiport equivalent circuit description of Fig. 1b, this situation corresponds to terminating the higher-order mode ports with their characteristic admittances. The multiport description reduces to the two-port description of Fig. 1c, where the accessible ports represent the dominant modes of both waveguides.

To compute the 2×2 admittance matrix of Fig. 1c from the $(N_1 + N_2) \times (N_1 + N_2)$ admittance matrix of Fig. 1b, the matching conditions at the higher-order mode ports are added to Eq. (3):

$$I_m^{(i)} = -y_{c,m}^{(i)} V_m^{(i)} \quad (7)$$

In (7) $y_{c,m}^{(i)}$ is the characteristic admittance of the equivalent transmission line, which has been assumed as the wave admittance of the waveguide mode $y_{c,m}^{(i)} = 1/\eta_m^{(i)}$, where

$$\eta_m^{(i)} = \begin{cases} \frac{\omega\mu}{\beta_m^{(i)}}, & \text{TE modes} \\ \frac{\beta_m^{(i)}}{\omega\varepsilon}, & \text{TM modes} \end{cases} \quad (8)$$

with

$$\beta_m^{(i)} = \left[\left(\frac{\omega}{c}\right)^2 - \left(k_{c,m}^{(i)}\right)^2 \right]^{1/2} \quad (9)$$

where c is the light velocity; $\beta_m^{(i)}$, the phase constant; and $k_{c,m}^{(i)}$, the eigenvalue of the m th mode. These equations refer to hollow waveguides or to waveguides totally filled with a homogeneous lossless dielectric. After rearranging and partitioning the admittance matrix (6) according to fundamental (subscript f) and higher-order modes

(subscript h)

$$[Y] = \begin{bmatrix} [Y_{ff}] & [Y_{fh}] \\ [Y_{hf}] & [Y_{hh}] \end{bmatrix} \quad (10)$$

the two-port admittance matrix description $[Y_{2p}]$ of the discontinuity is easily obtained from (7) and (3):

$$[Y_{2p}] = [Y_{ff}] - [Y_{fh}] \cdot ([Y_{hh}] + [Y_c])^{-1} \cdot [Y_{hf}] \quad (11)$$

In this relationship $[Y_c]$ is the diagonal matrix of the higher-order modes' characteristic admittances; it is defined as

$$[Y_c] = \text{diag} [y_{c,2}^{(1)}, \dots, y_{c,N_1}^{(1)}, y_{c,2}^{(2)}, \dots, y_{c,N_2}^{(2)}] \quad (12)$$

Alternative descriptions of the discontinuity can be obtained by either rearranging the discontinuity equations or using different electrical quantities rather than voltages and currents. In the former case, an impedance matrix description is obtained by expressing the voltages in terms of the currents:

$$[V] = [Z] \cdot [I] \quad (13)$$

By expressing the waveguide fields in terms of incident $[a]$ and reflected $[b]$ wavevectors, one can obtain a scattering matrix description of the discontinuity:

$$[b] = [S] \cdot [a] \quad (14)$$

The incident and reflected waves are related to voltage and current amplitudes as follows:

$$a_m^{(i)} = \frac{y_{c,m}^{(i)} V_m^{(i)} + I_m^{(i)}}{2 [y_{c,m}^{(i)}]^{1/2}} \quad (15)$$

$$b_m^{(i)} = \frac{y_{c,m}^{(i)} V_m^{(i)} - I_m^{(i)}}{2 [y_{c,m}^{(i)}]^{1/2}} \quad (16)$$

with $i = 1, 2$ and $m = 1, \dots, N_i$. As is well known from many textbooks, the interrelations among this matrix descriptions are

$$\begin{aligned} [Y_N] &= [Z_N]^{-1} = ([U] + [S])^{-1} \cdot ([U] - [S]) \\ [Z_N] &= [Y_N]^{-1} = ([U] + [S]) \cdot ([U] - [S])^{-1} \\ [S] &= ([Z_N] - [U]) \cdot ([Z_N] + [U])^{-1} \\ &= ([U] + [Y_N])^{-1} \cdot ([U] - [Y_N]) \end{aligned} \quad (17)$$

where $[U]$ is the unit matrix. The normalized (subscript N) admittance and impedance matrix elements are expressed

as

$$Y_{N,mn}^{(ij)} = \frac{Y_{mn}^{(ij)}}{\left[y_{c,m}^{(i)} y_{c,n}^{(j)} \right]^{1/2}} \quad (18)$$

$$Z_{N,mn}^{(ij)} = \frac{Z_{mn}^{(ij)}}{\left[z_{c,m}^{(i)} z_{c,n}^{(j)} \right]^{1/2}} \quad (19)$$

where $z_{c,m}^{(i)} = 1/y_{c,m}^{(i)}$ is the characteristic impedance of the equivalent transmission line.

The use of a lumped or distributed element equivalent circuit model to describe the discontinuity can be advantageous for many practical applications. The circuit model can be easily handled in more conventional engineering terms, and, when properly derived, reflects the physical behavior of the discontinuity. Moreover, it has the advantage of easily providing by mere inspection a description of the behavior of the discontinuity and the way the latter can be used for practical applications (e.g., filters).

From the discussion above it is apparent that a certain degree of arbitrariness is involved in the choice of the reference planes. As a consequence, different equivalent circuits can be assumed, depending on the location of the terminal planes. A proper choice of the reference plane locations can be exploited in some cases in order to reduce the complexity of the equivalent circuit. Observe that this ambiguity is inherent to the distributed nature of waveguide circuits, as opposed to lumped low-frequency circuits, where no ambiguity exists.

An additional ambiguity in the definition of the equivalent circuit models resides in the arbitrariness of the definition of the equivalence between waveguide mode and transmission line. In particular, the characteristic impedance $z_{c,m}^{(i)}$ of the m th transmission line can be changed by a factor of n^2 by transforming the voltages $V_m^{(i)}$ and currents $I_m^{(i)}$ into a new set $V_m'^{(i)}$ and $I_m'^{(i)}$

$$V_m'^{(i)} = n V_m^{(i)} \quad (20)$$

$$I_m'^{(i)} = \frac{1}{n} I_m^{(i)} \quad (21)$$

so that

$$z_{c,m}'^{(i)} = n^2 z_{c,m}^{(i)} \quad (22)$$

It is worth noting that the transformation represented by Eqs. (20) and (21) is such that power is conserved. The new definition is equivalent to the introduction of ideal transformers at the circuit terminals. By an appropriate selection of both the reference planes and the voltage-current definitions, different equivalent circuits with reduced complexity can be derived.

In the presence of multiple or cascaded discontinuities special caution should be employed in the use of equivalent-circuit models. If adjacent discontinuities are cascaded at a short distance, in fact, the reference planes cannot be chosen far enough from the discontinuities to make higher-order modes vanish. In this case, discontinuities

interact through higher-order modes. The models for isolated discontinuities may lead to significant errors. Multiport equivalent networks, including higher-order mode interactions, must be adopted instead. This is illustrated in Section 5 using a specific example.

3. GENERAL PROPERTIES OF WAVEGUIDE DISCONTINUITIES

This section presents a brief description of the general properties of waveguide discontinuities.

3.1. Losslessness

Losses in microwave circuits are due to imperfect dielectric materials (dielectric loss), finite conductivity of the conductors (conductor loss), and, for open structures, radiation (radiation loss). The impedance or admittance matrices of lossy discontinuities possess real as well as imaginary parts that are associated with the real and the reactive power, respectively.

In many practical cases losses may be neglected with good approximation so that the discontinuity behaves as a reactive circuit. The admittance and the impedance matrices are purely imaginary, and the scattering matrix is unitary. The latter property is obtained by expressing the balance between incident and reflected power in terms of wavevectors, (15), (16) as follows:

$$\frac{1}{2} [a]^T \cdot [a]^* = \frac{1}{2} [b]^T \cdot [b]^* \quad (23)$$

Using (14), one obtains the unitarity condition for the scattering matrix of a lossless discontinuity, where the asterisk * stands for complex conjugate:

$$[S]^T \cdot [S]^* = [U] \quad (24)$$

3.2. Reciprocity

As long as Lorentz' reciprocity theorem holds for the region occupied by the discontinuity, the latter behaves as a reciprocal network. This implies that the admittance, impedance, and scattering matrices are symmetric. As a consequence, a reciprocal N -port discontinuity is characterized by $N(N+1)/2$ complex parameters. Such parameters reduce to real parameters for lossless structures. Discontinuities containing anisotropic materials such as ferrite are examples of nonreciprocal circuits characterized by nonsymmetric matrix descriptions.

3.3. Symmetry

The presence of geometric symmetries of a discontinuity can be exploited to reduce the complexity of its analysis, as well as the number of unknown parameters of its equivalent network representation. For example, in the case of a two-port discontinuity, the existence of a central symmetry plane between the two outputs implies a corresponding symmetry of the matrix representations,

provided the terminal planes are chosen symmetrically (e.g., $Y_{11} = Y_{22}$). In such a case, the discontinuity, if reciprocal, is characterized by only two rather than three parameters, as in the general case. For a more detailed discussion on the exploitation of symmetry planes in three- or four-port structures, the reader is referred to Section 3.2 of Ref. 7.

4. CATEGORIZATION OF WAVEGUIDE DISCONTINUITIES

There is no unique way to classify waveguide discontinuities, since a number of different criteria can be adopted. Here we attempt at a categorization of discontinuities with reference to some geometric characteristics that are somewhat related to the corresponding electromagnetic problem. Examples of common discontinuities are shown in Tables 1–5. The examples discussed here are not exhaustive at all, but represent only a small fraction of what can be found in practical applications. The reader is also provided with some representative references taken from the immense amount of technical publications on this topic.

4.1. Uniaxial Junctions

In a uniaxial junction, two waveguides with different cross sections and coincident longitudinal axes are connected together. In the case of rectangular waveguides, examples of such discontinuities are: the *E*-plane (or capacitive) step Refs. 12–14, the *H*-plane (or inductive) step Ref. 15, and the *E*-plane and *H*-plane offsets. These discontinuities are illustrated in Table 1. As long as both waveguides are in

the monomodal regime, the corresponding equivalent networks have two ports. Other examples of uniaxial discontinuities are some particular kind of transitions (see later in the text), specifically, structures designed to transfer the microwave power from one waveguide system to another. In particular, we recall the transition between coaxial cable and a circular waveguide Ref. 16 and that between rectangular and circular waveguides Ref. 17.

4.2. Bifurcations and N-Furcations

One waveguide is joined to two or more waveguides with parallel longitudinal axes. A theoretical model of *N*-furcations has been presented in Ref. 18. In rectangular waveguide, the bifurcation can occur in either the *E* or the *H* plane, as shown in Table 2. The equivalent circuit may contain more than three ports, because the larger waveguide may support the propagation of higher-order modes.

4.3. Obstacles

Metallic or dielectric obstacles can be inserted in a waveguide to achieve specific electrical behaviors. Metallic obstacles may have infinitesimal or finite length along the waveguide axis. In the former case the equivalent circuit can be reduced to a shunt admittance. Typical examples are metal irises and metal posts. They have been widely employed as filter and matching network elements. In the case of rectangular waveguide, depending on the orientation with respect to the electric field of the dominant mode, such obstacles exhibit inductive or capacitive behavior, as shown in Table 3. Observe that irises are supposed to be

Table 1. Uniaxial Junctions in Rectangular Waveguide

Name	Structure	Equivalent Circuit	References/Comments
<i>H</i> -plane step			7 , pp. 296–302
<i>E</i> -plane step			7 , pp. 307–310
<i>H</i> -plane offset			
<i>E</i> -plane offset			

Table 2. Bifurcations in Rectangular Waveguide

Name	Structure	Equivalent Circuit	References/Comments
<i>H</i> -plane bifurcation			7 , pp. 383–386; TE ₁₀ mode in all waveguides; in addition, TE ₂₀ mode in the larger waveguide
<i>E</i> -plane bifurcation			7 , pp. 353–355

infinitesimally thin. A full-wave model of the inductive iris in rectangular waveguide can be found in Ref. 19. More complicated geometries involving circular irises Refs. 20,21, slanting and multiple rectangular irises Refs. 22,23 in rectangular waveguide, as well as irises in coaxial cable Ref. 24 and circular waveguides Refs. 25,26, have been investigated. Electromagnetic models of posts in rectangular waveguide have also been presented Refs. 27–29.

4.4. Multiaxial Junctions

Two or more waveguides with different longitudinal axes are connected together (see Table 4). In the case of uniaxial junctions, the associated boundary-value problem is a two-dimensional one. For multiaxial junctions, on the contrary, the analysis involves the solution of a 3D boundary-value problem Ref. 30. The simplest case of a biaxial junction is the right-angle junction between two rectangular

Table 3. Obstacles

Name	Structure	Equivalent Circuit	References/Comments
Inductive iris			7 , pp. 221–229
Capacitive iris			7 , pp. 218–221
Inductive post			7 , pp. 257–266
Capacitive post			7 , pp. 268–271

Table 4. Multiaxial Junctions

Name	Structure	Equivalent Circuit	References/Comments
<i>E</i> -plane corner			7, pp. 312–318
<i>H</i> -plane corner			7, pp. 318–322
<i>E</i> -plane tee			7, pp. 337–338
<i>H</i> -plane tee			7, pp. 355–356
Coupling hole, <i>E</i> plane			7, pp. 375–376
Coupling hole, <i>H</i> plane			7, pp. 379–380

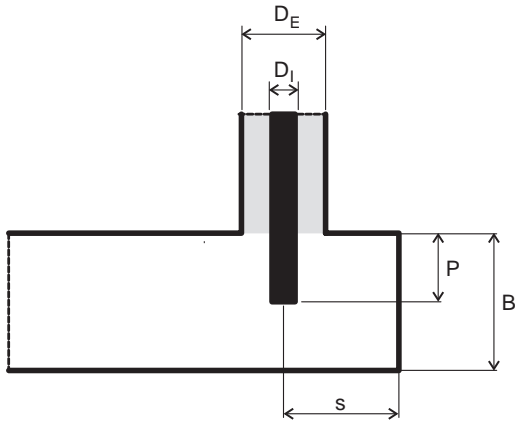


Figure 2. Coaxial to rectangular waveguide transition (side view).

waveguides. Depending on the plane of such junction, we have the *E*-plane or *H*-plane corner. This type of discontinuity realizes a 90° change of direction in the waveguide axis. To minimize reflections, alternative geometries can be adopted, such as the mitered bends Refs. 31,32 and the circular bends Refs. 33,34.

More complicated multi-axial junctions in rectangular waveguide technology are the *T* junctions in the *E* plane Refs. 35–37, or *H* plane Refs. 38–40. The matching of such a junction has been analyzed in detail in Ref. 41. The so-called magic (hybrid) tee is a well-known rectangular waveguide component where ports are decoupled in pairs Ref. 42. The aperture in the common wall of two rectangular waveguides Refs. 43,44 can also be seen as an example of a four-port multi-axial junction. An example of a

T-junction between rectangular and circular waveguide has been investigated Ref. 45.

The transitions, that is, the junction between two waveguide of different cross sections, can be considered as a particular case of multi-axial junctions. The purpose of these structures is to transfer the microwave power from one waveguide system to the other while minimizing the return loss in a band as wide as possible. As an example, we consider the transition between a coaxial cable and a rectangular waveguide as shown in Fig. 2. In its basic configuration, the center conductor of the coaxial line extends into the waveguide to form an electric probe. One of the two waveguide ends is short-circuited while the other is used as the output. The tuning of the structure is achieved by adjusting the probe penetration and/or the distance between probe and short circuit. Typically, the former is close to the 60% of the waveguide height, while the latter is between $\lambda_g/8$ and $\lambda_g/4$ at the operating frequency Ref. 4, pp. 471–484. If properly tuned, a 10% fractional bandwidth can be achieved for $S_{11} < -30$ dB. At the output side, a uniform waveguide section provides a suitable attenuation of the higher-order modes excited by the probe.

4.5. Open Discontinuities

In the examples presented so far, the discontinuities were completely bounded by metallic walls. An important category of waveguide discontinuities, however, is represented by open discontinuities, where the electromagnetic field can be radiated in outer space. The equivalent circuits of such discontinuities contain resistors that represent the radiation loss. Some examples are illustrated in Table 5.

Table 5. Radiating Discontinuities

Name	Structure	Equivalent Circuit	References/Comments
Open waveguide (with flange)			7 , pp. 193–194
Longitudinal slot			52

A first example is the open-ended waveguide. When the electromagnetic field impinges on such a termination, part of the associated power is reflected and part is radiated in the free space, so that the termination can be considered as an antenna. Such terminations, in fact, are widely used as secondary antennas (feeding antennas) in reflector-type antennas or as elements of an array antenna. The study of the radiation mechanism is rather complicated, and electromagnetic full-wave models are mandatory. The reader is referred to Refs. 46–48 for rectangular waveguide and to Refs. 49 and 50 for coaxial and circular waveguides.

Other radiating discontinuities are obtained by producing apertures in the waveguide walls. The aperture interrupts locally the conduction current flowing on the walls, producing both a distortion in the lines of flux and a displacement current in the aperture. The latter is necessary to maintain the continuity of the total current and constitutes the source of the radiated electromagnetic field. The most common example is the radiating slot in a rectangular waveguide. The longitudinal slot in the broad wall Refs. 51–53, and the slanting slot have been analyzed, Ref. 54, and the transverse slot has been investigated Refs. 55,56. These discontinuities are used to build slotted antennas.

5. ISOLATED AND INTERACTING DISCONTINUITIES

In Section 2 it was pointed out that the reduced equivalent circuit valid for an isolated discontinuity may not be adopted, in general, for adjacent discontinuities, because of the higher-order mode interaction occurring between them. To illustrate this phenomenon, consider as an example the symmetric capacitive step in rectangular waveguide depicted in Fig. 3a. The larger waveguide is the WR75 waveguide operating in the 10–15 GHz frequency range. The equivalent circuit of the step, supposed as isolated, is shown in Fig. 3b. The shunt capacitance represents the reactive energy stored in the proximity of the

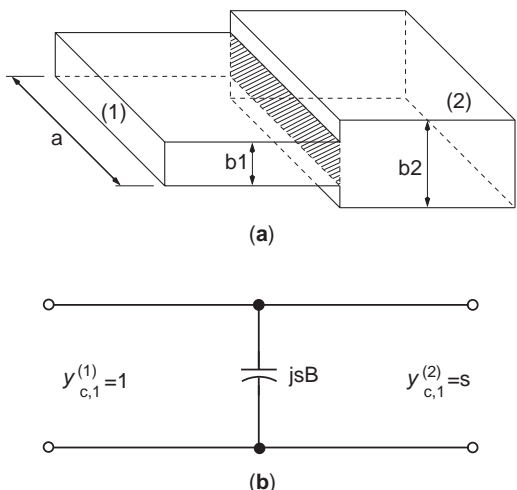


Figure 3. Capacitive step in rectangular waveguide: structure (a) and equivalent circuit (b). Geometric dimensions: $a = 19.05$ mm, $b_2 = 9.52$ mm, $b_1 = s b_2$.

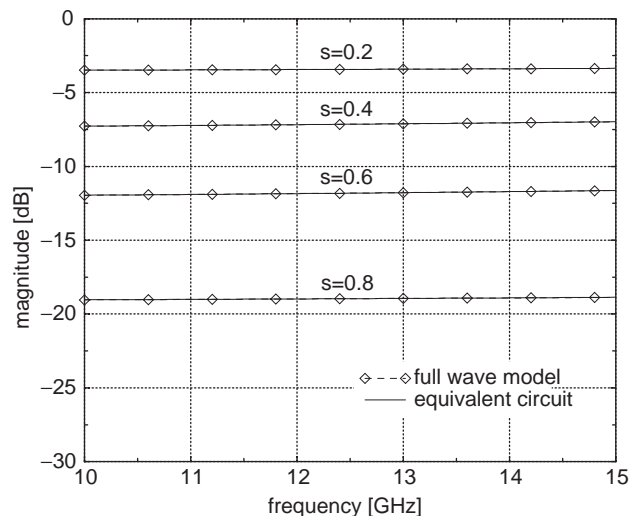


Figure 4. S_{11} of a capacitive step in rectangular waveguide for various step ratios $s = b_1/b_2$; comparison between the equivalent circuit and the full-wave mode-matching analysis.

step, due to attenuated higher-order modes excited at the junction between the two waveguides. The step susceptance is sB , where s being the step ratio

$$s = \frac{b_1}{b_2} \tag{25}$$

and B is easily computed by the approximate formula given in Ref. 7, p. 307. The scattering parameter S_{11} of the discontinuity, can be evaluated by elementary network analysis:

$$S_{11} = \frac{(1 - s) - jsB}{(1 + s) + jsB} \tag{26}$$

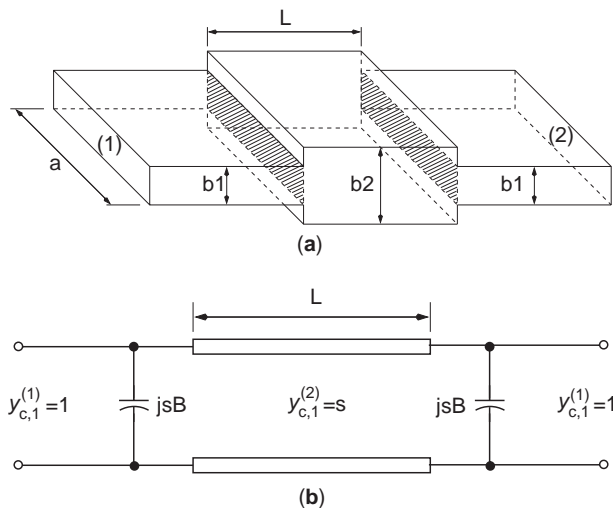


Figure 5. Capacitive double step in rectangular waveguide: structure (a) and equivalent circuit (b). Note that the equivalent circuit is derived under the approximation of isolated discontinuities. Geometrical dimensions: $a = 19.05$ mm, $b_2 = 9.52$ mm, $s = 0.20$, $b_1 = 1.90$ mm.

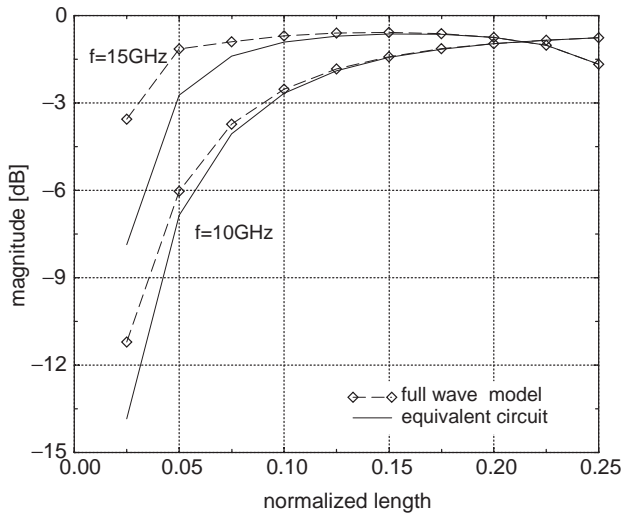


Figure 6. S_{11} of the double step versus the normalized length L/λ_{c1} of the central waveguide. Comparison between the equivalent circuit and the full-wave mode-matching analysis.

This parameter is shown in Fig. 4 as a function of frequency for different step ratios. For comparison, the scattering parameter computed by the rigorous mode-matching technique is also shown. The approximate formula is shown to be very accurate compared with the computationally more expensive mode-matching method.

Let us now consider two capacitive steps (step ratio $s = b_1/b_2 = 0.2$) cascaded through a uniform waveguide of length L as in Fig. 5a. The cascaded steps have been analyzed both by the equivalent circuit of Fig. 5b and by the mode-matching method. In the former case the higher-order mode interaction between the two steps is totally neglected, while in the latter case, higher-order mode interaction has been fully taken into account. Observe that higher-order modes, although evanescent, carry active power that flows between the two discontinuities. This causes the discrepancy observed between the two models, as illustrated in Fig. 6. In particular, such a figure shows the computed scattering parameter $S_{11} = S_{22}$ as a function of the normalized length L/λ_{c1} at the lower (10-GHz) and upper (15-GHz) ends of the frequency range of the WR75 waveguide; $\lambda_{c1} = 2a = 39$ mm is the cutoff wavelength of the waveguide. It is observed that the equivalent circuit of Fig. 5b, based on the hypotheses of isolated discontinuities, is accurate as long as the normalized distance exceeds $\lambda_{c1}/8$. For lower distances the error increases and becomes unacceptable below $\lambda_{c1}/20$. It can be noted that the error increases with frequency, as a result of the stronger excitation of higher-order modes.

BIBLIOGRAPHY

1. C. G. Montgomery, R. H. Dicke, and E. M. Purcell, *Principles of Microwave Circuits*, McGraw-Hill, New York, 1948.
2. L. Lewin, *Advanced Theory of Waveguides*, Pliffe, London, 1951.
3. R. Mittra and S. W. Lee, *Analytical Techniques in the Theory of Guided Waves*, The Macmillan, New York, 1971.
4. R. E. Collin, *Field Theory of Guided Waves*, IEEE Press, Piscataway, NJ, 1990.
5. D. Pozar, *Microwave Engineering*, Addison-Wesely, Reading, MA, 1990.
6. R. E. Collin, *Foundations for Microwave Engineering*, McGraw-Hill, New York, 1992.
7. N. Marcuvitz, *Waveguide Handbook*, McGraw-Hill, New York, 1951.
8. T. Itoh, *Numerical Techniques for Microwave and Millimeter Wave Passive Components*, Wiley, New York, 1988.
9. R. Sorrentino, *Numerical Methods for Passive Microwave and Millimeter Wave Structures*, IEEE Press, New York, 1989.
10. M. Sadiku, *Numerical Techniques in Electromagnetics*, CRC Press, Boca Raton, FL, 1992.
11. A. Wexler, Solution of waveguide discontinuities by modal analysis, *IEEE Trans. Microwave Theory Tech.* **15**:508–517 (Sept. 1967).
12. P. H. Mastermann and P. J. B. Clarricoats, Computer field-matching solution of waveguide transverse discontinuities, *IEE Proc.* **118**:51–63 (Jan. 1971).
13. R. Sorrentino, M. Mongiardo, F. Alessandri, and G. Schiavon, An investigation of the numerical properties of the mode-matching technique, *Int. J. Num. Model.* **4**:19–43 (1991).
14. T. Rozzi and M. Mongiardo, E-plane steps in rectangular waveguide, *IEEE Trans. Microwave Theory Tech.* **39**:1279–1288 (Aug. 1991).
15. M. Guglielmi, G. Gheri, M. Calamia, and G. Pelosi, Rigorous multimode network numerical representation of inductive step, *IEEE Trans. Microwave Theory Tech.* **42**:317–326 (Feb. 1994).
16. J. D. Mahony, A low-frequency investigation into the discontinuity capacitance of a coaxial line terminated in a lossless, dielectric loaded circular guide, *IEEE Trans. Microwave Theory Tech.* **35**:344–346 (March 1987).
17. P. Guillot, P. Couffignal, H. Baudrand, and B. Theron, Improvement in calculation of some surface integrals: application to junction characterization in cavity filter design, *IEEE Trans. Microwave Theory Tech.* **41**:2156–2160 (Dec. 1993).
18. F. Dai, Scattering and transmission matrix representations of multiguide junctions, *IEEE Trans. Microwave Theory Tech.* **40**:1538–1544 (July 1992).
19. M. Guglielmi and C. Newport, Rigorous, multimode equivalent network representation of inductive discontinuities, *IEEE Trans. Microwave Theory Tech.* **38**:1651–1659 (Nov. 1990).
20. C. Sabatier, Scattering at an offset circular hole in a rectangular waveguide, *IEEE Trans. Microwave Theory Tech.* **40**:587–592 (March 1992).
21. U. Papziner and F. Arndt, Field theoretical Computer-Aided-Design of rectangular and circular iris coupled rectangular or circular waveguide cavity filters, *IEEE Trans. Microwave Theory Tech.* **41**:462–471 (March 1993).
22. R. Yang and A. S. Omar, Analysis of thin inclined rectangular aperture with arbitrary location in rectangular waveguide, *IEEE Trans. Microwave Theory Tech.* **41**:1461–1463 (Aug. 1993).
23. R. Yang and A. S. Omar, Investigation of multiple rectangular aperture irises in rectangular waveguide using TE_{mn}^x modes, *IEEE Trans. Microwave Theory Tech.* **41**:1369–1374 (Aug. 1993).
24. G. L. James, Admittance of irises in coaxial and circular waveguide for TE_{11} mode excitation, *IEEE Trans. Microwave Theory Tech.* **35**:430–434 (April 1987).

25. R. W. Scharstein and A. T. Adams, Thick circular iris in a TE₁₁ mode circular waveguide, *IEEE Trans. Microwave Theory Tech.* **36**:1529–1531 (Nov. 1988).
26. Z. Shen and R. H. MacPhie, Scattering by a thick off-centered circular iris in circular waveguide, *IEEE Trans. Microwave Theory Tech.* **43**:2639–2642 (Nov. 1995).
27. J.-W. Tao and H. Baudrand, Multimodal variational analysis of uniaxial waveguide discontinuities, *IEEE Trans. Microwave Theory Tech.* **39**:506–516 (March 1991).
28. T. Rozzi, F. Moglie, A. Morini, W. Gulloch, and M. Politi, Accurate full-band equivalent circuit of inductive posts in rectangular waveguide, *IEEE Trans. Microwave Theory Tech.* **40**:1000–1009 (May 1992).
29. H.-W. Yao, K. A. Zaki, A. E. Atia, and R. Hershtig, Full wave modeling of conducting posts in rectangular waveguide and its application to slot coupled combline filters, *IEEE Trans. Microwave Theory Tech.* **43**:2824–2830 (Dec. 1995).
30. G. Conciauro, M. Guglielmi, and R. Sorrentino, *Advanced Modal Analysis—CAD Techniques for Waveguide Components and Filters: Electromagnetic Field Expansion in Waveguides*, Wiley, New York, 2000.
31. J. M. Reiter and F. Arndt, A full-wave boundary contour mode-matching method BCMM for the rigorous CAD of single and cascaded optimized H-plane and E-plane bends, *Proc. IEEE Int. Microwave Symp.*, San Diego, CA, May 1994, pp. 1021–1024.
32. F. Alessandri, M. Mongiardo, and R. Sorrentino, Rigorous mode matching analysis of mitered E-plane bends in rectangular waveguide, *IEEE Microwave Guided Wave Lett.*, **4**:408–410 (Dec. 1994).
33. M. Mongiardo, A. Morini, and T. Rozzi, Analysis and design of full-band matched waveguide bends, *IEEE Trans. Microwave Theory Tech.* **43**:2965–2971 (Dec. 1995).
34. B. Gimeno and M. Guglielmi, Multimode equivalent network representation for H- and E-plane uniform bends in rectangular waveguide, *IEEE Trans. Microwave Theory Tech.* **44**:1679–1687 (Oct. 1996).
35. E. D. Sharp, An exact calculation for a T-junction of rectangular waveguides having arbitrary cross sections, *IEEE Trans. Microwave Theory Tech.* **15**:109–116 (Feb. 1967).
36. T. Obata and J. Chita, Improved theory for E-plane symmetrical tee junctions, *IEEE Trans. Microwave Theory Tech.* **37**:624–627 (March 1989).
37. P. Lampariello and A. A. Oliner, New equivalent network with simple closed-form expressions for open and slit-coupled E-plane tee junctions, *IEEE Trans. Microwave Theory Tech.* **41**:839–847 (May 1993).
38. B. N. Das and N. V. S. N. Sarma, Analysis of E-H plane tee junction using a variational formulation, *IEEE Trans. Microwave Theory Tech.* **39**:1770–1773 (Oct. 1991).
39. X.-P. Liang, K. A. Zaki, and A. E. Atia, A rigorous three plane mode-matching technique for characterizing waveguide T junctions, and its application in multiplexer design, *IEEE Trans. Microwave Theory Tech.* **39**:2138–2147 (Dec. 1991).
40. T. Sieverding and F. Arndt, Field theoretical CAD of open or aperture matched T-junction coupled rectangular waveguide structures, *IEEE Trans. Microwave Theory Tech.* **40**:353–362 (Feb. 1992).
41. J. Hirokawa, K. Sakurai, M. Ando, and N. Goto, An analysis of a waveguide T junction with an inductive post, *IEEE Trans. Microwave Theory Tech.* **39**:563–566 (March 1991).
42. J. M. Rebollar, J. Esteban, and J. Page, Fullwave analysis of three and four-port rectangular waveguide junctions, *IEEE Trans. Microwave Theory Tech.* **42**:256–263 (Feb. 1994).
43. A. Datta, A. M. Rajeev, A. Chakrabarty, and B. N. Das, S matrix of a broad wall coupler between dissimilar rectangular waveguides, *IEEE Trans. Microwave Theory Tech.* **43**:56–62 (Jan. 1995).
44. A. M. Rajeev and A. Chakrabarty, Analysis of wide compound slot-coupled parallel waveguide coupler and radiator, *IEEE Trans. Microwave Theory Tech.* **43**:802–809 (April 1995).
45. B. N. Das, P. V. D. S. Rao, and A. Chakraborty, Narrow wall axial-slot-coupled T junctions between rectangular and circular waveguides, *IEEE Trans. Microwave Theory Tech.* **37**:1590–1596 (Oct. 1989).
46. H. Baudrand, J.-W. Tao, and J. Atechian, Study on radiating properties of open-ended rectangular waveguides, *IEEE Trans. Antenn. Propag.* **36**:1071–1077 (Aug. 1988).
47. B. N. Das, A. Chakraborty, and S. Gupta, Analysis of waveguides-fed thick radiating rectangular windows in a ground plane, *IEE Proc. H* **138**:142–146 (April 1991).
48. M. Mongiardo and T. Rozzi, Singular integral equation analysis of flange-mounted rectangular waveguide radiators, *IEEE Trans. Antenn. Propag.* **41**:556–565 (May 1993).
49. T. S. Bird, Cross-coupling between open-ended coaxial radiators, *IEE Proc. Microwave Antenn. Propag.* **143**:265–271 (Aug. 1996).
50. T. S. Bird, Improved solution for mode coupling in different-sized circular apertures and its application, *IEE Proc. Microwave Antenn. Propag.* **143**:457–464 (Dec. 1996).
51. G. J. Stern and R. S. Elliot, Resonant length of longitudinal slots and validity of circuit representation: theory and experiment, *IEEE Trans. Antenn. Propag.* **33**:1264–1271 (Nov. 1985).
52. L. G. Josefsson, Analysis of longitudinal slots in rectangular waveguides, *IEEE Trans. Antenn. Propag.* **35**:1351–1357 (Dec. 1987).
53. R. Kastner, On the convergence of matrix elements in planar and waveguide problems, *IEE Proc. H* **138**:532–536 (Dec. 1991).
54. S. R. Rengarajan, Compound radiating slots in a broad wall of a rectangular waveguide, *IEEE Trans. Antenn. Propag.* **37**:1116–1123 (Sept. 1989).
55. L. G. Josefsson, A waveguide transverse slot for array application, *IEEE Trans. Antenn. Propag.* **41**:845–850 (July 1993).
56. J. Joubert, A transverse slot in the broad wall of inhomogeneously loaded rectangular waveguide for array application, *IEEE Microwave Guided Wave Lett.* **5**:37–39 (Feb. 1995).

WAVEGUIDE JUNCTIONS

RALPH LEVY
R. Levy Associates
La Jolla, California

1. INTRODUCTION

A waveguide junction comprises two or more waveguides connected by a common metallic region having relatively small volume. The number of such waveguides is denoted by n , and for $n = 2$ we have a simple junction of two

waveguides. In some cases one or more of the waveguides may be a transmission line supporting the TEM mode, such as coaxial line, stripline, or microstrip. When $n=2$, such a junction is known as an *adapter*, and is a very important basic microwave component. Three- and four-port junctions are also very important, and occasionally one sees junctions having $n > 4$, but these are comparatively rare. Frequently several waveguide junctions are connected to form more complex effective n -port junctions that may be used as power dividers, typically in antenna feed networks. In other cases they are combined with other components to realize microwave subassemblies, such as duplexers, multiplexers, and monopulse arrays. In the case of $n=4$ having certain symmetry properties, the junction becomes a 0° or 180° hybrid, which, together with 90° hybrids treated in the article WAVEGUIDE DIRECTIONAL COUPLERS, are the most commonly used four-port waveguide junctions.

In general the junction regions have complex shapes with various types of discontinuities that are describable only in terms of higher-order modes, which frequently and most desirably lead to equivalent-circuit representations. The multiport junction is depicted in Fig. 1, where each port supports a single mode. Note that if a single waveguide supports more than one mode, say, m modes, then it is represented as m distinct "waveguides" with m ports.

An excellent description of n -port junctions (microwave networks) is given in Ref. 1, particularly in Chap. 3, and actually it is probably valid to state that there has been very little fundamental advancement in the state of the art since that work, which dates to the 1940s, at least in a basic sense. The main additions are probably due to the use of effective computer techniques to solve Maxwell's equations for the junction regions, thus deriving scattering matrices. An important general conclusion stated there [1] is that waveguide junctions always have equivalent-circuit representations. Any one junction will have a variety of such equivalent circuits, but usually there is one having the minimum number of circuit elements and possessing simple frequency dependence. Such a "natural" equivalent circuit can often be found by a suitable choice of reference planes, and sometimes also in the choice of terminating impedances of the ports. Further information

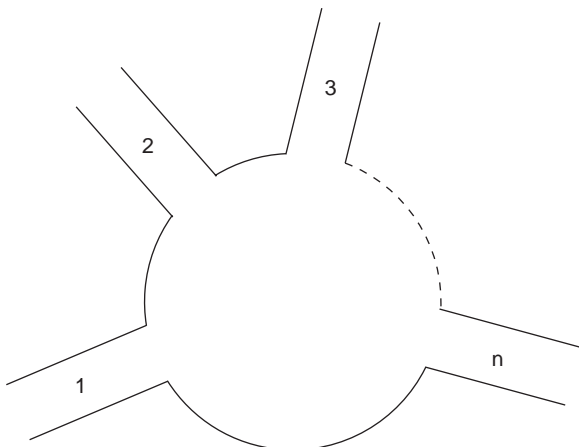


Figure 1. Schematic of an n -port waveguide junction.

on this general topic is given in Ref. 2, which also describes some methods for deriving equivalent circuits from numerically derived scattering matrices.

The treatment here is limited to passive reciprocal junctions, where the characteristic impedances of the ports are real. Ports having complex characteristic impedances may be handled using a simple modification [3]. We will be concerned primarily with the various waveguides at distances sufficiently far from the junction such that the dominant modes are the only ones of concern. As mentioned above, equivalent-circuit determination is very useful and important, and will be considered here in general terms.

The basic equations for the voltage and current at a port are

$$V = Ae^{-\gamma z} + Be^{\gamma z} \quad (1)$$

$$I = \frac{Ae^{-\gamma z} - Be^{\gamma z}}{Z_0} \quad (2)$$

where γ is the propagation constant and A and B have dimensions of voltage. At the arbitrary plane where $z=0$, we have $V=A+B$ and $I=(A-B)/Z_0$. If we now renormalize A and B so that $A=aZ_0^{1/2}$ and $B=bZ_0^{1/2}$, then at the plane $z=0$ (1) and (2) become

$$V = Z_0^{1/2}(a+b) \quad (3)$$

$$I = Z_0^{-1/2}(a-b) \quad (4)$$

Hence the net power flow into the port is

$$P = \text{Re}(VI^*) = \text{Re}\{(a+b)(a^* - b^*)\} = |a|^2 - |b|^2 \quad (5)$$

Thus $|a|^2$ and $|b|^2$ have the physical interpretation of incident and reflected powers, where a is the amplitude of the incident wave and b is the reflected wave amplitude. We now define the scattering matrix S according to

$$b_1 = S_{11}a_1 + S_{12}a_2 + \cdots + S_{1n}a_n$$

$$b_2 = S_{21}a_1 + S_{22}a_2 + \cdots + S_{2n}a_n$$

$$\vdots$$

$$b_n = S_{n1}a_1 + S_{n2}a_2 + \cdots + S_{nn}a_n$$

or

$$b = S \cdot a \quad (6)$$

where a and b are column vectors.

In the case of reciprocal networks each scattering matrix element satisfies the condition

$$S_{ij} = S_{ji} \quad i, j = 1, 2, \dots, n \quad (7)$$

or in scattering matrix representation, we have

$$S = S^{\text{tr}} \quad (8)$$

where S^{tr} denotes the transposed S matrix. When the network is lossless, then power conservation considerations lead to the unitary condition

$$S \cdot S^{tr*} = S \cdot S^* = \mathbf{1} \tag{9}$$

where $*$ indicates the complex conjugate matrix, and $\mathbf{1}$ is the unit matrix having entries of unity on the main diagonal and zero elsewhere. Sometimes $\mathbf{1}$ is denoted by I , meaning the identity matrix, but $\mathbf{1}$ is used here to avoid confusion with electric current I . Equation (9) is very important since it leads to a variety of basic and useful general properties for several types of n -port networks. It also leads to simpler expressions for other representations of microwave networks, such as the impedance, admittance, or transfer matrix representations.

2. IMPEDANCE MATRICES

The impedance matrix Z relates the voltages V_i and currents I_i ($i = 1, 2, \dots, n$) via the matrix equation

$$V = Z \cdot I \tag{10}$$

Where V and I consist of column vectors of the voltages V_i and currents I_i , and Z is, of course, an $n \times n$ square matrix having elements Z_{ij} . Using Eqs. (3) and (4) we can now relate the scattering and impedance matrices, and solving for a and b , we find

$$2Z_i^{1/2} a_i = (V_i + Z_i I_i) \tag{11}$$

$$2Z_i^{1/2} b_i = (V_i - Z_i I_i) \tag{12}$$

where Z_i is the real characteristic impedance of the i th port. Here the subscript i has been added to a and b to represent the forward and reflected wave amplitudes at the i th port. These equations may be expressed in matrix format if we define the characteristic impedance matrix of the n ports as

$$Z_0 = \begin{bmatrix} Z_1 & & & \\ & Z_2 & & \\ 0 & & \ddots & 0 \\ & & & Z_n \end{bmatrix} \tag{13}$$

where the positive real characteristic impedances of each port form the main diagonal, with zero entries elsewhere. Now Eqs. (11) and (12) may be expressed in matrix form as

$$a = Z_0^{-1/2} \frac{V + Z_0 \cdot I}{2} \tag{14}$$

$$b = Z_0^{-1/2} \frac{V - Z_0 \cdot I}{2} \tag{15}$$

and substituting for V using (10) we find

$$a = Z_0^{-1/2} \frac{(Z + Z_0)I}{2} \tag{16}$$

$$b = Z_0^{-1/2} \frac{(Z - Z_0)I}{2} \tag{17}$$

Substituting (16) and (17) into (6), we find

$$Z_0^{-1/2} \frac{(Z - Z_0) \cdot I}{2} = S \cdot Z_0^{-1/2} \frac{(Z + Z_0) \cdot I}{2} \tag{18}$$

which after a few cancellations and inverse multiplications gives S in the form

$$S = Z_0^{-1/2} (Z - Z_0) \cdot (Z + Z_0)^{-1} \cdot Z_0^{1/2} \tag{19}$$

which is the desired relationship giving the scattering matrix as a function of the impedance matrix.

It is usually more important to express the impedance matrix Z as a function of S , and this may be derived from Eq. (19) by carrying out the appropriate pre- and postmatrix multiplications, finally giving

$$Z = Z_0^{1/2} (\mathbf{1} - S)^{-1} (\mathbf{1} + S) Z_0^{1/2} \tag{20}$$

where $\mathbf{1}$ is the unit matrix. Note that in the case of a one-port network this equation becomes the familiar relationship

$$\frac{Z}{Z_0} = \frac{1 + S_{11}}{1 - S_{11}} \tag{21}$$

The n -port admittance matrix Y is given by an expression similar to Eq. (20)

$$Y = Y_0^{1/2} (\mathbf{1} + S)^{-1} \cdot (\mathbf{1} - S) \cdot Y_0^{1/2} \tag{22}$$

where Y_0 is, of course, similar to (13), and also $Y_0 = Z_0^{-1}$.

The scattering matrix of an n -port network always exists, but this is not always the case for the impedance and/or admittance matrices; for instance, $(\mathbf{1} + S)$ occasionally becomes a zero matrix or has a zero determinant; then $(\mathbf{1} + S)^{-1}$ is a singular matrix and Z as derived by (20) does not exist. In such a case Y probably exists, and if not, then the network may contain ideal transformers for which Z and Y do not exist.

An interesting special case is one where the scattering matrix is purely imaginary,

$$S = jS_i \tag{23}$$

where S_i is a real matrix. In this case we see that

$$SS^* = S_i^2 = -S^2 = \mathbf{1} \tag{24}$$

Here the unitary condition (9) has been used.

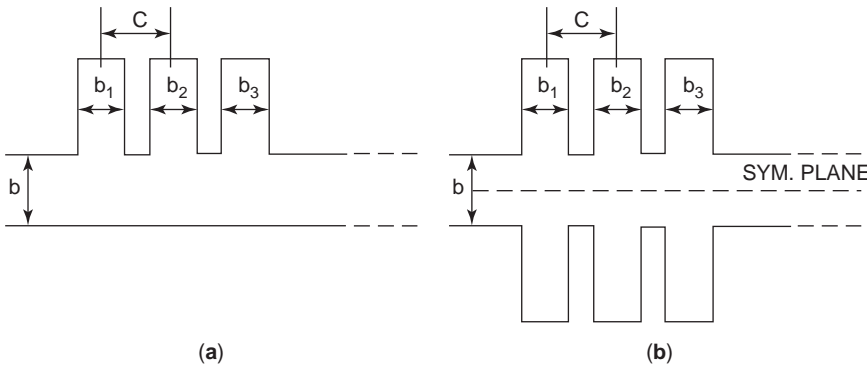


Figure 2. Interacting three- and four-port junctions spaced along a main waveguide to form a resonated stub bandstop filter: (a) asymmetric filter; (b) symmetric filter.

Hence we see that

$$(\mathbf{1} - S)(\mathbf{1} + S) = \mathbf{1} - S^2 = 2 \cdot \mathbf{1}$$

and therefore

$$(\mathbf{1} - S)^{-1} = \frac{\mathbf{1} + S}{2} \quad (25)$$

Consider the case where the port impedances are normalized to unity, that is, $Z_0 = \mathbf{1}$. Equation (20) becomes

$$Z = (\mathbf{1} - S)^{-1} \cdot (\mathbf{1} + S) = \frac{(\mathbf{1} + S)^2}{2} = \frac{1 + 2S + S^2}{2} = S \quad (26)$$

where we have used $S^2 = -\mathbf{1}$ from (24). Hence we have the remarkable result that the normalized impedance matrix of an n -port is identical to its scattering matrix when the latter is purely imaginary. An example of this situation is given in Section 5.2 on a four-port network, namely, a rat-race hybrid junction.

3. TWO-PORT NETWORKS

Numerous examples of two-port junctions of waveguides are given in Ref. 1 (where they are termed *four-terminal networks*) and elsewhere. Examples include inductive and capacitive irises in rectangular waveguides, E - and H -plane steps, and various junctions in circular cross-sectional waveguides. These are not dealt with in this article because the topic is well documented elsewhere as in Ref. 1, and also because the more interesting properties of waveguide junctions occur for three or more ports. A class of two-ports not treated in Ref. 1 is the coaxial-to-waveguide adapter, and readers are referred to the literature on this topic, such as Ref. 4, which also gives other pertinent references.

4. THREE-PORT NETWORKS

One of the most important properties of three-port networks is that it is impossible to obtain a match simultaneously at all three ports. If there were such a junction, it would have a scattering matrix having a zero main

diagonal:

$$S = \begin{bmatrix} 0 & \mathbf{S}_{12} & \mathbf{S}_{13} \\ \mathbf{S}_{12} & 0 & \mathbf{S}_{23} \\ \mathbf{S}_{13} & \mathbf{S}_{23} & 0 \end{bmatrix} \quad (27)$$

If we now apply the unitary condition (9) to this matrix, the following equations result:

$$\mathbf{S}_{12}\mathbf{S}_{12}^* + \mathbf{S}_{13}\mathbf{S}_{13}^* = 1$$

$$\mathbf{S}_{12}\mathbf{S}_{13}^* = 0 \quad \mathbf{S}_{12}\mathbf{S}_{23}^* = 0 \quad \mathbf{S}_{13}\mathbf{S}_{23}^* = 0 \quad (28)$$

From the last three equations (28) we see that two of \mathbf{S}_{12} , \mathbf{S}_{13} , and \mathbf{S}_{23} must be zero. In such case one row of the S matrix (27) will be all zero, which is impossible.

4.1. T Junctions

Among the important three-port networks are E -plane and H -plane T junctions and Y junctions. They received extensive treatment in Ref. 1, and in the case of T junctions more recent papers such as Ref. 5 have confirmed the validity of the early work. T junctions are an important component part of many microwave networks, such as filters with series or shunt stubs, and branch guide couplers. It is important to realize that the equations given for E - and H -plane T junctions in Ref. 1 are not accurate except in a rather restricted range of design parameters, but the information given in the various graphs is very good, as demonstrated in Ref. 5 (Figs. 9 and 10).

There is an important restriction on the validity of the results that is not well described in the literature, and this concerns the effect on the equivalent circuits when two or more T junctions are spaced along a connecting waveguide. This is indicated in the case of E -plane T junctions in Fig. 2a, and Fig. 2b shows a related situation where the junctions are also located across from one another, forming so-called cross-junctions. Considering one such junction of Fig. 2b with the short circuits in the vertical arm removed, we see that it is actually a four-port, but the device has a symmetry plane down the centerline of the main (horizontal) waveguide, and it may be treated as a three-port problem. The branchlines are shown short-circuited in Fig. 2 to form a type of waveguide filter known

as a resonated stub waveguide bandstop filter. When the spacing between the stubs c is sufficiently small, then the junctions interact, especially when the various b dimensions are somewhat large. The effect is observed as a considerable narrowing of the filter stop bandwidth. A discussion of means by which such interaction problems may be solved is given in Ref. 6, but the method has not yet been applied to the interacting stub situation.

Another useful class of T junctions are the E - and H -plane aperture coupled junctions, which are adequately treated in Ref. 1. They find application in E - and H -plane waveguide manifold multiplexers, where the filters are directly connected to the manifold rather than being offset by a length of waveguide, which forms an open T junction.

4.2. E -Plane Bifurcations

Another useful three-port junction treated in Ref. 1 is the E -plane bifurcation. This is shown in one of several possible formats in Fig. 3, which indicates it as a type of Y junction where the output arms are folded to become parallel and adjacent to one another. This is a very compact junction that is useful in the design of waveguide multiplexers. Thus, if bandpass filters tuned to different frequencies and having nonoverlapping passbands are introduced into the two folded output arms of Fig. 3 and their reference planes are correctly located with respect to the input or common port, a diplexer results. Several examples of the technique are given in Ref. 7.

5. FOUR-PORT NETWORKS

The types of four-port networks considered here have just one plane of symmetry; four ports with two such symmetry planes being considered in the article WAVEGUIDE DIRECTIONAL COUPLERS. The single plane of symmetry results in hybrid junctions where for one type of input port (the difference port) a pair of output ports have a phase difference of 180° and the remaining port is isolated. For a second type of input port, actually the isolated port of the previous 180° case, the phase difference is 0° , and this input port is known as the *sum port*. It can be shown that the scattering matrix of an ideal four-port 180° hybrid is given by

$$S = 2^{-1/2} \begin{bmatrix} 0 & 0 & j & j \\ 0 & 0 & j & -j \\ j & j & 0 & 0 \\ j & -j & 0 & 0 \end{bmatrix} \tag{29}$$

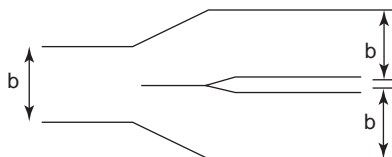


Figure 3. E -plane bifurcation.

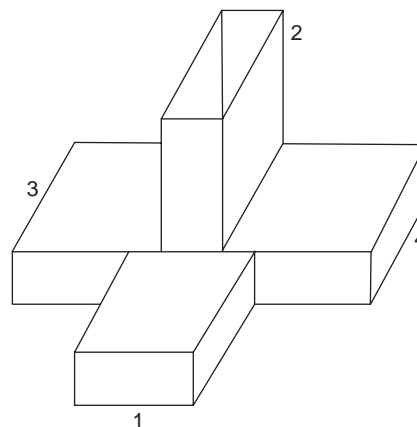


Figure 4. Magic-T junction.

We see that all ports are matched, ports 1 and 2 are isolated as are ports 3 and 4. The phase difference between S_{13} and S_{14} is zero in accordance with one of the initial conditions, and that between S_{23} and S_{24} is the required 180° . It is easily seen that the scattering matrix of (29) is unitary, satisfying the basic equation (9).

5.1. Magic-T Junctions

The abovementioned conditions hold for the magic-T shown in Fig. 4, where the input port is port 2 to give 180° phase difference between the output signals at ports 3 and 4, and port 1 is isolated. When the input is switched to port 1, output signals at ports 3 and 4 are in phase and port 2 is isolated. The phase properties may be deduced from the fact that with excitation at port 1 the hybrid degenerates to an H -plane three-port, and the electric fields in ports 3 and 4 of Fig. 5a are in phase. With excitation at port 2, the junction appears as an E -plane three-port and then, as indicated in Fig. 5b, the electric fields are in opposite phase in ports 3 and 4. Good match and isolation are ensured by incorporating irises or other obstacles in the common junction.

In practice it is perhaps more common to utilize more compact versions of the magic-T junction where waveguides 3 and 4 are folded to become parallel in either the E or H plane. Such T junctions give more compact physical realizations for diplexers and other sub-assemblies. Further information is given in Ref. 8 (pp. 162-163).

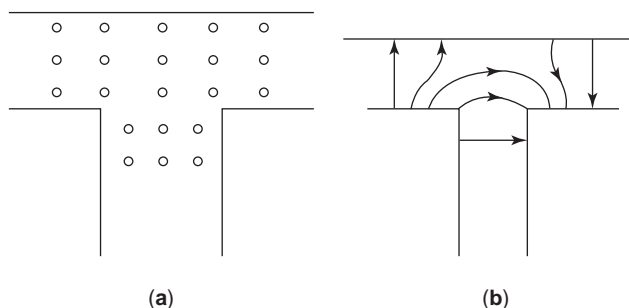


Figure 5. Electric field patterns of (a) H -plane T, (b) E -plane T.

5.2. Waveguide Ring (Rat-Race) Hybrids

A waveguide realization of a ring hybrid junction is shown in Fig. 6, where the plan view shows the narrow dimensions of the waveguide, with the uniform broad dimensions at right angles to the plane of the figure. Hence the ring is a composite of four E -plane T junctions. The characteristic impedance of the ring is lower than that of the input arms by a factor of $2^{1/2}$; specifically, the narrow dimension of the ring waveguide is smaller than that of the input ports. This is the dual of the similar ring hybrids built in TEM lines, such as coaxial, stripline, or microstrip, where the individual T junctions are of the shunt type, and the impedance of the ring is then *higher* than the input ports by the factor $2^{1/2}$. Note that in both cases the dimensions of the ring determining the characteristic impedance decreases, namely, the waveguide height, or the cross section of the inner conductor of the TEM line. The port nomenclature of Fig. 6 is chosen to make the scattering matrix identical to that for the magic-T junction, as given by Eq. (29). The sum port is port 1, and the difference port is port 2. Port 3 is also a sum port, and port 4 is a difference port, as deduced from Eq. (29).

It is now possible to consider the synthesis of the ring hybrid commencing from the scattering matrix (29), knowing that since it is purely imaginary, the impedance matrix is identical, as given by Eq. (26). Actually the rat-race realization shown in Fig. 6 becomes obvious, since a quarter-wavelength waveguide of characteristic impedance Z_0 between ports i and k gives a matrix entry jZ_0 , while if the waveguide is of length $\frac{3}{4}$ wavelength, the matrix entry is $-jZ_0$. A similar result may be obtained for the TEM line ring hybrid where one starts from an admittance matrix given by Eq. (29). The reasoning for this dual-admittance case is somewhat simpler and more familiar since the nodal admittance matrix has a more obvious synthesis in the form of the ring hybrid.

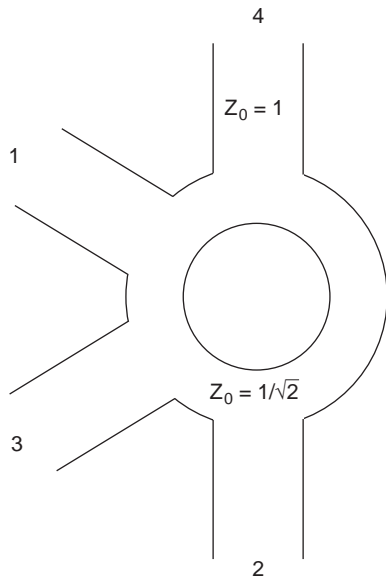


Figure 6. Waveguide rat-race or ring hybrid.

Numerous detailed reports on the various waveguide junctions and associated devices with actual example designs are given in several of the references listed below.

BIBLIOGRAPHY

1. N. Marcuvitz, ed., *Waveguide Handbook*, McGraw-Hill, New York, 1951.
2. R. Levy, Derivation of equivalent circuits of microwave structures using numerical techniques, *IEEE Trans. Microwave Theory Tech.* **47**:1688–1695 (Sept. 1999).
3. K. Kurokawa, Power waves and the scattering matrix, *IEEE Trans. Microwave Theory Tech.* **13**:194–202 (March 1965).
4. R. Levy and L. W. Hendrick, Analysis and synthesis of in-line coaxial-to-waveguide adapters, *2002 IEEE Int. Microwave Symp. Digest*, June 2002, Vol. 2, pp. 809–811.
5. X-P. Liang, K. A. Zaki, and A. E. Atia, A rigorous three plane mode-matching technique for characterizing waveguide T-junctions, and its application in multiplexer design, *IEEE Trans. Microwave Theory Tech.* **39**:2138–2147 (Dec. 1991).
6. R. Levy, Determination of simple equivalent circuits of interacting discontinuities in waveguides or transmission lines, *IEEE Trans. Microwave Theory Tech.* **48**:1712–1716 (Oct. 2000).
7. J. Dittloff and F. Arndt, Rigorous field theory design of millimeter-wave E-plane integrated circuit multiplexers, *IEEE Trans. Microwave Theory Tech.* **37**:340–350 (Feb. 1989).
8. R. Levy, Directional couplers, in L. Young ed., *Advances in Microwaves*, Academic Press, New York, 1966, Vol. 1, pp. 115–209.

WAVEGUIDE OSCILLATORS

ERIC L. HOLZMAN
Northrop Grumman
Corporation
Baltimore, Maryland

1. INTRODUCTION

Waveguide oscillators are DC-to-RF converters that function primarily as millimeter-wave power sources. Compared to more traditional millimeter-wave sources, such as klystrons, magnetrons, and traveling-wave tubes, these oscillators are lower in cost, and smaller in size, require lower operating voltages, and have higher reliability. A waveguide oscillator comprises two parts: (1) an *active element*, usually a packaged, two-terminal, solid-state device such as an *impact avalanche and transit time (IMPATT) diode* or *Gunn device*, which converts DC to RF power, and (2) a *passive element*, the waveguide circuit, which provides the DC power to the diode, the electromagnetic conditions required to sustain oscillation, a port for output of the RF power, and a stable thermal environment. The active device, mounted in an optimum circuit, determines the *conversion efficiency*, the ratio of RF output power to DC input power, a parameter that

decreases with frequency and is usually less than 20%. The principles governing IMPATT and Gunn device operation are complex and are described by Holzman and Robertson [1]. The key characteristic of these devices is that they exhibit a bias and temperature-dependent negative resistance at microwave frequencies.

Figure 1 shows a simplified internal view of a waveguide oscillator. A coaxial transmission line delivers DC power to the device, which is mounted on the floor of the waveguide in a gap under the coax center conductor. Unlike microwave transistors, IMPATT and Gunn devices will oscillate spontaneously without a feedback circuit when they are DC-biased. The waveguide circuit forms the resonator that tunes the *RF operating point* (output power and frequency) of the device.

The fundamental condition for oscillation is the oscillator equation, which states that the device impedance plus the circuit impedance equals zero ohms

$$Z_{\text{device}}(\text{frequency}, P_{\text{out}}, V_{\text{DC}}, I_{\text{DC}}, T) + Z_{\text{circuit}}(\text{frequency}, \text{geometry}) = 0 \tag{1}$$

where T = temperature. Kurokawa [2] showed that an oscillator’s output power is determined primarily by the resistive portion of the oscillator equation

$$R_{\text{device}}(P_{\text{out}}, V_{\text{DC}}, I_{\text{DC}}, T) = -R_{\text{circuit}}(\text{frequency}, \text{geometry}) \tag{2}$$

and an oscillator’s fundamental frequency of oscillation satisfies the reactive portion of the equation

$$X_{\text{device}}(\text{frequency}, P_{\text{out}}, V_{\text{DC}}, I_{\text{DC}}, T) = -X_{\text{circuit}}(\text{frequency}, \text{geometry}) \tag{3}$$

Since the circuit resistance must be greater than zero, the device must exhibit *negative resistance* to oscillate. A typical device’s resistance is on the order of a few ohms, while

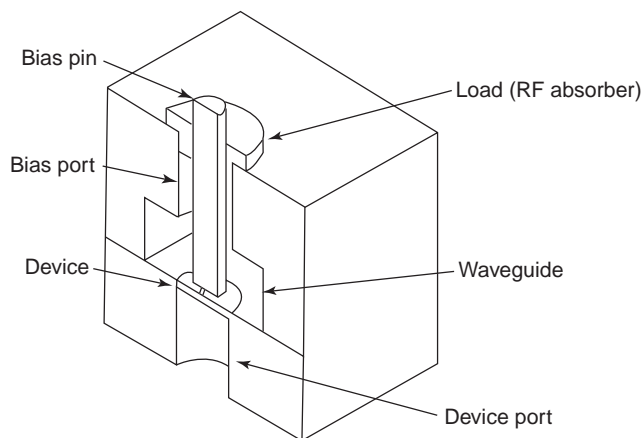


Figure 1. Cross-sectional view of a waveguide oscillator circuit. (Reprinted with permission from *Solid-State Microwave Power Oscillator Design* by E. L. Holzman and R. S. Robertson, Artech House Publishers, Norwood, MA, USA, www.artechhouse.com.)

the characteristic impedance of the dominant TE_{10} mode of the rectangular waveguide is a few hundred ohms. The oscillator circuit must be able to transform these widely varying impedances to satisfy Eqs. (2) and (3).

This article draws on material from the book by Holzman and Robertson [1] to discuss three different solid-state waveguide oscillator topologies:

- The single-device oscillator (SDO) is simply a single active device in a waveguide circuit. The frequency and power of an SDO can be tuned mechanically by changing the dimensions of the waveguide circuit or by adjusting the device’s DC bias point.
- A voltage-controlled oscillator (VCO) is an SDO plus an electronically adjustable, reactive tuning element such as a varactor diode placed in the waveguide circuit. The VCO frequency of oscillation can be adjusted with a separate DC voltage over a bandwidth that depends on the varactor’s range of reactance adjustment.
- A waveguide power combiner adds the power output of two or more active devices within a single waveguide circuit.

2. SINGLE-DEVICE OSCILLATORS

Single-device waveguide oscillators are used as bias tunable sources or device evaluation fixtures. Figure 2 shows four commonly used waveguide circuits. Each consists of waveguide/coaxial-line junction, with the coaxial-line center conductor supplying bias to the active device. The center conductor also influences the circuit impedance presented at the device terminals. The coaxial line is sized so that only the TEM-mode propagates, which requires that the sum of the inner and outer conductor diameters be less than $c/\pi f_{\text{max}}$, where c is the speed of light in the

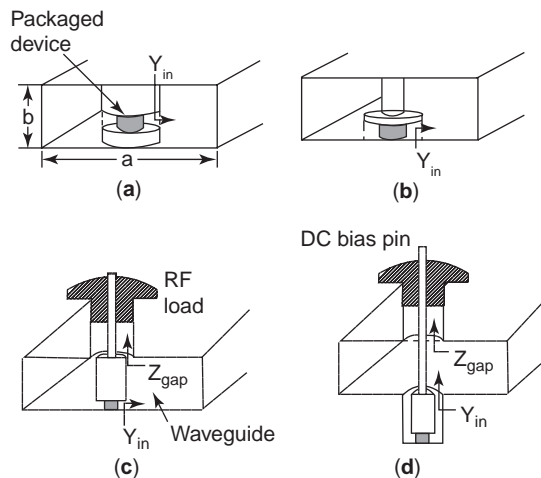


Figure 2. Waveguide oscillator circuits: (a) post gap; (b) top hat; (c) coaxial gap; (d) cross-coupled coaxial. (Reprinted with permission from *Solid-State Microwave Power Oscillator Design* by E. L. Holzman and R. S. Robertson, Artech House Publishers, Norwood, MA, USA, www.artechhouse.com.)

coax dielectric and f_{\max} is the maximum frequency of oscillation [3]. The RF-absorbing load material isolates the waveguide circuit from the external environment and presents a well-defined load impedance. It also maintains the coaxial-line center conductor concentric within the bias port.

In general, one of the two waveguide ports delivers the RF output power, while the other waveguide port is terminated in a short circuit, which often is adjustable. The output port may include a reactive tuning element such as an iris or post to further adjust the circuit impedance. The primary differences between the four circuits in Fig. 2 appear in the device mount region. In the post in Fig. 2a, a gap is placed at an arbitrary position above the waveguide floor. The diameter and the position of the gap determine how the propagating and evanescent modes in the waveguide couple to the device. Eisenhart and Khan discuss the behavior of the *post gap* circuit in some detail [4,5]. The *top hat* circuit in Fig. 2b is similar, but the device generally sits on the floor of the waveguide, and a radial disk transforms the circuit admittance Y_{in} to the device's package surface. This circuit is used when the device package becomes relatively large compared to the waveguide, at millimeter-wave frequencies. The circuit in Fig. 2c uses the RF-absorbing load in the bias port of the coaxial line to help tune the device operating point. Figure 2d shows the *Kurokawa* or *cross-coupled* circuit, which recesses the device below the waveguide floor so that the circuit admittance Y_{in} is transformed to the device by a section of coaxial line.

2.1. Waveguide Circuit Analysis

Oscillator circuits can be tuned by purely empirical means. However, to use the circuits in Fig. 2 effectively, an accurate electromagnetic model helps calculate the circuit impedance at the device terminals. Commercially available, generalized, three-dimensional frequency or time-domain simulators certainly can analyze these circuits. However, for speed and optimization, there are specialized, numerically efficient, and accurate, well-validated models for all four circuits [1,6–12]. With these circuit models, one can calculate the circuit admittance Y_{in} (see Fig. 2). Then, with a second transformation, depending on the device mount configuration, one can calculate the circuit impedance at the device package.

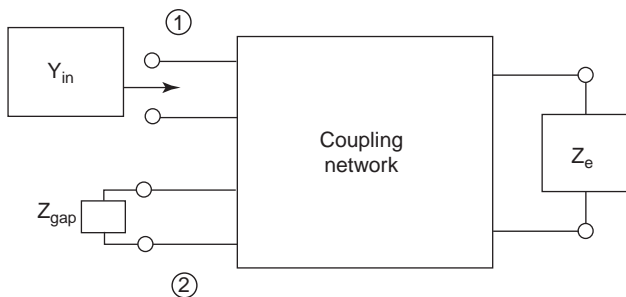


Figure 3. Waveguide oscillator circuit equivalent circuit. (Reprinted with permission from *Solid-State Microwave Power Oscillator Design* by E. L. Holzman and R. S. Robertson, Artech House Publishers, Norwood, MA, USA, www.artechhouse.com.)

All four circuits in Fig. 2 can be represented by an equivalent circuit of the form shown in Fig. 3. The desired circuit admittance is Y_{in} . Z_{gap} is the impedance presented at the reference plane where the coaxial line enters the waveguide (see, e.g., Fig. 2c), and Z_e is the total impedance presented by the waveguide, with equations for its computation given in Ref. 1. For the post gap circuits shown in Figs. 2a and 2b, Z_{gap} has an impedance of $0\ \Omega$ at the frequency of oscillation. However, the coax line delivers the bias to the device, so a lowpass filter is required in the bias port. Figure 4 shows a standard low–high–low filter. The cascading of three quarter-wave impedance transformers makes Z_{gap} a very low RF impedance as given by the following equation [1]:

$$Z_{\text{gap}} = \frac{1}{Z_L} \left(\frac{Z_{\text{c,lo}}^2}{Z_{\text{c,hi}}} \right)^2 \quad (4)$$

As shown in Fig. 4, dielectric sleeves are wrapped around the low-impedance section inner conductors to maintain their concentricity and to prevent the occurrence of a DC short circuit.

A nonzero Z_{gap} for the coax gap and cross-coupled coaxial circuits provides an extra variable for tuning the oscillator. One can use standard transmission-line equations to transform the load impedance of the RF absorber to the post gap as explained in Ref. 1, which also describes a way to measure the impedance of the absorber.

The equation giving the input admittance in terms of Y_{in} , Z_{gap} and Z_e is

$$Y_{\text{in}} = Y_{11} - Z_{\text{gap}} \frac{Y_{12}Y_{21}}{1 + Z_{\text{gap}}Y_{22}} \quad (5)$$

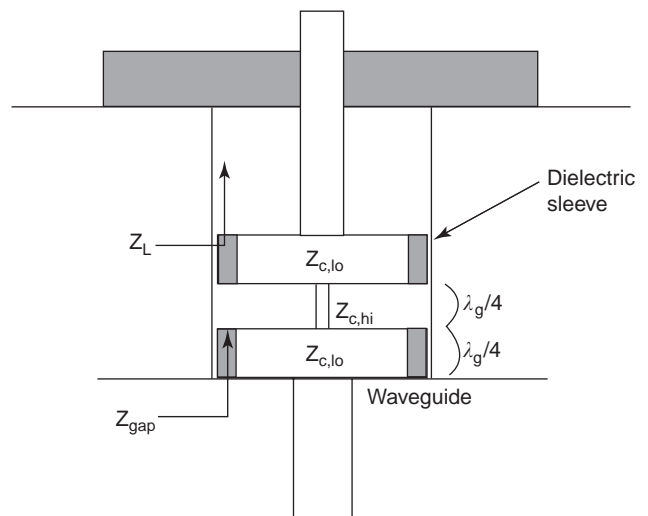


Figure 4. Low–high–low impedance transformer for applying DC bias and RF short-circuiting the coaxial waveguide bias port. (Reprinted with permission from *Solid-State Microwave Power Oscillator Design* by E. L. Holzman and R. S. Robertson, Artech House Publishers, Norwood, MA, USA, www.artechhouse.com.)

where

$$Y_{ii} = Z_{\text{gap}} \frac{1}{Z_e R_i^2} + jB_i, \quad i = 1, 2 \quad (6)$$

$$Y_{21} = Z_{\text{gap}} \frac{1}{Z_e R_1 R_2} + jB_{21} \quad (7)$$

Expressions for the terms in Eqs. (5)–(7) can be found in Ref. 1.

One uses Eq. (5) to compute the circuit admittance, and then transforms it through the device mount to the device terminals. This second calculation is relatively straightforward and involves simple equations. Figure 5 shows the

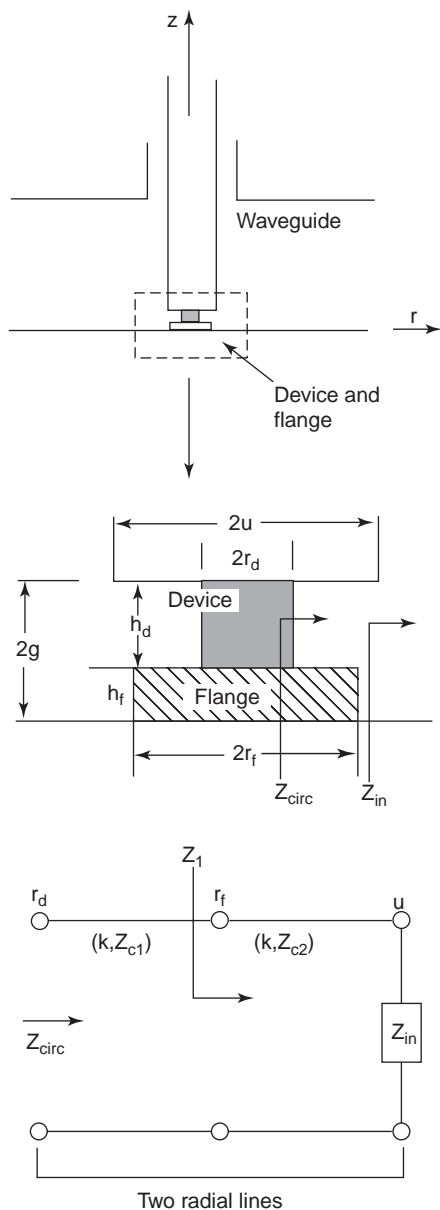


Figure 5. Coaxial gap oscillator circuit device mount and equivalent circuit. (Reprinted with permission from *Solid-State Microwave Power Oscillator Design* by E. L. Holzman and R. S. Robertson, Artech House Publishers, Norwood, MA, USA, www.artechhouse.com.)

post gap circuit (Fig. 2c) in detail. As long as the active device and gap are small relative to a wavelength, we can assume that the electromagnetic field in the gap is uniform, and that the electric field vector is vertical in orientation. One can use radial transmission-line equations to

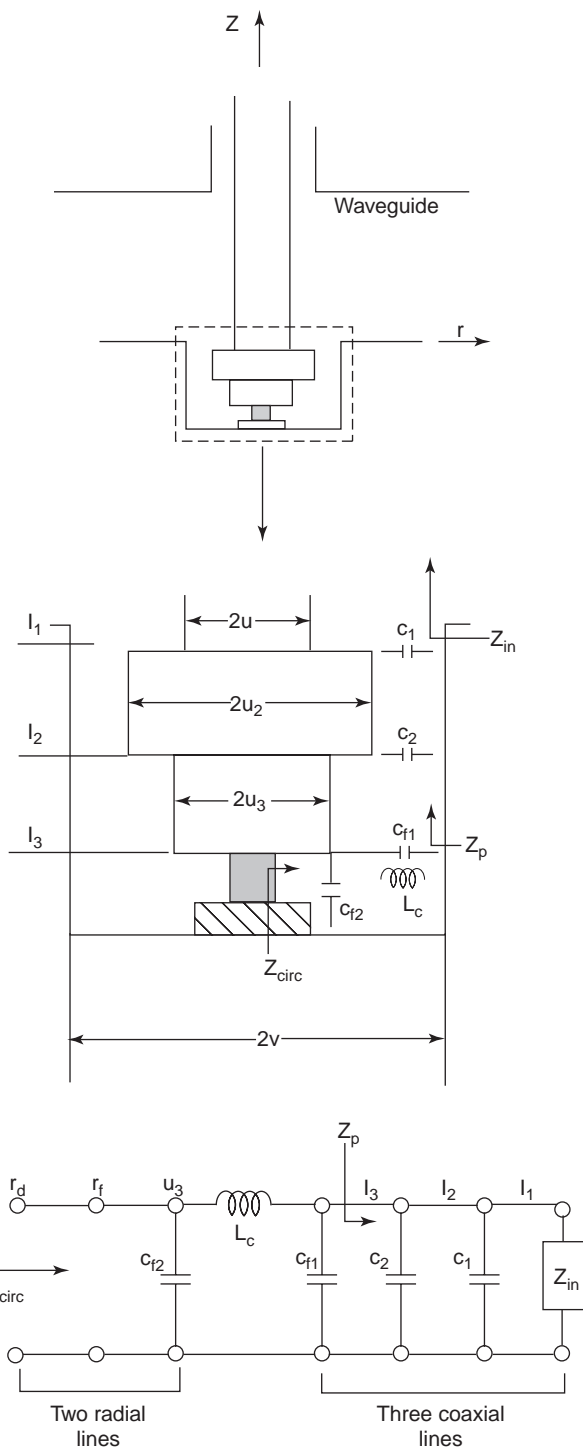


Figure 6. Device mount and equivalent circuit for the cross-coupled circuit. (Reprinted with permission from *Solid-State Microwave Power Oscillator Design* by E. L. Holzman and R. S. Robertson, Artech House Publishers, Norwood, MA, USA, www.artechhouse.com.)

transform the impedance Z_{in} ($1/Y_{in}$) to the device package [3]. Getsinger describes a package lumped inductance and capacitance model that gives the actual semiconductor chip impedance [13]. However, for oscillator design, this additional effort is seldom necessary since package characteristics tend to be repeatable. Further, above 40 GHz Getsinger’s model loses validity as most packages can no longer be modeled with lumped elements.

Figure 6 shows the details of the device mount for the cross-coupled circuit mount. The approach to calculating the circuit admittance at the device package is similar. A series of coaxial line transformations are applied to Z_{in} ($1/Y_{in}$) to obtain Z_p , and then Getsinger’s model in combination with radial line transformations gives Z_{circ} at the device package.

As an evaluation fixture for devices, a properly designed waveguide circuit allows users a wide range of mechanical tuning. They can tune a device to several different operating points. With an accurate electromagnetic model of their waveguide circuit, they can calculate the circuit impedance at the device terminals, and, in combination with the oscillation equations (2) and (3), predict the device impedance curve versus frequency. The device then can be mounted in a different waveguide circuit, and its resistance and reactance curves can be used to predict output power and frequency of oscillation.

2.2. Oscillator Circuit Hardware Design

Waveguide oscillator circuits are fabricated from metals such as copper, which have excellent electrical and thermal properties. Most circuits are nickel- and gold-plated to prevent oxidation. Since nickel is a relatively poor electrical conductor, the overlying gold should be a minimum of several skin depths thick. Figure 7 shows a Gunn oscillator DC bias circuit, and Fig. 8 shows a waveguide circuit housing that has been designed for maximum mechanical adjustment. There are two main parts to the housing: (1) bias port and rectangular waveguide cutout and (2) device port and rectangular waveguide floor. These parts are precision-aligned with metal dowel pins. One should choose a waveguide height that is below the standard to minimize higher-order-mode effects, which tend to create startup problems such as frequency hopping and spurious oscillations [17]. The active device is mounted in the device port. Device port shims are used to recess the device and adjust the circuit admittance. The coaxial-line center conductor slides through the RF-absorbing load to contact the device. For high-power oscillators, the load may have to be lengthened and a bias port filter may be needed to suppress *parametric oscillations* at multiples or fractions of the fundamental frequency [18–21]. A section of empty waveguide is attached to one waveguide port, and an adjustable short circuit is inserted for tuning. A good

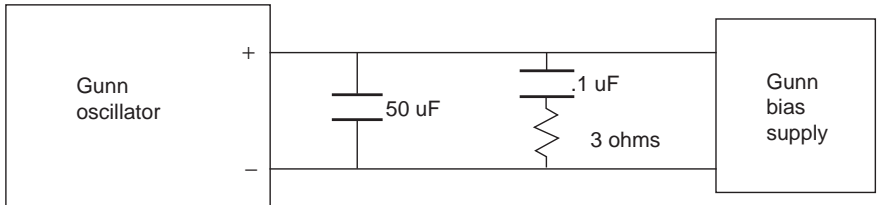


Figure 7. Gunn oscillator DC bias circuit schematic. (Reprinted with permission from *Solid-State Microwave Power Oscillator Design* by E. L. Holzman and R. S. Robertson, Artech House Publishers, Norwood, MA, USA, www.artechhouse.com.)

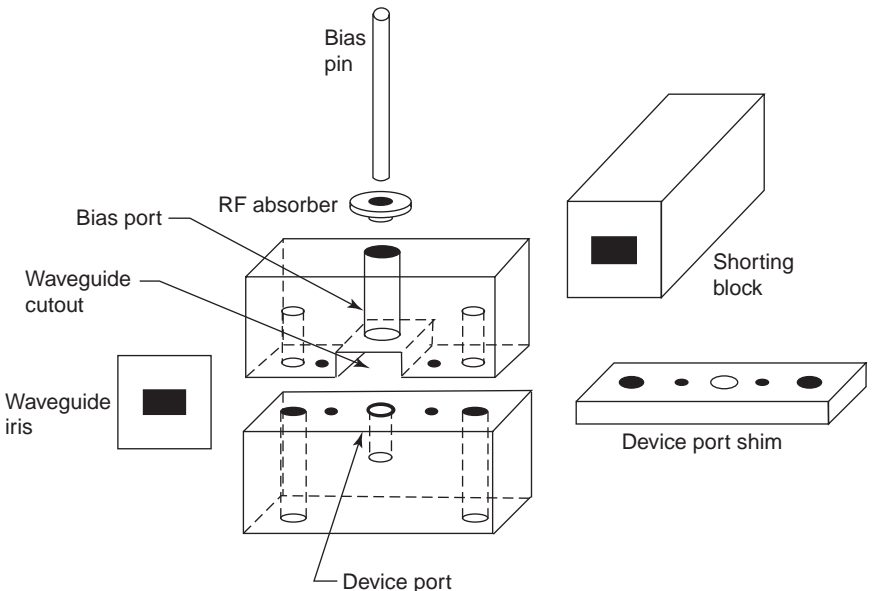


Figure 8. Waveguide oscillator circuit assembly. (Reprinted with permission from *Solid-State Microwave Power Oscillator Design* by E. L. Holzman and R. S. Robertson, Artech House Publishers, Norwood, MA, USA, www.artechhouse.com.)

waveguide short circuit, with a well-defined reference plane such as that designed by Eisenhart and Monzello [22], is important, especially if one is analyzing the circuit with a numerical model. At the other waveguide port, one can attach irises for further tuning. These can be etched from standard brass shim stock using a photolithographic print-and-etch process. An isolator at the output is often required to prevent external mismatched loads from tuning the oscillator frequency and output power.

2.3. External Bias Circuit Design

One must exercise caution when applying DC bias to two-terminal device oscillators. Voltage spikes or polarity changes can be catastrophic. A zener diode, shunted across the DC supply terminals, with its positive terminal connected to the negative of the supply, can limit such a polarity change. The zener diode reverse breakdown voltage must exceed the normal maximum DC bias voltage required for the active device, while its forward voltage should be less than one volt. If the polarity of the supply output changes, the zener forward voltage will limit the supply. If a zener diode provides inadequate protection, a voltage regulator may be needed.

Long wire leads to power supplies can behave as resonant circuits at frequencies as high as 100 MHz and cause unwanted bias circuit oscillations. To suppress these oscillations, one can place a capacitor close to the active device; a thin, annular, discoidal capacitor may have to be placed in the bias port coaxial line. It is wise to watch for bias circuit oscillations with voltage and current probes connected to an oscilloscope. Figure 7 shows the DC bias circuit for a Gunn oscillator driven by a regulator. Brackett [14] and Lee and coworkers [15,16] discuss IMPATT biasing in some detail.

2.4. Temperature Effects

An oscillator's power and frequency will change with temperature because the properties of solid-state materials and the circuit housing dimensions are temperature-dependent. If the circuit Q factor is high, thermal expansion of the housing can be the main cause of frequency drift. The differential metal expansion technique can be employed to cancel the changes in circuit size with temperature [17]. Alternatively, one can build the circuit out of a metal such as *invar*, a nickel-steel alloy that has a low thermal expansion coefficient. Even so, if the device is not well heatsunk, the oscillator frequency may exhibit *post-tuning drift* for minutes after the bias is applied. Sometimes the only way to eliminate temperature effects is to attach a heater to the housing.

Temperature effects also arise when an oscillator's DC bias is pulsed on and off. The active device reexperiences the startup phase at the beginning of each pulse. During the pulse, the device's junction temperature increases, causing the oscillator to *chirp* as its frequency drifts monotonically. Shaping of the chirp spectrum sometimes can be used to advantage in radar applications. If one applies a small amount of DC bias during the OFF-state portion of the waveform, chirp bandwidth can be reduced [23,24]. The *preheat bias* does not actually start oscillations, but

because the active device is warmed before the DC pulse turns it on, the temperature gradient is lessened, and so is the frequency drift.

3. VOLTAGE-CONTROLLED OSCILLATORS

A voltage-controlled oscillator (VCO) incorporates some means to vary the oscillation frequency with a separate external DC voltage. Although a variety of voltage control mechanisms exist, *varactor tuning* is the most popular choice for waveguide oscillators.

A VCO's *tuning range* is the frequency range over which the VCO meets its performance requirements such as output power. A typical waveguide VCO tuning bandwidth is about 5%. The *sensitivity* of a VCO is the ratio of the change in frequency to the change in tuning voltage in units of megahertz per volt. The ideal for most VCOs is a linear frequency-tuning voltage characteristic. The parameter *linearity* describes the degree to which the VCO response approximates a straight line

$$L = \frac{S_{\max} - S_{\min}}{S_{\max} + S_{\min}} \quad (8)$$

where S_{\min} and S_{\max} are the minimum and maximum values of sensitivity over the tuning range.

3.1. Varactor Diode Characteristics

One who uses a *varactor diode* to control the frequency of a VCO is simply making use of the bias voltage-varying capacitance of a p-n junction [1]. In the waveguide circuit, the capacitance is a reactance given by

$$X_j = \frac{1}{j\omega C_j} \quad (9)$$

where ω is 2π times the oscillation frequency and C_j is the varactor junction capacitance. To obtain a wide tuning range, a wide range of reactance is needed. Most varactors are packaged, so one must be sure that the package inductance and capacitance do not dominate the junction capacitance. In particular, the inductance of the leads connecting the semiconductor to the inside of the package can resonate with the junction capacitance and cause an excessive amount of current to flow through and potentially destroy the varactor.

The varactor capacitance-voltage slope is roughly proportional to $V_{\text{DC}}^{-0.5}$ [1], a nonlinear characteristic that does not naturally lead to a linear VCO. One technique for *linearizing* a VCO is to use an external bias circuit that is designed to compensate for the nonlinear varactor voltage characteristic. Another technique involves the use of linearizing circuit elements in the waveguide circuit. Last, semiconductor design engineers are always striving to adjust the varactor structure to produce a more linear response.

3.2. Waveguide Circuit Modeling

In a sense, a varactor is just another tuning element in the waveguide oscillator circuit. However, one must account for the varactor and its mounting structure if one is to model the waveguide VCO circuit analytically. Figure 9 shows a waveguide VCO circuit with the active device and varactor mounted under separate posts. For posts spaced apart so that only the dominant mode couples between them, one can create an equivalent circuit like that shown in Fig. 3 for each device and cascade the circuits. However, the two posts often are closely spaced to maximize the coupling between the two devices. Consequently, higher-order, evanescent waveguide modes must be included in the circuit model. Joshi and Cornick [25–27] have developed such a model based on the work of Eisenhart and Khan [4]. The details can also be found in Ref. 1.

3.3. VCO Circuit Design Practice

The amount of frequency tuning that can be achieved with a waveguide varactor-tuned VCO is controlled by the varactor capacitance range and the varactor to active device coupling. A VCO configured as in Fig. 9 has the most frequency tuning when the posts are centered in the waveguide, where the fields and coupling are the strongest. The coupling has a strong dependence on the post dimensions and spacing between posts, parameters that also can be used to linearize the VCO. Robertson and Poelker employed a top hat structure (see Fig. 2b) above their varactor diode and by adjusting the disk diameter achieved excellent linearity [28].

There are three basic steps to follow when designing a varactor VCO:

- Place the active device in a SDO circuit and characterize its impedance–frequency curve.
- Model the varactor as an impedance versus DC bias voltage [1].
- With both devices characterized, place them in a VCO circuit, and use a two-post analytical model to search for circuit dimensions that give the desired VCO tuning range and linearity.

If the active device resistance is constant with frequency in the tuning range (which is likely for tuning ranges of a few percent), design the oscillator so that the circuit resistance is also constant with varactor bias to maintain a constant level of output power with frequency [29].

4. WAVEGUIDE OSCILLATOR POWER COMBINERS

Power combining of several devices becomes necessary when higher-power devices are not available. Power combining can be accomplished at the device level, at the circuit level, or in free space. *Power combining efficiency*, the net power P_T at the combiner output divided by the sum of the powers of the individual devices P_O , is given by [1]

$$\eta_c = \frac{P_T}{NP_O} \quad (10)$$

where N is the number of devices being combined. The combining efficiency of a well-designed combiner should exceed 90%.

Two-terminal devices are usually power combined in resonant waveguide cavities, although both oscillators and amplifiers can be combined in resonant circuits. Resonant combiners have a number of excellent features, including very high efficiency. They also provide good heatsinking, since devices are mounted in the metal housing. The active devices tend to lock to each other in frequency, which leads to stable operation and compensates for device-to-device impedance variations. Further, resonant combiners can operate as high as 300 GHz, and they are compact in size. Some of their disadvantages include narrow bandwidth, limitations on the number of devices that can be combined without exciting unwanted cavity modes and electrical tuning complexity.

One advantage that a power combiner has over a SDO is that its performance will degrade in a gradual manner as active devices fail. Sarkar and Agrawal have performed an analytical study of gradual degradation due to device failure [30]. They derived an expression for the power *degradation* of the combiner by assuming that only a small number of the devices in the combiner fail and all devices are performing identically

$$GD = 10 \log_{10} \left(1 - \frac{F}{N} \right) \quad (11)$$

where F is the number of failed devices and N is the total number of devices. Equation (11) is optimistic. Holzman and Robertson remark that when IMPATT and Gunn devices fail, they mostly become short circuits rather than open circuits [1]. Short-circuited (shorted) devices cause a significant imbalance in the impedances presented to the other devices. A loss of 3 dB in output power is typical for a single shorted device, and the missing power often ends up in the shorted device's bias port load.

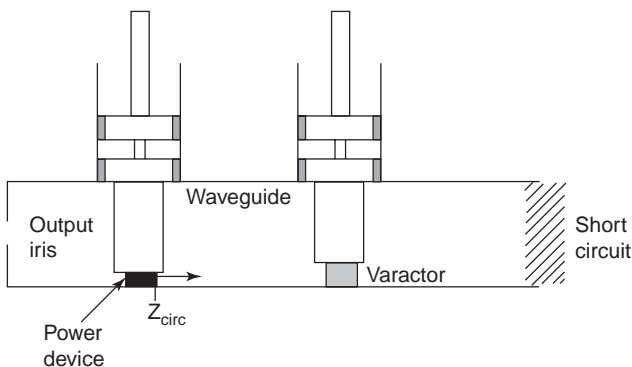


Figure 9. Waveguide VCO circuit. (Reprinted with permission from *Solid-State Microwave Power Oscillator Design* by E. L. Holzman and R. S. Robertson, Artech House Publishers, Norwood, MA, USA, www.artechhouse.com.)

4.1. Rectangular Waveguide Cavity Combiners

Kurokawa and Magalhaes designed the first resonant cavity combiner in 1971 using rectangular waveguide [31]. The circuit, shown in Fig. 10, comprises a multitude of coaxial-waveguide junctions. Each active device is recessed at the end of a coax transmission line, below the floor of the waveguide. Pairs of devices are placed in transverse planes spaced down the waveguide cavity at half-guide wavelength intervals such that each device couples to a maximum in the magnetic field. For an SDO circuit, typically only one mode is resonant. But, as the cavity is lengthened to accommodate more devices, more cavity modes become resonant within the operational frequency range. Because the spacing between devices is selected for the resonant mode of interest only, the other resonant modes will be excited only weakly, although any energy coupled into these modes will degrade the combiner efficiency. In addition, as the cavity is lengthened, its tuning bandwidth decreases because the circuit impedance of

devices farthest from the short circuit becomes more sensitive to frequency. To get optimum efficiency from a combiner, one should characterize a large number of active devices in a single-device evaluation circuit and select only those with similar characteristics.

One way to increase the output power of the combiner without increasing the length of the waveguide cavity is to increase the density of devices. The circuit in Fig. 11 has double the combiner density with two devices closely straddling each magnetic field maximum [32]. Figure 12 shows another way to increase device density by mounting three devices in each transverse plane of the combiner cavity [33]. In this combiner, the active devices near the cavity wall couple to the magnetic field, while a coaxial probe couples the center device to the TE₁₀₁-mode electric field maximum. The probe is connected to the bias port of one of the other devices with a wire.

4.2. Cylindrical Cavity Resonant Combiners

The cylindrical cavity resonant combiner is based on the circular waveguide cavity. The main benefit of this combiner, depicted in Fig. 13, is that a large number of devices can be combined with only the dominant, TM₀₁₀-mode resonant in the frequency band of operation. As shown in the figure, the devices are placed around the edge of the

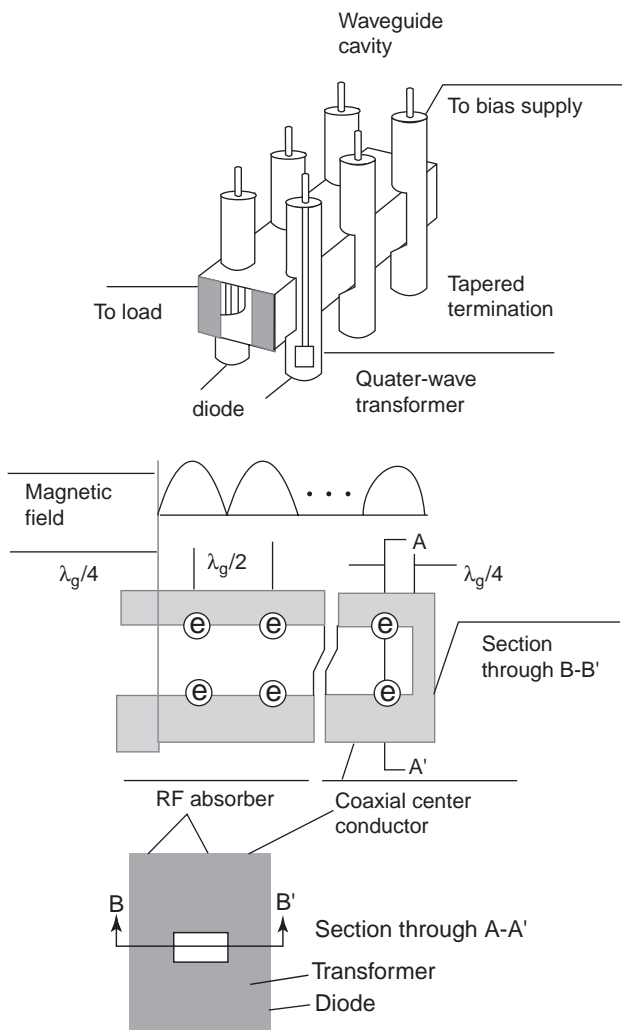


Figure 10. Kurokawa–Magalhaes rectangular waveguide resonant cavity combiner. (Source: K. Chang and C. Sun, Millimeter-wave power combining, *IEEE Trans. Microwave Theory Tech.* **31**(2):91–107 (1983). © 1983 IEEE. Reprinted with permission.)

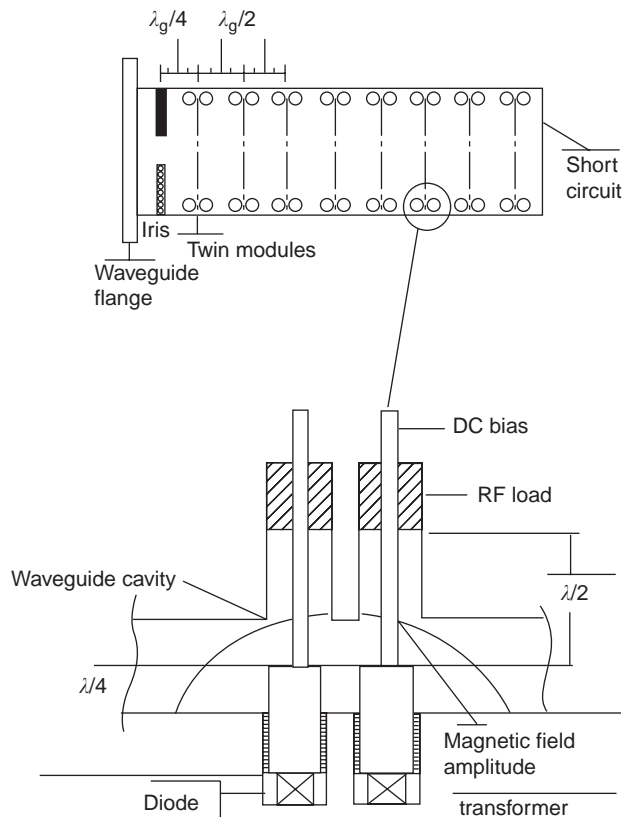


Figure 11. Kurokawa–Magalhaes rectangular waveguide cavity combiner with pairs of devices at each magnetic field maxima. (Source: K. Chang and C. Sun, Millimeter-wave power combining, *IEEE Trans. Microwave Theory Tech.* **31**(2):91–107 (1983). © 1983 IEEE. Reprinted with permission.)

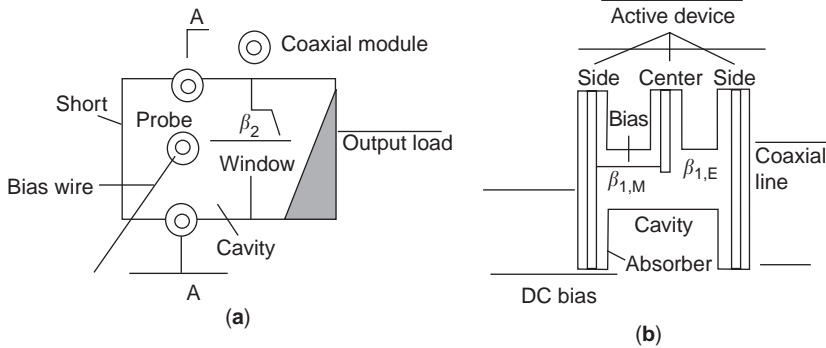


Figure 12. Rectangular cavity combiner with three devices in each transverse plane: (a) top view; (b) cross-sectional view in plane A–A'. (Source: M. Madhian, A. Materka and S. Mizushima, A multiple-device cavity oscillator using both magnetic and electric coupling mechanisms, *IEEE Trans. Microwave Theory Tech.* **30**(11):1939–1944 (1982). © 1982 IEEE. Reprinted with permission.)

cavity, where the magnetic field reaches its maximum level. A coax probe, placed in the center of the combiner, is the output. Both the coax TEM mode and cavity TM_{010} mode have similar axial field distributions, which enables good coupling between the devices and output. A mechanically adjustable tuning rod optimizes the combiner efficiency. The maximum number of devices that can fit

within a dominant mode combiner depends on the combiner’s *radius*, which is given by the formula for the resonant frequency of the TM_{010} mode [1]

$$r = \frac{c}{2\pi f_0} 2.4049 \tag{12}$$

where f_0 is the operational frequency of the combiner and c is the speed of light. The *height* h of the cavity is chosen so that the next higher-order mode, the TE_{111} mode (for $r > h$), resonates at a frequency outside the operational band. The resonant frequency of this mode is

$$f_{r,111} = \frac{c}{2\pi} \sqrt{\left(\frac{1.8412}{r}\right)^2 + \left(\frac{\pi}{h}\right)^2} \tag{13}$$

The cavity field is axially symmetric, so the magnetic field is constant with angle (see Fig. 13). Thus, the devices can be spaced as closely as physically and thermally possible. The dissipated heat can be better distributed by alternately reversing the locations of the device and absorber in adjacent locations [34]. Accurate models of cylindrical combiner structures have been developed using field matching [35,36]. Generalized, commercially available three-dimensional numerical electromagnetics software can be used also.

Cylindrical cavities are highly efficient with measured efficiencies sometimes exceeding 100%, implying that devices operate more efficiently in the combiner environment than as SDOs [37]. For a given cavity size, measured data show that the combining efficiency increases with device density. However, at *millimeter-wave frequencies*, the cylindrical cavity is less efficient, because the cavity size must be reduced to avoid higher-order modes. Unfortunately, the packaged devices do not decrease in size with higher operating frequency, so fewer devices can be combined. Further, the output coaxial probe dimensions must be very small for single-mode operation. The rectangular cavity may be a better choice at higher frequencies, because the number of unwanted modes increases comparatively slowly as its length increases.

One solution to the higher-order moding problem is the *window output* cylindrical combiner of Fukui and Nogi shown in Fig. 14 [38]. This combiner can be operated in axially varying modes with devices nonuniformly spaced, and it does not require a coaxial probe output. Another solution is to use an oversized combiner operating in a

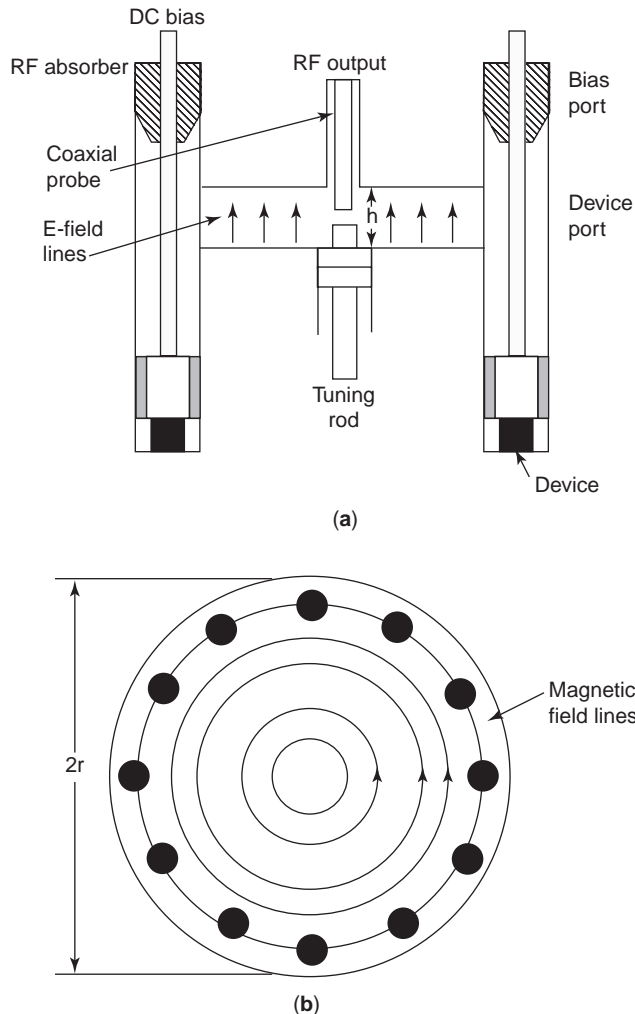


Figure 13. Cylindrical cavity resonant combiner: (a) cross-sectional view; (b) top view. [After K. J. Russell, Microwave power combining techniques, *IEEE Trans. Microwave Theory Tech.* **27**(5):472–478 (1979). © 1979 IEEE. Reprinted with permission.]

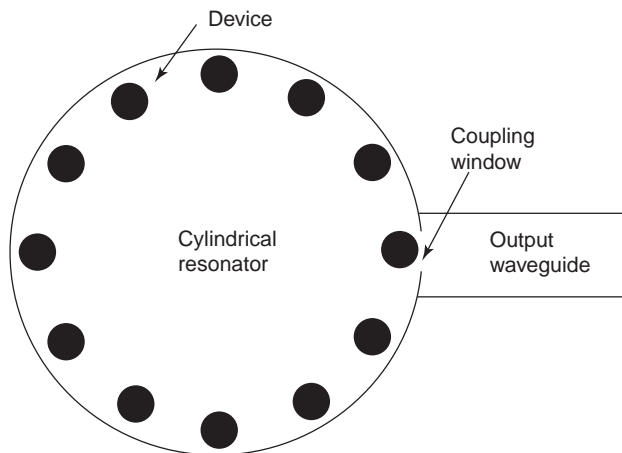


Figure 14. Window output cylindrical resonant cavity combiner. [Source: K. Fukui and S. Nogi, Mode analytical study of cylindrical cavity power combiners, *IEEE Trans. Microwave Theory Tech.* **34**(9):943–951 (1986). © 1986 IEEE. Reprinted with permission.]

higher-order cavity mode such as the TM_{0n0} ($n > 1$) or TM_{m10} ($m > 0$) mode. However, the unwanted modes must be suppressed without affecting the desired mode. TM_{020} -mode cavities have performed well [39–41], and even higher-order mode cavities have been designed and built [42,43].

5. CONCLUSION

Waveguide oscillators have lost favor as GaAs and InP microwave integrated circuit (MMIC) amplifier technology has advanced into the millimeter-wave frequency range. High-power diode multipliers have also encroached on the domain of Gunn and IMPATTs. Even with the good analytical models available today, waveguide oscillators are not easy to mass-produce, so they find use primarily as custom sources operating in the highest millimeter-wave frequency bands. The one exception is the cylindrical cavity combiner, which is employed as low as 10 GHz because of its capability to combine many devices with the highest possible efficiency.

BIBLIOGRAPHY

1. E. L. Holzman and R. S. Robertson, *Solid-State Microwave Power Oscillator Design*, Artech House, Norwood, MA, 1992.
2. K. Kurokawa, Some basic characteristics of broadband negative resistance oscillator circuits, *Bell Syst. Tech. J.* **48**:1937–1955 (1969).
3. S. Ramo, J. R. Whinnery, and T. van Duzer, *Fields and Waves in Communication Electronics*, 2nd ed., Wiley, New York, 1984.
4. R. L. Eisenhart and P. J. Khan, Theoretical and experimental analysis of a waveguide mounting structure, *IEEE Trans. Microwave Theory Tech.* **19**(8):706–719 (1971).
5. R. L. Eisenhart, Understanding the waveguide diode mount, *IEEE Int. Microwave Symp. Digest*, 1972, pp. 154–156.
6. A. G. Williamson, Analysis and modeling of a single-post waveguide mounting structure, *Proc. IEE* **129**(Part H)(5):271–277 (1982).
7. D. V. Otto, The admittance of cylindrical antennas driven from a coaxial line, *Radio Sci.* **2**(9):1031–1042 (1967).
8. A. G. Williamson, Analysis and modeling of “two-gap” coaxial line rectangular waveguide junctions, *IEEE Trans. Microwave Theory Tech.* **31**(3):295–302 (1983).
9. A. G. Williamson and D. V. Otto, Cylindrical antenna in a rectangular waveguide driven from a coaxial line, *Electron. Lett.* **8**:545–547 (1972).
10. A. G. Williamson, Analysis and modeling of a coaxial line rectangular waveguide junction, *Proc. IEE* **129**(Part H)(5):262–270 (1982).
11. A. G. Williamson and D. V. Otto, Analysis of a waveguide post mounting structure, *Proc. IREE Austral.* **34**:95–97 (1973).
12. M. E. Bialkowski, Analysis of disc-type resonator mounts in parallel plate and rectangular waveguides, *Int. J. Electron. Commun. AEU*, **38**:306–310 (1984).
13. W. J. Getsinger, The packaged and mounted diode as a microwave circuit, *IEEE Trans. Microwave Theory Tech.* **14**(2):58–69 (1966).
14. C. A. Brackett, The elimination of tuning induced burnout and bias circuit oscillations in IMPATT oscillators, *Bell Syst. Tech. J.* **52**:271–306 (1973).
15. C. A. Lee, R. L. Batdorf, W. W. Wiegmann, and G. Kaminsky, Analysis of the Q-factor, efficiency, stability, and the design of Read structures in the nonlinear range, *J. Appl. Phys.* **38**(7):2797–2809 (1967).
16. R. Kuvas and C. A. Lee, Nonlinear analysis of multifrequency operation of Read diodes, *J. Appl. Phys.* **41**(4):1756–1767 (1970).
17. C. M. Howell, Diode active layer sets operating points, Gunn-diode oscillators, part 1, *Microwaves RF*, 125–133 (1987).
18. J. J. Gloedbloed, Investigation of parametric IMPATT diode oscillators by a simple locus chart, *Electron. Lett.* **11**(3):54–56 (1975).
19. J. Gonda and W. E. Schroeder, IMPATT diode circuit design parametric stability, *IEEE Trans. Microwave Theory Tech.* **25**(5):343–352 (1977).
20. W. E. Schroeder, Spurious parametric oscillations in IMPATT diode circuits, *Bell Syst. Tech. J.* **53**(7):1187–1210 (1974).
21. M. E. Hines, Large signal noise, frequency conversion, and parametric instabilities in IMPATT diode networks, *Proc. IEEE* **60**(12):1534–1548 (1972).
22. R. L. Eisenhart and R. C. Monzello, A better waveguide short circuit, *IEEE Int. Microwave Symp. Digest*, 1982, pp. 360–362.
23. R. L. Eisenhart and R. S. Robertson, Controlled bias preheating for variable duty factor IMPATT transmitter, *IEEE Int. Microwave Symp. Digest*, 1985, pp. 529–530.
24. L. V. Kasatkin and N. F. Karushkin, Stabilization of RF parameters of injection-locked pulsed IMPATT oscillators, *Microwave J.* (Sept. 2000).
25. J. S. Joshi and J. A. F. Cornick, Analysis of waveguide post configurations: Part I—gap immittance matrices, *IEEE Trans. Microwave Theory Tech.* **25**(3):169–173 (1977).
26. J. S. Joshi and J. A. F. Cornick, Analysis of waveguide post configurations: Part II—dual-gap cases, *IEEE Trans. Microwave Theory Tech.* **25**(3):173–181 (1977).
27. J. S. Joshi and J. A. F. Cornick, Analysis of waveguide post configurations: Part III—influence of general waveguide

- terminations, *IEEE Trans. Microwave Theory Tech.* **26**(4): 319–320 (1978).
28. R. S. Robertson and J. N. Poelker, *Frequency Linearization Circuit for Microwave VCO in Ridged Waveguide*, U.S. Patent 5,014,021 (1991).
 29. H. A. Leach, *Design Procedure for Millimeter-Wave Gunn Diode Voltage Controlled Oscillators*, master's thesis, Cal State Univ., Northridge, CA, 1991.
 30. S. Sarkar and M. C. Agrawal, On the graceful degradation performance of multiple-device oscillators, *IEEE Trans. Microwave Theory Tech.* **33**(2):168–170 (1985).
 31. K. Kurokawa and F. M. Magalhaes, An X-band 10-Watt multiple-IMPATT oscillator, *Proc. IEEE* **59**(1):102–103 (1971).
 32. S. E. Hamilton, 32 diode waveguide power combiner, *IEEE Int. Microwave Symp. Digest*, 1980, pp. 183–185.
 33. M. Madihian, A. Materka, and S. Mizushima, A multiple-device cavity oscillator using both magnetic and electric coupling mechanisms, *IEEE Trans. Microwave Theory Tech.* **30**(11): 1939–1944 (1982).
 34. R. L. Eisenhart, *Microwave Power Combiner with Alternating Diode Modules*, U.S. Patent 4,588,963 (1986).
 35. M. E. Bialkowski and V. P. Waris, Electromagnetic model of a planar radial-waveguide divider/combiner incorporating probes, *IEEE Trans. Microwave Theory Tech.* **41**(6/7): 1126–1134 (1993).
 36. M. E. Bialkowski and V. P. Waris, Analysis of a N-way radial cavity divider with coaxial central port and waveguide output ports, *IEEE Trans. Microwave Theory Tech.* **44**(11):2010–2016 (1996).
 37. K. J. Russell, Microwave power combining techniques, *IEEE Trans. Microwave Theory Tech.* **27**(5):472–478 (1979).
 38. K. Fukui and S. Nogi, Mode analytical study of cylindrical cavity power combiners, *IEEE Trans. Microwave Theory Tech.* **34**(9):943–951 (1986).
 39. A. L. Hieber, C. A. Drubin, and G. Jerinic, *Microwave Power Combiner*, U.S. Patent 4,189,684 (1980).
 40. M. G. Alderstein and J. Fines, A multi-IMPATT injection-locked oscillator at 35 GHz, *IEEE Trans. Microwave Theory Tech.* **37**(3):571–579 (1989).
 41. L. C. Wagner, *Power Combiner with Reentrant Coaxial Diode Oscillators*, U.S. Patent 4,471,325 (1984).
 42. S. Nogi and K. Fukui, TM_{0n0} - and TM_{m10} -mode oversized cylindrical cavity power combiners, *IEEE Trans. Microwave Theory Tech.* **35**(9):835–842 (1987).
 43. S. Tanaka, S. Nogi, K. Fukui, and Y. In, Crucial factors in power combining by oversized cylindrical cavity multiple-device structures, *IEEE Trans. Microwave Theory Tech.* **32**(11):1755–1760 (1989).

WAVEGUIDES

ANDRÉ VANDER VORST
 Université Catholique de
 Louvain
 Louvain-la-Neuve, Belgium

In the electromagnetic spectrum, microwaves are the waves with wavelengths comparable to ordinary laboratory

dimensions. Furthermore, smooth surfaces of good conductors form very perfect reflectors for them. As a consequence, an electromagnetic wave in a reflecting pipe is reflected back and forth from wall to wall, so that it can travel to large distances with small attenuation. Hence we have “waveguides” as transmission lines, dealing with electromagnetic fields inside of hollow regions, rather than outside wires for more conventional electric applications, or waves in free space as in optics, and the propagating electromagnetic field is confined to the finite region of the guide by reflecting walls. The present article essentially reviews the basic theory and the different geometries used in the various applications of such hollow waveguides.

1. FUNDAMENTALS

1.1. Historical Evolution

J. C. Maxwell established the fundamentals of electromagnetic theory around 1880. In 1883, F. G. Fitzgerald suggested sources for electromagnetic emission. In 1888, H. Hertz proved that the concept of propagation was included in Maxwell's theory. At the same time, O. Lodge demonstrated the existence of maxima and minima on transmission lines. A group of experimental scientists was formed—the Hertzians—while J. C. Bose was experimenting with millimeter waves in India. In 1894, Lodge demonstrated radiation from circular hollow pipes—waveguides—as well as the effect of irises and resonant cavities, and illustrated the highpass properties of the device. Bose developed a semiconductor detector, rectangular waveguides and horns, at 60 GHz [1–5]. In 1893, Heaviside considered various possibilities for waves along wire lines from a theoretical standpoint and concluded that guided waves needed “two leads as a pair of parallel lines; or if but one is to be used, there is the earth, or something equivalent, to make another” [6]. J. J. Thompson gave a theoretical analysis of electric oscillations within a conducting cylindrical cavity of finite length. He found that there were permissible normal modes that were a function of the radius of the cylinder [7]. Shortly thereafter, J. Larmor similarly investigated the theory of resonant structures such as coaxial metallic cylinders and a single dielectric cylinder [8].

In 1897, Rayleigh showed that waves could indeed propagate within a hollow metallic cylinder [9]. He found that such waves existed only in a set of well-defined normal modes, with waves of two types: one with a longitudinal component of electric intensity only, while the other had a longitudinal component of magnetic intensity only. Both types had transverse components of both electric and magnetic intensity. He found that a fundamental limitation on the existence of such waves was that the frequency must exceed a lower limit—cutoff frequency—depending on mode number and the cross-sectional dimensions of the cylinder. He published the complete solutions in the case of rectangular and circular cross section, yielding all possible solutions.

Hertzian links, feeders, detectors, and even radioastronomy with an attempt by Lodge were on the horizon. In

fact, none of this happened, probably because of both the success of the long waves used by Marconi and the difficulty in generating microwaves. Lodge got interested in paranormal phenomena, and Bose in plant growth and biological effects of electromagnetic fields. Microwave electronics fell out of favor.

Almost 40 years later, G. C. Southworth, working with Schelkunoff, of Bell Telephone Laboratories (BTL), and W. L. Barrow, working with Chu, Stratton, and others, of the Massachusetts Institute of Technology (MIT), rediscovered the concept, each working independently for almost 5 years with no knowledge of the other. The question they investigated was the practical possibility of using waveguides for the transmission of microwave power. This work culminated in almost simultaneous presentations in 1936, when they claimed that they had discovered that electromagnetic waves would propagate in hollow tubes and had experimentally demonstrated the practicality of this phenomenon. They had become aware of each other's work about one month prior to the announcements, after publication of the programs for the meetings at which the presentations were to be made (3).

From the beginning, the most obvious application of waveguide had been as a communications medium. It had been determined by both Schelkunoff and Mead independently in 1933 that an axially symmetric electric wave in circular waveguide would have an attenuation factor that decreased with increased frequency [3]. This unique characteristic was believed to offer a great potential for wide-band multichannel systems, and for many years to come the development of such a system was a major focus of activity within the waveguide group at BTL. The use of a waveguide as a long transmission line, however, did not prove to be practical and Southworth himself concluded in 1939 that microwave radio with highly directive antennas was preferable, coming to the conclusion that the hollow cylindrical conductor would be valued as a new circuit element, a new type of toll cable.

The years from 1936 to 1940 saw great activity in microwave electronics, but hardly with important practical applications. The great impetus to its further development came with the application to radar in World War II. Generally, the development of experimental radar into an operational system is attributed to R. Watson-Watt, having convinced politicians to install a range of radar protection on the British coast. At the end of the summer of 1938, 5 stations were protecting London. In July 1940, 50 stations were operational. The efficiency of the system was determinant on the evolution of the war in Europe. During the war, the famous MIT Radiation Laboratory was the place where British and U.S. scientists and technicians worked together, developing microwave technology and electronics as well as the basic theory. The series of 28 books published after the war summarized the tremendous amount of high-quality work accomplished at that time [2,10].

Since then, waveguides have been very common in microwaves, especially in the centimeter and millimeter wave ranges, mostly because of their losses, lower than in coaxial cables. Another reason is that the waveguide forms a closed transmission line, which is an advantage in certain environments, in particular in the presence of

interferences or adverse tropospheric conditions. The tendency to go to higher frequencies has introduced particular configurations of loaded waveguides, essentially the fin line structure (see FINLINES).

For a few decades now most commercial applications have been based on planar transmission lines, especially in the lower frequency range, such as the microstrip, the most common planar line, although stripline came first. More recently, other configurations like slotlines and coplanar waveguides have become popular, because of their good properties at higher frequencies, namely, in the 30–60 GHz range. Planar technology developed with respect to waveguides for essentially two reasons. One is economical; producing a planar circuit is cheap, which compensates for the cost of research and development. The other is that planar technology easily combines with semiconductors, leading to microwaves monolithic integrated circuits (MMIC), while the combination waveguide-semiconductor has always been rather laborious, because of the significant differences in configuration as well as in impedance level.

1.2. Basic Theory

1.2.1. Electromagnetic Field in a Waveguide. Electromagnetic fields within any region of space are determined by solving Maxwell's equations in a coordinate system appropriate to the region. Such regions may be termed as either uniform or non-uniform. Uniform regions are characterized by the fact that cross sections transverse to a given symmetry, or propagation, direction are everywhere identical with one another in both size and shape. Examples of uniform regions are provided by regions cylindrical about the symmetry direction and having planar cross sections with, for example, rectangular or circular peripheries [2,4,5,10–12].

A waveguide is a metallic structure of arbitrary but constant cross section that extends in the direction of propagation of a wave and confines the wave energy within it. It is bounded by a conductor of high conductivity, filled with a dielectric of low loss, with arbitrary cross section. It may have more than one bounding surface, as the coaxial line, which consists of the annular space between two concentric circular cylindrical conductors. In practice the two most common cases are the rectangular and the circular guide. Hollow waveguide cross sections are limited by metallic boundaries. In the basic theory, those metallic boundaries are supposed to be made of perfect electric conductors. At microwaves, the actual losses in actual conductors are very small and are usually evaluated by a perturbation theory.

Within the enclosed region the electromagnetic field may be represented as the superposition of an infinite number of standard functions that form a mathematically complete set. The mathematical representation of the electromagnetic field within a uniform region is in the form of a superposition of an infinite number of modes or wave types. The electric and magnetic field components of each mode are factorable into form functions depending only on the cross-sectional coordinates transverse to the direction of propagation, and into amplitude functions depending

only on the coordinate in the propagation direction. The transverse functional form of each mode depends on the cross-sectional shape of the region and, save for the amplitude factor, is identical at every cross section. As a result the amplitudes of a mode completely characterize the mode at every cross section. The variation of each amplitude along the propagation direction is given implicitly as a solution of a one-dimensional wave or transmission-line equation. According to the mode in question the wave amplitudes may be either propagating or attenuating along the transmission line.

1.2.2. Transverse Electromagnetic, Transverse Magnetic, and Transverse Electric Modes. In physics, waves are usually classified according to two criteria. One is the geometric form of the wavefront, which describes the surface of constant phase, most generally planar, cylindrical, or spherical, more rarely elliptical or other. The second criterion is that the wave is said to be uniform or nonuniform, depending on whether the field has a constant amplitude in each point of the wavefront or not. As examples, the wave emitted from a point source is a uniform spherical wave while the wave propagating in a coaxial cable is a nonuniform plane wave. The term “pure mode,” or simply “mode,” refers to a wave whose field structure remains the same along the entire path of propagation. Different modes will, in general, have different field structures and different velocities of propagation. In uniform hollow waveguides, the waves, more often called the *modes*, are usually classified according to their properties with respect to the propagation direction and whether they have longitudinal components or not. A wave with longitudinal components for neither the electric nor the magnetic field is called a transverse electromagnetic (TEM) wave. It has only four field components. A wave with no longitudinal magnetic field component while having a longitudinal electric field component is called a transverse magnetic (TM) wave, and a wave with no longitudinal electric field component while having a longitudinal magnetic field component is called a transverse electric (TE) wave. TM and TE waves, or modes, each have five field components.

For a TEM mode to propagate on a guiding structure, at least two conductors are needed. The equations to be satisfied by a TEM mode *in the transverse plane* of such a structure are indeed identical to those of statics where two conductors at least are necessary, to impose a potential difference as a boundary condition. Hence a TEM mode cannot propagate on or in a hollow one-conductor waveguide, while it can propagate on or in a two-conductor waveguide of any cross section and any geometry, for instance, a coaxial cable or waveguide. A TEM mode has no cutoff frequency: because of the two or more conductors it can propagate down to zero frequency.

In a waveguide, an infinite number of TE and of TM modes can propagate. In the usual one-conductor waveguide, those two classes of modes cannot propagate down to zero frequency, since only one conductor is available. All the TE and the TM modes have a cutoff frequency below which they cannot propagate: the waveguide has a high-pass characteristic. The cutoff frequencies depend on the

dimensions of the waveguide and of the homogeneous medium filling the waveguide. In a waveguide with two or more conductors, like the coaxial cable or waveguide, the TEM, TE, and TM modes can propagate. The number of propagating modes is determined by the frequency: all the modes with a cutoff frequency lower than the generator frequency propagate while the others do not. If a waveguide is excited with a signal whose frequency is lower than the cutoff frequency, then instead of propagating, this signal is attenuated exponentially with distance. This phenomenon of attenuation in a nonabsorbing medium that occurs in a waveguide below cutoff is similar to the phenomenon of total reflection in optics, in which light is reflected going from an optically denser to an optically rarer medium. In the rarer medium there is an attenuated wave of the type discussed here. With a slightly absorbing medium inside the waveguide, the cutoff is no longer as sharp as it is in the nonabsorbing case. The attenuation is small in the range of frequency above cutoff, and rapidly becomes large when going to lower frequencies.

The mode with the lowest cutoff frequency is called the *dominant mode*. In general, most waveguides are operating at a frequency such that only the dominant mode propagates. In that case, the electromagnetic field is characterized by the amplitudes of this dominant mode. The amplitudes that measure the transverse electric and magnetic field intensities of this dominant mode are defined as voltage and current, respectively, as on appropriate transmission line. The knowledge of the wave impedance and propagation constant, that is, propagating, of the transmission line then permits one to describe the propagation of the dominant mode in familiar impedance terms.

When cross-sectional discontinuities are present in the waveguide, they require more boundary conditions to be satisfied than those characterizing the dominant mode, which are imposed by the longitudinal metallic walls. Mode voltages and currents are introduced as measures of the amplitudes of the transverse electric and magnetic field intensities of each of the higher-order modes. Each of these is represented by a transmission line, having however a reactive wave impedance and a real propagation constant, that is, attenuating. In this manner the complete description of the electromagnetic field in a waveguide may be represented in terms of the behavior of the voltages and currents on a infinite number of transmission lines.

1.2.3. Orthogonality Properties and Expansion of the Fields in Normal Modes. Solutions of the wave equation always have certain properties of orthogonality, which are particularly important when expanding a general solution as a sum of solutions for the various modes and when considering problems of energy. Several general theorems have been proved independently of the particular geometry of the cross section. The main orthogonality theorems are the following:

1. The integral over the cross section of the scalar product of either the transverse electric fields or the transverse magnetic fields of two different modes is zero.

2. The integral over the cross section of the product of either the longitudinal electric field components or the longitudinal magnetic field components of two different modes is zero.
3. The integral over the cross section of the longitudinal component of the vector product of the transverse electric field of one mode with the transverse magnetic field of another mode is zero.

These theorems hold when the two modes are both TE or both TM, as well as when the two modes are of opposite types. Several other theorems can be derived, relating to the integrals of squares of components of the electric and the magnetic fields, or of products of components with their conjugates.

Maxwell's equations within an one-conductor waveguide with perfectly reflecting walls have an infinite number of possible solutions, representing various normal modes, some TE and some TM. Furthermore, corresponding to each of these modes with propagation along the $+z$ direction, there is a possible wave propagated along $-z$. Each mode has a cutoff frequency, such that a disturbance in that mode at a frequency below cutoff is rapidly attenuated, whereas at a frequency higher than cutoff it is propagated.

The last problem to be considered is that of the most general field that can exist in the waveguide. Maxwell's equations, as well as the boundary conditions are linear. Hence, all the solutions that have been found can be superposed, with appropriate coefficients, to form another solution for the equations submitted to the boundary conditions. It can be proved that the most general solution, subject to the boundary conditions and to the additional condition that the guide contains no volume charge or current except what arises from Ohm's law in the imperfect dielectric filling it, can be represented by such a superposition. As usual when dealing with problems of expansion in orthogonal functions, the magnitude of the functions are normalized by determining their magnitudes so that their squares integrate to some convenient value, and by multiplying these normalized functions by an additional coefficient to secure an arbitrary value for the function. The complete field is obtained by superposing all possible fields, with waves traveling along the $-z$ direction as well as along $+z$ (2).

A quite general approach to waveguide theory is obtained by elevating Maxwell's equations into a dyadic form. This yields the concept of dyadic Green functions in electromagnetic theory. Vector wave functions can then be established for waveguides of specific cross sections [12,13].

2. THEORY

2.1. Electromagnetic Fields in a Waveguide

2.1.1. TEM Mode. TEM waves have longitudinal field components neither for the electric nor for the magnetic field. Hence they are fully determined by four components only, two for the transverse electric field and two for the

transverse magnetic field. Along a guiding structure, TEM waves can propagate only if at least two conductors are available, as is the case in a coaxial cable or waveguide. It can be shown indeed that those fields satisfy in the transverse plane the same equations as those of statics. To demonstrate the statement the vectors and operators appearing in Maxwell's equations are decomposed into their transverse and longitudinal components, which leads to decomposed equations [14]. These show that in the absence of the longitudinal components the purely transverse electric and magnetic fields do satisfy the equations of statics in the transverse plane. Furthermore, since neither electric nor magnetic variable field can exist in a perfect electric conductor, boundary conditions to be satisfied at the walls are also identical to those of statics. Hence two conductors at least are necessary for a TEM wave to propagate on a guiding structure: in a coaxial waveguide a TEM wave can propagate, while it cannot in a one-conductor hollow waveguide.

2.1.2. TE and TEM Modes. Only uniform waveguides are considered, where the cross section is identical along the propagation direction and limited by conducting walls surrounding a homogeneous and isotropic medium, usually with small losses. The propagation is interior to the guide. The walls are first supposed to be lossless. They can be either perfect electric or perfect magnetic, which can be used for the ease of calculation in some special cases. In practice, however, there are numerous materials that are very good electric conductors, although not perfect, which is not the case for magnetic conductors. Small losses in the walls will be evaluated later, using a perturbation method. Internal volume charge and current density are assumed to be zero. Steady-state sinusoidal solutions are calculated. Maxwell's equations are solved in the frequency domain and fields are represented by phasors (complex vectors).

Maxwell's equations are written as

$$\begin{aligned}\nabla \times \bar{\mathbf{E}} &= -j\omega\mu\bar{\mathbf{H}} \quad \text{or} \quad \nabla \times \bar{\mathbf{E}} = -jk\zeta\bar{\mathbf{H}} \\ \nabla \times \bar{\mathbf{H}} &= (j\omega\epsilon + \sigma)\bar{\mathbf{E}} \quad \text{or} \quad \nabla \times \bar{\mathbf{H}} = jk\eta\bar{\mathbf{E}} \\ \nabla \cdot \bar{\mathbf{E}} &= 0 \\ \nabla \cdot \bar{\mathbf{H}} &= 0\end{aligned}\tag{1}$$

by defining

$$\begin{aligned}jk &\triangleq \sqrt{j\omega\mu(\sigma + j\omega\epsilon)} \quad (\text{m}^{-1}) \\ \frac{\eta \triangleq 1}{\zeta} &\triangleq \sqrt{\frac{\sigma + j\omega\epsilon}{j\omega\mu}} \quad (\text{S})\end{aligned}\tag{2}$$

2.1.3. Transverse and Longitudinal Components for TE and TM Modes. Rewriting the first two equations of

Eq. (1) in detail yields

$$\begin{aligned}\frac{\partial E_z}{\partial y} - \frac{\partial E_y}{\partial z} &= -jk\zeta H_x \frac{\partial H_z}{\partial y} - \frac{\partial H_y}{\partial z} = jk\eta E_x \\ \frac{\partial E_x}{\partial z} - \frac{\partial E_z}{\partial x} &= -jk\zeta H_y \frac{\partial H_x}{\partial z} - \frac{\partial H_z}{\partial x} = jk\eta E_y \\ \frac{\partial E_y}{\partial x} - \frac{\partial E_x}{\partial y} &= -jk\zeta H_z \frac{\partial H_y}{\partial x} - \frac{\partial H_x}{\partial y} = jk\eta E_z\end{aligned}\quad (3)$$

Looking for a solution propagating in the $+z$ direction, the classical transmission line formalism yields a z dependence $e^{-\gamma z}$. Hence derivatives with respect to z are replaced by multiplications by $-\gamma$. TE and TM modes are most easily investigated by obtaining an equation for each of the longitudinal components separately. Extracting, for example, E_z from the last equation after replacing H_x and H_y by their values from the first two equations yields

$$E_z = \frac{1}{j^2 k^2} \left[\gamma \left(\frac{\partial E_x}{\partial x} + \frac{\partial E_y}{\partial y} \right) + \frac{\partial^2 E_z}{\partial x^2} + \frac{\partial^2 E_z}{\partial y^2} \right] \quad (4)$$

Usually the third Maxwell's equation yields

$$E_z = -\frac{1}{k^2} \left(\gamma^2 E_z + \frac{\partial^2 E_z}{\partial x^2} + \frac{\partial^2 E_z}{\partial y^2} \right) \quad (5)$$

or

$$[\nabla_t^2 + (k^2 + \gamma^2)]E_z = 0 \quad (6)$$

A similar equation can be obtained for any other component, and in particular for H_z . Defining

$$p^2 \triangleq \gamma^2 + k^2 \quad (7)$$

yields

$$(\nabla_t^2 + p^2)(E_z \text{ or } H_z) = 0 \quad (8)$$

the scalar eigenvalue Helmholtz equation. The eigenvalues are p^2 , defined by Eq. (7). To each eigenvalue there corresponds at least one eigenfunction, solution of the equation. If there is more than one eigenfunction, the solutions are said to be degenerate. This is the case, for instance, in a square waveguide for the solutions which have as the only difference the orientation of the electromagnetic field with respect to the two sides of the waveguide.

Equations similar to Eq. (8) can be obtained also for E_x and H_x , and for E_y and H_y , respectively. The fact, however, that the longitudinal components of electric and magnetic fields are not coupled—which is not the case when the medium filling the guide is inhomogeneous or anisotropic—makes solutions easy to calculate when the boundary conditions do not introduce a coupling between the two longitudinal components. It will be shown that this is the case for uniform waveguides filled with homogeneous and isotropic medium.

2.2. Waveguide Modes

The absence of coupling between the two longitudinal components in Eq. (8) yields separate solutions for modes with no H_z called *TM modes* (also sometimes called *E modes* because of nonzero E_z) and modes with no E_z called *TE modes* (also sometimes called *H modes* because of nonzero H_z). The general solution can be any linear combination of any TE and TM modes [2]. The separation of solutions for uniform, homogeneous, and isotropic waveguides in two classes, TE and TM modes, respectively, is particularly useful because, once solutions have been obtained either for TE or for TM modes, all the transverse components can be calculated from the longitudinal components. The appropriate rearrangement of Eq. (3) yields as an example

$$E_x = \frac{k}{p^2} \left(\frac{1}{j\eta} \frac{\partial H_z}{\partial y} - \frac{\gamma}{k} \frac{\partial E_z}{\partial x} \right) \quad (9)$$

and the relation between the transverse and longitudinal components can be rewritten as [14]

$$\begin{aligned}\bar{\mathbf{E}}_t &= \frac{1}{p^2} (-\gamma \nabla_t E_z + jk\zeta \bar{\mathbf{a}}_z \times \nabla_t H_z) \\ \bar{\mathbf{H}}_t &= \frac{1}{p^2} (-\gamma \nabla_t H_z - jk\eta \bar{\mathbf{a}}_z \times \nabla_t E_z)\end{aligned}\quad (10)$$

In summary, one has the general relations:

TE modes (H)	TM modes (E)
$(\nabla_t^2 + p^2)H_z = 0$	$(\nabla_t^2 + p^2)E_z = 0$
$\bar{\mathbf{H}}_t = -\left(\frac{\gamma}{p^2}\right)\nabla_t H_z$	$\bar{\mathbf{E}}_t = -\left(\frac{\gamma}{p^2}\right)\nabla_t E_z$
$\bar{\mathbf{E}}_t = \left(\frac{jk\zeta}{p^2}\right)\bar{\mathbf{a}}_z \times \nabla_t H_z$	$\bar{\mathbf{H}}_t = -\left(\frac{jk\eta}{p^2}\right)\bar{\mathbf{a}}_z \times \nabla_t E_z$

(11)

For both types of modes, boundary conditions are the vanishing of the tangential electric field at perfect electric walls and magnetic field at perfect magnetic walls, respectively.

2.2.1. Equivalent Transmission Lines. The previously obtained equations contain partial derivatives. An equivalence can be found between the expressions relating the transverse components and transmission line equations. Separating indeed the transverse and longitudinal variables by defining

$$\begin{aligned}\bar{\mathbf{E}}_t &\triangleq V(z)\bar{\mathbf{e}}_t(\bar{\mathbf{r}}_t) \\ \bar{\mathbf{H}}_t &\triangleq I(z)\bar{\mathbf{h}}_t(\bar{\mathbf{r}}_t)\end{aligned}\quad (12)$$

one observes that the vectors $\bar{\mathbf{e}}_t$ and $\bar{\mathbf{h}}_t$ are transverse but do not vary in z , while $V(z)$ and $I(z)$ are amplitude coefficients as a function of the coordinate z . It should be noted that at the right side of both equations each of the two terms of the products are only defined with respect to a complex arbitrary constant that may multiply one term

and divide the other: only their products are defined. Looking after an equivalence with transmission line equations, one has

$$\begin{aligned} V(z) &= V_+ e^{-\gamma z} + V_- e^{+\gamma z} \\ I(z) &= Y_0 (V_+ e^{-\gamma z} - V_- e^{+\gamma z}) \end{aligned} \quad (13)$$

where Y_0 is the characteristic admittance of the transmission line. The parameters Z_0 and γ are now to be calculated, in view of determining the parameters of the line: Z -series impedance in Ω/m , and Y shunt admittance in S/m . Those are different for TE and TM modes, respectively.

Investigating first the *TM modes*, the first Maxwell's equation shows that the transverse curl of \bar{e}_t is zero. Hence the transverse field derives in the transverse plane from a complex scalar *electric potential*:

$$\bar{e}_t = -\nabla_t \phi \quad (14)$$

This potential is proportional to E_z . Considering only one traveling wave, and introducing Eq. (12) into Eq. (10) yields

$$Y_0 \bar{h}_t = \left(\frac{jk\eta}{\gamma} \right) \bar{a}_z \times \bar{e}_t \quad (15)$$

Defining

$$Y_0 \triangleq \left(\frac{jk\eta}{\gamma} \right) K \quad (\text{S}) \quad (16)$$

where K is an arbitrary complex constant, depending on the complex constants unwritten in Eq. (12) to be determined, yields

$$\bar{h}_t = \left(\frac{1}{K} \right) \bar{a}_z \times \bar{e}_t \quad (17)$$

from which can be deduced

$$E_z = \frac{p^2}{jk\eta K} I(z) \phi \quad (18)$$

Hence, the potential is proportional to E_z and satisfies the same equation:

$$(\nabla_t^2 + p^2) \phi = 0 \quad (19)$$

When the wall is a perfect electric conductor, the longitudinal electric field vanishes at the wall, and so does the potential. There is a particular case, however—the potential may be a nonzero constant when p^2 is zero. This is the case for the TEM mode, which may exist if the guide has more than one conductor; the TEM mode is a special case of a TM mode. The parameters Z and Y of the equivalent transmission line *for the transverse components* can be

calculated using

$$Z = \frac{\gamma}{Y_0} \quad \text{and} \quad Y = \gamma Y_0 \quad (20)$$

which yields (Fig. 1)

$$Z = \frac{\gamma^2}{jk\eta K} (\Omega/\text{m}); \quad Y = jk\eta K \quad (\text{S}/\text{m}) \quad (21)$$

or:

$$Z = \frac{p^2 - k^2}{(\sigma + j\omega\epsilon)K} = \frac{p^2}{P(\sigma + j\omega\epsilon)K} + \frac{j\omega\mu}{K} \quad (22)$$

$$Y = (\sigma + j\omega\epsilon)K$$

It is observed that, if there are no losses in the medium filling the guide, the equivalent circuit has a highpass characteristic with a cutoff frequency given by:

$$\frac{\mu\omega_c}{K} = \frac{p^2}{\epsilon K \omega_c} \quad \text{from which} \quad \omega_c = pc \quad (23)$$

where c is the phase velocity in the medium supposed to be infinite.

Proceeding similarly for the *TE modes*, it can be shown that \bar{h}_t now depends upon a complex scalar *magnetic potential*, that the wave admittance also contains an arbitrary complex constant to be determined, that the potential is proportional to H_z , and that it satisfies the same equation as before:

$$(\nabla_t^2 + p^2) \Psi = 0 \quad (24)$$

The boundary conditions to be satisfied on perfect electric walls impose the normal derivative of the magnetic potential to vanish. The parameters of the equivalent transmission line are

$$\begin{aligned} Z &= \frac{\gamma}{Y_0} = \frac{jk\zeta}{K} = \frac{j\omega\mu}{K} \\ Y &= \frac{\gamma^2 K}{jk\zeta} = \frac{p^2 - k^2}{ik\zeta} K = \frac{p^2 K}{j\omega\mu} + (\sigma + j\omega\epsilon)K \end{aligned} \quad (25)$$

which are represented in Fig. 2. The equivalent circuit also exhibits a highpass characteristic, and the cutoff frequency is given by the same expression as for TM modes.

The equivalent circuits in Figs. 1 and 2 are not dual. This is because magnetic losses have not been introduced for the medium. The circuits would be dual if those losses were introduced. It can be seen that the equivalent circuits for the transverse components of TE and TM modes, respectively, are dual in the absence of any loss in the medium.

2.2.2. Eigenvalues, Power, and Impedance Level. Equations (19) and (24) are eigenvalue equations. They only have solutions—eigenfunctions—for an infinite number of

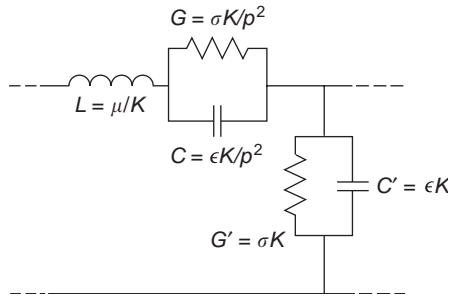


Figure 1. Equivalent circuit of TM modes, illustrating series impedance and parallel admittance.

discrete values of the eigenvalues p^2 . To each eigenvalue correspond one, or more in the case of degeneracy, eigenfunctions that determine the spatial distributions of the transverse fields. Those spatial distributions are called the *modes* of the waveguide. Equation (7) describes the dispersion characteristic of each mode: it expresses the variation of the propagation constant as a function of frequency and of the parameters of the medium. Certain properties of the eigenvalues can be demonstrated using Green's theorems [5]. In particular they are equal to the ratio of integrals over the cross section of the square of the absolute values of the gradient of the potential and of the potential, respectively, for TE as well as for TM modes:

$$p^2 = p^{*2} = \frac{\int_A |\nabla_t \theta|^2 da}{\int_A |\theta|^2 da} \quad \theta = \phi \text{ or } \Psi \quad (26)$$

Hence the eigenvalues

1. Are real and positive, even in the presence of losses in the medium
2. Do not depend on the properties of the medium filling the guide, as long as the medium is homogeneous and isotropic
3. Depend entirely on the geometry of the cross section of the guide

There is an interest in expressing the complex power traveling along the guide identically to the classical expression of lumped circuit theory $VI^*/2$. Calculating the complex power S in the $+z$ direction by using Poynting's vector integrated over the cross section A yields the classical expression:

$$S = \frac{1}{2} VI^* \quad (27)$$

provided one imposes

$$K^* \triangleq \int_A |\bar{e}_t|^2 da \quad (28)$$

This shows that to obtain Eq. (27) the unknown complex constant K must be real. It also shows that the value of K remains unknown, because no more equations can be used to specify the value of this constant; for TE and TM modes

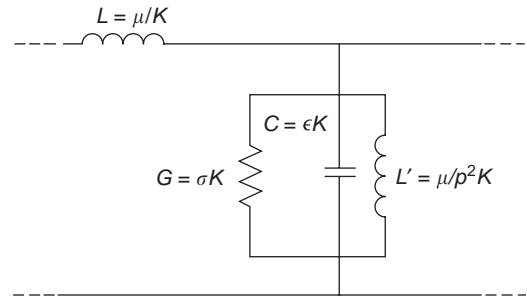


Figure 2. Equivalent circuit of TE modes, illustrating series impedance and parallel admittance.

the impedance of the equivalent transmission is not uniquely specified, and its level is arbitrary. This is why, when calculating the three expressions of power for TE and TM modes

$$\frac{V}{I}; \quad \frac{2S}{|I|^2}; \quad \frac{|V|^2}{2S} \quad (29)$$

identical values are not found [15]. The TEM mode is the only field configuration for which the concept of characteristic impedance is rigorously valid, and the three expressions in Eq. (29) yield the same value. Unfortunately, in most references the existence of the unknown constant for TE and TM modes is not stated explicitly. From this point on, it will be put equal to 1. This has consequences:

1. Equation (28) with $K^* = 1$ can be used as a normalization condition for the fields.
2. Equation (26) reduces to

$$p^2 \int_A |\theta|^2 da = 1 \quad (30)$$

which will be used to determine the integration constants when integrating the Helmholtz equation.

TE and TM modes, as well as the TEM mode in a more-than-one-conductor waveguide, have been shown to be the solutions of waves propagating in a waveguide. To actually exist in the guide, however, an adequate excitation transducer must be available. Its geometry has to be compatible with the geometry of the electromagnetic configuration of the launched modes, as will be demonstrated later.

2.2.3. Dispersion Diagram, Active and Reactive Power. Equation (7), defining the eigenvalues, can be written as

$$\gamma^2 = p^2 - \left(\frac{\omega}{c}\right)^2 \quad (31)$$

in the absence of losses in the medium filling the guide. It relates the propagation constant to the frequency. The propagation constant vanishes at the cutoff frequency, which determines the cutoff wavelength:

$$\omega_c = pc; \quad \lambda_c \frac{c}{f_c} = \frac{2\pi}{p} \quad (32)$$

Variations of γ^2 and $\gamma = \alpha + j\beta$ are represented in Fig. 3. At frequencies below cutoff the propagation constant is real. There is attenuation and the value of the attenuation constant is

$$\alpha = \sqrt{p^2 - \omega^2 \mu \epsilon} \tag{33}$$

At zero frequency the value of the attenuation constant is p and the curve $\alpha - \omega$ is an ellipse. At frequencies above cutoff the propagation constant is imaginary. There is propagation; the value of the propagation constant is

$$\beta = \sqrt{\omega^2 \mu \epsilon - p^2} \tag{34}$$

and the curve $\beta - \omega$ is hyperbolic with the straight line $\beta = \omega/c$ as an asymptote for any value of p . At high frequencies indeed the wavelength decreases, the electric distance between the walls increases, and the propagation approaches free-space propagation. At frequencies of operation the waveguide modes are dispersive and the dispersion increases when the frequency decreases down to the cutoff frequency. The mode having the lowest cutoff frequency, hence the smallest eigenvalue p , is called the *dominant mode*. It is most common to operate at a frequency located between the lowest cutoff frequency and the cutoff frequency of the next higher-order mode, so that only one mode propagates, the dominant one. To optimize this fre-

quency range, sometimes called the *bandwidth*, appropriate waveguide dimensions are chosen, in particular for the rectangular waveguide.

From Eq. (34) one determines the guide wavelength, the phase velocity, and the group velocity for each mode:

$$\lambda_g \triangleq \frac{2\pi}{\beta} = \frac{2\pi}{\sqrt{\left(\frac{\omega}{c}\right)^2 - p^2}} = \frac{1}{\sqrt{\left(\frac{1}{\lambda_0}\right)^2 - \left(\frac{p}{2\pi}\right)^2}} \tag{35}$$

$$v_{ph} = \frac{\omega}{\beta} = \frac{c\lambda_g}{\lambda_0}$$

$$v_g = \frac{\partial\omega}{\partial\beta} = \frac{c^2\beta}{\omega} = \frac{c\lambda_0}{\lambda_g}$$

It is observed that, for each mode, the product of the phase velocity and of the group velocity is equal to the constant c^2 . For only one traveling wave, the complex power of Eq. (27) can be written

$$S = P + jQ = \frac{1}{2} |V +|^2 Y_0^* e^{-2\alpha z} \tag{36}$$

with

$$P = \frac{1}{2} |V +|^2 e^{-2\alpha z} \text{Re } Y_0 \quad Q = - \left(\frac{1}{2}\right) |V +|^2 e^{-2\alpha z} \text{Im } Y_0 \tag{37}$$

where the admittance Y_0 is complex and is equal to

$$\text{For TM modes: } Y_{0E} = jk\eta/\gamma = \frac{\sigma + j\omega\epsilon}{\alpha + j\beta}$$

$$\text{For TE modes: } Y_{0H} = \gamma/jk\zeta = \frac{\sigma + j\beta}{j\omega\mu}$$

For no losses in the medium, these expressions reduce to the following:

1. For $\omega > \omega_c$: Real power is transmitted. There is no energy storage.
2. For $\omega < \omega_c$: Power is purely imaginary. No real power is transmitted and there is energy storage. The energy is capacitive for TM (E) modes and inductive for TE (H) modes: TM modes below cutoff store electric energy while TE modes below cutoff store magnetic energy. Hence, capacitors and inductors are designed at centimeter and millimeter wavelength by creating a limited region of space along the waveguide that concentrates the appropriate modes below cutoff. A resonant circuit is similarly designed around a frequency where the stored electric and magnetic energies of modes below cutoff compensate. Those regions of stored energy are centered on obstacles of the appropriate geometry, creating supplementary boundary conditions to be satisfied by higher-order modes, which are below cutoff.

Metallic waveguides can transport a significant power. Its value depends on the medium filling the guide, surface

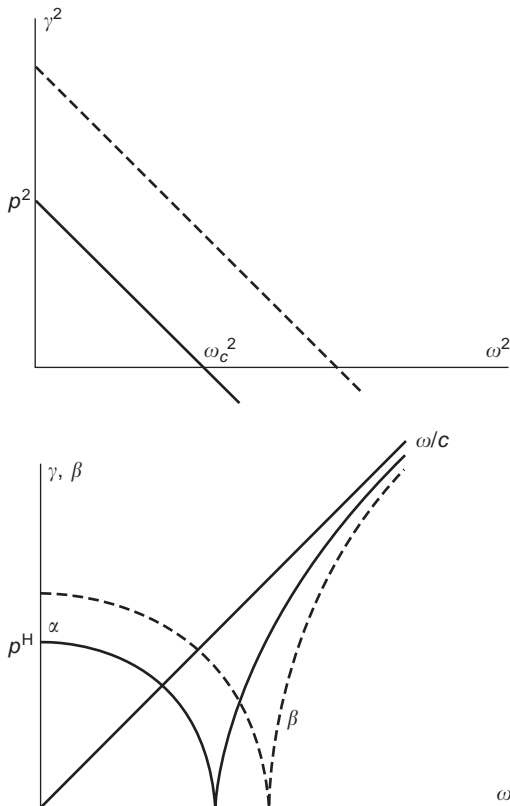


Figure 3. Dispersion diagram of typical modes, illustrating cut-off frequencies.

quality, humidity, pressure, possible temperature elevation, and frequency. If the guide is filled with dry air, the electric field may not go beyond 3 MV/m, which corresponds to a power range of 10 MW at 4 GHz and 100 kW at 40 GHz. Discontinuities and irregularities in the waveguide may impose a security factor of 4 or more. Furthermore, losses in copper walls are of the order of 0.03 dB/m at 4 GHz and 0.75 dB/m at 40 GHz (5).

2.2.4. Wall Losses. The losses in a metallic waveguide wall can be calculated by considering the metal wall as a perturbation of the perfectly conducting wall and using skin effect formulation. The formulation is valid as long as the skin depth is small compared with a distance around the periphery in which the magnetic field of the lossless guide changes considerably. Hence the formulation is not valid near corners unless that magnetic field is zero at the corner and may not be valid for modes of very high order, which, however, are seldom of great interest in practice. A number of results are given in 4 for rectangular and circular metal-walled guides, as well as for coaxial lines and other lines which are not of the guide type.

2.3. Specific Geometries

2.3.1. Rectangular Waveguide. The guide with a rectangular cross section has an inside horizontal width a (coordinate x) and vertical height b (coordinate y) with $a > b$. The identical eigenvalue Eq. (19) for TM modes and Eq. (24) for TE modes are solved by separation of variables and the potentials are the Cartesian eigenfunctions sine and cosine. The general solution for the potentials is

$$\text{Potential} = C(\cos ux \text{ or } \sin ux)(\cos vy \text{ or } \sin vy)$$

where C is an integration constant to be determined and u and v are constituents of the eigenvalue:

$$p^2 = u^2 + v^2 \neq 0 \quad (38)$$

Investigating first the TM modes, imposing the electric potential to vanish in $x=0$, a and in $y=0$, b yields the general solution

$$\phi_{mn} = C_{Emn} \sin \frac{m\pi x}{a} \sin \frac{n\pi y}{b} \quad (39)$$

where the product mn has to be different from zero, because of the sine functions. To each mn combination there corresponds a mode TM_{mn} . The integration constant C_{Emn} is determined by

$$p_{mn}^2 = u^2 + v^2 = \left(\frac{m\pi}{a}\right)^2 + \left(\frac{n\pi}{b}\right)^2 \quad (40)$$

and

$$p_{mn}^2 \int_A |\phi_{mn}|^2 da = 1 \quad (41)$$

from which

$$C_{Emn} = \frac{2}{p_{mn}\sqrt{ab}} \quad (42)$$

The transverse components are calculated using Eq. (14):

$$\begin{aligned} \bar{e}_{t,mn} &= -C_{mn} \left(\bar{a}_x \frac{m\pi}{a} \cos \frac{m\pi}{a} x \sin \frac{n\pi}{b} y \right. \\ &\quad \left. + \bar{a}_y \frac{n\pi}{b} \sin \frac{m\pi}{a} x \cos \frac{n\pi}{b} y \right) \\ \bar{h}_{t,mn} &= C_{mn} \left(\bar{a}_x \frac{n\pi}{b} \sin \frac{m\pi}{a} x \cos \frac{n\pi}{b} y \right. \\ &\quad \left. - \bar{a}_y \frac{m\pi}{a} \cos \frac{m\pi}{a} x \sin \frac{n\pi}{b} y \right) \end{aligned} \quad (43)$$

As for TE modes, the boundary conditions impose the normal derivatives of the magnetic potential to vanish at the walls, which yields cosine solutions

$$\Psi_{mn} = C_{H,mn} \cos \frac{m\pi x}{a} \cos \frac{n\pi y}{b} \quad (44)$$

where the sum $m+n$ has to be different from zero. To each mn combination corresponds a mode called TE_{mn} . The integration constant $C_{H,mn}$ is determined by the same equations as for TM modes, which yields

$$C_{H,mn} = \frac{2}{p_{mn}\sqrt{ab}} \quad (45)$$

when m and n are different from zero and

$$C_{H,mn} = \frac{\sqrt{2}}{p_{mn}\sqrt{ab}} \quad (46)$$

when m or n is zero. The transverse components are

$$\begin{aligned} \bar{e}_{t,mn} &= C_{mn} \left(\bar{a}_x \frac{n\pi}{b} \cos \frac{m\pi}{a} x \sin \frac{n\pi}{b} y \right. \\ &\quad \left. - \bar{a}_y \frac{m\pi}{a} \sin \frac{m\pi}{a} x \cos \frac{n\pi}{b} y \right) \\ \bar{h}_{t,mn} &= C_{mn} \left(\bar{a}_x \frac{m\pi}{a} \sin \frac{m\pi}{a} x \cos \frac{n\pi}{b} y \right. \\ &\quad \left. + \bar{a}_y \frac{n\pi}{b} \cos \frac{m\pi}{a} x \sin \frac{n\pi}{b} y \right) \end{aligned} \quad (47)$$

The smallest eigenvalue is obtained when the integer n related to the smallest dimension b is zero. Hence the dominant mode is the TE_{10} . For a lossless medium, its

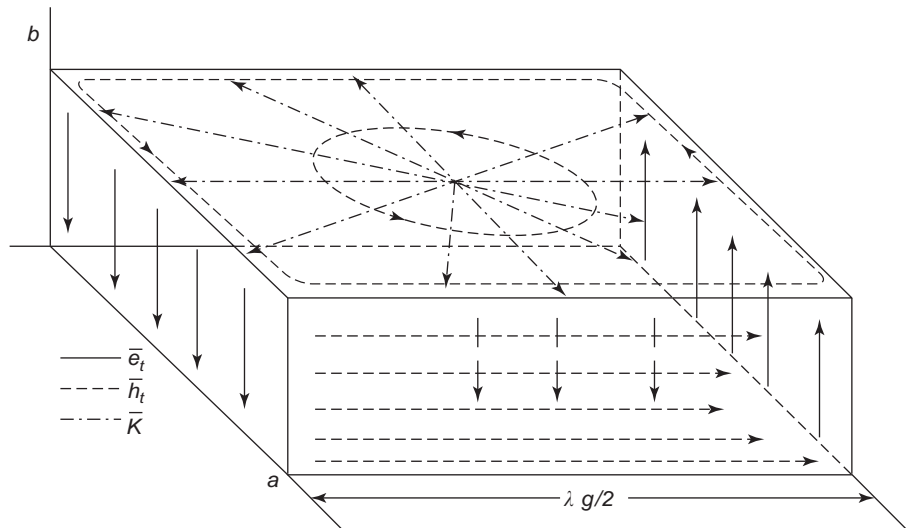


Figure 4. Fields and wall currents of dominant mode in rectangular waveguide, showing current source and sink.

parameters are

$$\begin{aligned} \Psi_{10} &= C_{10} \cos \frac{\pi x}{a} \\ C_{10} &= \frac{\sqrt{2a/b}}{\pi} \\ p_{10} &= \frac{\pi}{a} \\ \omega_{c10} &= \frac{\pi c}{a} \\ \lambda_{c10} &= 2a \\ \beta_{10} &= \left[\left(\frac{\omega}{c} \right)^2 - \left(\frac{\pi}{a} \right)^2 \right]^{1/2} \text{ at } \omega > \omega_c \\ \lambda_{g10} &= \left[\left(\frac{1}{\lambda_0} \right)^2 - \left(\frac{1}{2a} \right)^2 \right]^{-1/2} = \lambda_0 \left[1 - \left(\frac{\lambda_0}{2a} \right)^2 \right]^{-1/2} \end{aligned} \tag{48}$$

The fields of a traveling wave of the dominant mode have only three components:

$$\begin{aligned} \vec{E}_t &= -\bar{a}_y C_{10} V_+ \frac{\pi}{a} \sin \frac{\pi x}{a} e^{-j\beta_{10}z} \\ \vec{H}_t &= \bar{a}_x C_{10} V_+ \frac{\pi \beta_{10}}{\omega \mu} \sin \frac{\pi x}{a} e^{-j\beta_{10}z} \\ H_z &= C_{10} V_+ \left(\frac{\pi}{a} \right)^2 \frac{1}{j\omega \mu} \cos \frac{\pi x}{a} e^{-j\beta_{10}z} \end{aligned} \tag{49}$$

The transverse fields are in phase in time and in space, while H_z is out of phase with them, both in time and in space. Figure 4 represents the fields and surface current of the dominant mode along one-half guide wavelength. Hence the dominant mode is linearly polarized in the electric field. Calculating the cutoff frequencies of the first higher-order modes, it can be seen that to improve the bandwidth the height b must be chosen smaller than half the width a .

Calculating the three power expressions Eq. (29) for the dominant mode, normalized with respect to the factor $(b/a)Z_0$, respectively yields the values 1.57, 1.23, and 2.00, which shows that the differences are significant. Hence matching for instance a rectangular to a circular waveguide may offer serious difficulties. It seems that the square root of the product of 1.57 by 2.00 leads to the most convenient result for the power, although the reason is not certain [16]. The mode impedances and the parameters of interest for all the modes can be calculated according to the general theory developed earlier. Mode configurations can be found in a number of references [4,10,17,18].

Equation (40) shows that the eigenvalues, hence the cutoff frequencies, depend on the dimensions of both sides of the cross section of the guide. Furthermore, the height b must be smaller than $a/2$ to optimize the frequency range in which only the dominant mode propagates. For these reasons rectangular waveguides have specified dimensions [17] and corresponding normalized frequency bands have been defined. The most common bands are the following:

L	1.12–1.70 GHz
S	2.6–3.95 GHz
C	3.94–5.99 GHz
X	8.2–12.4 GHz
Ku	12.4–18.8 GHz
K	18.0–26.5 GHz
Ka	(or Q) 26.5–40 GHz
O	40–70 GHz
V	50–75 GHz
W	75–110 GHz

2.3.2. Ridge Waveguide. A waveguide that has the cross section as shown in Fig. 5 is called a *ridge waveguide*; it has a central ridge added either to the top or bottom or both of a rectangular section. Its interesting

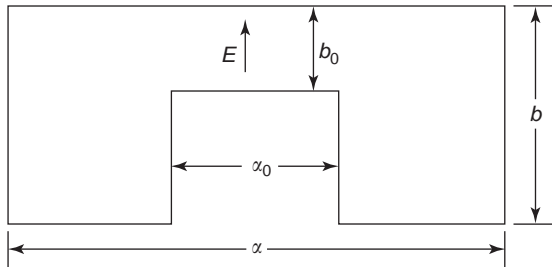


Figure 5. Cross section of a ridge waveguide.

electromagnetic property is that the cutoff frequency is lowered because of the capacitance effect at the center and could in principle be made as low as desired by decreasing the gap width sufficiently. Of course, the impedance of the guide also decreases as the gap is made smaller. Because of the increased effective length of the periphery, the attenuation is larger than in a usual rectangular waveguide. One of the important applications is as a nonuniform transmission system for matching purposes, obtained by varying the depth of ridge as one progresses along the guide [18].

Calculation of cutoff frequencies is rather easy if one remembers that, at cutoff, there is no variation in the z direction, so that waves reflect from sidewall to sidewall in a transverse direction at or below cutoff. Thus, at cutoff, the ridge waveguide can be considered as a short-circuited parallel-plane waveguide with infinite width in the z direction. The case of the dominant mode, like all the modes with no variation in the y direction, is particularly easy to calculate. Starting in the x direction from the vertical sidewall, which is a short circuit at the end of the transverse equivalent transmission line, one first has a parallel-plate waveguide per unit length in the z direction, then a capacitance because of the abrupt change in height, then again a parallel-plate waveguide with reduced height up to the middle of the cross section. There the impedance is either infinity or zero, depending on whether the mode is odd or even as a function of the electric field. The second half of the cross section is identical to the first half just described. The transverse resonance frequency, hence the cutoff frequency of the mode, can easily be calculated in terms of transmission-line parameters, as well as wavelength and impedance [19]. For the double-ridge waveguide, the impedance is twice that of the simple-ridge waveguide. Fundamental sources are Refs. 20 and 21.

2.3.3. Circular Waveguide. The circular waveguide has a circular cross section of radius a . The eigenvalue Eq. (19) for TM modes and Eq. (24) for TE modes are written in polar form for the transverse coordinates and solved again by separation of variables $r\phi$. The potentials are the polar eigenfunctions sine and cosine. The general solution for the potentials is

$$\theta = [A_m J_m(pr) + B_m y_m(pr)](\cos m\phi + \alpha \sin m\phi) \quad (50)$$

where m is an integer, possibly equal to zero, when the guide is of circular symmetry, which ensures a periodic solution in the polar angle, and where J_m and Y_m are the

Bessel functions of first and second kinds, respectively. The functions Y_m are sometimes called *Weber* or *Neumann functions*. They are singular at the origin $r = 0$. They have hence to be excluded from the solutions for a hollow guide. They have, however, to be included in the solutions for a coaxial cable or guide, and the general solution in that case will include a linear combination of both functions J and Y . In the case of the one-conductor circular waveguide, the general solution reduces to

$$\theta(r, \phi) = C_m J_m(pr)(\cos m\phi + \alpha \sin m\phi) \quad (51)$$

The choice of the cosine or sine function depends only on the polarization of the field, and all the modes are spatially degenerate. An elliptical polarization will be obtained by linearly combining the two orthogonal polarizations. In the following, only the cosine variation will be considered.

For *TM modes* the scalar potential must be zero at the wall:

$$J_m(p_e a) = 0 \quad (52)$$

which determines the eigenvalues p_{emn} from the arguments $em_n = p_{em}na$ for which the J_m functions vanish and yield:

$$\phi_m = C_{em} J_m(p_e r) \cos m\phi \quad (53)$$

where the first index m is the order of the function J_m and the second n relates to the order of the zeros with increasing argument.

For *TE modes* the normal derivative of the potential must vanish at the wall

$$J'_m(p_h a) = 0 \quad (54)$$

which determines the eigenvalues p_{hmn} from the arguments $hmn = p_{hm}na$ for which the J_m functions are extremum, and yields

$$\Psi_m = C_{hm} J_m(p_h r) \cos m\phi \quad (55)$$

where the first index m still is the order of the function J_m and the second n relates to the order of the extreme with increasing argument. There is a degeneracy that is typical of the circular waveguide—the TE_{0n} modes have the same eigenvalue as the TM_{1n} modes since a property of the Bessel functions is

$$J'_0(pr) = -J_1(pr) \quad (56)$$

For TM and for TE modes, the field configurations can be calculated from the general theory and the normalization conditions. The following results are obtained. TE

modes

$$\begin{aligned} \Psi_{mn} &= C_{hmn} J_m(p_{hmn}r) \cos m\phi \\ J'_m(h_{mn}) &= 0 \\ C_{hmn} &= \frac{1}{h_{mn} \sqrt{\pi} \sqrt{1 - (m/h_{mn})^2} J_m(h_{mn})} \\ &\text{multiplied by } \sqrt{2} \text{ if } m \neq 0; \text{ by } 1 \text{ if } m = 0 \\ \bar{h}_t &= C_{hmn} \left[-\bar{a}_r p_{hmn} J'_m(p_{hmn}r) \cos m\phi \right. \\ &\quad \left. + a_\phi \frac{m}{r} J_m(p_{hmn}r) \sin m\phi \right] \\ \bar{e}_t &= C_{hmn} \left[\bar{a}_r \frac{m}{r} J_m(p_{hmn}r) \sin m\phi \right. \\ &\quad \left. + \bar{a}_\phi p_{hmn} J'_m(p_{hmn}r) \cos m\phi \right] \end{aligned}$$

TM modes

$$\begin{aligned} \phi_{mn} &= C_{emn} J_m(p_{emn}r) \cos m\phi \\ J_m(e_{mn}) &= 0 \\ C_{emn} &= \frac{1}{e_{mn} \sqrt{\pi} J'_m(e_{mn})} \\ &\text{multiplied by } \sqrt{2} \text{ if } m \neq 0; \text{ by } 1 \text{ if } m = 0 \\ \bar{e}_t &= C_{emn} \left[-\bar{a}_r p_{emn} J'_m(p_{emn}r) \cos m\phi \right. \\ &\quad \left. + a_\phi \frac{m}{r} J_m(p_{emn}r) \sin m\phi \right] \\ \bar{h}_t &= C_{emn} \left[-\bar{a}_r \frac{m}{r} J_m(p_{emn}r) \sin m\phi \right. \\ &\quad \left. - \bar{a}_\phi p_{emn} J'_m(p_{emn}r) \cos m\phi \right] \end{aligned}$$

Comparing the successive order of zeros and extrema of Bessel functions shows that the *dominant mode* is the TE₁₁ mode. Its eigenvalue corresponds to the first maximum of the function J_1 and has the following characteristics:

$$\begin{aligned} p_{h11} &\cong \frac{1.84}{a} \\ \Psi_{11} &= C_{h11} J_1(p_{h11}r) \cos \phi \\ \omega_{h11} &= p_{h11}c \cong \frac{1.84c}{a} \\ \lambda_c &\cong \frac{2\pi}{1.84a} \end{aligned} \tag{57}$$

It is apparent that the wavelength at the cutoff frequency of the dominant mode is of the order of the guide circumference, while being larger than $2a$. Hence, the cutoff frequency of a circular waveguide of radius a is lower than that of a rectangular waveguide of width a . The transverse

fields of the dominant mode are

$$\begin{aligned} \bar{h}_t &= -\bar{a}_r C J'_1(pr) \cos \phi + \bar{a}_\phi \frac{C}{r} J_1(pr) \sin \phi \\ \bar{e}_t &= \bar{a}_r \frac{C}{r} J_1(pr) \sin \phi + \bar{a}_\phi C J'_1(pr) \cos \phi \end{aligned} \tag{58}$$

The TE_{0n} modes exhibit the interesting property of having losses that decrease when the frequency increases. As an example, the TE₀₁ mode has the following characteristics:

$$\begin{aligned} \Psi_{01} &= C J_0(p_{h01}r) \text{ with } p_{h01} \cong \frac{3.83}{a} \\ \bar{h}_t &= \bar{a}_r C p_{h01} J_1(pr); \bar{e}_t = -\bar{a}_\phi C p_{h01} J_1(pr) \end{aligned} \tag{59}$$

Hence the transverse fields vanish at the wall and induce no wall losses. The only wall losses are due to the field longitudinal component. Calculating the proportionality between the H_z component of a TE mode and the scalar potential yields

$$H_z = \frac{p^2}{jk\zeta} kV(z)\Psi \tag{60}$$

which shows that when the medium is lossless H_z is inversely proportional to the frequency. Hence losses decrease with increasing frequency. A number of mode configurations can be found in Refs. 4,10,17, and 18.

2.3.4. Coaxial Waveguide. Coaxial lines are among the most commonly used of all transmission lines, largely because of the convenient construction and the nearly perfect shielding between fields inside and outside of the line. They are commonly used up to 10–20 GHz. The range of impedances that may be obtained most conveniently in the TEM mode is about 30–100 Ω. Above 15 GHz and up to ~30 GHz the most common coaxial lines are rigid. In addition to the TEM mode, higher-order TE/TM-mode solutions can also exist. They are usually cutoff and are important essentially as reactive effects near junctions of the line, although they occasionally may enter as additional propagating modes in the transmission system. Higher-order TE and TM modes are calculated as indicated for the circular waveguide and the general solution is Eq. (50), where Bessel functions of both the first and second kind are to be used. The transcendental equations are more complicated than for the one-conductor circular guide. The solutions determine the values of the cutoff frequency, for any mode type and any particular sizes. Solution of the transcendental equations is obtained by graphical methods or by consulting published tables. More information is found in Refs. 10 and 18.

There are a number of normalized connectors for coaxial cables and waveguides. They are characterized by a maximum admissible standing wave ratio, due to very severe tolerances. In a rigid coaxial guide with no dielectric, the inside conductor is maintained in position by using special techniques [22].

The usual frequency limitation for using coaxial cable at microwaves is its specific attenuation, which is the sum of copper and dielectric losses. Analytical expressions are found for instance in Ref. 23. The specific attenuation of a good coaxial cable is of the order of 1 dB/m. When calculating the attenuation, the voltage breakdown, and the maximum power as a function of the ratio of the outside to the inside radii of an air-filled coaxial line, it appears that there is a minimum for the attenuation and a maximum for the voltage breakdown and for the maximum power in the approximate range of 30–80 Ω for the characteristic impedance, which explains why most coaxial lines and cables have an impedance of 50 or 75 Ω .

2.3.5. Elliptical Waveguide. An elliptical waveguide is a uniform region in which the transverse cross section is of elliptical form [24]. The rectangular coordinates xy of the cross section are related to the coordinates of the confocal ellipse and confocal hyperbola. The boundary ellipse is defined by the coordinate as a function of which the major and minor axes as well as the eccentricity and the focal distance can be expressed. Mode functions for TE and TM modes are derived from Mathieu functions, eigenfunctions of Helmholtz equation in elliptical coordinates [25]. When the eccentricity decreases, the elliptical boundary reduces to a circular one and the Mathieu functions degenerate into circular functions. Correspondingly, the confocal coordinates become the polar coordinates.

The field components can be calculated for each mode according to the general theory. The cutoff frequencies are expressed in terms of the roots of the functions, determined by the boundary conditions, and the semifocal distance. An alternative expression in terms of the eccentricity of the boundary ellipse is obtained by use of the elliptic integral formula for the length of the boundary ellipse. Computation of power flow and attenuation in elliptical guides involves numerical integration of the Mathieu functions over the guide cross section. Some mode patterns are shown in Ref. 10.

2.4. Radial Waveguide

2.4.1. Cylindrical Cross Section. The transverse cross section of a radial waveguide with cylindrical cross section is a complete cylindrical surface of a given height. The classical circular cylindrical coordinate system is appropriate to a region of this type. Radial waveguides are encountered in many of the resonant cavities used in microwave oscillator tubes, filters, and so on. Free space can be regarded as a radial waveguide of infinite height. The transverse electromagnetic field in radial waveguides cannot be represented, in general, as a superposition of transverse vector modes; there exists only a scalar representation that, for no H_z field, is expressible in terms of TM modes and, for no E_z field, in terms of TE-type modes [10].

In a radial waveguide the concept of guide wavelength loses its customary significance because of the nonperiodic nature of the field variation in the transmission direction. Consequently the usual relation between guide wavelength and cutoff wavelength is no longer valid. The cutoff wavelength however is still useful as an indication

of the propagating or nonpropagating character of a mode. The radial waveguide is a two-conductor system and supports a TEM mode. TE and TM modes are calculated according to the general theory (10).

2.4.2. Cylindrical Sector Cross Section. In this case the transverse cross section has a given aperture, limited by vertical metallic planes. Such devices have been used for quite some time as specific radar antennas. They have a wall formed by one conductor only, hence no TEM mode can propagate. Furthermore, there is no periodic symmetry in the horizontal plane, which alters the solutions with respect to the cylindrical situation. TE and TM modes are calculated according to the general theory [10].

2.5. Spherical Waveguide

Free space can be considered as a nonuniform transmission region or spherical waveguide. The cross sections transverse to the radial transmission direction are complete spherical surfaces. In practice many spherical cavities may be conveniently regarded as terminated spherical guides. The dominant mode is spherical TEM. TE and TM modes are based on the eigenfunctions in the spherical coordinate system, that is, the associated Legendre functions, or Legendre polynomials [15]. The corresponding fields are calculated for both types of mode [10]. The r dependence of the mode fields is determined by the spherical transmission-line behavior of the mode voltage and current. As for the modes in radial waveguide, the concepts of cutoff wavelength and guide wavelength lose their customary significance in a spherical waveguide because of the lack of spatial periodicity along the transmission direction. The cutoff wavelength of both TE and TM modes is, however, indicative of the regions wherein these modes are propagating or nonpropagating. For regions such that the wavelength is smaller than a given cutoff wavelength the mode fields decay spatially like $1/r$ and hence may be termed propagating; conversely, for wavelength larger than the cutoff wavelength the mode fields decay faster than $1/r$ and may, therefore, be termed *nonpropagating*.

2.6. Conical Waveguide

Conical waveguides are of a two-conductor type. The transmission direction is along the radius r and the cross sections transverse thereto are spherical surfaces bounded by the two cones. The conical waveguide is seen to bear the same relation to a spherical waveguide that a coaxial waveguide bears to a circular guide. Examples of conical guides are provided by tapered sections in coaxial guide, conical antennas [15], and others. Because of the two conductors, the conical waveguide propagates a TEM mode. The r dependence of this dominant mode voltage and current is determined by the spherical transmission-line equations, which reduce in this case to uniform transmission-line equations. The attenuation constant of this mode is given in Ref. 10, as well as some expressions related to TE and TM modes.

3. ADVANCED TOPICS

3.1. Periodic Waveguides

Periodic waveguides are periodically loaded waveguides. Hence, strictly speaking, they should not be considered in this article. The importance they have had, the fact that they are “empty” except for a periodic loading by infinitely thin obstacles, in most cases capacitive, and the beauty of their electromagnetic properties certainly deserves some attention [26].

Periodic waveguides have been used in the microwave-tube family as traveling-wave amplifiers and backward-wave oscillators, as microwave and video filters, and as linear particle accelerators. Most of the mathematics and point of view in studying such structures is the same as that used in analyzing the vibrations of a periodically weighted string or in studying the propagation of light or electrons through a crystal lattice [27]. The basic theorem is from Floquet [28]. The theorem applies to a second-order linear differential equation with periodic coefficients and is quite general [5]. It says that a solution of the equation differs from the solution one period away by only a complex factor. Applied to a periodically loaded transmission line it may be translated as follows [26]. For a given mode of propagation at a given steady-state frequency the fields at one cross section differ from those one period away only by a complex constant. The theorem is valid whether the structure contains loss or not so long as it is periodic.

The study reveals that periodic transmission lines have the following characteristics:

1. There are passbands and stopbands, which is to say certain frequencies can propagate down the structure with little or no attenuation, whereas other frequencies are attenuated at a rapid rate. These frequencies occur in bands.
2. There is no unique phase velocity. At any frequency for a given mode of propagation there is found to be an infinite number of discrete velocities characterizing the mode.
3. The fields may be analyzed in a Fourier series, often called *space harmonics* or *Hartree harmonics*, each component of the series having a different phase velocity but all having the same group velocity. Typically, there will be many components with phase velocities less than the velocity of light, yielding slow waves.
4. Structures can be treated from both the field and the circuit standpoint, each approach being useful in certain problems.

To understand what causes passbands and stopbands, assume that circular infinitely thin irises are placed periodically in a circular waveguide propagating the TM_{10} mode. This is the structure used in the linear electron accelerator. At each obstacle there will be transmission and reflection. An observer stationed in the plane of an iris will see that there are certain frequencies for which the reflections from the successive obstacles returning to her/

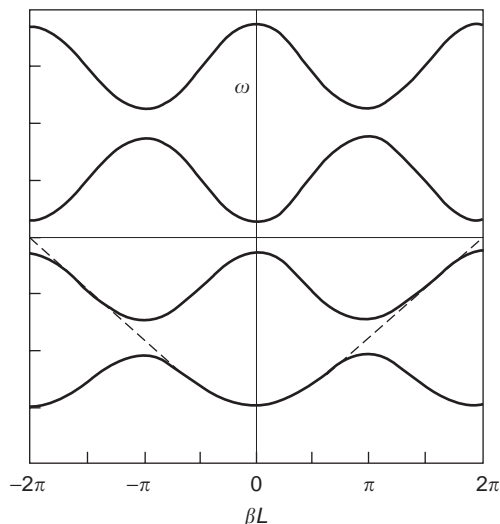


Figure 6. Dispersion diagram ($\omega - \beta$) for iris-loaded waveguide, with dashed line for unloaded waveguide.

him add in phase. These frequencies will be nearly equal to the frequencies for which the one-way phase shift between obstacles in the unperturbed guide is any multiple of π . These frequencies are the centers of the stopbands. At other frequencies the accumulated reflections from an infinite length of guide add up to zero, and transmission occurs. Those frequencies make up the passbands. Figure 6 shows an $\omega - \beta$ diagram for this structure. The dashed line represents the $\omega - \beta$ line for the waveguide without obstacles. Electric field representations illustrate the situation in more detail.

Two important theorems on lossless periodic transmission lines have been derived [26]. One is that the time-average electrical stored energy per period is equal to the time-average magnetic stored energy per period in the passbands. The other is that the time-average power flow in the passbands is equal to the group velocity times the time-average electrical and magnetic stored energy per period divided by the period.

3.2. Oversize Waveguides

As has already been mentioned, the TE_{0n} and in particular the TE_{01} modes in circular waveguides have received a good deal of attention for possible long-distance propagation of energy, especially at millimeter waves. The reason is that the amplitude of the fields at the wall decrease when frequency increases, and current and conductor losses approach zero at very high frequency. Attenuations as low as 1.3 dB/km have been attained. Since electric field lines are circular, modes of this class are often described as *circular electric modes* [18]. A major problem arises because the mode is not the dominant one. Such guides are known as *oversize guides*. For the TE_{01} mode, there are four other propagating modes, with cutoff frequency below the TE_{01} cutoff. Furthermore, since the frequency is well above cutoff, many other modes are in the propagating range. This raises several practical problems; for instance, the desired mode must be excited with reasonable purity, and, coupling from the desired mode to undesired

modes must be avoided. A general solution is to devise mode filters that discriminate against the undesired modes but cause negligible attenuation to the desired one [18].

Suggestions have been advanced also for using a large-size rectangular waveguide, whose transverse dimensions are just less than $\lambda \times 2\lambda$, to increase the CW power-handling capability. Trapped-mode resonance effects in such a system have been investigated experimentally, and it has been shown how to suppress them [29].

3.3. Mode Excitation

The general theory shows that an infinity of TE and TM modes may exist in a hollow waveguide. Furthermore, in a more-than-one-conductor waveguide a TEM mode may also exist. This possible TEM mode has a zero cutoff frequency while the TE and TM modes each have a specific cutoff frequency. Each of those modes will attenuate below cutoff, storing energy as has been seen, and propagate above cutoff. The modes however are only the possible solutions of the equations, submitted to the boundary conditions. As mentioned earlier, modes will actually exist in the waveguide only if they are properly excited, which requires an adequate transducer at the generator end of the waveguide. To adequately detect the power transmitted by those modes, such a transducer is also necessary at the detector end of the waveguide. For the sake of completeness, it should be mentioned that irregularities or non-uniformities in the waveguide may also excite other modes, causing what is called *mode conversion*. This may be an advantage or a disadvantage, depending on the application. This subject is, however, outside the scope of this article.

Equation (12) and the associated boundary conditions may yield the amplitudes of the fields, under specific excitation conditions. As already stated, a linear combination of all the modes, with adequate coefficients, is the general solution of Maxwell's equations for the waveguide [2]. If for a given excitation specific mode coefficients are found to be zero because the corresponding modes do not satisfy the boundary conditions of the excitation, those modes will not be excited and will not actually exist in the guide. Using Eq. (12) and adding the expressions of the longitudinal components [Eqs. (18) and (60)] for both directions of propagation yields the system:

$$\begin{aligned}\bar{\mathbf{E}}_t &= \sum_i (V_{+i}e^{-\gamma_i z} + V_{-i}e^{\gamma_i z})\bar{\mathbf{e}}_{t,i} \\ \bar{\mathbf{H}}_t &= \sum_i Y_{0i}(V_{+i}e^{-\gamma_i z} - v_{-i}e^{\gamma_i z})\bar{\mathbf{h}}_{t,i} \\ E_z &= \sum_i \frac{p_i^2}{jk\eta} Y_{0i}(V_{+i}e^{-\gamma_i z} - V_{-i}e^{\gamma_i z})\phi_i \\ H_z &= \sum_i \frac{p_i^2}{jk\zeta} (V_{+i}e^{-\gamma_i z} + V_{-i}e^{\gamma_i z})\psi_i\end{aligned}\quad (61)$$

The sums are on the indices m and n for TE as well as for TM modes. All the modes are considered, propagating and attenuating. The coefficients V are calculated from the

boundary conditions. To obtain a unique solution in a given volume the tangential electric field must be imposed on part of the bounding surface and the tangential magnetic field on the remaining part of the surface. In a waveguide with lossless conducting walls the tangential electric field is known to be zero on the walls. Hence it is sufficient to impose two conditions in reference planes; for instance, \mathbf{E}_{tan} in $z=0$ and \mathbf{H}_{tan} in $z=L$, or \mathbf{E}_{tan} and \mathbf{H}_{tan} in $z=0$, and so on. Use is then made of orthogonality conditions obtained from Green's theorems (see Green's function methods). As an example, if \mathbf{E}_{tan} is specified in $z=0$ and \mathbf{H}_{tan} in $z=L$, the following system is obtained:

$$\begin{aligned}V_{+j} &= (e^{\gamma_j L} + e^{-\gamma_j L})^{-1} \left[e^{\gamma_j L} \int_A \bar{\mathbf{E}}_{\text{tan}} \cdot \bar{\mathbf{e}}_{t,j}^* da + Z_{0j} \int_A \bar{\mathbf{H}}_{\text{tan}} \cdot \bar{\mathbf{h}}_{t,j}^* da \right] \\ V_{-j} &= (e^{\gamma_j L} + e^{-\gamma_j L})^{-1} \left[e^{-\gamma_j L} \int_A \bar{\mathbf{E}}_{\text{tan}} \cdot \bar{\mathbf{e}}_{t,j}^* da - Z_{0j} \int_A \bar{\mathbf{H}}_{\text{tan}} \cdot \bar{\mathbf{h}}_{t,j}^* da \right]\end{aligned}\quad (62)$$

If \mathbf{E}_{tan} and \mathbf{H}_{tan} are specified in $z=0$, for instance, by specifying a current sheet \mathbf{K} in part of the plane $z=0$, which could be a transverse electron pencil in that plane, and terming 1 the negative z region and 2 the positive z region yields as source conditions:

$$\bar{\mathbf{a}}_z \times (\bar{\mathbf{H}}_{t,1} - \bar{\mathbf{H}}_{t,2}) = \bar{\mathbf{K}}_t \quad \text{and} \quad \bar{\mathbf{E}}_{t,1} = \bar{\mathbf{E}}_{t,2}\quad (63)$$

Suppose that matching at both ends of the guide finally yields

$$V_{-j}^{(1)} = V_{+j}^{(2)} = \frac{Z_{0j}}{2} \int_A \bar{\mathbf{e}}_{t,j}^* \cdot \bar{\mathbf{K}}_t da\quad (64)$$

Hence, specifying \mathbf{K} yields the coefficients of the excited modes. Equation (64) clearly shows as an example that the modes for which the transverse fields are perpendicular to the current source are not excited.

4. SPECIFIC RECENT DEVELOPMENTS

4.1. Theory

A new causal power-normalized waveguide equivalent-circuit theory has been established very recently (as of 2003). Unlike its predecessors, it results in network parameters usable in both the frequency and time domains in a broad class of waveguides. Enforcing simultaneity of the voltages, currents, and fields and a power normalization fixes all the parameters of the new theory within a single normalization factor, including both the amplitude and phase of the characteristic impedance of the waveguide. Enforcing simultaneity also ensures that the network parameters of passive devices are causal [30]. On the other hand, an efficient finite-element method has been developed for

waveguide analysis. It uses Hermitian polynomials to interpolate the axial field component (E_z or H_z) and some of its derivatives at the nodal points, rather than the field components, as in the Lagrangian interpolation case, with significant advantages: (1) a significant reduction of the matrix order needed to compute the eigenvalues and eigenfunctions, (2) smooth axial components and continuous transverse field components, and (3) low-cost refinement of the mesh near nonconvex corners of the waveguide [31]. Furthermore, it has been shown that the upper and lower bounds of the cutoff frequencies of TE and TM modes in many waveguides bounded by metallic lossless walls and that may be hollow or comprise one or more inner conductor, can be computed using two independent methods. The methods are applicable whenever the cross section of the waveguide can be split up into several regions bounded by lines having a fixed coordinate and includes several cases of particular interest. The theory is illustrated with a rectangular coaxial line [32].

Mode coupling in waveguiding structures has been revisited using the theory of Morse critical points from catastrophe theory. The traditional coupled-mode formalism has a clear analytical connection with functional properties of the characteristic determinant in the vicinity of these points. Numerical results have been obtained for a variety of waveguiding structures like printed-circuit transmission lines, planar slab waveguides, and shielded microstriplike lines [33]. It has then been shown that two distinct regimes of modal behavior exist in the vicinity of the mode-coupling region, resulting from the presence of frequency branchpoints of the dispersion function. These branchpoint singularities are intimately associated with the Morse critical points [34]. Overmoded waveguides, with waveguide diameter large in terms of wavelength, have been a subject of interest for many years. These waveguides have been analyzed, when coated with a lossy material, particularly for their attenuation properties as a function of coating material, layer thickness, and frequency. It has been shown that, when the coating material is not too lossy, the low-order modes are highly attenuated even with a thin layer of coating. Hence, this coated waveguide may serve as a mode suppressor of the low-order modes, which can be particularly useful for reducing the radar cross section of a cavity structure such as a jet engine inlet [35,36].

On the other hand, how waveguide modes can transform into surface waves has been investigated. An asymptotic form of the characteristic equation that describes wave propagation at near-infrared wavelengths in small core hollow circular waveguides has been developed. Analytic solutions for the transverse and axial propagation constants have been obtained. They show that the TE_{11} and TM_{01} modes transfer to surface waves as the guide radius is increased to values much greater than at cutoff [37].

Twists may be required in oversized waveguide used for low-loss transmission at the higher microwave and millimeter-wave frequencies. The unwanted mode conversion in such twists has been calculated from numerical integration of the coupled mode equations, considering simultaneous coupling of the five lowest-order modes coupled in

a twist. Twists with tapered or linearly varying rates of twist have been shown to be superior in medium- or broad-band applications to those with uniform twist rate, such as those normally made commercially for single-mode waveguide [38].

An important problem is the determination of the input impedance of a probe when inserted into a waveguide [12]. A method-of-moments formulation based on a nonuniform surface current approximation and on the use of an impressed electric field arising from a semifinite rectangular waveguide Green function has been used to calculate the input impedance of a coaxial probe in a semifinite waveguide. The probe surface current was shown to vary significantly with probe angle [39]. Furthermore, the probe field distribution and mutual coupling between two probes arbitrarily located in a rectangular waveguide have been studied by means of dyadic Green's function, field transformation, and reaction concept. The waveguide is semi-infinite. Lengths, feeding points, and orientations of the two probes in the waveguide are arbitrary [40]. General formulas of the mutual impedance between probes have been established for a circular waveguide as well [41].

Nonuniform waveguides have been studied for some time with application to antennas and tapers. Furthermore, irregularities in waveguide walls are important to investigate as well. For typical tolerances the reflection coefficients are very small ($<10^{-3}$), but the results are important in precise six-port measurements. First-order results have been derived for the reflection coefficient of a waveguide with slightly uneven walls. Specific analytical and numerical results have been given for rectangular waveguides and coaxial transmission lines [42].

Finally, the expected properties of high- T_c superconductor waveguides have recently been evaluated. It has been shown that these devices would offer the potential of 100 GHz bandwidth for transmission over long distance with low attenuation, with a wider dynamic range than optical systems. The potential applications in local area networks have been investigated [43].

4.2. Arbitrary Cross Section

The treatment of waveguides with arbitrary cross section is a challenging task to solve on the computer, in particular when looking for speed and simplicity. A surface integral equation approach has been used where the E field is transformed into a matrix equation using the method of moments. The salient features of this method are speed, simplicity, and the absence of any spurious modes while treating waveguides of arbitrary cross section. It leads to the calculation of cutoff wavenumbers for a variety of cross sections and of modes [44].

On the other hand, it has been shown that the fields associated with the TM_{01} mode of an elliptical waveguide are qualitatively different from those that have appeared in the standard literature since the early 1950s. The method used was to solve the wave equation by numerical integration, using an iterative technique to obtain the relevant eigenvalues [45]. Cutoff frequencies of eccentric circular-elliptical metallic waveguides have also been

calculated [46]. A perturbation method has been used to obtain the attenuation constant and Q factor of several TEM, TE, and TM modes in confocal annular elliptic waveguides and resonators. Comparisons between the first higher-order mode in a confocal annular elliptic waveguide and a coaxial waveguide with the same cutoff frequency and cross-sectional propagating area reveals a lower attenuation in elliptical geometry. The Q factor has been found to be 20–40% higher in elliptical geometry than in a coaxial resonator with the same volume and resonant frequency [47].

Approximate analytical expressions have been derived by a perturbation technique for the cutoff wavenumbers and the corresponding modes in annular-cross-sectional waveguides having inner conductors of small radius. Waveguides with circular and rectangular outer boundary have been considered [48].

The mode analysis for parabolic waveguides has been performed. The approach is simple. It is based on one-dimensional analytic continuation. It yields exact values for parabolic cylinder functions. The difficulty in obtaining accurate values for these functions has long been an impediment to mode analysis for parabolic waveguides [49].

When looking at toroidal waveguides, it can be shown that the explicit solution of Maxwell's equations cannot be given. For small curvature the field equations can, however, be solved by means of an analytical approximation method. A perturbation method has provided eigenvalues and eigenfunctions containing first-order correction terms for the full spectrum of all modes including the degenerate ones [50].

A general analysis for the modal characterization of multiconnected uniform, hollow, conducting waveguides has been performed. It is relevant to waveguides with an outer conductor for which analytical Green functions are known and inner conductors described by integral equations. The TEM mode space is analyzed, and singularities of the integral equations are studied for determining the higher-order modes. Spurious solutions arise as a result of the structure of the integral equations for multiconnected waveguides; criteria to discard such modes are presented [51].

4.3. Ridged Waveguide

Ridged waveguides have found many applications in microwave and millimeter-wave devices. Their advantages include large single-mode broadband operation, large dominant cutoff wavelength, and low impedance characteristics. A magnetic field integral equation approach has been developed for the analysis and design of ridged waveguides. It has been pointed out that bandwidth estimates in previous works were erroneous because of the neglect of the TE_{11} mode. Design curves on cutoff frequency, bandwidth, attenuation, and waveguide impedance have been provided [52,53]. On the other hand, a coupled-integral equations technique has been used to determine the cutoff frequencies of all TE and TM modes of a ridged rectangular waveguide. The technique analyzes both symmetric and asymmetric situations. Basis functions, which include the edge conditions and mirror images in the waveguide walls, are used in the moment method solution of the integral equations [54]. Generalized rectangular and circu-

lar ridge waveguides have been analyzed using the mode-matching method, yielding the characteristic impedance, attenuation, and power-handling capability of several types of rectangular and circular ridge waveguides [55].

4.4. Grooved Waveguide

High-power devices such as gyrotrons have necessitated the development of specific structures, in particular grooved waveguides and, more specifically, axially multiple-grooved waveguides. A method has been developed to calculate the TE mode fields and cutoff frequencies of an axially multigrooved rectangular waveguide. The method has been extended to a rectangular waveguide with multiple grooves cut into two of its broad wall parallel surfaces [56]. The development of the gyrotron has also brought more attention to the corrugated waveguide, dielectric-loaded or not, in particular nonperiodic configurations. The Floquet theorem is used to express the field distribution in the vacuum region, while an eigenfunction expansion is employed in each dielectric region, with the appropriate boundary conditions applied at the interfaces, leading to an infinite number of equations. The system is solved numerically by truncation [57]. It should also be mentioned that radiation from the open end of a corrugated hybrid-mode circular waveguide has excellent properties, such as low sidelobes, cross-polarization levels, axial beam symmetry, and low attenuation. The general characteristics of electromagnetic scattering from a circular waveguide with rectangular corrugations have been calculated, in terms of frequency and waveguide geometry. Dyadic Green functions and Fourier transforms were used to get the field in terms of modal currents induced on the corrugation openings [58]. The grooved waveguide is considered for use at millimeter wavelengths as an alternative to classical waveguides such as the H guide and the rectangular guide. It is low loss, with low-dimensional tolerance and the ability to handle higher power capacities at high frequencies. Most of these properties are attributed to the open endedness of the guide, which reduces wall losses. The grooves in the guide trap the fields locally and prevent radiation from leaking out along the open parts of the guide. Multimodal analysis of an open rectangular groove waveguide is available for both TE and TM modes [59].

BIBLIOGRAPHY

1. K. L. Smith, Victorian microwaves: Millimetre transmissions before the Boer war, *IEEE AESS News*. 1–3 (June 1984).
2. J. C. Slater, *Microwave Electronics*, Van Nostrand, New York, 1950.
3. K. S. Packard, The origin of waveguides: A case of multiple rediscovery, *IEEE Trans. Microwave Theory Tech.* **MTT-32**: 961–969 (Sept. 1984).
4. R. A. Waldron, *Theory of Guided Electromagnetic Waves*, Van Nostrand Reinhold, London, 1969.
5. A. Vander Vorst and D. Vanhoenacker-Janvier, *Bases de l'ingénierie micro-onde*, De Boeck, Brussels, 1996.
6. O. Heaviside, *Electromagnetic Theory*, Benn, London, 1893.

7. J. J. Thompson, *Notes on Recent Researchers in Electricity and Magnetism*, Clarendon, Oxford, 1893.
8. J. Larmor, Electric vibrations in condensing systems, *Proc. Lond. Math. Soc.* **26**:119 (Dec. 1894).
9. Lord Rayleigh, On the passage of electric waves through tubes, or the vibration of dielectric cylinders, *Phil. Mag.* **43**:125–132 (1897).
10. N. Marcuvitz, *Waveguide Handbook*, McGraw-Hill, New York, 1948.
11. J. A. Stratton, *Electromagnetic Theory*, McGraw-Hill, New York, 1941.
12. R. E. Collin, *Field Theory of Guided Waves*, McGraw-Hill, New York, 1960.
13. C. T. Tai, *Dyadic Green Functions in Electromagnetic Theory*, 2nd ed., IEEE Press, New York, 1994.
14. A. Vander Vorst, *Transmission, Propagation et Rayonnement*, De Boeck, Brussels, 1995.
15. S. A. Schelkunoff, *Electromagnetic Waves*, Van Nostrand, New York, 1943.
16. R. M. Walker, Waveguide impedance: too many definitions, *Electron. Commun.* **1**(3) (May 1966).
17. *The Microwave Engineer's Handbook and Buyer's Guide*, Horizon House, Dedham, MA, 1966.
18. S. Ramo, J. R. Whinnery, and T. Van Duzer, *Fields and Waves in Communication Electronics*, Wiley, New York, 1965.
19. T. K. Ishii, *Microwave Engineering*, Ronald Press, New York, 1996.
20. S. B. Cohn, Properties of ridge waveguide, *Proc. IRE* **35**: 783–788 (1947).
21. W. J. Getsinger, Ridge waveguide field description and application to directional couplers, *IRE Trans. Microwave Theory Tech.* **MTT-10**:41–50 (1944).
22. G. L. Ragan, *Microwave Transmission Circuits*, MIT Rad. Lab Series, Vol. 9, Dover, New York, 1965.
23. G. L. Matthaei, L. Young, and E. M. T. Jones, *Microwave Filters, Impedance-Matching Networks, and Coupling Structures*, McGraw-Hill, New York, 1965.
24. L. J. Chu, Electromagnetic waves in elliptic hollow pipes, *J. Appl. Phys.* **9** (Sept. 1938).
25. M. Abramowitz and I. E. Stegun, *Handbook of Mathematical Functions*, Dover, New York, 1965.
26. D. A. Watkins, *Topics in Electromagnetic Theory*, Wiley, New York, 1958.
27. L. Brillouin, *Wave Propagation in Periodic Structures*, Dover, New York, 1953.
28. G. Floquet, Sur les équations différentielles linéaires à coefficients périodiques, *Ann. Ecole Norm. Sup.* **12**(47):1883.
29. A. L. Cullen, R. Reitzig, and P. N. Robson, Further considerations of overmoded rectangular waveguide for high-power transmission, *Proc. IEE* **112**(7):1301–1310 (1965).
30. D. F. Williams, B. K. Alpert, "Causality and waveguide circuit theory", *IEEE Trans. Microwave Theory Tech.* **MTT-49**:615–623 (April 2001).
31. M. Israel and R. Miniowitz, An efficient finite element method for nonconvex waveguide based on Hermitian polynomials, *IEEE Trans. Microwave Theory Tech.* **MTT-35**: 1019–1026 (Nov. 1987).
32. L. Gruner, Lower and upper bounds of cutoff frequencies in metallic waveguides, *IEEE Trans. Microwave theory Tech.* **MTT-40**:992–995 (May 1992).
33. A. B. Yakovlev and G. W. Hanson, Analysis of mode coupling on guided-wave structures using Morse critical points, *IEEE Trans. Microwave Theory Tech.* **MTT-46**:966–974 (July 1998).
34. A. B. Yakovlev and G. W. Hanson, Mode-transformation and mode-continuation regimes on waveguiding structures, *IEEE Trans. Microwave Theory Tech.* **MTT-48**:67–75 (Jan 2000).
35. C. S. Lee, S. -W. Lee, and S. -L. Chuang, Normal modes in an overmoded circular waveguide coated with lossy material, *IEEE Trans. Microwave Theory Tech.* **MTT-34**:773–785 (July 1986).
36. R. C. Chou and S. W. Lee, Modal attenuation in multilayered coated waveguides, *IEEE Trans. Microwave Theory Tech.* **MTT-36**:1167–1176 (July 1988).
37. F. E. Vermeulen, A. M. Robinson, C. R. James, and J. N. McMullin, Infrared surface waves in circular hollow waveguides with small core diameters, *IEEE Trans. Microwave Theory Tech.* **MTT-42**:1932–1938 (Oct. 1994).
38. J. L. Doane, Low-loss twists in oversized rectangular waveguide, *IEEE Trans. Microwave Theory Tech.* **MTT-36**: 1033–1042 (June 1988).
39. J. M. Jarem, A multifilament method-of-moments solution for the input impedance of a probe-excited semi-infinite waveguide, *IEEE Trans. Microwave Theory Tech.* **MMT-35**:14–19 (Jan. 1987).
40. B.-S. Wang, Mutual impedance between probes in a waveguide, *IEEE Trans. Microwave Theory Tech.* **MTT-36**:53–60 (Jan. 1988).
41. B.-S. Wang, Mutual impedance between probes in a circular waveguide, *IEEE Trans. Microwave Theory Tech.* **MTT-37**: 1006–1011 (June 1989).
42. D. A. Will, Reflection coefficient of a waveguide with slightly uneven walls, *IEEE Trans. Microwave Theory Tech.* **MTT-37**:244–252 (Jan. 1989).
43. J. H. Winters and C. Rose, High- T_c superconductor waveguides: Theory and applications, *IEEE Trans. Microwave Theory Tech.* **MTT-39**:617–623 (April 1991).
44. M. Swaminathan, E. Arvas, T. K. Sarkar, and A. R. Djordjevic, Computation of cutoff wavenumbers of TE and TM modes in waveguides of arbitrary cross sections using a surface integral formulation, *IEEE Trans. Microwave Theory Tech.* **MTT-38**:154–159 (Feb. 1990).
45. D. A. Goldberg, L. J. Laslett, and R. A. Rimmerl, Modes of elliptical waveguides: a correction, *IEEE Trans. Microwave Theory Tech.* **MTT-38**:1603–1608 (Nov. 1990).
46. J. A. Roumeliotis and S. P. Savaidis, Cutoff frequencies of eccentric circular-elliptic metallic waveguides, *IEEE Trans. Microwave Theory Tech.* **MTT-42**:2128–2138 (Nov. 1994).
47. J. C. Gutiérrez-Vega, R. M. Rodríguez-Dagnino, and S. Chávez-Cerda, Attenuation characteristics in confocal annular elliptic waveguides and resonators, *IEEE Trans. Microwave Theory Tech.* **MTT-50**:1095–1100 (April 2002).
48. M. Davidovitz and Y. T. Lo, Cutoff wavenumbers and modes for annular-cross-section waveguide with eccentric inner conductor of small radius, *IEEE Trans. Microwave Theory Tech.* **MTT-35**:510–515 (Jan. 1987).
49. C. S. Kenney and P. L. Overfelt, A simple approach to mode analysis for parabolic waveguides, *IEEE Trans. Microwave Theory Tech.* **MTT-39**:405–412 (March 1991).
50. K. W. Klark, Perturbation analysis of electromagnetic eigenmodes in toroidal waveguides, *IEEE Trans. Microwave Theory Tech.* **MTT-39**:631–637 (April 1991).

51. L. Carbonini, Modal analysis of multi-connected waveguides, *IEEE Trans. Microwave Theory Tech.* **MTT-40**:665–671 (April 1992).
52. W. Sun and C. A. Balanis, MFIE analysis and design of ridged waveguides, *IEEE Trans. Microwave Theory Tech.* **MTT-41**:1965–1971 (Nov. 1993).
53. W. Sun, and C. A. Balanis, Analysis and Design of quadruple-ridged waveguides, *IEEE Trans. Microwave Theory Tech.* **MMT-42**:2201–2207 (Oct. 1994).
54. S. Amari, J. Bornemann, and R. Wahldieck, Application of a coupled-integral-equations technique to ridged waveguides, *IEEE Trans. Microwave Theory Tech.* **MTT-48**:2256–2264 (Dec. 1996).
55. Y. Rong and K. A. Zaki, Characteristics of generalized rectangular and circular ridge waveguides, *IEEE Trans. Microwave Theory Tech.* **MTT-48**:258–265 (Feb. 2000).
56. K. P. Erickson and A. M. Ferendeci, TE modes of an axially multiple-grooved rectangular waveguide, *IEEE Trans. Microwave Theory Tech.* **MTT-43**:2001–2006 (Sept. 1995).
57. I. G. Tigelis, M. Pedrozzi, P. G. Cottis, and J. L. Vomvoridis, Calculation of eigenmodes in a nonperiodic corrugated waveguide, *IEEE Trans. Microwave Theory Tech.* **MTT-45**:236–244 (Feb. 1997).
58. H. S. Lee and H. J. Eom, Scattering from a cylindrical waveguide with rectangular corrugations, *IEEE Trans. Microwave Theory Tech.* **MTT-49**:315–320 (Feb. 2001).
59. M. Fernyhough and D. V. Evans, Full multimodal analysis of an open rectangular groove waveguide, *IEEE Trans. Microwave Theory Tech.* **MTT-46**:97–107 (Jan. 1998).

WAVELENGTH METER

MARTIN GUY
 Institut National d'Optique
 CHRISTINE LATRASSE
 Laval University
 BERNARD VILLENEUVE
 Nortel
 MICHEL T&TU
 PIERRE TREMBLAY
 Laval University

1. BASIC INFORMATION

1.1. Definition of Wavelength for a Monochromatic Source

Wavelength meters are instruments designed to measure the wavelength of an electromagnetic wave. Electromagnetic waves are the classic way to represent modifications of the space surrounding a moving electrically charged body. Time-varying electric and magnetic fields are produced and can be sensed. Wavelength is a well-established parameter when considering a monochromatic (single-frequency) plane wave propagating in vacuum. It is the distance between two planes, measured along the direction of propagation of energy, where the phase and its derivatives have the same values. For the purpose of electromagnetic

wave propagation, vacuum is a homogeneous, linear, isotropic, and nondispersive medium. This implies that the reaction of the medium to the electromagnetic wave's presence is instantaneous and does not depend on the location of the observation or on the amplitude and direction of propagation of the wave.

Nonconducting materials, like gases, ceramics, or polymers, are called dielectrics. They have electric charges, but the charges are not allowed to move freely within the medium. When an electromagnetic wave moves through such a medium, it stimulates the charges to oscillate around their equilibrium positions. These oscillating charges radiate an electromagnetic field that adds up to the impinging field. The resulting field is the field propagating in the medium. The reaction of the medium will then change the conditions of propagation when compared with those of vacuum. In general, a real medium is non-homogeneous, nonlinear, nonisotropic, and dispersive. This implies that the reaction will be dependent on location in the medium and the amplitude and direction of propagation of the field, that it will not be instantaneous, and that some of the wave energy will be transferred to other spectrum bands (harmonic generation). In a first approximation, it is useful to reduce the complexity of the medium reaction to something close to that of the vacuum, taking only into account a reduction of the propagation speed associated with the summing action. The speed of the wave in a perfect dielectric material is less than that in vacuum, and the ratio of the speed value in vacuum to the speed value in the medium is the index of refraction. It is then possible to reconsider the propagation of infinite plane waves and use the same definition for the wavelength. As the speed of propagation is less in the medium than in vacuum, the distance between the planes will be less, which implies that the wavelength in the material is less than that for vacuum. Consequently, the wavelength value is dependent on the medium in which the wave is propagating.

1.2. Wavelength or Frequency?

Wavelength is measured along the space (position) axis. However, if we measure the field associated with a monochromatic electromagnetic wave at a fixed position, we observe that this field oscillates regularly with time. The rate of this oscillation per unit of time is the frequency. The frequency is then measured along the time axis. The wavelength (λ) times the frequency (ν) is equal to the speed of light in the medium (v).

The two measurements, wavelength and frequency, are dual quantities. They reveal two aspects of the same physical interaction. The wavelength is related to the "wave" aspect of electromagnetic energy, whereas the frequency is related to the "corpuscular" aspect, the photon or quantum of energy. The wavelength is helpful for evaluating the probability of finding photons, which are the unit of exchange of electromagnetic energy with the surroundings during an interaction. The energy E of each photon is $E = h\nu$, where h is the Planck constant. The frequency ν is not dependent on the medium of propagation. The measurement of frequency is preferred by signal

engineers, whereas wavelength is the preferred choice for opticians.

1.3. Spectral Distribution

Another important aspect of wavelength measurement is the distribution of optical energy as a function of the wavelength. When a pure monochromatic wave is considered, there is no problem with the definition of wavelength because all the energy is concentrated on a single value. However, this is not realistic. Such a distribution would be generated by a noise-free source that evidently does not exist. This brings up a point related to the spectral distribution of the electromagnetic energy for which wavelength has to be measured.

Generally speaking, the energy emitted by a source is distributed over a given range of wavelengths or frequencies. This is called the *spectral distribution* of the source. If the spectral distribution is a symmetrically decreasing function around a central wavelength value, this value is defined as the nominal wavelength. If the distribution is not symmetrical and/or reveals many intense peaks, the wavelength definition is more complex. Giving a specific value of nominal wavelength is then somewhat arbitrary and must be justified by stating the prevailing conditions for the selection. In the next section, wavelength (or frequency) definitions will be given more in detail.

Particular cases that will require specifications are modulated and pulsed sources. According to the Fourier analysis of such signals, a periodically modulated source will produce a number of sidelobes, each being the replica of the unmodulated original source, whereas a pulse has a broad spectrum whose width is related to the reciprocal of its time duration.

1.4. Instruments Used for Wavelength Measurement

In the subsequent sections, we describe different instruments performing wavelength measurements. First, we present a brief overview of the principle of operation of the two most commonly used instruments, which are the spectrometer-based and the interferometer-based wavelength meters.

If the source has a broad spectrum, spectrometers are the instruments commonly used. The spectrum of the source is first analyzed using a dispersive element such as a prism or a grating. The intensity and central wavelength are then recorded by an appropriate detector for a number of dispersive element settings. This method results in a spectral analysis from which a nominal wavelength can be identified if the instrument has been previously calibrated.

As wavelength is defined in the space-domain, its accurate measurement will be done essentially through interferometric phenomena. Let us first consider a monochromatic source. The source signal is first split into space, allowing the various parts to travel different trajectories and recombine to produce interference patterns. Calibrated measurement of the periodicity revealed in the pattern gives an indication on the wavelength. We will later describe in detail the principle of operation of the

most commonly used type of interferometers used to measure wavelengths: Michelson, Fizeau, and Fabry–Perot interferometers.

Before we proceed with the description of the different wavelength meters encountered in research laboratories and in the industry, Section 2 gives some information regarding basic electromagnetic wave theory as well as useful wavelength-measurement definitions.

2. BASIC ELECTROMAGNETIC WAVE THEORY AND USEFUL WAVELENGTH-MEASUREMENT DEFINITIONS

2.1. Theoretical Background

The resolution of Maxwell's equations in vacuum gives rise to plane electromagnetic waves. Such waves are characterized by an electric field (units of volts per meter) and a magnetic field (units of amperes per meter), mutually oriented in perpendicular directions, which are themselves perpendicular to the direction of propagation of the plane wave, given by the direction of the Poynting vector (units of watts per square meter). The latter is defined as the cross-product between the electric and magnetic fields. The modulus of the Poynting vector represents the instantaneous intensity of the light beam. As both fields are perpendicular to the direction of propagation, such waves are called transverse electromagnetic (TEM) waves. Practical collimated laser beams are often well described by plane waves.

2.2. Fluctuating Electric Field

We define a Cartesian component of the electric field labeled $E^{(r)}(\mathbf{r}, t)$, which is a real field variable at a point represented by a position vector \mathbf{r} , at a time t . For any real light beam $E^{(r)}(\mathbf{r}, t)$, will be a fluctuating function of time. For example, laser fields exhibit intensity noise as well as phase noise.

In order to simplify the present analysis, we do not use the real field variable $E^{(r)}(\mathbf{r}, t)$. We rather consider its corresponding analytic signal $E(\mathbf{r}, t)$, which has only spectral components for the positive frequency part of the spectrum. This complex field is defined as

$$E(\mathbf{r}, t) = \frac{1}{2} E^{(r)}(\mathbf{r}, t) + j \frac{1}{2} \mathcal{H}\{E^{(r)}(\mathbf{r}, t)\} \quad (1)$$

where $\mathcal{H}\{E^{(r)}(\mathbf{r}, t)\}$ denotes the Hilbert transform of the real field.

The field intensity at the position \mathbf{r} and at time t is defined as

$$I(\mathbf{r}, t) = E^*(\mathbf{r}, t)E(\mathbf{r}, t) \quad (2)$$

The field intensity gives the beam power distribution over the beam shape.

We are usually concerned with stationary fields, in which case the statistical properties are independent of the origin of time. Such a field could be characterized by

the correlations of the field at two space-time points,

$$\Gamma(\mathbf{r}_1, \mathbf{r}_2, \tau) = \langle E^*(\mathbf{r}_1, t)E(\mathbf{r}_2, t + \tau) \rangle \quad (3)$$

where $\langle \rangle$ denotes an ensemble average. As the field is stationary, this ensemble average does not depend on t . This function is also called the mutual coherence function [1, Ch. 4]. When evaluated at the same position, it gives the autocorrelation function of the field $\Gamma(\mathbf{r}, \mathbf{r}, \tau)$ at position \mathbf{r} . Moreover, it follows that the autocorrelation function evaluated for a zero delay gives the ensemble average of the field intensity at position \mathbf{r} ,

$$\Gamma(\mathbf{r}, \mathbf{r}, 0) = \langle I(\mathbf{r}, t) \rangle \quad (4)$$

The intensity is constant over time for stationary fields.

According to the generalized Wiener-Khintchine theorem, the cross-spectral density is defined as the Fourier transform of the mutual coherence function,

$$W(\mathbf{r}_1, \mathbf{r}_2, \nu) = \mathcal{F}\{\Gamma(\mathbf{r}_1, \mathbf{r}_2, \tau)\} \quad (5)$$

The spectral density, also called the spectrum of the light beam at position \mathbf{r} , is then the Fourier transform of its autocorrelation function,

$$W(\mathbf{r}, \mathbf{r}, \nu) = \mathcal{F}\{\Gamma(\mathbf{r}, \mathbf{r}, \tau)\} \quad (6)$$

So the spread of the spectral density is directly related to the decorrelation time. Short decorrelation time gives rise to broad spectrum and vice versa. On proper normalization, the field spectral density could be related to the measured power spectrum.

Usually, the spectral density of the field has important components only over a frequency range much narrower than the frequencies of interest. This case is called quasimonochromatic light. For such situations, the spectral density of the field is often characterized by two global parameters: one giving the position of the spectrum and the other one estimating its width.

2.3. Parameter Definitions

The center frequency could be defined in many ways. We could use the median frequency ν_m , which is the frequency for which half the power of the signal is distributed on each side, so

$$\int_0^{\nu_m} W(\mathbf{r}, \mathbf{r}, \nu) d\nu = \int_{\nu_m}^{\infty} W(\mathbf{r}, \mathbf{r}, \nu) d\nu \quad (7)$$

A common way of specifying the position of the spectrum is the most probable frequency ν_{mp} , which is the frequency at which the spectral density of the field is maximum. Finally, the usual frequency value used and measured is the mean frequency, which is

$$\bar{\nu} = \frac{\int_0^{\infty} \nu W(\mathbf{r}, \mathbf{r}, \nu) d\nu}{\int_0^{\infty} W(\mathbf{r}, \mathbf{r}, \nu) d\nu} \quad (8)$$

The other parameter is the linewidth of the spectral density of the field. We could define the half-power bandwidth $\Delta\nu_{hp}$ as the symmetrical range around the median frequency containing half the power of the light,

$$\int_{\nu_m - \Delta\nu_{hp}/2}^{\nu_m + \Delta\nu_{hp}/2} W(\mathbf{r}, \mathbf{r}, \nu) d\nu = \frac{1}{2} \int_0^{\infty} W(\mathbf{r}, \mathbf{r}, \nu) d\nu \quad (9)$$

The root mean square (rms) width of the spectrum is also often encountered,

$$\Delta\nu_{rms}^2 = \frac{\int_0^{\infty} (\nu - \bar{\nu})^2 W(\mathbf{r}, \mathbf{r}, \nu) d\nu}{\int_0^{\infty} W(\mathbf{r}, \mathbf{r}, \nu) d\nu} \quad (10)$$

Usually, we use a more experimentally convenient definition, which is the full width at half maximum (FWHM) width. This width gives the frequency range over which the spectral density exceeds half its maximum value,

$$\Delta\nu = \nu_2 - \nu_1, \quad W(\mathbf{r}, \mathbf{r}, \nu_{1,2}) = \frac{1}{2} W(\mathbf{r}, \mathbf{r}, \nu_{mp}) \quad (11)$$

For quasimonochromatic light, the effective width of its power spectrum is much smaller than the mean frequency,

$$\frac{\Delta\nu}{\bar{\nu}} \ll 1 \quad (12)$$

All these definitions also apply to wavelength and to wave-number ($\sigma = \nu/\nu$).

2.4. Interference

Let us introduce the concept of interference through a simple experiment. Consider a light beam incident on an opaque screen having two distinct pinholes at positions r_1 and r_2 . The light emerging from these pinholes is observed on a second screen distant from the first one. The electric field at a position \mathbf{r} on the second screen is the sum of two components,

$$E_s(\mathbf{r}, t) = K_1 E(\mathbf{r}_1, t - t_1) + K_2 E(\mathbf{r}_2, t - t_2) \quad (13)$$

where K_1 and K_2 are constant factors and t_1 and t_2 are the propagation delays from the pinholes,

$$t_1 = |\mathbf{r}_1 - \mathbf{r}|/c \quad \text{and} \quad t_2 = |\mathbf{r}_2 - \mathbf{r}|/c \quad (14)$$

The average intensity observed on the second screen is

$$\begin{aligned} \langle I_s(\mathbf{r}, t) \rangle &= |K_1|^2 \langle I(\mathbf{r}_1, t - t_1) \rangle + |K_2|^2 \langle I(\mathbf{r}_2, t - t_2) \rangle \\ &\quad + 2 \operatorname{Re}[K_1^* K_2 \Gamma(\mathbf{r}_1, \mathbf{r}_2, t_1 - t_2)] \end{aligned} \quad (15)$$

This intensity differs from the sum of the intensities of the distinct components. A supplementary term develops, which takes into account the ‘‘correlation’’ between the two beams. This phenomenon is called interference.

For quasimonochromatic beams, the mutual coherence function could be expressed as

$$\Gamma(\mathbf{r}_1, \mathbf{r}_2, \tau) = g(\mathbf{r}_1, \mathbf{r}_2, \tau) e^{j2\pi\bar{\nu}\tau} \tag{16}$$

where $g(\mathbf{r}_1, \mathbf{r}_2, \tau)$ is a slowly varying function of τ , because its bandwidth is much smaller than the mean frequency of the field. In this case, the observed intensity on the second screen is

$$\begin{aligned} \langle I_s(\mathbf{r}, t) \rangle &= |K_1|^2 \langle I(\mathbf{r}_1, t - t_1) \rangle + |K_2|^2 \langle I(\mathbf{r}_2, t - t_2) \rangle \\ &+ 2|K_1 K_2| |g(\mathbf{r}_1, \mathbf{r}_2, t_1 - t_2)| \cos[2\pi\bar{\nu}(t_1 - t_2)] \\ &+ \angle(K_1^* K_2) + \angle g(\mathbf{r}_1, \mathbf{r}_2, t_1 - t_2) \end{aligned} \tag{17}$$

where \angle is defined as the angle. Thus, as we move along the second screen, the intensity varies sinusoidally at the spatial frequency $\bar{\nu}/c$. This variation is the interference fringe pattern. Fringe contrast is measured through their visibility, defined as

$$V(\mathbf{r}) = \frac{\langle I_s(\mathbf{r}, t) \rangle_{\max} - \langle I_s(\mathbf{r}, t) \rangle_{\min}}{\langle I_s(\mathbf{r}, t) \rangle_{\max} + \langle I_s(\mathbf{r}, t) \rangle_{\min}} \tag{18}$$

where the extreme values are evaluated in the neighborhood of the position \mathbf{r} .

When the mutual coherence function vanishes, the visibility is 0. This represents complete incoherence. The other extreme case is called complete coherence. In this case,

$$|\Gamma(\mathbf{r}_1, \mathbf{r}_2, \tau)| = \sqrt{\langle I(\mathbf{r}_1, t) \rangle \langle I(\mathbf{r}_2, t) \rangle} \tag{19}$$

which corresponds to the following visibility:

$$V(\mathbf{r}) = \frac{2|K_1 K_2| \sqrt{\langle I(\mathbf{r}_1, t) \rangle \langle I(\mathbf{r}_2, t) \rangle}}{|K_1|^2 \langle I(\mathbf{r}_1, t) \rangle + |K_2|^2 \langle I(\mathbf{r}_2, t) \rangle} \tag{20}$$

The visibility is 1 if the intensities associated with each beam are equal. Otherwise, perfect contrast is not achieved for complete coherence. In the general case, we experiment partial coherence, so the resulting visibility does not reach 1.

3. SPECTROMETER-BASED WAVELENGTH METERS

In this section, we describe instruments based on spectrometers using prism or diffraction gratings. We discuss their performances and limitations and explain their use as wavelength meters.

3.1. Basic Properties of Spectrometers

3.1.1. Spectrographs or Monochromators?. The difference between the two types of instruments is related to the detection of diffracted/dispersed light: in a spectrograph, a photographic plate or a charge-coupled device (CCD) array is placed in the output focal plane and records the entire spectrum. In a monochromator, a slit and a

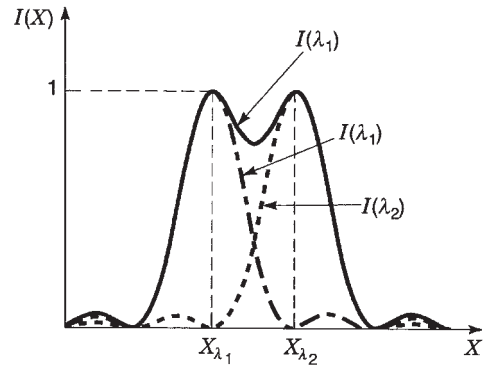


Figure 1. Rayleigh criterion for the definition of the spectral resolving power: two lines are resolved when the intensity profile corresponding to λ_1 has its maximum in coincidence with the minimum of the intensity profile corresponding to λ_2 . The interval $\Delta\lambda$ between two resolved wavelengths is the resolution limit.

photodetector are used so that only a portion of the output spectrum is recorded. It is therefore necessary to move the detection system in the output focal plane, or to rotate the dispersive/diffractive element, to obtain the complete spectrum. Both instruments are often referred to as spectrometers in the literature.

3.1.2. Spectral Resolving Power and Rayleigh's Criterion.

The spectral resolving power R is defined by

$$R = \frac{\lambda}{\Delta\lambda} = \frac{\nu}{\Delta\nu} \tag{21}$$

where $\Delta\lambda = \lambda_1 - \lambda_2$ is the smallest separation between two wavelengths λ_1 and λ_2 that the instrument is able to resolve. According to Rayleigh's criterion, illustrated in Fig. 1, two lines are resolved when the intensity profile corresponding to λ_1 has its maximum in coincidence with the minimum of the intensity profile corresponding to λ_2 . The interval $\Delta\lambda$ between two resolved wavelengths, known as the resolution limit, can also be expressed in terms of frequency $\Delta\nu$ or wavenumber $\Delta\sigma$.

The achievable resolving power of a spectrometer is in direct relation with the slit width and its linear dispersion $dx/d\lambda$, which is given by

$$\frac{dx}{d\lambda} = f \frac{d\theta}{d\lambda} \tag{22}$$

where f is the lens focal length and $d\theta/d\lambda$ the angular dispersion. If the entrance slit width is ε_1 , the slit image in the focal plane of the focusing lens will be

$$\varepsilon_2 = \frac{f_2}{f_1} \varepsilon_1 \tag{23}$$

where f_1 and f_2 are, respectively, the focal length of the collimating and focusing lenses of the spectrometer. If we want to be able to resolve two lines at λ_1 and λ_2 , the

separation of their image

$$\Delta x = f_2 \frac{d\theta}{d\lambda} \Delta\lambda = \frac{dx}{d\lambda} \Delta\lambda \quad (24)$$

must be greater than $2\epsilon_2$. It is therefore possible to increase the resolving power by decreasing the input slit width (at the expense of decreasing the amount of light to be detected). However, it will be limited because of diffraction because of the finite aperture a of the dispersive element. When the collimated beam is incident on the prism or grating, it experiences Fraunhofer diffraction resulting in an intensity distribution in $\sin^2(\gamma)(\sin(\pi\gamma)/\pi\gamma)$ with γ the diffraction angle. The central lobe of the distribution has a width equal to $2\lambda/a$ and contains 90% of the incident intensity. The distance between the two maxima in the output plane will be $f_2\lambda/a$, so that the condition for resolving λ_1 and λ_2 becomes

$$\Delta x \geq f_2 \frac{\lambda}{a} \quad \text{or} \quad \frac{\lambda}{\Delta\lambda} \leq a \frac{d\theta}{d\lambda} \quad (25)$$

giving the corresponding resolving power. One must notice that the spectral resolving power is limited by diffraction effects because of the finite aperture a (determined by the size of the prism or diffraction grating) and not by the entrance slit width. When taking into account the entrance finite slit width ϵ_1 , the condition is

$$\Delta x \geq \left(f_2 \frac{\lambda}{a} + \epsilon_1 \frac{f_2}{f_1} \right) \quad \text{or} \quad \Delta\lambda \geq \left(\frac{\lambda}{a} + \frac{\epsilon_1}{f_1} \right) \left(\frac{d\theta}{d\lambda} \right)^{-1} \quad (26)$$

However, there is a lower limit for ϵ_1 [2] resulting in a practical resolving power

$$R = \frac{\lambda}{d\lambda} = \frac{1}{3} a \frac{d\theta}{d\lambda} \quad (27)$$

3.1.3. Free Spectral Range. In the case of a spectrometer, the free spectral range is the wavelength region where the instrument has a one-valued relation between the wavelength and the position $x(\lambda)$ in the focal plane of the focusing lens. For prism spectrometers, it corresponds to the whole wavelength range of the instrument, whereas for grating spectrometers it is related to the diffraction order m .

3.2. Prism Spectrometers

3.2.1. Principle of Operation. A typical arrangement for a prism spectrometer is given in Fig. 2. The entrance slit S illuminated by the light source is placed in the focal plane of a collimating lens L_c . The prism P diffracts the incident collimated beam with an angle dependent on the wavelength. As shown in Fig. 3(a), the angle θ , relative to the incident direction, depends on the prism angle α , the angle of incidence of the beam θ_1 , and the refractive index of the prism material $n(\lambda)$. A focusing lens L_f is used after the prism to image the entrance slit so that the position $x(\lambda)$ of

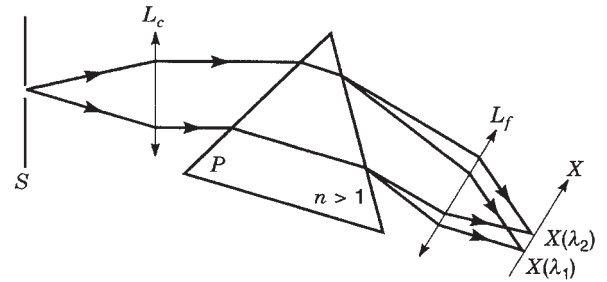


Figure 2. Typical configuration for a prism spectrometer: the light source illuminates the entrance slit S , which is placed in the focal plane of a collimating lens L_c . The prism P diffracts the incident collimated beam and a focusing lens L_f images the entrance slit so that the position $x(\lambda)$ of the focal point in the x plane is wavelength dependent.

the focal point in the x plane is a function of λ . A wavelength scan can be done either by rotating the prism while keeping the output slit fixed, or the contrary.

3.2.2. Angular and Linear Dispersion. When the prism is used at the minimum deviation [Fig. 3(a)], we have

$$\frac{1}{2} \sin(\theta + \alpha) = n \sin(\alpha/2) \quad (28)$$

Then, it is possible to derive the angular dispersion $d\theta/d\lambda$ by first evaluating $d\theta/dn$. We have

$$\frac{d\theta}{dn} = \frac{2 \sin(\alpha/2)}{\cos[(\theta + \alpha)/2]} = \frac{2 \sin(\alpha/2)}{\sqrt{1 - n^2 \sin^2(\alpha/2)}} \quad (29)$$

The angular dispersion is given by

$$\frac{d\theta}{d\lambda} = \frac{2 \sin(\alpha/2)}{\sqrt{1 - n^2 \sin^2(\alpha/2)}} \frac{dn}{d\lambda} \quad (30)$$

We see that dispersion increases with the prism angle α (and so does the size of the prism) but does not depend on the prism size. Therefore, small prisms can be used for small laser beams while keeping the same angular dispersion. However, the prism must be chosen large enough to prevent diffraction problems and to achieve a large

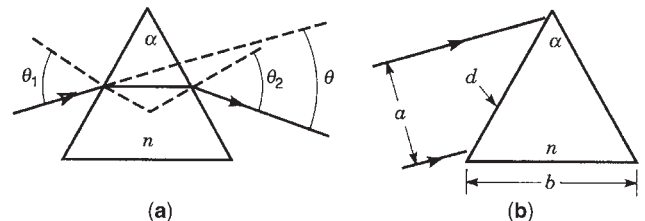


Figure 3. (a) Illustration of a diffraction prism used at minimum deviation: the beam exits the prism with an angle θ verifying the equation $\frac{1}{2} \sin(\theta + \alpha) = n \sin(\alpha/2)$, where α is the prism angle and n is its refractive index. (b) The limiting aperture of the prism a depends on the height of the prism d and on the incident angle θ_1 following the equation $a = d \cos \theta_1 = b[(\cos \theta_1)/2 \sin(\alpha/2)]$.

spectral resolving power. An equilateral prism with $\alpha = 60^\circ$ is usually chosen as the best compromise. In that case

$$\frac{d\theta}{d\lambda} = \frac{1}{\sqrt{1 - (n/2)^2}} \frac{dn}{d\lambda} \quad (31)$$

For values of n around 1.4 to 1.6, the angular dispersion reduces to

$$\frac{d\theta}{d\lambda} \cong n \frac{dn}{d\lambda} \quad (32)$$

The linear dispersion $dx/d\lambda$ depends directly on the prism material dispersion $dn/d\lambda$ and on the focal length f of L_f . It is given by

$$\frac{dx}{d\lambda} = f \frac{d\theta}{d\lambda} \quad (33)$$

3.2.3. Spectral Transmission and Dispersion of Prism Materials. The transparent spectral range for fused silica prisms is 180 nm to 3000 nm. For shorter wavelengths (VUV region), lithium or calcium fluoride can be used, whereas for longer wavelengths, CaF_2 , KBr, or NaCl are transparent up to 30 μm .

The spectral dispersion $dn/d\lambda$ increases greatly near a region of absorption, making glass (e.g., BK7) an attractive material in the visible and near-ultraviolet regions, whereas quartz is more interesting for the ultraviolet region.

3.2.4. Performance and Limitations. If the collimating and focusing lenses L_c and L_f are not achromatic, their focal length will decrease with wavelength. This effect can be compensated by tilting the image plane so that it matches the focal point for every wavelength. If the plane is tilted by an angle φ , the linear dispersion will be increased by a factor $1/\cos \varphi$.

The resolving power is

$$R = \frac{1}{3} a \frac{d\theta}{d\lambda} \quad (34)$$

where the limiting aperture of the prism a is given by [see Fig. 3(b)]

$$a = d \cos \theta_1 = b \frac{\cos \theta_1}{2 \sin(\alpha/2)} \quad (35)$$

with d the height of the input face of the prism and b the length of its base. At minimum deviation, we have

$$n \sin(\alpha/2) = \sin \theta_1 \quad (36)$$

so that

$$\frac{\lambda}{d\lambda} = b \frac{dn}{d\lambda} \quad (37)$$

is only limited by the size of the prism base and the dispersion. For example, if the prism material has a dispersion $dn/d\lambda$ of 500 cm^{-1} at 633 nm and the prism has a base $b = 50 \text{ mm}$, then $R \leq \frac{1}{3} \times 2500$. A spectrometer with such a prism is then able to resolve two lines separated by $\Delta\lambda = 0.75 \text{ nm}$ at 633 nm.

A prism spectrometer is interesting because it allows an unambiguous determination of wavelengths because of the nature of the equation $x(\lambda)$. Its cost can be low when using a small prism and it is simple to make and to adjust. However, as its spectral resolution is limited, it is mainly used for wavelengths scans over large spectral regions as a preliminary survey work.

3.3. Grating Spectrometers

3.3.1. Principle of Operation. Many configurations have been demonstrated for grating spectrometers. One possibility is to use an arrangement similar to the prism spectrometer (Fig. 2) and replace the prism by a diffraction grating used in transmission. Another way is to use the diffraction grating in reflection. Plane diffraction gratings can be used in a Littrow mounting [Fig. 4(a)] or in the Ebert mounting with a concave mirror [Fig. 4(b)]. A variation of the Ebert mounting is the Czerny–Turner mounting, where two adjacent concave mirrors are used. Many configurations have also been demonstrated using concave diffraction gratings [3].

The input light is first collimated by a lens or a concave mirror. It is then diffracted by the grating that separates the different wavelengths. The refracted light is focused in the detection plane. If an aperture is used, its width determines the wavelength resolution of the spectrometer.

In every case, the diffraction grating acts as a wavelength-selective reflector, by reflecting light into well-defined directions for each incident wavelength. The different reflected beams correspond to the orders of the grating. The general equation for the grating is

$$d(\sin \alpha \pm \sin \beta) = m\lambda \quad (38)$$

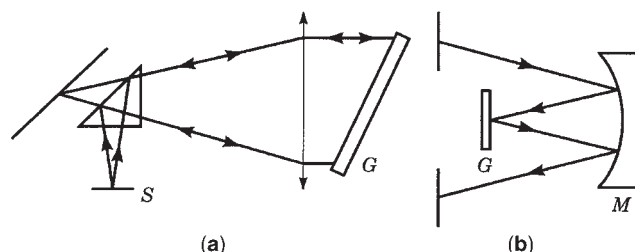


Figure 4. (a) Grating spectrometer using a Littrow-mounted grating: the light exiting the input slit is first reflected by the prism and diffracted by the grating. The diffracted light is imaged on the output plane. Note that the slit and the prism are placed in a different plane from the grating so that the light reflected by the grating does not pass twice in the prism. (b) Grating spectrometer using the Ebert mounting configuration: the light exiting the slit is collimated by a concave mirror, diffracted by the grating and imaged in the output plane after a second reflection on the concave mirror.

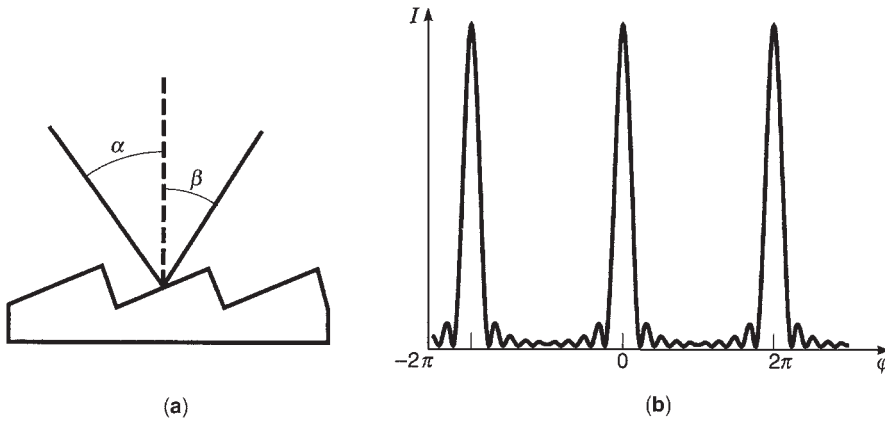


Figure 5. (a) The diffraction of a beam by a diffraction grating follows the equation $d(\sin \alpha \pm \sin \beta) = m\lambda$, where d is the groove dimension, α and β are the incidence and reflection angles relative to the grating normal, m is the grating order, and λ is the wavelength. (b) Intensity distribution of the reflected beam for $N = 10$. The amplitude of the wave reflected in the direction β results from the interference of the beams reflected by all the grooves illuminated. The corresponding intensity is $I = R_g I_0 \sin^2(N\varphi/2) / \sin^2(\varphi/2)$.

where d is the groove dimension, α and β are the incidence and reflection angles relative to the grating normal, m is the grating order, and λ the wavelength [see Fig. 5(a)]. The amplitude of the wave reflected in the detection β is the superposition of the amplitudes reflected by all the grooves illuminated.

The corresponding intensity is

$$I = R_g I_0 \frac{\sin^2(N\varphi/2)}{\sin^2(\varphi/2)} \quad (39)$$

where R_g is the reflectivity of the grating, I_0 the intensity of the incident wave on each groove, N the number of grooves illuminated, and

$$\varphi = \frac{2\pi}{\lambda} d(\sin \alpha \pm \sin \beta) \quad (40)$$

is the phase difference between two adjacent grooves. Figure 5(b) shows I as a function of φ for $N = 10$. Each maximum occurs when $\varphi = 2k\pi$. In terms of β , the line profile has a base half width of

$$\Delta\beta = \frac{\lambda}{Nd \cos \beta} \quad (41)$$

We can evaluate the angular dispersion from the grating equation to obtain

$$\frac{d\beta}{d\lambda} = \frac{m}{d \cos \beta} = \frac{\sin \alpha \pm \sin \beta}{\lambda \cos \beta} \quad (42)$$

which only depends on α and β and not on the number of grooves. The angular dispersion is reduced to

$$2 \tan \alpha / \lambda \quad (43)$$

in the case of a Littrow-mounted grating ($\alpha = \beta$).

3.4. Possible Monochromator Configurations

A double monochromator is a combination of two single monochromators placed in cascade. This configuration

improves the dynamic range, but the wavelength span is reduced and the losses are increased, degrading the sensitivity. Another possible configuration is the double-pass monochromator, which provides the dynamic range of a double monochromator while keeping the sensitivity and compactness of a single one.

3.4.1. Performance and Limitations. The resolving power R can be expressed from

$$\Delta\lambda = \Delta\beta \left(\frac{d\beta}{d\lambda} \right)^{-1} \quad (44)$$

so that

$$R = \frac{Nd(\sin \alpha \pm \sin \beta)}{\lambda} = mN \quad (45)$$

R depends on the number of illuminated grooves N and on the diffraction order m used. If the finite slit width and diffraction effects are considered, we have:

$$R = \frac{1}{3} mN \quad (46)$$

R is limited physically by the dimensions of the grating. It is advantageous to use a high-order m , but the grating reflectivity might decrease drastically. For example, a $5 \text{ cm} \times 5 \text{ cm}$ grating with 1200 grooves/mm used to first order has a practical resolving power of 2×10^4 . When used at 1550 nm, it is capable of resolving $\Delta\lambda = 0.075 \text{ nm}$.

The main disadvantage of grating spectrometers is the possible ambiguity in interpreting the output spectrum as the different orders will overlap for different wavelengths. A solution consists in using wavelength-selective filters in order to isolate one particular order of diffraction. However, the resolving power is much better than that obtained with a prism spectrometer. It can be increased by using a double-pass configuration where the beam is diffracted once by the grating, then passes into an aperture and diffracted again before being detected.

3.4.2. Wavelength Measurement Using Spectrometers. Both prism and grating spectrometers can be used as wavelength meters. To do so, it is necessary to tune the instrument over the unknown light-source spectrum. Another important aspect is to perform an accurate calibration for the wavelength determination.

One possibility for tuning monochromators is to rotate either the prism or the grating, which causes a different wavelength to be focused on the output slit, placed in front of a detector. Another possibility is to keep the prism or grating fixed and move the slit and photodetector in the output plane. In both cases, the prism or grating angle or the slit-photodetector movement must be controlled precisely and in a repeatable way to allow accurate tuning from measurement to measurement [4].

In the case of spectrographs (no moving parts), the spectrum is recorded at once using a photodetector array, and it is only necessary to know the wavelength calibration along the photodetector array. In order to make sure that the wavelength is correctly assigned, a calibration procedure is required for spectrometers as they do not have an internal wavelength reference. It is necessary to have external reference sources such as spectral lamps or lasers stabilized to atomic or molecular absorption lines. For an accurate calibration, the use of several wavelength references (at least three) is recommended and they should be distributed over the whole spectral range of the instrument. Some commercial instruments now include internal references based on the use of molecular resonances, such as acetylene, to perform internal calibrations (see Table 1).

4. INTERFEROMETER-BASED WAVELENGTH METERS

This section describes wavelength meters using interference phenomenon, including Michelson, Fizeau, and Fabry-Perot interferometers.

4.1. Classification of Interferometers

Optical interferometers can be used to perform a wide variety of precision measurements such as measurement of length, studies of surface structure, measurement of temperature, pressure, and particle velocities. Those measurements are based on the interference phenomena produced by light waves. Wavelength measurement can also be realized with very high precision. In fact, interferometers are the most accurate instruments for measuring the wavelength of an optical source.

Interferometers can be classified as two-beam interferometers or multiple-beam interferometers according to the number of interfering beams. The most common type of two-beam interferometers used to measure wavelength are the Michelson and Fizeau interferometers. The Fabry-Perot interferometer is the most usual type of multiple-beam interferometers.

Wavelength meters based on interference phenomena can be subdivided in two categories; dynamic and static

Table 1. Comparative Table of Commercial Instruments

Model	MS9710A	HP 71451B	WA-1500	HP 86120B	7711	LMW-6500B
Company	Anritsu	Hewlett Packard	Burleigh	Hewlett Packard	New Focus	ILX Lightwave
Configuration	Grating spectrometer	Double-pass grating Spectrometer	Michelson interferometer	Michelson interferometer	Fizeau Interferometer	Colored glass filter
Wavelength range (nm)	600–1750 nm	600–1700 nm	200–650 nm (UV) 600–1800 nm (NIR) 1500–4000 nm (IR)	700–1650 nm	400–1000 nm	400–1100 nm (OMH6722B) 950–1650 nm (OMH6727B)
Absolute Accuracy (nm)	± 0.05 nm	± 0.3 nm	± 1 × 10 ⁻⁷	± 0.005 nm @ 1550 nm	± 0.01 nm	± 0.5 nm
Resolving power (nm)	0.07 nm	0.08 nm	NA	0.16 nm @ 1550 nm	NA	NA
Sensitivity	- 90 dBm	-90 dBm	-10 dBm (UV) -17 dBm (other)	-25 dBm (0.8–1.2 μm) -40 dBm (1.2–1.6 μm)	-24 dBm (400 nm) -7 dBm (1 μm)	-20 dBm
Maximum input power (dBm)	20	30	20	Not available	11	30
Dynamic range (dB)	70	50	NA	25	NA	NA
Meas. rate	Δλ = ± 1 nm	Δλ > ± 1 nm	NA	Δλ = 0.8 nm	NA	NA
Input laser requirements	0.5 s/500 nm CW or pulsed	≥ 50 ms/40 nm CW or pulsed	1 Hz CW single mode	1 Hz CW up to 100 wavelengths	1–10 Hz CW or pulsed (pulse length ≥ 30 ps)	1, 4, or 16 Hz CW single-mode or pulsed
Calibration Source	Internal wavelength Reference(C ₂ H ₂)	External wavelength References	Internal stabilized He-Ne laser	Internal He-Ne laser	Plant calibration	Plant calibration

NA: not applicable.

wavelength meters. The former relies on the displacement of an element. It is the most accurate type of instrument, but it can only perform wavelength measurement on continuous wave (CW) sources. On the other hand, static wavelength meters have no moving parts and can be used to measure wavelength of CW or pulsed sources.

4.2. Michelson-Based Wavelength Meters

The principle of operation of the Michelson interferometer is presented in Fig. 6. The incident beam is first divided by a 50-50 beam splitter that can be either a partially reflecting metal mirror or dielectric film on a transparent substrate. The two beams are next recombined by the same beam splitter on a detector (or a screen). As the second beam passes only one time through the beam splitter, a compensating plate may be used in the second arm to equalize the optical path followed by the two beams, but is not always necessary for small collimated beams.

If the mirror M_2 is moved by Δx , the intensity of the interference pattern on the detector changes sinusoidally. A complete cycle is observed when the optical path difference between the two arms of the interferometer corresponds to one wavelength of the incident light beam. Thus, when a mirror displacement of $\lambda/2$ is performed, a complete cycle is observed.

The wavelength of the incident light beam can be deduced if the interference maxima frequency is measured when the mirror M_2 is displaced at constant speed

$$\lambda = \frac{2v_m}{f} \quad (47)$$

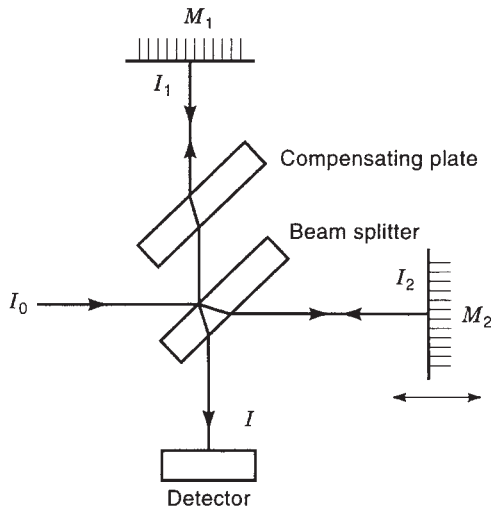


Figure 6. Principle of operation of a Michelson interferometer. An incident beam is divided by a 50–50 beam splitter. The two beams are next recombined by the same beam splitter on a detector. If the mirror M_2 is moved, the intensity of the interference pattern on the detector changes sinusoidally. The wavelength of the incident light beam is deduced if the interference maxima frequency is measured when the mirror M_2 is displaced at constant speed.

where v_m is the displacement speed of moving mirror M_2 and f is the frequency of apparition of interference maxima.

The main problem with the previously described Michelson-based wavelength meter resides in the determination and the accuracy of the displacement speed of the moving mirror. For that reason, Michelson interferometers are rarely used in that configuration unless low accuracy ($\sim 1 \times 10^{-4}$) is sufficient.

The most common type of Michelson-based wavelength meter uses a two-beam interferometry process [5]. In that configuration, a two-beam scanning Michelson interferometer compares the number of fringes obtained by both a reference laser, for which the wavelength is known very accurately, and an unknown laser. Absolute wavelength measurement or CW sources can then be performed. For the two beams, the optical path d is changed by the same and known amount. A typical optical configuration for that type of interferometer is presented in Fig. 7.

With this type of wavelength meter, the wavelength of the unknown laser can be determined by the following relation:

$$\lambda_U = \frac{N_R n_U \lambda_R}{N_U n_R} \quad (48)$$

where N_R and N_U are the number of fringes counted on the reference and input photodetectors (corresponding to the reference and unknown laser), n_R and n_U are the refractive index of the media at the reference and unknown wavelengths, and λ_R is the wavelength of the reference laser. From that equation, it is clear that all parameters in Eq. (48) must be known very accurately. The maximum relative uncertainty of the unknown wavelength λ_U is the sum of the relative uncertainty of each relevant parameter, which are the wavelength reference, number of fringes, the ratio of the refractive indexes, beam misalignment, and wave-front distortion [2, Ch. 4].

The measurement accuracy can be greatly enhanced by improving the wavelength reference's own accuracy.

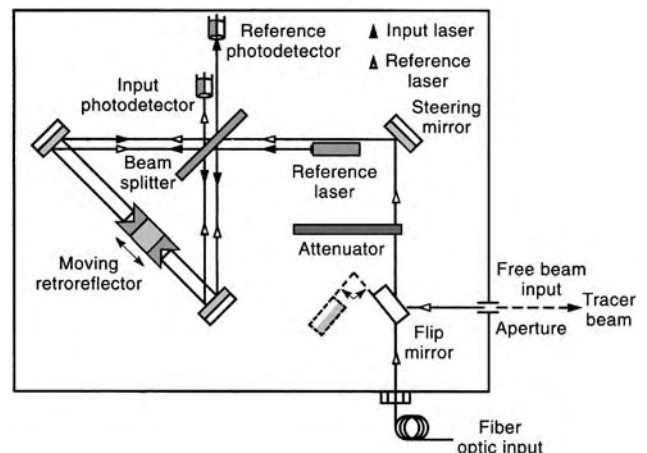


Figure 7. Commercially available two-beam scanning Michelson-based wavemeter™ (courtesy of Burleigh).

Wavelength references found in current laboratory instruments are relatively simple He–Ne gas lasers with about 10^{-7} absolute accuracy. A more accurate I_2 -stabilized He–Ne laser is often used in laboratory installations where size is of minor concern but is somewhat difficult to implement in a portable instrument. Those type of lasers are calibrated with an uncertainty smaller than 10^{-10} . Recently, some progress has been made in replacing He–Ne lasers at 633 nm by semiconductor lasers, providing a more compact and reliable source for the reference laser [6].

Other sources of error for wavelength determination come from the number of fringes seen by the input and reference detectors. One way to improve the accuracy is to count as many fringes as possible; this can be done by increasing the retroreflector mirror displacement. Unfortunately, this also increases the size of the instrument that, for a commercial instrument, is not suitable. Usually, this technique is implemented in a laboratory environment where space is not a concern. The maximum retroreflector mirror displacement is limited by the coherence length l_c of the reference and unknown laser sources. After a displacement corresponding to one coherence length, no interference pattern can be observed [7]. The coherence length is related to the spectral width of the source and is given by

$$l_c = c/\Delta\nu \quad (49)$$

where c is the speed of light in vacuum and $\Delta\nu$ is the spectral width of the source. From that relation, it is clear that the frequency of a source emitting in a very narrow band of frequency can be determined with greater precision than a broad-band source.

Another way to improve the wavelength-measurement accuracy without increasing the path displacement of the retroreflector mirror is to determine a fractional order number of interference fringes. Techniques such as phase-locking an oscillator to an exact multiple of the frequency of the ac signal from the reference laser [8] or using a vernier method in which the counting cycle starts and stops when the two signals coincide [9] have been proposed. With these techniques, fringe fractions can be determined with an uncertainty of $\frac{1}{500}$ of a fringe [10]. Moreover, vibrations during the measurement must be reduced to a minimum in order to eliminate the frequency jitter on the fringe signal [11].

To eliminate the dispersion of air, the wavelength meter is often operated in a vacuum chamber. If the instrument is operated in air, the index of refraction depends on the wavelength, the total air pressure, the partial pressures of H_2O and CO_2 , and the temperature. All those parameters must be controlled and/or recorded with great precision. Moreover, the ratio of the refractive indices depends on the wavelength difference $\Delta\lambda = \lambda_R - \lambda_U$. The relative uncertainty on the index of refraction depends on the wavelength range. Typically for visible wavelengths, the uncertainty ranges from 10^{-11} ($\Delta\lambda = 1$ nm) to 5×10^{-9} ($\Delta\lambda = 200$ nm).

There are other sources of systematic errors that can influence the achievable accuracy of a two-beam scanning Michelson-based wavelength meter. One of them is the

misalignment of the two beams that causes them to travel slightly different path lengths. As an example, if the two beams are slightly tilted against each other by 10^{-4} rad, the systematic relative error becomes 5×10^{-9} . In the wavelength meter proposed in Fig. 7, the corner cube retroreflector guarantees that the incoming light beam is reflected exactly parallel to its incident direction regardless of a slight misalignment.

Finally, the quality of the optical components can also limit the measurement accuracy. With a surface quality of $\lambda/10$, wavefront distortions are already visible in the interference pattern [2]. Moreover, to minimize diffraction effects particularly important in the infrared region, a large beam diameter should be used. The uncertainty because of diffraction is inversely proportional to the square of the beam diameter [11].

4.2.1. Laboratory and Commercial Instrument. In a laboratory experiment, Ishikawa, Ito, and Morinaga demonstrated a wavelength meter with an accuracy of 4×10^{-10} [10]. In that experiment, the main limitation was caused by a slight optical misalignment between the two beams. An improved version of that wavelength meter was later designed [11]. That time the wavelength uncertainty was evaluated at 7×10^{-11} and was limited by the accuracy of the I_2 -stabilized He–Ne laser.

For the most accurate currently available commercial instrument (Burleigh WA-1500), the wavelength of the unknown laser source can usually be determined to an accuracy of 10^{-7} . In that case, the accuracy is limited by the reference laser, which is a He–Ne gas laser stabilized on its gain curve. Temperature and pressure sensors are used to evaluate the index of refraction of air as the interferometer is not evacuated. Figure 8 presents a picture of that instrument.

4.2.2. Multiwavelength Measurement. One of the disadvantages of the previously described wavelength meter is that it can only perform a single wavelength measurement. However, the previous configuration can be modified to perform multiwavelength measurements. This task is particularly suited to dense-wavelength division multiplexing (DWDM) communication systems. The fringe pattern produced by the unknown laser can be sampled at regular intervals corresponding to the period of the reference-laser interference pattern. A Fourier transform on those data yields the complete spectrum. The resolution or the minimum frequency spacing $\Delta\lambda$ that can be measured by the instrument is directly related to the number of counted fringes [12].

$$\frac{\lambda}{\Delta\lambda} = 2N \quad (50)$$

As for the accuracy, the resolution can be improved by counting as many fringes as possible; this can be done by increasing the retroreflector mirror displacement.

A motionless Michelson interferometer with a fixed path difference Δs can also be used to measure the wavelength of pulsed sources [13]. In such a wavelength meter,



Figure 8. Front view of the Burleigh WA-1500 Michelson-based wavemeter (courtesy of Burleigh).

the incident signal enters the interferometer polarized at 45° . A phase difference $\Delta\phi = \pi/2$ is next introduced between the two polarized components. The interference signal at the exit of the interferometer is recorded separately for both polarizations. From the two interference signals obtained, it is possible to deduce the wavenumber $\sigma = 1/\lambda$ modulo $1/\Delta s$ as all wave numbers $\sigma_m = \sigma_0 + m/\Delta s$ ($m = 1, 2, 3, \dots$) give the same interference signals. If similar interferometers having a path difference in geometric ratios are used, the wavenumber can be deduced without ambiguity. As such an instrument measures the wavenumber, it is called a *sigmometer*.

4.3. Fizeau-Based Wavelength Meters

Fizeau interferometers can be used to perform wavelength measurement [14]. Those static wavelength meters have no moving parts and can measure the wavelength of CW and pulsed sources.

Fizeau interferometers consist of two plates inclined to form a wedge of angle α (see Fig. 9). When plane monochromatic light is incident on that type of interferometer, reflected light forms a series of uniformly spaced interference fringes for which the intensity will vary as

$$I(x) = \frac{1}{2} \left[1 + \cos\left(\frac{2\pi x}{\Lambda} + \phi\right) \right] \quad (51)$$

where $\Lambda = \lambda/(2\alpha)$, x is the distance along the detector array, and ϕ is the phase at $x = 0$. The fringes produced are imaged on a detector array. With a typical interferometer plate spacing of 1 mm and a wedge of 3 min, an accurate measurement of the fringe period can give a wavelength measurement accuracy of 10^{-4} . Moreover, if the phase of

the interference pattern on the detector array is determined accurately [15], the accuracy can go as high as 10^{-7} .

Such an accurate measurement can only be accomplished if the wedge angle and spacing are previously calibrated. Also, the fringe pattern on the detector must approximate as much as possible the sinusoidal pattern of Eq. (51). This is done by ensuring that the incident light has plane-wave fronts. This is accomplished by spatially

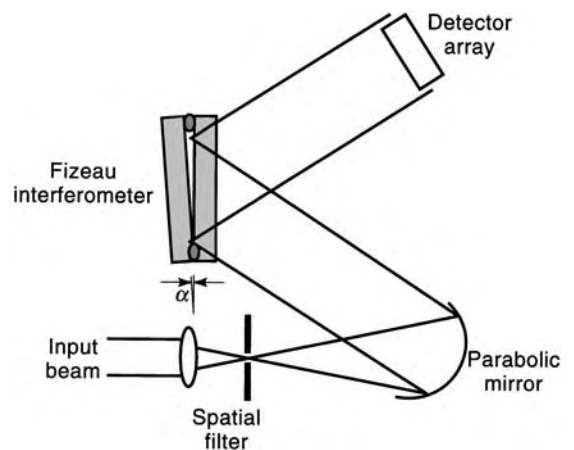


Figure 9. Principle of operation of a Fizeau-based wavelength meter. Fizeau interferometers consist of two plates inclined to form a wedge of angle α . When plane monochromatic light is incident on that type of interferometer, reflected light forms a series of uniformly spaced interference fringes for which the intensity will vary. The fringes produced are imaged on a detector array. The fringe period is computed and gives a wavelength measurement.



Figure 10. Front view of the New Focus Fizeau-based wavelength (courtesy of New Focus).

filtering the incident light and by using interferometer plates with excellent flatness. Dispersion effects must also be taken into account for very accurate wavelength measurement. The advantage of the Fizeau wavelength meter is its simple, compact, and robust design. However, the accuracy of such a wavelength meter is usually less than a scanning Michelson-based wavelength meter.

Figure 10 presents a commercially available Fizeau-based wavelength meter. It is worth mentioning that this instrument contains a thin fused silica etalon, a precision input aperture, and a silicon CCD array. As a result of the type of detector array used, this instrument can perform wavelength measurement from 400 nm to 1000 nm. The accuracy of the instrument is 10^{-5} . The instrument is wavelength calibrated at the factory using five different stabilized lasers. The calibration process allows for effective determination of the etalon thickness and to linearize the detector array signal. All the components are housed in a thermally isolated enclosure. The index of refraction of air is mathematically compensated for temperature and pressure variations.

4.4. Fabry–Perot-Based Wavelength Meters

Scanning Fabry–Perot interferometers can be used to perform wavelength measurement, although those instruments are usually used as optical spectrum analyzers. Figure 11 depicts the principle of operation of a Fabry–Perot interferometer. This type of interferometer is made of two highly reflecting mirrors (flat or concave) uniformly spaced by air or a dielectric material [16].

When coherent light is injected on one side of the interferometer, an interference phenomenon is created by the multiple reflections inside the cavity. For that reason, Fabry–Perot interferometers are called multiple-beam interferometers. The interference is constructive and a stationary wave is built when the distance between the two mirrors corresponds to an integer multiple of half wavelengths of the input beam. This condition is given by

$$L = \frac{m\lambda}{2n} \quad (52)$$

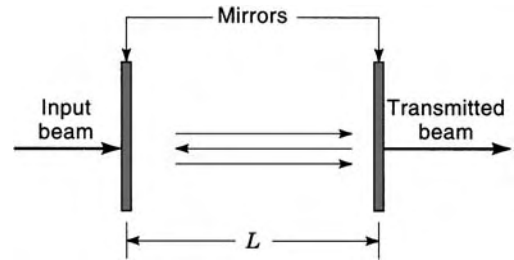


Figure 11. Principle of operation of a Fabry–Perot interferometer. This type of interferometer is made of two highly reflecting mirrors (flat or concave) uniformly spaced by air or a dielectric material. When coherent light is injected on one side of the interferometer, an interference phenomenon is created by the multiple reflections inside the cavity.

where L is the distance between the mirrors, m is an integer, and n is the refractive index of the material inside the cavity. When the condition in Eq. (52) is respected, light transmission through the interferometer is maximum. The frequency spacing between the transmission peaks is called the free spectral range (FSR) and is determined by the spacing between the mirrors and by the refractive index of the material inside the cavity. The FSR (in hertz) is given by

$$\text{FSR} = \frac{c}{2nL} \quad (53)$$

The transmission coefficient of an ideal Fabry–Perot interferometer is described by an Airy function [16]

$$\tau(\lambda) = \frac{I_t}{I_0} = \left[1 + \frac{4R}{(1-R)^2} \sin^2 \left(\frac{2\pi nL \cos(\theta)}{\lambda} \right) \right]^{-1} \quad (54)$$

where I_t and I_0 are the input and transmitted intensities, R and T are the mirror reflection and transmission intensity coefficients, and θ is the angle (relative to the mirror plane inside the cavity) of the input beam (usually the input beam is perpendicular to the mirrors, and this angle is 0). Figure 12 presents the transmission of an ideal Fabry–Perot interferometer for various mirror reflectivities at $\theta = 0^\circ$.

From Fig. 12, we see that another parameter, the finesse (F), gives information about the spectral width of each transmission peak. This parameter depends on the mirror reflectivities, optical quality, and alignment. The finesse is defined by

$$F = \frac{\text{FSR}}{\Delta\nu} \quad (55)$$

where $\Delta\nu$ is the full width at half maximum of the transmission peaks. If the finesse is much larger than 1 (which is usually the case), F can be approximated by

$$F = \frac{\pi R^{1/2}}{1-R} \quad (56)$$

Let us now return to the principle of operation of a scanning Fabry–Perot interferometer. If two signals are incident on the interferometer, and if the distance L between

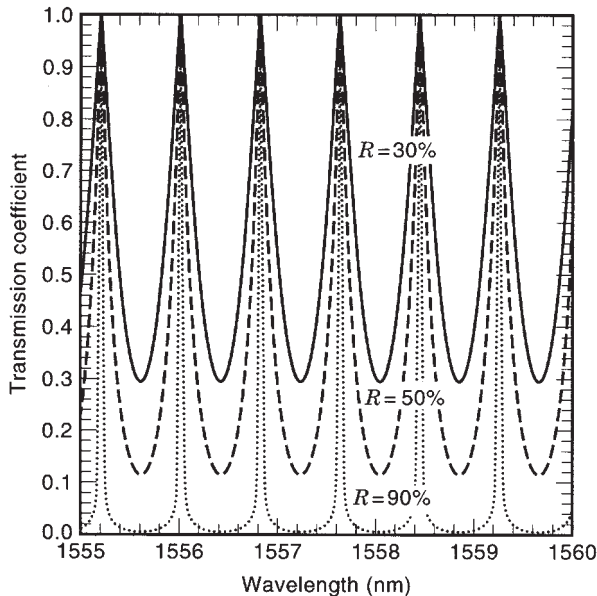


Figure 12. Transmission of an ideal Fabry–Perot interferometer for different mirror reflectivities ($\theta = 0^\circ$, $L = 1.5$ mm, $n = 1$, FSR = 99.9 GHz).

the two mirrors is changed, the interference patterns of both signals appear one after the other. For a given FSR, a high finesse allows the resolution of very closely spaced signals. The resolution is given by [12]

$$\frac{\lambda}{\Delta\lambda} = mF \quad (57)$$

where m is the mode number. The resolution can be increased if a high-order mode is used. This can be done by using a large distance L between the mirrors. In that case, the FSR is reduced; this means that the spectral range is also reduced. Depending on the application, tradeoffs have to be made. As we mentioned previously, that type of instrument is mainly used to perform high-resolution optical spectrum analysis over a relatively narrow spectral range.

However, by counting the fringes obtained by one reference and one unknown laser while the mirrors are scanned over a relatively long displacement, and by using a coincidence technique similar to the vernier technique, wavelength measurement with an accuracy of 1×10^{-7} can be obtained [17]. Also, by carefully calibrating the position of the mirrors against wavelength, and by carefully controlling parameters such as temperature, pressure and alignment, the instrument could be turned into a wavelength meter. Today, Fabry–Perot based wavelength meters are widely used for measuring the wavelength of pulsed lasers. In that case, a plane-mirror Fabry–Perot interferometer is operated in a static configuration (etalons). Such etalons, when illuminating with diverging light, produce a characteristic bull’s-eye fringe pattern corresponding to different angles of incidence. A CCD camera positioned across the fringe pattern is then used along with a computer to reconstruct the interferometer spectrum. The fringes of a Fabry–Perot etalon are

unequally spaced; for that reason, Fizeau etalons, which produce equally spaced fringes, can be used instead of the Fabry–Perot etalon. However, Fabry–Perot etalons have better shaped fringes. Let us also mention that high-accuracy (1 ppm) wavelength measurement of pulsed laser sources can also be performed using two different fixed Fabry–Perot etalons and a reference laser for continuous calibration. In that case, the interference patterns generated by both etalons are recorded by two CCD cameras. The patterns are finally analyzed in a computer and the wavelength is deduced.

5. APPLICATIONS AND ADVANCED TOPICS

5.1. Applications

5.1.1. Scientific Measurements. With the now generalized use of the laser as a scientific investigative tool, wavelength meters have established a firm presence in research and industrial environments. Laser-based measurement techniques reach well beyond the optics field into general physics, chemistry, biology, and engineering. The extremely coherent signal emitted from a laser, whether semiconductor, solid-state, gas, or dye-based, is ideal for probing materials in order to determine their composition or properties, measure dimensions or distances accurately, and much more. In such measurements, the laser wavelength must generally be known precisely, and often the parameter of interest can actually be transformed into a reading of wavelength or wavelength offset. This is where the accuracy of modern wavelength meters as instruments plays a vital role. Wavelength meters in general can also be used for spectral analysis, which expands even further their applicability.

Optical spectroscopy, in its various forms, is useful in a vast number of applications, because it deals with the precise measurement of atomic and molecular absorption or emission features. These features reveal fundamental characteristics of virtually any material, e.g., metals, gases, organic tissue, and crystals [18]. Possible wavelength ranges go from visible to infrared, which will guide the choice of a particular tunable laser, for example, semiconductor or dye [19], and of a particular wavelength meter. In a basic measurement, the frequency of an absorption feature is readily obtained by tuning the laser to it and measuring its wavelength with a wavelength meter. Simple spectral analysis can then be achieved by scanning the laser wavelength through the absorption feature and recording the amplitude versus wavelength for each step, as depicted in Fig. 13.

A different application of spectroscopy is the light detection and ranging (LIDAR), used for monitoring aerosols in the atmosphere. A pulsed (nanosecond timescale) laser signal is sent to a target zone, from which backscattered light is captured. Detailed optical frequency/spectrum measurement of this signal yields information about the target atmosphere. As this is a pulsed application, the typical scanned Michelson interferometer is not suitable and instruments with faster response times using Fabry–Perot or Fizeau interferometers are likely to be used. Calibrated with a reference He–Ne laser, such an instrument

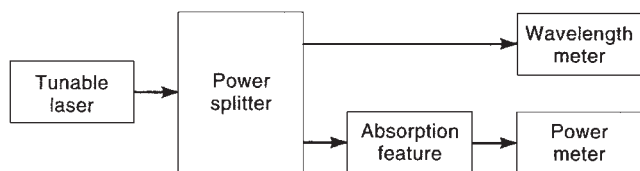


Figure 13. Use of the wavelength meter in a simple absorption spectroscopy experiment. Simple spectral analysis can be achieved by scanning the laser wavelength through the absorption feature and recording the amplitude versus wavelength for each step.

gives information about the absolute wavelength and spectral properties of the backscattered light, which in turn give information about the scattering medium properties.

5.1.2. DWDM Optical Communication. The laser has also enabled an area of significance for electrical engineering, that of optical communication, where wavelength meters find widespread use. After years of steady growth with single-wavelength systems at $0.8\ \mu\text{m}$, then $1.3\ \mu\text{m}$, the advent of the erbium-doped fiber amplifier (EDFA) has enabled a massive deployment of systems in the low-loss region at $1.5\ \mu\text{m}$ [20]. Accurate knowledge of the wavelength is generally not required in a single-wavelength system. However, technology advances coupled to the ever-increasing demand for bandwidth fueled by the Internet explosion have recently led to industrial implementation of dense-wavelength division multiplexing (DWDM). In such systems, up to tens of optical channels are transmitted on a single fiber with frequency spacing currently as low as 100 GHz (about 0.8 nm at $1.55\ \mu\text{m}$). Typical bit rates for individual channels in current high-capacity transport applications are 2.488 Gbit/s (Sonet OC-48) and 9.952 Gbit/s (Sonet OC-192). (Sonet is a multiplexing format and is the acronym for Synchronous Optical Network.)

The 100 GHz standard channel spacing has been endorsed globally through a recommendation of the International Telecommunication Union (ITU). This recommendation actually defines precisely each channel frequency to be used: at this time, 40 channels from $\nu = 192\ 100\ \text{GHz}$ to $\nu = 196\ 100\ \text{GHz}$ applying to the individual transmitters and receivers. Corresponding vacuum wavelengths can be computed with $\lambda = c/\nu$, where $c = 299\ 792\ 458\ \text{m/s}$, the speed of light. Each frequency (or wavelength) value is in essence absolute: no particular technique for obtaining it is specified. This allows various equipment manufacturers and users worldwide to work with a common set of specifications, easing interoperability while employing potentially different technologies. The frequency tolerance around the absolute value is not standardized rigidly and is evolving as manufacturers and users refine their designs. Current observed tolerances are in the $\pm 10\ \text{GHz}$ to $\pm 20\ \text{GHz}$ range for a 100 GHz channel spacing.

As every transmitter and receiver must be designed, constructed, verified, and maintained in accordance with such tolerances, the need for accurate and easy wavelength measurements is clear. DWDM transmitters

typically use distributed feedback (DFB) semiconductor lasers [21], which present a significant frequency dependence on operational parameters like temperature and current. As typical coefficients are $10\ \text{GHz}/^\circ\text{C}$ and $1.5\ \text{GHz}/\text{mA}$, and given the tight-frequency tolerance required, it follows that transmitter emission wavelengths need to be calibrated in terms of temperature and current. These parameters also influence markedly the laser's output power, a critical parameter that must also be mapped out.

Wavelength meters as instruments now find widespread industrial use in optical telecommunication manufacturers production facilities at various instances. At the DFB fabrication and testing stage, they are used for selecting a laser operating point (temperature and current within an acceptable range) resulting in a wavelength situated within a desired channel tolerance, this at a predefined power level. Devices for which such a setpoint cannot be found are rejected. At the transmitter subsystem assembly stage, they are used for setting up and verifying the laser initial operating conditions, always ensuring an output wavelength within prescribed tolerances. At the DWDM transmission system setup stage, they are used for final verification of the multiple channel wavelengths. Meters based on FFT techniques providing a multiwavelength function are particularly useful at this point because their spectral analysis capability provides a quick view of the entire transmitted signal. See the HP 86120B instrument in Table 1.

DWDM systems must be designed for very high reliability over many years, and laser frequency aging must be taken into account in order to guarantee that transmitter wavelengths will remain within the specified tolerances. Frequency stabilization external to the laser itself is then required and various schemes have been developed [22–24]. The basic approach is to compare the emitted wavelength with some active (reference laser) or passive (reference filter) wavelength standard, determine if the transmitter wavelength is adequate, and take corrective action if not. This will counteract the effect of laser wavelength aging and maintain a precise emission frequency over long periods of time. In a way, this comparison with a wavelength reference implements the wavelength meter function, although it does not necessarily return a reading of the wavelength itself. Of course, one possibility is to monitor the transmitter output with an actual wavelength meter instrument, and instruct a controller unit to slightly modify the laser operating conditions over time so as to maintain a prescribed wavelength. As represented in Fig. 14, a multiwavelength meter allows this concept to be extended simultaneously to every channel in the system [25].

DWDM receivers generally use demultiplexing filters with well-defined transmission responses that must be measured precisely. As in the electrical-domain, a simple way to achieve this measurement is to send the signal from a broad-band noise source through the filter and look at the transmitted shape on an Optical Spectrum Analyzer (OSA). For the $1.55\ \mu\text{m}$ communication band, an easily available noise source is the amplified spontaneous emission (ASE) found at the output of an EDFA [20]. The OSA, typically a grating-based monochromator-type instrument,

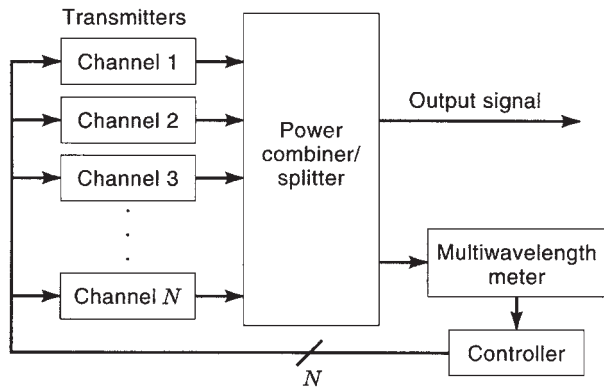


Figure 14. Use of a multiwavelength meter to control simultaneously the frequency of multiple laser transmitters in a DWDM communication system.

can measure wavelengths with less accuracy than a typical interferometer-based wavelength meter but offers more advanced spectral analysis capability. Again, wavelength meters with FFT-based spectral analysis capability can be used advantageously depending on the application. However, for precise transmission versus wavelength measurements, one can revert to the fundamental spectroscopic technique of scanning the wavelength of a tunable laser (typically a laboratory instrument based on an external-cavity laser design [19, Ch. 8], recording simultaneously the transmitted power and the wavelength with, respectively, a power meter and a wavelength meter, exactly as depicted in Fig. 13.

5.2. Advanced Topics

Let us now address some foreseen or desirable avenues for improvements of the wavelength meter instrument, as well as discuss the current state-of-the-art in wavelength measurement. In stand-alone instruments, one may wish to improve the resolution and accuracy of present units, in order to enable yet more precise measurements of all kinds. Improving the resolution means being able to sense a smaller wavelength change, and for the Michelson interferometer this requires a longer mirror travel. Although this can be achieved easily in a laboratory interferometer setup, it is harder to realize in an actual instrument because of size, reliability, and cost constraints. For example, a wavelength ratio uncertainty of 7×10^{-11} has been demonstrated in a laboratory configuration presenting a 60 cm mirror travel in vacuum and a 30 mm beam size [11]. Mechanically scanned interferometers tend also to have slow update rates, which will likely be slowed down further by longer travels. Simultaneous improvements in resolution and measurement speed appear difficult, although compromises toward either parameter can certainly be achieved.

Improving the measurement accuracy rests first on improving the wavelength reference's own accuracy. Semiconductor lasers stabilized to atomic or molecular features are a foreseen development in future instruments, featuring reduced size, increased reliability, and an improvement in reference accuracy to the 10^{-10} level [23,24]. Given an improved reference wavelength, one can then

refine the interferometer's intrinsic design. This implies a minimization and a precise characterization of the sources of error inherent in the design, its tolerance to misalignment, and the ultimate effect on the wavelength reading. Again, in the case of a commercial instrument, cost and reliability issues must be addressed at the same time as these refinements.

For the DWDM field, improvement paths may be oriented slightly differently, because the resolution and accuracy of commercial wavelength meters are basically sufficient for the needs of current and near-future systems. Emphasis should then be put on realizing wavelength meters that are smaller, cheaper, and more robust, particularly by developing solid-state designs with no moving parts. Resolution and accuracy may well be traded off for these considerations, depending on the particular application. Such developments might result in the ability to integrate an accurate wavelength meter function (as well as spectrum analysis) into optical transmission subsystems. Various possibilities for solid-state wavelength meters have been investigated [25,26].

Finally, let us touch on absolute wavelength measurement. Here, the term *absolute* means that the measurement must be related directly to the universal reference for frequency and time, the cesium primary standard. The SI unit of time, that is, the second, is defined with respect to a microwave transition from the ground state of cesium, around 9.192 GHz. Cesium primary standards, or "atomic clocks," exist as standalone instruments, but the most accurate and stable ones are fairly complex installations found at various national laboratories around the world. Their output usually consists of an RF signal in the 10 MHz range. One approach for absolute optical frequency measurement is to synthesize from the cesium reference, through frequency multiplication and heterodyning, phase-locked signals at progressively higher frequencies until the unknown wavelength has been reached [24, Ch. 5] This unknown wavelength can of course be measured with less accuracy prior to the absolute measurement with the help of a standard laboratory wavelength/optical frequency meter. The final determination of frequency is done by measuring a specific RF or microwave transfer frequency at a particular point in the chain. Such an absolute optical frequency measurement can then be transformed into an absolute vacuum wavelength measurement through the basic relation $\lambda_0 = c_0/v$. This was enabled by the 1983 redefinition of a meter by the Bureau International des Poids et Mesures (BIPM) [27], which effectively defined the speed of light in vacuum as $c_0 = 299,792,458$ m/s exactly. Measurement accuracies of 10^{-12} have been obtained in the visible range and also at the well-established $3.39 \mu\text{m}$ and $10 \mu\text{m}$ wavelengths of metrological He-Ne and CO_2 lasers. This is to be compared with the 10^{-7} basic accuracy of the most accurate currently available commercial instrument, the Burleigh WA-1500 depicted in Fig. 8.

Optical comb generation [28], that is the generation of precisely controlled optical sidebands at RF or microwave intervals from a precise reference wavelength, can also be used for creating signals in the vicinity of the unknown signal. This technique has recently been employed for

measuring accurately a series of molecular resonances of acetylene in the 1.5- μm communication band [29]. An accuracy in the 10^{-9} range was achieved.

6. CONCLUSION

Wavelength measurement is a fundamental and versatile function in many aspects of science and technology, as optical waves are prevalent in our everyday lives, in the scientific laboratory and in technology-based commercial ventures. As we have seen, wavelength measurement can take various shapes depending on the particular application, and it calls on diverse aspects of optics and both electrical and mechanical engineering.

One can use calibrated spectrometers based on prisms or gratings, or for better precision, Michelson, Fizeau, or Fabry-Perot interferometers. Each type of instrument presents advantages and limitations, so specific applications will dictate the choice of a particular configuration. Refined laboratory setups built for absolute measurements demand very accurate modeling and optical/mechanical design as well as construction, but size, complexity, and cost constraints are relaxed. Stand-alone laboratory instruments for scientific applications must be engineered so that a suitable level of performance is packaged in an easy to operate, robust, and cost-effective instrument. Finally, further improvements in the design of wavelength meters is leading the way toward the integration of this function into more and more compact subsystems, where size and cost are paramount.

BIBLIOGRAPHY

1. L. Mandel and E. Wolf, *Optical Coherence and Quantum Optics*, Cambridge, UK: Cambridge University Press, 1995.
2. W. Demtröder, *Laser Spectroscopy*, 2nd enlarged ed., Berlin:Springer-Verlag, 1996.
3. A. P. Thorne, *Electrophysics*, London: Chapman Hall & Science Paperbacks, 1974.
4. J. N. West and J. D. Knight, A high-resolution direct-drive diffraction grating rotation system, *Hewlett-Packard J.*, **44**(6):75–79 (1993).
5. F. V. Kowalski, R. T. Hawkins, and A. L. Schawlow, Digital wavemeter for cw lasers, *J. Opt. Soc. Amer.*, **66**:965–966 (1976).
6. A. Zarka et al., Intracavity iodine cell Spectroscopy with an extended-cavity laser diode around 633 nm, *IEEE Trans. Instrum. Meas.*, **46**:145–148 (1997).
7. M. Born and E. Wolf, *Principles of Optics*, 6th ed., Oxford, UK: Pergamon, 1980.
8. J. L. Hall and S. A. Lee, Interferometric real-time display of cw dye laser wavelength with sub-Doppler accuracy, *Appl. Phys. Lett.*, **29**:367–369 (1976).
9. A. Kahane et al., Vernier fringe counting device for laser wavelength measurements, *Rev. Sci. Instrum.*, **54**:138–142 (1983).
10. J. Ishikawa, N. Ito, and K. Tanaka, Accurate wavelength meter for cw lasers, *Appl. Opt.*, **25**:639–643 (1986).
11. J. Ishikawa, N. Ito, and A. Morinaga, Accurate wavelength measurement of the intercombination line of calcium, *Jpn. J. Appl. Phys.*, **33**:1652–1654 (1994).
12. K. D. Moller, *Optics*, Mill Valley, PA: University Science Books, 1988.
13. P. Jacquinot, P. Juncar, and J. Pinard, Motionless Michelson for high precision laser frequency measurement, in J. L. Hall and J. L. Carlsten, eds., *Laser Spectroscopy III*, Berlin: Springer-Verlag, 1977.
14. J. J. Snyder, Fizeau wavemeter, *Proc. SPIE*, **288**:258–262 (1981).
15. M. B. Morris, T. J. McIlrath, and J. J. Snyder, Fizeau wavemeter for pulsed laser wavelength measurement, *Appl. Opt.*, **23**:3862–3868 (1984).
16. B. E. A. Saleh and M. C. Teich, *Fundamentals of Photonics*, New York: Wiley, 1991.
17. R. Salimbeni and R. V. Pole, Compact high-accuracy wavemeter, *Opt. Lett.*, **5**:39–41 (1980).
18. L. J. Radziemski, R. W. Solarz, and J. A. Paisner, eds., *Laser Spectroscopy and Its Applications*, New York: Dekker, 1987.
19. F. J. Duarte, ed., *Tunable Lasers Handbook*, San Diego, CA: Academic Press, 1995.
20. I. P. Kaminow and T. L. Koch, eds., *Optical Fiber Telecommunications III*, San Diego, CA: Academic, 1997.
21. G. P. Agrawal and N. K. Dutta, *Semiconductor Lasers*, 2nd ed., New York: Van Nostrand-Reinhold, 1993.
22. M. de Labacherie et al., The frequency control of laser diodes, *J. Phys. (France), Sect. 3*, **2**:1557–1589 (1992).
23. T. Ikegami, S. Sudo, and Y. Sakai, *Frequency Stabilization of Semiconductor Laser Diodes*, Norwood, MA: Artech House, 1995.
24. M. Ohtsu, ed., *Frequency Control of Semiconductor Lasers*, New York: Wiley, 1996.
25. M. Guy et al., Simultaneous absolute frequency control of laser transmitters in both 1.3 and 1.55- μm bands for multi-wavelength communication systems, *J. Lightw. Technol.*, **14**:1136–1143 (1996).
26. J. C. Braasch, W. Holzapfel, and S. Neuschaefer-Rube, Wavelength determination of semiconductor lasers: Precise but inexpensive, *Opt Eng.*, **34**:1417–1420 (1995).
27. Documents concerning the new definition of the metre, *Metrologia*, **19**(4):163–178 (1984).
28. M. Kourogi, K. Nakagawa, and M. Ohtsu, Wide-span optical frequency comb generator for accurate optical frequency difference measurement, *IEEE J. Quantum Electron.*, **29**:2693–2701 (1993).
29. K. Nakagawa et al., Accurate optical frequency atlas of the 1.5- μm bands of acetylene, *J. Opt Soc. Amer. B*, **13**:2708–2714 (1996).

WAVELET TRANSFORMS

STANLEY R. DEANS
 JOHN J. HEINE
 DEEPAK GANGADHARAN
 WEI QIAN
 MARIA KALLERGI
 LAURENCE P. CLARKE
 University of South Florida

Functions that oscillate over time are often called waves. If the function is such that it oscillates only in a localized region and goes to zero outside the region it may be called

a wavelet. Thus we say wavelets are localized waves. This is analogous to many processes in nature. Consider a soundwave that starts out at zero, builds to some maximum, and then dies out to zero. If the duration of the sound is a few seconds, we say the scale for the process is on the order of seconds. Whenever examining some physical object, scale plays an important role. For example, when looking at another human at a scale of about a meter, you see the whole individual, but if you examine the same individual at a scale of about a centimeter, you can see details such as whorled ridges that form the fingerprint.

The fundamental role of the wavelet transform is to facilitate the analysis of signals or images according to scale. Wavelets are functions with some special mathematical properties that serve as a tool for efficiently dividing data into a sequence of frequency components without losing all information about position. This can be thought of in terms of viewing an object through different size windows. If a large window is used, we see gross features, and if a small window is used we only see small detail features. There are many similarities between wavelet analysis and classic windowed Fourier analysis. The goal in the latter is to determine the local frequency content of a signal by using sine and cosine functions multiplied by a sliding window. The wavelet analysis makes use of translations and dilations of an oscillating wavelet, called the *mother wavelet*, to characterize both spatial and frequency contents of a signal. The properties of this analyzing wavelet are very different from those of sines and cosines. These differences make it possible to approximate a signal contained in a finite region or a signal with sharp changes with a few coefficients, something not possible with classic Fourier methods.

Many of the principles that are the foundation for wavelet analysis emerged independently in mathematics, physics, geophysics, and engineering. In most cases, the concepts came from the motivation to solve some problem that related to resolution or scale. During the last decade, wavelets have been used with great success in a very wide variety of areas, including image compression, coding, signal processing, numerical analysis, turbulence, acoustics, seismology, and medical imaging.

There are some basic mathematical concepts that must be understood prior to a full explanation of the two types of wavelet transforms, the continuous transform and the discrete transform. Section 1 on basic concepts from linear algebra and Fourier analysis can be skipped by those who have already reached that level of mathematical sophistication.

1. BASIC CONCEPTS

1.1. Basis

One of the most fundamental ideas associated with many areas of mathematics is the concept of a *basis*. A simple illustration serves to get the idea across. Suppose we have a curve (waveform or signal) that looks somewhat complicated, as in Fig. 1. (In practice, this could be a voltage that varies in time.) How could you explain to someone who could not see the curve just what it looks like? One pos-

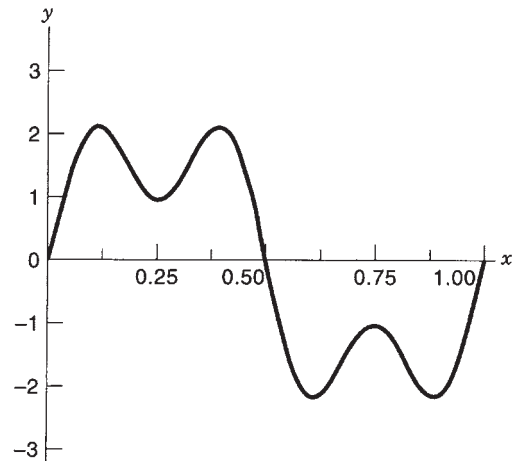


Figure 1. A complicated curve.

sible way is to think of the complicated curve as being made up of the sum of several simple curves. The complicated curve is selected so that it is exactly the sum of two simple curves shown in Fig. 2. The simple curves are known as sine curves. These fundamental curves can be described in terms of how many times they go through a complete cycle. Note that the low-frequency curve goes through one cycle and the higher frequency curve goes through three cycles. Also note that the low-frequency curve has two times the amplitude of the high-frequency curve. You could tell someone exactly how to reproduce the more complicated curve by giving the information about frequency and amplitude for the two basic curves. For those familiar with formulas for sine curves, the complicated curve is given by $y = 2 \sin(2\pi x) + \sin(6\pi x)$.

Technical Definitions: Motion that repeats in equal intervals of time is called periodic. The *period* is the time required for one complete cycle or oscillation. The *frequency* is the repetition rate of a periodic process, which is the number of cycles that occur over a given interval of time. If the period is given in seconds, the frequency is in hertz, abbreviated Hz. In Fig. 2, if the x axis represents time (in seconds), the frequencies are 1 Hz and 3 Hz for the two curves.

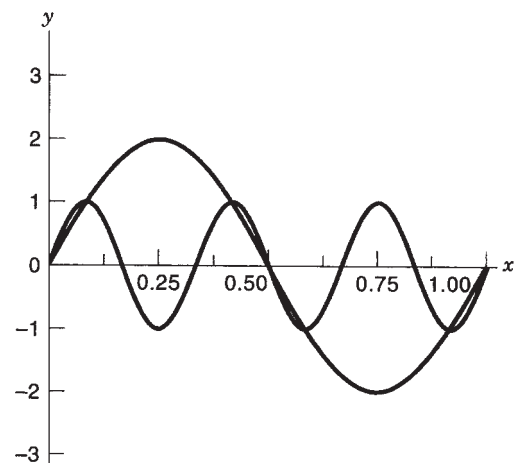


Figure 2. Two simple curves. The curve in Fig. 1 is the sum of these two curves.

The concept of a basis comes from an extension of the approach used to produce the curve in Fig. 1 from the sum of the curves in Fig. 2. If the basis is selected so that it is complete, an arbitrary curve can be replaced by a sum of basic curves. When this is done for periodic functions using sine or cosine curves with different frequencies and amplitudes, it is called a Fourier series decomposition. If the original function is not periodic and can be defined over the entire x axis such that its area is finite, a Fourier transform is used.

The important concept here is that there is a formal way to represent a function or waveform as a sum of basic parts. Fourier analysis corresponds to the language used, and a prescription for calculating the coefficients in the sum exists, which corresponds to finding the amplitudes in Fig. 2. You might think of this as a sort of mathematical prism. The prism breaks light into various colors in much the same way the Fourier analysis breaks the complicated waveform into component parts.

When considering all sorts of waveforms, an obvious question emerges. Under just what conditions is Fourier analysis the appropriate mathematical language to use to decompose the waveform? The complete answer to this question is the subject of the enormous literature on Fourier series and Fourier transforms. There are some simple answers that will suffice for our purposes. The sum in a typical Fourier series problem is an infinite sum. This means an infinite number of coefficients must be computed to represent the function. It seems we have made the problem more complicated! It turns out that in many physical situations only a few coefficients are needed to give an adequate description of the waveform. The coefficients associated with the high-frequency sines and cosines approach zero as the frequency increases. You can think about it this way: The large coefficients correspond to the case where there is a fair match between the original function and the basic sine or cosine. If the original waveform changes slowly relative to the high-frequency oscillations, there is a poor match, and consequently the coefficients are very small. More will be said about this in the sections that follow.

1.2. Orthogonality

Another concept that is essential is that of *orthogonality*. Recall from elementary geometry, if two line segments are perpendicular, we say they are orthogonal. If we make vectors out of line segments by giving them properties of magnitude and direction, we can determine whether they are orthogonal by computing their *scalar* product. This is sometimes called the *dot* or *inner* product. If the scalar product is zero, they are orthogonal. Another way to think about this is that orthogonal vectors do not have any components in common, or they contain completely independent information. The same type of thing can be defined for functions; however, the rule for doing the scalar product is different. It involves doing an integral of the product of two functions. The coefficients in a Fourier series expansion can be found by computing scalar products of the original waveform multiplied by sine and cosine functions with different frequencies. The important point is that the

building blocks, the sines and cosines of different frequencies, are orthogonal and complete. An important consequence is that the frequency content of the waveform can be determined in an unambiguous way. Also, an orthogonal transformation allows perfect reconstruction of the original waveform and eliminates redundancy. Generally, orthogonal transformations are more efficient and easier to use.

1.3. Sampling and the Fast Fourier Transform

In nature, many waveforms are continuous functions of time. If we want to work with these signals using digital computers, it is necessary to find a discrete representation. This means we have to *sample* the continuous function. There is an extremely important theorem known as the *Shannon sampling theorem* that is invoked in these situations. Proofs are given in most standard texts on Fourier analysis, for example, Bracewell [1] and Brigham [2]. The theorem states that a continuous signal can be represented completely by and reconstructed perfectly from a set of measurements (samples) of its amplitude made at equally spaced times. The time interval between samples must be equal to or less than one-half the period of the highest frequency present in the signal. For example, for a typical voice signal, the frequency range is from 0 Hz to 4,000 Hz. This signal must be sampled 8,000 times per second in order to describe it perfectly. In practice, the idea of perfect reconstruction must be compromised. When the amplitude is sampled with real physical apparatus, there must be some sort of round off. In speech transmission, an error of 1% is often sufficient for practical purposes.

Another development that helped usher in the digital communication revolution is the *Fast Fourier Transform* (FFT). For n sampled points, this reduces the number of computations from n^2 to $n \log n$. This is especially important for large values of n . A very interesting discussion of the FFT is given by Heideman, Johnson, and Burrus [3].

1.4. Time- and Frequency-Domains

When we look at the signal in the time-domain, we have full information about the amplitude of the signal at any time. When we do the Fourier decomposition, we have full information about the frequency content of the signal, but the time information is not apparent. The inverse transform yields the time information, but then the frequency spectrum is not apparent. Another way to think about this is to observe that a very sharp signal in the time-domain is flat in the frequency-domain. Inspection of the frequency spectrum does not tell when the sharp signal occurred in time. Some time-domain and frequency-domain transform pairs are shown in Fig. 3. The important point is that signals localized in time are spread in frequency and those spread in time are localized in frequency.

2. CLASSIFICATION OF SIGNALS

It is useful to give a broad classification of signals as *stationary*, *quasistationary*, and *nonstationary*. A signal is

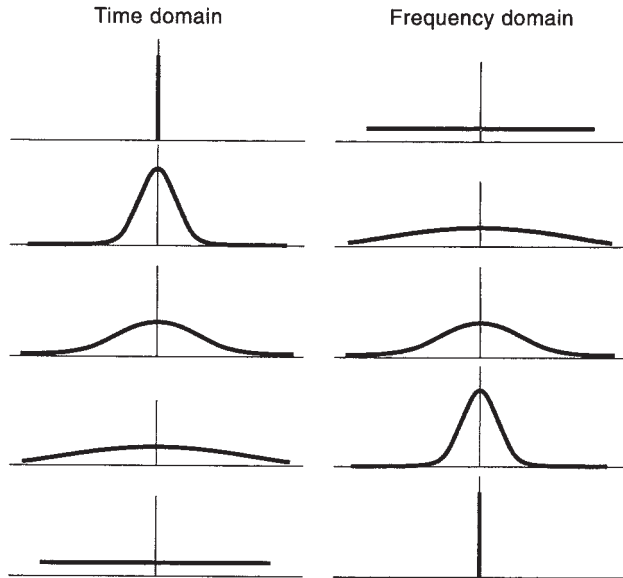


Figure 3. Signals concentrated in one domain are spread in the other domain.

stationary if its statistical properties are invariant over the time duration of the signal. For these signals, the probability of unexpected events is known in advance. If there are transient events (such as blips or discontinuities) in the signal that cannot be predicted, even with knowledge of the past, the signal is *nonstationary*. Consider viewing the signal through a window of some width; that is, look at a section of the signal. A signal is called *quasistationary* if the signal is stationary at the scale of the window.

The ideal tool for studying stationary signals is Fourier analysis. The study of nonstationary signals requires other techniques. One of these is the use of wavelets. An important technique for the study of quasistationary signals came before wavelets and will be discussed first.

The desire to maintain information about time when doing Fourier decompositions leads to the short-time Fourier transform (STFT), sometimes called the windowed Fourier transform. The idea is to select a window with fixed width and slide it along the signal. The Fourier decomposition is done for several short times of the signal rather than for the entire signal all at once. By a proper choice of the window, it is possible to maintain both time and frequency information; thus, this transformation is known as a time–frequency decomposition. When the window is a Gaussian, the transform is known as a Gabor transform in honor of early work done by Dennis Gabor [4]. Difficulties in connection with this approach involve both orthogonality and invertibility. An introduction to the STFT and the wavelet transform is given by Rioul and Vetterli [5]. The close connection with wavelets is illustrated in Fig. 4. Note that the main difference is that the functional form of the wavelet does not change, hence the name *mother wavelet*. The choices for the mother wavelet are virtually unlimited, which is in sharp contrast to Fourier analysis where the basis functions are sines and cosines.

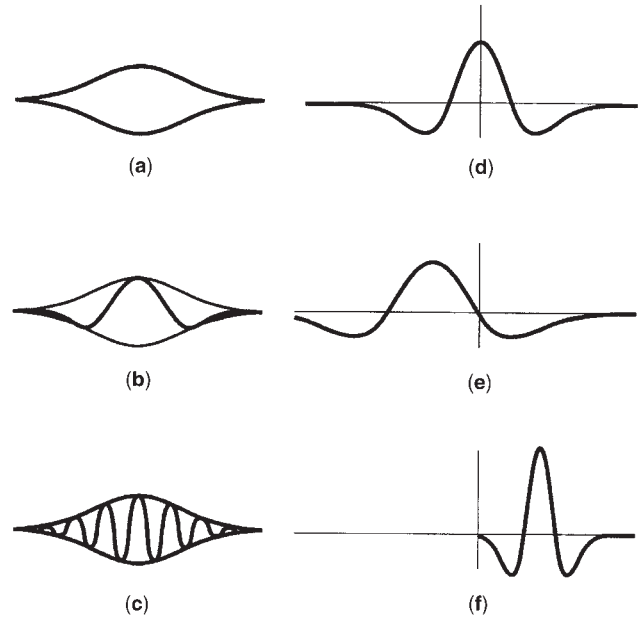


Figure 4. Comparison of STFT and wavelets. On the left, select the window and allow different frequency sinusoids to fill the window. On the right, select the mother wavelet, then translate and dilate the wavelet. The second wavelet is expanded and shifted to the left. The third wavelet is compressed and shifted to the right.

The mother wavelet is allowed to undergo translations and dilations. It is the various translations and dilations of the mother wavelet that form the basis functions for the wavelet transform. This stretching or compressing of the wavelet changes the size of the window and allows the analysis of signals at different scales. This is in some sense like a microscope; the wide stretched-out wavelets are used to give a broad approximate image of the signal, whereas the smaller and smaller compressed wavelets can zoom in on finer and finer details.

3. TIME-FREQUENCY RESOLUTION

We have already seen that sharp signals in the time-domain correspond to flatness in the frequency-domain. If the window for the STFT is selected as in the third row of Fig. 3, then the tiles that represent the essential concentration in the time–frequency plane are squares as indicated on the left in Fig. 5. For a window fixed at one position along the time axis, going up vertically corresponds to higher and higher frequency sinusoidal curves contained within the window. The corresponding tiles for the wavelet transform are shown on the right in Fig. 5. Here the wavelet that is stretched out over the time axis (low frequency) has a narrow concentration in the frequency-domain. As the wavelet is compressed (higher frequencies, smaller time window) the concentration in the frequency-domain is less and less concentrated. Think about this in terms of the curves in Fig. 3 where small time windows correspond to broad frequency windows. This helps in understanding how scale plays such an important role in the wavelet transform.

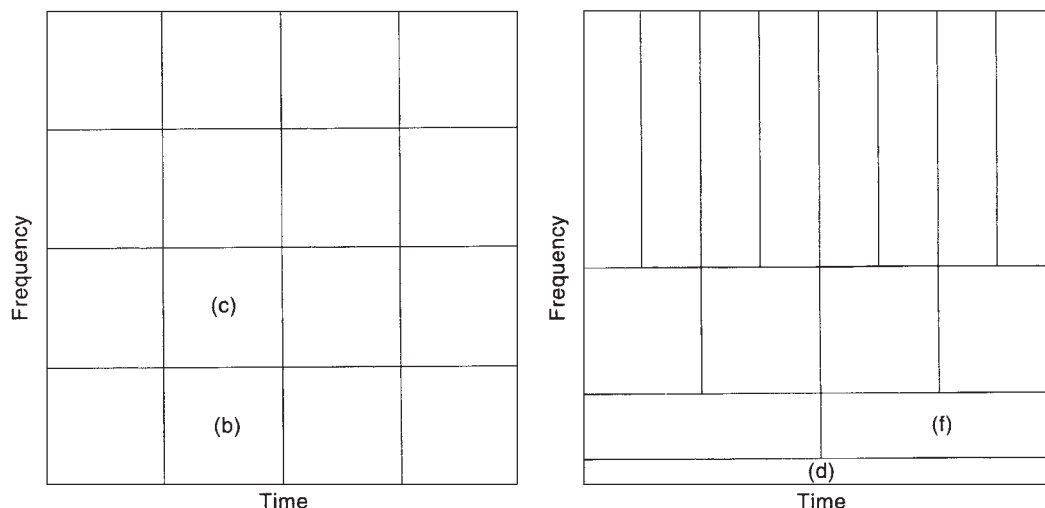


Figure 5. Left: Time and frequency resolution for STFT. Right: Time and frequency resolution for WT. The tiles indicate the region of concentration in the time–frequency plane for a basis function. As an illustration, if the tile labeled (b) corresponds to (b) in Fig. 4, then tile (c) could correspond to (c) in Fig. 4. The corresponding comparison for wavelets is for tiles labeled (d) and (f) with (d) and (f) in Fig. 4.

4. SOME HISTORY

There are many avenues that can be followed in trying to trace the history of wavelets. Barbara Burke Hubbard [6] has a quote in her beautiful discussion of wavelets by Yves Meyer. He says: “I have found at least 15 distinct roots of the theory, some going back to the 1930s.” Seven of these sources in pure mathematics are discussed in some detail in the translation of some of Meyer’s [7] lecture notes. The reader with some background in harmonic analysis will find this discussion covering 70 years of mathematics fascinating: the Haar basis (1909), the Franklin orthonormal system (1927), Littlewood–Paley theory (1930), Calderón–Zygmund theory (1960–1978), and the work of Strömberg (1980). In addition to the lecture notes by Meyer, references for this background include Haar [8], Franklin [9], Hernández and Weiss [10], Edwards and Gaudry [11] for Littlewood–Paley theory, Stein [12] for Calderón–Zygmund theory, and Strömberg [13].

This work done by mathematicians is now understood as part of the history of wavelets. The term “atomic decompositions” was used in place of the term wavelets. During this period from 1910 to 1980, mathematicians from the University of Chicago (location of Zygmund and Calderón) were leaders in harmonic analysis, but apparently they did not interact very much with the experts in physics and signal processing.

In physics, the ideas underlying wavelets are present in Nobel laureate Kenneth Wilson’s [14] work on the renormalization group. A review of some of Wilson’s work and other uses of wavelets in physics is given by Guy Battle [15,16]. Wavelet concepts also appear in the study of coherent states in quantum mechanics. This work dates from the early 1960s by Glauber [17] and Aslaksen and Klauder [18,19].

In parallel with advances in mathematics and physics, there were important ideas fundamental to wavelets being

developed in signal and image processing. This work was mostly in the context of discrete-time signals. As is often the case in applied science, much of this work was driven by the need to solve a problem. We have already mentioned the work by Gabor who introduced concepts very close to wavelets in speech and signal processing. A technique called subband coding was proposed by Croisier, Esteban, and Galand [20] for speech and image compression. This work and related work by Esteban and Galand [21] and Crochiere, Webber, and Flanagan [22] made use of special filters known as quadrature mirror filters (QMF). This led to important work in perfect reconstruction filter banks discussed in detail by Vetterli and Kovačević [23]. Other important relevant work was the development of pyramidal algorithms in image processing by Burt and Adelson [24], where images are approximated proceeding from a coarse to fine resolution. This idea is similar to the multiresolution framework currently used in connection with the discrete wavelet transform.

The important point of all of this is that the foundations of wavelet transforms were implicit in several areas of science, but those working in the various areas were not communicating outside their own field. The grand unification came as a surprise to many and is certainly one reason why this subject has become so popular. Several people made important contributions to this unification. Yves Meyer, in the foreword to the book by Hernández and Weiss [10], gives special tribute to Alex Grossmann and Stéphane Mallat.

In the early 1980s, Jean Morlet, a geophysicist with the French oil company Elf-Aquitaine, coined the name wavelet in connection with analysis of data in oil prospecting (see Morlet et al. [25]). Morlet’s early work was based on extensions of the Gabor transform coupled with the fundamental idea of holding the number of oscillations in the window constant while varying the width of the window.

Morlet developed empirical methods for decomposing a signal into wavelets and then reconstructing the original signal, but it was not clear how general the numerical techniques were. Morlet was referred to Alex Grossmann who had extensive experience in Fourier analysis as utilized in quantum mechanics. It took them about two years to determine that the inversion was exact, and not an approximation (Grossmann and Morlet [26]).

During 1985–1986, Stéphane Mallat [27,28], an expert in computer vision, signal processing, and applied mathematics, discovered some important connections among: (1) the quadrature mirror filters, (2) the pyramid algorithms, and (3) the orthonormal wavelet bases of Strömberg Meyer, building on the work by Mallat, constructed wavelets that are continuously differentiable, but they do not have compact support. (A function with compact support vanishes outside a finite interval.) A full discussion of these Meyer wavelets is given by Ingrid Daubechies [29], where she points out that Meyer actually found this basis while trying to prove the nonexistence of such nice wavelet bases. It requires a considerable amount of work to calculate the wavelet coefficients for the Meyer wavelets, and Daubechies wanted to construct wavelets that would be easier to use. She had worked with Grossmann in France on her Ph.D. research in physics, and she knew about Mallat and Meyer’s work before it was published. She demanded orthogonality, compact support, and some degree of smoothness (wavelets with vanishing moments). These constraints are so much in conflict that most people doubted such a task could be accomplished. After some very intense work, she had the construction by the end of March 1987. (See the revealing quote on page 47 of Hubbard [6]). This work is elegant, and the Daubechies wavelets have become the cornerstone of wavelet applications throughout the world. The first publication on her construction is in Ref. 30. Other relevant descriptions are in Refs. 29 and 31.

This concludes an all too brief history of a topic that has roots reaching into the core of pure and applied mathematics, physics, geophysics, computer science, and engineering. The reader with interest in these matters will find the informal discussion by Ingrid Daubechies [32] both enjoyable and enlightening. In that discussion, she does not cite specific references, but all of the characters in the story are identified in the bibliography or reading list for this article or in the books by Vetterli and Kovačević [23] and Daubechies [29].

5. THE CONTINUOUS WAVELET TRANSFORM

Families of continuous wavelets are found by shifting and scaling a “mother” wavelet $\psi(x)$

$$\psi_{a,b} = \frac{1}{\sqrt{a}} \psi\left(\frac{x-b}{a}\right), \quad a, b \in \mathbb{R}, \quad a \neq 0 \quad (1)$$

The parameter a is the scale parameter, b is the shift parameter, and \mathbb{R} is the set of real numbers. One possible

identification for ψ is the Mexican hat function,

$$\psi(x) = \frac{2}{\sqrt{3}} \pi^{-1/4} (1-x^2)e^{-1/2x^2}$$

This function is the second derivative of a Gaussian $e^{-1/2x^2}$. The normalization is such that its square integrated over the real line is unity, $L^2(\mathbb{R})$ norm equal to 1. This is the function used for illustration on the right side of Fig. 4. The reason for the name comes from the image generated by a rotation around its axis of symmetry [29]. Observe that for large a , the basis function $\psi_{a,b}$ is a stretched-out version of ψ and small a gives a contracted version.

If the basis functions are required to satisfy a completeness condition, then it is necessary for the wavelet to satisfy an “admissibility” condition [23]

$$C_\psi = \int_{-\infty}^{\infty} \frac{|\hat{\psi}(\xi)|^2}{\xi} d\xi < \infty$$

where $\hat{\psi}$ is the Fourier transform of ψ ,

$$\hat{\psi}(\xi) = \int_{-\infty}^{\infty} \psi(x)e^{-ix\xi} dx$$

This means that for practical cases we must require (Let $\xi \rightarrow 0$ in the formula for the Fourier transform):

$$\int_{-\infty}^{\infty} \psi(x) dx = \hat{\psi}(0) = 0$$

Thus, the wavelet function cannot be a symmetric positive “bump” function like a Gaussian, but must wiggle around the x axis like a wave. The zero of the Fourier transform at the origin and the decay of the spectrum $\hat{\psi}$ at high frequencies implies that the wavelet has a bandpass behavior.

The continuous wavelet transform of a function $f(x)$ is defined by

$$\tilde{f}(a, b) = \langle \psi_{a,b}, f \rangle = \int_{-\infty}^{\infty} \psi_{a,b}(x)f(x) dx \quad (2)$$

for a *real* set of basis functions. The function f is recovered from the transformed function \tilde{f} by the inversion formula

$$f(x) = \frac{1}{C_\psi} \int_{-\infty}^{\infty} \int_{-\infty}^{\infty} \frac{da db}{a^2} \tilde{f}(a, b) \psi_{a,b}(x) \quad (3)$$

For a proof, see Chapter 5 of Ref. 23. This last formula says that $f(x)$ can be written as a superposition of shifted and dilated wavelets.

The continuous wavelet transform has an energy conservation property that is similar to Parseval’s formula for the Fourier transform. The function $f(x)$ and its continuous wavelet transform $\tilde{f}(a, b)$ satisfy

$$\int_{-\infty}^{\infty} |f(x)|^2 dx = \frac{1}{C_\psi} \int_{-\infty}^{\infty} \int_{-\infty}^{\infty} \frac{da db}{a^2} |\tilde{f}(a, b)|^2 \quad (4)$$

The wavelet transform has localization properties. There is a sharp time localization at high frequencies, in marked contrast with Fourier transforms. For example, the

wavelet transform of a delta function centered at x_0 is

$$\frac{1}{\sqrt{a}} \int_{-\infty}^{\infty} \psi\left(\frac{x-b}{a}\right) \delta(x-x_0) dx = \frac{1}{\sqrt{a}} \psi\left(\frac{x_0-b}{a}\right)$$

For a given scale factor a , the transform is equal to a scaled and normalized wavelet centered at the location of the delta function.

6. DISCRETE WAVELET TRANSFORM

The wavelet transform has to be discretized for most applications. One way to approach this is to attempt to directly discretize the continuous wavelet transform and find a discrete version of the reconstruction formula given in Eq. (3). In effect, this means replace $\psi_{a,b}$ by $\psi_{m,n}$ with $m, n \in \mathbb{Z}$, where \mathbb{Z} is the set of integers. The appropriate replacements for a and b are [23,29]

$$a = a_0^m, \quad b = nb_0 a_0^m, \quad a_0 > 1, \quad b_0 > 0$$

When this is done, it turns out that in the discrete parameter case there is no direct generalization of Eq. (3); however, for certain ψ and appropriate a_0 and b_0 $\tilde{\psi}_{m,n}$ exist, such that

$$f = \sum_{m,n} \langle \psi_{m,n}, f \rangle \tilde{\psi}_{m,n}$$

This leads to the introduction of *frames* and *dual frames*. These represent an alternative to orthonormal bases in a Hilbert space (see Heil and Walnut [33]). This approach will not be pursued here. We refer the reader to standard references [10,23,29,33].

The approach presented here leads to the construction of orthonormal wavelet expansions for discrete sets of data. We *do not* start with a continuous wavelet and attempt to find a discrete counterpart. We make full use of multiresolution, the idea of looking at something at various scales or resolutions.

6.1. Multiresolution Analysis

In this approach, another function ϕ plays a fundamental role along with the wavelet function ψ . The simplest possible system that illustrates most of the fundamental properties of these functions is the Haar scaling function and Haar wavelet. In this case, the scaling function is the box function illustrated in Fig. 6(a) and the corresponding wavelet is shown in Fig. 6(b). We refer to these two functions as the *level 0* functions. The fundamental idea is to construct other scaling functions and wavelets from dilations and translations of the level 0 functions. Some of these are shown in Fig. 6. Note that scaling by $x \rightarrow 2x$ corresponds to a contraction, and scaling by $x \rightarrow \frac{1}{2}x$ gives an expansion. There are two scaling functions and two wavelet functions at level -1, with support on an interval of length $\frac{1}{2}$,

$$\phi(2x), \quad \phi(2x - 1), \quad \psi(2x), \quad \psi(2x - 1)$$

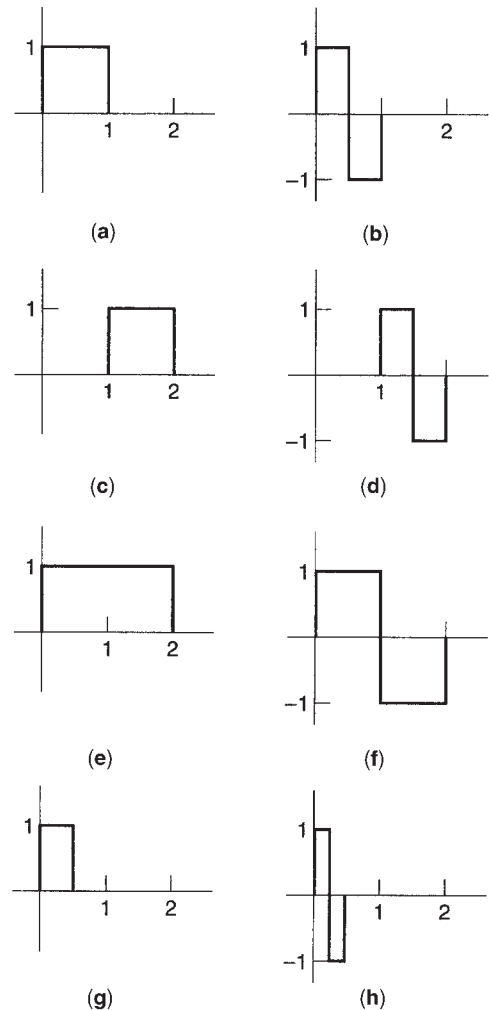


Figure 6. Scaling function ϕ and wavelet function ψ for the Haar system: (a) $\phi(x)$, (b) $\psi(x)$, level 0, basic; (c) $\phi(x - 1)$, (d) $\psi(x - 1)$, level 0, translated; (e) $\phi(\frac{1}{2}x)$, (f) $\psi(\frac{1}{2}x)$, level 1, basic; and (g) $\phi(2x)$, (h) $\psi(2x)$, level -1, basic.

Complete families of scaling functions and the wavelets are obtained by appropriate translations and dilations. The functions $\phi(x)$ and $\psi(x)$ are the functions at level 0. The move from $\psi(x)$ to $\psi(2x)$ is a dilation operation, whereas the shift from 0 to 1 is a translation operation. Starting from ϕ and ψ , the functions are shifted and compressed. The next level down (level -2) contains

$$\begin{aligned} &\phi(4x), \quad \phi(4x - 1), \quad \phi(4x - 2), \quad \phi(4x - 3); \\ &\psi(4x), \quad \psi(4x - 1), \quad \psi(4x - 2), \quad \psi(4x - 3) \end{aligned}$$

Each of these functions is supported on an interval of length $\frac{1}{4}$. A continuation of this process gives infinite families of functions,

$$\begin{aligned} \phi_{j,k}(x) &= 2^{-j/2} \phi(2^{-j}x - k); \\ \psi_{j,k}(x) &= 2^{-j/2} \psi(2^{-j}x - k) \end{aligned} \tag{5}$$

with $j, k \in \mathbb{Z}$. For the range of values ($j \leq 0$) and ($0 \leq k < 2^{-j}$), these functions form a basis over the interval $[0, 1]$.

Important Remark: The Haar system is used for illustration purposes because it is simple and easy to understand. The important point is that all of this holds for other scaling functions and wavelets that have increasing degrees of smoothness. Some of these will be discussed and illustrated later.

Suppose we designate the space spanned by functions of the form $\phi(x - k), k \in \mathbb{Z}$, by V_0 and the space spanned by functions of the form $\phi(2x - k), k \in \mathbb{Z}$, by V_{-1} . Clearly, the function $\phi(x)$ can be written as

$$\phi(x) = \phi(2x) + \phi(2x - 1)$$

As functions in V_0 can be written as a linear combination of functions in V_{-1} , we have the condition

$$V_0 \subset V_{-1}$$

This argument can be extended in either direction, for example

$$\phi\left(\frac{1}{2}x\right) = \phi(x) + \phi(x - 1), \quad V_1 \subset V_0$$

An example of the projection of a function onto V_0 and V_1 is shown in Fig. 7. By continuing this process, the nesting of the closed subspaces V_j follows,

$$\begin{aligned} \leftarrow \text{coarser} \dots V_2 \subset V_1 \subset V_0 \subset V_{-1} \\ \subset V_{-2} \subset \dots \text{finer} \rightarrow \end{aligned} \tag{6}$$

The nesting order is selected so that the spaces show less detail as the index increases. For example, in Fig. 7 the projection onto V_1 can be considered as a blurred version of the projection onto V_0 . This is an agreement with the choice made by Daubechies [29]. A caution for the reader is in order on this; about half of the wavelet literature uses the opposite convention, coupled with a change of $-j$ to $+j$ in Eq. (5). Properties of the V_j are summarized by the following definition of an orthogonal multiresolution analysis.

A *multiresolution analysis* of $L^2(\mathbb{R})$ consists of a sequence of closed subspaces V_j , for all $j \in \mathbb{Z}$, such that

- (M1) $V_j \subset V_{j-1}$
- (M2) $\overline{\bigcup_j V_j} = L^2(\mathbb{R})$ and $\bigcap_j V_j = \{0\}$
- (M3) $f(x) \in V_j \Leftrightarrow f(2x) \in V_{j-1}$
- (M4) $f(x) \in V_0 \Leftrightarrow f(x - k) \in V_0$ for all $k \in \mathbb{Z}$
- (M5) A function $\phi \in V_0$ exists, so that $\phi(x - k), k \in \mathbb{Z}$ form an orthonormal basis for V_0 .

Several remarks are in order in regard to this definition. In (M2), the bar over the union is to indicate *closure*. The closure of a set is obtained by including all functions that can be obtained as limits of sequences in the set. This terminology could be replaced by saying that the union is dense in L^2 . Condition (M5) is often relaxed by assuming that the set of functions $\phi(x - k)$ is a *Reisz basis* for V_0 . For a full treatment of this approach, see Refs. 10 and 34.

Now let us observe that, although we have the condition $V_0 \subset V_{-1}$, the basis functions in V_0 are not orthogonal to the basis functions in V_{-1} ,

$$\int \phi(x)\phi(2x) dx \neq 0 \quad \text{and} \quad \int \phi(x)\phi(2x - 1) dx \neq 0$$

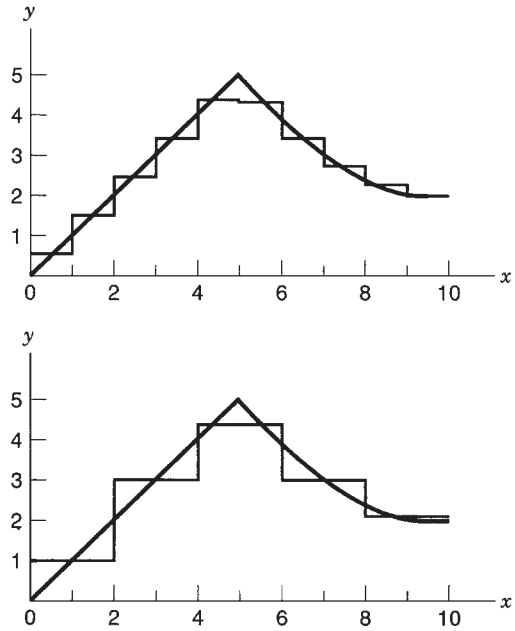


Figure 7. A function $y=f(x)$ (dots) projected onto V_0 (top), projected onto V_1 (bottom).

The integrals are over all x where the functions do not vanish. For the Haar case illustrated earlier, this would be over the interval $[0, 1]$. There is a clever way to fix this. Note that we can write

$$\phi(2x) = \frac{1}{2} [\phi(x) + \psi(x)] \quad \text{and}$$

$$\phi(2x - 1) = \frac{1}{2} [\phi(x) - \psi(x)]$$

If we designate the space spanned by the wavelets $2^{-j/2}\psi(2^{-j}x - k), j, k \in \mathbb{Z}$, by W_j , it follows that the direct sum of subspaces gives

$$V_{-1} = V_0 \oplus W_0$$

Moreover, it is easy to check that basis functions in V_0 are orthogonal to basis functions in W_0 . This idea can be extended in either direction

$$V_{-2} = V_{-1} \oplus W_{-1} \quad \text{and} \quad V_0 = V_1 \oplus W_1$$

The space W_j is said to be the *orthogonal complement* of V_j in V_{j-1} . In general, we have

$$V_{j-1} = V_j \oplus W_j, \quad W_j \perp W_{j'}, \quad \text{if } j \neq j' \tag{7}$$

If we designate the projection of $f(x)$ onto V_m by $P_m f$ and the projection of $f(x)$ onto W_m by $Q_m f$, then Eq. (7) implies that

$$P_{j-1} f = P_j f + Q_j f \tag{8}$$

If $j = 1, P_0 f = P_1 f + Q_1 f$. Projections $P_0 f$ and $P_1 f$ are shown in Fig. 7. The projection $Q_1 f$ contains the difference or

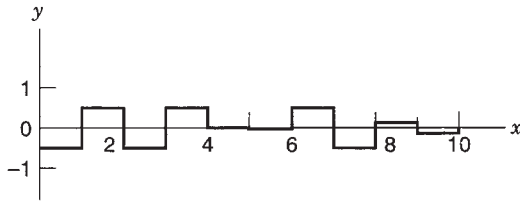


Figure 8. The detail information for the function from Fig. 7 in W_1 .

detail information, illustrated in Fig. 8. Note that this does indeed represent Haar wavelets at level 1.

To see how the general decomposition emerges, consider

$$V_0 = V_1 \oplus W_1 = V_2 \oplus W_2 \oplus W_1 = V_3 \oplus W_3 \oplus W_2 \oplus W_1$$

This could be extended as far as desired. The general formula is

$$V_j = V_j \oplus \bigoplus_{k=0}^{J-j-1} W_{J-k} \tag{9}$$

where all subspaces on the right are orthogonal, which means that any function can be represented as a sum of detail parts plus a smoothed version of the original function. This is often expressed by saying that the function is resolved into a low-frequency part plus a sum of high-frequency parts. To see this, think of Fourier transforms. The broad part in V_j has a Fourier transform concentrated at the origin in the Fourier domain, hence low frequencies. The parts in W_j have Fourier transforms that must vanish at the origin because the area of the wavelet is 0, hence high-frequency parts.

By use of (M2) and Eq. (9), it follows that

$$L^2(\mathbb{R}) = \bigoplus_{j \in \mathbb{Z}} W_j \tag{10}$$

(Note that $V_j \rightarrow \{0\}$ as $j \rightarrow \infty$.) The collection $\{\psi_{j,k}; j, k \in \mathbb{Z}\}$ is an orthonormal basis for $L^2(\mathbb{R})$. The spaces W_j also have the scaling property (M3), so the job is to find a $\psi \in W_0$, such that the $\psi(x - k)$ form an orthonormal basis for W_0 .

6.2. Orthonormal Wavelets with Compact Support

Before we embark on the task of determining other acceptable scaling and wavelet functions, it may be useful to examine the Haar system more closely. Keep in mind that what we are doing applies to any functions ϕ and ψ that satisfy the multiresolution analysis and decomposition, Eq. (9).

First, we observe that the scaling function $\phi_{j,k}$ from Eq. (5) satisfies an orthogonality condition at the same scale,

$$\langle \phi_{j,k}, \phi_{j,k'} \rangle \equiv \int_{\mathbb{R}} \phi_{j,k} \phi_{j,k'} dx = \delta_{kk'} \tag{11}$$

Here $\delta_{kk'}$ is the Kronecker delta defined to be 1 if $k = k'$ and 0 if $k \neq k'$. The wavelets are orthogonal at the same scale

and across scales,

$$\langle \psi_{j,k}, \psi_{j',k'} \rangle = \delta_{jj'} \delta_{kk'} \tag{12}$$

The wavelets and scaling functions also satisfy

$$\langle \phi_{j,k}, \psi_{j',k'} \rangle = 0 \tag{13}$$

We focus our attention on the containment $V_0 \subset V_{-1}$ and $W_0 \subset V_{-1}$ for the Haar system,

$$\phi(x) = \phi(2x) + \phi(2x - 1) \quad \psi(x) = \phi(2x) - \phi(2x - 1)$$

This is a special case of general expansions for ϕ or ψ where

$$\begin{aligned} \phi(x) &= \sum_{k \in \mathbb{Z}} c_k \phi(2x - k) \\ \psi(x) &= \sum_{k \in \mathbb{Z}} d_k \phi(2x - k) \end{aligned} \tag{14}$$

For the Haar system, there are only two coefficients needed; namely, $c_0 = c_1 = 1$. The d coefficients are found from these. We will see later that the condition is $d_k = (-1)^k c_{1-k}$. One way to obtain the coefficients for more general functions ϕ and ψ is to place constraints on the coefficients c_k in the expansion of the scaling function. The method here follows the pioneer work on this by Ingrid Daubechies [30].

The expansion for $\phi(x)$ in Eq. (14) is called a *dilation equation*. If only a finite number of the coefficients are nonzero, then ϕ must vanish outside a finite interval. This gives the property of *compact support*. Suppose the nonzero coefficients are c_m, c_{m+1}, \dots, c_n . If the original function ϕ has support on the interval $[a, b]$, then $\phi(2x)$ has support on the interval $[a/2, b/2]$. The shifted function $\phi(2x - k)$ has support on $[a + k/2, b + k/2]$. As the index k goes from m to n , we have

$$\phi(x) = \sum_{k=m}^n c_k \phi(2x - k) \tag{15}$$

The support on the left side is related to the support on the right side by

$$[a, b] = \left[\frac{a+m}{2}, \frac{b+n}{2} \right]$$

This requirement yields $a = m$ and $b = n$, hence the support is on $[m, n]$.

Example: Suppose $\phi(x)$ is the level 0 Haar box function, and let the sum go from 0 to n . If this function is substituted and used on the right side of Eq. (15), then the function on the left has support on $[0, 1 + n/2]$. If this function is now substituted on the right side the function on the left has support on $[0, 1 + 3n/4]$. If this procedure is continued, the limiting case is just the interval $[0, n]$.

A *consistency condition* can be established by integrating the dilation equation. This is easy and the details that involve a change of variables ($t = 2x - k$) are left for the reader,

$$\begin{aligned} \int_{-\infty}^{\infty} \phi(x) dx &= \int_{-\infty}^{\infty} \sum_k c_k \phi(2x - k) dx \\ &= \cdots = \frac{1}{2} \sum_k c_k \int_{-\infty}^{\infty} \phi(t) dt \end{aligned}$$

As the integral of the scaling function is assumed to be finite, there is a requirement that

$$\sum_k c_k = 2 \quad (16)$$

A convenient choice for the normalization on ϕ is such that

$$\int_{-\infty}^{\infty} \phi(x) dx = 1$$

Caution: Some authors use a slightly different convention for the constants. The other popular choice is to use $c_n = \sqrt{2}h_n$, where h_n corresponds to the notation used by Daubechies [29].

The *orthogonality* condition in Eq. (11) leads to another important relation. The reader may wish to see Alpert [35] for details.

$$\begin{aligned} \delta_{kl} &= \int_{-\infty}^{\infty} \phi(x - k)\phi(x - l) dx \\ &= \int_{-\infty}^{\infty} \sum_m c_m \phi[2(x - k) - m] \\ &\quad \times \sum_n c_n \phi[2(x - l) - n] dx \\ &= \frac{1}{2} \sum_{m,n} c_m c_n \delta_{2k+m, 2l+n} \\ &= \frac{1}{2} \sum_m c_m c_{2k-2l+m} \end{aligned}$$

As the sum is over all $m \in \mathbb{Z}$, we can make the change of index $m \rightarrow m + 2l$. This leads to the desired orthogonality condition

$$\sum_{m \in \mathbb{Z}} c_{2k+m} c_{2l+m} = 2\delta_{kl} \quad (17)$$

This equation ensures the orthogonality of the translates of the scaling function.

The coefficients d_k must be selected so that an orthogonality condition holds for the translates of the wavelet function $\psi(x)$. It is easy to show that this works for

$$d_k = (-1)^k c_{1-k} \quad (18)$$

The calculation makes use of Eqs. (14) and (17)

$$\begin{aligned} &\int_{-\infty}^{\infty} \psi(x - k)\psi(x - l) dx \\ &= \sum_{m,n} \int_{-\infty}^{\infty} d_m \phi[2(x - k) - m] d_n \phi[2(x - l) - n] dx \\ &= \frac{1}{2} \sum_m d_{2k+m} d_{2l+m} \\ &= \frac{1}{2} \sum_m (-1)^{2k+m} c_{1-2k-m} (-1)^{2l+m} c_{1-2l-m} \\ &= \frac{1}{2} \sum_m c_{1-2k-m} c_{1-2k-l} \\ &= \delta_{kl} \end{aligned}$$

Also, the choice made in Eq. (18) is adequate to establish the orthogonality

$$\int_{-\infty}^{\infty} \phi(x - k)\psi(x - l) dx = 0$$

This is left as an exercise; observe that you do not have to make use of Eq. (17).

The key conditions thus far are Eqs. (16), (17), and (18). These are not adequate for a unique determination of the coefficients that lead to the family of Daubechies that extend the Haar system in a natural way. The next condition relates to *approximation*.

The idea is to approximate polynomials of degree $j = 0, 1, \dots, N - 1$ as linear combinations of translates of the scaling function in V_0 . Thus, we look for coefficients α , such that

$$x^j = \sum_{k \in \mathbb{Z}} \alpha_{j,k}^N \phi(x - k), \quad (j = 0, 1, \dots, N)$$

By orthogonality

$$\alpha_{j,k}^N = \int_{-\infty}^{\infty} x^j \phi(x - k) dx$$

The scaling function depends on N and is often written as $N\phi$. Here, we suppress the N and just use ϕ . Recall that only two coefficients are needed for the Haar scaling function. In this case, polynomials of degree $N = 0$ can be represented with no error by scaling functions in V_0 for many situations as smoother scaling function is desired. We are looking for the conditions that must hold when we allow more than two coefficients, and require that polynomials of higher degree be represented exactly by functions in V_0 .

The space V_0 is orthogonal to W_0 ; consequently, for $j = 0, \dots, N - 1$,

$$\int_{-\infty}^{\infty} x^j \psi(x) dx = 0$$

Now, use Eq. (14) along with the trick (identity)

$$x^j = \left(\frac{2x - k + k}{2}\right)^j$$

which yields

$$\int_{-\infty}^{\infty} \sum_k \left(\frac{2x - k + k}{2}\right)^j d_k \phi(2x - k) dx = 0$$

The general binomial expansion

$$(a + b)^j = \sum_{r=0}^j \binom{j}{r} a^{j-r} b^r, \quad \binom{j}{r} = \frac{j!}{r!(j-r)!}$$

can be applied to give

$$2^{-j} \sum_{r=0}^j \binom{j}{r} \sum_k k^{j-r} d_k \int_{-\infty}^{\infty} (2x - k)^r \phi(2x - k) dx = 0$$

The change of variables $2x - k \rightarrow x$ leads to

$$2^{-j-1} \sum_{r=0}^j \binom{j}{r} \sum_k k^{j-r} d_k \int_{-\infty}^{\infty} x^r \phi(x) dx = 0$$

The integral over x cannot be zero because, by assumption, x^r can be written as a linear combination of translates of ϕ for $r = 0, \dots, N - 1$. It follows that we must require

$$\sum_{r=0}^j \binom{j}{r} \sum_k k^{j-r} d_k = 0$$

hold for individual values of j from 0 to $N - 1$. If you write this out for $j = 0$, then for $j = 1$ and $j = 2$, you see that the condition is

$$\sum_k k^j d_k = 0, \quad (j = 0, \dots, N - 1)$$

This is usually written in terms of the c_j coefficients from Eq. (18) with a slight modification. The index is usually shifted so the nonzero coefficients range from 0 to $2N - 1$ for the Daubechies coefficients [29]. This is accomplished by using the connection

$$d_k = (-1)^k c_{2N-1-k}$$

Then, the approximation condition becomes

$$\sum_{k=0}^{2N-1} (-1)^k k^j c_{2N-1-k} = 0, \quad (j = 0, \dots, N - 1) \quad (19)$$

Examples. The key equations are Eqs. (17)–(19). There are two coefficients for $N = 1$ that satisfy the conditions

$$c_0^2 + c_1^2 = 2, \quad c_0 - c_1 = 0$$

with region of support $[0, 1]$. These are the familiar Harr coefficients $c_0 = c_1 = 1$. For $N = 2$ we have four coefficients, known as the D4 coefficients. They satisfy orthogonality conditions

$$c_0^2 + c_1^2 + c_2^2 + c_3^2 = 2 \quad \text{and} \quad c_0 c_2 + c_1 c_3 = 0$$

and approximation conditions (for $j = 0$ and $j = 1$)

$$c_3 - c_2 + c_1 - c_0 = 0 \quad \text{and} \quad 0c_3 - 1c_2 + 2c_1 - 3c_0 = 0$$

The solution is unique up to a left–right reversal ($c_0 \leftrightarrow c_3, c_1 \leftrightarrow c_2$)

$$c_0 = (1 + \sqrt{3})/4 \quad c_1 = (3 + \sqrt{3})/4 \\ c_2 = (3 - \sqrt{3})/4 \quad c_3 = (1 - \sqrt{3})/4$$

Note that Eq. (16) is also satisfied by these D4 coefficients. Keep in mind that if the other popular normalization condition is used $c_n = \sqrt{2}h_n$, then each of these coefficients must be divided by $\sqrt{2}$. When this is done, then the sum of the squares is 1 rather than 2.

The region of support for the D4 scaling function and the wavelet function is $[0, 3]$. The graphs of these are shown in Fig. 9 across the top. The graphs for $N = 6$ (D12) are shown across the bottom. Here, the region of support is $[0, 11]$. Note that as the number of coefficients increases, the graphs get smoother and the region of support increases. Tables of coefficients for various values of N are given by Daubechies [29].

The functions in Fig. 9 are interesting, but knowing what these functions look like is absolutely unnecessary for implementation of the wavelet transform. The coefficients are all you need, coupled with an algorithm. An example is given in Section 7, and a method for obtaining Fig. 9 is indicated.

6.2.1. Other Wavelets. We have only touched the surface by indicating how to find the family of Daubechies wavelets. If the orthogonality and approximation conditions are modified, other sets of coefficients follow. For example, if you impose conditions of vanishing moments on ϕ as well as ψ , then the resulting wavelets are known as *coiflets*, after a suggestion by Ronald R. Coifman of Yale University. For more information on these, see Refs. 29, 36, and 37. Another example is provided by *biorthogonal wavelets*. The filter coefficients for the reconstruction are not the same as those for the decomposition, and there are two dual wavelet bases associated with two different multiresolution ladders. This leads to symmetric wavelets that are an advantage for some applications. Important references on these are by Cohen and Daubechies [38], Cohen, Daubechies, and Feauveau [39], and Vetterli and Herley [40].

6.2.2. Fourier Space Methods. Very powerful methods for finding wavelet coefficients are provided by Fourier techniques. These techniques can be used to find the family of Daubechies wavelets; also, they form a foundation for finding wavelets with other important properties.

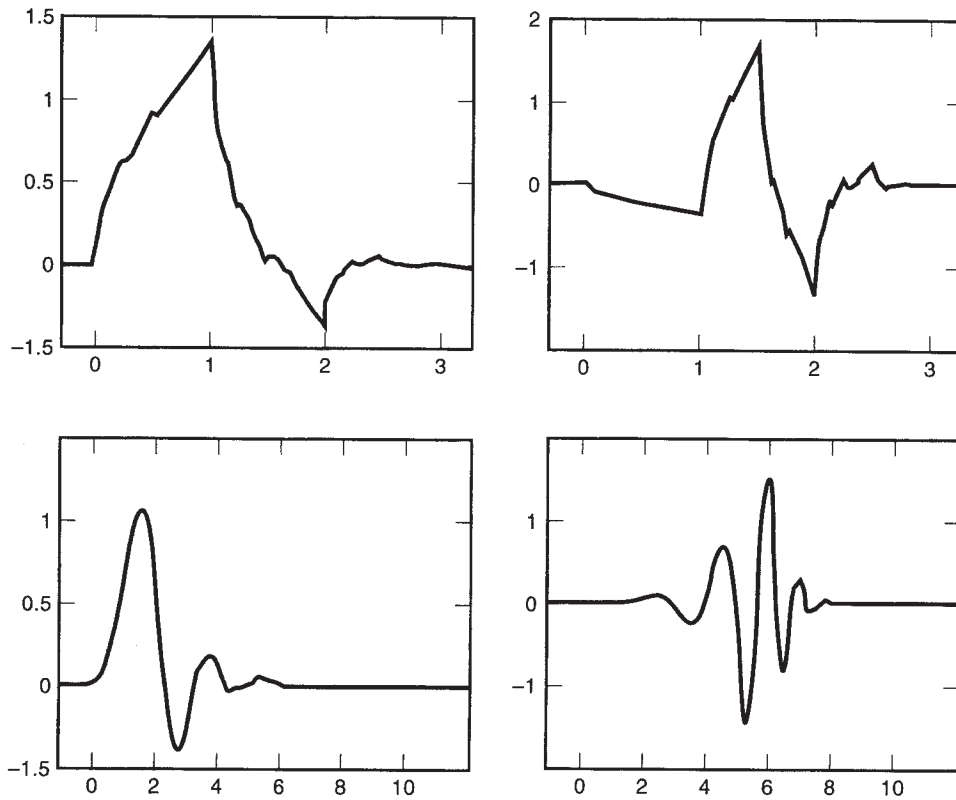


Figure 9. D4 scaling function (top left), D4 wavelet (top right), D12 scaling function (bottom left), and D12 wavelet (bottom right).

Here, we only indicate how this can be started and then refer the reader to some excellent references where this approach is utilized.

Start with the dilation equation for the scaling function

$$\phi(x) = \sum_k c_k \phi(2x - k)$$

The Fourier transform of this equation is

$$\hat{\phi}(\xi) = \sum_k c_k \int_{-\infty}^{\infty} \phi(2x - k) e^{-i\xi x} dx$$

The change of variables $t = 2x - k$ gives

$$\hat{\phi}(\xi) = \frac{1}{2} \sum_k c_k e^{-ik\xi/2} \int_{-\infty}^{\infty} \phi(t) e^{-i\xi t/2} dt$$

Observe that the integral is just $\hat{\phi}(\xi/2)$, which yields

$$\hat{\phi}(\xi) = m_0\left(\frac{\xi}{2}\right) \hat{\phi}\left(\frac{\xi}{2}\right)$$

where, in keeping with the notation of Daubechies [29], we define

$$m_0(\xi) \equiv \frac{1}{2} \sum_k c_k e^{-ik\xi}$$

Note that $m_0(0) = 1$ follows from

$$m_0(0) = \frac{1}{2} \sum_k c_k e^0 = \frac{1}{2} \sum_k c_k = 1$$

If we make the replacement $\xi \rightarrow \xi/2$, then

$$\hat{\phi}\left(\frac{\xi}{2}\right) = m_0\left(\frac{\xi}{4}\right) \hat{\phi}\left(\frac{\xi}{4}\right)$$

and

$$\hat{\phi}(\xi) = m_0\left(\frac{\xi}{2}\right) m_0\left(\frac{\xi}{4}\right) \hat{\phi}\left(\frac{\xi}{4}\right) = \left[\prod_{j=1}^2 m_0\left(\frac{\xi}{2^j}\right) \right] \hat{\phi}\left(\frac{\xi}{2^2}\right)$$

Clearly, this procedure can be continued to give

$$\hat{\phi}(\xi) = \left[\prod_{j=1}^N m_0\left(\frac{\xi}{2^j}\right) \right] \hat{\phi}\left(\frac{\xi}{2^N}\right)$$

As $N \rightarrow \infty$, $\hat{\phi}(\xi/2^N) \rightarrow \hat{\phi}(0) = 1$, because the area under the scaling function is normalized to 1. This means that as $N \rightarrow \infty$, the infinite product goes to the Fourier transform of the scaling function,

$$\hat{\phi}(\xi) = \prod_{j=1}^{\infty} m_0\left(\frac{\xi}{2^j}\right)$$

Example. Let us investigate how this works for the box function, the scaling function for the Haar case. If $c_0 = c_1 = 1$, then

$$m_0\left(\frac{\xi}{2}\right) = \frac{1}{2} (1 + e^{-i\xi/2})$$

and

$$\begin{aligned} m_0\left(\frac{\xi}{2}\right)m_0\left(\frac{\xi}{4}\right) &= \frac{1}{2^2} (1 + e^{-i\xi/2})(1 + e^{i\xi/4}) \\ &= \frac{1}{2^2} (1 + e^{-i\xi/4} + e^{-2i\xi/4} + e^{-3i\xi/4}) \end{aligned}$$

The part in parenthesis on the right is just the sum of $2^2 = 4$ terms of a geometric series, where the first term is 1 and the ratio term r is $e^{-i\xi/4}$. The sum of n terms is given by $(1 - r^n)/(1 - r)$. Thus

$$m_0\left(\frac{\xi}{2}\right)m_0\left(\frac{\xi}{4}\right) = \frac{1}{2^2} \frac{1 - e^{i\xi}}{1 - e^{-i\xi/4}}$$

In the general case, where there are 2^j terms, the result is

$$m_0\left(\frac{\xi}{2}\right) \dots m_0\left(\frac{\xi}{2^j}\right) = \frac{1}{2^j} \frac{1 - e^{i\xi}}{1 - e^{-\xi/2^j}}$$

Now let $2^{-j} = x$, then

$$2^j(1 - e^{-i\xi/2^j}) = \frac{1 - \cos x\xi}{x} + i \frac{\sin x\xi}{x}$$

In the limit as $j \rightarrow \infty$ and $x \rightarrow 0$, we get $i\xi$. It follows that

$$\prod_{j=1}^{\infty} m_0\left(\frac{\xi}{2^j}\right) = \frac{1 - e^{-i\xi}}{i\xi}$$

This is just the Fourier transform of ϕ where ϕ is the box function,

$$\hat{\phi}(\xi) = \int_{-\infty}^{\infty} \phi(x)e^{-i\xi x} dx = \int_0^1 e^{-\xi x} dx = \frac{1 - e^{-i\xi}}{i\xi}$$

just as expected.

A rich resource of information about wavelets comes from using Fourier techniques. The books by Hernández and Weiss [10], Vetterli and Kovačević [23], Strang and Nguyen [41], and Daubechies [29] are excellent sources.

7. MECHANICS OF DOING THE TRANSFORM

This example of how the wavelet transform can be implemented using matrices will be of value to those who wish to acquire an intuitive understanding about how the transform works. This is for illustration only, because in practice, efficient code may not be written in matrix form.

This example is for the simplest case, the Haar; however, the extension to smoother cases is easy, and we will indicate how easy following this example. The following operations are illustrated:

1. Generate the wavelet coefficients with downsampling.
2. Show how this is a dual-filter operation with a shrinking matrix and signal.
3. Mechanics of the reconstruction, the inverse transform.

There is a pyramidal structure to the procedure. At each level, the detail information is stored, whereas the smooth information may be transformed at the next higher scale. One way to indicate this is shown in Fig. 10, where we have carried the transform through three stages.

Let the transpose of the original signal vector for an eight-point transform be designated by

$$[16, 32, 64, 16, 6, 32, 16, 8]$$

The full smoothing operator (the lowpass part) with $c_0 = c_1 = 1$ is given by

$$S = \frac{1}{2} \begin{pmatrix} 1 & 1 & 0 & 0 & 0 & 0 & 0 & 0 \\ 0 & 1 & 1 & 0 & 0 & 0 & 0 & 0 \\ 0 & 0 & 1 & 1 & 0 & 0 & 0 & 0 \\ 0 & 0 & 0 & 1 & 1 & 0 & 0 & 0 \\ 0 & 0 & 0 & 0 & 1 & 1 & 0 & 0 \\ 0 & 0 & 0 & 0 & 0 & 1 & 1 & 0 \\ 0 & 0 & 0 & 0 & 0 & 0 & 1 & 1 \\ 1 & 0 & 0 & 0 & 0 & 0 & 0 & 1 \end{pmatrix}$$

The shift on the last row is to take into account edge effects, and is essential to ensure that the inversion is exact. The highpass operator associated with the detail is given

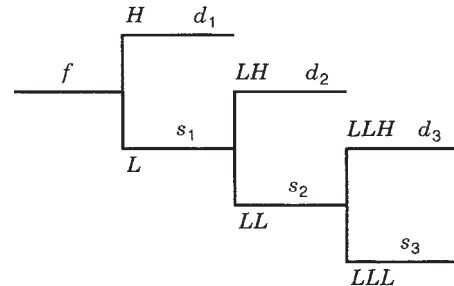


Figure 10. Pyramidal decomposition of a signal. The low- and highpass parts are indicated by L and H . The corresponding smooth and detail parts are designated by s and d with subscripts indicating the level.

by

$$H = \frac{1}{2} \begin{pmatrix} 1 & -1 & 0 & 0 & 0 & 0 & 0 & 0 \\ 0 & 1 & -1 & 0 & 0 & 0 & 0 & 0 \\ 0 & 0 & 1 & -1 & 0 & 0 & 0 & 0 \\ 0 & 0 & 0 & 1 & -1 & 0 & 0 & 0 \\ 0 & 0 & 0 & 0 & 1 & -1 & 0 & 0 \\ 0 & 0 & 0 & 0 & 0 & 1 & -1 & 0 \\ 0 & 0 & 0 & 0 & 0 & 0 & 1 & -1 \\ -1 & 0 & 0 & 0 & 0 & 0 & 0 & 1 \end{pmatrix}$$

Now we calculate the detail and smooth coefficients that lie in W_1 and V_1 , respectively

$$\begin{aligned} d_1 = Hf \downarrow &= [-8, -16, 24, 4, -12, 8, 4, -4] \\ \downarrow &= [-8, 24, -12, 4] \end{aligned}$$

and

$$\begin{aligned} s_1 = S_f \downarrow &= [24, 48, 40, 12, 20, 24, 12, 12] \\ \downarrow &= [24, 40, 20, 12] \end{aligned}$$

The use of the down arrow is to indicate downsampling. Every other value is discarded. You might think information has been lost by doing this, but note that you started with eight independent values in the signal and after downsampling you still have eight independent values, four detail and four smooth coefficients. These can be used to recover the original values. The next step is to contract the matrices S and H ,

$$S = \frac{1}{2} \begin{pmatrix} 1 & 1 & 0 & 0 \\ 0 & 1 & 1 & 0 \\ 0 & 0 & 1 & 1 \\ 1 & 0 & 0 & 1 \end{pmatrix}$$

$$H = \frac{1}{2} \begin{pmatrix} 1 & -1 & 0 & 0 \\ 0 & 1 & -1 & 0 \\ 0 & 0 & 1 & -1 \\ -1 & 0 & 0 & 1 \end{pmatrix}$$

The coefficients for W_2 and V_2 follow by applying these new contracted matrices to the s_1 vector,

$$\begin{aligned} d_2 = Hs_1 \downarrow &= [-8, 10, 4, -6] \downarrow = [-8, 4] \\ s_2 = Ss_1 \downarrow &= [32, 30, 16, 16] \downarrow = [32, 16] \end{aligned}$$

Once again, we contract S and H ,

$$S = \frac{1}{2} \begin{pmatrix} 1 & 1 \\ 1 & 1 \end{pmatrix} \quad H = \frac{1}{2} \begin{pmatrix} 1 & -1 \\ -1 & 1 \end{pmatrix}$$

The last two coefficients are found as before

$$d_3 = Hs_2 \downarrow = [8, -8] \downarrow = [8], \quad s_3 = Ss_2 \downarrow = [24, 24] \downarrow = [24]$$

This completes the eight-point transform. The eight points in the signal vector have been transformed by the Haar wavelet transform to eight points,

$$d_1 = [-8, 24, -12, 4] \quad d_2 = [-8, 4] \quad d_3 = [8] \quad s_3 = [24]$$

The inverse transform must start with the wavelet coefficients and end with the original signal coefficients. This is done by a clever reversal of the directions in Fig. 10, with a sum used to go from two branches on the right to one on the left, at a vertex where three lines meet. Here is how it works. Use the transpose of S and H without the factor of $\frac{1}{2}$ at each step and insert zeros where there were discarded values. This upsampling is indicated by the up arrow.

$$S^\dagger = \begin{pmatrix} 1 & 1 \\ 1 & 1 \end{pmatrix} \quad H^\dagger = \begin{pmatrix} 1 & -1 \\ -1 & 1 \end{pmatrix}$$

$$S^\dagger s_3 \uparrow = S^\dagger \begin{pmatrix} 24 \\ 0 \end{pmatrix} = \begin{pmatrix} 24 \\ 24 \end{pmatrix} \quad H^\dagger d_3 \uparrow = H^\dagger \begin{pmatrix} 8 \\ 0 \end{pmatrix} = \begin{pmatrix} 8 \\ -8 \end{pmatrix}$$

The s_2 signal is recovered by addition

$$\begin{pmatrix} 24 \\ 24 \end{pmatrix} + \begin{pmatrix} 8 \\ -8 \end{pmatrix} = \begin{pmatrix} 32 \\ 16 \end{pmatrix}$$

At the next step, we have

$$S^\dagger = \begin{pmatrix} 1 & 0 & 0 & 1 \\ 1 & 1 & 0 & 0 \\ 0 & 1 & 1 & 0 \\ 0 & 0 & 1 & 1 \end{pmatrix} \quad H^\dagger = \begin{pmatrix} 1 & 0 & 0 & -1 \\ -1 & 1 & 0 & 0 \\ 0 & -1 & 1 & 0 \\ 0 & 0 & -1 & 1 \end{pmatrix}$$

$$S^\dagger s_2 \uparrow = S^\dagger \begin{pmatrix} 32 \\ 0 \\ 16 \\ 0 \end{pmatrix} = \begin{pmatrix} 32 \\ 32 \\ 16 \\ 16 \end{pmatrix}$$

$$H^\dagger d_2 \uparrow = H^\dagger \begin{pmatrix} -8 \\ 0 \\ 4 \\ 0 \end{pmatrix} = \begin{pmatrix} -8 \\ 8 \\ 4 \\ -4 \end{pmatrix}$$

Again, by addition we recover the s_1 signal,

$$\begin{pmatrix} 32 \\ 32 \\ 16 \\ 16 \end{pmatrix} + \begin{pmatrix} -8 \\ 8 \\ 4 \\ -4 \end{pmatrix} = \begin{pmatrix} 24 \\ 40 \\ 20 \\ 12 \end{pmatrix}$$

In the final step we are back to the full matrices

$$S^\dagger = \begin{pmatrix} 1 & 0 & 0 & 0 & 0 & 0 & 0 & 1 \\ 1 & 1 & 0 & 0 & 0 & 0 & 0 & 0 \\ 0 & 1 & 1 & 0 & 0 & 0 & 0 & 0 \\ 0 & 0 & 1 & 1 & 0 & 0 & 0 & 0 \\ 0 & 0 & 0 & 1 & 1 & 0 & 0 & 0 \\ 0 & 0 & 0 & 0 & 1 & 1 & 0 & 0 \\ 0 & 0 & 0 & 0 & 0 & 1 & 1 & 0 \\ 0 & 0 & 0 & 0 & 0 & 0 & 1 & 1 \end{pmatrix}$$

$$H^\dagger = \begin{pmatrix} 1 & 0 & 0 & 0 & 0 & 0 & 0 & -1 \\ -1 & 1 & 0 & 0 & 0 & 0 & 0 & 0 \\ 0 & -1 & 1 & 0 & 0 & 0 & 0 & 0 \\ 0 & 0 & -1 & 1 & 0 & 0 & 0 & 0 \\ 0 & 0 & 0 & -1 & 1 & 0 & 0 & 0 \\ 0 & 0 & 0 & 0 & -1 & 1 & 0 & 0 \\ 0 & 0 & 0 & 0 & 0 & -1 & 1 & 0 \\ 0 & 0 & 0 & 0 & 0 & 0 & -1 & 1 \end{pmatrix}$$

The upsampling gives

$$S^\dagger s_1 \uparrow = S^\dagger \begin{pmatrix} 24 \\ 0 \\ 40 \\ 0 \\ 20 \\ 0 \\ 12 \\ 0 \end{pmatrix} = \begin{pmatrix} 24 \\ 24 \\ 40 \\ 40 \\ 20 \\ 20 \\ 12 \\ 12 \end{pmatrix} = H^\dagger d_1$$

$$\uparrow = H^\dagger \begin{pmatrix} -8 \\ 0 \\ 24 \\ 0 \\ -12 \\ 0 \\ 4 \\ 0 \end{pmatrix} = \begin{pmatrix} -8 \\ 8 \\ 24 \\ -24 \\ -12 \\ 12 \\ 4 \\ -4 \end{pmatrix}$$

The original signal vector is recovered by addition

$$f = \begin{pmatrix} 24 \\ 24 \\ 40 \\ 40 \\ 20 \\ 20 \\ 12 \\ 12 \end{pmatrix} + \begin{pmatrix} -8 \\ 8 \\ 24 \\ -24 \\ -12 \\ 12 \\ 4 \\ -4 \end{pmatrix} = \begin{pmatrix} 16 \\ 32 \\ 64 \\ 16 \\ 8 \\ 32 \\ 16 \\ 8 \end{pmatrix}$$

This concludes the Haar example; however, some additional things should be observed. It is possible to combine the matrix multiplication and the up- and downsampling. For a discussion of this, see Strang and Nguyen [41]. Also, one can combine the operations of finding the d and s parts along with the downsampling. A practical example of this is contained in Ref. 42, section 13.10, for the Daubechies D4 wavelet with four coefficients. In addition to Ref. 42, other sources of code for efficient implementation of the forward and inverse wavelet transform include Bruce and Gao [43] and Cody [44,45]. Also, see Section 10. Finally, note that if we start with

$$d_1 = [0, 0, 0, 0] \quad d_2 = [0, 0] \quad d_3 = [1] \quad s_3 = [0]$$

and apply the inverse transform, we get back the wavelet function

$$[1, 1, 1, 1, -1, -1, -1, -1]$$

This is one way to obtain the wavelets illustrated in Fig. 9. We simply run a unit vector, made up of 0's except for a 1 in a single location through the inverse transform.

8. OCTAVE BAND TREE STRUCTURE

The type of division of the spectrum for the tree structure of Fig. 10 is known as a *dyadic* or *octave* band. The part labeled s is the lowpass part and the part labeled d is the highpass part. At each level of the tree, the lower half of the spectrum is split into two equal bands. In Fourier space, this can be represented by Fig. 11. For an extensive discussion of tree structures and the corresponding frequency band splits, see Akansu and Haddad [46]. Another

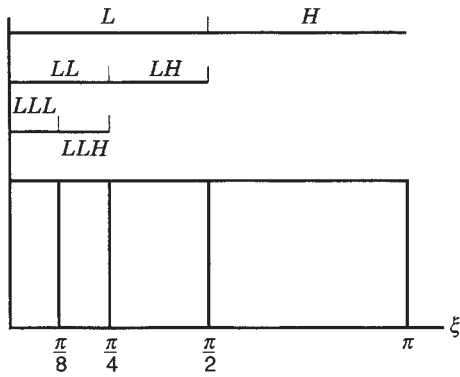


Figure 11. Relation of positive part of frequency spectrum to ideal high- and lowpass parts from Fig. 10.

important type of tree structure for wavelet analysis is that used in connection with wavelet packets and best basis algorithms pioneered by Coifman and Wickerhauser [47,48] and Wickerhauser [49]. In this type of tree, there is an option along both the highpass and lowpass branches to send the signal through more highpass and lowpass filters. This is part of an important and extensive area of wavelet theory known as *adaptive wavelet transform methods*. For a full discussion, we refer the reader to Refs. 47–49 and the Reading List.

An extension of the octave band tree structure to 2-D was suggested by Burt and Adelson [24]. The technique goes by the name of the *Laplacian pyramid*. The multi-resolution analysis can be extended to 2-D for functions $f(x, y)$, for details see Daubechies [29]. We define a scaling function of two variables and three wavelets. These come from tensor products of horizontal and vertical 1-D wavelets. Here, superscripts s, h, v , and d refer to smooth, horizontal, vertical, and diagonal, respectively.

$$\Phi^s(x, y) = \phi(x)\phi(y) \quad L(x)L(y)$$

$$\Psi^h(x, y) = \phi(x)\psi(y) \quad L(x)H(y)$$

$$\Psi^v(x, y) = \psi(x)\phi(y) \quad H(x)L(y)$$

$$\Psi^d(x, y) = \psi(x)\psi(y) \quad H(x)H(y)$$

This leads to a decomposition at levels 1 and 2 illustrated by Fig. 12. At level 2, the smooth part from level 1 is further divided to produce the parts in the upper left corner. To go to level 3, the upper left smooth-smooth part would be further broken down as in going from level 1 to level 2. This can go on as far as is practical. In an image, horizontal edges show prominently in the Ψ^h part, vertical edges in the Ψ^v part, and diagonal edges in the Ψ^d part. See Fig. 13 and the discussion and images in Chapter 10 of Ref. 29.

9. SOME INTERESTING APPLICATIONS

The range of fields, both pure and applied, where wavelets have had an impact is wide. The disciplines include mathematics, physics, geophysics, fluid dynamics, engineering,

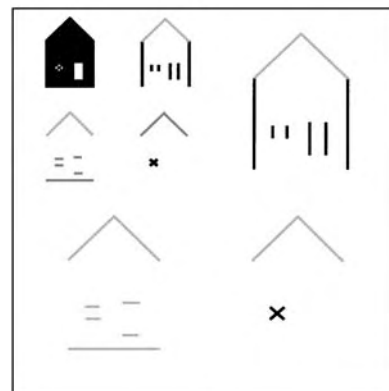
2 $L(x)L(y)$ $L(x)L(y)$	2 $L(x)L(y)$ $H(x)L(y)$	1 $H(x)L(y)$
2 $L(x)L(y)$ $L(x)H(y)$	2 $L(x)L(y)$ $H(x)H(y)$	
1 $L(x)H(y)$		1 $H(x)H(y)$

Figure 12. Decomposition of the 2-D transform into two levels. To go to the next level the lowpass part in the upper left is further broken down just as going from level 1 to level 2.

computer science, and medicine. The broad list of topics include Fourier analysis, approximation theory, numerical analysis, functional analysis, operator theory, group representations, fractals, turbulence, signal processing, image processing, medical imaging, various types of



(a)



(b)

Figure 13. (a) House to be decomposed using wavelet transform. (b) Decomposition through level 2. The gray scale has been reversed and rescaled to emphasize the important features. Note the prominence of the vertical, horizontal, and diagonal parts in the appropriate locations.

compressions, speech and audio, image, and video. In this section, we give a brief introduction to some of these applications and provide the reader with references to current literature for further study.

9.1. Compression

In many cases, a digitized image contains more information than is needed to convey the message the image carries. In these cases, we want to remove some of the information in the original image without degrading the quality too much; this is called *lossy compression*. This modified image can be stored more economically and can be transmitted more rapidly, using less bandwidth over a communications channel. Wavelets have been used for these kinds of problems with striking success. We illustrate this in Fig. 14. The original image is upper left. To obtain the image upper right, we performed a wavelet transform of the original image, kept 25% of the coefficients with the largest magnitude, replaced the other 75% with zeros, then did the inverse transform. The resulting image is clearly degraded, but not significantly. On the lower left, we did the same thing with 6.25% of the coefficients, and on the lower right with only 1.56%.

There is an enormous amount of literature on compression. Here we suggest only a few recent articles. These contain guidance to earlier work. Uses of wavelet transform maxima in signal and image processing are described by Mallat and Zhong [50] and Mallat [51]. Some new ideas on optimal compression are discussed by Hsiao, Jawerth,

Lucier, and Yu [52] and DeVore, Jawerth, and Lucier [53]. See Ref. 23 for a general discussion of video compression, and speech and audio compression. Acoustic signal compression with wavelet packets and a comparison of compression methods are given by Wickerhauser [54,55], and some general theorems on optimal bases for data compression are developed by Donoho [56].

9.2. Turbulence

Wavelet analysis has provided a new means for examining the structure of turbulent flow. They are especially useful when it is important to obtain some information about the spatial structure of the flow. Some of the pioneer work in this area along with a comparison of older methods is in the review by Marie Farge [57]. Also, see the paper on wavelets and turbulence by Farge, Kevlahan, Perrier, and Goirand [58] for a discussion of the main applications of wavelets and wavelet packets to analyze, model, and compute turbulent flows. Wavelet spectra of buoyant atmospheric turbulence are analyzed by Mayer, Hudgins, and Friehe [59], and an experimental study of inhomogeneous turbulence in the lower troposphere using wavelet analysis is discussed by Druilhet et al. [60]. Wickerhauser et al. [61] compare methods for compression of a two-dimensional turbulent flow and find that the wavelet packet representation is superior to the local cosine representation.

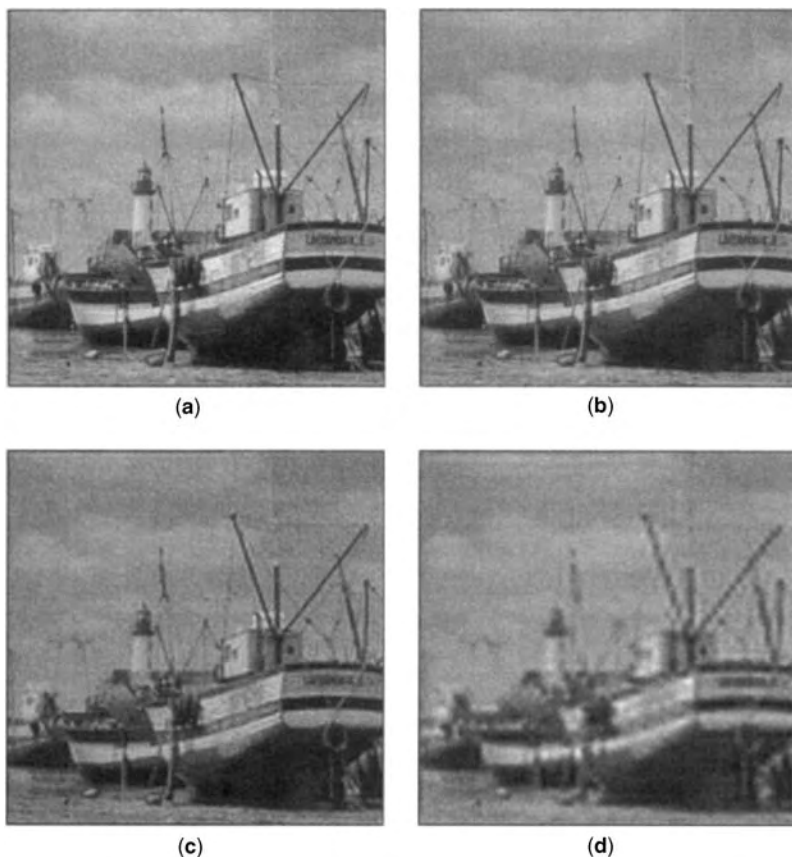


Figure 14. Boat figure to illustrate compression: (a) original, (b) use largest 25%, (c) use largest 6.25%, (d) use largest 1.56%. The degradation can be seen as fewer and fewer coefficients are used to reconstruct the boat.

9.3. Fractals

The wavelet transform is valuable for the efficient representation of scale-invariant signals. Fractal geometry is being used more and more to describe processes that do not fit naturally into traditional Euclidean geometry. Many fractals of interest have structure that is *similar* on different scales. These properties of wavelets and fractals lead to important foundations for scale-invariant signal models. The discrete wavelet transform algorithm is a key component for practical processing of scale-invariant signals and for estimating fractal dimensions. Signal processing with fractals using wavelets is an emerging area, one that is exciting with much work remaining to be done. An important resource in this field is the book by Wornell [62]. The local self-similarity aspect of fractals and the analysis through wavelet transforms is discussed by Holschneider [34], Chapter 4. These two references and the brief review by Hazewinkel [63] provide guidance to the rich literature in this field.

9.4. Medicine and Biology

Wavelets are playing an important role in many areas of medicine and biology. A review of one-dimensional processing in bioacoustics, electrocardiography (ECG), and electroencephalography (EEG) is given by Unser and Aldroubi [64]. This article also contains a brief review of biomedical image processing. Applications of importance include: *noise reduction* in magnetic resonance images [65] using methods systematized by Donoho and Johnstone [66,67] and DeVore and Lucier [68], *image enhancement and segmentation* in digital mammography to accentuate and detect image features that are clinically relevant [69–71], and *image restoration* to restore degradation because of photon scattering and collimator photon penetration with the gamma camera [72]. A general strategy for extraction of microcalcification clusters in digitized mammograms making use of wavelets is outlined by DeVore, Lucier, and Yang [73], and a multiresolution statistical method for the identification of normal mammograms with respect to microcalcifications has been developed [74]; the key to the method is the recognition of the statistical properties of the various levels of the wavelet decomposition. In *computer-assisted tomography* (CT) the Radon transform [75] is fundamental to the algorithms for reconstruction from projections. Several authors have successfully combined wavelet methods with Radon methods to obtain improved algorithms for certain areas of CT (see Refs. 64 and 76 and citations therein). Other medical applications are to *magnetic resonance imaging* (MRI) [77] and functional neuroimaging using *positron emission tomography* (PET) and *functional MRI* (fMRI). A review is given by Unser and Aldroubi [64].

9.5. Others

There are several other areas of application where the wavelet transform plays a key role. We have added a reading list at the end of the bibliography. A quick survey of this list will provide guidance to good starting points for various applications.

10. WAVELETS ON THE INTERNET

An increasing amount of wavelet resources are available on the Internet. Preprints of academic papers are available on the Internet long before they appear in print. Many researchers maintain Internet sites where they post their papers, software, and tutorial guides. In fact the World Wide Web (Web), the graphical interface of the Internet, was created by Tim Berners-Lee while he was at the CERN particle physics laboratory in Geneva. The particle physics community has pioneered in the use of the Internet and the Web in the exchange of ideas, abstracts, and papers since 1991.

A similar effort has been made by Wim Sweldens who founded the *Wavelet Digest* in 1992. The *Wavelet Digest* is a free monthly newsletter, edited by Sweldens, available to subscribers by e-mail. One can browse through past issues of the digest at the Wavelet Digest home page (<http://www.wavelet.org/wavelet/index.html>). The *Wavelet Digest* carries announcements of papers, books, conferences, and seminars in the field of wavelets. It is also a forum for subscribers to ask questions they have about wavelets. Given the wide reach of the *Wavelet Digest*, someone is likely to have an answer for almost any question.

The Collection of Computer Science Bibliographies at the Department of Computer Science of the University of Karlsruhe, Germany has a *Bibliographies on Wavelets* (<http://iinwww.ira.uka.de/bibliography/Theory/Wavelets/>). This is a fairly comprehensive collection of references, although many of them are not available on the Web.

The MathSoft Wavelet Resources page (<http://www.mathsoft.com/wavelets.html>) has a list of links to preprints and papers available on the Web.

Most wavelet pages on the Web have links to other wavelet resources on the Web. The wavelet page maintained by Andreas Uhl at the Department of Mathematics at the University of Salzburg, Austria (<http://www.mat.sbg.ac.at/~uhl/wav.html>) has a useful list of links to wavelet pages, and the Amara Graps wavelet page (<http://www.amara.com/current/wavelet.html>) has a comprehensive list of wavelet links. Also, the Amara Graps page provides a list of wavelet software available on the Internet along with a brief description of each software listed.

The WaveLab software for Matlab written by David Donoho, Iain Johnstone, Jonathan Buckheit, and Shaobing Chen at the Stanford University Statistics Department along with Jeffrey Scargle at NASA-Ames Research Center is available at (<http://stat.stanford.edu/~wave-lab/>). This site includes Macintosh, Unix, and PC versions of the software, including instructions on how to download and install the software.

MathWorks, the creators of Matlab, have introduced the Wavelet Toolbox. The Wavelet Toolbox is written by Michael Misiti, Yves Misiti, Georges Oppenheim, and Jean-Michel Poggi, who are all members of “Laboratoire de Mathématiques,” Orsay-Paris 11 University, France. The book *Wavelets and Filter Banks*, by Gilbert Strang and Truong Nguyen [41], comes with the Toolbox. The

exercises and examples in the book complement the Wavelet Toolbox. The Toolbox has both graphical user interface (GUI) and command line routines. Information on the toolbox can be found at the Matlab Wavelet Toolbox site (<http://www.mathworks.com/products/wavelettbx.shtml>).

An example of a wavelet application in the real world can be found at the Federal Bureau of Investigation (FBI) fingerprint image compression standard website (<http://www.c3.lanl.gov/~brislawn/FBI/FBI.html>). The FBI selected a wavelet standard for digitized fingerprints, and this site gives some of the reasons behind the choice.

Another interesting site on the Web is the Jelena Kovačević Bell Labs Wavelet Group page that includes a link to wavelet related Java applets (http://cm.bell-labs.com/who/jelena/Wavelet/w_applets.html).

This list is far from comprehensive. The interested reader can find wavelet-related links at these sites or by searching on any of the Internet search engines. There are some things one must keep in mind while browsing the Web. Not all information on the Web has been screened by any rigorous peerreview process. One must check the provenance of the information on the Web. Also note that Web addresses are not permanent. The author of a page may graduate or change jobs and the site could be removed. The Internet is a useful resource for any serious researcher. One cannot only get a lot of useful information on the Web, but one can contact other researchers to exchange ideas, data, and programs.

BIBLIOGRAPHY

1. R. N. Bracewell, *The Fourier Transform and Its Applications*, 3rd ed., New York: McGraw-Hill, 1986.
2. E. O. Brigham, *The Fast Fourier Transform and Its Applications*, Englewood Cliffs, NJ: Prentice-Hall, 1988.
3. M. T. Heideman, D. H. Johnson, and C. S. Burrus, Gauss and the history of the fast Fourier transform, *IEEE Acoust. Speech Signal Process. Mag.*, **1**(4):14–21 (1984).
4. D. Gabor, Theory of communication, *J. IEE*, **93**:429–457 (1946).
5. O. Rioul and M. Vetterli, Wavelets and signal processing, *IEEE Signal Process. Mag.*, **8**(4):14–38 (1991).
6. B. B. Hubbard, *The World According to Wavelets*, Wellesley, MA: A.K. Peters, 1996.
7. Y. Meyer, *Wavelets Algorithms & Applications*, Philadelphia: SIAM, 1993.
8. A. Haar, Zur theorie der orthogonalen funktionen-systeme, *Math. Ann.*, **69**:331–371 (1910).
9. P. Franklin, A set of continuous orthogonal functions, *Math. Ann.*, **100**:522–529 (1928).
10. E. Hernández and G. Weiss, *A First Course on Wavelets*, Boca Raton, FL: CRC Press, 1996.
11. R. E. Edwards and G. I. Gaudry, *Littlewood-Paley and Multiplier Theory*, Berlin: Springer-Verlag, 1977.
12. E. M. Stein, *Harmonic Analysis: Real-Variable Methods, Orthogonality, and Oscillatory Integrals*, Princeton, NJ: Princeton University Press, 1993.
13. J.-O. Strömberg, A modified Franklin system and higher-order spline systems on \mathbb{R}^n as unconditional bases for Hardy spaces, in W. Beckner et al., eds., *Conference on Harmonic Analysis in Honor of Antoni Zygmund*, vol. 2, Belmont CA: Wadsworth, 1983, pp. 475–494.
14. K. G. Wilson, Renormalization group and critical phenomems, II, Phase-space cell analysis of critical behavior, *Phys. Rev. B*, **4**:3184–3205 (1971).
15. G. Battle, Wavelets: A renormalization group point of view, in M. B. Ruskai et al., eds., *Wavelets and Their Applications*, Boston, MA: Jones and Bartlett, 1992, pp. 323–349.
16. G. Battle, Wavelet refinement of the Wilson recursion formula, in L. L. Schumaker and G. Webb, eds., *Recent Advances in Wavelet Analysis*, San Diego, CA: Academic Press, 1994, pp. 87–118.
17. R. J. Glauber, Coherent and incoherent states of the radiation field, *Phys. Rev.*, **131**:2766–2788 (1963).
18. E. W. Aslaksen and J. R. Klauder, Unitary representations of the affine group, *J. Math. Phys.*, **9**:206–211 (1968).
19. E. W. Aslaksen and J. R. Klauder, Continuous representation theory using the affine group, *J. Math. Phys.*, **10**:2267–2275 (1969).
20. A. Crosier, D. Esteban, and C. Galand, Perfect channel splitting by use of interpolation/decimation/tree decomposition techniques, *Int. Conf. Inform. Sci. Syst.*, Patras, Greece, 1976, pp. 443–446.
21. D. Esteban and C. Galand, Application of quadrature mirror filters to split band voice coding schemes, *Proc. IEEE Int. Conf. Acoust. Speech Signal Process.*, 1977, pp. 191–195.
22. R. E. Crochiere, S. A. Webber, and J. L. Flanagan, Digital coding of speech sub-bands, *Bell Syst. Tech. J.*, **55**:1069–1085 (1976).
23. M. Vetterli and J. Kovačević, *Wavelets and Subband Coding*, Englewood Cliffs, NJ: Prentice-Hall, 1995.
24. P. J. Burt and E. H. Adelson, The Laplacian pyramid as a compact image code, *IEEE Trans. Commun.*, **31**:532–540 (1983).
25. J. Morlet et al., Wave propagation and sampling theory—Part II: Sampling theory and complex waves, *Geophysics*, **47**:222–236 (1982).
26. A. Grossmann and J. Morlet, Decomposition of Hardy functions into square integrable wavelets of constant shape, *SIAM J. Math. Anal.*, **15**:723–736 (1984).
27. S. G. Mallat, A theory for multiresolution signal decomposition: The wavelet representation, *IEEE Trans. Pattern Anal. Mach. Intell.*, **11**:674–693 (1989).
28. S. G. Mallat, Multiresolution approximations and wavelet orthogonal bases of $L^2(\mathbb{R})$, *Trans. Amer. Math. Soc.*, **315**:69–87 (1989).
29. I. Daubechies, *Ten Lectures on Wavelets*, Philadelphia: SIAM, 1992.
30. I. Daubechies, Orthonormal bases of compactly supported wavelets, *Comm. Pure Appl. Math.*, **41**:909–996 (1988).
31. I. Daubechies, The wavelet transform, time-frequency localization and signal analysis, *IEEE Trans. Inf. Theory*, **36**:961–1005 (1990).
32. I. Daubechies, Where do wavelets come from?—A personal point of view, *Proc. IEEE*, **84**:510–513 (1996).
33. C. E. Heil and D. F. Walnut, Continuous and discrete wavelet transforms, *SIAM Rev.*, **31**:628–666 (1989).
34. M. Holschneider, *Wavelets an Analysis Tool*, Oxford, UK: Clarendon Press, 1995.
35. B. K. Alpert, Wavelets and other bases for fast numerical linear algebra, in C. K. Chui, ed., *Wavelets: A Tutorial in Theory*

- and Applications, San Diego, CA: Academic Press, 1992, pp. 181–216.
36. I. Daubechies, Orthonormal bases of compactly supported wavelets II. Variations on a theme, *SIAM J. Math. Anal.*, **24**:499–519 (1993).
 37. G. Beylkin, R. Coifman, and V. Rokhlin, Fast wavelet transforms and numerical algorithms I, *Comm. Pure Appl. Math.*, **44**:141–183 (1991).
 38. A. Cohen and I. Daubechies, A stability criterion for biorthogonal wavelet bases of compactly supported wavelets, *Duke Math. J.*, **68**:313–335 (1992).
 39. A. Cohen, I. Daubechies, and J.-C. Feauveau, Biorthogonal bases of compactly supported wavelets, *Comm. Pure Appl. Math.*, **45**:485–560 (1992).
 40. M. Vetterli and C. Herley, Wavelets and filter banks: Theory and design, *IEEE Trans. Signal Process.*, **40**:2207–2232 (1992).
 41. G. Strang and T. Nguyen, *Wavelets and Filter Banks*, Wellesley, MA: Wellesley-Cambridge Press, 1996.
 42. W. H. Press et al., *Numerical Recipes in C*, 2nd ed., Cambridge, UK: Cambridge University Press, 1992.
 43. A. Bruce and H.-Y. Gao, *Applied Wavelet Analysis with S-PLUS*, New York: Springer, 1996.
 44. M. A. Cody, The fast wavelet transform, *Dr. Dobbs's J.*, **17**(4):16–28 (1992).
 45. M. A. Cody, The wavelet packet transform, *Dr. Dobbs's J.*, **19**(4):44–54 (1994).
 46. A. N. Akansu and R. A. Haddad, *Multiresolution Signal Decomposition*, San Diego, CA: Academic Press, 1992.
 47. R. R. Coifman and M. V. Wickerhauser, Entropy-based algorithms for best basis selection, *IEEE Trans. Inf. Theory*, **38**:713–718 (1992).
 48. R. R. Coifman and M. V. Wickerhauser, Wavelets and adapted waveform analysis, in J. J. Benedetto and M. W. Frazier, eds., *Wavelets: Mathematics and Applications*, Boca Raton, FL: CRC Press, 1994, pp. 399–423.
 49. M. V. Wickerhauser, *Adapted Wavelet Analysis from Theory to Software*, Wellesley, MA: A. K. Peters, 1994.
 50. S. Mallat and S. Zhong, Wavelet transform maxima and multiscale edges, in M. B. Ruskai et al., eds., *Wavelets and Their Applications*, Boston, MA: Jones and Bartlett, 1992, pp. 67–104.
 51. S. Mallat, Wavelets for a vision, *Proc. IEEE*, **84**:604–614 (1996).
 52. C.-C. Hsiao et al., Near optimal compression of orthonormal wavelet expansions, in J. J. Benedetto and M. W. Frazier, eds., *Wavelets: Mathematics and Applications*, Boca Raton, FL: CRC Press, 1994, pp. 425–446.
 53. R. A. DeVore, B. Jawerth, and B. J. Lucier, Image compression through wavelet transform coding, *IEEE Trans. Inf. Theory*, **38**:719–746 (1992).
 54. M. V. Wickerhauser, Acoustic signal compression with wavelet packets, in C. K. Chui, ed., *Wavelets: A Tutorial in Theory and Applications*, San Diego, CA: Academic Press, 1992, pp. 679–700.
 55. M. V. Wickerhauser, Comparison of picture compression methods: Wavelet, wavelet packet, and local cosine transform coding, in C. K. Chui, L. Montefusco, and L. Puccio, eds., *Wavelets: Theory, Algorithms, and Applications*, San Diego, CA: Academic Press, 1994, pp. 585–621.
 56. D. L. Donoho, Unconditional bases are optimal bases for data compression and for statistical estimation, *Appl. Computat. Harmonic Anal.*, **1**:100–115 (1993).
 57. M. Farge, Wavelet transforms and their applications to turbulence, *Annu. Rev. Fluid Mech.*, **24**:395–457 (1992).
 58. M. Farge et al., Wavelets and turbulence, *Proc. IEEE*, **84**:639–669 (1996).
 59. M. E. Mayer, L. Hudgins, and C. A. Friehe, Wavelet spectra of buoyant atmospheric turbulence, in C. K. Chui, L. Montefusco, and L. Puccio, eds., *Wavelets: Theory, Algorithms, and Applications*, San Diego, CA: Academic Press, 1994, pp. 533–541.
 60. A. Druihet et al., Experimental study of inhomogeneous turbulence in the lower troposphere by wavelet analysis, in C. K. Chui, L. Montefusco, and L. Puccio, eds., *Wavelets: Theory, Algorithms, and Applications*, San Diego, CA: Academic Press, 1994, pp. 543–559.
 61. M. V. Wickerhauser et al., Efficiency comparison of wavelet packet and adapted local cosine bases for compression of a two-dimensional turbulent flow, in C. K. Chui, L. Montefusco, and L. Puccio, eds., *Wavelets: Theory, Algorithms, and Applications*, San Diego, CA: Academic Press, 1994, pp. 509–531.
 62. G. W. Wornell, *Signal Processing with Fractals: A Wavelet-Based Approach*, Upper Saddle River, NJ: Prentice Hall, 1966.
 63. M. Hazewinkel, Wavelets understand fractals, in T. H. Korowinder, ed., *Wavelets: An Elementary Treatment of Theory and Applications*, River Edge, NJ: World Scientific, 1995, pp. 207–219.
 64. M. Unser and A. Aldroubi, A review of wavelets in biomedical applications, *Proc. IEEE*, **84**:626–638 (1996).
 65. J. B. Weaver et al., Filtering noise from images with wavelet transforms, *Magn. Reson. Med.*, **24**:288–295 (1991).
 66. D. L. Donoho, De-noising by soft-thresholding, *IEEE Trans. Inf. Theory*, **41**:613–627 (1995).
 67. D. L. Donoho and I. M. Johnstone, Ideal spatial adaptation via wavelet shrinkage, *Biometrika*, **81**:425–455 (1994).
 68. R. A. DeVore and B. J. Lucier, Fast wavelet techniques for near-optimal image processing, *Proc. IEEE Military Commun. Conf.*, New York: IEEE, 1992, pp. 48.3.1–48.3.7.
 69. J. Fan and A. Laine, Multiscale contrast enhancement and denoising in digital radiographs, in A. Aldroubi and M. Unser, eds., *Wavelets in Medicine and Biology*, Boca Raton, FL: CRC Press, 1996, pp. 163–189.
 70. W. Qian et al., Computer assisted diagnosis for digital mammography, *IEEE Eng. Med. Biol. Mag.*, **14**:561–569 (1995).
 71. W. Qian et al., Tree structured wavelet transform segmentation of microcalcifications in digital mammography, *Med. Phys.*, **22**:1247–1254 (1995).
 72. W. Qian and L. P. Clarke, Wavelet-based neural network with fuzzy-logic adaptivity for nuclear image restoration, *Proc. IEEE*, **84**:1458–1473 (1996).
 73. R. A. DeVore, B. Lucier, and Z. Yang, Feature extraction in digital mammography, in A. Aldroubi and M. Unser, eds., *Wavelets in Medicine and Biology*, Boca Raton, FL: CRC Press, 1996, pp. 145–161.
 74. J. J. Heine et al., Multiresolution statistical analysis of high-resolution digital mammograms, *IEEE Trans. Med. Imaging*, **16**:503–515 (1997).
 75. S. R. Deans, *The Radon Transform and Some of Its Applications*, New York: Wiley, 1983; Malabar, FL: Krieger, 1993.

76. F. Rashid-Farrokhi et al., Wavelet-based multiresolution local tomography, *IEEE Trans. Image Process.*, **6**:1412–1430, (1997).
77. D. M. Healy, Jr. and J. B. Weaver, Adapted wavelet techniques for encoding magnetic resonance images, in A. Aldroubi and M. Unser, eds., *Wavelets in Medicine and Biology*, Boca Raton, FL: CRC Press, 1996, pp. 297–352.

FURTHER READING

In addition to Refs. [10,23,29,34,41,46,49], and [62] other possible texts are listed.

- A. C. Cohen and R. D. Ryan, *Wavelets and Multiscale Signal Processing*, London: Chapman & Hall, 1995.
- C. K. Chui, *An Introduction to Wavelets*, San Diego, CA: Academic Press, 1992.
- G. Kaiser, *A Friendly Guide to Wavelets*, Boston, MA: Birkhäuser, 1994.
- Y. Meyer, *Wavelets and Operators*, Cambridge, UK: Cambridge University Press, 1992.
- R. T. Ogden, *Essential Wavelets for Statistical Applications and Data Analysis*, Boston, MA: Birkhäuser, 1997.
- L. Prasad and S. S. Iyengar, *Wavelet Analysis with Applications to Image Processing*, Boca Raton, FL: CRC Press, 1997.
- B. W. Suter, *Multirate and Wavelet Signal Processing*, Boca Raton, FL: Academic Press, 1998.
- G. W. Walter, *Wavelets and Other Orthogonal Systems with Applications*, Boca Raton, FL: CRC Press, 1994.
- P. Wojtaszczyk, *A Mathematical Introduction to Wavelets*, Cambridge, UK: Cambridge University Press, 1997.

This list contains useful sources for applications. Most of these were not cited in the bibliography, but in a few cases there is overlap.

M. Akay, ed., *Time Frequency and Wavelets in Biomedical Signal Processing*, New York: IEEE Press, 1998.

This is excellent for engineers and applied scientists. It covers time–frequency analysis methods with biomedical applications; wavelets, wavelet packets, and matching pursuits with biomedical applications; wavelets and medical imaging; and wavelets, neural networks, and fractals. A. Aldroubi and M. Unser, eds., *Wavelets in Medicine and Biology*, Boca Raton, FL: CRC Press, 1996.

This covers many applications in medicine and biology. The main topics are wavelet transform: theory and implementation, wavelets in medical imaging and tomography, wavelets and biomedical signal processing, wavelets and mathematical models in biology.

J. J. Benedetto and M. W. Frazier, eds., *Wavelets: Mathematics and Applications*, Boca Raton, FL: CRC Press, 1994.

This is good for both foundations and applications. It contains core material, wavelets and signal processing, and wavelets and partial differential operators.

E. Foufoula-Georgiou and P. Kumar, eds., *Wavelets in Geophysics*, San Diego, CA: Academic Press, 1994.

A brief summary of wavelets is followed with applications directed toward turbulence and geophysics.

C. K. Chui, ed., *Wavelets: A Tutorial in Theory and Applications*, San Diego, CA: Academic Press, 1992.

This reference contains many articles on foundations for applications. There are sections on orthogonal wavelets,

semi-orthogonal and nonorthogonal wavelets, wavelet-like local bases, multivariate scaling functions and wavelets, short-time Fourier and window-Radon transforms, theory of sampling and interpolation, and applications to numerical analysis and signal processing.

L. L. Schumaker and G. Webb, eds., *Recent Advances in Wavelet Analysis*, San Diego, CA: Academic Press, 1994.

The articles here are mainly on recent advances related to mathematical properties of wavelets.

C. K. Chui, L. Montefusco, and L. Puccio, eds., *Wavelets: Theory, Algorithms, and Applications*, San Diego, CA: Academic Press, 1994.

Several fundamentals are covered. These include multi-resolution and multilevel analysis, wavelet transforms, spline wavelets, other mathematical tools for time–frequency analysis, wavelets and fractals, numerical methods and algorithms, and applications.

W. Dahmen, A. Kurdila, and P. Oswald, eds., *Multiscale Wavelet Methods for Partial Differential Equations*, San Diego, CA: Academic Press, 1997.

This will be of interest to people working with processes involving differential and integral equations, fast algorithms, software tools, numerical experiments, turbulence, and wavelet analysis of partial differential operators.

M. Farge, J. C. R. Hunt, and J. C. Vassilicos, eds., *Wavelets, Fractals, and Fourier Transforms*, Oxford, UK: Clarendon Press, 1993.

The papers here are based on the proceedings of a conference held at Newnham College, Cambridge in December 1990.

M. B. Ruskai et al., eds., *Wavelets and Their Applications*, Boston, MA: Jones and Bartlett, 1992.

There are some very useful articles in this reference. It includes signal analysis, numerical analysis, wavelets and quantum mechanics, and theoretical developments.

J. M. Combes, A. Grossmann, and Ph. Tchmitchian, eds., *Wavelets: Time-Frequency Methods and Phase Space*, 2nd ed., Berlin: Springer-Verlag, 1990.

The conference proceedings of a conference held at Marseille, France in 1988 are contained here. This brought together an interdisciplinary mix of participants, including many major contributors to the development of wavelet methods.

Y. Meyer, ed., *Wavelets and Applications*, Berlin: Springer-Verlag, 1992.

The proceedings of an international conference on wavelets held at Marseille are in this volume. This conference along with the previous one illustrates and captures some of the flavor and excitement of time.

A. Antoniadis and G. Oppenheim, eds., *Wavelets and Statistics*, Lecture Notes in Statistics 103, New York: Springer-Verlag, 1995.

This contains the proceedings of a conference on wavelets and statistics held at Villard de Lans, France in 1994.

T. H. Koornwinder, ed., *Wavelets: An Elementary Treatment of Theory and Applications*, River Edge, NJ: World Scientific, 1993.

This series of articles provides a good introduction to wavelets. It is available in paperback and could serve as a text for a one-semester course.

Finally, there are a few important issues of journals that have been devoted entirely to wavelets, and applications. These include: *IEEE Trans. Inf. Theory*, **38** (1992). Part II of two parts; *IEEE Trans. signal Process.*, **41** (1993). *Proc. IEEE*, **84** (1996). *Ann. Biomed. Eng.*, **23**(5) (1995). A fairly new journal is *Applied and Computational Harmonic Analysis*, started in 1993; many articles in this journal are devoted to wavelets and applications.

WAVELETS

BOJ N. TRAN
 The Boeing Company
 TIEN M. NGUYEN
 The Aerospace Corporation
 MAZEN M. SHIHABI
 Hughes Space and
 Communications Company

Wavelets have been found to be useful in many scientific and engineering applications, including signal processing, communication, video and image compression, medical imaging, and scientific visualization. The concept of wavelets can be viewed as a synthesis of ideas that originated during the last several decades in engineering, physics, and pure mathematics. Although wavelets are a rather simple mathematical tool with a great variety of possible applications, the subject of wavelets is often introduced at a high level of mathematical sophistication. The goal of this article is to develop a basic understanding of wavelets, their origin, and their relation to scaling functions, using the theory of multiresolution analysis.

1. HISTORICAL PERSPECTIVE [1–14]

Prior to the 1930s, the main tools of mathematics for solving scientific and engineering problems traced back to Joseph Fourier (1807) with his theory of frequency analysis. He proposed that any 2π -periodic function $f(t)$ can be represented by a linear combination of cosines and sines:

$$f(t) = a_0 + \sum_{k=1}^{\infty} (a_k \cos kt + b_k \sin kt) \tag{1}$$

The coefficients a_0 , a_k , and b_k are the *Fourier coefficients* of the series and are given by

$$a_0 = \frac{1}{2\pi} \int_0^{2\pi} f(t) dt \tag{2a}$$

$$a_k = \frac{1}{2\pi} \int_0^{2\pi} f(t) \cos kt dt \tag{2b}$$

$$b_k = \frac{1}{2\pi} \int_0^{2\pi} f(t) \sin kt dt \tag{2c}$$

After 1807, mathematicians gradually were led from the notion of frequency analysis to the notion of scale analysis—that is, analyzing $f(t)$ by creating a mathematical structure that varies in scale. A. Haar, in his thesis (1909), was the first to mention using wavelets. An important property of the wavelets he used is that they have compact support, which means that the function vanishes outside a finite interval. Unfortunately, Haar wavelets are not continuously differentiable, which limits their application.

From the 1930s to the 1960s, several groups, working independently, researched the representation of functions using scale-varying basis functions. By using one such function, the *Haar basis function*, Paul Levy investigated Brownian motion and thereby laid the foundation for the modern theory of random processes. He found that the Haar basis function is superior to the Fourier basis functions for studying small and complicated details in Brownian motion.

Also during the 1930s, research was done by Littlewood, Paley, and Stein on computing the *energy* of a function $f(t)$:

$$\text{energy} = \frac{1}{2} \int_0^{2\pi} |f(t)|^2 dt \tag{3}$$

Their computation produced different results when the energy was concentrated around a few points and when it was distributed over a larger interval. This observation disturbed many scientists, because it indicated that energy might not be conserved. Later on, they discovered a function that can both vary in scale and conserve energy at the same time, when computing the functional energy. David Marr applied this work in developing an efficient algorithm for numerical image processing using wavelets in the early 1980s.

Between 1960 and 1980, the mathematicians Guido Weiss and Ronald Coifman studied the simplest elements of a function space, called *atoms*, with the goals of finding the atoms for a common function and finding the *construction rules* that allow the reconstruction of all the elements of the function space using these atoms. In 1980, Grossman and Morlet recast the study of quantum physics in the context of wavelets using the concept of frames. Morlet introduced the term “wavelet” as an abbreviation of “wavelet of constant shape.” These new insights into using wavelets provided a totally new way of thinking about physical reality.

In the summer of 1985, Stephane Mallat applied wavelets to his work in digital signal processing. He discovered a relationship between quadrature mirror filters, the pyramid algorithm, and orthonormal wavelet bases. Inspired by these results, Y. Meyer constructed the first nontrivial wavelets. Unlike the Haar wavelets, the Meyer wavelets are continuously differentiable; however, they do not have compact support. In the early 1990s, Ingrid Daubechies used Mallat’s work to construct a set of orthonormal wavelet basis functions that are perhaps the most elegant, and have become the cornerstone of wavelet applications today.

The development of wavelets is an emerging field comprising ideas from many different fields. The foundations

of wavelet theory have been completed, and current research is in the refinement stage. The refinement involves generalizations and extensions of wavelets, such as extending wavelet packet techniques.

The future of wavelets depends on the possibility of applications. Wavelets have so far been limited in practical applications by their lack of compact support.

2. FOURIER ANALYSIS

Time-series data have traditionally been analyzed in either the time- or the frequency-domain. Fourier analysis is quite useful in identifying frequency components of a signal, but it cannot describe when those frequency components occurred, because it lacks time resolution. This is particularly important for signals with time-varying frequency content, as in human speech and video images.

The Fourier transform is characterized by the ability to analyze a signal in the time-domain for its frequency content. The transform works by first translating a function in the time-domain into a function in the frequency-domain. The signal can then be analyzed for its frequency content, because the Fourier coefficients of the transformed function represent the contribution of each sine and cosine function at each frequency. An Inverse transform does the opposite by transforming data from the frequency-domain into the time-domain. Although the time-series data can have infinitely many sample points, in practice one deals with a finite time interval using a sampling mechanism. The discrete Fourier transform (DFT) estimates the Fourier transform of a function from a finite number of its sampled points. The sampled points are supposed to be typical of what the signal looks like at all other times. The DFT has symmetry properties almost exactly the same as the continuous Fourier transform. To approximate a function by samples, and to approximate the Fourier integral by the DFT, requires multiplication by a matrix that involves on the order of n^2 arithmetic operations. However, if the samples are uniformly spaced, then the Fourier matrix can be factored into a product of just a few sparse matrices, and the resulting factors can be applied to a vector in a total on the order of $n \log n$ arithmetic operations. This technique is the so-called fast Fourier transform (FFT).

3. WAVELET VERSUS FOURIER TRANSFORM

The FFT and the discrete wavelet transform (DWT) are both linear operations that generate a data structure containing $\log_2 n$ segments of various lengths, usually filling it and transforming it into a different data vector of length 2^n .

The mathematical properties of the matrices involved in the transforms are similar as well. The inverse transform matrix for both the FFT and the DWT is the transpose of the original. As a result, both transforms can be viewed as a rotation in function space to a different domain [1]. For the FFT, this new domain contains basis

functions that are sines and cosines. For the wavelet transform, this new domain contains more complicated basis functions called wavelets, mother wavelets, or analyzing wavelets.

The two transforms have another similarity. The basis functions are localized in frequency, making mathematical tools such as power spectra (how much power is contained in a frequency interval) and scalegrams useful at picking out frequencies and calculating power distributions.

The most interesting dissimilarity between these two kinds of transforms is that individual wavelet functions are localized in space. Fourier sine and cosine functions are not. This localization in space, along with wavelets' localization in frequency, makes many functions and operators using wavelets *sparse* when transformed into the wavelet domain. This sparseness, in turn, makes wavelets useful for a number of applications such as data compression, feature detection in images, and noise removal from time series.

One way to see the time–frequency resolution difference between the two transforms is to look at the basis-function coverage of the time–frequency plane [7,14]. Figure 1 shows a windowed Fourier transform, where the window is simply a square wave. The square-wave window truncates the sine or cosine function to particular width. As a single window is used for all frequencies in the WFT, the resolution of the analysis is the same at all locations in the time–frequency plane. An advantage of wavelet transforms is that the windows vary. In order to isolate signal discontinuities, one would like to have some very short basis functions. At the same time, in order to obtain detailed frequency analysis, one would like to have some very long basis functions. A way to achieve this is to have short high-frequency basis functions and long low-frequency ones. This happy medium is exactly what you get with wavelet transforms. Figure 2 shows the coverage in the time–frequency plane with one wavelet function, the Daubechies wavelet.

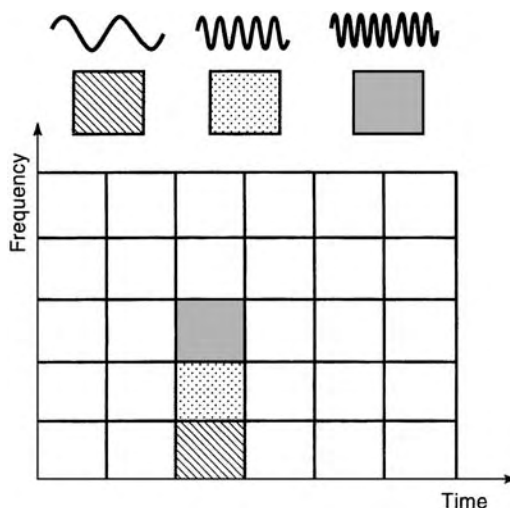


Figure 1. Fourier basis functions, time–frequency tiles, and coverage of the frequency plane [1].

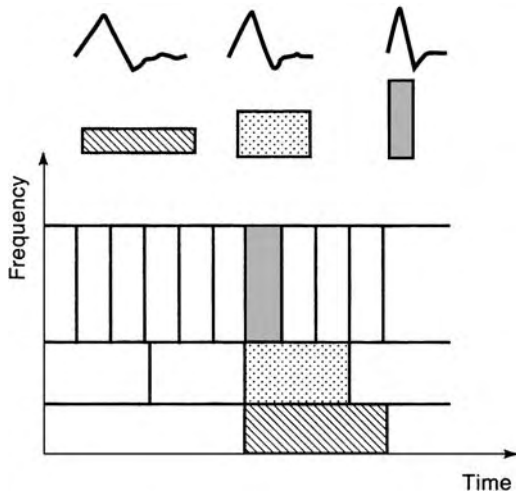


Figure 2. Daubechies wavelet basis functions, time–frequency tiles, and coverage of the frequency plane [1].

4. WAVELET ANALYSIS

Wavelets are a class of functions used to localize a given function in both space and scaling. The basic construction of wavelets is based on the family of *mother wavelets* ϕ , consisting of almost any function defined in a finite interval. *Daughter wavelets* are then formed by translation (b) and scaled contraction (a). An individual wavelet can be defined by

$$\phi_{[a,b]}(t) = |a|^{-1/2} \phi\left(\frac{t-b}{a}\right) \quad (4)$$

An example of a typical wavelet is $a = 2^{-j}$ and $b = ak$:

$$\phi_{[j,k]}(t) = 2^{j/2} \phi(2^j t - k) \quad (5)$$

More precisely, it can be written as a linear combination of scaling functions $\phi(2^j t - k)$, which are 2^{-j} -scaled and $k/2^j$ -translated version of $\phi(t)$, as follows:

$$\phi_{[j,k]}(t) = \sum_{k=-\infty}^{\infty} p_k \phi(2^j t - k) \quad (6)$$

This is often referred to as the two-scale function for the scaling functions, and the sequence $\{p_k\}$ is called the two-scale sequence of ϕ .

Given a scaling function ϕ , the basic assumption of multi-resolution analysis is that another function ψ exists, called a wavelet, such that ϕ forms a basis for the reconstruction of ψ , analogously to the relation for a scaling function. The reconstruction of the wavelet can be expressed as follows:

$$\psi_{[j,k]}(t) = \sum_{k=-\infty}^{\infty} q_k \phi(2^j t - k) \quad (7)$$

The two-scale relations in Eqs. (6) and (7) together are called the reconstruction relations. As both $\phi(2x)$ and

$\phi(2x - 1)$ are in the subspace of the analyzing function, Eqs. (6) and (7) can be combined to form the *reconstruction relations*:

$$\phi(2t - l) = \sum_{k=-\infty}^{\infty} [a_{l-2k} \phi(t - k) + b_{l-2k} \psi(t - k)] \quad (8)$$

Although many classes of wavelets exist, there are two main typical classes:

1. The wavelets defined on the real line, such as the Haar wavelet, the Daubechies wavelet, and B-spline wavelets in general. Linear, quadratic, and cubic wavelets have been studied.
2. Multiwavelets, or wavelet-like functions defined on finite intervals, such as Legendre wavelets and flat-let wavelets.

The interested reader is referred to Refs. 11–14.

4.1. Haar Wavelet

The Haar scaling function and Haar wavelet are a very simple example to illustrate many nice properties of scaling functions and wavelets, and are of practical use as well. The Haar scaling function is defined by

$$\phi(t) = \begin{cases} 1 & \text{for } 0 \leq x \leq 1 \\ 0 & \text{otherwise} \end{cases} \quad (9)$$

The two-scale relation can be expressed in a summation as shown below:

$$\phi_2^H(t) = \sum_{k=0}^2 p_k \phi(2t - k) \quad (10a)$$

or

$$\phi(t) = \phi(2t) + \phi(2t - 1) \quad (10b)$$

The Haar wavelet corresponding to the Haar scaling function is given by

$$\psi(t) = \begin{cases} 1 & \text{for } 0 \leq x \leq \frac{1}{2} \\ -1 & \text{for } \frac{1}{2} \leq x \leq 1 \\ 0 & \text{otherwise} \end{cases} \quad (11)$$

We can easily construct the two-scale relation for the Haar wavelet as

$$\psi(2t) = \phi(2t) - \phi(2t - 1) \quad (12)$$

The two-scale relations in Eq. (10b) express $\phi(t)$ in terms of $\phi(2t)$ and $\phi(2t - 1)$, whereas the two-scale relations in Eq. (12) for Haar wavelets express $\psi(t)$ in terms of $\phi(2t)$ and $\phi(2t - 1)$. The reconstruction relations can be

written in the matrix form

$$\begin{bmatrix} \phi(t) \\ \psi(t) \end{bmatrix} = \begin{bmatrix} 1 & 1 \\ 1 & -1 \end{bmatrix} \begin{bmatrix} \phi(2t) \\ \phi(2t-1) \end{bmatrix} \tag{13}$$

The decomposition relations are easily derived by just inverting the reconstruction relations as follows:

$$\begin{bmatrix} \phi(2t) \\ \pi(2t-1) \end{bmatrix} = \begin{bmatrix} \frac{1}{2} & \frac{1}{2} \\ \frac{1}{2} & -\frac{1}{2} \end{bmatrix} \begin{bmatrix} \phi(t) \\ \psi(t) \end{bmatrix} \tag{14}$$

4.2. Daubechies Wavelets

Another example of wavelets defined on the real line is Daubechies wavelets. The Daubechies scaling function ϕ_3^D is defined by the following relation:

$$\phi_3^D(t) = \sum_{k=0}^3 p_k \phi(2t-k) \tag{15}$$

where two-scale sequence $\{p_k\}$ are

$$\{p_1, p_2, p_3, p_4\} = \left\{ \frac{1+\sqrt{3}}{4}, \frac{3+\sqrt{3}}{4}, \frac{3-\sqrt{3}}{4}, \frac{1-\sqrt{3}}{4} \right\} \tag{16}$$

In general, the two-scale sequence for any scaling functions has the property

$$\sum_k p_{2k} = \sum_k p_{2k+1} = 1 \tag{17}$$

There is no closed form for ϕ_3^D ; however, one can use numerical computation to draw the graph of ϕ_3^D [1,2].

The Haar wavelet is the simplest one. It has found many applications. However, it has the drawback of discontinuity. It consists entirely of rectangular functions and cannot reproduce even linear functions smoothly in finite series for practical use. On the other hand, B-spline wavelets have higher continuity than Haar wavelets. They are more suitable for representing any continuous function. However, the complications of calculating its wavelet decomposition and reconstruction relation coefficients have limited its usefulness.

5. SUBBAND CODING [7,12–15]

One of the main applications of subband coding is compression. A key concept in signal analysis is that of *localization* in time and frequency. Another important intuitive concept is that of *multiresolution*, or the idea that one can consider a signal at different levels of resolution. These notions are particularly evident in image processing and computer vision, where coarse versions of images are often used as a first approximation in computational algorithms. In signal processing, a low-pass and subsampled

version is often a good coarse approximation for many real-life signals. This intuitive paradigm leads to the mathematical framework for wavelet constructions [12]. The wavelet decomposition is a successive approximation method that adds more and more projections onto *detail* spaces, or spaces spanned by wavelets and their shifts at different scales.

In addition, this multiresolution approximation is well suited to many applications. That is true in cases where successive approximation is useful, for example, in browsing through image databases, as is done for instance on the World-Wide Web. Rather than downloading each full image, which would be time-consuming, one only needs to download a coarse version, which can be done relatively fast. Then, one can fetch the rest, if the image seems of interest. Similarly, for communication applications, multiresolution approximation leads to transmission methods where a coarse version of a signal is better protected against transmission errors than the detailed information. The assumption is that the coarse version is probably more useful than the detail.

There are many techniques for image coding. Subband coding is the most successful today. Pyramid coding is effective for high bit rate compression, and transform coding based on the discrete cosine transform has become the JPEG standard. Subband coding using wavelets (the tree-structured filter-bank approach) avoids blocking at medium bit rates, because its basis functions have variable length. It uses an adapted basis (the transformation depends on the signal). Long basis functions represent flat background (low frequency), and short basis functions represent regions with texture. This feature is good for image enhancement, image edge detection, image classification, videoconferencing, video on demand, tissue and cancer cell detection [16], and so on. And because of its adapted basis functions, one can also develop a set of algorithms for adaptive filtering systems [7].

6. WAVELET APPLICATIONS

This section discusses the applications of wavelets in digital communication systems and in image and video compression. We will present a brief description of how wavelets can be used (1) to improve communication efficiency in digital communication systems, and (2) to remove redundant information (e.g., spatial redundancy, spectral redundancy, and temporal redundancy) in image and video compression for an FBI fingerprint application. Other applications in computer and human vision and for denoising noisy data are also described.

6.1. Wavelets in Digital Communications

The channel coding that follows source coding is designed to reintroduce—in a controlled manner—a prescribed level of redundancy into the source-coded streams to mitigate the anticipated effects of the channel, and best performance is achieved when the redundancy is tailored to the specific characteristics of the channel. Although channel coding and modulation applications have received comparatively little attention to date, wavelet theory has an

important complementary role to play in this aspect of the communications problem. Wavelet representation can be exploited to develop systems for reliable transmission over specific channels such as satellite or mobile wireless channels or a combination of both. The problem of multiple-user communication over a wireless channel is of greatest interest in practice. A wireless communication channel is subject to mutual interference among users and fading because of time-varying multipath propagation. To combat the interference and fading effects, a popular multirate modulation technique, referred to as *spread-spectrum code-division multiplexing access* (SS CDMA) has been used widely in the industry [17–22]. This subsection focuses on the use of wavelets for SS CDMA digital communication systems. In addition, a brief description of fractal modulation using wavelets is described.

6.1.1. Single-Scale Covert Communication Waveform.

The idea of wavelet-based SS CDMA was proposed in Ref. 18. The proposed algorithm is summarized below:

- k information bits are grouped together to form an M -ary set of sequences, where

$$M = 2^k \tag{18}$$

- A pseudonoise (PN) code selects a sequence (out of 2^k sequences) for each input information bit generated by the inverse discrete wavelet transform (IDWT).
- The coded data are sent as binary phase-shift keying (BPSK).
- The receiver reverses the above steps; that is, it performs BPSK demodulation, DWT, and data extraction.

Note that only one of 2^J wavelet coefficients is used for BPSK data and the remaining coefficients are unused, where J denotes the number of stages in the wavelet transform. If we let L be the length of the filterband of the DWT, then the processing gain equals the composite impulse response length, that is,

$$G = (2^J - 1)(L - 1) - 1 \tag{19}$$

This wavelet-based SS technique is equivalent to a single-scale covert communication waveform.

6.1.2. Multiple-Scale Covert Communications Waveform. A multiple-scale covert waveform employing a wavelet-transform-domain SS was proposed in Ref. 19. This technique is summarized as follows:

- Encode the data into an M -ary alphabet.
- Apply the PN code to the encoded data.
- Serial-to-parallel demultiplex the resultant into scale streams.
- Represent the SS chips as wavelet coefficients.
- Create a waveform by IDWT.

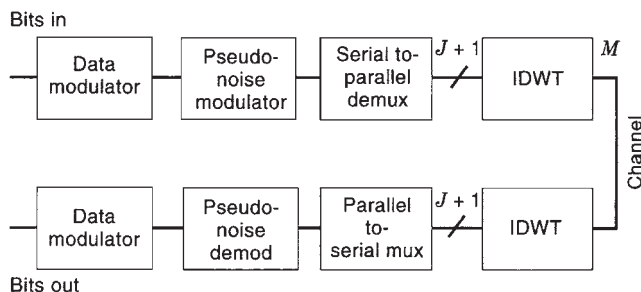


Figure 3. An illustration of a multiple-scale covert communications system using wavelet transforms [4, p. RO-72].

- Receiver reverses the above steps.
- Figure 3 [20, p. RO-72] illustrates the multiple-scale SS system.

6.1.3. Wavelets for Code-Division Multiplexing Access.

The above waveforms are suitable for multiple users where each user has the same waveform algorithm with fixed system parameters and independent PN drivers for the pseudorandom parameters. The design of a CDMA using wavelets has been addressed in Ref. 21, which concerns itself with the three key issues:

- *Channel Capacity.* The number of supportable users per unit bandwidth at a fixed bit error rate (BER) and bit signal-to-noise ratio (SNR), E_b/N_0
- *Near-Far Problem.* The effect of large interference because of a nearby user (this problem is discussed in another article in this encyclopedia)
- *Implementation.* Computational complexity

Regarding the channel capacity, the use of wavelets will lower the required bit SNR. This means that the multiple-access (MA) noise decreases on using a proper wavelet transform. As the wavelet transform is chosen to allow the user to operate at smaller bandwidth, one can impose tighter bandpass filtering at the transmitter. This means improved bandwidth efficiency. In addition to these features, modulation using wavelets occupies all available degrees of freedom in amplitude and phase.

Concerning the near-far problem, the Gaussian character of wavelet-based waveform makes the interference noiselike at all levels, and the near-far effects are perfectly predictable based on power levels.

Finally, the construction of a wavelet-based signal uses a finite number of subsequences, which allows the transmitter to be implemented with only load operations.

Sub-subsections 6.1.3.1. and 6.1.3.2. briefly explains the use of the single-scale and multiple-scale waveforms in CDMA, respectively.

6.1.3.1. Single-Scale CDMA. According to the sub-subsection 6.1.1., the single-scale CDMA waveform is generated using the following algorithm:

- For each input k information bits, we send one of the M complex-valued sequences a_n , where the index n denotes the n th of the M sequences, and M is given in Eq. (18).
- M complex-valued sequences are derived from the M -ary wavelet coefficient matrix. Note that these sequences have approximately Gaussian distribution.
- The set of sequences changes pseudorandomly for each transmission.

If we let the transform length N be k times the alphabet size M ,

$$N = kM \tag{20}$$

and the chip pulse with duration T be $P(t)$, then the signal model for the single-scale CDMA can be written as

$$S(t) = \sum_{n=1}^{N(M-1)} a_n P(t - nT) \tag{21}$$

For unfiltered BPSK or quaternary PSK (QPSK), the pulse shape is square. For filter BPSK/QPSK or wavelet use, the pulse shape is equivalent to the truncated approximation of a sinc pulse, defined as follows:

$$\text{sinc}(t) = \frac{\sin t}{t} \tag{22}$$

It should be noted here that the multiple user waveforms described above possess the following properties:

- Common structure with independent pseudorandom drivers
- Statistical orthogonality

Let us define U as the number of supportable users, G as the processing gain given by Eq. (19), $(E_b/N_0)_{\text{nom}}$ as the nominal bit SNR without MA noise, $(E_b/N_0)_{\text{act}}$ as the actual bit SNR with MA noise and intersymbol interference, and

$$\alpha = \frac{(E_b/N_0)_{\text{act}}}{(E_b/N_0)_{\text{nom}}} \tag{23}$$

The total number of supportable users for unfiltered QPSK is found to be [21]

$$U = \frac{3(1 - \alpha^{-1})G}{4(E_b/N_0)_{\text{nom}}} + 1 \tag{24}$$

whereas for filtered QPSK and a wavelet-based waveform it is

$$U = \frac{(1 - \alpha^{-1})G}{(E_b/N_0)_{\text{nom}}} + 1 \tag{25}$$

A plot of Eqs. (24) and (25) is shown in Fig. 4 [20, p. RO-90] for a QPSK signal with 16-ary simplex. This figure shows

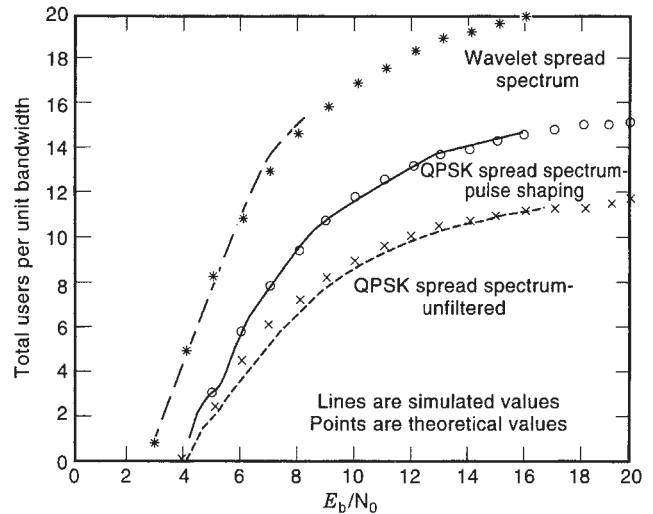


Figure 4. Supportable number of users per unit bandwidth as a function of bit SNR for various QPSK waveforms [4, p. RO-90].

that the wavelet SS can support more users than the filtered QPSK.

6.1.3.2. Multiple-Scale CDMA. According to the subsection 6.1.2., the multiple-scale CDMA waveform uses the wavelet transform domain structure shown in Fig. 3. In this figure, each user signal is driven by an independent PN modulator. The resulting signals will be statistically orthogonal (as good as the PN sequence orthogonality). The performance of the multiple-scale CDMA is as good as that of the single-scale, that is, it has the same channel capacity, BER, interference tolerance, and so on. However, the computational complexity for multiple-scale CDMA is less than for single-scale CDMA. Multiple-scale systems can acquire the signal without a training sequence [20,21], and they can be used for low probability of interception (LPI) and low probability of detection (LPD) networks.

6.1.4. Fractal Modulation. There are some noisy channels whose key characteristic is that the channel is open for some finite but unknown time interval, during which it has some finite but unknown bandwidth. Such models are useful for a range of wireless and secure communications applications, as well as for broadcast applications in which information is being transmitted to receivers whose front ends have different bandwidths and processing capabilities. A wavelet-based modulation model, referred to as *fractal modulation*, which makes efficient use of iterated multirate filter banks, has been shown to provide a novel diversity strategy for communication over such channels [23]. The essence of this scale diversity involves dividing the available transmit spectrum into multiple adjacent octave-spaced bands, and modulating periodic extensions of the symbol stream into these bands at corresponding rates. That is, the information stream is present on all time scales, providing a novel and efficient form of diversity for such applications.

6.2. FBI Fingerprint Compression

Between 1924 and today, the U.S. Federal Bureau of Investigation has collected about 30 million sets of fingerprints [24]. The archive consists mainly of inked impressions on paper cards. Facsimile scans of the impressions are distributed among law enforcement agencies, but the digitization quality is often low. Because a number of jurisdictions are experimenting with digital storage of the prints, incompatibilities between data formats have recently become a problem. This problem led to a demand in the criminal justice community for a digitization and compression standard. In 1993, the FBI's Criminal Justice Information Services Division developed standards for fingerprint digitization and compression in cooperation with the National Institute of Standards and Technology, Los Alamos National Laboratory, commercial vendors, and criminal justice agencies [25].

Let us put the problem of storing the data of digital fingerprints in perspective. Fingerprint images are digitized at a resolution of 500 pixels/in (200 pixels/cm) with 256 levels of gray-scale information per pixel. A single fingerprint is about 700,000 pixels and needs about 0.6 Mbyte of storage. A pair of hands, then, requires about 6 Mbytes of storage. So digitizing the FBI's current archive would result in about 200 terabytes of data. Obviously, data compression is important to bring these numbers down. The data compression standard *wavelet/scalar quantization* (WSQ) implements a hand-tuned custom wavelet basis developed after extensive testing on a collection of fingerprints. The best compression ratio achieved with these wavelets is 26 : 1.

6.3. Computer and Human Vision

In the early 1980s, David Marr began work at MIT's Artificial Intelligence Laboratory on artificial vision for robots. He is an expert on the human visual system, and his goal was to learn why the first attempts to construct a robot capable of understanding its surroundings were unsuccessful. Marr believed that it was important to establish scientific foundations for vision, and that while doing so, one must limit the scope of investigation by excluding everything that depends on training, culture, and so on, and focus on the mechanical or involuntary aspects of vision. This low-level vision is the part that enables us to re-create the three-dimensional organization of the physical world around us from the excitations that stimulate the retina. Marr asked these questions:

- How is it possible to determine the contours of objects from variations in their light intensity?
- How is it possible to sense depth?
- How is motion sensed?

He then developed working algorithmic solutions to answer each of these questions. Marr's theory was that the human visual system has a complicated hierarchical structure that involves several layers of processing. At each processing level, the retinal system provides a visual representation that scales progressively in a geometrical manner. His arguments hinged on the detection of inten-

sity changes. He theorized that intensity changes occur at different scales in an image, so that their optimal detection requires the use of operators of different sizes. He also theorized that sudden intensity changes produce a peak or trough in the first derivative of the image. These two hypotheses require that a vision filter have two characteristics: it should be a differential operator, and it should be capable of being tuned to act at any desired scale. Marr's operator is referred to today as a Marr wavelet.

6.4. Denoising Noisy Data

In diverse fields, from planetary science to molecular spectroscopy, scientists are faced with the problem of recovering a true signal from incomplete, indirect, or noisy data. Can wavelets help solve this problem? The answer is certainly yes, through a technique, called *wavelet shrinkage and thresholding*, that David Donoho of Stanford University has worked on for a number of years [26]. The technique works in the following way. When you decompose a dataset using wavelets, you use filters that act as *averaging* filters, and others that produce *details*. Some of the resulting wavelet coefficients correspond to details in the dataset. If the details are small, they might be omitted without substantially affecting the main features of the dataset. The idea of *thresholding*, then, is to set to zero all coefficients that are less than a particular threshold. The remaining coefficients are used in an inverse wavelet transformation to reconstruct the dataset.

7. REMARKS

There are many applications waiting for wavelet techniques to improve their usefulness beside those mentioned above. Examples are speech compression in mobile communication and digital answering machines; audio compression in digital broadcasting, HDTV, VSAT, storage devices, multimedia, high-fidelity audio, and music; and ECG heart waveform monitoring systems and archives for cardiologists.

In signal processing, wavelets make it possible to recover weak signals from noise. This has proven useful especially in the processing of X ray and magnetic resonance images in medical applications. Images processed in this way can be cleaned up without blurring or muddling the details [16].

In Internet communications, wavelets have been used to compress images to a greater extent than is generally possible with other methods. In some cases, a wavelet-compressed image can be as small as about 25% of the size of similar-quality images using the more familiar JPEG method. Thus, for example, a photograph that requires 200 kbyte and takes a minute to download in JPEG format might require only 50 kbyte and take 15 s to download in wavelet-compressed format.

Wavelet compression works by analyzing an image and converting it into a set of mathematical expressions that can then be decoded by the receiver. Wavelet compression is not yet widely used on the Web. The most common compressed image formats remain the GIF, used mainly for drawings, and JPEG, used mainly for photographs.

BIBLIOGRAPHY

1. A. Graps, An introduction to wavelets, in *IEEE Computational Science and Engineering*, Summer 1995, Vol. 2, No. 2, Los Alamitos, CA: IEEE Computer Society Press, 1995.
2. C. K. Chui, *An Introduction to Wavelets*, New York: Academic Press, 1992.
3. C. K. Chui, ed., *Wavelets: A Tutorial in Theory and Application*, New York: Academic Press, 1992.
4. I. Daubechies, Orthonormal bases of compactly supported wavelets, *Commun. Pure Appl. Math.*, **41**:909–996 (1998).
5. I. Daubechies, *Ten Lectures on Wavelets*, CBMS–NSF Regional Series in Applied Mathematics, Philadelphia, PA: SIAM, 1992.
6. I. Daubechies, Where do wavelets come from?—A personal point of view, *Proc. IEEE*, **84**:510–513 (1996).
7. G. Strang and T. Nguyen, *Wavelets and Filter Banks*, Wellesley, MA: Cambridge Press, 1996.
8. R. K. Young, *Wavelet Theory and its Applications*, Norwell, MA: Kluwer, 1993.
9. G. Beylkin, R. Coifman, and V. Rokhlin, Fast wavelet transforms and numerical algorithms I, *Commun. Pure Appl. Math.*, **44**:141–183 (1991).
10. G. Beylkin, R. Coifman, and V. Rokhlin, Wavelets in numerical analysis, in M. B. Ruskai, ed., *Wavelets and Their Applications*, Boston, MA: Jones and Bartlett, 1992.
11. M. Ueda and S. Lodha, Wavelets: An elementary introduction and examples, UCSC-CRL 94–47, 1995.
12. S. G. Mallat, A theory for multiresolution signal decomposition: The wavelet representation, *Commun. Pure Appl. Math.*, **41**:674–693 (1988).
13. K. Ramchandran, M. Vetterli, and C. Herley, Wavelets, subband coding, and best bases, *Proc. IEEE*, **84**:541–560 (1996).
14. M. Vetterli and C. Herley, Wavelets and filter banks: Theory and design, *IEEE Trans. Signal Process.*, **40**:2207–2232 (1992).
15. K. Cinkler, Very low bit-rate wavelet video coding, *IEEE J. Selected Areas Commun.*, **16**:4–11 (1998).
16. M. Unser and A. Aldroubi, A review of wavelets in biomedical applications, *Proc. IEEE*, **84**:1996 (626–638).
17. C. E. Cook et al., eds., *Spread-Spectrum Communications*, New York: IEEE Press, Wiley, 1983.
18. M. J. Medley, G. Saulnier, and P. Das, Applications of the wavelet transform in spread-spectrum communications systems, *Proc. NJIT Symp. Appl. Subbands and Wavelets*, March 1994, in *Proc. SPIE*, **2242**:54–68 (1994).
19. R. S. Orr, C. Pike, and M. J. Lyall, Wavelet transform domain communications, *Wavelet Applications II*, *Proc. SPIE*, **2491**:271–282 (1995).
20. R. S. Orr and P. P. Gandhi, Wavelets in communication systems, T06, *ICC'96 Tutorials and Workshop*, June 23, 1996.
21. R. S. Orr, C. Pike, and M. Bates, Multiple access communications using wavelet technology, *Wavelet Applications II*, *Proc. SPIE* **2491**:283–294 (1995).
22. G. W. Wornell, Emerging applications of multirate signal processing and wavelets in digital communications, *Proc. IEEE*, **84**:586–603 (1996).
23. G. W. Wornell and A. V. Oppenheim, Wavelet-based representation for a class of self-similar signals with application to fractal modulation, *IEEE Trans. Inf. Theory*, **38**:785–800 (1992).
24. V. Wickerhauser, *Adapted Wavelet Analysis from Theory to Software*, Boston, MA: A. K. Peters, 1994, pp. 213–214.
25. J. Bradley, C. Brislawn, and T. Hopper, The FBI wavelet/scalar quantization standard for gray-scale fingerprint image compression, Tech. Rep. LA-UR-93-1659, Los Alamos, NM: Los Alamos Ntl. Lab., 1993.
26. D. L. Donoho, Nonlinear wavelet methods for recovery of signals, densities, and spectra from indirect and noisy data, in I. Daubechies, ed., *Different Perspective on Wavelets*, Proc. Symp. Appl. Math. 47, Providence, RI: Amer Math. Soc., 1993, pp. 173–205.

WIDEBAND AMPLIFIERS

MYSORE NARAYANAN
Miami University
Oxford, Ohio

1. INTRODUCTION

Almost all signals received from transducers, sensors, radio/television antennas, and other broadcast equipment are always extremely small and are mostly in the microvolt range. Faithful amplification of these feeble signals is essential to activate any device or equipment, whether it is a cellphone or a sophisticated robotic navigator such as the Mars Pathfinder. An amplifier is expected to produce a *faithfully magnified* version of the input signal. It is easy to visualize an *audio amplifier* because the frequency range over which speech signals encountered are in the approximate range of 100–10,000 Hz. However, a *high-fidelity amplifier* may help amplify signals not only in the 100–10,000 Hz range, but also in the lower-frequency range, such as those that are between 35 and 300 Hz (bass) range. In addition, such amplifiers are helpful in the higher frequency ranges as well. The treble control acts to amplify signals beyond the 10,000 Hz range and may be up to 20,000 Hz. Therefore, *bandwidth* provides a measure over which the amplifier is capable of reproducing a magnified version of the input signal faithfully. Bandwidth values for some selected electronic signals are given in Table 1.

It is evident from Table 1 that when one encounters signals in the kilo-, mega-, and gigahertz ranges, it is essential that there be acute need for *wideband* amplifiers. It is recognized that the *gain* A_V of an amplifier is defined as

$$A_V = \frac{V_{\text{out}}}{V_{\text{in}}}$$

Table 1. Bandwidth Values for Selected Electronic Signals

Electrocardiograms	< 100 Hz
Audio signals	20–20,000 Hz
AM radiowaves	550–1600 kHz
FM radiowaves	88–100 MHz
Microwave and satellite signals	1–50 GHz

BIBLIOGRAPHY

1. A. Graps, An introduction to wavelets, in *IEEE Computational Science and Engineering*, Summer 1995, Vol. 2, No. 2, Los Alamitos, CA: IEEE Computer Society Press, 1995.
2. C. K. Chui, *An Introduction to Wavelets*, New York: Academic Press, 1992.
3. C. K. Chui, ed., *Wavelets: A Tutorial in Theory and Application*, New York: Academic Press, 1992.
4. I. Daubechies, Orthonormal bases of compactly supported wavelets, *Commun. Pure Appl. Math.*, **41**:909–996 (1998).
5. I. Daubechies, *Ten Lectures on Wavelets*, CBMS–NSF Regional Series in Applied Mathematics, Philadelphia, PA: SIAM, 1992.
6. I. Daubechies, Where do wavelets come from?—A personal point of view, *Proc. IEEE*, **84**:510–513 (1996).
7. G. Strang and T. Nguyen, *Wavelets and Filter Banks*, Wellesley, MA: Cambridge Press, 1996.
8. R. K. Young, *Wavelet Theory and its Applications*, Norwell, MA: Kluwer, 1993.
9. G. Beylkin, R. Coifman, and V. Rokhlin, Fast wavelet transforms and numerical algorithms I, *Commun. Pure Appl. Math.*, **44**:141–183 (1991).
10. G. Beylkin, R. Coifman, and V. Rokhlin, Wavelets in numerical analysis, in M. B. Ruskaied, ed., *Wavelets and Their Applications*, Boston, MA: Jones and Bartlett, 1992.
11. M. Ueda and S. Lodha, Wavelets: An elementary introduction and examples, UCSC-CRL 94–47, 1995.
12. S. G. Mallat, A theory for multiresolution signal decomposition: The wavelet representation, *Commun. Pure Appl. Math.*, **41**:674–693 (1988).
13. K. Ramchandran, M. Vetterli, and C. Herley, Wavelets, subband coding, and best bases, *Proc. IEEE*, **84**:541–560 (1996).
14. M. Vetterli and C. Herley, Wavelets and filter banks: Theory and design, *IEEE Trans. Signal Process.*, **40**:2207–2232 (1992).
15. K. Cinkler, Very low bit-rate wavelet video coding, *IEEE J. Selected Areas Commun.*, **16**:4–11 (1998).
16. M. Unser and A. Aldroubi, A review of wavelets in biomedical applications, *Proc. IEEE*, **84**:1996 (626–638).
17. C. E. Cook et al., eds., *Spread-Spectrum Communications*, New York: IEEE Press, Wiley, 1983.
18. M. J. Medley, G. Saulnier, and P. Das, Applications of the wavelet transform in spread-spectrum communications systems, *Proc. NJIT Symp. Appl. Subbands and Wavelets*, March 1994, in *Proc. SPIE*, **2242**:54–68 (1994).
19. R. S. Orr, C. Pike, and M. J. Lyall, Wavelet transform domain communications, *Wavelet Applications II*, *Proc. SPIE*, **2491**:271–282 (1995).
20. R. S. Orr and P. P. Gandhi, Wavelets in communication systems, T06, *ICC'96 Tutorials and Workshop*, June 23, 1996.
21. R. S. Orr, C. Pike, and M. Bates, Multiple access communications using wavelet technology, *Wavelet Applications II*, *Proc. SPIE* **2491**:283–294 (1995).
22. G. W. Wornell, Emerging applications of multirate signal processing and wavelets in digital communications, *Proc. IEEE*, **84**:586–603 (1996).
23. G. W. Wornell and A. V. Oppenheim, Wavelet-based representation for a class of self-similar signals with application to fractal modulation, *IEEE Trans. Inf. Theory*, **38**:785–800 (1992).
24. V. Wickerhauser, *Adapted Wavelet Analysis from Theory to Software*, Boston, MA: A. K. Peters. 1994, pp. 213–214.
25. J. Bradley, C. Brislawn, and T. Hopper, The FBI wavelet/singular quantization standard for gray-scale fingerprint image compression, Tech. Rep. LA-UR-93-1659, Los Alamos, NM: Los Alamos Ntl. Lab., 1993.
26. D. L. Donoho, Nonlinear wavelet methods for recovery of signals, densities, and spectra from indirect and noisy data, in I. Daubechies, ed., *Different Perspective on Wavelets*, Proc. Symp. Appl. Math. 47, Providence, RI: Amer Math. Soc., 1993, pp. 173–205.

WIDEBAND AMPLIFIERS

MYSORE NARAYANAN
Miami University
Oxford, Ohio

1. INTRODUCTION

Almost all signals received from transducers, sensors, radio/television antennas, and other broadcast equipment are always extremely small and are mostly in the microvolt range. Faithful amplification of these feeble signals is essential to activate any device or equipment, whether it is a cellphone or a sophisticated robotic navigator such as the Mars Pathfinder. An amplifier is expected to produce a *faithfully magnified* version of the input signal. It is easy to visualize an *audio amplifier* because the frequency range over which speech signals encountered are in the approximate range of 100–10,000 Hz. However, a *high-fidelity amplifier* may help amplify signals not only in the 100–10,000 Hz range, but also in the lower-frequency range, such as those that are between 35 and 300 Hz (bass) range. In addition, such amplifiers are helpful in the higher frequency ranges as well. The treble control acts to amplify signals beyond the 10,000 Hz range and may be up to 20,000 Hz. Therefore, *bandwidth* provides a measure over which the amplifier is capable of reproducing a magnified version of the input signal faithfully. Bandwidth values for some selected electronic signals are given in Table 1.

It is evident from Table 1 that when one encounters signals in the kilo-, mega-, and gigahertz ranges, it is essential that there be acute need for *wideband* amplifiers. It is recognized that the *gain* A_V of an amplifier is defined as

$$A_V = \frac{V_{\text{out}}}{V_{\text{in}}}$$

Table 1. Bandwidth Values for Selected Electronic Signals

Electrocardiograms	< 100 Hz
Audio signals	20–20,000 Hz
AM radiowaves	550–1600 kHz
FM radiowaves	88–100 MHz
Microwave and satellite signals	1–50 GHz

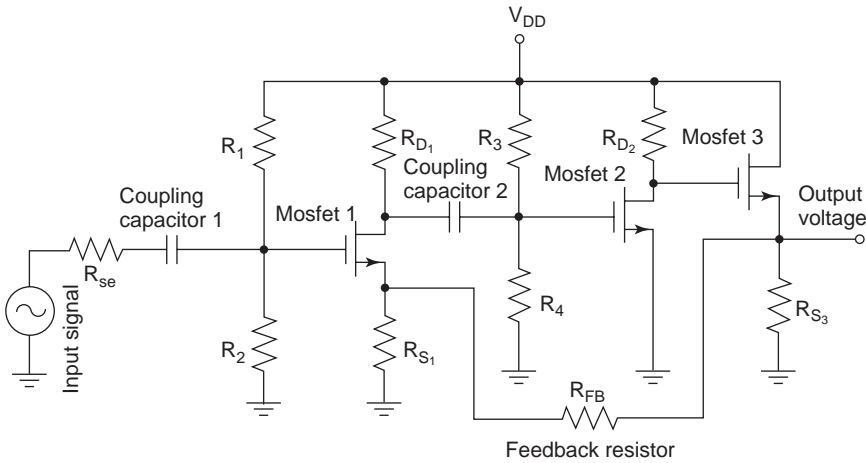


Figure 1. An example of a multistage amplifier.

Assuming that the amplifier utilizes a MOSFET (metal oxide semiconductor field-effect transistor) one can mathematically prove that

$$A_V = -g_m Z_L$$

where g_m is known as the *transconductance* or *mutual conductance* and Z_L is known as the load impedance connected at the *drain* of the transistor. Assuming an “inductance-free” RC load, it is possible to determine that the *uncompensated* bandwidth will be equal to $1/RC$. In other words, if one utilizes a common-source amplifier with a $150\ \Omega$ resistance and a one picofarad (10^{-12} Farad) capacitor would yield a frequency that is approximately 1,000,000,000 Hz. or *one gigahertz*.

When inductances are also utilized, it is possible to develop mathematical equations to govern special designs such as the *shunt peaking amplifier* or the *series peaking amplifier*. A complete discussion of *wideband amplifier* design can be found in many standard textbooks. The text *Highly Linear Integrated Wideband Amplifiers* by Henrik Sjöland of Lund University, Sweden has been completely devoted to the design and analysis techniques for frequencies from audiofrequencies to radiofrequencies.

Consider mathematically analyzing a multistage amplifier, symbolically shown in Fig. 1. The circuit is designed with three MOSFETs with two coupling capacitors. The exact values of the components are not included, because they may widely differ, depending on the design criteria. It should be observed that the input signal is fed to the gate of the first MOSFET via a coupling capacitor. The gate bias is derived from a potential divider circuit, consisting of two resistors. The first stage is designed as a common-source configuration. The output of the first stage is obtained from the drain of the first MOSFET and fed to the gate of the second MOSFET, via a second coupling capacitor. The third and final stage is a source follower and the final output is obtained at the source of the third MOSFET. This output signal is fed back to the source of the first MOSFET via a *feedback resistor*. This type of feedback helps increase the bandwidth of an amplifier. While analyzing such multistage amplifiers, one may conclude that the effect of inductive reactances are small; however, it should be recognized that the two coupling

capacitances incorporated in the circuit may have a pronounced effect on the gain and bandwidth calculations. This is because capacitive reactance is inversely proportional to the frequency. In other words, as the frequency increases, the capacitive reactance decreases because

$$X_C = \frac{1}{j(2\pi f C)}$$

Therefore, it is not advisable to use a grounded *bypass* capacitor, when high frequencies are being dealt with. This may result in signal currents being inadvertently diverted to ground instead of being transmitted through the circuit to the output. It can be seen from the equation above that bypass capacitors offer low reactances to signal currents at higher frequencies. However, the bypass capacitors offer high reactances to signals at lower frequencies, and therefore diversion of signal currents to ground do not pose a major problem, while encountering low-frequency signals.

The frequency plot of an amplifier is represented in Fig. 2. A measure of the magnitude of the output voltage is plotted against a range of frequencies (for a given constant input voltage). The frequency is normally plotted on a logarithmic scale along the x axis (abscissa). The output is plotted on the y axis (ordinate), and the unit is normally

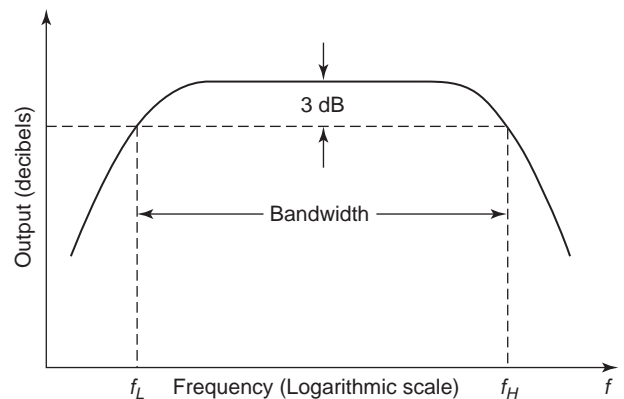


Figure 2. Frequency response characteristics of an amplifier.

decibels (dB):

$$\begin{aligned} \text{dB} &= 20 \log_{10} \frac{\text{voltage}_{\text{out}}}{\text{voltage}_{\text{in}}} \\ &= 10 \log_{10} \frac{\text{power}_{\text{out}}}{\text{power}_{\text{in}}} \end{aligned}$$

Consider the case when $\text{POWER}_{\text{OUT}} = (\frac{1}{2})\text{POWER}_{\text{IN}}$

$$\begin{aligned} \text{dB} &= 10 \log_{10} \left\{ \left(\frac{1}{2} \right) \frac{\text{power}_{\text{in}}}{\text{power}_{\text{in}}} \right\} \\ &= 10 \log_{10} \left\{ \frac{1}{2} \right\} \\ &= -3.0103 \end{aligned}$$

Therefore, design engineers focus at the point where the gain falls by 3 dB. The frequencies at which this occurs are called *half-power frequencies*. If the power is halved, the voltage level is decreased by its square root, because $P = (V^2/R)$. Taking the square root of $\frac{1}{2}$, it is seen that $\sqrt{(\frac{1}{2})} = 0.707$. If the maximum voltage level in the amplifier characteristic is identified as V , then the frequencies at which voltage levels have dropped to $0.707V$ can be identified as f_L and f_H . *Bandwidth* is defined as the range of frequencies that lies between f_L and f_H or in other words, as the frequency range over which the amplifier gain remains almost constant within 29.3% of its maximum value [3 dB level or $(1 - 0.707) = 0.293$].

2. PRINCIPLES OF FEEDBACK

For a simple amplifier, shown symbolically in Fig. 3a, the *voltage gain* is defined as the ratio of output voltage to input voltage. This is written as $A = V_{\text{out}}/V_{\text{in}}$. Addition of a feedback of magnitude F , as shown in Fig. 3b, will result in a modified value for the voltage gain G given by the equation

$$G = \left(\frac{A}{1 + AF} \right)$$

The term AF , called the *feedback factor*, can be either positive or negative. Effectively, Fig. 3c can “replace” Fig. 3b. A study of the variation of G with positive feedback is shown in Fig. 4a. Positive feedback boosts the gain toward infinity. However, positive feedback also greatly increases distortion levels in the output, and therefore it is not viewed as advantageous. Although mathematically the gain approaches infinity, oscillations set in. Therefore, positive feedback is not used in many circuit applications. Positive feedback is also called *regenerative* feedback. Feedback oscillators utilize this principle of positive feedback while designing frequency-selective circuits for audio amplifiers. Harry Nyquist of Bell Telephone Laboratories is credited with this development. His 1932 paper on *regenerative theory* provides more detailed mathematical analysis of positive-feedback circuits. A very simple numerical example may be used to illustrate the significance

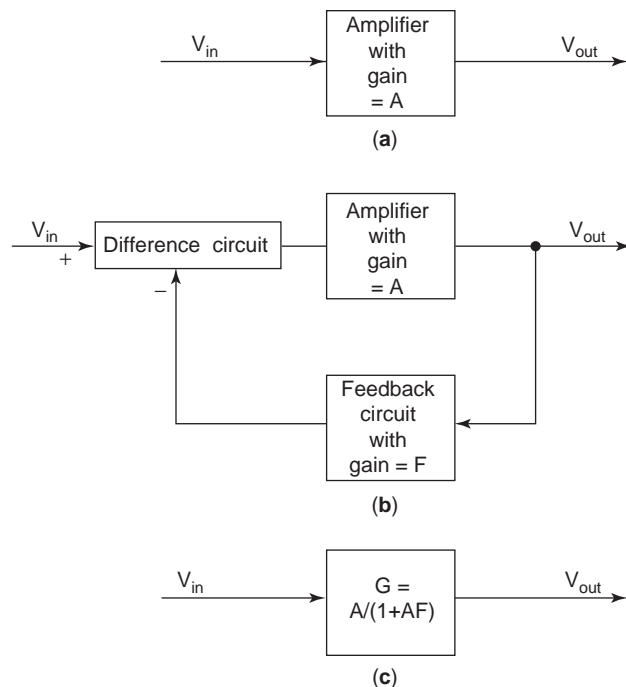


Figure 3. (a) Amplifier without feedback. (b) Amplifier with negative feedback. (c) Simplified version of Fig. 3(b).

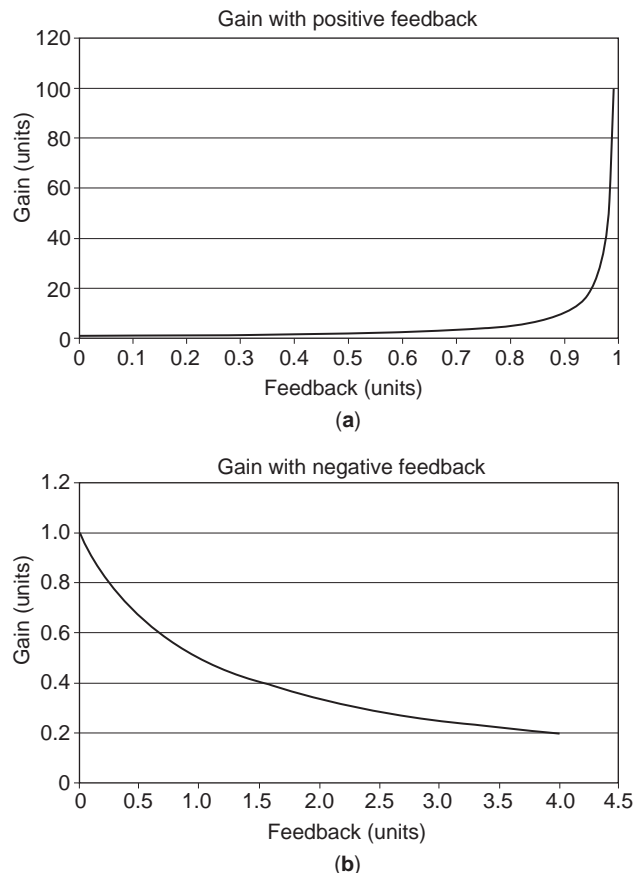


Figure 4. Gain with (a) positive and (b) negative feedback.

of the formula

$$G = \left(\frac{A}{1 + AF} \right)$$

Assume that the *midband gain* A_{MB} of a given amplifier is given as 500. This may be mathematically expressed as

$$A = \frac{(500)}{[1 + j(f/10 \text{ kHz})]}$$

where 10 kHz indicates the bandwidth.

If this is used with a negative-feedback configuration with a *feedback factor* $F = 0.01$, one can easily calculate the gain G for the negative-feedback amplifier as

$$G = \frac{500}{[1 + 500(0.01)]} = 83.33$$

The gain has fallen from the original value of 500 to 83.33.

The bandwidth with negative feedback is given by the formula

$$\begin{aligned} \text{BW}_{\text{neg FB}} &= \text{BW}(1 + AF) \\ &= 10[1 + 500(0.01)] = 60 \text{ kHz} \end{aligned}$$

It is seen that the gain has fallen by a factor of 6 but the bandwidth has improved by a factor of 6.

3. NEGATIVE FEEDBACK

As shown in Fig. 4b, negative feedback reduces the overall gain of an amplifier; hence the term, *degenerative* feedback. Here, a portion of the amplifier output is fed back to the input in such way that it opposes the input. Now it is possible to reexamine the frequency response characteristics with and without negative feedback. It is possible to prove that the bandwidth of the amplifier can be increased with negative feedback. This is the greatest advantage of negative-feedback amplifiers. In addition to extended bandwidth, negative feedback provides stabilized amplifier gain and reduced noise or distortion levels. Further, these types of negative-feedback amplifiers are very stable. It is possible to prove that series voltage feedback increases the input impedance of the circuit. The input impedance can be reduced by incorporating a parallel current feedback. Negative feedback also helps in reducing the circuit noise. In other words, signal-to-noise ratio is greatly improved.

4. SERIES AND SHUNT CONFIGURATIONS

The feedback signal can be obtained from the output voltage or output current. Further, this derived voltage or current can be incorporated into the input circuit in either a parallel or series configuration. Thus, it is possible to design four different types of feedback networks, and these are shown in Figs. 5a–d. It should be recognized that the

transfer function F in each case would be different. For a voltage–voltage feedback configuration, the feedback network takes the output voltage, and a fraction of this voltage is fed back to the input voltage. For a negative feedback circuit the *new* input voltage will actually be $V_{\text{in}} - V_{\text{F}}$ as shown in Figs. 5a and 5b. For a current–current feedback configuration, the feedback network takes the output current, and a fraction of this current is fed back to the input current. The corresponding input current for the ideal amplifier will now be $I_{\text{in}} - I_{\text{F}}$.

5. SIGNAL-TO-NOISE RATIO

While designing wideband amplifiers, it is extremely important to maintain the signal quality, faithfully. The characteristic identified as *signal-to-noise ratio* (SNR) is very helpful in determining the quality features of any amplifier. Consider the input signal of an amplifier expressed as

$$V_{\text{input}} = V_{\text{signal}} + V_{\text{noise}}$$

Here, the input consists of a pure signal that is of interest, but, in addition it has been corrupted with an unwanted component identified as V_{noise} . Circuit configurations may contribute toward electronic noise; however, the presence of harmonics and other extraneous signals such as the 60-Hz. “hum” from the power source may be considered undesirable. White noise, nonlinear distortion, and radio-frequency pickup also contribute toward unacceptable amplifier performance characteristics.

Signal-to-noise ratio is defined as

$$\text{SNR} = \frac{V_{\text{signal}}}{V_{\text{noise}}}$$

Even if one were to neglect the noise contained in the input, it should be recognized that the amplifier itself, introduces its own noise component. Now, one can rewrite the preceding equation as

$$[\text{SNR}]_{\text{open-loop amplifier}} = \frac{A[V_{\text{signal}}]}{V_{\text{noise,amp}}}$$

In this equation A represents the open-loop gain of the amplifier (without feedback) and $V_{\text{noise, amp}}$ is the unwanted noise introduced by the amplifier. Recall that the noise level of the input signal, which was identified simply as V_{noise} , has been ignored, indicating that the amplifier received high-quality input signal, *free* of any significant noise. If feedback F is now applied, it can be mathematically proved that

$$[\text{SNR}]_{\text{feedback amplifier}} = \frac{A[V_{\text{signal}}]}{V_{\text{noise,amp}}} (1 + AF)$$

It is easily seen that the SNR of the negative feedback amplifier is better than the SNR of the open-loop amplifier. It has improved by a factor of $(1 + AF)$.

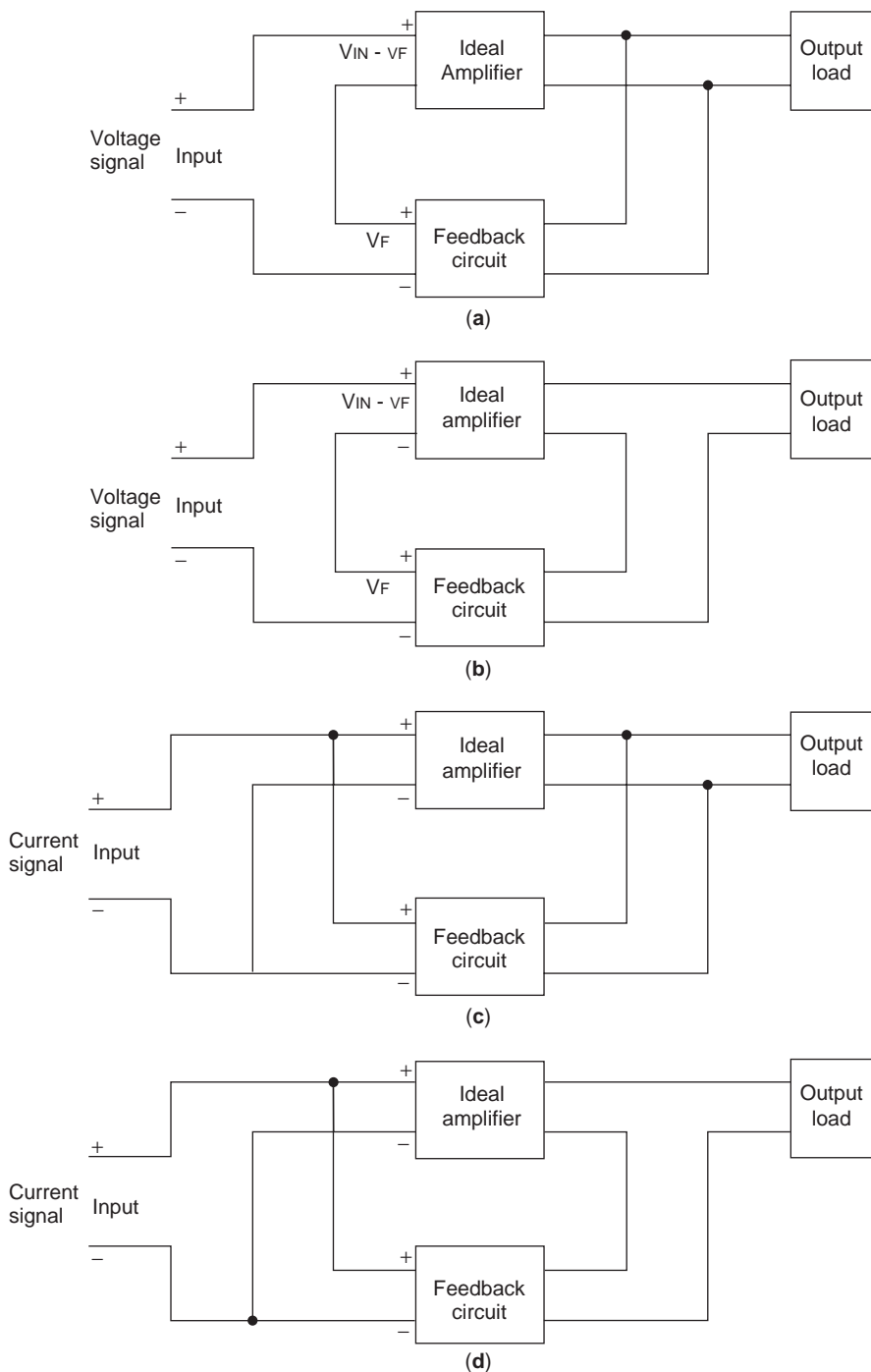


Figure 5. (a) Series–shunt amplifier (also called *voltage amplifier*); (b) series–series amplifier (also called *transadmittance amplifier*); (c) shunt–shunt amplifier (also called *transimpedance amplifier*); (d) shunt–series amplifier (also called *current amplifier*).

Similarly, one can prove that negative feedback helps greatly in reducing distortion:

$$\begin{aligned} & \% \text{ distortion with negative feedback} \\ &= \frac{\% \text{ distortion without negative feedback}}{(1 + AF)} \end{aligned}$$

Negative feedback *may* change to positive feedback at a certain frequency. This may occur as a result of the influence of certain types of reactive elements such as parasitic

capacitive circuit parameters. Oscillations will set in if care is not exercised while designing the wideband amplifier circuit.

6. MILLER EFFECT

While designing amplifiers, engineers may assume that the internal capacitances that exist in the transistor are very small compared to the external capacitances. But in reality, capacitances do exist between base and emitter

(C_{BE}) as well as between base and collector (C_{BC}). It can be mathematically shown that the total input capacitance

$$C_{in} = C_{BE} + (1 + A)(C_{BC})$$

In other words, the total input capacitance is the parallel combination of C_{BE} and $(1 + A) C_{BC}$. The base–collector capacitance has been amplified by a factor of $(1 + A)$. This is called the *Miller effect*.

As mentioned earlier, as the frequency increases, the value of the total input impedance reduces and thereby the frequency response characteristics are affected. The Miller effect has a pronounced effect with common-emitter amplifiers because they introduce a 180° phase shift between the input and the output. For example, the values of C_{BE} and C_{BC} may be small, say, 6 and 5 pF, for example. But when this transistor is used in an amplifier with a gain of 99, the total input capacitance will be large enough to affect the frequency output characteristics of the amplifier. This is because

$$\begin{aligned} C_{in} &= C_{BE} + (1 + A_V)(C_{BC}) \\ &= 6 + (1 + 99)(5) = 506 \text{ pF} \end{aligned}$$

It is recalled that at low frequencies the coupling capacitor and the emitter bypass capacitors offer high impedances, and therefore portions of signal voltage may be lost. The Miller effect is an extremely important concept that is utilized heavily while discussing feedback. Equations for calculating Miller *input impedance* and Miller *output impedance* can be developed, and are given here:

$$\begin{aligned} Z_{in,Miller} &= \frac{Z_{feedback}}{(1 - G)} \\ Z_{out,Miller} &= \frac{(G)Z_{feedback}}{(G - 1)} \end{aligned}$$

7. CASCODE AMPLIFIER STAGE

The drain–gate capacitance in a MOSFET or CMOS is normally designated as C_{gd} . The effect of this capacitance is actually magnified by a factor $(1 + A_V)$, according to the Miller effect, as described above. The *cascode amplifier stage* eliminates the *Miller effect* by isolating this capacitor. Figure 6 illustrates a cascode amplifier stage. Here, CMOS 2 converts the input voltage to an output current. CMOS 1 subsequently transfers this current to the load resistor at the output. It should be observed that the output is at the drain of CMOS 1 and the input is at the gate of CMOS 2. There is no *direct* capacitance across CMOS 2 gate and CMOS 1 drain. With this type of “capacitance isolation” it is possible to design circuits whose time constants are in the nanosecond range. It is possible to produce substantial improvement in bandwidth, with cascode amplifiers. Cascode stages are often used in combination with other methods that utilize inductive coils.

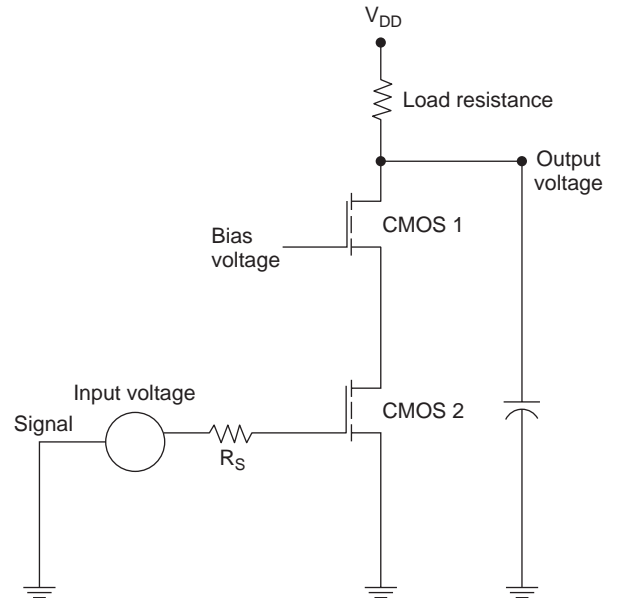


Figure 6. Cascode amplifier stage.

8. BANDWIDTH ENHANCEMENT

Bandwidth, of course, depends on the transistor *cutoff frequency* f_c . Recognizing that $(C_{gs} + C_{gd}) \approx C_{gs}$, then

$$\omega_C = 2\pi f_C \approx \frac{g_m}{C_{gs}}$$

This principle is utilized in the design of certain types of circuit designs. Bandwidth enhancement with *cutoff frequency doublers* can be accomplished by several circuit configurations such as the *Darlington pair* (Fig. 7). A circuit called the *differential pair doubler* is shown in Fig. 8. Another circuit, called the *Battjes doubler*, is also available; however, this does not exactly provide a doubling of the cutoff frequency. With these circuits it is often possible to accomplish a 50% increase in bandwidth, under certain specified conditions. A Bode plot is created using frequency on the x axis (logarithmic scale) and decibels on the y axis (linear scale, because decibels are already obtained from a logarithmic expression). Such a plot provides engineers with a visual picture of bandwidth enhancement, and this is shown in Figs. 9a and 9b. An amplifier without any feedback component has a gain of 100 dB within the frequency range 1–10 Hz. However, at this *breakpoint* frequency, the gain falls off at the rate of 20 dB/decade. With negative feedback incorporated into this amplifier, it can be seen that the new breakpoint frequency can be as high as 100 kHz. This, of course, is accomplished with a sacrifice in gain. Gain has fallen from the original 100 dB to a mere 20 dB, but increase in bandwidth has been accomplished.

9. SENSITIVITY AND GAIN STABILITY

Sensitivity, by definition, compares the fractional change of a dependent variable to the fractional change of an

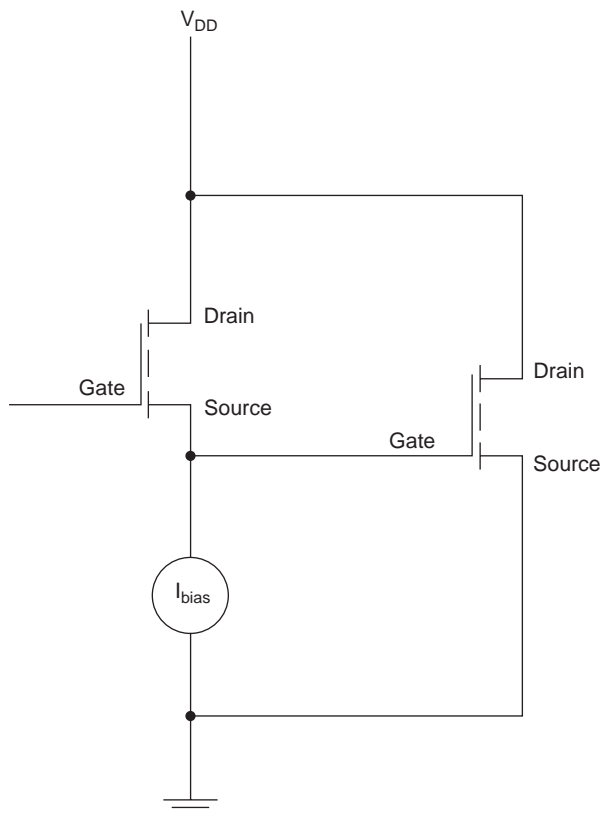


Figure 7. Darlington pair doubler.

independent variable. According to this definition, the sensitivity of V_{out} with respect to the gain A of the amplifier can be mathematically expressed as

$$\frac{(\partial V_{out})/(V_{out})}{(\partial A)/(A)}$$

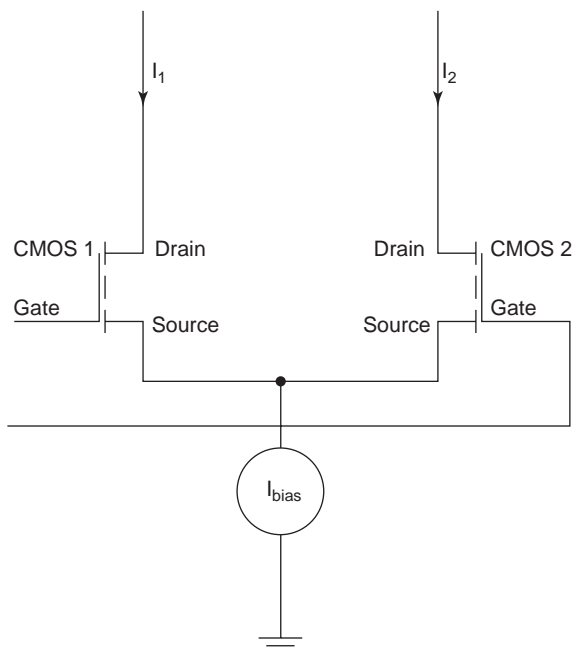


Figure 8. Differential pair doubler.

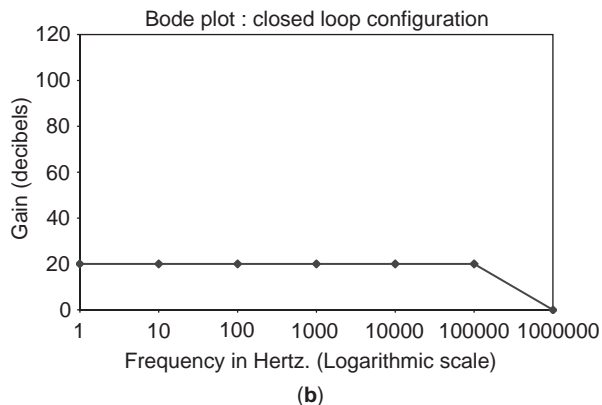
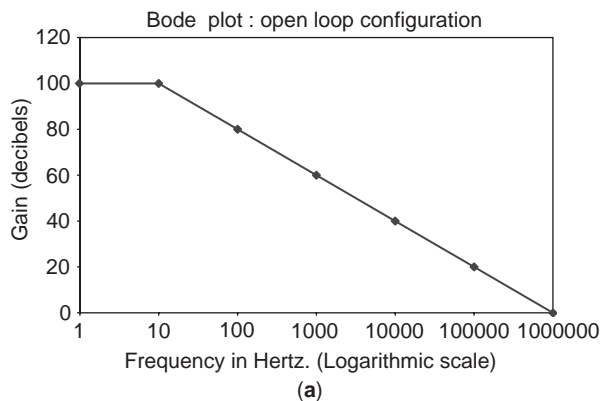


Figure 9. Bode plots with (a) open-loop and (b) closed-loop configurations.

With a closed-loop negative-feedback system it is possible to prove that the sensitivity of G with respect to A is

$$S_{G,A} = \frac{1}{(1 + AF)}$$

It can be observed that the overall gain reaches high stability as the denominator $(1 + AF)$ increases. Further examination of the closed-loop negative-feedback circuit equation indicates that the overall amplifier gain depends mainly on the feedback factor F . This is because

$$G = \frac{A}{1 + AF}$$

By choosing to design a high-gain amplifier with large feedback, it is possible to make $AF > 1$. Then, the equation above becomes

$$G \approx \frac{A}{AF} \approx \frac{1}{F}$$

indicating that the overall gain G is dependent only on the feedback, F and is insensitive to changes in A . This obviously is an extremely important feature of negative feedback.

With a closed-loop negative feedback system it is possible to prove that the gain sensitivity with respect to changes in feedback as

$$S_{G,F} = \frac{-AF}{(1 + AF)}$$

Again, if $AF > 1$, then $|S_{G,F}| = 1$.

Stability for most feedback amplifiers is usually calculated by determining the frequency at which the phase of AF equals $\pm 180^\circ$. Once this is obtained, the magnitude of AF can be easily calculated.

If the magnitude of the absolute value of AF is plotted on the y axis against radian frequency ω along the x axis, one can determine when $|AF|$ reaches unity. The amplifier circuit is then said to be marginally stable. At this instant, if θ is the phase shift, then one can define phase margin (PM) as

$$PM = 180 + \theta$$

The phase margin is therefore defined as a measure of the additional phase lag that is permitted before it reaches -180° . This is shown in Fig. 10. From the discussion above, it can be seen that phase margin also provides a measure of the stability of the amplifier. Addition of appropriate circuit elements in the feedback loop can help in stabilizing an unstable amplifier. A very common method used with operational amplifiers is called the *dominant pole compensation* method.

10. COILS

The coils realizable on a chip have enabled engineers to be very creative in their approach. Specifically designed coils may occupy only a very small area on a given circuit board. (e.g., approximately $50,000 \mu\text{m}^2$). Judiciously incorporating such inductances along with *bridging capacitances* can provide bandwidths in the gigahertz range. A circuit using coils is shown in Fig. 11. The input is

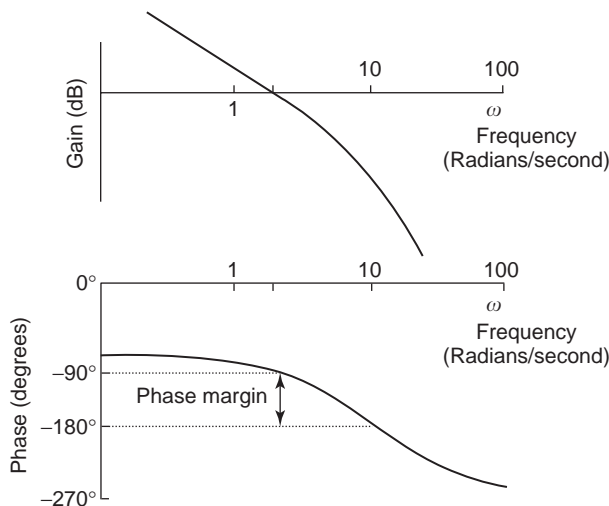


Figure 10. The example shown here records a phase margin of approximately 70° .

supplied to the gate of a single CMOS. The drain of the CMOS is connected to the DC supply via a series combination of two *coupled* coils and a small resistor. The output is taken from the midpoint junction of the coupled coils. Coupling coefficients are relatively small, of the order of 0.3 or 0.5. Each coil may have an inductance in the nanohenry range. The *bridging capacitor*, whose value is extremely small, may not be a separate circuit component. It may enter the circuit configuration as a result of the layout of the inductors on the board. Such circuits can provide a bandwidth improvement of the order of magnitude equal to $2\sqrt{2}$.

Since the early 1990s, world-class MMIC (monolithic microwave integrated circuit) design engineers have focused on the development of state-of-the-art millimeter-wave MMICs for digital radio applications. Bandpass cascode cell distributed amplifiers operating in the frequency range as high as 40 GHz have provided scientists and engineers with powerful tools to work with. Devices having extremely high performance utilizing the PHEMT (pseudomorphic high-electron-mobility transistor) process have enabled design engineers to work in frequency ranges from X band (8 GHz) to W band (110 GHz). Scientists have chosen mixed-topology configurations to obtain benefits of a bandpass topology circuit design keeping the drain line almost free of unnecessary circuit components. The basic idea is to judiciously incorporate a bandpass gate line with a lowpass drain line.

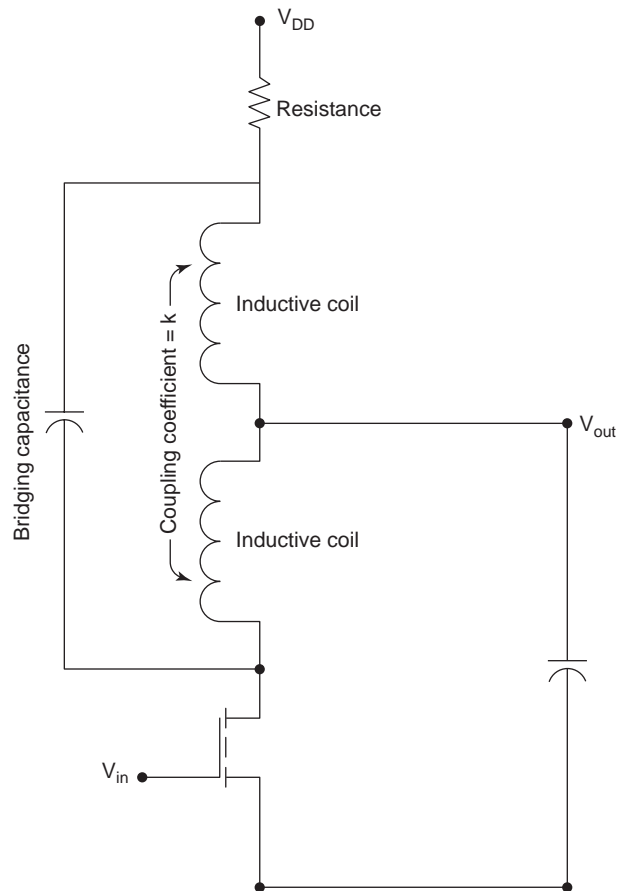


Figure 11. Amplifier with inductively coupled coils.

11. EPILOGUE

More recent developments in broadband communications systems have forced the development of circuit components that are more suited and more appropriate for broadband applications. In addition, the development of broadband communication systems has led the way to an increasing demand for use of wideband amplifiers. It should be recognized that distributed amplifiers have been critical *building blocks* in many such systems because of their performance characteristics, which are clearly *wideband*. However, the low efficiency and low output power of distributed amplifiers have made them unsuitable for high-power applications.

Broadband mixers have helped solve some of these problems, because mixers have always played a vital role in the design of efficient communication systems. In general, one can say that the input impedance of an amplifier can be decreased with shunt feedback and increased with series feedback. Further, the output impedance of an amplifier will increase with current feedback and decrease with voltage feedback. When series-feedback is applied, it is also called a *transadmittance amplifier*. An amplifier is called a *current amplifier* when shunt-series feedback is utilized. Advances in modern-day integrated-circuit design have enabled engineers to fabricate, and integrate miniaturized inductor coils and transformers into amplifier circuit boards. Although these coils do not possess excellent characteristics, they have helped the designers to successfully achieve amplifier bandwidth enhancement. Negative feedback has provided engineers with a method for accomplishing increased bandwidth. Further, the nonlinearities and distortion introduced by the amplifier circuit elements can be reduced by proper use of negative feedback. However, negative feedback suffers from a major disadvantage. The increased bandwidth is accomplished with a sacrifice in gain. Further, complexity itself may pose some problems for the circuit designers. There is also a tendency for the amplifier to oscillate.

WIDEBAND SLOT AND PRINTED ANTENNAS

ATEF Z. ELSHERBENI
 ABDELNASSER A. ELDEK
 CHARLES E. SMITH
 Center of Applied
 Electromagnetic Systems
 Research (CAESR) The
 University of Mississippi
 University, Mississippi

1. INTRODUCTION

Wideband antenna elements are essential for providing wideband scanning array antennas in industry and military applications. Such applications require several features such as wide scan, security, high-speed commu-

nication, and high reliability, and, in many cases, a compact size is required for space-limited mobile antenna systems. Because element size is a critical parameter in determining the scan angle in antenna array configurations, small size is desirable for the antenna arrays supporting wideband applications.

In many civilian and military applications, antenna size, weight, cost, performance, and ease of installation are constraints leading to the selection of low-profile antennas such as microstrip printed and slot antennas. Microstrip antennas were originally proposed in early 1953; however, it was not until the 1970s that further development was achieved in this field, due primarily to the advancement in substrate technology. By exploiting the low-profile, lightweight, conformal configuration, compatibility with integrated circuits and low fabrication cost of these printed circuit board (PCB)-type structures, antenna designers have developed many diversified printed and slot microstrip antenna applications. However, because of the inherent narrow bandwidth characteristics of this class of antennas, an enormous amount of research more recently has been devoted to broadbanding techniques for microstrip printed and slot antennas. Some of these techniques include the use of thicker substrates, odd or optimized shapes of the patch or the slot, aperture coupling, parasitic directors and/or reflectors, and stacks of more than one layer of substrate material, each supporting one or more antenna elements. Microstrip technology utilizing these techniques has enabled many designers to meet the demands of today's communication devices. However, with increasing demands for high-performance dual-band, triband, and wideband and ultraband antennas capable of providing adjustable beamwidth and direction of the mainlobe of the radiation pattern, more sophisticated designs are required.

As a result of these needs, the authors have originated several innovative designs to specifically address these requirements as reported in Refs. 1–5, where new designs of triangle slot antennas with tuning stubs, bowtie slot antennas with tapered tuning stubs, and microstrip-fed printed bowtie antennas for wideband phased-array systems are analyzed and presented. This article provides the detailed performance of one class of the more recently developed printed and slot Lotus antenna elements that support many applications in the X band.

For this, two novel antenna designs will be presented in this article: the coplanar waveguide (CPW)-fed slot Lotus antenna for ultra wideband applications and the microstrip-fed Lotus printed antenna for wideband phased-array systems. The two designs are obtained from smooth and idealized transitions from the feedlines to the antennas, which result in wide bandwidths and low return loss levels.

In addition to regular antenna design for wideband applications, this article also presents multiple band-reconfigurable printed and slot antennas. The multiple-band technology is more redundant to interference and requires lower peak power consumption. Wideband antennas, based on multiple-band technology, normally utilize bandlimited pulses through which information is transmitted with time-spaced pulses at different center frequencies. Thus, the antenna can be constructed from parts that are selected or reconfigured using switches, an

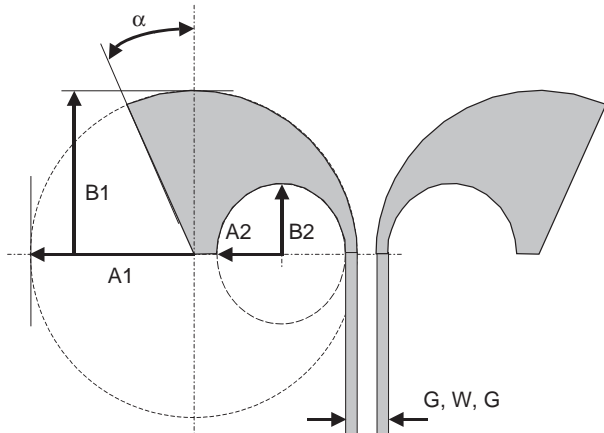


Figure 1. Geometry and parameters of the Lotus slot antenna.

approach that can be employed in most microstrip-based printed and slot antennas. The procedure for designing such reconfigurable antennas will be discussed and experimental verification for several basic antenna structures at X band will also be demonstrated for ideal switching configurations.

The analysis of these antennas will be based on the electromagnetic commercial software packages: momentum of the Agilent advanced design system (ADS), which is a method-of-moments (MoM)-based simulation computer program, and the Ansoft high-frequency structure simulation (HFSS), a finite-element based program. A finite-difference time-domain (FDTD) simulation package developed by the authors is also used in this study. Measurements of the return loss and radiation patterns are presented along with simulation results to further verify the presented designs. The primary objectives of this work is to present how the parameters that affect the characteristics of these new antennas are determined by simulation; to determine the limitations on bandwidth, radiation pattern stability, and antenna scanning capabilities in and array configuration; and to assemble and test a practical prototype antenna in order to validate the simulations and designs achieved.

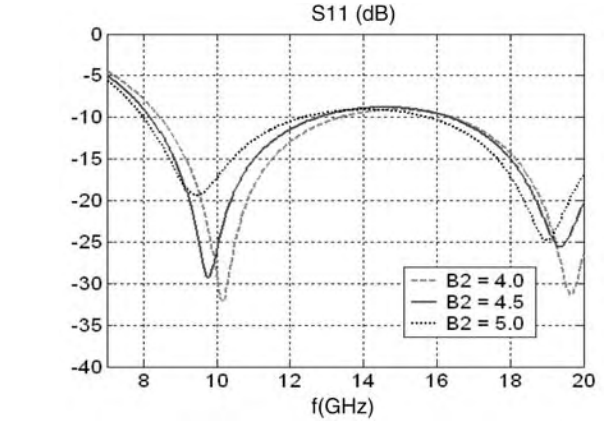


Figure 3. The effect on S_{11} of changing B_2 . (This figure is available in full color at <http://www.mrw.interscience.wiley.com/erfme>.)

2. ULTRAWIDEBAND CPW-FED SLOT LOTUS ANTENNA

In this section, a novel printed slot antenna design fed by coplanar waveguide, called the *Lotus slot antenna*, is introduced. This new antenna is a result of our more recent investigations for designing wideband slot antennas [1,2]. The suggested geometry is shown in Fig. 1, where the antenna consists of two ellipses with horizontal and vertical axes equal to A_1, B_1 and A_2, B_2 for the inner and outer ellipses, respectively. The tapering is truncated at an angle α from the vertical axis of the outer ellipse. The antenna is printed on Rogers RT/Duroid 5880 with $\epsilon_r = 2.2$ and substrate height $h = 1.57$ mm (62 mil).

A parametric study has been performed for this antenna using ADS Momentum. The initial design has A_1, A_2, B_1, B_2 and $\alpha = 9.8, 4.5, 9.8, 4.5$ mm and 0° . Figures 2–4 show that an increase of the radii of the ellipses shifts the resonance frequencies of the antenna to lower frequencies. The parameter B_1 has a significant effect on the resonance frequencies, since by changing B_1 from 9.8 to 17.15 mm, the lower resonance decreases by 2 GHz, while the upper decreases by 5 GHz. This is very important because it allows for shifting the operating band to lower frequencies

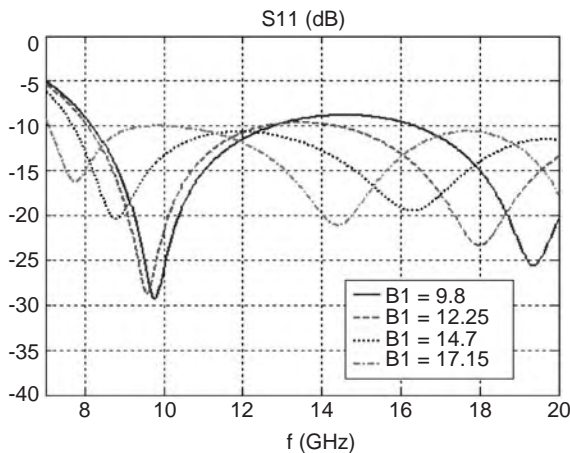


Figure 2. The effect on S_{11} of changing B_1 . (This figure is available in full color at <http://www.mrw.interscience.wiley.com/erfme>.)

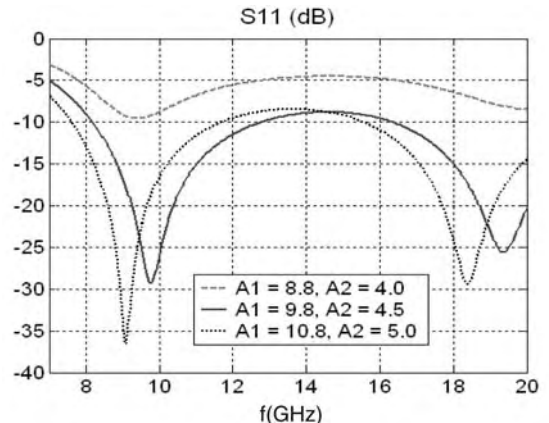


Figure 4. The effect on S_{11} of changing A_1 and A_2 . (This figure is available in full color at <http://www.mrw.interscience.wiley.com/erfme>.)

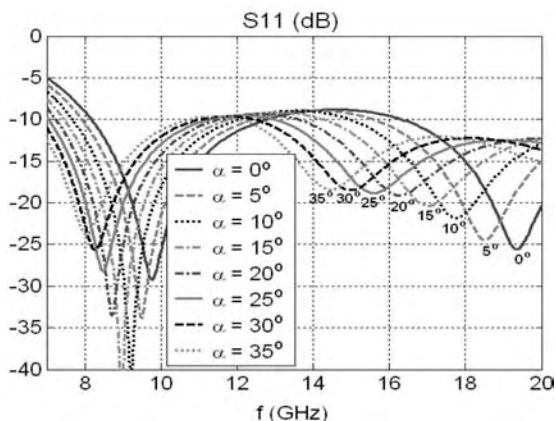


Figure 5. The effect on S_{11} of changing α . (This figure is available in full color at <http://www.mrw.interscience.wiley.com/erfme>.)

without increasing the antenna width. For this study, ultrawide bandwidth is obtained when $B_1 = 12.25$ and 17.15 mm. At the same time, the proper choice of A_1 and A_2 is essential for good return loss levels. From Fig. 5, one notices that the angle α has almost the same effect as B_1 ; whereas an increase of α increases the antenna width. Therefore, to keep the antenna size small α is set equal to zero in the present investigation.

In order to improve the return loss level, two additional parameters, d_1 and d_2 , are introduced and studied. These two parameters change the curvature of the antenna while keeping the slot area almost the same, and as a result a much smoother transition between the feedline and the antenna is obtained. As shown in Fig. 6, introducing d_1 and d_2 improves the return loss level, which results from decreasing the reflection coming from the transition between the narrow CPW slot and the wide Lotus slot.

A design of this antenna with $A_1, A_2, B_1, B_2, d_1, d_2 = 10.1, 4.5, 12.4, 4.25, 0.56, 0.76$ mm and $\alpha = 0^\circ$ is fabricated. The return loss for this design is computed from 5–50 GHz, and, as shown in Fig. 7a, the antenna operates over a large operating band starting from 8 up to >50 GHz. The measurements are compared to the simulation results in Fig. 7c, where good agreement is obtained between the

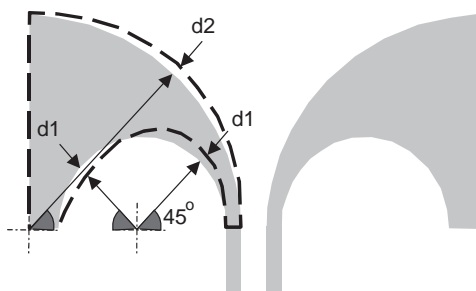


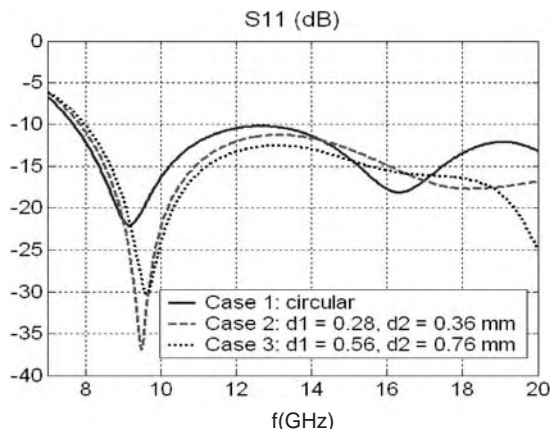
Figure 6. The effect of changing antenna curvature by d_1 and d_2 . (This figure is available in full color at <http://www.mrw.interscience.wiley.com/erfme>.)

two results. The computed radiation patterns using ADS Momentum are shown in Fig. 8 in the E and H planes at 8, 10, and 12 GHz. The radiation pattern is stable in this range, which covers the X band with a cross-polarization level of -6 dB in the H plane and zero in the E plane because of the antenna symmetry. Two elements of this antenna are simulated using ADS Momentum with a separation distance of 2 mm, and the computed coupling is depicted in Fig. 9. The coupling is less than -20 dB over the entire X-band range. The copolarized fields for 1, 8, and 16 elements of the slot Lotus antenna in the H plane are computed using ADS at 10 GHz, and are presented in Fig. 10. The maximum gain increases from 3.69 dB for one element to 12.47 and 15.49 dB for 8- and 16-element arrays, respectively.

3. MICROSTRIP-FED PRINTED LOTUS ANTENNAS

Printed microstrip antennas are widely used in phased-array applications. They are generally economical to produce since they are readily adaptable to hybrid and monolithic integrated circuit (IC) fabrication techniques at RF and microwave frequencies. In addition, they exhibit a very low profile, small size, light weight, low cost, high efficiency, and simple installation.

Among the most widely used printed antennas in phased-array systems are printed dipoles and quasi-Yagi antennas fed by coplanar stripline (CPS), which are usually used to obtain an endfire radiation pattern. In order to feed this antenna, some researchers suggested microstrip-to-CPS transition that includes a 180° phase shifter [6]. The phase shifter consists of a T junction with one side of the microstrip line delayed by a half-wavelength to produce a predominantly odd mode for the CPS. Other researchers feed the dipole with two microstrip lines, where the upper is an extension of the microstrip feedline and the lower is connected to the ground plane directly or through a tapered microstrip [7]. However, the latter method provides omnidirectional patterns and suffers from low bandwidth (BW) (19%). Other researchers used coplanar waveguide (CPW)-to-CPS transitions to feed



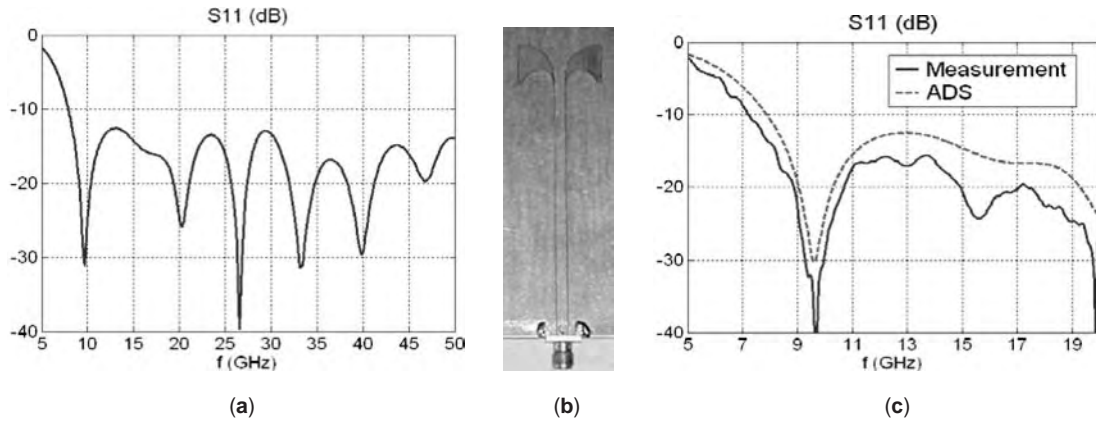


Figure 7. Return loss for the Lotus slot antenna: (a) simulation results up to 50 GHz; (b) printed Lotus prototype; (c) measured versus simulated return loss. (This figure is available in full color at <http://www.mrw.interscience.wiley.com/erfme>.)

printed dipole and bowtie antennas [8] that are designed for $100\ \Omega$ characteristic impedance.

An attractive quasi-Yagi antenna design that uses the transition in Ref. 6 is presented in Refs. 9 and 10 exhibiting wide BW (48%) and good radiation characteristics. The antenna consists of a half-wavelength dipole as a driver and an approximately quarter-wavelength rectangular director to increase the gain and improve the front-to-back ratio. While the driver and director are placed on one side of the substrate, the ground plane is placed on the other side and truncated to act as a reflector.

In this section, a novel printed antenna dual to the slot Lotus is designed and presented for additional improvements in terms of bandwidth and return loss level. The new antenna is called the *printed Lotus*, which supports wideband characteristics. The antenna is fed by microstrip line through a modified phase shifter that has a smaller size and better match with the new antenna than the one introduced in Ref. 10.

The proposed antenna element is printed on a Rogers RT/Duroid 6010/6010 LM substrate of a relative dielectric constant of 10.2, a thickness of 25 mil, and a conductor loss ($\tan \delta$) of 0.0023. The use of high-dielectric-constant sub-

strate material reduces radiation losses from the feedline because most of the electromagnetic field is concentrated in the dielectric between the conductive strip and the ground plane. Another benefit in having a high dielectric constant is that the antenna size decreases by the square root of the effective dielectric constant. To minimize conductor loss, the conductor thickness should be greater than 5δ [11], where δ is the skin depth, which is approximately $0.65\ \mu\text{m}$ for copper. The conductor thickness used to fabricate the antenna prototypes in this research is $34\ \mu\text{m}$.

The geometry of the proposed CPS-fed printed Lotus antenna is shown in Fig. 11a. The antenna is defined by two ellipses. The smaller ellipse is located completely in one half of the larger one. The larger ellipse has R_{h1} and R_{v1} as the semi-horizontal and semivertical axes, respectively; the smaller ellipse has R_{h2} and R_{v2} as the semi-horizontal and semivertical axes, respectively, and is rotated by an angle α . The vertical and horizontal distances between point P , shown in Fig. 11a, and the smaller ellipse centerpoint are L_1 and W_1 , respectively. The parameter L_2 defines the vertical dimension of the antenna, while L_3 is the distance between the substrate edge and the antenna in the y direction and L_4 is the length of the CPS.

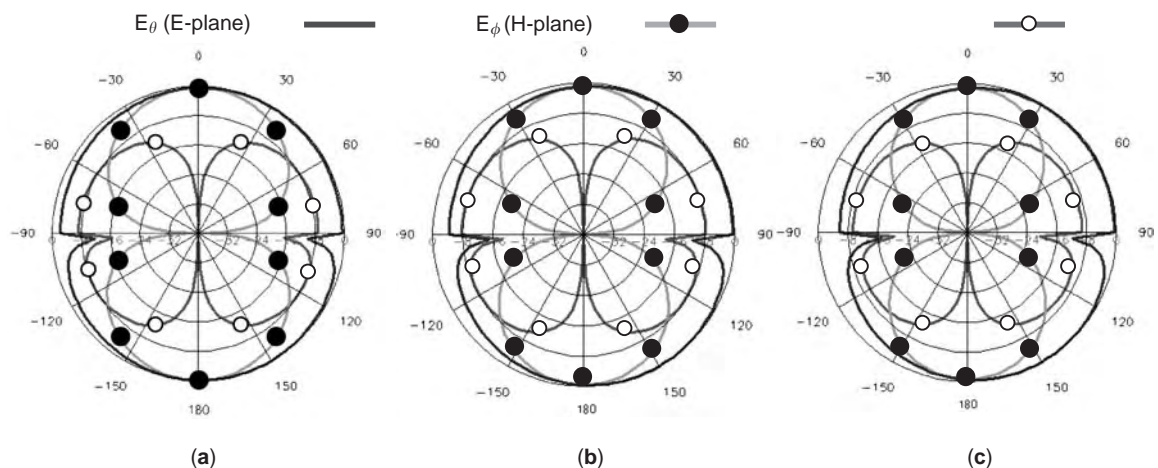


Figure 8. Computed radiation patterns for the Lotus slot antenna at (a) 8 GHz, (b) 10 GHz, and (c) 12 GHz. (This figure is available in full color at <http://www.mrw.interscience.wiley.com/erfme>.)

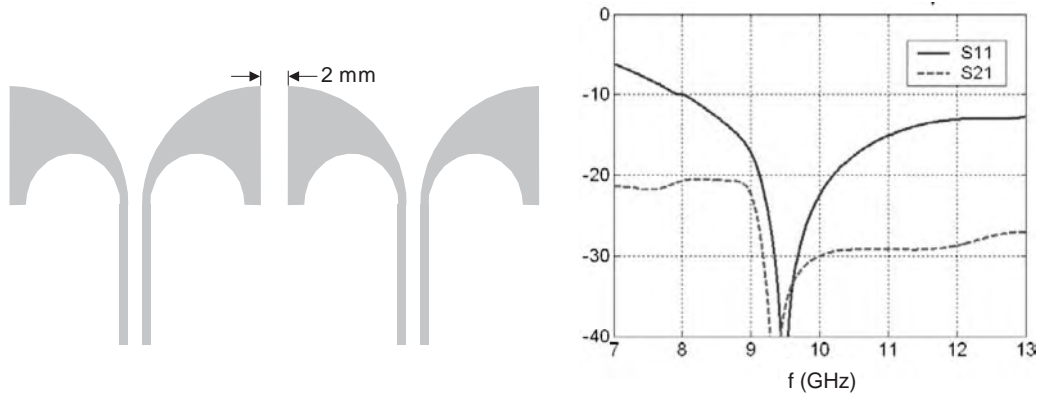


Figure 9. Computed coupling between two elements of the Lotus slot antenna. (This figure is available in full color at <http://www.mrw.interscience.wiley.com/erfme>.)

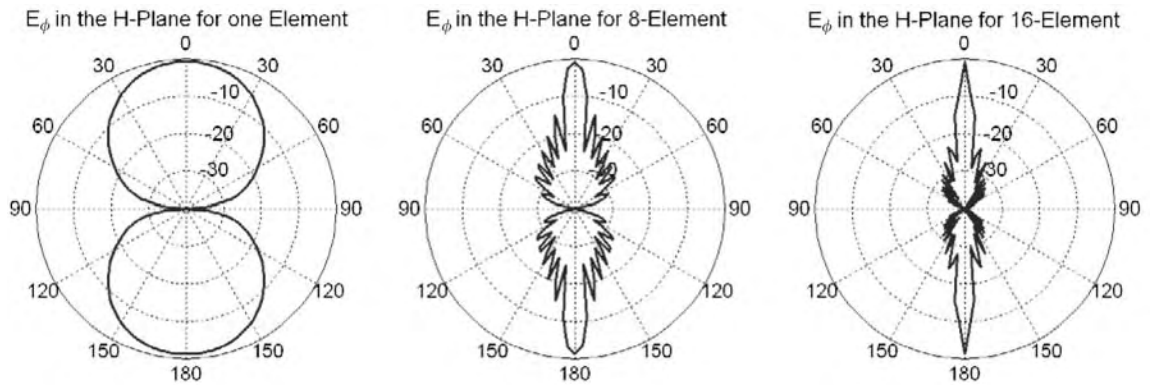


Figure 10. The copolarized field in the *H* plane for 1, 8, and 16 elements of the slot Lotus. (This figure is available in full color at <http://www.mrw.interscience.wiley.com/erfme>.)

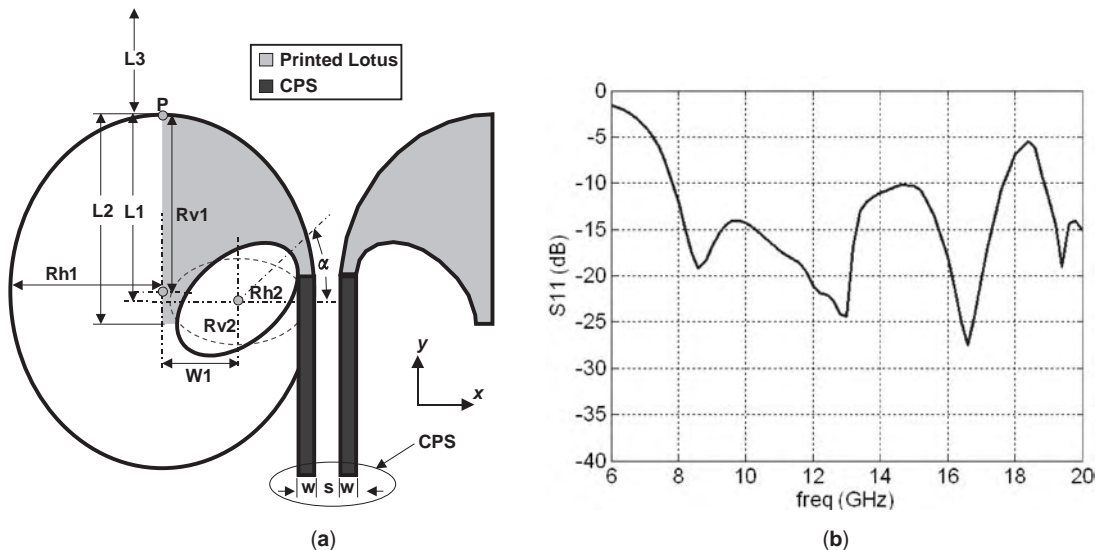


Figure 11. (a) Geometry of the printed Lotus antenna and (b) its computed return loss. (This figure is available in full color at <http://www.mrw.interscience.wiley.com/erfme>.)

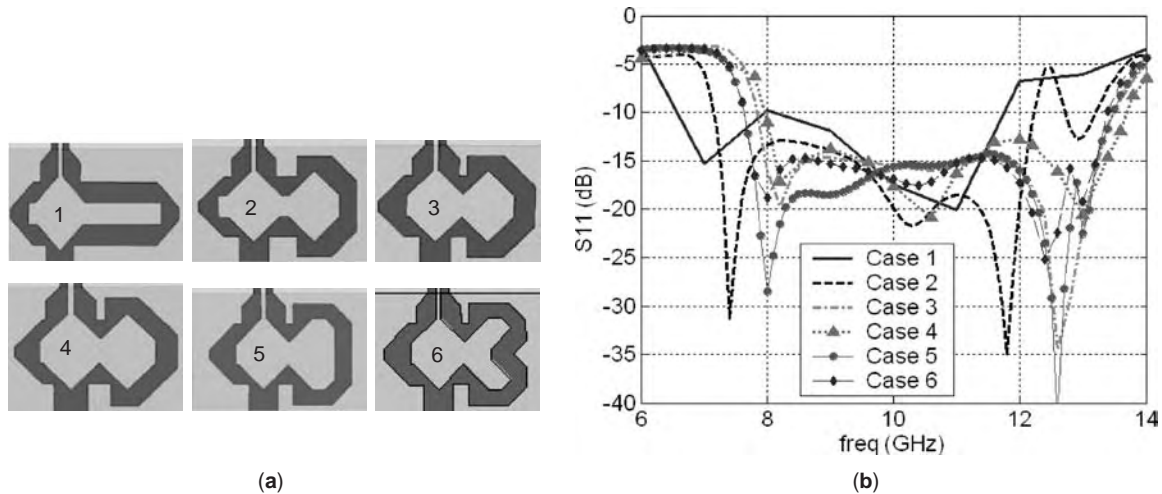


Figure 12. (a) Geometries of the conventional and modified phase shifters and (b) the computed return loss for the microstrip fed printed Lotus through these phase shifters. (This figure is available in full color at <http://www.mrw.interscience.wiley.com/erfme>.)

This study reveals that one of the proper dimensions of the parameters for this antenna R_{h1} , R_{v1} , R_{h2} , R_{v2} , L_1 , W_1 , L_2 , L_3 , and L_4 are equal to 3.4, 3.6, 1.57, 1.06, 3.87, 1.76, 4.2, 5.8 and 4.55 mm, and $\alpha = 41^\circ$, respectively. The CPS dimensional parameters w and s are 0.3 and 0.2 mm, respectively, for an approximate characteristic impedance of 100 Ω . Thus the total width of the antenna is 7 mm, which is 20% less than the quasi-Yagi antenna reported in Refs. 7 and 8. This antenna is simulated using Ansoft HFSS, and the computed return loss is shown in Fig. 11b. On the basis of the simulation results, the antenna operates over a wide frequency range that extends from 7.8 to >20 GHz, except for a small range from 17.7 to 18.7 GHz. This makes the printed Lotus antenna a very good candidate for many applications that require wideband operations.

To feed this design with a microstrip line, improvements for the microstrip-to-CPS transition are required for two reasons: reduction of its horizontal size to be comparable to the small antenna size and improving the matching with the new wideband antenna. The transition presented in the previous section along with five modified transitions, as shown in Fig. 12a as cases 1–6, is used to feed the designed printed Lotus antenna, while the return losses are depicted in Fig. 12b. An average $\lambda_g/2$ difference between phase shifter arms has been reserved for a 10 GHz center frequency. The horizontal dimension is decreased by 28% from 7.5 to 5.4 mm, which, in turn, decreases the coupling between elements in the array environment. The radiation patterns are calculated for these cases, and no significant difference is observed. However, modifying the phase shifter has a very obvious effect on the operating frequency band, return loss level, and BW. The return losses for these different cases are compared in Fig. 12b. The operating band is shifted from (6.6–11.8 GHz) for case 1 to (7.5–13.5 GHz) for cases 3–6. The return loss level decreases uniformly to -15 dB over a very wide range in cases 3, 5, and 6.

Because case 5 shows almost the best BW and return loss level, it will be used in all the following designs. It has a 57% bandwidth relative to -10 dB return loss level and

a 52% BW relative to -15 dB. The dimensions (in millimeters) of the transition section and a comparison between the measured and calculated return loss are shown in Fig. 13. A very good agreement is obtained with a slight increase in the -10 dB BW from 57% to 60% and in the -15 dB BW from 52% to 55.5%. The small discrepancies between measurement and simulation around 10 GHz are due to the imperfect fabrication of the SMA coaxial connector transition. However, one should note that these differences are well below the -15 dB level; thus, the simulations and measurements predict a wideband range of operation for this antenna.

Because of the high dielectric constant, the distance L_3 , shown in Fig. 11a, will have an effect on the radiation pattern in the H plane. As shown in Fig. 14, as L_3 increases from 5.8 to 10 mm, the pattern becomes more concentrated in the y direction, which results in gain enhancement from 5.7 to 7 dB while decreasing the 3 dB beamwidth. At the same time, varying L_3 has a negligible effect on the return loss. Since beamwidth is very important in phased-array applications, L_3 is chosen to be 5.8 mm on the basis of this study.

The radiation patterns at 10 GHz are shown in Fig. 15. The beamwidth is 74° and 143° in the E and H planes, respectively. The maximum gain is around 5.7 dB, and the front-to-back ratio is 17.9 dB. The cross-polarization level is -26 and -29 dB in the E and H planes, respectively, considering only the angles defined by the 3 dB beamwidth. The stability of the radiation pattern is illustrated in Fig. 16, where the copolarized fields in the E and H planes at 8, 10, and 13 GHz, which cover the entire operating band, are compared. The gain is found to vary from 4.2 to 5.7 dB. These characteristics make this antenna a very good candidate for phased-array systems.

A two-element array will be analyzed first in order to reduce the coupling between elements in the x (horizontal) and z (vertical) directions. The most significant source of coupling in the x direction is the surface waves traveling through the substrate from element to element. Introducing slits in the ground plane and gaps in the substrate can

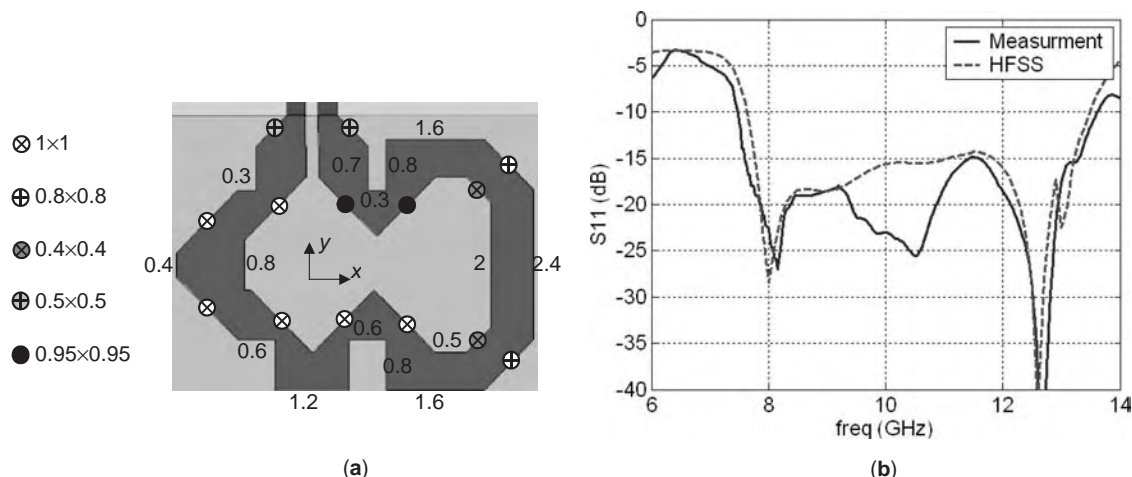


Figure 13. (a) Dimensions (in mm) of the modified phase shifter case 5 and (b) the measured computed return loss for the microstrip-fed printed Lotus through the phase shifter of case 5. (This figure is available in full color at <http://www.mrw.interscience.wiley.com/erfme>.)

reduce the effects of the surface waves. Three two-element arrays are designed: the normal case, a case with a gap in the substrate, and a case with both a slit in the ground plane and a gap in the substrate. Figure 17 presents the geometries of these three cases and compares their couplings. The gap improves the coupling from 8.5 to 14 GHz, while using both the slit and gap improves the coupling from 6.5 to 10.5 GHz and from 11.5 to 14 GHz. Since the area from 10.5 to 11.5 GHz is already less than -25 dB, the case with both the slit and gap is considered the best for these design parameters. The effect of the gap and slit on the radiation patterns of two elements is examined. Improvements are noticed in the gain and front-to-back ratio of the resulting radiation pattern. The gain increases from 7.2 dB for the normal case to 7.6 dB when using slit and gap, and the front-to-back ratio also improves from 17.5 to 20.5 dB. The second major source of coupling is the radiation coupling, which cannot be reduced in the x -directed array, whereas this is possible in the z -directed array by adding a metallic sheet in between the antenna elements to prevent the effect of the radiation from the

feedlines and the phase shifters. This is shown in Fig. 18, where the array geometries and the resulting couplings are shown. The metallic sheet improves the coupling in the range of 9.5 to almost 14 GHz; the gain improves from 8.5 to 9.3 dB, and the front-to-back ratio increases from 19.8 to 27.2 dB. However, it decreases the 3 dB beamwidth from 84° to 71° and from 63° to 56° in the E and H planes, respectively. This configuration also affects the radiation patterns for a two-element array in the x direction by increasing the gain from 7.2 to 8.5 dB and the front-to-back ratio from 17.5 to 21 dB. At the same time, it decreases the 3 dB beamwidth from 53° to 49° and from 129° to 103° in the E and H planes, respectively, which is considered an acceptable range for a two-element array.

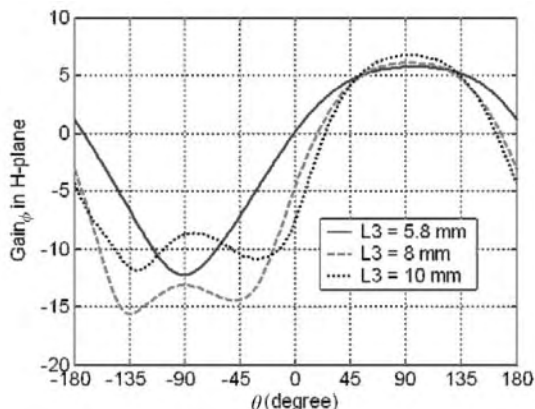


Figure 14. Effect of L_3 on the H plane copolarized field. (This figure is available in full color at <http://www.mrw.interscience.wiley.com/erfme>.)

CoPol ($E\phi$) – E Plane (xy)	●
XPol ($E\theta$) – E Plane (xy)	⊗
CoPol ($E\phi$) – H Plane (yz)	■
XPol ($E\theta$) – H Plane (yz)	⊗*

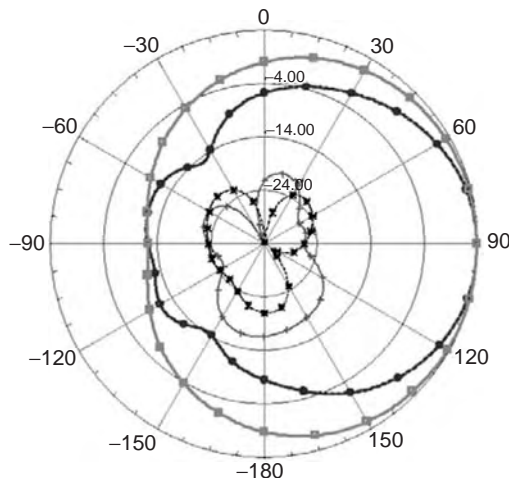


Figure 15. Radiation patterns at 10 GHz. (This figure is available in full color at <http://www.mrw.interscience.wiley.com/erfme>.)

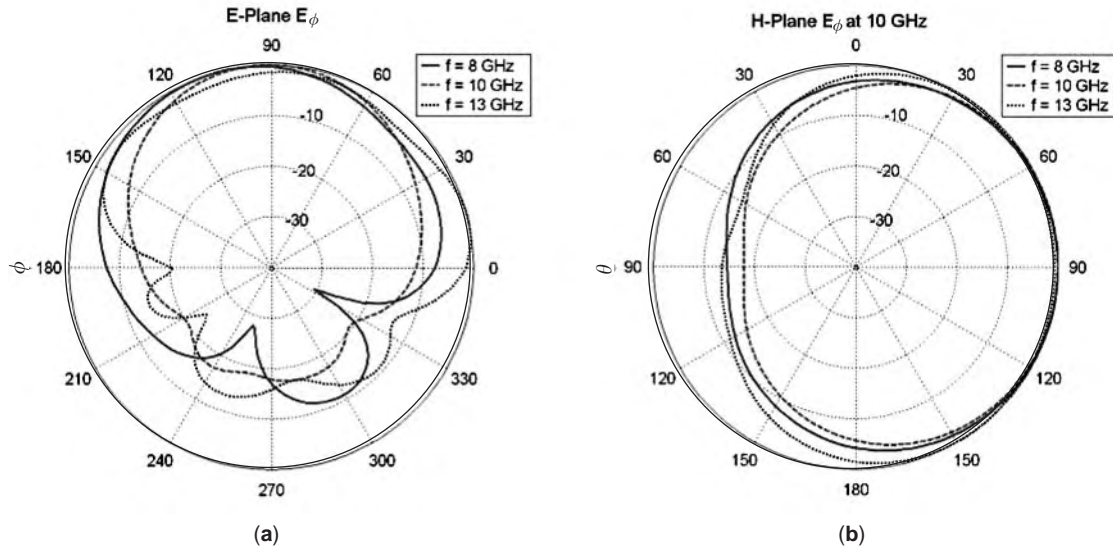


Figure 16. Comparison between the copolarized fields at 8, 10, and 13 GHz in the (a) *E* plane and (b) *H* plane. (This figure is available in full color at <http://www.mrw.interscience.wiley.com/erfme>.)

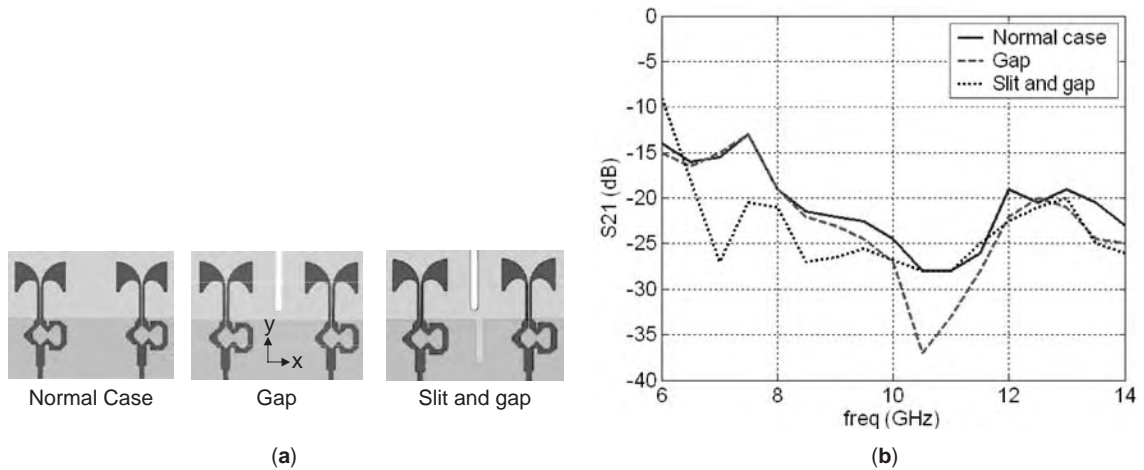


Figure 17. Antenna array configuration in the horizontal direction: (a) geometries; (b) computed coupling. (This figure is available in full color at <http://www.mrw.interscience.wiley.com/erfme>.)

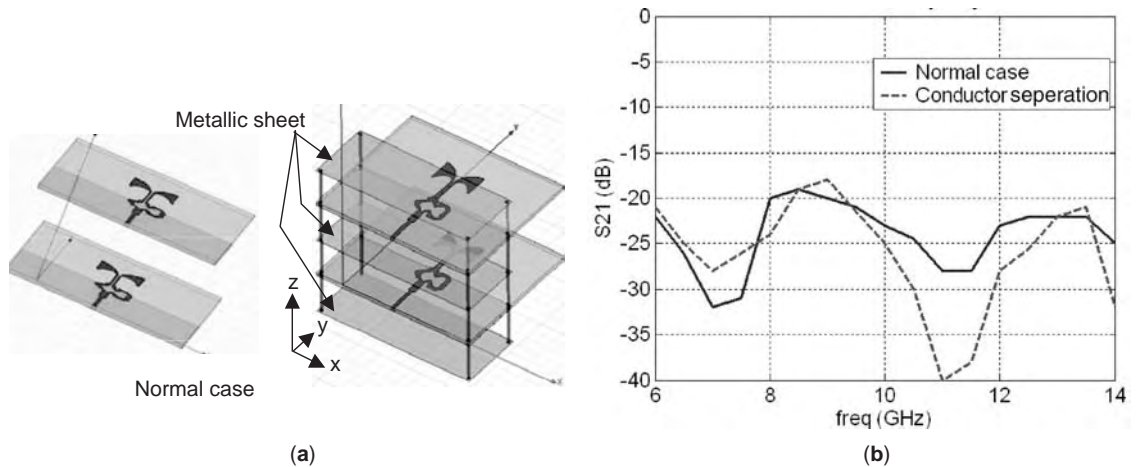


Figure 18. Antenna array configuration in the vertical direction: (a) geometries; (b) computed coupling. (This figure is available in full color at <http://www.mrw.interscience.wiley.com/erfme>.)

The ideal value of the center-to-center separation distance between elements in array environment (d) is free-space half-wavelength ($\lambda_0/2$) at the center frequency, which is 14.3 mm for an array of these elements. Much higher separation values will cause grating lobes, and much lower separation values will increase the array beamwidth. All the above mentioned two-element arrays are designed for d equal to 14 mm. Thus, the ratio of d/λ_0 for the frequency range 7.5–13.5 GHz ranges from 0.35 to 0.63, which is considered optimum for phased-array systems with the requirements of narrow beamwidth and low grating lobe within this wide range of frequencies.

To examine the maximum scanning angle, the radiation pattern of a 32-element array is analyzed at 10 GHz using the antenna design and visualization (ADV) software package [12] with Dolph–Chebyshev excitation factors calculated for 25 dB sidelobe level. The number 32 is considered for an array of total size less than 45 cm long. For an antenna in the x – y plane, the copolarized field E_ϕ is calculated for steering angles of 0° , 30° , 50° and 70° . Figure 19 shows E_ϕ in the E plane for an array along the x axis, while Fig. 20 shows E_ϕ in the H plane for an array along the z axis. The results in both figures show that the mainbeam of the antenna array starts to deteriorate when the steering angle approaches 70° .

Practical wideband arrays require wideband corporate feed networks to split and deliver the power to the array elements. Two designs are proposed for the microstrip feed network: design 1 and design 2, which are shown in Fig. 21 for a substrate of height = 0.635 mm and $\epsilon_r = 10.2$. In design 1, the power divider consists of two 50- Ω lines of width = 0.6 mm. The matching is obtained by using an impedance transforming line of length S and width D , and tapering the edges by 45° with a length of W , as shown in Fig 21a. In design 2, the power is divided through two 90- Ω branches of thickness = 0.1 mm, two 65- Ω impedance

transformers of thickness = 0.3 mm and length S , and a 50- Ω line of horizontal length L . The matching is obtained by controlling S and L , and tapering the edges 45° with a length of W . The parameters W , S , and L of the two designs are studied using the full-wave analysis of ADS Momentum to improve the return loss and transmission coefficient.

For design 1 with $L = 3$ mm and $S = 1.2$ mm, the effect of W is presented in Fig. 22, where improvement in S11 and S21 is observed as W increases from 0 to 0.9 mm. The effect of L is studied when $W = 0.9$ mm and $S = 1.2$ mm, and the results are presented in Fig. 23, where S is changed from 2.5 to 3.1 mm around the quarter-wavelength at 10 GHz. When increasing S , the null position shifts to lower frequencies. For best return loss at 10 GHz, S is chosen to be 2.75 mm. Finally, the effect of changing D from 0.8 to 1.2 mm is depicted in Fig. 24, with $W = 0.9$ mm and $S = 2.75$ mm. The value of D controls the return loss and transmission levels at the center frequency. The best values out of this analysis are $W = 0.9$ mm (1.5 times the feedline width), $S = 2.75$ mm ($\lambda_g/4$ at 10 GHz), and $D = 1.1$ mm (transformer characteristic resistance = 36 Ω). The average transmission coefficient is -3.2 dB (48%), while the return loss is less than -15 dB from 7 to 13 GHz, and -40 dB at 10 GHz.

For design 2 with $L = 3$ and $S = 1.2$ mm, the effect of W is presented in Fig. 25. As W increases from 0.6 to 0.9 mm, both return loss and transmission improve. Further increase in W results in improvement in the return loss level at the lower frequencies. Next, S is varied from 2.8 to 3.4 mm, where the operating band shifts to lower frequencies as S increases, as shown in Fig. 26. Figure 27 shows the effect of changing L from 0.8 to 1.4 mm, with $W = 0.9$ and $S = 3.2$ mm, where the operating band increases as L increases, but the return loss level at higher frequencies decreases.

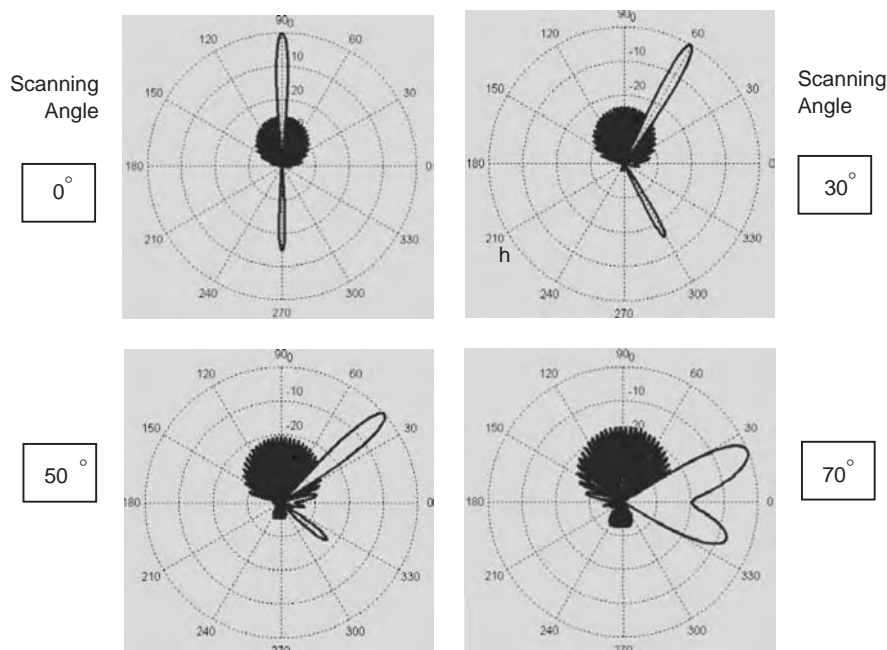


Figure 19. Mainbeam steering using 32-element array of Lotus antenna along the x axis. (This figure is available in full color at <http://www.mrw.interscience.wiley.com/erfme>.)

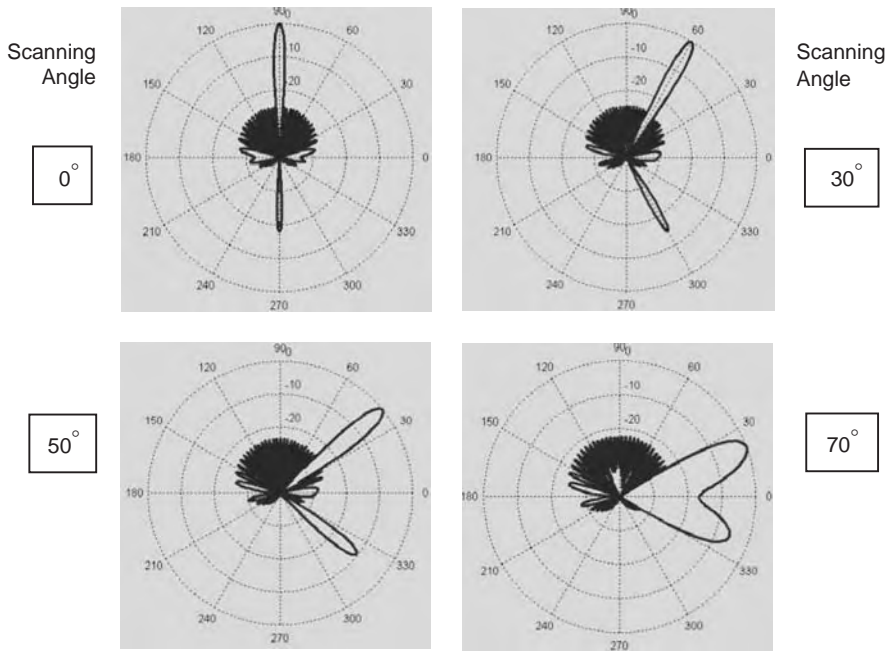


Figure 20. Mainbeam steering 32-element array of Lotus antenna along the z axis. (This figure is available in full color at <http://www.mrw.interscience.wiley.com/erfme>.)

The case of maximum bandwidth, with $W = 0.9$ mm, $S = 3.2$ mm, and $L = 1.4$ mm, is chosen for further study. To improve the return loss at higher frequencies, S is decreased from 3.2 to 3 mm, as shown in Fig. 28. In the final design $W = 0.9$ mm, $L = 1.4$ mm, and $S = 3$ mm, with an average return loss of -30 dB and a transmission coefficient of -3.16 dB from 8 to 13 GHz. Comparison between the two designs is shown in Fig. 29, where the second design has much wider bandwidth and almost constant transmission. However, accurate fabrication of this final design of the feeding network requires precision machining, due to the small thickness of the microstrip lines. With the available facilities, only the first design is fabricated and used to feed the printed Lotus antenna array.

Two 16-element arrays with one feed for 0° and 50° steering angles are built and measured. The 50° phase shift is obtained by decreasing the length of the feedline gradually, as shown in Fig 30a, and this introduces a progressive time delay that is equivalent to the progressive phase shift that steers the mainbeam 50° . Figures 30b and 30c show the measured return losses and copolarized patterns in the E plane for the two arrays. The bandwidths for the 0° and 50° cases are almost the same, and equal to

about 71%. The sidelobe level for the 50° array is around -12.5 dB with uniform excitation, but this can be significantly decreased by using Dolph–Chebyshev excitations for amplitude tapering.

To conclude this part, the printed Lotus antenna fed by a microstrip line through a modified phase shifter has a wide bandwidth of 55.5% relative to -15 dB and 60% relative to -10 dB. In addition to being very small in size, the antenna exhibits stable far-field radiation characteristics over the entire operating band with relatively high gain, low cross-polarization, very wide beamwidth, and high front-to-back ratio. The antenna arrays investigated have low coupling and high scanning capabilities, while the 16-element array with a feed network yielded 71% impedance bandwidth.

4. RECONFIGURABLE ANTENNAS

Antenna system performance depends on the parameters of the radiating elements, such as the size, shape, and position of each radiating element. Modifying or reconfiguring the parameters of these radiating elements enables

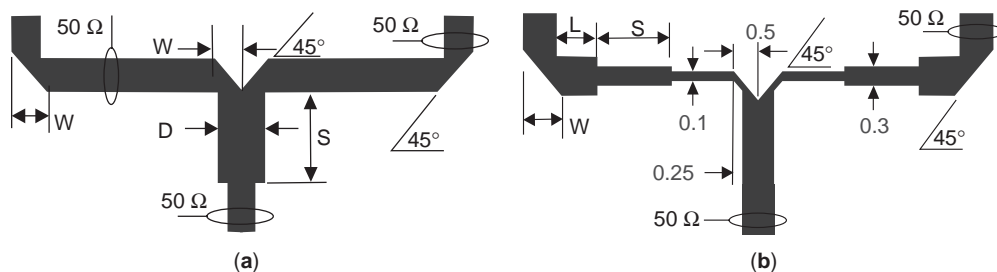


Figure 21. Proposed designs for microstrip feed network: (a) design 1; (b) design 2.

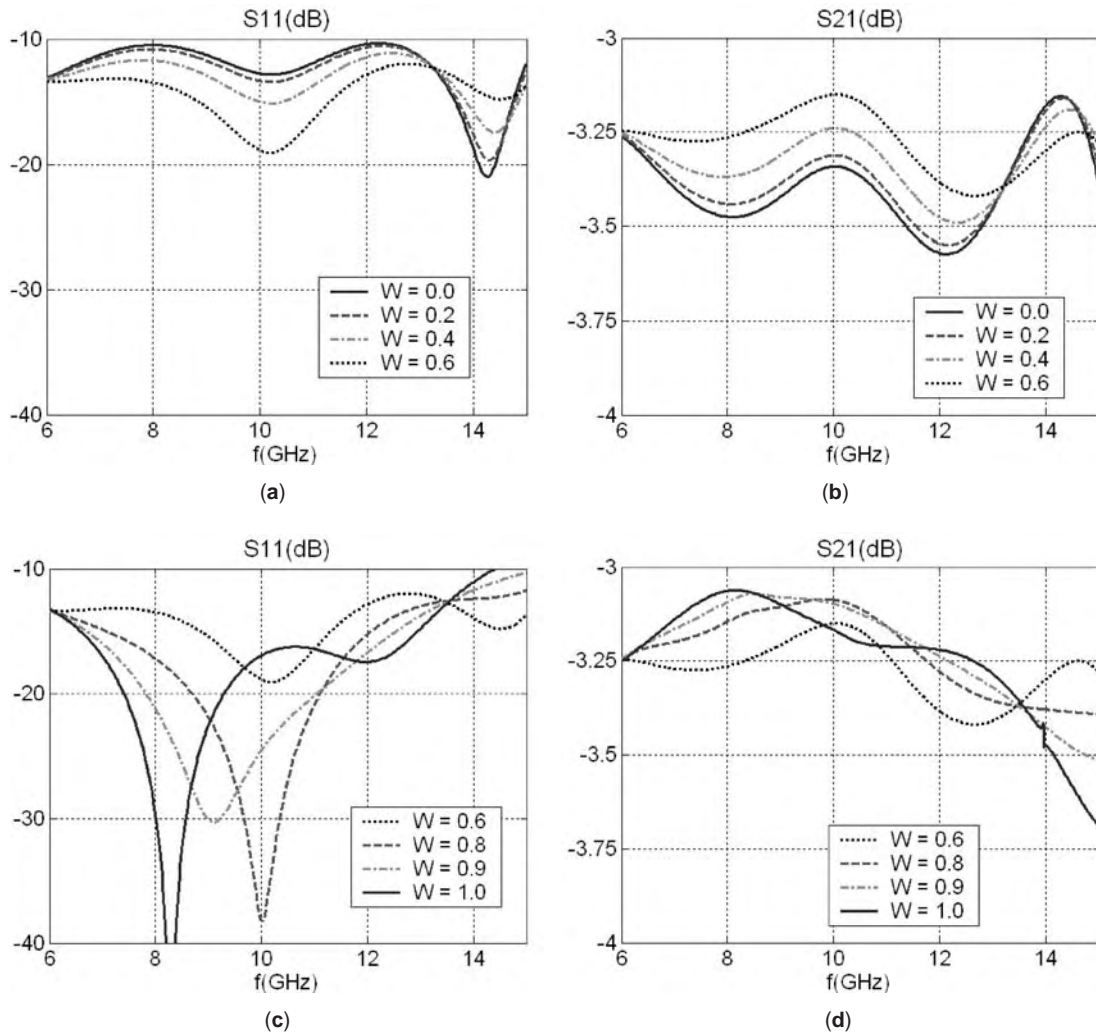


Figure 22. Effect of W on the return loss (a,c) and the transmission (b,d), for design 1. (This figure is available in full color at <http://www.mrw.interscience.wiley.com/erfme>.)

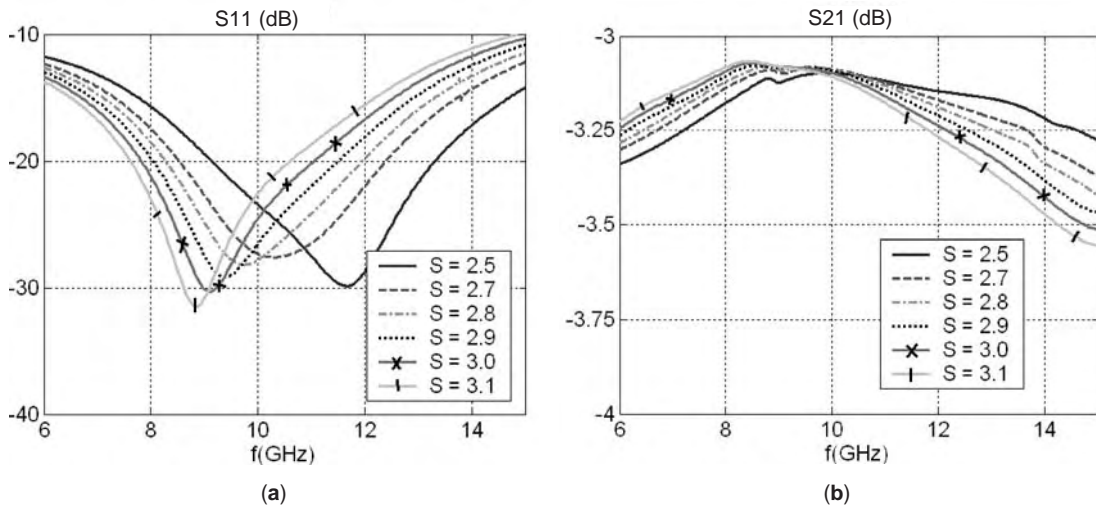


Figure 23. Effect of S on the return loss (a) and the transmission (b) for design 1. (This figure is available in full color at <http://www.mrw.interscience.wiley.com/erfme>.)

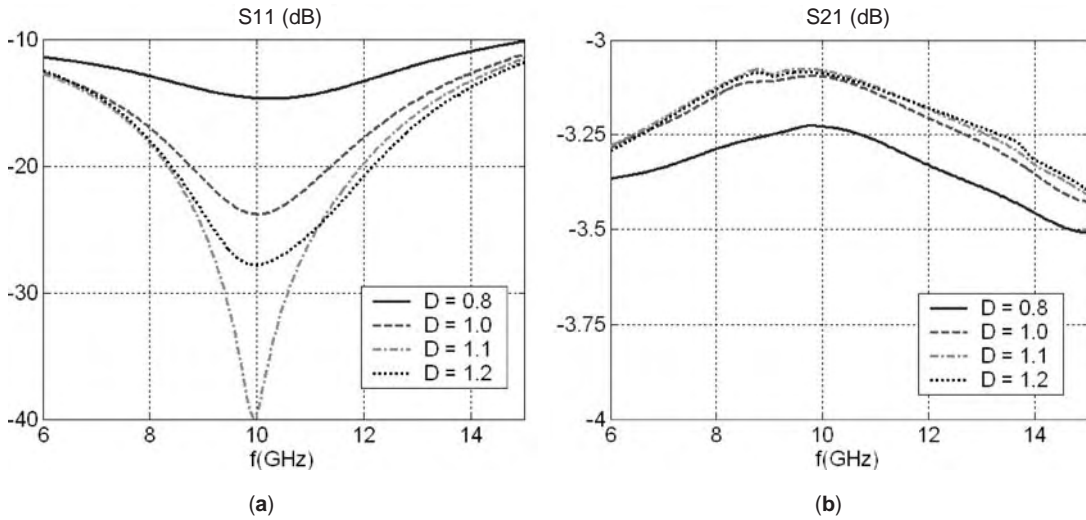


Figure 24. Effect of D on the return loss (a) and the transmission (b) for design 1. (This figure is available in full color at <http://www.mrw.interscience.wiley.com/erfme>.)

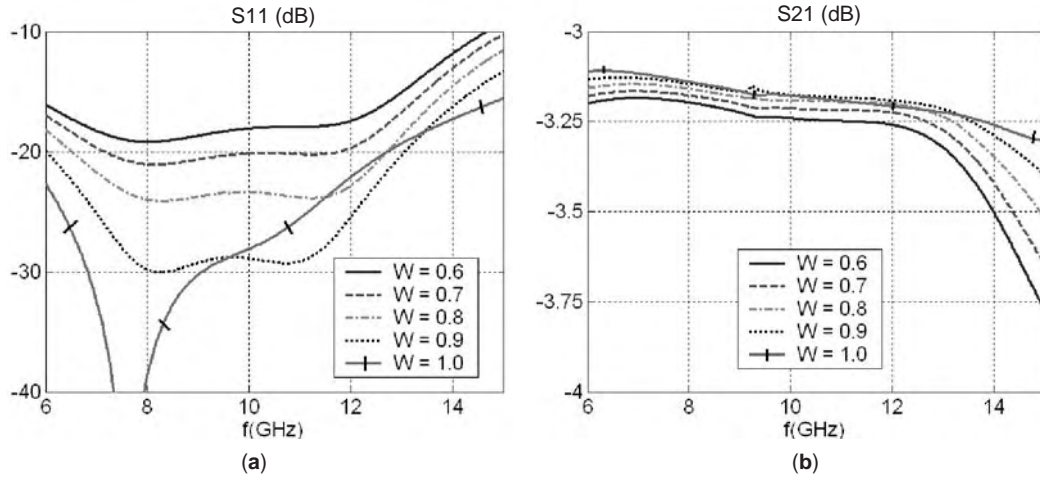


Figure 25. Effect of W on the return loss (a) and the transmission (b) for design 2. (This figure is available in full color at <http://www.mrw.interscience.wiley.com/erfme>.)

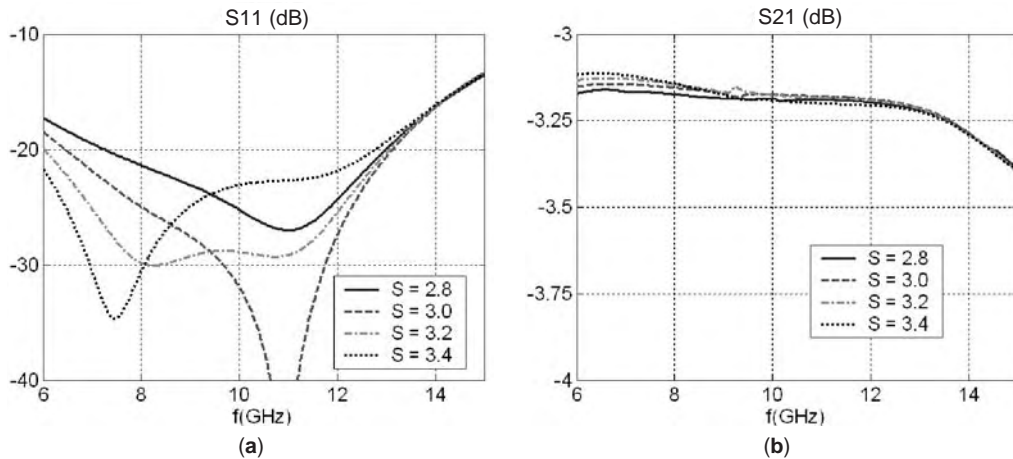


Figure 26. Effect of S on the return loss (a) and the transmission (b) for design 2. (This figure is available in full color at <http://www.mrw.interscience.wiley.com/erfme>.)

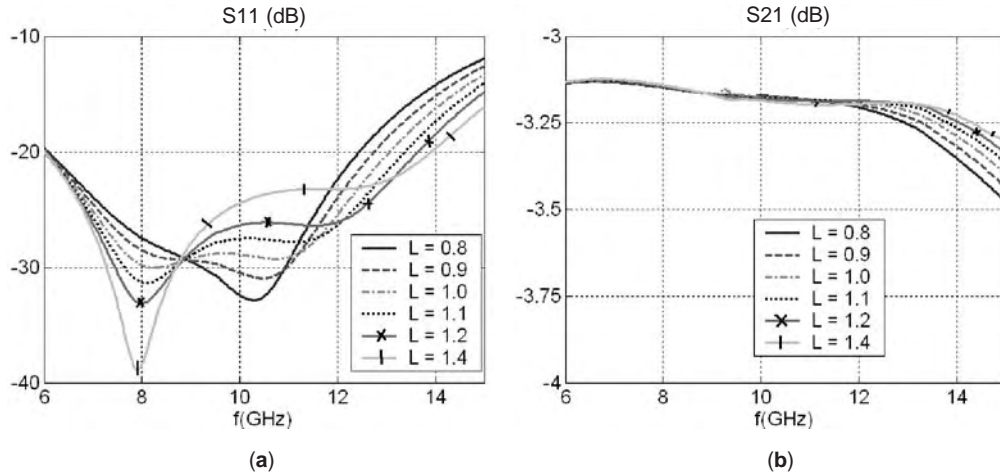


Figure 27. Effect of L on the return loss (a) and the transmission (b) for design 2. (This figure is available in full color at <http://www.mrw.interscience.wiley.com/erfme>.)

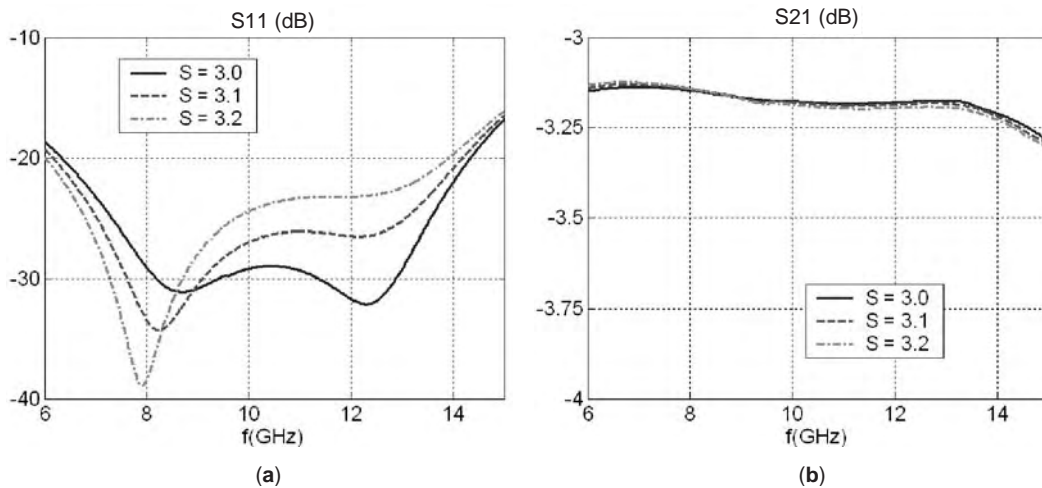


Figure 28. Effect of S on the final design return loss (a) and the transmission (b). (This figure is available in full color at <http://www.mrw.interscience.wiley.com/erfme>.)

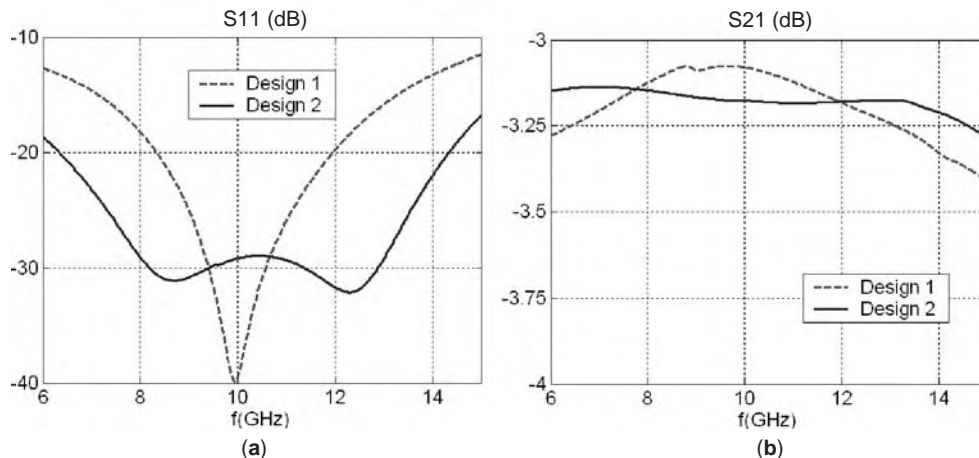


Figure 29. Comparison between the return loss (a) and the transmission coefficient (b) of the final cases of designs 1 and 2. (This figure is available in full color at <http://www.mrw.interscience.wiley.com/erfme>.)

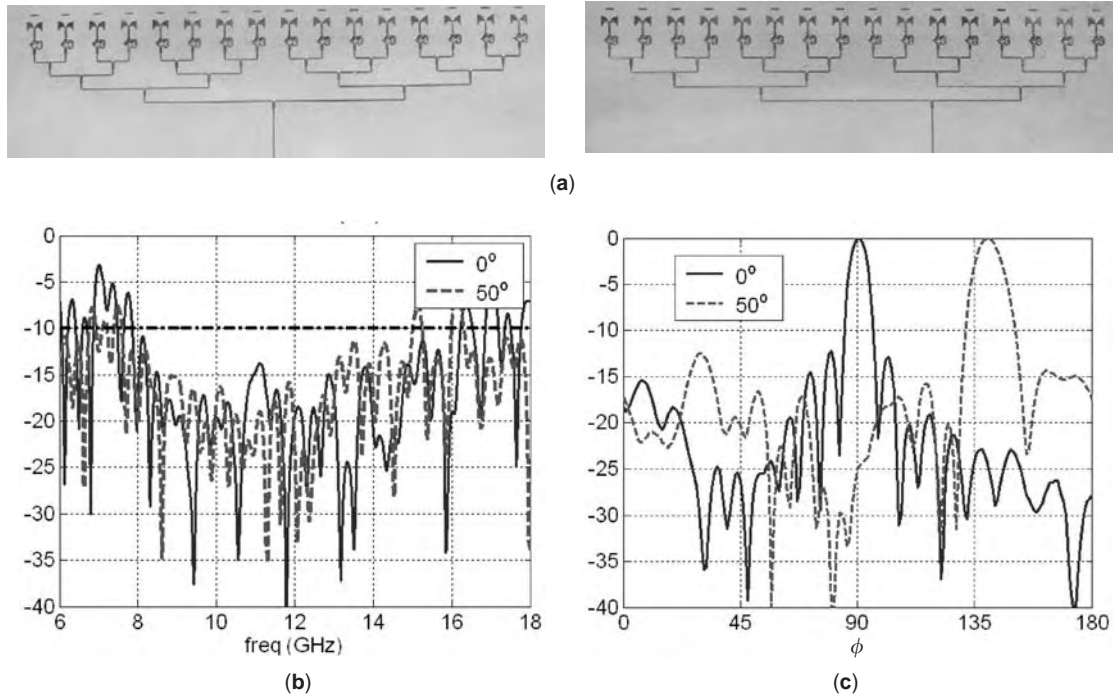


Figure 30. Prototypes of 16-element arrays for 0° and 50° steering angles (a), their measured return loss (b), and measured copolarized patterns in the E plane (c). (This figure is available in full color at <http://www.mrw.interscience.wiley.com/erfme>.)

one to use the same antenna for multiple functions at different frequencies or occasions. The conventional method for achieving reconfigurability is to allow reconfigurability between the various predefined conducting or slot regions by using multiple switches to modify the size or shape of the antenna radiating element. Thus, in order to have an additional degree of freedom for enhancing the antenna performance or to tailor its radiation characteristics for a specific application, it is desirable to have dynamic and reliable reconfigurable dimensions. This task can be achieved by using switches, provided these switches and their bias feeding network do not interfere with the antenna performance.

Conventional semiconductor switches are common components in today's microwave systems, and, depending on size and construction, they exhibit parasitic characteristics. The resulting high insertion loss of these switches, ranging from 1 dB to several decibels at millimeter-wave frequencies, is a serious issue for many applications. There is a crucial need for new switch technologies to address the loss issue for next-generation communication and phased-array systems.

The emerging microelectromechanical switch (MEMS) technology has attracted increased interest due to excellent switching characteristics over an extremely wide frequency band. Many RF MEM switching topologies have been reported, and they all show superior characteristics compared with their semiconductor-based counterparts. The low insertion loss, high isolation, and fast switching of MEM switches have been one of the most attractive devices for reconfigurable antennas and for developing wideband phase shifters for antenna arrays. These switches

provide circuits with reduced insertion loss for switching between different linewidths. With the loss reduction in switching components, smaller amplification is required or higher overall gain for the antenna system will be attained. The cost, weight, and heat dissipation problems can also be greatly reduced which improves the entire system efficiency.

A MEMS-switched reconfigurable multiband antenna is one that can be dynamically reconfigured within a few microseconds to serve different applications at drastically different frequency bands. In this article, we do not focus on the development of the MEMS switches themselves [13]. Rather, we use them as ideal control elements that are in an open or closed configuration in a reconfigurable antenna.

The concept of a frequency-reconfigurable rectangular ring slot antenna fed by slotlines or CPW is presented in Ref. 14. A reconfigurable patch antenna is obtained [15] by inserting slits at the nonradiating edges of the patch. A reconfigurable Yagi antenna has been presented [16] to operate at 2.4 and 5.78 GHz for wireless communications.

In this section we present multiple frequency-reconfigurable rectangular microstrip and slot antennas fed by a microstrip line or a coplanar waveguide (CPW) feedline. The reconfiguration for the microstrip antennas is carried out by connecting or disconnecting (switching on or off) appropriate rectangular strips surrounding the patch antenna to model the MEM switches. The shape and number of these strips along with the switching state and position are used to control the operating frequency of the antenna without changing the feeding mechanism. A

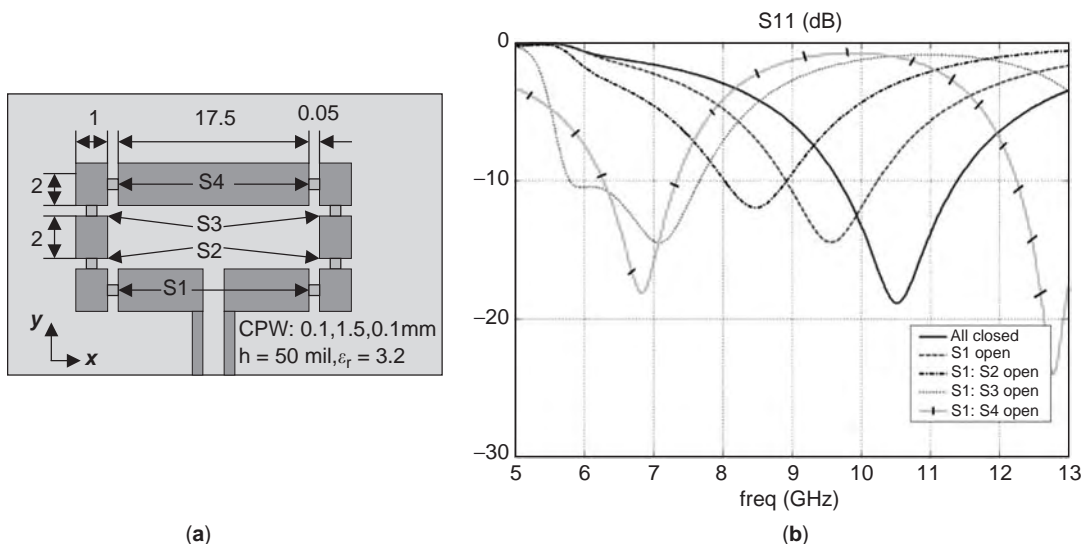


Figure 31. Reconfigurable CPWA (a) geometry and (b) return loss for different states of the switches. (This figure is available in full color at <http://www.mrw.interscience.wiley.com/erfme>.)

similar procedure is adapted for slot-type antennas. Full-wave EM simulations using Agilent’s Momentum have been carried out to demonstrate the feasibility of the proposed configurations. The procedure for designing such reconfigurable antennas is discussed, and experimental verification at X band is also conducted for ideal switching configurations. Detailed simulation results are presented for communication systems operating in the C and X frequency bands.

4.1. Reconfigurable Coplanar Patch Slot Antenna

A coplanar patch slot antenna (CPWA) is constructed from a rectangular metallic patch surrounded by a slot that separates the patch from the ground plane. The geometry and dimensions of this antenna along with the four pairs of switches, S_1 – S_4 , that perform the reconfiguration process of the antenna are shown in Fig. 31a, while the mechanism of controlling the return loss by these switches is indicated in the legend of Fig. 31b. Figure 32 shows the

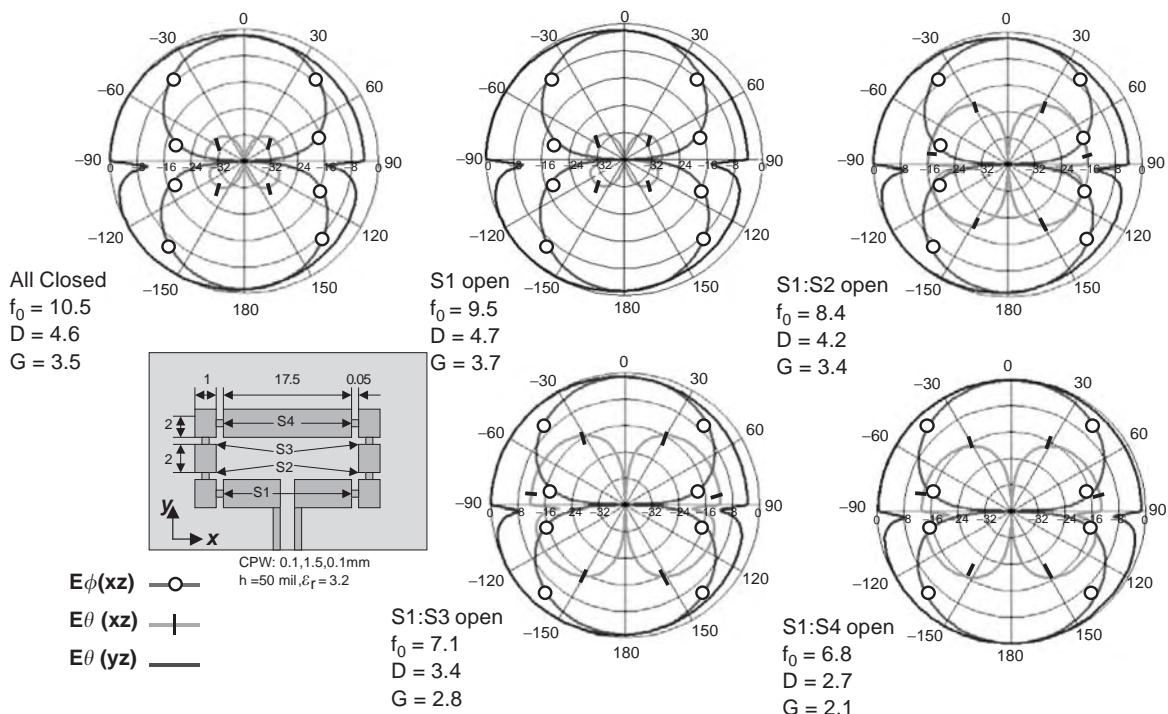


Figure 32. The radiation patterns of the reconfigurable CPWA at the operating frequencies. (This figure is available in full color at <http://www.mrw.interscience.wiley.com/erfme>.)

radiation pattern and lists the directivity D and gain G in decibels at the operating frequency f_0 for each configuration. The reconfiguration process here depends on transforming the antenna type from a slot dipole to a CSPA rather than changing the antenna width. When all switches are closed or only S_1 is open, the antenna acts as a slot dipole. The dominant contribution in these two cases comes from the main slot dipole in the presence of neighboring parasitic rectangular slots. The operating frequencies for these two cases are 10.5 and 9.5 GHz with bandwidths of 17% and 14%, respectively. The slot dipole length is around $0.82\lambda_g$, which is the resonance length of the slot dipole [17]. Very low cross-polarization is obtained, as shown in Fig. 32, because no vertical currents exist. When the other switches are opened one after another, the physical length of the slot antenna increases and, consequently, it operates at lower frequencies (8.4, 7.1, and 6.8 GHz), as shown in Fig. 31b. The bandwidth for these three cases is 10%, 23%, and 14%, respectively. Although the maximum bandwidth of the antenna in any of the five states is 23%, the usable bandwidth using the MEM switches extends from 5.7 to 11.4 GHz, which is equivalent to a 67% bandwidth. This is 3 times the maximum bandwidth of each individual case.

The cross-polarization level increases when S_2 and S_3 are opened because the vertical path of the magnetic currents is increased, which contributes to the cross-polarized field component. As shown in Fig. 32, the copolarized fields are almost constant for all cases, providing stable radiation characteristics at different operating frequencies. The maximum gain is found to decrease as the operating frequency increased. As shown in the figure, within the 6.8–10.5 GHz band the gain drops by 1.4 dB for this configuration.

4.2. Reconfigurable Printed Monopole Antenna

The printed monopole antenna presented here is designed for wideband applications. Its operating frequency depends mainly on its vertical length, which should be around $\lambda_g/4$, while the bandwidth depends on its width. Therefore, changing the vertical length would allow for controlling the operating frequency. The geometry and dimensions of this antenna along with four pairs of switches, S_1 – S_4 , that perform the reconfiguration process are shown in Fig. 33a, while Fig. 33b shows the return loss variation for five states of the switches. When the antenna vertical length increases using the switches, the operating band changes from 6–13.5 GHz to 5–11.3 GHz, 4.6–10.3 GHz, 4.2–9.6 GHz, and 3.9–7.1 GHz, with the corresponding bandwidths equal to 77%, 77%, 77%, 78%, and 58%, respectively. Therefore, the usable bandwidth using the MEM switches for this antenna extends from 3.9 to 13.4 GHz, which is equivalent to 110% bandwidth.

The radiation patterns shown in Fig. 34 are calculated for the case when S_1 – S_3 are closed (metal) at different frequencies within the entire operating band. Almost stable copolarized field patterns are obtained, while the highest cross-polarization level is -14 dB at 9 GHz.

4.3. Reconfigurable Slot Dipole Antenna

The geometry and dimensions of the CPW-fed slot dipole antenna with four pairs of switches, S_1 – S_4 , that perform the reconfiguration process are shown in Fig. 35a, while Fig. 35b shows the return loss variation for five states of the switches, and the corresponding radiation pattern, directivity, and gain at the center operating frequency for each case are shown in Fig. 36. The reconfiguration process for this antenna is obtained by changing the antenna

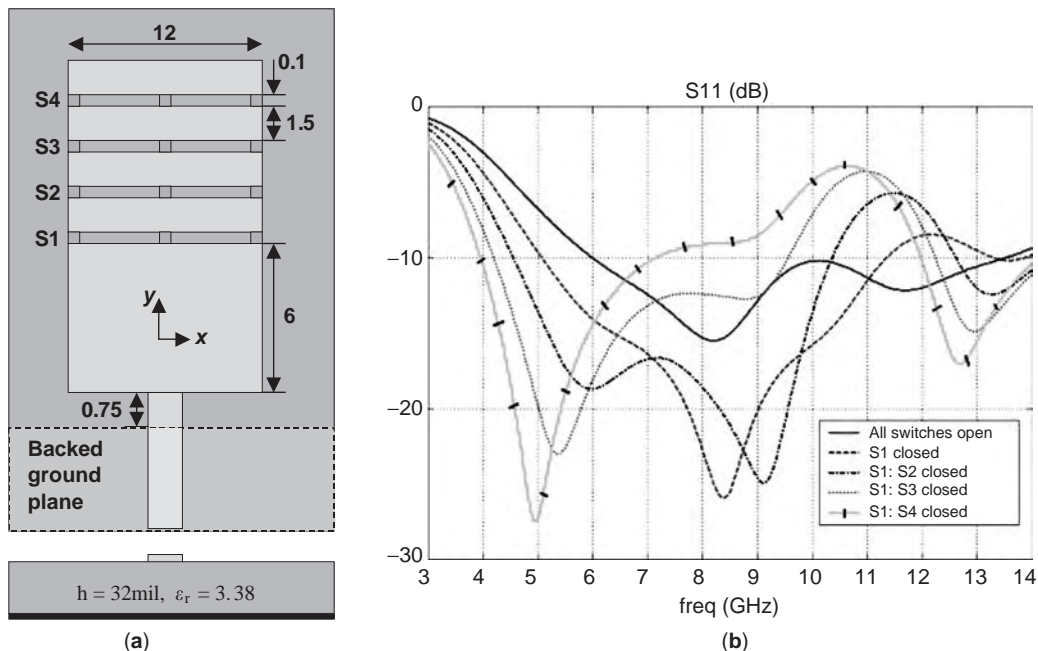


Figure 33. Reconfigurable printed monopole antenna (a) geometry and (b) return loss for different states of the switches. (This figure is available in full color at <http://www.mrw.interscience.wiley.com/erfme>.)

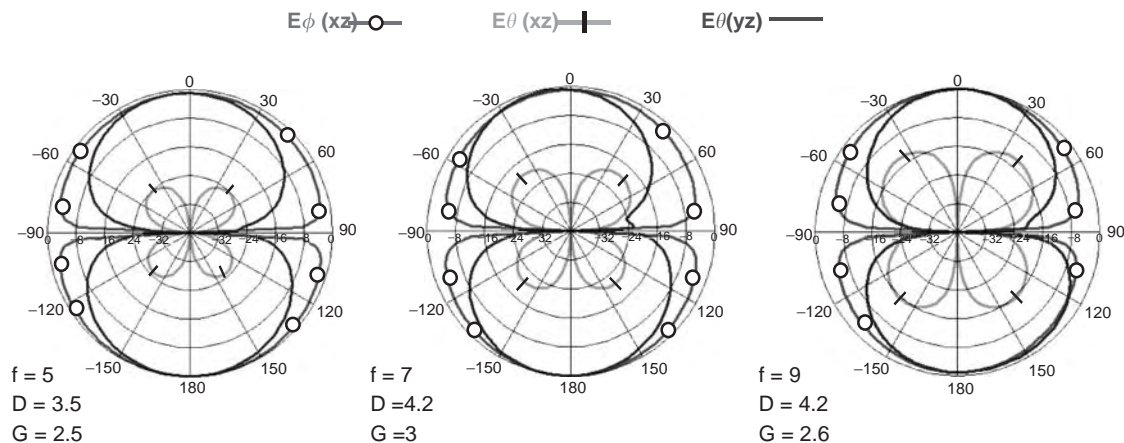


Figure 34. The radiation patterns of reconfigurable printed monopole antenna with S_1 – S_3 closed. (This figure is available in full color at <http://www.mrw.interscience.wiley.com/erfme>.)

width, which is approximately equal to $0.82\lambda_g$ [17]. The original width is 20 mm, and when a pair of switches is opened, the width increases by 2 mm to 28 mm for the case with all switches open. As shown in Fig. 35b, when the antenna width increases using the switches, the center operating frequency decreases from 11 GHz to 9.8, 8.8, 8.0, and 7.3 GHz, and the corresponding bandwidths change from 23% to 22%, 20.5%, 20%, and 20%, respectively.

This design has a stable radiation pattern and very low cross-polarization for all configurations presented, with an almost stable gain of 2.9 dB as shown in Fig. 36. It is also noticeable that the cross-polarization level decreases as the antenna width increases, because the antenna's of the vertical dimension–horizontal dimension (width) ratio decreases as its width increases.

The five configurations of the slot dipole antenna were fabricated, and their return loss and input impedance were measured using the network analyzer HP 8510C. The ground plane is truncated at 3 cm away from the slot antenna edges. A sample picture of one of these antennas

and the measured return loss are shown in Fig. 37. The measured operating frequency decreases from 10.9 to 9.8, 9, 8, and 7.5 GHz, which is very close to the simulation results. However, the bandwidth changes from 35% to 23.5%, 22.5%, 22.5% and 22.4%, which are slightly wider than the bandwidths calculated from the simulation results. A comparison between the simulation results and measurements for the cases with all switches closed, S_1 and S_2 open, and S_1 – S_4 open is shown in Fig. 38, where a very good agreement is observed. Although the maximum bandwidth of any of the five cases of this antenna is 35%, the usable measured bandwidth using the MEM switches extends from 6.6 to 13 GHz, which is equivalent to 65% bandwidth.

5. CONCLUSIONS

This article presents two novel antenna designs and a study of reconfigurable antennas for wideband applications.

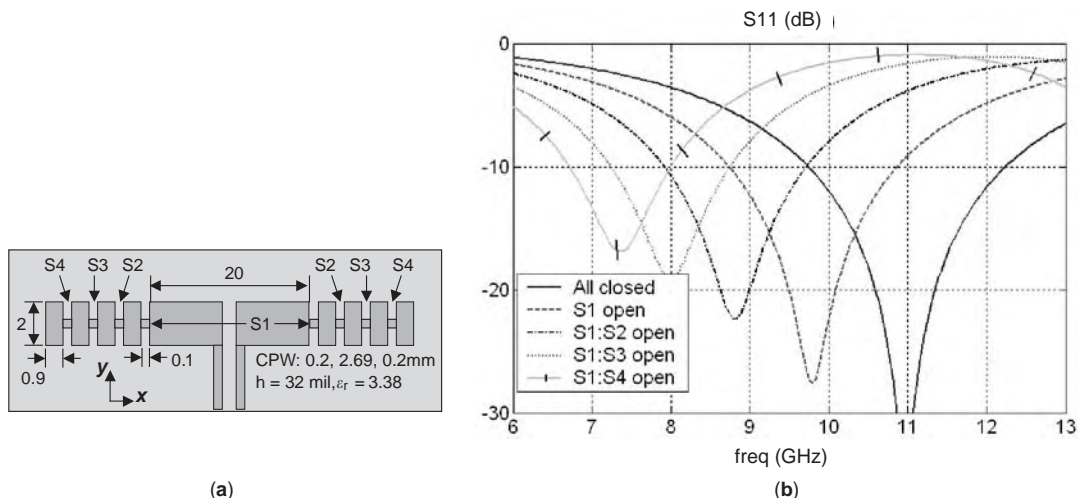


Figure 35. Reconfigurable slot dipole antenna (a) geometry and (b) return loss for different states of the switches. (This figure is available in full color at <http://www.mrw.interscience.wiley.com/erfme>.)

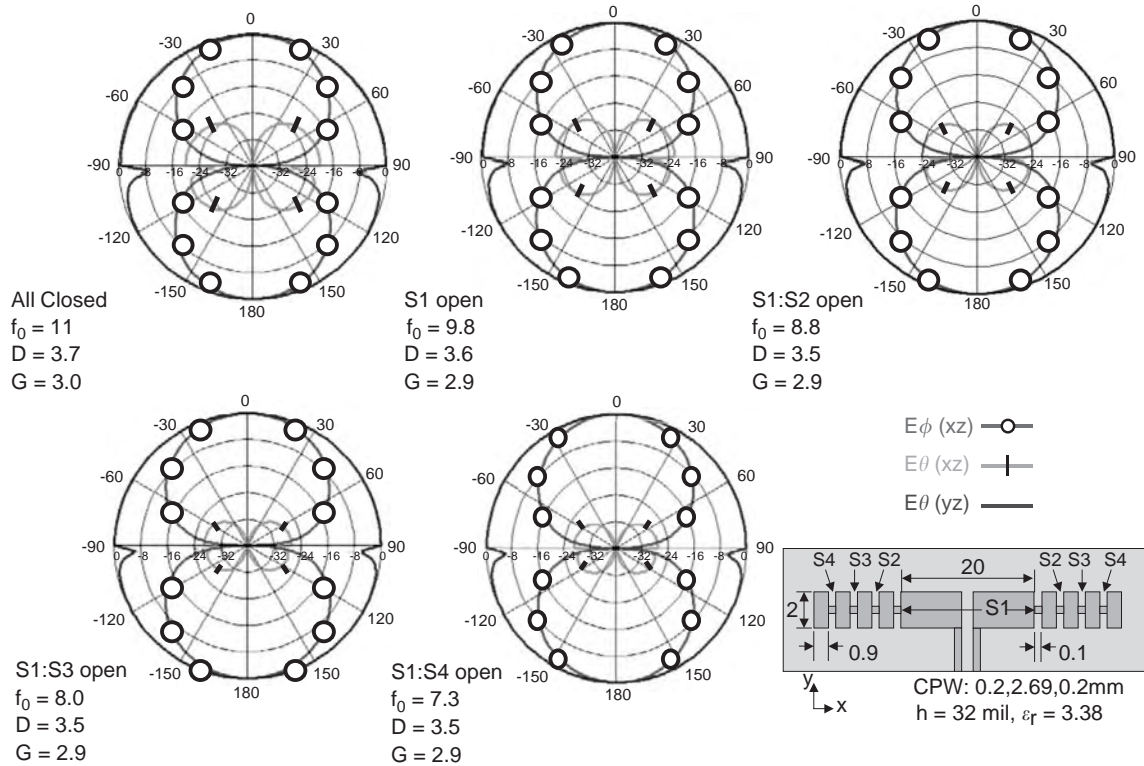


Figure 36. The radiation patterns of the reconfigurable slot dipole antenna at the operating frequencies. (This figure is available in full color at <http://www.mrw.interscience.wiley.com/erfme>.)

The presented slot Lotus antenna is a good candidate for ultrawideband applications. The printed Lotus antenna is also an excellent candidate for wideband phased-array systems because of its small size, wide bandwidth, low return loss level over the entire operating band, low coupling between elements, stable radiation patterns over

the entire operating band, and wide scanning capabilities. Finally, antenna reconfiguration using ideal switches shows great promise in controlling the antenna operating band without changing one of the antenna dimensions. This technique permits the antenna to operate at different frequency bands and, consequently, it increases the usable

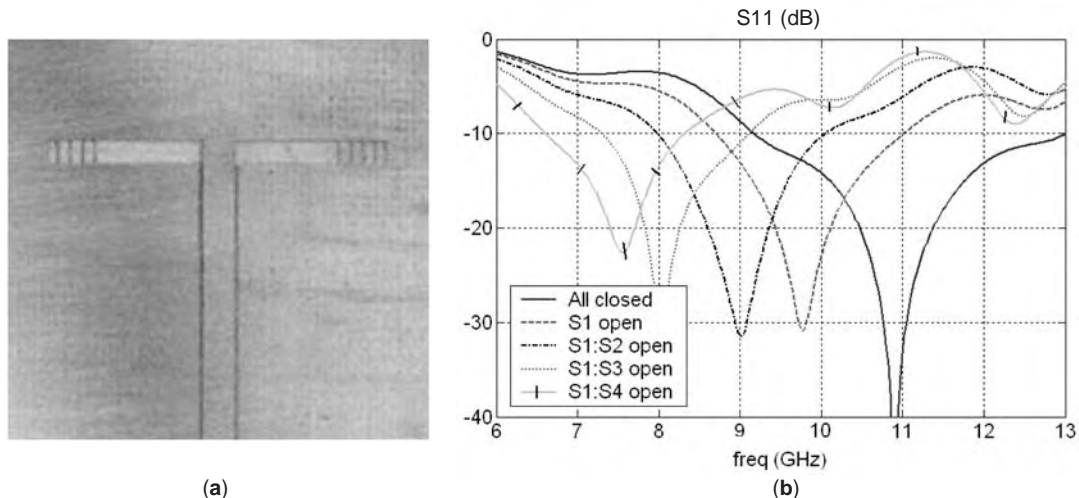


Figure 37. Reconfigurable slot dipole antenna (a) prototype and (b) measured return loss for different states of the switches. (This figure is available in full color at <http://www.mrw.interscience.wiley.com/erfme>.)

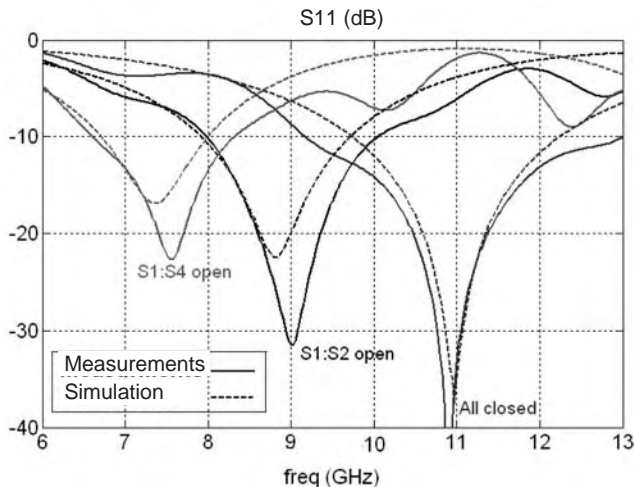


Figure 38. Comparison between the computed and measured return loss for the cases of the printed slot dipole with all switches closed, S_1 – S_2 open, and S_1 – S_4 open. (This figure is available in full color at <http://www.mrw.interscience.wiley.com/erfme>.)

bandwidth of the antenna to further expand the wideband or multiband operation of printed and slot antennas.

BIBLIOGRAPHY

1. A. A. Eldek, A. Z. Elsherbeni, C. E. Smith, and K.-F. Lee, Wideband rectangular slot antenna for personal wireless communication, *IEEE Anten. Propag. Mag.* **44**(5):146–155 (Oct. 2002).
2. A. A. Eldek, A. Z. Elsherbeni, C. E. Smith, and K.-F. Lee, Wideband planar slot antennas, *Appl. Comput. Electromagn. Soc. (ACES) Newsle.* **19**(1):35–48 (March 2004).
3. A. A. Eldek, A. Z. Elsherbeni, and C. E. Smith, *Design of Wideband Triangle Slot Antennas with Tuning Stub*, Electromagnetic Wave Monograph Series, Progress in Electromagnetic Research (PIER 48), (chief editor: J. A. Kong), vol. 48, 233–248, 2004.
4. A. A. Eldek, A. Z. Elsherbeni, and C. E. Smith, *Characteristics of Bow-Tie Slot Antenna with Tapered Tuning Stubs for Wideband Operation*, Progress In Electromagnetics Research (PIER 49), (chief editor: J. A. Kong), vol. 49, 53–69, 2004.
5. A. A. Eldek, A. Z. Elsherbeni, and C. E. Smith, Wideband Microstrip Fed Printed Bow-Tie Antenna for Phased Array Systems, *J. Microwave Opt. Technol. Lett.* **43**(2):123–126 (Oct. 2004).
6. N. Kaneda, Y. Qian, and T. Itoh, A broad-band microstrip-to-waveguide transition using quasi-Yagi antenna, *IEEE Trans. Microwave Theory Tech.* **47**(12):2562–2567 (Dec. 1999).
7. G. Y. Chen and J. S. Sun, A printed dipole antenna with microstrip tapered balun, *Microwave Opt. Technol. Lett.* **40**(4):344–346 (Feb. 2004).
8. C. W. Chiu, Coplanar-waveguide-fed uniplanar antenna using a broadband balun, *Microwave Opt. Technol. Lett.* **40**(1):70–73 (Jan. 2004).
9. W. Deal, N. Kaneda, J. Sor, Y. Qian, and T. Itoh, A new quasi-Yagi antenna for planar active antenna arrays, *IEEE Trans. Microwave Theory Tech.* **48**(6):910–918 (June 2000).

10. N. Kaneda, W. Deal, Y. Qian, R. Waterhouse, and T. Itoh, A broad-band planar quasi-Yagi antenna, *IEEE Trans. Antennas Propag.* **50**(8):1158–1160 (Aug. 2002).
11. L. G. Maloratsky, Reviewing the basics of microstrip lines, *Microwaves RF Mag.* 79–88 (March 2000).
12. A. Z. Elsherbeni and M. J. Inman, Antenna design and radiation pattern visualization, *J. Appl. Comput. Electromagn. Soc. (ACES)* (special issue on ACES 2003 Conference, Part I) 26–32 (Nov. 2003).
13. W. H. Weedon, W. J. Payne, and G. M. Rebeiz, MEMS-switched reconfigurable antennas, *Proc. IEEE Antennas Propagation Society Int. Symp.*, 2001, Vol. 3, pp. 654–657.
14. K. C. Gupta, J. Li, R. Ramadoss, and C. J. Wang, Design of frequency-reconfigurable rectangular slot ring antenna, *Proc. IEEE Antennas Propagation Society Int. Symp.*, Salt Lake City, UT, 2000, Vol. 1, p. 326.
15. S. Xiao, B. Z. Wang, and X. S. Yang, A novel frequency-reconfigurable patch antenna, *Microwave Opt. Technol. Lett.* **36**(4):295–297 (Feb. 2003).
16. P. F. Wahid, M. A. Ali, and B. C. Deloach, A reconfigurable Yagi antenna for wireless communications, *Microwave Opt. Technol. Lett.* **140**(2):140–141 (July 2003).
17. A. A. Eldek, A. Z. Elsherbeni, C. E. Smith, and K.-F. Lee, Wideband slot antennas for radar applications, *Proc. 2003 IEEE Radar Conf.* Huntsville, AL, May 2003, pp. 79–84.

WIRELESS COMMUNICATIONS SYSTEMS

ANA GARCÍA ARMADA
 JAVIER RAMOS LÓPEZ
 FRANCISCO J. GONZÁLEZ
 SERRANO
 Universidad Carlos III de
 Madrid, Madrid, Spain

1. INTRODUCTION

The birth of wireless communications systems can be traced back to G. Marconi's experiments to demonstrate the use of radio to contact with ships in the English Channel in 1897. Since then, wireless communications systems have experienced a tremendous evolution, and their use has spread throughout the world.

A brief historical view of the evolution of wireless communications can help us understand the impact of these communications systems in our lives nowadays. After Marconi's experiments, the first practical communication system involving vehicles was deployed by the police of Detroit (USA) at the end of the 1920s. This very first mobile network supported only unidirectional links (from central station to mobile terminals) and was based on amplitude modulation (AM). This unidirectional system was soon improved with bidirectional capability. In 1934 more than 200 police radio systems had been adopted for public safety in the United States, all based in amplitude modulation.

Because of the AM modulation characteristics, vehicle ignition noise was the factor that limited the quality of these early systems. In 1935, E. Armstrong demonstrated frequency modulation (FM) for the first time and, since then, FM became the preferred modulation technique for wireless applications.

After the remarkable improvement in manufacturing and miniaturization achieved during World War II, the number of mobile users experienced an enormous increase, and the main characteristics of wired telephony were introduced in wireless systems. Consequently these early-deployed systems began to saturate the spectrum and the need for more efficient planning of wireless communications systems was identified.

The solution was found during the 1950s and 1960s in AT&T Bell Labs and received the name of *cellular radio-telephony*. The main idea behind the cellular theory, as will be explained in Section 2 of this article, is the reuse of frequencies throughout the area of deployment of a given system. Technology was not ready to implement the cellular concept until the late 1970s.

The first commercial cellular telephone systems were those deployed by the Japanese Nippon Telephone and Telegraph (NTT) Company in 1979, the Nordic Mobile Telephone (NMT) system developed in 1981, and the U.S. Advanced Mobile Phone System (AMPS) implemented in 1983. The European Total Access Cellular System (ETACS) was deployed in 1985 and is virtually identical to AMPS.

These first-generation analog cellular systems were substituted by the second generation of digital cellular systems. In Europe, the different first-generation cellular systems were incompatible with each other because of the different frequency bands and protocols being used. This fact motivated the creation of a special group within CEPT (European Conference of Postal and Telecommunications Administrations) that received the name of GSM (Special Group for Mobile communications). The outcome of the GSM group gave birth to the first pan-European digital cellular system. The GSM standard was first deployed in 1990 using the 900-MHz band and it is gaining worldwide acceptance as the first digital cellular system with modern network features.

The U.S. Digital Cellular (USDC) standard was adopted as a means of increasing by 3 the capacity of AMPS in 1991. In Japan, the Pacific Digital Cellular (PDC) standard or Japanese Digital Cellular (JDC), very similar to the USDC, was adopted.

After the digital revolution in wireless communications, the need of what has been called *personal communication systems* (PCS) has arisen. The idea behind the term *personal communications* is that “anyone [should] be able to communicate anytime and anywhere.” Personal communication systems, also called *personal communication networks* (PCN), are being deployed above 1800 MHz using, among other standards, extended versions of GSM.

Both USDC and GSM are TDMA (time-division multiple-access) systems. A second-generation cellular system based in CDMA (code-division multiple access) was deployed by the U.S. company Qualcomm in 1993 and adopted as an Interim Standard (IS-95).

None of the systems described above has a worldwide projection. The idea of producing an enhanced worldwide standard led the ITU (International Telecommunications Union) to promote the creation of the family of standards named IMT-2000 (International Mobile Telecommunications for the year 2000). This IMT-2000, formerly called FPLMTS (future public land-mobile telephone system), will increase the amount of data that a wireless terminal is able to obtain from the network, giving rise to the possibility of multimedia wireless communications, that is, the third generation of mobile communications. The two main standards of the IMT-2000 family are called WCDMA and CDMA2000 and are being promoted by two international consortia: 3GPP and 3GPP2, 3GPP standing for 3rd-Generation Partnership Project.

The evolution toward 3G has produced some intermediate standards (receiving the name of 2,5G), and wireless local-area networks (WLAN) are receiving great interest as a complement to the existing mobile systems (either 2G, 2,5G, or 3G).

This means that although the history of wireless communications has been driven primarily by the evolution of mobile telephone systems, many different wireless standards are converging in the 3G scenario. A classification of wireless communications systems can give the reader some insight into the similarities and differences of these existing and future systems.

1.1. Classification of Wireless Communications Systems

Wireless communications systems can be classified according to different criteria. One of the preferred rules relies on whether the system is intended for public or private use:

Private mobile radio (PMR) systems are intended for private access and usually they are not connected to the Public Switched Telephone Network (PSTN). They are generally dedicated to management of vehicle fleets and dispatching tasks. They can serve different areas ranging from small local areas to nationwide.

Public mobile telecommunications (PMT) systems are intended to serve great areas, normally nation wide or larger. They are connected to the PSTN and offer similar services as those provided by wired PSTN terminals.

Most of the wireless communications systems used today can be considered to belong to either of these two categories. A comprehensive description is provided in Sections 2 and 4.

1.2. Evolution of the Demand For Wireless Products

The wireless systems industry has grown by orders of magnitude, mainly because of circuit fabrication improvements, large-scale circuit integration, and miniaturization, making small, portable, cheap wireless equipment a reality.

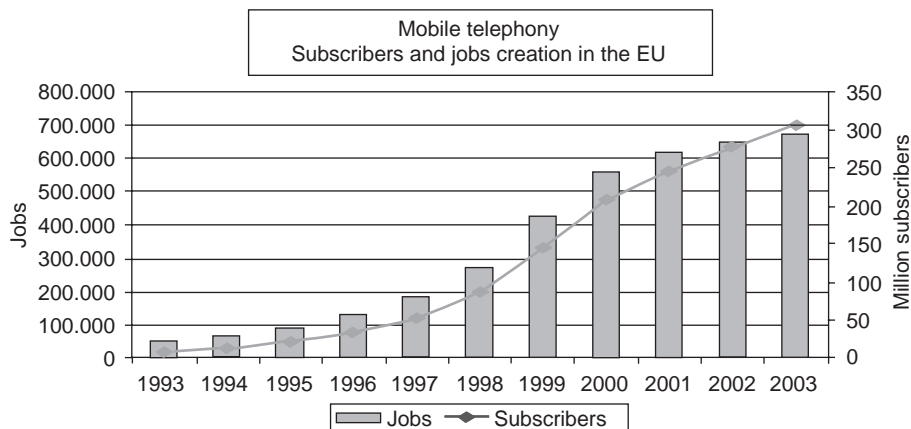


Figure 1. Mobile telephony subscribers and associated job creation in Europe. (This figure is available in full color at <http://www.mrw.interscience.wiley.com/erfme>.)

In the European Union (EU), the cellular mobile market is growing at an annual rate of 55%. Figure 1 [1] shows the evolution of subscribers of cellular products and the jobs, created in association with the mobile telephone market. This figure shows that more than 200 million EU citizens were “mobile” in year 2000, and some projections [2] indicate that 80% of the EU population by 2020 will have some form of mobile communication terminal.

On this basis, 280 million terminals need to be designed, manufactured, and provided to the customer. Even if this projection is halved, the number of mobile customers will still approach the present number of wired telephone connections within the EU [2].

In the United States, the number of cellular telephone users grew from 25,000 in 1984 to about 16 million in 1994, and, since then, wireless services have been experiencing customer growth rates up to 50% per year. According to the CTIA (Cellular Telecommunications Industry Association) [3], there were over 60 million wireless subscribers in the United States in June 1998 and more than 130 millions in June 2002 (see Fig. 2).

2. BASIC CONCEPTS AND FUNDAMENTALS OF WIRELESS COMMUNICATIONS

Radio, or wireless communication, is the use of radiated electromagnetic waves that permits the transmission and reception of information over a distance without the use of wires. At the transmitting or sending end, the information to be sent (e.g., a voice signal) is imposed on a locally generated radiofrequency (RF) signal called a *carrier*. The process of imposing the information signal on the carrier is called *modulation*. At the receiver, the information signal (e.g., voice) is extracted from the received signal in a process referred to as *demodulation*.

A pure, unmodulated radio carrier conveys no information and occupies only an infinitesimal amount of the spectrum. Modulation of the radio signal inevitably causes a spreading of the radiowave in frequency. Thus a radio signal conveying information occupies a range of frequencies called a *channel*. In general, the more information that is sent per unit of time, the wider the channel must

be. In addition to extracting the information from the radiowave through demodulation, it is also a principal-function of a receiver to accept only the information in the channel selected and reject other information sent simultaneously in other (e.g., adjacent) channels. The measure of the receiver’s ability to reject interfering signals on other channels is referred to as its *selectivity*. Hence, two or more radio systems can use the radio spectrum in the same area at the same time as long as (1) they are separated sufficiently in terms of frequency (i.e., so that their channels do not overlap) and (2) the receivers involved have sufficient selectivity to reject the signals on adjacent channels.

In many, if not most, communication systems, it is desirable to be able to communicate in both directions at the same time. This system characteristic, which is known as *full-duplex operation*, is desirable because it allows (1) one party in a voice conversation to interrupt the other with a question or (2) one device to immediately request a retransmission of a block of information received in error during a data communications session. There are two basic ways of providing for full-duplex operation in a radio system, as will be explained in Section 3. Once the most general principles of wireless communications have been explained, the fundamentals of the different wireless systems and the frequency bands allocated will be described in detail.

2.1. Cellular Systems

In the early mobile radio systems, the design objective was to achieve a large coverage area by using a single, high-powered transmitter. To avoid interference between users, the same carrier frequency could not be reused throughout the system. Hence, the overall system capacity was equal to the total number of channels: only a few thousand subscribers per system.

A cellular mobile communications system uses a large number of low-power wireless transmitters to create *cells*—the basic geographic service area of a wireless communications system. Variable power levels allow cells to be sized according to the subscriber density and demand within a particular region. As mobile users travel from cell

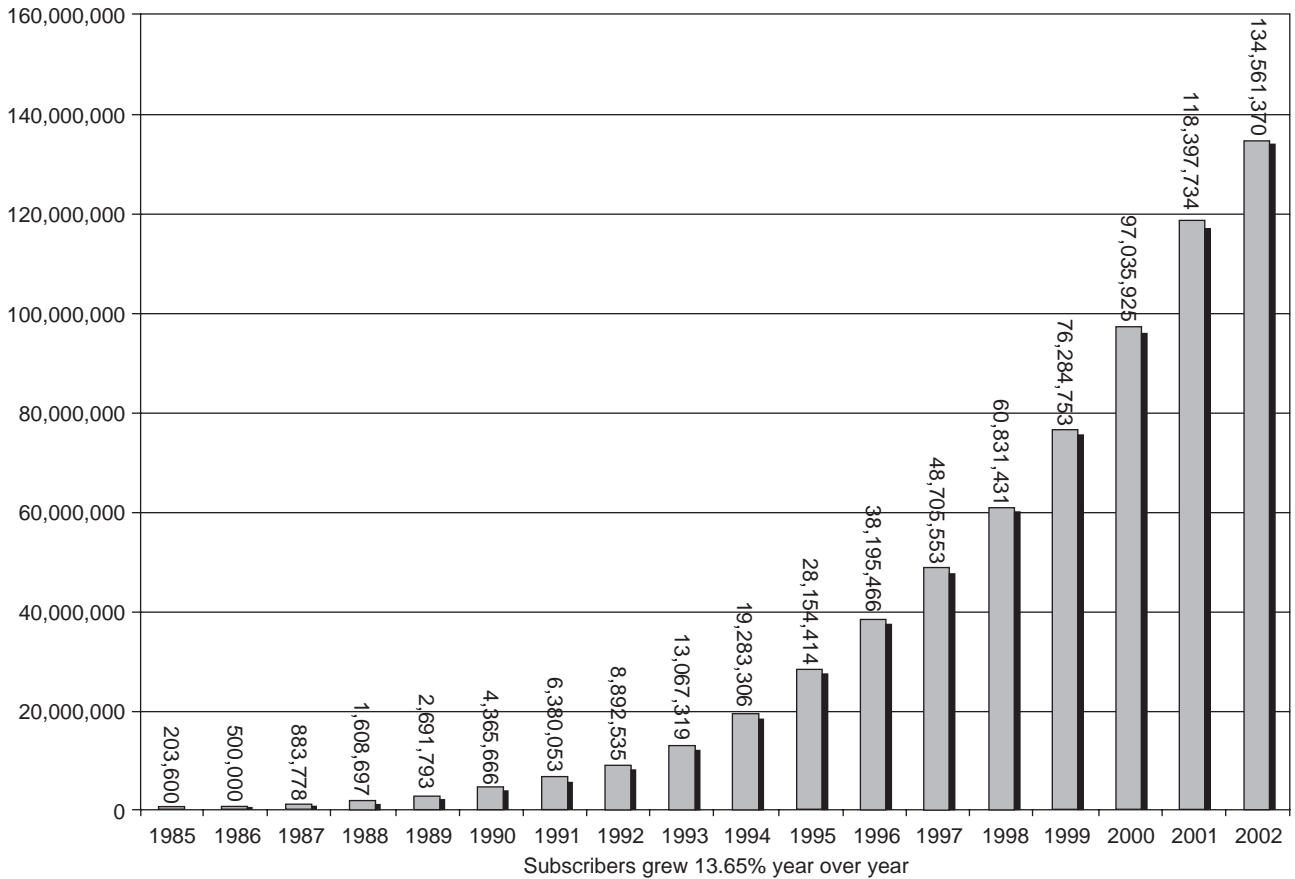


Figure 2. Evolution of wireless subscriber number in United States between June 1985 and June 2002.

to cell, their conversations are handed off between cells in order to maintain seamless service. Cells can be added to accommodate growth, creating new cells in unserved areas or overlaying cells in existing areas.

2.1.1. Frequency Reuse. In mobile systems, users share a pool of available channels (frequencies, timeslots, or codes). Let us assume that channels are associated with carrier frequencies. Since propagation losses are proportional to (a power of) the distance, the same frequency carrier, or channel, can be reused in cells at some distance away. The design process of selecting and allocating channel groups for all the cellular base stations within a system is called *network planning*. By reusing channels in multiple cells, the system can grow without geographical limits. In addition, this approach makes it possible to use small, battery-powered portable handsets with lower RF (radiofrequency) transmit power than the large vehicular mobile units used in earlier systems.

Reuse is critically dependent on the fact that the electromagnetic field attenuation in the cellular bands tends to be more rapid with distance (R) than it is in free space. As explained in more depth in Section 3, measurements have shown repeatedly that typically the field intensity decays like R^{-n} , with $3 < n < 5$ (in free space $n = 2$). If we assume that propagation attenuation does not depend on the azimuth angle, and that cell boundaries are at the

equisignal points, then a planar service area is optimally covered by the classical hexagonal array of cells.

Because the hexagonal geometry has exactly six equidistant neighbors, the size and geometry of a group of cells that collectively can use a complete set of available channels are limited [26]. Figure 3 shows an example in which seven sets of channels are used, one set in each colored cell. This seven-cell unit, also called *cluster*, is then replicated over the service area.

No similarly colored cells are adjacent, and therefore there are no adjacent cells using the same channel. While real systems never resemble these idealized hexagonal tilings of a plane, the seven-way reuse is typical of that achieved in practice. The preceding illustrations assume that the cells are using omnidirectional antennas. The system capacity, measured in users per square kilometer, can be increased by antenna *sectorization*. If each site is equipped with three sets of directional antennas, with their azimuths separated by 120° , the interference is reduced, allowing smaller clusters, which means an increase in capacity.

2.1.2. Cell Splitting. Economic considerations rendered the concept of creating full systems with many small areas impractical. To overcome this difficulty, system operators developed the idea of *cell splitting*. As a service area becomes full of users, this approach is used to split a single

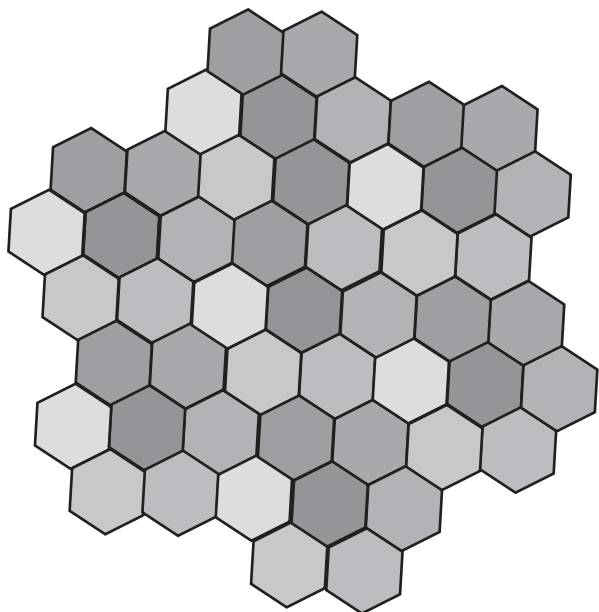


Figure 3. Illustration of the frequency reuse concept. Cells with the same color use the same set of frequencies. In this example, the cluster size K is equal to 7, and the frequency reuse factor is $\frac{1}{7}$. (This figure is available in full color at <http://www.mrw.interscience.wiley.com/erfme>.)

area into smaller ones. In this way, urban centers can be split into as many areas as necessary in order to provide acceptable service levels in heavy-traffic regions, while larger, less expensive cells can be used to cover remote rural regions (see Fig. 4).

The cell radii shown in Fig. 4 indicate that there are three types of cells in cellular networks: (1) *macrocells*, used mainly to cover large areas (1–10 km) with low traffic (rural areas); (2) the *microcells*, used in areas with high traffic density, such as suburban areas, with the cells 200-m and 200m–1 km in radius; and (3) *picocells*, or “indoor cells”, having radii between 10 and 200 m. Today, picocellular radio systems are used for wireless office communications.

2.1.3. Architecture of a Cellular Network. A cellular network is composed of three broad functional entities: the *mobile station* (MS) (normally a handset), carried by the subscriber; the *base station* (BS) subsystem, which controls the radiolink with the mobile station; and the *network subsystem*, the main part of which is the mobile services switching center (MSC), which performs the switching of calls between the mobile users, and between mobile and fixed network users. The MSC also handles the mobility management operations.

2.1.4. Handover. In a cellular network, the radiolinks and fixed links required are not permanently allocated for the duration of a call. *Handover*, also known as *handoff*, is the switching of an ongoing call to a different channel or cell (see Fig. 5).

A handover is performed in three stages. The MS continuously gathers information on the received signal level of the MS it is connected with, and all other BSs it can detect. This information is averaged to filter out temporary fluctuations in received-signal level. The averaged data are then passed on to the decision algorithm, which decides whether it will request a handover to another station. When it decides to do so, both the old BS and the MS execute handover.

2.2. Cordless Telephone Systems

Early cordless telephones operate solely as extension telephones to a dedicated base station, which is then connected to a dedicate telephone line with a specific telephone number on the Public Switched Telephone Network (PSTN). More recent cordless telephone systems employ the same technology as the digital cellular standards. However, the central difference is that cellular systems were developed for wide-area coverage, whereas the cordless standards are optimized for local coverage, with high densities of users.

The most recent digital cordless standards incorporate encryption, and support high-speed data (with circuit- and packet-switched modes) as well as fax and voice communications. The cordless standards provide higher speech

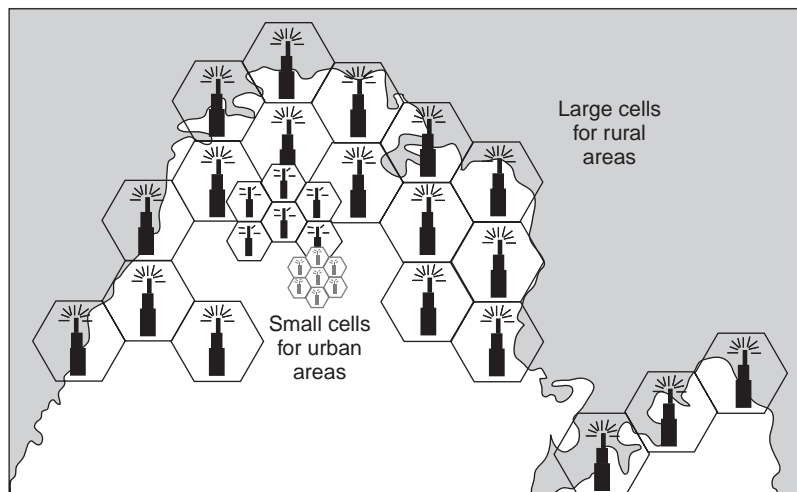


Figure 4. Cell splitting is the process of subdividing a congested cell into smaller cells, each with its own (low-powered) base station.

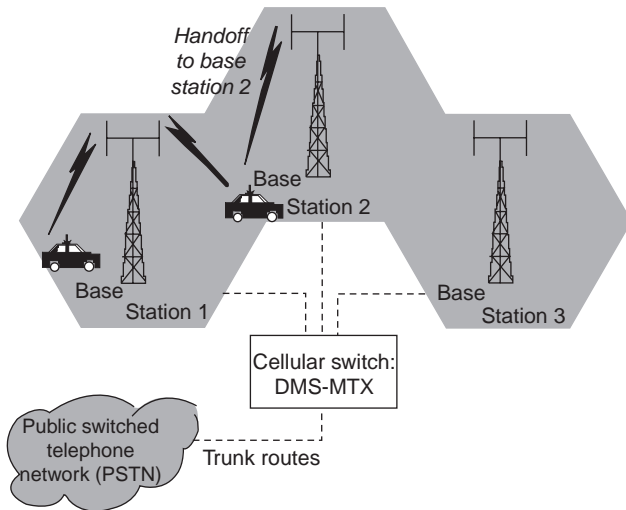


Figure 5. Handover, also known as *handoff*, is a process to switch an ongoing call from one cell to the adjacent cell as the mobile user approaches the cell boundary.

quality than do the mobile cellular standards (GSM, DCS 1800) and comparable with that of fixed networks. Even though digital cordless systems are more suited to stationary environments than vehicles, they also provide a limited degree of mobility in a local area.

Digital cordless systems are able to handle up to 100,000 users/km² in an office environment. They include dynamic channel selection/allocation (DCS/DCA) algorithms, which ensure that the best of the available radio channels are always used. This capability ensures that digital cordless systems can coexist with other systems in the same frequency band while providing high-quality, robust, and secure communications.

2.3. Trunking Systems

Radio trunking is a two-way communications technology where a number of users share a common pool of timeslots or frequencies that are dynamically allocated by the system as and when required. As it applies to radio, trunking is the automatic sharing of channels in a multiple-repeater system. Trunking concepts are based on the presumption that individual subscribers use the system only a small percentage of the time and that a large number of users do not use the system at the same time. Typical users of trunking systems are private corporations with large fleets (ambulances, buses), government departments (fire brigades, police) or utilities (electric power lines, oil pipelines, railways). Unlike other wireless systems, trunking systems can allow “direct mode” communications, that is, direct operation between mobile terminals without use of network infrastructure.

2.4. Differences between Cellular and Trunking Systems

One way of looking at the wireless communications systems is to chart the degree of customization required by users against traffic density. In such a model, the cordless technology is positioned as the technology that offers the

highest density and lowest degree of customization. Next to it are cellular systems, with medium traffic density, while the digital trunking technology is positioned to address low to medium traffic density with a higher degree of customization.

2.4.1. Large Cell Sizes. The different approach in these technologies is also reflected in the spectrum allocation and the cell sizes. At one end, in a dense urban environment, there are digital cordless systems, with cell sizes measured in hundreds of meters and operating at frequencies up to 2 GHz. Cellular systems, which address medium to high user densities with cells sizes measured in kilometers, operate at frequencies of 900 or 1800 MHz. In contrast, trunking systems address urban and suburban, low to medium user densities, with cell sizes of tens of kilometers and operating frequencies in the lower hundreds of megahertz.

2.4.2. Traffic Profile. Another important factor is the traffic profile. In cellular systems, call setup time is typically several seconds, in contrast to the fast push-to-talk operation of 300 ms for trunking systems. Also, while cellular calls are point-to-point (individual calls), the large percentage of trunking calls are group calls operating in an all-informed “open-channel mode.” The average duration of calls is also different: 2 min in cellular networks compared with 20 s for a trunking call.

2.4.3. Decentralized Architecture. The architecture of trunking systems is optimized for the predominance of local traffic. The need for fast call setup demands that the call switching and management be devolved to the lowest possible point in the network. This requires a decentralized, distributed system architecture, comprising distributed databases and loosely coupled autonomous parts. This, in turn, leads to an inherent reliability and fault tolerance with softer failure profiles.

2.5. Paging Systems

A radio paging system is a one-way wireless messaging system that allows continuous accessibility to someone away from the wired communications network. In its most basic form, the person “on the move” carries a palm-sized device (the pager) that has an identification number. The calling party inputs this number, usually through the public telephone network, to the paging system, which then signals the pager to alert the called party.

The paging system makes efficient use of the radio spectrum, enabling it to provide inexpensive functions satisfying customers’ demands. This has contributed to the steady expansion of the paging industry. The introduction of complementary products (e.g., pocket-sized cellular phones, cordless telephones, and multifunctional “communicators”) will inevitably spur the paging industry to provide more value-added services in the future. There will be more varied applications of paging such as sending e-mail, voicemail, faxes (facsimiles), or other useful information to a pager, which will also take on more attractive, innovative forms.

Paging systems vary widely in their complexity and coverage area. While simple paging systems may cover a limited range such as 2–5 km, or may always be confined to within individual buildings, wide-area paging systems can provide worldwide coverage. Although paging receivers are simple and inexpensive, the transmission system is quite sophisticated. Wide-area paging systems consist of a network of many base-station transmitters, and large radio towers that simultaneously broadcast a page from each base station (this is called *simulcasting*).

2.6. Wireless Local-Area Networks

A wireless local-area network (WLAN) is a flexible data communication system implemented as an extension to, or as an alternative for, a wired LAN. WLANs combine data connectivity with user mobility, and, through simplified configuration, enable movable LANs. With wireless LANs, users can access shared information without looking for a place to plug in, and network managers can set up or augment networks without installing or moving wires. Wireless LANs offer the following productivity, convenience, and cost advantages over traditional wired networks:

- *Mobility*—wireless LAN systems can provide LAN users with access to real-time information anywhere in their organization.
- *Installation speed and simplicity*—installing a wireless system can be fast and easy and can eliminate the need to pull cable through walls and ceilings.
- *Installation flexibility*—wireless technology allows the network to go where wire cannot go.
- *Reduced cost of ownership*—while the initial investment required for wireless LAN hardware can be higher than the cost of wired LAN hardware, overall installation expenses and lifecycle costs can be significantly lower.
- *Scalability*—wireless LAN systems can be configured in a variety of topologies to meet the needs of specific applications and installations.

2.6.1. WLAN configurations. The simplest WLAN configuration is an independent LAN that connects a set of PCs with wireless adapters. Any time two or more wireless adapters are within range of each other, they can set up an independent network. These on-demand networks typically require no administration or preconfiguration.

Access points can extend the range of ad hoc LANs by acting as a repeater, effectively doubling the distance between wireless PCs.

In infrastructure WLANs, multiple access points link the WLAN to the wired network and allow users to efficiently share network resources. The access points not only provide communication with the wired network but also mediate wireless network traffic in the immediate neighborhood. Multiple access points can provide wireless coverage for an entire building or campus.

2.7. Wireless Personal Area Networks

A wireless personal area network (WPAN) is a personal-area network — a network for interconnecting devices centered around an individual person — in which the connections are wireless. Because most PANs are wireless, these terms are virtually synonymous. Typically, a wireless WPAN uses some technology that permits communication within about 10 m — in other words, a very short range. One such technology is Bluetooth, which was used as the basis for a new standard, IEEE 802.15.

A WPAN could serve to interconnect all the ordinary computing and communicating devices that many people carry with them today — or it could serve a more specialized purpose such as allowing the surgeon and other team members to communicate during an operation.

A key concept in WPAN technology is known as “plugging in”. In the ideal scenario, when any two WPAN-equipped devices come into close proximity (within several meters of each other) or within a few kilometers of a central server, they can communicate as if connected by a cable. Another important feature is the ability of each device to lock out other devices selectively, preventing needless interference or unauthorized access to information.

The technology for WPANs is in its infancy and is undergoing rapid development. Proposed operating frequencies are around 2.4 GHz in digital modes. The objective is to facilitate seamless operation among home or business devices and systems. Every device in a WPAN will be able to plug into any other device in the same WPAN, provided they are within physical range of one another. In addition, WPANs worldwide will be interconnected

2.8. Frequency Bands Allocated for the Different Wireless Services

In response to rapid growth in the wireless personal communication services, regulatory authorities have steadily increased the amount of spectrum available through successive reallocations of the resource in the higher frequency ranges. Moving higher in frequency to avoid congestion has advantages and disadvantages. Generally speaking, the radiofrequency (RF) devices employed within the system get more costly at higher frequencies, and, in terms of propagation effects, the higher frequencies are subject to more blocking or shadowing by buildings or hills. However, the antennas involved are physically smaller, which is an important attribute for systems that seek to serve small portable units carried on one’s person. At some risk of overgeneralizing, it can be said that (1) the lower-frequency bands are best for economically covering wide areas (suburban and rural areas) where frequency reuse is not as important and (2) the higher-frequency bands are best for covering urban areas where high levels of frequency reuse are desired.

3. TECHNOLOGY

This section of the article addresses basic technical issues related to the transmission in wireless communications systems. The ideas presented herein will allow the reader

to understand the rationale behind the choices made for the standards described in Section 4 of this article.

3.1. A Brief Review of the Propagation Characteristics in Radio Bands

The use of radio propagation exhibits inherent advantages over “line” (copper, coaxial, optic fiber, waveguide) transmission. Some of these advantages are lower cost, faster deployment, and the capability to roam. However, the radio channel is less robust than line channels. Radio propagation is not a stationary phenomenon, but the propagation parameter depends on many factors that engineers cannot control, such as meteorology, or any moving object in the surroundings. This channel instability makes the radio transmission a much more difficult problem than line transmission and determines the design of the equipment.

Physical phenomena that affect both attenuation and delay are free-space propagation, shadowing, and reflections. Moreover, because of the multiple reflections, the path for the signal to travel from the transmitter to the receiver is not unique, but several propagation paths can occur simultaneously producing the phenomenon termed ‘*multipath*.’ This phenomenon affects both fixed and mobile radiolinks; however, channel variability is not an issue for fixed links. Propagation conditions in fixed links vary slowly or do not vary at all.

The radio channel affects amplitude attenuation, angular shift, time delay, and Doppler frequency shift of each propagation path between transmitter and receiver. In mobile links, these three parameters are time-varying and differ for each path. The sum of all these paths results in the following effects: variable signal attenuation, variable signal time delay, temporal spread, and Doppler frequency spread. In mobile communications, because of the many factors involved in the radio propagation and their unpredictable dynamics, these propagation parameters are modeled as random processes. Statistics for amplitude attenuation, time spread and Doppler spread are briefly summarized next.

The variable attenuation suffered by the received signal is usually referred to as “fading.” Fading can be modeled as the sum of three components: large-scale path loss, medium-scale (slowly-varying) fading, and small-scale (rapidly varying) fading.

The total fading is computed as the product (sum in logarithmic scale) of the three abovementioned factors. The large-scale path-loss model accounts for the average attenuation value for a geographic area ranging several hundreds of wavelengths in size. Large-scale loss is modeled as a constant and accounts for free-space attenuation, diffraction, refraction, and reflection. When the line between transmitter and receiver is not obstructed by any object [line of sight (LoS)], the large-scale loss is reduced to the free-space loss, and it can be modeled according to the following equation

$$L_{\text{free space}} = K \left(\frac{d}{\lambda} \right)^2 \quad (1)$$

where K is a constant and λ is the signal wavelength. This attenuation is known as ‘*free-space attenuation*’.

When the propagation environment does not correspond to the free-space scenario, large-scale loss can be modeled as

$$L_{\text{large - scale}} = K \left(\frac{d}{\lambda} \right)^\gamma \quad (2)$$

where γ is an empirical parameter that varies from 1.8 to 6 depending on the environment (outdoor or indoor, flat or mountainous, desert or forest, etc.).

The shadowing caused by natural or manmade objects close to the receiver is the physical effect responsible for slowly varying fading. Although this fading factor has slow dynamics, the shadowing causes the deepest variations of the received-signal level. The medium scale follows a lognormal distribution, where the received power, expressed in logarithmic units (dB), follows a normal (Gaussian) distribution. When designing the link equipment, this fading model has to be considered in one or both of the following ways: (1) the transmitted power has to be increased to compensate for this variable attenuation, typically with a signaling feedback from the receiver known as “closed-loop power control”, or (2) a scrambler must be included after the channel coder in such a way that it can be guaranteed that after descrambling at the receiver two consecutive bits do not simultaneously suffer a deep fading. Thus, the channel decoder is able to correct the errors caused by the deep fade. To guarantee the efficiency of the scrambler, its timelength has to be longer than the fading coherence time. This parameter is studied below.

The multipath is the phenomenon responsible for the fast varying fading. When two paths arriving either with close delays have the same phase, the resulting signal is stronger than those of either path.

However, when both paths arrive with a 180° phase difference, the resulting signal is smaller than the strongest path, or the signal can even vanish. The rapidly varying component follows a Rice or Rayleigh distribution, depending on the existence of LoS. When there is no LoS conditions, the probability distribution function for the received amplitude due to multipath follows a Rayleigh model. When there are LoS conditions, the amplitude pdf follows a Rice distribution.

Rapidly varying fading reduces the quality of the link, or in other words, increases the bit error rate (BER). The techniques usually employed to overcome this quality degradation are forward error-correcting codes, fast transmitted power control, or the usage of space or frequency diversity. Diversity utilizes the fact that the two signals with different carrier frequencies or antenna locations are unlikely to suffer a deep fading simultaneously. Then, proper combination of both frequencies, or antenna locations, can provide effective protection against the fast fading.

As mentioned before, knowledge of the temporal correlation of the fading is as important as the knowledge of the amplitude distribution for the correct system design. The *average fading* time is defined as the expected time the fading exceeds a given attenuation value. For a Rayleigh fading, the average fading time τ_f may be modeled as [4]

$$\tau_f = \frac{\exp(\rho^2) - 1}{\sqrt{2\pi}\rho f_d} \quad (3)$$

where ρ is the ratio between the fading level and its RMS (root-mean-square) value and f_d is the maximum Doppler frequency shift. f_d is calculated as

$$f_d = \frac{V}{\lambda} = \frac{fV}{C} \quad (4)$$

where V is the mobile speed, λ is the signal wavelength, and f is the carrier frequency.

Besides the variable attenuation, multipath causes several copies of the same signal to arrive at the receiver end with different delays. The time difference between the earliest and last paths is known as *delay spread*. Typical values for the delay spread in indoor environments are 50–250 ns for the 900-MHz band and 10–20 ns for the 2.4-GHz band [5]. Typical values in the 900-MHz band for outdoor environments are 10–25 μ s [6].

If the delay spread is smaller than the inverse of the signal bandwidth, the receiver is not able to resolve the different paths, and the multipath affects only the received amplitude; in this case, multipath causes fading but does not produce distortion on the received signal. This fading is known as *flat fading*. The mechanisms available to compensate for this type of fading are channel coding, scrambling, and space and frequency diversity.

However, if the delay spread is larger than the inverse of the bandwidth — comparable or larger than the symbol rate — the multipath causes intersymbol interference, namely, signal distortion. This fading is known as frequency-selective fading. The usage of equalizers can partially or totally overcome the intersymbol interference caused by the frequency-selective fading.

Because of user and/or environment motion, each path arrives with its own Doppler frequency shift, too, which causes a frequency spread of the received signal. This effect, known as *Doppler spread*, is closely related to the coherence time of the multipath channel and the average fading time. All these quantities describe the temporal correlation of the fading.

3.2. Modulations in Wireless Systems

Digital modulation is a simple concept. The transmitter groups the digital information to be sent into packets of N bits. Each of the $M = 2^N$ possible values of the N -bit packet is mapped into a signal, which is properly amplified and transmitted. At the receiver end, the signal arrives corrupted by noise and interference. An optimum receiver detects which signal, among the M possible ones, was transmitted in such a way that the probability of error is minimized.

Radio transmission requires the spectrum of the M possible signals to be centered around the frequency for which the antenna system is designed, which is modulating the signals with the proper carrier frequency. Summarizing, we could say in a very general way that radio digital modulations can be classified into four basic groups, each correspond to a different modulation scheme. So, we could say that there are ASK, PSK, FSK, and QAM digital modulation types, corresponding to amplitude,

phase, frequency, and amplitude–phase combination modulations, respectively.

Amplitude modulations are not advisable for mobile radiolinks. The wide amplitude variability caused by the radio channel fading would mask the changes of amplitude due to modulation. Although it could be envisaged that an automatic gain control (AGC) system in the receiver might compensate for the channel attenuation, it would unnecessarily complicate the system and would require the continuous transmission of a pilot signal to estimate the exact value of the channel attenuation. The same argument as that advanced for amplitude modulation can be applied for amplitude–phase combination, QAM, modulations. Thus, phase or frequency modulation, where amplitude does not carry information, is advisable for mobile communications.

According to the M -PSK (M -level phase shift keying) modulation scheme, pulses containing a sine wave with a constant frequency are transmitted. Each possible transmitted symbol shifts the phase of the sine wave by a different amount. To uniformly spread the phase of the M symbols, the phase shifted is a multiple of $2\pi/M$ radians. Thus the received signal, $s_i(t)$, when the i th symbol is transmitted, follows the expression

$$s_i(t) = \sqrt{\frac{2E}{T}} p(t) \cos\left(2\pi f_c t + i \frac{2\pi}{M}\right) \quad i = 0, \dots, M-1 \quad (5)$$

where E is the average received energy per symbol, T is the symbol timelength, f_c is the carrier frequency, and $p(t)$ corresponds to the pulse conformation. The symbol length T is related to the bit duration T_b as $T = T_b \log_2 M$. Therefore, the symbol rate R is

$$R = \frac{R_b}{\log_2 M} \quad (6)$$

The quality of any digital transmission is measured by the bit error rate (BER). The exact calculation of the BER of an optimum M -PSK receiver cannot be analytically calculated for an arbitrary value of M ; however, the exact expressions for BPSK ($M = 2$) and QPSK ($M = 4$) (binary and quadrature PSK) are

$$\text{BER}_{\text{BPSK}} = \frac{1}{2} \text{erfc}\left(\sqrt{\frac{E_b}{N_0}}\right) \quad (7)$$

$$\text{BER}_{\text{QPSK}} = \text{erfc}\left(\sqrt{\frac{E}{2N_0}}\right) \left[1 - \frac{1}{4} \text{erfc}\left(\sqrt{\frac{E}{2N_0}}\right)\right] = \text{erfc}\left(\sqrt{\frac{E_b}{N_0}}\right) \left[1 - \frac{1}{4} \text{erfc}\left(\sqrt{\frac{E_b}{N_0}}\right)\right] \quad (8)$$

where N_0 is the white Gaussian noise spectral power density, E_b is the average received energy per bit, and

$$\text{erfc}(x) = \frac{2}{\sqrt{\pi}} \int_x^\infty e^{-t^2} dt \quad (9)$$

Average received energy per symbol E , average received energy per bit E_b , and the average received power P are related by

$$E = E_b \log_2 M = PT = PT_b \log_2 M \quad (10)$$

The bandwidth required for the transmission of a M -PSK signal depends on the pulse $p(t)$ shaping. The minimum M -PSK bandwidth is

$$B_{M\text{-PSK}} = \frac{R_b}{\log_2 M} \quad (11)$$

where again R_b is the bit transmission rate. Equation (5) can be rewritten as

$$\begin{aligned} s_i(t) = & \sqrt{\frac{2E}{T}} p(t) \sin\left(i \frac{2\pi}{M}\right) \sin(2\pi f_c t) \\ & - \sqrt{\frac{2E}{T}} p(t) \cos\left(i \frac{2\pi}{M}\right) \cos(2\pi f_c t) \end{aligned} \quad (12)$$

It can be noted in this last equation that both in-phase (cos) and quadrature (sin) components are affected by the same envelope, $p(t)$. Therefore transitions between symbols occur at the same time in both components. When the available bandwidth is small, $p(t)$ is far from a rectangular pulse, and equal (synchronous) shaping for in-phase and quadrature components causes large RF amplitude variation; and amplitude variation represents a handicap for nonlinear power amplifiers, which have better power efficiency.

The straightforward solution for the problem of having amplitude variation in QPSK has been solved by staggering the envelope of the quadrature component by a time delay of $T/2$. This modulation is known as *offset QPSK* (OQPSK). The received signal, $s_i(t)$, when the i th symbol is transmitted follows the expression

$$\begin{aligned} s_i(t) = & \sqrt{\frac{2E}{T}} p(t) \sin\left(i \frac{2\pi}{M}\right) \sin(2\pi f_c t) \\ & - \sqrt{\frac{2E}{T}} p\left(t - \frac{T}{2}\right) \cos\left(i \frac{2\pi}{M}\right) \cos(2\pi f_c t) \end{aligned} \quad (13)$$

Besides lower-frequency spurious emission when it passes through a nonlinear amplifier, OQPSK has the same BER and bandwidth efficiency as does QPSK.

Another solution given to decrease the amplitude range of a QPSK signal under limited bandwidth conditions is the addition of a $\pi/4$ phase to every other transmitted symbol. In this way, the received signal $s_i(t)$ is

$$s_i(t) = \sqrt{\frac{2E}{T}} p(t) \cos\left(2\pi f_c t + i \frac{2\pi}{M} + \begin{cases} 0 \\ \pi/4 \end{cases}\right) \quad i = 0, \dots, 3 \quad (14)$$

where a 0 and $\pi/4$ phase are alternatively added to the carrier.

The second type of modulation with constant amplitude is FSK. According to the FSK modulation scheme, pulses containing a sine wave with a different frequency are transmitted. Each possible transmitted symbol shifts the carrier frequency by a different amount. Frequency modulation has the drawback of larger bandwidth. To overcome this problem to the maximum extent possible, frequency modulation with minimum frequency deviation has been proposed. This modulation is known as *minimum shift keying* (MSK), which is defined by the binary case, $M=2$. In this case, the received signal, $s_i(t)$, when the i th symbol is transmitted follows the expression

$$s_i(t) = \sqrt{\frac{2E}{T}} p(t) \cos\left(2\pi f_c t \pm \frac{\pi}{2T} t + \theta\right) \quad (15)$$

where the \pm signs mean a $\Delta f = 1/(4T)$ positive frequency shift when transmitting a “1” and the same negative frequency shift for the “0” transmission. The phase θ stands for a phase term that is added to each symbol in order to guarantee a continuous phase. For this reason MSK modulation is also known as CPFSK (continuous-phase FSK).

In the GMSK modulation, the “G” stands for Gaussian, and it refers to the fact that the MSK modulation is filtered with a Gaussian frequency response before its transmission. The Gaussian frequency response

$$H(f) = \exp\left(-\frac{\ln(2)}{2} \left(\frac{f}{B}\right)^2\right) \quad (16)$$

limits the 3dB-bandwidth of the transmitted signal to B . In order to increase the bandwidth efficiency, B is adjusted to satisfy $BT_b < 1$. The usual values for B are such that $0.2 \leq BT_b \leq 0.5$.

The exact value of the BER for an optimum GMSK receiver is very complex; however, an BER upper bound accurate enough for any practical propose is given by

$$\text{BER}_{\text{GMSK}} = \frac{1}{2} \text{erfc}\left(\sqrt{0.68 \frac{E}{N_0}}\right) \quad (17)$$

A common objective of all the digital modulations described above is to maximize the spectrum efficiency, which means that they try to minimize the occupied bandwidth for a given transmission bit rate. We introduce next a set of modulation techniques that try just the opposite, to maximize the bandwidth. These modulations are classified under the generic term *spread-spectrum techniques*.

Although it might seem that the usage of such spread-spectrum modulations is an unnecessary waste of spectrum, it can be proved that is not the case as spread-spectrum techniques allow a more efficient usage of the spectrum. In spread spectrum, the spectrum of transmitted signals is artificially spread by a code. This code is different for each link in the same geographic area of the radio network. Although we will not discuss this in detail in this article, the receivers can demodulate separately each link attending to its assigned code, so that the remaining signals in the same portion of the spectrum do not interfere.

As is mentioned in the next section, and explained in detail in the article entitled WIRELESS NETWORKS, the possibility of discriminating links from its code allows the multiple-access technique known as code-division multiple access (CDMA).

The spreading codes used in spread-spectrum modulations consist of a sequence of bits with random appearance. To distinguish the code bits from the information bits, the former are called “chips.” Although the spreading code auto- and cross-correlation functions resemble the auto- and cross-correlation of random sequences, they are generated deterministically by shift registers with specific feedback connections. Thus the receiver can generate an exact copy of the code used by the transmitter.

From a practical perspective, there are two kinds of spread-spectrum modulations: direct sequence (DS) and frequency hopping (FH). The former takes the transmitted bits and multiplies (performs exclusive OR) them by the code sequence before modulations. The chip rate of the spreading code has to be faster than the bit rate in order to spread the spectrum. The latter changes the carrier frequency according to a pattern dictated by the spreading code.

Because of practical implementation issues, DS uses BPSK or QPSK modulators, and FH is used in conjunction with bit FSK modulation. The BER in presence of additive white Gaussian noise is not altered from the expression corresponding to BPSK, QPSK, and FSK respectively.

3.3. Multiple Access

As explained in detail in the WIRELESS NETWORKS article multiple-access techniques can be classified into two generic types: scheduling and contention. The former assigns a fixed amount of resources (timeslot, frequency range, or code) to each link, so there is no possible interference among them. The latter allows several links to access the same resources but establish some mechanisms to minimize the probability of collision, with simultaneous usage of the same resources, and to detect the collision if it occurs.

The simplest and most straightforward multiple access method is known as *frequency-division multiple access* (FDMA). With FDMA, the available spectrum is divided into nonoverlapping slots in the frequency dimension or domain. These frequency slots or channels are then put into a pool and assigned to users on either a manual or automated basis for the duration of their particular call. For example, a 150-kHz block of spectrum could be divided into six channels or frequency slots, each 25 kHz wide. Such an arrangement would allow six simultaneous conversations to take place, each with their own carrier within their own frequency slot.

With *time-division multiple access* (TDMA), the available spectrum is divided into nonoverlapping timeslots in the time dimension or domain. These timeslots or channels are then put into a pool and assigned to users for the duration of their particular call. To continue the example given above, in a TDMA system the 150 kHz of spectrum would be divided into recurring groups (frames) of six timeslots, and each timeslot would carry a sequence of bits

representing a portion of one of six simultaneous conversations.

A third access method is known as *code-division multiple access* (CDMA). As explained above, CDMA is both a modulation and an access technique that is based on the spread-spectrum concept. In spread-spectrum systems, multiple conversations (up to some maximum) simultaneously share the available spectrum in both the time and frequency dimensions. Hence, in a CDMA system, the available spectrum is not channelized in frequency or time as in FDMA and TDMA systems, respectively. Instead, the individual conversations are distinguished through coding; that is, at the transmitter, each conversation channel is processed with a unique spreading code that is used to distribute the signal over the available bandwidth. The receiver uses the unique code to accept the energy associated with a particular code. The other signals present are each identified by a different code and simply produce background noise. In this way, many conversations can be carried simultaneously within the same block of spectrum.

3.4. Implementation of Duplex Channels

Duplex services are those that allow users in the network to send and receive information simultaneously. Obviously, the ability of sending and receiving requires the assignment of two links to each user. Although both links serve the same user, they can be viewed as two independent links; therefore a multiple-access technique has to be chosen. There are two options for the duplex implementation: time-division duplex (TDD), and frequency-division duplex (FDD).

Frequency-division duplexing (FDD) is used to assign two different frequency slots per conversation — one for transmitting and one for receiving. By separating the slots sufficiently in frequency (about 5% of the nominal RF), filters (say, in the portable radio) can be used to prevent the transmitted information from interfering with the simultaneously received information.

Time-division duplexing (TDD) uses the fact that it is possible to share a single radio channel in time. TDD is possible only with digital transmission formats and digital modulation, and is very sensitive to timing. For this reason, TDD has only recently been used for indoor or small-area wireless applications where the physical coverage distances (and thus the radio propagation time delay) are much smaller than the many kilometers used in conventional cellular telephone systems.

TDD simplifies the frequency planning when the service is not symmetric, with different bit rates for the “go and return.” On the other hand, TDD is not advisable for long links because of the long propagation time delays. Large propagation delays require large timeguard gaps between reception and transmission to avoid collisions between them, which results in a low spectral efficiency.

3.5. Recently Developed Modulation Techniques

3.5.1. Wideband CDMA. Wideband code-division multiple access (wideband CDMA) [17] has emerged as the mainstream air interface solution for third-generation

networks. In Europe, Japan, Korea, and the United States wideband CDMA systems are currently being standardized.

Wideband CDMA has a bandwidth of 5 MHz or more (multiples of 5 MHz). The nominal bandwidth for all third-generation proposals is 5 MHz. There are several reasons for choosing this bandwidth:

1. Data rates of 144 and 384 Kbps (kilobits per second), the main targets of third-generation systems, are achievable within 5 MHz bandwidth with a reasonable capacity. Even a 2-Mbps peak rate can be provided under limited conditions.
2. Lack of spectrum calls for reasonably small minimum spectrum allocation, especially if the system has to be deployed within the existing frequency bands already occupied by second-generation systems.
3. The 5-MHz bandwidth can resolve (separate) more multipaths than can narrower bandwidths, increasing diversity and thus improving performance. Larger bandwidths of 10, 15, and 20 MHz have been proposed to support higher data rates more effectively.

Several wideband CDMA proposals have been made for third-generation wireless systems. They can be characterized by the following new advanced properties:

- Provision of multirate services
- Packet-switched data
- Complex spreading
- A coherent uplink using a user-dedicated pilot
- Additional pilot channel in the downlink for beamforming
- Seamless interfrequency handover
- Fast power control in the downlink
- Optional multiuser detection

The third-generation air interface standardization for the schemes based on CDMA seems to focus on two main types of wideband CDMA: network asynchronous and synchronous. In network asynchronous schemes the base stations are not synchronized, while in network synchronous schemes the base stations are synchronized to each other within a few microseconds.

3.5.2. Orthogonal Frequency-Division Multiplexing (OFDM). OFDM is a multicarrier modulation [18] that is finding many wireless applications due to its ability to combat impulsive noise and multipath effects and make fuller use of the system available bandwidth. It has been adopted for the European Digital Audio Broadcasting (DAB) [19] and Digital Video Terrestrial Broadcasting (DVB-T) [20] standards and is under study for new wireless LAN generations (HIPERLAN: high-performance radio LAN).

In an OFDM-based system, the spectrum associated with each elemental piece of data is a small portion of the

total bandwidth (B), which is divided into N subchannels. Each of them is modulated with one information symbol, and they are all multiplexed in frequency.

If T represents the OFDM symbol duration, the N subcarriers are separated by $\Delta f = 1/T$, and thus placed in the following frequencies:

$$f_k = f_0 + k/T, \quad k = 0, 1, \dots, N - 1 \quad (18)$$

One of the main advantages OFDM is the possibility of an easy implementation using a fast Fourier transform algorithm (FFT) [21]. Among its weaknesses, sensitivity to phase noise, frequency offsets and nonlinear effects must be mentioned.

3.5.3. Combination of Multicarrier and CDMA Techniques.

Some ways of combining OFDM and CDMA have been suggested in attempts to obtain the advantages of both techniques. Depending on how they are combined, three different schemes have been developed: multicarrier (MC)-CDMA, multicarrier direct sequence (DS)-CDMA, and multi-tone (MT)-CDMA. They constitute different trade offs between transmitter-receiver complexity, spectral efficiency and bit error rate [22].

4. PRACTICAL WIRELESS SYSTEMS AND PRODUCTS

This section is devoted to describing in detail some practical wireless communications. Descriptions follow after an overview of their frequencies of operation:

Digital trunking systems operate the UHF band in the 400-MHz region:

TETRA (Trans European Trunked RAdio) release 1: 390.0125–392.9875 MHz and 420–425 MHz (digital 12.5–25 kHz channels)

Cordless telephone systems:

CT2 cordless phones: 854–870 MHz (this band will be reserved for CT2 until December 31, 2005)

(Pan European) cordless headphones: 863–865 MHz

DECT Digital European Cordless Telephones: 1880–1900 MHz

Cellular systems operate a band near 800/900 MHz, and, most recently, a band near 1.8/1.9 GHz:

Cellphones—GSM (Global System for Mobile communication; (124 × TDMA 200-kHz channels): 915–960 MHz, uplink (split – 45 MHz: 870–915 MHz, downlink)

ETACS/TACS: 917.0125–949.9875 MHz (25-kHz channels, 12.5-kHz offsets) to be phased out by 2005

EGSM—Extended GSM: 925.2–935 MHz

European Railways GSM system: 921–925 MHz

In-flight digital phones (air–ground): 1800.30–1804.969 MHz (164 × 30.303-kHz channels; ground at –130 MHz)

PCN mobile phones: 1805–1876.5 MHz (split – 95 MHz: 1710–1781.5 MHz)

Future UMTS (IMT-2000, third-generation mobile): 1900–2025 MHz (with 2110–2200) (– 190 MHz)

Wireless LAN: Three media can be used for transmission over wireless LANs. Infrared, radiofrequency and microwave.

Radiofrequency: industrial, scientific, and medical (ISM) frequency bands, 902–928 MHz, 2.4–2.4853 GHz, 5.725–5.85 GHz.

4.1. Cellular Systems

The concepts behind cellular systems were discussed in Section 2. This section briefly presents the networks commercially available nowadays and enumerates the services they provide and the main parameters and differences between them.

During the 1970s and 1980s several analog cellular systems were deployed with a successful acceptance among the public, including AMPS, TACS, and NMT. These systems were analog, and their low spectral efficiency severely limited the network capacity. Moreover, the lack of a unified standard prevented the users from roaming through different countries.

At the beginning of the 1980s, initiatives were taken to develop a new cellular standard with the following goals: digital transmission, high spectral efficiency, high network capacity, international roaming, provision of voice communications and low-bit-rate data (fax), small-size terminals, and digital signaling able to provide advanced services, among others.

The European initiative to provide a pan-European second generation was very successful, coming up with the GSM standard. The U.S. initiative produced the IS-54, which provides services similar to those of GSM. In the 1990s the United States also produced the IS-95, the first cellular system to employ spread-spectrum modulation.

4.1.1. GSM. Although GSM is now available in the frequency range of 1800 MHz, known as DCS-1800, the primary GSM band is 935–960 MHz for the downlink (base to mobile) and 890–915 MHz for the uplink (mobile to base). The duplex method is FDD with a constant go-and-return frequency separation of 45 MHz.

The multiple-access technique used by GSM is TDMA plus FDMA. The available spectrum is divided into frequency channels separated 200 kHz. Each of these frequency channels is divided into 8 timeslots of duration 0.577 ms each, which makes frames of length 4.615 ms. Both traffic and signaling channels are mapped into these TDMA/FDMA physical channels according to a established pattern. The transmitted raw (after channel coding) bit rate is 270.83 kbps for each carrier (i.e., eight TDMA channels). The modulation is GMSK with a bandwidth such that $BT_b = 0.3$, where $1/T_b = 270.83$ kbps.

The signaling of the GSM is an ISDN version adapted to the mobility and radio environment. Figure 6 shows GSM network structure.

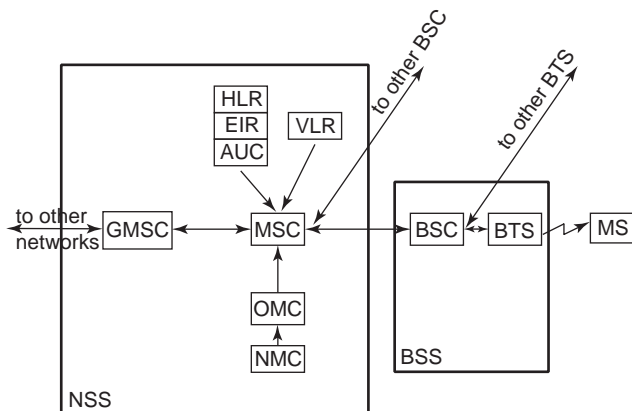


Figure 6. GSM network structure.

The GSM network is divided into three large segments: the mobile station (MS), the base-station subsystem (BSS), and the network switching subsystem (NSS).

BSS consists of the base transceiver station (BTS) and the base-station controller (BSC). BTS performs the physical-layer-related functions, while BSC contains the higher control functions. One BSC may control several (up to 10) BTSs.

The mobile (services) switching center (MSC) routes the calls toward the BSC closer to the MS. MSC gets the location of a particular MS from the home location register (HLR), which is updated so that it always contains the latest location of each mobile in the network. HLR also contains information about the user's profile. When a MS is roaming into a different network, the information in HLR regarding this user is copied to the visitors location register (VLR) of the host network.

The equipment identity register (EIR) and authentication center (AUC) are responsible for the network security and privacy. The operations management center (OMC) and network management center (NMC) handle the resources management and maintenance. Finally, the gateway mobile switching center (GMSC) connects the NSS to other networks.

The carrier services provided by GSM are voice and low-speed data with a maximum bit rate of 9.6 kbps. Voice is digitally coded at 13 K and 6.5 kbps. The former is known as *full-rate* (FR) and the later, as *half-rate* (HR). Although HR provides worse voice quality, it doubles the capacity of the network.

Additional services provided by the GSM network are calling-line identification, call forwarding, call waiting, call holding, multiparty, closed user group, advice of charge, reverse charging, user-to-user signaling, and barring outgoing and ingoing calls.

4.1.2. GPRS and EDGE. The General Packet Radio Service (GPRS) is a standard for data transmission across the GSM network. GPRS is part of the new services provided in phase 2+ of GSM. It supplements the GSM (phase 1) Circuit Switched Data Service by adding new functionalities in the core network that allow a packet-switched data transmission. Apart from the packet switching, GPRS has following novel features respect to GSM:

- *Bit Rate Transmission.* Theoretical maximum speeds of up to 171.2 kilobits per second (kbps) are achievable with GPRS using all eight timeslots at the same time. This is about 10 times faster than the maximum speed provided by circuit-switched GSM networks.
- *Immediacy.* GPRS facilitates instant connections whereby information can be sent or received immediately as the need arises. No dialup modem connection is necessary. This is why GPRS users are sometimes referred to be as being “always connected.” Immediacy is one of the advantages of GPRS when compared to circuit-switched GSM.
- *New Applications.* GPRS facilitates several new applications not previously available over GSM networks because of the limitations in speed of circuit-switched data (9.6 kbps) and message length of the short message service (160 characters).

EDGE (Enhanced Data for GSM Evolution), has been standardized within the European Telecommunications Standards Institute (ETSI) as the final evolution of data communications within the GSM standard. It uses a different modulation scheme to enable data throughput speeds of up to 384 kbps using existing GSM infrastructure.

Third-generation wireless systems will provide high-speed wireless access to wideband multimedia services where spectrum and licenses are made available. Today's GSM operators have two (nonexclusive) options for evolving their networks to third-generation wideband multimedia services: (1) use EDGE in the existing radio spectrum and in small amounts of a new spectrum or (2) use wideband CDMA in a new 2-GHz spectrum or in large amounts of an existing spectrum.

4.1.3. IS-95. In 1993 the Telecommunication Industry Association (TIA) produced the standard for the first CDMA cellular system under the nomenclature of IS-95. The usage of spread-spectrum techniques forecast a larger system capacity.

IS-95 uses a voice codec with variable bit rate. The IS-95 vocoder generates a bitstream at a 9600 bps rate, but it detects the silence periods and reduces the bit rate down to 1200 bps. Usage of a variable transmission rate further increases the network capacity.

Although they follow different spreading schemes, both downlink and uplink channels are spread by a pseudo-noise code of 1.2288 Mchip/s (megachips per second), such that the channel bandwidth is 1.25 MHz. IS-95 uses FDD duplexing with 45 MHz separation between the go-and-return. Frequency allocation is 869–894 MHz for the downlink and 824–849 for the uplink.

In addition to voice service, IS-95 also provides data transmission service at 9.6, 14.4, and 28.8 kbps.

4.1.4. IMT-2000. The goal of third-generation mobile systems is to provide users with worldwide coverage via handsets that have the capability to seamlessly roam between multiple networks (fixed and mobile, cordless and cellular) across regions that currently use different

technologies. Because their objective to provide larger capacity to accommodate multimedia transmission and better quality of service (QoS), third-generation (3G) mobile systems are one step beyond the digital cellular and cordless systems that are now in service. At the global level regarding 3G mobile systems, in ITU (International Telecommunications Union) there has been an initiative, IMT-2000, intended to settle the framework of the future telecommunication infrastructure. IMT-2000 will provide wireless access to the global telecommunications infrastructure through both satellite and terrestrial systems. It is being developed on the basis of the “family of systems” concept designed to be able to connect different radio transmission modules to the same core network equipment.

Different standards development organizations (SDOs)—ARIB (Japan), CWTS (China), TTA (USA), TTC (Korea), TTC (Japan), T1 (USA), and ETSI (Europe)—are participating in the development of this new “family of standards” including the creation of consortia and partnerships. There are two main active 3G partnership projects: 3GPP and 3GPP2. 3GPP is supported by the SDOs that were involved in specification of GSM systems and its evolution, while 3GPP2 comprises the SDOs involved in the ANSI/TIA/EIA-41 network evolution. 3GPP is working toward the definition of IMT-DS and IMT-TC air interfaces, which are better known as the UMTS (Universal Mobile Telecommunication System) on its FDD and TDD modes, respectively. 3GPP2 works toward the definition of an IMT-MC interface, which is better known as CDMA2000.

4.1.5. UMTS. UMTS defines a network architecture somewhat similar to GSM, as can be seen in Fig. 7, where three main functional entities, user equipment (UE), the UMTS terrestrial radio access network (UTRAN), and the core network are defined. The interfaces defined between the UE and the UTRAN is the Radio Interface (Uu) and the interface between the Core Network and the UTRAN, which is called Iu.

In order to simplify the migration from GSM to UMTS (see Fig. 8), the core network proposed for the first phase of UMTS deployment coincides with the GSM 2+ (GPRS) core network. Both the radio network subsystem (RNS) and UE are redefined by UMTS. For terrestrial applications, these two new subsystems, related to the radio interface, are defined by the UTRAN standard.

Functionalities of USIM, ME, Node-B, and RNC in UTRAN are equivalent to the functionalities performed by subscriber identity module (SIM), MT, BTS, and BSC in GSM. However, the specifications for these systems are modified in order to accommodate the higher capacity and better QoS. Maximum and minimum bandwidth of UMTS services are summarized in Table 1. As one of the main novelties of UMTS, the use of spread-spectrum modulation and CDMA can be highlighted to increase the overall network capacity (see Section 3).

4.1.6. CDMA2000. The CDMA2000 is the standard defined by 3GPP2 that includes air interface definition, minimum performance requirements, and definition of

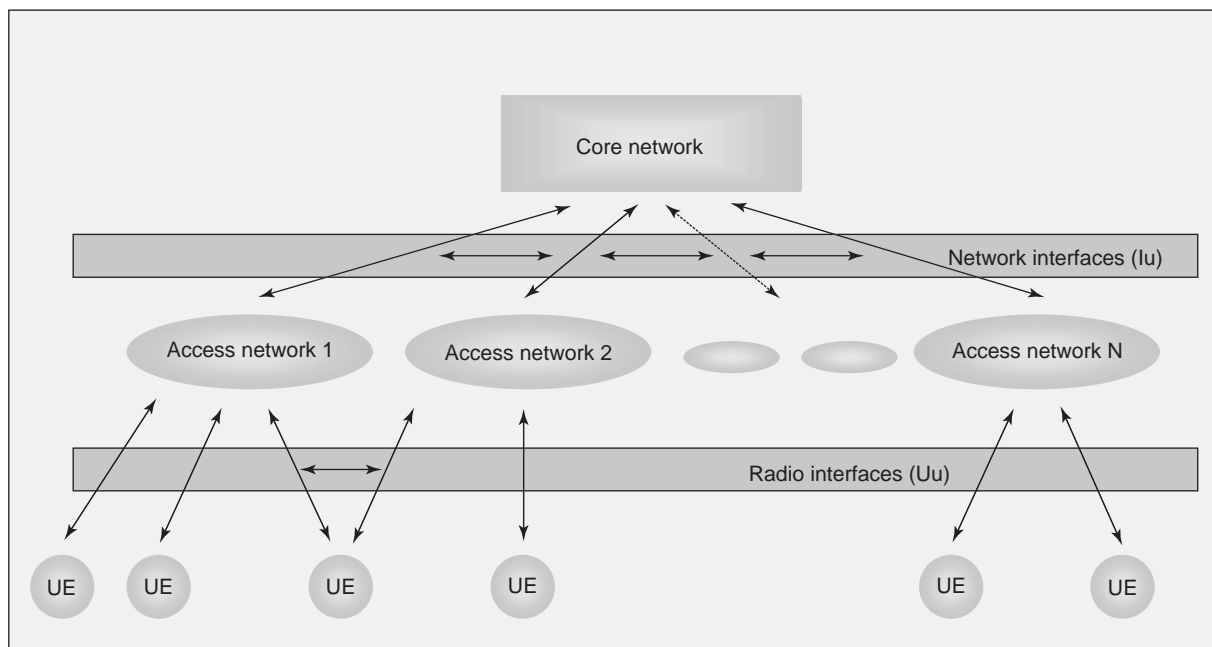


Figure 7. Functional entities in UMTS network architecture.

supported services. It meets all the requirements for the next-generation evolution of the current TIA/EIA-95-B (IS-95) standard and to be part of the “family of systems” concept designed by ITU to be able to connect different radio transmission modules to the same core network equipment. The CDMA2000 standard matches the ITU requirements for the IMT-2000 CDMA Multi-Carrier Mode (MC-CDMA).

The cdma2000 radio interface is a wideband, spread-spectrum interface that uses CDMA technology. It satisfies the ITU requirements for the indoor office, indoor-to-outdoor pedestrian, and vehicular environments. The key

design characteristics include a W-CDMA radio interface offering significant advances to increase performance and capacity, data rates ranging from 1.2 kbps to >2 Mbps, and support a wide range of RF channel bandwidths, advanced medium control access (MAC), turbo codes for higher transmission rates and increased capacity, and support for forward radio interface transmit diversity.

4.2. Cordless Systems

In contrast to cellular radio, cordless systems offer primarily an access technology rather than fully specified

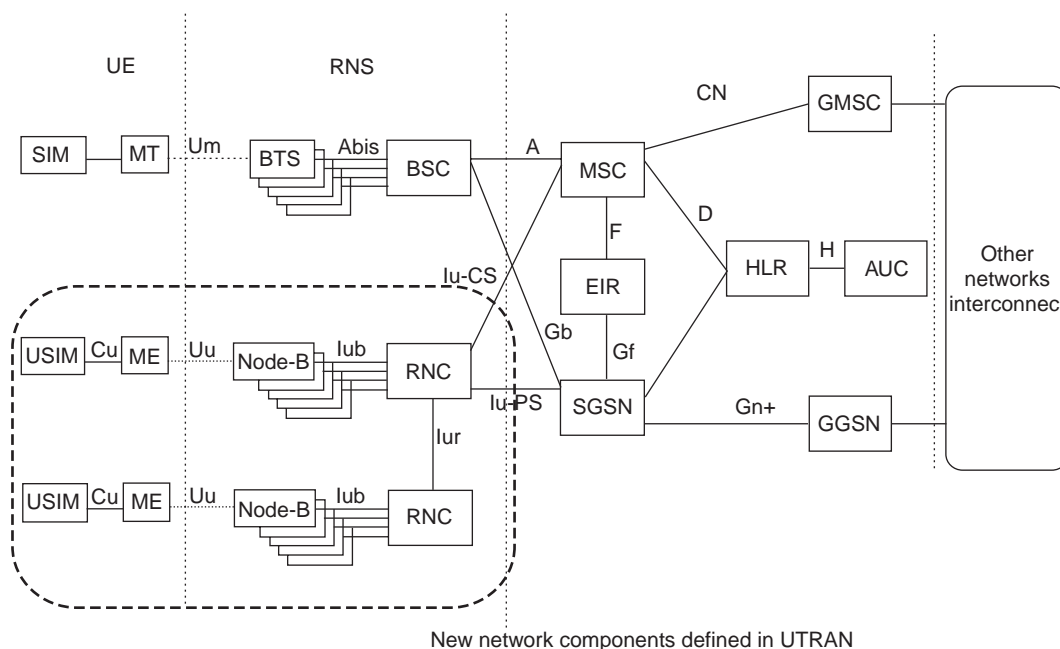


Figure 8. Comparison between GSM and UMTS architectures.

Table 1. Carrier Services Provided by UMTS^a

	FDD		TDD	
	Uplink Bit Rate	Downlink Bit Rate	Uplink Bit Rate	Downlink Bit Rate
Maximum	960	960	3840	3840
Minimum	15	7.5	240	240

^aIn kilobits per second (kbps).

networks. Cordless terminals generally transmit at lower power than cellular, using microcells with a range of a few hundreds of meters. In high-density environments, smaller cells are used to provide traffic densities higher than those obtained by cellular standards.

4.2.1. Services, Features, and Standards. Voice was the only service provided by early analog cordless systems. However, cordless technology has evolved and the cordless data market has become increasingly important as palm-top computers have emerged. DECT standard was specified to provide both voice and data services.

The potential of cordless access to permit user roaming between business and domestic applications was one of the key drivers of digital cordless standards. Also, the opportunity to offer public cordless access, generically known as *Telepoint*, was recognized. Thus, modern cordless telecommunications standards provide the following applications:

1. *Domestic Application.* The earliest application of cordless communication systems was the residential cordless telephone with a very simple base station giving service to the home environment and allowing the use of the telephone in such a small area. The domestic market was dominated by analog products because of the higher relative price of digital products.
2. *Business Application.* The potential business application of cordless telecommunications was one of the early drivers for development of the technology. Although early products focused on Telepoint, WPABX has shown significant progress. Wireless access in the PABX environment enables the user to obtain the wide range of PABX features while roaming across a business area. In new offices, the expense and delay of deploying a PABX can be avoided without the need of wiring up. ISDN as well as voice capabilities supported by the wired PABX can also be supported by WPABX. Also, mobility management functions must be incorporated so as to authenticate and locate users and route incoming calls.
3. *Telepoint.* *Telepoint*, also called *public access*, is a short-range radio system that enables a user with a portable handset to gain access to teleservices via a public fixed network like PSTN. CT2 was the first available Telepoint standard. DECT has also been specified to support public access. Although it is a European concept, the initial success of Telepoint has been in Asia, where early systems, combined with paging, have taken off in spite of the absence of the complementary domestic and business products. In contrast, early Telepoint experiences in Europe

failed to attract a significant number of users, probably because of the lack of standards and products at that time. New experiences were launched in 1992 using CT2 (“Rabbit” launched by Hutchison Telecom in UK, “Bibop” launched by France Telecom, “Birdie” launched by DBP Telekom in Germany, “Greenpoint” launched by PTT Netherlands, “Pointer” launched by Telecom Finland), which started showing greater success but ended up with unsatisfactory results (Rabbit and Birdie were phased out in 1993; Bibop continues with a number of users well below the self-sustaining level). Telepoint trials have also been carried out in Canada and the United States, under experimental FCC licenses. However, the implantation of low-cost personal communication services (PCS) has been a serious threat to the success of Telepoint.

4. *Wireless Access.* Although the applications mentioned in paragraphs 1–3 (above) led to the development of cordless standards and products, a fourth application has emerged with a new potential market for cordless telecommunications: the wireless local loop (WLL). Telecommunication services that used to be provided by wire from an exchange to the user’s premises are alternatively using cost-effective wireless standards. This use has been encouraged by the liberalization of telecommunications monopolies in Europe, leading to a number of potential service providers that do not own the wired infrastructure. Wireless local loops may be provided by different wireless technologies; cordless standards are one possible choice because of their low cost.

The main cordless standards, providing some of the applications listed above are as follows:

- CT0 (Europe) and CT1 (Europe): first-generation analog systems.
- CT2 (Europe): digital cordless FDMA standard using time-division duplex (TDD)
- PACS (USA), PHS (Japan) and DECT (Europe): the latest digital cordless telecommunication systems

Since DECT corresponds to the latest stage in the evolution of cordless systems, it will be explained in greater depth in the following section.

4.2.2. Digital European Cordless Telecommunications (DECT) Standard. DECT is based on a microcellular radio-communication system that provides low-power radio (cordless) access between portable parts (PPs) and fixed parts (FPs) at ranges up to a few hundred meters. The basic technical characteristics are as follows:

- Frequency band: 1880–1900 MHz
- Number of carriers: 10
- Carrier spacing: 1728 MHz
- Peak transmit power: 250 mW
- Carrier multiplex: TDMA; 24 slots per frame
- Framelength: 10 ms
- Basic duplexing: TDD using 2 slots on same RF carrier

- Gross bit rate: 1152 kbps
- Net channel rates: 32 kbit/s B-field (traffic) per slot; 6.4 kbps A-field (control/signaling) per slot

A connection is provided by transmitting bursts of data in the defined timeslots. These may be used to provide simplex or duplex communications. Duplex operation uses a pair of evenly spaced slots: one for transmission and one for reception. The simplest duplex service uses a single pair of timeslots to provide a 32 kbps digital information channel capable of carrying coded speech or other low-rate digital data. Higher data rates are achieved by using more timeslots in the TDMA structure, and a lower data rate may be achieved by using half-slot data bursts.

DECT is able to support a number of alternative system configurations ranging from single-cell equipment (e.g., domestic FPs) to large multiple-cell installations (e.g., large business WPABXs). Direct communication between portable parts (PPs) is also supported.

The protocols are designed to support uncoordinated system installation, even where the systems coexist in the same physical location. Efficient sharing of the radio spectrum (of the physical channels) is achieved using a careful mechanism of dynamic channel selection.

In addition, the DECT protocols provide two internal mechanisms to support rapid handover of calls in progress (both intracell and intercell handover are supported). These handover mechanisms allow a high quality of service to be maintained where the mobility of the PP requires transparent re-connection to another FP or where a new physical channel is required in response to disturbances in the radio environment. Detailed information about DECT standard may be found in Refs. 7–11. The latest introductions to the standard have dealt with interworking with GSM [12] and UMTS [13] and addition of a new packet service named DPRS (DECT Packet Radio Service) [14].

4.3. Trunking Systems

When we refer to a *trunked system*, or, equivalently a *private mobile radio* (PMR) system, we refer to a system where all the users share a pool with all the available channels. If a user wants to make a call, the system allocates one of the idle channels.

4.3.1. Features. The most important features of PMR systems are related to the special nature of their users.

1. PMR users, such as the emergency services, police, and firefighters handle incidents where calls are typically very short and speed of communication is vital. In contrast to cellular systems, where it takes several seconds to establish a call, the access to the PMR network takes tenths of a second.
2. PMR services allow group and broadcast calls.
3. PMR codecs are designed to provide good-quality speech in noisy environments.
4. New digital PMR systems can provide a user, on a dynamic basis, “bandwidth on demand.”

5. One powerful operational mode of PMR systems (not provided by cellular systems) is the so-called direct mode (DMO), the ability for radio handsets to communicate directly with each other without using the network infrastructure.

4.3.2. Standards. For completeness, we will summarize some of the digital technologies available.

The first one is the TETRA (Trans-European Trunked Radio). It is a radio open standard based on TDMA defined by ETSI (European Telecommunications Standards Institute). The TETRA standard contains high functionality for emergency services and is also very well suited for commercial trunked radio users.

There are other systems, all of which are proprietary and directed at users and markets similar to those for TETRA. The major ones are iDEN and ASTRO from Motorola, Aegis and PRISM from Ericsson, and Tetrapol from Matra. However, the majority of users have by now seen the benefits of standardization and are moving away from these proprietary systems.

In response, the manufacturers with their proprietary specifications have been increasingly attempting to have them adopted as a “standard” by national or international standardization bodies. The most active has been Matra, who developed a digital system called MatraCom, MC9600, a 12.5/10-kHz FDMA system initially sold to French Gendarmerie as Rubis and later its derivatives to other customers under various other names such as Acropolis, Pegas, and Nexus.

In order to promote these proprietary technologies as generic, Matra created the name Tetrapol and formed the so-called Tetrapol Forum. Also, as an active ETSI member, Matra has twice tried to have its technology selected by ETSI for the TETRA standard. Having failed on both occasions, the company has, this time as the Tetrapol Forum, declared its intent to have the Tetrapol specification considered for adoption as an ETSI deliverable under a so-called PAS (publicly available standard) procedures.

4.3.3. TETRA: The European Standard for Digital PMR.

TETRA (Trans-European Trunked Radio) is a radio open standard based on TDMA. In contrast to GSM, where manufacturers and operators have determined the specifications, the users, especially emergency service users, have contributed strongly in the creation of the standard. As a result, the TETRA standard contains high functionality for emergency services and is also very well suited for commercial trunked radio users. It is summarized as follows:

1. Technology
 - a. Physical-layer radio
 - i. Modulation: $\pi/4$ DQPSK
 - ii. Transmission rate: 36 kbps
 - iii. Duplex spacing: 10 MHz (45 MHz in 900-MHz band)
 - iv. RF carrier spacing: 25 kHz
 - b. Frequency bands. TETRA has been designed to work in the frequency range from VHF (150 MHz)

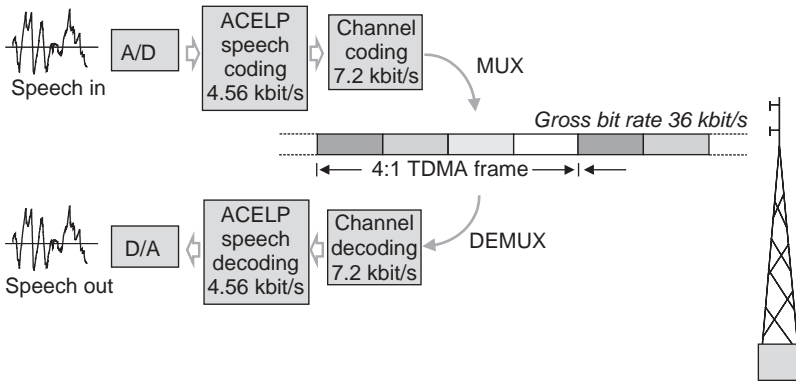


Figure 9. Speech coding and multiplexing in TETRA. Digitized speech is coded, using an ACELP coder, protected, by introducing redundancy, and inserted in a TDMA frame. (This figure is available in full color at <http://www.mrw.interscience.wiley.com/erfme>.)

to UHF (900 MHz). In particular, standardization bodies have released bands in the frequency range 380–400 MHz for public safety users.

- c. **Speech coding.** The TETRA codec was designed to provide good-quality speech in harsh environments and voice quality superior to that of GSM in the poor-signal conditions. In TETRA systems speech is digitized and coded using an ACELP (algebraic code-excited linear prediction) speech coder. In order to protect the transmitted information, a channel coder introduces additional redundancy. The resulting bit rate is 7.2 kbps. TETRA has the capability of using four TDMA slots, which allows managing four voice communications on the same carrier (see Fig. 9).
- d. **Data transmission.** TETRA can provide a user, on a dynamic basis, with up to four TDMA slots in a single communication channel, effectively “bandwidth on demand.” This applies to packet-mode and circuit-mode data, with data rates of ≤ 28 kbps.
- e. **TDMA frame structure.** The TETRA frame structure has four slots per TDMA frame. This is further organized as 18 TDMA frames per multiframe, where one frame per multiframe is always used for control signaling. Besides, there is a hyperframe imposed above the multiframe structure. This is for long repeat frame purposes such as encryption synchronization. Each timeslot has 510 (modulating) bits duration and has the basic structure shown in Fig. 10.

- f. **Spectrum efficiency.** TETRA is one the most frequency-efficient standard for mobile communication, equivalent to 6.25 kHz per channel, voice or data. This means that TETRA is currently 4 times more spectrum efficient than GSM, and twice as efficient when the half-rate codec is implemented. Regarding other PMR systems, TETRA can accommodate up to 4 times more users.
2. **Features.** In addition to the features of other public cellular systems, TETRA offers a series of additional services. The most important ones are.
 - a. **Group call and group communication**—a number of users share the same channel. This enables many users to cooperate on a specific task or to monitor the activities of other members of the group.
 - b. **Fast call setup**—TETRA makes it possible to set up calls in less than 0.3 s.
 - c. **Direct mode**—allows terminals to communicate directly with each other independently of the radio infrastructure, or in areas with no coverage.
 - d. **Mobile terminal used as repeater**—a mobile terminal can be used as a repeater and in this way extend the coverage of the TETRA network.
 - e. **Encryption**—TETRA offers a very high degree of encryption of both voice, data, signaling, and user identity. TETRA defines two methods of encryption: air interface encryption and an optional end-to-end encryption for the most critical applications.
 - f. **Broadcast**—transmission of messages to all users of the network.

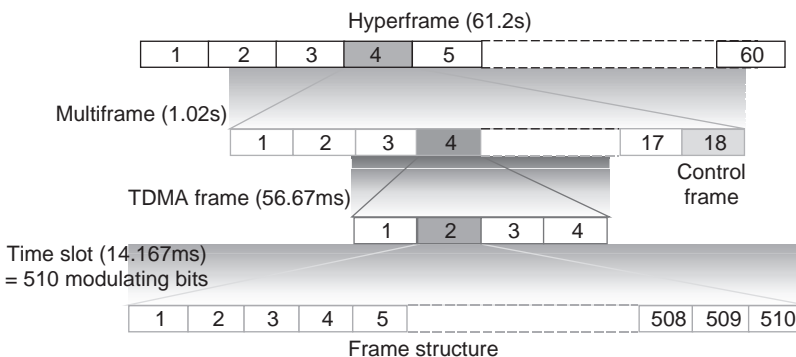


Figure 10. Hierarchical structure of frames in TETRA. (This figure is available in full color at <http://www.mrw.interscience.wiley.com/erfme>.)

- g. Priority—possibility of priority in up to eight levels; also, calls with high priority can “overrule” calls with low priority if no idle channels are available.
3. Typical of TETRA users
- a. Public safety and public security (police, fire, ambulance, customs, etc.)
 - b. Transport (airlines, ports, taxis, buses, railways, etc.)
 - c. Utilities (gas, electricity, water, oil, etc.)
 - d. Industry (manufacturing, plant, distribution, etc.)
 - e. Nonemergency authorities (government, public health, environment protection, etc.)

4.4. Paging Systems

A radio paging system is a wireless messaging system that allows continuous accessibility to someone away from the wired communications network. In its most basic form, the person on the move carries a palm-sized device (the pager) that has an identification number. The calling party inputs this number, usually through the public telephone network, to the paging system, which then signals the pager to alert the called party.

Pager types and existing standards are described in this section.

4.4.1. Pager Types. Several types of pagers are commercially available:

- *Tone-only*—pager alerts user; user takes predetermined action, such as calling a predetermined phone number.
- *Numeric pager display*—pager alerts user and displays numeric message; user calls phone number displayed.
- *Alphanumeric and ideographic display*—pager alerts user and displays text message; user can then take necessary action.
- *Tone and voice*—pager alerts user, then delivers short (10–20 s) voice message; user can then take necessary action.
- *Stored voice*—pager silently alerts and stores voice message for recall at user’s convenience.

4.4.2. Standards. Different manufacturers have developed an array of techniques to forward the required information to remote pagers. These techniques, known as *encoding formats*, define the techniques employed to represent the information-carrying data elements of the protocol as well as how to interpret the overall data content.

In many cases, encoding formats send additional data, known as *error detection and correction codes*, that are capable of detecting and recovering incorrectly received data. With error correction, pager receipt reliability is improved dramatically. Both analog and digital transmission techniques are used to transfer information to pagers.

Most paging formats are manufacturer-specific and often proprietary. A few paging protocols have been devel-

oped and put into the public domain so that many different manufacturers may produce compatible pagers. Among these public domain protocols are POCSAG, Swedish Format (MBS), the Radio Data System (RDS) format, and the European Radio Message System (ERMES) format. All of these formats were developed in Europe.

European Radio Message Standard (ERMES) Format.

The European Radio Message Standard (ERMES) is a standard that was developed by a subcommittee of the European Telecommunications Standards Institute (ETSI).

The ERMES digital encoding format supports tone-only, numeric, and alphanumeric paging in addition to data transfer capabilities. The format operates at 6250 bps. ERMES pagers operate on multiple frequencies, scanning for the best frequency for optimum reception.

The paging format uses a modulation mechanism known as “four-level pulse amplitude modulated FM.” In this mechanism, two binary bits of information are transmitted simultaneously through the transmission of one of four signaling frequencies. One set of frequencies is interpreted as the two binary bits “00,” another as “01,” another as “10,” and the final frequency as “11.” Therefore, with frequency transitions at the rate of 3125 per second, 6250 bits of information may be transferred. Under the ERMES protocol, every hour is broken up into 60 cycles, each one minute in duration (cycles 0–59). Each cycle is divided into five equal subsequences of 12 seconds each (subsequences 0–5). Finally, each 12-s period is divided into 16 separate batches (batches A–P). A batch contains separation partitions of information known as the *synchronization partition*, *system information partition*, *the address partition* and the *message partition*.

Within each batch, the address partition contains the first 18 bits (the initial address) of the unique pager number, a 35-bit address known as the *radio identity code* (RIC), ordered in descending order. This technique allows a pager to quickly determine whether its unique address is not part of this batch so that it may return to battery-saving mode. All pagers whose addresses are larger than the initial address can return immediately to battery-saver mode. Messages are transmitted directly after the address partition. The large (35-bit) address field accommodates a global address scheme that can support hundreds of millions of pagers.

4.5. Wireless Local-Area Networks (WLANS)

Wireless local-area networks (WLANS) constitute an evolution of the small-area data communication networks used to interconnect computers and peripherals, in which wired transmission is replaced by radiocommunications. They find their primary use inside buildings or in outdoors locations like the university campus.

The main features and the most commonly used standards are briefly described.

4.5.1. Services, Features, and Standards. The existing service scenarios for WLAN are mainly private local networks in workplaces, campuses, or public areas such as

airports. Universal access points in homes and nomadic access in public places can be provided by either WLAN or cordless standards and are experiencing an increasing interest. The WLAN market currently aims at five categories of applications: healthcare, factory floors, banking, educational institutions, and domestic applications.

Some examples of WLAN standards are

- IEEE 802.11: part of the IEEE 802 family of LAN standards, initially using either infrared (IR), direct-sequence spread spectrum (DSSS), or frequency-hopping spread spectrum (FHSS). Recent extensions looking for higher bit rates have included new modulation techniques (CCK—complementary code keying—in IEEE 802.11b and OFDM—orthogonal frequency-division multiplexing—in 802.11a).
- HIPERLAN: a family of standards prepared by ETSI (European Telecommunications Standards Institute) whose first outcome was HIPERLAN 1 (using GMSK modulation) with little success; the second outcome was HIPERLAN 2, using the same modulation as IEEE 802.11a.
- HomeRF: an WLAN standard specifically designed by the industry for in-home applications with special emphasis on voice services (using a modified version of DECT) and connection of the home computer to the Internet.

Table 2 summarizes the main characteristics of these standards. IEEE 802.11, the most commonly used WLAN standard nowadays, is described more deeply in the following section.

4.5.2. IEEE 802.11 Standard. The IEEE 802.11 standard for WLAN [15] has established itself as a mature standard presenting a well-defined technology that is being adopted by the manufacturers and accepted by users.

The earlier versions of IEEE 802.11 (1997) specified data rates of ≤ 2 Mbps using spread-spectrum technology (direct sequence or frequency hopping) in the 2.4-GHz band. IEEE 802.11b provides data rates of ≤ 11 Mbps in the same band, while IEEE 802.11a, an extension to the 5 GHz band, increases the data rate up to 54 Mbps. Alternatively, the version of 1997 allows infrared technology to be used at 850–950 nm.

Multiple access is based in CSMA/CA (carrier sense multiple access with collision avoidance), a contention-based scheme suitable for asynchronous applications. The

standard also supports a contention-free prioritized point coordination function (PCF) mechanism for time-bounded isochronous applications.

Two network topologies are considered: infrastructure-based and ad hoc.

4.6. Wireless Personal Area Networks (WPANs)

The term *wireless personal area networks* (WPAN) refers to a technology using short-range radiolinks, intended to replace the cable(s) connecting portable and/or fixed electronic devices. Its key features are robustness, low complexity, low power, and low cost, which make it especially suited to mobile handheld devices. The WPAN technology can also offer wireless access to LANs, PSTN, the mobile phone network, and the Internet for a host of home appliances and portable handheld interfaces.

The objective of the WPAN technology is to provide a uniform structure for a wide range of devices to communicate with each other, anywhere in the world, with minimal user effort. This feature introduces the “unconscious connectivity” paradigm, where WPAN devices can connect to those in the proximity almost without any user command or interaction.

4.6.1. Technical Challenges. The above mentioned requirements involve great technical complexity in terms not only of the functionalities to be provided but also of the power and size requirements. In this way, the WPAN technology must face the following technical challenges:

- The system has to use an unlicensed band for universal acceptance and usage. Thus, the industrial—scientific—medical (ISM) band is usually selected for this technology. The challenge here is to make the system robust to interference from other sources in this band, which include not only ISM band communication systems but also microwave ovens.
- Preferably, each transmitter itself should use the minimum power required so as not to increase the noise for other users.
- The transceivers should be able to adapt to a rapidly changing environment, as the devices will usually be mobile. The well-known problems in wireless systems such as multipath fading must be handled.
- The connection establishment and routing protocols must also operate in an environment where the number, location, and variety of WPAN devices will change dynamically with fair amount of rapidity.

Table 2. Characteristics of WLAN Products

	IEEE 802.11b	IEEE 802.11a	Hiperlan 2	HomeRF
Range (m)	30	50	50	50
Modulation	DSSS + CCK	OFDM	OFDM	FHSS
Main scenario	Office	Office	Office	Home
Power	100 mW	1 W	1 W	100 mW
Voice services	No	No	No	Yes
Minimum data rate (Mbps)	1	6	6	0.8
Maximum data rate (Mbps)	11	54	54	1.6

- The size of the implementation should be small for easy integration into handheld and mobile devices.
- The power consumption should not be more than a small fraction of the host device into which the WPAN capability is to be introduced.
- The technology should be adaptable to devices of varying computing power and memory resources. This will ensure that an increasing number of devices can interoperate.
- Automatic and unconscious connection establishment must be provided. The number and identity of devices in proximity will change quite frequently, and it will be very inconvenient to establish connections manually each time. Also, the number of devices will be too large for most users to be able to remember or search the device address of the device that they need to connect to.
- Synchronization of clocks among the communicating units will have to be achieved. As each unit will have its own free-running clock with its own drift, carrying out successful communication, especially CDMA, is a challenge in itself.
- Security considerations have to be satisfied. The WPAN devices will be part of people's personal usage and will contain and communicate their personal information, sensitive business information, or other data that must be protected from being spoofed or mutilated. The encryption facility must thus be provided among other security features.

4.6.2. Bluetooth. Bluetooth wireless technology is a specification designed to enable wireless communication between small, mobile devices. The inspiration behind this technology was the concept of eliminating the need for proprietary cables, which are currently required to enable device connectivity.

While Bluetooth wireless technology has many features unique to its own specification, it has borrowed heavily from several existing wireless standards, including Motorola's Piano, IrDA, IEEE 802.11, and Digital Enhanced Cordless Telecommunications (DECT). Motorola's Piano was developed with the concept of forming ad hoc "personal area networks." This concept was adopted by the Bluetooth SIG to expand the capabilities of the original Bluetooth concept beyond simple cable replacement. The voice data transmission capabilities of Bluetooth are derived from the DECT specification. The object exchange capabilities (the ability to share business card, contact information, messages, etc.) are derived from the IrDA specifications. Bluetooth also inherits the use of the 2.4-GHz ISM band, frequency-hopping spread spectrum (FHSS), authentication, privacy, power management, and LAN capabilities provided by the IEEE 802.11 specification.

There are four major components in any Bluetooth wireless technology system: a radio unit, a baseband unit, a software stack, and application software. The *radio unit* is the actual radio transceiver that enables the wireless link between Bluetooth devices. The *baseband unit* is hardware, consisting of flash memory and a CPU,

which interfaces with the radio unit and the host device electronics at the hardware level. The baseband hardware provides all required functionality to establish and maintain a Bluetooth wireless connection between devices. The *software stack* is essentially driver software or firmware that enables the application-level software to interface with the baseband unit. The *application software* implements the user interface and overall functionality of the Bluetooth device.

4.6.2.1. Bluetooth Radio. Bluetooth Radio uses the unrestricted 2.45-GHz ISM band, which is available globally with slight constraints in some locations relating to bandwidth and power output. Using a frequency hop transceiver with hops occurring at 1600 s^{-1} interference and fading effects are minimized since each packet is transmitted in a different hop frequency.

A time-division duplex scheme is used for full-duplex transmission. Within the range of 10 cm–10 m, a gross data rate of 1 Mbps can be achieved to service mobile and business users. The range can be extended beyond 100 m by increasing the transmit power. Second-generation plans are to increase the data rate to 2 Mbps.

Bluetooth can support an asynchronous data channel, up to three simultaneous synchronous voice channels, or a channel that simultaneously supports asynchronous data and synchronous voice. Each voice channel supports a 64 kbps synchronous (voice) link. The asynchronous channel can support an asymmetric link of 721 kbps maximum in either direction while permitting 57.6 kbps in the return direction, or a 432.6 kbps symmetric link allowing for easy integration of TCP/IP for networking.

Collections of devices connected via Bluetooth technology in an ad hoc fashion are called a *piconet* (Fig. 11a). Each unit can simultaneously communicate with up to seven other units per piconet (Fig. 11b). Although all devices are peer units, one acts as the "master" and the others as "slaves" for the duration of the connection to the piconet. The master unit provides the hopping sequence to synchronize all the devices in the piconet. A scatternet (Fig. 11c) is a collection of piconets that operate independently and are not synchronized. This allows a large group of devices to network with each other by means of smaller subnets. Since each piconet has the capacity of 1 Mbps between devices, scatternets allow the total throughput

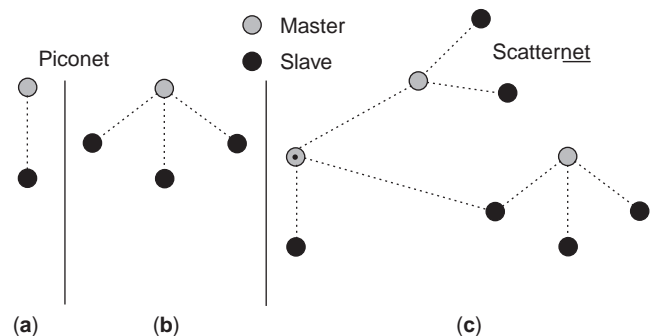


Figure 11. Bluetooth scatternet and piconet concepts.

accumulated over all piconets to increase as more piconets are added. Testing has proved that the overall speed reduction of a scatternet consisting of 10 piconets is less than 10% due to collisions. This results in the potential total network throughput of approximately 9Mbps.

5. ADVANCED TECHNOLOGIES AND SYSTEMS

Wireless communications are in continuous evolution [16]. We aim to introduce here some of the technologies and systems that today are yet to be fully developed and will constitute the wireless products of the next decades.

5.1. Advanced Wireless Technologies

Some of the advanced technologies being developed for wireless communications are briefly described as follows.

5.1.1. Multiuser Detection (MUD) and Blind Detection.

The continued expansion of the mobile cellular industry is translated to a need for increasing density of users within any given area without any corresponding increase in the frequency allocation. This heightens the probability of users and/or services interfering with one another, implying a need for new schemes to provide sophisticated interference cancellation approaches for a more efficient utilization of spectrum and space, at any time. Techniques known as *multiuser detection* (also as *joint detection*, *interference cancellation*, or *source separation*) consider multiple-access interference (MAI) not as a simple interference to be suppressed but as a composite signal that can be processed and separated.

The optimum MUD algorithm [23], based in a maximum-likelihood (ML) criterion, has a complexity growing exponentially with the number of users. That is the reason why many different suboptimal schemes are being developed.

Some of these algorithms do not need the introduction of reference sequences as an aid in the detection process, in what is known as *blind detection* [24]. The avoidance of overheads implies a more efficient use of the system capacity.

5.1.2. Smart Antennas. “Smart” antennas (or adaptive antennas) combine multiple antenna elements with a signal-processing capability in order to optimize the radiation and/or reception pattern automatically in response to the signal environment. This ability to adapt to a changing interference environment can dramatically increase the performance characteristics and capacity of a wireless system.

An overview of Smart Antenna applications can be found in Ref. 27.

5.1.3. Space-time Transmission Diversity (STTD). The concept of space-time transmission diversity (STTD) comes from the extrapolation of receivers’ antenna diversity widely used in 2G. The idea of receiver antenna diversity is to place two (several in general) antennas in different locations and select the output of the one with better signal-to-noise-plus-interference ratio (SINR).

Placing two antennas in reception defines two different radio channels, understanding as a channel the radiowave propagation between transmitter antenna and each of the receiving antennas. If the two receiving antennas are sufficiently separated, and for this purpose 10 times the wavelength is enough, the statistics of the two channels are independent. Therefore, the probability of having a deep fading on both channels simultaneously is the square of the probability of having a deep fading on one of them. In consequence the link quality is roughly speaking improved in 3 dB.

The extrapolation of the diversity concept to transmitting antennas is known as *spacetime transmit diversity* (STTD), which works as follows. Two (or several) transmitting antennas placed at relative distant location transmit simultaneously the same information but coded by different coding schemes. The coding schemes should be orthogonal; that is, the coded bit sequences transmitted by each antenna should be orthogonal to each other. In this way, the signal received from each antenna can be demodulated independently, and they can be used as two different copies of the same signal for the diversity purposes.

3G mobile systems may implement STTD techniques. The September 2000 release of 3GPP states that implementation of STTD will be optional for Node-B, but UE shall have the functionalities to support. There are multiple coding schemes for STTD; however, 3GPP adopted a reduced complexity algorithm proposed by Alamouti, which uses only two transmitting antennas [28].

5.2. Future Systems

The deployment of third-generation cellular systems with the provision of multimedia services over wireless networks represents the trends in wireless communications for the near future. Besides, satellite-based mobile services are expected to follow terrestrial systems toward a global 3G.

Now, a step further, the fourth generation, is already being investigated, mainly with two approaches in mind: software-defined radio (SDR) and integration of the multiple existing networks providing different but complementary services.

5.2.1. Mobile Satellite Systems. Because of the global coverage of satellites, mobile satellite services (MSS) systems will fill the gaps in areas where cellular terrestrial systems are physically or economically impractical to be implemented. Satellite systems may be classified according to the orbital altitude of the satellites being used: geostationary satellites (GEO), at an altitude of approximately 36000 km; low-Earth orbit satellites (LEO), at altitudes on the order of 1000 km; medium-Earth-orbit satellites (MEO), at intermediate altitudes between LEO and GEO; and highly elliptical orbit satellites (HEOS), with elliptical orbits of widely varying altitudes.

MSS systems have been implemented and are being designed with any of these types of satellites. One advantage of using GEOs is that global coverage (excluded polar latitudes) can be achieved with only three satellites. LEOs minimize the required transmitted power and propagation

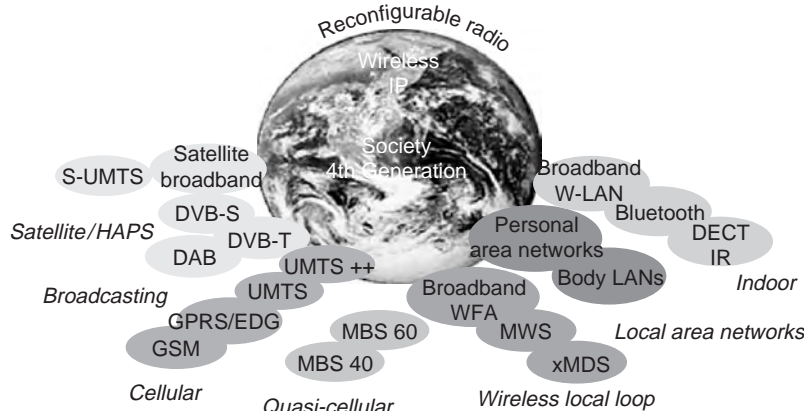


Figure 12. The multiple-system view of the European Commission. (This figure is available in full color at <http://www.mrw.interscience.wiley.com/erfme>.)

delay, but LEO systems have produced disappointing results in the deployment experiences of the last years (Iridium, Globalstar, etc.).

An alternative that is being tested in several trials are HAPS systems (high-altitude platform stations). They consist of stratospheric communication platforms that can be deployed in populated areas in order to complement the traffic capabilities of terrestrial systems.

Further details about future satellite systems may be found in Ref. 25.

5.2.2. Software-Defined Radio (SDR). Since the publication of J. Mitola's article in 1994 [29], many efforts have been carried out in order to achieve the so-called software-defined radio (or simply *software radio*). SDR are communication transceivers in which the tendency is toward programming as many functionalities as possible in software, using analog-to-digital and digital-to-analog converters, as close as possible to the antenna. One of the first experiments in the field of SDRs is the U.S. military software radio called "Speakeasy" [30]. After that, several projects have been carried out both in the United States and Europe, where SDRs were intended as a solution to the problem of different 3G standards defined in different parts of the world, contrary to the first idea of a universal unique 3G system.

Today SDRs are seen as the way toward the integration of many different systems, each achieving a different performance level in one of the various scenarios that constitute the target of the fourth generation of wireless communications.

System Integration: Toward Multisystem Multiservice Networks. At present we are witnessing a very wide span of wireless products, many of which have been described in this article, that aim to satisfying the needs of certain users in certain environments. Figure 12 shows as an example the vision of the European Commission with respect to this plethora of wireless communication standards and systems [1].

The current trend toward 4G is not just to invent some new systems, but mainly to take advantage of the capabilities of the many existing standards, making them work

together in a synergic way, so as to fulfill the communication demands of everybody. As mentioned above, one possible way to make different systems work together is through reconfigurable radios (SDRs).

The example of complementary use of wireless systems that is obtaining the greatest attention these days is the combination of cellular and WLAN systems. In this way, both systems satisfy the user's needs, the first achieving a wide coverage but with lower data rates, and the latter filling the data rate gap in small and crowded areas (hot-spots) such as meeting rooms, shopping malls, or airports.

A novel but promising application of the WLAN is what is being called "neighbor-area network" (NAN). This type of network is based on the idea of allowing users from a neighborhood to connect to an access point connected to WAN, typically an ADSL (asymmetric digital subscriber line) connection. In this way, users from that area can connect to the Internet sharing the cost of the WAN connection, so they can access to higher QoS at the same price. With an ordinary base station, wireless networking is possible within a range of about 75 m. But simply replacing the standard access point antenna by a simple rooftop antenna causes the range to increase considerably - certainly to 500 m, and maybe more.

As another example of the synergies that are being encouraged, we may mention the case of TETRA: ETSI Project TETRA release 1 was virtually completed during 2000. A new 3-year work program for TETRA release 2 was approved by the ETSI Board in September 2000. The main objectives of the new release are to enhance TETRA in order to provide packet data at much higher speeds, standardize additional speech codec(s), enable intercommunication between TETRA and other 3G networks without transcoding, and adopt new standards to provide improved interworking and roaming between TETRA and public mobile networks such as GSM, GPRS, and UMTS.

BIBLIOGRAPHY

1. CORDIS: Community Research and Development Information Service, <http://www.cordis.lu>.

2. J. S. Dasilva, B. Arroyo, B. Barani, and D. Ikononou, European third generation mobile systems, paper presented at ACTS Mobile Telecommunications Summit; Granada, Spain, November 27–29, 1996.
3. CTIA (Cellular Telecommunications Industry Association), <http://www.ctia.org/>.
4. R. Prasad, *Universal Wireless Personal Communications.*, Artech House, Norwood, MA, 1998.
5. H. Hashemi, The indoor propagation channel, *Proc. IEEE* **81**:943-968 (July 1993).
6. T. S. Rappaport, S. Y. Seidel, and R. Singh, 900MHz multipath projection measurements for U.S. digital cellular radio telephone, *IEEE Trans. Vehic. Technol.* 132-139 (May 1990).
7. ETSI EN 300 175-1, *Digital Enhanced Cordless Telecommunications (DECT), Common Interface (CI); Part 1: Overview.*
8. EN 300 175-2, *Digital Enhanced Cordless Telecommunications (DECT), Common Interface (CI); Part 2: Physical Layer (PHL).*
9. EN 300 175-3, *Digital Enhanced Cordless Telecommunications (DECT), Common Interface (CI); Part 3: Medium Access Control (MAC) Layer.*
10. EN 300 175-4, *Digital Enhanced Cordless Telecommunications (DECT), Common Interface (CI); Part 4: Data Link Control (DLC) Layer.*
11. EN 300 175-5, *Digital Enhanced Cordless Telecommunications (DECT), Common Interface (CI); Part 5: Network (NWK) Layer.*
12. ETS 300 756, *Digital Enhanced Cordless Telecommunications (DECT), Global System for Mobile Communications (GSM); DECT/GSM Interworking Profile (IWP); Implementation of Bearer Services.*
13. TS 101 863-1, *Digital Enhanced Cordless Telecommunications (DECT); DECT/UMTS Interworking Profile (IWP); Part 1: General Description and Overview.*
14. EN 301 649, *Digital Enhanced Cordless Telecommunications (DECT); DECT Packet Radio Services (DPRS).*
15. ISO/IEC 8802-11, 1999 (ANSI/IEEE Std 802.11, 1999 ed.), *Information Technology—Telecommunications and Information Exchange between Systems — Local and Metropolitan Area Network — Specific Requirements — Part II: Wireless LAN Medium Access Control (MAC) and Physical Layer (PHY) specifications.*
16. R. Schneiderman, *Wireless Personal Communications—the Future Talk*, IEEE Press, 1994.
17. Special issue on Wide-band CDMA: *IEEE Commun. Mag.* **36**(9) (Sept. 1998).
18. J. A. C. Bingham, Multicarrier modulation for data transmission: An idea whose time has come, *IEEE Commun. Mag.* **28**:5–14 (May 1990).
19. ETS 300 401, *Radio Broadcasting Systems; Digital Audio Broadcasting (DAB) to Mobile, Portable and Fixed Receivers*, ed.2 (1997-05).
20. EN 300 744; *Digital Video Broadcasting (DVB); Framing Structure, Channel Coding and Modulation for Digital Terrestrial Television*, V1.2.1 (1999-01).
21. S. B. Weinstein and P. M. Ebert, Data transmission by frequency-division multiplexing using the discrete Fourier transform, *IEEE Trans. Commun. Technol.* **COM-19**(5): 628-634 (Oct. 1971).
22. S. Hara and R. Prasad, Overview of multicarrier CDMA, *IEEE Commun. Mag.* **35**(12):126-133 (Dec. 1997).
23. S. Verdu, Minimum probability of error for asynchronous gaussian multiple access channels, *IEEE Trans. Inform. Theory* **IT-32**(1):85-96 (Jan. 1986).
24. M. L. Honig, U. Madhow and S. Verdu, Blind adaptive multiuser detection, *IEEE Trans. Inform. Theory* **41**(4):944-960 (July 1995).
25. J. Farserotu and R. Prasad, A survey of future broadband multimedia satellite systems, issues and trends, *IEEE Commun. Mag.* **38**(6):128-133 (June 2000).
26. V. H. MacDonald, The cellular concept, *Bell Sys. Tech. J.* **58**(1):15-43 (Jan. 1979).
27. K. Sheikh, D. Gesbert, D. Gore, and A. Paulraj, Smart antennas for broadband wireless access networks, *IEEE Commun. Mag.* **37**(11):100-105 (Nov. 1999).
28. S. M. Alamouti, A simple transmit diversity technique for wireless communications, *IEEE J Select. Areas Commun.* **16**(18) (Oct. 1998).
29. J. Mitola, The software radio architecture, *IEEE Commun. Mag.* **33**(5):26-38 (May 1995).
30. R. J. Lackey and D. W. Upmal, Speakeasy: The military software radio, *IEEE Commun. Mag.* **33**(5):56-61 (May 1995).

YAGI-UDA ANTENNA

NORIAKI KANEDA
 Lucent Technologies
 Holmdel, New Jersey
 W. R. DEAL
 Northrop Grumman Space
 Technology
 Redondo Beach, California

1. INTRODUCTION

The Yagi-Uda antenna, commonly used for broadcast television reception, is one of the most prevalent and recognizable antennas in existence. It has several desirable characteristics, including low cost and simple assembly, low weight, and radiation qualities adequate for many applications. While its popularity has waned in the United States in the past few decades because of the widespread availability of cable and dish-based satellite television services, it remains a familiar accompaniment on roofs throughout the world. Currently, with the introduction of high-definition broadcast television in the United States, the Yagi-Uda antenna is undergoing somewhat of a resurgence in popularity in many areas. It is true, however, that the Yagi-Uda is one of the most commonly found antennas in the world.

The Yagi-Uda was first described in English in 1926 [1] by Professor H. Yagi and (then) Instructor S. Uda at Tohoku University in Sendai city. More commonly referred to is Yagi's English language publication [2] of 1928, which was reprinted in 1997 [3]. The impact of this paper was significant. Included in Ref. 2 were the published comments of J. H. Dellinger, chief of the Radio Division of the Bureau of Standards: "I have never listened to a paper that I felt so sure was destined to be a classic." At this point in radio history, engineers had just begun to develop directional communications systems. The Yagi-Uda provided a practical higher-gain antenna.

The antenna has had a fascinating history, which is detailed by Gentai Sato [4]. According to Sato, although invented in Japan, it was largely forgotten until the Japanese military discovered its application to British radar in 1942. In addition to its common application in radars and television antennas, it is popular with ham radio aficionados.

This article is divided into three sections. In Section 2 the antenna is introduced and key concepts about its operation are discussed. In Section 3 some practical information on designing wire Yagi-Uda antennas is described along with a common graphical technique for determining the dimensions of the elements. In Section 4 a number of newer antennas that utilize the underlying concepts of the wire Yagi-Uda Antenna are described. These antennas are typically intended for higher-frequency applications.

2. THEORY OF OPERATION

A diagram of the typical Yagi-Uda antenna is shown in Fig. 1. It consists of a *driven* element, a single *reflector*, and a number of *director* elements (in this case, five directors are shown). The meaning of these terminologies will be detailed shortly. The configuration forms a directive, endfire array with the main beam focused in the y direction. Design variables are N (total number of elements), l_n (length of n th element), s_n (spacing between n th and $n + 1$ element), and a (radius of the element). Only the antenna elements are shown in the figure; a supporting boom for the elements is also required and may have some effect on the radiation qualities.

The Yagi-Uda's driven element is the only element in the array where the signal is directly fed or collected by transmission lines. The other array elements are parasitic elements that have no direct feeding, thus simplifying the construction of antenna array. Unlike ordinary antenna arrays where the amplitude and phase can be independently defined, the Yagi-Uda utilizes near-field mutual coupling between antenna elements. Although the feeding mechanism of the Yagi-Uda array has significant difference from the ordinary linear antenna array, the elements also line up in a straight line. Thus the majority of linear antenna array theory can be utilized to understand the nature of this antenna array.

From fundamental antenna theory, the far-field radiation pattern of an isotropic point source is proportional to, $I_0 e^{-j\beta r} / 4\pi r$, where I_0 is the current of the point source antenna, β is the free-space propagation constant, and r is the distance from source to the observation point. Now we consider the linear array consisting of isotropic radiators lined up in a straight line along the z axis with elements spaced an equal distance d as in Fig. 2. The contribution from each element forms a far-field radiation pattern as

$$\text{AF} \frac{e^{-j\beta r}}{4\pi r} \quad (1)$$

where AF stands for array factor, expressed in

$$\begin{aligned} \text{AF} = & I_1 + I_2 e^{j\beta d \cos \theta} + I_3 e^{j2\beta d \cos \theta} \\ & + \dots + I_{n+1} e^{jn\beta d \cos \theta} \end{aligned} \quad (2)$$

When a realistic antenna element, such as half-wavelength dipole antenna for typical Yagi-Uda array, is used rather than an isotropic source antenna, the final radiation pattern is obtained from the multiplication of the antenna array factor with the radiation pattern of the single element.

As a preparation for understanding the radiation pattern of Yagi-Uda array, we first consider a two-element array, as in Fig. 3. The array factor for two-element array is

$$\text{AF} = I_1 + I_2 e^{j\beta d \cos \theta} = |I_1| + |I_2| e^{j(\beta d \cos \theta + \alpha)} \quad (3)$$

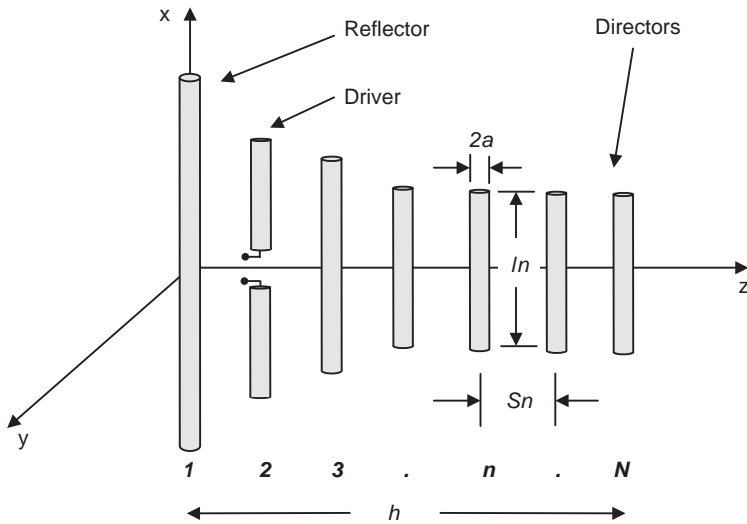


Figure 1. Geometry of the Yagi-Uda antenna. (This figure is available in full color at <http://www.mrw.interscience.wiley.com/erfme>.)

A phase progression α between currents on elements 1 and 2 is assumed. The normalized amplitude of the array factor is often referred to as the *universal radiation pattern*. When the currents have equal amplitude and phase difference α , the array factor can be simplified as a function of $\psi = \beta d \cos \theta + \alpha$:

$$AF = |I_1| (1 + e^{j\psi}) = 2|I_1| e^{j(\psi/2)} \cos\left(\frac{\psi}{2}\right) \quad (4)$$

Thus the normalized amplitude of array factor (universal radiation pattern) is simply written as a function of ψ as

$$f(\psi) = \left| \cos \frac{\psi}{2} \right| \quad (5)$$

The polar plot is a useful tool for visualizing operation of antenna arrays. We shall now explain the graphical procedure [5] for constructing a polar plot. The polar plot is the far-field radiation pattern constructed in a polar coordinate system by referring to the universal radiation pattern obtained from (3). With this arrangement, one can clearly see how the radiation pattern of the array can be obtained with regards to currents amplitude $|I_1|, |I_2|$, phase progression α , and the element spacing d . A few examples in Fig. 4 will give a good idea of how the plots are constructed. For the equal-amplitude excitation, where the conditions for (5) are

valid, we plot the universal radiation pattern $f(\psi)$ as in Fig. 4a. When $\alpha = 0$ and $d = \lambda/2$, the polar plot has its center at $\alpha = 0$ corresponding to $\psi = 0$ and its radius $\beta d = \pi$. The intensity of the far-field radiation at each θ can be found from the projection of θ to the corresponding universal radiation pattern $f(\psi)$. The resulting broadside radiation pattern is plotted in Fig. 4b with its highest peak at $\theta = \pi/2$ and $\theta = -\pi/2$. When $\alpha = \pi$ and $d = \lambda/2$, the center of the polar plot is shifted to $\alpha = \pi$, corresponding to $\psi = \pi$ with the same radius $\beta d = \pi$. The resulting endfire radiation pattern is plotted in Fig. 4c with the highest peak at $\theta = 0$ and $\theta = \pi$. When $\alpha = \pi/2$ and $d = \lambda/4$, the radiation pattern is still endfire but unidirectional with its highest peak at $\theta = \pi$ as plotted in Fig. 4d. From those plots, it is clear that in order for us to have a unidirectional endfire radiation pattern $d \leq \lambda/4$ must be satisfied. As in this example, although the universal radiation pattern is common to all three polar plots, it is possible to shift and scale the polar plot to obtain radiation patterns with different peak directions and shapes. The region in ψ where the radiation pattern is found is called the *visible region*.

The Yagi-Uda array can be discussed in the same manner as we have done for the ordinary endfire array, with the exception that the phase and the amplitude of the current and element spacing are no longer independent. The relationship between induced current on the parasitic element to the excited current on the driven element of the two-element Yagi-Uda array can be found using the

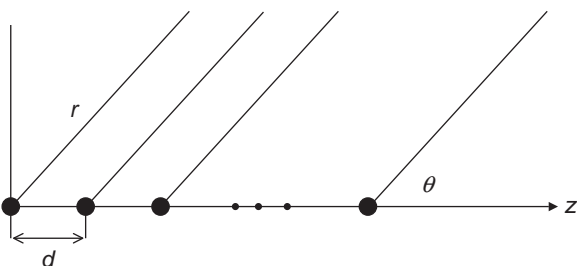


Figure 2. Antenna array made with ideal isotropic antenna source.

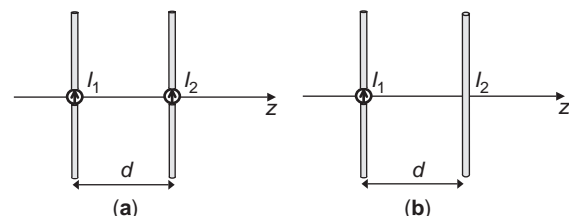


Figure 3. Two-element antenna array: (a) ordinary linear array; (b) Yagi-Uda array. (This figure is available in full color at <http://www.mrw.interscience.wiley.com/erfme>.)

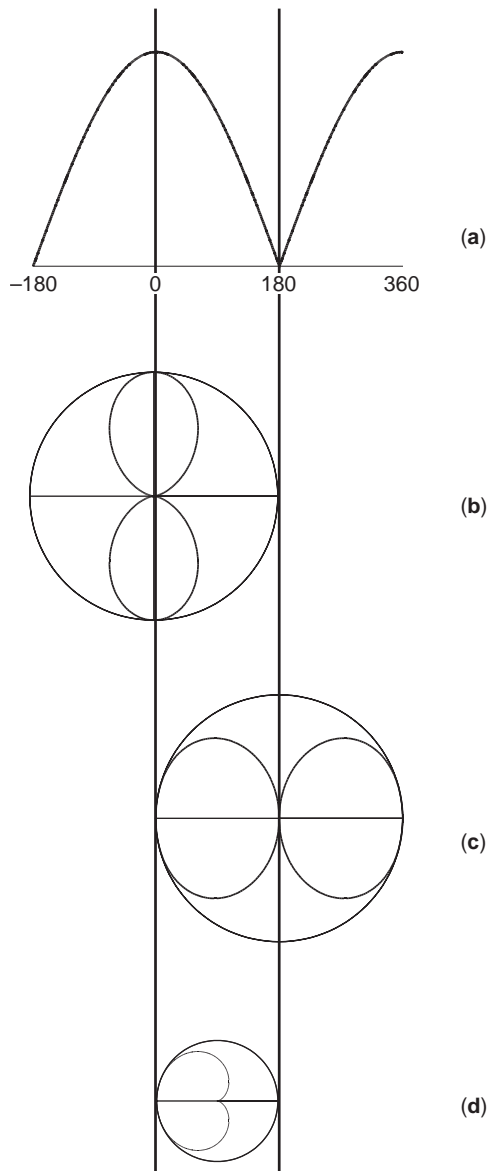


Figure 4. The universal radiation pattern and polar plots for equal amplitude two-element linear array: (a) universal radiation pattern; (b) polar plot for $\alpha=0$, $d=\lambda/2$; (c) polar plot for $\alpha=\pi$, $d=\lambda/2$; (d) polar plot for $\alpha=\pi/2$, $d=\lambda/4$.

concept of the two-port impedance network. Figure 3b shows the two-element Yagi-Uda array using half-wavelength dipoles as antenna elements. The impedance network can be defined as

$$V_1 = I_1 Z_{11} + I_2 Z_{12} \tag{6}$$

$$0 = I_1 Z_{21} + I_2 Z_{22} \tag{7}$$

The voltage at the parasitic element is zero since the middle of the dipole is short-circuited. Using (7), the current on element 1 (driven) and element 2 (parasitic)

can be related as

$$\frac{I_2}{I_1} = -\frac{Z_{12}}{Z_{22}} \tag{8}$$

In summary, the antenna array factor is the same as the ordinary linear array as in (3), although the phase and the amplitude of the currents on the Yagi-Uda array are no longer independent, but rather related to each other with both self- and mutual-impedances of the antenna elements as defined in (8). These facts state that Yagi-Uda antenna's array factor depends on the antenna's self- and mutual-impedances. Thus, the array factor needs to be specifically defined with the actual antenna element rather than isotropic point source. We will continue our discussion of Yagi-Uda array using half-wavelength dipole antenna. This is the most convenient and most popular antenna element for the Yagi-Uda array.

Closed-form expressions for the self- and mutual-impedances of a dipole array are not known, but it is true that impedances are subject to the antenna element spacing and length relative to the wavelength of interest. Although there are a number of analytical studies on characteristics of dipole and Yagi-Uda antennas with various approximations on the currents distribution to solve integral equations [6,7], a more versatile and accurate technique is available from the numerical electromagnetic technique based on the moment method. In this discussion, the numerical code known as *Numerical Electromagnetic Code* (NEC) [8] based on the method moment is utilized to analyze the full-wave characteristics of the Yagi-Uda array with wire dipole antennas. NEC is based on the moment method solution of the rigorous electric field integral equation (EFIE) constructed around the current induced on the wire dipoles with piecewise linear segmentation of the current distribution.

One important advantage of Yagi-Uda is that it can shape the unidirectional beam and thus achieve high directivity. Using the discussion based on polar plot and numerical simulation, we shall see how the dipole length and spacing affects the radiation pattern of the two-element Yagi-Uda antenna. As we discussed earlier, the element spacing d defines the radius of the polar plot while the phase progression α defines the center location of the polar plot. While this holds true for the Yagi-Uda array, the phase progression α is no longer independent from the spacing d . In order for us to control the phase progression independently from the element spacing, we may vary the length of the parasitic element. Uda [9] discussed the effect of varying parasitic element length with ample test results and analytical equations in his two-element array experiments. When the length of parasitic dipole antenna is longer than the resonance, the dipole is inductive (its reactance is positive), and the induced current lags behind the impinged electric field contributing to reflecting radiation backward. On the other hand, when the length of dipole is shorter than the resonance, the dipole is capacitive and the induced current leads the impinged electric field contributing to directing radiation forward.

Since our purpose is to have an antenna array of high directivity, as we have seen in the polar plot of Fig. 4, we

must avoid element spacing anything greater than a half-wavelength. For the first example, we choose dipole radius $a = 0.005\lambda$, a driven element length $l_1 = 0.463\lambda$, parasitic element length $l_2 = 0.496\lambda$, and element spacing $d = 0.2\lambda$. With the current amplitude $|I_1|, |I_2|$ and phase α obtained from numerical solution, we can calculate the universal array factor $|f(\psi)|$ of (3) and obtain the polar plots shown in Fig. 5. The computed phase progression is $\sim 200^\circ$ or 1.11π while the element spacing is $d = 0.2\lambda$, so that the polar plot has $\beta d = 0.4\pi$ radius and is located at 1.11π , contributing to the radiation pattern with the highest peak at $\theta = \pi$ direction and the small peak at the opposite direction. The radiation pattern constructed from element currents corresponds to the H -plane radiation patterns of the dipole Yagi-Uda. The numerically computed radiation patterns come very close to the radiation patterns constructed from the currents and array factor equation. The Yagi-Uda E -plane radiation pattern plotted in Fig. 5c can be obtained by multiplying the single element dipole's E -plane radiation pattern with the array factor polar plot (H -plane radiation pattern) of Fig. 5b. Note that since the current amplitude of the parasitic element is smaller than the one of the driven element, we do not have a null in H -plane radiation pattern even though we cross $\psi = \pi$ in the visible region of polar plot. Since the radiation peak is found in the direction opposite that of the parasitic element, the parasitic element acts as a reflector in this case. On the other hand, the radiation pattern with opposite peak direction can be obtained with shorter parasitic element as in Fig. 6 with parameters $a = 0.005\lambda$, $l_1 = 0.463\lambda$, $l_2 = 0.44\lambda$, and $d = 0.15\lambda$. The computed phase progression on parasitic element is 131° , or 0.73π , bringing the center of polar plot to the left of $\psi = \pi$ in uni-

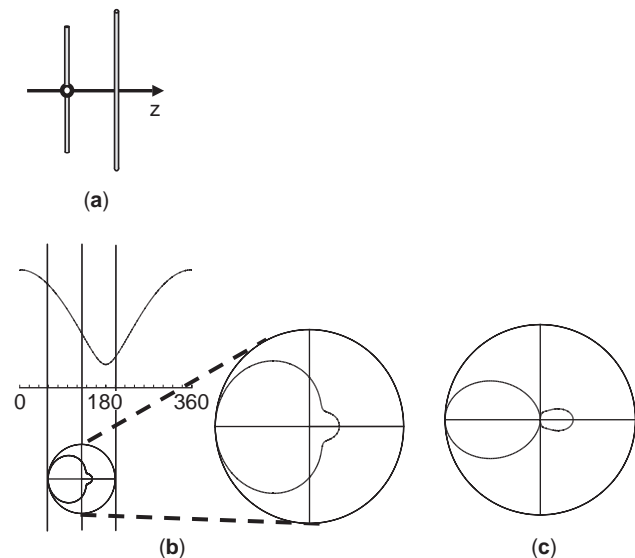


Figure 5. The two-element Yagi-Uda antenna with a driven element and a reflector element, with parameters $l_1 = 0.463\lambda$, $l_2 = 0.496\lambda$, $a = 0.005\lambda$, $d = 0.2\lambda$: (a) array configuration; (b) universal radiation pattern and corresponding polar plot of H -plane radiation pattern with radiation peak at $\theta = \pi$; (c) computed E -plane radiation pattern. (This figure is available in full color at <http://www.mrw.interscience.wiley.com/erfme>.)

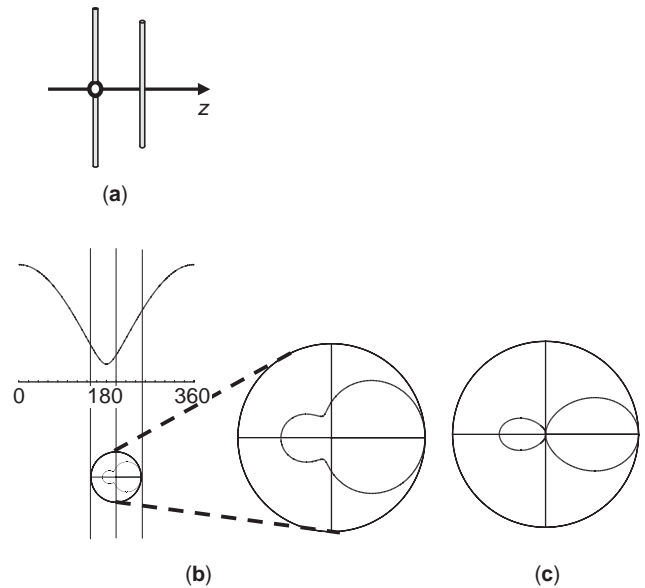


Figure 6. The two-element Yagi-Uda antenna with a driven element and a director element, with parameters $l_1 = 0.463\lambda$, $l_2 = 0.44\lambda$, $a = 0.005\lambda$, $d = 0.15\lambda$: (a) array configuration; (b) universal radiation pattern and corresponding polar plot of H -plane radiation pattern with radiation peak at $\theta = 0$; (c) computed E -plane radiation pattern. (This figure is available in full color at <http://www.mrw.interscience.wiley.com/erfme>.)

versal radiation pattern and a consequent radiation pattern with the highest peak at $\theta = 0$ and the smaller peak at $\theta = \pi$. Since the highest peak is in line with the direction of the parasitic element, the shorter parasitic element in this case acts as a director element.

As the array size increases, the Yagi-Uda antenna array can be discussed and understood as a surface-wave antenna. Provided an array has equal spacing d , the induced current on the element number m can be expressed as

$$I_m = e^{-j\beta_g m d} I_0 \zeta(x) \tag{9}$$

where $\zeta(x)$ describes the amplitude distribution along the x axis and β_g is the propagation constant of the array structure. Analytical studies on Poynting vector along the axis of array by Mailloux [10] reveals that in order for propagation along the axis to exist, and induce current on all the parasitic elements, the propagation along the axis has to be slower than the free-space propagation. The slow wave exists for $k_0 < \beta_g < \pi/d$. The Yagi-Uda is often referred to as a surface-wave antenna, due to the slow-wave excitation along the axis of the array as in surface-wave antennas. Ehrenspeck and Poehler [11] shows in their experimental study that the propagation constant of the Yagi-Uda is indeed slow and for the long Yagi antenna, the propagation constant approaches the Hansen-Woodyard [12] criteria of $\beta_g = \beta + \pi/h$. In their study, the terminal phase difference between driven element and the last director element of the Yagi array is measured near 60° for short array, comes close to 120° for h between 4λ and 8λ then gradually approaches to Hansen-Woodyard criteria of 180° for h is equal to 20λ . Using the condition for 100% efficiency of surface-wave excitation suggested by Zucker [13] as a lower bound,

the final Yagi propagation constant of any array length should remain inside:

$$\beta + \frac{\pi}{3h} < \beta_g < \beta + \frac{\pi}{h} \tag{10}$$

Further discussions regarding surface-wave antenna or traveling-wave antenna treatment of Yagi-Uda antenna are available in the literature [12–15].

Another important Yagi-Uda characteristic is its input impedance. From Eqs. (6) and (8) the input impedance is obtained as follows:

$$Z_{IN} = \frac{V_1}{I_1} = Z_{11} - \frac{Z_{12}^2}{Z_{22}} \tag{11}$$

The second term of this equation shows the strong dependence of the input impedance on the mutual coupling of two elements. A useful practice for matching the input impedance to the feeding transmission line is to slightly adjust the driven element's length so that an imaginary part of the total input impedance is canceled out to zero, enabling us to use a simple impedance transformer such as folded dipole feeding. Although self-impedance of a half-wavelength dipole antenna is about 70Ω, the final input impedance of the Yagi-Uda antenna is in general less than 50Ω. Elliott provides a more discussion on input impedance matching of two-element and three-elements Yagi-Uda antennas using closed-form expressions and tables for thin wire dipole's self-impedance and mutual impedance [16].

3. DESIGN OF THE YAGI-UDA ANTENNA

In this section, a design procedure for the dipole-based Yagi-Uda antenna is discussed. Because of the large number of optimization variables, the Yagi-Uda antenna is typically designed using design curves or tabulated data such as that presented in *Yagi Antenna Design* by Peter Viezbicke [17], in a technical note published by the National Bureau of Standards. The design data are intended to support designs in the HF, VHF, and UHF frequency

bands. Note that the design procedure provides an optimized design to obtain a desired gain at a specific frequency. It does not provide sufficient information on input impedance matching of antenna. This must be considered separately, either experimentally or through additional simulations.

The antennas in the study were constructed from aluminum rods. Mechanical support was provided by a Plexiglas rod perpendicular to and bisecting the Yagi-Uda elements. Effect of the Plexiglas support was studied in detail and is captured in the developed design guidelines. Note that the original reference specifically states that the supporting boom is constructed from *nonconducting Plexiglas*. A number of modern texts erroneously refer to the boom as being fabricated from metal.

Presented with the data is a design method for a specific gain in terms of the antennas physical geometry (element lengths, diameter, and spacing; reflector geometry and supporting boom). The design technique allows specific gains of 7.1, 9.2, 10.2, 12.25, 13.4, and 14.2 dB to be realized. Note that all gains given are relative to that of a λ/2 dipole located the same height above ground; isotropic gain can be obtained by adding 2.16 dB to these values. Note also that the design technique gives a specific array length (0.4, 0.8, 1.2, 2.2, 3.2, and 4.2λ), and are valid for a limited element thickness.

Graphical data supporting the design of the Yagi-Uda antenna are shown in Figs. 7 and 8 and Table 1. Figure 7 is the most important plot, and shows design curves as a function of 2a/λ₀. Figure 7 may be used to determine antenna performance provided that 0.001 ≤ 2a/λ₀ ≤ 0.04. Figure 8 shows compensation data of length of parasitic elements for the various diameters of Plexiglas boom on which the test antenna is mounted. This is used to obtain optimized values for the final design. In addition, Table 1 shows optimized lengths of parasitic elements of six different lengths and gains for the specific case of 2a/λ₀ = 0.0085. Each column represents an antenna design of a different gain.

The design is performed in the following manner. First, frequency and desired gain must be known. Note that gain is limited to one of six specific values, as shown in Table 1. Element and boom diameter should also be

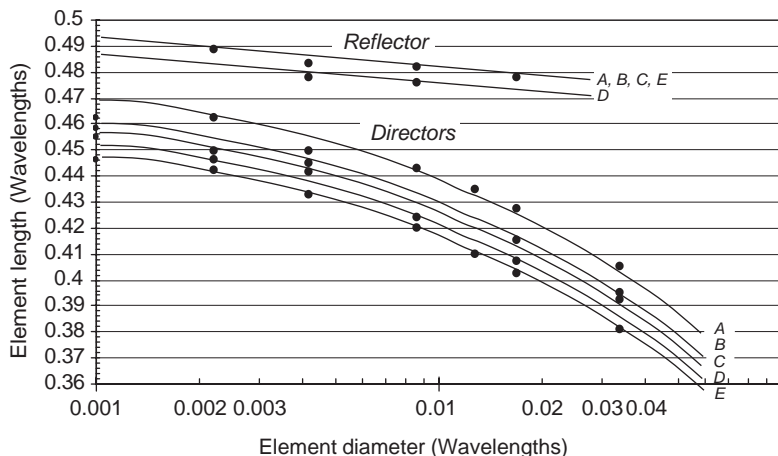


Figure 7. Yagi antenna design data showing relationship between element diameter and element length for different antennas, after Viezbickie [17].

Table 1. Optimized Length of Parasitic Elements for Yagi Antennas of Six Different Lengths^a

Length of Reflector (λ)	Length Of Yagi Antenna (λ)					
	0.4	0.8	1.20	2.2	3.2	4.2
Length of Reflector (λ)	0.482	0.482	0.482	0.482	0.482	0.475
Element length (λ)						
1st	0.424	0.428	0.428	0.432	0.428	0.424
2nd	—	0.424	0.420	0.415	0.420	0.424
3rd	—	0.428	0.420	0.407	0.407	0.420
4th	—	—	0.428	0.398	0.398	0.407
5th	—	—	—	0.390	0.394	0.403
6th	—	—	—	0.390	0.390	0.398
7th	—	—	—	0.390	0.386	0.394
8th	—	—	—	0.390	0.386	0.390
9th	—	—	—	0.398	0.386	0.390
10th	—	—	—	0.407	0.386	0.390
11th	—	—	—	—	0.386	0.390
12th	—	—	—	—	0.386	0.390
13th	—	—	—	—	0.386	0.390
14th	—	—	—	—	0.386	—
15th	—	—	—	—	0.386	—
Spacing between directors (λ)	0.20	0.20	0.25	0.20	0.20	0.308
Gain relative to half-wave dipole (dB)	7.1	9.2	10.2	12.25	13.4	14.2
Design curve (see Fig. 7)	(A)	(C)	(C)	(B)	(C)	(D)

^aElement Diameter = 0.0085 λ ; $f = 400$ MHz; reflector spaced 0.2 λ behind driven element. Source: After Viezbickie [17].

known. Referring to Table 1, choosing the column with the desired gain will provide the length of the antenna (in wavelengths), number of elements, and nonoptimized element length, as well as specifying the design curve for optimizing the element lengths. The element lengths are then plotted onto the correct design curve in Fig. 7 by drawing a horizontal line from the y axis. Then, a vertical line is drawn from the x axis at the desired element diameter and crosses the desired design curves for reflector and director. The director length without boom compensation is given by the value in the intersection of the director line. The highest-order director is assigned this point on the director design curve, and the other elements are translated along this curve, maintaining the same distance between each other as before they were compensated. This will determine the length of all elements without boom compensation, which is read from Fig. 8. The

length indicated for the corresponding boom diameter extends the length of each element. At this point the design is complete, and can be either fabricated or used as a starting point for further optimization. Figure 9 shows the computed H -plane and E -plane radiation patterns of a 17-element Yagi-Uda antenna constructed using parameters for 3.2 λ length array in Table 1. The front : back ratio for this example is approximately 20 dB, and sidelobes are more than 10 dB down from the mainlobe, illustrating how the Yagi-Uda could obtain high directive beam with relatively small antenna size. The normalized currents at the center segment of each of the 17 elements are also plotted in Fig. 10. The energy coupled into parasitic elements becomes smaller as it progresses further away from the driven element but stays at a certain level to the end of array indicating the slow-wave successfully propagates through the array structure as discussed in previous section.

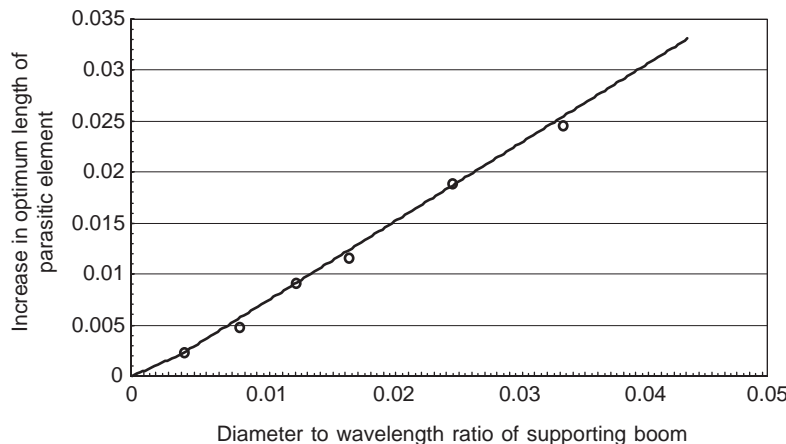


Figure 8. Graph showing effect of supporting boom on element length, after Viezbickie [17].

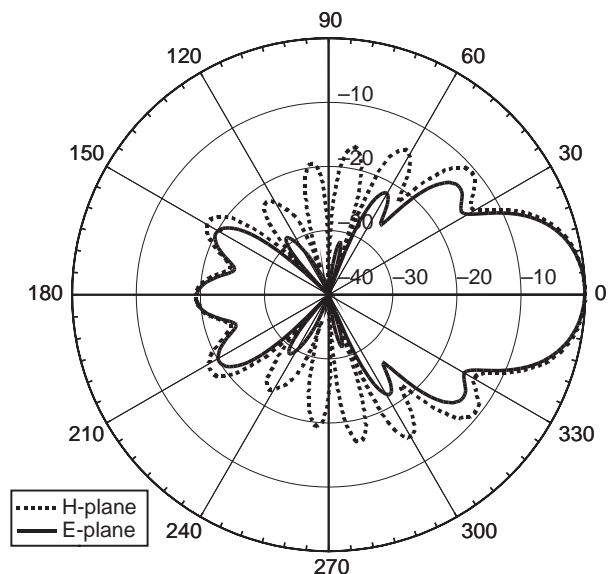


Figure 9. Radiation patterns for the 17-element Yagi-Uda array. Parasitic elements length and spacing of 3.2λ array in Table 1 are used. The dashed line indicates *H*-plane and solid line, *E*-plane radiation patterns.

While performing further optimizations into the design, either experimentally or through computer simulations, a few general trends have been observed and are well established in the literature [17,18]. First, for a given length of array, reflector spacing and size control the front-to-back ratio and can impact the impedance, but have small impact on the forward gain. The size of the driven element does not affect radiation pattern significantly but rather is chosen to control the input impedance (and is typically resonant). Finally, the director size and spacing have considerable impact on forward gain, front-to-back ratio, and input impedance. The directors must therefore be optimized carefully to obtain maximum performance. Optimization using perturbation techniques [19] and a search algorithm such as the genetic algorithm [20] have also been studied and reported.

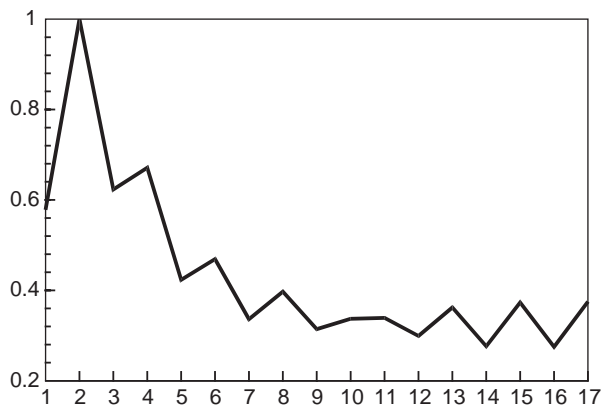


Figure 10. Normalized current amplitude at the center segment of a 17-element Yagi-Uda antenna. The array has equal element spacing 0.2λ .

The antenna will also need to be input-matched to the desired reference impedance. The Yagi-Uda is often fed using a twin-lead transmission line with a characteristic impedance of $300\ \Omega$. As stated in the previous section, the input impedance of the Yagi-Uda antenna is somewhat less than that of a half-wave dipole operating at its first resonance ($\sim 70\ \Omega$ for the dipole). For matching to a twin-lead transmission line, the same basic techniques that are used to match the half-wave dipole can be used with the Yagi-Uda antenna. One technique commonly used with dipoles is to use a folded dipole, which increases the driving impedance by a factor of 4. A larger number of folds can be used to achieve even higher impedance transformation. Additionally, stub tuners can be used to provide impedance matching.

The Yagi-Uda can also be stacked, either vertically or horizontally, to increase the gain; design information on this is also included in Ref. 17.

4. MODERN DEVELOPMENTS FOR THE YAGI-UDA ANTENNA

The traditional Yagi-Uda antenna is typically built of metal tubing and typically operates in the megahertz range to a few gigahertz. Many modern applications operate at much higher frequencies that are not compatible with this simple type of fabrication. In the decades since the Yagi-Uda antenna was originally introduced, the fundamental underlying concept has been applied to develop Yagi-Uda-type antennas using radiating elements other than the wire dipole. These antennas utilize the same traveling-wave concept to achieve an endfire radiation pattern, but often bear little visual resemblance to the antenna, which fostered their existence. In this section, a number of these are briefly introduced and discussed.

One practical planar version utilizes a coaxial fed patch antenna with parasitic microstrip patch antennas used as reflector and directors [21]. The structure of the antenna is shown in Fig. 11. The basic configuration of a patch antenna element includes a rectangular (or square in this case) metallic patch on one side of a dielectric substrate that is backed by a metallic ground plane. Feeding of the basic patch antenna can be done in a variety of manners, including edge fed microstrip, aperture coupling or by using a coaxial probe. Huang and Densmore [21] used coaxial probes to feed a square patch at two separate points, resulting in the formation of a circularly polarized beam. The patch antenna by itself has a broadside-directed radiation pattern (referring to the side view in Fig. 11, this would correspond to a mainbeam in the vertical direction). When combined with the reflector and two director parasitic patches, the mainbeam is tilted toward the endfire direction, but does not achieve true endfire operation as in the traditional Yagi-Uda antenna. Huang and Densmore [21] report a maximum directivity of 15 dBi.

According to Huang and Densmore [21], a number of other phenomena were observed with this antenna:

1. A conventional microstrip patch antenna achieves circular radiation by using orthogonal feed points

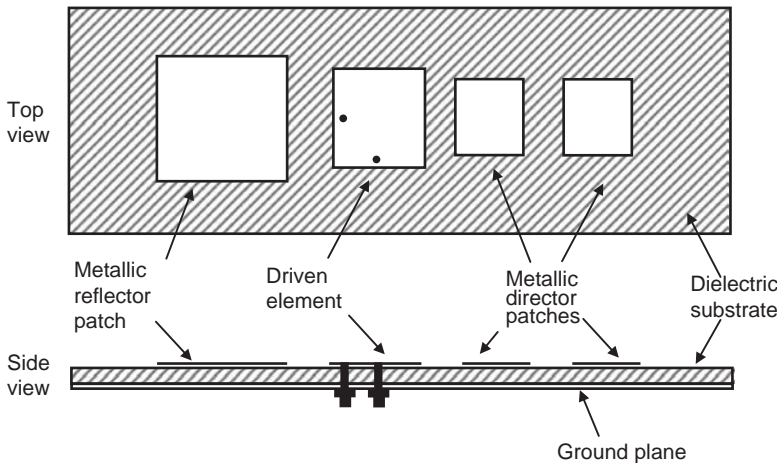


Figure 11. Microstrip Yagi array configuration, after Huang and Densmore [21].

excited 90° out of phase. For the microstrip Yagi antenna, a phase difference of 110° was required to achieve good circular polarization in the mainbeam direction.

2. The coupling at the two probes was reported to be affected by the parasitic patches. This results in optimal feeding points differing from those for the conventional patch antenna with circular polarization.
3. The addition of the parasitic patches had an impedance match bandwidth enhancement effect. Huang and Densmore [21] reported a 7.5% bandwidth on a 0.64-cm-thick substrate.

One attribute of the microstrip patch antenna is the ease with which multiple elements can be combined to form an array. This is also true of the microstrip Yagi antennas. Huang and Densmore [21], placed four microstrip Yagi antennas side by side to form a larger two-dimensional array. The composite array shown in Fig. 12 has

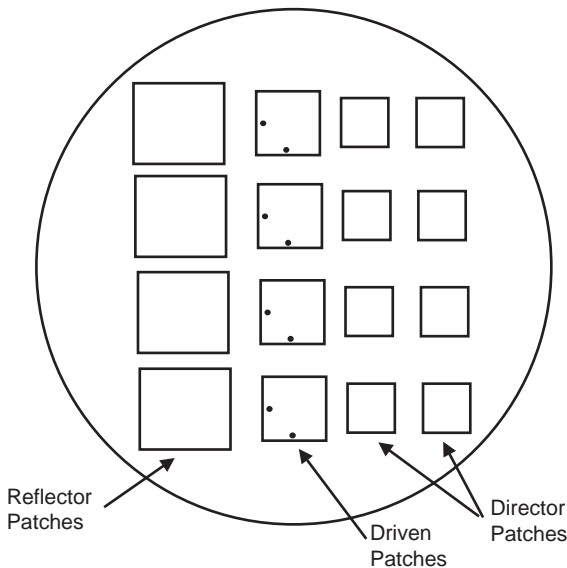


Figure 12. Two-dimensional microstrip Yagi array configuration, after Huang and Densmore [21].

a total of 16 patch antennas (including directors and reflectors), but only four elements are directly driven. To form a similar radiation pattern without using the Yagi-Uda concept, all 16 elements would have to be individually excited by a comparatively more complicated feed network. Other researchers have also used the microstrip Yagi antennas in a two-dimensional array. Figure 13 shows a six-sector Yagi-Uda array with a common parasitic element reported by Honma et al. [22], who use six microstrip Yagi antennas arrayed in a circular pattern intersecting at 60° of each other. The six antennas share a common director enabling a compact design. By switching between elements, the beam is steered in fixed directions. This results in a beamsteering array with a simple feeding structure.

A second class of planar antennas based on the Yagi-Uda concept includes the Yagi slot array. The radiation properties of a wire dipole antenna and an antenna formed from a slot in a metallic structure can be fundamentally related to each other by exchanging their electric and magnetic fields and multiplying by a proportionality constant. This strategy is based on an electromagnetic principle known as *duality*. Additionally, their impedances are directly related by Babinet's principle [23]. The development

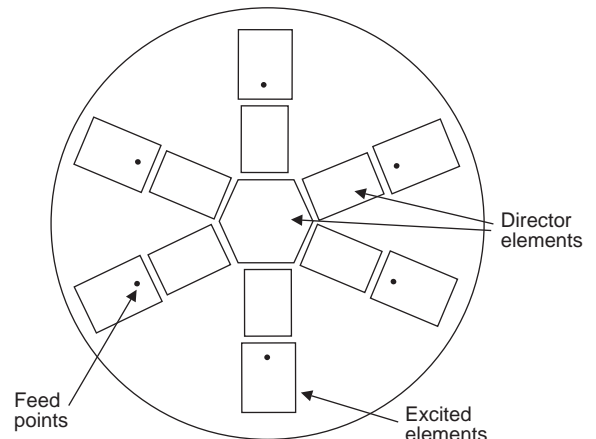


Figure 13. Configuration of six-sector patch Yagi-Uda antenna with a common parasitic elements, after Honma et al. [22].

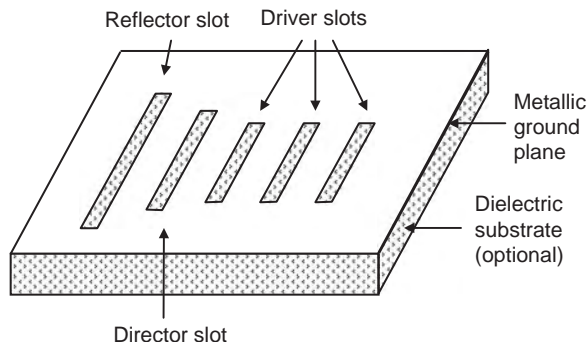


Figure 14. Geometry of Yagi-Uda array constructed from slot elements.

of a slot Yagi-Uda antenna array is therefore a natural extension of the wire Yagi-Uda array, one of the most common applications of the dipole antenna.

The basic geometry of a slot Yagi-Uda antenna is shown in Fig. 14. It can be fed by a variety of techniques, including coplanar waveguide (CPW), microstrip, coaxial probe or rectangular waveguide. The slot antenna ground plane is placed on a dielectric substrate if it is fed using CPW or microstrip. Note that the dielectric substrate is *not* essential if fed by other techniques. As with the microstrip Yagi antenna, the broadside-directed radiation pattern of the slot antenna results in a radiation pattern tilted between broadside and endfire. Additionally, radiation will be emitted into both the top and bottom hemispheres unless a technique is used to prevent this. Since it can be fed with CPW, this type of Yagi-Uda antenna could be potentially used well in to the millimeter range. In practice, high-frequency use may be limited because of the high probability of exciting surface waves in the conductor-backed dielectric substrate.

Although this type of Yagi-Uda antenna has been reported as early as 1963 [24], it appears to have found only limited application. One particularly interesting twist to this story is its application as an efficient TM_0 surface-wave exciter. Constructing the antenna on a relatively thick, high-permittivity substrate enhances the efficient excitation of surface waves. Consequently, the antenna emits almost zero radiation into the air. The majority of the energy is transmitted in the forward direction into the conductor-backed dielectric slab in the TM_0 surface wave. This type of Yagi-Uda surface wave launch can be fed by either CPW or microstrip, and has been demonstrated to be an efficient element for use in dielectric slab power combiners [25].

The planar Yagi-Uda-type antennas discussed in the last few paragraphs do not have a true endfire radiation pattern like that of the original dipole Yagi-Uda antenna. More recently, a planar antenna referred to as a “quasi-Yagi” antenna has been reported that does have this characteristic [26]. This printed dipole array is realized on a high-permittivity substrate with a microstrip feed, as shown in Fig. 15. Unlike the traditional Yagi-Uda antenna, this planar version uses the truncated microstrip ground plane as the reflecting element. This eliminates the necessity of a reflecting dipole element. The result is

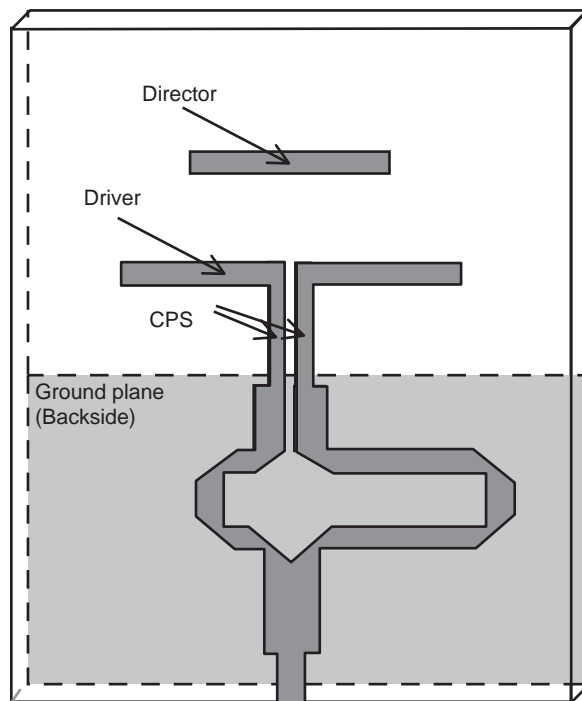


Figure 15. Geometry of the quasi-Yagi antenna, after Kaneda et al. [26].

very compact, with a length and width less than half those a free-space wavelength. The planar nature and microstrip feeding allow simple integration of active circuitry and electronics, thus making this antenna a candidate for dense active arrays and in applications requiring a high level of integration.

The antenna itself has proved capable of being scaled to a wide range of frequencies while maintaining good radiation qualities. An X-band version has been studied in detail. The antenna is constructed on a single substrate (0.635-mm-thick Duroid with a $\epsilon_r = 10.2$ for the X-band version) with metallization on both sides. Referring to Fig. 15, the top metallization consists of a microstrip feed, a broadband microstrip-to-coplanar stripline (CPS) balun,

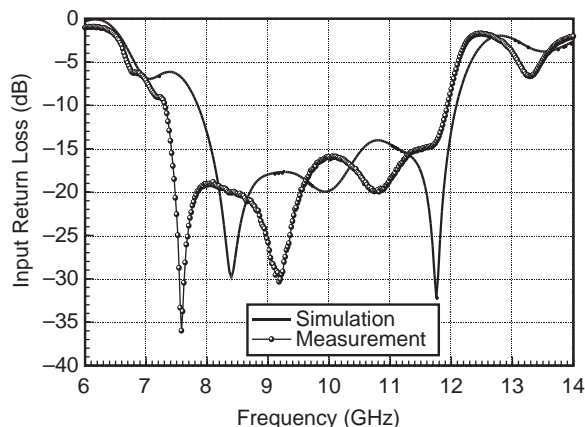


Figure 16. FDTD simulation and measured input return loss of the broadband quasi-Yagi antenna, after Kaneda et al. [26].

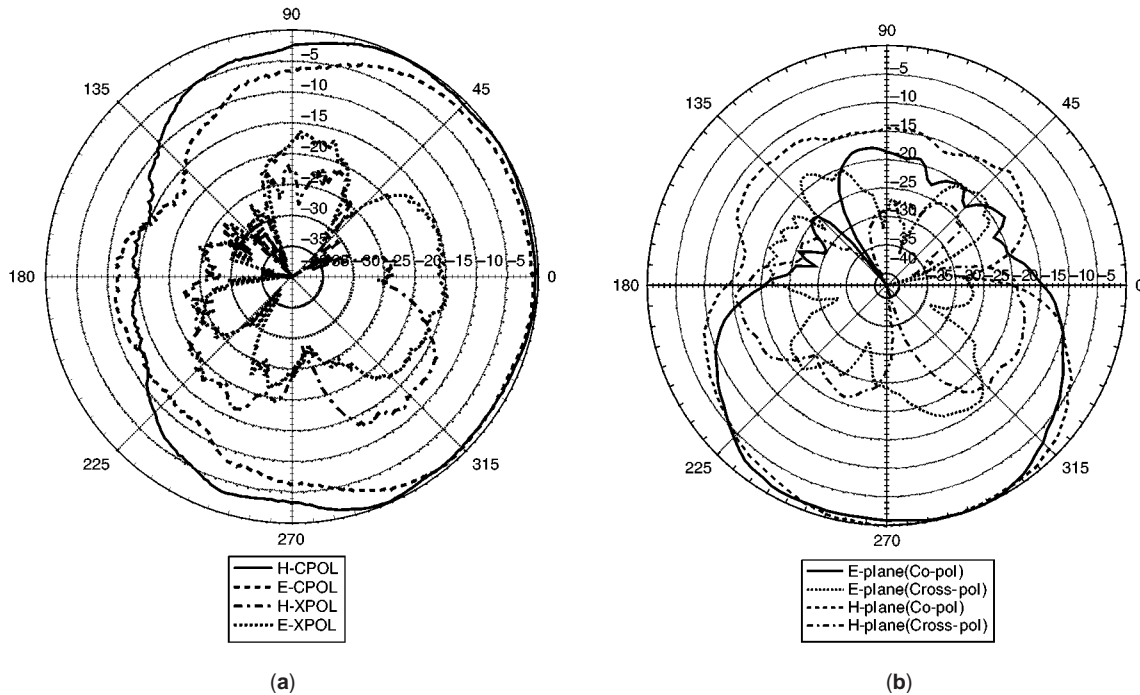


Figure 17. Measured E - and H -plane co- and cross-polarization radiation patterns for the (a) low-gain and (b) high-gain versions of the quasi-Yagi antenna. Note that the end direction in (a) is at 0° and is at 270° in (b) due to measurement setup after Kaneda et al. [26].

and two dipole elements (the driven element and the director). The metallization on the backside consists of a truncated ground plane, which acts as the reflector for the antenna. In addition to aiding the endfire radiation pattern, the director is also used for impedance matching.

As with the wire dipole Yagi-Uda antenna, proper design requires optimization of driver, director, and reflector parameters. By performing a parameter study, it was found that the quasi-Yagi could be either optimized for broadband (40–50% for $VSWR < 2$) characteristics with moderate gain (~ 4 dB), or narrow bandwidth (10–20% for $VSWR < 2$) with higher gains (~ 6.5 dB). Detailed dimensions for both of these cases can be found in Ref. 26. The simulated-measured input match for the broadband design is shown in Fig. 16. Note that the matched bandwidth covers the entire X-band. Radiation patterns for the low-gain (broadband) and high-gain (narrowband) versions of the quasi-Yagi antenna are shown in Figs. 17a and 17b, respectively. Note that the phase reference for the two polar plots varies by 90° between the two; the radiation pattern is in the same direction for the two, however. The gain in Fig. 17b is noticeably higher.

5. CONCLUSION

The Yagi-Uda antenna is one of these most recognizable and pervasive antennas in existence. In its classic form it features a remarkable feature set, including low profile, low weight, inexpensive manufacturing, and good radiation characteristics. The physics of its operation were detailed in Section 2. It was found that the antenna relies on a traveling-wave effect and operation relies on phasing of

each element. In Section 3 a classic graphical technique for obtaining specific optimized Yagi-Uda designs is outlined. In Section 4 three planar versions of the Yagi-Uda antenna are described, including the microstrip Yagi antenna constructed from patch antennas, the slot Yagi antenna, and a planar, printed dipole-based version referred to as the “quasi-Yagi” antenna.

BIBLIOGRAPHY

1. H. Yagi and S. Uda, Projector of the sharpest beam of electric waves, *Proc. Imperial Academy*, **2**:49–52 (Feb. 1926).
2. H. Yagi, Beam transmission of ultra short waves, *Proc. IRE*, **16**:715–741 (June 1928).
3. H. Yagi, Beam transmission of ultra short waves, *Proc. IEEE*, **85**(11):1864–1874 (Nov. 1997).
4. G. Sato, A secret story about the yagi antenna, *IEEE Antenn. Propag. Mag.* **33**(3):7–18 (June 1991).
5. W. L. Stutzman and G. A. Thiele, *Antenna Theory and Design*, 2nd ed., Wiley, New York, 1998. Chap. 3.
6. R. W. P. King, The linear antenna — eighty years of progress, *Proc. IEEE*, **55**(1):2–16 (Jan. 1967).
7. G. A. Thiele, Analysis of Yagi-Uda type antenna, *IEEE Antenn. Propag. Mag.* **AP-17**(1):24–31 (Jan. 1969).
8. W. A. Davis, D.G. Sweeney, and W. L. Stutzman, MiniNec II: An improved version of MiniNec for personal computers, Paper presented at 1987 URSI Radio Science Meeting, Blacksburg, VA, 1987.
9. S. Uda, *Short Wave Projector — Historical Records of My Studies in Early Days*, published by S. Uda, 1974, Chap. 1.
10. R. J. Mailloux, Antenna and wave theories of infinite Yagi-Uda arrays, *IEEE Trans. Antenn. Propag.* **13**(4):499–506 (July 1965).

11. H. W. Ehrenspeck and H. Poehler, A new method for obtaining maximum gain from Yagi antennas, *IRE Trans. Anten. Propag.* **AP-7**:379–386 (Oct. 1959).
12. W. W. Hansen and J. R. Woodyard, A new principle in directional antenna design, *Proc. IRE* **26**(3):333–345 (March 1938).
13. Z. J. Zucker, in R. C. Johnson, ed., *Antenna Engineering Handbook*, McGraw-Hill, New York, 1993, Chap. 43.
14. R. E. Collin and F. J. Zucker, *Antenna Theory – Part II*, McGraw-Hill, New York, 1969, Chap. 21.
15. E. A. Wolff, *Antenna Analysis*, Artech House, Norwood, MA, 1988, Chap. 8.
16. R. S. Elliott, *Antenna Theory and Design*, Prentice-Hall, Englewood Cliffs, NJ, 1981, Chap. 8.
17. P. Viezbickie, *Yagi Antenna Design*, NBS Technical Note 688, U.S. Government Printing Office, Washington, DC, Dec. 1976.
18. C. A. Balanis, *Antenna Theory Analysis and Design*, 2nd ed., Wiley, New York, 1997, Chap. 10.
19. C. A. Chen and D. K. Cheng, Optimum element length for Yagi-Uda arrays, *IEEE Trans. Anten. Propag.* **AP-23**(1):8–14 (Jan. 1975).
20. E. A. Jones and W. T. Joines, Design of Yagi-Uda antenna using genetic algorithm, *IEEE Trans. Anten. Propag.* **45**(9):1386–1392 (Sept. 1997).
21. J. Huang and A. C. Densmore, Microstrip Yagi array antenna for mobile satellite vehicle application, *IEEE Trans. Anten. Propag.* **39**(7):1024–1030 (July 1991).
22. N. Honma, F. Kira, T. Maruyama, K. Cho, and K. Mizuno, Compact six-sector antenna employing patch Yagi-Uda array with common director, *IEEE APS Int. Symp.*, June 2002, vol. 1, pp. 26–29.
23. H. G. Booker, Slot aeriels and their relation to Complementary wire aeriels, *J. IEE* **93**(Part IIIA):620–626 (1946).
24. R. J. Coe and G. Held, A parasitic slot array, *IEEE Trans. Anten. Propag.* **12**(1):10–16 (Jan. 1964).
25. A. R. Perkons, Y. Qian and T. Itoh, TM surface-wave power combining by a planar active-lens amplifier, *IEEE Trans. Microwave Theory Tech.* **46**(6):775–783 (June 1998).
26. N. Kaneda, W. R. Deal, Y. Qian, R. Waterhouse, and T. Itoh, A broad-band planar quasi-Yagi antenna, *IEEE Trans. Anten. Propag.* **50**(8):1158–1160 (Aug. 2002).

Index

Page references in **bold** type indicate a main article. Page references followed by italic *t* indicate material in tables.

<u>Index terms</u>		<u>Links</u>
A		
1/f noise	3459	
A/D and D/A conversion architectures and techniques	1	
Abbe sine condition	2330	
Aberrations	1788	2329
Absorbing boundary conditions	531	
finite-difference time-domain analysis	1575	
finite element analysis	1596	
Absorbing layers	2459	
Absorption isolator	1225	
Absorptive attenuators	453	463
Absorptive resonators	3948	
Accelerated life testing	3274	
Accessible modes	3167	
Acoustic microwave devices	24	
Acoustic sensors		
for buried-object detection	554	
Acoustic wave propagation	30	
Acquisition radar	4022	
Active antennas	34	
Active-array amplifiers		
quasioptical circuit application	3981	
Active arrays	2574	
Active attenuators	466	
Active diodes	2968	
Active elements		
in waveguide oscillators	5559	
Active filters		
overview of active-filter structures	56	
tools and techniques for active-filter design	68	
tuning	638	

<u>Index terms</u>	<u>Links</u>	
Active-impedance profile (AIP) technique	70	
Active mixers		
mm-wave integrated circuits	3030	
Active power		
waveguides	5575	
Active quasioptical components	3977	
Active radar cancellation	4038	
Active radiometry	4342	
Active RFID tags	4265	
Active shielding	1255	
Active transistor mixers	3105	
A/D and D/A conversion architectures and techniques	1	
<i>See also</i> Analog-to-digital converters; Digital-to-analog converters		
Adapter, waveguide junction	5555	
Adaptive antennas		
for mobile communications systems	164	
for wireless communications systems	5677	
Adaptive array antennas	87	224
	340	
antenna scanning arrays	256	
for mobile communications systems	165	
Adaptive array antennas for wireless local loop	341	
Adaptive beamforming	90	4153
	4154	
Adaptive finite-element method	1599	
Adaptive processing		
using conformal phased arrays	1065	
Adaptive wavelet transform methods	5617	
Adhesives		
insulating properties	151 <i>t</i>	
Adjacent-channel interference	4337	
Adjacent-channel power ratio (ACPR)	2879	
Admittance inverters	1562	1565 <i>t</i>
Advanced Mobile Phone Service (AMPS)	592	597
AFSATCOM systems	3019	
Agile mirror	1085	
Ad hoc networks		
adaptive array antenna application	91	
Air		
dielectric permittivity	939 <i>t</i>	

<u>Index terms</u>	<u>Links</u>	
Airborne electromagnetic methods	1267	
Airborne moving-target indication	4152	
Airborne radiation monitors	4223	4226
Aircraft		
patch array	756	
typical radar cross-section	4031 <i>t</i>	
Air defense	1334	
AIRSAR system	4106	4108
Air-to-air missiles (AAMs)	3087	
Air-to-surface missiles (ASMs)	3087	
Allan deviation	1724	
Allan variance	1723	
All-pole Chebyshev filters	1549	
Almost-periodic Fourier transform	3491	
Aloha multiple access scheme	3356	
Along-track interferometry	4113	
Altimeters	103	
Altimeter waveform	3995	
Altitude	103	
Alumina		
dielectric properties	945 <i>t</i>	2765 <i>t</i>
properties in microwave ICs	2775 <i>t</i>	
Aluminum gallium nitride/gallium nitride HEMTs	1760	
Aluminum-gallium-nitride/gallium-nitride MODFETs	3189	
Aluminum oxide		
dielectric properties	945 <i>t</i>	
Amber		
dielectric permittivity	939 <i>t</i>	
Ambiguity function	4143	
AM broadcasting		
and sky wave propagation at medium frequencies	4686	
Ammonia		
electric dipole moment	941 <i>t</i>	
Amplified noise	1730	
Amplifiers		
analytical and adaptive modeling of nonlinear high-power	127	
distributed	1086	
feedback	1418	
feedforward	1439	
intermediate-frequency	2175	

Index terms**Links**

Amplifiers (<i>Continued</i>)		
microwave parametric	2827	
mm-wave integrated circuits	3026	
quasi-optical circuits	3980	3984
radio on fiber systems	4312	
RF integrated circuits	4275	
Amplitron	2498	
Amplitude equalizers	1525	1541
Amplitude field pattern	226	
Amplitude-modulated laser altimeters	111	
Amplitude modulation		
mixer circuits	3111	
Amplitude shift keying	117	
AMPS (Advanced Mobile Phone Service)	592	597
AM radio waves	1281	
bandwidth value	5630r	
AM wireless	5656	
Analog cellular radio	592	597
Analog engineering		
Volterra modeling in	5507	
Analog intercept microwave receivers	2924	
Analog signals	1	
Analog television transmitters	5318	
Analog-to-digital conversion architectures and techniques	1	
Analog-to-digital converters	3	
cryogenically-cooled	883	
high-speed architectures	7	
microwave photonics application	2863	
mixed-signal CMOS RF integrated circuits	3098	
pipelined	12	
Analytical and adaptive modeling of nonlinear high-power amplifiers	127	
Analytical signal	4136	
Anechoic chambers, antenna	158	
Angle modulation		
mixer circuits	3112	
Angle spread at the receiver	168	
Angle spread at the transmitter	168	
Angle tracking	4178	
Angular spectrum of waves (ASoW) technique	34	
Anisotropic dielectrics	1219	

<u>Index terms</u>	<u>Links</u>	
Anisotropic perfectly matched layer absorbing boundary condition	1577	
Anisotropy	137	1449
Annular coaxial cavity resonators	579	
Annular elliptic waveguide cavity resonators	582	
AN/SPS-33 radar	4017	
Antenna accessories	147	
Antenna anechoic chambers	158	
Antenna arrays	224	289
dipole	1033	
feeds for	208	
fractal-shaped	1626	
for mobile communications	164	
Antenna arrays for mobile communications	164	
Antenna compact range	177	
Antenna cross-polarization discrimination	238	
Antenna directivity	278	
Antenna diversity	165	
Antenna efficiency	234	263
Antenna elements	218	
Antenna feeds	184	
leaky-wave antennas	2301	
linear antennas	2349	
radar antennas	4009	
reflector antennas	4466	
Antenna feed systems	211	
Antennafiers	52	
Antenna gain	221	263
	278	
dielectric loaded antenna enhancement	912	
feed antennas	189	
and radiation patterns	233	
Antenna impedance	272	
Antenna parameters	217	
Antenna polarization	221	263
and radiation patterns	235	
Antenna radiation intensity	232	
Antenna radiation patterns	219	225
measurement	263	
primary feed antennas	188	
reconfigurability	4409	

Index terms**Links**

Antenna radiation patterns (<i>Continued</i>)		
theory		273
Antenna radiation power density		231
Antenna reverberation chamber		239
Antennas		284
aperture		365
applications		290
bandwidth		282
calibration		268
compact range		177
conformal		750
conical		775
corrugated horn		847
dielectric loaded		893
dielectric resonator		960
dipole		1033
directive		1085
dual- and multi-frequency		1086
FE analysis application		1596
figures of merit		218
frequency bands and their usage		290 <i>t</i>
for ground-penetrating radar buried-object detection		547
helical		1925
for high-frequency broadcasting		295
horn		2021
integrated systems		2113
leaky-wave		2294
lens		2320
linear		2336
loop		2359
for low-power broadcasting		2387
for medium-frequency broadcasting		301
miniaturized packaged (embedded) antennas for portable wireless devices		3068
for mobile communications		319
monolithic		3203
monopole		3238
for monopulse tracking systems		3246
notch		3534
parameters		217
radar		292
reconfigurable		4405

Index terms**Links**

Antennas (<i>Continued</i>)		
rectifying	4418	
reflectarray	4428	
satellite	4585	
slot	4696	
small	4761	
spiral	4853	
standards	267	
terminology	263	
testing and measurements	262	
theory	269	
very high frequency range	5477	
Antenna scanning arrays	251	
Antennas for high-frequency broadcasting	295	
Antennas for low-power broadcasting	2387	
Antennas for medium-frequency broadcasting	301	
Antennas for mobile communications	319	
Antenna temperature	281	4347
Antenna testing and measurements	262	
Antenna theory	269	
Anti-Ballistic Missile (ABM) Treaty	3083	
Antiferroelectricity	1506	1515
Antiferromagnetism	1506	2416
Antijamming techniques	3009	
Antimony sulfoiodide		
ferroelectric properties	1512 <i>t</i>	
pyroelectric properties	1514 <i>t</i>	
Antireflection layers	2459	
Antispoofing techniques	3009	
Aperture antennas	365	
Aperture efficiency	222	
Aperture feed antennas	191	
Aperture theory	369	
Application of wavelets to electromagnetic problems	377	
Applied numerical electromagnetic analysis for planar high-frequency circuits	397	
Arbitrary cross section waveguides	5584	
Area radiation monitors	4222	
ARIES system	600 <i>t</i>	
Armstrong oscillator	5471	
Array antennas. <i>See</i> Antenna arrays		

<u>Index terms</u>	<u>Links</u>	
Array blindness	254	
Array factor	227	277
Array squint	252	
Artificial isotropic chiral media	614	
Artificial magnetic conductor	413	
Artificial neural networks	3390	
<i>See also</i> Neural networks		
ASK-OFDM	126	
Aspect angle	4031	
Assembly, in finite element analysis	1592	
Astable multivibrators	5473	5475t
	5494	
Astigmatism	1791	
Asymmetric Fabry-Perot resonators	1391	
Atmospheric noise	4304	
Atmospheric pressure	105	
Attenuation	435	452
circular waveguides	650	
measurement	443	
in troposphere	4475	
Attenuation standards	441	
Attenuators	436	452
design	147	
Audio cart machines	4238	
Audio compressors	4245	
Audio consoles	4231	
Audio distribution equipment	4235	
Audio processing equipment	4245	
Audio remote systems	4241	
Audio routing equipment	4235	4236
Audio routing switches	4236	
Audio signals		
bandwidth value	5630r	
Audio sources	4237	
Automatic direction finder (ADR) navigation	4296	
Autonomous circuit analysis	3492	
Avalanche noise	3417	
Axial ratio	263	

Index terms**Links****B**

Babinet's principle	1301	4697
	4700	
Backlobes	225	229
Backscatter	481	
approximating	484	
complex objects	490	
and radar cross-section	4032	
simple shapes	489	
Backscatter cross section	4098	
Backscattering	481	
Backscattering cross-section distribution	4022	
Backward wave materials	2303	
Bainter circuit	499	
Balanced-line attenuator	436	
Balanced transmission lines		
for high-frequency broadcasting	300	
Ballistic missiles	3083	3086
Ball grid array packages	4520	
Baluns	148	300
	810	2729
VHF range	5485	
Band-elimination filter	498	
Bandgap assisted bandpass filters	1117	
Bandpass filters	494	1522
CAD-based design using active-impedance profile (AIP)	74	
with coplanar striplines	787	
electromagnetic bandgap assisted	1117	
elliptic filters	1357	
frequency selective surfaces	1701	
microwave	2759	
microwave Fabry-Perot resonators as frequency	1394	
transformation of lowpass into	1539	1560
transformation relations	1561	
Bandpass signals	4135	
Band-reject filters	498	
elliptic filters	1358	
Bandstop filters	498	1522
frequency selective surfaces	1701	
microwave	2762	

Index terms**Links**

Bandstop filters (<i>Continued</i>)		
transformation of lowpass into	1539	1560
transformation relations	1561 <i>t</i>	
Bandwidth		
antennas	264	
cavity resonators	577	
distributed amplifiers	1090	
feed antennas	190	
feedforward amplifiers	1441	1446
ferrite isolators	1475	
lens antennas	2328	
linear antennas	2351	
microwave parametric amplifiers	2833	
microwave receivers	2920	
miniaturized antennas	3080	
mixers	3109	
on-off keying	118	
reflectarrays	4432	
selected electronic signals	5630 <i>t</i>	
waveguides	5576	
Bandwidth efficiency	117	
Bank-to-turn missiles	3089	
Barcodes	4263 <i>t</i>	
BARITT (Barrier injection transit time) diode		
description and applications	2968	2971
negative resistance	3389	
Barium cobalt fluoride		
ferroelectric	1505	
Barium iron fluoride		
ferroelectric	1505	
Barium nickel fluoride		
ferroelectric	1505	
Barium titanate	1229	
dielectric permittivity	939 <i>t</i>	
dielectric properties	945 <i>t</i>	
electrooptic dielectrics	1220 <i>t</i>	
ferroelectric properties	1512 <i>t</i>	
piezoelectric properties	1513 <i>t</i>	
pyrooptic properties	1515 <i>t</i>	
Barkhausen criterion	1433	
Barometric altimeters	103	

Index terms**Links**

Barretter	2737	
Base station, cellular networks	3132	5660
antenna scanning arrays	257	
antennas for	323	
downsizing	322	
Basis function approaches	1735	
Bathymetry, radar altimetry-based	3998	
Battjes doubler	5635	
Bayes criterion	4131	
Beacon magnetrons	2506	
Beam control arrays		
quasioptical circuit application	3983	
Beam efficiency	263	
Beam forming	4153	
Beamforming networks	211	
Beam rider guidance	3088	
Beam solid angle	233	
Beamsteering	34	
Beam waveguide	185	209
Beamwidth	220	263
antenna arrays	224	
Beamwidth between first nulls	230	
Beeswax		
dielectric permittivity	939	
Below-cutoff waveguide attenuator	5532	
Beltrami fields	615	
Beowulf clusters	1328	
Berenger's split-field perfectly matched layer absorbing boundary condition	1575	
Bessel filters	1550	
Bessel (Thomson) lowpass filter	1523	1534
Bianisotropic media	694	1225
Bianisotropy	137	
BiCMOS devices and RF integrated circuits	499	
Biconical antennas	776	
Biconical dipole antennas	1048	
Bifilar line	156	
Bifurcations	5548	
Biisotropic chiral media	702	
Binary unipolar ASK	118	

Index terms**Links**

Biological effects of radiofrequency energy	511	
Biomedical applications		
antennas for	292	
cryogenic electronics applications	890	
dielectric loaded antennas for	909	
electromagnetic inverse problems	1201	
magnetrons	2509	
monopole antennas	3243	
thermoacoustic tomography	2530	
Bipolar devices		
radiation effects	4211	
Bipolar multiplier	3117	
Bipolar symmetric MASK	122	
Bipolar transistors	4269	
Birds		
typical radar cross-section	4031 <i>t</i>	
Birefringence	140	
Bismuth vanadate		
pyrooptic properties	1515 <i>t</i>	
Bistatic radar	4062	
Bistatic radar cross-section	4033	
Bit error rate	118	
BJTs (Bipolar junction transistors)		
low noise behavior	2369	
noise	3423	
Blackbody radiation	4345	
Black box modeling approach	5510	
Blind channel estimation	173	
Blind spacetime processing	173	
Blind speeds	4152	4183
Blindspots	1022	
Block models	5511	
Bluestein-Gulyaev waves	31	
Bluetooth	5676	
personal area networking with	3711	
standard comparison	503 <i>t</i>	
Bluetooth application antennas	3074	
Bluetooth Radio	5676	
Boctor circuit	499	
Bode diagrams	625	

<u>Index terms</u>	<u>Links</u>	
Body enhancement, in body-worn loops	2366	
Body-worn loops	2366	
Bolometer mixers	1645	1647
Bolometers	2736	
Bomber aircraft		
typical radar cross-section	4031	
Bootface lens antennas	2331	
Borehole EM methods	1257	
Boresight direction	263	277
Borosilicate glass		
dielectric permittivity	939	
Boundary contour mode-matching method	3168	
Boundary-element method	1240	
Boundary integral resonant-mode expansion method	3168	
Boundary value problems	523	
Bowtie antennas	780	
Bowtie slot antenna	4708	
Bragg cell microwave receiver	2929	
Bragg peak	4187	
Branch-guide directional couplers	5541	
Branchline directional couplers	155	
Breast cancer		
early stage detection using microwave imaging	1585	
thermoacoustic tomography	2537	
Brightness temperature	223	
Broadband amplifiers		
mm-wave integrated circuits	3027	
Broadband dipole curtain arrays	1051	
Broadband microstrip antennas	2602	
Broadband MIMO channels	3060	
Broadband noise jamming	3008	
Broadband wireless access networks	4319	
Broadbeam leaky-wave antennas	2294	
Broadcast delay units	4240	
Broadcasting		
high-frequency	1981	
low-power	2385	
radio broadcast studio equipment	4227	
and sky wave propagation at medium frequencies in AM broadcasting	4686	
transmitters for FM	5337	

Index terms**Links**

Broadcasting satellite service (BSS) bands	1053	1059
	1061	
Broadcasting satellite service (BSS) expansion band	1064	
Broadcast recognition access method	3356	
Broadside antenna	229	278
Broadside antenna arrays	289	
Bruggeman formalism	143	
BSS expansion band	1064	
Bubnov-Galerkin method	1737	
Bulk acoustic wave resonators	24	
Bulk waves	30	
Buneman-Hartree equation	3003	
Buried-object detection	540	
Burns	518	
BUSFET (Body-under-source field-effect transistor)		
radiation resistant	4209	
Bus topology	2352	
Butterworth approximation	1532	1552
Butterworth characteristic	1552	
Butterworth lowpass filter	1523	1555
	2384	
C		
Cadmium iron niobate		
ferroelectric	1505	
Calibration		
circular loop antennas	560	
Capacitance extraction	565	
Capacitive iris, in waveguides	5549 <i>t</i>	
Capacitive post, in waveguides	5549 <i>t</i>	
Capacitors		
lumped-element microwave circuits	2724	
microwave integrated circuits	2779	
RF integrated circuits	4272	
VHF range	5484	
Carbon tetrachloride		
electric dipole moment	941 <i>t</i>	
Car phone systems	592	
Car radio monopole antennas	3242	
Carrier-sensing protocols	3357	

<u>Index terms</u>	<u>Links</u>	
Cartesian oval	1783	
Cartesian refracting surfaces	1783	
Cascaded elements	3166	
Cascaded single-stage distributed amplifiers		
mm-wave integrated circuits	3028	
Cascode amplifier stage	5635	
Cascode distributed amplifiers		
mm-wave integrated circuits	3028	
Cassegrain reflector	4460	
Cataracts	518	
Cauer lowpass filters	1524	1535
Cauer parameter filters	1550	
Cavities		
FE analysis application	1594	
Cavity backing	1687	
Cavity resonators	576	
C band radar	4031 <i>t</i>	4055 <i>t</i>
CDMA wireless standard	321	503 <i>t</i>
	5666	
and digital radio	1023	1030
optical, for radio on fiber systems	4322	
smart antennas	224	
specifications	599	
wavelet applications	5627	
CDMA2000 wireless standard	5657	5669
Cell-averaging constant false-alarm rate (CA-CFAR) radar signal processing	4156	
Cells	1022	5658
Cell splitting	90	5659
Cellular mobile communication systems	5658	5668
Cellular radio	592	1022
Cellular radiotelephony	5657	
Cellular telephone networks	1023	5660
Ceramic chip antenna	353	
Ceramic multichip modules	4524	
Ceramics		
insulating properties	151 <i>t</i>	
Cesium chloride		
electric dipole moment	941 <i>t</i>	
Chaff decoy countermeasures	1350	
Chain parameter matrix	877	

Index terms**Links**

Channel estimation		
forward link	175	
reverse link	172	
Channel fading	167	
Channelized microwave receiver	2927	
Channelizers	3362	
Channel propagation	1027	
military communication	3012	
Channel spreading	167	
Chaotic oscillators	5469	
Charge-balancing converters	5496	5499
Charge injection transistor (CHINT)	3388	
Chebyshev behavior	1522	1523
	1552	
Chebyshev filters	599	1549
Chebyshev lowpass approximation	602	1526
Chebyshev lowpass filters	1523	1555
	2384	
Chebyshev polynomials	601	1527 <i>t</i>
Chebyshev pseudospectral time-domain (PSTD) method	1408	
Chemosphere	105	
Chip-package integration		
RF integrated circuits	4289	
Chip-scale packaging	4523	
Chirality	610	
Chiral resonators	704	
Chiral slotlines	705	
Chiral striplines	705	
Chirowaveguides	703	
Circuit stability	622	
Circuit tuning	632	
Circular aperture antennas	372	
Circular aperture feed antennas	192	
Circular cone		
backscatter from	489	
Circular cylinder		
backscatter from	490	
Circular dichroism	611	
Circular electric modes	5582	
Circular ferrite-loaded waveguide	1491	

<u>Index terms</u>	<u>Links</u>
Circular loop antennas	
calibration of	560
Circularly polarized antenna	222
Circularly polarized dielectric resonator antennas	963
Circularly polarized waves	235
Circular polarization	235 4082
Circular waveguide cavity resonators	580
Circular waveguides	643 668
coupling holes in	5579 588
as transmission line	5529
Circulator-based isolators	1478
Circulator-coupled multiplexer	3364
Circulators	1448
CISPR (International Electrotechnical Committee on Radio Interference)	1138
Clapp oscillator	1434 5471
Clean-air observation radar	4027
Clear channel	302
Clockwise circularly polarized	236
Clockwise elliptically polarized	236
Cloud attenuation	4483
Cloud radar	4117
Clutter map constant false-alarm rate (CFAR) radar signal processing	4155
Clutter reduction	4128 4152
CMOS/BiCMOS	3025
CMOS RF integrated circuits	
mixed-signal	3095
Coaxial aperture feed antennas	192
Coaxial cable	
for antennas	150
Coaxial cavity resonators	577
Coaxial connectors	664
Coaxial fixed attenuators	453 460
Coaxial line attenuator	437
Coaxial-line microwave circuits	2711
Coaxial lines	658 662
discontinuities	653
Coaxial line steps	656
Coaxial resistive film attenuator	464
Coaxial waveguides	658 5580

<u>Index terms</u>	<u>Links</u>	
COBRA DANE	4017	
COBRA JUDY	4017	
Cochannel cells	592	
Cochannel interference	4337	
Code-division multiple access (CDMA) wireless standard. <i>See</i> CDMA wireless standard		
Codeword	3059	
Coherent radar	1316	
Coherent radar signal processing	4149	
Coherent waves	1294	
Coiflets	5612	
Cole-Cole equation	946	
Colpitts circuit	5471	
Colpitts oscillator	1434	
Coma	1790	
Combiners	3362	
Comb-line filters	674	
Command-to-LOS (line-of-sight) guidance	3088	
Compact-disk players	4237	
Compact microstrip antennas	2626	
Compact range antennas	177	
testing	266	
Companion modeling	401	
Compensated dual-offset reflectors	3331	
Compensation networks		
feedback amplifiers	1429	
Compensation temperature	2417	
Complex media	694	
Complex Poynting vector	1282	1284
Composites		
backscatter reduction for stealth technology	491	
radar cross-section reduction	4037	
Compound feed antennas	208	
Compressive microwave receiver	2930	
Computational electromagnetics	1232	
scattering models for microwave remote sensing	718	
Computer-aided design (CAD)		
active filter design	70	
dielectric resonator oscillators	996	
hybrid techniques	2040	
microwave circuits	2711	2731

Index terms**Links**

Computer-aided design (CAD) (<i>Continued</i>)		
microwave integrated circuits	2783	
microwave power amplifiers	2899	
nonlinear circuit design	3517	
RF integrated circuits	4274	
waveguide directional coupler applications	5543	
Computerized tomography (CAT)	1201	
Concave mirrors		
microwave Fabry-Perot resonators as	1397	
Concentric microstrip ring arrays	757	
Conditional access equipment, for direct-to-home broadcasting	1054	
Conductors	1218	
artificial magnetic	413	
Conflict-free multiple access schemes	3353	
Conformal antennas	288	750
Conformal arrays	750	757
	2573	
Conformal finite-difference time-domain technique	1362	
Conformal mapping techniques	760	
Conformal meshing	406	1323
Conformal phased arrays		
direction of arrival estimation and adaptive processing using	1065	
Conformal-strip-excited dielectric resonator antennas	961	
Conical antennas	775	
Conical arrays	759	
Conical horn aperture feed antennas	195	
Conical monopole antennas	3242	
Conical scan angle trackers	4178	
Conical scan radar	4024	
Conical waveguides	5581	
Constant false-alarm rate (CFAR) radar signal processing	4155	
Constrained lens antennas	2324	
Constrained lens dielectric antennas	901	
Contact currents	513	520
Contiguous band multiplexers	3367	
Continuity equation	1281	
Continuous active-diode distributed amplifiers	1086	1095
Continuous ferrimagnetic distributed amplifiers	1096	
Continuous groups of symmetry	700	

Index terms**Links**

Continuously variable attenuators	438	454
	462	
Continuous parametric varactor diode distributed amplifiers	1096	
Continuous transistor distributed amplifiers	1088	1096
Continuous-wave Doppler radar	4057	
Continuous wavelet transform	5607	
Convolution theorem, Fourier transform	1402	
Cooker magnetron	2493	
Cooley-Tukey FFT algorithm	1405	
Coplanar resonance isolators	1476	
Coplanar strip	2744	
Coplanar stripline components	780	
Coplanar stripline filters	787	
Coplanar stripline lowpass filters	790	
Coplanar stripline resonators	783	
Coplanar stripline-to-coplanar waveguide transitions	810	
Coplanar stripline-to-microstrip transitions	812	
Coplanar stripline-to-slotline transitions	814	
Coplanar stripline transitions	792	810
Coplanar waveguide aperture-coupled path antenna	820	
Coplanar waveguide components	816	
Coplanar waveguide-fed Lotus slot antenna	5638	5639
Coplanar waveguide microwave circuits	2719	
Coplanar waveguides	2744	
Coplanar waveguide transmission lines	672	821
MMICs	3218	
Copolarization	238	
Cordless Phone Two	599	3124
Cordless telephones	1022	1031
Cordless telephone systems	5660	5670
Cordless telephony	3124	
Corner reflector	4493	
Corner reflector decoys	1350	
Corning glass		
dielectric permittivity	939f	
Coronal mass ejections	4189	
Correlation theorem, Fourier transform	1402	
Corrugated horn antennas	847	

<u>Index terms</u>	<u>Links</u>	
Corrugated horn aperture feed antennas	195	
Costas loop	3973	
Coulomb gauge	833	
Counterclockwise circularly polarized	236	
Counterclockwise elliptically polarized	236	
Countertargeting	1335	1343
Coupled coplanar waveguide transmission lines	828	
Coupled microstrip line resonance isolators	1477	
Coupled-oscillator arrays		
quasioptical circuit application	3979	
Coupled transmission lines	863	
Couplers	2051	
into and out of cavity resonators	586	
Coupling		
distributed	1082	
mechanisms	1079	
Coupling holes, in waveguides	587	
Courant stability factor	1573	
Critical coupling	588	
Crossed dipoles	1052	
Cross-guide directional couplers	5540	
Cross-polarization	238	263
Crosstalk	863	
and electromagnetic compatibility	1147	
monolithic antennas	3211	
two microstrip lines	2285	
Cruise missiles	3089	
Cryogenically-cooled analog-to-digital converters	883	
Cryogenically-cooled low-noise amplifier	884	
Cryogenically-cooled microwave filters	885	
Cryogenically-cooled microwave mixers	884	
Cryogenically-cooled millimeter-wave mixers	884	
Cryogenically-cooled oscillators	888	
Cryogenic electronics	882	
Cryoperm		
electromagnetic properties	1223 <i>f</i>	
Cryostat altimeter	3990 <i>f</i>	3990
	4003	
Cryptography	3017	

Index terms**Links**

Crystal oscillators	5472	5475t
	5476	
feedback oscillators	1436	
Crystal video microwave receiver	2925	
CT-2 cordless phone standard	599	3124
Cuachy-Riemann equation	762	
Cubical quad loop antennas	2367	
Cubic spline interpolation	405	
Curie temperature	1224	
Curl slot antenna	4710	
Current gain	1419	
Current steering ratio	6	
Curvature of field	1791	
Curvilinear finite element analysis	1598	
Cutoff frequency doublers	5635	
Cylindrical arrays	758	
Cylindrical dielectric resonator filters	976	
Cylindrical waveguide cavity combiners	5566	
Cylindrical waveguides	5581	
D		
DAB (Digital Audio Broadcasting) standard	1018	
D/A conversion architectures and techniques	1	
<i>See also</i> Digital-to-analog converters		
D'Alembert's solutions	1282	
Damping factor		
cavity resonators	577	
Darlington pair	5635	
Data conversion	1	
oversampled	1	17
pipelined A/D	12	
Data converters	2	
architectures	5	
pipelined A/D conversion	12	
Daubechies wavelets	5612	5626
DC conductivity	916	
Decision feedback equalizer	173	
Decoy countermeasures	1349	

<u>Index terms</u>	<u>Links</u>	
DECT wireless standard	503 <i>t</i>	599
and adaptive array antennas	3123 <i>t</i>	5671
and digital radio	91	
Dedicated short-range communication (DSRC) systems		
Van Atta array reflector application	1032	
De-embedding algorithms	5465	
Deep-sub-micrometer (DSM) technology	410	
capacitance extraction		
Deep submicrometer MOS transistors	566	
Defense Satellite Communication System (DSCS)	3096	
Degenerate parametric amplifier	3019	
Delay-Doppler radar altimetry	2828	2833
Delay-line cancelers	3999	
Delay spread	4150	
Delta/sigma D/A modulator	168	
Demodulation	17	
wireless systems	117	
Dense media radiative transfer theory	5658	
Dense-wavelength division multiplexing (DWDM)	718	728
Depolarization	5600	
Depolarization dyadics	4481	
Deramp on receive	142	
Deterministic circuit tuning	3995	
Diagonal horn aperture feed antennas	633	634
Diamagnetic materials	203	
Diamagnetism	2412	
Diamond	2413	
dielectric permittivity	939 <i>t</i>	
Dichroic reflector feed antennas	210	
Dichromism	140	
Dielectric aging	956	
Dielectric constant	919	
Dielectric decrement	948	
Dielectric Fabry-Perot resonators	1394	
Dielectric-filled edge slot antennas	754	
Dielectric lens antennas	893	
Dielectric loaded antennas	893	
Dielectric-loaded circular horn aperture feed antennas	201	
Dielectric-loaded horns	904	

<u>Index terms</u>	<u>Links</u>	
Dielectric-loaded rectangular horn aperture feed antennas	203	
Dielectric-loaded waveguides	906	
Dielectric loss	942	
measurement on distributed parameter specimens	928	
measurement on lumped capacitance specimens	919	
Dielectric materials	1217	
anisotropic	1219	
Dielectric measurement	916	
Dielectric permittivity	938	
<i>See also</i> Permittivity		
selected solid dielectrics	939 <i>t</i>	
Dielectric polarization	938	940
Dielectric properties		
anisotropy included in boundary value problems	533	
selected materials	945 <i>t</i>	
Dielectric relaxation	938	946
Dielectric resonator antennas	960	
Dielectric resonator filters	974	
Dielectric resonator materials	1009 <i>t</i>	
Dielectric resonator oscillators	985	2824
Dielectric resonators	907	999
Dielectric resonator tuning	991	
Dielectric-rod feed antennas	207	
Dielectric spectroscopy	956	
Dielectric waveguide resonators	3054	
Dielectric waveguides	5530	
Dielectric oscillators		
feedback oscillators	1436	
Differential evolution strategy	1209	
Differential GPS	117	
Differential interferometry	4113	
Differential pair doubler	5635	
Differential time-domain reflectometry	4447	
Diffraction	1296	1298
and radar cross-section	4034	
uniform geometrical theory of	5433	
Diffused epitaxial varactors	2829	
Diffuse scattering	1295	1296
Diffusion noise	3421	
Digital-analog conversion architectures and techniques	1	

<u>Index terms</u>	<u>Links</u>	
Digital audio codecs	4241	
Digital audio storage systems	4244	
Digital audio systems	4242	
Digital bandpass filters	497	
Digital beamforming array antennas	95	
Digital cellular radio	593	1022
reasons for	596	
Digital cellular systems	1030	
Digital cordless telephony	1031	
Digital Doppler processing	4183	
Digital editing	4245	
Digital effects generators	4248	
Digital error correction	15	
Digital intercept microwave receivers	2932	
Digital microwave receivers	1014	
Digital modulation schemes	597	
Digital radio	1021	
Digital radiofrequency memory		
cryogenically-cooled	887	
Digital signals	1	
Digital television transmitters	5327	
Digital-to-analog converters	2	
architectures	5	
Diode mixers		
mm-wave integrated circuits	3029	
Diode ring mixers		
VHF range	5486	
Diodes	1033	2968
Diplexers	1649	3362
	3363	
microwave Fabry-Perot resonators as frequency	1394	
Diplexing		
feed antennas	211	
Dipole antenna arrays	1033	
for high-frequency broadcasting	298	
Dipole antennas	1033	
for electromagnetic field measurement	1190	
fields of ideal or very short	227 <i>t</i>	
monolithic	3206	
radiation from ideal	274	

Index terms**Links**

Dipole antennas (<i>Continued</i>)		
relationship to monopoles	3329 <i>t</i>	
Direct broadcast satellite systems	1053	
Direct-imaging radar	4025	
Directional antenna feeder systems	312	
Directional antennas	219	
radiation pattern	228	
Directional couplers	460	1076
for antennas	154	
for electromagnetic field measurement	1195	
Direction finding	4249	
Direction finding arrays	4254 <i>t</i>	
Direction of arrival estimation	165	
using conformal phased array	1065	
Directive antennas	1085	
Directivity	220	263
	278	
dielectric loaded antennas	893	
evaluation	238	
and radiation patterns	233	
Direct (line-of-sight) links	290	
Directors	206	
Direct satellite television broadcasting	1052	
Direct-sequence CDMA (DSCDMA)	174	
Direct-to-home satellite television broadcasting	1052	
Discontinuities		
coaxial line	653	
finline	1616	
leaky modes and high-frequency effects	2268	
in microstrip	2643	
mode-matching methods	3163	
waveguide	5543	
Discontinuous fast Fourier transforms (DFFT)	1414	
Discrete amplifiers	1086	
Discrete Fourier transforms	1401	1403
Discrete wavelet packet (DWT) transform	383	
Discrete wavelet transform	5608	
Dish antennas	4450	
Disk		
backscatter from semitransparent	489	

<u>Index terms</u>	<u>Links</u>	
Dispersion diagrams	5575	
Dispersive SAW delay lines	26	
Dissado-Hill model	950	
Dissipation constant	945	
Distance measuring equipment	4292	
Distributed amplifiers	1086	
mm-wave integrated circuits	3027	
Distributed circuits	153	
Distributed coupling	1082	
Distribution amplifiers		
for radio broadcasting	4236	
Diversity	3059	
adaptive array antennas	99	
Diversity channels	4339	
Domains	2415	
Dominant waveguide mode	5571	5576
Doppler ambiguities	4183	
Doppler beam sharpening	4098	4100
Doppler filtering	4182	
Doppler processing radar	4026	
Doppler spread	167	4391
	5664	
Doppler tracking	4182	
Dose	512	
Double-balanced mixers	1644	
Double-double-balanced mixers	1644	
Double-exchange materials	2418	
DOVATT (Double-velocity avalanche transit-time) diodes		
negative resistance	3389	
DOVETT (Double-velocity transit-time) diodes		
negative resistance	3389	
Dragone condition	4461	
DRM (Digital Radio Mondial)	1019	
Dual-beam base-station antennas	335	
Dual-curl slot antenna array	4713	
Dual-directional coupler	5536	
Dual-frequency base-station antennas	333	
Dual-frequency microstrip antennas	1098	
Dual-loop feedforward amplifiers	1447	

Index terms**Links**

Dual-mode ferrite phase shifters	1501	
Dual rhombic loop antenna	4427	
Dual-spiral slot	4713	
Dual-use radar altimetry	4004	
Ducting	4035	
Duplexers	1024	3363
comb-line filters	692	
ferrite circulators	1460	
Duplexing	1024	
DVX for DIRECTV JAPAN	1063	
(DWDM) Dense-wavelength division multiplexing	5600	
Dyadic Green's functions	141	835
	1411	
planar multilayers	1163	
Dyson equation	145	
E		
Earth Resource Technology Satellite-1 (ERTS-1)	293	
Earth's magnetic field		
effect on medium and high frequency sky waves	4688	4692
and radiation effects	4188	
Edge illumination	190	
Edge taper	190	
Effective isotropically radiated power (EIRP)	264	281
Effective number of bits	4	
<i>E</i> -field vectors	225	
Eikonal equation	1792	
Einstein relation	3444	
Eisenhart's transition	2656	
Electrets	1508	
Electrical boresight	263	
Electrical impedance tomography (EIT)	558	
Electrically small antennas	1627	3080
Electrically tunable oscillators	2824	
Electrical resistance		
negative	3385	
Electrical resonators	5469	
Electric coupling apertures	587	
Electric fields		
boundary value problems	523	

Index terms**Links**

Electric fields (<i>Continued</i>)	
near field measurement using modulated scatterer	2522
Electric field sensors	1190
Electric vector potential	238
Electrocardiograms	
bandwidth value	5630 <i>t</i>
Electromagnetic analysis	399
Electromagnetic bandgap assisted bandpass filters	1117
Electromagnetic bandgas structures	1117
Electromagnetic compatibility	1136
Electromagnetic ferrite tile absorber	1151
Electromagnetic field measurement	1190
Electromagnetic fields	833
computation in planar multilayers	1163
high-field effects	1970
measurement	1190
in waveguides	5570
Electromagnetic field sensors	1193
Electromagnetic induction (EMI) sensors	
for buried-object detection	552
Electromagnetic interpolation	405
Electromagnetic inverse problems	1200
Electromagnetic inverse scattering problems	1200
Electromagnetic materials	1216
Electromagnetic modeling	1232
Electromagnetic pulse (EMP)	1137
Electromagnetic radiation	4342
Electromagnetics, time domain	1318
Electromagnetic shielding	1248
electromagnetic analysis	407
and electromagnetic compatibility	1146
VHF range	5488
Electromagnetic simulation	
parallel algorithms and computing for large-scale	3614
parameter estimation using signal models	3646
Electromagnetic subsurface remote sensing	1256
Electromagnetic Surface Patch (ESP) Code	2348
Electromagnetic surface waves	1270
Electromagnetic wave absorbers	159

Index terms**Links**

Electromagnetic waves		
boundary value problems	523	
guided	1846	
in ionosphere	1303	
propagation	1280	
scattering	1295	
Electromagnetic wave spectrum	1281	
Electron acoustic phonon scattering	3465	
Electron-beam lithography		
Monte Carlo analysis	3266	
Electron cyclotron resonance (ECR) plasma	2935	
Electronically steerable parasitic array radiator (ESPAR)	97	
Electronic polarization	940	
Electronic toll collection (ETC) systems		
Van Atta array reflector application	5465	
Electronic warfare	1333	
and radar cross-section	4040	
Electrooptic limiters	2800	
Electrooptic dielectrics	1220	1220t
Electrostatics		
boundary value problems	523	
fast Fourier transform applications	1407	
Element factor	227	
ELF shielding	2474	
ELF waves	1281	
electromagnetic effect in ionosphere	1306	
Ellipsoid-hyperbolic waveguide cavity resonators	584	
ELLIPSO system		
system characteristics	600r	
Elliptical horn aperture feed antennas	199	
Elliptically polarized antenna	222	
Elliptically polarized vector	232	
Elliptically polarized waves	235	
Elliptical polarization	235	4081
Elliptical waveguide cavity resonators	580	
Elliptical waveguides	5581	
Elliptic filters	1353	1524
	1535	1550
Elliptic function characteristic	1553	
Elliptic function filters	1549	

Index terms**Links**

Elliptic function lowpass filters	1557	
Elliptic waveguides	669	
Embedded antennas, for portable wireless devices	3068	
Emissivity	4345	
EN 55022	1139	
Enantiomers	611	
Encryption	3017	
Endfire antenna	229	278
Endfire antenna arrays	289	
Enhancements of finite difference time domain method	1361	
Envelope detection	4137	
Environmental noise	4297	
<i>E</i> -plane	219	
<i>E</i> -plane antenna radiation pattern	225	
<i>E</i> -plane bifurcations	5549 <i>t</i>	5558
<i>E</i> -plane circuits	1601	1609
	5530	
<i>E</i> -plane corner	5550 <i>t</i>	
<i>E</i> -plane coupling hole	5550 <i>t</i>	
<i>E</i> -plane diplexers	5534	
<i>E</i> -plane junctions	5557	5558
<i>E</i> -plane offset	5548 <i>t</i>	
<i>E</i> -plane pattern	229	274
<i>E</i> -plane step	5548 <i>t</i>	
<i>E</i> -plane tee	5550 <i>t</i>	
<i>E</i> -plane waveguide bends	5531	
<i>E</i> -plane waveguide filters	5533	
Epoxy resin		
dielectric permittivity	939 <i>t</i>	
insulating properties	151 <i>t</i>	
Equal-time combining	166	
Equiangular spiral antennas	1679	
Equiripple	1355	1522
	1523	1552
Equivalent circuit-state space equation-neural networks	3395	
ERMES (European Radio Message Standard)	5674	
Error cross section	4193	
ERS-1 altimeter	3990 <i>t</i>	3991
ERS-2 altimeter	3990 <i>t</i>	3991

<u>Index terms</u>	<u>Links</u>
ESPIRIT algorithm	165
Essential boundary conditions	1739
ETACS (European Total Access Cellular System)	5657
ETHERNET	2356
Euler differential equation	1738
European norm	1139
European Radio Message Standard (ERMES)	5674
European Total Access Cellular System (ETACS)	5657
Exposure	512
External Q -factor	3938 3952
 F	
Fabry-Perot interferometers	1381
wavelength measurement	5598
Fabry-Perot resonators	1381
Fabry-Perot resonators-based antennas	1395
Fading	2948
Fading statistics	2948
Failure rate	3270
Fan-beam antenna pattern	228
Faraday chiral medium	706
Faraday rotation	1225
and electromagnetic effect in ionosphere	1313
Faraday rotation isolator	1475 2788
Faraday rotation phase shifters	1501
Far-field exposure	514
Far-field (Fraunhofer) region	218
Far-field patterns	225
Far-field region	230
testing	264
Fast Fourier transforms	1401 5604
Fast inverse scattering methods	1411
Fast time-domain nonlinear circuit analysis	3486
FBI fingerprint compression	5629
FCC regulations	1138
FDMA wireless standard	597 5666
and digital radio	1023
multiple access schemes	3351 3353
Feature extraction	3017

<u>Index terms</u>	<u>Links</u>
Feed antennas	184
Feedback	1418
wideband amplifier	5632
Feedback amplifiers	1418
Feedback equation	1420
Feedback oscillators	1432 5470
Feedback systems	622
Feeder links	3150
Feedforward adaptation	1447
Feedforward amplifiers	1439
Feedforward operation	1440
Fermat's principle	1781
Ferrimagnetic materials	1451
Ferrimagnetic resonance	1454
Ferrimagnetism	2417
Ferrite circulators	1448
Ferrite isolators	1473
Ferrite junction circulators	2434
Ferrite limiters	2799
Ferrite-loaded finlines	1494
Ferrite-loaded loop antennas	2365
Ferrite-loaded microstrip lines	1493
Ferrite-loaded parallel-plate waveguide	1493
Ferrite-loaded slotlines	1494
Ferrite-loaded waveguides	1486
Ferrite nonreciprocal resonators	2445
Ferrite phase shifters	152 1497
Ferrites	1224 1483
in anechoic chambers	160
defined	1452
electrodynamics	1486
magnetization	1452
permittivity tensor	702
wave propagation in	1453
Ferrite tile absorber, electromagnetic	1151
Ferroelectric devices	
microwave	2742
Ferroelectric film deposition	1516
Ferroelectricity	1505

<u>Index terms</u>	<u>Links</u>	
Ferroelectric lens antenna	2747	
Ferroelectric materials	1229	1504
and high-temperature superconductors	2742	
permittivity tensor	2749	
Ferrofluids	699	
Ferromagnetic materials	2424	
Ferromagnetic materials	1451	2412
Ferromagnetic resonance	1478	
Ferromagnetism	2413	
FET (Field effect transistor)		
description and applications	2968	2972
frequency multipliers	3529	
low noise behavior	2369	
microwave photonics	2853	
microwave power amplifiers	2873	
mixer circuits	3104	
MMICs	3214	
nonlinear circuit design	3505	
source of photodetection method	2852 <i>t</i>	
as switching device	2847	
Fiberoptic distributed amplifiers	1089	
Fiberoptic links		
microwave photonics	2853	
phased-array antennas	2860	
Fibers-to-the-home system	4310	
Fiber-to-the-air system	4310	4319
Fiber-to-the-curb system	4310	
Fibre Channel	2358	
Field displacement isolators	2790	
Field effect transistors. <i>See</i> FET; MESFET; MOSFET		
Field oxides	4206	
Field pattern	225	226
Field regions, of antennas	230	
Fields. <i>See</i> Electromagnetic fields; Magnetic fields		
Fighter aircraft		
typical radar cross-section	4031 <i>t</i>	
Figures of merit, antennas	218	
Filtered noise	1730	
Filtering	600	

<u>Index terms</u>	<u>Links</u>	
Filters	1548	
dielectric resonator	974	
finlines	1601	
microwave	2751	
multimode equivalent network representation	3347	
RF integrated circuits	4284	
transformation relations	1561 <i>t</i>	
tuning	638	
VHF range	5487	
Filter synthesis	1521	
Filter tables	1524 <i>t</i>	1524
Filter theory	1548	
Finite difference method	1238	
boundary value problems	523	
Finite-difference time-domain analysis	524	1241
enhancements of	1320	1567
and fast Fourier transform	1361	
hybrid method	1407	
nonlinear circuit analysis	1245	
3487	3487	
Finite differencing	524	
Finite element analysis	1589	
and Galerkin method	1746	
Finite-element/boundary integral method	1598	
Finite-element method	1239	
Finite-element time-domain method	1324	1599
Finite impulse response (FIR) digital bandpass filters	497	
Finline amplifiers	1606	
Finline antennas	1603	
Finline components	1601	
Finline couplers	1602	
Finline discontinuities	1616	
Finline mixers	1604	
Finline oscillators	1606	
Finlines	1609	
transitions to other transmission media	1617	
First-hop footprint	296	
Fixed attenuators	437	460
Fixed phase shifters	152	
Fixed satellite service (FSS) bands	1053	1061

Index terms**Links**

Fixed-value coaxial attenuator	437	
Fixed-value waveguide attenuators	439	
Fizeau interferometers	5594 <i>t</i>	
wavelength measurement	5597	
Flap (movable-vane) attenuators	462	
Flare decoys	1351	
Flash (A/D) converters	7	
Flat fading	5664	
Flicker noise	3459	
Flip-chip technology	4521	
Floquet phase number	1385	
FLTSATCOM systems	3019	
Flux shunting	2476	
FM broadcasting antennas	5124	
FM broadcasting transmitters	5337	
FM radio waves	1281	
bandwidth value	5630 <i>t</i>	
FM wireless	5657	
Fog attenuation	4483	
Folded dipole antennas	1049	
Folded monopole antennas	3240	
Folding (A/D) converters	10	
Foldy-Lax equation	732	
Foods		
dielectric properties	2765 <i>t</i>	
Forward bias	1034	1037
and low-level injection	1039	
Forward gain	1419	
Fourier transforms	1401	
Four-port waveguide junctions	5557	5558
Fractal modulation	5628	
Fractals	1620	
Fractal shaped antennas	2598	
review	1620	
Fraunhofer region	231	
Free-space Lorentz	836	
Free-space power combining	53	
Free-space transmission		
Friis formula for	1733	

<u>Index terms</u>	<u>Links</u>	
Frequency	5587	
Frequency conversion	1637	
Frequency conversion arrays		
quasioptical circuit application	3983	
Frequency converters	1635	
Frequency dispersion	1287	
Frequency dividers		
nonlinear circuits	3523	
resonant tunneling diodes	4489	
Frequency-division duplex (FDD) systems	17	597
and digital radio	1024	
Frequency-division multiple access (FDMA). <i>See</i> FDMA wireless standard		
Frequency-division multiplexers	1649	
Frequency-domain circuit analysis	1659	
Frequency doublers	5486	
Frequency downconversion	1637	
Frequency-independent antennas	288	1674
Frequency licensing	3129	
Frequency mixers	1635	
nonlinear circuit design	3503	
Frequency modulation	1691	
Frequency modulation waveforms	4158	
Frequency multiplication	1637	
Frequency multipliers		
microwave and radio frequency	2663	
mm-wave integrated circuits	3033	
nonlinear circuits	3528	
resonant tunneling diodes	4489	
Frequency reconfigurability	4406	
Frequency remapping	3491	
Frequency response		
feedback amplifiers	1422	
Frequency reuse	3129	
multibeam antennas	3317	
Frequency reuse by polarization isolation	3317	
Frequency reuse by sidelobe isolation	3317	
Frequency-selective channels	4334	
Frequency selective surfaces	1700	
Frequency shift keying (FSK)	118	5665
Frequency stability	1706	1721

Index terms**Links**

Frequency standards, characterization	1720	
Frequency synthesizers	1729	3120
	3767	
Frequency thinner	1651	
Frequency-to-voltage converter	5489	
Frequency translation		
mixer circuits	3113	
Frequency tunable recursive filters	66	
Frequency upconversion	1637	
Fresnel reflectivity	2956	
Fresnel region	230	
Fresnel zone plate lenses	2325	2335
Friend biquad circuit	499	
Friis free-space transmission formula	1733	
Fringing capacitance	568	
Front-fed offset Cassegrain	3332	
Fully depleted silicon on insulator MOSFET (FD-SOI MOSFET)	3278	
Functional circuit tuning	633	
Fused quartz		
dielectric permittivity	939 <i>t</i>	
insulating properties	151 <i>t</i>	
G		
Gain		
distributed amplifiers	1090	
feedback amplifiers	1419	1420
microwave receivers	2921	
Gain, antennas. See Antenna gain		
Gain circles	4513	
Gain margin	1429	
Galactic cosmic rays	4189	
Galerkin (Rayleigh-Ritz) method	1735	
Gallium arsenide		
comparison with SiGe elements using active-impedance profile (AIP)	81 <i>t</i>	81
HBT	3024	
HEMT	3022	
MMIC substrate properties	3216	3217 <i>t</i>
properties in microwave ICs	2775 <i>t</i>	
resonant tunneling diodes	4484	
technology and applications	1749	

<u>Index terms</u>	<u>Links</u>	
Gallium arsenide NMESFET attenuators	470	479
Gallium nitride		
for electronics	1757	
HEMT	3023	
MMIC substrate properties	3217 <i>t</i>	
Gap-fed loop antenna	2363	
Garnets		
characteristics as circulators	1459 <i>t</i>	
as ferrites	1452	1484
Gaseous limiters	2798	
Gate-level simulation	566	
Gate mixer	3505	3508
Gate oxides	4201	
Gaussian noise	3400	
Gaussian optics	1784	
Geiger-Mueller tubes		
as radiation monitors	4222	
Generalized admittance matrix	1767	3167
Generalized Chebyshev characteristic	1553	
Generalized Chebyshev filters	1550	
Generalized Chebyshev lowpass filters	1557	
Generalized impedance matrix	3167	
Generalized plane wave	270	
Generalized scattering matrix	1767	3165
Generalized scattering matrix technique	1767	
General Packet Radio Service (GPRS)	5668	
Generation-recombination noise	3458	
Genetic algorithms	1208	
Geometrical optics	1298	1777
Geometrical theory of diffraction	5433	
GEOS-3 altimeter	3990 <i>t</i>	
Geosat altimeter	3990 <i>t</i>	
Germanium-silicon alloys and devices	1796	
Ge-Si alloys and devices	1796	
GFO altimeter	3990 <i>t</i>	
Gilbert cell	3104	3115
Gilbert cell mixer	3031	
Glass		
dielectric permittivity	939 <i>t</i>	

Index terms**Links**

Glass (<i>Continued</i>)		
dielectric properties	2765t	
insulating properties	151t	
Glass transition temperature		
selected polymers	955t	
Global dynamic topography	3991	
Global Positioning System (GPS)	113	4297
military application	3018	
Grating antennas	1806	
Grating lobes	253	
and frequency selective surfaces	1703	
Gratings	1806	
Grating spectrometers	5592	5594t
Gravity		
radar altimetry	3998	
Green Bank Radio Telescope	4451	4462
Green functions, dyadic	141	
Green's function methods	1817	
Gregorian reflector	4460	
Grid amplifiers		
quasioptical circuit application	3981	
Grid arrays	2574	
Grid-dip meters	3938	
Grid oscillators		
active antennas	53	
quasioptical circuit application	3979	
Grooved waveguides	5585	
Ground conductivity maps	303	
Grounded-timing-capacitor oscillator	5474	
Ground/foilage penetrating radar	4028	
Ground moving-target indicator	4078	
Ground penetrating radar	1261	1833
	4028	
for buried object detection	541	
electromagnetic inverse problems	1202	
Ground plane	272	
Group delay, filters	1552	
Group velocity	1288	

<u>Index terms</u>	<u>Links</u>	
GSM wireless standard	321	3123 <i>t</i>
	3123	5657
	5668	
and digital cellular radio	596	1031
physical-layer parameters	598 <i>t</i>	
Guided electromagnetic waves	1846	
Guided waves	1292	
Gunn (transferred-electron) devices and circuits	1857	
Gunn diodes	2968	2971
	3387	
in waveguide oscillators	5559	
Gunn oscillators	2823	
Gyrator	1225	
Gyrators	1874	
Gyroelectric media	700	
Gyrotron oscillator	3001 <i>t</i>	3004
Gyrotrons	1883	
Gyrotropic materials	1454	
 H		
Haar scaling function	390	5608
	5623	
Haar wavelet	5608	5625
Half-power beamwidth	220	230
	277	
Handoff	1022	5660
Handover, in cellular systems	5660	
Handset antennas	356	
Hankel transforms	1893	
Hard errors	4186	4195
Hard magnets	2422	
Harmonic balance method	3487	3506
Harmonic circuits	1915	
Harmonic injection frequency dividers	3523	3525
Harmonic mixers	1638	1644
	3110	
Harmonic oscillators	1915	5490
Hartley oscillator	1434	5471
Havriliak-Negami function	948	
Hazard function	3270	

<u>Index terms</u>	<u>Links</u>	
HBTs (Heterostructure bipolar transistors)		
active antennas	45	
description and applications	2977	
gallium arsenide	1756	
microwave photonics	2853	
microwave power amplifiers	2872	
MMICs	3214	3220
mm-wave integrated circuits	3023	
Monte Carlo analysis	3260	
noise in	3423	3429
source of photodetection method	2852 <i>t</i>	
Helical antennas	1925	
Helical radar pattern	4022	
Helmholtz equations	1282	1936
HEMTs (High-electronic mobility transistors)		
active antennas	45	
aluminum gallium nitride/gallium nitride	1760	
cryogenic electronics	882	
description and applications	2968	2973
gallium arsenide	1754	
microwave and radio frequency multipliers	2663	
microwave photonics	2853	
mixer circuits	3104	
MMICs	3214	3220
mm-wave integrated circuits	3022	
Monte Carlo analysis	3261	
noise mechanisms	2380	
source of photodetection method	2852 <i>t</i>	
Hertzian dipole antenna	1046	2338
Heterojunction bipolar transistors (HBTs)	1946	
See also HBTs		
Heterostructure devices	1963	
Hexaferrite	2444	
HF band radar	4031 <i>t</i>	4055 <i>t</i>
HFETs (Heterostructure field-effect transistors)		
noise in	3421	3439
<i>H</i> -field vectors	225	
HF shielding	2474	
HF waves	1281	
electromagnetic effect in ionosphere	1307	
High-electronic mobility transistors (HEMTs). <i>See</i> HEMTs		

<u>Index terms</u>	<u>Links</u>	
High-field effects	1970	
High-frequency backscattering region	483	
High-frequency broadcasting	1981	
High-frequency broadcasting antennas	295	
High-frequency circuits		
applied numerical electromagnetic analysis for planar	397	
High-frequency effects		
in microwave integrated circuits	2268	
High-frequency noise	3417	
High-frequency noise generation	3414	
High-frequency permittivity	944	
High frequency sky wave propagation	4690	
High frequency sky waves	4686	
High-frequency transmission lines	1989	
High-order recursive filters	67	
Highpass filters	1522	
elliptic filters	1357	
microwave	2761	
transformation of lowpass into	1540	1560
transformation relations	1561 <i>t</i>	
High- <i>Q</i> millimeter-wave filters	1018	
High-resolution imaging radar	4025	
High-speed electronics		
FDTD analysis application	1583	
time-domain reflectometer application	4449	
High-temperature superconductors	2005	
and cryogenic electronics	882	
and ferroelectrics	2749	
film growth	2032	
Hilbert monopole	1627	
HIPERLAN	5675	
HIPPI (High-performance parallel interface)	2358	
History of wireless communication	2015	
Hologram	4026	
Holographic processing radar	4026	
Home RF	5675	
Homing missiles	3088	
Horizontal polarization	4083	
Horn antennas	288	2021

<u>Index terms</u>	<u>Links</u>	
Hot carrier noise effects	3439	
Hot-electron bolometer mixers	1647	
Hot-electron noise	3440	
Hot electrons	3429	
<i>H</i> -plane	219	
<i>H</i> -plane antenna radiation pattern	225	
<i>H</i> -plane bifurcation	5549 <i>t</i>	
<i>H</i> -plane corner	5550 <i>t</i>	
<i>H</i> -plane coupling hole	5550 <i>t</i>	
<i>H</i> -plane junctions	5557	5558
<i>H</i> -plane offset	5548 <i>t</i>	
<i>H</i> -plane pattern	229	274
<i>H</i> -plane step	5548 <i>t</i>	
<i>H</i> -plane tee	5550 <i>t</i>	
<i>H</i> -plane waveguide bends	5531	
HTS film growth	2032	
Hull cutoff condition	3003	
Human beings		
typical radar cross-section	4031 <i>t</i>	
Hybrid CAD techniques	2040	
Hybrid-coupled multiplexer	3364	
Hybrid coupler	5536	
Hybrid feedforward amplifiers	1448	
Hybrid Opticelectronic analog-to-digital converters	2864	
Hybrid ring	155	
Hybrids and couplers	2051	
Hydrogen chloride		
electric dipole moment	941 <i>t</i>	
HYPERchannel	2358	
Hypersil		
electromagnetic properties	1223 <i>t</i>	
Hysteresis loops	1223	
I		
IBOC (In-band/on-channel) radio	1019	
IDEN (Integrated digital enhanced network)	598	
IEEE 802.2	2353	
IEEE 802.3	2353	2356
IEEE 802.4	2353	2356

<u>Index terms</u>	<u>Links</u>	
IEEE 802.5	2352	2353
	2357	
IEEE 802.11	503t	5675
IEEE 802 LAN standards	2352	
IFM microwave receiver	2926	
IGFET (Insulated gate field effect transistor)	3278	
Ilmenite		
ferroelectric	1505	
Image compression		
FBI fingerprint compression wavelet application	5629	
wavelet transforms	5618	
Image enhancement	3017	
Image-rejection mixers	3107	
Impact avalanche transit time (IMPATT) diodes and circuits. <i>See</i> IMPATT diodes		
Impact ionization noise	3421	
IMPATT (impact avalanche transit time) diodes	2067	2968
	2970	
negative resistance	3389	
in waveguide oscillators	5559	
IMPATT oscillators	2824	
Impedance	272	
Impedance element filters	27	
Impedance inverters	1562	1565t
Impedance transformers	2079	
Impulse noise	4336	
Impulse radar	4062	
Impurity scattering	3465	
IMT-2000 wireless standards	321	322
	593	3125
	5657	5669
specifications	600	
Incident	1248	
Incoherent scatter radar	1317	
Incoherent waves	1294	
Indium phosphide	2092	
HBT	3024	
HEMT	3023	
MMIC substrate properties	3217t	
resonant tunneling diodes	4484	
Induction near-field region	230	

Index terms**Links**

Inductive iris, in waveguides	5549t	
Inductive post, in waveguides	5549t	
Inductive strips	1616	
Inductive-voltage divider	441	
Inductors		
lumped-element microwave circuits	2723	
magnetic materials	2420	
microwave integrated circuits	2780	
RF integrated circuits	4273	
Infinite impulse response (IIR) digital bandpass filters	497	
Infinitesimal dipole antenna	1046	2338
Infinitesimal loop antenna	2359	
Input impedance		
antennas	220	
feedback amplifiers	1424	
Insects		
typical radar cross-section	4031t	
Insertion loss		
attenuators	456	
filters	1551	
Insertion voltage gain	1521	
Insertion voltage loss	1521	
Instantaneous frequency	1706	
Instructional television fixed service (ITFS)	2385	2388
	2391	
Instrument landing systems	4295	4297
Insulated antennas	907	
Insulated gate field effect transistor (IGFET)	3278	
Insulators		
for antennas	151	
Integral equations	2103	
Integrated antenna systems	2113	
Integrated circuit-antenna modules	2732	
Integrated circuits	2147	
<i>See also</i> Microwave integrated circuits		
capacitance extraction	565	
Monte Carlo analysis of circuit yield	3267	
radiation effects	4186	
RFID tags	4263	
tuning	640	

<u>Index terms</u>	<u>Links</u>	
Integrated finlines	1607	1610
Integro-differential equations	2166	
Intelligent Transportation System (ITS) radio service standards and wireless access in vehicular environments (ITS-wave) at 5.9 GHz	2241	
Intelsat-9	4467	
Intercept receiver	2919	
Intercontinental ballistic missiles	3083	
Interdigitated interdigital transducers (IIDTs)	27	
Interference	5589	
and electromagnetic compatibility	1136	
military communication	3007	
modeling	3397	
Interference suppression	4148	4340
Interferometer-based wavelength meters	5594	
Interferometers	5594	
Interferometric synthetic aperture radar	4165	4170
Intermediate-frequency amplifiers	2175	
Intermediate-frequency piston attenuator	442	
Intermodulation	1638	2189
measurement	2215	
Intermodulation distortion	2877	
Intermodulation measurement	2215	
Internal photoconductive effect	2852	
International Space Year-microwave power transmission in space (ISY-METS) experiment	4426	
Interrogating signal	4493	
Intersatellite links	3150	
Intervallic wavelets	383	
Intrinsic layer	3176	
Inverse Chebyshev lowpass approximation	603	
Inverse Fourier transform	1402	
Inverse nonuniform discrete Fourier transforms (NUDFT)	1413	
Inverse synthetic aperture radar	4062	4070
	4075	
Inverted-F antenna	351	
Ion implantation	3264	
Monte Carlo analysis	3264	
Ionization	4192	
radiation effect	4192	
Ionizing radiation	4217	

Index terms**Links**

Ionosphere		
electromagnetic waves in	1303	
reflection of high frequency waves from	4687	
reflection of low frequency waves from	4681	
reflection of medium frequency waves from	4690	
Ionospheric absorption		
low frequency sky waves	4675	
medium and high frequency sky waves	4686	4687
Ionospheric imaging by radio	1315	
Ionospheric modification	1315	
Ionospheric scintillation	1313	
Ionospheric storms	4686	
Iridium system	600 <i>t</i>	
Iron		
electromagnetic properties	1223 <i>t</i>	
Iron sulfide		
ferroelectric	1505	
Irregular stratified layers		
radar remote sensing	4122	
Isolated port	5536	
Isolators	1473	
ferrite circulators	1460	
Isotropic antennas	219	263
Isotropic antenna source	227	
Isotropic chiral media	611	612
artificial	614	
Beltrami fields in	615	
scattering in	618	
Isotropic radiator	220	227
Isotropic scatterer	2949	
IS-95 wireless standard	3123 <i>t</i>	3124
	5669	
Iterative methods	2231	
ITS radio service standards and wireless access in vehicular environments (ITS-wave) at 5.9 GHz	2241	
J		
Jamming	3008	
Jason-1 altimeter	3990 <i>t</i>	
Jason-2 altimeter	3990 <i>t</i>	
Joint Strategic Target Attack Radar System (Joint STARS)	4078	

Index terms**Links****K**

Ka band radar	4031 <i>t</i>	4055 <i>t</i>
	4056	
K band radar	4031 <i>t</i>	4055 <i>t</i>
	4056	
Kelvin-Varley divider	441	
Klystron	2257	
Klystrons	3001 <i>t</i>	3003
Knowledge-aided design	2732	
Knowledge-based neural networks	3394	
Koch monopole	1627	
Kolrauch-Williams-Watts function	947	
Kramers-Kronig relations	943	1218
Krylov subspace methods	1410 <i>t</i>	
<i>k</i> -Space method	1409	
Ku band radar	4031 <i>t</i>	4055 <i>t</i>
	4056	
Kuroda's transformation	1562	1563

L

Ladar (Laser detection and ranging)	4027	
Lambertian radiators	4346	
Lambert's law	4346	
Laminate multichip modules	4524	
Landing rights	1060	
Landmine detection	1201	
Landsat	115	
Lange coupler	155	
Laplacian pyramid	5617	
Large-scale electromagnetic simulation		
parallel algorithms and computing for	3614	
Lark guided missile	3083	
Larmor frequency	2463	
Laser altimeters	111	
Laser-based wavelength measurement	5599	
Laser detection and ranging (ladar)	4027	
Laser piston attenuator	465	
Laser radar systems	4027	
Lasers		
quasioptical power combining	3978	

<u>Index terms</u>	<u>Links</u>	
L attenuator		
insertion loss	459	
Layered media		
electromagnetic field computation	1163	
L band radar	4031t	4055t
LC filters		
tuning	637	
LC oscillators		
feedback oscillators	1434	
LC-tuned oscillators	5471	5475t
LC two-port filters	1530	
Lead niobium zirconium titanate		
ferroelectric properties	1512t	
pyroelectric properties	1514t	
pyrooptic properties	1515t	
Lead titanate	1229	
ferroelectric	1509	
ferroelectric properties	1512t	
pyrooptic properties	1515t	
Lead zirconate		
piezoelectric properties	1513t	
pyroelectric properties	1514t	
Lead zirconate titanate	1229	
ferroelectric	1509	
ferroelectric properties	1512t	
Leakage constant	2294	
Leaky modes and high-frequency effects in microwave integrated circuits	2268	
Leaky-wave antennas	287	2294
Leaky-wave arrays	2299	2571
Leaky waves	31	1293
	2295	
Left-handed elliptically polarized	236	
Left-handed materials for microwave devices and circuits	2303	
Left-handed polarized waves	236	
Lens antennas	287	2320
feeds supplying	185	
Lens-corrected dielectric-loaded horns	905	
Leslie-Singh architecture	17	
LF waves	1281	
electromagnetic effect in ionosphere	1307	

<u>Index terms</u>	<u>Links</u>	
Lidar (Light detection and ranging)	112	4027
	5599	
Lifetime probability models	3270	
Light detection and ranging (Lidar)	112	4027
	5599	
Lightning arresters	152	
Lightwave distributed amplifiers	1095	
Limiters	4245	
MMICs	3232	
Linear anisotropy	137	
Linear antennas	285	2336
Maxwellian circuits	2520	
Linear bianisotropy	137	
Linear circuit stability	625	
Linear dipole antennas	1047	
Linear feed antennas	206	
Linear interpolation	405	
Linearity, Fourier transform	1402	
Linearly polarized antenna	222	
Linearly polarized waves	235	
Linear mixing	1637	
Linear polarization	235	
Linear slot arrays	5520	
Linear spacetime beamformer	171	
Line-source feed antennas	207	
Link margin	263	
List-type equalizers	3067	
Lithium niobate		
dielectric properties	945t	
for SAW device substrates	27	28
Lithium tantalate		
pyroelectric properties	1514t	
for SAW device substrates	27	28
Loaded line microwave phase shifters	2839	
Loaded Q -factor	3938	3952
Load-line matching condition	2880	
Lobe on receive only (LORO)	4179	
Lobes, antenna	219	225
	229	263
	277	

Index terms**Links**

Local-area networks (LANs)	2352	
Local channel	302	
Localized modes	3167	
LOCUS software tool	61	
Lognormal distribution	4395	
Log-periodic antenna arrays	224	
Log-periodic antennas	1679	
applications	1050	
for high-frequency broadcasting	296	
Log-periodic dipole arrays	1680	
Log-periodic folded slot antennas	1681	
Loop antennas	285	2359
for electromagnetic field measurement	1190	
for magnetic field measurement	2401	
Loop gain	1420	
Loop slot antenna	4709	
Loral/QUALCOMM system		
system characteristics	600r	
LORAN (Low-frequency long-range navigation)	4296	
Lorent-reciprocal media	139	
LORO (Lobe on receive only)	4179	
LOS (line-of-sight) guidance	3088	
Loss factor	238	
Loss resistance	220	234
Lossy line attenuators	437	438
	460	
Lossy wall attenuators	462	463
Lotus slot antenna	5639	
Lower limit of detection	4225	
Lower-sideband adjacent-channel power ratio	2879	
Low-frequency long-range navigation (LORAN)	4296	
Low-frequency noise	3458	
Low frequency sky wave propagation	4675	
Low-noise amplifiers	2368	
mixed-signal CMOS RF integrated circuits	3097	
MMICs	3231	
mm-wave integrated circuits	3026	
modulation-doped FETs (MODFETs)	3183	
noise characterization and design	2379	
RF integrated circuits	4275	

<u>Index terms</u>	<u>Links</u>	
Lowpass filters	1521	1523
comb-line	1524	2383
microwave	677	
transformation into other filters	2751	2756
transformation relations	1539	1560
Lowpass-to-bandpass transformation	1561 <i>t</i>	
Lowpass-to-bandstop transformation	2754	
Lowpass-to-highpass transformation	2754	
Lowpass-to-lowpass transformation	2754	
Low-power broadcasting	2385	
Low-power television (LPTV) station	2385	2388
Low-sidelobe arrays	1631	
Low temperature co-fired ceramic (LTCC) technology	2393	
Low-temperature thermal plasmas	2934	
Lumped amplifiers	1086	
Lumped-element circulators	2441	
Lumped-element ferrite circulators	1464	
Lumped-element microwave phase shifters	2843	
Lumped element transmission line	5488	
Luneburg lens	902	904 <i>t</i>
	2325	2333
M		
Mach-Zender interferometer	1195	
Macrocells	168	
Magic-T (waveguide) junctions	5558	
Magnetic conductors		
artificial	413	
Magnetic coupling apertures	587	
Magnetic field measurement	2400	
Magnetic fields		
boundary value problems	523	
measurement	2400	
near field measurement using modulated scatterer	2522	
Magnetic field sensors	1192	2401
Magnetic field strength meters	2401	
Magnetic field units	2400	
Magnetic materials	2412	
Magnetic microwave devices	2425	

<u>Index terms</u>	<u>Links</u>
Magnetic recording media	2423
Magnetic resonance imaging	2462
Magnetic shape memory	1228
Magnetic shielding	2473
Magnetic solitons	2455 2497
Magnetic vector potential	238
Magnetite	1486 2412
Magnetization	1222
Magnetization vector	1224
Magnetoelastic damping	1228
Magnetoelectric kernels	613
Magneto optic devices	2457
Magnetostatic wave delay lines	2449
Magnetostatic wave directional couplers	2450
Magnetostatic wave filters	2450
Magnetostatic wave resonators	2451
Magnetostatic waves	2430 2448
Magnetostriction	1227
Magnetotelluric methods	1264
Magnetron oscillator	3001 <i>t</i> 3002
Magnetrons	2482
power applications	2491
Magnitude-balanced condition, feedback oscillators	1433
Mainbeam	229 263
Mainlobe	219 225
	229 277
Mainlobe solid angle	233
Major lobe	219 229
	277
Manifold-coupled multiplexer	3365
Man-made noise	4298 4304
Man-pack devices	3068
Manual step attenuators	453 462
MAP (Manufacturing Automation Protocol)	2356
Marble	
dielectric permittivity	939 <i>t</i>
MASH architecture	17
MASK (<i>M</i> -ary ASK)	118 120
bipolar symmetric	122
MPSK contrasted	126

<u>Index terms</u>	<u>Links</u>	
MASK (<i>M</i> -ary ASK) (<i>Continued</i>)		
unipolar	123	
Matched filters	4128	4133
and radar signal processing	4148	
Matrix distributed amplifiers		
mm-wave integrated circuits	3028	
Matrix solvers	1594	
Maximally flat time-delay filters	1550	1554
Maximally flat time-delay lowpass filters	1558	
Maximum-likelihood decision criterion	4130	
Maximum-likelihood sequence detection (MLSD)	172	
Maximum-ratio combining	166	
Maxwell Garnett homogenization formalism	143	
Maxwellian circuits	2514	
Maxwell's equations	1281	1319
Meanderline antenna	349	
Mean path loss	167	
Measured Equation of Invariance (MEI) method	2540	
Measurement of near fields using modulated scatterer	2522	
Mechanical boresight	263	
Mechanical oscillators	5469	
Medical applications. <i>See</i> Biomedical applications		
Medical imaging		
thermoacoustic tomography application	2530	
Medium-frequency broadcasting antennas	301	
Medium frequency sky wave propagation	4690	
Medium frequency sky waves	4686	
MEI (Measured Equation of Invariance) method	2540	
Memoryless Volterra model	5512	
MEMS (Microelectromechanical systems)		
and coaxial lines	665	
microwave switches	2991	2998
Mercuric chloride		
electric dipole moment	941t	
MESAR radar	4017	
MESFET attenuators	470	479
MESFET limiters	2797	
MESFET (Metal-semiconductor FET)	470	
active antennas	45	
active filters	65	

Index terms**Links**MESFET (Metal-semiconductor FET) (*Continued*)

cryogenic electronics	882	
description and applications	2968	
dielectric resonator oscillator	995	
gallium arsenide	1753	
microwave parametric amplifiers	2828	
microwave power amplifiers	2872	
microwave switches	2992	2998
mixer circuits	3104	
MMIC active devices	3219	
MMICs	3213	
nonlinear circuit analysis	3485	
nonlinear circuit design	3505	3515
Metal detectors	552	1201
Metallorganic chemical vapor deposition	1752	
Metal oxide field effect transistor (MOSFET). <i>See</i> MOSFET		
Metamagnetism	2418	
Meteor scatter	4368	
Method of lines	1237	2548
Method of moments	1233	2554
and Galerkin method	1746	
Meyer wavelets	5623	
MFSK (<i>M</i> -ary FSK)	118	
MF waves	1281	
electromagnetic effect in ionosphere	1307	
Mica		
dielectric permittivity	939 _t	
dielectric properties	945 _t	
Michelson interferometers	5594 _t	
wavelength measurement	5595	
Microcavity lasers		
FDTD analysis application	1586	
Microcells	168	593
	5660	
Microcell technology	593	
Microcellular phone systems		
antennas for	338	
Microphone processors	4247	
Microphones	4238	
Microstrip antenna arrays	2568	

<u>Index terms</u>	<u>Links</u>	
Microstrip antennas	289	2580
broadband	2602	
compact	2626	
dual- and multi-frequency	1098	
Microstrip circuits	2637	
Microstrip edge-guided-mode isolators	1477	
Microstrip-fed coplanar stripline T junction	791	
Microstrip-fed Lotus printed antenna	5638	5640
Microstrip feed antennas	205	
Microstrip filter		
CAD-based design using active-impedance profile (AIP)	74	
Microstrip lines	153	669
	2647	
leaky modes and high-frequency effects	2268	2277
MMICs	3217	
Microstrip-line Y-junction ferrite circulators	1464	
Microstrip resonators	907	
Microstrips	2744	
microwave circuits	2716	
Microstrip-to-coax transitions	2656	
Microstrip-to-TEM transmission line transitions	2655	
Microstrip-to-waveguide transitions	2658	
Microstrip transitions	2654	
Microstrip wraparound antennas	755	
Microwave active filters	56	
Microwave and radio frequency multipliers	2663	
Microwave applicators	2766	
Microwave bandpass filters	2759	
Microwave bandstop filters	2762	
Microwave circuits	2704	
capacitance extraction	565	
left-handed materials for	2303	
neural networks for	3390	
Microwave detectors	2736	
Microwave devices		
acoustic	24	
FE analysis application	1595	
left-handed materials for	2303	
magnetic	2425	
Microwave distributed amplifiers	1095	

<u>Index terms</u>	<u>Links</u>	
Microwave elliptic filters	1359	
Microwave engineering		
Volterra modeling in	5507	
Microwave Fabry-Perot resonators	1381	1390
applications	1394	
Microwave feedback oscillators	1435	
Microwave ferroelectric devices	2742	
Microwave filters	2751	
high- Q millimeter-wave	1018	
Microwave heating	2763	
Microwave highpass filters	2761	
Microwave integrated circuits	153	2773
leaky modes and high-frequency effects in	2268	
Microwave isolators	2786	
Microwave landing systems	4297	
Microwave limiters	2792	
Microwave lowpass filters	2751	2756
Microwave magnetrons	2485	
Microwave measurements	2801	
Microwave mixers	2812	
Microwave multipliers	2663	
Microwave oscillators	2818	
Microwave ovens	2767	
Microwave parametric amplifiers	2827	
Microwave phase shifters	2836	
Microwave photonics		
technological evolution and applications	2851	
Microwave photonic signal processors	2862	
Microwave power amplifiers	2871	
Microwave power transmission	2906	
Microwave Q factors	3937	3948
Microwave radiation	2763	
Microwave receivers	2919	
digital	1014	
Microwave remote sensing		
computational electromagnetic scattering models for	718	
rough-surface scattering simulations	4549	
Microwave resonant plasma source	2934	
Microwave resonators		
cavity resonators	576	

<u>Index terms</u>	<u>Links</u>	
Microwave resonators (<i>Continued</i>)		
Q factor	3937	3949
Microwave scattering		
models for Earth terrain	2948	
Microwave signals		
bandwidth value	5630 <i>t</i>	
Microwave solid-state devices	2968	
Microwave superconductor devices	2980	
Microwave switch elements	2994	
Microwave switches	2991	
Microwave tomography	2537	
Microwave transistors	2968	2972
Microwave tubes	2999	
Middleton noise	3405	
MILAX (Microwave lifted airplane experiment)	4426	
Military communications	3007	
Military satellite communication systems	3018	
Miller effect	5635	
Millimeter band radar	4031 <i>t</i>	4055 <i>t</i>
Millimeter-wave filters, high- Q	1018	
Millimeter-wave integrated circuits	3021	
Millimeter-wave measurement	3046	
Millimeter-wave mixers	2813	
Millimeter-wave phase-conjugating arrays	4504	
Millimeter-waves		
atmospheric absorption	3978	
Millimeter-wave sampling head	1020	
Millimeter-wave systems		
quasioptical circuit application	3977	
Millimeter-wave Van Atta arrays	4503	
MILSATCOM systems	3018	
Milstar	3019	
MIL-STD 883	4209	
MIMO channel equalization	3068	
MIMO-MRC systems	3062	
MIMO systems	3059	
adaptive array antenna application	92	
Miniature wideband patch antennas	2617	
Miniaturized packaged (embedded) antennas for portable wireless devices	3068	

Index terms**Links**

Minimum coverage area directivity	3319	
Minimum detectable concentration	4225	
Minimum detectable level	4225	
Minimum error probability criterion	4131	
Minimum mean-squared error		
forward link	175	
reverse link	173	
Mininumerical Electromagnetic Code (MININEC)	2349	
Minislotted alternating priority (MSAP) schemes	3355	
Minor lobes	225	229
	277	
Minor-lobe solid angle	233	
Missile guidance	3082	
Missile defense	3084	
Missile treaties	3083	
Missile warning systems	3084	
MITATT (Mixed-tunnel-avalanche transit-time) diodes		
negative resistance	3389	
Mixed-signal CMOS RF integrated circuits	3095	
Mixer circuits	3102	
Mixers		
MMICs	3232	
mm-wave integrated circuits	3029	
resonant tunneling diodes	4489	
RF integrated circuits	4283	
Mizugutch condition	4461	
mm band radar	4031t	4055t
MMIC oscillators	2825	
Mobile communication	3121	
antennas	291	
Mobile communications systems		
adaptive array antennas for	88	
antenna arrays	164	
antennas	319	
antenna scanning arrays	257	
CAD-based active filter design using active-impedance profile (AIP)	74	
channel effect	3061	
MOBILE [Monostable-Bistable (Transition) Logic Element]	4491	
Mobile phone antennas	3069	
Mobile phone systems	592	

<u>Index terms</u>		<u>Links</u>
Mobile radio channels	3125	3132
Mobile radio monopole antennas	3242	
Mobile radio on fiber systems	4317	
Mobile satellite communications	3150	
Mobile satellite systems	599	600t
	5677	
Mobile station, cellular networks	5660	
antennas for	342	
Mobile telephone health effects	518	
Mobile terminal antennas	342	
Mode-matching methods	1234	3162
Mode transducers	5531	
MODFETs (Modulation-doped FETs)	3176	
Modified Allan deviation	1725	
Modulated scatterer		
near field measurement using	2522	
Modulation		
digital radio	1025	
mixer circuits	3110	
radar remote sensing	4099	
very high frequency range	5482	
wireless systems	5658	5664
Modulation-doped FETs (MODFETs)	3176	
Modulators		
RF integrated circuits	4283	
Molecular-beam epitaxy	1751	
Molybdenum disulfide		
pyrooptic properties	1515t	
Monolithically integrated mode-locked laser	2857	
Monolithic analog bandpass filters	496	
Monolithic antennas	3203	
Monolithic microwave integrated circuit (MMIC) waveguides	5531	
Monolithic microwave integrated circuits (MMICs)	2773	3022
	3213	
development milestones	3225t	
electromagnetic simulators	3227t	
feedforward amplifiers	1448	
gallium arsenide	1749	1751
multifunctional	3233	
packaging	3235	

Index terms**Links**

Monolithic microwave integrated circuits (MMICs) (<i>Continued</i>)		
VHF range	5487	
wideband amplifiers for	5637	
Monopole antenna arrays	3241	
Monopole antennas	3238	
relationship to dipoles	3329 <i>t</i>	
Monopole mobile terminal antennas	348	
Monopulse angle sensing	4179	
Monopulse feed antennas	212	
Monopulse processors	3249	
Monopulse reflector radar antennas	4009	
Monopulse tracking feed antennas	213	
Monopulse tracking radar	4024	
Monopulse tracking systems	3244	
Monostatic radar cross-section	4033	
Monte Carlo analysis	3255	
Monte Carlo simulation		
in reliability	3269	
MOSFET attenuators	472	
MOSFET (Metal oxide field effect transistor)		
active antennas	45	
description and applications	2968	
microwave switches	2998	
mixer circuits	3104	
modeling	3278	
radiation effects	4201	
in wideband amplifiers	5631	
MOSFET modeling	3278	
Movable-vane (flap) attenuators	462	
Moving-target indication		
and radar signal processing	4148	4150
Moving-track detecting radar	4058	
MPEG standard	1063	4241
	4244	
MPSK (<i>M</i> -ary PSK)	118	5664
MASK contrasted	126	
Mueller matrix	4085	
Multiaxial waveguide junctions	5549	
Multibeam antennas	3317	
Multibeam arrays	2573	

<u>Index terms</u>	<u>Links</u>	
Multichannel multipoint distribution service (MMDS)	2385	
Multiconductor transmission lines	3335	
Multidimensional Fourier transform	1403	3491
Multidimensional mobile communications networks	323	
Multiferroic magnetoelectrics	1515	
Multifrequency antenna elements	1621	
Multi-frequency microstrip antennas	1098	
Multilayer arrays	2571	
Multilayer microwave circuits	2726	
Multilayer microwave Fabry-Perot resonators	1393	
Multilayer perceptrons neural network	3390	
Multilooking	4104	
Multimedia mobile communications	322	
Multimode circular horn aperture feed antennas	198	
Multimode equivalent network representations	3342	
Multimode rectangular horn aperture feed antennas	202	
Multipactor	2799	
Multipath fading	4332	
digital radio	1028	
Multipath propagation	168	
Multiple access schemes	3351	
Multiple-antenna synthetic aperture radar	4078	
Multiple-beam reflector radar antennas	4008	
Multiple-reflector radar antennas	4009	
Multiple-target tracking	4184	
Multiplexers	3362	
comb-line filters	692	
microwave circuits	2710	
Multiplexing		
ferrite circulators	1461	
Multiplying D/A converters	6	
Multipoint distribution service (MDS)	2385	2388
	2391	
Multiresolution technique	3369	
Multiresolution time-domain scheme	1325	3369
Multiresolution time-domain technique	1366	
Multiresolution time-domain wavelet (MRTD) method	387	
Multistage (A/D) converters	11	
Multitone jamming	3009	

Index terms**Links**

Multivibrators	5473	5475t
	5494	
Mumetal		
electromagnetic properties	1223t	
MUSIC algorithm	165	
Mutual coupling	254	
microstrip antenna arrays	2577	
radar antennas	4016	
Mutual impedance	254	
N		
Nakagami distribution	4394	
Nanostructured biomaterials	2944	
Narrowband amplifiers		
low-noise	2376	
Narrowband digital microwave receiver	2932	
NA-TDMA wireless standard	598	
Natural boundary conditions	1739	
Natural radio noise	4297	
Navigation radar	4024	
Near-far-field transformation	1582	
Near-far interference	4337	
Near-field exposure	514	
Near-field patterns	225	
Near-field region	230	
measurement using modulated scatterer	2522	
testing	267	
Near-infrared (NIR) optical spectroscopy	2866	
NEAR laser rangefinder	113	
Negative feedback	1419	
wideband amplifier	5633	
Negative-index-of-refraction materials	2303	
Negative permeability materials	2303	
Negative permittivity materials	2303	
Negative-phase-velocity materials	2303	
Negative resistance	3385	
Negative-resistance diode mixers	1645	
Negative-resistance field effect transistor (NERFET)	3388	
Negative-resistance oscillators	5472	

Index terms**Links**

Neoceram		
dielectric properties	2765t	
Neoprene		
dielectric permittivity	939t	
dielectric properties	945t	
NERFET (Negative-resistance field effect transistor)	3388	
Netwon-Kantorovitch algorithm	1207	
Network analyzers	4896	
Network subsystem, cellular networks	5660	
Neumann functions	5579	
Neural networks		
for microwave circuits	3390	
for modeling memoryless TWT amplifiers	131	
radar target recognition modeling	4166	
reflector antenna synthesis	4473	
training	3392	
News format radio studio	4228	
Neyman-Pearson criterion	4131	4134
<i>N</i> -Furcations	5548	
Nodal harmonic balance	3488	3497
Nodding radar pattern	4022	
Noise		
antennas	281	
attenuators	478	
distributed amplifiers	1091	
feedforward amplifiers	1444	
frequency synthesizers	1730	3120
high-frequency	3417	
hot carrier effects	3439	
low-frequency	3458	
magnetrons	2502	
microwave oscillators	2822	
microwave parametric amplifiers	2832	
microwave receivers	2921	
mixers	3108	
modeling	3397	3408
modulation-doped FETs (MODFETs)	3195	
MOSFETs	3308	
nonlinear circuits	3522	
radio on fiber systems	4315	
statistical description	3397	

Index terms**Links**

Noise (<i>Continued</i>)		
very high frequency range	5482	
wavelet applications	5629	
Noise and interference modeling	3397	
Noise circles	4512	
Noise equivalent backscatter cross section	4099	
Noise equivalent circuits	3419	
Noise factor	4299	4508
Noise figure	3419	
Noise generators	3408	
Noise matching	3420	
Noise-matching networks	4509	
Noise reduction systems	4247	
Noise temperature	4510	
Nominal angular frequency	1721	
Noncontiguous band multiplexers	3367	
Nonhomogeneous Poisson process	3274	
Nonionizing radiation	4217	
Nonlinear anisotropy	144	
Nonlinear circuits		
analysis	3482	
design	3502	
Nonlinear high-power amplifiers		
analytical and adaptive modeling	127	
Nonlinear phase equalizers		
feedforward amplifiers	1447	
Nonpolar optical phonon scattering	3466	
Nonradiative dielectric waveguides	910	
Nonstationary signals	5604	
Nonuniform discrete Fourier transforms (NUDFT)	1401	1412
Nonuniform fast Fourier transforms (NUFFT)	1401	1412
Normalized antenna power pattern	233	
Normalized backscatter cross section	4099	
Normal magnetization curve	1223	
Normal-mode helical antenna (NMHA)	349	
Normal polarization	238	
Notch antennas	3534	
Notch filter	498	
Nuclear-blast induced plasma	3012	

<u>Index terms</u>	<u>Links</u>	
Nuclear power plants		
radiation monitoring in	4219	
Nylon 6	6	
dielectric properties	945t	
Nyquist filter	28	
Nyquist-rate (oversampled) data conversion	1	17
Nyquist sampling theorem	1404	
 O		
Obscuration burnthrough	1345	
Obstacles		
in waveguides	5548	
Ocean altimeter	4115	
Ocean scatterometer	4114	
Odyssey system	600t	
Offset-keyed quadrature phase shift keying (OQPSK)	3965	
Offset reflectors	3328	
Okumura-Hata model	3126	
Omnidirectional antennas	219	
radiation pattern	228	
Omnidirectional microstrip antennas	754	
On-off keying	118	
Open-boundary truncation	531	
Open-circuit gain	46	
Open-ended coaxial line	654	
Open-ended strip resonator	783	785
Open-ended waveguides	5551	5552
Open-loop gain	1419	
Open resonators		
microwave Fabry-Perot resonators as	1397	
OpenTV	1063	
Operating system noise factor	4298	
Operational transconductance amplifiers	496	
Opposite polarization	238	
Optical activity	610	
Optical amplifier		
radio on fiber systems	4312	
Optical analog-to-digital converters	2863	
Optical CDMA		
for radio on fiber systems	4322	

<u>Index terms</u>	<u>Links</u>	
Optical detectors		
for buried-object detection	557	
Optical rotation	611	
Optical systems	1783	
Optical TDMA		
for radio on fiber systems	4321	
Optical WDM		
for radio on fiber systems	4321	
Optics	2320	
Optimized circular horn aperture feed antennas	198	
Ordered-statistics constant false-alarm rate (OS-CFAR) radar signal processing	4156	
Orientational polarization	940	
Orthogonal frequency-division multiplexing (OFDM)	5667	
Orthogonality, of eigenmodes	3166	
Orthogonal multibeam antennas	3323	
Orthomode transducers	3547	
Oscillation	5469	5470
Oscillators	5468	5490
cryogenically-cooled	888	
design	3563	
dielectric resonator	985	
feedback	1432	
microwave	2818	
microwave Fabry-Perot resonators as	1398	
mm-wave integrated circuits	3032	
noise generators	3410	
nonlinear circuit design	3511	
quasi-optical circuits	3979	3984
resonant tunneling diodes	4489	
RF integrated circuits	4279	
stability	628	
OTA-C bandpass filter	496	
Output impedance		
feedback amplifiers	1424	
Overlapped subarray feeds	261	
Overlapped transform feeds	261	
Overlearning, neural networks	3393	
Oversampled data conversion	1	17
Oversampled data converters	1	
Oversize waveguides	5582	

Index terms**Links****P**

Packaged (embedded) antennas	3068	
Packaging		
monolithic microwave integrated circuits (MMICs)	3235	
RF devices and modules	3590	
RF/wireless	4516	
PACS (Personal access communication system)	599	
and digital radio	1032	
Padé rational polynomial interpolation	405	
Pads (fixed attenuators)	460	
Paging systems	1032	5661
	5674	
Palmer radar pattern	4022	
Paper		
dielectric properties	2765	
Parabaloidal reflector radar antennas	4008	
Parabolic antennas	4450	
Parabolic cylinder	4460	
Parabolic cylinder radar antennas	4008	
Parabolic reflectors	186	
Parabolic torus	4460	
Paraboloid		
backscatter from	489	
Paraffin wax		
dielectric permittivity	939	
Parallel algorithms and computing for large-scale electromagnetic simulation	3614	
Parallel cascade Volterra model	5512	
Parallel-plate waveguides	667	2745
Paramagnetic materials	2412	
Paramagnetism	1506	2413
Parameter estimation from electromagnetic simulations using signal models	3646	
Parametric frequency dividers	3523	
Parasitic array antennas		
adaptive array antennas	96	
Parasitic extraction	566	
Parasitic monopole antennas	3241	
Partial-band noise jamming	3008	
Partial-body exposure	514	
Partial polarization	4083	
Passivation	3669	

Index terms**Links**

Passive attenuators	455	
Passive bandpass filters	495	
Passive diode mixers	3104	
Passive diodes	2968	
Passive filters		
tuning	637	
Passive mixers		
mm-wave integrated circuits	3029	
Passive quasioptical components	3985	
Passive radar cancellation	4038	
Passive radiometry	4342	
Passive RFID tags	4265	
Passive weapons sensors	1336	
Patch antennas		
monolithic	3208	
Patch panels	4235	
Path loss	4326	
PATRIOT radar	4017	
Pattern multiplication	227	
Pattern pair multiplication	309	
Pattern reconfigurable antenna arrays	4411	
Pattern reconfigurable horn antennas	4411	
Pattern reconfigurable microstrip antennas	4410	
Pattern reconfigurable reflector antennas	4411	
PDC wireless standard	598	3124
and digital radio	1031	
Pearson-Moskowitz sea surfaces	4126	
Peltier device	4312	
Pencil-beam antenna pattern	228	
People		
typical radar cross-section	4031	
Perfect reconstruction	1692	
Perimeter radiation monitors	4224	
Periodically loaded active-diode distributed amplifiers	1087	1091
Periodically loaded Gunn diode distributed amplifiers	1092	
Periodically loaded transistor distributed amplifiers	1088	1093
Periodically loaded tunnel diode distributed amplifiers	1091	
Periodically loaded varactor diode distributed parametric amplifiers	1092	
Periodic slow-wave coplanar waveguide transmission lines	829	

<u>Index terms</u>	<u>Links</u>	
Periodic structures	3675	
Periodic waveguides	5582	
Permanent magnets	2422	
Permittivity		
measurement	3698	
measurement on distributed parameter specimens	928	
measurement on lumped capacitance specimens	919	
and radar cross-section	4036	
Perovskite structure	1509	
Personal access communication system. <i>See</i> PACS		
Personal area networking		
with Bluetooth	3711	
Personal communication networks	5657	
Personal communication systems	5657	
antennas for	291	
Personal digital cellular system. <i>See</i> PDC wireless standard		
Personal handy-phone (PHS) system	599	3124
antennas for	339	362
and digital radio	1032	
Perturbation theory	3725	
Phase arrays	4154	
Phase-balanced condition, feedback oscillators	1433	
Phase center		
corrugated horn antennas	858	
feed antennas	189	
Phase-coded waveforms	4159	
Phase-conjugating arrays	4495	
Phased-array antennas		
adaptive array antennas	94	
fiber optic distribution for	2860	
microwave ferroelectric devices	2747	
Phased-array radar antennas	4013	
Phased arrays	2572	
Phase delay, filters	1552	
Phase equalizers	1525	1541
Phase locked loops	3735	
Phase locked oscillators	3767	
Phase margin	1429	
Phase noise	3802	
feedback oscillators	1435	

Index terms**Links**

Phase noise (<i>Continued</i>)		
measurement	3806	
nonlinear circuits	3522	
Phase shifters	152	3810
ferrite	152	1497
finlines	1606	
microwave	2836	
MMICs	3232	
mm-wave integrated circuits	3036	
radar antennas	4016	
Phase shift keying	118	
Phase shift oscillator	5470	
Phase velocity	1283	
Photoconductive effects	2852	
Photodetectors		
radio on fiber systems	4313	
Photon flux	4345	
Photonic band gap	3823	
Photonic bandgap materials	1117	
Photonic electromagnetic field sensors	1194	
Photonic integrated circuits		
FDTD analysis application	1585	
Photonics	2851	
Physical optics	1299	
Physical properties, their symbols and units	1508	
Pi attenuator	437	
fixed	460	461
insertion loss	458	
Picocells	5660	
Picocellular phone systems		
antennas for	338	
Piecewise harmonic balance	3490	3498
Piezoelectric effect	1504	
Piezoelectricity	1228	1512
	3846	
Piezoelectric materials	1229	
Piezoelectric transducer controlled circuits	3838	
Pilot signal	4493	
Pin diode	2970	
Pin diode attenuators	438	466

<u>Index terms</u>	<u>Links</u>	
Pin diode limiters	2793	
PIN diodes	3858	
inline applications	1603	
microwave phase shifters	2837	
microwave photonics	2853	
source of photodetection method	2852t	
use with variable-frequency oscillators	5475	
Pipelined analog-to-digital converters	12	
Piston attenuators	438	442
	464	
Planar high-frequency circuits		
applied numerical electromagnetic analysis for	397	
Planar inverted-F antenna	353	
Planar isolators	1476	
Planar multilayers		
electromagnetic field computation	1163	
Planar transmission lines	153	
Plane-polarized waves	235	
Plane-wave propagation	139	
Plane waves	1283	
Plasma chemistry	2945	
Plasma frequency	1218	
Plastic deformation magnetic assembly	4406	
Plastics		
dielectric properties	2765t	
insulating properties	151t	
<i>p-n</i> junctions	1035	
Pockels cell	1194	
Poincare. sphere	237	4083
Point group symmetry	139	140t
Polar diagrams	229	
Polar formatting	4070	4074
	4076	
Polarimetric interferometry	4113	
Polarimetric passive microwave remote sensing		
wind on foam-covered ocean surface	725	
Polarimetric target decomposition	4092	
Polarization	1283	
antennas	221	263
backscatter field	486	

Index terms**Links**

Polarization (<i>Continued</i>)		
feed antennas	189	
and radar cross-section	4032	
Polarization efficiency	222	238
Polarization ellipse	235	
Polarization fork	4084	
Polarization isolation, frequency reuse by	3317	
Polarization loss factor	237	
Polarization mismatch	238	
Polarization pattern	238	
Polarization reconfigurability	4409	
Polarization reuse	181	
Polarization scattering matrix	4084	
Polarization sense	236	
Polarization signature	4081	4087
Polarization synthesis	4086	
Polarized electromagnetic waves	4081	
Polarized waves	235	
Polar optical phonon scattering	3466	
Polar patterns	229	
Polder permeability tensor	2425	
Polling schemes	3354	
Polycarbonate		
dielectric properties	945 <i>t</i>	
Polyester		
dielectric properties	945 <i>t</i>	
Polyethylene		
dielectric permittivity	939 <i>t</i>	
dielectric properties	945 <i>t</i>	
insulating properties	151 <i>t</i>	
Polymers		
glass transition temperature of selected	955 <i>t</i>	
Polynomial interpolation	405	
Polypropylene		
dielectric properties	2765 <i>t</i>	
Polystyrene		
dielectric properties	945 <i>t</i>	
Polytetrafluoroethylene		
dielectric properties	945 <i>t</i>	
insulating properties	151 <i>t</i>	

<u>Index terms</u>	<u>Links</u>	
Poly(vinyl chloride)		
dielectric permittivity	939 <i>t</i>	
dielectric properties	945 <i>t</i>	
Poly(vinylidene fluoride)		
piezoelectric properties	1513 <i>t</i>	
pyroelectric properties	1514 <i>t</i>	
Porcelain		
dielectric permittivity	939 <i>t</i>	
dielectric properties	945 <i>t</i>	
Portable wireless devices		
embedded antennas for	3068	
Poseiden altimeter	3990	3990 <i>t</i>
Position-location-based services		
adaptive array antenna application	92	
Potassium dihydrogen phosphate		
ferroelectric properties	1512 <i>t</i>	
Potassium niobate		
ferroelectric	1509	
ferroelectric properties	1512 <i>t</i>	
Potassium tantalate niobate		
ferroelectric	1509	
ferroelectric properties	1512 <i>t</i>	
POTS codecs	4242	
Power amplifiers		
analytical and adaptive modeling of nonlinear high-power	127	
gallium nitride	1763	
microwave	2871	
mixed-signal CMOS RF integrated circuits	3098	
MMICs	3231	
mm-wave integrated circuits	3026	
modulation-doped FETs (MODFETs)	3185	
RF integrated circuits	4277	
VHF range	5488	
Power budget	4325	
Power combiners	155	
Power combiners and dividers	3869	
Power density	220	
Power dividers	155	3869
Power patterns	225	226
	231	

<u>Index terms</u>	<u>Links</u>	
Power spectral density	117	
modeling	3399	
Poynting vector	231	1281
and left-handed materials	2303	
Preamplifiers	3891	
Precipitation measurement radar	4027	
Prefractals	1621	
Primary feed antennas	185	188
Primary ferroics	1506	
Primary field	187	
Primary pattern	187	
Principal plane patterns	225	229
	274	
Printed-circuit leaky-wave antennas	2300	
Printed E-plane circuits	5530	
Printed inductors	3905	
Prior knowledge input method	3395	
PRISM	4690	
Prism spectrometers	5591	
Private mobile radio (PMR) systems	5657	5672
Process radiation monitors	4222	
Professional mobile radio	3124	
Profiled horn antennas	858	
Profiled horn aperture feed antennas	198	
Programmable attenuators	462	
Programmable noise generators	3411	
Propagation constant	270	
Proportional hazards model	3274	
Protocol layering, LANs	2354	
Proton-induced effects	4197	
Proximity coupling	4711	
Proximity detection		
active antennas	54	
Pseudoelliptic characteristic	1553	
Pseudoelliptic filters	1550	
Pseudoelliptic lowpass filters	1557	
Pseudomorphic modulation-doped FETs (PMODFETs)	3176	3184t
Pseudospectral time-domain (PSTD) methods	1407	
Public mobile telecommunications (PMT) systems	5657	

<u>Index terms</u>	<u>Links</u>	
Pulse compression	3915	4149
	4158	
Pulsed jamming	3009	
Pulsed laser radar	112	
Pulse-limited altimeters	3994	
Pulse modulation		
mixer circuits	3113	
Pulse radar	4057	
range tracking with	4176	
Pulse-shaping circuits	3927	
Pumped cutoff frequency	2831	
Pure Aloha multiple access scheme	3356	
Pyrex glass		
dielectric permittivity	939 <i>t</i>	
dielectric properties	945 <i>t</i>	
Pyroelectric effect	1504	
Pyroelectricity	1513	
Pyrooptic effect	1514	
Q		
<i>Q</i> -factor	3937	3949
	5470	
antenna reverberation chamber	247	
cavity resonators	577	
comb-line filters	690	
dielectric resonator oscillators	988	
dielectric resonators	1007	
measurement	3948	
<i>Q</i> meters	3938	
QPSK demodulators	3967	
QPSK modulators	3965	
Quad loop antennas	2367	
Quadruplexers	1651	
Quadrature phase shift keying (QPSK)	3964	5665
Quality factor. <i>See Q</i> factor		
Quantum electronic distributed amplifiers	1093	
Quartz		
dielectric properties	945 <i>t</i>	
piezoelectric properties	1513 <i>t</i>	
for SAW device substrates	27	28

Index terms**Links**

Quasimemoryless Volterra model	5512	
Quasi-optical arrays	3984	
Quasi-optical backscattering	483	
Quasi-optical circuits	3977	
Quasi-optical power combiners		
microwave Fabry-Perot resonators as	1398	
Quasi-optical power combining	3978	4837
Quasiorthogonal multibeam antennas	3326	
Quasistatic backscattering	481	
Quasistationary signals	5604	
Quasi-Yagi-Uda antenna	5699	
Quintaplexers	1651	
QWITT (Quantum-well injection transit-time) diodes		
negative resistance	3389	
QZERO for Windows	3945	
R		
RA-2 altimeter	3990 <i>t</i>	3991
Radar	263	4005
	4056	
<i>See also</i> Ground penetrating radar; Synthetic aperture radar		
spaceborne	4823	
Radar absorbing materials	4037	
backscatter reduction for stealth technology	491	
Radar altimeter satellites	3989	
Radar altimetry	108	3989
Radar ambiguities	4183	
Radar antennas	292	4005
Radar applications	4018	
Radar cancellation	4038	
Radar cross section	1302	4030
antenna compact range for measuring	179	
and backscatter	481	
measurement	4041	
reduction	4036	
typical objects	4031 <i>t</i>	
Radar displays	4067	
Radar equation	4040	
Radar equipment	4055	
Radar frequencies	4055 <i>t</i>	4055

<u>Index terms</u>	<u>Links</u>	
Radar imaging	4069	4096
high-resolution	4160	
Radar polarimeter antennas	4089	
Radar polarimetry	4080	
synthetic aperture	4106	
Radar remote sensing	4096	
irregular stratified layers	4122	
Radar scanning	4065	
Radar signal detection	4128	
Radar signal processing	4148	
Radar signal processor	4149	
Radar sounder	4117	
Radar target acquisition	4174	
Radar target detection	4174	
Radar target recognition	4165	
Radar targets	4063	
Radar tracking	4172	
Radial waveguides	5581	
Radiated susceptibility problem	1137	
Radiating near-field	230	
Radiating near-field (Fresnel) region	218	219
Radiation effects	4186	
Radiation efficiency	220	
Radiation intensity	220	232
Radiation monitoring	4217	
Radiation pattern reconfigurability	4409	
Radiation patterns, antennas. <i>See</i> Antenna radiation patterns		
Radiation power density	231	
Radiation region	230	
Radiation resistance	220	234
Radioactive materials	4220	
Radio altimetry	110	
Radio astronomy	263	292
Radio broadcasting		
station classification	302	
Radio broadcast studio equipment	4227	
Radio communications		
signal fading	4619	
Radio consoles	4231	

<u>Index terms</u>	<u>Links</u>	
Radio direction finding	4249	
Radiofrequency chokes	150	
Radiofrequency circuits		
nonlinear circuit analysis	3482	
Radiofrequency energy		
biological effects	511	
Radio-frequency identification systems (RFID)	4263	
microwave power transmission application	2913	
Radio-frequency integrated circuits	499	4269
applied numerical analysis	397	
CMOS	4270	
CMOS mixed-signal	3095	
Radio frequency multipliers	2663	
Radio highway	4310	4320
Radio interferometer	292	
Radiometers	4342	
Radiometric brightness	4347	
Radiometry	4342	
Radio navigation	4292	
Radio noise	4297	
Radio on fiber (RoF) systems	4310	
Radio paging systems	5661	
Radio propagation	5663	
Radio receivers	1029	
Radio reception	4324	
Radio signals	1281	
Radio spectrum	1304	
Radio studio	4227	
Radiotelemetry	4350	
Radio trunking	5661	5672
Radiowave propagation	4365	
ground effects	4371	
in multipath channels	4389	
Radomes	365	4012
Radon transform	5619	
Radon-Wigner transform	4145	
Rain attenuation	4480	
Rain radar	4118	
Randomly polarized waves	235	
Random noise	3400	

<u>Index terms</u>	<u>Links</u>	
Range ambiguity	4104	4105
Range eclipsing	4183	
Range processing radar	4025	
Range tracking	4175	
Rao-Wilton-Glisson basis functions	1748	
RASCAL (Raster scanning airborne laser)	112	
Raster radar pattern	4022	
Rat-race ring hybrids	5559	
Ray equation	1781	
Rayleigh distribution	4393	
Rayleigh fading	90	4395
Rayleigh quotient criterion	1736	
Rayleigh region	481	
Rayleigh-Ritz (Galerkin) method	1735	
Rayleigh scattering	1302	
Rayleigh waves	31	
Ray transfer matrices	1786	
RC active bandpass filters	496	
RC oscillators	5470	5475t
feedback oscillators	1436	
Reactive near-field region	218	219
	230	
Reactive power		
waveguides	5575	
Reactive region	230	
Reactive resonators	3948	
Read heads	2421	
Real aperture radar	4100	
Real-space transfer devices	3387	
Real-time circuit evaluation	4695	
Rear-radiating feed antennas	204	
Receiver coil		
metal detector	553	
Receiver noise	4297	4298
Receiver noise factor	4299	
Receivers		
RF integrated circuits	4287	
Receive spacetime processing	172	
Reciprocal ferrite switch	1461	

<u>Index terms</u>	<u>Links</u>	
Reciprocity, antennas	272	
Reconfigurability	4405	
enabling	4416	
frequency	4406	
polarization	4409	
radiation pattern	4409	
Reconfigurable antennas	289	4405
multibeam	3322	
reflectors	4469	
wideband slot and printed	5647	
Reconfigurable aperture antennas	4413	
Reconfigurable coplanar path slot antenna	5652	
Reconfigurable printed monopole antenna	5653	
Reconfigurable slot dipole antenna	5653	
Rectangular aperture antennas	369	
Rectangular dielectric-loaded waveguides	5530	
Rectangular ferrite-loaded waveguide	1492	
Rectangular horn aperture feed antennas	201	
Rectangular loop antennas	2367	
Rectangular waveguide cavity combiners	5566	
Rectangular waveguide cavity resonators	579	
Rectangular waveguides	667	2745
	5577	
coupling holes in	587	
as transmission line	5527	
uniaxial junctions	5548	
Rectenna array	210	
Rectennas	2916	4418
Rectifying antennas (rectennas)	4418	
Redundancy		
digital error correction using	15	
Reel-to-reel tape recorders	4238	
Reentrant coaxial cavity resonators	578	
Reflectarray antenna	186	4428
Reflectarrays	2574	
Reflection	1778	
plane waves	1289	
and radar cross-section	4034	
and scattering	1295	
Reflection resonators	3948	

<u>Index terms</u>	<u>Links</u>	
Reflective attenuators	453	
Reflectometers	1078	5536
time-domain	4436	
Reflector antenna isolation	4470	
Reflector antennas (parabolic antennas, dish antennas)	286	4450
Reflector radar antennas	4008	
Reflectors		
feeds supplying	185	
upgrading	4467	
Refraction	1780	
plane waves	1289	
and scattering	1296	
spherical interface	1788	
in troposphere	4475	
Refractive ducts	4477	
Regenerative frequency dividers	3523	
Regional channel	302	
Register insertion ring	2357	
Regulatory requirements		
for electronic systems	1138	
Relativistic magnetrons	2509	
Relaxation oscillations	5469	
Relaxation oscillators	5469	5472
	5493	
Reliability		
Monte Carlo simulation	3269	
Reliability function	3270	
Remote sensing	115	
<i>See also</i> Microwave remote sensing; Radar remote sensing		
antennas for	263	293
electromagnetic subsurface	1256	
Repeat-track interferometry	4112	
Reproductive system		
effect of RF energy on	518	
Residual magnetism	1222	
Residual-wave current	2269	
Resistive card attenuators	438	460
Resistive mixer	3505	
Resistors		
lumped-element microwave circuits	2724	

Index terms**Links**

Resistors (<i>Continued</i>)		
microwave integrated circuits	2780	
RF integrated circuits	4272	
VHF range	5485	
Resonance backscattering	481	
Resonance isolator	1476	2789
Resonant antennas	287	
Resonant tunneling bipolar transistors (RTBTs)	3386	4490
Resonant tunneling diodes	4484	
Resonant tunneling structures	3385	
Resonated stub waveguide bandstop filter	5558	
Resonators		
Q factor	3937	
Q factor measurement	3948	
Resz basis	5609	
Retrodirective systems	4493	
Retrodirectivity		
microwave power transmission	2913	
Retroreflectors		
active antennas	54	
Return losses		
feedforward amplifiers	1444	
filters	1551	
Reuse within cell	176	
Reverberation chamber for antenna	239	
Reverse bias	1034	1037
	1041	
RF circuit noise	4507	
RF distributed amplifiers	1094	
RF engineering		
Volterra modeling in	5507	
RF feedforward amplifiers	1440	
RFID tags	4263	
RF magnetic permeability tensor	1486	
RF noise measurement	3420	
RF packaging devices and modules	3590	
RF Q factors	3937	
RF resonators		
Q factor	3937	

<u>Index terms</u>	<u>Links</u>	
RF SoP modules	4525	
RF switches		
mm-wave integrated circuits	3034	
RF system-on-chip	508	
RF/wireless packaging	4516	
Rice distribution	4393	
Richards' transformation	1561	
Ridged waveguides		
as transmission line	5529	
Ridge waveguides	5578	5585
Right-handed materials	2304	
Right-handed polarized waves	236	
Ring antennas	4542	
Ring circuits	4537	
Ring filters	4540	
Ring oscillators	4547	5472
feedback oscillators	4575 t	5492
feedback oscillators	1436	
Ring resonators	4537	
Ring topology	2353	
<i>RLC</i> bandpass filters	495	
Rochelle salt	1505	
ferroelectric properties	1512 t	
Root locus	630	
Rotary-field ferrite phase shifters	1502	
Rotary-vane attenuators	439	442
	462	
Rotary-vane waveguide attenuator	5532	
Rotman lens antennas	2325	2331
Rough-surface scattering		
numerical simulations and applications in microwave remote sensing	4549	
radar cross-section	4040	
<i>R</i> -2R lens	2325	2333
RTBTs (Resonant tunneling bipolar transistors)	3386	4490
RTHEMT (Resonant tunneling high-electron-mobility transistor)	4491	
Rubber		
dielectric permittivity	939 t	
Rutile		
dielectric properties	945 t	

Index terms**Links****S**

Sallen-Key lowpass circuit	2384	
Sampling oscilloscope	4436	
Sapphire		
permittivity tensor	699	
properties in microwave ICs	2775 <i>t</i>	
Satellite altimetry	108	
Satellite antennas	4585	
Satellite communications	290	
Satellite radar altimetry	3989	
Satellite signals		
bandwidth value	5630 <i>t</i>	
Satellite subchannelizers	28	
Satellite television broadcasting	1052	
Satellite transponder	1060	
Sawtooth edge-mode isolators	1477	
S band radar	4031 <i>t</i>	4055 <i>t</i>
SCALARQ	3946	
Scanned holography	4026	
Scattering		
finite element analysis	1597	
Scattering coefficient	722 <i>t</i>	2948
Scattering matrix technique, generalized	1767	
Scattering phase function	2949	
Schmitt trigger converters	5496	
Schottky barrier diodes	2969	4595
Schottky barriers	4607	
Schottky diode mixers	1639	
Schwarz-Christoffel transformation	764	
Scrimp horn aperture feed antennas	197	
Search radar	4022	
Seasat altimeter	3990 <i>t</i>	
SEASAT synthetic aperture radar	4112	
Secondary antennas		
feeds supplying	185	
Second-order bandpass filter	495	
Segmentation	3017	
Seismic sensors		
for buried-object detection	554	

Index terms**Links**

Selection diversity	165	
Self-oscillating mixers	1645	
Semiconductors	1218	
III-V	5237	
Semiconductor switches	3387	
Semirigid cables	664	
Semitransparent disk		
backscatter from	489	
Sense of polarization	236	
Sensitivity, circuit tuning	634	
Sequential lobe angle sensing	4179	
Sequential lobing radar	4024	
Sequentially fed arrays	2571	
Series peaking amplifier	5631	
Series sampling	1426	
Series slot	1617	
Setback layer	3176	
Sextaplexers	1651	
Shadowing	4392	
Shape-based buried-object detection	557	
Shaped-beam antenna pattern	228	
Shaped-reflector radar antennas	4008	
Shielded cables	1253	
Shielded electromagnetic analysis	407	
Shielding. See Electromagnetic shielding		
Ships		
typical radar cross-section	4031	
Short-backfire feed antennas	205	
Shorted-turn damping	1502	
Short-ended strip resonator	785	
Short-time Fourier transform	5605	
Shortwave	295	
Shot noise		
defined	3402	
high-frequency	3417	3421
low-frequency	3458	
Shunt-fed dipole antennas	1049	
Shunt-fed monopole antennas	3241	
Shunt peaking amplifier	5631	

<u>Index terms</u>	<u>Links</u>	
Shunt sampling	1426	
Shunt-shunt feedback	1426	
Shuttle Radar Topography Mission (SRTM)	4110	
SiC device technologies	4613	
Side-fed offset Cassegrain	3332	
Sidelobe isolation, frequency reuse by	3317	
Sidelobe level	219	229
Sidelobe ratio	229	
Sidelobes	219	225
	229	263
	277	
Side-looking aperture radar	4100	
Sidewall directional couplers	5540	
Sierpinski monopole	1621	1624
Signal enhancement	4148	
Signal fading in radio communications	4619	
Signal models		
parameter estimation from electromagnetic simulations using	3646	
Signal propagation		
very high frequency range	5482	
Signals	1	
Signal-to-noise-and-distortion ratio (SNDR)	3	
Signal-to-noise ratio	4	4128
	4141	
Signal-to-noise ratio criterion	4134	
Signal-to-quantization-noise ratio (SQNR)	3	
Silicon		
MMIC substrate properties	3217t	
properties in microwave ICs	2775t	
Silicon carbide		
device technologies	4613	
MMIC substrate properties	3217t	
Silicon-germanium	4626	
BiCMOS devices and RF integrated circuits	499	
comparison with GaAs elements using active-impedance profile (AIP)	81t	81
HBT	3024	3026
	4270	
modulation-doped FETs (MODFETs)	3196	
Simulation	3269	
Simulator Program with Integrated Circuit Emphasis. <i>See</i> SPICE		

Index terms**Links**

Simultaneous acquisition of spatial harmonics (SMASH)	2472	
Sine wave	1706	
Single-balanced mixers	1643	
Single-ended mixers	1643	
Single-event burnout	4197	
Single-event effects	4186	4199
Single-event functional interrupt	4195	
Single-event gate rupture	4186	4196
Single-event latchup	4195	
Single-event transients	4195	
Single-event upsets	4186	4193
mitigation	4198	
Single-phase unidirectional transducers (SPUDTs)	27	
Single-port cavity resonator	588	
Single-surface dielectric lens antennas	2321	
Sinusoidal antennas	1683	
Sinusoidal oscillations	5469	
Sirius Satellite Radio	1019	
SIS mixers	1646	
Six-port junctions		
mode-matching methods	3167	
Six-port networks	4641	
Skid-to-turn missiles	3089	
Skin effect	4669	
Skylab altimeter	3990 <i>t</i>	
Sky noise	4298	
Sky wave diffraction		
low frequency waves	4684	
Sky wave propagation		
at low frequencies	4675	
at medium and high frequencies	4686	
Sleeve dipole antennas	1049	2347
Slewing dipole arrays	299	
SLF waves	1281	
Slot antennas	4696	
Slot dipole antennas	1048	
Slotline components	4717	
Slotline field displacement isolators	1478	

Index terms**Links**

Slotlines	671	2744
	4736	
Slot-loop antennas		
monolithic	3205	
Slotted Aloha multiple access scheme	3356	
Slotted ring	2357	
Slow fading	167	
Slow wave structures	4744	
Small antennas	4761	
Small mobile terminal antennas	342	
Smart antennas		
adaptive array antennas	88	
for wireless communications systems	5677	
Smart jamming	3009	
Smart materials	4799	
Smith chart	4814	
VHF range	5482	
Snapback	4197	
Snell's law	1780	2320
Snow		
frequency dependence of scattering	718	
microwave scattering from	2949	2965
Soft errors	4186	
Software-defined multiple-standard tuner platform	1018	
Software-defined radio	5678	
Soil surfaces		
microwave scattering from	2949	2956
Solar flares	4189	
Solenoid attenuators	462	
Solid-state magnetoplasmas	700	
Solitons	2455	
Sol/SoS technologies	3025	
Sommerfeld-Goubau surface	1274	
Sommerfeld's radiation condition	2540	
South Atlantic anomaly	4189	
Spaceborne Imaging Radar	4090	
Spaceborne radar	4823	
Space diversity	172	
Space-division multiple access	91	
Space factor	227	

<u>Index terms</u>	<u>Links</u>	
Space groups	139	
Space-mapped neural networks	3395	
Space mapping	401	402
Space solar power		
microwave power transmission application	2906	2916
	2917	
and rectennas	4418	
Spacetime block codes	3065	
Spacetime codes	3060	3062
	3064	
Spacetime coding	176	
Spacetime processing	166	
algorithms for forward link	175	
algorithms for reverse link	172	
applications	176	
Space-time transmission diversity (STTD)	5677	
Spacetime trellis codes	3065	
S parameters	1330	
Spatial multiplexing	3065	
Spatial power combining	4837	
Spatial sampling density	1573	
Spatial (temporal) scaling	1402	
Spatial (temporal) shifting	1402	
Speckle		
synthetic aperture radar	4103	
Spectral distribution	5588	
Spectral (frequency) scaling	1402	
Spectral (frequency) shifting	1402	
Spectrometer-based wavelength meters	5590	
Spectrum management	3128	
Specular scattering	1295	
Speech coding	1024	
Spherical aberration	1790	
Spherical arrays	757	
Spherical waveguide cavity resonators	583	
Spherical waveguides	5581	
SPICE (Simulator Program with Integrated Circuit Emphasis)	4844	
nonlinear circuit analysis	3483	
Spillover	190	

Index terms**Links**

Spinels		
characteristics as circulators	1459f	
as ferrites	1452	1484
Spin glass state	2418	
Spin-wave zone	2431	
Spiral antennas	4853	
Spiral radar pattern	4022	
Spiral slot antenna	4713	
Splash-plate feed antennas	210	
Split Gaussian microwave transmitting aperture	2908	
Splitters		
VHF range	5485	
Spoofing	3008	3009
Spotlight synthetic aperture radar	4062	4073
Spread-spectrum code-division multiplexing access (SS CDMA)	5627	
Square-law detection	4137	
Square-ring-shape open-ended strip resonator	785	
SQUIDS (Superconducting QUantum Interference Devices)	891	4869
Squint angle	4024	
Squinted stripmap synthetic aperture radar	4070	
Stability		
of circuits	622	
distributed amplifiers	1091	
feedback amplifiers	1428	
feedback oscillators	1434	
feedforward amplifiers	1445	
low noise amplifiers	2373	
microwave plasma sources	2941	
nonlinear circuits	3519	
of nonlinear systems	4881	
Stacked microstrip antennas	289	
Standard atmosphere	105	
Standing-wave antennas	287	
Standing-wave arrays	5520	
Standing wave meters	4896	
Star topology	2353	
Stationary high-altitude relay program (SHARP)	4425	
Stationary signals	5604	
Stealth antennas	1085	

<u>Index terms</u>	<u>Links</u>	
Stealth technology		
backscatter reduction for	491	
and radar cross-section	4039	
Steatite		
dielectric permittivity	939 <i>f</i>	
dielectric properties	945 <i>f</i>	
Stein limit	3323	
Step attenuators	439	461
Stepped circular horn aperture feed antennas	198	
Stepped-frequency waveforms	4159	
Step response	623	
Stiff systems	3486	
Stokes vector	4082	
Storm observation radar	4027	
Strategic Arms Reduction Treaty (START)	3083	
Stratified layers		
radar remote sensing of irregular	4122	
Stratopause	105	
Stratosphere	105	
Striped-channel modulation-doped FETs (SC-MODFETs)	3176	
Stripline components	4931	
Stripline resonance isolators	1477	
Striplines	153	2648
	4918	
leaky modes and high-frequency effects	2268	2283
microwave circuits	2712	
Stripline standard	403	
Stripline Y-junction circulator	1225	
Stripline Y-junction ferrite circulators	1463	
Stripmap-mode synthetic aperture radar	4071	
Strip transmission lines	4918	
Structurally chiral media	620	
Studio monitors	4237	
Subband coding	5626	
Sub-Gaussian noise	3404	
Submarine antennas	4937	
Subsurface microwave tomography	558	
Subsurface object detection	540	
Subsurface remote sensing	1256	
Summing four-amplifier biquad circuit	499	

Index terms**Links**

Sum port	5558	
Sunspots		
effect on medium frequency sky waves	4691	
Superconducting cavity resonators	4951	
Superconducting electromagnets	4965	
Superconducting filters and passive components	4974	
Superconducting microwave filters	2980	
Superconducting microwave limiters	2800	
Superconducting microwave technology	4990	
Superconducting mixers	1645	
Superconductors	1218	
Superheterodyne microwave receiver	2925	
Supermagnetostrictive materials	1227	
Supermalloy		
electromagnetic properties	1223t	
Superparamagnetism	2418	
Super-PHS-WLL	341	
Surface acoustic wave applications	5002	
Surface acoustic wave chirp Fourier transform	29	
Surface acoustic wave delay lines	24	5012
Surface acoustic wave devices	24	5029
Surface acoustic wave filters	1543	5046
Surface acoustic wave ladder networks	27	
Surface acoustic wave oscillators	29	
Surface acoustic wave resonators	26	
Surface acoustic wave transversal filter	25	
Surface height measurement	116	
Surface leakage	4012	
Surface meshing electromagnetic analysis	400	
Surface mount technology	5058	
Surface resistivity		
measurement	918	
Surfaces		
frequency selective	1700	
treatment using microwave plasma sources	2943	
Surface scattering	2948	
Surface-to-air missiles (SAMs)	3086	
Surface-to-surface missiles (SSMs)	3086	
Surface transverse waves	31	

<u>Index terms</u>	<u>Links</u>	
Surface-wave antennas	287	
Surface waves	1293	
electromagnetic	1270	
and radar cross-section	4034	
Surveillance radar	4022	
Survivor function	3270	
Switched-beam systems	176	
adaptive array antennas	93	
Switching circuit phase shifters	153	
Switching-mode power amplifiers	2889	
Switch isolation	2991	
Symmetric Fabry-Perot resonators	1391	
Synchronization	3492	
Synchronized circuit analysis	3492	
Synchronous detector	4149	
Synthetic aperture processing radar	4026	
Synthetic aperture radar	4070	4096
	4100	5067
equipment for	4061	
signal processing	4160	
target recognition	4165	
Synthetic aperture radar interferometry	4110	
Synthetic aperture radar polarimetry	4106	
Synthetic imaging radar	4025	
System-on-chip (SoC)	4525	
System-on-package (SoP)	4525	
 T		
Talk format radio studio	4228	
Target identification		
military communication	3018	
Target recognition		
military communication	3017	
Target tracking	5081	
T attenuator	437	
fixed	460	461
insertion loss	457	
TDMA wireless standard	593	597
	5666	
and digital radio	1023	1030

Index terms**Links**

TDMA wireless standard (<i>Continued</i>)		
multiple access schemes	3351	3353
optical, for radio on fiber systems	4321	
specifications	597	
Teflon		
dielectric properties	2765t	
Telecommunications Act Bill	596	
Telemedicine	5097	
Telemetry	5106	
Telephone frequency extenders	4241	
Telephone hybrids	4239	
Television		
transmitters for analog	5318	
transmitters for digital	5327	
Television antennas	5132	
Television audio consoles	4233	
Television broadcasting		
antennas	5124	
direct satellite	1052	
transmission standards	5143	
Television signals	1281	
Television studio	4228	
Terahertz science, engineering, and systems	5175	
Terminated circulators	2787	
Tesla coil	2914	
TETRA wireless standard	5672	5678
Thermal analysis and design of electronic systems	5194	
Thermal noise	4297	
defined	3401	
high-frequency	3417	3421
low-frequency	3459	
Thermionic traveling-wave distributed amplifiers	1089	1093
Thermistor	2738	
Thermoacoustic tomography	2530	
Thermocouples	2736	2738
Thick stripline benchmark	404	
Thin-film attenuators	437	
Thin-film bulk acoustic wave resonator	24	
Thin film resistors	5213	

<u>Index terms</u>	<u>Links</u>	
Thin films	5226	
magnetic materials	2419	
Thin lens	1785	
3G wireless systems	3124	
and adaptive array antennas	89	
Thomson filters	1550	
Thomson lowpass filter	1523	1534
Three-antenna measurements	268	
Three-box Volterra model	5511	
Three-dimensional lens antennas	2323	
III-V Semiconductors	5237	
radiation effects	4211	
Three-port waveguide junctions	5557	
Time-division duplex (TDD) systems	175	599
and digital radio	1024	
Time-division multiple access wireless standard. <i>See</i> TDMA wireless standard		
Time domain electromagnetics	1318	
Time-domain reflectomers	4436	
Time-domain reflectometry	4437	
Time-frequency distributions	1691	
Tissue		
dielectric properties of selected	512	
T-junctions	5533	5557
	5558	
coaxial line discontinuities	657	
mode-matching methods	3167	
Token-passing bus	2357	
Token ring	2357	
Tomato can	193	
TOPEX altimeter	110	3989
	3990t	3990
	4117	
design of	3996	
height accuracy	3992t	3993
TOPSAR system	4106	
TOP (Technical and Office Protocol)	2357	
Toroidal ferrite phase shifters	1499	
Total internal reflection	1780	
Total stopping power	4187	
Tracking radar	4024	

<u>Index terms</u>	<u>Links</u>	
Track-while-scanning systems	3244	
Track-while-scan radar	4024	
Transadmittance amplifier	5638	
Transceivers	5254	
RF integrated circuits	4286	
Transconductance	1419	
Transconductors	496	
Transducers		
mode	5531	
orthomode	3547	
piezoelectric transducer controlled circuits	3838	
Transfer functions		
feedback systems	623	
filters	1521	1550
Transferred electron (Gunn) devices and circuits	1857	3387
<i>See also</i> Gunn diodes		
Transfer voltage ratio	1521	
Transformers		
VHF range	5485	
Transient analysis	5268	
Transient antenna fields	284	
Transimpedance amplifiers		
mm-wave integrated circuits	3029	
Transistors	2968	
heterojunction bipolar	1946	
Transition bands, in bandstop filters	498	
Translators		
for low-power broadcasting	2385	2391
Transmission line matrix (TLM) method	1321	5286
Transmission lines	659	5310
coplanar waveguide	821	
coupled	863	
MMICs	3217	
theory	5297	
waveguide types	5527	
Transmission resonators	3948	
Transmit spacetime processing	174	
Transmitter coil		
metal detector	553	

Index terms**Links**

Transmitters		
for analog television	5318	
for digital television	5327	
for FM broadcasting	5337	
for low-power broadcasting	2388	
RF integrated circuits	4286	
Transresistance	1419	
Transverse electric mode	5571	5572
Transverse electric wave	5571	
Transverse electromagnetic mode	5571	5572
Transverse electromagnetic waves	1283	5571
Transverse magnetic mode	5571	5572
Transverse magnetic wave	5571	
Transverse resonance techniques	5357	
TRAPATT (Trapped plasma avalanche-triggered transit) diodes		
description and applications	2968	
negative resistance	3389	
Trapped surface waves	1277	
Traveling-wave antennas	287	5363
Traveling-wave arrays	5522	
Traveling-wave feed antennas	206	
Traveling-wave slot feed antennas	207	
Traveling-wave tube amplifiers	3001 <i>t</i>	3001
Traveling wave tubes	5373	
Tree scattering	732	
Triangular (bowtie) antennas	780	
Triglycerine sulfate		
ferroelectric properties	1512 <i>t</i>	
pyroelectric properties	1514 <i>t</i>	
pyrooptic properties	1515 <i>t</i>	
Triplate line	2648	
Triple-band base-station antennas	335	
Triplexers	1651	
Tropical rainfall measuring mission (TRMM)	4118	
Tropopause	105	
Troposphere		
refraction and attenuation in	4475	
Tropospheric scintillation	4478	
Truncated fractals	1621	

<u>Index terms</u>	<u>Links</u>	
Truncated sphere		
backscatter from	490	
Trunking systems, for wireless communications	5661	5672
T-slot resonators	784	
T-strip resonators	783	
TSUNAMI project	91	
Tunable cavity resonators	586	
Tunable filters		
microwave ferroelectric devices	2746	
Tunnel devices	5380	
Tunnel diodes	2968	2972
	3385	
TUNNETT (Tunnel injection transit time) diodes		
description and applications	2968	
negative resistance	3389	
Turbulence measurement radar	4027	
Turntables	4237	
TV guided missiles	3089	
Twin-lead line	156	
Two-box Volterra model	5511	
Two-port cavity resonator	589	
Two-port waveguide junctions	5557	
Two-step (A/D) converters	8	
 U		
UFO	3019	
UHF band radar	4031 <i>t</i>	4055 <i>t</i>
	4055	
UHF receivers	5391	
mixer circuits	3103	
UHF waves	1281	
electromagnetic effect in ionosphere	1308	
ULF waves	1281	
Ultem		
dielectric properties	2765 <i>t</i>	
Ultrawideband antennas	283	
Ultrawideband arrays	2571	
Ultrawideband CPW-fed Lotus slot antenna	5639	
Ultra-wideband radio	5402	
Ultra-wideband wireless systems	5411	

Index terms**Links**

UMTS wireless standard	3125	5669
Underground propagation	5423	
Underlearning, neural networks	3393	
Undersampled arrays	1629	
Uniaxial waveguide junctions	5548	
Uniform geometrical theory of diffraction	5433	
Uniform line source antenna	275	
Uniplanar compact PBG structure (UCPBGS)	1117	
Unipolar MASK	123	
Universal relaxation law	948	
Unloaded Q -factor	3938	3952
Unmanned aerial vehicles (UAVs)		
microwave power transmission	2906	2918
Unpolarized waves	235	
Unstructured meshing	1594	
Upper-sideband adjacent-channel power ratio	2879	
V		
van Allen radiation belt	4188	
Van Atta array reflector	4495	5456
Varactor diodes	2829	5564
microwave phase shifters	2846	
Varactor parametric amplifier	1087	
Varactors	5472	
microwave ferroelectric devices	2745	
Variable attenuators	461	
Variable coupler attenuator	463	
Variable-frequency oscillators	5468	
Variable phase shifters	152	
Variable T attenuators	464	
Variable-value coaxial attenuator	438	
Variable-value waveguide attenuators	439	
V band radar	4055 <i>t</i>	
V-BLAST	3062	
Vector effective length(height), antenna	221	
Vector network analyzer	2802	
Vector potentials	238	
Vegetated areas		
microwave scattering from	2949	2961

<u>Index terms</u>	<u>Links</u>	
Verdet constant	1225	
Vertical polarization	4083	
Very high frequency range	5477	
Very Large Array	4451	
Very-large-scale integrated (VLSI) circuits		
capacitance extraction	566	
VHF band radar	4031 <i>t</i>	4055 <i>t</i>
	4055	
VHF band radio	5478	
VHF circuitry	5488	
VHF components	5483	
VHF inductors	5483	
VHF omnidirectional range equipment	4294	
VHF radio technology	5478	
VHF range	5477	
VHF receivers		
mixer circuits	3103	
VHF waves	1281	
electromagnetic effect in ionosphere	1307	
VLW waves	1281	
electromagnetic effect in ionosphere	1306	
VLSI	566	
Vocal quality	4247	4248 <i>t</i>
Voltage-controlled filter (VCF) PLL	78	
Voltage-controlled oscillators		
feedback oscillators	1437	
microwave ferroelectric devices	2745	
mixed-signal CMOS RF integrated circuits	3098	
MMICs	3232	
nonlinear circuit design	3518	
Voltage-controlled waveguide oscillators	5564	
Voltage gain	1419	
Voltage-to-frequency converters	5489	
as oscillator	5474	5475 <i>t</i>
Voltage-tuned magnetrons	2506	
Volterra modeling	5507	
nonlinear high-power amplifiers	133	
Volterra series analysis	5508	
nonlinear circuit design	3506	

Index terms**Links**

Voltage breakdown strength		
measurement	933	
Volume meshing electromagnetic analysis	399	
Volume resistivity		
measurement	916	
VSAT (Very-small aperture-terminal) systems	4452	
VSWR/return loss	263	
W		
Water		
dielectric properties	2765 <i>t</i>	
electric dipole moment	941 <i>t</i>	
Wave attenuation	1287	
Wave equation	1281	
Waveguide antennas	5515	
Waveguide attenuators	148	439
	5531	
Waveguide below cutoff attenuators	464	
Waveguide cavity resonators	579	
Waveguide components	5527	
Waveguide coupling slot antennas	5519	
Waveguide diplexers	5532	
Waveguide directional couplers	5536	
Waveguide discontinuities	5543	
Waveguide feeds	192 <i>t</i>	
Waveguide ferrite isolators	1475	
Waveguide filters	5531	
Waveguide junctions	5554	
discontinuities	5548	
Waveguide linear slot arrays	5520	
Waveguide microwave circuits	2706	
Waveguide modes	5571	5573
excitation	5583	
Waveguide multiaperture couplers	5537	
Waveguide multiplexers	5532	
Waveguide oscillators	5559	
Waveguide planar arrays	5523	
Waveguide radiating slot antennas	5516	
Waveguide resonators	5531	
Waveguide ring hybrids	5559	

<u>Index terms</u>	<u>Links</u>	
Waveguides	665	1292
	5569	
FE analysis application	1595	
ferrite loaded	1486	
geometries	5577	
transitions to finlines	1617	
Waveguide terminators	5531	
Waveguide-to-microstrip transitions	2658	
Waveguide Y-junction ferrite circulators	1462	
Wavelength	1283	5587
Wavelength meter	5587	
Wavelet packets	383	
Wavelets	5602	5623
application to electromagnetic problems	377	
transforms	379	5602
Wavelet/scalar quantization (WQS) standard	5629	
Wavelet shrinkage	5629	
Wavelet transforms	379	5602
Wavenumber	270	
Wave number	1282	
W band radar	4055 <i>t</i>	
WCDMA (wireless CDMA) standard	322	503 <i>t</i>
	5657	5666
Weather observation radar	4026	
Weather Service Radar	4063	
Weber functions	5579	
Whistlers	1314	4368
Whitening filter	4134	
White noise	3400	
Whole-space dyadic Green functions	1184	
Wide-angle lens antennas	2330	
Wideband amplifiers		
low-noise	2377	
Wideband amplifiers	5630	
Wideband code-division multiple access (wideband CDMA)	5666	
Wideband digital microwave receiver	2933	
Wideband microstrip antennas	2599	
Wideband mixers		
mm-wave integrated circuits	3031	
Wideband slot and printed antennas	5638	

Index terms**Links**

Wide-swath ocean altimeter (WSOA)	4004	
Widowed Fourier transform	5605	
Wiener-Hammerstein model	133	
Wiener model	133	
Wiener noise	3401	
Wigner-Ville distribution	1696	4143
Wind observation radar	4027	
Wire antennas	285	
Wirebond	4522	
Wireless communications	290	
Wireless communications systems	5656	
adaptive array antennas for	88	
antenna scanning arrays	257	
history of	2015	
MIMO systems	3059	
miniaturized packaged (embedded) antennas for portable wireless devices	3068	
RF integrated circuit design	502	
standards comparison	503 <i>t</i>	
superconducting microwave devices for	2986	
Wireless LANs	2358	
Wireless local area networks (WLANs)	3125	5657
	5662	5674
Wireless local loop		
adaptive array antennas for	341	
Wireless personal area networks (WPANs)	5662	5675
Wireless power transmission	2906	
Wireless transceivers	1029	
Wire-loop antennas		
monolithic	3206	
WITTEX	4004	
WLAN application antennas	3074	
Wood		
dielectric properties	2765 <i>t</i>	
Wood's anomaly	1704	
Worst-case partial-band jamming	3009	
Write heads	2421	
X		
X band radar	4031 <i>t</i>	4055 <i>t</i>
	4056	

Index terms**Links**

X-junctions		
mode-matching methods	3167	
XM Satellite Radio	1019	
X-ray scattering		
for buried-object detection	558	
Y		
Yagi-Uda antenna	224	287
	5680	
Yagi-Uda dipole array	1051	
Yee central difference approximation	1571	
Yee space grid	1570	
YIG. See Yttrium iron garnet		
Y-junctions	5557	
Yttrium iron garnet (YIG)		
as ferrite	1452	1484
film devices	2448	
Z		
Zenneck waves	1270	
Zero-length coupled line	404	
Zinc oxide		
piezoelectric properties	1513f	
Zoned dielectric lens antennas	899	
Zoned lens antennas	2322	